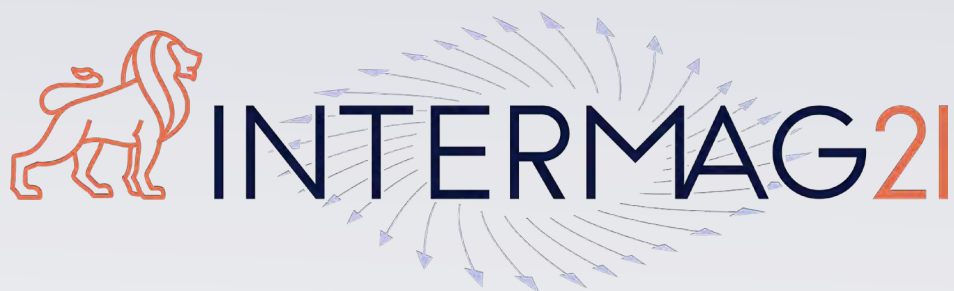


IEEE International Magnetics
Virtual Conference
26-30 April 2021



DIGEST BOOK



MONDAY, 26 APRIL 2021

LIVE Q&A SESSIONS, 3:00 PM EUROPE CEST

Session TU

TUTORIAL: MAGNETISM AND THE ENVIRONMENT

Johan Paulides, Chair

Advanced Electromagnetics Group, Waalwijk, Netherlands

INVITED PAPERS

TU-01. Magnetic Refrigeration: From Fundamentals to Applications.*O. Gutfleisch¹**1. Material Science, Technical University Darmstadt, Darmstadt, Germany*

Magnetic materials are key components in energy technologies, robotics, sensors and information technology. Magnets are inseparable from our everyday life. “Green” energy technologies such as wind turbines, electro-mobility and solid state cooling, rely on high performance magnetic materials which have to be available in bulk quantities, at low-cost and with tailored magnetic hysteresis. Gas-vapour compression technology for refrigeration, heating, ventilation, and air-conditioning has remained unchallenged for more than 120 years. Energy spent for domestic cooling is expected to outreach that for heating worldwide over the course of the twenty-first century. There is a huge demand for a smarter, more flexible and more efficient cooling technology. Magnetic refrigeration could be that alternative working without gas-based refrigerants. The magnetocaloric effect (MCE) is the reversible temperature change of a magnetic material upon application and removal of a magnetic field. Its potential for room-temperature refrigeration utilizing a regenerative cycle was initially demonstrated using the heavy rare earth element gadolinium. I will introduce the basics of the magnetocaloric effect, illustrate its great potential in magnetic refrigeration, will derive the required materials attributes of a magnetic heat exchanger, give guidelines for material selection and will look into the challenges of developing an efficient prototype. Further, I will address the criticality of strategic metals in magnetic cooling, their potential for substitution and how the ecological footprint of the magnetic fridge can be improved by using recycled permanent magnets. Finally, a brief outlook will be given into Heusler compounds for multifunctional applications with special emphasis on their elastocaloric, barocaloric, and magnetocaloric properties. Their multi-responsiveness to stimuli such as strain, pressure and magnetic field enable a variety of new design concepts for sensors, actuators and caloric cooling concepts. Acknowledgements: Funded by the Deutsche Forschungsgemeinschaft (DFG, German Research Foundation) – Project-ID 405553726 – TRR 270. This work was also supported by the European Research Council (ERC) under the European Unions Horizon 2020 research and innovation programme (Grant No. 743116-project Cool Innov).

O. Gutfleisch, J.P. Liu, M. Willard, E. Brück, C. Chen, S.G. Shankar, *Magnetic Materials and Devices for the 21st Century: Stronger, Lighter, and More Energy Efficient* (review), *Advanced Materials* 23 (2011) 821–842. O. Gutfleisch, T. Gottschall, M. Fries, D. Benke, I. Radulov, K. P. Skokov, H. Wende, M. Gruner, M. Acet, P. Entel and M. Farle, *Mastering hysteresis in magnetocaloric materials*, *Phil. Trans. R. Soc. A* 374 (2016) 20150308. F. Scheibel, T. Gottschall, A. Taubel, M. Fries, K. P. Skokov, A. Terwey, W. Keune, K. Ollefs, H. Wende, M. Farle, M. Acet, O. Gutfleisch, M. E. Gruner, *Hysteresis design of novel magnetocaloric materials - from basic mechanisms to applications*, *Energy Technology* 6 (2018) 1397 – 1428. T. Gottschall, K.P. Skokov, M. Fries, A. Taubel, I. Radulov, F. Scheibel, D. Benke, S. Riegg, O. Gutfleisch, *Making a cool choice: the materials library of magnetic refrigeration*, *Progress Report in Advanced Energy Materials* (2019) 1901322. J. Liu, J.D. Moore, K.P. Skokov, M. Krautz, K. Löwe, O. Gutfleisch, *Exploring La(Fe,Si)₁₃-based magnetic refrigerants towards application*, *View Point Paper, Scripta Mat.* 67 (2012) 584-589. T. Gottschall, D. Benke, M. Fries, A. Taubel, I. A. Radulov, K. P. Skokov, O. Gutfleisch, *A matter of size and stress: Understanding the first-order transition in materials for solid-state refrigeration*, *Adv. Funct. Mater.* 27 (2017) 1606735. D. Benke, M. Fries, T. Gottschall, I. Radulov, K. Skokov, A. I. Bevan, D. Prosperi, C. O. Tudor, P. Afiuny, M. Zakotnik, O. Gutfleisch, *Magnetic refrigeration with recycled permanent magnets and free rare earth magnetocaloric La-Fe-Si*, *Energy Technology*, submitted. J. Liu, T. Gottschall, K.P. Skokov, J.D. Moore, O. Gutfleisch, *Giant magnetocaloric effect driven by structural transition*, *Nature Mat.* 11 (2012) 620. T. Gottschall, A. Gracia-Condal, M. Fries, A. Taubel, L. Pfeuffer, L. Manosa, A. Planes, K.P. Skokov, O. Gutfleisch, *A multicaloric cooling cycle that exploits thermal hysteresis*, *Nature Materials* (2018).

TU-02. Magnetics of Motor Drive System for Electrical Vehicle.K. Fujisaki¹*1. Toyota Technological Institute, Nagoya, Japan*

Magnetic Material for Electrical Vehicle Recent trends of magnetic material research about electrical motor drive system for electrical vehicle are shown in this lecture for magnetic material and electrical researcher and engineers. Motor drive system consists of electrical motor and power electronics circuit, and magnetic material are used and an important role in both equipment. The purpose of the electrical motor is to make an electromagnetic torque to drive a vehicle based on Maxwell stress equations. The power electronics circuit such as inverter or DC-DC converter is an electrical power source in controlling the variable voltage and/or variable frequency based on a switching operation of power semiconductors [1]. Soft magnetic material is used in the stator core and the rotor core in the electrical motor, and permanent magnet is used in the field part of the motor. The electromagnetic torque is almost proportional to square of magnetic flux density. So higher magnetic flux density is required to obtain higher electromagnetic torque. Soft magnetic material is much useful to obtain a higher magnetic flux density in smaller electrical current, which is supplied by the power electronics circuit. Magnetic Material for Motor Most of the electrical motor uses an electrical steel with a few % silicon due to high performance of magnetic characteristics with low price. Mechanical stress in manufacturing the motor core, magnetic non-linearity, and magnetic anisotropy, magnetic hysteresis, magnetic flux distribution base on grain shape and orientation, magnetic vector property of magnetic field and magnetic flux density, higher harmonics components derived from the slot shape of the stator core as well as the power electronics circuit base on the switching operation are main properties of the electrical steel to be discussed and researched. Mutual interaction between the power electronics circuit and the magnetic material or motor are often observed [2, 3]. To reduce the motor core loss, low iron loss magnetic materials such as amorphous and nano-crystal material are reported to be applied to the motor core [4, 5]. The details are shown in the presentation. Hard magnetic material is used in the field of the motor due to no electrical current supply and no slip ring. So most of electrical vehicle are driven by permanent magnetic synchronous motor, because the higher efficiency and the downsizing of the electrical motor can be realized. Due to almost the same electrical conductivity of the NdFeB permanent magnet as the stainless steel, the temperature of the permanent magnet increases and the demagnetization phenomena occur. To avoid it, rare earth problem generates such as Dy or so. Weakening field control scheme is used in the PM motor for the high speed rotation. So higher coercive force is required for the permanent magnet. Magnetic Material for Power Electronics In the electrical vehicle, variable speed operation is required to move from a starting point to a stopping point. So variable speed control is required for electrical motor. Variable voltage and variable frequency are required for the power source of the electrical PM motor, due to the electromotive force theory and the synchronous condition of the mechanical rotational speed and the magnetic rotation speed. The power electronics technology is possible to be realized by the switching operation of the power semiconductors. So the higher frequency operation can be realized by the high performance power semiconductor such as IGBT or GaN-FET or SiC-FET devices because it realizes the downsizing of the power electronics circuits. However, the bottle neck technology for the realization is a soft magnetic material in high frequency and high power operation. Nowadays, the hindrance for the realization of power electronics technology might be said to be a high frequency magnetic material in a point of view of the downsizing, high efficiency and the low cost [6-8]. Ferrite is mainly used in the high frequency magnetic material up to 100 MHz or so. However, it has the low saturation magnetization such as 0.4 or 0.5 T, the thermal runaway phenomena of self-heating in high temperature, and the weakening of mechanical vibration which often occurs in automobile car. Metal material such as iron or steel is possible to solve the problems. Iron powder has good performance as the high saturation magnetization, no thermal runaway phenomena and no problem for the mechanical vibration. However, magnetic permeability is relative small due to the demagnetization in a small particle. So, as far as high frequency transformer which is quite useful for electrical circuit insulation, leakage magnetic flux may increase and then the low loss transformer might be difficult. Thin plate

shape of the steel or iron has no demagnetization phenomena, and then high magnetic permeability can be realized. Micro-meter order steel is trial manufactured by sputtering method, rolling or so [9]. The details will be shown in the presentation at that time.

(1) Editor and author: Keisuke Fujisaki, "Magnetic Material for Motor Drive System - Fusion Technology of Electromagnetic Fields-", Material Engineering, Springer-Nature, 2020. (2) N. Denis, M. Inoue, K. Fujisaki, H. Itabashi, T. Yano, "Iron Loss Reduction of Permanent Magnet Synchronous Motor by Use of Stator Core Made of Nanocrystalline Magnetic Material," IEEE Transactions on Magnetics, Volume: 53, Issue: 11, 8110006, 2017. (3) S. Okamoto, N. Denis, M. Ieki, K. Fujisaki, "Core Loss Reduction of an Interior Permanent Magnet Synchronous Motor Using Amorphous Stator Core," IEEE Transactions on Industry Applications, vol.52, no.3, pp.2261-2268, May/June 2016. (4) K. Fujisaki, S. Liu "Magnetic Hysteresis Curve Influenced by Power-Semiconductor Characteristics in PWM Inverter," Journal of Applied Physics, Vol. 115, 17A321, 2014. (5) A. Yao, K. Tsukada, and K. Fujisaki, "Investigating Iron Loss Properties in an Amorphous Ring Excited by Inverters based on Silicon and Gallium Nitride," IEEE Journal of Industry Applications, Vol. 7, No. 4, p. 321-328, 2018. (6) J. W. Kolar, Future Challenges for Research and Teaching in Power Electronics, Presentation held at the 14th Int. Conf. Optimization of Electrical and Electronic Equipment (OPTIM 2014), Brasov, Romania, May 22-24, 2014. (7) Tim Heidel, "ARPA-E Initiatives in High Efficiency Power Conversion," APEC Plenary Session Ft. Worth, TX, March 14, 2014. (8) J.S. Glaser, et. al. "A 900 W, 300V to 50 V dc-dc power converter with 30 MHz switching frequency," In Proc. Twenty-Fourth Annual IEEE Applied Power Electronics Conf. and Exposition APEC 2009, pp. 1121-1128, 2009. (9) J. Tanase, E. Tsuchida, K. Fujisaki, "Magnetic characteristics of 1 μ m-thick pure iron sheets for power electronics circuits with GaN devices," IEEE Intermag2020, CW-02, 2020.

TU-03. Rare Earth Magnet Recycling: the Missing Link in a Circular Economy.

*K. Mugerma*¹

1. Geomega Resources Inc., Montreal, QC, Canada

Rare earth elements (REE) are crucial for many applications including clean energy, transportation, high-tech devices, medicine, advanced manufacturing and military. The most important usage of REE by value is the NdFeB permanent magnet. Rare earths recycling was always presented as a negligible amount (<1%) and the low price of REO was blamed for that. On the other hand, China has been recycling REE from magnetic scrap for over a decade and the amounts are growing. What are the main drivers of REE recycling in China vs the main prohibitors of REE recycling outside of China? What are the advancements in REE recycling from permanent magnets outside of China? What are the main feeds that are recycled and how can one drive an increase of REE recycling in the future?

TUESDAY, 27 APRIL 2021

LIVE Q&A SESSIONS, 10:30 AM EUROPE CEST

Session YA

FOCUS SESSION: BENCH TO BEDSIDE TRANSITION OF BIOMAGNETIC RESEARCH: HOW CLOSE ARE WE?

Ravi L Hadimani, Chair

Virginia Commonwealth University, Richmond, VA, United States

INVITED PAPERS

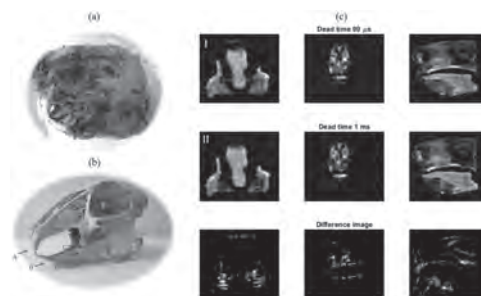
YA-01. Hard Tissue Magnetic Resonance Imaging With Fast Control of Intense Magnetic Fields.

J. Algarín^{1,2}, E. Díaz-Caballero³, J. Borreguero^{1,2}, F. Galve^{1,2},
D. Grau-Ruiz³, J. Rigla³, R. Bosch^{1,2}, J. González³, E. Pallás^{1,2},
C. Gramage^{1,2}, A. Ríos³, J. Benloch^{1,2} and J. Alonso^{1,2}

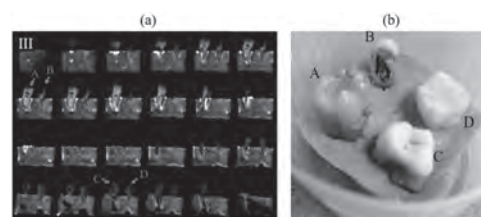
1. Institute for Molecular Imaging and Instrumentation (i3M), Consejo Superior de Investigaciones Científicas, Madrid, Spain; 2. Institute for Molecular Imaging and Instrumentation (i3M), Universitat Politècnica de Valencia, Valencia, Spain; 3. Tesoro Imaging S.L., Valencia, Spain

Magnetism plays an instrumental role in biomedical applications and health-care, both from the perspectives of devices and techniques. In particular, Magnetic Resonance Imaging (MRI, [1]) addresses the magnetization induced on the patients' constituent matter when subject to a magnetic field, and exploits the time-varying signal resulting from the contribution of the ubiquitous hydrogen nuclei spins for high quality spatial reconstructions. At present, MRI is the only available medical imaging technique known to deliver high resolution images of deep biological tissues *in vivo* and without harmful ionizing radiation. However, MRI does not come without its own limitations. In particular, it is much more efficient at detecting soft tissues and fluids than hard, solid samples. This is due to the weak, short-lived signals emitted by the latter, by cause of dipolar magnetic interactions between neighboring spins in the sample, which constitute a noisy environment that decoheres the quantum nature of the MR signal. The environment's contribution averages out for soft tissues, but not so for solids, where nuclei are approximately fixed with respect to each other in the laboratory reference frame. This explains the scarcity of useful (with diagnostic value) MR images of dental tissues [2-4], the hardest in the human body. Furthermore, the MRI scanners employed so far use static magnetic field strengths ranging from 4 to 12 T, which makes them large and expensive. At around 1 M\$ per Tesla [5], this precludes their penetration in dental clinics. In this symposium, devoted to evaluating the transition of biomagnetic research from laboratory to clinical environments, we present a new, inexpensive approach to MRI of combined hard and soft biological tissues, with a view on dental applications [6]. We will show 3D reconstructions of human teeth (Figures 1 and 2), as well as a rabbit head and a cow femur, all obtained at a field strength of only 260 mT. These images are, to the best of our knowledge, the first featuring soft and hard tissues simultaneously at sub-Tesla fields, and have been acquired in a home-made special-purpose MRI scanner designed with the goal of demonstrating dental imaging at low field settings. We also present two recently patented sequences for efficient encoding of spatial information and image reconstruction: VIEWS (Volumetric Image Encoding Without k-Space) and MASSIF (Magic Angle Spinning of Spatially Inhomogeneous Fields). These are key players in the roadmap we envision to shorten scan times from several hours, as in our first prototype, to a few minutes, as desired for clinical applications.

[1] Haacke, E. Mark, et al. *Magnetic resonance imaging: physical principles and sequence design*. Vol. 82. New York: Wiley-Liss, 1999. [2] Weiger, Markus, et al. "High-resolution ZTE imaging of human teeth." *NMR in Biomedicine* 25.10 (2012): 1144-1151. [3] Idiyatullin, Djaudat, et al. "Dental magnetic resonance imaging: making the invisible visible." *Journal of endodontics* 37.6 (2011): 745-752. [4] Mastrogiacono, Simone, et al. "Magnetic Resonance Imaging of Hard Tissues and Hard Tissue Engineered Bio-substitutes." *Molecular Imaging and Biology* (2019): 1-17. [5] Sarracanie, Mathieu, et al. "Low-cost high-performance MRI." *Scientific Reports* 5 (2015): 15177. [6] Algarín, José Miguel, et al. "Simultaneous imaging of hard and soft biological tissues in a low-field dental MRI scanner." *Scientific Reports* 10 (2020): 21470.



(a) Picture of the scanned rabbit head. (b) Picture of a rabbit skull. (c) Top: Single slices for 90 us dead time with PETRA; middle: the same slices for 1 ms dead time; bottom: difference between the above images.



(a) 2 dimensional slices of four human teeth embedded in a piece of pork ham (PETRA). (b) Photograph of the sample.

YA-02. Nanoviber: Magnetic Nanovibrations for Brain Tumor Therapy: the Translational Road Also Needs Innovation.

F. Berger¹

¹. BrainTech Lab U1205 INSERM-UGA, Grenoble, France

The median survival of glioblastoma, the main primitive brain tumor, is 15 months. The progress of imaging, surgery, robotic, chemoradiotherapy, as well as last generation molecular biology and targeted therapy did not provide any curative strategies. Innovative therapies are warranted to increase our therapeutical efficacy. Magnetic nano and micro particles are widely studied for biomedical applications such as contrast agents for MRI, regenerative medicine, cell sorting, tissue engineering, protein purification, hyperthermia or magnetofection. For cancer therapy, Magnetic Particles (MP) offer new perspectives for untreated diseases such as glioblastoma. Indeed, new pharmacotherapies struggle to prove their efficacy while therapies based on physical effect, such as Tumor Treating Fields demonstrate promising results. An approach based on mechanical destruction of cancerous cells by low-frequency vibration of magnetic particles, that we call Treatment by Magneto-Mechanical Effect of Particles (TMMEP) has been studied for several years. Kim et al. first showed that they were able to reduce glioma cancer cells viability from 90% by applying a 20 Hz alternating field on cells incubated with permalloy microdisks. Master et al. put superparamagnetic iron oxide nanoparticles (SPIONs) on breast cancer cells and applied a 100 kA/m alternating magnetic field at 50 Hz for a total of 30 min, with 10 min on / 5 min off patterns. They demonstrated a reduction in cell viability up to 75%. Interestingly, they showed that healthy cells were less affected by the treatment because of different cell mechanical properties. A comparative study of cylindrical particles with different length and diameter was conducted by Wong et al. They showed that MP with smaller diameter have a better efficacy with about 75% of cell viability after application of a biaxial pulsed magnetic field thanks to 4 coils. *In vivo* study on an orthotopic model of glioblastoma was conducted by Cheng et al. In a preliminary approach, they injected cancerous cells mixed with disks microparticles in brain mice and showed a better survival of mice submitted to a daily exposition of a 1 T rotating magnetic field at 20 Hz for 1 h. In this work, we used permalloy microdisks submitted to a Rotating Magnetic Field (RMF) and optimized in *in vitro* assay the particle concentration, magnetic field amplitude, and duration of exposure. We demonstrate here a strong lethal effect of TMMEP *in vitro*. We conducted *in vivo* assay on an orthotopic model of glioblastoma on mice but could not demonstrate efficacy of the treatment. We explain this failure by a strong difference in cell mechanical properties between *in vitro* and *in vivo* assay. To face this difficulty, we propose an *in vitro* 3D model by the use of spheroids put in a gel which can then be treated as a tumor and enable to mimic particle injection and RMF exposure. We also developed a 3D gel model mimicking peri-tumoral invasion of glioblastoma cells. Similarly, to the spheroid model, no effect was observed on the tumor proliferating cell in the core of the tumor. Moreover, migrating cells outside the core were strongly altered in their migration by the mechanical stimulation. Indeed, the data in the literature that supported our approach to TMMEP are essentially *in vitro* experimental results and no evaluation of TMMEP had yet been performed on an *in vitro* 3D model. Only a few articles showed *in vivo* efficacy, but the only survival benefit has been obtained with particles injected at the same time as the cells. The use of spheroids and organoids for the study of cancer and its treatments is now booming. Taking into account the importance of mechanical properties in tumor development, this model, placed in between 2D cell culture and animal experiments, mimics the architecture and heterogeneity of the tumor microenvironment. Closer to the *in vivo* tumor environment, this technique enables to better optimize and test *in vitro* treatments before moving to the preclinical phase, thus reducing the number of animals used in medical research. Preclinical models have been also extensively questioned, poorly mimicking the human disease. We demonstrated that results obtained in 2D culture are not relevant for the *in vivo* situation. Similarly, classical animal models are also poorly relevant, harboring a few invasive cells in the peritumoral area that is the main driver for tumor relapse. The model developed in this study will be crucial to modelize potential effect of magnetic vibration. The anti-invasive properties of magnetic vibration discovered using this innovative model could be explained by the specificity of the cell cytoskeleton in the

migrating machinery, potentially highly sensitive to mechanical impact. A new preclinical strategy is emerging using new models to detect potential therapeutical effect of nano-magnetic vibrations. Similarly, a new design of the clinical trials should be implemented using highly cognitive trials, multimodal imaging including mechanical imaging and *in situ* molecular and cellular analysis of the tumor after local delivery of magnetic particles and mechanical actuation. These new translational paradigms also warrant a rigorous ethical analysis.

Cécile Naud, François Berger, Hélène Joisten *et al.* Cancer treatment by magneto-mechanical effect of particles, a review. *Nanoscale Adv.*, 2020, 2, 3632. Jain KK. A Critical Overview of Targeted Therapies for Glioblastoma. *Front Oncol.* 2018;8(October):1–19. Kim D-H, Rozhkova EA, Ulasov I V, Bader SD, Rajh T, Lesniak MS, et al. Biofunctionalized magnetic-vortex microdisks for targeted cancer-cell destruction. *Nat Mater.* 2010;9(2):165–71. Master AM, Williams PN, Pothayee N, Zhang R, Vishwasrao HM, Golovin YI, et al. Remote Actuation of Magnetic Nanoparticles for Cancer Cell Selective Treatment Through Cytoskeletal Disruption. *Sci Rep.* 2015;1(919):1–13. Zhang E, Kircher MF, Koch XM, Eliasson L, Goldberg SN, Renstrom E. Dynamic Magnetic Fields Remote-Control Apoptosis via Nanoparticle Rotation. *ACS Nano.* 2014;8(4):3192–201. Leulmi S, Chauchet X, Morcrette M, Ortiz G, Joisten H, Sabon P, et al. Triggering the apoptosis of targeted human renal cancer cells by the vibration of anisotropic magnetic particles attached to the cell membrane. *Nanoscale.* 2015;7(38):15904–14. Wong DW, Gan WL, Liu N, Lew WS. Magneto-Actuated cell apoptosis by biaxial pulsed magnetic field. *Sci Rep.* 2017;7(1):1–8. Cheng Y, Muroski ME, Petit DCMC, Mansell R, Vemulkar T, Morshed RA, et al. Rotating magnetic field induced oscillation of magnetic particles for *in vivo* mechanical destruction of malignant glioma. *J Control Release.* 2015 Feb;223:75–84. Mansell R, Vemulkar T, Petit DCMC, Cheng Y, Murphy J, Lesniak MS, et al. Magnetic particles with perpendicular anisotropy for mechanical cancer cell destruction. *Sci Rep.* 2017;7(1):1–7. Fong ELS, Harrington DA, Farach-Carson MC, Yu H. Heralding a New Paradigm in 3D Tumor Modeling. *Biomaterials.* 2016;108:197–213.

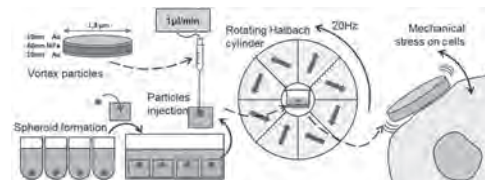


Figure 1: Spheroid model for preclinical mechanical stimulation testing. 1) mechanical stimulation using Halbach cylinder 2) *in situ* local delivery of magnetic nanoparticles.

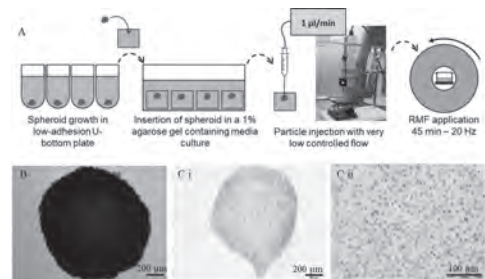


Figure 2

YA-03. Imaging and Quantifying Transition Metal Ion Distribution in the Human Brain for Early Detection and Diagnosis of Neurodegenerative Disorders.

J. Collingwood¹

1. School of Engineering, University of Warwick, Coventry, United Kingdom

Transition metal elements play many essential roles in the normal functioning of the human brain. These elements are transported, stored, and used by a vast range of proteins and enzymes. In most examples they are bound as individual metal ions (such as cobalt in vitamin B12), but some mineralized forms (such as the iron oxide core in ferritin) are also present. Neurodegenerative disorders (an umbrella term encompassing many forms of dementia and movement disorders), exhibit complex pathological changes within the central nervous system and beyond. Among these changes, altered patterns of transition metal element storage and utilization are generally observed in neurodegenerative disorders, as reviewed by others (*e.g. Mezzaroba 2019*). Magnetism plays key roles both in distinguishing the post-mortem materials properties of transition metals in biology, and in the clinical detection of transition metals in brain tissues (*Collingwood & Telling, 2016*). To advance the field, it is necessary to be able to image and quantify these transition metal elements in the human brain with sensitivity and specificity. From an analytical perspective, these brain compartments are effectively dilute systems, and the abundance, distribution, and material properties of the respective metal elements in their local environments vary greatly between cell types, tissues, and brain regions, and this in turn has implications for detection. The earliest histochemistry studies of post-mortem tissue revealed the heterogeneity of elements throughout the brain architecture, for example with Perls staining for iron. The ways in which these metals are bound affects staining efficacy, and efforts have been made to quantify metal ion concentrations in brain tissue as a function of brain region and ageing (*e.g. Hallgren & Sourander 1958*). Imaging transition metals within the living human brain with sensitivity and specificity presents many challenges. Transcranial sonography has shown sensitivity to tissue iron concentration, and scope to apply Dual-Energy Computed Tomography to image the most abundant elements is being explored. The most widely recognised opportunity came with the advent of Magnetic Resonance Imaging (MRI), which created the opportunity for sensitive, if not specific, clinical imaging of iron in the human brain (*Drayer 1986*). Subsequent efforts to improve specificity have included i) Bartzokis' approach with sequential MRI scans using two distinct (B_0) magnetic fields, which enable measurement of the field-dependent transverse relaxation increase associated with ferritin-encapsulated iron oxide nanoparticles (*e.g. Bartzokis 2000*), and ii) Quantitative Susceptibility Mapping, a method utilizing phase images to determine magnetic susceptibility distributions within tissues to thereby infer chemical composition (*e.g. Haacke 2015*). Post-mortem analysis continues to play an important role in testing the relationships between the properties of transition metals in brain tissue, and the signals detected with clinically-applicable methods. Magnetometry methods enable the proportion of iron present as iron oxide to be distinguished and characterized, although historically this has been applied to bulk samples, so spatial distribution information has not been preserved. Opportunities for magnetic imaging continue to evolve, and recently we demonstrated the application of synchrotron X-ray Magnetic Circular Dichroism to image the magnetic properties of post-mortem tissue from Alzheimer's disease patients at sub-micron spatial resolution (*Everett 2018*). Meanwhile, the relative distribution of transition metals can be measured with outstanding sensitivity and specificity using focused beam synchrotron X-ray fluorescence imaging, creating the opportunity to correlate these distributions with high resolution quantitative MRI (*Finnegan 2019*). These findings can in turn inform interpretation of clinical MRI data. In conclusion, current developments in both post-mortem and clinical imaging are supporting efforts to determine whether altered patterns of transition metals can be used as biomarkers, and to investigate the extent to which disease-associated changes in the regulation of transition metals may provide insight into the pathogenesis of neurodegenerative disorders.

G. Bartzokis and T. Tishler, *Cell Mol. Biol.*, Vol. 46, p.821 (2000) J. Collingwood and N. Telling, *Iron Oxides: from Nature to Applications*,

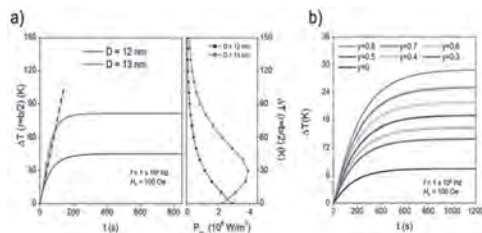
Chap. 7, p143 (2016) B. Drayer, P. Burger, R. Darwin et. al., *AJR Am. J. Roentgenol.* Vol. 147, p.103 (1986) J. Everett, J. Collingwood, V. Tjendana-Tjhin et. al., *Nanoscale*, Vol. 10, p.11782 (2018) M. Finnegan, N. Visanji, I. Romero-Canelon et. al., *J. Neurosci. Methods*, Vol. 319, p.28 (2019) E. Haacke, S. Liu, S. Buch et. al., *Magnetic Resonance Imaging*, Vol. 33, p.1 (2015) B. Hallgren and P. Sourander, *J. Neurochem.* Vol. 3, p.41 (1958) L. Mezzaroba, D. Alfieri, A. Simão, and E. Reiche, *Neurotoxicology*, Vol. 74, p.230 (2019)

CONTRIBUTED PAPERS

YA-04. Heating Efficiency of Magnetic Nanoparticles for Magnetic Hyperthermia: Effects of Temperature and Driving-Field Waveform.G. Barrera¹, P. Allia¹ and P. Tiberto¹*1. Advanced Materials and Life sciences, Istituto Nazionale di Ricerca Metrologica, Torino, Italy*

The power released by magnetic nanoparticles (MNPs) submitted to an alternating driving field in the typical frequency range used in therapeutic treatments based on magnetic hyperthermia is studied using a rate-equation approach in which MNPs are modelled as double-well systems with randomly distributed easy axes. Taking into account the temperature dependency of MNP magnetization and anisotropy, a detailed picture of their hysteretic properties and of the resulting heating efficiency. The temperature variation in a host medium is then studied by solving a simple, radial Fourier equation with two typical boundary conditions. The time evolution of the temperature increment of the medium turns out to be strongly affected by the non-monotonic temperature dependence of the power released by NPs (see Figure 1a); the direct consequences on the heating efficiency make the determination of the specific loss power (SLP) and the resulting maximum temperature from the initial slope of the heating curve misleading. An alternative, sounder method to measure the average power released by magnetic nanoparticles and the SLP is proposed [1]. Another way of optimizing the performance of MNPs as heat generators consists in applying non-harmonic driving-field waveforms, with notable advantages with respect to the effects of harmonic magnetizing fields of same frequency and amplitude [2]. This improvement is related to the presence of fast, quasi-adiabatic transformations where the occupancy numbers in the two potential wells are virtually frozen, resulting in largely off-equilibrium magnetization states and in hysteresis loops with a greater area. In particular, changes of the inclination of the trapezoidal waveform's lateral sides are also shown to induce controlled changes in the specific loss power generated by the activated nanoparticles (Figure 1b). Specific issues typical of the therapeutic practice of hyperthermia, such as the need for fine tuning of the optimal treatment temperature in real time, the possibility of combining sequential treatments at different temperatures, the ability to substantially reduce the heating transient in a hyperthermia treatment are properly addressed and overcome by making use of versatile non-harmonic driving fields of trapezoidal shape [3]. In the light of our results, features, methods, advantages and dangers of MNP-assisted precision nanomedicine are assessed in a more accurate way, and the efficiency of magnetic hyperthermia treatments is improved.

[1] G. Barrera, P. Allia, P. Tiberto, *Nanoscale*, 2020,12, 6360. [2] P. Allia, G. Barrera, P. Tiberto, *Phys. Rev. Applied*, 2019, 12, 034041. [3] G. Barrera, P. Allia, P. Tiberto, *Nanoscale Advances*, 2020, 2, 4652.



(a) Left: Time evolution of the temperature increment. Right: released power by NPs as a function of temperature. (b) Temperature increment as a function of time for selected inclination of the trapezoidal waveform lateral sides.

YA-05. Magnetic Bio-Sensing of Plasma-Derived Extracellular Vesicles for Cancer Screening.

A. Moyano^{1,2}, E. Serrano-Pertierra², M. Salvador^{1,3}, J.L. Marqués¹, J.C. Martínez-García¹, M.C. Blanco-López² and M. Rivas¹

1. Universidad de Oviedo Departamento de Física, Gijón, Spain;

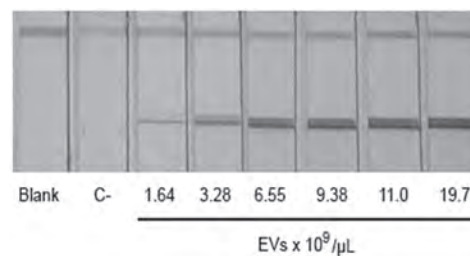
2. Department of Physical and Analytical Chemistry, University of Oviedo,

Oviedo, Spain; 3. Istituto di Struttura della Materia Consiglio Nazionale delle Ricerche, Roma, Italy

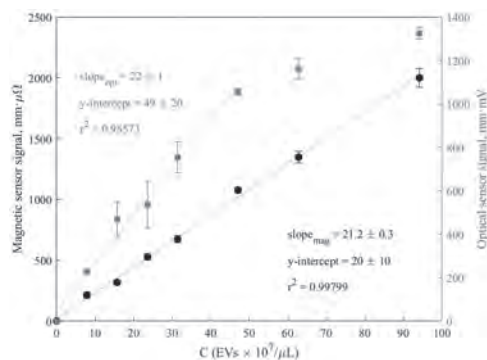
In the last months, due to the COVID-19 pandemic, we have become familiar with the expression “rapid tests” referred to fast and easy-to-use bioanalytical devices to detect viral proteins or antibodies generated by the patient’s immune system in response to the infection. The same type of rapid tests is extremely interesting to detect cancer biomarkers for disease screening and early diagnosis. Besides the fast response, the optimal technology should be low-cost, easy to use, and portable. The rapid tests rely on the lateral flow immunoassay (LFIA) technique [1]. The LFIA substrate is a strip of nitrocellulose membrane along which the liquid sample containing the molecule of interest can flow by capillary action. Before this flow, the analyte is specifically tagged with fluorescent enzymes or particles to make it visible. Two lines of recognition molecules are immobilized across the strip: (i) the test line, formed by a molecule that captures the tagged molecule of interest, and (ii) the control line, at which the unbound tags are trapped. The LFIA technique is used for point-of-care detection of various biomarkers; the best known is the pregnancy hormone in the popular home pregnancy tests that we can buy in the pharmacy and use ourselves with no prescription. There are some limitations for LFIA expansion, mainly their sensitivity and limit of quantification, which are not sufficient for some biomedical applications. Despite their limitations, WHO highly encourages the research into their performance and utility for disease surveillance [2]. There are two crucial ways in which magnetism can contribute effectively to improve the performance of rapid diagnostic tests: magnetic nanotags and magnetic sensing. The use of magnetic particles to tag the biomolecule of interest can have several advantages compared to non-magnetic tags (used for optical detection): magnetic immuno-concentration, magnetic detection, and long-lasting signal. Once the biomolecule is tagged by magnetic particles, the magnetic pre-concentration or isolation of the target biomolecule can be achieved by a magnetic gradient that attracts them and allow their separation from the original medium. This is enormously advantageous to increase the sensitivity of any technique that is applied after it. We can then detect the particles through a magnetic sensor without interferences from the paper strip or the biological fluid. Finally, the magnetic signal coming from the particles in the test line perdures in time and is insensitive to the paper strip aging or staining [3]. We recently developed a bio-detection method based on LFIA using superparamagnetic labels combined with an inductive sensor for reading out their signal. We proved the viability of the technique for quantifying prostatic cancer biomarkers [3] and toxic biogenic amines [4] in the range of interest. In this work, we have developed a lateral flow immunoassay (LFIA) system to detect plasma-derived extracellular vesicles (EV). These small (micro- or nano-sized) membrane structures are released by cells to mediate intercellular communication. Given that they carry proteins and micro-RNA specific to their cell of origin, they are nowadays thoroughly studied as disease biomarkers. We used superparamagnetic iron oxide nanoparticles coated with a double layer of oleic acid [5] as reporter labels. They were conjugated to antibodies against proteins expressed in the EVs surface, specifically CD-63 and CD-147. The latter is in higher concentrations in patients with colorectal cancer [6]. We used different concentrations of EVs purified from human plasma to perform LFIA tests to calibrate the system. Fig. 1 shows some of the LFIA strips obtained for such calibration. Subsequently, the strips were analyzed by a commercial reflectance sensor and our magnetic inductive sensor. The results for the assays with CD63 are shown in Fig. 2. We can appreciate that the linear range extends to all the concentration range understudy for the magnetic sensor. The tendency to saturation that we observe with the optical reader is typical of the immunoassays and is caused by the available antibodies’ occupation. Given that the reflectance signal comes only from the particles at the surface of the membrane, the saturation is achieved at lower concentrations than in the magnetic one, which comes from the whole volume. Besides this obvious advantage, the

magnetic sensor provides better linearity (even taking a reduced linear range of concentration for the optical signal) and a lower limit of detection (three times smaller for CD63 and two times smaller for CD147). We must emphasize that the analyte has not been magnetically pre-concentrated for these measurements. Such a technique will be studied in an ongoing investigation to increase further the sensitivity of the magnetic LFIA aiming at a rapid, portable technology for liquid biopsy applied to colorectal cancer screening. Acknowledgements This work was supported by the Spanish Ministry of Economy and Competitiveness (grant MAT2017-84959-C2-1-R), the Principality of Asturias (IDI/2018/000185) and the Council of Gijón/IUTA (SV-20-GIJON-1-22).

[1] C. Parolo, A. Sena-Torralba, J.F. Bergua, et al., Nat Protoc., Vol. 15(12), p.3788 (2020) [2] <https://www.who.int/news-room/commentaries/detail/advice-on-the-use-of-point-of-care-immunodiagnostic-tests-for-covid-19> [3] D. Lago-Cachón, M. Oliveira-Rodríguez, M. Rivas, et al., IEEE Magn. Lett., Vol. 8, p. 1 (2017) [4] A. Moyano, M. Salvador, J. C. Martínez-García, et al., Anal. Bioanal. Chem, Vol. 411, p. 6615 (2019) [5] D. Bica, L. Vékás, M.V. Avdeev, et al., J. Magn. Magn. Vol. 311, p. 17 (2007). [6] Y. Yoshioka, N. Kosaka, Y. Konishi, et al., Nat. Commun. Vol. 5, p. 1 (2014)



LFIA strips performed to test the concentration of human-plasma circulating EVs expressing CD63.



Calibration of CD63 LFIA using the magnetic (black) and optical (orange) readers.

YA-06. Potential Effects of TMS Magnetic Fields Beyond the Conventional Neurostimulation.

A. Guller^{1,2}, S. Clement¹, P. Sowman³ and E. Goldys¹

1. ARC Centre of Excellence for Nanoscale BioPhotonics, The Graduate School of Biomedical Engineering, University of New South Wales, Sydney, NSW, Australia; 2. The Institute for Regenerative Medicine, Sechenov University (I.M. Sechenov First Moscow State Medical University), Moscow, Russian Federation; 3. Macquarie University, Sydney, NSW, Australia

Transcranial magnetic stimulation (TMS)^{1,2} is a widely available technology employing strong (up to 4 T) pulsed (up to 300 Hz) magnetic fields for diagnostics of brain functions and treatment of various brain disorders. It is currently approved for clinical application in patients with drug-resistant depression^{2,3}, while a spectrum of new indications is emerging⁵⁻¹⁰. The current paradigm of TMS biological effects implies magnetic induction of Eddy currents in the brain cortical neurons as the leading action mechanism. However, the effects of the TMS-like magnetic fields on non-neuronal cells and some artificial systems is almost unknown. Based on literature analysis^{4,11-24} and our pilot experimental data, we hypothesize, that the transcranial and extracranial repetitive magnetic stimulation employing pulsed magnetic fields (MFs) generated by TMS devices can have immunomodulatory effects, affect the growth of brain and extracranial malignant tumours and applied in drug delivery control to the cells. This motivated us to explore the effects of designed 18 regimes of patterned repetitive magnetic stimulation (PRMS) on tumor cells of brain (glioblastoma multiforme, GBM) and pancreatic (pancreatic ductal adenocarcinoma) cancers and on microglia (immune cells of the brain). We also tested the effect of PRMS on a drug release from polymer nanoparticles in aqueous environment. A standard TMS device “Magstim Rapid2” with Double 70mm Air Film Coil was applied to the cell cultures spatially configured to correspond to a peak MF of 0.6 T, 0.25-50 Hz frequency, with sessions of 300 or 600 pulses. PRMS selectively modulated the viability and functional polarisation of immune-stimulated microglia in a frequency/intensity-dependent manner (Figure 1) and affected the proliferation/viability of GBM astrocytes and pancreatic cancer cells (frequency- and pulse number-dependent up- and downregulation) (Figure 2). Finally, we show the triggering of the efficient drug release from biocompatible polymer nanoparticles by the 50 Hz/2 min PRMS mode. Our pioneering findings demonstrate the potential of PRMS performed with using of re-purposed TMS equipment for immunomodulation, cancer treatment, brain repair and regeneration. We thank Sydney Vital Translational Cancer Centre (for seed grant) and Medilink Australia (for providing the “Magstim”).

1. Barker AT, et al.: Neurosurgery 1987, 20:100-9.
2. Rossini PM, et al. U: Clinical neurophysiology 2015, 126:1071-107.
3. Post A, Keck ME: Journal of Psychiatric Research 2001, 35:193-215.
4. Funk RH, et al.: Prog Histochem Cytochem 2009, 43:177-264.
5. Nardone R, et al.: Brain research bulletin 2020, 159:44-52.
6. Gao F, et al.: J Neurosurg Sci 2017, 61:514-22.
7. Rose DK, et al.: Stroke Res Treat 2014, 2014:305236.
8. Jin Y, et al.: Pain Physician 2015, 18:E1029-46.
9. Pérocheau D, et al.: Joint, bone, spine : revue du rhumatisme 2014, 81:22-6.
10. Peng L, et al.: Medicine 2019, 98:e15572.
11. Vazana U, et al.: J Neurosci 2016, 36:7727-39.
12. Antov Y, et al.: Biophysical journal 2005, 88:2206-23.
13. Shankayi Z, et al.: Electromagn Biol Med 2014, 33:154-8.
14. Towhidi L, et al.: Radiol Oncol 2012, 46:119-25.
15. Adey WR, Sheppard AR: in Mechanistic Approaches to Interactions of Electric and Electromagnetic Fields with Living Systems: Springer, 1987. pp. 365-87.
16. Cullen CL, Young KM: Front Neural Circuits 2016, 10:26.
17. Yamaguchi S, et al.: Bioelectromagnetics 2006, 27:64-72.
18. Golovin YI, et al.: Journal of controlled release 2015, 219:43-60.
19. Kim DH, et al.: Nat Mater 2010, 9:165-71.
20. Master AM, et al.: Scientific reports 2016, 6:33560.
21. Wong W, et al.: Scientific reports 2017, 7:10919.
22. Maniotis N, et al.: Journal of Magnetism and Magnetic Materials 2019, 470:6-11.
23. Pickard M, Chari D.: Nanomedicine 2010, 5:217-32.
24. Pickard MR, Chari DM: Int J Mol Sci 2010, 11:967-81.

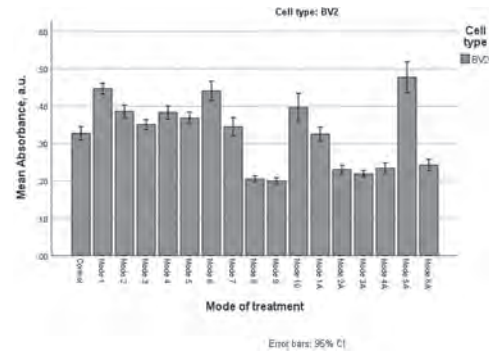


Figure 1. Effect of PRMS generated by a TMS device on viability of murine microglial BV-2 cells cultured in vitro. The cells’ viability was evaluated by MTT assay in 24 h after performing magnetic treatment. Mean absorbance is directly proportional to the number of viable cells. The left bar represents absorbance in control (untreated group), and the next bars to the right represent the measurements in the cells’ cultures treated with different regimes of PRMS.

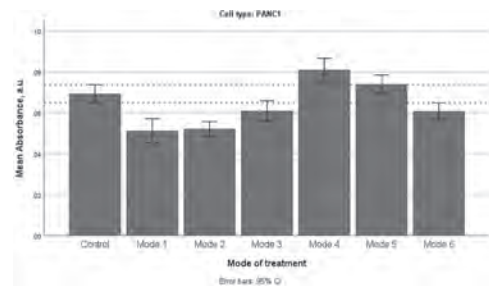


Figure 2. Effect of PRMS generated by a TMS device on viability of human pancreatic cancer cells (PANC-1) cultured in vitro. The cells’ viability was evaluated by MTT assay in 24 h after performing magnetic treatment. Mean absorbance is directly proportional to the number of viable cells. The left bar represents absorbance in control (untreated group), and the next bars to the right represent the measurements in the cells’ cultures treated with different regimes of PRMS. Green dashed lines indicate the borders of CI_{95%} for mean absorbance in control (untreated group; the left bar).

Session YB

FOCUS SESSION: MAGNETORHEOLOGICAL COMPOSITE MATERIALS AND APPLICATIONS

Norman Wereley, Chair

University of Maryland, College Park, MD, United States

INVITED PAPERS**YB-01. Magnetorheology in Unsteady Triaxial Fields.**

M.B. Terkel¹, J.R. Morillas¹, G. Camacho¹ and *J. de Vicente*¹

1. Applied Physics, Universidad de Granada Facultad de Ciencias, Granada, Spain

Conventional magnetorheological (MR) fluids are colloidal suspensions prepared by dispersion of magnetisable particles in non-magnetic liquid carriers. Interestingly, they exhibit a remarkable rheological change (so-called MR effect) upon the application of a magnetic field. The reason for this is the magnetic field-guided colloidal assembly of the dispersed magnetisable particles. The self-assembly can be controlled through the field configuration (DC, AC or combinations) and most of the investigations reported in the literature focus on DC fields. In this communication we show that the use of AC fields alone or in combination of DC fields are capable to generate exotic structures with enhanced MR effect (i.e. larger viscoelastic moduli and yield stresses).

YB-02. Disassembling Blood Clots and Improving Blood Oxygenation With Magnetorheology for Covid-19 Patients.

R. Tao¹

1. Physics, Temple University, Philadelphia, PA, United States

As the fight against Covid-19 pandemic continues, we have learned that the blood clotting caused by Covid-19 is the main issue making this disease much more severe than any flu or pneumonia. Doctors are seeing an alarming number of COVID-19 patients with blood clots — gel-like clumps in the blood that cause serious problems: internal bleeding, heart attack and stroke [1]. Autopsies have also found blood clots not only in the lungs of these victims, but throughout their bloodstream [2]. The microscopic image in Fig.1 illustrates that as the red blood cells stack together to form clots, their surfaces are blocked, compromising their oxygen function. When the blood clots get bigger, they can block blood circulation and trigger heart attack or stroke. Dr. Kanthi et.al recently claim that severe Covid-19, same as AP Syndrome, induces antibody to attack the phospholipid in red cell membrane, triggering blood clotting [3]. These blood clots take most platelets, creating high risk for internal bleeding. Currently blood thinners are the only medicine used to reduce the blood clot formation in severe Covid-19 patients. Unfortunately, blood thinner medicines do not disassemble the blood clots. Moreover, they increase the risk of bleeding, serious, or even life threatening. In fact, many patients were not saved by these medicines. Therefore, a new, safe and reliable approach to disassemble blood clots for Covid-19 patients is urgently needed. Here I am presenting our magnetorheology (MR) technology [4] to treat Covid-19 patients with thrombosis: applying a strong magnetic field along the patients' arm. When the blood clots come to the magnetic field with blood circulation, they will be disassembled. Red cells will be freed, the blood oxygenation function will be recovered, internal bleeding can be avoided, the blood viscosity along the flow direction will be reduced, turbulence will be suppressed, and cardiovascular accident can be prevented. Blood is a liquid suspension consisting mainly of red cells in plasma. The volume fraction of red cells is 40-50%. The amount of white blood cells and platelets in the blood is very small. Therefore, blood clots are actually aggregates of red cells (Fig.1). A typical human red cell is a biconcave disk (Fig.2a), with its diameter about 7.7 μm and the thickness decreasing from 2.5 μm at its edge to 0.8–1 μm at its center. The cytoplasm of the red cell contains hemoglobin, a metalloprotein containing heme groups that temporarily bind oxygen molecules taken up from the lungs and release them throughout the body. To allow efficient diffusion of oxygen, the full surface area of the red cells need to be available. When the blood form clots such as in Fig.1, surfaces of red cells are blocked and oxygen uptake and delivery is impeded. As the hemoglobin in red cells is an iron containing protein, deoxygenated red cells are paramagnetic. We are utilizing this property to disassemble blood clots (Fig.2). Red cells are polarized in a magnetic field. Because red cell is a disk, the strongest polarization is along the diameter direction. In a strong magnetic field, red cells will tilt to make their disk surface parallel to the field. Each red cell obtains an induced magnetic dipole moment. As shown in Fig.2b, when the red blood cells stack each other as in the clots, the interaction between neighboring red cells is strongly repulsive. This force is proportional to the square of magnetic field. If the applied magnetic field stronger than one Tesla, this repulsive force is strong enough to break the toughest blood clots, rouleaux [4,5]. As blood clots are mainly aggregates of red cells, once red cells are disassembled, platelets and other components are also released; internal bleeding risk is reduced. The magnetic field will further align the released red cells to form short chains along the diameter direction (Fig.2c). In such chains, the surface of red cells is fully exposed, excellent for their normal oxygen functions. Fig.2d shows a microscopic image of such short chain. Also shown in Fig.2d, we apply the magnetic field along the blood flow direction. The short chains is parallel to the blood flow. As the chains are streamlined in the flow direction, the blood viscosity along the flow direction is considerably reduced. Meanwhile, the short chains resist any motion in the directions perpendicular to the flow. The treated blood thus suppresses turbulence or disturbed motion as any disturbed flow cannot survive without motions in the directions perpendicular to the flow [4,6]. The blood circulation and red cell function will thus be greatly improved and cardiovascular accident can be prevented. Of course, after the magnetic field is turned off, these short chains will be eventually

broken and the red cells will become wholly independent, flowing inside the plasma (Fig.2e). Our lab tests [4] have confirmed that this MR technology can effectively disassemble rouleaux [6]. As the newly formed blood clots in Covid19 patients should be weaker than rouleaux, we expect that this technology can safely and effectively disassemble them and help the patients to recover.

1. Z. Varga, *et al*, *www.thelancet.com* Vol 395, pp 1417-1418, May 2, 2020. 2. <https://www.webmd.com/lung/news/20200424/blood-clots-are-another-dangerous-covid-19-mystery> 3. Y. Zuo et al, *Science Translational Medicine*, 12. eabd3876 (2020) 4. R. Tao, *et al.*, Systems and method for reducing the viscosity of blood, suppressing turbulence in blood circulation, and curing rouleaux. PCT/US2017/059446 (<https://patentscope.wipo.int/search/en/detail.jsf?docId=WO2018085330>) 5. N. Abramson, *BLOOD*, V107, I 11, 4205-4205 (2006) 6. R. Tao, K. Huang, *Physical Review E* 84, 011905 (2011).

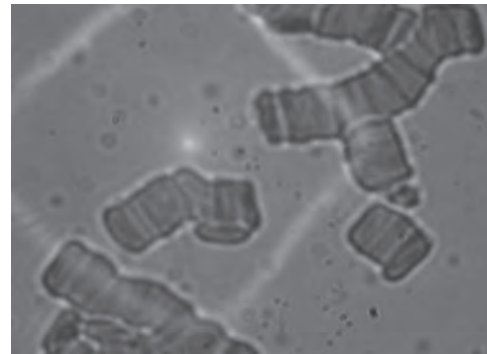


Fig.1 Blood clots found in coronavirus patients' blood.

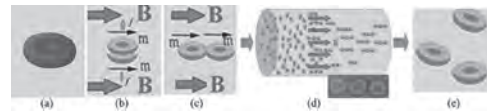


Fig.2 (a) Red blood cell. (b) The strong magnetic field breaks the blood clot. (c) The released red cells form short chains along the diameter-magnetic field direction. (d) The microscopic image of a short red-cell chain. The magnetic field improves blood circulation. (e) After the magnetic field is off, the red cells will eventually become wholly independent within the plasma.

YB-03. Controllable Stress of Magnetorheological Fluid Encapsulated Elastomers.

Y. Choi¹ and N. Wereley¹

¹. Department of Aerospace Engineering, University of Maryland at College Park, College Park, MD, United States

Smart materials can change key physical properties in response to external stimuli. To achieve adaptive design performance regardless of environmental changes, demand for smart materials technology has greatly increased. Magnetorheological (MR) composites are a class of smart materials that can rapidly and reversibly control adjust their damping and stiffness properties in response to external magnetic field. MR composites consist of micron-size soft magnetic particles in a non-magnetic carrier matrix. MR composites can be divided into three major classes based on matrix materials: MR fluids (MRFs), MR foams, and MR elastomers (MREs). The rheological properties of MRFs, which use liquid as the carrier matrix, can be controlled in response to an external magnetic field. MRFs have been widely applied to a variety of hydraulic actuators to produce a controllable damper force or torque. MR foams are composed of either non-magnetic porous metal foam filled with MRF or have particles embedded in a porous elastomeric foam. Because of their light weight and high compliance, MR foams exhibit large changes in baseline stiffness and are candidate smart materials for space applications, as well as vibration and acoustic absorption applications. MREs, which use a non-porous solid elastomer as the carrier matrix, have controllable viscoelastic properties. MREs can be used to retrofit passive rubber isolators and mounts in vibration and shock mitigation systems to provide improved and adaptive performance. MRFs typically exhibit sedimentation because of the large density difference between carbonyl Fe particles (density of 7.9 g/ml) and the non-magnetic carrier fluid (e.g., silicone oil has a density of 0.97 g/ml). Unlike MRFs, the Fe particles in MR foams and MREs are permanently dispersed. Because particles are embedded in the carrier matrix, MR foams and MREs show less MR effect than MRFs where particles can migrate and agglomerate. To increase MR effects in MREs, research [1-4] to encapsulate MRFs in MREs has been reported. It should be noted that MR foams have porous carrier matrix and may be not possible to encapsulate MRF into MR foam. In this study, MRF encapsulated elastomers (MREEs) are fabricated and their controllable stress behaviors are experimentally evaluated. Two design configurations are studied for MREEs: the first is MRF and permanent magnet (PM) embedded inside MREEs, and the second is MRF only embedded in MREEs. MREEs with PM can be passively and actively activated, but MREEs without PM can be only activated by external magnetic field produced by an electromagnet. A sample MREE (Figure 1) encapsulates an MRF composed of 35 vol% carbonyl Fe dispersed in a 1,000 cSt silicone oil. The silicone rubber was as soft as 00-20. The diameter and height of this sample was nominally 2.6" and 0.37", respectively. The compressive stress-strain curve of the MREEs both without and with applied magnetic field were measured by a MTS machine. Figure 2 presents the measured field-dependent compressive stress curves of the MREE. As seen in this figure, the compressive stress curves of the MREE can be continuously adjusted in response to current input. Also, the hysteresis loop also increased as the applied current inputs. This physically implies that the dissipated energy increased. In the full paper, the effect of two different magnetic flux directions (i.e., positive and negative coil currents) will be presented. The compressive stress curve of the MREEs can also be affected by the strain rate, as in impact events. To illustrate such strain rate effects, the compressive stress curves over a range of strain rates will be also presented. From the measured hysteresis loop, the dissipated energy can also be determined. In addition, the MREEs can be stacked for accommodating larger compressive displacement. In this study, the effect of two different stackable situations (one is attractive PMs configuration and the other is repulsive PMs configuration) on the compressive stress curve will be evaluated. From the results presented in this study, the controllable stress capability of the MREEs will be presented for a range of operating conditions.

[1] D. York, X. Wang, and F. Gordaninejad, "A new MR fluid-elastomer vibration isolator," *J. Intel. Mater. Syst. and Struct.*, 18: 1221-1225 (2007).

[2] D. York, X. Wang, F. Gordaninejad, "A new magnetorheological mount

for vibration control," *J. Vibr Acoust.*, 133: 031003 (2011). [3] A. K. Bastola, L. Li and M. Paudel, "A hybrid magnetorheological elastomer developed by encapsulation of magnetorheological fluid," *Journal of Materials Science*, Vol. 53, pp. 7004-7016 (2018). [4] A. K. Bastola, E. Ang, M. Paudel, L. Li, "Soft hybrid magnetorheological elastomer: gap bridging between MR fluid and MR elastomer," *Colloids and Surfaces A*, Vol. 583, 123975 (2019).

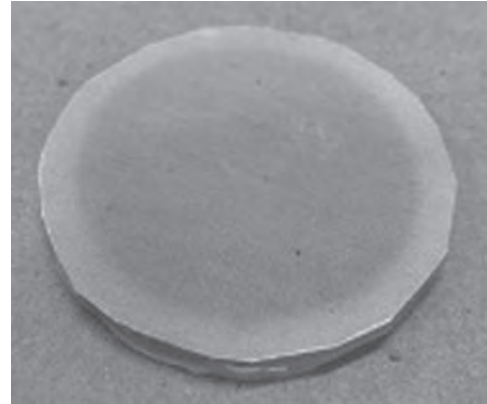


Figure 1. MRF encapsulated elastomers (MREEs).

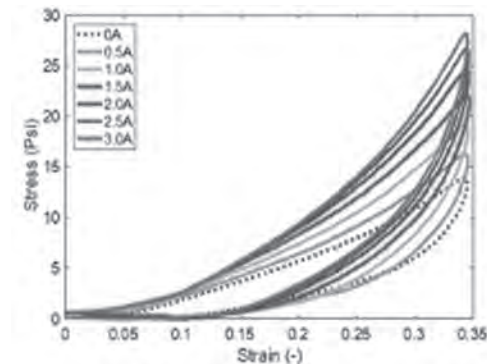


Figure 2. Field-dependent compressive stress curves of the MREE.

CONTRIBUTED PAPERS

YB-04. Magnetorheological Elastomers – Material Properties and Actuation Capabilities.

H. Böse¹, J. Ehrlich¹ and T. Gerlach¹

1. Fraunhofer Institute for Silicate Research ISC, Würzburg, Germany

Magnetorheological (MR) elastomers as composite materials of magnetizable particles in an elastomer matrix are the soft solid relatives of the better known MR fluids [1]. They preferably consist of silicone elastomer filled with dispersed iron particles [2]. MR elastomers exhibit interesting viscoelastic properties, which strongly depend on the elastomer stiffness and the particle concentration and are controllable by a magnetic field. With rising iron particle concentration, the basic stiffness in terms of the elastic storage modulus increases, as expected. In a strong magnetic field, the storage modulus can be enhanced by a factor of about 10 (see Figure 1). A corresponding increase is observed also for the viscous loss modulus (see Figure 1). These effects are particularly pronounced for MR elastomers with soft silicone matrices, which exhibit low molecular crosslinking densities. In common MR elastomers, the iron particles are randomly distributed in the surrounding matrix material due to the mixing of the particles with the liquid silicone precursors in the preparation process. However, it is also possible to prepare MR elastomers with anisotropic particle distribution [3]. In order to achieve this modification, a magnetic field is applied already in the preparation procedure before and during the chemical crosslinking of the silicone elastomer in a thermal process, where the particles are arranged to chains along the magnetic field, in analogy to MR fluids. The magneto-mechanical properties of anisotropic MR are significantly different from those of their isotropic counterparts. A strong increase of the storage modulus of the anisotropic composites is observed already with lower iron particles concentrations. In other investigations, the magnetic properties of MR elastomer cubes with isotropic and anisotropic particle arrangements were studied and compared. Similar to MR fluids, even with high concentrations of iron particles, the magnetic susceptibility of MR elastomers is extremely low in comparison with pure solid iron, which is due to the dispersed distribution of the iron particles in the composite. The measured susceptibility of the anisotropic MR elastomer with a magnetic field perpendicular to the iron particle chains is comparable to the corresponding values of the isotropic samples. However, it could be shown that the susceptibility parallel to the particle chains in the anisotropic MR elastomer is significantly higher due to the particle contacts in this direction. Numerous interesting applications become possible with MR elastomers. Generally known are applications in vibration reduction. Here, the focus is on tunable vibration absorbers due to the dominant elastic behavior of elastomers [4] in contrast to the more viscous characteristics of MR fluids. However, promising exploitation potential of MR elastomers arises also for actuation devices, where an MR elastomer body deforms in a magnetic field. A speciality of these MR elastomer-based actuators is the possibility to realize different types of actuation depending on the orientation of the magnetic field. A basic type of actuation is caused by the linear deformation of an MR elastomer body in a corresponding magnetic field. Due to magnetic attraction forces on the soft-magnetic iron particles by a specially shaped yoke part in the magnetic circuit, the MR elastomer body such as a disk is deformed into a preferred direction. This type of actuator can be used for human-machine interfaces, where haptic feedback is required, when the user touches the interface. Another interesting application of linear MR elastomer actuators are pumping units. In these units, the periodic linear deformation of the actuator sucks the medium to be transported through a non-return valve into a chamber and pushes it out through another non-return valve. Moreover, with MR elastomers also another type of actuators with radial motion may be realized. In a magnetic field with radial orientation between an inner yoke and an annular outer yoke, a ring-shaped body of MR elastomer between the two yokes leaving an annular gap to the inner yoke can expand radially and close the gap (see Figure 2). This unusual kind of radial actuation offers a high potential for various applications. Especially interesting are valves with a ring-shaped opening, where the degree of closing is controlled by the magnetic field strength, i.e. the current in the coil of the electromagnet, and the corresponding radial deformation of

the MR elastomer ring. With this mechanism, proportional valves can be realized. Another possible application of radial MR elastomer actuators are locking devices. Here, MR elastomer rings bridge the annular gaps between an inner rotatable shaft and an outer housing, thereby blocking the rotation, when the magnetic field is activated. It could be demonstrated that locking torques of about 5 Nm can be achieved in a device with two MR elastomer rings. The locking effect is stronger than with an MR fluid in a device with a corresponding geometrical configuration. In this symposium contribution, material properties of MR elastomers and various actuator designs for different applications are discussed.

[1] J. D. Carlson and M. R. Jolly, MR fluid, foam and elastomer devices. *Mechatronics* 10, 555-569 (2000) [2] W. H. Li and M. Nakano, Fabrication and characterization of PDMS based magnetorheological elastomers, *Smart Materials and Structures* 22, 055035 (2013) [3] H. Böse and R. Röder, Magnetorheological Elastomers with high variability of their mechanical properties, *J. Phys.: Conf. Ser.* 149, 012090 (2009) [4] X. Z. Zhang and W. H. Li, Adaptive Tuned Dynamic Vibration Absorbers Working with MR Elastomers, *Smart Structures & Systems* 5, 517-529 (2009)

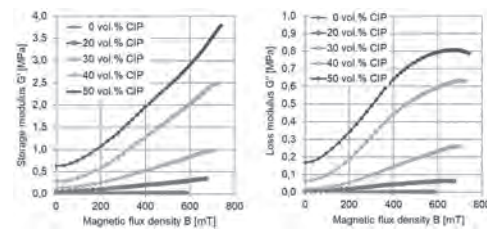


Figure 1: Dependence of the storage modulus (left) and the loss modulus (right) of MRE composites with different carbonyl iron particle (CIP) concentrations on the magnetic flux density

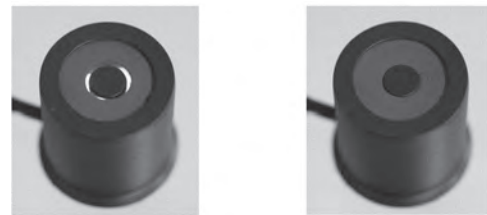
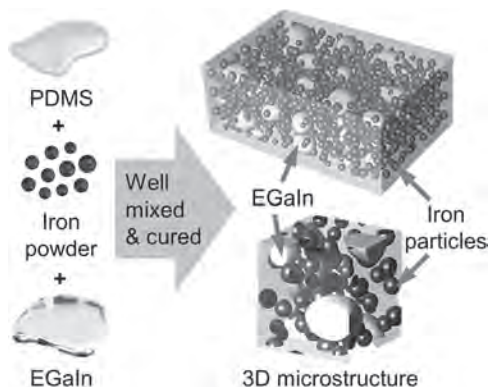
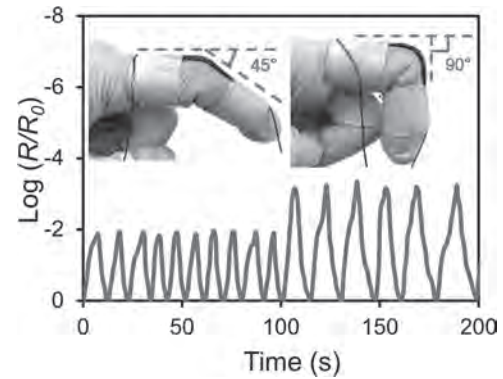


Figure 2: MRE actuator with radial expansion for proportional valve applications in the inactivated state (annular gap open, left) and activated state (annular gap closed, right)

YB-05. Study of Liquid Metal Filled Magnetorheological Elastomers.G. Yun¹, S. Tang² and W. Li¹¹. School of Mechanical, Materials, Mechatronic and Biomedical Engineering, University of Wollongong, Wollongong, NSW, Australia;². Department of Electronic, Electrical and Systems Engineering, University of Birmingham, Birmingham, United Kingdom

The work presents the fabrication and characterisation of a new liquid metal filled magnetorheological elastomer (LMMRE) comprising liquid metal microdroplets and metallic magnetic microparticles¹. The conductive network formed by liquid metal droplets and solid metal microparticles in the matrix imparts conductivity to LMMRE (Fig. 1). Both isotropic and anisotropic LMMREs were fabricated either without or with an external magnetic field. For the case of isotropic LMMRE, compared to conventional composites, this LMMRE uniquely reaches a maximum resistance in the relaxed state and can drop sharply under any mechanical deformation, including compression, stretching, bending, and twisting. This indicates that the LMMRE can exhibit an unconventional negative piezoresistive effect. The mechanical and thermal properties of LMMRE were further studied. Several proof-of-concept applications based on LMMRE such as wearable joint sensors and intelligent heating devices were also demonstrated. For example, the LMMRE can be used to detect the movement of human joints. A LMMRE strip was attached to the index finger, then the finger bent repeatedly with the maximum bending angles of 45° and 90°, respectively. The resistance change-time curve reflects the accurate response of the LMMRE sensor to different angles and its stability under cyclic loading (Fig. 2). Therefore, this LMMRE has the potential to be applied for developing highly sensitive flexible sensors for wearable devices. After that, we created and studied an anisotropic LMMRE using the magnetic field alignment method. We show that magnetically aligning the particles prior to curing the LMMRE produces different results. Namely, the conductivity of the anisotropic LMMRE—in the absence of deformation—improves significantly by several orders of magnitude in all directions compared to the isotropic LMMRE with the same composition. In addition, the resistivity changes of the anisotropic LMMRE under mechanical deformation and its anisotropic piezoresistive properties are also significantly different from isotropic LMMRE. Along the particle alignment direction, the resistivity of anisotropic LMMRE increases sharply with strain. In contrast, in the direction perpendicular to the particle chains, its resistivity decreases monotonically with strain. Besides, the anisotropic LMMRE is also more sensitive to mechanical deformation along the particle alignment direction. Furthermore, we discovered that the mechanical, magnetic and thermal properties of the anisotropic LMMRE also exhibit significant anisotropy. Harnessing these unique properties, we demonstrated several applications based on anisotropic LMMRE such as soft tactile logic devices and an improved intelligent heating device.

1. G. Yun, S.Y. Tang, S. Sun, D. Yuan, Q. Zhao, L. Deng, S. Yan, H. Du, M.D. Dickey and W. Li, Nature Communications, Vol. 10, p.1300 (2019)



YB-06. Magnetic Particle Reinforced Elastomer Composites for Additive Manufacturing.

J. Park¹, A. Becnel¹, A. Flatau¹ and N. Wereley¹

¹. University of Maryland at College Park, College Park, MD, United States

Magnetorheological elastomer (MRE) is a magnetic particle reinforced elastomer composite, which its mechanical properties can be controlled with the application of a magnetic field.¹ The magnetorheological effect induces changes in stiffness and damping properties in the composite with the response of the magnetic particles to the external magnetic field.² Smart sensor and actuator components can be fabricated for adaptive vibration control systems where mechanical properties can be controlled by the application of magnetic field. Typically, composites are prepared by mixing magnetic particles with the uncured rubber matrix and then the mixture is poured into a mold for curing. Recently low-cost 3D printers are widely available, utilizing various polymers. Manufacturability of MRE composites using additive manufacturing (AM) process has gained great attention so the geometrical design of the MRE composite fabrication can be achieved.³ In this research, development of filament of MRE for fused filament fabrication based on additive manufacturing is performed. The magnetorheological effect depends on the particle's magnetic properties and volume fraction, and distribution, etc. Filament materials are developed by mixing thermoplastic polyurethane (TPU) pellets with the magnetic particles (iron oxide, carbonyl Fe particles), followed by extrusion process to produce rolls of filament. Due to the nature of the mixing process relying on gravity to feed material into the extruder, denser and much smaller magnetic particles (~10 μm) than the TPU pellets (~mm) tend to fall to the bottom of the hopper, leading non-uniform distribution of magnetic particle along the filament thru extrusion process. Therefore, the trickling systems with a screw feeder were developed to provide consistent trickling rate of each TPU and magnetic particles respectability. [Figure 1 (a)] The trickling rate of TPU was fixed at ~4.9 g/min and the trickling rate of iron oxide was varied from 0.0 to 2.5 g/min. Five sets of filaments were produced with different trickling rates of iron oxide.[Figure 1(b)]. Diameter ranges from 1.45 ± 0.01 to 1.55 ± 0.06 mm. The density of filament increases with the higher trickling rate of magnetic powder and the densities change from 1.33 ± 0.05 to 1.46 ± 0.05 g/cc, indicating that the volume fraction control of magnetic particles in the extrusion process was successful. The grayscale level plot [Figure 1 (c)] indicates the iron oxide concentration in each filament in the yellow box region. The grayscale plot profiles the images with each point represents the average pixel intensity. This data shows that the filaments produced with lower trickling rate (0.6 and 1.0 g/min) did not show significant difference but the lower gray scale values of filaments with 1.5 and 2.5 g/min indicate that there are more iron oxide particles. Micro-focus X-ray tomography scans were performed on the produced composite filament (Figure 2). The results show that magnetic particles are well dispersed in the matrix. The small grains are < ~30 μm and the larger grains are ~60 μm . The iron oxide volume fraction ranges from 9.31% to 12.95%. This demonstrates that MRE filament feedstock materials can be successfully manufactured for use in fused filament deposition processes.

1. S. S. Kang, K. Choi, and J. D. Nam, *Materials.*, Vol.13, p.4597 (2020) 2. O. Padalka, H. J. Song, N. M. Wereley, J. A. Filer, *IEEE Transactions on Magnetics*, Vol. 46, p.2275 (2010) 3. A. K. Bastola, M. Paudel, L. Li, *Smart Materials and Structures*, Vol. 29, p.123002 (2020)

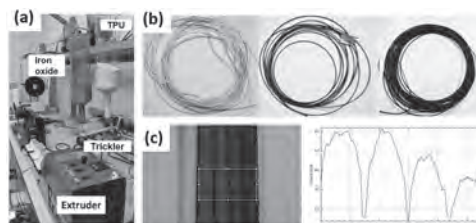


Figure 1 (a) Schematic drawing and image of developed trickling system. (b) coils of TPU filaments produced with different amount of iron oxide. (c) image of extruded filaments and plot profile of the yellow box.



Figure 2 X-ray tomography scan performed on the produced composite filament. Iron oxide particles are highlighted with color coding by volume. The TPU matrix is colored in light gray to easily visualize the pores and iron oxide dispersions.

MONDAY, 26 APRIL 2021

LIVE Q&A SESSIONS, 5:00 PM EUROPE CEST

Session AA

PROGRESS AND PROSPECTS OF ADVANCED MAGNETIC MICROSCOPIES

Olivier Fruchart, Chair

Univ. Grenoble Alpes, CNRS, CEA, Grenoble, France

INVITED PAPERS

AA-01. Advanced Scanning Transmission X-Ray Microscopy for the Investigation Magnetic Phenomena.

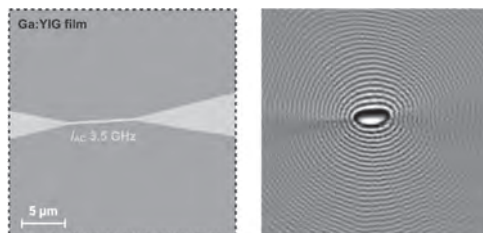
M. Weigand^{2,1}, S. Wintz¹, J. Gräfe¹ and G. Schütz¹

1. Max-Planck-Institute Stuttgart, Stuttgart, Germany;

2. Helmholtz-Zentrum Berlin für Materialien und Energie GmbH, Berlin, Germany

X-ray circular magnetic dichroism (XMCD) is a powerful tool for highly-sensitive and element-specific investigations of magnetic materials. This effect can be utilized in Scanning Transmission X-ray Microscopy (STXM) in the soft X-ray range for magnetic imaging at spatial resolutions down to 20 nm. When combined with a pump-probe excitation and single-photon detection scheme, magneto-dynamic imaging can be achieved with a stroboscopic time-resolution of the order of 20 ps. These capabilities have been widely used in the field of magnetism, including vortex core dynamics [1], magnonics in real-space on the scale of tens of nm[2,3,4] and room temperature skyrmionics [5,6] As a photon-based technique, STXM is very tolerant to the sample environments and allows for diverse detection methods. For example, the use of strong magnetic fields can be combined with surface sensitive electron yield imaging, as well as with helium cryostats to provide sample temperatures down to 20K at multi-GHz bandwidths for dynamic excitation. Examples for research utilizing these features will be presented, as well as recent developments such as CCD-Ptychography for super-resolution or using a high- repetition-rate laser as an optical pump source for time-resolved measurements. As an outlook, it will be discussed how STXM can profit from the current developments in high-brilliance x-ray sources.

[1] Van Waeyenberge et al., Nature 444, 461 (2006). [2] S Wintz et al., Nat. Nanotech. 11, 948 (2016). [3] V. Sluka et al., Nat. Nanotech. 14, 328 (2019). [4] N. Träger et al., Phys. Status Solidi RRL, 14: 2000373 (2020). [5] S Woo et al., Nat. Mater. 15, 501 (2016). [6] K Litzius et al., Nat. Phys. 13, 170 (2017). [7] S. Mayr et al. (unpublished) (2020).



Schematics and time-resolved STXM image (normalized snapshot) revealing the coherent flow of magnons in a ferrimagnetic insulator [7]

AA-02. Quantum Sensing of Quantum Materials Using NV-Center Microscopy.*A. Yacoby*¹*1. Physics, Harvard University, Cambridge, MA, United States*

The magnetic fields generated by spins and currents provide a unique window into the physics of correlated-electron materials and devices. Proposed only a decade ago, magnetometry based on the electron spin of nitrogen-vacancy (NV) defects in diamond is emerging as a platform that is exceptionally suited for probing condensed matter systems [1]: it can be operated from cryogenic temperatures to above room temperature, has a dynamic range spanning from DC to GHz, and allows sensor-sample distances as small as a few nanometers. As such, NV magnetometry provides access to static and dynamic magnetic and electronic phenomena with nanoscale spatial resolution. While pioneering work focused on proof-of-principle demonstrations of its nanoscale imaging resolution and magnetic field sensitivity, now experiments are starting to probe the correlated-electron physics of magnets and superconductors and to explore the current distributions in low-dimensional materials [1]. In this talk, I will review some of our recent work that uses NV center magnetometry to image skyrmions in thin magnetic films [2], measure the spin chemical potential in magnetic insulators [3], and image hydrodynamic electron flow in layered materials [4,5].

1. F. Casola et al., Nat. Rev. Mater. 2018 2. Y. Dovzhenko et al., Nature Comm. 2018. 3. C. Du et al., Science 2017. 4. M. Ku et al., Nature 2020. 5. Uri Vool et al., arXiv2009.04477

AA-03. Imaging 3D Magnetic Configurations With X-Rays.

C. Donnelly¹, M. Guizar-Sicarios², S. Gliga², S. Finizio², K. Metlov^{3,4}, V. Scagnoli^{2,5}, M. Holler², A. Hrabec^{2,5}, S. Mayr^{2,5}, N. Bingham^{2,5}, N.R. Cooper¹, J. Raabe² and L. Heyderman^{5,2}

1. University of Cambridge, Cambridge, United Kingdom; 2. Paul Scherrer Institut, Villigen, Switzerland; 3. Donetsk Institute for Physics and Engineering, Donetsk, Ukraine; 4. Institute for Numerical Mathematics RAS, Moscow, Russian Federation; 5. ETH Zurich, Zurich, Switzerland

Three dimensional magnetic systems promise significant opportunities for applications, for example providing higher density devices and new functionality associated with complex topology and greater degrees of freedom [1,2]. For the experimental realisation of these new properties, appropriate characterisation techniques are required to determine both the three-dimensional magnetic structure, and its response to external stimuli. In this talk, I will describe our recent progress in the development of new capabilities for the imaging of three-dimensional magnetic systems, and their dynamic behaviour. For three-dimensional magnetic imaging, we have developed X-ray magnetic nanotomography [3]. By measuring high resolution 2D XMCD projections [4] of the sample for many angles about a dual rotation axis experimental setup, and combing these with a new iterative reconstruction algorithm [5], we determine the complex three-dimensional magnetic patterns within the bulk of a micrometre-sized soft magnetic pillar with 100 nm spatial resolution, as shown in Figure 1. The internal magnetic configuration reveals a complex network of topological magnetic features such as vortices, antivortices and domain walls and, at the crossing points of these structures, we observe the presence of Bloch point singularities [3]. The identification, and interpretation, of nanoscale topological objects within the complex reconstructed magnetic configurations – that consist of millions of pixels – represents a significant challenge. To address this, we have recently implemented calculations of the magnetic vorticity [6,7], a vector that represents the *flux* of the skyrmion number density, and thus encodes the topology of the magnetic configuration. In this way, not only can we locate and identify the presence of topological structures (Figure 1e,f), but we gain new insights into 3D magnetic solitons, leading to the first observation of magnetic vortex rings [7], as shown in Figure 1g. Lastly, in addition to the static magnetic configuration, the *dynamic* response of the 3D magnetic configuration to excitations is key to our understanding of both fundamental physics, and applications. With our recent development of X-ray magnetic laminography [8,9] (Figure 2), it is now possible to determine the magnetisation dynamics of a three-dimensional magnetic system [8]. In this way, we have been able to map the dynamics of a magnetic microdisc in response to the excitation of a 500 MHz magnetic field, revealing the motion of vortex domain walls within the bulk of the structure, as well as mapping the coherent rotation modes of the magnetisation in three dimensions (Figure 2c,d), with spatial and temporal resolutions of 50 nm and 70 ps, respectively. These new experimental capabilities of X-ray magnetic imaging open the door to the elucidation of complex three-dimensional magnetic structures, and their dynamic behaviour.

[1] A. Fernández-Pacheco, *et al.*, “Three-dimensional nanomagnetism” Nat. Comm. 8, 15756 (2017) [2] C. Donnelly & V. Scagnoli, “Imaging three-dimensional magnetic systems with X-rays” J. Phys. D: Cond. Matt. (2019). [3] C. Donnelly *et al.*, “Three-dimensional magnetization structures revealed with X-ray vector nanotomography” Nature 547, 328 (2017). [4] C. Donnelly *et al.*, “High-resolution hard x-ray magnetic imaging with dichroic ptychography” PRB 94, 064421 (2016). [5] C. Donnelly *et al.*, “Tomographic reconstruction of a three-dimensional magnetization vector field” NJP 20, 083009 (2018). [6] N. R. Cooper, “Propagating magnetic vortex rings in ferromagnets.” PRL. 82, 1554 (1999). [7] C. Donnelly *et al.*, “Experimental observation of vortex rings in a bulk magnet” Nat. Phys. (2020) [8] C. Donnelly *et al.*, “Time-resolved imaging of three-dimensional nanoscale magnetization dynamics”, Nat. Nano. 15, 356 (2020). [9] K. Witte *et al.*, “From 2D STXM to 3D Imaging: Soft X-ray Laminography of Thin Specimens”, Nano Lett. 20, 1305 (2020).

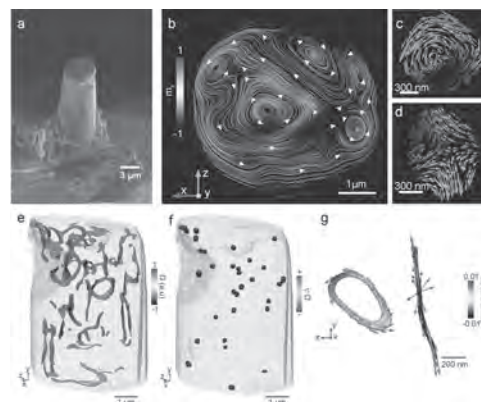


Figure 1. X-ray magnetic tomography of a GdCo micropillar (a) reveals a complex internal magnetic configuration. A horizontal slice (b) contains a number of vortices (c) and antivortices (d). Through calculations of the magnetic vorticity vector, we can identify the presence of topological structures (e) and magnetisation singularities (f) within the bulk of the micropillar. By plotting the magnetic vorticity, we identify magnetic vortex rings of circulating vorticity (g). a-d are reproduced from [3], and e-g are reproduced from [8].

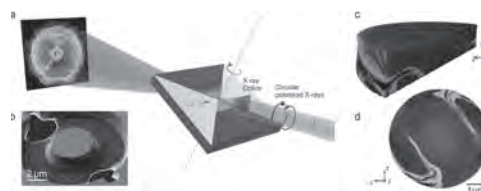


Figure 2 Pump-probe X-ray magnetic laminography (a) allows for the mapping of the magnetization dynamics of a magnetic microdisc (b) with spatial and temporal resolutions on the order of nanometers and picoseconds, respectively. Coherent rotation modes of the magnetization are shown for a cross section (c) and a lower slice of the structure containing vortex domain walls (d). a-d reproduced from [8].

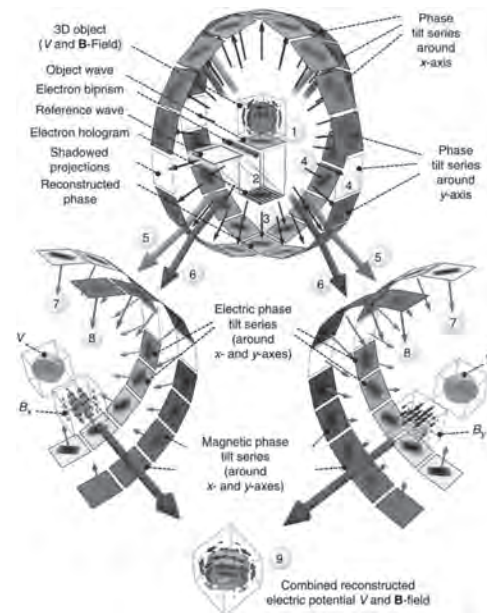
AA-04. 3D Mapping of Magnetic Nanotextures With Nanometer Resolution Using Holographic Vector-Field Electron Tomography.

D. Wolf¹, I. Andersen², S. Schneider³, A. Kovacs⁴, L. Rodriguez⁵ and A. Lubk¹

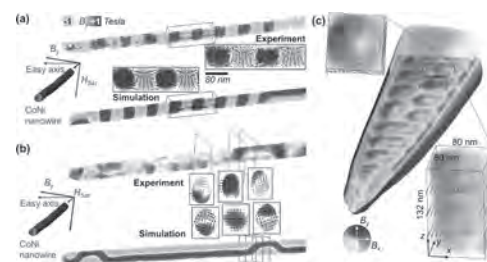
1. Leibniz-Institut für Festkörper- und Werkstofforschung Dresden eV, Dresden, Germany; 2. Centre d'Elaboration de Materiaux et d'Etudes Structurales, Toulouse, France; 3. Technische Universität Dresden, Dresden, Germany; 4. Forschungszentrum Julich GmbH, Julich, Germany; 5. Universidad del Valle, Cali, Colombia

The increasing exploration of nanomagnetism into the third dimension lead to the discovery of novel frustration mechanisms and ensuing magnetic configurations and textures, many with unprecedented properties [1]. The fundamental understanding of these configurations and the interactions stabilizing them requires a quantitative microscopy technique revealing 3D magnetic structures with a spatial resolution below characteristic magnetic length scales pertaining to a given problem. In our contribution we introduce holographic vector-field electron tomography (VFET), a combination of off-axis electron holography (EH) and electron tomography in the transmission electron microscope (TEM), facilitating sub-10 nanometer spatial resolution [2, 3]. Off-axis EH utilizes an interferometric setup to determine the phase shift of an electron wave that passed through the sample. The Aharonov-Bohm phase shift of ferro-magnetic samples is proportional to projections of both electric potential (mainly mean inner potential) and magnetic flux density (B -field), which allows to reconstruct them in 3D from a tilt series of 2D phase images by tomographic methods [2]. The principle and workflow of holographic VFET is illustrated in Fig. 1. In addition to the comprehensive workflow of recording and reconstructing the 3D data, crucial steps of alignment and image processing, e.g., precise displacement correction of 2D projections and 3D tomograms, phase unwrapping, denoising, etc. are addressed. Fig. 2 shows two examples, how holographic VFET is applied to reveal 3D magnetic configurations in nanoscale magnetic materials. In Figs. 2a,b, we present 3D remanent states in a Co-rich CoNi cylindrical nanowire (NW) with a diameter of 70 nm and the hcp c-axis oriented almost perpendicular to the NW axis [4]. We observed two different remanent states after the application of an external saturation field of 2 T perpendicular (Fig. 2a) and parallel (Fig. 2b) to the NW axis. The external field direction perpendicular to both the wire axis and the magnetocrystalline easy axis resulted in a transverse-vortex chain configuration, whereas a field direction parallel to the wire axis produced longitudinal vortex domains with their cores aligned along the applied field, but with alternately opposite chirality. Micromagnetic simulations confirm our findings and enable us to understand the origin of the observed complex magnetic states, in particular, reveal a large influence of the NW morphology on the remanent state. In Fig. 2c, the first 3D reconstruction of Bloch-Skyrmions in a FeGe needle-shaped FIB sample taken at 90K temperature is depicted. The reconstructed textures provide insights into a variety of previously unseen local deviations from a homogeneous Bloch character within the skyrmion tubes (SkTs), details of the collapse of the skyrmion texture at surfaces, and a correlated modulation of the SkT in FeGe along their tube axes. [5]

[1] A. Fernandez-Pacheco *et al.*, Nat Commun 8, p.15756 (2017) [2] D. Wolf *et al.*, Chem Mater 27, p. 6771 (2015) [3] D. Wolf *et al.*, Comm Phys 2, p. 87 (2019) [4] I.M. Andersen *et al.*, submitted (2021) [5] D. Wolf *et al.*, to be submitted (2021) [6] DW and AL have received funding from the European Research Council (ERC) under the Horizon 2020 research and innovation program of the European Union (grant agreement number 715620). AL, and SS acknowledge financial support through the Priority Program SPP2137 of the German Research Foundation (DFG) within projects LU-2261/2-1 and RE-1164/6-1.



Principle and workflow of holographic vector-field electron tomography (VFET) in the transmission electron microscope (adapted from Ref. [3]). (1) Modulation of electron waves by magnetic sample, (2) Interference of modulated object wave with unmodulated reference wave by an electrostatic biprism building up an electron hologram, (3) Reconstruction of hologram yielding amplitude and phase shift of object wave, (4) Acquisition of two tilt series around two tilt axes, X and Y, providing two (ideally 360°) phase tilt series, (5/6) Calculation of half the sum/difference of opposite projections (green/red arrow) resulting in electric/magnetic phase tilt series, (7) 3D reconstruction of electric potential from electric phase tilt series, (8) 3D Reconstruction of the two magnetic B -field components B_x (B_y) from the derivatives in y (x) - direction of the magnetic phase tilt series, (9) Computation of B_z component by solving $\text{div}B=0$.



Holographic VFET of magnetic nanostructures. (a,b) Volume rendering of the B_y component of the reconstructed magnetic induction B of two remanent magnetic states (a) and (b) in a Co-rich CoNi nanowire (70 nm diameter) after external field H_{Sat} applied perpendicular (a) and parallel (b) to the wire axis. The magnified regions with vectors slices show transverse vortex chains in (a) and longitudinal vortex domains of alternating chirality separated by a domain wall in (b). (c) Volume rendering of the in-plane components B_x, B_y according to the colorwheel and iso-surface of the mean inner potential reconstruction highlighting the FeGe FIB-prepared specimen shape (grey, bottom half only). The magnified views visualize a single skyrmion tube (SkT) in which the three vectors slices plot the 3D spin texture inside the SkT at different z-heights.

AA-05. Progress in Magnetic Force Microscopy.

E. Berganza^{1,2}, M. Jaafar^{1,3} and A. Asenjo¹

1. ICMM, Consejo Superior de Investigaciones Científicas, Madrid, Spain;

2. Karlsruhe Institut für Technologie, Karlsruhe, Germany; 3. Física de

la Materia Condensada, Universidad Autónoma de Madrid Facultad de Ciencias, Madrid, Spain

Since its early days, magnetic force microscopy (MFM) has become a truly widespread and commonly used characterization technique that has been utilised in a variety of fundamental and applied research and in industrial applications. In this work, we review the current state-of-the-art, analyse the challenges and outline the future of this fascinating field [1]. In comparison to other magnetic imaging techniques, MFM presents some advantages: high spatial resolution, down to 10nm; ability to work in different environments as vacuum, air or liquids [2] (despite the technical difficulties that are solved, MFM in liquids facilitates the study of biomagnetic materials) and under applied magnetic fields [3] (to study the magnetization reversal process of thin films, nanoparticles and nanostructures). Additionally, MFM exhibits high versatility and simplicity in operation. Advanced operation modes based on Variable Field MFM have proven to be very useful to visualize the magnetization reversal process [4] in one dimensional nanostructures (Figure 1). Isolated multisegmented nanowires (120nm in diameter) formed by segments of FeCo with variable length (increasing from 250nm at the left edge to 400nm the right edge) separated by Cu segments of 30nm have been characterized. The reversal process propagates always unidirectionally (ratched effect) irrespectively of the external field direction, due to the broken symmetry induced by the increasing length of the magnetic segments. Moreover, MFM studies allow us to determine the pinning centers (associated to Cu layers) that may vary from scan to scan. The so called 3D MFM imaging is used in these experiments to obtain a non-standard image where the slow scan corresponds to a continuous variation of the external magnetic field. Some emerging aspects of MFM imaging are also tackled in this work. It is worth mentioning the challenging quantitative and accurate interpretation of the MFM images [5], the probe-engineering alternatives [6] (including the analysis of the active role of the probe what could be used to gain information about the sample stray field with ultra-high resolution) or the MFM experiments on complex magnetic configurations as the skyrmionic states [7,8]. Variable Field MFM and customized MFM probes [6] (growth by Focused Electron Beam Induced Deposition onto AFM probes) have been used for studying skyrmionic states. Figure 2 shows that permalloy hemispherical nanodots with a diameter of 70 nm and height of 30 nm (prepared by hole mask colloidal lithography) are able to host half-hedgehog spin textures with non-zero topological charge. Notice that they are observed at room temperature, in absence of DMI interaction and they can be further stabilized by the magnetic field arising from the Magnetic Force Microscopy probe. The movement of the structure core depends on its chirality and it is controlled by the tip stray field. Micromagnetic simulations have been used to determine the low energy magnetic configuration compatible with the MFM results. Future perspectives of MFM imaging as the characterization of 2D materials and devices for spintronic or straintronic are also address in this work; namely, the in situ combination of magnetic imaging with magnetoelectric, thermoelectric or thermomagnetic characterization.

[1] O. Kazakova et al., J. Appl. Phys. 125, 060901 (2019) [2] P. Ares et al., Small, 11, 4731-4736 (2015) [3] E. Berganza et al., Sci. Rep. 7,11576 (2017) [4] C. Bran et al., Acs. Nano. 12, 5932-5939 (2018), [5] D. Martínez-Martín et al., Phys. Rev. Lett. 105, 257203 (2010) [6] M. Jaafar, et al., Nanoscale 12, 10090-10097 (2020) [7] M. Bačani et al., Sci Rep 9, 3114 (2019). [8] E. Berganza et al., Nanoscale,12, 18646-18653 (2020)

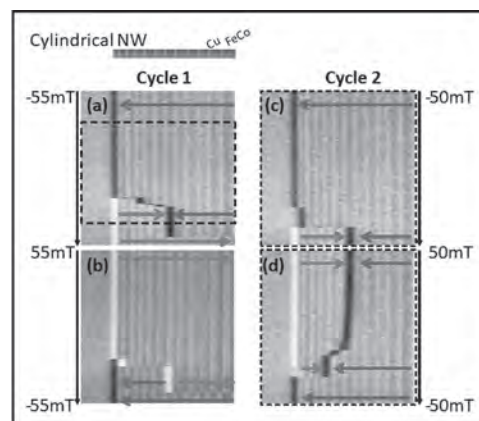


Fig1: 3D MFM images corresponding to four branches of two pseudo-hysteresis loops. The MFM tip moves continuously along the NW axis (fast scan) while the external magnetic field sweeps (slow scan) from negative to positive fields in (a) and (c) and vice versa in (b) and (d).

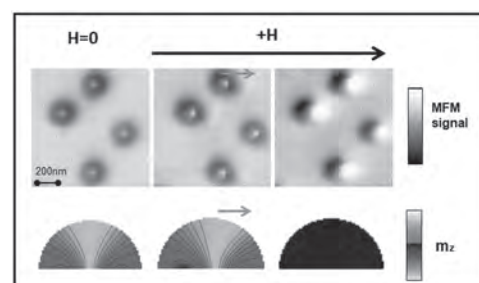


Fig 2. Sequence of MFM images corresponding to Py hemispherical nanodots. The images are obtained at different external magnetic fields applied along the X axis. The OOMMF simulations calculated for different in-plane magnetic fields reproduce the parallel to the magnetic field movement of the core, in good agreement with the MFM experiments.

AA-06. Brillouin Light Scattering Revisited.

*K. Schultheiss*¹ and H. Schultheiss¹

1. Helmholtz-Zentrum Dresden-Rossendorf, Dresden, Germany

Since the 80's, when Brillouin light scattering emerged as a powerful tool for investigating magnetization dynamics in thin films and multilayers, it developed into a versatile microscopic probe for studying collective spin excitations. Following a short introduction on studies of millimeter-sized films, we will give examples how to investigate individual magnetic structures down to tens of nanometers in dimension. We will introduce the concepts of time- and phase-resolved Brillouin light scattering which give full access to the spatio-temporal evolution of the optically accessible spin-wave spectrum. During our talk, we will provide hands-on demonstrations how to drive spin waves via spin currents and microwave excitations in magnetic nanostructures using the build in dc/ac probe station in our laboratory and show the capabilities of Brillouin light scattering for quantifying spin-wave phenomena. Furthermore, we will highlight similarities and differences to other optical scanning probe techniques such as time-resolved magneto-optical Kerr microscopy and optically detected magnetic resonance based on vacancy centers. We will outline how those techniques can potentially be combined with Brillouin light scattering to access complementary information.

Session AB
MAGNETIC MICROSCOPY AND IMAGING
Trevor Almeida, Chair
CEA-SPINTEC, Grenoble, France

CONTRIBUTED PAPER

AB-01. Microstructural and Residual Stress Evaluation of Bulk Martensitic Steels With Micrometer-Sized Grains Through Magneto-Optical Kerr Effect.

M. Jovičević-Klug^{1,2}, P. Jovičević-Klug^{1,3}, L. Thormählen², J. McCord² and B. Podgornik^{1,3}

1. Institute of Metals and Technology, Ljubljana, Slovenia;

2. Christian-Albrechts-Universität zu Kiel, Kiel, Germany;

3. Jozef Stefan International Postgraduate School, Ljubljana, Slovenia

The modernization of steel industry has brought up an interest in development of novel and fast characterization techniques that analyze the material from different aspects with the same instrument setup. In recent years, development of magnetic characterization techniques arose for investigating the microstructure and mechanical properties of certain steels [1]. However, these techniques display limited flexibility in terms of surface specific measurements and defect analysis that can become an important part in quality assurance of a produced material. Within this work, a novel utilization of magneto-optical Kerr effect (MOKE) microscopy for microstructural and stress evaluation of martensitic steels is discussed. MOKE has been proven to be a very powerful and versatile characterization technique [2], that allows investigation of magnetic domains and magnetic properties that emerge from the investigated material's surface. With domain analysis and evaluation of magnetization change with external magnetic field, the surface magnetic properties can be correlated to the bulk magnetic properties of the material [3]. Furthermore, the technique allows high-resolution imaging and investigation of microstructural characteristics of the material without the usage of etchants that can potentially modify the microstructure and ending results. By correlating the microstructural attributes to the magnetic behavior of the material's surface, the different phases of the material can be distinguished and morphologically analyzed. The method also allows clear identification of austenite in the matrix of martensitic steels, since austenite is non-magnetic opposite to other matrix phases. As a result, the method is highly versatile and allows investigation of steels on different aspects of its properties on a microstructural level. We present the applicability of MOKE on an example of martensitic high-speed steels with micrometer sized microstructural features. The presented data will provide insight into the correlation of the magnetic information to the microstructure. The novelty of this research lies in the application of MOKE microscopy on steels that are relatively magnetically hard and have a fine grain size (under 10 μm). The utilization of MOKE microscopy for phase and microstructure investigation on such steels has until now not been performed. To further display the practicality of MOKE, the steel is investigated with two different processing states, conventionally heat treated and deep cryogenic treated (DCT) [4]. DCT exposes the steel to sub-zero temperatures down to the temperature of liquid nitrogen (-196 °C) inducing further transformation of retained austenite into martensite, which is beneficial for the mechanical properties [5]. The presented examples display the capability of MOKE to identify small quantities of retained austenite of volumetric fraction under 1 %, which is challenging to evaluate with other commonly used techniques such as electron back scattering diffraction (EBSD) and X-ray diffraction (XRD) [6]. In addition to microstructural analysis, we also explore the possibility to use MOKE for residual stress analysis. The technique involves the application of a Vickers indenter that imposes localized stress changes through an indentation imprint on the material's surface. The resulting stress extends radially from the indentation and decreases in magnitude with distance from the edge of the indentation. With local magnetometry and domain analysis of the material's surface before and after the stress state modification, a correlation to the residual stress of the material is established. The applicability of the method is presented on the example of the conventionally treated and DCT steel, for which the DCT is reported to reduce tensile residual stresses. MOKE analysis confirms the reduction of residual stresses as well as confirms the change of tensile residual stresses to compressive residual stresses as reported by previous researchers [7]. With the discussed results we present that MOKE microscopy shows high potential as a fast and

in-depth microstructural and stress characterization technique applicable on an industrial scale.

[1] J. Liu, J. Wilson and M. Strangwood, *J. Magn. Magn. Mater.*, vol. 401, pp. 579–592 (2016). [2] J. McCord, *J. Phys. D. Appl. Phys.*, vol. 48, no. 33, p. 333001 (2015). [3] F. Qiu, M. J. Klug and G. Tian, *J. Phys. D. Appl. Phys.*, vol. 52, no. 26, p. 265001 (2019). [4] B. Podgornik, V. Leskovsek, and J. Vizintin, *Mater. Manuf. Process.*, vol. 24, no. 7–8, pp. 734–738 (2009). [5] P. Jovičević-Klug, B. Podgornik, *J. Mater. Res. Technol.* Vol. 9, 13118–27 (2020). [6] Y. Zhang, P. Lai and H. Jia, *Metals*, vol. 9, no. 1, p. 94 (2019). [7] D. Senthikumar, I. Rajendran and M. Pellizzari, *J. Mater. Process. Technol.* Vol. 211, pp. 396–401 (2011).

INVITED PAPERS**AB-02. Imaging the Dynamical Switch of Antiferromagnetic Domains by Optical Microscopy INVITED.**

Y. Wu¹, J. Xu¹, X. Zhang², J. Xia², C. Zhou¹, H. Chen¹, D. Shi¹ and Y. Zhou²

1. Physics department, Fudan University, Shanghai, China; 2. School of Science and Engineering, The Chinese University of Hong Kong, Shenzhen, China

Spintronic devices based on antiferromagnetic (AFM) materials has drawn significant attention due to its potential for information storage with low power consumption and ultrafast switching speeds. Since all the information storage in AFM spintronics devices rely on the switching of AFM domains, there is an urgent requirement to directly measure the AFM domain in real space during the spin switching process. Recently, we developed a novel method to image the AFM domains in single crystal CoO and NiO thin films grown on MgO(001) substrates with the magneto-optical birefringence effect[1,2]. The magneto-optical birefringence effect is found to strongly depend on the photon energy of incident light. Utilizing this optical method, we demonstrated the first real-time imaging of the AFM domain switching process in Fe/CoO system through the spin-flop coupling. While applying a constant field, the domain nucleation dominates the switching process, but while applying an alternative field, the AFM domain switching process is found to be dominated by domain wall motion. Our studies demonstrate that the AFM domain imaging under external fields or current pulse can be achieved in real time, which could be helpful for the understanding of the dynamics of AFM materials and the development of AFM spintronics storage devices.

Jia Xu, et. al, New J. Phys. 22, 083030 (2020). Jia Xu, et. al, Phys. Rev. B 100, 134413 (2019).

AB-03. Developing High-Resolution Magnetic Microscopy Applications Using NV Centers in Diamond INVITED.

*P. Kehayias*¹

1. Sandia National Laboratories, Albuquerque, NM, United States

A quantum diamond microscope (QDM) uses a uniform sheet of magnetically-sensitive nitrogen-vacancy (NV) centers in diamond placed on top of a flat magnetic sample [1,2]. In a QDM, we illuminate the NVs with laser light, probe the NV transitions with a microwave field, and image the NV fluorescence with a microscope and camera. This allows us take pictures of the magnetic field in every pixel. Compared to other magnetic imaging tools (SQUID, MOKE, and MFM), the recently-developed QDM has the following advantages, enabling new measurements that were previously unfeasible and generating interest in the physics, geomagnetism, and biomagnetism communities: 1. Large field of view (~1 mm) 2. Parallelized camera readout of 1E6 pixels, with no raster scanning 3. Minimal sample-sensor separation (as small as a few nanometers), which enables high signal-to-noise ratio and sub-micron spatial resolution 4. Capability for full-vector or scalar-projection magnetic imaging, over a wide range of magnetic field frequencies (DC to 100 GHz) and temperatures (0 to 600 K) This talk will discuss how we apply the QDM instrumentation techniques in interdisciplinary applications in related physics and engineering disciplines. I will highlight our recent success with imaging fabricated 2D magnetic materials, reconstructing the electric currents in integrated circuits to troubleshoot and diagnose their behavior, hunting for failures in fabricated silicon electronics, and measuring previously-inaccessible characteristics of ion chip traps used for quantum computing. I will conclude this talk with a preview of upcoming new directions for NV diamond magnetic imaging with color centers, such as NV magnetic sensing in extreme environments and promising alternative color-center candidates. Sandia National Laboratories is a multi-mission laboratory managed and operated by National Technology and Engineering Solutions of Sandia, LLC, a wholly owned subsidiary of Honeywell International, Inc., for the DOE's National Nuclear Security Administration under contract DE-NA0003525.

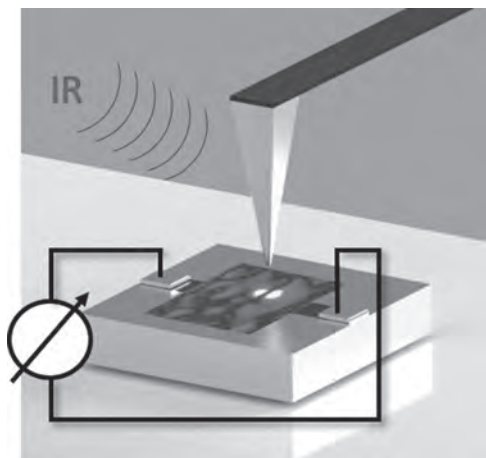
1. *Geochem. Geophys. Geosyst.* 18, 8 (2017) 2. *Nanophotonics* 8 11 1945-1973 (2019).

AB-04. Magneto-Seebeck Microscopy of Domain Switching in Collinear Antiferromagnet CuMnAs INVITED.

T. Janda^{1,3}, J. Godinho^{2,3}, T. Ostatnicky³, Z. Soban², H. Reichlova⁴, V. Novak², T. Jungwirth², B. Kästner⁵ and J. Wunderlich^{1,2}

1. Universitat Regensburg Institut fur Experimentelle und Angewandte Physik, Regensburg, Germany; 2. Institute of Physics, Czech Academy of Sciences, Cukrovarnická 10, Prague, Czechia; 3. Faculty of Mathematics and Physics, Charles University, Prague, Czechia; 4. Dresden University of Technology, Dresden, Germany; 5. Physikalisch-Technische Bundesanstalt, Braunschweig, Germany

We introduce a novel microscopy for antiferromagnetic nanostructures based on the local generation and detection of photocurrents, and apply it to the collinear and fully compensated antiferromagnet CuMnAs. By using the optical near field generated by a scattering near-field microscope, we display narrow 180deg domain walls (DWs) and provide the first experimental evidence of reversible current-pulse-driven 180deg DW displacements in agreement with theoretically predicted Néel spin-orbit torque DW motion. In CuMnAs, photocurrents result from the local magneto-Seebeck effect (MSE). MSE-based microscopy can be applied to the entire class of conductive antiferromagnets, and in contrast to the established X-ray linear dichroism microscopy which is based on large scale synchrotrons, it can be easily performed with common laboratory equipment.



AB-05. Coherent Correlation Imaging: High-Resolution Imaging of Stochastic Dynamic INVITED.

C. Klose¹, F. Buettner^{2,3}, W. Hu³, C. Mazzoli³, I. Lemesh², J. Bartell², M. Huang², C.M. Günther⁴, M. Schneider¹, A. Barbour³, S.B. Wilkins³, G. Beach², S. Eisebitt¹ and B. Pfau¹

1. Max-Born-Institut für Nichtlineare Optik und Kurzzeitspektroskopie, Berlin, Germany; 2. Massachusetts Institute of Technology Department of Materials Science and Engineering, Cambridge, MA, United States; 3. National Synchrotron Light Source II, Brookhaven National Laboratory, Upton, NY, USA, Upton, NY, United States; 4. Technische Universität Berlin Institut für Optik und Atomare Physik, Berlin, Germany

Fluctuations are ubiquitous in magnetically and charge ordered systems. Spanning multiple orders of magnitude in space and time, they often lead to a wealth of fascinating physical effects. Recent examples of such dynamics are fluctuations of spin- and charge density waves in antiferromagnets [1], diffusion-like motion of magnetic skyrmions in low pinning magnetic multilayer or spontaneous fluctuations between ordered stripe and skyrmion lattices phases [2]. High-resolution real-space imaging can resolve the spatial information. However, due to insufficient signal on a timescale faster than the relevant dynamics, averaging over an extended period of time (or repetitions) is key for the majority of high-resolution imaging experiments. So far, averaging has been performed blindly and continuously, leading to a trade-off between extracting either spatial or temporal information, especially in weak contrast systems. Here, we present coherent correlation imaging (CCI) – a high-resolution, full-field imaging technique that realizes multi-shot, time-resolved imaging of stochastic processes. The key of CCI is the classification of camera frames that correspond to that same physical state by combining a correlation-based similarity metric with powerful classification algorithm developed for nanoparticle tomography and genome research (see Fig. 1) [3]. CCI extends these algorithms to the temporal domain, realizing informed, non-sequential signal averaging while maintaining single frame temporal resolution. CCI does not require prior knowledge of the imaged system, rendering it the first time-resolved x-ray imaging technique capable of accessing systems with entirely unknown dynamics. To develop and demonstrate CCI, we study thermal hopping of magnetic domain walls – a prototypical example of stochastic nanometer-scale dynamics – on timescales ranging from sub-seconds to hours under equilibrium conditions. Our material is [Pt (2.7 nm)/Co₆₀Fe₂₀B₂₀ (0.8 nm)/MgO (1.5 nm)]₁₅, a chiral ferromagnet with magnetic pinning low enough to exhibit stochastically recurring dynamics that resemble thermally induced Barkhausen jumps near room temperature [4]. Imaging is performed through Fourier-transform x-ray holography with contrast provided by the x-ray magnetic circular dichroism [5]. CCI reconstructs sharp, high-contrast images of all domain states and, unlike previous approaches, also tracks the time when these states occur (see Fig. 2). This uniquely reveals not only the occupation probabilities of all states, but further, the complex network of stochastic transition trajectories between states. The full potential of this technique will manifest at the next generation of pulsed high-coherence x-ray sources, where it promises to resolve a wealth of previously hidden dynamic processes, such as the nucleation dynamics of externally-induced phase transitions and the intrinsic fluctuations of weakly pinned textures in spin and charge ordered systems.

[1] - Shpyrko, O. G. *et al.* Direct measurement of antiferromagnetic domain fluctuations. *Nature* 447, 68–71 (2007) [2] - Seaberg, M. H. *et al.* Nanosecond X-Ray Photon Correlation Spectroscopy on Magnetic Skyrmions. *Physical Review Letters* 119, 067403 (2017) [3] - Eisen, M. B. *et al.* Cluster analysis and display of genome-wide expression patterns. *Proceedings of the National Academy of Sciences* 95, 14863–14868 (1998) [4] - Lemesh, I. *et al.* Current-Induced Skyrmion Generation through Morphological Thermal Transitions in Chiral Ferromagnetic Heterostructures. *Advanced Materials* 30, 1805461 (2018) [5] - Eisebitt, S. *et al.* Lensless imaging of magnetic nanostructures by X-ray spectro-holography. *Nature* 432, 885–888 (2004)

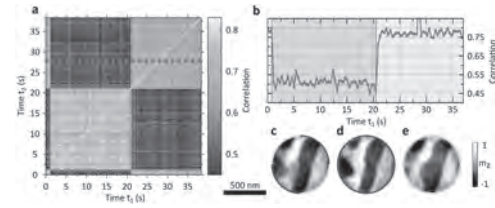


Figure 1 | Single-frame correlation and single-frame imaging. a, CCI two-time correlation analysis showing the similarity between the states recorded at different times. b, Cross-section of the two-time correlation function at $t_2 = 28$ s (red line in (a)). The colored shades define the frames that correspond to the same physical state of the system. c, Image corresponding to the blind average of all frames. High-contrast regions indicate stationary behavior of the local out-of-plane magnetization m_z , while seemingly semi-transparent features correspond to a superposition of two different magnetic states. d,e, Images obtained by selectively averaging the blue and yellow shaded regions in (b), respectively.

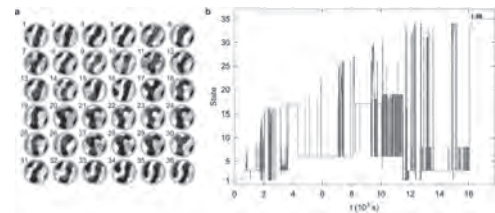


Figure 2 | CCI-resolved dynamics in our sample. a, Real-space images of all domain states. Field of view is 720 nm in diameter. b, Temporal evolution of the states. The horizontal axis indicates the measurement time. The vertical axis shows which state has existed at the given time.

CONTRIBUTED PAPERS

AB-06. Withdrawn

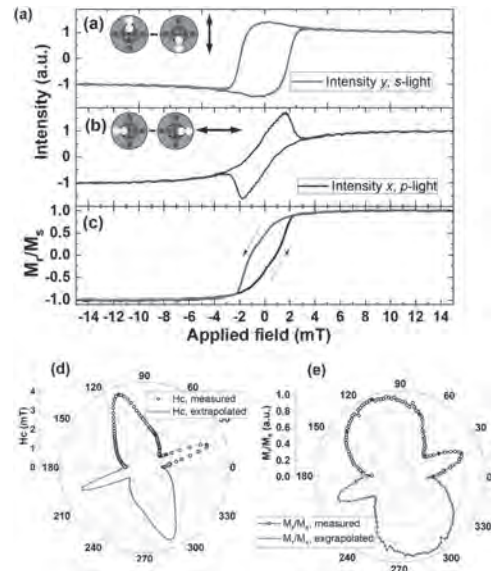
AB-07. Advanced, Kerr-Microscopy-Based MOKE Magnetometry for the Anisotropy Characterization of Magnetic Films.

I. Soldatov¹, J. Zehner¹, K. Leistner¹, T. Kang², D. Karnaushenko² and R. Schäfer^{1,3}

1. Leibniz Institute for Solid State and Materials Research (IFW) Dresden, Institute for Metallic Materials, Dresden, Germany; 2. Leibniz Institute for Solid State and Materials Research (IFW) Dresden, Institute for Integrative Nanosciences, Dresden, Germany; 3. Technische Universität Dresden, Dresden, Germany

Among other properties of magnetic films, the evaluation of the magnetization in response to changing external magnetic fields (magnetization reversal loops) and especially the dependence of the reversal on the magnetic field angle, which reflects the anisotropy of the material, is of particular interest for both fundamental and applied research. Measuring reversal loops at various field angles by magnetometry requires that the sensitivity of the magnetometer is aligned along the field direction for all field angles. For the commonly applied vibrating sample magnetometry (VSM) or its more advanced variants of vectorial VSM, this involves the complexity of a mechanical rotation of the sample. The anisotropic magnetoresistance can also be utilized by electric transport measurements, which requires, however, lithography and sample patterning. A powerful and extensively applied alternative method is magneto-optical Kerr Effect (MOKE) magnetometry. Apart from magnetometry, the Kerr effect is also employed in wide-field Kerr microscopy, which is an effective tool for both magnetic domain imaging. Several approaches to realize vectorial MOKE magnetometry have been reported in literature mostly based on systems that apply the longitudinal Kerr effect. However, in most cases the angular dependence is again achieved by mechanical adjustment like in VSM, i.e. the specimen has to be physically rotated to achieve alignment of the field and the sensitivity axis, possibly resulting in experimental error and spurious signals. Furthermore, it is usually assumed that the axis of the longitudinal Kerr sensitivity (the direction of magnetization at the surface, which produces the maximum Kerr signal) is precisely aligned along the plane of light incidence. As we will show in this paper, this assumption is only valid in limited cases while in general there may be transverse Kerr contributions superimposed leading to rotated sensitivity directions. In this work, we have theoretically analyzed the contrast generated in a wide-field Kerr microscope, specifically its dependence on the polarization of light and the plane of incidence, and verified it experimentally. An analytical expression for the magnetization reconstruction along the direction of an externally applied field was derived. This allowed us to develop a fully automated method for the measurement of magnetization reversal loops in magnetic films with in-plane anisotropy without any mechanical adjustment of the system or sample displacement. The subsequent analysis of the angular dependencies of the coercive field and remanent magnetization (see figure) provides insights into the magnetic anisotropy of the film. Although the method is experimentally not restricted to magnetic films, it should be granted that the magnetization does not change across the thickness if bulk specimens are investigated. The applicability and functionality of the technique was demonstrated on an FeO/Fe thin magnetic film [1], which is dominated by a uniaxial anisotropy.

[1] J. Zehner, I. Soldatov, S. Schneider, R. Heller, N. B. Khojasteh, S. Schiemenz, S. Fäähler, K. Nielsch, R. Schäfer, and K. Leistner, *Adv. Electron. Mater.* n/a, 2000406 (2020). [2] I. Soldatov and R. Schäfer, *Review of Scientific Instruments* 88, 073701 (2017).



(a) and (b) Hysteresis loops, obtained with complimentary sensitivities: (a) s-polarised light along the y-axis and (b) p-polarised light along the x-axis. In (c) the field is applied at an angle of 40° to the x-direction. The magnetisation along this field direction was reconstructed from (a) and (b) The incidence plane is defined by activating proper LEDs as indicated by the circular insets that show the ends of the glass fibre cross in the conoscopic imaging mode [2]. (b) and (c) Angular dependencies of coercive field and remanent magnetisation, respectively (the black points are measured and the red curve is an extrapolation by mirroring with respect to the y-axis). The data is obtained on the Fe/FeO film with 10 nm thickness

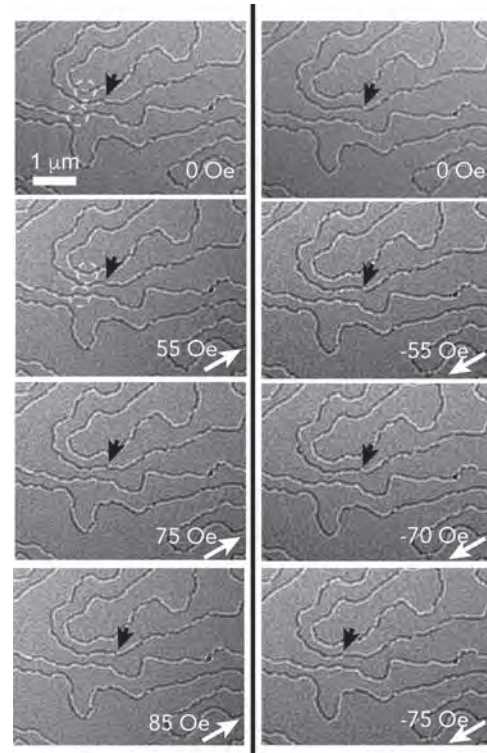
AB-08. Direct Observation of Vertical Bloch Line Manipulation via in-Plane Magnetic Fields.

M.P. Li¹, C. Phatak², M. De Graef¹ and V.M. Sokalski¹

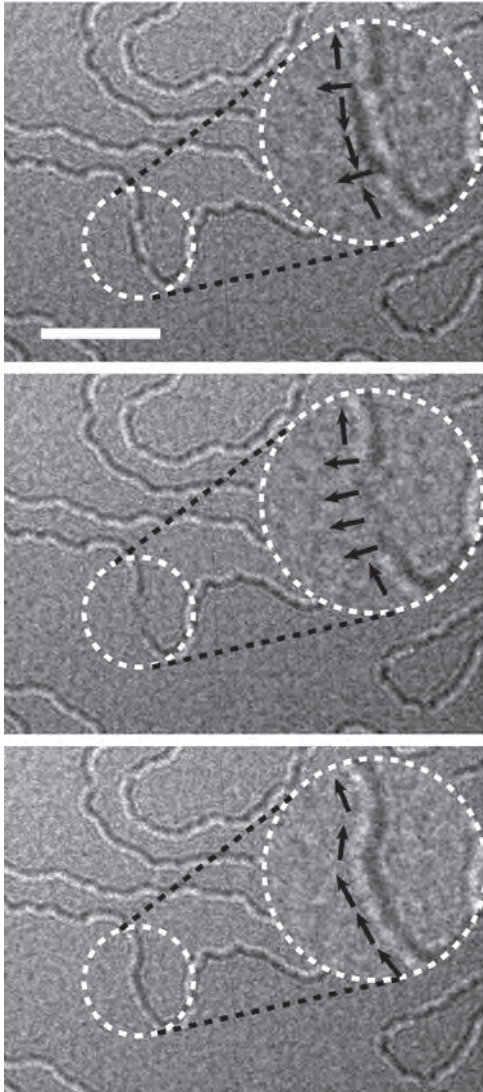
1. *Materials Science & Engineering, Carnegie Mellon University, Pittsburgh, PA, United States*; 2. *Argonne National Laboratory Materials Science Division, Lemont, IL, United States*

Discovery of the Dzyaloshinskii-Moriya Interaction (DMI) in magnetic thin films has launched an intense research effort into its effects on the structure of magnetic bubbles and domain walls including the formation of topological excitations like skyrmions. While it is well established that the internal structure of a DW transitions from a Bloch to a Néel domain wall when there is sufficient DMI, less attention has been paid to excitations contained within the domain wall. For example, recently, a new feature known as a domain wall (DW) skyrmion has been theoretically predicted and observed experimentally [1,2]. These are 360 degree rotations of the internal magnetization of a DW, which are the post-DMI analogue of a vertical Bloch line (VBL), where there is a 180 degree rotation. Moving forward, it will be important to probe excitations like these *in situ* to understand their dynamic behavior. Here we demonstrate the manipulation of VBLs via in-plane magnetic fields observed *in situ* using Lorentz transmission electron microscopy (LTEM). In this work, $(\text{Co/Ni})_M$ multi-layers are deposited via magnetron sputtering directly onto custom-sized Si_3N_4 TEM membranes. We chose to examine an $M=10$ sample as we have previously observed an abundance of $1-\pi$ and $2-\pi$ VBLs along its DWs [3]. We note that $2-\pi$ VBLs are topologically equivalent to DW skyrmions. Fresnel mode Lorentz TEM was performed on an FEI Tecnai F20 in Lorentz mode (objective lens turned off). In-plane magnetic fields are applied *in situ* through the use of a Hummingbird Scientific magnetic biasing holder; the specific holder used here has a field range of ± 300 Oe. In the as-prepared state, many VBLs are observed along Bloch DWs in Fresnel-mode micrographs (Fig. 1). Upon application of in-plane magnetic fields of increasing strength, we observe the movement of VBLs along DWs. When the field direction is reversed, we observe the same VBLs to move in the opposite direction. Additionally, we observe the annihilation of VBLs following the impingement of their movement by VBLs of the same winding direction. The winding of these VBLs can be reasoned to be the same sign as one another because those with opposite winding would have a zero-energy barrier to annihilation as seen in Fig. 2. Details regarding challenges to imaging, observations in high-DMI samples, and other implications of this technique will be further discussed in this presentation [4].

[1] R. Cheng, M. Li, A. Sapkota, A. Rai, et al., *Phys. Rev. B*, Vol. 99, p. 184412 (2019). [2] M. Li, A. Sapkota, A. Rai, A. Pokhrel, et al., *arXiv*: 2004.07888, (2020). [3] M. Li, D. Lau, M. De Graef, and V. Sokalski, *Phys. Rev. Mater.*, Vol. 3, p. 064409, (2019). [4] This research is supported by the Defense Advanced Research Project Agency (DARPA) program on Topological Excitations in Electronics (TEE) under grant number D18AP00011. The authors also acknowledge use of the Materials Characterization Facility at Carnegie Mellon University supported by grant MCF-677785.



Micrographs of magnetic domain walls in $[\text{Co/Ni}]_{10}$ samples with magnetic fields applied in the (left) “positive” and (right) “negative” directions. Arrows highlight positions of vertical Bloch lines whereas dotted circles indicate locations of $2-\pi$ vertical Bloch lines that have annihilated.



Micrographs of two vertical Bloch lines “unwinding” as magnetic field strength is increased. Insets depict magnified view of circled regions with potential domain wall configuration labeled with arrows. Scale bar is 1 μm .

AB-09. Quantitative Magnetic Force Microscopy: Tip Transfer Function Method Revisited With High-Quality Data.

Y. Feng^{2,1}, A. Mandru² and H.J. Hug^{2,1}

1. Physics Department, Universität Basel Philosophisch-Naturwissenschaftliche Fakultät, Basel, Switzerland; 2. Magnetic and Functional Thin Films, Empa, Dübendorf, Switzerland

Magnetic force microscopy (MFM) is a versatile technique used to image the micromagnetic state of a sample and its dependence on an applied magnetic field and/or on the sample temperature with a spatial resolution down to about 10 nm. The high resolution and the ease of implementation in existing atomic force microscopy (AFM) tools make the MFM technique particularly desirable for the investigation of magnetic thin films and nanoscale devices. The measured signal in MFM is a change of the dynamic properties of the imaging cantilever arising from the interaction of the magnetic cantilever tip with the stray field emanating from the sample surface. The obtained MFM images are therefore only indirectly connected to the micromagnetic state of the sample. However, if the perturbations to the micromagnetic states of the tip and sample are negligible during the measurement process, the measured MFM signal can be described as the convolution of the magnetic moment of the tip with the stray field of the sample. This allows for a quantitative analysis of the stray field by the deconvolution of MFM data. Such a deconvolution of the stray field from the measured MFM signal requires the calibration of the imaging properties of the tip. The latter can be achieved by fitting multipole moments to the tip in order to fit MFM data obtained on samples with a known stray field. Nevertheless, the success of such procedures remained limited: the size and position of the tip monopole and dipole moments were found to be dependent on the size of the imaged sample structures. A concept of tip transfer function (TF) was proposed two decades ago by van Schendel *et al.* [1]. This approach is used to specify the imaging properties of the probe and thus to access the quantitative information about the stray field emanating from the sample surface. More precisely, the method calibrates the response of the MFM tip on different spatial wavelengths of the stray field. This calibration method was then used by our group for the determination of the closure domain structure in thick Cu/Ni/Cu trilayer samples [2], for the measurement of the local density of pinned uncompensated spins in exchange-biased thin films [3], for the measurement of stray fields arising from skyrmions and the determination of the chirality in thin film systems with DMI [4], and for the detailed analysis of the complex dependence of the micromagnetic state on the external field in exchange-coupled Co/Pt-TbFe [5]. Despite these successes, the tip calibration method presented by van Schendel *et al.* has only been taken up slowly. Examples include the reconstruction of magnetic vortex state at the end of FeCo nanowires [6] and the characterization of the 3D stray field landscape above a Ir17Mn83/Co70Fe30 exchange-biased multilayer system with engineered domain walls [7]. However, more recently, quantitative MFM methods have gained renewed interest. Hu *et al.* have for example analyzed the reproducibility of the tip calibration methods following the TF approach in round robin tests [8]. The results presented by different groups were however based on data acquired with MFM instruments operated under ambient conditions. The limited sensitivity of these instruments and consequently the low signal-to-noise ratio largely affect the final results obtained by the quantitative procedure. Moreover, the tip-sample distance control in most of the existing work was achieved by lift-mode operation, where the sample topography is first scanned with the tip in intermittent contact with the sample. Although the reproducibility of the measurements can be ensured to some extent, tip wear is almost unavoidable as also pointed out in Ref. [8]. To exploit all the advantages of quantitative MFM in the investigation of magnetic thin films and nanostructures, the instrument is preferably operated under vacuum conditions. Furthermore, a noncontact technique for tip-sample distance control should be applied to avoid the tip wear. In this work, we present a state-of-the-art MFM tip calibration procedure based on measurements performed in vacuum and with high-quality factor (Q) cantilevers. We also discuss the subtleties in data treatment specifically during tip calibration procedure, which have been largely overlooked in the past. In addition, the advantages and the limits of this TF-method are addressed.

- [1] Schendel, H. J. Hug, B. Stiefel *et al.*, *J. Appl. Phys.* 88, 435 (2000). [2] M. A. Marioni, N. Pilet, T. V. Ashworth *et al.*, *Phys. Rev. Lett.* 97, 027201 (2006). [3] A. Benassi, M. A. Marioni, D. Passerone *et al.*, *Sci Rep* 4, 4508 (2014). [4] M. Bačani, M. A. Marioni, J. Schwenk *et al.*, *Sci Rep* 9, 3114 (2019). [5] M. Heigl, C. Vogler, A-O Mandru *et al.*, *ACS Appl. Nano Mater.* 3, 9, 9218–9225 (2020). [6] S. Vock, C. Hengst, M. Wolf *et al.*, *Appl. Phys. Lett.* 105, 172409 (2014). [7] N. Zingsem, F. Ahrend, S. Vock *et al.*, *J. Phys. D: Appl. Phys.* 50 495006 (2017). [8] X. Hu, G. Daia, S. Sievers *et al.*, *J. Magn. Magn. Mater.* 511, 166947 (2020).

AB-10. Withdrawn

AB-11. Quantitative Imaging of Antiferromagnetic Spin Cycloidal Textures on Strain Engineered BiFeO₃ Thin Films With a Scanning Nitrogen-Vacancy Magnetometer.

H. Zhong¹, J. Fischer², A. Haykal³, A. Finco³, A. Stark¹, F. Favaro¹, P. Maletinsky¹, M. Munsch¹, K. Bouzehouane², S. Fusil², V. Garcia² and V. Jacques³

1. Qnami AG, Muttens, Switzerland; 2. Unité Mixte de Physique, CNRS, Thales, Université Paris Saclay, Palaiseau, France; 3. Laboratoire Charles Coulomb, CNRS, Université de Montpellier, Montpellier, France

Antiferromagnetic thin films attract significant interest for future low-power spintronic devices. They are largely insensitive to external magnetic fields, exhibit negligible cross-talk between neighboring memory cells and they can be switched at THz frequencies [1]. Multiferroics, such as bismuth ferrite BiFeO₃, in which antiferromagnetism and ferroelectricity coexist at room temperature, appears as a unique platform for spintronic [2] and magnonic devices [3]. The nanoscale structure of its ferroelectric domains has been widely investigated with piezoresponse force microscopy (PFM), revealing unique domain structures and domain wall functionalities [4, 5], but nanoscale magnetic textures present in BiFeO₃ and their potential for spin-based technology remain concealed. Depending on the strain, growth conditions and crystal orientation, the magnetic state of BiFeO₃ thin films can either show different types of non-collinear cycloids, canted G-type antiferromagnetic orders, or even a mixture of these [6]. In this report, we present two different antiferromagnetic spin textures in multiferroic BiFeO₃ thin films with different epitaxial strains, using a non-invasive scanning Nitrogen-Vacancy magnetometer (Qnami, ProteusQ™) based on a single nitrogen-vacancy (NV) defect in diamond (Qnami, Quantilever™ MX), with a calibrated NV flying height of ~35 nm and proven dc field sensitivity of ~1 μT/√Hz. The two BiFeO₃ samples were grown on DyScO₃ (110) and SmScO₃ (110) substrates using pulsed laser deposition. The striped ferroelectric domains in both samples are first observed by the in-plane PFM as shown in Figs. (a) and (b), respectively. The corresponding scanning NV magnetometry (NV) images in Figs. (c) and (d) confirm the existence of the spin cycloid texture, with zig-zag wiggling angles of 90° and 127°, and the propagation wavelength of λ_{DSO} ≈ 64 nm and λ_{SSO} ≈ 94 nm, respectively. At the local scale, the combination of PFM and scanning NV magnetometry allows to identify the relative orientation of the ferroelectric polarization and cycloid propagation directions on both sides of a domain wall. For the BiFeO₃ grown on DyScO₃ (110) substrate, the 90-degree in-plane rotation of the ferroelectric polarization imprints the 90-degree in-plane rotation of the cycloidal propagation direction along $k_1 = [-1 \ 1 \ 0]$ direction, corresponding to the type-I cycloid as shown in Fig. (c). On the contrary, in the BiFeO₃ film grown on SmScO₃ (110) substrate, the propagation vectors are found to be along $k_1' = [-2 \ 1 \ 1]$ and $k_2' = [1 \ -2 \ 1]$ directions in the neighboring domains separated by the 71° domain wall, cf. Fig. (d). It is worth to mentioned that in the previous report [6], BiFeO₃ grown on SmScO₃ (110), prepared in another growth chamber, showed G-type antiferromagnetic textures, compared to the observed type-II cycloid here in Fig (d). Our results here shed the light on future potential for reconfigurable nanoscale spin textures on multiferroic systems by strain engineering.

[1] V. Baltz, *et al.*, *Rev. Mod. Phys.* 90, 015005 (2018). [2] J. T. Heron *et al.*, *Nature* 516, 370–373 (2014). [3] P. Rovillain *et al.*, *Nat. Mater.* 9, 975–979 (2010). [4] N. Balke *et al.*, *Nat. Phys.* 8, 81–88 (2011). [5] G. Catalan, *et al.*, *Rev. Mod. Phys.* 84, 119–156 (2012). [6] A. Haykal, *et al.*, *Nat. Commun.* 11, 1704 (2020).

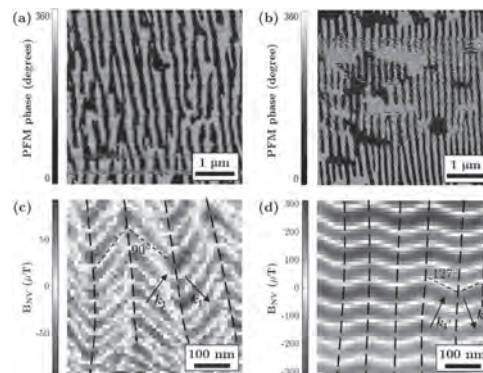


Figure: (a-b) In-plane PFM phase images of BiFeO₃ films grown on DyScO₃ (110) and SmScO₃ (110) substrates with resulted strains of -0.35% and +0.5%, respectively. (c-d) NV magnetometry images corresponding to the ferroelectric domains depicted in (a-b). The dashed lines in (c-d) are guides to the eyes, reflecting a change of the cycloid propagation vector associated to the ferroelectric domain walls.

Session AC

INSTRUMENTATION AND MEASUREMENT TECHNIQUES

Marcin Sikora, Co-Chair

AGH University of Science and Technology, Krakow, Poland

Jose R. L. Mardegan, Co-Chair

DESY, Hamburg, Germany

CONTRIBUTED PAPERS

AC-01. Electromagnetic Non-Destructive Testing of Wire Rope Inside Composite Steel Belts.

X. Yan¹

1. University of Harbin Institute of Technology, Shenzhen, Shenzhen, China

I. Introduction As a new type of elevator drive and load-bearing member, the composite steel belt has been used widely. Inside the composite steel belt, there are multiple small-diameter steel wire ropes side by side, and the rope spacing is small. The surface of these side-by-side wire ropes is covered with a special plastic material. So, the composite steel belt has large traction capability and high flexibility, which makes the main engine volume smaller than that of the traditional elevator product mainframe. Furthermore, the composite steel belt has more steel wires than the conventional wire rope, which is more durable and has a longer service life. In addition, the composite steel belt is lighter in weight, and it can effectively reduce the vibration and noise during the operation of the elevator. A number of elevator manufacturers are also gradually adopting and promoting the use of composite steel strips in elevators. However, the surface of the composite steel strip is covered with a wear-resistant plastic material such as polyurethane. In the process of use, if the internal steel wire rope has defects such as warping, breaking, misalignment, and thinning, it cannot be recognized by the naked eye, which affects the safety of the elevator. If the internal wire rope has potential defects at the time of leaving the factory, it is easy to scratch the surface rubber material, which is more likely to cause an accident. Therefore, the damage detection of the composite steel belt plays an important role in the safe operation of the elevator [1]. The rope in the composite steel belt belongs to ferromagnetic component, electromagnetic detection methods is ideal for its non-destructive testing [2]. In addition, the electromagnetic detection method has also been used for fine steel wire rope detection and achieved a good detection effect [3]. The wire ropes inside the composite steel belt are just fine steel wire ropes. Electromagnetic finite element simulation analysis (FEA) can provide magnetic field status reference for electromagnetic detection of wire rope [4]. The application of some magnetic dipole model analysis and related algorithms in electromagnetic detection also provides relevant references for the detection of wire rope defects[5,6]. II. Simulation and Excitation Structure Design The schematic diagram of the common composite steel strip structure is shown in Fig. 1(a), and the excitation structure is established as shown in Fig. 1(b). By selecting the appropriate size of permanent magnet and yoke, the wire ropes in the composite steel belt are excited to near saturation. In the simulation, three defects appear on the first, fifth and ninth wire ropes at the same time. Extract the radial magnetic flux leakage directly above and below each wire rope and above and below both sides of the 1st and 10th wire ropes, as shown in Fig. 1(c) and Fig. 1(d). It can be seen that on the defective wire ropes, the radial magnetic flux leakage is large, and on the wire rope without defects, the magnetic flux leakage is very small. Therefore, magnetic detection sensors (such as hall, anisotropic magneto-resistive, giant magneto-resistive, fluxgate, tunnel magneto-resistive, etc.) can be arranged above and below each wire for picking up the magnetic flux leakage signal, thereby detecting the defect. III. Experimental and Results Since the diameter of the wire rope and the distance between the ropes inside the composite steel belt is small. The hall element having a small volume and high sensitivity is selected as the detecting sensor. The halls are placed above and below each wire rope. For the signal processing, the hall output signals above and below each wire are first summed up. Then the noise and interference signals are filtered out by a bandpass filter. Subsequent use of a comparator to determine the defect. Fig.2a) shows a photograph of a steel belt with three defects, each of which is located on a wire rope inside. Fig.2b) shows the design of the steel wire rope detection device inside the composite steel strip and the detection result when the second defect is detected.

[1] H.M. Lei, G.Y. Tian, "Broken wire detection in coated steel belts using the magnetic flux leakage method," *Insight*, vol. 55, no. 3, pp.126-31, 2013. [2] H. R. Weischedel, R. P. Ramsey, "Electromagnetic testing, a reliable method for the inspection of wire ropes in service," *NDT&E Int.*, vol. 22, no. 3, pp.155-161, 1989. [3] X. L. Yan, D. L. Zhang, and S. M. Pan, "Online nondestructive testing for fine steel wire rope in electromagnetic

interference environment", *NDT E Int.*, no. 92, pp. 75-81, 2017. [4] R. H. Priewald, C. Magele, and P. D. Ledger, et al. "Fast magnetic flux leakage signal inversion for the reconstruction of arbitrary defect profiles in steel using finite elements". *IEEE Trans. Magn.*, vol. 9, no. 1, pp. 506-516, 2013. [5] Li E, Kang Y, Tang J. et al. "Analysis on Spatial Spectrum of Magnetic Flux Leakage Using Fourier Transform". *IEEE Trans. Magn.*, vol. 54, no. 8, pp. 6201810, 2018. [6] Hosseingholizadeh S, Filleter T, Sinclair A. "Evaluation of a Magnetic Dipole Model in a DC Magnetic Flux Leakage System". *IEEE Trans. Magn.*, vol. 55, no. 4, pp. 6200407, 2019.

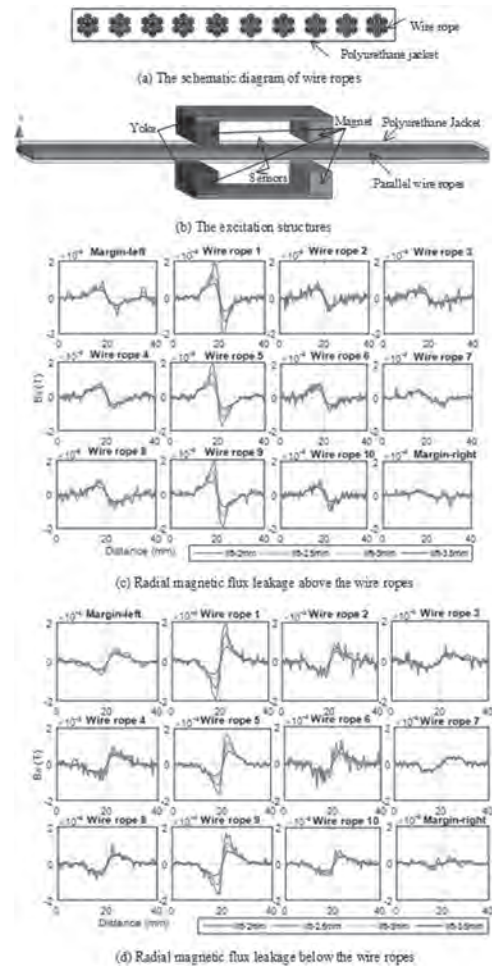


Fig. 1. The schematic diagram of wire ropes, the excitation structure and the radial magnetic flux leakage

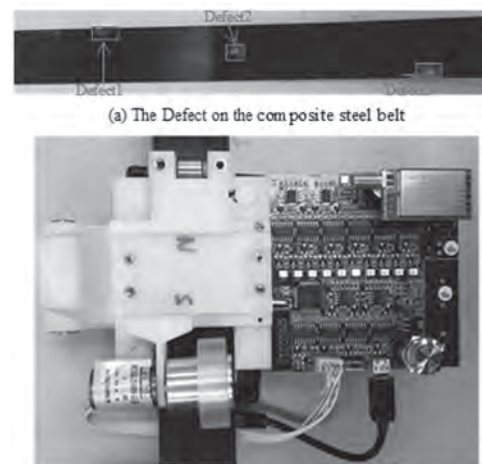


Fig. 2. The experiment and test result

AC-02. Anisotropic Magnetoresistance Zero-Field Domain Wall Depinning in Cylindrical Nanowires.

J.A. Moreno¹ and J. Kosel^{2,3}

1. Materials Science and Engineering, King Abdullah University of Science and Technology, Thuwal, Saudi Arabia; 2. Electrical Engineering, King Abdullah University of Science and Technology, Thuwal, Saudi Arabia; 3. Sensor Systems Division, Silicon Austria Labs GmbH, Graz, Austria

Investigations the current-driven domain wall (DW) motion in cylindrical nanowires (CNWs) are more valuable if performed at zero applied external field for their use in prospective electronic devices. Here, we present an all-magneto-electrical method to pin DWs in multi-segmented CNWs, maintain them pinned at zero field and de-pin them using current pulses. We test this in compositionally modulated nickel/cobalt ($\sim [10/14]$ μm) and nickel/cobalt/nickel ($\sim [3/7/3]$ μm) CNWs of c.a. 150 - 190 nm diameter where DWs can be pinned in a predictable and reproducible way and their soft/hard magnetic texture has been fairly studied [1]–[3]. Furthermore, we perform micromagnetic simulations to interpret and study the behavior of the magnetoresistance as a function of segment length. The method is based on the anisotropic magneto-resistance (AMR) measurement of a CNW with a pinned DW [4] for which we show the relevant range of one branch in Figure 1 (solid line). This branch starts from a saturated magnetization state in the “right” direction (3000 Oe, not shown) and moves to a saturated state in the “left” direction (-3000 Oe, not shown), as indicated by the arrow at the bottom. The CNW’s long axis is parallel to the applied field. Simplifying, AMR gives an overall measure of the portion of the CNW’s magnetization that is not along the direction of the applied electrical current: at ± 3000 Oe, most of the CNW’s magnetization is in the same direction as the electrical current, i.e., along the CNW’s long axis, resulting in a saturated high resistance state. As the field decreases, magnetization vortices appear at the ends of the CNW, driving magnetization away from the axial direction and resulting in a low resistance state. When the field is ramped in the opposite direction, a DW propagates from one of the ends and is pinned at some point within the nickel segment [1], increasing the axial component of the magnetization as indicated by the rapid increase in resistance in Figure 1 (“Domain wall pinning”). Finally, when the field is further increased, the DW de-pins and propagates to the opposite end from where it was initially nucleated leaving most of the magnetization in the axial direction, as indicated by the second resistance change in Figure 1 (“Domain wall de-pinning”). Note that pinned DWs and vortices at the ends of the CNW lower the resistance as they are mainly composed of magnetization textures out of axis. To test current-driven DW motion at zero field, a DW has to be pinned first by saturating the magnetization to +3000 Oe, decreasing the field, inverting it and increasing it only until the first resistance jump is reached (red, open squares in Figure 1). After this, the field is reduced to 0 (blue, open triangles in Figure 1), at which point current pulses are applied. To verify whether the DW is still pinned after reducing the field to zero and/or that a current pulse has de-pinned it, the field is ramped up again in the negative direction (towards -3000 Oe). If the DW had de-pinned as a consequence of reducing the field, the CNW’s magnetization would return to a “right” state and the domain wall pinning resistance jump would be registered again, which we never observed. If the DW remained pinned, even after the application of a pulse, only the DW de-pinning resistance jump was observed, as seen in Figure 2 (solid red squares), where a current pulse of 9.21×10^{11} A/m² and 10 ns width was applied. On the other hand, if a current pulse de-pinned the DW, neither of the resistance jumps would be observed, as seen in Figure 2 (solid blue triangles), where a pulse of 1.38×10^{12} A/m² and 20 ns width was used. This method resembles recent ones in the sense that the state of the CNW is known after the current pulse is sent, for example using MFM [5] or TEM [6]. As the DW is de-pinned at high enough current densities, the width of the pulse can be used to estimate the DW speed by successively reducing the pulse width until no de-pinning event is found. With this, the velocity is estimated as the length of the cobalt segment over the current pulse width. We find that the de-pinning event is dependent on the direction of the applied current and that the magnetoresistance value for pinned domain walls increases as the length of the segments increases, which is consistent with our simplified view of AMR. This suggests that, for long enough CNWs, the DW width remains constant as the segment length increases, which we also

confirmed with micromagnetic simulations. We believe this method can be used to study current-induced DW de-pinning at zero applied field in soft/hard magnetic CNWs with known magnetic configurations.

[1] Y. P. Ivanov, *et al*, *ACS Nano*, vol. 10, no. 5, pp. 5326–5332 (2016) [2] S. Lopatin, Y. P. Ivanov, J. Kosel, and A. Chuvilin, *Ultramicroscopy*, vol. 162, pp. 74–81 (2016) [3] C. Bran *et al*, *ACS Nano*, vol. 14, no. 10, pp. 12819–12827, (2020) [4] H. Mohammed, E. V. Vidal, Y. P. Ivanov, and J. Kosel, *IEEE Trans. Magn.*, vol. 52, no. 7 (2016) [5] M. Schöbitz *et al*, *Phys. Rev. Lett.*, vol. 123, no. 21, pp. 1–5 (2019) [6] Y. P. Ivanov, *et al*, *ACS Appl. Mater. Interfaces*, vol. 9, no. 20, pp. 16741–16744 (2017)

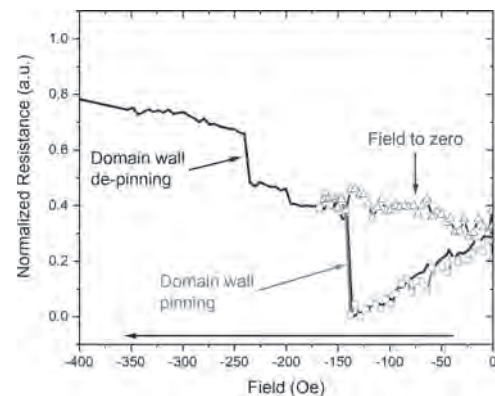


Figure 1. Anisotropic magneto-resistance measurement of a cylindrical nanowire with a pinned domain wall rescaled to the domain wall pinning and de-pinning field range and the subsequent reduction of external field to zero where nanosecond square current pulses are applied.

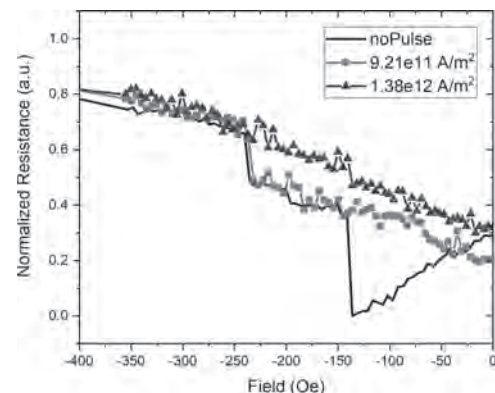


Figure 2. Magnetoresistance profile after two different current pulses are applied at zero field: 9.21×10^{11} A/m², 10 ns width (red squares), the de-pinning resistance jump indicates the domain wall was not de-pinned; 1.38×10^{12} A/m², 20 ns (blue triangles) results in the de-pinning of the DW as the depinning resistance jump is not observed.

AC-03. The Application of Unsupervised Learning to the AC Susceptibility Measurements of High-Temperature Superconductors.

M. Kowalik¹, R. Zalecki², M. Giebultowski², J. Niewolski² and W. Tokarz²
 1. Rzeszow University of Technology, Rzeszow, Poland; 2. AGH University of Science and Technology, Krakow, Poland

Introduction High-temperature superconductors (HTS) are materials which exhibit properties like zero electrical resistance and expulsion of an external magnetic field from the interior of a superconductor [1]. These unique properties are used in state of the art applications in medicine (NMR machines), science (particle accelerators), transportation (magnetic levitation trains) and the electrical industry (power transmission, fault current limiters). The greatest drawback of HTS is that they only function in low temperatures up to 134 K for HgBa₂Ca₂Cu₃O₉ at ambient pressure [2]. Scientists are still pursuing the discovery of a room-temperature superconductor. The phenomenon of high-temperature superconductivity is still not fully understood. Machine learning (ML) is the study of computer algorithms that improve automatically through experience [3]. ML algorithms are built on a mathematical model based on data, in order to make predictions or decisions without being explicitly programmed to do so [4]. Unsupervised learning (UL) is a subfield of ML. UL algorithms look for previously undetected patterns in a dataset with no pre-existing labels and with a minimum of human supervision [5]. Great progress has been made in a quest to discover, develop or refine various machine learning algorithms in recent years and new ways of data analysis (Artificial Neural Network autoencoders [6], t-SNE [7]) have been shown. The ML application to the analysis of datasets is a state of the art technique which allows to make breakthroughs in various areas of science and engineering. Our work aims to provide a first insight into application of clustering techniques to the large dataset of AC susceptibility measurements of HTS. It should allow recovering known relationships between different types of high-temperature superconductors and their superconducting properties. Theory The AC magnetic susceptibility can be written as a complex number by the formula $\chi = \chi' + i\chi''$, where χ' is the dispersion and χ'' is the absorption part of the AC susceptibility. The value of the dispersion part corresponds to the diamagnetic nature - a negative magnetization of the HTS sample when an external magnetic field is applied [8]. The values of χ' and χ'' for HTS change with temperature. Above the critical temperature T_c , both parts of AC susceptibility are equal to zero. On the other hand, below the critical temperature T_c , the χ' part has negative values and the χ'' part is positive or equal to zero. The shapes of $\chi'(T)$ and $\chi''(T)$ curves strongly depend on superconductor properties, therefore the temperature dependence of the complex AC susceptibility χ is the most common measurement method used for characterizing the properties of a HTS sample. A single AC susceptibility vs temperature measurement $\chi(T)$ can be treated as a sequence of several hundred data points (sentence). Therefore it can be represented as a collection of smaller subsequences (words). The data point is a 3D vector consisting of values of sample temperature, real χ' and imaginary χ'' parts of AC susceptibility. Our hypothesis is that the $\chi(T)$ single measurement (sentence) can be represented as a collection of only a few unique subsentences (words). Using the Bag Of Words (BOW) model, for any $\chi(T)$ measurement word occurrences a histogram can be created which is tied to the physical properties of a sample. A histogram preserves the most important features of the $\chi(T)$ curve. Computation details All $\chi(T)$ measurements were normalised and split into words of the size of about several dozen data points. Next, the reduction of the dimensionality of the words to 9D vectors was performed by using a 1D convolutional autoencoder. Its task was to learn the most efficient representation for a given word. Then, the set of words were analysed by K-means and DBSCAN clustering algorithms to find groups of words with unique features and create a dictionary of words. The results of the clustering were evaluated by visualisation of the words dataset on a 2D plane using the t-SNE algorithm. The most reasonable results were achieved by the k-Means with a number of classes set to 5. In the final step, the trained autoencoder and created dictionary were used to transform the $\chi(T)$ measurement into a 5D vector. The vector coordinates correspond to word occurrence in a single $\chi(T)$ measurement. Results It is possible to represent the most significant features of a single $\chi(T)$ measurement of an HTS sample as 5 numerical values by using a Convolutional 1D Autoencoder and the Bag Of Words model. The

most distant 5D representations of $\chi(T)$ are for samples, which have the most different superconducting properties i.e. thin layer HTS and grinded and pressed polycrystalline HTS so the 5D representation of the $\chi(T)$ dataset preserves the most important features of the measurement of the HTS sample. However the cluster analysis of the 5D $\chi(T)$ dataset by two clustering algorithms did not reveal the existence of clearly distinct classes of $\chi(T)$ measurements. Though a t-SNE visualisation (Fig 1) in 3D space shows that some clustering exists and part of the measurements are mainly arranged on some sort of cluster boundary. Therefore, more advanced analysis should be performed. Acknowledgements This work was supported by The National Science Center Poland under Project No. DEC-2018/02/X/ST3/01741.

[1] M. Tinkham, G. McKay, Introduction to superconductivity, 2nd ed., McGraw-Hill Inc., New York (1996) [2] A. Schilling, M. Cantoni, J. D. Guo, Nature, vol. 363, p. 56 (1993) [3] T. Mitchell, Machine Learning, McGraw Hill (1997) [4] C. M. Bishop, Pattern Recognition and Machine Learning, Springer, Heidelberg (2006) [5] G. Hinton and T. Sejnowski, "Unsupervised Learning: Foundations of Neural Computation", MIT Press, Terrence (1999) [6] M. A. Kramer, AIChE Journal, vol. 37, p. 233 (1991) [7] L. J. P. van der Maaten, G. Hinton, Journal of Machine Learning Research, vol. 9, p. 2579 (2008) [8] F. Gömöry, Supercond. Sci. Technol., vol. 10, p. 523 (1997)

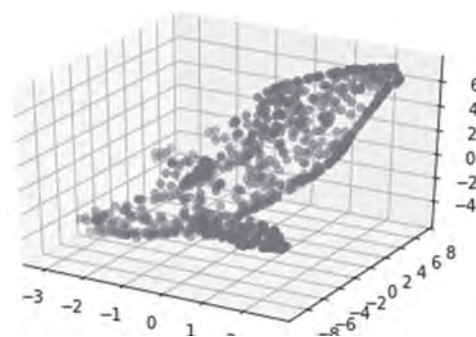


Fig 1. Visualisation of about 1000 $\chi(T)$ measurements of HTS samples in 3D space by t-SNE. A single measurement is a 5D vector and it is represented as a single circle. The x, y and z axes represents the t-SNE features.

AC-04. Residual Flux Measurement of Power Transformer Based on Transient Current Difference.

Y. Wang^{1,2}, Y. Ren^{1,2} and C. Liu^{1,2}

1. Hebei University of Technology State Key Laboratory of Reliability and Intelligence of Electrical Equipment, Tianjin, China; 2. Hebei University of Technology, Tianjin, China

I Introduction The iron core residual flux density is one of the two reasons that cause the no-load closing of the large power transformer to generate magnetizing inrush current^[1]. In order to effectively weaken the residual flux density to reduce the occurrence probability of magnetizing inrush current, it is necessary to measure the magnitude and direction of the residual flux density. In the existing research, the empirical estimation method^[2] and the voltage integration method^[3] are mainly used to estimate the residual flux density in the core, but these methods have some limitations in the residual flux measurement of large power transformer. Therefore, the accurate measurement of the residual flux density in the core is of great theoretical significance for the efficient operation of the whole power grid. The main purpose of this paper is to study the most effective method to measure the residual flux density of transformer. **II Theoretical analysis of measurement methods** When the transformer core structure is fixed, the excitation inductance is mainly affected by differential permeability. Residual flux will lead to the change of core differential permeability. By using the method of field-circuit coupling, the magnetic field problem with closed magnetic circuit structure is transformed into the circuit problem with equivalent inductance. Based on the electromagnetic transient characteristics of iron core materials, this paper proposes a residual flux density measurement method of externally applied voltage. The residual flux results in different transient current waveforms under positive and reverse voltage applied in the windings. The relation expression between the extreme value of transient current difference and residual flux is derived theoretically. In order to improve the accuracy of residual flux density measurement, modeling and analysis were carried out on the measured square core, and a set of appropriate test circuit parameters were optimized based on the differential permeability characteristics of the core material. It can be seen from Fig.1 that the transient current differential extremum parameter t_s , ΔI_{max} change with residual flux changes obviously, but the parameter t_s is more sensitive to the change of residual flux in the core. Therefore, t_s is selected as the basis for quantitative detection of residual flux. **III Conclusion** By using the finite element method, the effects of different circuit parameters on the transient process can be compared, and some valuable conclusions are obtained, which will provide a theoretical reference for the subsequent application of the measurement method. Finally, experimental verification was carried out on the measured core, and the estimated residual flux in the core was compared with the actual value. As shown in Figure 2, the maximum measurement error did not exceed 5.4%. Therefore, it was considered that the measurement method proposed in this paper was reliable. This method can be used to test the residual flux of large power transformer without any requirement for transformer, which laid a foundation for the quantitative detection of residual flux in transformer core.

[1] Y. Wang, Z. Liu and H. Chen, "Research on Residual Flux Prediction of the Transformer", IEEE Transactions on Magnetics, Vol. 53, no. 6, pp. 1-4, June 2017. [2] Colombo E, Santagostino G. "Results of the enquiries on actual network conditions when switching magnetizing and small inductive currents and on transformer and shunt reactor saturation characteristics", Electra, 1984, 94: 35—53. [3] W. Wei, Y. Liu, S.W. Mei and et al. "Study on Residual Flux Evaluation Method Based on Variable-Regional Integral during the Voltage Attenuation Process," 2019 IEEE Innovative Smart Grid Technologies - Asia (ISGT Asia), Chengdu, China, 2019, pp. 954-959.

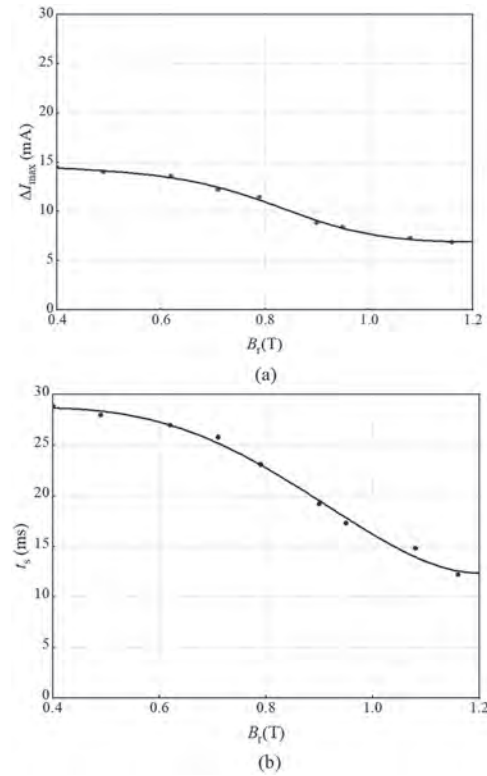


Fig.1 The curves of transient current difference extremum parameters versus B_r

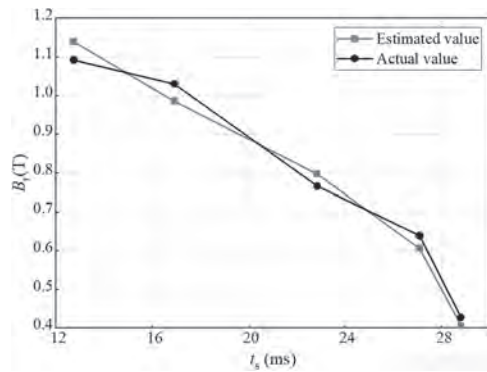


Fig.2 The comparison of experimental residual flux density and estimated residual flux density

AC-05. Pulse Eddy Current Signal Analysis Using Machine Learning and Artificial Intelligence Techniques.

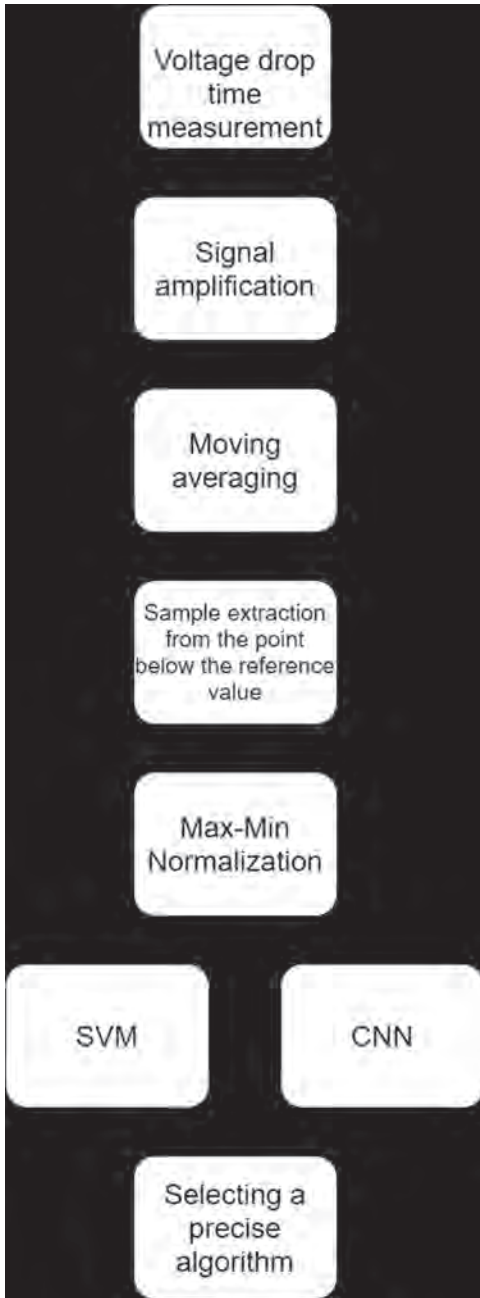
J. Kim^{1,2}, J. Shin³, H. Seo¹, K. Kim¹ and D. Park^{3,1}

1. Korea Atomic Energy Research Institute, Daejeon, The Republic of Korea; 2. University of Science and Technology, Daejeon, The Republic of Korea; 3. AIPIT, Daejeon, The Republic of Korea

1. Introduction Eddy current testing technology has been widely used for corrosion testing in use for safe and economical management of nuclear power plants. Corrosion detection by ultrasonic waves and eddy currents is widely used for its utility and reliability, but has limitations in some areas where direct access is difficult. Pulsed Eddy Current (PEC) is used to compensate for the limitations of this technique. The PEC system was designed and manufactured to detect the local wall thinning such as corrosion under insulation (CUI) and flaw accelerated corrosion (FAC). The purpose of this study is to develop the new technology which identify these defects without removing the insulation. 2. Experimental After learning the degree of damage determined by analyzing the eddy current signal through machine learning and deep learning, preprocessing (normalization and denoising) of signal data is performed so that it can be used to develop a non-destructive evaluation AI that estimates the degree of damage from an unknown eddy current signal. We tried to select a preprocessing condition that can improve the estimation accuracy. The test material is a 1500mm long, 12.85mm stair A106 Gr.B pipe. It was covered with a 50mm thick plastic insulation, and a 0.5mm stainless steel cladding was installed outside the insulation. PEC measurements were performed using a prototype machine developed in the laboratory. The sample was marked with the axial and circumferential directions in consideration of irregularities according to the measurement point, and the axial direction was divided into position (x-axis) and the circumferential direction into 8 waves (A, B, ... H). To receive the measured signal change with high vertical precision, the signal was amplified, and the amplified data was applied moving averaging to reduce the discrete characteristics of the digitally converted data. The amplitude decreased and the delay characteristics were measured differently in the time domain depending on the step and inflection. However, the change in the time delay and the average value of the amplitude is data that has a large room for modulation according to various experimental conditions, as well as whether there is a step or inflection, and there was an error in the data itself measured 10 times at the same point. It was affected by the manipulation of the experimental equipment. Therefore, it was necessary to solve the problem that the thickness of each step is not clearly distinguished due to the occurrence of an unclear section due to the time delay and simple amplitude change characteristics. When the average voltage of 1000 sample data was extracted from the time it fell below 7V, the thickness division for each step became clear, but it was impossible to distinguish the thickness of the test piece at the thin point. To solve this problem, Support Vector Machine (SVM) and Convolutional Neural Network (CNN) were introduced. Among SVM algorithms, Polynomial and Radial Basis Function (RBF) were used, and VGG19 and Inception were used as CNN models. Fitting:New = 9:1 (72:8) The dataset was used as the Train:Test dataset, and the diagnostic performance was compared with Mean Squared Error (MSE), but in order to reduce the sensitivity to unusual issues during training, If the Mean Absolute Error (MAE) did not decrease in more than 10 learning processes (Epoch), further learning was set to stop. For all five models, the initial Learning Rate (LR) was set to 0.0001, and if the MAE did not decrease even in more than five learning processes (Epoch), the LR was reduced by 0.5 times. 3. Results and discussion CNN, a deep learning algorithm, has successfully identified trends that were previously difficult to identify. For the test data, the performance difference according to the batch size (8, 16, 32) and sampling (500, 1000, 1500, 2000) was shown as in the attached table. When Inception (Batch Size: 8) is used, Sequence At Length = 2000, MSE was the lowest at 0.00082, showing the best performance among 28 measurement criteria. In the case of the Inception model, when the batch size was 8, the MSE values showed little change as 0.00106 and 0.00098, respectively, but when the sequence length was 500, the MSE was 0.00224, showing a marked decrease in accuracy. The batch size was 16, and the MSE values at the sequence length=1500 and 2000 points were 0.00102 and 0.00114, respectively. The VGG19 model showed results that were not affected by the sequence length

and were affected by the batch size. At the point where the sequence length was 500, the result was better than Inception with MSE=0.00151, but even if the amount of calculation was increased by increasing the length, it did not show a remarkable improvement in accuracy. 4. Conclusion It was possible to improve the accuracy of PEC by inputting sufficient data and selecting a signal analysis method suitable for the situation. The Inception model showed high accuracy, and the application of the VGG19 model is expected in the interval where the amount of reliable data is small. Through these, it was possible to analyze the pipes of the specimens covered with 50mm-thick plastic insulation and 0.5mm stainless steel cladding without disassembly and showed the possibility of being sufficiently applied to industrial sites. In addition, it was confirmed that in order to further improve the performance of PEC measurement equipment, it is necessary to secure a high-quality database and apply signal processing technology.

1. Xiaou Li, Wen Yu 2013, International Journal of Computational Intelligence Systems 7(2):197-212 2. Karen Simonyan, Andrew Zisserman, 2015, Very Deep Convolutional Networks for Large-Scale Image Recognition, arXiv 3. N. Nair, V. Melapudi, J. Hector, X. Liu, Y. Deng, Z. Zang, L. Udpa, J. M. Thomas and S. Udpa, 2006, "A GMR based eddy current system for NDE of aircraft structures", IEEE Trans. Magn. 42, 3312 4. C. J. Renken, 2001, "The use of personal computer to extract information from Pulsed eddy currents, Materials Evaluation", 59(3), 356.



Model	SVM Poly		SVM RBF		VQNN				Description
	1E-07	1E-07			8	16	32	64	
Number of Parameters	11,407	11,407			8,478,257				18,933,127
Sequence Length	16	16							
500	0.33192	0.10233	0.89157	0.20151	0.00773	0.00224	0.00411	0.07987	
1000			0.86111	0.60788	0.00305	0.00088	0.00175	0.00943	
1500			0.00725	0.00307	0.00321	0.00108	0.00102	0.00738	
2000	0.33284	0.05842	0.90211	0.00172	0.00418	0.00051	0.00114	0.00286	

AC-06. System for Testing non-Persistent Switching and Retention Faults of STT-MRAM Arrays.

S. Salimy¹, I. Joumard², G. Zahnd¹, B. Blanc¹, A. Chavent¹, S. Cussac¹, R. Sousa², K. Garello² and L. Lebrun¹

1. Hprobe, Eybens, France; 2. SPINtronique et Technologie des Composants, Grenoble, France

Spin transfer torque magnetic random-access memory (STT-MRAM) is one of the promising non-volatile memory (NVM) technology resolving scalability issue, current consumption, and current leakages of traditional transistor-based memories. Due to the intrinsic STT-switching stochasticity and thermal fluctuation dependance of MRAM technology, potential transitions and retention faults may happen during chip operating life [1]. Consequently, each bit writing and reading should be tested many times ($> 10^6$ iterations) to quantify the fault event occurrence, and validate that each fault is well detected and addressed by the error correction code (ECC) algorithms. For large memory arrays ($> \text{MB}$), non-persistent faults with ppm occurrences are difficult to test. Extrapolating the transition faults of large array in 10 years operation within few microseconds is challenging and does require the use of faults acceleration factors to limit the testing time [2], as well as the use of on-chip BIST (Built In-Self-Test) circuitry with algorithms optimized for testing MRAM arrays at higher speed than with external electrical tester. The MRAM switching behavior dependance with temperature is usually used to compress the retention time through application of weak but long disturb current [1,4], and application of temperature while testing [3]. Although these approaches are helping in reducing the retention testing time for each bit cell of the array, it is still very problematic for addressing full testing of large arrays. As example, the testing of each bit using different proposed algorithms leads to test time of 0.5 to 3 sec per bit cell, which is way too long for large array testing [1-4]. To further improve testing time, it is interesting to apply a magnetic field as an additional acceleration factor, as applying an offset field in opposite direction to the anisotropic field of free layer will help in further compressing the retention [2]. Importantly, testing MRAM arrays under magnetic field also allows to evaluate the immunity of the bit cells to parasitic external field [5]. The difficulty for testing MRAM arrays at wafer level for such purpose is the need of using an external magnetic field, perpendicular to the wafer and covering the entire array surface area in the range of 1 to 10mm² while testing electrically at high temperature. It requires both a good field strength and uniformity on the covered area. In this presentation, we propose a new magnetic head designed for the testing of large arrays, aiming in both optimizing the identification of non-persistent faults related to STT-switching stochasticity and reducing retention testing time. The system can also be used for evaluating bit cells persistence to magnetic interference through magnetic disturbance test. The proposed magnetic test head system is integrating a new 5-poles design from Hprobe proprietary 3D magnetic generator. In test operation, the magnetic head is docked on the head plate of 300mm wafer probing station (figure 1) with the probe card placed underneath. The system is driven by external software interface or operating with triggered signals enabling field application synchronized with electrical measurements. The test head integrates two robotic systems enabling three modes of operations. (i) Field calibration mode to generate and optimize the field patterns to be used in testing; (ii) testing mode for electrical probing and under static or variable magnetic field; and (iii) field monitoring mode to verify that the field stimulus is under the specification limits required by application. A hexapod robot is handling the electro-magnet with six degrees of freedom (X, Y, Z, roll, pitch and yaw). Other two axis system is used for controlling the position of the 3D hall sensor used to sense the magnetic field, scanning the entire area of the array in 3D with step resolution of less than 10 μm . The system enables to work with standard probe cards having hundreds of needles and is designed to do the field calibration at the exact DUT position above the chuck. STT-MRAM anisotropy is oriented perpendicular to the wafer, and compression scheme for non-persistent fault testing requires magnetic field strength at the upper range of the free layer switching field (100-400mT). The proposed system can generate a perpendicular field up to 700mT (Fig.1) and is sufficient for time acceleration testing of bit cell switching and retention, as well as for field immunity testing. The last would be beneficial to be made also by applying disturbance field in the planar direction to the wafer, the system

can generate 3D fields and a maximum planar field amplitude of 100mT is obtained. The achieved non-uniformity is less than 5% over an area above 5mm² (Fig.2), which is enough to cover arrays of $> 64\text{Mb}$ considering an average density of $< 0.08 \text{ mm}^2/\text{Mb}$ [6].

[1] H. Naeimi et al., "STTRAM scaling and retention failure," Intel Technology Journal, vol. 17, 2013, <https://www.intel.com/content/dam/www/public/us/en/documents/research/2013-vol17-iss-1n-intel-technology-journal.pdf#page=54>. [2] Wu, Lizhou & Taouil, M. & Rao, Siddharth & Marinissen, Erik & Hamdioui, Said. (2020). Survey on STT-MRAM Testing: Failure Mechanisms, Fault Models, and Tests. (<https://arxiv.org/abs/2001.05463>) [3] A. Iyengar, S. Ghosh, and S. Srinivasan, "Retention testing methodology for STTRAM," IEEE Design & Test, vol. 33, pp. 7–15, 2016, doi:10.1109/MDAT.2016.2591554. [4] I. Yoon and A. Raychowdhury, "Test challenges in embedded STTMRAM arrays," in Int. Symp. Quality Electronic Design, Mar. 2017, doi:10.1109/ISQED.2017.7918289. [5] Y. Chih et al., "13.3 A 22nm 32Mb Embedded STT-MRAM with 10ns Read Speed, 1M Cycle Write Endurance, 10 Years Retention at 150°C and High Immunity to Magnetic Field Interference," 2020 IEEE International Solid-State Circuits Conference - (ISSCC), San Francisco, CA, USA, 2020, pp. 222-224, doi: 10.1109/ISSCC19947.2020.906295 [6] S.H. Han et al, "28-nm 0.08 mm²/Mb Embedded MRAM for Frame Buffer Memory", in International Electron Device Meeting 2020

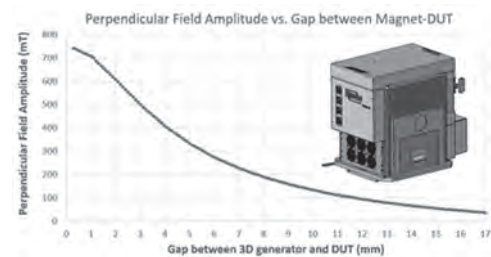


Fig. 1 – Perpendicular field versus the gap between 3D generator and DUT and an illustration of the test head mounted on wafer probing station

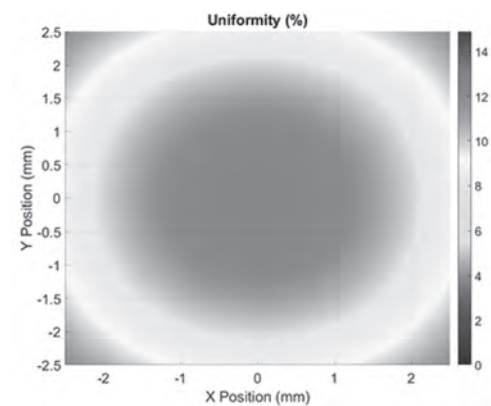


Fig. 2 – Field area uniformity (at 4mm gap) of perpendicular field

AC-07. Towards a Wideband Induction-Based AC Magnetometer for a Fast Characterization of Magnetic Nanoparticles.

M. Saari^{1,2}, M. Sulaiman¹, H. Ahmad³, N. Che Lah⁴ and K. Tsukada⁵

1. Faculty of Electrical and Electronic Engineering Technology, Universiti Malaysia Pahang, Pekan, Malaysia; 2. Automotive Engineering Centre, Universiti Malaysia Pahang, Pekan, Malaysia; 3. College of Engineering, Universiti Malaysia Pahang, Kuantan, Malaysia; 4. Faculty of Manufacturing and Mechatronic Engineering Technology, Universiti Malaysia Pahang, Pekan, Malaysia; 5. Graduate School of Interdisciplinary Science and Engineering in Health Systems, Okayama University, Okayama, Japan

Magnetic susceptibility methods particularly, AC susceptibility measurement have shown high potential to provide a fast characterization and standardization technique of magnetic nanoparticles (MNPs) [1]–[4]. Depending on the applications, AC magnetometers have been developed to measure magnetic responses from MNPs where Neel and Brown relaxation parameters are mostly characterized and utilized in these applications. From the acquired Brownian and Neel relaxation, physical and magnetic properties of the MNPs can be estimated such as the hydrodynamic size and magnetic anisotropy energy ratio. However, the characterization frequency range of the Neel and Brownian relaxations plays an important role where a wider frequency range may reveal further information on the MNP properties. In this study, to realize a simple, wideband, and sensitive AC magnetometer for bio-sensing applications and characterization of magnetic nanoparticles (MNPs), we report the improvements in the detection unit of our previously developed induction-based AC magnetometer [5] for achieving a larger usable range of the detection frequency. In order to obtain a linear sensitivity response, the induction coil is typically operated below its self-resonance frequency where its inductive property becomes dominant and not affected by the parasitic capacitance. This self-resonance frequency is governed by the coil's inductance and parasitic impedance, and increasing the self-resonance frequency by reducing the coil's inductance will extend the usable frequency range of the coil. However, it should be noted that there is a trade-off between the coil's usable frequency range and sensitivity where an increase of the self-resonance frequency may reduce the coil's sensitivity at the low-frequency region. In the attempt to achieve a wide frequency range yet sufficiently sensitive pickup coil, we compared the sensitivity and usable frequency range of 6 different designs of pickup coils by investigating the effect of inductance and parasitic capacitance. The number of turns and coil section separation were varied from 400 to 200 turns, and 1 to 4 sections, respectively. We found that the usable frequency range was greatly affected by the pickup coil's inductance due to the self-resonance phenomena compared to parasitic capacitance. A low noise amplification circuit was designed based on two AD8429 instrument amplifiers and fabricated on a 2-layer printed circuit board as shown in Fig. 1 (a). For the field excitation unit, the excitation coil was designed to produce a field uniformity of more than 90% and constructed using a Litz wire with 60 strands of 0.1-mm Cu wire. The acquisition of the magnetization signal was realized by implementing a generalized Goertzel algorithm to achieve fast signal and phase extractions [6] in comparison to the conventional use of Fast Fourier Transform and lock-in amplifier techniques. As a result, the developed magnetometer showed a sensitivity of 10^{-8} Am²/sqrt(Hz) at 6 Hz and a frequency range of up to 158 kHz. We then demonstrated the developed AC magnetometer by evaluating the effect of viscosity on the frequency response of thermally blocked, single-core nanoparticles (SHP30, Ocean Nanotech, USA). The viscosity of the carrier liquid was varied by different weights of glycerol mixed in a constant volume of purified water and the Fe-concentration was fixed at 0.5 mg/mL. The excitation frequency was swept from 5 Hz to 158 kHz at a maximum field of 0.55 mT_{pp} to obtain discrete 51 measurement points within the acquisition time of 5 minutes. As a result, the peak for the imaginary part was observed to be shifted towards lower frequency values when the wt/V% of the glycerol solution was increased. From the real and imaginary magnetization curves, the hydrodynamic size and the average anisotropy energy ratio s were estimated to be 60.6 nm and 25, respectively. It can be expected that the developed AC magnetometer can be a valuable tool in providing a simple, fast, and reliable assessment of MNPs for bio-sensing applications. Acknowledgments This work was

supported by the Ministry of Higher Education of Malaysia under the grant number of FRGS/1/2019/TK04/UMP/02/4 (RDU1901154), the Research Management Center of Universiti Malaysia Pahang under the grant number of RDU1903100, and the "Strategic Promotion of Innovative R&D" of the Japan Science and Technology Agency (JST).

[1] J. Wells *et al.*, "Standardisation of magnetic nanoparticles in liquid suspension," *J. Phys. D: Appl. Phys.*, vol. 50, no. 38, p. 383003, Sep. 2017, doi: 10.1088/1361-6463/aa7fa5. [2] P. Schier *et al.*, "European Research on Magnetic Nanoparticles for Biomedical Applications: Standardisation Aspects," *Curr. Trends Biomed. Eng. Bioimages Anal. PCBEE 2019. Adv. Intell. Syst. Comput.*, vol. 1033, no. May, pp. 316–326, 2020, doi: 10.1007/978-3-030-29885-2_29. [3] M. M. Saari *et al.*, "Influence of Viscosity on Dynamic Magnetization of Thermally Blocked Iron Oxide Nanoparticles Characterized by a Sensitive AC Magnetometer," *J. Supercond. Nov. Magn.*, vol. 32, no. 9, pp. 2765–2772, Sep. 2019, doi: 10.1007/s10948-019-5031-6. [4] S. Ota *et al.*, "Effects of size and anisotropy of magnetic nanoparticles associated with dynamics of easy axis for magnetic particle imaging," *J. Magn. Mater.*, vol. 474, no. September 2018, pp. 311–318, 2019, doi: 10.1016/j.jmmm.2018.11.043. [5] M. M. Saari, N. S. Suhaimi, N. A. C. Lah, K. Sakai, T. Kiwa, and K. Tsukada, "A Sensitive AC Magnetometer using A Resonant Excitation Coil for Magnetic Fluid Characterization in Nonlinear Magnetization Region," in *2018 IEEE International Magnetics Conference (INTERMAG)*, Apr. 2018, pp. 1–4, doi: 10.1109/INTMAG.2018.8508784. [6] P. Sysel and P. Rajmic, "Goertzel algorithm generalized to non-integer multiples of fundamental frequency," *EURASIP J. Adv. Signal Process.*, vol. 2012, no. 1, p. 56, Dec. 2012, doi: 10.1186/1687-6180-2012-56.

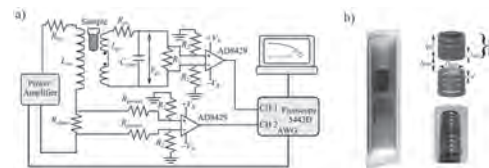


Fig. 1. a) Diagram of the developed AC magnetometer. b) The arrangement and configuration of the excitation coil with respect to the sample and pickup coil.

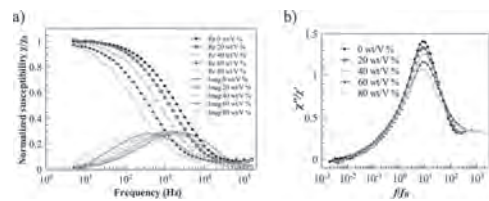


Fig. 2. (a) The normalized real and imaginary susceptibilities of the SHP30 particles at different glycerol wt/V % in the solutions with respect to the frequency. (b) The ratio between the imaginary and real susceptibilities of the SHP30 solutions with respect to the frequency normalized by each Brownian frequency f_B .

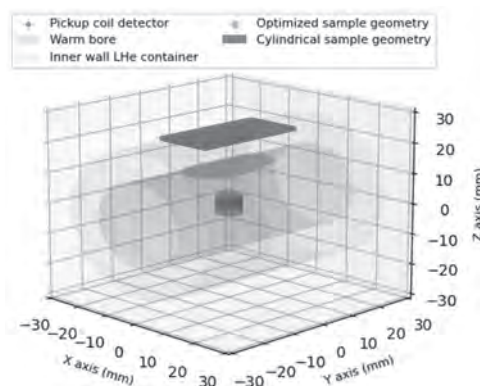
AC-08. Thermal Noise Power Properties of Magnetic Nanoparticles: Theory and Experiment.

K. Everaert^{1,2}, M. Liebl¹, D. Gutkelch¹, B. Van Waeyenberge², F. Wiekhorst¹ and J. Leliaert²

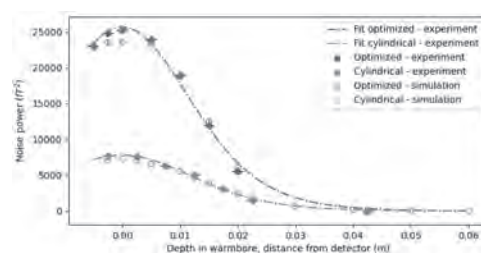
1. Department 8.2 Biosignals, Physikalisch-Technische Bundesanstalt, Berlin, Germany; 2. Department of Solid State Sciences, Ghent University, Ghent, Belgium

Magnetic nanoparticles are powerful tools in biomedical applications, where they are employed in both diagnosis and therapy. A prerequisite for the efficiency of these applications are precisely characterized particles. To this end, several magnetic measurement techniques are established. They all have in common that they measure the magnetic response of the particles exposed to an externally applied magnetic field, which may change the aggregation state of the particles [1]. To overcome this limitation, the method of Thermal Noise Magnetometry (TNM) has been developed to characterize magnetic nanoparticle ensembles without the use of an external magnetic excitation [2]. Amplitude variations in the net magnetic moment of the sample are measured, which are caused by thermal fluctuations in the system. Rather than measuring the dissipation or impedance in the system as a result of the application of the external field, the thermal fluctuations are studied in the absence of the external excitation. The dissipation-fluctuation theorem describes the accordance between the conventional dissipation characterization techniques such as Magnetorelaxometry (MRX) or AC-Susceptibility (ACS) measurements [4, 5], and the fluctuation-based TNM technique. The total switching rate of the magnetic moments depends on volume, anisotropy, aggregation of the particles and the viscosity and temperature of the suspension. TNM measurements have been proven to be feasible, and complementary to other characterization techniques due to its diminutive impact on the sample [2, 5]. In this contribution we present a numerical framework which we use to mirror our TNM measurements, in order to further establish this characterization method. First, we numerically investigate and explain the dependence of the stochastic TNM signal on basic parameters such as the number of particles and their volume. The linear dependence on the number of particles is experimentally verified. Next, we designed a sample holder geometry by solving an optimization problem, maximizing the noise power in our setup (see Fig. 1). Its performance is compared to that of a cylindrical sample holder, typically used for MRX measurements. This was done by measuring the noise power as a function of the sample distance from the detector (i.e. the depth profile of the experimental setup), both computationally and experimentally (Fig. 2). We obtained an increase in noise signal by a factor of 3.5 for the optimized sample holder, while the volume of the sample decreased by more than half. The superior signal amplitude of our optimized sample holder and the match between computed and measured depth profile demonstrate the accuracy and importance of our TNM simulations. The theoretical framework allows us to study aspects of TNM which are hard to accomplish experimentally, making it possible to visualize them and gain insight in the experiment. Our results therefore contribute to the further establishment of TNM as a magnetic nanoparticle characterization method.

[1] Myrovali, E. et al., *Sci. reports*, Vol. 6, p. 37934 (2016) [2] Leliaert, J. et al., *Appl. Phys. Lett.*, Vol. 107, p. 222401 (2015) [3] Wiekhorst, F., Steinhoff, U., Eberbeck, D. & Trahms, L., *Pharm. Res.*, Vol. 29, p. 1189 (2012) [4] Ludwig, F., Guillaume, A., Schilling, M., Frickel, N. & Schmidt, A. M., *J. Appl. Phys.*, Vol. 108, p. 33918 (2010) [5] Leliaert, J. et al., *J. Phys. D: Appl. Phys.*, Vol. 50, p. 085004 (2017)



The geometry for the regular cylindrical and the optimized 200 μ l sample in the experimental setup



The measured and simulated noise power as a function of the depth in the warm bore of both sample geometries

AC-09. Virtualizing CoFeB/MgO Reconstruction Effects on the STT-PMTJ's Performance.

A. Ramesh^{1,2}, K. Chen¹, Y. Lin¹, P. Singh², J. Wei³, Y. Hsin³ and Y. Tseng¹
 1. National Chiao Tung University, Hsinchu, Taiwan; 2. Indian Institute of Technology Delhi, New Delhi, India; 3. Industrial Technology Research Institute, Hsinchu, Taiwan

Modern MRAM technology relies on the magnetic tunnel junction (MTJ) consisting of the state-of-the-art CoFeB/MgO heterostructure. Although current studies support the importance of this heterostructure to the technology, the concern of MgO dielectric breakdown limits MRAM lifetime. We found that inserting an ultra-thin Mg (0.4nm) layer between CoFeB and MgO could promote lifetime and change polarity dependence on applied voltage (Fig.1). However, it traded off the perpendicular magnetic anisotropy and tunneling magneto-resistance. In this work we visualized the modified CoFeB/MgO with Mg insertion against dielectric breakdown by using an in-situ x-ray absorption spectroscopy technique. We find this technique very helpful to understand the origin of interface reconstruction in association with the changes of energy barrier-height and electronic occupation, which are invisible but essential to the MTJ's performance. This is due to the uniqueness of the element-/orbital specificity and the real-time design of the setup. We established a bridge correlating the heterostructure' microscopic and macroscopic properties, by cross-utilizing the x-ray technique with spin transport measurements and atomistic magnetic simulation (Vampire). This thus offers us comprehensive insights which may improve contact engineering of the MTJ technology.

[1] Van Beek, Simon, et al. "Impact of processing and stack optimization on the reliability of perpendicular STT-MRAM." *2017 IEEE International Reliability Physics Symposium (IRPS)*. IEEE (2017). [2] Van Beek, Simon, et al. "Understanding and empirical fitting the breakdown of MgO in end-of-line annealed MTJs." *2020 IEEE International Reliability Physics Symposium (IRPS)*. IEEE (2020).

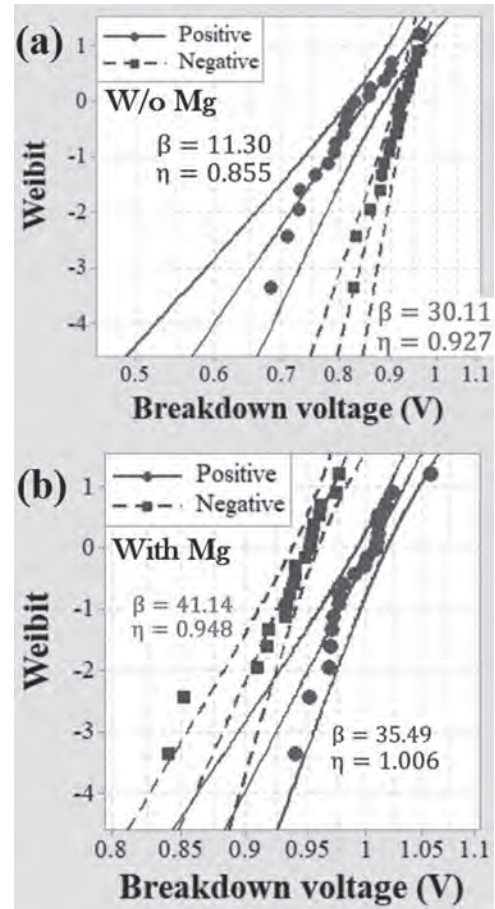


Fig. 1: Weibull distribution versus breakdown voltage for the pMTJ stack consisting of (a) SAF/CoFeB(8Å)/MgO(10Å)/CoFeB(11.5Å)/Ta(3Å) (referred to w/o Mg sample), (b) SAF/CoFeB(8Å)/MgO(10Å)/Mg(4Å)/CoFeB(11.5Å)/Ta(3Å) (referred to with Mg sample). Blue and red data correspond to positive and negative voltages applied to the MTJ, respectively. SAF refers to synthetic antiferromagnetic layer which consists of [Co(4Å)/Pt(3Å)]₁/Co(6Å)/Ru(8Å)/[Co(4Å)/Pt(3Å)]₂/Co(4Å). β and η refer to slope parameter and extrapolated breakdown voltage, respectively.

AC-10. Analysis of Magneto-Tactic Bacteria Using an Open-Source Optical Density Meter.

L. Abelmann^{1,2}, M. Welleweerd² and T. Hageman²

1. Korea Institute of Science and Technology Europe Forschungsgesellschaft mbH, Saarbrücken, Germany; 2. Universiteit Twente, Enschede, Netherlands

We present a simple device that measures the optical transmission of a suspension of magneto-tactic bacteria under application of a magnetic field. The system consists of a measurement head with a RGB LED, a photodetector and three sets of orthogonal coils that generate a field up to 3.5 mT. In addition we realized a module based on an ESP32 microprocessor that sets the coil currents, performs data collection, and features a touchscreen and Wifi access. Source files such as source code for the software as well as links to the designs for hardware (3D prints, circuit boards) are available online at <https://github.com/LeonAbelmann/MagOD>, so that anyone with average electronic skills (for instance EE students) can construct such a magnetic Optical Density meter (MagOD) for under 1000 Eu. We demonstrate to application of the MagOD system on two types of magneto-tactic bacteria. Magnetospirillum bacteria (MSR-1) are elongated and have very different scattering properties depending on the direction of the incident light. Figure 1 shows that there is a clear change in transmitted light when the magnetic field is rotated from parallel to perpendicular to the light path. The signal difference (red lines) is a measure for the fraction of magnetic bacteria in the culture. Since the MagOD meter measures at data acquisition rates up to 800 Hz, we can also time-resolve the rotation of the bacteria (blue lines). The time constant for rotation is a measure for the ratio between bacteria length and their magnetic moment. Unlike MSR-1, which swim along the magnetic field lines but reverse frequently in direction, Magnetococcus bacteria (MC-1) swim in one direction only. This allows us to perform marathon experiments, as shown in figure 2. First, the bacteria are collected at the bottom of the container by a vertical magnetic field. After reversal of the field, the entire groups swim up and passes the photodetector after some time. From the reduction in transmission, we can obtain the distribution in swimming velocity. These are just two examples of the wealth of information one can obtain with such an inexpensive system. Not all possibilities have been explored yet. Next to magneto-tactic bacteria, also suspensions of magnetic nanoparticles can be analyzed with respect to sedimentation and clustering. Since the LED used for the light beam has three different wavelengths, which can be individually tuned in intensity, simple spectral analysis methods can be applied. Moreover next to transmitted light also the scattered light can be detected. Since the housing is 3D printed, other geometries can be easily realized. By making the source code available, we hope that researchers in other fields will make use of and expand on our efforts.

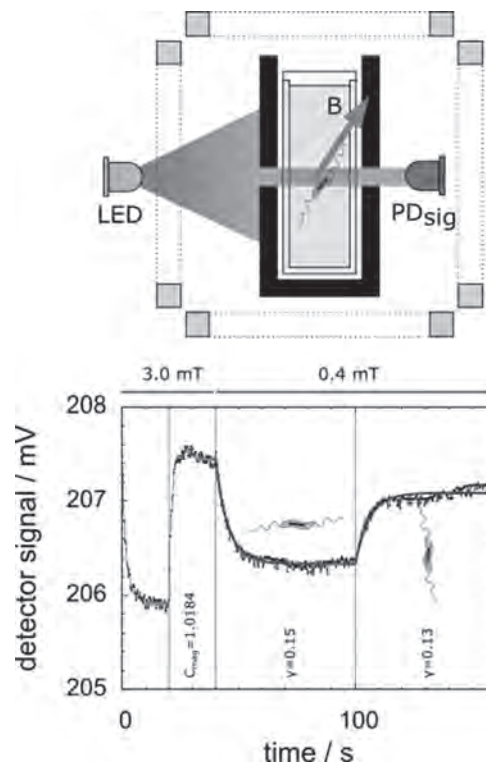


Fig 1. The scattering properties of magnetospirillum bacteria is dependent on their orientation with respect to the incident light beam. By rotating the magnetic field, we can obtain information on the amount of magnetic bacteria in the suspension from the amplitude of the signal (C_{mag}) and information on the magnetic moment from the time response (γ).

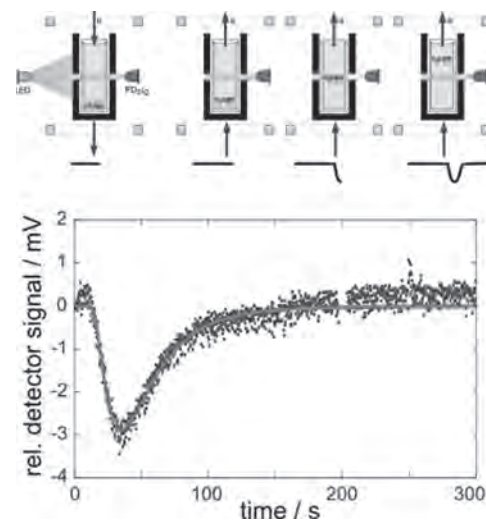


Fig. 2. Magnetococcus bacteria can be sent to the bottom of the container by a vertical magnetic field. When the field is reversed, the entire group swims up (like in a marathon). From the resulting dip in transmission, we can determine the velocity distribution of the bacteria.

**AC-11. Exploring Magnetic Materials by Means of XMCD and XRM
Methods at Beamline P09 at Petra III/DESY.**

J.R. Mardegan¹, O. Leupold¹, D. Graulich², J. Bergholdt¹, T. Kuschel² and S. Francoual¹

1. Petra III, Deutsches Elektronen-Synchrotron, Hamburg, Germany;

2. Department of Physics, Bielefeld University, Bielefeld, Germany

Electronic structure and magnetism of complex materials have been a field for decades extensively investigated in materials science. Although the scientific community has in hands outstanding tools to probe such properties in a microscopic level, resonant x-ray techniques are still a unique instrument for probing electronic and magnetic properties with chemical and site selectivity. In particular, x-ray techniques are ideal for providing additional information for AC/DC susceptibility, electrical resistivity, neutron scattering, etc. In order to grant the community with a powerful instrument for investigating 4d/5d transition metals, lanthanide and actinide complex magnetic materials, beamline P09 at Petra III/DESY has employed diverse x-ray scattering, diffraction and absorption techniques. [1] Particular attention has been drawn to x-ray methods that employ circular radiation and able to probe interfacial magnetism. A few recent examples include measurements carried out by means of x-ray magnetic circular dichroism (XMCD) [2-6] and x-ray resonant magnetic reflectivity (XRM)[6], in which a wide variety of samples, such as powder, single crystals, thin films can be investigated. Using an in vacuum double phase retarder system, P09 is able to provide full polarization control (e.g. linear or circular polarization) between 2.7 and 15 keV [7]. Dichroic magnetic x-ray data combined with magneto-optical sum rules [8] are able to individually provide spin and angular momentum of the probed ions. Hereby I will present a few experimental set-ups currently available at P09 along with some of novel scientific results obtained mainly by means of XMCD and XRM methods.

[1] J. Stempfer, S. Francoual, D. Reuther, J. Synchrotron Rad. 20, 541 (2013) [2] J. Mardegan, S. Francoual, G. Fabbris, Phys. Rev. B 93, 024421 (2016) [3] A. Khanas, S. Zarubin, A. Dmitriyeva, Adv. Mater. Interfaces, 2000411, 1 (2020) [4] Y. Liu, A. Luchin, S. M. Sanchez, ACS Appl. Mater. Interfaces 12, 8780 (2020) [5] Z. Liu, X. Wang, X. Ye, accepted Phys. Rev. B (2021) [6] D. Graulich, J. Krieff, A. Moskaltsova, Appl. Phys. Lett. 118, 012407 (2021) [7] S. Francoual, J. Stempfer, D. Reuther J. Phys.: Conf. Ser. 425 132010 (2013) [8] B. T. Thole, P. Carra, F. Sette, Phys. Rev. Lett. 68, 1943 (1992)

AC-12. Development of a Magneto-Mechanical Bench and Experimental Characterization for Magneto-Rheological Elastomers.

M. Savary¹, S. Hermann^{1,2}, C. Espanet¹ and V. Préault¹

1. Moving Magnet Technologies, Besançon, France; 2. Mécanique, Franche-Comte Electronique Mecanique Thermique et Optique Sciences et Technologies, Besançon, France

Magneto-rheological materials are composites consisting of hard or soft magnetic particles embedded in a cross-linked elastomer with various filling ratios. They belong to the class of smart materials whose stiffness and damping can be controlled by an external stimuli as magnetic field. Due to their great flexibility and potential strain amplitude under a various magnetic field, they can find an interest in the field of mechatronic systems such as, soft-robotic or medical technologies. Magneto-mechanical coupling of flexible magnet needs to be clearly understood for development of applications in which they can be submitted to magnetic and mechanical loads. Some researchers have already worked on a full magneto-mechanical experimental characterization for soft magneto-rheological elastomer in case of large deformation [1-3]. However, due to high deformation range, the distances between magnetic particles increase. Thus, the magneto-rheological effect, which is defined by an increase of the stiffness under various magnetic field, is lowered. In the first part of this work we present the recent development of a magneto-mechanical bench for magneto-rheological elastomer filled with hard or soft ferromagnetic particles (figure 1). Concerning the mechanical part, the setup is composed by a system which consist of a displacement loading with a stress controller. By monitoring the displacement, we are able to work up to 1% of its deformation. This deformation mode allows to avoid non-linearities in case of large deformation range. The magnetic loading consists of a reluctant magnetic circuit which is able to produce homogeneous and large magnetic field (up to 40kA/m) in a variable air gap. Mechanical stress and magnetic loading are oriented toward the same direction. A 3D simulation analysis has been performed with a finite element simulation software (Altair Flux ©) for sizing and optimization of the magnetic loading such as intensity and homogeneity. The goal of this study is to expand as large as possible the magnetic field range to which our material would be submitted. For the numerical study, we have chosen a permanent magnet made of NdFeB ($B_r = 1.3T$) and the magnetic flux is driven through a pure iron core. Various magnetic strength field can be reached by adjusting the air-gap thickness of the device. In case of hard magneto-rheological elastomer, composed by silicon-based elastomer filled with 36% vol of NdFeB particles, we are able to explore 10% of the demagnetization curve. The second part of this work focuses on the experimental characterization of magneto-mechanical coupling based on the setup developed. Thanks to this characterization tool, we are able to perform mechanical loading and unloading cycles with and without magnetic field. We observe, without any magnetic field applied, a hysteretic behavior and a remanent deformation specific to elastomeric material (figure 2) [4]. From this unloading stress state, a magnetic field strength of 40kA/m is applied. As it can be seen (figure 2), a tensile stress around 6.5kPa is induced due to magnetic particles interaction in response of the magnetic field applied. These first results are very promising and confirm the ability of the setup to characterize the magneto-mechanical coupling of hard flexible magnet. Further tests will be performed on composites with different elastomeric matrices with various Young's moduli, different filling ratios and polarization orientation.

[1] C.bellan, & Bossis, Georges. (2012). *Field dependence of viscoelastic properties of MR Elastomers*. Int J Mod Phys B;16(17n18):2447-2453 [2] Schubert, Gerlind & Harrison, Philip. (2015). *Large-strain behaviour of Magneto-Rheological Elastomers tested under uniaxial compression and tension, and pure shear deformations*. Polym Test; 42:122-134 [3] Pössinger, Tobias. (2015). *Experimental Characterization, Modeling and Simulation of Magneto-Rheological Elastomers*. PhD THESIS. Ecole Polytechnique, France. [4] Chagnon, Gregory. (2003). *Modélisation de l'effet Mullins dans les élastomères*. PhD THESIS. Ecole Centrale de Nantes, France.

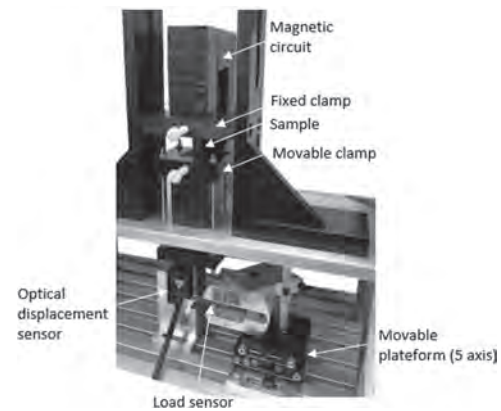


Figure 1: Illustration of the magneto-mechanical bench

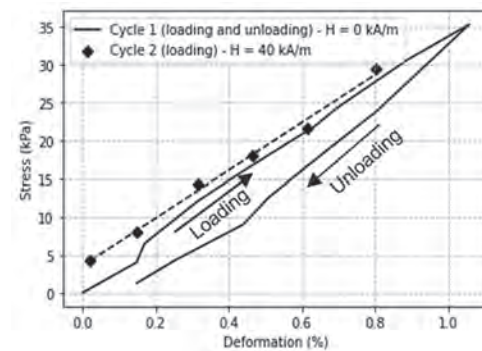


Figure 2: Experimental characterization of the mechanical behavior of a hard magneto-rheological elastomer

AC-13. Magnetic Nanoparticle for Thermal and Magnetic Particle Imaging.

T.Q. Bui¹, A. Biacchi¹, E. Correa¹, W. Tew¹, A.R. Hight Walker¹, C. Dennis¹ and S. Woods¹

1. National Institute of Standards and Technology, Gaithersburg, MD, United States

The prospect of thermal imaging and control in magnetic particle imaging (MPI) is an important advancement for non-invasive medical diagnostics and therapeutics. Current MPI systems focus on imaging only, from measurement of magnetic nanoparticle concentrations, while leaving out the important *in vivo* diagnostic of temperature. Here, we report on our progress toward accurate thermal imaging with high resolution MPI and discuss our achievement of 410 mK total temperature uncertainty at 100 ms integration time near room temperature using a high-precision magnetic field-stabilized magnetic particle spectrometer. The magnetic field is stabilized to ~ 14 nT_{RMS} uncertainty, which allows for precise and accurate determination of magnetic nanoparticle temperature by measurement of magnetization under AC driving fields. Figure 1 shows the obtained temperature Allan deviation plot extracted from the measurement of magnetization in 10 nm ferrite magnetic nanoparticles driven by a 2.5 kHz magnetic field [1]. It has been reported that the imaging resolution of MPI is critically impacted by nanoparticle relaxation dynamics [2]; specifically, spin relaxation under AC drive fields causes a lagged response that results in image blurring. The dynamic response of magnetic nanoparticles in magnetic fields is intricate, depending strongly on the particles' inherent magnetic and structural properties, inter-particle interactions, as well as the local environment in which they are suspended. Thus, comprehensive understanding of these effects requires high sensitivity over a broad parameter space. We have recently developed an arbitrary-wave magnetic particle spectrometer for characterizing relaxation dynamics for particles ranging in sizes from 10 – 70 nm. The combined advantage of arbitrary drive waveforms (sine, pulse, chirp, composite, etc.) and high drive amplitudes in our system allows for facile characterization over a large parameter space, using magnetic field frequencies from DC to 50 MHz at amplitudes 0-10 mT_{RMS}. This capability to drive and observe magnetization dynamics occurring on the order 20 ns is required for isolating independent Brownian and Néel relaxation processes, as well as their dependence on particle environment and magnetic field amplitude. We have characterized the dynamic AC susceptibility of magnetic nanoparticles ranging in diameter from 10 nm to 70 nm and in composition (ferrite, cobalt-doped ferrite, zinc-doped ferrite, core-shell, etc.), and we have observed peaks in the imaginary part of the AC susceptibility (χ'') at frequencies from as low as 50 Hz to > 50 MHz, on particle size and composition. As an example, Figure 2 show the χ'' peak frequency for 15 nm (blue arrow) and 20 nm (green arrow) Fe₃O₄ nanoparticles suspended in water. This peak is an indication of the effective relaxation timescale ($\tau \sim 16$ ms for 20 nm, and $\tau \sim 160$ ns for 15 nm), which will impact the spatial resolution of MPI, depending on the excitation frequency used. This knowledge will eventually inform strategies for design and synthesis of magnetic nanoparticles with properties targeted for accurate and sensitive thermal imaging using MPI.

[1] Think Q. Bui, Weston L. Tew, Solomon I. Woods. AC magnetometry with active stabilization and harmonic suppression for magnetic nanoparticle spectroscopy and thermometry. *J. Appl. Phys.* 128, 224901 (2020). [2] Zhi Wei Tay, Daniel W Hensley, Erika C Vreeland, Bo Zheng, Steven M Conolly. The Relaxation Wall: Experimental Limits to Improving MPI Spatial Resolution by Increasing Nanoparticle Core size. *Biomed Phys. Eng. Express*, 3 (3), 035003 (2017)

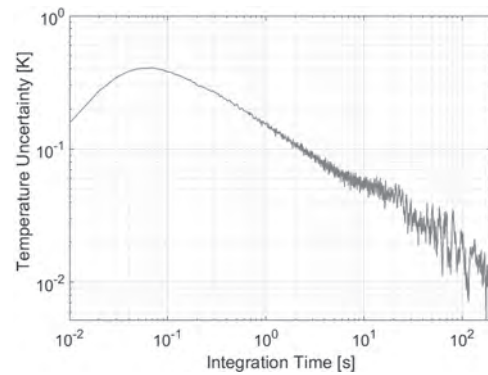


Figure 1: Temperature Allan deviation for 10 nm ferrite nanoparticles at 2.5 kHz and 2.5 mT_{RMS}

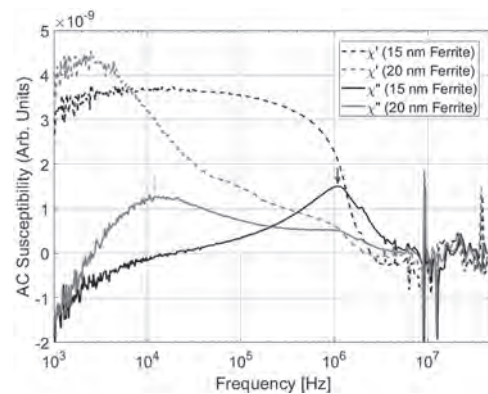


Figure 2: AC susceptibility for 15 and 20 nm ferrite nanoparticles. χ' and χ'' are the real and imaginary components, respectively.

AC-14. RIXS-MCD as Selective *in-Situ* Probe of Structure and Magnetization of Nanoparticles Throughout Synthesis.

J. Kuciakowski¹, K.T. Pitala¹, A. Kmita¹, M. Wyrwal-Sarna¹, D. Lachowicz¹, S. Lafuerza-Bielsa², D. Koziej³, A. Juhin⁴ and M. Sikora¹
 1. AGH University of Science and Technology, Krakow, Poland; 2. ESRF, Grenoble, France; 3. Universitat Hamburg, Hamburg, Germany; 4. Institut de Mineralogie de Physique des Materiaux et de Cosmochimie, Paris, France

Thorough characterization of magnetic nanoparticles (MNP) is a demanding task. Still, due to growing usability and demand, there is a constant pressure to develop better means of MNP characterization, especially in a solution, which is a typical environment for majority of MNP applications. Techniques well developed so far are well suited to probe nanopowders or thin films, but are scarce in case of magnetic nanoparticles embedded in a matrix, due to short probing distance, weak selectivity, or incompatibility of method's characteristic time and MNP' relaxation time. It has been shown that RIXS-MCD (Magnetic Circular Dichroism in Resonant Inelastic X-ray Scattering) is a sensitive, element selective probe of structure, environment and magnetic moment of transition metals in solids, nanomaterials and frozen solutions of MNP [1-3]. 1s2p RIXS-MCD is a high-resolution second-order optical transition spectroscopy (K absorption followed by K α relaxation) resulting in dichroism effect comparable to L-edge XMCD. Any material embedded in a hard X-ray transparent matrix can be studied volumetrically with weak self-absorption. By the use of bend crystal analyzers K α emission can be recorded free of background, omitting constituents not containing studied element, what results in a high sensitivity often required for nanoparticles in solutions. Well-resolved spectral features in the K pre-edge energy range holds information on ion coordination and MCD signal in that region can be used to quantitatively determine magnetic moment projection onto the beam/magnetic field direction. MNP solution magnetization can be measured free of diamagnetic or paramagnetic contributions from carrier or chemical additives in the solution, what is especially important for the evaluation of the smallest nanoparticles that are very hard to magnetize and easy to disregard as background (fig. 1) [4]. We demonstrate applicability of RIXS-MCD to study structural and magnetic state of ferrites nanoparticles being synthesized via decomposition reaction starting from pure precursors. Growth of MNP by means of thermal decomposition of iron/cobalt acetylacetonates syntheses were studied on-the-fly both on iron and cobalt edges using a special cell designed for *in-situ* synchrotron experiments on solutions (fig.2) [5]. Recorded spectra are used to discern main components taking part in the MNP growth process and to follow evolution of local atomic coordination and valence of transition metal ions. Development of magnetization in iron and cobalt ferrites MNP are linked to changes in atomic structure and chemical state. RIXS-MCD supported by ex-situ characterization (TEM, SAXS, Mössbauer spectroscopy) provides a comprehensive characterization of magnetic nanoparticles in solution. It opens a new pathway for controlled synthesis of MNP with defined magnetic response.

1. A. Juhin, A. Lopez-Ortega, M. Sikora, et al., *Nanoscale*, Vol. 6, 11911 (2014) 2. N. Daff , M. Sikora, M. Rovezzi, et al., *Advanced Materials Interfaces*, Vol. 4, 1700599 (2017) 3. N. Daff , J. Ze evi , A. Juhin, et al., *Nanoscale*, Vol. 12, 11222 (2020) 4. J. Kuciakowski, M. Sikora, D. Koziej, et al., *Nanoscale*, Vol. 12, 12640 (2020) 5. M. Staniuk, O. Hirsch, N. Kr nzlin, et al., *Chemistry of Materials*, Vol. 26, p. 2086-2094 (2014)

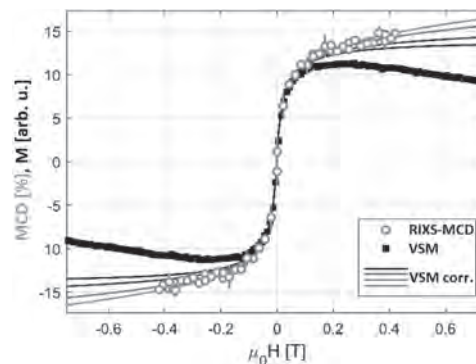


Fig. 1. Magnetization profiles of $Zn_xFe_{3-x}O_4$ MNP in solution measured using VSM (black squares) and RIXS-MCD (orange circles). Lines correspond to VSM signal corrected for diamagnetic background using different approaches [4].

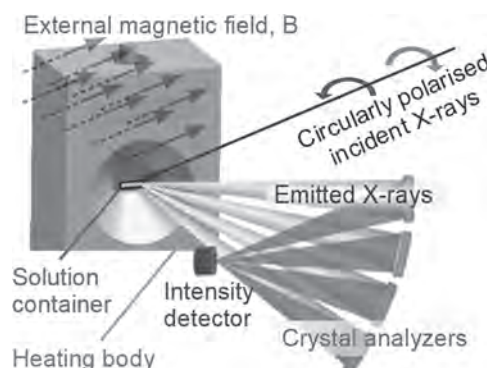


Fig. 2. Sketch of RIXS-MCD experimental setup with reaction cell for *in-situ* experiments on solutions [5].

AC-15. Withdrawn

AC-16. Withdrawn

AC-17. New Polarized Neutron Diffraction Setup for Precise High-Field Investigations of Magnetic Structures up to 8 T at the MLZ.

V. Hutamu¹, H. Thoma³, H. Deng¹, G. Brandl³, A. Weber³, V. Rubanskyi³, J. Peters⁶, W. Lubertetter¹, T. Krist², G. Roth⁴, L. Peters⁴, S. Mattauch³ and T. Brückel²

1. Institute of Crystallography & JCNS outstation at MLZ, RWTH Aachen University, Rheinisch-Westfälische Technische Hochschule Aachen, Aachen, Nordrhein-Westfalen, DE, academic, Garching, Germany;

2. Juelich Centre for Neutron Science JCNS and Peter Gruenberg Institut PGI JCNS-2 & PGI-4, Forschungszentrum Juelich, Jülich, Germany;

3. Jülich Centre for Neutron Science JCNS at Heinz Maier-Leibnitz Zentrum (MLZ), Forschungszentrum Julich GmbH Jülich Centre for Neutron Science, Jülich, Germany;

4. Institut für Kristallographie, RWTH Aachen University, Rheinisch-Westfälische Technische Hochschule Aachen, Aachen, Nordrhein-Westfalen, DE, Berlin, Germany;

5. NOB Neutron Optic Berlin, Berlin, Germany;

6. Forschungs-Neutronenquelle Heinz Maier-Leibnitz (FRM II), Garching b. München, Germany

Polarized neutron diffraction (PND) is a powerful method for investigating magnetic structures. It gives unique access to contributions from nuclear and magnetic scattering, their interference terms, magnetic chirality, and permits to distinct between them. In contrast to non-polarized neutron diffraction, where the scattered intensity depends on the square of the magnetic structure factor, PND has a linear nuclear-magnetic interference term as part of the scattered intensity. This increases the precision in the determination of the ordered magnetic moment by at least one order of magnitude. In the classical PND the sample is situated in a strong magnetic field. For each Bragg reflection, two scattered cross sections are measured for the two antiparallel oriented directions of the incoming neutron spin, and the ratio between them is built. PND measurements are used for the refinement of magnetization density distribution maps [1,2] and the determination of local anisotropy in the magnetic susceptibility at the unit-cell level [3]. It is also used for the high-quality determination of magnetic form factors [4,5], to untangle complex (e.g. chiral) magnetic structures and to follow the movement of magnetic domains [6]. Recently, a first PND setup using a compact high T_c superconducting magnet and a ^3He spin filter polarizer has been successfully implemented [7,8] on the hot neutrons single crystal diffractometer POLI at Maier-Leibnitz Zentrum (MLZ) in Garching near Munich, Germany. Although this setup performs well and first scientific output from it starts to appear [1], it suffers from the relatively low maximal available field of only 2.2 T. For studying many modern-topic (e.g quantum, topologic-order, complex frustrated, etc.) magnetic materials with small ordered magnetic moment, the field-limit of about 2 T is insufficient to produce significant measurable signal, even for PND. To overcome this limitation, a new 8 T split-coil superconducting magnet has been procured and implemented for measurements on POLI. It provides a large angular acceptance for the scattering beam of 300° in the horizontal and 30° ($-5^\circ/+25^\circ$) in the vertical plane respectively, permitting both a right- and left-handed scattering geometry, the registering of the out-of-plane reflections and the usage of large 2D detectors. The field polarity can be swiped between positive and negative. The vertical asymmetric field configuration is realized as the standard operation mode to shift the zero-field node out of the beam path to avoid a neutron depolarization. The magnet is equipped with a re-condensing liquid He cryostat using a Joule-Thomson cold head on top to liquefy the exhaust He gas back into the cryogen bath. Under a constant temperature condition, a zero He boil-off rate could be maintained over a long time (weeks or even month). This significantly reduces the operation costs and maintenance effort for the regular refilling during the neutron experiments. Using two sample rods with dedicated thermometry, sample temperatures between 1.7 and 800 K are available. An extension to the mK range is planned. The sample rod is equipped with an axial rotation and a vertical translation for precise sample centering and diffraction measurements. The spacious sample tube ($\varnothing=34$ mm) and large coil-split space of 53 mm facilitates multiparameter studies by fitting e.g. pressure cells inside [9]. The installation of high-voltage lines for an additional electric field at the sample position is ongoing. Although this new magnet is actively shielded, reducing the stray field by an order of magnitude compared to the classical design (50 Oe at 1 m radial distance from the magnets center), its fringe fields are still too large to be used with

the sensitive ^3He polarizer of the previous setup. To overcome this issue, a new large-beam-cross-section solid-state supermirror bender polarizer (BP) has been developed for POLI. It was realized by a Fe/Si multilayer coating on both sides of the thin Si wafers ($m=3$) by the NOB company. An additional Gd oxide layer is deposited on the convex side of each wafer to absorb the neutrons with the wrong polarization. An existing shielded Mezei-type flipper is used between the magnet and BP. A dedicated guide field construction was numerically simulated, optimized and built to link the magnetic field of the BP to the flipper and to the stray field of the magnet. The neutron beam path between the monochromator-drum to the sample magnet is shown in the Fig. 1. The new setup was successfully tested using a ^3He spin filter as analyzer at low fields (< 1 T), and a high quality Cu_2MnAl single-crystal situated in the magnet as analyzer at high fields (> 2 T). An almost loss-free spin transport within the instrument for the complete field range of the new magnet was achieved. A high polarization efficiency of above 99% even for short wavelength neutrons could be experimentally reached using the new BP (Fig.2). The new high-field PND setup is now available for precise magnetic structure investigations on POLI for the internal and external user communities.

[1] J. Jeong, B. Lenz, A. Gukasov et al., Phys. Rev. Lett. 125, 097202 (2020). [2] M. Deutsch, B. Gillon, N. Clauser et al., IUCrJ 1, 194 (2014). [3] A. Gukasov, P. J. Brown, J. Phys. Condens. Matter 14, 8831 (2002). [4] B. Lebeck, B. D. Rainford, P. J. Brown et al., J. Magn. Magn. Mater. 14, 298 (1979). [5] C. Wilkinson, D. A. Keen, P. J. Brown et al., J. Phys. Condens. Matter 1, 3833 (1989). [6] R. Nathans, S. J. Pickart, H. A. Alperin et al., Phys. Rev. 136, A1641 (1964). [7] H. Thoma, H. Deng, G. Roth et al., J. Phys.: Conf. Ser. 1316, 012016 (2019). [8] H. Thoma, W. Lubertetter, J. Peters et al., J. Appl. Cryst. 51, 17 (2018). [9] A. Eich, M. Hölzle, Y. Su et al., High Pressure Research (2020).

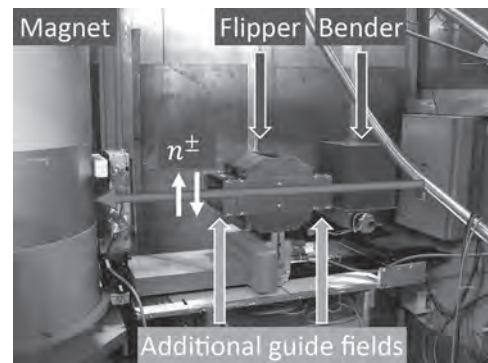


Fig.1: Components of the PND setup on POLI.

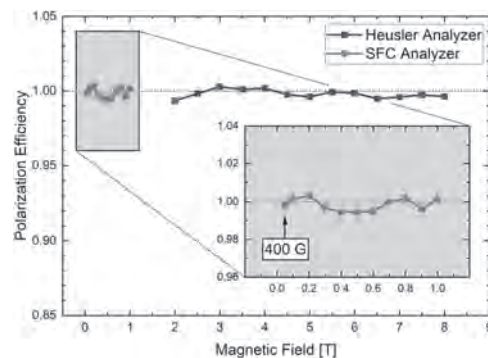


Fig.2: Experimentally measured polarization efficiency of the new PND setup on POLI. Above 1 T, the spin filter cell (SFC) gets magnetized and the Heusler crystal is not yet fully saturated up to 2 T. Thus, both analyzers are not perfectly suitable for the calibration in this field portion. Nonetheless, further measurements with magnetic samples showed a continuous high polarization efficiency in this field region as well.

AC-18. Magnetic Stimulation Reduced Electroencephalography Beta Band Excitability in Insomniacs.

H. Yu¹, M. Qiao¹, S. Ba¹, G. Xu¹ and L. Guo¹
 1. Hebei University of Technology, Tianjin, China

Abstract: Insomnia is a common sleep disorder that affects a great percentage of the population. Magnetic stimulation technology is a new non-invasive and painless treatment for brain disorders. However, the effectiveness of magnetic stimulation technology in the treatment of insomnia has not been fully studied. In this paper, magnetic stimulation was used to stimulate acupuncture points (acupoints). 64-channel electroencephalography (EEG) signals under different states (healthy subjects' resting state, sub-healthy insomnia subjects' resting state before and after magnetic stimulation) were recorded. The brain functional networks based on EEG were constructed and analyzed to investigate the effects of magnetic stimulation on insomnia. The results showed that after magnetic stimulation, the connection and characteristic parameters of brain function network in EEG beta band of insomniacs were improved. Keywords: Magnetic stimulation; Electroencephalography (EEG); Brain functional network; Insomnia I. Introduction Insomnia is a functional disorder caused by the imbalance of brain function. Magnetic stimulation technology has the advantage of safe and painless, and it could stimulate deep tissues and nerves [1]. The synchronization of EEG signals could reflect the correlation between various brain regions [2]. II. Materials and methods Eighteen (nine insomnia and nine healthy) right-handed subjects were chosen in this experiment. According to traditional Chinese medicine, Neiguan (PC6), Shenmen (HT7) and Sanyinjiao (SP6) acupoints were selected in this experiment. Stimulation frequency was 1Hz. Intensity was 1.76 T (80% of the maximal). Each subject was stimulated for three days. 64-channel EEG signals were recorded before and after magnetic stimulation. Pearson correlation coefficient of EEG beta band was calculated. III. Results For insomnia subjects, after magnetic stimulation, the connections and the characteristic parameters of brain in EEG beta band were tending to those of healthy subjects, as shown in Fig.1 and Table 1. IV. Conclusion The results showed that after magnetic stimulation, insomnia subjects' connections and characteristic parameters of brain functional network were improved. It suggested that magnetic stimulation of acupoints might be an effective treatment for insomnia.

[1] Penghui S, Hua L, Siran L, Sleep Med., vol.56, pp.157-163 (2019) [2] Yunna K, Chorom B, Sunhye C, Int J Psychophysiol.,vol.124, pp.26-32 (2018)



Fig.1 Node degree of brain information maps of EEG beta band under different sates

Table 1 Characteristic parameters of brain functional networks of EEG beta band under different states

Different states	Healthy subjects	Insomniacs before stimulation	Insomniacs after stimulation
Average degree	11.29 ± 1.87	18.81 ± 8.03 [*]	13.71 ± 3.98 ^{**}
Average clustering coefficient	0.82 ± 0.42	0.67 ± 0.10 [*]	0.84 ± 0.10 ^{**}
Average path length	2.72 ± 0.42	2.45 ± 0.27 [*]	2.49 ± 0.10 ^{**}
Global efficiency	0.4774	0.5278	0.5113
Small-world property	2.0811	2.5055	2.1333

Note: * indicates that there were significant differences between healthy subjects and insomnia subjects. ** indicates that there were significant differences between the insomniacs before the stimulation and those of after stimulation. (p < 0.05)

Table 1 Characteristic parameters of brain functional networks of EEG beta band under different states

Session AD
HYSTERESIS MODELLING
Salvatore Perna, Chair
University of Naples Federico II, Naples, Italy

CONTRIBUTED PAPERS

AD-01. Exploring Effects of Magnetic Nanowire Arrangements and Imperfections on First-Order Reversal Curve Heat-Maps.M. Zamani Kouhpanji¹ and B. Stadler¹¹. University of Minnesota, Minneapolis, MN, United States

The first-order reversal curve (FORC) method is one of the most appealing magnetic characterization methods that has been used over decades for detailed analyses of nanoscaled magnetic systems. These detailed analyses are accompanied by numerous magnetic features in FORC heat-maps that usually cannot be fully explained¹. In this direction, several theoretical studies have been done to provide a coherent framework to demonstrate those features^{1,2}. However, due to computational limitations, the theoretical models consider mostly perfect arrangements of ideal nanomagnets, such as magnetic nanowires (MNWs), that do not match the real experiments^{3,4}. Here, the FORC heat-maps of several MNW arrays were modeled and discussed. First, several MNW arrays with different arrangements (e.g. hexagonal, square, and random) are modeled and the effect of arrangement on the interaction fields (H_u) are explored. Next, the FORC heat-maps of these MNW arrays are calculated to visualize the importance of the arrangement on the magnetic characteristics of these systems. Then, geometrical imperfections (e.g. variations in shape and size) of MNWs were modeled and randomly assigned to investigate their effects on the FORC heat-maps. Figure 1 shows simulation results for different MNWs arrangements and geometrical imperfections that dictate the H_u among MNWs and the FORC heat-maps, respectively. It was found that the average interaction field (H_u^{ave}) in hexagonal arrangements is higher than those in square arrangements regardless of the filling factor (defined as the area of MNWs to the total area of the simulation box). That is because the hexagonal arrangement has an odd number of MNWs in which the middle one is always in a frustrated state. The MNWs in random arrangements have significantly higher H_u variations (defined as the difference between the interaction field maximum (H_u^{max}) and minimum (H_u^{min})) because the interwire distance in this arrangement is not constant, as opposed to hexagonal and square arrangements. Thus, the H_u is less uniform, and the mean-field effect theory ceased to be a reasonable approximation for simulating these randomly arranged MNWs. Moreover, modeling the geometrical imperfections as variations in coercivity (H_c) will result in presence of the well-known “Wish-bone” and “T-shape” features in the FORC heat-maps. Interestingly, we show that the presence of these features not only depends on the variation of the H_c but also depends on the relative strength of both H_c and H_u .

1 C.-I. Dobrotă and A. Stancu, *J. Appl. Phys.*, 2013, 113, 043928. 2 D. A. Gilbert, G. T. Zimanyi, R. K. Dumas, M. Winklhofer, A. Gomez, N. Eibagi, J. L. Vicent and K. Liu, *Sci. Rep.*, 2014, 4, 1–5. 3 M. R. Zamani Kouhpanji, A. Ghoreyshi, P. B. Visscher and B. J. H. Stadler, *Sci. Rep.*, 2020, 10, 15482. 4 M. R. Zamani Kouhpanji and B. J. H. Stadler, *Nano Express*, 2020, 1, 010017.

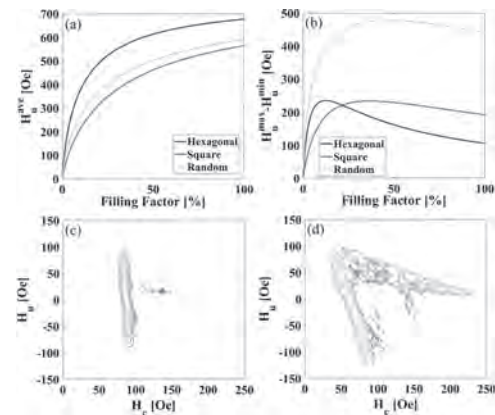


Figure 1: Subfigures (a) and (b) show the average interaction field (H_u) and the difference between the maximum and minimum H_u for various MNW arrangements. Subfigures (c) and (d) show the FORC heat-maps for the hexagonal arrangement, where the filling factor and average coercivity (H_c) are 5% and 100 Oe, respectively, for both cases. The H_c standard deviation is 10 Oe and 50 Oe for (c) and (d), respectively. As the ratio of H_u standard deviation (which is constant here because both cases have the same filling factor) to H_c standard deviation decreases from 10 to 2, the FORC heat-map of MNWs changes from “T-shape”, (c), to “Wish-bone”, (d), respectively.

AD-02. A Dynamic Model for the Hysteresis of CoPt Multilayers and its use for the Interpretation of MOKE Hysteresis Loops Acquired at Different Field Ramp Rates.

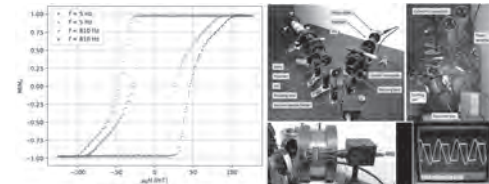
J. Haupt^{2,1}, G. Atcheson¹, K. Borisov^{2,1}, N. Teichert¹, J. Bepas¹, W. Wernsdorfer² and P.S. Stamenov¹

1. School of Physics and CRANN, The University of Dublin Trinity College, Dublin, Ireland; 2. Physikalisches Institut, Karlsruhe Institute of Technology, Karlsruhe, Germany

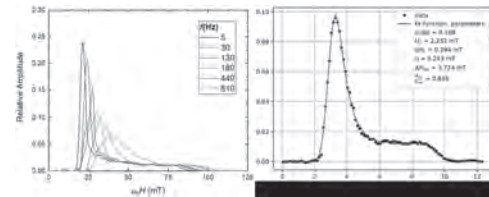
For more than 30 years, the properties of Co/Pt multilayers have intrigued magneticians for their high coercivity and well-developed perpendicular magnetic anisotropy (PMA) [1], with a view to applications in magneto-optical recording and perpendicular magnetic recording media and MRAM, to name but a few. The magnetic and structural properties of this system usually rely on the induction of <111> crystallographic texture and do vary substantially with thickness of the component layers within and number of repetitions of the Co/Pt bi-layer building block [2]. The quality of PMA typically deteriorates beyond 10-20 repetitions and mechanisms of magnetisation reversal complicate as a result. Here we describe the measurement of dynamic hysteresis loops from essentially DC to about 1 kHz in this type of multilayer using an in-house developed MOKE dynamic hysteresiograph and their interpretation within a model of viscous dynamics, accounting for both hysteretic switching and magnetisation rotation. The samples are prepared by DC magnetron sputtering in a Shamrock multi-chamber deposition tool and have the following structure SiO₂/Ta(5)/Pt(2)/[Co(0.4)/Pt(0.8)]₁₀/Co(0.4)/Pt(2), where the dimensions in brackets are given in nanometre. The measurement setup, shown on fig. 2, consists of an optical system utilizing a crossed polarizer/analyser close-to-polar geometry, with a CW He-Ne laser light source (focused down to about 30 μm) and high-speed biased (> 1 MHz bandwidth) photo-diode detector. The magnetic field excitation is provided by an air-gap resonant coil, connected in series to a variable capacitance bank and a high-bandwidth linear operational power amplifier. The system is able to swing over 60 V and at least 5 A of current and deliver fields > 250 mT at low frequency and 150 mT at 1 kHz. Fundamental frequency current resonance is maintained by adjusting the magnitude of the series capacitance, for each magnetic field ramp rate of interest. Two typical hysteresis loops are shown on fig. 1, demonstrating two distinct regions – one of relatively abrupt magnetisation reversal, followed by another, consisting primarily of magnetisation rotation. The behaviour of the normalized differential susceptibility is illustrated on fig. 2, for a number of frequencies in the region 5 – 810 Hz (linear ramp rates of up to 100 T/s). The same is computed using a statistical β-spline (of 3rd order) interpolation of the normalized hysteresis curves, in time domain. The peak in the differential susceptibility is becoming lower and broader as the frequency increases, while the plateau (associated with rotation) remains constant in amplitude, while shifting towards larger fields. To account for this behaviour a model is constructed, comprised of a statistical ‘normal’ hysteretic distribution and constant ‘rectangular profile’ plateau, time-convolved with a function (convolution kernel), which is a decaying exponent for positive times and zero for negative times, the time-constant of which is related to both the magnetic viscosity of the system and the magnetic field ramp rate. The resulting integral model yields excellent non-linear least squares fits to the experimental data, as demonstrated of fig. 2, and allows for the quantification of the quasi-static coercive field H_c, its distribution ΔH_c, the rotational torque amplitude ΔH, and the magnetic viscosity parameter η, at different magnetic field ramp rates. The scaling of the amplitude of the model is essentially constant in the frequency range DC-1 kHz, while the extracted values of the average coercive field, the width of the hysteretic distribution and effective viscosity parameter, all scale linearly, with factors of 25 %, 50 % and 500 %, respectively. As the rotational plateau of the normalized differential susceptibility is essentially unchanged up to field ramp rate of ~100 T/s, it can be inferred that both the magnetisation reversal and rotational dynamics (ferromagnetic resonance frequencies are expected to range between 0.5 and 3 GHz, in the field region of interest) is governed by timescales much shorter than 1 ms, and the probing spot size chosen, is sufficiently small, to not impact significantly the results even for domain wall viscous propagation velocities as low as 0.1 m/s. It is hoped that the here-illustrated simple dynamic model of the dynamic hysteresis in perpen-

dicular anisotropy thin films will also help with the parametrisation, interpretation and analysis (in broad regions of field, frequency and temperature) of experimental data on systems of great practical interest, other than Co/Pt, such as L1₀ FePt, FeNi and CoPd, to name just a few.

[1] C.-J. Lin, G.L. Gorman, C.H. Lee, R.F.C. Farrow, E.E. Marinero, H.V. Do, H. Notarys and C.J. Chien “Magnetic and structural properties of Co/Pt multilayers”, Journal of Magnetism and Magnetic Materials 93 194-206(1991). [2] D. M. Donnet, V. G. Lewis, J. N. Chapman, K. O’Grady and H. W. van Kesteren “Microstructure and hysteresis in Co/Pt multilayers”, Journal of Applied Physics 26 (1993).



(left) Illustrative dynamic hysteresis loops of a Co/Pt multilayer, measured via MOKE, at two different frequencies of the triangular profile drive field (5 Hz and 810 Hz). (right) Views of the various components of the experimental setup and, including the optical and magnetic field sub-systems and the sample mounting. Also shown is a real-time oscillogram of the field and MOKE sample signal, for sinusoidal excitation.



(left) Normalized differential susceptibility of the Co/Pt multilayer described in the text, at several different frequencies in the range (5 - 810 Hz). (right) A non-linear least squares fit to the data obtained at 440 Hz, using the integral model described in the text and the corresponding fitting parameters, as an inset.

AD-03. Coarse-Graining in Micromagnetic Simulations of Dynamic Hysteresis Loops.

R. Behbahani^{1,2}, M.L. Plumer¹ and I. Saika-Voivod¹

1. *Physics and Physical Oceanography, Memorial University of Newfoundland, St. John's, NL, Canada*; 2. *Applied Mathematics, Western University, London, ON, Canada*

We use micromagnetic simulations based on the stochastic Landau-Lifshitz-Gilbert (sLLG) equation to calculate dynamic magnetic hysteresis loops relevant to magnetic nanoparticle hyperthermia. Our simulation model is inspired by a preclinical study reported by Dennis et al. [1] using iron oxide nanoparticles for cancer treatment in mice. The nanoparticles consist of nanorods nominally 6.7 nm x 20 nm x 47 nm in size. Instead of simulating atomic spins, micromagnetics suggests assuming uniformly magnetized cells with dimensions of the cubic unit cell ($a_0=0.839$ nm), resulting in a rod composed of 10752 cells. The approximation that all spins within a cell are uniformly aligned via a relatively strong exchange interaction is valid at zero temperature for cell sizes smaller than the exchange length. At finite temperature, spin decorrelation must be taken into account, and a coarse-graining procedure is required to determine how micromagnetic parameters vary with cell size and temperature. To avoid unwanted heating of surrounding healthy tissues due to Eddy currents, restrictions on the applied field frequency and amplitude limit the field sweep rate to $SR=4H_{max}f < 0.25$ Oe/ns [2, 3]. Simulating a rod made of cells with size a_0 takes months, so using fewer but larger cells is computationally attractive. Our study models the rods using larger cells (of length $a_b = b a_0$ for $b > 1$) to be able to simulate complex nanoparticles in a reasonable time (see Fig. 1). As the cell size affects the system's simulated properties, magnetic parameters need to be scaled to keep the model's magnetic response, i.e., m - H hysteresis loops, invariant with the simulation cell size. Scaling also appears within the realm of phase transitions and critical phenomena, driven by thermodynamic considerations, resulting in the powerful renormalization group (RG) approach based on the correlation length. In the present study, we use the RG approach of Grinstein and Koch [4] to determine how the field $H(b)$, anisotropy constant $K(b)$, and exchange constant $A(b)$ should scale with b (see Fig. 1) at finite temperature. We modify their approach to describe the scaling of the magnetization $m(b)$ by introducing a phenomenological parameter δ that accounts for the nonlinear magnetization temperature dependence [5]. We also extend their approach to include magnetostatic interactions that were not considered in Grinstein and Koch's work. The scaling algorithm produces nearly identical loops over several decades in the model grain volume, as shown in the top four curves of Fig. 2; for details, see Ref. [6]. Larger cell sizes also allow using a larger Δt when solving the equations of motion. Using the scaling approach decreases the rod's simulation time from months to days. At the heart of the LLG equation is α , responsible for describing energy loss from the macroscopic motions of the local magnetization to microscopic thermal motion [7]. A larger α signifies a faster loss of energy and a shorter relaxation time required to align the magnetic moments to the field and results in a smaller hysteresis loop. Likewise, a slower SR is equivalent to a longer measurement time and consequently yields a smaller loop. Considering Sharrock's work [8], which relates the coercive field to the relaxation time and attempt frequency, we argue that, for the small α , so long as $SR/\alpha = \text{constant}$, the coercive field should remain the same. In Fig. 2, we plot the m - H hysteresis loops for two sets of values for SR and α , such that $SR/\alpha = 2.5$, and interestingly even for large values of α , the loops overlap. Using this approach reduces the simulation time from days to hours, for details see Ref. [5]. To summarize, we show here that the RG approach of Grinstein and Koch yields a scaling of magnetostatic, exchange and anisotropy parameters that, with some modification for the rescaling of the resulting magnetization, yields finite temperature nanorod hysteresis loops that are, to approximately 10%, invariant with cell size. Scaling results hold even to the point where the nanorod is represented by a single magnetization vector that experiences only anisotropy and self-demagnetization. In addition to the computational speedup resulting from the use of fewer micromagnetic cells, the invariance of loops when SR/α is fixed provides another avenue for computational efficiency by allowing one to use a larger SR than the target value. This paves the way for efficient simulations of nanoparticles

(composed of nanorods) and their response to AC fields [6], in support of experimental studies of hyperthermia.

[1] C. L. Dennis, et al. *Nanotechnology*, 20(39), 395103 (2009). [2] S. Dutz, and R. Hergt, *Int. J. Hyperth.*, 29(8), 790-800 (2013). [3] R. Hergt, and S. Dutz, *J. Magn. Magn. Mater.*, 311(1), 187-192 (2007). [4] G. Grinstein, and R. H. Koch, *Phys. Rev. Lett.*, 90(20), 207201 (2003). [5] R. Behbahani, M. L. Plumer and I. Saika-Voivod, *J. Phys.: Condens. Matter*, 32, 35LT01 6pp (2020). [6] R. Behbahani, M. L. Plumer and I. Saika-Voivod, arXiv:2010.08848 (2020). [7] T. L. Gilbert, *IEEE Trans. Magn.*, 40(6), 3443-3449 (2004). [8] M. Sharrock, and J. McKinney, *IEEE Trans. Magn.*, 17(6), 3020-3022 (1981).

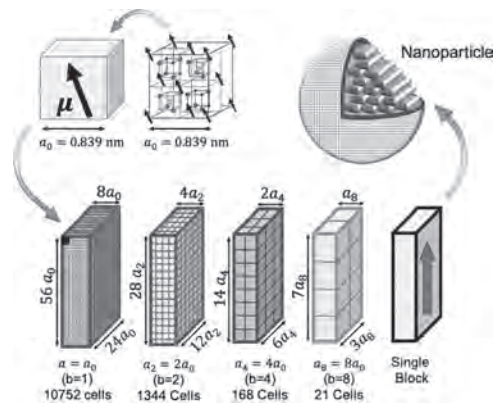


Figure 1. Coarse-grained modelling of a magnetite nanorod. The smallest micromagnetic cell models eight atomic spins within a cubic unit cell of length $a_0 = 0.839$ nm with a single magnetic moment. Ultimately, the nanorod is modelled as a single block, corresponding to $b = 22$. Spherical magnetic nanoparticles studied in Ref. 2 are made up of magnetite nanorods.

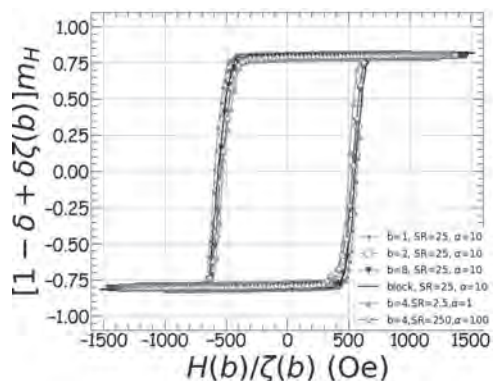


Figure 2: Hysteresis loop invariance. The top four loops show invariance with cell size when magnetic parameters are scaled according to a modified RG prescription in addition to the magnetostatic interactions scaling. The last two loops show the invariance of MH loops when the ratio SR/α is constant.

AD-04. Using a Random Forest Regressor to Predict First-Order Reversal Curves of hcp-Co Particle Ensembles.

L. Breth¹, T. Schrefl¹, J. Fischbacher¹, A. Kovacs¹, H. Oezelt¹, M. Schwarz², C. Storf², J. Pachthofer², C. Czettel² and H. Brückl¹
 1. Department for Integrated Sensor Systems, Donau-Universität Krems, Krems, Austria; 2. R&D Carbide and Coating, Ceratizit Austria GmbH, Reutte, Austria

First Order Reversal Curve (FORC) diagrams have over 30 years of history as a tool to characterise ensembles of magnetic particles reaching from applications in geophysics to detect the prevalence of carriers of paleomagnetic signals [1] to the measurement of magnetic recording media properties [2]. Using FORC diagrams as a purely quantitative tool remains an open topic of active research (see e.g. [3]), but they have proven to be useful as semi-quantitative instrument to determine traces of magnetic phases in a material mixture [4]. Based on this present understanding we introduce the idea of using FORC diagrams to detect the crystalline structure of the cobalt binder phase in tungsten carbide (WC-Co), a hard metal used in a wide range of high-tech applications (e.g. drills or cutting inserts) [5]. The goal is to interpret FORC diagrams from experimental measurements by micromagnetic simulations as a source of “big data” for a fast characterisation of tungsten carbide binders. Our proposed method goes significantly beyond state-of-the-art techniques used for characterisation of WC-Co in particular, but also makes a contribution to the interpretability of FORC diagrams in general by applying machine learning to the large amount of data points available through FORCs. Here, we present our first results towards such an automated interpretation of FORC diagrams, which requires a substantial amount of training data from micromagnetic simulations. Such simulations provide the opportunity to assemble mixtures of particles with a known distribution of various properties, which should serve as labelled training data. We use energy minimization [6] to compute the magnetization curves of Co particles with sizes of 100 nm and uniaxial anisotropy. A reversal curve is computed starting at each point Hr on the major loop where the magnetization M has changed by a defined amount. Depending on the alignment of the anisotropy axes with respect to the field H different numbers and configurations of domain wall nucleation-propagation-annihilation sequences occur during a full reversal loop, leading to a large variation in the number of generated FORCs. To mitigate the necessary computational efforts to acquire the training data of large ensembles of more than 100 particles we developed a Python-based FORC analysis framework and used scikit-learn’s Random Forest Regressor [7] to predict the surface $M(H, H_r)$ from a subset of simulations. Our first results for an ensemble of non-interacting cubes with varying anisotropy axes show that the FORC diagrams calculated from the predicted $M(H, H_r)$ surface give a valid representation of the FORC diagram calculated directly from the fully simulated ensemble (Fig.1). This approach will enable us to speed up the generation of training data considerably, which provides the basis to understand the microstructure of WC-Co samples containing Co particles with dimensions beyond the 100 nm scale by using FORCs as a fast and non-destructive characterisation tool. Fig. 2 shows two examples of simulated FORCs and their respective FORC diagrams. In Fig. 2a the external field is aligned more parallel to the particle’s easy axis than in Fig. 2b. As FORC diagrams only show pronounced peaks for irreversible processes, they can be directly associated with the jumps present in the FORCs shown in the upper part. Analytical models to explain the peaks’ positions and heights can only be found for simplified models. Following [8], the two peaks in Fig. 2a can be modelled analytically using a curvilinear hysteresis loop, but this model does not reveal the exact reversal process in the material. Combining micromagnetic simulations with machine learning will enable us to train models using realistic assumptions about the material of interest. As a first step the presented approach will make it possible to get data for the interpretation of FORC diagrams within minutes instead of weeks by replacing time-consuming micromagnetic simulations with sufficiently trained machine learning models. The financial support by the Austrian Federal Ministry of Climate Action, Environment, Energy, Mobility, Innovation and Technology (BMK) in the KI-Carbide project (#877141) is gratefully acknowledged.

[1] A. R. Muxworthy and D. J. Dunlop: *Earth and Planet. Sci. Lett.* 203, pp 369-382 (2002) [2] M. Winklhofer and G. T. Zimanyi, *J. Appl. Phys.* 99, 08E710 (2006) [3] D. A. Gilbert, G.T. Zimanyi, R.K. Dumas et al., *Sci. Rep.* 4, 4204 (2014) [4] C. Carvallo et al.: *Phys. Earth Planet. Inter.* 154, pp 308–322 (2006) [5] J. García et al., *Int. J. Refr. Met.* 80, pp 40-68 (2019) [6] L. Exl, J. Fischbacher, A. Kovacs et al., *Comp. Phys. Comm.* 235, pp 179-186 (2019) [7] F. Pedregosa et al, *JMLR* 12, pp 2825-2830 (2011) [8] C. Pike and A. Fernandez, *J. Appl. Phys.* 85, pp 6668-6676 (1999)

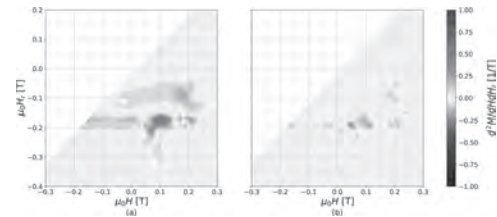


Fig. 1 FORC diagrams computed (a) directly from simulating a full ensemble of 125 non-interacting hcp-Co particles with varying alignment of the anisotropy axis with respect to the external field and (b) by using only a subset of 20 simulations as input to a Random Forest Regressor to predict the $M(H, H_r)$ surface

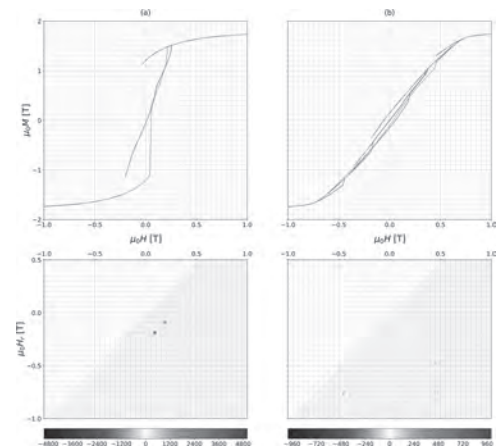


Fig. 2 Examples of simulated FORCs and calculated FORC diagrams for a 100 nm cube of hcp Co (uniaxial anisotropy). Colorbars indicate the peak height of the FORC distribution (see also Figure 1). The external field in (a) is aligned more parallel to the easy axis than in (b). The visible peaks in the FORC diagrams (bottom) correspond to irreversible jumps of the magnetization (top).

AD-05. Two-Dimensional Dynamic Magnetization Model of Steel Sheets Including Vector Hysteresis Effect.

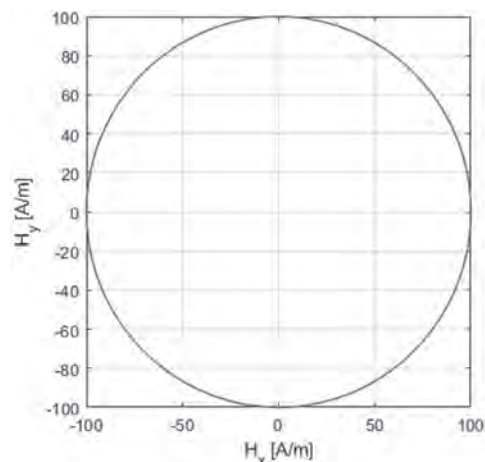
R. Zeinali¹, D. Krop¹ and E. Lomonova¹

¹. Electrical Engineering, Eindhoven University of Technology, Eindhoven, Netherlands

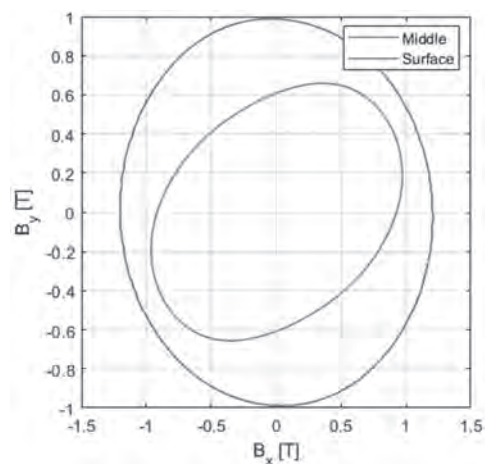
The accurate estimation of dissipated energy in ferromagnetic steel sheets is essential for electric machine designers. This requires considering three coupled phenomena, i.e. magnetic hysteresis, eddy currents, and excess field in the electromagnetic analysis. The magnetic hysteresis is referred to as the static component of the dynamic lamination dynamic model. There exist several physical and phenomenological models in the literature to model static hysteresis [1-3]. In [4], a congruency-based hysteresis model is proposed. This model yields higher accuracy than the Preisach model. In this model, first and second-order reversal curves are used to approximate any third or higher-order reversal curves. When a magnetic material is exposed to a time-varying magnetic field, in addition to the static hysteresis field, the excess field is created, as well. The excess field is created because of the viscose property of the domain walls in magnetic materials. As a result, there is always a time delay between the local flux density and the local field strength. Since the physical process of domain wall movement is not well understood yet, the excess field effect is modeled using engineering phenomenology. This field is modeled using Bertotti empirical model for the excess field [1]. By adding the excess field component to the static hysteresis component modeled by the congruency-based model proposed in [4], the scalar hysteresis model is obtained. Due to the anisotropy effect, magnetic materials show different magnetic characteristics when uniaxial measurements are applied in different directions to the material rolling direction. To achieve an accurate material characterization, the anisotropy effect should be taken into account. To generalize the developed scalar hysteresis with the anisotropy effect, two isotropic scalar models in parallel and perpendicular to the material rolling direction are developed. Then the anisotropic scalar model is developed by interpolating the obtained two isotropic scalar models. When a magnetic material is subjected to a rotating field, the scalar hysteresis models are not applicable anymore, and the so-called vector hysteresis models are required to model the hysteretic behavior. Mayergoyz proposed a vector generalization of the scalar Preisach model in [5]. In this generalization, the input data is projected into a finite number of directions, and the model output is obtained by a vectorial sum of the established scalar Preisach models. In general, the proposed vector generalization by Mayergoyz can be applied to the other scalar hysteresis models. In this study, the Mayergoyz vector generalization is applied to the developed anisotropic scalar model to obtain the vector hysteresis model. Based on Faraday's law, when a magnetic material is exposed to a varying magnetic flux, eddy currents are induced, due to the conductivity of the material. The induced eddy currents create a magnetic field opposing the change of the magnetic flux density. This behavior is described by the so-called diffusion equation. Owing to the thin long dimensions of steel lamination, edge effects can be neglected, and the diffusion equation is then simplified into a 1D spatial Partial Differential Equation (PDE). The developed vector hysteresis model is employed as the material constitutive relation. Finite Element Method (FEM) is used to solve the diffusion equation coupled with the vector hysteresis model. Figure 1 shows the H -loci of a circular rotating magnetic field applied to a lamination sheet of NO27 magnetic material. The associated B -loci on the surface and in the middle of the lamination thickness is depicted in Fig. 2. As seen in the figure, due to the skin depth effect, the flux density in the middle of lamination is lower than the flux density on the lamination surface. To validate the accuracy of the proposed 2D dynamic magnetization model, the model results will be compared with the measurements obtained from a rotational magnetic tester. This comparison will be presented in the full paper.

[1] G. Bertotti, I. Mayergoyz, The science of hysteresis: Hysteresis in materials, Vol. 3, 1st edn. (Academic Press, 2005) [2] Steentjes, Simon, et al. "Iron-loss and magnetic hysteresis under arbitrary waveforms in NO electrical steel: A comparative study of hysteresis models." *IEEE Transactions on Industrial Electronics* 64.3 (2016): 2511-2521. [3] Zirka, Sergey E., et al. "Congruency-based hysteresis models for transient simulation." *IEEE transactions on magnetics* 40.2 (2004): 390-399. [4]

Zeinali, Reza, Dave CJ Krop, and Elena A. Lomonova. "Comparison of Preisach and congruency-based static hysteresis models applied to non-oriented steels." *IEEE Transactions on Magnetics* 56.1 (2019): 1-4. [5] I. D. Mayergoyz, "Vector Preisach models of hysteresis," *Journal of Applied Physics*, vol. 8, no. 69, pp. 4829-4831, 1991.



H -loci of the applied magnetic field strength to the lamination sheet.



B -loci obtained from the proposed 2D dynamic magnetization model

AD-06. Hysteresis Branch Crossing and the Stoner-Wohlfarth Model.S.A. Mathews¹, A. Ehrlich² and N. Charipar¹

1. *Materials Science and Technology Division, US Naval Research Laboratory, Washington, DC, United States;* 2. *Leidos Inc Arlington, Arlington, VA, United States*

The Stoner-Wohlfarth model [1], first published in 1948, describes the magnetic behaviour of anisotropic, ferromagnetic particles, which magnetize via coherent rotation. This widely used model predicts the crossing of the ascending and descending branches of the magnetization curve when the applied field is close to the magnetic hard-axis. However, experimental observation of this hysteresis branch crossing has not been acknowledged in the literature. In fact, the crossing of hysteresis branches has been labelled as being nonphysical [2] and a problem [3] with the Stoner-Wohlfarth model. Here we show that the crossing of the ascending and descending branches of the magnetization curve does occur and is consistent with the Stoner-Wohlfarth model. Contrary to previous reports, we show that the crossing of hysteresis branches is physically realistic [4] and violates no fundamental law.

[1] Stoner, E.C. and Wohlfarth, E.P., *Phil. Trans. Roy. Soc. of London Series A*, 240, no. 826, pp.599-624 (1948). [2] Vajda, F. and Della Torre, E., *IEEE Trans. Mag.*, 28, no. 5, pp.2611-2613 (1992). [3] Tannous, C. and Gieraltowski, J., *Physica B*, 403, pp.3563-3570 (2008). [4] Heslop, D. and Roberts, A., *Jour. Geophys. Res.*, 117, B03103 (2012).

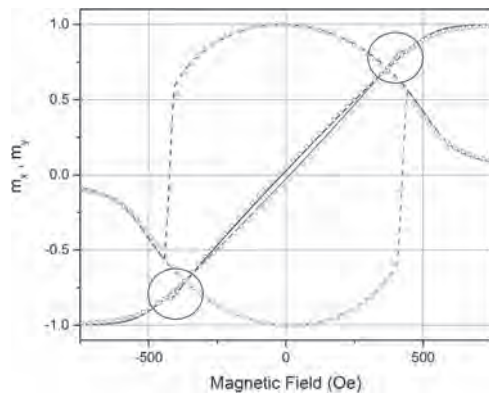


Figure 1: The reduced x- and y-components of the magnetization as a function of applied field for an angle of $\alpha=2^\circ$. Circles and triangles represent the x- and y-components of the measured magnetization, respectively. Solid and dashed lines represent numeric solutions to a temperature-dependant Stoner-Wohlfarth model. Ascending and descending data are shown in red and blue, respectively. Black circles highlight the hysteresis branch crossings.

AD-07. Estimation of Magnetostrictive Hysteresis Properties of Electrical Steel Sheet Under External Stress Using Multi-Scale Domain Energy Model.

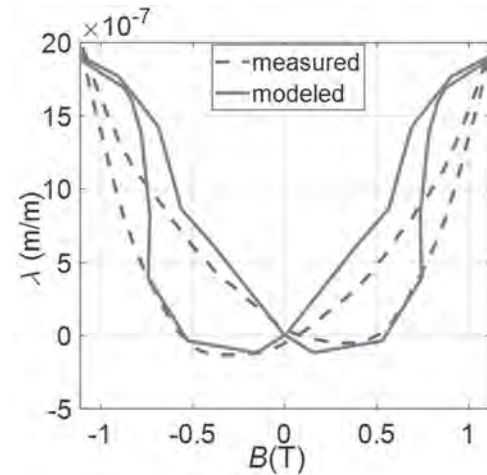
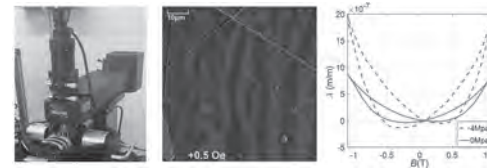
M. Li¹, Y. Zhang¹, W. Jiang¹, D. Xie¹ and C. Koh²

1. School of Electrical Engineering, Shenyang University of Technology, Shenyang, China; 2. Cheongju, Chungbuk, Chungbuk National University, Cheongju, The Republic of Korea

I. Introduction The iron losses, permeability and magnetostriction of electrical steel sheet are sensitive to mechanical stress, and the presence of mechanical stress may bring out the deformation of the magnetostrictive hysteresis loops, the increase of core loss, and the aggravation of vibration and noise in electrical machines or transformers. The accurate prediction of magnetic characteristics under stress is significant for optimum design of high power density motor. The multi-scale domain energy models [1-2], such as the assembled domain structure model (ADSM) have been conducted to represent the magnetic hysteretic behavior in an electrical steel sheet based on the minimization principle of total magnetic energy. In comparison with some phenomenon models such as Preisach, the domain energy model interprets the magnetic domain wall movements and rotation with the magnetic field applied and builds a relevance between the microstructure and magnetic hysteresis properties. However, due to the complexity of the parameter identification, the establishment of domain model is at the cost of large computation time and its modeling accuracy to the magnetostrictive loops is also to be improved. In this paper, a multi-scale domain energy model is improved to estimate the magnetostrictive characteristics under different external stresses, in which the hysteresis energy function is introduced instead of pinning energy in order to reduce the computation time. To identify the parameters in the model, the magnetic domain wall movements in an electrical steel sheet during the magnetization process are observed by a magnetic domain observation microscope, and the magnetostrictive hysteresis loops under several external stresses are measured. The validity of proposed model is verified by comparing the measured magnetostrictive loops with computed ones. **II. Experiments and Approaches** **A. Experiments** With the presence of external magnetic field intensity H , the balance state with the total inner energy in the ferromagnetic materials keeping the minimum is disturbed, and then the wall movements and magnetic moment rotation in the magnetic domains is occurring. This magnetization process in an electrical steel sheet is observed with a polished sample of with the size of 8mm width and 8mm length, as shown in Fig.1(a), by means of a magnetic domain observation microscope, BH-782PI-SHG, Japan. Fig.1(b) represents a domain figure under a 0.5Oe field in a non-oriented silicon steel, in which the difference between grey levels indicates different magnetization direction domains. Further, the magnetic hysteresis and magnetostrictive loops with different mechanical stresses applied are measured, as shown in Fig.1(b), by a laser magnetostrictive tester from Brockhaus, Germany, in which the shape and magnitude and area of magnetostrictive loops occur to increase after applying a 4Mpa compressive stress. **B. Improved Multi-Scale Domain Energy Model** The magnetic domain moment is alignment with the easy directions of the crystal in a grain when the material is in the demagnetized state. According to the ADSM model each grain is assumed to be composed of six magnetic domains along the easy directions, and the unit magnetization vector m of each domain is denoted by the variables θ and Φ as a vector $[\sin\theta\sin\Phi, \sin\theta\cos\Phi, \cos\theta]$. The θ_i , Φ_i and the existence probability r_i ($i=1,2,\dots,6$) of magnetization vector for each domain can be determined according to the principle of local energy minimum. The total magnetic domain energy is expressed as the summation of Zeeman energy, the crystal-line anisotropic energy, the magnetostatic energy and magnetoelastic energy in the ADSM. Further in order to model the magnetic hysteresis effect, the pinning energy have been added into the total energy. In this paper, in order to estimate the behavior of magnetostrictive hysteresis behavior, a hysteresis energy density function in (1) instead of the pinning energy is employed into the total domain energy in terms of simplifying the parameter identification process. $E_h = -\mu_0 M_s \chi_0 (\alpha_{1,i} m_{x-p} + \alpha_{2,i} m_{y-p} + \alpha_{3,i} m_{z-p})$ (1) where $[\alpha_{1,i}, \alpha_{2,i}, \alpha_{3,i}]$ is direction cosine of the unit magnetization vector of the i -th domain with respect to the three easy axes; $(m_{x-p}, m_{y-p}, m_{z-p})$ is three components of magnetization vector at previous moment, M_s is the saturation magnetization. The hysteresis energy density function can take the effect of the

magnetization history, and explain the hysteresis phenomenon as an inertia. Further, the effect of external stress on the magnetostriction in the magnetoelastic energy is described as: $E_\sigma = -3/2 \lambda_{100} \sigma (\alpha_{2,1}^2 \gamma_1^2 + \alpha_{2,2}^2 \gamma_2^2 + \alpha_{2,3}^2 \gamma_3^2) - 3 \lambda_{111} \sigma (\alpha_{1,1} \alpha_{2,1} \gamma_1 \gamma_2 + \alpha_{2,1} \alpha_{3,1} \gamma_2 \gamma_3 + \alpha_{3,1} \alpha_{1,1} \gamma_3 \gamma_1)$ (2) where $(\gamma_1, \gamma_2, \gamma_3)$ is the cosine of the angle between the stress and the three easy axes; λ_{100} and λ_{111} are saturation magnetostrictive coefficients along the [100] direction and the [111] direction; σ is the stress applied on the sample; Fig. 2 shows the measured and modeled results of magnetostriction loops, and more discussion will be presented in detail in the extended paper.

[1] S. Ito, T. Mifune, T. Matsuo, et al. Energy-Based Magnetization and Magnetostriction Modeling of Grain-Oriented Silicon Steel under Vectorial Excitations. *IEEE Trans. Magn.* vol 52, no. 5, pp. 1-4, 2016. [2] D. Vanoost, S. Stentjes, J. Peuteman, et al. Magnetic hysteresis at the domain scale of a multi-scale material model for magneto-elastic behaviour. *J. Magn. Magn. Mater.* vol 414, no. sep., pp. 168-179, 2016. [3] T. Moses. Relevance of microstructure and texture to the accuracy and interpretation of 1 and 2 directional characterisation and testing of grain-oriented electrical steels. *International Journal of Applied Electromagnetics & Mechanics*, vol. 55, pp. 1-11, 2017.

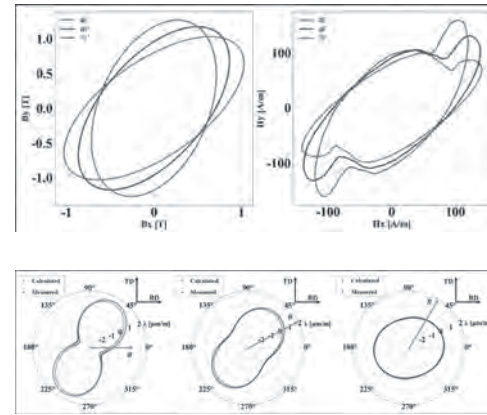


AD-08. A 2D Vector Magnetostriction Model in an Electrical Steel Sheet Taking the Pining Hysteresis Effect Into Account.

D. Li¹, Y. Zhang¹, W. Jiang¹, C. Koh² and D. Xie¹

1. School of Electrical Engineering, Shenyang University of Technology, Shenyang, China; 2. College of Electrical and Computer Engineering, Chungbuk National University, Cheongju, The Republic of Korea

Magnetostriction is one of main factors causing the core vibration and noise of electromagnetic equipment, and the magnetostriction at the stator core and T-joint in transformers has the vector characteristics due to the two-dimensional (2D) rotational magnetization. Recently, the 2D vector magnetostriction models[1,2] have been researched based on the Fourier analysis of measured 2D magnetostrictive waveforms and magnetic flux density ones. But, owing to the complexity of rotational magnetization, it is more significant to describe the magnetostrictive characteristics in terms of magnetization mechanism. In this paper, with the reference to the hysteresis behavior and irreversibility in the Jiles-Atherton model, the hysteresis characteristics between the magnetostriction λ and the magnetization M are attempted to be explained by the pinning effect. After that, a 2D vector magnetostriction model is proposed and its validity is verified with experimental data from a 2D rotational magnetization tester. I. The Proposed 2D Vector Magnetostriction Model The magnetostriction λ and magnetization M are usually expressed as a square function relationship when they are static and do not consider saturation, $\lambda = pM^2$ (1) A large number of experimental observations show that the change of magnetostriction λ lags behind the variation of magnetization M within one magnetization time period. For the ferromagnetic material, with the magnetic field applied, the domain wall displacement may be hindered by the pinning effect, which results from the impurity and cavity in the material, so the quantitative hysteresis behavior and irreversibility are mainly caused by overcoming the pinning. As a result, the hysteresis behavior of magnetostriction can be also explained by the pinning effect, in which the magnetostriction is mainly due to the movement of domain walls whose spontaneous magnetization is not alignment with the applied magnetic field. By adding the irreversibility of magnetostriction into (1) and taking the vector properties of 2D magnetization into account, a 2D vector magnetostriction model is proposed as $\lambda_{xx} = p\lambda_{xx}[c\lambda_{xx}M_{anx} + (1 - c)\lambda_{xx}M_{irr}\lambda_x]^2/M_{sx}^2 + p\lambda_{yy}[c\lambda_{yy}M_{any} + (1 - c)\lambda_{yy}M_{irr}\lambda_y]^2/M_{sy}^2$ $\lambda_{xy} = q\lambda_{xy}[c\lambda_{xx}M_{anx} + (1 - c)\lambda_{xx}M_{irr}\lambda_x]^2/M_{sx}^2 + q\lambda_{yy}[c\lambda_{yy}M_{any} + (1 - c)\lambda_{yy}M_{irr}\lambda_y]^2/M_{sy}^2$ (2) $\gamma_{xy} = r\gamma_{xy}[c\lambda_{xx}M_{anx} + (1 - c)\lambda_{xx}M_{irr}\lambda_x][c\lambda_{yy}M_{any} + (1 - c)\lambda_{yy}M_{irr}\lambda_y]/(M_{sx}M_{sy})$ where λ_{xx} is the normal strain in x direction, λ_{yy} is the normal strain in y direction, and γ_{xy} is the shear strain; M_{sx} and M_{sy} are two components of saturation magnetization; M_{anx} and M_{any} are two components of ideal anhysteretic magnetization in the x,y direction; the parameters of $c\lambda_{xx}$, $c\lambda_{yy}$, $p\lambda_{xx}$, $p\lambda_{yy}$, $q\lambda_{xx}$, $q\lambda_{yy}$, and $r\gamma_{xy}$ are to be determined from the experimental data of 2D magnetic properties; $M_{irr}\lambda_x$ and $M_{irr}\lambda_y$ denote the irreversible component of the magnetization and can be described as $M_{irr}\lambda = M_{an} - k\lambda\delta(dM_{irr}\lambda/dH_e)$ (3) where $k\lambda$ is the pinning constant and obtained through experimental data; $\delta = (dH_e/dt)/|dH_e/dt|$; H_e is the effective field. II. Experiments and Model Verification A 2D magnetic properties tester with a rosette strain gauge detecting the magnetostrictive strain signals in [3] is used to provide the data with identifying the parameters in (2) and (3). Fig. 1 shows the measured magnetic flux density B loci and magnetic field intensity H trajectories. Fig. 2 shows the comparison of the calculated and measured values of magnetostriction at three time moments with respect to a B trajectory with the axis ratio $\alpha = 0.2$, $B_{max} = 0.9T$, and the inclination angle $\theta_B = 45^\circ$.



[1] Yamagashira M, Wakabayashi D, Enokizono M. "Vector magnetic properties and 2-D magnetostriction of various electrical steel sheets under rotating flux condition," IEEE Trans. Magn., vol. 50, no. 4, pp. 1-4, Apr. 2014, Art. no. 6100404. [2] L. Zhu, H.-S. Yoon, H.-J. Cho, D.-J. Um, and C.-S. Koh, "Finite-element analysis of magnetostriction force in power transformer based on the measurement of anisotropic magnetostriction of highly grain-oriented electrical steel sheet," IEEE Trans. Magn., vol. 52, no. 3, pp. 1-4, Mar. 2016, Art. no. 6100304. [3] Z. Wang, Y. Zhang, D. Zhang, D. Xie, C.-S. Koh, and O. A. "Modelling of magnetostrictive property of electrical steel sheet under vectorial excitation," IEEE Trans. Magn., vol. 55, no. 6, pp. 1-4, Jun. 2019, Art. no. 7300304.

AD-09. Optimized Magnetic Hysteresis Management for Electromagnetic Space Discretization Simulation Tool.

P. Fagan^{1,2}, B. Ducharme^{2,3} and A. Skarlatos¹

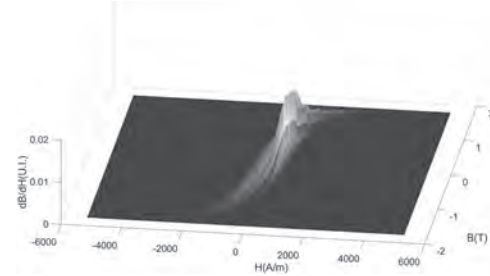
1. CEA – DISC, CEA-LIST, CEA Saclay Digiteo Labs, Saclay, France;

2. LGEF INSA Lyon, Villeurbanne, France; 3. ELYTMAX UMI 3757, CNRS – Université de Lyon – Tohoku University, International Joint Unit, Tohoku University, Sendai, Japan, Sendai, Japan

The treatment of hysteresis models in the numerical solution of Maxwell equations represents major issues as large computational times and significant memory space allocations are required [1][2]. Stability issues of the iterative solution are also a non-negligible source of concern. The Jiles-Atherton (J-A) [3] and the Preisach models [4] are the most used and commented hysteresis models. On the one hand, memory management in the Jiles-Atherton model is simple but convergence often goes through large temporal discretization. On the other hand, Preisach model can work with a limited time discretization but it requires huge memory space and complex memory management. In [5][6], authors proposed an interesting way to take into account hysteresis solving both the J-A and the Preisach models issues. Hysteresis is taken into account through the following hypothesis: the slope dB/dH (reciprocally dH/dB) inside and over the major hysteresis loop envelope is supposed to be dependent on only three parameters: the magnetic excitation field H , the magnetic induction field B , the sign of the time derivation of the model input (B or H). Based on this simple assumption, a new way to take into account the quasi-static scalar hysteresis for ferromagnetic materials was described. This new method also called DSHM for “Derivative Static Hysteresis Model” is an elegant alternative technique, it can be implemented with a simple memory management and reduced memory allocation demands in respect to more classical approaches. Convergence and precise simulation results can be reached with a relatively coarse temporal discretization. This hysteresis taken into account is also easily reversible (from $B(H)$ to $H(B)$) and easily exportable. Fig. 1 – Illustration of the DSHM matrix. Up to now, the filling step of the DSHM matrix (Fig. 1) has always been through a set of experimental first-order reversal curves (as illustrated in [5]). It is evident that getting such experimental results can be complicated in particular situations, including electromechanical converters design or electromagnetic nondestructive testing but in this study we propose to fill the DSHM model’s matrix with a reduced number of experimental data thanks to assumptions also used to parameter the Preisach and the Jiles-Atherton models. The principles of the new method can be detailed as follows: _ The Preisach or the J-A models are implemented first. It implies to determine an adequate combination of parameters for the J-A model or an adequate triangle density for the Preisach model. Such implementation can be done with a limited number of experimental results (a single major hysteresis cycle in the extreme case). _ Reversal curves are plotted numerically using the classic hysteresis models. _ The numerical reversal curves are used to fill the DSHM matrix. The DSHM model provides correct simulation results even under unsymmetrical waveform situations. Implemented in a nonlinear dynamic finite differences numerical scheme for the resolution of the magnetic field diffusion through the cross section of a magnetic lamination [7][8], it allows considerable speed-up of the simulation process while conserving very reasonable level of accuracy. To summarize: the hysteresis law is considered in a generalized input vector space, in which an interpolation matrix is constructed with the columns and rows denoting respectively the discrete values of H and B and whose values stand for the dB/dH (reciprocally dH/dB) slope at the corresponding points. In the end of this study, the resolution of the non-linear magnetic field diffusion through a ferromagnetic lamination is chosen as a benchmark simulation. It allows to compare the performances of space discretized based numerical solvers and to confirm the improved efficiency of the proposed method versus the J-A and the Preisach ones.

[1] P. Zhou & al., IEEE Trans. On Mag. Dev., vol. 40, Iss. 4, pp. 1803 – 1809, (2004) [2] B. Ducharme & al., J. Phys. D: Appl. Phys., Vol. 40, pp. 551-555, (2007) [3] D.C. Jiles & al., J. App. Phys. 55, pp. 2115, (1984) [4] Y. Bernard & al., vol. 25, Iss. 1-4, pp. 729-733, (2007) [5] R. Scorretti & al., proceedings of compumag 2011, 8. Mat. modelling, 11. Num. techniques, (2011) [6] T-P Do & al. & al., proceedings of compumag 2009, (2009)

[7] B. Gupta & al., IEEE Trans. on Mag., Vol. 54, Iss. 3, (2018) [8] M. A. Raulet & al., IEEE Trans. on Mag., vol. 40, n° 2, pp. 872 – 875, (2004)



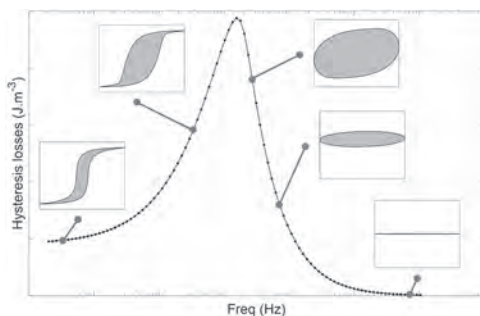
AD-10. Ferromagnetic Hysteresis Model Using Fractional Derivative Resolution Developed for the Simulation of Viscoelastic Phenomena.

B. Ducharne^{1,2} and G. Sebald¹

1. ELYTMAX UMI 3757, CNRS – Université de Lyon – Tohoku University, International Joint Unit, Tohoku University, Sendai, Japan, Sendai, Japan;
2. LGEF INSA Lyon, Villeurbanne, France

Ferromagnetic materials are used in a wide range of electromagnetic applications (energy converters, sensors, inductances ...). Ferromagnetic materials are characterized by a strong answer under the influence of a magnetic field [1]. These properties are of huge advantages in many applications but they are also strongly non-linear and frequency dependent. In this domain, we observe a growing interest in the development of simulation tools reducing the experimental campaigns and improving the knowledge and the performances. Accurate simulation results can only be obtained by coupling precise electromagnetic equations to the exact material laws (hysteresis, saturation, frequency dependence). Under the influence of an external magnetic excitation, the local magnetic state through the ferromagnetic specimen is ruled by the combination of both the magnetic domain kinetics and the external magnetic field diffusion. Fig. 1, Illustration of the ferromagnetic hysteresis frequency dependence. The usual methods for the simulation of the magnetic behavior are all based on the separation of the magnetic contributions, where the microscopic Eddy currents due to the domain wall motions and the macroscopic ones due to the external magnetic field variations are considered separately [2]. This separation remains artificial, since practically both losses mechanisms occurs simultaneously and interact on each other. Alternative solutions for the simulation of these phenomena have already been proposed through the resolution of an anomalous fractional magnetic field diffusion (1, 2 or 3D depending on the experimental situation) [3][4]. The fractional order constitutes an additional degree of freedom in the simulation scheme. It is identified through comparisons to experimental results. By adjusting precisely this order, very accurate local and global simulation results can be obtained on a very broad frequency bandwidth [5]. It allows to predict precisely the dynamic magnetic behavior of classic ferromagnetic components. Fractional diffusion equation is an interesting method but this is not the only way to take into account the hysteresis frequency dependence using fractional derivative operators. Lump models based on time fractional differential equations is another option [6][7]. In both methods (the fractional diffusion equation and the time fractional differential equation), a numerical resolution of the Riemann-Liouville definition is required. Recent works have demonstrated the effectiveness of using quadrature techniques to approximate the Riemann-Liouville definition for fractional derivatives in the context of nonlinear viscoelastic model [8]. In this manuscript, the quadrature methods are implemented and tested in the case of the ferromagnetic hysteresis. Theoretical results are compared to experimental ones, and conclusions and perspectives are drawn such as possible improvements.

[1] R. M. Bozorth, Wiley-IEEE Press, Michigan University, (1993) [2] G. Bertotti, IEEE Trans. Magn., vol. 24, iss. 1, pp. 621-630, (1988) [3] B. Ducharne & al., Com. in Nonlin. Sci. and Num. Sim., vol. 92, 105450, (2020) [4] B. Ducharne & al., The Eur. Phys. J. Plus, 135:325, (2020) [5] B. Ducharne & al., under revision, AIP advances, (2021) [6] B. Zhang & al., IEEE Trans. Magn., Iss. 99, pp. 1-5, (2018) [7] B. Zhang & al., IEEE Trans. Magn., Vol. 54 iss. 3, (2017) [8] P.R. Miles & al., J. Int. Mat. Syst and Struct., (2020)



Session AE**MICROMAGNETIC MODELLING**

Daria Gusakova, Co-Chair

SPINtronique et Technologie des Composants, Grenoble, France

Joo-Von Kim, Co-Chair

Université Paris-Saclay, Palaiseau, France

INVITED PAPER

AE-01. Dzyaloshinskii Domain Wall Creep INVITED.

V.M. Sokalski¹*1. Materials Science & Engineering, Carnegie Mellon University, Pittsburgh, PA, United States*

The discovery of a significant interfacial Dzyaloshinskii-Moriya Interaction (iDMI) in multi-layer thin films launched a fervent research effort into its impact on the behavior of chiral magnetic objects including domain walls (DWs).[1] The field driven creep of these Dzyaloshinskii domain walls as observed by Kerr microscopy remains a popular tool for evaluating the strength of the iDMI, but results are notoriously challenging to interpret. In this talk, we focus on experimental and theoretical investigations into the asymmetric field-driven expansion of magnetic domains in thin films with iDMI, which provide a fascinating landscape to understand creep of 1D elastic manifolds with an internal order parameter.[2] We will review early models of creep based on the DW energy, which matched well with certain experimental observations – namely, that an in-plane field (H_x) coupled with a perpendicular driving field (H_z) leads to asymmetric expansion of the domain as well as minima in the plot of x-velocity vs H_x . However, other common observations were not explained by this model including that, at large values of H_x , the high energy wall orientations reached or exceeded the velocity of low energy orientations. To explain this, Pellegren et al considered the more general elastic energy of the DW, given by the stiffness $[\sigma(\theta) + \sigma''(\theta)]$. [3] By introducing a dispersive stiffness, which accounts for the finite lengthscale over which the wall deforms, it was indeed shown that the elastic energy of opposite extrema on the domain converge as $H_x \rightarrow \infty$. This more general model explains some of the features that have also been explained by an attempt frequency that depends on wall chirality (via a chiral damping parameter).[4] The possible role of chiral damping will be discussed briefly. In more recent experiments, Brock et al showed that, in some cases – especially for weak DMI, the domain adopts a highly preferred growth direction with a dendritic structure that is neither parallel or anti-parallel to H_x . [5] The results cannot be explained by a chiral Bloch component to the DW, which would violate the symmetry of the system. Instead, we identify a steady-state DW substructure that results from the z-field torque on the internal DW magnetization (see figure 1c). This breaks the energetic mirror symmetry along the x-axis and leads to orientations of the DW with vanishing elastic energy (i.e. rapidly increased creep velocity). Remarkable agreement between an augmented form of the dispersive stiffness model (now accounting for steady-state configurations) and the experimental measurements is found. The material parameters that give rise to this seemingly anomalous behavior will be discussed. Other important factors such as internal DW excitations, field-dependent pinning, and a field-dependent DW width will be considered in this presentation as well.

[1] Thiaville, A., Rohart, S., Jué, É., Cros, V. and Fert, A., 2012. Dynamics of Dzyaloshinskii domain walls in ultrathin magnetic films. *EPL (Europhysics Letters)*, 100(5), p.57002. [2] Fournier, J. B. "Generalized gibbs-thomson equation and surface stiffness for materials with an orientational order parameter." *Physical review letters* 75.5 (1995): 854. [3] Pellegren, J.P., Lau, D. and Sokalski, V., 2017. Dispersive stiffness of Dzyaloshinskii domain walls. *Physical Review Letters*, 119(2), p.027203. [4] Jué, E., Safeer, C.K., Drouard, M., Lopez, A., Balint, P., Buda-Prejbeanu, L., Boule, O., Auffret, S., Schuhl, A., Manchon, A. and Miron, I.M., 2016. Chiral damping of magnetic domain walls. *Nature materials*, 15(3), pp.272-277. [5] Brock, J., Medapalli, R. and Fullerton, E., 2020. Chirality-driven growth of stripe domains in Co/Ni/Pt-based multilayers. *Bulletin of the American Physical Society*, 65.

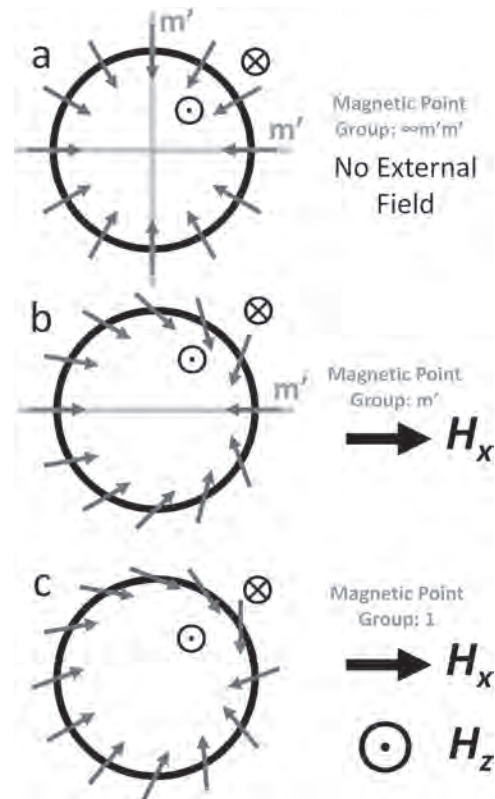


Fig 1. Schematic of a Néel bubble subject to external magnetic field. Arrows indicate the direction of internal magnetization along the circumference. Green lines indicate time-reversal mirror planes, m' . a) No external field. Magnetic point symmetry: $\infty m' m'$. b) H_x only. Magnetic point symmetry: m' . c) H_x and H_z field. Magnetic point symmetry: 1.

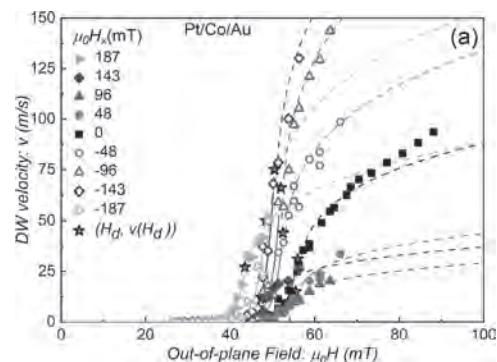
CONTRIBUTED PAPERS

AE-02. Interaction of Chiral Domain Walls With Pinning Disorder in Thin Ferromagnetic Films.V. Jeudy¹, P. Géhanne¹, S. Rohart¹ and A. Thiaville¹¹. Laboratoire de Physique des Solides, Orsay, France

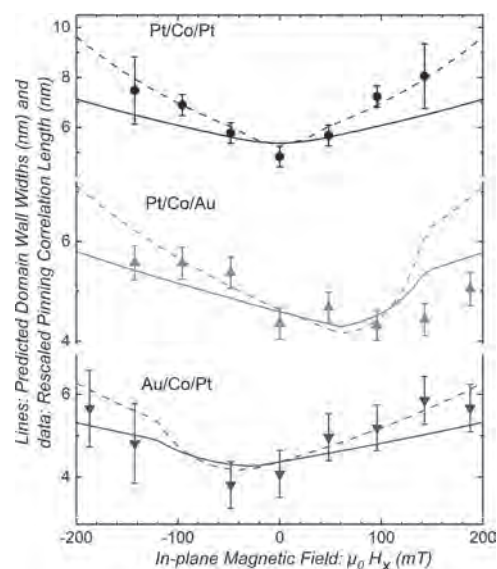
Abstract. Despite numerous recent studies focusing on the dynamics of pinned chiral magnetic textures [1-6], their interactions with weak pinning disorder is far from being understood. Basic issues such as the length-scale and the strength of interaction between domain walls (DWs) and defects in magnetic materials remain open. Our works [7] evidence a strong correlation between controlled variations of DW width and the characteristic length of pinning. The DW-disorder interaction strength is also shown to depend on DW energy and width. These findings should be also relevant for a wide variety of elastic interfaces moving in weak pinning disordered media. We explore the magnetic field-driven motion of domain walls with different chiralities in thin ferromagnetic films made of Pt/Co/Pt, Au/Co/Pt, and Pt/Co/Au. The displacement of DWs was observed by polar Kerr microscopy. An in-plane magnetic field H_x was used to control the magnetization direction in the DW, as well as its width. A pulse out-of-plane field H was used to move DW. The measured velocity corresponds to the ratio between the measured DW displacement and the pulse duration. The velocity curves obtained for Pt/Co/Au with different values of H_x are reported in Fig. 1. Their analysis with the self-consistent description of the universal creep and depinning regimes [8] was used to extract parameters (depinning field H_d and temperature T_d) characterizing the interaction between domain wall and weak random pinning disorder of the films. Surprisingly, the values of H_d and T_d vary (not-shown) with the in-plane magnetic field H_x , which strongly suggests that the pinning properties of DWs depend on their magnetic texture, in contrast to the usual assumption found in the literature [1-6]. To predict accurately the variation of DW energy and structure with in-plane and DMI fields, we have calculated the orientation of the magnetization $M(x)$ for a DW plane perpendicular to H_x , from numerical micromagnetic calculations (MuMax3), using the micromagnetic parameters of the three samples (not-shown). For the DW width, we both use the geometrical Hubert and dynamic Thiele definitions. Upon varying H_x away from the magnetic field H_{DMI} associated to the Dzyaloshinskii-Moriya interaction (DMI), the magnetization within the DW progressively switches from Bloch to Néel configuration, and the DW width increases due to the Zeeman contribution, as expected. The DW surface energy decreases as H_x departs from H_{DMI} , in qualitative agreement with the predictions of simplified models [3-5]. In order to discuss the DW pinning at microscopic scale as a function of in-plane field H_x , we use standard scaling arguments [8] based on the variation of the energy produced by the deformation of a DW. The DW energy is assumed to be controlled by the gain of Zeeman energy due to magnetization reversal, the elastic energy produced by the increase of DW length, and the pinning energy due to the fluctuations of DW energy produced by the weak disorder. From scaling arguments, we obtain the relations which link the characteristic range and force of the interaction between DW and pinning defects, to the measured depinning field $H_d(H_x)$, temperature $T_d(H_x)$, and the predicted DW surface energy. For a comparison (see Fig. 2) with the predicted variations of the DW width, the values of the pinning range were rescaled with a constant factor, which is the only adjustable parameter. As it can be observed, there is a strong correlation between the variations of the pinning range and the DW width. This strong correlation suggests that the variations of domain wall structure, controlled by an in-plane field, modify the characteristic lengthscale of pinning, whatever the DW chirality and the interaction strength between domain wall and pinning defects.

[1] S.-G. Je, D.-H. Kim, et al., Phys. Rev. B 88, 214401 (2013). [2] R. Lavrijsen, D. M. F. Hartmann, et al., Phys. Rev. B 91, 104414 (2015). [3] D. Lau, V. Sundar, et al., Phys. Rev. B 94, 060401 (2016). [4] J. P. Pellegren, D. Lau, and V. Sokalski, Phys. Rev. Lett. 119, 027203 (2017). [5] D. Lau, J. P. Pellegren, et al., Phys. Rev. B 98, 184410 (2018). [6] D. M. F. Hartmann, R. A. Duine, et al., Phys. Rev. B 100, 094417 (2019). [7] P. Géhanne, S.

Rohart, A. Thiaville, and V. Jeudy, Phys. Rev. Res. 2, 043134 (2020). [8] V. Jeudy, R. Diaz Pardo, et al., Phys. Rev. B 98, 054406 (2018).



Domain wall velocity versus out-of-plane magnetic field measured for a Pt/Co/Au film and different values of the in-plane field. The solid and dash lines are predictions for the creep and depinning regimes. The stars correspond to the coordinates of the depinning thresholds $H_d(H_x)$.



Domain wall widths (Hubert: solid line) and (Thiele: dash line), and correlation length of the pinning versus in-plane magnetic field for the three films. For each film, the correlation length was rescaled to highlight its strong correlation with the DW widths.

AE-03. On Dynamics of Domain Walls With Internal Degrees of Freedom.*L. Laurson*¹*1. Tampereen Yliopisto, Tampere, Finland*

I will present an overview of our recent results on modelling field-driven dynamics of domain walls in ferromagnetic thin films and strips with perpendicular magnetic anisotropy, focusing on the effect of internal degrees of freedom on the domain wall dynamics. In the geometries considered, the dynamics associated with the internal degrees of freedom are given by that of the magnetisation at the domain wall mid-point, and is manifested as repeated nucleation, propagation and annihilation of topological defects known as *Bloch lines* within the moving domain wall. Our aim is to understand the effect of such internal dynamics on the large-scale dynamics of domain walls. First, I will discuss micromagnetic simulations of magnetic field-driven domain wall dynamics in thin ferromagnetic strips with perpendicular magnetic anisotropy which demonstrate that in wide enough strips the *Walker breakdown* - the sudden drop of domain wall velocity as the field is increased above the Walker field - is a multistep process: It consists of several distinct velocity drops separated by short linear parts of the velocity vs field curve. These features originate from the repeated nucleation, propagation, and annihilation of an increasing number of Bloch lines within the domain wall as the driving field magnitude is increased [1]. Second, I will consider micromagnetic simulations of Barkhausen noise in disordered Pt/Co/Pt thin films due to precessional motion of domain walls. In this regime the domain walls contain Bloch lines which repeatedly nucleate, propagate, and annihilate within the domain wall during the Barkhausen jumps. In addition to bursts of domain wall propagation, the in-plane Bloch line dynamics within the domain wall exhibits crackling noise and constitutes the majority of the overall spin rotation activity [2]. Finally, I will present our very recent work on developing a reduced model of line-like domain walls in thin films with perpendicular magnetic anisotropy including a description of internal degrees of freedom, i.e., Bloch lines and their dynamics. The model, which is computationally much more efficient than full micromagnetic simulations, is applied to study the depinning transition of field-driven domain walls in disordered ferromagnetic thin films [3].

[1] J. Hütner, T. Herranen, and L. Laurson, Phys. Rev. B 99, 174427 (2019).

[2] T. Herranen and L. Laurson, Phys. Rev. Lett. 122, 117205 (2019). [3] A.

Skaugen and L. Laurson, in preparation (2020).

AE-04. Micromagnetics of Frustrated States and High-Frequency Modes in Artificial Buckyball Nanostructures.

R. Cheenikundil¹ and R. Hertel¹

1. Institut de Physique et Chimie des Matériaux de Strasbourg, Centre National de la Recherche Scientifique, Strasbourg, France

With recent advancements in fabrication techniques, in particular through FEBID technology, three-dimensional (3D) nanomagnetism has emerged as a new field of interest [1]. Over the past decades, extensive studies on patterned two-dimensional thin-film elements have demonstrated that the properties of magnetic nanostructures are significantly affected by their shape, such that certain magnetic features can be generated and modified by changing the geometry. Following this principle, the access to an additional degree of freedom in 3D nanomagnetism can introduce new effects unknown in planar structures and may open up possibilities for new devices with artificially designed properties [2]. In this context, a promising category of novel nanomagnetic nano-architectures with remarkable potential for applications are 3D arrays of interconnected magnetic nanowires. The assembly of magnetic nanowires into an interconnected array can lead to interactions and magnetic structures with features known from artificial spin ice (ASI) lattices. A particular micromagnetic situation occurs at the intersections of the wires, where the magnetization must adapt to a change of both the geometry and the magnetization direction. At the vertices, characteristic magnetic configurations and phenomena of magnetic frustration unfold. Here we show that these frustrated states can strongly impact the overall properties of a bucky-ball type geometry, which can be considered a prototype of a 3D ASI. Using finite-element micromagnetic simulations, we investigate the hysteretic behavior, the static magnetization structure, and the high-frequency properties of the magnetization in artificial buckyball-type nanostructures. The buckyball geometry [3, 4] acts as a model system to study the transition from two-dimensional to three-dimensional ASI structures. It has, on one hand, important similarities with a two-dimensional Kagomé lattice, while, on the other hand, it also incorporates distinct three-dimensional properties resulting from the spatial arrangement of the nanowires and the spherical shape of the network that they form. The geometry consists of 90 nanowires connected at 60 vertices, resulting in a closed network of hexagons and pentagons. Our model system is made of soft-magnetic Co, and its size is typically in the micron range. More specifically, we have investigated various buckyball-type geometries with individual nanowire lengths ranging between 25 nm and 250 nm. At zero field, the static magnetization structure of the magnetic bucky-balls is characterized by their configurations at the vertices. Due to the prevailing impact of shape anisotropy, each nanowire is magnetized along its axis. Based on the orientation of the magnetization in the three nanowires meeting at a vertex, the magnetic structures at the vertices can be classified into four types: two-out / one-in, two-in / one-out, three-out, and three-in. A specific magnetic charge, +1, -1, +3 and -3, can be assigned to each of these configurations, as is done in Kagomé lattices [5]. Neglecting the sign of the charges, one can distinguish between ice-rule obeying single-charge and defect-like triple-charge configurations. By means of hysteresis loop simulations, we find that triple-charged vertices can be created and removed through minor loops: If the field is reduced to zero from saturation, two triple-charge vertex configurations form at diametrically opposite sites. These triple charge defects dissolve after applying a moderate negative field, and they do not reappear if the field is subsequently removed again. Hence, we show that in these 3D ASI geometries, it is possible to inject and to remove magnetic triple-charge defect structures in a controlled way by varying the external magnetic field within a specific range. Going further in the study, we analyze the fundamental high-frequency modes of the magnetization in these geometries and their dependence on the magnetic structure. To extract the modes, the equilibrium states at zero field are excited by a picosecond field pulse, leading to a magnetic ringing over several nanoseconds. From these high-frequency dynamics, the magnetic modes are derived by using spatially-resolved windowed Fourier analysis [6]. We observe a distinct correlation between the distribution of magnetic charges at the vertices and the frequency of the modes. The modes can be distinguished as oscillations that are localized either at the vertices or within the nanowires. In particular, we find that the dynamics of the triple-charge states is very different from the dynamics at the single-charge

vertices. The triple-charge states generate a strong, often dominating signal at low frequencies, which is absent in configurations without triple-charge defects. Moreover, we show that the frequency of this mode can be varied in an almost linear fashion by an external magnetic field. The combination of this feature with the particular hysteretic properties of the system opens a promising perspective to develop tailored devices with desired high-frequency properties that can be manipulated by varying the type of magnetic frustrations.

[1] A. Fernández-Pacheco et al., Nat Commun 8, 15756 (2017) [2] P. Fischer et al., APL Materials 8, 010701 (2020) [3] L. Keller and M. Huth, Beilstein J. Nanotechnol. 9, 2581 (2018) [4] C. Donnelly et al., Phys. Rev. Lett. 114, 115501 (2015) [5] F. Montaigne et al., Sci. Rep. 4 : 5702 (2014) [6] M. Yan, R. Hertel, C. M. Schneider, Phys. Rev. B 76, 094407 (2007)

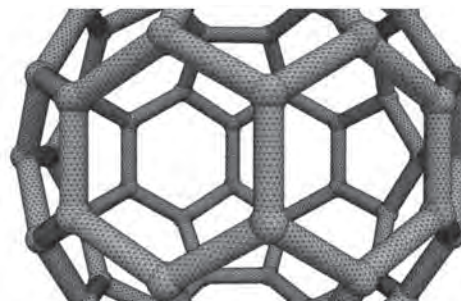


Fig. 1: Finite-element discretization of a 3D buckyball-type nanostructure. Depending on the buckyball size, we use up to 1.9 million elements.

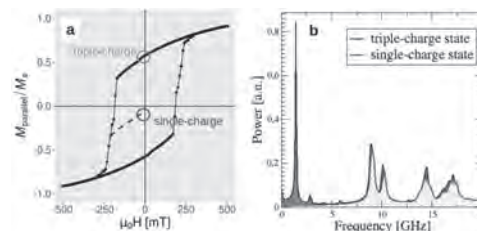


Fig. 2: a) Different zero-field configurations can be accessed through hysteresis loops and minor loops, in particular the triple-charge state and the single-charge state. b) Simulated Fourier spectrum of the magnetic modes of the triple-charge and single-charge state.

AE-05. Micromagnetic Modelling of Ferro-, Ferri-, and Antiferromagnetic Materials.

L. Sánchez-Tejerina^{1,2} and V. Puliafito³

1. Department of Mathematical and Computer Sciences, Physical Sciences and Earth Sciences, Università degli Studi di Messina, Messina, Italy;

2. Department of Biomedical, Dental, Morphological and Functional Imaging Sciences, Università degli Studi di Messina, Messina, Italy;

3. Department of Engineering, Università degli Studi di Messina, Messina, Italy

The manipulation of magnetic textures in ferromagnets (FM) has been the focus of intense research in recent years. More recently, this focus has been displaced towards the use of antiferromagnets (AFM), and ferrimagnets (FiM), which are more robust against external perturbation and can sustain faster magnetization dynamics. In this context, simplified models have been proved very useful to describe and clarify the phenomenology on FM [1], AFM [2], and FiM [3] materials giving in some cases also good quantitative predictions. Nevertheless, AFM and FiM are described by two sublattices strongly couple through an exchange interaction while FM are described by only one magnetic lattice. In order to recover the FM case from the FiM description, one needs not only to set the second sublattice magnetization to zero but also its corresponding energy densities. It is possible to describe all these cases in a unified framework by a simple renormalization of the energy densities to the squared of the sublattices magnetization modulus. To give an example, considering K_{u1} and K_{u2} the common uniaxial anisotropy parameters, we substitute them by $k_{u1}*(M_{S1})^2$ and $k_{u2}*(M_{S2})^2$ respectively. This procedure is followed for all the energy density terms and included in Petaspin micromagnetic solver [4]. Here, we focus on the statics and dynamics of domain walls (DWs) when excited by spin-orbit torque (SOT). Regarding the static states of AFM, we show that as in FM, AFM also may exhibit periodic patterns due to the interfacial Dzyaloshinskii-Moriya interaction (iDMI) [5]. In this case, the ‘effective’ inhomogeneous exchange accounting for the two intralattice inhomogeneous exchange contributions and the one interlattice inhomogeneous exchange plays the role of the exchange interaction in FM. Correspondingly, the ‘effective’ iDMI to consider is the sum of the iDMI parameter of the two sublattices. Additionally, we show that similarly to FM, iDMI promotes the nucleation of new domains at the edges of and AFM strip even for moderate current densities [6]. Differently from FM, in AFM this effect is more efficient due to the robustness of the Néel DW against SOT excitation dynamics. This effect is one of our main results since it could limit the maximum DW velocity in and AFM racetrack memory because the nucleation of new domains would change the stored information, thus limiting the maximum current density that can be applied. We have also compared full micromagnetic simulations with a collective coordinates (CC) model which also includes the DW width changes due to the SOT and the spatial tilting of the domain wall [7] for different saturation magnetization ratios. The CC model properly predicts the domain wall width at equilibrium. On the other hand, when the magnetic texture is excited by a current through the SOT we can find three scenarios: (i) when the exchange and anisotropy parameters are larger enough, the DW dynamics can be described by the CC model even if we neglect the DW tilting and width variation. When we neglect these effects we talk about the ‘rigid CC model’. (ii) The cases where the exchange is lower but the anisotropy is large enough cannot be properly described by the rigid CC model. In these cases, the effect of the tilting and the DW width reduced the stationary DW velocity and, thus, they should be taken into account to describe the dynamics. This is shown in Fig. 1 where the solid linear line corresponding to the rigid CC model cannot predict the stationary DW velocities from the full micromagnetic simulations. Nonetheless, the dashed line corresponding to the CC model follows the saturation of the velocity due to the DW tilting. (iii) For low anisotropy parameters the excitation of self-oscillation threshold can be found for moderate current densities (red line in Fig. 2). We observe that before this threshold, where the Gilbert damping is almost compensated by the antidamping term induced by the SOT, the DW velocity increases faster than the usual linear trend being able to reach much larger velocities. Neither the rigid CC model nor the CC model can describe this effect and these cases required a full micromagnetic approach. From a fundamental point of view, this super-linear trend is another of our main results. The

threshold current for self-oscillations depends on the anisotropy [8] which can be tuned, opening a path to exploit the super-linear DW mobility under moderate current densities.

[1] S. Emori, U. Bauer, S.-M. Ahn, *et al.*, Nat. Mater., Vol. 12, 611 (2013).
 [2] H. V Gomonay and V. M. Loktev, Phys. Rev. B, Vol. 81, 144427 (2010).
 [3] L. Sánchez-Tejerina, *et al.*, IEEE Magn. Lett., Vol. 11, 2505005 (2020).
 [4] A. Giordano, G. Finocchio, L. Torres, *et al.*, J. Appl. Phys., Vol. 111, 07D112 (2012). [5] R. Tomasello, *et al.*, Phys. Rev B, Vol. 102, 224432 (2020) [6] L. Sánchez-Tejerina, *et al.*, Phys. Rev. B, Vol. 101, 14433 (2020). [7] E. Martinez, S. Emori, N. Perez, *et al.*, J. Appl. Phys., Vol. 115, 213909 (2014). [8] V. Puliafito, R. Khymyn, M. Carpentieri, *et al.*, Phys. Rev. B, Vol. 99, 024405 (2019).

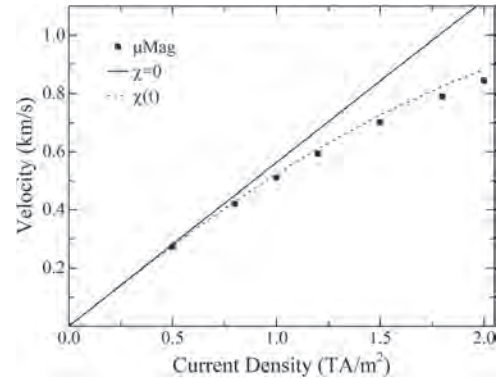


Fig. 1 Domain wall velocity near the angular momentum compensation point as a function of the current density for a case with low exchange and large anisotropy. Dots stand for full micromagnetic simulations, solid lines for the rigid domain wall model, and the dashed line for the non-rigid domain wall model.

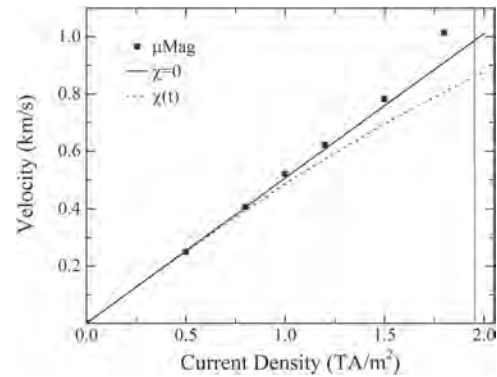


Fig. 2 Domain wall velocity near the angular momentum compensation point as a function of the current density for a case with low exchange and low anisotropy. Dots stand for full micromagnetic simulations, solid lines for the rigid domain wall model, and the dashed line for the non-rigid domain wall model.

AE-06. Micromagnetic Simulations of Artificial Spin ice Lattices and Vertices.

L. Connell^{1,2}, K. Esien¹ and S. Felton¹

1. School of Maths and Physics, Queen's University Belfast, Belfast, United Kingdom; 2. University of Glasgow, Glasgow, United Kingdom

Research into geometrical frustration over the past two decades has revealed fundamentally new exotic behavior [1]. The magnetic interactions of the structure, coupled with the specific geometry causes frustration in the system, referred to as artificial spin ices. Several geometries exist, but for the purpose of this research, the kagome arrangement was used. In general, the geometry of these frustrated systems follows the ice rule, that being two interacting moments point in while two point out. The kagome however follows the modified ice rule of two moments pointing in while one points out or vice versa. These systems appear as 2D analogues to the 3D structure and it is the lattice configuration along with the specific frustration created that causes these exotic behaviors. Presented here are the magnetoresistances obtained for kagome magnetically frustrated systems in a single vertex and lattice format. Both geometries are compared in a magnetically connected format and a magnetically disconnected format in order to observe the exchange and dipolar energies. The structures were simulated with parameters for permalloy, using BORIS [2], and dimensions of $1\mu\text{m}$ long, 100nm wide and 10nm thick. The aim was to evaluate the magneto resistance, which was done assuming the current density aligns with the long axis and a basic resistor network. By comparing the simulated data for the connected and disconnected single vertex with the measurements taken previously for a lattice, a greater understanding of the effect of the disconnected versus connected structures can be achieved. Measurements of the kagome lattice showed that the disconnected lattice had a change in magnetoresistance that was 2-3 times greater than the connected lattice, experimentally. The simulations of the single vertex's magnetoresistance differ by approximately an order of magnitude to those of the experiments. While the simulations are not for the full lattice, they shed some light on the experimental results obtained and the single vertex interactions that occur within the lattice. The simulation of the hybrid vertex appears to mirror that of the experimental data obtained for the hybrid lattice while the simulation of the connected vertex appears to differ somewhat from the experimental data obtained for the connected lattice. This highlights the implications of the experimental work in that the connected kagome has more complex interactions throughout the lattice while the magnetically disconnected hybrid is rather a simplified system. The subtle difference in the geometries of the connected and disconnected lattices aids in the explanation of the effects and interplay of both the spin structures and the current density. This work demonstrates the potential for using simulations to expose magnetic interactions in a lattice type structure and other interesting geometries, along with the enhanced magnetoresistance signals that were obtained.

References [1] Nisoli, C., Moessner, R., & Schiffer, P. (2013). Colloquium: Artificial spin ice: Designing and imaging magnetic frustration. *Reviews of Modern Physics*, 85(4), 1473. [2] Lepadatu, Serban. (2019). Boris Computational Spintronics User Manual.

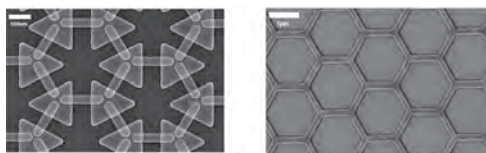


Figure 1. SEM images of an electrically connected but magnetically disconnected (hybrid) lattice (left). Also shown is the standard honeycomb lattice for comparison.

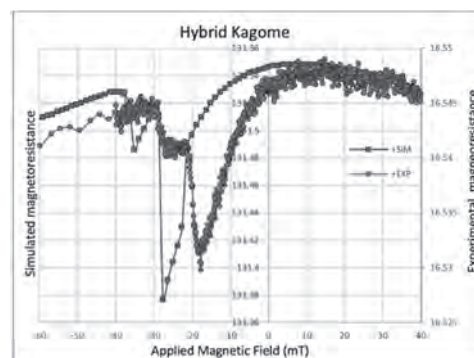


Figure 2: Simulated single vertex and experimental lattice for the magnetically disconnected, electronically connected (hybrid) kagome plotted against the applied magnetic field. Data shown is the positive part of a full sweep of the magnetic field i.e. from a positive applied field through to the negative of the same applied field.

AE-07. Concentric Target Domains in Magnetic Nanodisks.

R. Morel¹, S. Ponomareva¹, H. Joisten², S. Philippe¹ and B. Dieny¹

1. Univ. Grenoble Alpes, CNRS, CEA, Grenoble INP, SPINTEC, 38000, Grenoble, France, Grenoble, France; 2. Univ. Grenoble Alpes, CEA, LETI, 3800 Grenoble, France, Grenoble, France

The micromagnetic configuration of a ferromagnetic sample results from the balance between different energy terms, in particular the magnetic anisotropy, the exchange energy and the magnetostatic energy. A very large variety of domain structures is observed depending on the intrinsic properties of the ferromagnetic material (anisotropy, exchange, spontaneous magnetization) and on its shape. Of particular interest are domains presenting a cylindrical symmetry that appear in thin films or patterned cylindrical micro/nanostructures. As examples, magnetic bubble domains have been extensively studied in micron-thick rare-earth orthoferrites films where they were considered for magnetic recording applications. A theory linking the static stability of these structures to both the material properties and sample geometry was developed, highlighting the requirement that the uniaxial anisotropy must overcome the stray field energy in order to stabilize the bubble. Stable cylindrical target domains have also been observed in a variety of patterned magnetic thin films, characterized by multiple nested concentric magnetic rings. Such micromagnetic configurations have been reported in systems with out-of-plane magnetization such as high magnetic anisotropy Co and FePt films [1] or perpendicular anisotropy multilayers [2,3], as well as in low anisotropy NiFe and Ni films [4,5] in which the magnetization is mostly in-plane with a weak out-of-plane component. Several numerical simulation studies have been undertaken to investigate these magnetic configurations [1-3,5-7]. Most of these simulations assumed the presence of a strong perpendicular anisotropy. Numerical simulations with low anisotropy systems have received less attention [4,5], and still require to consider a rather large perpendicular uniaxial anisotropy - attributed to built-in magnetostriction or resulting from a columnar grain structure [8] - to explain the formation of bubble or target domains. In this paper, we present experimental and numerical results obtained on patterned micron-size permalloy disks showing magnetic target domains. We conducted a thorough investigation of the evolution of the magnetic structure as a function of the Py thickness. Arrays of microdisks were patterned by optical lithography, e-beam evaporation and lift-off step. Disks diameter is constant at 1.3 μm and the thicknesses was varied from 90 nm to 400 nm. The MFM imaging of the remanent magnetization for disks in the as deposited state are shown in Figure 1. Thinner disks exhibit the expected vortex structure (Fig. 1a, b). For thicker disks, imaging reveals a structure with spiraling or concentric ring domains with alternating, up and down, perpendicular component of the magnetization (Fig. 1c - 1h). Micromagnetic numerical simulation have been carried out where we consider that the disks exhibit a columnar magnetic grain structure with variable inter-grain coupling and, in contrast with previous calculations, no contribution from magnetocrystalline or intrinsic uniaxial anisotropies. In our case, the inter-grain coupling intensity σ allows for the modulation of the demagnetizing field energy, giving rise to various magnetic configurations that will be described in details (Fig. 2). It is found that, for the thinnest disks, despite the columnar structure, the most stable magnetic structure is the vortex structure. Above a critical thickness the lowest energy structure evolves into a target domain structure, with a number of concentric domains that decreases as the thickness increases. It is also observed that, in addition to the target structure, less symmetrical spiral or disordered metastable structures can be observed. These observations closely match the experimental results for disks with similar aspect ratio, indicating that, together with σ , these are the two governing parameters in this case. We will also present details of the different energy contributions and describe the internal structure of the magnetization. This model based on a columnar texture of the film constitutes an alternative to explain the formation of target domain structures without relying on the existence of a perpendicular anisotropy difficult to justify in materials such as permalloy.

[1] C. Moutafis, S. Komineas and C. A. F. Vaz, Phys. Rev. B 76, 104426 (2007). [2] F. Garcia, H. Westfahl and J. Schoenmaker, Appl. Phys. Lett. 97, 022501 (2010). [3] T. Liu, V. Puliafito and F. Montaigne, J. Phys. D: Appl. Phys. 49, 245002 (2016). [4] P. Eames and E. Dan Dahlberg, J. Appl.

Phys. 91, 7986 (2002). [5] G. D. Skidmore, A. Kunz and C. E. Campbell, Phys. Rev. B 70, 012410 (2004). [6] J. K. Ha, R. Hertel and J. Kirschner, Europhys. Lett. 64, 810 (2003). [7] S. Komineas, C. A. F. Vaz and J. A. C. Bland, Phys. Rev. B 71, 060405 (2005). [8] S. Finizio, S. Wintz and D. Bracher, Phys. Rev. B 98, 104415 (2018).

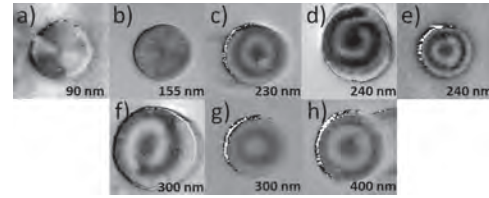


Fig. 1: MFM images of permalloy disks with 1.3 μm diameter, in the as-deposited state, with different thicknesses. (a, b) Vortex structure; (c, e) Four concentric ring domains structure; (d, f) Spiraling domains structure; (g, h) Three concentric ring domains structure.

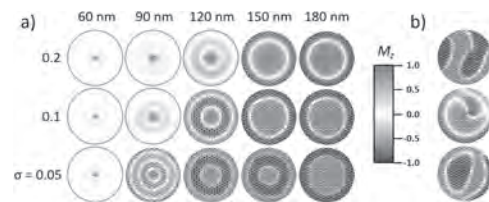


Fig. 2: (a) Calculated magnetic structure in the median plane of the disk (plane at half thickness), as a function of the thickness and σ coupling parameter. (b) Examples of metastable configurations with disordered, spiral or incomplete ring domains, obtained with $\sigma = 0.1$ and 180 nm thickness (top); $\sigma = 0.2$ and 150 nm (middle); and $\sigma = 0.1$ and 150 nm (bottom). The red/blue colors refer to the $\pm M_z$ magnetization component.

AE-08. Micromagnetic Study of Stable Skyrmions in Dot-Patterned Graphene-Based Magnetic Trilayers.

P. Olleros-Rodríguez¹, R. Guerrero¹, J. Camarero^{1,2}, O. Chubykalo-Fesenko³ and P. Perna¹

1. *Fundacion IMDEA Nanociencia, Madrid, Spain*; 2. *Departamento de Física de la Materia Condensada, Universidad Autonoma de Madrid, Madrid, Spain*; 3. *Instituto de Ciencia de Materiales de Madrid, Madrid, Spain*

Recent advances on the stabilization and manipulation of chiral magnetic configurations hosted by systems that consist in alternating atomic layers of ferromagnetic and non-magnetic materials hold promise of innovative spintronic devices. The low dimensionality of the systems promotes spin-orbit driven interfacial effects[1] like the antisymmetric Dzyaloshinskii-Moriya interaction (DMI) and interfacial magnetic anisotropy (iMAE), whose relative strengths may be tuned to achieve stable nanometer sized magnetic objects with fixed chirality called magnetic skyrmions[2], which are proposed as information carriers in future spin-orbitronics technologies. While in most of the cases this is obtained by engineering complex multilayers stacks in which interlayer dipolar fields become relevant[3], we consider here a simple epitaxial trilayer in which a ferromagnet (namely Cobalt, Co), with variable thickness, is embedded between a heavy metal and graphene[4]. The latter enhances the perpendicular magnetic anisotropy of the system, promotes a Rashba-type DMI, and can sustain very long spin diffusion length. The work consists in the development of a layer-resolved micromagnetic model capable to account for the interfacial nature of the interactions[5], which leads to macroscopic parameters that depend on the thickness of the ferromagnetic layer. We demonstrate that our model correctly reproduces the experimental magnetization configurations and the spin reorientation transition (SRT) of a gr/Co(t_{Co})/Pt sample[4]. Next, we study the stabilization of magnetic skyrmions in patterned magnetic nanodots with a diameter of 256 nm. In particular, we analyze the thickness-dependent stability of the skyrmionic state in contrast with a single domain state. Our results demonstrate that, for samples with Co thicknesses larger than 3.6 nm, intrinsic mixed Bloch-Néel (predominantly Bloch-type) skyrmions are stabilized in 256 nm wide dots. For thicknesses larger than ~ 5 nm, the results show that the geometrical confinement imposed by the nanodot promotes the stabilization of chiral spin textures similar to skyrmions but with complex and fluctuating domain walls.

[1] A. Soumyanarayanan, N. Reyren, A. Fert and C. Panagopoulos, *Nature*, Vol. 539, p. 509-517 (2016) [2] A. Fert, N. Reyren and V. Cros, *Nature Reviews Materials*, Vol. 2, p. 170301 (2017) [3] W. Legrand, J.-Y. Chaudreau, D. Maccariello et al., *Science Advances*, Vol. 4(7), p. eaat0415 (2018) [4] F. Ajejas, A. Gudin, R. Guerrero et al., *Nano Letters*, Vol. 18(9), p. 5364-5372 (2018) [5] P. Olleros-Rodríguez, R. Guerrero, J. Camarero et al., *Applied Materials and Interfaces*, Vol. 12(22), p. 25419-25427 (2020)



Fig.1 Sketch of modelled magnetic nanodots at selected cobalt thicknesses. The stabilized spin textures are represented by the arrows at the top of the structures. The color of the arrows represents the out-of-plane component of the magnetization. The color of the surface represents the X-component of the magnetization.

AE-09. Néel Type Skyrmions Formation in Nanodots and Antidot Arrays.

M.K. Zelent¹, S. Saha^{4,5}, I. Vetrova², M. Mruczkiewicz^{2,3} and M. Krawczyk¹

1. Faculty of Physics, Adam Mickiewicz University in Poznan, Poznan, Poland; 2. Institute of Electrical Engineering, Slovak Academy of Sciences, Bratislava, Slovakia; 3. Centre For Advanced Materials Application CEMEA, Slovak Academy of Sciences, Bratislava, Slovakia; 4. Laboratory for Multiscale Materials Experiments, Paul Scherrer Institut, Villigen, Switzerland; 5. Laboratory for Mesoscopic Systems, Department of Materials, ETH Zurich, Zurich, Switzerland

Magnetic skyrmions in ferromagnetic materials are mainly stabilized by the interplay of several magnetic energy contributions, i.e. exchange, dipole, anisotropy, and Zeeman. In particular, the asymmetric Dzyaloshinskii-Moriya exchange interaction (DMI) introduces chiral canting between neighboring spins and favors skyrmion stability [1]. Skyrmions are particle-like chiral spin textures found in magnetic films and patterned nanostructures with out-of-plane anisotropy and are considered to be potential candidates as information carriers in next-generation data storage devices [2]. The challenge of the experimental study of skyrmions is to find an efficient technique for forming stable skyrmions. In particular, the outstanding issues are the reproducible generation, stabilization, and confinement of skyrmions at room temperature [2,3,4]. It is well known that various magnetic textures can be stabilized by geometrical confinement using artificial nanostructures, however, there are several key challenges like reproducible skyrmion formation that still need to be addressed. We present two methods of skyrmions formation in nanodots and antidot arrays. For these first structures, we have shown the formation of skyrmion using the tip of a magnetic force microscope [3], and during the remagnetization process for antidot arrays [4]. Here, we present the results of the investigation of a skyrmion formation in Pt/Co/Au nanodots. We demonstrate that the high magnetic momentum probe induces individual skyrmions during the scan. A specific path of the MFM tip causes a systematic change in the state of the magnetic domains during scanning. The process of annihilation of remaining domains is ruled by magnetostatic interactions where the magnetic domains are simultaneously repelled from the edges of the nanodots and from the tip field. Micromagnetic simulations have shown that specific conditions restricting the movement of magnetic domains must be met in order to form the magnetic skyrmion [3]. In this work, we present a method to form nanometer-sized magnetic skyrmions in an array of magnetic topological defects in the form of an antidot lattice. In particular, the introduction of the holes in a thin magnetic film modifies the spatial distribution of the effective field, which has a profound influence on the formation mechanism of the skyrmions. The position of skyrmion formation was recognized at the saddle point of the lattice as a result of the spatial distribution of the effective field. With micromagnetic simulations, we elucidate the steps of the skyrmion formation process and showed that this process depends on the antidot lattice parameters. This behavior is confirmed with scanning transmission x-ray microscopy measurements [4]. The work was supported by National Science Centre of Poland, Projects Nos. UMO-2017/27/N/ST3/00419 and UMO-2018/30/Q/ST3/00416.

[1] Fert et al. "Magnetic skyrmions: advances in physics and potential applications", Nat. Rev. Mater. 2, 17031 (2017). [2] C Back et al. "The 2020 skyrmionics roadmap", J. Phys. D: Appl. Phys. 53 363001 (2020). [3] Iu. V Vetrova et al. "Skyrmion formation in nanodisks using magnetic force microscopy tip", arXiv preprint arXiv:2002.11685. [4] S. Saha et al. "Formation of Néel-type skyrmions in an antidot lattice with perpendicular magnetic anisotropy", Phys. Rev. B 100, 144435.

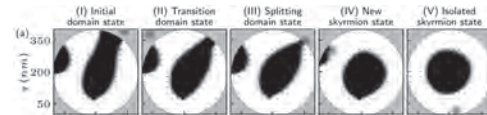
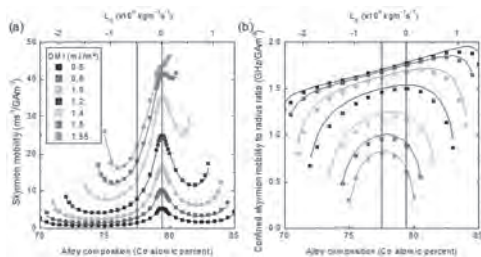


Fig. 1: Simulated images of the evolution of the magnetic configuration in nanodots for random initial state and different positions of the tip field. x (nm) Simulations were performed for 400 nm disks with 4 repetition of the stack with DMI=1.0 mJ/m². The red circle represents the z-component of the magnetic field induced by the high-momentum tip. The amplitude of tip field was 200 mT at center of the spot, and spot diameter was equal to 25 nm. The colors represent the orientation of the magnetization.

AE-10. Smaller and Faster Skyrmions in Compensated Ferrimagnets and Synthetic Antiferromagnets.

S. Rohart¹, E. Haltz¹, S. Mallick¹, L. Berges¹, A. Mougin¹ and J. Sampaio¹
 1. Laboratoire de Physique des Solides, Université Paris-Saclay Faculté des Sciences d'Orsay, Orsay, France

Skyrmions in magnetic thin films are solitonic excitations that could open new possibilities for spintronic devices. The recent successes obtained in ferromagnetic films have shown some limitations, with dipolar-coupling induced large skyrmion sizes and topology induced gyrotropic deflection. Antiferromagnetic films and their artificial equivalents that are ferrimagnets and synthetic antiferromagnets could overcome these limitations. In this talk, we explore the skyrmion dynamics in such materials. Separating them into two antiferromagnetically coupled sublattices, we show that the dynamics can be described by two coupled Thiele equations. This framework is used to address the consequences of the small skyrmion size and the angular momentum compensation. It provides a simple approach to describe this problematic. Small skyrmions, that are possible due to the vanishing total magnetization, are shown to be significantly slower (velocity proportional to radius) than larger ones (size independent velocity). This result is a direct consequence of the skyrmion topology, which induces an excess of dissipation per size unit at small sizes. Angular momentum compensation is shown to cancel the gyrotropic deflection, without the need to modify the topology and maximizes the velocity. In a track, where the edge repulsion cancels the gyrotropic deflection, the angular momentum compensation has no effect and skyrmions travel faster than non confined skyrmions. From an applied perspective, the data rate is given by the velocity to radius ratio and correspond to the inverse of the time needed for a skyrmion to jump from one site to another. This shows that small skyrmions in ferrimagnetic films would still be preferable to large ones, providing fast and dense devices.



(a) Variation of the skyrmion velocity in a CoGd thin film and (b) variation of the skyrmion velocity to skyrmion radius ratio (proportional to an application data rate), when the skyrmion is confined in a track, as a function of the alloy composition, close to the angular momentum (L_S) composition (79.4%), and for different DMI values. The points are the results of simulations, and the lines are the result of the model. Note that the skyrmion size increases with DMI at a given composition, and that the size is minimal at the magnetic moment compensation (77.5%).

AE-11. Statics and Dynamics of Skyrmions in Synthetic Antiferromagnets : Benefits and Micromagnetic Understanding.

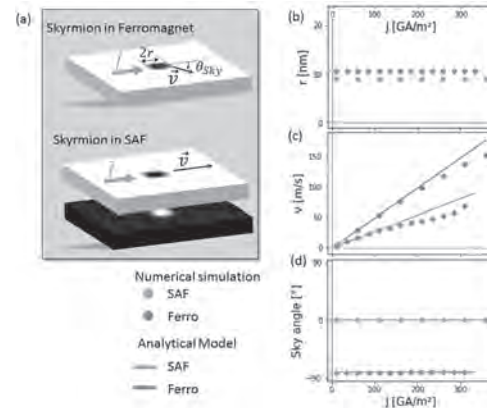
E. Haltz¹, C. Barker¹ and C. Marrows¹

1. Physics, University of Leeds School of Physics and Astronomy, Leeds, United Kingdom

In this last decade, experimental results and their understanding have led to magnetic skyrmions becoming promising candidates for the storage and processing of digital information [1]. However, some key barriers such as reducing their size, enhancing their stability at room temperature, or their low-power manipulation under electrical current have not yet been overcome, meaning that they are rarely integrated in actual devices [2]. To surmount these limitations, it has been proposed to study these magnetic textures in antiferromagnets or synthetic antiferromagnets (SAFs) instead of the conventional ferromagnetic layers that are usually considered [3,4]. In this more complex system, multiple ferromagnetic layers are coupled antiferromagnetically through a non-magnetic spacer layer *via* the RKKY interaction (Fig a) [4,5]. By switching to these systems, two crucial points need to be addressed. First, a drastic reduction of stray fields is expected in SAFs due to the anti-alignment of magnetization, which should reduce the size of the skyrmions [6]. Second, it is not possible to manipulate a conventional skyrmion in the driving force direction in a ferromagnet due to its topology that intrinsically induces a deflection known as the skyrmion Hall effect [7]. In SAF systems, since the magnetisation of the skyrmions in each magnetic layer are opposite, it is expected that the two deflections cancel each other out and the two skyrmions move in the current direction [3]. Even if skyrmions have recently been observed in SAFs [4,8,9], a clear and simple micromagnetic description of both the static and dynamic properties of such skyrmions is so far lacking to further understand this phenomenon. In order to improve the description of these properties and highlight the expected benefits of using SAFs rather than conventional ferromagnets, we simulate numerically the behavior of skyrmions in bilayer SAFs for a large range of parameters. We also adapt the ferromagnetic analytical formalism [10] to SAF systems. This leads to results that are in good agreement with the numerical simulations whilst also highlighting the underlying mechanisms. First, we investigate the stability region of SAF skyrmions and how their radii r evolve with micromagnetic parameters. We show that they are only slightly smaller than for ferromagnetic systems (Fig b), but that they exist for a larger range of parameters. Second, we study the dynamics of these skyrmions under spin currents. We find, as expected, that SAF skyrmions move at a faster velocity v than in a conventional ferromagnet (Fig c) for a given current density J , and move in the applied current direction (Fig d) with zero skyrmion Hall angle θ_{SKy} . By using the analytical model based on the Thiele equation, we are able to recover these dynamics (Fig c and d) and identify the required condition for the vanishing of the topological deflection. Finally, we unbalanced the SAF by asymmetricizing the skyrmions in each layer in different ways in order to verify the condition for vanishing deflection. The results obtained highlight the qualitative benefits of SAF skyrmions and propose some methods for more quantitative optimizations.

[1] The 2020 skyrmionics roadmap: C. Back et al., J. Phys. D: Appl. Phys. 53 (2020) [2] Magnetic skyrmions: advances in physics and potential applications: A. Fert, et al. Nat. Rev. Mat. 2, 17031 (2017) [3] Static and dynamical properties of antiferromagnetic skyrmions in the presence of applied current and temperature: J. Barker, et al. Phys. Rev. Lett. 116, 147203 (2016) [4] Room-temperature stabilization of antiferromagnetic skyrmions in synthetic antiferromagnets. W. Legrand et al., Nat. Mat. 19, 34–42 (2020) [5] Oscillatory magnetic exchange coupling through thin copper layers: S. S. P. Parkin, et. al. Phys. Rev. Lett. 66, 2152–2155 (1991) [6] Theory of isolated magnetic skyrmions: from fundamentals to room temperature applications: F.Büttner, et al., Sci. Rep. 8 4464 (2018) [7] Nucleation, stability and current-induced motion of isolated magnetic skyrmions in nanostructures: J. Sampaio, Nat. Nano. 8, 839-844 (2013) [8] Imaging non-collinear antiferromagnetic textures via single spin relaxometry: A. Finco et al., arXiv:2006.13130v1 (2020) [9] Exploring different facets of magnetic skyrmion nucleation and dynamics in ultra-thin films: R. Juge, PhD Thesis, Université Grenoble-Alpes (2020) [10] The

skyrmion-bubble transition in a ferromagnetic thin film: A. Bernard-Mantel et.al. SciPost Phys. 4, 027 (2018)



(a) Sketch of the skyrmion structure and motion under current in ferromagnetic and SAF systems. Radii (b), velocity (c) and deflection (d) for a ferromagnetic skyrmion (in blue) and a SAF skyrmion (in red) with the same micromagnetic parameters versus the current density J . Points correspond to the micromagnetic numerical simulations and lines to the analytical model.

AE-12. The Effects of Field History on Magnetic Skyrmion Formation in [Pt/Co/Ir]_n Multilayers.

A.T. Clark¹, X. Wang¹, A. Stuart², W. Jiang^{3,4}, S.G. te Velthuis³,
A. Hoffmann^{3,5}, K. Buchanan² and X. Cheng¹

1. Department of Physics, Bryn Mawr College, Bryn Mawr, PA, United States; 2. Department of Physics, Colorado State University, Fort Collins, CO, United States; 3. Materials Science Division, Argonne National Laboratory, Lemont, IL, United States; 4. Department of Physics, Tsinghua University, Beijing, China; 5. Department of Materials Science and Engineering, University of Illinois at Urbana-Champaign, Urbana, IL, United States

Magnetic skyrmions are chiral, topologically-protected magnetic spin textures known for their rich physics and potential for future data storage devices. Recently, magnetic multilayers with interfacial Dzyaloshinskii-Moriya interactions (DMI) have attracted great attention because they can support stable Néel-type magnetic skyrmions at room temperature. Here, we report on micromagnetic simulations of the effect of initial magnetic field treatment on skyrmion formation in [Pt/Co/Ir]_n magnetic multilayers. The multilayer system was modeled with MuMax3 using parameters determined from experimental measurements on [Pt/Co/Ir]_{n=3,5,8} multilayer thin films. The simulations show that the application and subsequent removal of a nearly in-plane magnetic field can transition the originally labyrinth domains into bubble skyrmions, which agrees well magneto-optical Kerr effect imaging results. Systematic simulations of the magnetic configuration of the [Pt/Co/Ir]_n as a function of angle and magnitude of the applied magnetic field reveal that the formation of bubble skyrmions occurs for field magnitudes that are close to but below the in-plane saturating field and that an additional out-of-plane component will help the skyrmion formation. Skyrmion formation is observed over a wider magnetic field range as the repetition number is increased, which corresponds to increasing importance of the demagnetization field coupling. Work at Bryn Mawr College was supported by the National Science Foundation CAREER DMR-1053854 and DMR-1708790. Work at Colorado State University was supported by the National Science Foundation DMR-1709525 and work at Argonne National Laboratory was supported by the U.S. Department of Energy, Office of Science, Materials Science and Engineering Division.

AE-13. Dependence of Curvature in HAMR Transitions on Bit Length.

K. Xue¹ and R. Victora¹

1. Electrical and Computer Engineering, University of Minnesota Twin Cities, Minneapolis, MN, United States

Heat Assisted Magnetic Recording (HAMR) technology has reached an areal density of over 2Tb/in², but the Signal to Noise Ratio (SNR) as well as the overall recording quality clearly decreases with the recording bit length (BL). In HAMR, recording patterns typically have a crescent shape due to the moving heat spot. The curvature of this crescent shape is of great significance as it is a significant source of transition broadening of the readback signal[1][2]. Various methods have been applied to determine and modify this curvature for better recording performance[3][4][5]. Thus, investigating how this curvature varies with different bit lengths and studying the change of this curvature during the HAMR writing process may help improve HAMR performance at the highest linear densities. In this digest, a detailed study of the dependence of curvature in HAMR transitions on bit length is presented. With the help of micromagnetic simulations, HAMR transition patterns for three different bit lengths, 10.5nm, 15nm and 21nm, were obtained and analyzed. For each bit length, 128 bits were written on multiple media and overlapped. Curvatures were then calculated using these averaged patterns. AC-erased thermal Exchange Coupling Composite (ECC) media was used, where a superparamagnetic layer with high Curie temperature forms the writing layer and a doped FePt layer with relatively low Curie temperature serves as the storage layer[6]. The change in curvature during the cooling process was also tracked for pure FePt media. Curvatures of DC-erased thermal ECC media were tested as well for comparison. Introduction of intergranular exchange was also implemented to find potential optimizations of HAMR system designs. Micromagnetic simulations in this study are guided by the Landau-Lifshitz-Gilbert equation. Renormalization group theory is applied to enable inclusion of atomic level phenomena[7]. Media dimension is 384nm x 48nm x 9nm. For a certain bit length, the 128 written bits were overlapped and averaged, as shown in Fig. 1. The left edge of the -1 bit (blue-colored) was chosen for curvature calculation. This curve was fitted to a parabolic curve and the reciprocal value of its second order coefficient was taken as its curvature. In HAMR, the cooling process could potentially modify the written bits as magnetic properties of the media materials, such as saturation magnetization and magneto-crystalline anisotropy, change greatly with temperature. Curvatures before and after the cooling process for both AC-erased thermal ECC media and pure FePt media with BL10.5nm, 15nm and 21nm are presented in Fig. 2. For thermal ECC media, curvatures before the cooling process for all the three bit lengths were close to each other, as shown with the cyan solid line in Fig. 2. After the bits were cooled down to room temperature, a decrease in curvature was seen for both BL10.5nm and 15nm while no obvious curvature change was observed for BL21nm. The BL10.5nm curvature experienced a bigger drop than the BL15nm curvature. This means that curvatures are reduced more during the cooling process for smaller bit lengths. The reason lies in the distance between the bit edge and the heat spot. When a -1 bit is just written, the left edge of this bit is about twice the bit length away from the heat spot. For BL10.5nm case, this distance is 21nm, which is much smaller than that for BL15nm and BL21nm cases. This implies that for BL10.5nm case, this bit edge is under a much higher temperature and spins here have a greater chance to be switched due to their reduced anisotropy fields. When the magnetic field switches as the head moves on, some spins at the center of this left bit edge area would get flipped, which will flatten the curve and thus cause the curvature to decrease. This leads to the interesting conclusion that the enhanced erase-after-write found in the thermal ECC media is actually beneficial owing to the resulting reduction in curvature. FePt media shows a very similar erase-after-write effect, with the 10.5 nm bits showing before and after cooling curvatures very close to the thermal ECC media. Interestingly, the 21 nm bits, while showing reduced erase-after-write as expected, have overall larger values of the curvature in comparison to the thermal ECC media, possibly owing to the differing magnetostatics. Curvatures for DC-erased thermal ECC media are found to be larger than those for AC-erased media in all the three BL cases. This is because the +1 background of DC-erased media provides stronger dipole interaction than the averaged 0 background of AC-erased media. Spins have a higher switching probability, especially in the middle of the

track. For AC-erased thermal ECC media, when intergranular exchange was introduced, a decrease in curvature was seen in all the three BL cases. This results from the weaker intergranular exchange effect received by two transition corner areas than by the central areas due to the averaged 0 background. The two corners are then removed and the curvature is reduced.

[1] Liu, Z. and Gilbert, I., *IEEE Transactions on Magnetics*, 55(3). (2019) [2] Tseng, C. Y. and Hurben, M. J., *IEEE Transactions on Magnetics*, 47(10), 2974–2976. (2011) [3] Hashimoto, M. and Salo, M., *INTERMAG 2006 - IEEE International Magnetics Conference*, 43(7), 448. (2006) [4] Zhu, J. G. J. and Li, H., *IEEE Transactions on Magnetics*, 53(2). (2017) [5] Scholz, W. and Batra, S., *IEEE Transactions on Magnetics*, 41(10), 2839–2844. (2005) [6] Liu, Z., Jiao, Y. and Victora, R. H., *Applied Physics Letters*, 108(23). (2016) [7] Victora, R. H. and Huang, P. W., *IEEE Transactions on Magnetics*, 49(2), 751–757. (2013)

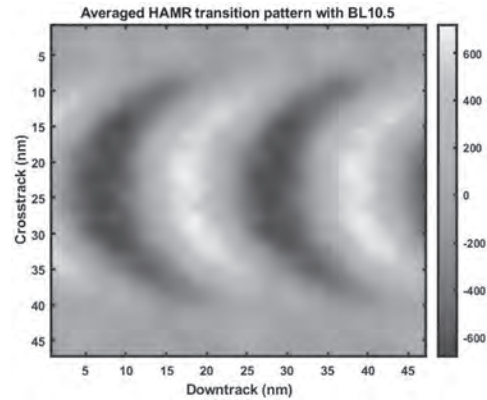


Fig. 1 Averaged HAMR transition patterns with BL 10.5nm.

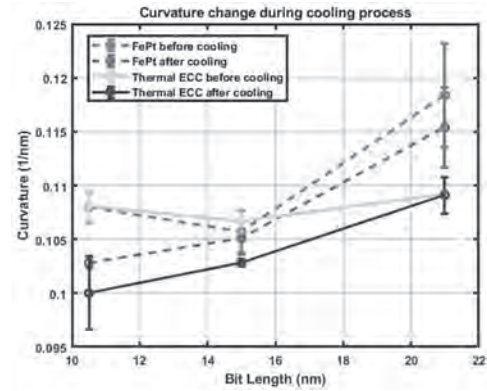


Fig. 2 Curvature change during HAMR cooling process. Solid lines are for thermal ECC media while dashed lines are for FePt media.

Session AP**ADVANCES IN (SEMI)-ANALYTICAL AND NUMERICAL TECHNIQUES FOR DESIGN I****(Poster Session)**

Yacine Amara, Chair

GREAH, University of Le Havre, Le Havre, France

AP-01. A Space-Time Domain Decomposition Method for the Finite Element Analysis of Transient Magnetic Field.

Y. Zhang¹, X. Yang², D. Shao¹, C. Zhang², H. Wu³ and W. Fu³

1. School of Mechatronic Engineering and Automation, Shanghai University, Shanghai, China; 2. Hebei University of Technology State Key Laboratory of Reliability and Intelligence of Electrical Equipment, Tianjin, China; 3. Department of Electrical Engineering, The Hong Kong Polytechnic University, Kowloon, Hong Kong

I. Introduction In order to reflect the reality more accurately, high resolution discretization is required for the numerical analysis of electric machines to consider the model details. Due to the large mesh scale, the numerical analysis process is costly and time-consuming. This problem is further aggravated when using the time stepping analysis to estimate the transient performance. Domain decomposition methods (DDMs) [1] are developed to divide the original problem into sub-problems and then solve them in parallel. Similarly, several time decomposition methods (TDMs) [2] are reported to make the time stepping process work in parallel. As the number of subdomains increases, the convergence performance of the global algebraic system deteriorates, and more communication costs are required for the parallel processors. In other words, DDMs are not scalable with respect to the number of subdomains. The computational efficiency can be further improved by using the DDMs in combination with the TDMs. In this paper, we propose a novel space-time DDM, which combines the non-overlapping Schwarz method with the block direct solver based TDM, for the transient magnetic field analysis. The entire time-stepping process is divided into several subdivisions, in which multiple time steps are solved at a time. Meanwhile, the Schwarz method is embedded in the finite element method (FEM) to make the computation of each time step parallel. II. The Space-Time Domain Decomposition Method The governing equations of transient magnetic problems can be fully discretized using the finite element method and backward Euler method, and the algebraic equations for the entire time stepping process can be written in the block matrix form, forming a compact equation. Since solving this compact equation at a time is very costly and difficult, it is straightforward to partition the time stepping process into several subdivisions. Two adjacent subdivisions are coupled by the final time step of current subdivision and the first step of next subdivision. Similarly, the computational domain of one single time step can be further divided into subdomains, which are then solved by domain decomposition methods in parallel. The domain decomposition is realized by the partition program Metis, and a non-overlapping domain decomposition method, namely, the dual-primal finite element tearing and interconnecting method, is used in this paper. It is worth noting that the partition of space and time domain should adapt to the processors to realize a maximum computation speedup. A preliminary study is conducted to solve a surface-mounted permanent magnet synchronous motors with four pairs of poles and twenty-four slots. Based on the generated mesh, which contains 11788 triangle elements and 5970 degrees-of-freedom, the entire computational domain is decomposed into 15 sub-domains. The magnetic potential derived by the domain decomposition method is shown by the contours in Fig. 2, which is in good agreement with the results of traditional finite element method. The implementation details of this proposed method will be reported with more numerical problems in the full paper.

[1] Y. Takahashi, et al. IEEE Transactions on Magnetics, Vol. 55(6), p.1-4 (2019) [2] B. He, et al. Progress in Electromagnetics Research-Pier, Vol. 160, p.1-8(2017)

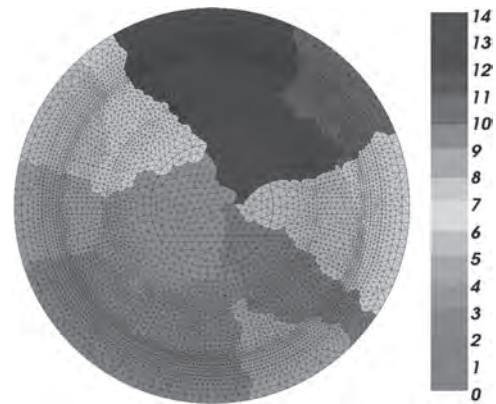


Fig. 1 The discrete mesh of the permanent magnet synchronous motor and the decomposed subdomains.

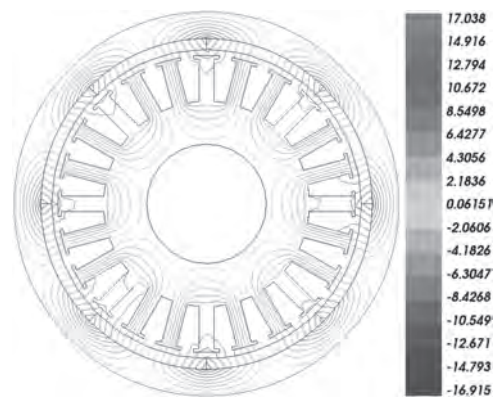


Fig. 2. The derived contours of magnetic potential.

AP-02. Analytical Computation of Inductance for Spoke-Type Permanent Magnet Synchronous Motor Accounting for Saturation.

P. Liang¹

¹ Northwestern Polytechnical University, Xi'an, China

I. Introduction Spoke-Type permanent magnet synchronous motors (STPMSMs) are widely applied in the industry, especially for the electric vehicle where the high efficiency and high power density are required [1]. As a basic parameter of motor design, the inductance affects the performance, such as flux-weakening capability and control strategy [2]. It is necessary to accurately calculate the inductance. Various researches on inductance with analytical method have been carried out. However, the effect of saturation is normally neglected in the past. This paper presents an analytical method to calculate the d- and q-axis inductances accounting for saturation. II. Proposed Method The proposed analytical method is based on the subdomain model. Firstly, the STPMSM is divided into several types of simple subdomains. The analytical expression of each subdomain is derived and the field solution is obtained by the boundary conditions. Then, the lumped magnetic circuit model (LMCM) is established to calculate the stator reluctance. According to the iterative method, the flux linkage in the case of saturation is calculated. At last, the d- and q-axis inductances under saturation can be obtained. The solution process is summarized in Fig. 1. III. Results and Analysis The finite element method (FEM) is employed to validate the accuracy of the proposed model. Fig.2 shows the d- and q-axis inductances of a 18-slot/16-pole STPMSM. As the current increases, the effect of saturation on the inductance is more pronounced. Compared with the analytical method without saturation, the result of the proposed method is closer to that of FEM. Hence the proposed method is more advantageous for the inductance calculation. IV. Conclusion This paper presents an analytical method for inductance calculation which combines the advantages of subdomain model and LMCM. The effect of saturation on the inductance is fully considered, which improves the accuracy of the inductance calculation. The validity of the analytical technique is verified by FEM. In addition, the method can also be used in the inductance calculation for other types of motors.

[1] W. Zhao, J. w. Kwon, X. Wang, T. A. Lipo, and B. i. Kwon, "Optimal Design of a Spoke-type Permanent Magnet Motor with Phase-group Concentrated-coil Windings to Minimize Torque Pulsations," *IEEE Trans. Magn.*, vol. 53, no. 6, Jun. 2017, Art. no. 8104604. [2] J. Y. Kim, D. W. Kang, T. C. Jeong, D. H. Jeong, J. Lee, and S. G. Lee, "Optimal Rotor Design of an 150 kW-Class IPMSM by the 3-D Voltage-Inductance-Map Analysis Method," *IEEE Trans. Magn.*, vol. 53, no. 11, NOV. 2017, Art. no. 8206805.

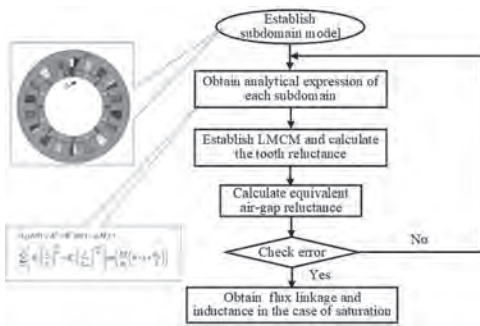


Fig.1 Solution process

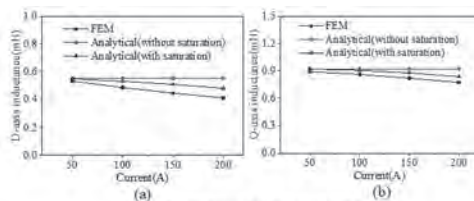


Fig.2 Inductance: (a) D-axis. (b) Q-axis.

AP-03. Optimization Method for Setting Resonance of Multi-Module Wireless Charging Systems With Various Circuit Topologies.

J. Lee¹, C. Byeon² and S. Lee¹

1. Jeonbuk National University, Jeonju, The Republic of Korea;

2. Wonkwang University, Iksan, The Republic of Korea

I. Introduction In order to meet the increased demand for convenience and safety of electrical devices, wireless power transfer (WPT) systems have been applied to a variety of electrical products from portable electronics to electric vehicles [1]-[2]. Recently, there are strong needs for the development of multi-module WPT systems in order to enhance the competitiveness for the price and efficiency. Nevertheless, there is little research for multi-module WPT systems that are composed of a “single transmitter and multiple receivers (S-M) with various circuit topologies (i.e. series (transmitter) to series and/or parallel (receiver) circuit topology)”. As the number of receiver modules with various circuit topologies increases, it becomes increasingly difficult to design the optimal system that can maximize the power transfer efficiency while satisfying the required functional requirements and regulations. In the literature to date, there was the resonance setting for S-M WPT systems with the series (transmitter) to series (each receiver) circuit topology [3]. However, there has been little research to determine the resonance setting for S-M WPT systems with the series-to-combinations (i.e. integrated receiver part they are composed of the series and/or parallel modules). In this paper, the optimization method which can design the resonance setting of the S-M WPT systems with various circuit topologies (series and/or parallel circuit) is proposed. Note that it assumes that the resonance condition is the condition when the total power transfer efficiency of the S-M WPT systems is maximized while satisfying the rated power required by each receiver module. II. Optimization Framework The proposed optimization was composed of the optimization module, which can determine the resonance condition for the S-M WPT system with various circuit topologies, and the analysis module, which can evaluate the electromagnetic and electrical performances of the target system. The in-house code for optimizing the target system was programmed to automatically exchange information (e.g. design variables, efficiency, rated power, etc.) between the optimization module and the analysis module (i.e. ANSYS Maxwell and Simpler in this paper) during the optimization process. For the gradient-based optimization, the modified method of feasible direction was chosen as an optimization algorithm, which has determined the reliable optimum solution for the WPT systems [4]-[8]. As indicated in the flow chart in Figure 1, the optimization module provides the value of the design variables, which are related to the objective function and constraint functions, to the analysis module. Then, the analysis module makes the circuit model for the S-M WPT systems and analyzes the model to evaluate the electrical performances. After the evaluation, the electrical performances are delivered to the optimization module in order to calculate the objective function, constraint functions, and the sensitivity of the objective and constraint functions with respect to the design variables. And then, the value of the design variables is updated in order to determine the optimum resonance condition through the search direction and step size calculated by using the sensitivities. Through the iterations, if the convergence criteria are satisfied, the process of the optimization is finished and then the optimized model is determined. If not, this updated process is repeated until the criteria are satisfied. III. Application This section will cover that the proposed framework is applied to an S-3M WPT system consisting of one transmitter (series circuit topology) and three receivers (one parallel circuit and two series circuit topology). A. Model description The application model was composed of three-receiver modules required by rated power of 12.5W (Receiver 1 with the series circuit) and two 5W (Receiver 2 with the parallel circuit and Receiver 3 with the series circuit). B. Optimization for the resonance condition In this application model, the design variables were set by the input voltage, transmitter resistance, inductances of the transmitter and receivers, and capacitances. The optimization formulation was formulated to maximize the total power transfer efficiency of the S-3M WPT systems while all rated power of each receiver module is satisfied. As described in the optimization history in Fig. 2, the optimizer found the feasible model that are satisfied all the constraint functions until 24 iterations and then maximized the objective function (i.e. total power transfer efficiency in this paper) while satisfying all

the constraints. Therefore, it can be concluded that the proposed framework successfully designs the resonance condition for multi-module WPT systems with different circuit topologies. IV. Conclusion The new resonance optimization for multi-module wireless power transfer systems with various circuit topologies was proposed. The method was composed of the optimization module and analysis module to maximize the total power transfer efficiency while the constraints (i.e. rated power for each receiver module) are satisfied. Through the application model, it was validated that the proposed method can determine the optimal resonance condition for the multi-module WPT systems with different circuit topologies.

[1] Siqi Li and C. C. Mi, “Wireless Power Transfer for Electric Vehicle Applications,” *IEEE J. Emerg. Sel. Top. Power Electron.*, vol. 3, no. 1, pp. 4–17, Mar. 2015. [2] J. Kim, H. Son, D. Kim, and Y. Park, “Optimal design of a wireless power transfer system with multiple self-resonators for an LED TV,” *IEEE Trans. Consum. Electron.*, vol. 58, no. 3, pp. 775–780, Aug. 2012. [3] S. B. Lee and I. G. Jang, “Determination of the Optimal Resonant Condition for Multi-receiver Wireless Power Transfer Systems Considering the Transfer Efficiency and Different Rated Powers with Altered Coupling Effects,” *IEEE J. Emerg. Sel. Top. Power Electron.*, Mar 2020, Accepted. [4] S. B. Lee and I. G. Jang, “Coil Layout Optimization for Maximizing the Power Transfer Efficiency of Wireless Power Transfer Systems with Multiple Transmitter Coils,” *IEEE J. Emerg. Sel. Top. Power Electron.*, vol. 8, no. 3, pp. 2672 - 2681, 2019. [5] S. B. Lee and I. G. Jang, “Layout Optimization of the Receiver Coils for Multi-transmitter Wireless Power Transfer Systems,” *IEEE J. Emerg. Sel. Top. Power Electron.*, vol. 5, no. 3, pp. 1311–1321, Sep. 2017. [6] S. B. Lee, S. Ahn, and I. G. Jang, “Development of the Optimization Framework for Low-Power Wireless Power Transfer Systems,” *IEEE Trans. Microw. Theory Tech.*, vol. 63, no. 3, pp. 813–820, Mar. 2015. [7] S. B. Lee, S. Ahn, and I. G. Jang, “Simulation-Based Feasibility Study on the Wireless Charging Railway System With a Ferriteless Primary Module,” *IEEE Trans. Veh. Technol.*, vol. 66, no. 2, pp. 1004–1010, Feb. 2017. [8] S. B. Lee, C. Lee, and I. G. Jang, “Precise Determination of the Optimal Coil for Wireless Power Transfer Systems Through Postprocessing in the Smooth Boundary Representation,” *IEEE Trans. Magn.*, vol. 53, no. 6, pp. 1–4, Jun. 2017.

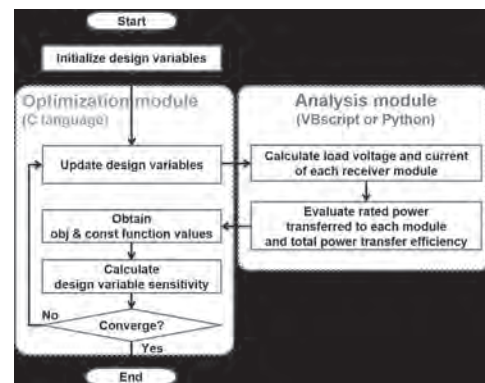


Fig. 1. Flow chart of the proposed method for determining the optimal resonance condition.

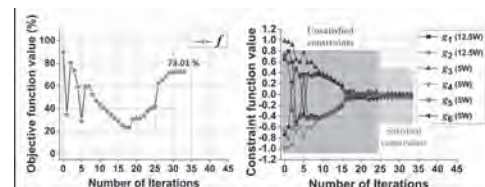


Fig. 2. Optimization history of the objective function and the constraint functions for three-receiver modules (one parallel and two series circuit topology).

AP-04. Analytical Method of Form-Wound Winding Loss Calculation Considering Circulating Current Effect.

Y. Jiang¹, J. Chen¹, H. Wang¹ and D. Wang¹

1. Naval University of Engineering, Wuhan, China

I. Introduction Form-wound winding is one of the common forms of electrical machine windings, which owns many advantages, such as simple structure and good insulation. It is widely used in medium and large capacity electrical machines. In order to estimate the AC loss of the form-wound winding, researchers have proposed many analytical models and finite element models [1-6]. Among these analytical methods, many researches focused on the uneven current distribution inside the wire bars. Meanwhile, the circulating currents between parallel wire bars of one coil is usually neglected due to the torsion at the end winding. In fact, the torsion at the end winding cannot completely eliminate the circulating current, especially in the case of multi-bar parallel windings and high frequency conditions. It is a challenging task to establish a complex external circuit in order to simulate connections of wire bars. In this paper, an analytical calculation method to estimate the AC copper loss of the form-wound winding, taking the circulating current effect into consideration, is presented. Firstly, the current of each wire bar is calculated by building the electric circuit model. Consequently, the current density distribution inside each wire bar is obtained by introducing the previous 1-D analytical method. Finally, the accuracy of the model is validated by FEM simulations. II. Analytical Model of Circulating Current Assuming that the main flux difference between parallel wire bars of one coil, the uneven current distribution inside the wire bar, the MMF drop inside the core and the magnetic field x component are neglected. The voltage equation of the p th wire bar of the i th coil is written as Eq. 1. Considering all voltage equations of wire bars in the same coil, two adjacent equations can be subtracted from each other, thus eliminating the induced voltage caused by main flux, as shown in Eq. 2. With total current constraint shown in Eq. 3, currents can be obtained. The mutual leakage inductances of the wire bars are the key parameters. As shown in Fig. 1 (b), the leakage inductance matrix of bars in one slot is firstly derived through the analytical method. By introducing the directional incidence matrix C between coil bars and slot bars, the mutual leakage inductance matrix of coil bars can be finally obtained, as shown in Fig. 1(c). It's worth to mention that the positive and negative sides of one coil need to be considered separately to simulate the torsion at the end winding. III. Analytical Model of Uneven Current Distribution inside Bars The currents of bars calculated above are considered as inputs of the analytical model for calculating the current density inside bars. Assuming that the length of the slot opening is infinite and the flux lines are parallel to the slot bottom, the computation of the uneven current distribution inside bars can be simplified to 1-D problem. Based on the Maxwell equations and continuous boundary conditions and current constraints, the partial differential equation of the magnetic field can be derived and solved by analytical method [7]. IV. FEM Validation A 12-pole 72-slot PM generator with six phases is taken for FEM validation. The simplified structure of one coil is shown in Fig. 2(a). Due to the torsion at the end winding, the orders of bars placements in positive side and negative side of one coil are opposite. The currents of bars in one coil is shown in Fig. 2(b). It shows a good agreement between FEM and the proposed method results. Furthermore, the calculation error increases with frequency and the maximum amplitude error of current vectors is about 6.58% (@1000Hz). The current density distribution is shown in Fig. 2(c). The proposed method shows a high accuracy compared with the FEM result. Fig. 2(d) shows the variation curves of the AC loss factor with frequency, which are obtained by the FEM method, the conventional analytical method and the proposed method, respectively. These results show that the conventional method ignoring circulating current effect can cause significant error, especially in high-frequency conditions. Obviously, the accuracy of the AC copper loss estimation has been greatly improved by the proposed method in this case. V. Conclusion An analytical method for estimating form-wound winding loss considering circulating current effect was presented, the accuracy is validated by FEM method. For the case in this paper, the new proposed method greatly improved the accuracy compared with the conventional method. The proposed method provided a fast and accurate copper loss calculation approach for electrical machine optimization design.

[1]P. L. Dowell, Proceedings of the Institution of Electrical Engineers, Vol. 113, No.8, p. 1387-1394 (1966) [2]A. S. Thomas, Z. Q. Zhu, and G. W. Jewell, IEEE Transactions on Magnetics, Vol. 45, No. 10, pp. 4748-4751 (2009) [3]L. J. Wu, Z. Q. Zhu and D. Staton, IEEE Transactions on Magnetics, Vol. 48, No. 7, p. 2138-2151 (2012) [4]Y. Wang, J. Pries and K. Zhou, IEEE Transactions on Magnetics, Vol. 56, No. 4, p. 1-9 (2020) [5] P. Mellor, R. Wrobel and N. Simpson, The Energy Conversion Congress and Exposition, p. 5563-5570 (2014) [6]H. Hamalainen, J. Pyrhonen and J. Nerg, IEEE Transactions on Magnetics, Vol. 49, No. 6, p. 2967-2973 (2013)

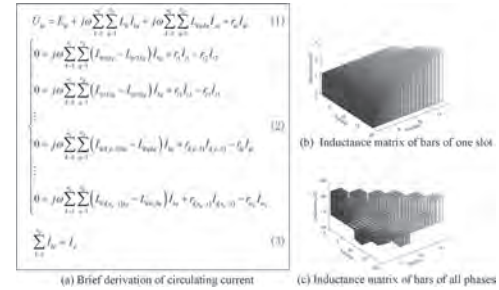


Fig.1 Brief derivation of circulating current and inductance matrix

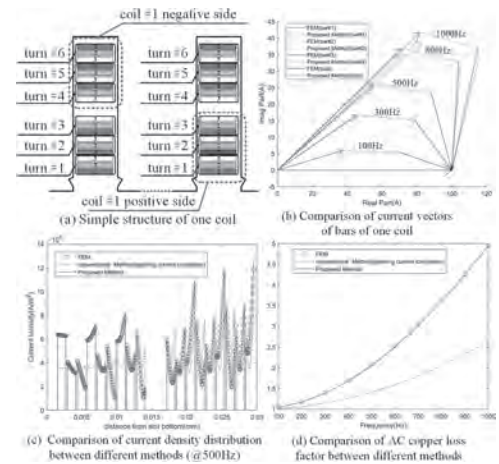


Fig.2 Test model and results comparison

AP-05. Magnetic Field Model of Flux Switching Permanent Magnet Machines Considering Harmonic Analysis and Slot Shape.

F. Liu¹, J. Hu¹ and Y. Li¹

¹. Harbin Institute of Technology, Harbin, China

Owing to the structures of the magnetic resistance rotor and hybrid excited stator, the flux switching permanent magnet (FSPM) machine achieves many advantages, including the structural robustness, wide flux-weakening capability, high torque density and efficient cooling [1], [2]. As the basis in the electromagnetic design and parameter optimization of the FSPM, an accurate but efficient calculation model of the motor magnetic field is of great significance. Compared with the magnetic permeance function (MPF) model [3] and finite element (FE) model [4], the sub-domain method (SDM) model can provide a direct insight to the modeling of the magnetic field, and has high accuracy close to that of the FE model [5]. As the re-modeling and re-meshing are not needed when the dimension is changed, the SDM model is attractive in the FSPM motor optimization. In the SDM model, the potential and flux density of the magnetic field are expressed in the Fourier series forms of the field harmonics. Since it is impossible to calculate the field harmonics from 1th to infinite, the general SDM model only includes 1th to n th harmonics when the effect of $n+1$ th harmonics on the final result is small enough. However, due to the double-salient pole effect, the air gap magnet field of the FSPM motor contains a large number of high-order harmonics. Compared with the SDM model of the ordinary permanent magnet motor, it is more difficult and time-consuming to determine the appropriate n . On one hand, n has a large value. On the other hand, it is easy to fall into the local optimal choice of n , since the effect of higher harmonics is not intuitive and determined. Besides, the magnetic permeability of the iron region is considered to be infinite in the SDM model. To simplify the magnetic field equation of the slot surrounded in the iron region, the slot structure in the SDM model is generally equivalent to fan-shaped. As a result, the SDM model can hardly consider the influence of the actual slot structure on the magnetic field results. However, as discussed in [6], the detent force and load torque ripple of the FSPM motor can be optimized by the selection of a proper slot structure. In [7], the actual structures of permanent magnet (PM) and slot are equivalent to multiple fan-shaped regions. However, the dimension of the SDM solving matrix is increased, and the SDM calculation needs more solving time. In a word, the existing SDM model needs to be further improved to make it more suitable for the FSPM motor optimization. In this paper, an improved SDM model combined with the MPF is proposed to determine the effective harmonics in the magnetic field calculations of the FSPM motor. As we discussed, the amplitude of the field harmonics can be easily observed by the Fourier analysis of the MPF results. Based on this idea, the appropriate n of the highest harmonic can be obtained. Moreover, not all 1th to n th harmonics are the effective components of the air gap magnet field in FSPM motors. The dimension of the SDM solving matrix and time consumption can be significantly reduced by excluding the invalid harmonics. According to the proposed model, the influence of the slot shape on the magnetic field result can also be considered by the correction of the air magnetic permeability in the slot region. Finally, the validity of the proposed model is verified based on a detailed comparison between the SDM and FE calculation results.

[1] W. Xu, J. G. Zhu, Y. C. Zhang, Y. G. Guo, and G. Lei, "New axial laminated-structure flux-switching permanent magnet machine with 6/7 poles," *IEEE Trans. Magn.*, vol. 47, no. 10, pp. 2823-2826, Oct. 2011. [2] D. H. Wang, X. H. Wang, and S. Y. Jung, "Reduction on cogging torque in flux-switching permanent magnet machine by teeth notching schemes," *IEEE Trans. Magn.*, vol. 48, no. 11, pp. 4228-4231, Nov. 2012. [3] B. L. J. Gysen, E. Ilhan, K. J. Meessen, J. J. H. Paulides, and E. A. Lomonova, "Modeling of flux switching permanent magnet machines with Fourier analysis," *IEEE Trans. Magn.*, vol. 46, no. 6, pp. 1499-1502, Jun. 2010. [4] J. D. McFarland, T. M. Jahns and A. M. EL-Refai, "Analysis of the torque production mechanism for flux-switching permanent-magnet machines," *IEEE Trans. Ind. Appl.*, vol. 51, no. 4, pp. 3041-3049, Aug. 2015. [5] M. Desvaux, B. Traullé, R. L. G. Latimier, S. Sire, B. Multon, and H. B. Ahmed, "Computation time analysis of the magnetic gear analytical model," *IEEE Trans. Magn.*, vol. 53, no. 5, pp. 7000409, May. 2017. [6] Z. Z. Wu

and Z. Q. Zhu, "Analysis of air-gap field modulation and magnetic gearing effects in switched flux permanent magnet machines," *IEEE Trans. Magn.*, vol. 51, no. 5, pp. 8105012, May. 2015. [7] P. X. Liang, F. Chai, Y. Li, and Y. L. Pei, "Analytical Prediction of Magnetic Field Distribution in Spoke-Type Permanent-Magnet Synchronous Machines Accounting for Bridge Saturation and Magnet Shape," *IEEE Trans. Ind. Electron.*, vol. 64, no. 5, pp. 3479-3488, May. 2017.

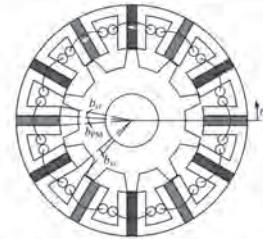


FIGURE 1. 2D model of the flux switching permanent magnet motor.

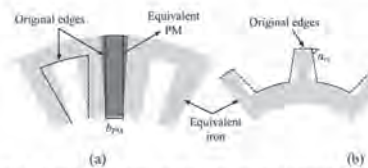


FIGURE 2. Shape equivalence in the SDM model: (a) stator slot and PM; (b) rotor slot.

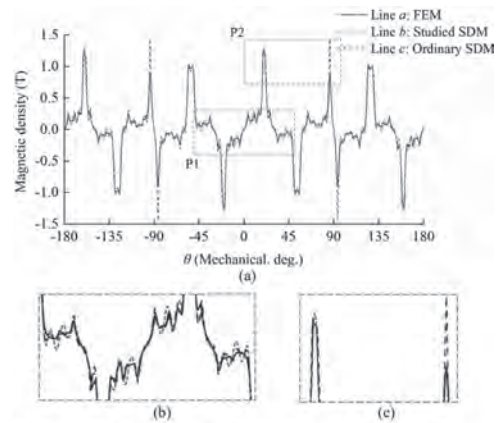


FIGURE 3. Result comparison of: (a) radial air gap magnetic density ($\theta=0^\circ$); (b) at position 1; (c) at position 2.

AP-06. A General Analytical Expression to Model the air gap Permeance of Electrical Machines.

J. Marault¹, A. Tounzi¹, F. Gillon¹ and M. Hecquet¹

¹. Univ. Lille, Arts et Metiers Institute of Technology, Centrale Lille, Junia, Lille, France

1. Introduction Nowadays, Finite Element Model (FEM) is considered as the most accurate approach to design and study electrical machines as it is able to consider many physical phenomena. However, its computation time can constitute a real drawback when several machines have to be tested thus making analytical approaches more suitable. Analytical model that involves winding functions and airgap permeance remains one of the more accurate and widely used approach. It is based on different assumptions including that of a regular stator and rotor slot pitches. As such, analytical expressions leads to an accurate representation of the air gap permeance [1]–[3]. However, recent studies show that spatial harmonic content of the stator Magneto Motive Force (MMF) can be reduced using non-regular slot pitches [4], [5]. Therefore, to be able to quantify the interest of such proposition or even optimize the location of the slots with limited time calculation, an analytical approach which makes it possible to take into account any location of the slots is needed. To achieve that, a generic analytical expression to model the air gap permeance of electrical machines is proposed. It enables to accurately calculate the air gap permeance in all cases i.e. with regular and non-regular stator and/or rotor slot pitches. Results obtained using the proposed approach are compared to the ones given by FEM in the case of an example of slotless rotor electrical machine with regular and non-regular stator slot pitches. 2. Analytical model permeance Quantifying the performance of an electrical machine is based on an accurate calculation of the magnetic flux density in the air gap whose permeance is the key quantity. To obtain the latter through a general analytical expression, the air gap can be split into three areas as showed in the Figure 1: - Mechanical air gap, δ_e , of constant thickness all around the circumference of the machine - Additional air gap due to stator slots, δ_s , which depends on θ_s - Additional air gap due to rotor slots, δ_r , which depend on θ_r and θ , θ represents a given position in the airgap with respects to a fixed stator axis and θ is the relative position of the rotor with respects to the stator. At steady state with a constant speed Ω , $\theta = \Omega.t$. The total air gap thickness $g(\theta_s, \theta)$ is then the sum of these three air gaps allowing to obtain the permeance through the calculation of $g^{-1}(\theta_s, \theta)$. Air gap permeance calculation is usually made considering one regular slot pitch but if the latter is non-regular, it is more relevant to consider the entire air gap circumference. In the proposed approach, each additional air gap due to a stator slot i or rotor slot j is represented by an elementary function $\delta_{s_i}^{elem}(\theta_s, \alpha_i)$ or $\delta_{r_j}^{elem}(\theta_r, \alpha_j)$ where α_i and α_j are the spatial shift phases related to the positions of the stator slot i and the rotor slot j with respect to reference stator and rotor axes respectively. The superposition of the elementary functions of all the slots enables to obtain the complete functions of $\delta_s(\theta_s)$ and $\delta_r(\theta_r, \theta)$ and hence the global air gap as $g(\theta_s, \theta) = \delta_e + \delta_s(\theta_s) + \delta_r(\theta_r, \theta)$. 3. Application In order to highlight the accuracy of the proposed model, a simple structure, i.e. slotless rotor, has been chosen. The proposed approach has then been used in the case of regular (Figure 2.a) and non-regular (Figure 2.b) slot pitch cases as proposed in the literature [4], [5]. The comparison between the magnetic flux density in the air gap obtained by both approaches under the assumption of linear behavior of the magnetic material are given in the Figure 2.c and 2.d. Results are very similar and show the accuracy of the proposed analytical expression of the air gap permeance. In the extended version, the analytical calculation of the air gap permeance will be presented in detail. Then, the proposed approach will be used in the case of non-regular rotor slot pitch and in the case of both non-regular stator and rotor slot pitches. Results will be given and discussed.

[1] D. Zarko, D. Ban, et T. A. Lipo, « Analytical calculation of magnetic field distribution in the slotted air gap of a surface permanent-magnet motor using complex relative air-gap permeance », *IEEE Transactions on Magnetics*, vol. 42, n° 7, p. 1828-1837, juill. 2006, doi: 10.1109/TMAG.2006.874594. [2] Z. Q. Zhu, D. Howe, E. Bolte, et B. Ackermann, « Instantaneous magnetic field distribution in brushless permanent magnet DC motors. I. Open-circuit field », *IEEE Transactions on Magnetics*, vol. 29, n° 1, p. 124-135, janv. 1993, doi: 10.1109/20.195557. [3] B. Gaussens, E. Hoang, O. de la

Barriere, J. Saint-Michel, M. Lecrivain, et M. Gabsi, « Analytical Approach for Air-Gap Modeling of Field-Excited Flux-Switching Machine: No-Load Operation », *IEEE Transactions on Magnetics*, vol. 48, n° 9, p. 2505-2517, sept. 2012, doi: 10.1109/TMAG.2012.2196706. [4] J. Marault, F. Gillon, M. Hecquet, et A. Tounzi, « Optimization of the MMF spatial harmonic content to design electrical machine winding », *International Journal of Applied Electromagnetics and Mechanics*, vol. Preprint, n° Preprint, p. 1-16, janv. 2020, doi: 10.3233/JAE-209508. [5] N. Bekka, M. E. H. Zaïm, N. Bernard, et D. Trichet, « A Novel Methodology for Optimal Design of Fractional Slot With Concentrated Windings », *IEEE Transactions on Energy Conversion*, vol. 31, n° 3, p. 1153-1160, sept. 2016, doi: 10.1109/TEC.2016.2552546.

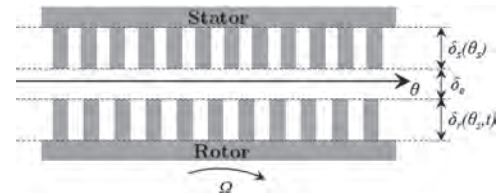


Fig 1. Air gap permeance function

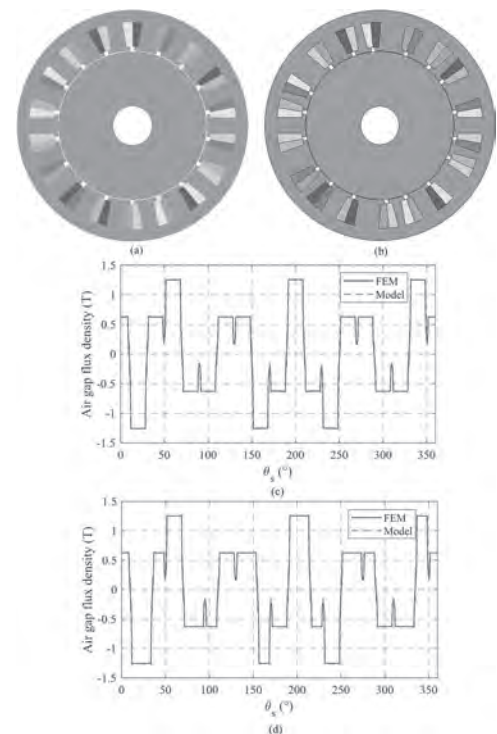


Fig 2. 18 slots, 10 poles simplified structure, (a) cross section with regular slot pitch, (b) cross section with non-regular slot pitch, (c) air gap flux density waveform for regular slot pitch, (d) air gap flux density waveform for non-regular slot pitch

AP-08. A Novel DiG-DE Algorithm for Multi-Objective Design Optimization of Electrical Machine.

J. Wu¹, J. Yin¹, W. Cao¹, B. Zhuang³, V. Rallabandi² and D.M. Ionel²

1. Department of Electrical Engineering, Zhengzhou University of Light Industry, Zhengzhou, China; 2. University of Kentucky, Lexington, KY, United States; 3. Ansys, Shenzhen, China

I. INTRODUCTION Differential evolution (DE) is a powerful evolutionary algorithm that is widely used to solve global optimization problems because of its ease of use, simple structure, efficiency, and robustness. It has been pointed out that the optimization methods, especially of electrical machine designs, are shifting from response surface method toward varieties of DE algorithm [1]–[4]. However, some previous work indicated that DE faces significant difficulty particularly with problems that are not linearly separable [5]. It has been observed that DE sometimes has a limited ability to move its population through large distances across the search space if the population is clustered in a limited portion of it, and in such cases it also has a tendency to find the local rather than global optima due to this lack of movement abilities. Sutton *et al.* found strong evidence that DE becomes more reliant on differential mutation, and less so on orthogonal steps produced by crossover when the function is non-separable. This paper proposes a hybrid multi-objective optimization method for electrical machines with directed graph (or digraph, DiG) and DE. The proposed method, called DiG-DE, is able to keep the balance of exploration and exploitation in search. The operation of the proposed method is verified, and its performance is compared with that of the standard DE method, for electric machine optimization problem. According to the results, the proposed DiG-DE can solve the problem faster than classic DE. Additionally, for the same computing time, the DiG-DE can always find better candidate designs than classic DE. II. APPLICATION TO ELECTRICAL MACHINE OPTIMIZATION To verify its superiority in terms of optimization for electrical machine design, the proposed DiG-DE is applied to the optimal design of a special modular external rotor switched reluctance motor and compared with classic DE. Fig. 1 displays the fitness of all designs found by classic DE and DiG-DE. From the distribution point of view, the designs found by DiG-DE are more densely distributed near the target Pareto front. All the designs are found by classic DE, but DiG-DE would select those designs that are closer to Pareto front. With the accumulation of selection preferences over time, there is a difference in evolutionary speed. This indicates that the DiG-DE is able to provide higher selective pressure than classic DE. It has been noted that the selective pressure will lead to the loss of diversity. In DiG-DE, the population size of parents is increasing in every generation, and the population grows exponentially, which compensates for this loss of diversity. Fig. 2 shows the candidate designs found by DiG-DE and classic DE for four different solution times. It may be observed that DiG-DE's solutions are closer to the target Pareto front as compared with the classic DE's. After a long solution times, the results obtained by the two methods tend to be close. Therefore, there is sufficient evidence to show that the proposed DiG-DE has faster convergence and higher search efficiency than classic DE. III. CONCLUSION In this work, a new algorithm, DiG-DE, based on differential evolution, which uses a digraph to rank candidate designs is proposed and compared with classical DE for electric machine optimization. In contrast with the classic DE approach in which the parents produce the same number of children in every generation, the DiG-DE method shows features that are closer to natural evolution. Under the pressure of selection, the individuals with higher rankings in DiG-DE are more likely to be selected, resulting in more offspring. The conducted comparative studies show that this unique selective scheme gives DiG-DE faster convergence and higher search efficiency than classic DE.

[1] Y. Duan, and D.M. Ionel, IEEE Trans. Ind. Appl., vol. 49, p. 1268–1275 (2013). [2] C.T. Krasopoulos, I.P. Armouti, A.G. Kladis, IEEE Trans Magn., vol. 53 (2017). [3] Y. Wang, D. Ionel, D.G. Dorrell, and S. Stretz, IEEE Trans. Magn., vol. 51 (2015). [4] M.E. Beniakar, A.G. Sarigiannidis, P.E. kakosimos, and A.G. Kladis, IEEE Trans. Magn., vol. 50 (2014). [5] S. Das, and P.N. Suganthan, IEEE Trans. Evol. Comput., vol. 15, p. 4–31 (2011).

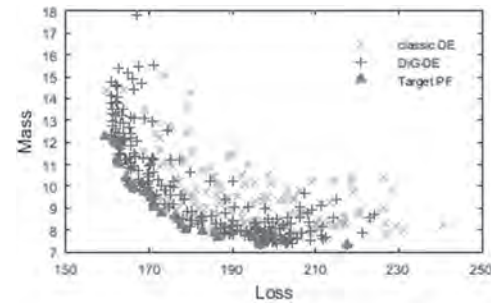


Fig. 1 All designs by classic DE and DiG-DE.

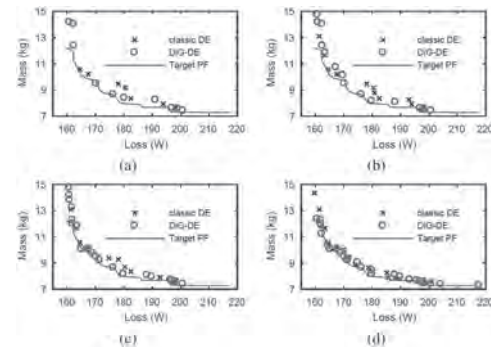


Fig. 2 Solutions of classic DE and DiG-DE computed within (a) 4 hours, (b) 6 hours, (c) 10 hours, and (d) 17 hours.

AP-09. Low Weight Halbach UAM Motor Design Based on Subdomain Analysis.

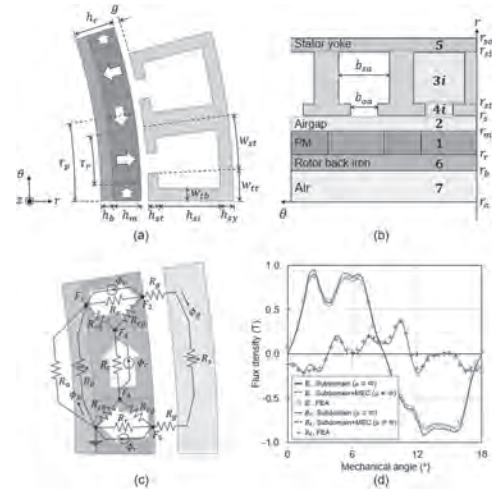
B. Koo¹, M. Lee¹ and K. Nam¹

1. Pohang University of Science and Technology, Pohang, The Republic of Korea

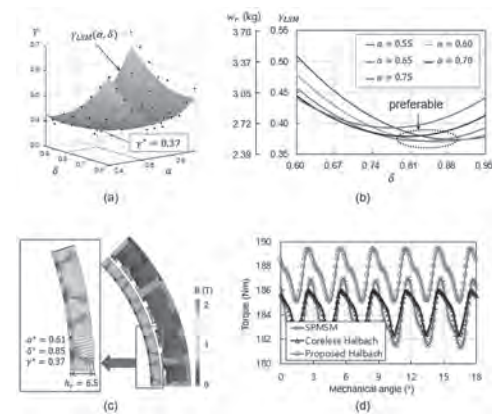
Urban air mobility (UAM) motors must be designed for light weight and high power density. This is because reducing an aircraft's curb weight increases the aircraft's efficiency and cruising range. UAM motors are basically high torque low speed machines, so they are designed with high poles [1]. The fractional slot structure allows for higher pole numbers with fewer slots and provides a concentrated slot winding, thus reducing the weight of the stator. In addition, the Halbach array rotor can reduce or eliminate back iron cores, thus reducing the weight of the rotor. Therefore, the fractional slot Halbach motor can reduce weight, making it a very suitable for UAM applications. Fig. 1 (a) shows the basic layout of UAM motor, and the design target specifications are as follows: 40-pole 48-slot, DC voltage 600 V, maximum power 50 kW, maximum torque 180 Nm, maximum speed 3 krpm, power density 4 kW/kg. The rotor has a two-segment Halbach array, so only two kinds of magnetization are used: radial and circumferential. The wider the radial magnet, the higher the field density. For this, radial magnets are designed wide and circumferential magnets are narrow. Then the height of the circumferential magnet is not enough to provide complete flux return in the back. The design shown in Fig. 1 (a) has a shallow back iron core at the bottom of permanent magnets (PMs). It supports flux return that is not managed by circumferential PM. Therefore, it is necessary to efficiently determine the ratio of radial to circumferential PMs, and the ratio of magnet to back iron. There are three design variables for optimal design of the rotor. One is the radial magnet coverage ratio $\alpha = \tau_r / \tau_p$, the other is the PM height ratio $\delta = h_m / h_r$, the other is the rotor height ratio $\gamma = h_r / \tau_p$, where τ_r is the angle for radial magnets, τ_p is the pole pitch angle, h_m is the magnet height, and h_r is the rotor height. The design goal is to minimize the weight of the rotor while meeting the output torque requirements. To meet the design requirements in the proposed two-segment Halbach motor, three design variables α , δ , and γ must be found that ensure that $w_r(\gamma)$ is minimized at the same time $T_e(\alpha, \delta, \gamma) > 180$ Nm. T_e is the electromagnetic torque and w_r is the weight of the rotor. In finite element analysis (FEA)-based design, the number of models to be analyzed increases exponentially as the number of design variables increases. Therefore, FEA design is not suitable for such multivariate optimization. The subdomain can find the optimal design much faster because the result can be obtained by simply changing the design variables. In this paper, the subdomain method was combined with the magnetic equivalent circuit (MEC) analysis to account for the core saturation occurring under load conditions [2]. Fig. 1 (b) shows the domain setup of the subdomain analysis, and (c) shows the MEC model [3]. Fig. 1 (d) shows the airgap flux density compared to the FEA results. It more accurately matches the FEA results when saturation is considered through the MEC. With the combined method, we can find the minimum rotor height ratio $\gamma(\alpha, \delta)$ that satisfies the torque specification $T_e \geq 180$ Nm, which is shown as dots in Fig. 2 (a). Furthermore, $\gamma(\alpha, \delta)$ can be approximated as a concave function with minimum values at a certain point (α^*, δ^*) and is: $\gamma_{LSM}(\alpha, \delta) = p_{00} + p_{10}\alpha + p_{20}\alpha^2 + p_{01}\delta + p_{11}\alpha\delta + p_{02}\delta^2$, where p_{xy} is the coefficient of $\alpha^x\delta^y$ in γ_{LSM} . By applying the least square method (LSM), we can find the best fitting coefficients. $\gamma \approx XP$, where P is the matrix of coefficients p_{xy} and X is the matrix of variables α and δ . Let the cost be defined by $J = 1/2 * (\gamma - XP)^T (\gamma - XP)$. Then, the cost minimizing solution is obtained as $P = (X^T X)^{-1} X^T \gamma$. The resulting function $\gamma_{LSM}(\alpha, \delta)$ with the fitted coefficients are depicted as planes shown in Fig. 2 (a). The minimum point can be found by solving $\partial \gamma_{LSM} / \partial \alpha = 0$ and $\partial \gamma_{LSM} / \partial \delta = 0$, and is obtained such that $\alpha^* = (2p_{10}p_{02} - p_{01}p_{11}) / (p_{11}^2 - 4p_{20}p_{02})$, $\delta^* = (2p_{20}p_{01} - p_{10}p_{11}) / (p_{11}^2 - 4p_{20}p_{02})$. While satisfying the required torque, the minimum rotor height is obtained as $\gamma^* = 0.37$ when $\alpha^* = 0.61$ and $\delta^* = 0.85$. That is, when the rotor height is $h_r = 0.37\tau_p = 6.5$ mm, the desired torque can be achieved with the minimum rotor weight. Fig. 2 (b) shows rotor weights, and (d) shows an optimized design using the proposed method. To verify the optimized design algorithm, the proposed Halbach motor is compared with SPMSM and a coreless Halbach motor without rotor back irons. For comparison, SPMSM uses the same amount of magnets as the proposed Halbach motor and raises the height of the back iron until it meets the torque spec-

ification. For coreless Halbach motors, radial and circumferential magnets are designed to have the same arc according to the existing design. Note that the stator remains the same for accurate comparison. Fig. 2 (d) shows the torque waveform through FEA when $I_{ph} = 90$ A_{rms}. The torque of the proposed Halbach motor is 187.4 Nm, and it has the highest torque. At this time, the rotor weight is 2.54 kg, which has a high power density of 4.17 kW/kg. The SPMSM and coreless Halbach motors have similar torque, but for SPMSM, the rotor height must be increased to 10.5 mm to achieve similar torque levels. Thus, the power density decreases to 3.71 kW/kg.

[1] T. F. Talerico, Z. A. Cameron, and H. Hasseeb, "Outer Stator Magnetically-Geared Motors for Electrified Urban Air Mobility Vehicles," *AIAA/IEEE Electric Aircraft Technologies Symposium (EATS)*, pp. 1-25 (2020) [2] M. Lee, B. Koo and K. Nam, "Analytic Optimization of Halbach Array Slotless Motor Considering Stator Yoke Saturation," in *IEEE Trans. on Magn.*, (2020) [3] S. Wu, X. Zhao, and C. Jiu, "Multi-Objective Optimal Design of a Toroidally Wound Radial-Flux Halbach Permanent Magnet Array Limited Angle Torque Motor," in *IEEE Trans. on Ind. Electron.*, vol. 64, no. 4, pp. 2962-2971 (2017)



(a) A pole pair of Halbach motor model, (b) simplified subdomain model, (c) MEC model, and (d) comparison of airgap flux density.



(a) $\gamma(\alpha, \delta)$ that satisfies $T_e > 180$ Nm and fitted curve $\gamma_{LSM}(\alpha, \delta)$ using LSM, (b) rotor weights versus δ for different α , (c) flux density of the optimized motor, and (d) torque comparison when $I_{ph} = 90$ A_{rms}.

AP-10. Calculation and Decomposition of Zig-Zag Leakage Flux Losses in a Wet Submersible Induction Machine by the Virtual Permanent Magnet Harmonic Machine Model.

J. Yan¹, C. Di¹ and X. Bao¹

1. School of Electrical Engineering and Automation, Hefei University of Technology, Hefei, China

1. Induction: The accurate estimation of the harmonic losses caused by the zig-zag leakage flux which occupies a high proportion of stray losses is of great significance in the efficiency calculation as well as the optimization design for the wet submersible induction machine [1]. To precise estimate the zig-zag leakage flux losses at the nominal load, it is necessary to determine losses induced by a particular order of the air-gap flux density harmonic. 2. Analysis and Calculation: In this paper, a two-dimensional finite element method is presented to separate zig-zag leakage flux losses produced by the stator slot harmonic, rotor slot harmonic and interaction harmonic between them, respectively. The air-gap magnetic flux density is decomposed by the two-dimensional fast Fourier transform at a sampling frequency of 5000 Hz. The hybrid excited virtual permanent magnet harmonic machine model is applied to reconstruct the air-gap magnetic field and excited the stator and rotor separately, in which the iron core node magnetic flux density is extracted and decomposed [2]. Each node harmonic iron loss is acquired through the modified Bertotti’s iron loss model with the consideration of high frequency power losses as a function of the magnetic flux density. The losses caused by a single harmonic are obtained by subtracting the losses resulted from the hybrid excitation [3]. Fig. 1(a) shows rotor iron losses density distribution induced by the -17th harmonic, which denotes the first order stator slot harmonic. The rotor is equipped with the closed slot because of the machine’s water-filled operating environment, where the mixed mesh subdivision through triangular mesh and rectangular mesh are employed. It can be seen in Fig. 1(a) that the -17th harmonic penetrates into the rotor surface where the mapped mesh exists. Meanwhile, Fig. 1(b) and Fig. 1(c) display rotor bar and stator winding eddy-current density distributions respectively, where the current density engendered by the -17th harmonic close to the air gap is higher than the rest in other positions. 3. Results: The zig-zag leakage flux losses calculated includes the surface and pulsation losses in the stator and rotor as well as eddy-current losses in the stator winding and squirrel cage. Different proportion of losses caused by corresponding harmonics have important reference for the optimization of the power density of the machine. Table I displays the losses caused by the first and second order stator slot harmonics, together with the first order rotor slot harmonic (-20th and 22nd). In Table I, ‘Nan’ expresses that the corresponding values are small or approach zero. It can be represented that the losses reduce with the order of harmonic, therefore, the iron losses in the stator can be neglected. Meanwhile, the rotor losses generated by the rotor slot harmonic is not listed in the table, because the rotor slot harmonic rotates synchronously with the rotor itself. It can be concluded that the eddy-current losses in the squirrel cage caused by -17th harmonic account for the largest proportion among the overall zig-zag leakage flux losses. Hence, to improve the power density of the machine, effective measures (e.g. rotor skew, semimagnetic wedge) can be taken to reduce the -17th harmonic. The method shown in this paper separates the zig-zag leakage flux harmonic losses and lays a fundamental for the machine design as well as the optimization.

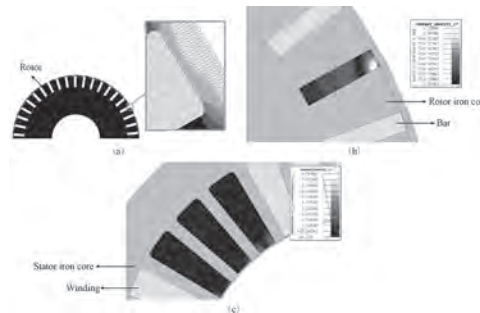


Fig. 1 Losses density and current density distributions produced by -17th harmonic at the nominal load. (a) Rotor iron losses. (b) Rotor bar eddy-current. (c) Stator winding eddy-current.

TABLE I
Main Harmonic Amplitude and Zig-Zag Leakage Losses

Harmonic order	Amplitude (T)	Iron losses in the stator, W	Eddy-current losses in the rotor winding, W	Iron losses in the rotor, W	Eddy-current losses in the squirrel cage, W
-17	0.1790	0.804	313.95	17.371	1426.79
19	0.1339	Nan	92.19	22.931	399.81
-20	0.1091	Nan	91.7	Nan	Nan
22	0.1084	Nan	60.42	Nan	Nan
-25	0.08069	Nan	5.22	5.285	20.14
37	0.05959	Nan	1.81	5.112	11.31

Table I Main Harmonic Amplitude and Zig-Zag Leakage Losses

[1] R. Hagen, T. Knopik, and A. Binder, IEEE Int. Elect. Mach & Drives Conf., p. 1325-1330 (2009) [2] C. Di, I. Petrov, and J. J. Pyrhönen, IEEE Trans. Magn., Vol. 54, p. 1-12 (2018) [3] C. Di, I. Petrov, and J. J. Pyrhönen, IEEE Access, Vol. 7, p. 27746–27755 (2019)

AP-11. Analytical Modeling for the Flux Reversal Permanent Magnet Machine With Halbach Array Magnets in Rotor Slot.

K. Yang¹, T. Zhang¹, F. Zhao¹ and Y. Wang¹

1. Harbin Institute of Technology Shenzhen, Shenzhen, China

I. INTRODUCTION In recent years, due to the merits of easy thermal management, alleviated torque ripple and robust rotor, flux reversal permanent magnet (FRPM) machines have attracted more and more attention [1]. However, since the large leakage flux leads to the limitation of its output, a series of novel topologies are proposed, such as the consequent-pole FRPM machine [2], the FRPM machine with asymmetric-stator pole configuration [1] and the FRPM machine with Halbach array magnets in rotor slot (HAM-FRPM) [3], etc. This study presents an analytical sub-domain model for the characteristic evaluation of the HAM-FRPM machine. By dividing the HAM-FRPM machine into seven sub-domains and solving the Maxwell equations in polar coordinate for each region according to the boundary conditions, the vector magnetic potential can be obtained. Subsequently, the radial and tangential flux density can be calculated. Finally, the analytical results are compared with the finite element method (FEM) to verify the accuracy. II. ANALYTICAL SUB-DOMAIN MODEL One 12-stator slot/17-rotor tooth HAM-FRPM machine with double-layer winding is investigated in this paper to verify the proposed method. As shown in Fig. 1, the permanent magnet (PM) arrangement in the stator of the HAM-FRPM machine is identical to that of the consequent-pole FRPM machine. In addition, the PMs in each rotor slot are the same, which contain a radially magnetized middle PM and two tangentially magnetized side PMs. In this analytical sub-domain modeling, some essential assumptions have been made in advance: (1) The permeability of iron is regarded as infinite. Also, the relative permeability of PMs and coils is assumed to be 1; (2) The end effect and the magnetic field component on the axial direction are neglected; (3) The geometrical structure side of the HAM-FRPM machine is parallel to either r or θ direction in polar coordinate. As shown in Fig. 2, the HAM-FRPM machine is divided into several regions: stator slot (Region i), stator slot opening (Region l and Region u), PM (Region s and Region g), air gap (Region l) and rotor slot (Region j). Maxwell equation is satisfied in each region as equation (1), which can be expressed as a Poisson equation or a Laplace equation and further solved by the separation of variables method. According to the law of magnetic flux continuity and Neumann condition, the unknown coefficients can be derived. Finally, the radial flux density B_r and tangential flux density B_θ can be obtained by (2). where J and M are the current density vector and magnetization vector of magnets, respectively. μ_0 is the magnetic permeability of vacuum. III. RESULTS AND DISCUSSION The air gap flux density comparisons between the analytical prediction and FEM results are exhibited in Fig.3-4, which present a good agreement between the analytical results and FEM solution for both radial and tangential air gap flux density. Hence, the proposed analytical model is verified to be used to predict the performances of the HAM-FRPM machines. Fig.5-6 show the back-EMF and torque waveforms, which validate the correctness of analytical model. More detailed derivation and analysis will be shown in the full paper.

[1] H. Yang, H. Lin, Z. Q. Zhu, S. Lyu, and Y. Liu, "Design and Analysis of Novel Asymmetric-Stator-Pole Flux Reversal PM Machine," *IEEE Transactions on Industrial Electronics*, vol. 67, no. 1, pp. 101-114, 2020. [2] Y. Gao, R. Qu, D. Li, J. Li, and G. Zhou, "Consequent-Pole Flux-Reversal Permanent-Magnet Machine for Electric Vehicle Propulsion," *IEEE Transactions on Applied Superconductivity*, vol. 26, no. 4, pp. 1-5, 2016. [3] K. Yang, F. Zhao, Y. Wang, and Z. Bao, "Consequent-Pole Flux Reversal Permanent Magnet Machine with Halbach Array Magnets in Rotor Slot," *IEEE Transactions on Magnetics*, pp. 1-1, 2020.

$$\frac{\partial^2 A(r, \theta)}{\partial r^2} + \frac{1}{r} \frac{\partial A(r, \theta)}{\partial r} + \frac{1}{r^2} \frac{\partial^2 A(r, \theta)}{\partial \theta^2} = -\frac{J_r}{\mu_0} \quad r = i \quad (1)$$

$$\frac{\partial A(r, \theta)}{\partial r} = 0 \quad r = i, s, g \quad (2)$$

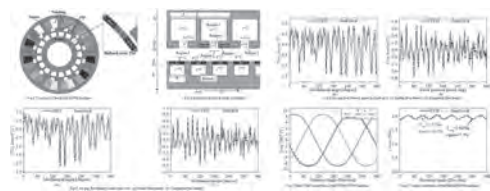
TABLE I. GENERAL SOLUTION OF THE VECTOR MAGNETIC POTENTIAL IN EACH REGION

Region	General solution
1	$A(r, \theta) = A_0 - \frac{1}{2} \mu_0 J_r r^2 + \sum_{n=1}^{\infty} \left[\frac{C_n}{r} + \frac{D_n r}{r} \right] \cos(n\theta) + \sum_{n=1}^{\infty} \left[\frac{E_n}{r} + \frac{F_n r}{r} \right] \sin(n\theta) + \sum_{n=1}^{\infty} \left[\frac{G_n}{r} + \frac{H_n r}{r} \right] \cos(n\theta) + \sum_{n=1}^{\infty} \left[\frac{I_n}{r} + \frac{J_n r}{r} \right] \sin(n\theta)$
2	$A(r, \theta) = A_0 - \frac{1}{2} \mu_0 J_r r^2 + \sum_{n=1}^{\infty} \left[\frac{C_n}{r} + \frac{D_n r}{r} \right] \cos(n\theta) + \sum_{n=1}^{\infty} \left[\frac{E_n}{r} + \frac{F_n r}{r} \right] \sin(n\theta) + \sum_{n=1}^{\infty} \left[\frac{G_n}{r} + \frac{H_n r}{r} \right] \cos(n\theta) + \sum_{n=1}^{\infty} \left[\frac{I_n}{r} + \frac{J_n r}{r} \right] \sin(n\theta)$
3	$A(r, \theta) = A_0 - \frac{1}{2} \mu_0 J_r r^2 + \sum_{n=1}^{\infty} \left[\frac{C_n}{r} + \frac{D_n r}{r} \right] \cos(n\theta) + \sum_{n=1}^{\infty} \left[\frac{E_n}{r} + \frac{F_n r}{r} \right] \sin(n\theta) + \sum_{n=1}^{\infty} \left[\frac{G_n}{r} + \frac{H_n r}{r} \right] \cos(n\theta) + \sum_{n=1}^{\infty} \left[\frac{I_n}{r} + \frac{J_n r}{r} \right] \sin(n\theta)$
4	$A(r, \theta) = A_0 - \frac{1}{2} \mu_0 J_r r^2 + \sum_{n=1}^{\infty} \left[\frac{C_n}{r} + \frac{D_n r}{r} \right] \cos(n\theta) + \sum_{n=1}^{\infty} \left[\frac{E_n}{r} + \frac{F_n r}{r} \right] \sin(n\theta) + \sum_{n=1}^{\infty} \left[\frac{G_n}{r} + \frac{H_n r}{r} \right] \cos(n\theta) + \sum_{n=1}^{\infty} \left[\frac{I_n}{r} + \frac{J_n r}{r} \right] \sin(n\theta)$
5	$A(r, \theta) = A_0 - \frac{1}{2} \mu_0 J_r r^2 + \sum_{n=1}^{\infty} \left[\frac{C_n}{r} + \frac{D_n r}{r} \right] \cos(n\theta) + \sum_{n=1}^{\infty} \left[\frac{E_n}{r} + \frac{F_n r}{r} \right] \sin(n\theta) + \sum_{n=1}^{\infty} \left[\frac{G_n}{r} + \frac{H_n r}{r} \right] \cos(n\theta) + \sum_{n=1}^{\infty} \left[\frac{I_n}{r} + \frac{J_n r}{r} \right] \sin(n\theta)$
6	$A(r, \theta) = A_0 - \frac{1}{2} \mu_0 J_r r^2 + \sum_{n=1}^{\infty} \left[\frac{C_n}{r} + \frac{D_n r}{r} \right] \cos(n\theta) + \sum_{n=1}^{\infty} \left[\frac{E_n}{r} + \frac{F_n r}{r} \right] \sin(n\theta) + \sum_{n=1}^{\infty} \left[\frac{G_n}{r} + \frac{H_n r}{r} \right] \cos(n\theta) + \sum_{n=1}^{\infty} \left[\frac{I_n}{r} + \frac{J_n r}{r} \right] \sin(n\theta)$
7	$A(r, \theta) = A_0 - \frac{1}{2} \mu_0 J_r r^2 + \sum_{n=1}^{\infty} \left[\frac{C_n}{r} + \frac{D_n r}{r} \right] \cos(n\theta) + \sum_{n=1}^{\infty} \left[\frac{E_n}{r} + \frac{F_n r}{r} \right] \sin(n\theta) + \sum_{n=1}^{\infty} \left[\frac{G_n}{r} + \frac{H_n r}{r} \right] \cos(n\theta) + \sum_{n=1}^{\infty} \left[\frac{I_n}{r} + \frac{J_n r}{r} \right] \sin(n\theta)$

Abbreviation: A_0, A_n, B_n, C_n are the cosine coefficients of each space (respectively); J_r is the DC component of the current density; J_n is peak value of the harmonic component of the current density; M_n is the peak value of the harmonic component of the radial magnetization of the inner PM; M_n is the peak value of the harmonic component of the radial magnetization of the rotor PM; M_n is the peak value of the harmonic component of the tangential magnetization of the inner PM.

Definition: $\theta_1(i, j) = \frac{2\pi}{p} \left(\frac{r}{R} - \frac{1}{2} \right)$; $\theta_2(i, j) = \frac{2\pi}{p} \left(\frac{r}{R} + \frac{1}{2} \right)$

Unknown coefficients: $A_0, A_n, B_n, C_n, D_n, E_n, F_n, G_n, H_n, I_n, J_n, K_n, L_n, M_n, N_n, O_n, P_n, Q_n, R_n, S_n, T_n, U_n, V_n, W_n, X_n, Y_n, Z_n$



AP-12. Analytical Study and Comparison of Electromagnetic Characteristics of 8-Pole 9-Slot and 8-Pole 12-Slot Permanent Magnet Synchronous Machines According to Rotor Eccentricity.

H. Lee¹, T. Bang¹, J. Woo¹, K. Shin² and J. Choi¹

1. Chungnam National University, Daejeon, The Republic of Korea;

2. Power System Engineering, Chonnam National University, Yeosu, The Republic of Korea

Permanent magnet synchronous motors have become necessary in several industries that develop home appliances, industrial tools, and electrical vehicles; in addition, there is a growing interest in resolving motor malfunctions. Data provided in [1] show that 41% of motor faults are bearing faults, 37% are stator faults, 10% are rotor faults, and 12% are other faults. One of the main causes of malfunction is rotor eccentricity, wherein the center of the rotor axis deviates from the center of the stator, so that the air gap is not uniform. Static eccentricity, a type of rotor eccentricity, is a condition where the position of the minimum radial air gap is fixed [2]. This can be caused by stator core ovality, incorrect positioning of the stator core, or bearing at commissioning or following a repair, and its level does not change over time [3]. As the magnetic flux density in the air gap is an important characteristic of the machine performance [4] [5], the characteristics of the permanent magnet machine and the impact of rotor eccentricity on the magnetic field distribution must be analyzed. Finite element and analytical methods are employed to design a permanent magnet synchronous motor or perform characteristic analysis. The finite element method (FEM) is a numerical process that can be performed using a commercial tool. However, it is necessary to learn to use each commercial tool and have a disadvantage depending on the experience of the designer for accurate analysis. The analytical method analyzed the electromagnetic field characteristics using Maxwell's equation. Magnetization modeling is applied to the design of the machine using the Fourier series and partial differential equations derived using the magnetic vector potential. It must be preceded by deriving a solution that considers various boundary conditions. Several studies are being conducted because the analytical method can quickly predict the characteristic variation according to the design parameters. This study compared electromagnetic characteristics based on rotor eccentricity using the analytical method. Magnetic flux density, induced voltage, and unbalanced magnetic force were derived using the analytical models. The results were verified by experiments and the FEM. Figure 1(a) shows the experimental setup, and Fig. 1(b) shows the manufactured test motors. An experimental setting was constructed to control rotor eccentricity. To measure the back-EMF at the rated speed, a back-to-back system was constructed, wherein one servo motor and one test motor were arranged successively. In addition, the rotor eccentricity was precisely controlled using two gap sensors. The analysis model was simplified based on several assumptions obtained from the analytical method. Based on the electromagnetic field and perturbation theories, the governing equations of the air-gap region were derived. Furthermore, the relationship between the magnetic vector potential in each region and appropriate boundary conditions was used to obtain undefined coefficients to derive magnetic flux density characteristics in each region. Figures 2(a) and (b) exhibit the magnetic flux density derived using the analytical method and the radial and tangential components with a 25% eccentricity ratio. The induced voltage was derived using the magnetic flux density, and Figs. 2(c) and (d) show the comparison of the induced voltages of the 8-pole 12-slot and 8-pole 9-slot models. The induced voltage of the 8-pole 12-slot model was expressed by each branch of winding because of the symmetry of the winding distribution. The induced voltage of the 8-pole 9-slot model differs in magnitude for each of the three phases owing to the asymmetry of the winding distribution. These no-load characteristics affect the load and reduce the life of the machine. The analytical results were validated by comparing the FEM and experimental results. Detailed results, discussions, and desired effects will be presented in the main paper.

[1] J. R. Cameron, W. T. Thomson, and A. B. Dow, "Vibration and current monitoring for detecting airgap eccentricity in large induction motors," *Proc. IEE Electr. Power Appl. B*, vol. 133, no. 3, pp. 155–163, May 1986. [2] Q. Zhu, D. Howe, E. Blöte, and B. Ackermann, "Instantaneous magnetic field distribution in brushless permanent magnet DC motors, Part I: Open-circuit

field", *IEEE Trans. Magn.*, vol 29, pp. 124-135, Jan. 1993. [3] U. Kim and D. K. Lieu, "Magnetic field calculation in permanent magnet motors with rotor eccentricity: Without slotting effect", *IEEE Trans. Magn.*, vol. 34, no. 4, pp. 2242-2252, Jul. 1998. [4] A. Rahideh and T. Korakianitis, "Analytical open-circuit magnetic field distribution of slotless brushless permanent magnet machines with rotor eccentricity", *IEEE Trans Magn.*, vol 47, no. 12, pp. 4791-4808, Jun. 2011. [5] U. Kim and D. K. Lieu, "Effects of magnetically induced vibration force in brushless permanent magnet motors", *IEEE Trans. Magn.*, vol. 41, no. 6, pp. 2164-2172, Jun. 2005.

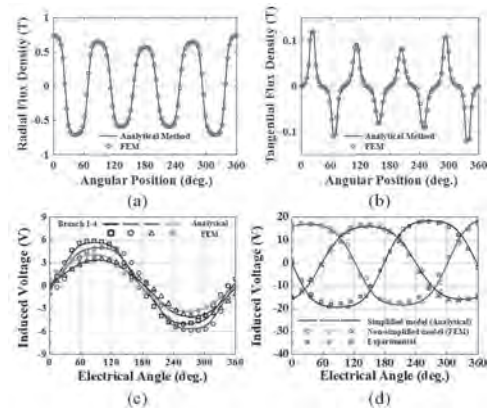
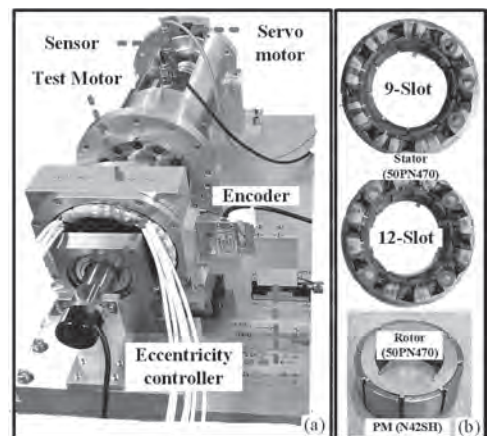


Fig. 2. Electromagnetic characteristic according to rotor eccentricity: (a) radial flux density, (b) tangential flux density, (c) induced voltage of 8-pole 12-slot model, and (d) induced voltage of 8-pole 9-slot model.



Figs. 1. (a) Experimental setup, and (b) manufactured test motor.

AP-13. Particular Reduced Scalar Potential Formulation for End Winding Magnetic Circuits Modeling Enabling Increased Field Weakening in PM Motors.

E.K. Karamanis¹ and A.G. Kladas¹

1. Electrical and Computer Engineering, National Technical University of Athens, Zografou, Greece

Permanent magnet machines are now-a-days very popular in electric traction applications requiring a wide constant-power speed range. However, the field weakening action, necessary in higher speeds creates important air gap field distribution distortion and increased losses leading to particular configurations search, such as conjunction with variable reluctance rotors [1], pole shoe configurations [2], flat embedded magnet topologies [3], convenient stator windings and permanent magnet arrangements [4], axial flux topologies [5]. In the present paper a convenient configuration of stator windings in permanent magnet motors is proposed involving appropriate additional end winding magnetic circuits in order to achieve inductance management. Such a technique can be applied in all permanent magnet motor configuration cases and enables increased flux weakening capability in high rotor speeds, resulting in substantial efficiency improvements. The optimal design of these extra iron cores can be modeled by adopting a particular reduced scalar potential formulation and the resulting finite element model can be facilitated considering appropriate two dimensional configurations. The overall analysis is performed through co-simulation of the additional magnetic circuits simultaneously with the permanent magnet synchronous machine active part. The proposed methodology enables appropriate handling of increased flux weakening effects in traditional surface mounted permanent magnet motors. It exploits the end zone part of the windings, which does not contribute in the machine torque and performance. The main concept involves introduction of convenient magnetic circuits in the end zone parts of stator coils. These magnetic circuits enable magnetic coupling with auxiliary windings which are connected to appropriate varistors and are energized in desired electromotive force values developed at specific speed ranges through convenient selection of turns ratios. The magnetic material proposed for the additional magnetic circuits is a particular Ferrite ensuring low losses in order not to compromise the machine efficiency. Moreover, the increase of the stator windings leakage inductance is reduced when the auxiliary windings are not energized and is greatly increased when the varistors are activating them. The representation of such configurations necessitates in general a 3D finite element modeling of the whole machine, which is very demanding in computational means. However, an important reduction in computation requirements can be achieved by adopting an appropriate reduced scalar potential formulation, involving one unknown per node. A further calculation simplification can be obtained by implementing an appropriate two dimensional axisymmetric representation for the additional magnetic circuits in conjunction with a two dimensional Cartesian representation of the motor active part and by adopting a direct coupling of field and circuit equations [6]. The methodology developed has been applied in a permanent magnet synchronous machine case with surface permanent magnet rotor configuration and rated power of 100 kW. The motor end winding geometry for one pole part illustrating the additional ferrite toroidal magnetic circuits positioning is shown in Fig. 1. The obtained efficiency maps in cases without and with the additional magnetic circuits are shown in Figs. 2a and 2b, respectively, illustrating the important efficiency improvement resulting in high speed ranges. It may be noted that the proposed technique can offer great services in field weakening action and respective efficiency improvements at high speed ranges of all permanent magnet machine configurations implemented in electric traction applications.

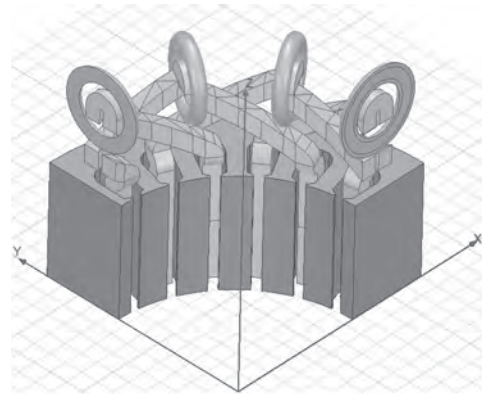


Fig. 1 Stator windings end zone geometry of one pole part of the machine illustrating the additional magnetic circuits positioning.

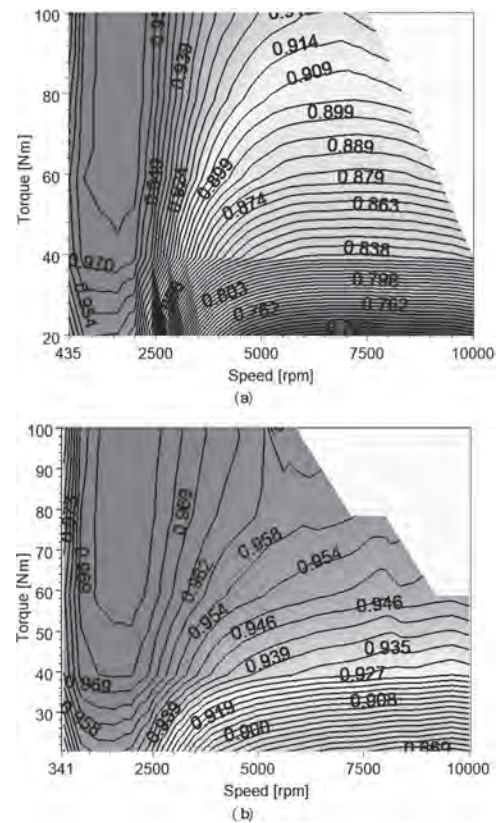


Fig. 2 Efficiency maps of the permanent magnet motor in cases (a) without additional end winding magnetic circuits (b) with additional end winding magnetic circuits.

[1] C. Tang, W.L. Soong, T.M. Jahns, et al., IEEE Transactions on Industry Applications, Vol. 51, p.3761 (2015) [2] N. Zhao and N. Schofield, IEEE Transactions on Magnetics, Vol. 53, p. 8112607 (2017) [3] S. Chaithongsuk, B. Nahid-Mobarakeh, J.P. Caron et al., IEEE Transactions on Industrial Electronics. Vol. 59, p.2484 (2012) [4] M.S. Toulabi, J. Salmon and A.M. Knight, IEEE Transactions on Industry Applications, Vol. 53, p.1892 (2015) [5] A. Hemeida, M. Taha, A. Abdallah, et al., IEEE Transactions on Energy Conversion, Vol. 32, p.111 (2017) [6] E. Karamanis and A. Kladas, 2020 International Conference on Electrical Machines (ICEM), p.332 (2020).

Session AQ**ADVANCES IN (SEMI)-ANALYTICAL AND NUMERICAL TECHNIQUES FOR DESIGN II
(Poster Session)**

Guillaume Parent, Chair
Université d'Artois, Béthune, France

AQ-01. An Acceleration Method for Reaching Steady-State Performance in Time-Stepping Finite Element Analysis.

Y. Li¹, Y. Feng¹, S. Huang¹, B. Ma¹, G. Wu¹ and J. Zhu²
1. College of Electrical and Information Engineering, Hunan University, Changsha, China; 2. School of Electrical and Information Engineering, University of Sydney, Sydney, NSW, Australia

Introduction: Time-step finite element method is widely used in the transient simulation because the harmonic of magnetic fields and the nonlinear characteristics of the material can be processed simultaneously [1]. However, the steady-state solution of the transient simulation convergence slowly due to the time constant characteristic in field-circuit coupling computation [2-3]. Aiming at this problem, this paper proposes an acceleration method based on the estimation of initial values in time step simulation by time harmonic analysis. With the precalculated initial solution, the iteration steps for each point calculation and time for convergence to the steady state are effectively saved. Meanwhile, the advantages of the traditional time step method are well retained. A permanent magnet assisted synchronous reluctance motor (PM-assisted SynRM) is investigated by the proposed method. The comparison results with traditional FEM demonstrate the effectiveness of the proposed method in reducing the iterations step for searching a steady-state solution in the transient simulation. The proposed approach: Firstly, the governing equation for the electromagnetic field can be formulated as equation (1) in Fig. 1. The problem formula also includes the following two equations (2) and (3) in Fig. 1, which describe the connection of the circuit. We can establish field-circuit coupling equations through (1), (2), and (3). Secondly, in time-harmonic analysis, time dependence can be eliminated from the equations by using complex field quantities (4) in Fig. 1. By Galerkin discretization in time-harmonic, the weak formulas (1) and (3) are formed into (5) and (6) in Fig.1. The complex system of equations can be written in the matrix form (7), (8), (9), and (10) in Fig.1. Newton's method is adapted for the nonlinear solution. Taylor expansion is applied to the Jacobian matrix as (11) and (12) in Fig.1 to satisfy the Cauchy-Riemann differential equations. The unknown vector in the time-harmonic simulation is then solved by (13) in Fig. 1 iteratively and only a small number of steps is required for convergence. In the harmonic analysis, the vector potential a can be described as a periodic function in Fig1. (14). The achieved time-harmonic solution is then transferred into the time domain system (16) according to (15) as the initial value at $t=0s$. Since the time-harmonic simulation results are very close to the steady-state solution in the transient simulation, the iteration for each time-stepping solution can be fast with fewer steps than the traditional method. Also, the time step required for convergence to the steady-state is shortened further. Thereby the total calculation time significantly reduced. The effectiveness of the presented method is verified by the following simulation case. Numerical example: Fig. 2 (a) illustrates the mesh diagrams for the FE model of the PM-assisted SynRM. The time-step simulation is performed at a frequency of 100Hz, and the motor is power by a sinusoidal voltage source with 350V RMS line voltage and -28.3 load angle. Two simulation models run in Matlab on the same workstation. The total cost for the 0.3s simulation of the traditional time-stepping method and the proposed method is 58 mins and 16 mins, respectively. As shown in Fig. 2 (b), the simulation convergence to steady-state at 0.15s, and the corresponding computation cost is 8.5 mins, which means the proposed method is 6 time faster. The good agreement of both methods in steady-state torque calculation in Fig. 2 (b) also demonstrates the accuracy of the proposed method. Conclusion: The effectiveness of the proposed method is verified by the PM-assisted SynRM example. Moreover, due to the universality of the model derivation, it is also applicable to other electrical machines e.g. induction machines.

[1] Shinji Wakao, Masato Tokuhisa, and Atsushi Maeda, "Acceleration of convergence characteristics of time-stepping FE analysis for rotating machines," IEEE Trans. Magn., vol.37, no.5, pp. 3558-3561, 2001. [2] W. N. Fu, S. L. Ho, and Ping Zhou, "Reduction of computing time for steady-state solutions of magnetic field and circuit coupled problems using time-domain finite-element method," IEEE Trans. Magn., vol. 48, no. 11, pp. 3363-3366, 2012. [3] Oszkár Bíró and Kurt Preis, "An efficient time-

domain method for nonlinear periodic eddy current problems," IEEE Trans. Magn., vol. 42, no. 4, pp. 695-698, 2006.



Fig. 1

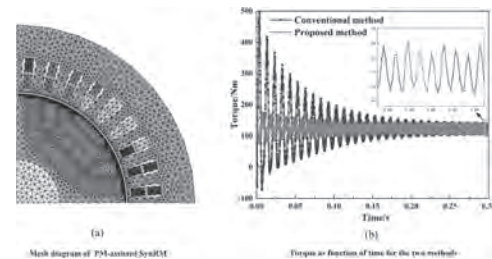


Fig. 2

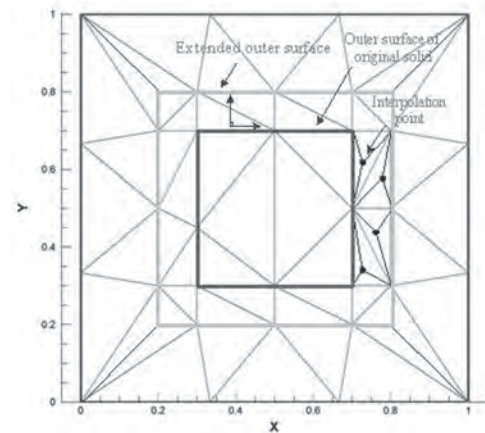
AQ-02. An Automatic Local Mesh Refinement Method on Material Interfaces for Enhancing the Solution Accuracy in Electric Field Computation.

Y. Zhao¹, S. Cheng¹ and W. Tao¹

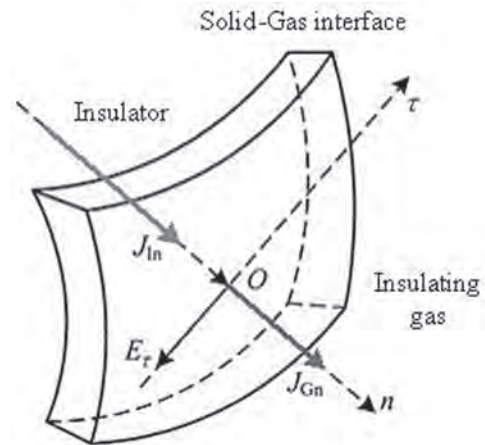
¹. Wuhan University, Wuhan, China

When applying finite element method (FEM) to solve electromagnetic field distribution, it is often ideal to refine the mesh near the interface or surface of the concerned equipment locally in order to ensure the solution accuracy along these surfaces. For example, in the calculation of the electric field distribution within a valve hall of large converter station, the distance between the outlet bushing and the equalizing device is very close, and the valve hall contains a lot of metal and dielectric material interfaces. Since the electric field on the metal surface is important to know for the insulation design, special treatment of the finite element mesh elements there is an essential problem. If we create a fine mesh everywhere for the whole model, it will lead to a huge amount of unnecessary computing resources, so how to establish a well-distributed locally refined mesh so as to get accurate resolution of the electric field distribution is worth being investigated. How to automatically generate the ideal mesh is proposed in this work. In [1-3], the adaptive mesh generation method is studied by choosing the best discretization method, and gradually adjusting the mesh according to the estimated error to improve the solution accuracy. This method has better accuracy and less calculation overhead, but it is difficult to realize the adaptive mesh generation of complex model automatically. In [4], the electric field of valve hall is calculated by a sub model method. Although the accuracy of local calculation results is improved, the transfer error will be formed in boundary interpolation, and the process of sub model method is cumbersome and the efficiency is low. For example, with more and more use of gas insulated metal enclosed transmission lines(GIL), for which surface charge accumulation is the main cause of insulator flashover or failure, when the voltage polarity is reversed, the electric field distortion effect caused by surface charge accumulation will be more prominent [5]. In [6], many thin layers are established on the interface between GIL basin insulator and insulating gas, which can be ignored compared with insulator. The charge in the thin layer can be regarded as the surface charge in this area, and the direction from insulator to gas is set as the normal direction of electric field. Based on this, the surface charge accumulation of insulator is studied. For post insulator, the shape is more complex, the thickness of thin layer, the size of area and the number of nodes will directly affect the results of surface charge accumulation. The main idea of the proposed method is given here. For complex geometry model of an electrical power equipment, the coordinates of the nodes on the object interface can be obtained during the initial mesh generation. Based on this, the normal vectors of any node on the surface can be obtained easily, and then the whole interface can be extended along the normal vectors, and the extension distance can be controlled based on suitable criteria. Then we get the same or similar mesh surface layers as the original solid surface, insert a given number of nodes between the two surfaces and on the two surfaces, and finally complete the mesh generation. Fig.1 is the schematic diagram of equipment surface extension. By using this method, any region of the model can be expanded along the surface and nodes can be inserted to refine the mesh. When the distance of power fittings is very close, it is also convenient to obtain the interface of the expansion area and divide the material properties, or judge in advance which expansion distance the two surfaces will be connected and make constraints, so as to reduce the subsequent assignment of the material properties of the interface. For the valve hall of high voltage converter station, due to the large number of equipment parts, the mesh can be refined only on the surface of the equipment object that needs to be concerned. At the same time, because the expanded thickness and the number of inserted nodes can be controlled, the calculation accuracy of surface electric field of GIL insulator can be improved by adding these layered elements, and the area division and mesh refinement of surface charge accumulation can be more flexible. Fig.2 is the schematic diagram of insulator gas interface. In the full paper, detailed algorithm and implementation will be demonstrated, numerical examples will also be presented to demonstrate the advantages of this adaptive mesh refinement technique by adding arbitrary number of nodes along the extended layers of the selected object.

- [1] D. Lee, J.-W. Kim, C.-G. Lee, et al., IEEE Transactions on Magnetics, Vol.47(10), p.3232-3235(2011). [2] B. Kaciewicz, Numerical Algorithms, Vol.77(1), p.57-75,(2018). [3] R.-X. Tao, Z.-Z. Wang, Transactions of China Electrotechnical Society, Vol.33(2), p.225-231(2018)(in Chinese). [4] D.-C. Huang, J.-J. Ruan, W. Cai, et al., IEEE Transactions on Dielectrics and Electrical Insulation, Vol.16(1), p.88-98,(2009). [5] A. Winter, J. Kindersberger, IEEE Transactions on Dielectrics and Electrical Insulation, Vol.19(5), p.1732-1739(2012). [6] H.-Y. Zhou, G.-M. Ma, S.-P. Liu, et al., Chinese Journal of Electrical Engineering, Vol.37(04), p.1251-1260(2017) (in Chinese).



Schematic diagram of equipment surface extension



Schematic diagram of insulator gas interface

AQ-03. A Novel 3D Finite Element Modelling Approach for Calculating Axial Flux Permanent Magnet Machines Based on Scaling Air Gap Method.

Y. Bi¹, F. Chai¹ and Y. Pei¹






1. Harbin Institute of Technology, Harbin, China

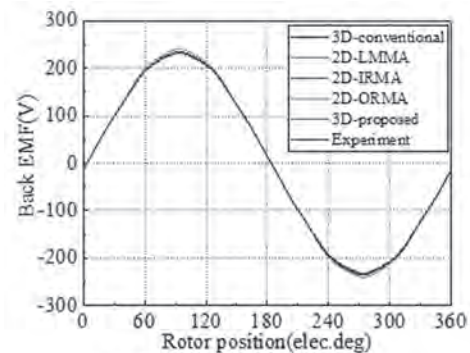
I. Introduction Axial flux permanent magnet (AFPM) machines are getting popularity in various applications. Due to the complex structure of the AFPM machine, 3 dimensional finite element analysis (3D FEA) is normally employed [1]. In order to save the computation time, several 2D FE modelling approaches have been adopted and studied by researchers. 2D linear motor approach (LMMA) is commonly used not only in the performance calculation but also in the analytical study [2]. 2D inner rotor modelling approach (IRMA) and 2D outer rotor modelling approach (ORMA) are proposed and compared with LMMA in [3]. Generally, 2D FE modelling approaches use the geometrical parameters at the average radius of the machine. Considering the variation of geometrical parameters along radial direction, geometrical parameters at different radius are taken into account by the multi-layer 2D FE modelling approaches [3, 4]. However, errors are still existed between the results gotten by 2D FEA and 3D FEA. In order to shorten the computation time and to ensure the accuracy, a 3D FE modeling approach based on scaling air gap method is proposed in this paper. II. The Principle of the Scaling Air Gap Method Basing on the expression of reluctance, the changing of geometrical parameters of an element can be balanced by the adjustment of its relative permeability. In the 3D FE modelling of an AFPM machine, the resizing of the air gap has no influence on the sizes of the other parts. It provides an opportunity to customize the air gap with equivalent relative permeability. If the air gap length is scaled to k ($k > 1$) times, its relative permeability in axial direction should be adjust to k times and its relative permeability in circumferential and radial direction should be adjust to $1/k$ times. The electromechanical energy conversion happens in the air gap, so the meshing of the air gap region is very important. Sometimes the air gap may be over meshed due to its small dimension. At this time, the scaling air gap method provides a way to reduce the number of meshes and to refine the meshing quality. III. Comparison among FEA Approaches and Experiments All the 2D and 3D FEA approaches for AFPM machines are implemented to a double-stator single-rotor AFPM machine. In this paper, we focus on the computation time and accuracy of motor performance including back electromotive force (EMF), torque output, and torque ripple. All the 2D FEA is based on multi-layer model to consider the variation of geometrical parameters at different radii. In order to make the study comprehensive, motors with different slot-pole combinations and magnet shapes are employed. Taking a 30-pole 36-slot motor with fan-shape magnets as an example, the comparison based on mesh profile and computation time are presented in Table 1. The comparison of motor performance is shown in Figure 1. It illustrates that all the 2D FEA approaches have advantages in the computation time, but there is a decrease in accuracy. The proposed 3D FEA approach based on scaling air gap method can reduce the computation time with good accuracy compared with the traditional 3D FEA approach. For further verification of the proposed method, a prototype is manufactured and tested. IV. Conclusions A 3D FE modelling approach for calculating AFPM machines based on scaling air gap method is proposed in this paper. The axial length and relative permeability of the air gap can be changed based on the scaling air gap method. In this way, the mesh setting for the air gap will be more flexible and the mesh of the whole machine can be adjusted to be more reasonable. The proposed approach is proved to have shorter computation time than the traditional 3D FEA approach and to be more accurate than 2D FEA approaches. The accuracy of the proposed approach is also verified by experiments.

[1] S. H. Won, J. Choi, and J. Lee, "Axial-Gap Type Permanent Magnet Motor Modeling for Transient Analysis," *IEEE Trans. Magn.*, vol. 44, no. 11, pp. 4085-4088, Nov. 2008. [2] F. Zhao, T. A. Lipo, and B. Kwon, "A Novel Dual-Stator Axial-Flux Spoke-Type Permanent Magnet Vernier Machine for Direct-Drive Applications," *IEEE Trans Magn.*, vol. 50, no. 11, pp. 1-4, Nov. 2014. [3] M. Gulec, M. Aydin, "Implementation of different 2D finite element modelling approaches in axial flux permanent magnet disc machines," *IET Electr. Power Appl.*, vol. 12, no.2, pp. 195-202, 2018.

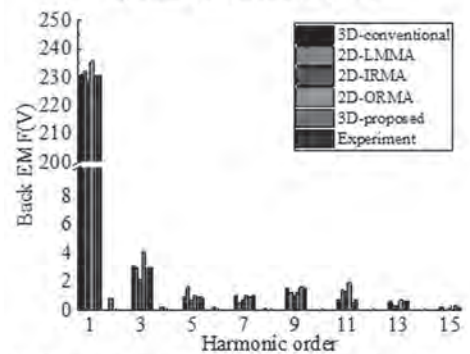
[4] C. Bianchini, F. Immovilli, E. Lorenzani, etc., "Axial flux permanent magnet machine desing and optimization using multi-layer 2-D simulation," in *Proc. Ann. Conf. Ind. Electron. Soc.*, 2013, pp. 2620-2625.

Table 1. Comparison based on mesh profile and computation time

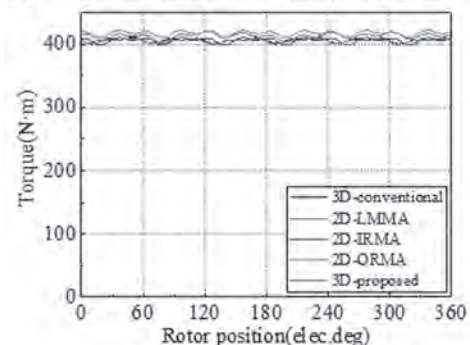
Approach	Number of Meshes	Computation time of one period of back EMF	FEA model
3D-conventional	3131746	8h5min	
2D-LMMA	47766	16min51sec	
2D-IRMA	18900	4min54sec	
2D-ORMA	16680	4min30sec	
3D-proposed	1589723	3h5min	



(a) Comparison of back EMF



(b) Comparison of harmonic contents of back EMF



(c) Comparison of torque output

Figure 1. Comparison of motor performance

AQ-04. Comparison of Electromagnetic Field Distribution Estimated by Three-Channel U-net Neural Network.

Y. Chen^{1,2}, Q. Yang³, C. Zhang^{1,2}, Y. Li^{1,2} and H. Zhang^{1,2}

1. Hebei University of Technology, Tianjin, China; 2. Hebei University of Technology State Key Laboratory of Reliability and Intelligence of Electrical Equipment, Tianjin, China; 3. Tianjin University of Technology, Tianjin, China

I. Introduction Multi-physics coupling analysis of electrical equipment has becoming more and more important in industrial design. However, the multi-physics fields simulation often relies on finite element method (FEM) which is generally time-consuming and not very efficient in genetic optimization algorithm of electrical equipment. As a result, the surrogate model of optimization needs to be both numerical highly precise and highly efficient [1]. Convolutional neural network (CNN) can be a potential alternative for the surrogate model with its powerful abilities of nonlinear mapping and layered extraction of information features. Neural networks have been widely applied in the estimation of fluid field [2], stress field [3]. U-net, a kind of full convolutional neural network (FCN), is used for magnetic field estimation for its great advantage in small sample sets of restoring images through the jump structure which extract the features from input images and map them to output [4-6]. The estimation of electromagnetic field is essentially a dense regression problem. In this paper, the simplified model of three-phase dry-type transformer is presented and the distribution of electromagnetic field is calculated by FEM software. The image dataset of the electromagnetic simulation is established which contains the geometric information, material properties and current excitations. Based on TensorFlow 2.0, parameters of U-net model are trained to solve the problem of pixel-level dense regression. And accurate estimation of electromagnetic field distribution in electrical equipment is realized. II. Deep Learning model structure A. Structure of neural network This paper adopts the U-net structure of [8], which is composed of 6 encoder layers and 6 decoder layers. Each layer contains an activation function, a batch normalization, and a convolution or up-convolution. The size of the convolution kernel is 4×4 with a stride of 2. The back-propagation algorithm is used to reduce the mean square error (MSE). Deep learning (DL) model structure is shown in Fig.1(a). B. Generation and pre-processing of datasets The quality and scale of dataset have a crucial effect on the training of DL networks parameters. Although the U-net can perform well on small dataset, high quality dataset is crucial to avoid overfitting and improve the convergence of model parameters. Based on Maxwell's parameterized modeling, a simplified two-dimensional finite element calculation model of single-phase dry-type transformer is established. The sweeping parameters including geometric information, material characteristics and current excitations ranges in constant step size. The model and the computed magnetic density distribution are denoted as input X and label Y . Cropping and noise filtering are carried out on samples to avoid the interference from redundant information. In order to explore the influence of multi-channels images dataset and single-channel images dataset on training, RGB images dataset and gray-scale images dataset are generated both. To improve the generalization ability of the U-net, the original training set has been enhanced by the actions of translation, rotation, scaling and shearing. An extended dataset of 2100 images is generated, including 1800 in training set, 200 for validation set and 100 for test set. The generating and pre-processing of dataset are shown in the Fig.1(b). The selection of hyper-parameters is very important for model training. In the proposed model, learning rate is set as 0.0001, the optimization algorithm as Adam, batchsize as 10, epoch as 200 and the loss function as MSE which is widely used in regression analysis. III: Results and Discussion Trained by the two datasets, the magnetic field estimated by U-net is shown in the Fig.2(a). The training curves with two different datasets are shown in Fig.2(b). It can be seen from the training curves that the performance of the model trained by three-channel dataset is almost the same with the model trained by the single-channel dataset on the verification set in the early stage. However, when the epoch is greater than 100, three-channel model performs significantly better than single-channel model. It is partially because the three-channel dataset contains more information of material properties and excitations, which improves the efficiency of neural network training and predicting accuracy. The precisions of the models trained by

single-channel model and three-channel are 7.87% and 5.23%. IV. Conclusion The three-channel images dataset containing material properties, current excitations and geometric information can more effectively improve the training speed and precision than the single-channel images dataset only containing geometric information. The validity of estimating electromagnetic field distribution through neural network is verified.

- [1] J. Yaochu, Swarm and Evolutionary Computation., Vol.1, p.61-70 (2011)
 [2] L. Julia, A. Kurzawski, and J. Templeton, Journal of Fluid Mechanics., Vol.807, p.155-166 (2016) [3] N. Zhenguo, H. Jiang, and L. B. Kara (2018)
 [4] R. Olaf, P. Fische, and T. Brox, International Conference on Medical Image Computing and Computer-Assisted Intervention (2015) [5] A. Khan, V. Ghorbanian, and D. Lowther. IEEE Transactions on Magnetics., Vol.55, p.1-4, (2019) [6] G. Ruohan, Z. Tang, COMPEL - The international journal for computation and mathematics in electrical and electronic engineering., Vol.39, p.959-970 (2020)

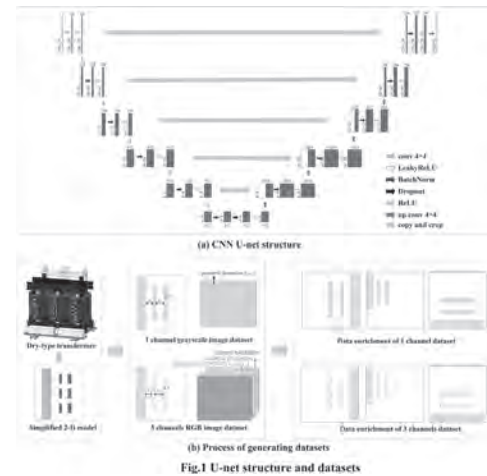


Fig.1 U-net structure and datasets

Fig.1 U-net structure and datasets

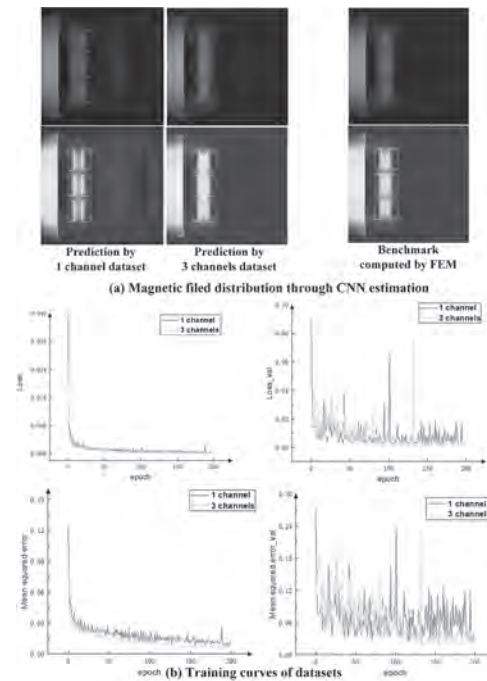


Fig.2 Estimation results and training curves

Fig.2 Estimation results and training curves

AQ-05. Efficiency Improvement for Submersible Motors by Optimizing the Ratio of Diameter to Shaft Length.

J. Li¹, C. Di¹, X. Bao¹, Z. Ke¹ and J. Yan¹

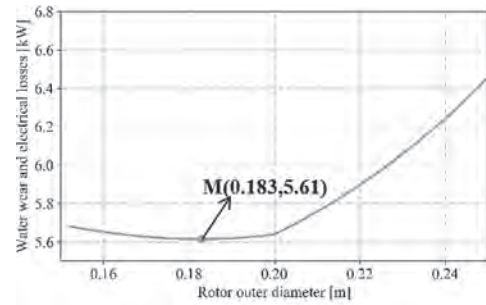
1. School of Electrical Engineering and Automation, Hefei University of Technology, Hefei, China

Introduction: Nowadays, with the rapid development of the computer science, numerical methods have been widely used during all the design stages of an electrical machine, such as the electromagnetic design, mechanical structure optimization, thermal estimation etc. We may select the main dimension of the motor, according to the existing electromagnetic design scheme of the induction motor with the same power level. This approach is suitable for the conventional induction motor design, because the main performance is highly determined by the main dimension [1]. However, different from traditional induction motors, the water friction losses of wet submersible motors are much greater than the wind mill losses of air-cooled induction motors. As shown in Fig 1, unlike traditional industrial motors, submersible motors have a larger ratio of diameter to shaft length. The water wear of the water-filled submersible motor accounts for a large proportion of the overall losses, so how to reduce the water wear of the submersible motor has become the key to improving the efficiency of the submersible motor. Many scholars have put forward the numerical calculation method of water wear of water-filled submersible motor, which are shown in Formula (1)-(4) in Figure 2 [2-3]. It can be seen that the main factors affecting the water wear of submersible motors are the surface roughness of the rotor, rotor speed, outer diameter of the rotor and motor shaft length. The literature [4] verified the influence of surface roughness on water wear. For a submersible motor with a given output power, the speed and surface roughness are constant. In this paper, the diameter and shaft length ratio of the motor are optimized to achieve the purpose of reducing the water wear in the design stage. Optimization Method: It can be known from the main relation formula of AC motor that the motor power with constant effective volume of rotor is also approximate. Therefore, keeping the effective volume of the rotor constant, reducing the outer diameter of the rotor and increasing the shaft length can ensure the output power and reduce the water wear of the motor. However, reducing the water wear through the above methods will also increase the electrical losses of the motor. In this paper, the electrical losses of a series of size motors are solved by electromagnetic simulation, and the curve of electrical losses as a function of the rotor outer diameter is fitted by the cubic spline interpolation. A new curve is obtained by adding the water wear and electrical losses of the motor, and the minimum of the curve is the optimal rotor outer diameter. Results: As shown at point M in Fig.2, when the rotor outer diameter is 0.183 m, the sum of electrical losses and water wear of the motor are the minimum. Compared with the loss when the outer diameter of the rotor is 0.225, the loss is reduced by 360 W. This method realizes the optimization of the diameter-axle-length ratio of the submersible motor and reduces the water wear of the submersible motor in the design stage. Detailed results and discussion will be given in the full text.

[1] J. Pyrhonen, T. Jokinen, and V. Hrabovcova. Design of Rotating Electrical Machines, 2nd ed. Hoboken, NJ, USA; wiley, (2014). [2] S. Li and S. Liu, Pump Technol., vol. 33, pp. 21–25(1988). [3] H. Liu, M. Tan, and S. Yuan, Trans. Chin. Soc. Agricult. Eng., vol. 22, pp. 107–109(2006). [4] X. He, W. Jiao, C. Wang, et al. IEEE Access, vol. 7, pp. 105331-105341(2019).



Fig. 1 A submersible motor with large ratio of diameter to shaft length.



$$P_m = 0.1435 \times 10^{-6} k n_2^3 D_2^4 (D_2 + 5L) \quad (1)$$

$$P_m = 0.133 \times 10^{-3} \rho R_d^{0.134} \omega^3 (D_2/2)^3 D_2^2 \quad (2)$$

$$P_m = 0.35 \times 10^{-2} \times k \rho \omega^3 (D_2/2)^5 \quad (3)$$

$$P_m = 1.1 \times 75 \times 10^{-6} \times \rho g u_2^3 D_2^2 \quad (4)$$

where $R_d = 106 \times \omega(D_2/2)^2$ and $\omega = 2\pi n/60$, ω is the angular velocity (in rad/s), ρ is the density of the fluid (in kg/m³), $k=0.8-1.6$, u_2 is the circumferential speed of impeller outlet (in m/s).

Fig. 2 Losses at different rotor outer diameters.

AQ-06. Electromagnetic Performance Analysis of a Hybrid Excitation Machine Based on Equivalent Magnetic Network.

W. Tong¹, P. Wang¹, S. Wu² and S. Li¹

1. National Engineering Research Center for Rare-Earth Permanent Magnet Machines, Shenyang University of Technology, Shenyang, China;

2. School of Electrical Engineering, Shenyang University of Technology, Shenyang, China

Abstract—This paper proposes an equivalent magnetic network (EMN) model for predicting the electromagnetic performances of hybrid excitation machines. In addition to the influence of flux leakage and iron saturation, the proposed EMN model also takes the change of rotor position into consideration. A new node connection method is proposed to make the dynamic analysis easier. Moreover, the reasonable simplification of stator yoke and teeth further reduces the calculation time and ensures the accuracy of the proposed EMN model. In addition, the proposed model in the motor hybrid excitation part can consider the electromagnetic characteristics under different DC excitation conditions. Finally, the prototype is manufactured, and the effectiveness of the EMN model is verified by comparison with the finite-element analysis (FEA) and experimental tests.

I. Introduction Hybrid excitation machines not only has many advantages of permanent magnet machine, but also has the advantages of smooth and adjustable air gap magnetic field, wide speed range in electric operation, and wide voltage regulation ability in power generation operation [1]. Therefore, it has received a lot of attention from scholars. In order to analyze the performance of the machine, the finite-element analysis (FEA) method is usually used [2]. However, the hybrid excitation machine is a three-dimensional magnetic circuit structure, which requires a large number of grids, which is very time-consuming. In order to reduce the calculation time, the analytical method is also used to reveal the machine performance [3]. However, the effect of iron saturation is mostly considered, resulting in low accuracy. The equivalent magnetic network method has attracted more and more attention due to its short calculation time and moderate accuracy. In this paper, a dynamic magnetic network analysis model is proposed to predict the electromagnetic performance of consequent pole hybrid excitation machines. The EMN model considers the magnetic flux leakage, the nonlinearity saturation of iron materials and the magnetic bridge, which has high calculation accuracy. The calculated results are compared with the FEA and experimental test results.

II. PROPOSED EMN MODEL FOR HYBRID EXCITATION MACHINES Generally, the yoke and tooth magnetic circuit of the machine is regular, and the Simplified EMN modeling method can be used to establish the model. However, the tooth tip, air gap and magnetic bridge magnetic circuit are irregular, and complex magnetic network needs to be established to improve the accuracy and be used for dynamic analysis. At the same time, the DC excitation source should be considered when the hybrid excitation motor is built for three-dimensional magnetic circuit. Figure 1 shows the topology of the machine. The following is a brief introduction to the modeling process:

A. Simplified Stator EMN Model The magnetic circuit of the yoke and teeth of the stator is regular. Therefore, a simplified stator EMN model can be used to reduce the calculation time without affecting the accuracy requirements.

B. Air Gap EMN Model and Dynamic Analysis The tooth tip of the machine is seriously saturated due to the quasi-closed slot. It is necessary to consider the influence of saturation in order to establish the cross-shaped mesh model. The air gap is the key part of the model, which connects the stator and the rotor. In the dynamic analysis, the stator and rotor depend on the air gap EMN model node connection. It is important to consider the rotor position change with time for the dynamic analysis. Therefore, it is necessary to build cross-shaped mesh model in the air gap. This makes dynamic analysis more effective and faster.

C. EMN Model of Rotor and Hybrid Excitation Part When modeling the rotor part, the saturation of the magnetic bridge part is serious, and the cross-shaped mesh model needs to be established. Under the influence of DC excitation, the iron-pole generates magnetic field in the hybrid excitation section of the machine. The permanent magnet and DC magnetic source can be considered separately in the modeling to avoid the complex situation caused by two magnetic sources in the model. It should be noted that the alternating existence of permanent magnet and iron-pole also makes the modeling difficult.

III. Results Verification In order to verify the effectiveness of the proposed EMN model,

a hybrid excitation machine prototype is developed. The experimental test platform is shown in Fig. 2. The electromagnetic performances, such as the air-gap field distribution, phase flux linkage and back-electromotive force (EMF), d-axis and q-axis inductances, and electromagnetic torque, are predicted by the proposed EMN method. Finally, the results obtained from the EMN method are compared with those obtained by the FEA and experimental tests.

IV. CONCLUSIONS In this paper, an equivalent magnetic network analysis model is proposed to predict the electromagnetic performance of hybrid excitation machine. The new node connection form is established in the tooth tip and air gap for considering dynamic analysis. The proposed EMN model considers the influence of flux leakage and Nonlinear saturation of iron materials. The calculated results are compared with the FEA and experimental test results, which proves the effectiveness of the proposed EMN model. The detailed modeling process and calculation results will be given in the full paper.

- [1] Z. Q. Zhu, I. A. A. Afinowi, and Y. Guan, "Hybrid-Excited Stator Slot Permanent Magnet Machines—Influence of Stator and Rotor Pole Combinations," in *IEEE Transactions on Magnetics*, vol. 52, no. 2, pp. 1-10, Feb. 2016, Art no. 8100710. [2] K. Wang, J. Li, and C. Liu, "Novel hybrid-pole rotors for consequent-pole PM machines without unipolar leakage flux," *IEEE Trans. Ind. Electron.*, vol. 66, no. 9, pp. 6811–6823, Sep. 2019. [3] S. G. Min, and B. Sarlioglu, "Fast and systematic design optimization of surface-mounted PM machines using advanced analytical models and subharmonic elimination methods," *IEEE Trans. Magn.*, vol. 55, no. 1, Jan. 2019, Art. no. 8100216.

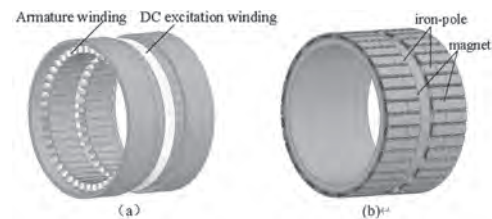


Fig. 1. Topology of hybrid excitation machine. (a) Topology of stator. (b) Topology of rotor.



Fig. 2. Test platform of a hybrid excitation prototype.

AQ-07. Electromagnetic Performance Analysis of Permanent Magnet Synchronous Machine Considering Axial Leakage Flux Using Subdomain Analytical Method.

K. Shin¹, H. Park², T. Bang³, H. Cho³ and J. Choi³

1. Power System Engineering, Chonnam National University, Yeosu, The Republic of Korea; 2. Hyundai Mobis, Yong-in, The Republic of Korea; 3. Chungnam National University, Daejeon, The Republic of Korea

Permanent magnet synchronous machine (PMSM) has been widely used in various applications such as industries, home appliances, and electric propulsion systems due to the technological progress for producing permanent magnets with high energy density and power electronics [1], [2]. The design of PMSM requires a lot of electromagnetic analysis depending on various design variables, so the two-dimensional (2D) analysis, which allows faster analysis than the three-dimensional (3D) analysis requiring a large number of meshes, is mainly used. The electromagnetic design of PMSM is required to have a high-power per unit volume to improve system performances and to satisfy the maximum voltage limit under rated conditions. However, since the 2D electromagnetic analysis cannot consider the axial leakage magnetic flux, it is difficult to accurately predict the machine performance under the rated condition. To overcome these problems, the axial leakage magnetic flux can be considered through a 3D electromagnetic analysis. The 3D analytical method is rarely studied due to the complexity and difficulty of the analysis, and the 3D finite element (FE) method requires a long time and high-performance computing technology due to numerous meshes. Therefore, in this study, the electromagnetic analysis of PMSM considering axial flux leakage is proposed using a 2D subdomain analytical method. In the design phase, 2D subdomain analytical methods not only provide insights into the relationship between design variables and performances but can also consider end effects by applying permeability to slot and slot opening regions. Fig. 1(a) shows the structure of PMSM to verify the validity of the 2D subdomain analytical method considering axial magnetic flux leakage. To consider the axial magnetic flux leakage in the 2D subdomain analytical model, the leakage component due to the leakage part of the winding as shown in Fig. 1(b) and the leakage components according to the 3D structure in the slot and slot opening as shown in Fig. 1(c) should be analyzed. Fig. 1(d) shows a 2D subdomain analytical model considering 3D axial leakage flux. The simplified model is defined using 2D polar coordinates and some assumptions [3], [4]. To consider the axial flux leakage and end winding flux leakage [2], a proposed analytical model is defined that applies corrected permeability to slot and slot-opening regions. The entire domain of the field problem is divided into four subdomains: Region I (air-gap subdomain); Region II (PM subdomain); Regions III, i (Slot opening subdomain, $i = 1, 2, \dots, Q$; Q : number of stator slots); Regions IV, j (slot subdomain, $j = 1, 2, \dots, Q$). The governing equation in all subdomains can be solved, and the field distribution can be obtained by applying the boundary conditions on the interfaces between the subdomains. Based on these solutions, the electromagnetic performances such as back-EMF, inductance, electromagnetic torque, and torque-speed curve can also be determined analytically. The magnetic field and the electromagnetic performance obtained using the proposed analytical method were compared with those obtained using the FE analysis, and experimental measurement in this paper. To measure the operating characteristics, a back-to-back system with a prototype and load generator is constructed as shown in Fig. 2(a). Fig. 2(b) compares torque-speed characteristics from the proposed analytical method with the conventional 2D FE and experimental results. Under the rated conditions, the conventional 2D FE analysis includes high torque and a wide operating range, and the proposed analytical method and experimental results show similar operating performances. Therefore, the proposed analytical method can predict an accurate characteristic analysis by considering the axial leakage flux in the initial design stage. The analytical approach, analysis, and experimental results will be presented in more detail in the full paper.

[1] E. Sulaiman, T. Kosaka, and N. Matsui, "High power density design of 6-slot-8-pole hybrid excitation flux switching machine for hybrid electric vehicles," *IEEE Trans. Magn.*, vol. 47, no. 10, pp. 4453–4456, Oct. 2011. [2] J. Jung, H. Park, J. Hong, and B. Lee, "A novel approach for 2-D electromagnetic field analysis of surface-mounted permanent magnet

synchronous motor taking into account axial end leakage flux," *IEEE Trans. Magn.*, vol. 53, no. 11, Nov. 2017, Art. no. 8208104. [3] K.-H. Shin, H. I. Park, H.-W. Cho, and J.-Y. Choi, "Analytical calculation and experimental verification of cogging torque and optimal point in permanent magnet synchronous motors," *IEEE Trans. Magn.*, vol. 53, no. 6, Jun. 2017, Art. no. 8106204. [4] T. Lubin, S. Mezani, and A. Rezzoug, "Two-dimensional analytical calculation of magnetic field and electromagnetic torque for surface inset permanent-magnet motors," *IEEE Trans. Magn.*, vol. 48, no. 6, pp. 2080–2091, Jun. 2012.

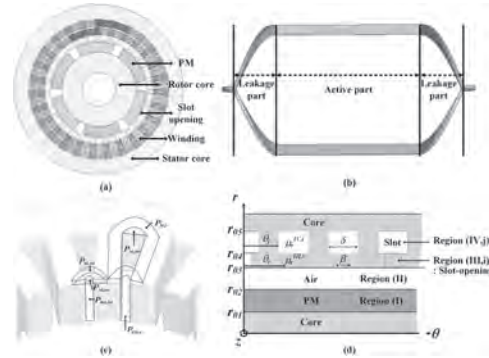


Fig. 1. Structure of PMSM: (a) analysis model, (b) winding with active and leakage part, (c) stator with permeances and (d) simplified analytical model.

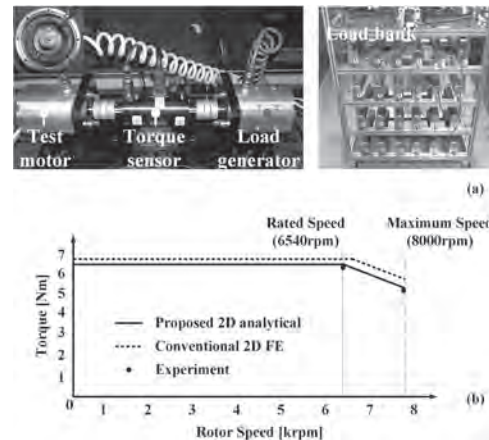


Fig. 2. (a) Experimental setup and (b) torque-speed curve obtained by 2D FE analysis, analytical and experimental results.

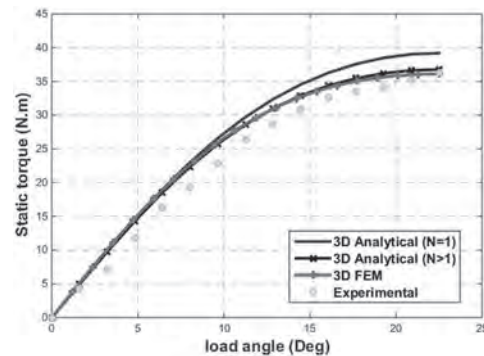
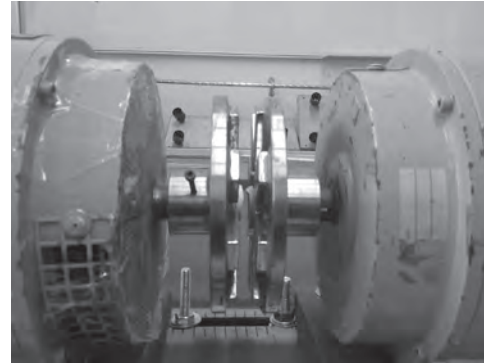
AQ-08. Improved 3D Electromagnetic Analytical Model of an Axial Flux Magnetic Coupling With Rectangular Shaped Permanent Magnets.

A. Zerioul¹, L. Hadjout¹, S. Mezani² and Y. Ouazir¹

1. LSEI-Université des Sciences et Technologie Houari Boumediene (USTHB), Algiers, Algeria; 2. Laboratoire GREEN - FST, Université de Lorraine, Nancy, France

Nowadays some industrial applications require contactless motion transmission. The use of magnetic couplers is the most appropriate solution. The synchronous version of this solution, based in PM excitation, can be adopted in radial or axial topologies. In these topologies the most common shapes of permanent magnets are rectangular, sector and circular. The electromagnetic torque of a magnetic coupler, required to transmit motion, is usually calculated using numerical methods or even 3D analysis which takes into account all the geometric and physical effects. However, in the design process, you need a fast and precise model that does not require a lot of computation time. Firstly, a purely 3D analytical model for axial coupler (with sector shape magnets), based on magnetic scalar potential formulation, is developed. So, the magnetic field distribution in different regions (PM, air gap and iron disks) leads to solve the Laplace's equation. In low-permeability sub domains, the fields due to the two PM rotors of the magnetic coupler are calculated separately. The solutions form of the partial differential equations expressed in cylindrical coordinates are determined using the method of separation of variables. Secondly, we extend the above developed model to calculate the field in the magnetic coupler with magnets of rectangular shape. So, it is necessary to divide the geometry of the rectangular magnet into a number of elementary geometric elements where each element is approximated by a sector-shaped one keeping the same volume of magnet. The approach adopted can be summarized as follows:- Subdivide each rectangular Magnet in N radial Elementary Blocks; - Approximate the elementary block by a sector shape with the same volume; - Compute the magnetic Field of each sector shape block with the developed model;- The total magnetic field, torque and axial force are computed by using the superposition principle. Hence, the total torque developed by the magnetic coupler is obtained by summation of all torques produced by the interaction of each block of the first inductor with all blocks of the second inductor. The results obtained by the proposed 3D analytical model are compared to those obtained by 3D finite elements and to those determined experimentally. A close agreement is noticed (relative error on the static torque don't exceed 2 %) between the measured and the predicted torques, which demonstrates the validity of the proposed model. The low computing time of the developed model provides an efficient and quick tool for assessing the influence of the geometrical and physical parameters of a magnetic coupler as a part of a design optimization process.

[1] L. Belguerras and L. Hadjout, "Study of HTS Magnetic Coupler Using Analytical and Numerical Computations" *IEEE Trans. Applied Superconductivity*, Vol. 24, No. 6, December 2014 [2] Jian Wang and all, "A General Analytical Model of Permanent Magnet Eddy Current Couplings", *IEEE Trans. Magn.*, Vol. 50, No. 1, January 2014. [3] Hyeon-Jae, Shin and all, "Design and Analysis of Axial Permanent Magnet Couplings Based on 3D FEM" *IEEE Trans. Magn.*, Vol. 49, No. 7, JULY 2013. [4] T. Lubin, S. Mezani and A. Rezzoug, "Simple analytical expressions for the force and torque of axial magnetic couplings". *IEEE Trans. on Energy Conversion*, volume 27, N°2, pp. 536-546, 11 pages, Juin 2012.



AQ-09. Modeling and Electromagnetic Performance Analysis of the Novel DC Hybrid Magnetic Bearing With Crossed Poles.

T. Zhang¹ and Z. Wang¹

1. Huaiyin Institute of Technology, Huaian, China

I. Introduction Hybrid magnetic bearings (HMBs) have several merits, such as no friction and abrasions, no lubrication and no sealing, high speed, high precision and long life. In HMBs, the permanent magnet is adopted to generate bias flux for the low power consumption and small volume. However, in existing HMBs, several suspension poles are designed in the same stator core. The suspension force is generated by the interaction of the bias flux and control flux. The HMB of this structure realizes the radial two-degree-of-freedom (2-DOF) suspension in one stator core, especially when the rotor is deviated from unbalance position, the suspension force coupling in the X-Y direction is severe and the control is complicated. To compensate for this deficiency, a novel DC HMB with crossed poles is studied. The suspension poles in the X and Y direction are designed different stator cores. Therefore, it can solve the radial 2-DOF coupling of traditional four-pole HMBs and simplify the control. A simple mathematical models are presented, which can make the maximum magnetic levitation force in the X and Y directions. The nonlinearity of suspension forces and the coupling of electromagnetic among this four-pole magnetic bearing are analyzed by MagNet 3D. The finite element simulation is carried out to verify the theoretical analysis. II. Configuration and Suspension Principle The configuration and magnetic circuit of a novel DC HMB with crossed poles are presented in Fig. 1. As shown in Fig. 1(a), the main parts of this HMB are two slice stators, namely X-stator and Y-stator, axial magnetized permanent magnets and two slice rotor irons. Two symmetrical suspension poles in the X direction are evenly distributed along the circumference of X-stator, and the suspension poles in the Y direction are crossed in the Y-stator. Radial control windings are wound on each stator. The magnetic circuit of radial suspension control flux and static bias flux is represented in Fig. 2(b). The solid lines denote the static bias flux generated by the permanent magnets. The dotted lines describe the radial suspension control flux generated by radial control current. If the rotor irons are displaced from the balance position in the radial position by the radial disturbances, the fluxes between the magnetic flux and the bias flux are overlapped, which results in force to bring the rotor to the radial balance position. According to the equivalent magnetic circuit method, the radial suspension forces in the X and the Y directions are deduced as follows: $F_j = F_{pm} + k_{ij} \times ij$ (1) where the subscript “j” denotes x and y. F_{pm} is the magnetic attraction force produced by the bias flux at the equilibrium position. k_{ij} is the radial force-current stiffness. F_{pm} and k_{ij} can be given as: $F_{pm} = S \times \mu_0 \times F_m \times F_m \div g^3$ $K_{ij} = 2S \times \mu_0 \times F_m \times N \div g^2$ (2) where F_m is the magnetomotive force. μ_0 is vacuum permeability. S is radial magnetic pole area. g is radial air gap length. N is number of radial control coils. III. Models, Design and Analysis Based on above-mentioned analysis, electromagnetic performance of the presented HMB is manufactured by the MagNet software. The prototype is simulated to analyze the electromagnetic performance by the three-dimensional finite element method, and the different simulation cases are given in Fig. 2. Fig. 2(a) shows the distribution of the bias flux. The radial air-gap magnetic flux density of each pole is 0.6T symmetrically. In Fig. 2(b), the radial control winding in the X direction is electrified with 3A current, and the control flux density distribution in the X direction is generated. It can be seen from Fig. 2(c) that there is an increase of air-gap flux in the positive X direction and a decrease in the negative X direction by the superposition of the control flux in the X direction and bias flux. Therefore, only the suspension force in the X direction is produced. To verify the correctness of the mathematical models, the control current is applied to generate radial suspension force only in the positive X direction. The relationships between the suspension force and control current are shown in Fig. 2(d). The currents change from 0 to 3 A. The maximum suspension force reaches 260 N. It can be seen that the finite element simulation results are in good agreement with the theoretical values, and there is a linear force-current relationships. IV. Conclusion This paper aims to construct a novel DC HMB with crossed poles to simplify the structure, obtain the maximum bearing capacity and solve the radial two-degree-of-freedom coupling. The simulation results have shown that the suspension forces produced by the crossed poles have better linearity around the balance

position and no movement. There is no coupling of two directions for the independent magnetic circuit. The research results verify the correctness of magnetic circuit, suspension mechanism and mathematical model.

[1]D. Ning, H. Kai, and J. Long, “Review on High Speed Permanent Magnet Machines Including Design and Analysis Technologies,” in *Proceedings of the CSEE*, vol. 34, no. 27, pp. 4640-4653, Sep, 2014. [2]J. Ju, H. Zhu and C. Zhao, “Radial Force-Current Characteristic Analysis of Three-Pole Radial-Axial HMB,” *2016 IEEE Vehicle Power and Propulsion Conference (VPPC)*, Hangzhou, 2016, pp. 1-6.

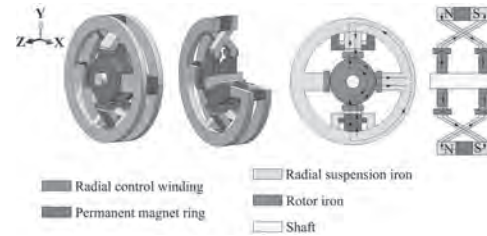


Fig. 1. The configuration and magnetic flux path of the proposed HMB.

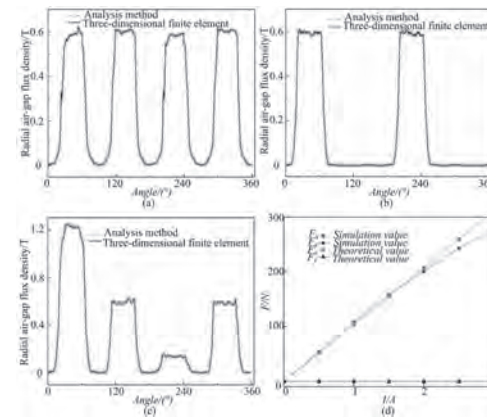


Fig. 2. Flux distribution and the force-current relationships. (a) Bias flux. (b) Control flux. (c) Resultant flux. (d) Force-current relationship.

AQ-10. Quickly and High-Precision Digital Twin Device-Level Simulation Modeling of Permanent Magnet Synchronous Generator and Voltage Stabilizing System.

R. Sun¹, D. Yang¹, D. Shi¹, L. Zhuo^{1,2} and H. Peng¹

1. National Engineering Research Center for Small and Special Precision Motors, Guizhou Aerospace Linquan Motor Co., Ltd, Guiyang, China;

2. Department of Electrical Engineering, Harbin Institute of Technology, Harbin, China

Abstract: The traditional finite element model of permanent magnet synchronous generator(PMSG) needs nonlinear iteration for each grid, and time-consuming. Besides, the performance of various components of the voltage regulator controller (VRC) will be affected by the operating environment. The traditional component library cannot meet the accurate digital twin effect. Taking an emergency power supply system for an unmanned aerial vehicle as an example, this paper uses the device-level modeling method to build a digital twin simulation model (DTSM) of a PMSG and its AC-DC regulated power supply system, which simulation speed can guarantee real-time output results in synchronization with the experiment, and has an agile digital twin effect. Finally, the calculated results are compared with the experimental values to verify the accuracy of the proposed digital twin device-level model, which is of great significance to the combined design of PMSGs and VRCs.

Index Terms : Permanent magnet synchronous generator (PMSG); Digital twin ;Voltage regulator controller.

I. Introduction The performance of permanent magnet synchronous generator (PMSG) is closely related to its control method and load characteristics. When the AC-DC step-down chopper voltage stabilization control strategy is adopted, it can ensure the output of stable DC power while reducing the three-phase line current of the generator, reducing the motor winding loss greatly, and optimizing the matching design of the generator and the power converter. The power stabilization system is stable and efficient. Therefore, the research of PMSG and its AC-DC conversion and voltage stabilization system (VSS) simulation can promote the development of PMSG and VSS technology, improve system design accuracy effectively, and realize the perfect match to improve the stability and reliability of the VSS [1][2][3][4].

II. Composition of VSS Circuit After studying the load characteristics and actual working environment, the power supply system adopts a PMSG combined with a three-phase uncontrolled rectifier bridge and a BUCK converter. The actual power supply system consists of PMSG, three-phase uncontrolled bridge rectifier circuit, power regulator circuit, filter circuit, feedback circuit, control circuit, drive circuit and auxiliary power supply circuit.

III. Digital Twin Device-Level Simulation Modeling In order to improve the simulation speed of the simulation model and achieve a fast digital twin effect, this paper uses the ECE reduced-order model extraction method to convert the generator finite element model into a data matrix model, and establishes the PWM main control chip SG1525 and the device-level modeling method. The digital twin simulation model (DTSM) of the AC-DC VSS of the PMSG is built as shown in Fig.1. The simulation speed can ensure the real-time output results in synchronization with the experiment results, and realize the fast and accurate digital twin effect.

IV. Experimental Verification The PMSG and its VSS were tested on a dedicated test bench, which is shown in Fig. 2. The oscilloscope is used to display the output DC voltage waveform in real time, and the DTSM is run on the computer at the same time. The simulation data is highly consistent with the measured data.

V. Conclusion This paper proposed a high-precision DTSM based on the actual prototype of an emergency power supply system for an unmanned aerial vehicle. Firstly, the ECE reduced-order mathematical model is extracted by the alternating-direct-axis periodic current scanning method, which accelerates the simulation speed greatly. Secondly, according to the actual circuit structure of the emergency voltage stabilization control power converter, a DTSM of the entire VSS circuit is built. Finally, the accuracy of the DTSM is verified by experiments. The reduced-order model extraction and device-level modeling techniques used in this paper are in line with the development trend of digital twin technology. The research results can provide a reference for the design of PMSG and the optimal matching design of VSS.

[1] A. Rassölkin, V. Rjabtšikov and T. Vaimann. "Digital twin of an electrical motor based on empirical performance model," 2020 XI

International Conference on Electrical Power Drive Systems (ICEPDS), Saint Petersburg, Russia, 2020. [2] N. Khaled, B. Pattel and A. Siddiqui. "Digital twin development and cloud deployment for a DC motor control embedded system", 2020. [3] R. Goraj. "Digital twin of the rotor-shaft of a lightweight electric motor during aerobatics loads", Aircraft engineering and aerospace technology, 2020. [4] N. Khaled, B. Pattel and A. Siddiqui. "Digital twin development for an inverter circuit for motor drive systems", Digital Twin Development and Deployment on the Cloud, PP. 163-201, 2020.

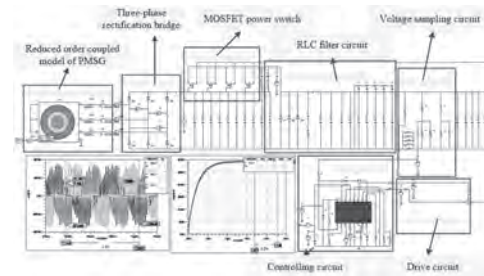


Fig.1. The DTSM of the AC-DC VSS of the PMSG.



Fig.2. The test bench of PMSG and its VSS.

AQ-11. Robust Multi-Objective Optimization Design of Permanent Magnet Motors Based on Objective-Dimension-Reduced Method.

L. Quan¹, Y. Lu¹ and J. Wu¹

¹. Jiangsu University, Zhenjiang, China

I. Introduction Recently, permanent magnet (PM) motors have been widely applied in various application fields, such as electric vehicles, aerospace, and household appliances, owing to the inherent advantages of high torque density, high energy efficiency, and compact structure. With the increasingly severe and diversified application scenarios of PM motors, higher and more complicated requirements are raised for optimization design. It is noted that the motor system is actually a multi-disciplinary, nonlinear, strong coupled system, hence the objectives are often in conflict with each other in the design process. In previous studies, multi-objective optimization design is considered as an effective solution for obtaining high-performance PM motors, and some optimization methods are often utilized, such as a multi-objective genetic algorithm (MOGA) [1]. However, the traditional optimization method is a deterministic design approach and has not investigated the uncertainties in engineering manufacturing, such as material diversity, manufacturing error, and assembly inaccuracy. These will result in design parameter fluctuation affecting the reliability and quality of the machine. To deal with this problem, the robust optimization design approach is proposed and gradually becomes a hotspot in machine design research orientation. Generally, the design for the six sigma (DFSS) technique is an effective optimization approach, which is often adopted to provide direct and reliable evaluation for the assessment of robustness. In [2], a soft magnetic composite (SMC) motor is optimized based on DFSS, which takes robustness into consideration in not only motor but also integrated control schemes. In [3], the robust design of a surface-mounted permanent magnet (SPM) motor is realized by the particle swarm optimization (PSO) instead of genetic algorithm (GA) due to long computational time of DFSS. Yet, it is noted that in the DFSS method, the mean and variance of the optimization objectives should be optimized at the same time, which greatly improves the dimension and complexity of the motor optimization model. Thus, for the machine robust design, ensuring the optimization convergency is a big challenge. It is necessary to propose an optimization method to improve the efficiency and accuracy of DFSS, effectively achieving machine robust design. To address this problem, this paper proposes an efficient machine robust design approach, where the dimension of the robust optimization model can be reduced according to the assessment of the relationship between objectives. To better clarify the proposed method, an interior PM machine with a multi-layer flux barrier is investigated as a design example. By implementing the proposed optimization method, it can be found that the performance and design reliability of the machine can be effectively improved.

II. Proposed optimization method As is shown in Fig. 1, the design concept from the traditional deterministic optimization to robust design optimization is described for better presentation. Fig. 2(a) gives the configuration of the design example, an interior PM motor with a multi-layer flux barrier. It can be seen that the motor adopts the 36/8 slot/pole combination and NdFeB-PM is embedded in the middle of each arc-shaped magnetic barrier. Fig. 1(b) shows the parameter model of the motor and structural parameters for optimization is marked. Based on the parametric model, the process of robust optimization is given as the flowchart in Fig. 3. Firstly, in order to reduce the computation of FEA, Latin hypercube sampling (LHS) was utilized to approximate random sampling from multivariate parameter distributions. Then, parameters are divided into two layers by the result of sensitivity analysis. In Layer 1, the parameters with low sensitivity are optimized for objectives that have relatively strong relevance with them by parameter sweeping. In addition, robust factors of the performance fluctuation caused by sensitive parameters are considered in Layer 2. And then, a non-parametric measure of conflict method is adopted for objective reduction, then, the objectives with high conflict have remained for multi-objective optimization. Finally, the filtered objectives are optimized by NSGA-II (Non-Dominated Sorting Genetic Algorithm-II). III. Analysis and results Based on the robust optimization method proposed above, the analysis results are obtained. According to Spearman's rank correlation coefficient, five objectives with relatively high assessed conflict value are remained in the process of multi-objective optimization, and the result is shown in Fig. 4 (a). In addition, the solution

set corresponding to all objectives based on parameters determined above is shown in Fig. 4 (b). The torque and torque ripple of the proposed interior PM motor are calculated and compared in Fig. 5 (a), it can be seen that the average torque has been improved from 23.56 Nm to 25.95 Nm, while the torque ripple decreases from 10.14% to 9.50%. In order to evaluate the robust performance, 1000 points are sampled separately around initial and optimized parameters by Monte Carlo analysis method, as is shown in Fig. 5 (b), the variance μ of the distribution is decreased from 0.43 Nm to 0.27 Nm. Additionally, the improvement of core loss performance is given in Fig. 6. In conclusion, it can be seen that deterministic and robust performances of the proposed motor are improved simultaneously. More detailed design process description and experimental verification will be given in the full paper.

[1] X. Zhu, W. Wu, L. Quan, Z. Xiang, and W. Gu, "Design and Multi-objective Stratified Optimization of a Less-rare-earth Hybrid Permanent Magnets Motor with High Torque Density and Low Cost," *IEEE Trans. Energy Convers.*, vol. 34, no. 3, pp. 1178-1189, Sept. 2019. [2] G. Lei, T. Wang, J. Zhu, Y. Guo and S. Wang, "System-Level Design Optimization Method for Electrical Drive Systems—Robust Approach," *IEEE Trans. Ind. Electron.*, vol. 62, no. 8, pp. 4702-4713, Aug. 2015. [3] V. Rafiee and J. Faiz, "Robust Design of an Outer Rotor Permanent Magnet Motor Through Six-Sigma Methodology Using Response Surface Surrogate Model," *IEEE Trans. Magn.*, vol. 55, no. 10, pp. 1-10, Oct. 2019, Art no. 8107110.

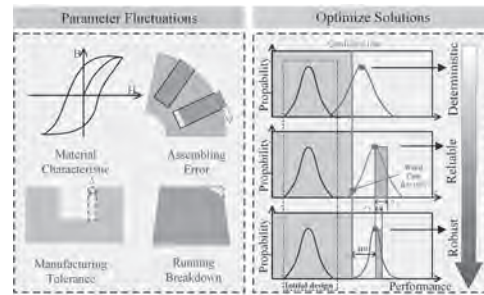


Fig. 1. Robust design concept

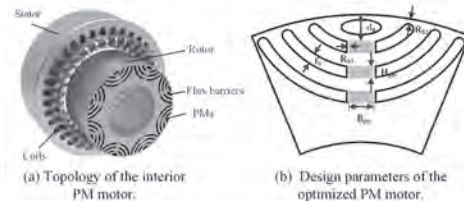


Fig. 2. Configurations of the interior PM motor



Fig. 3. Robust multi-level optimization design process based on trade-off strategy.

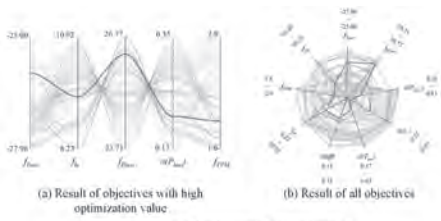


Fig. 4. Multi-objective Optimization result.

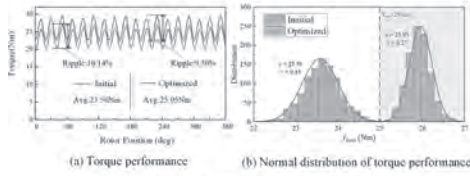


Fig. 5. Comparison of torque performance between initial and optimized motor.

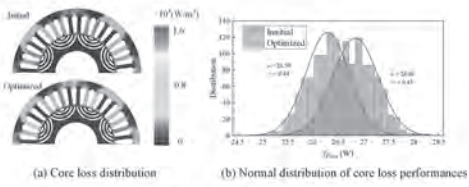


Fig. 6. Comparison of core loss performance between initial and optimized motor.

AQ-12. Robust Optimization Design for PMBL Machine Considering Permanent Magnet Material Uncertainties.

J. Wu¹, X. Zhu¹ and D. Fan¹

1. Jiangsu University, Zhenjiang, China

I. Introduction In recent years, permanent magnet brushless machines (PMBL) have been widely applied in various applications thanks to the merits of high efficiency, high power density, and free maintenance. For this type of machine, PMs are crucial components, whose quality has a significant influence on motor performance. However, there are many uncertainty factors in the PM material characteristic and manufacturing, which often lead to machine performance deviate from the design results. For example, for PM magnetic characteristics, there exists inconsistency between different batches of PM on magnetization magnitude and direction, which leads to PMs remanence and magnetization angle slightly deviate from a given reference. On the other hand, since some PM material machining precision is relatively lower, there is often a discrepancy between the actual and nominal size. During the assembly, this discrepancy might cause a gap between PM and core, which will seriously influence machine performance. Thus, how to design PMBL machines in a robust way to resist PM material uncertainty factor has attracted much attention. To address this problem, researchers have paid plenty of effort, proposing multiple optimization design methods. In reference [1], a robust optimization method is proposed for transverse flux PM motor, in which the influence of inconsistency of magnetic characteristics of PM material is considered. Then, in order to reduce the influence of PM machining error during the motor manufacturing process, a robust optimization method is utilized for a novel double-sides air-core PM linear synchronous motor. [2]. Besides, many engineering probability uncertainty analysis methods are employed to improve PM machine design robustness. [3] Yet, it is noted that these researches generally treated uncertainties as single random variables, lacking the consideration about the specific influence of uncertainties on PM material. In this paper, a robust optimization method is proposed to improve PMBL machine design reliability, where PM material uncertainty factors are sufficiently considered. To better clarify the optimization method, a double PM brushless machine (DPMBL) is investigated as a design example, where NdFeB-PM and ferrite-PM are adopted together to improve machine torque density and reduce the Rare-earth PM usage. The detailed design process and optimized results are presented specifically. By implementing the proposed optimization method, it can be found that the performance and design reliability of the DPMBL machine can be improved. II. Design case and design method Fig.1(a) gives the configuration of the investigated DPMBL machine. It can be seen that the machine adopts a 12/10 slot/pole combination, where two types of permanent, NdFeB and ferrite, are parallelly arranged in the rotor. Fig 1(b) shows the parametric rotor model, where the corresponding design variables are marked out. It is noted that there are two kinds of uncertainty factors in the PM material. The first one is the ferrite width, which might lead to a gap between steel and PM. The second one is the material characteristic of ferrite and NdFeB, including remanence and magnetization direction. Fig.2 describes the proposed robust optimization design process, where PM material uncertainty factors are treated as disturbance parameters. In the implement, the NdFeB and ferrite dimensions are set as design parameters, and the ferrite width, the width of the gap between ferrite and steel, the NdFeB and ferrite remanence, and magnetization direction are regarded as disturbance parameters. Based on multi-objective optimization and uncertainty analysis, the proposed approach conducts the optimization of the design parameters for machine performance enhancement. III. Results After optimization, the design scheme of the DPMBL machine is obtained. Fig 3 gives a comparison of output torque between before and after optimization. It can be seen that in the case of PM without any uncertainty factor, the average torque obtains an improvement from 35.87Nm to 38.21Nm and the torque ripple decreases from 11.26% to 8.78%. As the same PM uncertainty factor is applied to these two machines, the torque quality of the initial machine suffers an obvious decline while the optimized machine can maintain stability. To better validate the effectiveness of the optimization method, Fig 3(b) and Fig.3(c) give the torque and torque ripple distribution of a batch of machines with random PM uncertainty factors. It can be observed that the optimized machine possesses more concentrated performance. In conclusion, the proposed opti-

mization method can resist the PM uncertainty factor and benefit the manufacturing of good quality PMBL machines. More detailed design process descriptions and experimental validation will be presented in the full paper.

[1] G. Lei, T. Wang and J. Zhu, "System-Level Design Optimization Method for Electrical Drive Systems—Robust Approach," *IEEE Trans. Ind. Electron.*, vol. 62, no. 8, pp. 4702-4713, Aug. 2015. [2] F. Dong, J. Zhao and J. Zhao, "Robust Optimization of PMLSM Based on a New Filled Function Algorithm with a Sigma Level Stability Convergence Criterion," *IEEE Transactions on Industrial Informatics*, doi: 10.1109/TII.2020.3020070. [3] B. Ma, J. Zheng and J. Zhu "Robust Design Optimization of Electrical Machines Considering Hybrid Random and Interval Uncertainties," *IEEE Trans. Energy Convers.*, vol. 35, no. 4, pp. 1815-1824, Dec. 2020.

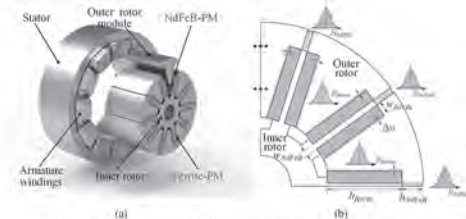


Fig. 1 DPMBL motor Topology and PMs design parameters (a) 3D topology (b) Design parameters and uncertainty disturbance

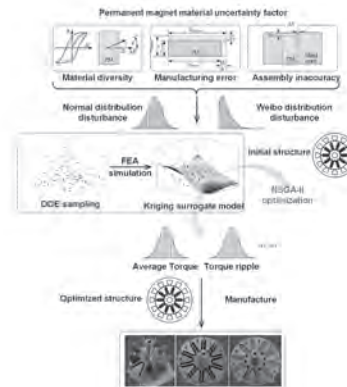


Fig. 2 The flowchart of DPMBL machine robust optimization

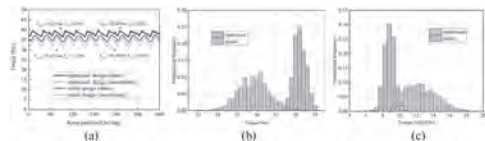


Fig. 3 Optimization results comparison (a) Torque quality (b) Average torque distribution (c) Torque ripple distribution.

Session AR
DESIGN OPTIMIZATION OF PERMANENT MAGNET ELECTRICAL MACHINES
(Poster Session)

Metin Aydin, Chair
Kocaeli University, Umuttepe, Izmit, Turkey

AR-01. Topology Optimization of Consequent-Pole PMSM Using on/OFF Method.

Z. Sun^{1,2}, K. Watanabe¹ and X. Xu²

1. Muroran Institute of Technology, Muroran, Japan; 2. Henan Polytechnic University, Jiaozuo, China

I. INTRODUCTION PM machines have obtained wide applications in the last several decades because of the high efficiency, high torque and high power density. Most PM machines adopt rare-earth PMs as magnetic potential source for high performance. However, due to the unstable supply of rare-earth PMs, the price of PMs is becoming a major issue. Therefore, many machines with less or no PM have been developed in the last a couple of years. Although less or no PM machines such as hybrid PM motors and synchronous reluctance motors can reduce the usage of PMs significantly, they still suffer from poor torque density. Adopting consequent-pole(CP) structure in PM machines is another solution to save PMs[1]-[3]. However, the rotors in CP motors are difficult to design and there is seldom design experience for reference. Topology optimization(TO) is an approach for shape optimization. It searches optimal shape by making free modifications in the distribution of material, and has potentialities to provide novel design. In this paper, The TO method based on ON/OFF method and immune algorithm (IA) was applied on the rotor core of a consequent-pole permanent magnet synchronous motor (CP-PMSM) to improve its torque quality. II. STRUCTURE AND OPERATION PRINCIPLE OF CP-PMSMS Fig.1(a) shows the 1/4 models of PMSMs with surface-mounted PM(SPM) and CP. For a CP-PMSM, the magnetic direction of all the PMs are the same, and each PM pole is set between two silicon steel poles. The magnetic circuits of two motors are established to explain the working principle of the CP motor. Then, torque waveforms are simulated for comparison. The average torque of SPM motor and CP motor are 3.25N and 2.09N, respectively. The average thrust will not reduce half with the missing of half PM poles, which means the PM has higher utilization in the CP-PMSM. Additionally, the motors still have potential to be optimized for better torque quality. III. TOPOLOGY OPTIMIZATION BASED ON ON/OFF METHOD AND IMMUNE ALGORITHMS The authors have proposed a TO method based on ON/OFF method with IA [4]. The ON/OFF method divides the search space into numerous finite element meshes to represent material distribution, each finite element mesh is associated with a binary value, indicating either the presence or absence of material. The area to be optimized is the search space of ON/OFF method. Consequently, the optimized shape could be represented by the presence (silicon steel) or absence (air) of silicon steel material. IA is used to search the optimal shape by changing the material distribution in the meshes. The TO procedures of ON/OFF method based on IA can be summarized as follows: 1) Generate initial antibodies of N_{pop} candidate solutions, create random initial shapes; 2) Smoothen surface and eliminate holes by filter process; 3) Evaluate the objective function for each antibody, list them up from high value to low value; 4) Generate clones for each antibody, the antibodies with high evaluation function will be cloned more to generate more offspring; 5) Apply affinity maturation (small modifications) on material surface to the clones; 6) Smoothen surface and eliminate holes by filter process; 7) Evaluate each clone and list them up, if one clone is better than its parent, it will replace its parent; 8) Keep $N_s\%$ ($0 < N_s < 1$) clones with high ranking and weed others out. Then add randomly generated antibodies as step 1-2 to keep the population size constant; 9) Back to step 4 until the optimization targets are met. IV. OPTIMIZATION RESULT OF THE CP-PMSM The rotor core is chosen to be the search space of ON/OFF method. The search space is defined in $0^\circ-45^\circ$ range, the optimized shape of this range is reversing copied to $45^\circ-90^\circ$ range, so as to make the rotor symmetrical and reduce computation cost. Both the average torque and torque ripple were considered in the evaluation function in optimization. Fig.1(b) shows the evolution of the rotor topologies during optimization. At first, the profile of silicon steel poles emerged in the surface of rotor core, and there were many big holes inside the rotor. Then, the holes inside the core gradually decreased and became smaller, and the shape of the silicon steel poles became more obvious. Finally, the holes inside the rotor core almost disappeared, and the silicon steel poles gradually became a 'W' shape. Torque characteristics before and after optimization are compared in Fig.2. The components of output torque, i.e., electromagnetic torque and

cogging torque, are simulated for analysis. It can be found that the output torque of the CP-PMSM is greatly improved after optimization, the average torque is increased from 2.09N to 2.32N, and the torque ripple is reduced from 126.6% to 13.7%. Moreover, the improvement of output torque is contributed by both the improvement of cogging torque and electromagnetic torque. In the future, we plan to extend this TO method to PM poles and stator core so as realize comprehensive TO.

[1]S. U. Chung, J. W. Kim, and Y. D. Chun, "Fractional slot concentrated winding PMSM with consequent pole rotor for a low-speed direct drive: reduction of rare earth permanent magnet," IEEE Transactions on Energy Conversion, Vol.30, No.1, pp. 103-109, Mar. 2015. [2]L. Wei and T. Nakamura, "Optimization Design of a Dual-Stator Switched Flux Consequent Pole Permanent Magnet Machine With Unequal Length Teeth," IEEE Transactions on Magnetics, Vol. 56, No. 2, pp. 1-5, Feb. 2020. [3]S. Teymoori, A. Rahideh, and H. Moayed-Jahromi, "2-D analytical magnetic field prediction for consequent-pole permanent magnet synchronous machines," IEEE Transactions on Magnetics, Vol.6, No.6, pp. 1-14, Jun.2016. [4]K. Watanabe, T. Suga and S. Kitabatake, "Topology Optimization Based on the ON/OFF Method for Synchronous Motor," IEEE Transactions on Magnetics, Vol. 54, No. 3, pp. 1-4, March 2018.

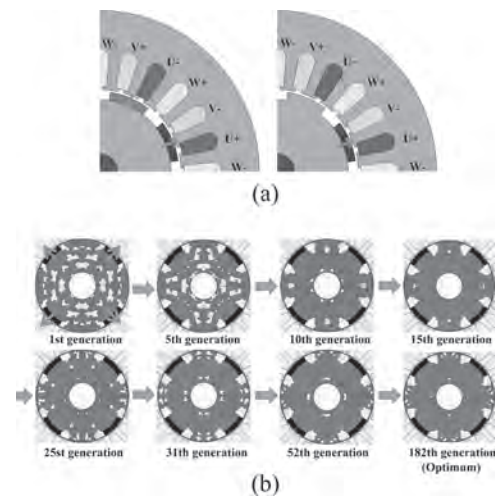


Fig. 1. (a) Comparison of surface-mounted PM motor and consequent-pole motor. In consequent-pole motor, each PM pole is set between two silicon steel poles, so as to save PM volume. (b)Variation of rotor topologies during evolution(Evolutions takes 15 hours in total). The rotor shape varies sharply in the beginning generations and gradually tends to be fixed in a 'W' shape.

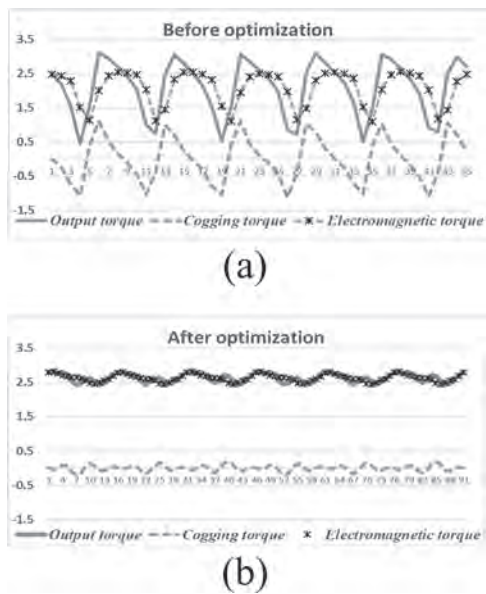


Fig. 2. (a) Torque characteristics before optimization. (b) Torque characteristics after optimization. It can be found the improvement of output torque is contributed by both the improvement of cogging torque and electromagnetic torque

AR-02. Influence of Split Ratio on Field Modulation Effect in Consequent-Pole Permanent Magnet Machine.

Y. Li¹, H. Yang¹ and H. Lin¹

1. Southeast University School of Electrical Engineering, Nanjing, China

I. Introduction Permanent magnet (PM) machines have been extensively investigated and employed in various industrial applications due to their inherent merits of high torque and high efficiency. Nevertheless, because of the ever-increasing price and unstable supply, the rare-earth material cost is a major concern [1]. In order to address above-mentioned issue, the electrical machines with no or less rare-earth PM material are widely developed [1]. Because half of magnetic poles are replaced by iron core, the consequent-pole PM (CPM) machines [2]-[13] exhibit higher PM utilization ratio and comparable torque capability compared with conventional surfaced-mounted PM (SPM) structures. Therefore, various CPM machines in terms of surface-inset [2] [3], interior [4]-[7] and hybrid pole [8]-[10] configurations are reported and extensively investigated, which shows that the CPM design exhibits better field-weakening capability, higher PM utilization ratio, similar torque capability and efficiency compared with SPM machines. Recently, the field modulation effect (FME) concept has been extended to the CPM machines [11]-[13]. It can be found that the CPM machines exhibit more air-gap field harmonics responsible for torque generation compared with the SPM counterparts [11]-[13], which is mainly due to its doubly salient structure, unipolar PM magneto-motive force (MMF) distribution. The split ratio is a key design parameter of the PM machines, which significantly reflects the torque capability, iron loss, efficiency and thermal behavior [14]. However, the influences of split ratio on the FMEs in CPM machines remain unreported hitherto. Therefore, in order to provide an in-depth understanding of their torque production mechanism, the influence split ratio on FME of the CPM machines is investigated in this paper.

II. Machine Topology and Preliminary Electromagnetic Performance The topology of the proposed CPM with 12-stator-slot/14-rotor-pole is illustrated in Fig. 1(a). The fractional slot concentrated windings are adopted to reduce the end winding length and improve the efficiency. The split ratio γ can be defined as $\gamma=r_{si}/r_{so}$ (1) where r_{si} and r_{so} are the stator inner and outer diameters, respectively. The average torque variations of the CPM machine with different split ratios are illustrated in Fig. 1(b). It can be seen that the average torque rises first, and then drops steadily when split ratio exceeds 0.55, which is mainly due to the increased first and then decreased electrical load. In order to quantify the torque contributions of the various working harmonics, the Maxwell stress tensor method is employed. The electromagnetic torque can be expressed as $T_e=\sum(\pi l_{stk} r_g^2/\mu_0) B_{rk} B_{tk} \cos[\theta_{rk}(t)-\theta_{tk}(t)]=\sum T_k(t)$ (2) where r_g is the air-gap radius. l_{stk} is the active stack length. T_k is the electromagnetic torque generated by the k^{th} harmonics of radial and tangential air-gap flux densities, respectively. Thus, the contributions of the k^{th} field harmonics to the total electromagnetic torque can be separated when the k^{th} radial and tangential air-gap field harmonics are obtained. The average torque proportion can be defined as $\lambda=(T_k/T_e)\times 100\%$ (3) The torque contributions of FME can be expressed as $\lambda_{\text{FME}}=(1-T_{Z_r}/T_e)\times 100\%$ (4) where T_{Z_r} is the average torque generated by Z_r order air-gap field harmonic. The corresponding torque proportions of the various air-gap flux density harmonics can be obtained (2)-(4), as shown in Figs. 2(c) and (d). Due to the slightly increased air-gap flux density amplitudes, the torque proportions of 5th, 19th and 21th are increased with split ratio, as shown in Fig. 2(c). Similarly, the torque proportion of 7th harmonic is decreased with split ratio, which is mainly due to its decreased 7th air-gap flux density amplitude. The corresponding torque proportion of FME can be obtained by (4), as shown in Fig. 1(e). Because of the decreased amplitude and torque proportion of the Z_r order air-gap flux density, the torque proportion of FME is increased with split ratio, which indicates that the more pronounced FME can be obtained in relatively higher split ratio. III. Experimental Validation In order to verify the FE simulation, a 12-slot/14-pole CPM machine prototype is manufactured, as shown in Figs 2. The test results are illustrated in Figs. 2(c) and (d), respectively. It can be seen that the measured back-EMF values are slightly lower than FE predictions, as shown in Fig. 2(d), which is mainly due to the fact that the end-winding effect and mechanical tolerance are not considered in FE analysis. The detailed analysis and experimental measurements will be presented in the full paper.

[1] H. Tahanian, M. Aliahmadi and J. Faiz, IEEE Transactions on Magnetics, Vol. 56, Art. no. 900120, (2020) [2] S. U. Chung, S. H. Moon and D. J. Kim, IEEE Transactions on Industrial Electronics, Vol. 63, p.302-309, (2016) [3] J. Li, K. Wang and F. Li, IEEE Transactions on Industrial Electronics, Vol. 66, p.1736-1747, (2019) [4] M. Onsal, B. Cumhuri and Y. Demir, IEEE Transactions on Magnetics, Vol. 54, Art. no. 8206005, (2018) [5] W. Liu and T. A. Lipo, IEEE Transactions on Industry Application, Vol. 54, p.5918-5929, (2018) [6] X. Ren, D. Li and R. Qu, IEEE Transactions on Energy Conversion, Vol. 33, p.2112-2121, (2018) [7] J. Li, K. Wang and H. Zhang, IEEE Transactions on Industrial Electronics, Vol. 67, p.3374-3385, (2020) [8] K. Wang, J. Li and S. S. Zhu, IEEE Transactions on Industrial Electronics, Vol. 66, p.6811-6823, (2019) [9] G. Dajaku, IEEE Transactions on Magnetics, Vol. 56, Art. no. 8200409, (2020) [10] G. Xu, W. Zhao and G. Liu, IEEE Transactions on Transportation Electrification, accepted, (2020) [11] Y. Li, H. Yang and H. Lin, in Proc. XIII International Conference Electrical Machine (ICEM), pp.65-71, (2018) [12] D. Jang and J. Chang, IEEE Transactions on Energy Conversion, Vol. 34, p.2019-2028, (2019) [13] Y. Li, H. Yang and H. Lin, IEEE Transactions on Energy Conversion, accepted, (2020) [14] Y. Shen and Z. Q. Zhu, IEEE Transactions on Magnetics, Vol. 47, p.4187-4190, (2011)

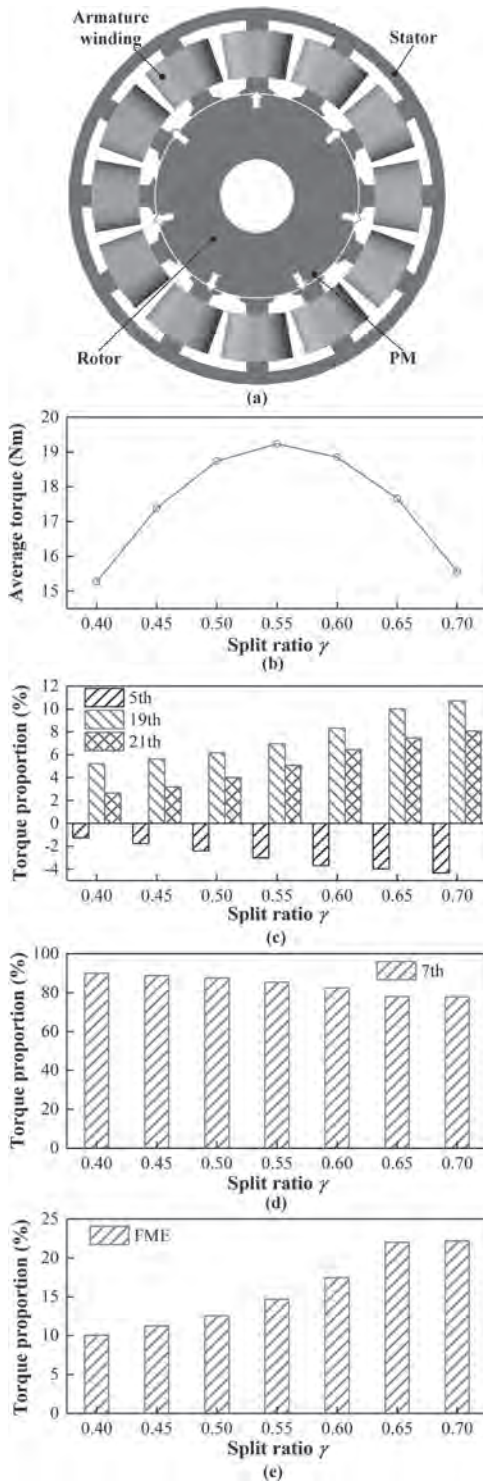


Fig. 1. (a) Configuration of 12-stator-slot/14-pole CPM. Torque characteristics of the CPM machine with different split ratio. (b) Average torque. Torque proportions of the various working harmonics (c) field modulated harmonics, (d) 7th, (e) FME.

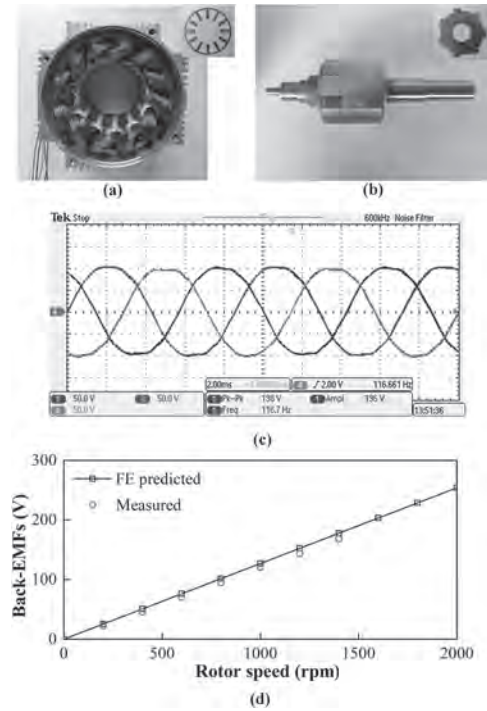


Fig. 2. 12-slot/14-pole CPM machine prototype and measured results. (a) Stator. (b) Rotor. (c) Measured open-circuit back-EMFs. (d) Comparison of the measured and FE predicted open-circuit fundamental amplitudes of back-EMFs.

AR-03. Design and Optimization of Fractional Slot Concentrated Windings Interior Permanent Magnet Traction Motor Considering Anti-Demagnetization Capability.

T. Huynh¹, J. Peng¹, M. Hsieh¹ and P. Huang²

1. Electrical Engineering, National Cheng Kung University, Tainan, Taiwan; 2. Electrical Motor Technology Research Center, National Cheng Kung University, Tainan, Taiwan

Abstract— This work focuses on the analysis of rotor geometry parameters and added flux barriers design to improve the anti-demagnetization capability of fractional slot concentrated windings interior permanent magnet motor (IPM) for electric vehicle (EV) traction applications. A 2.5kW V-shape IPM motor (12 slots and 8 poles) is designed to achieve high torque density and wide constant power speed range (CPSR), which is selected to study in this paper. The influence of rotor geometry parameters variation (such as the magnet position and angle, the width and thickness of magnet) on the relation of characteristic current (I_{ch}) and demagnetization in wide-speed range operation is firstly investigated under high-temperature and high current density operation. Then, the impact of added flux barriers design on the anti-demagnetization capability of the IPM motor is evaluated. The analysis results show that the increase of magnet angle of V-shape IPM would improve the anti-demagnetization capability but would reduce I_{ch} ; meanwhile, the increase of magnet thickness would increase I_{ch} and simultaneously improve the anti-demagnetization capability. In addition, the added flux barriers design significantly affects the anti-demagnetization capability of the V-shape IPM motor. Finally, a unique multi-objective genetic algorithm is applied for the rotor geometry optimization of the V-shape IPM motor to achieve good anti-demagnetization capability, excellent CPSR, and high efficiency. Finite element analysis (FEA) is used for evaluation, and experiments are conducted to validate the analysis. I. Introduction In order to achieve the power and torque requirements of an EV motor, magnetic loading and electrical loading need to be improved. However, due to the saturation of the electrical steel sheet, a high current density design is unavoidable. In a high current operating environment, due to the high temperatures and strong armature magnetic field presented in the motor, the magnetic field provided by the magnet is usually reduced. Under these conditions, the magnet can suffer from irreversible demagnetization. For this reason, a higher current will be required to achieve the originally expected performance. To avoid this type of problem is very important to design a motor with high resistance to demagnetization for the safety and reliability of the product. II. Target Models and Analysis Method A 2.5 kW fractional slot concentrated windings V-shape IPM motor with 12 slots and 8 poles is applied to study here. The rotor configuration of V-shape IPM with the design parameters is shown in Fig. 1(a) and the design of different flux barriers is presented in Fig. 1(b). Finite element analysis (FEA) is utilized to comprehensively evaluate the impact of rotor geometry parameters variation and design characteristic of added flux barriers on the relation of characteristic current (I_{ch}) and the anti-demagnetization capability of the V-shape IPM motor. The details will be reported in the full paper. III. Analysis Results and Experiments Fig. 2 shows the comparison of magnetic flux density distribution on PM without and with added flux barriers design during no-load and load conditions. It can be seen that the added flux barriers design significantly affects the demagnetization risk on PM. Fig. 3 presents the comparison of back EMF of V-shape IPM motor without and with the added flux barriers design before and after demagnetization. The result shows that the added flux barriers design significantly reduces the demagnetization risk on PM of V-shape IPM motor. Fig. 4(a) shows the rotor configuration after optimized of the V-shape IPM motor which is made as a prototype for validating the analyses. Fig. 4(b) shows the comparison of back EMF of V-shape IPM motor between the simulation and experiment at 1500 rpm speed. The phase voltage of back EMF is 13.45 V in the simulation, thus the peak-to-peak of back EMF is 23.3 V; meanwhile, the measured back EMF is 24.8 V. The error between the simulation and experiment is only 6%, thus the analysis results are reliable. Fig. 5(a) shows the torque and power versus speed curves of the V-shape IPM motor. The output torque of the motor is 9.17 Nm for simulation and 8.9 Nm for the experiment, respectively. Fig. 5(b) presents the comparison of back EMF of IPM motor before and after demagnetization in the experiment. The back EMF of the motor after fully demagnetized magnets only

has an error of 2%. The accuracy of the simulation is thus verified by the experiment results. Detail analysis and experiment will be reported in the full paper. IV. Conclusion This digest has analyzed the impact of rotor geometry parameters variation and design characteristic of added flux barriers on the performance and the anti-demagnetization capability of fractional slot concentrated windings V-shape IPM motor. The added flux barriers design significantly affects the performance and anti-demagnetization capability of the V-shape IPM motor. The detail analysis and experimental results will be reported in the full paper.

[1] H. Chen, R. Qu, J. Li and D. Li, "Demagnetization Performance of a 7 MW Interior Permanent Magnet Wind Generator With Fractional-Slot Concentrated Windings," IEEE Transactions on Magnetics, vol. 51, no. 11, pp. 1-4, Nov. 2015. [2] K. Imamura, M. Sanada, S. Morimoto, and Y. Inoue, "Improvement of Demagnetization by Rotor Structure of IPMSM with Dy-Free Rare-Earth Magnet," in Proceeding of IEEE International Electrical Machines and Systems Conference, Sapporo, 2012.

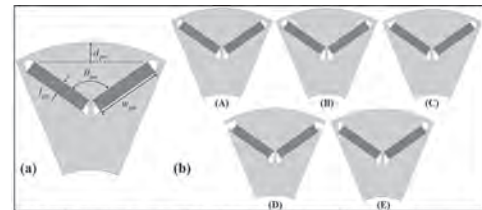


Fig. 1 (a) Rotor configuration of 2.5kW V-shape IPM motor with design parameters for study; (b) The different added flux barriers design applied for study.

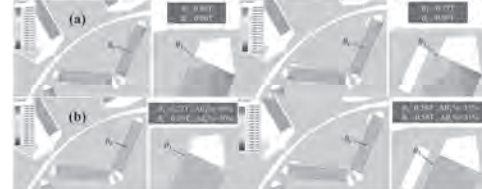


Fig. 2 Comparison of the magnetic flux density distribution on PM without and with the added flux barriers design during no-load and load conditions. (a) no-load condition; (b) load condition.

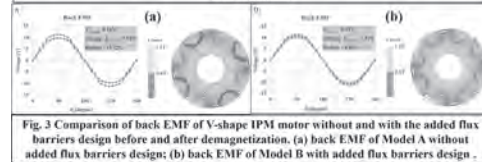


Fig. 3 Comparison of back EMF of V-shape IPM motor without and with the added flux barriers design before and after demagnetization. (a) back EMF of Model A without added flux barriers design; (b) back EMF of Model B with added flux barriers design.

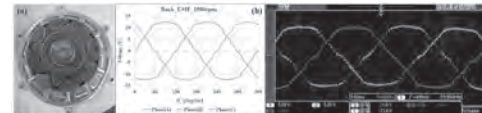


Fig. 4 (a) Prototype of 2.5kW V-shape IPM motor; (b) Back EMF comparison of 2.5kW V-shape IPM motor between simulation and experiment at 1500 rpm speed before demagnetization.

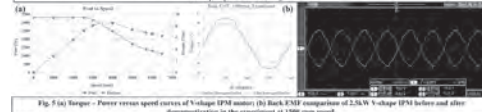


Fig. 5 (a) Torque - Power versus speed curves of Voltage IPM motor; (b) Back EMF comparison of 2.5kW V-shape IPM before and after demagnetization in the experiment at 1500 rpm speed.

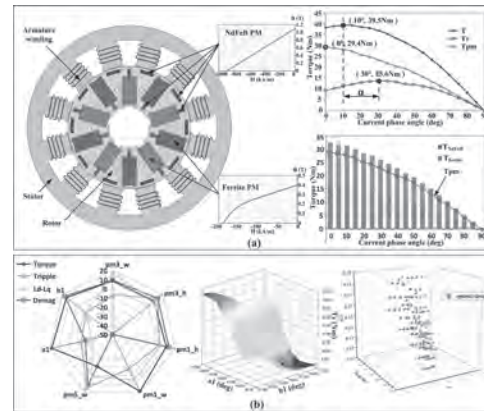
AR-04. Optimization of a New Asymmetric-Hybrid-PM Machine With High Torque Density and Low Torque Ripple Considering the Difference of Magnetic Materials.

Y. Chen², T. Cai², X. Zhu¹ and Y. Ding²

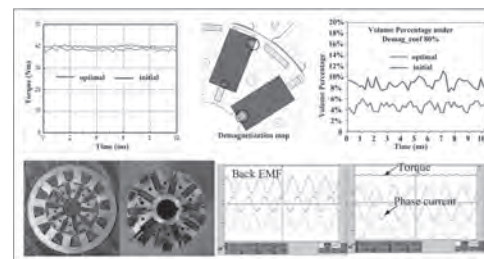
1. Jiangsu University, Zhenjiang, China; 2. Yangzhou University, Yangzhou, China

I. Introduction With the large-scale application of rare-earth permanent magnet motors, the consumption of rare-earth PM material has increased sharply [1]. As a non-renewable resource, such excessive consumption increases the potential risks of further larger scale application of rare-earth PM motors. Recently, to alleviate the dependence on the rare-earth PMs, a type of less rare-earth permanent magnet (LRE-PM) machines has attracted much attention since the adoption the low cost of non-rare-earth Ferrite-PMs [2]. In this paper, a new asymmetric-PM-placed rotor topology is applied to the conventional LRE hybrid magnet machine, where such new placement of hybrid magnets can be designed to improve the torque performance effectively. Considering the complexity of rotor structure and the difference between two magnetic materials, the relationship among the size of the hybrid magnets (NdFeB-PMs and Ferrite-PMs), torque density and torque ripple is investigated through theoretical derivation and finite element analysis. And, some key size parameters are optimized to improve torque performances. II. Optimization Design and Analysis of Torque Performance In this paper, a new frozen permeability method is used to separate the components of total torque [3], and the design factors influencing torque ripple are deduced theoretically. According to the principle of equivalent magnetomotive force, the initial design of hybrid magnets is carried out. Then for the key size of hybrid magnets, the sensitivity analysis of multiple optimization objectives is conducted to obtain the optimal solution [4]. The effectiveness of the proposed method is verified by comparing the torque performance and anti-demagnetization property of the initial machine with that of the optimized one. Fig. 1(a) shows the proposed asymmetric-hybrid-PM machine structure. In the rotor, the NdFeB-PMs and Ferrite-PMs are asymmetric arranged in mixed series-parallel connection. It can be seen that the permanent magnet torque (T_{pm}) decreases due to the coupling effect of the two different magnets. However, by properly designing the size of spoken hybrid magnet element arranged asymmetrically, the reluctance torque (T_r) can be improved and the maximum torque approximation angle can be optimized to improve the torque density. Fig. 1(b) shows the sensitivity analysis results of key parameters and the optimal solution. The improvement of torque capabilities and anti-demagnetization ability is shown in Fig. 2, which verifies the validity of the proposed optimal method. III. Verification by FEM and Experimental Results In order to further verify the feasibility of the motor topology and the effectiveness of the proposed optimal method, an experimental prototype is fabricated, and more detailed electromagnetic performance analysis and experimental results will be presented in the full paper.

Xianxian Zeng, Li Quan, Xiaoyong Zhu, et al., Investigation of an asymmetrical rotor hybrid permanent magnet motor for approaching maximum output torque. *IEEE Trans. Appl. Supercond.*, 2019, vol. 29, no. 2, Article No. 0602704. Qian Chen, Gaohong Xu, Guohai Liu, et al., Reduction of torque ripple caused by slot harmonics in FSCW spoke-type FPM motors by assisted poles, *IEEE Trans. Ind. Electron.*, 2020, Vol. 67, No. 11, pp. 9613-9622. Xiaoyong Zhu, Deyang Fan, Zixuan Xiang, et al., Systematic multi-level optimization design and dynamic control of less-rare-earth hybrid permanent magnet motor for all-climatic electric vehicles. *Appl. Energy*, 2019, 253, 113549. B.Ma, G. Lei, J. Zhu, Y. Guo, et al., Application-oriented robust design optimization method for batch production of permanent-magnet motors, *IEEE Trans. Ind. Electron.*, vol. 65, no. 2, pp. 1728-1739, Feb. 2018.



The asymmetric-hybrid-PM machine structure and the optimal design.



The performance improvement of the proposed machine.

AR-05. Design and Optimization of New Flux-Concentrating Rotors Combining Halbach PM Array and Spoke-Type IPM for PMSM.

J. Wang¹, W. Geng¹, Q. Li¹ and L. Li¹

1. College of Automation Engineering, Nanjing University of Science and Technology, Nanjing, China

I. INTRODUCTION This paper proposed a new flux-concentrating rotor for PM machine, taking advantages of spoke-type and Halbach array PM flux-concentrating. As shown in Fig. 1 (a), it is the evolution of the proposed rotor. The upper part of tangentially magnetized magnets still remain the spoke-type flux-concentrating property, while the bottom tangentially magnetized magnets and the radially magnetized magnets form a primitive Halbach array [1] [2]. Since the ratio match tangentially/radially magnetized magnets directly affects the effect of flux-concentrating, as well as the saliency ratio and torque performance, this paper focuses on the optimization of the size of permanent magnets on the rotor on the basis of keeping the same amount of PMs and the polar arc coefficient. II. OPTIMAL DESIGN OF NEW FLUX-CONCENTRATING ROTOR Response surface method (RSM) is a set of statistical and mathematical techniques to find the “best fitted” response of the physical system through experiment or simulation [3]. In RSM, a polynomial model, called a fitted model, is generally constructed to represent the relationship between the performance and design parameters. As shown in Fig. 1 (a), it is the evolution of the proposed rotor. Ensuring the same volume of PM in three rotors, the new rotor was optimized. The geometric parameters of the new rotor are shown in Fig. 1 (b). In order to quantitatively compare with the motor whose pole-arc coefficient is 0.8, including in various electromagnetic characteristics. b is determined as 8 mm. The volume of PM is defined as (1), where p is pole pairs, l is stack length, m is the volume of PMs. The optimized objective is formulated to maximize the air-gap flux density under the constraint of keeping the PM volume. Tab. I shows electromagnetic analysis results under various combinations of l_x and h_y . The relationship between air-gap flux density and l_x , h_y is shown in Fig. 2 (a). Two optimized points are found, where the analysis result is better than the predicted value. The regression equations of air-gap flux density obtained by RSM analysis is as (2). As shown in Fig. 2 (b), the predicted value and the actual result maintain a high consistency. It can be concluded that the regression equation obtained by the RMS is reliable. As shown in Fig. 3, The result of optimization is to maximize the air-gap magnetic density. l_x is determined as 16.5 mm, and h_y is determined as 3.75 mm. Fig. 4 shows the comparison of two rotors. The final optimized model is built by 2-D FEA, as shown in Fig.5. III. FEA AND EXPERIMENTAL VERIFICATION Tab. II gives the main parameters of optimized rotor. Fig. 6 (a) compares the air-gap flux density of the motors with optimized rotor and the original rotor. The air-gap flux density in the motor with optimized rotor is higher than that in the initial one. As shown in Fig. 6 (b), the line back electromotive force (EMF) of the motor with optimized rotor increases slightly due to the higher air gap flux density. Fig. 6 (c) shows the C-T relationship under maximum torque per ampere (MTPA) control and $i_d=0$ control. The results show that under MTPA control and $i_d=0$ control, the output torque of the optimized rotor is higher than the initial model. In Fig. 6 (d), the saliency ratio is higher in the optimized rotor than in the original one. so the flux-weakening ability is stronger. Considering the manufacturing process, the actual rotor structure is shown in Fig. 7 the shape of the radially magnetized PMs are rectangular. The stator, rotor and test platforms are shown in Fig. 8. Fig. 9 compares the experimental and FEA results. Fig. 9 (a) is the comparison between the experimental and analytical result about back EMF without load, Fig. 9 (b) shows the C-T relationship of the motors with original rotor and optimized rotor under MTPA control and the results present a high consistency and error is less than 2%. But the error is large in the relationship between experiment and analysis under $i_d=0$ control due to the reluctance torque is fully utilized with the large current. IV. CONCLUSION In this paper, a new flux-concentrating rotor for PM machines is designed to combing spoke-type IPM rotor and Halbach PM array The size parameters of PM of the new rotor are optimized by the response surface method for the maximum air-gap flux density and torque capacity considering the constant pole-arc coefficient and the volume of PM. The 72-slot/16-pole PM motor with the optimized rotor is developed by 2-D FEA and experiments. The experimental result the air-gap flux density is increased by 6.7%and the torque is increased by 7.5%.

[1]Igor P. Wiltuschnig, Paulo R. Eckert, David G. Dorrell, “A Study of the influence of quasi-Halbach arrays on a torus machine,” *IEEE Trans. Magn.*, vol. 52, no. 7, pp. 1325-1328. July 2016. [2]M. M. Rahman, K.-T. Kim, and J. Hur, “Design and optimization of neodymium-free spoke-type motor with segmented wing-shaped PM,” *IEEE Trans. Magn.*, vol. 50, no. 2, Feb. 2014, Art. ID 7021404. [3]Byeong-Hwa Lee; Jung-Pyo Hong; Jung-Ho Lee, “Optimum Design Criteria for Maximum Torque and Efficiency of a Line-Start Permanent-Magnet Motor Using Response Surface Methodology and Finite Element Method,” *IEEE Trans. Magn.* vol. 48, no. 2, pp. 863-866. Feb. 2012.

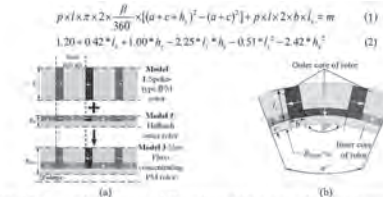


Fig. 1 The proposed new structure. (a) The evolution of the new rotor. (b) Geometric parameters

Tab. I

	l_x /mm	h_y /mm	Lq/Ld	Air-gap flux density/T	Max torque/N m
1	18.8	3.00	1.544	1.287	200.56
2	18.0	3.25	1.550	1.285	200.59
3	17.2	3.50	1.570	1.281	201.38
4	16.5	3.75	1.599	1.280	202.94
5	16.0	4.00	1.623	1.276	203.45
6	14.7	4.25	1.644	1.266	202.23
7	13.9	4.50	1.672	1.253	201.40
8	13.0	4.75	1.729	1.227	200.96
9	12.2	5.00	1.735	1.228	200.61

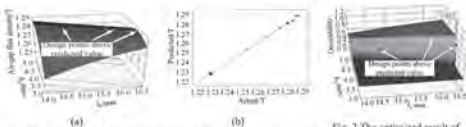


Fig. 2 Results of response surface method. (a) The relationship between air-gap flux density and l_x , h_y . (b) Fitting of prediction and actual.

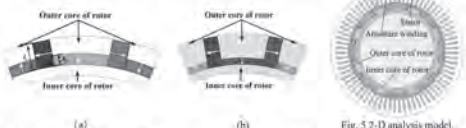


Fig. 4 Comparison of rotors. (a) The original rotor. (b) The analysis rotor.

No. 200 Xiaolingwei, xuanwu district, Nanjing, 210094, Jiangsu Province, PR, China
E-mail: arwein@ust.edu.cn, Tel: +86-10850724704

Tab. II

Parameter	Value
Rated current/A	100
Peak current/A	200
Rated power/kW	30
Peak power/kW	60
Rated voltage/V	300
Magnet poles/Stator slots	16/72
Pole-arc coefficient	0.8
PM weight/kg	1.6
Rotor outer diameter/mm	188
Rotor inner diameter/mm	146
Stator outer diameter/mm	260
Stack length/mm	40

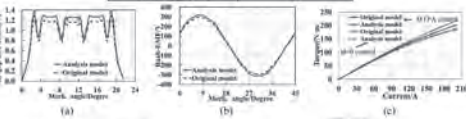


Fig. 6 Electromagnetic properties. (a) Air-gap flux density. (b) Line back EMF. (c) Current VS torque under MTPA and $i_d=0$ control. (d) Saliency ratio.



Fig. 7 Sectional view of the final prototype. (a) Stator. (b) Rotor. (c) Test platform.



Fig. 8 Prototype and test platform. (a) Stator. (b) Rotor. (c) Test platform.

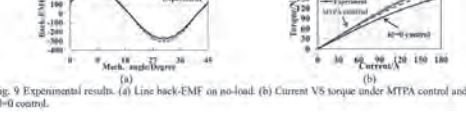


Fig. 9 Experimental results. (a) Line back-EMF on no-load. (b) Current VS torque under MTPA control and $i_d=0$ control.

AR-06. Multi-Objective Tradeoff Designs of Rotor Flux-Barrier in a Multi-Layered IPM Machines for EV Applications.

Z. Chen¹

1. Nanjing University of Aeronautics and Astronautics, Nanjing, China

I. Introduction Interior permanent magnet (IPM) machines are very attractive for the electric vehicle (EV) traction applications due to its excellent performance such as high torque density, and good flux-weakening capability. The multi-layered magnet rotors are more and more adopted in IPM machines, such as the 2008 Lexus LS600H, 2012 Nissan Leaf, 2016 BMW i3, and 2017 Prius which are delta-shape and 2U-shape magnet configuration. A multi-objective tradeoff design method is proposed in a multi-layered IPM machine for EV applications. The multi-objective including the cogging torque, average torque at different loads, torque ripple at different loads, iron loss, and magnet eddy-current loss. Firstly, the single-objective according to the variation of rotor flux-barriers are investigated individually. It is hard to tradeoff design between them, because there have seven targets. Then, a novelty method synthesize the torque on different loads, torque ripple on different loads, and total iron loss which can reduce the targets number from seven to three. The center of gravity of the three points are selected as the eventual angles of rotor flux-barriers. Finally, the multi-layered IPM machine is prototyped and experimented to verify the tradeoff design results. II. Main Body Fig. 1(a) shows the multi-layered magnet configurations. The rib1-rib5 are the bridges and ribs, $PM_{a2} - PM_{a3}$ are the angle of magnets, $b_{a1} - b_{a3}$ are the angle of barriers. The magnets are inserted in the rotor barriers. Multi-layer magnet has adopted to enhancing saliency ratio for improving reluctance torque. The rated power of the machines is 48 kW, the continuous rated current (rated load) is 200 A, the maximum current (over load) is 400 A, and the maximum speed of the machines is 12000 r/min. The torque ripple is generated by the harmonic interaction of the stator magnetic force harmonic and the rotor magnetic field. It will also cause the vibration, and noise, affecting the comfort of passengers in the EV. In the design of IPM machines, it is desire to minimize the torque ripple. Not only just about the rated load, also about over load condition. The torque ripple at different loads according to the variation of ba_3 and ba_6 are shown in Fig. 2(a) and Fig. 2(b). The minimum torque ripple under rated load condition is located at point A. The minimum torque ripple under over load condition is located at point B. With different loads, the location of point A, and B are different. To considerate the overall torque ripple, synthesize the rated load, and the over load condition. In the design of IPM machines, it is desire to minimize the core loss and magnet eddy-current loss. The core loss and magnet eddy-current loss at 12000 r/min according to the variation of ba_3 and ba_6 are shown in Fig. 2(c) and Fig. 2(d). The minimum core loss is located at point C. The minimum magnet eddy-current loss is located at point D. Therefore, it is hard to achieve minimum core loss and magnet eddy-current loss simultaneously. In order to verify the results of the previous analysis, a prototype machine with multi-layered magnet rotor is manufactured. Fig. 1(b) shows photographs of the rotor. The FEA predicted and measured no-load phase EMF at 1500 r/min of multi-layered IPM machines are compared. It can be seen that the measured EMF waveforms consist of three steps corresponding to the pole-arc to pole-pitch ratios of three PM layers, which agrees well with the results of the FEA. The torque and efficiency are measured by a digital meter, the measured results are also agrees well with the results of the FEA. III. Conclusion This paper has presented a multi-objective tradeoff design method in a multi-layered IPM machine for EV traction applications. The novelty method synthesize the torque on different loads, torque ripple on different loads, and total iron loss, which can reduce the targets numbers. The selected of the center of gravity of the three targets can consider the global performances simultaneously, it is a reasonable tradeoff design. It is demonstrated that the effects of angles of rotor flux-barriers on torque ripple and core loss is significant. Therefore, rotor flux-barrier angles is an important issue in the design of multi-layered IPM machine. Finally, the prototype machine with multi-layered magnet rotor is fabricated and experimented.

Salimi1, Min Li, "Visualization and Analysis of Tradeoffs in Many-Objective Optimization: A Case Study on the Interior Permanent Magnet Motor Design," IEEE Trans. Magn., vol. 52, no. 3, pp. 8102404, Mar. 2016.

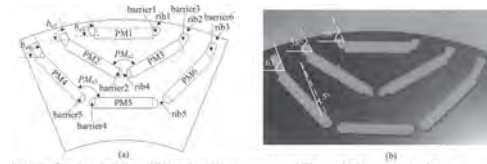


Fig. 1. Configuration of multi-layered IPM machine. (a) Design parameters. (b) Photograph of the prototype machine rotor.

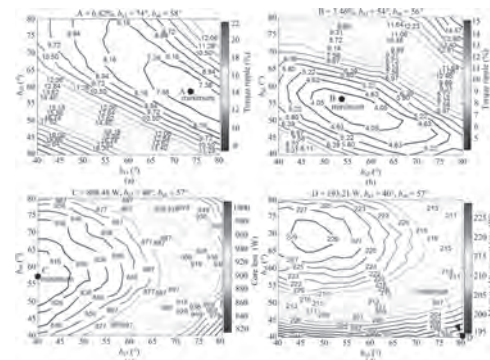


Fig. 2. The torque ripple at different loads, the core loss and magnet eddy-current loss at 12000 r/min according to the variation of ba_3 and ba_6 . (a) Rated load. (b) Over load. (c) Core loss. (d) Magnet eddy-current loss.

[1] Burak Ozpineci, "Oak Ridge National Laboratory Annual Progress Report for the Electric Drive Technologies Program," Oak Ridge National Laboratory, ORNL/SR-2016/640, Oct. 2016. [2] Rodrigo Silva, Armin

AR-07. Robust Design Optimization Based on Separated Surrogate Model Method for IPMSM.

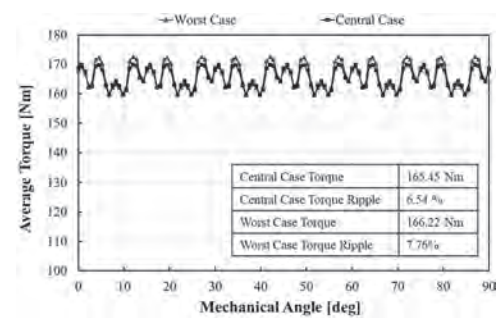
C. Kim¹, S. Jun¹ and S. Jung¹

1. Department of Electrical and Computer Engineering, Sungkyunkwan University College of Information and Communication Engineering, Suwon, The Republic of Korea

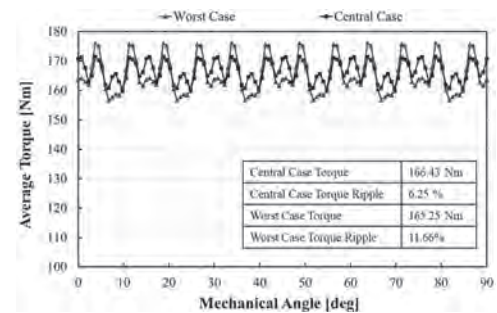
I. Introduction There has been a growing demand for permanent magnet electric machines with high torque and power density per unit current. Furthermore, electric machines are increasingly required to have high efficiency by regulation of energy efficiency. Many optimization algorithms are being studied to achieve high efficiency of IPMSM. Practically, manufactured electric machines can't expect high performance for all products due to material deviations and dimensional tolerances. Therefore, we must consider the problems that occur while manufacturing to perform an optimization algorithm. However, considering the manufacturing tolerances along with many of the design variables of IPMSM requires a lot of time and cost. Therefore, we propose to apply multiple regression method to improve the performance of the conventional particle swarm optimization (PSO) algorithm. In addition, we can estimate the function formula for the design variables and derive the global solution by using estimated function formula. The convergence speed of the conventional PSO algorithm is improved by using the information of the solution obtained by performing the multiple regression. In addition, we will ensure the robustness of the design by estimating the appropriate regression equation for each design space. II. Particle Swarm Optimization with Multiple Regression Method Since the PSO algorithm finds the optimal solution using the information of each individual, the optimal solution can be found only when the particle moves. In this paper, multiple regression analysis is performed on the accumulation data obtained through the PSO algorithm. Then, an approximate solution can be obtained by using multiple regression. PSO with multiple regression algorithm has the same main loop as conventional PSO algorithm. First, initial particles are created with random locations, and update the velocity and position to find the global solution every iteration. If the amount of data for multiple regression is considered to be sufficient, then regression analysis is performed. We iterate this process until we reach the defined objective function. We selected seven numerical test functions to validate the proposed algorithm. The data obtained from performing the PSO algorithm is used to construct the Multiple Regression Model. Multiple regression is performed within the overall design space, and the result is a rough model. However, it is not a problem because it is used to improve the convergence speed. III. Robust Design Optimization of IPMSM A robust solution is the solution that has the lowest variability of the objective function in the design space that meets the requirements of the objective function. Constraints are needed to solve the problem of finding a robust solution. Constraints are obtained through multiple regression analysis. In particular, in order to consider the variability of design variables, the surrogate model must be configured in all solutions to find a robust solution. However, multiple regression analysis over the entire design space can improve the convergence of the algorithm, but it is challenging to construct an accurate surrogate model. Therefore, we used a method of reducing the design space into limited space that can be explained by multiple regression. A detailed procedure to find a robust solution is as follows. First, perform the modified PSO algorithm to save the data of the particles and find the first solution. When finding a solution, convergence speed is improved by performing multiple regression in the total design space. Second, Construct a multiple regression model around the first solution. The construct region of the multiple regression model limits the region to the adjusted coefficient of determination above 0.95. Multiple regression models verify the variability of the objective function. Third, the first and second process is repeated except for the multiple regression areas obtained in the second section. This procedure is repeated to the extent that it does not violate the constraints of the objective function. We have applied the proposed algorithm to the robust design optimization of IPMSM. We considered the variability of the objective function according to manufacturing tolerances. Target model was selected as IPMSM with eight poles and 48 slots as the target model for driving a vehicle. The constraint condition is over 165 Nm of average torque at 3000 RPM and objective function is minimization of the torque ripple. The central case torque and central case

torque ripple are the average torque and torque ripple at the reference point. The worst case torque and worst case torque ripple are the average torque and torque ripple at the design variable values that represent the largest variation within the manufacturing tolerances. As a result of optimization using proposed algorithm, global solution and robust solution were found as shown in Fig. 1, 2. The robust solution has smaller torque ripple variability in Fig. 1. however, global solutions are large variability when considering manufacturing tolerance in Fig. 2. The engineers have the problem of selecting a global solution with higher torque at a similar torque ripple level without considering manufacturing tolerances. However, considering manufacturing tolerances, engineers can choose a robust solution with low variability.

B. D. S. G. Vidanalage, M. S. Toulabi, S. Filizadeh, IEEE Transactions on Energy Conversion., vol. 33, p.1547 (2018) C. Ma, L. Qu, IEEE Transactions on Energy Conversion., vol. 30, p.1144 (2015) J. Ou, Y. Liu, R. Qu, IEEE Transactions on Industrial Electronics., vol. 65, p.3772 (2018) J. H. Lee, J. Song, D. Kim, IEEE Transactions on Industrial Electronics., vol. 65, p.1791 (2018) B. Ma, G. Lei, C. Liu, IEEE Transactions on Magnetics., vol. 54, p.8102404 (2018)



Average torque variability of robust solution



Average torque variability of global solution

AR-08. Tornado Optimization With Pattern Search Method for Optimal Design of IPMSM.

C. Wi¹ and D. Lim¹

1. University of Ulsan, Ulsan, The Republic of Korea

Abstract – In this paper, a novel global search algorithm tornado optimization (TO) and its hybridization with pattern search method (PSM) are proposed to solve the multimodal optimization problem. The TO enhances capability of global searching with two strategies, intensification strategy and diversification strategy. The hybridization with PSM supports the exact and fast convergence on adjacent optima from the points that are discovered in global search using TO. Outstanding performance of the proposed algorithm is verified by comparison with niching genetic algorithm at the test function and the algorithm is applied to the optimal design of the interior permanent magnet synchronous motor for electric vehicle. I. Introduction To analyze the accurate characteristics of the electric motors for electric vehicle (EV), finite element method (FEM) analysis, which takes a lot of time, is required because of the nonlinear magnetic saturation of the motors [1]. Computational problem of FEM becomes worse when it is applied to the multimodal optimization problem, such as an optimal design of motor. To solve this problem, several algorithms such as niching genetic algorithm (NGA) have been studied. The NGA is an improved algorithm of GA for the multimodal function [2]. However, the NGA still have a problem with calculation time because it takes a lot of function calls to converge to the accurate peak point [3]. To reduce the number of function calls and to enhance the convergence characteristic, this paper proposes the tornado optimization (TO) hybridized with pattern search method (PSM). The TO is an algorithm to search overall area and to designate some points as candidates for several optima. The performance of the algorithm is maximized with the usage of the PSM, which is a kind of deterministic algorithm. II. TORNADO OPTIMIZATION WITH PSM In hybrid algorithm for the multimodal function, adopting strategy and role sharing of each search algorithm are important. Global search algorithm adopts diversification strategy to search overall area and to find undiscovered candidates. On the other hand, local search algorithm converges candidates to each adjacent optimum quickly and precisely by adopting intensification strategy [4]. In TO, the processes of being sucked into tornadoes and searching the opposite side by Zone 1 are employed as intensification strategy. On the other hand, thunder strike of Zone 2 is used as a diversification strategy to prevent particles from being trapped in a local optimum. First, the superior initial particles are generated by Latin hypercube sampling (LHS), which scatters samples evenly, and search each location [5]. With their results, tornadoes occur with their own zones. The rest of particles are sucked into tornado. When they enter the zone of tornado, they will be moved in two ways. As seen in Fig. 1, if they enter in Zone 1 which is the half of the zone, they are swept away by tornado and fly to the opposite side of the tornado. On the other hand, if they enter in Zone 2 which is the inside of the zone, they will be scattered outside the tornado, just as thunder strikes from inside to outside of the real tornado. They will continue to be sucked into the tornado at the relocated area. And then, the searched tornado extends its zone to the location of the absorbed particle. At the same time, the proportion of Zone 2 increases. Zone 1 reduces the number of function calls in advance before the PSM to be executed and helps to find optima hiding beyond the tornado. Zone 2 prevents meaningless re-discovery of discovered tornado and it helps to find new candidates that has not been found yet. In addition, expansion of Zone 2 increases the weight of thunder strikes instead of being swept away. It means that the proportion of diversification strategy increases with each iteration of the search. After repeating this process, new tornadoes occur in potentially optimal candidates recorded during the process. After enough tornadoes are created by TO, those candidates are converged to adjacent optimum by the PSM. The hybridization with the PSM makes TO to find the accurate peak point without being trapped to the local optima [3]. III. VERIFICATION OF PROPOSED ALGORITHM To verify the performance of the proposed algorithm, TO and NGA are applied to the mathematical test function. Test was carried out 100 times with each algorithm. As shown in Fig. 2, there is no doubt that the TO shows outstanding performance than the NGA. The $D_{st_{avg}}$ means the average distance from the found peak point to the actual peak point. When the function calls of TO and NGA are 1108 and 1380, respectively, the $D_{st_{avg}}$ of

the TO is 72% less than the result of NGA. The TO consumed 19% less function calls than the NGA, even though the accuracy was higher. The application of the TO to the optimal design of the interior permanent magnet synchronous motor (IPMSM) will be covered in full paper. IV. CONCLUSION This paper introduces a novel hybrid algorithm on the purpose of both reducing function call and increasing accuracy of multimodal problem. The outstanding performance of the TO was confirmed through a test function, compared with NGA. The TO was applied to the optimal design for minimizing the cogging torque of IPMSM for EV and successfully derived the optimum model. Acknowledgement This work was supported by a National Research Foundation of Korea (NRF) grant funded by the Korean government (Ministry of Science and ICT) (No. 2019R1F1A1061132).

- [1] M. Caruso, A. O. Di Tommaso, L. Ferraris, 2017 Twelfth International Conference on Ecological Vehicles and Renewable Energies (EVER)(2017)
 [2] B.-K. Son, G.-J. Park, J.-W. Kim, *IEEE Trans. Magnetics.*, vol.52, No.3 (2016)
 [3] Emanuele Diletto, Nunzio Salerno, *IEEE Trans. Magnetics.*, vol.42, No.4, pp.1203-1206 (2006)
 [4] K. Lei, F. Wang, Y. Qiu, *Proc. Auto. Decentralized Syst. (ISADS)*, pp. 513–519 (2005)
 [5] Y.-R. Kang, J.-C. Son, D.-K. Lim, *IEEE Access.*, vol.8, pp. 117405-117412 (2020)

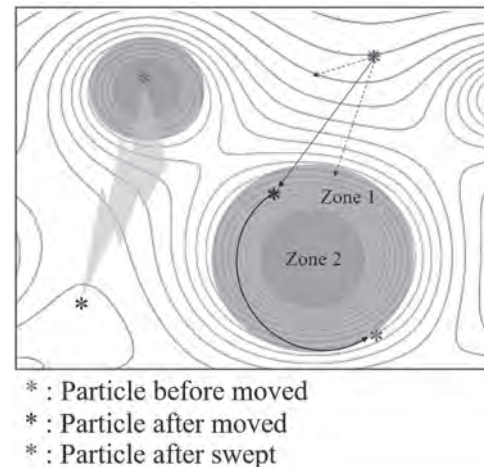


Fig 1. Concept of Tornado Optimization

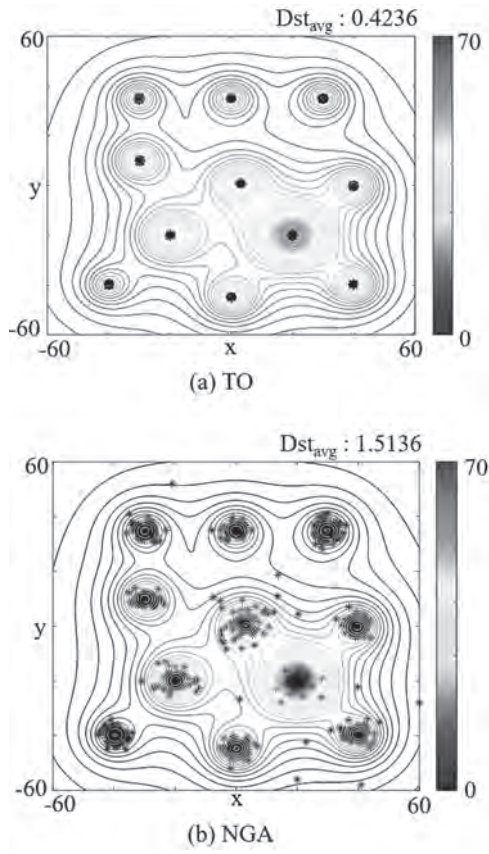


Fig 2. Result of test function. (a) TO, (b) NGA

AR-09. Torque Ripple and Cogging Torque Reduction Method of IPMSM Using Asymmetric Shoe of Stator and Notch in Stator.

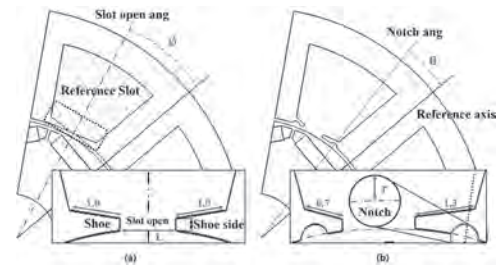
J. Moon¹, D. Lee³ and D. Kang²

1. Dept. of Electrical and Electronic Convergence System Engineering, Keimyung University, Daegu, The Republic of Korea; 2. Dept. of Electrical Energy Engineering, Keimyung University, Daegu, The Republic of Korea; 3. Dept. of Electronic and Electrical Engineering, Keimyung University, Daegu, The Republic of Korea

This paper suggests asymmetric stator shoe and stator notch design method to reduce torque ripple and cogging torque of Permanent Magnet Synchronous Motors(PMSM). In this paper, we analyze an Interior Permanent Magnet Synchronous Motors(IPMSM) with 6 poles and 9 slots. Analysis of proposed design method is analyzed using Finite Element Method(FEM). The proposed design method in this paper is advantageous for torque ripple and cogging torque reduction with minimizing torque reduction. We propose improved design method thorough comparing basic model and improved model, and the experiment of the improved model is conducted to verify the validity of this design method. As environmental regulations become more severe, research has been conducted to develop high efficiency and high power motors. Permanent Magnet Synchronous Motors(PMSM) commonly use rare earth magnets, which is advantageous for high power output. In addition, PMSM does not require a device to generate flux, so the loss in the rotor is very small, which is advantageous for the development of high efficiency motors. Interior Permanent Magnet Synchronous Motors(IPMSM) can increase torque by using reluctance torque, it is widely used in industries requiring high power motors. However, back EMF and the difference in reluctance cause the torque ripple and cogging torque of the motor. The skew-applied model can reduce torque ripple and cogging torque, but reduces the torque and makes manufacturing difficult[1-3]. In addition, many studies such as pole and slot number combinations[4], magnetic barriers[5], and magnet shapes[6, 7] have been conducted to reduce torque ripple and cogging torque. Torque ripple and cogging torque can be reduced by changing design of the stator teeth, back yoke and shoes without changing design of the rotor. However, it is not easy to improve torque ripple and cogging torque with maintaining output power. In this paper, we suggest design method of asymmetric stator shoe and stator notch that can reduce torque ripple and cogging torque with minimizing torque reduction. Fig. 1 shows examples of parameters, basic model and improved model of this study. In this paper, we analyze torque ripple and cogging torque by asymmetric shoe structure. Cogging torque is caused by the difference in reluctance, and reluctance depends on the shape of the shoe. Therefore, the analysis of notch structure is performed after finding the optimal point of the asymmetric shoe structure. The design is based on the values shown in Table 1. The slot area and current of all models are the same, and the minimum size of the slot opening is limited to 4.3 mm when considering the possibility of manufacture. In this study, the direction in which the rotor rotates is CCW(Counter Clockwise), and the reference axis of the parameter for the angle is centered between the reference slot and the previous slot. The design parameters for the analysis of the asymmetric shoe structure are the slot opening width L and the angle Φ of the center of L . The magnetic flux of the stator generated by the applied current is most saturated in the shoe. The magnetic saturation of the shoe lowers the permeability and increases the harmonic component, increasing torque ripple and cogging torque. Therefore, the magnetic saturation of the shoe will change with the length of parameter L , and the harmonic components will change as the flow of magnetic flux changes. In addition, the asymmetric structure of the shoe, which is changed by parameter Φ , changes the harmonic components. Analysis of the change of two parameters is performed by FEM to find the optimal design parameters of torque ripple and cogging torque. The asymmetric structures of the shoe are applied to the improved model, and the relationship between torque ripple and cogging torque is compared with the basic model. The design parameters for analyzing the notch structure are the notch radius r and the angle θ of the center for the notch. The design parameters of the notch are analyzed after applying the optimal design parameters of the preceding asymmetric shoe structure to the basic model. Asymmetrical shoes make the permeability of the stator asymmetrical due to the magnetic flux of the permanent magnet. And increases the difference in reluctance

between the stator and the air gap. Therefore, depending on the length of the parameter r , the notch shape of the stator and the difference in reluctance between the stator and the air gap change. In addition, the position of the notch is moved by the parameter θ , and the movement of the notch changes the difference in reluctance between the stator and the air gap. The parameter r and θ are analyzed by FEM to find the optimal design parameters for torque ripple and cogging torque. The asymmetric and notched structures of the shoe are applied to the improved model, and the relationship between torque ripple and cogging torque is compared with the basic model. Finally, optimal model will be created and experimented, and the experiment results will verify the advantage of the proposed design method.

[1] K. Kim, IEEE Trans. Magn., vol. 50, no. 2, pp. 793-796 (2016) [2] D. C. Hanselma, IEE Proceedings - Electric Power Applications, vol. 144, no. 5, pp. 325-330 (1997) [3] W.Q Chu, IEEE Trans. Magn., vol. 49, no. 3, pp. 1211-1220 (2013) [4] Y. Yang, IEEE Trans. Magn., vol. 42, no. 4, pp. 1135-1138 (2006) [5] L. Fang, IEEE Trans. Magn., vol. 46, no. 6, pp. 2183-2186 (2010) [6] W. Ren, IEEE Trans. Magn., vol. 52, no. 7, pp. 1-5 (2016) [7] S. Han, IEEE Trans Power Syst, vol. 25, no. 1, pp. 118-127 (2010)



Classification	Parameter	Unit	Value
Specification	Rated torque	Nm	6.6
	Base speed	rpm	6000
Dimension	Stator outer diameter	mm	95.9
	Rotor outer diameter	mm	50.1
	Air gap length	mm	0.65
	Shoe side	mm	0.53
	Minimum size_Slot open	mm	4.3
Material	Stator/Rotor core	-	35PN250
	Magnet	-	40UH

AR-10. A Novel Structure Design About Nonidentical Slotted Concentric Winding.

H. Kim¹, D. Kang¹, S. Kang¹, Y. Kim² and S. Jung¹

1. Department of Electrical and Computer Engineering, Sungkyunkwan University, Jongno-gu, The Republic of Korea; 2. Department of Electrical Engineering, Chosun University, Gwangju, The Republic of Korea

This paper focuses on designing a optimal novel structure for high power density of a concentric winding integer slots permanent magnet synchronous motor(PMSM). This research shows the motor design possibility with a higher power density than a typical distributed winding model, within the same size. If the number of slots per phase per pole(NSPP) of PMSM is larger than 1, distributed windings are applied mostly. The distributed winding is a winding method that the number of turns is distributed into each slot according to NSPP. The distributed winding can make a sinusoidal magnetomotive force(MMF) waveform. Also, harmonics can be reduced. Distributed Windings can be classified into lap winding and concentric winding according to the number of pitch of each coil. In lap winding, the number of pitch of each coil is same. On the other hand, the number of pitch of each coil is different maintaining same center of each coil in concentric winding. The distinction between the winding methods is shown in Fig. 1. The concentric winding is divided into identical concentric winding and nonidentical concentric winding according to the number of each coil. Identical concentric winding is that the number of turns in each coil is identical. Nonidentical concentric winding, maintaining a sinusoidal waveform even if the number of turns in each coil is nonidentical, has the advantage of adjusting the number of turns in each coil can obtain a higher winding factor than the lap winding[1-3]. The winding factor is the determinant by the MMF at the air gap and is proportional to the fundamental amplitude of back electromotive force (BEMF)[4-5]. Consequently, the nonidentical concentric winding has potential to enhance a power density of motors according to winding factor. In general, all slots in the stator are the identical shape, so if each coil has a different number of turns, slot fill factors vary from each slot. As a result of slot fill factor differences, some slots are inefficient in utilizing space. It affects the BEMF's fundamental wave amplitude as well, which the output performance of the nonidentical concentric winding motors could be worse than the identical concentric winding one. To improve this problem, we need to design the structure of stator with optimization algorithm to make each slot shape efficiently. In this paper, we study about nonidentical slotted concentric winding in the following ways. A concentric winding integer slots model is selected with 3-phase 4-pole 24-slots PMSM that NSPP is 2. the winding factors of identical concentric winding type and various nonidentical concentric winding types are calculated and compared in case of the number of turns distribution for nonidentical one. nonidentical concentric winding is selected to the winding factor higher than identical concentric winding. For improving the above mentioned problem, a new structure of the stator, nonidentical slotted concentric winding, is optimized and designed. the winding factors of identical concentric winding type and various nonidentical concentric winding types are calculated and compared in case of the number of turns distribution for nonidentical one. Variable shown in Fig. 2. for algorithm is composed of factors which control a slot area. The purpose of optimization is power density and performance. Therefore, objective functions are average torque and torque ripple, and they are minimized as the following two objective function equations. $obj_1 = 1/T_{avg}$ $obj_2 = T_{c, ripple} = (T_{e,max} - T_{e,min}) / T_{e, avg} * 100$ $T_{e, avg}$ is the average torque and $T_{e, ripple}$ is the torque ripple ratio. $T_{e, max}$ and $T_{e, min}$ are the maximum and minimum of the instantaneous torque, respectively. Through a finite element analysis(FEA) of designed models, we ultimately compared the performance of motor models according to identical concentric winding, nonidentical concentric winding and nonidentical slotted concentric winding. Finally, we propose a novel structure of stator with each different slot areas and nonidentical concentric winding. it is called nonidentical slotted concentric winding. This research shows the motor design possibility with a higher power density than a typical distributed winding model, within the same size.

Transactions of the American Institute of Electrical Engineers, vol. 62, no. 10, pp. 664-666, Oct. 1943. [3] G. R. Slemon, A. Straughen "Electric Machines" University of Toronto, pp. 369-383, 1980. [4] Wen Ouyang, A. El-Antably, Surong Huang and T. A. Lipo, "Analysis of optimal stator concentric winding patterns design," 2005 International Conference on Electrical Machines and Systems, Nanjing, vol. 1, pp. 94-98, 2005. [5] J.R. Hendershot, T.J.E. Miller, "Design of Brushless Permanent-Magnet Machines" Magna Physics Publishing & Oxford University Press, pp. 180-181, 2010 [6] J. H. Lee, J. Kim, J. Song, Y. Kim and S. Jung, "A Novel Memetic Algorithm Using Modified Particle Swarm Optimization and Mesh Adaptive Direct Search for PMSM Design," in IEEE Transactions on Magnetics, vol. 52, no. 3, pp. 1-4, March, 2016.

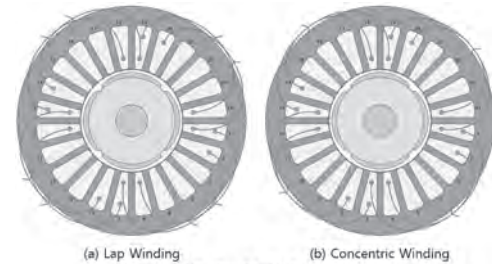


Figure 1. Winding Method(only a-phase)

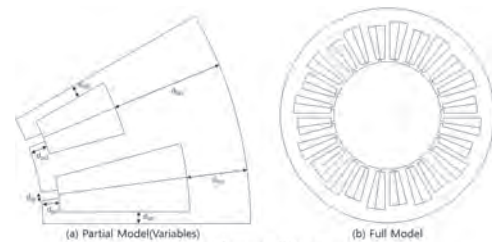


Figure 2. Nonidentical Concentric Winding Stator Structure

[1] T.A. Lipo, "Introduction to AC Machine Design", University of Wisconsin, pp. 53-82, 2004. [2] M. M. Liwschitz, "Distribution Factors and Pitch Factors of the Harmonics of a Fractional-Slot Winding," in

AR-11. Optimization Design Method of Radial-Radial Flux Compound-Structure Permanent-Magnet Synchronous Machine to Improve the Energy Transfer Efficiency of Hybrid Electric Vehicles.

W. Du¹, S. Zhao¹, J. Gao¹ and Z. Zheng¹
 1. Xi'an Jiaotong University, Xi'an, China

Abstract : As a new type of electromechanical coupling device, double rotor motor is suitable for energy transmission and power distribution in hybrid electric vehicles. In recent years, many scholars have done a lot of research on it and put forward a variety of novel dual- rotor motors. In this paper, starting from the performance requirements of hybrid electric vehicles, the goal is to improve the overall efficiency of engine and powertrain as much as possible. Taking the radial-radial dual-rotor motor as an example, the main parameters of the inner motor and the outer motor of the dual-rotor motor are optimized. The results show that by reasonably selecting the parameters of internal and external motors, the engine and motor can work in high efficiency range under common road conditions, and the overall efficiency of the powertrain can be improved.

1 Introduction Hybrid electric vehicles are considered to be one of the effective solutions to alleviate energy problems and reduce exhaust pollution[1]. Different from pure electric vehicles, the powertrain of hybrid electric vehicles is more complex, usually there are one or two motors. According to the connection mode of motor and engine, it can be divided into three types: series connection, parallel connection and hybrid connection [2]. The application of dual-rotor motor in hybrid electric vehicles (HEV) can decouple the engine working point and load completely, and improve fuel economy. It is a very promising scheme. Many scholars have studied it and put forward many novel dual-rotor motors[3-4]. However, the existing research focuses on how to develop high-performance dual-rotor motor. In the driving process of hybrid electric vehicles, the dual-rotor motor should also work in the high efficiency range as far as possible. In this paper, based on the performance requirements of hybrid electric vehicles, the speed and torque of the engine are decoupled by the dual-rotor motor to improve the working efficiency of the engine. This paper studies how to select the parameters of the dual-rotor motor, so that the dual-rotor motor can work in the high efficiency range as far as possible, and further improve the efficiency of the powertrain.

2 Introduction of hybrid powertrain based on dual-rotor motor The structure of hybrid electric vehicles based on dual-rotor motor is shown in Fig. 1. The dual-rotor motor has two rotors, one stator and two sets of windings. There is a set of winding on the inner rotor and another on the stator. The inner rotor and outer rotor constitute the inner motor, and the outer rotor and stator constitute the outer motor. When the powertrain works, the internal motor decouples the speed of engine and the external motor decouples the torque of engine, so that the working points of the engine has nothing to do with the load. When the load changes, the engine always works in the high efficiency range.

3 Parameter optimization design of double rotor motor In order to improve the fuel economy of hybrid electric vehicles, the efficiency of dual-rotor motor should be further improved on the basis of engine working in high efficiency range. The purpose of this paper is how to select the parameters of the dual-rotor motor reasonably, so that the engine and motor are in the high efficiency range in common working points. Taking the radial-radial permanent magnet dual-rotor motor as an example, the efficiency distribution of the motor is similar. After the rated working point of the motor is determined, the efficiency distribution of the whole working area can be calculated. Therefore, the optimization variable are the rated power and speed of the internal motor and the rated power and speed of the external motor. Taking the vehicle parameters and engine parameters of Toyota Prius as an example, the genetic algorithm and dynamic programming algorithm are combined to optimize the variable of dual-rotor motor under UDDS condition[5]. The specific optimization process is shown in Fig. 2.

4 Conclusion The initial parameter selected in this paper is ; the optimized parameter is. The average efficiency of internal and external motors is 78.2% before optimization, and 83.5% after optimization, which increases by 6.77%. It can be seen that the efficiency of the powertrain can be further improved by selecting the parameters of the dual-rotor motor reasonably.

and J.M. Miller, Hybrid Electric Vehicles: Architecture and Motor Drives, Proceedings of the IEEE, vol. 95, p. 719-728 (2007) [3]Y. Li, D. Bobba and B. Sarlioglu, Design and Optimization of a Novel Dual-Rotor Hybrid PM Machine for Traction Application, IEEE Transactions on Industrial Electronics, vol. 65, p. 1762-1771 (2017) [4]E. Yildiriz, M. Güleç and M. Aydın, An Innovative Dual-Rotor Axial-Gap Flux-Switching Permanent-Magnet Machine Topology With Hybrid Excitation, IEEE Transactions on Magnetics, vol. 54, p. 1-5 (2018) [5]W Du, S D Zhao and L Y Jin, Optimization design and performance comparison of different powertrains of electric vehicles, Mechanism and Machine Theory, vol. 156 (2021)

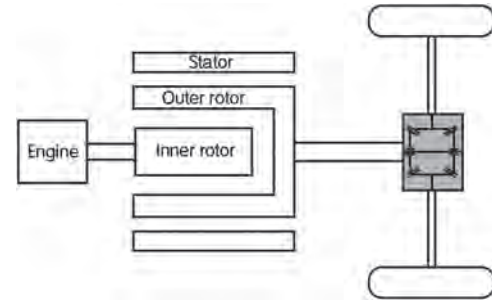


Fig. 1 The structure of powertrain based on dual-rotor motor

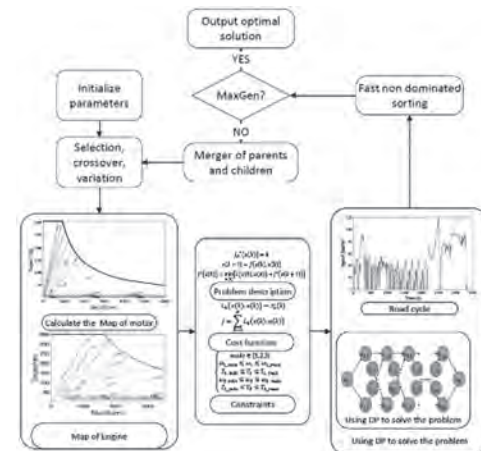


Fig. 2 The flow chart of optimization algorithm

[1]C.C Chan, The state of the art of electric, hybrid, and fuel cell vehicles, Proceedings of the IEEE, vol. 95, p. 704-718 (2007) [2]M. Ehsani, Y. Gao

AR-12. Optimal Design of IPMSM for EV Using Subdivided Kriging Multi Objective Optimization.

J. Ahn¹, S. Park², M. Baek² and D. Lim¹

1. University of Ulsan, Ulsan, The Republic of Korea; 2. Korea Electrotechnology Research Institute, Changwon, The Republic of Korea

Abstract – In this paper, subdivided kriging multi objective optimization (SKMOO) is proposed for the optimal design of interior permanent magnet synchronous motor (IPMSM). The SKMOO with inverse searching can obtain uniform and accurate pareto front set with reduced computation cost compared to conventional algorithms. In the SKMOO algorithm, Fill blank method is applied to prevent premature convergence. In addition, the subdivided kriging grid is proposed to make well distributed and precise pareto front set. Superior performance of the SKMOO is confirmed the by compared conventional MOO algorithms with the test function and applied it to the optimal design of IPMSM for electric vehicle. I. Introduction The interior permanent magnet synchronous motor (IPMSM) has the torque caused by the magnet and reluctance torque. Therefore, the IPMSM torque greater than surface mounted PMSM [1]. However, such a permanent magnet type motor has a disadvantage of high cogging torque and torque ripple which causes in the motor’s noise, vibration, and efficiency reduction. This is important to electric vehicle for comfortable driving [2]. Therefore, we aim to design the IPMSM with reduced cogging torque and torque ripple. Finite element method (FEM) analysis is required since the accurate analysis is difficult by using simple mathematical models due to the nonlinear characteristic of the IPMSM [3]. However, the actual motor design using FEM analysis should meet several requirements. It takes a lot of time and effort to simultaneously consider multi objective functions in motor design that require FEM interpretation [4],[5]. To solve this problem, a lot of studies are in progress [6],[7]. The most widely used algorithms are multi objective particle swarm optimization (MOPSO) and non-dominated sorting genetic algorithm-II (NSGA-II). However, the MOPSO and NSGA-II still need many function calls to get the accurate and well distributed pareto front set. Therefore, subdivided kriging multi objective optimization (SKMOO) is proposed which applies the surrogate model to reduce function calls. Outstanding performance of the proposed algorithm is verifyverified through comparison of results with the MOPSO and NSGA-II. And the optimal design was derived by applying the SKMOO to design of the IPMSM with reduced cogging torque and torque ripple. II. Proposed Algorithm MOO performance can be determined based on the accuracy, uniform distribution, and number of function calls while consisting the SKMOO uses the following methods to improve algorithm performance. Pareto front set are extracted from samples using non-dominated sorting and sorted one objective function. The Euclidean distance of adjacent solutions is calculated to obtain a uniform pareto front set and predicted solution is added directly between the two solutions with the longest distance. The spline interpolation is used to increase the accuracy of the solution as shown in Fig. 1. Design variables are inversely searched to generate a real solution. The most similar combination of design variables is found by comparing the objective function value of the surrogate model with the predicted value and the function call is executed to the explored design variables. Fill blank method is used to prevent premature convergence. This method is greatly efficient because it does not overlap the area already explored. When the algorithm converges after the set number of iterations, subdivided kriging grid is proposed to improve performance. The same methods are used to adds solutions, but more accurate solutions can be added because the kriging grid is finely divided. Also, the solution with the closest distance is deleted, if the distance is less than a set distance and if it is more than a set distance, a new solution is added as the intermediate point of before and after solution to obtain more uniform distribution. Fig. 1 shows that the solution is directly added in objective function area. However, the solution is added only at the grid points. Therefore, there is a difference between predicted and real solution. In this case, solutions are uneven and inaccurate. Subdivided grid is a method to solve this problem by dividing kriging grid finely as shown in right of Fig. 1. III. verification of proposed algorithm The SKMOO, the NSGA-II and MOPSO are applied to the test functions. GD indicates how similar the pareto set to the real pareto set and SP indicates how uniformly the solution is distributed. GD and SP value mean better performance if values close to zero. Table. I summa-

ize the results and shows that the SKMOO has superior performance on GD, SP, and the number of function calls than NSGA-II and MOPSO. IV. Conclusion In this paper, SKMOO based on surrogate model is presented to solve MOO problems. The SKMOO can reduce computation cost and show superior performances in the MOO problems. The proposed algorithm is validated by comparing with MOPSO and NSGA-II. Finally, we applied the SKMOO to the optimal design of IPMSM. Taguchi method is used to select variables among several variables that are sensitive to the objective function. The application of the SKMOO to optimal design of the IPMSM will be covered in full paper. V. Acknowledgment This research was supported by Korea Electrotechnology Research Institute (KERI) Primary research program through the National Research Council of Science & Technology (NST) funded by the Ministry of Science and ICT (MSIT) (No. 21A01082).

[1] Guo Hong, Tian Wei, and Xiaofeng Ding, IEEE Access, Vol. 6, pp. 23568-23581, (2018). [2] Young-Rok Kang, Ji-Chang Son, and Dong-Kuk Lim, IEEE Access, Vol. 8, (2020). [3] M. Caruso, A. O. Di Tommaso, L. Ferraris, R. Miceli, F. Viola, 2017 Twelfth International Conference on Ecological Vehicles and Renewable Energies (EVER), (2017) [4] Min Li, Fabien Gabriel, Maria Alkadri, IEEE Transactions on Magnetics, Vol. 52, (2016) [5] Siguang An, Shiyong Yang, Osama A. Mohammed, IEEE Transactions on Magnetics, Vol. 54, (2018) [6] Khalil Alkebsi, Wenli Du, IEEE Access., Vol. 8, (2020) [7] Vikas Palakonda, Rammohan Mallipeddi, IEEE Access, Vol. 8, (2020)

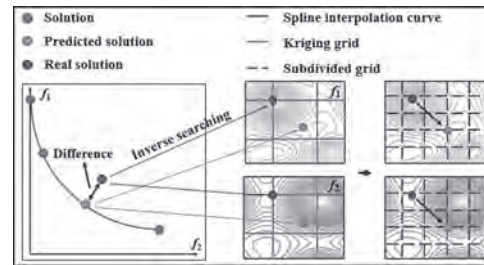


Fig.1 Conceptual diagram of SKMOO

Test Function	GD	SP	Function calls
NSGA-II	0.0158	0.0786	720
MOPSO	0.0163	0.0901	700
SKMOO	0.0144	0.0234	602

Table. I Test function results

AR-13. Design and Analysis of a Low Torque Ripple Inset-Permanent-Magnet Motor Considering Multi-Harmonic Injection.

Y. Xu¹, L. Quan¹ and W. Pu¹

1. Jiangsu University, Zhenjiang, China

I. Introduction Due to the outstanding advantages, such as simple structure, high torque density and excellent dynamic performance, permanent magnet motors (PMMs) have been widely applied over the past four decades. Yet, the implementation of PMSM is limited in servo system with high demand for low torque ripple. In this background, the research on how to reduce torque ripple has become a hot spot for many scholars. In order to reduce the high torque ripple of PMM, different methods have been put forward, which can be concluded as rotor skewing, auxiliary slots or teeth, magnet shaping and flux barriers etc. Among these methods, magnet shaping has been developed as an effective method. A rotor consists of several different PM segments arranged in the axial direction is proposed in [1], which is validated by the effectiveness of reducing torque ripple. However, the shape of PM is random and lack of pertinence. By injecting the optimal third harmonic into PM shape, torque performance can be improved with analysis of airgap flux density in [2]. However, only one harmonic is considered into magnet design process. Hence, the influence of different harmonic injection methods on PM shape design is investigated comprehensive in [3], in which various magnet shape is explored to reduce torque ripple. However, the consequents of different initial phase angles of injected harmonics are neglected. In this paper, a magnet design method considering multi-harmonic injection is proposed, which selects an inset-permanent-magnet motor (Inset-PMM) as research subjective. The key of the study is to extensively consider the factor of harmonic phase angle into the design process. Then, based on different harmonic combination and phase angle consideration, two feasible rotor topologies are proposed. Based on the reasonable design, the torque ripple can be reduced effectively, while the motor can also offer a relatively high output torque. II. Motor features and Analysis Inset-PMMs with two optimal phase angle of injected harmonics and four optimal phase angle of injected harmonics are shown in Fig. 1. The principle of initial phase angle of injected harmonics into rotor design process is listed in Fig. 2, which confirms the effectiveness of proposed method. The relationships between torque ripple and different initial phase angle of injected harmonics are given in Fig. 3, meanwhile, the Inset-PMM without phase angle of injected harmonics, considering two optimal phase angle of injected harmonics and four optimal phase angle of injected harmonics are proposed. The comparisons of the initial phase angle of the proposed Inset-PMM are listed in Table I. The flux density, harmonic spectrum, magnetic field distributions and flux distributions of three Inset-PMM are shown in Fig. 4 and Fig. 5, which can be seen that the amplitudes of injected harmonics are almost same. The comparisons of torque performance of three Inset-PMM are presented in Fig. 6, which validates the effectiveness of the proposed method on reducing torque ripple. III. Conclusion Based on the analysis above, the initial phase angle of injected harmonics into rotor design process on torque performance in Inset-PMMs are investigated. Torque ripple is reduced from 37.9% to 13.7% when the factor of harmonic phase angle is considered, the results not only verify the effectiveness of the proposed method on reducing torque ripple, but also prove the validity of the Inset-PMM which can realize the low-cost design and enhance torque capability simultaneously, providing the new orientation for reducing the torque ripple. More detailed electromagnetic performance analysis and FEA results will be presented in the full paper.

[1] W. Zhao, T. A. Lipo and B. Kwon, "Material-Efficient Permanent-Magnet Shape for Torque Pulsation Minimization in SPM Motors for Automotive Applications," *IEEE Transactions on Ind Electron.*, vol. 61, no. 10, pp. 5779-5787, Oct. 2014. [2] K. Wang, Z. Q. Zhu and G. Ombach, "Torque Enhancement of Surface-Mounted Permanent Magnet Machine Using Third-Order Harmonic," *IEEE Trans Magn.*, vol. 50, no. 3, pp. 104-113, March 2014. [3] Y. Zeng, M. Cheng, G. Liu and W. Zhao, "Effects of Magnet Shape on Torque Capability of Surface-Mounted Permanent Magnet Machine for Servo Applications," *IEEE Transactions on Ind Electron.*, vol. 67, no. 4, pp. 2977-2990, April 2020.

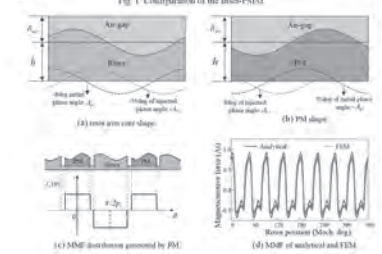
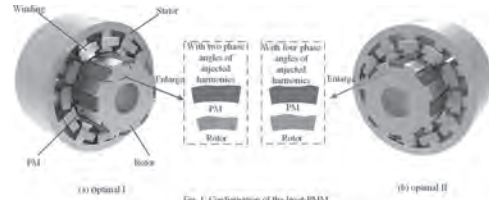


Fig. 2 Principle of phase angle of 16th injected harmonic.

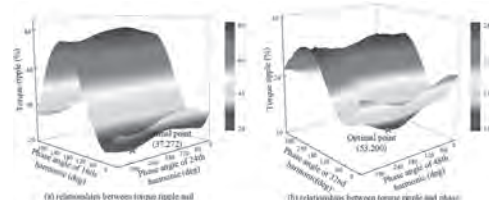


Fig. 3 Relationships between torque ripple and phase angles of injected harmonics.

TABLE I
Comparisons of the Phase Angle of Injected Harmonics

Harmonic order	Amplitude (%)	Initial phase angle (deg)	Optimal I	Optimal II
16th	0.28	27	37	37
24th	0.11	180	272	272
32nd	0.09	180	180	51
48th	0.04	24	-24	-309

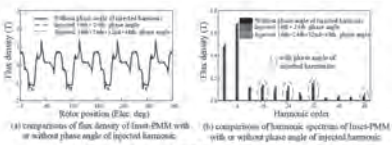


Fig. 4 Comparison of flux density and harmonic spectrum of Inset-PMM with or without phase angle of injected harmonic.



Fig. 5 Comparison of magnetic field distributions and flux distribution of Inset-PMM with or without phase angle of injected harmonic.

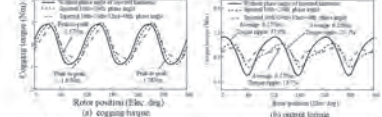


Fig. 6 Comparison of torque performance of Inset-PMM with or without phase angle of injected harmonic.

AR-14. Multi-Variable Multi-Objective Optimization Algorithm for Optimal Design of PMA-SynRM for Electric Bicycle.

J. Son¹, K. Lee² and D. Lim¹

1. Department of Electrical and Computer Engineering, University of Ulsan, Ulsan, The Republic of Korea; 2. Korea Railroad Research Institute, Uiwang, The Republic of Korea

Abstract-In this paper, internal division point genetic algorithm (IDP-GA) was proposed to lessen the computational burden of multi-variable multi-objective optimization problem using finite element analysis such as optimal design of electric vehicles. The IDP-GA could consider various objectives with normalized weighted sum method and could reduce the number of function calls with novel crossover strategy and vector-based pattern search method. The superiority of the proposed algorithm was verified by comparing performances with conventional optimization method at the test functions. Finally, the applicability of the IDP-GA in practical electric machine design was verified by successfully deriving an improved design of electric bicycle propulsion motor. I. Introduction Electric bicycles (EBs) are getting more attention in many countries for their convenience, long travelling distance and environment friendly features, therefore, EB propulsion motor with low cost and high performance is needed [1]. When designing a motor for EBs, high torque density and improved riding impression is required [2]. Permanent magnet assisted synchronous reluctance motor (PMA-SynRM) has advantage of high torque density as it utilizes both magnet torque and reluctance torque. Also, with the usage of inexpensive ferrite magnet, PMA-SynRM is competitive for the manufacturing cost. Hence, PMA-SynRM is selected for the EB propulsion motor. To relieve the noise and vibration of the motor, various performances such as cogging torque, and torque ripple should be considered, and those characteristics can be adjusted with optimization of the variables related to the structure of the motor [3], [4]. Therefore, optimal design of the PMA-SynRM can be defined as multi-objective multi-variable (MVMO) problem. Finite element analysis (FEA) is required for accurate analysis of electric machines. However, the FEA has the disadvantage of huge computational cost, and such burden becomes more worse when FEA is applied to optimization of MVMO problems. Therefore, this paper proposes the novel optimization algorithm that reduces the number of function calls. II. Proposed Algorithm GA is one of the heuristic algorithms and can successfully converges to the global solution [5]. However, the GA has problem with requiring many function calls to enhance the converge rate and cannot consider various objective functions at once. The IDP-GA reduces function calls with novel crossover strategy and VPSM. Also, multi-objective can be considered with NWSM. The NWSM is one of the multi-objective methods and can simply reduce several objectives to one objective. The total fitness is calculated by multiplying each normalized fitness by assigned weight and adding them all together. The designer can perform optimization by giving the desired weight to each objective with the NWSM. Conventional GA converges to global solution by selecting superior entities as parents and generating crossover on the middle of selected two parents. To enhance the convergence speed, the proposed algorithm applies internal division point (IDP) concept. The IDP literally generates crossover not on the middle point, but on the point divided by objective values of two parents. Fig. 1 shows the difference of conventional approach and IDP. Conventional crossover, which is blue dot, is generated on the center of two parents. However, the location of the red dot is determined considering objective values of parents. With the usage of IDP, superior crossover can be obtained. At the end of the algorithm, if the populations are regarded as gather near the global solution, VPSM is executed on the estimated solution to find the actual global solution, preventing unnecessary function calls, and enhancing convergence characteristic. The VPSM has pattern move and exploration move. On the pattern move step, unit direction vector is determined using objective value of infinitesimal displacement of starting point. Fig. 2(a) shows an example of calculating direction vector. Assuming that the problem region is continuous, with two function calls on the point DX and DY, the values of DX' and DY' can be interpolated. Then, increasing direction of each variable is determined, and the unit direction vector can be calculated. Secondly, as shown in Fig. 2(b), the exploration move is performed on the best particle with preset initial moving distance to determined direction, until the objective value decreases. If the value of next

point decreases, pattern move is repeated on the previous point and exploration move with reduced moving distance. To verify the performance, the IDP-GA and conventional GA was applied to two mathematical test functions. The number of function calls of IDP-GA was decreased as 56% and 64% of GA in two tests, and the convergence rate was improved as well. The detailed explain of the IDP-GA, test functions, and application to optimal design of PMA-SynRM for EB will be described in a full paper. III. Conclusion This paper introduces IDP-GA to relieve the computational burden of the MVMO optimization problem applying FEA. The proposed algorithm was validated by applying to mathematical test functions and comparing performance with conventional algorithm. The applicability of the optimization of actual electric machines was also verified by deriving design with improved performances, when the IDP-GA is applied to optimal design of PMA-SynRM for EBs.

[1] Y. Li, J. Hu, F. Chen, S. Liu, Z. Yan, and Z. He, *IEEE Trans. Power Electronics*, vol. 33, no. 10, pp. 8226-8230 (2018) [2] D. Lim, Y. Cho, J. Ro, S. Jung and H. Jung, *IEEE Trans. Magnetics*, vol. 52, no. 3, pp. 1-4 (2016) [3] Ji-Chang Son, Young-Rok Kang, and Dong-Kuk Lim, *Energies*, 13, 3395 (2020) [4] Young-Rok Kang, Ji-Chang Son, and Dong-Kuk Lim, *IEEE Access*, vol. 8, pp. 117405-117412 (2020) [5] K. Lee, H. Oh, S. Jung and Y. Chung, *IEEE Trans. Magnetics*, vol. 55, no. 6, pp. 1-4 (2019)

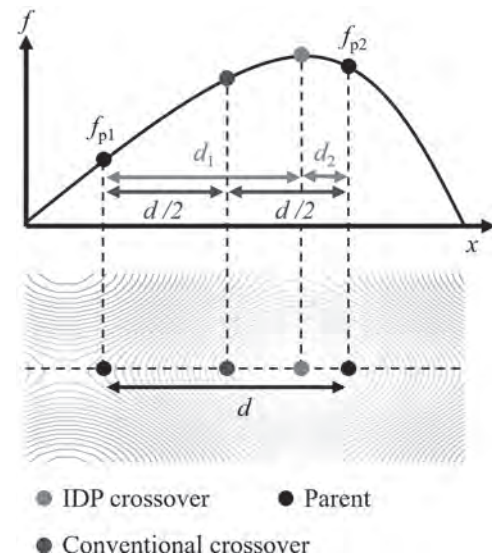


Fig. 1. Comparison of conventional crossover and IDP.

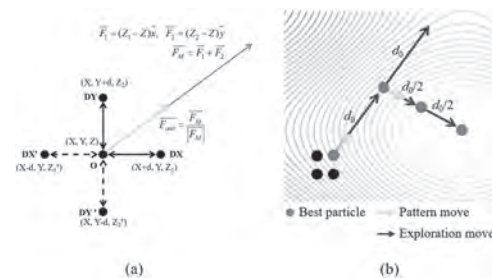


Fig. 2. Conceptual schematic of VPSM. (a) Pattern move. (b) Exploration move.

AR-15. A Study on the Optimal Design and Analysis of Outer Rotor Surface Permanent Magnet Synchronous Generator for Charging Battery of Electric Vehicle.

H. Kim¹, Y. Park¹, S. Oh¹ and J. Lee¹

1. Electrical Engineering, Hanyang University, Seongdong-gu, The Republic of Korea

1. Abstract Recently, as interest of electric vehicle increase, several researches are being studied on electric vehicle parts such as the electric power steering (EPS), the alternator, and shift by wire (SBW). In particular, the alternator for the charging battery is actively studied for the electric vehicle and drone. This paper is the design and analysis of alternator considering the constant current charging mode. First, the pole-slot combinations are analyzed based on finite element analysis (FEA), the 14pole-18slot is selected considering the total harmonic distortion (THD) of the back electromotive force (BEMF). Next, the optimal design is performed to minimize THD and the cogging torque using the response surface method (RSM). The optimal design parameters are the rotor and stator design parameters such as the thickness of teeth, pole-arc ratio, and slot opening, etc. Finally, the optimal generator is designed, and analyzed considering the constant current mode of battery based on co-analysis with FEA and circuit simulation. 2. Introduction As increasing the environment problem such as the greenhouse effect and CO₂ emissions, interest in the electric vehicle has been focused [1]. Furthermore, as increase of electric power consumption, the power density and efficiency of alternator must be improved. Therefore, the study on the alternator must be performed. However, most of the researches have studied with wind or wave power generator [2] and MW class generator of electric ship. This paper discusses the design of alternator for charging the battery of 48Vdc. In general, the alternator requires the low cogging torque and the total harmonic distribution (THD) of back electromotive force (BEMF) due to the pulsating speed and the link of the battery system [3]. Therefore, the design methods of alternator must be studied to minimize the cogging torque and THD of BEMF. In this paper, the design of outer rotor surface permanent magnet synchronous generator (PMSG) is performed based on finite element analysis (FEA). In step I, four pole-slot combinations are compared with the total harmonic distribution (THD) of back electromotive force (BEMF). One pole-slot combination is selected as the initial model considering the magnitude and THD of BEMF. In step II, the optimal design is performed to minimize the cogging torque and THD of BEMF based on the initial model. The design parameters are selected as the rotor and stator design parameters such as the thickness of teeth, pole-arc ratio, and slot opening, etc. Finally, the performances of the optimal PMSG are analyzed considering the constant current mode of battery using the co-analysis with FEA and circuit simulation. 3. Design and Analysis of PMSG THD of BEMF is important performance index of PMSG because of the link to battery. THD of PMSG is expressed as Eq. (1). $THD = \sqrt{(\sum V_n^2) / V_1} = \sqrt{(V^2 - V_1^2) / V_1}$ Where THD is the total harmonic distribution of BEMF, V_n is the rms value of nth BEMF, V is the rms value of BEMF, and V_1 is the rms value of 1st BEMF. In order to reduce THD of PMSG, the harmonics of BEMF are reduced, and methods are used such as the fractional slot, skew of rotor, and the tapering. However, the skew of rotor and tapering decrease the power density. For this reason, the fractional slot is used in this paper. Furthermore, the multi-pole structure can improve the power density in the outer rotor. Therefore, the pole-slot combinations are compared in the outer rotor PMSG considering THD and the cogging torque. Fig. 1 shows the comparison models of pole-slot combinations under the same operating speed. Among the pole-slot combination models, the 14pole-18slot is selected as the initial model considering THD of BEMF. The detail comparison with the pole-slot combinations will be discussed in the full paper. In order to minimize cogging torque and THD of BEMF, the optimal design is performed by the rotor and stator design parameters. Fig. 2(a) shows the optimal design parameters, and Fig. 2(b) shows the optimal model. In the full paper, the co-analysis is added to the constant current mode of the charging battery. 4. Conclusion In this paper, the optimal design is performed to minimize the cogging torque, THD, and maximize the output power. Through the pole-slot combinations, the initial PMSG is selected as 14-pole/18-slot. Based on the initial PMSG, the optimal design is performed by the stator and rotor design parameters such as the pole-arc ratio, thick-

ness of teeth, slot opening, and thickness of bridge. In the full paper, the detail comparisons will be discussed considering THD and cogging torque. Furthermore, the detail optimal design method will be discussed, and the performances of the optimal design model will be analyzed using co-analysis with FEA and circuit simulation considering the constant current charging mode of the battery.

[1] J.-H. Seo, S.-M. Kim, and H.-K. Jung, IEEE Trans. Magnetics, Vol. 46, pp. 2458-2461 (2010) [2] T.P.M. Bazzo, J.F. Kolzer, and L. Gerbaud, IEEE Trans. Ind. Electron. Vol. 64, pp. 9815-9823 (2017) [3] S.-H. Lee, Y.-J. Kim, and S.-J. Kim, IEEE Trans. Appl. Superconductivity, Vol. 26, Art no. 5202605 (2016)

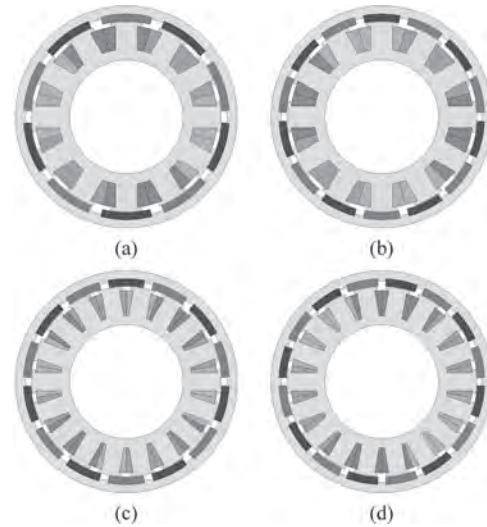


Fig 1. Pole-slot combinations (a) 10-pole/15-slot (b) 14-pole/15-slot (c) 14-pole/18-slot (d) 16-pole/18-slot

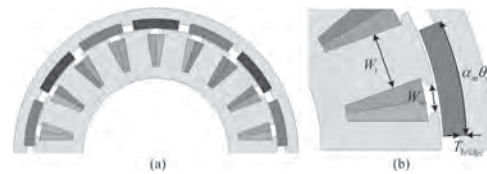


Fig 2. FEA model for the optimal design (a) the initial model (b) design parameters

AR-16. A Study on the Comparison of Power Characteristics of Slotless Motor by the Permanent Magnet Shape.

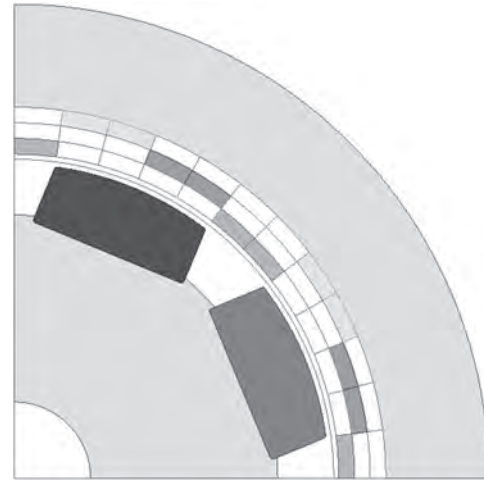
Y. Park¹, H. Kim¹, S. Oh¹, C. Jin² and J. Lee¹

1. *Electrical Engineering, Hanyang University, Seongdong-gu, The Republic of Korea*; 2. *Electrical Engineering, Wonkwang University, Iksan, The Republic of Korea*

1) Introduction As the requirements for motors (high power, high efficiency, miniaturization, etc.) in various industries, research and development of motors that can comprehensively satisfy these requirements are actively progressing. Recently, with the development of driving systems such as robots, vehicles, and aerospace industries, there is a demand for weight reduction, miniaturization, and control precision of electric motors, which are key components of the driving system. Slotless motors are advantageous for implementing high-speed and high-power performance because there are good driving stability, low noise and low vibration, and no cogging torque based on the structural advantages of no slot structure. Accordingly, research and development of slotless motors is actively progressing. 2) Body In this paper, the power characteristics of the slotless motor according to the shape and arrangement of the rotor permanent magnets were compared and analyzed. A slotless motor has a structure consisting of only a coil without a slot in the stator and is miniaturization and has no cogging torque and low loss, so its performance is superior compared to conventional a slotted motor. On the other hand, in a slotless motor, since the stator does not have a slot structure, the air gap is wider than a slotted motor, so that magnetic flux density of the air gap is low. Due to the wide air gap, there is almost no difference between d-axis inductance and q-axis inductance value, so the reluctance torque component is very small. Hence, in slotless motors, magnetic torque becomes an important factor in determining the power of the motor [1]. In order to maximize the power characteristics of the slotless motor, the design was conducted on the permanent magnet shape and arrangement of the rotor that can ensure the maximum magnetic torque. The power characteristics of each permanent magnet shape were compared by selecting a slotless motor for a banding machine that is common in the construction industry field as a target. The design specifications and constraint conditions of the target slotless motor were analyzed by measuring and analyzing the drawing, no-load back EMF and torque at the rated speed. Based on the basic specifications and conditions of the motor secured through spec generation, the FEM model of the target slotless motor was derived. With the same stator conditions as the target slotless motor, and the same power characteristics appeared according to the shape or arrangement of the permanent magnet of the rotor were analyzed. In general, surface permanent magnet (SPM) motors have larger magnetic flux due to their large sectional area of permanent magnet compared to interior permanent magnet (IPM) motors [2]. In addition, the magnetic resistance does not change depending on the position of the rotor, so the effective air gap in the magnetic flux path are the same. In terms of inductance, the permanent magnet of the rare earth series is regarded as air, so the value of d-axis and q-axis inductance is always constant [3]. Since the SPM has a permanent magnet attached to the surface, a mechanical stress analysis was conducted to prevent the permanent magnet from scattering by centrifugal force that could occur at high speed. Spoke-type motors have high magnetic flux concentration due to the reluctance torque and permanent magnetics, so they can generate high torque and high power, and the motor can miniaturize when the same power. However, in the structure of the spoke-type, cogging torque was generated due to a large difference in magnetic resistance in the air gap, and a design was proceeded to reduce this. There is also a halbach structure as a permanent magnet arrangement method that can concentrate magnetic flux. The Halbach structure can reduce the leakage magnetic flux and concentrate the main magnetic flux by adjusting the magnetizing direction of the permanent magnet. When the Halbach structure is applied, the trend was analyzed by conducting a design on the pole ratio and magnetization direction that can concentrate the magnetic flux to the maximum. 3) Conclusion The power characteristics of slotless motor are analyzed according to the rotor shape in order to achieve the high torque and high power performance. Finite element method (FEM) design was conducted on three structures : the SPM motor, the spoke type motor, and the Halbach structure motor. By analyzing the power characteristics of each type of motor, a study on a slotless motor with an optimal

permanent shape was conducted. The FEM rotor model of a slotless motor that can improve the power was derived by comparing and analyzing the power characteristics according to the arrangement and shape and pole ratio.

Reference [1] Kais Atallah, "Armature Reaction Field and Winding Inductances of Slotless Permanent-Magnet Brushless Machines", IEEE Transactions on Magnetics, vol. 34, no. 5, pp. 3737~3744, (1998) [2] Jianning Dong, "Comparative Study of Surface-Mounted and Interior Permanent-Magnet Motors for High-Speed Applications", IEEE Transactions on Applied Superconductivity, vol. 26, no. 4, (2016) [3] Tae-Jong Kim, "Comparison of Dynamic Responses For IPM and SPM Motors by Considering Mechanical and Magnetic Coupling", IEEE Transactions on Magnetics, vol. 37, no. 4, pp. 2818~2820, (2001)



target slotless motor FEM model

AR-17. Research on Flux Regulating Characteristics of Built-in Permanent Magnet IPM Synchronous Motor for Multiple Operating Conditions.

W. Wu¹, Y. Sun¹, Q. Chen¹ and L. Gao¹

1. School of Automotive Engineering, Changsu Institute of Technology, Changshu, China

Automotive industry applications are oriented increasingly toward more energy-efficient and environmentally friendly drive-train technologies. This trend is mainly attributed to the detrimental effects of greenhouse gas emissions causing by vehicle emissions. Thus, the diffusion of pollution-free electric cars in urban environment has become an irreversible trend. As one of the key devices in an EV, the choice of electric drive-train most suited to EV's application is still matter of discussions. In particular, the permanent magnet synchronous motors are widely chosen for their higher torque density and efficiency. In general, EVs require a constant-torque performance at low speed and a constant-power one at high speed. The continuous torque at low speed is determined by the wanted up-hill behavior, while the maximum continuous power determines the maximum speed of the vehicle. Besides, the high efficiency of the entire speed region is extremely desired. To achieve the above requirements, scholars have conducted a great deal of exploration on the innovation of machine structure in past years. As for interior permanent magnet (IPM) machines, therein two kinds of machines are widely reported in the literatures. One is the PM-assisted synchronous reluctance machine and the other is the field intensify interior permanent magnet synchronous machine. The former utilizing a high rotor anisotropy to achieve a low PM flux linkage. The later generally owning the inverse-saliency characteristic of $L_d > L_q$, and a high PM flux linkage. Both kinds of machines have been proven to be feasible candidate in EV's driving circle. In this paper, by combinations of PM pieces and magnetic barriers in rotors, two kinds of IPM machines respectively operating with PM-assisted effect and flux-intensifying effect are established, a comparative study is carried out to clarify the influence of PM flux linkage on the high-speed properties. The structures of the two machines, named PMA-IPM machine and FI-IPM machine, are shown in Fig.1(a) and (b). In PMA-IPM machine, the PM pieces are inserted in magnetic barriers of q -axis, with a magnetization direction opposite to flux generated by armature reaction. Thus, the main function of the PMs is to saturate the rotor bridges and increase power factor of the machine, and only an assisted contribution is made for its output torque. As for the FI-IPM machine, although the PM piece cuts the magnetic barriers in the middle, resulting in a marked obstacle for the d -axis flux guide, it should be noted that the magnetic field of d -axis can be intensified by applying a positive d -axis current, which really offsets the reduction of the reluctance torque causing by resistance effect of PM pieces. Fig.2 (a)\(b) shows the variation rules of flux linkage in different current amplitudes of the two machines. Fig.2 (c) and Fig.2 (d) compares the inductance characteristics and torque characteristics of the two machines.

[1]M. Obata, S. Morimoto, M. Sanada, and Y. Inoue, "Performance of PMASynRM with ferrite magnets for EV/HEV applications considering productivity," *IEEE Trans. Ind. Appl.*, vol. 50, no. 4, pp. 2427-2435, Jul./Aug., 2014. [2]N. Limsuwan, T. Kato, K. Akatsu, and Robert D. Lorenz, "Design and evaluation of a variable-flux flux intensifying interior permanent magnet machine," *IEEE Trans. Ind. Appl.*, vol. 50, no. 2, pp. 1015-1024, Mar. 2014.

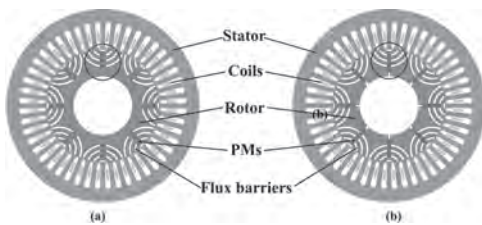


Fig 1. The PM-assisted IPM motor and field-intensified IPM motor

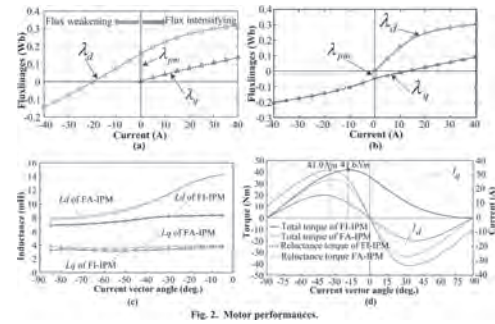


Fig.2 Motor performance

AR-18. Research on Polar Anisotropic Molding Yoke Shape to Reduce Dead Zone of Ring Type Bond Magnets.

J. Min¹, D. Nam¹ and W. Kim¹

1. Electrical Engineering, Gachon University, Seongnam, The Republic of Korea

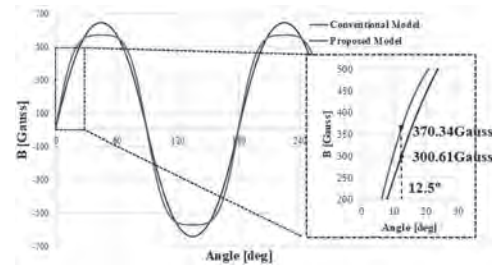
Introduction - Recently, as the demand for robots and the supply ratio of renewable energy have increased, the usage of electric motors and generators has increased. Therefore, sensors required for detecting the position of the rotor has also increased. Of these, the safety window motor for preventing accidents in which an automobile window is pinched is based on the principle that a ring type bond magnet is attached to the lower part of the rotor of the motor to detect the magnetic flux and detect the position. At this time, a dead zone, which is a section where the magnetic flux is very weak, is generated between the N pole and the S pole of the ring-type bond magnet and the hall sensor does not detect the magnetic flux in this section. When the range of this dead zone is large, the region where the magnetic flux can be detected is limited, so that accurate position detection is impossible. In this paper, we provide the optimum model of a polar anisotropic molding yoke with a magnetic flux-concentrated structure for the dead zone reduction plan of ring type bond magnets for accurate control of electric motors and generators. Equation - In order to concentrate the magnetic flux generated from the permanent magnet of the molding yoke, a structure having a high magnetic flux concentration factor is required. This indicates that the more magnetic flux passing through the magnet than the air gap, the more the magnetic flux is concentrated. Therefore, if the magnetic flux-concentrated structure is used, when a magnetic field is applied, the air gap flux density can be higher than that of the conventional model, and the dead zone of the ring type bond magnet can be reduced. Analysis & Result – In the case of the conventional model, the structure is such that a magnetic field is directly applied to a very different ring type bond magnet with a permanent magnet. Therefore, the magnetic flux does not penetrate deeply into the magnet, and a large Dead Zone is generated. To reduce this dead zone, this paper designed a model that could be molded with a high air gap flux density by inserting a magnetic flux concentration core. The thickness of the inner and outer teeth and the direction of the magnetic field applied to the permanent magnet were used as the design variable. In this paper, the results were analyzed through finite element analysis. The design variable of inner and outer teeth thickness was set range of 0mm to 12mm and the angle degree of the magnetic field applied to the permanent magnet was set the range of 0° to 90°. a) Air gap flux density according to magnetization angle When the inner teeth thickness is 11mm and the outer teeth thickness is 0mm, the change in air gap flux density according to the magnetization direction was analyzed. When the angle of the magnetization direction is too large or too small, the magnetic flux leaks to the permanent magnet and the outside. So it can be confirmed that the maximum air gap flux density is generated around 40°. b) Air gap flux density according to the thickness of the inner teeth When the angle of the magnetization direction is 40° and the thickness of the outer teeth is 0mm, the change in air gap flux density according to the thickness of the inner teeth was analyzed. Analyzing the results at 12.5° where the dead zone occurs in a ring type bond magnet, the magnetic flux leaks to the adjacent core when the thickness of the inner teeth is too large. So it can be confirmed that the magnetic flux is most concentrated on the pole of the ring type bond magnet when the thickness of the inner teeth is 11mm. c) Air gap flux density according to the thickness of the outer teeth When the angle of the magnetization direction is 40° and the thickness of the inner teeth is 11mm, the change in air gap flux density according to the thickness of the outer teeth was analyzed. It is confirmed that when the thickness of the outer teeth is 0mm, the magnetic flux leaked to the outside is minimized and the maximum air gap flux density is generated. Therefore, an optimum model that can be molded to the highest air gap flux density was obtained. Comparing the waveforms of the air gap flux density of the proposed model and the conventional model, the proposed model increased the air gap magnetic flux density by 23% compared to the conventional model. As a result, dead zone decreased by about 22%. Conclusion – In this paper, a flux-concentrated core was inserted to reduce the dead zone range of the ring type bond magnet. As a result, it is possible to reach a higher air gap flux density than the conventional model. Finally, the validity of this paper

was verified through the finite element analysis method. Based on this, it is expected that the market share of the safety window can be expanded, and further, the technological competitiveness of domestic sensor industries can be improved. Acknowledgment - This work was supported by the National Research Foundation of Korea(NRF) grant funded by the Korea government(MSIT). (No. 2020R1A2C1013724) NRF - 2020R1A2C1013724

H. J. Kim et al, IEEE Trans. Magn., vol. 46, no. 6, pp. 2314-2317, Jun. 2010



Magnetic Flux Density of Conventional & Proposed Model



Waveform Comparison of Conventional & Proposed Model

Session AS
ELECTRIC DRIVE APPLICATIONS, TRANSFORMERS AND WIRELESS POWER TRANSFER II
(Poster Session)

Kyung-Hun Shin, Chair
Chonnam National University, Yeosu, The Republic of Korea

AS-01. The Electric Vehicle Wireless Charging Application Oriented Coupler Robust Optimization Design With Multiple Series Unipolar Coils.

L. Li¹, Z. Wang¹, Z. Feng¹, J. Deng¹, S. Wang¹ and D.G. Dorrell²

1. Faculty of Mechanical Engineering, Beijing Institute of Technology, Beijing, China; 2. The University of Witwatersrand, South Africa, Johannesburg, South Africa

Introduction In the field of wireless charging for electric vehicles, the limitation of vehicle-mounted space is a major constraint for the on-board device. It is impossible to ask the drivers to park their vehicle at the same exact position and drivers often park the car with more than a few centimetres of misalignment [1]. Currently, unipolar coils are widely used; these have an upper limit for the coupling coefficient k . With a certain secondary coil size and air gap, a maximum coupling coefficient of the coupler at the aligned position can be estimated using a Dagum distribution [2]. However, the horizontal misalignment has a significant impact on the coupling coefficient, which makes it difficult to tune the resonance of the compensation. With the decrease in k , the primary inverter output may operate in an over-current mode with series-series compensation. This is a challenge for the power semiconductors. At the same time, the misalignment will affect the power transfer capability and efficiency. The system performance, within reasonable misalignment, should be robust which will make the system usable for practical charging systems. Proposed Primary Coupler In order to enhance the power transfer capability with a relatively large misalignment, this work investigates a unipolar transmitter coil and its robust optimization design process. Several design parameters of the coupler are shown in Fig. 1, including the pitches, the length and width of the coil, the types of Litz wire. The coupler is analysed and verified with finite element (FE) modelling. Earlier research has shown that by reducing the main coil inductance and connecting with the assistive coil in series, a superposition effect in the magnetic field can be produced to a certain extent. By optimizing the design parameters, a higher coupling coefficient can be obtained under a specific primary inductance. For example, the analysis results show that by increasing gap B between the Litz wires, the self-inductance can be reduced which effectively enhances the lateral and longitudinal freedom of movement of the magnetic coupler. Reducing the centre distance G between the assistive coils and the main coil can increase the self-inductance linearly, but this will weaken the smoothness of the magnetic field. Analysis and Comparison The magnetic field of the receiver pad is more consistent within the controllable misalignment range, and comparing to [3], all the coils are series connected with one high frequency power source. Fig. 2 shows a comparison of the simulation results of the traditional unipolar coil, which is fully optimized using the Dagum distribution, and the proposed coil proposed in this work. These results are with the same offset condition, same receiver coil, and other external conditions. The X and Y directions are the driving and door-to-door direction respectively. The newly designed emitter coil produces a smoother coupling coefficient over a wider range. Inductive Charging Coupler Robust Design Optimization To achieve less performance variation in the face of misalignment variation caused by the vehicle driver, which is off the control in the design phase, a robust design can be introduced. The misalignment distribution is regarded as the uncertainty parameter in the robust design. The relationship between the coupler design parameter and the coupler circuit parameter is analysed through the FE simulation. The system performance parameters are derived from the circuit. The primary inverter output current, the output power and efficiency of the inductive power transfer system are combined with the distribution of the misalignment in the robust design optimization to form the robust design object. The coupler is optimized using the robust design object. Conclusion and Future work In the full paper, the impact of the additional coil on the magnetic field will be analysed extensively. A robust optimization design process based on the coupler design will be described. A prototype will verify the simulation results.

Type Structure Magnetic Coupler for Wireless Electric Vehicle Charger,” in *2020 IEEE ISIE*, Delft, Netherlands. [3] S. Wang, D. G. Dorrell, Y. Guo, and M.-F. Hsieh, “Inductive Charging Coupler With Assistive Coils,” *IEEE Trans. Magn.*, vol. 52, no. 7, pp. 1–4, 2016.

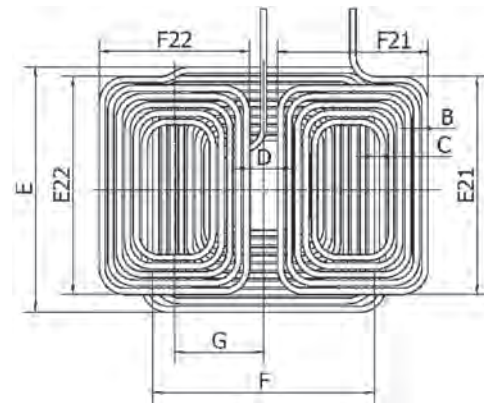


Fig. 1 The proposed coupler design and optimization parameters

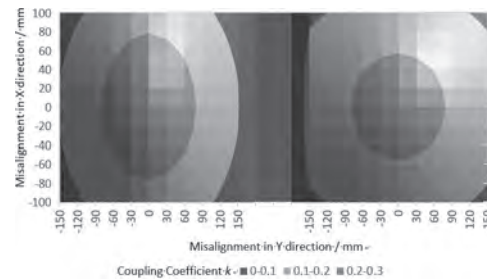


Fig. 2. The FEA simulation result comparison of misalignment tolerance a) Traditional unipolar coil, b) Proposed unipolar coil.

[1] S. A. Birrell, D. Wilson, C. P. Yang, “How driver behaviour and parking alignment affects inductive charging systems for electric vehicles,” *Transportation Research Part C: Emerging Technologies*. [2] L. Li, Z. Wang, F. Gao, “FEA-Assisted Optimization Design of Asymmetric DD

AS-02. Decoupled-Double D Coils Based Dual-Resonating-Frequency Compensation for Wireless Power Transfer.

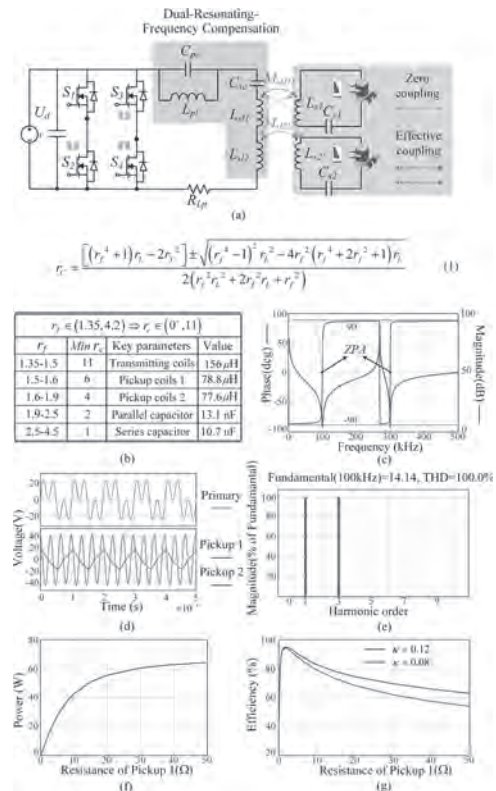
H. Pang¹, K. Chau¹, W. Han³, W. Liu¹ and Z. Zhang²

1. University of Hong Kong, Hong Kong; 2. Tianjin University, Tianjin, China; 3. University of Toronto, Toronto, ON, Canada

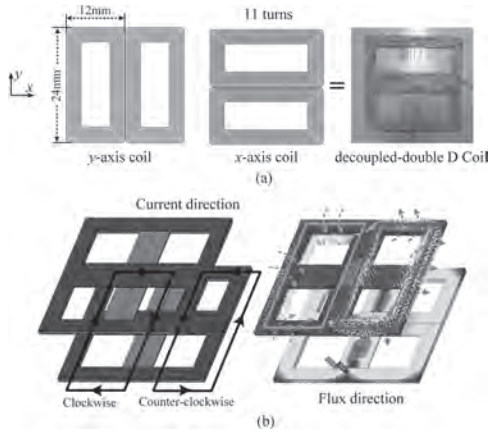
I. Introduction By reducing the over-dependence on current battery technologies, wireless power transfer (WPT) provides a brand-new power-supply solution and changes the traditional style of the energy utilization for electric-driven devices [1]. Accompanied by the increasing utilization of practical application, the diverse requirements of customers and various standards of manufacturers pose challenging issues on this technique, for example, Wireless Power Consortium (WPC) regulates the operating frequency of 87-205 kHz, while AirFuel (AF) alliance holds the operating frequency of 277-357 kHz. Thus, a number of efforts have been focused on the multiple frequencies multiple pickups based WPT, which can be divided into three aspects: 1) single-inverter single-transmitter [2-4], 2) multiple-inverters single-transmitter [5], and 3) single-inverter multiple-transmitters [6]. Due to the simplicity and low cost, single-inverter single-transmitter becomes the optimal choice. However, in [2], energies are transmitted by time division method, which fails to concurrently transfer multiple frequency power, in [3], the distribution of multiple frequency power cannot be adjusted arbitrarily, and in [4], the cross-coupling effect among the pickups will significantly deteriorate the transmission performance. Accordingly, how to randomly transmit multiple frequency power simultaneously without unnecessary coupling becomes a critical technical concern. In this paper, a dual-resonating-frequency compensation topology is adopted and implemented for exciting the decoupled-double D transmitting coils. Concretely speaking, two double D coils are located orthogonally to obtain the effect of magnetically decoupled in both primary side and pickup side. Meanwhile, the proposed system can provide two randomly predefined operating frequencies and the power distribution of two different frequencies can be arbitrarily regulated based on the users' requirement by adopting the proposed frequency overlay modulation (FOM). Moreover, owing to the nonexistent cross-coupling between decoupled-double D pickup coils and the characteristic of compact integrated, each pickup can maintain the maximum efficiency respectively. II. Methodology Fig. 1(a) depicts the WPT system with a single-transmitter for two pickups, where the configuration of dual-resonating-frequency compensation topology which consists of a series-connected LC ($C_{sc} L_{s1} L_{s2}$) tank and a parallel-connected LC ($C_{pc} L_{p1}$) tank is presented. Meanwhile, the parameters design procedure needs massive calculation based on equation (1), thus this paper specifies the operating frequency of 100kHz and 300kHz and each of them satisfies WPC and AF standards, respectively. Then, a simplified lookup table design method for randomly predefined operating frequency is shown in Fig. 1(b). Fig. 1(c) testify the effectiveness of the proposed compensation topology. Besides, the proposed FOM can overlap randomly dual frequencies with various magnitudes, where Fig. 1(d) elaborates the proposed FOM with the same magnitude for 100kHz and 300kHz, which can be confirmed by Fig. 1(e). As shown in Fig. 1(g), both simulation and practical experiments validate that the proposed system can maintain a high transmission efficiency of over 90% for each pickup of more than 10W. From the perspective of the magnetic, since the y-axis coils and x-axis coils are located orthogonally, the magnetic fluxes are symmetrical regarding the central axes. It indicates that when the current flows in y-axis coils as shown in fig.2 (b), the amount of magnetic flux from y-axis coils that passes through the x-axis equals to that passes out of it. Consequently, the coupling between y-axis coils and x-axis coils is theoretically zero which means the y-axis coils and x-axis coils are decoupled. In this paper, the y-axis coils and x-axis coils are orthogonally compactly placed and series-connected as the transmitting coils. While y-axis coils and x-axis coils are only orthogonally compactly placed in the pickup side and are utilized to energized pickups independently. Specifically speaking, y-axis coils in the transmitting side are fully coupled with the y-axis in the pickup side, and so do x-axis coils. This mechanism can boost the coupling thus promoting the efficiency for both pickups. Fig. 1(g) quantitatively analyses the efficiency under the coupling of 0.08 (traditional circular coils) and 0.12 (decoupled-double D Coils), respectively, which indicates a maximum efficiency improvement of 25.2%. III. CONCLUSION

This paper proposes an artfully designed dual-resonating-frequency compensation topology with a simplified parameter design procedure. Meanwhile, the proposed FOM regulation method can arbitrarily produce the compound excitation. By adopting decoupled-double D coils, the dual-frequency WPT system holds the merit of zero cross-coupling in the pickup side, thus can promote the transmission efficiency for each pickup. Theoretical analysis, simulation, and experimental results will be given in more detail to verify the feasibility. Acknowledgment This work was supported by a grant (Project No. T23-701/20-R) from the Hong Kong Research Grants Council, Hong Kong Special Administrative Region, China.

[1] Z. Zhang, H. Pang, A. Georgiadis and C. Cecati, "Wireless power transfer—an overview," *IEEE Trans. Ind. Electron.*, vol. 66, no. 2, pp.1044-1058, 2019. [2] Z. Zhang, H. Pang, S. H. K. Eder, and R. Kennel, "Self-balancing virtual impedance for multiple-pickup wireless power transfer," *IEEE Trans. Power Electron.*, vol. 36, no. 1, pp. 958-967, 2021. [3] W. Liu, K. T. Chau, C. H. T. Lee, C. Jiang, W. Han, and W. H. Lam, "Multi-frequency multi-power one-to-many wireless power transfer system," *IEEE Trans. Magn.*, vol. 55, no. 7, pp. 8001609: 1-9, 2019. [4] Z. Zhang, Xing. Li, H. Pang, H. Komurcugil, Z. Liang, R. Kennel, "Multiple-frequency resonating compensation for multichannel transmission of wireless power transfer," *IEEE Trans. Power Electron.* doi: 10.1109/TPEL.2020.3027916. [5] F. Liu, Y. Yang, Z. Ding, X. Chen, and R. Kennel, "A multifrequency superposition methodology to achieve high efficiency and targeted power distribution for a multiload MCR WPT system," *IEEE Trans. Power Electron.*, vol. 33, no. 10, pp. 9005-9016, 2018. [6] C. Zhao, D. Costinett. "GaN-based dual-mode wireless power transfer using multifrequency programmed pulse width modulation," *IEEE Trans. Ind. Electron.*, vol. 64, no. 11, pp. 9165-9176, 2017



Schematic of proposed dual-frequency WPT systems. (a) Configuration. (b) Simplified design scheme and key parameters. (c) Impedance characteristics. (d) Waveforms. (e) FFT analysis. (f)-(g) Characteristics of the transmission power and transmission efficiency.



(a) Structure of decoupled double-D coils. (b) Magnetic field distributions of coils.

AS-03. Design, Manufacture, and Test of a Contactless Power Transfer Device for Rotating System.

Y. Zhang¹, J. Yang¹, D. Jiang¹, D. Li¹ and R. Qu¹

1. Huazhong University of Science and Technology, Wuhan, China

Abstract—A CPT (contactless power transfer) device is designed in this paper. It removes the traditional contact slip-ring in the device where power transfer from stationary to rotary side is needed. The structure is designed and simulated. Compensation are added to improve the coupling coefficient between the primary and secondary sides. To improve the system power rate, high frequency power converter is utilized. At last, a prototype is built and tested. From the results, the performances of the device are well verified.

I. Introduction Mechanical slip ring is widely used as a method of power transfer from a stationary component to a rotary one. However, mechanical slip ring is very easy to wear and needs frequent maintenance.[1] CPT solves this problem. System diagram of the system is shown in Fig. 1. The low frequency AC source is first rectified, and then converted by the high frequency inverter circuit. Through electromagnetic induction, voltage is induced in the secondary winding. At last, the power is transferred from the stationary to the rotary side load after rectifying. II. System Design The CPT device is like a rotating transformer in structure. The device is consisting of iron core and windings. The basic structure of the device is shown in Fig. 2(a). There is an air gap between the device primary side and secondary side. Thus, one side could rotate relatively to the other side. However, the system is operating at high frequency, producing large losses in both ferromagnetic materials and copper windings. To overcome this problem, high frequency ferrite and litz wires are utilized. Due to the fragile mechanical performances of the ferrite, pre-manufactured U-shape ferrite pieces are utilized and assembled as shown in Fig. 2(b). III. Simulations Results The device is modeled and simulated using FEM method. No-load and load condition is calculated and the system inductance is obtained. Results are shown in Table I. As the device magnetic circuit will change while rotating in this special design, the inductances of teeth-to-teeth and teeth-to-air position are compared IV. Experimental Analysis The prototype is manufactured and its electromagnetic performances is tested. The test platform is shown in Fig. 3. The voltage and current waveform under load condition are shown in Fig. 4. From the figure, the voltage and current have identical phase in both primary and secondary side. Under this condition, the load power reaches 1kW with efficiency of 92% and no obvious temperature rise is monitored. V. Conclusion This paper analyzes the contactless power transfer system applied to rotating application. The special design of the device could decrease the system loss and increase the couple between primary and secondary sides. Electromagnetic parameters of the device are simulated by FEA. It shows good consistency with the measurement results. Also, the experiments are carried out and it turns out that the power is transferred successfully with high efficiency.

References [1] J. Yang, Y. Zhang and D. Jiang, “A Contactless Power transfer Device Applied to the CT System,” 2019 22nd International Conference on Electrical Machines and Systems (ICEMS), Harbin, China, 2019, pp. 1-5.

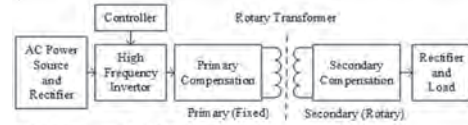


Fig. 1 CPT system block diagram



Fig. 2 CPT device 3D structure. (a) rotating transformer structure. (b) rotating transformer manufactured by ferrite pieces.

TABLE I
SIMULATION AND MEASUREMENT RESULTS OF PARAMETERS

		Simulations	Measurements
Teeth to teeth	Excitation inductance	42uH	38uH
	Primary leakage inductance	183uH	179uH
	Secondary leakage inductance	42uH	54uH
Teeth to air	Excitation inductance	42uH	37uH
	Primary leakage inductance	168uH	172uH
	Secondary leakage inductance	42uH	47uH

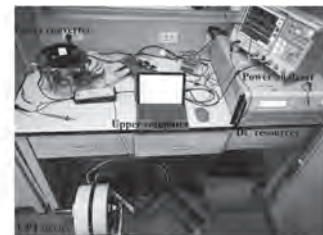


Fig. 3 Experimental platform

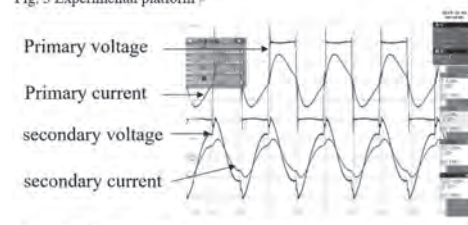


Fig. 4 Waveform of load voltage and current

AS-04. Active Shielding Coil Design for Wireless Charging System of Electric Vehicle.

M. Mi¹, Y. Li¹, Q. Yang¹, P. Zhang¹ and W. Zhang¹

1. State Key Laboratory of Reliability and Intelligence of Electrical Equipment, Hebei University of Technology, Tianjin, China

1 Introduction High-intensity magnetic field around the system will be generated when the wireless charging system of electric vehicles(EV) is working, which will reduce the transmission efficiency of the system and pose risks to human health[1]. Ferrite core has been widely used to shield the magnetic flux leakage on the back side of the coil and improve the magnetic coupling between the primary and the secondary sides due to its high permeability and large resistivity. However, this shielding method is not very effective in shielding the magnetic field in the non-working area on the side of the system. As a supplement to the passive shielding method, the main idea of the active shielding method is to use the reverse magnetic field generated by the shielding coil to cancel the magnetic field leakage in the target area. The reactive shielding method based on resonance of a passive compensation loop has been proven to be an effective method to offset the magnetic leakage in the target area, but adjustment of the shielding circuit impedance is complicated[2]. The shielding coil with independent power supply can be controlled to produce a magnetic field that is completely opposite to the incident magnetic field, but it inevitably reduces the overall transmission efficiency of the system[3]. A good solution is to make active shielding coil be in series with the branch where the energy transfer coil is located[4]. It should be noted that the active shielding coil may be coupled with the main magnetic linkage. Under this condition, the equivalent magnetic coupling between the primary and the secondary sides becomes smaller, which will reduce the output power of the system. In this paper, a dual-loop active shielding coil directly connected in series with the primary side is designed to reduce the reverse magnetic coupling between the primary and the secondary sides and the magnetic flux leakage around the wireless charging system of EV. The parameters of the shielding coil are determined by multi-objective optimization. Finally, a prototype with an input power of 1.2kW is built. The proposed active shielding coil has superior performance in system transmission efficiency and shielding effect on the target surface comparing to conductor shielding. 2 Active Shielding Coil Design Circuit theory is adopted to model the wireless power transmission system with double LCC compensation topology as shown in Fig. 1, where L_1 and L_2 are self-inductances, L_3 is the self-inductance of shielding coil. To prevent load power from being affected by the shielding coil, what we need to do is to minimize the mutual inductance M_{23} between the active shielding coil and the secondary side. The proposed dual-loop active shielding coil shown in Fig. 2 is only arranged on the primary side, since the steel plate of the car chassis has a good shielding effect on the magnetic field around the secondary side. The inner diameters of the inner loop coil is set to a fixed value of 50cm, and the target surface is set at a distance of 55cm from the center of the coil. The number of turns and outer diameter of the shielding coil are optimized through ANSYS simulation. The outer diameter of the shielding coil is optimized in the range of 29cm to 44cm with a step length of 3cm. In addition, the number of turns of the inner loop and outer loop is optimized in the range of 1 to 3 and 1 to 4, respectively. The optimization targets are the mutual inductance between the active shielding coil and the secondary side, the maximum magnetic flux density on the target surface, and the length of the active shielding coil. To solve the multi-objective optimization problem, the constraints are set as follows: $M_{23} \leq 0.5\mu\text{H}$ $B < 27\mu\text{T}$ $L \leq 13\text{m}$ To further determine the optimal solution, an evaluation function $F(d)$ is constructed and defined as the normalized objective function f_i multiplied by their respective weight coefficients ω_i as follows: $F(d) = \sum \omega_i |f_i - f_i^*| / (f_{\text{set}} - f_i^*)$ ($i=1,2,3$) where f_i^* is the ideal value with a value of 0, and f_{set} is the constraint value of the objective function. The solution with the smallest evaluation function value is adopted for subsequent simulation and experimental verification. The magnetic field distribution on the target surface is compared in three condition through ANSYS simulation: no shielding, with aluminum shielding and active shielding. When the active shielding is applied, the maximum magnetic flux density of the target surface is reduced to 16.2uT comparing to the case of 33.05uT when only the ferrite core is applied. However, the maximum magnetic flux density is 20.01uT in the case of

aluminum shielding. The proposed active shielding design is verified by a prototype with an output power of 1.2kW. To investigate the effect of shielding methods on transmission efficiency, the input voltage needs to be adjusted to keep the system input power constant. The results of the experiment will be presented in the final paper. 3 Conclusion This paper introduced a dual-loop active shielding coil connected in series with the primary side to reduce the magnetic leakage around the system. An evaluation function has been proposed to optimize the number of turns and outer diameter of the shielding coil. The proposed shielding method obtains a superior shielding effect on the target surface than conductor shielding, and has less passive impact on the transmission efficiency of the system.

[1] S. Park, IEEE Transactions on Magnetics., vol. 54, p.1-8 (2018). [2] H. Moon, S. Kim and H. H. Par, IEEE Transactions on Magnetics., vol. 51, p.1-4 (2015). [3] T. Campi, S. Cruciani and F. Maradei, IEEE Transactions on Electromagnetic Compatibility., vol. 62, p.1398-1405 (2020). [4] S. Y. Choi, B. W. Gu and S. W. Lee, IEEE Transactions on Power Electronics., vol. 29, p.5770-5783 (2014).

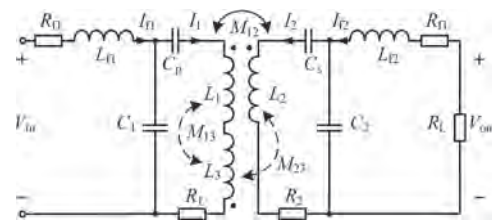


Figure. 1: Equivalent circuit of the system with active shielding coil

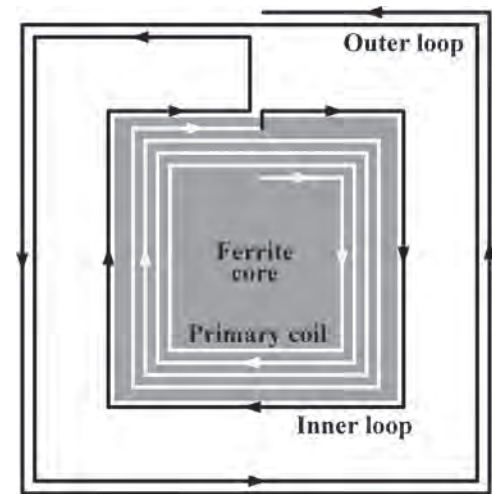


Figure. 2: Design of dual-loop active shielding coil

AS-05. Propulsion of Magnetic Material Embedded Microrobot in Tubes Based on Wireless Power Transfer System.

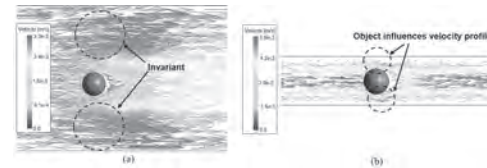
D. Kim¹

¹. Automotive Engineering, Yeungnam University, Gyeongsan, The Republic of Korea

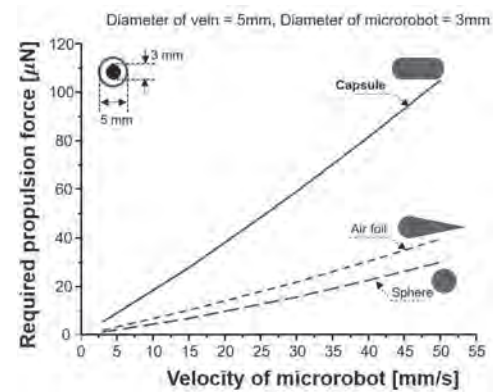
Microrobots have been studied for medical applications, allowing surgical operations with minimal invasion to the human body [1, 2]. Due to the small size of the microrobot, it has the advantage of being able to move freely within the vessel and perform various missions. For this reason, a lot of research groups have worked on the propulsion of microrobot. Most prevalent microrobot propulsion method is external magnetic field based microrobot propulsion [2-4]. However, due to the lack of electric power source, these kinds of microrobots are able to perform only limited missions. To expand their utilization, wireless power transfer system applied microrobot have been proposed. One of them, microrobots that can simultaneously receive electrical energy and generate propulsion force have been introduced [5-8]. They verified the propulsion of microrobot through the water surface movement experiments. However, since the microrobot supposed to be located inside of blood vessel, moving motion of microrobot should be consider their environment as inside of a tube. In this paper, a mm-sized magnetic material embedded microrobot, located in the tube is analyzed. Depending on their dimensional differences the environment of microrobot can be regarded as free-stream or non-free stream conditions. Fig. 1 (a) and (b) represents the velocity profile of internal flow condition and external flow condition. In case of external flow condition, the diameter of the tube is large enough, so the effect of fluid bypassing the object does not change the entire flow of the fluid. On the other hands, if the size of an object is comparable to its internal diameter, the flow of fluid that bypasses the object has a significant impact on the velocity profile and therefore, the fluid velocity profile of the internal flow condition is more influenced by duct as illustrated in Fig. 1(b). If we assume that the diameter of vein is 5 mm and the microrobot designed in this research has the 3.5 mm diameter with 10 mm length, interpreting the microrobot inserted in tube as internal flow condition is reasonable. Fig. 2 illustrates the propulsion force that required to achieve certain velocity of microrobots depending on their various structure shape. As illustrated, under the condition of that the surface diameter which is face to the stream is identical, the sphere and air foil structure have much more efficient for the propulsion. However, in this research, a bar-type magnetic material is applied, a capsule shaped structure is applied for enclose the microrobot. In this case, for example, if the microrobot tried to reach the speed of 3 mm/s, it requires 7 μ N propulsion force. The magnetic force when the incident time-varying magnetic field applied to the magnetic material, can be derived as follows; $F(t) = 2\pi\mu_m r^3 \times ((\mu_p \mu_m) / (\mu_p + 2\mu_m)) \nabla H(\sin(\omega t))^2$, where, $\mu_m, \mu_p, r, \nabla H$, and ω are represents permeability of magnetic material, permeability of media, radius of magnetic material, gradient incident magnetic field and angular frequency of incident magnetic field, respectively [9]. When we considered that the size of transmitting coil is 170 mm x 170 mm and the distance between transmitting coil and microrobot is 50 mm away, the required current to achieve 7 μ N is determined as 200 Ampere-turn. To verify theoretically obtained value, simulation with 3D FEM simulator, Ansys Electronics Maxwell, is conducted. As expected, by exciting 200 Ampere-turn in the transmitting coil, it is able to generate 7 μ N magnetic force which is enough to move the velocity of 3 mm/s in the tube whose diameter is 5 mm.

[1] J. Li, et al., "Micro / nanorobots for biomedicine : Delivery, surgery, sensing, and detoxification," *Sicenc Robotics*, vol. 2, pp. 1-10, 2017. [2] B. J. Nelson, et al., "Microrobots for Minimally Invasive Medicine," *Annu. Rev. Biomed. Eng.*, vol. 12, pp. 55-85, 2010. [3] A. M. Maier, et al., "Magnetic Propulsion of Microswimmers with DNA-Based Flagellar Bundles," *Nano Lett.*, vol. 16, pp. 906-910, 2016. [4] G. Bin Jang, et al., "A Spiral Microrobot Performing Navigating Linear and Drilling Motions by Magnetic Gradient and Rotating Uniform Magnetic Field for Applications in Unclogging Blocked Human Blood Vessels," *IEEE Trans. Magn.*, vol. 51, p. 9100404, 2015. [5] D. Kim, et al., "Magnetic resonant wireless power transfer for propulsion of implantable micro-robot," *J. Appl. Phys.*, vol. 117, p. 17E712, 2015 [6] R. Narayamoorthi, et al., "Frequency splitting-

based wireless power transfer and simultaneous propulsion generation to multiple micro-robots," *IEEE Sens. J.*, vol. 18, pp. 5566-5575, 2018. [7] A. Hajiaghajani, et al., "Patterned Magnetic Fields for Remote Steering and Wireless Powering to a Swimming Microrobot," *IEEE/ASME Trans. Mechatronics*, vol. 25, pp. 207-216, 2020. [8] D. Kim, et al., "Propulsion and Rotation of Microrobot Based on a Force on a Magnetic Material in a Time-Varying Magnetic Field Using a Wireless Power Transfer System," *IEEE Trans. Magn.*, vol. 56, pp. 1-5, 2020. [9] D. Kim, et al., "Instantaneous Magnetic Force Evaluation on a Magnetic Material for Wireless Power Transfer Based Microrobot Propulsion," 2020 IEEE Wireless Power Transfer Conference (WPTC 2020).



Velocity profile depending on the flow types. Simulation results of external flow (a) and internal flow (b).



Required propulsion force depending on the velocity of microrobot in tube.

AS-06. Modelless Prediction of Variable Coupling Effect for Multiple-Pickup Wireless Power Transfer.

S. Shen¹, Z. Zhang¹ and Y. Wu¹
 1. Tianjin University, Tianjin, China

I. Introduction By means of the high power density, the low cost as well as the compact design, the wireless power transfer (WPT) with one single transmitter for multiple pickups (STMP) has obtained increasing attentions for both academic researchers and the industrial engineers in recent years. In order to simplify the circuit modeling, the cross-coupling effect among pickup coils is normally ignored in the theoretical analysis. In practical applications, however, the cross-coupling effect cannot be taken as zero since multiple pickup coils locate within a limited and narrow area. As a result, the corresponding coupling effect between the transmitting coil and each pickup coil is inevitably affected by the cross-coupling effect. In addition, the variation of relative position between the transmitter and the pickup also results in the fluctuation of the mutual inductance. The resulted non-constant coupling effect cannot be measured directly and accurately, which means that STMP-WPT faces with more challenged by comparing with 1-to-1 transmission. This paper proposes a modelless prediction scheme by using the neural network (NN) to predict variable mutual inductance between the transmitting and the pickup coils for STMP-WPT systems. In traditional model-based predictive control, the accuracy significantly depends on parameters of the system model. However, the parameters such as the inductance and the capacitance inevitably deviate from the normal value due to the variable working temperature and the operating frequency. Accordingly, the proposed modelless prediction scheme can realize the prediction of the mutual inductance by using the offline-trained NN instead of the system model, which cannot only avoid the impact of the parameter disturbance on the prediction accuracy but also enhance the dynamic response performance by means of the parallelism of data processing and the generalization ability of NN. II. Proposed Modelless Prediction In this paper, a WPT system with one single transmitter for three pickups is adopted as an exemplification. Fig. 1(a) shows the circuit diagram, where the primary current (i_p) and the secondary currents (i_{s1} , i_{s2} , and i_{s3}) can be measured by using the current sensor and then taken as inputs of NN-based controller. By adopting the offline training, the NN-based controller generates the coupling coefficients between the transmitting coil and each pickup coil, such as K_{ps1} , K_{ps2} , and K_{ps3} . The corresponding mutual inductance can be obtained, accordingly. Additionally, the experimental prototype is set up as shown in Fig. 1(b), which consists of a H-bridge inverter (MOSFET C3M0065090D) to produce the 100-kHz AC exciting power, a DSP28335 microcontroller to implement the proposed NN-based prediction and generate the PWM for the inverter, a current sensor (LA25-NP/AD637) to measure primary and secondary currents, a DC power supply (ITECH IT6722A), a transmitting coil, and three pickup coils. In order to verify the feasibility of the proposed modelless prediction scheme, simulation and experimental verifications are both carried out by adjusting the relative positions between the transmitting coil and each pickup coil to vary the coupling effect. By using JMAG for the magnetic field analysis and the MATLAB/SIMULINK for the circuit analysis, Fig. 2(a)-(c) shows primary and secondary currents as well as the corresponding mutual inductance, namely 8.97 μ H, 5.29 μ H, and 7.67 μ H. Meanwhile, the experiment is also carried out by taking into account the variation of the coupling effect caused by the transmission distance as shown in Fig. 2(d)-(f) and the load as shown in Fig. 2(g)-(i). Accordingly, the simulated results well agree with the experimentally measured results, which illustrates the feasibility of the proposed modelless prediction scheme for the coupling effect between the transmitting and multiple pickup coils. Besides, the detailed parameters, comparison with traditional method, theoretical analysis, simulated results, and experimental waveforms will be presented in the full manuscript. III. Conclusion This paper proposes a modelless prediction scheme to predict variable coupling effect between the transmitting and the pickup coils for STMP-WPT systems. The proposed data-driven prediction scheme only requires the value of currents rather than the detailed parameters of the equivalent mutual inductance model, thus effectively enhancing the accuracy of the coupling effect prediction under parameter disturbances. By using the offline trained NN, the primary and secondary currents can be fitted to the mutual inductance. Accordingly, it can effectively predict

the non-constant coupling effect caused by the variation of relative position between the transmitting coil and each pickup coil as well as the load. ACKNOWLEDGEMENT This work was supported in part by the National Natural Science Foundation of China (Project No. 51977138), and in part by the Humboldt Research Fellowship (Ref 3.5-CHN-1201512-HFST-P) and in part by Carl Friedrich von Siemens Research Fellowship (Ref 1201512).

[1] Z. Zhang, H. Pang, and A. Georgiadis, *IEEE Trans. Ind. Electron.*, vol. 66, no. 2, pp. 1044-1058, 2019. [2] Z. Zhang, X. Li and R. Kennel, *IEEE Trans. Power Electron.*, DOI: 10.1109/TPEL.2020.3027916. [3] X. Li, Z. Zhang, and Z. Liang, *IEEE Trans. Magn.*, DOI: 10.1109/TMAG.2020.3017804.

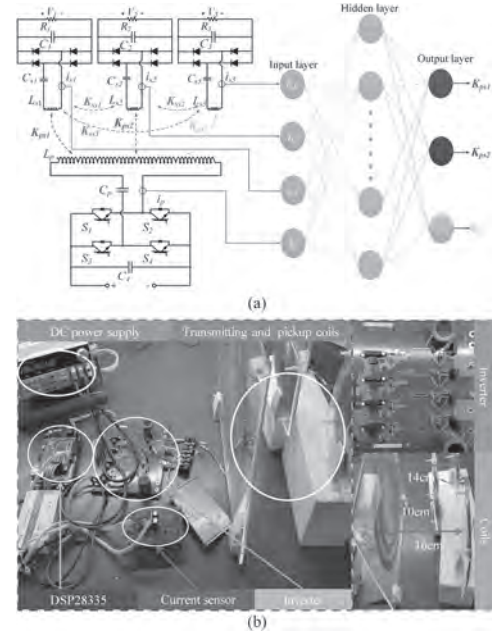


Fig. 1. STMP-WPT with modelless prediction scheme: (a) Circuit; (b) Prototype.

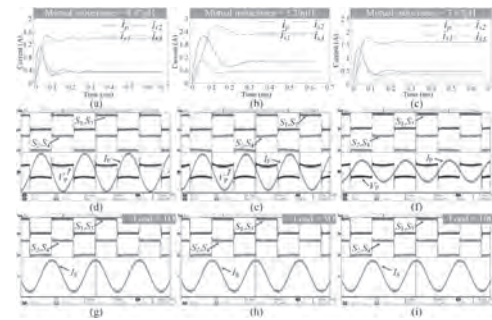


Fig. 2. Results: (a) Simulated currents at Position 1; (b) Simulated currents at Position 2; (c) Simulated currents at Position 3; (d) Measured primary current at Position 1; (e) Measured primary current at Position 2; (f) Measured primary current at Position 3; (g) Measured secondary current (load=1 Ω); (h) Measured secondary current (load=5 Ω); (i) Measured secondary current (load=10 Ω).

AS-07. Brushless DC Motor Driver and Control System Based on Simultaneous Wireless Information and Power Transfer.

Y. Li¹, H. Zhang¹, J. Wu¹, J. Yin¹, M. Wang¹ and J. Zhang¹
 1. Zhengzhou University of Light Industry, Zhengzhou, China

I. Introduction Currently, the wireless power transfer (WPT) system is mainly used to wirelessly supply power to resistive loads [1]. In industrial application scenarios, the loads are mostly motors, which brings challenges to the wide application of WPT technology [2]. This paper proposes to apply simultaneous wireless information and power transfer (SWIPT) technology to drive permanent magnet brushless DC (BLDC) motors. The power transmission part is used to provide power to the motor, and the information transmission part is used to control the motor. This paper studies the equivalent impedance characteristics of the motor port in the SWIPT-BLDC system, establishes a mathematical model including the SWIPT system and the BLDC system, provides the conditions for the stable operation of the system, and builds an experimental platform to verify the scheme. II. Theoretical Analysis The SWIPT-BLDC system consists of a SWIPT system modulated by MFPWM [3], a motor controller and a BLDC motor. The SWIPT system uses MFPWM modulation to transmit two frequencies at the same time, which are used to drive the BLDC motor and control the motor speed. In order to reduce the volume of the coil and improve the transmission performance, a coil with a tap is designed in this paper to simultaneously transmit power and information. 2.1 System Structure and Control Method As shown in Fig. 1(a), the SWIPT module and the BLDC module form the SWIPT-BLDC motor system. On the primary side, the MFPWM inverter generates a dual-frequency signal. The capacitor and the tapped coil form a magnetic coupling resonance tank. On the secondary side of the system, two rectifiers respectively convert AC signals of different frequencies into DC. The BLDC driver contains a three-phase inverter. The rectified low frequency signal is input to the BLDC controller to drive the motor. The rectified high frequency signal is input to the BLDC controller as the given speed of the motor. The motor speed is proportional to the voltage of the given speed signal. 2.2 Magnetic Field Analysis of Coupled Coils The tapped coil reduces the system volume. As shown in Fig. 2(b), a finite element simulation model of the tapped coil is established. The magnetic fields of the two frequencies have overlapping regions. The simulation results show that the mutual inductance of the inner and outer coils is very small, and the tapped coil does not affect the signal transmission efficiency. 2.3 Analysis of Loading BLDC motor load is different from resistive load. The equivalent impedance of the motor load includes inductance and back electromotive force (EMF). The back-EMF of the motor load is related to the phase angle, torque and magnetic flux of the motor. During the motor operation, the back-EMF is constantly changing. This paper analyzes the voltage when the motor is loaded, and establishes the transfer relationship from the SWIPT system to the motor load. The deduction process and results will be presented in the full manuscript. III. Results and Discussion The simulation result of SWIPT-BLDC motor system is shown in Fig. 2. The blue line is the voltage to drive BLDC motor on the secondary side, the yellow line is the DC voltage of desired speed, the green line is the motor drive current in one phase, and the red line is motor speed. As shown in Fig. 2, giving the speed signal and the primary DC voltage, the induced voltage on the secondary side can drive the motor. The motor starts smoothly and the speed is stable. With the speed setting signal switching at 5s and 10s, the motor speed changes. The simulation results show that the structure proposed in this paper realizes motor driving and speed control. The actual measured results will be shown in the full manuscript. The research has also been experimentally verified. Due to the space limitation, the specific theoretical analysis and experimental results will be presented in the full manuscript.

[1] X. Li, Z. Zhang, W. Si, R. Wang and Z. Liang, IEEE Trans. on Magnetics., doi: 10.1109/TMAG.2020.3017804. [2] L. Yang, Z. Q. Zhu, H. Bin, Z. Zhang and L. Gong, IEEE Trans. on Industry Applications., vol. 57, p.306-315 (2021) [3] J. Wu, H. Zhang, P. Gao, Z. Dou, N. Jin and V. Snášel, Sustainability., vol. 12(10), p.4189 (2020)

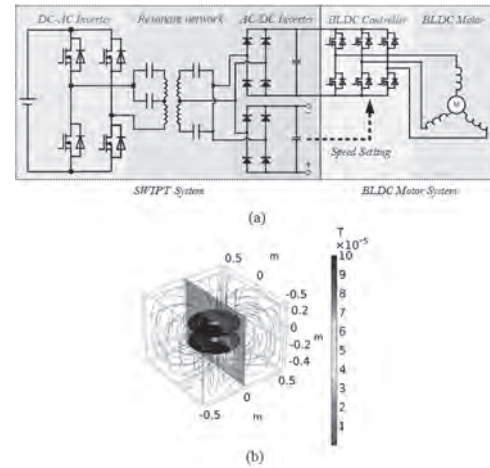


Fig. 1 (a) Circuit diagram of BLDC motor system based on SWIPT. (b) Finite element simulation model of tapped coil. The blue streamline represents the magnetic flux density. The colored section represents the magnetic flux density magnitude (T).

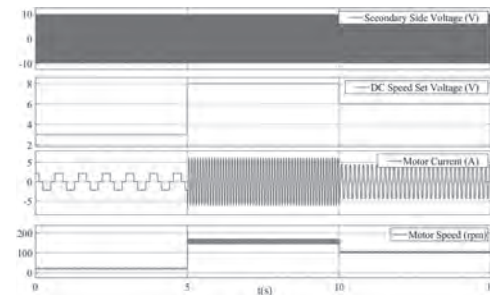


Fig. 2 Circuit Simulation Waveform of BLDC Motor System based on SWIPT.

AS-08. Analysis and Comparison of Variable Positioning Wireless Power Transfer Using Multi-Axis Coil.

Y. Kim¹, D. Um¹ and G. Park¹

1. Electrical Engineering, Pusan National University, Busan, The Republic of Korea

Abstract—Recently, omnidirectional wireless power transfer(WPT) systems with high flexibility compared to single-directional wireless power transmission systems have been actively studied. In this paper, we compare a system with a WPT structure in one direction and with a multi-axis transmitting coil(Tx) structure. The location of the receiver and the degree of flexibility and efficiency of the angle were compared in many cases, depending on the angle from the center axis of the Tx and the distance from the virtual sphere center, which is mainly influenced by the magnetic field induced from the Tx. In both cases, the input frequency was set to 60kHz under the same magnetomotive force and constructed a structure that considered the actual type. We construct a circuit in which magnetic fields occur in the direction of the Z and X axis in the Tx. The experiment allowed us to analyze the changes in electromotive force according to the distance and the angle tilted from the center axis when the Tx was composed of multiple axis. **Keywords**— WPT, Inductively Coupled Power Transfer (ICPT), multi-axis, spherical structure, induced electromotive force I. Introduction Wireless power transfer(WPT) technology is rapidly gaining traction and is used in a variety of applications, starting with Tesla coil and charging electric cars, cell phones and hearing aids [1]-[2]. WPT technology has been studied divided into magnetic resonance and magnetic induction methods [3]-[4]. Magnetic inductive methods have the disadvantage of reducing transmission distances, but have been used in various fields as they enable the coil to be compact. It is researched to increase the efficiency of transfer to loads in a magnetic inductive method [5]. In various fields, WPT is becoming more important, and as devices are compacted, it becomes more difficult to match the receiver of the device to the axis of the transmitter. For example, medical devices are developing due to the aging and diseases, and wirelessly charged hearing aids often require to be placed in the correct position and direction, even though they are wirelessly charged. Therefore, in this paper, we have adopted a charging method as long as it is located within the case, regardless of position and angle, to make it easier for the elderly to use, and we analyze its tendency. In Bowl-Shape hearing aids, the analysis of the distance-dependent magnetic field was conducted [2]. Bowl-Shape’s hearing aids have only Z-axis directions of magnetic fields induced by the Tx and adjust the diameter of the coil inducing the magnetic field of the Z-axis to make the radial-directional magnetic field perpendicular to the Z-axis. In contrast, in this paper, we set the Tx to multi-axis to control the direction of the induced magnetic field and compare it to a single-axis system. II. SIMULATION AND EXPERIMENT Figure1(a) sets the structure with the change in angle and (b) sets the structure with the change in position as FEM (Finite Element Method) and predicts the results. At this time, the magnetomotive force was 6.66 [At] for both the single and the multi-axis under the same conditions. In the experiments, the input frequency was set to 60 kHz, taking into account the range that does not interfere with the trunked radio system in the multi-axis experiment. In the case of Tx, a 1.8mm litz wire was wound around 9 turns, and the inner diameter of the coil forming the magnetic field in the z-axis was set to 75mm and the inner diameter of the coil forming the x-axis was set to 85mm. In the case of Receiving coil(Rx), a 0.3mm copper wire was used to wind 40 turns, and the inner diameter was set to 20mm. III. ANALYSIS Experiments were conducted with the same conditions as FEM. From the center of the Tx, the distance was increased by 2mm from 0mm to 20mm, moving in the z axis and measuring the electromotive force at the Rx. The Tx voltage was the same at 6V and 60kHz, and the electromotive force measured at the receiver tends to decrease as the distance increases to 3.36V when the distance is 0mm and 1.84V when the distance is 20mm. Measurements of electromotive force, moving in the X-axis direction, from 0mm to 20mm, and increased the size of electromotive force at the receiver as it moved from the center of the coil to the edge. In addition, electromotive force at the receptor decreased from 0 to 70 deg and increased from 70 to 90 deg as the angle increased by 10deg relative to 0deg in the same direction as the x-axis Tx. IV. CONCLUSION A single axis has high efficiency but low flexibility for location, while

a multi-axis has low efficiency but high flexibility. This trade-off needs to be studied in depth and will be dealt with in full-paper.

[1] C. C. Mi, G. Buja, S. Y. Choi and C. T. Rim, “Modern Advances in Wireless Power Transfer Systems for Roadway Powered Electric Vehicles,” in IEEE Transactions on Industrial Electronics, vol. 63, no. 10, pp. 6533-6545, Oct. 2016 [2] J. Kim, D. Kim, K. Kim and Y. Park, “Free-positioning wireless charging system for hearing aids using a bowl-shaped transmitting coil,” 2014 IEEE Wireless Power Transfer Conference, Jeju, 2014, pp. 60-63 [3] H. Hu and S. V. Georgakopoulos, “Wireless power transfer in human tissue via Conformal Strongly Coupled Magnetic Resonance,” 2015 IEEE Wireless Power Transfer Conference (WPTC), Boulder, CO, 2015, pp. 1-4 [4] H. Nong and J. Lin, “Design of loosely coupled inductive power transfer systems for instrumented wheelset,” 2009 9th International Conference on Electronic Measurement & Instruments, Beijing, 2009, pp. 1-670-1-674 M. Pinuela, D. C. Yates, S. Lucyszyn and P. D. Mitcheson, “Maximizing DC-to-Load Efficiency for Inductive Power Transfer,” in IEEE Transactions on Power Electronics, vol. 28, no. 5, pp. 2437-2447, May 2013

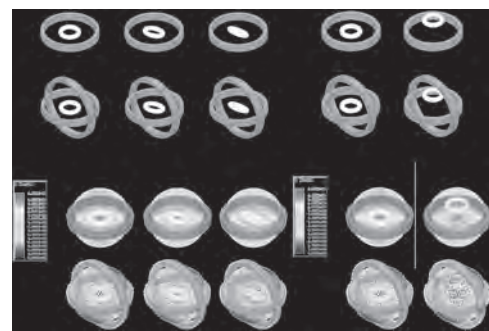


Fig. 1. (a) Structure according to angular changes, (b) position changes

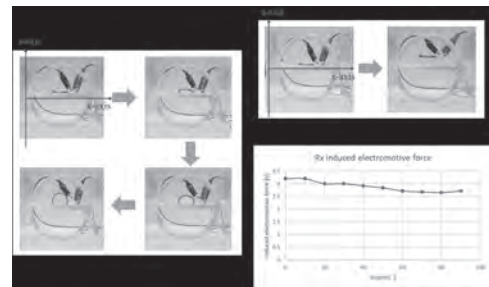


Fig. 2. (a) Experiment of position changes, (b) angular changes, (c) Data of experiments on angles

AS-09. Thermal Network Model of a SCB2500kVA Dry-Type Transformer Coupled With Electromagnetic Loss.

Y. Chen^{2,1}, Q. Yang³, C. Zhang^{2,1}, Y. Li^{2,1} and X. Li^{2,1}

1. Hebei University of Technology, Tianjin, China; 2. Hebei University of Technology State Key Laboratory of Reliability and Intelligence of Electrical Equipment, Tianjin, China; 3. Tianjin University of Technology, Tianjin, China

Abstract The research for the temperature distribution of the transformer is significant for design [1]. Methods applied pervasively in academic field are thermal-network method [2], finite element method [3] and Computational Fluid Dynamics (CFD) [4]. Although CFD method can improve the accuracy of the transformer temperature field calculation, it is time-consuming and difficult to mesh finely for some sophisticated structures such as the insulating paper between foil windings. In this paper, an equivalent thermal-network model for a SCB2500kVA dry-type transformer with foil winding as low-voltage (LV winding) and subsection and layer winding as high-voltage (HV winding) is established under natural convection. Considering the nonuniformity of the power loss density in LV winding [5], the heat sources at different positions need to be corrected by using correction factor. The cooling conditions are different with the varying locations in transformer such as the airways with asymmetric one-adiabatic-side heat flux density between HV winding and insulating barrier and the groove surrounded by LV coils with approximately symmetrical heat flux density [6]. To settle this, corresponding experimental formulas are applied to solve the convective heat dissipation coefficients and the thermal parameters like thermal resistances, heat capacities and heat sources of each part [7]. After all of this, temperature rise curves are obtained. Simulation by computational fluid dynamics (CFD) is conducted to verify the validity of thermal network model. The results are consistent with the data from analytical method and experiments.

I. The Establishment of Thermal Network Model Separated by DMD insulation prepreg papers, each layer of LV winding is one turn. Consisted of enameled rectangular copper wires, the HV segmented layers windings are divided into four sections, which are insulated by glass fiber mesh cloth. Upon core part, 9 nodes are selected as shown in Fig1(a), among which 5 points are from the core limb, 2 from half of core yokes and 2 from the lapping joints of core limb and yoke. The LV winding is divided into 6 sections along the axial direction as shown in Fig1(b), so 6 nodes are achieved. The HV winding is segmented into 9 sections as shown in Fig1(c) according to the location of the heat source distribution. The single-phase thermal network model of the transformer is set up.

II. Calculation of Thermal Parameters Thermal parameters in the thermal network model are heat source, heat resistance and heat capacity. The heat sources mainly come from core loss and winding loss. Due to the existence of the transverse leakage magnetic field, eddy currents are induced in the ends of foil coils, which lead to inhomogeneous distributions of currents and power losses among the LV winding. The current density can surge up to be 3 times at the ends than in the middle. Based on electromagnetic FEM computing software, parameter C_e is introduced to characterize this effect and correct the input power loss at end. The thermal resistances contain the conduction thermal resistance, the convection heat resistance and the radiant thermal resistance, which happen to be the three heat transfer pathways. The equivalent thermal conductivity can be obtained by Fourier's law. According to the diverse thicknesses, spatial directions, heat transfer areas and material compositions in different positions, thermal resistances between nodes can be calculated respectively. The radiant thermal resistance is related to the surface temperature and emissivity, which can be calculated by the Stephen Boltzmann equation. In view of the fact that when the dry-type transformer reaches heat dissipation equilibrium, the temperature in most areas can up to more than 100 degrees, the heat emitted to the environment by radiation is too considerable to neglect. Since the convective heat transfer coefficients are affected by the internal structural complexity of the transformer, the asymmetry heat sources and the buoyancy lift of natural convection, it is obviously inaccurate to apply an average value for the whole plane. By analyzing the heat dissipation conditions at different planes as shown in Fig1(d), the Nusselt number of vertical surface and horizontal are calculated.

III. Numerical Simulation The methods for solving convective heat dissipation coefficient include analytical method, experimental method and

numerical analysis method. The numerical analysis is a wide used method for solving the problems of various shapes and boundary conditions at present. By finite volume method, the results of temperature rise and velocity distribution can be obtained not only, but also the convective heat dissipation coefficient on different surfaces.

IV. Experiment In order to verify the validity of the model, the temperature rise experiment of load is carried out. The experimental results show that the hottest spot is located in the highest disc of outer HV winding with the temperature of 425.15K, which is in good agreement with the results of thermal network model and CFD simulation.

V. Conclusion: According to the thermoelectric analogy effect, the thermal network method simulates the temperature field through the method of circuit. By considering the heat source, thermal resistance and heat capacity of different structures respectively, the average temperature rise curve of every node is obtained. The precision of the hottest spot by thermal network method is reliable.

[1] M. Xiao and B. X. Du, IEEE Transactions on Dielectrics and Electrical Insulation., Vol. 23, p.2413–2420 (2016) [2] Cremasco, Andrea, and Wei, COMPEL - The international journal for computation and mathematics in electrical and electronic engineering., Vol. 37, p.1039-1053 (2018) [3] Ahn. H. M, Oh. Y. H, and Kim J K, IEEE Transactions on Magnetics., Vol.48, p.819-822 (2012) [4] L. Caibo, IEEE Transactions on Magnetics., Vol.50, p.1-4 (2014) [5] L. Yongjian, IEEE Transactions on Magnetics., Vol.55, p.1-5 (2019) [6] L. moonhee, Electric Power Systems Research., Vol.80, p.121-129 (2010) [7] F. P. Incropera, D. P. Dewitt, and T. L. Bergman, Chemical Industry Press (2007)

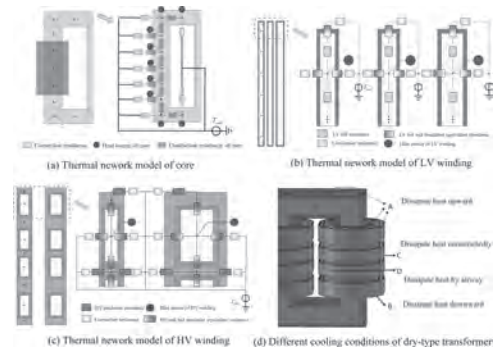


Fig.1 The establishment of thermal network model

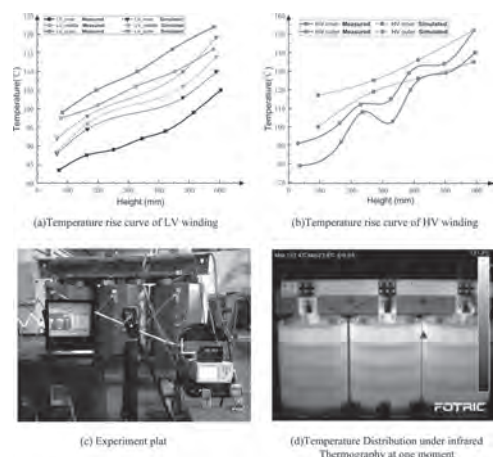


Fig.2 Results of simulation and experiment

AS-10. Fourier-Based Semi-Analytical Method for Current Distribution of Foil Wound Solid-State Transformers.

S. Pourkeivannour¹, M. Curti¹ and E. Lomonova¹

1. Electrical Engineering, Technische Universiteit Eindhoven Faculteit Industrial Engineering and Innovation Sciences, Eindhoven, Netherlands

Introduction Foil-wound transformers exhibit higher heat dissipation as well as high utilization of window area in SSTs, compared with Litz-wound ones. However, the frequency related winding loss becomes a dominating component in analyzing the general system operation performance in foil conductors. The predictions of the current distribution and the AC losses due to skin and proximity effects have been addressed in several studies. The most preferred method is a “ready-to-use” Dowell’s 1D expression for AC resistance of transformer windings [1]. This method assumes the length of the windings equal to the length of the winding window, which enables the one-directional magnetic field and current density distribution along the foil height. Nevertheless, due to the electric field insulation requirements in higher voltage applications, the height of the winding is limited within the window area of the transformer. This constraint introduces some deviations from Dowell’s method. The magnetic field gets a second-dimensional component causing high current density concentrations in the foil corners, called the edge effect. Accurate estimation of the 2D current distribution in high-frequency applications is mostly done using FEM analysis, showing a good level of accuracy. However, FEMs require extra fine mesh implying high computational cost/time, making it a less-preferable choice for daily use by design engineers. Fig. 1 shows the deviation of Dowell’s method in calculating the AC resistance factor compared with FEM. It can be concluded from Fig. 1 that the accuracy of 1D Dowell’s approach reduces as the operating frequency increases. While the operating frequency is aimed to be increased for novel designs to utilize the high-frequency related advantages of MFTs, the deviation becomes dominant. Several researches contributed to 2D eddy loss calculations by either introducing geometry-based correction coefficients [2] and [3] or using empirical approaches [4]. However, these methods are mainly valid for specific geometries and not flexible for a wide range of designs. This study aims to develop a mesh-free, frequency-independent, accurate Fourier-based method to calculate the magnetic field distribution in the window area of foil-wound SSTs. Fourier-based magnetic field analysis is a well-known semi-analytical method to solve the differential form of Maxwell equations in Electromagnetic devices [5]. The proposed method is implemented on a foil-wound SST to find a 2D expression for magnetic vector potential inside the window area of the SST. *Methodology* The geometric assumptions and the implemented boundary conditions are shown in Fig. 2. This method utilizes harmonic decomposition of position-dependent current excitation and conductivity. In this method, the core is assumed as infinite permeable material due to the high relative permeability of core materials compared with the insulation, air, and conduction material. The window area has been divided into multiple conducting and non-conducting regions. To model the imposed and induced currents in the conducting regions, the segmentation approach introduced in [6] is used. For this purpose, the imposed current density and the conductivity of the foils is imaged with a periodicity in the x-axis using the complex form of the Fourier series. The magnetic field distribution is calculated based on the solution of the Laplace (1) and Poisson (2) equations for non-conducting and conducting regions, respectively. In (2) the current density is composed of two terms: the imposed current and the induced eddy current. Consequently: $\nabla^2 A_z(x,y) = 0$ (1) $\nabla^2 A_z(x,y) = -\mu [J_{imp}(x) + \sigma(x) \cdot \partial A_z(x,y) / \partial t]$ (2) To solve the equations (1-2), a set of boundary conditions is used: 1-the continuity of the tangential component of flux density; 2-the continuity of normal component of magnetic field intensity; 3-zero tangential component for the flux density on the upper and lower boundaries of the window area. The developed linear equations are solved for the established boundary conditions. To overcome the numerical errors coming from the geometric characteristics of the model the scaling method is used as explained in [5].

[1] P. L. Dowell, *Proc. Inst. Electr. Eng.*, vol. 113, p. 1387, 1966. [2] F. Robert, P. Mathys, J. P. Schauwers, *IEEE Trans. Power Electron.*, vol. 16, p. 437–444, 2001. [3] D. Whitman, M. K. Kazimierczuk, *IEEE Trans. Power Electron.*, vol. 34, p. 10425–10432, 2019. [4] F. Robert, P. Mathys,

IEEE Trans. Magn., vol. 34, p. 1255–1257, 1998. [5] B. L. J. Gysen, K. J. Meessen, J. J. H. Paulides, and E. A. Lomonova, *IEEE Trans. Magn.*, vol. 46, p. 39–52, 2010. [6] C. H. H. M. Custers, E. A. Lomonova, *IEEE Trans. Magn.*, vol. 53, p. 1–6, 2017.

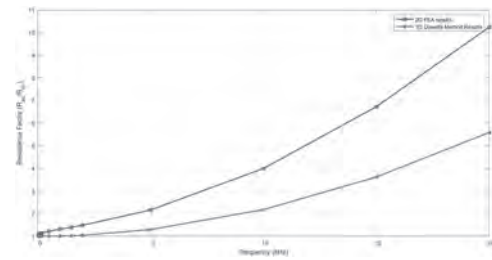


Figure 1 The Comparison of Resistance Factor for 1D Dowell’s Method and 2D FE Method

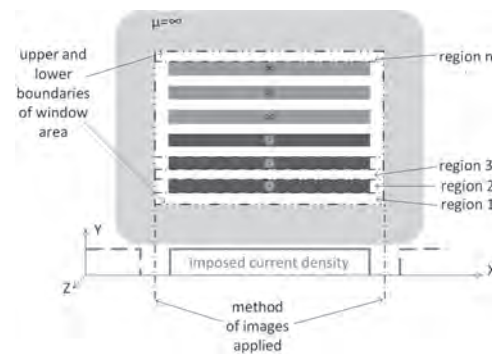


Figure 2 The Geometric Model of the Window Area of a MFT and the Boundaries of the Implemented Method

AS-11. Study of Vibration and Noise Considering DC Bias in Power Transformer.

Z. Xin¹, D. Chen¹, H. Yao¹, B. Bai¹ and D. Fang²
 1. School of Electrical Engineering, Shenyang University of Technology, Shenyang, China; 2. Tieling Power Supply Company, State Grid Liaoning Electric Power Supply Co Ltd, Shenyang, China

Abstract: This paper aiming to solve the vibration and noise problem of transformer core under DC bias, the magnetostrictive characteristics of 30ZH120 oriented silicon steel sheet in rolling direction and vertical rolling direction were studied firstly based on the measurement system of silicon steel sheet, and the influence rules of different DC bias on the magnetostrictive butterfly characteristics in different directions were studied. Secondly, the vibration and noise of transformer under the condition of DC bias are simulated, and the calculation results under different DC bias conditions are given. Thirdly, by means of modal numerical calculation and modal experimental study, the elastic modulus assignment methods and intervals suitable for modal calculation of transformers of different sizes are obtained and determined. Finally, the vibration and noise of the transformer are studied experimentally, and the correctness of the simulation content is verified. **Key words:** DC bias, vibration noise, magnetostriction, modal analysis

Introduction DC transmission grid, geomagnetic changes and other reasons can cause the ground potential of the transformer neutral point to rise, the presence of DC magnetic flux in the core, resulting in increased transformer no-load losses, vibration noise, and bring safety hazards to the power system transmission and distribution networks. Therefore, the study of transformer vibration noise is important. [1] simulated the 2-D magnetic properties of a silicon steel sheet and proposed a vector J-A hysteresis model considering the non-hysteresis magnetization intensity, and simulated its rotational magnetic properties. In [2], the magnetic properties of silicon steel sheets were studied at different temperatures and DC bias conditions, and the magnetization curves, permeability curves and loss curves were given. In [3], the magnetostriction characteristics of the silicon steel sheet were measured and the results were taken into the MagNet finite element software to study the vibration and noise of the power transformer, but the effect of DC bias on the vibration and noise of the transformer was not considered. This paper investigates the vibration noise of the transformer under DC bias through simulation and experimental verification. As in the research flowchart of Fig.1, the measured magnetic characteristic curves of the silicon steel sheet under DC bias magnetism can be brought into the transformer FEM model to obtain more accurate results. Finally, modal numerical calculations and modal experimental studies of transformers are also carried out to obtain and determine the elastic modulus assignment methods and intervals applicable to modal calculations of transformers of different sizes.

2 Simulation and experiment of vibration and noise under DC bias of transformer The results obtained by substituting the magnetic characteristic curves in Fig. 1 into the transformer FEM model considering the boundary conditions are shown in Table 1. The results show that the vibration and noise of the transformer increase with the increase of the DC bias. When the DC bias is greater than 2.3A, the vibration displacement reaches 0.4442 μm and the noise reaches 72.96 dB. In addition, the noise distribution curve of the transformer under DC bias shows that the noise increases with the increase of DC bias, but the noise remains stable when the DC bias is greater than 2.3A, indicating that the transformer core is saturated.

3 conclusion This paper first measures the magnetic properties of silicon steel wafers, and then uses finite element analysis to investigate the vibration noise performance of transformers under DC bias magnetism, and conducts experimental verification. The results show that the vibration and noise simulation results are in good agreement with the experimental results. Detailed experimental results and comparisons as well as modal analysis results will be shown in the full paper.

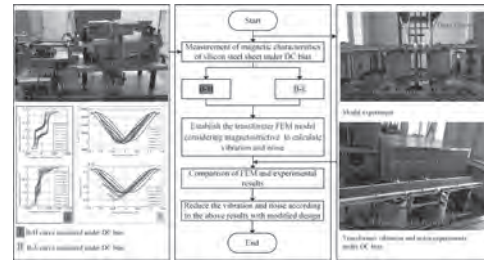


Fig.1 Research process flowchart

Item	Simulation		Modal experiment
	DC bias is 1.2A	DC bias is 2.3A	
Distribution of vibration displacement in core [μm]			
Distribution of sound pressure level [Pa]			

Table.1 Simulation and modal experiment results

[1] X. Wang, Y. Zhang and W. Jiang, Transactions of China Electrotechnical Society., Vol. 12(33), p.257-262 (2016) [2] D. Chen, L. Fang and B. Kwon, AIP Advances., Vol. 7(5), 056682 (2017) [3] D. Chen, W. Zhao and B. Bai, International Journal of Applied Electromagnetics and Mechanics., Vol. 52(3-4), p.1477-1484 (2016)

AS-12. Study on Vibration and Noise Characteristics of Nanocrystalline High-Frequency Transformer.

P. Zhang¹, L. Li², Y. Jia¹ and L. Li³

1. School of Mechanical Electronic and Information Engineering, China University of Mining and Technology (Beijing), Beijing, China; 2. North China power control sub-center of State Grid, Beijing, China; 3. State Key Laboratory of Alternate Electrical Power System with Renewable Energy Sources (North China Electric Power University), Beijing, China

Abstract: The high-frequency transformer (HFT) will produce sharp noise when working and the long-term excessive vibration will not only accelerate the aging of the equipment but also influence the surrounding environment, so it is great significance to study the vibration and noise characteristics of the HFT. In this paper, the core-type nanocrystalline high frequency transformer with capacity of 5400kVA and frequency of 5000Hz is simulated and analyzed by two factors of magnetostrictive and Maxwell. At last, a high frequency transformer is designed and a test platform is set up. The vibration and noise is tested and analyzed, and compared with the simulation results.

Index Terms—Nanocrystalline, high frequency transformer, vibration, noise

Introduction The high-frequency transformer (HFT) of large capacity in DC/DC converter will be able to achieve voltage and power transmission in the electric power system, high and low voltage side electrical isolation between inverter and rectifier circuit through the magnetic coupling, which can more easily achieve the electrical control of DC/DC converter on both sides. The vibration and acoustic noise emission of electromagnetic devices is not a new research area. However, the focus in the past has been on electrical machines and line frequency transformers, which have been thoroughly investigated in [1-3]. A clear understanding of the vibration and noise characteristics of HFT is necessary for detecting electrical and mechanical faults in a transformer using vibration-based monitoring strategies. Vibration mechanism of iron core There are two main factors in the vibration of HFT, the first factor is the magnetostriction effect of the iron core and the second factor is Maxwell force at the air gap. From the perspective of conservation of mechanical and internal energy, the magnetostrictive intrinsic model which is suitable for grain oriented silicon steel sheets is established. The test platform is built to test the vibration and noise of the core-type HFT, the test platform is shown in Fig. 1(a). The measuring points are shown in Fig.1 (b), and the noise is measured at the front and side of HFT. The simulation results show that the displacement of point 3 at 1000Hz is 5.5×10^{-7} m when the flux density in the core is 0.6T, and the displacement of point 4 is 7.9×10^{-7} m. The displacement increased by 43.63% compared with point 3, which indicates that the air gap is greatly influenced by Maxwell force due to the large leakage magnetic field. The time domain vibration of three points working at 1000Hz and 0.6T is shown in Fig. 2(a), it can be seen that the vibration of the upper part of the iron core is more serious. The vibration and noise trend of HFT at different frequencies is shown in Fig. 2(b). It can be seen that the vibration and noise of HFT gradually become larger with the increase of the frequency of excitation. At the same time, the vibration and noise are much larger than the conventional transformers, and the noise values are completely beyond the tolerable range. Therefore, it is necessary to study the vibration and noise characteristics of the high frequency transformer. Acknowledge This work was supported in part by National Natural Science Foundation of China under Grant 52007192. and in part by the Fundamental Research Funds for the Central Universities (2020XJJD02).

[1] B. Weiser, H. Pftzner, and J. Anger, "Relevance of magnetostriction and forces for the generation of audible noise of transformer cores," IEEE Transactions on Magnetics, vol. 36, no. 5, pp. 3759–3777, 2000.
 [2] R. S. Masti, W. Desmet, and W. Heylen, "On the influence of core laminations upon power transformer noise," in Proceedings of ISMA, 2004, pp. 3851–3862. [3] A. Moses, P. Anderson, T. Phophongviwat, and S. Tabrizi, "Contribution of magnetostriction to transformer noise," in 45th International Universities Power Engineering Conference (UPEC), 2010, pp. 1–5.



Fig. 1 The experiment set-up and the structure and the vibration measuring points

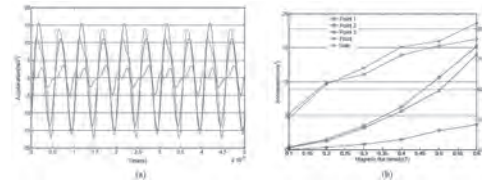


Fig. 2 The vibration time domain waveform and the change of vibration and noise with magnetic flux density

AS-13. Study of Electromagnetic Characteristics of Silicon Steel Sheet and Transformer Vibration Under Different Tension/Compression Stress.

H. Yao¹, D. Chen¹ and B. Bai¹

1. School of Electrical Engineering, Shenyang University of Technology, Shenyang, China

Abstract: In order to study the electromagnetic and vibration performance of transformer under different tensile and compressive stresses. This paper firstly studies the magnetic properties of core silicon steel sheets for transformers under different tensile and compressive stresses, the B-H curves, B-P curves, and permeability curves of silicon steel sheets under different tensile and compressive stresses are given. Secondly, based on the test results of magnetic characteristics of the silicon steel sheet, the electromagnetic performance and vibration of a 3kVA transformer are simulated and analyzed. In the simulation process, the influence of different tensile and compressive stresses on the performance of the silicon steel sheet core of the transformer is considered. It provides a new idea for the electromagnetic-vibration analysis of transformers.

1 Introduction The magnetostrictive property of silicon steel sheet is the main reason for the vibration and noise of electrical equipment such as transformers and reactors, and its characteristics are particularly sensitive to the mechanical stress[1]. Based on the analysis of the mechanism of core vibration noise and experimental verification, the influence of magnetic properties and magnetostrictive effect of electrical steel sheet on the performance of power transformer under different stress is studied. This paper, by using a magnetostriction stress effect of the magnetic properties of measuring equipment and measuring instrument system, on oriented silicon steel (brand: 27 sqgd090) along the rolling direction under different tension and compression stress and magnetic properties of magnetostrictive properties were tested and the research of silicon steel sheet under different tension and compression stress are given B-H curve, B-P curve and permeability curve and curve of single value, as shown in figure 1 flow chart of research. Secondly, based on the above-mentioned measurement results, the model material library was established. Based on the finite element analysis software COMSOL, the finite element analysis was carried out on a 3KVA transformer under different tensile and compression stress conditions. Finally, an experimental study is carried out to verify the correctness of the proposed scheme, which provides a reference for the study of power transformer vibration noise under different tension and compression stresses.

2 Simulation study of power transformer under different stresses The results obtained by substituting the magnetic characteristic curves in Fig. 1 into the transformer FEM model considering the boundary conditions are shown in Fig. 2. The compressive stress increases the magnetostriction, while the tensile stress reduces the magnetostriction, magnetostriction is particularly sensitive to the compressive stress. The stress reduces the magnetic conductivity of electrical steel sheet. When there is no external force, the maximum magnetic density reaches 1.7T.

3 conclusion In this paper, the magnetic characteristics and magnetostrictive characteristics of silicon steel sheet are measured firstly, and then the electromagnetic and vibration characteristics of power transformer under different stresses are studied by using finite element analysis software. The results show that the compressive stress increases the magnetostriction, and the tensile stress decreases the magnetostriction, and the compressive stress is especially obvious. Detailed test results and simulation analysis will be shown in the full text.

Anderson P I, Moses A J, Stanbury H J. An automated system for the measurement of magnetostriction in electrical steel sheet under applied stress [J]. Journal of Magnetism and Magnetic Materials, 2000, 215: 714-716.

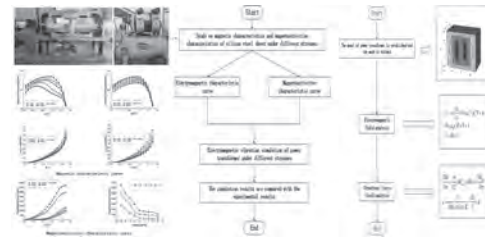


Fig.1 Research process flowchart

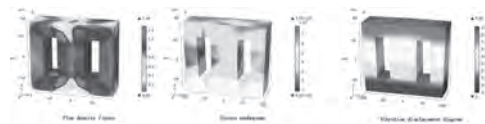


Fig.2 Simulation result

AS-14. Study of Magnetic Properties of Ultra-Thin Silicon Steel Sheet and Medium Frequency Transformer.

X. Cao¹, D. Chen¹, Y. Wang¹, S. Zhang¹ and B. Bai¹

1. School of Electrical Engineering, Shenyang University of Technology, Shenyang, China

To improve the thermal stability, reduce vibration/noise and system cost of mediate frequency transformers for DC-DC converters in low-voltage DC distribution networks. This paper presents a design study of a 20kW three-winding medium frequency transformer using 0.15mm oriented silicon steel sheet. First, the magnetic properties of silicon steel wafers at different frequencies were measured based on a single silicon steel wafer magnetic property measurement system, and the B-H curve, B-P curve and excitation curve at different frequencies were given. Next, a three-winding mediate frequency transformer with 537V input and 375V and 48V output is designed using particle swarm algorithm with loss minimization as the optimization objective, and finite element simulation and magnetic performance experiments are conducted. The flux density, loss and temperature field distribution curves of mediate frequency transformers under different operating conditions, and B-H curves, hysteresis lines and B-P curves at different frequencies are given. Finally, the experimental platform of DC-DC converter is built and its characteristics under different load conditions (no-load, rated load and overload) are experimentally studied to verify the correctness of the proposed scheme.

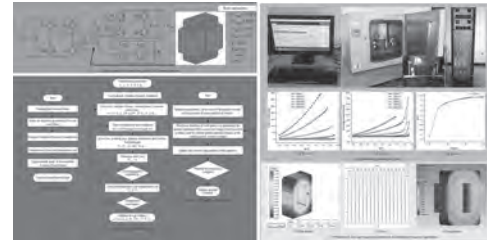
1. Introduction Compared with AC distribution networks, DC distribution networks have significant advantages in terms of distributed energy access, improving system efficiency, reducing line losses and operating costs, and increasing system capacity. As one of the main links of the DC distribution network, the bi-directional full-bridge converter (power electronic transformer), through the introduction of power electronic converters on the primary and secondary sides of the primary and secondary side of the voltage amplitude and phase of real-time digital control, compared to the traditional power transformer, power electronic transformer can be more accurate, flexible, stable and reliable regulation of the output side voltage^[1]. As shown in Fig. 1(a), the mediate frequency transformer, as an important component of the bi-directional DC-DC converter, has an important impact on the size, weight, loss, and price of the power electronics transformer^[2]. This paper takes low-voltage DC distribution network as the application background, converts PV power generation into DC 375V and DC 48V through DC-DC converter, and directly enters the home to supply power for TV sets, refrigerators, washing machines, lighting, etc. in the home, eliminating the loss generated by the AC-DC link and saving energy significantly. Fig. 1(b) shows the technical roadmap of this paper. Firstly, the topology of power electronic transformer is analyzed and bi-directional CLLC resonant converter topology is adopted. Secondly, the magnetic characteristics of 0.15mm electrical steel sheet are tested to lay the foundation for the subsequent design, performance analysis and prototype development of mediate frequency transformer. Then, the design study of mediate frequency transformer is carried out, and one three-port mediate frequency transformer is designed based on particle swarm optimization algorithm with loss minimization as the goal, and finite element analysis is carried out. Finally, a power electronic transformer is fabricated and experiments under no-load, load and overload are completed to verify the correctness of the proposed scheme.

2. Simulation and Experiment on the Medium Frequency Transformers Fig. 1 (c) shows the design process of the three-port mediate frequency transformer proposed in this article; Fig. 1 (d) shows the optimization flow chart of the mediate frequency transformer; Fig. 1(e) shows the 0.15mm electrical steel sheet test platform and test results; Fig. 1(f) shows the magnetic flux density, loss and temperature field distribution of the mediate frequency transformer. It can be seen from Fig. 1 that the medium frequency transformer has a flux density of 0.5T, core loss of 137W, copper consumption of 123W, and an average temperature of 84.4°C at rated load. The design scheme meets the system requirements.

3. Conclusion This paper has carried out systematic research work on power electronic transformers in low-voltage DC distribution networks. Based on the monolithic silicon steel wafer measurement system, the test work of magnetic characteristics of silicon steel wafers at different frequencies was completed. A 537V/375V/48V three-port mediate frequency transformer was designed with the goal of loss minimization. A three-dimensional finite

element model with electromagnetic-temperature field coupling was established to analyze the magnetic properties and temperature characteristics of the mediate frequency transformer under different operating conditions, which provides guidance for the design of the mediate frequency transformer. Detailed experimental results and comparisons are shown in the full paper.

[1] T. F. Wu, C. H. Chang, L. C. Lin. DC-Bus Voltage Control With a Three-Phase Bidirectional Inverter for DC Distribution Systems[J]. IEEE Transactions on Power Electronics, 2013, 28(4):1890-1899. [2] Posada Contreras J, Ramirez J M. Multi-Fed Power Electronic Transformer for Use in Modern Distribution Systems[J]. IEEE Transactions on Smart Grid, 2014, 5(3):1532-1541.



AS-15. Study of Loss and Temperature Considering Different Shielding Structure in Power Transformer.

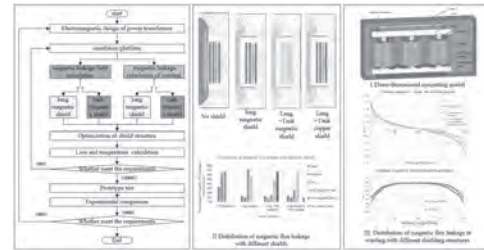
B. Bai¹, X. Cui^{1,2} and D. Chen¹

1. *Shenyang University of Technology, Shenyang, China*; 2. *Shenyang Institute of Engineering, Shenyang, China*

Abstract: This paper investigates and optimizes processes on the influencing of the magnetic shunts design to reduce the generated losses and temperature in power transformers are done. An 3D FEM model is established based on the OSFPSZ-200000/230 power transformer, considering the influence of magnetic flux leakage distribution with different shielding structure. Calculation and experiment of loss and temperature of power transformer are supplied to obtain the optimal shield structure, which are required for safe operation. Finally, the simulation results of the loss and temperature of the three-phase power transformer verified by the experimental results under the different shielding structure. 1Introduction Magnetic shielding is generally laid on the transformer tank and clamps to reduce the eddy current loss, which can prevent overheating. However, the leakage flux will be concentrated, if the design of the magnetic leakage shielding structure is unreasonable. Thus, it is necessary to analyze the the best geometrical size and electrical, magnetic, thermal, and mechanical considering different shielding structures effect. [1] is proposed that the the tank magnetic shields can reduce stray losses of structural parts, and horizontal shunts are as effective as vertical shunts in reducing stray load losses. However, he did not consider the effect of yoke shielding on the magnetic flux leakage distribution. Whereas, In [2], it is presented an application of yoke shunts to control the leakage flux on a case study transformer. However, the structure of yoke shielding is not reasonable, which results in the waste of materials. The effect of yoke shielding on the magnetic flux distribution at the end of the winding is not considered. In [3] a transient FEM analysis was used to optimize the magnetic shunts for minimum eddy current loss and temperature rise, considering different taps of the windings, without relevant experimental data to verify the theoretical analysis. This paper investigates the effects of different shielding structures on power transformer losses and temperature by theory analysis and experiment verification. As in the research flowchart of Fig.1, the shielding structure is optimized by analyzing the distribution of magnetic flux leakage and the distribution of magnetic flux leakage at the winding ends. Then based on the requirements of the IEC standard, the FEM model considering shielding structure is completed to judge whether the loss and temperature rise of the structural parts meet the requirements. If not, modify the shielding structure and perform FEM analysis again until the loss and temperature rise meet the requirements of the IEC standard. and modified for better performance. Simulation results of distribution of power transformer loss and hot spot are shown in Table 1, where the experimental results of the three-phase power transformer also lists to verify the simulation results. 2Simulation and experiment on power transformers with different shielded structures Established 3D model and shielding structure are shown in Figure 1-I. Divided four types shielding structure are shown in Figure 1. Calculated the leakage flux distribution of the transformer and winding with different shielding structures. The results are shown in Figure 1-II and Table 1. It shows that the improved structure of the shielding can effectively reduce the leakage flux into the structural parts(tank, lamp, pull plate), which can minish the loss of the structural parts, thus mitigating the extent of local overheating. Adding the lung magnetic shields can particularly effective influence the loss of structural parts. When the tank adopts magnetic shielding, it can significantly reduce the leakage flux into the tank. 3Conclusion This paper investigates the losse and temperature of power transformers considering the different shielding structures. The coupled 3D-FEM model in electromagnetic-temperature field is established based on OSFPSZ-200000/230 power transformer. The leakage flux distribution of the transformer and winding analyzed, which provides guidance for the usual transformers magnetic shielding design. It shows that the temperature simulation is in a reasonable agreement with the experimental (error=4.8%), verifying the validity of the proposed method. Detailed experimental results and comparison will be shown in the full paper.

[1] M. Moghaddami, A. I. Sarwat, and F. de Leon. Reduction of Stray Loss in Power Transformers Using Horizontal Magnetic Wall Shunts,

DOI 10.1109/TMAG.2016.2611479, IEEE Trans. Magn., 2016. [2] Leonardo Štrac, Three-Phase Shunts for Stray Magnetic Field, Procedia Engineering 202, pp. 183–188, 2017. [3] H. Yang and Y. Zhang, Analysis on the magnetic shunt structure of large power transformer, IET Generation, Transmission & Distribution, vol. 12, no. 11, pp. 2755-2761, 2018. (doi: 10.1049/iet-gtd.2017.1490)



Item	100% load	Simulation	130% load	loss	Experiment
Flux density distribution (T)				Core loss: 1.2W Winding loss: 1.5W Total loss: 2.7W	
Temperature field distribution (°C)				Core temperature: 65°C Winding temperature: 75°C Tank temperature: 55°C	

AS-16. Research on Structure Loss Separation of Power Transformer.

X. Cui^{1,2}, D. Chen¹ and B. Bai¹

1. Shenyang University of Technology, Shenyang, China; 2. Shenyang Institute of Engineering, Shenyang, China

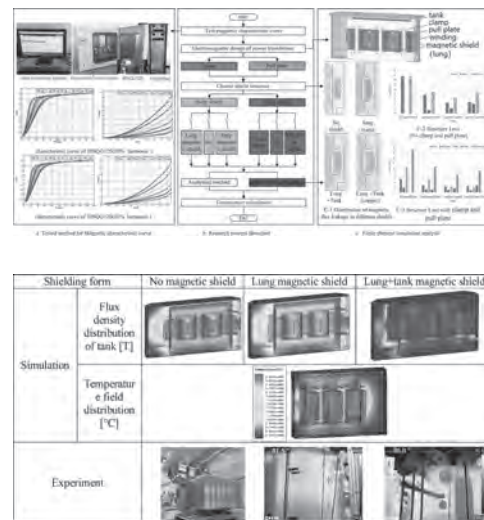
Abstract: How to effective control losses of large power transformer, such as tank and structural parts, shielding and others, which is significant to reduce the manufacturing cost of power transformer and the safety of network operation. Based above, this paper investigated on the structural parts (pull plates, clamps and others) loss of power transformer with analytical and experimental method under different harmonic conditions. First, measured the B-H, B-P and permeability curves of different materials (silicon steel sheet, non-magnetic steel and steel) under different frequencies. Second, established the loss calculation model of power transformer based on analytical method; at the same time, calculated the losses of the structural parts under different shields with the finite element method. Finally, an experimental study is carried out to verify the correctness of the proposed simulation results.

1 Introduction Due to the increasing of the capacity of power transformer, the leakage magnetic field and the effect of the stray loss caused in the tank and structural parts have increased significantly. It is contrary to the national policy of “energy saving priority” for sustainable development. Therefore, it has great potential for energy saving by reducing structural parts loss. So, it is significance for analysising the leakage magnetic field, eddy current loss and temperature field of the tank and the internal structural parts of transformer deeply and accurately. At present, domestic and foreign scholars have carried out extensive research work on electrical steel sheets for electromagnetic devices. In reference [1], the magnetic properties of oriented silicon steel sheets under different temperature and harmonic conditions were tested. The magnetic properties of electrical steel sheet for transformer are studied in reference [2,3]. In [4], the horizontal mounted tank magnetic shunts were proposed to reduce stray losses in power transformers. But there is no comparative analysis of different shielding structures. In [5] a transient FEM analysis was used to optimize the magnetic shunts for minimum eddy current loss and temperature rise, considering different taps of the windings, without relevant experimental data to verify the theoretical analysis. This paper investigates the loss of structural parts with different structures and materials under different shielding structures, through theoretical analysis and experimental verification. As shown in Figure 1, first, measured the B-H, B-P and permeability curves of different materials under different frequencies. Second, designed structural parts and shielding structure, then optimize the shielding structure by analyzing the distribution of magnetic flux leakage, adopt 3-D FEM analysis and analytical method to calculate the loss and temperature of the power transformer, then judge the loss and temperature rise of the structure based on the requirements of the IEC standard. If not, the shielding structure is modified, and do it again until the loss and temperature rise meet the requirements. Finally, an experimental study is carried out to verify the correctness of the proposed simulation results. The simulation results of power transformer loss distribution and hot spot distribution are shown in Table 1, which also lists the experimental results of the three-phase power transformer.

2 Simulation and experiment on the loss of power transformer Substitute the data of B-H and B-P curves from Fig.1 (a) into the FEM model of transformer in Fig.1 (c) considering different shielding condition, then the results can be obtained as in Table 1 and Fig.1 (c). It can be seen from Fig.1 (a) results that when the harmonic content is a constant, with the increase of the harmonic power, the magnetic permeability of the silicon steel sheet will gradually decrease, and the loss will gradually increase obviously. It can be seen from Fig.1 (c) the calculation results: 1) In the case of each shielding structure, the total loss with clamps and pull plates is higher than without them, but the structural loss of tank is the opposite. So, it is difficult to directly measure the stray loss, and it is also difficult to accurately separate the loss on the component from the total loss. 2) With the addition of body shielding, the total loss of structural parts will be reduced by 17.1%-21%, so a reasonable arrangement of the shielding structure will effectively reduce structural parts loss and hot spot temperature rise. 3) Whether to use magnetic shielding, it is still necessary to consider the increase in magnetic shielding loss and the decrease in tank loss, as well as the shielding material and size. Specific comparison data will be given in the full text. 4) The magnetic shielding effect of tank is better

than the copper shielding. 3 Conclusion This paper investigates the losses of transformer structural parts (pull plates, clamps and others) considering the different structural parts, materials and shielding structures from two methods (FEM and analytical). The coupled 3D-FEM model in electromagnetic- temperature field is established based on SZ-50000/110 model. The structural losses calculation results of FEM method, analytical method and experimental results are compared and analyzed, which provides guidance for the usual transformers design. It shows that the loss simulation is in a reasonable agreement with the experimental one (error=5.9%, error <7K), verifying the validity of the proposed method. Detailed experimental results and comparison will be shown in the full paper.

[1]Chen D., Fang L., Kwon B I., et al: Measurement research on magnetic properties of electrical sheet steel under different temperature, harmonic and dc bias. *AIP Advances*, 7.5 (2017), 056682. [2]Oda, Yoshihiko, M. Kohno, and A. Honda: Recent development of non-oriented electrical steel sheet for automobile electrical devices. *Journal of Magnetism & Magnetic Materials*, 320.20 (2008), 2430-2435. [3]Freitag, C, C. Joost, and T. Leibfried: Modified Epstein frame for measuring electrical steel under transformer like conditions. *International Conference on High Voltage Engineering & Application*, (2014), 1-4. [4]M. Moghaddami, A. I. Sarwat, and F. de Leon, “Reduction of Stray Loss in Power Transformers Using Horizontal Magnetic Wall Shunts”, DOI 10.1109/TMAG.2016.2611479, *IEEE Trans. Magn.* 2016 [5]H. Yang and Y. Zhang, “Analysis on the magnetic shunt structure of large power transformer”, *IET Generation, Transmission & Distribution*, vol. 12, no. 11, pp. 2755-2761, 2018.



Session AT
MAGNETIC BEARINGS AND MAGNETIC LEVITATION
(Poster Session)

Somporn Ruangsinchaiwanich, Chair
Naresuan University, Thailand, Phitsanuloke, Thailand

AT-01. New Levitation Scheme With Traveling Magnetic Electromagnetic Halbach for EDS MAGLEV System.

W. Qin¹

1. Electrical Engineering, Beijing Jiaotong University, Beijing, China

I. INTRODUCTION The Maglev train have aroused worldwide research efforts due to numerous advantages over the conventional wheel-on-rail system, such as less maintenance costs, lower noise and vibration, higher grades and curves and so on [1-3]. There are two types of levitation technologies: 1) electromagnetic suspension; 2) electrodynamic suspension; The EDS system is based on a repulsive force of magnets. Therefore, EDS, which is highly suitable for high-speed operation and freight, is so stable magnetically that it is unnecessary to control the air gap. Because of its significant advantages of high speed, large levitation gap and no need for any active control, the EDS train has attracted a wide research [4-5]. However, this system needs sufficient speed to acquire enough induced currents for levitation and so, a wheel like a rubber tire is used below a certain speed (around 100 km/h). This paper proposes a new EDS MAGLEV scheme which needs no auxiliary wheels. II. MACHINE TOPOLOGIES The configuration of the EDS maglev system is shown in Fig. 1(a). The main structure of this maglev system includes one mover (primary) and one stator (secondary). In order to increase the thrust density as possible, a novel Traveling Magnetic Electromagnetic Halbach Array (TMEHA) was proposed to the EDS maglev as the primary windings, of which is composed of three-phase windings. Three phase coils are displaced symmetrically at every 120 electrical angle and the current waveform in the phases is a 120 wave. Each phase winding consists of two coils and the coils are divided into two general arrangements, i.e., vertical-piece and horizontal-piece arrangements. The vertical-piece arrangement is spatially displaced by 90 electrical angle from horizontal-piece arrangements. The TMEHA, of which has inherent self-shielding property shown as in Fig. 1(b), have ability for creating magnetic flux enhanced on one side (strong side) of the array while the flux cancelled on the other side (weak side). By placing the windings as Traveling Magnetic Electromagnetic Halbach Array, the higher flux density and more sinusoidal magnetic Field in the air-gap (strong side) can get as possible than rectangular coil forms, so that the thrust density is increased and ripple decreased. Therefore, the proposed TMEHA is suitable for the future ultra-high-speed transportations because of high thrust density and low ripple. The secondary made of Aluminum or copper facing the primary windings embedded in ground. Different geometric of the winding will generate different air gap magnetic and influence the performance of the EDS maglev system. The vertical-piece and horizontal-piece arrangements in TMEHA can be utilized in a few different manners. The arrangements options focusing on the offset, shown as in Fig. 1(c), between the vertical-piece and horizontal-piece are investigated in full paper in detail. III. RESULTS AND VALIDATION By using an improved analytical method and the 2-dimensional finite element analysis (2D-FEA), the dimensional parameter optimization design of the proposed EDS maglev system is conducted, and the performance comparison with a conventional primary with core is also carried out to prove the TMEHA superiority of the proposed design (not shown here due to space limits). Finally, a prototype is fabricated for experimental testing, shown as in Fig.2(a), and the measured results are in good agreement with the FEA and analytical method, shown as in Fig.2(b), which verifies the validity of the proposed EDS maglev system topology and its theoretical flux-regulation principle analysis. More results will be present in the full paper.

[1]K. Dong-Hun, L. Ji-Kwang, H. Song-Yop, *IEEE Trans. Magn.*, vol. 32, no. 5, pp. 5151-5153, 1996. [2] J. Z. Bird, *2019 12th International Symposium on Linear Drives for Industry Applications (LDIA)*, pp. 1-6, 1-3 July 2019 2019. [3]T. Gong, G. Ma, Y. Cai, *IEEE Transactions on Applied Superconductivity*, vol. 29, no. 5, pp. 1-6, 2019. [4] T. Fujimoto, M. Aiba, T. Umeki, H. Suzuki, and S. Nakamura, J-STAGE Quarterly Report of RTRI, vol. 41, no. 2, pp. 63-67, 2000. [5] K. Kuwano et al., *IEEE Trans. Appl. Supercond.*, vol. 17, no. 2, pp. 2125-2128, 2007.

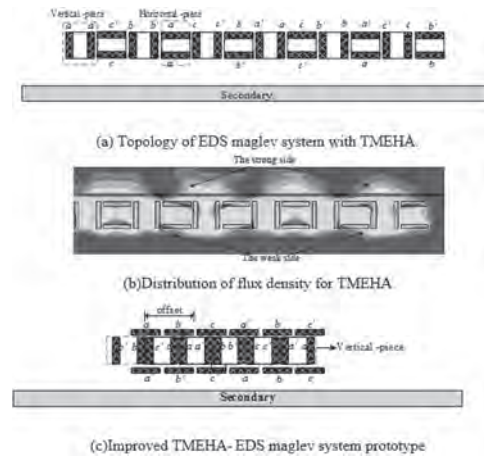


Fig.1 Proposed EDS maglev system configuration

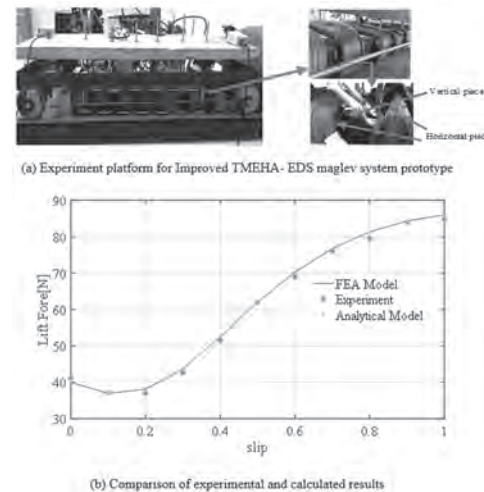


Fig.2 Proposed EDS maglev system prototype and part of results.

AT-02. Levitation Force and Lateral Force Analysis of a Large-Load Magnetic Levitation Gravity Compensator With Two-Dimensional Permanent Magnet Array.

H. Zhang¹, L. Zhou¹, B. Kou¹ and Y. Liu¹

1. Harbin Institute of Technology, Harbin, China

I. Introduction Magnetic levitation technologies are widely used in many fields, such as the electromagnetic bearings in high-speed compressor, the maglev in transportation, and the magnetic levitation planar motor in ultra-precision positioning systems. In addition, there are also potential application for magnetic levitation technology in some special fields [1-6]. For instance, the passive magnetic force between permanent magnets could be used to compensate the gravity of the large optical loads to achieve the ground test. Compared with the air bearings or air springs, the magnetic levitation gravity compensator (MLGC) can realize multiple degrees of freedom and vacuum compatibility. Furthermore, the complex air supply system can be removed. According to Earnshaw's theorem, the stable levitation state cannot be realized only with permanent magnets. Therefore, the non-contact actuators are required to achieve the active control. Generally, a constant passive levitation force within effective stroke is expected in order to reduce the active force level and the volume of the actuators. In this paper, a large-load magnetic levitation gravity compensator with two-dimensional permanent magnet array is analyzed in aspects of levitation force and lateral force.

II. Topology and Model The large-load MLGC composed of three two-dimensional permanent magnet arrays. The middle PM array is the mover. The top PM array and bottom PM array are the stator. The mover is attracted by the top stator and repelled by the bottom stator, so a levitation force can be generated to compensate the load mass [7]. Each PM array are composed of 36 pieces of cuboid PM distributed in a checkerboard pattern. Basically, the passive force between two cuboid PM can be calculated using the magnetic charge model [8-9] or the equivalent current model. However, the relative permeability in both two classical models is assumed to 1.0, which causes a negligible error for MLGC. In [10], the actual working point of PM in magnetic spring is considered, using which the accurate model of the large-load MLGC can be built. III. Levitation Force and Lateral Force Analysis In this section, the influence of the parameters on the levitation force level and levitation force variation are analyzed based on the model and FEM. The levitation force level of the large-load MLGC is determined by some structural parameters. Compared with the PM thickness and pole arc coefficient, the pole pitch and air gap length are two critical parameters to decide the levitation force level. When the structural parameters are selected, the levitation force with different vertical and lateral displacement are analyzed. The maximum and minimum levitation force within 2mm vertical displacement is 17282N and 17155N. The maximum and minimum levitation force within 2mm lateral displacement is 17155N and 17108N. The change rate of levitation force is less than 1%. Additionally, the value of the lateral force is also very low. However, it should be noted that the lateral force increases with the increase of the vertical displacement. The maximum lateral force is 102N within 2mm lateral displacement when the vertical displacement is 1mm. IV. Experiment To verify the accuracy of the model and the correctness of the related analysis, a prototype of the large-load MLGC is manufactured. In order to maintain the relative position of the PM in each layer, all of the PM are inserted into the slots of aluminum plates. As shown in Fig. 1, the testing platform consists of base plate, adjusting bolts, multimeter, load sensor, sensor transmitter and power supply, in which the adjusting bolts are used to change the vertical displacement of the large-load MLGC. The measurement range of the load sensor is 25000N. To improve test accuracy, the components on the test platform should be made of non-magnetic materials as many as possible. As shown in Fig. 2, the levitation force increases with the vertical displacement, and the test value of the levitation force in the center position is 16860N. the error between the experiment and FEM is less than 2%. The levitation force variation within 2mm vertical displacement is 1.2%.

V. Conclusion In this paper, a large-load magnetic levitation gravity compensator is analyzed and tested. To achieve a high levitation force, the 2-D permanent magnet array are used. To reduce the levitation force variation, the double-sided stator is applied. The ultimate load capacity of the prototype is 16860N (i.e., 1720kg). The testing results match well with the 3D FEM.

- [1] W. Robertson, B. Cazzolato, and A. Zander, *IEEE Trans. Magn.*, vol. 41, no. 10, pp. 3826–3828, Oct. 2005. [2] S. A. J. Hol, E. Lomonova, and A. J. A. Vandepuut, *Precision Eng.*, vol. 30, no. 3, pp. 265–273, Jul. 2006. [3] H. Zhang, B. Kou, Y. Jin, *IEEE Trans. Magn.*, vol. 50, no. 11, pp. 8001304, Nov. 2014. [4] H. Zhang, B. Kou, Y. Jin, *IEEE Trans. Ind. Electron.*, vol. 62, no. 6, pp. 3629–3639, Jun. 2015. [5] J. L. G. Janssen, J. J. H. Paulides, J. C. Compter, *IEEE Trans. Magn.*, vol. 46, no. 6, pp. 1748–1751, Jun. 2010. [6] J. L. G. Janssen, J.J.H. Paulides, E.A. Lomonova, *Mechatronics*, vol. 23, no. 2, pp. 197–203, Mar. 2013. [7] H. Zhang, B. Kou, Y. Zhou, *ICEMS Conference, Harbin, 2019*. [8] M. F. J. Kremers, J. J. H. Paulides, E. Ilhan, *IEEE Trans. Magn.*, vol. 49, no. 5, pp. 2299–2302, May. 2013. [9] J. M. M. Rovers, J. W. Jansen, and E. A. Lomonova, *IEEE Trans. Magn.*, vol. 49, no. 6, pp. 2913–2919, Jun. 2013. [10] H. Zhang, B. Kou, L. Zhou, *IEEE Trans. Magn.*, Early Access, Nov. 2020.

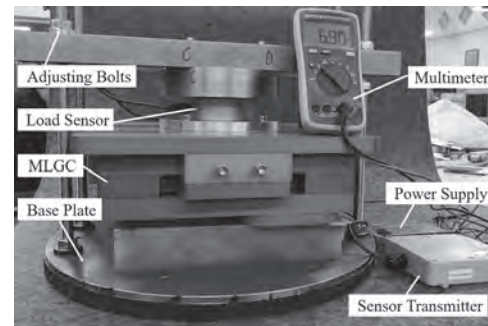


Fig. 1. Prototype and testing device of the large-load MLGC.

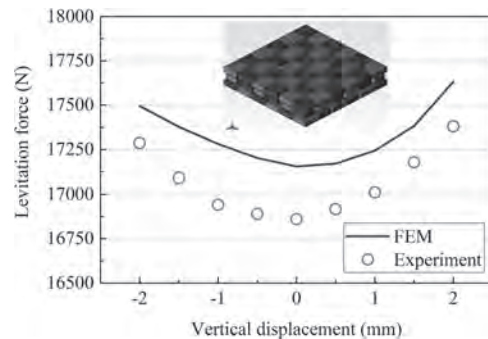


Fig. 2. Comparison of the levitation force characteristic curves.

AT-03. Modeling and Finite Element Analysis on the Novel Double-Stator Hybrid Magnetic Bearing.

X. Ye¹, Z. Wang¹, T. Zhang¹ and Q. Lu¹
 1. Huaiyin Institute of Technology, Huai'an, China

I. Introduction Magnetic bearing (MB) is a new support bearing, which can suspend a rotor in the space by magnetic forces without machinery contact between the rotor and the stator. It has the advantages of no-friction, no-abrasion, high precision of rotor position, support high speed rotor, no-lubricant. The MBs have a wide application prospect in the fields of energy, transportation, machinery, life science. At present, the permanent magnet in hybrid magnetic bearings (HMBs) is adopted to produce the bias magnetic field, which saves the energy, reduces the size and improves the bearing capacity. However, the structure of the traditional HMBs is single-rotor or single-stator, and the radial suspension force is only produced on the inner or outer of the rotor. It leads to the low suspension force density, which makes it difficult to satisfy the performance requirements of some special applications. Therefore, the aim of this work is the investigation of a novel double-stator hybrid magnetic bearing to solve this drawback. This DSHMB consists of an inner stator and an outer stator, which are designed to share the same rotor. It has the compact structure and can decrease the power consumption. In addition, the control windings are wound on the outer stator and the inner stator so that it can reduce the axial length and increase the radial bearing capacity. The model of proposed DSHMB is constructed and analyzed by the method of equivalent magnetic circuit. Then, the air-gap magnetic fields and radial suspension forces are analyzed through 3-D finite element analysis (FDA). The research results prove the correctness of the structure and suspension principle of this novel DSHMB.

II. Configuration and Suspension Principle Fig.1 shows the configuration of the proposed DSHMB which consists of double stator cores, two axial magnetized permanent magnets (PMs) and a rotor core. Each stator core has four stator poles. The inner stator and the outer stator place the relative position. The rotor core is separated into two blocks by the nonmagnetic material between double stator cores. Two PMs are located between two outer and inner stator cores. Two PMs have opposite magnetization directions. Radial control windings are wound on the inner and outer stator poles. The magnetic circuit of the static bias flux and radial suspension control flux is shown in Fig.1. The static bias flux is generated by the magnetized permanent magnet ring, and the radial suspension control flux is generated by radial control coils. The static bias flux and the control flux are superimposed or subtracted in each air gap. When the rotor suspends stably, the rotor locates in the center under the action of the static magnetic suction produced by permanent magnet. Based on the equivalent magnetic circuit analysis, the mathematical models of suspension force are deduced. The radial suspension force can be written as $F_j = k_j \times j + k_{ij} \times ij$ (1) where the subscript "j" denotes x and y. k_j is the radial force-displacement stiffness. k_{ij} is the radial force-current stiffness. k_j and k_{ij} can be given as $k_j = F_m \times F_m \times \mu_0 \times S_i \times S_o \div [2g(S_i + S_o) \times (S_i + S_o)]$ $k_{ij} = F_m \times \mu_0 (N_i S_i + N_o S_o) \div [g^2(S_i + S_o)]$ where F_m is the magnetic potential of permanent magnets. μ_0 is vacuum permeability. S_o is the outer pole face area. S_i is the inner pole face area. g is the average length of inner and outer air-gap. radial air gap length. N_i is number of inner radial control coils. N_o is number of outer radial control coils. III. Models, Design and Analysis According to the 3D model, the distribution of the flux in different cases is obtained by finite element analysis. Fig.2 (a) shows the bias flux distribution. The magnetic flux is symmetrical in the radial direction, and the permanent magnetic induction of each air gap is equal. Fig.2 (b) shows the magnetic density diagram generated only by the control current in the X direction. The excitation current of 3 A is applied to the radial control winding according to the design result. As can be seen from Fig.2 (c), the resultant magnetic density diagram is generated by the control current in the X direction and the permanent magnet ring. The control flux and the bias flux overlap increases in positive X direction, while overlap decreases in negative X direction. The inner and outer air gap bias flux density has the same magnitude. Therefore, the correctness of magnetic circuit and suspension mechanism is proved. The force-current relationships are measured on a four-pole DSHMB in Fig. 2 (d). Inject control current into radial control windings in the X direction from 0 to 3 A. It can be seen that the finite element simulation results are in good agreement with the theoretical values. The trends of suspension force-current

curves are the same. IV. Conclusion The flux distribution and suspension force in proposed DSHMB are calculated and analyzed in this paper. The inner and outer stators are designed to produce the larger suspension force at the same time. It can be seen that the final scheme can meet the design indexes proposed in the beginning with the mathematical models of suspension force and the verification by finite element calculation.

[1]D. Ning, H. Kai, and J. Long, "Review on High Speed Permanent Magnet Machines Including Design and Analysis Technologies," in *Proceedings of the CSEE*, vol. 34, no. 27, pp. 4640-4653, Sep, 2014. [2]J. Ju, H. Zhu and C. Zhao, "Radial Force-Current Characteristic Analysis of Three-Pole Radial-Axial HMB," *2016 IEEE Vehicle Power and Propulsion Conference (VPPC)*, Hangzhou, 2016, pp. 1-6. [3]R. Zhu, W. Xu, C. Ye, J. Zhu, G. Lei and X. Li, "Design Optimization of a Novel Heteropolar Radial Hybrid Magnetic Bearing Using Magnetic Circuit Model," in *IEEE Transactions on Magnetics*, vol. 54, no. 3, pp. 1-5, March 2018, Art no. 8201105.

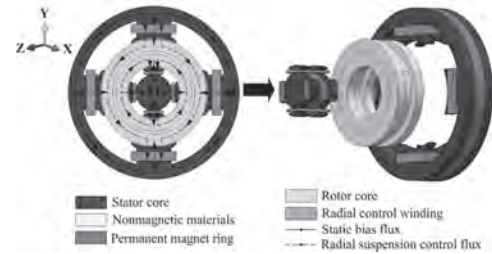


Fig. 1. Structure and magnetic circuit of the proposed DSHMB.

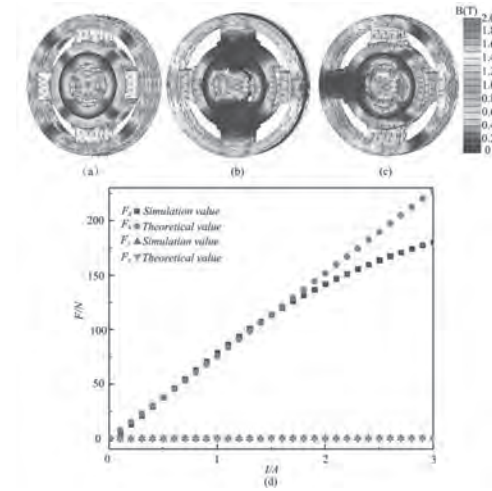


Fig. 2. Flux distribution and the force-current relationships.

AT-04. Electromagnetic Analysis of a Novel Axial-Radial Four-Pole DC Hybrid Magnetic Bearing.

S. Wu¹, Z. Wang¹ and T. Zhang¹

1. Huaiyin Institute of Technology, Huaian, China

I. Introduction Hybrid Magnetic bearing (HMB) is a kind of high-performance bearing which can realize magnetic suspension of the rotor without mechanical contact. Therefore, it has many advantages, such as no contact, no friction, no lubrication, low noise and so on. It has been widely employed in some industrial applications, such as flywheel energy storage system, compressor and turbine. HMBs have easier controllability and higher stiffness than the passive magnetic bearings. However, the area of magnetic pole is small, which make a small magnetic force. In addition, the traditional HMBs has the shortcoming of low mechanical strength. To solve these drawbacks, an improved axial-radial four-pole DC HMB with integrated stator poles is put forward in this paper. Moreover, compared with the existing radial four-pole three degrees of freedom HMBs, it can effectively increase the radial magnetic pole area, thus increasing the suspension force. The structure and working principle of the designed HMB is introduced, and its mathematical model is also derived. The prototype is established by finite element analysis. The electromagnetic simulation is carried out by software MagNet 3D to verify the theoretical analysis. II. Configuration and Suspension Principle As shown in Fig. 1 (a), the proposed HMB is composed of axial stator, radial stator, four radially magnetized permanent magnets (PMs) and a rotor. The radial stator and PM are divided into four parts by four non-magnetic materials. The outer of each stator core is provided with four axial cores. Radial control coils are wound on eight axial cores. In the proposed HMB, the static bias flux is generated by the radial magnetized PMs. Radial and axial control flux is generated by radial and axial control coils. The magnetic circuit is shown in Fig.1 (b). If an external force acts on the rotor and the rotor move to one direction, control current is applied to generate the control flux. The control flux adds to the static bias flux in the opposite direction, and then an active restoring force will bring the rotor back to the equilibrium position. According to the equivalent magnetic circuit method, the axial suspension force in the Z direction and the radial forces in the X and the Y directions are deduced as follows: $F_z = k_z \times z + k_{iz} \times i_z$, $F_j = k_{ij} \times j + k_{ij} \times i_j$, $K_z = -F_m \times F_m \times \mu_0 \times \{ [g_z \div S_z + 2g_r \div (3S_r)] 2g_z \times S_z \}$, $K_{iz} = F_m \times N_z \times \mu_0 \div \{ [g_z \div (2S_z) + g_r \div (3S_r)] \times g_r \}$ where the subscript "j" denotes x, and y. k_j is the radial force-displacement stiffness. k_{ij} is the radial force-current stiffness. k_z is the axial force-displacement stiffness. k_{iz} is the axial force-current stiffness. F_m is the magnetic potential of permanent magnets. μ_0 is vacuum permeability. S_m is radial magnetic pole area. g_r is radial air gap length. g_z is axial air gap length. N_r is number of radial control coils. N_z is number of axial control coils. III. Models, Design and Analysis The electromagnetic performances of the proposed HMB are analyzed by MagNet 3D, which verifies the correctness of the structure and suspension mechanism. The distribution of the flux in different cases is shown in Fig.2. Fig. 2(a) shows the bias flux distribution produced by the PMs. The values under four suspension poles are approximately equal. When current is only applied to the radial control coils to generate the force in the X direction, the distribution of control flux is illustrated in Fig.2 (b). Fig. 2 (c) shows the radial resultant flux distribution. The bias flux is superimposed by the control flux in the radial air gap for producing the radial suspension force in the positive X direction. Fig. 2(d) shows the axial resultant flux distribution, in which the axial suspension force is produced in the negative Z direction. Therefore, the correctness of magnetic circuit and suspension mechanism is proved. Fig. 2(e) demonstrates the calculated radial and axial force-current relationship curves respectively. The simulation value is close to the theoretical value. The suspension forces of the proposed HMB are changing linearly with the control current. IV. Conclusion This paper presents a novel axial-radial four-pole DC HMB with integrative stator poles. The area of the radial suspension poles is to the maximum, thereby effectively improving the radial suspension force. The research results verify the correctness of magnetic circuit, suspension mechanism and mathematical model.

[1]H. Q. Zhu, Y. X. Shen, and Q. H. Wu, "Modeling and control system for AC hybrid magnetic bearing," Proceedings of the CSEE, vol 29, no. 18, pp. 100-105, 2009. [2]J. Ju, H. Zhu and C. Zhao, "Radial Force-Current

Characteristic Analysis of Three-Pole Radial-Axial HMB," 2016 IEEE Vehicle Power and Propulsion Conference (VPPC), Hangzhou, 2016, pp. 1-6.

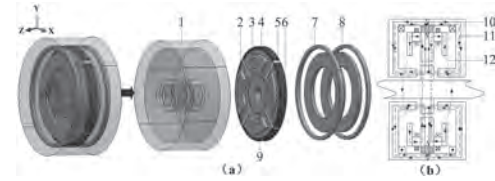


Fig. 1. Structure and magnetic circuit of the HMB. (a) Structure. 1-axial stator, 2-radial control coil, 3-axial core, 4-radial stator, 5-non-magnetic material, 6-permanent magnet ring, 7-axial control coil, 8-non-magnetic part, 9-rotor core, 10-static bias flux, 11-axial control flux, 12-radial control flux. (b) Magnetic circuit.

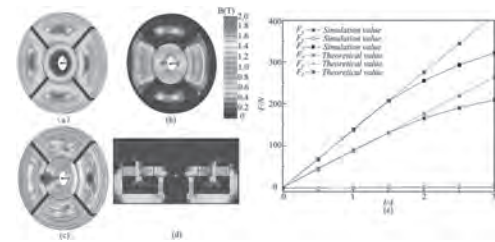


Fig. 2. Flux distribution and the force-current relationships.

AT-05. Development of a 120W Bearingless Maglev Motor for Centrifugal Pumps.

C. Wang¹, S. Nain¹, S. Liou¹ and G. Chen¹

1. Industrial Technology Research Institute, Hsinchu, Taiwan

For the past two decades, conventional centrifugal pumps continued to face the challenge. Lubrication oil and fluid leakage cause pump failures. The conventional centrifugal pump separates the pump and the motor, and it needs a seal placed between the shaft and the pump housing. As the seals age and harden, it results in leakages. According to the studies [1], in the chemical industry, 80% of centrifugal pump failures are caused by the mechanical seals, and 20% are caused by bearing, couplings and others. It is possible to remove the seal by using 2-in-1 pump and canned motor design or a magnetic coupler, but sleeve bearings are needed. Chemical slurries such as CMP slurry aid cooling and lubricating the sleeve bearings. They generate abrasive particles stuck in the gap between the bearing and the shaft. The condition accelerates bearing wear. To eliminate the problem of bearing wear, bearingless maglev motors (BLMMs) [2]-[4] have recently emerged as a potential alternative solution in the chemical pump market. Although, there are other alternative solutions [5], BLMM meets the size and the energy saving demand of the market. Centrifugal pumps with BLMM can be totally bearing free. BLMM centrifugal pumps are contactless, oil-free, particle-free, compact, cost-effective, and produce much lower vibrations. Our institute is devoted to developing BLMM for use in centrifugal pumps. The target of the first phase is to develop the BLMM with a maximum shaft output power and speed of the motor which are 120W and 5,000 rpm. However, high-speed, high-power density BLMM has levitation stability, thermal, and centrifugal stress issues which may result in unstable levitation, permanent-magnet (PM) demagnetization[6], and blade deformation. In addition, the coupling effect between magnetic circuits of magnetic bearing and motor has to be considered. Therefore, the main goal of this paper is to propose a total solution to overcome the aforementioned issues. We present the design, analysis, fabrication and test results of our BLMM pump prototype. Due to the non-linear nature of the rotor position sensors, we designed a tunable eddy-current sensor with a sensing circuit which incorporates control algorithms from a digital signal processor (DSP). A measurement method for validating the linearity and sensitivity of a single-pair position sensor (Fig. 1) is demonstrated in this paper. After the position of the rotor is correctly detected, the rotor is levitated with precision bearingless levitation control which includes start up, steady state, dynamic, and shut down processes. Furthermore, key magnetic indices such as current density, torque ripple to output torque ratio, back-EMF are calculated to evaluate motor performance. CFD and mechanical analysis and simulations are completed to predict static and dynamic stabilities at high-speed revolution to demonstrate the thermal distribution, shear strength, unbalance, and deformation of the PM blade. The heat sources of whole system are also monitored to avoid PM demagnetization and system failure. A new BLMM centrifugal pump (Fig. 2) with a delta pressure of 0.36 bar and a flow rate of 5 LPM is designed based on our analysis, and a rotor orbit < 20% radial air gap can be maintained at 120W/5,000 rpm.

[1]R. Schob, World Pumps, Vol. 2002, p. 34 (2002). [2]S. Silber, W. Amrein, and P. Boesch, IEEE Trans. on Mechatronics, Vol. 10, p. 611 (2005). [3]X. Sun, L. Chen, and Z. Yang, IEEE Trans. Ind. Electron., Vol. 60, p. 5528 (2013). [4]J. Asama, D. Kanehara, and T. Oiwa, IEEE Trans. Ind. Appl., Vol. 50, p. 288 (2014). [5]D. Guangren and D. Howe, IEEE Trans. on Control Systems Technology, Vol. 11, p. 204 (2003). [6]R. N. Johnson, G. B. Kliman, and Y. F. Liao, U.S. Patent 5 801 470 (1998).

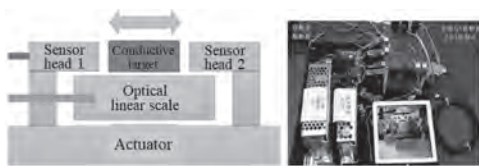


Fig. 1. Position sensor test rig.

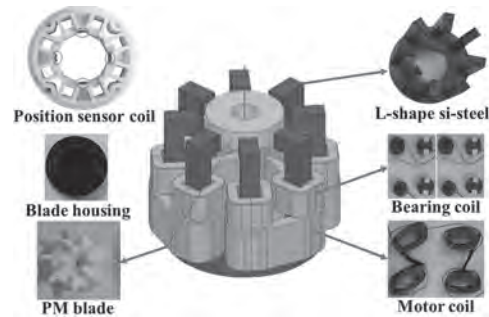


Fig. 2. BLMM components.

AT-06. Design of the HTS Magnetic Bearing Rotor Incorporated the Secondary of the Induction Motor.

M. Minamitani¹, S. Takimura¹ and S. Ohashi¹
 1. Kansai University, Suita, Japan

The magnetic levitation using the pinning force of the high temperature superconductor (HTS) has an advantage to achieve stable levitation without control. Applications for the contact less magnetic bearing system have been developed [1][2]. For example, there is application to a flywheel electric power storage device. In this study, the magnetic bearing using the HTS has been developed. The rotor is supported by the pinning effect of the HTS. The rotor is rotated using the principle of induction motor. An iron core with a slot, and a winding with distributed winding are installed on the fixed side. The rotor is rotated by a rotating magnetic field from the stator. A rotating field is generated by applying a three-phase voltage to the stator. The rotating field generates an eddy current in the aluminum part on the outer periphery of the rotor, and torque is generated. On the other hand, the flux inside the rotor is disturbed by the influence of the rotating field. Therefore, it is necessary to examine the effects of rotational torque and rotating field on the rotor when using an induction motor. This paper proposes the design of HTS magnetic bearing rotor incorporated the secondary of the induction motor. In this study, the yoke equipped ring type rotor is proposed. Fig. 1 shows the system of the yoke equipped ring type rotor. In this rotor, the ring type permanent magnet is covered the yoke to increase the linkage flux to the HTS. The flux is distributed widely because of the ring type permanent magnet. The flux of this rotor is concentrated to the outer peripheral part of the HTS[3]-[5]. In this rotor, the aluminum is installed to generate torque from the rotating field. The flux of the permanent magnet is disturbed by the effect of the rotating field generated from the stator. To solve this problem, the iron is installed as a shield and it is defined as the magnetic shield. The air gap and the magnetic shield are attached between the yoke and the aluminum. The magnetic shield and the air gap are used to guide the rotating field to the outside without getting inside the rotor. The air gap increases the reluctance and suppresses the flux from the inside of the magnetic shield toward the yoke. As a result, the influence of the rotating field on the inside the rotor decreases. The diameter of this magnetic circuit is 86[mm]. If the rotor becomes large than the HTS, the stability decreases. Total diameter of this rotor is 100[mm] in consideration of the HTS whose diameter is 80[mm]. The thickness of the aluminum W_{Al} , the magnetic shield W_{Shield} and the air gap W_{Air} are defined. These W are changed, and the effect of the torque generated by the rotating field, and of the rotating field on the magnetic circuit are considered. However, total width W makes 7[mm], and the levitation gap between the upper surface of the HTS and the lower surface of the rotor is 10[mm]. In addition, the analysis is performed using the 3D FEM software JMAG Designer. The analysis conditions are coil current 4[A], frequency 60[Hz] and the number of turns 300[turn]. And the rotation conditions are sliding $s = 0.01$ that provides sufficient torque, and the number of rotations 1782[rpm]. The thickness of the aluminum W_{Al} is changed. At that time, the generate rotational torque is analyzed. The torque of the three-phase induction motor using in this experiment is 0.25 [Nm]. It is converted torque value into dimension of the rotor. When W_{Al} is 1[mm], generated rotational torque is 0.13 [Nm]. When W_{Al} is 2[mm], generated rotational torque is 0.27[Nm]. From the result, W_{Al} is defined as 2[mm] that generates enough torque to rotate the rotor. The effect of the rotating field on the magnetic circuit of the rotor is considered. Because of the $W_{Air}=2$ [mm], the sum of W_{Shield} and W_{Air} is 5 [mm]. When the thicknesses are $(W_{Shield}, W_{Air}) = (1,4)$, (3,2), the flux density distribution is analyzed on the outer side of the aluminum and the yoke. Fig. 2 shows the analysis result. From the result, as W_{Shield} increases, the flux density on the outer peripheral side of aluminum increases. This is because the flux is moved to the magnetic shield inside the aluminum. On the other hand, the flux density on the outer peripheral side surface of the yoke decreases. This is because the magnetic shield prevents the flux generated by the rotating field from entering the inside of the rotor. However, at $W_{Shield} = 4$ [mm], the flux density increases. This is because the magnetic resistance is small at $W_{Air} = 1$ [mm], and the flux leaked from the magnetic shield reaches the yoke. Consequently, when $(W_{Shield}, W_{Air}) = (3,2)$, the influence of the rotating field is most suppressed. In conclusion, by installing a magnetic shield inside the aluminum and setting an air gap

between the shield and the yoke, the influence of the rotating field on the magnetic circuit is suppressed. The HTS magnetic bearing rotor incorporated the secondary of the induction motor is designed.

[1] F. C. Moon, "Superconducting Levitation", John Wiley & Sons, New York, (1994) [2] J. Hull, M. Murakami, "Applications of Bulk High Temperature Superconductors", Proc. of IEEE, Vol.92, 2004, pp1705-1718 [3] T. Minami, S. Sakai, S. Ohashi, "Improvement of Stability against Vibration at the Mechanical Resonance in Attractive type HTS Permanent Hybrid Magnet Bearing", (TENCON2016), 16657805, pp3294-3297, (2016) [4] S. Sakai, K. Oguni, S. Ohashi, "Effect of the Magnetic Configuration on the Rotational Motion in the Attractive type HTS-Permanent Magnet Hybrid Bearing", IEEE Trans. On Applied Superconductivity, Vol. 26, No.4, 3601204, (2016) [5] S. Takimura, T. Arai, T. Minami, S. Ohashi, "Basic Characteristics of the Yoke Equipped Rotors in the Magnetic Bearing using HTS Pinning effect", IEEE Xplore Digital Library IEEE, 12th International Symposium on Linear Drives for Industry Applications (LDIA2019), 8770991, (2019)

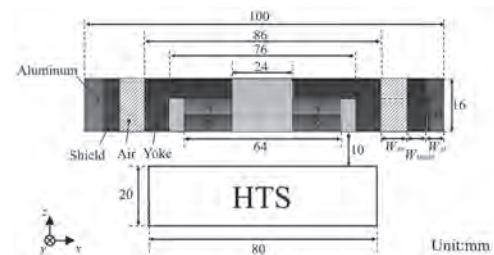


Fig.1 System of the yoke equipped ring type rotor

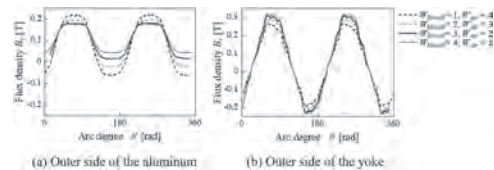


Fig.2 Flux density distribution

AT-07. A Suspension Performance Comparison of the Bearingless Axial Motor With Different Number of the Rotor Poles and Stator Slots.

T. Pei¹, D. Li¹, J. Liu¹, W. Kong¹ and R. Qu¹

1. Huazhong University of Science and Technology State Key Laboratory of Advanced Electromagnetic Engineering and Technology, Wuhan, China

Abstract-This paper has proposed two bearingless axial motors (BLAM) with different combination of the number of the rotor poles and the stator slots. The proposed BLAMs are analyzed by 3D finite element analysis (FEA) when the suspension currents are imposed. The winding in the BLAM with the high number of the rotor poles is designed carefully to limited the coupling of different degree of freedoms (DOF) and the ripple of the active suspension force as well as the active restoring torque. The suspension performances are compared between the proposed BLAMs and it shows that ripple of the active suspension force and ripple of the active restoring torque of the BLAM with high number of the rotor poles has at least 33.6 times less than that of the BLAM with low number of the rotor poles. At the same time, the average of the radial suspension force of the BLAM with high number of the rotor poles is 2.65 times larger than that of the BLAM with low number of the rotor poles. I. Introduction The bearingless motor (BLM) is attractive in high speed applications, special environment applications and so on, since it has no lubricant, no pollution, less friction, long device lifetime and maintenance-free [1]-[3]. In the traditional bearingless radial motor (BLRM), the output torque is limited by the volume of the rotor which is limited by the active suspension force. The output torque of the BLAM is not limited due to the active suspension force varies directly as the square of the rotor radius. The BLAM can be performed as an all DOF active suspension motor, which is difficult to achieve in the traditional BLRM [4]-[6]. To further enhance the suspension performance of the BLAM, the BLAMs with different combine of the number of the rotor poles and the number of the stator slots are proposed and compared in this paper, and the result shows a well-designed BLAM can reduce the ripple of the active suspension force and restoring torque obviously, and can limited the coupling of different DOF. II. Topologies of BLAM The topology of proposed BLAMs are shown in Fig. 1, which can be divided into two stators and a rotor. The concentrated winding is applied to simplify the manufacture and reduce the length of the end winding. The BLAM-HP has 14 rotor poles combined with 18 stator slots and the BLAM-LP has 4 rotor poles combined with 6 stator slots. Each coil is controlled independently so two kind of armature fields can be controlled. For the BLAM-HP, 12/14 armature fields are imposed and the former is used to control the radial active suspension force as well as the radial active restoring torque, the latter is used to control the output torque as well as the axial active suspension force. For the BLAM-LP, 2/4 armature fields will be imposed and used to control all DOF. The outer radius, the inner radius the gap thickness, the line current density and the axial length of the proposed BLAMs are uniform. III. Performance Comparison of BLAM Topologies The suspension performance comparison between the two BLAMs when only produces the x-axis active suspension force is shown in fig.2. As shows in fig.2, the x-axis active suspension force created by the BLAM-LP is 16.2N in average with 148.6% ripple, which is 43N and 4.4% for the BLAM-HP. It shows the BLAM-HP can enhance the radial active suspension force and reduce the ripple remarkable. From a different perspective, the max unexpected suspension force in the BLAM-LP is 12N, 74.1% of the average active suspension force. For the BLAM-HP, the max unexpected suspension force is 1.02N, 2.4% of the average active suspension force. It confirms that the BLAM-HP can restrain the coupling of different DOF effectively. IV. Conclusions Two BLAMs with different combine of number of rotor poles and stator slots are proposed in this paper. The suspension performances are analyzed by the FEA. According to the comparison of the results, it shows an impressively enhance of the active suspension force and reduce of the ripple and the coupling of the other DOF when the high number of the rotor poles and stator slots are chosen. Compare to the BLAM-LP, the average active suspension force is 2.65 times larger, the ripple is 33.6 times less and the coupling of different DOF is 31.2 times less when the BLAM-HP is applied.

[1] X. Sun, L. Chen, Z. Yang. "Overview of Bearingless Permanent-Magnet Synchronous Motors," *TIE*, vol. 60, no. 2, pp. 5528-5538, Dec. 2013. [2] T. Nussbaumer, P. Karutz, F. Zurcher, J. W. Kolar. "Magnetically Levitated Slice Motor – An Overview," *TIA*, vol. 47, no. 2, pp. 754-766, Mar. 2011. [3] B. Warberger, R. Kaelin, T. Nussbaumer, J. W. Kolar, "50-Nm/2500-W Bearingless Motor for High-Purity Pharmaceutical Mixing" *TIE*, vol. 59, no. 5, pp. 2236-2247, May. 2012. [4] M. Takemoto, S. Iwasaki, H. Miyazaki, A. Chiba, and T. Fukao, "Experimental evaluation of magnetic suspension characteristics in a 5-axis active control type bearingless motor without a thrust disk for wide-gap condition," in *2009 IEEE Energy Conversion Congress and Exposition*, pp. 2362-2367, 2009. [5] S. Ueno, K. Nakazawa and C. Jiang, "Improvement of Stability of an Tilt-Controlling Axial Gap Self-bearing Motor with Single Stator," in *2019 12th Asian Control Conference (ASCC)*, pp. 1216-1221, 2019. [6] M. Osa, T. Masuzawa, R. Orihara, and E. Tatsumi, "Compact maglev motor with full DOF active control for miniaturized rotary blood pumps," in *2017 11th International Symposium on Linear Drives for Industry Applications (LDIA)*, pp. 1-6, 2017.

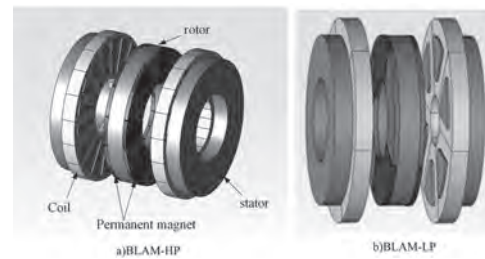


Fig.1 The topology of the proposed BLAM. a) shows the BLAM with high number of rotor poles and b) shows the BLAM with low number of rotor poles.

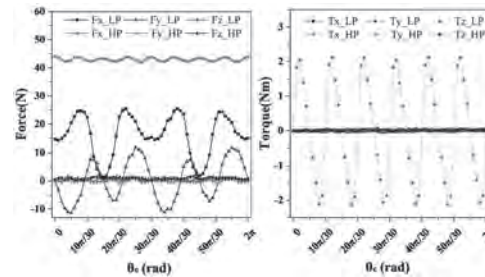


Fig.2 The suspension performance comparison when only the x-axis active suspension force is produced.

AT-08. Electromagnetic Analysis of a Novel AC Six-Pole Hybrid Magnetic Bearing.

T. Zhang¹, Z. Zhou¹ and Z. Ding¹

1. Huaiyin Institute of Technology, Huai'an, China

I. Introduction Because the hybrid magnetic bearing (HMB) has the advantages of long life, high precision and low loss, the high-speed rotor supported by HMBs instead of traditional bearings can obtain higher speed and higher power. It is widely used in life science, flywheel energy storage, aerospace and other occasions [1]-[2]. According to the bias magnetic circuit, radial HMBs can be divided into homopolar HMBs and heteropolar HMBs. However, the axial length of homopolar HMB is long, which limits the critical speed of rotor. Comparing with DC 4-pole HMB and AC 3-pole HMB, the AC 6-pole HMB not only has the advantages of symmetrical structure, but also can be driven by the three-phase inverter to decrease the volume and cost. Therefore, a novel AC 6-pole HMB are proposed in this paper. Firstly, the structure and suspension mechanism of the proposed HMB are introduced. Secondly, the equivalent magnetic circuit is established. Then the main parameters of the HMB are designed. Finally, the electromagnetic simulation is carried out by software MagNet to verify the theoretical analysis. II. Configuration And Suspension Principle The proposed novel AC 6-pole HMB includes stator, permanent magnets, control coils and rotor, as shown in Fig. 1. Six permanent magnets arrange with $NS-SN-NS-SN-NS-SN$, embedded in the stator slots of each pole, which forms heteropolar magnetic flux distributions. There are three outer air gaps under pole A, B and C , and the air gap reluctance are noted as $R_A \sim R_C$. The air gap reluctance of the inner air gaps are noted as $R_1 \sim R_6$. The control windings, marked as A, a, B, b, C, c , and c , are wound on the poles. The solid lines denote the control flux, and the dotted lines describe the bias flux. The bias flux generated by permanent magnet starts from N pole and return to S pole, one passing through internal stator core, inner air gap, the other passing through internal stator core, outer air gap, stator suspension pole and external stator core. The coils of A and b, B and c, C and a , are respectively connected in series. Then the coils of A, B and C , the coils of a, b and c , are respectively connected in parallel as three phase control winding. Then, the three-phase winding is electrified by one three-phase inverter. Assume that the rotor has the displacement to the pole b , the three phase symmetrical currents flow into $A \sim c$ coils. As a result, the air gap flux density increases under the poles A, a and c , while decreases under the poles b, B and C . Thus, the suspension force pointing to pole A will pull the rotor back to the balance position. III. Main Parameter Design The average inner air-gap length, noted as g_m , is 0.5mm and the outer air-gap length noted as g_w is 2mm. The diameter of the rotor is 50.5mm. The outer diameter of the stator is 106 mm. The turn number of coil A, B and C is 200T, and the turn number of coil a, b and c is 40T. The axial length of the stator is 45mm. The equivalent magnetic circuits are analyzed. According to the equivalent magnetic circuit, the resultant suspension forces of the rotor in the x and y directions, are deduced as $F_{xmax} = (B_s \times B_s + B_0 \times B_s) S_n + (2\mu_0) F_{ymax} = \sqrt{3} \times B_s \times B_s \times S_n + (2\mu_0)$ where μ_0 is the permeability of vacuum, B_s is the saturated flux density, B_0 is bias flux density, S_n is the internal pole area. A. Inner and Outer Air-Gap In order to avoid magnetic saturation, the saturation magnetic induction (B_s) is 1.2T, inner air gap bias flux (B_0) is designed as 0.6T. $R_i = R_n$ ($i=1,2,3,4,5,6$), $R_j = R_w$ ($j=A,B,C$). According to the equivalent control magnetic circuit, the relationship of the inner and outer air-gap can be obtained $(g_n + S_n) \times (S_w + g_w) = 1/4 B$. Number of Coil Turns According to equivalent control magnetic circuit, the relationship of the turn number of coil A, B, C , noted as N_w , and the turn number of coil a, b, c , noted as N_m , as described by $N_w : N_m = 5 : 1$ IV. Finite Element Analysis The analysis model is established by MagNet 3D. Fig. 2(a) presents the permanent magnetic static bias flux density distribution in the bearing. Fig. 2(b) shows the control flux in produced by coil A, B and C . Fig. 2(c) shows the control flux in produced by coil a, b and c . And the corresponding resultant flux is shown in Fig. 2(d). Fig. 2(e) shows the maximum suspension force can be obtained in $+x$ direction, while the force in y direction is close to zero, which shows a good linearity. And the theoretical value is consistent with the calculated value. V. Conclusions In this paper, the novel AC 6-pole HMB is proposed and designed. The structure and suspension mechanism are analyzed. The magnetic circuits are presented. According to the main design parameters, the analysis model is established by MagNet 3D. Then, the electromagnetic

performances of the novel AC 6-pole HMB are researched. The simulation results have shown that correctness of the structure, magnetic circuit and mathematical models.

[1]T. Schuhmann, W. Hofmann, and R. Werner, "Improving operational performance of active magnetic bearings using Kalman filter and state feedback control," IEEE Transactions on Industrial Electronics, vol. 59, no. 2, pp. 821-829, 2012 [2]H. Q. Zhu, Y. X. Shen, and Q. H. Wu, "Modeling and control system for AC hybrid magnetic bearing," Proceedings of the CSEE, vol 29, no. 18, pp. 100-105, 2009.

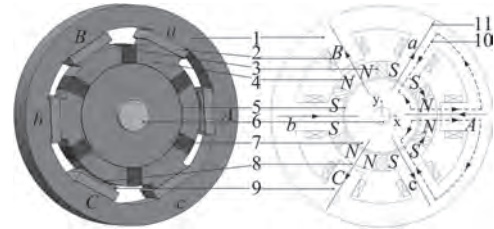
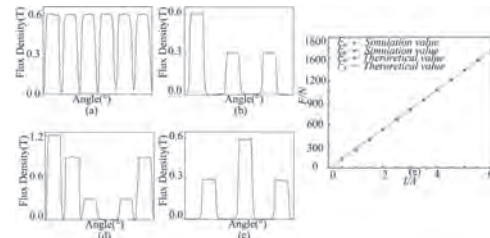


Fig. 1. Structure of novel AC 6-pole RHMB: 1-external stator core, 2-control windings, 3-permanent magnet, 4-internal stator core, 5-inner air gap, 6-shaft, 7-rotor core, 8-outer air gap, 9-stator suspension teeth, 10-bias flux, 11-control flux.



Flux distributions and the force-current relationships

Session AU

ELECTRIC DRIVE APPLICATIONS, TRANSFORMERS AND WIRELESS POWER TRANSFER III

(Poster Session)

Kazuhiro Muramatsu, Chair
Saga University, Saga, Japan

AU-01. Magnetolectric Inductor Tuned by Electric and Magnetic Fields.

D.V. Savelev¹, L.Y. Fetisov¹, D.V. Chashin¹ and Y.K. Fetisov¹

1. MIREA - Russian Technological University, Moscow, Russian Federation

Magnetolectric (ME) inductors are one of the promising elements of tunable energy efficient electronics. The main attention is paid to the possibility of controlling the inductance of such devices by electric field [1]. In this paper, we consider magnetic and electric tuning for two ME ring inductors of different geometries. The devices were manufactured as follows. Ferromagnetic (FM) layers of an amorphous magnetic alloy Metglas 2605SA1, 23 μm thick and 5 mm wide, were glued using cyanoacrylate adhesive to the outer (sample 1) or inner (sample 2) side of the piezoelectric PbZrTiO_3 (PZT) ring (see Fig.1). The rings with Ag-electrodes had an inner diameter of 16 mm, thickness of 1 mm, and height of 1 mm. The rings were poled in the radial direction. The samples were placed inside a plastic frames and then 100 turns of wire with a diameter of 0.2 mm were wound around them. A constant electric voltage of up to 1 kV was applied to the PE rings parallel to the direction of polarization, which generated inside PE an electric field up to $E=1$ kV/cm. A constant magnetic field $H=0-200$ Oe, created by Helmholtz coils, was applied along or perpendicular to the axis of the devices. The frequency dependences of the inductance $L(f)$ were measured in the frequency range 100 Hz – 5 MHz, and the inductance tuning coefficient $\gamma = (L_0 - L)/L$, at a frequency $f=300$ Hz was calculated. Here L is the inductance in a given electric or magnetic field, L_0 is the inductance in the absence of fields. The possibility of tuning the inductance with the simultaneous application of electric and magnetic fields is also shown for both samples. Fig. 1 shows measured dependences of the devices' inductance on the electric field. With an increase in E , a decrease in the inductance of the structures was observed from 74 μH to 41.4 μH for sample 1. The inductance tuning coefficient in a field $E = 1$ kV/cm was $\gamma \approx 78\%$ for sample 1, and $\gamma \approx 34\%$ for the sample 2. Fig. 2 shows similar dependences when a constant magnetic field was applied to the structure. With an increase in H , the tuning coefficient nonlinearly increased and then saturated following the saturation of the FM layer. The tuning coefficient for sample 1 reached 1000% for in-plane magnetization at $H = 20$ Oe and 700% for magnetization along the axis at $H = 200$ Oe. Tuning coefficients for the sample 2 reached 1300% for both directions of magnetization. When the structures were magnetized with a field created by additional coil, the tuning coefficient reached $\sim 850\%$ at $H \approx 9$ Oe. The observed dependences can be explained as follows. When an electric field E is applied to the PZT ring, it deforms as a result of the inverse piezoelectric effect. This deformation is transferred to the FM layer and generates an effective uniaxial magnetic anisotropy field as a result of the Villari effect. Thus, magnetic permeability μ and L becomes proportional to $\sim 1/E$. Since the magnitude of tensile strains on the outer side of the PE ring exceeds the magnitude of compression strains on the inner side, the tuning coefficient for the sample 1 is almost 2 times higher [2]. During magnetization of the FM layer with external magnetic field H , the change in inductance L is associated with a change in the magnetic permeability μ . The magnetic field inside the FM layer is $H_m \approx H/(1+\chi \times N)$, where χ is magnetic susceptibility, N is the demagnetizing factor [3]. Thus, upon in-plane magnetization of the samples, a decrease in the tuning coefficient was observed in an order of magnitude smaller magnetic fields. We have shown a possibility of creation ME inductors which inductance can be tuned by both electric and magnetic fields. The control of inductance by an electric field is more effective for the structure with a FM layer on the outer side of the PZT ring. At the same time, a larger magnetic field tuning coefficient was observed for a structure with an FM layer on the inner side of the PZT ring. The work was supported by the Russian Science Foundation, grant 19-79-10128.

1. G. Srinivasan, N.X. Sun, SPIN, v. 2, p. 1240004 (2012). 2. Y. Yan, L.D. Geng, L. Zhang et al, Scientific reports, v.7, p. 16008 (2017). 3. J.A. Osborn, Phys. Rev., v. 67, p. 1351-1357 (1945).

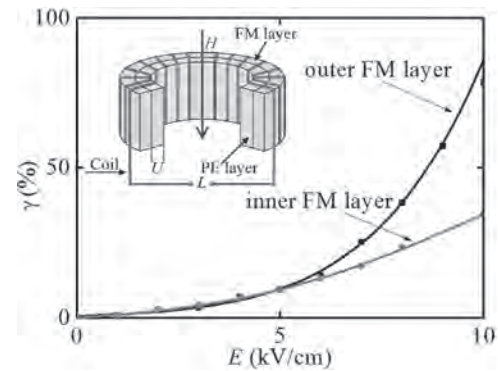


Fig. 1. Dependences of the inductance tuning coefficient γ on the electric field E for both samples.

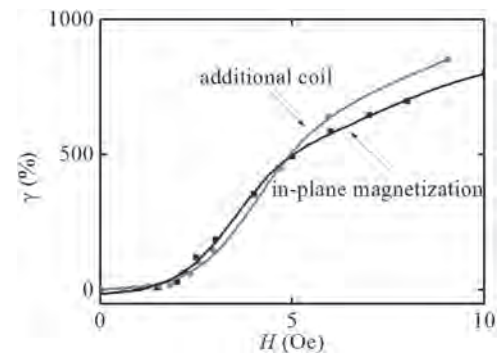


Fig. 2. Dependences of the inductance tuning coefficient γ on the magnetic field H for in-plane magnetization and for magnetic field created by additional coil for sample 1.

AU-02. High Efficiency Eddy Current Couplings.

S.J. Alshammari¹, P. Lazari¹ and K. Atallah¹

1. Electronic and Electrical Engineering, University of Sheffield, Sheffield, United Kingdom

Permanent magnet eddy current coupling (PMECCs) are electromagnetic devices which can transmit power from a motor to a load with no electrical or mechanical connections. Therefore, resulting in vibration isolation, low maintenance, and overload protection. However, PMECCs which have been considered so far, exhibit relatively lower efficiencies due to their torque slip- speed characteristics. Consequently, their industrial applications as power transmission devices has been limited, and they have mostly been employed in braking and damping applications. PMECCs topologies described in the literature have mainly employed plain copper sheets as a conducting material [1][2]. Although, these were simpler and more cost-effective solutions, they suffered from relatively lower efficiencies. The efficiency, η , of a PMECC is given by: $\eta=1-\Delta\Omega/\Omega$ (1) Where, Ω is the input speed and $\Delta\Omega$ is the slip-speed corresponding to the transmitted torque. From (1), it can be seen that the efficiency of PMECCs increase with larger speeds and reduced slip-speeds. In [3], it was theoretically shown that employing short-circuited conductors in slots (SCCSs), has the potential to improve efficiency, and it was proposed that high efficiency PMECCs can be employed as limited-slip differentials in electric vehicles. Nevertheless, in more recent investigations, SCCSs have been used in configurations which didn't fully exploit their potential in improving efficiency, thereby, resulting in PMECCs, with efficiencies similar to those using conductor sheets [4] [5]. Therefore, in this paper an investigation into the design and analysis of PMECCs for power transmission applications, where efficiency is a primary requirement, is undertaken. The performances of radial and axial field topologies, using conductor sheets and SCCSs, in terms of torque slip-speed characteristics and efficiency are compared. It is shown, that when appropriately employed, SCCSs result in significant improvement in efficiency, even when less conductive materials, such as Aluminium, are employed. Fig. 1 shows schematics of radial and axial field PMECCs employing SCCSs, and Fig. 2 shows the variation of transmitted torque with slip-speed for a prototype radial field PMECC employing SCCSs. It can be seen that a good agreement between measured and predicted results exists. It can also be seen that the slip-speed corresponding to the maximum transmitted torque is only 100rpm. This represents a significant improvement when compared to previously published PMECCs [1][2][4][5], where the slip-speed corresponding to the maximum transmitted torque can typically vary between hundreds of rpm to more than a 1000rpm.

[1] A. Canova and B. Vusini, *IEEE Transactions on Industrial Applications*, Vol. 39 (2003). [2] A. S. Erasmus, M. J. Kamper, *IEEE Energy Conversion Congress and Exposition*, (2015) [3] K. Atallah, J. Wang, *IEEE Transactions on Magnetics*, Vol. 47, (2011) [4] X. Dai, Q. Liang, J. Cao, Y. Long Y, J. Mo J and S. Wang, *IEEE Transactions Magnetics*, Vol. 52, (2016) [5] Z. Li, L. Yan, B. Qu and K. Fu, *International Journal Applied Electromagnetics and Mechanics*, Vol. 62, (2020)

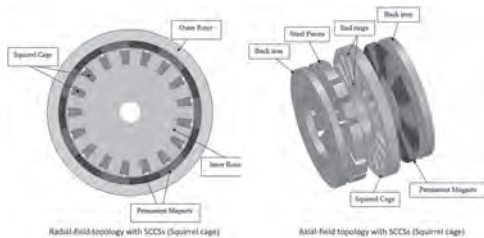


Fig. 1 Radial and axial field PMECCs with SCCSs.

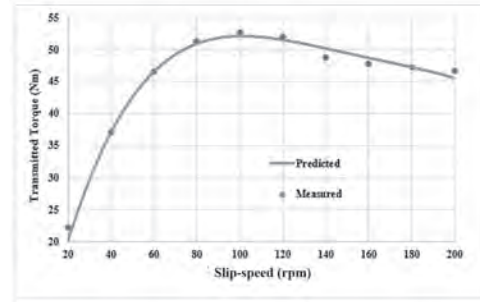


Fig. 2 Variation of transmitted torque with slip-speed.

AU-03. Compact Wireless Motor Drive Using Decoupled Bipolar Coils for Coordinated Operation of Robotic Arms.

W. Han¹, K. Chau², Z. Hua² and H. Pang²

1. Department of Electrical and Computer Engineering, University of Toronto, Toronto, ON, Canada; 2. Department of Electrical and Electronic Engineering, The University of Hong Kong, Hong Kong

I. INTRODUCTION As one of the epoch-making technologies, the wireless power transfer (WPT) has significantly changed the power-accessing pattern owing to the distinctive merits of high convenience, reliability and security [1]. Possessing the capability to cordlessly transmit the energy via a long air gap, the emerging WPT has been widely investigated by many researchers [2]-[3]. Recently, the study objectives of WPT concentrate on efficiency enhancement, topology development, coil optimization and fresh applications such as the wireless lighting, wireless heating and wireless-powered implant [4]-[6]. In particular, the concept of wireless motor was newly conceived which can eliminate the metallic connection to facilitate the motor operation in an isolated environment [7]. By integrating the selective WPT with the motor drive, the wireless switched reluctance motor was proposed to remove the converter in the receiver side and centralize all controls in the transmitter side [8]. With the adoption of self-driving circuits and a full-bridge inverter in the receiver, the wireless shaded-pole induction motor was developed as tagged as the first wireless AC motor [9]. And the frequency-modulated wireless direct-drive motor was established for the underground in-pipe pumping application [10]. It should be noted the aforementioned wireless motor systems are universally evolved from the multifrequency selective WPT system which is designed to energize receivers by operating at different resonant frequencies. Nevertheless, it unavoidably adopts complicated switched capacitors, bulky transmitter coil and multiple independent receiver coils which in turn will result in a clumsy system and the unbalanced phase current of motor. To address concerns of previous wireless motor drives, a new wireless motor drive using decoupled bipolar coils is proposed and implemented for the coordinated operation of robotic arms. Specifically, two bipolar coils are orthogonally integrated to form a compact magnetic coupler while two magnetic couplers serve as the transmitter and receiver coils, respectively. The same-side coils are magnetically decoupled which indicates the transmitter-side bipolar coils can be independently controlled to facilitate the coordinated operation of two permanent magnet (PM) DC motors in the receiver side. Meanwhile, the series-inductor-capacitor-capacitor (S-LCC) compensation is adopted to ensure high transmission efficiency over a wide load range. Therefore, the proposed system is highly suitable for cordless robotic arms operating in an isolated or watery environment with electrocution free and high reliability.

II. METHODOLOGY As depicted in Fig. 1 (a), the proposed system involves two half-bridge inverters, magnetic couplers, S-LCC compensations, diode rectifiers and PMDC motors. By independently controlling bipolar coils in coupler #1 in the transmitter, the motors can be separately excited by bipolar coils in coupler #2 in the receiver due to the magnetic decoupling characteristics of the same-side coils. Instead of adopting multiple resonant frequencies and multiple power-transfer channels, the proposed system can readily activate two motors with a single resonant frequency through the single power-transfer channel which in turn will significantly shrink the system volume and reduce the system complexity. In order to intuitively illustrate the magnetic coupling characteristics of the proposed coil, the finite element method (FEM) based simulations are conducted for better visualization as shown in Fig. 1 (b). It can be observed that two horizontal bipolar (Hb) coils and two vertical bipolar (Vb) coils are strongly coupled, respectively. However, the net amount of magnetic flux flows from the Hb coil to Vb coil is zero due to the symmetrical distribution of the magnetic flux. Consequently, the Hb and Vb coils are naturally decoupled which indicates the independent and wireless excitation of two PMDC motors can be realized by separately control the Hb and Vb coils from the transmitter side.

III. EXPERIMENTAL VERIFICATION The experimental prototype and testing setup are built as shown in Fig. 2 (a) in which two gallium nitride (GaN) half-bridge inverters serve as the high-frequency AC source and two 150 W PMDC motors act as the load, respectively. All coils are made by Litz wires and all rectifiers are made by Schottky diodes to reduce the undesired power loss. Fig. 2 (b) shows the measured waveforms of three basic modes,

namely, Mode I: motor A is active while motor B is idle; Mode II: motor A is idle while motor B is active; Mode III: both motor A and B are active. Meanwhile, it can be observed that no unexpected currents appear in the idle motor which well illustrates the good decoupled characteristics between Hb and Vb coils. Moreover, the ZVS can be readily achieved at the resonant frequency of 85 kHz in all modes. Finally, the measured results well confirm the feasibility and flexibility of the proposed wireless motor drive for the coordinated operation of robotic arms. This work was supported by Hong Kong Research Grants Council, Hong Kong, China under project 17207420.

[1] G. A. Covic, and J. T. Boys, "Inductive power transfer," *Proceedings of the IEEE*, vol. 101, no. 6, pp. 1276-1289, Jun. 2013. [2] Z. Zhang, H. Pang, A. Georgiadis and C. Cecati, "Wireless power transfer – an overview," *IEEE Trans. Ind. Electron.*, vol. 66, no. 2, pp.1044-1058, Feb. 2019. [3] S. Li and C. C. Mi, "Wireless power transfer for electric vehicle applications," *IEEE J. Emerg. Sel. Topics Power Electron.*, vol. 3, no. 1, pp. 4-17, March 2015. [4] W. Han, K. T. Chau, C. Jiang, W. Liu and W. H. Lam, "High-order compensated wireless power transfer for dimmable metal halide lamps," *IEEE Trans. Power Electron.*, vol. 35, no. 6, pp. 6269-6279, Jun. 2020. [5] W. Han, K. T. Chau, and Z. Zhang, "Flexible induction heating using magnetic resonant coupling," *IEEE Trans. Ind. Electron.*, vol. 64, no. 3, pp. 1982-1992, Mar. 2017. [6] C. Liu, C. Jiang, J. Song and K. T. Chau, "An effective sandwiched wireless power transfer system for charging implantable cardiac pacemaker," *IEEE Trans. Ind. Electron.*, vol. 66, no. 5, pp. 4108-4117, May 2019. [7] L. Wang, J. Li, H. Nie, J. Liu and S. Ke, "Coaxial nested couplers-based offset-tolerance rotary wireless power transfer systems for electric excitation motors," *IEEE Access*, vol. 8, pp. 44913-44923, 2020. [8] C. Jiang, K. T. Chau, C. Liu, and W. Han, "Design and analysis of wireless switched reluctance motor drives," *IEEE Trans. Ind. Electron.*, vol. 66, no. 1, pp. 245-254, Jan. 2019. [9] H. Wang, K. T. Chau, C. H. T. Lee, L. Cao and W. H. Lam, "Design, analysis and implementation of wireless shaded-pole induction motors," *IEEE Trans. Ind. Electron.*, doi: 10.1109/TIE.2020.3007116. [10] W. Liu, K. T. Chau, C. H. T. Lee, L. Cao and C. Jiang, "Frequency-modulated wireless direct-drive motor control," *IEEE Trans. Magn.*, doi: 10.1109/TMAG.2020.3021708.

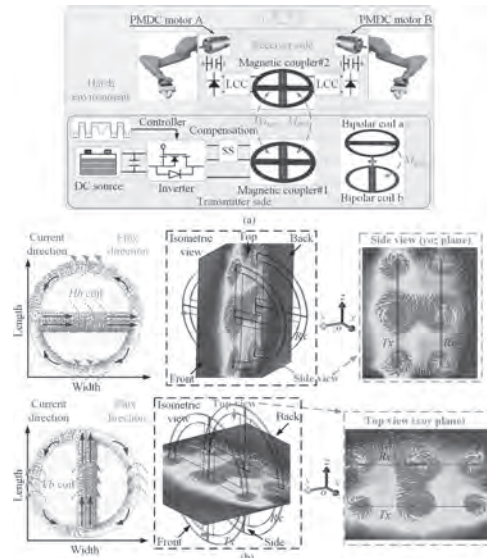


Fig.1 Proposed wireless motor drive. (a) Configuration. (b) Magnetic field distributions of bipolar coils.

AU-04. A Study on Optimal Design of Induction Heater for Electric Vehicle Considering Proximity Effect and Skin Effect.

H. Shin¹, C. Lee¹, I. Song¹ and B. Lee²

1. Hanbat National University, Daejeon, The Republic of Korea;

2. Samhyun, Changwon, Gyeongsangnam-do, The Republic of Korea

Battery Electric Vehicles can significantly shorten battery life if not maintained at the proper temperature. PTC heater is used as a temperature control system for commercial vehicles. But PTC is heavy so the mileage of the vehicle is reduced. In addition, the insulation structure of PTC is complicated. Research on induction heaters is underway to compensate for the shortcomings of PTC in the ventilation industry. The structure of the induction heater consists of a workpiece and a coil. An alternating magnetic flux is generated by the coil to which the AC current is applied. Core loss occurs as heat in the workpiece by the alternating magnetic flux. This heating method does not require an insulating structure between the workpiece and the electrode, so it can increase mileage by reducing the volume and weight of the vehicle. The induction heater operates in a high frequency region, and the skin effect occurs due to the operation of the high frequency. Thus, the current is concentrated on the coil surface. Since a magnetic skin effect occurs in the workpiece, the magnetic flux generated by the current is concentrated on the inner and external workpiece surfaces adjacent to the coil. Due to the concentrated magnetic flux on the surface of the workpiece, the magnetic flux density from the surface of the workpiece rapidly with rising. So the relative permeability of the workpiece is high before the saturation point. Additionally, the coil is wound several times inside the induction heater. Therefore, a proximity effect occurs between coils by magnetic force generated when current flows. The current that is affected of the magnetic force is tilted inside the coil according to the direction and magnitude of the magnetic force, and the tilted direction and magnitude change continuously for a very short time by high frequency. The workpiece is directly affected by these phenomena. The skin effect and proximity effect occur due to the magnetic force between the coils and the high-frequency current, so these effects should be reduced for efficiency of induction heating. In this paper, the design of an optimal model was studied to increase the efficiency of the induction heater by considering skin effect and proximity effect. The induction heater is composed of a series resonance circuit among LC series resonance circuit and LC parallel resonance circuit. When the LC series resonance circuit operates at the resonance frequency, the reactance becomes 0 and the power factor approaches to 1. Since the reactance is zero at the resonant frequency, the impedance is minimized. Therefore, maximum current and magnetic flux can be generated with the same voltage. In other words, it is possible to maximize the output of the induction heater through the operation of the resonant frequency. For the operation of the resonance frequency of the induction heater, the required capacity of the capacitor is determined according to the inductance of the workpiece. And the capacity of the capacitor is proportional to the size and price. Small capacitors require high inductance to operate at resonant frequencies. For high inductance, proper workpiece design of induction heater is required. For example, if the workpiece is thicker more material is required. However, the magnetic flux is concentrated only on the workpiece surface due to the skin effect. Thus, the surface of the workpiece adjacent to the coil is saturated. Other regions except the surface have low flux linkage. As a result, the overall inductance of the workpiece is lowered. Conversely, if the workpiece is too thin, it becomes saturated due to overheating. So the inductance decreases and the required output is not obtained. Relative permeability is a parameter that directly affects inductance. In order to measure the exact relative permeability of the workpiece according to the skin effect, the magnetic flux density was derived by electromagnetic field analysis. After considering the saturation of magnetic flux density, the relative permeability of the workpiece was derived according to the distance from the coil. The average of the derived relative permeability was calculated to obtain the depth of penetration. The relative permeability of the workpiece was highest at the point depth of penetration, which is the result of calculation. Also, the magnetic force influencing the proximity effect was analyzed. The magnetic force was calculated by deriving the current density inside the coil by electromagnetic field analysis. And then a design flow chart was established and a basic model was selected. The 6kW induction heating model was chosen as the base model,

a total of 101 coils consisted of two layers, and the workpiece was made of SUS430 material. For the basic model analysis, capacitance that satisfies the operation of capacity, voltage, and resonance frequency was derived using electromagnetic field analysis. In addition, a sensitivity analysis of the design parameters was performed and a high sensitivity parameter was derived. High sensitivity parameters included the height and thickness of the workpiece, the distance between the workpiece and the coil, the diameter of the workpiece, and the diameter of the coil. The optimal model was derived by comparing and analyzing the basic model with the model in which the height, thickness of the workpiece, and diameter of the coil were changed.

- [1] Hiroyuki Kagimoto, Daisuke Miyagi and Norio Takahashi, IEEE Trans. Magn., vol.46, no.8, pp.3018-3021 (2010) [2] Alexander Boadi, Yuji Tsuchida and Takashi Todaka, IEEE Trans. Magn., vol.41, no.10, pp.4048-4050 (2005) [3] M. Messadi, L. Hadjout and Y. Ouazir, IEEE Trans. Magn., vol.52, no.3 (2016) [4] Jesus Acero, Claudio Carretero and Rafael Alonso, IEEE Trans. Magn., vol.49, no.4, pp.1382-1389 (2013) [5] Nikolaos Tsopelas and Nicolaos J. Siakavellas, IEEE Trans. Magn., vol.44, no.12, pp.4711-4720 (2008)

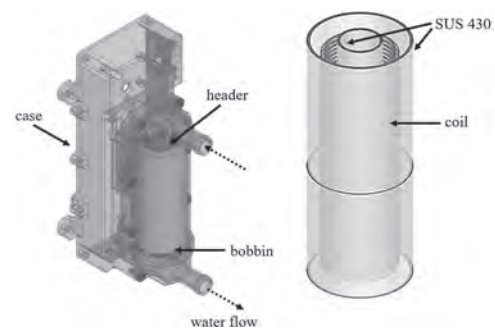


Figure 1. 3D Base Model of the Induction Heater

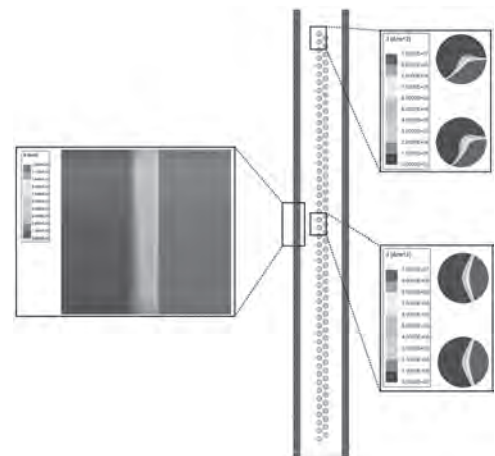


Figure 2. Magnetic Flux Density Distribution and Current Density Distribution

AU-05. Research on Iron Loss Characteristics of a Variable-Leakage-Flux Permanent Magnet Motor Considering Multiple Operation Conditions.

Z. Wan¹, X. Zhu¹ and X. Zhou¹

¹. Jiangsu University, Zhenjiang, China

I. Introduction Nowadays, electric vehicles (EVs) have developed rapidly for reducing environmental pollution and alleviating the scarcity of resources. With the driving environment of EVs becoming increasingly complex, the performance requirements of traction motor are more and more strict, such as the high efficiency and high torque density. As is known, interior permanent magnet (PM) motors have been the popular machine type for EV applications, however, the air gap magnetic field of conventional PM motors keeps constant, which leads to the disadvantages of the limited speed range and low efficiency in flux-weakening control region. So, to realize the flux regulation in PM motors, a variable leakage flux permanent magnet (VLF-PM) motor has aroused widespread attention due to the characteristics of variable flux leakage [1]. This kind of motor can control the flux leakage by regulating the q -axis current, then the magnetic flux leakage region can be effectively adjusted and wide speed range can be realized [2]. Moreover, the different saturation degrees under various operation conditions may cause the variation of magnetic density fluctuation. Based on above analysis, VLF-PM motor uses different magnetic flux leakage and saturation degrees under different operation conditions to improve the performance of the motor. At the same time, the magnetic density fluctuation caused by different saturation degrees will have a great impact on the fluctuation of iron loss. Thus, to VLF-PM motors, exploring the magnetic flux leakage characteristics to reduce the average and fluctuation of iron loss and ensure the stability of efficiency is extremely meaningful. In this paper, the key of research is to solve the problem of high iron loss and fluctuation, which caused by the distinctly various magnetic density of the rotor flux leakage region in VLF-PM motor under different operation conditions. For further research, this paper proposes a method that the magnetic flux leakage region is divided from the perspective of magnetic circuit change and each region selects the representative point, which has contributed to evaluating the fluctuation of magnetic density and iron loss. Finally, by optimizing the size of motor, the iron loss and its fluctuation can be reduced. II. Motor topology and analysis of the performance Fig. 1(a) shows the configuration of the proposed VLF-PM motor. Fig. 1(b) shows urban operation conditions. It can be found that low-speed operation condition of the motor accounts for 86% and it is worthy to be focused. Fig. 1(c) shows magnetic circuit under different loads. Based on Fig. 1(c), Fig. 1(d) shows the selections of typical magnetic density region. In Fig. 1(e), through the analysis of flux leakage regions under different operation conditions, different points are selected for the analysis of magnetic density, it can be seen that the magnitude and amplitude of the magnetic density of the selected points change because of the variation of saturation degree, which explains the phenomenon that the iron loss of VLF-PM motor fluctuates greatly after reaching a stable level. Fig. 2(a), Fig. 2(b) and Fig. 2(c) optimize parameters R_{fv} and R_{sw} from perspectives of the average of core loss, the fluctuation of core loss and the torque. Fig. 2(d) and Fig. 2(e) shows comparison of iron loss between initial motor and optimal motor. It can be seen that the average and fluctuation of optimal motor both decrease through optimizing. III. Conclusion In this paper, the iron loss characteristics are studied and improved based on VLF-PM motor under multiple operation conditions. The average and fluctuation of iron loss are reduced by optimizing the size of the motor. The results provide a new orientation for studying the iron loss characteristics of VLF-PM motor. More detailed electromagnetic performance analysis and experimental results will be presented in the full paper.

[1] M. Minowa, H. Hijikata, K. Akatsu and T. Kato, in *Proc. IEEE ECCE*, 2014, pp. 3828-3833. [2] W. Wu, Q. Chen and X. Zhu, *IEEE Trans. Magn.*, doi: 10.1109, Aug. 2020, Art no. 3015784.

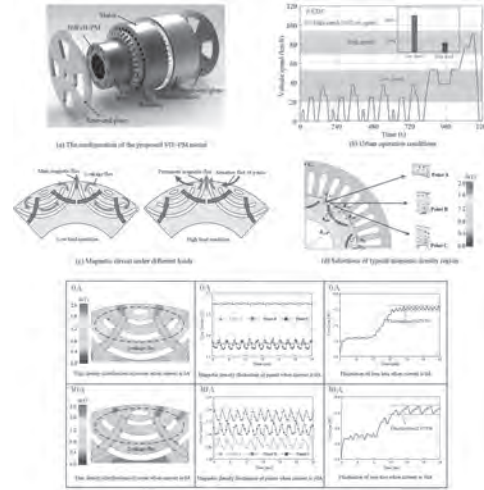


Fig. 1. The configuration of the motor and analysis of magnetic circuit

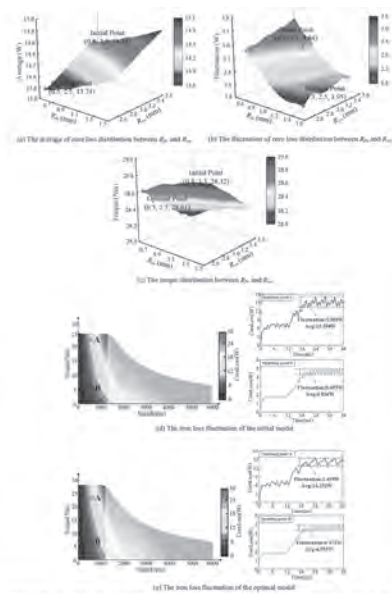


Fig. 2. Distributions with surface analysis and comparison of iron loss between initial motor and optimal motor

AU-06. Closed-Form Electromagnetic Field Coupling to Transmission Line Model Exploiting the Reciprocity Theorem.

T. Liang¹ and Y. Xie¹

1. School of Electrical Engineering, Xi'an Jiaotong University, Xi'an, China

I. Background Transmission line (TL) is a fundamental structure that can easily be identified in an electric system by various forms, for instance, the external incoming/outgoing line and internal windings of an electrical machine, etc. [1]–[4]. These TLs represent dominant propagation paths for radiated noises coupling into an apparatus, resulting in potential susceptibility effects like over-voltage breakdown, insulation failure. As a result, with the objective to ensuring safety operation of system in complex electromagnetic environment and assessing its radiated immunity, it is of great interest to predict the voltage/current responses of TL under the illumination of external electromagnetic interferences. In this connection, the TL model based on solving telegrapher's equation receives undoubtedly the most attention. To incorporate the impinging field contribution into TL model, pioneer works by Taylor et al. [5], Agrawal et al. [6] and Rachidi et al. [7] argued three different but equivalent approaches to cast the field contributions as a set of equivalent circuit sources. Besides, researches started to look outside of classic FC models for alternatives approaches, the motivation includes interpreting Taylor's, Agrawal's and Rachidi's approach in a unified theory [8], predicting transient field responses [9], analyzing the worst-case load responses [10]–[12], etc. Lorentz reciprocity theorem, which was exploited in [8]–[12], demonstrated great potentials in modeling the FC problem. However, a simple concise FC model in parallel to Agrawal's model was still missing in the literature. In this study, we re-consider the FC problem by taking advantage of the reciprocity theorem, specifically, through solving the TL in transmitting mode, analytical solution of far-field radiation pattern and input impedance are obtained, which leads to closed-form expressions of equivalent voltage sources accounting for the field contributions. The sources are then incorporated into a passive TL model, resulting in a solvable two-port network with active feeding sources and terminal impedances connecting to the terminals. II. The Proposed FC Approach As shown in Fig.1, a lossless single conductor transmission line of length l and radius r_w is placed parallel above the ground plane at height h . The system can be regarded as a two-port system under the assumption $h \ll c_0/f$, where c_0 is speed of light in free space, f is frequency. The TL is illuminated by a linearly polarized uniform plane wave of electrical field E , magnetic field H , and propagates vector k . Incidence angles (θ , Φ) and polarization angle (η), are defined in the spherical coordinates. In this regard, the TL under study can be treated as a two-port network with two voltage sources connected to two ports, representing the contribution of external field, resorting to the generic multi-port reciprocity theorem discuss in [13], the sources can be cast as function of radiation pattern and input impedance, which needs to be solved by considering TL in transmitting mode, namely, a dummy voltage source is connected to the port whereas the opposite terminal is left open. According to passive TL model and solution in [14], [15], the far-field radiation field can be solved analytically, which finally leads to the proposed closed-form TL model. The proposed method is verified by comparing to the classic FC model [16]. Without the loss of generality, we consider a TL of $l=1$ m, $h=1$ cm, $r_w=1$ mm and impedances $Z_L=10$ Ω , $Z_R=50$ Ω . Let $|E|=1$ V/m. Different impinging waves are considered, namely, wave #1 ($\theta=138.6^\circ$, $\Phi=40.9^\circ$, $\eta=184.1^\circ$), wave #2 ($\theta=90^\circ$, $\Phi=73^\circ$, $\eta=180^\circ$), wave #3 ($\theta=90^\circ$, $\Phi=73^\circ$, $\eta=270^\circ$). The magnitude of the induced voltage across the left load $|V_L|$ predicted by both proposed reciprocity model and classic TL model from 1 MHz to 1 GHz, the results are summarized in Fig. 2. The predicted load voltages by two methods agree perfectly with each other for all three cases. Therefore, it can be concluded that the proposed model could offer trustworthy predictions to the FC problems. III. Conclusions An algorithm for computing the field-to-wire coupling problem is proposed based on the reciprocity theorem. The contributions due to the external field are modeled as equivalent voltage sources, whose expressions are obtained in closed-form. Owing to the non-conventional definitions of incidence and polarization angles, the proposed method offers a more concise and physical interpretation for the field-to-wire coupling phenomena, the effects of incidence and polarization angles are conveniently decoupled in the closed-form

solution. In this connection, the proposed method is more advantageous in addressing the wave angles associating to maximal/minimal coupling efficiency.

[1] Y. Ryu, B. Park, and K. J. Han, "Estimation of High-Frequency Parameters of AC Machine From Transmission Line Model," *IEEE Transactions on Magnetics*, vol. 51, no. 3, pp. 1–4, Mar. 2015, doi: 10.1109/TMAG.2014.2355718. [2] Y. Huangfu, L. D. Rienzo, and S. Wang, "FDTD Formulation Based on High-Order Surface Impedance Boundary Conditions for Frequency-Dependent Lossy Multi-Conductor Transmission Lines," *IEEE Transactions on Magnetics*, vol. 56, no. 1, pp. 1–4, Jan. 2020, doi: 10.1109/TMAG.2019.2950603. [3] Q. Zhang et al., "Application of an Improved Multi-Conductor Transmission Line Model in Power Transformer," *IEEE Transactions on Magnetics*, vol. 49, no. 5, pp. 2029–2032, May 2013, doi: 10.1109/TMAG.2013.2245874. [4] H. D. Gersem and A. Muetze, "Finite-Element Supported Transmission-Line Models for Calculating High-Frequency Effects in Machine Windings," *IEEE Transactions on Magnetics*, vol. 48, no. 2, pp. 787–790, Feb. 2012, doi: 10.1109/TMAG.2011.2172197. [5] C. D. Taylor, R. S. Satterwhite, and C. W. Harrison, "The response of a terminated two-wire transmission line excited by a nonuniform electromagnetic field," *IEEE Transactions on Antennas and Propagation*, vol. 13, no. 6, pp. 987–989, 1965, doi: 10.1109/TAP.1965.1138574. [6] A. K. Agrawal, H. J. Price, and S. H. Gurbaxani, "Transient response of multiconductor transmission lines excited by a nonuniform electromagnetic field," *IEEE Transactions on Electromagnetic Compatibility*, vol. EMC-22, no. 2, pp. 119–129, 1980, doi: 10.1109/TEMC.1980.303824. [7] F. Rachidi, "Formulation of the field-to-transmission line coupling equations in terms of magnetic excitation field," *IEEE Transactions on Electromagnetic Compatibility*, vol. 35, no. 3, pp. 404–407, 1993, doi: 10.1109/15.277316. [8] M. Stumpf and G. Antonini, "Electromagnetic Field Coupling to a Transmission Line—A Reciprocity-Based Approach," *IEEE Transactions on Electromagnetic Compatibility*, pp. 1–9, 2018, doi: 10.1109/TEMC.2018.2884038. [9] R. G. Olsen and A. G. Tarditi, "EMP Coupling to a Straight Conductor Above Ground: Transmission Line Formulation Based on Electromagnetic Reciprocity," *IEEE Transactions on Electromagnetic Compatibility*, pp. 1–9, 2018, doi: 10.1109/TEMC.2018.2838080. [10] F. Vanhee, D. Pissort, J. Catrysse, G. A. E. Vandenbosch, and G. G. E. Gielen, "Efficient Reciprocity-Based Algorithm to Predict Worst Case Induced Disturbances on Multiconductor Transmission Lines due to Incoming Plane Waves," *IEEE Transactions on Electromagnetic Compatibility*, vol. 55, no. 1, pp. 208–216, Feb. 2013, doi: 10.1109/TEMC.2012.2208754. [11] T. Liang and Y.-Z. Xie, "Determining Incidence and Polarization of Electromagnetic Field for Maximal/Minimal Coupling to Transmission Line System," *IEEE Microwave and Wireless Components Letters*, vol. 30, no. 11, pp. 1021–1024, Nov. 2020, doi: 10.1109/LMWC.2020.3021695. [12] T. Liang, G. Spadacini, F. Grassi, and S. A. Pignari, "Coupling of wideband radiated IEMI to cables above ground," *IEEE Transactions on Electromagnetic Compatibility*, vol. 61, no. 6, pp. 1–9, 2018, doi: 10.1109/TEMC.2018.2877508. [13] T. Liang, G. Spadacini, F. Grassi, and S. A. Pignari, "Worst-Case Scenarios of Radiated-Susceptibility Effects in a Multiport System Subject to Intentional Electromagnetic Interference," *IEEE Access*, vol. 7, pp. 76500–76512, 2019, doi: 10.1109/ACCESS.2019.2921117. [14] R. Ianculescu and V. Vulfin, "Radiation from transmission lines PART I: free space transmission lines," *arXiv preprint arXiv:1701.04878*, vol. 2, no. 1, pp. 1–9, 2017, [Online]. Available: <http://arxiv.org/abs/1701.04878>. [15] R. Ianculescu and V. Vulfin, "Radiation from free space TEM transmission lines," *IET Microwaves, Antennas & Propagation*, Jun. 2019, doi: 10.1049/iet-map.2018.6061. [16] C. R. Paul, *Analysis of multiconductor transmission lines*. New York: IEEE, 2007.

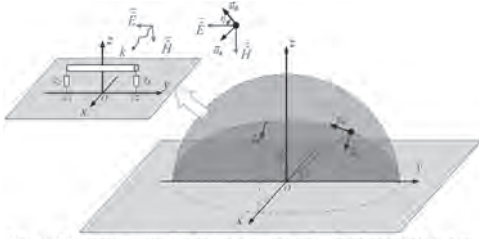


Fig. 1. TL above ground plane under analysis illuminated by a plane electromagnetic field defined in spherical coordinates.

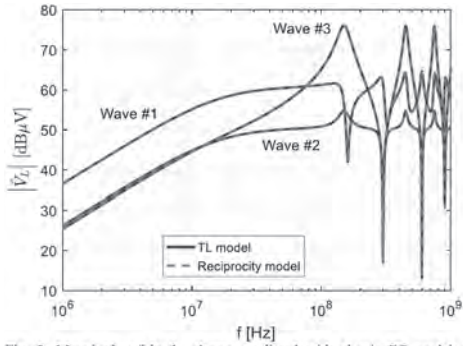


Fig. 2. Magnitude of load voltages predicted with classic FC model and proposed model.

AU-07. Design and Experimental Verification of DC Superconducting Current-Limiting Switch.

Z. Cai¹, I. Ren¹, X. Tan¹, H. Zheng¹, Z. Li¹ and Y. Tang¹

1. State Key Laboratory of Advanced Electromagnetic Engineering and Technology, Huazhong University of Science and Technology, Wuhan, China

I. Introduction When a short-circuit fault occurs on the DC side of the ship DC system, the peak short-circuit current on the DC side can reach 100kA, and the current rise rate can reach 20kA/ms, which is difficult for the existing DC circuit breaker (DCCB) to remove the fault circuit [1], [2]. The coordination of superconducting fault current limiter (SFCL) and DCCB is a good current limiting and breaking scheme. However, there is a lack of feasibility experimental studies of SFCL in short-circuit faults of ships. The topology of DC superconducting current-limiting switch (SCLS) is shown in Fig. 1(a). The structure of SCLS is designed, then the prototype is manufactured and its principle experimental tests are conducted. II. Principle and Structure of SCLS Superconducting flux-coupling coil is one of core component of SCLS, its principle mainly includes two aspects. The first is the principle of branch current sharing, in which reverse-coupled coils can maintain the same current in two branches. The second is the principle of current limiting, which uses the quench characteristics of R-SFCL to increase the line impedance and reduce the short-circuit current level [3]. Due to R-SFCL usually use non-inductive coils and the two branches of SCLS are connected in series with a DCCB, there are mainly two coil winding methods for SCLS: pancake-winding (PW) and layer-winding (LW) both made of 4 mm wide 2G YBCO tape [4], [5]. These two coils are manufactured and the structure diagram are shown in Fig. 1(b). By calculating the distribution of the leakage magnetic field of the two coils in COMSOL, it is found that the gap between each cake in PW coil makes the magnetic field distribution uneven and there is a larger leakage magnetic field than LW coil. It can also be calculated from Formula (1) and (2) that the LW coil has a higher m by measuring the inductance of the two coils with the LCR instrument. Therefore, the following principle verification experiment uses LW coil. $L_{eq} = M + (L_1 - M) / (L_2 - M) = M + (L - M) / 2 = (L + M) / 2$ (1) $m = -M / L$ (2) (where L_1 and L_2 are the branch inductance, $L_1 = L_2 = L$, M is the mutual inductance, L_{eq} is the actually measured coupling inductance, and m is the coupling degree.) III. Experimental results and discussion The current sharing test is completed. Put SCLS into DC source circuit, and the currents of the two branches $i_1 = i_2 = 8A$. With or without LW coil, the branch current sharing effects of DCCB breaking at different times are compared. At t_1 , t_3 , the DCCB of branch 1 is opened, and at t_2 , t_4 the DCCB of branch 2 is opened. The experimental results are shown in Fig. 2(a), (b). Before t_1 , from Fig. 2(a), the two branch currents are different due to the minor difference in branch impedance; However, before t_3 in Fig. 2(b), $i_1 = i_2$ due to the existence of the LW coil. During $t_1 \sim t_2$ in Fig. 2(a), all current in branch 1 is gradually transferred to branch 2; However, during $t_3 \sim t_4$ in Fig. 2(b), the current of branch 2 can basically remain unchanged. Therefore, SCLS has a good current sharing effect, which verifies the effectiveness of the current sharing principle. The current limiting effect of the LW coil of SCLS is tested experimentally. Since this huge surge in the fault current is caused by the discharge of the DC-link capacitor [6], an RLC DC impact platform is built to simulate the fault current waveform. Set the main parameters of the circuit are $R=0.2\Omega$, $L=0.1mH$, $C=6mF$ so that the rise time of the fault current is within 1ms. And the current peak value can be gained by adjusting the capacitor charging voltage. The comparison of current limiting effect before and after installation of LW coil is shown in Fig. 2(c). The current limiting effect of the LW coil is obvious, the peak value of impulse current is limited from 3.0kA to 1.3kA, and current limiting ratio can reach 56.67%. In addition, the time of the peak is also delayed from the original $t_5=0.83ms$ to $t_6=0.97ms$. It can also be seen from Fig. 2(d), the quench resistance of each branch can increase from 0Ω to 0.7Ω in 1ms, which has a fast current limiting response speed. Therefore, the LW coil of SCLS has a good current limiting effect, which verifies the efficiency of the current limiting principle. IV. Conclusion In this research, the structures of PW coil and LW coil are designed and compared, and the principles of SCLS are experimentally studied. The experimental results are as follows: (1) Compared with PW coil, the LW coil has a more uniform magnetic field distribution and a higher m . (2) Due to the existence of the coupling coil, SCLS can ensure that

the currents of the two branches are equal and can also reduce the current deviation caused by the two switches not being opened at the same time. (3) The superconducting coil plays a key role in restraining short-circuit current level and absorbing DCCB breaking capacity, which is conducive to the smooth removal of the fault.

[1] "IEEE Recommended Practice for 1 kV to 35 kV Medium-Voltage DC Power Systems on Ships," in IEEE Std 1709-2018 (Revision of IEEE Std 1709-2010), vol., no., pp.1-54, 7 Dec. 2018. [2] K. Satpathi, A. Ukil. "Modeling and real-time scheduling of DC platform supply vessel for fuel efficient operation," IEEE Transactions on Transportation Electrification, vol. 3, no. 3, pp. 762-778, 2017. [3] Z. Cai and L. Ren, "Design and Analysis of Superconducting Current-Limiting Switch in Ship MVDC System," 2020 IEEE International Conference on Applied Superconductivity and Electromagnetic Devices (ASEMD), pp. 1-2, Tianjin, 2020. [4] S. Yan, Y. Tang, L. Ren and Z. Wang, "AC loss analysis of a flux-coupling type superconducting fault current limiter," 2018 IEEE International Magnetics Conference (INTERMAG), pp. 1-2, Singapore, 2018. [5] L. Chen, "Current limiting characteristics of a novel flux-coupling type superconducting fault current limiter", IEEE Trans. Appl. Superconduct., vol. 20, no. 3, pp. 1143-1146, Jun. 2010. [6] Satpathi, Kuntal, Abhisek Ukil. Short-circuit fault management in DC electric ship propulsion system: protection requirements, review of existing technologies and future research trends [J]. IEEE Transactions on Transportation Electrification, 4 (1): 272-291, 2017.

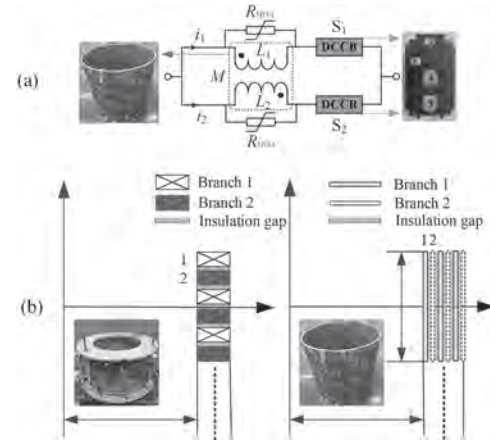


Figure 1: (a) The topology of SCLS; (b) The structure and physical diagram of PW coil and LW coil.

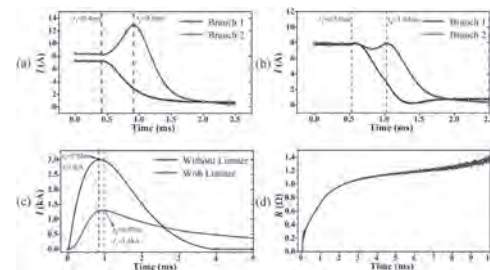


Figure 2: Current sharing experiment: (a) without superconducting coupling coil; (b) with superconducting coupling coil; Current limiting experiment: (c), (d) Current limiting result.

AU-08. Influence of Current Harmonics on Mechanical Noise of Interior Permanent Magnet Synchronous Motor Driven by SVPWM Control.

H. Shin¹, G. Jang¹, T. Bang¹, G. Park², Y. Baek² and J. Choi¹
 1. Chungnam National University, Daejeon, The Republic of Korea; 2. LG Electronics First Changwon Plant, Changwon, The Republic of Korea

Interior permanent magnet synchronous motors (IPMSMs) are used for applications that require high torque and an extended operational speed range. In IPMSMs, both magnetic torque and reluctance torque are generated due to the difference of inductance between the d- and q-axis. Therefore, torque utilization is high. Moreover, IPMSMs have a wide operating range because of flux-weakening control, which increases the d-axis flux in the negative direction [1, 2]. In general, current source analysis based on sinusoidal current is employed for the design of IPMSMs. This process can simplify the design, and the obtained values of the overall electromagnetic characteristics are almost identical to experimentally measured values. In the IPMSM drive system, the space vector pulse width modulation (SVPWM) technique is widely used due to high voltage utilization rate. SVPWM generates current harmonics through switching processes. These harmonic components increase torque ripple and loss, as well as vibration and noise. Therefore, current source analysis considering current harmonics provides highly accurate predictions of the electromagnetic characteristics of IPMSMs, because it enables more accurate loss prediction than sinusoidal current source analysis does [3]. Moreover, by comparing the mechanical analysis of IPMSMs considering sinusoidal and harmonic currents, the influence of current harmonics on mechanical noise can be determined. In this study, mechanical analysis of IPMSM based on SVPWM control is performed to analyze the influence of current harmonics on mechanical noise. Harmonic current can be obtained via experiment and simulation, as shown in Figure 1. (a) and (b). Figure 1. (a) shows the back-to-back experimental setup used for the IPMSMs. Current is applied to the motor through the SVPWM inverter and contains harmonics due to the switching in the SVPWM inverter. The load torque to the motor is generated by the generator on the other side of the motor through the torque sensor. The torque of the generator can be adjusted using the DC load machine. The analysis model used in this study, as shown in Figure 1. (a), is a V-shape IPMSM with 6 poles, 9 slots, and a concentrated winding. The experiment is performed at the rated speed of the analysis model, and the current applied to the motor is measured and used in the mechanical noise analysis. Figure 1. (b) shows the SVPWM control block of the IPMSMs in simulation. Moreover, the current-generating technique of the SVPWM inverter identified. SVPWM inverter contains proportional and integral (PI) controllers for adjusting the current and speed. To improve the control performance, dq-axis coordinate transformation is used. Park's transformation converts the stationary dq-axis coordinates to rotating dq-axis coordinates. Clark's transformation converts the Cartesian coordinates to stationary dq-axis coordinates. Feedback of speed and position information is obtained from the motor to ensure that the motor can follow the reference speed and current closely. Figure 2. (a) shows the measured current waveform obtained through the experiment, and harmonic component can be seen in this figure. Figure 2. (b) presents the harmonic spectrum of the measured current. We can confirm that the 3rd, 5th, 7th, 11th, and 13th harmonics have a significant influence on the harmonic current. Figure 2. (c) and (d) present the mechanical vibration analysis results for the sinusoidal and measured current, respectively. The noise from the current containing harmonics is greater than that from the sinusoidal current; the majority of the noise is generated by the 6th, 12th, 18th, 21st, and 24th harmonics. From Figure 2, it can be seen that multiples of 6th order component of the current harmonic affects the mechanical noise although the harmonic magnitude is small. In finalized of version of this paper, the current harmonic in the SVPWM control simulation will be discussed, and its mechanical analysis will be presented. In addition, a more detailed discussion and more results will be provided.

[1] K. H. Shin, J. Y. Choi, and H.W. Cho, "Characteristic Analysis of Interior Permanent-Magnet Synchronous Machine With Fractional-Slot Concentrated Winding Considering Nonlinear Magnetic Saturation," *IEEE Trans. Appl. Supercond.*, vol. 26, no. 4, June. 2016, ID 5200404. [2] S. H. Lee,

Y. J. Kim, and S.Y. Jung, "Numerical Investigation on Torque Harmonics Reduction of Interior PM Synchronous Motor With Concentrated Winding," *IEEE Trans. Magn.*, vol. 48, no. 2, pp. 927-930, Feb. 2012. [3] T. C. Jung, W. H. Kim, M. J. Kim, K. D. Lee, J. J. Lee, J. H. Han, T. H. Sung, H. J. Kim, and J. Lee, "Current Harmonics Loss Analysis of 150-kW Traction Interior Permanent Magnet Synchronous Motor Through Co-Analysis of d-q Axis Current Control and Finite Element Method," *IEEE Trans. Magn.*, vol. 49, no. 5, pp. 2243-2246, May. 2013.

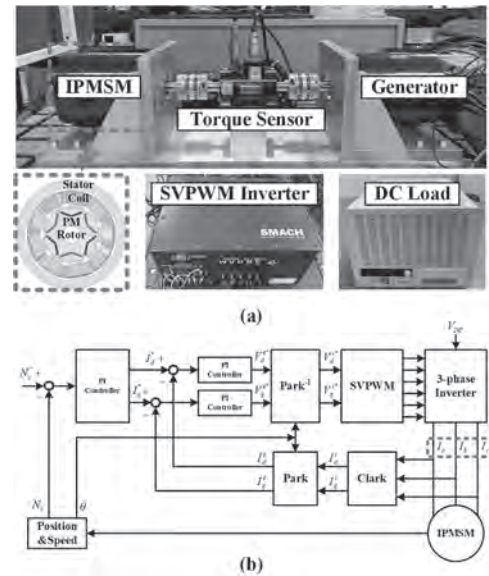


Figure 1. (a) Back-to-back experimental setup for IPMSMs. (b) SVPWM control block of IPMSMs.

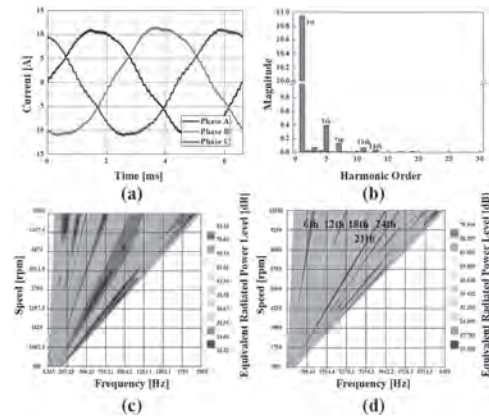


Figure 2. (a) Measured current waveform. (b) Harmonic spectrum of measured current waveform. Results of mechanical noise analysis for (c) sinusoidal current and (d) measured current.

AU-09. Analysis and Calculation of Magneto-Thermal-Structure Coupling of Double-Skewed Induction Motor Based on Multiphysics Field.

G. Chen¹, X. Bao¹, C. Di¹, W. Xu¹, R. Zhu¹ and J. Li¹

1. Hefei University of Technology, Hefei, China

Induction motors are widely used in production due to their simple structure, no-winding rotor, low cost, and convenient maintenance. In order to further improve the electromagnetic performance, some researchers have proposed a new topology structure of the double skewed rotor, which has the advantages of low noise and low vibration [1], and solved the problem that the single skewed rotor induction motor is prone to axial movement and the shortcomings of synchronous additional torque cannot be completely eliminated [2]. In recent years, researchers have optimized the main rotor parameters, but only briefly introduced the intermediate ring (IR) parameters in this type of center ring rotor [3]. In addition, the lack of design strategies for thermal simulation can lead to potential motor failures. This article puts forward a point of view, due to the difference in the electrical density of the middle ring (IR) and the conductive bar will cause greater thermal stress at the junction. Taking into account that under certain operating conditions, when the instantaneous load is huge, the thermal stress at the start time is likely to cause broken bars and broken shafts. Therefore, this article believes that the thermal stress at the moment of startup is considered the main cause of IR electrical failure. Figure 1 a is an electromagnetic model, b is a thermal simulation model and c is the experimental prototype. Compared with the electromagnetic model, thermal simulation model it considers parts such as the casing and wind blades that cannot be ignored. Fig. 2 a is the steady-state thermal analysis of the squirrel cage rotor and shaft in case of locked rotor, and b is the thermal stress analysis of the squirrel cage rotor and shaft. It can be seen from the figure that due to the temperature difference between the guide bar and the middle ring, the maximum thermal stress of the squirrel cage appears at the junction of the guide bar and the middle ring, while the maximum temperature of the rotating shaft is at the location of the middle ring. The simulation situation is roughly consistent with that of the prototype. Detailed results and discussion will be given in the full text.

[1] L. Wang, X. Bao, C. Di and J. Li, "Effects of novel skewed rotor in squirrel-cage induction motor on electromagnetic force and vibration characteristics," 2015 IEEE International Magnetics Conference (INTERMAG), Beijing, 2015, pp. 1-1, doi: 10.1109/INTMAG.2015.7157420. [2] L. Wang, X. Bao, C. Di, et al. Analysis of synchronous parasitic torque in dual skew cage rotor induction motors with equivalent slot number[J]. Iet Electric Power Applications, 2017, 11(8):1357-1365. [3] W. Xu, X. Bao, C. Di, L. Wang and Y. Chen, "Optimal Angle Combination for Improving Electromagnetic Torque in Induction Motor With Double-Skewed Rotor," in IEEE Transactions on Magnetics, vol. 53, no. 11, pp. 1-5, Nov. 2017, Art no. 8206405, doi: 10.1109/TMAG.2017.2707239.

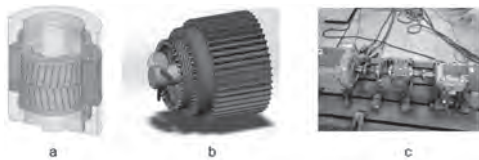


Fig1 double skewed induction motor model

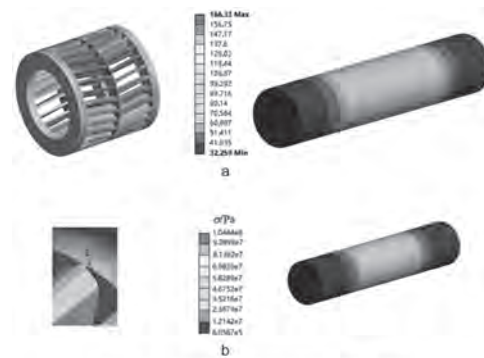


Fig1 steady-state thermal analysis and thermal stress analysis

AU-10. Prediction of Iron Loss With Combined Nonlinear and Linear Finite Element Analysis Considering Current Harmonics by PWM.

X. Gu¹, J. Ryu¹, J. Chin¹ and M. Lim¹

1. Automotive Engineering, Hanyang University, Seoul, The Republic of Korea

I. Introduction Motor characteristics are calculated considering sinusoidal current in a conventional design stage. However, pulse width modulation(PWM) is used to generate alternating current(AC), which will lead to a current distortion. The harmonics in the PWM current cause considerable losses on the iron core [1]. For this reason, considering fundamental current for analysis leads to the decrease of the accuracy of the prediction results. Therefore, it is essential to predict motor characteristic considering harmonic current for electromagnetic design [2]. However, Conventional method considering PWM current needs to put all the large number of analysis step of PWM current into nonlinear finite element analysis(FEA), which leads to the increase of analysis steps and computational time. Therefore, this paper proposes a combined nonlinear and linear FEA method to reduce computational time. In order to reduce the number of analysis step, fundamental current is used to calculated permeability of each element through nonlinear FEA. Then the permeability at each step is interpolated and PWM current is used to predict the motor characteristic through linear FEA. The proposed method is applied to a 130kW IPMSM for traction to calculate iron loss. Comparing with a conventional method that considered PWM current, the proposed method has a high accuracy with a low computational time. II. The proposed analysis method The proposed analysis method is shown in Fig.1. Since the difference between fundamental current and PWM current is small enough not to affect the saturation in iron core as shown in Fig.2 (a), the saturation considering fundamental and PWM current are assumed to be the same. Therefore, the fundamental current can be used to calculate the saturation of the core, and the number of nonlinear analysis step can be reduced. Then, the permeability of each element can be calculated by nonlinear FEA. In order to perform the linear FEA by PWM current which has a lot of data, permeability is interpolated to satisfy all the linear analysis points. Finally, the iron loss can be calculated by linear FEA. A. Determination of non-linear analysis steps First of all, since the PWM current has a large number of data, the number of nonlinear analysis step needs to be large enough, which leads to an increase in computational time. In order to reduce the computational time and maintain the correctness of the analysis, the fundamental current is used to perform a nonlinear FEA. Secondly, gradually reduce the number of step while ensuring the magnetic flux waveform is almost constant. Then, by comparing with the magnetic flux waveform at different positions, it can be known that rib has the highest correlation between the magnetic flux density and step number. And 91 steps are the minimum analysis steps that can describe the original waveform best. Therefore, 91 steps are selected as the minimum analysis steps in this paper. B. Magnetic permeability extraction and interpolation After selecting 91 steps as the minimum analysis steps, the permeability of each element of nonlinear analysis is extracted. And then, considering that the PWM current has a lot of steps, the permeability is interpolated, in order to well describe the PWM current. C. Linear analysis After interpolating the permeability, the number of linear analysis step is increased in order to well describe the PWM current. Then put the interpolated permeability into each element to perform the linear analysis. D. Comparison with conventional method From the analysis results, as shown in the Fig.2 (b), the iron loss calculated by the conventional PWM current method, conventional fundamental current method and the proposed PWM current method can be obtained. Comparing the above three, it can be seen that the iron loss calculated by conventional fundamental current method is quite different from conventional PWM current method, with a difference of 29.7%. However, iron loss calculated by proposed PWM current method is similar with conventional PWM current method, only with a 1% difference. At the same time, computational time is reduced by 88.5% compared with conventional PWM current method. III. Conclusion In this paper, a combined nonlinear and linear analysis method based on PWM current is proposed, which can greatly shorten the analysis time on the premise of ensuring the accuracy of analysis. Compared with the conventional nonlinear analysis which considering the PWM current, this method has high accuracy with only 1% difference. And the computational time is also dramatically

reduced. The method proposed in this paper is reliable and feasible. The experimental verification will be conducted in the final paper.

[1] Y. Miyama, M. Hazeyama, S. Hanioka, "PWM Carrier Harmonic Iron Loss Reduction Technique of Permanent-Magnet Motors for Electric Vehicles," in IEEE Transactions on Industry Applications, vol. 52, no. 4, pp. 2865-2871, July-Aug. 2016. [2] R. Mayuri., N. R. Sinnou and K. Ilango, "Eddy current loss modelling in transformer iron losses operated by PWM inverter," 2010 Joint International Conference on Power Electronics, Drives and Energy Systems & 2010 Power India, New Delhi, 2010, pp. 1-5.

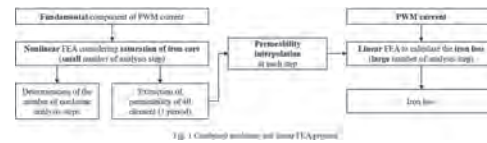


Fig. 1 Combined nonlinear and linear FEA process

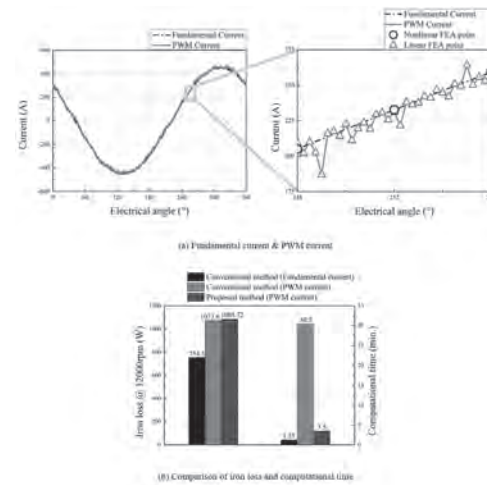


Fig. 2 The influence of harmonics on the analysis results

(a) Fundamental current & PWM current (b) Comparison of iron loss and computational time Fig. 2 The influence of harmonics on the analysis results

AU-11. Magnetic-Thermal Coupling Analysis of Anode Saturable Reactor.

Y. Chen^{1,2}, Q. Yang³, C. Zhang^{1,2}, Y. Li^{1,2} and J. Wang^{1,2}
 1. Hebei University of Technology, Tianjin, China; 2. Hebei University of Technology State Key Laboratory of Reliability and Intelligence of Electrical Equipment, Tianjin, China; 3. Tianjin University of Technology, Tianjin, China

I. Introduction The anode saturable reactor is a critical element in the thyristor converter valve of HVDC (high voltage direct current) transmission system, which is designed for limiting the current rise of the thyristor so as to protect it. However, the non-uniform distribution of core loss of anode saturable reactor can cause overheating and thermal aging of the insulating material, eventually lead to the failure of the reactor [1-2]. It is difficult to measure the local core loss of reactor directly so we have to monitor real-time temperatures with the infrared thermocamera [3]. Because of the complex working current waveform of saturable reactor, Bertotti core loss separation model suitable to sinusoidal excitation is no longer available [4]. Therefore, the dynamic core loss calculation method is used to calculate core loss of the reactor [5-6]. In this paper, the model of saturable reactor is established, and the core loss is analyzed by electro-magnetic finite element method (FEM). To couple the data from magnetic field to temperature field accurately, core loss is mapped between heterogeneous meshing. Meanwhile, the thermal network model of the saturable reactor is built up. Based on the calculation results of computing fluid dynamics (CFD) software, the convective heat transfer coefficients on the reactor surfaces are extracted for thermal resistances calculation. Finally, the steady-state temperature distribution is obtained. The validity of the FEM and thermal network is verified by the temperature rise experiment.

II. Anode saturable reactor model The model of the saturable reactor is shown in Fig.1(a). Located inside the reactor, the hollow aluminum winding consists of 5 turns, which is wrapped by epoxy resin and cooled by circulated water in the aluminum tubes. The 9 pairs of cores, epoxy resin and winding are encapsulated into the reactor fiberglass enclosure with polyurethane elastomer. The outside surfaces of the reactor dissipate heat by natural convection, while the inside surfaces of the reactor can transfer the heat through the circulation aluminum tubes due to highly efficient forced water cooling. In addition, because of the geometric symmetry of the reactor, a one-ninth model of saturable reactor is established for temperature simulation, as shown in Fig.1(b). Other boundary conditions of the model are shown in Fig.1(c).

III. Magnetic-thermal- fluid coupling analysis
A. Magnetic field calculation In order to reduce eddy loss, the core is made of ultra-thin silicon steel sheets with 0.1mm thickness. The leakage magnetic flux penetrates into the silicon steel normally, so the outermost layers silicon steel sheet have significant eddy current. The exact laminated model of sheet-by-sheet reactor is difficult to computed. In order to simulate the surface local eddy current, the homogenous numerical technique is adopted for FEM modelling. The distribution of magnetic flux density is shown as Fig.2(a). Under the impact of air gap, winding structure and leakage magnetic field, the eddy loss is concentrated in the core surfaces and the air gap as shown in Fig.2(b).
B. Calculation of temperature field and fluid field In traditional magneto-thermal coupling method, the loss from magnetic field is obtained by integrating over the whole region and then distributed evenly to each element. This coupling mode with equally distributed loss density underestimates the highest hot-spot so as not to be accurate enough for the reactor model. Consequently, the node-to-node mapping method can predict the loss distribution inside the saturable reactor more precisely. The triangulation element in magnetic field calculation is tetrahedron, while the element in the solid region of CFD is hexahedron. Namely, the meshes of the two physical fields are heterogeneous, so the data cannot be delivered directly. The method of interpolation between the adjacent nodes is proposed in the paper to map the core loss to CFD. The heat sources of saturable reactor are consisted of core loss and hollow aluminum winding loss. Since the temperature in aluminum winding is lower than that in epoxy resin and core, and the cooling water inside winding is a fluid with stable flow rate, the convection heat transfer coefficient is constant. So the winding can be regarded as an internal convective heat transfer boundary condition, which convection heat transfer coefficient on the interface of the winding is $6 \text{ W}/(\text{m}^2 \cdot \text{K})$ by experiment [7]. Contacting with air, the exterior surfaces of

reactor dissipate heat by natural convection. By solving energy conservation, momentum conservation and mass conservation equations, the distributions of reactor temperature and air velocity are shown in Fig.2(c) and Fig.2(d).
IV. Experimental results and discussion The current of the reactor under actual operating conditions is excited into the winding. When the overall temperature is stable, the infrared thermograph is used to record the temperature distribution on the reactor housing. The experimental results show that the highest temperature on the shell is located in the inner toroidal surface, which is 317.15K and in good agreement with CFD simulation results.
V. Conclusion The average surface temperature of the saturable reactor is 315.15K, and the highest temperature is 317.15K at the top of the inner ring surface. Affected by the buoyancy and the uneven distribution of loss, the hottest spot of core is located at the inner and upper position with 354.15K.

[1] C. Peng, S. Baokui, and J. Feng, High Voltage Engineering., Vol.42, p.2612-2617 (2016) [2] Z. Yang, 2019 IEEE 10th International Symposium on Power Electronics for Distributed Generation Systems., p.294-298, (2019) [3] J. Cao, F. Ji, and J. Liu, IET Science, Measurement & Technology., Vol.10, p.77-83 (2016) [4] G. Wenjun, H. Shaogang, and Y. Yuwen, Motor and Control Application., Vol.43, p.82-85 (2016) [5] S. Barg, K. Ammou and H. Mejri, IEEE Transactions on Power Electronics., Vol.32, p.2146-2154 (2017) [6] D. Lin, P. Zhou, and W. N. Fu, IEEE Transactions on Magnetics., Vol.40, p.1318-1321 (2004) [7] M. Yan, D. Shengchu, and G. Lu, High Voltage Engineering., Vol.44, p.3359-3367 (2018)

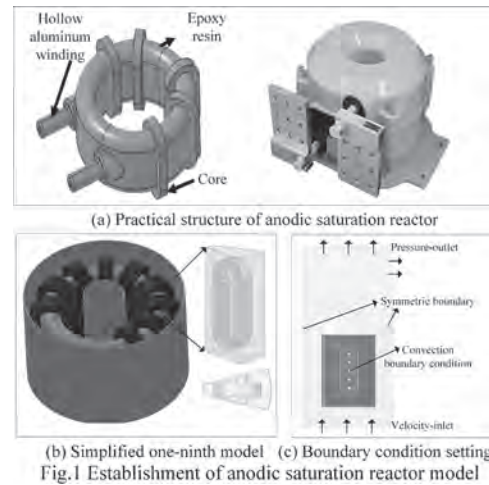


Fig.1 Establishment of anodic saturation reactor model

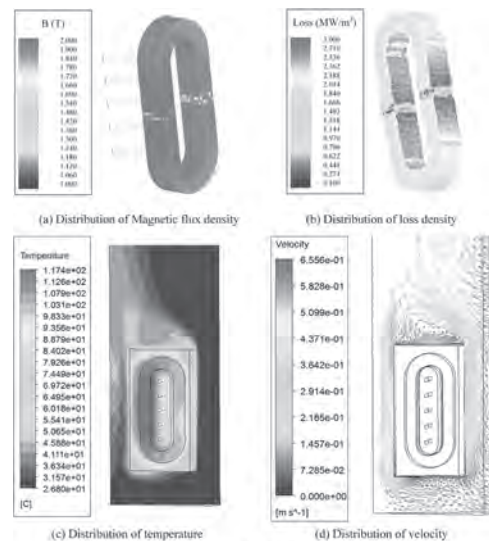


Fig.2 Simulation results of one-ninth model

Fig.2 Simulation results of one-ninth model

AU-12. Influence of Uneven Axial Temperature Distribution on Axial Unbalanced Magnetic Force in PM Machines With Different Rotor Skew Types.

Y. Du¹, L. Wu¹ and H. Wen¹

1. College of Electrical Engineering, Zhejiang University, Hangzhou, China

I. Introduction Permanent magnet (PM) machines have been widely used in many applications, such as wind power generator and electric vehicles, due to their high torque density and efficiency. However, PM machines still face some problems, such as vibration and noise, which can be caused by torque ripple. It has been proved in literature that the torque ripple can be suppressed by rotor skew. Nevertheless, the employment of rotor skew leads to additional problems, such as axial unbalanced magnetic force (UMF) [1]. Axial UMF can also lead to vibration in the axial direction, which further deteriorates bearing life. Although axial UMF due to rotor skew has been investigated in much previous literature, almost all literature assumes PM temperature is uniform in the axial direction. This assumption may be reasonable in PM machines with a short active length and natural cooling method. When active length of PM machines is long or cooling fans are used, axial PM temperature distribution is usually uneven [2]. It is known PM remanence heavily depends on temperature and thus axial UMF can be different from that under uniform PM temperature, which is rarely investigated. This digest is dedicated to fill in this gap. II. FE Model for Investigation 12-slot/8-pole surface-mounted PM (SPM) machines with the same stator yet different rotors are selected for investigation, which are shown in Fig. 1(a)-Fig. 1(c). The parameters will be detailed in the full paper. Due to the complex manufacturing process of continuous rotor skew, three-step skew is applied for the two rotors. They share the same angle displacement 5 mechanical degrees between two adjacent PM segments to mitigate cogging torque yet with opposite directions. It is defined that the rotor skew in Fig. 1(b) is the counter-clockwise (CCW) type and the one in Fig. 1(c) is the clockwise (CW) type. III. Uneven Axial Temperature Distribution The thermal circuit method is employed to calculate the temperature distribution, where Motor-CAD is used. For SPM machines, $I_d=0$ control strategy is usually employed and thus $I_q=13$ A is input to stator windings, which leads to a copper loss of 219W. The rotor speed is assumed to be 500rpm and the other losses are neglected. It is also assumed that the ambient temperature is 20 degrees Celsius. The natural convection is applied outside the machine frame and the inside of machine is cooled down through ventilation. The cooling air blows from the rear to the front of the SPM machines with a constant flow rate 0.004m³/s. The steady temperature distribution in the axial direction is shown in Fig. 1(d). It can be seen that the PM close to the air inlet exhibits the lowest temperature 34.3 degrees Celsius, which is about 12.4 degrees Celsius smaller than that for the PM close to the air outlet, which cannot be neglected. For the two rotor skew types, the axial temperature distribution is almost the same. IV. Axial Unbalanced Magnetic Force Three-dimensional finite element method is used to calculate the axial UMF under $I_q=13$ A. In order to simplify the analysis, it is assumed the temperatures for each PM segment are uniform, which are 46, 41 and 36 degrees Celsius, respectively. Assuming the PM remanence is 1.2T and its temperature coefficient is about -0.12%, the axial UMF waveforms and spectra are shown in Fig. 2(a) and (b). It can be seen that the axial UMF has the same magnitude for both skew types yet with opposite directions under uniform axial temperature 41 degrees Celsius. When the uneven axial temperature distribution is considered, the axial UMF becomes smaller for CW skew and larger for CCW skew. The average axial UMF for CCW skew is about 7.8% larger than that of CW skew whilst the UMF ripple is about 3.6% larger. Then the influence of temperature difference between side and middle PM segments and middle PM temperature is analyzed. When the middle PM temperature keeps unchanged and the temperature difference increases, both the average axial UMF and UMF ripple further increase for CCW rotor skew whilst they decrease for CW rotor skew, as shown in Fig. 2(c) and (d). It can be seen that when the temperature difference is 10 degrees Celsius, the CCW skew exhibits 16.2% larger average UMF and 7.2% larger UMF ripple than the CW skew. When the middle PM temperature increases and temperature difference keeps fixed, the axial UMF decreases for both CW and CCW skew. V. Conclusions This digest investigates the influence of uneven axial

temperature distribution on axial UMF in PM machines. It shows that CW rotor skew is recommended when designing PM machines from the perspective of mitigating axial UMF. The conclusions are applicable to the conditions with different middle temperature when the temperature difference is fixed. Furthermore, the advance of CW skew increases with the temperature difference under the same middle temperature. In the full paper, the influence of uneven axial temperature distribution on the axial UMF for herringbone skew type will be investigated. In addition, more analytical analysis and experimental validation will be presented.

[1] C. H. Kang, K. J. Kang, and J. Y. Song, *IEEE Transactions on Magnetics*, vol. 53, pp. 1-5 (2017). [2] M. T. Bin Tarek, J. Herbert, and S. Choi, *IEEE International Electric Machines and Drives Conference*, pp. 1-6 (2017).

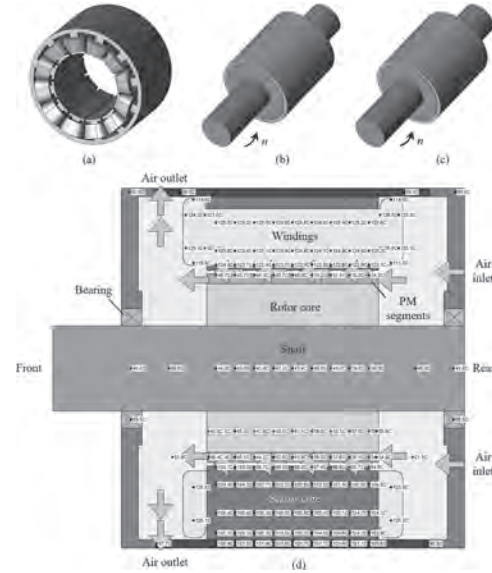


Fig.1. FE model and axial temperature distribution. (a) FE model. (b) CCW rotor skew. (c) CW rotor skew. (d) Axial temperature distribution.

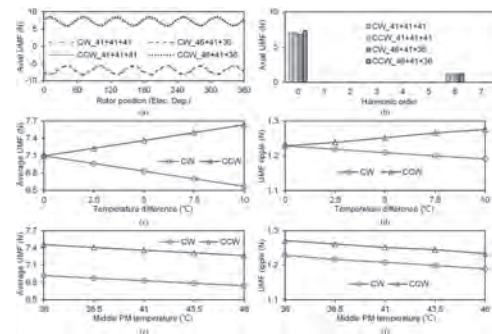


Fig.2. Axial UMF. (a) Axial UMF waveforms. (b) Spectra of axial UMF. (c) Average axial UMF under different temperature differences. (d) Axial UMF ripple under different temperature differences. (e) Average axial UMF under different middle PM temperatures. (f) Axial UMF ripple under different middle PM temperatures.

AU-13. Withdrawn

AU-14. Research on Electromagnetic Control of Robot Arm Using Smart Motor Combined With Internet of Things.

C. Hsu¹

1. Mechanical Engineering, Oriental Institute of Technology, Panchiao, Taiwan

1. Abstract This research aims to study the edge computing devices with a faster processing and signal connecting function based on development of the physical layer and magnetic sensing devices. It is important matter for smart robot in multi-axis motor control. Based on the variable robot properties, it includes humanoid robots, wheeled machines, and fixed robots, respectively, are contented. This research is constructed as follows: to establishing an edge computing device system, the image vision system with neural-network learning theory to control robot arm path, multiple magnetic sensors in physical layer to analyze the signals of the motor, voltage, current, temperature, etc., are transmitted signal to the edge computing device and IoTs computing server system. 2. Introduction The Industry 4.0 concept represents the trend of data exchange and automation in the manufacturing industry. It is defined by cloud computing, cyber-physical systems and the IoTs. In Industry 4.0, computers and automation technologies are integrated with robots and their components [1,2]. These robots and other components are remotely connected to a computer system, and the computer system is equipped with algorithms that can control and learning robots with minimal human intervention. For the motor device, the robot composes the control of the DC motor and relate to the accessories vital role. However, there are many factors that can misguide the controller’s work, to make an unable to accurately control and/or have the desired dynamic behavior. For example, the resistance (Ohmic) of the coil winding of the motor is changed due to the temperature is different. If the vibration level is high and the wear of the rotor ball bearing becomes larger, the friction coefficient will also be affected. Therefore, the cloud computing environment of industrial factories, a continuous processing is required to re-evaluate the precise values of motor parameters and update the corresponding controller settings. In addition, it should be noted that the torque and speed sensors of the motor must have the correct selection to assist for achieving the correctness of the program. 3. Theory and methods: multi-axis motor sensing and visual images of robotic arms Collaborative robots focus on intelligent motor control. Based on this construction, multiple sensor component signals are added. The physical information such as voltage, current, vibration, electric heating, magnetic flux sensing, and motor position is diagnosed through integrated control. This study, the artificial intelligent motor with the sensing signals, is used to control motor speed, positioning, constant horsepower, constant torque, force feedback, vibration resistance, overheating, overload, and instantaneous short circuit, as shown in Figure 1. The electromagnetic control of this paper is as follows: A. Single robotic arm function automation: Directly control the robot motor, at the same time, it has higher precision and speed to perform specific tasks repeatedly, but most of them cannot clearly actuate without an electromagnetic sensor. B. Part of the arm automation: It assists decision-making through environmental sensing input signals. In this study, robots use vision and sensors to determine the decision-making process, which is not easy to deal with accidental arm interference. C. Conditional autonomous robot: Control the arm according to the environmental monitoring behavior, but the external server can operate in real time. D. Highly autonomous robot: an environment that needs to be defined in an area or any situation without human operation. 4. Experimental results and discussion Based on the motor control of intelligent robots, this research proposes a better and faster algorithm structure, which is a neural network-like combined with particle swarm method, which is used to calculate the convergence result of a lower loss function, which can accurately control the motor parameters and combine the IoTs, as shown in Figure 2. First, the robotic arm establishes multi-input sensing values, using the above algorithm to evaluate the robotic arm motor parameters, the prevention of interference from peripheral physical sensing, and the signal processing of external visual images. The issues raised based on past research experience include:(1) Establish edge and fog calculations to control the voltage and current of the motor, (2) establish neural network algorithm to calculate motor parameter, (3) construct the image vision system, (4) establish a smart robot platform, including wheel-shaped and human-shaped robots as experi-

ments, which uses the above-mentioned deep learning theory to construct the test of the robot’s motor motion and signal transmission response, (5) to use the multiple sensors, motor electromagnetic signals, piezoelectric sensors, and load signals, as the force feedback of the robot to calculate and judge. Finally, (6) to integrate the edge computing of the sensing layer, the fog computing of the signal processing layer, and faster computing layer through the IoTs cloud server. The IoTs chip is to use the dual-core Linkit-7697 (Taiwan’s MediaTek Inc). The chip can perform as a cloud computing and remote device, which indeed meet the requires of providing multi-sensing force feedback for cooperative robot handling objects.

[1]. Chang-Hung Hsu*, et. al., “Effect of Magnetostriction on the Core Loss, Noise, and Vibration of Fluxgate Sensor Composed of Amorphous Materials,” IEEE Trans. on Magnetics, vol. 49, no. 9, pp: 3862-3865, 2013.
 [2]. Chang-Hung Hsu*, “Fractional Order PID Control for Reduction of Vibration and Noise on Induction Motor, IEEE Transactions on Magnetics, vol. 55, no. 11, pp. 6700507-1-7, Nov. 2019.

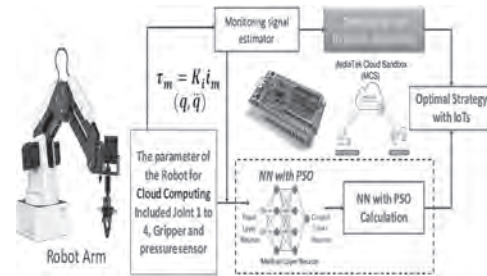


Figure 1 The artificial intelligent motor with the sensing signals including as motor speed, positioning, horsepower, torque, force feedback signals.

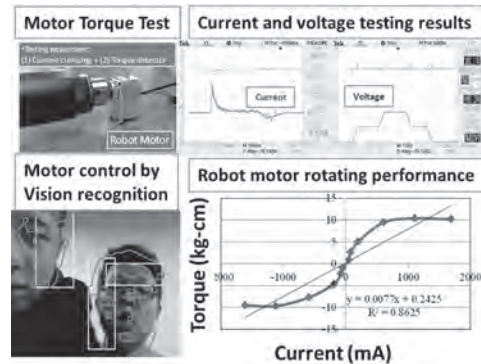


Figure 2 The smart motor of the robot performance testing results and AI vision detection.

Session AV
VIBRATION ANALYSIS AND ENERGY HARVESTING APPLICATIONS
(Poster Session)

Daniele Davino, Chair
Universita degli Studi del Sannio Dipartimento di Ingegneria, Benevento, Italy

AV-01. Dependence of the Vibration Energy and Frequency on the Charging Characteristics and the Damping Characteristics of the Linear Synchronous Generator.

T. Azuma¹, T. Maruyama¹ and S. Ohashi¹

1. Electrical and Electronic Engineering, Kansai University, Suita, Japan

The renewable energy is introduced because of global environmental problems. The vibration energy generated by the electric vehicle and the buildings is considered. Using the linear synchronous generator, this energy is converted to electric energy. The charging circuit with the EDLC (Electric Double-Layer Capacitor) for the linear synchronous generator is introduced. The linear synchronous generator extends the cruising distance of the electric vehicle and lighting of the buildings. In addition, it also suppresses vibration. Thus it is used as the damping device such as the mechanical damper [1]. Fig.1 shows the linear synchronous generator. The electric energy is generated by using the linear synchronous generator. The linear synchronous generator consists of the stator part and the vibration part. The permanent magnet and the iron yoke are set on the stator part. The coil for the generation is set on the vibration part. The vibration is generated by giving the initial energy (the elastic energy by the mechanical spring) to the vibration part. When the coil moves in the x -axis direction on the permanent magnet, the linkage flux from the permanent magnet is changed. The electromotive force in the coil is generated by the linkage flux is changed [2]. In this paper, the charging characteristics and the damping characteristics of the linear synchronous generator are studied. The charging characteristics are determined by the charging energy of the EDLC. The vibration waveform is damped by the charging energy of the EDLC, the power consumption in the wire-wound resistance of the coil and the internal resistance of the EDLC, the mechanical loss. The mechanical loss is calculated as the loss proportional to the velocity using the viscosity coefficient $c = 2.0$ derived from the vibration waveform of the linear synchronous generator. Their characteristics are examined by changing the initial energy given to the vibration part and the frequency of the vibration waveform. The initial energy is changed by the initial displacement of the vibration part. The frequency is changed by the spring constant [3]. In this study, MATLAB/Simulink and PSIM (the electronic circuit simulation software) are used for analysis. The generated voltage V_m is converted to DC voltage by the rectifier. The analysis conditions are as follows; the coil inductance $L = 1.4$ mH and the wire-wound resistance of the coil $R_L = 3.0$ Ω , the EDLC capacitance $C = 0.141$ F and the internal resistance of the EDLC $R_C = 6.67$ Ω . The charging characteristics and the damping characteristics are studied by changing the initial energy (0.073 ~ 7.3 J). The initial displacement of the vibration part is changed (10 ~ 100 mm) and the spring constant is 1465 N/m. The frequency is 5 Hz. From the result, the charging energy of the EDLC is increased proportionally as the initial energy increases. This is because the electromotive force in the coil is increased as the initial energy increases. And charging efficiency of the EDLC is increased as the initial energy increases. The linear synchronous generator can be charged with high efficiency as the initial energy increases. The stop time of the vibration part compared to the case that the charging circuit is not connected is the fastest and the vibration part is stopped 38.6% faster when the initial energy is 7.3 J. But the power consumption in the wire-wound resistance and in the internal resistance of the EDLC, and the mechanical loss are increased. The charging characteristics and the damping characteristics are studied by changing the frequency (1 ~ 10 Hz). The initial energy is fixed at 0.36 J. Figs.2(a) shows the vibration waveform (1, 5, and 10Hz), and Figs.2(b) shows the charging energy of the EDLC by changing the frequency (1 ~ 10 Hz). From the result, the charging energy of the EDLC is decreased as the frequency increases. This is because the current in the circuit and the velocity of the vibration part is increased as the frequency increases, and the power consumption in the wire-wound resistance and in the internal resistance of the EDLC, and the mechanical loss is increased. The stop time of the vibration part is shortened as the frequency increases. To improve the charging characteristics, the circuit switching the EDLC is created. Switching uses two EDLCs. The charging characteristics are improved. This is because a low voltage that isn't charged can be charged. And the damping characteristics are improved because the kinetic energy of the vibrating part is consumed faster. In conclusion, the charging characteristics are improved when the initial energy is large and the frequency

is low. The damping characteristics are improved when the initial energy is large and the frequency is high. When using as the power generator, the vibration with the large energy amount and low frequency is effective. And when using as the vibration damping device, the vibration with the large energy amount and high frequency is effective. The circuit that switching the EDLC is effective for both the charging characteristics and the damping characteristics.

[1] M. Mueller, P. Brooking and J. Xiang, "Low Speed Linear Electrical Generators for Renewable Energy Applications," *Proc. of Int. Symposium on Linear Drives for Industry Applications*, pp.29 -32 (2003) [2] K. Ishida, J. Muranishi, T. Aoki, S. Ohashi, "The Generation Characteristics of the Improved Configuration of the Stator and the Mover in the Linear Generator Using Vibration Energy," *IEEE Region 10 Conference (TENCON)*, pp.2634-2637 (2016) [3] S. Ohashi, T. Matsuzuka, "Basic Characteristics of the Linear Synchronous Generator Using Mechanical Vibration," *IEEE Trans. Magnetics*, vol.41, No.10, pp.3829-3831 (2005)

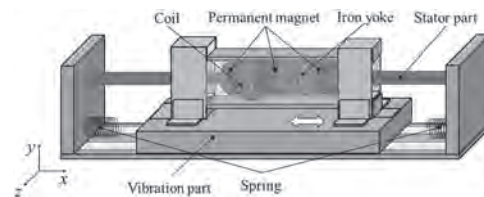


Fig.1 The linear synchronous generator

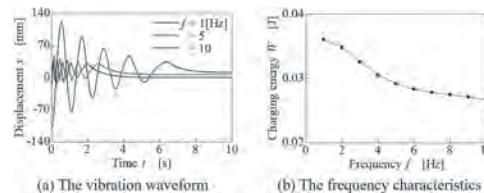


Fig.2 The charging characteristics and the damping characteristics by changing the frequency

AV-02. Modal Frequency Calculation of Stator Assembly of the Electrical Machine Considering Interference Fit and Orthogonal Properties of Materials.

F. Liu¹, P. Zheng¹, M. Wang¹, G. Qiao¹ and S. Zhang¹

1. School of Electrical Engineering & Automation, Harbin Institute of Technology, Harbin, China

1. Abstract: In this paper, an improved modal frequency calculation theory of the stator assembly of the electrical machine is proposed based on the first-order shear deformation laminated theory. The frame, stator core and windings of the assembly are modeled as multilayer cylindrical shell, which are laminated along the radial direction. In order to increase the accuracy, the interference fit is considered in the proposed model, which is widely used in manufacture of the assembly. Due to the lamination characteristics of stator core and the arrangement of copper and insulation of windings, the orthogonal properties of these materials are considered in the modeling. The motion and boundary equations are deduced via variational method, and the modal frequency can be obtained by calculating the eigenvalues of the equations. Then, the experiments is conducted by hammer impact test. The experimental results of the free and simply supported boundary conditions are compared with the calculated results, and the comparison shows good arrangement for the proposed model. 2. Introduction: Electrical machines are widely used in electric vehicles, washing machines, compressors and other people involved areas, and the concomitant electromagnetic vibration and noise have aroused attention to comfort. Based on the modal superposition method, the vibration response can be obtained depending on pressure distribution, excitation frequencies, modal frequencies and shapes. In order to avoid coincidence between excitation frequencies and natural frequencies, the modal frequency of the machine stator should be accurately calculated [1]. Because machine stator assembly contains many parts, such as frame, windings, end covers and stator core, some simplifying assumptions have been made in existing studies [2]-[3]. The ring type model takes all the parts as a single ring and neglects the axial direction, but it can only calculate the pure radial modes and cannot consider the boundary conditions. Other researchers propose different simplification method of teeth, windings and frame, but the calculated modes are only in partial agreement with experimental. As for the materials, most studies consider them as isotropic and continuous. However, this can lead to a noticeable discrepancy between the mode of the analytical result and that of the test result. The interference fit will increase the equivalent stiffness of the stator assembly, but the effect of the fit on the modal frequency are not deeply investigated. In this paper, a modal frequency calculation method is proposed, and the orthogonal properties of materials and the interference fit are considered. 3. Calculation model: A nature frequency calculation theory is proposed based on the first-order shear deformation laminated theory. In the proposed method, the stator assembly is modeled as multilayer cylindrical shell laminated along radial direction. Due to the lamination characteristics of silicon steel sheet and the arrangement of copper and insulation of winding, these two materials can be model as orthotropic materials. In order to approach the realistic situation, the interference fit is modeled in the proposed method, which is a single layer between the frame and stator core. Then, the motion and boundary equations are deduced via the variational method, as shown in Fig. 1. The modal frequencies of three translational and two rotational directions can be obtained by calculating the eigenvalues of the equations. The modal frequencies of the stator assembly under free and simply support boundary condition are calculated, and compared with simulation results of the finite element method. In addition to calculating the modal frequency of the radial-flux electrical machines, the proposed model can also be applied to calculated modal frequency of the axial-flux machines. 4. Experimental verification: To verify the accuracy of the proposed model, a 27-slot stator assembly of a radial-flux machine is utilized. The hammer-impact test of the free boundary condition is realized by suspending the assembly using an elastic cord, as shown in Fig. 2 (a) and (b). Then, the force and vibration signals of the impact test are input into the signal-processing model to obtain the modal frequency, and the experimental result is shown in Fig. 2 (c). The modal frequencies calculated from isotropic model, the proposed method excluding and including interference fit are compared with the experimental results. The errors between isotropic model and experimental results are

up to 30%, especially the interested low-order modal frequencies. Due to considering the interference fit, the calculation results of the proposed model are closer to the experimental results. Then, the experiment of simple support boundary conditions is conducted by fixing the stator assembly on the bench, and the results are compared with the proposed model. The maximum errors between the proposed method and the results are within 5%, which verifies the accuracy of the proposed method.

[1] Lin F., S. Zuo and W. Deng, IEEE Trans. on Ind. Electron., Vol. 63 (12), p.7455-7466, (2016) [2] J. Le Besnerais, V. Lanfranchi and M. Hecquet, IEEE Trans. Ind. Appl., vol. 46(4), pp. 1367-1373, (2010) [3] D. Torregrossa, B. Fahimi and F. Peyraut, IEEE Trans. Ind. Electron., vol. 59(2), pp. 839-847, (2012)

$$\begin{aligned} & \frac{\partial}{\partial r} \left(\frac{1}{r} \frac{\partial u}{\partial r} \right) + \frac{\partial}{\partial r} \left(\frac{1}{r} \frac{\partial v}{\partial r} \right) + \frac{\partial}{\partial r} \left(\frac{1}{r} \frac{\partial w}{\partial r} \right) + \frac{\partial}{\partial r} \left(\frac{1}{r} \frac{\partial \theta}{\partial r} \right) + \frac{\partial}{\partial r} \left(\frac{1}{r} \frac{\partial \psi}{\partial r} \right) = 0 \quad (1) \\ & \frac{\partial}{\partial r} \left(\frac{1}{r} \frac{\partial u}{\partial r} \right) + \frac{\partial}{\partial r} \left(\frac{1}{r} \frac{\partial v}{\partial r} \right) + \frac{\partial}{\partial r} \left(\frac{1}{r} \frac{\partial w}{\partial r} \right) + \frac{\partial}{\partial r} \left(\frac{1}{r} \frac{\partial \theta}{\partial r} \right) + \frac{\partial}{\partial r} \left(\frac{1}{r} \frac{\partial \psi}{\partial r} \right) = 0 \quad (2) \\ & \frac{\partial}{\partial r} \left(\frac{1}{r} \frac{\partial u}{\partial r} \right) + \frac{\partial}{\partial r} \left(\frac{1}{r} \frac{\partial v}{\partial r} \right) + \frac{\partial}{\partial r} \left(\frac{1}{r} \frac{\partial w}{\partial r} \right) + \frac{\partial}{\partial r} \left(\frac{1}{r} \frac{\partial \theta}{\partial r} \right) + \frac{\partial}{\partial r} \left(\frac{1}{r} \frac{\partial \psi}{\partial r} \right) = 0 \quad (3) \\ & \frac{\partial}{\partial r} \left(\frac{1}{r} \frac{\partial u}{\partial r} \right) + \frac{\partial}{\partial r} \left(\frac{1}{r} \frac{\partial v}{\partial r} \right) + \frac{\partial}{\partial r} \left(\frac{1}{r} \frac{\partial w}{\partial r} \right) + \frac{\partial}{\partial r} \left(\frac{1}{r} \frac{\partial \theta}{\partial r} \right) + \frac{\partial}{\partial r} \left(\frac{1}{r} \frac{\partial \psi}{\partial r} \right) = 0 \quad (4) \\ & \frac{\partial}{\partial r} \left(\frac{1}{r} \frac{\partial u}{\partial r} \right) + \frac{\partial}{\partial r} \left(\frac{1}{r} \frac{\partial v}{\partial r} \right) + \frac{\partial}{\partial r} \left(\frac{1}{r} \frac{\partial w}{\partial r} \right) + \frac{\partial}{\partial r} \left(\frac{1}{r} \frac{\partial \theta}{\partial r} \right) + \frac{\partial}{\partial r} \left(\frac{1}{r} \frac{\partial \psi}{\partial r} \right) = 0 \quad (5) \end{aligned}$$

Fig. 1 Motion equations of the proposed modal frequency calculation theory

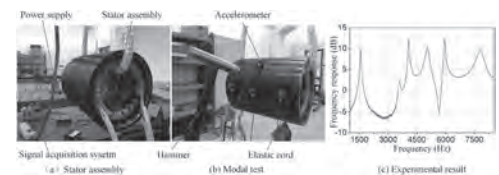


Fig. 2 Modal test and experimental result

AV-03. Vibration Reduction of IPMSM With Asymmetric Rotor Shape Under Certain Load Condition.

S. Woo¹, J. Kim¹, J. Park¹, S. Park¹ and M. Lim¹

1. Automotive Engineering, Hanyang University, Seongdong-gu, The Republic of Korea

I. Introduction The electric motors have been widely used in various applications such as automobiles, and home appliances. Among the various types of electric motors, the interior permanent magnet synchronous motors (IPMSM) in which permanent magnets (PM) are inserted in the rotor receive a lot of attention due to the advantage of high efficiency and high power density. Since these applications are closely related with daily life, the vibration and noise reduction of IPMSM used in these applications are important. Further, most of these applications require continuous driving under certain load condition. Thus, it is important to reduce the vibration and noise of IPMSM used for continuous driving under certain load condition [1]. To reduce the vibration of IPMSM under certain load condition, the asymmetric rotor design which changes mechanical air-gap length has been proposed in [2]. However, the average torque is decreased as mechanical air-gap length is changed. Therefore, in this paper, arrangement of the PM and flux barrier is modified to make the asymmetric rotor shape which changes magnetic air-gap length instead of mechanical air-gap length. Through this method, the vibration can be reduced maintaining average torque under certain load condition. To confirm the vibration reduction of IPMSM with asymmetric rotor shape under certain load condition, the vibration analysis of the 4-pole 24-slot IPMSM with the symmetric and asymmetric rotor shape is conducted using 2-dimensional finite element analysis (2D FEA). II. Relationship between radial force density and air-gap magnetic flux density The radial force density can be expressed by the Maxwell stress tensor method. The radial force density generates the stator displacement which causes the vibration of motors. The spatial harmonic order of the radial force density is called as the vibration order. The stator displacement is inversely proportional to the fourth power of the vibration order [3]. Thus, the radial force density with low vibration order should be decreased to reduce the vibration. As a result, it is necessary to make the radial air-gap magnetic flux density sinusoidal. The radial air-gap magnetic flux density can be calculated by multiplying the sum of the air-gap magnetic flux density neglecting slotting effect by the PM and armature with the relative specific permeance of the stator and rotor. Therefore, to make the radial air-gap magnetic flux density sinusoidal, the rotor permeance should be uniform. In this paper, the arrangement of the PM and flux barrier is modified to make the rotor permeance uniform. III. Vibration analysis using FEA The configuration of the 4-pole 24-slot IPMSM with the symmetric and the asymmetric rotor shape is shown in Fig. 1. The symmetric and asymmetric model have same geometric shapes only except for the rotor. Under the load condition of 1.92 Nm at 5000 rpm, the radial force density is calculated from (1) using 2D FEA. The spectrum analysis result of the radial force density using 2D fast Fourier transform is shown in Fig. 2(a). As shown in Fig. 2(a), at most time harmonic orders, the radial force density of the asymmetric model is less than that of the symmetric model. Specifically, at the 2nd time harmonic order, the radial force density with the lowest vibration order of 4 is decreased by 12.4% from 125.62 kN/m² to 110.04 kN/m². Also, at the 10th time harmonic order, the radial force density with the lowest vibration order of -4 is decreased by 44.5% from 12.79 kN/m² to 7.10 kN/m². Next, the vibration analysis is conducted to calculate the stator displacement using 2D FEA by applying the radial force density on the stator. The time harmonic analysis result of the stator displacement of the symmetric and asymmetric model is shown in Fig. 2(b). As shown in Fig. 2(b), at most time harmonic orders, the stator displacement of the asymmetric model is reduced. Particularly, at the 2nd, 10th, and 22nd time harmonic orders, the stator displacement of the asymmetric model is decreased by 16.1%, 45.0%, and 68.4%, respectively. According to these results, the vibration reduction of the asymmetric model compared with that of the symmetric model is confirmed under the load condition of 1.92 Nm at 5000 rpm. This is because under the load condition, rotor permeance of the asymmetric model is more uniform than that of the symmetric model due to the current phase angle. IV. Experimental verification and conclusion In this paper, the vibration analysis of the symmetric and asymmetric model is conducted using 2D FEA under the load condition of

1.92 Nm at 5000 rpm. As a result, the vibration reduction of the asymmetric model is confirmed. This is because the radial force density with a low vibration order is decreased as the rotor permeance becomes uniform. Therefore, it is expected that the 4-pole 24-slot IPMSM with asymmetric rotor shape is effective to reduce the vibration. To verify the vibration reduction of the asymmetric model, the vibration experiments will be conducted under the same load condition of 1.92 Nm at 5000 rpm.

[1] C.-H. Lin and C.-C. Hwang, "Multiobjective optimization design for a six-phase copper rotor induction motor mounted with a scroll compressor", *IEEE Trans. Magn.*, vol. 52, no. 7, July 2016. [2] Y.-H. Jung, M.-R. Park, and M.-S. Lim, "Asymmetric rotor design of IPMSM for vibration reduction under certain load condition", *IEEE Trans. Energy Convers.*, vol. 35, no. 2, pp. 928-937, June 2020. [3] J.-F. Gieras, C. Wang, and J.-C. Lai, "Magnetic fields and radial forces in polyphase motors fed with sinusoidal currents", in *Noise of Polyphase Electric Motors*, 1st ed., Boca Raton: CRC Press, 2006, ch. 2, pp. 21-64.

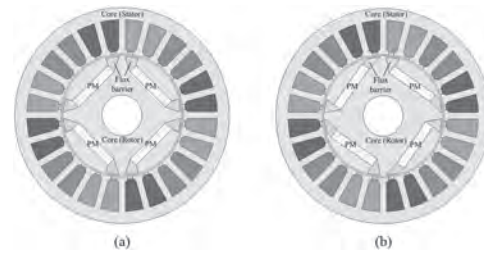


Fig. 1. Configuration of the 4-pole 24-slot IPMSM with (a) the symmetric rotor shape (b) the asymmetric rotor shape

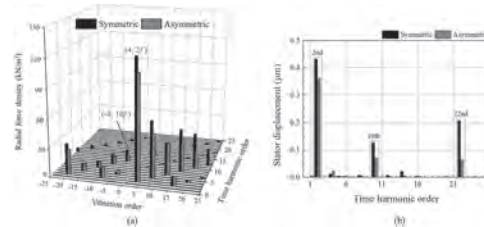


Fig. 2. Under the load condition of 1.92 Nm at 5000 rpm (a) spectrum analysis result of the radial force density (b) time harmonic analysis result of the stator displacement

AV-04. Modeling and Low-Power Design of Advanced Galfenol Non-linear Coupled Energy Harvesting System.

S. Cao¹, C. Zhao¹, J. Zheng¹ and R. Yan¹

1. Hebei University of Technology, Tianjin, China

I. Introduction Galfenol [1]–[6] and piezoelectric (PZT) [7] cantilever energy harvesters (CEHs) have wide applications in powering wireless sensors in Internet of Things. Especially, Galfenol with high tensile strength is more suitable as CEHs than PZT. However, Galfenol [1]–[3] and PZT single-degree-of-freedom (SDOF) traditional CEHs (TCEHs) exhibit high-frequency narrowband, which is not suitable for low-frequency broadband vibration in the sensor environment. Also, Galfenol CEHs have inherent nonlinear mechanical-magnetic-electric coupled (NMMEC) behaviors. The two-DOF (2DOF) improved CEHs (ICEHs) [6],[7] by introducing nonlinearity and elastic magnifier (EM) have larger low-frequency broadband power than the SDOF ICEHs [4], [5], but have more complex behaviors. Different models of Galfenol CEHs are presented, including dynamic [1], [2], [6] and finite element [5] models. These models are important for designing CEHs, but simplify energy extraction circuits (EECs) as a resistance. In practical EECs design, harvesters are often simplified as a voltage source, and the circuit model [3] cannot describe nonlinearities of the CEHs. To improve and evaluate the performances of the systems, the challenge is to model and design an advanced system including ICEH and EEC for adapting environmental frequency changes. II. Modeling and Design of Harvesting System In the paper, the NMMEC equivalent circuit models of a TCEH [1] and a ICEH [6] are firstly established, where the mechanical, magnetic and mechanical-electro coupled terms are represented by electronic components. It is noted that the nonlinear magnetic force F_m , nonlinear piezomagnetic coefficient d_1 , NMMEC coefficient e and nonlinear magnetic induction B are obtained by the controlled voltage sources. Then, a simple low-power consumption EEC is proposed, and its components' type and value are determined. The EEC includes a AC-DC converter [8] with two n-MOSFETs M_{n1} and M_{n2} , a voltage regulator, an oscillator, and a positive DC supply V_+ . The CEHs' inductance L_c is used for boost operation in the positive and negative half-cycle of AC voltage V_a . The converter is operated in discontinuous conduction mode (DCM) to provide a resistance R_c to the CEHs. The regulator LT3009-3.3 is used to stabilize the storage capacitor voltage V_{Cs} to a DC voltage $V_d=3.3V$. It is noted that in the designed EEC, the PI-control circuit [8] with many passive components is replaced by a voltage regulator. Moreover, the EEC, which does not require external sawtooth power supply and DC supply V_+ in [3], can use a simple oscillator to produce the fixed duty cycle $D \approx 0.7V$ for ensuring that the load power of the CEHs are bigger. These improvements are important for the CEHs with low power. Finally, the TCEH and ICEH systems with the EEC are modeled in a circuit simulator LTSpice for system-level evaluation. III. Results and Analysis The equivalent circuit models can describe and predict NMMEC behaviors of the TCEH [1] and ICEH [6], which will be shown in full paper. Here, under bias field $H_b=3580$ A/m and base acceleration $a=a_m \sin(2\pi ft)$, the curves calculated by the circuit simulator LTSpice are shown in Fig.1 and Fig.2. Fig.1 shows that the circuit models can accurately describe open-circuit voltage nonlinear curves of the TCEH, and can predict low-frequency-broadband power output behaviors of the ICEH, which oscillates in the medium-, high- or chaotic-energy orbits. From Fig.2, the performances of the TCEH and ICEH systems with the EEC are as follow: 1) Under varying load resistance R_d and f , load current I_d , AC voltage V_a and storage capacitor voltage V_{Cs} will vary, but steady DC voltage $V_d \approx 3.3V$ is maintained; 2) In the initial stage of the systems, the EEC is powered by a 2V battery. The battery maximum discharging power $P_{E1} \approx -72\mu W$ (in Fig.2 (b)) shows that the EEC is a very low-power consumption circuit; 3) With the increase of the harvested energy, the DC supply V_+ is bigger than the battery voltage $V_{E1}=2V$, thus the EEC is powered and charged even by the harvested small energy (in Fig.2(b) and (c)) to maintain self-sustaining and future start-up operations; 4) Compared to the TCEH system, the ICEH system can harvest and store more energy to persistently satisfy the load requirements (3.3V DC) in the wider low-frequency range [30Hz, 51Hz]. IV. Conclusion In short, a general NMMEC circuit modeling method of Galfenol CEHs is presented. The CEH systems with complicated mechanical structure and a low-energy consumption EEC are modeled and designed, and their complex NMMEC behaviors

are effectively evaluated. It is found that under varying f and R_d , the systems with EEC can use harvested low power (e.g., 0.73mW) to convert changeable and low AC voltage (e.g., 0.6V) to a steady 3.3V voltage, and maintain self-sustaining and future start-up operations. The advanced ICEH system can harvest and store more energy to persistently provide 3.3V voltage in the broader frequency range [30Hz, 51Hz] for adapting environmental frequency changes.

[1] J. -H. Yoo and A. B. Flatau, *J. Intell. Mater. Syst. Stru.*, vol. 23, no. 6, pp. 647–654(2012) [2] H. Liu, L. Wei, Q. Liang, *et al.*, *Mechatronics*, vol.63, no.12, Art no. 102264(2019) [3] S. Cao, X. Wang, J. Zheng, *et al.*, *IEEE Trans. Magn.*, vol. 54, no. 11, Nov. Art no. 8207 005(2018) [4] S. Furumachi and T. Ueno, *Proc. SPIE, Smart Materials and Nondestructive Evaluation for Energy Systems*, 9806, 98060X(2016) [5] Z. Deng and M. J. Dapino, *J. Intell. Mater. Syst. Stru.*, vol. 27, pp. 1–11(2016) [6] S. Cao, L. Liu, J. Zheng, *et al.*, *IEEE Trans. Magn.*, vol. 55, no. 6, Art no. 8200905(2019) [7] B.P. Bernard and B.P. Mann, *J. Intell. Mater. Syst. Struct.*, vol. 29, no.6, pp. 1196–1205(2018) [8] R. Dayal and L. Persa, *IET Power Electron.*, vol.5, no.9, pp.1923–1933(2012)

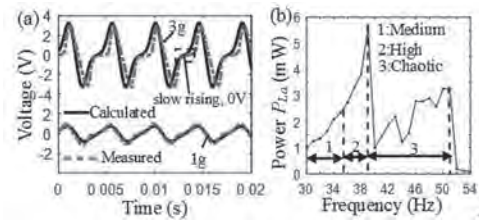


Fig. 1. (a) open-circuit voltage of TCEH. (b) average load power of ICEH under $R_L=100\Omega$.

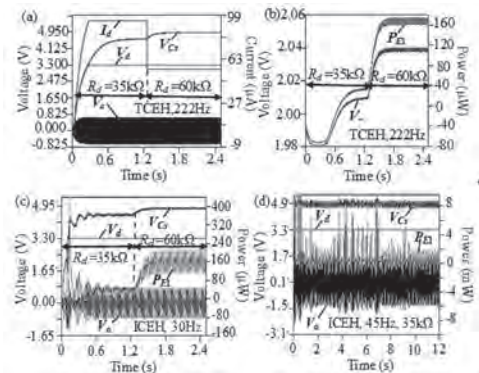


Fig. 2. Performances of TCEH and ICEH systems with the EEC under $a_m=1g$. (a) AC voltage V_a , capacitor voltage V_{Cs} , DC voltage V_d , load current I_d , and (b) DC supply V_+ , battery power P_{E1} of TCEH system under varying R_d , $f=222Hz$. AC voltage V_a , capacitor voltage V_{Cs} , DC voltage V_d , battery power P_{E1} of ICEH system under (c) varying R_d , $f=30Hz$, (d) $R_d=35k\Omega$, $f=45Hz$.

AV-05. Research on Performance of Magnetic Fluid Triboelectric Nanogenerator.

X. Yang¹, Y. Chen², Y. Zhang¹ and W. Yang²

1. Hebei University of Science and Technology, Shijiazhuang, China;
2. Hebei University of Technology, Tianjin, China

I Introduction With the rapid development of wireless sensor networks, portable electronics and wearable devices, widely distributed sensors have been used in health monitoring, health care, environmental protection, infrastructure monitoring and security^[1]. How to supply power for these devices in a long-term and stable way has become an urgent problem^[2]. In order to solve these problems, the vibration energy in the environment can be converted into available electric energy through the design of a reasonable energy harvesting device. At present, the research focus of vibration energy harvesting technology is piezoelectric energy harvester, electromagnetic generator and triboelectric nanogenerator (TENG). The structure of piezoelectric energy harvester is simple, and there is no need to add additional power supply, but the piezoelectric sheet is hard and brittle, which is easy to cause fatigue and damage. Electromagnetic generator has simple structure and good low-frequency output performance, but the output voltage is relatively small. The TENG based on solid-solid friction has the problems of material wear and thermal effect^[3], while TENG based on liquid-solid contact has much less friction. Based on the above problems, this paper proposes a TENG based on magnetic fluid (MF-TENG). When subjected to external mechanical vibration, the base fluid and the polymer container shell generate electricity by friction. The sealing structure of the magnetic fluid TENG can reduce the external environmental interference, and the high stability of the magnetic fluid ensures the durability of the device. MF-TENG can improve the energy conversion efficiency and reduce the friction heat effect, which has good research value and application prospect in the field of energy harvesting of low-frequency vibration. II Theoretical Analysis MF-TENG consists of aluminum electrode, cylindrical PTFE container and magnetic fluid, as Fig.1. The aluminum electrode is close to the outside of the PTFE container. When MF-TENG is working, the aluminum electrode is grounded through the wire. When the external vibration occurs, the magnetic fluid sloshes in the container. With the instantaneous interface rising on the surface of PTFE, the positive charge will be induced on the surface close to PTFE. When the magnetic fluid leaves the surface of PTFE, the same amount of positive charge will be transferred from the earth to the aluminum electrode. With the fluctuation, a continuous charge transfer will be formed between the copper electrode and the earth, so that the external circuit will be closed and an electrical signal is formed in the system. The amount of positive charge transferred in the electrode (Q) is related to the charge density (σ_0) and the liquid-solid contact area (S), and the relationship is shown in (1). $Q = \sigma_0 * S = \sigma_0 * w * x$ (1) σ_0 is related to the liquid-solid contact electrification, $S = w * x$: w is the electrode width, and x is the instantaneous wave height. According to the theory of single electrode mode TENG, the open circuit voltage V_{OC} between electrode and ground is related to the charge transfer quantity Q , as follows (2). $V_{OC}(x) = k_q * Q(x) = k_q * \sigma_0 * w * x$ (2) where k_q is the scale factor. The output voltage of MF-TENG will change linearly with the instantaneous wave height and is independent of the wave frequency. The sensitivity of MF-TENG is related to electrode width and charge density. Therefore, the sensor sensitivity can be enhanced by widening the electrode and enhancing the surface hydrophobicity. III Simulation and analysis The charge accumulation process of MF-TENG is simulated by finite element simulation software, and the output potential of mf-teng is obtained, as Fig.2. The simulation results show that the potential difference of the aluminum electrode reaches the peak value when the liquid surface swings to the highest point on one side during the sloshing process, and the peak potential difference of mf-teng changes approximately linearly with the change of the sloshing height. The simulation analysis verifies the rationality of mf-teng, which lays a theoretical foundation for the later experimental design.

[1] Hensley D, Tay Z W, Dhavalikar R, et al. Combining magnetic particle imaging and magnetic fluid hyperthermia in a theranostic platform[J]. Physics in Medicine and Biology, 2017, 62(9):3483-3500. [2] Kim Y S. Induced Voltage Characteristics by Back-Iron Effect for Electromagnetic Energy Harvester Using Magnetic Fluid[J]. IEEE Transactions on Applied

Superconductivity, 2018, 28(3): 5000504. [3] Seol M L, Jeon S B, Han J W, et al. Ferrofluid-based triboelectric-electromagnetic hybrid generator for sensitive and sustainable vibration energy harvesting[J]. Nano Energy, 2017, 31:233-238.

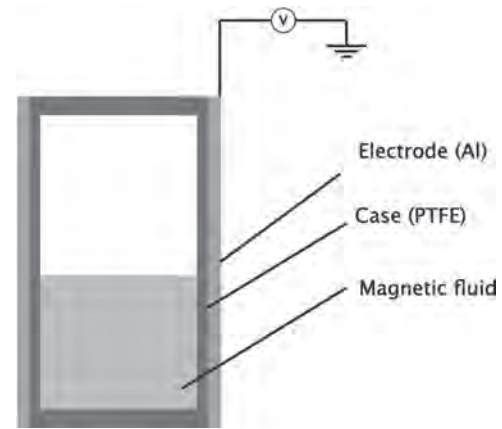


Fig.1 Structure of the MF-TENG

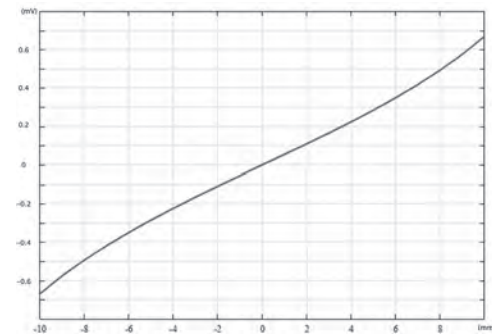


Fig.2 The relationship between the height of liquid sloshing and the potential difference of electrode

Session BA
ELECTRICAL MACHINES AND DRIVES 2020 AND BEYOND

Amr Adly, Chair
Cairo University, Giza, Egypt

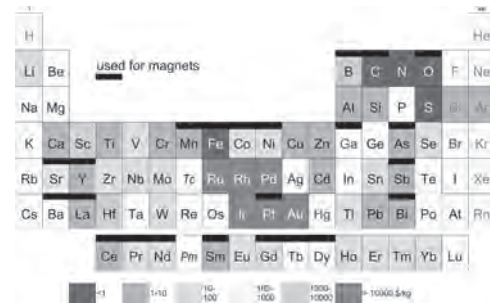
INVITED PAPERS

BA-01. Getting rid of Critical raw Materials in Hard Magnets: is it Feasible?F. Mazaleyrat¹*1. Electrical engineering, Ecole Normale Supérieure Paris-Saclay, Gif-sur-Yvette, France*

Critical raw materials are key issues in many applications in the field of energy and transportations since their stock market price is highly unstable due to geopolitical reasons and increase of the demand. The problem is that all efficient hard magnets needs critical materials, either cobalt, platinum, rare-earth (RE) in a small or large extend (see Fig. 1). Everybody knows that the problem with Pt is its low abundance in earth-crust and relatively high demand in jewelry, for catalysis and magnetic recording, but its price is quite stable around 35 000 \$/kg. In contrast, cobalt market is volatile. It oscillates between 20 and 100 \$/kg depending mainly on the political situation in Democratic Republic of Congo, (because RDC produces 60%, i.e. 90 kt in 2018) and, more recently, because of the speculation crisis mainly linked with Chinese demand. The situation with RE is more complicated, one can classify RE into 2 categories: heavy RE (64Gd to 71Lu), light RE (57La to 63Eu) from which 57La, 58Ce and 39Y are almost free, though Y is not exactly a RE but chemically behaves as such. Dy oxide price was around 125\$/kg in 2009, grows to 2300\$ during summer 2011 and then stabilized between 150 and 300\$. RE market is controlled by China where 70% of RE ore is produced though having 30% only of reserves. So the question is why this critical materials are necessary and in which extend we can get rid of them? The answer to this question is not straightforward because many factors have to be taken into account : price of raw elements, volatility of their market, processing cost, added value, application class and life cycle. More than the price itself, volatility can affect the profit if the cost of raw material changes appreciably between design and production stages of a product. The processing cost may be involved if substituting a expensive element or material by a cheaper one is counterbalanced by an increase in processing cost. In contrast, added value can compensate the price of raw elements if it stands only for a tiny part of the total cost. For example, a luxury watch can use a 0.1g PtCo magnet because its cost would be negligible compared to advertising, total cost of precious metals or stones, trade mark rights... The class of application is a key parameter : the 3 main classes are aeronautics, energy production and automobile. In aeronautics price doesn't matter compared to weight (or safety), so any element can be used if for a given energy the magnet is lighter. For energy production, e.g. in a wind turbine, the price of magnet is easily balanced by the cost of Joules losses summed over 30 years if a DC excitation is used instead of a hard magnet. By opposition, a car runs typically 1000h in 3 years, so the situation is reversed compared to the wind turbine. At last, life cycle is an important issue, magnets can be either milled and reprocessed – to the price of downgrading – or reused from the first step of synthesis. In the latter case, separation of RE elements would be necessary and this process is costly. Among magnets, it is well known that the RE-based are the harder, this is typically due to the strong spin-orbital coupling of RE elements which arises from the unfilled inner electronic shell and to the two fold symmetry of the crystal. FeNdB is the most powerful magnet known, but its coercive field has a quite large dependence on temperature. Dysprosium substitution is therefore necessary for power applications. A strategy to reduce the Dy content will be described [2]. Another way could be getting rid of heavy RE by cooling more efficiently the magnets. In this case, even reducing the Nd content can be envisaged, using cerium [3] or mischmetal, which is a mix of RE containing Ce, La, Nd and Pr obtained at an intermediate step of separation and therefore cheaper. SmCo can be synthesized into two structures having RE-TM ratio 1-5 or 2-17. Both are very good at high temperature though having lower energy product than NdFeB. Sm is not expensive and can be substituted by Y, but the problem is that they contains mainly cobalt [4]. Also magnet with a 1-12 ratio, thus containing less RE, can be synthesized but at the present date the phase is difficult to stabilize. Hexagonal ferrites remains still an interesting option because they are near perfect magnets and

have a positive thermal dependence of coercivity. They were discovered 60 years ago, but they have been improved continuously and remained cheap. There are many possibilities to make RE free magnets based on cobalt: alnico, carbides, Co-Zr, nanowires. Some have quite good properties, but actually not better than SmCo and not cheaper. Lastly, research on RE free hard magnets based on manganese will be reviewed. Focus will be done on Mn-Al which exhibits a good potential and uses only almost free elements. At last, a comparison will be tried on the basis of cost per Joule.

[1] JMD Coey, *Scripta Materialia* 67 (2012) 524–529 [2] H. Nakamura, K. Hirota, M. Shimao, T. Minowa, M. Honshima, *IEEE Trans. Magn.* 41 (2005) 3844 [3] Z.B. Li et al., *Journal of Alloys and Compounds* 628 (2015) 325–328 [4] K.P. Skokov, O. Gutfleisich, *Scripta Materialia* 154 (2018) 289–294 [5] A.M. Gabay, G.C. Hadjipanayis, *Scripta Materialia* 154 (2018) 284–288 [6] Muriel Tyrman, *AIP Advances* 8 (2018) 056217



Cost periodic table (reviewed 2020) in \$ per kg of pure element.

BA-02. Integration of Electrical Machine and Drive.*J.J. Paulides¹ and L. Encica¹**1. R&D, AE-Group www.ae-grp.nl, Waalwijk, Netherlands*

Amidst burgeoning attention for local manufacturing, manufacturing must adopt innovations that lie at the heart of the Industry 4.0 transformation. All need to offer (or at least start to think about offering) a unique combination of high-quality electric drives that incorporate electrical machines, software, mathware, mechatronics, electronics, assembly and predictive maintenance. In integrated drives data driven rapid development will be paramount to the electric drive systems (motor with power electronics drive and embedded intelligence). This will allow for predictive maintenance to illustrate the state of both the electrical machine as the power electronics. Integrating or bringing the power electronics in very close proximity to the electrical machines is not new. Engineers have been pursuing this for a few decades due to the obvious potential benefits including: higher system power density/smaller system footprint, reduced system cost, reduced cabling, reduced EMI issues, and more potential for modular systems [1]. However, integrating power electronics components as close as possible to an electrical machine is not an easy task, because inside an electrical machine is a very disturbed environment: strong electric and magnetic fields can occur, temperature conditions are way beyond power electronics standards and the drives may be subjected to unusual mechanical vibrations and stress [2]. Although all the aforementioned arguments are in effect true, and integrated drive with predictive maintenance using motor current signature analysis (MCSA) and condition monitoring will introduce a paradigm shift for future electric drive applications by utilizing the full potential of electrical motor drives. For example, by implementation of GaN-based inverters with the addition of condition monitoring. This shift is essential to embrace the advantages of smaller footprint/higher power density, minimization of cost and implementation, increased system efficiency, reduced Electromagnetic Emission (EME) issues. For many years the condition monitoring industry relied on vibration analysis and other traditional techniques to identify developing faults in electric motors. In recent years, however, condition monitoring based on motor current signature analysis has begun to provide a more effective and efficient alternative to traditional techniques [3]. As such we have identified research challenges and will highlight their current status, these include: - Thermal/cooling management - Hard- and soft magnetic materials - Power electronics that can tolerate higher temperatures - Distribution of the power electronics using modular/segmented machine topologies - Synchronization of the commutation control algorithms - Integrated condition and predictive maintenance algorithms - Coil/teeth/Magnet configurations - Cabling, manufacturing and integration challenges Within this invited symposium, Electrical Machines and Drives 2020 and Beyond these various aspects will be highlighted. We look forward to your presence to discuss these truly multi-disciplinary challenges!

[1] Ayman M. EL-Refaie, 2015, "Integrated Electrical Machines and Drives: An Overview", 2015 IEEE International Electric Machines & Drives Conference (IEMDC), 10.1109/IEMDC.2015.7409083 [2] Hossam Al Ghossini, Thu Thuy Dang, and Stéphane Duchesne, 2019, "A New Concept for Deeper Integration of Converters and Drives in Electrical Machines: Simulation and Experimental Investigations", Open Physics Volume 17: Issue 1, 10.1515/phys-2019-0084 [3] <https://www.semioticlabs.com/resources/motor-current-signature-analysis>

BA-03. HTS Machines.

S. Mezani¹, B. Dolisy¹, L. Belguerras¹, T. Lubin¹, J. L ev eque¹ and A. Rezzoug¹

1. Groupe de Recherche en Energie Electrique de nancy, Universite de Lorraine, Nancy, France

In 1911, Heike Kamerlingh Onnes discovered the superconducting state of the mater. After more than a century of intensive researches worldwide, significant improvement of the performance of high temperature superconducting wires and the cryogenic cooling systems has been done. This led to a rising motivation and interest of users and manufacturers to develop HTS electrical machines for their energy savings potential. Furthermore, the HTS motor will also be smaller in size than its conventional motor counterpart, particularly for high torque/low speed applications like marine propulsion and wind energy generation. Among the problems encountered in HTS motor drive systems, the torque transmission from the cryogenic environment to the load at room temperature is a key factor. Contactless torque transmission devices like magnetic couplings and gears constitute interesting solutions. The following items will be discussed in the presentation: 1- *Operating current of an HTS coil* HTS materials exhibit a non-linear relation between the electric field E and the current density J. This non-linearity is usually described by the power law which depends on an important parameter called the critical current I_c [1]. The operating current is defined as the maximal allowable current avoiding thermal limits. It depends on magnetic flux density components, cooling temperature and mechanical constraints [2]. A simple method to determine the operating current of a coil made from HTS tapes and supplied with a current I_s is to determine the intersection between the $I_c(B)$ curve of the tape and the $I_s(B)$ curve of the coil. An illustrative example for a stack composed of 4 tapes is given in Fig. 1. 2- *HTS electrical machines and HTS magnetic couplers design* The design of HTS machines is different from that of conventional machines because it is necessary to include operating current calculation during the sizing procedure. Furthermore, the inclusion of a magnetic coupling to transmit the torque from the cryogenic environment to the load increases the design difficulties. An example of an HTS machine with integrated coupling is shown in Fig. 2. It is an axial flux topology intended for high torque/low speed applications. The modelling and optimization of such a machine topology will be detailed [3], [4]. Finally, the potential of HTS motors/generators with integrated HTS torque transmission in making a real jump in performance will be discussed.

[1] Y. Kim, C. Hempstead, and A. Strnad, Physical Review Letters, Vol. 9, p. 306–309 (1962). [2] J. Pitel, Supercond. Sci. Technol., Vol. 26, p.1-13 (2013). [3] L. Belguerras, S. Mezani, T. Lubin and al., *Superconductor Science and Technology*, Vol. 28, p. 095003 (2015). [4] B. Dolisy, S. Mezani, T. Lubin, and al., *Superconductor Science and Technology*, Vol. 30, p. 35015 (2017).

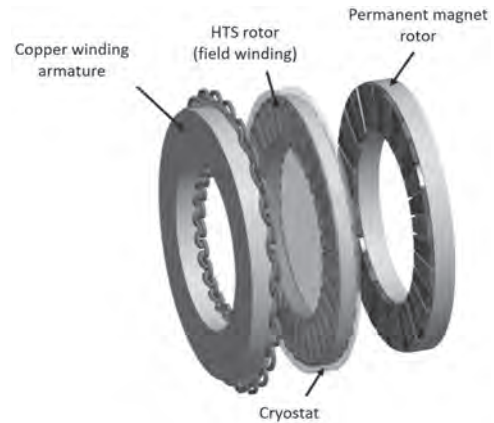


Fig.2 Axial HTS motor with integrated HTS magnetic coupling

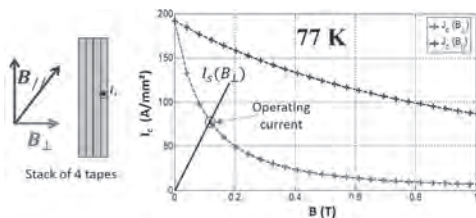


Fig.1 Definition of the operating current

BA-04. A Review of Electric Aircraft Drivetrain Motor Technology.J. Bird^{1,2}

1. Portland State University, Portland, OR, United States; 2. FluxMagic, Inc., Portland, OR, United States

In order to develop the next generation of fixed wing and vertical lift aircraft, the aircraft efficiency, emissions, reliability, and noise needs to be improved [1]. An electric aircraft drivetrain needs to operate at a very high mass torque density whilst also being exceptionally reliable, efficient, robust and environmentally benign. Mechanically geared drivetrains are often utilized as they enable the aircraft drivetrain to be more compact. However, the use of mechanical gears within an aircraft introduces a number of system level consequences such as the need for a lubrication system to reduce tooth friction and remove heat [2]. A back up lubrication system is then also required to meet certification requirements in the advent of loss of lubrication performance. The mechanical gearing system also introduces significant cabin noise due to the gear-tooth vibrations [2]. To mitigate tooth wear and failure, the aircrafts need to be grounded periodically for inspection and maintenance. One of the main alternatives to using mechanical gearing is the use of a direct-drive permanent magnet (PM) motors [3]. The use of a direct-drive PM motor removes the reliability concerns with respect to the mechanical gearbox. However, the torque density of a direct-drive PM motor is thermally limited (by current) and therefore a PM motor does not normally achieve torque densities much greater than 50Nm/L [4-10]. For this reason, direct-drive PM generators become very large when scaled-up in size. Superconducting motors are being considered for use in electric aircraft as the torque density can be much higher [11], however the required cooling system is highly complex. Recently the use of magnetic gearing (MG) within an aircraft drivetrain has been proposed as a means of achieving a higher mass torque density and power density that is competitive to mechanically geared systems [1, 2]. Magnetic gears (MGs) utilize magnetic field space modulation to create speed amplification without any physical contact [12]. As a MG does not rely on current excitation, the MG can sustain a very high magnetic air-gap shear stress value. MGs can operate with low noise and vibration and its noncontact operation means that no gear lubrication is required. In addition, MGs have the unique ability to pole slip when overloaded rather than catastrophically failing, thereby providing built-in overload protection [2]. Recently, MGs have been shown to be able to operate at 99% efficiency [13]. The MG can be nested internally with a much smaller motor or connected in series with a motor thereby enabling a compact electric drivetrain typology. This presentation will review the performance potential of MGs relative to alternative direct-drive aircraft drivetrains. The paper will provide an up-to-date review of electric aircraft drivetrain motor research conducted at government agencies, such as NASA [1, 2], as well as at universities and companies (such as Magnix and Siemens [14]) The performance potential of utilizing a magnetically geared aircraft drivetrain relative to the alternative direct drivetrain technology will be discussed.

[1] J. J. Scheidler, V. M. Asnani, and T. F. Tallerico, "NASA's magnetic gearing research for electrified aircraft propulsion," presented at the AIAA Propulsion and Energy Forum, Cincinnati, Ohio, July 9-11, 2018. [2] V. Asnani, J. Scheidler, and T. Tallerico, "Magnetic gearing research at NASA," presented at the AHS International 74th Annual Forum & Technology Display, Phoenix, Arizona, USA, May 14-17, 2018. [3] I. Pazdera, P. Prochazka, D. Cervinka, and B. Klima, "Electrical drivetrain of the small airplane and mutual interaction of this drivetrain," presented at the 39th Annual Conference of the IEEE Ind. Elect. Society, Vienna, 2013. [4] M. R. J. Dubois, "Optimized Permanent Magnet Generator Topologies for Direct-Drive Wind Turbines," Ph.D. Thesis, Delft University of Technology, Delft, Netherlands, 2004. [5] W. M. Arshad, T. Backstrom, and C. Sadarangani, "Analytical design and analysis procedure for a transverse flux machine," in *IEEE Inter. Elect. Mach. Drives Conf.*, Cambridge, MA, pp. 115-121, June, 2001. [6] M. R. Harris, G. H. Pajooman, and S. M. A. Sharkh, "Comparison of alternative topologies for VRPM (transverse-flux) electrical machines," in *IEE Coll.on New Topologies for Perm. Magnet Mach.*, London, pp. 2/1- 2/7, 1997. [7] M. R. Harris, G. H. Pajooman, and S. M. A. Sharkh, "The problem of power factor in VRPM (transverse-flux) machines" presented at the 8th Inter. Elect. Mach. Driv. Conf., Sep., 1997.

[8] S. Jinhao, L. Yongbin, and Z. Wenpeng, "Survey on the development of transverse flux machines," in *Inter. Conf. Elect. Mach.*, Beijing, China, pp. 127-141, 2003. [9] P. Kasinathan, A. Grauers, and E. S. Hamdi, "Force density limits in low-speed permanent-magnet machines due to saturation," *IEEE Trans. Energy Conv.*, vol. 20, no. 1, pp. 37-44, Mar. 2005. [10] D. G. Dorrell, S. S. Ngu, and C. Cossar, "Comparison of high pole number ultra-low speed generator designs using slotted and air-gap windings," *IEEE Trans. Mag.*, vol. 48, no. 11, pp. 3120-3123, Nov. 2012. [11] K. S. e. al., "Development of a High Speed HTS Generator for Airborne Applications," *IEEE Trans. Applied Super.*, vol. 19, no. 3, pp. 1656-1661, June 2009. [12] K. Atallah, J. Wang, S. Mezani, and D. Howe, "A novel high-performance linear magnetic gear," *IEEJ Trans. Ind. Appl.*, vol. 126, no. 10, pp. 1352-1356, 2006. [13] M. C. Gardner, M. Johnson, and H. A. Toliyat, "Performance Impacts of Practical Fabrication Tradeoffs for a Radial Flux Coaxial Magnetic Gear with Halbach Arrays and Air Cores," presented at the IEEE Energy Conversion Congress and Exposition (ECCE), Baltimore, MD, USA, 2019. [14] M. Duffy, A. Sevier, R. Hupp, E. Perdomo, and S. Wakayama, "Propulsion Scaling Methods in the Era of Electric Flight," presented at the AIAA/IEEE Electric Aircraft Technologies Symposium Cincinnati, Ohio, July, 9-11, 2018.

BA-05. Novel Asymmetric Rotor Pole Interior Permanent Magnet Machines With Enhanced Torque Density: an Overview.

Z. Zhu¹ and Y. Xiao¹

1. The University of Sheffield, Sheffield, United Kingdom

ABSTRACT This paper overviews recent developments and novel topologies of a new class of asymmetric rotor pole interior permanent magnet (AIPM) machines for torque enhancement. The principle for torque enhancement by utilizing magnetic-field-shifting is introduced firstly. AIPM machine topologies are then categorized in terms of asymmetries of PM configurations and rotor core geometries. Subsequently, various AIPMs in each category are described and analyzed with respect to merits and demerits. Finally, electromagnetic performances of selected AIPM machines are compared. **INDEX TERMS:** Asymmetric interior permanent magnet (AIPM), Magnetic-field-shifting (MFS), PM torque, Reluctance torque I. Introduction Interior permanent magnet (IPM) machines having PMs buried inside the rotor cores are of growing interests due to superior torque density, high efficiency, wide constant power operating speed range, and high rotor robustness [1]. In IPMs, the reluctance torque resulted from the rotor saliency can be utilized to enhance the torque density without increasing the PM usage. However, in conventional IPM machines with symmetrical rotor structures, the maximum PM and reluctance torque components are achieved at different current angles whose difference is theoretically 45 electrical degrees. Consequently, only a portion of both torque components can be utilized at the current angle of maximum synthetic torque. To deal with this issue, a novel design concept for torque enhancement of IPMs by making the maximum PM and reluctance torque components to be reached with a smaller difference of current angles has been firstly proposed by setting the optimal displacement angle between the surface-mounted PM rotor and the reluctance rotor in a two-part rotor PM machine [2] and by employing asymmetric rotor flux barriers in a V-shape IPM [3], respectively. To utilize the concept designated as magnetic-field-shifting (MFS) effect in this paper, the PM field and reluctance axes of IPM machines need to be shifted, resulting in a new class of novel asymmetric rotor IPM machines. The torque enhancement principle of AIPM is illustrated in Fig. 1. This paper overviews various novel AIPM topologies which are categorized in terms of asymmetries of PM configurations and rotor core geometries, analyses various AIPMs in each category with respect to merits and demerits, and compares electromagnetic performances of selected AIPM machines. II. AIPM Machine Topologies In this section, novel AIPM machine topologies in literature are categorized according to whether their PM configurations and rotor core geometries are symmetrical or asymmetric, respectively. The proposed categorization method and some examples reported in references for each category are shown in Fig. 2 (a). An AIPM topology with the asymmetric hybrid-layer PM configuration and asymmetric rotor cavity has been proposed in [4], which achieves torque enhancement with simple structure due to utilizing MFS effect and also shows reduced torque ripples. A hybrid-pole AIPM machine is proposed in [5] that employs V-shape and inset PMs in adjacent poles alternatively, which has asymmetric PMs due to shifted positions of inset PMs but symmetrical rotor core geometry. This hybrid-pole AIPM has higher torque density compared with a V-shape IPM with the same PM usage. An AIPM machine with asymmetric PMs and symmetrical rotor structure is also reported in [6] that can achieve fully aligned maximum PM and reluctance torque components, although the increase of synthetic torque is not notable compared with a PM-assisted reluctance machine because of significant reduction of maximum reluctance torque. The asymmetric flux barrier in one side of symmetrical V-shape PMs in each pole is used in [3] to utilize the MFS effect by shifting the angle of reluctance axis and to clearly increase the synthetic torque. Similar to [2], a two-part rotor design with a SPM rotor and a multi-layer reluctance rotor is proposed in [7] that exhibit symmetrical PM configuration and rotor cavity design, respectively. The MFS effect is utilized by adjusting the displacement angle between both rotor parts, which can also achieve fully aligned maximum PM and reluctance torque components and shows a clear torque enhancement. Four selected AIPM machines with rotor topologies proposed in references [3]-[5] and [7] are redesigned by using the same stator, rotor diameter and PM usage to the conventional Toyota Prius 2010, and their torque performances at 750

r/min and 236A are compared in Fig. 2 (b). Comprehensive overview of more AIPM topologies will be given in the full paper.

[1] Z. Zhu and D. Howe, *Proc. IEEE*, vol. 95, p.746-765 (2007). [2] P. Winzer and M. Doppelbauer, *2014 Int. Conf. Electr. Mach. (ICEM)*, Berlin, 2014, p. 641-647. [3] W. Zhao, F. Zhao, T. A. Lipo, and B.-I. Kwon, *IEEE Trans. on Magn.*, vol. 50, no. 11, p. 1-4 (2014). [4] Y. Xiao, Z. Q. Zhu, J. T. Chen, D. Wu, and L. M. Gong, *2020 Int. Conf. Electr. Mach. (ICEM)*, Gothenburg, 2020, p. 26-32. [5] G. Xu, G. Liu, W. Zhao, Q. Chen, and X. Du, *IEEE Trans. Ind. Electron.*, vol. 66, no. 4, p. 2580-2591 (2018). [6] F. Xing, W. Zhao, and B.-I. Kwon, *IET Electr. Power Appl.*, vol. 13, no. 5, p. 573-580 (2018). [7] H. Yang, Y. Li, H. Y. Lin, Z. Q. Zhu, et al., *2017 IEEE Energy Convers. Congr. Exposition (ECCE)*, Cincinnati, 2017, pp. 2362-2367.

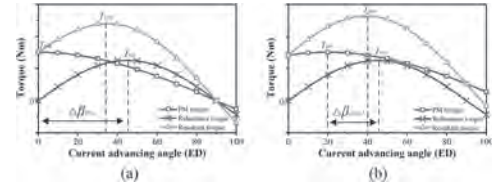


Fig.1. Principle of torque enhancement of AIPM. (a) Conventional IPM. (b) AIPM with reduced $\Delta\beta$. T_{syn} , T_{pm} and T_{rel} denote maximum synthetic, PM, and reluctance torques, respectively, and $\Delta\beta$ denote the current angle difference between maximum PM and reluctance torque components.

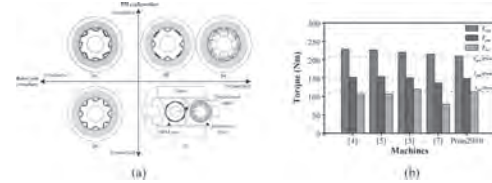


Fig.2. Categorization of some typical AIPM machine topologies. In (a), PMs in red and blue denote N- and S-poles.

BA-06. Hybrid Excited Synchronous Machines.

S. Hlioui¹, M. Gabsi², H. Ben Ahmed³, G. Barakat⁴ and Y. Amara⁴

1. SATIE Laboratory, Conservatoire National des Arts et Metiers, Paris, France; 2. SATIE Laboratory, Ecole Normale Supérieure Paris-Saclay, Gif-Sur-Yvettes, France; 3. SATIE Laboratory, Ecole Normale Supérieure de Rennes, Bruz, France; 4. GREAH Laboratory, Université du Havre, Le Havre, France

I. Introduction Hybrid excited synchronous machines (HESM) combine permanent-magnet (PM) excitation with wound field excitation. The goal behind the principle of hybrid excitation is to combine the advantages of PM excited machines and wound field synchronous machines. The principle of hybrid excitation allows responding to many problematic related to electric machines: flux weakening [1], energy efficiency [1], and fluctuations of permanent magnets price [2]. Due to their advantageous characteristics, this type of machines is gaining more and more attention [1]–[8]. They have been identified as one of the emerging technologies of modern energy conversion systems [3]–[5]. They have been the subject of many review papers [6]. Figure 1 shows the evolution of the number of contributions dedicated to HESM in the IEEE Xplore Digital Library, between 1989 and 2019. As can be seen this number is in constant evolution, going from one contribution in 1989 [6], to more than 350 contributions in 2019. In this contribution, after a description of the operating principal of HESM, a brief literature review of scientific and technical literature dedicated to HESM will be established. Then, the use of this type of electric machines for different applications (constant and variable speeds applications) will be discussed. The design and operation of three particular structures will be presented. Two of them have been designed as generators for transportation applications [7] [8], and the third one has been designed as generator for renewable energies conversion [2]. All of them are flux switching structures. II. Hybrid Excitation Synchronous Machines The hybrid excitation principle allows a wide variety of structures to be realized. Figure 2 shows three different structures of rotating HESM. All of them are flux switching hybrid excited synchronous machine (FSHESM). Due to their advantageous characteristics FSHESM are the subject of increasing attention. This figure illustrates the variety of HESM structures. More structures will be presented in the full version of the contribution. In most references dedicated to HESM, it is mainly rotating machines which are studied. Nevertheless, many linear HESM are also studied. Examples will be provided in the full version. III. Study of Three HESM Prototypes HESM characteristics make them well suited for transportation applications [1] [5] [7] [8]. Nevertheless, HESM could also be used as renewable energy conversion generators [2], even if, in these applications, it is not all of their advantageous characteristics which are exploited. In fact, it is mainly economic considerations which are driving the use of an electric machine technology [2]. The use of HESM in renewable energies applications is mainly driven by fluctuations of rare earth PM price and their availability [2]. Another important reason is the fault tolerance characteristic which could be brought by HESM. Considering the evolution of wind energy market toward the use of large power rated offshore wind turbines, the fault tolerance characteristic is very important. In fact, the HESM allow controlling the air-gap magnetic field, even with the presence of permanent magnets, and they therefore offer a protection against faults as stator short circuits, for example. The fault tolerance allows the reduction of maintenance requirements, and consequently exploitation costs. The fault tolerance they bring increases their attractiveness in many applications. The design studies of three HESM prototypes (Fig. 2) will be presented. The first one [Fig. 2(a)] has been studied for an aircraft DC electric power generation [7]. This prototype weight 3.5 kg, and was designed to deliver 6 kW at 6000 rpm. It is a 2D flux switching structure. The second prototype can be used as a car alternator [Fig. 2(b)] [8]. Instead of having a distributed excitation windings, the excitation coil is annular without end windings. The excitation flux has a 3D nature, which requires the use of massive ferromagnetic material to channel it. This prototype was able to deliver 2.5 kW at a speed of 11 krpm. The third prototype [Fig. 2(c)] was designed to be used as a generator for renewable energy conversion (10 kW at 300 rpm). As compared to transportation applications, where the speed is relatively high, renewable energy conversion systems operate at relatively low speed, which requires the development of high torque machines. This

prototype includes the Vernier effect in order to be able to cope with the torque production requirement. It is a water cooled machine. It has a 2D structure. The full version will include more details about the three prototypes. HESM machines may seem more complicated as compared to classical machines, as PM machines for example, but regarding the worldwide shift toward a greener economy, economic considerations will be in the favor of the development of even more complex electric machines technologies [5]. Indeed, considering the number of pieces required for the construction of even the simplest IC engine, the construction of even the much complex electric machines requires much more less operations, and simpler production lines.

[1] Y. Amara, S. Hlioui, A. H. Ben Ahmed and M. Gabsi, “Power capability of hybrid excited synchronous motors in variable speed drives applications,” *IEEE Trans. Magn.*, vol. 55, no. 8, paper 8204312, August 2019. [2] A. S. McDonald, “Hybrid Excitation of Synchronous Generators for Wind Turbines,” *Proceedings of the 2nd IET Renewable Power Generation Conference (RPG2013)*, 9-11 September 2013, Beihang University (BUAA), Beijing, China. [3] G.-A. Capolino and A. Cavagnino, “New trends in electrical machines technology—Part II,” *IEEE Trans. Ind. Electron.*, vol. 61, no. 9, pp. 4931–4936, Sep. 2014. [4] C. Liu et al., “Guest Editorial Emerging Electric Machines and Drives for Smart Energy Conversion,” in *IEEE Transactions on Energy Conversion*, vol. 33, no. 4, pp. 1931–1933, Dec. 2018. [5] K. Akatsu et al., “Message from Editors,” *CES Transactions on Electrical Machines and Systems*, vol. 3, no. 3, pp. 231–232, Sept. 2019. [6] E. Spooner, S. A. W. Khatab and N. G. Nicolaou, “Hybrid excitation of AC and DC machines,” in *Proc. 1989 Fourth International Conference on Electrical Machines and Drives Conf.*, London, UK, 1989, pp. 48–52. [7] A. Nasr, S. Hlioui, M. Gabsi, M. Mairie, and D. Lalevee, “Design optimization of a hybrid-excited flux-switching machine for aircraft-safe DC power generation using a diode bridge rectifier,” *IEEE Trans. Ind. Electron.*, vol. 64, no. 12, pp. 9896–9904, Dec. 2017. [8] A. Dupas, S. Hlioui, E. Hoang, M. Gabsi and M. Lécivain, “Investigation of a new topology of hybrid-excited flux-switching machine with static global winding: experiments and modeling,” *IEEE Trans. Ind. Appl.*, vol. 52, no. 2, pp. 1413–1421, March/April 2016.

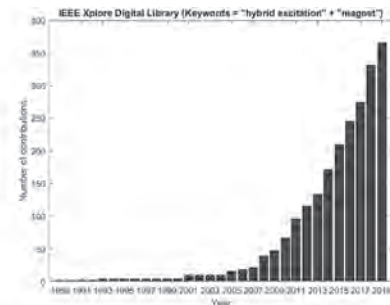


Fig. 1. Evolution of the number of contributions dedicated to HESM.

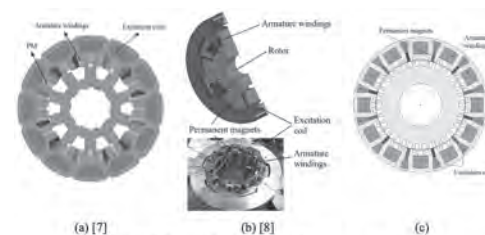


Fig. 2. Different hybrid excited synchronous structures.

Session BB

DUAL WINDING AND PERMANENT MAGNET MEMORY MACHINES

Jonathan Bird, Co-Chair

Portland State University, Portland, OR, United States

Johan Paulides, Co-Chair

Advanced Electromagnetics Group, Waalwijk, Netherlands

CONTRIBUTED PAPERS

BB-01. Split Ratio Investigation of Double Stator Permanent Magnet Motor Considering Multimode Operation.

D. Fan¹, Z. Xiang¹ and X. Zhu¹
 1. Jiangsu University, Zhenjiang, China

I. Introduction With the rapid development of electric vehicles and hybrid electric vehicles, they put forward more critical and complicated requirements for driving motor drive systems. Double stator permanent magnet (DSPM) motors have become promising candidates for driving motors, due to its advantages of high torque/power density and relatively compact structure. DSPM motor can be considered as the integration of inner and outer motors. By the flexible control of inner and outer motors of double stator motors, different operation modes of motors can be realized. In [1], a double stator permanent magnet motor is proposed, and corresponding multi-mode characteristics are investigated. It is noted that current research on double stator motors mainly biased on proposing novel motor topologies, realizing different operation modes, and verifying motor electromagnetic performances. However, the reasonable power split and allocation of inner and outer motors are seldom investigated, especially for the multi-mode operation. Hence, it is very necessary and essential to purposefully determine power ratio of inner and outer motors, considering design requirements of multiple operation modes. Split ratio, which termed as the ratio of inner and outer diameter of stator, often determines motor magnetic and electrical loading. It possesses significant influences on motor performances, including torque output capability, loss characteristics, and efficiency. So, motor split ratio is considered as one of most crucial motor design parameters and often investigated during the motor initial design stage. In [2], the split ratio of surface-mounted permanent magnet motor is analyzed and the optimal motor split ratio is decided by analytical method. While for double stator motors, split ratios of inner and outer motors determine not only motor magnetic and electrical loading, and but also the power split characteristics of the whole motor. However, it is noted current publications of motor split ratio mainly focus on the split ratio of single-stator motors which mainly work on rated condition. Since double stator motor are required to work in different operation modes, traditional design methods of motor split ratio cannot be applied for double stator motors directly. Consequently, it has been a hot but challenging issue on how to determine split ratio of double stator permanent magnet motors during the initial design stage, considering the design requirements of multiple operation modes. In this paper, a double stator permanent magnet (DSPM) motor is investigated, and the relationship between motor split ratio and power split characteristics of different motor operation mode is analyzed in detail. Furthermore, by the purposeful design and optimization of motor split ratio, design requirements of multiple operation modes can be satisfied comprehensively. II. Motor topology and split ratio investigation Fig. 1 presents the configuration of the investigated DSPM motor. As can be seen, inner stator and middle rotor form inner motor, while outer motor consists of outer stator and middle rotor. In order to realize multimode operation effectively, the torque-speed curves of inner and outer motor are designed purposefully, as shown in Fig. 2. The inner motor is designed to have a relatively flat torque curve over a wide speed range, which is utilized to augment the output torque of outer motor, especially in the range of torque of outer motor is dropping off. In addition, driving requirements of whole DSPM motor are arranged purposefully as optimization objectives for the inner and outer motors of DSPM motor. So, by the purposeful and reasonable design and optimization of split ratios of inner and outer motors, design requirements of multi-mode operation can be satisfied. III. Optimization results and performances validation In order to satisfy design requirements of multiple operation modes, response surface method and multi-objective genetic algorithm are utilized for DSPM motor, the optimal motor split ratio and pole teeth ratio can be determined. Distribution of optimization objectives and design parameters are presented in Fig. 3 and Fig. 4 respectively. And, based on finite element analysis, electromagnetic performances of DSPM motor can be obtained. Fig. 5(a) depicts the flux lines and flux densities distributions of DSPM motor after optimization. Table I presents the multi-mode performance comparison

of initial and optimal DSPM motor. And, torque performances of overall DSPM motor before and after optimization are shown in Fig. 5(b). As can be seen, after optimization, the average output torque increases from 71.83Nm to 82.81Nm, while the torque ripple reduces from 10.93% to 7.78%. Electro-magnetic performances verify that, by the reasonable design and cooperation of inner and outer motors of DSPM motor, design requirements of different operation mode can be realized more effectively, which provides a research path for the optimization design of multi-port PM motors. More detailed theoretical analysis, optimization design results, and experimental validations will be presented in the full paper.

[1] Y. Wang, W. Xu, X. Zhang, and W. Ma, "Harmonic analysis of air gap magnetic field in flux-modulation double-stator electrical-excitation synchronous machine," *IEEE Trans. Ind. Electron.*, vol. 67, no. 7, pp. 5302-5312, Jul. 2020. [2] Y. Ni, Z. Liu, B. Xiao, and Q. Wang, "Optimum split ratio in surface-mounted permanent magnet machines with pieced halfbach magnet array," *IEEE Trans. Energy Convers.*, vol. 35, no. 4, pp. 1877-1885, Dec. 2020.

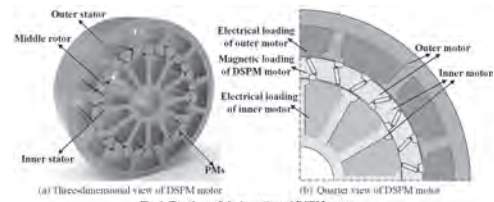


Fig. 1 Topology of the investigated DSPM motor

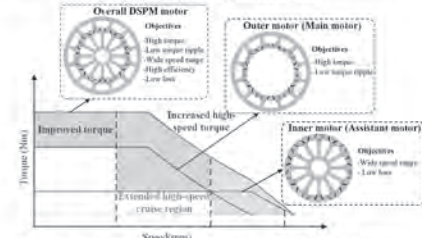


Fig. 2 Design requirements of inner motor, outer and overall DSPM motor considering multi-mode operation

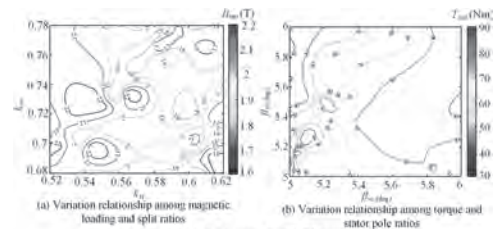


Fig. 3 Optimization results of DSPM motor

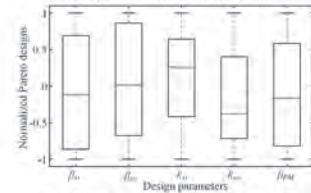


Fig. 4 Distribution of design parameters of DSPM motor

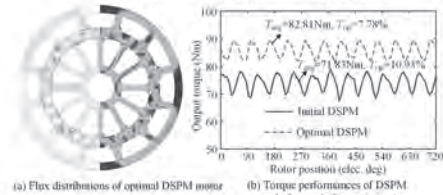


Fig. 5 Electromagnetic performances of DSPM motor

TABLE I
 MOTOR PERFORMANCE OF INITIAL AND OPTIMAL DSPM MOTOR

Items	Initial DSPM	Optimal DSPM
Inner motor		
Average torque	22.41Nm	23.68Nm
Torque ripple	18.9%	15.3%
Speed range	1/20rpm	230rpm
Outer motor		
Average torque	53.78Nm	63.15Nm
Torque ripple	20.7%	13.2%
Item loss	93.5%	99.2%
DSPM motor		
Average torque	71.83Nm	82.81Nm
Torque ripple	10.93%	7.78%
Efficiency		93.7%

BB-02. Analytical Modelling, Optimization and Electromagnetic Performance Analysis of Electrically Excited Flux Switching Motor.

B. Khan¹, F. Khan¹, W. Ullah¹, E. Sulaiman² and B. Ullah¹
 1. Electrical & Computer Engineering, COMSATS University Islamabad, Abbottabad, Pakistan; 2. Department of Electrical Power Engineering, Universiti Tun Hussein Onn Johore, Johore, Malaysia

High torque-density, high efficiency and robust rotor structure are the key features of flux switching motors (FSMs) [1]. Permanent magnet (PM) FSMs are preferred choice, however, these machines consume high amount rare-earth magnet and its resources are depleting with the passage of time. The degradation of performance with increase in temperature and uncontrolled flux are the other concerns with PMFSMs. The flux of electrically excited (EE) FSM can be controlled electronically, performance is not degraded with increase in temperature and overall cost is low. The simple manufacturing process of single phase EEFSM, easy maintenance, longer lifetime and low cost are the main characteristic that prioritized it for high speed applications [2-3]. Authors [4-6] have proposed novel single phase EEFSM designs, they have successfully accomplished their targets in the form of good average torque and efficiency etc. These designs have overlapped windings and segmented or modular rotor. High copper losses are caused by overlapped windings and segmented or modular rotor is not suitable for high speed applications. High power density, torque and efficiency are key factors for motors used in high speed applications. Flux switching motor (FSM) designs with the conventional stator slot have relatively good average torque but high copper losses and low efficiency. This paper has proposed an optimized octane modular stator (OMS) 8slots-6poles (8S-6P) single phase electrically excited (EE) FSM design. The geometric representation of the OMS design is given in Fig.1 (a), R_{se} , R_{re} , $\beta_s\theta_s$, $\beta_r\theta_r$, and θ are stator outer radius, rotor outer radius, stator slot opening, rotor slot opening and rotor position respectively. The proposed OMS design has high copper slot filling factor and high efficiency than the conventional stator trapezoidal slot [3]. Moreover, the purpose of this paper is to analyze OMS EEFSM design by means of simplified analytical method. For electromagnetic performance investigation numerical based technique finite element analysis (FEA) is powerful tool. But, computational complexity, high computational time and high drive storage compel researchers to model and analyze electric machines and especially FSMs analytically. In this paper, doubly-salient air-gap permeance, magneto-motive force (MMF) and inductance calculation is performed to obtain radial magnetic flux density distribution in the air-gap and electromagnetic torque, accounts the influence of all parts of EEFSM. This simplified approach has reduced the computational time, drive storage and computational complexity. Geometric optimization (GO) is implemented in multiple steps to optimize the initial design. The analytical results are validated via JMAG v18.1 finite element analysis (FEA) simulator. Finally, prototype stator is fabricated and experimentally tested. Prototype stator without windings and with windings are shown in Fig.1 (b) and (c) respectively. The analytical results has good agreement with FEA and experimental results and the deviancy is from 3 to 4%. Overall GO implementation, average torque of the proposed optimized EEFSM design is enhanced 42.5% and comparison of the electromagnetic performance is plotted in Fig.2.

[1] X. Sun, Z. Shi, G. Lei, Y. Guo, and J. Zhu, "Multi-objective design optimization of an IPMSM based on multilevel strategy", IEEE Transactions on Industrial Electronics (2020). [2] M. Lihong, Z. Gangxu, Z. Tao, L. Qing and L. Baolian, "Multi-level optimization design for a Flux-Concentrating Permanent-Magnet Brushless Machine Considering PM demagnetization limitation", IEEE Transactions on Magnetics (2020). [3] B. Khan, F. Khan, W. Ullah, M. Umair and S. Hussain, "Slot Filling Factor Calculation and Electromagnetic Performance of Single Phase Electrically Excited Flux Switching Motors", Applied Computational Electromagnetics Society Journal, 35(8), pp.922-928, (2020). [4] M. F. Omar, E. Sulaiman, M. Jenal, R. Kumar and R. N. Firdaus, "Magnetic flux analysis of a new field-excitation flux switching motor using segmental rotor", IEEE Transactions on Magnetics, 53(11), pp.1-4, (2017). [5] Y. J. Zhou and Z. Q. Zhu, "Comparison of low-cost single-phase wound-field switched-flux machines", IEEE Transactions on Industry Applications, 50(5), pp.3335-3345, (2014). [6] J. Yuan, D. Meng, G. Lian, J. Zhang, H. Li and F. Ban,

"The stator slot-type optimization of electrical excitation flux-switching motor and its maximum torque/copper loss control", IEEE Transactions on Applied Superconductivity, 29(2), pp.1-5, (2019).

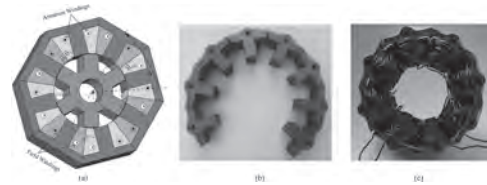


Fig.1: Proposed OMS single phase 8s-6p EEFSM (a) geometry (b) stator (c) stator with windings

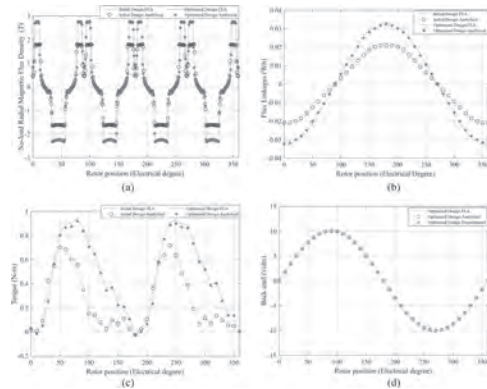


Fig.2: Performance of OMS 8S-6P EEFSM (a) Flux density (b) Flux linkage (c) Torque (d) Back-emf

BB-03. A Novel Stator Cooling Construction for Yokeless and Segmented Armature Axial Flux Machine With Heat Pipe.

W. Le¹, M. Lin¹, L. Jia¹ and S. Wang¹

1. Southeast University, Nanjing, China

I. Introduction Yokeless and segmented armature axial flux machine (YASA) is being considered for an advanced electric traction and propulsion in electric vehicles applications, since it has compact construction and high torque density. Compared with other axial flux machine, YASA could have higher winding fill factor and lower stator iron losses because of the absence of the stator yoke [1]. However, it is very difficult to design the stator cooling structure of YASA especially large power motor for electric vehicles as its stator is in the middle of two rotors. [2] gives a stator water-cooling structure for a 30KW YASA machine, in which fins are insert the space between stator modules with U-shape water-cooling pipe. But the manufacturing process is very complicated. Recently, heat pipe, as a small size but highly efficient passive cooling element, is attracting more and more attention [3]. Therefore, in this paper, a novel stator cooling structure combined flat heat pipe with housing water-cooling is presented. II. Stator Cooling Structure of YASA For an electric drive motor, the sealing is the primary consideration. As a result, open fan cooling can not be applied and the entire machine must be assembled in a housing. In addition, the weight of the motor should be as light as possible ensuring the mechanical strength. [4] introduces a stator mechanical construction of YASA with a excellent plastic material named polyetheretherketon (PEEK), which verifies the feasibility of stator support made by PEEK. Considering the low density, high thermo-stability, workability and nonelectroconductibility of PEEK, it is chosen as the material of stator carrier. In consideration of the fixation improvement of stator modules and the accuracy enhancement of rotor assembly, the ultimate cooling structure is shown in Fig. 1. It is obvious that the stator irons and concentrated windings are imbedded in two plates made of PEEK for full fixation. And the PEEK plates are bolted to the protruding middle part of the inner surface of the housing. A aluminum alloy ring is placed inside to secure the bearing to avoid unbalance air gap. What's more, several heat pipe is inserted in the gap in parallel between stator modules to enhance the heat transfer efficiency of stator to housing water-cooling. Considering the space limitation, the flat instead of round heat pipe is selected. And The thickness, height and length of flat heat pipe selected are 2mm (one third of the total gap width), 4mm and 85mm, respectively. For the reducing thermal contact resistance and improving mechanical strength, the remainder of stator support is impregnated with epoxy resin. The spiral type of housing cooling structure is adopted, because of its simple processing. III. CFD simulation of cooling structure Before simulation, the properties of epoxy resin and heat pipe should be identified. The selection principle of epoxy is high thermal conductivity, low thermal expansivity, low viscosity and high mechanical stability [5]. Finally, EP2000 from Lord is chosen after comparison. And the thermal conductivity of EP2000 is 1.9 W/mK. The heat pipe is the heat-transfer device which combines the principles of both thermal conductivity and phase transition to transfer heat between two solid interfaces effectively [6]. Its equivalent heat conductivity can reach hundreds of times more than copper, which is the metal with the best thermal properties. In simulation, a heat pipe is usually equivalent to a copper bar of high thermal conductivity [7]. But its performance should be determined in detail. Different size of heat pipes have been measured in laboratory under different conditions. And it is found that the performance of them depends on their size and the input power of heat source. With the increase of input power, the equivalent heat conductivity will get higher, and finally plateau. But the relationship between performance with size is still under study. In the most extreme case, the input power is 5W, the average temperature of a 100mm long, 2.5mm high and 0.8mm thick heat pipe is 308K. And the equivalent thermal conductivity is calculated as 14801W/mK. Therefore, the thermal conductivity of heat pipe in CFD is set as 10000W/mK tentatively. The stator temperature distribution of CFD simulation with heat pipes is shown in Fig. 2 (a), whereas the result without heat pipes is given in Fig. 2 (b). As is shown in Fig. 2, it is evident that the heat pipes accelerate the release of heat from the stator, and reduce the temperature of the stator significantly. The average temperature of stator reduces from 480K to 352K, which is 128K lower. IV. Conclusion In this paper, a novel stator cooling system for yokeless and segmented armature

axial flux machine with flat heat pipe is developed. The proposed structure can increase the heat transfer efficiency of stator and improve the temperature of stator sufficiently. And the validity of this cooling structure is verified by CFD simulation. However, there are also many works to be done in the future. The thermal properties of heat pipes, especially the relationship between size parameters with thermal conductivity, should be identified. And the mechanical stability of above construction needs to be confirmed.

[1] A. Gerlando, G. Foglia and M. Iacchetti, IEEE Transactions on Energy Conversion, Vol. 31, no. 2, pp. 750-758, 2016. [2] J. Chang, Y. Fan and J. Wu, IEEE Transactions on Industrial Electronics, early access. [3] J. Huang, S. Naini and R. Miller, IEEE Transactions on Vehicular Technology, vol. 68, no. 5, pp. 4467-4478, 2019. [4] B. Zhang, T. Seidler and R. Dierken, IEEE Transactions on Industrial Electronics, vol. 63, no. 4, pp. 2062-2071, 2016. [5] S. Nategh, A. Boglietti and D. Barber, IEEE Transactions on Energy Conversion, vol. 35, no. 2, pp. 1026-1035, 2020. [6] A. Faghri, Heat Pipe Science and Technology, Global Digital Press, 2016. [7] G. Fang, Y. Wei and Z. Yan, Applied Thermal Engineering, vol. 152, pp. 594-604, 2019.

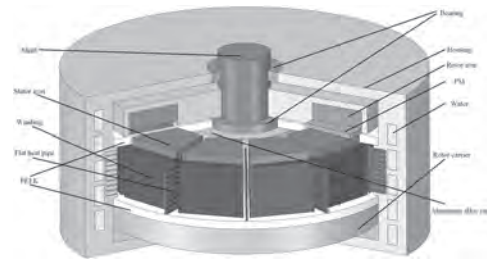


Fig. 1 Stator cooling structure of YASA with flat heat pipe

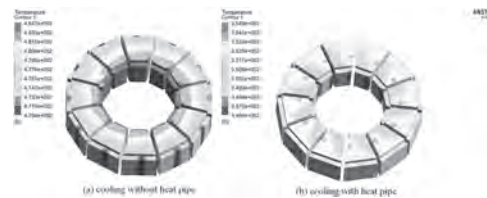


Fig. 2 Temperature distribution of stator (a) cooling without heat pipe (b) cooling with heat pipe

BB-04. Research on an Asymmetric-Primary Axis-Flux Hybrid-Excitation Generator for the Vertical Axis Wind Turbine.

J. Liu¹, Q. Zhang¹ and J. Chen¹

1. China University of Petroleum Huadong, Qingdao, China

I. Introduction The vertical axis wind turbine has been widely concerned because of its advantages such as multiphase wind, stable force, easy installation and maintenance, and small starting wind speed. Vertical axis wind turbines mostly use permanent magnet synchronous generators or doubly fed induction wind turbines, and most of them are axial flux permanent magnet generators^[1]. Compared with doubly fed induction wind turbine, permanent magnet synchronous generator (PMSG) has the advantage of high power density and is the main research object of vertical axis wind turbine. However, the direct coupling of the high power axial flux permanent magnet synchronous generator and wind turbine causes the starting of the wind turbine to become more difficult. In order to improve the starting performance of vertical axis wind turbines, maglev technology is considered to reduce the starting resistance as the development direction of vertical axis wind turbines. Therefore, an asymmetric-primary axis-flux hybrid-electricity generator is proposed in this paper, and the decoupling control of levitation force and output power is implemented using asymmetric primary and hybrid excitation. II.operation principle The proposed asymmetric-primary axis-flux hybrid-excitation generator for the vertical axis wind turbine structure is shown in the Fig.1. The generator is composed of double stator primary and single actuator. The double stator primary has an asymmetric structure design, and the rotor shaft is connected with the wind turbine shaft to realize direct drive wind power generation. The rotor adopts the spacing design of permanent magnet and modulating tooth to reduce the consumption of permanent magnet. Both the excitation winding and the armature winding are located in the primary stator, so the mixed excitation and magnetic field can be adjusted without adding any mechanism such as brush slip ring, which reduces the complexity of the structure. In general, the proposed generator has the following characteristics (1) The flat structure shortens the axial length of the generator and is suitable for direct drive of vertical axis wind power generation system. (2) The levitation force is provided by bilateral unbalance design of axial flux. The two sides adopt different primary sizes, and then the axial electromagnetic force imbalance of the bilateral air gap forms the suspension force, which avoids adding active and passive levitation mechanisms and reduces the complexity of the overall system. (3) The levitation force and output power are controlled by hybrid excitation. The primary tooth DC excitation is adopted to realize zero crosslinking of the excitation with permanent magnet and armature, and the levitation force regulation does not affect the output power. The system can start at low wind speed, and the levitation force and total output power can be adjusted according to the change of wind speed. Through free distribution of bilateral power to achieve the total power following the wind speed and the levitation force following the lift force of the wind turbine. (4) Using magnetic field modulated axial magnetic field structure, the rotor structure is simple and reliable. If the pole pair numbers of rotor and armature are p_r and p_s , and the number of the stator tooth is p_n , there is $p_r = p_n \pm p_s$. The design makes it have the magnetic field modulation effect, which can increase the magnetic field change rate under the low speed, thus increasing the generation power. (5) The use of concentrated armature windings and excitation windings reduces the end, thus reducing magnetic leakage and losses. III.simulation and results A three-dimensional finite element model of the asymmetric-primary axis-flux hybrid-excitation generator is established, and the no-load characteristics and load characteristics of the generator are obtained. The no-load characteristics under different excitation current are simulated, and the flux linkage of armature coils and DC excitation coils are shown in Fig.2. We can see that when different excitation currents are applied, the crossing flux linkage between DC excitation winding and secondary permanent magnet is almost 0, and DC flux has little effect on the armature flux. Therefore, When the excitation changes, the unilateral levitation force changes only in amplitude, but there is no harmonic phase shift, and positioning torque is almost unaffected. he proposed generator has good decoupling performance of levitation force, output power, and DC excitation. In addition, the optimization design of the generator is further studied such as pole arc coefficient, positioning moment and pole slot ratio. IV.conclusion In this paper, we proposed

an asymmetric-primary axis-flux hybrid-excitation generator, studied the no-load characteristics, load characteristics and excitation characteristics, and optimized the structural parameters of the generator. The simulation results are obtained, and state that the generator can realize the decoupling of the levitation force of excitation and power, which is suitable for vertical axis wind turbine.

[1]Ghulam Ahmad, Uzma Amin, Design, construction and study of small scale vertical axis wind turbine based on a magnetically levitated axial flux permanent magnet generator[J]. Renewable Energy, 101(2017): 286-292, 2017

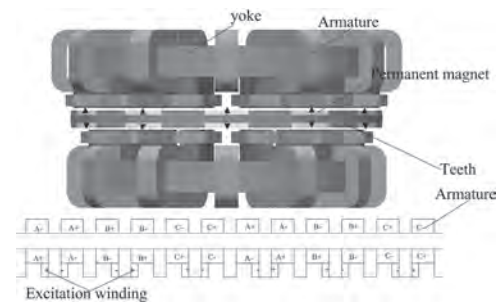


Fig.1 The structure of the proposed asymmetric-primary axis-flux hybrid-excitation generator

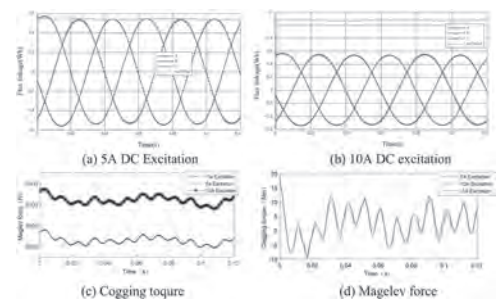


Fig.2. The performance under different excitation current

BB-05. An Improved Dual-Stator Cup Rotor Interior Permanent Magnet Synchronous Machine.

M.M. Zaid^{1,2}, H. Ahmad¹, I. Sami¹ and A. Waheed¹

1. Chung-Ang University, Seoul, The Republic of Korea; 2. Milim Syscon Co, Ltd., Seongnam-si, The Republic of Korea

Interior permanent magnet synchronous machine (IPMSM) is considered the best candidate for various applications such as traction and electric vehicle applications [1] [2]. In some cases, the IPMSM must have a high amount of torque density, power density, and wide speed range [3]. Recently, researchers have tried to increase the torque density of the vernier motor [4]. However, the vernier motor suffers a low power factor because of a high reluctance due to a large amount of leakage flux in the airgap [5] [6]. In this draft, a new dual stator interior permanent magnet synchronous motor (DS-IPMSM) is developed, comprised of 72 slots and 8 pole-pairs. In the proposed design, a new inner stator is inserted using the unused space of the rotor. The slots of inner stator are shifted by half pole pitch to attain the maximum amount of torque and to aid the flux lines of an inner and outer stator with each other. Although the torque of the proposed design increases; however, due to a new stator, the amount of losses increases. Hence, instead of silicon steel (50A1000), a soft magnetic amorphous material (2605SA1) is used in the outer and inner stator to reduce the proposed design losses. Fig. 1 (a) shows the configuration of the proposed designs. To reduce the inner winding temperature, a cup rotor is presented, as shown in Fig. 1 (b). It shows that the inner stator is attached to the inner stator shaft to support it mechanically. The rotor is attached to the shaft in the form of a cup. Moreover, the bearing is used between the inner stator support shaft and output rotor shaft to align the rotor. Because of cup shape rotor configuration, the inner windings' heat is removed from one side of the motor. The slot area of the inner and outer stators is not the same because of its geometry. To reduce the inner winding temperature, the inner stator's current density is less than the outer stator. Therefore, the proposed design uses two inverters, as shown in Fig. 1 (c). The proposed DS-IPMSM using conventional steel sheets are presented by PD-1; however, the design using the amorphous material is presented by PD-2. Fig. 2 shows the analysis and comparison of the proposed and conventional designs. Fig. 2 (a) shows the back EMF of the conventional and proposed designs. Additionally, the back EMF of outer stator PD-1 and PD-2 is identical with the back EMF of a conventional single stator model. Fig. 2 (b) shows the dramatic improvement in the torque compared to the conventional model. In the end, the losses of PD-1, PD-2, and conventional design (CD) are compared. It shows that although the torque performance of the PD-1 and PD-2 increased by a huge amount as compared to conventional modal. Contrary, the losses are also increased by 25 % due to a second stator in the conventional design. The total losses in the conventional design are 556.3 W, and the losses in the PD-1 are 753.2 W. The efficiency of the conventional design is 98.45 %, whereas it is decreased to 98.39% due to an increase in motor losses. To cope with the problem of increased losses, the amorphous material is introduced to the stator; thus, decreasing the overall losses of the motor up to 493.5 W, resulting in increased efficiency of 98.90 %.

[1] Toba and T.A. Lipo, "Generic torque-maximizing design methodology of surface permanent-magnet vernier machine," vol. 36, no. 6, pp. 1539-1546, 2000. [2] F. Zhao, T. A. Lipo, and B. Kwon, "Magnet flux focusing design of double stator permanent magnet vernier machine," in Proc. COMPUMAG, 2013. [3] C. Liu, K. Chau, J. Zhong, W. Li, and F. Li, "Quantitative comparison of double-stator permanent magnet vernier machines with and without HTS bulks," vol. 22, no. 3, pp. 5202405-5202405, 2011. [4] Y. Wang, M. Cheng, M. Chen, Y. Du, and K. J. I. E. p. a. Chau, "Design of high-torque-density double-stator permanent magnet brushless motors," vol. 5, no. 3, pp. 317-323, 2011. [5] Y. Gao, R. Qu, D. Li, H. Fang, J. Li, and W.B. Kong, "A novel dual-stator Vernier permanent magnet machine," vol. 53, no. 11, pp. 1-5, 2017. [6] Y. Shi and T.W. Ching, "Power Factor Analysis of Dual-Stator Permanent Magnet Vernier Motor with Consideration on Turn-Number Assignment of Inner and Outer Stator Windings," 2020.

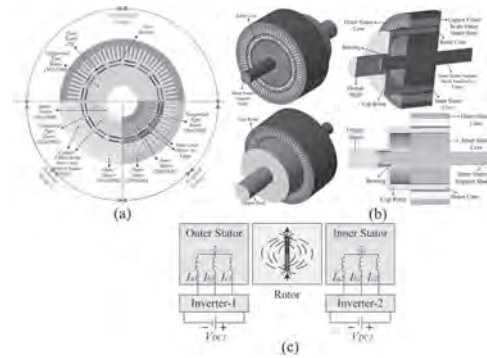


Fig. 1. (a) Geometry of the proposed and conventional designs; (b) Proposed dual stator cup type rotor; (c) Configuration of the inner and outer stator with the inverter.

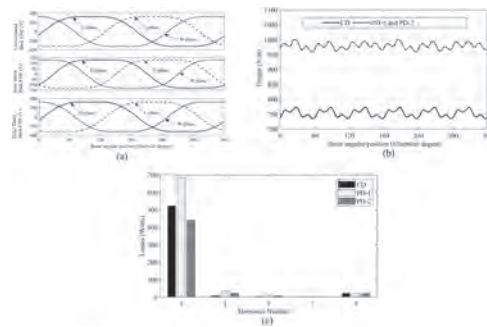


Fig. 2 (a) Back EMF of the conventional and proposed designs; (b) torque comparison; and (c) losses comparison.

BB-06. Fault-Tolerant Control for a Six-Phase Two-Controllable-Rotor Motor.

H. Suzuki¹, K. Hirata¹, N. Niguchi¹ and K. Takahara¹
 1. Graduate School of Engineering, Osaka University, Suita, Japan

1. Introduction The electrification of a vehicle has been gaining momentum recently, and more and more vehicles are being equipped with many electric motors and their inverters. In particular, a series-parallel hybrid electric vehicle and coaxial helicopter have two motors in its drive train [1-2]. In order to reduce the space of the motors, we proposed a two-controllable-rotor motor [3]. The proposed motor has two axially-arranged rotors and a common stator. The two rotors can be independently controlled using 3- and 6-phase superimposed currents created by a 6-phase inverter. One rotor is driven by a 3-phase current and the other is driven by a 6-phase current. In the transportation applications, it is important to continue the drive operation under fault conditions. Therefore, a fault tolerant control for multiphase motors have been studied [4-5]. In this paper, we propose a fault-tolerant control for a two-controllable-rotor motor using a 6-phase inverter, and its effectiveness is verified using finite element analysis. 2. Structure and Operational Principle Fig. 1 shows general and sectional views of our proposed motor with two axially-arranged rotors. The proposed motor has a common stator and two rotors: 6- and 12-pole rotors. The common stator has 36 slots and 6-phase distributed winding from A-phase to F-phase, and the in-phase coils are connected in series. This motor has a high heat dissipation because the stator is located outside. The two rotors can be easily supported because the two rotors are axially located with each other, and the 6-pole rotor shaft is mounted in the 12-pole rotor shaft through bearings. The 6- and 12-pole rotors are driven as 3- and 6-phase permanent magnet synchronous motors, respectively, by using superimposed currents created by a 6-phase inverter. Furthermore, it is known that the 3- and 6-phase currents do not mathematically interfere with each other [6]. In the proposed motor shown in Fig. 1, the stator and rotors diameters are $\Phi 110$ mm and $\Phi 64$ mm, respectively, the radial air gap length is 1 mm, and the rotor, stator thickness, and axial air gap length are 30 mm, 62 mm, and 2 mm, respectively. The winding factors of the 6- and 12-pole rotors are 0.7 and 1.0, respectively. The Maximum current density is 10Arms/mm². 3. Fault-Tolerant Control A multiphase motor can be used for a fault-tolerant operation due to its additional degrees of freedom. This is because, under fault conditions, the remaining healthy phases in a multiphase machine can be used to compensate the faults and to continue the drive operation [4-5]. A two-controllable-rotor motor needs at least 5 phases to independently control the both rotors [7]. Therefore, a two-controllable-rotor motor using a 6-phase inverter can be driven although one phase is in a fault condition. In this paper, we propose a fault-tolerant control for a two-controllable-rotor motor when one phase is in an open circuit. In order to investigate the torque ripple due to a superimposed current when one phase is in an open circuit, an electromagnetic field analysis using finite element method is conducted. Figs. 2 (a) and (b) show the drive current waveforms for the 6- and 12- pole rotors under normal condition, respectively. Figs. 2 (c) and (d) show the drive current waveforms for the 6- and 12- pole rotors in A-phase open condition, respectively. Figs. 2 (e) and (f) show the torque waveforms of the 6- and 12- pole rotors, respectively under the normal and fault conditions. From Figs. 2 (e) and (f), the torque ripple rate of both rotor torque under the fault condition due to the superimposed current hardly changes. Therefore, the both rotors can be independently controlled under the fault condition. 4. Conclusion In this paper, we propose a fault-tolerant control for a two-controllable-rotor motor using a 6-phase inverter. The torque ripple rate of both rotor torque due to a superimposed current when one phase in an open circuit hardly changes compared with a normal condition. Therefore, the both rotors can be independently controlled under the fault condition. In the final paper, a mathematical model of the fault-tolerant control is described in detail. Furthermore, the torque ripple and N-T characteristics in normal and fault conditions are compared using a prototype.

no. 2, pp. 476-485 (2011) [5]W. Zhang, X. Liang, F. Yu, IEEE Trans. Magnetics, vol. 54, no. 11 (2018) [6]N. Tan, M. Arimitsu, Y. Naruse, The International Power Electronics Conference, pp 1482-1488 (2005) [7]H. Suzuki, K. Hirata, N. Niguchi, IEEE ICES, pp. 5-11 (2020)

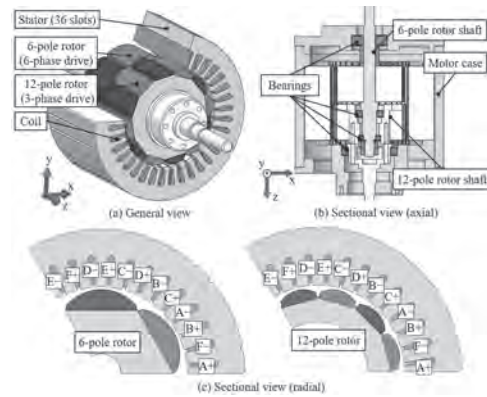


Fig. 1 Our proposed two-controllable-rotor motor.

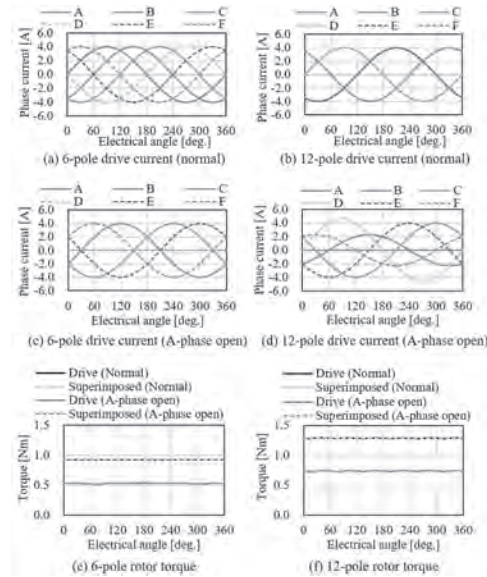


Fig. 2 Current and torque waveforms.

[1]H. A. Borhan, A. Vahidi, A. M. Phillips, American Control Conference, pp. 3970-3976 (2009) [2]J. Paulos, B. Caraher, M. Yim, IEEE ICRA, pp. 7011-7016 (2018) [3]H. Suzuki, K. Hirata, N. Niguchi, IEEE INTERMAG (2018) [4]S. Dwari, L. Parsa, IEEE Trans. Industrial Electronics, vol. 58,

BB-07. Ultra High-Field, High-Efficiency Superconducting Machines for Offshore Wind Turbines.

T. Balachandran¹, D. Lee¹, A. Yoon¹ and K. Haran¹

¹. Hinetics LLC, Champaign, IL, United States

Offshore wind has gained traction worldwide as an alternative to fossil-fuel based power plants. Coastal US states have started incentivizing the development of offshore wind farms, with at least 24,135 MW currently planned for deployment. To make offshore wind more cost-competitive, major turbine OEMs like GE, Siemens, and MHI Vestas have been steadily increasing the power produced per turbine from 1.6 MW in 2000 to 12 MW in 2020. Increasing the turbine power reduces balance-of-plant costs, increases electromagnetic efficiency, and boosts capacity factor, leading to lower levelized cost of electricity (LCOE) for power purchasers [1]. However, even at 12 MW per turbine, the cost of shipping, installing, and maintaining thousands of wind turbines makes the price of electricity prohibitively expensive. Traditional permanent-magnet turbine technologies make it pointless to increase the power rating beyond 15 MW since their size and weight are significantly increased by their installation cost. Low temperature superconducting (SC) generators were explored for a long time for high-power application where volume and weight requirements are strict [2]-[3]. Recent technology development in low temperature and high temperature SC cables renewed SC machines interest in wind turbine applications [3]-[4]. Achieving ambitious goals of harvesting 24,135 MW of offshore wind energy hinges on the successful development of superconducting generator technology. Superconducting generators can produce extremely high specific power and run at higher efficiency than commercial, permanent-magnet generators because they can produce up to 10X more magnetic flux density which reduces the weight significantly. This shows that with 10X power per turbine is possible at same PM generator specification. To demonstrate these benefits, a 12 MW superconducting wind turbine has been investigated for 3 different generator topologies: fully active, hybrid and fully passive. 12 MW power was chosen instead of the theoretical limit of 120MW to show that partial SC machines can outperform the best commercial 12 MW turbines while maintaining a 10T flux densities which have already been demonstrated in MRI applications. Low temperature Nb_3Sn [2] cables and high temperature VIPER [3] cables are analyzed for field windings with Litz wire armature windings. A multi objective optimization is performed on machine designs to achieve less than 60 Ton machine weight while reaching greater than 98% efficiency. Two studies are conducted at outer diameter (OD) of 4.2 m and 7.2 m to analyze the reduction in LCOE due to transportation and installation cost. Fig. 1 shows the obtained Pareto-front for motor active weight Vs motor efficiency at 7.2 m OD. Results show that targeted weight and efficiency can be achieved at ultra-high-field designs. The best designs have 10-12 T peak field at field windings and 3-5 T peak field at airgap. The optimization performed here equally weighted the mass and efficiency of the generator to reach the final design. However, LCOE is sensitive to superconductor length than the mass and efficiency-related cost penalties. This will be considered to further refine design optimization study presented here. The thermal design studies will also be refined using temperature-dependent thermal conductivities ranging all the way from room temperature to the proposed 4K operating temperature. Along the same lines, there is an outstanding need to identify cryocoolers which can reach 4K while satisfying the heat load requirements from ambient conduction and radiation. Upon completion of the electromagnetic, thermal, and mechanical design, the weight estimates for the generator will be refined to include both the generator and its supporting systems for comparison with the weight of commercial turbines. This is an important research study which also translates to a concrete value proposition for the feasibility of SC offshore wind turbines. An integration scheme was explored by mounting the proposed generator inside of a commercial turbine with the associated aerodynamic, mechanical, electrical, and thermal systems needed for operation in an offshore wind farm. Fig. 2 shows the cross-section and full turbine structure and the detail winding arrangements of a selected 7.2 m OD design. The proposed turbine would output 200% of the rated power for a commercial turbine of the same size. As it can be seen in the figure, the volume of the turbine nacelle is not fully occupied, leaving additional room to increase the turbine power even further with larger-diameter SC machines. In conclusion, this paper will produce

electromagnetic, thermal, mechanical and cost analysis to support the feasibility of using ultra-high-field superconducting generators for offshore wind applications.

[1]. A. B. Abrahamsen et al., IEEE Transactions on Applied Superconductivity, vol. 28, no. 4, (2018). [2]. S. Minnich et al., IEEE Transactions on Magnetics, vol. 15, no. 1, (1979). [3]. H. Southall and C. Oberly, IEEE Transactions on Magnetics, vol. 15, no. 1, (1979). [4]. M. Hsieh, C. Lin, I. Lin, IEEE Transactions on Magnetics, vol. 49, no. 5, (2013). [7]. D. Liu, H. Polinder, A. B. Abrahamsen, IEEE Transactions on Applied Superconductivity, vol. 27, no. 5, (2017). [5]. A. Godeke, B. ten Haken, H. H. J. ten Kate, Supercond. Sci. Technol., vol. 19, no. 10, (2006). [6]. Z. S. Hartwig, R. F. Vieira, B. N. Sorbom, Supercond. Sci. Technol., Volume 33, no. 11, (2020).

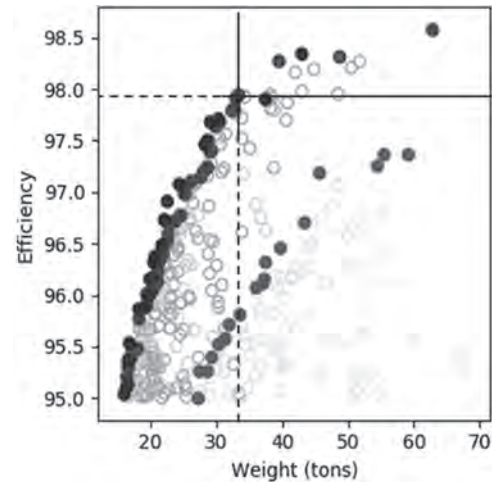
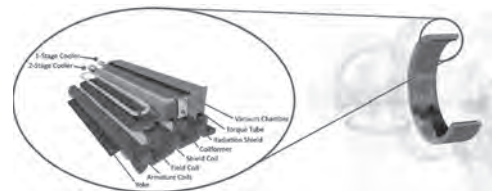


Fig. 1 Optimal Pareto-front of weight Vs efficiency



Detailed mechanical design of proposed SC machine inside a commercial turbine and detail winding arrangement

BB-08. A sub-Harmonically Excited Novel Brushless Wound Rotor Synchronous Machine Using a new two-Layer Winding Topology.

S.H. Rafin¹ and Q. Ali²

1. *Electrical and Electronic Engineering, Northern University Bangladesh, Dhaka, Bangladesh;* 2. *Electrical Engineering, Sukkur IBA University, Sukkur, Pakistan*

This digest introduces a novel BL-WRSM having a unique two-layer stator winding configuration that surpasses the performance of the BL-WRSMs presented in [1] - [5]. Moreover, the new two-layer stator winding is such that it utilizes all the slot space available, and it can produce fundamental MMF components for torque generation and sub-harmonic MMF components for field excitation. As it can be seen from Fig. 1, two sets of series-connected stator windings, ABC and XYZ, are wound in a two-layer arrangement. Although the bottom layer's slots are entirely covered by the ABC winding, the top layer consists of both ABC and XYZ winding, where every other slot has XYZ winding conductors in the whole periphery of the top layer, which is shown in Fig.2. By this arrangement, a single current source inverter can drive the machine with a maximum number of slots utilization. It is important to state that the rotor of the machine is also comprised of two separate windings itself and they are: the field winding and the harmonic winding. While the field winding is wound in an 8-pole manner, the rotor harmonic winding is a 2-pole winding that is employed for inducing the sub-harmonic MMF generated by the XYZ winding of the stator. Both the rotor windings are connected via a diode bridge rectifier circuit mounted on the periphery of the rotor. To extend the understanding, the fundamental MMF component is produced by winding ABC, and it has an 8-pole arrangement with the frequency of ω_m , where ω_m is the frequency in the mechanical space domain. Whereas in the case of winding XYZ with its 2-pole configuration, it delivers the sub-harmonic MMF component with the frequency of $(\omega_m)/4$. Thus, the two components rotate at a different speed. In the rotor, on the other hand, the harmonic winding is placed on the rotor such that it aligns magnetically with the stator's XYZ winding, and both are wound in a 2-pole manner. Adjacent to the harmonic winding, which is connected through the diode rectifier, field winding having an 8-pole arrangement aligns magnetically with winding ABC having 8 poles. Given all that, the novel BL-WRSM achieves its brushless operation by inducing the sub-harmonic MMF to the rotor harmonic winding and by magnetically locking the stator fundamental MMF with the rotor field winding. The main manuscript of this topic will cover an extensive literature review, structure of the machine, winding configuration, and working principle of the proposed BL-WRSM. Along with these, a 2-D finite element analysis (2-D FEA) has been performed to test the validity of the machine, which is also partially reported in this digest. An 8-pole, 48-slot BL-WRSM with a 3-phase, 2-layer distributed stator winding is designed to validate the proposed topology. Based on the stator winding structure, both ABC and XYZ windings are placed throughout the 360-mechanical degree of the stator, and the rated power of the machine is considered 1281 W having a constant speed of 900 rpm. To examine the effectiveness of the proposed machine, its performance is compared with the conventional WRSM used in [3] and the single inverter BL-WRSM in [4]. For the proposed machine, however, all design parameters are kept exactly similar to the BL-WRSM presented in [4], which includes, outer diameters, air-gap length, stack length, the current density in the stator, and rotor winding to name but a few. While all the machines are supplied with an RMS current of 4.5 A, the rotor field current is found in the proposed BL-WRSM (21.61 A) is remarkably higher than that of the BL-WRSM (9.8 A) in [4]. The reason for the higher current is 2-pole sub-harmonic component and the proposed 2-layer stator winding arrangement. As a result, the 2-D FEA shows that the average torque of the new machine is found 12.03 Nm that is approximately 65% more than the average torque production of the machine in [4]. Despite the performance enhancement in torque generation, the torque ripple is found 34%. Moreover, the flux density and flux lines are somewhat evenly distributed throughout the stator rotor frame for the novel BL-WRSM, unlike in the case of BL-WRSM in [4], where the distribution was found uneven because of the under-utilized stator slot space. It also shows the proposed BL-WRSM works under the flux density of 2 T. The focal point of this work is to develop a brushless wound rotor synchronous machine. To study the performance and feasibility the new machine has

substantiated with the 2-D finite element method. Although operation wise it resembles the BL-WRSMs, performance-wise it surpasses many crucial aspects, and it demonstrates some certain advantages over the newly developed BL-WRSMs in [2] to [5]. Hence, the proposed machine could be an alternative solution considering all the attractive features provided, and they are listed as follows, 1. Single inverter brushless operation. 2. Utilizes the maximum allowable slot capacity. 3. No need for implying complex current control to mitigate unbalanced current circulation in the stator. 4. No need for imposing a complex unbalanced-cooling system. 5. Greater torque generation. With all these advantages, it can certainly be a competitive alternative not only to the BL-WRSMs but also with the state of the art PMSMs those are used in contemporary electrified transportation application. Moreover, the proposed topology could potentially adopt the design presented in [6] to [9], and used in converter topologies presented in [10], [11]. These designs will extensively be covered in the main manuscript.

1. F. Yao, D. Sun, L. Sun, and T. A. Lipo, "Dual third-harmonic-current excitation principle of a brushless synchronous machine based on double three-phase armature windings," in *Proc. 22nd Int. Conf. Electr. Mach. Syst. (ICEMS)*, Harbin, China, Aug. 2019, pp. 1-4. 2. Q. Ali, T. A. Lipo and B. Kwon, "Design and Analysis of a Novel Brushless Wound Rotor Synchronous Machine," in *IEEE Transactions on Magnetics*, vol. 51, no. 11, pp. 1-4, Nov. 2015, Art no. 8109804. 3. Ali, Q., Atiq, S., Lipo, T. A., & Kwon, B. (2016). PM Assisted, Brushless Wound Rotor Synchronous Machine. *Journal of Magnetics*, 21(3), 399-404. 4. Hussain, A., & Kwon, B. (2017). A new brushless wound rotor synchronous machine using a special stator winding arrangement. *Electrical Engineering*, 100(3), 1797-1804. 5. Hussain, A., Atiq, S., & Kwon, B. (2018). Optimal Design and Experimental Verification of Wound Rotor Synchronous Machine Using Subharmonic Excitation for Brushless Operation. *Energies*, 11(3), 554. 6. M. Ayub, S. Atiq, Q. Ali, A. Hussain and B. Kwon, "Dual-Mode Wound Rotor Synchronous Machine for Variable Speed Applications," in *IEEE Access*, vol. 8, pp. 115812-115822, 2020. 7. G. Jawad, Q. Ali, T. A. Lipo and B. Kwon, "Novel Brushless Wound Rotor Synchronous Machine With Zero-Sequence Third-Harmonic Field Excitation," in *IEEE Transactions on Magnetics*, vol. 52, no. 7, pp. 1-4, July 2016, Art no. 8106104. 8. M. Ayub, A. Hussain, G. Jawad and B. Kwon, "Brushless Operation of a Wound-Field Synchronous Machine Using a Novel Winding Scheme," in *IEEE Transactions on Magnetics*, vol. 55, no. 6, pp. 1-4, June 2019, Art no. 8201104. 9. A. Hussain, S. Atiq and B. Kwon, "Consequent-Pole Hybrid Brushless Wound-Rotor Synchronous Machine," in *IEEE Transactions on Magnetics*, vol. 54, no. 11, pp. 1-5, Nov. 2018, Art no. 8206205. 10. Rafin, S. M., Lipo, T. A., & Kwon, B. (2014). A novel topology for a voltage source inverter with reduced transistor count and utilizing naturally commutated thyristors with simple commutation. *2014 International Symposium on Power Electronics, Electrical Drives, Automation and Motion*. doi:10.1109/speedam.2014.6872057. 11. Rafin, S. M., Lipo, T. A., & Kwon, B. (2015). Performance analysis of the three transistor voltage source inverter using different PWM techniques. *2015 9th International Conference on Power Electronics and ECCE Asia (ICPE-ECCE Asia)*.

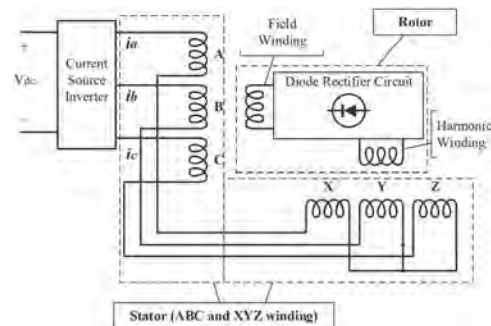


Fig.1

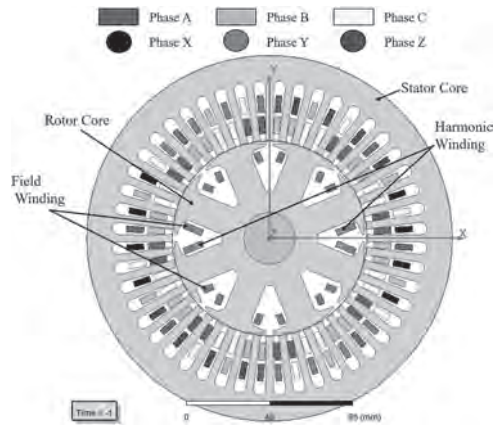


Fig.2

BB-09. Investigation of a Novel Consequent-Pole Variable Flux Memory Machine With Reduced Magnetization Current.

H. Yang^{1,2}, R. Tu¹ and H. Lin¹

1. School of Electrical Engineering, Southeast University, Nanjing, China;
2. The Hong Kong Polytechnic University, Kowloon, Hong Kong

I. Introduction Variable flux memory machine (VFMM) [1]-[4] is becoming a hot research focus with its merits of flexible flux adjustment capability, and high efficiency over a wide operation range. Normally, VFMMs [1]-[4] utilize a transient *d*-axis current pulse generated by armature windings to change the magnetization states (MSs) of low coercive force (LCF) magnets, eliminating the continuous flux-weakening excitation copper loss. Nevertheless, the conventional VFMMs generally require large amplitudes of magnetization currents due to the high magnetic reluctance of two LCF magnets located on adjacent rotor poles, which inevitably leads to increased inverter power rating. Therefore, this paper proposes a novel consequent-pole VFMM (CP-VFMM) to address the above-mentioned issues for the existing VFMMs [1]-[4]. The combination of flux memory concept [5]-[6] and consequent-pole (CP) [7]-[8] structure exhibits the following strengths: 1) The usage and cost of AlNiCo magnet can be effectively reduced. 2) The flux regulation current magnitude can be reduced due to the replacement of half number of LCF magnets. 3) The iron poles provides additional magnetic circuit for armature reaction, which can reduce the risk of unfavorable demagnetization. II. Machine Topology and Operating Principle The topologies of CP-VFMM and conventional VFMM are shown in Figs. 1(a) and (b), respectively. For CP-VFMM, nearly half of the magnet poles are replaced by iron ones, forming a CP structure, which can reduce the usage of AlNiCo PM. Fig. 1(c) shows the hysteresis model of AlNiCo. When flux regulation magnetomotive force (MMF) is applied, the working point of LCF PMs will move along the recoil lines and finally stabilize at the load line. Thus, the MSs of the LCF PMs can be flexibly changed with different current pulses. III. Preliminary Electromagnetic Performance Analysis In order to better clarify the advantages of the proposed CP-VFMM, the electromagnetic performance is preliminarily evaluated and compared with the benchmark VFMM by using finite element method (FEM). Figs. 2(a)-(c) illustrate the flux line distributions, flux linkage and open-circuit back electromotive force (EMF) under different MSs, respectively. The results indicate that both topologies have excellent flux regulation capability. Fig. 2(d) compares the variations in back-EMF subject to different demagnetizing current amplitudes. It is revealed that the difficulty of flux regulation for CP-VFMM is significantly reduced. The torque versus angle curves in Fig. 2(e) verify that both topologies exhibit a reverse saliency, ensuring their excellent demagnetization withstand capabilities under load condition. In addition, the proposed CP-VFMM exhibits comparable torque capability with the conventional counterpart, by saving approximately 40% PM usage. The design optimization and experimental validation of the proposed CP-FIMM will be detailed and given in the full paper.

[1] V. Ostovic, "Memory motors," *IEEE Ind. Appl. Mag.*, vol. 9, no. 1, pp. 52-61, Jan./Feb. 2003. [2] J. Song, J. H. Lee, D. Kim, Y. Kim and S. Jung, "Analysis and modeling of concentrated winding variable flux memory motor using magnetic equivalent circuit method," *IEEE Trans. Magn.*, vol. 53, no. 6, pp. 1-4, Jun. 2017. [3] X. Zhu, S. Yang, Y. Du, Z. Xiang and L. Xu, "Electromagnetic performance analysis and verification of a new flux-intensifying permanent magnet brushless motor with two-layer segmented permanent magnets," *IEEE Trans. Magn.*, vol. 52, no. 7, pp. 1-4, Jul. 2016. [4] H. Yang, Z. Q. Zhu, H. Lin and S. Lyu, "Comparative study of hybrid PM memory machines having single- and dual-stator configurations," *IEEE Trans. Ind. Electron.*, vol. 65, no. 11, pp. 9168-9178, Nov. 2018. [5] N. Limsuwan, T. Kato, K. Akatsu and R. D. Lorenz, "Design and evaluation of a variable-flux flux-intensifying interior permanent-magnet machine," *IEEE Trans. Ind. Appl.*, vol. 50, no. 2, pp. 1015-1024, Mar./Apr. 2014. [6] M. Ibrahim, L. Masisi and P. Pillay, "Design of variable-flux permanent-magnet machines using Alnico magnets," *IEEE Trans. Ind. Appl.*, vol. 51, no. 6, pp. 4482-4491, Nov./Dec. 2015. [7] J. Li, K. Wang and C. Liu, "Comparative study of consequent-pole and hybrid-pole permanent magnet machines," *IEEE Trans. Energy Convers.*, vol. 34, no. 2, pp. 701-711, Jun. 2019. [8] H. Yang, S. Lyu and H. Lin, "A variable-mode stator consequent

pole memory machine," *AIP Advances*, vol. 8, no. 5, Art no. 056612, pp. 1-5, 2018.

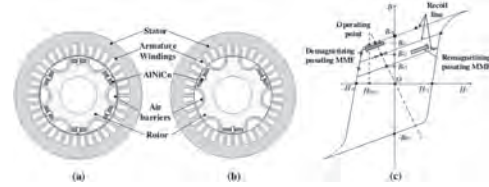


Fig. 1 Topology of (a) FIMM and (b) CP-FIMM. (c) Hysteresis model of AlNiCo PM.

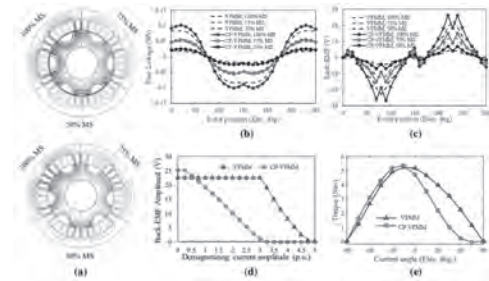


Fig. 2. Performance comparison of FIMM and CP-FIMM. (a) Flux line distributions. (b) Flux linkage. (c) Back-EMF. (d) EMF subject to different demagnetizing currents. (e) Torque versus current angle.

BB-10. Design and Analysis of a Novel Series-Parallel Variable Flux Machine With Segmented Hybrid Permanent Magnets.

M. Wang¹, P. Zheng^{1,2}, C. Tong¹, G. Qiao¹ and F. Liu¹

1. School of Electrical Engineering & Automation, Harbin Institute of Technology, Harbin, China; 2. State Key Laboratory of Robotics and System, Harbin Institute of Technology, Harbin, China

I. Introduction. With the merits of broad speed range and high efficiency at high-speed region, variable flux machine (VFM) is gaining more and more attentions in the wide-speed applications, such as electric vehicle, railway traction and numerical control machine tool. With the high coercive-force (HCF) and low coercive-force (LCF) permanent magnets (PMs) both utilized, VFMs with hybrid PMs are widely investigated. According to the combination way of hybrid PMs, VFM can be divided into series scheme and parallel scheme. Parallel VFMs are proven with relatively small demagnetization current and wide speed-adjusting range. But the HCF PM of parallel VFM has demagnetization effect on LCF PM, which will reduce the stability of LCF PM. While the LCF PM of series VFM is relatively stable, but the demagnetization current of series scheme is always large. This digest proposes a novel series-parallel VFM, which improves the stability of LCF PM by applying segmented PMs. The structure of the machine is introduced firstly, and then the magnetization-regulation principle is analyzed. The influences of V-shape pole parameters on electromagnetic torque and speed adjusting range of the machine are investigated.

II. Machine Structure and Magnetization-Regulation Principle The structure of the proposed series-parallel VFM with segmented PMs is shown in Fig.1, which is evolved from traditional V-shape PM synchronous machine (PMSM). The magnetic pole of the machine is composed of NdFeB and AlNiCo, and each side of the V-shape PM is divided into three parallel segments along the long-side direction of PM slot. The inner and outer PM segments are composed of series NdFeB and AlNiCo, and the middle PM segment is pure AlNiCo. Compared with the traditional parallel VFM, the proposed VFM has higher stability at load state, because of the NdFeB PM placed at the outer part of V-shape pole, where is more likely to be demagnetized by q -axis armature reaction. In addition, the series segments composed of NdFeB and AlNiCo has weaker demagnetization effect on middle AlNiCo than pure NdFeB, which can also improve the stability of the magnetic pole. The no-load flux distributions of the proposed VFM at forward and reverse magnetization state are shown in Fig. 1. It is illustrated that the flux provided by inner and outer PM segments are shorted by middle AlNiCo at reverse magnetization state, and the fundamental amplitude of no-load back electromotive force (EMF) is decreased from 73.00V to 5.94V, which proves the wide speed-adjusting range of the proposed VFM.

III. Research on Electromagnetic Torque and Speed-Adjusting Range Electromagnetic torque and speed-adjusting range are important characteristics of VFM, and thus influence laws of V-shape pole parameters on them are investigated. Since the change of PM dimensions will influence the magnetization result of middle AlNiCo when the same forward magnetization current is applied, the magnetization states of middle AlNiCo in VFMs with different PM dimensions at fully forward magnetization state are different. Therefore, the influences of V-shape pole parameters are different from traditional interior PMSM. According to the relationship between NdFeB thickness and the average flux density of series segments at no-load state, it can come to the conclusion that the equivalent remanence of the series segment can be adjusted by changing NdFeB thickness with the series-segment thickness unchanged. Afterwards, the influence of middle-AlNiCo position on electromagnetic torque and back EMF is investigated. It is found that moving the middle AlNiCo closer to the air gap can decrease the total harmonic distortion (THD) of back EMF at reverse magnetization state, and almost has no impact on electromagnetic torque and back EMF at forward magnetization state. The influence of PM ratio is analyzed, and it is indicated that VFM with larger PM ratio has wider speed-adjusting range, but the average torque is relatively low. With PM ratio kept unchanged, the average torque increases firstly, and then decreases with the increase of PM-pole width. Moreover, the difference between d - and q -axis inductances is found having the same variation law with the average torque. The reason is that changing PM-pole width will change the distance between poles, which will change the d - and q -axis magnetic circuits distribution of the machine. When the thickness of the PM pole is increased, the

average torque is increased firstly, and then decreased, while the torque ripple is increased continuously. The efficiency maps of the proposed VFM at forward and reverse magnetization states are shown in Fig. 2. It is illustrated that when VFM is reversely magnetized, the maximum speed of the machine is increased, and the efficiency at high-speed region is increased. The maximum torque of the machine at high speed region is also increased.

IV. Conclusions A novel series-parallel VFM with segmented hybrid PMs is proposed, and the selection principles for PM parameters of the machine is proposed. The speed-adjusting ability of the machine is elaborated by analyzing the magnetization-regulation progress, and the speed-adjusting performance is revealed by efficiency maps at different magnetization states.

[1] H. Yang, H. Zheng, and H. Lin, in Proc. IEMDC, CA, USA, pp. 2259-2264 (2019) [2] M. Wang, C. Tong, and P. Zheng, IEEE Trans. Magn., vol. 55, no. 7, pp. 1-7 (2019) [3] G. Qiao, M. Wang, and F. Liu, IEEE Trans. Magn., doi: 10.1109/TMAG.2020.3013624 (2020)

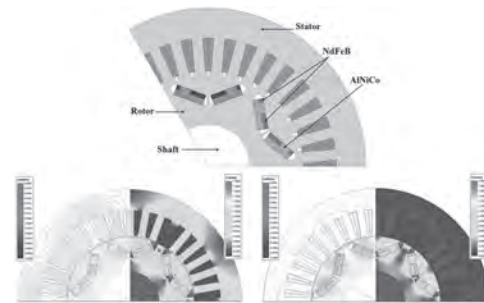


Fig. 1. Structure of the proposed VFM and no-load flux distributions at forward and reverse magnetization states.

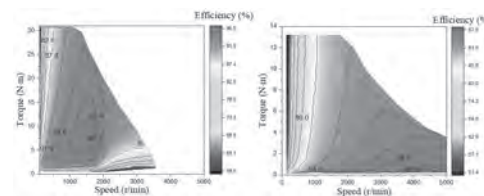


Fig. 2. Efficiency maps of the proposed VFM at forward and reverse magnetization states.

Session BC

HIGH-SPEED MACHINES AND RELUCTANCE MACHINES

Jian-Xin Shen, Chair
Zhejiang University, Hangzhou, China

INVITED PAPER

BC-01. Permanent Magnet Synchronous Reluctance Machines With Axially Combined Rotor Structure INVITED.

J. Shen^{1,2}, X. Qin¹, Y. Lin¹, Y. Sun¹, W. Wan¹ and S. Cai^{3,1}

1. College of Electrical Engineering, Zhejiang University, Hangzhou, China; 2. Zhejiang Provincial Key Laboratory of Electrical Machine Systems, Hangzhou, China; 3. Nanyang Technological University, Singapore, Singapore

A synchronous machine can have both mutual torque due to the permanent magnet (PM) excitation and reluctance torque due to the rotor saliency. According to the ratio of these two torque components, the machine can be classified as (i) the salient permanent magnet synchronous machine (PMSM) in which the mutual torque is dominant or (ii) the permanent magnet-assisted synchronous reluctance machine (PMA-SynRM) in which the reluctance torque is dominant. Both categories can be called permanent magnet synchronous reluctance machines (PMSynRM). Of course, the PMSM with no rotor saliency and the SynRM with no PM assistance can be regarded as special PMSynRM which have no reluctance torque or mutual torque, respectively. In the salient PMSM, there are many interior permanent magnet (IPM) rotor structures, such as the V-shaped and the Delta-shaped structures. The magnets not only produce magnetic excitation but also act as flux barriers to make the rotor magnetically salient. Basically, the Delta-shaped structure brings better rotor saliency than the V-shaped structure, as it has more layers of flux barriers. On the other hand, in the PMA-SynRM, there are even more layers (usually 3~5 layers) of flux barriers to further enhance the rotor saliency, but the magnets inserted in these flux barriers have inefficient utility due to the severe leakage in the circumferential bridges of the rotor and the series structure of all the magnets in each pole. In the conventional PMSynRM, the rotor is identical in the axial direction, but in the radial direction, from the rotor center to the airgap, there are iron core, flux barriers and magnets which are all merged, therefore, this kind of rotor can be called radially merged rotor structure (RMRS). A characteristic of the RMRS is that the PM excitation is along the d-axis of the rotor, whilst the rotor saliency is symmetric about the d-axis as well as the q-axis. In the RMRS machines, referring to Fig. 1(a), the current vector should be located along the q-axis to maximize the mutual torque per ampere, and ideally located in the middle between the q-axis and d-axis to maximize the reluctance torque per ampere. In other words, it is not achievable to maximize both torque components simultaneously, and thus the current vector has to be located at a compromised phase angle (see Fig. 1(a)). In this paper, the d-axis is re-defined as that about which the rotor saliency is symmetric, and the q-axis is away from the d-axis by 90 electric degrees. If the PM excitation vector is shifted from the conventional position (i.e., the d-axis) towards the q-axis by 45 electric degrees, as shown in Fig. 1(b), the back EMF vector will then be located in the middle between the q-axis and d-axis. In this case, the current vector can be simply placed at the same phase angle as the EMF vector, so that both the mutual torque and the reluctance torque can be maximized simultaneously. Fig. 1. Vectors in permanent magnet synchronous reluctance machines. (a) for conventional RMRS machines, (b) for proposed ACRS machines. An asymmetric rotor structure with extra flux barriers is proposed in [1], where the flux barriers force the PM flux to shift from the original d-axis towards the q-axis. However, it is very difficult to make the shifting angle as large as 45 electric degrees. Therefore, the current vector still has to be located at a compromised phase angle. In order to better shift the PM flux vector, it is proposed to use two types of rotor segments [2], one is the conventional surface-mounted permanent magnet (SPM) rotor, and the other is the conventional SynRM rotor without permanent magnet assistance. As shown in Fig. 2, these two types of rotor segments are axially combined on the shaft. Hence, this is called axially combined rotor structure (ACRS). Clearly, any shifting angle of the PM flux from the d-axis can be achieved. Fig. 2. Schematic of axially combined rotor structure (ACRS). In the full presentation, pros and cons of the ACRS machines will be detailed. For example, when using the same stator, the SPM rotor and the SynRM rotor can be optimized individually. Moreover, the SPM rotor has

less leakage than the IPM rotor, hence the permanent magnets can be utilized more efficiently. And, the SynRM rotor contains no permanent magnet, so that the circumferential bridges suffer from less stress due to the centrifugal force, thus the bridges can be thinner and the rotor saliency can be better. Furthermore, in the full presentation, different criteria will be described to determine the shifting angle and the axial length ratio of the two rotor segments, so as to maximize the two torque components simultaneously as well as the machine torque density, or to enhance the power factor for increasing the voltage utilization, or to make the torque ripple on the two rotor segments cancel each other and consequently reduce the overall torque ripple. Moreover, each of the SPM and SynRM rotors can be divided into several segments, so that the axial combination will be more flexible though the 3D effect will be severer.

[1] W. Zhao, et al, IEEE Trans. Mag., Vol. 50, p.8104504 (2014). [2] J.X.Shen, et al, Chinese Patent No.202020519211.7.

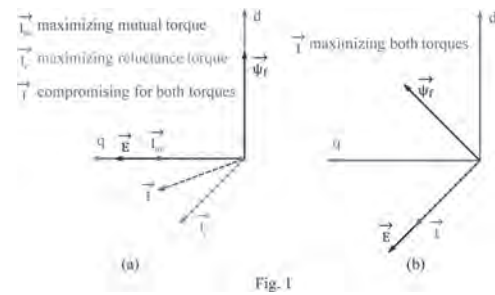


Fig. 1. Vectors in permanent magnet synchronous reluctance machines. (a) for conventional RMRS machines, (b) for proposed ACRS machines.

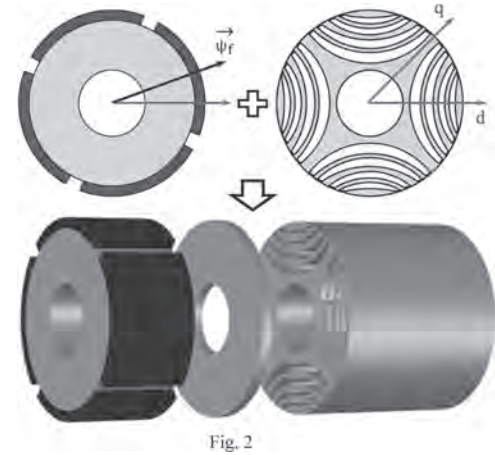


Fig. 2. Schematic of axially combined rotor structure (ACRS).

CONTRIBUTED PAPERS

BC-02. Analytical Analysis of the Eccentricity Effect in Slotted Ultra-High Speed Axial Flux Permanent Machines.G. Cao¹, W. Cheng¹, Z. Deng¹, L. Xiao¹ and M. Li¹¹. College of Science, Xi'an University of Science and Technology, Xi'an, China

For axial flux permanent magnet machines (AFPMMs), eccentricities may occur due to the manufacturing process, assembly error and operation fault. Therefore, the performances of the machines will be affected, which leads to vibration, noise and the reduction of motors' service life [1]. Analytical and semi-analytical methods to analyze the eccentricity effects of AFPMMs are concluded as the following. An analytical model of AFPMMs with mixed eccentricity (rotor radial deviation and angular eccentricity) was derived by the coordinate transformation and air gap length function, and the slotting effect was considered by relative complex permeance [1]. An improved conformal mapping method for static angular eccentricity was reported in literature [2]. The conformal mapping needs a Schwarz-Christoffel (SC) transformation which is difficult to deal mathematically. In addition, the conformal mapping method seems only suit to static eccentricity from published literatures. And the circumferential flux density may not be predicted accurately by this method. In [3-5], the superposition method was advised, which divided the eccentric machine into several uniform sections and achieved the air-gap flux density by synthesising the results of each concentric parts. However, it would be relatively time-consuming if the section number is large. Recently, an equivalent transformation method is proposed. It hypothetically transforms the original eccentric machine into a concentric one with redistributed PM remanence and current density. However, the method can only modify the radial flux density [6]. A 3-dimension field reconstruction method was proposed in [7] to consider the rotor eccentricity. In fact, the method still needs the results of finite element method (FEM), and hence time consuming. Another one is the perturbation method which can be used to describe the rotor eccentricity effect. Moreover, this model can account the slotting effect, the mutual influence between slots accurately. Literature [8] applied the perturbation method to predict the magnetic field of the mounted PM machines (radial flux typed). But there are few papers analyzing AFPMMs by using the perturbation method. This paper uses the combination of subdomain method and perturbation method to study the eccentricity of the slotted ultra-high speed AFPMMs. The open circuit field in the airgap under normal and eccentricity are calculated. In addition, the unbalanced magnetic force (UMF) and the corresponding incidental moment are obtained by the Maxwell stress tensor method. These results are verified by the finite-element method (FEM), which shows the effectiveness of the analytical method.

[1] W. Tong, S. Dai and S. Li, *IEEE Trans. Energy Convers.*, Vol. 35, p. 2181 (2020) [2] B. C. Guo, Y. K. Huang and F. Peng, *Journal of Magnetics*, Vol. 23, p.27 (2018) [3] Y. Li, Q. Lu and Z. Q. Zhu, *IEEE Trans. Magn.*, Vol. 52, p.1 (2016) [4] Y. Li, Q. Lu and Z. Q. Zhu, *IET Electr. Power Appl.*, Vol. 11, p.1095 (2017) [5] W. Tong, S. Li and X. Pan, *IEEE Trans. Energy Convers.*, Vol. 35, p. 2191 (2020) [6] J. Ren, X. H. Wang and W. L. Zhao, *IET Electr. Power Appl.*, Vol. 14, p. 192 (2020) [7] E. Ajily, M. Ardebili and K. Abbaszadeh, *IEEE Trans. Energy Convers.*, Vol. 31, p. 486 (2016) [8] J. Fu and C. Zhu, *IEEE Trans. Magn.*, Vol. 48, p. 1906 (2012)

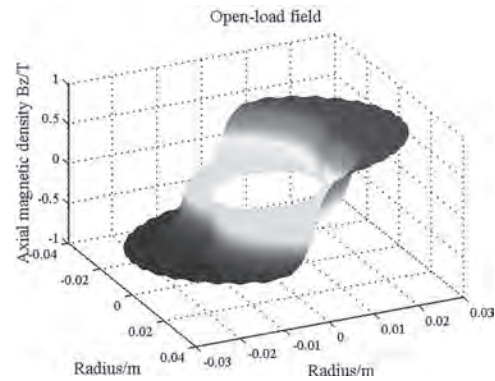


Fig.1 The axial magnetic density of open-load field under normal

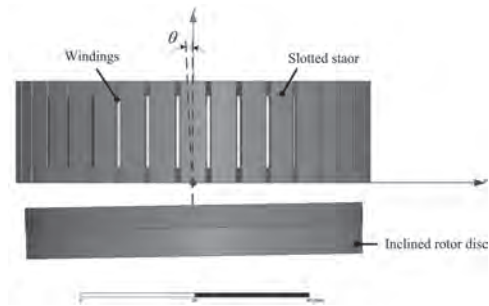


Fig. 2 The FEM model under eccentricity

BC-03. Design and Optimization of a Slotless High-Speed Permanent-Magnet Synchronous Motor With Non-Magnetic Fillers in Stator.

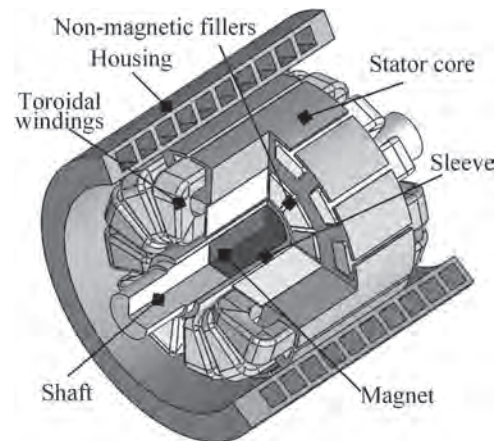
Y. Wan¹, L. Zhu¹, Y. Jia², N. Meng¹, J. Guo¹ and X. Jiang¹

1. School of automation, Nanjing University of Science and Technology, Nanjing, China; 2. Aviation Key Laboratory of Science and Technology on Aero Electromechanical system integration, AVIC Nanjing Engineering Institute of Aircraft System, Nanjing, China

INTRODUCTION: Recently an increasing demand for high-speed permanent-magnet synchronous motor (HSPMSM) emerges in the high-power density, high-efficient and limited-installation space applications, such as electric vehicles and aircraft [1,2]. However, high-power density inevitably results in high-loss density and limited heat dissipation surface, which will pose great difficulty in motor cooling. Besides, a high-strength sleeve is usually necessary to guarantee the mechanical strength of the surface-mounted HSPMSM rotor. But additional loss will be generated in the conductive sleeve, further increasing the difficulties on cooling. The overheating of magnets, which will cause the irreversible demagnetization, is regarded as one of the biggest problems in the HSPMSMs [3]. The slotless HSPMSM was thought has less rotor eddy-current loss, since without high-frequency space harmonics of the magnetic field in the airgap caused by stator slotting [4]. Nevertheless, it's well known that the flux density of the airgap is usually lower. But the power density is closely related with it. So as to counteract the shortage, higher electrical load of the winding can be regarded as a feasible approach, but which in turn increases the copper loss. Both the efficiency and heating of HSPMSM are determined by the losses. And the losses mainly consists of copper loss, iron loss, rotor eddy-current loss and friction loss, all of which are closely correlates with dimensions [5, 6]. Therefore, it is essential to find the optimal design to achieve the competitive power density and minimum losses in the limited space for the slotless HSPMSM. This paper introduces a slotless toroidal-winding HSPMSM with non-magnetic fillers in stator for fuel cell air compressor application. A multi-objective optimization process was discussed and carried out to find the best compromise between power density and efficiency for a 15 kW, 120 000 rpm HSPMSM. Based on optimization results, the optimal design scheme was selected and compared with a slotted scheme. **BASIC TOPOLOGY AND PRELIMINARY DESIGN CHOICES:** The configuration of the proposed HSPMSM was shown in Fig. 1. Slotless configuration was chosen in order to reduce the electric losses in the sleeve and magnet. The toroidal winding was adopted. Some slots are machined on the outside edge of stator core and the part of toroidal windings outside of the stator core are embedded in these slots. So the leakage flux will increase in the outside slots and the inductance of windings are accordingly increased. Moreover, the toroidal windings is tightly surround the stator core, so the fixation of slotless windings is very convenient. Litz wires was employed to alleviate the eddy-current losses of windings, due to skin effect and proximity effect. So as to achieve the good insulation between different phases of windings, some non-magnetic insulating fillers are desired to be mounted between them. The inside edge of stator core are machined with some notches, and the fillers are inserted to them with epoxy resin glue. After impregnation processing, the stator becomes a strong overall structure. The fillers are also beneficial to withstand the tangential electromagnetic force of the winding, consequently protecting the insulation of magnet wires. In addition, the fillers can help transfer the heat of windings to iron lamination. Boron nitride ceramics was selected as the candidate of non-magnetic fillers material, because of the good electrical insulation and thermal conductivity. **MULTI-OBJECTIVE OPTIMISATION:** Power density and efficiency were selected as the objective functions to be maximized. The key design variables and constraint variables were described and discussed in detail, as well as the multi-objective modeling method based on genetic algorithm and finite-element analysis of electromagnetic field. **OPTIMISATION RESULTS AND DISCUSSION:** In order to achieve the optimum design for the studied HSPMSM, 2246 evaluations has been performed and about 15 offspring populations was generated until the optimization converged. The optimization results were provided in Fig. 2, where all the feasible designs explored are represented by colored points. Besides, the solid black line is the Pareto front. The best designs are those that located on the Pareto front or closest to it. It can be clearly seen that the two optimization objectives are conflicting, which means that an

increase in power density is generally associated with a reduction in efficiency, and vice versa. A large number of design schemes were generated in the optimization process. Weighing a tradeoff between power density and efficiency, the final scheme was selected and the candidate point was also indicated in Fig. 2. As a comparison, a common slotted-configuration HSPMSM was also designed. The performance of the final scheme was analyzed and compared with the slotted scheme. The axial length of windings for the slotless HSPMSM is 24.8% lower than the slotted one, which is beneficial to improve the critical speeds of the rotor. The self-inductance calculated was higher than the slotted scheme. Besides, the slotless scheme has higher copper loss. But thanks to the removal of stator teeth, the iron loss was significantly decreased. So the total stator loss are basically the same for the two scheme. Finally, the slotless schemes exhibits higher efficiency and power density than the slotted scheme.

[1] D. Hong, B. Woo, and J. Lee, and D. Koo, IEEE Trans on Magn., vol. 48, no. 2, pp. 871-874 (2012). [2] N. Uzhegov, A. Smirnov, and C. H. Park, IEEE Trans. Ind. Electron., vol. 64, no. 11, pp. 8427-8436 (2017). [3] D. Gerada, A. Mebarki, and N. L. Brown, IEEE Trans. Ind. Electron., vol. 61, no. 6, pp. 2946-2959 (2014). [4] F. Luise, A. Tassarolo, and F. Agnolet, 2014 International Symposium on Power Electronics, 18-20 June 2014, pp.1237-1244. [5] G. H. Jang, J. H. Ahn, and B. O. Kim, IEEE Trans on Magn., vol. 54, no. 11, pp. 1-6, (2018). [6] W. D. Zhao, X. J. Wang, and C. Gerada, IEEE Trans on Magn., vol. 54, pp. 1-5(2016).



Configuration of the proposed HSPMSM

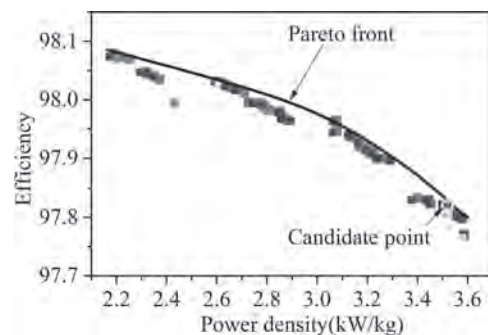


Fig.2 Optimization results

BC-04. Experimental Study on Remanence Variation of Permanent Magnets for High-Speed Machines.

J. Shen^{1,2}, H. Cao¹, Y. Zhang¹ and Y. Wang^{1,2}

1. College of Electrical Engineering, Zhejiang University, Hangzhou, China; 2. Zhejiang Provincial Key Laboratory of Electrical Machine Systems, Hangzhou, China

High-speed permanent magnet synchronous machines (PMSM) are widely used. However, there are challenges in the machine design [1-3]. To protect the magnets against the centrifugal force, a retaining ring is often employed on the rotor with interference fit, applying a strong compressive stress on the magnets. When the machine runs at high speed, the centrifugal force further enlarges the compressive stress on the magnets. On the other hand, high-speed machines have a disadvantage of high loss density which results in high temperature rise [1] [4]. Since different materials on the rotor have different thermal expansion, the high temperature rise produces more stress on the magnets. Therefore, the magnets in the high-speed PMSM suffer from high stress which may be up to 90 MPa, as well as high temperature such as 130 °C or higher. It has been well studied that the property of the permanent magnets varies (usually deteriorates) at high temperature, and such variation of property is usually considered in the machine design. However, it is hardly reported in existing literatures how the magnet property changes under high compressive stress. Therefore, an experimental study on this issue is carried out, by measuring the magnet property under various stress and temperature. A test rig is designed and built, and 7 types of NdFeB and 2 types of SmCo magnets are tested. Fig. 1 shows the test results of the NdFeB 42SH magnet at 24°C. When the compressive stress is applied on the magnet, its remanence increases slightly and then stays almost constant, as the curve of test-1 shows. However, when the pressure is released, it is found that the magnet remanence decreases. Then, compressive stress is applied again, and the remanence increases more remarkably, as shown as the curve of test-2. If the pressure is released again, the remanence returns with no extra decrease. Pressure is applied and released repeatedly, and the magnet property variation also repeats (see the curves of test-3, 4, and 5). Moreover, the same property variation trend is observed for the other NdFeB magnets and the SmCo magnets, i.e., the magnet property under the second application of compressive stress is lower than that under the first application of stress, but, the property will not become worse when the stress is applied more times. Therefore, it can be said that the magnet property is stabilized by the compressive stress. Fig. 2 shows the stabilized property variation versus the compressive stress for the other NdFeB magnets at room temperature. Each grade of NdFeB magnet has its own significance of property variation, and so is the case of the SmCo magnets. Similarly, the property variation versus the compressive stress at other temperature is also measured, demonstrating the negative thermal coefficient of the magnet remanence. In high-speed PMSM, the magnets suffer from significant compressive stress and temperature rise, therefore, their property of remanence is different from the data given by the manufacturer, as the manufacturer's data does not take into account the stress influence. Clearly, the stress influence is negligible in regular-speed machines, but should be considered in the high-speed machine designs. Acknowledgement This work was supported by the Natural Science Foundation of China under the grants

[1] J. Shen, et al, CES Transactions on Electrical Machines and Systems, Vol.2, p.23 (2018). [2] D. Gerada, et al, IEEE Trans. Industrial Electronics, Vol.61, p.2946 (2014). [3] F. Zhang, et al, IEEE Transportation Electrification Conference and Expo, Busan, Korea, p.843 (2016). [4] W. Li, et al, IEEE Trans. Industrial Electronics, Vol.61, p.3056 (2014).

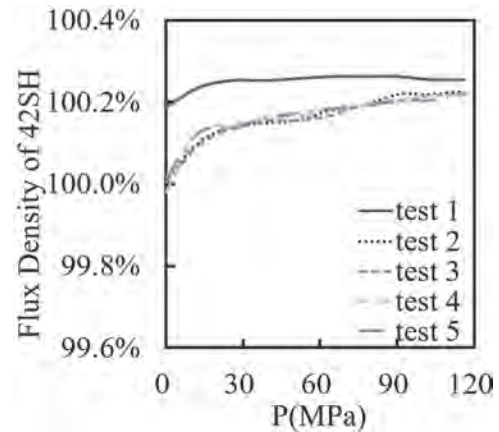


Fig.1 Remanence variation of NdFeB 42SH magnet versus compressive stress at room temperature.

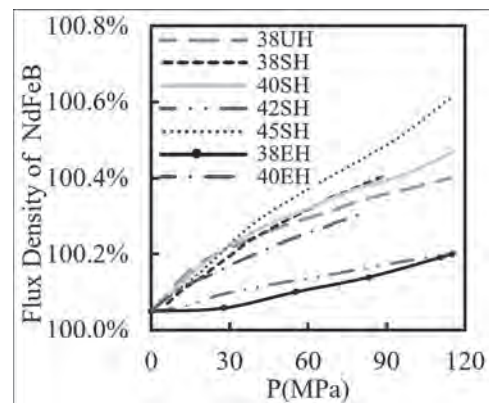


Fig.2 Stabilized remanence variation of different NdFeB magnets versus compressive stress at room temperature.

BC-05. Analysis and Experimental Verification of Segmented Rotor Structure on Rotor Eddy Current Loss of High-Speed Surface-Mounted Permanent Magnet Machine.

W. Tong¹, M. Hou¹, L. Sun¹ and S. Wu¹

1. National Engineering Research Center for Rare-Earth Permanent Magnet Machines, Shenyang University of Technology, Shenyang, China

Abstract—The eddy current loss in the permanent magnet (PM) and the sleeve of high-speed surface-mounted permanent magnet synchronous motors (HS-SPMSMs) increases the temperature rise of the rotor, which increases the risk of irreversible demagnetization of the PM. In order to reduce the rotor eddy current loss (RECL) of HS-SPMSM, this paper analyzes the suppression effect of four different segmented rotor structures (axially segmented sleeve, circumferentially segmented PM, axially segmented PM, PM and sleeve are simultaneously segmented) on the RECL of HS-SPMSM. On this basis, the applicability of the rotor segmented structure to the RECL with different sleeve materials is further analyzed. Finally, the C-core experiment was used to verify the influence of different segmented rotor structures on the RECL. I. Introduction High-speed permanent magnet synchronous motors (HS-PMSMs) have the characteristics of high-power density, but they also have the characteristics of high loss density and high temperature rise [1]. The high temperature of the rotor not only affects the performance of the motor, but also increases the risk of irreversible demagnetization of the PMs [2]. In order to suppress the RECL of the PMSM, the PM is usually divided into pieces [3-4]. This method is usually applied to conventional speed motors without sleeves. For HS-SPMSM, which is widely used in HS-PMSM, the RECL is mainly concentrated in the PM and sleeve [5], and the segmentation of the PM will affect the eddy current loss in the sleeve. However, there is little research on the effect of permanent magnet segmentation on the RECL of HS-SPMSM with sleeve structure. In this paper, four segmented rotor structures are established, including axial segmented sleeve, circumferential segmented PM, axial segmented PM, PM and sleeve segmented simultaneously. This paper uses different segmented rotor structures with three commonly used sleeve materials (carbon fiber, titanium alloy, stainless steel), and analyzes the influence of different segmented rotor structures on the RECL of HS-SPMSM. Finally, the C-core experiment is used to verify the influence of different rotor structures on RECL. II. Segmented Rotor Structure and Analysis A 15 kW, 30000 rpm HS-PMSM is taken as an example to analyze the RECL under different sleeve structures. When the motor is running at the rated speed, the four segmented rotor structures are analyzed for their suppression effect on RECL. The four segmented rotor structures are shown in Fig. 1. This paper analyzes the RECL of HS-PMSM with several commonly used sleeve materials (carbon fiber, titanium alloy, stainless steel), and studies the influence of segmented rotor structure on the RECL of HS-PMSM by using the four structures shown in Fig. 1. According to the calculation results, for the high conductivity sleeve material, when the number of axial segments reaches a certain degree, it is helpful to reduce the RECL, while for the carbon fiber sleeve, the axial segmentations have little effect on the RECL. When the PM is segmented axially or circumferentially, the RECL can be significantly reduced for the carbon fiber sleeve, and the effect of axial segmentation is better than that of circumferential segmentation. However, for the sleeve made of high conductivity material, the shielding effect on the eddy current magnetic field is weakened due to the segmentation of the permanent magnet, which makes the sleeve produce more eddy current loss and increases the total RECL. If the rotor structure shown in Fig. 1 (d) is used, the RECL can be reduced for all three sleeve materials, but the number of segments of PMs and sleeves needs to be reasonably configured. III. Experimental Verification In order to verify the influence of various sleeve materials on rotor eddy current loss and the suppression effect of sleeve axial segment structure on rotor eddy current loss. This paper verifies the influence of different sleeve structures on the eddy current loss of the rotor through the C-core experiment. The C-core experimental platform and different sleeve materials are shown in Fig. 2. IV. CONCLUSIONS This paper compares and analyzes the RECL of HS-SPMSM with different rotor structures. The RECL generated by the high-conductivity material sleeve is relatively high, but it can shield the eddy current loss of the permanent magnet. For high-conductivity sleeves, the axial segmentation can reduce

the eddy current loss of the sleeve by increasing the equivalent resistance of the sleeve and further suppress the RECL, when using PM segments, the sleeve will generate more eddy current loss, resulting in increased RECL. However, for carbon fiber sleeves, circumferentially or axially segmented PMs can help reduce the RECL, but the axial segmentation of the sleeve has almost no effect on the RECL. For the three sleeve materials, segmenting the sleeve and the PM at the same time will reduce the RECL, but the number of segmentations of the sleeve and the PM should be reasonably configured.

[1] C. Chen, Y. Wang and J. Wei, "Research on method for reducing eddy current loss of magnet in high-speed permanent magnet synchronous motor," 2019 22nd International Conference on Electrical Machines and Systems (ICEMS), Harbin, China, 2019, pp. 1-4. [2] J. Dong, Y. Huang, and L. Jin, "Thermal Optimization of a High-Speed Permanent Magnet Motor," IEEE Transactions on Magnetics, vol. 50, no. 2, pp. 749-752, Feb. 2014. [3] J. Shen, H. Hao, and M. Jin, "Reduction of Rotor Eddy Current Loss in High-Speed PM Brushless Machines by Grooving Retaining Sleeve," IEEE Transactions on Magnetics, vol. 49, no. 7, pp. 3973-3976, July 2013. [4] K. Yamazaki, M. Shina, and Y. Kanou, "Effect of Eddy Current Loss Reduction by Segmentation of Magnets in Synchronous Motors: Difference Between Interior and Surface Types," IEEE Transactions on Magnetics, vol. 45, no. 10, pp. 4756-4759, Oct. 2009. [5] H. Jun, J. Lee, and H. Lee, "Study on the Optimal Rotor Retaining Sleeve Structure for the Reduction of Eddy-Current Loss in High-Speed SPMSM," IEEE Transactions on Magnetics, vol. 51, no. 3, pp. 1-4, March 2015.

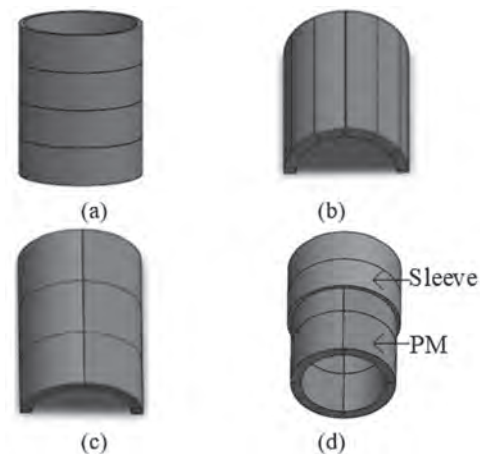


Fig. 1. Various rotor structures. (a) Axial segmented sleeve. (b) Circumferential segmented PM. (c) Axial segmented PM. (d) PM and sleeve are segmented simultaneously.

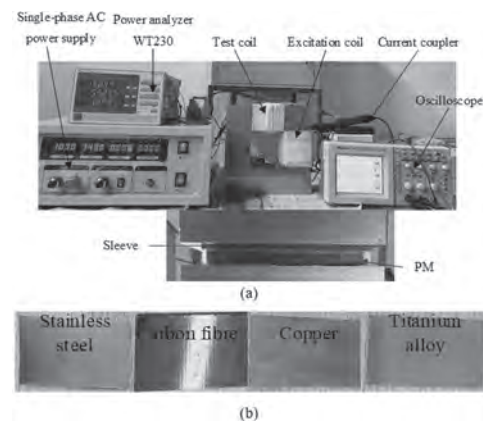


Fig. 2. Experimental verification. (a) C-core loss test experiment platform. (b) Sleeve materials.

BC-06. Impact of Rotor Eccentricity and Current Harmonics on High-Speed Permanent Magnet Generator Performance for Microturbine Applications.

T. Huynh¹ and M. Hsieh¹

1. Electrical Engineering, National Cheng Kung University, Tainan, Taiwan

Abstract This digest investigates the effect of rotor eccentricity and current harmonics on the performance of high-speed permanent magnet generators (HSPMG) with multi-physical analysis. First, the impact of magnetic flux density and electromagnetic force distribution due to rotor eccentricity in the no-load and load conditions on vibration and mechanical strength is studied and the allowed tolerance of rotor eccentricity is determined. Then, the current harmonics generated by the rectifier are injected into the generator armature to study the distribution of core loss, eddy current loss, and temperature rise (particularly on the rotor). Moreover, the resonance impact of rotor eccentricity and current harmonics on the electromagnetic force distribution is also evaluated. The results show that the increase of losses, temperature, vibration, and mechanical strength in HSPMG depends on the amplitude and percentage of total current harmonic distortion injected into the HSPMG under an allowable rotor eccentricity. Finally, the performance of the generator in multi-physical fields is validated through experimental studies.

I. Research Method and Target Model

A. Background The critical factors affecting the performance and operation of the high-speed generator the most are the increase of electromagnetic and mechanical losses, thermal, mechanical strength, vibration, and acoustic noise [1]. These can be produced by current harmonics due to low winding inductances, nonlinear characteristics of its converter, nonlinear loads, and rotor eccentricity. Here, the effects of current harmonics and rotor eccentricity are the main target. The force density between the stator and rotor surfaces of permanent magnet (PM) machines can be determined and divided into two components as [1] [2]: $f_r = (B_r^2 - B_t^2)/2\mu_0$ (1) $f_t = B_r B_t / \mu_0$ (2) where f_r and f_t are the radial and tangential components of the force density and B_r and B_t represent the radial and tangential components of the magnetic flux density in the air gap. The eccentricity of the rotor is defined as the radial distance between the stator and rotor cores and is calculated by [3]: $e = \varepsilon g$ (3) where ε is the eccentricity ratio and g is the nominal air gap length. Then, the effect of the static and dynamic eccentricity in the air gap length is the function of time and space as [4]: $g(\theta, t) = g(1 - \varepsilon \cos(\theta - \omega_m t))$ (4) where θ is the mechanical angle, t is the time, and ω_m is the rotor angular velocity. Note that only dynamic eccentricity is considered in this digest as it reflects the actual condition of the target high speed generator. Therefore, the effect of static and dynamic eccentricity on the radial electromagnetic force density related to the air gap permeance can be defined as $P_{ecc} = \mu_0 / k_c g(1 - \varepsilon \cos(\theta - \omega_m t))$ (5) where P_{ecc} is the air gap permeance considering the eccentricity. The permeance can be further used to calculate the flux, flux density and force density in the air gap considering eccentricity.

B. High-Speed Generator Model and Analysis Method

A. 200 kW high-speed generator is studied here, as shown in Fig. 1(a) and the current harmonics (with 16.8% total harmonic distortion) generated due to the rectifier that is connected to a load of 375 A output current is injected when the generator reached the peak power at the 45000 rpm speed, as shown in Fig. 1(b). Finite element analysis (FEA) is utilized to comprehensively evaluate the impact of rotor eccentricity and current harmonics on the electromagnetic field, loss distribution, temperature field, vibration, and mechanical strength of the high-speed generator.

II. Results

Fig. 2 shows the comparison of eddy current loss of high-speed generator with and without the effect of current harmonics when the generator reached 200 kW of power at the 45000-rpm speed and 375A output current. It can be observed that the eddy current loss reaches 1.25 times on the stator core and 4.2 times on the rotor core with current harmonics [Fig. 2(b)], respectively. This results in a winding temperature increase from 142°C to 166°C and rotor core temperature increase from 133°C to 156°C. Moreover, the temperature distribution on the rotor core under the effect of current harmonics almost focuses on the sleeve and the magnet near the sleeve, as shown in Fig. 3. This is a critical problem for high-speed machines. Fig. 4 shows the expansion and mechanical stress of the rotor core at 45000 rpm without the impact of the eccentricity. As can be seen, a rotor expansion of 0.03 mm and a rotor mechanical stress of 300 MPa are produced in this condition. The expansion seems

to be safe as the air gap is over 1 mm. However, the stress is close to the yield stress of the electrical steel and hence it needs to be carefully considered. The prototype of a 200 kW high-speed generator and the experimental setup to measure the magnetic flux density distribution on the rotor core are presented in Fig. 5. The measurement result for the magnetic flux density distribution on the rotor core is shown in Fig. 6. This result shows that the magnetic flux density distribution is unbalanced on the overall rotor length, which would significantly affect the mechanical strength and vibration of the high-speed generator.

III. Conclusion This digest has analyzed the effect of rotor eccentricity and current harmonics on the performance of a high-speed generator. The analysis results show that the iron loss and temperature of the generator are worsened with the effect of current harmonics. The detail analysis and experimental results will be reported in the full paper.

[1] F. Lin, S. Zuo, W. Deng, and S. Wu, *IEEE Transactions on Industrial Electronics*, vol. 63, no. 12, pp. 7455-7466 (2016). [2] K. H. Yim et al, *IEEE Transactions on Magnetics*, vol. 48, no. 11, pp. 2981 - 2984 (2012). [3] T.-J. Kim et al, *IEEE Transactions on Magnetics*, vol. 37, no. 4, pp. 2818 – 2820 (2001). [4] Ferhat Çıra, *Results in Physics*, vol. 10, pp. 760–765 (2018).

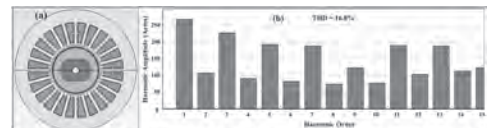


Fig. 1 (a) Model of 200 kW high-speed generator for study; (b) The total harmonic distortion of current injected into the generator in this study.



Fig. 2 Comparison of eddy current loss of generator with and without the effect of current harmonics: (a) without the effect of current harmonics; (b) with the effect of current harmonics.

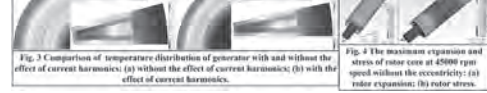


Fig. 3 Comparison of temperature distribution of generator with and without the effect of current harmonics: (a) without the effect of current harmonics; (b) with the effect of current harmonics.



Fig. 5 The prototype of 200 kW high-speed generator and the experimental setup to measure the magnetic flux density distribution on the rotor core: (a) Stator core with the winding, Permanent magnet, and assembled rotor core; (b) the experimental setup to measure the rotor core.

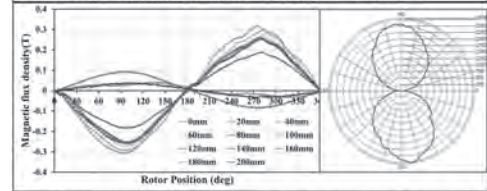


Fig. 6 The experimental results of the magnetic flux density distribution on the rotor core with the different positions on the rotor length.

Session BD

LINEAR MACHINES, ELECTROMAGNETIC ACTUATORS AND APPLICATIONS

David Bowen, Chair

University of Maryland, College Park, MD, United States

CONTRIBUTED PAPERS

BD-01. Analysis of Magnetic Gearing Effect in Field-Modulated Hybrid Excitation Transverse Flux Linear Generator for Direct Drive Wave Energy Conversion.

M. Chen¹, L. Huang¹, Y. Li¹, P. Tan¹, G. Ahmad¹, Y. Liu¹ and M. Hu¹

¹. School of Electrical Engineering, Southeast University, Nanjing, China

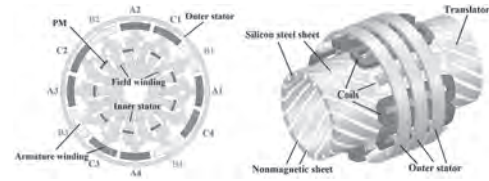


Fig.1 Sectional view and trimetric view of FM-HE-TFLG

I. Introduction Direct drive wave energy conversion (DD-WEC) is a typical low-speed long-stroke application, harvesting wave energy presents enormous challenges, because wave energy naturally exists in the form of extremely low speed, high force, or torque motion [1]. In DD-WEC, linear generators with multi-pole design all suffer from drawbacks such as low power density [2]. However, the frequency of flux linkage in field-modulated machine can be increased by the magnetic gear effect, and the output voltage and power density can also be effectively enhanced. Therefore, field-modulated machines have attracted more attentions in DD-WEC. A magnetic field-modulated linear permanent magnet (PM) generator for DD-WEC is proposed. The generator with a high power density converts wave energy effectively and enhances power density in DD-WEC [2]. A mover separated linear magnetic-field modulated motor for long stroke applications is proposed, the motor exhibits high thrust force by effectively employing the magnetic-field modulation effect [3]. A large-scale inner stator radial flux magnetically geared generator for wave energy conversion is proposed, the magnetic gear will not be damaged when exposed to overload torques [1]. Most recent work on field-modulated machines in DD-WEC focuses on the radial flux and axial flux machine, there is few literature about field-modulated transverse flux machine. In this paper, based on the field modulated principle, a field-modulated hybrid excitation transverse flux linear generator (FM-HE-TFLG) is proposed. Different combinations of PM pole pair, armature winding pole pair and translator pole pair are selected and their performances are compared and analyzed. II. Machine Configuration and Operation Principle Fig.1 In the proposed structure, as shown in Fig. 1, the armature winding is placed in outer stator slots. Excitation methods include electric excitation and PM excitation. Direct current (DC) field winding and PM are both located in inner stator. The translator consists of spiral silicon steel sheets and nonmagnetic sheets. In the proposed FM-HE-TFLG, armature winding pole pair p_{aw} , translator pole number N_p , and PM pole pair match p_{PM} : $N_p = p_{PM} + p_{aw}$ (1) The relationship between the translator position in electric and mechanical degrees is as follows: $\theta_e = N_p \theta_m$ (2) where θ_e and θ_m are translator positions in electric and mechanical degrees respectively. III. Results Fig.2 The 18/12/17 topology has higher electric frequency, and the amplitude of flux linkage is lower than 12/12/11 counterpart. As the armature current increases, the saturation of 12/12/11 topology is earlier than that of 18/12/17, so the structure with higher modulation ratio is more suitable for high current applications. IV. Conclusion The simulation results support several interesting conclusions. As the modulation ratio increases, the electric frequency is enhanced. The structure with higher modulation ratio is more suitable for high current applications. The proposed 18/12/17 FM-HE-TFLG is a good candidate for DD-WEC.

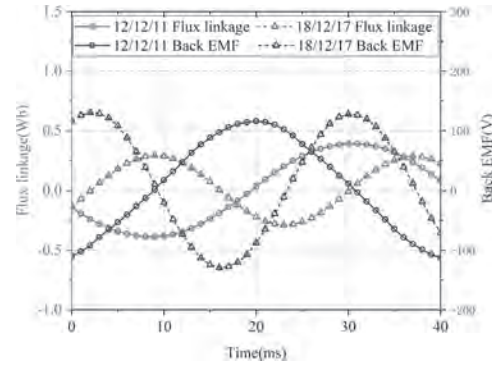


Fig. 2. Waveforms of flux linkage and back EMF in 12/12/11 and 18/12/17 FM-HE-TFLG

[1] M. Johnson, M. C. Gardner, H. A. Toliyat, S. Englebretson, W. Ouyang and C. Tschida, "Design, Construction, and Analysis of a Large-Scale Inner Stator Radial Flux Magnetically Geared Generator for Wave Energy Conversion," in *IEEE Transactions on Industry Applications*, vol. 54, no. 4, pp. 3305-3314, July-Aug. 2018. [2] N. Feng, H. Yu, M. Zhao, P. Zhang and D. Hou, "Magnetic field-modulated linear permanent-magnet generator for direct-drive wave energy conversion," in *IET Electric Power Applications*, vol. 14, no. 5, pp. 742-750, 5 2020. [3] W. Zhao, S. Wang, J. Ji, L. Xu and Z. Ling, "A New Mover Separated Linear Magnetic-Field Modulated Motor for Long Stroke Applications," in *IEEE Transactions on Magnetics*, vol. 53, no. 11, pp. 1-5, Nov. 2017, Art no. 4002205.

BD-02. Design and Analysis of a Three-Degree-of-Freedom Linear Oscillatory Actuator Integrated With Support Mechanism.

R. Nakamura¹, A. Heya² and K. Hirata¹

1. Division of Materials and Manufacturing Science, Osaka University, Suita, Japan; 2. Department of adaptive machine systems, Osaka University, Suita, Japan

< I. INTRODUCTION > Recently, oscillatory actuators have been applied in various fields, including consumer electronics, entertainment, and industrial equipment. Especially, haptic devices that induce a virtual force are attracting attention. Haptic display systems using oscillatory actuators utilize the non-linearity of human perception, and it is possible to illusion a continuous unidirectional force by an asymmetric vibration [1]. Such oscillatory actuators are expected to become smaller and can be three-dimensionally (3-D) driven to display 3-D traction, for improving portability and functionality. Kato et al. developed a three-degree-of-freedom linear oscillatory actuator (3-DOFLOA) [2]. This actuator consists of four sets of coils has mutual interference of force for driving to each axis. Moreover, Heya et al. proposed a 3-DOFLOA that consists of three sets of coils and can be driven in three axes without interference [3]. However, the conventional 3-DOFLOAs need complex and large support mechanisms outside the magnetic circuit, which increase the size and weight of the device. Then, we propose a novel magnetic structure of a 3-DOFLOA in this paper. The magnetic pole and permanent magnet shapes are designed to integrate with the elastic support mechanism using mechanical springs. The proposed structure contributes to reduce the size and weight of the actuator. The force characteristics are clarified using a magnetic field analysis modeled with a 3-D finite element method (3-D FEM). The calculated results show that the proposed actuator can be independently driven for each axis. < II. PROPOSAL OF MAGNETIC STRUCTURE AND OPERATING PRINCIPLE > << A. DESIGN >> Conceptual scheme of the magnetic structure is shown in Fig. 1(a). In the case of the conventional support mechanisms, mechanical springs are attached to the outside of the magnetic circuit sections. On the other hand, by adopting magnetic pole and permanent magnet shapes that allow the mover and stator to be connected by mechanical springs, it is possible to reduce the size without losing the function as a support mechanism. Fig. 1(b) shows the overview of the proposed a 3-DOFLOA. The inner mover has cylindrical permanent magnets for installing mechanical springs inside the stator. The stator consists of six sets of coils and the stator yoke. The coil is wound around the iron core with a hole of the same size as the permanent magnet. The mechanical springs made of non-magnetic material are used to support the mover. A total of six springs are arranged, two for each shaft, through the holes of the permanent magnet and the iron core. From this design, the proposed actuator can be integrated the support mechanism. The movable range is ± 0.5 mm to each axis. Fig. 1(c) illustrates the magnetic circuit. The magnetization direction of the permanent magnets arranged in the x-axis and y-axis directions is outward, and the magnetization direction of the permanent magnets arranged in the z-axis direction is inward. Therefore, the magnetic flux generated from the permanent magnets passes through the stator yoke and forms a closed magnetic circuit. << B. OPERATING PRINCIPLE >> Fig. 1(d) shows the operating principle of the proposed actuator. When the Coil-X1 and Coil-X2 are excited, a magnetic pole is induced and the mover moves in the x-axis direction due to magnetic attraction and repulsion forces. Similarly, the mover can move in the y-axis and z-axis directions by the excitation of the Coil-Y1/2 and Coil-Z1/2. < III. STATIC FORCE ANALYSIS > The static force is calculated employing a magnetic field analysis using 3-D FEM. The inner yoke and stator yoke are made of SUY. The residual magnetic flux density of the permanent magnets is 1.3 T. The number of turns of each Coil-X1/2 and Coil-Y1/2 is 85 turns, and the number of turns of each Coil-Z1/2 is 68 turns. The input current is 0.3 A. The detent and excitation forces when the mover is moved in the x-axis, y-axis, and z-axis directions are shown in Fig. 2(a), (b), and (c), respectively. From Fig. 2(a), the magnetic spring constant in the x-axis direction due to the detent force is 2.10 N/mm, and the average excitation force in the x-axis is 0.23 N. From Fig. 2(b), the magnetic spring constant in the y-axis direction is 2.10 N/mm, and the average excitation force in the y-axis is 0.23 N. From Fig. 2(c), the magnetic spring constant in the z-axis direction is 2.25 N/mm, and the average excitation force in the z-axis is 0.22 N. The detent and exci-

tion forces are generated only in the direction of the driving direction. In addition, the linear detent force characteristics are obtained. Therefore, it has to become a stable system at the origin by incorporating mechanical springs to cancel the detent force. From these analyzed results, it is confirmed that the proposed actuator can be independently driven in three axes, and the interference of forces between each axis is not observed. < IV. CONCLUSION > The novel small 3-DOFLOA was proposed in this paper. It can be driven three axes, and has not interference between each axis. The proposed actuator can contribute to the miniaturization of 3-D haptic devices.

[1] T. Amemiya, and T. Maeda, Asymmetric oscillation distorts the perceived heaviness of handheld objects, *IEEE Trans. Haptics*, vol. 1, no. 1, pp. 9–18, (2008) [2] M. Kato, and K. Hirata, Control of Three-Degree-of-Freedom Resonant Actuator Driven by Novel Vector Control, *TRANSPORTATION SYSTEMS AND TECHNOLOGY*, Vol. 4, No. 3, pp. 90-101, (2018) [3] A. Heya, K. Hirata, T. Matsushita, and Y. Kono, Design and Analysis of a Three-Degree-of-Freedom Linear Oscillatory Actuator, *IEEE Transactions on Magnetics*, Vol. 56, No. 2, 6701404, (2020)

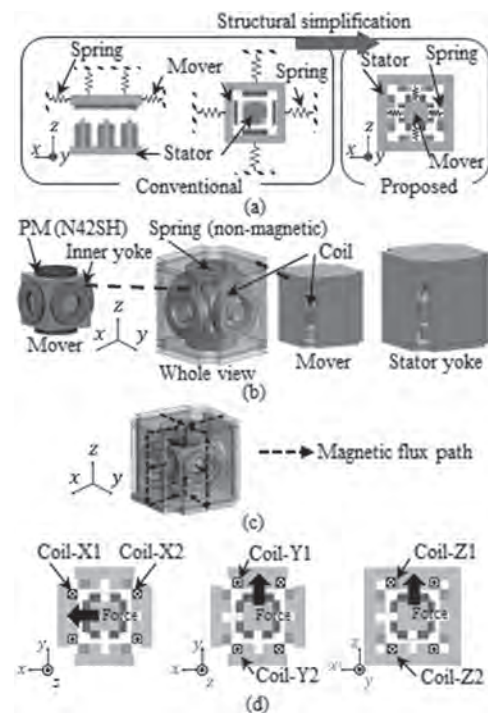


Fig. 1. Proposed 3-DOFLOA (a) Conceptual scheme of the structure., (b) The overview of the proposed actuator., (c) Magnetic circuit., and (d) Operating principle.

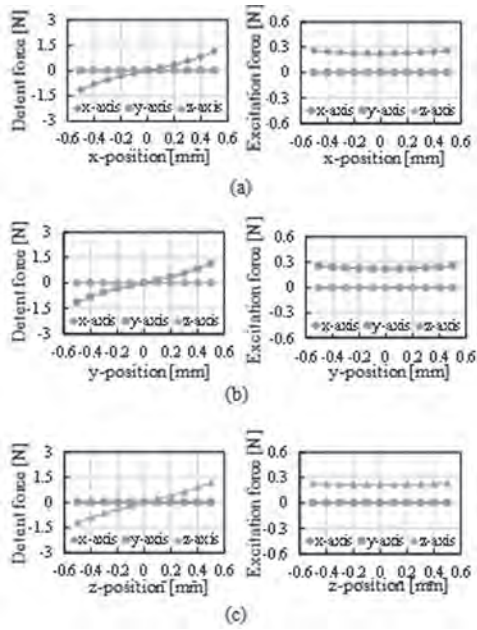


Fig. 2. Analysis results of the static force (a) When the mover moves in the x-axis., (b) When the mover moves in the y-axis., and (c) When the mover moves in the z-axis.

BD-03. Eddy Current Analysis and Optimization Design of Linear Induction Motors With Different Secondary Topologies Based on XGBoost.

S. Wu¹ and Q. Lu¹

1. College of Electrical Engineering, Zhejiang University, Hangzhou, China

Abstract—This paper presents an efficient multi-objective optimization method for linear induction motors (LIMs). With this modified method, the eddy current analysis and optimization design can be realized with speediness and accuracy. To ensure the consideration of skin effect, transverse end effect and longitudinal end effect, the raw data are obtained from 3D finite element model (FEM). Latin hypercube sampling (LHS) is adopted to facilitate the extraction of data, including every structural parameter of secondary. With these samples, eXtreme Gradient Boosting (XGBoost) is utilized to establish a multiple analysis model. Assuredly, the analysis model of thrust force, vertical force, eddy current and magnetic flux density owns concurrency and precision. Considering the limitation and rationality of designing structure and velocity, an objective function is specified to determine the ultimate optimization scheme. I. INTRODUCTION As a vital component of an LIM, secondary induces eddy current and generates thrust force. Therefore, the rectification method and optimization design of eddy current plays a crucial role in performance improvement. Due to the complexity of approximate analytical method, finite element analysis (FEA) is a conventional analysis method for eddy current distribution and magnetic flux density instead. Evidently, 2D FEM is inadequate for eddy current analysis [1]. 3D FEM can ensure the reliability of the calculation, and yet has the fatal flaw of being laborious and time-consuming. Therefore, this paper proposed a modified analysis and optimization method based on XGBoost and LHS. The mathematical modeling method can explore the output characteristic and electromagnetic performance under different secondary topologies with efficiency and accuracy. II. TOPOLOGY AND EDDY CURRENT DENSITY DISTRIBUTION To weaken the impact of skin effect and end effect, modifying eddy current path can apparently improve the performance, but the optimization capability is bound up with the selection of secondary topology. Figs. 1(a)-(c) show the topologies and eddy current density distributions of LIMs with different types of secondary. Obviously, the existence of back-iron strengthens the eddy current. Compared with the distribution in single-slit structure, the transverse component of current density at the edge is higher, while the longitudinal component at the active zone and overhang area shows an opposite trend. III. ALGORITHM AND PRINCIPLE Considering correctness, efficiency and generalization are the core of optimization, the mainstay of proposed strategy is streamlined as follows. As shown in Fig. 2, the optimization process can be divided into five main steps. Objective to determine the general value range of structural parameters, equivalent circuit is effective for preliminary assessment. Then, Latin hypercube sampling (LHS), as a method can ensure the maximum of feature information and minimum of sample points, is adopted to obtain data with good rationality and coverage. Respecting that the analysis model erected by XGBoost has the combination of accurateness and speediness, the relationship between structural parameters and analysis objectives will be observed intuitively [2]. Thereinto, the structural parameters contain overall dimension and ladder structural dimension of secondary; thrust force, vertical force, current density and magnetic flux density are taken into consideration as analysis objectives. The objective function can conveniently judge the comprehensive performance of analysis targets, so as to select the most appropriate optimization scheme. IV. CHARACTERISTIC ANALYSIS Figs. 1(b)-(e) show the distributions of eddy current density and the force characteristics of LIMs under different secondary topologies. Through the analysis and optimization method proposed in this paper, both electromagnetic properties and force characteristics achieved modification. Crucially, the ultimate optimization scheme is in good agreement with the FEA result, but the achievement only takes a little time after the analysis model is erected. V. CONCLUSION In this paper, the proposed analysis method, which adopts LHS and XGBoost, realizes the speedy and accurate optimization of electromagnetic properties and force characteristics by selecting the most suitable secondary scheme. The superiorities are listed as follows. (1) The proposed method can analyze the relationship between secondary structural parameters and performance

indexes with efficiency. Both electromagnetic properties and force characteristics are taken into consideration. (2) With LHS, random samples in the whole range possess a balance of distribution and representativeness. (3) Excluding the speediness of modeling and prediction, XGBoost has a great imputation capability of missing data. Additionally, the autonomy of objective function and evaluation function is a high guarantee for the adjustability of multi-objective optimization. Therefore, this proposed multi-objective analysis method can achieve an efficient, accurate and reliable optimization for LIMs. The detailed analysis will be listed in the full paper.

[1] Q. F. Lu, L. X. Li, J. W. Zhang, X. Y. Huang, J. J. Cai, "Design Optimization and Performance Investigation of Novel Linear Induction Motors With Two Kinds of Secondaries," *IEEE Trans. Ind. Appl.*, vol.55, no.6, Nov.-Dec. 2019. [2] B. S. Bhati, G. Chugh, F. Almilurjman, N. S. Bhati, "An improved ensemble based intrusion detection technique using XGBoost," *Trans. Emerg. Telecommun. Technol.*, 2020.

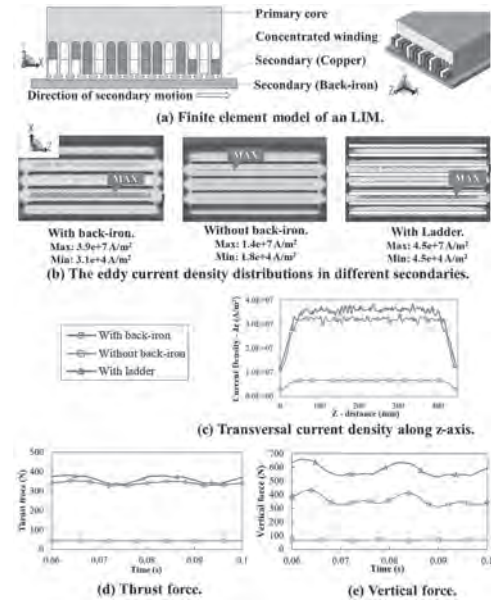


Fig. 1. 3D finite element models and results of LIMs.

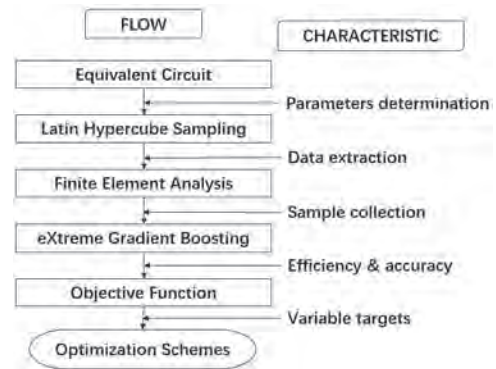


Fig. 2. Flow chart of proposed multi-objective method.

BD-04. An Ironless Planar Translational Permanent Magnet Generator for sea-Wave Energy Conversion.

M. Trapanese¹, D. Curto¹ and V. Franzitta¹

1. Dipartimento di Ingegneria, Università di Palermo, Palermo, Italy

Several approaches to harvest sea wave energy have been recently proposed; almost all of them introduce a mechanical conversion device between the waves and the electromagnetic generator. This stage converts the mechanical energy contained in the motion modes of the converter placed on the waves (heave, sway, surge, yaw, pitch, and roll) into a more usable mechanical energy; it may be a hydraulic coupling device or a mechanical gear and, in any case, introduces additional losses, weakness in the reliability of the system and additional maintenance requirements. In order to solve these issues a generator directly coupled to the sea waves entirely contained in a vessel has been proposed. These systems are known as Inertial Wave Energy Converter and up to now, they have been designed to exploit only one motion mode of the wave converter. The most proposed solutions are linear generators for heave motion in point absorber technology and a rotating generator coupled to a flywheel for rolling motion mode. In this approach, only one motion mode is exploited to harvest the energy contained in sea waves, on the contrary, this paper presents a permanent magnet planar translational generator able to exploit more motion modes of the mechanical converter coupled to the waves fig.1. The linear and planar electrical generators have been recently studied for the exploitation of sea wave energy [1-2] but, to our best knowledge, no planar ironless translational generator has been proposed. In this paper, in order to maximize the energy extraction, all the motion modes of the waves have been considered and included in the mathematical model of the system. The principle of operation of the generator can be summarized as follows: the sea-waves hitting the floating body containing the planar generator induce on the moving part (translator) of the generator relative motion with respect to the armature and, doing so, induces an emf on the winding mounted on the armature. The movement of the translator is two-dimensional and therefore all the movement modes of the wave, but heave motion can be exploited. The mathematical model includes the dynamic equations of the moving part of the generator and the electric equations of the windings. The coupling parameters (inductances, fluxes, etc.) have been determined by a FEM analysis (which includes a careful analysis of the boundary conditions, because of the fact that the machine is working in a conductive medium). The design (fig.2) has been optimized by including in the mathematical model used for the optimization the following aspects: the dynamic and stochastic features of the waves, a dynamic model of the mechanical system, a parametric circuit model of the magnetic circuit as well as of the electric windings, a circuit model of the power electronics converter used to connect the generator to the utility. The main innovation of the optimization approach proposed is that the speed of the machine is neither supposed known nor supposed fixed, but the stochastic features of the imposed movement are the factors that most influence the optimization process. The optimization has been performed by finding the maximum of an objective function that has been built on the basis of the mathematical model developed. The variables of the function were related to the magnetic circuit of the converter, the parameters to the stochastic features of the waves as well as to the characteristics of the hydraulic system and of the power electronics converter.

[1] N.M. Kimoulakis; A. G. Kladas; J.A. Tegopoulos, IEEE Trans. on Magnetics, vol.45, issue 3 (2009) [2] M. Trapanese; D.Curto; V. Franzitta et al, IEEE Trans. on Magnetics, vol. 55, issue 12, (2019)

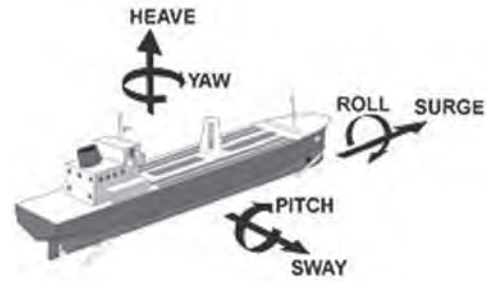


Fig.1 Motion modes of a floating body

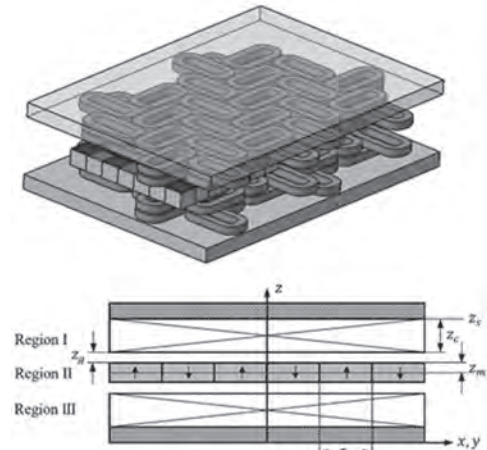


Figure 2: (a) 3D Model of the machine. (b) Planar machine cross-section geometry.

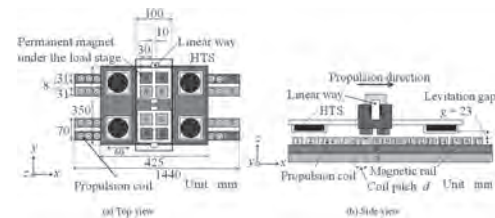
BD-05. Optimization of the Excitation Method of the Propulsion Coils in the Permanent Magnet-HTS Hybrid Magnetically Levitated Conveyance System.

S. Ohashi¹

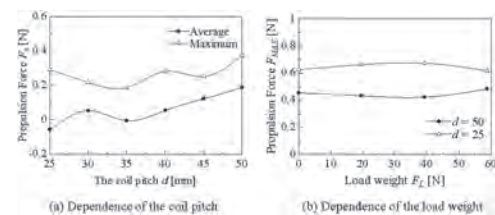
1. Electrical and Electric Engineering, Kansai University, Suita, Japan

Conventional conveyance systems using wheels and belt conveyors occur friction and wear at the contact portions. In order to solve these problems, a noncontact conveyance system has been developed[1][2]. In this research, a permanent magnet repulsion levitation system and superconducting magnetic levitation system are adopted. The permanent magnet repulsion levitation system cause a large levitating force at the loading part. Superconducting magnetic levitation system cause a stable levitation at the carrier body. There is no influence of large load weight on the levitation of the carrier because the loading part and the carrier body are connected by the linear way. The carrier moves above the magnetic rail. The coils are installed on magnetic rail, and the magnetic field gradient is generated by the exciting coils. The carrier is propelled by the magnetic field gradient. By increasing the flux of the coil behind the HTS in the propulsion direction and reducing the flux of the HTS in the propulsion direction, magnetic field gradient is generated and the carrier propels. The coil pitch is optimized and propulsion force is examined by adding the exciting coils [3] [4] Fig.1 shows the experimental device[4]. The change of the magnetic field gradient is analyzed when changing the coil pitch by 5mm in the range of 25~50mm with the FEM analysis software JMAG-Designer[5]. The propulsion force is confirmed by the experimental results. The experimental condition is as follows; current of the coil $I=2.0A$ and levitation gap $g=23mm$. The propulsion force is measured by the load cell installed in front of the carrier. From the analytical result, when the coil pitch is changed, the position of peak value of the flux density due to the magnetization and demagnetization on the magnetic rail changes, but the crest value of the magnetic field gradient is not changed. In the range of coil pitch 40~50mm, the excitation coils are separated. The flat section is formed between the positive peak value and the negative one in the magnetic gradient field. Thus, in the z-axis direction, the surface flux density of the HTS is the strongest at the center. Fig.2 (a) shows the average value and the maximum value of the propulsion force at each the coil pitch. At the coil pitch 50mm, both the average propulsion force and the maximum propulsion force are largest. As a result, the optimum value of the coil pitch under the HTS is 50mm. Center of the HTS keeps the largest flux from the permanent magnet. The coils are arranged on the magnetic rail at the coil pitch 50mm, as the diameter of the coil used in this research is 22mm, only the odd number coil in Fig.1 (b) will be installed. Thus, the excitation switching interval becomes large. Thus, as shown in Fig.1 (b), coils are installed at intervals of 25mm. At first, No.1 coil and No.3 coil in Fig.1 (b) are excited. Next, No.2 coil and No.4 coil are excited. In this way, the coils to be excited are switched, and coil pitch 50mm is realized. The case of exciting the coil between the two excited coils is considered. No.1 coil shown in Fig.1 (b) is magnetized, No.2 and No.3 coils are demagnetized. The flux density in the y-axis direction at that time is analyzed with the magnetic analysis software JMAG-Designer. In the range of $x=-20\sim 20$, the flux density in the y-axis direction in three excitation coil case is smaller than that in two excitation coil case. As the magnetic rail is composed of Halbach array, the y-axis direction flux density is strong on the magnetic rail. Therefore, the change of the flux due to the excitation of the coil tends to occur in the y-axis direction. The propulsion force is compared when exciting two coils at intervals of 50mm with the propulsion force when three coils are excited at intervals of 25mm. No.1 coil in Fig.1 (b) is magnetized, No.2 and No.3 coils are demagnetized. The load weight up to 58.8N is placed on the carrier. Fig.2 (b) shows the maximum propulsion force for each load weight. Larger propulsion force is given when No.1, No.2 and No.3 coil in Fig.1 (b) are excited t at all load weight. This is because the range of the magnetic field gradient is increased by adding a coil to be excited. In the case of three coils excitation, as the change of flux density in the y-axis direction is large, it is necessary to consider the magnetic gradient field in the y-axis direction. In the case of two coils excitation, it is suitable to install the coils at intervals of 50mm so as to catch the center of the HTS. In addition, in the case of three coils excitation the propulsion force increases by generating a gradient in the flux density in the y-axis direction.

[1]F. C. Moon, Superconducting levitation, John Wiley & Sons, New York, 1994. [2]J. Hull, M. Murakami, "Applications of bulk high-temperature Superconductors", Proc. of IEEE, vol.92, 2004, pp1705-1718. [3]S. Ohashi, D. Dodo, "Influence of the Propulsion System on the Levitation Characteristics of the HTSC-Permanent Magnet Hybrid Magnetically Levitated System", IEEE Transactions on Applied Superconductivity, vol.17, no.2, 2007, pp2083-2086. [4]Y. Takaki, T. Sumida, S. Ohashi, "Improvement of Velocity Control in the Permanent Magnet-HTS Hybrid Magnetically Levitated Conveyance System", IEEE Region 10 Conference (TENCON), 2016, pp3105-3108 [5] T. Sumida, Y. Kamitani, N. Yamada, S. Ohashi, "Propulsion Characteristics using Pinned flux of the HTS in the Permanent Magnet-HTS Hybrid Magnetically Levitated Conveyance System", IEEE Transaction on Applied Superconductivity, 2016, Vol.26, No.4, 3600905.



Experimental device of the conveyance system



Propulsion force between HTS and the permanent magnet

BD-06. Reduction of Rotational Vibration Using Coriolis Force Generated by Electromagnetic Oscillatory Actuator Moving in Radial Direction.

M. Kato¹ and F. Kitayama¹

¹ Ibaraki University, Hitachi, Japan

1 Introduction Reciprocating engines generate torque only during the explosion process and this causes a large ripple in output torque. When the torque ripple is transmitted through the engine drive system, torsional vibration is induced in a drive shaft, resulting in uncomfortable vibration and noise. This rotational vibration is a problem not only in automobiles, but also in ships, cableways, and other transportation equipment. Various vibration suppression methods have been proposed to solve this problem. Matsuhsa et al. proposed a dynamic vibration absorber (DVA) with an additional mass that oscillates in the radial direction of the cableway to suppress rotational vibration caused by wind [1]. When the natural frequency of the added mass is set to about twice the natural frequency of the gondola, the Coriolis force generated by the radial vibration of the added mass has been shown to be effective in damping the rotational vibration. However, since the additional mass is passively vibrated by the centrifugal force of the gondola, it is not possible to control the magnitude of the Coriolis damping force. This paper proposes a new hybrid DVA to reduce rotational vibration of a rotor. The additional mass operates as the mover of the electromagnetic linear oscillatory actuator (LOA). The LOA actively oscillates the mover by current control and obtains the variable damping force caused by the Coriolis effect. LOAs have been applied to various industrial equipment due to their simple structure, direct drive, and high efficiency [2]. They have also been applied to an active control device for automobiles [3]. In this paper, we describe the structure and mathematical model of the proposed hybrid DVA. Moreover, we evaluate numerically the vibration suppression effect under the active operation of the LOA.

2 Hybrid DVA Using Electromagnetic Oscillatory Actuator

2.1 Basic Structure and Operational Principle Fig. 1 shows the basic configuration and operational principle of the proposed hybrid DVA. 1-DOF LOA is embedded on the surface of a rotor and oscillates in the radial direction (r -direction). Excitation of the coil generates an electromagnetic force in the r -direction, which works to increase the mover stroke of the LOA. Consequently, the Coriolis force is produced in the circumferential direction (θ -direction), which suppresses the rotational vibration in the θ -direction. Since the coil of the LOA rotates synchronously with the rotor, we need to discuss power supply. We assume a direct power supply from a battery mounted on the rotor surface. Therefore, we include the equivalent moments of inertia of the stator and the battery in the moment of inertia for the rotor. Our hybrid DVA can be also understood as a opposite phenomenon of a parametric excitation (parametric damper). Fig. 1(b) shows an example of the mover trajectories under parametric excitation and parametric damper. This figure clearly suggests that the vibration in the θ -direction increases after one oscillation period because of the positive energy provided by the parametric excitation. When the trajectory becomes reversed, the vibration decreases because of the negative energy provided by the parametric damper. The important point is that both cases require to satisfy the following relationship, $\omega_r \cdot \omega_\theta = 2:1$.

(1) Here, ω_r and ω_θ are the natural frequency in the r - and θ -directions, respectively.

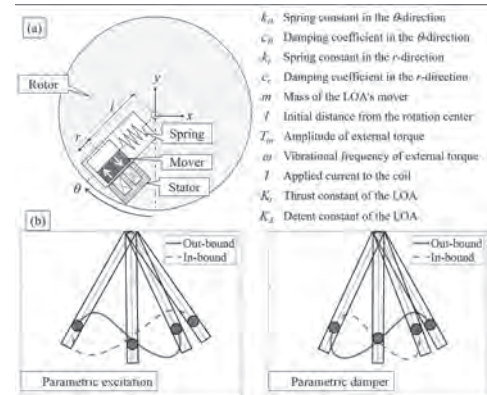
2.2 Equations of Motion for Hybrid DVA The Euler-Lagrange equation gives the following equations of motion in the r - and θ -directions, (2) $Jd^2\theta/dt^2 = m(l+r)d^2\theta/dt^2 + c\theta d\theta/dt + 2m(l+r)d\theta/dt \cdot dr/dt + k\theta = T_m \cos\omega t$, (3) $md^2r/dt^2 + c_r dr/dt + k_r r = m(l+r)(d\theta/dt)^2 + K_r l + K_r r$.

(3) Here, the fourth term on the left-hand side of equation (2) is the Coriolis force, which works to decrease the vibration in the θ -direction. The first term on the right-hand side of equation (3) is the centrifugal force, which works to increase the vibration in the r -direction. The kinetic parameters of the hybrid DVA are determined as follows so that equation (1) holds, $2\sqrt{k\theta/(J+mI^2)} = \sqrt{(k_r - K_r)/m}$.

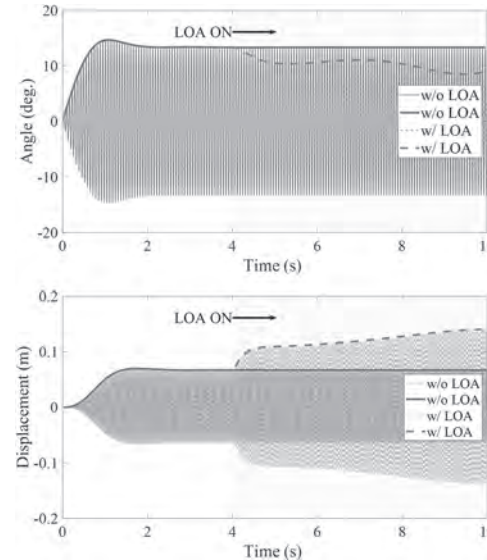
(4) 3 Reduction of Rotational Vibration under Active Control In this section, we solve the above equations of motion and verify the effectiveness of the proposed hybrid DVA through numerical simulation. Fig. 2 shows the rotational vibration of the rotor and the displacement of the mover with and without the LOA. In this simulation, The mover is oscillating passively until 4s. After that, Electromagnetic force generated by the LOA starts to oscillate the mover actively. Focusing on the envelopes of the waveform (blue solid line: without LOA, orange dashed line: with LOA), the active

operation with LOA reduced the rotational vibration of the rotor by about 30%. In response to the decrease in the rotational vibration, the amplitude of the mover displacement is approximately doubled. We are able to conclude that the electromagnetic force generated by the LOA increases the displacement of the mover and the resulting damping effect by the Coriolis force also increases. In the final paper, we will describe the detailed design of the hybrid DVA and evaluate performances of the LOA through finite element analysis. Because this technique may also be applied to reduce torque ripple in AC motors, the rotational vibration by torque ripple will also be discussed.

[1] L.D. Viet, N.D. Anh, H. Matsuhsa, Journal of Sound and Vibration, Vol. 330, no. 9, pp. 1904–1916 (2011) [2] M. Kato, Y. Kono, K. Hirata, and T. Yoshimoto, IEEE Transactions on Magnetics, Vol. 50, no. 11, 8206404 (2014) [3] F. Kitayama, K. Hirata, N. Niguchi, and M. Kobayashi, Sensors, Vol. 16, No. 377 (2016)



(a) Basic structure of the proposed hybrid DVA. (b) The trajectories of the mover under parametric excitation and damper.



Rotational vibration of the rotor and the displacement of the mover with and without the LOA.

BD-07. Design and Experimental Analysis of Novel Hybrid Excited Linear Flux Switching Machine With Unequal Primary Tooth Width and Segmented Secondary.

N. Ullah^{1,2}, F. Khan¹ and A. Basit²

1. Department of Electrical and Computer Engineering, COMSATS University Islamabad, (Abbottabad Campus), Abbottabad, Pakistan;

2. Department of Electrical Energy System Engineering, University of Engineering and Technology, Peshawar, Pakistan

I. INTRODUCTION Deficiency of controllable air-gap flux and continuous increasing cost of rare earth PM materials in case of Linear PM Flux Switching Machines (LPMFSMs) and inherent low thrust force capability of Linear Field Excited Flux Switching Machines (LFEFSMs) compels researchers and scientists to investigate new topologies. Hybrid Excited Linear Flux Switching Machine (HELFSM) is the new class of Linear Flux Switching Machines (LFSMs) that combines advantages of LPMFSM and LFEFSM and provides high thrust force density with controllable air-gap flux. All three excitation sources i.e. PMs, DC, and AC are confined to short mover and completely passive secondary makes this design a strong candidate for high speed long stroke direct-drive applications [1]. Double sided topology of the HELFSM wiped out undesired normal/attraction force problem, when compared with single sided design [2, 3]. The property of dual excitation i.e. PMs and electromagnets, makes this design economical in terms of PM volume consumption and enables flux weakening/strengthening. Yokeless or segmented secondary reduces length of flux paths and improves performance [4]. This paper investigates a novel Double Sided Hybrid Excited Linear Flux Switching Machine with Unequal Primary Tooth Width and Segmented Secondary (DSHELFSM-UPTWSS) having complementary coil design and combination of series/parallel magnetic circuit. Adjustment of primary tooth width technique is another advancement of the proposed design that provides appropriate low reluctance path where high flux is recorded during initial tests. Additional assistant teeth at all four end points of the mover design is installed to balance magnetic circuit and reduce end-effect. Additionally, segmented secondary design provides low reluctance short paths for flux linkage and reduce secondary material consumption. Furthermore, complementary coil design and combination of series/parallel magnetic circuit enables more symmetrical and sinusoidal flux linkages, resulting in a reduced thrust force ripple ratio. II. DESIGN SPECIFICATION AND FINITE ELEMENT ANALYSIS Topology of proposed machine is shown in Fig. 1(a). Main design parameters such as number of mover teeth (N_m), number of DC coil pairs (N_{DC}), number of AC coil pairs (N_{AC}), and stator to mover pole pitch ratio (τ_s/τ_m) are obtained by following equations; $N_m = 4jm + 1$ $N_{DC} = 2jm + 1$ $N_{AC} = 2jm$ $\tau_s/\tau_m = 4jm/(2jm + 2)$ Where, m represents number of phases, j is a positive integer and represents each AC phase winding pair repetition in the machine, τ_s is the stator pole pitch, and τ_m is mover pole pitch. DSHELFSM-UPTWSS having dual stator topology with single side specifications of $m=3$; $j=2$; $N_m=25$; $N_{DC}=13$; and $N_{AC}=12$ leading to $\tau_s/\tau_m = 24/14$ are investigated in this paper. Initial design parameters are simulated and optimized using JMAG commercial FEA package v18.1 utilizing single variable geometric optimization approach. Simulated unidirectional thrust force of optimized design parameters is shown in Fig. 1(b). Analysis of thrust force profile indicates that both PM and FE flux is summed up to strengthen overall performance of the machine. Average thrust force of 1952N is achieved by using 0.0455Kg NdFeb PMs in combination with DC and AC current densities of 1.37A/mm² and 4.57A/mm², respectively. III. EXPERIMENTAL VALIDATIONS A full scale prototype with simulated current densities of the proposed machine was developed (as shown in Fig. 2(a)) to validate the predicted performance. Measured no-load B-EMF at velocity of 1.5 m/s (50Hz) is compared with corresponding simulated one in Fig. 2(b). Detailed analysis of open circuit flux linkage, B-EMF, detent force, geometric parameters optimization procedure, and on-load test results will be provided in the final version of the paper. Fig.1: Proposed DSHELFSM-UPTWSS; (a) Topology, (b) Simulated thrust force. Fig.2: Experimental Setup; (a) Test bed, (b) Comparison of simulated and measured B-EMF.

Nov. 2018. [3] Shen, Y., Lu, Q., Li, H., IEEE Trans. Ind. Electron., vol. 65, no. 2, 2018. [4] M. F. Omar, E. Sulaiman, M. Jenal, IEEE Trans. Magn., vol. 53, no. 11, Nov 2017.

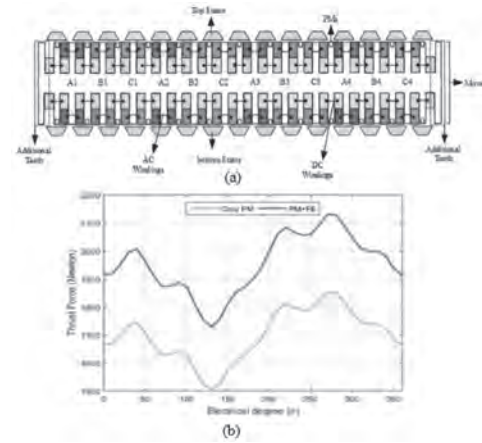


Fig.1: Proposed DSHELFSM-UPTWSS; (a) Topology, (b) Simulated thrust force.

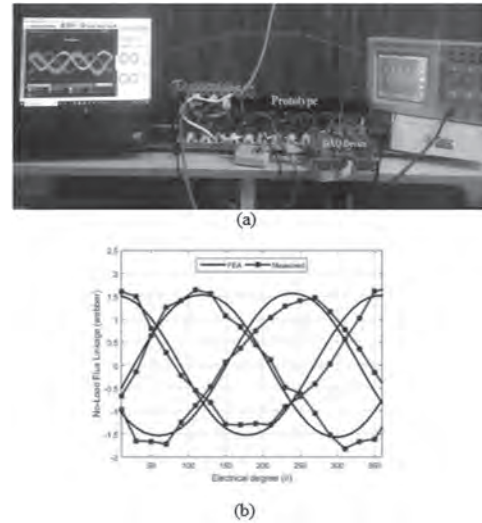


Fig.2: Experimental Setup; (a) Test bed, (b) Comparison of simulated and measured B-EMF.

BD-08. Numerical Analysis of Magnetic Soliton Excited on Nonlinear LC Ladder Circuit Array Using Permanent Magnet Flux Biased Inductor.

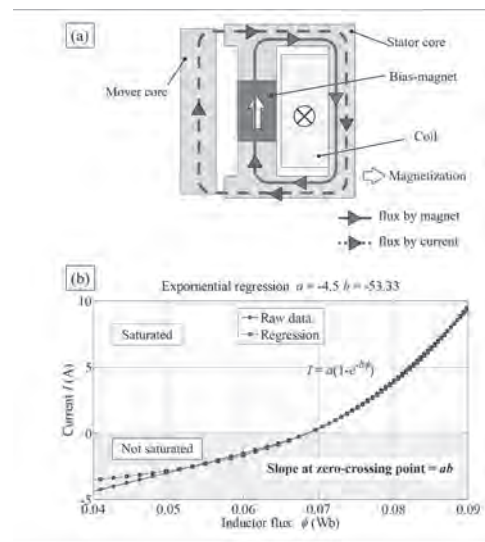
M. Kato¹, S. Lee² and K. Hirata²

1. Ibaraki University, Mito, Japan; 2. Osaka University, Suita, Japan

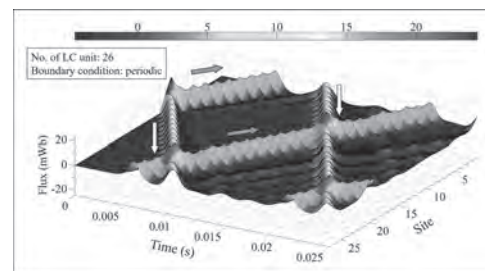
I Introduction A soliton is a wave that maintains its shape while it propagates at a constant velocity. The soliton exists in various nonlinear systems such as fiber optics, biology, magnetics, and electric circuit. In particular, Hirota proposed an LC ladder circuit, in which inductors and capacitors are connected like a ladder [1], [2]. Hirota experimentally proved the magnetic soliton was excited on the LC ladder circuit by using the capacitor whose capacitance is an exponential function of voltage. The observed magnetic soliton propagates along the LC ladder circuit at a constant velocity while maintaining the shape [3]. In other words, the magnetic soliton corresponds to a kind of rotating magnetic field. The rotating magnetic field is produced by a three-phase alternating current (AC) and is essential for AC motors. The current technology requires to use Pulse Width Modulation (PWM) inverters for generating the rotating magnetic field. On the other hand, the magnetic soliton can be generated by applying a pulsed voltage only at one point on the LC ladder circuit, which is expected to simplify the PWM inverter and its control algorithm [4]. This paper proposes an LC ladder circuit consisting of linear capacitors and nonlinear inductors. We also show the magnetic soliton can be excited if the inductance of the inductor becomes an exponential function of the current. However, the coil inductance wound on soft magnetic materials becomes symmetric with respect to the positive and negative currents, not exponential. To solve this problem, we propose a permanent magnet flux biased inductor (PMFB inductor) in which a permanent magnet is mounted into the magnetic circuit and the operating point of the iron core is biased. Finite element analysis (FEA) reveals that the inductance varies exponentially with the current. Finally, we solve numerically the differential equation of the LC ladder circuit consisting of the PMFB inductors and capacitors, and show the magnetic soliton propagates at a constant speed in the LC ladder circuit. II Permanent Magnet Flux Biased Inductor Fig. 1(a) shows the basic structure of the PMFB inductor. It consists of a stator core, a mover core, a coil, and a permanent magnet (PM). Its magnetic circuit is axisymmetric. An axially magnetized permanent magnet is embedded in the stator core. Here, we explain the reason why the inductance of the PMFB inductor changes exponentially as follows. The flux by PM mainly flows through the stator core as shown by the solid blue line. This leads to biasing the B-H curve of the stator core. When a positive current is applied, the flux by current strengthens the flux by PM. This results in magnetic saturation of the stator core and the inductance decreases with the current. When a negative current is applied, the flux by current weakens the flux by PM. This results in eliminating the magnetic saturation of the stator core and the inductance increases with the current. Therefore, exponential inductance characteristics is obtained when we design the shape of the PM, stator and mover cores property. Fig. 1(b) shows the analyzed relation between the flux and current obtained through FEA. The slope of this curve corresponds to the inductance. The solid line shows the bias flux provides asymmetric characteristics for positive and negative current. The dashed line is an approximation using the exponential function shown below, $I = a(1 - e^{-b(\Phi - \Phi_{PM})})$ (1) Here, a and b are the parameters and Φ_{PM} is the bias flux by PM. The exponential function is a good approximation of the $I-\Phi$ property. This result implies the magnetic soliton can be excited on the LC ladder circuit consisting of the PMFB inductors and linear capacitors. III Numerical Results and Discussion In this chapter, we numerically solve the differential equation of the nonlinear LC ladder circuit mentioned in the previous chapter, and presents the successful excitation and propagation of the magnetic soliton. Kirchhoff's voltage law gives the following differential equation, $d_t \Phi_n / d_t^2 = a/C(2e^{-b\Phi_n} - e^{-b\Phi_{n+1}} - e^{-b\Phi_{n-1}})$ (2) Here, Φ_n is the flux through the n th inductor and C is the capacitance of the capacitor. The internal resistance of the PMFB inductor and capacitor is neglected. Note that this differential equation has a similar form to the one presented in [1] and [2]. Fig. 2 shows the numerical result of the differential equation in Equation (2). The number of LC units is 26 and the capacitance is 100 μ F. The start and end of the LC ladder circuit are connected and periodic. One magnetic soliton excited at 0s propagates at a constant speed in the positive

and negative directions while maintaining its shape. Since the LC ladder circuit is periodic, the two magnetic solitons collide at a certain time. The waveform before and after the collision clearly shows the solitons are not affected by the collision. This is one of the most important properties of solitons. These results concludes magnetic solitons has a potential to be applied as a kind of the rotating magnetic field. In the final paper, we will describe the detailed design procedure for the PMFB inductor because this digest paper only presents the straight type PMFB inductor, not an annular one. Moreover, we will visualize and evaluate the rotating magnetic field produced by the magnetic soliton through FEA.

[1] R. Hirota and K. Suzuki, Journal of the Physical Society of Japan., Vol. 28, pp. 1366–1367 (1970) [2] K. Muroya and S. Watanabe, Journal of the Physical Society of Japan., Vol. 50, pp. 2762–2769 (1981) [3] D.L. Sekulic, M.V. Sataric, M.B. Zivanov, and J.S. Bajic, Electronics and Electrical Engineering., Vol. 121, pp. 53–58 (2012) [4] M. Kato, S. Lee, and K. Hirata, IEEE Transactions on Magnetics., to be published, DOI:10.1109/TMAG.2020.3018118 (2020)



(a) Basic structure of PMFB inductor. (b) Analyzed relation between flux linkage and current.



Numerical result of magnetic soliton excited on the nonlinear LC ladder circuit.

BD-09. Proposal of Novel Multiple-Degree-of-Freedom Voice Coil Actuator.

A. Heya¹ and K. Hirata²

1. Department of Adaptive Machine Systems, Osaka University, Suita, Japan; 2. Division of Materials and Manufacturing Science, Osaka University, Suita, Japan

I. INTRODUCTION Environment recognition is a crucial task for autonomous mobile systems such as robots and drones, and vision information obtained by a camera is important. These systems require a high spatial awareness while undergoing various disturbances in an unknown environment. However, there are some problems: degradation of recognition accuracy caused by vibration and increase in size of the structure using a multi-degree-of-freedom (DOF) driving mechanism. Therefore, we focused on a multi-DOF actuator. Various types of multi-DOF actuators have been proposed, which use principles based on synchronous motors [1], stepping motors [2]. Nevertheless, the conventional actuators have a large structure and control device, for high torque density and continuous rotation. For applying to a driving source of a camera attitude control system, an actuator that can be configured with a few components and driven by a simple control device is required. Therefore, a multi-DOF voice coil actuator (DOF-VCA) is discussed in this paper, which has high responsiveness because it has only a few components. Kim et al. proposed a two-DOF-VCA with four-coils and permanent magnets [3,4]. This actuator can generate two-DOF motion driven by two H-bridge circuits. Moreover, our group proposed a three-DOF-VCA with eight-coils driven by three H-bridge circuits [5]. However, further simplification of a structure and control device is required for robotic eyes in humanoid robots. In this paper, we propose novel multiple-DOF-VCA: two-DOF actuator driven by a three-phase half-bridge circuit and three-DOF actuator driven by a four-phase half-bridge circuit. The proposed actuators can be driven by a smaller number of switching elements and coils compared to the conventional actuators. The proposed magnetic structure and driving principle are described. The torque characteristics are clarified by a magnetic field analysis using a three-dimensional finite element method (3D-FEM), and it is shown that the proposed actuator can be driven by the proposed principle. II. PROPOSAL OF NOVEL STRUCTURE AND PRINCIPLE Figs. 1(a) and (b) show the proposed two-DOF-VCA driven by three-phase and three-DOF-VCA driven by four-phase, respectively. The mover consists of three-coils arranged at intervals of 120 degrees. The stator consists of an outer stator yoke and an inner stator with a yoke and permanent magnets. This actuator can be driven two-DOF by combined torques generated in each coil. The coils are connected at a neutral point, and the coils are excited in a balanced state. Thus, the actuator can be driven by only a three-phase half-bridge circuit. The proposed three-DOF-VCA has a structure that coils and permanent magnets are arranged at intervals of 90 degrees, and the mover consists of four-coils. This actuator can be driven by combined torques in each coil connected at a neutral point and can be operated by a four-phase half-bridge circuit. III. TORQUE CHARACTERISTICS The evaluated models are designed for verifying the proposed principle. The static torques are calculated by the 3-D FEM when the mover is forcibly rotated. The torque characteristics of the proposed VCAs are shown in Fig. 2. Fig. 2(a) shows the calculated torque of the proposed two-DOF-VCA when the current is applied to generate torque in the x-axis direction. The torque in the y- and z-axis directions are not generated, and the torque in the x-axis can be only obtained. The torque is maximum at the origin position and decreases by increasing the rotational angle. This is because the centers of poles in permanent magnets and coils are close together, and the magnetically attracted torque decreases. Fig. 2(b) shows the torque characteristics of the proposed three-DOF-VCA. From the analyzed results, it is found that the torque can be generated by the proposed principle. The decrease of the torque by rotation is also occurred due to the same reason in that of the two-DOF-VCA. The maximum torque in the z-axis is times compared with that of the x- and y-axis. This is because the permanent magnets are arranged with tilts of 45 degrees. From this result, it is suggested that the maximum torque in each axis direction can be adjusted by changing the tilt angle of the permanent magnets. IV. CONCLUSION The novel multi-DOF-VCAs were proposed in this paper, which can be driven by a small number of switching elements and components. The structure and principle were

shown, and it was clarified that the actuators can generate torque, through 3-D FEM analysis.

[1] K. Kahlen, I. Voss, C. Priebe, and R. De Doncker, "Torque Control of a Spherical Machine With Variable Pole Pitch", *IEEE Transactions on Power Electronics*, Vol. 19, No. 6, pp. 1628-1634, 2004. [2] G. S. Chirikjian and D. Stein, "Kinematic Design and Commutation of a Spherical Stepper Motor", *IEEE/ASME Transactions on Mechatronics*, Vol. 4, No. 4, pp. 342-353, 1999. [3] H. Kim, H. Kim, D. Ahn, and D. Gweon, "Design of a new type of spherical voice coil actuator", *Sensors and Actuators A: Physical*, Vol. 203, pp. 181-188, 2013. [4] H. Y. Kim, H. Kim, D.-G. Gweon, and J. Jeong, "Development of a Novel Spherical Actuator With Two Degrees of Freedom", *IEEE Transactions on Mechatronics*, Vol. 20, No. 2, pp.532-540, 2015. [5] A. Heya, K. Hirata, and N. Niguchi, "Dynamic Modeling and Control of Three-Degree-of-Freedom Electromagnetic Actuator for Image Stabilization", *IEEE Transactions on Magnetics*, Vol. 54, No. 11, 8207905, 2018.

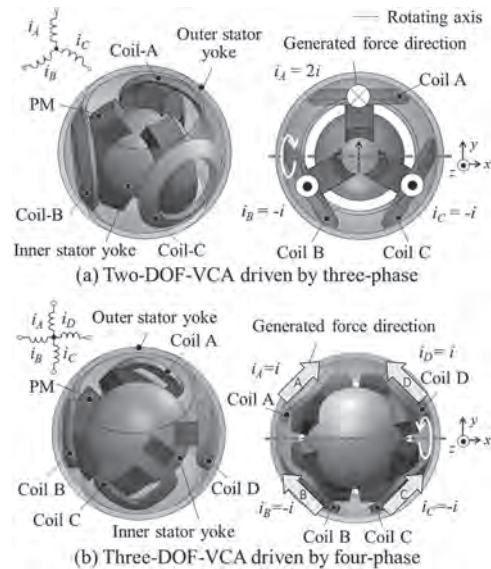


Fig. 1. Proposed multi-DOF-VCAs

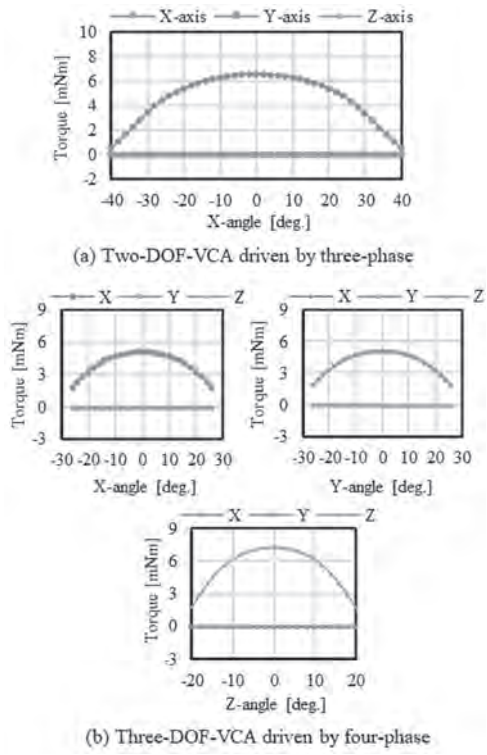


Fig. 2. Analysis results

BD-10. Core Loss Reduction of Tubular Flux-Switching Permanent Magnet Machine With Hybrid Magnetic Core.

S. Wang^{1,2}, Y. Wang^{1,2}, C. Liu^{1,2}, G. Lei³, Y. Guo³ and J. Zhu⁴

1. Hebei University of Technology, Tianjin, China; 2. State Key Laboratory of Reliability and Intelligence of Electrical Equipment, Hebei University of Technology, Tianjin, China; 3. University of Technology Sydney, Sydney, NSW, Australia; 4. School of Electrical and Information Engineering, University of Sydney, Sydney, NSW, Australia

I. INTRODUCTION Tubular flux-switching permanent magnet machine (TFSPMM) inherits the advantages of tubular machine and flux-switching machine with simple structure, strong robustness and no radial force[1]. However, it is not practical to make a TFSPMM entirely from axially stacked silicon steel sheet in machine manufacturing, because the flux will pass vertically through the silicon steel at the yoke of stator and mover and cause eddy current loss. Soft Magnetic Composite (SMC) material can solve the problem of three-dimensional permeability due to its magnetic isotropy[2]. However, TFSPMM with a magnetic core made only by SMC have low thrust due to low permeability and saturation magnetic density of the material. Moreover, core loss of the SMC is very high at low frequency. In order to change the above situation, hybrid magnetic core combined silicon steel sheet and SMC is proposed in this paper, which combines the high permeability of silicon steel and the magnetic isotropy of SMC. In hybrid magnetic core, the silicon steel sheet and SMC have a parallel and series relationship in the magnetic field, so the distribution of the two materials will affect the performance of the machine, including the core loss. Therefore, core loss reduction is important in hybrid magnetic core. II. MAIN CONTENT Fig. 1 shows the configuration of the TFSPMM with hybrid magnetic core and stacking direction of the silicon steel sheet. The silicon steel sheets in hybrid magnetic core are stacked along several tangential directions, and each part of the silicon steel is of the same stack width. The remaining space on the circumference, which cannot be stacked by silicon steel sheet, will be filled by SMC. Fig. 2 (a) shows the position of the point on the yoke when the silicon steel sheet stack width is 21mm. Point 1 is on the end of the silicon steel sheet and point 5 is on the middle silicon steel sheet. W_{ss} is the stack width of the silicon steel sheet. As the position of the point is farther from the end, the amplitude of B_y decreases. B_y is the component of magnetic density in the stacking direction of silicon steel sheet. According to Faraday's law of electromagnetic induction, eddy current loss will be generated on the silicon steel sheet affected B_y . The larger the amplitude of B_y , the larger the eddy current loss will be. Therefore, it is considered to reduce the stack width and increase the number of blocks with appropriate stack width. Fig. 2 (b) shows the B_y of point 1 with different stack widths and different silicon steel sheet blocks. 4 parts 12mm means number of silicon steel blocks is 4 and the stack width is 12mm and 8 parts 12mm means number of silicon steel blocks is 8 and stack width is 12mm shown in Fig. 1 (a). As can be seen, with the reduction of stack width, the amplitude of B_y decreases. When the stack width is 12mm, the amplitude of B_y of 8 silicon steel sheets is smaller than that of 4 silicon steel sheets. Compared with the silicon steel sheet located in the radial direction, the larger the stack width is, the larger B_y is on the silicon steel sheet at the end. Fig. 2 (c) shows the core loss of TFSPMMs with different hybrid magnetic cores. The results show that the loss difference is not significant, because the material is not assigned electrical conductivity, and the software does not calculate the eddy current loss at the end. If the silicon steel is set as a solid in the calculation, the solid loss calculated by the finite element method is shown in Fig. 2 (d). In practice, large eddy currents are not generated in the axial section because there is an insulating layer between the silicon steel sheets. But in the software, lamination setting cannot simulate the insulation layer. Therefore, solid manual partitioning is needed to approximate the actual situation. III. CONCLUSION In this paper, core loss of TFSPMMs with hybrid magnetic core are compared and analyzed. The stacking direction and width of silicon steel sheet as well as the match with SMC are described. Although the silicon steel sheet and the flux path are parallel to each other, the magnetic flux is not strictly limited to the plane of the silicon steel sheet. The component of magnetic density in the stacking direction of silicon steel sheet varies with the stack width. As the stack width of the silicon steel sheet decrease, B_y of point 1 will decrease. Since B_y is the magnetic density component perpendicular to the silicon steel

sheet, the smaller B_y is, the smaller the eddy current loss generated on the silicon steel sheet will be. When the number of silicon steel blocks is 4, the eddy current loss at the end decreases with the reduction of stack width, but the reduction of the proportion of silicon steel in the hybrid magnetic core will reduce the flux linkage and reduce the thrust. Therefore, when the stack width is 12mm, the number of silicon steel blocks is increased to 8, so as to increase the proportion of silicon steel in the hybrid magnetic core, ensuring small eddy current loss at the end and increased thrust.

[1] R. Cao et al., "Quantitative comparison of linear flux-switching permanent magnet motor with linear induction motor for electromagnetic launch system," IEEE Trans. Ind. Electron., vol. 65, no. 9, pp. 7569_7578, Sep. 2018. [2] C. Liu et al., "Performance evaluation of an axial flux claw pole machine with soft magnetic composite cores," IEEE Trans. Appl. Supercond., vol. 28, no. 3, Apr. 2018, Art. no. 5202105.

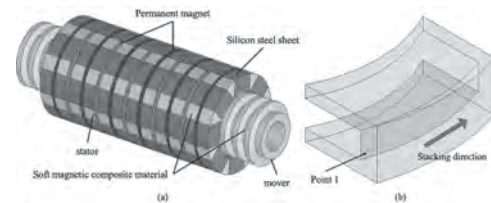


Fig. 1 (a) Configuration of TFSPMM with hybrid magnetic core; (b) point 1 on stator yoke and stacking direction of silicon steel sheet.

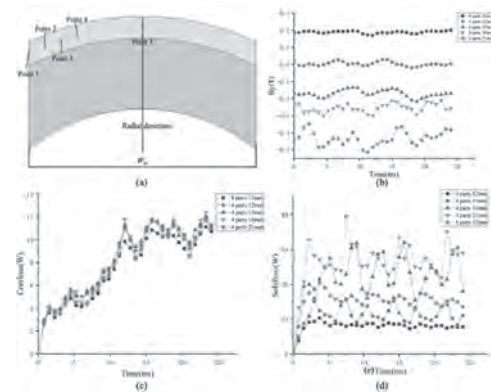


Fig. 2 (a) point on stator yoke; (b) B_y at point 1 under different stack widths; (c) core loss of TFSPMMs with different hybrid magnetic cores; (d) solid loss of TFSPMMs with different hybrid magnetic cores.

BD-11. Translator Eccentricity Analysis in Tubular Linear Machines Using Quasi-3D Finite Element Method Modeling.

H. Diab¹, Y. Amara¹, G. Barakat¹ and M. Ghandour²
 1. GREAH, Université du Havre, Le Havre, France; 2. Université Libanaise Faculte de Genie, Beirut, Lebanon

Tubular linear permanent magnet machines (TLPM) have gained increasing popularity over the past years due to their versatile nature. Whether used as actuators for linear motion applications or as generators for energy production applications, these machines can provide accurate and precise motion with relatively compact structures and simpler control systems [1]-[3]. Like any other mechanical application, TLPMS might suffer from different structural deformations during either operation or assembly. The moving part of the machine called the translator is the most vulnerable to such mechanical deformations. One commonly occurring deformation happens at the level of the translator shaft and is usually called a translator eccentricity where the translator shaft is no longer aligned perfectly with the central axis of the machines’s cylindrical structure. Eccentricity can take different forms and has been studied previously by some authors [4]-[7]. In [4] [5], eccentricity analysis was done using analytical and 3D FEM modeling and the calculated results were compared and validated by experimental results. In [6], eccentricity effects were studied for a surface mounted TLPM structure using the 3D finite element method (3D FEM). The study was continued in [7] by analyzing the eccentricity effects on another TLPM structure, also using 3D FEM, and comparing the eccentricity effects on the two structures. The authors of [6] [7] noted the extensive amount of time and effort required to compute some of the 3D FEM models and generate the results. Hence, an alternative modeling technique for eccentricity analysis that can provide relatively good results with less computation time is needed. The aim of this paper is to present a quasi-3D modeling technique that can represent the 3D problem using the superposition of multiple 2D models. It will be shown that the proposed model takes much less computation time and effort and produce relatively accurate results in comparison to the 3D model. Translator eccentricity unbalances the radial electromagnetic forces acting on the translator by forming a non-uniform air gap between it and the primary. Static eccentricity, which is a common eccentricity form, is the state of having the translator axis displaced by a constant distance ϵ from the primary axis while both axes remain parallel to each other. This work only focuses on the static eccentricity form leaving other forms for future works. The proposed quasi-3D model is achieved by dividing the 3D structure in the tangential direction (θ direction) into a certain number of sections (see Fig. 1). Since the air gap is non-uniform around the translator in the tangential direction, there is a different air gap value e (Fig. 1) for each θ along the tangential direction where $\theta \in [0, 2\pi]$. Hence, each section in the tangential direction is modeled as a standalone 2D linear machine having an air gap equal to the air gap value at the central angle of the corresponding section. Then, for each 2D linear machine model, the magnetic induction in the air gap is calculated where it will have two components x and y corresponding to the axial (z -direction) and normal (r -direction) cylindrical components of the 3D model respectively. The tangential component can be associated with a z component which is impossible to determine in a 2D model that has only x and y directions, and hence it will be neglected. After gathering the results from all the 2D modeled sections, using the Maxwell stress tensor the electromagnetic forces acting on the translator in the axial and radial directions are calculated. Both the 2D and 3D models used are finite element method based models, and for this work, they were constructed using the FLUX commercial software. The quasi-3D model will be used to study two TLPM structures having static eccentricity. The first one is a surface-mounted PM structure, the second one is an inserted PM flux focusing structure, and the two have similar dimensions. Both open circuit and on load operations will be studied, and the two cases of linear and non-linear ferromagnetic materials will be considered as well. Studying the different cases will provide an insight into the accuracy and efficiency of the proposed quasi-3D model. Fig. 2 shows a comparison between the quantities (cogging force and attraction force) calculated using the quasi-3D and the 3D FEM models for the surface mounted TLPM having an eccentricity value ϵ equal to 0.75mm (75% of the air gap value). For this comparison, the ferromagnetic materials were defined in their linear case with a constant $\mu_r = 10000$. Also, the relative

permeability of the PM was defined as $\mu_r = 1$ and its magnetic remanance as $B_r = 1T$. Noting that the attraction force computed is acting along the axis aligned with the angles having the minimum and maximum air gap values. The results shown in Fig. 2 are relatively accurate and acceptable especially that the solution of 65 time steps of the quasi-3D model with 32 tangential divisions took only around 15 minutes with much less construction effort, while it took around 3 days to solve 33 time steps of the 3D FEM model with much more construction and computation efforts. Computation time differences will be even more noticeable and remarkable when solving non-linear models that will be presented and compared in the full paper release.

[1] N. Bianchi, S. Bolognani, D. D. Corte and F. Tonel, “Tubular linear permanent magnet motors: an overall comparison,” in IEEE Transactions on Industry Applications, vol. 39, no. 2, pp. 466-475 (2003) [2] J. Wang, W. Wang and K. Atallah, “A Linear Permanent-Magnet Motor for Active Vehicle Suspension,” in IEEE Transactions on Vehicular Technology, vol. 60, no. 1, pp. 55-63 (2011) [3] L. Szabo, C. Oprea, I. Viorel and K. A. Biro, “Novel Permanent Magnet Tubular Linear Generator for Wave Energy Converters,” IEEE International Electric Machines & Drives Conference, pp. 983-987 (2007) [4] F. Marignetti, P. Cancelliere, and M. Scarano, “Analytical formulation of the no-load magnetic field in IPM tubular machines with translator eccentricity,” in IECON 2006 - 32nd Annual Conference on IEEE Industrial Electronics, pp. 829–835 (2006) [5] L. Cappelli, Y. Coia, F. Marignetti and Z. Q. Zhu, “Analysis of Eccentricity in Permanent-Magnet Tubular Machines,” in IEEE Transactions on Industrial Electronics, vol. 61, no. 5, pp. 2208-2216 (2014) [6] D. Sarr Lo, H. Lawali Ali, Y. Amara, G. Barakat, and F. Chabour, “3D Finite Element Analysis of Eccentricity in a Tubular Linear Permanent Magnet Machine,” in 2018 XIII International Conference on Electrical Machines (ICEM), Alexandroupoli, p. 1996–2001 (2018) [7] H. Diab, Y. Amara and G. Barakat, “Comparison of Two Tubular Linear Permanent Magnet Machines with Translator Eccentricity,” 2020 International Conference on Electrical Machines (ICEM), Gothenburg, pp. 612-618 (2020)

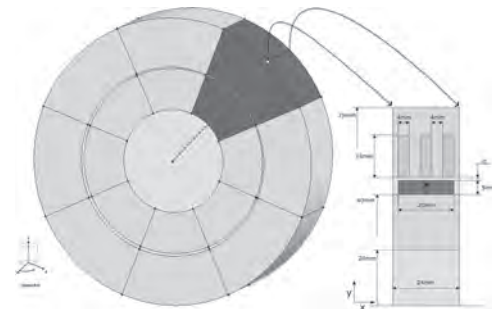


Fig.1 A 3D TLPM structure divided in the tangential direction with a 2D axial cross-section view with dimensions

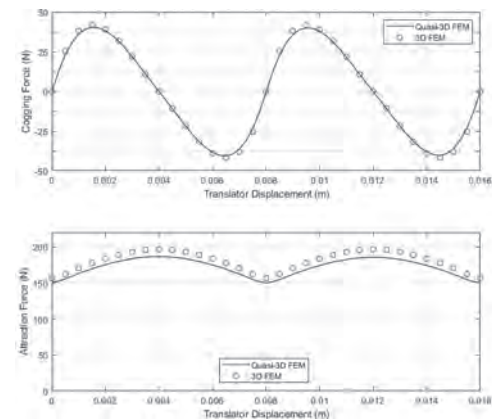


Fig.2 Comparison of the cogging and attraction forces generated by the quasi-3D and 3D FEM models

Session BE

MAGNETIC BEARINGS AND MOTOR MATERIAL MODELLING

Jonathan Bird, Co-Chair

Portland State University, Portland, OR, United States

Wei Qin, Co-Chair

Beijing Jiaotong University, Beijing, China

CONTRIBUTED PAPERS

BE-01. Parameter Identification of Preisach Model Based on the Conjugate Gradient Method and Velocity-Controlled Particle Swarm Optimization.

L. Chen^{1,2}, Q. Yi^{1,3}, T. Ben^{1,2}, Z. Zhang^{1,3} and Y. Wang²

1. College of Electrical Engineering and New Energy, China Three Gorges University, Yichang, China; 2. State Key Laboratory of Reliability and Intelligence of Electrical Equipment Hebei University of Technology, Hebei University of Technology, Tianjin, China; 3. Hubei Provincial Engineering Technology Research Center for Power Transmission Line, China Three Gorges University, Yichang, China

I. INTRODUCTION Ferromagnetic materials have complex nonlinear hysteresis characteristics, which play a decisive role in simulating electrical equipment’s magnetic properties, such as the power loss and the magnetic remanence of the core in transformers and motors[1]. Therefore, the accurate and efficient hysteresis model is fundamental to improving the power equipment’s operational efficiency. As a fast and precise hysteresis model, the Preisach model is widely used in analyzing the magnetic properties of the electromagnetic device coupled with the FEM method. However, some problems remain to exist in the current Preisach model parameter identification methods, such as the convergence speed and the accuracy need to be further improved[2,3]. To develop a more efficient parameter identification method of the Preisach model, a hybrid algorithm combining conjugate gradient method (CGM) and velocity-controlled particle swarm optimization (VCPSO) algorithm is proposed in this paper: Firstly, a one-dimensional magnetic property test system is built to measure the hysteresis loop data of B30P150 steel sheet under quasi-static conditions. Secondly, the parameters of the Preisach model with closed-form Everett function are identified based on the proposed hybrid optimizing algorithm. Finally, in the full paper, the proposed method’s accuracy is discussed by comparing the convergence speed and calculation accuracy of the proposed hybrid algorithm with other single intelligent algorithms. II. THE IMPLEMENT AND IDENTIFICATION OF PREISACH MODEL A. The Preisach model based on the closed-form Everett function The traditional Preisach model is implemented by the double integral of the distribution function in the Preisach plane, which is time-consuming and inefficient. To overcome the complex parameters identification process of the traditional Preisach model, the distribution function is simplified to the product of two single-valued functions, and a numerical Preisach model based on the closed-form Everett function is established. The improved model only needs a series of basic operations and a few parameters to be identified, which implement efficiency is much improved. B. Parameters identification of the Preisach model by combing the CGM and VCPSO algorithm A hybrid intelligent algorithm based on the conjugate gradient method (CGM) and a velocity-controlled particle swarm optimization (VCPSO) algorithm is proposed to overcome the low convergence speed and easily fall into a locally optimal solution. The identification process of a hybrid algorithm is shown in Fig 1. Firstly, according to the fast optimization of the VCPSO algorithm, finding the optimal solution range of parameters. Secondly, the searching range of VCPSO is taken as the initial parameter of the conjugate gradient method. Then the optimal solution is determined by local search. Finally, the optimal parameters are obtained by CGM. The measured and simulated hysteresis loop are compared after the identification process. The efficiency of the hybrid algorithm with other single optimal identification algorithms will be discussed in the full paper. III. RESULT AND DISCUSSION The simulated and measured hysteresis loops of the B30P150 silicon steel sheet are shown in Fig 2. It can be found that the model parameters identification results can well simulate the hysteresis loop of the B30P150 silicon steel sheet. The error is due to the approximate substitution of the Everett function, and increasing the number of relevant terms of the Everett function can improve the Model accuracy. What’s more, considering the reversible and irreversible magnetization, the simulation accuracy at the model’s turning point can also be improved. IV. CONCLUSION In this paper, a hybrid optimization algorithm combining a velocity-controlled particle swarm optimization algorithm and the conjugate gradient method is proposed to identify the parameters of the Preisach

model. The hybrid algorithm is an effective means for parameter identification of the Preisach model and contributes to the design and upgrading of electrical equipment.

[1]Szabo Z, Fuezi J, Journal of magnetism and magnetic materials, 406(may):251-258(2016). [2] N. Duan et al., IEEE Trans. Magn. 51, 7300904 (2015) [3]Stoleriu L, Andrei P, Journal of Applied Physics, 103(7p.3):132-134(2018).

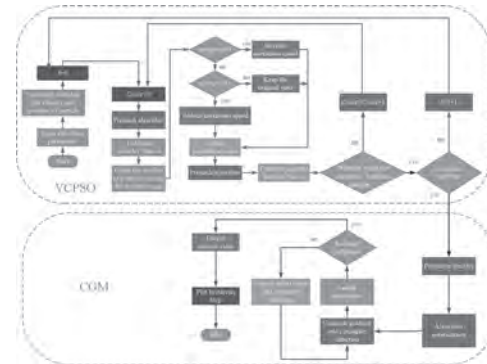


Fig. 1 Identification process based on the hybrid algorithm of CGM and VCPSO

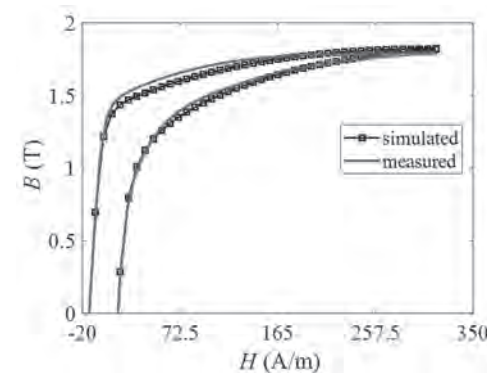


Fig. 2 Comparison between the measured and the simulated hysteresis loops

BE-02. Design of Innovative Radial Flux Permanent Magnet Motor Alternatives With Non-Oriented and Grain-Oriented Electrical Steel for Servo Applications.

B. Ozdincer² and M. Aydin¹

1. *Mechatronics Engr., Kocaeli Universitesi, Kocaeli, Turkey;* 2. *Akim Metal Sanayi ve Ticaret A S, Istanbul, Turkey*

I. ABSTRACT Permanent magnet (PM) synchronous motors have become excellent alternatives for asynchronous motors as well as DC motors in numerous applications in recent years. Therefore, torque density and efficiency improvements in development of PM synchronous motors has become a significant issue. In this study, various PM synchronous motor alternatives are proposed with both non-oriented and grain-oriented silicon steel material in the same stator in order to increase the power density and the efficiency. Detailed performance comparison using 2D/3D FEA is completed and a feasible stator designs manufactured. The proposed design is also compared with a conventional PM motor with a non-oriented stator. As a result of the investigations, it is observed that the proposed motor with both materials in the stator have higher torque density and efficiency. II. INTRODUCTION In this study, detailed investigation on the stator design with both non-oriented and oriented electrical steel is conducted so as to increase the performance of conventional permanent magnet synchronous motors. Different motors with the same stator dimensions and the same rotor are examined with six different cases as in Fig.1: Case-1 (Entire stator made of non-oriented silicon steel), Case-2 (Entire stator made of grain oriented silicon steel), Case-3 (Entire stator made of grain oriented silicon steel with 1/3rd segments), Case-4 (Stator yoke made of non-oriented silicon steel and the conventional teeth made of grain-oriented steel), Case-5 (Stator yoke made of non-oriented silicon steel and the Screw shaped teeth made of grain-oriented steel), Case-6 (Stator yoke made of non-oriented silicon steel and the wedge shaped teeth made of grain-oriented steel). Detailed FEA simulations of all of the 6cases are performed and compared. Detailed performance tests of the promising prototype motors are performed. Torque output, losses and efficiencies of the motors are obtained and compared in order to illustrate the benefits of the proposed solution. III. FEA of PROPOSED SKEWED MODELS AND EXPERIMENTAL VERIFICATION Detailed FEA is performed for both proposed and reference PM motors. Since the flux density in stator teeth is higher than that of stator yoke, stator teeth are modeled and manufactured with grain-oriented material. The model structure of the two motors is shown in Fig 2. Detailed analyses including cogging variations, back EMF, losses, torque-speed curves and output torque of both motors are performed. Flux densities and flux lines obtained by both simulations are obtained. A prototype motor is manufactured and tested to show the promising benefits. It is seen that the torque and losses shows the potential performance benefits of the proposed motor. III. CONCLUSION In this paper, the design of innovative PM motors with two different materials in the stator is proposed. Promising alternatives are investigated and summarized. Detailed FEA results are presented. The motor with promising oriented silicon steel material is manufactured and tested. Detailed test results will be provided in the final version of the paper. Based on the initial results of the analyses, the output torque is increased by 1.88% and the stator tooth losses is decreased by 51.1%. The test results and comparisons will also be given in the last version of the paper.

V. REFERENCES [1] Stefano Cicalé, Luciano Albin, Francesco Parasiliti, Marco Villani, Design of a Permanent Magnet Synchronous Motor with Grain Oriented Electrical Steel for Direct-Drive Elevators, IEEE, 2012, 978-1-4673-0142-8 [2] Nuwantha Fernando, Fuad HaninMagnetic, Materials for Electrical Machine Design and Future Research Directions: A Review, IEEE, 2017, 978-1-5090-4281-4 [3] Damian Kowal, Peter Sergeant, Luc Dupré, Alex Van den Bossche, Comparison of Nonoriented and Grain-Oriented Material in an Axial Flux Permanent-Magnet Machine, IEEE, 2010, 0018-9464 [4] Andreas Lindner, Ingo Hahn, Investigation of a large air-gap E-core flux-switching machine with arbitrary magnet shape and grain-oriented material, IEEE, 2016, 978-1-5090-2538-1

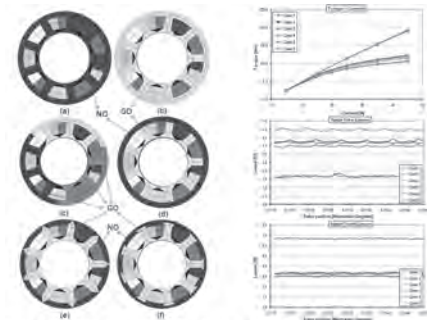


Figure 1. PM motors alternatives with Non-Oriented and Grain Oriented silicon steel

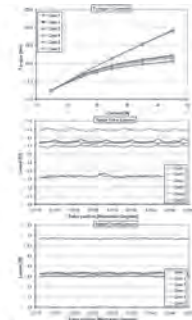


Figure 2. Torque vs. current, Teeth and back-iron losses with Non-Oriented and Grain-Oriented silicon steel materials

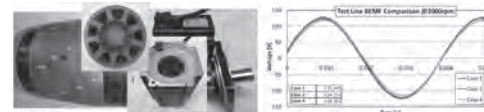


Figure 3. Prototype machine and experimental validation

BE-03. Additively Manufactured Fe-3Si Stator for High-Performance Electrical Motor.

T. Lamichhane¹, C. Chinnasamy², F. List¹, K. Carver¹, B. Andrews¹ and P.M. Paranthaman¹

1. Oak Ridge National Laboratory, Oak Ridge, TN, United States;

2. Carpenter Technology Corporation, Philadelphia, PA, United States

Additive manufacturing technology carries its potential to develop high-performance electrical machines enabling direct printing of complex shapes and incorporating the complex sequence of feedstock materials in a single build to optimize the demanding physical parameters such as low weight, cost, energy loss, and high mechanical strength and corrosion resistance. We printed Fe-3%Si stator core using selective laser melting and machined it down to thin laminates to assemble a prototype brushless permanent magnet electric motor. The magnetic and electrical properties of the thin heat-treated laminates and back emf of the electrical motors are studied. The thin laminates exhibit maximum relative permeability of 7494 with an approximate 0.8 T applied field and core-loss of 0.473 watts/lb at 60 Hz. We will report in detail about the magnetic and mechanical properties of Fe3Si soft magnets and their influence on the electrical motor. The designed machine is analyzed using finite element analysis and compared with measured electrical parameters.

BE-04. Reduction of Materials Criticality in Hybrid Manufacturing of Halbach Arrays Using Sintered NdFeB Magnets and Additively Manufactured Soft Magnetic Frame.

*T. Lamichhane*¹, *B. Andrews*¹, *A. Dalganan*¹, *T. Charlton*², *M. Doucet*², *V. Lauter*², *J. Katsaras*² and *P.M. Paranthaman*¹

1. Chemical Science, Oak Ridge National Laboratory, Oak Ridge, TN, United States; 2. SNS, Oak Ridge National Laboratory, Oak Ridge, TN, United States

The main goal of this research is to build a novel prototype Halbach ring magnet for the Magnetism Reflectometer at the Spallation Neutron Sciences using additively printed magnets. Using sintered magnet cubes, additively manufactured PLA and steel frames, we report on the enhancement mechanism of the lateral magnetic field inside cylindrical magnetic dipolar magnet Halbach arrays introducing nested Halbach rings. The inner Halbach was designed with 8 dipolar NdFeB N48 magnets while the outer Halbach ring was designed with tightly fitted similar 24 cubes. The increase in a lateral magnetic field was only 5% with the introduction of the second ring with the 8 magnets. About 27% of the axial field was increased when 16 identical steel cubes were added to the outer ring. Interestingly, the increase in the lateral field with 8 dipolar magnets cubes and 16 steel cubes was equal to all 24 magnet cubes in the outer Halbach rings. The same set up with one-inch magnet cubes was fabricated to study the influence of the thickness of the slabs. This demonstrates the true potential of reduction of the criticality of high-quality materials in industrial manufacturing using 3D printing. Additionally, the results are being validated using EMS simulations and optimal geometries for the potential enhancement of the field will be predicted.

BE-05. A Novel Hybrid Axial Magnetic Bearing That Produces a Unidirectional Electromagnetic Force.

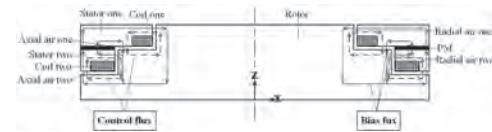
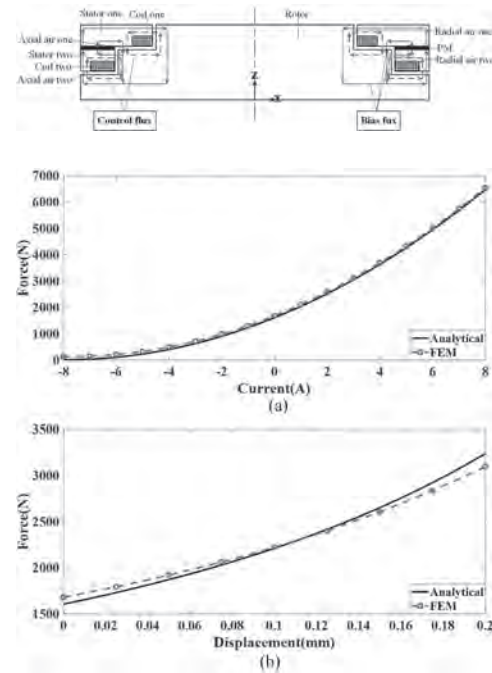
C. Yu¹, Z. Deng¹, L. Mei², C. Peng¹ and S. Chen¹

1. College of Automation Engineering, Nanjing University of Aeronautics and Astronautics, Nanjing, China; 2. College of Electrical Engineering and Control Science, Nanjing Tech University, NanJing, China

This paper proposed a novel hybrid axial magnetic bearing (HAMB) for a vertical system, which can produce a unidirectional magnetic force. The principle of the new HAMB is analyzed. When the rotor is suspended in the equilibrium position, the bias force offsets the gravity of the rotor and the current is zero, which can reduce the copper loss. According to the magnetic field distribution, an equivalent magnetic circuit is established. Based on the analytical model, the curve of force-current, curve of force-displacement and bearing capacity are calculated. The results of analytical are consistent with the ones of the finite element method (FEM). *Index Terms*—Hybrid, axial magnetic bearing, magnetic circuit, finite element. I. Introduction Magnetic bearings (MBs) are widely used in high-speed rotating machinery, such as compressors, flywheel energy storages for the merits of contactless property and long life[1]. To reduce copper loss, hybrid MB has become the research feature combing the characteristics of active MB and passive MB [2]-[4]. Several axial MB are significant in vertical levitation rotor systems. A novel hybrid axial MB is proposed in [5], which reduces the reluctance of the control path and power loss of axial MB and through constructing the second air gap. In [6], an improved magnetic circuit model is introduced for a novel axial hybrid MB, which provides a reference for the MB design. In [7], an equivalent magnetic circuit with the conformal mapping method and Laplace's equation is developed for axial MB with multiple air gaps. The results of analysis are consistent with the ones of finite element analysis. In this paper, a novel hybrid axial magnetic bearing (HRMB) is proposed for the vertical system, which produces a unidirectional electromagnetic force to replace the traditional bidirectional force. There is no need for the current to control the MB when the rotor is in the equilibrium position, which reduces the copper loss greatly. Then, the equivalent magnetic circuit method is adopted to analyze the performances of the HRMB. Ultimately, the accuracy of the analytical model is validated by the finite element method (FEM). II. Principle of Hybrid Axial Magnetic Bearing A. Principle of HAMB The structure of HAMB is shown in Fig.1. The blue solid line represents the bias flux, and the red dotted line represents the control flux. B. Magnetic circuit model The equivalent magnetic circuit models of the bias flux and control flux are established. III. Analysis of HRMB The variation of force with current and displacement can be obtained in Fig.2. The analytical results are in agreement with the results of FEM. The bias force and maximal force are calculated and compared with the finite element method. The margin of error is within 10%. IV. Conclusion A novel hybrid axial magnetic bearing is proposed in this paper and the principle of HAMB is analyzed. The structure has low copper loss when the rotor is stable in the suspension position. According to magnetic field distribution, an equivalent magnetic circuit is established. The curve of force-current, curve of force-displacement and bearing capacity are calculated by analytical and FEM respectively. The accuracy of the analytical model is confirmed by FEM.

[1] J. X. Zhou, S. Q. Zheng, B. C. Han, et al. "Effects of Notch Filters on Imbalance Rejection With Heteropolar and Homopolar Magnetic Bearings in a 30-kW 60000-r/min Motor." *IEEE Trans. Ind. Electron.*, vol. 64, no. 10, pp. 8033-8041, Oct. 2017. [2] K. D. Bachovchin, J. F. Hoburg, and R. F. Post, "Magnetic fields and forces in permanent magnet levitated bearings," *IEEE Trans. Magn.*, vol. 48, no. 7, pp. 2112-2120, Jul. 2012. [3] W. Zhang and H. Zhu, "Improved model and experiment for AC-DC three-degree-of-freedom hybrid magnetic bearing," *IEEE Trans. Magn.*, vol. 49, no. 11, pp. 5554-5565, Nov. 2013. [4] B. C. Han, S. Q. Zheng, X. Wang, et al. "Integral design and analysis of passive magnetic bearing and active radial magnetic bearing for agile satellite application," *IEEE Trans. Magn.*, vol. 48, no. 6, pp. 1959-1966, Jun. 2012. [5] J. C. Fang, J. J. Sun, Y. L. Xu, et al. "A New Structure for Permanent-Magnet-Biased Axial Hybrid Magnetic Bearings." *IEEE Trans. Magn.*, vol. 45, no. 12, pp. 5319-5325, Dec. 2009. [6] X. X. Liu, J. Y. Dong, Y. Du, et al. "Design and Static Performance Analysis of a Novel Axial Hybrid Magnetic Bearing." *IEEE Trans. Magn.*, vol. 50, no.

11, pp. 1-4, Nov. 2014. [7] K. Wang, D. Wang, H. Y. Lin, et al. "Analytical Modeling of Permanent Magnet Biased Axial Magnetic Bearing With Multiple Air Gaps." *IEEE Trans. Magn.*, vol. 50, no. 11, pp. 1-4, Nov. 2014.



BE-06. Design of a Stiffness Control Actuator Utilizing Magneto-Elastic Actuation.

L. Cheng¹ and J. Chang¹

1. Power Mechanical Engineering, National Tsing Hua University, Hsinchu, Taiwan

To achieve the force/torque control feature for robotic applications, some robotic devices such as robotic grippers or robotic arms use servo motors' current or the structures' mechanical strain to measure torques and forces. Additional commercial torque sensors are also commonly used to detect the output forces. Although these sensors can detect motor torques or contact forces, they are too stiff to render a soft stiffness [1]. If the load environment is stiff and the actuator is also stiff, the force controller will lead to low accuracy, as any tiny movements will cause a large force variety and components are rigid. To make robotic actuators perform more compliant with torque control and stiffness control, a series elastic actuation method was proposed [2]. The series elastic actuator (SEA) is constructed with an actuator and an elastic spring which can be added between the motor and the load to provide compliant features [3]. With displacement sensors attached at two sides of the spring, the output torque can be computed [4] by measuring the relative movement. With the SEA, a force control can then be transferred into a position control whatever the load environment is stiff or not. Magnetic coupling is a component that transmits torque from the motor to load without any direct mechanical contact, as attractive forces between N and S poles are used to transmit the force. When there is a relative angle difference between N and S poles, the attractive forces, which can be separated into axial forces and shear forces, generate a relative force that can be utilized as a virtual spring in the SEA system. The torsional stiffness of magnetic coupling was reported in [5] to be sensitive to strength of magnetic forces and air gap, axial displacement, and angular misalignment. When the load exceeds maximum torque that can be transmitted by the magnetic coupling, it then switches to pole-slipping mode to avoid possible permanent deformation in structure [6]. To form a magnetic SEA (mSEA) system, an elastic magnetic coupling must be placed within the actuator and the load. This configuration of SEA connects the elastic component to the load directly, which apparently is sensitive to changes of the external load. By using the magnetic coupling, the attraction forces between two magnets can be transferred to the rotary torque when angular rotation occurs. With the angle solver attached to the load, the angular displacement of mSEA can be measured by the angle difference between the load's angle solver and the motor's encoder. The mathematic relation between output torque and rotating angle is the stiffness of magnetic coupling, which is an important variable for a mSEA controlling system. In this study, a 4-pole axially magnetized NdFeB ring magnet (Magtech Corp., TW) was chosen. The magnet's outer and inner diameters are 24 and 13mm, respectively. The magnet's thickness 3mm with flux density of 3530G. Because of its flat ring structure, the mSEA is more compact in size than other types of magnetic coupling. Beyond the size and material of the magnet, some other parameters affecting characteristics of the mSEA, like airgap length, pole number, and angular displacement were studied and analyzed in this paper toward understanding the torsional stiffness and attractive force for the axial magnetic coupling. The relation between airgap length and angular displacement is shown in Fig. 1(a), from which one can observe that the torque is a parabola curve with a saturation region between 30° and 60°, with decreasing of torque when angular displacement is over 60°. The maximum torque is observed to decrease significantly when the airgap, indicated as "e" in the figure, becomes larger. On the other hand, the axial force renders a linear relationship with the angular displacement as shown in Fig. 1(b). When the angle between the two magnets goes in Fig. 1(b), the axial force decreases linearly, leading to zero value where the two magnets are separated. Along with these results, the airgap is found to be provide significant influence in axial attractive force and pull-out torque. With higher airgap, attractive force and pull-out torque both go lower. From this study, the torque for the magnetic couple is also found to be affected by the angular displacement of two magnets and the number of pole pairs. When the angular displacement goes higher, the pull-out torque follows a parabola curve, reaching to the maximum torque value 150 mN-m around 15° with the airgap is 1mm as showed in Fig. 1. The range of angular displacement beyond the saturation region is the magnet coupler's effective region. By

using the model 4-pole axially magnetized ring magnet, the transmitting torque for the coupler can be then controlled, as the torsional stiffness can be rendered by the model of magnetic coupling. The proposed mSEA can render various magnitudes of torsional stiffness and the rendered results are showed in Fig. 2. The mSEA system can be controlled to perform desired motion when a virtual spring stiffness is set between 50 to 300mN-m/rad with ~5% stiffness rendering error compared to ideal stiffness. The maximum output torque of the mSEA is 130mN-m with force resolution of 0.1mN and control error less than 1mN. With the proposed mSEA put between actuator and load, the output torque and stiffness can certainly be controlled for robotic applications with fragile objects or human.

- [1] Y. Yu and C. Lan, "Design of a Miniature Series Elastic Actuator for Bilateral Teleoperations Requiring Accurate Torque Sensing and Control," *IEEE Robotics and Automation Letters*, vol. 4, no. 2, pp. 500-507 (2019)
 [2] J. Pratt, B. Krupp, and C. Morse, "Series elastic actuators for high fidelity force control," *Industrial Robot: An International Journal*, vol. 29, pp. 234-241, 06/01 (2002) [3] C. Lee, S. Kwak, J. Kwak, and S. Oh, "Generalization of Series Elastic Actuator Configurations and Dynamic Behavior Comparison," *Actuators*, vol. 6, p. 26, 08/22 (2017) [4] S. Oh and K. Kong, "High-precision robust force control of a series elastic actuator," *IEEE/ASME Transactions on Mechatronics*, vol. 22, no. 1, pp. 71-80 (2016)
 [5] T. Lubin, S. Mezani, and A. Rezzoug, "Simple Analytical Expressions for the Force and Torque of Axial Magnetic Couplings," *IEEE Transactions on Energy Conversion*, vol. 27, no. 2, pp. 536-546 (2012) [6] R. Montague, C. Bingham, and K. Atallah, "Servo Control of Magnetic Gears," *IEEE/ASME Transactions on Mechatronics*, vol. 17, no. 2, pp. 269-278 (2012)

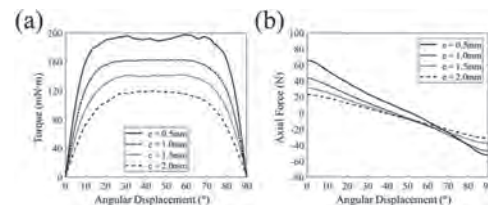


Fig. 1 (a) torque and (b) axial force caused by angular displacement between the magnetic rings.

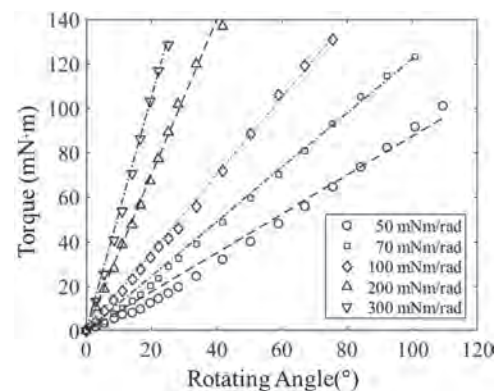


Fig. 2 Measured and predicted torque for the model mSEA.

BE-07. A Constant Stiffness Magnetic Bearing.

R. Bjørk¹ and C.R. Bahl¹

1. Department of Energy Conversion and Storage, Danmarks Tekniske Universitet, Lyngby, Denmark

With the increasing focus on energy efficiency for the green transition, there is a desire to identify and reduce all losses possible. For rotary machines losses occur as friction at the bearings, and therefore frictionless magnetic bearings can be an important upgrade to high-speed machinery. However, as proven by Samuel Earnshaw in 1842 magnetic bearings are inherently unstable. Typically, magnetic bearings are stable in the lift (often vertical) direction. This results in instability in the radial direction and therefore some kind of stabilizing force is required in this direction [1]. For a magnetic bearing, the radial stiffness determines the active force needed to keep the bearing stable. Thus there is a compromise in designing a magnetic bearing which can both lift as high a load as possible and at the same time have a low and constant radial instability [2-5]. Here we describe a new magnetic bearing aiming to fulfill these requirements [6]. The bearing consists of two nested conical axi-symmetric permanent magnet rings with quadratic cross-sections, as shown in Fig. 1. This configuration is a superposition between a radially magnetized bearing and an axially magnetized bearing. The rotor and stator are centered on the same axis, and when load is applied on the rotor bearing this will move along the z-axis. The stator has a magnetization direction that is along the inwards normal to its surface, while the rotor has a magnetization direction outwards normal to its surface. Thus, there is repulsion between the rings. The idea behind this design is that the magnetic forces will both have a component providing a lifting force along the z-axis, but also a component along the radial direction, which might allow the stiffness along this direction to be controlled. Such a design of tilted conical rings of permanent magnets can easily be made of cubes of permanent magnets placed in a ring. We consider a design where there is a minimum distance between rotor and stator of 0.2 mm and where the conical rings that make up both the rotor and the stator have quadratic cross-section side lengths of 3 mm. The radius of the center of the tilted ring in the stator is fixed at 24 mm, while it is varied for the rotor. We consider different tilt angles of the stator/rotor rings in the bearing and we also consider ring geometries with twice the cross-section and different magnetization directions. The “single” bearing consists of two tilted concentric rings with opposite magnetization as described above, the “double” bearing has two magnets in each tilted ring, and finally the “alternating” bearing has the magnetization of one part of the ring reversed in both the stator and rotor. All configurations are illustrated in Fig. 1. We assume that the permanent magnets in the bearing have a remanence of 1.4 T and a relative permeability of 1. We determine the force and stiffness of the bearing using a magnetostatic finite element (FEM) axi-symmetric model in Comsol Multiphysics. As the simulations are 2D axi-symmetric a very high mesh resolution can be used, eliminating the known convergence issues with bearing models in 3D [7]. We have conducted a variation study to determine the optimal geometry of the bearing as function of the tilt angle and the bearing type. Tilt angles from 0 to 90 degrees in steps of 15 degrees were modelled. Combined with the three bearing types studied, this gives a total of 21 bearings modelled. For each of these we use an adaptive routine to determine the optimal rotor radius to a precision of 0.1 mm. We show that the optimal value of the rotor radius is almost identical for the different bearing geometries considered, with decreasing rotor radius for increasing tilt angle. Following this we determine which bearing would be easiest to control, i.e. has a constant stiffness value, but which also provides a high lifting force. We investigate this by calculating the relative standard deviation for both the axial force and stiffness. This is shown in Fig. 2 for all studied bearings which are stable in the axial direction. Choosing the best bearing depends on the desired characteristics of the bearing. If one desires a bearing that is easy to control, i.e. has a mostly constant stiffness, for a 3 mm axial displacement the double geometry with a tilt angle between 60-75 degrees is clearly the best. When a smaller axial displacement of 1 mm is considered, all bearings with a tilt angle of 60 degrees display almost constant stiffness. This is a remarkable property, as such a bearing is very easy to control with an active bearing. In this bearing the exact load on the rotor is not of importance, as long as it is between the minimum and maximum lift, and at the same time the stiffness is constant

regardless of the load. We thus show that by varying the tilt angle and the bearing geometry it is possible to tailor a bearing to the desired characteristics and achieve an easily controllable bearing with a high lifting force.

[1] J. P. Yonnet, IEEE Transactions on Magnetics, Vol. 17, p.1169-1173 (1981) [2] J. G. Detoni, Proceedings of the Institution of Mechanical Engineers, Part C: Journal of Mechanical Engineering Science, Vol. 228, p.1829-1844 (2014) [3] J. Sun, D. Chen and Y. Ren., IEEE Transactions on Instrumentation and Measurement, Vol. 62, p.2960-2965 (2013) [4] L. Zhang, H. Wu, P. Li, Y. Hu and C. Song, Mathematical Problems in Engineering, Vol. 2019, p.4265698 (2019) [5] K. K. Nielsen, C. R. H. Bahl, N. A. Dagnaes, I. F. Santos and R. Bjørk, IEEE Transactions on Magnetics, 10.1109/TMAG.2020.3042957 (2020) [6] R. Bjørk and C. R. H. Bahl, “A conical passive magnetic bearing with constant stiffness”, submitted for publication (2021) [7] N. A. Dagnæs-Hansen and I. F. Santos., Proceedings of the Institution of Mechanical Engineers, Part C: Journal of Mechanical Engineering Science, Vol. 233, p.5280-5293 (2019)

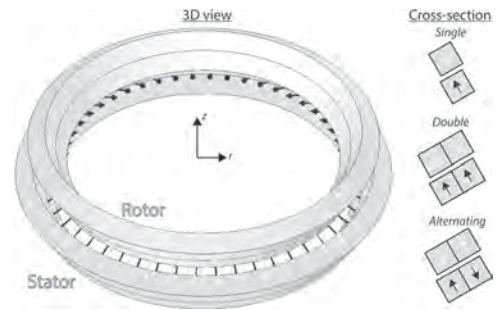


Fig.1: The bearing geometry considered. The stator, shown in green, and the rotor, shown in grey, each consists of two tilted rings of permanent magnets with a quadratic cross-section. Their direction of magnetization is also indicated. On the right is shown a cross-section of the bearing, with the three types of magnet configurations considered. The bearing illustrated here has a tilt angle of 30 degrees.

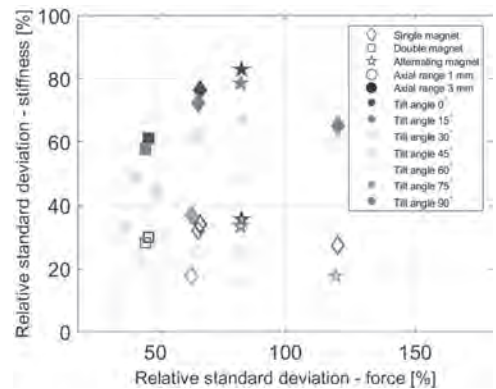


Fig.2: The relative standard deviation of the stiffness in the z-direction in percent as function of the relative standard deviation of the force in the z-direction in percent.

Session BF

MAGNETIC GEARING

Kais Atallah, Chair

University of Sheffield, Sheffield, United Kingdom

CONTRIBUTED PAPERS

BF-01. Design of Bridged Flux Modulators in Coaxial Magnetic Gear Considering Mechanical Stress.

Y. Zhan¹, K. Wang¹, Z. Ying¹, G. Xu¹ and H. Zhao¹

1. School of Electrical and Electronic Engineering, North China Electric Power University, Beijing, China

I. Introduction The conventional modulating ring in a coaxial magnetic gear is composed of separate pieces of laminated steel known as flux modulators. The assembly of the separate modulators is not easy because the laminations of each modulator must be firmly held together by using a clamping rod. A modulating ring with bridges that integrate the steel pieces into a whole laminated ring can greatly save the assembly efforts [1]. From the electromagnetic perspective, thin bridges are undoubtedly preferred as thick bridges compromise the modulating effect and hence downgrade the pull-out torque [2], [3]. However, thin bridges challenge the mechanical design of the modulating ring considering the stress due to the magnetic pull. Fernando and Saha investigated the effect of different numbers of flux modulators, thicknesses and positions of bridge on the shear stress in the modulating ring, and ended with a double-bridge design [3]. Due to the effectively thick bridges, this design has a large loss of torque capacity though the double-bridge structure is very robust mechanically. This digests proposes a design procedure of bridged modulators that reduces the mechanical stress at the cost of torque capacity as small as possible. II. Magnetic Gear With Bridged Modulators Fig. 1 shows the prototype magnetic gear with bridged modulators. This magnetic gear was originally presented with separate modulators, and more information about its construction can be found in [4]. For the study in this paper, the separate modulators are replaced with a modulating ring integrated by the bridges near the high-speed rotor (HSR), as shown Fig. 1. Such a position of bridges was proved to have larger torque capacity than any other positions [2], [3]. The modulating ring laminations are kept together by using the end plates and the clamping rods that are inserted into three of the modulators. III. Design of Modulating Ring Considering Stress A. With Different Thicknesses of Bridge Two modulating ring designs with different thicknesses of bridge and equal ratio of pole arc to pole pitch (δ) (designs 1 and 2) are presented in Table I. The time-varying torques and stress distributions in these magnetic rings are calculated by three-dimensional (3-D) time-stepping finite element method (T-S FEM). The maximum mean torques extracted from the torque curves with different initial relative positions of the rotors, known as pull-out torques, are 15.70 Nm and 16.24 Nm at the outer rotors of designs 1 and 2, respectively. Table I shows the maximums of the fluctuating stress under approximately equal load condition. The stress of the thinner bridge is apparently higher than that of the thicker bridge. The maximum stress occurs at the junction of the bridge and the modulator that encloses a clamping rod. It should be noted that the modulating ring bears wildly fluctuating stress which is more prone to cause failure than a static stress of equivalent magnitude in a long-term operation, due to the metallic fatigue. Therefore, a sufficient margin of safety for yield must be reserved. B. With Different Ratios of Pole Arc to Pole Pitch Previous research indicates that the pull-out torque does not deviate significantly from the maximum for a certain large variation of δ in the vicinity of δ_m corresponding to the maximum pull-out torque [2]. This feature suggests that an appropriate value of δ can reduce the stress without downgrading the torque capacity. For the bridge thickness of 0.8 mm, the calculated pull-out torques with the δ values of 0.33, 0.375, 0.41, 0.45, 0.5 and 0.58 are 16.00 Nm, 16.33 Nm, 16.44 Nm, 16.53 Nm, 16.17 Nm and 15.11 Nm, respectively. When δ equals 0.33 to 0.5, the torque capacity is not apparently different from the maximum. Table I shows the maximum stress in the modulating ring with that range of δ , at approximately equal load. In comparison to the δ_m design, the design with δ of 0.33 reduces the maximum stress by 24.1% at the cost of only 3.2% lower torque capacity. C. With Different Fillet Radii at Junctions Filleting the sharp or right-angle corner is a commonly used mechanical design approach to reducing the stress concentration in a junction. Designs 1 to 6 all have right-angle junctions. Table I shows the maximum stresses with different δ and fillet radii (designs 7 to 15) at approximately equal load. In those cases, the increase of fillet radius relieves

the stress only when δ equals 0.5. Filleting the junction may not relieve the stress in the modulating ring because the distribution of the magnetic load force changes together with the shape of bridge, unlike a mechanical load force. IV. Conclusion This digest proposes a design procedure for reduced mechanical stress in the bridged modulating ring of coaxial magnetic gear, at minimum cost of torque capacity. Step 1 of the design procedure is to place the bridges near the side of high-speed rotor and minimize the thickness of bridge for maximum torque capacity and acceptable stress. Step 2 is to vary the pole-arc-to-pole-pitch ratio of the modulating ring for reduced stress at acceptable cost of torque capacity. Step 3 is to fillet the junctions for the potential further reduction of stress. These steps could be repeated until the desired torque capacity and stress are achieved. Using more clamping rods could be another approach to reducing the stress. The full paper will investigate the effects of adding clamping rods on the stress and the eddy current loss in the modulating ring.

[1] D. Z. Abdelhamid and A. M. Knight, *IEEE Trans. Magn.*, vol. 53, no. 11, Art. no. 8112804 (2017). [2] Y. Zhan, *et al*, *IEEE Trans. Magn.*, vol. 55, no. 6, Art. no. 8103904 (2019). [3] N. Fernando and S. Saha, *IEEE Trans. Energy Convers.*, vol. 33, no. 1, pp. 49–58 (2018). [4] Y. Ge, Q. Xin, and C. Nie, *Journal of Mech. Trans.*, vol. 36, no. 4, pp. 5–8, 13 (2012).

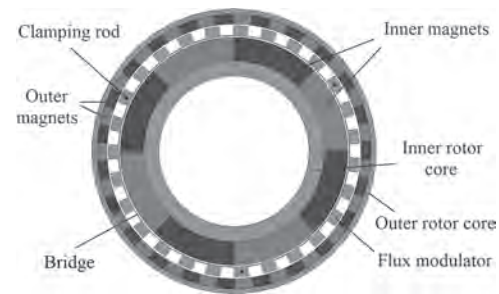


Fig. 1. Magnetic gear

Designs	Thickness of bridge (mm)	Ratio of pole arc to pole	Fillet radius (mm)	Mean outer torque (Nm)	Maximum stress (MPa)
1	1.0	0.5	NA	13.66	121.12
2	0.8	0.5	NA	13.53	198.19
3	0.8	0.45	NA	13.62	196.78
4	0.8	0.41	NA	13.55	179.69
5	0.8	0.375	NA	13.60	153.21
6	0.8	0.33	NA	13.67	149.41
7	0.8	0.5	1	13.67	193.87
8	0.8	0.5	2	13.65	186.06
9	0.8	0.5	3	13.66	170.94
10	0.8	0.41	1	13.68	165.95
11	0.8	0.41	2	13.61	174.71
12	0.8	0.41	3	13.63	164.26
13	0.8	0.33	1	13.64	154.19
14	0.8	0.33	2	13.65	152.47
15	0.8	0.33	3	13.62	156.59

Table I Load torques and stresses

BF-02. Influence of Magnetic Interaction on Power Factor and Efficiency of IPM-Type Magnetic-Geared Motor.

K. Ito¹ and K. Nakamura¹

1. Graduate School of Engineering, Tohoku University, Sendai, Japan

The electrification of vehicles and ships has been required to reduce the carbon dioxide emissions on global environment. In many cases, a general drive system of electric vehicles and ships consists of an electric motor and a mechanical gearbox to obtain desired speed and torque in terms of reducing size and weight. However, the mechanical gearbox has inherent problems caused by mechanical contacts, e.g., acoustic noise, wear and tear, vibration, and periodical maintenance. To solve the above problems, a magnetic-geared motor (MGM) has attracted attention [1]. The MGM consists of a permanent magnet (PM) motor and a flux-modulated type magnetic gear (MG), and they can transmit the torque without any contacts by an electromagnetic force. In addition, the MGM has the structure that a PM motor and an MG are combined magnetically and mechanically as one electric machine so that it can offer the higher torque density than the conventional drive system. Hence, the MGM is expected to be put into practical use. In previous studies, Refs. [2] and [3] have reported about a magnetic interaction of the MGM caused by magnetically coupling between a PM motor part and an MG part. These studies have discussed about the relationship between the magnetic interaction and the output torque of MGM. The magnetic interaction may influence only the output torque, but also the efficiency and the power factor. However, the influence of the magnetic interaction on the efficiency and the power factor have not been clarified. This paper investigates that the influence of the magnetic interaction on the efficiency and the power factor of the MGM by using a three-dimensional finite element method (3D-FEM). Furthermore, in order to verify the validity, the experimental results are compared to the calculated ones. Fig.1 shows the specifications of the MGM used for examinations. It consists of a PM motor part and an MG part, which share one high-speed rotor (HSR). The PM motor part consists of an armature and the shared HSR, while the MG part consists of the shared HSR, a magnetic modulator called pole-pieces (PP), and a low-speed-rotor (LSR). The numbers of pole-pairs of the shared HSR and the LSR are 4 and 23, respectively. Hence, the gear ratio is 5.75 which is given by the pole-pair ratio of the shared HSR and the LSR. First of all, the phase of the armature voltage is calculated by 3D-FEM in various load angles, namely, in various load torques, to clarify the influence of the magnetic interaction on the armature voltage. In 3D-FEM, the rotational speed and the current phase are kept constant. Fig. 2(a) indicates the calculated waveforms of the armature voltage at various load angles of 0 (no-load), 30, 45, and 90 degrees. In addition, an input current is also indicated in the figure as a reference of the phase. It is understood that the phase of the armature voltage is gradually shifted by increasing the load angles, i.e. load torque. The reason why the phase of the armature voltage is shifted is discussed based on the rotational coordinate system synchronized with HSR. Fig. 2 (b) shows the vector diagram of MGM based on the rotational coordinate system of the HSR when a load angle is δ and a current phase is β . In the figure, the no-load induce voltage is e_a , the armature voltage is V_a , the armature current is i_a , the phase difference between V_a and i_a is Φ , d - and q -axis inductance are L_d and L_q , the magnetic flux of HSR magnet is ψ_h , the modulated magnetic flux of LSR magnet is ψ_{ml} due to the magnetic interaction, respectively. The sum of four magnetic fluxes, which are $L_d i_a$, $L_q i_a$, ψ_h , and ψ_{ml} , is represented as the combined magnetic flux ψ_o . The phase of ψ_{ml} changes with the load angle δ , thereby the phase of ψ_o changes too. Hence, the phase of V_a shifts due to the magnetic interaction when the load angle changes, because the phase difference between V_a and ψ_o is always 90 degrees. Based on the above discussions, it is considered that power factor also changes due to the magnetic interaction. Fig. 2 (c) indicates the calculated results of the displacement power factor of MGM in various load torques and current phases. The figure reveals that the displacement power factor changes with the load torques. Moreover, it is understood that the maximum point of the displacement power factor varies in each load torque. Therefore, it is concluded that if the current phase is advanced in accordance with increasing the load torque, the MGM can be a high-power-factor drive. Fig. 2 (d) indicates the measured results of the displacement power factor of the prototype MGM. The figure reveals that the measured displacement power factor changes with the load

torque in the same way as the calculated ones shown in Fig. 2(c). Hence, the validity of the calculated results is proved.

[1] K. T. Chau, Z. Dong, J. Z. Jiang, L. Chunhua, and Z. Yuejin, *IEEE Trans. Magn.*, Vol. 43, pp. 2504-2506 (2007) [2] H. Suzuki, K. Hirata, N. Niguchi, A. Kohara and K. Takahara, *Proc. of 19th International Symposium on Electromagnetic Fields in Mechatronics, Electrical and Electronic Engineering* (2019) [3] K. Ito and K. Nakamura, *IEEE Trans. Magn.*, doi: 10.1109/TMAG.2020.3020121 (2020)

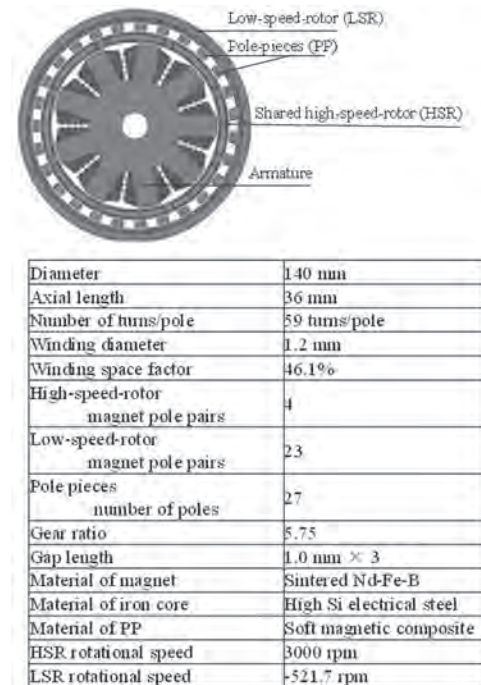


Fig. 1 Specifications of the MGM used for examinations.

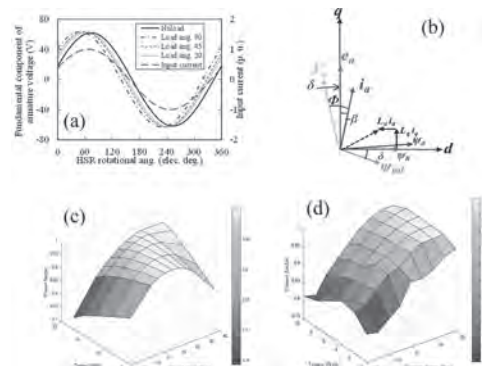


Fig. 2 Calculation and experimental results, (a) Calculated waveforms of the armature voltage at various load angles, (b) Vector diagram considering the magnetic interaction, (c) Calculated results of the displacement power factor, (d) Measured results of the displacement power factor.

BF-03. Pseudo Direct Drive Electrical Machine for a Floating Marine Current Turbine.

R. Dragan¹, R. Barrett¹, S.D. Calverley¹, J. Moreu³ and K. Atallah²

1. Magnomatics Ltd, Sheffield, United Kingdom; 2. Electronic and Electrical Engineering, University of Sheffield, Sheffield, United Kingdom; 3. Seaplace, Madrid, Spain

Tidal stream offers predictable electrical energy generation at higher power densities than other renewable energy sources, such as wind. However, compared to wind turbines, the tidal turbine technology is arguably still in its infancy, and various types of drivetrains are being considered [1][2]. These include permanent magnet (PM) generators and doubly-fed induction generators. The paper presents an investigation into the application of magnetically geared Pseudo Direct Drive (PDD) electrical machine to a floating tethered 6kW, 100rpm marine current turbine. The turbine is designed to harness the energy from tidal and ocean currents, in regions with relatively high-speed water flows at depths, that are a long distance from the seabed, and cannot be economically exploited by conventional fixed turbines. The marine current turbine is a robust, easy to service and cost-effective solution for regions with variable or fixed sea depth of more than 60 metres. Fig. 1 shows the prototype tidal current turbine and cross-sectional view of the PDD generator, where the magnetic gear element consists of a 4-pole pair high speed PM rotor, 31 ferromagnetic pole piece output rotor and a 27-pole pair stationary Halbach PM array. The high-speed rotor of the magnetic gear is magnetically coupled to the stator, which employs a double layer concentrated winding, forming the PM brushless machine element. The PDD generator was designed for a rated torque of 580Nm at 100rpm, while the pull-out torque requirement of the magnetic gear was fixed at 640Nm. Fig. 2 shows the PDD generator efficiency for a range of input load torque and speed points. It can be seen, that the 6 kW PDD generator is capable of an efficiency of 94-95% for a substantial range of operation. The paper will present the electromagnetic design and analysis of the PDD generator, and predicted performance such as efficiency, will be compared with dynamometer measurements on a prototype PDD generator. Furthermore, test results on a demonstrator marine turbine in a towing tank will also be presented.

[1] S. Benlghali, M. E. Benbouzid, J. F. Charpentier, IEEE Transactions on Oceanic Engineering, Vol. 37 (2012) [2] K. Touimi, M. Benbouzid and P. Tavner, IEEE International Power Electronics and Application Conference and Exposition (PEAC), (2018)

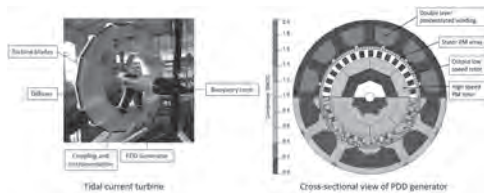


Fig. 1 Prototype tidal current turbine and PDD generator.

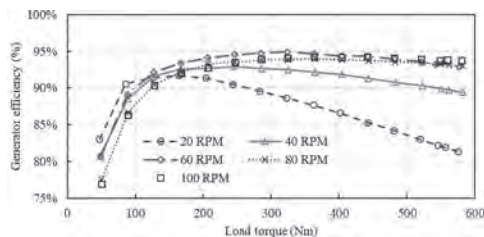


Fig. 2 Variation of PDD generator efficiency with torque.

BF-04. Magnetically Geared Propulsion Motor for Subsea Remote Operated Vehicle.

G. Cooke¹, R. Barrett¹, R. Dragan¹, D. Powell¹, S. Graham³ and K. Atallah²
 1. Magnomatics Ltd, Sheffield, United Kingdom; 2. Electronic and Electrical Engineering, University of Sheffield, Sheffield, United Kingdom; 3. Soil Machine Dynamics Ltd, Wallsend, United Kingdom

Currently, subsea remote operated vehicles (ROVs) are equipped with hydraulically or electrically powered thruster units. For the former, the surface powered on-board electric motors are only used to drive hydraulic pumps, which distribute hydraulic power to hydraulically driven thrusters and auxiliary toolings [1]. For the electrically powered thruster, direct-drive brushless permanent magnet (PM) machines are normally employed [2] [3]. A novel all-electric ROV, which employs 25kW electric thruster units, exhibits increased system efficiency, in addition to a 20% reduction in weight/size of the power delivery and drive systems, when paired with a high voltage DC supply umbilicals. Thus, enabling operation from smaller vessels. This paper presents an investigation into the electromagnetic design and analysis of a magnetically geared thruster motors, which can operate in closed loop control providing accurate tracking of designated routes or position holding of the ROV. Additionally, the novel thrusters provide 20% more thrust with 50% fewer moving parts, reducing the maintenance requirement, while providing hot-swap capability to reduce down-times of the ROV. The torque limit capability of the magnetic gear unit can passively isolate the propeller from the electric motor and re-engage normal operation when the excess load, on the output shaft, has been removed. In addition, the hermetically sealed magnetic gear topology, isolates the active electrical part of the thruster from the passive output stage of the magnetic gear. Thus, sea water ingress will not affect normal operation and the oil leak severity is reduced, since the output stage of the gear only requires a small quantity of oil for pressure compensation. Fig. 1 shows the main components of the novel magnetically geared thruster, and a cross-sectional view of the magnetic gear connecting the high-speed PM motor to the propeller, which is driven by the low speed rotor (LSR) of the magnetic gear. Furthermore, high-speed side of the thruster is hermetically sealed from the output LSR by the stationary pole piece structure. The high speed rotor (HSR) of the magnetic gear is rigidly connected to the rotor of the PM motor, which is designed for a rated output of 25kW. Fig. 2 shows the predicted efficiency map of the magnetically geared thruster. It can be observed that a high system efficiency is possible, despite the entire thruster being filled with mineral oil for pressure compensation. The paper will present the electromagnetic design and analysis of the magnetic gear and PM motor, and predictions are compared with experiments undertaken on a prototype. It is shown for the magnetic gear an airgap shear stress in excess of 100kPa can be achieved.

[1] F. Zhou et al. OCEANS, 2013 [2] D. Uygun et al. IEEE 5th International Conference on Power Engineering, Energy and Electrical Drives (POWERENG), 2015. [2] H. Tian, Z. Mao, B. Song and Y. Li, OCEANS, 2018.

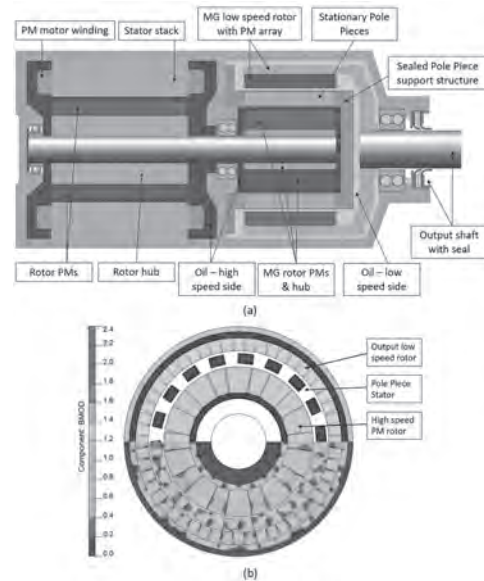


Fig. 1 a) Magnetically geared thruster topology (b) Magnetic gear cross-section

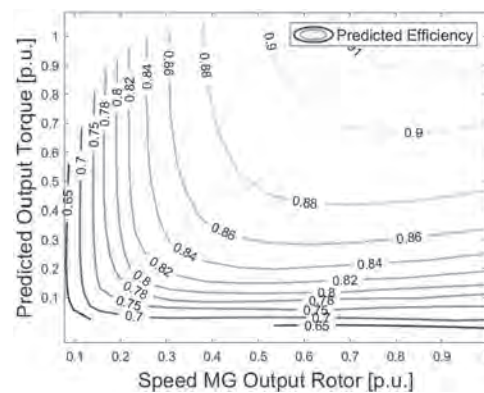


Fig. 2 Efficiency map of the thruster system

BF-05. Optimization Algorithms for Performance Calculation of Rotating Cylinder Planetary Gear.

Y. Zhan¹, Z. Zhang¹, X. Yuan¹, H. Zhao¹ and G. Xu¹

1. School of Electrical and Electronic Engineering, North China Electric Power University, Beijing, China

I. Introduction The conventional modulating ring in a coaxial magnetic gear is composed of a sequence of ferromagnetic blocks. The rotating cylinder planetary gear (RCPG) proposed by Davey *et al* borrowed the conventional topology but replaced the ferromagnetic blocks with free-spinning magnetized cylinders called planet gears [1]. The planet gears enhance the modulating effect and hence the torque density, since they themselves are a source of magnetomotive force (MMF). Davey’s team reported 79% increase of torque density over a conventional coaxial gear of comparable dimension [1]. In the operation of the RCPG, the planet gears move to new angular position corresponding to each updated relative position of the two rotors. It is a prerequisite to know these angular positions of planet gear for the calculation of the performance such as torque. Since the planet gears are unconstrained, they move to zero-torque positions. However, finding these positions is mathematically a difficult optimization with a large number of unknowns and strong internal coupling. A custom optimization algorithm combining splines, quadratic interpolation and response surface method was implemented for these positions that minimize the maximum torque on the planet gears. This algorithm was proved to be the most effective though it converged more slowly than the other algorithms that Davey’s team had tried [1]. Alternatively, Wang *et al* proposed that the total magnetic energy stored in the gear should be minimum (or maximum magnetic coenergy) when all the planet gears settle in their equilibrium positions [2]. Wang’s team found the positions of planet gear corresponding to the minimum stored magnetic energy, by using gradient-based Broydon–Fletcher–Goldfarb–Shanno (BFGS) and three preconditioning techniques, respectively. The BFGS algorithms converge apparently faster than Davey’s custom algorithm. However, two of the preconditioning techniques need flux-tracing finite element (FE) calculation with or without non-magnetized cylinders. The other technique seems analytical and consequently saves the preconditioning cost, but it was not described in detail [2]. This digest proposes a BFGS algorithm with an alternative analytical preconditioning technique for the angular positions of planet gear corresponding to the minimum stored magnetic energy. The algorithm can quickly find these angular positions for each relative position of the two rotors in the operation of the gear.

II. Description of Proposed Preconditioned BFGS The proposed preconditioning technique estimates the angular position of a planet gear depending on the polarities of the closest neighboring magnets on the rotors. This estimate can be easily formulated if the two closest neighboring magnets have different polarity, but it is difficult for some special relative positions of the planet gear and the two rotors. For example, the closest neighboring magnets have same polarity, as shown in Fig. 1 (a) and (b), or the distances from the planet gear to the two neighboring magnets on a rotor are equal, as shown Fig 1 (c) and (d). The angular position of planet gear (given by the direction of polarity, shown as the red arrow in Fig. 1) in each special case is found by the BFGS without preconditioning. The preconditioned BFGS relies on this result to formulate the presetting of angular position for each special case in the performance calculation of RCPG. The calculation of gradient in the BFGS algorithm was also improved to ensure the convergence to the global optimum. The formulation of the proposed preconditioning and the improved gradient calculation will be given in the full paper.

III. Performance Calculation With Preconditioned BFGS The proposed preconditioned BFGS was used to calculate the torque for each relative position of the planet gears and the rotors in the running of a magnetic gear with 4 inner poles, 40 outer poles and 22 planet gears. Randomly initialized and flux-tracing preconditioned BFGS algorithms were also used respectively to calculate the torque. The latter algorithm makes two-dimensional (2-D) FE calculation of the flux distribution in the magnetic gear with the conventional modulators of the same dimension as the planet gears, and initializes each planet gear’s angular position for the BFGS optimization according to the field direction in the center of the corresponding conventional modulator. Fig. 2 (a) compares the performances of the three BFGS algorithms for the optimization at a certain relative position of the planet gears and the rotors.

The randomly initialized, flux-tracing preconditioned and proposed preconditioned BFGS algorithms made 21, 16 and 14 iterations, and calculated the stored magnetic energy by FE for 474, 348 and 279 angular position cases in total, respectively, until the convergence. The running of the magnetic gear with different initial angles of the inner rotor was simulated by FE and the proposed preconditioned BFGS. Fig. 2 (b) shows the torque-initial-angle curve given by this simulation.

IV. Conclusion This digest proposes an analytically preconditioned BFGS algorithm for the performance calculation of RCPG. With the preset angular positions of planet gear, the BFGS converges fast and significantly saves the cost for the FE simulations of the full-range operation of RCPG. The full paper will discuss the application of other algorithms to the analysis of RCPG.

[1] K. Davey, *et al*, IEEE Transactions on Industry Applications, vol. 52, no. 3, pp. 2253–2260 (2016) [2] R. Wang, *et al*, IEEE Magnetics Letters, vol. 7, Art. no. 1303805 (2016)

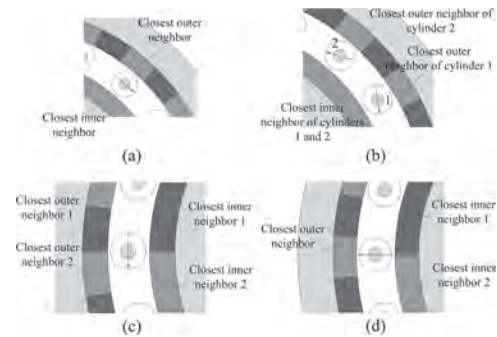


Fig. 1. Special preconditioned cases

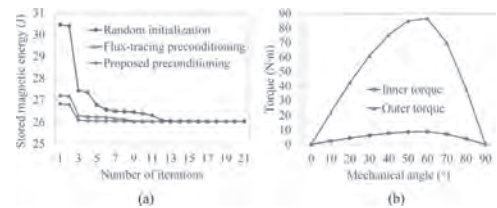


Fig. 2. Performances of BFGS algorithm and torque capacity curve.

BF-06. Analytical Modeling of an Axial Flux Magnetic-Gearing Double-Rotor Machine With Interior-Modulating-Rotor.

J. Lang¹, C. Tong¹, J. Bai¹, P. Zheng¹ and J. Liu¹

1. Electrical Engineering, Harbin Institute of Technology, Harbin, China

Abstract— Axial flux magnetic-gearing double-rotor machines (AMGDRMs) are characterized as a potential core component of the power splitting system in hybrid electric vehicles (HEVs). Conventional AMGDRMs suffer from low mechanical strength due to high axial magnetic force. In this paper, an interior-modulating-rotor axial flux magnetic-gearing double-rotor machine (IMR-AMGDRM) is proposed to solve this problem. An analytical model of the IMR-AMGDRM is proposed to predict the magnetic field distribution and electromagnetic performances. Since analytical model is based on 2-D geometry, a 2-D approximation of IMR-AMGDRM which has similar output performance to 3-D finite element analysis (FEA) is presented based on the permanent magnet (PM) magnetic energy equivalent principle. Utilizing subdomain method, the magnetic field distribution and electromagnetic performances are calculated. Finally, the accuracy of the proposed analytical model is validated by 3-D FEA. Index Terms—Analytical model, axial flux, magnetic-gearing machine, double-rotor machine. I. Introduction Axial flux magnetic-gearing double-rotor machines (AMGDRMs), which enable high torque density, have been considered a promising candidate for power splitting in hybrid electric vehicles (HEVs) [1]. However, conventional AMGDRMs suffer from low mechanical strength due to high axial magnetic force. To enhance mechanical strength, an interior-modulating-rotor axial flux magnetic-gearing double-rotor machine (IMR-AMGDRM) which can reduce axial magnetic force dramatically is proposed in this paper. Fig. 1 (a) and (b) illustrate the configuration of the proposed IMR-AMGDRM. As axial flux type machine, IMR-AMGDRMs have complex 3-D magnetic circuits. 3-D finite element analysis (FEA) can offer accurate results by taking into account the nonlinear factors such as magnetic saturation and flux leakage. But the major drawback of 3-D FEA is serious time cost. Analytical model which is much lower time-consuming provides an alternative for electromagnetic performance prediction in the initial design procedure. In this paper, an analytical model of the IMR-AMGDRM is proposed. The geometry of analytical model is derived based on PM magnetic energy equivalent principle to guarantee similar output performance to 3-D FEA. The solution to analytical model is calculated by subdomain method. To evaluate the accuracy of the proposed analytical model, the results computed by analytical model and that of 3-D FEA are compared. II. Configuration of IMR-AMGDRM In conventional configuration, the inner and outer rotors are the permanent magnet (PM) rotor and the modulating rotor, respectively. Since the modulating rotor is closer to the PM rotor than stator, the modulating rotor suffers from high axial magnetic force. Furthermore, the modulating rotor is hollow and thus the low mechanical strength of modulating rotor becomes the major drawback of conventional configuration [1]. To solve this problem, the IMR-AMGDRM which switches positions of the PM rotor and the modulating rotor is proposed. In interior-modulating-rotor configuration, as shown in Fig. 1 (a) and (b), the PM rotor is between the modulating rotor and stator, i.e. the inner and outer rotors are the modulating rotor and the PM rotor, respectively. Owing to that the PM rotor suffers from reverse axial magnetic forces from both sides simultaneously, the total axial magnetic force is dramatically reduced. Hence, although the outer rotor is hollow in both configurations, the axial magnetic force of interior-modulating-rotor configuration is significantly decreased, leading to higher mechanical strength and reliability. III. Geometry of 2-D Approximation Generally, the unrolled section of axial flux machine at mean radius is used as 2-D approximation. However, few references are found to evaluate the electromagnetic performance equivalence of such approximation. To make the electromagnetic performance of 3-D model and 2-D approximation equal, the amount of magnetic energy of the PM should remain unchanged after approximation, i.e. PM magnetic energy equivalent principle [2]. A 2-D approximation of IMR-AMGDRM which has identical output performance is presented by using PM magnetic energy equivalent principle. IV. Analytical Calculation of IMR-AMGDRM The proposed analytical model is illustrated in Fig. 1 (c). It can be seen that the model consists of four subdomains. Region i , I, II and III represent the i th slot of the modulating rotor, the inner air gap, the PM rotor and the outer air gap, respectively. Utilizing subdo-

main method, the magnetic field distributions in the inner and outer air gaps are obtained by the solution of Laplace's and Poisson's equations. Then, the electromagnetic performances such as no-load back EMF, torque and axial force can be derived from the calculated magnetic field distributions. Comparisons of computation accuracy between analytical model and 3-D FEA is shown in Fig. 2. As can be observed, the results of analytical model are well consistent with that of 3-D FEA, validating the proposed method.

[1] M. Q. Wang, D. C. Tong and P. Zheng, *IEEE Trans. Ind. Electron.*, vol. 66, no. 1, pp. 806-817(2019). [2] Kim J S, Lee J H, Song J Y, and Kim D W, *IEEE Trans. Magn.*, vol. 53, no. 6, 8105304(2017).

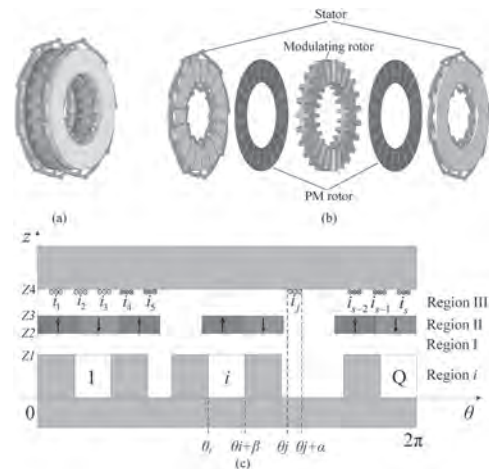


Fig. 1. IMR-AMGDRM. (a) Overall view of configuration. (b) Exploded view of configuration. (c) Analytical model.

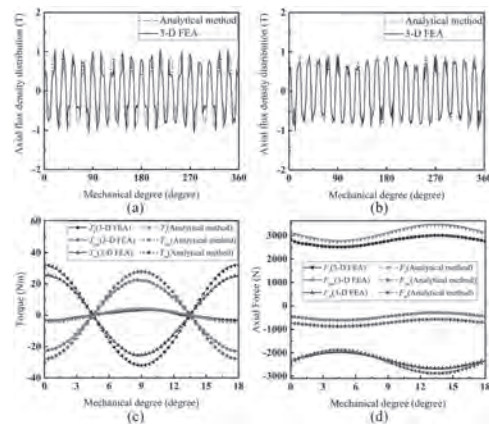


Fig. 2. Comparisons between analytical model and 3-D FEA. (a) Axial flux density distribution in the inner air gap. (b) Axial flux density distribution in the outer air gap. (c) The static torque characteristic. (d) The static axial force characteristic.

BF-07. Optimization Design of Performance and its Cost of a Novel Magnetic Lead Screw by Combination of Different Permanent Magnet Materials.

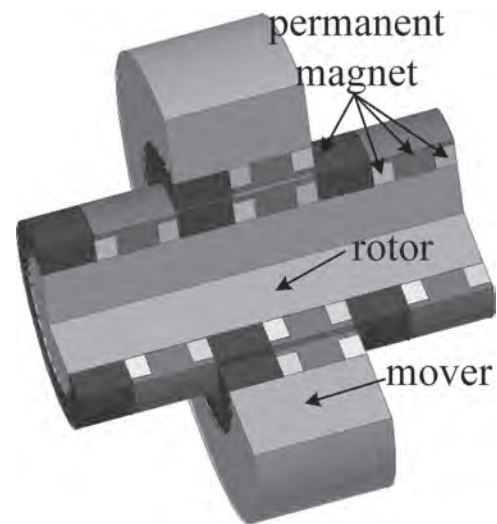
Y. Liu¹, H. Yu¹, Y. Wang¹, Q. Zhang¹ and M. Chen¹

1. College of Electrical Engineering, Southeast University, Nanjing, China

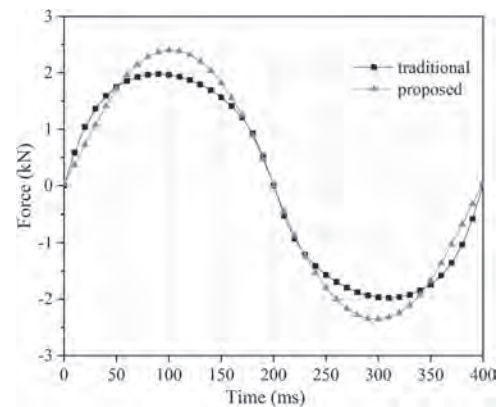
Abstract — Magnetic lead screw (MLS) is a new type of linear actuator with high force density. Its output force depends not only on the arrangement of the permanent magnet (PM), but also on the materials used for the PMs, and the different materials of the PM directly affect the cost of the MLS. Therefore, based on this, a proposed MLS is given based on the combination of PM structure and magnetization direction and the combination of different PM materials. Compared with the traditional structures, it can not only improve the output force of the MLS, but also reduce the cost of the MLS. The results show that the size of air gap, the size of PM and the proportion of different materials combinations have great influence on the performance and cost of MLS. Finally, the performance of the proposed structure is compared with the traditional structures. The results show that the output force is increased by 21.5% and the cost is reduced by 21.4% under the same volume of MLS and PM. Index Terms — MLS, PM structure, magnetization direction, output force, cost. I. Introduction In recent years, as a new type of high force density linear actuator, magnetic lead screw (MLS) has been widely used in many fields, ranging from CNC machine tools, wave power generation to artificial heart [1-3]. MLS is similar to mechanical lead screw, which can convert linear motion into rotary motion, and vice versa. Compared with mechanical lead screw, MLS has the characteristics of inherent overload, minimum friction and low maintenance [4]. But for the existing applications and MLS structure, in addition to its output force is still low, there is also a problem of high cost caused by the use of high-performance PM materials in order to improve the output force of the MLS. Based on the above problems, a proposed MLS is given based on the combination of PM structure and magnetization direction and the combination of different PM materials, which improves the output force and decreases its cost. Detailed proposed structure introduction and operation principle are introduced in the second part. In the third part, the influence of the main parameters on the output force and cost is designed and optimized, and finally the size parameters of the structure are given. Finally, the performance of the proposed model is simulated and compared with the traditional structures to verify the superiority and economy of the proposed model. II. Structure and Operation Principle Compared with the traditional MLS structures, the proposed structure is shown in Fig. 1. The blue block and red block are radially magnetized PMs, in which the blue block is rectangular shape and the red block is salient pole shape, and both are made of NdFeB material. Green and yellow block are axially magnetized PMs with rectangular shape, and are made of other materials. Compared with the traditional halbach magnetizing array, this structure has higher output force and lower cost, and the structure is not difficult to process. The detailed operation principle of MLS is introduced in this paper. Fig.1. The proposed model. III. Design and Optimization The main design point of MLS is how to design the 3D structure of PM. There are three kinds of processing and installation structures, which are cylindrical, spiral and discrete surface mounted. In this part, the three structures will be compared in detail and the advantages and disadvantages of the description, and finally choose the appropriate shape for processing. After the structure is determined, the structure of the PM is optimized, mainly discussing the influence of the size of the air gap and PM on the output force and its cost of the MLS. In addition, the combination of different materials also has a great impact on the performance and cost of MLS, such as NdFeB, Ferrite, SmCo and Alnico. Finally, the best set of structural parameters of the MLS is obtained through the optimization, and the specific description is shown in the full text. IV. Results and Conclusion After design, optimization and analysis, the output force of the proposed model is shown in Fig. 2. It can be seen that the output force has increased by 21.5%. Moreover, after calculation, the cost of the proposed MLS is reduced by 21.4%, and the weight of the proposed MLS is also reduced by 8.6% due to the use of the combined materials of NdFeB and Ferrite, in which the proportion of NdFeB is 75.9% and Ferrite is 24.1%. In particular, limited by the number of words and pictures, we choose the traditional MLS for comparison, in which the PMs are rect-

angular and are made of NdFeB material. Fig.2. Performance comparison of the proposed model.

[1] R. K. Holm, N. I. Berg, M. Walkusch, P. O. Rasmussen and R. H. Hansen, "Design of a Magnetic Lead Screw for Wave Energy Conversion," in IEEE Transactions on Industry Applications, vol. 49, no. 6, pp. 2699-2708, Nov.-Dec. 2013. [2] N. I. Berg, R. K. Holm and P. O. Rasmussen, "Theoretical and Experimental Loss and Efficiency Studies of a Magnetic Lead Screw," in IEEE Transactions on Industry Applications, vol. 51, no. 2, pp. 1438-1445, March-April 2015. [3] J. Ji, Z. Ling, J. Wang, W. Zhao, G. Liu and T. Zeng, "Design and Analysis of a Halbach Magnetized Magnetic Screw for Artificial Heart," in IEEE Transactions on Magnetics, vol. 51, no. 11, pp. 1-4, Nov. 2015, Art no. 8108604. [4] Z. Ling, J. Ji, J. Wang and W. Zhao, "Design Optimization and Test of a Radially Magnetized Magnetic Screw with Discretized PMs," in IEEE Transactions on Industrial Electronics, vol. 65, no. 9, pp. 7536-7547, Sept. 2018.



The proposed model



Performance comparison of the proposed model

BF-08. Dinamyc Magnetic Gear: Different Topologies and Magnetization and Demagnetization Assessment.

K. Marques de Andrade Júnior¹, C.G. da Costa Neves², A.F. Flores Filho³ and G. Teixeira de Paula¹

1. Universidade Federal de Goiás Escola de Engenharia Eletrica Mecanica e de Computacao, Goiania, Brazil; 2. Universidade Federal de Pelotas, Pelotas, Brazil; 3. Universidade Federal do Rio Grande do Sul, Porto Alegre, Brazil

In the global conjuncture regarding the searching for more efficient equipment and machines and renewable energy resources, the magnetic gear is attracting more attention since this type of system can improve the efficiency of any mechanical torque transmission system when compared to the traditional gear. The magnetic gear is present in numerous applications in the modern life that requires a high precision and efficiency (over 99%), low maintenance, such as in traction systems, sanitation, industry applications and robotics. All these advantages presented in the magnetic gear is due to the contactless rotors that are responsible for the transmission of torque. The torque transmission is accomplished thanks to the interaction between the magnets present in the rotors and the modulators present in the contactless interface between the rotors. On the other hand, magnetic gears generally have only one input/output speed ratio (gear ratio) [1]-[3] and is quite expensive due to the permanent magnets, usually NdFeB, in both rotors. In order to overcome the high cost of using permanent magnet in both rotors, here, the authors propose two combination of the usage of low coercivity magnets: the first one is the usage of these magnets in both rotors; and the second one is the usage of these magnet in only one rotor. Furthermore, a magnetizing winding is introduced in the modulators to make the low coercivity magnets capable of been magnetized, demagnetized and re-magnetized according to the gear operation point and torque demand. The modulators are kept stationary and their geometry reshaped in order to accommodate the magnetizing winding. This way, a more flexible magnetic gear is achieved and can operate within a wide range of torque and speed and with a lower production cost despite the more complex operation (online magnetization and demagnetization process) and the usage of copper. The demagnetization and magnetization process can be done in two different moments: before the gear starts its operation, i.e., when the gear is stopped and the position of the rotors related to the position of the magnetizing field is well known; or, while the gear is running, which requires the orientation of the magnetizing field and the magnet field to proper magnetization or demagnetization [4]. The later one is the most complex one and requires an encoder or a set of hall sensor which increase the cost of the magnet gear. Last but not the least, the results of the dynamic behavior of the proposed gears are compared to the conventional one with permanent magnet showing that for low to medium torque applications a compact gear using low coercivity magnets can be employed. A full detailed assessment of the magnetization, demagnetization and re-magnetization has been carried out and demonstrated the suitability of the proposed techniques. Detail analysis, discussions and results will be given in the full paper which will describe the magnetization and demagnetization process along with the proposed gear topologies.

[1] M. Chen, K. T. Chau, W. Li, C. Liu and C. Qiu, "Design and Analysis of a New Magnetic Gear With Multiple Gear Ratios", in *IEEE Transactions on Applied Superconductivity*, vol. 24, no. 3, p. 1-4, (2014). [2] D. Fodorean, "State of the art of magnetic gears their design and characteristics with respect to EV application" in Modeling and Simulation for Electric Vehicle Applications, Rijeka, Croatia, InTech, (2016). [3] Neves, C.G.C.; Flores, A.F.F. "Magnetic Gearing Electromagnetic Concepts. Journal of Microwaves, Optoelectronics and Electromagnetic Applications", Vol. 16, p.108-119, (2017). [4] H. T. Anh and M. Hsieh, "Analysis of Local Demagnetization in Magnet for PM-Assisted Synchronous Reluctance Motors.," 2018 IEEE International Magnetics Conference (INTERMAG), Singapore, (2018).

BF-09. Analysis of Magnetic Coupling Between Armature and Field Windings of Variable Flux Reluctance Machine.

H. Gurleyen¹

1. Usak Universitesi, Usak, Turkey

I. INTRODUCTION Non-permanent magnet machines are having growing interest recently due to the volatility of permanent magnet (PM) prices. Variable flux reluctance machine (VFRM) is a non-permanent magnet machine and it is a candidate for high-performance applications such as electric vehicles [1,2]. There are several slot/pole combinations of VFRM, such as 6/4, 6/5, 6/7, and 12/10 [3,4]. The 6/4 topology has a large torque ripple [5]. The 6/5 and 6/7 topologies have low torque ripple, but they have an unbalanced magnetic force (UMF) issue which causes mechanical stress and acoustic noise due to the odd rotor poles [6]. The 12/10 topology has a low torque ripple and balanced UMF. Although the structure of the VFRM is similar to the switched reluctance machine (SRM), VFRM has DC winding in the stator as well as three-phase AC windings. Therefore, the back-EMF waveform of the armature winding is sinusoidal. The control of the VFRM is easier than SRM due to the sinusoidal back-EMF. There is a magnetic coupling between armature and field winding because they have a common flux path as seen in Fig. 1. However, the field winding is fed by a DC current while armature windings have an AC current. In this study, the magnetic coupling between armature and field winding is analyzed and how VFRM can operate having DC and AC windings is explained. II. FLUX LINKAGE ANALYSIS OF FIELD WINDING Every tooth of VFRM has a field winding as shown in Fig. 1. Blue ones are field windings, red, green and yellow ones are armature windings. Firstly, the field winding is separated and called DC1, D2, D3, DC4, DC5, and DC6. Field windings are excited by DC current while armature windings are not excited. The flux of a single excited magnetic circuit is determined by Eq. (1). $\theta = NI/R(\theta)$ (1) Where N is turns number, I is current, R is magnetic reluctance and θ , is rotor position. The magnetic reluctance of the motor depends on rotor position because effective airgap changes with rotor position. Flux linkages of DC field windings and resultant flux linkage of field winding are obtained using the FEA, as shown in Fig. 2. Reluctance function of DC1 winding is obtained by FFT analysis of flux linkage, turns number and DC current. $R_{DC1} = R_0 + \sum R_n \sin(n\theta_r + \alpha)$ (2) Flux linkage of DC1 winding is obtained using Eq. 1 and Eq. 2. Each of stator and rotor poles are not aligned at the same time, so there is a phase difference between DC windings. Therefore, the flux linkage of the DC2 winding is given in Eq. 4. $\lambda_{DC1}(\theta_r) = \lambda_0 + \sum \lambda_n \sin(n\theta_r + \alpha)$ (3) $\lambda_{DC2}(\theta_r) = \lambda_0 + \sum \lambda_n \sin(n\theta_r + \alpha + \pi/3)$ (4) Eventually, resultant flux linkage of when all DC windings are connected series is obtained by Eq. 5. $\lambda_f(\theta_r) = 6\lambda_0 + \sum \lambda_n \sin(n\theta_r + \alpha) + \sum \lambda_n \sin(n\theta_r + \alpha + \pi/3) + \sum \lambda_n \sin(n\theta_r + \alpha + 2\pi/3) + \sum \lambda_n \sin(n\theta_r + \alpha + 3\pi/3) + \sum \lambda_n \sin(n\theta_r + \alpha + 4\pi/3) + \sum \lambda_n \sin(n\theta_r + \alpha + 5\pi/3)$ (5) $\lambda_f(\theta_r) = 6\lambda_0$ (6) As shown in Fig. 2, all of the AC components eliminate each other and the resultant flux linkage has only a DC component. In this analysis, armature windings are not excited. Also, both field and armature windings are excited and flux linkage of the field winding is obtained by FEA, core material is assumed it has infinite magnetic permeance. Although magnitudes of the harmonic orders are changed, all AC components are eliminated and resultant flux linkages consist of DC components. Flux linkage of field winding has little harmonic if core material is steel, due to the magnetic saturation and leakage flux. These results could not be presented in this digest due to the figure limits. However, all of the results will be given in the final paper. III. CONCLUSION VFRM has DC field winding and armature windings in the stator. Although armature and field windings have a common flux path and magnetic coupling, field winding can be excited by DC current. Thus, the flux linkage of the DC field winding is analyzed while armature windings are excited by AC current. The field winding is separated, and flux linkages of every winding are obtained by FEA. Every winding has a DC biased AC flux linkage. However, all DC windings are connected series, AC components of resultant flux are eliminated. Eventually, field winding has only a DC component even if there is a magnetic coupling between armature and field windings. The magnetic circuit of analysis and results at full load will be given in the final paper due to the figure limits of the digest.

1. T. Raminosa, D. A. Torrey and A. M. El-Refae, IEEE Trans. on Industry Applications, Vol. 52, p. 2129, (2016) 2. T. Raminosa, A. M. El-Refae and D. A. Torrey, IEEE Trans. on Industry Applications, Vol. 53, p. 3496, (2017) 3. X. Liu and Z. Q. Zhu, IEEE Transactions on Magnetics, vol. 49, p. 3020 (2013) 4. J. T. Shi, X. Liu and Z. Q. Zhu, IEEE Transactions on Magnetics, Vol. 50, (2014). 5. J. Feng, L. Huang and Z. Q. Zhu, IEEE Transactions on Energy Conversion, Vol. 34. p.1135 (2019) 6. X. Liu and Z. Q. Zhu, IEEE Transactions on Industry Applications, Vol. 50. p. 3675 (2014)



Fig. 1 Structure and windings of 12/10 VFRM

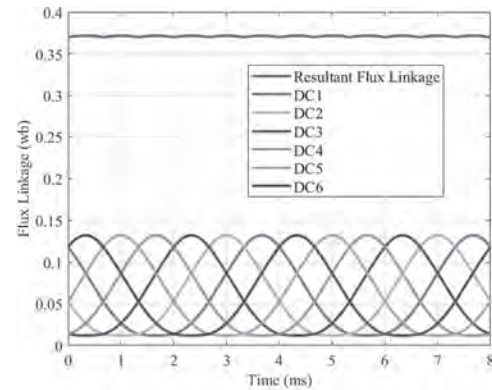


Fig. 2. Flux linkage variation of DC windings

BF-10. Investigating the Performance Potential of High Gear Ratio Coaxial Magnetic Gears.

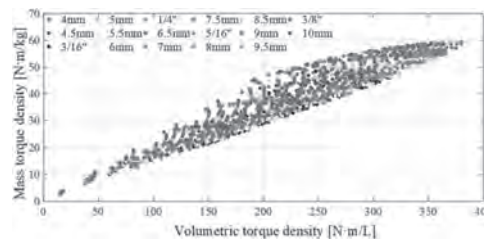
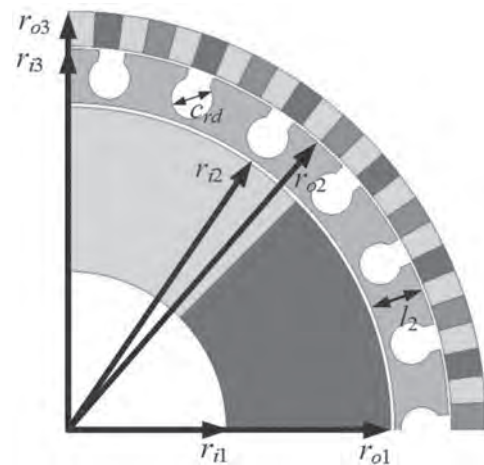
H. Wong¹ and J. Bird¹

¹ Maseeh College of Engineering and Computer Science, Portland State University, Portland, OR, United States

Coaxial magnetic gears (MGs) create non-contact speed change by using a ferromagnetic slotted rotor between an inner and outer magnetic rotor with dissimilar magnet pole-pairs. In 2001, Atallah et al. demonstrated that a coaxial surface mounted permanent magnet MG with a gear ratio $G_r = 5.5$, could be designed to operate with a peak volumetric torque density of 100Nm/L [1]. This is approximately twice the continuous operating torque density of a motor. If a higher gear ratio is utilized, then the motor size can be reduced thereby increasing the overall performance of a magnetically geared drivetrain. To-date most studies have concluded that coaxial MGs are only capable of operating at a high volumetric torque density at a relatively low gear ratio, typically less than 1:8 [2]-[5]. The reason for the reduction in torque density at higher gear ratios is explained by the increased discrepancy between the inner and outer rotor magnet pole count as well as the pole pitch. For instance, Gouda [2] conducting a limited sweep analysis in which the magnet thickness and modulation thickness was varied and concluded that the peak volumetric torque density was close to a $G_r=5$ gear ratio and the torque density greatly reduced with increased gear ratios. More recently Gardner [3] came to the same conclusion. Gardner studied three different coaxial MG designs and computed that the lowest gear ratio design, $G_r = 4$, had a significantly higher torque density. In many applications a high gear ratio is required. In order to design a coaxial MG with a high gear ratio multistage MG designs must currently be utilized [6]. However, using a multistage MG complicates the mechanical structure and decreases the torque-per-kilogram of the rare earth permanent magnets. The object of this paper is to further investigate the performance of higher gear ratio designs, $G_r > 20$. In this paper the authors demonstrate, for the first time, that a coaxial MG can be simultaneously designed with both a high gear ratio, $G_r > 20$, and high torque density. In order to do this a complete design sweep of three key radial geometric sweep parameters (r_{i1} , r_{o1} , l_2) is conducted using the MG design illustrated in Fig. 1. In this MG design the laminated (M19) modulator is supported using an inner bridge and G11 Garolite rods (not shown). A pole-slot combination defined as $(p_1, n_2, p_3) = (1, 22, 21)$ is used to demonstrate the performance capability. When the outer rotor is stationary, a gear ratio of $G_r = n_2/p_1 = 22$ is obtained. In the design study the outer rotor is composed of a four-segment Halbach array (N48) rotor structure and the inner rotor is composed of a single pole-pair created by a single diametrically magnetizing NdFeB (N48) cylinder magnet. Note that the torque ripple is mitigated by choosing a pole-slot combination that minimizes the greatest common divisor (gcd) defined as: $C_T = \text{gcd}(2p_1, n_2)$ [7]. However, when $C_T = 1$, an odd number modulation rotor slot number is obtained but this then creates a large radial force on the cage rotor due to the unsymmetrical slot number. Thus, the design with a $C_T = 2$ was selected. In the illustrated design a 2-D finite element analysis model was used in which the outer rotor radius was fixed at $r_{o3} = 60\text{mm}$ and the axial stack length was $d = 60\text{mm}$. The active material mass and volumetric torque density performance for the design example is shown in Fig. 2. Fig. 2 was created by simultaneously sweeping the three radial parameters. The inner rotor values were swept across values: $(r_{i1}, r_{o1}) = ([8, 10, \dots, 30], [30, 32, \dots, 50])$ and the cage rotor radial thickness was simultaneously swept across the range shown in the legend of Fig. 2. The resulting pareto-front is evident. The peak volumetric torque occurred when $(r_{i1}, r_{o1}, l_2) = (8\text{ mm}, 44\text{ mm}, 5/16")$ and this yielded a peak computed volumetric and mass torque density of $T_v = 380.5\text{ Nm/L}$ and $T_m = 59.4\text{ Nm/kg}$ respectively. The peak torque for the design was $T = 258.2\text{ Nm}$. The volumetric and mass torque density were computed using $T_v = T / (d\pi r_{o3}^2)$ and $T_m = T / (m_m + m_s)$, where $m_m = \text{mass of the magnets}$ and $m_s = \text{mass of the laminations}$. By studying Fig. 2, it can be seen that a design can be obtained that has an impressively high torque density whilst still having a high gear ratio. The authors believe this has not been demonstrated before. In order to understand the reason for this high performance, the full paper presents a comparison in performance for the lower performing high gear ratio design presented in [2] – [5] with the MG design presented here. A field and torque harmonic analysis are used to demonstrate that whilst a higher gear ratio does

lead to a lower torque density, if a complete sweep analysis is used, then the reduction in torque density performance with a high gear ratio is much less than previously demonstrated.

[1] K. Atallah and D. Howe, IEEE Trans. Magn., vol. 37, no. 4, p. 2844, July 2001. [2] E. Gouda, S. Mezani, L. Baghli, IEEE Trans. Magn., vol. 47, no. 2, p. 439, Feb. 2011. [3] M. C. Gardner, M. Johnson and H. A. Toliyat, 2018 IEEE Energy Conv. Congress and Expo., Portland, OR, 2018, p. 5005. [4] D. J. Evans, Z. Q. Zhu, 2011 IEEE Intern. Elect. Mach. Drives Conf., Niagara Falls, ON, 2011, p. 1403. [5] E. Park, C. Kim, S. Jung, Intern. Conf. Elect. Mach. Sys., Jeju, Korea, p. 2529, Oct. 7-10, 2018. [6] M. C. Gardner, M. Johnson, H. A. Toliyat, IEEE Trans. Energy Conv. Vol. 34, no. 2, p. 665, June 2019. [7] G. Jungmayr, J. Loeffler, B. Winter, IEEE Trans. Ind. App., vol. 52, no. 5, p. 3822, Sept.-Oct. 2016.



BF-11. Design and Analysis of Dual-Stator Flux-Switching Permanent Magnet Machine-Compressor With Asymmetric Rotor Poles.

B. Li¹, J. Zhu², C. Liu¹ and Y. Li¹

1. Hebei University of Technology, Tianjin, China; 2. The University of Sydney, Sydney, NSW, Australia

I. Introduction Recently, compressed air has been used in many applications and compressors tend to high energy efficiency and high-power density, which becomes a hot issue and draws more and more interest. As a powerful candidate, permanent magnet (PM) machine including PM located on rotor and stator is an excellent candidate for the compressors [1]. However, due to the increase of rotation speed and rotor diameter, the rotor integrity for PM located on rotor becomes a critical issue. Although bandings have been installed in rotor, they inevitably increase the air-gap width and rotor loss and hence reduce the torque capability of the machine. Meanwhile, the electrical machines driven compressors has challenges in machines cooling, sizing and loss. The PM located on the stator, namely the flux-switching PM machines (FSPMMs), have been an intense topic of research for the high-speed compressors. And the torque density is comparable to the conventional rotor-PM machines. By combining the armature winding and excitation source in the stator, its rotor is a robust steel sheet lamination, a passive single material and salient pole rotor, making it inherently suitable for high-speed applications. Hence, there is a feasible solution to integrate the machine with the compressor, which combines the function of motor drive and compressor. In additional, the self-cooling capability of this topology is another important advantage due to its forced convection flow to the stator, rotor, magnet and winding generated by the rotor rotation, especially in high power density applications, which is robust in harsh environment. Even though the conventional topology (12/10 FSPMMs) can achieve more symmetrical phase back-EMF waves, it is not optimistic in terms of core loss under high-frequency excitation. A feasible design with the lowest possible slot-poles (6/4 FSPMMs) for three-phase windings is proposed by Li *et al.* [2], which possesses the lowest fundamental frequency for the given speed. The purpose of this paper gives a suitable structure for high-speed axial flow compressors based on the topology of FSPM machines. In order to minimize the size of compressor system, a design of dual-stator 6/4 FSPM machine-compressor is proposed. The electromagnetic performance of C-core and E-core topology is calculated and analyzed by the 3-D finite element analysis (FEA). The design is electromagnetically and aerodynamically coupling since the structure of rotor has significant effects on both the machine and compressor. For better fitting high-speed operation and generating compressed air, the rotor with asymmetric pole-width is used and optimized. II. Machines Topology The FSPM machines are attractive in ultra-high-speed application due to its robust rotor. A specification of 10 kW, 30 krpm dual-stator FSPM machines is designed and analyzed by 3-D FEA. For given speed, the dual-stator structure is a promising solution to minimize the fundamental frequency of the source system. Fig. 1 (a) and (b) show the topology of C-core and E-core stator of FSPM. The electromagnetic performance of two stator topology is analyzed and compared such as average torque, torque ripple and over load capability. As shown in Fig. 1 (c), the front rotor is offset-ed by 45° mechanically with respect to the rear rotor and the even harmonics are counteracted in the total flux linkage based on this topology. In order to better air flow, the asymmetric rotor poles are used in the integrated 6/4 FSPM machines. The parameters of the rotor are optimized in terms of electromagnetics and aerodynamics. III. Results The design of integrated machines-compressor based on the lowest slot-pole numbers is proposed. By the FEM analysis, the electromagnetic and aerodynamic performance of the proposed machines is calculated and compared. Fig. 2 (a) and (b) show the 3-D flux density distribution of the C-core and E-core 6/4 FSPM machines at no-load condition. Fig.2 (c) show the torque characteristic of two FSPM machines with different stator cores at on-load condition. The torque ripple of the machine with E-core stator reduce 25.7% than the one with C-core stator. The optimized E-core FSPM machine-compressor is verified to generate better torque characteristic and overload capability. Furthermore, after optimizing rotor topology, the E-core stator FSPM machines is a good candidate for axial-flow compressors, especially in higher rotation speed.

[1] Gerada D, Mebarki A, Brown N L, et al. High-speed electrical machines: Technologies, trends, and developments[J]. IEEE Transactions on Industrial Electronics, 2013, 61(6): 2946-2959 [2] Liu M, Li Y, Sixel W, et al. Design and Testing of Low Pole Dual-stator Flux-Switching Permanent Magnet Machine for Electric Vehicle Applications[J]. IEEE Transactions on Vehicular Technology, 2019, PP(99):1-1.

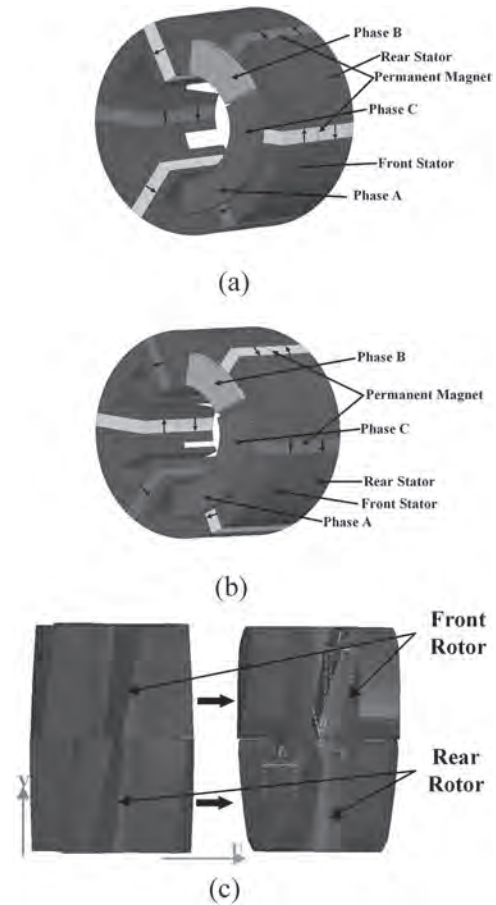


Fig. 1. Topology of 6/4 FSPM machines. (a) C-core dual-stator. (b) E-core dual-stator. (c) Design parameters of rotor.

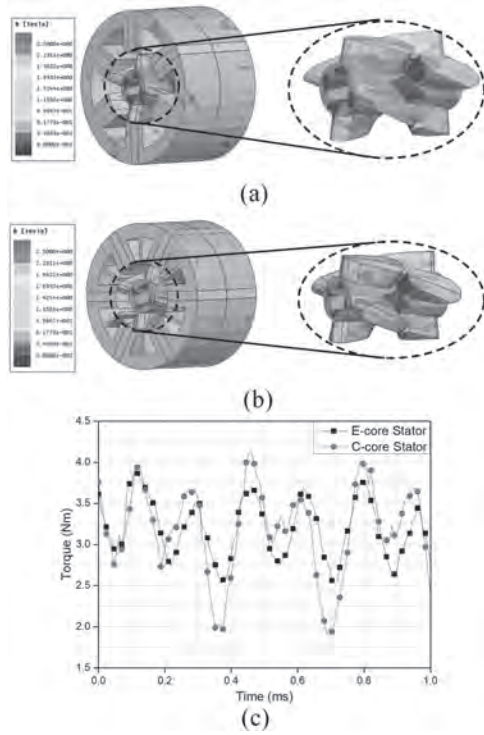


Fig. 2. The performance characterization of the FSPM machines. (a) Flux density distribution of C-core FSPMMs at no-load condition. (b) Flux density distribution of E-core FSPMMs at no load condition. (c) The torque characteristic of the machines with different stator cores.

BF-12. A Transversely-Dislocated Brushless Double-Rotor Machine Based on Magnetic-Field Modulation for Contra-Rotating Propeller.

Y. Wang¹, Y. Sui¹, J. Liu¹, G. Liu¹, P. Zheng¹ and L. Sun¹
 1. School of Electrical Engineering and Automation, Harbin Institute of Technology, Harbin, China

The contra-rotating propeller (CRP), a complex propulsion device that produces thrust by two oppositely rotating propellers, can be used for applications like unmanned underwater vehicles, power generations and aero propulsions [1]. The CRP propulsion system requires two output shafts with equal and opposite torques. Nowadays, there are three ways to achieve the above function. Compared with the schemes which are driven by two independent machines or one conventional machine connected to gear box, the contra-rotating double-rotor machine (CRDRM) directly drives the CRP, which is the most competitive scheme due to the advantages like as high transmission efficiency, low noise and compact volume. However, the existing CRDRM schemes have several inevitable problems. Due to the existence of electric brushes, slip rings and rotating windings, the CRDRM scheme which is achieved by the coaxial rotation of armature winding and rotor has problems of poor reliability and difficult dynamic balance. Moreover, the heat dissipation becomes more difficult when the rotating winding is placed inside the machine. The other kind of CRDRMs adopts the way of double-rotor and stator with two sets of windings in the middle of two rotors, which has the severe heat dissipation problems [2]. Therefore, the research of the brushless CRDRM with easier heat dissipation is a main developed direction in CRP propulsion applications. In this paper, a transversely-dislocated magnetic-field modulated brushless double-rotor machine (TDMFM-BDRM) is proposed to solve the above problems. The TDMFM-BDRM is composed of a stator, a transversely-dislocated modulating (TDM) rotor and a permanent-magnet (PM) rotor, as shown in Fig. 1 (a)-(b). The stator ring windings, which is similar with the tubular linear machine, are distributed along the axial direction. The spoke-type PMs of the PM rotor are distributed along the circumferential direction. Moreover, the special structure of the TDMFM-BDRM is its TDM rotor, as shown in Fig. 1 (c)-(d), which is composed of the magnetic blocks and non-magnetic support. The magnetic blocks of one modulating group are regularly distributed along the oblique direction, and the number of modulated groups is equal to the pole-pair number of PMs. The proposed TDMFM-BDRM combines the structural characteristics of transverse-flux machines and the modulated theory of magnetic-field modulated machines. Therefore, the proposed TDMFM-BDRM has the following advantages: (1) it has high reliability due to the elimination of electric brushes and slip rings; (2) it has better heat dissipation condition because the stator is next to the frame; (3) compared with conventional machine, it has more design freedom because of the decoupling of electric load and magnetic load; (4) the stator ring winding has no end winding, which can save a lot of space of the machine system. Different from the conventional magnetic-field modulated machines, the main flux path of the TDMFM-BDRM is three-dimensional, and its operating principle cannot be explained by the conventional magnetic-field modulated theory. Therefore, the special magnetic-field modulated principle of the TDMFM-BDRM is investigated in detail. According to the theoretical analysis, the equal and opposite torques can be generated on the two rotors of the TDMFM-BDRM, and the speed difference of the two rotors can be controlled by the adjusting the frequency of stator currents. Therefore, the coaxial contra-rotating operating mode of the two rotors can be achieved. Furthermore, the operating principle and design method of the TDMFM-BDRM are analyzed in detail. The torque and speed characteristics are shown in Fig. 2 (a), where $p_s, f_s, \tau_s,$ and v_s are the pole-pair number, frequency, pole pitch, and speed of stator axial magnetic-field, respectively; $T_m, n_m,$ and T_{PM}, n_{PM} are the electromagnetic torques and rotation speeds of transversely-dislocated modulating ring rotor and PM rotor, respectively; p_{PM} is the pole-pair number of the PM rotor; p_m is the number of magnetic blocks of one modulating group. In order to verify the validity of the proposed structure and theory, a 3-D finite element model is established and the calculated results are shown in Fig. 2 (b)-(e). The calculated results agree well with the theoretical results. The full paper will present the detailed magnetic-field modulated theory, design principle and contra-rotating performance analysis of the proposed TDMFM-BDRM.

[1] H. Shin, J. Chang, and D. Hong, "Design and characteristics analysis of coaxial magnetic gear for contra-rotating propeller in yacht," *IEEE Transactions on Industrial Electronics*, vol. 67, no. 9, pp. 7250-7259, Sep. 2020. [2] G. Liu, G. Qiu, J. Shi, et al, "Study on counter-rotating dual-rotor permanent magnet motor for underwater vehicle propulsion," *IEEE Transactions on Applied Superconductivity*, vol. 28, no. 3, Apr. 2018, Art. no. 0601905.

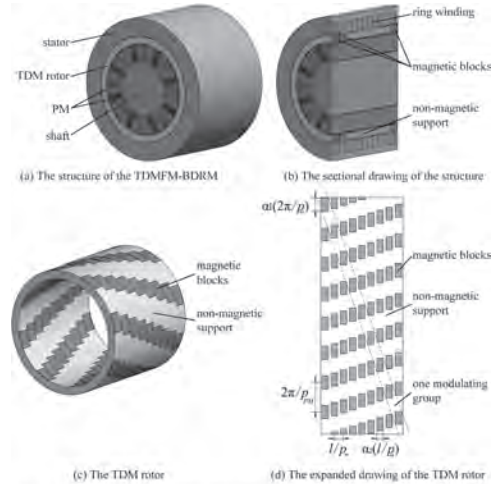


Fig. 1 The structure, sectional drawing, and expanded drawing of the TDMFM-BDRM

The structure, sectional drawing and expanded drawing of the TDMFM-BDRM

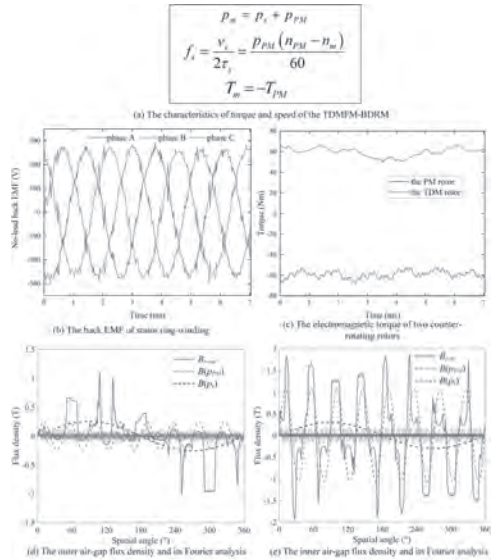


Fig. 2 The characteristics and simulation results of the TDMFM-BDRM

The characteristics and simulation results of the TDMFM-BDRM

INVITED PAPER

BF-13. Design, Build and Test of a Magnetically Geared Generator for Wind Turbine Applications INVITED.

S.D. Calverley¹, R. Dragan¹, G. Cooke¹ and D. Powell¹
 1. Magnomatics Ltd, Sheffield, United Kingdom

For many low-speed electrical machine applications it is usually cost effective to employ a high-speed machine together with a mechanical gearbox. This can also minimise system size and weight. The gearbox however brings disadvantages in terms of reliability, acoustic noise, mechanical vibration and the need for lubrication and maintenance. For the case of offshore wind turbines with high service life the disadvantages are compounded by the high cost of gearbox replacements. To eliminate these concerns in offshore wind applications, it is commonplace to delete the gearbox and use a direct drive machine, but care is required to ensure the size, mass and cost of the system do not become unfeasible. The Pseudo Direct Drive (or PDD®) is a magnetic and mechanical integration of a magnetic planetary gear with a permanent magnet generator. A magnetic equivalent to a planetary gear is embedded within a permanent magnet generator. This integrated approach is used to reduce the size and mass of the machine without recourse to a mechanical gearbox. By doing this the disadvantages of using a mechanical gearbox are avoided, but the size of the generator is minimised. This paper discusses the design, build and test results of a 200,000Nm, 500kW PDD machine shown in Fig 1. This is the world's largest PDD machine and serves as a technology demonstrator for a larger 10MW project, providing validated data for this new class of machine at this size. The discussion presented includes the principle of operation of magnetically geared machines, and specifically how this is applied in the design of very large machines. The magnetic gear embedded in the generator is described and the equivalence of a mechanical planetary system with analogous components (sun, planets and ring) is detailed. The high torque is reacted magnetically and there is no mechanical contact between the shafts. The inclusion of this single stage magnetic gear gives the same uplift in performance to the generator system, i.e. increased rotor speed, reduced airgap torque and increased efficiency whilst allowing the size and mass of the generator to be minimised. The key design features of a highly integrated magnetic gear are discussed:-

- The magnetic components service both the generator and the gear; hence the losses can be assumed to be shared and minimised, leading to very high system efficiencies
- The compliant nature of the gear leads to the attenuation of drive train oscillations and reduces acoustic noise.
- There is no lubrication of the gear element (except bearings) and the service interval can be extended accordingly.
- The integrated magnetic gear is placed in the centre of the machine and does not increase the overall volume envelope.
- Small size means higher power machines may be built with existing facilities designed for direct drive generators. This paper gives quantitative experimental data of a 500kW, 200,000Nm magnetically geared PDD wind turbine generator that was designed, built and tested as part of the DemoWind Programme funded under the European Research Area Network. Key operating data is shown, including verified electromagnetic parameters. Component thermal traces verify the thermal and operation models with an exemplar case presented at 80% load showing a 70°C rise in winding temperature. Dynamic operating data is presented as a measured 10minute recorded trace of speed, torque, current and electrical power whilst the machine is operated with a real-world input profile example at nominal 10m/s wind speed conditions, this verifies the performance of the machine in realistic wind conditions. The results presented confirm both the accuracy of the underlying analysis models and the suitability of the generator system as a wind turbine machine. Finally, the verified data is used to provide Levelized Cost of Energy (LCOE) analysis for a 10MW system (performed independently). The LCOE calculations are based on OPEX, CAPEX and Energy production models comprising 17 sub-categories upon which the influence of the PDD efficiency, mass, CAPEX and operational parameters can be individually evaluated. The results show a reduction in LCOE of 2.8% and 2.5% when the PDD system is compared to the equivalent direct-drive and mid-speed geared systems respectively as detailed in Fig.2

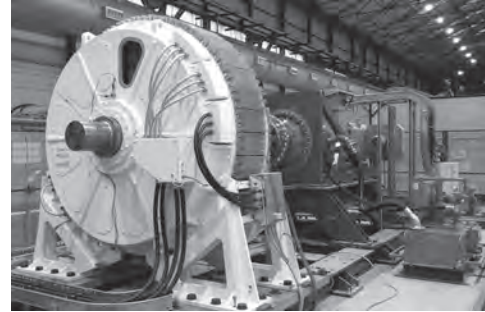


Fig. 1. 200,000Nm, 500kW PDD generator on test

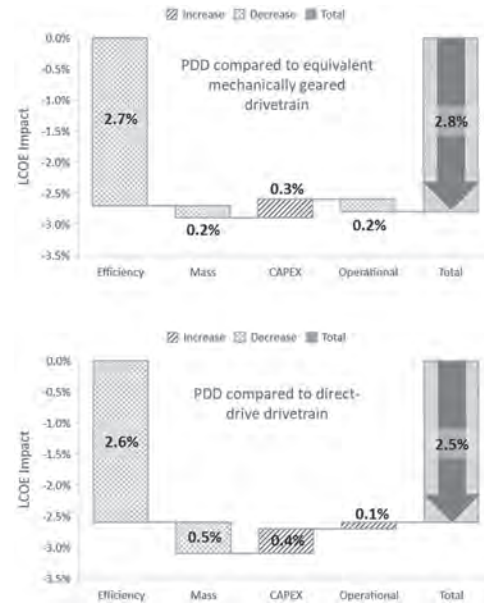


Fig. 2. Source of LCOE savings of PDD compared to alternative drivetrains

Session BG

SURFACE MOUNTED AND INTERIOR MOUNTED PERMANENT MAGNET ELECTRICAL MACHINES

Thierry Lubin, Chair
Lorraine University, Nancy, France

INVITED PAPER

BG-01. Flooded Permanent Magnet Direct-Drive Generator for Tidal Turbines INVITED.F. Wani¹ and H. Polinder¹*1. Maritime & Transport Technology, Technische Universiteit Delft, Delft, Netherlands*

Tidal turbine generators are submerged in water, which means reliability is a critical criterion, arguably even more than efficiency. The objective of this paper is to discuss the main electromagnetic design aspects of a flooded permanent magnet (PM) direct-drive generator for tidal turbines. In a flooded generator design, the stator-rotor gap is filled with sea water instead of air, as shown in Fig. 1. The reasons to consider flooded direct-drive generators are to get rid of highly pressurized rotary seals that keep the water outside the nacelle which holds the generator; additionally, a flooded design could also improve cooling. This could result in a higher power density generator and/or potentially better performance. As a ramification of the flooded design, however, protective sleeves (also called cans) are needed to shield the magnets, iron and windings from sea water [1]. The paper mainly focuses on the following three aspects of the generator, which could provide useful guidelines for the design of flooded generators. *I. WINDING TYPE SELECTION* Fractional slot windings are cheaper and easier to manufacture than distributed windings [2]. In large direct-drive generators, it may also result in lower copper losses, improving the lifetime cost of the generator. However, because of the higher space harmonic content of the fractional slot windings, they could cause high eddy current losses in the rotor magnets and the rotor sleeve if it is conductive [3]. In contrast, a distributed winding is costlier to manufacture, especially in a flooded design due to larger end windings, but contains much lower space harmonics. These aspects need to be carefully considered while selecting a winding layout for the flooded generator. *II. SLEEVE MATERIAL SELECTION* For the stator, a non-conductive sleeve is strongly preferred. Even at no-load, the losses in a conductive stator sleeve due to rotating magnets would be too high for a reasonable design. On the other hand, for the rotor a conductive sleeve may be acceptable. In this study, we compared the eddy-current losses in the rotor sleeve of a flooded generator with different sleeve materials, ranging from highly conductive metallic materials, such as stainless steel to non-conductive glass fiber. Whereas the glass fiber has no loss, it is not as robust against water ingress as metallic materials [4]. Consequently, a thicker layer of glass fiber would be necessary compared to the metallic sleeve. This would increase the volume of the magnets required, increasing the generator cost. Thus, the selection of sleeve material should be based on multiple aspects, such as losses in the sleeve, material strength, water-proofing properties, thermal performance of the generator, winding layout, etc. rather than just losses. *III. THERMAL ANALYSIS* The effect of flooding the generator on the temperature distribution is analyzed in this section. For this purpose, a flooded generator was compared with a similarly sized airgap generator (both are 300 kW at 30 rpm and both contain a rotor sleeve). Consequently, we assumed that the loss distribution in the airgap and the flooded generator is the same. Figure 2 shows the influence of flooding the stator-rotor gap on the magnet and the slot temperatures in a flooded and an airgap PM generator with fractional slot windings (non-negligible rotor losses). The figure also illustrates the effect of using materials with different electrical conductivities on the temperature distribution inside the machine. It is clearly seen that the materials with higher conductivity exhibit higher temperature in the magnets and in the stator slots on account of higher eddy current losses in the rotor. For the corresponding decrease in the magnet temperature on flooding, there is an increase in the temperature of the stator slot. This is because of the better heat transfer in the flooded stator-rotor gap compared to the airgap. Whether the net heat transfer is from the rotor-to-stator or vice-versa would depend on the losses in the rotor and the stator, rotor-to-ambient thermal path via the stator iron and rotor-to-ambient thermal via the shaft and bearings, etc [5]. In the case of glass fiber (GRP) sleeve, it is seen that the magnet temperature in the airgap design is more than the flooded design. This is because in this case magnet (or rotor) temperature is less than the slot (or stator) temperature in the

airgap design. As a result, on flooding the heat transfer improves enhancing the heat transfer to the rotor, which increases the magnet temperature rather than decreasing it [5].

- [1] O. Krovel, R. Nilssen and S. Skaar, in *Proceedings of ICEM*, 2004. [2] A. El-Refaie, *IEEE Transactions on Industrial Electronics*, vol. 57, no. 1, pp. 107-121, 2009. [3] F. Wani, U. Shipurkar and H. Polinder, in *13th European Wave and Tidal Energy Conference*, Napoli, Italy, 2019. [4] L. Bian, J. Xiao and J. Zeng, *Journal of Composite Materials*, vol. 46, no. 25, pp. 3151-3162, 2012. [5] F. Wani, J. Dong and H. Polinder, in *13th International Conference on Electrical Machines (ICEM)*, Alexandroupolis, Greece, 2018.

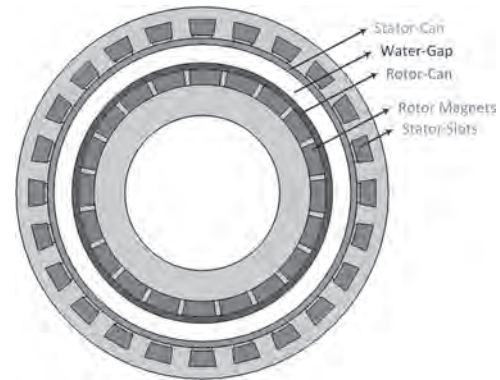


Fig. 1. A representative diagram of a flooded permanent magnet generator (not drawn to scale).

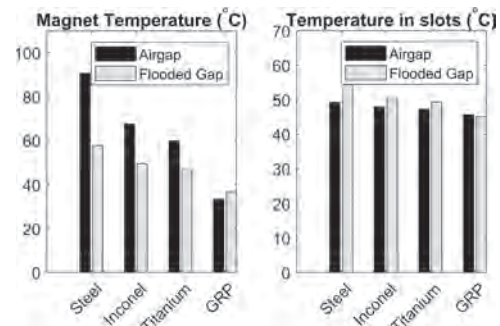


Fig. 2. Temperature of the magnets and the slots is shown as a function of different rotor sleeve materials. Electrical conductivities of the materials are: Stainless steel 304L— 1.30×10^6 S/m ; Inconel alloy 718— 0.80×10^6 S/m ; Titanium SP700— 0.61×10^6 S/m ; Glass reinforced plastic (GRP)— 0 S/m [5].

CONTRIBUTED PAPERS

BG-02. Electromagnetic Performance Analysis of a New Hybrid Excitation Synchronous Generator With Decoupling Magnetic Field.

C. Wang¹, Z. Zhang¹, Y. Liu¹, X. Kong^{1,2} and Y. Hua¹

1. College of Automation Engineering, Nanjing University of Aeronautics and Astronautics, Nanjing, China; 2. Jiangsu Province Key Laboratory of Aerospace Power System, Nanjing, China

I. Introduction With the development of more electric aircraft (MEA), higher demand for electrical energy is put forward in generation systems. In order to reduce the weight of the aircraft generation system, the requirement on the power density of generator becomes higher [1]. Wound rotor synchronous machines (WRSMs) are most widely used in aircraft applications. However, the reliability of rotating rectifier is low. In addition, the starting processing is complex. Hybrid excitation synchronous machines (HESMs) are recently proposed as the potential candidates for EV drive systems, wind power generation and more electric aircraft, for the air-gap flux can be regulated by field current efficiently. This paper proposes a new hybrid excited starter-generator (HESG) with magnetic field decoupling topology for MEA applications. The predicted electromagnetic performance is validated by the 3-D finite-element analysis (FEA) model. Finally, the results of FEA are confirmed by the experiments on a 60kVA HESG. The contribution of this paper is to propose a promising HESG to replace WRSMs in aircraft starter-generator applications. II. Operation Principle and Machine Specification Table I presents the design requirements of a starter-generator for aircraft generation system. The structure of the HESG with decoupling magnetic field is shown in Fig. 1, it can be seen that the PM side air-gap is larger than EE side air-gap. In order to implement high air-gap flux density, the Halbach-array PM rotor is preferred for the flux concentrating characteristic, low harmonic components and low inductance characteristic. Fig. 2 shows the HESG topology. It can be seen that the PM rotor and the two EE rotors can be installed on the shaft together seamlessly, which can greatly improve the compactness, torque density and power density. As shown in Fig. 3, the magnetic flux path can be divided into axial part and radial part. There is no axial flux in the stator core so that the stator can keep the same with that in WRSM and brings sinusoidal back EMF, which makes it suitable for starter-generator system. Table II provides the main parameters of the designed HESG with decoupling magnetic field. III. Electromagnetic Performance Analysis In order to verify the applicability of the new HESG magnetic field decoupling topology for AC starter-generator system, the electromagnetic performance analysis mainly focus on the power characteristics and flux regulation capability. Fig. 4 shows the distribution of magnetic field with different field currents. As shown in Fig. 5, the back-EMF magnitude increases with field current. Fig. 6 shows the output voltage versus output current at 8000r/min for different field currents. It can be seen that the output characteristics can be regulated by field current. The output power versus speed for different field currents is shown in Fig. 7. A 60kVA prototype is manufactured and measured for the verification of previous analysis. The photos of the motor are shown in Fig. 8. The experimental results will be supplemented in the later formal paper. IV. CONCLUSION In this paper, a new HESG is proposed for aircraft generation system. The topology and operating principle are described in detail. In addition, the electromagnetic performance of HESG is investigated to verify the applicability of the HESM to a starter-generator system for aircraft applications.

[1] Y. Liu, Z. Zhang and X. Zhang, "Design and Optimization of Hybrid Excitation Synchronous Machines With Magnetic Shunting Rotor for Electric Vehicle Traction Applications," in *IEEE Transactions on Industry Applications*, vol. 53, no. 6, pp. 5252-5261, Nov.-Dec. 2017.

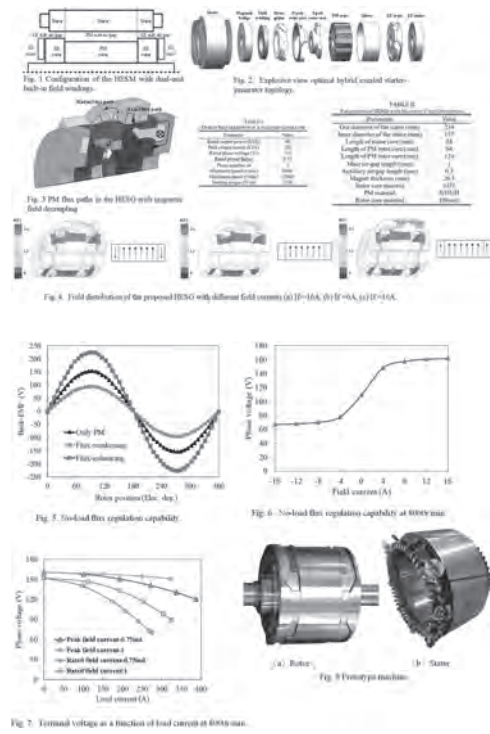


Fig. 7. Terminal voltage as a function of field current at 6000 r/min.

BG-03. Design of a Novel Axial-Radial Flux Permanent Magnet Machine With Halbach-Array Permanent Magnets.

R. Huang^{1,2}, C. Liu^{1,2}, Z. Song^{1,2} and H. Zhao^{1,2}

1. School of Energy and Environment, City University of Hong Kong, Hong Kong SAR, China; 2. Shenzhen Research Institute, City University of Hong Kong, Shenzhen, China

I. Introduction There are many studies on axial flux permanent magnet machines (AFPMMs) due to their compactness [1]. The conventional AFPMMs comprise a stator and two rotors. In general, the stator with toroidal windings or overlapping windings is sandwiched between two rotors [2][3]. Toroidal windings have shorter ends than overlapping windings, which can reduce copper loss and ending effect. However, this structure also wastes the ends of windings, which means that the windings are not utilized sufficiently. To some extent, it reduces the torque density of the machine. This paper proposes a novel axial-radial flux permanent magnet machine (ARFPMM) to solve the problem. In the ARFPMM, the endings of windings are also used to produce torque with little increase of volume, which results in the improvement of torque density. II. Structure of ARFPMM The proposed ARFPMM integrates both axial-flux and radial-flux machines in a compact space, which improves the torque density. As shown in Fig. 1(a), the ARFPMM is composed of one stator, two axial rotors and one radial rotor. Because the end of overlapping windings is useless, the machine adopts toroidal windings. Thus, the stator is equipped with opening slots on three faces. Permanent magnets are mounted on the surface of rotors. The radial rotor is fixed and aligned with two axial rotors, which can avoid the tilt of axial rotors and generation of harmonics in flux density per phase. The inner and outer diameters of permanent magnets on axial rotors are the same as those of stator. Similarly, the height of permanent magnets on radial rotor is equal to that of stator. In order to suppress air-gap flux density harmonics and get more sinusoidal waveform of air-gap flux [4], the permanent magnets are arranged as Halbach-array. It can also increase the flux density in the air gap. The magnetization direction of PMs is related to the number of segments per pole pair. As shown in Fig. 1(b), each pole pair is divided into six segments, so the magnetization direction of each segment varies 60° in turn. III. Design and Analysis Compared with integer-slot concentrated windings, fractional-slot concentrated windings can enhance flux-weakening capability and reduce cogging torque [5]. Therefore, a 20 pole 24 slot fractional-slot concentrated-winding machine is chosen. In the case, the winding factor is 0.966. It is related to the no load back electromotive force (EMF) which can be calculated as equation (1). $E_0=4.44fk_wN\Phi_{10}$ (1) Where f is the electric frequency of the machine, k_w is the winding factor, N is the number of coils per phase in series, Φ_{10} is the magnetic flux. In the ARFPMM, three rotors are used to increase the magnetic flux in air gap. The result of 3D FEA for back EMF is shown in Fig. 2(a). Fig. 2(b) is the fast Fourier transform of back EMF. It shows that the maximum harmonic is the third order harmonic, which can be neglected due to the star-connection of three phase windings. Because the magnetic flux in air gap is increased under the same operating state, the torque of ARFPMM is also increased. Fig. 2(c) shows the torque of the machine at rated conditions when the current is 7 A and rotor speed is 600 rpm. In the condition, the average torque is 41.63 Nm and the torque density is 28.58 Nm/L. The torque ripple is 3.4 Nm, 8.1% of the rated torque. As shown in Fig. 2(c), the peak-peak value of cogging torque is 3.26 Nm. IV. Conclusion This paper proposes a novel ARFPMM with a unique structure of two axial rotors and one radial rotor, and implements its design and FEA. Due to the Halbach-array PMs, the main harmonics of back EMF is the third order harmonic, which is negligible when the windings are connected in star-connection. Compared with conventional AFPMM, the structure increases the torque through increasing the magnetic flux through windings per phase. Thus, the ARFPMM reaches an extremely high torque density of 28.58 Nm/L. On the other hand, fractional-slot concentrated winding configuration reduces the cogging torque, of which the peak-peak value is only 3.26 Nm. Acknowledge This work is supported in part by NSFC (52077186&51677159), in part by STIC of Shenzhen Municipality (JCYJ20180307123918658), and in part by ITF (ITP/027/19AP), HK.

[1] W. Tong, S. Wang, S. Dai and S. Wu, et al, "A Quasi-Three-Dimensional Magnetic Equivalent Circuit Model of a Double-Sided Axial Flux Permanent

Magnet Machine Considering Local Saturation," in IEEE Transactions on Energy Conversion, vol. 33, no. 4, pp. 2163-2173, Dec. 2018. [2] M. F. H. Khatib, Z. Q. Zhu, H. Y. Li and Y. Liu, "Comparative study of novel axial flux magnetically geared and conventional axial flux permanent magnet machines," in CES Transactions on Electrical Machines and Systems, vol. 2, no. 4, pp. 392-398, Dec. 2018. [3] M. Aydin and M. Gulec, "Reduction of Cogging Torque in Double-Rotor Axial-Flux Permanent-Magnet Disk Motors: A Review of Cost-Effective Magnet-Skewing Techniques With Experimental Verification," in IEEE Transactions on Industrial Electronics, vol. 61, no. 9, pp. 5025-5034, Sept. 2014. [4] Z. Song, C. Liu, K. Feng, H. Zhao and J. Yu, "Field Prediction and Validation of a Slotless Segmented-Halbach Permanent Magnet Synchronous Machine for More Electric Aircraft," in IEEE Transactions on Transportation Electrification, vol. 6, no. 4, pp. 1577-1591, Dec. 2020. [5] G. De Donato, F. Giulii Capponi, A. Rivellini and F. Caricchi, "Integer-slot vs fractional-slot concentrated-winding axial-flux permanent magnet machines: Comparative design, FEA and experimental tests," 2011 IEEE Energy Conversion Congress and Exposition, Phoenix, AZ, 2011, pp. 3120-3127.



Fig. 1 Structure of ARFPMM. (a) Topology overview, (b) Halbach array PMs

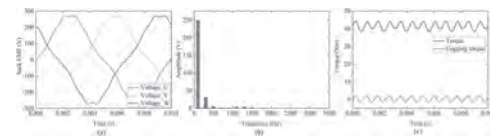


Fig. 2 Back EMF and torque analyzed by FEA. (a) Back EMF waveform, (b) Fast Fourier transform of back EMF, (c) Electromagnetic torque and cogging torque

BG-04. Impact of Asymmetric and Symmetric Overhangs on Torque Quality and Axial Magnetic Force Computations in Surface Mounted PM Synchronous Motors.

M. Onsal², Y. Demir² and M. Aydin¹

1. Kocaeli Universitesi, Kocaeli, Turkey; 2. MDS Motor Ltd., Kocaeli, Turkey

I. ABSTRACT Permanent magnet (PM) motors have become great alternatives to traditional motors. Overhang, either on the rotor or the stator, is commonly used in these motors. In this study, various alternatives of stator or rotor overhang in PM synchronous motors are investigated in detail. Both asymmetric and symmetric overhang cases are considered in the paper. Impact of overhang on the torque quality and torque densities are investigated using 3D Finite Element Analysis (3D-FEA). Axial magnetic forces during assembly with and without overhang are also simulated and variation of axial forces for different cases of overhangs are explored. A prototype PM motor with rotor overhang is used to validate the analyses experimentally. II. INTRODUCTION Rotor overhang is commonly used in different types of permanent magnet motors for numerous reasons. There are various studies in literature covering rotor overhang including magnetic modelling, 2D and 3D-FEA mostly for linear permanent magnet and induction motors, axial flux motors and brushless DC motors. Very limited studies exist on radial flux PM synchronous motors. Most studies are focused on analytical modelling of overhang and 2D/3D simulations [1-4]. However, no detailed investigation on both symmetric and asymmetric overhangs on the motor performance are conducted. Influence of torque quality, cogging and back-EMF harmonics are not covered especially for asymmetric overhang cases since some applications do require asymmetric placement of the rotor. In this paper, both asymmetric and symmetric overhang cases will be investigated in detail. Impact of such cases on the motor performance and torque quality are covered. Axial magnetic forces are also explored for PM motors since it is a crucial issue in assembly of framed and frameless PM motors. III. INVESTIGATED PM MOTOR CASES AND FEA SIMULATIONS AND IV. EXPERIMENTAL VERIFICATION Detailed 3D-FEA is performed for different cases of overhang. The motor is selected as a low speed surface mounted permanent magnet synchronous motor as shown in Fig. 1. The prototype motor in a test system is also shown in Fig. 2. Various cases of overhang is investigated in great detail using 3D-FEA. Case-1 does not have any overhang. Case-2 has rotor overhang and Case-3 has stator overhang. In each case, rotor stack is kept the same and torque quality as well as motor performance is explored. Axial magnetic forces acting on the rotor are also covered in 3D-FEA as seen in Fig3, 4 and 5. A prototype motor with rotor overhang is also manufactured and tested for different cases and some of the 3D-FEA simulations including axial magnetic forces are verified. The test results and comparison with the FEA simulations will also be given in the final version of the paper.

V. REFERENCES 1. Yon-Do Chun; Ju Lee; S. Wakao, 'Overhang effect analysis of brushless DC motor by 3-D equivalent magnetic circuit network method', *IEEE Trans. Magn.*, vol. 39, pp. 1610-1613, May. 2003. 2. P. Upadhyay; K. R. Rajagopal, 'Permanent magnet overhang effect in PM BLDC motor using 2D & 3D finite element analysis', 2012 Nirma University International Conference on Engineering, India. 3. Jung-Moo Seo, In-Soung Jung, Hyun-Kyo Jung, and Jong-Suk Ro, 'Analysis of Overhang Effect for a Surface-Mounted Permanent Magnet Machine Using a Lumped Magnetic Circuit Model', *IEEE Trans. Magn.*, vol. 50, Issue: 5, May. 2014. 4. Kyu-Yun Hwang; Hai Lin; Se-Hyun Rhyu; Byung-Il Kwon, 'A Study on the Novel Coefficient Modeling for a Skewed Permanent Magnet and Overhang Structure for Optimal Design of Brushless DC Motor', *IEEE Trans. Magnetics.*, vol. 48, Issue: 5, May. 2012. 5. Han-Kyeol Yeo; Hyeon-Jeong Park; Jung-Moo Seo; Sang-Yong Jung; Jong-Suk Ro; Hyun-Kyo Jung, 'Electromagnetic and Thermal Analysis of a Surface-Mounted Permanent-Magnet Motor with Overhang Structure', *IEEE Trans. Magnetics.*, vol. 53, Issue: 6, June 2017.

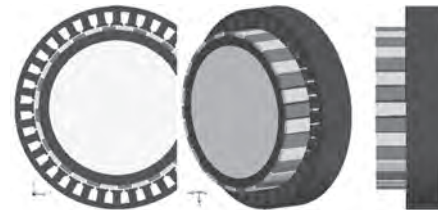


Fig. 1. 3D FEA model for the different rotor displacement cases



Fig. 2. Test system to investigate overhang and magnetic force during rotor moving along z-axis

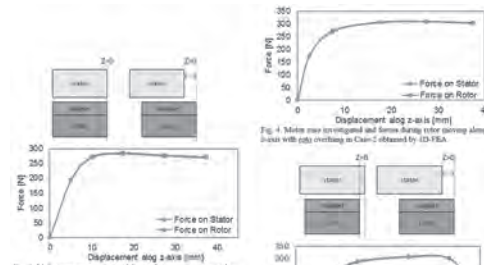


Fig. 1. Motor case investigated and force during rotor moving along z-axis without any overhang in Case-1 obtained by 3D-FEA.

Fig. 4. Motor case investigated and force during rotor moving along z-axis with rotor overhang in Case-2 obtained by 3D-FEA.

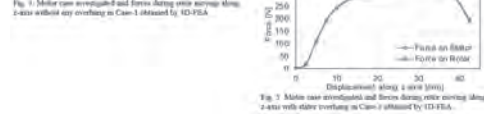


Fig. 3. Motor case investigated and force during rotor moving along z-axis with stator overhang in Case-3 obtained by 3D-FEA.

Fig. 5. Motor case investigated and force during rotor moving along z-axis with stator overhang in Case-3 obtained by 3D-FEA.

BG-05. Design Optimization for Torque Ripple Reduction Using Asymmetric Rotor in IPMSM Considering Forward and Reverse Directions.

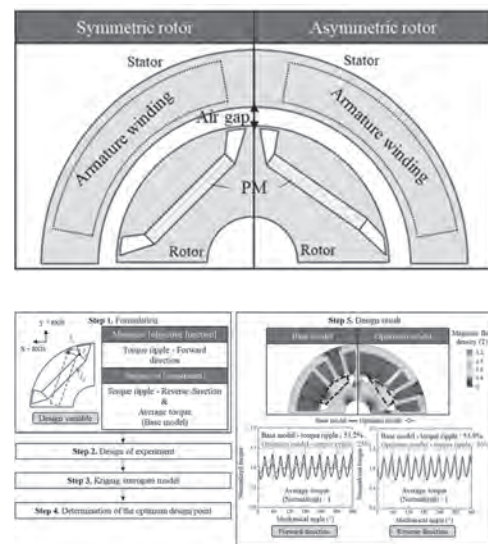
J. Park¹, J. Kim¹, S. Park¹, S. Lee¹, K. Kim¹ and M. Lim¹

¹. Department of Automotive Engineering, Hanyang University, Seongdong-gu, The Republic of Korea

1. Introduction The advantage of interior permanent magnet synchronous motor (IPMSM) is known for having high power density by utilizing not only magnetic torque but also reluctance torque. Accordingly, the IPMSM is used in various industrial components such as robots, electric vehicles (EVs), and home appliances to exert high-performance. The performances required for the industrial components are high power density and low torque ripple. The torque ripple is related to noise and vibration characteristics of the IPMSM. Thus, it is necessary to reduce the torque ripple when designing the IPMSM. Many design method has been reported for torque ripple reduction, such as rotor eccentricity, skew, notch, and chamfer. These methods are related to changing the length of the air-gap [1]. However, changing the air-gap length makes the average torque decrease because the effective air-gap length increases [2]. To reduce the torque ripple while maintaining the average torque, a design method of asymmetric rotor shape has been proposed [3]. The symmetric and asymmetric rotor shapes are illustrated in Fig. 1. The significant difference between the symmetric and asymmetric rotors is the effects of the rotating directions on the torque ripple. When applying the symmetric rotor, the torque ripple is constant regardless of the rotating directions. On the other hand, the torque ripple is different depending on the rotating directions when applying the asymmetric rotor. Since some applications such as an EV traction motor require rotating in the forward and reverse directions, it is necessary to consider the rotating directions in the design for the torque ripple reduction of an IPMSM. In this paper, the design of an IPMSM for an EV traction to reduce the torque ripple is performed considering the rotating directions of the asymmetric rotor. Unlike the conventional design method for torque ripple reduction, the average torque is maintained with an asymmetric rotor. In the EV traction motor, the driving time in the forward direction is longer than the driving time in the reverse direction. Therefore, the torque ripple of the forward direction is minimized, and the torque ripple of the reverse direction is designed at the same level as the base model. To verify the result of the design optimization, prototypes of the base and the optimum models are fabricated and the experimental results of the base and optimum models are compared. 2. Design Optimization Process By applying the asymmetric rotor, the air-gap magnetic field distribution at load conditions can be sinusoidal compared with the base model. Considering that the magnetic permeance of the rotor is determined by the shape of the rotor, the three design variables are selected as shown in Fig. 2. In the figure, the l_x and l_y represent the x-axis and y-axis directional displacements. l_a represents the positional angle of the permanent magnet (PMs) which implies the degree of the asymmetry of the rotor. For comparison, the same stator of the base model is used in the asymmetric rotor design. Moreover, the PM size, the pole angle, the rib thickness, and the rib angles are the same as those of the base model. The objective function and the constraints for the torque ripple minimization are defined considering the rotational directions: the forward and reverse directions. Since the targeted system mainly rotates in the forward direction, the torque ripple when rotating the forward direction is set as the objective function while the torque ripple when rotating in the reverse direction is considered in the constraint. Besides, the average torque is maintained with the value of the base model. In the optimization process, the objective and constraints values are predicted using kriging surrogate models based on the finite element analysis (FEA). As the design of experiment (DOE) technique for constructing the kriging surrogate models, a combination of optimal Latin hypercube (OLHD) and sequential maximin distance design (SMDD) are adopted [4]. Using the constructed kriging surrogate models, the design optimization is performed and the optimum model of the asymmetric rotor is determined. Using the constructed kriging surrogate models, the design optimization is performed and the optimum model of the asymmetric rotor is determined. 3. Design Result In Fig. 2, the FEA results are compared to the base model with the symmetric rotor and the optimum model with the asymmetric rotor. The average torque in the forward and reverse directions is

the same. The torque ripple in the forward direction is reduced in the optimal model compared to the base model. The torque ripple in the reverse direction is similar between the base model and the optimum model. 4. Experiment Verification and Conclusion The test result is used to compare and verify the base model and the optimum model. The test of the base model and the optimum model will be performed under the same load conditions. In conclusion, a design for torque ripple reduction using the asymmetric rotor was performed considering the forward and reverse directions. The torque ripple in the reverse direction and the average torque are similar to that of the base model, while the torque ripple in the forward direction is reduced. Therefore, the design result can be applied to various applications having the forward and reverse rotations.

[1] T. Ishikawa, M. Yamada, and N. Kurita, *IEEE Trans. Magn.*, vol. 47, pp. 1290–1293, (2011) [2] Y.H. Jung, M.S. Lim, and J.-P. Hong, *IEEE Trans. Energy Convers.*, vol. 33, pp. 333–340, (2018) [3] W. Ren, Q. Xu, Q. Li, and L. Zhou, *IEEE Trans. Magn.*, vol. 52, Art. ID 8104105, (2016) [4] S.K. Kim, S.G. Lee, and M.S. Lim, *IEEE Trans. Energy Convers.*, vol. 35, pp. 2056–2065, (2020)



BG-06. A Novel Hybrid Excited Machine With H-Type Modular Stator and Consequent Pole PM Rotor.

W. Ullah¹, F. Khan¹, E. Sulaiman², B. Khan¹ and M. Umair¹

1. Electrical and Computer Engineering, COMSATS Institute of Information Technology - Abbottabad Campus, Abbottabad, Pakistan;
 2. Electrical Power, Universiti Tun Hussein Onn Malaysia, Batu Pahat, Malaysia

Flux Switching Machines (FSMs) are competent applicant for high speed brushless AC applications due to double-salient robust rotor structure, high torque, efficiency, and power density. Hybrid excited FSM (HEFSM) are widely applicable to many industrial applications, Electric Vehicles (EVs), Hybrid Electric Vehicles, electric propulsion, electric craft, electric power-assisted steering, renewable and automotive application due to high power and torque density and flux controllability [1]. However, the compact stator structure of conventional HEFSM (as shown in Fig. 1(a)) [2] suffer from parasitic effects of iron loss, demagnetization due to spatial harmonics in non-overlapped winding. This effect greatly effects electromagnetic performance i.e. average torque (T_{avg}), torque density (T_{den}), average power (P_{avg}), power density (P_{den}), efficiency (η), flux controllability, flux focusing effects and fault tolerant capability. To overcome the aforesaid demerits, in this research a novel H-type stator core (as shown in Fig. 1(b)) is proposed to improve electromagnetic performance and flux controllability. Furthermore, the proposed model is converted to modular stator by introducing flux gaps in all and alternate stator teeth as shown in Fig 1(c, d), because considering steel lamination in modular topologies with segmented stator, manufacturing process i.e. winding process is made at ease. Moreover, modular structure offers thermal, mechanical, and physically magnetic separation between armatures winding hence, on-site maintenance is reduced, and fault tolerant capability is improved [3]. In mechanical aspect, it is noteworthy that combination of consequent pole rotor with modular stator structure effectively results higher PM utilization and ease manufacturing process, transportation, assembly and on-site maintenance when design in large-dimension for wind power application whereas in electromagnetic analysis, modular structure shows dominant influence on electromagnetic performance. In order to show effectiveness of the proposed modular H-type HEFSM, a comprehensive electromagnetic performance analysis is investigated (as shown in Fig. 2(a-d)) at armature current density (J_a) of 15 at constant magnetic loading in both conventional and proposed design. Analysis concludes that in proposed design, T_{avg} is improved by 42.35% whereas P_{avg} is enhanced by 48.48%. Moreover, T_{den} is increased by 42.04% and P_{den} by 48.68% in comparison with conventional design. In additional, the proposed design offers highest efficiency of 98.68% whereas conventional design has efficiency of 87.20%. thus, improving the efficiency by 13.07%. Despite of electromagnetic performance proposed modular structure improve flux focusing effects by decoupling mutual phase coupled flux linkage which greatly enhanced fault tolerant capability and improve flux weakening capability and overload capability. This analysis is comprehensively investigated under varying flux gap at all stator teeth and alternate stator teeth. Analysis concludes that flux gap (FG) increases self-inductance and reduces mutual inductance thus, mitigating short circuit current and separate healthy and faulty phases during fault and hence improve fault tolerant capability.

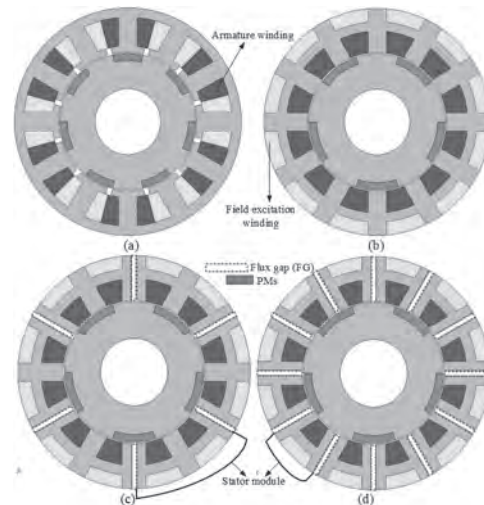


Fig. 1: Cross sectional view (a) conventional design (b) proposed non-modular (c) proposed modular with alternate stator teeth FGs and (d) proposed modular with all stator teeth FGs

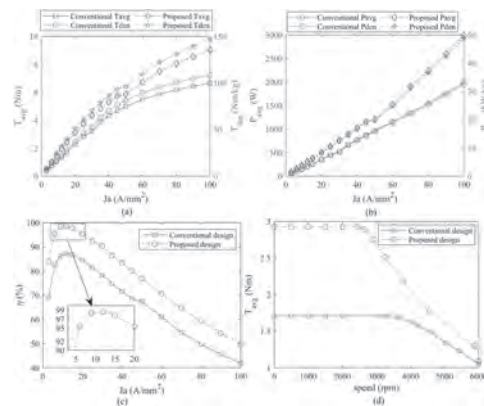


Fig. 2: Electromagnetic performance analysis (a) T_{avg} and T_{den} (b) P_{avg} and P_{den} (c) η and (d) Torque speed curve

[1] W. Ullah, F. Khan, E. Sulaiman, M. Umair, N. Ullah and B. Khan, "Analytical validation of novel consequent pole E-core stator permanent magnet flux switching machine," in IET Electric Power Applications, vol. 14, no. 5, pp. 789-796, 5 2020 [2] S. Cai, Z. -Q. Zhu, C. Wang, J. -C. Mipo and S. Personnaz, "A Novel Fractional Slot Non-Overlapping Winding Hybrid Excited Machine With Consequent-Pole PM Rotor," in IEEE Transactions on Energy Conversion, vol. 35, no. 3, pp. 1628-1637, Sept. 2020 [3] R. Zhou, G. -J. Li, K. Zhang, Z. Q. Zhu, M. Foster and D. Stone, "Performance Investigation of Consequent-Pole PM Machines with E-core and C-core Modular Stators," in IEEE Transactions on Energy Conversion, doi: 10.1109/TEC.2020.3027366.

BG-07. A New Harmonic Current Injection Technique to Reduce Cogging Torque in Axial Flux Permanent Magnet Motors.

M. Tetik Girgin² and M. Aydin¹

1. Kocaeli Universitesi, Kocaeli, Turkey; 2. Akim Metal Sanayi ve Ticaret A S, Istanbul, Turkey

I. ABSTRACT In this paper, a new two-stage harmonic current injection (TSHCI) technique is proposed for permanent magnet synchronous machines to reduce the cogging torque and torque ripple components at low speeds. The developed algorithm is validated for different AFPM motors experimentally. It has been shown that the proposed technique help reduce the cogging components significantly especially at very low speeds. II. INTRODUCTION The use of permanent magnet (PM) synchronous motors is increasing in industrial applications compared to conventional AC and DC motors due to their high torque density and efficiency. Axial flux permanent magnet (AFPM) motors move forward in many applications due to their geometric benefits, high efficiency and high power density. Such motors may suffer from high torque ripple in some slot-pole combinations. At high speeds, torque ripple can be filtered by the system inertia. However, it would be imperative to reduce the cogging torque components at low speeds in some applications. Harmonic current injection is used to reduce the torque ripple in some PM motors [1-5]. However, it has been observed that such studies are generally carried out at high speeds [6-7]. In this paper, a harmonic current injection algorithm is proposed to reduce both torque ripple and cogging torque at very low speeds. Two AFPM prototype motors is used so as to validate the developed proposed algorithm. The proposed algorithm is validated with and without harmonic current injection for such PM motors at different speed levels. III. EXPERIMENTAL VERIFICATION OF PROPOSED TWO-STAGE HARMONIC CURRENT INJECTION The proposed two-stage harmonic current injection method is used for two different AFPM synchronous motors. In order to adapt the algorithm, shown in Fig. 1, the cogging torque and its harmonics are determined first as shown in Fig. 2. After the harmonic current injection, the variation of cogging component and its harmonics are shown in Fig. 3. It has been observed that the effect of the cogging torque can be reduced from 55.91% to 36.2% with the proposed method. The reduction of the impact of the cogging torque by the harmonic current addition method applied to the q-axis current when the AFPM motor is running at 4.5Nm at 10rpm speed. It has been observed that the impact of the cogging torque can be reduced from 55.91% to 30.9% with the proposed method. IV. CONCLUSIONS In this paper, two-stage harmonic current injection is proposed and the algorithm is validated for AFPM motors at very low speeds. Torque ripple at low speeds are reduced by more than 51% with the developed method. The validity of the proposed technique is shown in 2 different AFPM motor.

[1] Hongyun Jia, M. Cheng, W. Hua, Zhengzhan Yang and Yunqian Zhang, "Compensation of cogging torque for flux-switching permanent magnet motor based on current harmonics injection," 2009 IEEE IEMDC, Miami, FL, 2009, pp. 286-291. [2] A. Ebrahimi, "A Novel Harmonic Current Control Algorithm for Torque Ripple Reduction of Permanent Magnet Synchronous Motors for Traction Application," 2018 IEEE International Conference on Electrical Systems for Aircraft, Railway, Ship Propulsion and Road Vehicles & International Transportation Electrification Conference (ESARS-ITEC), Nottingham, 2018, pp. 1-5. [3] H. Le-Huy, R. Perret and R. Feuillet, "Minimization of Torque Ripple in Brushless DC Motor Drives," in IEEE Transactions on Industry Applications, vol. IA-22, no. 4, pp. 748-755, July 1986. [4] Ma, Y.; Li, Y. Active Disturbance Compensation Based Robust Control for Speed Regulation System of Permanent Magnet Synchronous Motor. Appl. Sci. 2020, 10, 709. [5] Y. A. I. Mohamed and E. F. El-Saadany, "A Current Control Scheme With an Adaptive Internal Model for Torque Ripple Minimization and Robust Current Regulation in PMSM Drive Systems," in IEEE Transactions on Energy Conversion, vol. 23, no. 1, pp. 92-100, March 2008. [6] M. Lukaniszyn, M. JagieLa and R. Wrobel, "Optimization of permanent magnet shape for minimum cogging torque using a genetic algorithm," in IEEE Transactions on Magnetics, vol. 40, no. 2, pp. 1228-1231, March 2004. [7] P. Mattavelli, L. Tubiana and M. Zigliotto, "Torque-ripple reduction in PM synchronous motor drives using

repetitive current control," in IEEE Transactions on Power Electronics, vol. 20, no. 6, pp. 1423-1431, Nov. 2005.



Fig. 1. The proposed harmonic current injection algorithm to reduce cogging torque



Fig. 2. AFPM Motor used in the experimental results

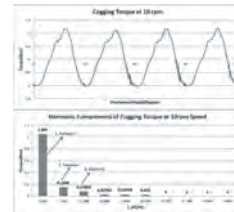


Fig. 3. Cogging torque variations and cogging harmonics without any harmonic current injection (test data)

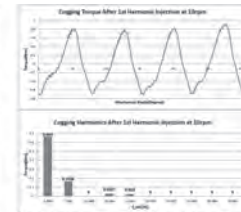


Fig. 3. Cogging torque variations and cogging harmonics after 1st harmonic current injection (test data)

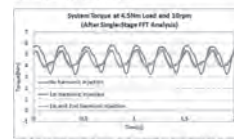


Fig. 4. System torque after single-stage FFT analysis (test data)

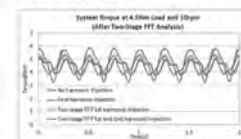


Fig. 4. System torque after the proposed two-stage TCI analysis (test data)

BG-08. Dual Stator Drum Rotor Interior Permanent Magnet Synchronous Motor With Improvement in Torque Density, and Rotor Alignment.

M.M. Zaid^{1,2}, A. Waheed¹, H. Ahmad¹ and I. Sami¹

1. Chung-Ang University, Seoul, The Republic of Korea; 2. R&D, Milim Syscon Co. Ltd, Songnam, The Republic of Korea

Interior permanent magnet synchronous motor (IPMSM) are widely used for industrial and traction applications. IPMSM's are known for high efficiency, reliability, and power density. For certain applications, like traction in hybrid electric vehicles, a high torque and power density with wide range of speed is of high importance. The efficiency of the motors can be increased in two ways: (1) increasing the output torque of the motor or (2) reducing the losses of the motor. The torque of various motors has been improved by introducing dual rotor structure and dual excitation using the unused space in electrical machine [1, 2]. The authors in [3] compares number of electrical motors. A quantitative analysis of three types of dual stator flux modulation permanent magnet (PM) motors including magnetic geared motor, and vernier machine. High torque density has been achieved in [4] for double stator brushless PM motors. The design has also been optimized based on split ratio to achieve maximum torque density. Recently, a lot of research has been carried out on vernier permanent magnet motors (VPMMs). The authors proposed a dual stator VPMMs and performs a comparative analysis of proposed design with regular VPM [5]. The proposed design achieved high efficiency and torque density and lower cogging torque. Similarly, power factor based analytical and FEM analysis have been provided in [6] on dual stator VPMM. A high torque density VPMM with dual stator topology has been proposed in [7]. This draft proposes a drum type configuration of dual stator IPMSM with improvement in the torque density, rotor alignment and inner winding temperature compared to single stator IPMSM by utilizing the unused space in the motor. The new design of dual stator IPMSM with 16-poles and 72-slots in each stator are presented with the aim of improving the average torque and torque ripple for industrial and traction applications. The presented design is then compared with the commercial design of single stator IPMSM to show the direct and fair comparison. Fig. 1 (a) shows the proposed design (PD) and conventional design (CD). The CD uses tangential type rotor with rare-earth PMs mounted inside the surface of rotor. The conventional IPMSM offers a good torque capability, but this torque capability can be improved by utilizing the unused space of the rotor. For this purpose, another stator with the same number of stator slots has been added to replace the unused space of rotor resulting in a proposed dual stator IPMSM. To increase the torque of the proposed models, the inner stator is shifted by a half slot pitch to aid the flux lines of outer stator with the inner stator. As the slots of inner stator are aligned with the outer stator-teeth, hence the slot area of an inner stator is somewhat smaller compared to the outer stator-slots. The number of turns of the inner stator-slots are double compared to the outer stator-slots to reduce the current density and inner winding temperature. Due to the addition of an inner stator, the cup rotor is the suitable. However, the cup type rotor configuration decreases the rotor alignment because of only one bearing towards the rotor shaft. Hence, in this draft, the drum type rotor is introduced comprising of two bearing on both sides of stator to support the inner stator shaft and to improve the alignment of the rotor. Furthermore, to reduce the inner winding temperature, the curve-windows are introduced in the drum configuration for the air inlet to reduce the inner winding temperature as presented in Fig. 1 (b). The analysis is performed on the conventional and proposed designs to show the competency of the proposed model. The Fig. 2 (a), and (b) shows the back EMF of the inner and outer stator. Moreover, the back EMF of the conventional design is identical to the outer stator back EMF of the proposed model due to same geometry of outer stator. Moreover, the Fig. 2 (b) shows the substantial improvement in the average torque and torque ripple of the proposed model compared to the conventional design.

[1] A. Toba and T. A. Lipo, "Generic torque-maximizing design methodology of surface permanent-magnet vernier machine," vol. 36, no. 6, pp. 1539-1546, 2000. [2] F. Zhao, T. A. Lipo, and B. Kwon, "Magnet flux focusing design of double stator permanent magnet vernier machine," in *Proc. COMPUMAG*, 2013. [3] C. Liu, K. Chau, J. Zhong, W. Li, and F. J. I.

T. o. a. s. Li, "Quantitative comparison of double-stator permanent magnet vernier machines with and without HTS bulks," vol. 22, no. 3, pp. 5202405-5202405, 2011. [4] Y. Wang, M. Cheng, M. Chen, Y. Du, and K. J. I. E. p. a. Chau, "Design of high-torque-density double-stator permanent magnet brushless motors," vol. 5, no. 3, pp. 317-323, 2011. [5] Y. Gao, R. Qu, D. Li, H. Fang, J. Li, and W. J. I. T. o. M. Kong, "A novel dual-stator Vernier permanent magnet machine," vol. 53, no. 11, pp. 1-5, 2017. [6] Y. Shi and T. J. I. T. o. M. Ching, "Power Factor Analysis of Dual-Stator Permanent Magnet Vernier Motor with Consideration on Turn-Number Assignment of Inner and Outer Stator Windings," 2020. [7] N. Baloch, B.-i. Kwon, and Y. J. I. T. o. M. Gao, "Low-cost high-torque-density dual-stator consequent-pole permanent magnet Vernier machine," vol. 54, no. 11, pp. 1-5, 2018.

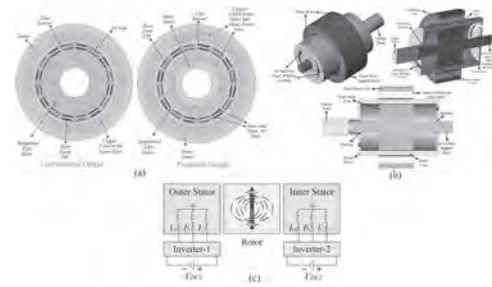


Fig. 1. (a) Geometry of the proposed and conventional designs; (b) Proposed dual stator drum type rotor; (c) Configuration of the inner and outer stator with the inverter.

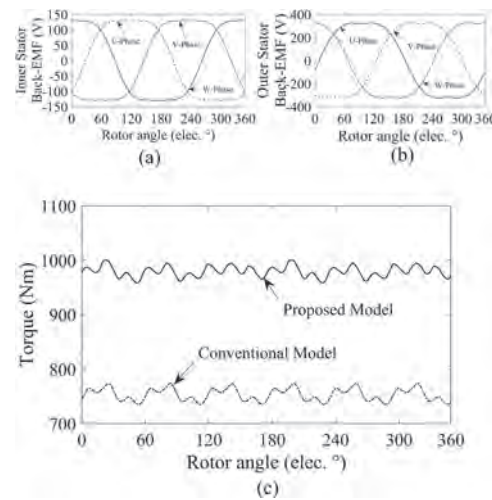


Fig. 2. Back EMF of the (a) Inner Stator; (b) Outer Stator; and (c) torque comparison.

BG-09. Comparative Analysis of Axial-Radial, Axial, and Radial Flux Permanent Magnet Machines.

R. Huang^{1,2}, C. Liu^{1,2}, Z. Song^{1,2} and H. Zhao^{1,2}

1. School of Energy and Environment, City University of Hong Kong, Hong Kong SAR, China; 2. Shenzhen Research Institute, City University of Hong Kong, Shenzhen, China

I. Introduction Conventional radial flux permanent magnet machines (RFPMMs) and axial flux permanent magnet machines (AFPMMs) are always the research hotspot high performance drive systems. RFPMMs have simple structure and magnetic circuit, which makes them easy to design and analyze [1]. As for the AFPMMs, they are paid attention for their compactness [2]. The merit makes them more suitable for direct-drive system [3] [4]. However, for some special applications such as industrial robotic arms, machines with higher torque density are required [5]. In this case, the axial-radial flux permanent magnet machines (ARFPMMs) may meet the requirements. Compared with the AFPMM and RFPMM, the proposed ARFPMM has the merits of compactness, high utilization of windings and high torque density. In this paper, The structures of ARFPMM, AFPMM and RFPMM are introduced. A detailed performance comparison between the three topologies is also conducted. 3D models of different topologies are built and 3D finite element method (FEM) is used to analyze them. The performances such as back electromotive force (EMF), torque density, and torque ripple are compared to specify the best topology for particular applications. II. Three Topologies In order to exclude factors which may affect the comparison results, some parameters of the machines are kept consistent. The inner/outer diameter and axial length of three machines are the same. As shown in Fig. 1, the pole/slot combinations of three topologies are all 20 poles 24 slots. In addition, toroidal windings are also adopted in the RFPMM to keep consistent with the AFPMM and ARFPMM. They are all placed in the opening slots. Permanent magnets which are mounted on the surface of rotors are arranged as Halbach array. It can suppress the harmonics of air-gap flux density [6]. Each pole pair contains six segments, so the angle of magnetization direction between permanent magnets is 60° . Fig. 1 shows that the numbers of rotors of three machines are different. The RFPMM and the AFPMM has a radial rotor and two axial rotors, respectively, while the ARFPMM has a radial rotor and two axial rotors. It makes the active part of windings of the ARFPMM the longest and that of the RFPMM the shortest. Those differences lead to different performances. III. Operation Principles of Three Topologies Due to the different configurations, the equivalent magnetic circuits of three machines are different. The magnetic flux of RFPMM goes from rotor to stator in radial direction. There are circumferential and radial components of magnetic flux in the stator core. The electromagnetic torque is generated by the reaction between the radial magnetic field and the outside components of windings. As for the AFPMM, the magnetic flux goes through air gap in axial direction. There are circumferential and axial components in the stator core. The electromagnetic torque is due to the reaction between the axial magnetic field and the radial components of windings. The magnetic flux of ARFPMM is the combination of that of RFPMM and AFPMM. It flows in the stator core in circumferential, radial, and axial direction. Similarly, the electromagnetic torque is also the combination of that of RFPMM and AFPMM. IV. Performance Comparison The three machines are analyzed through FEM. Considering the ending effect, a 3D model is also built for the RFPMM. Fig. 2(a) shows the back EMFs of three machines obtained through 3D finite element analysis. The amplitude of ARFPMM is the largest, while that of RFPMM is the smallest. The waveforms show that the distortion of back EMF in the ARFPMM is the most serious. However, as shown in Fig. 2(b), the largest harmonic of back EMF in the ARFPMM is the third harmonic, which can be neglected due to the star connection of three phase windings. V. Conclusion This paper has described the structures and operation principles of ARFPMM, AFPMM, and RFPMM. The results of 3D FEA show that the proposed ARFPMM has the highest torque density. Because the slots and PMs of RFPMM are all rectangular, while the PMs of AFPMM are fan-shaped and slots are rectangular, the percentage of torque ripple to average torque of the RFPMM is the largest. The ARFPMM is equipped with the characteristics of both AFPMM and RFPMM. Thus, the percentage of torque ripple of ARFPMM is in the middle. Acknowledge This work is supported in part by

NSFC (52077186&51677159), in part by STIC of Shenzhen Municipality (JCYJ20180307123918658), and in part by ITF (ITP/027/19AP), HK.

[1] H. Zhao, C. Liu, Z. Song and W. Wang, "Exact Modeling and Multi-Objective Optimization of Vernier Machines," in IEEE Transactions on Industrial Electronics, early access. [2] M. Aydin, Surong Huang and T. A. Lipo, "Torque quality and comparison of internal and external rotor axial flux surface-magnet disc machines," in IEEE Transactions on Industrial Electronics, vol. 53, no. 3, pp. 822-830, June 2006. [3] C. Liu, K. T. Chau, and C. H. T. Lee, "A Critical Review of Advanced Electric Machines and Control Strategies for Electric Vehicles," in Proceedings of the IEEE, early access. [4] M. Wang, C. Tong, Z. Song, J. Liu and P. Zheng, "Performance Analysis of an Axial Magnetic-Field-Modulated Brushless Double-Rotor Machine for Hybrid Electric Vehicles," in IEEE Transactions on Industrial Electronics, vol. 66, no. 1, pp. 806-817, Jan. 2019. [5] A. Dwivedi, S. k. Singh and R. K. Srivastava, "Analysis and Performance Evaluation of Axial Flux Permanent Magnet Motors," in IEEE Transactions on Industry Applications, vol. 54, no. 2, pp. 1765-1772, March-April 2018. [6] Z. Song, C. Liu, K. Feng, H. Zhao and J. Yu, "Field Prediction and Validation of a Slotless Segmented-Halbach Permanent Magnet Synchronous Machine for More Electric Aircraft," in IEEE Transactions on Transportation Electrification, vol. 6, no. 4, pp. 1577-1591, Dec. 2020.

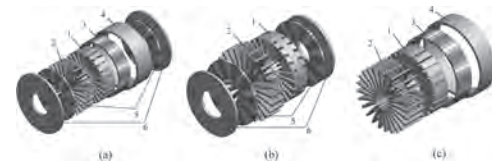


Fig. 1 Topologies of three machines. (a) ARFPMM, (b) AFPMM, (c) RFPMM. 1-Stator, 2-Windings, 3-Radial PMs, 4-Radial back iron, 5-Axial PMs, 6-Axial back iron.

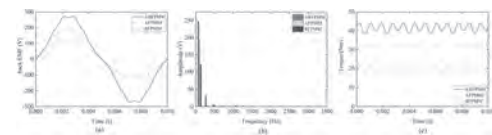


Fig. 2 Back EMF and torque analyzed through 3D FEM. (a) Back EMF, (b) Fast Fourier transform of back EMF, (c) Electromagnetic torque.

BG-11. A New IPMSM With Hybrid Rotor Structure for Electrical Vehicle With Reduced Magnet Loss.

W. Cui¹, L. Ren¹, J. Zhou¹ and Q. Zhang¹

1. Shanghai University, School of Mechatronic Engineering and Automation, Shanghai University, Shanghai, China

Fractional-slot concentrated-winding permanent magnet synchronous motors (FSCW-PMSMs) have been widely used in the field of electric vehicles (EVs) due to their high-power density, high efficiency, short end turns, low cogging torque, good flux weakening capability and so on [1]. However, these machines usually exhibit high amount of sub-harmonic spatial fields, which will lead to high rotor eddy current loss, particularly in NdFeB magnets. This part of loss will increase significantly as the speed goes up, causing the rising temperature and hence the potential irreversible demagnetization of NdFeB magnets [2]. Aiming at the reduction of magnet loss, a hybrid rotor structure FSCW-PMSM is proposed in the paper. The key is to introduce additional ferrite magnets in D and Q axis magnetic flux paths, respectively. Compared with traditional all-NdFeB structure, the proposed design can effectively curb the magnet loss due to the low conductivity of ferrite magnets. Fig.1 shows the comparison of existing all-NdFeB rotor structure and proposed hybrid rotor design for 12 slots/8 poles IPMSM with only the cross section of one pole illustrated, from which it can be seen that part of the tangentially magnetized NdFeB magnets are replaced with ferrite magnets and additional ferrite magnet is introduced to fill up the air at the bottom between the two tangentially magnetized magnets. Fig.2 shows the comparison of total magnet loss and the magnet loss in the tangentially magnetized magnets between existing and proposed FSCW-PMSM with respect to rotor speed. It can be seen that as the rotor speed goes beyond the rated value of 3700rpm with field-weakening operation, the total magnet loss of traditional all-NdFeB structure increases rapidly with the contribution mainly coming from tangentially magnetized NdFeB magnets. It can be well explained by the fact that as a result of increasing leading angle of current vector against Q-axis under field-weakening operation, more and more armature harmonic flux will cross-link with the tangentially magnetized NdFeB magnets and hence lead to high magnet loss in them. Despite of the significant loss reduction by partially replacing the tangentially magnetized NdFeB with ferrite magnets, the magnet loss in the radially magnetized NdFeB magnets still remain high. Therefore, additional ferrite magnets should also be introduced in the d-axis flux-path just as shown in Fig.1. As a result, the introduced ferrite magnets can not only effectively curb the magnet loss in the radial magnets but also contribute to the air-gap flux density and hence improve the output torque. Although the proposed design effectively diminishes the magnet loss, it inevitably leads to the decrease of output torque due to the reduced usage of NdFeB magnets as well as increased torque pulsation. Further optimization is still needed for the proposed structure to improve its competitive edge against the traditional design. Fortunately, the hybrid rotor structure leaves more scope for the improvement of saliency ratio so that it can be possible to enhance the reluctance torque. Furthermore, by adopting auxiliary slots design on the rotor surface, the torque pulsation is effectively curbed and the magnet loss in the radially magnetized NdFeB magnets is further reduced. As a result of the Finite Element analysis, compared with traditional NdFeB IPMSM with the maximum torque of 172N.m, the prototype with the proposed design can accomplish a maximum torque of 158N.m, nearly 92% of that of traditional one due to the contribution of enhanced reluctance torque through optimization, as well as reduced torque ripple from 10.6% to 6.9%, while the total cost of magnets is reduced by 39%. As a conclusion, the proposed hybrid rotor structure can not only solve the problem of excessive magnet loss of traditional NdFeB motor at high speed, but also present a cost-effective design approach for IPMSM for EV applications with less usage of expensive NdFeB magnets as well as enhanced reluctance torque capability.

[1] Ayman M. EL-Refaie, Fractional-Slot Concentrated-Windings Synchronous Permanent Magnet Machines: Opportunities and Challenges. IEEE Transactions on Industrial Electronics, VOL. 57, NO. 1(2010) [2] Xinggang Fan, Bin Zhang, Ronghai Qu, Comparative Thermal Analysis of IPMSMs With Integral-Slot Distributed-Winding (ISDW) and Fractional-

Slot Concentrated-Winding (FSCW) for Electric Vehicle Application. IEEE Transactions on Industry Applications, VOL. 55, NO. 4(2019)

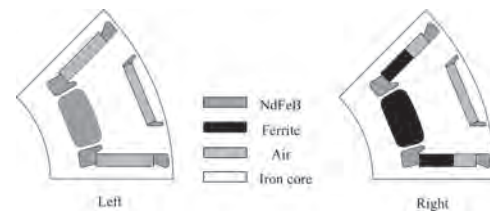


Fig.1 Comparison of the two rotor structures. Left. The traditional rotor structure. Right. The hybrid rotor structure.

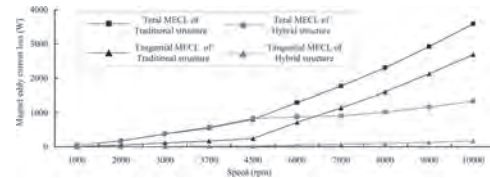


Fig.2 Comparison of magnet eddy current loss (MECL) between the traditional and hybrid rotor structure in full speed range

BG-12. A Novel Two-Step Flux Linkage Identification for PMSMs Considering Magnetic Saturation and Spatial Harmonics.

Y. Zuo¹, S. Afrasiabi¹ and C. Lai¹

1. Electrical and Computer Engineering, Concordia University, Montreal, QC, Canada

I. INTRODUCTION In order to achieve reliable and high-performance control of permanent magnet synchronous machines (PMSMs), the accurate model of electromagnet characteristics of PMSMs under different load conditions is critical [1]. The conventional method is to use the finite element analysis (FEA) to derive the magnetic model of PMSM [2]. However, this method requires accurate geometric parameters and material information of the machine and the results must be validated by experiments. Therefore, it is desirable to obtain accurate machine model from measurable terminal signals. To date, considerable research work has been conducted to deal with the flux linkage identification problem for PMSMs [3]-[5]. However, either magnetic saturation or spatial harmonics effects have been ignored during the flux linkage identification in the existing methods. Therefore, this paper proposes a novel two-step flux linkage identification method for PMSMs considering both magnetic saturation and spatial harmonics. Step one is an offline estimation of the flux linkages considering magnetic saturation based on genetic algorithm (GA), while the spatial harmonics effect has been mitigated compared with the existing method. In the second step, a state-space observer is employed to estimate the spatial harmonics online with the estimated offline data in step one. In addition, Kalman filter is applied in dq-axis inductances harmonics estimation to reduce the influence of noise and high order harmonics in the motor drive system. Therefore, the proposed method achieves to consider both magnetic saturation and spatial harmonics for PMSM flux linkage identification. The proposed approach is validated on both the surface-mounted and interior PMSMs. II. Magnetic Saturation Modeling and Parameter Estimation using GA To consider magnetic saturation in the machine model, the dq-axis flux linkages are modeled using the quadratic equation as in (1). $\Psi_d(i_d, i_q) = \alpha_0 + \alpha_1 i_d + \alpha_2 i_q + \alpha_3 i_d^2 + \alpha_4 i_q^2 + \alpha_5 i_d i_q$; $\Psi_q(i_d, i_q) = \beta_0 + \beta_1 i_d + \beta_2 i_q + \beta_3 i_d^2 + \beta_4 i_q^2 + \beta_5 i_d i_q$. (1) Where i_d, i_q, Ψ_d, Ψ_q are dq-axis currents and flux linkages; α_0 denotes the fundamental PM flux linkage; β_0 is adopted to generalize the quadratic form of the model and compensate the offset for Ψ_q ; α_1 and β_1 denote self-inductances in the dq-axis; $\alpha_2, \dots, \alpha_5$ and β_2, \dots, β_5 denote the cross-coupling effect and the influence of magnetic saturation. There are 12 parameters to be estimated, while the rank number is two. Therefore, the coefficients of flux linkages equations cannot be solved directly as it is rank-deficient. To solve this issue, a GA based estimation approach is proposed. Suppose that, for a given pair of (i_d, i_q) , the (u_d, u_q) under a certain speed ω_m during the period T seconds ($T=2\pi n/\omega_m$, where $n=1,2, \dots, N$ represents the number of rotations) are recorded in order to mitigate the influence of spatial harmonics. To estimate the coefficients of flux linkages, two fitness functions are designed as follows: $F_d = \sum_{i=1}^N \sum_{j=1}^J [\alpha_0 + \alpha_1 i_d(i) + \alpha_2 i_q(j) + \alpha_3 i_d^2(i) + \alpha_4 i_q^2(j) + \alpha_5 i_d(i) i_q(j) - \Psi_d(i_d(i), i_q(j))]$; $F_q = \sum_{i=1}^N \sum_{j=1}^J [\beta_0 + \beta_1 i_d(i) + \beta_2 i_q(j) + \beta_3 i_d^2(i) + \beta_4 i_q^2(j) + \beta_5 i_d(i) i_q(j) - \Psi_q(i_d(i), i_q(j))]$, (2) where $i=1, \dots, N$ and $j=1, \dots, J$ are directories of (i_d, i_q) . Based on (2), the coefficients of dq-axis flux linkages at each pair of (i_d, i_q) can be obtained by using GA to achieve the minimization of F_d and F_q . III. Online Parameter Estimation Considering Spatial Harmonics Considering spatial harmonics, dq-axis voltage equations of a PMSM can be written as (3) under the steady state. $u_d = R i_d - \omega_e L_{dq,0} i_q - \omega_e \Psi_{d6} \sin(6p\theta) + \sin(6p\theta) (-6p\omega_e L_{dd,6} i_d - \omega_e L_{dq,6} i_d) + \cos(6p\theta) (6p\omega_e L_{dq,6} i_q - \omega_e L_{qq,6} i_q) + \varepsilon_d$; $u_q = R i_q + \omega_e L_{dd,0} i_d - \omega_e \Psi_{q6} \cos(6p\theta) + \sin(6p\theta) (-6p\omega_e L_{dq,6} i_d - \omega_e L_{dq,6} i_q) + \cos(6p\theta) (6p\omega_e L_{dq,6} i_d - \omega_e L_{dd,6} i_d) + \varepsilon_q$, (3) where u_d, u_q are dq-axis voltages; θ is the electrical rotor position; p is the number of pole pairs; R is the resistance; ω_e is the rotor speed; Ψ_{d6} and Ψ_{q6} are the magnitudes of the 6th permanent magnet (PM) flux-linkage harmonics in dq-axis. $L_{dd,0}, L_{qq,0}, L_{dd,6}, L_{qq,6}$ are the magnitudes of fundamental and the 6th harmonic of self-inductances in the dq-axis; $L_{dq,6}$ is the magnitude of the 6th harmonic of mutual-inductance; ε_d and ε_q are high order harmonics and high frequency noise components in the dq-axis. The harmonic magnitudes of the PM flux linkage can be easily obtained by using FFT analysis of the back-electromotive force. To achieve an online identification of the dq-axis inductances harmonics, a state observer is employed. The state observer model is firstly built based on (3) to get the magnitude of the 6th harmonic of the self-in-

ductance and mutual-inductance in the dq-axis. The state vector is built as: $x=[L_{s6} \cos(6p\theta); L_{m6} \sin(6p\theta); -6p\omega_e L_{s6} \sin(6p\theta); 6p\omega_e L_{m6} \cos(6p\theta)]$, (4) with $L_{s6}=L_{dd,6}$ and $L_{m6}=L_{dq,6}$. The estimated dq-axis flux linkage maps are shown in Fig.1 and Fig.2. Detail analysis and experimental results will be given in the full paper. IV. CONCLUSION This paper proposes a novel two-step method to identify flux linkages in PMSMs considering both the effects of magnetic saturation and spatial harmonics during the estimation process. In step one, GA is used to estimate the magnetic saturation coefficients of flux linkage. With the results obtained from GA, the Kalman filter based online method is proposed to estimate the spatial harmonics to achieve an accurate estimation of the flux linkage map. The co-simulation results show that the proposed approach is effective for flux linkage estimation.

[1] E. Armando, R. I. Bojoi, P. Guglielmi, G. Pellegrino and M. Pastorelli, in IEEE Transactions on Industry Applications, vol. 49, no. 5, pp. 2116-2125, Sept.-Oct. 2013. [2] N. Bianchi and S. Bolognani, in Proc. Int. Conf. IEEE Ind. Appl., Oct. 1998, pp. 27-34. [3] Z. Li, G. Feng, C. Lai, W. Li and N. C. Kar, in IEEE Transactions on Transportation Electrification, vol. 5, no. 4, pp. 1430-1440, Dec. 2019. [4] Q. Chen, W. Zhao, G. Liu, Z. Lin, in IEEE Transactions on Industrial Electronics., vol. 66, no. 2, pp. 944-955, Feb. 2019. [5] K. Liu, J. Feng, S. Guo, L. Xiao and Z. Zhu, in IEEE Transactions on Industrial Informatics, vol. 14, no. 2, pp. 556-568, Feb. 2018.

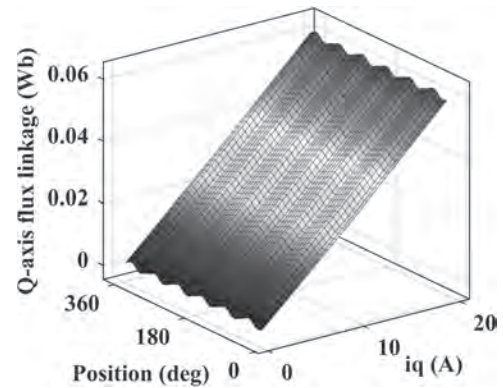


Fig. 1. SPMSM q-axis flux linkages estimation results.

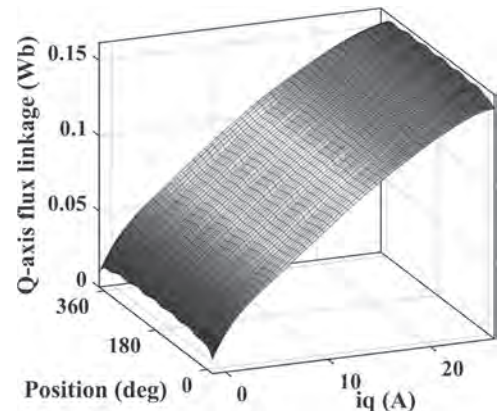


Fig. 2. IPMSM q-axis flux linkages estimation results.

BG-13. Design of a New Consequent-Pole Segmented Dual-Stator Permanent Magnet Machine.

G. Qu¹ and Y. Fan¹

1. School of Electrical Engineering, Southeast University, Nanjing, China

I. INTRODUCTION The permanent magnet (PM) machine has attracted wide attention in many application areas such as electric vehicles (EVs) for high output torque, high efficiency and high reliability. For the traditional PM machine, its maximum output torque is constricted by the current density supplied from the power source, which may lead to the insufficient output torque, especially at low speed [1-2]. Furthermore, in the direct-drive PM machines, the number of the pole-pair is usually relatively high to maintain the large output torque within the low speed range. However, due to the high pole-pair number, the PM dosage and the production cost are both increased accordingly. Therefore, the consequent-pole structure seems to be an appropriate choice to reduce the rare-earth materials and increase the pole-pair number in the limited space [3-4]. In this paper, a new consequent-pole segmented dual-stator permanent magnet (CPSDSPM) machine is proposed for some high-torque & low-speed applications. Compared with the traditional PM machines, this proposed CPSDSPM machine, which reasonably utilizes the internal space of the intermediate rotor, realizes the low-demagnetization, the low dosage of the rare earth, the flexible control strategy and the large output torque by a particular coupling effect between two stators. **II. MACHINE TOPOLOGY** As shown in Fig. 1(a), the topology of the proposed CPSDSPM machine mainly includes three parts: the external stator, the internal stator and the intermediate rotor. First, the external stator is divided into three sub-parts, in which the phase difference of two adjacent sub-parts of the external stator is a complete 360 electrical angle. Second, for convenient maintenance and low cost, the internal stator located inside the intermediate rotor is designed as an integrative structure. Third, the intermediate rotor, which adopts 12 V-type PMs and 6 iron cores, is sandwiched between the external stator and the internal stator. Forth, all the PMs and the iron cores located in the intermediate rotor are alternately distributed as the sequence of N-iron-N-S-iron-S. Fifth, two sets of windings, which are mounted in the external and the internal stator respectively, are adopted in this proposed topology. The five-phase winding is composed of three sub-windings connected in series. It's placed in the external stator and designed to produce the main output torque. The three-phase winding, which is housed in the internal stator, can not only be used as the field coil, but also offers an additional output torque directly when it's needed. **III. WORKING PRINCIPLE** According to the analysis result mentioned above, the flux paths in the proposed CPSDSPM machine are summarized in Fig. 1(b). These flux paths can be mainly divided into three types. First, the flux path 1 includes two PMs in different polarity. It can be seen that the flux path 1 exists in the external stator and the intermediate rotor. Second, the flux path 2 includes one PM and one iron core. Compared with the flux path 1, the ability of the PM excitation in the flux path 2 is weakened, but the total magnetic conductance is improved. Third, the flux path 3 needs to cross both the inner air gap and the outer air gap. It can be easily obtained that the flux density of both iron cores and PMs in the outer air gap can be adjusted by the three-phase winding. Therefore, the three-phase winding can also be regarded as the supplemental excitation source for the external stator. At last, the flux directions of these two iron cores marked in Fig. 1(b) are different. Because of the downward direction of the flux, the iron core on the left can be regard as S-pole. Similarly, the iron core on the right can be defined as N-pole. Therefore, these two iron cores can be regarded as one pole-pair equivalently in the intermediate rotor. **IV. ELECTROMAGNETIC PERFORMANCE ANALYSIS** First, the no-load phase back-EMF waveforms at rated speed of the five-phase winding presented in Fig. 2(a) are calculated by finite element method (FEM). It can be seen that the back-EMF of the proposed machine is extremely sinusoidal owing to the segmented structure, which can contribute to the electromagnetic performance of the external stator of the proposed CPSDSPM machine. Second, for the proposed machine, the cogging torque is mainly caused by the external stator. As shown in Fig. 2(b), it can be obviously found that the total cogging torque generated from the whole machine is decreased considerably, compared with the single part of the external stator. Third, due to the segmented structure, it can be obtained in Fig. 2(c) that the torque ripple generated by the external stator

is quite low (around 0.4%). Furthermore, under the vector control strategy, the maximum total output torque waveform generated by both the external stator and the internal stator is shown in Fig. 2(c). **V. CONCLUSION** In this paper, a new CPSDSPM machine is proposed and analyzed. First, the configuration is introduced. Second, the working principle and the main flux paths of this machine are analyzed and classified. Third, the electromagnetic properties, such as the no-load phase back-EMF waveforms, the cogging torques and the output torques are all calculated by FEM, which can verify the correctness of the theoretical analysis and the superiority of the proposed CPSDSPM machine.

[1] S. Niu, S. L. Ho and W. N. Fu, "A Novel Direct-Drive Dual-Structure Permanent Magnet Machine," *IEEE Trans. Magn.*, vol. 46, no. 6, pp. 2036-2039, June 2010. [2] H. Yang et al., "Novel Dual-Stator Machines With Biased Permanent Magnet Excitation," *IEEE Trans. Energy Convers.*, vol. 33, no. 4, pp. 2070-2080, Dec. 2018. [3] W. Li, T. W. Ching and K. T. Chau, "A New High-Temperature Superconducting Vernier Permanent-Magnet Machine for Wind Turbines," *IEEE Trans. Appl. Supercond.*, vol. 27, no. 4, pp. 1-5, June 2017. [4] H. Hua, Z. Q. Zhu and H. Zhan, "Novel Consequent-Pole Hybrid Excited Machine With Separated Excitation Stator," *IEEE Trans. Ind. Electron.*, vol. 63, no. 8, pp. 4718-4728, Aug. 2016.

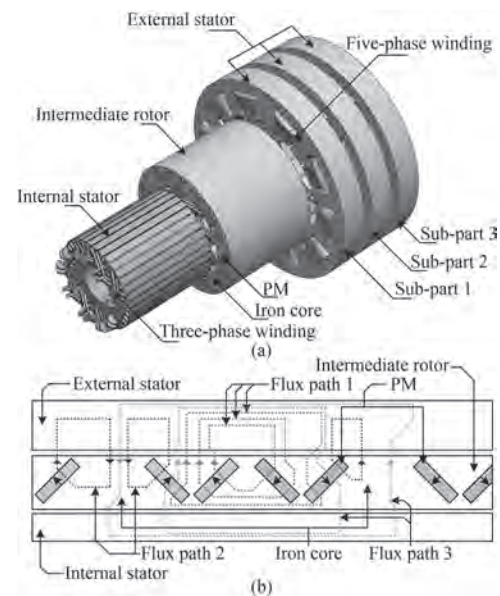


Fig. 1. CPSDSPM machine. (a) Topology. (b) Magnetic paths.

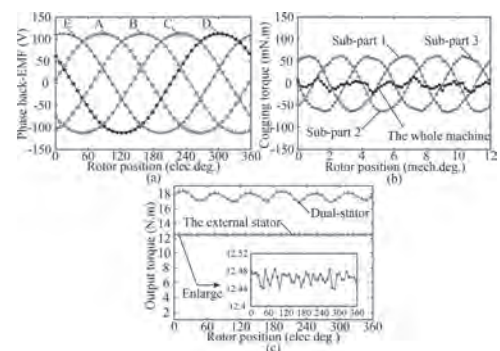


Fig. 2. Electromagnetic field analysis of the proposed CPSDSPM machine. (a) No-load phase back-EMF waveforms. (b) Cogging torques. (c) Output torques.

BG-14. Optimization of Pole Segmentation Technique Applied to Permanent Magnet Synchronous Machines to Reduce the Cogging Torque Peak.

H. Emerenciano Santos¹, K. Marques de Andrade Júnior¹, A.F. Flores Filho², C.G. da Costa Neves³ and G. Teixeira de Paula¹

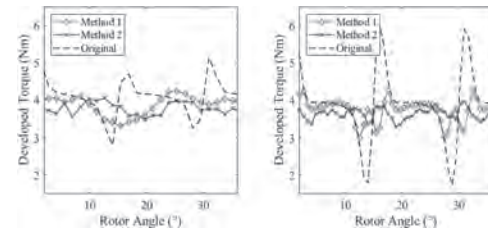
1. EMC, Universidade Federal de Goiás Escola de Engenharia Eletrica Mecanica e de Computacao, Goiania, Brazil; 2. Universidade Federal do Rio Grande do Sul, Porto Alegre, Brazil; 3. Universidade Federal de Pelotas, Pelotas, Brazil

Permanent magnet synchronous machines are once again gaining attention due to the increasing quality of magnets and the global concern regarding the efficiency of electromagnetic systems, and, particularly, to achieve IE5. This kind of machine presents great advantages over induction machines, such as smaller volume for the same power, thus higher energy density, low inertia and easier control [1]. On the other hand, they present a characteristic ripple in the output torque, known as cogging torque, caused by the tendency of alignment between rotor poles and stator slots. Many techniques have been developed to reduce the peak of this component and here the authors discuss one, the pole segmentation technique [2-3]. Here, the authors propose two optimization processes to determine both the width and distribution of the segments. This technique consists in dividing the poles in smaller segments, being the width and distribution of these segments the difference between different researches. The first proposed method considers that all segments have equal width and are equal spaced in a pole. As for the second one, both segments width and space between them have different values for each segment. See Fig. 1. The objective of the optimization process is to determine the values of the mentioned variables in order to minimize a multi-objective function, similarly to the one realized in [3]. This function takes into account the value of the cogging torque peak, permanent magnet volume and the amplitude of the fundamental harmonic of the airgap flux density, which influences the value of the output torque. All these variables were analytically calculated for each set of possible solutions, using adaptations of the expressions obtained in [4] for the tangential and radial components of the airgap flux density and the maxwell stress tensor for the cogging torque peak. Finite elements analysis has been employed to validate the proposal. Machines with four and eight poles were considered, with equal rotor and teeth dimensions. To guide the optimization process, constraints were added, regarding the construction feasibility of the machine and to maintain the airgap flux density at a minimum of 95% of the original value. It has been verified that both proposals allowed a reduction in the cogging torque, satisfying all geometry constraints, but in some cases the airgap flux density constraint was not satisfied. A reduction by up to 84% in the cogging torque peak was achieved in the eight-pole machine with unequal segments, maintaining about 95% of the original airgap flux density. The developed torque waveforms obtained for all machines are shown in Fig. 2.

[1] T. J. E. Miller and J. R. Hendersot, Jr., *Design of Brushless Permanent Magnet Motors*. London, U.K.: Oxford Univ. Press, 1995. [2] R. Lateb, N. Takorabet and F. Meibody-Tabar, *IEEE Transactions on Magnetics*, vol. 42, no. 3, pp. 442-445 (2006). [3] M. Ashabani and Y. A. I. Mohamed, *IEEE Transactions on Magnetics*, vol. 47, no. 4, pp. 795-804 (2011). [4] Zhu, Z. Q. et al., *IEEE Transactions on Magnetics*, v. 29, n. 1, p.124-135 (1993).



Rotor geometries (left) Method 1; (right) Method 2.



Developed torque waveforms (left) 4-pole machine; (right) 8-pole machine.

BG-15. Sinusoidal, Trapezoidal and Harmonic Injection PWM Techniques Applied to the Pole Segmentation of Permanent Magnet Synchronous Machine to Reduce the Torque Ripple.

K. Marques de Andrade Júnior¹, A.F. Flores Filho², C.G. da Costa Neves³ and G. Teixeira de Paula¹

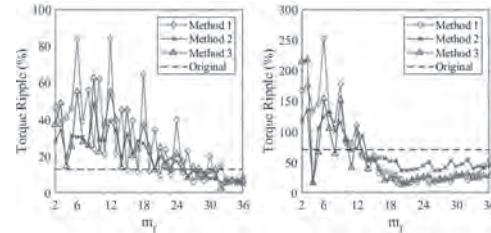
1. EMC, Universidade Federal de Goiás Escola de Engenharia Eletrica Mecanica e de Computacao, Goiania, Brazil; 2. Universidade Federal do Rio Grande do Sul, Porto Alegre, Brazil; 3. Universidade Federal de Pelotas, Pelotas, Brazil

The demand for more efficient and green process of electromechanic energy conversion resulted in an increase in the utilization of permanent magnet (PM) synchronous machines. These machines present high energy density and efficiency, low inertia and easy control when compared with induction machines [1]. On the other hand, they suffer from an intrinsic ripple in their electromagnetic torque, known as cogging torque, arisen from the tendency of alignment between slot openings and magnet edges. Numerous techniques considering the mitigation of this torque can be found in the literature [2-5], including the pole segmentation technique addressed here. As the name suggests, this technique consists in dividing the poles into smaller segments and the arrangement (distance between and width of segments) is the problem to be solved and the main difference between researches. The pole segmentation can substantially reduce the cogging torque peak, but it also affects negatively the output torque, therefore there is a need for new approaches to address this problem. In this paper, the width and distance between each segment are determined using the sequence obtained with three different pulse width modulation (PWM) techniques. Each of these PWM techniques is assigned to a new method, with Method 1 considering the sinusoidal PWM, Method 2 the trapezoidal PWM and Method 3 the sinusoidal with harmonic injection PWM, this being the novelty differing from [4] and [5]. The output sequence of the PWM techniques is obtained comparing one modulating wave with two triangular carriers. The modulating waveform is the desired waveform for the airgap flux density distribution; thus, a sinusoidal waveform is chosen for Method 1, a trapezoidal is chosen for Method 2 and a sinusoidal waveform with specific injected harmonics is chosen for Method 3. For each positive pulse in the PWM output sequence, a north pole magnet is assigned accordingly in the rotor surface; whereas for negative pulses, a south pole magnet is assigned. The rotor geometries obtained are shown in Fig. 1. These methods ensure a reduction in the cogging torque peak, due to a reduction in the number of alignments between slot openings and magnets. This phenomenon is analytically modeled in this paper in terms of the ratio between the frequency of the modulating and the carrier waves (frequency modulation index, mf). Furthermore, the methods grant an airgap flux density distribution similar to the modulating wave with a harmonic spectrum defined by mf . To validate the proposed methods a finite elements analysis is carried out for machines with four and eight poles with equal rotor and teeth dimensions. It has been verified that all machine output parameters, such as PM flux linkage, back electromotive-force (back-emf) and developed torque, are high dependent with mf , as can be seen in Fig. 2. All methods are able to reduce the cogging torque peak value, but the Method 1 has achieved the best result with a reduction of 78,54% in the original value of the eight-pole machine. In addition, it has been verified that the back-emf waveform (and its harmonic content) is almost equal to the modulating waveform. It is worth mentioning that the machine construction feasibility is directly linked to the mf value, since a high value results in a pole with high number of segments with reduced dimensions. Furthermore, a constraint regarding this feasibility has been added in the analysis, comprising the elimination of distances between segments smaller than 0.2° (mechanical).

[1] T. J. E. Miller and J. R. Hendersot, Jr., London, U.K.: Oxford Univ. Press (1995). [2] R. Lateb, N. Takorabet and F. Meibody-Tabar, IEEE Transactions on Magnetics, vol. 42, no. 3, pp. 442-445 (2006). [3] M. Ashabani and Y. A. I. Mohamed, IEEE Transactions on Magnetics, vol. 47, no. 4, pp. 795-804 (2011). [4] S. Chaithongsuk, N. Takorabet and F. Meibody-Tabar, IEEE Transactions on Magnetics, vol. 45, no. 3, pp. 1736-1739 (2009). [5] S. Chaithongsuk, N. Takorabet, B. Nahid-Mobarakeh and F. Meibody-Tabar, 45th International Universities Power Engineering Conference UPEC2010, Cardiff, Wales, pp. 1-6 (2010).



Rotor geometries (left) Method 1; (middle) Method 2; (right) Method 3.



Torque ripple as a function of mf (left) 4-pole machine; (right) 8-pole machine.

Session BH

ADVANCES IN (SEMI)-ANALYTICAL AND NUMERICAL TECHNIQUES FOR DESIGN, AND INNOVATIVE DESIGNS

Pierre-Daniel Pfister, Chair
Zhejiang University, Hangzhou, China

CONTRIBUTED PAPERS

BH-01. Convolutional Neural Networks for Inverse Design of Magnetic Structures.S. Pollok¹, R. Bjørk¹ and P.S. Jørgensen¹¹. Department of Energy Conversion and Storage, Danmarks Tekniske Universitet, 2800 Kgs. Lyngby, Denmark

Abstract – Electric motors, magnetic resonance imaging and many other modern applications are built out of systems of multiple permanent magnets, which are arranged so that the magnetic field that they produce has the required properties. Here, starting from a given magnetic field, we invert the design procedure to predict a matching magnetic structure using deep learning. A convolutional neural network (CNN) learns the mapping from a desired magnetic field to a simple magnetic structure with an error of 0.22%. We further extend the method to work with multiple permanent magnets. **Introduction** Systems of multiple magnets are the basis for many modern applications like magnetic resonance imaging, frictionless bearings in flywheels or electric motors. In these applications permanent magnets of different shapes and magnetic properties are assembled to produce a magnetic field, whose field strength and homogeneity match the requirements for the given application. In order to provide better medical devices, store energy or pave the way to green mobility with electric vehicles, optimized structures of multiple magnets are essential. Traditionally, the design procedure for producing optimized structures of permanent magnets is by selecting a known design that produces a field close to the desired field and then optimizing the structure through modeling. As an example, consider the Halbach cylinder [1] where in real-world applications manufacturing tolerances mean that its actual field will not be exactly equal to the analytically calculated field. In this case one can e.g. use a genetic algorithm to incorporate the manufacturing variations of the single magnetic segments in a traditional design optimization approach [2]. However, this optimization approach is limited in scope, as it relies on a design structure to start from and is computationally intense. **Problem** Here we consider the general inverse problem of determining a magnetic structure that generates a desired magnetic field. We investigate this through the use of a deep neural network, with the network learning the mapping of Maxwell’s equations in an inverse manner. We want to predict the properties of a system of multiple permanent magnets from a part of the magnetic field, as illustrated in Fig. 1. We consider complicated structures of permanent magnets formed out of different simple geometries, e.g. prisms, tetrahedrons or cylindrical tiles. Previously, artificial intelligence has been used to approximate the solution of Maxwell’s equations for electromagnetic structures [3], in order to calculate the magnetic field in a computationally cheap manner. Here, however we invert this problem to use deep learning to predict magnet structures from the magnetic field. A major challenge is to find an invariant representation for systems of a varying number of magnets. Each of the permanent magnets is specified by its geometric appearance, location, and magnetic properties. The output space easily explodes with an increasing number of magnets, when a poor representation is chosen. Additionally, the problem becomes complex when predicting the properties of the magnetic system from a magnetic field, which does not contain the structure itself. There may exist several solutions for the given desired field. **Method** The magnetic field in a so-called “design area” is calculated point-wise, which results in a matrix of field values in each of the spatial dimensions. That tensor is fed into a neural network of multiple convolutional layers. As baseline model, we use a convolutional neural network (CNN) inspired by the ResNet architecture [4]. The output shape of the structural design depends heavily on the chosen magnetic system representation. The model parameters are then updated by backpropagation of the difference between the ground-truth and the predicted target structure. To train such models of millions of tunable parameters artificial neural networks require a large amount of data. We produce accurate field-structure-pairs fast and efficiently with MagTense [5], an open-source magnetostatic and a micromagnetism calculation framework. The learned network parameters are then able to infer magnetic structures of unseen magnetic fields. Initially we limit the input space to be a two-dimensional magnetic field by setting the z-component of the single magnet magneti-

zations to 0 T. We further only use prisms with a constant height and omit rotations of the geometries. The primarily two-dimensional “design area” lies in the plane, which cuts the single tiles in their center point. **Results** We show in [6] that the prediction of the properties of a single permanent magnet from its magnetic field has an average error rate of 0.22%, which is much below magnet manufacturing tolerances. Predictions of the trained CNN are hardly distinguishable from its ground-truth, when given a previously unseen magnetic field, as exemplified in Fig. 2. We discuss the error rates in extending this to multiple magnets and finally discuss how to represent magnetic structures with multiple permanent magnets of different shapes.

- [1] K. Halbach, Nuclear Instruments and Methods, Vol. 169, pp. 1-10 (1980)
 [2] K.K. Nielsen et al., Journal of Magnetism and Magnetic Materials, Vol. 514, p. 167175 (2020) [3] A. Khan, V. Ghorbanian and D. Lowther, IEEE Transaction on Magnetics, Vol. 55, no. 6 (2019) [4] K. He et al., CVPR, “Deep Residual Learning for Image Recognition” (2016) [5] R. Bjørk and K.K. Nielsen, www.magtense.org, https://doi.org/10.11581/DTU:00000071 (2019) [6] S. Pollok, R. Bjørk and P.S. Jørgensen, “Inverse Design of Magnetic Fields using Deep Learning”, Under review (2021)

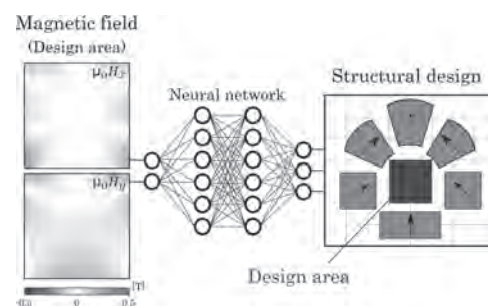


Fig. 1. Deep learning pipeline for inverse design of magnetic structures. The magnetic field in a so-called “design area” serves as input to the neural network, which predicts a systems of permanent magnets required to produce such a field.

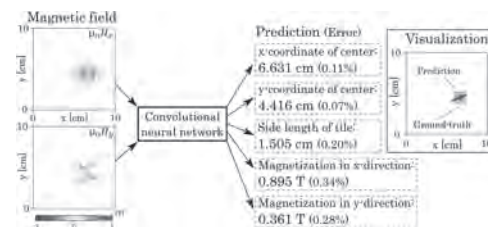


Fig. 2. Prediction of a trained convolutional neural network from an unseen magnetic field. When plotting the predicted single permanent magnet it is visually indistinguishable from its ground-truth.

BH-02. Influence of Rotor Pole Number on Electromagnetic Performance of Hybrid-Magnetic-Circuit Variable Flux Memory Machine.

Y. Ge¹, H. Yang¹ and H. Lin¹

1. Electrical Machines and Apparatus Technologies (EMAT), Nanjing, China

I. INTRODUCTION Hybrid-magnetic-circuit variable flux memory machine (HMC-VFMM) [1] can combine the advantages of wide flux adjusting range in parallel type [2] and beneficial on-load demagnetization withstand capability in series type [3]. The rotor pole number plays an essential role in the electromagnetic performances of conventional PM machines [4]-[6]. In addition, the design process of HMC-VFMM needs to consider not only the basic performance metrics, such as the torque capability, but also flux regulation range and on-load magnetic stability of low coercive force (LCF) magnet. Thus, it is crucial to provide and generalize a utility design guideline for choosing proper pole number for VFMM. This paper attempts to analyze the electromagnetic performances of HMC-VFMMs with different rotor pole numbers. The influence rules of different rotor pole numbers on the performance metrics of the HMC-VFMMs are then provided, and a 4-pole machine prototype is manufactured and tested to experimentally validate the theoretical analyses. II. TOPOLOGIES AND WINDING LAYOUTS OF HMC-VFMM The investigated objectives of this paper refer to HMC-VFMMs with 36-slot/4-pole, 36-slot/6-pole and 48-slot/8-pole combinations, which are all characterized by integer slot structures. The double-layer and full-pitch windings are utilized in all machine models, as shown in Fig. 1. For the parallel branch, the “U”-shaped hybrid magnets are employed. For the series branch, the HCF PMs feature a spoke-type configuration. And only A-phase winding is shown here. III. ELECTROMAGNETIC PERFORMANCE AND COMPARISON Fig. 2 (a) shows the rated-load torque waveforms of HMC-VFMMs with different rotor pole numbers under the conditions of flux-enhanced and flux-weakened states, respectively. It can be seen that with the increase of rotor pole number, the average torque shows an increasing trend, while the torque ripple decreases. These results indicate that the increase of rotor pole number can improve the torque performance to a certain extent. The variations of LCF PM working point subject to an intermediate on-load operation in HMC-VFMM are illustrated in Fig. 2 (b). The excellent on-load demagnetization withstand ability can be observed in all machines. The variations of the back-EMF fundamental magnitudes with the remagnetizing and demagnetizing currents are plotted in Fig. 2 (c). It can be seen that the increase of rotor pole number enlarges the adjusting range of the fundamental back EMF. However, higher current magnitudes are required for full magnetization in the high rotor pole cases at the same time. The detailed characteristics analysis, comparison results and experimental verification will be presented in the full paper.

[1] H. Yang, S. Lyu, H. Lin, Z. Zhu, H. Zheng and T. Wang, “A Novel Hybrid-Magnetic-Circuit Variable Flux Memory Machine,” *IEEE Trans. Ind. Electron.*, vol. 67, no. 7, pp. 5258-5268, July 2020 [2] K. Sakai, K. Yuki, Y. Hashiba, N. Takahashi, and K. Yasui, “Principle of the variable-magnetic-force memory motor,” in *Proc. Int. Conf. Electr. Mach. Syst.*, Tokyo, Japan, 2009, pp. 1-6. [3] A. Athavale, K. Sasaki, B. S. Gagas, T. Kato, and R. D. Lorenz, “Variable flux permanent magnet synchronous machine (VF-PMSM) design methodologies to meet electric vehicle traction requirements with reduced losses”, *IEEE Trans. Ind. Appl.*, vol. 53, no. 5, pp. 4318-4326, Sep./Oct. 2017. [4] J. T. Chen and Z. Q. Zhu, “Winding Configurations and Optimal Stator and Rotor Pole Combination of Flux-Switching PM Brushless AC Machines,” *IEEE Trans. Energy Convers.*, vol. 25, no. 2, pp. 293-302, Jun. 2010. [5] M. Ibrahim, L. Masisi and P. Pillay, “Design of Variable Flux Permanent-Magnet Machine for Reduced Inverter Rating,” *IEEE Trans. Ind. Appl.*, vol. 51, no. 5, pp. 3666-3674, Sep./Oct. 2015.

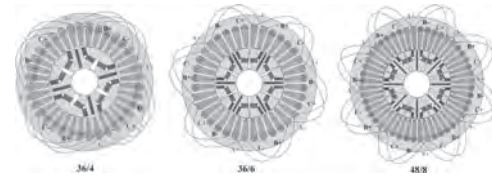


Fig. 1. Topologies and winding layouts (A-phase) of three HMC-VFMMs.

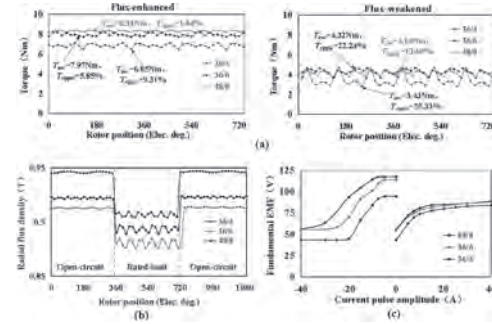


Fig. 2. (a) Steady-state torque waveform @ rated load. (b) Working point variations of the LCF PM in the HMC-VFMMs subject to an intermediate on-load operation. (c) Back-EMF magnitudes versus the current pulses (1500r/min).

BH-03. Multicriteria Optimal Latin Hypercube Design-Based Surrogate-Assisted Design Optimization for a Permanent-Magnet Vernier Machine.

Y. Ma¹, Y. Xiao², J. Wang¹, L. Zhou¹ and Z. Zhu²

1. State Key Laboratory of Advanced Electromagnetic Engineering and Technology, School of Electrical and Electronic Engineering, Huazhong University of Science and Technology, Wuhan, China; 2. Department of Electronics and Electrical Engineering, The University of Sheffield, Sheffield, United Kingdom

Abstract This paper proposes an efficient surrogate-assisted design optimization method based on multicriteria optimal Latin hypercube design (LHD) for multi-objective optimization of a permanent-magnet vernier machine (PMVM). By combining simulated annealing algorithm, the uniformity and orthogonality of spatial distribution of the LHD are optimized to efficiently capture data features over the optimization parameter ranges. Consequently, an accurate surrogate model with high generalization capability can be built with a small training set by using the optimal LHD. The optimal design of the PMVM is obtained by multi-objective design optimization based on the surrogate model. A prototype is made and tested to validate the proposed method. I. Introduction Due to high torque capability at low speeds, permanent-magnet vernier machines (PMVMs) are suitable for direct-drive applications such as wind power generation and electric drilling [1]. To deal with the issue of massive finite-element analysis (FEA) for multi-objective design optimization, this paper proposes a novel surrogate-assisted multi-objective design optimization method for PMVMs. A multicriteria optimal Latin hypercube design (LHD) employing simulated annealing (SA) algorithm is proposed for efficient data feature capturing that enables to use a small training dataset for obtaining an accurate surrogate model. The sparrow search algorithm (SSA)-optimized multi-output least squares support vector machine (MLS-SVM) [2] and the non-dominant sorted genetic algorithm-III (NSGA-III) [3] are combined to build the multi-output surrogate model and to perform the multi-objective design optimization. A prototype is made based on the obtained optimal design and tested for validation. II. PMVM and Sensitivity Analysis A surface-mounted PMVM with 18 slots and 15 pole pairs is studied as an example, whose topology is illustrated in Fig. 1 (a). The four optimization objectives are average torque, power factor, THD of back-EMF, and cogging torque. To improve the optimization efficiency, a global sensitivity analysis (GSA) of four optimization targets is performed using the Sobol's method [4], the stack bars of total sensitivity coefficient (TSC) for optimization parameters are given in Fig. 1 (b), which shows the geometrical parameters that have the greatest influence on design objectives. Thus, five geometrical parameters including PM thickness (t_{PM}) and width (w_{PM}), yoke thickness (t_y), slot width (w_s), and stator split ratio ($k=R_{st}/R_{so}$) are selected for optimization while stator outside diameter, axial length, air-gap length, and current density are fixed. III. Surrogate-Assisted Optimization with LHD The optimal LHD employs SA to minimize a composite indicator ψ_p that consists of the Morris-Mitchell index Φ_p and the correlation coefficient of the test factors ρ^2 to guarantee the spatial distribution uniformity and orthogonality as given in (1), where ω_1 and ω_2 are the weight factors. Subsequently, a 270×5 LHD is built to capture the data feature over the optimization parameter ranges more efficiently as shown in Fig.2 (a), in which 20 sets of data are used for testing the regression results. $\min \psi_p = \omega_1 \Phi_p + \omega_2 \rho^2$ (1) Finite element analysis (FEA) simulations are only performed within the optimal LHD to acquire the training data. The surrogate model based on MLS-SVM are trained using the data of the optimal LHD. The radial basis function (RBF) kernel is adopted for MLS-SVM and SSA is combined with MLS-SVM to find an optimal hyper-parameter set that produces a surrogate model with the highest average determination coefficient R^2 . The four-objectives optimization is performed by NSGA-III and an optimal design is selected from the Pareto front shown in Fig. 2 (b). A prototype is made based on the optimal design and tested, Figs. 2 (c) and (d), to validate the proposed method and the optimization. The proposed method needs only 270 FEA simulation cases during the whole design optimization procedure. For the conventional FEA-based parametric optimization method, even when only 5 levels are selected for each of the five geometrical parameters, 3125 FEA cases are required. Meanwhile, since the parameter space is discretized, the results of the conventional optimization method are likely to be

locally optimal. For the method employing randomly generated LHDs [5], it requires nearly 500 FEA cases to achieve consistent R^2 s, which consumes 2 times the time of the proposed method. Thus, the proposed method can secure both efficient and accurate global design optimization of PMVMs. IV. Conclusions This paper proposes a novel optimal LHD-based surrogate assisted design optimization method for multi-objective optimization of PMVMs, which can perform high efficiency and high validity simultaneously. The proposed method and optimal design are validated by experiments on a prototype. Details of the design optimization and test results will be given in the full paper.

[1] Y. Oner, Z. Q. Zhu and L. J. Wu, IEEE Trans. Ind. Electron., Vol. 63, No. 7, pp. 4105–4117 (2016). [2] S. Xu, X. An and X. Qiao, Pattern Recognit. Lett., Vol. 34, No. 9, pp. 1078–1084 (2013). [3] A. M. Usman, U. K. Yusof and S. Naim, IEEE Access, Vol. 8, pp. 76333–76356 (2020). [4] J. Yin, X. Zhu, L. Quan and C. Zhang, IET Electr. Power Appl., Vol. 11, pp. 72–79 (2017). [5] J. B. Kim, K. Y. Hwang and B. I. Kwon, IEEE Trans. Magn., Vol. 47, No. 5, pp. 1078–1081 (2011).

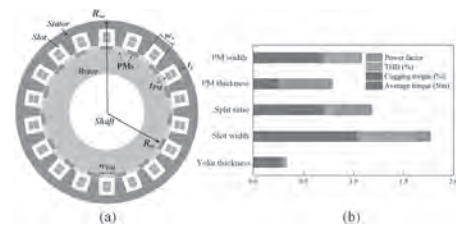


Fig. 1 Topology of PMVM and GSA results. (a) PMVM. (b) GSA results characterized by TSCs.

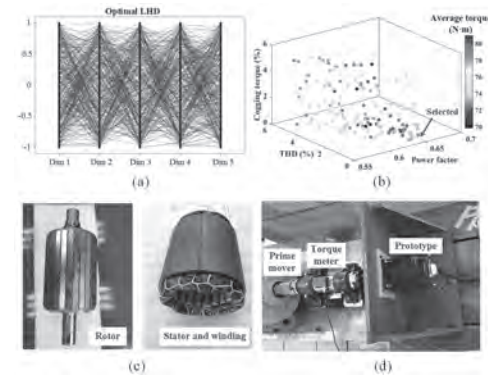


Fig. 2 Surrogate-assisted optimization. (a) Optimal LHD. (b) Pareto front of multi-objective optimization. (c) Rotor and stator of the prototype. (d) Test platform.

BH-05. Parametric Geometric Metamodel of Nonlinear Magnetostatic Problem Based on POD and RBF Approaches.

A. Boumesbah¹, T. Henneron¹ and S. Clénet¹

1. Univ. Lille, Arts et Metiers Institute of Technology, Centrale Lille, Inreca Hauts-de-France, ULR 2697 - L2EP, F -59000 Lille, France

The finite element method (FEM) is widely used to model electromagnetic devices. This method ensures precise results at the expense of a consequent computation time, especially when dealing with parametric problems. Model order reduction methods had proven their efficiency in reducing the computation time for parametric problems. The proper orthogonal decomposition (POD) is a popular model order reduction approach [1]. Based on the solutions of the FE model for different values of parameters (called snapshots), the POD approximates the solution of the FE model in a reduced basis. The parametric FE model is projected onto a reduced basis, decreasing the order of the numerical model to be solved. Another approach consists in constructing a metamodel by interpolation of the parametric FE solution expressed into a reduced basis. A hybrid approach has also been proposed combining the POD with an interpolation-based method such as the radial basis functions (RBF) interpolation method [2]. Moreover, when the problem involves geometric parameters, an adaption of the FEM mesh is required. Remeshing the geometry at each modification can deteriorate the precision of the FEM model by introducing significant numerical noise. A solution to preserve the problem's consistency is to deform the initial mesh using the RBF interpolation [3][4]. The method consists of imposing a displacement on a set of nodes and interpolating the remaining nodes' position. Then, a metamodel of a FE solution taking into account geometric and electric parameters, can be defined by using the POD approach and the RBF interpolation. In this work, we propose to build a metamodel of a nonlinear magnetostatic parametric problem involving geometric parameters using the POD-RBF approach. The study case is a single-phase EI inductance, with one electrical parameter and two geometrical parameters. An initial geometry is meshed with 36859 elements; the number of nodes is 18553. The geometric parameters are the thickness of the airgap varying from 0.1 mm to 0.9 mm, the width of the central column of the magnetic core varying from 20 mm to 40 mm. The phase current varying from 0 to 50 A is also a parameter of the model. The mesh deformation is modeled using the RBF interpolation with a multi-quadratic function for two consecutive times to consider the two varying geometric parameters. The results of the original FEM model are taken as a reference. The POD-RBF approach is applied to the parametric FEM model. The method consists of first gathering a set of data, using the method of snapshots, by solving the original FEM model for a set of inputs. The snapshots matrix is decomposed using the singular value decomposition (SVD). The left orthogonal matrix of the SVD decomposition corresponds to the reduced basis, and the right orthogonal matrix is composed of the FE solution projected into the reduced basis for each snapshot parameter. An RBF interpolation is then performed on the right orthogonal matrix to interpolate the solution expressed in the reduced basis for the new inputs set. Finally, an approximation of the FE solution is defined by projecting the reduced solution into the FE basis. The choice of snapshots is made using a greedy algorithm [2], which consists of an iterative process. The metamodel is then improved at each iteration until the required precision is reached. The stop criterion to the greedy algorithm is set to an error between the FE solution and the metamodel solution lower than 0.1%. The evolution of error represented by Frobenius norm as a function of the iterations' number of the greedy algorithm is represented in "Fig. 1". In order to satisfy the selected criterion, 158 snapshots are required. The magnetic flux cartography as a function of phase current and the central column width for an airgap width fixed at 0.1 mm is represented in "Fig.2". The global mean absolute error between the flux cartographies obtained using the metamodel and the original FEM model is 1.7%, while the maximal local error is 4.96%. Then, the metamodel of the parametric FE solution can be used in an optimization process for different applications or to be coupled with other numerical models in order to simulate a system.

[1] L. Sirovich, Quarterly of applied mathematics, vol. 45, no 3, pp.561-571, (1987). [2] T. Henneron, A. Pierquin and S. Clénet, IEEE Transactions on Magnetics, vol. 56, no. 1, pp. 1-4, (2020). [3] A. de Boer, M.S. van

der Schoot and H. Bijl, Conference on Computational Fluid and Solid Mechanics, vol. 85, pp. 784-795, (2007). [4] T. Henneron, A. Pierquin and S. Clénet, IEEE Transactions on Magnetics, vol. 55, no. 6, pp. 1-4, (2019).

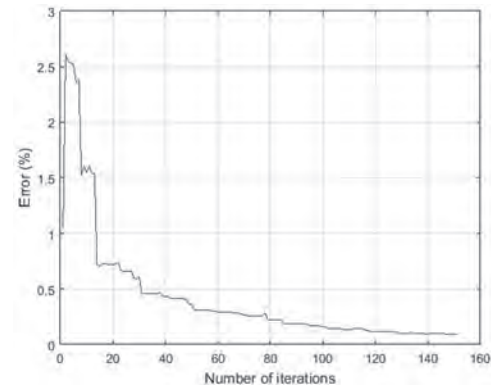


Fig.1 Error as a function of the number of iterations

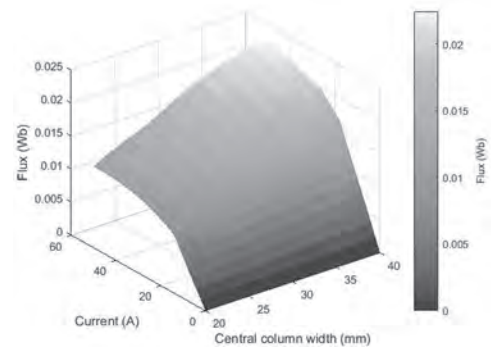


Fig. 2 Flux cartography as a function of current and central column width

BH-06. A New Permanent Magnet Biased Eddy Current Brake With Both AC and DC Windings for Low Speed Applications.

M. Gulec¹ and M. Aydin¹

¹ Kocaeli Universitesi, Kocaeli, Turkey

Eddy current brakes (ECB) are frequently used in many applications due to their simple structures and almost infinite working life compared to conventional friction-type brakes. They have numerous topologies such as radial or axial flux ECBs and rotational or linear type ECBs [1-3]. The aim of all ECB topologies is to generate retarding force or torque in the moving rotor. Owing to Faraday's law of induction, altering magnetic fields create circular electric fields and these fields cause eddy currents. In low speeds applications, eddy currents are not generated sufficiently so that the braking force or torque characteristic of ECB does not usually fulfill the requirements [3-6]. In general, most ECBs in the literature and in the industry utilizes DC excitation coils. There is almost no study in the literature that covers axial flux AC ECB [7]. In this study, a new PM biased ECB is proposed with both DC and AC windings. This new PM biased ECB has an axial flux single-rotor single-stator configuration with DC and AC windings placed in the same slots. The main advantage of the proposed structure is that it is possible to obtain more braking torque at low speeds compared to conventional ECB due to additional AC winding. The DC winding is activated during both low and high speeds in the proposed ECB. Nevertheless, AC winding is used only at low speeds to increase the eddy currents in the rotor. Thus, more braking torque at low speeds is achieved by both DC and AC windings. In addition, the proposed PM biased hybrid winding ECB has other advantages that it is possible to control PM flux paths by using excitation coils alone. PM flux can be controlled in terms of flux switching by windings. Therefore, flux driven by PMs is forced to complete its path over the rotor during braking and much more braking torque is obtained. The proposed PM biased hybrid winding ECB topology is illustrated in Figure 1. PM magnetizations and hybrid coils are also provided in the figure. The general braking torque equations for a reference conventional axial flux ECB [8-9] are modified for the proposed PM biased ECB and used in the design process which will be given in the final paper. A series of FEA simulations are carried out to validate the design. Magnetic flux density variations for braking and no-braking operations are also given in Figure 2. Results show that it is possible to control the magnet flux by the proposed ECB. Braking torque characteristics at low speeds are also investigated and results are provided in Figure 3. It can clearly be said that more braking torque can be obtained by the proposed hybrid winding at low speeds compared to conventional ECB. This is the first paper covering axial flux ECB with hybrid windings. More details of the study will be provided in the final version of the paper.

[1] B. Lequesne, L. Buyun, T.W. Nehl, "Eddy-current machines with permanent magnets and solid rotors", *IEEE Trans. on Ind. Appl.*, vol. 33, no. 5, pp. 1289-1294, 1997. [2] R. Yazdanpanah, M. Mirsalim, "Hybrid electromagnetic brakes: Design and performance evaluation," *IEEE Trans. on Energy Con.*, vol. 30, no. 1, pp. 60-69, 2015. [3] S. E. Gay, M. Ehsani, "Parametric analysis of eddy-current brake performance by 3-D finite-element analysis," *IEEE Trans. on Magnetics*, vol. 45, no. 2, pp. 319-328, 2006. [4] K. Baoquan, J. Yinxi, Z. He, Z. Lu, Z. Hailin, "Analysis and design of hybrid excitation linear eddy current brake", *IEEE Trans. on Energy Conv.*, vol. 39, no. 2, pp. 496-506, 2014. [5] H. Shin, J. Choi, H. Cho, S. Jang, "Analytical torque calculations and experimental testing of permanent magnet axial eddy current brake", *IEEE Trans. on Magn.*, vol. 49, no. 7, pp. 4152-4155, 2013. [6] Y. Lezhi, L. Desheng, M. Yuanjing, J. Jiao, "Design and performance of a water-cooled permanent magnet retarder for heavy vehicles," *IEEE Trans. on Energy Conversion*, vol. 26, no. 3, pp. 953-958, 2011. [7] K. Karakoc, A. Suleman, E. J. Park, "Optimized braking torque generation capacity of an eddy current brake with the application of time-varying magnetic fields," *IEEE Trans. on Vehicular Tech.*, vol. 63, no. 4, pp. 1530-1538, 2014. [8] M. Gulec, E. Yolacan, M. Aydin, "Design, analysis and real time dynamic torque control of single-rotor-single-stator axial flux eddy current brake," *IET Elect. Power Appl.*, vol. 10, no. 9, pp. 869-876, 2016. [9] M. Gulec, M. Aydin, "Modelling and analysis of a new axial flux permanent magnet biased eddy current brake," in *Proc. of International Conference on Electrical Machines*, pp. 459-465, 2016

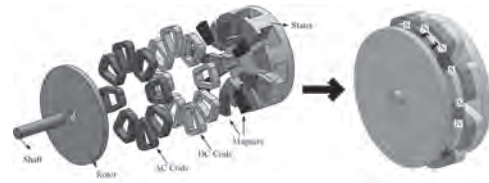


Fig. 1. Proposed PM biased hybrid winding ECB

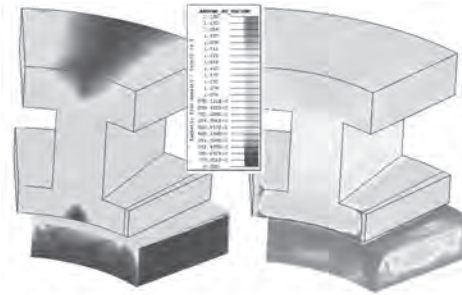


Fig. 2. Magnetic flux density distribution of proposed ECB for (a) no braking and (b) braking operations

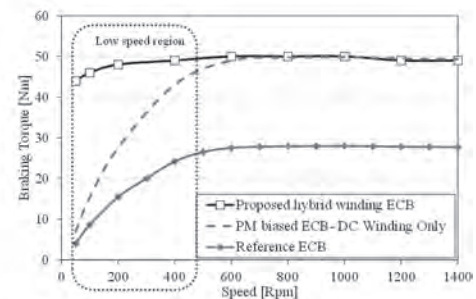


Fig. 3. Torque-speed curve of proposed PM biased hybrid windings ECB

BH-07. Magnetic Energy Minimization for Suppressing Magnetic Field Intensity of Inductive Power Transfer Systems.

Y. Narusue¹ and H. Morikawa¹

¹. Graduate School of Engineering, The University of Tokyo, Bunkyo-ku, Japan

I. INTRODUCTION Although inductive power transfer technology is under development with consideration for the protection of the human body and electromagnetic compatibility for practical use [1], further magnetic field strength reduction methods are necessary to accommodate the trend of increasing transmission power. Coil structures and shielding structures to suppress the magnetic field intensity [2,3]; however, further measures are required to build safer and higher-power inductive power transfer systems. Among the components comprised in inductive power transmission systems except the coils and shielding, the load is the only component that strongly affects the magnetic field intensity. The load impedance indirectly affects the magnetic field intensity because of the dependence of the amplitude and phase of the currents flowing through the transmitter and receiver on the load impedance. In this study, we design the load impedance based on a magnetic energy minimization problem. As the magnetic energy stored in the inductive power transfer system is positively correlated with the magnetic field intensity, solving the magnetic energy minimization problem leads to the load impedance at which the magnetic fields generated by the transmitter and the receiver cancel each other as much as possible. Because the proposed method does not assume the physical structures of the coils to be incorporated into the system, it can be applied along with existing magnetic field intensity suppression methods to achieve enhanced suppression. **II. METHODOLOGY** To solve the magnetic energy minimization problem for the load impedance Z_{load} , the equivalent circuit and circuit parameters shown in Fig. 1 are used. Although minimizing the magnetic field intensity with the equivalent circuit is not straightforward because the magnetic field intensity depends on the three dimensional structures of the coils, the magnetic energy stored in the inductances can be minimized with the equivalent circuit. The magnetic energy E_{L1} stored in the inductance L_1 of the transmitter can be calculated as $E_{L1} = L_1 i_1^2 / 2$. Similarly, the magnetic energy E_{sum} stored in inductances L_1 and L_2 and their mutual inductance M is expressed by $E_{sum} = L_1 i_1^2 / 2 + L_2 i_2^2 / 2 + M i_1 i_2$. In addition, for the angular frequency and the phasor current in the transmitter I_1 , the phasor current I_2 in the receiver is expressed as $I_2 = -j\omega M I_1 / (r_2 + j\omega L_2 + Z_{load})$. Z_{load} can determine the amplitude and phase of I_2 in the receiver with respect to I_1 in the transmitter, thereby manipulate the magnetic energy. Under the condition of constant received power, we derive the Z_{load} that minimizes the time average of E_{sum} . We omit the derivation process here for conciseness; however, when the quality factor of the receiving coil is sufficiently high such that r_2 approximates zero, the load impedance is formulated as: $Z_{load} = \omega |k| \sqrt{(1-k^2)} L_2 + j\omega(k^2-1) \times L_2$, (1) where k is the coupling coefficient between the transmitting and receiving coils. The effectiveness of the derived Z_{load} was confirmed using electromagnetic field simulations via Altair FEKO. The parameters of the transmitting and receiving coils were set assuming a power supply system for electric vehicles, with reference to [4]. Specifically, the outer diameter of the coil was 450 mm, the inner diameter was 115 mm, the number of turns was 50, the winding pitch was 3.35 mm, the diameter of the copper wire was 1.6 mm, and the operating frequency was 100 kHz. Simulation of a single coil yielded the inductance of 660.3 μ H. The coupling coefficient, calculated by simulation with a transmission distance of 100 mm in the vertical direction, was 0.3470. The optimum Z_{load} calculated from (1) was $135.0 - j364.9 \Omega$. When a load of $135.0 - j364.9 \Omega$ is connected and 1 kW is transferred to the load, the magnetic field intensity is shown in Fig. 2(a) with a drawing range of 1 m \times 1 m. When the Z_{load} value for maximizing power efficiency [5] is connected and 1 kW is transferred, the magnetic field intensity is as shown in Fig. 2(b). Although the magnetic field intensity with the proposed method is not suppressed uniformly, it is significantly suppressed in the space between the transmitting and receiving coils. At the central point in this space, the magnetic field intensity is weakened by 16%. The power efficiencies are nearly equal at 98.77% and 98.84% for the cases of magnetic energy minimization and power efficiency maximization, respectively. Z_{load} in (1) asymptotically approaches the value at which the power efficiency is maximized as the coupling coefficient decreases; therefore, it is considered that the power

efficiency is not significantly impaired. **III. CONCLUSION** In this study, the load impedance that minimizes the magnetic energy per transmission power is formulated by equivalent circuit analysis to suppress the magnetic field intensity generated by an inductive power transmission system. The validity of the theoretical formula is confirmed by electromagnetic field simulations. It is shown that in a system with a coupling coefficient of 0.35, the magnetic field intensity can be suppressed by up to 16% with a deterioration of approximately 0.1% in power efficiency.

[1] S.W. Park, IEEE Transactions on Magnetics, Vol.54, pp.1–8 (2018) [2] J. Kim, J. Kim, S. Kong, H. Kim, I.-S. Suh, N. P. Suh, D.-H. Cho, J. Kim, and S. Ahn, Proceedings of the IEEE, Vol.101, pp.1332–1342 (2013) [3] J. Park, C. Park, Y. Shin, D. Kim, B. Park, J. Cho, J. Choi, and S. Ahn, Applied Physics Letters, Vol.114, pp.1–5 (2019) [4] M. Kato, T. Imura, and Y. Hori, in Proceedings of 2012 IEEE International Telecommunications Energy Conference, pp.1–5 (2012) [5] I. Awai and T. Ishizaki, in Proceedings of 2012 IEEE MTT-S International Microwave Workshop Series on Innovative Wireless Power Transmission: Technologies, Systems, and Applications, pp.105–108 (2012)

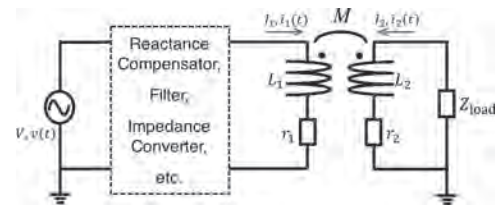


Fig.1 Equivalent circuit of an inductive power transfer system.

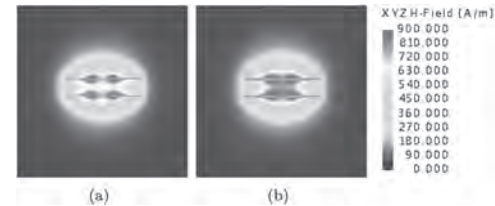


Fig.2 Comparison of the magnetic field intensity using different load impedances when the received power is 1 kW. (a) The proposed load impedance for minimizing the magnetic energy, (b) the load impedance for maximizing power efficiency.

BH-09. Back-EMF Characteristics of Two-Degree-of-Freedom Rotary-Linear Flux-Switching PM Machine.

P. Wang¹, K. Liu¹, H. Zhang¹ and W. Hua¹

1. School of Electrical Engineering, Southeast University, Nanjing, China

Abstract—Two-degree-of-freedom rotary/linear flux-switching permanent magnet (2DoFRL-FSPM) machine, which capable of rotary, linear and helical motion, has a wide application in automated lines, grinders, robot arms, etc. In this paper, the back-EMF characteristics of 2DoFRL-FSPM machine are investigated by the 3D finite element model, including the effect of motion forms and coupling effect. In addition, a prototype machine of 2DoFRL-FSPM machine is manufactured and tested. I. Introduction With the increasing requirement of machine tools, grinders, robot arms, automated lines, etc., two-degree-of-freedom (2DoF) machines have attracted more and more attention. 2DOF machines capable of rotary, linear and helical motions through the use of a single motor, seem to be an excellent solution to the problems of large volume, mechanical errors of the traditional plans which realized by the combination of multiple motors. Amiri E was the pioneer of 2DoF machines and proposed the first 2DoF machine named two-armature rotary-linear induction motor, which stator adopts a rotary armature connecting with a linear armature in series [1]. Afterward, several topologies of 2DoF machines had been proposed and investigated. To realize 2DoF motion form, special structures such as multi stators, spiral grooves, and windings, Halbach structure were designed and applied in 2DoF machines [2,3]. Previously, a Halbach PM array and a multi-winding array were adopted in an air-cored linear and rotary Halbach permanent magnet actuator [4]. The motion forms of the machine were determined by the mode of power supply. Normally, a long mover was always adopted in most 2DoF machines, which use more permanent magnets and result in low utilization of permanent magnets because there are always some permanent magnets beyond the stator. To overcome the above problems, 2DoFRL-FSPM machine whose permanent magnets are arranged in the stator part was proposed to increase the utilization and reduce the cost. In this paper, the back-EMF characteristics of 2DoFRL-FSPM machine are investigated. A 3D FE model considering the end and coupling effects are constructed to predicted the back-EMFs in different motion forms. In addition, experiments concerning 2DoFRL-FSPM machine are conducted based on its prototype machine. II. Topology of 2DoFRL-FSPM Machine A 2DoFRL-FSPM machine consists of two split arc-shaped stators (rotary and linear stators) and a long solid salient-poles mover to achieve rotary, linear and helical motions. In order to analyze the back-EMF characteristics of 2DoFRL-FSPM machine, a 3D FE model, which can simulate multi-degrees of freedom motions, is constructed as shown in Fig. 1. III. Back-EMF characteristics The stators of 2DoFRL-FSPM machine are arc-shaped, hence, the longitudinal end effect exists in the two parts of 2DoFRL-FSPM machine, which results that the back-EMF of one phase is larger than that of the other two phases. Due to the mover with an array of salient-poles on its surface, the coupling areas between the rotary or linear stator and the mover are variable in helical motion. In addition, the coupling effect between rotary and linear stators exists in helical motion, which leads to an increase of back-EMF harmonics. IV. Experiment In order to verify the above back-EMF characteristics, a prototype machine of 2DoFRL-FSPM machine is manufactured and tested. The rotary stator, linear stator, mover, and assembled machine are shown in Fig. 2. The predicted results are almost consistent with the measured, i.e., the back-EMF of one phase is larger than that of the other two phases.

[1] E. Amiri, P. Gottipati, and E. A. Mendrela, "3-D space modeling of rotary-linear induction motor with twin-armature," *in 2011 1st International Conference on Electrical Energy Systems*, 2011, pp. 203-206 [2] K. Guo, S. Fang, and H. Lin, "3-D Analytical Analysis of Magnetic Field of Flux Reversal Linear-Rotary Permanent-Magnet Actuator," *IEEE T. Magn.*, vol. 6, no. 53, pp. 1-5, 2017. [3] P. Jin, S. Fang, and H. Lin, "Analytical Magnetic Field Analysis and Prediction of Cogging Force and Torque of a Linear and Rotary Permanent Magnet Actuator," *IEEE T. Magn.*, vol. 10, no. 47, pp. 3004-3007, 2011. [4] P. Jin, Y. Yuan, and G. Jian, "Static Characteristics of Novel Air-Cored Linear and Rotary Halbach Permanent Magnet Actuator," *IEEE T. Magn.*, vol. 2, no. 50, pp. 977-980, 2014.



Fig.1 3D FE model of 2DoFRL-FSPM machine.

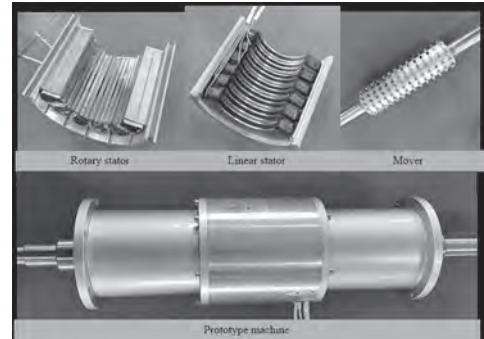


Fig.2 Prototype machine of 2DoFRL-FSPM machine.

BH-10. Influence of Rotor Pole Number on Electromagnetic Performance of Novel Asymmetric-Stator-Pole Flux Reversal PM Machine.

C. Qian¹, H. Yang¹ and H. Lin¹

¹. Southeast University, Nanjing, China

I. INTRODUCTION The novel asymmetric-stator-pole flux reversal permanent magnet (ASP-FRPM) machine [1] is recently developed to resolve the key problem of significant magnetic leakage in the conventional FRPM machine with uniform “NS-NS-NS” PM sequence [2]-[5]. The novel ASP-FRPM machine is characterized by a “NSN-S-NSN” stator magnet arrangement, which can significantly reduce the interpolar PM flux leakage, further improving the torque capability. However, the influence of the rotor pole number (RPN) on the ASP-FRPM machine has not been researched hitherto. Hence, this paper investigates the underlying mechanism and the influence rule of the RPN on the electromagnetic performance of ASP-FRPM machines, which can provide a generic design guideline for this type of machine.

II. TOPOLOGIES AND ROTOR POLE NUMBER DESIGN The topology of 12-stator-slot/17-rotor-pole ASP-FRPM machine is shown in Fig. 1(a). The stator slot number is set as 12 similar to conventional FRPM machines. In order to obtain a symmetrical and bipolar phase flux linkage, the stator-slot/rotor-pole numbers N_s and N_r should satisfy [6] $N_s/GCD(N_s, N_r)=2k, k=0,1,2,\dots(1)$ where GCD denotes the Greatest Common Divisor. Besides, the effective torque is proportional to the product of the flux linkage and the RPN, which is governed by [1] $T_e = 3/2N_r\Psi_m I_q$ (2) where T_e denotes the effective torque, Ψ_m denotes the flux linkage, and I_q is the q -axis current. Consequently, the RPN should not be too low. Hence, the RPN of ASP-FRPM can be 11, 13, 17, and 19 in this paper (higher RPNs will cause significant flux leakage, which are ignored in this case).

III. INFLUENCE OF ROTOR POLE NUMBER ON ELECTROMAGNETIC PERFORMANCE The no-load flux lines with various RPN are shown in Figs. 1(c)~(f). Apparently, more significant flux leakage can be observed when RPN decreases, as evidenced by the flux distributions on the stator yoke. In addition, the open-circuit phase back-EMFs of the ASP-FRPM machines with different RPNs are shown in Fig. 2(a). When the RPN is 17, the back-EMF is highest, which indicates that highest average torque can be accordingly obtained in this case, as evidenced in Fig. 2(b). Besides, when the RPN is less than 17, the average torque increases with the RPN, while decreases as the RPN is greater than 17. This is because the flux linkage is highest when RPN is 17, as visualized in Fig. 2(c), and the PM flux leakage becomes significantly serious when RPN is 19.

IV. EXPERIMENTAL VERIFICATION As shown in Fig. 1(b), the optimized 12-stator-slot/17-rotor-pole ASP-FRPM machine prototype is manufactured and tested. Fig. 2(d) shows the FE predicted and measured static torque against rotor position. The experiments agree well with FE results, confirming that the feasibility of the proposed design. The detailed design methodology, characteristics analyses, parametric optimization, and test results will be given in the full paper.

[1] H. Yang, H. Lin, Z. Q. Zhu, S. Lyu and Y. Liu, “Design and analysis of novel asymmetric-stator-pole flux reversal PM machine,” *IEEE Trans. Ind. Electron.*, vol. 67, no. 1, pp. 101-114, Jan. 2020. [2] R. P. Deodhar, S. Andersson, I. Boldea and T. J. E. Miller, “The flux-reversal machine: a new brushless doubly-salient permanent-magnet machine,” *IEEE Trans. Ind. Appl.*, vol. 33, no. 4, pp. 925-934, July/Aug. 1997. [3] C. Wang, S. A. Nasar and I. Boldea, “Three-phase flux reversal machine (FRM),” *IEE Proc. Elect. Power. Appl.*, vol. 146, no. 2, pp. 139-146, March. 1999. [4] D. Li, Y. Gao, R. Qu, J. Li, Y. Huo, H. Ding, “Design and analysis of a flux reversal machine with evenly distributed permanent magnets,” *IEEE Trans. Ind. Appl.*, vol. 54, no. 1, pp. 172-183, Jan./Feb. 2018. [5] H. Y. Li and Z. Q. Zhu, “Influence of magnet arrangement on performance of flux reversal permanent magnet machine,” in *Proc. Int. Electr. Mach. Drives Conf. (IEMDC)*, May 2017, pp. 1–8. [6] Y. Wang and Z. Deng, “Hybrid excitation topologies and control strategies of stator permanent magnet machines for dc power system,” *IEEE Trans. Ind. Electron.*, vol. 59, no. 12, pp. 4601-4616, Dec. 2012.

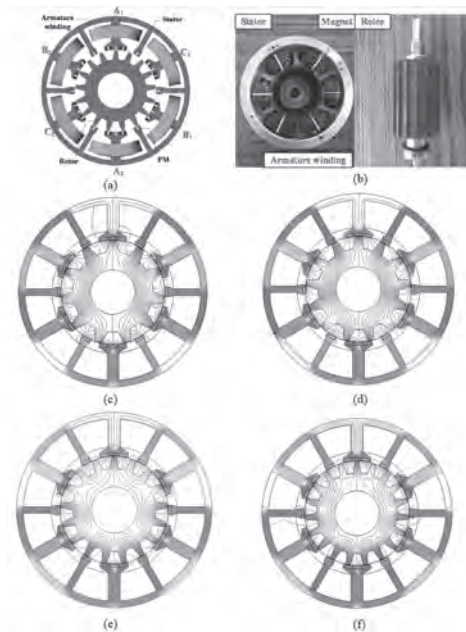


Fig. 1. (a) Topology of 12/17-pole ASP-FRPM machine. (b) The 12/17-pole ASP-FRPM machine prototype, and No-load flux line with various RPN. (c) RPN=11. (d) RPN=13. (e) RPN=17. (f) RPN=19.

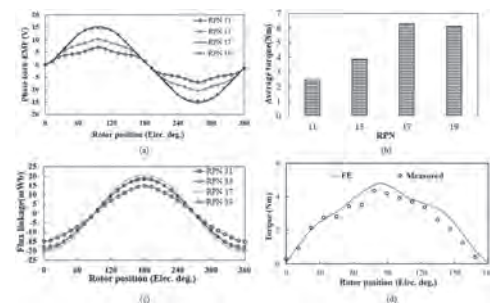


Fig. 2. (a) The open-circuit phase back-EMFs of the ASP-FRPM machine. (b) The average torque variation with different RPNs. (c) The flux linkage subject to different RPNs. (d) Comparison of FE and measured static torque against rotor position curves. ($I_a=-2I_b=-2I_c=10A$)

BH-11. Optimal IPT System Design Using Spiral Rectangular Coils for E-Tricycle Scooters Charging.

E. Yildiriz¹, S.B. Kemer² and B. Murat³

1. *Duzce Universitesi, Duzce, Turkey*; 2. *NURIS Technology, Ankara, Turkey*; 3. *FARBA Lighting Facility, Kocaeli, Turkey*

Although e-bikes are widely used today, there is no detailed system design for their wireless charging. In this study, the effects of switching frequency, quality factor, current density of the windings and critical coupling value have been examined and their boundaries have been determined for low power contactless charge system. According to these design constraints; an optimized Inductive Power Transfer (IPT) system has been analytically designed, which transfers the required power (120W) for the charging of the e-tricycle scooter from 100 mm air-gap. In view of previous studies in the literature [1, 2], the required power for e-bikes can be transmitted contactless at a frequency of 20-360 kHz. As the operation frequency increases, the size and quantity of coils to be used will decrease. The weight and volume of the coils are constraints in the system, that's why the operating frequency may increase as in small household appliances and biomedical applications. However, as in the case of electric vehicles where the power is relatively high; operating at high frequencies can be risky for human health. In addition, working at high frequencies, can increase switching losses and may cause noise in the communication system. Using ferrite cores can also reduce coil sizes [3]. But, the efficiency will decrease as core losses occur, and also the system weight will increase. On the other hand, in order to transfer the same power at low frequencies, the coil dimensions and number of turns increase. Therefore, an optimal design is required for IPT using air-core windings. The most important step affecting the system design performance is to calculate the real inductance values of the coils analytically. An IPT optimization used rectangular windings is described in ref [4] for 2kW and 200kW. But in ref [4], the average winding dimensions has been used in the calculation of self and mutual inductances. However, when the coil dimensions become smaller or the number of turns increases, the inductance calculation with this method gives unacceptable incorrect results. Therefore, we need to make separate calculations for each turn of spiral coils. For this, magnetic flux is calculated for each side of each winding in the spiral rectangular coil and all the results are summed for mutual inductance calculation [5]. Thus, the gaps between each winding can also be taken into account. The optimized IPT system is expected to operate under any operating conditions. The equivalent impedance of the batteries change during charge and discharge. The bifurcation event occurs when the load changes or in the misalignment condition. Therefore, primary and secondary quality factors should be carefully determined. Critical parameters are maximum switching frequency, the maximum current density of the coils, and quality factors in IPT design. Optimal system design is decided by the proper combination of critical parameters [4]. In this study, in addition to other optimization parameters, the critical coupling value is also considered in IPT optimization to avoid bifurcation [6]. The input impedance has been observed at different frequencies when the amplitude of load (Fig1a) and the coupling changes (Fig1b). Optimized design parameters for the inductive power transfer link are given in Figure 2. A controlled rectifier is used on the secondary-side to increase the overall system efficiency. Details of the optimum IPT design and experimental results of the system will be provided in the final version of the paper.

[1] N. Campagna, V. Castiglia, R. Miceli and F. Pellitteri, "A Bidirectional IPT system for Electrical Bicycle Contactless Energy Transfer," 2019 8th International Conference on Renewable Energy Research and Applications (ICRERA), Brasov, Romania, 2019, pp. 1063-1068, doi: 10.1109/ICRERA47325.2019.8996640. [2] A. Ahmad, M. S. Alam and R. Chabaan, "A Comprehensive Review of Wireless Charging Technologies for Electric Vehicles," in IEEE Transactions on Transportation Electrification, vol. 4, no. 1, pp. 38-63, March 2018. DOI: 10.1109/TTE.2017.2771619. [3] D. Iannuzzi, L. Rubino, L. Pio Di Noia, G. Rubino, and P. Marino, "Resonant inductive power transfer for an E-bike charging station," Elect. Power Syst. Res., vol. 140, pp. 631-642, Jun. 2016. [4] J. Sallan, J. L. Villa, A. Llombart and J. F. Sanz, "Optimal Design of ICPT Systems Applied to Electric Vehicle Battery Charge," in IEEE Transactions on Industrial Electronics,

vol. 56, no. 6, pp. 2140-2149, June 2009. DOI: 10.1109/TIE.2009.2015359. [5] P. Venugopal, S. Bandyopadhyay, P. Bauer and J.A. Ferreira, "A Generic Matrix Method to Model the Magnetics of Multi-Coil Air-Cored Inductive Power Transfer Systems," Energies 2017, 10, 774. DOI: 10.3390/en10060774 K. Aditya and S. S. Williamson, "Design Guidelines to Avoid Bifurcation in a Series-Series Compensated Inductive Power Transfer System," in IEEE Transactions on Industrial Electronics, vol. 66, no. 5, pp. 3973-3982, May 2019, doi: 10.1109/TIE.2018.2851953.

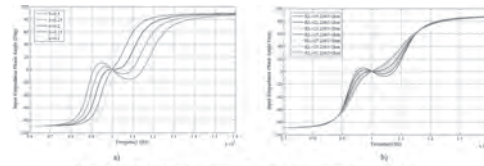


Figure 1. The effect of a) load and b) coupling change on the input impedance phase angle

Parameter	MATLAB	Measured	Parameter	MATLAB	Measured
d (mm)	100	100	V_p (Volt)	41,1	41,1
N_p	25	25	V_{c-} (Volt)	317,7077	318,7
N_s	24	24	V_{c+} (Volt)	287,9340	286,14
R_p (Ω)	0,3698	0,433	I_p (A)	2,9087	2,95
R_s (Ω)	0,3501	0,4067	I_s (A)	2,8465	2,86
L_p (μ H)	205,1179	207	f_0 (kHz)	84,7513	85,2
L_s (μ H)	189,9593	191	P_{in} (Watt)	113,5818	114,51
M (μ H)	26,4054	26	R_{eq} (Ω)	14,0183	14
C_p (nF)	17,1927	16,8	$V_{s'}$ (Volt)	39,9027	40,17
C_s (nF)	18,5646	18,3	η (%)	95,01	94,4

Figure 2. The design parameters achieved analytically and experimentally for optimal 120 W inductive power transfer link

Session B1

ADVANCES IN (SEMI)-ANALYTICAL AND NUMERICAL TECHNIQUES FOR MODELING

Shuangxia Niu, Chair

The Hong Kong Polytechnic University, Kowloon, Hong Kong

INVITED PAPER**BI-01. Core Losses and AC Winding Losses in Finite-Element and Lumped-Parameter Analysis of PMSMs – Pragmatism Versus Number Crunching INVITED.**

*J. Gyselinck*¹ and *R. Sabariego*²

1. BEAMS, Universite Libre de Bruxelles, Bruxelles, Belgium; 2. ELECTA, Katholieke Universiteit Leuven, Leuven, Belgium

Since the early days in the 1980's, the finite-element (FE) analysis of electrical machines has evolved enormously, both regarding software and hardware, and both in academia and industry. Finding the right balance between accuracy and computational cost for the analysis task at hand is key. Thanks to parameter extraction from the FE model and/or experimental identification, the numerical analysis can be started/continued in a circuit simulator, e.g. Simulink, with consideration of power-electronic supply and the wider system. There is still a big margin for progress in terms of computational cost and accuracy, in particular by devising and cleverly using new modelling techniques. This will be demonstrated in this presentation by focusing on permanent-magnet synchronous machines (PMSMs) and the consideration of core losses, i.e. hysteresis and eddy-current (EC) losses in core and permanent magnets (PMs), and AC winding losses due to skin and proximity effect. This includes homogenization techniques for lamination stacks and multi-turn windings in a FE model, as opposed to their detailed brute-force modelling; implementation/exploitation complexity, computational cost and accuracy will be discussed. An overview of hysteresis models will also be given. A recurrent (sometimes open) question throughout the presentation is: is our modelling approach sufficiently pragmatic or are we only having our computer do overtime.

CONTRIBUTED PAPERS

BI-02. Reluctance Network Model of Switched Reluctance Motor Considering Magnetic Hysteresis Behavior.

Y. Hane¹, K. Mitsuya¹ and K. Nakamura¹

1. Graduate School of Engineering, Tohoku University, Sendai, Japan

In recent years, it is strongly required to establish a practical calculation method for iron loss of electric machines including magnetic hysteresis behavior, in order to develop high-efficient electric machines. However, magnetic hysteresis is not considered in general-purpose numerical analysis programs due to a long calculation time. To overcome the above problem, this paper proposes a reluctance network analysis (RNA) [1]. The RNA expresses an analytical object by one reluctance network. All the reluctances can be determined by B-H curve of the material and dimensions. The RNA has some advantages such as a simple model, fast calculation, and easy coupling with external electric circuit and motion equation. The RNA has been applied to the calculation of characteristics of various electric machines including transformers and motors. In previous papers, a novel RNA model incorporating a play model [2], which is one of the phenomenological models of magnetic hysteresis behavior, was presented. So far, this method was applied to the analyses of a permanent magnet synchronous motor [3] and a variable inductor [4], and its calculation accuracy was proved by comparing the measured and calculated values. However, the voltage and current waveforms are almost sinusoidal in these devices. Therefore, in this paper, the versatility of this method is experimentally demonstrated by using a switched reluctance (SR) motor, which has stronger nonlinear magnetic properties and is excited by a square voltage waveform, as an object of discussion. In this paragraph, a deriving method for the RNA model of the SR motor incorporating the play model is described [5]. First, the analytical object is divided into multiple elements. To allow consideration of leakage flux flowing between the stator pole and yoke, and between the adjacent stator poles, surrounding space is also divided. In the core region, each reluctance is needed to be determined by considering magnetic hysteresis. Thus, the dc hysteresis is represented by the play model, which can express an arbitrary hysteresis loop by multiplying play hysterons with different widths by shape functions. Although the play model generally requires a large number of measured dc hysteresis loops with different maximum flux densities to derive the shape functions, the proposed method requires only one or two measured dc hysteresis loops because the Landau-Lifshitz-Gilbert (LLG) equation is used to calculate the dc hysteresis loops [6]. Fig. 1(a) shows the hysteresis loops calculated by the LLG equation. As shown in this figure, a large number of hysteresis loops which are used to derive the play model can be obtained without experiments. On the other hand, the classical and anomalous eddy current losses are denoted by the inductance and controlled-source, respectively. In addition, since an SR motor has a salient pole structure, the magnetic flux distribution around the stator and rotor pole tips change dynamically with rotation. Thus, the magnetic circuit around poles and the air gap is represented by variable reluctances depending on the rotor position angle as shown in Fig. 1(b), so that the local magnetic saturation and the fringing magnetic flux can be taken into consideration. Fig. 1(c) shows a schematic diagram of the proposed RNA model incorporating the play model. The controlled-sources at the stator poles are the MMFs generated from the winding current. Using the proposed RNA model, the characteristics of the SR motor are calculated when the excitation voltage is 9 V, the excitation starting angle is 0 deg., and the excitation width is 70 deg. Fig. 2(a) and (b) show the measured and calculated winding rms current density versus torque and torque versus rotational speed characteristics, respectively. As shown in these figures, the measured and calculated values are in good agreement. Next, Fig. 2(c) and (d) show the measured and calculated iron loss and efficiency characteristics, respectively. In the experiment, iron loss is measured by subtracting the sum of mechanical output and copper loss, and mechanical loss measured separately in advance, from electrical input. From these figures it is clear that the measured and calculated values are in good agreement. Furthermore, Fig. 2(e) indicates calculated hysteresis loops in certain divided elements of the RNA model. As shown in the figure, the magnetic hysteresis inside the core, which is generally difficult to measure

and calculate, can be drawn by the proposed method. In the future, we plan to verify the validity of such local hysteresis loops in the experiment. This work was supported by Grant-in-Aid for JSPS Fellows (JP19J20572).

[1] C. P. Steinmetz, "On the law of hysteresis", Proc. IEEE, Vol. 72, No. 2, pp. 197-221 (1984). [2] D. C. Jiles and D. L. Atherton, "Theory of Ferromagnetic Hysteresis", J. Magn. Magn. Mater., Vol. 61, No. 1-2, pp. 48-60 (1986). [3] G. Friedman, "New Formulation of the Stoner-Wolfarth Hysteresis Model and the Identification Problems", J. Appl. Phys., Vol. 67, No. 9, pp. 5361-5563 (1990). [4] G. S. Park, S. Y. Hahn, K. S. Lee, and H. K. Jung, "Implementation of Hysteresis Characteristics Using the Preisach Model with M-B Variables", IEEE Trans. Magn., Vol. 29, No. 2, pp. 1542-1545 (1993). [5] S. Bobbio, G. Miano, C. Serpico, and C. Visone, "Models of Magnetic Hysteresis Based on Play and Stop Hysteresis", IEEE Trans. Magn., Vol. 33, No. 6, pp. 4417-4426 (1997). [6] H. Tanaka, K. Nakamura, O. Ichinokura, "Magnetic Circuit Model combined with Play Model Obtained from Landau-Lifshitz-Gilbert Equation", Journal of Physics: Conference Series, Vol. 903, 012047 (2017). [7] K. Nakamura and O. Ichinokura, "Reluctance Network Based Dynamic Analysis in Power Magnetics," IEEE Trans. FM, Vol.128, No.8, pp. 506-510 (2008). [8] K. Nakamura, K. Kimura, and O. Ichinokura, "Electromagnetic and motion coupled analysis for switched reluctance motor based on reluctance network analysis," Journal of Magnetism and Magnetic Materials, Vol. 290-291, pp. 1309-1312 (2005).

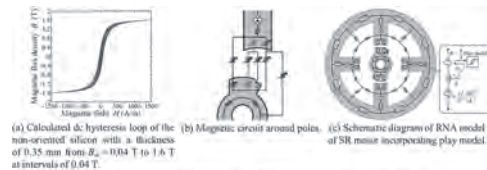


Fig. 1 Proposed RNA model of SR motor incorporating play model.

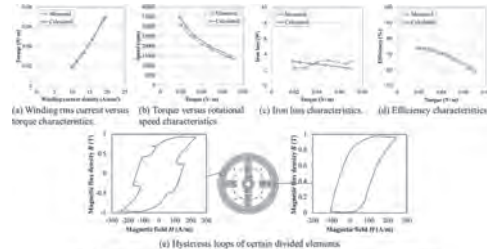


Fig. 2 Simulation results of the RNA model of SR motor incorporating play model

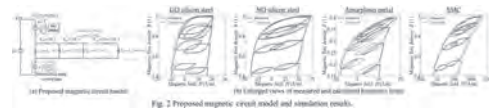
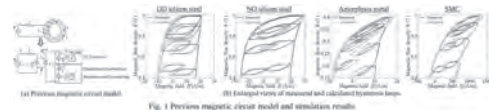
BI-03. Dynamic Hysteresis Modeling Considering Skin Effect for Magnetic Circuit Analysis.

Y. Hane¹ and K. Nakamura¹

1. Graduate School of Engineering, Tohoku University, Sendai, Japan

In recent years, quantitative analysis of iron loss taking magnetic hysteresis behavior into account is essential to development of high-efficiency electric machines. In a finite element method (FEM)-based design and analysis, iron loss of electric machines is approximately calculated based on Steinmetz's equation [1], although its calculation accuracy is not necessarily sufficient in the case of PWM and dc-biased excitation conditions. Thus, various hysteresis models have been proposed so far [2]-[4], in order to accurately simulate the magnetic hysteresis behavior. However, most of the general-purpose FEM programs neglect magnetic hysteresis since its calculation takes a lot of time in general. Therefore, establishment of a simple and practical method for calculating iron loss including magnetic hysteresis behavior is strongly required. In a previous paper, a magnetic circuit model incorporating a play model [5], which is one of the phenomenological models of magnetic hysteresis behavior, was proposed [6]. It was clear that the proposed model can calculate the hysteresis loop of the magnetic reactor with high-speed and high-accuracy. However, there is a possibility for further improvement in the calculation accuracy of the minor loop generated from carrier harmonics under PWM excitation because the influence of the skin effect cannot be considered. Therefore, in this paper, the magnetic circuit model is improved to be that the dynamic hysteresis characteristics including the skin effect can be considered, so that the minor loop can be calculated with higher accuracy. The validity of the improved model is proved by using ring cores made of various materials, such as grain-oriented (GO) and non-oriented (NO) silicon steels, an amorphous alloy, and a soft magnetic composite (SMC). Fig. 1(a) shows the previously proposed magnetic circuit model incorporating the play model. As shown in the figure, the dc hysteresis is represented by the play model. The play model can express an arbitrary hysteresis loop by multiplying play hysterons with different widths by shape functions. To derive the shape functions, the play model generally requires a large number of measured dc hysteresis loops with different maximum flux densities [1]. On the other hand, the classical eddy current loss and the anomalous eddy current loss are denoted by the inductance and the controlled-source, respectively. Fig. 1 (b) shows the comparison of the measured and calculated hysteresis loops under PWM excitation for each core material. This figure reveals that the previous magnetic circuit model can calculate the major loop with high accuracy, while there are errors in the shape of the minor loops. The cause of the errors is not to consider the influence of the skin effect by carrier harmonics. Therefore, in order to calculate minor loops with higher accuracy, the magnetic circuit model is improved as shown in Fig. 2(a). In the previous model, the eddy current loss is given by single inductance element. On the contrary, in the proposed model, the influence of the skin effect is represented by a ladder circuit in which inductances and resistances are repeatedly connected in parallel and in series. This ladder circuit represents the frequency characteristic of the complex permeability at higher frequencies as the number of circuit stages is larger. The parameters L_m and R_m of the circuit elements are given by the following equations: $L_m = (4/\sigma d^2) \times (l/S)$ (1) $R_m = (1/\mu) \times (l/S)$ (2) where the magnetic path length is l , the cross-sectional area is S , the conductivity is σ , the thickness of the silicon steel is d , and the permeability is μ , respectively. The validity of the proposed model is proved by comparing the measured and calculated hysteresis loops under PWM excitation, as shown in Fig. 2(b). In the analysis, the ladder circuit is terminated by the second inductance L_{m1} . From this figure, it is clear that the minor loops can be calculated with much higher accuracy comparing with the previous model for GO and NO silicon steels and a SMC. On the other hand, the calculation accuracy hardly changes for an amorphous metal since the values of σ and d is quite small. The cause of the error of the minor loops is considered to be the overestimated anomalous eddy current loss, which is one of the issues to be solved in the future. In the future, we plan to apply the proposed method to the analysis of reactors and transformers, which are used for switching power supplies, in order to calculate the iron loss considering magnetic hysteresis behavior including the minor loop with higher accuracy. This work was supported by Grant-in-Aid for JSPS Fellows (JP19J20572).

[1] C. P. Steinmetz, "On the law of hysteresis", Proc. IEEE, Vol. 72, No. 2, pp. 197-221 (1984). [2] D. C. Jiles and D. L. Atherton, "Theory of Ferromagnetic Hysteresis", J. Magn. Magn. Mater., Vol. 61, No. 1-2, pp. 48-60 (1986). [3] G. Friedman, "New Formulation of the Stoner-Wolfarth Hysteresis Model and the Identification Problems", J. Appl. Phys., Vol. 67, No. 9, pp. 5361-5563 (1990). [4] G. S. Park, S. Y. Hahn, K. S. Lee, and H. K. Jung, "Implementation of Hysteresis Characteristics Using the Preisach Model with M-B Variables", IEEE Trans. Magn., Vol. 29, No. 2, pp. 1542-1545 (1993). [5] S. Bobbio, G. Miano, C. Serpico, and C. Visone, "Models of Magnetic Hysteresis Based on Play and Stop Hysteresis", IEEE Trans. Magn., Vol. 33, No. 6, pp. 4417-4426 (1997). [6] H. Tanaka, K. Nakamura, O. Ichinokura, "Magnetic Circuit Model combined with Play Model Obtained from Landau-Lifshitz-Gilbert Equation", Journal of Physics: Conference Series, Vol. 903, 012047 (2017).



BI-04. Vector Hysteresis Modeling of a Variable Flux Reluctance Machine Combined With the Hybrid Analytical Modeling.

D. Ceylan¹, R. Zeinali¹, B. Daniels¹, K.O. Boynov¹ and E. Lomonova¹
 1. Department of Electrical Engineering, Technische Universiteit Eindhoven, Eindhoven, Netherlands

Variable flux reluctance machine (VFRM) attracts many researchers' attention because of its permanent magnet (PM)-free and robust structure [1]. It has both ac- and dc-field windings in the stator, while it exhibits double saliency without any source in the rotor. The additional dc field in the stator makes VFRM capable of on-line adjusting the flux-linkage [2]. Therefore, VFRM can implement the flux weakening at high efficiency without any risk of demagnetizing PMs or an additional mechanical flux adjuster. Moreover, VFRM performs a sinusoidal flux-linkage and back-EMF [3]. On the other hand, the existence of dc-field windings in the stator comes with a disadvantage which is the fact that they contribute to the magnetic flux density in the electrical steel as an off-set. The magnetic flux density with a non-zero average in the soft-magnetic material decreases the accuracy of the single-valued nonlinear magnetic characteristics approximation. Therefore, using a single-valued B-H curve for the analysis of VFRM results in unrealistic magnetic field distribution which causes inaccurate core loss and torque calculation. In this paper, the effect of including the vector hysteresis modeling in the analysis of a VFRM will be investigated. The hybrid analytical modeling (HAM) technique [4] will be employed to perform the magnetostatic analysis aiming to calculate the torque variation with respect to the rotor position for different ac- and dc-excitation levels. The proposed method will be verified with experiments in terms of the ac winding voltage dependent on the flux-linkage. I. Modeling method HAM is a combination of the magnetic equivalent circuit (MEC) and the Fourier analysis (FA) methods [5]. The stator and rotor are modeled as a MEC network, while the magnetic field distribution in the airgap is calculated analytically using FA. The fixed-point method (FPM) is coupled with HAM to take the nonlinear magnetic characteristics of the soft-magnetic material into account iteratively. FPM uses the magnetic flux density values calculated by HAM and gives the remanent flux density and the incremental permeability defining the tangential line on the saturation curve. The tangent line is used to calculate an additional magnetic saturation related magneto-motive force (MMF). The convergence analysis of FPM with HAM is investigated in [6]. FPM is modified such that an anisotropic congruency-based vector hysteresis model is used instead of the single-valued saturation curve to update the saturation related MMF. In the hysteresis calculation, a scalar congruency model [7] is employed as the main building-block for the vectorial model. The scalar model is extended to include the anisotropy effect. The Mayergoyz vector generalization is applied to the developed anisotropic scalar model. The flowchart of the proposed method consisting of both HAM and the vector hysteresis is illustrated in Fig. 1. The proposed method starts with an initial guess of the incremental permeability (μ_{init}) for the MEC elements located in the iron regions. HAM calculates the magnetic flux density (B) and the torque (T). Then, the stopping criterion is checked using the relative error in the torque between the successive iterations. If it is decided to continue iterations, the hysteresis model updates the remanent flux density (B_r) and the permeability (μ) which changes the reluctance (R) and MMF in HAM formulation. II. Results VFRM benchmark designed and tested in [8] is analyzed using the developed 2-D nonlinear HAM combined with a static vector hysteresis model. The magnetostatic analysis of the benchmark with a constant speed is carried out for different saturation levels as well as different dc over ac current ratios. In Fig. 2(a), the magnetic flux density in the radial direction in the middle of an arbitrary stator tooth is presented with respect to the displacement. In the first case, dc and the peak of ac currents are selected as 40 and 28 A, while the rotor is rotated with 500 rpm to be in the constant torque region. Then, the dc current is reduced to 20 A for 5000 rpm to perform the flux weakening with a reduced dc current and increased speed. Fig. 2(b) presents the results of the hysteresis model, which is set up to represent static curves of NO27 material. It is observed that increasing the dc over ac current ratio causes the minor loop to move upward in the hysteresis diagram. Therefore, an accurate hysteresis modeling is significant for VFRM with a large dc excitation level which is the case in the constant torque region. In the full paper of this study, the listed further investigations

will be presented: • The proposed modeling method combining HAM technique with an anisotropic congruency-based vector hysteresis model will be explained in detail. • The effect of dc over ac current ratio and the saturation level on the minor hysteresis loops and the total hysteresis loss will be investigated. • The results of the hybrid analytical model with and without the hysteresis model will be compared in terms of the magnetic flux density distribution. • The improvement in the modeling will be verified experimentally. In the experiments, the stator windings will be excited with the same ac and dc currents, while the rotor is rotated by an external motor. The winding voltage depending on the flux-linkage will be measured for the verification of the proposed modeling method.

[1] J. T. Shi, X. Liu and D. Wu, IEEE Trans. Magn., vol. 50, no. 11, pp. 1-4, (2014) [2] X. Liu and Z. Q. Zhu, IEEE Trans. Magn., vol. 49, no. 6, pp. 1-9, (2013) [3] X. Liu and Z. Q. Zhu, IEEE Trans. Magn., vol. 50, no. 11, pp. 1-4, (2014) [4] K. J. W. Pluk, J. W. Jansen and E. A. Lomonova, IEEE Trans. Magn., vol. 51, no. 8, pp. 1-12, (2015) [5] S. Ouagued, Y. Amara and G. Bakarar, IEEE Trans. Magn., vol. 52, no. 7, pp. 1-4, (2015) [6] D. Ceylan, L. A. J. Friedrich and K. O. Boynov, IEEE Trans. Magn., early access, (2020) [7] R. Zeinali, D. C. J. Krop and E. A. Lomonova, IEEE Trans. Magn., vol. 56, no. 1, pp. 1-4 (2020) [8] J. Bao, Ph.D. dissertation, Eindhoven University of Technology (2019)

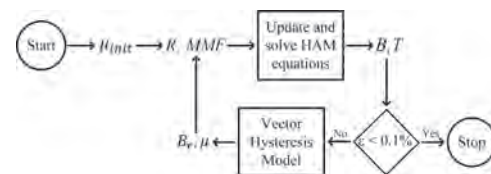


Fig. 1: The flowchart of the proposed method.

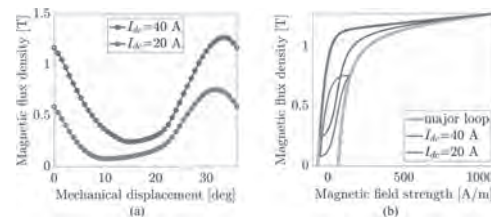


Fig. 2: a) The magnetic flux density variation for two different dc excitation levels, b) The resultant hysteresis loops.

BI-05. Analytical Calculation for Magnetic Field in Spoke-Type Permanent Magnet Machines Based on a Rotor Magnetic Potential Model.

S. Wu², H. Wang³, L. Guo³, Z. Wang³, Z. Song² and T. Shi¹

1. Zhejiang University, Hangzhou, China; 2. Tianjin University, Tianjin, China; 3. Tiangong University, Tianjin, China

I. Introduction The spoke-type permanent magnet (PM) machines are widely used in many industrial fields because of their excellent performance of concentrating flux from the PM. Accurate calculation of the magnetic field is the premise for predicting the machine performances [1]-[3]. The analytical calculation methods of the magnetic field commonly used for spoke-type machines include the lumped magnetic circuit (LMC) model [1], subdomain model [2], and the method combining the two above [3]. The rotor magnetic potential (RMP) model is another analytical method to accurately calculate the magnetic field [4], which has been widely used in interior radial PM machines but has not been applied to spoke-type machines. In this paper, the RMP models of the spoke-type machine are proposed. Furthermore, a method is provided by combining the proposed RMP model and the winding function, which can realize a fast and accurate calculation of the magnetic field in spoke-type machines. The modeling processes of the RMP model proposed in this paper are straightforward, and it has fewer variables to be solved. Moreover, the proposed method does not need to consider the change of the relative position between the stator and rotor caused by rotor rotation.

II. The Proposed RMP Model The RMP model is used to reflect the rotor surface magnetic potential distribution. In this paper, the magnetic field is divided into d-axis magnetic field (the magnetic field generated by the interaction of PM and d-axis current component) and q-axis magnetic field (the magnetic field generated by the q-axis current component). When there is only the d-axis magnetic field, it can be seen from Fig. 1(a) that the pole cap region is not saturated. Therefore, the RMP of the pole cap region is equal to that of the corresponding PM surface. Due to symmetry, the magnetic potentials on the left and right PM surfaces are opposite to each other. Hence the zero-crossing point of the RMP is located in the middle of the bridge (point B in Fig. 1(a)). According to the flux lines distribution in the bridge region, the RMP in this region changes linearly to both sides as the distance from point B increases. Therefore, the d-axis RMP model is obtained, as shown in Fig. 1(c). When there is only the q-axis magnetic field, it can be seen from Fig. 1(b) that the flux lines do not pass through the PMs; hence the RMP in the pole cap region is equal to zero. In the bridge region, the flux lines are separated in the middle of the bridge. Since the d-axis magnetic field is larger than the q-axis magnetic field, the influence of the d-axis magnetic field should be taken into account in the q-axis RMP model. Therefore, the q-axis RMP reaches the maximum value in the middle of the bridge (point B in Fig. 1(b)) and decreases to both sides along the flux lines. Therefore, the q-axis RMP model is obtained, as shown in Fig. 1(d). It should be noted that the position of points A and B in Fig. 1(a) and Fig. 1(b) are same. III. The Solution of the Proposed RMP Model The d-axis and q-axis LMC models are established to solve the unknown parameters (U_{d1} and U_{q1}), as shown in Fig. 1(e) and Fig. 1(f). R_{au} and R_{ad} are nonlinear reluctances corresponding to the upper and lower bridge regions, respectively. R_{gd} is d-axis air-gap reluctance. R_m is PM reluctance. F_c is PM magnetomotive force (MMF). F_d is the equivalent stator MMF, and its value is $F_d=(F_{d1}+F_{d2}+F_{d3}-F_{d4}-F_{d5}-F_{d6})/3$. $F_{d1}-F_{d6}$ are the MMF at the corresponding stator teeth generated by the d-axis current component. R_{gq} is q-axis air-gap reluctance. F_q is the MMF generated by the q-axis current component. It should be noted that when there is only q-axis magnetic field, the bridge region is not saturated. Therefore, the reluctance R_{au} is only affected by the d-axis magnetic field. Moreover, there is a saturation overflow phenomenon in the bridge region (the width of the saturation region is wider than the actual bridge width). To reflect this phenomenon, the flux density value of point A in Fig. 1(a) is set as 1.6T (the magnetic potential drop in the core with flux density value less than 1.6T is ignored). Therefore, the length l_{ro} of the saturation overflow region (as shown in Fig. 1(a)) changes with different excitation conditions. The value of l_{ro} can be solved by using the continuity principle of flux, and then the value of abscissa x_1 of point A can be obtained. Since the dq-axis cross-coupling effect has been taken into account in the above models, the total RMP model can be obtained by adding the d-axis and q-axis RMP models

directly. Then the magnetic field and related parameters can be calculated by combining winding function with the proposed RMP model. IV. FEA Verification The basic parameters of the machine are listed in Table I. The validity of the proposed method (ANA) is verified by FEA. The comparison results of no-load air-gap flux density and back EMF are shown in Fig. 2 (a) and Table II. Under different current effective value I (20A to 200A) and different current angle φ (0° to -90°), the corresponding results of the air-gap flux density fundamental amplitude (FA) and average torque are shown in Fig. 2 (b) and Fig. 2 (c), respectively. As shown in Fig. 2, the maximum error of air-gap flux density FA does not exceed 8%, and the maximum error of average torque does not exceed 2%.

[1] Q. Chen, G. Liu, and W. Zhao, *IEEE Transactions on Magnetics.*, vol. 49(9), pp. 5150–5157 (2013). [2] P. Liang, F. Chai, and Y. Li, *IEEE Transactions on Industrial Electronics.*, vol. 64(5), pp. 3479–3488 (2017). [3] P. Liang, F. Chai, and Y. Bi, *Journal of Magnetism and Magnetic Materials.*, vol. 417, pp. 389-396 (2016). [4] Q. Li, T. Fan, and X. Wen, *IEEE Transactions on Magnetics.*, vol. 49(3), pp. 1193-1201 (2013).

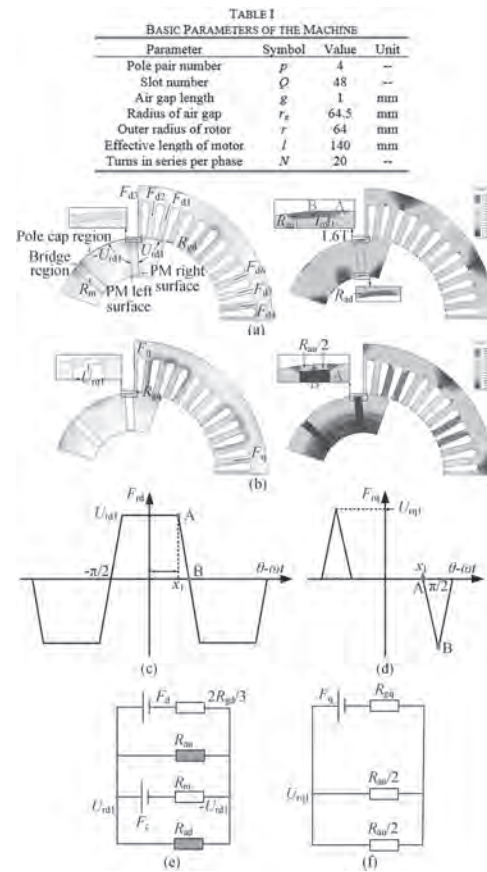


Fig. 1. (a) d-axis magnetic field (b) q-axis magnetic field (c) d-axis RMP model (d) q-axis RMP model (e) d-axis LMC model (f) q-axis LMC model

Parameter	Symbol	Value	Unit
Pole pair number	p	4	--
Slot number	\varnothing	48	--
Air gap length	δ	1	mm
Radius of air gap	r_s	64.5	mm
Outer radius of rotor	r	64	mm
Effective length of motor	l	140	mm
Turns in series per phase	N	20	--

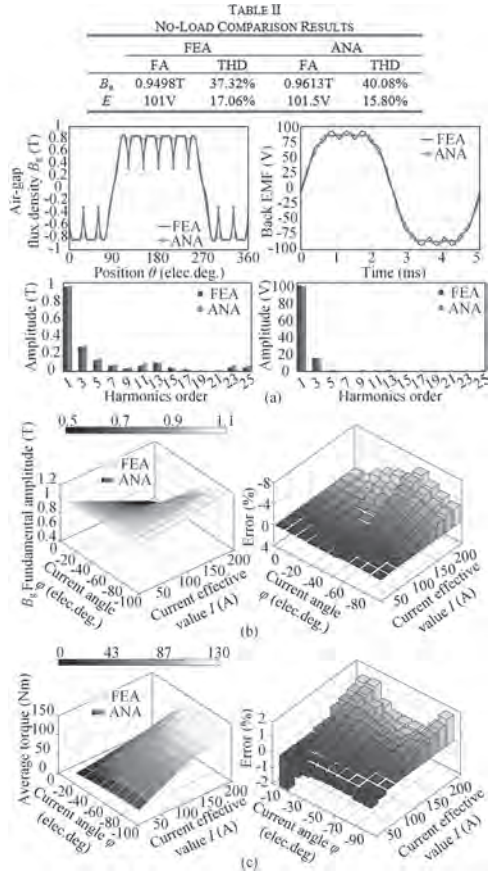


Fig. 2. The comparison results (a) no-load (b) air-gap flux density at load (c) average torque

BI-06. A Surrogate Model Assisted With a Subdomain Model for Permanent-Magnet Machine.

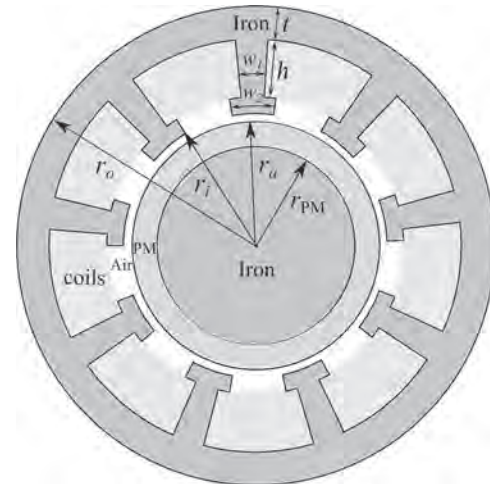
C. Tang¹, P. Pfister¹ and Y. Fang¹

1. Zhejiang University, Hangzhou, China

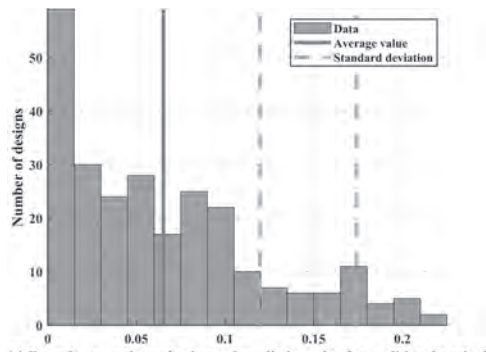
1 Introduction High-torque-density permanent-magnet (PM) motors are widely used in many industrial applications. They often work in overload situations. The magnetic saturation effect should hence be considered in the optimization process. These motors can have many slots and pole-pairs combinations, which makes optimization difficult. In the initial design step, analytical models allow a quick selection of the best candidates. However, most analytical models, such as subdomain models [3], are linear. The error of such models is important when the motor works in an overload situation. Researchers have provided hybrid models, which combine a reluctance network or a finite element model (FEM) with a subdomain model [5], [4]. These hybrid models are general and precise for different motors. However, they are slow, which is a major drawback compared to analytical models. Another quick nonlinear model is the surrogate model [1], [2]. The traditional surrogate model uses design parameters as the input and performance parameters as the output. Machine learning is used to build a mapping between input and output. However, PM motors always have many design parameters which may induce a large design parameters space. For this reason, this method can only build a surrogate model of the PM motors in a small local region of the design space. To overcome these drawbacks, we combine the subdomain and surrogate model into a new surrogate model assisted with a subdomain model (SMASM), which allows a very quick optimization and takes magnetic saturation into account. 2 Surrogate model assisted with a subdomain model (SMASM) We use more general features generated by the subdomain model to replace the design parameters as the input. The ratio of performance parameters between the linear (subdomain model) and nonlinear model (FEM) is used as output. Then, we use the Gaussian process regression (GPR) to build a mapping between them. We build a traditional surrogate model and SMASM which use the design parameters and features generated by the subdomain model as input separately. The ratio of the flux-linkage generated by PMs in no-load conditions between the linear and nonlinear model is selected as the output. Then, we use GPR to build two surrogate models. Finally, the test datasets are used to compare the performance between the two models. The topology of the test motors are surface-mounted PM (SPM) motors is shown in Fig. 1. The design parameters of the test motor include: 1. r_o , the outer radius of the stator, 2. t , the thickness of yoke, 3. h , the depth of slot, 4. r_i , the inner radius of the stator, 5. $a=r_i-r_a$, the air-gap, 6. $t_{PM}=r_a-r_{PM}$, the thickness of PM, 7. w_1 , the ratio of the tooth, 8. w_2 , the ratio of tooth-tip, 9. B_r , the remanence of PM, and 10. μ_r , the relative permeance of PM. The parameters include t , h , r_i , a , and t_{PM} divided by r_o to scale motors of different sizes into similar motors. The μ_r does not change too much in different SPM motors. In the traditional method, 8 design parameters are needed to be selected for the training dataset except for r_o and μ_r . However, in the SMASM, 5 features are selected which can contain the most information on these design parameters. 2.1 Training dataset for SMASM For SMASM, we select five features which include: 1. B_{tooth} , the maximum of the magnetic density in the tooth during the rotation, 2. B_{yoke} , the maximum of the magnetic density in the yoke during the rotation, 3. Φ/r_2 , the maximum of the flux in the tooth during the rotation divided by the radius of yoke $r_2=r_o-0.5t$, 4. P/r_2 , the equivalent air-gap $P=t_{PM}/\mu_r+a$ divided by the radius of yoke r_2 , and 5. h/r_2 , the depth of the slot divided by the radius of yoke r_2 . The ranges of the features are: 1. B_{tooth} from 1.5 T to 2.5 T; 2. B_{yoke} from 1.5 T to 2.5 T; 3. Φ/r_2 from 0.023 to 0.027; 4. P/r_2 from 0.03 to 0.05; 5. h/r_2 from 0.1 to 0.15. 2.2 Training dataset for the traditional method For a fair comparison, the five design parameters which change the features in the SMASM are selected correspondingly in the traditional method. They include w_1/r_2 , t/r_2 , B_r , t_{PM}/r_2 and h/r_2 . The range of these design parameters are: 1. w_1/r_2 from 1.0 to 1.5; 2. t/r_2 from 0.15 to 0.20; 3. B_r from 1.1 T to 1.3 T; 4. t_{PM}/r_2 from 0.02 to 0.04; 5. h/r_2 from 0.1 to 0.15. 2.3 Test dataset The test datasets of SMASM and the traditional method have eight features. Five of them are inherited from the training dataset separately. The other three design parameters are a/r_2 , w_2 and w_3 . We fix them in the training dataset and change them in the test dataset. The range of these design parameters are : 1. a/r_2 from 0.005 to 0.015; 2. w_2 from

0.45 to 0.75; 3. w_3 from 0.7 to 1.0. 2.4 Model verification The prediction error distribution is shown in Fig. 2. The average and maximum errors of the traditional method are 6.5% and 21.3%. The average and maximum errors of the SMASM are 1.1% and 3.5%. Despite that only 5 features are used, the performance of the SMASM is better. 3 Conclusion The SMASM uses five features to generate the surrogate model which can reduce the size of the training dataset and keep the accepted precision. If we sample 4 points for every feature, we can reduce the size of the training dataset from $4^8=65536$ to $4^5=1024$ sample points. Acknowledgment This work was supported by the National Natural Science Foundation of China under Grant 51851110761. Corresponding author: P.-D. Pfister (e-mail: pierredaniel.pfister.public@gmail.com).

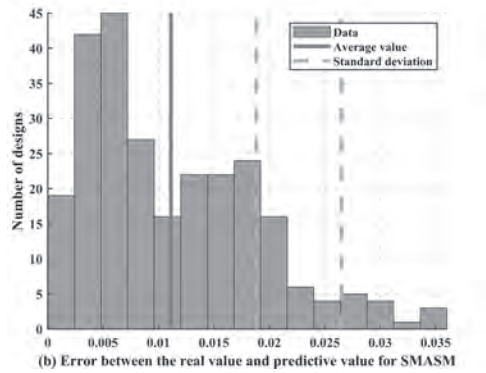
[1] Y. Fujishima, S. Wakao, A. Yamashita, T. Katsuta, K. Matsuoka, and M. Kondo. Design optimization of a permanent magnet synchronous motor by the response surface methodology. *Journal of Applied Physics*, 91(10):8305–8307, May 2002. [2] J. Gong, H. Zhang, B. Zhao, D. Fu, and F. Gillon. Proposal of a Bi-Objective Kriging Adapted Output Space Mapping Technique for Electromagnetic Design Optimization. *IEEE Transactions on Magnetics*, 55(6):1–5, June 2019. [3] P.-D. Pfister, X. Yin, and Y. Fang. Slotted permanent-magnet machines: General analytical model of magnetic fields, torque, eddy currents, and permanent-magnet power losses including the diffusion effect. *IEEE Transactions on Magnetics*, 52(5):1–13, May 2016. [4] M. Shen, P.-D. Pfister, C. Tang, and Y. Fang. A hybrid model of permanent-magnet machines combining Fourier analytical model with finite element method, taking magnetic saturation into account. *IEEE Transactions on Magnetics*, pages 1–5, 2020. [5] L. Wu, H. Yin, D. Wang, and Y. Fang. On-Load Field Prediction in SPM Machines by a Subdomain and Magnetic Circuit Hybrid Model. *IEEE Transactions on Industrial Electronics*, 67(9):7190–7201, September 2020.



The topology of the test motors



(a) Error between the real value and predictive value for traditional method



(b) Error between the real value and predictive value for SMASM

Flux linkage produced by the PMs calculated by the traditional and the SMASM methods: prediction error distribution

BI-07. Lagrange Based Model for Non-Linear Airgap Analytical Optimization in a Transverse Flux Motor, With Reference to an Electric Bicycle.

B. Mukherjee¹, J. Vannier¹ and F. Bernot²

1. *Energie, CentraleSupélec, Gif-sur-Yvette, France; 2. FranceCol Technology, Tours, France*

Abstract—This paper presents an analytical model of a transverse flux motor accounting for airgap shape between the rotor poles and the stator teeth. The major focus is in visualizing the impact of the airgap on the motor performance parameters as well as optimizing the airgap. The magnetic field distribution and electromagnetic performance of the motor is calculated by solving the governing functions based on boundary and interface conditions. The analytical predictions of the motor under both no-load and on-load conditions (cogging torque, back-EMF, rated torque etc.) are calculated and compared by finite element method. **Keywords**—Analytical model; transverse flux motor; low-traction. **I. Introduction** The authors envisage a future where public transportation is the optimal method to reduce carbon footprint in crowd movement in urban areas [1]. To allow this to happen mass adoption of light weight single person transportation modes is necessary. The paper focuses on electric bicycles which correspond to the most widely used single person transport medium till date. Although an unorthodox approach to the industry standard, a transverse flux motor powered electrical bicycle has several advantages over conventional motors used presently. The minimal to zero use of permanent magnets as well as a design optimized for industrial production (modularity, standardized parts, ease of assembly etc.) can help bring the production cost down. Bicycling is a relatively high torque low speed application which can make use of the variable excitation magnetic flux in a transverse flux motor [2]. However, the methodology for designing and optimizing transverse flux machines has not yet reached the sophistication that is visible with conventional motor geometry. Perusal of the existing literature points out that finite element method is mostly followed due to its accuracy in modelling for the non-conventional motor topology. But an alternative to the processor heavy and time-consuming modelling method during the initial design and optimization stage is needed. To accurately and quickly predict the magnetic field distribution and electromagnetic performance for TFM machines, an analytical model of machine accounting for effect of airgap on the performance is proposed in this paper. The analytical results of both no-load and on-load conditions (back-EMF, torque, cogging torque etc.) are analyzed and verified by FE method. **II. Analytical Modelling** A simplified (linearized) model of a field excited machine is shown in Fig. 1(a). For simplifying the model, the end effect is neglected, the current density is assumed to be uniformly distributed in slot area, the permeability of iron lamination is assumed to be infinite and the vector potential has only z-axis component. Example shown in the digest considers a flux excitation DC current coil wound on an iron rotor. Accounting for the varied types of transverse flux machine in the literature, permanent magnet regions on the rotor can be considered but the project is customized for a novel magnetless fractionnair transverse flux motor geometry whose rotor can be simplified into the presented diagram. The machine is divided into various regions based on field domains. The airgap is modelled in a greater detail by tracing the geometrical curves of the stator tooth shape and the rotor poles shape in a spatio-temporal reference frame. Then the current distribution integral and the airgap are used to get the magnetic flux density considering the partial differential equations for magnetic field determined in each region by the following: the airgap and slot opening regions satisfy the Laplace’s equation, the rotor poles region satisfies the Poisson’s equation, the slot region satisfies the Laplace’s equation for open-circuit condition and Poisson’s equation for on-load condition [3]-[5]. Once the magnetic flux density and other electromagnetic performances are tabulated with respect to variations in the airgap shape, an optimal airgap structure can be determined. **III. Electromagnetic Performance** The model considers a magnetless fractionnair transverse flux motor geometry of 3 phase 18-slot, 20-pole machine. The primary focus of the model is the airgap optimization. To this effect several models with different airgap shapes are considered. Fig. 1(b) shows two types of airgap geometry in 2D by swapping the shape of the stator tooth (the rotor remains same): parallel airgap and sinusoidal airgap. For simplification, the graphs are traced using a 18-slot, 18-pole single phase machine and the no load

flux density and on load flux density given by the model is compared in the Fig. 2(a) and Fig. 2(b) respectively. The optimized airgap as well as the electromagnetic performances of the full 3-phase motor model including back-EMF, cogging torque, rated torque etc. as well as its comparison to FEA model will be presented and analyzed in the full paper.

- [1] A. Olivares, J. Solé and O. Osychenko, “Transportation in a 100% renewable energy system,” *Energy Conversion and Management*, vol. 158, p. 266-285 (2018)
- [2] J. Gieras and N. Bianchi, “Electric Motors for Light Traction,” *European Power Electronics and Drives*, vol. 14, p. 12-23 (2004)
- [3] M. Azeem, M. Humza and B. Kim, “Analytical investigation of air-gap flux density distribution of a PM vernier motor,” *International Journal of Applied Electromagnetics and Mechanics*, vol. 59, no. 3, p. 943-949 (2019)
- [4] L. Roubache, K. Boughrara, F. Dubas, and R. Ibtouen, “New subdomain technique for electromagnetic performances calculation in radial-flux electrical machines considering finite soft-magnetic material permeability,” *IEEE Trans. Magn.*, vol. 54, no. 4, p. 1-15, (2018).
- [5] I. Hasan, T. Husain and Y. Sozer, “Analytical Model-Based Design Optimization of a Transverse Flux,” *Machine,” IEEE Energy Conversion Congress and Exposition* (2016)

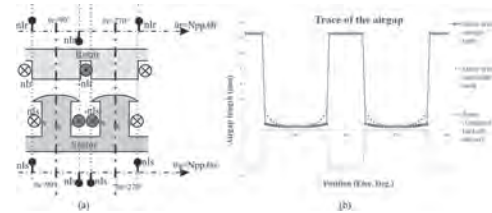


Fig. 1 (a) simplified (linearized) model of a field excitation machine (b) trace of two types of airgap: parallel and sinusoidal

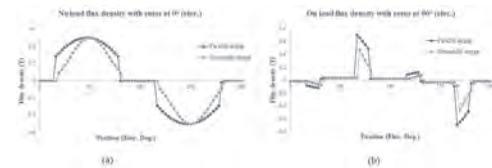


Fig. 2 Flux density comparison between the two airgap types (a) no load flux density at $\theta_e=0^\circ$ elec. angle (b) on load flux density at $\theta_e=90^\circ$ elec. angle

BI-08. 3-D Analytical Modeling and Optimization of Axial Flux Coreless PM Motor.

W. Qin¹, F. Wang¹ and J. Zhao¹

¹. Electrical Engineering, Beijing Jiaotong University, Beijing, China

I. INTRODUCTION Coreless axial-flux permanent-magnet synchronous machines (AFPMSMs) have many advantages such as high power density, simple structure, high overload capability, no cogging torque and so on. It has been used more and more widely in many applications, such as flywheel energy storage systems, wind energy power generation, electric vehicles, and ultra-precision positioning and processing areas [1-3]. However, it is difficult to accurately model AFPMSM as 3D electromagnetic problems, such as the curvature effect and fringing effect. The electromagnetic characteristics, such as air-gap flux density, back electromotive force (EMF), and electromagnetic torque, are critical in motor design. Precise design methods and fast performance estimations for coreless AFPMSM would be necessary. The most accurate method to design the AFPMSM is the 3D finite-element analysis, which is exceedingly time-consuming [4-5]. To solve this problem, a three-dimensional analytical approach, based on the volume integral method and second order vector potential (SOVP), is developed to calculate the coreless AFPMSM's steady-state and transient performances. II. ANALYTICAL MODEL The 3-D geometric model of the coreless AFPMSM is shown in Fig. 1 (a). This coreless AFPMSM consisting of one stator with ironless winding and two rotors with Halbach magnet array mounted on nonmagnetic supports. Such a Halbach rotor can be modeled using equivalent current sheets, thereby enabling the field at any point in 3-D space to be calculated using the Biot-Savart law [3]. For instance, the axial magnetized magnet can be created by the radial and circumference current filament model, as shown in Fig. 1(b), and then a volume integral approach is proposed to obtain the field for the current sheet shown as in Fig. 1(c) and ironless winding. The calculation of the magnetic field using the integral equations is obtained in very short times thanks to the use of particular volumetric basis elements for which the solution is obtained analytically. The field solution from volume integral approach is then used as the magnetic charge source term for an equivalent magnetic charge model. The replace function of the field for winding and Halbach rotor were given by Fourier series, thus the program difficulty (not shown here due to space limits) for three-dimensional distribution of the magnetic field will be reduced. The 3-D torque equations are derived using a magnetic charge sheet approach that enables the final torque equation to be expressed by a single equation without the need for a large number of summations. III. RESULTS AND VALIDATION The accuracy of the approach was validated 3D finite element analysis shown as in Fig 1 (d). The flux density calculated with the proposed approach are in good accordance with that obtained by 3D FEM simulation. Currently, we have designed and established a coreless AFPMSM prototype in laboratory as shown in Fig.2. Performance of the AFPMSM such as the flux density and torques are measured with the prototype. The experiment results are validated by FEA and proposed approach results and they will be included in the full paper. IV. CONCLUSIONS A three-dimensional analytical approach based on the volume integral method and magnetic charge sheet for the flux density and torque calculations in a coreless AFPMSM. These results will be compared to the 3D FEA and experiment results in the full paper.

[1] Z. Kohari, Z. Nadudvari, L. Szlama, M. Keresztesi, and I. Csaki, IEEE Trans. Appl. Supercond., vol. 21, no. 3, pp. 1497–1501. (2011). [2] T. F. Chan, L. L. Lai, IEEE Trans. Energy Convers., vol. 22, no. 1, pp. 86–94. (2007). [3] N. Taran, V. Rallabandi, G. Heins, and D. M. Ionel, IEEE Trans. Ind. Appl., vol. 54, no. 6, pp. 5907–5917. (2018). [4] Xu L, Xu Y, Gong J. IEEE Transactions on Magnetics, vol. 54, no. 11, pp. 1-5.(2018). [5] Daghigh A, Javadi H, Torkaman H. IEEE Transactions on Magnetics, vol.52, no.9.(2016).

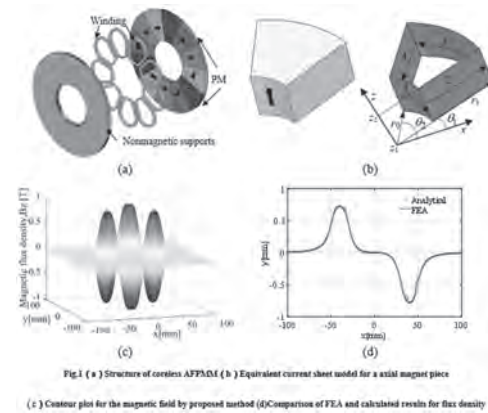


Fig. 1 (a) Structure of coreless AFPMSM (b) Equivalent current sheet model for a axial magnet piece (c) Contour plot for the magnetic field by proposed method (d) Comparison of FEA and calculated results for flux density

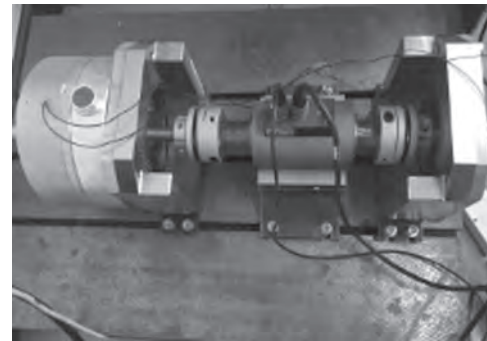


Fig. 2 Experimental setup to test the coreless AFPMSM

BI-10. Genetic Algorithm Optimal Design of SMPMSM Using Analytical Subdomain Model.

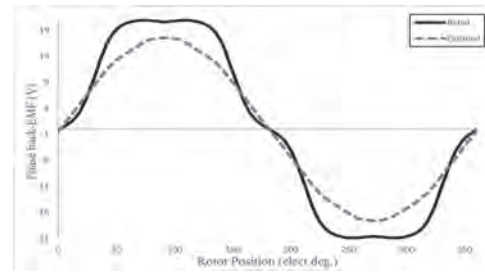
S.A. Mohd Shafiri¹, T. Tiang¹, D. Ishak², J. Leong¹, C. Tan³, H. Ong⁴ and M. Ahmad¹

1. Faculty of Electrical Engineering Technology, Universiti Malaysia Perlis, Arau, Malaysia; 2. Universiti Sains Malaysia, Minden, Malaysia; 3. Wawasan Open University, Penang, Malaysia; 4. Universiti Malaysia Perlis, Arau, Malaysia

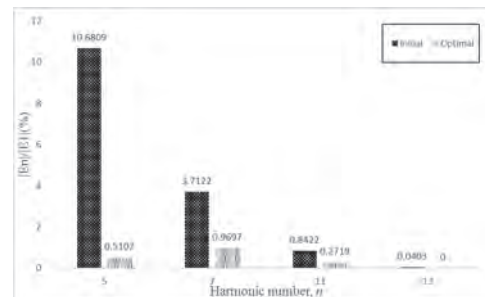
Introduction In recent years, SMPMSM is quietly famous compared with other conventional motors in industrial applications due to higher efficiency, higher reliability, low cost, and smooth torque [1]–[3]. In general, several objective optimizations need to be consider, which required an optimization technique for an electrical motor. This paper deals with an optimal design of a surface-mounted permanent magnet synchronous machine (SMPMSM) with an exact analytical subdomain model by using a genetic algorithm method. To analyze the characteristic of permanent magnet (PM) motors, the classical optimization method, such as the finite element method (FEM), is intensively used. However, FEM has several time problems that require a longer computational time to evaluate the performance of PM motors. This problem can be overcome by using a genetic algorithm (GA) method combined with a subdomain model (SD), which developed an improved performance of SMPMSM, for instance, total harmonic distortion (THD_v) and phase back-EMF. In this design, a three-phase 12-slot/8-pole PM motor is established with an exact SD model with radial magnetization patterns. Then, the GA ensemble with SD model to search the optimality of SMPMSM machine design. In the final analysis, the optimal new design of SMPMSM demonstrated by comparing with the initial design that is investigated by FEM. The result of induced back-EMF, and magnetic flux density of optimal design is compared with the initial design to show the advantages of GA optimization method. Analytical Model, Genetic Algorithm and Parameter of optimization The purpose of this analysis is to investigate the optimization design of a three-phase 12-slot/8-pole SMPMSM with a radial magnetization pattern. This optimization problem has been solved by obtains the minimum THD_v as a fitness function. In order to process the optimization design of SMPMSM, several parameters need to be optimized i.e magnet pole-pitch, α_p and slot-opening angle, b_{oa} . The roulette method is used to select the objective function of optimization with 50 maximum generations per iteration. The cross and mutation probability need to be set which requires linear and uniform recombination which is 0.89 and 0.025 respectively. The parameters of 12-slot/8-pole SMPM motor as follows: radius of the rotor, $R_r = 23\text{mm}$, the radius of PM surface $R_m = 26\text{mm}$, the inner radius of the stator $R_{sb} = 42.5\text{mm}$, axial length, $l_a = 50\text{mm}$, air-gap length, $l_g = 1\text{mm}$, remanence of the magnet, $B_r = 1.12\text{T}$, relative coil permeability, $\mu_r = 1.05$ with the number of pole pairs, N_p is 8 and number of stator slots, N_s is 12. The result, Discussion and Conclusion The phase back electromotive force has a significant relationship with flux-linkage because phase back electromotive force is derived from the rate of change of flux-linkage. In Fig. 1. show the waveform of phase back electromotive force against rotor position of initial and optimal design in radial magnetization patterns. The initial design of phase back electromotive force waveform shows more trapezoidal compare with the optimal design which has a sinusoidal waveform. The comparison of total harmonic distortion between the initial and optimal design of SMPMSM are demonstrated in Fig. 2 below. The result from Fig.2. shows the highest total harmonic distortion of 12-slot/8-pole motor is an initial design which is 11.34% compared with the optimal design where 1.3%. The magnitude of harmonic in phase back electromotive force $|E_n|$ of initial design shows 22.24 V compare to optimal design which is 17.4 V. This shows a good agreement that the optimal motor design gives lowest total harmonic distortion compare with the initial design. The optimizes of SMPMSM motor with the following parameters are given in Table 1.

[1] S. Wang *et al.*, “Multilevel optimization for surface mounted PM machine incorporating with FEM,” *IEEE Trans. Magn.*, vol. 45, no. 10, pp. 4700–4703, 2009, doi: 10.1109/TMAG.2009.2024875. [2] K. Sindhya, A. Manninen, K. Miettinen, and J. Pippuri, “Generator Using Interactive,” vol. 64, no. 12, pp. 9776–9783, 2017. [3] H. Li, Z. Chen, and H. Polinder, “Optimization of multibrid permanent-magnet wind generator systems,”

IEEE Trans. Energy Convers., vol. 24, no. 1, pp. 82–92, 2009, doi: 10.1109/TEC.2008.2005279.



The comparison of phase back electromotive force between initial and optimal design of 12-slot/8-pole SMPMSM under radial magnetization pattern.



The comparison of total harmonic distortion between initial and optimal design of 12-slot/8-pole SMPMSM under radial magnetization pattern.

Session BJ

ELECTRIC DRIVE APPLICATIONS, TRANSFORMERS AND WIRELESS POWER TRANSFER I

ChaoQiang Jiang, Chair

University of Cambridge, Cambridge, United Kingdom

CONTRIBUTED PAPERS

BJ-01. New Core Loss Model for Ferrite Cores Based on a Meta-Material Approach.T. Dimier¹ and J. Biela¹¹. HPE / D-ITET, ETH Zurich, Zurich, Switzerland

Introduction MnZn ferrites are widely used in power electronics for high frequency transformers and inductors since they offer a good compromise between low core losses, permeability and saturation flux density. For properly designing magnetic components, the effective permeability and the core losses must be determined. Different phenomena, like magnetic hysteresis or eddy-currents, lead to core losses. State-of-the-art loss models are often based on the Steinmetz equation or extensions such as Generalized Steinmetz Equation [1]. These approaches aim to model the overall losses at once using a power law based on three (or more) coefficients. A given set of parameters is only accurate around the operating point used for determining these parameters, for the various phenomena scale differently with frequency and flux density. This results in reduced operating ranges in which the methods are accurate. In contrast, with the Bertotti method [2] hysteresis and classical eddy current losses as well as an extra term, called excess losses, are considered separately. The three terms are calculated as with the Steinmetz model but with specific coefficients for each loss term. Even if using three loss components widens the frequency and flux density ranges, the parameters remain frequency dependent and the excess losses lack a proper physical explanation. Therefore, this work presents a physical approach based on the combination of an electrical model of the material structure with the flux distribution resulting from solving Maxwell equations. The new model is used to explain and estimate the frequency dependency of complex permeability as well as the eddy-current and excess core losses that can be then combined with hysteresis losses predicted by classical methods. Equivalent electrical model of material structure The sintering process leads to a meta-material made of grains that are insulated one from each other. Such a structure reduces significantly eddy-current losses since the effective conductivity is small due to the insulating layer between grains. However, the apparent conductivity and permittivity of ferrite depend on frequency because the grain boundary interface acts like a capacitor (Fig 1. a). Its impedance reduces at higher frequencies what short-circuits the high resistivity of the boundary (cf. [3] for NiZn ferrites and [4] for MnZn ferrite). As proposed in [3], a two series cells model could be used to describe the grain and the boundary (Fig. 1. b) for calculating the overall conductivity and permittivity. Each cell is composed of a parallel conductance and capacitance, representing for one cell the admittance of the grains and for the other cell the admittance of the boundaries. By taking the limit of the admittances when the cross section dA and the length dl converges to zero, one can obtain the apparent conductivity and permittivity. These quantities are then a function of the frequency and of the material parameters, i.e.: conductivities and permittivities of the boundary and of the grain. Model of flux distribution vs. frequency The dielectric and ferromagnetic nature of ferrite results in standing waves in the core when the frequency increases. This affects the flux density distribution and induces eddy-currents. To model those effects, two approaches can be considered: lumped elements circuit [5] or full wave equation solution [6]. The first one assumes that induced currents flow only around the cross section in concentric loops, which is satisfied if only the first mode is excited. A more general approach is to solve the wave equations, as proposed in [6] for toroid and pot cores. The solution given in [6] converges quickly with respect to the number of considered spatial harmonics, reducing the computational cost. Proposed model Based on the electrical model of the material structure and on the solution for the flux distribution, a new core loss model is presented in this paper. This model allows to compute the complex permeance of a toroid core, even if the electrical material parameters of the material change with frequency. The effective complex permeability is derived by dividing the complex permeance by the ratio of the effective cross section over the effective magnetic length of the core. The overall core losses are calculated by adding the losses associated with the imaginary part of the permeance to the hysteresis losses. The latter are obtained from low frequency measurements and are then scaled

linearly with frequency (similar to Bertotti model). Experimental validation The proposed approach is validated on a R36 toroid core made of N87. The complex effective permeability and the core losses are measured between 10 kHz and 1 MHz for various flux densities, at room temperature using an IWATSU SY-8219 BH Analyzer. The model is then fitted with complex permeability measurements using MATLAB curve fitting toolbox. Results and discussion As shown in Fig 2, the presented model captures accurately the variations of both the complex permeability and the core losses. Furthermore, it can be concluded that the so-called excess losses are due to additional eddy-current losses due to the excitation of wave modes in the core and to the increasing effective conductivity with frequency.

[1] J. Li, T. Abdallah and C.R. Sullivan, Conference Record of the 2001 IEEE Industry Applications Conference. 36th IAS Annual Meeting, IEEE, (2002) [2] G. Bertotti, IEEE Transactions on Magnetics, Vol. 24, p. 621-630 (1988) [3] C. G. Koops, Physical Review, Vol. 83, p. 121-124 (1951) [4] M. Kacki, M.S. Rylko, J.G. Hayes and al., 2020 IEEE Applied Power Electronics Conference and Exposition (APEC) (2020) [5] C.R. Sullivan, PSMA 2019 Magnetics Workshop (2019) [6] W. Hauser, Modellbildung für strukturabhängige Effekte in Ferritkernen (2018)

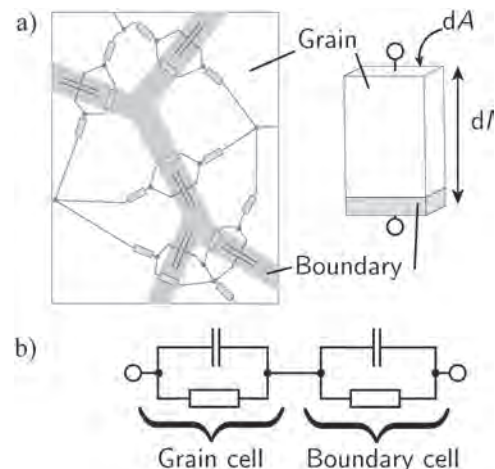


Fig. 1: a) The granular microstructure of Ferrites leads to a capacitive behaviour that can be represented by a 1D model. b) Equivalent two cells model for the permittivity and conductivity of ferrites.

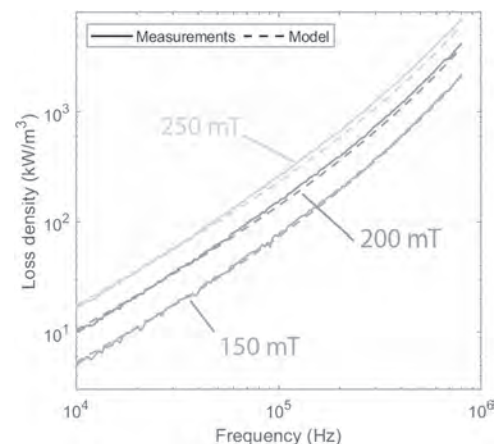


Fig. 2: Loss density against frequency for various flux density values.

BJ-02. Concept and Process Development Using Ex-Situ Fabricated High Density Interconnect Plugs for Circuit-Board Embedded Magnetic Components.

D. Bowen¹, D. Basu² and G. Stackhouse²

1. The Laboratory for Physical Sciences, College Park, MD, United States;

2. Electrical and Computer Engineering, The University of Maryland College Park, College Park, MD, United States

Closed core magnetic circuit components have long been the most difficult circuit component to miniaturize. Loss of cross sectional core area and available space to wrap windings trades off inductance as the component becomes smaller. For both circuit compactness and high frequency performance, there has been interest in the embedding of magnetic core materials within planar substrate (printed circuit board, PCB) and fabricating the windings lithographically [1-5]. This allows precise winding fabrication with control of capacitances, as well as being able to reclaim the circuit board area of the formerly surface mounted package. However, high turn numbers are difficult to achieve using PCB via fabrication methods. In standard PCB via fabrication, via diameters are limited by the aspect ratio of the hole that needs to be drilled. In-situ via fabrication in full 1.6mm thickness boards is limited to about a 1:8 aspect ratio. This translates to a ~200 micron via diameter, with a required via-to-via gap of about the same. This limits the number of turns that can be wrapped around the embedded core. Wire-wound magnetic components can use wire with diameters of 50 microns, and gaps equal to the varnish thickness of a couple of microns; wire-wound components can fit significantly more winding turns than embedded components using PCB via fabrication, and thus will have a much higher inductance for the same sized core. In this digest, an alternative ex-situ via forming method is presented, which uses embedded z-conductive via plugs, to fabricate embedded transformers. The effective aspect ratio is theoretically unlimited, but is 1:40 in the process presented here, competitive with wire-wound components. The general embedding process has six steps (Fig. 1): 1. Mill pocket for via plug, 2. Insert via plug and embed with epoxy, 3. Planarize both sides to reveal plug faces, 4. Mill pocket for magnetic core material, 5. Embed magnetic core with epoxy and planarize, 6. Double sided photolithography to form windings. The ex-situ fabricated via plug is the enabling part of the process; the plug is z-conductive in that it electrically conducts along the plug’s length, but is electrically isolating over the plug’s cross-section. When the plug is embedded in the PCB, the plane of the PCB is considered the xy plane, and the thickness of the PCB is in the z-direction. The major advantage of this process compared to alternative ex-situ via fabrication methods is how there is no precise pattern in the z-conductive plug. The plug, ideally, creates an xy continuum of z-direction conduction. Interlayer electrical connections occur wherever a circuit pattern on the top layer overlaps the circuit pattern on the bottom layer; precise alignment to the via plug is not required. Thus, the resolution of the lithography, not the via fabrication, is what determines the maximum number of turns on the winding. To fabricate the z-conductive plugs, commercial litz wire (660 strand bundle/ 46 American wire gauge strands) is epoxy cast into a bar, then cut into 1.6mm thick segments (“plugs”, fig. 2b and c). The 46 gauge strands effectively create 40µm diameter vias (fig. 2c), with a strand-to-strand gap of a few microns. A racetrack core [1, 6] size of 2.1mm outer diameter, 1.0mm inner diameter, leg length of 6.25mm, and a thickness of 1.0mm (fig. 2) is used for embedding. After step 5 (fig 1), the samples are polished with 1 micron slurry to reduce surface roughness and repair surface smearing of the copper litz wire. The transformer winding design has 14 turns per winding (200 µm lines, fig. 2). The lithography process developed is an etch process, where copper is deposited over the entire sample, after step 5, by e-beam evaporation or wet chemical plating. A photolithography process using microelectronics tools was developed, but is difficult to perform given the bulky board materials and the samples having a surface that was not precisely planar. One non-functioning 14-turn sample was completed using photolithography. As a novel alternative approach, spray paint was applied to a sample as an etch mask, and a 3D laser writer, which is less sensitive to surface non-uniformity, was used to ablate the negative image of the 14-turn winding pattern. The winding pattern was successfully etched using this robust approach, but windings were found to be consistently shorting. To help trace the path of the current shorting through the windings, a magneto-optical garnet was used,

where a DC current was applied through the shorting path, and the garnet was placed on the windings and observed through a polarizing light microscope. The garnet indicates optically the magnetic fields emanated by the current, showing the shorting current path (Fig. 2d). To correct the shorting defect, high DC current was applied to thermally decompose the assumed high-resistance shorting anomaly. The approach effectively opened the shorting path, but collateral damage occurred destroying the device. In summary, we present this work as innovative both in approach and diagnostic technique. Support for this project has ended and work will not continue, but others working with the same miniature, high-frequency, high-inductance application requirements should consider this approach.

References: [1] D. Bowen, D. Basu, C. Krafft and I. Mayergoyz, “Fabrication and Evaluation of PCB-Embedded Broadband Signal Transformers With Custom Machined Racetrack-Shaped Ferrite Cores for Ethernet Applications,” in *IEEE Transactions on Magnetics*, vol. 53, no. 11, pp. 1-5, Nov. 2017, Art no. 8401805 [2] D. Bowen, A. Lee, C. Krafft and I. D. Mayergoyz, “Design Control of Performance in Nested and Interleaved Winding Printed Circuit Board Transformers for Ethernet Applications,” in *IEEE Transactions on Magnetics*, vol. 49, no. 7, pp. 4013-4016, July 2013. [3] D. Bowen, A. Lee, C. Krafft and I. D. Mayergoyz, “Zero-footprint Ethernet transformers using circuit-board embedded ferrites,” *Journal of Applied Physics* 115, 17E716 (2014) [4] J. Quilici, “Embedded magnetics technology overview,” see http://www.radial-e.com/?page_id=2for Radial Electronics Technology Brief. [5] “Planarmag Product Technology From TE Brings Automated Embedded Magnetic Products To The Ethernet Market,” *Electronic Specifier*, Feb. 2011, retrieved from <https://www.electronicspecifier.com/communications/new-planarmag-product-technology-from-te-brings--automated-embedded-magnetic-products-to-the-ethernet-market> Jan. 2020 [6] D. Bowen, C. Krafft and I. D. Mayergoyz, “Inductance optimization of miniature Broadband transformers with racetrack shaped ferrite cores for Ethernet applications,” *AIP Advances* 7, 056663 (2017)

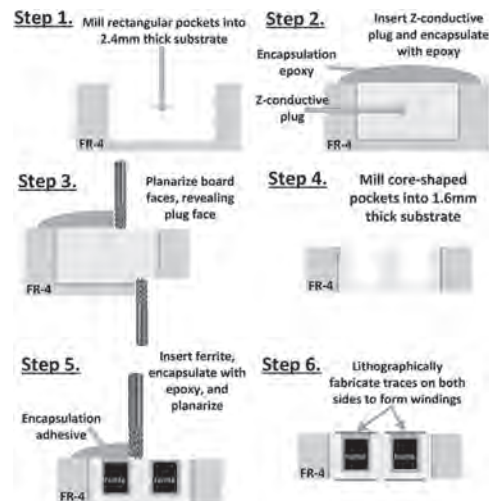


Figure 1. Process for embedding a Z-conductive plug to fabricate a magnetic circuit component.

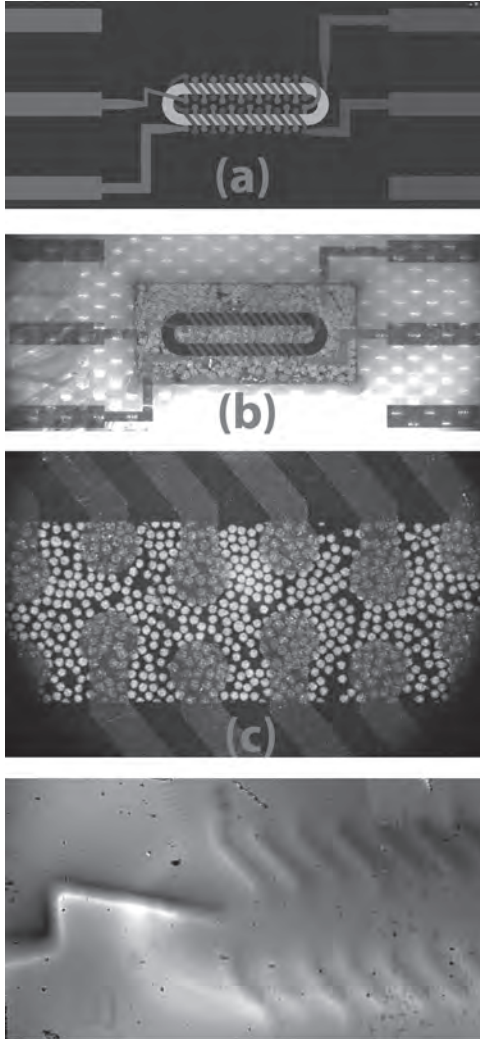


Figure 2. 14-turn racetrack core transformer (a) Layout (b) Top Image (c) Image of turns overlapping via plug (d) Magneto-optic image of current flowing between primary and secondary windings

BJ-03. Prediction of Cylindrical Magnetic Shielding Performance by Considering the Magnetic Field Strength Inside the Material.

M. Sakakibara¹, G. Uehara¹ and Y. Adachi¹

¹. Kanazawa Institute of Technology, Kanazawa, Japan

I. INTRODUCTION Magnetoencephalographs (MEGs) require a magnetically shielded room (MSR) made of mu-metal to protect against very slow and small range of magnetic field (micromagnetic field) noise. As magnetic shields tend to be very expensive, the evaluation of the magnetic shielding factor SF of the MSR in advance is crucial. The permeability μ of the shielding material is the main factor affecting the magnetic properties, which influence the SF . Conventionally, an index of permeability at $H = 4$ mA/cm, which we denote as “ μ_4 ” in this paper, is used to evaluate the performance of a mu-metal. However, as we explained in a previous study [1], permeability at a lower range than 4 mA/m, such as the Rayleigh region [2], is important for magnetic shielding materials in MSRs used for MEGs. We also explained that the measurement system of permeability against a very low-frequency micromagnetic field fluctuation and heat treatment process can improve the permeabilities of a mu-metal [3]. The SF is also affected by the shape of the magnetic shield. As a first step for predicting the SF of an MSR model, we examined a cylindrical-shell magnetic shield (material thickness, $t = 1$ mm; length, $L = 640$ mm; diameter, $D = 100$ mm), which can be considered as infinitely long and can be applied with $SF = 1 + \mu t/D$ [4]. We propose a prediction method for the SF by using this formula and the estimated μ . The permeability index, μ , of a ring-shaped test piece (ring TP) was measured at a magnetic field strength of 0.001–0.675 A/m, which comprises the linear region in the μ - H curve, to detect the initial permeability, μ_i , and Rayleigh constant ν ; Rayleigh’s law states the μ - H curve is present for $\mu = \mu_i + \nu H$. Before we apply two equations to calculate SF , we need to know the internal magnetic field of the material $H = H_i$, whose value is attenuated from applied magnetic field H_e due to the demagnetization effect of its cylindrical-shell shape. Although the demagnetizing factors of spheres and ellipsoids are known, it is difficult to calculate these values for other shapes. Therefore, we used magnetic field analysis to estimate the internal magnetic field H_i of the cylindrical shell. In this study, a prediction method of the SF for a cylindrical shell was demonstrated for three types of mu-metals, and its accuracy was verified by an experiment on the SF . II. METHOD We prepared three types of mu-metals (mu-metals 1, 2, and 3), which exhibited different properties. A ring TP and cylindrical shell were fabricated from mu-metals 1, 2, and 3. The ring TPs and cylindrical shells were simultaneously magnetically annealed in the same heat-treatment furnace. The prediction of the SFs was performed in three steps. First, ring TPs were measured in an alternating magnetic field of 1 Hz, and μ_i and ν were obtained via the least-squares method that was applied to the μ data of the linear region. Second, the H_i values of the cylindrical shells were estimated using magnetic simulation software ELF/MAGIC (ELF corporation). A cylindrical shell was modeled as a 3D object that was divided into 180 cells along its circumferential direction, 64 along the length, and using a single cell along the thickness. H_i was obtained as the average value of all dividing elements; H_e was varied as 0.01, 0.1, 1, and 10 A/m (0 to peak); and H_i was calculated for each level of H_e . Third, SF was predicted as $SF = 1 + \mu t/D$ using the equation $\mu = \mu_i + \nu H_i$. Fourth, the cylindrical shells fabricated from mu-metals 1, 2, and 3 were placed in a uniform magnetic field strength of H_e that varied at 1 Hz, and the magnetic field at the center of the shell H_p was measured. The SF was obtained as H_e/H_p and compared with the predicted result. III. RESULT AND DISCUSSION The μ - H curve, μ_i and ν of the ring TPs are displayed in Fig. 1. The internal magnetic fields H_i of the cylindrical shell calculated using the magnetic simulation software were 1/1608 to 1/418 of H_e , and were in the Rayleigh region. Fig. 2 shows the predicted SF using H_i values of each H_e and the experimental results for the three types of cylindrical shells. It showed that mu-metal 3 has the highest μ in the Rayleigh region, mu-metal 2 has the lowest μ , and so as the order of the SF . Both results of the prediction and experiment show the tendency that the SF increases with an increase in H_e , and are in good agreement. IV. CONCLUSION To develop an accurate prediction method for the magnetic shielding factor in the design of an MSR, we proposed a prediction method for cylinders as a preliminary step and verified its accuracy via the comparison with the result of the experiment. The value of H_i indicate that only few of H_e can penetrate

inside the material of cylindrical shell, and thus μ of micromagnetic field such as the Rayleigh region is important for a magnetic shield against even large magnetic field noise of 10 A/m. As shown in Fig. 2, it was confirmed that the value of μ calculated using Rayleigh’s law is linked to the magnetic shielding effect, and the result also indicated the possibility of applying it to predict SF of MSR.

[1] M. Sakakibara, S. Muto, M. Okuda, Y. Adachi, and G. Uehara, IEEJ Trans. Magn. 140, 331 (2020). [2] R. M. Bozorth, IEEE Magnetics Society, 489 (1993). [3] M. Sakakibara, Y. Adachi, and G. Uehara, T. Meguro, IEEE Trans. Magn. (2020). [4] Wills, A.P., Phys. Rev. 9 pp. 193 213 (1899)

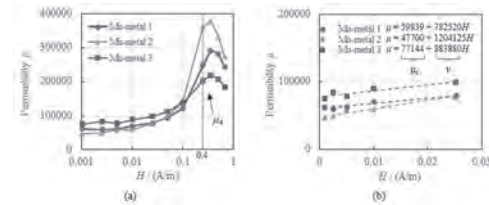


Fig.1 Plots of μ - H . In (a) and (b), H denotes values in the range of 0 – peak. μ_4 is an index of permeability at $H = 4$ mA/cm, which is conventionally used to evaluate the shielding factor.

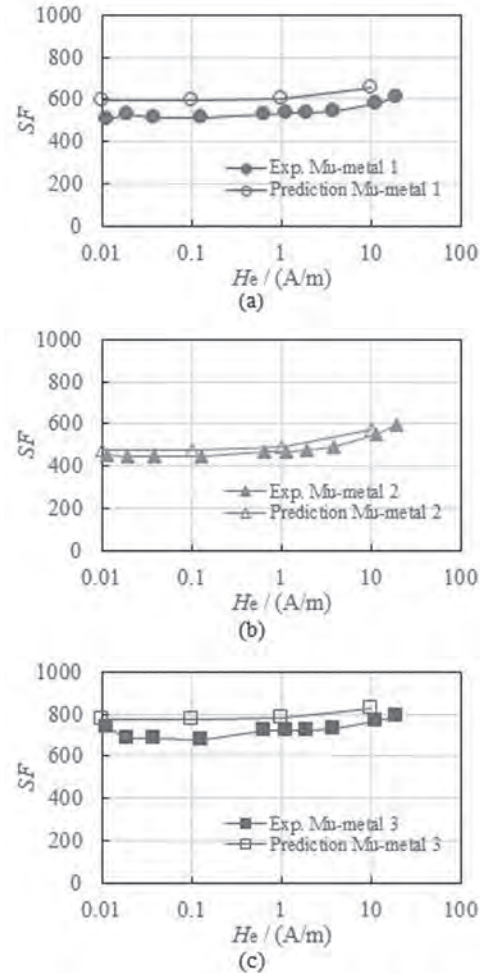


Fig.2 Estimated value of the shielding factor SF compared with the experimental results; (a) mu-metal 1, (b) mu-metal 2, and (c) mu-metal 3.

BJ-04. A Novel Output Voltage Regulation Method for Three-Phase Three-Level Wireless Power Transfer Based on a Simplified System Model.

Y. Liu^{1,2}, C. Liu^{1,2}, X. Gao^{1,2} and Y. Xiao^{1,2}

1. School of Energy and Environment, City University of Hong Kong, Hong Kong SAR, China; 2. Shenzhen Research Institute, City University of Hong Kong, Shenzhen, China

1. INTRODUCTION Wireless power transfer (WPT) has been widely used in various applications due to its great convenience of contactless energy delivery [1,2]. Generally, WPT systems can be categorized into single-phase type and multi-phase type. Compared to traditional single-phase WPT systems, the multi-phase type WPT systems can have more uniformed magnetic field, more compact coil structure and less output current ripple [3]. However, additional interphase mutual inductance is a problem in multi-phase WPT system, making the modeling and control more difficult [3,4]. Also, most multi-phase WPT systems are based on two-level inverters, and three-level inverters surpass traditional two-level inverters in many applications because of advantages like lower voltage stress on power switches and smaller electromagnetic interference (EMI). Among the various three-level topologies, the T-type neutral point clamp (TNPC) topology has high overall efficiency and equal conduction loss of all used power switches [5]. In this paper, a three-phase three-level WPT system based on TNPC inverter is proposed. First, a compact three-phase coil structure are designed to achieve symmetric interphase mutual inductance. Next, with a simplified modeling method, each phase of the three-phase system is simplified to a single-phase system. Further, a novel output regulation method with specific switching sequence is proposed to control the amplitude of the output voltage. Finally, the effectiveness of the proposed three-phase WPT system is verified by both the simulation and experimental results. 2. SYSTEM CONFIGURATION The main topology of the proposed WPT system with series-series compensation is shown in Fig. 1(a). The 3D coil structure is shown in Fig. 1(d) where every two of the six coils have a mutual inductance. The primary coils and the secondary coils have the identical shape. The three coils on the same side are in the same plane and occupy 120° of a circle. With this unique coil structure, the space is highly utilized, and the three-phase coils keep symmetric and has the same interphase mutual inductance. M_{pp} is the mutual inductance of the primary coils, M_{ss} is the mutual inductance of the secondary coils, M_{sp1} is the mutual inductance of the aligned coils from the primary side and secondary side, and M_{sp2} is the mutual inductance of the coils which are not aligned from the primary side and secondary side. Based on the first harmonic approximate (FHA) method, the equivalent circuit is shown in Fig.1 (b), where $R_L=6R_{dc}/\pi^2$ [6]. When the three phases keep balanced, the voltage across o_1 and n_1 , $U_{1on}=0$, and the voltage across o_2 and n_2 , $U_{2on}=0$. Therefore, a simplified equivalent circuit can be derived, as shown in Fig.1 (c). In Fig.1 (c), each phase of the system is approximately equivalent to a single-phase system, where the inductance of the primary side is L_1-M_{pp} , the inductance of the secondary side is L_2-M_{ss} , and the mutual inductance is $M_{sp1}-M_{sp2}$. 3. OUTPUT VOLTAGE REGULATION METHOD The inverter output voltage U_{1xo} is subject to the switching states. Supposing the switching state of the phase x is $S=[S_{x1} S_{x2} S_{x3} S_{x4}]$, when $S_{x1}=[1 1 0 0]$, $U_{1xo}=+0.5U_{dc}$; when $S_{x1}=[0 1 1 0]$, $U_{1xo}=-0.5U_{dc}$; when $S_{x1}=[0 0 1 1]$, $U_{1xo}=-0.5U_{dc}$. In order to reduce the state change of each controlled switches and make the control signal symmetric, a specific switching sequence is chosen for the proposed WPT system, that is $S_0-S_{x1}-S_0-S_{x1}-S_0$. As shown in Fig. 2 (a) and (b), each of S_{x1} and S_{x1} account for $0.5aT$ in a period time T . The drive signals of each power switches are symmetric in half a period time, and the states of each controlled switches only change twice in a single period time, which makes the driver signals easy to produce. By using fourier decomposition method, the amplitude of the first harmonic can be expressed as $m_1=2U_{dc}\sin(a\pi/2)/\pi$ ($0\leq a\leq 1$). Also, the ratio of U_{2xn} and U_{1xn} in Fig.1 (c) can be obtain by $U_{2xn}/U_{1xn}=[j\omega(M_{sp1}-M_{sp2})]/[(R_2+R_L)R_1+4\pi^2f^2(M_{sp1}-M_{sp2})^2]$. Therefore, by regulating the value of a , the transferred power can be controlled. 4. SIMULATION AND EXPERIMENTS In order to verify the effectiveness of the proposed WPT system, simulations are done in MATLAB/SIMULINK. Also, as shown in Fig.2(c), a 500W three-phase prototype is established. Fig.1(b) is the experiment results of the three-phase current and the voltage of U_{1xo} at $a=0.3$. More analysis and experiment

results will be given in full paper. 5. CONCLUSION In this paper, a three-phase three-level WPT system is proposed. Each phase of the system is approximately equivalent to a single-phase system which effectively simplify the system model. A novel output regulation method is proposed to control the output voltage. Simulation and experiment results show a good performance of the proposed WPT system and effectiveness of the control and modeling method, and indicate the proposed WPT system has a better output voltage spectrum and reduced voltage stress compared to traditional three-phase two-level WPT system. Acknowledge This work is supported in part by NSFC (52077186&51677159), in part by STIC Shenzhen Municipality (JCYJ20180307123918658), and in part by ITF (ITP/027/19AP), HK.

[1] X. Gao, C. Liu, Y. Huang, "Design of An UAV-Oriented Wireless Power Transfer System with Energy-Efficient Receiver," *IECON 2020*, Singapore, 2020, pp. 2025-2030. [2]Y. Xiao and C. Liu, "Direct Load Voltage Control for Electrolytic Capacitor-less Wireless Power Transfer System Without DC/DC Converter," in *IEEE Transactions on Industrial Electronics*. doi: 10.1109/TIE.2020.3013780 [3]J. Pries *et al.*, "A 50-kW Three-Phase Wireless Power Transfer System Using Bipolar Windings and Series Resonant Networks for Rotating Magnetic Fields," in *IEEE Transactions on Power Electronics*, vol. 35, no. 5, pp. 4500-4517, May 2020. [4]G. A. Covic, J. T. Boys, M. L. G. Kissin and H. G. Lu, "A Three-Phase Inductive Power Transfer System for Roadway-Powered Vehicles," in *IEEE Transactions on Industrial Electronics*, vol. 54, no. 6, pp. 3370-3378, Dec. 2007. [5]Z. Yuan *et al.*, "Design and Evaluation of Laminated Busbar for Three-Level T-Type NPC Power Electronics Building Block With Enhanced Dynamic Current Sharing," in *IEEE Journal of Emerging and Selected Topics in Power Electronics*, vol. 8, no. 1, pp. 395-406, March 2020. [6]C. Wang, C. Zhu, G. Wei, J. Feng, J. Jiang and R. Lu, "Design of Compact Three-Phase Receiver for Meander-Type Dynamic Wireless Power Transfer System," in *IEEE Transactions on Power Electronics*, vol. 35, no. 7, pp. 6854-6866, July 2020.

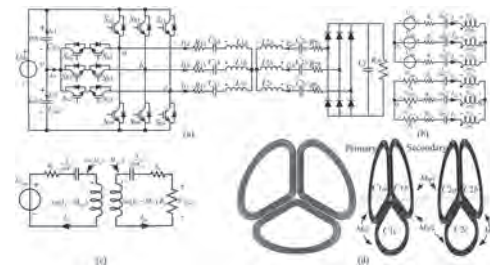


Fig. 1. Proposed three-phase three-level WPT system. (a) Main topology. (b) Equivalent circuit. (c) Simplified equivalent circuit. (d) 3D model of the primary coils and the secondary coils.

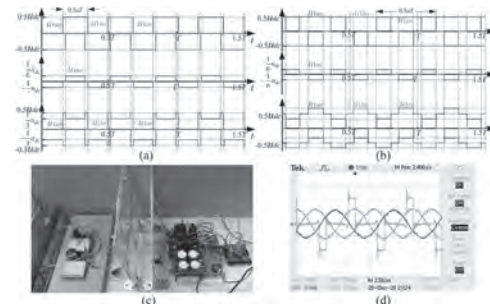


Fig. 2 Primary voltage and experiment of the proposed WPT system. (a) Voltage waveform when $a=0.37$. (b) Voltage waveform when $a=0.88$. (c) Testbed. (d) Inverter output voltage in phase A and three-phase currents.

BJ-05. Analysis of Highly Reliable Electric Drive System Based on Dual-Winding Fault-Tolerant Permanent Magnet Motor.

X. Jiang¹, D. Wu¹, L. Li¹ and Y. Li¹

1. Nanjing University of Science and Technology, Nanjing, China

I. INTRODUCTION Due to the ability to maintain system operation after electrical failure, fault-tolerant machines are increasingly used in safety-critical applications, for instance, automobiles, aviation and armament [1]-[2]. In this paper, based on the dual-winding fault-tolerant permanent magnet motor (DFPMM) which not only inherits permanent magnet synchronous motors' advantages of high torque density and high efficiency but also has high-performance of fault-tolerance, a novel electric machine drive system is proposed and studied. The 12-slot/10-pole DFPMM, with two separate sets of three-phase single-layer concentrated windings wound on alternate teeth, is capable of restricting fault propagation. The drive system is equipped with two independent drive circuits, while only one DC power supply is needed. With the proposed drive system, fault-tolerant performance to cope with open-circuit faults can be implemented by applying corresponding control strategies. Especially when the one-phase open-circuit fault occurs, system utilization rate is larger compared with the traditional drive system. Simulation and experimental results incorporating current, torque and speed under conditions of one-phase open circuit fault are exhibited respectively. The results verify the effectiveness of the proposed fault-tolerant control strategies and the high reliability of the proposed DFPMM motor drive system.

II. THE DFPMM SYSTEM CONFIGURATION AND DESIGN The structure of the proposed electric drive system is shown in Fig. 1(a), which contains a DFPMM, two sets of three-phase full-bridge drive circuits, two triacs, six fuses, and an independent 270V DC power supply. The two sets of windings of the DFPMM are independent of each other, and the ABC windings are controlled by T1 to T6, while the XYZ windings are controlled by T7 to T12. The triac TR1 is connected to the neutral point of the ABC windings and the midpoint of the capacitors, and TR2 is in a similar way. Fuses F1-F6 prevent a shoot-through fault caused by a simultaneous breakdown of power switches in the same phase. During normal operation, two independent three-phase bridge drive circuits control the two windings, each with the same power output which is 50% of the total output power, and the two triacs are kept off.

III. FAULT TOLERANT CONTROL STRATEGIES Based on the principle of constant magnetomotive force, control strategies after faults occur will be introduced in the full paper in detail. With the double d-q mathematical model of DFPMM, it is a vector control system that consists of two separate speed controllers, current controllers and SVPWM modules for both two sets of windings. When an open-circuit fault occurs in one set of the windings, the corresponding triac will be turned on, forming a power conversion circuit with a neutral point, as the conductive triac will add a degree of freedom to control the system under the fault condition. Meanwhile, two capacitors are used to perform amplitude and phase modulation on the remaining two-phase currents.

IV. SIMULATION AND EXPERIMENTAL VERIFICATION Simulation and experiments are carried out under the conditions of open-circuit faults occurring in one phase, to verify the effectiveness of the proposed electric drive system and its control strategies. The test platform is shown in Fig. 1(b). The results are shown in Fig. 2, including three-phase current of the fault set of windings, speed and torque waveforms. Simulation waveforms of current, torque and speed when an open-circuit fault occurs in phase-A with and without the fault-tolerant control strategies are shown in Fig. 2(a) and Fig. 2(b), respectively. And experimental waveforms of current, torque and speed when an open-circuit fault occurs in phase-A with and without the fault-tolerant control strategies are compared in Fig. 2(c) and Fig. 2(d). From these results, the motor with the proposed drive system maintains the normal performance after the fault occurs, by applying the corresponding control strategy. Thus, the damage caused by open-circuit faults can be avoided.

V. CONCLUSION In this paper, a highly-reliable DFPMM drive system aiming at ensuring a normal operation after open-circuit faults is proposed. By applying the control strategies and corresponding actions to typical types of faults, both simulation and experiments have done, proving the effectiveness of the proposed highly-reliable electric drive system. It can cope with open-circuit faults in different situations, and it is suitable for safety-critical applications. More detailed theoretical analysis and experimental verification will be presented

in the full paper. **ACKNOWLEDGEMENT** This work was supported in part by the National Natural Science Foundation of China under Project 51807094, and in part by the Project funded by China Postdoctoral Science Foundation under Project 2020M671499, and in part by Jiangsu Planned Projects for Postdoctoral Research Funds under Grant 2020Z145.

- [1] B. Wang, J. Wang and A. Griffo, "Stator Turn Fault Detection by Second Harmonic in Instantaneous Power for a Triple-Redundant Fault-Tolerant PM Drive", IEEE Transactions on Industrial Electronics, vol. 65, no. 9, pp. 7279-7289 (2018) [2] X. Jiang, D. Xu and L. Gu, "Short-Circuit Fault-Tolerant Operation of Dual-Winding Permanent-Magnet Motor Under the Four-Quadrant Condition", IEEE Transactions on Industrial Electronics, vol. 66, no. 9, pp. 6789-6798 (2019)

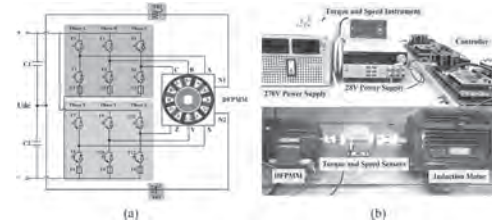


Fig. 1. The proposed DFPMM drive system. (a) Configuration topology. (b) Test platform.

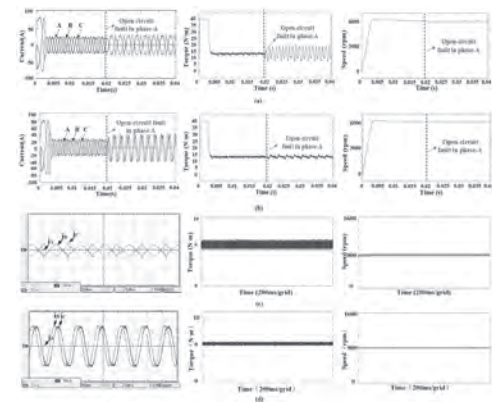


Fig. 2. The waveforms of three-phase currents, torque, and speed under conditions of phase-A open-circuit fault. (a) Simulation waveforms when no fault-tolerant control strategy is adopted. (b) Simulation waveforms when the fault-tolerant control strategy is adopted. (c) Experimental waveforms when no fault-tolerant control strategy is adopted. (d) Experimental waveforms when the fault-tolerant control strategy is adopted.

BJ-06. Iron Loss Calculation Based on Loss Surface Hysteresis Model and Its Verification.

W. Li¹, Y. Sun¹, X. Fan¹ and Q. Wu¹

1. College of Electronic and Information Engineering, Tongji University, Shanghai, China

1. Introduction Due to the rapid growth in global energy consumption, it is imperative to improve the efficiency of electrical machines and other electrical devices. Iron loss is a crucial part of electrical machines, and has received increasing attention in the past few years. It is significant for both optimizing electrical machine design and improving thermal efficiency. Over the years, several iron loss models have been developed, such as the loss separation models [1] and various hysteresis models [2]. In order to evaluate the iron loss, the most traditional way is to analyze the machine using finite element method (FEM), and calculate the iron loss employing a loss separation model. However, it is deficient, especially when dealing with inverter-fed electrical machines, in which higher-order harmonics exist. In some cases, the estimation error exceeds one hundred percent [3], which is critical for iron loss prediction. On the other hand, in order to precisely describe the materials properties, several hysteresis models are developed. One benefit of hysteresis models is that the iron loss can be directly obtained if the B-H hysteresis loops are known. This paper introduces an iron loss estimation method based on the loss surface (LS) hysteresis model and has applied it on several specimens. The verification process is shown in Fig. 1. The LS hysteresis model is constructed based on the B-H hysteresis loops measured from a toroidal specimen laminated of non-oriented electrical steel sheets. A C-type specimen constructed by the same material is taken as the test object, and is analyzed using the finite element method. The obtained field results combined with the LS hysteresis model are used for iron loss calculation. The calculation results are compared with measured ones. The verification is carried on for both sinusoidal and non-sinusoidal cases. 2. The Proposed Procedure As the iron loss can be calculated directly from the integral of the hysteresis loop without the empirical values. Therefore, it is important to get the magnetic field intensity (H) from the flux density (B) and its derivative (dB/dt). The method begins with the measurement of the B-H hysteresis loops, which is performed on a toroidal specimen according to the International Standard IEC 60404-6 [4]. A primary winding is used for the excitation, and another winding is the measuring coil. The B-H hysteresis loops under different magnetic flux density magnitudes B_m have been measured to demonstrate the material behavior more precisely. The LS model, therefore, can be represented by the function between the magnetic field intensity (H) and the flux density (B) and its derivative (dB/dt) and its maximum value (B_m). The calculated object is first performed field analysis by using finite element method. The magnetic flux density distribution can be computed in all elements, which is also taken as the input of the LS model. Combined the derivative of magnetic flux density (dB/dt) and the magnitude B_m , the corresponding magnetic field intensity (H) can be obtained, therefore, the B-H hysteresis loops for arbitrary waveforms can be construed, from which iron loss can be calculated. 3. Verification First, a C-type specimen with the same material is manufactured to verify the proposed procedure, as shown in Fig. 1. In order to check the LS hysteresis modeling accuracy, a magnetic flux density with 0.8T amplitude and 50Hz fundamental frequency, combined with 35% of the third harmonic with a phase shift of 90° is taken as the input, and the magnetic field intensity and hysteresis loops are shown in Fig. 2. The modeled results match well with measured ones. The iron loss of the test C-type specimen is calculated by using both the proposed method and the loss separation model. The measured iron loss is 1.699W, and for the proposed method, the calculated iron loss is 1.530W, whereas for the loss separation models, the calculated iron loss is 1.282W. 4. Conclusion The proposed iron loss calculation procedure based on the LS hysteresis model has been developed and the verification of a C-type specimen has been done. Compared with actual measured results, the proposed iron loss calculation method is more accurate than loss separation model. Verification and analysis on more topologies will be discussed in the full paper.

[1] G. Bertotti, "General properties of power losses in soft ferromagnetic materials," in *IEEE Transactions on Magnetics*, vol. 24, no. 1, pp. 621-630, Jan. 1988. doi: 10.1109/20.43994. [2] Chevalier, T., Kedous-Lebouc, A. and

Cornut, B. et al. A new dynamic hysteresis model for electrical steel sheet. *Physica B: Condensed Matter*, 275(1-3), 197-201. [3] Tekgun, B., Sozer, Y., and Tsukerman, et al. Core loss estimation in electric machines with flux-controlled core loss tester. *IEEE Transactions on Industry Applications*, 55(2), 1299-1308. [4] Methods of measurement of the magnetic properties of magnetically soft metallic and powder materials at frequencies in the range 20hz to 200khz by the use of ring specimens", *International Standard IEC 60404-6*: 2003.

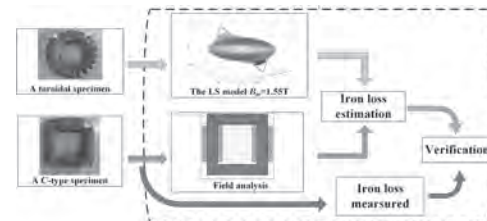


Fig 1 The LS model Verification Process

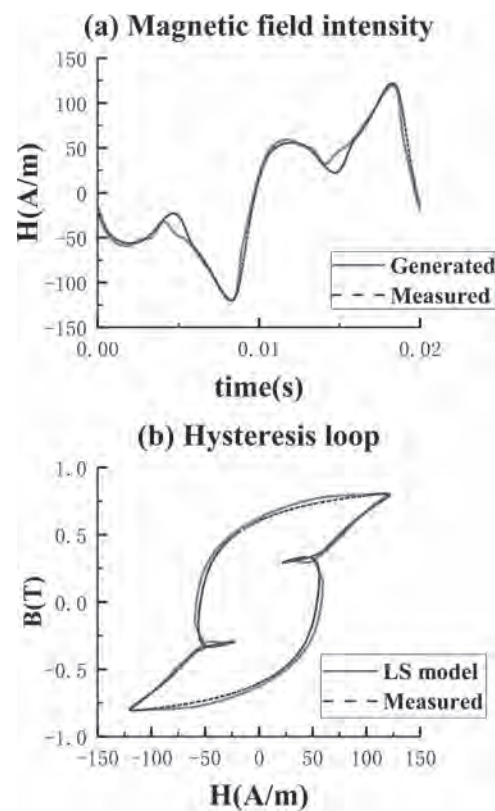


Fig 2 LS Model Estimated And Measured Results

BJ-07. Withdrawn

BJ-08. Experimental Study of a Hybrid Bonding in Ferromagnetic Stacks for Electrical Machine Applications.

A. Giraud¹, M. Nomdedeu¹ and B. Nogaredé¹

¹. NOVATEM, Toulouse, France

The aim of this paper is to investigate the feasibility of a hybrid ferromagnetic bonding in a stack used in electrical machines. In a context of growing energy needs and the absolute need to reduce greenhouse gases, the stakes are high. For instance, with the electrification of aircraft in full development, it is essential to improve the power density of on-board electric actuators. Beyond aeronautics, the advantage of improving machine performance through its intrinsic performance of its materials is that this increase in efficiency does not depend on the application and becomes possible in all sectors of activity. This study which is supported by the French ADEME (Agency of the Environment and the Control of Energy) focuses on steel sheet stack intrinsic performance improvement for electrical machine applications. Generally, a laminated stack is composed by electrical steel sheet. An epoxy-based bonding is often used to ensure a structural cohesion of the stack in order to be manipulated and integrated. It also helps to keep a proper electrical insulation between sheets, limiting eddy current circulation. This study proposes to add iron powder to the epoxy bonding as described on Fig. 1, in order to improve the permeability of the bonding, which is magnetically neutral, becoming then a SMC. However, SMCs are generally used as a magnetic yoke [1] and not as an adhesive layer. The powder load is only intended to exploit a magnetically inert volume. The magnetic flux which will circulate in the packet will do so essentially through the sheets, but the gain in permeability envisaged to make pass more flux under the same magnetic field. The powder load could also improve the thermal conduction along the z axis, improve the thermal performance of the sheet package. Nevertheless, the circulation of eddy currents must remain limited between the sheets and the composite joints. It is necessary to limit the powder load to ensure this. Actually, the method proposed here does not really reproduce the SMC manufacturing process (pressure at temperature of the dielectric mixture - magnetic powder). In the case of a conventional SMC, the process ensures inter-grain isolation [2], making these materials particularly efficient at high-frequency. In the composite joint proposed here, the inter-grain (and therefore inter-sheet) insulation relies only on the residue of the epoxy adhesive around the grains once the sheets have been bonded. The distribution and the quantity of the adhesive being difficult to control, it is essential to keep a sufficient margin, and therefore to limit the powder load. On the other hand, the addition of a magnetic filler has been shown to improve the permeability of a mixture, especially at high frequency [3]. This feasibility study is based on ring core characterization. In order to limit parameters, the thickness and the number of sheets are set, respectively at 0.2 mm and 10 per stack. The thickness of the composite joint is also set at 50 μm . Actually, the powder grains must be large enough to retain interesting magnetic properties. A thickness of 50 μm is a good compromise in the context of a feasibility study. Finally, the only variable parameter is the powder charge. It has been decided to set it at 25%, 50% and 75% of the mass of the composite joint. A joint of the same thickness but loaded at 0% will be used as a reference. The magnetic permeability of the joint is actually determined by the powder volume / joint volume ratio. However, it is much simpler to proceed by mass ratio and to use density to calculate the corresponding volume ratio (4.5%, 13% and 30%). Besides, two types of iron powder are used (AHC 300 and MH300, both 300 mesh for grain size), each with specific properties. Therefore, each ring core corresponds to electrical steel sheet stack with a determined load of specific type of iron powder. Then, ring cores are manufactured and their windings are designed to reach 2 T at 400 Hz and 1000 Hz, and 1 T at 5000 Hz. Specific iron losses (W/kg) are measured and gathered in Fig. 2. This study demonstrates that adding iron powder to adhesive bonding of steel sheet is technically possible. The gain observed is significant and appears promising from the perspective of a more developed study. However, some technical points must be improved. More measurement should be proceeded, including reproducibility measurement. It would appear interesting to charge the adhesive with a metal powder of the same thermal conductivity as iron (or similar) but which would be non-magnetic. It could then be determined whether the performance is improved via magnetic permeability or via thermal conduction. In order to fully characterize these

samples, optimization by numerical simulation could be considered, in order to precisely determine the parameters essential to performance. Finally, it seems essential to perform tests on a machine and not on ring cores, in order to ensure the real potential gains.

- [1] A. Jakubas, P. Gebara, S. Seme, "Magnetic properties of SMC cores produced at a low compacting temperature". *Acta Phys. Pol. A*, 131(5), 1289-1293. [2] Y. X. Pang, S. N. B. Hodgson, J. Koniarek, "The influence of the dielectric on the properties of dielectromagnetic soft magnetic composites. Investigations with silica and silica hybrid sol-gel derived model dielectric." *Journal of magnetism and magnetic materials*, 310(1), 83-91. [3] Belyaev, B. A., & Tyurnev, V. V. (2018). "Electrodynamic calculation of effective electromagnetic parameters of a dielectric medium with metallic nanoparticles of a given size." *Journal of Experimental and Theoretical Physics*, 127(4), 608-619.

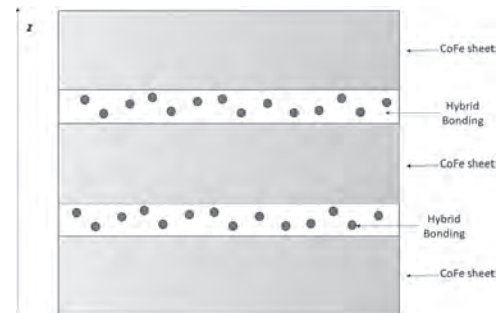


Fig. 1: Representation of the hybrid bonding in an electrical steel sheet stack.

F (Hz)	B (T)	0%	AHC25	AHC50	AHC75	MH25	MH50	MH75
400	1	14.12	10.64	10.26	8.42	9.51	9.76	8.80
	2	42.70	47.57	46.77	38.59	43.71	44.99	40.87
1000	1	52.34	56.042	54.99	44.10	49.92	44.16	45.93
	2	163.09	177.29	173.21	142.19	158.23	165.60	148.22
5000	1	697.42	740.65	745.78	567.02	689.26	690.31	592.68

Fig. 2: Results of specific iron losses measured in the samples for AHC300 and MH300 iron powder, at several frequencies and magnetic flux densities.

BJ-09. Magnetic Hysteresis: a Reliable Technique for Condition Monitoring of Magnetic Cores.

H. Hamzehbahmani¹

1. Engineering, Durham University, Durham, United Kingdom

I. Introduction Condition monitoring of magnetic cores of power transformers and electrical machines has been an active research field and engaging topic for electrical steel manufacturers and designers of the magnetic cores. During the last few decades, analytical and experimental approaches have been developed and effectively employed to monitor quality of the magnetic cores of power transformers and rotating machines [1-2]. Most of these work, however, are focused on measuring the localised power loss and hot spot, as well as on the overall power loss of the magnetic cores. Hysteresis phenomenon, and more specifically magnetic hysteresis, is a distinctive technique to classify and characterise magnetic materials and magnetic cores [3]. During one magnetising cycle, magnetic field strength $H(t)$ and flux density $B(t)$ may not reach the peak values at the same instant. Therefore, two distinctive points with different definitions can be observed (B_m, H_m) and (B_m, H_b) . H_m is the peak magnetic field strength and H_b is magnetic field strength corresponding to the peak flux density B_m [4-6]. In this paper, a new approach based on the measured dynamic hysteresis loops (DHLs) is developed for condition monitoring of the magnetic cores. The proposed technique can be implemented to detect inter-laminar fault between laminations of the clamped magnetic cores, over a wide range of magnetisation. II. Experimental Results The experimental work were carried out on stacks of four Epstein size laminations (305 mm × 30 mm) of 0.3 mm thick CGO 3 % SiFe, with standard grades of M105-30P. Stacks of four laminations were prepared and labelled as: Stack #1, with no ILF, Stack #2, with minor ILF at one set point, Stack #3, with minor ILFs at three set points, and Stack #4, with ILF throughout the laminations. Lead-free solder was used to replicate artificial ILFs on the test samples. The test samples were magnetised using a standard double yoke single strip tester (SST) [7] under controlled sinusoidal induction of 50 Hz and peak flux densities of 1.3 T, 1.5 T and 1.7 T. Impact of each ILF on the magnetising process and magnetic parameters of the test samples was studied by analysing the measured DHLs and interpreting the most distinctive parameters. DHLs of the samples at 50 Hz, 1.7 T are shown in Fig 1-a. To study impact of the ILFs on magnetising processes, instantaneous waveforms of corresponding magnetic field strength $H(t)$ for one magnetising cycle at 50 Hz, 1.7 T are shown in Fig 1-b. Fig 1-a evidently shows that loop area of the DHLs, which measure the total energy loss per unit volume per cycle, is significantly increased for different types of ILFs. Furthermore, shape of the hysteresis loops is remarkably changed for different fault scenario. Fig 1 also shows that peak magnetic field strength H_m is remarkably increased by increasing number of the shorted laminations. In contrast, H_b of all of the test samples coincide with the peak flux density B_m . This can be interpreted to the impact of core failure on total energy loss and its components. In a recent study conducted by the author [5], it was experimentally shown that ILFs do not affect the hysteresis energy loss. Fig 1 evidently proves this, even for Stack #4 where all laminations are completely shorted on either side. It is widely recognised that core failures have direct impact on eddy current distribution and hence eddy current loss at the defected zone of the core, which increase the magnetic field associated with the eddy current, and hence total magnetic field $H(t)$. Therefore, even at high inductions two distinct points (B_m, H_m) and (B_m, H_b) can be observed during each magnetising cycle, as shown in Figs 1-a and 1-b. In the last part of this study, total energy loss W_{tot} and relative permeability μ_r of the test samples were calculated from the measured DHLs, the results at magnetising frequency of 50 Hz and peak inductions of 1.3 T, 1.5 T and 1.7 T are shown in Fig 2. Fig 2 shows a significant increase in the total energy loss of the test samples. Specific energy loss at $B_{pk}=1.7$ T for Stack #1 and Stack #4 increased from 172 J/m³ per cycle to 722 J/m³ per cycle. As stated earlier, the increased energy loss is purely due to the dynamic energy loss components. Fig 2 also shows that relative permeability of the test samples is significantly reduced by increasing number of the shorted laminations, as a result of increased peak magnetic field strength H_m for a given peak flux density B_m . In fact, this experiment provides a new insight regarding the effects of core failure on overall quality of the magnetic cores, which can be implemented in condition monitoring of magnetic cores

and relevant studies. III. Conclusion In this paper a practical technique was proposed for condition monitoring of magnetic cores based on the magnetic hysteresis. In this technique total energy loss W_{tot} , relative permeability μ_r , peak flux density B_m , peak magnetic field strength H_m and magnetic field at peak flux density H_b are the most important quantities to be considered. The results of this study showed that condition monitoring of magnetic cores can be effectively performed by monitoring the DHLs of the cores, and analysing these quantities.

[1] H. Hamzehbahmani, P. Anderson, J. Hall, and D. Fox, "Eddy Current Loss Estimation of Edge Burr Affected Magnetic Laminations Based on Equivalent Electrical Network-Part I Fundamental Concepts", IEEE Trans. on Power Delivery, Vol. 29, No. 2, pp. 642-650, April 2014 [2] D. Bertenshaw, C. Ho, A. Smith, M. Sasi, and T. Chan, "Electromagnetic modelling and detection of buried stator core faults" IET Electric Power Applications, Vol. 11, Issue 2, pp. 187-196, March 2017 [3] G. Bertotti, "Hysteresis in Magnetism, For Physicists, Materials Scientists and Engineers", Academic Press 1998 [4] Z. Cheng, N. Takahashi, B. Forghani, Y. Du, Y. Fan, L. Liu, Z. Zhao, and H. Wang., "Effect of Variation of B-H Properties on Loss and Flux Inside Silicon Steel Lamination," in IEEE Transactions on Magnetics, Vol. 47, No. 5, pp. 1346-1349, May 2011 [5] H. Hamzehbahmani, "A Phenomenological Approach for Condition Monitoring of Magnetic Cores Based on the Hysteresis Phenomenon," in IEEE Transactions on Instrumentation and Measurement, Vol. 70, pp. 1-9, 2021, Art no. 6003409. [6] S Zirka, Y Moroz, S Steentjes, K Hameyer, K Chwastek, S Zurek, R Harrison, "Dynamic magnetization models for soft ferromagnetic materials with coarse and fine domain structures", Journal of Magnetism and Magnetic Materials, Vol. 394, Nov. 2015, pp 229-236 [7] BS EN 10280:2001 + A1:2007, Magnetic Materials - Methods of measurement of the magnetic properties of electrical sheet and strip by means of a single sheet tester, British Standard, 2007

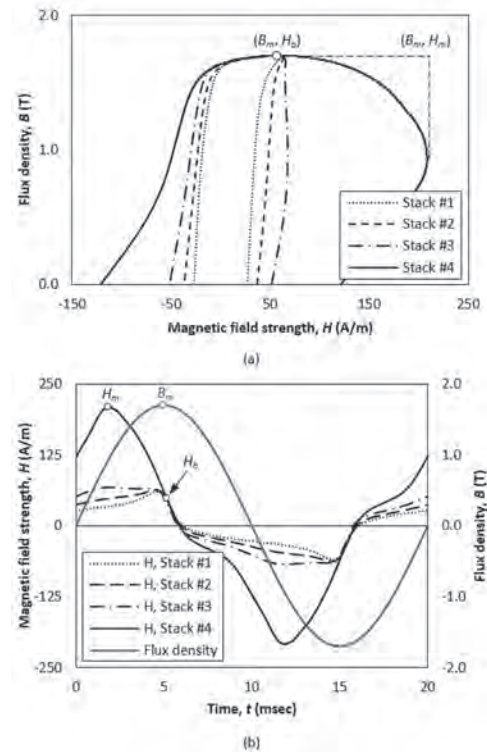


Fig 1 (a) Dynamic hysteresis sloops and (b) Instantaneous wave shapes of $H(t)$ and $B(t)$ of the test samples under sinusoidal induction of 50 Hz and peak flux density of $B_{pk}=1.7$ T

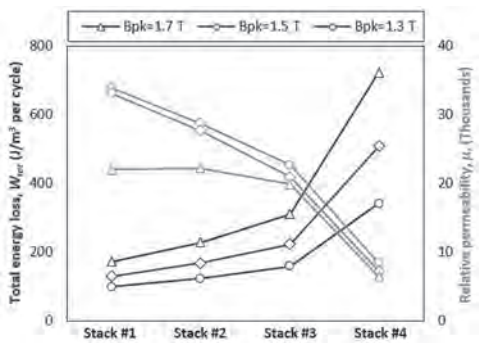


Fig 2 Total energy loss and relative permeability of the test samples

BJ-11. Additive Manufacturing for Soft Magnetic Materials.

V. Martin¹, F. Gillon¹, D. Najjar², A. Benabou¹, J. Witz², M. Hecquet¹ and P. Quaegebeur²

1. Univ. Lille, Arts et Metiers Institute of Technology, Centrale Lille, Junia, ULR 2697 - L2EP, Lille, France; 2. Univ. Lille, CNRS, Centrale Lille, UMR 9013 - LaMcube - Laboratoire de Mécanique, Multiphysique, Multiéchelle, Lille, France

Introduction. Additive manufacturing, also known as 3D printing, has experienced a tremendous development over the past twenty years. This process enables fast prototyping and it offers the ability to create complex shapes that would otherwise be difficult to produce using classical techniques. This process has been applied to a wide range of polymer, nowadays different research interests [1] focus on functional materials, such as metals or ceramics, to create components with enhanced physical properties. In this way, electromagnetic systems and power applications could exploit printed soft magnetic materials to be designed in a shorter amount of time and benefit from a wider range of feasible shapes. In this work, additively manufactured inductor made using two different printing feedstock types are presented. The simulation of a new geometry is made using finite element method in an attempt to explore the influence of the form on the flux density distribution. Finally, modeling and magnetic characterizations were carried out to compare the performances with a reference material. The specificity of this work consists in the usage of magnetic materials shaped with 3D printing.

1. Additive manufacturing of magnetic materials. Fabrication of objects is realized through the Fused Deposition Modeling technic. A first approach is to use a feedstock that comes as a filament loaded with metallic particles [2]. For this, two filaments from Proto Pasta and Virtual Foundry were used to produce shapes that could be used in an electrical system, like toroidal or E-shaped inductor. To achieve a greater concentration of the target materials, a pellet type feedstock was also used to perform MIM-like additive manufacturing with material from PolyMIM. In order to get good magnetic performances, the binding polymer has to be removed from the final part, so that it is only composed of the loaded material. Finally, the densification of the object has to be performed through a heat treatment. These last two steps are called debinding and sintering. Both processes will be undertaken in future works. 2. Modeling. In order to predict the behavior and performances of a toroidal inductor, a multi-physical modeling has been realized. It takes into account the analytical computation of the flux density, the thermal behavior due to the losses and the impact of heat on magnetic permeability. This model was then compared to a finite element simulation for validation. The simulation was performed using the software Opera-3D. The whole is put into perspective with practical tests. 3. New printable geometry. The main benefit from creating 3d printed objects is the variety of shapes that becomes accessible [3]. Complex geometry could be considered in the design process to suit requirements or even to modify the behavior of a component without using a different material [4]. To explore this possibility, an inductor with a complex shape was studied using finite element method. It consists in a torus that is distorted, along its axis, in a cyclic manner. The result is a wavy body that can be seen on figure 1.a. This core will be coiled and simulated as if it was made out of a ferromagnetic material. The geometry has been created to follow a wrapped-up sinus curves and to ensure a constant section along the path. This way, the circulation of the magnetic field can be modified without increasing the torus radius. Conductor were placed around each antinodes of the waves. Finally, different amplitudes were tried and the distribution of the magnetic field inside the core was observed. In figure 1.b, we can see that the magnetic field repartition can be tilted depending on the ripple range. 4. Magnetic characterization. To evaluate the performance of the different printed materials, a serie of magnetic characterizations was conducted. For this, the TX42/26/13 ferrite core from Ferroxcube was taken as a reference and several components with the same dimensions were printed with the feedstocks stated previously. Some examples of wound components are shown in figure 2.a. Magnetic variables such as magnetic permeability, maximum flux density and iron losses were observed. As it can be seen in the work of Bollig *et al.* [5], performances are way smaller than the reference material. This is due to the fact the first materials tested were made out of powder enclosed in a polymer binder, hence the density of magnetic material is very low. In figure 2.b, the magnetic permeability versus the density of the

material is presented. Conclusion. To conclude, the use of additive manufacturing with magnetic materials offers a wide range of feasible shapes that can be used advantageously in the design process. However, the performances of such objects need to be improved. In future work, the density of the printed parts will be greatly enhanced by using a pellets based printing process and by going through the thermal treatments. Furthermore, a soft magnetic material that is similar to the reference presented earlier, will be used as feedstock for future prints.

- [1] Y. Yan, J. Moss, K. D. T. Ngo, Y. Mei, et G.-Q. Lu, « Additive manufacturing of toroid inductor for power electronics applications », in *2016 IEEE Energy Conversion Congress and Exposition (ECCE)*, Milwaukee, WI, USA, sept. 2016, p. 1-6, doi: 10.1109/ECCE.2016.7854826. [2] Y. Wang, F. Castles, et P. S. Grant, « 3D Printing of NiZn ferrite/ABS Magnetic Composites for Electromagnetic Devices », *MRS Proc.*, vol. 1788, p. 29-35, 2015, doi: 10.1557/opl.2015.661. [3] F. Lorenz, J. Rudolph, et R. Wemer, « Design of 3D Printed High Performance Windings for Switched Reluctance Machines », in *2018 XIII International Conference on Electrical Machines (ICEM)*, sept. 2018, p. 2451-2457, doi: 10.1109/ICELMACH.2018.8506845. [4] L. Liu *et al.*, « Design and Additive Manufacturing of Multi-Permeability Magnetic Cores », p. 6, 2017. [5] L. M. Bollig, P. J. Hilpisch, G. S. Mowry, et B. B. Nelson-Cheeseman, « 3D printed magnetic polymer composite transformers », *J. Magn. Magn. Mater.*, vol. 442, p. 97-101, nov. 2017, doi: 10.1016/j.jmmm.2017.06.070.

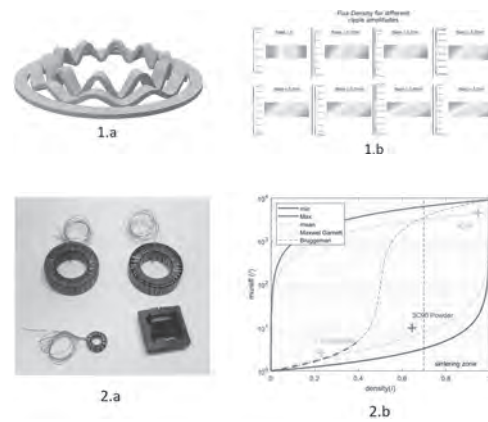


Fig.2 Printed samples and magnetic characterization results (effective permeability over material density)

BJ-12. Coupled Electromagnetic and Thermal Analysis of Permanent Magnet Rectifier Generator Based on LPTN.

H. Wang¹, Y. Jiang¹, D. Wang¹ and J. Chen¹

1. The Key Laboratory of Science and Technology on Vessel Integrated Power System, Naval University of Engineering, Wuhan, China

1 Introduction In aviation field, direct drive permanent magnet (PM) rectifier generator is often used in Multi Electric Airplane (MEA). Multiphase AC windings and rectifier technology make DC generator an excellent DC source with low torque ripple and low voltage ripple. And by regulating the engine speed within specified range, the DC-link voltage can be maintained constant with various electric loading. The key point of designing such a kind of generator, is to predict the electromagnetic and thermal field accurately. To solve the problem above, most research focused on electromagnetic thermal coupling analysis based on computational fluid dynamics (CFD), which can accurately predict temperature distribution [1]. Obviously, CFD-based coupling analysis method is not fit for optimization of direct drive PM rectifier generator for CFD process is time-consuming. In this paper, we aim to adopt lumped parameter thermal network (LPTN) as a substitute to replace the CFD process, implementing an electrical circuit-electromagnetic field-thermal network coupling analysis algorithm, enabling a much faster solution to analyze and optimize a PM rectifier generator.

2 Coupling Analysis

2.1 Electrical Circuit and Electromagnetic Field Coupling Analysis Electrical circuit and electromagnetic field are coupled by electromotive force (EMF). Electromagnetic field analysis takes winding current as the input, and outputs EMF. Electrical circuit analysis takes EMF as the input, and outputs winding current. Electromagnetic field is usually solved by 2D time stepping FEM method. Electrical circuit is solved by branch current method. The coupling relation is so strong that magnetic vector potential and winding current can only be analyzed simultaneously.

2.2 Electromagnetic Field and Thermal Network Coupling Analysis Electromagnetic field analysis takes winding current as input, and outputs iron loss, copper loss, solid loss, etc. Thermal networks analysis takes loss as input, and output temperature of generator parts. The above is just one way coupling (designated as unidirectional) from electromagnetic field to thermal network, which is carried out by transferring and mapping loss data. In this paper, we have also considered the coupling from thermal network to electromagnetic field, involving material property, which will be described in Section 2.3. Here this is called bidirectional coupling method. As for the LPTN model of generator, thermal resistance of each part refers to Mellor's T-shaped model [2]. The structure of each part is equivalent to a hollow cylindrical structure. Conduction, natural and forced convection are considered in the LPTN model. Model parameters and assumptions will be detailed in the full paper.

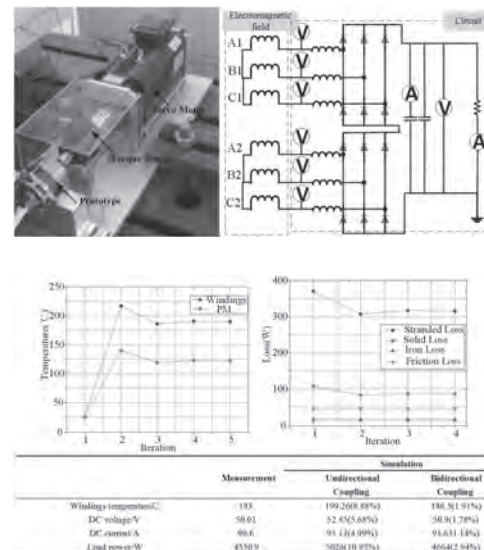
2.3 Material Property The temperature dependent material property is measured in the lab. The result is as follows: (1) For permanent magnet, coercivity and remanence decrease with temperature. (2) For silicon steel, the iron loss decreases with temperature. (3) For copper and permanent magnet, the resistivity increase with temperature.

2.4 Implementation Thermal network of generator is modelled and solved in Matlab, and electrical circuit and electromagnetic field are solved in ANSYS/Maxwell. Because the electromagnetic field and the temperature field have different time constant, during each iteration, several periods of electromagnetic field-circuit calculation are need to reach a steady state, followed by LPTN calculation. A control program is coded in Matlab to call thermal solver and Maxwell solver, and to transfer and map loss and temperature dependent material property. The convergence criterion is met if the temperature difference between adjacent iterations is less than 1°C.

2.5 Experiment Validation This prototype machine is an inner rotor PM generator with an integrated fan on the same shaft as rotor. The designed output power is 4.5kW at 7250rpm, and the DC link voltage is 50V. The generator is of 10 poles and 12 slots, filled with six phase double layer winding. The surface mounted PM is sintered SmCo30H. After 5 iterations, the coupled field analysis quickly reached convergence. The PM and winding temperature at each iteration and the corresponding loss is shown in Fig 2. As shown in Fig 1, a load test has been carried out to validate the accuracy of the bidirectional coupling method. The servo motor drives the prototype at a constant speed and torque meter measures the mechanical torque. The rectifier circuit is connected to the terminal of the prototype. Two thermocouples are embedded in the end

windings. Fig 2 shows the measured and simulated results. To illustrate the effect of temperature on electromagnetic field, the simulated result by unidirectional method is provided where the initial temperature is set to 25°C. Due to the consideration of thermal effect on material properties, the simulated result by bidirectional method is more accurate than unidirectional method. The prediction error of the bidirectional coupling method is within 5%. This paper proposed a much faster method to predict the electromagnetic and thermal field of direct drive PM rectifier generator. Lumped parameter thermal network (LPTN) is used as a substitute to replace the CFD process, greatly shortens the solution time. Furthermore, temperature effect on material property is considered, enabling a bidirectional coupling analysis in the paper. The experimental validation shows that the proposed method is enough accurate. The method can be applied to analyze and optimize a PM rectifier generator, as well as other typed motor.

[1] Yapeng Jiang, Dong Wang, Junquan Chen, "Electromagnetic-Thermal-Fluidic Analysis of Permanent Magnet Synchronous Machine by Bidirectional Method," *IEEE Transactions on Magnetics*, vol.3, no.54, pp. 1-5, 2018. [2] Mellor P.H, Roberts D, Turner D.R, "Lumped parameter thermal model for electrical machines of TEFC design," *IEEE PROCEEDINGS-B*, vol.138, no.5, pp.205-218, 1991.



BJ-13. Investigation of Balanced Bidirectional-Magnetization Effect of a Novel Hybrid-Magnet-Circuit Variable Flux Memory Machine.

R. Tu¹, H. Yang^{1,2}, H. Lin¹, Z. Zhu³, S. Niu² and S. Lyu¹
 1. Southeast University, Nanjing, China; 2. The Hong Kong Polytechnic University, Kowloon, Hong Kong; 3. The University of Sheffield, Sheffield, United Kingdom

I. Introduction Variable flux memory machines (VFMM) equipped with low coercive force (LCF) aluminum-nickel-cobalt (AlNiCo) magnets [1]-[4] can achieve high efficiency over a wide operation range by applying a current pulse to magnetize the LCF magnets with negligible copper loss. Thus, VFMM is widely recognized as a competitive candidate for traction applications. For elevating the the electromagnetic performance of VFMMs, hybrid usage of high coercive force (HCF) and LCF magnets is applied in VFMMs. A novel hybrid-magnet-circuit VFMM (HMC-VFMM) is proposed in [5], which combines the design concepts and strengths of VFMMs with parallel and series magnetic circuit of HCF and LCF magnets. Due to the special hybrid magnetic circuit design, it is essential to provide an insightful understanding about the nonlinear hysteresis behavior of the LCF working point considering the resultant effects of parallel and series branches and to analyze the magnetic field variation phenomenon of the developed HMC-VFMM due to the transient current pulse by an effective solution. This paper attempts to reveal and investigate a balanced bidirectional-magnetization effect of the proposed HMC-VFMM, i.e., the required demagnetizing and remagnetizing current levels are basically similar, which will benefit the inverter rating reduction and online flux control. The balanced bidirectional-magnetization effect is analytically revealed by using a simplified Fourier-series based hysteresis model. In addition, the numerical hysteresis model is programmed with FE model so as to accurately investigate the magnetization characteristics of HMC-VFMM. Finally, the experimental results on a prototype are carried out to verify the theoretical analyses. II. Machine configuration and working principle The proposed 21-slot/4-pole HMC-VFMM is investigated, in which the cross-section is illustrated in Figs. 1(a). The proposed HMC design is characterized by a dual-layer PM structure. For the parallel branch, the “U”-shaped hybrid PM arrangement is employed. For the series branch, the HCF PMs form a spoke-type flux concentration type. The proposed HMC-VFMM can combine the advantages of wide flux regulation range in parallel type and excellent on-load demagnetization withstand capability in series type. The variable-flux principle of the proposed HMC-VFMM can be illustrated by the open-circuit field distributions under different magnetization states (MSs) in Fig. 1(b). It can be observed that the air-gap flux can be flexibly adjusted by applying a transient magnetizing or demagnetizing current pulse. Meanwhile, due to the variable flux property, the losses at different speeds and loads can be also manipulated to realize efficiency improvement over a wide operating range. III. Analytical Analysis of Balanced Bidirectional-Magnetization Effect The nonlinear hysteresis characteristics of the LCF PMs used in the proposed HMC-VFMM can be characterized by a simple Fourier-series based hysteresis model as shown in Fig. 2(a). The PM working point can track along different recoil lines by applying a specific remagnetizing or demagnetizing current pulse. The underlying mechanism of the balanced bidirectional-magnetization effect can be physically characterized by hysteresis curves of the LCF PM in Fig. 2(b). The load line of the HMC design is placed between the two load lines of the parallel and series cases, which allows a better balance between the magnetizing and demagnetizing current amplitudes. Meanwhile, the oversized inverter rating issue for either parallel or series VFMMs can be well avoided by appropriately reducing maximum remagnetizing currents. The detailed analysis and investigation of magnetization characteristics of HMC-VFMM will be given in the full paper.

[1] V. Ostovic, “Memory Motors,” *IEEE Ind. Appl. Mag.*, vol. 9, no. 1, pp. 52-61, Jan./Feb. 2003. [2] H. Liu, H. Lin, Z. Q. Zhu, M. Huang, and P. Jin, “Permanent Magnet Remagnetizing Physics of a Variable Flux Memory Motor,” *IEEE Trans. Magn.*, vol. 46, no. 6, pp. 1679-1682, 2010. [3] Yu, C. and K. T. Chau. “Design, Analysis, and Control of DC-Excited Memory Motors,” *IEEE Trans. Energy Convers.*, vol. 26, no. 2, pp.479-489, 2011. [4] N. Limsuwan, T. Kato, K. Akatsu, and R. D. Lorenz, “Design and Evaluation of a Variable-Flux Flux-Intensifying Interior Permanent-Magnet

Machine,” *IEEE Trans. Ind. Appl.*, vol. 50, no. 2, 2014. [5] H. Yang, S. Lyu, H. Lin, Z. Q. Zhu, H. Zheng and T. Wang, “A novel hybrid-magnetic-circuit variable flux memory machine,” *IEEE Trans. Ind. Electron.*, vol. 67, no. 7, pp. 5258-5268, 2020.

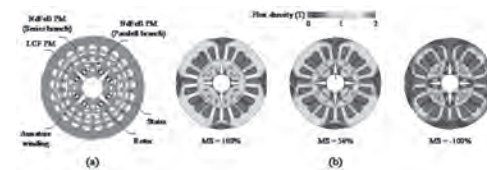


Fig. 1 VFMM topology and open-circuit field distributions under different magnetization states. (a) Topology. (b) Open-circuit field distributions under different magnetization states.

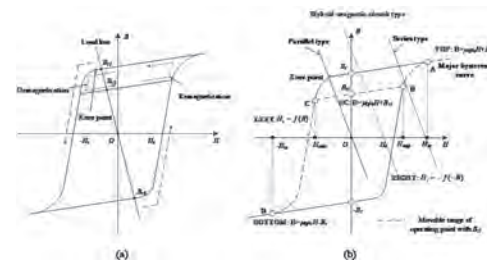


Fig. 2 Illustration of Fourier-series based hysteresis model. (a) Simplified view for illustrating the variable flux principle. (b) Numerical representation.

BJ-14. Impact of Hysteresis Phenomena in Time and Frequency Analysis for Inrush Currents in Power Transformers.

S. Perna¹, D. Lauria¹, A. Del Pizzo¹ and C. Visone¹

1. Università degli Studi di Napoli Federico II, Napoli, Italy

The first energization of a power transformer in an energy distribution system is a critical issue in the transformer's lifetime since the high currents experienced by the device in these conditions. Such currents are primarily due to magnetization of the iron core, which exhibits memory phenomena and saturation. Further, the initial phase strongly affects dynamics and could push the core in a saturation state, which, in turn, reduces the primary coil impedance and hence enables the current to rise (up to 10-15 times the full load current). This transient current is usually referred to as inrush current [1,2] and can be very dangerous for the device, causing electrodynamic stress, dissipations and consequent heating of the electrical insulations, harmonics production and their circulation in the power system. Such magnetizing currents focused great attention in the analysis of large transformers. The latest research activity was basically focused on the modeling, at the macroscopic scale, of the magnetization processes taking place in the transformer's core, strongly affecting the circuit's dynamics. The effort was therefore aimed to plug into the circuit model a suitable hysteresis operator. Different proposals discussed the effects of hysteresis models (e.g., Preisach, Jiles Atherton (J-A), etc., [3,4]) on the global behavior of the transformer dynamics, with particular emphasis to model's accuracy and computational weight, [5,6]. The J-A model offers a tool to describe hysteresis, but it is able to describe too simplified memory phenomena, [3] and requires a nontrivial parameters identification (e.g., through a nonlinear optimization). Conversely, Preisach model (PM) provides a memory description that fits with the real macroscopic processes but requires some expertise and a large of measured data (i.e., first order reversals), which limits its use in non-specialized frameworks, as power circuits and industrial electronics. Therefore, the availability of well-behaved hysteresis operator suitably simplified with respect to, e.g., the Preisach model, would represent an interesting contribution to this field. In the present contribution, the core magnetization modeling of a power transformer in a network is provided through a Preisach-based operator (i.e., it is characterized by the Preisach memory updating rules), [7] offering a simpler implementation, inverse operator availability and a reduced set of measured data, than PM. Such operator, as detailed hereafter, is based on a weighted linear superposition of elementary operators (Play operators, see, [7]) and will be referred to as Prandtl-Ishilinskii (P-I) operator. Further, due to its simpler structure and reduced numbers of parameters, it allows the inrush current process analysis in a wide range of magnetization conditions with low effort. The P-I model, describing the B-H characteristic, along with the circuit's equations, referred to the same circuit as in [6], are reported in Fig. 1. In the first frame, $P_i[\cdot]$ is the play operator, while $\mu(r)$ is a weight function and the saturation magnetization, $M_s = 1.5T$. In the second frame, R_1 is the primary resistance, E the voltage amplitude, while F is the hysteresis operator linking the flux linkage to the primary current. The secondary current is assumed zero during the analysis. The model so conceived is able to fairly describe the behavior of a realistic core, as shown in the same figure. The circuit's behavior has been preliminary tested in the same conditions as in [6]. However, in Fig. 2 its behavior has been studied in conditions where the great arise of (inrush) currents clearly appears. In the same figure the impact of hysteresis with respect to a memoryless description is outlined. Aim of the paper will be a thorough testing of the proposed model, in terms of accuracy, computational efficiency for the analysis of inrush currents phenomena in power transformers. The characteristics of the hysteresis operator would allow an immediate analysis of the basic magnetic parameters affecting the inrush currents dynamics. In particular, the influence of remanence, coercive field and permeability at current reversal, will be investigated. For the latter (initial permeability at the branch start), during the transient, the material experiences an up and forth current variation, allowing the branching to arise and to affect (in the starting part of the branch characterized by low permeability) the whole current dynamics. Such effect, which strongly relies on the initial magnetization state of the iron core (M_r), could be easily described by the proposed model and of course, cannot be taken into account when a nonlinear memoryless modeling is employed.

[1] R. Yacamini, C. Eng., and A. Abu-Nasser, IEE Proceedings, Vol. 133, Pt. B, No. 1, 1986. [2] J.C. Yeh, C.E. Lin, C.L. Huang, Electric Power Systems Research 30, 93-102, 1994. [3] I. D. Mayergoyz, Springer, 1991. [4] D.C. Jiles, D.L. Atherton, J. of Magnetism and Magnetic Materials, vol. 61, 1-2, pp. 48-60, 1986. [5] A. A. Adly, IEEE Trans on Magnetics, vol. 37, no. 4, 2001. [6] X. Wang, D. W. P. Thomas, M. Sumner, IEEE Trans. on Magnetics, 44, 3, 2008. [7] C. Visone, M. Sjöström, Physica B: Condensed Matter, vol. 343, 1-4, pp. 148-152, 2004.

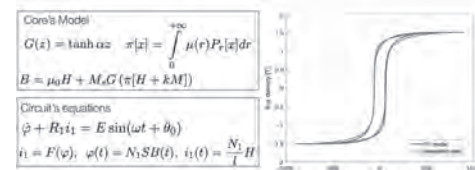


Figure 1 – Left: the P-I operator and the core characteristic, along with the circuit's equations. Right: The simulated and measured B-H characteristic.

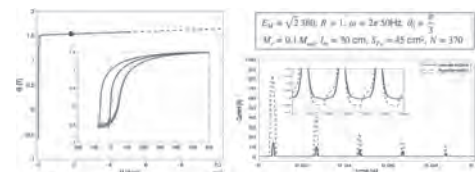


Figure 2 – Left: B-H characteristic experienced during transient, with a saturation magnetization $M_{sat} = 1.5T$. Right: inrush currents time behavior for a memoryless nonlinear and hysteretic characteristic, along with the core and circuit's parameters.

Session BK

VIBRATION ANALYSIS AND ENERGY HARVESTING APPLICATIONS

Mauro Zucca, Chair
INRIM, Torino, Italy

CONTRIBUTED PAPERS

BK-01. Vibration Analysis of the Multi-Unit Permanent Magnet Synchronous Machine in the non-Mechanical-Load Indirect-Testing Situation.

D. Zeng¹, J. Zou², Y. Xu² and Q. Wei¹

1. Harbin Engineering University, Harbin, China; 2. Harbin Institute of Technology, Harbin, China

The vibration of the machine is always cared, since it may influence the stability and reliability characteristics. Some indirect-testing methods for the multi-unit permanent magnet synchronous machine have been proposed in order to measure the parameters and characteristics of the machine without any mechanical load. The aim of this paper is to calculate and analyze the vibration of the machine in the indirect-testing method, and discuss the difference of the vibration characteristics between the indirect-testing situation and the direct-testing situation. The calculation error is discussed in this paper. To validate the analysis, the calculated radial electromagnetic force and vibration are compared with the test results of a multi-unit PMSM prototype. I. Introduction The high-power low-speed permanent magnet synchronous machine (PMSM) is typically applied in high-power fields, such as electric propulsion, for their excellent operating characteristics of high efficiency and high torque density. To reinforce the reliability and reduce the power capacity of one phase, a novel multi-unit structure has been proposed [1]. Much effort has been devoted to the electromagnetic analysis, the drive strategy and the testing method of the multi-unit PMSM [2]-[6]. In order to avoid using the mechanical load, non-mechanical-load indirect-testing methods for some important characteristics of the multi-unit PMSM have been proposed. The important characteristics are tested in the non-mechanical-load testing situation, where some unit-motors run as motor and some unit-motors run as generator. However, the vibration analysis of the multi-unit PMSM in the non-mechanical-load testing situation have not been mentioned in literature so far. The PMSM is always required to have a smooth and quiet operation when used in electrical propulsion or military appliances [7]-[9]. If the vibration characteristics of the electrical machine are too bad, it may cause the mechanical fault of the system. Thus, vibration and acoustic noises in the PMSM are considered a critical issue [10]-[11]. In this paper, the radial electromagnetic force and vibration of the multi-unit PMSM in the non-mechanical-load testing situation are calculated and analyzed. The difference of the vibration between different operating situations are discussed. II. The calculation of the radial electromagnetic force and vibration The principle of virtual work is now used as a matter of routine to compute the electromagnetic torque for its excellent advantages of high accuracy and minor calculation. According the virtual work method, the electromagnetic torque of the multi-unit PMSM can be expressed. And combining the voltage equations, the magnetic flux of the machine can be expressed by the function of the electromagnetic parameters. The multi-unit PMSM can perform in the situation that some unit-motors are running as the motor and some unit-motors are running as the generator. In this situation, the parameters and characteristics (including the currents, losses, torque, etc) of the machine can be obtained without using the mechanical load. It can be considered the non-mechanical-load indirect-testing situation. Thus, the magnetic density distribution in the non-mechanical-load indirect-testing situation can be obtained. Furthermore, the radial electromagnetic force are calculated according to the magnetic density. To calculate the vibration, besides the radial electromagnetic force, the modal analysis is also necessary. In this paper, the transient structural analysis is performed using the modal superposition method. The mechanical structure model of the multi-unit PMSM is established. And the natural frequencies of the structure are obtained. The displacement response of the calculated radial electromagnetic force can be calculated based on the established mechanical structure modal model. To validate the calculated displacement response, the modal test and the response test are performed. The test bench for the vibration of the PMSM prototype in the non-mechanical-load indirect-testing situation is shown in Fig. 1. The frequencies of the harmonic components in the calculated results are in a satisfactory agreement with those in the test results. The displacement response in the non-mechanical-load indirect-testing situation

is shown in Fig.2. It can be seen in Fig.2 that there are some additional harmonic components of the acceleration because of the additional radial electromagnetic force in the non-mechanical-load indirect-testing situation. The variety of the additional harmonic components are influenced by the rotating speed fluctuation and the asymmetric currents in the phases. The additional harmonic components in the displacement response are also discussed in this paper.

- [1] B. Zhang, Y. Liu, and G. Feng, "Study on low voltage high power multi-branch permanent magnet synchronous motor," in *Proc. Conf. Power and Energy Engineering*, Aug. 2010. pp. 747-755. [2] P. Zhao, G. Yang, and J. Liu, "Multi-unit motor parallel drive system for electric vehicle application," in *Proc. IEEE conf. Vehicle Power and Propulsion*, Aug. 2008. pp. 747-755. [3] B. Zhao, J. Zou, G. Hao, J. Zou, and Y. Xu, "Asymmetry of inductance and torque ripple of multi-unit permanent magnet synchronous motor," in *Proc. Conf. International Conference of Electrical Machines and Systems*, Aug. 2011. pp. 747-755. [4] Zeng Depeng, Zou Jibin, Xu Yongxiang, "An Indirect Testing Method for the Torque Ripple of Multiunit Permanent Magnet Synchronous Machines," *IEEE Transactions on Industrial Electronics*, 2020, 67(4): 2734-2743. [5] Zeng Depeng, Zou Jibin, Xu Yongxiang, "Analysis and Discussion of the Indirect Testing Method for the Losses of Permanent Magnet Synchronous Machines," *IEEE Transactions on Magnetics*, 2018, 54(11). [6] Zou Jibin, Zeng Depeng, Xu Yongxiang, "An Indirect Testing Method for the Mechanical Characteristic of Multiunit Permanent-Magnet Synchronous Machines With Concentrated Windings," *IEEE Transactions on Industrial Electronics*, 2015, 62(12): 7402-7411. [7] Islam, R, and I. Husain. "Analytical Model for Predicting Noise and Vibration in Permanent-Magnet Synchronous Motors." *IEEE Transactions on Industry Applications* 46.6(2010):2346-2354. [8] Fakam, Mathias, M. Hecquet, and V. Lanfranchi. "Design and Magnetic Noise Reduction of the Surface Permanent Magnet Synchronous Machine Using Complex Air-Gap Permeance." *2014 Ninth International Conference on Ecological Vehicles and Renewable Energies (EVER)* IEEE, 2014. [9] Xing, Zezhi, et al. "Reduction of Radial Electromagnetic Force Waves Based on PM Segmentation in SPMSMs." *IEEE Transactions on Magnetics* PP.99(2020):1-1. [10] Zhang, Qinghu, et al. "Analysis and Calculation of Radial Electromagnetic Force of Circular Winding Brushless DC Motor." *IEEE Transactions on Industrial Electronics* PP.99(2019):1-1. [11] Shin, Hyeon Jae, et al. "Vibration Analysis and Measurements Through Prediction of Electromagnetic Vibration Sources of Permanent Magnet Synchronous Motor Based on Analytical Magnetic Field Calculations." *IEEE Transactions on Magnetics* 48.11(2012):4216-4219.



Fig.1 The test bench for the vibration

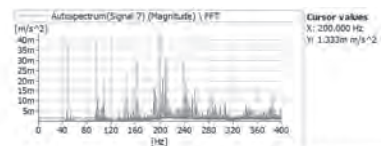


Fig.2 The displacement response in the non-mechanical-load indirect-testing situation.

BK-02. A New Method to Control Intrinsic Localized Mode Using a Variable Magnetic Spring Structure.

S. Lee¹, M. Kato² and K. Hirata¹

1. Division of Materials and Manufacturing Science, Osaka University, Suita, Japan; 2. Electrical and Electronics Systems, Ibaraki University, Mito, Japan

1 Introduction In a dynamical mass-spring system with many discrete mass points, when the spring has nonlinearity, a special localized vibration mode occurs in which only a limited number of masses vibrate. This is called the intrinsic localized mode (ILM) [1]. Many researchers have been interested in the ILM because of its unique features that are not found in the linear systems. Particularly in mobile ILMs [2], in which the kinetic energy of the system is localized in a small number of masses and the localized energy propagates to adjacent masses, have high potential for engineering applications through experiments [3,4]. However, the shape, frequency and speed of the ILM were determined by the parameters of the dynamic vibration system (mass, spring constant, and initial vibration). Hence, control of the generated ILM was not possible and therefore, there has been no significant progress in engineering applications. Here, we propose a new magnetic spring structure that can variably handle the nonlinear spring characteristics of dynamic vibrating systems. In this paper we would like to describe the ILM in dynamic vibrating systems. Then, a variable magnetic spring structure (VMS structure) is proposed, and the variable magnetic spring properties are verified from the finite element analysis (FEA) results of the proposed structure. Lastly, by solving the differential equations of the dynamic oscillating system, we show the possibility of controlling the ILM by varying the nonlinear spring properties of the dynamic vibrating system. 2 Variable magnetic spring structure For ILM generation, multi-mass and nonlinear springs are required. Since we are dealing with rotating bodies, the mass is replaced by inertia and the nonlinear spring has restoring torque. A large number of rotating bodies with the same inertia are connected by nonlinear restoring torques with neighboring rotating bodies. The nonlinear restoring torques structure with VMS is shown in Fig. 1(a). The VMS consists of two rotors, the outer rotor with electromagnets and the inner rotor with interior permanent magnets (IPM). The outer rotor coil consists of two phases with opposite phases and applies DC current. The magnetic flux due to permanent magnet is shown by the solid blue loop, and the magnetic flux due to the applied current is shown by the dotted red loop. The restoring torque of the VMS is generated by the relative angle between the inner and outer rotors. Fig. 1(b) shows the relationship between the relative angle and the restoring torque when 2A/mm² to 8A/mm² is applied to the two-phase coil with opposite phases obtained from the FEA. The restoring torque T can be approximated as follows: $T=k_3\theta^3+k_1\theta$..(1) Here, θ is the relative angle (rad), k_1 (Nm/rad) is the spring constant, and k_3 (Nm/rad) is the nonlinear coefficient. Also, the nonlinear ratio is defined as. It decreases continuously from 20.52 at an applied voltage of 2A/mm² to 11.99 at 8A/mm². 3 Control of ILM In this chapter we numerically solve the differential equations for a rotating nonlinear mass-spring system. The equation of motion with consideration of the nonlinear coefficients of the rotating spring in Fig. 2(a) is the following differential equation $Jd^2\theta_n/dt^2=k^1_{n+1}(i)(\theta_{n+1}-\theta_n)+k^3_{n+1}(i)(\theta_{n+1}-\theta_n)^3-k^1_n(i)(\theta_n-\theta_{n-1})-k^3_n(i)(\theta_n-\theta_{n-1})^3$..(2) Here, J is the inertia of the VMS, θ_n is the absolute angle of the nth VMS, $k^1_n(i)$ is the linear spring constant at current density i between the (n-1)th and nth VMS, and $k^3_n(i)$ is the nonlinear spring coefficient at current density i between the (n-1)th and nth VMS. Fig. 2 shows the numerical results of the differential equation (2). There are 21 VMS's used, and the inertias are all 1.34×10^{-4} kg×m². Initially, the oscillations were such that the ILM was generated from the center. Magnetic springs of 2A/mm² (nonlinear ratio 20.52) and 4A/mm² (nonlinear ratio 16.25) were used as shown in Fig. 1(b). In (b-1), a magnetic spring with a nonlinearity factor of 20.52 was used for the entire simulation time. This resulted in the initial ILM remaining centered until the end of the simulation. In (b-2), we used a magnetic spring of 20.52 for the simulation time of 0-1 sec, and changed $k^{1,3}_{5-10}$ to a magnetic spring of 16.25 for 1-2 sec. In 2-3 seconds, $k^{1,3}_{5-10}$ were changed to magnetic springs of 16.25. From (b-1) and (b-2), it is clear that the ILM can be controlled by changing the nonlinear rate of the magnetic spring. In the final paper, we will discuss the cause of the nonlinear magnetic spring property of the proposed VMS structure by FEA,

and furthermore, discuss the movement speed and trend of ILM according to the nonlinear rate.

[1] S. Takeno, K. Kisoda, and A.J. Sievers, Progress of Theoretical Physics Supplement, No. 94, pp. 242-269 (1988). [2] M. Kimura, R. Tsujisaka, T. Hikiyama, Y. Taniguchi, and Y. Matsushita, A study on reflection of moving intrinsic localized modes at a junction of two different nonlinear lattices, 2014. [3] Y. Watanabe, M. Nishimoto, and C. Shioyama, Nonlinear Theory and Its Applications, IEICE, vol. 8, pp. 146-152, 2017. [4] S. Lee, K. Hirata, M. Kato, *Electrical and Electronic Engineering (ISEF)*, Nancy, France, 2019, pp. 1-2, doi: 10.1109/ISEF45929.2019.9097039.

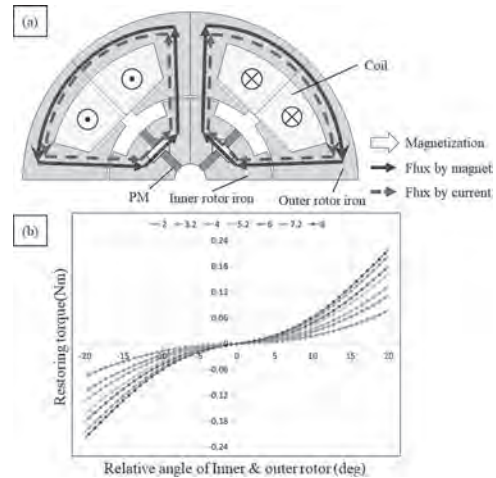


Fig.1 (a) Proposed VMS structure. (b) The relative angle and the restoring torque by applied current density.

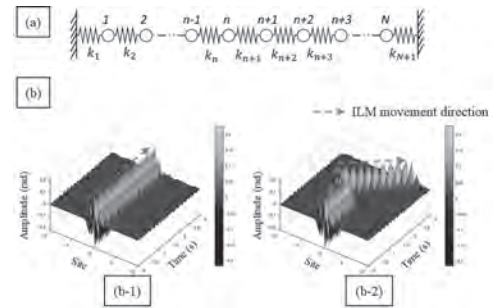


Fig.2 (a) Spring-mass system. (b) Numerical result of ILM with VMS.

BK-03. Design Study of a Two-Dimensional Electromagnetic Vibration Energy Harvester.

C. Imbaquingo¹, C.R. Bahl¹, A.R. Insinga¹ and R. Bjørk¹

1. Energy Conversion and Storage, Danmarks Tekniske Universitet, Lyngby, Denmark

This work investigates a two-dimensional electromagnetic vibration energy harvester (2-D EMVEH) that uses magnetic interactions to convert ambient vibrations into electrical energy. This work focuses on a specific prototype design, which consists of two parts. The first part is a free-to-move two-ring magnetic structure with a set of coils located between the rings. The second part is a fixed system of a top and bottom plate with a set of cylindrical magnets placed at the centre. Fig 1 depicts the schematic of the 2-D EMVEH. The top lid of the prototype and the set of coils are not shown in Fig 1 so that the internal parts can be seen. In the structure, the central two-ring structure is free to move relative to the fixed plate and the fixed cylindrical magnets in the centre of the fixed plate. When the prototype is exposed to ambient vibrations in one or more dimensions, the two-ring structure moves until the repulsive force, due to the interaction with the fixed cylindrical magnets pushes it back. The movement of the two-ring structure relative to the fixed cylindrical magnets simultaneously generates an electromagnetic force on the fixed winding coils that are located in the gap in the two-ring structure. In the two-ring structure, the distance between the top and bottom rings is kept with nine equally-distributed columns. There is a total of 48 block permanent magnets in each top and bottom ring. Similarly, the distance between the top and bottom fixed plates is maintained with nine outer columns. The magnetic polarity of each ring structures and the cylindrical permanent magnet is such that the magnetic flux line distribution is as shown in Fig 2, given as a result a repulsive force. Furthermore, the two-ring structure has a set of bearings on the bottom and top sides so that the friction with the fixed plates is considerably reduced. Two-dimensional electromagnetic vibration energy harvesters have only been considered very briefly in literature. Ref. [1] considers a somewhat similar structure as discussed above, but where the moving part is the middle magnet and also with coils placed on the outside of the design. Moreover, the analysis of the harvested power was done for a vertically mounted design and with a mathematical model that considers the same expressions as for a 1-D EMVEH. Thus, the reason for employing this configuration was only to decrease friction but not scavenging energy from two-dimensional vibrations. Likewise, Ref. [2] consists of a spherical permanent magnet inside a capsule which is wound with two coils. Due to the lack of a repulsive force, this prototype needs stoppers on the inner walls of the capsule so that the spherical magnet does not break. Finally, other potential prototypes are discussed in [3], where mostly 1-D EMVEH's, but also a couple of 2-D EMVEH's are discussed, e.g. [4] who considers how an eccentric mass brings about an oscillatory motion which, under certain conditions, results in a rotary motion. However, as it is clear from the above literature an analysis of the behaviour of a true two-dimensional electromagnetic energy harvester has not been performed. How such a device responds to two-dimensional vibrations is not known, nor has such devices been analyzed neither with modelling or experimental characterization. In this study, a thorough analysis of the device presented above is performed. First, the optimal harvester is designed with respect to the repulsive force provided by the magnets by carrying out a parametric analysis. Some dimensions are chosen such as the gap between the ring holder, size and number of the cylindrical magnets, coil shape, and so on. With these fixed parameters, the ideal size of the fixed cylindrical magnets is determined by calculating the repulsive magnetic force and the magnetic flux in the coils with the help of a finite element method software. With the optimal design determined, the force and flux are tabulated and saved as functions of the position of the two-ring structure. Subsequently, by using this data, a modelling study of the performance of the device is realized. A two-dimensional ordinary differential equation solver is constructed and by using the tabulated force and flux it is determined the three state variables of the system as a function of time for a given set of vibrations. The state variable solved for are the position and speed of the two-ring structure and the electrical current in the coils. Finally, a prototype of this 2-D EMVEH is built and tested in a two-axis shaker at different frequencies and displacement amplitudes. Especially, the prototype is tested at low frequencies and small amplitudes to determine its ability to

overcome the mechanical friction and the amount of harvester power with such operating conditions. The experimental results are compared with the results of the mathematical model.

[1] Manuel Gutierrez, Amir Shahidi, David Berdy, and Dimitrios Peroulis. Design and characterization of a low frequency 2-dimensional magnetic levitation kinetic energy harvester. *Sensors and Actuators, A: Physical*, 236, 2015. [2] Benjamin J. Bowers and David P. Arnold. Spherical, rolling magnet generators for passive energy harvesting from human motion. *Journal of Micromechanics and Microengineering*, 19(9), 2009. [3] Clemens Cepnik, Roland Lausecker, and Ulrike Wallrabe. Review on Electrodynamic Energy Harvesters - A Classification Approach. *Micromachines*, 4:168–196, 2013. [4] Ken Sasaki, Yuji Osaki, Jun Okazaki, Hiroshi Hosaka, and Kiyoshi Ito. Vibration-based automatic power-generation system. In *Microsystem Technologies*, volume 11, 2005

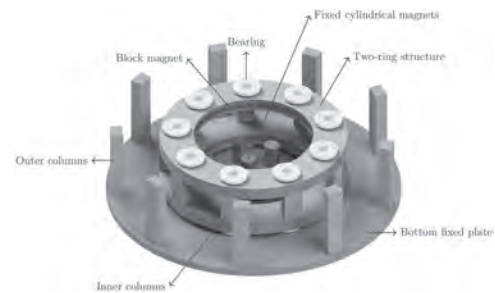


Fig. 1 Schematic of the 2-dimensional electromagnetic energy harvester. The top lid of the prototype and the set of coils are not shown.



Fig 2 Cross-section of the 2-D EMVEH and magnetic flux lines between the two-ring structure(left and right) and fixed cylindrical magnet (centre).

BK-04. Spin-Orbit Torque Rectifier for Energy Harvesting From Weak Radio-Frequency.

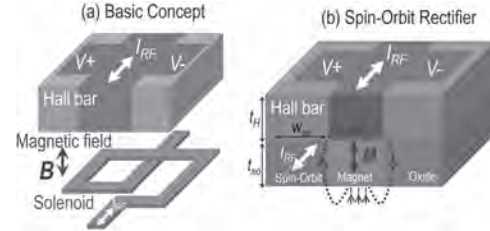
S. Sayed¹, S. Salahuddin¹ and E. Yablonovitch¹

1. Electrical Engineering and Computer Sciences, University of California Berkeley, Berkeley, CA, United States

Harvesting of the ambient radio-frequency (RF) energy is of great interest to address the increasing energy demand for emerging applications, e.g., the internet of things, wearable devices, various sensors and implants, and 3D integrated circuits. To use the weak ambient RF power density for such applications, we need rectifiers capable of operating much below 1 μ W RF power with high efficiencies. However, the development of such technologies is severely limited by the conventional semiconductor rectifiers [1], which fail to operate in the weak RF limit. We propose a new rectifier concept [2], simultaneously utilizing the spin-orbit torque (SOT) and the Hall effect, that can provide \sim 200 μ V DC voltage from a 500 nW of radio-frequency (RF) power using existing materials, with a power conversion efficiency as high as 71%. The DC voltage strength can be efficiently enhanced to \sim 300 mV from the same RF power with a series array of such devices while matching the low impedance of the receiver antenna. We estimate a very high curvature coefficient of the proposed rectifier, in the order of 10^4 V^{-1} , where the theoretical limit of conventional Schottky diodes is determined by the inverse of the thermal voltage $q/k_B T \sim 40$ V^{-1} [3]. Various SOT materials are being extensively studied for efficient current-induced switching of scaled ferromagnets for memory applications (see, e.g., Ref. [4] and references therein). Here, we propose a new application of SOT in the rectification of weak RF by coupling it to conventional Hall devices. The basic idea can be explained using a Hall bar and a solenoid connected in parallel, see figure. A current-carrying conductor placed in a magnetic field (B) exhibits a voltage drop in the direction orthogonal to both the current and the B-field, known as the Hall effect. If a fraction of the current flows through a solenoid underneath the Hall bar to generate the B-field, the Hall voltage will be unidirectional irrespective of the current direction, leading to a rectification. We propose a structure where such a solenoid is replaced with a bilayer consisting of a material exhibiting SOT and a ferromagnet (FM) with a low anisotropy energy barrier. We design the device such that the current equally divide between the Hall and the SOT layers. The FM magnetization, on average, follows the fraction of the current flowing in the SOT layer, provided that the current can produce sufficiently strong SOT. The FM applies an effective B-field to the Hall layer and thus leads to a similar rectification case as described in the solenoid case. The Hall effect and spin-orbit-torque are both proportional to current density, which improves inversely with device cross-sectional area, providing the largest signals at the nanoscale. To make the proposed rectifier sensitive to weak RF current, we need a material with a high SOT factor, an FM with low anisotropy energy, and a low Gilbert damping constant. An FM with low anisotropy energy is typically achieved by lowering the total magnetic moment or by tuning the FM thickness to optimize near the transition point between in-plane and perpendicular anisotropies or by using isotropic geometries. We consider a soft ferrite with a very low anisotropy field and a low total magnetic moment, that is expected to easily follow a SOT induced by a weak RF current. Such a low anisotropy energy magnets can achieve a wide frequency bandwidth of operation, depending on the total magnetic moment in the FM and the angular momentum conservation [5]. We simulate the magnetization dynamics using the stochastic-Landau Lifshitz Gilbert equation, which considers the stochastic nature of such low anisotropy energy magnets due to the presence of thermal noise. We can further optimize the device structure and use emerging materials to enhance the figure-of-merits at even lower RF power. The proposed device can lead to important new technologies addressing the alarming energy issues in the era of the internet of things, wearable devices, and densely integrated 3D circuits. This work is supported by the Center for Energy Efficient Electronics Science (E3S), NSF Award 0939514.

[1] S. Hemour et al. IEEE Trans. Microw. Theory Tech. 62, 965–976 (2014). [2] S. Sayed, S. Salahuddin, and E. Yablonovitch, to appear in Appl. Phys. Lett. (2021). [3] J. Karlovský, Solid-State Electronics 10, 1109 – 1111

(1967). [4] S. Sayed et al., arXiv:2010.01484 (2020). [5] S. Sayed et al., Phys. Rev. Applied 11, 054063 (2019).



(a) Basic concept of rectification explained using a Hall bar and a solenoid sharing the same current. The magnetic field on the Hall bar, applied by the solenoid reverses when we reverse the current direction. Thus the Hall voltage remains of the same polarity irrespective of the current direction. (b) The proposed spin-orbit torque (SOT) rectifier, where the solenoid is replaced with a bilayer of a SOT material and a soft ferromagnet (FM). The FM follows in the current in the SOT material and applies a magnetic field to the Hall layer, similar to the solenoid case.

BK-05. Design Optimization of Tapered Wideband Nonlinear Electromagnetic Vibration Energy Harvesters for Powering IoT.

K. Paul¹, A. Amann^{2,3} and S. Roy^{1,4}

1. Micro-Nano-systems Center, Tyndall National Institute, Cork, Ireland;
2. School of Mathematical Science, University College Cork, Cork, Ireland;
3. Photonics Centre, Tyndall National Institute, Cork, Ireland;
4. Department of Physics, University College Cork, Cork, Ireland

The ongoing development in the landscape of low power electronics has paved the way for the emergence of autonomous wireless sensor networks (WSNs) to create a smart and responsive environment around us through the Internet of Things (IoT). For instance, efficient WSN performs structural health monitoring of heavy-duty vehicles like train and reports on vital physical parameters and alerts if there are any probable failure to reduce the chances of accidents. Perpetually powering these sensors is one of the critical bottlenecks in realizing a WSN system. The associated maintenance and installation cost [1] of the batteries limits the widespread deployment of the WSNs. The demand for the implementation of battery-less microsystems and the ubiquity of ambient vibrations in an industrial and domestic environment has made the electromagnetic vibration energy harvesters (EM-VEHs) [2] a striking sustainable energy source for powering the WSNs. Compared with the conventionally used narrowband linear VEHs, the nonlinear counterparts [3,4] are much more efficient in harnessing mechanical energy from real-world broadband vibrations owing to their intrinsic wideband frequency response. An effective way of realizing nonlinearity is by tailoring the stiffness of the spring geometry [5,6], which on the other hand depends critically on the thickness of the spring material limiting the scope of geometric alterations. Tapered spring structures on the other hand open up the scope for optimizing the degree of nonlinearity and hence the bandwidth of the VEHs by changing the taper ratio of the spring structure [7]. In this work, we exploit exponential and parabolic tapering to induce stretching based nonlinearity in the spring structure and we explore the overall performance of an optimized tapered EM-VEH that could be a potential candidate for powering WSN involved with railway infrastructure monitoring system. The EM transducer under consideration works on the Faraday's principle, in which the relative motion between a pair of coil and magnet induces voltage across the coil, which could be harvested in the form of usable electrical energy. Among the other conventional transducers, owing to the reliability, longevity and large tunable parameters offered, the EM transducers are the most promising ones. We have used the structural mechanics module of COMSOL Multiphysics to explore the effect of tapering on the force-displacement relationship of the spring structures. The broad arm of the spring (length w_1) is fixed with the frame and the shorter arm (w_2) is attached to the moving load, which is the magnet assembly as shown in Figure 2. We have varied the taper ratio ($= w_2/w_1$) of the spring structures from 0.2 to 0.35, keeping the length of the shorter arm fixed to 4mm. Figure 1 depicts the first eigenmodes of the structures exhibiting out of plane displacements. Owing to the atypical stress distribution of these tapered structures, at a larger amplitude of excitation, the vertical displacement of the spring varies nonlinearly with the force. Hence, the restoring force of the spring consists of the linear part responsible for bending of the springs and the nonlinear part responsible for the stretching of the same. As compared with the parabolically tapered spring architectures, the exponentially tapered counterpart exhibits larger displacements for the same taper ratio. This can be attributed to the larger stress distribution on the springs owing to the exponentially reducing area. We further designed a nonlinear EM-VEH employing exponentially tapered spring having the taper ratio of 0.25 as shown in figure 2. The central paddle of the spring holds the magnet assembly comprising of four NdFeB magnets arranged such that it forms a close loop of magnetic field lines across the coil. To further eliminate the fringing of magnetic field lines and enhance the EM-coupling, block of soft magnetic steel is arranged on both sides of the magnet assembly, resulting in an EM-coupling of 15.2Wb/m. At low acceleration (0.1g), the system's frequency response resembles with that of a linear VEH, the load power maximizing at 124Hz. As the excitation amplitude increases from 0.1g to 1g, the frequency response becomes gradually non-resonant in nature. When the frequency is swept in the forward direction, the load power changes from 235 μ W at 124Hz to 1.6mW at 154Hz with 1g acceleration, beyond this point the response suddenly falls off the high

energy branch, which is a signature of the effect of induced nonlinearity. But when the frequency is swept in the backward direction, the response follows a lower energy branch, giving rise to the phenomena of multistability, which in turn aids in enhancing the operable bandwidth of frequency that the device offers. At 1g acceleration, the system offers 20Hz of bandwidth. The typical vertical acceleration of a diesel train is around 0.93g [8] with substantial mechanical energy distributed around 100-300Hz (Fig.2d). This developed VEH could be employed to harness this mechanical energy from trains to power the WSNs associated with the railway system responsible for structural health monitoring.

[1] J. P. Amaro, R. Cortesão, J. Landeck *et al*, *IEEE Transactions on Instrumentation and Measurement*, vol. 64, no. 7, pp. 1847-1857 [2] W. Hwang *et al.*, *Applied Energy*, vol. 243, pp. 313-320, 2019. [3] S. Roy, P. Podder, and D. Mallick, *IEEE Magnetics Letters*, vol. 7, pp. 1-4, 2016. [4] P. Constantinou and S. Roy, *Smart Materials and Structures*, vol. 25, no. 9, p. 095053, 2016. [5] B. Marinkovic and H. Koser, *Applied Physics Letters*, vol. 94, 2009. [6] D. Mallick, A. Amann, and S. Roy, *Smart Materials and Structures*, vol. 24, no. 1, p. 015013, 2014. [7] K. Paul, A. Amann, S. Roy, *Applied Energy*, 2020, 116267, ISSN 0306-2619. [8] Real vibration, NIPS lab, <https://realvibrations.nipslab.org/node/1093>.

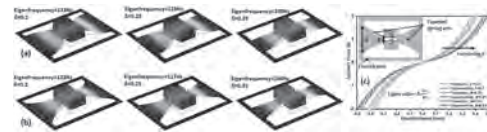


Fig 1: First eigenmodes of parabolically (a) and exponentially (b) tapered spring structure with different taper ratio is shown. The force-displacement relation of springs is shown in (c).

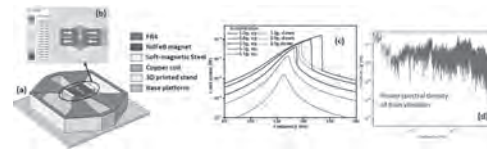


Fig 2: Exponentially tapered EM-VEH (a) is designed with taper ratio 0.25. The EM interaction is depicted in (b). Frequency response of the nonlinear VEH is shown in (c) and power spectral density of train vibrations in (d).

Session BP
PERMANENT MAGNET ELECTRICAL MACHINES FOR ELECTRIC VEHICLE
(Poster Session)

Rong-Jie Wang, Chair
Stellenbosch University, Stellenbosch, South Africa

BP-01. Research on the Influence of Harmonics Back-EMFs on the Flux-Weakening Performance of IPMSM.

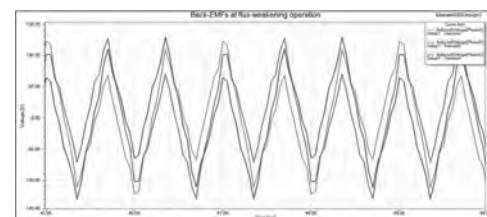
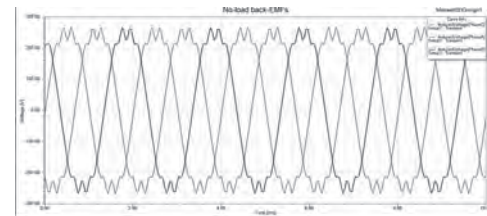
L. C¹, J. Hu¹, K. Li¹ and J. Shang¹

1. Harbin Institute of Technology, Harbin, China

Abstract This paper analyzes the influence of harmonic back-EMFs, especially the third harmonic back-EMF, on the flux-weakening performance of interior permanent magnet synchronous motor (IPMSM). First, IPMSM model and the back-EMF harmonics components of IPMSM are studied. Then, the commonly used flux-weakening control methods are introduced briefly. Finally, the influence of back-EMF harmonics on the flux-weakening performance is analyzed in detail from the perspective of voltage limit. The analysis is validated with the simulation. 1. Introduction IPMSM has been widely explored due to its excellent performance such as high efficiency and high power density. In many applications of IPMSM such as electric vehicles, a wider speed range is usually required, and flux-weakening control is usually adopted to obtain higher speeds. The flux-weakening range of permanent magnet motor is very limited, because the magnetic field of the permanent magnet cannot be adjusted. Generally speaking, IPMSM has a wider flux-weakening speed range than surface permanent magnet synchronous motor (SPMSM) because of the salient-pole structure [1]. Based on the current vector control, there are two typical flux-weakening control methods [2]: one is the feedforward control method, which requires the accurate IPMSM mathematical model parameters. The other is the feedback control method, which uses the PI regulator to compensate the demagnetizing current. The feedback control method can be further divided into two categories: flux-weakening control based on dual current regulators and flux-weakening control based on variable voltage angle. The dual current regulators method is still based on current vector control, but suffers from the conflict of two voltages saturation. There is no current regulator in the initial variable voltage angle method. However, the single d-axis current regulator or single q-axis current regulator methods are developed to plan the current locus and improve the dynamic performance [3]. Regardless of the different flux-weakening methods, its essence is to offset the permanent magnet back-EMF at high speeds by applying the demagnetizing current, and relieve the conflict of back-EMF and inverter voltage limit. However, the demagnetizing current can only counteract the fundamental back-EMF. The back-EMF of IPMSM has rich harmonic back-EMFs. The reason is that the permanent magnet flux linkage contains the harmonic components. Among these harmonics, the third harmonic is the most obvious. At high speeds, the high third harmonic back-EMF can also reach the inverter voltage limit like the fundamental back-EMF. However, there is no demagnetizing current offsetting it. This paper will analyze the influence of the harmonics back-EMFs on the flux-weakening performance of IPMSM. The rest of the paper is organized as follows: Section 2 introduces the IPMSM model and harmonics back-EMFs; Section 3 gives a profile of existing flux-weakening method; Section 4 analyzes the influence of harmonics back-EMFs on the flux-weakening performance of IPMSM. 2. IPMSM Model and back-EMF harmonics Flux-weakening control is based on the current vector control architecture, which is implemented in synchronous rotating (d-, q-axis) coordinate system. Through coordinate transformation, all variables in the IPMSM mathematical model, including the back-EMF, become DC components. However, this mathematical model only considers the fundamental back-EMF and does not consider the harmonic components in the back-EMF. In fact, due to the permanent magnet shape and the magnetization direction, the back-EMF contains rich harmonic components. Especially for IPMSM, since its permanent magnets are embedded in the rotor, it is more difficult to optimize the permanent magnets shape than the surface mount structure. Therefore, IPMSM contains more harmonics in the back EMF than SPMSM. Fig.1 shows a IPMSM's back-EMFs. It can be seen that they are not standard sine waves. Through FFT analysis, the THD of back-EMF reaches 10.25%, and the main harmonics are the third harmonic. 3. Dual current regulators based flux-weakening method This paper adopts the commonly used dual current regulators based flux-weakening method. The principle of this method is adding a voltage feedback regulator. When the reference voltage exceeds the inverter voltage limit, a negative demagnetizing current is generated through the PI regulator, and then a voltage that cancels the fundamental back-EMF is generated to eliminate the saturation

of the reference voltage. 4. The influence of harmonic back-EMFs on the flux-weakening performance. The essence of flux-weakening control is to counteract the high back-EMF through the voltage generated by the demagnetizing current. However, the demagnetizing current in the d-axis can only offset the fundamental back-EMF. The harmonic back-EMFs are also very large at high speeds, and can also cause saturation of the inverter voltage. Fig.2 shows the back-EMFs of the IPMSM operating in the flux-weakening condition. In the simulation, the inverter voltage limit is set as 150V. It can be seen that through applying d-axis demagnetizing current, the fundamental back-EMF has been suppressed. But the amplitudes of the harmonics back-EMFs reach 130V, which is very close to the inverter voltage limit. In other words, for higher speeds, the harmonics back-EMFs will reach the inverter voltage limit, which will prevent the speed from continuing to rise. This proves that the harmonics back-EMFs will seriously affect the range of flux-weakening control.

- [1] N. Bedetti, S. Calligaro and R. Petrella, "Analytical Design and Autotuning of Adaptive Flux-Weakening Voltage Regulation Loop in IPMSM Drives With Accurate Torque Regulation," in *IEEE Transactions on Industry Applications*, vol. 56, no. 1, pp. 301-313, Jan.-Feb. 2020 [2] Wang J, Wu J, Gan C, et al. Comparative study of flux-weakening control methods for PMSM drive over wide speed range[C]. 2016 19th International Conference on Electrical Machines and Systems (ICEMS) 2016: 1-6. [3] Z. Zhang, C. Wang, M. Zhou and X. You, "Flux-Weakening in PMSM Drives: Analysis of Voltage Angle Control and the Single Current Controller Design," in *IEEE Journal of Emerging and Selected Topics in Power Electronics*, vol. 7, no. 1, pp. 437-445, March 2019.



BP-02. Design of Hybrid-Type PM Motor for Electric Vehicle Traction Using Trapezoidal Ferrite-PM to Improve Reluctance Torque.

J. Park¹, R. Tsunata¹, M. Takemoto², K. Orikawa¹ and S. Ogasawara¹
 1. Hokkaido University, Sapporo, Japan; 2. Okayama University, Okayama, Japan

I. Introduction The electric vehicle market is expanding, and the demand for components related to electrification of powertrains is increasing rapidly. There is a traction motor as a related key component, and interior permanent magnet synchronous motor (IPMSM) having excellent efficiency and power density is mainly applied [1]. In addition, NdFeB permanent magnet (NdFeB-PM) with high energy product is used for traction IPMSM. However, NdFeB-PM is expensive and there is an issue with stable supply. As a traction motor without NdFeB-PM, there have been representative studies in terms of permanent magnet assisted-synchronous reluctance motor (PMA-SynRM) using ferrite-PM, switched reluctance motor (SRM) and separately excited synchronous motor (SESM) [2-4]. However, PMA-SynRM with ferrite-PM has a lower power density than conventional IPMSM. SRM structurally has a major issue with acoustic noise and SESM has a disadvantage that requires a separate device for generating the field flux of the rotor. Recently, in order to reduce the amount of NdFeB-PM in IPMSM, there is a study on a hybrid-type PM motor (HPMM) that simultaneously applies ferrite-PM to the rotor [5-7]. However, if the HPMM does not have a stator, there is a problem that ferrite-PM become demagnetized due to the strong leakage flux of NdFeB-PM [5-6]. In addition, in order to achieve the same torque density as the target IPMSM, there are problems in that the use of ferrite-PM must be increased by reducing the inner diameter of the rotor [7]. Therefore, in this paper, we solve these problems and propose a new HPMM based on a trapezoidal ferrite-PM that has the same torque density as the traction motor of Nissan Leaf electric vehicle commercialized in 2018, the target motor. At the same time, the proposed HPMM reduces the use of NdFeB-PM by 30% and the total PM cost by 14.8% compared to the target motor. II. Structure of the Proposed HPMM Fig. 1 (a) and (b) show the ¼ rotor cross-sectional view of the proposed HPMM and the target motor. The stator of the two motors is identical, which is the stator of the 2018 Nissan Leaf traction motor. In the proposed motor, NdFeB-PM and ferrite-PM are arranged on the d-axis direction. When the two types of PM are arranged in the d-axis direction, the leakage flux of NdFeB-PM converges by itself or is aligned in the same direction as the magnetization direction of ferrite-PM, so that demagnetization of ferrite-PM does not occur. However, since the permeability of the magnet is almost similar to that of air, this structure generates a high reluctance of the d-axis, resulting in a decrease in magnet torque of IPMSM. To overcome this point, the q-axis flux path is enlarged by applying trapezoidal ferrite-PM. That is, the d-axis inductance decreases as the d-axis reluctance increases, but the q-axis inductance is maintained or increased according to the expansion of the q-axis flux path, thereby improving the reluctance torque. These characteristics are expressed in Fig. 1 (a), the performance of the proposed HPMM and the target motor are predicted by FEM using commercial software, JMAG-Designer and Solidworks under the same operating condition. III. FEA Verification Fig. 1 (c) is the flux density distribution of the rotor in the absence of a stator. The temperature of the PM was selected as -40 degC considering the low-temperature demagnetization of ferrite-PM and the automotive environment temperature range. As described in Chapter II above, it is shown that demagnetization of ferrite-PM is not generated by the leakage flux of NdFeB-PM. The lowest flux density of ferrite-PMs is 0.3 T, which is not less than knee point of 0.05 T. Fig. 1 (d) shows the average torque for each phase angle β of the proposed HPMM and target motor. The input current is 465 A, the maximum current of the target motor, and PMs temperature is 100 degC. In $\beta = 0$ deg, which means magnet torque, the magnet torque of the proposed HPMM is 198 Nm, which is 27.5 Nm lower than that of the target motor. However, with the improved reluctance torque of the proposed HPMM, the maximum torque is 336.9 Nm, which is almost the same as the target motor. Fig. 1 (e) shows the results of the mechanical stress analysis of the rotor at a maximum speed of 10,500 rpm. Since the traction motor for an electric vehicle performs variable speed operation control over a wide speed range, it is required to secure a safety factor for rotor rigidity at the maximum speed. In Fig 1 (e), based on the same analysis

conditions and material properties, the maximum stresses of the proposed HPMM and the target motor are 305 MPa and 351 MPa. Based on the yield stress of the electrical steel sheet, 420 MPa, the safety factors are 1.38 and 1.2, respectively. Table I shows the specifications of the proposed HPMM and target motor. The proposed HPMM realizes the same torque density as the target motor, and at the same time reduces the usage of NdFeB-PM by 30 % and the total PM cost by 14.8 %. IV. Summary This paper proposes a new HPMM for electric vehicle traction motor. The proposed HPMM solves the problem of existing HPMM and realizes the same torque density as the target motor, Nissan leaf traction motor. At the same time, the proposed HPMM reduces the usage of NdFeB-PM by 30 % and the total PM cost by 14.8 % compared to the target motor.

[1] K. T. Chau, et al, IEEE Trans. Ind. Electron., vol. 55, no. 6, pp. 2246–2257 (2008) [2] M. Obata, et al, in Proc. Eur. Conf. Power Electron. Appl., pp. 1–9 (2013) [3] K. Kiyota, et al, IEEE Trans. Ind. Appl., vol. 48, no. 6, pp. 2303–2309 (2012) [4] C. Stancu, et al, IEEE Trans. Ind. Appl., vol. 54, no. 1, pp. 223–232 (2018) [5] C. L. Lim, et al, IEEE Trans. Magn., vol. 53, no. 11, Art. no. 8110904 (2017) [6] C. L. Lim, et al, IEEE Trans. Ind. Appl., vol. 55, no. 5, pp. 4692-4701 (2019) [7] Z. Zhang, IEEE Energy Conversion and Exposition, DOI: 10.1109/ECCE44975.2020.9235708 (2020)

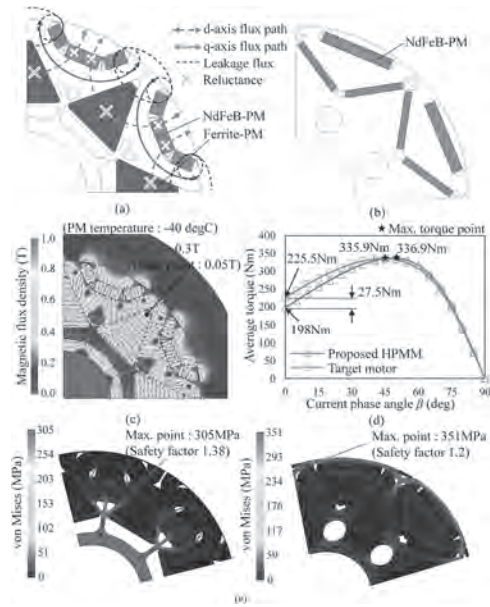


Fig. 1. Rotor structure and FEA results (a) Proposed HPMM (b) Target motor (c) Magnetic flux density distribution without stator (d) Average torque by current phase angle β (e) Mechanical stress analysis results at rotational speed 10,500rpm

Items	Specification	
	Target motor	Proposed HPMM
DC-link voltage (Vdc)	360	360
Max. current (A)	456	456
Max. torque (Nm) ^a	335.9 ^a	336.9 ^a
Number of poles and slots	8 / 48	8 / 48
Max. motor speed (rpm)	10,500	10,500
Stator outer diameter (mm)	Ø220	Ø220
Rotor outer diameter (mm)	Ø130	Ø130
Rotor inner diameter (mm)	Ø45	Ø45
Stack length (mm)	140	140
Airgap length (mm)	0.5	0.5
Electrical steel sheet	27PNX1350F	27PNX1350F
PM grade	N39UZ	N39UZ / NMF-15J
PM volume	NdFeB-PM (mm ³)	246,355 (100%)
	Ferrite-PM (mm ³)	-
Total PM cost (%) ^b	100	85.2

^a FEA Result
^b The cost of NdFeB-PM is assumed to be 10 times that of ferrite-PM

BP-03. Design, Modelling, and Analysis of a Novel Series-Parallel-Connected Hybrid-PM Variable-Flux PMSM.

G. Qiao¹, P. Zheng¹, M. Wang¹, F. Liu¹ and Y. Liu¹

1. Harbin Institute of Technology, Harbin, China

I. Introduction Permanent magnet synchronous machines (PMSMs) have been widely used in electric vehicles. However, traditional PMSMs need continuous flux-weakening current in high-speed region, which can reduce the operating efficiency and increase the demagnetization risks of PMs. Variable-flux PMSMs have gained a lot of attention for their ability to expand speed range and reduce loss by manipulating the magnetization state dynamically. Variable-flux machines employ low coercive force magnets, whose magnetization state can be adjusted by d -axis current pulses [1]. The PM excitation field is adjustable and the need for continuous flux-weakening current is reduced. The power density of the variable-flux machine firstly proposed in [1] is relatively low since only AlNiCo is used. The variable-flux PMSMs that employ both AlNiCo and NdFeB are proposed to improve the power density, in which two kinds of magnets are arranged in either series or parallel magnetic circuits [2-4]. Moreover, the magnetic circuit of PM flux is complicated and changeable in hybrid-PM variable-flux PMSMs under different magnetization states, which brings inconvenience to the modelling and analysis of machines. A novel hybrid-PM variable-flux PMSM with series-parallel magnetic circuits is proposed in this paper. The machine topology and operating principle are analysed. The equivalent magnetic circuit model of the machine is established and proven with good precision under different magnetization states. The electromagnetic performances are analysed and compared with the series-connected and parallel-connected variable-flux PMSMs. The results prove that the proposed machine has high torque density, wide magnetization state adjustment range, stable PM working points and high efficiency. II. Machine Topology and Operating Principle The proposed machine employs both AlNiCo and NdFeB, as shown in fig. 1, where red coloured magnets are AlNiCo and blue coloured ones are NdFeB. Two layers of magnets are placed in the proposed machine. In the upper V-shape layer, NdFeB is connected with AlNiCo in series near q -axis, and these two series-connected magnets are connected with another AlNiCo located near d -axis in parallel. In the lower U-shape layer, NdFeB and AlNiCo are connected in series. Under reverse magnetization state, AlNiCo near d -axis in the V-shape layer can be reversely magnetized by negative d -axis current pulses, and most PM flux of the V-shape layer is short-circuited in rotor core. Under forward magnetization state, the flux of U-type magnets flow through the upper V-type magnets and help to stabilize PM working points. The proposed machine combines the advantages of the parallel-connected and series-connected machines. III. Equivalent Magnetic Circuit Model The magnetic circuit in the proposed machine is complicated and changeable since the amplitude and direction of PM flux vary with machine's magnetization state. It's necessary to establish the equivalent magnetic circuit model, which can provide an effective way for the operating principle and performance analysis. The equivalent magnetic circuit model of the proposed machine under different magnetization states is established, with PMs substituted by equivalent flux sources and reluctances, and iron core and air gap replaced by equivalent reluctances, as shown in fig. 1. More details are presented in full paper. The air-gap flux density, back-EMF and PM operating points are obtained by this model, and compared with the FEA results. The calculation errors are below 5%, which proves the accuracy of the proposed equivalent model. The complicated and changeable series-parallel-connected magnetic circuit in the proposed machine under different magnetization states is equivalently simplified by this model, which brings more convenience to the machine modelling and the fast performance analysis and calculation. IV. Performance Analysis The electromagnetic performances, including back-EMF, torque capacity, operating points of AlNiCo, magnetization state adjustment range and operation efficiency, of the proposed machine are analysed and compared with the parallel-connected and series-connected variable-flux machines. The fundamental amplitudes of no-load EMF of these three machines under fully forward magnetized state are 180V, 165V and 187V. And those under fully reversed magnetized state are 60V, 38V and 120V. The magnetization state adjustment ratios, which are the important index for variable-flux PMSMs, are 66.7%, 77.0% and 35.8%. For the parallel-connected machine, the

working points of AlNiCo will move below the knee points when the load current angle is less than -37° . AlNiCo is demagnetized unexpectedly then. For the proposed machine, the working points of AlNiCo are stable. The operating loss for the proposed machine under different magnetization states and operation conditions is evaluated, as shown in fig. 2. A low magnetization state is suitable for the high speed, low torque condition; A high magnetization state is suitable for the low speed, high torque condition. The operating efficiency is significantly improved by adopting proper magnetization states under different operating conditions. The performances are analysed in detail in full paper. The results prove that the proposed machine has the characteristics of high torque density, wide magnetization state adjustment range, stable PM working points and high efficiency.

[1] V. Ostovic. "Memory Motors," *IEEE Ind. Appl. Mag.*, 9(1): 52-61, 2003. [2] K. Sakai, K. Yuki, Y. Hashiba, et al. "Principle of the Variable-Magnetic-Force Memory Motor," in *Proc. Int. Conf. Electr. Mach. Syst.*, 2009. [3] H. Hua, Z. Q. Zhu, A. Pride, et al. "Comparative Study on Variable Flux Memory Machines with Parallel or Series Hybrid Magnets," *IEEE Trans. Ind. Appl.*, 55(2): 1408-1419, 2019. [4] J. H. Chen, J. Li, R. H. Qu et al. "Magnet-Frozen-Permeability FEA and DC-Biased Measurement for Machine Inductance: Application on a Variable-Flux PM Machine," *IEEE Trans. Ind. Electron.*, 65(6): 4599-4607, 2018.

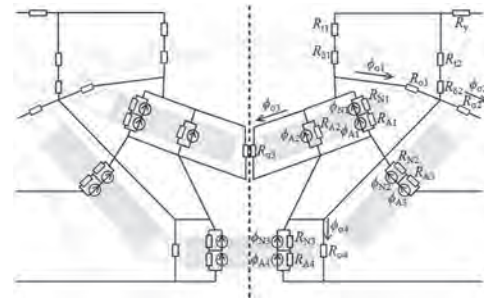


Fig. 1. Equivalent magnetic circuit of the proposed machine.

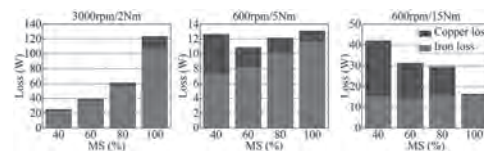


Fig. 2. Loss evaluation under different magnetization states and load conditions.

BP-04. A Design of IPMSM High-Power Electric Vehicles With Wide Field Weakening Control Region.

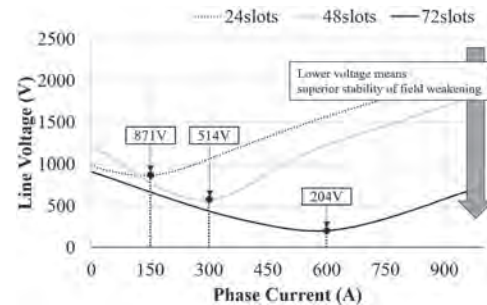
C. Song¹, I. Song², H. Shin² and C. Lee²

1. Taesung SNE, Seoul, The Republic of Korea; 2. Hanbat National University, Daejeon, The Republic of Korea

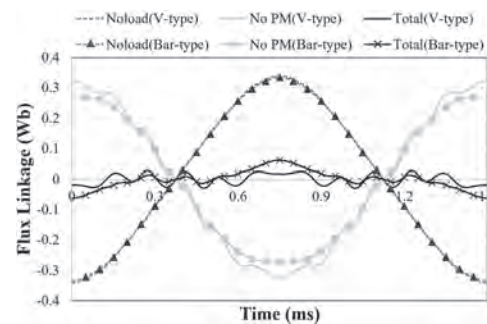
The Interior Permanent Magnet Synchronous Motor (IPMSM) is mainly used as a driving motor for Electric Vehicles (EVs) due to its advantage for high-power density and wide speed operation range. Because of the characteristics of EVs motor, it is necessary to perform high-speed driving at a small load condition. Thus, IPMSM is controlled by the field weakening control method to meet a wide operation range, which controls the phase angle through the d- and q-axis transformation. However, as the phase angle increases, the air-gap magnetic flux contains more harmonics and thus becomes less controllable, which has the drawback that there is a limit to the operation range. Moreover, in the case of large commercial EVs, high torque is required at low speed for the driving stability and the gradeability. Thus, to perform high torque at low speed, the motor should have a large permanent magnet in the motor. As the field magnetic flux increases, the back EMF also increases, so a larger phase angle is required for high-speed operation. However, the maximum speed that can be driven through the field weakening control is decreased because of the harmonics. For high-speed driving of commercial EVs, an optimal design method is needed to expand the field weakening region. The reason why the existence of a maximum speed limit is the increased harmonic component as the phase angle increases. In this paper, we divided the design part into the rotor and the stator. And then the effect on the field weakening control is analyzed when the design variables are changed. Finally, a motor design method for high-power at low-speed mode with a wide operation range is proposed by reducing harmonics and enhancing the back EMF controllability. To analyze the effects of the harmonics and the field weakening control characteristics as the design variable changed, no-load analysis is performed according to the number of slots per phase per pole. In the load analysis, the variation of line voltage is analyzed according to the current value when the maximum demagnetizing magnetomotive force is applied. Fig.1 represents that the larger the number of slots per phase per pole, the more stable voltage can be controlled. Namely, the voltage can be decreased by varying the current value and phase angle at a specific speed. It means that the limitation of the field weakening region can be possible calculated. Next, the field weakening control characteristic is analyzed according to the variation of the number of conductors per slot. Although the number of conductors per slot can reduce copper loss, it needs to prepare the countermeasure against voltage rising for field weakening control. To compare the effect according to the number of conductors in the field weakening region, the voltage values according to the number of turns are analyzed under the condition given the maximum demagnetizing magnetomotive force. The maximum operating speed considering the voltage limitation is selected. In consequence, fewer conductors in the slot are more advantageous for high-speed operation, but the rising current for voltage control and torque generation must be considered. The characteristic of field weakening control is analyzed by changing the magnet layer and shape, and the harmonic reduction analysis is implemented by the skewed method. Prior to the design of permanent magnet shape, permanent magnet with multi-layer structures, the air-gap magnetic flux is relatively sinusoidal compared to the single-layer. Moreover, the torque generation is flexible by securing the q-axis flux path. In other words, the multi-layer structure is used despite the difficulties of productivity due to this advantage. It is analyzed how the multi-layer structure affects the field weakening region. Additionally, the Total Harmonics Distortion (THD) and reluctance torque are analyzed according to changes in the number of magnet layers. As a result, the higher the number of layers, the lower the THD and the greater the proportion of the use of reluctance torque. It is indicated that the voltage controllability in the field weakening control range is more effective if the rotor flux linkage is small when the maximum demagnetizing magnetomotive force is applied. Depending on the shape of the permanent magnet, the barrier changes simultaneously, and the d- and q-axis flux path also changes. So, the air gap magnetic field distribution and voltage control performance are changed. The performance of voltage controllability according to the shape of the magnet is compared by representing the magnetic flux density

in the air gap. In Fig.2, if the flux linkage is small, the voltage controllability in the field weakening control region is more stable when the maximum demagnetizing magnetomotive force is applied. As a result, V-type models demonstrate effectively reducing total flux linkage over Bar type models. Lastly, the skew is applied for optimized design to reduce harmonics. The lowest voltage curve can be investigated in both the skew and the non-skew models for comparison of harmonic reduction using FFT analysis. In this paper, with the main aim of optimizing the characteristics in the field weakening control region and improving the voltage control performance, the design of a motor for driving 300kW commercial EVs with a wide range of field weakening control region is presented.

[1]Ki-Chan Kim, "A Novel Magnetic Flux Weakening Method of Permanent Magnet Synchronous Motor for Electric Vehicles", IEEE Transactions on Magnetics, Vol.48, No.11, p.4042-4045 (2012) [2]J. A. Guemes, A. M. Iraolagoitia, and P. Fernandez, "Torque Analysis in Permanent-Magnet Synchronous Motors: A Comparative Study", IEEE Transactions on Energy Conversion, Vol.26, No.1 p.55-63 (2011) [3]Jung-Min Mun, Yong-Jae Kim, and Sang-Yong Jung, "Design Characteristics of IPMSM With Wide Constant Power Speed Range for EV Traction", IEEE Transactions on Magnetics, Vol. 53, No.6 (2017) [4]Mohammad Sedigh Toulabi, John Salmon, and Andrew M. Knight, "Concentrated Winding IPM Synchronous Motor Design for Wide Field Weakening Applications", IEEE Transactions on Industry Application, Vol.53, No.3 p.1892-1900 (2017)



Comparison of the lowest line voltage with different number of slots



The comparison of the total flux linkage between 2-layers V-type and Bar-type model

BP-05. Study of a High-Efficiency Series-Parallel-Connected Hybrid-PM Variable-Flux Permanent Magnet Synchronous Machine.

G. Qiao¹, P. Zheng¹, M. Wang¹, F. Liu¹ and Y. Liu¹

1. Harbin Institute of Technology, Harbin, China

I Introduction Permanent magnet synchronous machines (PMSMs) have been widely used in electric vehicle industry for their characteristics of high efficiency and power density. However, the development of PMSMs is limited by the unalterable permanent magnet (PM) excitation field. The flux-weakening control used in PMSMs can bring about high copper loss, low efficiency, and PM demagnetization. Variable-flux PMSMs are considered as a good candidate for EV propulsion because the speed range is wider and the operation efficiency is higher than traditional PMSMs. Variable-flux PMSMs employ low coercive force magnets, whose magnetization state can be adjusted by d -axis current pulses [1]. The PM excitation field is adjustable and the need for continuous flux-weakening current is reduced. Two schemes of novel hybrid-PM variable-flux PMSMs with series-parallel magnetic circuits are proposed in this paper. The performances of these two machines are analysed and compared with series-connected and parallel-connected machines. Moreover, the efficiency characteristic of the proposed machine under different magnetization states and load conditions is evaluated. A control strategy of appropriately combining magnetization state adjustment control and flux-weakening control is proposed, which can obviously improve the efficiency in full speed range, especially in high-speed region, by manipulating the magnetization state. II Machine Topology and Operating Principle Two schemes of variable-flux PMSMs with series-parallel magnetic circuits are proposed, as shown in fig.1, which are the single-layer V-type and two-layer V-U-type machines. The red coloured magnets are AlNiCo and blue coloured ones are NdFeB. As shown in fig. 1(a), the V-shape magnets are placed in the V-type machine. The NdFeB is connected with AlNiCo in series near q -axis, and these two series-connected magnets are connected with another AlNiCo located near d -axis in parallel. As shown in fig. 1(b), two layers of magnets are placed in the V-U-type machine. The series-connected U-shape NdFeB and AlNiCo magnets are placed under the V-shape magnets. The magnetization state of proposed machines can be adjusted by manipulating the magnetization direction of AlNiCo near d -axis in V-shape magnets and the flux amplitude of all AlNiCo. More details about the operating principle are analysed in full paper. III Performance Comparisons Electromagnetic performances, including back-EMF, torque capacity, stability of AlNiCo and magnetization state adjustment range, of the proposed machines are analysed and compared with parallel-connected and series-connected machines. Under fully forward magnetized state, the fundamental amplitudes of no-load EMF of V-type and V-U-type series-parallel-connected, parallel-connected and series-connected machines are 168V, 180V, 165V and 187V respectively. And those under fully reversed magnetized state are 58V, 60V, 38V and 120V. The magnetization ratios are 65.5%, 66.7%, 77.0% and 35.8%. Other performances are also compared in detail in full paper. After the comprehensive comparison, the proposed V-U-type series-parallel-connected machine is selected. The magnetizing/demagnetizing current density of V-U-type machine is 17.5A/mm², which is smaller than that in [2-4]. The torque density of V-U-type machine is nearly the same with that in [3-4], and larger than that in [2]. The analysis results show that the proposed V-U-type series-parallel-connected machine combines the advantages of parallel-connected and series-connected variable-flux PMSMs. IV Efficiency Improvement through Magnetization State Adjustment The expanded speed range and efficiency improvement in high-speed region are the distinct advantages of the proposed machine. The maximum achievable torque-speed ranges at 4 typical magnetization states are evaluated. The speed range is significantly expanded by manipulating the magnetization state. The operating efficiency of the proposed machine at 4 magnetization states are evaluated. The efficiency can be significantly improved by adopting appropriate magnetization states at different working points. A control strategy to improve efficiency by adjusting magnetization state is proposed. For uncertain working conditions, a steady-state efficiency maximizing control strategy is proposed. The magnetization states whose operating efficiency is highest at every torque-speed working point are selected based on the efficiency characteristic at different magnetization states, as shown in fig. 2. A LUT is formed by the selected magnetization

states. A hysteresis integral comparator is proposed to minimize the unnecessary magnetization state adjustment. The steady-state efficiency maximizing control is achieved by choosing magnetization states through the LUT and minimizing unnecessary magnetization state adjustment through the hysteresis integral comparator. For certain working conditions, like WLTC, an efficiency maximizing control strategy considering magnetization state adjustment loss is proposed. Optimal magnetization states at every working point are selected based on Genetic Algorithm. The optimization target is to minimize the whole drive cycle loss including the steady-state loss at each working point and the magnetization state adjustment loss. The results prove that the operation efficiency is significantly improved by adopting the proposed magnetization state adjustment strategy.

- [1] V. Ostovic. "Memory Motors," *IEEE Ind. Appl. Mag.*, 9(1): 52-61, 2003. [2] N. Limsuwan, T. Kato, K. Akatsu, et al. "Design and Evaluation of a Variable-Flux Flux-Intensifying Interior Permanent-Magnet Machine," *IEEE Trans. Ind. Appl.*, 50(2): 1015-1024, 2014. [3] A. Athavale, K. Sasaki, B. S. Gagas, et al. "Variable Flux Permanent Magnet Synchronous Machine (VF-PMSM) Design Methodologies to Meet Electric Vehicle Traction Requirements with Reduced Losses," *IEEE Trans. Ind. Appl.*, 53(5): 4318-4326, 2017. [4] H. Hua, Z. Q. Zhu, A. Pride, et al. "Comparative Study on Variable Flux Memory Machines with Parallel or Series Hybrid Magnets," *IEEE Trans. Ind. Appl.*, 55(2): 1408-1419, 2019.

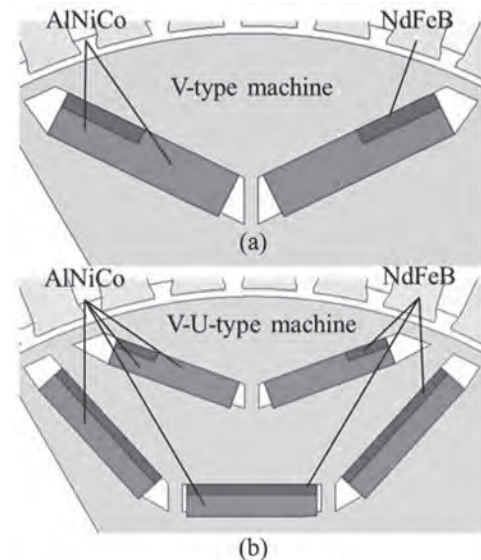


Fig.1 Two schemes of the proposed machines.

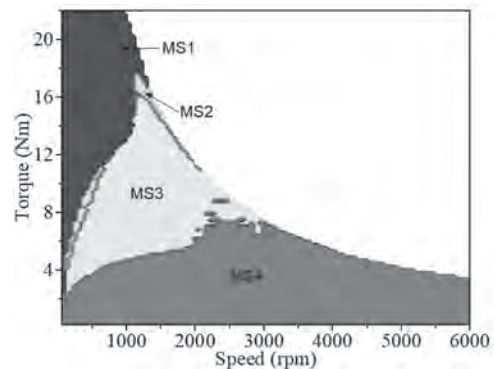


Fig.2 Selected magnetization states with highest efficiency at each working point.

BP-06. Maximum Torque per Ampere Control for Variable-Flux PMSMs Considering the Influence of Magnetization State Adjustments and Load Condition Variations.

G. Qiao¹, P. Zheng¹, M. Wang¹, F. Liu¹ and Y. Liu¹
 1. Harbin Institute of Technology, Harbin, China

I Introduction Variable-flux permanent magnet synchronous machines (PMSMs) have gained a lot of attention for their ability to expand speed range and reduce copper loss by manipulating the magnetization state dynamically. Variable-flux PMSMs employ low coercive force magnets, whose magnetization states can be adjusted by d -axis current pulses [1-2]. The PM excitation field is adjustable and the need for continuous flux-weakening current is reduced. To maximize output torque and operation efficiency, the maximum torque per ampere (MTPA) control is widely used in interior PMSMs [3-4]. However, the parameters, like PM flux-linkage, d - and q -axis inductances, of variable-flux PMSMs are influenced by not only the load condition variations but also the magnetization state adjustments. The precise MTPA control for variable-flux PMSMs is highly affected by the nonlinear parameter properties. The operating principle of a novel variable-flux PMSM is analysed. The nonlinear load flux-linkage model is established to simplify the modelling of nonlinear parameter properties. The MTPA current trajectory search method based on Golden Selection method is proposed to obtain the current trajectory considering the influence of magnetization state adjustments and load condition variations. Moreover, the on-line MTPA control method based on neural-network algorithm is proposed to provide an effective way of on-line MTPA control for variable-flux PMSMs. II Operating Principle of Variable-flux PMSMs and Nonlinear Load Flux-Linkage Model A novel series-parallel-connected hybrid-PM variable-flux PMSM is proposed and shown in fig. 1. The magnetization state of this machine can be adjusted by manipulating the magnetization direction of AlNiCo near d -axis in V-shape magnets and the flux amplitude of all AlNiCo. The machine saturation degree varies significantly with magnetization state adjustments and load condition variations. Then the machine parameters, such as PM flux-linkage, d - and q -axis inductances, vary nonlinearly too. The nonlinear load flux-linkage model is established to simplify the modelling of nonlinear parameter properties. The amplitude-phase sequences of current working points are selected to calculate the corresponding d -, q -axis flux-linkage by FEA or experiment. And the permeability of any two adjacent selected points is nearly the same. The nonlinear load flux-linkage model is formed using the selected current working points and corresponding d -, q -axis flux-linkage. The separation of load PM flux-linkage and calculation of d -, q -axis inductances are no longer needed. The load flux-linkage model that presents the nonlinear parameter properties is used in the MTPA current trajectory search process. III MTPA Current Trajectory Search based on Golden Selection Method The proposed MTPA current trajectory search method includes two iterative loops which are both based on Golden Selection method. The current phase iterative loop is implemented firstly, and the optimization target is to minimize corresponding current amplitude at a given torque reference and a given magnetization state. The amplitude is optimized to the minimum value when the iteration interval of phase is within a given minuscule number. However, the corresponding amplitude of phase cannot be obtained directly due to nonlinear parameter properties. The current amplitude iterative loop is nested in the phase iterative loop to obtain corresponding amplitude of each phase. The target of amplitude iterative loop is to optimize the difference between present torque and torque reference to zero. During the amplitude iteration process, the value of present torque under different amplitudes and phases is calculated by the nonlinear load flux-linkage model. MTPA current trajectories of the proposed machine under 4 magnetization states are obtained by the proposed search method, and compared with the trajectories obtained by traditional method, as shown in fig. 2. The current trajectories are evaluated by FEA and experiments. The results prove that the proposed search method can find MTPA current trajectories precisely considering the influence of magnetization state adjustments and load condition variations. IV On-Line MTPA Control based on Neural-Network Algorithm The on-line generation of current commands by the proposed search method is time-consuming. The neural-network-based MTPA control method is proposed to implement MTPA control in real-time control system. The MTPA current trajectory

generated by proposed search method under different magnetization states and torque references are selected as sample data. The on-line MTPA control neural-network model is trained, tested and validated using sample data. The model input is magnetization state and torque reference, and the output is current amplitude and phase. Once the train, test and validation process are finished, the knowledge about input-output relationship is acquired and the on-line MTPA control neural-network model is established. MTPA current trajectories at any magnetization state and torque reference can be predicted by this model. The mathematical expressions of established model are easily programmed and quickly executed by DSP for on-line MTPA control. The calculation speed and accuracy are evaluated by simulations and experiments. The results prove that the proposed neural-network model can realize on-line MTPA control for variable-flux PMSMs quickly and precisely.

[1] V. Ostovic. "Memory Motors," *IEEE Ind. Appl. Mag.*, 9(1): 52-61, 2003. [2] H. Hua, Z. Q. Zhu, A. Pride, et al. "Comparative Study on Variable Flux Memory Machines with Parallel or Series Hybrid Magnets," *IEEE Trans. Ind. Appl.*, 55(2): 1408-1419, 2019. [3] S. Kim, Y. D. Yoon, S. K. Sul, et al. "Maximum Torque per Ampere (MTPA) Control of an IPM Machine Based on Signal Injection Considering Inductance Saturation," *IEEE Trans. Power Electron.*, 28(1): 488-497, 2013. [4] J. H. Chen, J. Li and R. H. Qu. "Maximum-Torque-per-Ampere and Magnetization-State Control of a Variable-Flux Permanent Magnet Machine," *IEEE Trans. Ind. Electron.*, 65(2): 1158-1169, 2018.

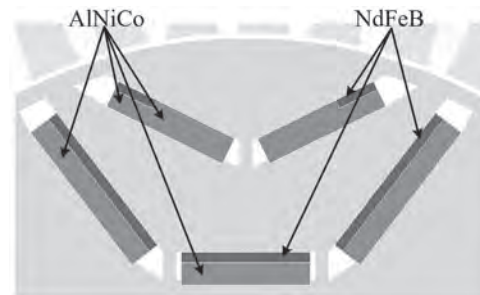


Fig.1 Structure of proposed machine.

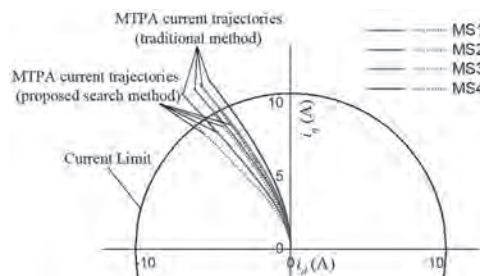


Fig.2 Current trajectories obtained by proposed method and traditional method.

BP-07. Flux Intensifying Features of Permanent Magnet Assisted Synchronous Reluctance Motor With High Torque Density.

D. Ngo¹ and M. Hsieh²

1. Vinh University of Technology Education, Nghean, Vietnam;

2. Electrical Engineering, National Cheng Kung University, Tainan, Taiwan

Abstract This digest investigates the flux intensifying (FI) characteristics for permanent magnet assisted synchronous reluctance motor (PMA-SynRM) to achieve high torque density with a small amount of PM. This motor is particularly denoted as “FI-PMA-SynRM”. The developed FI-PMA-SynRM is then compared with two other counterparts, i.e., a surface permanent magnet synchronous motor (SPMSM) and a synchronous reluctance motor (SynRM). The analysis is conducted using finite element method through flux linkage and inductances so that the effectiveness of FI characteristics is demonstrated. The analysis shows that a high torque density (24.8 Nm/L) can be achieved with a small amount of PM (0.72% motor volume). I. Motor Models Flux intensifying (FI) rotor configuration has been of recent interest as an alternative to conventional permanent magnet synchronous motors (PMSMs) which usually adopt flux weakening feature [1], [2]. By using a moderate amount of PM, the FI configuration can be applied to synchronous reluctance motor (SynRM), which leads to the introduction of FI permanent magnet assisted SynRM (FI-PMA-SynRM) [3]. In order to minimize the amount of PM used, a surface-inset PM design is employed, indicating that the rotor configuration can be considered as the combination of a SynRM with multiple flux barriers (FBs) and a surface PMSM (SPMSM), as shown in Fig. 1(a). This configuration (PM placed along d -axis) differs from common PMA-SynRM (PM placed along q -axis) so that PM flux linkage is intensified by part of the armature flux. This is called “FI” as illustrated in Fig. 1(b), making PM not easily demagnetized in such a configuration. Two other models with the same rotor shapes are used for comparison: the first one is an inset SPMSM (only eliminating interior FBs when compared to the developed FI-PMA-SynRM) that represents the flux weakened motor while the second one is a SynRM (only removing PMs based on the FI-PMA-SynRM) with only reluctance torque, as indicated in Fig. 1(a). The motor specifications are presented in Table I. II. Analysis and Results A. Distribution of magnetic field - The no-load condition is considered first, where the flux lines and flux densities are shown in Fig 1(c). It can be seen that for the FI-PMA-SynRM the flux focuses on the region between two adjacent interior FBs. For the inset SPMSM the flux focuses around the PMs. However, the PM operating conditions are similar since the flux density distributions in the PMs are basically affected by their relative positions to the stator slots. - Fig. 1(d) shows the motor flux densities under the maximum torque per ampere (MTPA) control where the FI-PMA-SynRM and SynRM operated with negative current phase advance angles with the SynRM having a greater phase advance. These all correspond to the phasor diagrams presented in Fig. 1(b). - The PM flux densities of the FI-PMA-SynRM and inset PMSM at -25 degrees (current phase advance) based on MTPA control of FI-PMA-SynRM are shown in Fig. 1(e). The negative current phase advances indicate that these motors operate in the FI mode. As can be seen, the overall flux densities in the PM seem to increase with applied current although part of the PMs may still suffer lower operating points. However, when the inset SPMSM operates in the MTPA condition, a positive current phase advance (19 degrees) is required, and the PM operating points are much lower due to flux weakening, which is also shown in Fig. 1(e). These imply that the PM is more secure with FI and the torque density can be possibly improved without suffering demagnetization. B. Inductance variation The inductances vs current amplitude when applying current on the d -axis are shown in Fig. 1(f). It can be seen that, for both the FI-PMA-SynRM and SynRM, L_d is higher than L_q so that the saliency, i.e. L_d/L_q of these models is higher than 1. Nevertheless, L_d of the SynRM is rapidly reduced with current increase while that of the FI-PMA-SynRM maintains. For the inset SPMSM, L_d is slightly lower than L_q and they both decrease when current magnitude increase so that the saliency is slightly lower than 1. C. Torque production Fig. 1(g) shows the torque vs current angle of these motors at both rated and peak currents. The MTPAs of the FI-PMA-SynRM and SynRM are achieved with negative current phase advance and that for the inset SPMSM is achieved with a positive phase advance. Moreover, with an added PM amount of

just 0.72% of motor volume, the FI-PMA-SynRM has 1.77 and 1.34 times torque of that of the SynRM at rated and peak currents, respectively. On the other hand, by adding some FBs, the FI-PMA-SynRM produces 1.4 and 1.73 times torque of that of the inset SPMSM at the rated and peak currents, respectively. This indicates that the FI-PMA-SynRM is capable of effectively combining reluctance torque or PM torque compared to the other types of motors. As a result, this motor achieved high torque density, i.e. 13.45 Nm/L and 24.8 Nm/L at rated and peak conditions, respectively. D. Measurements The experimental results based on the prototype shown in Fig. 1(a) will be reported in the full paper. III. Conclusion This digest compares the characteristics of the designed FI-PMA-SynRM and its counterparts. The results revealed that the target FI-PMA-SynRM can achieve higher torque density than its counterparts by using a small amount of PM.

[1] N. Limsuwan et al, *IEEE Trans. Ind. Appl.*, vol. 50, no. 2, pp. 1015–1024, Mar. 2014. [2] M.-T. Chui et al, *2015 18th International Conference on Electrical Machines and Systems (ICEMS)*, Oct. 2015, pp. 232–236. [3] D.-K. Ngo, M.-F. Hsieh, and T. A. Huynh, *IEEE Trans. Magn.*, vol. 55, no. 7, pp. 1–8, Jul. 2019.

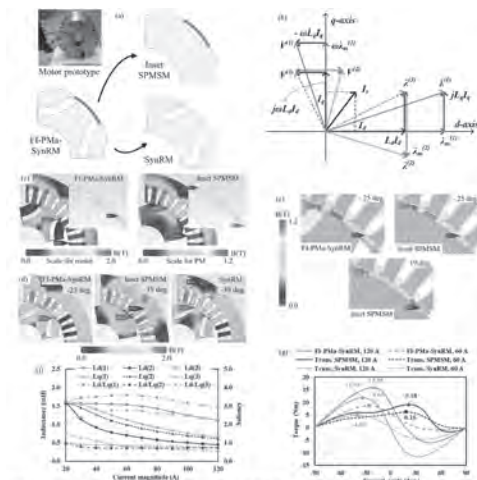


Fig. 1. Motor model and analysis results: (a) Motor prototype; (b) Comparison of phase diagrams of FI-PMA-SynRM, inset SPMSM, and SynRM which shows the same inductance and current vectors; (c) Flux density distributions; (d) MTPA flux densities; (e) MTPA PM flux densities; (f) Inductance and saliency vs current magnitude for FI-PMA-SynRM, inset SPMSM, and SynRM; (g) Torque production.

TABLE I
MOTOR SPECIFICATIONS

Parameter	Unit	Value
Motor volume	l	0.6434
PM volume	l	0.0046
PM/motor volume ratio	%	0.72
Rated current	A	60
Peak current	A	120
Rated torque	Nm	8.65
Peak torque	Nm	15.95
Rated torque density	Nm/l	13.45
Peak torque density	Nm/l	24.79

BP-08. Torque Characteristics Investigation of a Flux-Controllable Permanent Magnet Motor Considering Different Flux-Leakage Operation Modes.

H. Hu¹, Z. Xiang¹, X. Zhu¹, S. Zheng¹ and W. Fan¹
 1. Jiangsu University, Zhenjiang, China

I. Introduction Permanent magnet (PM) motors have been widely used in electric vehicles due to its high torque/power density and high efficiency. Yet, a relatively constant airgap magnetic field of PM motors may limit the speed range to large extent, which is still the shortfall for the further applications in EVs. In recent years, a type of variable-flux-leakage PM motor is emerged, which draws intense interest from academics of motor field because of the achievement of flux-controllable capability [1]. In this type of motors, the leakage flux can be varied by designing flux bridge and magnetic barrier, and it can be controllable through the change of q -axis current of winding. Compared with conventional PM motor, the variable flux is essentially derived from active design of flux leakage. So, the magnetic field distribution of leakage flux is sensitively linked to the flux controllability. Then, in [2], a variable-flux-leakage PM Motor is proposed, where a unique flux leakage path is purposely considered by arranging the PM position and magnetic barrier reasonably. The results indicate that the relatively obvious capability of flux regulation is achieved by effectively controlling the leakage flux. Yet, in flux-regulated process, the magnetoresistance characteristic of the motor is changed appreciably caused by the variation of leakage flux. It means that different flux-leakage operation modes of the motor will bring the characteristic differences of output torque. For instance, the varied main flux caused by leakage flux greatly leads to the change of PM torque, while the variation of inductance characteristics induced by magnetic saturation bring about the change of reluctance torque. Therefore, to the variable-flux-leakage PM motor, it is necessary and meaningful to comprehensively consider the torque characteristics at various flux-leakage operation modes. And, in this case, how to realize the optimal distribution of different torque components is full of challenge. In this paper, a flux-controllable permanent magnet (FC-PM) motor is proposed. The key of the study is to conduct torque characteristics analysis and optimization by combining with typical operation conditions. Then, based on different flux-leakage operation modes, a reasonable optimization strategy considering torque components is developed. The results reveal that, based on optimization, the comprehensive torque is effectively improved while maintaining a desirable flux regulation region. II. Motor Topology and Simulation Result Fig.1(a) shows the structure of the FC-PM motor with independent separated flux leakage branches. It can be seen that the q -axis is equipped with multi-layer arc and ellipse magnetic barriers to obtains good magnetic flux leakage controllable performance, which further broadens the motor speed regulation range. Fig.1(b) shows the magnetic density distributions of the FC-IPM motor under different flux-leakage operation modes, and the corresponding requirements of torque components distribution are listed. In Fig. 2(a) and (b), the sensitivity of each design variable to different design objectives is evaluated, and three variables with high sensitivity are selected for further optimization. Fig. 2(c) and (d) show the result of torque distribution under different flux-leakage Operation Modes, which can be seen that through the multi-objective optimization proposed in this paper, the torque quality is improved as expect. The torque performances and corresponding torque component distribution under different modes are shown in Fig.2 (d) and (f). The prototype of proposed FC-IPM motor and corresponding experiment result of back-EMF are shown in Fig. 2(g) and Fig. 2(h), respectively. In additional, III. Conclusion In this paper, a FC-PM motor is purposely designed, and a multi-objective optimization method is also newly proposed, where the optimal distribution of torque components under different flux-leakage operation modes is considered. Through optimization, the PM torque becomes the main component under less flux leakage, and the reluctance torque as the main component under more flux leakage. It means that the optimal proportion of different torque components of the FC-PM motor is realized. Both the simulation and experiment results not only verify the reasonability of the proposed motor but also confirm the effectiveness of the proposed optimization method. The more electromagnetic performance analysis and experimental results will be provided in the full paper.

[1] X. Zhu, W. Wu, S. Yang, Z. Xiang and L. Quan, in *IEEE Transactions on Energy Conversion*, vol. 33, no. 4, pp. 2260-2269, Dec. 2018. [2] T. Kato, M. Minowa, H. Hijikata, K. Akatsu and R. D. Lorenz, in *IEEE Transactions on Industry Applications*, vol. 51, no. 5, pp. 3811-3821, Sept.-Oct. 2015.

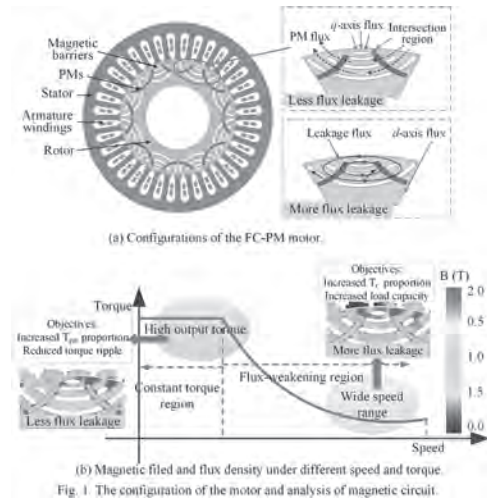


Fig. 1 The configuration of the motor and analysis of magnetic circuit.

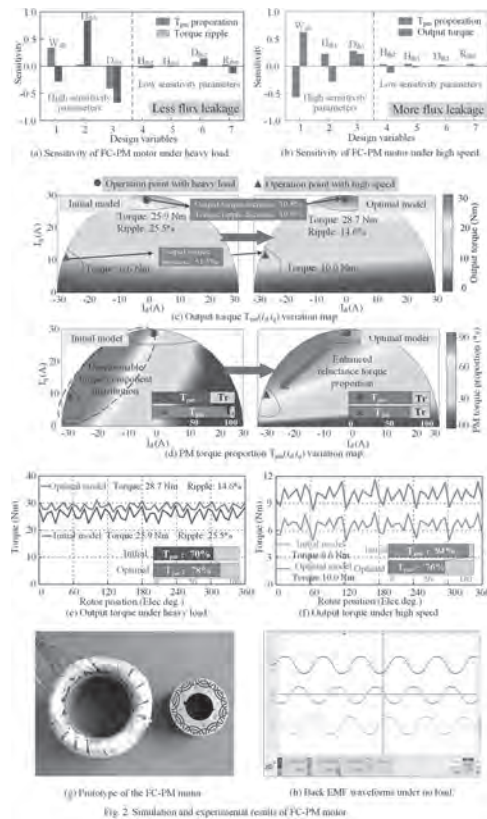


Fig. 2 Simulation and experimental results of FC-PM motor.

BP-09. Influence of MMF Space Harmonic on PM Eddy-Current Losses in a Modular Fault-Tolerant in-Wheel Motor Under Open-Circuit Faulty Operations.

Y. Tang¹, F. Chai¹, Y. Yu¹ and T. Chen¹

1. Electrical Engineering, Harbin Institute of Technology, Harbin, China

I. INTRODUCTION The traditional three-phase PMSMs are confronted with severe challenge, and some researchers turn to investigate modular motor systems for better fault-tolerant capability [1]. The modular motor system is composed of several modules, and each module could be equivalent to an independent sub-motor. The better the independence of electric, magnetic, thermal, and physics between the modules, the better fault-tolerant performance of the motor is. The fractional slot concentrated winding (FSCW) has some advantages in non-overlapping end winding, large inductance and small coupling between phases, so it is very suitable for the application in modular fault-tolerant motors [2]. However, the MMF of the motor with FSCW contains quantities of space harmonics which will cause PM eddy-current losses. The open-circuit fault is a typical fault in all kinds of motor faults [3], and the fault-tolerant capability of the motor is mostly determined by the output performance under open-circuit faults [4]. This paper investigates the influence of magneto motive force (MMF) space harmonic on permanent magnet (PM) eddy-current losses in a modular fault-tolerant in-wheel motor under various open-circuit faulty operations. First, reconfiguring maximum round MMF with constant amplitude of current is taken as the fault-tolerant (FT) strategy for the open-circuit of one phase. The fault-tolerant strategies for various faults are derived respectively based on this strategy. Second, the harmonic components of MMF under various faults and corresponding fault-tolerant control are analyzed respectively. Then, an analytical model based on multi-loop method for PM eddy current losses is proposed. The losses induced by each harmonic components of MMF can be obtained from the model. The analytical results agree well with the finite element method (FEM) results. The space harmonics are composed of slot harmonics and other harmonics. The proportions of eddy current losses caused by these two types of harmonics under various faults are derived. Finally, PM eddy-current losses induced by the fault-tolerant current under the overload condition are analyzed, and the results have a certain reference value for the fault-tolerant strategy which makes the faulty motor operates safer and more stable.

II. MODULAR MOTOR SYSTEM WITH FAULT-TOLERANT CAPABILITY For design a better fault-tolerant motor, the entire fault-tolerant system needs to be considered comprehensively. Not only design the motor itself, but also should consider the topology of the controller and the fault-tolerant control strategy. The motor consists of 4 modules, as shown in Fig. 1. Each module is controlled by an independent drive with a three-phase four-wire control circuit, which ensures electrical isolation between the modules.

III. ANALYSIS OF CHARACTERISTICS OF MMF UNDER VARIOUS OPEN-CIRCUIT FAULTY OPERATIONS

1) Reconfiguring Maximum Round Fundamental MMF With Constant Current When A1 is in open-circuit condition, the performance of MMF will be declined. Quantities of sub-harmonics and high order harmonics closed to the working wave emerge, and the amplitude of working wave decreases, as shown in Fig. 2. Through the proposed fault-tolerant control, the performance of MMF is improved.

2) Spatial Harmonic Analysis of MMF under Various Faults The overall performance evaluation of the MMF is established by the two following aspects: 1 The amplitude of the working wave; 2 Total harmonic distortion (THD). The performance of MMF for the modular motor under various open-circuit faults can be effectively improved through the proposed fault-tolerant strategies.

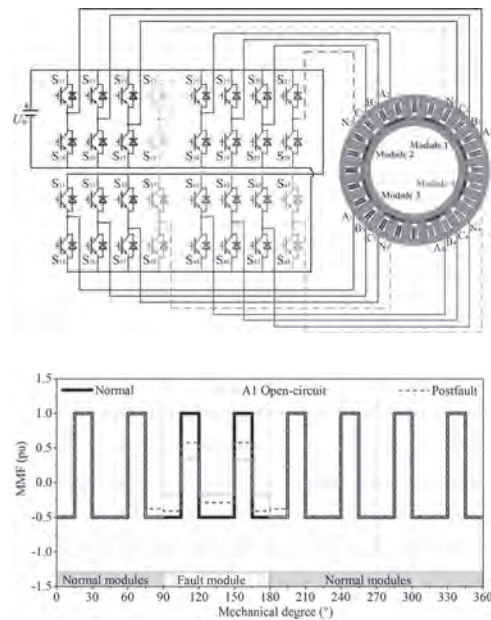
IV. ANALYSIS OF PM EDDY-CURRENT LOSSES UNDER VARIOUS LOSSES UNDER VARIOUS OPEN-CIRCUIT FAULTY OPERATIONS

1) Analytical Model An analytical model based on multi-loop method for PM eddy current losses is proposed. 2) Verification by FEM The eddy-current losses of PMs by FEM consist of two parts. One is the slot ripple losses in PMs, which are the most important losses in PMs and generated by the fundamental frequency magnetic flux due to the stator slot openings. The other one is the losses in PMs induced by the space harmonics. The analytical results agree well with the FEM results. 3) Analysis of PM Eddy-Current Losses under Overload Fault-Tolerant Control When the overload FT controls are adopted, the motor can operate safely for a period of time rather

than a long time. If we want the motor operates stably during the time, the PM losses should be considered.

V. CONCLUSIONS An analytical model based on multi-loop method for calculating PM eddy-current losses is proposed. The analytical results agree well with the FEM result, which proves the correctness of the model. The proposed model is more accordant with the actual situation and the physical meaning is clearer. The eddy-current losses caused by high order slot harmonics are very small. Among the newly emerged harmonics, the sub-harmonics and high order harmonics closed to working wave will cause relatively large eddy-current losses. As the fault level increases, the proportion of eddy-current loss induced by slot harmonics decreases, while the proportion of eddy-current loss induced by other harmonics increases. If the overload fault-tolerant strategy is adopted, not only the copper losses but also the eddy-current losses of PMs should be considered.

[1] Ifedi C. J., Mecrow B. C., Brockway S. T. M., "Fault-tolerant in-wheel motor topologies for high-performance electric vehicles". *IEEE Trans. Ind. Appl.*, 2013, 49, (3), pp. 1249-1257. [2] Heins G., Ionel D., Thiele M., "Winding factors and magnetic fields in permanent magnet brushless machines with concentrated windings and modular stator cores". *IEEE Trans. Ind. Appl.*, 2015, 51, (4), pp. 2924-2932. [3] Li Y. X., Zhu Z. Q., Thomas A. S., "Novel modular fractional slot permanent magnet machines with redundant teeth". *IEEE Trans. Magn.*, 2019, 55, (9), pp. 1-10. [4] Liang P. X., Pei Y. L., Chai F., "An improved method for armature-reaction magnetic field calculation of interior permanent magnet motors". *IEEE Trans. Magn.*, 2016, 52, (7), pp. 1-4.



BP-10. Comparative Study of Field Modulation Effects on Consequent-Pole PM Machines With Different Stator Slot Configurations.

Y. Li¹, H. Yang¹ and H. Lin¹

1. Southeast University, School of Electrical Engineering, Nanjing, China

Abstract—This paper presents a comparative study of the field modulation effects (FMEs) on consequent-pole permanent magnet (CPM) machines with different stator slot configurations, i.e., open-slot, semi-closed slot and close-slot. Due to the asymmetrical PM magneto-motive force (MMF) distributions and double-side slotting effect, the CPM machines exhibit more air-gap field harmonics for the torque production. In order to quantify the torque contributions of the various effective harmonics, the Maxwell stress tensor method (MSTD) is adopted. The torque proportions due to various air-gap field harmonics in the CPM machines with different stator slot configurations are subsequently investigated by finite element (FE) method, which confirms that the stator slot configurations have a great influence on FME. It can be found that the highest and the lowest torque proportion contributed by the modulated field harmonics can be observed in closed-slot and open-slot structures, respectively. Finally, some experimental measurements on a 12-slot/14-pole CPM machine prototype with a semi-closed slot configuration are carried out to validate the theoretical and FE analyses.

I. Introduction In order to reduce permanent magnet (PM) consumption, consequent-pole PM (CPM) machines are widely investigated with hybrid excited [1], modular design [2] and multi-phase [3] in recent years. Besides, some interior CPM machines with different PM arrangements, i.e., V-shaped [4], U-shaped [5] and spoke-type [5]-[7] are studied. It demonstrates that the proposed designs exhibit comparable torque performance, high-efficiency region and relatively lower PM consumption than conventional counterparts. Moreover, the field modulation effect (FME) on CPM machine is comparatively studied with surfaced-mounted PM (SPM) machine, which shows that the CPM machine exhibits more pronounced FME than SPM case due to its double-side slotting effect [8] [9]. However, the influence of stator slot on FME of the CPM machines remain unexplained hitherto. Thus, this paper comparatively study of the FME on CPM machines with different stator slots, i.e., open-slot, semi-closed slot and closed-slot. **II. Machine Topologies** The illustrations of 12-slot stators with open-slot, semi-closed slot and closed-slot structures are given in Fig. 1(a), (b) and (c), respectively. In order to perform a fair comparison, the three CPM machines share the same 14-pole rotor, as shown in Fig. 1(d). Besides, in order to identify and compare the effective air-gap field harmonics for the torque production in a fair way, the same stator outer diameter, air-gap length, active stack length and current density are employed in the three CPM machine topologies. **III. Comparison of Torque Contributions of Dominant Magnetic Field on CPM Machines** The torque characteristics of the three CPM machines are illustrated in Fig. 1(e) and (f). It can be observed that the semi-closed slot structure exhibits the highest torque, as shown in Fig. 1(e), which is mainly due to its the lowest flux leakage. According to Maxwell stress tensor method, the instantaneous electromagnetic torque T_e can be calculated by $T_e = (l_{stk} r_g^2 / \mu_0) \int B_r B_t d\theta = \sum (\pi l_{stk} r_g^2 / \mu_0) B_{rk} B_{tk} \cos[\theta_{rk}(t) - \theta_{tk}(t)] = \sum T_k(t)$ (1) where r_g is the air-gap radius. l_{stk} is the active stack length. T_k is the instantaneous electromagnetic torque generated by the k^{th} harmonics of radial and tangential air-gap flux densities, respectively. Thus, the contributions of the k^{th} field harmonics to the total electromagnetic torque can be separated when the k^{th} radial and tangential air-gap field harmonics are obtained, as illustrated in Figs. 1(f). It should be noted that, apart from the Z_r order magnetic harmonic, various modulated field harmonics engage in the torque generation, which confirm that the pronounced FME in CPM machines. Besides, the Z_r order harmonic contributes the highest and lowest torque proportion in open-slot and closed-slot, respectively. As a result, the highest and the lowest torque production contributed by the modulated field harmonics can be observed in closed-slot and open-slot structures, respectively. **IV. Experimental Validation** The stator and rotor assemblies of the CPM machine prototype with semi-closed slot configuration are shown in Figs. 2(a) and (b), respectively. The comparison of the FE predicted and measured back-EMF and average torque values are illustrated in Figs. 2(c) and (d), respectively. Because the end flux leakage and mechanical tolerance are not considered in the FE analyses, the slight difference between the FE predicted and measured results can

be observed in Figs. 2(c) and (d). Overall, a satisfactory agreement between the measured and FE predicted results confirms the theoretical analyses. The detailed analysis will be presented in the full paper.

[1] J. A. Tapia, F. Leonardi and T. A. Lipo, IEEE Transactions on Industry Application, Vol. 39, p.1704-1709 (2003) [2] S. U. Chung, J. W. Kim and B. C. Woo IEEE Transactions on Magnetics, Vol. 47, p.4215-4218 (2011) [3] H. Dhulipati, E. Ghosh and S. Mukundan, IEEE Transactions on Energy Conversions, Vol. 34, p.2041-2051 (2019) [4] J. Li, K. Wang and H. Zhang, IEEE Transactions on Industrial Electronics, Vol. 67, p.3374-3385 (2020) [5] J. Li and K. Wang, IEEE/ASME T Transactions on Mechatronics, Vol. 24, p.2182-2192 (2019) [6] W. Liu and T. A. Lipo, IEEE Transactions on Industry Application, Vol. 54, p.5918-5929 (2018) [7] X. Ren, D. Li and R. Qu, IEEE Transactions on Energy Conversions, Vol. 33, p.2112-2121 (2018) [8] Y. Li, H. Yang and H. Lin, in Proc. XIII International Conference Electrical Machine (ICEM), pp. 65-71 (2018) [9] Y. Li, H. Yang and H. Lin, IEEE Transactions on Energy Conversions, accepted. (2020)

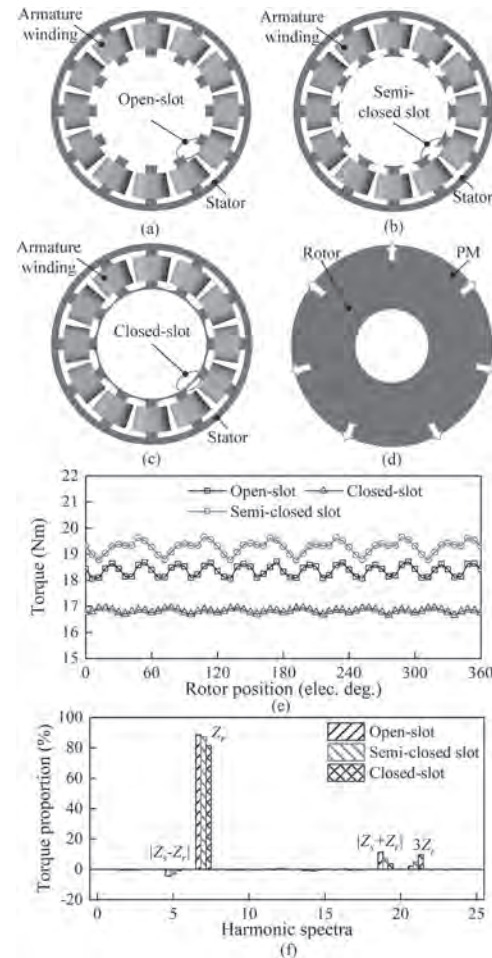


Fig. 1. Machine Topologies of the CPM design with different stator slot configurations. (a) Open-slot. (b) Semi-closed slot. (c) Closed-slot. (d) CPM rotor. Torque characteristics of the CPM machines with different stator slot configurations. (e) Steady-state torque. (f) Torque proportion of the main working harmonics.

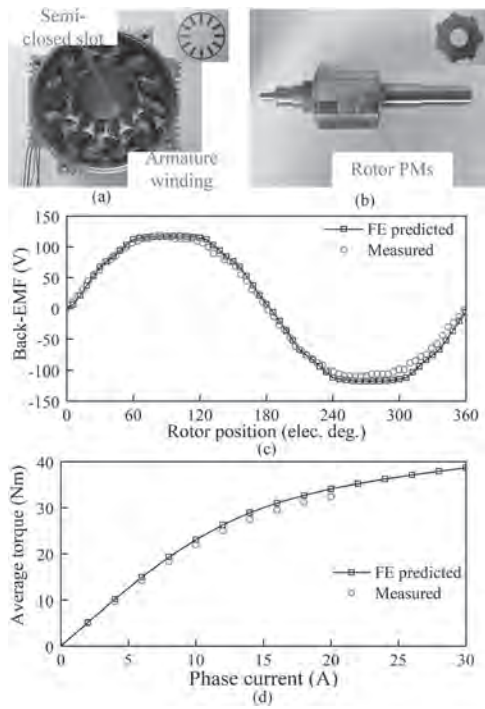


Fig. 2. The CPM machine prototype with semi-closed slot. (a) Stator. (b) Rotor. Comparison of the measured and FE predicted back-EMF and average torque values. (c) Back-EMFs. (d) Average torque versus phase current.

BP-11. A Study on the Electromagnetic Multi-Step Transmission Characteristics of Interior Permanent Magnet Synchronous Motor.

C. Lee¹, I. Song¹, H. Shin¹ and D. Kim²

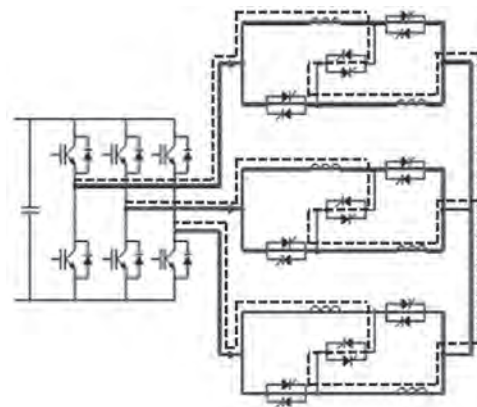
1. Hanbat National University, Daejeon, The Republic of Korea;

2. Global Engineering, Hwaseong, Gyeonggi-do, The Republic of Korea

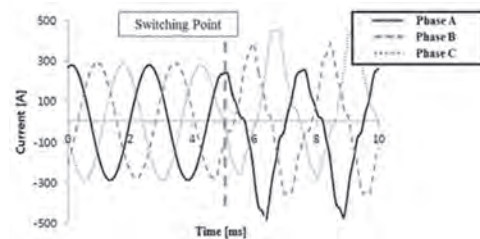
Recently, regulations on carbon dioxide emissions caused by environmental problems have been promoted worldwide. In the automotive industry, engine vehicles are being regulated and will disappear on the road in the next 10 years. As a result, the market for low-carbon Fuel Cell Electric Vehicles and electric vehicles is expanding, and much research on electrical components is underway. Compared to engine vehicles, electric vehicles have better efficiency of the drive unit itself without using a transmission. However, it has the disadvantages of the high vehicle price, low All-Electric Range(AER), and long charging time. These reasons are due to the high price of batteries that go into electric vehicles. To reduce the price of the vehicle, it is necessary to improve the performance of the battery and AER. In other ways, the efficiency of electric motors, inverters can affect the improvement of mileage when the same battery is used. Therefore, research to minimize the loss of both motors and inverters is also needed. Due to the characteristics of the electric motor, it does not come out efficiently in all operating ranges. Especially when the electric motor enters the high-speed region, the efficiency will be further reduced. The model is IPMSM used in electric vehicles, and the concept of electromagnetic multi-step transmission is introduced. The electromagnetic multi-step transmission is a method in which the parallel branch of the stator is changed at a constant speed by using the switch. Using this method, high torque and efficiency in the low-speed range, high efficiency in the high-speed range, and the operating range were expanded. The operating characteristics were analyzed using the finite element method (FEM). Additionally, phenomena occurring in the shifting process were analyzed. To proceed with the analysis, a 2D model was made by using a simulation tool. The model was analyzed into two models to select the parallel branch conversion point. The model's size is the same, and it is divided into two models of parallel branch 2 and 4. The base speed and maximum speed of parallel branch 2 are 3,000rpm and 8,000rpm, and the base and maximum speed of parallel branch 4 are 6,000rpm and 10,000rpm. The efficiency characteristics of both models were derived and analyzed for expanding the high-efficiency operating range. By combining the efficiency characteristics of both models, the conversion point of the parallel branch in which the high-efficiency section at the time of shifting is formed most widely was selected at 6,000 rpm. Fig. 1 shows a circuit diagram for electromagnetic multi-step shifting. The stator winding is Y-connected, and the dotted line is the circuit in the low-speed range, and the number of parallel circuits for each A, B, C phase is 2. The solid line shows the circuit when the number of parallel circuits of each phase is changed to 4 through a switch. Change the number of parallel branch The switch used for contact used a thyristor and consisted of 12 terminal terminals. The phenomenon that may be displayed when the number of parallel branch increases in the same model is that the torque decreases. And it is possible to operate up to a higher speed region than the model in which the number of parallel branch is small in voltage saturation. In addition, it was derived that the current density is reduced, which is advantageous in terms of heat. This motor operates with parallel branch 2 in the low-speed range, and changes the number of parallel branch of the stator to 4 through a switch at 6,000rpm. The electric motor used in the model is driven by parallel branch 2 in the low-speed section and changes the number of parallel branch of the stator to 4 by using the switch at 6,000rpm. The parallel branch 2 is called 1-step, and the voltage is saturated in the low-speed range. Therefore, it generates high torque at low speed, and the maximum efficiency point appears at low speed due to voltage saturation. After 6,000rpm, it is referred to as 2-step, driven by parallel branch 4. And the voltage is saturated at 6,000rpm. Therefore, in the case of parallel branch 4, the range of maximum efficiency point is displayed at around 6,000rpm. Fig. 2 shows the waveform of the current flowing through the stator winding in the process of shifting from 1-step to 2-step through FEM analysis. It was derived that the current waveform was unbalanced when shifting from 1-step to 2-step. In addition, a current unbalance phenomenon appeared in the process of shifting from 2-step to 1-step. current imbalance generates an impact during the shifting process,

and is defined as a shift shock. It was analyzed that the shift shock was caused by a phenomenon in which the current was delayed by inductance in the process of changing the switch to shift. A study was conducted on the phenomena and characteristics of the electric motor when the electromagnetic transmission system was introduced into the IPMSM for electric vehicles. As a method of expanding the high-efficiency range of the motor, a method of changing the number of parallel branch through the shift process was used. However, it was confirmed that a shift shock was generated by an unbalanced current during the shifting process. In order to alleviate the shift shock, additional research was conducted to reduce the shock by selecting a parameter related to the stator.

[1] Ho-Chang Jung, Gyeong-Jae Park, and Sang-Yong Jung, IEEE Trans. Magn, Vol. 53, No. 6 (2017) [2] Liang Fang, Jae-woo Jung, and Jung-Ho Lee, IEEE Trans. Magn, Vol. 44, No. 11, pp. 4393-4396 (2008) [3] Se-Young Oh, Su-Yeon Cho, and Ju Lee, IEEE Trans. Magn, Vol. 50, No. 2 (2014) [4] Ho-chang Jung, Deokjin Kim, and Sang-Yong Jung, IEEE Trans. Magn, Vol. 50, No. 2 (2014) [5] SangHyeok Seo, Gyeong-Jae Park, and Sang-Yong Jung, IEEE Trans. Magn, Vol. 53, No. 6 (2017)



Circuit diagram for electromagnetic multi-step transmission



Current waveform from 1st to 2nd step

BP-12. Design Methodologies for Variable-Flux Machines for Fully Utilizing the Material Properties of the Magnet.

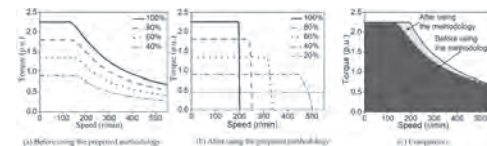
F. Liu¹, P. Zheng¹, M. Wang¹, G. Qiao¹ and S. Zhang¹

1. School of Electrical Engineering & Automation, Harbin Institute of Technology, Harbin, China

1. Abstract: In order to extending the operating speed range and increasing the maximum torque, two design methodologies of variable-flux machines (VFMs) are proposed, which make full utilizing of the material properties of the low coercive force (LCF) magnet. The inner relationship between the permanent-magnet (PM) flux variation range and speed-torque curves is comprehensively analyzed. The variation boundary of the PM flux for non-salient-pole with $i_d=0$ control method is investigated by analytic method. Due to the complexity of the transcendental equations, the per unit system is utilized for other types of machine and control method. Because the hysteresis loops of the LCF magnet employed in VFMs are quite different, which makes it difficult for machine designers to select suitable magnet. Therefore, an ideal determination model of hysteresis loop is established considering the remanent flux density, permeability of the recoil line, knee point and coercive force of the LCF magnet. A custom method is proposed to obtain the hysteresis loop calculated from the determination model. By using the proposed methodologies, the material properties of the magnet can be fully utilized and provide guidance to the scholars in the initial design stage of the VFM. 2. Introduction: Owing to the controllability of the permanent-magnet (PM) magnetic field, the variable-flux machine (VFM) become a good candidate for wide-speed operating demanding areas. By applying instantaneous demagnetizing current pulse, the PM flux of the VFM can be changed with negligible copper loss [1]. Compared with the conventional PMSMs, the negative d -axis current control (flux-weakening control) used under high speed condition is superseded by the instantaneous current pulse, so the overall efficiency of the VFM can be improved. Moreover, since the no-load back electromotive force proportional to the PM flux is reduced, the machine can operate under higher speed. There are many VFM topologies proposed by scholars, which has demonstrated the concepts and verified the merits of the VFM in detailed. In order to improve the torque output capability, the hybrid-PM variable flux machines (HPM-VFMs) are proposed [2-5]. The low coercive force (LCF) magnet employed in the above mentioned VFMs are AlNiCo, SmCo and Ferrite. However, there are little design methodologies to improve the machine performance in terms of the full utilizing of the material properties of the LCF magnet. In order to address the issues mentioned above, the design methodologies of the VFM are studied in this paper. 3. Design methodology of the boundary of the PM flux variation range: Conventionally, in order to obtain wider speed range, the minimum PM flux is designed to be low enough. However, during the deeply studying of the relationship between the torque-speed curves and PM flux variation ratio, the curves of several flux variation ratio is always lower than other ratios, as shown in Fig. 1 (a). The result shows that it is unnecessary to pursuit wider flux variation range. In order to investigate the inner relationship between the flux variation ratio and speed-torque curves and find the boundary of the PM flux variation range, the machine performance is comprehensively analyzed considering the PM flux linkage, machine inductance, saliency ratio, bus voltage and current limit. The operation equations of the non-salient-pole VFM with $i_d=0$ control method is deduced, and then the PM flux variation boundary is obtained. For the non-salient-pole VFM, if the PM flux linkage after saturation magnetization is larger than the product of the d -axis inductance and the current limit, all machine always possesses speed extension capability by demagnetization process. The comparison of the torque-speed areas of the VFM with and without adopting the proposed methodology is shown in Fig 1 (c). The torque-speed curves after adopting the proposed in Fig 1 (c) is composed of many PM variation ratios. It can be seen from Fig 1 that machine 1 can obtain extra speed region after adopting the proposed methodology. The then boundaries of other types of machines and control methods are investigated. Due to the complexity of the transcendental equation, the per unit system is used. For the other machines, we can conclude that the minimum PM flux should be larger than the product of the d -axis inductance and the current limit. 4. Design methodology of the Optimum PM hysteresis loop: By comparing the hysteresis loops of the AlNiCo, SmCo and Ferrite, the hysteresis loops are

quite different from each other, and it is necessary to find the suitable loop. An ideal determination model of hysteresis loop is established considering the remanent flux density, permeability of the recoil line, knee point and coercive force of the LCF magnet. The overall performance of the VFM are also considered, including maximum torque, re/demagnetization difficulty and anti-passive demagnetization ability, and the ideal hysteresis loop can be obtained. By connecting the LCF and the high-coercive force magnet in series and adjusting the ratio of the two magnet, we can customize the hysteresis loop. Based on the proposed model and the custom method of the hysteresis loop, a VFM with optimum PM hysteresis loop is designed. The simulation result shows that the PM torque of the VFM can be increased. By using the proposed methodologies, the material properties of the LCF magnet can be fully utilized.

[1] V. Ostovic, IEEE Ind. Appl. Mag., Vol. 9, p. 52 (2003) [2] M. Ge, J. Li and R. Qu, IEEE Trans. on Appl. Sup. Vol.28(3), p. 1-5 (2018) [3] H. Yang, Z. Q. Zhu and H. Lin, IEEE Trans. on Mag. Vol.53(5), p. 1-4 (2017) [4] A. Athavale, K. Sasaki, and R. D. Lorenz, IEEE Trans. on Ind. Appl. Vol.53, p.4318-4326 (2017) [5] Z. Q. Zhu, H. Hua, A. Pride, IEEE Trans. on Mag. Vol.53(11), p. 1-4 (2017)



Comparison of the torque-speed areas of the VFM with and without adopting the proposed methodology

BP-13. Current Map Refinement of Interior Permanent Magnet Synchronous Motor Using the Magnetic Flux Map Obtained by Experiment.

J. Jung¹, S. Chai¹, J. Park¹ and B. Lee²

1. Electrification Business Unit, Hyundai Mobis, Yoingin, The Republic of Korea; 2. Katech, Daegu, The Republic of Korea

1. Introduction For control systems of permanent magnet synchronous motors (PMSM) for automotive applications, stator flux-based current maps are widely used to efficiently control a PMSM even when the DC voltage changes [1]. In general, the current map constructed based on the magnetic flux map which is measured at a constant rotational speed does not reflect iron loss and mechanical loss which are changed by source frequency. Therefore, when the conventional current map is applied to the motor control, torque control accuracy is deteriorated in particular high speed range. To solve this problem, the current value can be compensated for by estimating power loss due to source frequency variation. However, there is a drawback that the compensation factor must be obtained by frequent experiments, trial and error or complex control algorithms [1]. In the magnetic circuit design and analysis, finite element analysis (FEA) is applied to calculate the d and q-axis inductance and the linkage flux by the permanent magnet (PM) according to the current and current phase angle. Then, the characteristic analysis is performed by using d and q-axis equivalent circuit analysis (ECA) based on the parameters calculated through FEA [2]. When the d and q-axis ECA is carrying out, iron loss and mechanical loss can be reflected to the motor characteristics. However, if the input parameters in particular d and q-axis inductance profiles are incorrect, the exact motor characteristics cannot be obtained. The limitations of the direct torque control using current map processed through magnetic flux map and the characteristic analysis through the d and q-axis ECA have the respective limitations as described above. To overcome these technical limitations, this paper presents the current map improvement method using the d and q axis ECA and the flux map obtained by the experiment. 2. Method of current refinement First, to measure the flux map, the PMSM is rotated at a constant speed by the servo motor. After measuring the d-axis and q-axis voltages with the current and current phase angles applied, we convert the d-axis and q-axis magnetic flux through the relationship between the voltage drop by the resistance and the rotational speed. At this time, torque can also be measured. The q-axis inductance can be calculated simply by dividing the q-axis flux by the q-axis current. However, since the d-axis flux includes the linkage flux generated by the PM, flux separation is required for the d-axis inductance calculation. The d-axis inductance can be extracted by subtracting the linkage flux by the PM obtained through FEA from the d-axis flux obtained through the experiment and dividing by the d-axis current. The extracted d and q axis inductances can be used as input parameters for d and q axis ECAs to build current maps for all operating ranges. Through analysis of the d- and q-axis ECAs, iron and mechanical losses can be considered. In addition, characterization can be performed using inductances close to the actual values, which improves the reliability of the calculated current map. Figure 1 is a simplified representation of proposed method. The full paper will cover the theoretical background of flux separation and the effect of improving the torque control using current maps obtained by this method.

[1] Bon-Ho B, Patel N, Schulz S, et al. "New field weakening technique for high saliency interior permanent magnet motor," *Proc. Conference Record of the 2003 IEEE Industry Applications Conference 38th IAS Annual Meeting*, IEEE Press, 2003, pp.898-905. [2] B. H. Lee, S. O. Kwon, T. Sun, J. P. Hong, G. H. Lee, and J. Hur, "Modeling of Core Loss Resistance for d-q Equivalent Circuit Analysis of IPMSM considering Harmonic Linkage Flux," *IEEE Trans. Magn.*, vol.47, no. 5, pp. 1066-1069, May 2011.

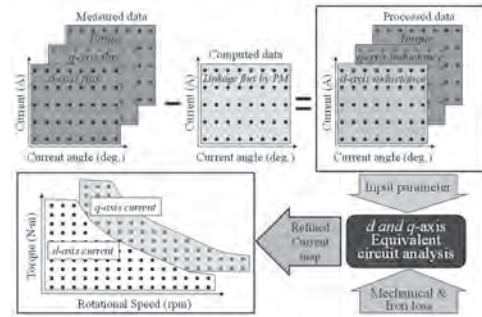


Fig. 1. Process of current map refinement.

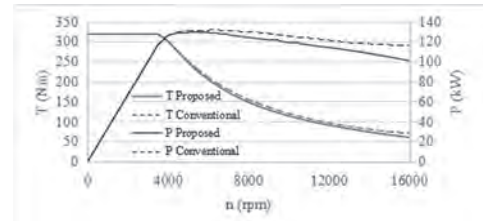
BP-14. Torque-Speed Characteristics Evaluation for Permanent Magnet Synchronous Motors With Rectangular Conductors.

C. Huang^{1,2}, D. Meng¹ and Y. Gong²

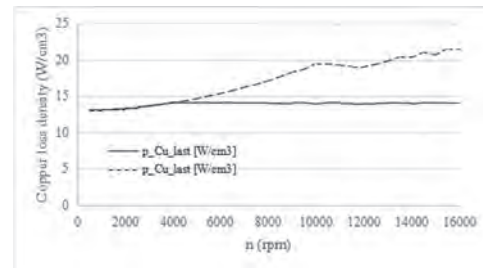
1. Tongji University, Shanghai, China; 2. Schaeffler Group, Anting, Shanghai, China

Recently, new energy electrical vehicles have a great development. To achieve longer driving range and higher acceleration performance at defined battery capacity and driving conditions, there is a demand of high efficiency and high torque-speed characteristics for electrical drive machines [1-2]. One of solutions is to use rectangular conductors, e.g. hair-pin winding. It can enhance the slot filling ratio to simultaneously decrease resistance and increase heat transfer ability. Furthermore, the tooth can be kept enough width and benefits for peak performance. The peak performance in new energy electrical vehicles generally require short duration (10-60 seconds) at each speed within an allowable temperature rise (Depend on the insulation level of winding and starting temperature). However, due to the strong skin effect, the current distribution in conductors become more and more uneven with speed rising. This will bring overheat risks at high speed because the temperature rising rate in short duration is closely related to the copper loss density. In this paper, a new peak torque-speed characteristics estimation method for these machines is proposed. Not only supplied maximal voltage and current limitation are considered, but also the skin effect of conductors and transient thermal issues are investigated. The copper loss density in the last conductor which has severest skin effect can be theoretically kept constant from some speed. Firstly, the supplied maximum voltage (U_m) and current (I_m) are defined according to the capability of battery and power electronic unit (PEU). The electromagnetic torque (T_e), d-axis voltage (U_d), q-axis voltage (U_q) and terminal voltage (U_s) are calculated under specified lead angle and current intervals. By scanning all points and based on MTPA and MTPV, the conventional peak torque-speed curve is acquired. Secondly, to apply the temperature rising limitation, an analytical equation on basis of the conductor size, position and frequency is used and the AC resistance of active parts of conductors is calculated [3]. $r_N/r_{dc}=\varphi(\xi)+N(N-1)\psi(\xi)$ r_N represents the AC resistance at some speed due to the skin effect and r_{dc} represents the DC resistance. Both are only related to the conductors in stator lamination core. The functions $\varphi(\xi)$ and $\psi(\xi)$ are related to the frequency and conductor size because ξ is expressed by the ratio of conductor height and skin depth. To keep the highest copper loss density constant with speed rising, the current limitation I_m shall be decreased with speed rising according to below question. $I_m=I_b/\sqrt{(\varphi(\xi)+N(N-1)\psi(\xi))}$ where I_b is the current limitation at the base speed n_b . At this base speed, the copper loss density reaches the maximum allowable value. It can be defined through thermal simulation or measurement. N represents the ID of conductors in stator slot which starts counting from slot bottom. $\varphi(\xi)=\xi(\text{sh}(2\xi)+\sin(2\xi))/(\text{ch}(2\xi)-\cos(2\xi))$ $\psi(\xi)=2\xi(\text{sh}(\xi)-\sin(\xi))/(\text{ch}(\xi)+\cos(\xi))$ In the end, the maximum torque at each speed with similar temperature rising level in short duration will be found out and improved peak torque and power curves are finally outputted. A typical PMSM with 8 poles and 48 slots are investigated. Figure 1 and 2 show the comparison results between the conventional and proposed methods. Based on CFD simulation or measurements, the maximum copper loss density can be defined under specified S2 work condition. The special prototype with 20 thermal couples in the stator is built. The simulated torque-speed curve and measured hotspots are compared. It verifies the good effectiveness of the proposed method.

[1] Z.Q. Zhu and D. Howe, Proceedings of the IEEE, Vol:95, 2007. [2] L. Sepulchre, M. Fadel, IEEE Transactions on Industry Application, p6081-6089, Vol:54, 2018. [3] D. Lin and P. Zhou, ICEMS, p3810-3814. Nov. 2008. [4] J. Brauer, IEEE Transactions on Magnetics, Vol: 18, Mar 1982



Comparison of peak torque and power performance between conventional and proposed methods



Comparison of copper loss densities in the last conductor of stator slot between conventional (dash line) and proposed (solid line) methods

BP-15. Performance Analysis of a PMASynRM Machine for Light Electric Vehicle.

V. Manescu Paltanea¹, G. Paltanea¹, I. Hantila¹, M. Maricarul¹, P. Minciunescu², B. Varaticeanu², L. Demeter² and M. Pesteri²

1. *Electrical Engineering, Universitatea Politehnica din Bucuresti, Bucuresti, Romania;* 2. *Servomotor Division, ICPE S.A., Bucharest, Romania*

Today, electrical motors for electric vehicle traction applications have restrictive requirements on torque and power density that must have the highest possible values. Mechanical power has to be constant for a wide range of speeds and an overall high efficiency of the machine must be attained. Usually, these conditions are met when are used synchronous motors with permanent magnets based on rare earth materials as NdFeB, SmCo₅, Sm₂Co₁₇, La_{0.6}Sr_{0.4}FeO₃ and CeNdFeB. These permanent magnets are expensive, and they increase the entire price of the machine. The context of the global dynamics regarding imports and exports of rare earth minerals, price evolution and even the availability of rare earth minerals, can generate a shock wave that will affect companies worldwide. This fact determines an increased attention on research, which must develop alternative solutions to permanent magnet synchronous motor (PMSM) [1-3]. A viable solution can be found in the variable reluctance synchronous motor (SynRM), a motor that no longer includes rare earth minerals. In order to improve the torque density, power factor and efficiency of such an electric machine is to assist the motor with permanent magnets based on ferrite (SrO₆Fe₂O₃) and thus obtaining the so-called synchronous motor with variable reluctance assisted by permanent magnets (PMASynRM), which does not contain rare earth. It is well known that ferrite magnets have a lower residual magnetic flux density, compared to neodymium magnets, they are also characterized by a higher Curie temperature point. Also, in the context outlined above, ferrite permanent magnets have another special advantage, given by the fact that the materials from which they are made, do not fall into the group of deficient materials. The performance of the PMASynRM motor depends decisively on the value of the magnetization on the two machine axes, *d* and *q* respectively. The PMASynRM type motor is characterized by two torque components, the component given by the magnetic flux of the permanent magnets and the component given by the variable reluctance of the motor (due to the degree of magnetic asymmetry of the rotor). The number of flux barriers influences the degree of magnetic asymmetry of the rotor, while the volume of permanent magnets inserted in the rotor flux barriers influences the magnetic flux generated by the coils in the no-load mode of the motor. We want to design a PMASynRM model, with six poles that will be produced as a new series of electrical machine by the Romanian manufacture ICPE S.A. Servomotor Division (Fig. 1). This new production line will be addressed to light electric vehicle traction and it can assure a constant power through a large speed scale. The main advantages of this prototype refer to the much more compact construction compared to that of asynchronous motors, obtaining a high-power density and efficiency, and a constant power for a wide range of speeds. It does not require a complicate maintenance and the torque ripple is reduced. It is well known that the magnetic aspects are very important in the electrical machine design and they will be addressed in the paper, using finite element (FEM) method simulations. A geometrical design of an electrical machine prototype is drawn in AutoCAD and then is introduced in 2D magnetic FEA software FEMM 4.2. (a free and friendly software). This environment is compatible with Octave package and interconnected programs that uses the geometry introduced in FEMM are developed. As results there can be obtained cogging torque values, magnetic flux density maps (Fig. 2) and air-gap magnetic field distribution. When electric currents are fed through the stator coils, different determinations are made such as electromagnetic torque and machine power. The magnetic saturation and transversal magnetic saturation are analyzed. The phenomena will be put in evidence through flux linkage analysis on *d* and *q* axis, respectively as a function of the electrical currents on these axes. The machine efficiency will be investigated. The whole number of stator slots on the pole and on the phase, allows solving the magnetic field problem only on one teeth step. The reduction of the cogging torque can be easily done using two rotor pieces along the length of the machine, offset by a smaller angle than the tooth step (e.g. 1/2 tooth step). Acknowledgment The work was supported

by a grant of the Romanian Ministry of Education and Research, CCCDI - UEFISCDI, project number PN-III-P2-2.1-PTE-2019-0423 (47PTE/2020), within PNCDI III.

- [1] G. Pellegrino, A. Vagati, B. Boazzo and P. Guglielmi, IEEE Transactions on Industry Applications, vol. 48, 6, p. 2322 – 2332 (2012)
 [2] B.D. Varaticeanu, P. Minciunescu, and S. Matei, Design of Permanent Magnet Assisted Synchronous Reluctance Motor for Light Urban Electric Vehicle, Proceedings of International Symposium on Fundamentals of Electrical Engineering, 2014 [3] B.D. Varaticeanu, P. Minciunescu, and S. Matei, Performance Evaluation of Permanent Magnet Assisted Synchronous Reluctance Motor for Micro Electric Vehicle, Lecture Notes in Mobility, Advanced Microsystems for Automotive Applications, 2015.

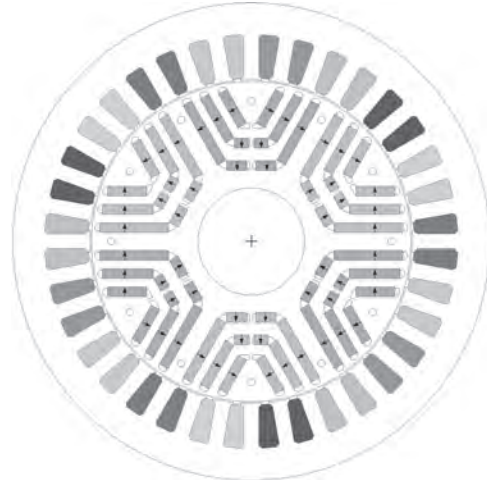


Fig. 1. Distribution and magnetizing direction of the rotor ferrite magnets and three phased stator windings.

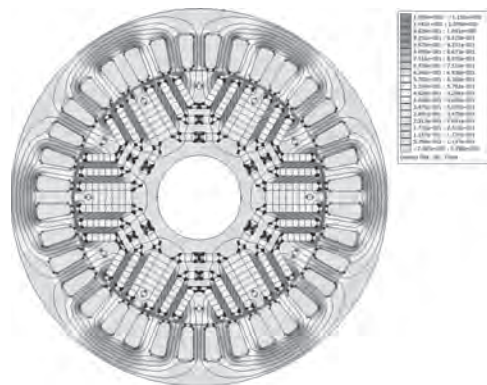


Fig. 2. Magnetic flux density map at no-current stator coil configuration.

BP-16. Torque Analysis of High Power Density Permanent Magnet Synchronous Machines by Considering Core Reluctance.

C. Li¹, J. Gao¹, W. Zhang², W. Zhou¹ and S. Huang¹

1. College of Electrical and Information Engineering, Hunan University, Changsha, China; 2. Department of Electronic and Electrical Engineering, Changsha University, Changsha, China

Abstract—Most mathematical torque models for the permanent magnet synchronous machines (PMSMs) are established based on neglecting the core reluctance. In order to analyze the torque of high power density PMSMs more effectively in the saturated state, this paper has considered the core reluctance in the torque analysis and a novel torque model is proposed to adapt magnetic saturation condition. It is demonstrated by simulation and experiment that the proposed torque model is closer to the actual torque.

Index Terms—Torque, permanent magnet synchronous machines (PMSMs), core reluctance, high power density. I. Introduction Various torque analysis studies have been presented for permanent magnet synchronous machines (PMSMs). For instance, when the machine is gradually saturated, it is considered with the variation of dq-axis self-inductances depending on operating conditions [1] and the cross-magnetization phenomenon in the electrical machine has been subjected to detailed scrutiny [2]. In order to deal with saturation and cross-saturation, an extension of the d-q model is proposed in [3]. However, those studies have not analyzed the effect of core reluctance on magnet torque. With the saturation level in PMSMs is getting severer, this will cause the magnetic conductivity of the core to decrease rapidly, in this case, the core reluctance cannot be ignored. Although some literatures have analyzed the influence of core reluctance on the magnetic circuit, there is no specific analysis of the influence on magnet torque [4]. This paper has considered the core reluctance on the magnetic circuit and analyzed the influence of the core magnetic motive force (mmf) generated by the core reluctance on the magnet torque, then a novel magnet torque model is proposed to adapt magnetic saturation condition. Finally, the validity of the proposed torque model is verified by experiment and simulation.

II. Analysis of Magnet Torque *A. Neglecting the Core Reluctance* In the conventional analysis of magnet torque, core reluctance can often be made much smaller than that of the air gap, in this case, the reluctance of the core can be neglected, the dominant reluctance is that of the air gap. Therefore, the stator mmf F_s is equal to the air gap mmf F_{sg} provided by the stator and the rotor mmf F_r is equal to the air gap mmf F_{rg} provided by the rotor. It can be known from the literature [5], the general expression for the magnet torque for the multi-pole non-salient-pole machines could be expressed as $Te = -p(\mu_0 \pi D l / 2g) F_s F_r \sin \delta_{sr}$ (1) Where μ_0 is the permeability of free space, p is the number of pole-pairs and g is the length of the air gap. D is the average diameter of the air gap; l is the axial length of the air gap and δ_{sr} is the angle between the mmf of the stator and the rotor. *B. Considering the Core Reluctance* When the machine is in the saturated state, this will cause the magnetic conductivity of the core to decrease rapidly, the core reluctance should be considered. In this case, the mmf includes the air gap mmf and the core mmf, the expression (1) could be rewritten as $Te' = -p(\mu_0 \pi D l / 2g) (F_s - F_{sr})(F_r - F_{rt}) \sin \delta_{sr}$ (2) Then, through a series of simplification, (2) could be expressed as $Te' = Te (F_{gd} / (F_{gd} + F_{id}))^2$ (3) Where F_g is the resultant air gap mmf and F_r is the resultant core mmf. F_{gd} and F_{id} are the d-axis components of the F_g and F_t respectively. Further detailed derivation formula and calculation method will be reported in the full paper. III. Simulation and Experiment In order to verify the analysis, a 350kW high power density interior PMSM is studied as an example. The conventional $id=0$ control strategy is applied to eliminate the influence of reluctance torque. The air gap magnetic field intensity H_{gd} and the magnetic field intensity of stator teeth H_{id} in the d-axis direction are obtained by finite element software. The magnetic field intensity of the machine is illustrated in Fig. 1. Because most of the core mmf is in the stator teeth, the yoke mmf is ignored. $F_{gd} = H_{gd} * g$, $F_{id} = H_{id} * l$, and l is the calculated length of the magnetic circuit of the stator teeth. Then a 350kW high power density interior PMSM has been prototyped and tested for validation. As shown in Fig. 2, through comparison, the magnet torque Te obtained by conventional calculation has large error. The magnet torque Te' obtained by the modified torque model is very close to the actual torque and simulation torque, which verifies the validity of the torque analysis proposed in this paper.

[1] G. H. Kang, J. P. Hong, G. T. Kim, and J. W. Park, "Improved parameter modeling of interior permanent magnet synchronous motor based on finite element analysis," *IEEE Trans. Mag.*, vol. 36, pp. 1867–1870, July 2000. [2] E. Levi and V. A. Levi, "Impact of dynamic cross-saturation on accuracy of saturated synchronous machine models," *IEEE Trans. Energy Conversion*, vol. 15, pp. 224–230, June 2000. [3] Stumberger, B.; Stumberger, G.; Dolinar, D.; Hamler, A.; Trlep, M.; "Evaluation of saturation and cross-magnetization effects in interior permanent-magnet synchronous motor," *IEEE Transactions on Industry Applications*, vol.39, no.5, pp. 1264- 1271, Sept.-Oct. 2003 [4] Gabriel Forstner, Andreas Kugi, Wolfgang Kemmetmüller, "A Magnetic Equivalent Circuit Based Modeling Framework for Electric Motors Applied to a PMSM With Winding Short Circuit," *IEEE Transactions on Power Electronics*, vol. 35, no. 11, pp. 12285–12295, Nov. 2020. [5] S. D. Umans, *Fitzgerald & Kingslye's Electric Machinery*. New York, NY, USA: McGraw-Hill, Jan. 2013.

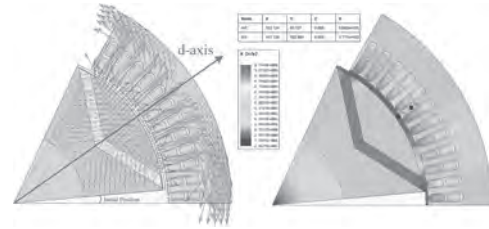


Fig. 1. The machine model and magnetic field intensity distribution.

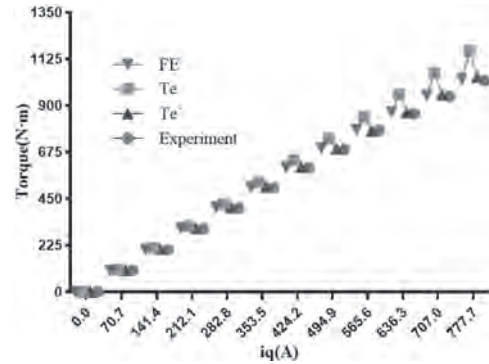


Fig. 2. Comparison of the torque.

BP-17. Optimized Rotor Shape for Reducing Torque Ripple and Electromagnetic Noise.

H. Ge¹, X. Qiu¹, B. Guo¹ and H. Wang¹

1. Nanjing Normal University School of Electrical and Automation Engineering, Nanjing, China

Abstract — This paper proposes a rotor design method suitable for double-layer interior permanent magnet synchronous motor (BIPMSM), which can reduce electromagnetic torque ripple and at the same time reduce the electromagnetic noise of the motor. In previous studies, the inverse cosine function (ICF) has been used for torque ripple reduction by making the air gap flux density distribution sinusoidal under a no-load condition. However, ICF can only be used in a single-layer interior rotor structure. Therefore, this article proposes a piecewise inverse cosine function (PICF) based on ICF, which can be applied to BIPMSM. To verify the validity of the proposed design method, the characteristics of 8-pole, 36-slot motors that have different rotor shapes are analyzed using finite element analysis. 1. INTRODUCTION there are a number of advantages of shaping the salient pole shoes of interior permanent magnet (IPM) synchronous machines to produce a sinusoidal air-gap flux density distribution [1]. Firstly, the phase electromotive force (EMF) will be more sinusoidal which will reduce the electromagnetic torque ripple from the machine when using sinusoidal phase currents. Secondly, cogging torque will also be reduced. Thirdly, the magnitude of the radial force in the air-gap is proportional to the square of the radial component of the air-gap flux density. Therefore, the radial force space distribution in the air-gap will contain much reduced number of space harmonics which will lower the probability of exciting stator core resonances. All of these aspects will have a positive effect on the noise and vibration behavior of the machine. In [1], the application method of inverse cosine function in single-layer interior permanent magnet synchronous motor is demonstrated in detail. After optimizing the rotor structure through the inverse cosine function, a more sinusoidal air gap flux density can be obtained under no-load conditions. In [2], the author, through finite element analysis, found that ICF can reduce the torque ripple of the motor, but at the same time it can also cause the torque to drop. In this article, PICF makes the air gap magnetic density of BIPMSM more sinusoidal, thereby reducing torque ripple and electromagnetic noise, and improving the performance of the motor. 2. PRINCIPLES OF BICF The traditional ICF can be expressed by the following formula: $B_{max} \cos\theta = \mu_0 F_g / l_g(\theta)$, where B_{max} is the maximum value of the air gap flux density, $l_g(\theta)$ is the air gap length using, μ_0 is the permeability of vacuum and F_g is the air gap magnetic potential by PM. In the traditional ICF, the magnetic potential generated by the permanent magnet can be regarded as a fixed value, but the magnetic potential generated by the permanent magnet in BIPMSM is not a fixed value, as shown in Fig.1. Therefore, it is necessary to calculate the magnetic potential in sections according to θ_1 and θ_2 , so that the air gap flux density generated by each section meets the same sinusoidal distribution. 3. FINITE ELEMENT SIMULATION VERIFICATION In order to verify that based on PICF, the rotor structure designed in this paper can reduce the torque ripple and electromagnetic noise of the motor, and the finite element simulation of the designed motor rotor is carried out. It can be seen from Fig.2(a) that after the use of PICF to improve the motor rotor structure, the electromagnetic torque ripple is well suppressed, but the torque amplitude is slightly reduced, which is consistent with the conclusion in [2]. Fig.2(b) shows the two-dimensional Fourier decomposition results of the radial force before and after the optimization. PICF greatly weakens the amplitude of most electromagnetic force components, which will effectively reduce the electromagnetic noise of the motor under different operating conditions. 4. DISCUSSION Through PICF, the torque ripple of BIPMSM can be significantly reduced and the motor control accuracy can be improved. As the air gap distance increases, the electromagnetic torque of the motor will inevitably be reduced. However, PICF can greatly reduce the electromagnetic noise of the motor, and it can effectively attenuate the noise of the motor at different operating speeds.

G. Ombach and W. Chlebosz, “Optimal rotor shape with third harmonic for maximizing torque and minimizing torque ripple in IPM motors,” 2012 XXth International Conference on Electrical Machines, Marseille, 2012, pp. 397-403.

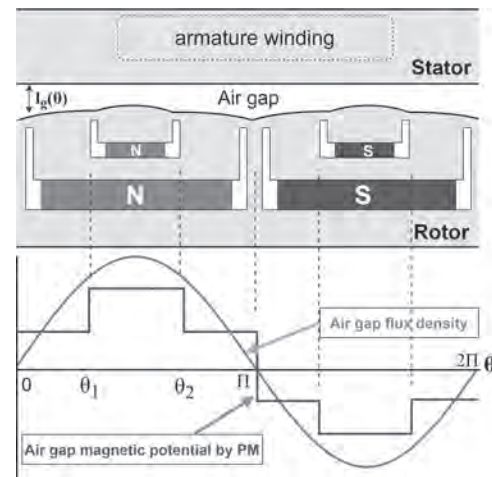


Fig.1

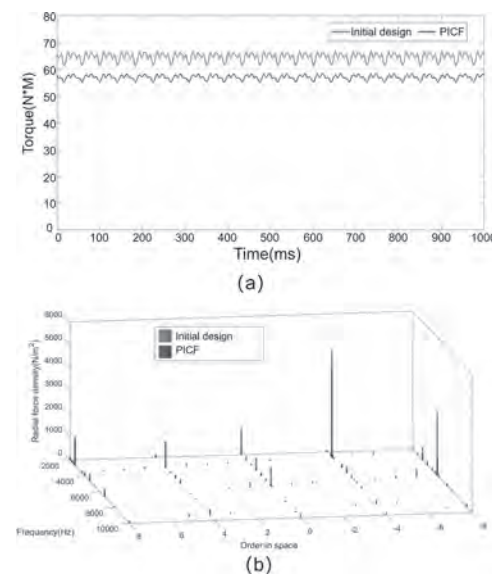


Fig.2

[1] S. A. Evans, “Salient pole shoe shapes of interior permanent magnet synchronous machines,” The XIX International Conference on Electrical Machines - ICEM 2010, Rome, 2010, pp. 1-6. [2] K. Wang, Z. Q. Zhu,

Session BQ
HIGH-SPEED MACHINES AND ENERGY STORAGE MACHINES
(Poster Session)

Chang-Hung Hsu, Co-Chair
Oriental Institute of Technology, New Taipei City, Taiwan
Christopher H. T. Lee, Co-Chair
Nanyang Technological University, Singapore, Singapore

BQ-01. Kriging Surrogate Model-Based Design of Ultra-High-Speed Surface-Mounted Permanent Magnet Synchronous Motor Considering Stator Iron Loss and Rotor Eddy Current Loss.

S. Im¹, S. Lee¹, D. Kim¹, X. Gu¹, S. Shin¹ and M. Lim¹

1. Automotive Engineering, Hanyang University, Seongdong-gu, The Republic of Korea

1. Introduction Ultra-high-speed (UHS) surface-mounted permanent magnet synchronous motor (SPMSM) is widely used for driving air compressor [1]. The electromagnetic losses generated by the UHS SPMSM include iron loss, copper loss, rotor eddy current loss, and etc. Especially, the UHS SPMSM can have large stator iron loss and rotor eddy current loss due to its high rotational speed [2]. The stator iron loss is related to the magnetic properties of the stator iron core, and the rotor eddy current loss is related to the electrical properties of the rotor sleeve and permanent magnet (PM). In addition, the magnitude of these losses can be influenced by the armature magnetomotive force (MMF), which is the product of the number of turns and current. Accordingly, in order to determine the armature MMF, it is necessary to determine the appropriate number of turns and current magnitude in the motor design process. Since the magnetic flux density of stator iron core is different according to the armature MMF, the nonlinearity of the stator iron core must be considered in the motor design process. The contribution of this research is to propose the kriging surrogate model-based design process of UHS SPMSM considering stator iron loss and rotor eddy current loss. In the proposed design process, the nonlinearity of the stator iron loss and rotor eddy current loss according to the magnetic saturation is considered through the kriging surrogate model. The kriging surrogate model is suitable for use in electric motor design because it has high predictive ability for responses with nonlinear characteristics [3]. For the verification, a prototype is fabricated and the experiments will be conducted. 2. Kriging surrogate model-based design process Using the constructed kriging surrogate models, the motor is designed through the motor design process shown in Fig. 1. The kriging surrogate model-based design process is divided into two stages: size determination and loss minimization. In both stages, optimization techniques are applied. First, the optimization problem is defined to minimize the objective function while satisfying the constraints. Next, the design of experiments for the selected design variables is performed, and a kriging surrogate model is created. Finally, the kriging surrogate models are used to determine the optimal model that satisfies the objective function and constraints. As a result, the model designed using the kriging surrogate model improves as follows compared to the model designed using the conventional design methodology: 1.4% reduction in stator outer diameter, 11.8% reduction in stack length, and 6.4% reduction in total losses. A. Size Determination The radial dimension of the rotor is determined in consideration of the mechanical stiffness and air gap magnetic flux density. Optimization technique is applied in the size determination. The objective function is set to minimize the stack length, and the constraints are defined considering the electrical specifications. The tooth width, yoke thickness, and the number of turns are selected as design variables. Then, the responses to be predicted by the kriging surrogate models are the stator outer diameter, stack length and line to line voltage. When kriging surrogate models are used in the motor design process, the tendency according to design variables and the nonlinearity of the core can be considered. In particular, when the current is the same, the change in the armature MMF according to the number of turns affects the magnetic flux density of the stator core. Since saturation of core is an important parameter in determining the motor size, it is considered by using the kriging surrogate model. B. Loss Minimization In this paragraph, the loss of the motor is minimized by changing the stator shape. The considered losses are iron loss, rotor eddy current loss, alternation current (AC) copper loss, and windage loss. As mentioned in section 2. A, optimization technique is applied to minimize motor losses. UHS SPMSM is designed through the kriging surrogate model for losses because the ratio of the stator core loss and the rotor eddy current loss due to the high rotational speed is large. Another major loss to consider in UHS SPMSMs is AC copper loss. As mentioned in section 1, since the frequency of the input current is large in the UHS SPMSM, the AC copper loss is also large, which is considered through kriging surrogate model. The windage loss generated in the air gap and increases with increasing rotational speed. The windage loss is also consid-

ered through the kriging surrogate model. The constraints for motor loss minimization are electrical specifications and target torque. Design variables are selected as tooth tip and slot open. Using the kriging surrogate model, the optimal model is obtained that minimizes motor loss while satisfying the constraints. 3. Result and Conclusion In this paper, a kriging surrogate model-based design process is proposed. Through the process, a motor that satisfies the required motor size and specifications is determined. As a result, the model designed using the kriging surrogate model reduced the stator iron loss by 7.6% and the rotor eddy current loss by 24.9% compared to the model designed using the conventional design methodology. As shown in Fig. 2, a prototype of the designed model is fabricated. Through the test, the validity of the designed model will be verified.

[1] Z.Zhang, Z. Deng, and Q. Sun, IEEE Transactions on Magnetics., Vol. 55, p.1-11 (2019) [2] F. Zhou, J. Shen, and W. Fei, IEEE Transactions on Magnetics., Vol. 42, p. 3398-3400 (2006) [3] S. Kim, S.-Y. Lee, and J.-M. Kim, IEEE Transactions on Energy Conversion., Vol. 35, p.2056-2065 (2020)

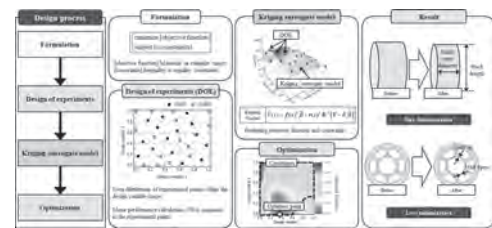


Fig. 1 Proposed kriging surrogate model-based design process

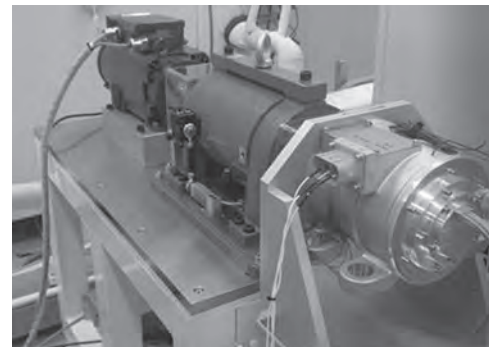


Fig. 2. Experimental setup for no-load test of prototype

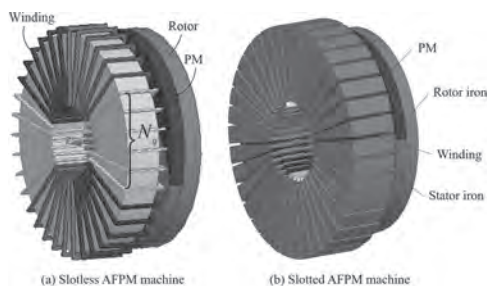
BQ-02. Torque Comparison Between Slotless and Slotted Ultra-High Speed AFPM Motors.

W. Cheng¹, G. Cao¹, Z. Deng¹, L. Xiao¹ and M. Li¹

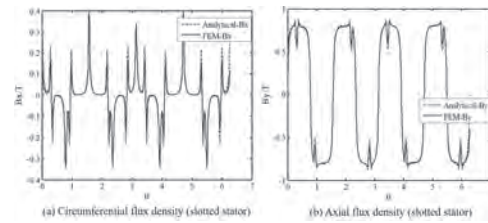
1. College of Science, Xi'an University of Science and Technology, Xi'an, China

Comparing with the radial flux permanent magnet (RFPM) motor, axial flux permanent magnet (AFPM) motor has higher power density, higher torque density. Especially, if the AFPM motor is designed to work at a high speed, its size will be further reduced, leading to a more compact size and a significant volume saving. In addition, the AFPM motor has a superior cooling structure. The above features will boost the application of the high speed AFPM in many potential fields, such as flywheel energy storage system, man-portable power platforms, turbo-compressors, and machining spindles, and so forth [1-3]. A 3,2000r/min, 200W AFPM generator with a slotless stator core and toroidal coils was reported in literature [4]. Literature [5] designed a single-sided AFPM machine with 100W shaft output power at 50,000r/min, and stator core is slotless and made of powder composite material. Literature [6] developed a 15kW, 25,000 r/min AFPM motor, the stator core is slotted and used amorphous alloy. A 30kW, 16,000 r/min AFPM motor has been developed for the flywheel in which a slotted stator core and distributed winding are applied [7]. A 30kW, 30,000 r/min AFPM generator having 2 stators and 3 rotors was propounded [8]. It can be found that, in low power field such as hundreds of watts, high speed AFPM machines generally apply the slotless stator. Because the stator windings occupy the air gap, which leads to a wider air gap, then the air gap flux density is low, whereupon, the power can not be designed very large. However, for kilowatt power level field, a slotted stator is necessary. Moreover, the power can be further increased by the combination of multi-layer stator and rotor. It is well known that the slotless stator core also can eliminate the cogging torque. However, slotted stator will increase ripple torque. Relative to the AFPM motor with slotless stator, how much the motor power and the torque ripple can increase for the one with the slotted stator. It is an interesting, challenging question. However, rare researches about this are reported. Therefore, first, the paper will solve the electromagnetic field of the AFPM motor analytically. Then, electromagnetic torque will be obtained by Maxwell stress tensor method (MSTM). Thirdly, an example will be carried out for the cases in which both slotless and slotted stators are considered. Finally, results of torque comparison will be given and discussed. The analytical solution is verified by 3D finite element method (FEM) and experiment data.

[1]S. Neethu, S. P. Nikam and S. Pal, et al. *IEEE T Ind Electron.*, vol. 67, no. 7, pp. 5269-5277 (2020) [2]M. G. Kesgin, P Han and N. Taran, et al. in *Proc. Conf. (ICRERA)*, pp. 1026-1031 (2019). [3]WJ Cheng, ZK Deng and L Xiao, et al. *Journal of Electrical and Computer Engineering*, vol. 2019, pp. 1469637 (2019) [4]S. Kumar, T. A. Lipo and B. I. Kwon, et al. *IEEE Trans. Magn.*, vol. 52, no. 7, pp. 8205004 (2016) [5]L Zheng, TX Wu, K. B. Sundaram, et al. *IEEE International Conference on Electric Machines and Drives* (2005) [6]WM Tong, YP Ci. *Electric Machines and Control*, vol. 20, no. 6, pp. 68-76 (2016) [7]F. Sahin, A. M. Tuckey, and A. Vandenput. *IEEE Industry Applications Conference* (2001) [8]M. Sadeghierad, H. Lesani, and H. Monsef, et al. *Journal of Applied Sciences*, vol. 9, no. 10, pp. 1915-1921 (2009)



Models of AFPM motor with slotless/slotted stator



Comparison of results from analytical model and FE model

BQ-03. Reduction of Torque Ripple and Rotor Eddy Current Losses by Closed Slots Design in a High-Speed PMSM for EHA Applications.

Y. Hu¹

1. Nanjing Engineering Institute of Aircraft Systems, Nanjing, China

I. Introduction The electro-hydrostatic actuators (EHA) are very attractive for the More-Electric Aircraft (MEA) due to its excellent performance such as safety, reliability, weight and cost [1]. Because of the advantages of high torque density, high efficiency, the permanent magnet synchronous machine (PMSM) can be used for the EHA [2]. When the PMSM is running at high speed, the torque ripple will cause the vibration and noise of the EHA, and the machine magnetic field will produce a lot of eddy current loss in the rotor [3]. Excessive eddy current loss of permanent magnet will lead to irreversible demagnetization at high temperature. Therefore, it is of great significance to study the torque ripple and rotor eddy current loss of high-speed PMSM for EHA applications. II. Main Body The high-speed PMSM consists of the stator, rotor, and enclosure. The structural diagram of the high-speed PMSM is shown in Fig. 1. The stator has the iron core and three phase windings, and the rotor has the stainless steel retaining sleeve, magnets, and the shaft. The rated power of the high-speed PMSM is 4 kW, and the rated speed is 18000 r/min. Fig. 2 shows the stator core losses and rotor eddy current losses density distribution at different stator slot openings of the high-speed PMSM, where the B_{s0} is the width of stator slot openings. The current I is 15.5 A, and the frequency is 600 Hz. The stator core losses of the closed slot are 118.35 W, $B_{s0} = 2$ mm are 116.54 W. It can be found that the rotor eddy current losses are focus on the retaining sleeve and magnets. The rotor eddy current losses of the closed slot are 2.43 W, $B_{s0} = 2$ mm are 18.64 W. The rotor eddy current losses are the minimum when the stator slot openings selected as the close slot. The cause is the larger the slot opening is, the severer the permeance variation, and the more significant the rotor eddy current losses. The torque waveforms of different stator slot openings are studied. It shows that the average torque of the $B_{s0} = 2$ mm is 2.5 Nm, and the closed slots is 2.494 Nm, which is almost the same. The torque ripple of the $B_{s0} = 2$ mm is 15.38%, the $B_{s0} = 0$ is 6.56%. The torque ripple of the closed slots is almost decreasing 60% than that of the stator slot openings is 2 mm. The EMF waveforms also measured and compared with the FEA, which agrees well with the results of the FEA. The torque ripple are measured by a digital torque meter, the measured results are also agrees well with the results of the FEA. III. Conclusion This paper has analyzed the stator slot openings width for the reduction of torque ripple and rotor eddy current losses in a high-speed PMSM for the electro-hydrostatic actuator applications. It is demonstrated that when the stator slot openings selected as the closed slot, the torque ripple and rotor eddy current losses can be extremely reduced. Finally, the prototype machine with the closed slots is fabricated and experimented.

[1] A. Trentin, P. Zanchetta, P. Wheeler, J. Clare, "Power flow analysis in electro-mechanical actuators for civil aircraft," IET Electr Power Appl., vol. 5, no. 1, pp. 48-58, 2011. [2] Wenping Cao, Barrie C. Mecrow, et al. "Overview of Electric Motor Technologies Used for More Electric Aircraft (MEA)," IEEE Trans. Ind. Electron, vol. 59, no. 9, pp. 3523-3531, Sep. 2012. [3] D. Gerada, A. Mebarki, N. L. Brown, C. Gerada, A. Cavagnino, and A. Boglietti, "High-speed electrical machines: Technologies, trends, and developments," IEEE Trans. Ind. Electron, vol. 61, no. 6, pp. 2946-2959, Jun. 2014.

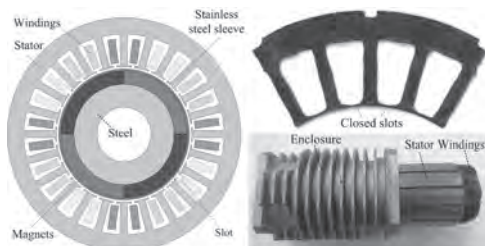


Fig. 1. Machine specification and the prototype machine with closed slots.

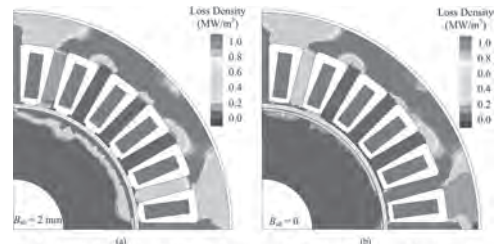


Fig. 2. Stator core losses and rotor eddy current losses density distribution at different stator slot openings. (a) $B_{s0} = 2$ mm, (b) $B_{s0} = 0$, (current is 15.5A, speed is 18000 r/min)

BQ-04. Optimization of a High-Speed PMSM Based on the Quantum Evolutionary Bat Algorithm and Deep Neural Network.

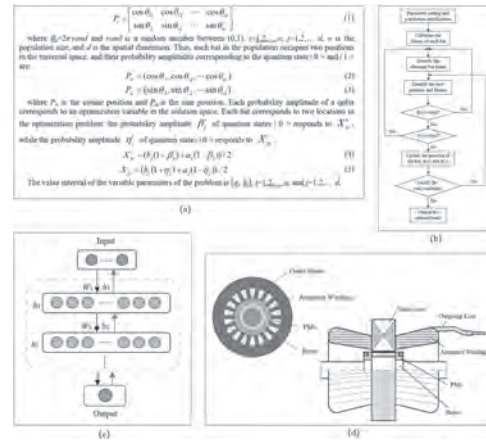
X. Liu¹ and B. Yuan²

1. Chongqing Normal University, Chongqing, China; 2. Chongqing University, Chongqing, China

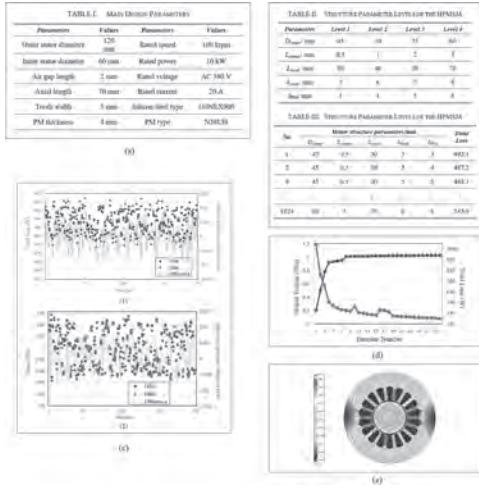
1 Introduction Compared with ordinary motors, high-speed permanent-magnet synchronous motors (HPMSMs)[1] have obvious advantages [2]. However, under the collective influence of temperature, armature reaction and other factors, a serious temperature rise in the inner components of the motor will cause demagnetization of the permanent magnet [3]. The problems of achieving the global optimization of the motor structure parameters include the selection of a global optimization algorithm and the establishment of a fast calculation model. The bat algorithm [4] is a new heuristic algorithm. Quantum evolutionary computation [5] makes full use of the theory of quantum bits and superposition states in quantum computation. At present, the combination of quantum theory and intelligent algorithms has become a popular research method [6]. The quantum bat algorithm (QBA) [7] introduces the idea of quantum evolutionary computation into the bat algorithm and gives full play to its advantages. This algorithm is a very effective global optimization algorithm. In this paper, a regression modeling method based on a deep neural network (DNN) [8] for HPMSM structure optimization is employed. Through the network structure of the DNN multi hidden layer, the model accuracy is improved by learning the parameters layer by layer, and the calculation model of the HPMSM is established to provide high-precision and high-efficiency model support for global optimization. Based on the QBA with the DNN model, the structure parameters of the HPMSM are optimized to obtain the optimal combination to minimize the loss of the motor. The performance of the optimized HPMSM is verified by finite element simulation analysis and prototype experiments. 2 Quantum Bat Algorithm In the QBA, the probability amplitude of a qubit is directly used as the code of the current position of the bat. Considering the randomness of coding during population initialization, the coding scheme in Fig. 1(a) is adopted. The position of the bat changes according to a quantum revolving gate. Therefore, the update of the bat movement speed in the ordinary bat algorithm (BA) is converted to the update of the quantum revolving gate angle, and the update of the bat position is converted to the update of the qubit probability amplitude for the bat. Suppose that the optimal position searched by the whole population is P_g , then, the bat status update rules are as Fig. 1(b). 3 Deep Neural Network Model The DNN model is composed of multilayer adaptive nonlinear elements [16], and it continuously reduces the model prediction error by learning layer by layer. The structure of the DNN algorithm can be divided into a visual layer and hidden layer. The visual layer includes the input layer and the output layer. Its basic structure is shown in Fig. 1(c). The DNN adopted in this paper is a fully connected neural network, where each layer can be expressed as a weight W multiplied by a vector x and is composed of neurons, and the deviation quantity b is added. 4 Design Optimization of the HPMSM Fig. 1 (d) shows an HPMSM that has 18 slots and 2 inner rotor pole pairs. With the initial main design parameters, which take into account the limitation of the current density of the conductors in the stator slots, the magnitude of the ampere conductors of the total electric loading are obtained based on magnetic circuit computations; they are shown in Fig. 2(a). According to the constraint conditions of the structural parameters, a 5-factor 4-level variable scale is given, as shown in Fig. 2(b), and there are 1024 orthogonal combination modes in total. Since the temperature rise of the HPMSM is directly related to the loss of the motor, the loss under different structural parameters is used to build the sample library. To verify the accuracy of the DNN rapid calculation model established in this paper, sample points are randomly selected in the solution domain. The total loss and the output torque of the test samples simulated by the FEM and DNN model are predicted and compared. The difference between the DNN model and FEM simulation is calculated by η . The accuracy verification of the DNN model is shown in Fig. 2(c). To achieve better overall performance, the HPMSM is optimized through a single-objective problem. The output torque and total loss for different iteration numbers are shown in Fig. 2(d). The final design parameters after optimization are given in Fig. 2(e). When the HPMSM is working at the rated working point, as shown in Fig. 8, in which the rated speed is 100 krpm, and the output

torque is 1.026 Nm, the efficiency can reach 96%. Within the speed range of 20 krpm to 120 krpm, the efficiency can be maintained at higher than 93%. 4 Conclusion This paper systematically studies the QBA optimization method combined with a DNN model for the structure optimization problem of HPMSMs. The DNN models for the objective functions of the loss and torque are proven to be accurate enough to replace the FEM simulation. Instead of calculating a FEM simulation for each particle, applying DNN models can shorten the working time of the optimization process. The QBA optimization algorithm has a faster convergence speed than the traditional PSO algorithm.

[1] J. Ahn, C. Han, C. Kim, and J. Choi, "Rotor Design of High-Speed Permanent Magnet Synchronous Motors Considering Rotor Magnet and Sleeve Materials," *IEEE Transactions on Applied Superconductivity*, vol. 28, no. 3, pp. 1-4, 2018. [2] H. L. Shuhua Fang, Haitao Wang, Hui Yang, Heyun Lin, "High Power Density PMSM With Lightweight Structure and High-Performance Soft Magnetic Alloy Core," *IEEE Transactions on Applied Superconductivity* vol. 29, no. 2, pp. 1-5, 2019. [3] Y. Chen, J. Zhou, Y. Fang, Y. Gao, Y. Xia, "Multi-field coupling finite-element analysis of the temperature rise in permanent magnet synchronous motor applied for high speed train," presented at the 2016 19th International Conference on Electrical Machines and Systems (ICEMS), Chiba, Japan, 13-16 November, 2016, 16650589. [4] H. Liang, Y. Liu, Y. Shen, F. Li, Y. Man, "A Hybrid Bat Algorithm for Economic Dispatch With Random Wind Power," *IEEE Transactions on Power Systems*, vol. 33, no. 5, pp. 5052 - 5061, 2018. [5] S.L. Ho, S. Yang, P. Ni, J. Huang, "A Quantum-Inspired Evolutionary Algorithm for Multi-Objective Design," *IEEE Transactions on Magnetics* vol. 49, no. 5, pp. 1609 - 1612, 2013. [6] Y. Li, S. Yang, Z. Ren, "A Methodology Based on Quantum Evolutionary Algorithm for Topology Optimization of Electromagnetic Devices," *IEEE Transactions on Magnetics* vol. 55, no. 6, p. 7204004, 2019. [7] H. T. ul Hassan, M.U. Asghar, M.Z. Zamir, H.M. Aamir Faiz, "Economic load dispatch using novel bat algorithm with quantum and mechanical behaviour," presented at the 2017 International Symposium on Wireless Systems and Networks (ISWSN), Lahore, Pakistan, 19-22 November 2017, 2017. [8] Z. L. L. Bai, "Evaluating the supplier cooperative design ability using a novel support vector machine algorithm," presented at the 2008 12th International Conference on Computer Supported Cooperative Work in Design, Xi'an, China, 16-18 April 2008, 2008.



(a) Quantum Bat Algorithm. (b) The flow chart of the QBA. (c) Basic structure of the DNN. (d) Configuration and mechanical structure of the proposed machine.



(a) Main Design Parameters (b) Structure Parameter Levels of the HPMSM (c) Accuracy verification of the model. (d) Output torque and total loss for different iteration numbers. (e) The optimized HPMSM

BQ-05. Experimental Verification and Analytical Approach for Electromagnetic Characteristics of a High-Speed Permanent Magnet Motor With two Different Rotors and Winding Patterns.

J. Woo¹, T. Bang¹, H. Lee¹ and J. Choi¹

1. Electrical Engineering, Chungnam National University, Daejeon, The Republic of Korea

Recently, high-speed permanent magnet (PM) motors have high output and efficiency by using rare-earth PMs. However, rare earth magnets with such advantages have major environmental disadvantages, owing to the serious environmental pollution caused during the separation and purification of rare earth materials. In addition, rare earth magnets are highly dependent on rare earth production, which is likely to lead to a surge in rare earth values. From an industrial perspective, an increase in manufacturing costs owing to dependence on rare earth PMs is inevitable, which causes production disruptions. Therefore, research on the reduction of the amount of rare earth PMs used and rare earth PM alternatives are being actively pursued. For most high-speed motors, a lower frequency is advantageous from a control viewpoint. Accordingly, a two-pole cylindrical magnet rotor that has an advantage in terms of output is often used. Because this requires a large amount of magnet usage, in this study, research was conducted to reduce the number of magnets in the conventional high-speed motor. We applied a hollow rotor shaft to reduce the number of magnets used while maintaining the magnetic loading ratio of conventional high-speed motors. The reduction in motor power by reducing PM usage is complemented by the redesign process through the analytical method and finite element method (FEM). A manufacturing model based on the design results was then used to conduct the experimental verification. The model in this study is a high-speed motor with two poles, and in early design, we compare the characteristics of concentrated and distributed windings in a 6-slot stator. The electromagnetic properties were analyzed according to each winding method, and based on this, the MMF(magneto-motive fore) characteristics on a high-speed rotor were compared and analyzed. Then, comparative verification was performed by experimenting with a hollow-shaft rotor model with concentrated windings finally applied by comparing the electromagnetic and mechanical properties according to the type of rotor considering windings. Figure 1(a) shows the 3D structure of two different winding patterns, (b) shows the rotor shape 3D structure along the hollow shaft. Figure 1(c) shows the manufacturing model to which the hollow shaft and concentrated windings are applied. Fig. 2(a) shows the magnetic flux line according to the winding method of the 2 pole 6-slot model. It can be confirmed that the magnetic flux lines are different according to each model with a concentrated winding with a coil pitch of one and a distributed winding with a coil pitch of two. Accordingly, to analyze the winding method influence on the motor, an MMF analysis was first performed, and the mechanical properties were considered based on the results. The MMF analysis was performed as follows. When the air gap is uniform, the relative permeance is constant; therefore, the distribution of the magnetic flux density of the air gap has the same distribution as that of the MMF [3]. Therefore, MMF analysis was performed based on the magnetic flux density of the air gap owing to the armature reaction of the winding method. A space harmonic method, which is an analytical method, is used to derive the air gap magnetic flux density. The space harmonic method is an electromagnetic field analysis technique that obtains magnetic vector potential from the Maxwell equation, which was used to perform an MMF analysis according to the winding methods of a high-speed PM motor [4]. Fig. 2(b) shows the MMF analysis results of the analytical method and FEM. When comparing these two methods, the results obtained are found to be generally well matched, although there are slight harmonic differences. When a current of 15-Arms is applied in the distributed winding case and 25.5-Arms in the concentrated winding case, a similar MMF is observed. Fig. 2(c) shows the density distribution of electromagnetic losses. This result compares the electromagnetic losses generated in the rotor and stator when a hollow shaft is applied to the rotor. It was confirmed that the reduction in stator saturation owing to the reduction in the number of magnets decreased the core loss generated in the stator, and the current increase to match the same existing model output had a slight effect on the eddy current loss. Finally, Fig. 2(d) shows the line voltage according to the rotor shape under load conditions. As a result, it was confirmed that 3D analysis considering

leakage through the hollow rotor shaft shape was most similar to the actual experimental results. This suggests the validity of the design results of a high-speed PM motor. Further discussion and results, including mechanical properties, are provided in the full paper.

[1] A. Damiano, A. Floris, G. Fois, I. Marongiu, M. Porru, and A. Serpi, "Design of a High-Speed Ferrite-Based Brushless DC Machine for Electric Vehicles", IEEE Trans. Ind. Appl., vol. 53, no. 5, pp. 4279-4287, Sep./Oct. 2017. [2] S. Musuroi, C. Sorandaru, M. Greconici, V.N. Olarescu, M. Weinman, "Low-cost ferrite permanent magnet assisted synchronous reluctance rotor an alternative for rare earth permanent synchronous motors", Industrial Electronics Society, IECON 2013- 39th Annual Conference of the IEEE, 10-13 Nov. 2013, Vienna, pp. 2966-2970. [3] Hulin Kang, Libing Zhou, Jin Wang, "Harmonic winding factors and MMF analysis for five-phase fractional-slot concentrated winding PMSM", 2013 International Conference on Electrical Machines and Systems (ICEMS), 16 January 2014 [4] P. Virtic, M. Hadziselimovic, T. Marcic, B. Stumberger, "Torque analysis of an axial flux permanent magnet synchronous machine by using analytical magnetic field calculation", IEEE Trans. Magn., vol. 45, no. 3, pp. 1036-1039, Mar. 2009.

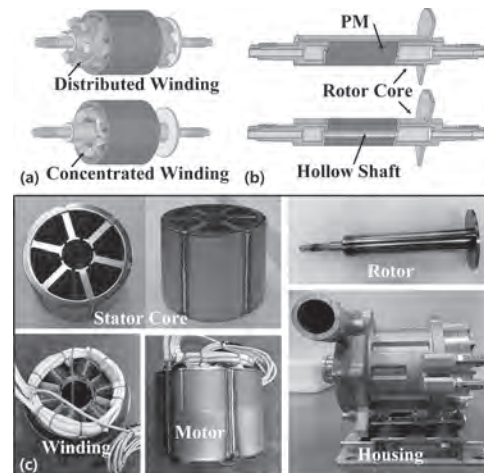


Figure 1. 3D structure of (a) two different winding patterns, (b) two different rotors and (c) Manufacturing model of concentrated winding motor

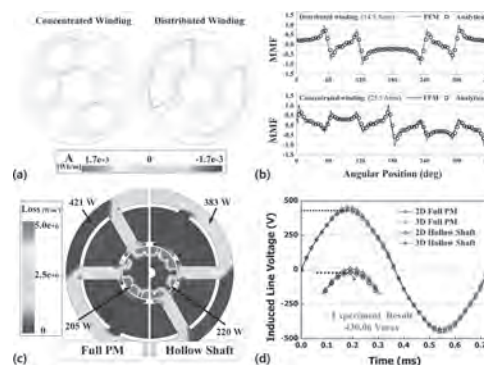


Figure 2 (a) Magnetic flux lines due to winding patterns and (b) MMF waveform comparison between analytical method and FEM, (c) The electromagnetic loss density distribution, (d) line voltage according to the rotor condition

BQ-06. Electromagnetic Loss Analysis of High-Speed Permanent Magnet Motors for High-Speed and High-Head Centrifugal Pump Using Co-Simulation Method With Controller.

G. Jang¹, C. Kim¹, H. Shin¹, D. Kwon¹ and J. Choi¹

1. Chungnam National University, Daejeon, The Republic of Korea

This study deals with the electromagnetic loss analysis through the coupling analysis of the controller motor considering the SVPWM control of a high-speed permanent magnet motor for driving a centrifugal pump. High-speed mechanical systems are suitable for applications such as compressors, vacuum pumps, turbine generators, flywheel energy storage systems, drilling machine tools, and electric vehicle propulsion motors in various industries such as transportation, defense, energy, aviation, and general industry. They are being developed for many industrial applications. It is not an exaggeration to say that the proportion of high-speed motors in the modern industry is on the rise. High-speed motors are operated by a power conversion device and a controller, and owing to the development of power conversion elements, high-speed and high-power motors are becoming possible [1]. In addition, there is a growing interest in the analysis of the loss and heat of high-speed motors in industry and academia. In the existing studies, the loss analysis of the motor is primarily performed through the current source analysis, which has the disadvantage of not considering the current harmonics caused by the switching of the controller. Therefore, it is difficult to predict the electromagnetic loss caused by current harmonics. In addition, few researchers have published a study on the characteristic analysis of the motor considering the current harmonics, but it is difficult to obtain accurate analysis results in all operating areas because only a single parameter of the motor is considered [2]. In addition, there is significant interest in reducing the loss and heat generation of high-speed permanent magnet motors. There are certain motor problems because of reduced efficiency and increased calorific value owing to electromagnetic losses that were not considered in the design stage. In particular, the heat generated in the rotating body of high-speed motors using sleeves in the industry is transferred to both bearings along the shaft. It also causes serious problems such as failure of bearings and shortening of life [3]. Hence, the electromagnetic loss analysis of the motor based on the controller and motor co-simulation analysis are important. Therefore, this study deals with the electromagnetic loss and dynamic characteristics analysis considering the inverter drive of a high-speed permanent magnet synchronous motor for a centrifugal pump. The motor and the SVPWM inverter were modeled, and the environment for the co-simulation analysis of the controller and the motor was established. The designed motor was manufactured, and the motor performance was evaluated. As illustrated in Fig. 1(a), a co-simulation analysis system was constructed using the analyzed motor model and the controller conceptual diagram. Results such as current applied to the motor according to the speed command and load torque, speed response characteristics, torque characteristics, and torque ripple were obtained. Fig. 1(b) depicts an experimental setup for the evaluation of a high-speed permanent magnet motor. The high-speed permanent magnet motor was combined with a centrifugal pump and a torque sensor and was operated through a controller. Fig. 1(c) presents the voltage and current waveforms of the motor measured in the rated speed and rated output range. It could be verified that the rated current was applied to the motor within the range not exceeding the voltage limit. Fig. 2(a) presents a comparison of the sinusoidal current and the incoming current waveforms of the motor during the coupling analysis. It could be verified that harmonics were included in the current waveform by the SVPWM switching frequency and were introduced into the motor. Fig. 2(b) shows the order and magnitude of the harmonic components included in the current waveform. Figs. 2(c) and (d) depict the analysis results of the loss of iron and permanent magnet rotors that occur during general sinusoidal current analysis and coupling analysis. Notably, the iron loss and eddy current loss increased owing to the harmonic components included in the current. Therefore, coupling analysis is important for detailed electromagnetic loss analysis. Based on the results presented here, it is judged that this study will contribute to the related industries by designing, developing, and evaluating the performance of a motor that can be used for industrial 12,500 rpm and 100 hp class centrifugal pumps. In addition, the co-simulation analysis method used in this disserta-

tion is considered to be useful in the design of high-speed motors that can be applied to various industrial applications.

[1] D.-K. Hong, D. Joo, Y.-H. Jeong, and D.-H. Koo, IEEE Transactions on Magnetics, vol.49, no.7, p. 4072, 2013. [2] Yunkai Huang, Jianning Dong, Long Jin, Jianguo Zhu, and Youguang Guo, IEEE Trans. Magnetics, Vol.47, No.10, October 2011. [3] Ziyuan Huang, Jiancheng Fang, Member, IEEE, Xiquan Liu, and Bangcheng Han, IEEE Trans. on Industrial Electronics, Vol.63, No.4, APRIL 2016.

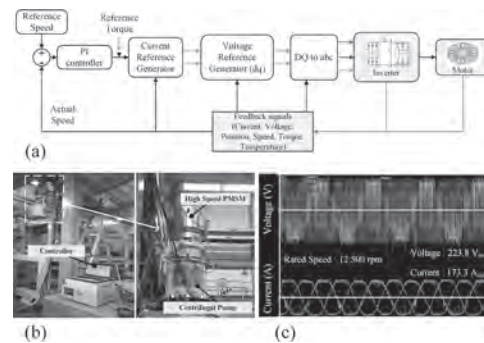


Fig. 1. (a) Concept diagram of the co-simulation analysis of motor including speed controller and current controller. (b) Motor performance test bed combined with centrifugal pump. (c) Motor voltage and current measurement results at rated speed and rated output.

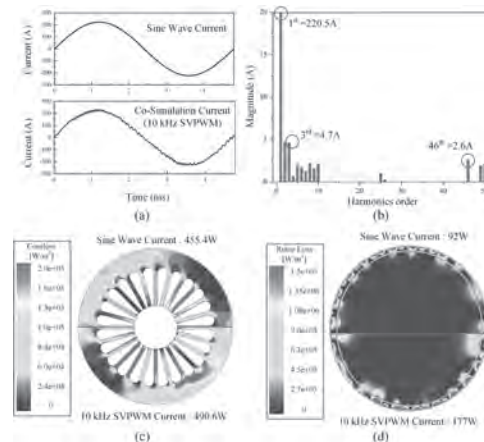


Fig. 2. (a) Comparison of sinusoidal current and PWM current waveforms using co-simulation method. (b) Harmonic analysis result of motor current using co-simulation analysis. (c) Core loss analysis result according to current waveform. (d) Rotor loss analysis result according to current waveform.

BQ-07. Design and Optimization of a High-Speed Permanent Magnet Synchronous Machine for gas Compressors.

Z. Yu¹, F. Zhao¹ and J. Cao²

1. Harbin Institute of Technology Shenzhen, Shenzhen, China;

2. Harbin Institute of Technology, Harbin, China

I. INTRODUCTION Recently, high-speed electrical machines have attracted much attention in the application of gas compressors [1], which have the advantages of high power density, small volume, small moment of inertia and fast response speed. In addition, the gearbox could be eliminated, because the gas compressor could be directly driven by a high-speed electrical machine. So that the maintenance costs and noise can be reduced [2]. Moreover, compared with the squirrel cage induction machine and the switched reluctance machine, the permanent magnet synchronous machine (PMSM) has higher efficiency and has been widely used in high speed applications [3-4]. Therefore, a high speed PMSM, which is rated at 15kW, 120krpm for a gas compressor, has been designed and analyzed in this paper. The performance of the proposed machine is verified by finite element method (FEM). Furthermore, the proposed machine has been optimized to reduce wind friction loss and increase power density. II. TOPOLOGY AND OPERATION PRINCIPLE OF THE FRPM MACHINE According to the design specifications given in the left column of TABLE I, the main dimensions of the machine are designed and listed in the right column of TABLE I. Fig.1 shows the prototype of the proposed machine. The structural strength and thermal constraints are the two main design constraints of high speed PMSM [2]. Therefore, various measures are used to ensure the strength of the rotor and reduce the losses of the proposed machine. Firstly, since the permanent magnet (PM) is weak in tension, a glass fiber sleeve is applied to protect the PM in high speed operation condition. Secondly, silicon steel sheets with a smaller core loss coefficient are used for stator to reduce core loss. Moreover, the toroidal windings are applied for easy installation and reducing the end length of the wire caused by one pole pair design, thereby reducing copper loss. FEM model of the proposed machine is established to obtain the output performances, e.g., output torque, core loss. The air gap computational fluid dynamics (CFD) model of the proposed machine is established to calculate the wind friction loss of the machine. The results show that the performance of the proposed machine can meet the design specifications, with a wind friction loss of 64.22W, an efficiency of 97.85% and a power density of 6.398kW/kg. Considering the sensitivity of different parameters to the objective function, the motor optimization is divided into two steps. Considering that the wind friction loss has a significant effect on the temperature rise of the rotor, the slot width b_0 and the slot height h_0 are optimized and the reduced wind friction loss is selected as one optimal object function in step 1. The relationship between them is shown in Fig.2. The stator tooth width b_1 , stator slot depth h_1 and PM thickness h_{PM} are optimized to maximize the power density in step 2. The optimization process of each step is as follows. Firstly, the output characteristics of the proposed machine under different design parameters are obtained as sample data through FEM/CFD. After that, a total of 50 sample data has been taken for analysis and an interpolation model has been established by Kriging interpolation. The interpolation model can be used to obtain the objective function value under different design parameters. Finally, the optimal values of the design parameters are obtained by using genetic algorithm. III. RESULTS AND DISCUSSION Through FEM analysis, the electromagnetic performance of the proposed machine is verified to be satisfactory. Further, the proposed machine has been optimized. As shown in Fig.3, the wind friction loss of the optimized machine is 57.28W, the power density is 6.865kW/kg. The main output characteristics of the proposed machine and the optimized machine are compared in TABLE II. The maximum relative error between the interpolation model and the CFD/FEM is less than 1.2%, which indicates that the interpolation model is accurate. Compared with the proposed machine, the wind friction loss of the optimized machine is reduced by 9.72%, and the power density is increased by 7.25%. Note that the efficiency of two machines is almost the same, while the efficiency of the optimized machine is 97.84%. Detailed characteristics and comparison results will be discussed in the future full paper.

[1] F. Zhang, G. Du, T. Wang, F. Wang, W. Cao, and J. L. Kirtley, "Electromagnetic Design and Loss Calculations of a 1.12-MW High-Speed Permanent-Magnet Motor for Compressor Applications," *IEEE Transactions on Energy Conversion*, vol. 31, pp. 132-140, Jan. 2016. [2] D. K. Hong, B. C. Woo, Y. H. Jeong, D. H. Koo, and C. W. Ahn, "Development of an ultra high speed permanent magnet synchronous motor," *International Journal of Precision Engineering & Manufacturing*, vol. 14, pp. 493-499, 2013. [3] D. Gonzalez, "Performance validation of a high-speed permanent-magnet motor for centrifugal compressors," in *2016 XXII International Conference on Electrical Machines (ICEM)*, 2016, pp. 545-549. [4] Z. Huang and J. Fang, "Multiphysics Design and Optimization of High-Speed Permanent-Magnet Electrical Machines for Air Blower Applications," *IEEE Transactions on Industrial Electronics*, vol. 63, pp. 2766-2774, 2016.

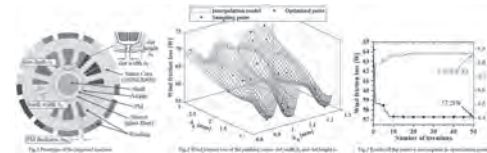


TABLE I. MAIN PARAMETERS OF THE MACHINE

Design Specifications		Main Dimensions (mm)	
Rated power	15kW	Stator inner/outer radius	16.5/15
Rated speed	120krpm	Rotor inner/outer radius	16.5/15
Rated voltage	300V	Air gap thickness	1.2
Phase number	3	Axial length	48
Efficiency	>96%	Slot/Slot number	3/42
Permanent magnet	NdFeB	PM thickness	3.3
Sleeve material	Glass Fiber	Slot thickness	1.2

TABLE II. MAIN OUTPUT PARAMETERS OF THE PROPOSED MACHINE AND THE OPTIMIZED MACHINE

Items	h_0/h_1 (mm)	b_0/b_1 (mm)	Wind friction loss (W)	Power density (kW/kg)	Efficiency (%)
Proposed machine	1.571	4.3/16.4/3.3	64.22	6.398	97.85
Optimized machine (interpolation model)	-0.031/0.005	5.3/16.56/2.7	57.28	6.865	97.84
Optimized machine (FEM/CFD)			57.98	6.864	97.84

BQ-08. A Novel High-Speed Dual-Stator Flux Switching Permanent Magnet Machine.

W. Yu¹, K. Liu¹, W. Hua¹, M. Hu¹, Z. Zhang¹ and J. Hu¹
 1. Southeast University, Nanjing, China

Abstract: This paper proposes a novel axial dual-stator flux-switching permanent magnet (FSPM) machine for high-speed (HS) applications. The machine adopts a fractional slot distributed winding, which has a higher winding factor, power and torque density. Firstly, the HSFSPM machine topology and operating principle are introduced. By using the principle of winding complementarity, the HSFSPM machine can counteract the even harmonics of a single stator and generate the standard sinusoidal waveform flux linkage. Besides, it can effectively reduce the cogging torque and torque ripple. Secondly, based on the three-dimensional (3D) finite element method (FEM), the no-load and load performance of the machine is obtained. Finally, a HSFSPM prototype is manufactured, and a test platform is built to test the no-load and load performance of the machine, which verified the correctness of the theoretical analysis.

I. Introduction High-speed (HS) machines are widely used in many civil and industrial applications, such as flywheel energy storage transportation electrification, air compressor, etc. The rotor permanent magnet (PM) machines are used in most applications. However, the PMs in the rotor are exposed to strong centrifugal forces particularly at high speed. They are easy to be damaged due to their vulnerability even if they are protected by a retaining sleeve or the iron core [1]. The stator PM machine has neither windings nor PMs on the rotor. It has a simple structure and is suitable for high-speed operation. The PMs and the armature winding are located in the stator, which makes the PMs easy to cool [2]. The HSFSPM machine is more promising and widely studied due to its higher torque density.

II. Topology and operation principle The topology of a three-phase HSFSPM machine with six stator-slots and four rotor-poles is shown in Fig. 1. There are two stators in the axial direction, named Stator_A and Stator_B. The magnetization directions of PMs in different stators are opposite. The two rotor poles differ from each other by 45° in mechanical angles. Six distributed armature winding coils are wound around 12 stator teeth. Fig. 2 shows the flux-linkage and back electromotive force (EMF) for phase winding. It can be seen that the flux linkage and back EMF generated in a single stator contain a large number of second harmonics. With the dual stator structure proposed in this paper, the axial complementarity of the windings can be used to generate a flux linkage and back EMF close to the sinusoidal waveform. The detailed motor design process and performance analysis of no-load and load conditions will be given in the full text. Fig. 1 Proposed dual-stator HSFSPM machine Topology Fig. 2 Flux-linkage and EMF for phase windings

III. Experimental verification To verify the HSFSPM machine operating principle, no-load and load performance, a HSFSPM machine is manufactured, and a prototype test platform is built as shown in Fig. 3(a). Figs. 3 (b), (c) and (d) show the waveform and harmonic content of the measured results compared with the predicted values. Fig. 3 The HSFSPM machine experimental platform and test results.

V. Conclusion In this paper, a novel axial dual-stator HSFSPM machine for high-speed (HS) applications is proposed. The operating principle, no-load and load performance of the machine is studied, and the correctness of the theoretical analysis is verified through experiments.

Reference [1]D. Gerada, A. Mebarki, N. L. Brown, C. Gerada, A. Cavagnino, and A. Boglietti, "High-Speed Electrical Machines: Technologies, Trends, and Developments," IEEE Trans. Ind. Electron., vol. 61, no. 6, pp. 2946–2959, Jun. 2014, doi: 10.1109/TIE.2013.2286777. [2]M. Liu, W. Sixel, and B. Sarlioglu, "Comparative Study of 6/4 FSPM and SPM Machine for High-Speed Applications," IEEE Transportation Electrification Conference and Expo (ITEC), Jun. 2019, pp. 1–7, doi: 10.1109/ITEC.2019.8790622.

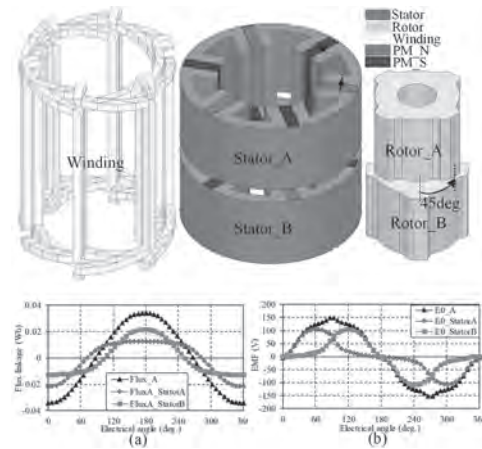


Fig. 1 Proposed dual-stator HSFSPM machine Topology and Flux-linkage and EMF for phase windings

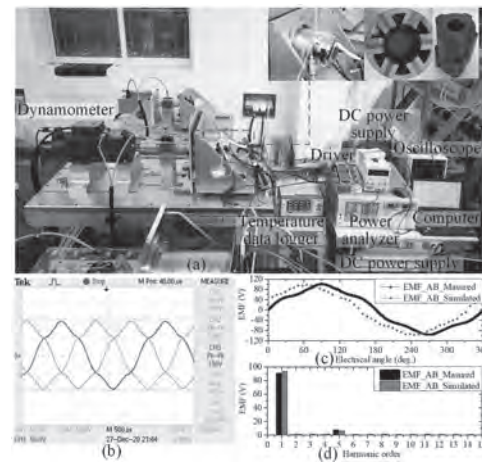


Fig. 3 The HSFSPM machine experimental platform and test results.

BQ-09. Design of High-Speed Permanent Magnet Synchronous Generator With Two Different Shaft Materials Considering Overhang Effect and Mechanical Characteristics.

J. Lee¹, T. Bang¹, K. Shin² and J. Choi¹

1. Chungnam National University, Daejeon, The Republic of Korea;

2. Chonnam National University, Yeosu, The Republic of Korea

Recently, permanent magnet machines have been widely used in various industrial fields, such as devices using permanent magnets having high coercive force and residual magnetic flux density due to the development of manufacturing technology. Machines rotating at high speed have the advantage of miniaturization and cost reduction through the application of a direct-drive system connected directly to the shaft of an electric device without using a gear system [1],[2]. In addition, it has the advantage of high device output and efficiency according to the power conversion device development. Owing to these advantages, they are used in various fields such as turbine generators, machine tools, and electric vehicle propulsion motors [3]. However, because the high-speed machine rotates at such high speed, the problem of damage and loss of the rotor caused by centrifugal force still exists. To prevent damage to the rotor owing to this problem, the scattering of permanent magnets is prevented through the sleeve, and the shaft uses materials with excellent mechanical rigidity [4]. However, depending on the shaft material, it has a significant influence on the electromagnetic and mechanical properties of high-speed devices. In this study, the design of high-speed permanent magnet synchronous generator with two different shaft materials considering overhang effect and mechanical characteristics was performed. As for the shaft material, two materials were used: STS420J2, which has lower stiffness(740Mpa) than Inconel 718, but is cheaper and has paramagnetic properties, and Inconel 718, which is expensive but has excellent stiffness(1100Mpa) characteristics and is non-magnetic. Fig. 1 (a) shows the result of leakage magnetic flux analysis according to each shaft material. In the case of Inconel 718 material, the leakage magnetic flux hardly occurs due to the non-magnetic material. However, although STS420J2 has paramagnetic properties, it is deformed into ferromagnetic properties through heat treatment during rotor assembly, resulting in a large leakage magnetic flux. The leakage inductance increases due to the effect of the leakage magnetic flux, and the increase in reactance becomes a factor of the voltage drop as shown in Fig. 1 (b). Therefore, the result was obtained that the output of the generator decreased due to the voltage drop. It is important for high-speed machines to accurately predict the natural frequency mode of the rotating body during high-speed rotation. The critical speed is a phenomenon where the vacuum space rapidly increases because of resonance. This phenomenon is a direct cause of rotor damage, stator collision, noise, and bearing damage. Therefore, it is essential to analyze the critical rotor speed of a high-speed machine. The rotating body can be divided into rigid body and bending modes according to its shape, and the design should be accomplished while avoiding the bending mode frequency as much as possible. Therefore, in this study, the critical speed characteristics of the rotor were analyzed to check the resonant frequency range when the rotor designed for each material rotates at the rated speed (36,000 rpm). Resonant generation of critical speed is generally analyzed through Campbell diagram. The Campbell diagram shows the natural frequency change related to rotational speed with the rotational axis speed as the horizontal axis and the structure frequency as the vertical axis. Fig. 1 (c) is the result of the STS420J2 material, and Fig. 1 (d) is the Campbell diagram characteristics of the Inconel718 material. As a result of the characteristic analysis, the critical speed mode closest to the rated speed is the 3rd mode, and deformation occurs at approximately 41 873 rpm for STS420J2 and 52 106 rpm for Inconel 718. It was confirmed that there was no problem in the rotor design because both materials had no intersection of critical speed and bending mode when rotating at the rated speed. It can be seen that the critical speed of the rotor is formed higher as the rigidity of the Inconel 718 material is stronger. The rotor was manufactured using two materials, STS420J2 and Inconel 718, as shown in Fig. 2(b), based on the shape used for critical speed analysis, as shown in Fig. 2(a). In general, performance verification of electric machines are performed using a dynamo system or a Back-to-Back system. However, the generator designed and manufactured in this study has high rated speed and output power. Therefore, as shown in Fig. 2(c), the back-to-back system

was configured using a high-speed motor, and the generator was evaluated through commercial inverter control. The design, analysis results, and measurements of the high-speed synchronous generators will be presented in more detail in the final paper.

[1] H. Qiu, B. Tang, W. Yu, S. Yuan, J. Wu, C. Yang, and G. Cui, "Analysis of the super high-speed permanent magnet generator under unbalanced load condition", IET Electr. Power Appl., vol. 11, no. 8, pp. 1492-1498, 2017. [2] Y. Zhang, S. McLoone, W. Cao, F. Qiu and C. Gerada, "Power Loss and Thermal Analysis of a MW High-Speed Permanent Magnet Synchronous Machine", IEEE Trans. Energy Convers., vol. 32, no. 4, pp. 1468-1478, 2017. [3] X. Jannot, J. C. Vannier, C. Marchand, M. Gabsi, J. S. Michel, and D. Sadarnac, "Multiphysics Modeling of a High-Speed Interior PermanentMagnet Synchronous Machine for a Multiobjective Optimal Design", IEEE Trans. Energy Convers., vol. 26, no. 2, pp. 457-467, Jun. 2011. [4] K. H. Shin, T. K. Bang, H. W. Cho, J. Y. Choi, "Design and Analysis of High-Speed Permanent Magnet Synchronous Generator With Rotor Structure Considering Electromechanical Characteristics", IEEE Trans. Appl. Supercond., vol. 30, no. 4, Art. no. 5204305, 2020.

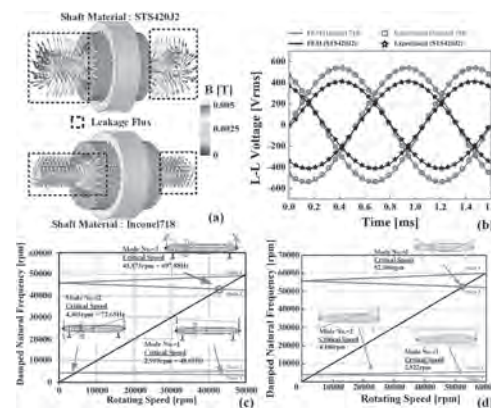


Fig. 1. (a) Leakage flux according to shaft material (b) Voltage characteristics at load according to shaft material (c) Campbell diagram: STS420J2 (d) Campbell diagram: Inconel 718.

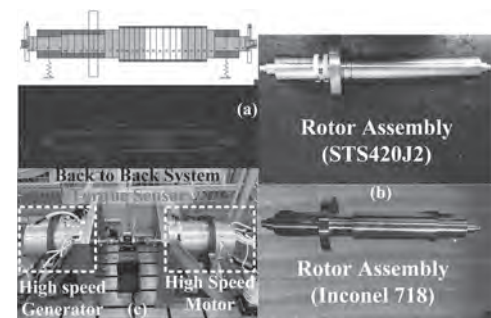


Fig. 2. (a) Rotor shape of designed (b) rotor assembly (c) Test bed of high-speed permanent magnet synchronous generator.

BQ-10. Characteristic Analysis and Experimental Study for Accurate Prediction of Electromagnetic Losses Considering Current Harmonics in High-Speed Permanent Magnet Synchronous Motors.

K. Shin¹, H. Park², T. Bang³, H. Cho³ and J. Choi³

1. Chonnam National University, Yeosu, The Republic of Korea;

2. Hyundai Mobis, Yong-in, The Republic of Korea; 3. Chungnam National University, Daejeon, The Republic of Korea

High-speed permanent magnet synchronous motors (PMSMs) are developed in direct-drive applications such as centrifugal compressors and vacuum pumps because of the advantages of compact size and high efficiency [1]. However, due to the small size, it has a high loss density and a limited heat dissipation surface, which causes difficulties in cooling [2]. Therefore, the accurate prediction of electromagnetic losses is very important in the design stage of high-speed PMSM. Particularly, in the case of a high-speed PMSM, it includes many harmonic components in the current applied to the machine due to pulse width modulation (PWM) inverter. Although the amplitude of harmonic components is small, they produce additional losses over and above the fundamental component. In this study, electromagnetic analysis considering PWM inverter and effective three-dimensional (3D) electromagnetic structure is proposed for predicting accurate electromagnetic losses of high-speed PMSM. Fig. 1 shows the 3D structure and side view of the high-speed PMSM and the evaluation system of the prototype. To accurately predict the applied current, it is necessary to derive the back EMF constant, resistance, and inductance using the 3D finite element method (FEM). Using the dynamic model based on the derived machine constants, it is possible to predict the applied PWM current similar to the experimental results as shown in Figs. 2(a) and (b). As shown in Fig.2(c), mechanical losses according to speed can be calculated by subtracting the core losses calculated from FEM from the measured no-load losses. Using the proposed effective 3D model, accurate electromagnetic losses such as AC and DC copper losses, core loss, and rotor loss can be predicted. Considering mechanical losses, the error between the proposed electromagnetic loss analysis and the experiment is within 3% according to the operating condition as shown in Fig. 2 (d). The analysis, discussions, and measurements of high-speed PMSM will be explained in more detail in the full paper.

[1] D. Gerada, A. Mebarki, N. L. Brown, C. Gerada, A. Cavagnino, and A. Boglietti, "High-speed electrical machines: Technologies, trends, and developments," IEEE Trans. Ind. Electron., vol. 61, no. 6, pp. 2946–2959, Jun. 2014. [2] D.-K. Hong, B.-C. Woo, and D.-H. Koo, "Ultra High Speed Motor Supported by Air Foil Bearings for Air Blower Cooling Fuel Cells," IEEE Trans. Magn., Vol. 48, No. 2, pp. 871–874, 2012.

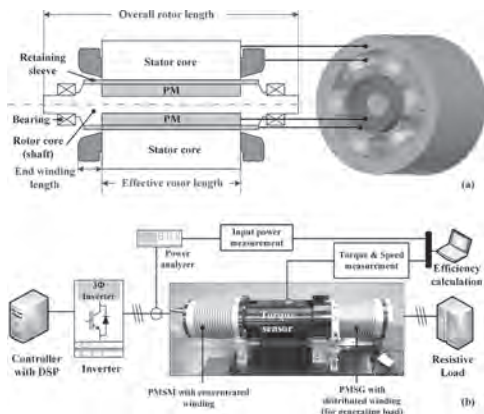


Fig. 1. (a) Structure of HPMSM with concentrated winding and (b) performance evaluation system.

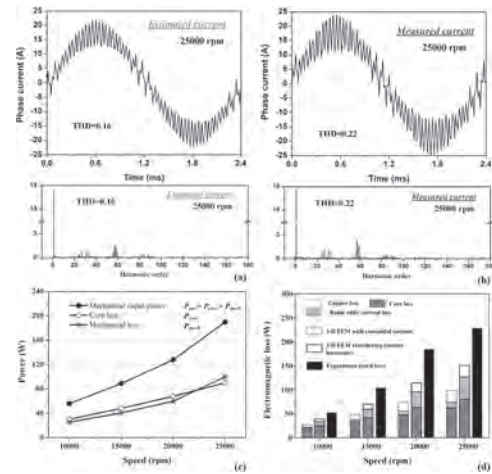


Fig. 2. Comparison with analysis and experimental results: (a) estimated, (b) measured phase current, (c) measured mechanical loss, and (d) electromagnetic losses.

BQ-11. Accurate Calculation of Iron Loss of High Temperature and High Speed Permanent Magnet Synchronous Generator Under the Conditions of SVPWM Modulation.

L. Zhuo^{1,2}, D. Yang², R. Sun², D. Shi², J. Zou¹ and Y. Xu¹

1. Electrical Engineering, Harbin Institute of Technology, Harbin, China;

2. National Engineering Research Center for Small and Special Precision Motors, Guizhou Aerospace Linquan Motor Co., Ltd, Guiyang, China

In this paper, a 40kW, 36000rpm high-speed permanent magnet synchronous generator(HSPMSG) with the ambient temperature of 350 Celsius is taken as an example to study the accurate calculation of iron loss. Considering the influence of high temperature and high frequency on the loss and electromagnetic performance of electromagnetic materials, the corresponding iron loss coefficient is fitted according to the variable coefficient iron loss separation model. Then, based on the field-circuit co-simulation method, the influence of switching frequencies and modulation ratios on the iron loss characteristics of the HSPMSG under the conditions of SVPWM modulation is studied. The calculation accuracy of the iron loss is improved. Finally, the effectiveness of the proposed method is verified by the experimental results, which provides a reference for the precise analysis of iron loss of the same type of HSPMSG. I. Introduction High-speed permanent magnet synchronous generators have drawn more and more attention due to the advantages of high-power density and high efficiency in the fields of aerospace applications. However, due to the poor heat dissipation conditions, it may lead to the excessive temperature of the PMs and increase the risk of irreversible demagnetization. A method combining 2-D nonlinear finite element analysis with 3-D frequency-domain harmonic analysis is proposed in [1], the motor loss under the influence of the harmonic field generated by the inverter is calculated. The iron loss analysis of HSPMSM considering the influence of multi-physical factors is proposed in [2], but the influence of harmonic current under inverter PWM modulation is not considered. The total loss value of a 100kW, 32000rpm HSPMSM is calculated by numerical analysis and verified by test results in [3], but it did not separate the calculation of each loss. The novelty of this paper is as follows. Considering the influence of temperature and frequency on the iron loss. The influence of switching frequencies and modulation ratios on the iron-loss characteristics of high-temperature HSPMSG under the conditions of SVPWM modulation is studied based on the method of field-circuit coupling co-simulation, which improves the calculation accuracy of the iron-loss of the HSPMSGs. II. Loss Performance Test The magnetization and loss characteristics of electromagnetic materials are not only related to temperature, but also related to frequency. Therefore, it is necessary to evaluate the temperature-frequency-magnetization characteristics and temperature-frequency-loss characteristics of electromagnetic materials. The loss characteristics of 1J22 soft magnetic alloy materials at the frequency of 1000Hz is shown as Fig.1. III. Variable Coefficient Iron Loss Separation Model In this paper, based on the orthogonal decomposition model, an improved variable coefficient orthogonal decomposition model is used to study the iron core loss, which takes into account the magnetization mode and the skin effect, and the variable coefficient orthogonal decomposition model suitable for calculating the iron loss of the HSPMSG is obtained. IV. Iron Loss Calculation and Analysis Based on the field-circuit co-simulation method, the influence of switching frequencies and modulation ratios on the iron loss characteristics of the HSPMSG under the conditions of SVPWM modulation is studied. The calculation accuracy of the iron loss is improved. V. Experimental Verification The HSPMSG test platform was built as shown in Fig.2. And the iron loss of the HSPMSG was tested. The test results are in good agreement with the calculated results, which verifies the accuracy of the previous calculation results. VI. Conclusion In this paper, the loss characteristics and electromagnetic performance of electromagnetic materials under high temperature and high frequency are tested, and the corresponding iron loss coefficients are fitted according to the variable coefficient iron loss separation model. Based on the field-circuit co-simulation method, the influence of switching frequencies and modulation ratios on the iron loss characteristics of the HSPMSG under the conditions of SVPWM modulation is studied, and the accuracy of the calculation method is verified by comparison with the test results, which is of great significance for the accurate analysis of the iron loss of the HSPMSGs.

[1] K. Yamazaki and S. Watari, "Loss analysis of permanent-magnet motor considering carrier harmonics of PWM inverter using combination of 2-D and 3-D finite-element method," *IEEE Trans Magn*, vol. 41, no. 5, pp. 1980-1983, May 2005. [2] G. Liu, M. Liu and Y. Zhang, "High-speed permanent magnet synchronous motor iron loss calculation method considering multi-physics factors," *IEEE Trans. Ind. Electron.*, vol. 67, no. 12, pp. 10109-10120, Dec. 2020. [3] Z. Huang, Fang, J and Liu, X, "Loss calculation and thermal analysis of rotors supported by active magnetic bearings for high-speed permanent-magnet electrical machines," *IEEE Trans. Ind. Electron.*, vol. 63, no. 4, pp. 2027-2035, Apr. 2016.

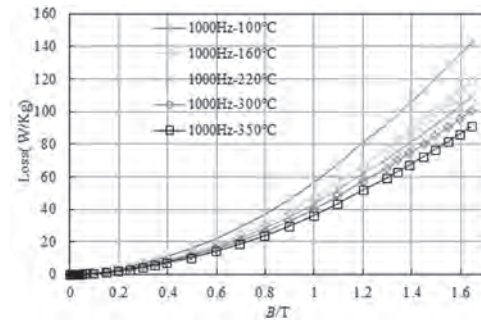


Fig.1. The loss characteristics of 1J22 at the frequency of 1000Hz

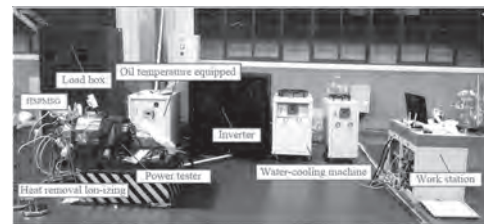


Fig.2. The HSPMSG test platform

BQ-12. Current Waveform for Vibration Analysis of High-Speed Switched Reluctance Motor With Amorphous Alloy Core.

F. Chai¹, Z. Li¹, L. Chen¹ and Y. Wu²

1. Harbin Institute of Technology, Harbin, China; 2. Midea Welling Motor Technology, Shanghai, China

I. Introduction At present, high-speed switched reluctance motors (SRM) have been widely used in different applications, such as electric vehicle, aircraft, turbine and compressor, due to low manufacturing cost, high reliability, robustness, possible operation at high temperature, and high rotational speed [1]. However, stator loss will reduce the reliability of high-speed motor, and low loss material has been attractive candidates in motor design. In addition, the acoustic noise of high-speed SRM is relatively higher than that of induction machines and permanent magnet synchronous machines (PMSMs). It has limited the widespread development of high-speed SRM, especially for noise-sensitive applications [2]. It is widely recognized that radial force is caused by motor excitation, and radial vibration is transmitted through the stator structure and emitted from motor surface [3]. Vibration and acoustic noise will be especially intensified when excitation or its harmonic frequency is close to any natural frequencies of the motor. Therefore, it is meaningful to analyze the natural frequency and mode shapes of high-speed SRM. In addition, the effect of different control strategies on current waveform is also very obvious, which will lead to the difference of radial force and vibration. Therefore, the current optimization has been attractive research for high-speed SRM. This paper focused on modal frequency calculation and vibration analysis of high-speed SRM with amorphous alloy core. Firstly, this paper compared different current waveforms and analyzed the effect of current waveforms on radial force. Radial force calculation method was improved to adapt to amorphous alloy material. Secondly, natural frequency of high-speed SRM was calculated with properties of amorphous alloy core considered. Modal shapes of stator system were analyzed and compared. Then, the modal frequency experiment was carried out to verify the calculation method. Finally, magnetostriction of amorphous alloy core was introduced to the vibration analysis of high-speed SRM. II. Radial force of high-speed SRM A. Theoretical analysis of radial force Considering the magnetic flux density and permeability of amorphous alloy core, this paper proposed the calculation method of radial force. In addition, the harmonic distribution of stator magnetomotive force of switched reluctance motor is related to phase current and control strategy. B. Effect of current waveforms on radial force Through theoretical model, radial force could be calculated. And radial force produced by different current waveforms were compared in this paper, the comparison result was shown in Fig. 1. For angle position control (APC), current chopper can increase the fundamental wave component and reduce the dc component. From the comparison of radial force density, dc component will produce more severe radial force. III. Natural frequency calculation and experiment A. Analytical model of amorphous alloy core Different motor components, such as stator core, housing, bearings and end plates, have great effect on modal frequency and dynamic performance at high speed. All of them are related to the reliability and output performance of high-speed SRM indirectly. Based on traditional natural frequency calculation method, the effect of axial mode on high-speed motor and the properties of amorphous alloy is considered in this paper. B. Experiment and verification With axial mode considered, the natural frequency was calculated and compared with the experimental result. Mode shapes and experiment platform were shown in Fig. 2. IV. Vibration analysis of high-speed SRM with amorphous alloy core The vibration characteristics of amorphous alloy core are different from those of silicon steel core. Amorphous alloy materials have high magnetostrictive coefficient and magnetostrictive strain is related to magnetic field distribution. Through theoretical model, the relationship between magnetostrictive stress and magnetic field in the core was analyzed, and the vibration performance of amorphous alloy core can be more accurately predicted. A 20kW high-speed SRM with amorphous alloy core was manufactured and vibration experiment has been carried out, see the Fig. 1. V. Conclusion In this paper, effect of current waveform on radial force and vibration was analyzed. Through improved natural frequency calculation method, natural frequency and mode shapes of amorphous alloy core were calculated more accurately with axial mode considered. The experimental results verify that

high-speed SRM with amorphous alloy core shows more severe vibration. From analysis of current harmonic distribution and radial force component, high harmonics of phase current will cause more severe radial force, which will produce high frequency vibration. By using the current chopper of the controller, certain harmonic could be effectively removed.

[1] J. Furqani, M. Kawa, K. Kiyota, "Current Waveform for Noise Reduction of a Switched Reluctance Motor Under Magnetically Saturated Condition," in IEEE Transactions on Industry Applications, vol. 54, pp. 213-222(2018). [2] X. Guo, R. Zhong, M. Zhang, "Fast Computation of Radial Vibration in Switched Reluctance Motors," in IEEE Transactions on Industrial Electronics, vol. 65, pp. 4588-4598(2018). [3] A. H. Isfahani and B. Fahimi, "Comparison of Mechanical Vibration Between a Double-Stator Switched Reluctance Machine and a Conventional Switched Reluctance Machine," in IEEE Transactions on Magnetics, vol. 50, no. 2, pp. 293-296, Feb. 2014.

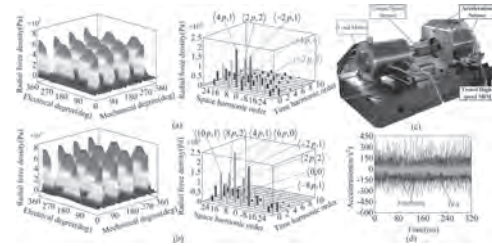


Fig. 1. Vibration analysis and experiment verification, (a) radial force analysis with ideal square-wave current, (b) radial force analysis with angle position control (APC), (c) Vibration experiment platform of high-speed SRM, (d) Experimental results of stator surface.

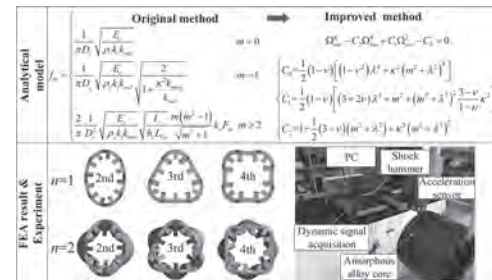


Fig. 2. Analytical model, corresponding FEA result and Experiment platform.

BQ-13. Research of a Hybrid Excitation Synchronous Machine Integrated With Magnetic Bearings.

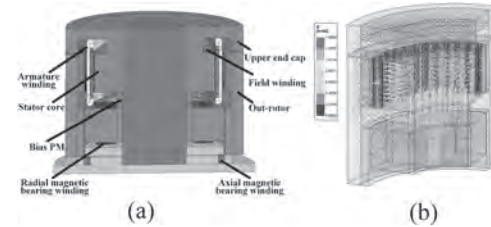
D. Yu¹, C. Ye¹, C. Deng¹ and Y. Du¹

1. Huazhong University of Science and Technology, Wuhan, China

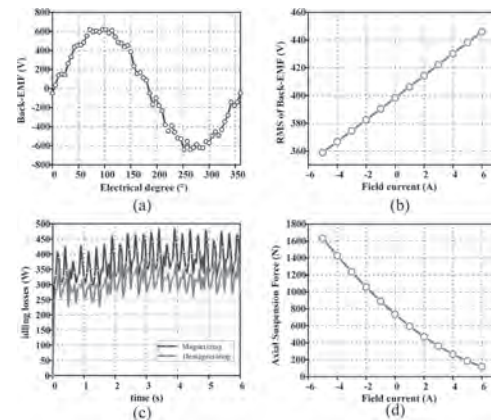
Abstract- As the core component of the flywheel energy storage system (FESS), the flywheel energy storage motor requires low self-loss, high power density, and a wide working speed range. This paper proposes a hybrid excitation synchronous machine integrated with magnetic bearing (HESM-IMB), which is suitable for FESS. First, the structure and operation principle of the proposed HESM-IMB are explained. Afterward, the influence of field current on the electromagnetic performance of HESM-IMB is researched by the magnetic equivalent circuit (MEC). Then, the performance of HESM-IMB is present by finite element analysis (FEA). The results indicate that HESM-IMB has the advantages of adjustable air-gap flux density, high integration, and low idling loss. I. Introduction Permanent magnet (PM) synchronous machines are widely used in FESS. However, the PM machine suffers from large idling losses and poor field weakening ability. Besides, the FESS usually requires at least one axial magnetic bearing and two radial magnetic bearings, which causes an influence on rotor dynamics. In order to solve the above problems, this paper proposes a hybrid excitation synchronous machine integrated with magnetic bearing (HESM-IMB), with the advantage of adjustable air-gap flux density, high integration, and low idling loss. II. Structure and operation principle The structure of HESM-IMB is shown in Fig. 1(a). The machine adopts a hybrid excitation structure. The upper section of the out-rotor is a structure in which iron core poles and permanent magnet poles are alternately distributed, and the lower section is a bearing rotor, as a part of radial magnetic bearing. Field winding, bias permanent magnet, and rotor permanent magnet provide working magnetic flux for the machine at the same time. Fig. 1(b) shows the magnetizing flux path of HESM-IMB. Since the magnetic resistance of the permanent magnet poles is much greater than that of the iron cores, the magnetic flux on the surface of the permanent magnet poles is almost unchanged. On the contrary, the magnetic permeability of the iron core pole is large, by adjusting the magnitude and direction of the field current, the air-gap flux density distribution on the surface of the iron core pole can be changed to meet the needs of the system under different working conditions flexibly. Similarly, the axial air gap magnetic flux on the rotor will also change with field current adjustment, so the axial force on the rotor will change greatly. Thus, an axial magnetic bearing winding at the bottom needs to be used to balance the axial force, keeping the total axial force on the rotor is around zero. As for radial magnetic bearing, the magnetic resistance of the bias permanent magnet is very large, so the flux generated by the permanent magnet poles and the field winding will hardly pass through the core of the radial magnetic bearing, the bias magnetic flux on the bearing rotor is almost unchanged, which provides convenience for control of rotor radial force. III. Simulation and analysis The back EMF waveform of HESM-IMB is shown in Fig. 2(a). In Fig. 2(b), as the field current increases, the RMS of the back EMF increases linearly, which proves that HESM-IMB has a high performance of adjusting air-gap magnetic density. Fig. 2(c) shows the idling loss in the state of field weakening and field increasing. It can be seen that field weakening can reduce the loss of the machine effectively and improve the efficiency of the system. Fig. 2(d) represents the change curve of the axial force on the rotor with the field current when the bottom axial magnetic bearing winding is not energized, which is consistent with the previous analysis. IV. Conclusion The HESM-IMB proposed in this paper can adjust the air-gap flux density flexibly, which increases power during charging and discharging, and reduces idling loss during energy storage standby. Besides, HESM-IMB integrates a radial magnetic bearing and an axial magnetic bearing in the magnetic circuit, with the advantages of high integration.

[1] J. A. Tapia, F. Leonardi and T. A. Lipo, "Consequent-pole permanent-magnet machine with extended field-weakening capability," in IEEE Transactions on Industry Applications, vol. 39, no. 6, pp. 1704-1709, Nov.-Dec. 2003. [2] T. D. Nguyen, K. Tseng, S. Zhang, "A Novel Axial Flux Permanent-Magnet Machine for Flywheel Energy Storage System: Design and Analysis," in IEEE Transactions on Industrial Electronics, vol. 58, no. 9, pp. 3784-3794, Sept. 2011. [3] E. Severson, R. Nilssen, T. Undeland,

"Magnetic Equivalent Circuit Modeling of the AC Homopolar Machine for Flywheel Energy Storage," in IEEE Transactions on Energy Conversion, vol. 30, no. 4, pp. 1670-1678, Dec. 2015.



(a) Topology. (b) Magnetizing flux paths.



(a) The back-EMF waveform. (b) The RMS of back-EMF versus field current curve. (c) Comparison of idling loss before and after field weakening. (d) The axial force on rotor versus field current curve.

BQ-14. Structure and Control of Modular Frequency-Multiplying Inverter With Low-Carrier-Ratio for High Speed Machine.

J. Yin¹, W. Kong¹, J. Wu¹, Q. Zhang¹, J. Zhang¹ and G. Han²
 1. Zhengzhou University of Light Industry, Zhengzhou, China;
 2. Xidian University, Xian, China

I. Introduction In recent years, with the gradual development of wind power technology from land to sea, the unit capacity of its generating units has developed from low voltage (690V) and medium power (2-3MW) to medium voltage (3.3kV) and high power (5-10MW). For the medium-voltage high-power wind power converters with power level of 5-10MW, the switching frequency of the equipment is usually required to be within 1kHz, which brings many difficulties to the control of the converter [1]. In particular, for semi-direct drive wind power system, the operating frequency of the generator is relatively high, while the switching frequency of the converter is relatively low, which results in the problem of low sampling rate. This further increases the control difficulty of the medium voltage high power converter [2-3]. In addition, in the permanent magnet semi-direct drive wind power generation system, the operating frequency of the generator is usually greater than 100Hz, so the sampling rate is low. It also deteriorates the dynamic and steady-state performance of the traditional model predictive control with low switching frequency, and affects its stability. In order to realize the low switching frequency control of medium-voltage high-power permanent magnet synchronous generator with low sampling ratio, this paper proposes a structure and a control method of a modular frequency-multiplying inverter with low-carrier-ratio. II. System Topology and Principle The modular frequency-multiplying inverter adopts a nested H-Bridge structure. For example, a modular frequency-tripling inverter includes an inner layer, a middle layer and an outer layer. A_1 - A_4 constitute the outer layer module, B_1 - B_4 constitute the middle layer module, and C_1 - C_4 constitute the inner layer module. The outer module uses independent IGBTs, and the middle and inner modules employ bidirectional switches composed of two anti-parallel IGBTs. The two anti-parallel IGBTs share a gate switch signal. The input voltage of the inverter is V_{in} . The output of the upper module is used as the input of the next module, and so on. The final output voltage of the inverter is V_o . The specific structure is shown in Fig. 1(a). A control signal is applied to each IGBT, where the switch at the diagonal position in the H bridge is turned on and off at the same time, the upper and lower switches on the same arm are turned on complementary, and the phase shift between each layer of modules is 120° electric angle. It can be seen from Fig. 1(b) that the frequency of the inner output voltage V_o of the inverter is three times the frequency of the outer output voltage V_1 . That is, a triple frequency output voltage is obtained at the fundamental switching frequency. III. Simulation According to Fig. 1(a), a simulation model is established, and the IGBT is controlled by SPWM. The input voltage V_{in} is 20V, and the fundamental frequency is 50Hz. Assuming that the carrier ratio of the outer switching tube is M, since the switching frequency of the three layer modules is the same, and the output frequency of the inner layer is three times the fundamental wave, the carrier ratio of the entire inverter is reduced to one third of the outer layer, i.e. $M/3$. The simulation results verify the proposed method. Under the condition that the fundamental frequency is 50Hz and the switching frequency of tube is not increased, an output voltage frequency of 150Hz is achieved. Analyzing the output voltage through FFT, the result shows that the third harmonic component is the highest, which is consistent with the desired result. The output voltage FFT analysis result is shown as in Fig. 2. IV. Discussion and Conclusion The structure and control method of the low-carrier-ratio frequency-multiplying inverter proposed in this paper can output voltages of several times the fundamental frequency without increasing the switching frequency. Simulations and experiments verify the method. The inverter system is simple in structure and easy to implement, and can solve the low carrier ratio control of medium-voltage high-power permanent magnet synchronous generators at low sampling rates. The inverter system can also be expanded to a more layered structure to achieve higher frequency output. The detailed analysis process and experimental results will be provided in the full manuscript.

IEEE Trans. on Magnetics., Vol. 56, p. 1-5 (2020). [3] W. Xu, R.D. Lorenz, IEEE Trans. on Industry Applications., Vol. 51, p. 3932-3942 (2015).

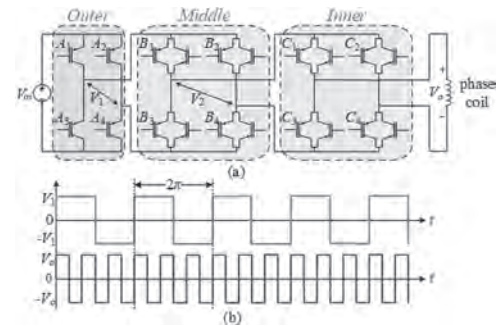


Fig. 1 (a) Low carrier ratio modular frequency-multiplying inverter structure; (b) Output of V_1 and V_o

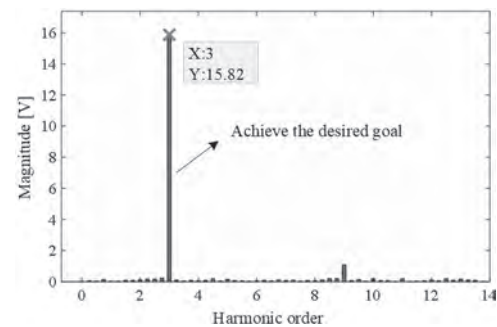


Fig. 2 Spectrum of load voltage

[1] H. Bizhani, R. Noroozian and S. M. Muyeen, IEEE Trans. on Power Electronics., Vol. 34, p. 3407-3417 (2019). [2] X. Zhao, S. Niu and W. Fu,

BQ-15. A Study on High Reliability Sensorless Control of High Speed Permanent Magnet Synchronous Motor Using Line Drive Method.

S. Oh¹, H. Kim¹, Y. Park¹, C. Kim², C. Jin³ and J. Lee¹

1. Electrical Engineering, Hanyang University, Seongdong-gu, The Republic of Korea; 2. Electrical Engineering, Vision University of Jeonju, Jeonju, The Republic of Korea; 3. Electrical Engineering, Wonkwang University, Iksan, The Republic of Korea

1) Introduction As the use of high-efficiency and high-performance motors as motors for drones and home appliances increases, the use of PMSM (Permanent Magnet Synchronous Motor) type motors is increasing. To this end, many studies are being conducted on speed control in high-speed areas, and studies on sensorless control are also actively being conducted to reduce space constraints and weight and cost. [1][2] However, as the high-speed range increases, the position estimation signal of the sensor becomes unstable due to harmonics and inductance components, and it is greatly affected when small noise and disturbance occur. These errors degrade the performance of the high-speed control algorithm and the reliability of the motor. In this paper, to solve the sensorless error problem from low speed to high speed range, we use the signal output method of line drive method. The line drive output method generates signals that are complementary to each other, and through calculation, it can have strong characteristics against electrical noise and disturbance. Based on this, sensorless control in the high-speed region with high reliability was performed through detection and correction of signal distortion and disturbance in the signal generated at high speed due to inductance and harmonics. The PMSM simulation was configured to compare before and after application of the algorithm and verified its validity. 2) Methodology The sensorless control algorithm of the PMSM method generally includes current-based sensorless control and back EMF-based sensorless control. The current model-based sensorless control is used to estimate the speed and initial position using information of voltage and current, and the back EMF-based sensorless control estimates the position information through the estimated value of the back EMF. For current-based sensorless control, a lambda gamma-axis voltage equation that estimates the position from the existing dq-axis voltage equation is required, and the magnitude of the current is converted into an equation for the change of inductance to detect the position of the rotor. However, as the high-speed region increases, the delay of the current due to the inductance component and the positional error due to harmonics increase, so in the high-speed region, a sensorless control method using a back EMF model is used. Back EMF sensorless control includes a back EMF term as shown in Equation (1), and it is possible to establish voltage equations for lambda and gamma that estimate the position as a difference by θ . Through this, the back EMF equation can be expressed as Equation (2). Using this, you can estimate the position for θ as in Equation (3). $V\gamma = (R + pLd)i\gamma - (\omega rLq)i\delta + e\gamma$, $V\delta = (\omega rLd)i\gamma + (R + pLq)i\delta + e\delta$ (1) $\hat{e}\gamma = E\cos(-\sin\Delta\theta)$, $\hat{e}\delta = E\cos(-\cos\Delta\theta)$ (2) $\Delta\theta = \tan^{-1}(\hat{e}\gamma/\hat{e}\delta)$ (3) However, when the motor reaches the high speed range, the distortion of the waveform becomes severe and it is more affected by disturbances such as vibration. Through this, the accuracy of sensorless control based on back EMF is deteriorated. In order to improve this, there is a harmonic injection method or an extended back EMF method, but the calculation is complicated and the system configuration cost increases due to an increase in the amount of operation. To improve this, we propose a signal correction method of the line drive method applied to the encoder. The basic concept of the line drive method is that the sum of the two signals must always be 1 by calculating the normal signal and the reverse signal at the same time. Therefore, even if an incorrect signal comes into one signal due to interference or disturbance, if a value other than 1 is output through the calculation of the normal component and the reverse component, the instantaneous count is not performed. By applying the method, the A-phase normal signal is processed using the existing signal for the A, B, and C-phase signals, and the reverse-phase signal is made based on the result obtained through the back EMF estimation method. Therefore, even if the A-phase normal signal is changed through disturbance and distortion of the signal, an error of the signal can be detected through comparison of the reverse-phase signal. Fig. 1 briefly shows the disturbed A-phase normal component and reverse phase component, and the resulting error values. As shown in Fig. 1, the position and magnitude of the error value can be detected by calculating the normal and inverse

components. Based on this, the accuracy of the sensorless control algorithm can be improved by applying the compensation signal generated with the magnitude of the phase opposite to the error value to the signal generated by the disturbance. 3) Conclusion In order to verify the sensorless control algorithm in the high-speed region using the line drive method, the simulation was conducted after artificially adding noise using Matlab Simulink. In the case of using only the existing sensorless method, control was broken by noise and it was not able to operate properly. On the other hand, when the compensation of the line drive method was performed, the initial error was gradually compensated as shown in Fig 2, and it was confirmed that the motor operates stably after 0.4 seconds. Through this, we verified the validity of the algorithm proposed in this paper.

[1] X. Song, J. Fang, B. Han, and S. Zheng, "Adaptive compensation method for high-speed surface PMSM sensorless drives of EMF-based position estimation error," IEEE Trans. Power Electron., Vol. 31, No. 2, pp. 1438-1449, Feb. 2016. [2] G. Wang, H. Zhan, G. Zhang, X. Gui, and D. Xu, "Adaptive compensation method of position estimation harmonic error for emf-based observer in sensorless IPMSM drives," IEEE Trans. Power Electron., Vol. 29, No. 6, pp. 3055-3064, Jun. 2014.

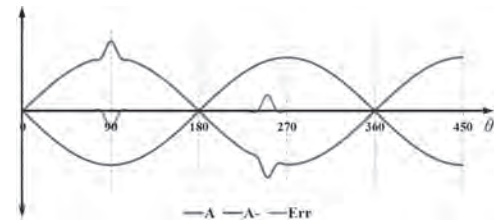


Fig. 1 A, A-, Err graph using line drive method

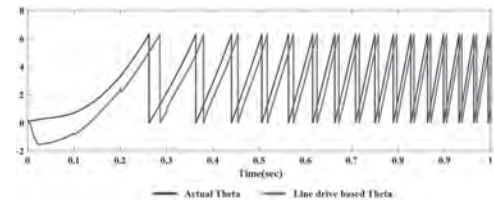


Fig. 2 Actual angle and angle of line drive method

BQ-16. Investigation of a Novel Homopolar Inductor Machine With Flux Memory for the Flywheel Energy Storage System.

J. Yang¹, S. Huang¹ and C. Ye²

1. Hunan University, Changsha, China; 2. Huazhong University of Science and Technology, Wuhan, China

Abstract—Electrically excited homopolar inductor machine (EE-HIM) has good application in the field of flywheel energy storage system (FESS) due to its merits of simple structure, brushless exciting and little idling electromagnetic losses. However, the copper loss of field winding in the charge/discharge operation state would decrease the efficiency of energy conversion. To improve the efficiency of charge/discharge and inherit the merit of little idling electromagnetic losses, a novel HIM with flux memory (HIM-FM) is proposed. Firstly, the structure and operation principle of HIM-FM are illustrated. Then, the key structure parameters, including the rotor tooth width and slots depth are optimized. Finally, the electromagnetic performance, including the air-gap flux density, flux linkage, back-EMF and output torque and losses of HIM-FM are analyzed by finite element method. The result indicates that the proposed HIM-FM has the merit of little idling electromagnetic losses and no copper loss, which can be help to improve the energy conversion efficiency. I. Introduction An electrical machine is the key component of flywheel energy storage system (FESS), whose performance would directly affect the ration of energy conversion of FESS. Among the various electrical machine topologies, an electrically excited homopolar inductor machine (EE-HIM) has attracted much attention in the FESS due to its merits of robust rotor structure, brushless exciting. Moreover, the idling electromagnetic loss of EE-HIM can be eliminated by cutting off the field current [1]. However, the copper loss of field winding would decrease the charge/discharge efficiency of EE-HIM. Addressing this issue, a NdFeB permanent magnet (PM) HIM is proposed in [2]. While the idling loss would be caused due to the no-load high frequency magnetic field generated by PM. To improve the efficiency of charge/discharge and inherit the merit of little idling electromagnetic losses, a novel HIM with flux memory (HIM-FM) is proposed in this paper. II.Topology and operation principle The topology of proposed HIM-FM is shown in Fig. 1. As shown, the rotor is made of solid steel and has teeth on its both ends. The left and right teeth axes are differed by 180° electrical degree. Two stator cores are made of laminated steels and sandwich a magnetizing coil, which is used to demagnetize and magnetize the circular Al-Ni-Co permeant magnet (PM). Two segment shells are placed on both sides of Al-Ni-Co PM and provide the flux path for fluxes generated by the PM or the magnetizing coil. The PM would be magnetized when the HIM-FM works at charge/discharge state and demagnetized when the HIM-FM works at idling state. III.Performance evaluation Fig. 2(a) shows the air-gap flux density distribution of HIM-FM when the Al-Ni-Co PM has different remanence. It can be found that the maximum and minimum air-gap flux density is 0.848 and 0.021T. Fig. 2(b) gives the phase back electromotive force (EMF) of HIM-FM under different demagnetization. The amplitude of back-EMF can be regulated by 97.2% compared with the zero demagnetization. The stator core loss of HIM-FM are respectively 13.3 W and 0.0284W and the rotor eddy current loss of HIM-FM are respectively 0.85 W and 0.00197W under zero and severe demagnetization. Compared with the zero demagnetization, the stator core loss and eddy current loss can be reduced by 99.91% and 99.77%, which indicates that the proposed HIM-FM can be greatly reduced the idling electromagnetic loss. IV.Conclusion This paper proposed a novel HIM with flux memory (HIM-FM) for the application of flywheel energy storage system. The performance of HIM-FM is evaluated, which indicates that the proposed HIM-FM helps to reduce the idling electromagnetic loss and improve the efficiency of charge/discharge. The other electromagnetic performance of HIM-FM, such as the flux linkage, output torque and losses, would be presented in full paper.

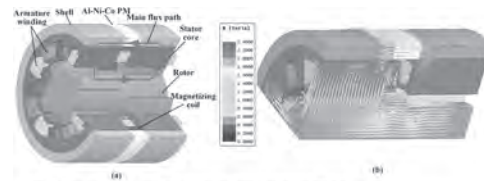


Fig. 1. (a) Structure of the proposed HIM-FM. (b) Flux density distribution of HIM-FM.

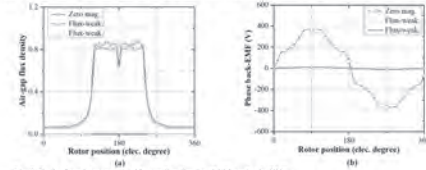


Fig. 2. No-load performance. (a) Air-gap flux density. (b) Phase back-EMF.

[1] P. Tsao, M. Senesky, and S. Sanders, “An integrated flywheel energy storage system with homopolar inductor motor/generator and high-frequency drive,” *IEEE Trans. Ind. Appl.*, vol. 39, no. 6, pp. 1710–1725, Nov./Dec.2003. [2] Z. Q. Liu, K. Wang and F. Li, “Design and Analysis of Permanent Magnet Homopolar Machine for Flywheel Energy Storage System,” *IEEE Trans. on Magn.*, vol. 55, no. 7, pp. 1-6, Jul. 2019.

Session BR
SURFACE MOUNTED AND INTERIOR MOUNTED PERMANENT MAGNET ELECTRICAL MACHINES
(Poster Session)

Smail Mezani, Chair
Université de Lorraine, Vandoeuvre lès Nancy CEDEX, France

BR-01. Novel Dual-Stator Single Rotor Consequent Pole PM Machine.

J. Yang¹, S. Huang¹ and C. Ye²

1. Hunan University, Changsha, China; 2. Huazhong University of Science and Technology, Wuhan, China

Abstract—A novel dual-stator single-rotor consequent pole permanent magnet (PM) machine (DSCP-PMM) is proposed in this paper. Firstly, the special structure and operation principle of the DSCP-PMM are presented. Then, the key structure parameters of DSCP-PMM are optimized. Finally, the electromagnetic performance indexes including the air-gap flux density, back-EMF, output torque and losses of the proposed machine are evaluated. It indicates that the proposed DSCP-PMM2 has higher torque density and lower torque ripple. *Index Terms*—Dual-stator single-rotor, consequent pole PM machine, torque density and torque ripple. I. Introduction Consequent pole permanent magnet (PM) machines (CP-PMMs) have attracted much attention due to its high efficient utilization ratio of PM materials and low cost [1]. While the power density of CP-PMM would be lower than that of the conventional surface-mounted PM (SPM) machine. Meanwhile, the torque ripple would be deteriorated by the even-order harmonic components of phase back electromotive force (back-EMF) [2]. Addressing those issues, a novel dual-stator single-rotor CP-PMM (DSCP-PMM) is proposed and investigated in this paper. II. Structure and Operation Principle To improve the power density of CP-PMM, a dual-stator single-rotor consequent pole PM machine (DSCP-PMM) with N-iron-N-iron poles is proposed, as shown in Fig. 1(a), which is defined as DSCP-PMM1. To reduce the torque ripple, the rotor structure of DSCP-PMM is further improved, as shown in Fig. 1(b) and defined as DSCP-PMM2. Its rotor consists of two layers, one layer is N-iron-N-iron, and the other is iron-S-iron-S. The armature windings on the inner and outer stator of DSCP-PMM2 are connected to counteract the even-order harmonic component of the phase back-EMF. III. Performance Comparison The back-EMF waveforms of DSCP-PMM1 and DSCP-PMM2 are shown in Fig. 2(a). It can be found that the waveform of DSCP-PMM1 is different with that of the DSCP-PMM2 due to the even-order harmonic components of air-gap flux density in the DSCP-PMM1. The harmonic components of back-EMFs for both machines are given in Fig. 2(b). The back-EMF of DSCP-PMM1 contains even-order harmonic components, while the DSCP-PMM2 only consists of odd-order harmonic components. Fig. 3 shows the output torques of both machines. The average torques of DSCP-PMM1 and DSCP-PMM2 are 3.65 Nm and 3.81Nm, and the torque ripples of both machines are 79.6% and 21.8%, respectively. Thus, higher torque density and lower torque ripple could be obtained by the DSCP-PMM2. More analysis results would be presented in the full paper due to the limitation of space. IV. Conclusion A novel dual-stator single-rotor consequent pole permanent magnetic machine (DSCP-PMMs) is proposed in this paper. Its electromagnetic performance indexes are investigated. Relevant results indicate that the proposed DSCP-PMM2 has higher torque density and lower torque ripple.

[1] S. U. Chung, H. J. Lee, B. C. Woo, J. W. Kim, J. Y. Lee, S. R. Moon and S. M. Hwang, "A feasibility study on a new doubly salient permanent magnet linear synchronous machine," *IEEE Trans. Magn.*, vol. 46, no. 6, pp. 1572–1575, Jun. 2010. [2] J. Li, K. Wang, F. Li, S. S. Zhu and C. Liu, "Elimination of Even-order-Order Harmonics and Unipolar Leakage Flux in Consequent-Pole PM Machines by Employing N-S-Iron-S-N-Iron Rotor," *IEEE Trans. Ind. Electron.*, vol. 66, no. 3, pp. 1736-1747, Mar. 2019.

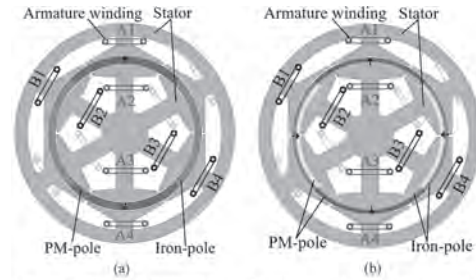


Fig. 1. Topologies of 6-slot/4-pole DSCP-PMM with different rotors. (a) DSCP-PMM1. (b) DSCP-PMM2.

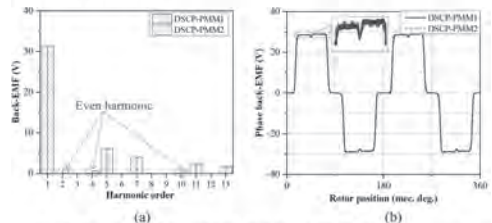


Fig. 2. Phase back-EMFs of DSCP-PMM1 and DSCP-PMM2. (a) Waveform. (b) Harmonic components.

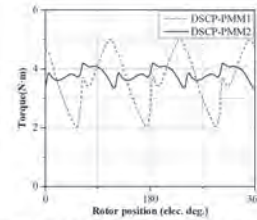


Fig. 3. Output torques of DSCP-PMM1 and DSCP-PMM2.

BR-02. Comparative Studies of Winding Short-Circuit Currents of Six-Phase PMSMs With Different Armature Magnetomotive Force Distributions.

L. Cheng¹, Y. Sui¹, P. Zheng¹, Z. Yin¹ and S. Yang¹
 1. Harbin Institute of Technology, Harbin, China

I Introduction Owing to high efficiency, high power density and inherently high fault-tolerant capacity, multiphase permanent magnet synchronous machines (PMSMs) equipped with the fractional-slot concentrated windings (FSCWs) have been drawing much attention [1]. Unfortunately, they are still limited by the excessive armature magnetomotive force (MMF) harmonics which will produce high eddy current loss in the PMs. To improve this situation, some new stator and winding arrangements, which can reduce the content of armature MMF harmonics, are proposed. But, it should be noted that the amplitude of the winding short-circuit current of these new topologies will increase due to the reduction of the harmonic leakage inductance. In this paper, the winding short-circuit faults of three six-phase PMSMs with different stator configurations whose contents of armature MMF harmonics are different are compared.

II Six-Phase PMSMs with Different Armature MMF Distributions The well-known six-phase 12-slot/14-pole PMSM with traditional single-layer FSCW is shown in Fig. 1(a). The MMF distribution produced by the traditional single-layer FSCW contains a large content of harmonics as shown in Fig. 1(d). The two harmonics of order $\nu=1$ and $\nu=5$ are the main components, which are both the main contributors to PM eddy loss and harmonic leakage inductance. To improve the quality of armature MMF distribution produced by the traditional single-layer FSCW, two low armature MMF harmonic topologies are proposed, as shown in Fig. 1 (b) and (c). By employing modular stator as shown in Fig. 1(b), the amplitude of the harmonic of order $\nu=1$ can be significantly reduced. By using the concept of stator shifting [5], a double-layer 2-pitch 24-slot/14-pole six-phase PMSM can be obtained, as shown in Fig. 1(c). It can be seen that the main harmonic components, i.e. harmonics of order $\nu=1$ and $\nu=5$, are significantly reduced in the 24-slot/14-pole six-phase PMSM. In this way, three six-phase PMSMs with different contents of armature MMF harmonics are obtained for the comparison studies.

III Winding Short-Circuit Currents and Demagnetization Analyses The winding short current will contain a transient component and a steady component when the winding short current occurs in a PM machine. In order to compare the surface-mounted PM demagnetization withstand ability of the three six-phase PMSM, the peak negative d-axis current during the whole short-circuit fault should be firstly obtained. The transit short current trajectories are shown in Fig. 2. It can be found that for the three six-phase PMSMs, the peak d-axis components of the winding short currents are -29.8 A, -39.5 A and -74.8 A, respectively. The amplitudes of the peak d-axis currents are increase with the decrease of the content of the armature MMF harmonics. A high winding short-circuit current will destroy the balance thermal distribution, which is the main drawback of the low armature MMF harmonic designs. Fortunately, owing to more even armature MMF distributions, even with higher negative d-axis current, the minimum flux densities of the PMs of the low armature MMF harmonics designs will be lower than the traditional one, as shown in Fig. 3.

[1] F. Barrero and M. J. Duran, "Recent advances in the design, modeling, and control of multiphase machines—Part I," *IEEE Trans. Ind. Electron.*, vol. 63, no. 1, pp. 449–458, Jan. 2016. [2] P. B. Reddy, K.-K. Huh, and A. M. El-Refaiie, "Generalized approach of stator shifting in interior permanent-magnet machines equipped with fractional-slot concentrated windings," *IEEE Trans. Ind. Electron.*, vol. 61, no. 9, pp. 5035–5046, Sep. 2014.

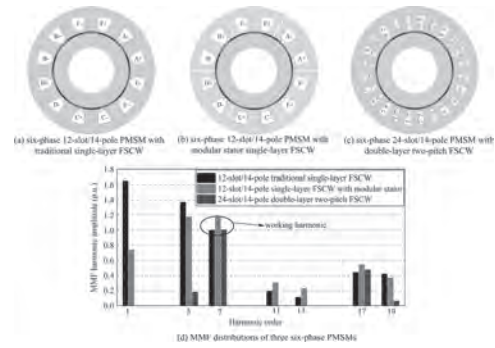


Fig. 1 Three six-phase PMSMs and MMF distributions

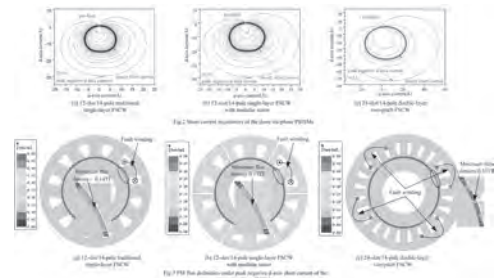


Fig. 2 Peak negative d-axis current trajectories of the three six-phase PMSMs

BR-03. Cogging Torque Dynamic Reduction Based on Regional Magnetic Compensation.

J. Gao¹, Z. Xiang¹, S. Huang¹ and L. Dai¹
 1. Hunan University, Changsha, China

Abstract—In order to reduce the cogging torque of the permanent magnet (PM) machine more effectively, a novel conception of the regional magnetic compensation (RMC) is introduced. An effective approach from the perspective of dynamic control for cogging torque reduction based on RMC is then proposed, by which the cogging torque could be reduced. **Index Terms**—Cogging torque, permanent magnet machines, dynamic reduction method, regional magnetic compensation. **I. Introduction** The cogging torque is an significant issue of the PM machines, which is an inherent shortcoming of PM machines. It leads to mechanical vibration, noise, and deteriorate the performances of the PM machines [1]. A wide variety of design methods for minimizing the cogging torque of PM machines have been comprehensively studied [1-3]. The existing cogging torque reduction methods can be mainly divided into two types: stator design and rotor design techniques. Undoubtedly, these methods can weaken the cogging torque but may result in the degradation of other machine performances, such as the unnecessary harmonics introduction, cost increase, and efficiency reduction, etc. On the other hand, it is impossible to weaken the cogging torque of a PM machine that has already been manufactured. Therefore, weakening the cogging torque from the perspective of dynamic control is worth considering, but few scholars have carried out related research on this. In this paper, a novel cogging torque reduction method based on regional magnetic compensation (RMC) has been proposed. The imbalance property of the magnetic field between adjacent stator teeth has been investigated and the compensation strategy of the regional magnetic field has been researched. The case studies of interior and surface-mounted PM machines show that the proposed method could help to dynamic minimize the cogging torque. **II. Finite Element Analysis Of Cogging Torque** Cogging torque is caused by the construction of the magnetic circuit of the machine, which is the interaction between the rotor magnetic flux and variable permeance of the air gap due to the geometry of stator slots [4], and it also exists when the machine is not energized. By making accurate analysis and calculation of the cogging torque, the basis for its compensation of the PM machines is created. The net cogging torque at any rotor position, which produced by a surface/interior PM machine can be calculated by [5] $T_c = \sum_{k=1}^{Q_s} (L_a \int_0^{h_s} (B\theta_{b1}^2(r) - B\theta_{b2}^2(r)) / (2\mu_0)) (1)$ where $B\theta_{b1}$ and $B\theta_{b2}$ are the tangential components of flux densities near the adjacent stator teeth, respectively; Q_s is the number of slots; L_a is the effective length; h_s is the radius of the slot opening. The cogging torque calculation of PM machines will be illustrated and analyzed in this part. **III. Regional Magnetic Compensation Strategy** According to the analytical formula of cogging torque, it can be known that the tangential flux density on both sides of the slot wall can be compensated by supplying current or voltage on the stator side, the magnetic close component of the cogging torque can be balanced, thus weakening the cogging torque. The cogging torque analytical calculation and the regional magnetic field compensation is shown in Fig. 1. Take a 2-pole, 12-slot surface-mounted PM machine as an example, the current injection scheme for different slots is illustrated in Fig. 2. Further detailed regional magnetic compensation schemes of different machine topologies and their cogging torque reduction results will be reported in the full paper.

Permanent Magnet brushless motors,” *IEEE Trans. Magn.*, vol. 28, no. 2, pp. 1371–1374, Mar. 2009.

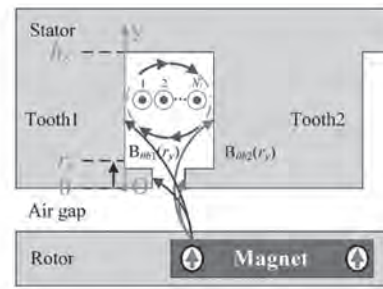


Fig. 1. Diagram of the cogging torque analytical calculation and the regional magnetic field compensation.

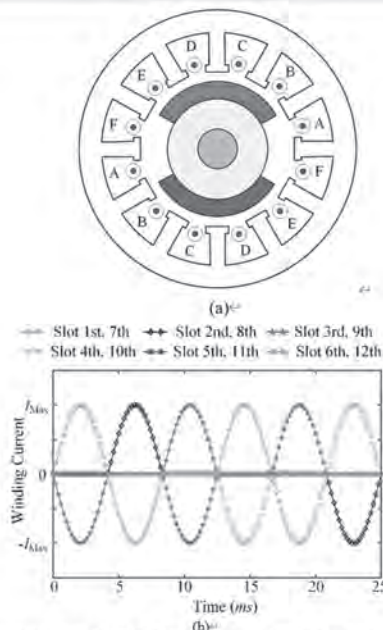


Fig. 2. (a) 2-pole 12-slot PM machine (b) Current injection scheme for different slots.

[1] W. Fei and Z. Q. Zhu, “Comparison of cogging torque reduction in permanent magnet Brushless machines by conventional and herringbone skewing techniques,” *IEEE Trans. Energy Convers.*, vol. 28, no. 3, pp. 664–674, Mar. 2013. [2] J. Gao, G. Wang, X. Liu, W. J. Zhang, S. D. Huang, and H. M. Li, “Cogging Torque Reduction by Elementary-Cogging-Unit Shift for Permanent Magnet Machines,” *IEEE Trans. Magn.*, vol. 53, no. 11, p. 8208705, Nov. 2017. [3] L. Zhu, S. Z. Jiang, Z. Q. Zhu, and C. C. Chan, “Analytical methods for minimizing cogging torque in permanent-magnet machines,” *IEEE Trans. Magn.*, vol. 45, no. 4, pp. 2023–2031, Apr. 2009. [4] E. H. Abd-Elhameed and M. Iwasaki, “Pulsating torque modeling and compensation for high precision positioning control,” 2009 IEEE International Conference on Mechatronics, Malaga, 2009, pp. 1-5. Z. Q. Zhu and D. Howe, “Analytical Prediction of the Cogging Torque in Radial-field

BR-04. Hybrid Spoke-Type Permanent Magnet Synchronous Generator for Wind Power Generation System.

D. Kim¹, S. Kim², S. Song³, I. Yang¹ and W. Kim³

1. Electrical Engineering, Hanyang University, Seongdong-gu, The Republic of Korea; 2. Korea Electronics Technology Institute, Gwangju-si, The Republic of Korea; 3. Electrical Engineering, Gachon University, Seongnam, The Republic of Korea

1. Introduction In recent wind power generation systems, a permanent magnet synchronous generator(PMSG) using rare earth magnets has been widely used for high power density and miniaturization per unit volume[1]. However, rare earth magnets have the disadvantage of high prices and high instability in supply and demand due to the characteristics of resources produced mostly in specific countries[2]. On the other hand, ferrite magnets have the advantage of stable material supply and demand and low cost compared to rare earth magnets. However, ferrite magnets have a low magnetic flux density, about 1/3 of that of rare earth magnets, and a spoke-type structure was developed to compensate for this. The spoke-type is a structure in which magnetic flux is concentrated by arranging two magnets in a radial direction on the rotor. By combining the magnetic fluxes of two magnets facing each other, the magnetic flux can be increased to obtain a high airgap magnetic flux density[3]-[4]. Currently, various research and development of spoke-type are carried out and used in the motor field, but application cases, research and development are still insufficient in generators. In this paper, a 10-pole 36-slot spoke-type PMSG was designed using a 3kW class wind turbine as a model, and a hybrid magnetic flux intensive PMSG with improved performance of the conventional spoke-type was proposed. 2. Conventional spoke-type shape and features A spoke-type rotor structure typically has two feature types, as shown in Figure 1 (a) and (b). There are types of non-conductors, such as (a), that are designed to prevent magnetic flux from flowing into the inside of the rotor, and (b), such as the inside of the rotor is designed extremely small, to rapidly saturate the inner core of the rotor to reduce the leakage magnetic flux. For the first method, high output density can be expected because it essentially removes passes from the leakage magnetic flux, but it has the disadvantage of high manufacturing difficulty and production costs due to the need for another material component inside the rotor. Additional structures are also needed for binding to non-elastic bodies and cores to support the release of the pole piece. The second method is advantageous in terms of manufacturability and production cost, but even though the rotor shape has an extremely small inner side, leakage magnetic flux occurs and the output density decreases. If the inner side is too shortened, there is a limit to reducing the inner side because it is disadvantageous in terms of rigidity.[5]-[6]. 3. Hybrid spoke-type permanent magnet synchronous generator design and characteristic analysis In this paper, the shape of a hybrid spoke-type permanent magnet synchronous generator for wind power generation system is proposed. The hybrid spoke-type PMSG is a shape in which the inner and outer bridges of the rotor are arranged in zigzag as shown in Fig. 1(c), and they are intersected when stacked. Since it does not require additional components, it has better fabrication than the (a) type, and the inner leakage magnetic flux is reduced by using only half of the inner bridge, and the stiffness is supplemented by adding an outer bridge. Cogging torque related to the starting performance of wind turbines, efficiency during load operation, and voltage fluctuation rate are compared and analyzed for each model using finite element analysis(FEA). The cogging torque was 3.6, 3.5, and 2.3[Nm], respectively, and the proposed model had the best cogging torque performance. During load operation, the efficiency was 96.2, 95.7, and 95.6[%], respectively, and there was a difference of about 0.6%P between the (a) model and the proposed model, in which the internal leakage was blocked. As a result of the 3D analysis, the voltage fluctuation rate during load operation occurred above the target specification value of 15% for each model[7]. As the voltage fluctuation rate increases, the target output and efficiency cannot be satisfied. The voltage decrease during load operation is due to the armature reaction, so the number of turns and the voltage drop are proportional. Therefore, the number of turns was reduced by applying the overhang model, and as a result, the voltage fluctuation rate was reduced, and the final model was designed that satisfies the target specifications of cogging torque, voltage fluctuation rate, efficiency, and output. 4. Performance test and Conclusion To confirm the

validity, a prototype was produced based on the final design model and a performance test was performed. The comparison of the test values with the FEA analysis results is shown in Table 1 and shows that the test values are similar to the analysis results. In this paper, a hybrid spoke-type PMSG for wind turbines was designed. By comparing the performance with the existing spoke-type models, it was confirmed that the cogging torque, an important performance specification of the wind turbine, was reduced, and the final model with overhang was designed to reduce the voltage drop that occurs during load operation. The performance was reviewed through 2D and 3D FEA, and a prototype was produced to verify the validity of the analysis results. Acknowledgments This work was supported in part by Technology Innovation Program (No. 20000401) funded By the Ministry of Trade, Industry & Energy(MOTIE), Korea and in part by the National Research Foundation of Korea(NRF) grant funded by the Korea government(MSIT) (No. 2020R1A2C1013724).

[1] Zaijun Wu, Xiaobo Dou, Jiawei Chu and Minqiang Hu, "Operation and Control of a Direct-Driven PMSG-Based Wind Turbine System with an Auxiliary Parallel Grid-Side Converter", *Energies* 2013, pp. 3405-3421, 12. July. 2013. [2] J. Seaman, "Rare Earths and Clean Energy: Analyzing China's Upper Hand," 2010. [3] W. Zhao, T. A. Lipo, and B. I. Kwon, "Torque pulsation minimization in spoke-type interior permanent magnet motors with skewing and sinusoidal permanent magnet configurations," *IEEE Trans. Magn.*, vol. 51, no. 11, Nov. 2015 [4] S. I. Kim, S. Park, T. Park, J. Cho, W. Kim, and S. Lim, "Investigation and experimental verification of a novel spoke-type ferrite-magnet motor for electric-vehicle traction drive applications," *IEEE Trans. Ind. Electron.*, vol. 61, no. 10, pp. 5763-5770, Oct. 2014. [5] Sandra M. Castano;Ehab Sayed;James Weisheng Jiang;Jianbin Liang, " Design of a Spoke-Type Ferrite Magnet Generator for a Hybrid Electric Vehicle Application," 2019 IEEE Transportation Electrification Conference and Expo (ITEC), 08 August 2019 [6] Mohammad Kimiabeigi; James D. Widmer; Raymond Long; Yi Gao; James Goss, On Selection of Rotor Support Material for a Ferrite Magnet Spoke-Type Traction Motor," *IEEE Transactions on Industry Applications* Volume: 52, Issue: 3, May-June 2016 [7] Sung Gu Lee;Jaenam Bae;Myungchin Kim;Won-Ho Kim, " Study on the Improvement of the Correction Coefficient Considering the 3-D Effect of Spoke-Type Permanent-Magnet Synchronous Motor " *IEEE Transactions on Magnetics*, Volume: 56, Issue: 3, March 2020.

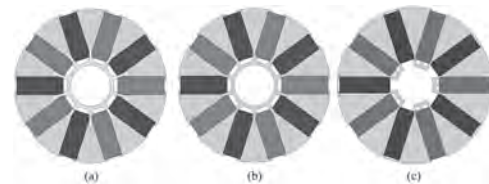


Fig.1 Shape cross section for each rotor type

Specifications		FEA	Test Model	Unit
No-Load	Back-EMF	130.06	136	V _{emf}
	Cogging Torque	2.7	2.5	Nm
	Torque	103.64	107.31	Nm
	Voltage	126.28	122.9	V _{emf}
Load	I _{2L}	210.17	212.79	V _{emf}
	THD	1.01	0.52	%
	Current	7.92	8.66	A _{emf}
	Copper Loss	97.8	106.5	W
	Core Loss	48.53	99.82	W
	Output Power	2996.42	3160	W
	Efficiency	95.82	93.7	%
Voltage fluctuation rate		6.48	8.47	%

Table.1 Comparison of FEA and Test results

BR-05. Comparison of Short Circuit and Irreversible Demagnetization Between Different Winding Connections in Surface-Mounted PM Machines.

Y. Du¹, L. Wu¹ and H. Zhan¹

1. College of Electrical Engineering, Zhejiang University, Hangzhou, China

I. Introduction PM machines have become more and more popular in various applications due to high torque density and efficiency. There are two typical winding connection methods for PM machines, of which star connection is more widely used. Delta connection is the other one, which leads to higher line current yet smaller line voltage compared to star connection. Therefore, delta connection is usually employed in high-voltage applications. However, circulating currents are likely to occur in delta connection, which can lead to additional copper loss and thus reduced efficiency. In addition, a hybrid star-delta connection has been proposed in the past few years [1]. Compared to star connection, the winding factor is maximized and thus torque density is enhanced by approximate 5.2%. Nevertheless, little literature is found regarding short circuit (SC) and demagnetization for these winding connections. SC and demagnetization are detrimental to the reliabilities of PM machines. SC currents are usually several times larger than working currents, which can generate more heat and accelerate winding insulation aging. In addition, SC can lead to large torque ripple, which can result in vibration and further damage machine components. Moreover, SC current can yield huge magnetic fields against PMs and thus cause irreversible demagnetization. Average torque can be reduced and torque ripple can deteriorate once demagnetization happens [2]. Therefore, comparing SC currents and demagnetization between different winding connections helps determine which connection should be selected when designing PM machines, especially those for safety-critical applications. In this digest, three-phase SC (3PSC) and two-phase SC (2PSC) for star and delta connections are investigated, together with their resultant demagnetization. II. Finite Element Model and Drive Schemes for Star and Delta Connections Finite element method coupled with circuit is employed. A 10-pole/12-slot surface-mounted PM machine is selected for investigation. Practically, SC faults are more likely to happen in the converter than the SPM machine itself because the power electronic devices are usually easier to be damaged than the well-insulated windings. Therefore, the drive schemes for both connections are shown in Fig. 1(a) and (b) for the following analysis. III. Three-Phase Short Circuit and Demagnetization It is assumed that 3PSC happens when all upper switches in Fig.1 (a) and (b) are closed whilst all lower ones are opened to prevent shoot-through. The equivalent circuits are shown in Fig. 1(c) and (e). The 3PSC starts at the rotor position $\pi/2$ from open-circuit state and the rotor speed is assumed to be 500rpm during 3PSC. As shown in Fig. 2(a), the star connection shows slightly larger peak currents. Since SC current usually produces a voltage against the back-EMF, the terminal voltage of each phase is approximately 0V during 3PSC for star connection. Therefore, when only the fundamental back-EMF is considered, the 3PSC currents for both winding connections are almost the same. For the star connection, the 3rd back-EMF harmonics are compensated in each loop and does not contribute to the 3PSC currents. However, the 3rd harmonic cannot be compensated in the delta connection and leads to additional 3PSC current component, which reduces peak currents in this 10-pole/12-slot SPM machine. In addition, the demagnetization level is evaluated by torque loss, which is defined as the ratio of the reduction of average torque to pre-demagnetization value. The torque loss for the star and delta connection are 1.84% and 1.53%, respectively. IV. Two-Phase Short Circuit and Demagnetization It is assumed that 2PSC happens when the switches VT1 and VT3 in Fig.1 (a) and (b) are closed whilst the others are opened. The equivalent circuits are shown in Fig. 1(d) and (f). 2PSC heavily depends on start rotor position and only SC currents starting from rotor position $\pi/2$ are analyzed as an example. As shown in Fig. 2(b), for the delta connection, the phase B current is approximately twice the SC currents of phase A and C in the opposite directions. This is because the SC loop of winding A and C has twice larger impedance than that of winding B, as shown in Fig.1 (f). Compared to the star connection, the phase B and C peak currents are larger and the phase A current is smaller under this start rotor position. The 2PSC peak currents under different start rotor positions are shown in Fig. 2(c). In addition, the

torque loss after 2PSC for delta connection is larger under most start rotor positions, as shown in Fig. 2(d). V. Conclusions It can be concluded which winding connection causes larger 3PSC peak currents and severer demagnetization heavily depends on the 3rd back-EMF harmonic. In addition, delta connection exhibits larger 2PSC peak currents and severer demagnetization under most start rotor positions. In the full paper, hybrid star-delta connection and single-phase SC will be considered. In addition, more analytical analysis and experimental validation will be presented.

[1] M. N. F. Ibrahim, A. S. Abdel-Khalik and E. M. Rashad, *IEEE Transactions on Energy Conversion*, vol. 33, pp. 1015-1024 (2017). [2] L. Wu, Y. Du and Z. Chen, *IEEE Transactions on Industry Applications*, vol. 56, pp. 2427-2440 (2020).

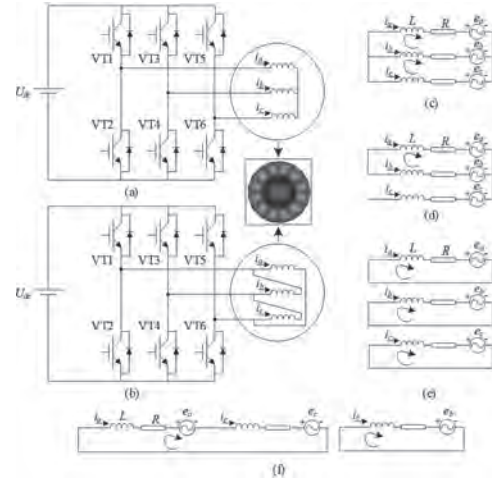


Fig. 1. Drive schemes for star and delta winding connections and SC equivalent circuits. (a) Drive scheme, star. (b) Drive scheme, delta. (c) 3PSC equivalent circuit, star. (d) 2PSC equivalent circuit, star. (e) 3PSC equivalent circuit, delta. (f) 2PSC equivalent circuit, delta.

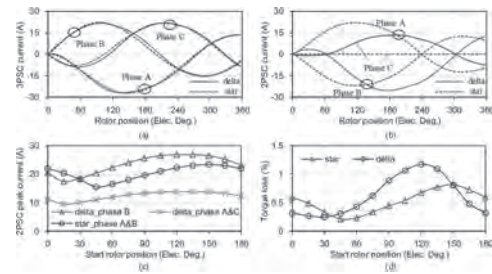


Fig. 2. SC currents and torque loss. (a) 3PSC current waveforms. (b) 2PSC current waveforms. (c) 2PSC peak currents under different start rotor positions. (d) Torque loss due to 2PSC under different start rotor positions.

BR-06. Analysis and Experimental Study for Electromagnetic and Mechanical Characteristic of Permanent Magnet Synchronous Machines According to Eccentricity.

T. Bang¹, K. Shin², J. Lee¹, H. Lee¹, H. Cho² and J. Choi¹

1. Electrical Engineering, Chungnam National University, Daejeon, The Republic of Korea; 2. Electric. Electro. & Comm. Eng. Edu., Chungnam National University, Daejeon, The Republic of Korea; 3. Power System Engineering, Chonnam National University, Yeosu, The Republic of Korea

Permanent magnet synchronous machines (PMSMs) are widely used in transmission and air-conditioning systems owing to several advantages such as high power density, high efficiency, and compact structure. However, PMSMs have the drawbacks of noise, vibration, and harshness (NVH) caused by the interaction between the magnetic motive force (MMF) of the stator winding and rotor magnets having a high coercive force, significantly affecting the machine characteristics. The NVH of PMSMs is influenced by serious machine operation problems such as eccentricity, rotor mass asymmetry, and axis misalignment, which causes machine faults and breakage. Therefore, it is necessary to consider these problems during the initial design stage. However, among these problems, the rotor mass asymmetry and axis misalignment have an influence on the change in mechanical characteristics, while eccentricity affects the change in the electromagnetic characteristic, which causes an increase in the electromagnetic NVH sources. Previous research has shown that eccentricity affects not only electromagnetic performance but also NVH sources that are related to the machine's characteristics. Electromagnetic NVH sources can be divided into two types: torque and electromagnetic force characteristics. The torque characteristics are classified as cogging torque and torque ripple. Previous research has shown that NVH characteristics are improved by reducing the torque characteristics. The electromagnetic force characteristics are classified as unbalanced electromagnetic force (UMF) and magnetic pull force (MPF). The MPF is the distribution of the magnetic flux density owing to the MMF of the stator winding, rotor magnets, and slotting effect. Numerous studies emphasizing MPF symmetry have been published. The UMF is caused by changing the magnetic flux density according to the rotating operation, which has been actively studied as the primary cause of NVH along with rotor eccentricity in induction machines. There are a few studies on the UMF of PM machines. Wu, et al. analyzed the UMF harmonic orders using an analytical method along with experimental results. Zhu, et al. analyzed the UMF generated in the models according to different winding patterns with equal specifications and changes in the current waveform according to the shape of the machines. However, the electromagnetic source influence on the NVH caused by eccentricity was not confirmed. Therefore, to analyze the eccentricity influence on each electromagnetic NVH source, we proposed the design of a PMSM with a fractional pole/slot combination, derived the dominant model of the pole/slot combination for each electromagnetic NVH source through a finite element analysis, and carried out a comparative results analysis of the results of the electromagnetic characteristic analysis. The derived pole-slot combination of the models are 8-pole/9-slot. The dominant components of 9-slot is electromagnetic force characteristics, respectively. However, if it is applied eccentricity conditions that increased the torque characteristics. Thus, we analyzed the influence of each NVH source by conducting experiments and electro-mechanical coupled analysis using FEM, and then compared the results with two different operating conditions. The analysis model and concept of eccentricity used for the electromagnetic excitation analysis are shown in Fig. 1(a). The derived pole-slot combination is the 8-pole/9-slot and 8-pole/12-slot. The concept of the NVH experimental system is shown in Fig. 1(b), to generate eccentricity, an apparatus for moving the stator is applied to the test motor. The characteristic analysis results of electromagnetic excitation are shown in Figs. 1(c) and (d). The NVH source, in the eccentricity condition is higher than that in a healthy condition. Therefore, the influence on each source can be analyzed. Figs. 2(a) and (b) show the electro-mechanical NVH characteristic analysis results of PMSMs according to the eccentricity. Figs. 2(c) and (d) show the measurement NVH results. This indicates that eccentricity significantly influences the NVH of the PMSMs. Detailed analysis and measurement results are discussed in the full paper.

[1] J. Zou, H. Lan, Y. Xu, and B. Zhao, "Analysis of Global and Local Force Harmonics and Their Effects on Vibration in Permanent Magnet Synchronous Machines," *IEEE Trans. Energy Convers.*, vol. 32, no. 4, pp.1523-1532, Dec. 2017. [2] D. Torregrossa, F. Peyraut, B. Fahimi, J. MBoua, and A. Miraoui, "Multiphysics finite-element modeling for vibration and acoustic analysis of permanent magnet synchronous machine," *IEEE Trans. Energy Convers.*, vol. 26, no. 2, pp. 490-500, Jun. 2011. [3] H. Yang and Y. Chen, "Influence of radial force harmonics with low mode number on electromagnetic vibration of PMSM," *IEEE Trans. Energy Convers.*, vol. 29, no. 1, pp. 38-45, Mar. 2014. [4] P. Beccue, J. Neely, S. Pekarek, and D. Stutts, "Measurement and control of torque ripple-induced frame torsional vibration in a surface mount permanent magnet machine," *IEEE Trans. Power Electron.*, vol. 20, no. 1, pp. 182-191, Jan. 2005. [5] Z. Q. Zhu, Y. Liu, and D. Howe, "Minimizing the influence of cogging torque on vibration of PM brushless machines by direct torque control," *IEEE Trans. Magn.*, vol. 42, no. 10, pp. 3512-3514, Oct. 2006. [6] D. Y. Kim, M. R. Park, J. H. Sim, and J. P. Hong, "Advanced Method of Selecting Number of Poles and Slots for Low-frequency Vibration Reduction of Traction Motor for Elevator," *IEEE/ASME Trans. Mechatron.*, vol. 22, no. 4, pp. 1554-1562, Aug. 2017. [7] J. F. Gieras, C. Wang, and J. C. Lai, *Noise of Poly-phase Electric Motors*. New York, NY, USA: Taylor & Francis, 2006.

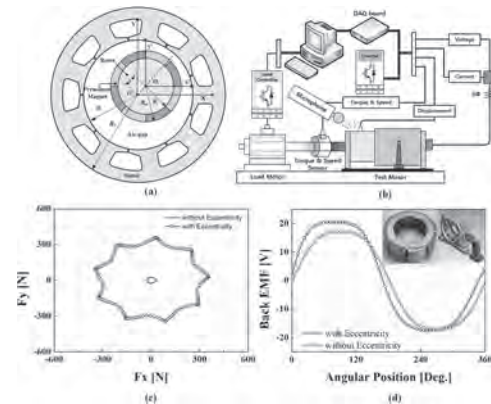


Figure 1 (a) Analysis model (b) the concept of experimental system (c) UMF analysis results according to Eccentricity (d) Back EMF analysis results according to Eccentricity

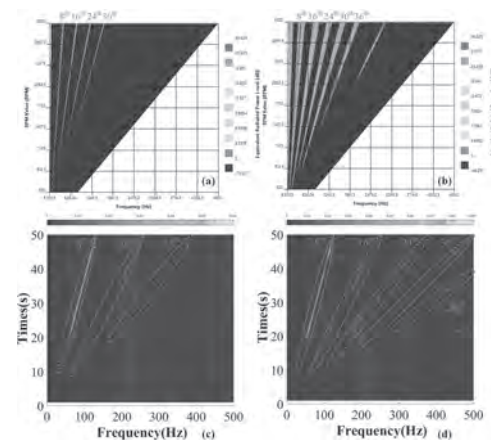


Figure 2 Experimental and analysis results of NVH according to eccentricity: (a) healthy conditions analysis results (b) eccentricity conditions analysis results (c) healthy conditions measurement results (d) eccentricity conditions measurement results

BR-07. Comparative Studies of Six-Phase PMSMs With Modular Stator Under Pre-Fault and Post-Fault Conditions.

L. Cheng¹, Y. Sui¹, P. Zheng¹, Z. Yin¹ and S. Yang¹
 1. Harbin Institute of Technology, Harbin, China

I Introduction Owing to their characteristics of easy manufacturing, convenient transportation and high fault-tolerant capacity, the modular permanent magnet synchronous machines (PMSMs) are favored by various industrial applications, such as electric vehicle and wind turbine applications [1]. However, due to the manufacturing tolerance, the additional mechanical gaps between the modules are inevitable which will affect the magnetic field distribution and hence the electromagnetic performances. The influences of the inevitable mechanical gaps between the modules in a three-phase PMSM has been investigated in [2-5]. Unfortunately, the influences of the additional gaps between the modules in a six-phase modular machine have not been covered. Moreover, the different influences of the modular structures on PMSMs with symmetrical or asymmetrical six-phase winding layouts are not investigated. II Development of the different six-phase winding layouts and the modular machines The symmetrical and asymmetrical six-phase windings layouts 12-slot/14(10)-pole PMSMs can be obtained by analyzing the slot star diagram of a conventional 12-slot/14(10)-pole three-phase PMSM with double-layer FSCW as shown in Fig. 1. The mutual inductances between adjacent phases are nonzero as shown in Table I, which will decrease their magnetic isolation capacity. To improve this situation, all the double-layer slots are divided into two single-layer slots so that three 24-slot/14(10)-pole six-phase PMSMs with unequal teeth can be obtained. And, the modular stators are employed. For the asymmetrical six-phase machine, there is only one modular method—one module with one coil (Design A). For the symmetrical six-phase machine, there can be two different modular methods—one modular with one coil (Design B) and one modular with one-phase (Design C) (one phase possesses two adjacent coils). The different modular methods will introduce different additional mechanical gaps which cannot be avoided resulting from the manufacture limitations and tolerances, as shown in Fig. 1. These mechanical gaps will have significant influences on the electromagnetic performances of the modular machine. III Influences of the modular stators on the performances In this section, the performance such as winding factor, no-load air-gap flux density, on-load torque and short-circuit current, are investigated. For the sake of comparison, all the dimensions of the three modular stator PMSMs are the same as shown in Table II and Fig. 2. Since the slot area is fixed, the sum of the width of coil-wound tooth (t_1) and the width of non-wound tooth (t_2) is the same when the width of the coil-wound tooth varies. The additional mechanical gap varies from 0.5 mm to 5 mm. By injecting rated sine currents, the on-load torques can be obtained as shown in Fig. 3. It can be clearly found that the average torques of the three machines all decrease with the increase in mechanical gap width. When the mechanical gaps are relative small, i.e. 0~1 mm, the average torques are in direct proportion to t_1 . However, due to the serious saturation in the non-wound teeth, this rule will disappear. This is why, the average torques drop more rapidly with the increase in mechanical gap width when t_1 is relatively large. The average torques of Design C are the most smooth ones, which indicates that the modular method of Design C can avoid deep saturation. The fault-tolerant machine requires that the short-circuit current should be closed to the rated current. The short-circuit currents of the three modular machines are investigated as shown in Fig. 4. For Design A and B, it can be seen that the short-circuit current decreases with the increase in mechanical gaps when t_1 smaller than 24mm, which results from the reduced back-electromagnet force (back-EMF). The short-circuit will rapidly increase with the increase in mechanical gap width when t_1 bigger than 24mm, which results from the reduced self-inductance when deep saturation occurs. For Design C, with different winding tooth width, the amplitudes of the short current are almost deprived of the influence of the width of the mechanical gaps. IV Conclusion This paper presents three different modular six-phase PMSMs. For the asymmetrical six-phase machine, there is only one modular method—one module with one coil (Design A). For the symmetrical six-phase machine, there can be two different modular methods—one modular with one coil (Design B) and one modular with one-phase (Design C) (one phase possesses two adjacent coils). For Design A and B, the mechanical gaps between the modules

will make the performances bad significantly. While, Design C almost insulates from the influence of the additional mechanical gaps.

[1] B. Bickel, J. Franke, and T. Albrecht, "Manufacturing cell for winding and assembling a segmented stator of PM-synchronous machines for hybrid vehicles," in Proc. 2nd Int. EDPC, Oct. 2012, pp. 1-5. [2] Z. Q. Zhu, Z. Azar, and G. Ombach, "Influence of additional air gaps between stator segments on cogging torque of permanent-magnet machines having modular stators," IEEE Trans. Mag., vol. 48, no. 6, pp. 2049-2055, Jun. 2012. [3] G. Dajaku and D. Gerling, "Low costs and high-efficiency electric machines," in Proc. 2012 2nd Int. Electr. Drives Prod. Conf. (EDPC), Oct. 15-18, 2012, pp. 1-7. [4] G. J. Li, Z. Q. Zhu, W. Q. Chu, M. P. Foster, and D. A. Stone, "Influence of Flux Gaps on Electromagnetic Performance of Novel Modular PM Machines," IEEE Trans. Energy Convers., vol. 29, no. 3, pp. 716-726, Sept. 2014. [5] G. J. Li, Z. Q. Zhu, M. Foster, and D. Stone, "Comparative Studies of Modular and Unequal Tooth PM Machines Either With or Without Tooth Tips," IEEE Trans. Magn., vol. 50, no. 7, 8101610, July 2014.

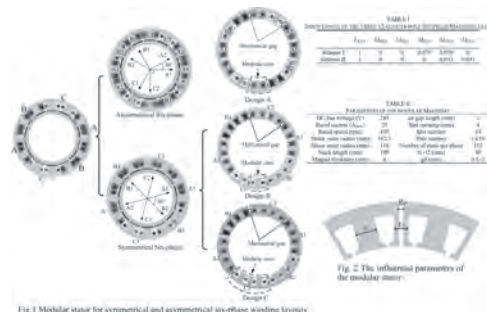


Fig. 1 Modular stator for symmetrical and asymmetrical six-phase winding layouts

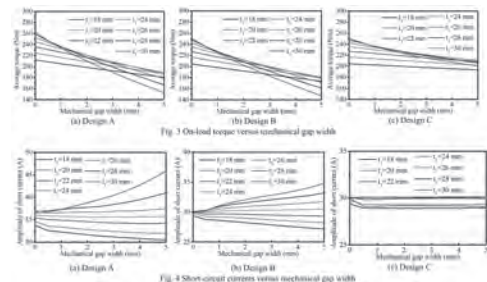


Fig. 3 On-load torque versus mechanical gap width

Fig. 4 Short-circuit current versus mechanical gap width

BR-08. Segmented Asymmetrical Stator Structure of PMSM to Reduce Torque Ripple.

C. Liu¹, J. Zou¹, Y. Xu¹, G. Yu¹ and L. Zhuo¹

1. Harbin Institute of Technology, Harbin, China

Abstract: this paper proposes segmented asymmetrical stator design to reduce torque ripple for permanent magnet synchronous motor (PMSM). By changing the design parameters of the segmented stator, a specific phase difference of the two torque ripples can be generated by two sections of the stator, so the ripples can offset each other to reduce the torque ripple. A 14-pole 12-slot PMSM is carried out to analyze the proposed stator design, and the correctness of the method is verified by finite element analysis (FEA). I. Introduction Permanent magnet synchronous motor (PMSM) is widely used in industrial fields because of the advantages of high power density and high efficiency [1]. However, torque ripple of PMSM can cause vibration and noise, which are not conducive to the smooth operation of the motor. So, it's of great necessity to reduce the torque ripple. Generally, magnet shape optimization is carried out to reduce torque ripple, but this method also decreases the average torque [2]- [3]. Consequently, this paper proposes segmented asymmetrical stator design, which can reduce torque ripple without significant drop of average torque. II. Mechanism of Torque Ripple Electromagnetic torque is generated by back EMF and current. Assuming that the input current is a standard sinusoidal wave, then average torque is generated by the current and the fundamental of back EMF, while torque ripple is generated by the current and the harmonics of back EMF. The conventional method is to optimize the shape of permanent magnet. In this way, the amplitude of back EMF harmonics can be reduced so as to achieve the decrease of the torque ripple. However, the fundamental of back EMF is also reduced so the average torque decreases obviously. The proposed method is not to reduce the back EMF harmonics, but to create two groups of harmonics which are staggered by a certain phase to make them cancel each other. In this way, the torque ripple is reduced and the average torque can be maintained. III. segmented stator design A 14-pole 12-slot PMSM is carried out to analyze the proposed stator design. For the conventional symmetrical structure, the average torque is 53Nm and the torque ripple is 3.05%. Then segmented asymmetrical design is carried out to optimize the stator. The main parameters are θ and W . θ is the degree from the middle of teeth to the middle of slot opening. W is the width of the slot opening. Given several θ and W , finite element analysis (FEA) is used to calculate the performance of the motor. A total of 120 schemes are calculated by FEA and the results are analyzed. Fast Fourier Transform (FFT) are applied to the torque results to obtain the harmonics distribution of the torque ripples. From the analysis, it's easy to find two torques which have similar ripple amplitude and opposite phase. The model A is that when θ is 12° and W is 4.4, and the model B is that when θ is 18° and W is 4.4. The details of the torque results are shown as Fig.1. It can be seen from Fig.1 that the amplitudes of sixth torque ripple are 0.4664 and 0.7719, and the phases are -109° and 74° . The amplitudes of twelfth torque ripple are 0.1484 and 0.1512, and the phases are -165° and 28° . Both the sixth and the twelfth torque ripples of the two models have similar amplitude and opposite phase. So the torque ripple can be reduced sharply if the two torque waveforms are superimposed. According to the above analysis, the stator core can be designed in sections. The stator core can be divided into two parts in the axial direction, and the laminations of the two parts are made according to model A and model B respectively. Then the segmented stator is used for FEA calculation, the average torque is 52.5 Nm and the torque ripple is 0.93%. The torques of segmented stator and relevant comparison models are shown in Fig.2. It can be seen from Fig.2 that although the FEA results of segmented stator structure are not entirely consistent with the average results of model A and model B, the torque ripple of the motor can be effectively reduced without obvious reduction of average torque. The torque ripple is obviously reduced from 3.05% to 0.93%, and the average torque is only reduced from 53Nm to 52.5Nm. IV. Conclusion This paper proposes a segmented asymmetric stator structure. By segmenting the stator and designing each section, the torque ripples generated by different sections can cancel each other, so as to weaken the torque ripple. This method doesn't require permanent magnet shape optimization, so the torque will not decrease significantly. The validity and accuracy of the segmented asymmetrical stator structure are verified by FEA calculation.

1. J. Si, S. Zhao, H. Feng and R. Cao, *Chinese Journal of Electrical Engineering*, vol. 44, p. 67-73(2018) 2. W. Zhao, T. A. Lipo and B.-I. Kwon, *IEEE Transactions on Industrial Electronics.*, vol. 61, p. 5779-5787(2014) 3. D. Wu and Z. Q. Zhu, *IEEE Transactions on Magnetics*, vol. 51, p. 1-4(2015)

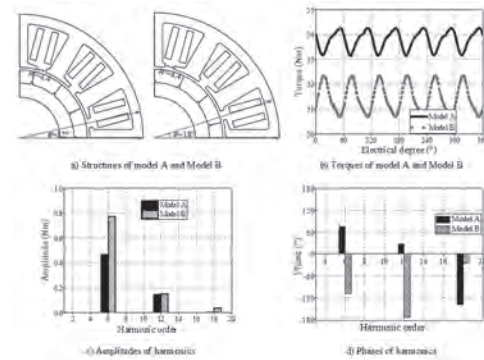


Fig.1 Structures and torque analysis of asymmetrical models

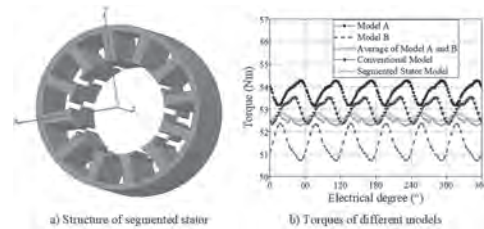


Fig.2 Segmented asymmetrical stator structure and torque results of the models

BR-09. Comparison and Analysis of Dual-Winding Fault-Tolerant Permanent Magnet Motor for Aviation Fuel Pump Applications.

J. Li¹, X. Jiang², Y. Chen², W. Jiang¹ and W. Huang¹

1. College of Automation Engineering, Nanjing University of Aeronautics and Astronautics, Nanjing, China; 2. College of Automation Engineering, Nanjing University of Science and Technology, Nanjing, China

I. INTRODUCTION With the development of electric drive technology, all electric and hybrid control has been more and more used in aerospace, and the integrated electric engine fuel pump on the aircraft has many potential advantages: compared with the traditional system using mechanical drive pump, the fuel control system is lighter, smaller, simpler and more efficient. Therefore, the fuel pump motor also plays an important role in electric drive control. The existing dual-winding fault-tolerant permanent magnet machine (DWFT-PMM) is generally designed with a rated speed of 5000rpm, rated power of 10kW and rated torque of 20Nm, the cooling mode is air cooling [1]. In [1], the optimized DWFT-PMM owns the advantages of physics isolation, strong magnetic isolation, inhibiting the short circuit current, small cogging torque ripple and high fault tolerance by designing and optimizing the air gap surface shape and anti short-circuit reactance parameters. It is precisely because of these advantages that existing DWFT-PMM as a fuel pump motor has a broad application and the idea of continuing to optimize this motor is worthwhile. However, in practical application, due to the speed demand of aviation fuel pump motor reaching 6000rpm or even higher, the demand for power and torque is relatively reduced, and the cooling mode is changed from air cooling to oil cooling. This paper aims to optimize the parameters of the existing DWFT-PMM. To improve the performance of DWFT-PMM and make it successfully used in the aviation field, the design and optimization of aviation fuel pump motor based on DWFT-PMM are proposed and studied in this paper. Firstly, according to the design specifications, the design and performance optimization scheme of the fuel pump motor is proposed and finally determined. Then, to verify the performance of the motor, the comparative analyses of the DWFT-PMM are showed in simulation and experiment, and the finite element analysis (FEA) results are given in terms of the sizing and volume, electromagnetic torque, no-load back EMF in simulation and experiment, etc. Based on the design and optimization results, the prototype is manufactured, and the experimental results of loss analysis are given. Finally, the conclusion is drawn. II. DESIGN AND PERFORMANCE OPTIMIZATIONS Fig.1 shows the comparison of two-dimensional (2-D) model and three-dimensional (3-D) model of DWFT-PMM before and after optimization along with the optimized prototype. It is indicated from models in Fig. 1(a) that the inner and outer diameters of the stator and rotor are reduced to achieve the optimization goal. The optimization goal also includes reducing the peak value of no-load back EMF to increase the speed, the cooling mode changed from air cooling to oil cooling, and reducing the copper loss, iron loss and mechanical loss. Fig. 1(b) shows the prototypes before and after DWFT-PMM optimization. III. FINITE ELEMENT ANALYSIS VERIFICATION According to the design and optimization parameters, no-load back-EMF waveforms of DWFT-PMM are shown in Fig. 2(a) before and after optimization. The electromagnetic torque waveforms of DWFT-PMM before and after optimization are shown in Fig. 2(b). More detailed simulated verification will be presented in the full paper. IV. EXPERIMENTAL VERIFICATION The no-load back-EMF waveforms in experiment are respectively shown in Fig. 2(c). The former is when DWFT-PMM is running at the 2000r/min, and the latter is when the optimized DWFT-PMM is running at the 5000r/min. V. CONCLUSION This paper presents and studies the comparison and analysis of DWFT-PMM. According to the actual requirements, the speed of the fuel pump motor is higher and the cooling mode is oil cooling. So, the flow chart of the design and performance optimization of the existing DWFT-PMM is established. Then, the size of the stator and rotor and the number of coil turns of the fuel pump motor are designed and optimized. The performance of the optimized DWFT-PMM is analyzed by FEM from the aspects of inductance, cogging torque ripple, no-load back EMF, short circuit current, electromagnetic torque, and loss. Finally, the simulated and experimental results show that the optimized DWFT-PMM has the advantages of higher speed, better heat dissipation, smaller size, higher reliability, and more practicability. More detailed theoretical analysis, simulated and experimental verification

will be presented in the full paper. ACKNOWLEDGMENT This work was supported in part by the National Natural Science Foundation of China under Project 51807094, and in part by the Project funded by China Postdoctoral Science Foundation under Project 2020M671499, and in part by High-level Innovative Entrepreneurial Talent Introduction Program of Jiangsu Province under Project [2019]20, and in part by Jiangsu Planned Projects for Postdoctoral Research Funds under Grant 2020Z145.

[1] Xuefeng Jiang, Shaoshuai Wang, Qiang Li, Yufei Gao, "Design and optimization of dual-winding fault-tolerant permanent magnet motor," CES Transactions on Electrical Machines and Systems, vol.3, no.1, pp.45- 53, (2019).

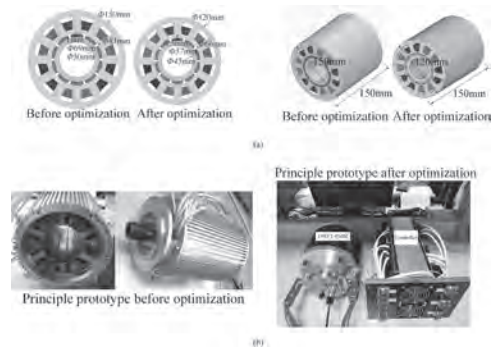


Fig. 1. The proposed DWFTPMM. (a) Comparisons the 2-D of and the 3-D model. (b) Comparison of prototype.

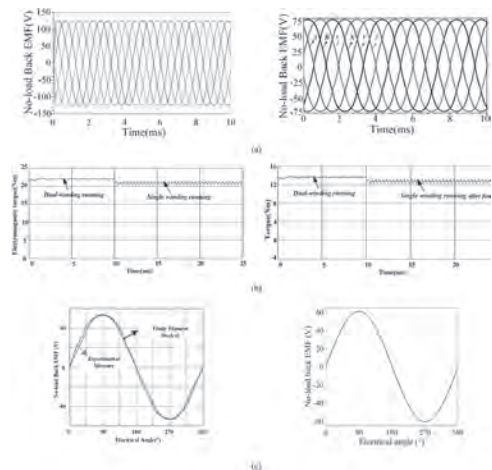


Fig. 2. Simulation and experimental comparison results of DWFT-PMM before and after optimization. (a) The comparison of no-load back EMF in simulation. (b) The comparison of the electromagnetic torque in simulation. (c) The comparison of no-load back EMF in experiment.

BR-10. Research on Improving Magnetic Flux of Permanent Magnet Synchronous Generator Shell With Amorphous Alloy.

C. Hsu¹

1. Mechanical Engineering, Oriental Institute of Technology, Panchiao, Taiwan

1. Abstract In recent years, electromagnetic renewable energy systems such as wind turbines have become an important research direction. It can be seem more and more commonly to use surface-mounted permanent magnet generators and mostly installed in coastal areas. In order to improve the reliability of the generator, permanent magnet elements are used in the internal structure. In the research of this article, an enhanced permanent magnet salient pole generator that improving the magnetic flux is proposed. The demagnetization phenomenon of the motor is the transient magnetic performance of the fault. The two-pole alternator device is shown as Figure 1. For concept of the rotor core structure, a sinusoidal waveform is generated between the surface and the air gap magnetic flux density. At each magnetic pole of the two permanent magnet phenomena, it shown the symmetry magnetization directions with mirror condition are embedded. In two pole generators, non-magnetic materials are generally used to guide the path of magnetic flux [1]. Due to the placement of permanent magnets, the radial magnetic field will be stronger. To change the angle between the two left and right permanent magnets, it will show the demagnetization performance of the magnetic field in the magnetic pole. Therefore, the AC two-pole generator in this research with two forms is proposed. The first one, it is the naked motor form of the No Cover (NC), as shown in Figure 1, and the other is an iron-based amorphous alloy material is used to cover the whole generator. Due to this changing of the magnetic pole and the spatial magnetic field, it apply a different permanent magnet motors with a magnetic material shell and a shell-less structure to observer their magnetic field distribution, is obtained. The demagnetization area of the demagnetization area is measured by the power analyzer and Tesla measuring instrument. The harmonic measurement results of different shell shapes are shown in Figure 2, which the demagnetization area is magnetized in the direction magnetic flux density node coverage. As shown in Figure 2, the amorphous alloy shell-clad magnetic pole generator has the highest demagnetization rate in the permanent magnet area near the bottom of the pole shoe. This is because the side frame of the pole shoe is certainly changed the leakage flux. The magnetic flux path is affected by the demagnetization performance. In contrast, due to the magnetic field distribution characteristics of the different casings, the demagnetization of the generator armature in the two forms of magnetic field distribution is not completely symmetrical. The experimental measurement of the surface of the amorphous shell shows that the magnetic flux at the inner and outer center points is about 1.2-2.4 (mT), and the magnetic flux distribution at the four corners is about 0.6-1.0 (mT), which is relatively weak before NC type of the generator. The experimental target is to define the influence of demagnetization on electromagnetic parameters, and summarize the magnetic flux distribution of permanent magnet salient pole motors in the demagnetization and amorphous housings, which is used as a reference for the design of such type motors. 2. Theory and Method The rotating field alternator shown in the figure below is the most widely used generator [2,3]. In this type of generator, direct current from another power source flows through the windings on the rotor by means of slip rings and brushes is obtained. By this way, a rotating electromagnetic field with a fixed polarity can be maintained, and the rotating magnetic field of the rotor extends outward and passes through the armature windings embedded in the surrounding stator. When the rotor rotating, an AC voltage is induced in the windings because the magnetic field of the first polarity and the other polarity penetrates them. Because the output power comes from a fixed winding, the output can be connected through a fixed terminal. The advantage of this structure is indicated that there are no sliding contacts and the entire output circuit is continuously insulated and can handle a large amount of current. 3. Experimental discussion and conclusion This research is a single-phase two-pole alternator, which apply a NC type of the generator, to produce an average AC voltage of 37V, current of 0.11A, power factor of 0.99, P power of 4.11 watts, Q of 0.48VAR, and S of 4.14VA during operation. Besides, for CO type of the generator with amorphous material, it is produce an average AC voltage of 37.03V, current of 0.14A, power factor

of 0.99, P power of 3.97 watts, Q of 0.43VAR, and S of 4 VA. This results of the CO type is much better than NC type of the generator. This research focuses on observing the comparison between the bare generator and the structure covered with the amorphous shell. At the same time, it observes the electric energy generated by the generator and the harmonic state. It can be carried out by measuring the voltage and current without interrupting the generator. From the perspective of THD (Total harmonic distortion) performance, the third, fifth, and seventh order waves have the most serious impact on the generator. Of course, the generator with an amorphous shell structure has better magnetic properties and power.

1. Chang-Hung Hsu* and Yi Mei Huang, "Performance of the Noise and Vibration of the AC/DC Signal for a Permanent Magnetic DC Motor," IEEE Transactions on Magnetics, Early Access Articles. Accepted Publishing on the web 28 July 2020.
2. Chang-Hung Hsu* and Chia Wen Chang, "Permanent Magnetic Brushless DC Motor Magnetism Performance depends on Different Intelligent Controller Response," Transactions of the Canadian Society for Mechanical Engineering, Accepted Publishing on 6 August 2020.
3. Chang-Hung Hsu*, "Fractional Order PID Control for Reduction of Vibration and Noise on Induction Motor," IEEE Trans. on Magnetics, vol. 55, no. 11, pp. 6700507-1-7, 2019.(SCI, Impact Factor: 1.651)

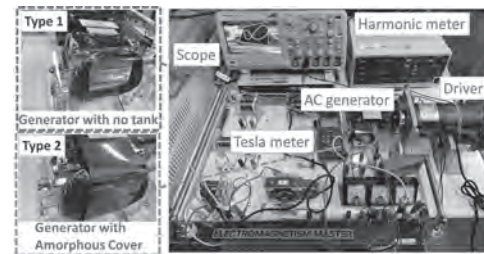


Figure 1. The AC generator with (without) tank composited with amorphous alloy in magnetic flux and performance testing results

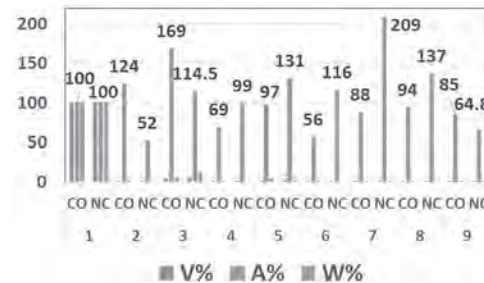


Figure 2. The experimental results of the two types of AC generator in harmonic performance with cover (CO) or without cover (NC, No cover).

BR-11. Annual Energy Production Design Optimization for PM Generators Considering Maximum Power Point Trajectory of Wind Turbines.

W. Zhang², L. Dai¹, S. Huang¹ and J. Gao¹

1. College of Electrical and Information Engineering, Hunan University, Changsha, China; 2. College of Electronic and Electrical Engineering, Changsha University, Changsha, China

Abstract— This paper presents a design optimization method for improving annual energy production (AEP) of wind direct-drive permanent magnet generators. Unlike the traditional efficiency optimization method that only improves the rated point efficiency, the proposed method is to improve the overall efficiency of the generator during the operation cycle by matching the maximum power point trajectory of the wind turbine. The periodic loss model of the permanent magnet synchronous generator (PMSG) is established and further constituted as the objective functions, and the genetic algorithm is used to find the Pareto solution between multiple objective functions. Compared with the traditional design method, higher AEP is achieved by the proposed method. 1. Introduction Design optimization for generators is an important approach to promote wind energy conversion systems (WECSs) more efficient, reliable, and cost-effective. Some studies have discussed the optimization methods to maximize the operating efficiency of the PMSGs in WECSs [1-3]. The works of literature adopt stochastic algorithms to optimize the analytical efficiency to find the preferable generator structural parameters, such as the genetic algorithm in [1], deterministic optimization algorithm in [2], and evolutionary algorithm in [3]. However, most of the efficiency models in the literature are based on the single function, which is usually rated conditions with rated speed, which means that only the efficiency in the rated state is optimized without considering the entire operating cycle. This is not suitable for WECSs, because of climatic and geographical factors, wind turbines rarely work under rated conditions. Therefore, the classical efficiency optimization method is likely to cause a reduction in AEP. In this paper, a novel design optimization method for PMSGs is presented to maximize the AEP. First, the aerodynamic model of the wind turbine is introduced to predict the relationship between maximum output power and optimum shaft speed, and the wind speed distribution is investigated to obtain the featured operating points with multiple wind speeds. Second, the generator loss models of the multiple featured points are formulated as objective functions, and the genetic algorithm is utilized to solve multi-objective issues. Finally, the proposed optimization is verified by simulation and experiment. 2. Maximum Power Point Trajectory of Wind Turbines The achievable mechanical power obtained from the wind turbine is given by $P_m=0.5\rho R^2V\omega^3C_p$ where C_p is the wind turbine power coefficient. To maximize C_p , the optimal mechanical speed ω_r must match the wind speed $V\omega$. Based on the aerodynamic model, the optimal mechanical speeds at different operating powers are obtained, as shown in Fig. 1. Therefore, the typical operating conditions (power, speed) of the generator have been obtained and can be used to assist in the construction of periodic loss models. 3. Optimization Process The loss models of PMSG under the 5 typical wind speeds are established and used as the objective functions, and their weighting coefficients are derived based on the Rayleigh distribution of wind speed. Next, the genetic algorithm is selected to simultaneously optimize the operating efficiency of PMSG at multiple speeds and powers. The efficiency is about 94.78% at the wind speed of 4 m/s, 95.58% at 6 m/s, 96.14% at 8 m/s, 96.69% at 10 m/s, 97.31% at 12m/s, respectively. Considering the wind distribution of the site, the overall efficiency can be achieved by about 96.18%. Finally, the prototype of the designed PMSG is manufactured according to the optimized solution, as shown in Fig. 2. The detailed optimization process and results will be reported in the full paper.

[1] Q. Wang, S. Niu, and L. Yang, "Design Optimization of a Novel Scale-Down Hybrid-Excited Dual Permanent Magnet Generator for Direct-Drive Wind Power Application," *IEEE Trans. Magn.*, vol. 54, p. 8100904, (2018). [2] T. Bazzo, J. Kolzer, R. Carlson, "Multiphysics Design Optimization of a Permanent Magnet Synchronous Generator," *IEEE Trans. Ind. Electron.*, vol. 64, pp. 9815–9823, (2017). [3] C. L. Sabioni, M. F. O. Ribeiro, and J. A. Vasconcelos, "Robust Design of an Axial-Flux Permanent Magnet

Synchronous Generator Based on Many-Objective Optimization Approach," *IEEE Trans. Magn.*, vol. 54, p. 8101704, (2018).

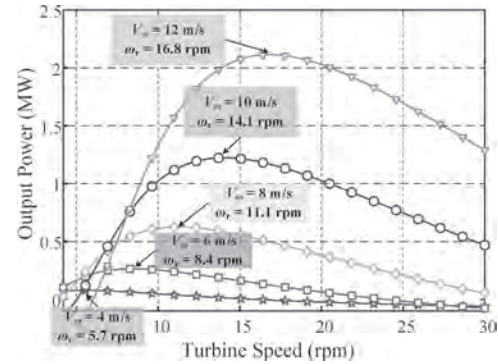


Fig. 1. Characteristics of output power and rotational speed of wind turbine at several typical wind speeds

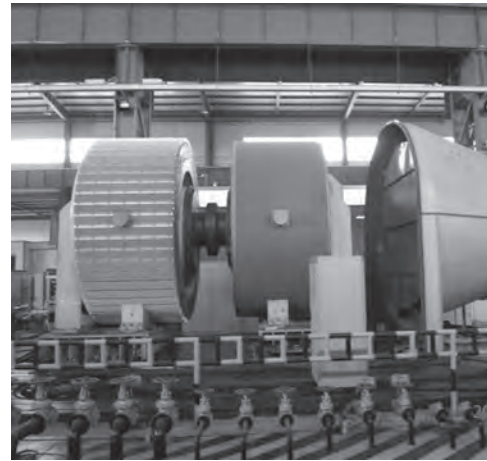


Fig. 2. The prototype of 2 MW wind direct-drive PMSG.

BR-12. A Study on the Improvement of Powerfactor of LSPM Motor by Rotor bar Material and Stator Winding Considering Irreversible Demagnetization of Permanent Magnet.

S. Lee¹, D. Shin¹, W. Kim¹ and K. Lee²

1. Electrical Engineering, Gachon University, Seongnam, The Republic of Korea; 2. Intelligent Mechatronic Research Center, Korea Electronics Technology Institute, Seongnam, The Republic of Korea

This paper is a study on the improvement of powerfactor according to the material of the rotor bar, the number of turns of the stator winding, and the winding method of a super premium efficiency(IE4 class) LSPM motor. In order to satisfy the IE4 class based on the 2.2kW 6-pole induction motor, an efficiency of 88.5% or higher was selected as the target variable, and the material of the rotor bar, the number of windings of the stator, and the winding method as design variables. By analyzing the characteristics of the motor during start-up and operation, the final model that satisfies the target value was selected and produced by comparing and reviewing the rated characteristics, such as demagnetization of the permanent magnet and the motor's powerfactor, efficiency, and torque ripple through Finite Element Analysis(FEA). Through the test, it was confirmed that the target value was satisfied. The motor is an energy converter that occupies a high proportion of electric energy, and the improvement effect is very great when designing a high-efficiency and high-powerfactor. Therefore, it is a situation of researching high-efficiency motors worldwide. In particular, induction motors with simple structure and easy maintenance are widely used in industrial fields. Accordingly, various studies are being conducted on the high-efficiency of induction motors. One of the ways to improve the efficiency of an induction motor is an LSPM(Line Start Permanent Magnet)motor with a permanent magnet inserted into the rotor. It is a structure in which a conductor bar and a permanent magnet are inserted into the rotor, and it is possible to start by simply supplying power like an induction motor. Therefore, unlike general synchronous motors, there is no need for an inverter or a control sensor, so the system cost is low. In addition, after synchronization, no current flows through the rotor bar and the copper loss of the rotor of the induction motor disappears. This enables high-efficiency operation like a BLDC motor. However, compared to the general IPMSM(Interior Permanent Magnet Synchronous Motor), there is a possibility that excessive current flows instantaneously during start-up, resulting in irreversible demagnetization of the permanent magnet. Therefore, it is necessary to accurately calculate the starting current of the motor and design it so that demagnetization does not occur in the permanent magnet. In addition, the phase of the current is also an important design variable to improve the powerfactor, and is determined by the stator winding and the number of turns. Therefore, the diameter of the winding, the optimal number of turns, and the winding method were selected in consideration of the slot fill factor. In this paper, in order to improve the powerfactor of an LSPM motor that satisfies IE4 class, the material and number of rotor bars, the number of turns of the stator winding, and the powerfactor characteristics during rated operation according to the winding method are compared and analyzed by considering the irreversible demagnetization of the permanent magnet. 6-pole 36-slot LSPM motor was selected as the analysis model, and the material of the rotor bar of the motor, the number of turns of the stator winding, and the powerfactor characteristics during rated operation according to the winding method were analyzed through FEA. A model that satisfied the target value was selected and fabricated in consideration of the manufacturability, powerfactor, and magnetism. It was confirmed that the final model satisfied the target specifications through the actual test.

[1] S. Saha, G. Choi and Y. Cho, "Optimal Rotor Shape Design of LSPM With Efficiency and Power Factor Improvement Using Response Surface Methodology," in *IEEE Transactions on Magnetics*, vol. 51, no. 11, pp. 1-4, Nov. 2015, Art no. 8113104, doi: 10.1109/TMAG.2015.2448754. [2] S. Saha and Y. Cho, "Optimal rotor shape design of LSPM with efficiency and power factor improvement using response surface methodology," 2015 IEEE International Magnetics Conference (INTERMAG), Beijing, 2015, pp. 1-1, doi: 10.1109/INTMAG.2015.7157403.

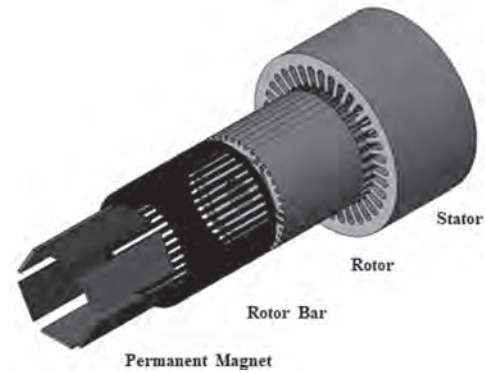


Fig 1. view of LSPM(Line Start Permanent Magnet) motor (3D)



Fig 2. LSPM motor Test

BR-13. Study on the Design of Six Phase Surface Inset Permanent Magnet Synchronous Generator and Motor Considering the Power Factor and Torque Ripple.

H. Kim¹, Y. Park¹, W. Kim², C. Jin³ and J. Lee¹

1. Electrical Engineering, Hanyang University, Seongdong-gu, The Republic of Korea; 2. Electrical Engineering, Gachon University, Seongnam, The Republic of Korea; 3. Electrical Engineering, Wonkwang University, Iksan, The Republic of Korea

1. Abstract In this paper, the optimal design of six phase surface inset permanent magnet synchronous generator and motor (SIPMSGM) is proposed considering the power factor and torque ripple. Because of the reluctance torque component by q-axis core thickness of rotor, SIPMSGM has the high torque density but the poor torque ripple. In order to reduce the torque ripple, the tapering is applied to magnet, but the torque density and power factor are decreased. Therefore, the optimal design is proposed using the performance map based on the tapering of magnet and q-axis thickness of core. First, pole-slot combinations are compared with the efficiency and power factor of SIPMSGM. Considering the efficiency and power factor, the initial SIPMSGM is selected for the optimal design. Based on the initial SIPMSGM, the optimal design is performed based on the optimal design parameters. considering the power factor and torque ripple. 2. Introduction As increasing the environment problems such as the greenhouse gas emissions, the ship demands the high efficiency and environmentally friendly. By this trend, the shaft generator and motor (SGM) of hybrid electric ship have been received the attention because of the energy efficiency, noise, and reliability [1]. Therefore, there are the studies on the torque ripple reduction, the high efficiency, the high power factor, and multi-phase winding. Six-phase surface inset permanent magnet SGM (SIPMSGM) has the high power density, the efficiency, the power factor, the reliability because of the reluctance torque and multi-phase winding [2], [3]. However, the torque ripple is increased by the reluctance torque ripple component. Therefore, the design method of the torque ripple reduction must be studied such as the tapering and winding method. This paper is the optimal design of six-phase SIPMSGM considering the power factor and torque ripple based on finite element analysis (FEA). Through the comparison with performance of pole-slot combinations, the initial SIPMSGM is selected. The optimal design parameters are selected as the q-axis core thickness and tapering of magnet. The selected optimal design parameters have the relationship with torque density, power factor, and torque ripple. Therefore, the optimal design is performed through the performance maps considering the objective function and constraints such as the power and voltage limit. Finally, the PTI/PTO performances of the optimal SIPMSGM are analyzed based on FEA. 3. Optimal Design of SIPMSGM SIPMSGM has the reluctance torque by the q-axis core thickness which determines by the q-axis inductance. The reluctance torque of SIPMSGM is expressed as Eq. (1). $T_r = mP(L_d - L_q)i_d i_q / 4$ (1) Where T_r is the reluctance torque, m is the number of phase, P is pole, L_d and L_q are d- and q-axis inductance, respectively, and i_d and i_q are d- and q-axis current. From Eq. (1), the reluctance torque is determined by the q-axis inductance. Furthermore, the q-axis inductance increases as the q-axis core thickness increases. Fig. 1(a) shows the definition of the q-axis core thickness and FEA result according to the q-axis core thickness. As the q-axis core thickness increases, the torque is improved due to the reluctance torque, but the torque ripple increases. In order to reduce the torque ripple, another design parameter is required. The tapering of magnet can reduce the torque ripple because the sinusoidal magnetic flux density. Therefore, the tapering of magnet is selected as the optimal design parameter. Fig. 1(b) shows the definition of the tapering of magnet and FEA result according to the tapering of magnet. According to the tapering of magnet, the torque ripple is reduced as shown Fig. 1(b). As a result, the q-axis core thickness and tapering of magnet are selected as the optimal design parameters considering the torque density and ripple. The optimal design is performed using the performance maps according to the q-axis core thickness and the tapering of magnet. Fig. 2 shows the performance maps according to the design parameters. Considering the constraints of the power, the current density, and voltage limit, the optimal design point is selected to maximize the power factor and minimize the torque ripple. 4. Conclusion In this paper, the optimal design of SIPMSGM is proposed considering the power

factor and torque ripple. First, the comparison of pole-slot combinations are performed considering the efficiency, the current density, and power factor. Furthermore, the optimal design is performed using performance maps according to the design parameters. As a result, the optimal design is selected considering the various objective functions. In the full paper, the pole-slot combinations will be added, and the characteristics according to the design parameters will be detail discussed. Moreover, PTI/PTO mode characteristics of the optimal SIPMSGM will be discussed.

[1] A.G. Sarigiannidis, E. Chatzinikolaou, and A.G. Kladas, IEEE Trans. Transport. Electric., Vol. 2, pp. 558-569 (2016) [2] B. Qu, Q. Yang, and Z. Li, Symmetry, Vol. 12, pp. 1-14 (2020) [3] Y. Sun, W. Zhao, and Y. Cheng, IEEE Trans. Veh. Technol., Vol. 69, pp. 9601-9612 (2020)

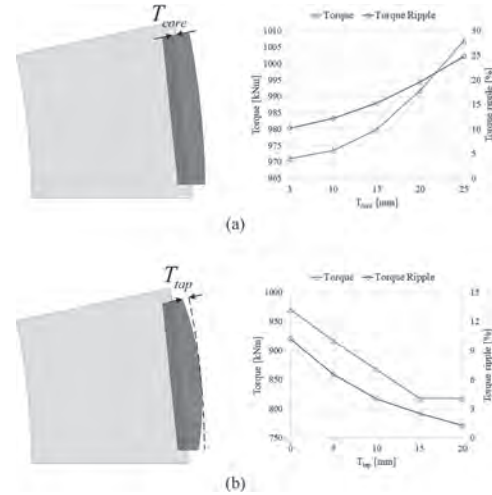


Fig 1. FEA result according to the design parameters (a) q-axis core thickness (b) tapering of magnet

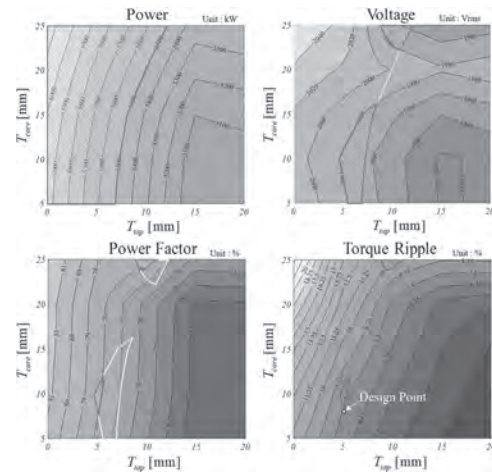


Fig 2. Performance map according to design parameters

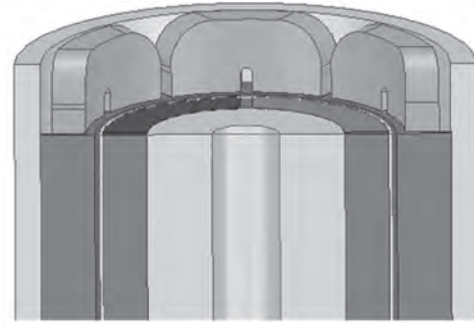
BR-14. A Study on Improving the Power Density of Slotless Motor Applying 3D Printing Technology.

Y. Park¹, S. Oh¹, H. Kim¹, S. Kim² and J. Lee¹

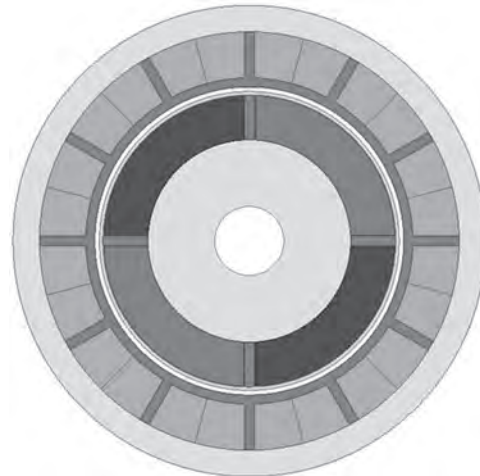
1. *Electrical Engineering, Hanyang University, Seongdong-gu, The Republic of Korea*; 2. *Electrical Engineering, Yuhan University, Bucheon, The Republic of Korea*

1) Introduction Slotless permanent magnet (PM) motors has no tooth and slot structure compared to the slot type motor. Hence, slotless PM motor, there are no cogging torque and low vibration, low noise, high power density, low iron loss [1]. However, since the slotless PM motor does not have a tooth-slot structure, the manufacturing process of the coil is complicated and a lot of time and cost is required. By using 3D printing technology, non-magnetic material tooth-slot structure can be produced, thereby solving the difficulties of manufacturing the conventional slotless PM motor winding. Using the proposed structure, it is structurally simple to manufacture the windings, and the electromagnetic characteristics of the conventional slotless PM motor can be equally taken. 2) Body In this paper, a design method for slotless PM motor that can replace the conventional slotless motor by conducting a study on the non-magnetic material tooth-slot structure using 3D printing technology is proposed. Additionally, in order to improve the power density on the proposed slotless PM motor, a design using an end-turn was conducted. In general slotted motors, cogging torque occurs because the permeance is uneven in the air gap, whereas in slotless PM motors, since slot structure do not exist, the air gap permeance is even and cogging torque does not occur. When the overall size is the equal, slotless PM motor can increase the fill factor more than slotted motor, which can result in greater Back-EMF. In addition, there are the moment of inertia of the rotor is low, so it is advantages high responsive, and the driving safety and control precision are high [2]. Despite these advantages of a slotless PM motor, it is more difficult to manufacture than a slotted motor. The windings of a general slotted motor are overlapped and made into ellipse shape. In this case, if each coil does not be made to the same shape, the coils are meshed. Eventually, this leads to a phase unbalance due to the shape of the windings [3]. In order to solve this difficulty of slotless PM motor manufacturing, a slotless PM motor design using 3D printing technology was conducted. By using 3D printing technology, a non-magnetic (polycarbonate material) tooth-slot structure is printed to structurally support the coil. Then, while having a structurally slotted structure, it is possible to take the power characteristics of a slotless PM motor in terms of electromagnetic. In this process, the response surface method (RSM) was used to conduct optimal design of the slotless PM motor applying 3D printing technology. The objective function was set as torque, power, and efficiency to derive the optimal values of major design parameters. In addition, when a winding is manufactured as the method of a slotted motor, the end-turn of the coil does higher than the stacking length of the stator, which occurs to leakage magnetic flux. An Additional design, high-height stator design, was conducted to improve the power density of the slotless PM motor by using magnetic flux leakage from the end-turn of the winding. A motor design algorithm was established by applying a high-height stator structure that increases the stacking length of the stator by the length of the end-turn that occurs when winding manufacturing. Slotless PM motor applied with this algorithm are designed, manufactured, and experimented. Conventional target slotless motors had a torque of 0.2Nm and a power density of 0.267W/g, whereas the improved slotless PM motor had a torque of 0.25Nm and a power density of 0.326W/g, indicating that the power characteristics were improved. 3) Conclusion In order to solve the difficulty of manufacturing the windings of a slotless Pm motor, a motor design incorporating 3D printing technology was conducted. A method combining the 3d printing injection molded structure with the stator in the motor was derived. When 3D printing injection molded structure was applied, the major design parameters were selected to derive optimal results using RSM to proceed with the optimal design of the motor. Furthermore, in order to improve the power density within a limited size, the design using the leakage magnetic flux of end-turn was additionally conducted. The motor design algorithm that goes through this process was established, and a prototype of the proposed motor was manufactured, and the finite element method (FEM) result and the actual experimental result were compared to verified that the power density was improved.

Reference [1] Jung-Moo Seo, "Design and Analysis of Slotless Brushless DC Motor", IEEE Transactions on Industry Applications, vol. 47, no. 2, pp. 730~735, (2011) [2] Nicola Bianchi, "High speed drive using a slotless PM motor", IEEE Transactions on Power Electronics, vol. 21, no. 4, pp. 1083~1090, (2006) [3] Jin Hur, "Three-dimensional characteristic analysis of micro BLDC motor according to slotless winding shape", IEEE Transactions on Magnetics, vol. 39, no. 5, pp. 2989~2991, (2003)



(3D image) proposed motor by applying 3d printing injection molded structure and high-height stator structure



(2D image) proposed motor by applying 3d printing injection molded structure

BR-15. A Study on Improving Magnetization Performance of Spoke Type Motor Through Asymmetric Magnetization Method.

M. Jeong¹, K. Lee², H. Pyo¹, D. Nam¹ and W. Kim¹

1. Gachon University, Seongnam, The Republic of Korea;

2. Hanyang University, Seongdong-gu, The Republic of Korea

In the process of manufacturing a permanent magnet motor, magnetization of a permanent magnet is essential. Permanent magnet magnetization methods include Single product magnetization and post-assembly magnetization. Single product magnetization is a method of magnetizing individual or multiple magnets, and since a magnetizing magnetic field is directly applied to the magnet, complete magnetization is possible. However, in this method, not only is it difficult to assemble in the rotor due to the attraction force of the magnet, but also the iron powder is attached to the magnet, creating a tolerance. Therefore, the Single product magnetization method is not suitable for mass production. In order to solve the problem of Single product magnetization described above, a method of magnetizing after assembling a permanent magnet to a rotor is widely used. The post-assembly magnetization method is a method of applying a magnetized magnetic field after inserting an unmagnetized magnet into the rotor. Since an unmagnetized magnet is inserted into the rotor before magnetization, there are no difficulties and tolerances in assembly due to attraction force. Therefore, many magnetization companies currently use the magnetization method after assembly. However, the above method is difficult to apply to all permanent magnet motors. For example, in the case of a surface-mounted Permanent Magnet Synchronous Motor (SPMSM), a permanent magnet is attached to the surface of the rotor, so that it can receive a magnetic field completely. However, in the case of spoke-type PMSM, the permanent magnets are arranged in the radial direction in the rotor, so the magnetic field is divided in half and flows during magnetization. That is, only half of the magnetizing magnetic field is applied to the permanent magnet, so the magnetization performance is greatly degraded. Also, during magnetization, the magnetic flux does not reach the permanent magnet located inside the rotor due to magnetic saturation of the pole piece of the rotor (the part of the rotor between the magnet and the magnet). Spoke type motors are motors that are in the spotlight as motors that use non-rare earth to generate high magnetic energy. However, because of a fact that it is not fully magnetized during magnetization, there are restrictions on its use, so research is needed to solve this. Therefore, in this paper, a study was conducted on the asymmetric magnetization method to improve the magnetization performance of the spoke type motor. As mentioned above, extant magnetization method has a symmetrical structure, so when the spoke type magnetization is performed, the magnetizing field is divided in half and flows through the permanent magnet. Therefore, in this paper, a different magnetization path was created by applying the asymmetric magnetization method, and by using this, the magnetization performance compared to extant magnetization method was greatly improved.

[1] Min-Fu Hsieh, Yao-Min Lien and David G. Dorrell, "Post-Assembly Magnetization of Rare-Earth Fractional-Slot Surface Permanent-Magnet Machines Using a Two-Shot Method", IEEE Trans. Ind. Appl., Vol. 47, no.6 Nov./Dec. 2011. [2] Kyu-Seob Kim, Min-Ro Park, Hae-Joong Kim, Seung-Hee Chai, and Jung-Pyo Hong, "Estimation of Rotor Type Using Ferrite Magnet Considering the Magnetization Process", IEEE Trans. Magn., Vol. 52, no. 3, Mar. 2016. [3] S. L. Ho, H. L. Li, and W. N. Fu, "A Post-Assembly Magnetization Method of Direct-Start Interior Permanent Magnet Synchronous Motors and Its Finite-Element Analysis of Transient

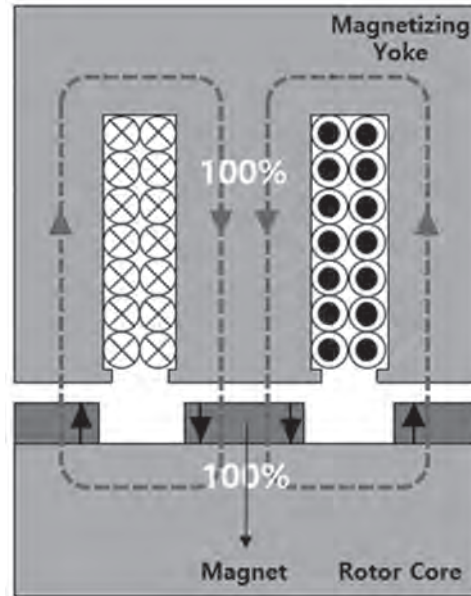


Fig. 1 Magnetization of SPMSM

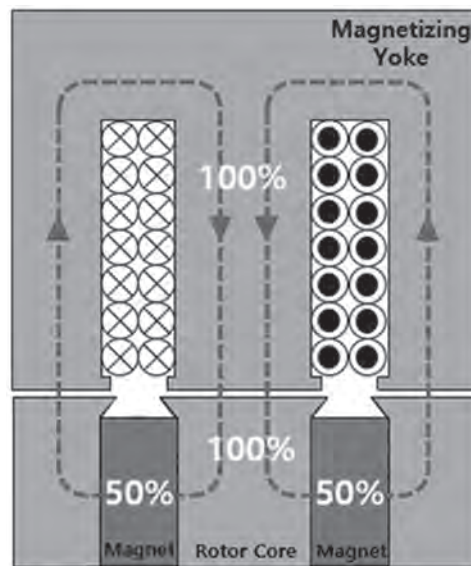


Fig. 2 Magnetization of Spoke type PMSM

BR-16. A Study on Electrical Power Steering Motor's 2-Stage Skew Shape Design to Reduce Cogging Torque and Torque Ripple.

D. Shin¹, S. Lee¹, S. Song¹, K. Kim¹ and W. Kim¹

1. Electrical Engineering, Gachon University, Seongnam, The Republic of Korea

The development of permanent magnets (PM) and the growing interest in electric motors with high torque high output power and high efficiency Brushless Permanent Magnet Direct Current motors are used in industry and various fields and have high output power As the interest in these BLDC motors which satisfy high efficiency and high torque grows the supply is unstable due to the high price of rare earth which is the raw material of permanent magnets and export restrictions so the production cost and future environment Considering the problem we provide a model of the rotor shape and rotation of the Neodymium-Free EPS (Electric Power Steering) Motor In the case of EPS Motor which is used in the steering system of Electric mobility EPS which is an electronic steering system provides steering performance that controls the motor with high precision based on the conditions of the vehicle without utilizing the existing hydraulic system Therefore it is important to reduce the cogging torque and torque ripple components at design as steering feel responsiveness and stability are paramount Therefore in order to satisfy high output and high performance the Spoke-Type rotor shape in which magnets are arranged in the radial direction and the Skew rotor shape in consideration of vibration and noise due to torque ripple of cogging torque are provided To do In the case of the Spoke-Type rotor shape the magnets are arranged in the radial direction and the d-axis and q-axis iron cores are inserted to concentrate the magnetic flux In the case of the Spoke-Type rotor shape high output and high torque can be satisfied even with the same amount of magnet used In the case of the Spoke-Type rotor shape the performance of the motor changes according to the size of the magnet When the length of the magnet becomes long a leakage magnetic flux is generated on the rotor Therefore the optimum magnetic length that can minimize the leakage magnetic flux was analyzed and the thickness of the magnet was increased in order to maintain the performance An important requirement from EPS motors other than high torque and high output is a cogging torque and torque ripple reduction design to minimize vibration and noise Of the several proposals for reducing cogging torque and torque ripple we are proceeding with a design that utilizes the skew produced by twisting the rotor angle For skew a continuous skew design that continuously reflects the twist angle is effective in reducing cogging torque and torque ripple but the creation is significantly reduced Therefore in this paper we provide a multi-stage skew that divides the stack into two in consideration of the second preparation A 3D analysis is required to reflect the axial asymmetry when designing the skew motor Since this has the drawback of dramatically increasing the analysis time the individual stages are analyzed two-dimensionally and added up and design errors are analyzed via three-dimensional FEA (Finite Element Analysis) to verify the validity did Therefore in this paper we provide the rotor shape of the EPS motor that satisfies high torque and high output and considers vibration and noise

Wenliang Zhao; Thomas A. Lipo; Byung-Il Kwon IEEE Transactions on Magnetics (Volume: 51, Issue: 11, Nov. 2015) Mizanoor Rahman Mohammad; Kyung-Tae Kim; Jin Hur IEEE Transactions on Magnetics (Volume: 49, Issue: 5, May 2013) Shanming Wang; Jianfeng Hong; Yuguang Sun IEEE Transactions on Industrial Electronics (Volume: 67, Issue: 6, June 2020)

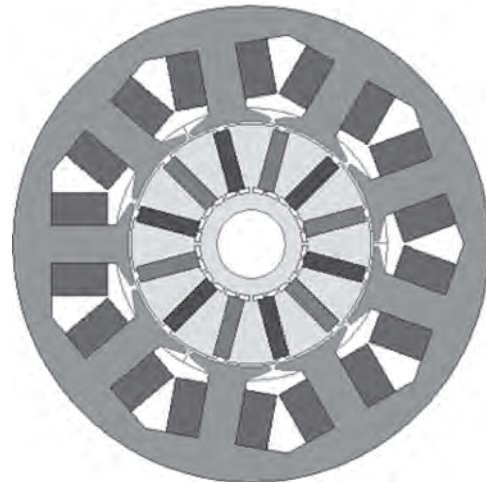


Fig.1. Rotor Shape of Spoke Type

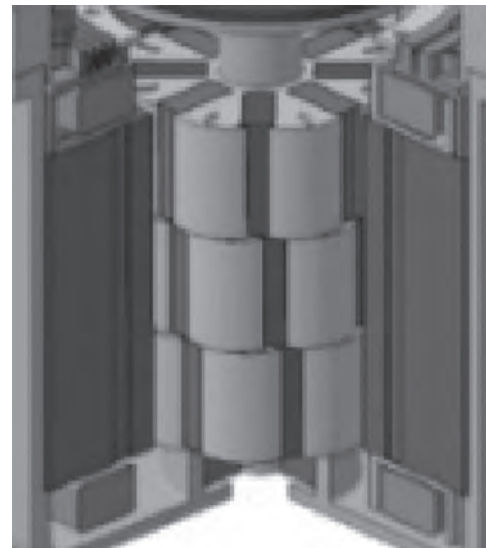


Fig.2. Skew of Rotor Shape

BR-17. A Study on Core Skew for Performance Improvement of Double-Layer Spoke Type PMSM.

D. Nam¹, K. Lee², H. Pyo¹, M. Jeong¹ and W. Kim¹

1. *Electrical Engineering, Gachon University, Seongnam, The Republic of Korea;* 2. *Hyundai Kia Motors Namyang Institute, Hwaseong, The Republic of Korea*

Abstract: The spoke type permanent magnet synchronous motor (PMSM), which is a general ferrite magnetic flux concentrated motor, has a low portion of reluctance torque at the total torque magnitude. Therefore, as a way to increase the reluctance torque, there is a double-layer spoke type PMSM that can maximize the difference in inductance between the d-axis and the q-axis. However, in the double-layer spoke type PMSM, cogging torque, torque ripple, and total harmonic distortion (THD) increase as reluctance torque is maximized, which is the main cause of vibration and noise. In this paper, a method is proposed that provides the same effect as skew without dividing stages of the permanent magnet by dividing the core of the rotor into two types so that it is easy to manufacture according to the number of stages unlike extant skew methods. Based on the method, the reduction of cogging torque and THD was verified by Finite Element Analysis (FEA). 1. Introduction The general interior permanent magnet synchronous motor (IPMSM) uses NdFeB magnets to take advantage of the high airgap magnetic flux density. However, it had an adverse impact on cost of the motor because there are fluctuation of the cost from limited sources of heavy rare earth. Therefore, for stable supply of permanent magnets, a lot of development of a spoke type permanent magnet synchronous motor (PMSM), which is a structure capable of concentrating magnetic flux by using a ferrite magnet having a low magnetic flux density, has been conducting. The spoke type PMSM concentrates the magnetic flux density and can replace the NdFeB magnet used in the extant PMSM with a ferrite magnet. However, in general spoke type PMSM, the portion of reluctance torque is low because the difference in inductance between the d-axis and the q-axis is not large. In order to further utilize this reluctance torque, a double-layer spoke type shape that can maximize the difference in inductance between the d-axis and the q-axis can be used to bigger reluctance torque to improve motor performance. However, increasing the reluctance torque increases cogging torque, torque ripple, and total harmonic distortion (THD), which in turn leads to vibration and noise problems. Therefore, the double-layer spoke type PMSM needs a design that can reduce cogging torque and THD. As a representative method, it can be solved by applying skew to the rotor, but the conventional method of applying skew is not a good method in terms of productivity because it is difficult to manufacture because it divides the stages of the permanent magnet. For ameliorate of the limitation, the shape of the rotor core is divided and cross-stacked into stack1 and stack2 so that the permanent magnet can be inserted in one shape as the conventional shape. Therefore, the shape of the rotor core is divided into stack1 and stack2 so that the permanent magnet can be inserted in one shape as before and cross-stacked. The stack1 cuts the left part fixing the permanent magnet, and the stack2 cuts the right part fixing the permanent magnet to apply the same effect as skew. In this paper, this is expressed as a core skew, and through this core skew, the design to reduce cogging torque, torque ripple, and THD is conducted while considering productivity. 2. Concept of Core Skew The core skew represents the stacking of only cores of opposite shapes when stacking the rotor cores of the motor. The contents of the basic theory are as follows. Fig. 1 shows stack No. 1 and stack No. 2, respectively. Due to the shape of the rotor core, the phases of the airgap magnetic flux density of stack No.1 and stack No.2 are shifted, and when the two stacks are synthesized due to the phase of the shifted airgap magnetic flux density. As shown in Fig. 2, the cogging torque decreases. Also Fig. 1 shows the shape of applying core skew to the conventional model by intersecting and stacking stack No. 1 and stack No. 2. Through this core skew structure, research to reduce cogging torque, torque ripple, and THD is conducted. Most of the original skew research is conducted in 3D FEA, but since 3D FEA requires a lot of time, first calculate the optimal model using 2D FEA and then proceed with 3D FEA according to the number of steps considering 3D effect. The final result will be revealed on full paper. Acknowledgment This work was supported by the Technology Innovation Program (No. 20011495) funded by the Ministry of Trade, Industry & Energy(MOTIE, Korea), in part by the

National Research Foundation of Korea (NRF) Grant funded by the Korean government. (No. 2020R1A2C1013724).

References [1] D. G. Dorrell, M.-F. Hsieh, and A. M. Knight, "Alternative rotor designs for high performance brushless permanent magnet machines for hybrid electric vehicles," *IEEE Trans. Magn.*, vol. 48, no. 2, pp. 835–838, Feb. 2012. [2] M. M. Rahman, K.-T. Kim, and J. Hur, "Design and optimization of neodymium-free SPOKE-type motor with segmented wing-shaped PM," *IEEE Trans. Magn.*, vol. 50, no. 2, Feb. 2014, Art. ID 7021404. [3] S. I. Kim, S. Park, T. Park, J. Cho, W. Kim, and S. Lim, "Investigation and experimental verification of a novel spoke-type ferrite-magnet motor for electric-vehicle traction drive applications," *IEEE Trans. Ind. Electron.*, vol. 61, no. 10, pp. 5763–5770, Oct. 2014 [4] K.-C. Kim, "A novel method for minimization of cogging torque and torque ripple for interior permanent magnet synchronous motor," *IEEE Trans. Magn.*, vol. 50, no. 2, Feb. 2014, Art. ID 7019604. [5] C. Bianchini, F. Immovilli, E. Lorenzani, A. Bellini, and M. Davoli, "Review of design solutions for internal permanent-magnet machines cogging torque reduction," *IEEE Trans. Magn.*, vol. 48, no. 10, pp. 2685–2693, Oct. 2012. Z. Q. Zhu, Y. Liu, and D. Howe, "Minimizing the influence of cogging torque on vibration of PM brushless machines by direct torque control," *IEEE Trans. Magn.*, vol. 42, no. 10, pp. 3512–3514, Oct. 2006.

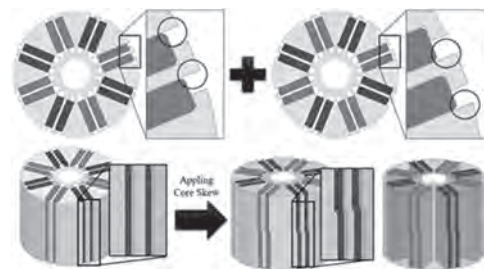


Figure 1. Concept diagram of core skew

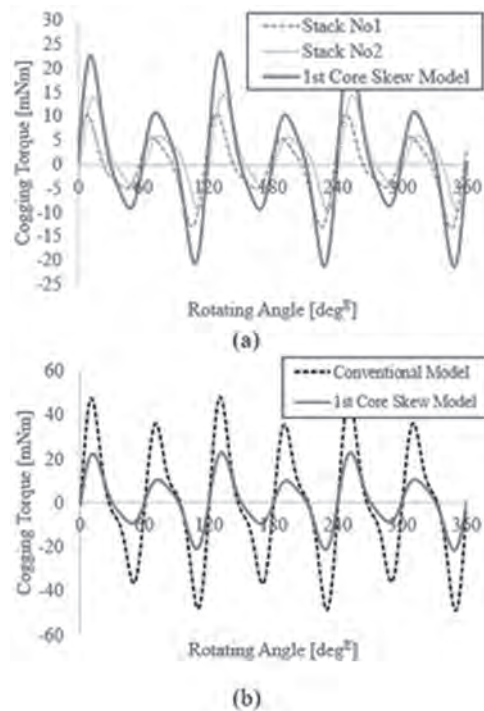


Figure 2. Cogging torque comparison. (a) 1st core skew model cogging torque; (b) Comparison between the conventional model and 1st core skew model.

Session BS
LINEAR MACHINES, ELECTROMAGNETIC ACTUATORS AND APPLICATIONS
(Poster Session)

Mohamed Ibrahim, Co-Chair
Ghent University, Ghent, Belgium

Salvatore Perna, Co-Chair
University of Naples Federico II, Naples, Italy

BS-01. Optimal Design of Short-Stroke Linear Oscillating Actuator for Minimization of Side Force by Using Response Surface Methodology.

W. Kim¹, C. Kim¹, H. Shin¹, S. Jeong² and J. Choi¹
 1. Electrical Engineering, Chungnam National University, Daejeon, The Republic of Korea; 2. LG Electronics, Yeongdeungpo-gu, The Republic of Korea

Most of the modern industrial machinery and automation equipment obtain a straight thrust by using a rotary motor and a gear, which is a power converter. However, in such power transmission, mechanical noise and friction are produced, and vibration loss occurs. Thus, position control, system, and efficiency deteriorate [1]. In contrast, linear motors do not require gears, ball screws, racks, or pinions, which are used for linear motion conversion in general rotating equipment. Hence, they are not affected by problems such as heat generation, inertia, and stiffness deterioration. Thus, they can function at high speed and offer high precision. Among linear motors, permanent-magnet linear synchronous motors are used in various types of equipment, such as compressors, pumps, and Stirling low-temperature coolers, because of their high efficiency, thrust density, and excellent control performance [2]. However, a disadvantage of the permanent magnet linear synchronous motor is the side force, which is inevitably generated by the magnetically coupled structure of the stator and mover. The side force imparts eccentricity to the rotor. Eccentricity of the rotor is that the center of the shaft is not located at the center of the stator. This causes noise and vibration during operation, and in severe cases, renders the motor inoperable [3]. Eccentricity thus decreases the reliability of a system. Once design and manufacture are completed, a spring with higher rigidity should be used to reduce eccentricity. Therefore, side-force reduction is essential at the design stage to secure system reliability and prevent system complexity. In this study, an optimal design of the side force of a short-stroke linear oscillating actuator (LOA) was performed. Owing to the numerous design variables, the optimum design of the motor requires a considerable analysis time. Particularly, the required analysis time increases exponentially for three-dimensional analysis, such as that required for an LOA, if stochastic algorithms such as genetic and particle swarm optimization algorithms are used. To address this problem, approximate optimal design methods that require relatively fewer experimental points have garnered attention [4]. In this study, the response surface methodology (RSM) was used for the optimal design. The RSM can determine the curvature effect and yield a precise optimal solution through repetition of center points and axis points. The main factors causing the side force were investigated through factorial design in this study [5]. The residual magnetic flux density of the permanent magnet, the inner and outer air gaps, and the magnet fill factor were selected as the optimization variables based on factorial design. Based on the selected variables, experimental points were selected via central composite design, which is most commonly used in response surface design. The side force was set as the objective function of the optimization. The back EMF of the original model was set as a constraint to minimize the reduction in the output power. The reliability of the optimization was determined through FEM and experiments involving the manufactured initial LOA model. Fig. 1 (a) show the 3-D analysis model and manufactured initial LOA model. The LOA consists of an outer core, inner core, a coil, and moving magnet. The moving magnet performs reciprocating motion along the z-axis and generates an electromagnetic force. Fig. 1 (b) shows the experimental setup for the LOA. Fig. 2 (a) and (b) show the flux paths of the initial and optimized LOA models, respectively. In the optimized model, the residual magnetic flux density of the permanent magnet was reduced from 1.3 to 1.1, the inner air gap was increased from 0.3 mm to 0.5 mm, and the magnet fill factor was increased from 0.7 to 1. Fig. 2 (c) presents the side force regression model obtained via RSM according to the magnet specifications. Fig. 2 (d) shows the side force optimization result. The side force was reduced by 50% and the back EMF was maintained at 90% when compared with those of the initial LOA model. Further discussions, analysis results, and experimental results are presented in the final paper.

[1] I. Boldea and S. A. Nasar, IEEE Trans. Energy Conversion, vol. 14, no.3, pp. 712–717, [2] Chang-Woo Kim, Gang-Heyon Jang, Kyung-Hun Shin, IEEE Transactions on Applied Superconductivity, VOL. 30, NO. 4, June

2020 [3] Navneet Behra, IEEE International Conference on Technologies for Smart-City Energy Security and Power (ICSESP-2018), March 28-30, 2018 [4] Yoshifumi Okamoto, Yusuke Tominaga, Shinji Wakao, IEEE Transactions on Magnetics, VOL. 50, NO. 2, February 2014 [5] W. Yim, K. An, J. Seo, D. Woo and H. Jung, 2010 International Conference on Electrical Machines and Systems, Incheon, 2010, pp. 1268-1272.

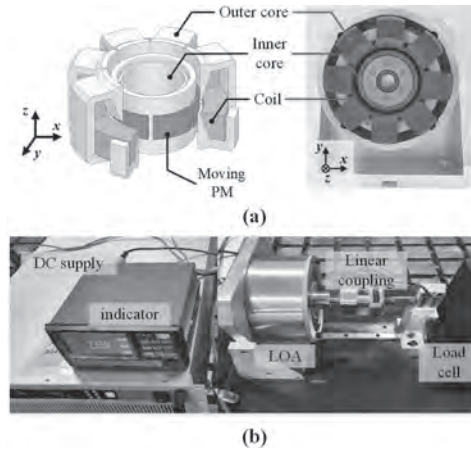


Fig. 1. (a) 3-D analysis model and manufactured initial LOA model, (b) Initial LOA model experiment setup

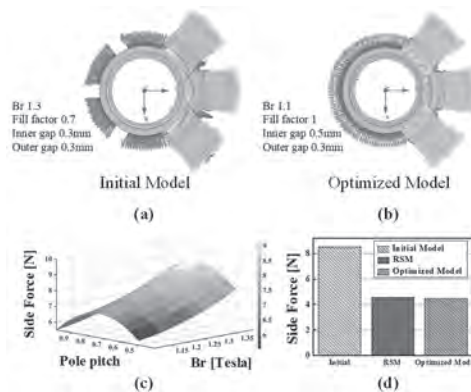


Fig. 2. (a) flux path of initial model, (b) flux path of optimized model, (c) side force according to magnet specifications (d) side force reduction result

BS-02. Characteristics Analysis and Experimental Study on Reduction of Vibration and Noise in Permanent Magnet Synchronous Machines.

K. Shin¹, T. Bang² and J. Choi²

1. Chonnam National University, Yeosu, The Republic of Korea;

2. Chungnam National University, Daejeon, The Republic of Korea

Permanent magnet synchronous machines (PMSMs) are becoming popular as a key technology for applications such as home appliances, industrial tools, and electric vehicles because of their high efficiency, high power density, and low maintenance costs. However, PMSMs have the drawback of vibration caused by the interaction between the stator teeth and the rotor magnets, significantly affecting the machine's performance [1]. The vibration of machine can be classified into three categories based on its source: 1) aerodynamic; 2) mechanical; and 3) electromagnetic. The electromagnetic source is the dominating one in low- to medium-power rated machines. Cogging torque, torque ripple, and unbalanced magnetic forces are the major electromagnetic vibration sources. Therefore, it is desirable to account for these electromagnetic sources at the design stage itself. Accurate calculations of the magnetic field are essential for the accurate performance prediction of PMSMs; hence, magnetic field analysis using the finite element method (FEM) is preferred. However, this analysis is often time consuming and has poor flexibility. In this paper, an analytical solution based on Fourier analysis is proposed to compute the cogging torque, torque ripple, and unbalanced magnetic forces in PMSMs, as shown in Figs. 1(a) and 1(b). The magnetic field solutions are obtained using a magnetic vector potential and a boundary condition [2]. Based on these solutions, the electromagnetic torque and force are determined analytically. The analytical results for flux density and magnetic pull force are validated with FEM results, as shown in Fig. 1(c). To verify the analytical results of the proposed method, an experimental system (as shown in Fig. 2(a)) was implemented on a servomotor with a torque sensor and a gap sensor. Fig. 2(b) shows a schematic diagram of a system for measuring rotor vibrations in a PMSM. Position the gap sensor at 90° intervals in the x and y directions and measure the displacement by rotation. In this study, PMSM was designed based on combination of pole / slot combination and slot opening / pole arc ratio which can minimize the electromagnetic excitation component as well as electromagnetic analysis of PMSM using analytical method. Fig. 2(c) shows the results of the loci graph for the displacement of the rotor in the x and y direction when the AC load operation is performed under the rated condition. According to KS B 0411, the shaft diameter of the machine is 35 mm and the machining error of the rotor shaft is 0.3 mm. From the measurement results, it was confirmed that the vibration of the generator is less than the machining error, and the generator is hardly vibrated when the AC load is operated. From the FFT analysis, it can be seen that the main vibration components are primary and secondary components, and the vibration components of the generators are mostly generated from mechanical imbalance and mechanical looseness. From the analysis results, it is possible to select the electromagnetic design variables such as pole slot combinations, width of slot opening, and optimal pole arc ratio that can reduce the major electromagnetic vibration sources. Therefore, the proposed method could be very useful in the initial design and optimization process of PMSMs for improving electromagnetic performances. The detailed analysis results, discussions, and measurements of the PMSMs will be presented in the full paper.

[1] V. Simon-Sempere, M. Burgos-Payan, J.-R. Cerquides-Bueno, "Cogging Torque Measurement Using the Electromotive Force in Surface-Mounted Permanent-Magnet Motors", *IEEE Trans. Magn.*, vol. 51, no. 7, 8105910, Jul. 2015. [2] B. L. J. Gysen, K. J. Meessen, J. J. H. Paulides, E. A. Lomonova, "General formulation of the electromagnetic field distribution in machines and devices using Fourier analysis", *IEEE Trans. Magn.*, vol. 46, no. 1, pp. 39-52, Jan. 2010.

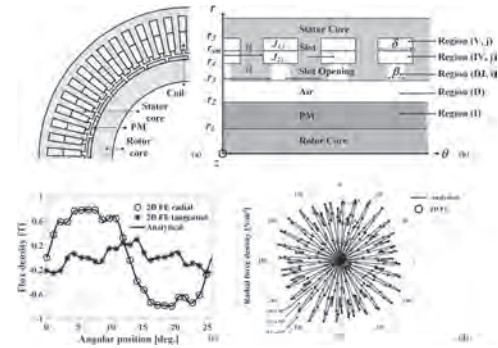


Fig. 1. (a) Analysis model of PMSM, (b) analytical model, (c) magnetic flux density from analytical and FEM results, and (d) magnetic pull force from analytical and FEM results.

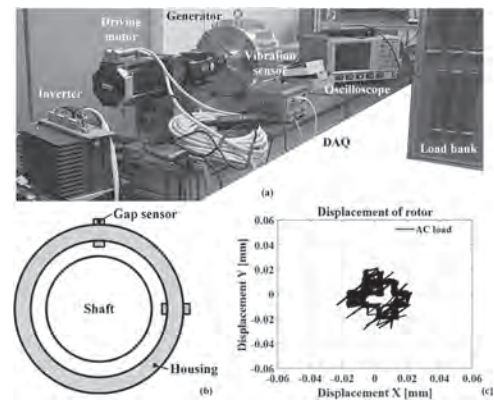


Fig. 2. (a) Experimental setup for force and torque measurement, (b) a conceptual view of a rotor vibration measurement system, and (c) displacement of the rotor under AC load conditions.

BS-03. Design and Optimization of a Novel Dynamic Relieving-DC-Saturation Transverse Variable Flux Tubular Linear Memory Machine.

Z. Li¹, X. Zhang², S. Niu¹ and W. Fu¹

1. Department of Electrical Engineering, The Hong Kong Polytechnic University, Hong Kong, Hong Kong; 2. Shenzhen In-Drive Amperex Co. Ltd, Shenzhen, China

Abstract Due to the constant flux of slot PM for relieving-saturation, the effect is limited when it is applied to the variable biased flux machine(VBFM). To address this issue, low coercivity permanent magnet (LC-PM) is applied to slot PM of transverse variable flux tubular linear machine (TVFTLM) to accomplish the dynamic relieving-DC-saturation in the stator core in this paper, and the method to verify the value of magnetizing current is also illustrated. The novel transverse variable flux tubular linear memory machine (TVFTLMM) has merits of higher thrust density, higher overload capacity and lower leakage flux. The key to achieve this is that the remanence of the LC-PM can be varied in coordinate with the magnetizing current which is adjusted online for dynamic-relieving-DC-saturation. **I. Introduction** Locating tangential magnetization PM at slot opening of motor is an effective method to relieve saturation in the stator core [1]. However, the saturation in the stator core of VBFM is variable, while the flux excited by conventional slot PMs are constant. Therefore, conventional relieving-DC-saturation method cannot cancel VBFM saturation perfectly and may cause further leakage flux. The low coercivity PM (LC-PM) such as Al-Ni-Co is a kind of material whose magnetic status is relatively easy to change via pulsing magnetizing current [2]. Therefore, the LC-PM is a quite suitable candidate for VBFM to alleviate saturation in the core. The transverse flux tubular machine (TFTM) achieving much smaller normal force and decoupling three phases windings has wide application in industry [3]. On the other hand, It is also a kind of VBFM suffered from variable saturation and leakage flux. In this paper, LC-PM material whose magnetization can be regulated online is applied to a novel TVFTLM to increase its overload capability. In this way, when DC excitation changes, the magnetization degree of LC-PM can be adjusted accordingly to cancel the saturation in the core. The methodology of this online flux regulation is also discussed in this paper. **II. Design Mechanism and Analysis Method** The stator of the motor is composed of 3 separate parts, which have 12 teeth and is arranged alternately with armature windings, field windings and magnetizing windings wound on teeth, as shown in the Fig.1. The other parts of phase B and C is arranged in line with phase A, and the distance between two neighboring phases is $2k\tau+2/3\tau$, where k is an integer, and τ is pole pitch. The mover of this proposed motor is composed of the laminations with stack thickness of τ , and switched by 60 degrees every τ distance. The LC-PMs are located at slot opening. Together with armature windings, the magnetizing windings are wound on the armature teeth. When armature teeth A1, A3 and A5 aligned with mover teeth at $z=0$, the magnetic loop of A2, A4 and A6 is open, and the pulsing magnetizing current is applied on M2, M4 and M6 to generate magnetization flux for part of slot LC-PMs, as shown in Fig.1 (a). Vice versa, at $z=\tau$, current is applied on M1, M3 and M5 to magnetize the rest of LC-PMs, which is shown in Fig.1 (c). Fig.1 (e) compares the distribution of no-load flux linkages with constant PMs (CPM) and LC-PMs, where TVFTLM with changeable LC-PMs could cancel the DC components of flux linkages perfectly, regardless of the value of DC excitation. The hysteresis model presented in Fig.1 (f) could demonstrate the operation points of the LC-PMs intuitively. The operation points of the LC-PMs can be determined by magnetic field intensity H_{mk} and load line. With different excitation modes (e.g., light, rated and over excitation), the operation points of the slot PM can be switched among P_1 , P_2 , and P_3 by applying magnetizing/demagnetizing current. Hysteresis model is utilized and coupled with transient finite element method (FEM) for calculation. **III. Design Consideration and Results** The main initial design parameters of the proposed motor are set as follows. Radius of outer stator $R_{so}=50\text{mm}$, the split ratio $r_{sp}=0.6$, field windings turns per slot $N_{dc}=75$, armature winding turns per slot $N_{ac}=75$, and the ratio of pole arc between stator and mover $r_{pole}=0.9$. The coercivity of the LC-PMs H_{c1} is set as -119366 A/m and the remanence $B_r=1.05\text{T}$. In Fig.2, no-load magnetic field distribution of proposed TVF-TLM with LC-PMs and CPMs are compared. It can be seen that with same DC-excitation, the

flux density in the core with LC-PMs is lower than that with CPMs regardless of DC excitation, especially when the excitation current comes to 12A. Therefore, from the perspective of flux distribution, comparing with CPMs, the LC-PMs could further alleviate saturation and improve the performance of motors. **IV. Conclusion** In this paper, a dynamic relieving-DC-saturation transverse variable flux tubular linear memory machine (TVF-TLMM) is proposed. The memory LC-PMs are innovatively applied on the biased-flux TVF-TLMM to relieve saturation in the core dynamically. The comprehensive design consideration and optimization of the proposed machine will be presented in the full paper. **Acknowledgement** This work was supported in part by grants from the Hong Kong Research Grants Council, Hong Kong, China, under Project PolyU 152058/17E and PolyU 152143/18E.

[1] X. Zhao, S. Niu and X. Zhang, IEEE Trans. Ind. Electron., vol. 67, p.9571 (2020) [2] H. Yang, Z. Q. Zhu and H. Lin, IEEE Trans. Ind. Electron., vol. 65, p.9168 (2018) [3] X. Zhao and S. Niu, IEEE Trans. Ind. Electron., vol. 66, p. 494 (2019)

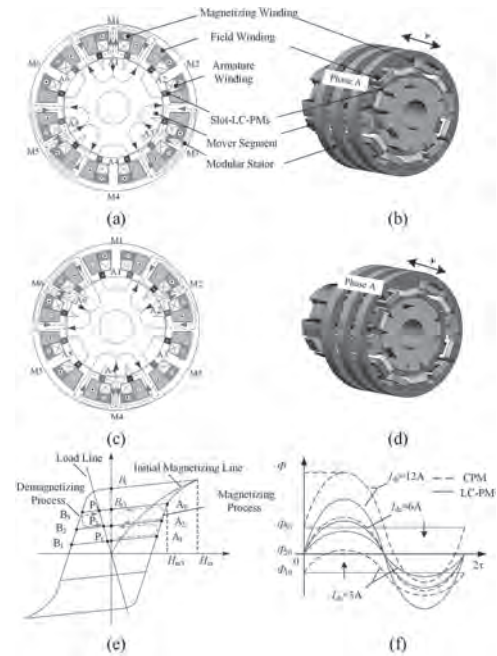


Fig.1 Operation Principle of the Proposed Machine (a) 2D Cross section at $z=0$ (b) 3D Model at $z=0$ (c) 2D Cross section at $z=\tau$ (d) 3D Model at $z=\tau$ (e) Operation Principle of LC-PMs (f) Hysteresis Model

Fig.1 Operation Principle of the Motor (a) 2D Cross section at $z=0$ (b) 3D Model at $z=0$ (c) 2D Cross section at $z=\tau$ (d) 3D Model at $z=\tau$ (e) Operation Principle of LC-PMs (f) Hysteresis Model

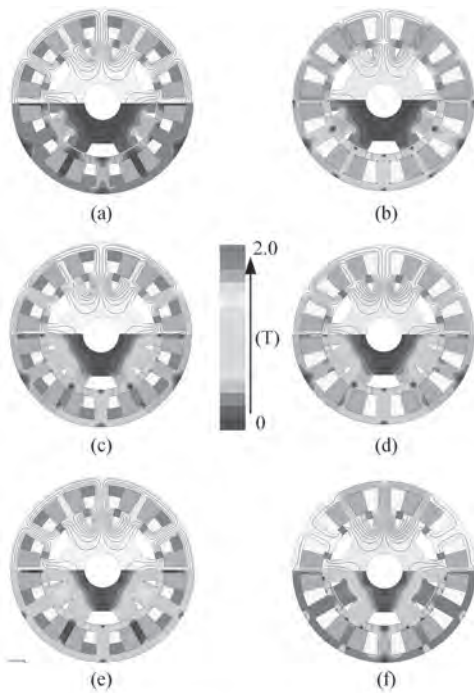


Fig. 2. Comparison of Field Distribution. (a) $I_{dc}=3A$ (LC-PMs) (b) $I_{dc}=3A$ (CPMs)
 (c) $I_{dc}=6A$ (LC-PMs) (d) $I_{dc}=6A$ (CPMs) (e) $I_{dc}=12A$ (LC-PMs) (f) $I_{dc}=12A$ (CPMs)

Fig. 2. Field Distribution. (a) $I_{dc}=3A$ (LC-PMs) (b) $I_{dc}=3A$ (CPMs) (c) $I_{dc}=6A$ (LC-PMs) (d) $I_{dc}=6A$ (CPMs) (e) $I_{dc}=12A$ (LC-PMs) (f) $I_{dc}=12A$ (CPMs)

BS-04. Optimization of Detent Force in Linear Oscillatory Generator With Assisted Permanent Magnet and Stacking Effect for Stirling Engines Using Subdomain Analytical Method.

K. Shin¹, T. Bang², J. Choi², H. Cho², K. Lee³ and S. Lee³

1. Chonnam National University, Yeosu, The Republic of Korea;
2. Chungnam National University, Daejeon, The Republic of Korea;
3. Korea Institute of Industrial Technology, Gwangju, The Republic of Korea

The cogeneration system using recycling waste heat is one of the most effective ways to generate electricity without environmental pollution, and the Stirling engine power generating system has been actively studied [1]. The free-piston Stirling engine system connected to the electric machines performs thermo-mechanical-electrical energy conversions. Linear oscillatory generators (LOGs) applied to Stirling engines have the advantage of high transmission efficiency and maintenance by performing energy conversion without rotary to linear conversion mechanisms [2]. In addition, LOG with permanent magnet (PM) has high power density, high efficiency, high reliability, and compactness due to the use of a PM with high energy density and a tubular structure. However, one of the disadvantages of LOG with a PM is that it generates a high detent force between the PM and the iron core, which increases thrust force ripple, vibration, and noise, and worsens controllability. Therefore, research to improve the detent force is required at the design stage of the LOG. In this paper, a design method applying assisted PM and superposition principle in a circumferential direction to improve the detent force of LOG is presented using a subdomain analytical method. The application of assisted PMs to the LOG reverses the direction of the detent force and generates a restoring force that aligns the mover to the center, which improves the electro-mechanical performances of the LOG system by improving the spring coefficients [2]. Also, by determining the ratio of assisted PMs in the circumferential direction along with stacking effects, it is possible to derive an optimal model compared to the amount of PM usage within the stroke range of LOG. In particular, the subdomain analytical method was used for fast analysis and insight into the relationship between design variables and performances of LOG in electromagnetic optimization. Fig. 1 shows the prototype and design model of LOG with assisted PM, a two-dimensional (2D) finite element (FE) model, and a simplified model. As shown in Figs. 1(b) and 1(c), the 2D FE model and the analytical model can take into account the 3D effect by using the superposition principle according to the presence or absence of magnetization of the assisted PM. As shown in Fig. 1(c), the proposed model is divided into seven regions: air (I, III), main PM and assisted PM (II), slot opening (IV), slot (V), and end (VI, VII) regions. The magnetic fields and the electromagnetic performances obtained by the analytical method were compared with those obtained by the FE analysis and experimental results of the prototype; the comparison validates the analytical methods presented in the full paper. As shown in Figs. 2(a) and 2(b), the analytical results for the magnetic field according to assisted PM are in good agreement with the FE analysis results. With the stacking factor and superposition principle of the LOG, the Maxwell stress tensor was used to determine the electromagnetic forces according to a width of assisted PMs [3], [4]. Fig. 2(c) shows the analysis result of the detent force according to the width of assisted PMs at a minimum position of -13mm. As the width of the assisted PM increases, the detent force changes to the restoring force. Therefore, it is very important to select the optimal width of assisted PM considering the rated thrust force. Fig. 2(d) shows the comparison of analysis results according to initial and optimal design. It is observed that the direction of the detent force changes in the optimal design with assisted PM and the force is hardly generated in the stroke region. From the analysis results, it can be seen that the analytical method and optimization proposed in this paper were valid. The analytical modeling, analysis results, discussions, and measurements of the LOG will be presented in detail in the full paper.

for Free-Piston Stirling Engine Systems”, AIP adv., vol. 7, no. 5, May 2017, Art. no. 056667. [3] K. H. Shin, K. H. Kim, K. Hong, and J. Y. Choi, “Detent Force Minimization of Permanent Magnet Linear Synchronous Machines Using Subdomain Analytical Method Considering Auxiliary Teeth Configuration”, IEEE Trans. Magn., vol. 53, no. 6, June 2017, Art. no. 8104504. [4] K. H. Shin and J. Y. Choi, “Electromagnetic Analysis of Single-Phase Linear Oscillatory Actuator Based on Subdomain Analytical Model with End and Stacking Effects”, IEEE Trans. Magn., in press, 2020.

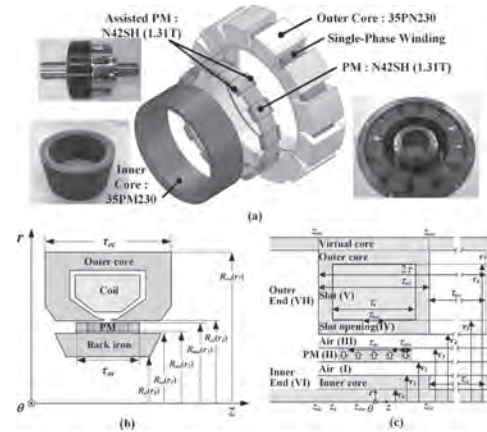


Fig. 1. Structure of LOG with PM: (a) main structure with a prototype, (b) analysis model, and (c) simplified analytical model.

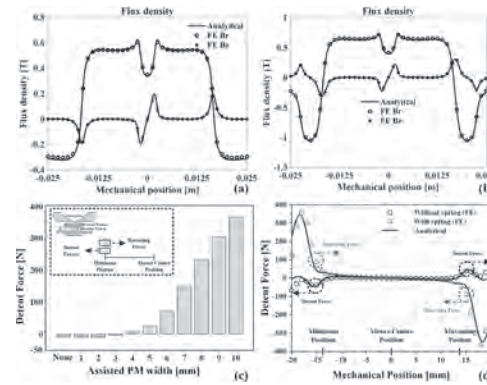


Fig. 2. Comparison of analysis results obtained by analytical model and 2D FE analysis: (a) flux density without assisted PMs, (b) flux density with assisted PMs, (c) detent forces according to a width of assisted PM, and (d) detent forces with initial and optimal models.

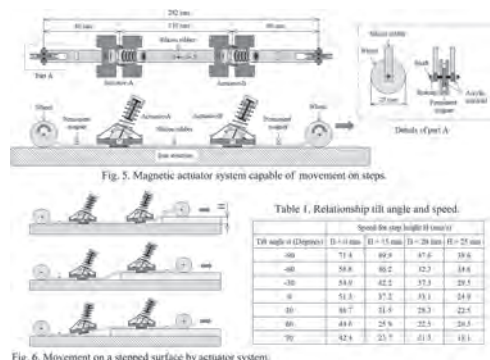
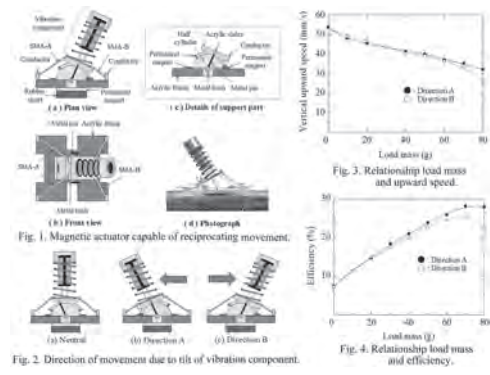
[1] M. Hadziselimović, G. Srpić, I. Brinovar, Z. Praunseis, S. Seme, and B. Štumberger, “A Novel Concept of Linear Oscillatory Synchronous Generator Designed for a Stirling Engine”, Energy, vol. 180, no. 1, pp.19-27, Aug. 2017. [2] J. M. Kim, J. Y. Choi, K. S. Lee, and S. H. Lee, “Design and Analysis of Linear Oscillatory Single-Phase Permanent Magnet Generator

BS-05. A Novel Magnetic Actuator System for Appearance Inspection of Complex Iron Structures.

H. Yaguchi¹ and Y. Itoh¹

1. Tohoku Gakuin University, Tagajo, Japan

In recent years, aging of social infrastructure such as bridges and industrial tanks has become a problem. Therefore, robots capable of working in difficult environments are desired. In this study, a novel magnetic actuator system capable of an appearance inspection on complex steel structures with steps was proposed. Fig. 1 shows a diagram of the magnetic actuator capable of a reciprocating movement on a magnetic substance. The magnetic actuator consists of a vibration component, an acrylic frame, four shape memory alloy (SMA) coil springs, eight electrodes, an acrylic semi-cylinder, an acrylic slider and two permanent magnets attached to the bottom of the frame. The vibration component consists of a permanent magnet of ring type, a translational spring, an electromagnet with iron core of the bobbin-type proposed by the authors in a previous paper [1]. The permanent magnet of ring type is NdFeB and is magnetized in the axial direction. The permanent magnet of ring type has an outer diameter of 12 mm, an inner diameter of 9 mm, and a thickness of 8 mm. The surface magnetic flux density measured using a tesla meter was 322 mT. The translational spring was a stainless steel compression coil type having an outer diameter of 12 mm, a free length of 25 mm. The bobbin-type electromagnet was inserted in the translational spring. The actuator has a height of 42 mm, a length of 40 mm, a width of 38 mm, and a total mass of 19 g. This actuator can move in the direction that the vibration component is tilted. Therefore, as shown in Fig. 1, the actuator support part was made to be rotatable. The reciprocating movement of the actuator was realized by tilting the vibration component using the expansion and contraction of four shape memory alloy (SMA) coil springs. After the vibration component is tilted, the acrylic semi-cylinder and the acrylic slider are held by the attractive force of the two permanent magnets even if the input current to SMA coil spring is stopped. Fig. 2 shows the direction of movement due to the expansion and contraction of SMA coil springs. Fig. 3 shows the relationship between the load mass and the vertical upward speed for two directions of movement. This figure shows that the actuator is able to climb upward at 32.1 mm/s while pulling a load mass of 80 g. Fig. 4 shows the relationship between the load mass and the efficiency. The maximum efficiency of the actuator was 28.1%. In both figures, almost the same movement characteristics were shown even if the direction of movement changes. There are many complicated steps in steel structures such as bridges and tanks. In order to realize the movement of these steps, a magnetic actuator system has been proposed in which two actuators are arranged on flexible silicon rubber as shown in Fig. 5. In this actuator system, two acrylic discs and a ring-type permanent magnet are combined at both ends of the silicon rubber. In addition, two permanent magnets A and B are arranged on the silicon rubber. The total length of this actuator system is 307 mm, and the total mass is 70 g. The diameter of the acrylic disc, the attractive force and position of the permanent magnet, and the rigidity and length of the silicon rubber material were determined in consideration of both step movement and traction characteristics for the actuator system. Details will be shown in a full paper. Fig. 6 shows a situation in which the actuator system moves the step of height H by the cooperative operation of two actuators. This actuator system can move on the step surface very smoothly. The moving situation will be shown as a video at the presentation. Table 1 shows the relationship between the tilt angle of the actuator system α and the speed when the step length L is fixed at 200 mm and the height H is changed to 15 mm, 20 mm, and 25 mm, respectively. The measurement distance with the step length was set at 600 mm. The tilt angle was varied from $\alpha = -90^\circ$ (straight down) to $\alpha = 90^\circ$ (straight up). This actuator system can move in the complex steel structure with the step height of 25 mm.



[1] Hiroyuki Yaguchi and Shun Sakuma : Improvement of a Magnetic Actuator Capable of Movement on a Magnetic Substance, *IEEE Transactions on Magnetics*, Vol. 52, No. 7, Article#: 10.1109/TMAG.2016.2533433 (2016).

BS-06. Force Control of a Bilateral Linear Permanent Magnet Switched Reluctance Motor.

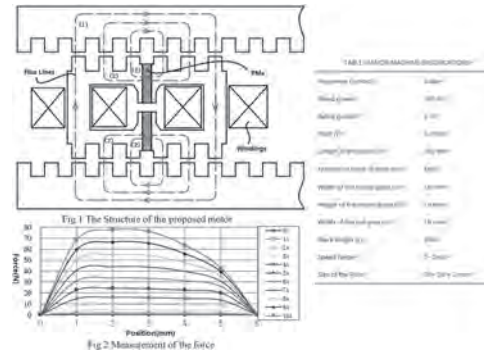
Y. Zou¹

1. Research Centre, Goal Technology (Shenzhen) Limited Company, , China

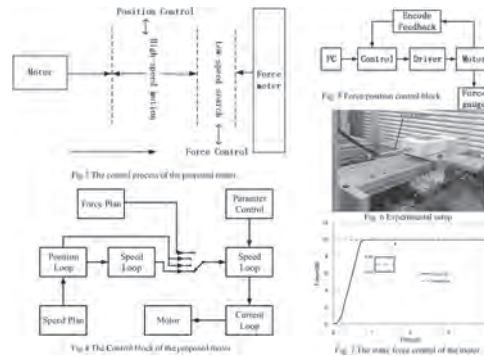
I. INTRODUCTION Force control is an important part of linear motors for industrial applications nowadays [1]. A stable and swift transient step between the position control of the mover and the force output plays a key role to affect the positioning accuracy and working efficiency for automatic equipment [2, 3]. However, traditional methods to change the operation mode of the linear motor from position control to force control have an negative effect to the entire performance, resulting in an obvious overshoot of the force response [4, 5]. This paper presents a speed regulator to regulate the control mode change from position control to force control. The controller introduces a speed regulator that the parameters of the speed loop can be regulated properly to stably change the control mode of the linear motor, eliminating the overshoot of the force output when the motor is governed from position control to force control. Importantly, the vibration of the mover is effectively suppressed during the force control mode. II. STRUCTURE OF THE MOTOR The bilateral linear permanent magnet structure is shown in Fig. 1. It mainly consists of two stators, a moving unit wrapped by two coils and two permanent magnets embedded in the moving unit. Two coils construct a winding on one phase of the motor. There are three phases of the linear motor and three moving units are fixed together to construct the mover of the motor. Two stators are mounted on the basement and the mover is guided by a pair of linear guides that are also installed on the basement. When one phase is excited, the flux lines are shown in Fig. 1. The flux lines are generated by the embedded permanent magnet (1) and the excited winding (2) simultaneously. Force outputs at different positions of the mover under different current excitations are shown in Fig. 2. Main specifications are listed in Table I. III. CONTROL OF THE MOTOR The position control can be divided by a high-speed control stage and a low-speed searching stage as shown in Fig.3. The force control can be achieved during the low-speed searching stage. Initially, the motor is governed by position control and the mover is far away from the destination. The controlled current amplitude could be very large depending on the error of the position signal, so the acceleration of the mover will be very large. The mover will enter the high-speed stage instantly. During this stage, the proportion of the controller should be increased and the integral coefficient should be decreased. With the mover approaching the destination, the speed of the mover will be adjusted quickly and it decreases according to the control command. The control system enters a stable adjustment stage and the proportional coefficient of the controller should be small. At this stage, the integral coefficient should be large to eliminate the stable error. The whole system can realize a swift response, highly accurate positioning and force outputs without overshoot. The control command of the PID controller is $u(t) = K_p(v(t)) * e(t) + K_i(v(t)) * \int [e(t) dt] + K_d(v(t)) * de(t)/dt$ (1) $v(t)$ is the moving speed. $K_p(v(t)), K_i(v(t)), K_d(v(t))$ are the proportional coefficient, the integral coefficient and the derivative coefficient. They are related with the speed of the mover. To realize the highly accurate control for force output regulation, the optimized PID controller can regulate the force output indirectly. Parameters of the PID controller are $K_p(v(t)) = K_{p.max} - (K_{p.max} - K_{p.min}) * \exp[-k_1(v_r(t) - v(t))]$ (2) $K_i(v(t)) = K_{i.max} - (K_{i.max} - K_{i.min}) * \exp[-k_2(v_r(t) - v(t))]$ (3) $K_d(v(t)) = K_{d.max} - (K_{d.max} - K_{d.min}) * \exp[-k_3(v_r(t) - v(t))]$ (4) where $v_r(t)$ is speed reference, k_1, k_2, k_3 are positive values. As shown in Fig.3, the control mode changes during the low-speed stage according to threshold values of the position error and the phase current error. When the threshold values are achieved, the position mode will be switched to a combination control mode that governs the speed-loop control and the current-loop control of the system. Consequently, the speed of the mover can be suppressed dramatically and precisely so that the force mode can achieve a smoothing transient change from other operation modes. As shown in Fig.4, when the control mode of the motor changes from the position control to the force control, a force planner will be added to quickly switch the control mode for the motor. The force control can stabilize quickly and the force output overshoot will be eliminated. The speed regulator can be realized by adjusting the parameters of the speed control loop. The speed control loop is always effective and

the speed regulator can be designed for a highly precise force output. IV. EXPERIMENTAL RESULTS The experimental control scheme is plotted as shown in Fig.5 and the experimental setup is shown in Fig.6. The force control result is shown in Fig.7. The force control error can be limited within 0.01 N when the motor is governed by the force controller. V. Conclusion This paper presents a force control method for the linear motor. The construction of the motor has been introduced and the current loop control for the motor is the most significant section to precisely control the force output. The transfer functions for the current loop are discussed. The force control method for the motor has been proposed and the PID parameters can be calculated according to the designed method. Experiments demonstrate the force output error can be limited within the precision of 0.01 N.

[1]O. Kukrer, "Discrete-time current control of voltage-fed three-phase PWM inverters", IEEE Trans. Ind. Electron., vol. 11, no. 2, pp. 260–269, Mar. 1996. [2]M. P. Kazmierkowski, R. Krishnan, and F. Blaabjerg, Control in PowerElectronics. New York: Academic, 2002. [3]N. Mohan, T. M. Undeland, and W. P. Robbins, Power Electronics, 2nd ed. New York: Wiley, 1995. [4]H. Le-Huy, K. Slimani, and P. Viarouge, "Analysis and implementation of a real-time predictive current controller for permanent-magnet synchronous servo drives", IEEE Trans. Ind. Electron., vol. 41, no. 1, pp. 110–117, Feb. 1994. [5]L. Malesani, P. Mattavelli, and S. Buso, "Robust dead-beat current control for PWM rectifier and active filters", IEEE Trans. Ind. Appl., vol. 35, no. 3, pp. 613–620, May/June 1999.



Structure and main specifications



Control and experimental results

BS-07. Operating Characteristic Analysis and Verification of Short-Stroke Linear Oscillating Actuators Considering Mechanical Load.

C. Kim¹, D. Kwon¹, H. Shin¹, G. Jang¹, S. Jeong² and J. Choi¹

1. Electrical engineering, Chungnam National University, Daejeon, The Republic of Korea; 2. LG Research and Development, Seoul, The Republic of Korea

Linear oscillating actuators (LOAs) are devices that make reciprocating movements at a certain frequency. Therefore, LOAs can be classified according to the movement type, such as the moving-core type, moving-coil type, and moving-magnet type. The moving-core-type LOA has the advantage of easily increasing the permanent magnet usage and the output, but the price of the LOA becomes more expensive as the magnet usage increases. The moving-coil-type LOA has the highest output density compared to other types, but its disadvantage is that it is difficult to manufacture. Most LOAs used in practical applications are of the moving-magnet type. The moving-magnet type makes the mover light and suitable for high-speed operation, which is the most efficient way of increasing LOA output [1]. A novel design of a single-phase short-stroke LOA has been developed for application in refrigeration compressors and other similar equipment because of its advantages, such as high transmission efficiency and simple structure [2]. However, the performance of the LOA is difficult to evaluate due to its reciprocating linear motion. Additionally, unlike rotating machines, measuring the magnetic force of LOAs can be complicated. Therefore, LOA analysis and performance evaluation are essential not only via applying the finite-element method (FEM) analysis but also experimental verification. Experimental studies of the electromagnetic force and output of LOAs have been conducted by various researchers [3]. In this study, the structural and magnetic characteristics of a moving-magnet-type LOA are determined and verified through the analysis and experiment of mover stroke and current based on the operating frequency and applied voltage. Because the operation of the LOA is most efficient at the resonance frequency, it is essential to consider the operating frequency in the electromagnetic design. Finally, the change of the resonance frequency according to the mechanical load is confirmed, and the most efficient operation range is confirmed. Figure 1(a) illustrates the structure of the LOA. The LOA is fixed to the outer core, coil, and inner core, and has a structure in which the permanent magnet makes a linear reciprocating motion in the z-axis direction. The flux path and flux density are depicted in Figure 1(b). The permanent magnet makes a reciprocating motion in the z-axis direction and changes the direction of the main magnetic flux flowing in the outer core, which generates a counter electromotive force. Figure 1(c) shows a manufactured LOA component and experimental set. AC power is applied through the function generator and the voltage is amplified through the amplifier. The mover's stroke is measured through a displacement sensor. Figure 2(a) displays an analysis model considering both the electrical system and mechanical load of the LOA. The mechanical loads include the spring coefficient, damping coefficient, and mover mass. Under no-load conditions, the spring coefficient and mover mass act as mechanical loads, and the effects of force and damping from the loads are negligible. Figure 2(b) shows the current and stroke based on the applied voltage and frequency. Both cases show the most efficient operation at the resonance frequency. Therefore, the operating frequency of the LOA should be similar to the resonance frequency, and the LOA operation becomes less efficient as the difference between the resonance frequency and operating frequency increases. Detailed analysis and experimental results will be presented in the full paper.

[1] J. Wang, D. Howe, and Z. Lin, "Design Optimization of Short-Stroke Single-Phase Tubular Permanent-Magnet Motor for Refrigeration Applications," *IEEE Trans. Industry App.*, vol. 57, no. 1, pp. 327–334, Jan., 2010. [2] T. Ibrahim, J. Wang, and D. Howe, "Analysis and Experimental Verification of a Single-Phase, Quasi-Halbach Magnetized Tubular Permanent Magnet Motor with Non-Ferromagnetic Support Tube," *IEEE Trans. Mag.* vol. 44, no. 11, pp. 4361–4387, Nov., 2008. [3] Z. Q. Zhu, and X. Chen, D. Howe, and S. Iwasaki, "Electromagnetic Modeling of a Novel Linear Oscillating Actuator," *IEEE Trans. Mag.* vol. 44, no. 11, pp. 3855–3858, Nov., 2008.

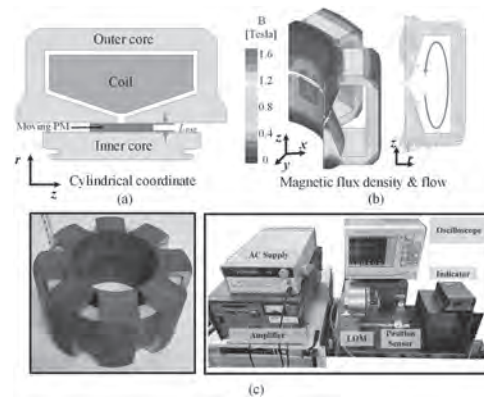


Fig. 1 (a) Analysis model of linear oscillating machine, (b) magnetic flux density and flow of linear oscillating machine due to PM, (c) outer core and experimental set.

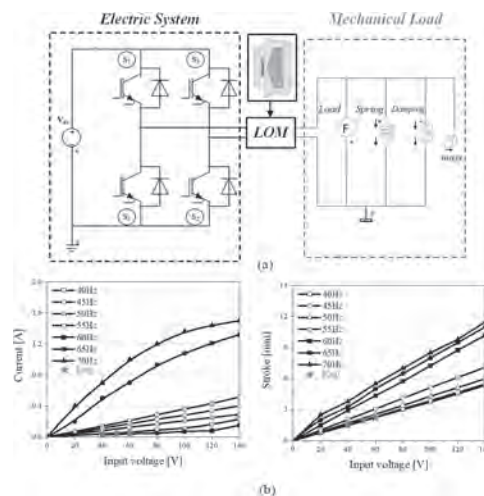


Fig. 2 (a) Analysis model of linear oscillating machine considering mechanical load, (b) stroke and current analysis results and experimental results based on applied voltage and frequency

BS-08. Design and Analysis of a High Thrust Linear Voice Coil Motor Using for the Stiffness Test of Linear Motor Servo System.

H. Zhang¹, B. Kou¹, Q. Ge¹ and Y. Liu¹

1. Harbin Institute of Technology, Harbin, China

I. Introduction The electrical energy can be directly converted to the linear mechanical energy through linear motors. Containing no transmission mechanisms, linear motors have many remarkable advantages, such as high speed and high positioning accuracy. Therefore, linear motor servo systems have received more and more attentions in academic and industrial fields in recent decades [1-6]. However, the testing methods for the linear motor servo systems is not well elaborated and researched compared with conventional rotary motors. Among all the indexes of the linear motor servo systems, the position loop stiffness defined as the ratio between the dynamic disturbing force and the consequent maximal position deviation is an important one to evaluate the closed-loop performances of linear motor servo systems. In the conventional position loop stiffness testing systems, the weight lifting, hydraulic, and the rotating motor plus ball screw are three common loading methods. Nevertheless, some inherent defects exist in these loading methods, such as low repeatability, complex system structure, and low dynamic response. In [7], a novel position loop stiffness testing method for the linear motor servo systems is proposed, in which a high thrust linear voice coil motor is served as the loading motor. This paper will focus on the electromagnetic analysis and cooling design of the proposed high thrust linear voice coil motor. II. Configuration and Model The configuration of the position loop stiffness testing platform for linear motor servo system is shown in Fig. 1. The linear voice coil motor is connected to the tested linear motor by a load sensor, and the tested linear motor operates in position loop state. The thrust generated by the linear voice coil motor can be seen as a step disturbance for the linear motor servo system. Therefore, low thrust ripple performance of the loading motor is required to improve the testing accuracy of position loop stiffness. The cooling structure is also needed to increase the force density and decrease the motor mass. Basically, the magnetic charge method can be used to calculate the magnetic flux density of permanent magnet, and the image method is applied to consider the influence of ferromagnetic boundary [8-9]. The thrust expression with different parameters is obtained using Lorentz force equation. III. Thrust Analysis and Cooling Design In this section, the influence of the parameters on the thrust and thrust ripple are analyzed based on the established model. To enhance the structural strength of primary, two layers arrangement are selected and two layers coils are inserted into a common coil frame. Additionally, the cooling structure for the high thrust linear voice coil motor is designed. The water channels are evenly distributed in the coil frame. To further improve the cooling effect and realize thermal shielding of primary, two aluminum sheets are fixed onto both sides of the primary with heat-conducting glue. The cooling effect is analyzed using temperature field simulation. IV. Experiment To verify the related analysis, a prototype of the high thrust linear voice coil motor is manufactured. The thrust linearity test shows that the thrust varies linearly with the current. The rated thrust is 800N when the current is 9.6A. the experiment values of thrust match well with the ones from analysis and FEM. The thrust ripple within 4mm displacement is less than 1%, which could provide a nearly constant thrust during stiffness testing. In addition, the temperature test is achieved. The temperature rises of the primary with and without the cooling water are compared. The aluminum sheets could quickly transfer the coils heat to the coil frame, and the surface temperature of primary with cooling is 37 degrees under 12A coil current. V. Conclusion In this paper, a linear voice coil motor is analyzed and designed. Considering the practical requirements in the stiffness testing of linear motor servo system, high thrust and low thrust ripple are two critical indexes. Additionally, the effective cooling structure is important. The related experimental results show a good agreement with the analytical model and finite element simulation results.

[1] W. Zhao, J. Zheng, J. Wang, IEEE Trans. Ind. Electron., vol. 63, no. 4, pp. 2072–2082, Apr. 2016. [2] Q. Lu, Y. Li, X. Huang, IEEE Trans. Magn., vol. 51, no. 11, pp. 8108804, Nov. 2015. [3] Y. Fujimoto, T. Kominami, and H. Hamada, IEEE Trans. Ind. Electron., vol. 56, no. 5, pp. 1383–1392, Mar. 2009. [4] Y. Gao, R. Qu, J. Li, D. Li, and F. Chen, IEEE Trans. Magn., vol.

53, no. 6, 7001905, Jun. 2017. [5] Z. Liu, W. Zhao, J. Ji, IEEE Trans. Magn., vol. 51, no. 7, 8105807, Jul. 2015. [6] H. Zhang, B. Kou, Z. Q. Zhu, IEEE Trans. Ind. Electron., vol. 65, no. 12, pp. 9853–9862, Dec. 2018. [7] H. Zhang, B. Kou, Y. Zhou, ICEMS Conference, Harbin, 2015. [8] S. A. Nasar and G. Y. Xiong, IEEE Trans. Magn., vol. 24, no. 3, pp. 2038–2044, May 1988. [9] S. H. Lee, S. B. Park, S. O. Kwon, IEEE Trans. Magn., vol. 42, no. 4, pp.1327-1330, Apr. 2006.

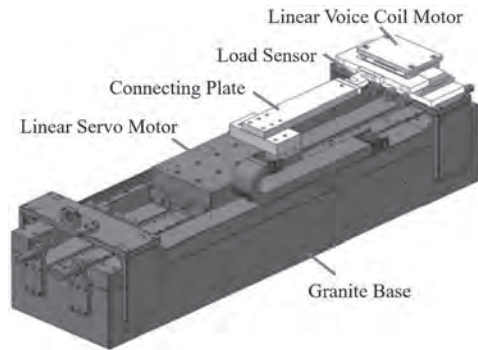


Fig. 1. Configuration of the position loop stiffness testing platform for linear motor servo system.

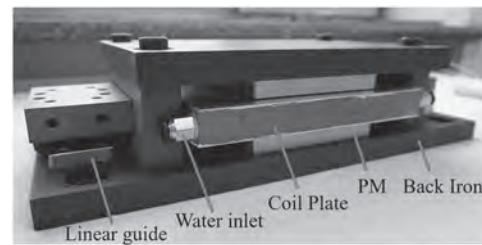


Fig. 2. Prototype of the high thrust linear voice coil motor.

BS-09. Study on the Optimal Shape and Installation Position of the Damper Coils at the Low Velocity Range in Electrodynamic Suspension System.

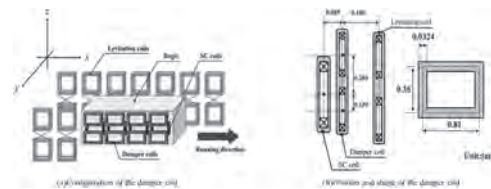
R. Yamamoto¹, R. Betsunoh¹ and S. Ohashi¹

1. Department of Electrical and Electronic Engineering, Kansai University, Suita, Japan

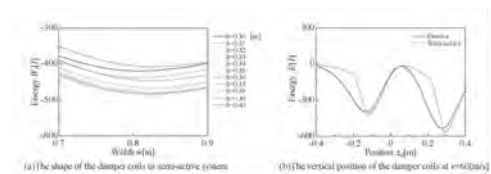
The electrodynamic suspension system (EDS) is used for levitation and guidance[1]. The principle of the EDS system is electromagnetic induction. This system has basically no damping factor against the vertical oscillation of the bogie. Once the vertical oscillation of the bogie occurs by the external disturbance, it does not converge immediately. Thus, the additional damping system is needed. Fig.1 shows the coils for the EDS system[2]. Passive damper system is installed to improve the damping factor. However, the damper coil current of this system is delayed by its self-inductance. When the direction of the bogie oscillation is same to the direction of the damping force, the damper coils amplifies the oscillation. To improve the damping factor, the semi-active damper system is installed. The damper coils are switched according to the oscillation velocity of the bogie and the magnetic force generated by the damper coils. The operation velocity of the train is $v = 120$ [m/sec]. At this speed, the bogie is capable of levitation stability because the electromagnetic force is large. However, at low speed such as the velocity $v = 60 - 80$ [m/sec], the damping factor is small. So, it is difficult to keep levitation stability[3]. This paper examines optimal shape and installation position of the damper coil at the low speed. As a typical application of the EDS system, this paper discusses about the JR Maglev system. EDS system is used for levitation and guidance. The levitation force is generated by the SC coil attached to the bogie. The eight-figure null-flux connection is used for the levitation coils on the ground. When the bogie passes the center of the eight-figure coils, the levitation force is generated to the bogie. The current induced in the levitation coils is calculated. EDS system has an air coil system and modeled as electric circuits. The mutual inductance between the SC coils and levitation coils is calculated from the electric circuit equations. And, to solve the electric circuit equations, the current of the levitation coils is calculated. Also, the motion of the bogie is calculated from the motion equations. By repeating these procedures, the transient motion of the bogie is given. Runge-Kutta method is used to solve these equations[4]. The optimal shape of damper coils is analyzed using the energy consumption. The bogie is forced to oscillate in the vertical direction and run at the velocity $v = 60 - 80$ [m/sec]. The bogie oscillates based on free oscillation of the bogie without the damper coils. The energy consumption of the damper coil in one cycle of the oscillation is considered to evaluate damping factor. When the energy W_d takes negative peak, the damper coils are optimal shape. According to previous research[5], the width of the damper coils indicated as optimal around the width $w = 0.8$ [m] because change in the number of flux linkage is greatest. Therefore, the width of the damper coils is considered at $w = 0.7 - 0.9$ [m]. The height of the damper coils indicated as optimal around the height of the levitation coils because electromagnetic force works between the damper coils and levitation coils. Therefore, the height of the damper coils is considered at $h = 0.30 - 0.40$ [m]. Fig. 2(a) shows energy consumption. the weight of the damper coil is constant at 10.31[kg]. The optimal height of the damper coils is around $h = 0.35$ [m] regardless of velocity and switching system. This is almost the same as the height of levitation coils. The width of the damper coils in the semi-active system is smaller than in the passive system. This result is thought to be related to the chain flux change. At the high speed, change in the number of flux linkage of the damper coils increase. So, the energy W_d at the velocity $v = 80$ [m/sec] is larger than at the velocity $v = 60$ [m/sec]. Optimal installation position of the damper coils on the bogie is discussed. In this study, for damper coils are installed on each side of the bogie as the installation position of the damper coils $z_d = -0.40 - 0.40$ [m]. Fig. 2(b) shows the dependence of energy on the position of the damper coils at the velocity $v = 60$ [m/sec]. From Fig. 2(b), there are two position where the energy becomes small regardless of the velocity and damper system. This position is related to the position of the levitation coils. So, the result is that there are two optimal installation positions of the damper coils. In the semi-active damper system, the energy W_d change sharp in value at the position $z_d = -0.12, 0.29$ [m]. This is because the number of switching change around this position. The optimal installation

position of the damper coils is the same regardless of velocity. However, in the passive damper system, at the velocity $v = 80$ [m/sec], the optimal installation position of damper coils is lower than at the velocity $v = 60, 70$ [m/sec]. Because the weight of the bogie balances with the levitation force. The levitation position of the bogie at the high speed is higher than at the low speed. In conclusion, the optimal shape of the damper coils at the velocity $v = 60 - 80$ [m/sec] is almost the same as at the velocity $v = 120$ [m/sec]. However, the optimal installation position of the damper coils at the velocity $v = 60 - 80$ [m/sec] is higher than at the velocity $v = 120$ [m/sec]. Because the levitation position of the bogie at the low speed is lower than at high speed.

[1] A. Seki, J. Kitano and S. Miyamoto, "Dynamics of the bogie of a maglev system with guideway irregularities", IEEE Trans. on Magnetics vol.32, No.5, pp5043-5045, 1996. [2]Takenori Yonezu;Ken Watanabe;Erimitsu Suzuki;Takashi Sasakawa, "Study on Electromagnetic Force Characteristics Acting on Levitation/Guidance Coils of a Superconducting Maglev Vehicle System", IEEE Trans. on Magn. Vol. 53, no. 11, 2017. [3]T. Okubo, S. Ohashi, N. Ueda, "Effective Control Method of the Active Damper System against the Multi Directional Vibration in the Superconducting Magnetically Levitated Bogie", IEEE Trans. on Appl. Supercond., Vol.26, No.4, Jun. 2016, Art. no. 3601804. [4]S. Ohashi and T. Ueshima, "Control Method of the Semi-Active Damper Coil System in the Superconducting Magnetically Levitated Bogie Against Vertical and Pitching Oscillation", IEEE Trans. on Magn. vol.48, No.11, pp4542-4544, 2012. [5]S. Ohashi, "Weight Reduction of the Damper Coils in the Superconducting Magnetically Levitated Bogie", IEEE Trans. on Magn. Vol. 54, no. 11, 2018.



Superconducting magnetically levitation system and the damper coil



Energy consumption

BS-10. Nonlinear Permanent Magnet Degradation Model and its Application in Magnetic System Optimization.

J. You¹, X. Feng¹, H. Liang¹, X. Tan² and H. Wang¹

1. School of Electrical Engineering and Automation, Harbin Institute of Technology, Harbin, China; 2. Shaanxi Qunli Electric Co., Ltd, Baoji, China

1. Introduction Aiming at the nonlinear permanent magnet(NPM) degradation modeling problem in a type of differential magnetic system, firstly, for the NPM magnetization and demagnetization process, the first-order reversal curves of the permanent magnet of different segments is solved based on the Preisach model^[1]. Based on this model, a finite element simulation model of the electromagnetic system of a Small Rotation Actuator(SRA) is built, and the model is verified by actual measurement. Combining the simulation data with the physical model, a NPM degradation model is proposed. Based on this model, the single factor analysis of the electromagnetic system is carried out to determine the key parameters of SRA, and a fast calculation model of the degradation process is built. Kriging method^[2] is used to perform error fitting, and the SRA magnetic system is optimized with the degradation degree of PEM as the target. The actual measurement results of the prototype are made to verify the effectiveness of the model. 2. Permanent magnet degradation model based on Preisach theory Usually in the finite element simulation, the permanent magnet B-H curve is set according to the return line model^[3], but there are still large errors for the magnetic system after the magnetization and demagnetization process. An operating point model of PEM is built based on the Preisach theory and applied to the finite element simulation model considering the process of magnetization and demagnetization. The simulation results of the model's suction characteristics have a smaller error with the actual measurement, and the simulation accuracy is significantly better than the traditional model. At the suction position, the error is the largest, which is only 6.7%. As shown in Figure 1. After the calculating of the initial state of the actuator, through accelerated tests, the permanent magnet magnetic performance degradation data with time and temperature is obtained, and the function relationship between the degradation degree of magnetic properties of the NPM and temperature and time based on data is deduced. Firstly, analyze the degradation mechanism of the NPM, and the demagnetization rate based on the surface magnetic intensity is determined as the characteristic parameter of magnetic properties of the NPM. The permanent magnets are subjected to degradation tests at different temperatures. Based on the measured data, select the logarithmic function model, combined with Preisach model to build degradation model based on Arrhenius equation. The calculation shows that the model is in good agreement with the measured data. 3. Fast calculation model of electromagnetic system of SRA considering degradation In order to optimize the structure of the electromagnetic system, it is necessary to determine the key size parameters that have a greater impact on the performance of the electromagnetic system, and build a fast calculation model based on them. First, through the single factor simulation, the key size parameters are determined, and then based on the self-defined model, establish a fast calculation model that takes voltage, armature rotation angle, permanent magnet remanence, and the size parameters as input, and static suction torque as output. Kriging method is used for error correction. The calculation error using this model is not more than 3%. The average calculation time of a single group of electromagnetic torque is 1.07s, which meets the requirements of optimal calculation accuracy and speed. 4. Optimized design and test verification of principle prototype Based on the completed permanent magnet degradation model and the fast calculation model of the static magnetic torque of the magnetic system which takes voltage, armature rotation angle, permanent magnet remanence, and size parameters as inputs, the optimization objective is the absolute value of the static magnetic torque of the armature at the release position when there are no excitation and pull-in voltage, and at the same time, the tolerance during production and processing is considered, the optimization problem is solved using the NSGAI algorithm. After optimization, the static magnetic torque of the armature at the release position is increased by 29.6% when no excitation is applied. The static magnetic torque under the pull-in voltage is increased by 41.5%, as shown in Figure 2.

[1] S. R. Naidu, "Simulation of the hysteresis phenomenon using Preisach's theory," in IEE Proceedings A - Physical Science, Measurement and Instrumentation, Management and Education, vol. 137, no. 2, pp. 73-79, March 1990. doi: 10.1049/ip-a-2.1990.0010. [2] Krige, D.G. A statistical approach to some basic mine valuation problems on the Witwatersrand[J]. Journal of the Southern African Institute of Mining and Metallurgy, 1952, 52(9): 201-203. [3] Huimin Liang, Jiabin You, Wenyang Yang, and Guofu Zhai. A Type of Subsection Model for a Permanent Magnet Bar and its Leakage Permeance Calculation Method in an Open Magnetic Circuit[J]. Journal of Magnetics, 2014, 19(1), 37-42.

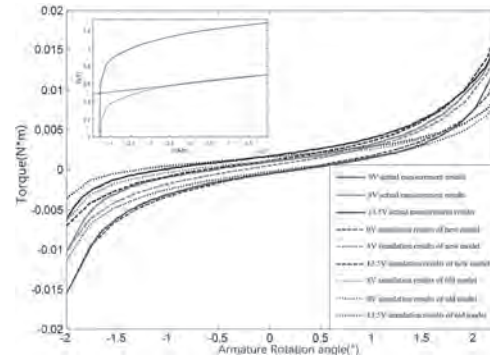


Figure.1 Comparison of simulation calculation results based on Preisach theory and actual measurement results

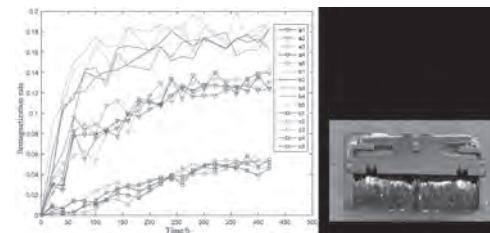


Figure.2 The performance degradation calculation result of the SRA and the degeneration formula

BS-11. Design of a Slim-Width Linear Vibration Motor Used for Automotive LCD Display Panel.

Z. Jiang¹, K. Park¹ and S. Hwang¹

1. Mechanical engineering, Pusan National University, Busan, The Republic of Korea

1. Background Nowadays, more and more vehicles are starting to use an automotive display to enhance vehicle infotainment function with high resolution, large screen, and highly accurate in-touch technology, especially haptic feedback. The linear vibration motor is attached to the automotive display to provide efficient haptic performance. A permanent magnet with high remanence can generate massive flux inside a linear vibration motor and cause high acceleration. However, it also causes lots of static magnetic flux leakage in front of the display, potentially having indirect adverse effects on passenger's implanted medical devices. International Commission on Non-Ionizing Radiation Protection (ICNIRP) guidelines [1] are applied to occupational exposures and exposure of the general public. Many individuals are wearing implanted ferromagnetic or electronic medical devices sensitive to magnetic fields. ICNIRP guidelines mention that the static magnetic field at or below the 0.5 mT will not create a health hazard on implanted medical devices from studies to date. The prototype linear vibration motors are designed for use in an organic light-emitting diode (OLED) display panel, a thin display that each pixel emits light itself individually. Owing to the display's thinness, the prototype linear vibration motor were placed around the center of the display. In contrast, liquid crystal display (LCD) pixels require backlight units (BLUs) to emit lights. The BLUs cover the entire display that makes the LCD panel thicker than the OLED panel; thus, the prototype can no longer be used. The available space for placing linear vibration motors are in the bezels around the LCD panel, requiring a slim-width linear vibration motor with acceptable haptic performance and less static magnetic flux leakage (< 0.5 mT). 2. Analysis methods Maxwell's equations [2] are employed to do the magnetostatic analysis by considering the nonlinearity and hysteresis of magnetic material. The electromagnet-mechanical coupled method is used to verify the linear vibration motor's haptic performance with the finite element method. 3. Prototype The linear vibration motor consists of an electromagnetic system and a mechanical system. The electromagnetic system includes a voice coil, a top plate, a permanent magnet, and a yoke. The mechanical system consists of an inserted frame, an upper frame, a lower frame, and a plate. The full model, half model, an exploded view of the prototype are shown in Figure 1(a). The final slim linear vibration motor has a smaller size than the prototype, and it has an added magnet to provide an opposite magnetic flux to lower magnetic flux leakage at the measured position, shown in Figure 1(b). The magnetic flux leakage is defined as the magnetic flux that does not pass through the air gaps of the voice coil or other parts of the electromagnetic system. The measured positions are in front and behind of linear vibration motor with an 11.30mm distance. The measurement results in front and behind the prototype are 1.60 mT and 11.70mT, while the analysis results are 1.59 mT and 11.69 mT. The experiment setup to measure magnetic flux leakage is Kanetec Tesla Gauss meter, and the measurement results are shown in Fig. 2(a). Based on the E-M coupled method, the analysis results of displacement and acceleration on dummy jig of the prototype are obtained and verified by the experiment results. The measurement setups for measuring displacement and acceleration are Klippel and vibration tester (Type BK 2120C2). 4. Novel design The slim model is designed to satisfy the requirement of the automotive LCD display panel. With a new upper frame shape, the slim model can be inserted into an automotive display in two directions, while the prototype only can be inserted in one direction. Based on a previous study [3] (application of magnetic shielding), the upper frame of the slim model is made by magnetic material (sus 430), which can create another magnetic circuit to make magnetic flux coming back to yoke. Magnetic circuit design includes voice coil design, added yoke design, added magnet design, and magnetic circuit optimization. Secondly, the movable parts of the linear vibration motor include yoke, magnet, and top plate. The inserted frame is treated as spring, and the thickness of the inserted frame's bridge has a dominant influence on resonance frequency. To maintain the same resonance frequency as the prototype (around 130Hz), the thickness of the inserted frame's bridge is changed from 2.30mm to 1.90mm. With a combination of

the above designs, the final slim model's analysis results show that magnetic flux leakages in front and behind the slim model are 0.10 mT and 0.43 mT. Both sides are lower than 0.5 mT. There are 93.71%, 96.32% decreased from the prototype. Samples are manufactured and used to do the experimental measurement. 5. Conclusion The current study proposes a width slim linear vibration motor with a novel magnetic circuit design to achieve low static magnetic flux leakage. Haptic performance of linear vibration motor includes the displacement of movable mass and acceleration on dummy jig, shown in Fig. 2(b). The final slim model has the same resonance frequency as a prototype, around 130 Hz, and it has higher displacement than the prototype due to the smaller movable mass. Eventually, the experiment results are in good agreement with the analysis results.

1. International Commission on Non-Ionizing Radiation Protection. Guidelines on limits of exposure to static magnetic fields. Health Physics., Vol. 96(4), pp. 504-14 (2009 Apr 1) 2. Monk P. Finite element methods for Maxwell's equations. Oxford University Press., (2003 Apr 17) 3. Jiang ZX, Park KH, Kim JH. Analysis and Design of a New Linear Vibration Motor Used to Reduce Magnetic Flux Leakage in In-Vehicle Infotainment. Applied Sciences., Vol.10(10), pp. 3370 (2020 Jan)

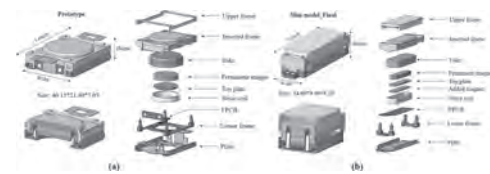


Fig.1 Model comparison between prototype and slim model_Final

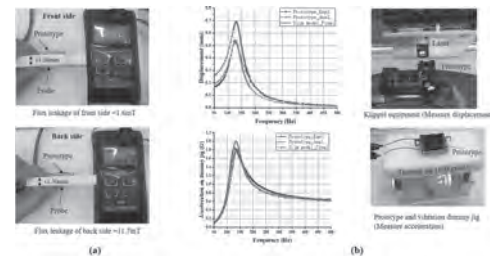


Fig.2 Results comparison between experiment and analysis

BS-12. Novel Dual Coil Microspeaker With Reduced Back Volume.

K. Park¹, Z. Jiang¹ and S. Hwang¹

1. Mechanical engineering, Pusan National University, Busan, The Republic of Korea

-Introduction Smartphones are widely used in daily routines, and microspeakers are widely used in these devices for sound generation. The sound is important since they provide immersive experience when consuming multimedia contents. Therefore, acoustic performance of the microspeaker is an important feature for consumers when selecting smartphones. A round shape microspeaker was widely used in earlier version of cellular phones. The circular or elliptical microspeaker was designed and analyzed [1]. A rectangular microspeaker was developed to utilize the internal space in cellular phone more efficiently [2]. Lee et al. developed a rectangular microspeaker for acoustic performance improvement. Using a piezoelectric effect, engineers developed a piezoelectric speaker [4]. For smartphone featuring bezel-less display, indirect- and direct-vibration actuators were developed [5,6]. In the past, a few components inside the smartphone provided sufficient space for the microspeakers. However, recent design trend to bezel-less display and the slimmer design started to limit the allowable space for the microspeaker. In addition, many components such as sensors, stylus pen, etc., are mounted around the microspeaker that limit the allowable space. These trends reduce back volume of microspeaker that affect the acoustic performance which is SPL (Sound Pressure Level). The back volume is a sealed air volume under the diaphragm that affects acoustic performance. Reduced back volume adds an additional stiffness to the microspeaker system that increase the resonant frequency and decrease SPL at low frequencies. The smaller the back volume, the lower the SPL at low frequency. The prototype microspeaker termed as 1410_1VC consists of single coil with resistance of 6 Ω (DCR). The 1410_1VC can't provide sufficient SPL at low frequency when placed in small back volume of 0.25 cc. To address this problem, a new microspeaker must be designed. In this paper, while remaining identical exterior size to the prototype, a novel dual-coil microspeaker termed as 1410_2VC is designed and analyzed for low frequency SPL enhancement. - Analysis methods and verifications by experiment (Prototype) The microspeaker is multiphysics system that consists of three domains which are electromagnetic, mechanical and acoustic domain, and they are coupled with certain parameters. The SPL can be obtained by solving these multiphysics system with coupled analysis. Coupled analysis are conducted for obtaining SPL and displacement using 3D FEA (Finite Element Analysis). The SPL measurement of the prototype 1410_1VC was conducted in an anechoic chamber shown in Fig. 2 (a). The SPL and displacement are measured by B&K equipment and Klippel equipment, respectively. The analysis methods are verified comparing experimental and simulated data which show good agreement. The acoustic performance of the microspeaker at low frequency can be represented by arithmetic mean (average) of SPL at four frequencies which are 200 Hz, 300 Hz, 500 Hz and 700 Hz. The SPL at low frequency of the 1410_1VC is 80.98 dB. -New Microspeaker Design The moveable mass of the speaker consists of coil, center diaphragm, side diaphragm. Increasing moveable mass will decrease the resonant frequency leading to enhanced low frequency SPL. Among components consisting moveable mass, the coil is the heaviest component, and has the highest mechanical density. Maintaining same resistance, the coil mass can be increased by using large diameter coil. Changes in coil design cause magnetic circuit design modifications and affects electromagnetic force which is Lorentz force. The magnetic circuit includes top plates, coil, yoke and magnets. Thus, coil design is an important factor for the performance improvement. The 1410_1VC has a single coil with resistance, diameter, mass and total length as 6Ω, 0.077mm, 69.93mg, 1675.7mm, and 0.499N, respectively. Maintaining same DCR 6 Ω, dual coil can be connected in series with each coil of 3Ω, or parallel with each coil of 12Ω. The coil diameter is chosen to match height of the prototype 1410_1VC coil. The parallel connection shows the inferior force to the series because thicker coil resulted in lower flux density. Two 3Ω coils connected in series are designed with the diameter of 0.084 mm. Instead of two permanent magnets used in 1410_1VC, total seven magnets are used. The yoke is identical to the prototype. Put together, newly designed 1410_2VC has total mass, total length and Lorentz force as 93.4 mg, 1929.2 mm and 0.542 N, respectively. The structure and manufac-

tured sample are shown in Fig. 1 (a) and (b). The SPL and displacement of 1410_2VC are measured through experiments. - Result The experimental data of the prototype and newly designed microspeaker are compared as shown in Fig. 2 (b). The results show that average SPL of 1410_2VC at low frequencies is 83.25 dB. It is 2.27 dB higher than 1410_1VC which is significant improvement. Remaining same exterior size, using dual coils and novel magnetic circuit, low frequency SPL is improved.

[1]. S.M. Hwang, G.Y. Hwang, J.H. Kwon, et al. "Performance comparison between circular and elliptical type micro-speakers for cellular phones." IEEE Trans. Magn., Vol. 39, p. 3256-3258 (2003) [2] J.H. Kwon, S.M. Hwang, K.S. Kim, et al. "Development of slim rectangular microspeaker used for minimultimedia phones." IEEE Trans. Magn., Vol.43, p. 2704-2706 (2016) [3] C.M. Lee, and S.M. Hwang, "Development of advanced rectangular microspeakers used for wide liquid-crystal display mobile phones." J. Appl. Phys., Vol.109, p. 07E504 (2011) [4] S.H. Tseng, S.C. Lo, Y. J. Wang, et al. "Sound Pressure and Low Frequency Enhancement Using Novel PZT MEMS Microspeaker Design." In Proceedings of the 2020 IEEE 33rd International Conference on Micro Electro Mechanical Systems (MEMS), p. 546-549 (2020) [5] J.H. Kim; Y.W. Jiang and S.M. Hwang, "Analysis and Design of New Actuator Used for Full-Wide Screen LCD." Appl. Sci., Vol.9, p. 4599 (2019) [6] K. H. Park, Z.X. Jiang, Y. W. Jiang, et al. "Development of Direct-Vibration Actuator for Bezel-Less Display Panels on Mobile Phones." Appl. Sci., Vol. 10, p. 4975 (2020)

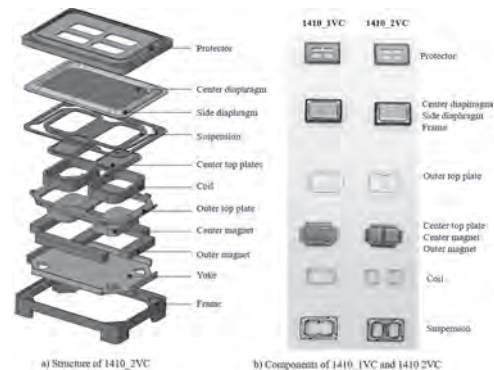


Fig 1. Structure and manufactured components of new microspeaker

Fig. 1 Structure and manufactured components of new microspeaker

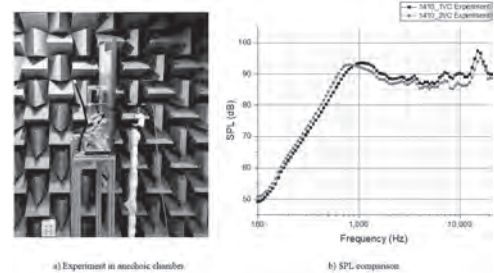


Fig 2. Experiment setup and result

Fig.2 Experiment setup and result

BS-13. Crawling Biopsy Robot Magnetically Actuated in Tubular Environments.

E. Jung¹, W. Lee¹, J. Nam³ and G. Jang²

1. Mechanical Convergence Engineering, Hanyang University, Seongdong-gu, The Republic of Korea; 2. Mechanical Engineering, Hanyang University, Seongdong-gu, The Republic of Korea; 3. Electronics and Information Engineering, Kwangwoon University, Nowon-gu, The Republic of Korea

A biopsy is a medical test to examine the presence or extent of a disease using tools such as a scalpel, a needle, and forceps to extract sample tissues from a patient's body. While excisional or needle aspiration biopsies take a tissue sample close to human skin, endoscopic or cardiac biopsies collect sample tissues located deep inside the human body by inserting a long tube or catheter along the tubular structure of the human body. Conventional wired biopsies have low steering ability and controllability, and mostly depend on the experience of physicians. Since a target region is sometimes located in a complicated and twisted tubular environment, conventional methods have limitations on reaching the narrow target region. Also, there is a possibility of causing bacteremia due to the penetration of external bacteria into the patient's body through the wires [1], [2]. This may cause sepsis in patients who have low levels of immunity and could lead to death [3], [4]. To overcome these problems, many researchers have studied wireless biopsy robots. Previous researchers have mainly explored biopsy robots for capsule endoscopes. However, such robots do not have their own propulsive force and are driven by the passive peristaltic motion of the intestine. In this paper, we propose a crawling biopsy robot (CBR) that can wirelessly crawl and perform biopsies in tubular environments. The proposed CBR performs various mechanical actions under the control of an external magnetic field, such as a crawling motion with the needle covered, an uncovering motion to expose the needle, the insertion of the needle into the target area, and a covering motion of the needle after the collection of sample tissues. Fig. 1 shows the structure of the proposed CBR, composed of a crawling part and a biopsy part. The crawling part is composed of three crawling bodies, and each crawling body contains an axially magnetized cylindrical magnet (CM) and two flexible legs. Each crawling body is freely rotatable with respect to the y-axis, and the motion of the crawling body is controlled using an external precessional magnetic field for stable navigation and needle insertion. When the CBR reaches a target area, the CBR is designed to open the cover to expose a needle to a target area by controlling the external magnetic field. Once the cover opens, the forward crawling motion of the CBR inserts the needle into the target area. Then, the backward crawling motion takes the needle out of the target area and automatically closes the cover to carry the needle and sampled tissues independently of the crawling motion; this is accomplished by controlling the external magnetic field. To verify the functions of CBR, we made a prototype of CBR using 3D printing technology except for the legs and magnets. The crawling legs are made of silicon rubber, and all magnets are NdFeB 45. The first experiment using the prototype of CBR was measuring the puncturing force of CBR. The proposed CBR should generate a puncturing force enough to insert a needle into the tissue to collect sample tissue. According to Yang et al. [5], a minimum force of 0.3 N is required to puncture the liver tissue of pigs. To verify the puncturing force of CBR, an experiment was done using load cell (Honeywell, Morris Plains, NJ, USA). The pseudo glass tube containing the CBR was fixed in a water container, and a jig connected to the load cell was placed in front of the pseudo glass tube. The experimental setup was then placed inside of the magnetic navigation system which generated external magnetic field [6]. The puncturing force was 0.46 N when the magnitude and the rotational frequency of the external precessional magnetic field were 14 mT and 25 Hz. The second experiment was to evaluate the crawling motion and biopsy performance of the CBR. We used a pseudo tissue made of agar filled at one end of a Y-shaped watery glass tube with a diameter of 14 mm, as shown in Fig. 2(a). In step 1, the CBR crawled to a target point, propelled by the external precessional magnetic field ($B=8$ mT, $f=15$ Hz, $\delta=30^\circ$), and the cover was closed during navigation as shown in Fig. 2(b). In the bifurcated branch, we controlled the joystick to change the unit vector of the rotating axis (N), which can be accomplished by controlling the applied currents of the developed MNS. In step 2, the cover was opened by a uniform magnetic

field of 12 mT. In step 3, the uncovered biopsy needle punctured the tissue by the crawling motion generated by the external precessional magnetic field ($B=14$ mT, $f=25$ Hz, $\delta=30^\circ$). In step 4, the turning motions of the crawling bodies and flexible legs along the y-axis as well as the covering motion of the biopsy needle were performed by rotating the uniform magnetic field of 12 mT by 180° along the y-axis. Finally, in step 5, the CBR crawled back to the original point, propelled by the external precessional magnetic field ($B=12$ mT, $f=15$ Hz, $\delta=30^\circ$). Fig. 2 (c) shows the uncovered needle before the biopsy needle was inserted into the pseudo tissue. Fig. 2(d) shows a sampled tissue of 1-mm thickness extracted through this experiment. We confirmed from this experiment that the proposed CBR could crawl through a tubular structure and extract sample tissue successfully.

[1] J. Rizzo, D. Bernstein, and F. Gress, *Gastrointest. Endosc.*, vol. 51, no. 3, pp. 257–261, Mar. 2000. [2] K. A. Marr, *Ann. Intern. Med.*, vol. 127, no. 4, p. 275, Aug. 1997. [3] C. Brun-Buisson, F. Doyon, and J. Carlet, *Am. J. Respir. Crit. Care Med.*, vol. 154, no. 3, pp. 617–624, Sep. 1996. [4] M. H. Samore, M. A. Wessolossky, and A. W. Karchmer, *Am. J. Cardiol.*, vol. 79, no. 7, pp. 873–877, Apr. 1997. [5] H. Yang, P. X. Liu, and J. Zhang, *IEEE International Conference Mechatronics and Automation, 2005*, 2005, vol. 2, p. 592–595 Vol. 2. [6] S. Jeon, G. Jang, H. Choi, and S. Park, *IEEE Trans. Magn.*, vol. 46, no. 6, pp. 1943–1946, Jun. 2010

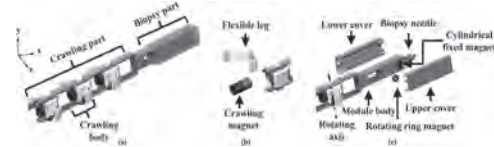


Fig. 1. (a) Proposed CBR composed of a crawling part and a biopsy part. (b) Structure of a crawling body. (c) Structure of a biopsy part.

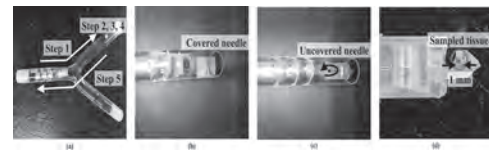


Fig. 2. (a) Experiment testing the crawling and biopsy motions. (b) Covered needle. (c) Uncovered needle. (d) Collected sample tissue.

BS-14. Development of Linear Oscillatory Actuator With 4 Poles and 8 Poles Movers.

F. Kitayama¹ and R. Kondo¹

1. Ibaraki University, Mito, Japan

Recently, Inertia Force Generators (IFGs) was reported to reduce undesirable vibrations in automobiles and precision devices, which consists linear oscillatory actuators (LOAs), sensors and a controller. In the IFG, inertia force for reducing vibrations that generated by the LOA is controlled by a controller and sensors [1]. Here, the LOA should effectively generate inertia force at wide frequency range because the frequency range of undesirable vibrations is wide. However, the conventional LOA can effectively generate inertia force at narrow frequency range because of one mechanical resonance. In this abstract, a LOA with two movers which can effectively drive using two mechanical resonance is developed and the pole configuration is discussed. The proposed LOA mainly consists a stator, an outer mover (0.485 kg) and an inner mover (0.545 kg), as shown in Fig. 1. The stator and outer mover are connected by two leaf springs (totally 139.4 N/mm), and the stator and inner mover are also connected by two leaf springs (totally 44.4 N/mm). The stator is mainly composed of 16 coils and yokes, and the outer and inner movers are mainly composed of magnets and a yoke. Magnets are magnetized at positive or negative radial-direction, and these are axial-directionally arranged with 4 magnetic poles in outer mover, and these are arranged with 8 magnetic poles in inner mover. Coil 1, 2, 5, 6, 9, 10, 13 and 14 are wound clockwise and others are wound counterclockwise. Then, Coil 1, 4, 5, 8, 9, 12, 13 and 16 are connected in series that are called as coil group 1, and others are connected in series that are called as coil group 2. Same-phase or reverse-phase current is applied to coil groups. Here, the former is sinusoidal current with same-amplitude and same-phase in coil groups, and the latter is sinusoidal current with same-amplitude and reverse-phase in coil groups. The 4 poles outer mover is reacted with magnetic fluxes generated by same-phase current, and the 8 poles inner mover is reacted with magnetic fluxes generated by reverse-phase current. In this way, two movers can be independently driven by controlling current. Also, the two movers simultaneously oscillate by superimposing with same- and reverse-phase current. By driving of movers, inertia force is effectively generated at two frequency range because of two mechanical resonance. Next, it is compared between a LOA with 2 and 3 poles movers [2] and the proposed LOA which has 4 and 8 poles movers. In the former, unintentional attractive force was generated between a 3 magnetic-poles and 2 magnetic-poles movers when no current was applied at initial condition because pole-combination of movers is odd and even numbers. So, it must be canceled out by mechanical springs that may have manufactured error or deterioration. In the latter, unintentional attractive force is made to theoretically be zero because that is different even and even numbers. By electromagnetic analysis using 2-D EFM [3], attractive force in the former LOA was calculated as 28.5 N and -9.5 N at each mover, and that in the latter LOA was calculated as 0 N at all movers. Thus, it was verified that the pole combination of the proposed LOA is effective to reduce the attractive force. The prototype of the proposed LOA is manufactured as shown in Fig. 1. The accelerations of outer and inner movers are measured when same-phase or reverse-phase currents with amplitude 0.5 A is applied at each frequency. Then, inertia force is calculated by multiplying measured accelerations and mover's mass together. As shown in Fig. 2, an outer mover was mainly oscillated when applying same-phase current, and an inner mover was mainly oscillated when applying reverse-phase current. Then, large inertia force was obtained with two frequency at 37 and 84 Hz because of mechanical resonances of the outer and inner movers. For comparison, each mover positions are calculated using motion equations with current thrust and detent characteristics that derived from electromagnetic analysis, and analyzed inertia force is calculated. As shown in Fig. 2, measured results almost agreed with analyzed results.

[1] M. Tagami, T. Yamashita and Y. Tagawa et al., Journal of System design and Dynamics., Vol. 2, No. 2, pp. 507-517 (2008) [2] F. Kitayama, K. Hirata and R. Kondo, Proceedings of XXIIIrd International Conference on Electrical Machines., pp. 1586-1592 (2018) [3] A. Yoshitake, K. Harada and T. Todata et al., IEEE transactions on Magnetics, Vol. 33, No.2, pp. 1662-1665 (1997)

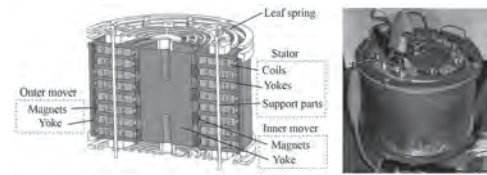


Fig. 1 Proposed LOA.

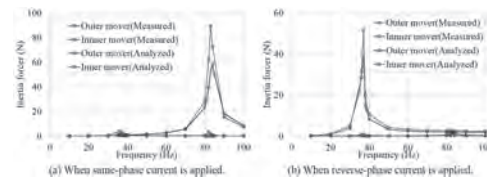


Fig. 2 Measured and analyzed inertia force.

BS-15. Analysis of Magneto-Mechanical Coupled Effect on Electro-magnetic Propulsion.

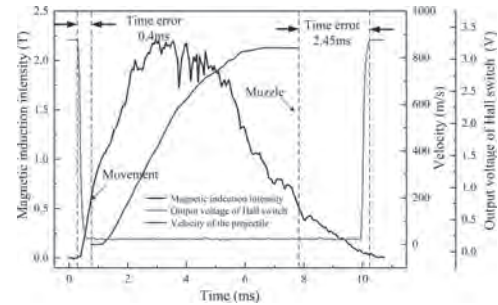
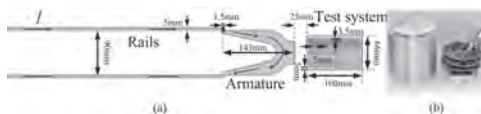
Y. Yang¹, P. Liu¹ and Q. Yin²

1. Nanjing University of Science and Technology, Nanjing, China;

2. Southwest Institute of Technical Physics, Chengdu, China

In recent years, electromagnetic propulsion technology has made many breakthroughs in the fields of aircraft launch and advanced artillery [1]. With the help of pulse strong current, electromagnetic propulsion technology can achieve a target speed of 2000 m/s or higher in a few milliseconds [2]. During the propulsion, the strong magnetic field generated by input pulse current interacts with the armature current to produce electromagnetic force, which propel the armature and the load. At the same time, the high-velocity of the armature will change the current distribution inside the rail and armature, and affect the magnetic field around the armature. However, the magneto-mechanical coupled simulation of moving armature cannot be solved by commercial software. Many scholars have overcome this problem by using various simplified, but it is not sure whether these methods will affect the accuracy of simulation results [3]. Therefore, the measurement is a relatively intuitive research method. In this work, we propose a multi-parameter measurement method of magneto-mechanical coupled effect. The acceleration sensor, linear Hall sensor, Hall switch, signal processing module, memory module and control module are integrated into a 27*30 mm storage testing system. Fig.1a is a simulation model of electromagnetic propulsion system considering velocity skin effect. The influence of velocity skin effect on the current distribution in the rail and armature is simulated by reducing the thickness of the rail and the contact area between the rail and armature. Fig.1b is the storage testing system. Fig.2 is the comparison of dynamic storage test results, in which the velocity signal is obtained by integrating the acceleration signal. According to the test value, we can divide the electromagnetic propulsion process into three phases. In the first phase of 0 - 0.75 ms, the armature is stationary due to the influence of preload and static friction. The magnetic induction intensity is affected by the current in armature and rails, and continuously rises to 0.58 T; The second phase is 0.75 - 7.8 ms, when the armature is moving, the velocity increases continuously and reaches the maximum of 844 m/s in 7.8 ms. After that the armature flew out of the rails. At this phase, the maximum magnetic induction intensity is 2.2 T, and it is reduced to 0.54 T when the armature flew out. The third phase is 7.8 - 10.75 ms, as the armature flew out of the rails. The circuit disconnected, and the magnetic induction intensity is reduced to 0. Among them, the change of Hall switch corresponds to the value of magnetic induction. The jumping time of Hall switch signal partly reflects the starting time and muzzle time of armature movement, which can be used as a simple method to judge muzzle time. However, the time error at the starting time and muzzle time is 0.75 ms and 2.45 ms, which needs to be corrected by introducing a correction coefficient.

[1]. H. D. Fair. Advances in electromagnetic launch science and technology and its applications[J]. IEEE Transactions on Magnetics, vol. 45, no. 1, pp. 225-230, Jan. 2009. [2]. Li J, Li S, Liu P, et al. Design and Testing of a 10-MJ Electromagnetic Launch Facility[J]. IEEE Transactions on Plasma Science, vol. 39, no. 4, pp.1187-1191, Apr. 2011. [3]. Yin Q, Zhang H, Li H J, et al. Analysis of in-bore magnetic field in C-Shaped armature railguns[J]. Defence Technology, vol. 15, pp. 83-88, Feb. 2019.



Session BT
VERNIER AND FLUX MODULATED MACHINES
(Poster Session)

Xiao Chen, Chair
The University of Sheffield, Sheffield, United Kingdom

BT-01. A Design Method of Multi-MMF Halbach PM Array and its Application in Flux Reversal Machines.

H. Huang¹, D. Li¹, X. Ren¹ and R. Qu¹

1. Huazhong University of Science and Technology State Key Laboratory of Advanced Electromagnetic Engineering and Technology, Wuhan, China

Abstract-This paper investigates a design method of a Halbach magnet array which can produce multiple MMFs with desired amplitudes and phase position. The construction process and the operation principle of this new type of Halbach array is introduced in this digest. It reveals that through adjusting the proportion of two main working MMFs, higher back EMF and torque density can be achieved than the Halbach flux reversal machines with only one fundamental MMF. I. Introduction Flux modulation machines are attractive for their high torque density due to the magnetic gear effect. It has been validated that multiple airgap flux harmonics can both contribute to the back EMF and torque in flux modulation machines [1]. In stator PM flux modulation machines such as flux switching and flux reversal machines [2], multiple static MMF harmonics can be modulated by single rotor permeance and generate multiple airgap flux harmonics with same frequency, therefore can both contribute to the total back EMF. Different from regular stator PM machine with only fundamental MMF and its odd harmonics, recently a new kind of stator PM flux modulation machines with unequal magnet thickness has been proposed in [3]-[4]. By adjusting the pole arc of each magnet, several other stator MMFs can be generated, and more airgap working harmonics can be introduced to enhance 10% back EMF and torque capacity of machines. However, the oriented design of each working MMF has not been achieved yet in these papers. In [5], the analytical model of Halbach PM array with unequal pole arcs and arbitrary magnetizing directions has been proposed, which can be optimized with algorithm to get multiple main MMFs, but the processing and manufacturing is difficult. In this paper, a design method of Halbach PM array with only radial and tangential magnets has been proposed to produce multiple MMF harmonics with required amplitudes and phase angles. Then, the method is applied into the optimization of Halbach flux reversal machines. II. Forming Process of Multi-MMF Halbach PM Array The forming process of Halbach PM array with two main MMFs is illustrated in Fig. 1. At first, the amplitudes and phase angle of each required MMF harmonic are given, the ideal sine wave of these two MMFs can be presented, respectively. By the accumulation of these two sinusoidal MMFs, a composite MMF can be presented, which has irregular shape and is hard to process. Then, through setting positive and negative threshold values, the composite MMF can be simplified into 3-step PWM composite MMF form. According to this form, the arc length and the magnetization direction of each radial magnet can be determined. On the other hand, the tangential magnets are placed between the radial magnets with different polarities, and the magnetization directions of tangential magnets are determined by the mechanism of conventional Halbach PM array to achieve strong magnetic field on the airgap side. In addition, the gaps are left between two radial magnets with the same polarity. Based on these procedures, the magnet arrangement of Halbach PM array with two MMFs can then be derived. Similarly, the Halbach PM array with more than 2 MMFs can be built by adding the sine wave ideal MMFs at the first step. The simulation results, which will be given in the full paper, validate the accuracy of this method on the construction of required MMFs. III. Application of Multi-MMF Halbach Array in Flux Reversal Machines As one of its interesting applications, the proposed Halbach PM array can be used to increase the airgap working field harmonics in the stator PM flux modulation machines. As shown in Fig. 2 (a), a 6-slots-4-poles flux reversal machine (FRM) with 16-salient-pole rotor is selected as the research object. The proposed Halbach PM array with 12th and 18th MMFs is mounted under the stator teeth of this machine. According to the flux modulation theory, the 12th and 18th MMFs are modulated by 16th rotor permeance and generate 4th and 2nd airgap flux harmonics separately, which both contribute to the back EMF but with different coefficients [3]. Fig. 2 (b) shows the back EMF and cogging torque of proposed machine varied with the proportion of 12th MMF. Since 2nd harmonic has two times pole ratio than the 4th harmonic, the FRM with only 18th MMF has higher back EMF than with only 12th MMF. Also, since the least common multiple between 18 and 16 is 144, which is much larger than the least common multiple between 12 and 16, 18th MMF can bring lower cogging torque than the 12th MMF in proposed FRM. However, it is interesting that when

increasing the proportion of 12th MMF from 0 to 0.3, the back EMF of proposed machine can still get 10% increased on the basis of Halbach FRM with 18th MMF under the same magnet usage. The reason analysis and the theoretical upper limit of this growth under Halbach PM array with 2 and 3 MMFs will be studied in the full paper. IV. Conclusions A design method of multi-MMF Halbach PM array has been proposed, and its application in a 6-slots-16-poles flux reversal machine has been researched. Compared to regular flux reversal machines with single MMF, the proposed flux reversal machine with composite MMFs can achieve 10% higher back EMF and torque capacity under the same magnet usage. The influence of pole ratio and the selection of threshold values on the performance of machine will be given in the full paper.

[1] Tianjie Zou, Dawei Li, Canruo Chen, etc., "A Multiple Working Harmonic PM Vernier Machine with Enhanced Flux-Modulation Effect," *IEEE Transactions on Magnetics*, vol. 54, no. 11, June. 2018. [2] Dawei Li, Ronghai Qu, Jian Li, etc., "Synthesis of Flux Switching Permanent Magnet Machines," *IEEE Transactions on Energy Conversion*, vol. 31, no. 1, Mar. 2016. [3] Yuting Gao, Dawei Li, Ronghai Qu, etc., "A Double-Stator Flux Switching PM Machine with Multi-PM MMF Harmonics," *IEEE Transactions on Magnetics*, vol. 55, no. 6, June. 2019. [4] You Zhou, Ronghai Qu, Yuting Gao, etc., "A Novel Flux Modulation Linear Machine with Dual-Sided Modular Primary and Multi Pole Pitches," *IEEE International Electric Machines & Drives Conference (IEMDC)*, May. 2019. [5] Hailin Huang, Libing Jing, Ronghai Qu, etc., "Analysis and Application of Discrete Halbach Magnet Array with Unequal Arc Lengths and Unequally Changed Magnetization Directions," in *IEEE Transactions on Applied Superconductivity*, vol. 28, no. 3, pp. 1-5, April 2018.

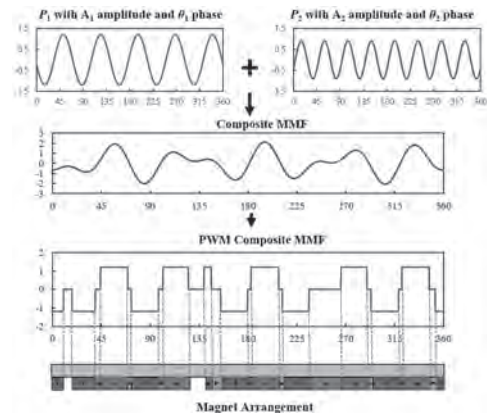


Fig. 1. The Forming method of Halbach PM array with two main MMFs.

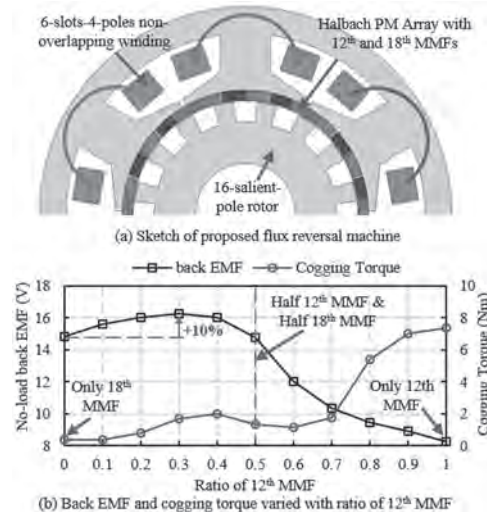


Fig. 2. Sketch and performance of Halbach flux reversal machine with 12th and 18th MMF.

BT-02. Investigation of a Dual-Winding Dual-Flux-Concentrated Magnetic-Field Modulated Brushless Compound-Structure Machine.

G. Liu¹, P. Zheng^{1,2}, J. Bai¹, J. Liu¹ and Y. Wang¹

1. School of Electrical Engineering & Automation, Harbin Institute of Technology, Harbin, China; 2. State Key Laboratory of Robotics and System, Harbin Institute of Technology, Harbin, China

Abstract In this paper, dual-winding dual-flux-concentrated magnetic-field modulated brushless compound-structure machine (DDMFM-BCSM) is proposed, combining the magnetic-field modulated brushless dual-rotor machine (MFM-BDRM) and permanent magnet synchronous machine (PMSM) into one. Proposed machine has two sets of windings in stator slots and spoke type PMs on dual rotors. Besides, there are flux barrier on inner rotor to improve the performance of MFM-BDRM. First, the performance of proposed machine is analyzed, including MFM-BDRM part, PMSM part and the whole DDMFM-BCSM. Second, in order to analyze the influence of flux barrier on performance of DDMFM-BCSM, a DDMFM-BCSM without flux barrier is designed to compared their performance. I. Introduction Combination of planetary gear and permanent magnet synchronous machine (PMSM) is widely used in hybrid electric vehicles (HEVs). Considering its maintenance and reliability problem, scholars are searching for new structure to replace this combination. Due to high reliability and low maintenance cost, the magnetic-field modulated brushless dual-rotor machine (MFM-BDRM) has high potential in HEVs. But in HEVs, MFM-BDRM need work together with a PMSM, which raise the system cost and volume. MFM-BDRM with dual windings, which is combination of MFM-BDRM and PMSM, is an alternative solution. In this paper, dual-winding dual-flux-concentrated magnetic-field modulated brushless compound-structure machine (DDMFM-BCSM), which is combination of MFM-BDRM and PMSM, is proposed. Magnetic field modulation principle, working principle of DDMFM-BCSM, is introduced [1,2]. Electromagnetic performance of DDMFM-BCSM, such as back EMF, torque and efficiency, are analyzed and obtained. In order to verify the function of proposed machine, performance of MFM-BDRM and PMSM are also analyzed separately. II. Structure and Working Principle The structure of the proposed DDMFM-BCSM is shown in Fig. 1. The stator iron core is similar to that of common PMSM. But there are two sets of windings in stator slots, regular winding and modulation winding. The outer and inner rotor are formed by the alternant placement of magnetic blocks and spoke type PMs whose flux-concentrating effect could improve the flux density efficiently. The difference of two rotors are the magnetic blocks of inner rotor connect together and flux barrier is added in the end of PMs of inner rotor. The MFM-BDRM part consists of modulation winding, magnetic blocks on outer rotor and PMs on inner rotor, while the PMSM part consists of regular winding and PMs on outer rotor. Working principle of DDMFM-BCSM is magnetic field modulation principle which is also the working principle of magnetic gears, magnet-g geared machines and vernier machines. Based on analysis of magnetic field modulation principle, torque and speed characteristic of DDMFM-BCSM can be obtained. III. Performance Analysis By finite element method (FEM), the performance of DDMFM-BCSM is analyzed at the inner and outer rotor speed of 1000rpm. Spectrum analysis result of air gap flux density verifies the magnetic field modulation principle. From low mutual-inductance of two sets of windings, we can see the interaction between two sets of windings could be weakened efficiently with reasonable motor design. The power factor of MFM-BDRM is low (0.58), which is the disadvantage of all machines based on magnetic field modulation principle. Loss and efficiency of DDMFM-BCSM is also analyzed. To verify the function of MFM-BDRM part and PMSM part, torque performance of two parts is analyzed respectively and shown in Fig. 2. It's obvious that both of MFM-BDRM part and PMSM part could put out stable torque. The torque of outer rotor and inner rotor of MFM-BDRM satisfies the torque characteristic mentioned above. Dimension parameters of magnetic blocks and spoke array PMs of two rotors are changed to improve the amplitude of needed flux density harmonics. In DDMFM-BCSM model simulated by FEM, flux density harmonics of 4 and 11 PM pole-pairs could generate fundamental wave of back EMF in modulation winding and regular winding respectively. IV. Influence of flux barrier In order to prove the flux barrier effect on performance, DDMFM-BCSM without flux barrier is also simulated. Torque, efficiency and power factor of two topologies are compared.

The result shows that flux barrier could improve the torque of MFM-BDRM while the power factor of MFM-BDRM and torque of PMSM is weakened. V. Conclusion A new DDMFM-BCSM topology is proposed, combining the MFM-BDRM and PMSM together. Magnetic field modulation principle, the working principle of DDMFM-BCSM, is introduced. FEM result shows that proposed machine could realize function of two machines. Flux barrier could improve the torque of MFM-BDRM while the power factor of MFM-BDRM and torque of PMSM is weakened.

- [1] J.G. Bai, P. Zheng, C.D. Tong, et al, "Characteristic Analysis and Verification of the Magnetic-Field-Modulated Brushless Double-Rotor Machine", *IEEE Trans. Ind. Electron.*, vol. 62, pp. 4023-4033, Jul. 2015.
- [2] G.P. Liu, Y. Sui, J.Q. Liu, et al, "Comparison of Vernier Machines with Different Rotor PM Configurations", *2019 22nd Int. Conf. on Electrical Machines and Systems (ICEMS 2019)*, Harbin (China), Aug. 2019, pp. 1-4.

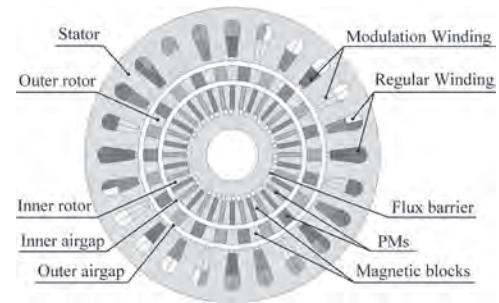


Fig.1. Structure of proposed DDMFM-BCSM

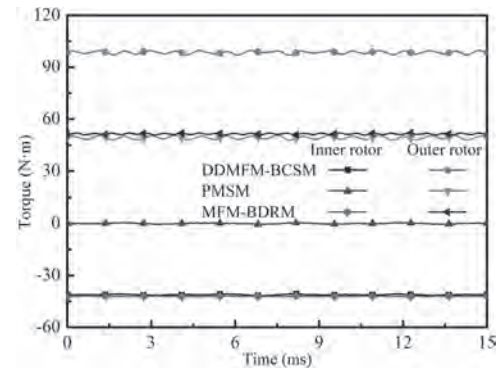


Fig.2. Torque waveform of DDMFM-BCSM, PMSM part and MFM-BDRM part

BT-03. Design and Analysis of a New Partitioned Stator Hybrid-Excited Flux Reversal Machine With Dual-PM.

Y. Meng¹, S. Fang¹, Z. Pan¹ and L. Qin¹

¹. School of Electrical Engineering, Southeast University, Nanjing, China

1. Introduction. Due to the merits of simple structure, mechanical robustness and high power density, flux reversal permanent-magnet machine (FRPMM) has been an appealing choice in many industrial applications [1]. However, similar to other solely PM-excited machines, the constant-power operation range of FRPMM is restricted by the uncontrollable PM flux [2]. To improve the flux regulation ability, the hybrid-excited design concept is introduced into flux reversal machine [3]. With the participation of direct current (dc) excitation, the air-gap flux density can be regulated flexibly. However, the dc-field winding and armature winding placed in the same stator results in a serious space confliction, which deteriorates the torque production and flux regulation ability. To cope with the space problem, the partitioned stator hybrid excited flux reversal machine (PSHEFRM) is developed [4], in which the armature windings and field windings are placed separately in the inner and outer stators. Nevertheless, the solely stator-PM excitation limits the torque capability of PSHEFRM. To further enhance the torque production and obtain the flexible flux regulation ability, this paper proposes a new partitioned stator hybrid-excited flux reversal machine with dual-PM (DP-PSHEFRM), in which the field windings are placed in the inner stator and the PMs are employed on both the rotor and outer stator. The topology and operation principle of the proposed DP-PSHEFRM are described. The electromagnetic performances of the machine are investigated by finite element analysis (FEA). 2. Machine topology and operation principle. Fig. 1 shows the topology of the proposed DP-PSHEFRM, which consists of two stators and one sandwiched rotor. It can be seen that the machine employs the outer stator to accommodate three-phase armature windings and PMs, and inner stator to place field winding. The PMs mounted on the top of outer stator teeth are separated by iron poles, which composes a consequent-pole PM arrangement. The non-overlapping armature windings and field windings are wound on the teeth of outer and inner stators, respectively, which offers the merits of short ending-length and low copper loss. In addition, the outer stator teeth are aligned with inner stator slots, which means the two stators have half teeth pitch displacement. Moreover, the alternate PMs and iron poles composes a consequent-pole PM rotor structure. The PMs on the rotor and outer stator are magnetized with the identical radially direction to enhance the flux densities in the air-gap and stator core. The operation principle of the proposed DP-PSHEFRM is based on the flux modulation effect, and the torque of machine is generated by taking advantage of the modulated air-gap field harmonics. In addition, the dc flux is mainly used to regulate the air-gap flux density to improve the flux weakening capability. 3. Electromagnetic performance evaluation. Fig. 2(a) shows the no-load back-electromotive forces (back-EMFs) of the proposed DP-PSHEFRM excited by stator-PM only, rotor-PM only and dual-PM at the field current density of 0 A/mm². It can be seen that the back-EMFs excited by different PM excitations all have a symmetrical and sinusoidal waveform. In addition, compared with stator-PM, rotor-PM makes more contribution for the back-EMF production. Fig. 2(b) compares the torques of proposed machine under different PM excitation at the armature current of 6 A. It can be seen that the torque with dual-PM excitation is 82% higher than that with stator-PM excitation only and 47% higher than that with rotor-PM excitation only, which illustrates a great enhancement of torque production by using dual-PM excitation. Then, in order to verify the flux regulation ability of DP-PSHEFRM, the dual-PM excited outer air-gap flux density and its harmonic spectra at different field current density are evaluated, as shown in Fig. 2(c) and (d). It can be observed that the amplitudes of working harmonics can be continuously regulated with the change of the field current density. Thus, the flux linkage at armature terminal can be effectively adjusted, as shown in Fig. 2(e). When the armature current is fixed as 6 A, the variation of average torque with field current density is investigated. As shown in Fig. 2(f), the average torque decreases by 9.2Nm from J=0A/mm² to J=-15A/mm², which illustrates the excellent flux weakening capability of the proposed DP-PSHEFRM. More detailed design considerations and electromagnetic performance analysis will be presented in the full paper.

[1] Y. Gao, R. Qu, D. Li, "Torque performance analysis of three-phase flux reversal machines," *IEEE Trans. Ind. Appl.*, vol. 53, no. 3, pp. 2110–2119 (2017). [2] X. Zhao, S. Niu, and W. Fu, "Design of a novel parallel-hybrid-excited dual-PM machine based on armature harmonics diversity for electric vehicle propulsion," *IEEE Trans. Ind. Electron.*, vol. 66, no. 6, pp. 4209–4219 (2019). [3] L. Xu *et al.*, "Design and analysis of a new linear hybrid excited flux reversal motor with inset permanent magnets," *IEEE Trans. Magn.*, vol. 50, no. 11, Art. ID 8202204 (2014). [4] Z. Zeng, Q. Lu and X. Huang, "Analysis of a new partitioned-primary flux-reversal hybrid-excited linear motor," in *Proc. IEEE Int. Elect. Mach. Drives Conf. (IEMDC)*, pp. 74-79 (2019).

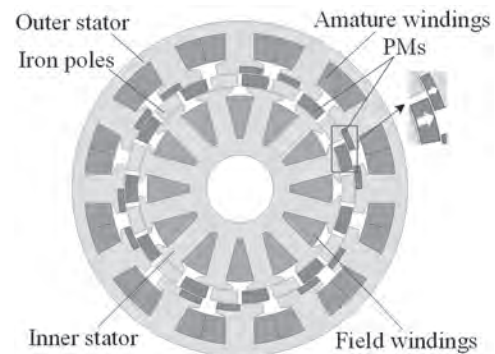


Fig. 1 Topology of the proposed DP-PSHEFRM

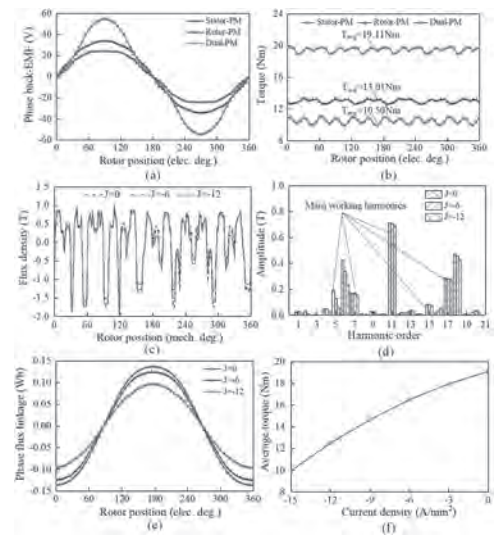


Fig. 2 Electromagnetic performances analysis

BT-04. Investigation of Consequent-Pole Flux-Switching Permanent Magnet Machines With Magnets in Stator Slot Opening.

C. Chen¹, D. Li¹ and R. Qu¹

1. Huazhong University of Science and Technology, Wuhan, China

Abstract — This paper proposes a novel consequent-pole flux-switching permanent magnet (FSPM) machine with magnets in stator slot opening to improve the torque density, which is a critical concern of FSPM machines. The working principle of the proposed topology is investigated based on the magnetomotive force (MMF)-permeance model and numerical finite element analysis (FEA). The electromagnetic performance such as back EMF and electromagnetic torque is compared with the conventional consequent-pole FSPM machine. It is demonstrated that the proposed machine can achieve 27.8% larger back EMF and 20.2% higher torque density than the conventional counterpart. I. Introduction Recently, permanent magnet (PM) machines have been used in many industry applications, such as servo motors and electric vehicle. Flux-switching permanent magnet (FSPM) machine was first proposed in [1]. Due to simple rotor structure and excellent flux-weakening capability [2] [3], FSPM machines have received much attention in recent decades. To improve torque density of FSPM machines, many topologies have been proposed and investigated. Z. Q. Zhu et al. analyzed a novel multi-tooth FSPM machine [4] and the optimal slot/pole pair combination is determined by a simple analytical method in [5]. H. Yang et al. proposed a consequent-pole FSPM machine to increase the contents of low-order harmonics to enhance the torque capability in [6]. In this paper, a consequent-pole FSPM machine with magnets in the slot opening is proposed to increase the torque density. In Section II, the working principle of the proposed topology is analyzed based on magnetomotive force (MMF)-permeance model and numerical finite element analysis (FEA). The electromagnetic performance, such as back EMF and electromagnetic torque, is compared with the conventional consequent-pole FSPM machine in Section III. It is found that the proposed topology can achieve 27.8% larger back EMF and 20.2% higher torque capability than the conventional counterpart. In Section IV, some conclusions are drawn. II. Machine Topology and Working Principle The conventional consequent-pole and proposed FSPM machines are shown in Fig. 1(a) and Fig. 1(b) respectively. Different from the conventional consequent-pole FSPM machine, there are Halbach-type magnets in stator slot opening in the proposed topology. The magnetization directions of the magnets are represented by the yellow arrows. Owing to the unique structure of consequent-pole FSPM machine, there are relatively lower reluctance paths for low-order flux density harmonics. It can be demonstrated that the non-working 6-pole-pair flux density harmonic can be reduced by the magnets in the stator slot opening. Thus, the working flux density harmonics can be enhanced while comparable saturation degrees can be realized in the conventional and proposed FSPM machines. III. Electromagnetic Performance Fig. 2 shows the FEA-predicted phase back-EMF waveforms, FFT analysis results of back EMF and electromagnetic torque curves. It can be seen from the figure that the proposed machine can achieve 27.8% larger back EMF and 20.2% higher torque density than the conventional counterpart. It should be noted that the phase current of proposed machine is smaller than the conventional consequent-pole FSPM machine due to the smaller slot area when the copper losses are kept constant. IV. Conclusion In this paper, a novel consequent-pole FSPM machine with magnets in stator slot opening is proposed to enhance the torque capability. It is demonstrated that the proposed topology can realize 27.8% larger back EMF and 20.2% higher torque density than the conventional counterpart.

[1] S. E. Rauth and L. J. Johnson, "Design principles of flux-switching alternators," *AIEE Trans.*, vol. 74, pt. III, no. 3, pp. 1261-1268, Jan. 1955. [2] D. Li, R. Qu, J. Li, W. Xu, and L. Wu, "Synthesis of flux switching permanent magnet machines," *IEEE Trans. Energy Convers.*, vol. 31, no. 1, pp. 106-117, Mar. 2016. [3] W. Hua, M. Cheng, and G. Zhang, "A novel hybrid excitation flux-switching motor for hybrid vehicles," *IEEE Trans. Magn.*, vol. 45, no. 10, pp. 4728-4731, Oct. 2009. [4] Z. Q. Zhu, J. T. Chen, Y. Pang, D. Howe, S. Iwasaki, and R. Deodhar, "Analysis of a novel multi-tooth flux-switching PM brushless AC machine for high torque direct-drive applications," *IEEE Trans. Magn.*, vol. 44, no. 11, pp. 4313-4316, Nov. 2008. [5] J. T. Chen, Z. Q. Zhu, and D. Howe, "Stator and rotor pole combinations

for multi-tooth flux-switching permanent-magnet brushless AC machines," *IEEE Trans. Magn.*, vol. 44, no. 12, pp. 4659-4667, Dec. 2008. [6] H. Yang, Y. Li, H. Lin, Z. Q. Zhu and S. Lyu, "Principle investigation and performance comparison of consequent-pole switched flux PM machines," *IEEE Trans. Transport. Electrifi.*, doi: 10.1109/TTE.2020.3022991.

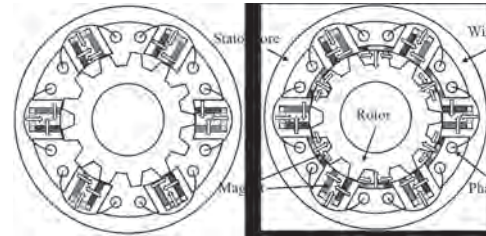


Fig. 1. Basic topologies. (a) Conventional consequent-pole FSPM. (b) Proposed FSPM.

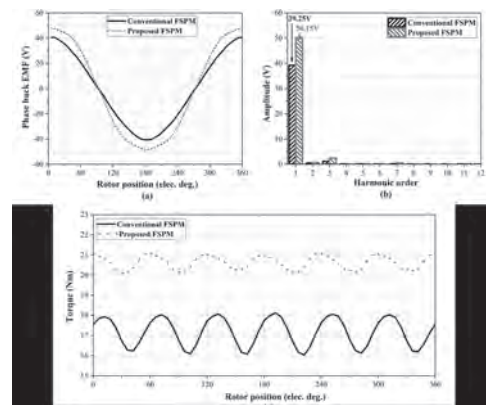


Fig. 2. Electromagnetic performance. (a) Back EMF. (b) FFT analysis results of back EMF. (c) Electromagnetic torque.

BT-05. Quantitative Identification of Airgap Flux Density Harmonics Contributing to Back-EMF in Dual-Permanent-Magnet-Excited Machine.

Y. Shi^{1,2}, L. Jian² and T. Ching¹

1. Department of Electromechanical Engineering, University of Macau Faculty of Science and Technology, Taipa, China; 2. Southern University of Science and Technology Department of Electrical and Electronic Engineering, Shenzhen, China

1. Background and Literature Review Since permanent-magnet vernier machines (PMVMs) can offer high torque directly without the aid of intermediate transmission devices such as mechanical gearbox, they are extremely suitable for low-speed large-torque direct-drive (LLDD) applications [1], such as industrial robots, wind power generation, ship propulsion, etc. Generally, PMVMs can be classified into three types according to the location of permanent magnets (PMs), i.e., stator type (ST), rotor type (RT) and stator and rotor type (SRT). The former two types mean that either PMs are only on stator or only on rotor, while the latter type signifies that PMs are on both stator and rotor. Since there are two PM excitation sources, the SRT type of PMVM is also called “dual-permanent-magnet-excited (DPME) machine” [2]. Clearly, DPME machine has one more PM excitation source than the other two types, so it can output higher torque compared with the other two types, which has been demonstrated in [2,3]. Thus, DPME machine has more advantages in the LLDD field, and much research on it is also growing increasingly. However, according to the literature review, research on DPME machine concentrates on the qualitative explanation of the bidirectional field modulated effect (BFME) [2], new structures [4], design and optimization [5], comparative study [6] and control strategies [7]. 2. Motivation Back-EMF is an important physical quantity in electrical machine (EM), which many designers often care about, as nonsinusoidal back-EMF may cause torque ripple, and increase inverter capacity [8]. For DPME machine (see Fig. 1), it has two PM excitation sources with different pole-pair numbers (PPNs), i.e. stator PMs and rotor PMs; it also has double-salient structure. Due to the double-salient structure, the magnetic field generated by stator PMs or rotor PMs can be modulated into abundant airgap field harmonics through rotor teeth or stator teeth. So, the airgap harmonics of DPME machine are more abundant and more complex than those of traditional PM machine. Regarding the back-EMF of DPME machine, two questions (Qs) arise naturally, i.e., Q1: do all airgap flux density harmonics make contribution to back-EMF? Q2: For these harmonics which contribute to the back EMF, do they all produce positive or negative back EMF? According to the previous literature review, only [4] answered Q1 by qualitative analysis, and pointed out that only specific harmonics can contribute to back-EMF. However, as far as we know, there is no literature to answer Q2. So, it is necessary to quantitatively identify the airgap flux density harmonics contributing to back-EMF, thus helping to suppress the harmonics which produce negative back EMF. 3. Method Magneto motive force (MMF) permeance analytical model (MPAM) is used to identify the airgap flux density harmonics contributing to back-EMF. Firstly, establish the MPAM of DPME machine. Next, derive the expressions of airgap flux density harmonics generated by stator and rotor PMs respectively based on the MPAM, and classify the harmonics into six types (see Table I). Then, deduce the expressions of PM flux-linkage by means of winding function and the derived airgap flux density harmonics. Afterwards, get back-EMF expressions by the derived PM flux-linkage. Finally, identify the airgap flux density harmonics contributing to back-EMF. 4. Results As shown in Fig. 1, a 12/10 DPME machine is selected as an example for analysis. Fig. 2(a) compares back-EMFs obtained by theoretical analysis and FEM. As can be seen from Fig. 2(a), the back-EMF obtained by the MPAM basically coincides with that obtained by FEM. The error between the analytical and FEM results is about 8.7%, which indicates that the MPAM is feasible. By means of the MPAM, one can also identify the airgap flux density harmonics contributing to back-EMF. Fig. 2(b) gives the identification results of the airgap flux density harmonics contributing to the fundamental back-EMF. Apparently, S-II and R-II types of harmonics generate negative back-EMFs, which weakens the total back-EMF; S-III, R-I and R-III types contribute to positive back-EMFs, and R-III type contributes nearly half the back-EMF; S-I type makes no contribution to back-EMF. 5. Note Limited by the length

of the digest, 1) not all the references are given in the digest body, and the others will add in the full paper; 2) the derivation of the MPAM for DPME machine as well as the derived expressions will be elaborated in the full paper; 3) other results such as waveforms of flux density will be added in the full paper.

[1] F. Wu and A. M. El-Refai, *IET Electr. Power Appl.*, Vol. 13, p. 127–137 (2019) [2] L. Jian, Y. Shi and C. Liu, *IEEE Trans. Magn.*, Vol. 49, p. 2381–2384 (2013) [3] W. Zhao, X. Sun and J. Ji, *IEEE Trans. Appl. Supercond.*, Vol. 26, p. 1-5 (2016) [4] L. Xu, W. Zhao and G. Liu, *IEEE Trans. Veh. Technol.*, Vol. 69, p. 7104-7115 (2020) [5] Q. Lin, S. Niu and W. N. Fu, *IEEE Trans. Magn.*, Vol. 56, p. 1-5 (2020) [6] Q. Wang, S. Niu and L. Yang, *IEEE Trans. Ind. Electron.*, Vol. 64, p. 9924-9933 (2017) [7] S. Niu, S. L. Ho and W. N. Fu, *IEEE Trans. Magn.*, Vol. 50, p. 805-808 (2014) [8] X. Ren, D. Li and R. Qu, *IEEE Trans. Ind. Electron.*, Vol. 67, p. 6248-6258 (2020)

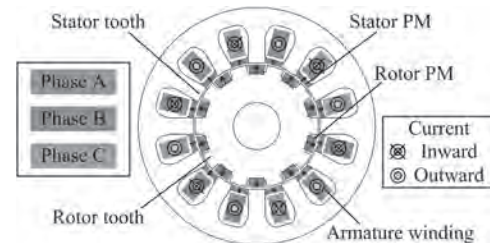


Fig. 1. 12/10 DPME machine

TABLE I
TYPES OF AIR-GAP FLUX DENSITY HARMONICS

Harmonics produced by stator PMs		Harmonics produced by rotor PMs	
Type	PPN	Type	PPN
S-I	$m_s p_s$	R-I	$m_r p_r$
S-II	$m_s p_s + k_s p_s$	R-II	$m_r p_r + k_r p_r$
S-III	$ m_s p_s - k_s p_s $	R-III	$ m_r p_r - k_r p_r $

Fig. 1 and Table I

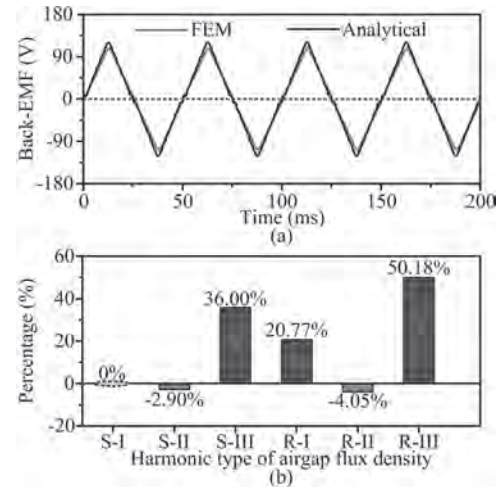


Fig. 2. (a) Back-EMFs. (b) Contribution of airgap flux density harmonics to the fundamental back-EMF.

BT-06. Design of a Axial-Modular Flux-Switching Permanent Magnet Machine.

Y. Wang¹, P. Su¹, Y. Shen¹ and Y. Li¹

1. Hebei University of Technology School of Electrical Engineering, Tianjin, China

I. Introduction Recently, the flux-switching permanent magnet (FSPM) machines have been recognized as attractive candidates for electric vehicle (EV) and hybrid electric vehicle (HEV) propulsion on account of their high torque (power) density and robust rotor structure. The 6s/5p FSPM machine is considered for the high speed condition, since it reduces the fundamental frequency and exhibits improved torque performances. However, the topology utilization is restricted due to the unbalanced magnetic force in automotive applications. In order to address the above issues, this paper proposes a axial-modular flux switching permanent magnet (AM-FSPM) machine, as shown in Fig. 1. It contains two axial modular parts, namely front modular part and rear modular part, where the PMs of each part are sandwiched between the two U modular cores. It is worth noting that the PMs magnetization directions are opposite at the same stator position of two axial modular parts. The phase armature winding is composed of two toroidal coils, which are wound around the stator yokes. It can be found from Fig. 1(a) that the integrated toroidal windings are shared by the two axial modular parts, and then the winding function is different from that of the conventional FSPM machine. Meanwhile, the winding factor of the AM-FSPM machine is improved by the toroidal windings, which is helpful to increase the torque density. The rotor poles in the rear part are shifted relative to the front part by 180° mechanically. II. Electromagnetic performances of AM-FSPM machine For the AM-FSPM machine, the PM magneto-motive-forces (MMFs) of two axial modular parts are modulated by the corresponding salient rotor cores. Then the PM air gap flux density is produced, and the harmonic amplitudes in two modular parts are identical due to the same PM-MMF and rotor permeance model. However, the PMs magnetization directions of the two modular parts are opposite and the rotor positions are different, which leads to the flux density harmonic phase difference. Based on the PM flux density expression, the phase difference between two modular parts is obtained as $|(2n-1)P_{PM} \pm kP_r|\pi$, where P_{PM} and P_r is the PM pole-pair number and rotor pole number, respectively. Meanwhile, the winding functions of two axial modular parts are the same due to the sharing of the integrated toroidal armature windings. Hence, the phases difference of the PM flux linkage between the front modular part and the rear modular part is $|(2n-1)P_{PM} \pm kP_r|\pi$. When k is an even number, the harmonics with even orders in flux linkages of two coils are cancelled, and then the sinusoidal flux linkage will be obtained as shown in Fig. 2(a). It can be found from Fig. 2(b) that the total harmonic distortion (THD%) of the single coil flux linkage is 31.57% in the modular part, where the harmonic with 2nd order is the highest (30.95%). Nevertheless, the THD% in the same coil of whole machine is 6.19% due to the cancelled harmonics with even orders. Moreover, the coil flux linkage harmonic distortion with 3rd orders is 6.18%, which is not contributed to the electromagnetic torque. In order to verify the merits and disadvantages of AM-FSPM machine, a comprehensive comparison between AM-FSPM and conventional 6s/5p FSPM machine is conducted. Two machines have the same outer diameter, axial stack length and air gap length. Meanwhile, the same PM and silicon steel materials are utilized and the rated current density of two machines are equal. Fig. 2(c) shows the electromagnetic torque waveforms of two machines. It can be found that the average torque of the AM-FSPM machine is 14.05Nm, which is 1.09 times of that of the FSPM machine. The reason is that the winding factor of AM-FSPM is 1, which is higher than 0.866 of traditional 6s/5p FSPM machine. In addition, the cogging torque in AM-FSPM (0.62Nm) is approximately identical to the FSPM machine. However, the torque ripple of AM-FSPM is 6.6%, which is 0.7% higher than that of FSPM machine. It is worth noting that the torque ripples without cogging torques are 3.6% and 4.1% in AM-FSPM and FSPM machines, respectively. Hence, the torque ripple is dominantly influenced by the cogging torque, which will be investigated and suppressed in the full paper. The electromagnetic torque with different current densities of two machines are shown in Fig. 2(d). It can be found that the average torque increases linearly as the current density rises, then the two machines exhibit the attractive overload capability. III. Conclu-

sion This paper proposes a novel AM-FSPM machine and the flux density harmonics characteristics are deduced. Then the sinusoidal flux linkage of the toroidal coil can be obtained due to the flux density harmonics phases difference between two modular parts of the AM-FSPM machine. In addition, compared with the 6s/5p FSPM machine, the proposed machine with the same geometric parameters exhibits higher torque density, and lower torque ripple, which is suitable for the EV and HEV applications.

[1] Y. Li, D. Bobba and B. Sarlioglu, "Design and Performance Characterization of a Novel Low-Pole Dual-Stator Flux-Switching Permanent Magnet Machine for Traction Application," in IEEE Transactions on Industry Applications, vol. 52, no. 5, pp. (2016) [2] C. Di, I. Petrov and J. J. Pyrhönen, "Unbalanced Magnetic Pull Compensation With Active Magnetic Bearings in a 2 MW High-Speed Induction Machine by FEM," in IEEE Transactions on Magnetics, vol. 54, no. 8, pp. (2018)

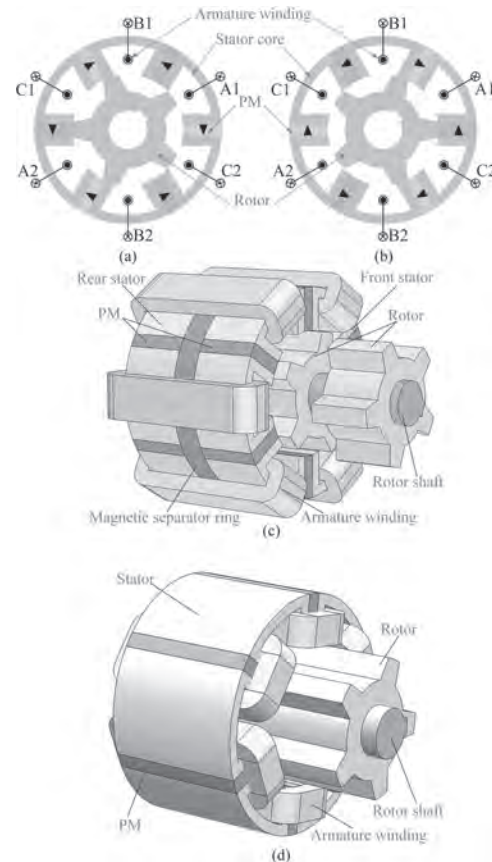


Fig. 1. AM-FSPM machine and traditional 6s/5p FSPM. (a) front modular part of AM-FSPM, (b) rear modular part of AM-FSPM, (c) AM-FSPM. (d) 6s/5p FSPM.

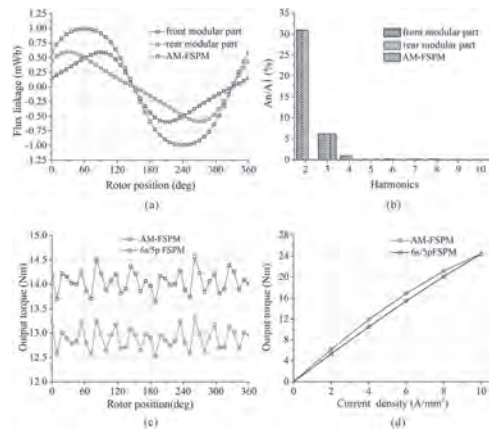


Fig. 2. 2D and 3D finite element analysis results of AM-FSPM and traditional 6s/5p FSPM parameters (a) flux linkage, (b) corresponding Fourier spectra, (c) electromagnetic torque, (d) current density.

BT-07. A Novel Winding Switching Strategy of a Consequent-Pole Ferrite-PM Hybrid-Excited Machine for Electric Vehicle Application.

J. Jiang¹, X. Zhang² and S. Niu¹

1. Electrical Engineering Department, The Hong Kong Polytechnic University, Hong Kong, Hong Kong; 2. Shenzhen In Drive Amperex Co. Ltd., Shenzhen, China

Abstract: In this paper, a novel winding switching strategy is proposed to extend the speed range of a consequent-pole ferrite-PM hybrid-excited machine (CPFPM-HEM) for electric vehicle application. The key is that in low-speed range, the ac armature winding and dc field winding are connected in series to achieve large starting torque, while in high-speed range, dc field winding are injected with different dc currents to realize constant back-EMF with flux-weakening effect. Furthermore, consequent-pole rotor is used to reduce the dosage of the permanent magnet (PM). In the meantime, ferrite PM is used to replace rare-earth PM to reduce the cost with the shortage of rare earth resources. In this paper, the machine configuration, winding switching concept are illustrated in detail. Then, the electromagnetic performance of CPFPM-HEM in different speed ranges are investigated. Finally, the speed range which greatly extended with the same back-EMF is testified by the Maxwell/Simplorer co-simulation. 1. Introduction Nowadays, permanent magnet synchronous machine (PMSM) has attracted more and more attention in electronic vehicle application with excellent advantages such as high-power density and high efficiency [1-2]. However, the fixed PM flux of PMSM has limited the speed range of electronic vehicle. In order to extend speed range of the electric vehicle, hybrid excited machine, which incorporates PM excitation and dc field excitation, is proposed [3-4]. For hybrid excited machine, the flux regulation range has a limitation with dc field current control. In order to extend the flux regulation range, a novel winding switching strategy is proposed. 2. Machine configuration and winding switching concept A. Machine configuration Fig. 1 shows the configuration of consequent-pole ferrite permanent magnet hybrid-excited machine (CPFPM-HEM). It is composed of 8 pole pair inner rotor and 12-slot outer stator. The rotor consists of consequent-pole ferrite PMs and the magnetization direction of these PMs is radial outward as denoted in Fig. 1. The stator comprises ac armature winding and dc field winding. Both ac armature winding and dc field winding are made of single layer concentrated windings. The ac armature winding and dc field winding are connected in series in low-speed operation, while which are separately excited in high-speed operation. B. Winding switching concept Fig. 1 presents the winding switching manipulation circuit which consists of ac armature winding, dc field winding, rectifier, dc voltage source as well as some switches. There are two speed modes. Mode 1: Low speed mode S1 and SW1 is OFF. The ac armature winding and dc field winding are connected in series when the machine is in low-speed operation. The back-EMF is the sum of the voltage from ac armature winding and dc field winding. Due to the low speed, the back-EMF provided by the powertrain does not need to be high. Mode 2: High speed mode S1 and SW1 is ON. The ac armature winding and dc field winding are separately excited. While ac armature winding is provided by powertrain, the dc field winding is provided by dc voltage source. By regulating the dc source voltage value, the back-EMF provided by the powertrain can keep the same. 3. Electromagnetic performance Fig. 2 shows variable speed constant back-EMF with winding switching operation and dc excitation regulation. It can be noticed that in 0 to 20 ms, the machine operates in mode 1 with 300 rpm, the ac armature winding and dc field winding are connected in series to provide large starting torque. At 40 ms, the ac armature winding and dc field winding are separately excited and the machine switches to mode 2. Between 40 ms to 80 ms, the machine speed is 600 rpm and the dc excitation current is zero. Between 80 ms to 120 ms, the machine speed changes to 900 rpm and dc excitation current changes to -3 A. Between 120 ms to 160 ms, the machine speed attains 1200 rpm and the dc excitation current reaches -6 A. It can be concluded that, the amplitude of back-EMF is almost unchanged when the speed changes from 300 rpm to 1200 rpm with resort to winding switching operation and dc excitation regulation. 4. Conclusion This paper proposes a novel winding switching strategy to enhance the flux regulation capability of CPFPM-HEM, thus whose speed range can be greatly extended. The ac armature winding and dc field winding are connected in series to provide large torque in low-speed

mode, while which are separately excited to realize variable speed constant back-EMF in high-speed mode. The paper has verified variable speed constant back-EMF through Maxwell/Simplorer co-simulation. In addition, consequent-pole ferrite PMs are used to save the cost and avoid the usage of rare-earth resources. In the full paper, the machine operation principle, flux regulation principle, as well as winding switching concept will be illustrated in detail. In addition, more electromagnetic analysis will be performed and more conclusions will be drawn from the finite element results. Moreover, a prototype of the machine will be manufactured and relative tests will be carried out. Acknowledgement This work was supported in part by grants from the Hong Kong Research Grants Council, Hong Kong, China, under Project PolyU 152058/17E and PolyU 152143/18E.

[1] S. Niu, Y. Luo, W. Fu and X. Zhang, "Robust Model Predictive Control for a Three-Phase PMSM Motor With Improved Control Precision," *IEEE Trans. Ind. Electron.*, vol. 68, no. 1, pp. 838-849, Jan. 2021. [2] S. Niu, Y. Luo, W. Fu and X. Zhang, "An Indirect Reference Vector-Based Model Predictive Control for a Three-Phase PMSM Motor," *IEEE Access*, vol. 8, pp. 29435-29445, 2020. [3] X. Zhao and S. Niu, "A New Slot-PM Vernier Reluctance Machine With Enhanced Zero-Sequence Current Excitation for Electric Vehicle Propulsion," *IEEE Trans. Ind. Electron.*, vol. 67, no. 5, pp. 3528-3539, May 2020. [4] Y. Fan, G. Qu, and C. Tan, "Design and Analysis of a New Five-Phase Dual-Stator Consequent-Pole Brushless Hybrid Excitation Machine," *IEEE Trans. Magn.*, vol. 55, no. 1, pp. 1-10, Jan. 2019.

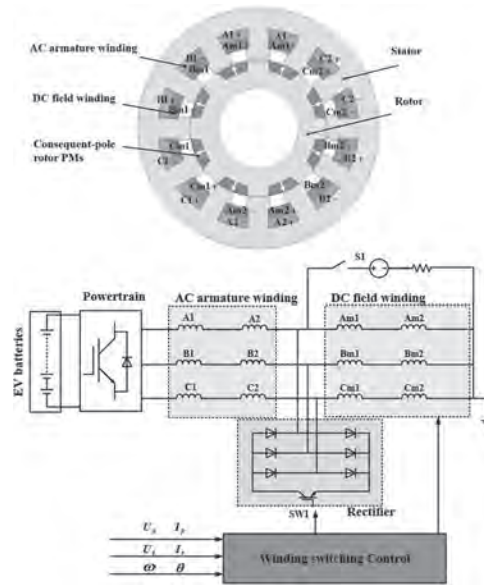


Fig. 1. Configuration of CPFPM-HEM and winding switching manipulation circuit.

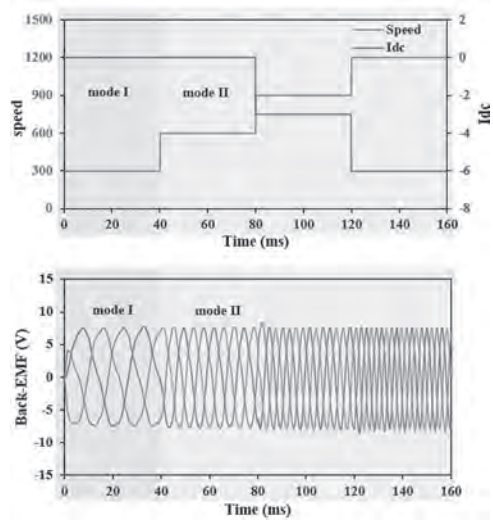


Fig. 2. Variable speed constant back-EMF with winding switching operation and dc excitation regulation. (a) Speed variation and given dc excitation current. (b) Variable speed constant back-EMF.

BT-08. Analysis of Axial Modular Flux Reversal Permanent Magnet Machine.

Y. Shen¹, P. Su¹, Y. Wang¹ and Y. Li¹

1. Hebei University of Technology School of Electrical Engineering, Tianjin, China

I. INTRODUCTION The flux reversal permanent magnet (FRPM) machine, as a speed PM machine with a simple rotor configuration, is suitable for high speed electric propulsion applications. However, the conventional 6-slot and 8-pole (6s/8p) FRPM machine has some disadvantages, such as low torque density and large torque ripple. An axial modular flux reversal permanent magnet (AM-FRPM) machine is proposed in this paper as shown in Fig. 1. It contains two modular parts including front modular part 1 and rear modular part 2, and the modular part topology evolves from the conventional 6s/8p FRPM machine. It is worth noting that the PMs of two modular parts have opposite magnetization directions at the same stator position. Meanwhile, the rotor poles in the rear part are shifted by 22.5° mechanically relative to those in the front part. In addition, the toroidal windings are wound around the yokes of the AM-FRPM machine, which are different from those of conventional FRPM machines. Besides, the winding factor is set as 1 to obtain a high torque density. II. PRINCIPLES AND PERFORMANCE Based on the magnetic field modulation theory, the operating principle of AM-FRPM machine is analyzed from three perspectives, including PM field modulation, armature reaction field modulation and torque production mechanism. For the PM field, the PM magneto-motive-force (MMF) of each modular part is modulated by the corresponding modular salient rotor teeth [1]. Then the air gap flux density expression B_g can be deduced, which contains the harmonics components (HCs) with $|nP_s \pm kP_r|$ order, where P_s is the number of stator slots, P_r is rotor poles number, $n=1, 2, \dots$, and $k=0, 1, 2, \dots$. The air-gap flux density harmonics distributions of the PM field are shown in Fig. 2(a). It can be found that harmonics distributions of two modular parts are similar, and the dominant harmonics components are 2nd, 4th, 6th, 12th, 14th and 24th orders, which verifies the HCs results by the field modulation theory. PMs of the two modular parts have opposite magnetization directions at the same stator position, so the phases differences of the flux density harmonics generated by the PM MMF, such as 6th, 12th and 24th, are 180° between two parts. Besides, the PM-MMFs are modulated by two rotor parts with different initial angles, so the phases of modulated harmonics in two parts are also different. In addition, based on the flux density harmonics phases analysis, the PM flux linkages harmonics with even orders are cancelled as shown in Fig. 2(b). The armature reaction MMF mathematic model of the AM-FRPM machine cannot be obtained by three phases overlapping directly because its winding function is different from that of the conventional FRPM machine. The reason is that the armature coils of the AM-FRPM machine are with the same direction. Hence, the armature reaction MMF distributions need to consider three phases synchronously. In addition, the armature reaction MMF in two modular parts is modulated by the front and rear rotors in Fig. 1(a), respectively, then the armature reaction air gap flux density harmonics distributions can be obtained. It can be found from Fig. 2(c) that the number of HCs can be expressed as $2k$ ($k=1, 2, \dots$), and the dominant harmonic orders are 2nd, 4th, 6th, 10th and 12th. It is worth noting that the rotors in two modular parts have different initial angle, and then the armature reaction flux density harmonic distributions of two parts obtain different harmonic performances, including amplitudes and phases. The harmonics characteristics analysis will be illustrated in detail in the full paper. Here it is clearly shown in Fig. 2(c) that the amplitudes of 4th harmonic in front and rear modular parts are 0.22T and 0.11T, respectively, which influence the harmonics contribution of electromagnetic torque. Based on the analysis of the PM field and the armature reaction field, it can be concluded that the electromagnetic torque is mainly contributed by the harmonics with 2nd, 4th, 6th and 12th orders. The 6th and 12th harmonics are generated by the PM MMF, while the 2nd and 4th harmonics are produced by the modulation of salient pole rotor on PM MMF. The electromagnetic torque waveforms are shown in the Fig. 2(d). It can be found that the torque ripples of front and rear modular parts are 8.4% and 8.3%, respectively, and the torque ripple of AM-FRPM machine is only 6.4%. Besides, the torque of front and rear modular are 5.23Nm and 5.24Nm, and the torque of AM-FRPM machine is 10.64Nm. The torque is generated by overlapping of two modular

parts is 1.6% less than that of the whole machine, so the magnetic flux leakage between modular parts is small and the structure is compact. III. CONCLUSION The proposed AM-FRPM machine contains two modular parts and integrated toroidal windings. In this paper, the operating principle of the proposed machine was explained by the air gap field modulation theory. It can be found that the armature reaction flux density harmonic distributions of two parts obtain different harmonic performances. Besides, the AM-FRPM machine exhibits a high torque density and the torque ripple is suppressed effectively, which is suitable for electric vehicle applications.

[1] X. Zhu and W. Hua, "An Improved Configuration for Cogging Torque Reduction in Flux-Reversal Permanent Magnet Machines," in IEEE Transactions on Magnetics, vol. 53, no. 6, pp. 1-4, (2017). [2] X. Zhu, W. Hua and W. Wang, "Analysis of Back-EMF in Flux-Reversal Permanent Magnet Machines by Air Gap Field Modulation Theory," in IEEE Transactions on Industrial Electronics, vol. 66, no. 5, pp. 3344-3355, (2019).

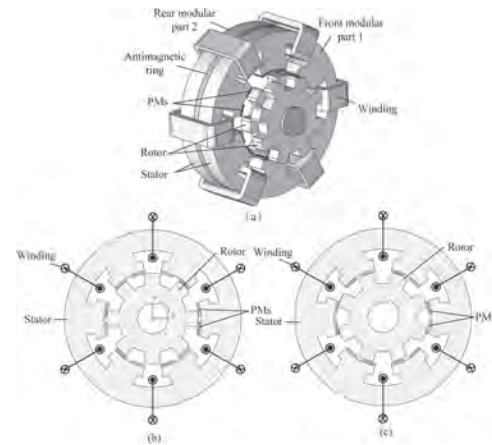


Fig.1 (a) The topology of AM-FRPM machine. (b) front modular part (c) rear modular part.

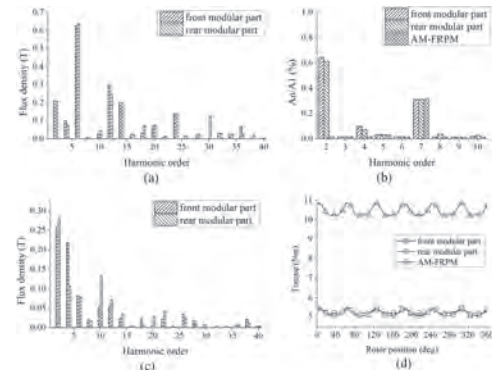


Fig.2 (a) The air-gap flux density harmonics distributions of PM field. (b) The harmonic spectrum of line flux linkage. (c) The air-gap flux density harmonics distributions of armature field. (d) Torque waveforms.

BT-09. A Novel Brushless Dual-Electrical-Port Dual-Mechanical-Port Machine With Opening Stator Slot.

Z. Liang¹, X. Ren¹, D. Li¹ and R. Qu¹

1. Huazhong University of Science and Technology, Wuhan, China

Abstract A novel brushless dual-electrical-port dual-mechanical-port machine with opening stator slot is proposed to improve the torque density. Compared to the regular BLDD machine, which can be regarded as the combination of the magnetic gear machine (MGM) and permanent magnet synchronous machine (PMSM), the proposed BLDD is formed by MGM and vernier PM machine (VPM). The stator teeth are not only used to go through the main flux, but also worked as a modulator to change the pole pairs and construct the VPM part. Due to the flux modulation effect and reduced effective air-gap, the torque density is significant improved. The operation principle is introduced and electromagnetic performances of the regular and proposed BLDD machine are compared by 2-D finite element analysis (FEA). I. Introduction Continuously variable transmission (CVT) is the key component of the hybrid power system, which has the advantages between the electric drive system and engine [1]-[3]. With the development of the flux modulation principle [4], a new type of CVT called brushless dual-electrical-port dual-mechanical-port (BLDD) machine, which can realize the function of a generator, a motor and the planetary gear in the hybrid power system, has been proposed in [5]. This paper proposes a higher torque density BLDD machine with opening stator slot, as shown in Fig. 1. II. Structure and operation principle The proposed BLDD machine has the same outer and inner rotors structure with the regular BLDD machine [6]. The major difference is the stator configuration. A split-teeth stator structure is used and two sets of windings are placed in the auxiliary teeth and main teeth respectively. In the regular BLDD machine, the auxiliary teeth are closed slot structure, and only used to provide flux path. In the proposed BLDD machine, the auxiliary teeth are opening slot structure, and not only used to go through the magnetic path, but also worked as a modulator to change the PM pole-pair to vernier winding pole-pair. As shown in Fig.1 (a2) and (b2), the MGM part is composed of the modulation winding, teeth in the inner rotor and spoke-array PMs in the outer rotor, which is the same for both regular and proposed BLDD machines. The operation principle of the MGM portion is based on the magnetic gear effect, and the modulation winding pole-pair is equal to the difference between the PM pole-pair and inner rotor teeth number. The other portions of regular and proposed BLDD machines are completely different, one is PMSM portion, and the other is VPM portion. The PMSM portion of the regular BLDD machine in Fig.1 (a3) is formed by regular winding, stator with closed slot and spoke-array PM outer rotor. PMSM works on the same operation principle as a conventional PM machine, and the regular winding pole-pair is equal to PM pole-pair. Nevertheless, the VPM portion of the proposed BLDD machine in Fig.1 (b3) consists of vernier winding, stator with opening slot and spoke-array PM outer rotor. The operation of VPM is based on the flux modulation principle, in which stator auxiliary teeth work as a pole pair transformer and the vernier winding pole-pair is equal to the difference between the stator auxiliary teeth number to PM pole-pair. III. Comparison of the Regular and Proposed BLDD Machines The two BLDD machines with the same machine volume and current density are used to compare the electromagnetic performance. The two BLDD machines have been optimized respectively. Compared to the regular BLDD machine, the proposed BLDD machine has 53.3% higher MGM torque due to increased pole ratio (ratio of PM pole-pair to winding pole-pair) and 77.8% higher VPM torque because of flux modulation effect. IV. Conclusion This paper proposes a novel BLDD machine with opening stator slot. The proposed BLDD machine can significantly improve the back EMF and torque density. Because the composite structure of the proposed BLDD machine is changed and the operation principle is different. More details about machine operation principle, operation features and some design considerations of the proposed BLDD will be given in the full paper.

[1] Z. Q. Zhu and S. Cai, "Hybrid excited permanent magnet machines for electric and hybrid electric vehicles," *CES Trans. on Electrical Machines and Systems*, vol. 3, no. 3, pp. 233-247, Sept. 2019. [2] A. Emadi, Y. J. Lee and K. Rajashekara, "Power Electronics and Motor Drives in Electric,

Hybrid Electric, and Plug-In Hybrid Electric Vehicles," *IEEE Trans. Ind. Electron.*, vol. 55, no. 6, pp. 2237-2245, June 2008. [3] X. Zhang, C. T. Li, D. Kum etc., "Prius+ and volt- : configuration analysis of power-split hybrid vehicles with a single planetary gear," *IEEE Trans. Veh. Technol.*, vol. 61, no. 8, pp. 3544-3552, Oct. 2012. [4] D. Li, R. Qu and T. A. Lipo, "High-Power-Factor Vernier Permanent-Magnet Machines," *IEEE Trans. Ind. Appl.*, vol. 50, no. 6, pp. 3664-3674, Nov.-Dec. 2014. [5] D. Li, R. Qu, X. Ren etc., "Brushless dual-electrical-port, dual mechanical port machines based on the flux modulation principle," in *Proc. IEEE Energy Convers. Congr. Expo.* 2016. [6] Z. Liang, X. Ren, D. Li, etc., "Analysis of a Spoke-Array Brushless Dual-Electrical-Port Dual-Mechanical-Port Machine With Reluctance Rotor," *IEEE Trans. Ind. Electron.* vol. 68, no. 4, pp. 2999-3011, April 2021.

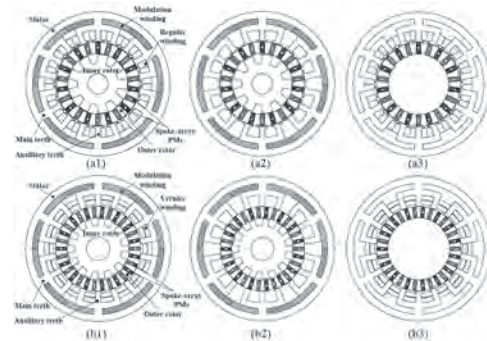


Fig.1 Configurations. (a1) Regular BLDD machine. (a2) MGM portion of regular BLDD machine. (a3) PMSM portion of regular BLDD machine. (b1) Proposed BLDD machine. (b2) MGM portion of proposed BLDD machine. (b3) VPM portion of proposed BLDD machine.

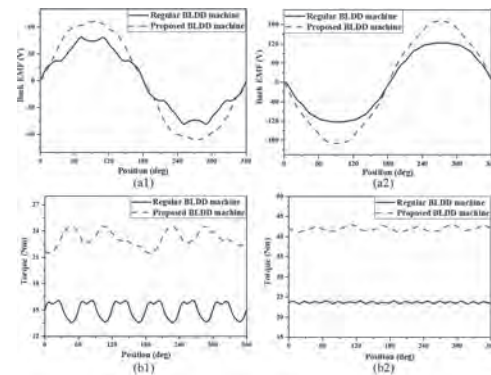


Fig.2 Comparison of regular and proposed BLDD machines. (a1) Back EMFs of modulation winding. (a2) Back EMFs of regular or vernier windings. (b1) MGM torque component. (b2) PMSM or VPM torque component.

BT-10. Flux-Modulated DC-Saturation-Relieving Hybrid Reluctance Machine Using Zero-Sequence Current Excitation for Electric Vehicle Application.

J. Jiang¹, X. Zhao¹, S. Niu¹ and K. Wong²

1. Electrical Engineering Department, The Hong Kong Polytechnic University, Hong Kong, Hong Kong; 2. Division of Science, Engineering and Health Studies, The Hong Kong Polytechnic University, Hong Kong, Hong Kong

Abstract This paper proposes a novel hybrid reluctance machine with dual-layer slot PMs and zero-sequence excitation. Dual-layer slot PMs are utilized to evoke DC-saturation-relieving and flux modulation effect respectively. By introducing zero-sequence current excitation which functions as virtual DC field source, extra dc field winding can be removed. Moreover, flux can be flexibly controlled through regulating zero-sequence current, thus speed range can be greatly extended. In this paper, the machine configuration, DC-saturation-relieving principle, flux modulation effect, and zero-sequence current control are introduced. Electromagnetic performance of the proposed machine is evaluated by finite element analysis (FEA), including variation of flux-linkage, back-EMF, as well as torque density with different zero-sequence currents. Furthermore, a prototype is manufactured and relevant experiments are performed to verified the correctness of FEA.

1. Introduction Nowadays, electric vehicles have attracted more and more attention due to fossil fuel depletion and severe environment pollution [1]. It is required that the motor operates at wide speed range [2]. Reluctance machine has come to be a good solution for electric vehicle application, which includes switched reluctance machine (SRM) [3], doubly salient machine (DSM), flux switching machine (FSM) [4], flux reversal machine (FRM), as well as variable flux reluctance machine (VFRM) [5]. In this paper, a novel DC-saturation-relieving flux-modulated hybrid reluctance machine with zero-sequence current excitation is proposed. Zero-sequence current, which acts as dc field excitation, is injected into ac and dc integrated winding, thus dc field winding is removed.

2. Machine configuration and operation principle The structure of flux-modulated DC-saturation-relieving hybrid reluctance machine with integrated ac and dc winding is presented in Fig. 1. Inner rotor consists of only iron core which provides mechanical robustness. Outer stator comprises only one set of winding, namely ac and dc integrated winding. Zero-sequence current, which acts as dc field excitation, is injected into ac and dc integrated winding. There are two layers of PMs on the slot opening. Inner layer slot PMs are radial magnetized to generate effective torque with flux modulation effect. Meantime, outer layer slot PMs are tangential magnetized to enhance torque density through relieving DC saturation. A dual inverter drive circuit is also showed in Fig. 1. Each phase winding is split into two sub-phase windings. Two sub-phase winding groups are driven by two inverters respectively and the neutral points of which are connected. The advantages of proposed machine are listed as following.

(1) Since all excitation sources are mounted in the stator side and the rotor consists of only iron, no brush and slip rings are needed, which enhances mechanical robustness. (2) Radial magnetized PMs are mounted in the slot opening, which provides valid torque with flux modulation effect. Tangential magnetized PMs are placed in the slot opening, which improve torque density through relieving DC saturation. (3) Independent dc field winding is eliminated, which will leave more space for ac and dc integrated winding, thus more load current can be reached. (4) Through regulating zero-sequence current, flux can be flexibly regulated, thus extensive speed range can be realized.

3. Electromagnetic performance Fig. 2 shows on-load steady torque and no-load back-EMF with different zero-sequence currents. It can be seen that the on-load average torque is 3.4 Nm without zero-sequence current, 0.8 Nm with -10 A zero-sequence current, and 5.4 Nm with 10 A zero-sequence current. Also, the peak-to-peak value of no-load back-EMF is 12.8 V without zero-sequence current, 2.1 V with -10 A zero-sequence current, 28 V with 10 A zero-sequence current. By regulating zero-sequence current, on-load steady torque and no-load back EMF can be controlled, thus speed range of the proposed machine can be greatly extended.

4. Conclusion In this paper, the flux-modulated DC-saturation-relieving hybrid reluctance machine with zero-sequence current excitation is proposed. Zero-sequence current, acting as dc field excitation source, is injected into ac and dc integrated winding, thus dc field winding can be eliminated. Initial finite element analysis shows

that the on-load steady torque and no-load back-EMF can be controlled by regulating zero sequence current, thus speed range of the proposed machine can be greatly extended. Later, DC-saturation-relieving principle and flux regulation principle will be illustrated in detail. In addition, more electromagnetic analysis will be performed and more conclusions will be drawn from the FEA results. Furthermore, a prototype of the proposed machine will be manufactured and relative tests will be performed. This work was supported in part by grants from the Hong Kong Research Grants Council, Hong Kong, China, under Project PolyU 152058/17E and PolyU 152143/18E.

[1] X. Zhao, S. Niu, and X. Zhang, "Design of a New Relieving-DC-Saturation Hybrid Reluctance Machine for Fault-Tolerant In-Wheel Direct Drive," *IEEE Trans. Ind. Electron.*, vol. 67, no. 11, pp. 9571-9581, Nov. 2020. [2] S. Hemmati and T. A. Lipo, "Field weakening of a surface mounted permanent magnet motor by winding switching," International Symposium on Power Electronics Power Electronics, Electrical Drives, Automation and Motion, Sorrento, 2012, pp. 736-740. [3] X. D. Xue, K. W. E. Cheng, and T. W. Ng, "Multi-objective optimization design of in-wheel switched reluctance motors in electric vehicles," *IEEE Trans. Ind. Electron.*, vol. 57, no. 9, pp. 29-29, Sep. 2010. [4] C. Yu and S. Niu, "Development of a magnetless flux switching machine for rooftop wind power generation," *IEEE Trans. Energy Convers.*, vol. 30, no. 4, pp. 1703-1711, Dec. 2015. [5] J. T. Shi, X. Liu, and D. Wu, "Influence of stator and rotor pole arcs on electromagnetic torque of variable flux reluctance machines," *IEEE Trans. Magn.*, vol. 50, no. 11, pp. 1-4, Nov. 2014

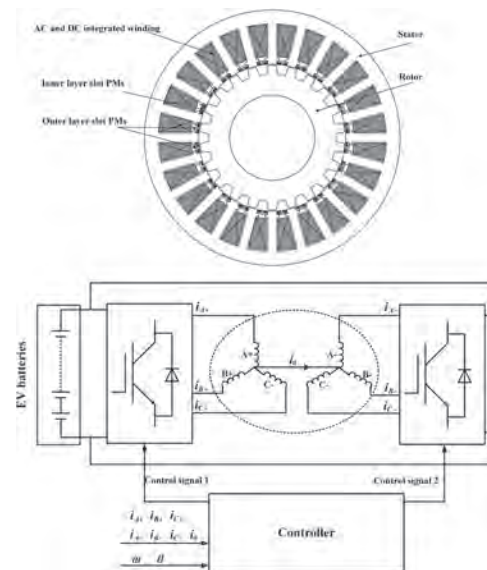


Fig. 1. Structure of flux-modulated DC-saturation-relieving hybrid reluctance machine and dual inverter drive control system.

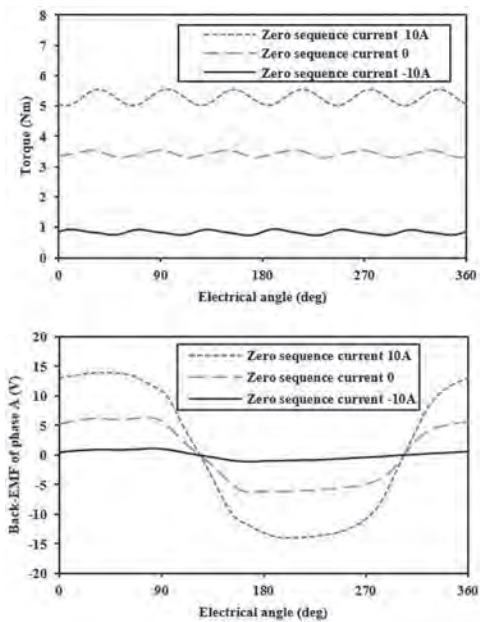


Fig. 2. On-load steady torque and no-load back-EMF with different zero-sequence currents.

BT-11. Comparative Study of Winding Configuration on a Multi-Tooth Flux Switching Permanent Magnet Machine.

Z. Li¹, G. Zhao¹, W. Hua², X. Jiang¹ and P. Su²

1. School of Electrical and Automation Engineering, Nanjing Normal University, Nanjing, China; 2. Southeast University, Nanjing, China

I. Introduction The multi-tooth flux-switching permanent magnet (PM) (FSPM) machines have attracted wide attention due to the advantages of fewer permanent magnet materials and higher torque density, compared with the conventional FSPM machines[1]. Recently, a 6-stator-coil/17-rotor-pole (6/17) multi-tooth FSPM machine with concentrated windings, namely, the C-multi-tooth FSPM machine, was proposed in paper [2], as shown in Fig 1(a). In this paper, in order to evaluate the electromagnetic performance of the multi-tooth FSPM machines with different winding configurations, the full-pitch windings are adopted as is shown in Figure 1 (b), called the FP-multi-tooth machine. II. Performance comparisons In this paper, the electromagnetic performance of the 6/17 multi-tooth machine with different winding configurations is evaluated by finite element analysis (FEA), which is mainly in terms of no-load back EMF, harmonic components, air-gap flux density, cogging torque, electromagnetic torque, etc. Figure 2(a) shows the no-load phase back-EMF per turn waveforms of the two multi-tooth machines at 1500r/min. It can be seen that the winding configuration has an impact on the amplitude of the back-EMF for the multi-tooth machine. The amplitude of the FP-multi-tooth machine is much larger than the C-multi-tooth one with concentrated windings. Figure 2(b) presents the FFT results of the no-load phase back-EMF waveform of the 6/17 multi-tooth machine shown in Figure 2(a), where it is adopted different winding configurations. The fundamental wave amplitudes are respectively 2.45 V (C-multi-tooth machine) and 4.47V(FP-multi-tooth machine), moreover, the total harmonic distortion (THD) is 2.21%, 1.38%, and that the harmonic components are the same, mainly odd-numbered harmonics. Hence, in terms of the 6/17 multi-tooth FSPM machine, the motor with the full-pitch winding exhibits larger amplitude of the fundamental component than the concentrated winding one, and the THD is slightly smaller. Figure 2 (c) shows the two multi-tooth machines air-gap flux density distribution in the air-gap region of coil A1 and A2. Furthermore, for the C-multi-tooth and the FP-multi-tooth machine, the average values of B_r are -0.391T and -0.603T respectively, which means the no-load PM fluxes flowing through the coil A1 and A2 of the FP-multi-tooth machine are larger. Correspondingly, its back EMF should be larger than the C-multi-tooth one, since part of the magnetic flux of the C-multi-tooth machine will flow through other phases to form a closed-loop magnetic circuit. Figure 2(d) presents the cogging torque waveforms of the two multi-tooth machines. The result indicates that the cogging torque waveforms phase of two multi-tooth machines is not the same, since their rotor position is different when the peak value of the maximum back EMF is obtained. To compare the torque performance of the 6/17 multi-tooth machines with different winding configurations, the study is conducted by 2-D-FEA with Flux software under $i_d=0$ control, where the slot package factor is $k_{pf}=0.45$, as shown in Fig. 2(e) and (f). When the current density is changed from 1A/mm² to 10A/mm², the FP-multi-tooth machine with full-pitch windings exhibits greater average torque and smaller torque ripples than the C-multi-tooth one. Figure 2(g) shows the electromagnetic torque waveform at the rated current density $J_{sa}=5A/mm^2$, where the load is 1.0. It can be seen that the average torque of the FP-multi-tooth machine with full-pitch windings (16.8Nm, 4.96%) are greater than that of the C-multi-tooth one (12.7Nm, 11.1%), and that the torque ripple of the FP-multi-tooth machine is smaller than the C-multi-tooth one. III. Conclusion In this paper, the study on the electromagnetic performance of the multi-tooth machine with different winding configuration is conducted by FEA. The results indicate that for the 6/17 multi-tooth FSPM machine, the FP-multi-tooth machine with full-pitch windings exhibits higher no-load phase back EMF, torque density, and smaller harmonic distortion and torque ripple, hence, the FP-multi-tooth machine with full-pitch windings is superior to the multi-tooth one with concentrated windings. A comparative study of other types of multi-tooth machines, such as the 6/10 multi-tooth FSPM machine, will be shown in the full paper.

[1]Y. Du, C. Zou, and X. Zhu, "A Full-Pitched Flux-Switching Permanent-Magnet Motor," in *IEEE Transactions on Applied Superconductivity*, vol. 26, no. 4, pp. 1-5, June 2016, Art no. 0604505, doi: 10.1109/TASC.2016.2541308. [2]G. Zhao and W. Hua, "Comparative Study Between a Novel Multi-Tooth and a V-Shaped Flux-Switching Permanent Magnet Machines," in *IEEE Transactions on Magnetics*, vol. 55, no. 7, pp. 1-8, July 2019, Art no. 8104908, doi: 10.1109/TMAG.2019.2900749.

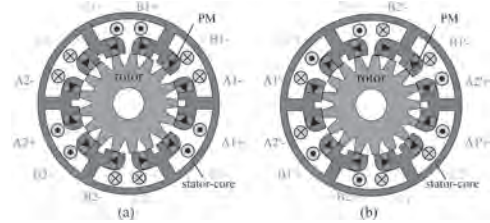


Fig. 1 Topologies of 6/17 multi-tooth FSPM machines. (a) C-multi-tooth machine. (b) FP-multi-tooth machine.

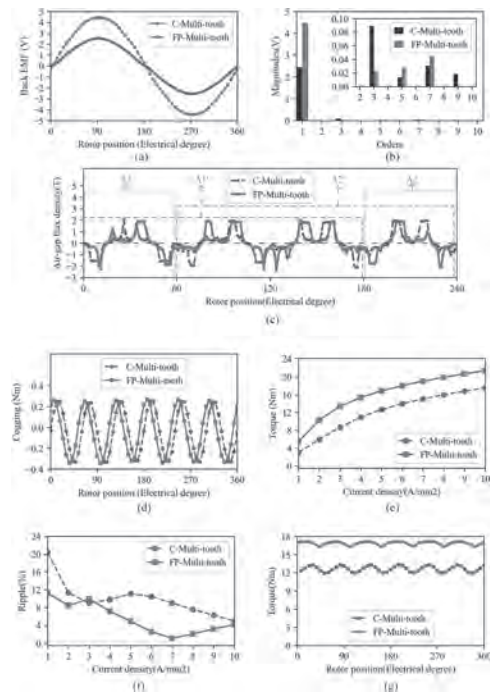


Fig. 2 Performance comparisons. (a) Phase back-EMF per turn waveforms at 1500r/min. (b) Harmonics of back-EMF. (c) Radial air-gap flux density B_r in the air-gap region of coil A1 and A2 (d) cogging torque. (e) Electromagnetic torque waveforms versus current densities. (f) Torque ripple waveforms versus current densities. (g) Electromagnetic torque waveforms under $J_{sa}=5A/mm^2$.

BT-12. Development of Slot-PM-Assisted Reluctance Generator With Self-Excited DC Source for Stand-Alone Wind Power Generation.

J. Jiang¹, X. Zhao¹, S. Niu¹ and K. Wong²

1. Electrical Engineering Department, The Hong Kong Polytechnic University, Hong Kong, Hong Kong; 2. Division of Science, Engineering and Health Studies, The Hong Kong Polytechnic University, Hong Kong, Hong Kong

Abstract: This paper proposed a new slot-PM-assisted reluctance generator with self-excited DC source for stand-alone wind power generation. The key is that several ac armature coils are used to provide electrical power to dc field winding through a rectifier. Compared with separately excited dc source, self-excited dc source is more suitable for stand-alone wind power generation and greatly reduces device costs since no independent dc source is needed. In this paper, the machine configuration and operation principle are introduced. Some leading dimension parameters are optimized to obtain maximum torque and minimum torque ripple. The feasibility of the optimal design with this novel structure is verified by finite element analysis and prototype testing.

1. Introduction: When it comes to provide energy to remote area, stand-alone wind power system with battery appeals to an excellent solution with relatively maintenance simplicity and low system cost [1-2]. The most important part of wind power generation system is the generator. Permanent magnet (PM) machine has been widely used as wind power generator due to simple structure, high efficiency, as well as high power density [3-4]. However, PM machines have no flux regulation ability. In this case hybrid excited machine, which excited by both PMs and dc field source, has been applied. The problem is that they all need independent dc excitation sources, which are not suitable for stand-alone wind power system. To solve abovementioned problem, several ac armature coils are used to supply electrical power to dc field winding through a rectifier, which are called ac rectifier winding. In this way, a novel slot-PM-assisted reluctance generator (SPMA-RG) with self-excited DC source (SEDC) is proposed.

2. Machine configuration and operation principle As shown in Fig. 1, a novel slot-PM-assisted reluctance generator (SPMA-RG) with self-excited DC source (SEDC) has three sets of stator windings, namely dc field winding, ac armature winding as well as ac rectifier winding. Radial magnetized PMs are placed in the slot opening of stator to enhance the torque density compared with traditional variable flux reluctance machine. Reluctance rotor consists of only iron core which provides mechanical robustness. The current produced by ac rectifier winding passes through controlled rectifier to provide excitation current to dc field winding. The advantages of the proposed generator are listed as following. (a) Since all excitation sources are placed in the stator side and the rotor comprises only iron, there are no brush and slip rings, which provides mechanical robustness. (b) Radial magnetized PMs are mounted in the slot openings which enhances the torque density compared with traditional variable flux reluctance machines. (c) Flux produced by dc field winding does not pass through the slot PMs, which will not lead to demagnetization of slot PMs. (d) Output voltage of ac armature winding can be controlled through regulating the dc field excitation, thus variable speed constant voltage can be realized in wind power generation system. (e) Several ac armature coils, namely ac rectifier winding, are used to provide excitation current to dc field winding through a controllable rectifier. In this way, no extra dc source is needed, which not only improves independent characteristic of wind power generation system, but also realizes energy feedback utilization.

3. Electromagnetic performance Fig. 2 shows rectified voltage and current generated from ac rectifier winding and rectified by the controllable rectifier. Furthermore, output voltage of the ac armature winding appears to be stable and achieves three-phase symmetric when rectified voltage and current arrive a stable value. It verified the feasibility of proposed wind power generation system. The ac rectifier winding can be used to provide dc excitation current to dc field winding through the controllable rectifier.

4. Conclusion In this paper, a novel slot-PM-assisted reluctance generator with self-excited DC source is proposed for wind power generation. Several ac armature coils, namely ac rectifier winding, provide electricity to dc field winding through a rectifier. This self-excited dc source greatly reduces device cost and improves the independent characteristic of the wind power system. In the full paper, the electromagnetic performance of proposed SPMA-RG is analyzed in detail.

The prototype of proposed generator is manufactured and relative testing is conducted. This work was supported in part by grants from the Hong Kong Research Grants Council, Hong Kong, China, under Project PolyU 152058/17E and PolyU 152143/18E.

[1] Ming-Shun Lu, Chung-Liang Chang, Wei-Jen Lee and Li Wang, "Combining the Wind Power Generation System with Energy Storage Equipment", *IEEE Trans. Ind. Appl.*, Vol.45, No.6, pp.2109-2115. November / Dec. 2009. [2] Ronan Doherty, Ronan Doherty and Mark O'Malley, "Establishing the Role That Wind Generation May Have in Future Generation Portfolios", *IEEE Trans. Power Sys.*, Vol.21, No.3, pp.1415-1422. Aug. 2006. [3] Y. Fan, K. T. Chau, and M. Cheng, "A new three-phase doubly salient permanent magnet machine for wind power generation," *IEEE Trans. Ind. Appl.*, vol. 42, no. 1, pp. 53-60, 2006. [4] Y. Chen, P. Pillay, and A. Khan, "PM wind generator topologies," *IEEE Trans. Ind. Appl.*, vol. 41, no. 6, pp. 1619-1626, 2005.

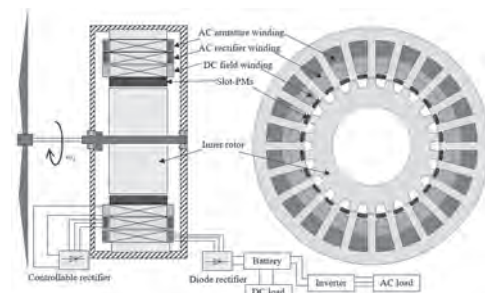


Fig. 1. Wind power generation system based on the proposed SPMA-RG.

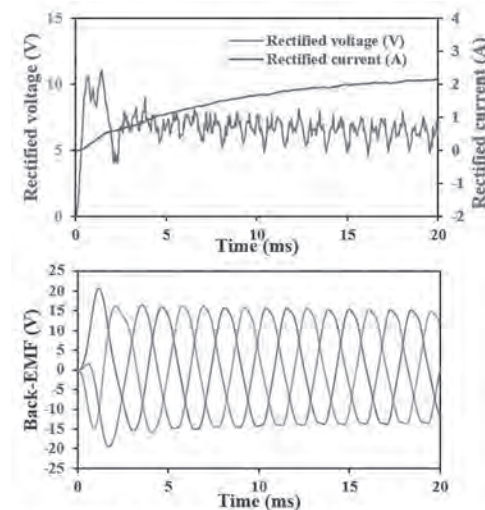


Fig. 2. Rectified voltage/current and Back-EMF.

Fig. 2. Rectified voltage/current and Back-EMF.

BT-13. A Novel Relieving-DC-Saturation Hybrid-Excited Machine With Skewed Permanent Magnets for Electric Vehicle Application.

S. Wang¹, S. Niu¹, X. Zhao¹ and K. Wong²

1. *Electrical Engineering, The Hong Kong Polytechnic University, Hong Kong, Hong Kong;* 2. *Division of Science, Engineering and Health Studies, The Hong Kong Polytechnic University, Hong Kong, Hong Kong*

Abstract This paper proposes a novel hybrid-excited outer-rotor machine with skewed permanent magnets (PM) placed at the stator slot opening. The key novelty is that the skew-magnetized PMs can achieve both torque production promotion and stator core saturation relieving. Compared with DC-excited reluctance machine, the proposed machine with skewed PMs has higher torque production and efficiency. Compared with synthetic slot PM excited machine, it is easier for machine assembly and manufacture, and the manufacture cost is reduced. In this paper, the machine structure of the proposed machine is presented. Then, the working principle are introduced briefly, including the relieving-DC-saturation effect and the flux modulation effect. The derivation will be presented in more detail in the full-page paper. Finally, the machine performance under different DC field current is presented. **I. Introduction** The DC-excited reluctance machine is a promising solution for electric vehicle because of its inherent reliable and simple rotor structure, good thermal dissipation ability and wide speed range [1]. However, the torque production and efficiency are not satisfying, because the excitation ability of DC winding is usually lower than PM [2]. Besides, the saturation in stator core limits the DC current due to the biased field [3]. To address the two problems, this paper proposes a novel skewed PM structure. The radical component of the PMs can provide an effective flux to the armature winding, so that the torque production can be promoted directly. The tangential component of the PMs can relieve the saturation in the stator core, so that higher DC field current can be applied, and hence the torque production can be raised accordingly. **II. Machine structure** The structure of the proposed machine is presented in Fig. 1(a). The rotor consists of iron core only, so, it is reliable and easy for manufacture. In the stator side, there are two groups of windings, one is the DC field winding and another one is the 3-phase armature winding. The skewed PMs are placed at the slot-openings. The radical component of magnetization of every PM is outwards direction, but the tangential component of magnetization has alternate polarity in every tooth. The purpose of radical component is to provide an additional field linked to armature windings, so that the torque production can be raised directly. The purpose of tangential component is to provide a constant flux in the stator core, of which the direction is opposite with the flux from DC current, so that higher DC current can be applied. The armature winding configuration is presented in Fig. 1(b). The concentrated single-layer winding configuration is used. **III. Working principle** In this part, to introduce the working principle of skew-magnetized PM clearly, the tangential magnetization component and the radical magnetization component are introduced respectively. For the radical magnetization component of PMs, the following relationship should be satisfied. $N_{PM} \cdot N_r + N_w = 0$ N_{PM} , N_r and N_w represent the pole pair number of PM, rotor teeth number and the order of working harmonic. In this case, the values of N_{PM} , N_r and N_w are 12, 22 and 10, respectively. The pole pair number of armature winding is the same with the order of working harmonic. Hence, 10-pole-pair armature winding is used. The flux path of the tangential magnetization component is presented in Fig. 2(a) together with the flux from DC current. The tangential component contributes little torque production directly if the current is kept unchanged, because the flux from the tangential component of PM is a constant biased flux. But the stator saturation is largely relieved because the directions of flux of DC current and the tangential component of PM are opposite. Hence, higher DC current can be applied when the PMs are used, and hence the torque production can be raised accordingly. **IV. Machine performance** To show the effectiveness of the skew-magnetized PMs, an FEA model is built. The maximum diameter is 150 mm, stack length is 80 mm, and air gap length is 0.5 mm. DC windings have the same number of turns and rated current as armature windings, the values are 52 turns and 6 A respectively. The torque production under different field excitation is presented in Fig. 2(b). Either the DC field current or skew-magnetized PMs can be used for excitation individually. The torque production from skewed PMs is higher, but the torque production from DC field current is easier to

regulate. **IV. Conclusion** In this paper, a novel hybrid-excited machine with skew-magnetized PM is proposed. The radical magnetization component of PM is used to promote the torque directly, and the tangential magnetization component of PM is used to relieve the saturation. The flexible DC excitation current provide a wide speed range, and the additional skewed PM raises the torque production. An FEA model is built and the torque production is presented to verify the effectiveness of the proposed machine. The other features of the proposed machine will be presented and analyzed in the full-page paper. **Acknowledgement** This work was supported in part by grants from the Hong Kong Research Grants Council, Hong Kong, China, under Project PolyU 152058/17E and PolyU 152143/18E.

[1] C. H. T. Lee, K. T. Chau and C. Liu, *IEEE Trans. Magn.*, Vol. 49, p.3969-3972 (2013) [2] Q. Wang and S. Niu, *Renew. Sust. Energ. Rev.*, Vol. 68, p.475-491 (2017) [3] X. Zhao, S. Niu and W. Fu, *IEEE Trans. Magn.*, Vol. 55, p.1-5 (2019)

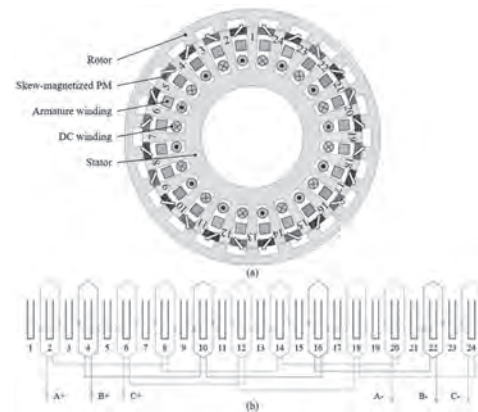


Fig. 1. The proposed machine. (a) Machine structure. (b) Armature winding configuration.

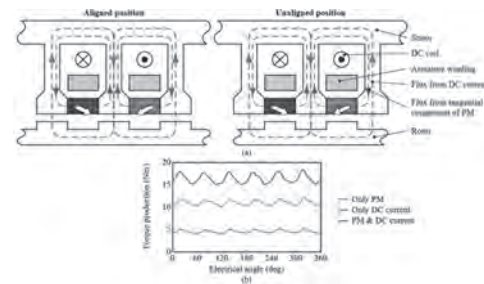


Fig. 2. Main flux path and torque production. (a) Flux path of DC current and tangential component of PM. (b) Torque production under rated armature winding.

BT-14. Influence of DC/AC Winding Split Ratio on Electromagnetic Performance of Hybrid Reluctance Machine With Synthetic Slot PM Excitation.

S. Wang¹, X. Zhao¹, S. Niu¹ and K. Wong²

1. Electrical Engineering, The Hong Kong Polytechnic University, Hong Kong, Hong Kong; 2. Division of Science, Engineering and Health Studies, The Hong Kong Polytechnic University, Hong Kong, Hong Kong

Abstract This paper investigates the influence of DC/AC winding split ratio on electromagnetic performance of hybrid reluctance machine with synthetic slot PM excitation. The machine structure and working principle are introduced briefly at first. Then, the machine performance, including power factor, torque production, loss, efficiency, and voltage regulation rate, are investigated with different DC/AC winding ratio. It is found that the machine has higher torque production and efficiency when the AC windings take up more space. But higher voltage regulation rate can be achieved when the space used for DC windings is close to AC winding. More detailed investigation will be presented in the further version.

I. Introduction Recently, the DC-excited reluctance machine has attracted lots of research interests and it is a very promising solution for electric vehicles because of its reliable rotor structure and wide speed range [1]. However, the torque production and efficiency are not satisfying. To address this issue, a novel hybrid reluctance machine with synthetic slot PM is proposed in [2]. But the influence of DC/AC winding split ratio, which is one of key design parameters on machine performance, has yet to be comprehensively studied. To give a design guideline for this hybrid reluctance machine, this paper will fully investigate the power factor, torque production, loss, efficiency and voltage regulation rate with different DC/AC winding ratio.

II. Machine structure and working principle The machine structure is presented in Fig. 1(a). The rotor consists of iron core only, so it is reliable and easy to manufacture. There are two groups of winding, one is the 3-phase armature winding and another one is the DC field winding. There are two groups of PMs located at slot openings. One group is radially magnetized PMs with the same magnetization direction. Another group is tangentially magnetized PMs with alternate polarity in every tooth. In the proposed machine, the flux excited by DC current varies as rotor permeance to provide an effective flux. However, the biased flux can cause saturation in stator core. To address this issue, the tangentially magnetized PMs are used to relieve saturation. They produce a constant biased flux with opposite direction with DC current field in the stator core, so that the flux density can be reduced. As for the radially magnetized PMs, they are used to provide an effective flux linked to armature winding to enhance the torque production directly.

III. Machine performance In this part, the machine performance under different DC/AC winding split ratio is presented based on FEA result. The maximum diameter is 150 mm, the stack length is 80 mm, the air gap length is 0.5 mm, the slot filling factor is 0.7 and the rated current density is 6A/mm². The DC/AC winding split ratio is defined as follow. $k_{dc} = N_{dc} / (N_{ac} + N_{dc})$, $k_{ac} = N_{ac} / (N_{ac} + N_{dc})$, k_{dc} and k_{ac} are the winding split ratios of DC and AC winding, respectively. And N_{dc} and N_{ac} are the number of conductors of DC field winding and armature winding in one slot, respectively. The rated torque, loss, efficiency and voltage regulation rate are presented in Fig. 2. The higher rated torque and can be achieved when less space is used for DC field winding, because the excitation ability of DC field current is poorer than PMs. The higher torque production brings with higher efficiency when armature winding takes up more space in slot, in spite of higher core loss. High power factor can be obtained when DC field winding takes up more space because it brings stronger excitation ability. As for voltage regulation rate (k_{VRR}), it is defined as follows. $k_{VRR} = (V_{2r} - V_0) / V_r$, V_0 , V_r and V_{2r} are the open-circuit back EMF when the DC field current is at zero, rated value and twice of rated value. It reflects the voltage regulation ability of the DC field winding and it is directly related to the speed range. When DC field winding split ratio is very small, the excitation ability of DC current is also very small. When DC field winding ratio is very large, the saturation effect becomes very severe. Hence, the voltage regulation rate is not high when DC field winding ratio is either too high or too low. From Fig. 2(d), it can be found that the highest voltage regulation rate can be achieved when the AC winding ratio is at around 40%.

IV. Conclusion This paper presents the machine performance of the hybrid-excited reluctance machine with synthetic slot PM excitation under various DC/AC winding split ratio.

It is concluded that when the more slot space is used for armature winding, the higher rated torque, core loss and efficiency can be achieved, but the power factor is lower. The highest voltage regulation rate can be obtained when the armature winding ratio is at around 40%. *Acknowledgement* This work was supported in part by grants from the Hong Kong Research Grants Council, Hong Kong, China, under Project PolyU 152058/17E and PolyU 152143/18E.

[1] E. Trancho, E. Ibarra and A. Arias, IEEE Trans. Ind. Electron. Vol. 65, p.2986-2995 (2018) [2] X. Zhao, S. Niu and X. Zhang, IEEE Trans. Ind. Electron. doi: 10.1109/TIE.2020.2996140 (2020)

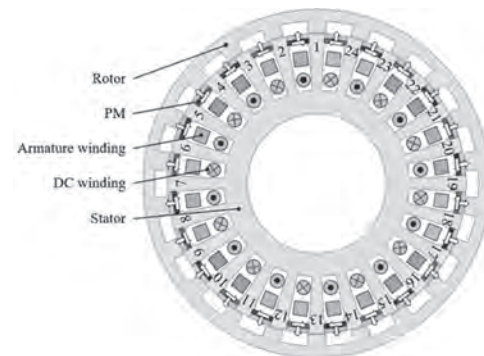


Fig. 1. Machine structure.

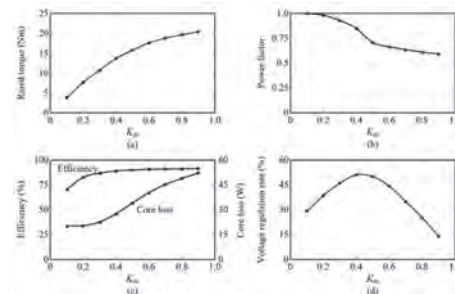


Fig. 2. Machine performance under different armature winding ratio. (a) Rated torque. (b) Power factor. (c) Core loss and efficiency. (d) Voltage regulation rate.

BT-15. Electromagnetic Performance Analysis and Comparison of Fractional-Slot Non-Overlapping Winding Dual-Rotor Axial Flux Permanent Magnet Vernier Machines With Segmented Stators.

L. Jia¹, M. Lin¹ and W. Le¹

1. School of Electrical Engineering, Southeast University, Nanjing, China

I. INTRODUCTION Axial flux permanent magnet (AFPM) machines with tooth-wound concentrated windings (TCWs) and segmented stator were founded a growing interest for high-performance drive applications such as electric vehicles, aircrafts, ships, etc. [1] Four dual-rotor single-stator (DRSS) axial flux permanent magnet vernier (AFPMV) machines with segmented stator and consequent-pole (CP) embedded rotors are proposed and compared in this paper. The configuration and operating principle of AFPMV machines are introduced first. Then, the critical design parameters and electromagnetic performances of proposed AFPMV machines are analyzed and compared both in no-load and load conditions. Finite element analysis (FEA) results demonstrate that the machine with Halbach arrays employed on the stator split teeth features higher torque capability and lower rotor eddy current loss compared to its counterparts with conventional PMs or stator magnet less machines. In addition, for better flux-weakening capability, the AFPMV machine with hybrid field excitation from both rotor PM and stator DC coils is also discussed. **II. MACHINE CONFIGURATIONS AND OPERATION PRICIPLE** The proposed AFPMV machine A is shown in Fig.1(a) as the benchmark. The machine has a single stator sandwiched between two-disc rotors which embedded CPs. The stator consists of 12 segments, each with three split teeth on the major tooth. TCWs are employed to shorten the end length and suppress copper loss. With the absent of the stator yoke, such machines take the advantageous performance of lower stator core loss. Furthermore, as shown in the Fig.1(b) and Fig.1(c), the radially magnetized PMs and the Halbach arrays are equipped in the split slots to form machine B and C, respectively. Finally, each stator segment of machine D is wound with a DC field winding on the middle split tooth, which is illustrated in the Fig.1(d). The flux modulation effect has enhanced the torque producing capability according to the pole ratio of rotor and AC windings [2]. In the vernier machine with modulation poles fixed on the stator, the angular speed of the working flux harmonic component is $\omega_p = -N_{PM}\omega_{PM} / (N_m - N_{PM})$ where N_{PM} and N_m are the pole-pair number of the magnetic fields excited with PM and the number of modulation teeth, respectively, ω_p and ω_{PM} are the speed of the working rotation magnetic field produced by the stator windings and the speed of the PMs, respectively. **III. PERFORMANCE ANALYSES AND COMPARISONS** **A. No-Load Flux Linkage and No-Load Back-EMFs** The flux distributions of four investigated machines were conducted by the FEA, the simulation results show that the machine C tend has lower flux leakage in the stator split teeth and higher magnetic density compared with the machine B because of the PM with circumferentially magnetization. Lower magnetic density is distributed in machine D when the DC winding produces the reverse flux, that is, the flux adjustment can be realized through the DC winding in the split teeth. The waveforms of no-load back-EMFs of the models are illustrated in Fig.2, in which the DC winding of the machine D operates in the flux-weakening condition. It can be seen that the amplitude of the no-load back-EMFs increase with the introduction of the PM in the split teeth. For the machine C, with the increase of circumferential PM volume, the amplitude of the back-EMF first increases and then decreases, that is, it is necessary to balance the flux leakage and the main flux. **B. Output Torque and Losses** Fig. 3 shows the output torque of the machines, the average output torque of the machines with PMs in the stators generate an average output torque at least 37% higher than those of the machines without PMs in the stators. The results of comprehensive comparison are shown in table I, which verify that the machine with Halbach arrays employed in the split slots tend to have higher output torque and lower stator core loss and rotor PM loss. And the parametric sensitivity studies and design optimizations will be presented in the final paper. **III. CONCLUSION** This paper extends the theory of magnetic field modulation into AFPM machines with DRSS and TCWs, making it particularly suitable for low-speed, high-torque, and axial length limited applications. The comparative analyses of four topologies of AFPVM machines are conducted by FEA. The results verify that it is a feasible method to modulate the magnetic field in the air gap with

the split teeth in the segmented stator modules of the AFPM machine. By comparing the relative merits and disadvantages of the performances of the proposed machines, it is concluded that the machine with Halbach PMs embedded in the stator split slots shows the characteristics of higher torque density and lower loss compared with other topologies, and machine with DC field winding in the stator split slots shows the adequate flux-weakening performance.

[1] F. Giulii Capponi, G. De Donato and F. Caricchi, "Recent Advances in Axial-Flux Permanent-Magnet Machine Technology," *IEEE Trans. Ind. Appl.*, vol. 48, no. 6, pp. 2190-2205, (2012). [2] R. Qu, D. Li and J. Wang, "Relationship between magnetic gears and vernier machines," *2011 International Conference on Electrical Machines and Systems*, Beijing, pp. 1-6, (2011).

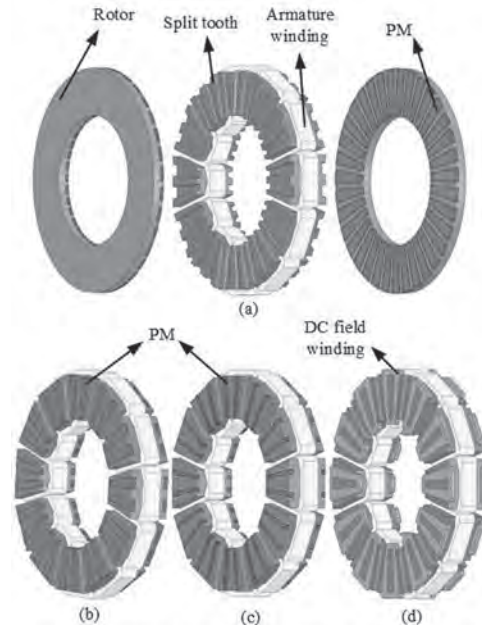


Fig. 1. 3-D view of the proposed machines. (a) Machine A. (b) The stator of machine B. (c) The stator of machine C. (d) The stator of machine D.

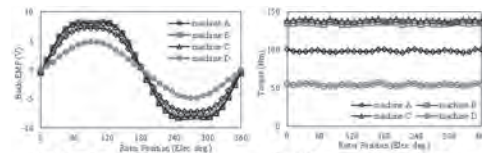


Fig. 2. Back-EMF waveforms of the machines.



Fig. 3. Output torque waveforms of the machines.

TABLE I
PERFORMANCE COMPARISON

Machine	A	B	C	D
Eff. Output Torque (Nm)	100	137	139	139
Max. EMF (V)	0.52	0.42	0.47	0.33
Stator Core Loss (W)	28.67	148.97	118.53	24.72
Output Torque (Nm)	1.72	1.31	1.36	1.31
Stator Core Loss (W)	3.26	6.66	5.27	2.82
Rotor PM Loss (W)	1.78	1.52	0.81	0.76

BT-16. Investigation on Electromagnetic Torque of a Flux-Switching Permanent Magnet Motor From Perspective of Flux Density Harmonic Deterioration Rate.

Y. Pu¹, Z. Xiang¹, M. Jiang¹ and X. Zhu¹
 1. Jiangsu University, Zhenjiang, China

I. Introduction Flux-switching permanent magnet (FSPM) motor, possessing the potential merits of high torque and power density, has aroused considerable attention and extensive research in recent years [1]. Electromagnetic torque, which is the most important evaluation index of the FSPM motor, is researched in majority of the existed papers. For the FSPM motor, the magnetic density of the motor has a decisive influence on the electromagnetic torque. As the excitation source, PMs serve to generate the magnetic power, which goes through stator, airgap and rotor to form the effective magnetic path. In other words, the electromagnetic torque relies heavily on the magnetic flux density of the stator, airgap and rotor. Actually, the improvement of the magnetic flux density of the stator, airgap and rotor may contribute to the increasing of electromagnetic torque. In [2], from the perspective of the magnetic flux density of the stator, different types of PM arrangement are investigated, which indicates that the arrangement of V-shaped PMs is superior to that of the I-shaped and Arc-shaped PMs in the stator in terms of torque output capability. On the other hand, from the perspective of the magnetic flux density of airgap, various parameters close to the airgap are selected during the multi-layer design of the FSPM motor for improved torque in [3]. Based on the above research, many attempts are made to study the magnetic flux density of stator and airgap related to airgap for the torque improvement. Yet, few efforts are made to analyzing the effective magnetic flux density of the rotor which contributes to the magnetic energy transmission and torque production. Hence, the concept of flux density harmonic deterioration rate is introduced to analyze the rotor effective magnetic flux in this paper, which eventually reflects the loss of magnetic energy transmission from the airgap. By analyzing the influence of harmonic flux density variation from airgap to rotor yoke on electromagnetic torque, the relevant between electromagnetic torque and flux density harmonic deterioration rate is explored, and the resulting torque represents to be increased, which provides a new perspective for motor performance analysis. II. Motor topology and analysis of the performance The topology of the studied I-shaped FSPM motor is shown in Fig. 1 (a), with the related structure parameters marked in Fig. 1 (b). In order to select the harmonic for research use, the torque contribution of different harmonic is obtained as depicted in Fig. 2, and contributions of the 4th-, 18th-, 28th-, 30th- and 40th-order harmonic are chosen as the basis of the comprehensive deterioration rate. The flux density and harmonic amplitude of airgap and rotor yoke are illustrated in Fig. 3 (a) and (b). It is obvious that the 4th- and 18th-order harmonic remain high amplitude at both airgap and rotor yoke, while the 28th-, 30th- and 40th-order harmonic present a sharp decline. The single harmonic deterioration rate is also calculated in Fig. 3 (b), where the positive value denotes an actual downward trend while the negative one indicates the opposite. To further investigate the relationship between torque capability and harmonic deterioration rate, the parameters are selected from both stator and rotor side, and the partial results are shown in Fig. 4 (a) and (b). With the PM cost keeping constant and the PM width b_{pm} and the rotor tooth width b_r increasing, the total torque decreases while the comprehensive deterioration rate mainly represents uptrend as expected. Considering the lowest comprehensive deterioration rate, the final value of b_{pm} and b_r are chosen to be 2deg and 3.4deg for comparison. Moreover, the magnetic field and flux distribution of the initial and final motor are shown in Fig. 5, which indicates that the final motor possesses less flux leakage. Meanwhile, the back-EMF and torque of the motors are presented in Fig. 6 and Fig. 7. The rationality of analysis perspective of flux density harmonic deterioration rate is confirmed by the higher back-EMF and torque with lower comprehensive deterioration rate of the final motor. III. Conclusion In conclusion, the above results reveal that during the process of magnetic energy transmission, the proposed flux density harmonic deterioration rate has the certain relevant with the electromagnetic torque. The decrease of the comprehensive deterioration rate contributes to the improvement of the flux modulation effect and electromagnetic torque to some degree, which verifies the effectiveness of

deterioration rate concept. Finally, more theoretical analysis, performance simulations and experimental results will be presented in the full paper.

[1] X. Zhu, M. Jiang, Z. Xiang, L. Quan, W. Hua and M. Cheng, "Design and Optimization of a Flux-Modulated Permanent Magnet Motor Based on an Airgap-Harmonic-Orientated Design Methodology," *IEEE Trans. Ind. Electron.*, vol. 67, no. 7, pp. 5337-5348, July 2020. [2] T. Fukami, Y. Ueno and K. Shima, "Magnet Arrangement in Novel Flux-Modulating Synchronous Machines with Permanent Magnet Excitation," *IEEE Trans. Magn.*, vol. 51, no. 11, pp. 1-4, Nov. 2015, Art no. 8206104. [3] L. Mo, T. Zhang and Q. Lu, "Design and Analysis of an Outer-Rotor-Permanent-Magnet Flux-Switching Machine for Electric Vehicle Applications," *IEEE Trans. Appl. Super.*, vol. 29, no. 2, pp. 1-5, March 2019, Art no. 3601305.

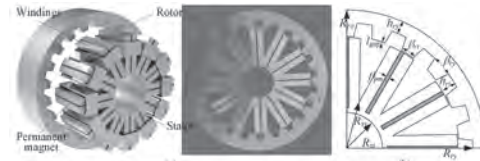


Fig. 1 The topology of the I-shaped FSPM motor (a) The topology of the I-shaped FSPM motor (b) The geometric parameter model of the VS-FSPM motor

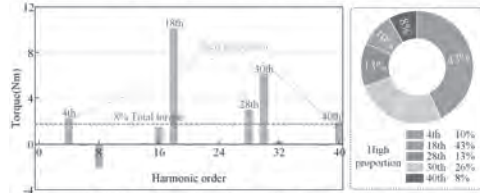


Fig. 2 The contribution of airgap harmonics to the torque performance

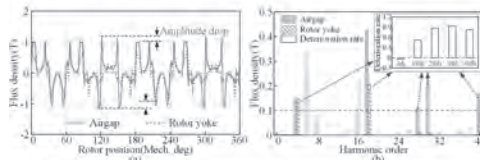


Fig. 3 The magnetic flux density and the corresponding harmonics distribution on the rotor yoke (a) The magnetic flux density (b) The corresponding harmonics distribution

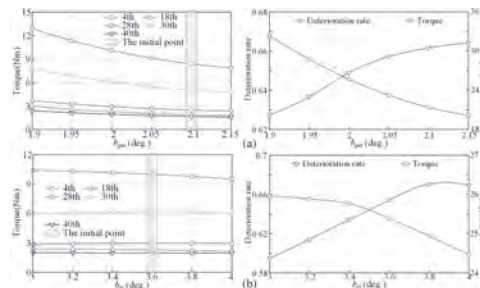


Fig. 4 The effects of the parameters on the output torque generated by the airgap harmonics (a) b_{pm} (b) b_r

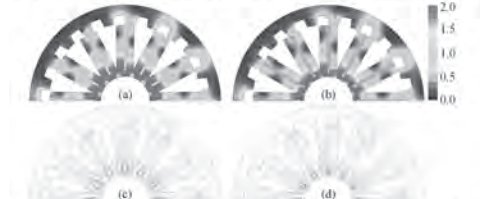


Fig. 5 Magnetic field distributions and flux distributions of the I-FSPM motor (a) Flux distribution of initial motor (b) Flux distribution of the optimal motor (c) Magnetic field distribution of initial motor (d) Magnetic field distribution of the optimal motor

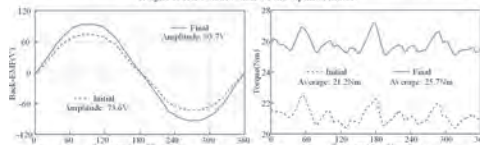


Fig. 6 No-load back-EMF waveforms

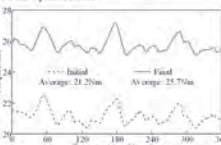


Fig. 7 The torque performance of initial and optimal I-FSPM motor

Session BU
MAGNETIC GEARS AND VERNIER MACHINES
(Poster Session)

Siavash Pakdelian, Chair
University of Massachusetts Lowell, Lowell, MA, United States

BU-01. A High Torque Density Magnetic-Geared Dual-PM Split-Tooth Vernier Machine With Halbach Consequent Poles.

H. Huang¹, D. Li¹ and R. Qu¹

1. Huazhong University of Science and Technology State Key Laboratory of Advanced Electromagnetic Engineering and Technology, Wuhan, China

Abstract--This paper has proposed a 3-airgap magnetic geared vernier machine for low-speed direct-drive applications. By combining dual PM split-tooth vernier machine with magnetic gear, an impressive 150 Nm/L output torque density under 140 mm outer diameter can be achieved. The Halbach consequent pole structure is applied to the dual-layer-magnet rotor, which can largely reduce the thickness of rotor back iron compared to regular magnet arrangement, while increasing the airgap flux density. The performances of magnetic gear machines with different topologies are compared in this paper, it shows that proposed MG-DPSTM has at least 40% higher torque density than all the previous MGM topologies. I. Introduction The magnetic geared machine (MGM) is attractive in continuous low speed direct-drive applications since it has remarkable torque density under relatively low electrical load. The contactless feature of magnet gear makes it more suitable for occasions when maintenance is difficult, such as wind/tide power generation, marine propulsion, oil pumping. In recent years, many MGM topologies were proposed for high torque density between 60-110 Nm/L^{[1]-[5]}. To further enhance the torque density of MGM to a new level, a magnetic-geared dual PM vernier machine is proposed in this paper, which can exceed 150 Nm/L active torque density under low heat load, which also remains 0.8 power factor under rated load. II. Topologies of MG-DPVM The topology of proposed MG-DPVM is shown in Fig. 1, which can be divided into magnetic gear (MG) part and vernier machine (VM) part radially. The structure of proposed machine has been carefully designed for higher torque density. One of the distinct structures is PM rotor, which has two layers of Halbach consequent pole (HCP) magnets with different pole pairs. Compared to surface mounted magnets in [6], this topology can minimize the magnetic circuits and the thickness of back iron between two layers of magnets, while maximum the airgap flux density in both airgaps. For the VM part, there are consequent pole magnets on the stator. Through dual flux modulation effect^[7], it can increase the torque density by introducing additional airgap working flux, and the power factor is also higher than regular vernier machines. III. Performance Comparison of MGM Topologies As shown in Table I, under the same outer radius and gap thickness, several MGM topologies are compared in this paper, including pseudo direct drive machine in [2], vernier pseudo direct drive machine in [5], 3-airgap outer rotor magnetic geared machine in [3], and magnetic geared vernier machine newly proposed in this paper. Considering slip risk and operating point of machine, the output torque is selected as 80% of the MG stall torque, and the heat load as well as copper loss (considering the winding) of each model can then be derived. It is obvious that proposed MG-DPVM has the highest MG stall torque density and output torque density, and the DC copper loss is also the lowest. IV. Conclusions A novel 3-airgaps magnetic geared split-tooth vernier machine is proposed in this paper. Through dual stage of magnet gear effect, high output torque density can be achieved under low current density and copper loss. It is impressive that proposed machine has achieved 150 Nm/L active torque volume density and 23 Nm/kg active mass density. According to the comparison, this value is much higher than the existing topologies of MGM, which makes it competitive in long-term low-speed high-torque industrial fields such as wind generation and marine propulsion. The power factor of proposed machine is lower than other MGMs due to the application of vernier machine, however the copper loss and heat load are largely reduced, therefore higher efficiency can be expected.

[1] K. T. Chau, D. Zhang, J. Z. Jiang, C. Liu, and Y. Zhang, "Design of a Magnetic-Geared Outer-Rotor Permanent-Magnet Brushless Motor for Electric Vehicles," *IEEE Transactions on Magnetics*, vol. 43, no. 6, pp. 2504-2506, Jun. 2007. [2] K. Atallah, J. Rens, S. Mezani, and D. Howe, "A Novel 'Pseudo' Direct-Drive Brushless Permanent Magnet Machine," *IEEE Transactions on Magnetics*, vol. 44, no. 11, pp. 4349-4352, Nov. 2008. [3] S. Gerber and R.-J. Wang, "Design and Evaluation of a Magnetically Geared PM Machine," *IEEE Transactions on Magnetics*, vol. 51, no. 8, pp. 1-10, Aug. 2015. [4] L. Jian, W. Gong, G. Xu, J. Liang, and W.

Zhao, "Integrated Magnetic-Geared Machine with Sandwiched Armature Stator for Low-Speed Large-Torque Applications," *IEEE Transactions on Magnetics*, vol. 48, no. 11, pp. 4184-4187. [5] X. Yin, Y. Fang, X. Huang, and P.-D. Pfister, "Analytical Modeling of a Novel Vernier Pseudo-Direct-Drive Permanent-Magnet Machine," *IEEE Transactions on Magnetics*, vol. 53, no. 6, pp. 1-4, Jun. 2017. [6] M. Johnson, M. C. Gardner, H. A. Toliyat, S. Englebretson, W. Ouyang, and C. Tschida, "Design, Construction, and Analysis of a Large-Scale Inner Stator Radial Flux Magnetically Geared Generator for Wave Energy Conversion," *IEEE Transactions on Industry Applications*, vol. 54, no. 4, pp. 3305-3314, Jul. 2018. [7] S. Niu, S. L. Ho, and W. N. Fu, "A Novel Stator and Rotor Dual PM Vernier Motor with Space Vector Pulse Width Modulation," *IEEE Transactions on Magnetics*, vol. 50, no. 2, pp. 805-808, Feb. 2014.

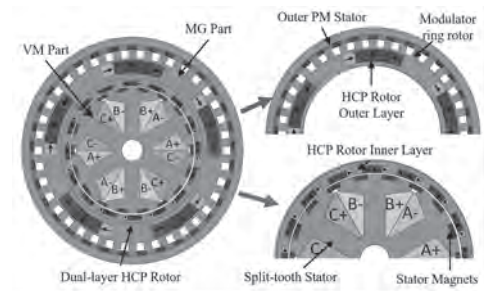


Fig. 1 The topology of proposed MG-DPVM

MGM topologies	PDD	VPDD	OMGM	MGVM
Outer diameter, mm			140	
Axial length, mm			50	
Airgap length, mm			0.6	
Heat load, A/cm · A/mm ²	2307	795	1467	920
DC Copper loss, W	74	84	41	22
MG stall torque, Nm	75	77	99	143
MG Stall torque density, Nm/L	97	100	129	186
Output torque, Nm	60	62	79	116
Output torque density, Nm/L	78	80	103	151
Power factor	0.89	0.85	0.96	0.80
Gear ratio	9.5	14	7.2	7.6
Magnet mass, kg	0.86	2.27	0.89	1.37
Total active mass, kg	4.22	5.35	3.87	4.94
Torque/magnet mass, Nm/kg	69.8	27.3	88.8	84.7
Torque/active mass, Nm/kg	14.2	11.6	20.4	23.3

BU-02. Design of an Axial-Type Magnetic Gear With an Auxiliary Flux-Enhancing Structure.

H. Zhao^{1,2}, C. Liu^{1,2}, Z. Song^{1,2} and R. Huang^{1,2}

1. *SEE, City University of Hong Kong, Kowloon, Hong Kong;* 2. *Shenzhen Research Institute, City University of Hong Kong, Shenzhen, China*

I. Introduction: Magnetic gears are good candidates to replace mechanical gearboxes, since it has higher efficiency, lower noise and self-protection characteristic [1], [2]. Radial-type magnetic gears (RMGs) are sometimes not suitable for special application scenarios where there is strict requirement for space. Axial-type magnetic gears (AMGs) have an even higher torque density than RMGs and a shorter axial length, [3]. Therefore, AMGs can be applied in scenarios where the weight is a crucial concern. However, one drawback of AMGs is the large amount usage of permanent magnets (PMs), which significantly increases manufacture cost. In this paper, an iron-made flux-enhancing plate is added to the outside of AMGs to increase the output torque. Then, the flux-enhancing principle is elaborated by analyzing the flux path variation before and after the installation of the auxiliary flux-enhancing slice. Finally, the performances of three AMGs are compared, and it is proved that the proposed structure has the highest torque density. II. Machine Configuration The proposed auxiliary flux-enhancing structural axial-type magnetic gear (AFS-AMG) contains four slices, and its structure together with the magnetic flux density distribution are depicted in Fig. 1 (a), (b). Two rotors are those with surface-mounted PMs on them, and the one with less PM pieces is the high-speed rotor, while the one with more PM pieces is the low-speed rotor. The first and third slices from the left to the right are steady slices, and they formed as one stator component. The PMs on the high-speed rotor are magnetized on the axial direction, while the PMs on the low-speed rotor are magnetized on the circumferential direction. To produce a steady electromagnetic torque, the pole-pair number of high-speed and low-speed rotor PMs P_{high} and P_{low} and the number of modulator pieces $Q_{modulator}$ must satisfy Eq. (1) [4]. Additionally, since the auxiliary flux-enhancing slice serves as a complementary structure for the magnetic flux to form a shorter loop, its tooth number Q_{teeth} should be equal to the number of modulator pieces, as given in Eq. (2). Then, based on the operating principle of magnetic gear, the rotating speed and output torque relations between the high-speed and low-speed rotor satisfy Eq.(3) and (4), where T_{high} and T_{low} are the electromagnetic torques on the high-speed and low-speed rotor, respectively. Ω_{high} and Ω_{low} are the rotating speeds of the high-speed and low-speed rotor, respectively. III. Flux Enhancing and AMG Evolution The flux-enhancing effect of the auxiliary slice can be illustrated by the flux line path, as shown in Fig. 1 (c). It can be observed that without the auxiliary slice, the magnetic flux path passes through the air region several times to form a close loop. Since the permeability of air is much lower than that of the iron, the magnetic reluctance of the whole loop is very large, leading to a small magnetic flux density and a low torque. When the auxiliary slice is added to the outside of the spoke-type PMs, the corresponding flux line changes to pass through a path with smaller reluctance. Hence, the magnetic flux density on the air gap increases, leading to a larger electromagnetic torque. In fact, the structures of AMGs can be derived from its RMG counterparts, as illustrated in Fig. 2 (a)-(c) [5]. The operating principle of AMGs and RMGs are similar, and their differences lie in two aspects. First, the magnetic flux density direction of the two types of magnetic gears are different: the main flux paths in AMGs are in axial direction, and in radial direction for RMGs. Second, the different rotors are distributed on axial direction for AMGs, making it more suitable to have multi-slice structure. However, adding an auxiliary structure in RMG will lead to a very large size. Therefore, the flux-enhancing slice can maximize its effect for AMGs. IV. Validation and Comparison: To obtain a better electromagnetic performance, three AMGs with the same inner and outer radii are constructed in JMAG to compare their performances, whose parameters are provided in TABLE I. The corresponding simulation results are provided in TABLE II and Fig. 2 (d). It can be observed that AMG (c), namely the proposed AMG, has the highest efficiency and the highest torque density per PM usage. The axial component magnetic flux density distributions and the corresponding Fast Fourier Transform of the AMG (b) and (c) outside the low-speed rotor with the same radius are depicted in Fig. 3 (e), (f). It can be observed that for AMG (c), the amplitude of working harmonic (14th) is

much larger than AMG (b), leading to a torque increase. IV: Conclusion In this paper, a novel AFS-AMG is proposed. By introducing an auxiliary flux-enhancing slide to shorten the flux path, the proposed AFS-AMG has a higher torque density per PM usage and a higher efficiency compared to conventional AMG structure. This work was supported by a grant (Project No. 52077186 and 51677159) from NSFC of China; a grant (Project No. JCYJ20180307123918658) from STIC of Shenzhen Municipality, China; a grant (Project No. SGDX2019081623101559) from Shenzhen – Hong Kong Innovation Circle Category D Project from the Science Technology and Innovation Committee of Shenzhen Municipality, China.

[1] H. Zhao, C. Liu, Z. Song and J. Yu, "A Fast Optimization Scheme of Coaxial Magnetic Gears Based on Exact Analytical Model Considering Magnetic Saturation," in IEEE Transactions on Industry Applications (Early Access). [2] P. O. Rasmussen, T. O. Andersen, F. T. Jorgensen and O. Nielsen, "Development of a high-performance magnetic gear," in IEEE Transactions on Industry Applications, vol. 41, no. 3, pp. 764-770, May-June 2005. [3] Y. Chen, W. N. Fu, S. L. Ho and H. Liu, "A Quantitative Comparison Analysis of Radial-Flux, Transverse-Flux, and Axial-Flux Magnetic Gears," IEEE Trans. Magnetics, vol. 50, no. 11, pp. 1-4, Nov. 2014. [4] K. Atallah and D. Howe, "A novel high-performance magnetic gear," IEEE Trans. Magnetics, vol. 37, no. 4, pp. 2844-2846, July 2001. [5] X. Zhang, X. Liu and Z. Chen, "A Novel Dual-Flux-Modulator Coaxial Magnetic Gear for High Torque Capability," in IEEE Transactions on Energy Conversion, vol. 33, no. 2, pp. 682-691, June 2018.

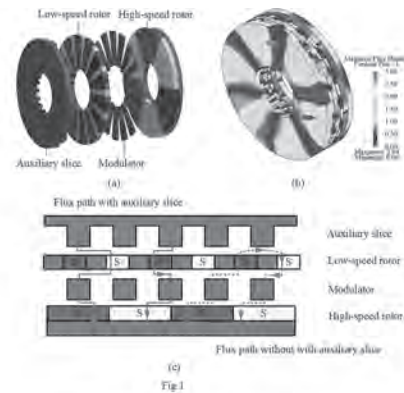


Fig.1

TABLE I GEOMETRICAL PARAMETERS OF STUDIED AMGS

Symbol	Parameter	Value
P_{low}	Low-speed rotor PM pole pairs number	18
P_{high}	High-speed rotor PM pole pairs number	3
Q	Modulation pieces number	17
R_{out}	Outer radius of the AFS-AMG	80 mm
R_{in}	Inner radius of the AFS-AMG	50 mm
Ω_{low}	Rotating speed of low-speed rotor	300 r/min
Ω_{high}	Rotating speed of high-speed rotor	1800 r/min

TABLE II ELECTROMAGNETIC PARAMETERS OF STUDIED AMGS

	T_{out}/Nm	Torque ripple	Iron loss/W	PM eddy current loss/W	Efficiency
AMG (a)	72.76	5.06 %	13.95	63.78	96.71 %
AMG (b)	72.23	2.31 %	9.14	33.32	98.15 %
AMG (c)	93.38	5.77 %	9.38	2.23	99.61 %

$$P_{low} + P_{high} = Q_{modulator} \quad (1)$$

$$Q_{teeth} = Q_{modulator} \quad (2)$$

$$\frac{T_{high}}{T_{low}} = \frac{P_{high}}{P_{low}} \quad (3)$$

$$\frac{\Omega_{high}}{\Omega_{low}} = \frac{P_{low}}{P_{high}} \quad (4)$$

Fig.1 The proposed AFS-AMG: (a) Explosive view; (b) magnetic flux density distribution, (c) illustration of flux path.

It can be observed that for AMG (c), the amplitude of working harmonic (14th) is

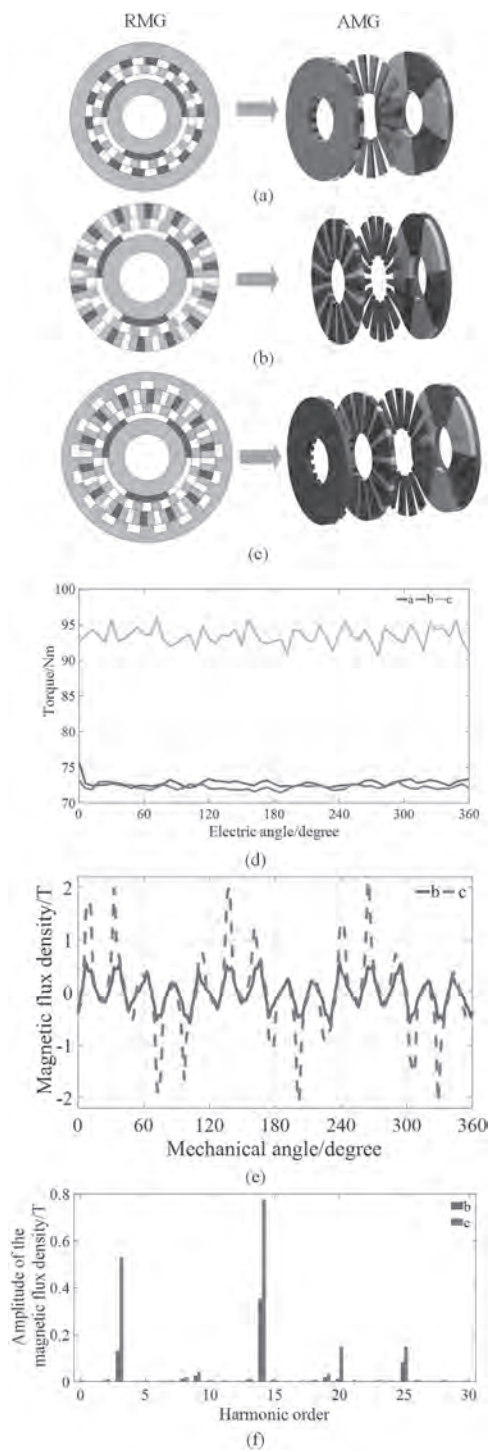


Fig.2 (a) Conventional AMG, (b) Circumferentially magnetized AMG, (c) AFS-AMG, (d) torque waveform comparisons, (e) magnetic flux density distribution, (f) the corresponding FFT.

BU-03. Design and Analysis of an Effective Fault-Tolerant Dual-Winding Axial-Flux Magnetic-Geared Machine for in-Wheel Electric Vehicle.

Y. Chen¹, W. Fu¹, S. Ho¹ and S. Niu¹

1. Electrical Engineering, The Hong Kong Polytechnic University, Kowloon, Hong Kong

Abstract—In this paper, a novel dual-winding axial-flux magnetic-geared machine (DAMGM) is presented for in-wheel electric vehicle driving. By using armature windings for replacing the high speed rotor and utilizing the space between the modulators with sets of auxiliary winding, the torque density and the fault-tolerant ability can be enhanced significantly since it can operate normally with the excitation of either armature winding or auxiliary winding. Compared with dual-winding radial-flux magnetic-geared machine (DRMGM), axial-flux magnetic-geared machine (AMGM) and conventional axial-flux PM motor, the proposed motor has huge improvement in torque density, efficiency and fault-tolerant capacity. The pole-pair combination and geometric parameters are carefully compared and optimized by using three-dimensional finite-element method for getting the best performance of the proposed structure and verifying the validity of the proposed machine design. 1. Introduction Magnetic gear (MG) and magnetic-geared machine provide the solutions for many high-torque-density applications with the advantages of easy maintenance, inherent overload protection, and low working noise. For electric vehicle, two general solutions have been adopted: the first type consists of a high-speed motor and a mechanical gear box while the second only employs a direct-drive motor. However, the former has the disadvantages of high transmission loss, overload damage, heavy weight and high noise. The latter is limited by efficiency issue and bulky size since the efficiency of the machine is lower when it works at a low level power and the size of the machine will increase with the reduction of nominal speed. Magnetic-geared machine (MGM) can overcome the shortages by integrating a magnetic gear and an electric machine together, hence, it becomes the hotspot among researchers. Nevertheless, most of researches focus on radial-flux magnetically geared machine (RMGM), including traditional MGM, dual-flux-modulated MGM and vernier MGM [8]. For the space constrains in some specific applications, such as electric vehicles, the traditional RMGM is not suitable for direct coupling of the motor with a wheel. Hence an axial-flux magnetically geared machine (AMGM) [1] was proposed to solve these problems. However, none of the existing solutions for axial-flux MGM can fully utilize the space between the modulators, which can actually be used for placing sets of auxiliary winding and strengthening the magnetic field generated by the armature winding. In such case, for getting a higher torque density and fault-tolerance capacity, this paper presents a novel dual-winding axial-flux magnetic-geared machine (DAMGM) to solve those problems. 2. Working Principle and Motor Structure The overall structure of the proposed machine is shown in Fig.1 (a), which consists of two rotors, two sets of modulators and a shared stator. The total axial length, outer radius of the outer-rotor and the inner radius of the stator with a modulator are 60mm, 92mm and 64mm, respectively. Fig. 1 (b) and (c) shows the corresponding coil-emf vectors in electrical degrees for the armature winding and auxiliary winding, whose slot numbers are 45 and 27, respectively. The DAMGM complies with the fundamental rule of magnetic gears, which is expressed as: $P=N_L \pm S (1)$ where N_L is the number of pole pairs of rotor, P is the number of modulator and S is the number of pole pairs of armature winding. For improving the torque density, P is equal to $S+N_L$ [2]. In this paper, the P , N_L and S are 27, 24 and 3, respectively. Besides, the speed of rotor is 300 r/min, which is close to the rated operation speed of electric vehicle driving system. 3. Performance Comparisons and Analysis The performance comparisons are shown in Fig. 2, where Motor 1, 2, 3 and 4 are the proposed machine, the axial-flux PM machine, DRMGM and axial-flux magnetic-geared machine. For the torque performance, as shown in Fig.2 (a), the proposed machine has the best torque output capacity, whose output torque is increased by 71.13% compared to Motor 2, 104.93% compared to Motor 3 and 110.12% compared to AMGM, reaching 166.13 Nm with the ripple of 7.38% under the current density 6A/mm² and slot package factor 0.6. Besides, the Fig. 2 (c) shows the fault-tolerance capacity of the proposed machine, which can operate with either auxiliary winding or armature winding. Simulation result shows that it can operates

normally with the sole excitation of armature winding under the current density reaching about 18A/mm² or excited by auxiliary winding solely under the current density nearly 10A/mm². Furthermore, Fig. 2(b) shows the distributions of radial flux density B_r in the air gap under no load condition while the back EMF of those machines can be found in Fig. 2 (d). Finally, the proposed machine has the highest efficiency compared among motor 2, 3, and 4, reaching 93.78% with the copper loss of 226 W and the iron loss of 75.3 W. 4. Conclusion This paper proposes an effective fault-tolerant dual-winding axial-flux magnetic-geared machine. The structure, corresponding coil-emf vectors and working principle are introduced. Then, the performance comparison among the proposed machine, axial-flux PM machine, DRMGM and axial-flux magnetic-geared machine are conducted to verify the efficiency of the design.

[1] M. Johnson, M. C. Gardner and H. A. Toliyat, "Design and Analysis of an Axial Flux Magnetically Geared Generator." *IEEE Trans. Industry Applications*, vol. 53, no. 1, pp. 97-105, Jan.-Feb. 2017. [2] S. L. Ho, S. Niu and W. N. Fu. "Design and Analysis of a Novel Axial-Flux Electric Machine." *IEEE Trans. Magnetics*, vol. 47, no. 10, pp. 4368-4371, Oct, 2011.

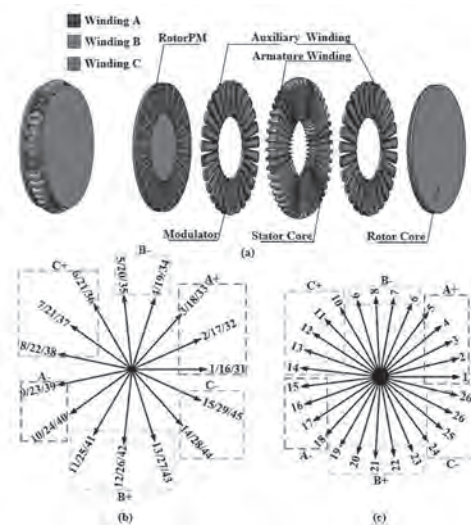


Figure 1

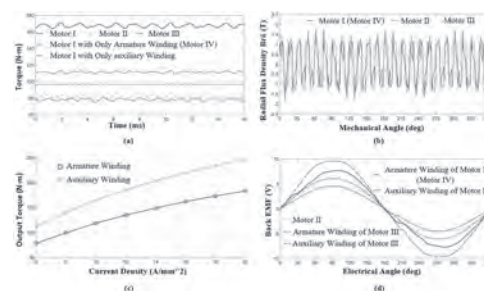


Figure 2

BU-04. Design and Comparison Study of a Yokeless Magnetic Gear With Trapezoidal Halbach PM Array for Electric Vehicle Driving.

Y. Chen¹, W. Fu¹, S. Ho¹ and S. Niu¹

1. Electrical Engineering, The Hong Kong Polytechnic University, Kowloon, Hong Kong

Abstract—In this paper, a novel yokeless magnetic gear (YMG) with trapezoidal Halbach PM array is presented for direct drive of electric vehicles. Compared to traditional structures, the proposed machine has huge performance improvement in the following two aspects: Firstly, by using the aluminum to replace the silicon steel as the rotor iron core, the iron loss and motor weight can be reduced and the torque density can be increased significantly; Secondly, the generated torque and ripple can be optimized by adopting a trapezoidal Halbach PM array, whose leakage flux is far more lower than YMG with Halbach PM array and YMG with conventional PMs. The performance of the proposed motor is compared and analyzed by using three-dimensional finite-element method and the best parameter combination of the proposed machine is found using optimization method.

1. Introduction Magnetic gears provide solutions for replacing the mechanical gearbox in electric vehicle driving system since it inherently has the advantages of high transmission efficiency, overload protection, low working noise and physical isolation. In order to tap the potentials of industrial application, more researchers focus on the magnetic gears, including radial-flux, axial-flux magnetic gear and magnetic-gearing machines, for finding high efficiency, high torque density and better performance solutions. Papers [1] proposed the types of a magnetic gear with Halbach PM array and discussed how the arrangement of Halbach PM affects the performance of the machine. However, due to the limit of machine structures, all of these magnetic gears have the rotor iron core, which is used to form the magnetic circuit of PM and reduce the magnetic resistance. However, the performance of the machine is weakened severely with adopting the yokeless structure since it introduces of great leakage flux. Hence, although the design and research in this topology have made some progress, in terms of its own design thought, the improvement level is very limited. In this paper, a novel yokeless magnetic gear (YMG) with trapezoidal Halbach PM array is proposed to solve the drawbacks mentioned above. Compared to the designs of the magnetic gears with Halbach PM array, the proposed machine has a better performance in the torque output capacity, torque density and efficiency.

2. Working Principle and Motor Structure The overall structure of the proposed yokeless magnetic gear with trapezoidal Halbach PM array is shown in Fig. 1. As shown in Fig. 1, the proposed machine contains four kinds of magnetized PM and aluminum supporter for reducing the leakage flux and weight. The total axial length, outer radius of outer-rotor and inner radius of stator are 220 mm, 120 mm and 65.8 mm, respectively. All magnetic gears, including the proposed one, comply with the fundamental rule, which is expressed as: $P=N_L \pm N_H$ (1) where N_L , N_H and P are the number of pole pairs of low speed rotor (LSR), high speed rotor (HSR) and modulator, respectively. For getting a better performance, P should be equal to N_H+N_L . Besides, similar to the above equation, the operation speed of MG should also follow the following relationship: $\omega_H/\omega_L = -N_L/N_H = -G_r$ (2) where ω_L and ω_H are the mechanical speed of LSR and HSR. The proportion of the two speed G_r is the gear ratio, which is used to indicate that the speed ratio of MG equals the inverse ratio of the PM pole-pair numbers in two rotors. In this paper, the rated operation speed for the HSR and LSR are 2400 r/min and 300r/min, respectively, which is close to the rated operation speed of direct-drive electric vehicle system.

3. Performance Comparisons and Analysis The output torque comparison between the proposed machine, conventional magnetic gear (MG), yokeless magnetic gear (YMG) and YMG with conventional Halbach PM array are shown in Fig. 2 (a). Simulation results show that the output torque of the proposed machine increases by 169.1%, 97.2% and 21.0% compared to YMG, YMG with conventional Halbach PM array and conventional MG, reaching 1840.5 Nm with the ripple of 1.28%. Besides, the proposed machine has a minimum iron loss and the highest efficiency compared to the other types of MG, reaching 110 W and 99.38%, respectively. Furthermore, the torque density of proposed machine reaches 51.18 Nm per kilogram and 88.1 Nm per PM weight (Kg), which increased by 96.8% and reduced by 7.3% compared to conventional MG. Fig. 2(b) shows the distributions of radial flux density B_r in the air gap under no load condi-

tion. The comparison of leakage flux between YMG with conventional Halbach PM array and proposed machine, YMG and proposed machine are indicated in Fig.4 (c) and (d), respectively. Compared to those two types of YMG, the proposed machine has the lowest density of magnetic flux line in both the outer region of outer PMs and inner region of inner PMs, which means the leakage flux of the proposed machine is the lowest and that is the reason for the high torque density of the proposed machine.

4. Conclusion This paper proposes a yokeless magnetic gear with trapezoidal Halbach PM array for electric vehicle driving. First, the structure, PM arrangement and working principle are introduced. Then, the performance comparison among the proposed machine, conventional MG, YMG and YMG with Halbach array are conducted. Finally, the simulation results verify the efficiency of the novel structure.

[1] Yiduan Chen; W. N. Fu; Wei Li. "Performance analysis of a novel triple-permanent-magnet-excited magnetic gear and its design method". *IEEE Trans. Magnetics*, vol. 52, no.7, pp. 1-4, 2016.

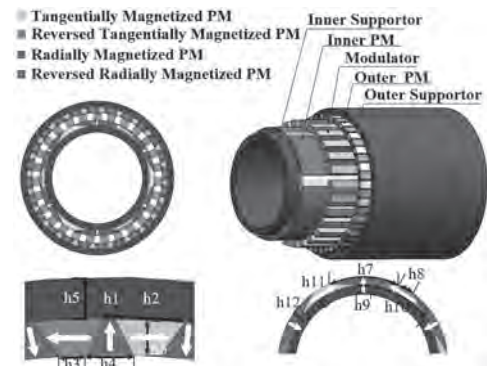


Figure 1

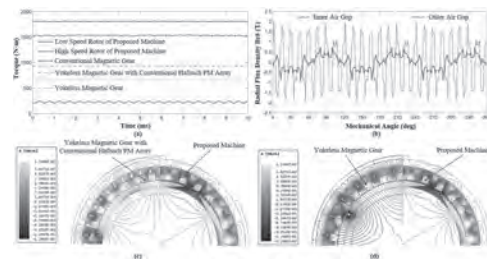


Figure 2

BU-05. Design and Analysis of a Novel Active Magnetic Gear for Low-Speed Large-Torque Applications.

Y. Chen¹, W. Fu¹, S. Ho¹ and S. Niu¹

1. Electrical Engineering, The Hong Kong Polytechnic University, Kowloon, Hong Kong

Abstract—In this paper, a novel active magnetic gear (AMG) is presented for low-speed large-torque applications. Compared to traditional solutions, the proposed machine has two key advantages: Firstly, by introducing an auxiliary winding, the overload protection, torque output and fault-tolerant capability can be improved significantly. Secondly, the dynamic performance and anti-perturbation capability of the low speed rotor can be enhanced by introducing a zero-variation control strategy applied to auxiliary winding. The validity of the control strategy and structure design is proved by the co-simulation of control program and ANSYS Maxwell. 1. Introduction Magnetic gears (MGs) are an ideal alternative choice for replacing the mechanical gear box in driving system of many low-speed large-torque applications since they can provide inherent overload protection ability, low working noise and physical isolation between rotors [1]. However, for most MGs, since the low speed rotor (LSR) in MG is driven by the high speed rotor (HSR) solely, which means the output torque is determined by the space angle difference between the resultant magnetic field vector (RMFV) generated by PMs on two rotors. Hence, compared to general PI (Proportional-Integral) controller, the conventional MG can be regarded as a PM machine applied the proportional controller to control the output rotor since output torque is determined by relative position of RMFV solely. In such case, the MGs have the drawbacks as the PM machine applied proportional controller, including high steady state error, low anti-interference capability and low controllability. Besides, the overload protection and torque output capability of conventional MGs are limited, which means the designed power should be increased for the requirement of extreme working condition and it will increase the volume of MG inevitably. Furthermore, conventional MG is only driven by external electric machine, which means it will stop operating if the external motor or transmission shaft is broken, and even result in serious consequences. In this paper, a novel active magnetic gear is proposed for solving those problems mentioned above. 2. Working Principle and Machine Structure The overall structure of the proposed active magnetic gear is shown in Fig. 1(a). An auxiliary winding is placed among modulators. Fig. 1 (b) shows the corresponding coil-emf vectors in electrical degrees for the auxiliary winding, whose number of slots is 27. The total axial length, outer radius, inner radius, rated operation speed for the HSR and LSR are 220 mm, 120 mm, 65.8 mm, 2400 rpm and 300rpm, respectively. After introducing the auxiliary winding, the output torque T_{output} can be expressed as: $T_{Output} = T_{Auxiliary} + T_{MG}$ (1) where T_{MG} and $T_{Auxiliary}$ are the torques generated by HSR and auxiliary winding, respectively. In this paper, the variation control strategy will be applied for enhancing the dynamic performance and anti-perturbation capability, which uses the variation of LSR speed and torque as the control objective. This is because when an output torque or operating speed is stable, the variation of it should be equals to zero nearly. The space vector diagram of AMG is indicated in Fig.1. (c). The ψ_{fl} and the ψ_{fl} are the flux linkage vectors generated by LSR and HSR, while ψ_s is that produced by the auxiliary winding. In such case, the torque generated by the auxiliary winding can be described as: $T_{Auxiliary} = p[\psi_{fl}i_q + (L_d - L_q)i_d i_q]$ (2) Since the electromagnetic torque is generated by the interaction between magnetic fields produced by LSR and the summation of auxiliary winding and HSR, hence, in this formula, the flux linkage ψ_{fl} in this formula is that of LSR and the p is the pole pairs of LSR. 3. Performance Comparisons and Analysis The output torques with and without the excitation of auxiliary winding are shown in Fig. 2(a). The auxiliary winding can increase the output torque, reaching 1733.2 Nm compared to that without auxiliary winding 1531.9 Nm, all with the current density of 6A/mm² and slot package factor 0.6. Besides, The AMG torque performances with different values of current density driven by HSR and auxiliary winding, and by auxiliary winding solely are indicated in Fig.2 (b). For the AMG driven by HSR and auxiliary winding, the output torque can increase from 1733 Nm to 2657 Nm with the current density from 6 to 50A/mm², which shows a strong overload protection capability. As for the fault condition, the AMG will be driven by auxiliary winding solely and the output torque can grow from 242 Nm with the current density 6A/mm²

to 1751 with 50A/mm². The load change and given speed change situation with and without the zero-variation control strategy are shown in Fig. 3 (c) and (d) under undamped situation. Simulation results indicate that the speed and torque will become stable within 0.25 second with the control strategy when working condition change, which means the proposed control strategy can improve the dynamic performance of LSR and enhance anti-perturbation capability compared to traditional MGs. 4 Conclusion This paper proposes a novel active MG with an auxiliary winding. First, the structure, working principle and control strategy are introduced. Then, the performance of the proposed structure and control strategy is conducted. Finally, the simulation results verify the efficiency of the novel structure and control strategy.

[1] S. Niu, N. Chen, S. L. Ho, and W. N. Fu. "Design optimization of magnetic gears using mesh adjustable finite-element algorithm for improved torque." *IEEE Trans. Magnetics*, vol.48, no.11, pp. 4156-4159, 2012.

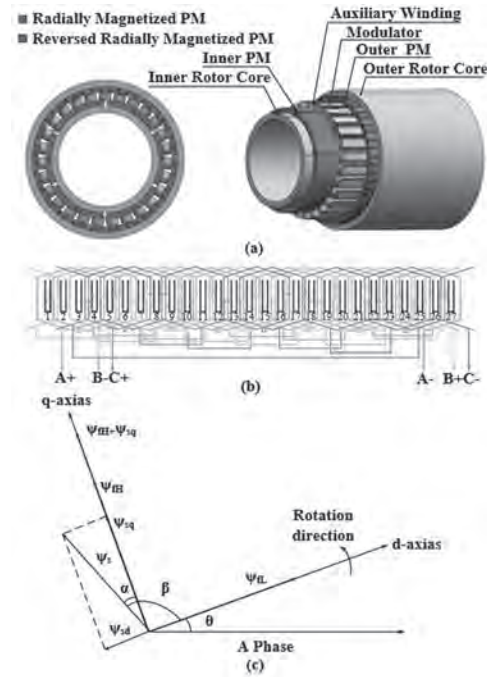


Figure 1

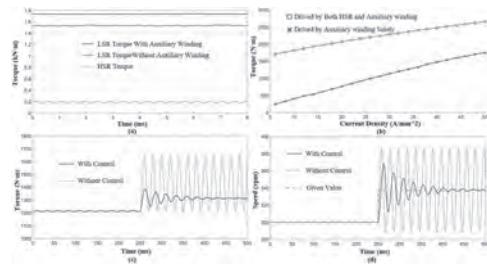


Figure 2

BU-06. Design and Analysis of a Ferrite-Assisted Hybrid Reluctance Machine for Electric Vehicle Propulsion.

W. Wang¹, X. Zhao¹ and S. Niu¹

1. Department of Electrical Engineering, The Hong Kong Polytechnic University, Kowloon, Hong Kong

Abstract— Reluctance machines with DC field coil in stator is a competitive candidate for electric vehicle propulsion due to the elimination of rare-earth permanent magnets (PM), robust structures and controllable excitation. However, their torque density cannot be compared with permanent magnet (PM) machines. Introducing rare-earth PMs into reluctance machines can be an effective way to boost torque density, but the costs will greatly increase as well. To solve this problem, this paper proposes a hybrid reluctance motor using ferrite magnets for torque density improvement. The key is to evoke flux modulation effect by introducing ferrite magnets in stator slots. Based on finite element analysis, with ferrite assisted design, machine torque density can be improved by 25% while the efficiency boosts up by 5%, respectively. **Index Terms**— hybrid reluctance machine (HRM), ferrite magnets, flux modulation, torque density I. Introduction Permanent magnet (PM) machines are widely researched for electrical vehicle (EV) applications because of their characteristics of high performance in power factor and torque density. However, PM, as a rare-earth resource, greatly increases the costs of the machines. Therefore, the research of non-PM reluctance machines in EV applications have attracted extensive attention and became an important research hotspot[1]. As a typical non-PM machine, switched reluctance machine (SRM) has been studied widely due to its simple structure, high reliability and low cost. However, since each phase of the SRM is only energized in first quadrant of BH curve, the torque ripple is serious and the torque density is poor[2]. To improve torque density, rare-earth PM auxiliary SRM in analyzed by introducing PMs into stator slots[3], thus the extended BH working range can be acquired. Doubly-fed doubly salient motor has a similar structure with SRM, while it has both DC and AC coils in the stator. Alternating excitation flux can be established by DC field coils, which enables it to work in a whole electrical period[4]. But the torque density is lower than that of SRM since the space of the stator slot is shared by DC and AC coils. Variable flux reluctance motors have symmetrical voltage and inductance characteristics and the torque ripples and noises can be decreased[5]. But the torque density is still lower than that of SRMs. An innovative method of embedding PMs in the slots of a hybrid reluctance machine (HRM) has been confirmed as an important strategy to increase the torque density through flux modulation effect[6]. The field windings and the PMs produce the flux linkages with the same phase angle. As rare-earth resources, PMs are still desired to be replaced by more accessible materials completely. The application of ferrite magnets in electrical machines is also another effective way to replace rare-earth PM materials[6]. Although its coercivity and remanence are lower than those of widely applied NdFeB35. As an artificial material, ferrite magnets have quite lower prices than NdFeB35 and are expected to be widely used in HRMs. Based on the comprehensive consideration of production costs and torque density performance, a HRM using ferrite magnets for electric vehicle propulsion was researched under finite element analysis. Optimal design and prototype experiment are going to be conducted. II. Configuration and principle The structure of the proposed HRM is shown in Fig. 1. It contains DC field coils, AC armature coils, ferrite magnets, 12 stator teeth and 11 rotor teeth. Ferrite magnets are magnetized in the radial outward direction. In order to further explain the flux modulation principle of the field winding flux linkage and the ferrite magnets flux linkage, the field excitation winding and the ferrite magnets magnetic circuit are shown. it is clear to see that the magnetic circuit of the DC field winding is mainly along the wounded stator teeth, meshing rotor teeth and adjacent rotor teeth. The magnetic circuit of ferrite magnets is along the stator slot and the rotor slot, which has a longer magnetic circuit than that of DC. However, at the stator teeth, the magnetic circuit generated by the two excitation methods has the same trend in amplitude changes. This effect can enhance the magnetic circuit. In addition, the torque performance is also improved by flux harmonics. III. Performance analysis The finite element analysis results flux distributions of ferrite magnets only and DC (6A) excitation only are shown in Fig. 2(a) and Fig. 2(b), respectively. Consistent with the above analysis, the DC excitation

magnetic circuit mainly follows the wounded stator teeth, adjacent stator teeth and meshing rotor teeth. Due to the bipolarity of the ferrite magnets magnetic circuit and the phase consistency with the DC excitation magnetic circuit, the variation range of the composite magnetic circuit is enhanced. This appearance is more obvious in the synthetic magnetic circuit which is shown in Fig. 2(c). It can be seen from the torque curves that ferrite magnets HRM can effectively increase the torque density compared with dc excitation only. Conclusion This paper proposes a ferrite-assisted hybrid reluctance machine. With the effect of flux modulation, the torque density and the efficiency can be improved by 25% and 5%, respectively.

[1] I. Boldea, L. N. Tutelea and L. Parsa, IEEE Trans. Ind. Electron., Vol. 61, p. 5696-5711 (2014) [2] J. Ye, B. Bilgin and A. Emadi, IEEE Trans. Power Electron., Vol. 30, p. 1457-1470 (2015) [3] S. Ullah, S. P. McDonald and R. Martin, IEEE Trans. Ind. Appl., Vol. 55, p. 298-305 (2019) [4] Z. Bian, Z. Zhang and L. Yu, IEEE Trans. Power Electron., Vol. 35, p. 6070-6081 (2020) [5] X. Liu and Z. Q. Zhu, IEEE Trans. Ind. Appl., Vol. 50, p. 3675-3684 (2014) [6] X. Zhao, S. Niu and W. Fu, IEEE Trans. Ind. Electron., Vol. 66, p. 4209-4219 (2019) [7] A. Fasolo, L. Alberti and N. Bianchi, IEEE Trans. Ind. Appl., Vol. 50, p. 3708-3716 (2014)

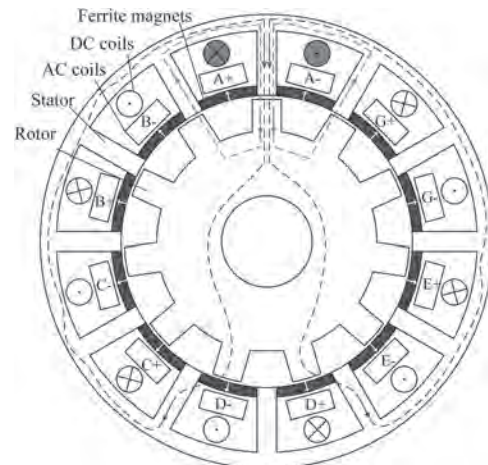


Fig. 1. Structure of the proposed HRM.

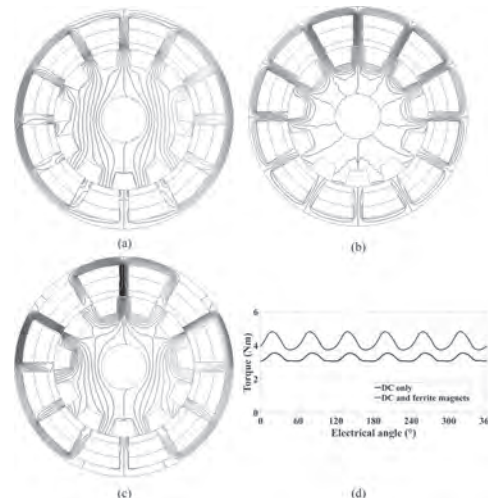


Fig. 2. (a) Flux distribution of ferrite magnets only. (b) Flux distribution of DC only. (c) Flux distribution of DC and ferrite magnets. (d) Steady torque curves.

BU-07. Design and Implementation of New Axial-Radial Bevel Magnetic Gear Based on Magnetic 3D Printing.

P. Huang¹, H. Huang¹, I. Jiang¹, T. Chang¹ and M. Tsai^{1,2}

1. *Electrical Motor Technology Research Center, National Cheng Kung University, Tainan, Taiwan;* 2. *Department of Mechanical Engineering, National Cheng Kung University, Tainan, Taiwan*

Introduction In recent years, there has been an increase in requirements for motors, as well as its characteristics of high torque transmission, low vibration, low noise, maintenance free and overload protection. In particular, the coaxial magnetic gear (CMG) has become an attractive potential alternative to the traditional mechanical gear boxes [1][2]. Due to its complicated structure and multiple air gaps, however, the conventional radial type CMG is difficult to be manufactured and assembled, as a result its applications are restricted. The axial-radial magnetic gear (ARMG) could be a possible way to simplify such fabrication problems by putting the steel pole pieces around the outside of the two rotors instead of between them, but the longer flux paths between the two rotors lowers the torque and energy transmission. To overcome this drawback while retaining the advantages of the ARMG, this paper proposes a new axial-radial bevel magnetic gear (ARBMG), with new high-performance magnet additive manufacturing (or 3D printing) process to fabricate bevel shape structure. The design of the ARBMG not only shortens the total flux paths, but also increases the efficiency. These results are proved by the FEA simulation and measurement results of a prototype. Model Description and Simulation Fig. 1 shows the comparison between a traditional ARMG as well as an ARBMG with the same gear ratio. The pole pairs of the high-speed rotor (Rotor 1) are 4, while the low-speed rotor's (Rotor 2) pole pairs are 13, and the number of steel pieces which surround the rotors on the outside are 15. It can be observed that the flux paths between the two rotors of ARBMG are shorter, as a result flux leakage is negligible therefore achieving higher efficiency. Fig. 2 (a) shows the assembly entity of ARBMG, and Fig. 2 (b) shows the ARBMG and ARMG efficiency at different input speeds with the same volume torque density, illustrating that the ARBMG has higher efficiency. Conclusion This paper proposes a new ARBMG with bevel type magnetic gear. With a bevel shaped magnet design, the new ARBMG has shorter flux paths, higher efficiency and much smaller structural volume when compared to the ARMG. Less flux leakage and higher efficiency are assumed, investigated and achieved via analytical as well as Finite Element Analysis (FEA) solutions. A prototype and experimental results based on magnetic 3D printing method are also provided to verify the proposed design.

[1] W. Bomela, J. Z. Bird and V. M. Acharya, "The Performance of a Transverse Flux Magnetic Gear," in *IEEE Transactions on Magnetics*, vol. 50, no. 1, pp. 1-4, Jan. 2014, Art no. 4000104, doi: 10.1109/TMAG.2013.2277431. [2] Y. Li, J. Xing, Y. Lu and Z. Yin, "Torque Analysis of a Novel Non-Contact Permanent Variable Transmission," *IEEE Transactions on Magnetics*, vol. 47, no. 10, pp. 4465-4468, October 2011.

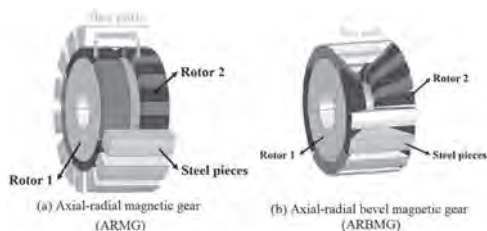


Fig. 1. Structure diagram

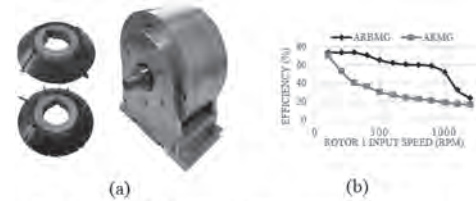


Fig. 2. (a) ARBMG bevel shape magnet and assembly entity (b) ARBMG & ARMG efficiency at different input speed

BU-08. Series Coupled Coaxial Magnetic Gear Design for High Gear Ratio and High Torque Density.

E. Park¹, S. Jung² and Y. Kim¹

1. Chosun University, Gwangju, The Republic of Korea; 2. Sungkyunkwan University College of Engineering, Suwon, The Republic of Korea

I. Torque Density Limit of High Gear Ratio Coaxial Magnetic Gears Gearing system is a useful device used to get higher torque. Due to the advantages of non-contact power transmission and easy maintenance of magnetic gears, movement to apply them to gearing systems by replacing mechanical gears is becoming active. Early magnetic gears had a low torque density of 5 kNm/m³ and could not be considered as gearboxes [1]. However, after the coaxial magnetic gear (CMG) proposed by Atallah achieved a high torque density exceeding 100 kNm/m³, the total system torque density coupled with a motor has reached higher than the one motor, indicating the possibility of replacing the mechanical gears [1, 2]. Previous research has shown a high system torque density at a high gear ratio [2], and it is limited to the case where the magnetic gear shows the same torque density (about 100 kNm/m³) regardless of the gear ratio. However, it was observed that the higher the gear ratio, the lower the torque density [1-14]. Fig. 1 tendency shows that gear torque density is decreased when gear ratio is rising and the system torque density is increased up to specific gear ratio and decreased after that. In this paper, a series coupled magnetic gear is proposed to improve the torque density limit of high gear ratio CMGs. In addition, this structure shows reducing-loss effect, its superiority is demonstrated. II. Loss Issue and Series Coupled Coaxial Magnetic Gear In the high gear ratio model, the problem of not only torque density but also efficiency was confirmed. In this paper, a single CMG with a gear ratio of 63:1 was designed and the efficiency of 58.9% was confirmed with a torque density of 21.4kNm/m³. This is because it is accompanied by a rapid change in magnetic flux at once to show a high gear ratio. That is, each change must be magnetically separated while using the stepwise change of magnetic flux. Therefore, in this paper, a series coupled CMG is proposed. Fig. 2 shows a concept of the series coupled coaxial magnetic gear. The gear ratio of 63:1 was divided into 7:1 and 9:1, and each torque density is about 85kNm/m³ and 75 kNm/m³ according to Fig. 1. In addition, losses can theoretically be reduced by 3 and 2.6 times, respectively. In this paper, various series coupling methods were considered, and a model favorable for improving torque density and one for improving loss were finally selected. As a result of the study, the proposed series coupled CMG improves torque density of 3 times and reduces loss of 90% compare to the single high gear ratio CMG. The detailed design of the series coupled CMG will be presented in full paper. Acknowledgment: This research was supported by Korea Electric Power Corporation. (Grant number: R19X001-34)

[1] K. Atallah and D. Howe, "A novel high-performance magnetic gear," *IEEE Trans. Magn.*, vol. 37, no. 4, pp. 2844-2846, July. 2001. [2] K. Atallah, S. D. Calverley, and D. Howe, "Design, analysis and realisation of a high-performance magnetic gear," *IEE Proceedings - Electric Power Applications*, vol. 151, no. 2, pp. 135-143, 2004. [3] Y. Wu, c. Chan, "A novel bicycle rear hub transmission with a magnetic gear mechanism," *Advances in Mechanical Engineering*, vol. 10, no. 7, pp. 1-9, 2018. [4] M. Desvaux, B. Traulle, R. Latimier, S. Sire, B. Multon, H. Ahmed, "Computation Time Analysis of the Magnetic Gear Analytical Model," *IEEE Trans. Magn.*, vol. 53, no. 5, pp. 7000409, 2017. [5] M. Kowol, J. Kolodziej, M. Jagiela, M. Lukaszyn, "Impact of Modulator Designs and Materials on Efficiency and Losses in Radial Passive Magnetic Gear," *IEEE Trans. Energy Conversion*, vol. 34, no. 1, pp. 147-154, 2019. [6] H. Shin, J. Chang, "Comparison of the Characteristics in the Surface Mounted Permanent Magnet and Flux Concentrating Coaxial Magnetic Gears Having the Solid Cores," *J. Electr. Eng. Technol.*, vol. 13, no. 3, pp. 1275-1284, 2018. [7] Y. Chen, W. Fu, S. Ho, H. Liu, "A Quantitative Comparison Analysis of Radial-Flux, Transverse-Flux, and Axial-Flux Magnetic Gears," *IEEE Trans. Magn.*, vol. 50, no. 11, pp. 8104604, 2014. [8] D. Jang, J. Chang, "Effect of Stationary Pole Pieces with Bridges on Electromagnetic and Mechanical Performance of a Coaxial Magnetic Gear," *Journal of Magnetism*, vol. 18, no. 2, pp. 207-211, 2013. [9] X. Zhang, X. Liu, Z. Chen, "A Novel Coaxial Magnetic Gear and Its Integration With Permanent-Magnet Brushless Motor," *IEEE*

Trans. Magn., vol. 52, no. 7, pp. 8203304, 2016. [10] X. Liu, Y. Zhao, X. Zhang, J. Gao, S. Huang, "Investigation of the Dynamic Characteristics of a Coaxial Magnetic Gear under Loading Condition Based on Analytical Model," *International conference on electrical machines and systems*, 2017. [11] M. Filippini, P. Alotto, "An optimization tool for coaxial magnetic gears," *The international journal for computation and mathematics in electrical and electronic engineering*, vol. 36, no. 5, pp. 1526-1539, 2017. [12] O. Molokanov, P. Dergachev, V. Kiruhin, P. Kurbatov, "Analyses and Experimental Validation of Coaxial Magnetic Planetary Gear," *International symposium on electrical apparatus and technologies*, 2014. [13] E. Gobl, G. Jungmayr, E. Marth, W. Amrhein, "Optimization and Comparison of Coaxial Magnetic Gears With and Without Back Iron," *IEEE Trans. Magn.*, vol. 54, no. 11, pp. 8001604, 2018. [14] G. Jungmayr, J. Loeffler, B. Winter, F. Jeske, W. Amrhein, "Magnetic Gear: Radial Force, Cogging Torque, Skewing, and Optimization," *IEEE Trans. Industry Applications*, vol. 52, no. 5, pp. 3822-3830, 2016.

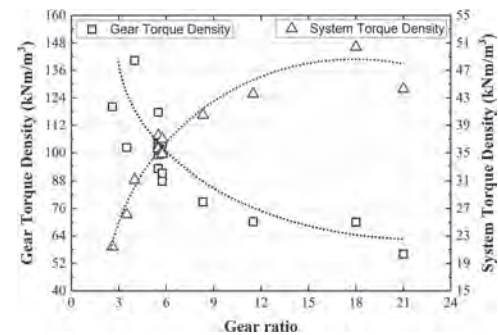


Fig. 1. System torque density of preceding researches. (Using same torque density motors)

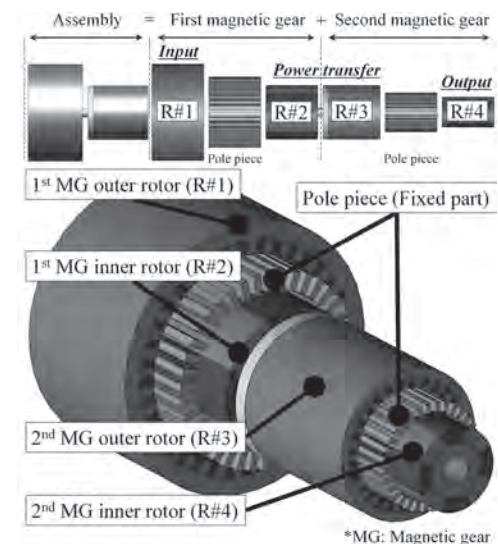


Fig. 2. Concept of the series coupled coaxial magnetic gear

BU-09. Topology Optimization of the Reluctance Trans-Rotary Magnetic Gear.

R. Safarpour¹ and S. Pakdelian¹

1. *Electrical and Computer Engineering, University of Massachusetts Lowell, Lowell, MA, United States*

This paper shows that by using topology optimization, force density of a reluctance trans-rotary magnetic gear (TROMAG) can be improved significantly. TROMAG is a magnetic device that converts high-force, low-speed linear motion to low-torque, high-speed rotation, and vice versa [1]. The device is also referred to as magnetic screw [2] and magnetic lead screw [3]. As shown in Fig. 1a, a TROMAG consists of an inner and an outer component which are separated by an air gap. One component serves as a rotor and the other as a translator. The linear to rotary motion conversion is achieved via helically-shaped permanent magnet (PM) poles. TROMAG can offer large values of shear stress and gear ratio; resulting in light-weight and compact designs. In addition, similar to other types of magnetic gears, TROMAG offers low noise and high reliability. Advantages of TROMAG have made it a strong contender for a wide range of high force, low speed applications. Helical PM poles can assume different magnetization patterns. Radially-magnetized TROMAG (RMT), axially-magnetized TROMAG (AMT), and Halbach-magnetized TROMAG (HMT) have been proposed. Another configuration, shown in Fig. 1b, is reluctance TROMAG in which one component is furnished by helical PM poles while the other component has a variable reluctance structure. Reluctance TROMAG offers less shear stress compared to configurations having PMs on both components. However, lack of PMs on the variable reluctance component makes it potentially advantageous, for example, in applications with a long stroke. Reluctance TROMAG is investigated in multiple works; with radially-magnetized PMs (R-RMT) in [2], with Halbach-magnetized PMs (R-HMT) in [3], and with axially-magnetized PMs (R-AMT) in [4]. In all these works, teeth in the variable reluctance component are of rectangular shape. This paper aims to find the optimum tooth shape using topology optimization. Noting that 2D approximation of TROMAG introduces no more than a few percent error in force calculation compared to the 3D model, the former is used for topology optimization. Topology optimization has been applied to different electromagnetic devices [5]-[8]. The essence of topology optimization is to divide the design region into small elements and use an optimization algorithm to assign to each element a set of specific materials in order to achieve the optimum topology. In [5] and [6], a genetic algorithm (GA) is used along with the so-called on/off method in which each element can be either air or a pre-defined material. Since elements are triangular or quadrilateral, resultant topologies may have sharp corners. Hence, in [7], topology optimization is performed in two main stages. First, GA and on/off method are used to run a global search and obtain the optimum topology. Then, the level set approach which is gradient based is employed to smooth the corners and create a more practical design. Recently, a topology optimization method based on the normalized Gaussian network (NGnet) has been presented [8]. Here, the on/off method is applied to Gaussian circles mapped to the design region. The method is incorporated in JMAG-Designer software, which is employed in this paper for optimizing the reluctance TROMAG. First, the three reluctance TROMAG configurations, R-RMT, R-AMT, and R-HMT with rectangular teeth are optimized by sweeping teeth dimensions while keeping other design variables fixed. For all cases the results of which are presented here, the pole pitch is 10 mm, PM thickness along radial direction is 10 mm, and air gap length is 1 mm. Optimum values of shear stress for the three designs are 82, 95, and 119 kN/m² respectively. Then, JMAG is used to apply topology optimization coupled with genetic algorithm to the three configurations. The design region has been divided into quadrilateral elements. Each element area is 0.25 mm² and the number of circles in the design region is set to 21. The optimization objective is to maximize the shear stress. Fig. 2 shows two cases resulted from topology optimization of R-RMT, offering largest values of shear stress. It was revealed that 1) For R-RMT, trapezoidal tooth shape shown in Fig. 2a offers 10% higher, and elliptical tooth shape with non-magnetic material yoke, shown in Fig. 2b, offers 30% higher shear stress compared to R-RMT with optimized rectangular tooth. 2) Optimum shape for R-AMT is rectangular; i. e., topology optimization algorithm converges to a rectangular shape. 3) For R-HMT, trapezoidal tooth

shape offers 5% higher shear stress, and elliptical tooth shape with non-magnetic material yoke offers almost the same shear stress compared to R-HMT with optimized rectangular teeth. Note that although the case of R-HMT with elliptical tooth shape and non-magnetic material yoke does not offer an appreciable increase in shear stress, it has the advantage of replacing iron yoke of the variable reluctance structure with non-magnetic material, resulting in significant weight reduction. The full paper will include detailed topology optimization results for the three configurations.

[1] S. Pakdelian, N. W. Frank and H. A. Toliyat, *IEEE Trans. Magn.*, vol. 49, no. 2, pp. 883-889, Feb. 2013. [2] H. M. Mohamed and K. Atallah, *IEEE Trans. Magn.*, vol. 55, no. 7, pp. 1-4, July 2019, Art no. 8001504. [3] N. I. Berg, A. B. Christiansen, R. K. Holm and P. O. Rasmussen, in *Proc. Int. Elect. Mach. Drives Conf.*, 2017, pp. 1-8. [4] M. Cirolini, A. F. Flores Filho, Y. C. Wu and D. G. Dorrell, *IEEE Trans. Magn.*, vol. 55, no. 7, pp. 1-6, July 2019, Art no. 8001906. [5] Chang-Hwan Im, Hyun-Kyo Jung and Yong-Joo Kim, *IEEE Trans. Magn.*, vol. 39, no. 5, pp. 2163-2169, Sep. 2003. [6] N. Takahashi, T. Yamada, S. Shimose and D. Miyagi, *IEEE Trans. Magn.*, vol. 47, no. 5, pp. 1262-1265, May 2011. [7] Y. Hidaka, T. Sato and H. Igarashi, *IEEE Trans. Magn.*, vol. 50, no. 2, pp. 617-620, Feb. 2014, Art no. 7015204. [8] T. Sato, K. Watanabe and H. Igarashi, *IEEE Trans. Magn.*, vol. 51, no. 3, pp. 1-4, March 2015, Art no. 7202604.

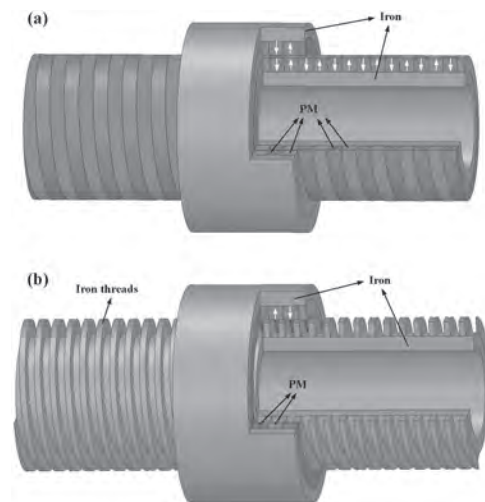


Fig. 1. 3D views of (a) RMT; and (b) Reluctance RMT.

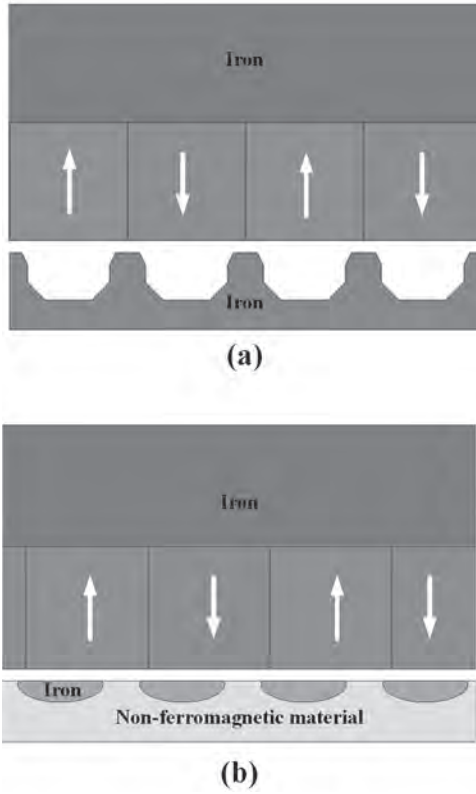


Fig. 2. 2D views of promising R-RM topologies; (a) trapezoidal tooth; (b) elliptical tooth with non-magnetic yoke. Topologies are created by JMAG and reproduced in ANSYS Maxwell.

BU-10. Hybrid Excitation Dual Stator/Rotor Armature Winding Vernier Machine With Alternate Stator PM.

S. Jia¹, S. Feng¹, D. Liang¹ and X. Dong¹
 1. Xi'an Jiaotong University, Xi'an, China

Abstract—This paper proposes a novel hybrid excitation alternate stator PM dual stator/rotor armature winding vernier machine with the DC-biased current. Due to the both armature windings and alternate stator PM interact with each other, this proposed machine contain six torque components. Compared with traditional stator permanent magnet machines and flux modulated machines, this machine makes full use of the space in rotor cavity, and giving full play to the flux modulation effect. This digest will introduce the coil-connection, current configuration, and the simulation results, such as flux density, back-EMF, and electromagnetic torque, which are predicted by finite element analysis (FEA). *Index Terms*—Hybrid excitation, DC-biased current, Vernier machine (VM), Dual stator/rotor armature winding. **I. Introduction** Recently, stator permanent magnet (PM) machines are gaining more and more research attention for their benefit of a robust rotor structure[1]. In the meantime, the flux modulated machines due to the natural high torque density characteristic are gaining more research interest, too [2]. Combining the advantages of both machines, the DC-biased hybrid excitation stator PM vernier machines (HEPMVMs) are proposed [3]. Compared with the stator PM machines, the DC-biased HEPMVMs improve the shortcomings of the inherent limited magnetic field adjustment ability, meanwhile, improve the torque density. However, these machines don't make full use of the space in the rotor cavity, and the reliability of torque output is poor, due to only contain stator armature winding. In this paper, the topology of DC-biased hybrid excitation alternate stator PM dual stator/rotor armature winding vernier machine (DAWVM) is proposed. As shown In Fig. 1, the stator has two phase DC-biased winding and the teeth located PMs alternately, the rotor has three phase winding. Therefore, high torque will be generated. The drive circuit, operation principle, and the electromagnetic characteristics will be illustrated in the full paper. **II. Electromagnetic Performance Evaluation** The simulation results of flux density, back-EMF, and electromagnetic torque are analyzed by the finite element analysis (FEA). The no-load flux distribution is shown in Fig. 2. The back-EMF and electromagnetic torque with various excitation modes are shown in Fig. 3. This machine exhibits larger torque due to contain six torque components, which will be illustrated in the full paper.

[1] Z. Zhu, H. Hua, D. Wu, J. Shi, and Z. Wu, *IEEE Trans. Ind. Appl.*, vol. 52, no. 1, pp. 199–208, Jan./Feb. 2016. [2] S. Jia, R. Qu, W. Kong, D. Li, and J. Li, *IEEE Trans. Ind. App.*, vol. 54, no.2, Jul./Aug., pp:3187-3196, 2018. [3] S. Jia et al., *IEEE Trans. Ind. Appl.*, vol. 54, no. 2, pp. 1339-1348, March-April 2018.

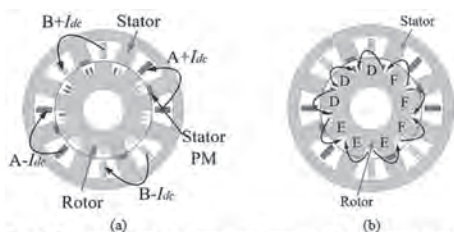


Fig. 1. Coil connections and current configuration of the proposed topology. (a) Stator part winding connection. (b) Rotor part winding connection.



Fig. 2. No-load flux distributions when the stator DC/AC current is 14/0 A, rotor current is 0A.

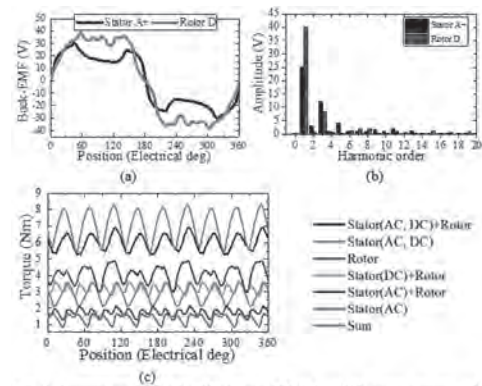


Fig. 3. Comparison of back-EMF (stator DC/AC: 14/0A, rotor current: 0A) and electromagnetic torque (stator DC/AC: 14/14A, rotor current: 15A). (a) back-EMF waveforms. (b) back-EMF harmonics. (c) Torque waveforms with various excitation modes.

BU-11. A Novel Permanent Magnet Generator With Dual-Electric and Dual-Mechanical Port for Stand-Alone AC/DC Power Supply System.

Q. Lin¹, S. Niu¹, X. Zhao¹, F. Cai² and W. Fu¹

1. *Electrical Engineering, The Hong Kong Polytechnic University, Kowloon, Hong Kong*; 2. *Xiamen Tungsten Co Ltd, Xiamen, China*

1. Introduction Hybrid AC and DC power supply system has been applied to various situations [1]. A stand-alone system (SAS) is one of these situations. Due to the limited space in SAS, the power supply system in it should be small and light. Usually, there are three ways to realize hybrid AC/DC power supply system. One is to use an AC synchronous generator to provide AC power and a DC generator to provide DC power. Although high-quality power can be obtained, two generators make the whole system large and heavy. Moreover, it is not economic. The slip rings and brushes for the DC generator will reduce the reliability and increase the maintenance cost of the system. Another method is adopting an AC synchronous generator and high-power converters. This method may decrease the volume and weight of the system. But the AC and DC power is electrically connected, the mutual influence between AC and DC power is significant and the robustness of the system is poor. The last approach which is also the trend is using a hybrid AC/DC power supply system. It possesses a small weight and volume and can achieve electrical isolation between AC and DC power. A hybrid AC/DC generator with salient poles was first proposed in [2]. Two sets of star-connected armature windings are installed in stator slots. One set of winding provides AC power and the other set provides DC power after rectification. But the coupling between these two sets of windings may strong. In [3], an induction generator with a static excitation controller is proposed. It provides DC power controlled by ISFC controller and variable frequency AC power. In [4], a new dual-winding Vernier permanent magnet (PM) wind power generator is proposed for hybrid AC and DC power supply. Machines mentioned above modulate their output voltage through the out voltage modulation circuit. The high power electric circuit is usually high cost. Moreover, the introducing of the outer electric circuit also reduces the reliability of the whole system. In this paper, a novel generator with dual-electric and dual-mechanical ports for hybrid AC/DC power supply system is proposed in this paper. The voltage modulation circuit is eliminated through the adjustment of the inner rotor. With the special design of stator teeth, and the flux modulation effect between stator teeth, inner salient rotor, and outer rotor with PM-iron structure, abundant harmonics will be generated in the outer airgap. Two sets of armature winding are installed in stator slots and they have different pole pairs. Two sets of armature winding share one rotation rotor, with different pole pairs of their winding, they have different frequencies. Detailed introduction of the machine topology and the initial simulation results of the proposed generator are introduced in the following parts. 2. Machine Topology The machine topology is shown in Fig. 1. The stator structure is specially designed. The modulation effect is realized through the modulation effect between the inner rotor and the outer rotor. The outer rotor has PM-iron structure. The pole pairs of it are 23. The inner rotor has 13 pole pairs and it has salient poles. The inner rotor is connected to a step motor. Through control of the step motor, the position of the inner rotor will be adjusted. Through the rotation of the inner rotor, the relative position between the stator and the inner rotor is adjusted and the volume of the flux in the outer airgap will be modulated, thus the amplitude of the output voltage will be modulated. 3. Initial Simulation Results The initial simulation result is shown in Fig. 2. The waveform of the no-load air gap flux density of the proposed machine is shown in Fig. 2 (a). The harmonic components of it are obtained through Fast Fourier Transform and the result is shown in Fig. 2 (b). It can be found that there are mainly two pole pairs of harmonics, namely, 10 pole pairs and 23 pole pairs. The 10 pole pairs are obtained through the modulation between the inner rotor and the outer rotor. And the 23 pole pairs is obtained due to the outer rotor poles. Due to the limitation of the length of the abstract, the detailed analysis of the proposed generator will be presented in the full paper, including the operation principle of the proposed machine, as well as its theoretical analysis, optimization, and electromagnetic performances.

[1] Y. Li, X. Wang, S. Wang, P. Su and W. Ma, *Proceedings IPEDMC*, vol.1, pp. 476-481(2000) [2] P. W. Franklin, *IEEE Transactions on Power*

Apparatus and Systems, vol. PAS-92, no. 2, pp. 543-551(1973) [3] F. Bu, W. Huang, Y. Hu and K. Shi, *IEEE Transactions on Energy Conversion*, vol. 27, no. 3, pp. 810-812(2012) [4] Q. Wang, S. Niu and T. W. Ching, *IEEE Transactions on Magnetics*, vol. 54, no. 11, pp. 1-5(2018)

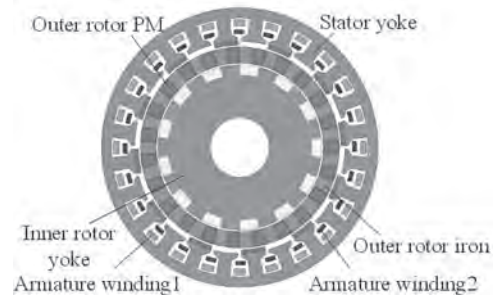


Fig. 1. The configuration of the proposed generator.

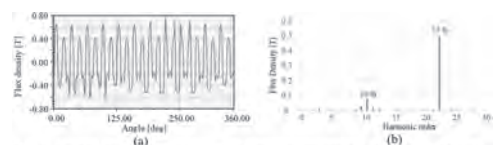


Fig. 2. No-load airgap flux density and its harmonic components. (a) The waveform of the airgap flux density. (b) The harmonic components of it.

Fig. 2. No-load airgap flux density and its harmonic components. (a) The waveform of the airgap flux density. (b) The harmonic components of it.

BU-12. Analysis of Split-Tooth Stator-Slot Permanent-Magnet Machines With Different PM Arrangements.

L. Cao¹, K. Chau¹, C. Lee² and T. Yang¹

1. University of Hong Kong, Hong Kong; 2. Nanyang Technological University, Singapore, Singapore

I. Introduction Permanent-magnet (PM) machines, which exhibit the merits of high torque/power density and high efficiency, have been widely employed in many industrial applications in recent decades, such as wind power generation and electric vehicles [1-5]. As these applications are safe-critical, the development of new machine structures with improved reliability is speeding up [6, 7]. To achieve the feature of fault tolerance, various design techniques of PM machines have been put forward, such as the redundant designs with multi-phase windings [8] or dual three-phase windings [9], and the modular designs with modular windings [10] or modular stator [11], etc. Recently, the stator-slot PM (SSPM) machine with inherent fault-tolerant ability is proposed to achieve high failure-safe capability during uncontrolled generator operation or winding short circuits [12]. However, relatively low torque density puts this structure at a disadvantage, particularly at light load condition. To improve the torque performances, the split-tooth (ST) structure is introduced in the machine [13], where the PMs are placed between the split tooth and tangentially magnetized with opposite polarities in the adjacent PMs, as shown in Fig. 1(a). In this paper, three new types of split-tooth stator-slot PM (ST-SSPM) machines are proposed as shown in Fig. 1(b)-(d), which are designated as Type-2, Type-3, and Type-4 machine, respectively. Four types of machines share the same structure with the split-tooth stator and salient-pole rotor but the PMs are arranged with different positions and polarities. The operation principles are introduced while the electromagnetic performances of four types of machines are comprehensively analyzed and compared by using finite-element analysis (FEA). Based on the analyzed results, the merits and demerits of four types of machines with different PM arrangements are concluded. II. Methodology Similar to the other stator-PM machine with salient rotor poles, the operation principle of four types of machines can be explained by the field modulation theory [14]. Then, the slot-pole combinations of Type-1 and Type-3 machines can be derived as $P_a = \min(|iN_s/2 \pm N_p|)$, ($i=1, 3, 5, \dots$) while those of Type-2 and Type-4 machines can be derived as $P_a = \min(|iN_s \pm N_p|)$, ($i=1, 2, 3, \dots$), where P_a is the pole-pair number of armature winding, N_s is the stator slot number, N_p is the rotor pole number, and i is a positive integer. By performing FEA in JMAG-Designer, the torques and torque ripples of machines with various slot-pole combinations are optimized in Fig. 2. It can be seen that Type-1 to Type-4 machines can produce the largest torque with $N_p=22, 16, 23$ and 17 respectively, while the torque of Type-4 machine with $N_p=17$ is the largest among all the machines. However, Type-3 machine with $N_p=23$ and Type-4 machine with $N_p=17$ produce large unbalanced magnetic force due to the odd number of N_p , thus undesired electromagnetic vibration and noise will be incurred. To resolve this concern, it is desirable to achieve good torque performances with an even number of N_p . One can see that the torques of Type-3 and Type-4 machines with $N_p=22$ are the highest among all the machines with even numbers of N_p , despite slightly lower than those of Type-3 machine with $N_p=23$ and Type-4 machine with $N_p=17$, respectively. Therefore, the optimal N_p of Type-1 to Type-4 machines are preliminarily selected as 22, 16, 22, and 22, respectively. Furthermore, the torque ripples of these four machines are all lower than 10 %, and hence are acceptable. Finally, taking into consideration all the above factors, Type-1 to Type-4 machines are globally optimized with optimal $N_p=22, 16, 22, 22$, respectively, which are further investigated, including the cogging torque, back-EMF, steady torque, PM utilization ratio, loss, efficiency, power factor and PM demagnetization. III. Conclusion Based on the analyzed results of four types of machines, some findings are listed as follows. a) Type-1 machine has the lowest cogging torque due to the circulation of PM flux in the stator at no load condition, whereas Type-2 machine shows the highest cogging torque due to the largest cogging torque factor. b) Type-1, Type-2 and Type-4 machines have the similar and largest average torque at rated condition. However, Type-4 and Type-2 machines offer the highest and lowest PMs utilization ratio, respectively. c) Type-4 machine exhibits the best torque performance at rated and light load conditions, while Type-1 machine has the best overload capability. Type-2 machine shows

good torque performances both in light and overload conditions, despite not the best, d) Type-4 machine offers the highest power factor, despite the power factors of four types of machines tend to be low. However, their power factors can be improved by increasing the value of stator inner radius/airgap. e) Type-1 to Type-3 machines show irreversible PM demagnetization with different degrees at the inner corner of PMs under over load and high temperature condition, whereas this does not happen in Type-4 machine with the best PM demagnetization withstand. More detailed analysis and results will be given in the full paper. Acknowledgment This work was supported by a grant (Project No. 17205518) from the Hong Kong Research Grants Council, Hong Kong Special Administrative Region, China.

[1] K. T. Chau, C. C. Chan, and C. Liu, "Overview of permanent-magnet brushless drives for electric and hybrid electric vehicles," *IEEE Trans. Ind. Electron.*, vol. 55, no. 6, pp. 2246-2257, May 2008. [2] Z. Q. Zhu, and D. Howe, "Electrical machines and drives for electric, hybrid, and fuel cell vehicles," *Proc. IEEE*, vol. 95, no. 4, pp. 746-765, Apr. 2007. [3] J. Li, K. T. Chau, J. Jiang, C. Liu, and W. Li, "A new efficient permanent-magnet vernier machine for wind power generation," *IEEE Trans. Magn.*, vol. 46, no. 6, pp. 1475-1478, May 2010. [4] C. Liu, K. T. Chau, J. Z. Jiang, and S. Niu, "Comparison of Stator-Permanent-Magnet Brushless Machines," *IEEE Trans. Magn.*, vol. 44, no. 11, pp. 4405-4408, Nov. 2008. [5] L. Cao, K. T. Chau, and C. H. T. Lee, "A new parallel-hybrid-excited permanent-magnet machine with harmonic-differential effect for electric vehicles," *IEEE Trans. Veh. Technol.*, vol. 69, no. 11, pp. 12734-12750, Sept. 2020. [6] A. M. E.-. Refaie, M. R. Shah, and K. Huh, "High-power-density fault-tolerant PM generator for safety-critical applications," *IEEE Trans. Ind. Appl.*, vol. 50, no. 3, pp. 1717-1728, Sept. 2014. [7] W. Zhao, L. Xu, and G. Liu, "Overview of permanent-magnet fault-tolerant machines: Topology and design," *CES Trans. Elect. Mach. and Syst.*, vol. 2, no. 1, pp. 51-64, Mar. 2018. [8] F. Barrero, and M. J. Duran, "Recent advances in the design, modeling, and control of multiphase machines—Part I," *IEEE Trans. Ind. Electron.*, vol. 63, no. 1, pp. 449-458, Jun. 2016. [9] X. Jiang, W. Huang, R. Cao, Z. Hao, and W. Jiang, "Electric drive system of dual-winding fault-tolerant permanent-magnet motor for aerospace applications," *IEEE Trans. Ind. Electron.*, vol. 62, no. 12, pp. 7322-7330, Dec. 2015. [10] P. Zheng, Y. Sui, J. Zhao, C. Tong, T. A. Lipo, and A. Wang, "Investigation of a novel five-phase modular permanent-magnet in-wheel motor," *IEEE Trans. Magn.*, vol. 47, no. 10, pp. 4084-4087, Oct. 2011. [11] G. J. Li, Z. Q. Zhu, M. Foster, and D. Stone, "Comparative studies of modular and unequal tooth PM machines either with or without tooth tips," *IEEE Trans. Magn.*, vol. 50, no. 7, pp. 1-10, Jul. 2014. [12] I. A. A. Afinowi, Z. Q. Zhu, Y. Guan, J. Mipo, and P. Farah, "A novel brushless AC doubly salient stator slot permanent magnet machine," *IEEE Trans. Energy Convers.*, vol. 31, no. 1, pp. 283-292, Mar. 2016. [13] H. Qu, and Z. Q. Zhu, "Analysis of split-tooth stator slot PM machine," *IEEE Trans. Ind. Electron.*, 2020, doi: 10.1109/TIE.2020.3031535 (Early Access). [14] M. Cheng, P. Han, and W. Hua, "General airgap field modulation theory for electrical machines," *IEEE Trans. Ind. Electron.*, vol. 64, no. 8, pp. 6063-6074, Mar. 2017.

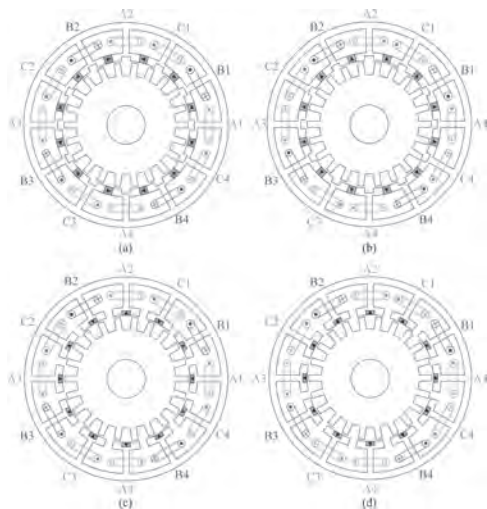


Fig. 1. ST-SSPM machines with different PM arrangements. (1) Type-1. (b) Type-2. (c) Type-3. (d) Type-4.

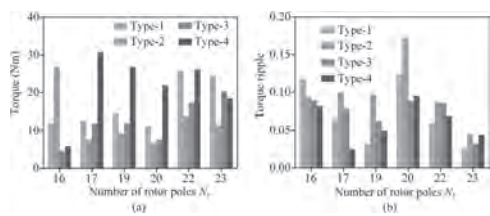


Fig. 2. Torques and torque ripples of four types of machines with different numbers of rotor poles. (a) Torques. (b) Torque ripples.

BU-13. A Novel Split-Teeth Vernier Pseudo-Direct-Drive Permanent-Magnet Machine With Concentrated Winding.

Q. Gan¹, P. Pfister¹ and Y. Fang¹

1. Zhejiang University, Hangzhou, China

1. Introduction The demand for low-speed and high-torque electrical machines is increasing in different industrial applications. Vernier permanent-magnet machines (VPM) and Pseudo-direct-drive machines (PDD) are especially suitable for this situation due to their magnetic gearing effect [1,2]. Generally, the power factor of the conventional VPM can be as low as 0.66 [3]. PDDs have the capability of high power factor as well as high torque density [2]. To output higher torque density compared with PDDs, a novel Vernier Pseudo-direct-drive machine (VPDD) is proposed in [4] as Fig. 1 (a) shows. In this paper, the subdomain analytical model is used to analyze and preoptimize a VPDD. After the preoptimization, a finite element model (FEM) is also used to optimize the slot opening and check the demagnetization. However, in this machine, the winding has not been optimized to reduce the size of end-winding, and as a result, the real torque density taking the end-winding into account is much lower. Our research focuses on further improving the torque density of the VPDD considering a structure that reduces the size of end-winding. A concentrated winding split-teeth VPDD topology (ST-VPDD), shown in Fig. 1 (b), is hence proposed. 2. Modeling and optimization The ST-VPDD can be regarded as a combination of a magnetic gear and a VPM. For the part that functions as a magnetic gear [4], the speed ratio can be expressed as $G_r = \Omega_s / \Omega_r = p_r / p_s = T_r / T_s$, where Ω_s , Ω_r are the rotational angular speed of the transmitter and of the low-speed (LS) rotor; p_s , p_r are the pole-pairs of permanent-magnets (PM) of the transmitter and of the LS rotor; T_r , T_s are the torque of the transmitter and of the LS rotor. The rotating magnetic field created by the armature winding drives the transmitter. The LS rotor will be driven by both the transmitter and by the field created by the armature winding. If the transmitter is removed, the ST-VPDD can be regarded as a VPM. According to [5], if $P_r = nZ = p_r \neq p_s$ is satisfied, the rotating field of armature winding can drive the LS rotor. n is the number of split teeth per tooth, Z is the number of slots and p_s is the pole-pairs of armature winding. The gear ratio can be expressed as $G_{st} = \Omega_s / \Omega_r = p_r / (nZ - p_r) = p_r / p_s$, where Ω_s is the rotational angular speed of the field created by the winding. We keep $p_s = p_r$, so that $G_{st} = G_r$. Therefore, the part of the magnetic gear and the VPM will drive the low-speed rotor together at the same speed. The ST-VPDD is analyzed through a FEM. Its ferromagnetic material is made of M-45 steel. Fig. 2 (b) shows the proposed concentrated winding model. For comparison, the distributed winding model of the prototype VPDD is put in Fig. 2 (a). In the figure, l_w is the length of the half-width of a slot, and l_s depends on the winding material. According to the winding model, a mathematical model is built to calculate the torque density taking end-winding into account. The torque density of the ST-VPDD is optimized. The variable parameters are: 1. r_1 is the radius of the transmitter iron; 2. h_{mt} is the thickness of the transmitter PM; 3. h_{mr} is the thickness of the rotor PM; 4. l_s is the length of the split teeth; 5. $c_1 = \alpha_1 / \alpha_2$; 6. $c_2 = l_r / l_s$; 7. $c_3 = \beta_1 / \beta_2$. Once the optimization is done, we do the demagnetization check on the optimized ST-VPDD. 3. Results The following parameters of the ST-VPDD are assumed to be similar to the parameters of the VPDD [4]: $Z=9$, $n=5$, $p_r=p_s=3$ and $p_r=42$, and its out radius r_o is 90 mm and active length l_a is 75 mm. The optimized ST-VPDD can output 172.1 Nm of torque in theory. Without taking the end-winding into account, it provides 90.2 Nm/L of torque density, which is slightly lower than the torque density of 91.8 Nm/L of the VPDD in [4]. From the winding model of the VPDD and of the ST-VPDD, we get that the lengths of end-winding of VPDD and ST-VPDD are 96 mm and 49.6 mm, respectively. So, taking the end-winding into account, the torque density of VPDD and ST-VPDD are 40.3 Nm/L and 54.3 Nm/L. There is a 34.7% improvement in the torque density. The PM used for this design is VACODYM AP 776 [6]. When the temperature is 60 Celsius degree, its remanent flux density is 1.25 T and the demagnetization field is 1300 kA/m. No demagnetization occurs. 4. Conclusions With concentrated winding, the optimized ST-VPDD topology improves the torque density capability compared with the VPDD. And the concentrated winding is less complicated, which simplifies manufacture and hence decrease its cost. The split tooth allows more combinations of poles and slots, so the structure can be further optimized. 5. Acknowledgment This work was supported by the National Natural Science Foundation of China

under Grant 51851110761. Corresponding author: P.-D. Pfister (e-mail: pierredaniel.pfister.public@gmail.com).

[1] A. Toba and T. A. Lipo, "Generic torque-maximizing design methodology of surface permanent-magnet vernier machine," in IEEE Transactions on Industry Applications, vol. 36, no. 6, pp. 1539-1546, Nov.-Dec. 2000, doi: 10.1109/28.887204. [2] K. Atallah, J. Rens, S. Mezani and D. Howe, "A Novel "Pseudo" Direct-Drive Brushless Permanent Magnet Machine," in IEEE Transactions on Magnetics, vol. 44, no. 11, pp. 4349-4352, Nov. 2008, doi: 10.1109/TMAG.2008.2001509. [3] D. Li, R. Qu and T. A. Lipo, "High-Power-Factor Vernier Permanent-Magnet Machines," in IEEE Transactions on Industry Applications, vol. 50, no. 6, pp. 3664-3674, Nov.-Dec. 2014, doi: 10.1109/TIA.2014.2315443. [4] X. Yin, Y. Fang, X. Huang and P. Pfister, "Analytical Modeling of a Novel Vernier Pseudo-Direct-Drive Permanent-Magnet Machine," in IEEE Transactions on Magnetics, vol. 53, no. 6, pp. 1-4, June 2017, Art no. 7207404, doi: 10.1109/TMAG.2017.2660241. [5] D. Li, T. Zou, R. Qu and D. Jiang, "Analysis of Fractional-Slot Concentrated Winding PM Vernier Machines With Regular Open-Slot Stators," in IEEE Transactions on Industry Applications, vol. 54, no. 2, pp. 1320-1330, March-April 2018, doi: 10.1109/TIA.2017.2778686. [6] VACUUMSCHMELZE. Rare Earth Permanent Magnets: VACODYM VACOMAX. Accessed: January 05, 2021. [Online]. Available: https://vacuumschmelze.de/Assets-Web/VACODYM-VACOMAX-PD002_2015_en.pdf.

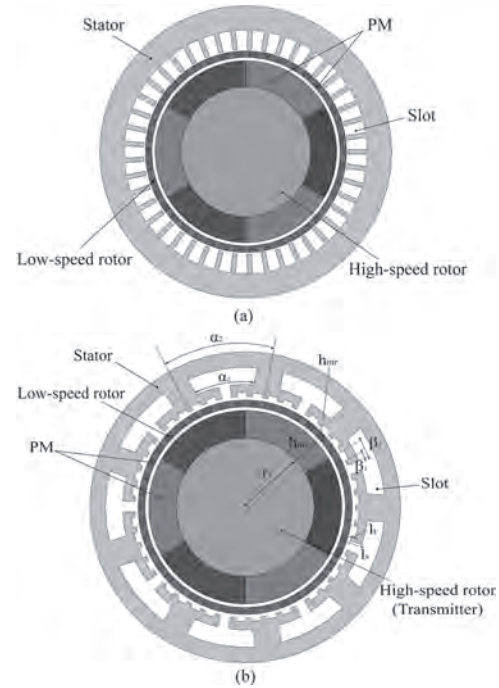


Figure 1: (a) The structure of the VPDD [4]. (b) The structure of the proposed ST-VPDD.

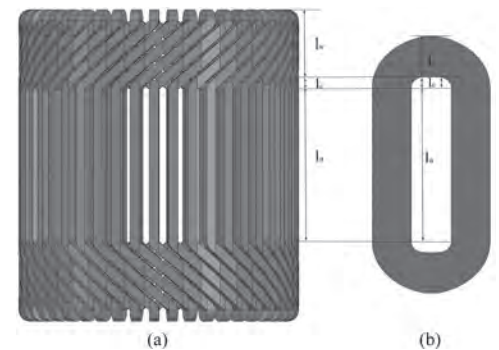


Figure 2: (a) The distributed winding model of the prototype VPDD. (b) The concentrated winding model of the proposed ST-VPDD.

BU-14. Design of a Quasi-Halbach Permanent Magnet Vernier Machine.

W. Guendouz¹, A. Tounzi² and T. Rékioua¹

1. Université Béjaïa, Béjaïa, Algeria; 2. Univ. Lille, Arts et Metiers Institute of Technology, Centrale Lille, Junia, ULR 2697 - L2EP, Lille, France

1. Introduction Direct drive machines are more and more used in several applications involving low speed operation at standard frequencies. This replaces conventional systems which use classical machines coupled to gear-boxes thus improving the dynamic and the efficiency of the system while avoiding the maintenance drawbacks of classical solutions. The simplest way to obtain a direct drive machine consists in increasing the pole pair number of a classical machine and more specifically a PM synchronous machine. However, this leads to large diameters which are not well adapted for applications with limited volume. This is the case of traction applications as the mass and the volume of the machine are key points. PM Vernier machine is well known for its capacity to provide high torque density with reduced ripples. It requires smaller stator slot and pole pair numbers than classical PM machine with the same rotor pole pairs [1-2]. Therefore, it could constitute a good candidate to be used as a traction motor. In its common configuration, PM are mounted on the rotor surface with a radial magnetization and several studies have been dedicated to give the rules to well design a PM Vernier structure or to propose topologies to improve the torque density and power factor which is considered as the main drawback [3-4]. Recently some of them focused on another way to arrange the magnets on the rotor [5-6]. The present paper deals with the study of PM Vernier machine with a quasi-Halbach configuration of the magnets. The effects of the ratio between the tangential and the radial parts of the magnets on the machine performance (torque density, torque ripple) are evaluated using finite element analysis (FEA) method. Using an analytical approach with a pure radial magnetization of PM, a prototype is first designed and sized under the specifications of an urban traction application. Simulations are then carried out on the prototype with different stator slot openings and ratios of the tangential part of the magnet to quantify the effect of the two variables in term of average torque, ripples and harmonics of the no load emf. 2. Operation principle PM Vernier machine achieves the electromagnetic energy conversion on the basis of the interaction of the armature magnetic field with the one of the rotating magnets. As the pole pair numbers of both magnetic fields are different, the variation of the air gap permeance, which is due to the only stator slots, plays a key role by modulating the two fields so that they can interact. The analytical expression of the whole magnetic energy in a PM Vernier machine under the assumption of high permeability of the magnetic material shows that the latter is constituted of different terms. Only some of them are function of the rotor position and can then generate an electromagnetic torque. Therefore, to select one of these terms thus achieving an electromagnetic conversion in a continuous manner, a strong relationship should link the rotor PM pole pairs p_r , to the stator winding pole pairs p_s and the number of stator slots N_s : $N_s = |p_s \pm p_r|$. In the case of radial magnetization of the PM, previous studies have shown that the best arrangement is when the magnets are contiguous. Thus, for a given mechanical air gap thickness, only the opening of the stator slot influences the interaction and therefore the performance. In the case of a quasi-Halbach configuration, in addition to the opening of the stator slot, the tangential magnetization part of PM will also have a significant effect in terms of the average value of the electromagnetic torque but also in terms of torque ripples and harmonics of the no load emf. 3 Application A first prototype has been designed with PM magnetized in the only radial direction and its main geometries sized using analytical approach for the desired application with rated power 65 kW at 300 rpm and 55Hz. The rotor and stator pole pair numbers are 11 and 1 respectively. Thus, the slots number is equal to 12. The machine air gap radius is 0.177m and its active length is 0.532m. Figure 1a shows the magnetic flux density distribution in a cross section of the designed machine. It clearly looks like just 1 pole pair machine even if the rotor has 11 pole pairs. Figure 1b presents the two variables whose effects are evaluated, i.e. λ_{H1} which represents the tangential angular part of a pole magnet and λ_{S1} which is the angular opening of a stator slot. While keeping the same magnet and mechanical airgap thicknesses, different stator slot opening and tangential parts of the magnets have been investigated using FEA while taking into account the non-linear behavior of magnetic

materials. Figure 2a shows the no load emfs for a ratio of the tangential part of the magnets equal to $\lambda_{H1}/\lambda_r = 10\%$ and $\lambda_{S1}/\lambda_s = 43, 50$ and 57% . Figure 2b presents the electromagnetic torque at load when the machine is supplied by three phase rated currents for $\lambda_{S1}/\lambda_s = 45\%$ and 3 $\lambda_{H1}/\lambda_r = 5, 10$ and 15% . It can clearly be seen that both variables have non negligible effect on the no load emf in terms of magnitude and harmonic content and on the average value of the electromagnetic torque along with its ripples. In the final paper, more details about the design of the first prototype will be given and results leading to an optimal prototype with a quasi-Halbach configuration of the magnets will be presented and discussed.

[1] D. Li, R. Qu, J. Li, L. Xiao, L. Wu and W. Xu, "Analysis of Torque Capability and Quality in Vernier Permanent-Magnet Machines," in *IEEE Transactions on Industry Applications*, vol. 52, no. 1, pp. 125-135, Jan.-Feb. 2016. [2] B. Kim and T. Lipo, "Operation and design principles of a PM vernier motor," *IEEE Trans. Ind. Appl.*, vol. 50, no. 6, pp. 3656-3663, Nov./Dec. 2014. [3] L. Wu, R. Qu, D. Li and Y. Gao, "Influence of Pole Ratio and Winding Pole Numbers on Performance and Optimal Design Parameters of Surface Permanent-Magnet Vernier Machines," in *IEEE Transactions on Industry Applications*, vol. 51, no. 5, pp. 3707-3715, Sept.-Oct. 2015. [4] D. Li, R. Qu, and T. Lipo, "High power factor vernier permanent magnet machines," *IEEE Trans. Ind. Appl.*, vol. 50, no. 6, pp. 3664- 3674, Nov./Dec. 2014 [5] L. Xu, G. Liu, W. Zhao, J. Ji and X. Fan, "High-Performance Fault Tolerant Halbach Permanent Magnet Vernier Machines for Safety-Critical Applications," *IEEE Trans. Magn.*, vol. 52, no. 7, July 2016 [6] Y. Kataoka, Y. Anazawa, 'Analysis of counter Electromotive force in a surface permanent magnet-type Vernier Motor using a Halbach array', The 23rd ICEMS, 2020, pp: 1257-1262

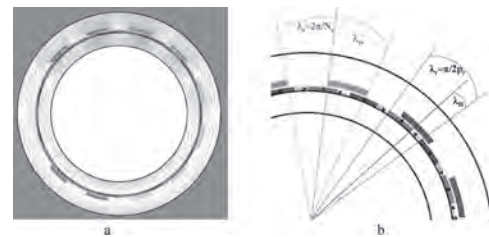


Fig. 1. a) No load magnetic flux density in the cross section of the first prototype b) The two variables studied

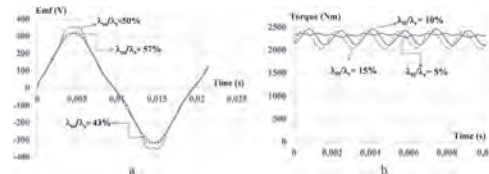


Figure 2. No load emfs and rated electromagnetic torque for different configurations

BU-15. Design and Analysis of Novel Split-Pole Fault-Tolerant Vernier Permanent Magnetic Machine.

B. Xu¹, Q. Wu¹, J. Ma¹, X. Liu¹, L. Wu¹, L. Qiu¹, J. Zhang¹ and Y. Fang¹
 1. Zhejiang University, Hangzhou, China

I. Introduction Vernier permanent-magnet (VPM) machine takes advantage of high torque density and low rotational speed, which makes it a promising candidate in direct-drive applications. The industrial application prospect makes it a research interest in recent years. A fault-tolerant structure is proposed in [1], which can decouple the interaction between different phases and hence improve the fault-tolerant ability. However, as the fractional slot concentrated winding (FSCW) configuration is adopted, the torque capability is consequently reduced [2]. This paper proposes a split-pole fault-tolerant (SPFT) VPM machine as is shown in Fig. 1(a). The consequent-pole PM structure is adopted to improve the torque density with less magnet usage [3]. Meanwhile the stator affiliated PMs are employed to further enhance the torque capability. Last but not least, the inner stator is composed of alternately arranged modular teeth and fault-tolerant teeth. The modular tooth consists of root part and split-pole structure, and the split-pole structure plays the role of flux modulation poles (FMPs). The concentrated windings are wound around the modular teeth, so the fault-tolerant teeth can segregate the adjoining phases. The stator only has one modular tooth for each phase, and the winding pole pair is set to one. Thus, the coils can link nearly 120 mechanical degree of the flux linkage even if the FSCW configuration is adopted. In this way the torque capability can be maximized. In this paper the operation principle and working mechanism of proposed machine are described. The influences of the key parameters on electromagnetic performances are investigated by finite element analysis (FEA) method. A comparison between conventional FTVPM machine and proposed machine is discussed. Besides, the analytical model of proposed machine is illustrated and analyzed. The prototype is manufactured and tested which verifies the feasibility of calculation results. The analytical model and experiment results are not shown in the digest for space limitation, and will be added in the full paper. II. Parameter Optimization and Electromagnetic Performance Comparison The influences of the key parameters on electromagnetic performances are investigated to optimize the proposed structure. As can be seen in Fig. 1(b), the optimal stator modular tooth width is 18mm. It is because the proposed structure only has 3 stator teeth for windings. When the d-axis and the modular tooth coincide, all the flux linkage will pass through one of the modular teeth, so that the saturation problem is heavier. Therefore the modular teeth have to be wide enough. When the width is larger than 18mm the area for armature winding is reduced, thus the torque decreases instead. When the fault-tolerant tooth width increases, there is a small drop at first as is shown in Fig. 1(c). The reason is when fault-tolerant teeth is very thin, the split-pole occupies larger air-gap angle, so there will be more flux linkage passes through the coils. The stator and rotor PM thickness are also confined by the winding area since the outer diameter is fixed. The rotor yoke thickness has to be large enough to prevent the saturation problem, which is concluded in Fig. 1(e). It should be noted that when the rotor yoke thickness is large, the air-gap volume which stores the magnetic field energy is reduced as well as the winding area. The comparison between proposed machine and conventional FTVPM machine is discussed. The same main parameters are shown in Fig. 2(a). The proposed machine is 18/17-pole with one-pole-pair winding and the conventional topology is 18/13-pole with five-pole-pair winding. The no-load flux density at the air-gap is investigated to find out the harmonic characteristic of proposed machine. As can be seen in Fig. 2(c), the 5th and 13th harmonic of FTVPM are both larger than the fundamental and 17th harmonic of proposed machine. But as a VPM machine, the rotor with 17 pole-pair has larger pole ratio, which means the modulated magnetic field rotates faster. Meanwhile the proposed topology makes phase coil link more flux linkage, so the open circuit back-EMF is 2.45 times that of the conventional one. Moreover, according to Fig. 2(e), the proposed structure can provide larger average torque while maintain a low torque ripple. It is because the magnitude of torque ripple is inversely proportional to the lowest common multiple (LCM) of the number of stator and rotor pole pairs. III. Conclusion The split-pole fault-tolerant VPM machine is proposed in this paper. The topology and operation principle are presented. The FEA results show that the proposed structure takes advantage of large torque, low torque

ripple, short end turn length and fault-tolerant capability. Compared with conventional FTVPM machine, the proposed machine can produce 145% higher output torque under the same copper loss. The analytical analysis and experiment results will be added in the full paper.

[1] G. Liu, J. Yang and W. Zhao, IEEE Trans. on Magn., vol. 48, no. 11 (2012) [2] L. Xu, G. Liu and W. Zhao, IEEE Trans. on Energy Conversion, vol. 30, no. 4 (2015) [3] D. Li, R. Qu and J. Li, 2014 IEEE Energy Conversion Congr. and Expo., (2014)

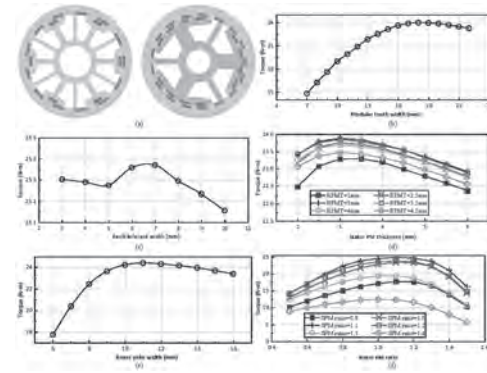


Fig. 1. (a) Topologies of both machines. (b) Influence of modular tooth width on torque. (c) Influence of fault-tolerant tooth width on torque. (d) Influence of stator and rotor PM thickness on torque. (e) Influence of rotor yoke thickness on torque. (f) Influence of stator and rotor PM ratio on torque.

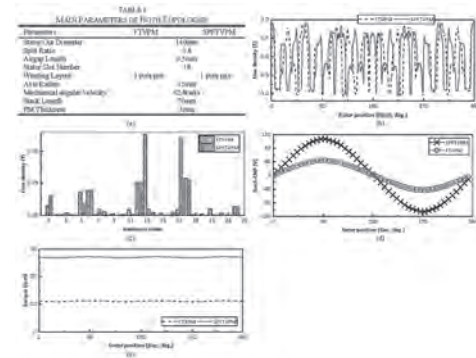


Fig. 2. (a) Main parameters of both topologies. (b) Flux density wave-forms at the air-gap. (c) Flux density spectra at the air-gap. (d) Open-circuit back-EMF. (e) Torque performances

BU-16. Analysis of a Novel Dual-PM Vernier Machine With High Torque Density and Low Torque Ripple and Unbalanced Force.

J. Huang¹, W. Fu¹ and S. Niu¹

¹. Department of Electrical Engineering, The Hong Kong Polytechnic University, HongKong, Hong Kong

Abstract—A novel dual permanent magnet (PM) dual three phase vernier machine is proposed for electric vehicles in this paper. Compared with conventional dual PM vernier machines, a dual three-phase winding connection is adopted to reduce sub-harmonics and improve working harmonics at the same time. The dual three-phase windings supplied by two separate converters can improve the reliability of the machine driving systems, which is an important issue in electric vehicles. Therefore, this proposed machine exhibits higher torque density, higher reliability, lower force ripple, and lower unbalanced force. The simulation result shows that with the proposed dual three phase winding, the torque is improved by 3.9% while the torque ripple and unbalanced force are reduced about 50% and 72.5%, respectively.

Index Terms—Concentrate winding, permanent magnet, torque density, vernier machine. Introduction With the emergence and widespread use of automobiles, people's lives have been highly improved. However, while the cars bring convenience in our lives, they also cause excessive consumption of non-renewable energies and the emission of greenhouse gases at the same time, which have aggravated environmental pollution. To solve these problems, electric vehicles are a potential solution. Therefore, the motors, which are the key components in the electric vehicles' driving system, have attracted a lot of attention in recent years. The induction motor and permanent magnet (PM) motor are the two main types of motors used in electric vehicles. Compared to the induction motor, the PM motor has higher power density, lower copper loss and smaller volume; hence it has become the mainstream in academia and commercial applications. However, there are only limited pole and slot combinations which have been investigated due to the high iron loss and unbalanced force under high-speed operation in electric vehicles. In this paper a novel dual three phase dual PM vernier machine with high torque density and low unbalanced force is proposed. Its structure will be presented first. Then the operation principle is illustrated, and the performance of the motor is shown. Structure, Operation Principle and Performance The structure of the proposed motor is shown in Fig. 1. The outer diameter is 220mm and the rated speed is 3980rpm. It has 12 slots and 10 poles; PMs are employed on both the rotor and stator. The windings on the stator are fractional slot concentrated windings (FSCWs). All the armature windings can be divided into two sets of 3 phases windings which are supplied by two separate converters. The two converters supply phase A1, B1 and C1, and phase A2, B2 and C2, which has $\pi/6$ shift. This arrangement can improve the fault tolerance capability since the motor can operate under one set of winding when a failure occurs in the other one. Referring to [1], the MMF of armature windings adopting dual three structure can be given as $F_i(t, \theta) = \sum_{k=1,5,7,\dots} \alpha (12NI/k\pi) \sin(k\pi/12) \sin((k-1)\pi/12) \sin(k\theta - \omega t - (k-1)\pi/12)$ According to the equation, it is obvious that by adopting dual three structure, the subharmonic can be eliminated, and the 5th, 7th, 17th and 19th harmonics can be increased. Considering the modulation effect, the working harmonics of the proposed motor can be obtained which are 5th, 7th and 17th. Therefore, the output torque of the proposed motor is increased, and the torque ripple reduced. The analytical result is verified by 2-D FE analysis. Fig. 2 shows the torque comparison between the conventional dual PM vernier machine and the proposed one. It can be seen that the output torque increases 3.9% from 148Nm to 154Nm and the torque ripple reduces about 50% from 2.75% to 1.4%. The proposed machine not only improves the torque performances, but also the core loss and unbalanced force. After applying this structure, the unbalanced force is reduced a lot, which is from 1158.2N to 318.54N. The efficiency and torque density are also improved a little bit from 96.63% to 96.77% and $3.54 \times 10^{-5} \text{ Nm/mm}^3$ to $3.68 \times 10^{-5} \text{ Nm/mm}^3$. Conclusion A novel dual three phase dual PM machine is proposed in this paper. The structure, operation principle and the performance are analyzed. The simulation result shows that adopting this novel structure can reduce the subharmonics and improve the working harmonics. It increases the output torque, reduces the torque ripple and unbalanced force. It is a very effective way to improve the performance and more detailed characteristics will be reported in full paper.

[1] A. S. Abdel-Khalik, S. Ahmed and A. M. Massoud, IEEE Trans. Magn., Vol. 51, p. 1-10 (2015). [2] Q. Wang, S. Niu and L. Yang, IEEE Trans. Ind. Electron., Vol. 64, p. 9924-9933 (2017).

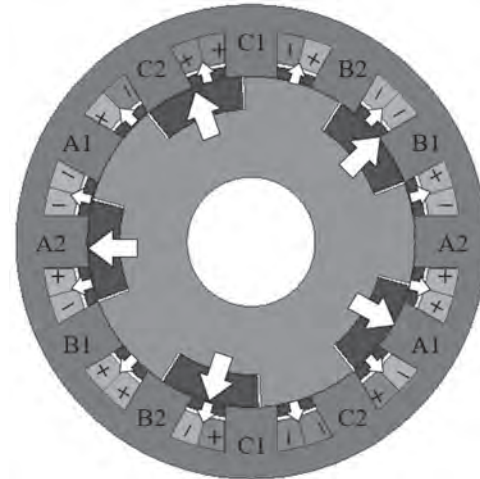


Fig.1. Structure of the proposed motor.

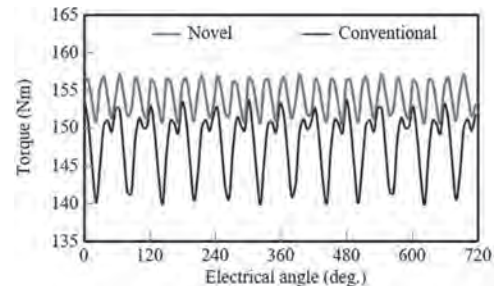


Fig. 2. Output torque comparison.

BU-17. Analysis of 12 Slots Novel DC-Biased Dual-PM Vernier Machines With Slot-Opening PMs.

J. Huang¹, W. Fu¹ and S. Niu¹

1. Electrical Engineering, The Hong Kong Polytechnic University, Hong Kong, Hong Kong

Abstract—This paper proposes and compares two different 12 slots DC-biased dual-PM vernier machines. Both machines have tangentially magnetized magnets located in the slot openings, and an integrated winding is adopted to produce the armature field and excitation field at the same time. The slot-opening PMs not only improve the machine torque performance but also relieve the saturation caused by the DC-biased. The results show that both structures exhibit high torque density and slot-opening PMs in machine 1 contribute more to torque improvement while PMs in machine 2 are more for dc-saturation relief. *Index Terms*—DC-bias, dual PM, finite-element method, vernier machine. Introduction With the emergence of the magnetic gear and the proposal of a unified theory of flux modulation, vernier machine has attracted people’s attention. Due to its high torque density and wide operation range, vernier machine becomes the potential candidate for many applications such as electric vehicles and wind power generation. To further increase the torque density under the constrain dimension, dual-PM vernier machine is proposed, and several structures have been investigated. In order to achieve a more compact structure and wider flux weakening range, the integrated winding with DC-biased structures have also been studied. In this paper, two novel DC-biased dual-PM vernier machines with slot-opening PM are proposed and investigated. To showcase the effectiveness of the slot-opening PMs, the conventional DC-biased dual PM vernier machines will be presented first. Then the operation principle of proposed novel machines will be presented, and the comparison between different structures will be conducted. Structure, Operation Principle and Performance The structure of the proposed motors and their conventional structures are shown in Fig.1. To make a relatively fair comparison, the main dimensions of all the structures are the same. The outer diameter is 90mm, the air gap is 0.5mm, and the stack length is 80mm. As shown in Fig. 1, PMs are located on both the rotor and stator. The PMs in the rotor and stator tooth are both radially magnetized, while the slot-opening PMs are tangentially magnetized. The main difference between the two novel machines is the PMs in the stator teeth region, which is directly attached to the teeth surface in machine 1 while embedded in machine 2. The phase windings are arranged as follows. $I_{a1}=I_{ac}\cos(2\pi ft)+I_{dc}$ $I_{b1}=I_{ac}\cos(2\pi ft-2\pi/3)+I_{dc}$ $I_{c1}=I_{ac}\cos(2\pi ft+2\pi/3)+I_{dc}$ $I_{a2}=I_{ac}\cos(2\pi ft)-I_{dc}$ $I_{b2}=I_{ac}\cos(2\pi ft-2\pi/3)-I_{dc}$ $I_{c2}=I_{ac}\cos(2\pi ft+2\pi/3)-I_{dc}$ The machines can achieve different operation mode by simply adjust the DC-bias. The magnetic field can be strengthened by applying the positive DC biased, while negative DC biased can weaken the magnetic field. The 2-D FE analysis is conducted to analyze the machine performances. Fig. 2 shows the torque comparison between the conventional and novel structures. It is obvious that both conventional and novel structures of machine 1 have better torque performances than machine 2. They have higher output torque and lower torque ripple. The output torque of conventional and novel machine 1 are 11.44 Nm and 13.25Nm while machine 2 are 10.75Nm and 11.77Nm, respectively. The output torque of novel machine 1 improves 12.57% compares to novel machine 2. It also can be found that structures of machine 2 have better flux regulated capability. By injecting different direction of DC biased, the output torque can increase 6.68% and decrease 14.6% in conventional machine 1 while output increases 10.98% and decreases 22.98% in conventional machine 2. It also can be seen that the slot-opening PMs are more effectively in torque improvement in machine 1 and saturation relief in machine 2. The output torque increases by 15.82% after adopting the slot-opening PMs in machine 1, while machine 2 only increases by 9.49%. Furthermore, the torque improvement percentage with DC biased have a different degree of increase. After applying the slot-opening PMs, the percentage increases from 6.68% to 9.81% in machine 1 while 10.98% to 24.47% in machine 2. Conclusion Two novel DC-biased dual PM machine with slot-opening PM are proposed and compared in this paper. The structure, operation principle and performance are analyzed. The simulation result shows that the machine 1 has better torque performance while machine 2 has better flux regulation capability. More detailed characteristics will be reported in the full paper.

[1] X. Zhao, S. Niu and W. Fu, IEEE Trans. Magn., vol. 55, p. 1-5 (2019)
 [2] Q. Wang, S. Niu and X. Luo, IEEE Trans. Ind. Electron., vol. 64, p. 6908-6919 (2017)

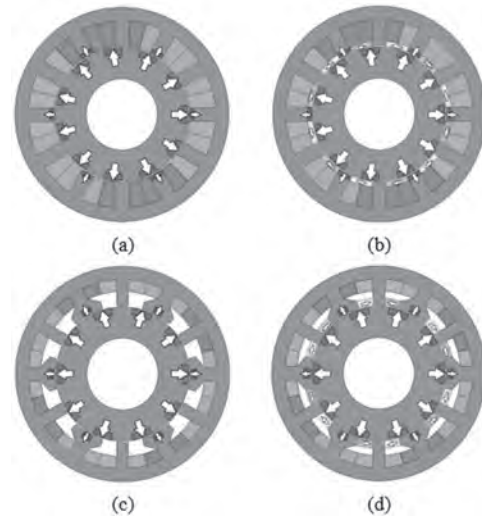


Fig. 1. Structure of the proposed motors. (a) Conventional machine1. (b) Novel machine1. (c) Conventional machine2. (d) Novel machine2

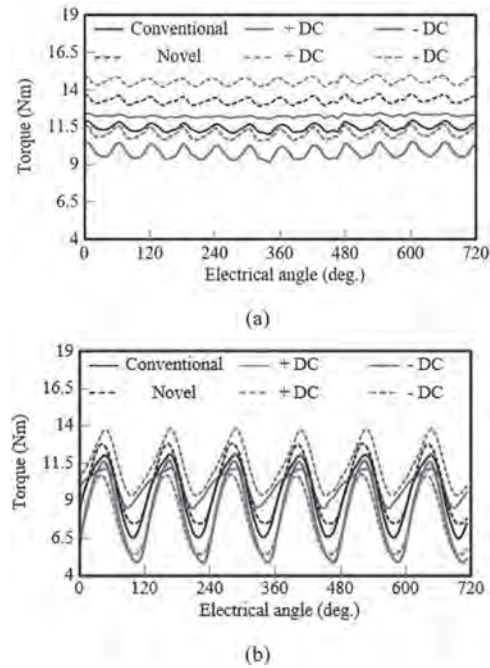


Fig. 2. Output torque comparison. (a) Machine 1 (b) Machine 2

BU-18. A Novel Approach for Power Factor Improvement in Dual-Stator Vernier Permanent Magnet Machines.

Q. Lin¹, S. Niu¹, X. Zhao¹, F. Cai² and W. Fu¹

1. *Electrical Engineering, The Hong Kong Polytechnic University, Kowloon, Hong Kong;* 2. *Xiamen Tungsten Co Ltd, Xiamen, China*

1. Introduction Vernier permanent magnet machines (VPMM) have a simple structure and high torque density due to the so-called magnetic-gear effect and are very suitable for direct drive applications, such as wind power turbines and electric vehicles [1]. In addition, the VPMM has low pulsing torque due to its more sinusoidal back-EMF, compared with traditional designs of PM machines [2]. However, the power factor of the VPMM is relatively low (sometimes even below 0.3), which requires a converter with a larger capacity for the fixed output power [1]. Many researchers have been carried out to address this problem and some improvements in structure have also been studied in recent decades. Vernier structure was proposed in the early 19th century and then applied to stepping motors [3]. The VPMM as a unique electromechanical device is firstly derived from the earlier Vernier reluctance machine [4-5]. Further, dual-excitation VPMM is invented with a dual stator and toroidal winding, which not only has high torque density at low speed but also improves space utilization [6]. In [7-8], dual-excitation VPMM is further investigated. A generic torque maximizing design methodology for the motor is proposed to improve the torque density in the machine in [6], and a new structure constructed with interior PM, spoke-array rotor, and dual-stator with a displacement of half slot is proposed to improve the power factor and the pole shoe was also investigated to further improve the torque performance [7-8]. In this paper, a novel effective, and convenient method aiming to improve the torque density and power factor of DS-VPMM is proposed. The key is to rotate the inset-type PMs in the rotor with a certain electrical angle as well as the excitation direction and it is found that the flux leakage is significantly reduced in the air-gaps and the flux distribution in the inner and outer stator windings can be compensated with each other. Hence not only the back-EMF and torque are boosted but also the power factor is greatly improved. The paper is organized as follows. The operation principles including the structure and magnetic field analyses are introduced first. In the third section, the electromagnetic characteristics of this machine are evaluated based on FEM analyses, including flux density in the two air gaps and their harmonic investigation to find the effective components of the flux density. Besides, back-EMF, cogging torque, and on-load torque, as well as torque density and power factor will be analyzed. Machines with different rotation angles are studied and compared. The power factor improving method proposed in this paper can also be extended to other machines to improve the torque density within a limited peripheral.

2. Machine Topology The original design of DS-VPMM is as shown in Fig.1 (a). A flux concentrating structure using spoke-array magnets rotor to increase the useful magnet flux and decrease the flux leakage between adjacent PMs is adopted. The stator has a tooth-pole structure, which functions as modulation pieces in a flux modulate machine. The windings with yellow, green, and red color refer to phase A, B, C respectively. Fig. 1 (b) shows the DS-VPMM that adopts the proposed method to rotate the inserted PMs as well as their excitation directions with a certain angle. The other parts of DS-VPMM are kept the same. Windings of inner and outer stators can be connected independently or series according to the applications. In order to investigate more explicitly, the windings of two stators are connected independently in this paper. This machine follows the following rule [7]: $Z_2 = Z_1 - p$ or $Z_1 + p$ (1) where p , Z_1 , Z_2 are the pole-pair number (PPN) of winding, stator teeth, and rotor, respectively. According to the modulation effect of magnet gear, the main effective harmonic order will be 1st and 11th order harmonics.

3. Initial Investigation Results Fig. 2 shows the variations of torque and power factor when changing the rotation angle of the inset-type PMs in the rotor iron core. It can be found that the highest torque density is 24.275 KN/m³, whereas the power factor is 0.726. Since a rotation angle of 15 degrees exhibits a more preferable power factor, the torque of the machine with a 15-degree rotation angle versus the current control angle is investigated and shown in Fig. 12. It is found that when the current control angle is 55 degrees, the power factor can reach nearly 0.8. The torque reaches the highest value when the current control angle is nearly 30 degrees and the power factor is around 0.7 at this control angle. In this

abstract, only one machine topologies and its investigation results are shown. More machines applied with this method will be investigated in the full paper. 4. Conclusion A novel method to improve the power factor of VPMM machine is proposed in this paper and the analyses are strongly proved that this method is efficient and the power factor can be improved nearly to 0.8 which is significantly higher than the traditional VPMM. In addition, through the rotation of PMs, the machine can get more space for PMs, thus obtaining higher torque density within the limited volume.

[1] G. Eason, B. Noble, and I. N. Sneddon, *Phil. Trans. Roy. Soc. London*, vol. A247, pp. 529-551(1955) [2] A. Ishizaki, T. Tanaka, K. Takasaki, *Electrical Machines and Drives Seventh International Conference(2002)* [3] C. H. Lee, *IEEE Trans. Power App. And Syst.*, vol.82, no. 66, pp. 343-349(2007) [4] T. Toba, T. A. Lipo, *Conference Record of the 1999 IEEE Industry App. Conference*, vol.4, pp.2539-2544(2002) [5] A. Toba, T. A. Lipo, *IEEE Trans. Indus. Appl.*, vol. 36, no. 6, pp. 1539-1546(2002) [6] Dawei Lin, Ronghai Qu, Thomas A. Lipo, *IEEE Trans. Indus. Appl.*, vol.50, no.6, pp. 3664-3674(2014) [7] Dawei Li, Ronghai Qu, Jian Li, *IEEE Energy Conversion Congress and Exposition*, pp. 1885-1891(2015) [8] Ronghia Qu, Dawei Li, Jin Wang, *2011 International Conference on Electrical Machines and Systems*, pp. 1-6(2011)

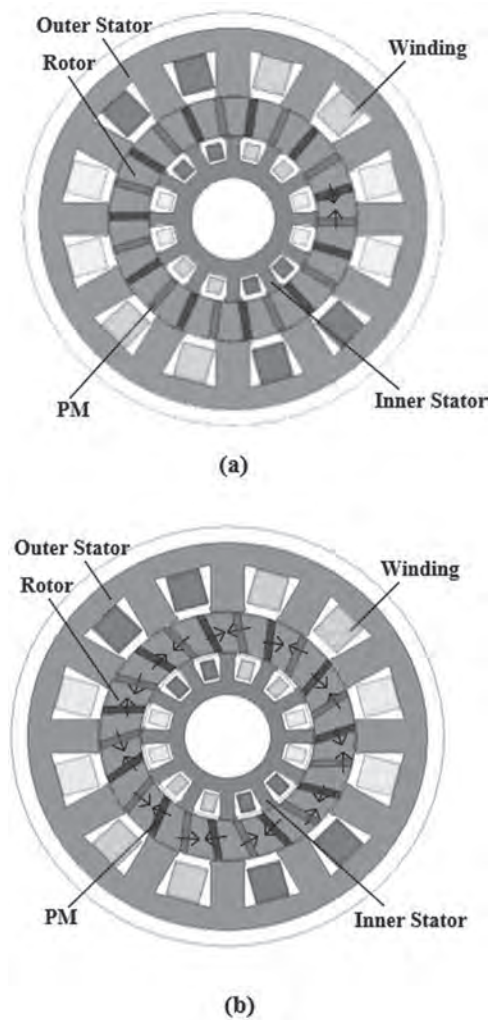


Fig. 1. The topology of the DS-VPMM. (a) Initial machine structure. (b) Machine with the rotated PMs.

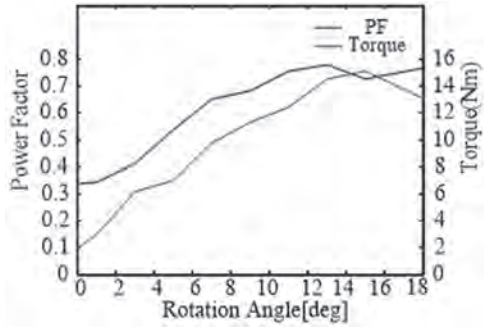


Fig. 2. Power factor and torque versus rotor-PM rotation angle.

BU-19. Comparative Study of Novel Dual Stator Machines Having Different Biased PM Configurations.

X. Zhang³, H. Yang^{2,1} and S. Niu¹

1. Electrical Engineering, The Hong Kong Polytechnic University, Kowloon, Hong Kong; 2. Southeast University, Nanjing, China; 3. Shenzhen In Drive Ampere Co. Ltd., Shenzhen, China

I. INTRODUCTION Nowadays, the demands of high torque/power rating in critical industrial applications usually lead to bulky size and excessive material consumption in the conventional permanent magnet (PM) machines [1]. Thus, torque density improvement is widely recognized as a challenging issue for traditional PM machines [1]. As a common practice, doubling the stator is normally employed to increase the torque density within a limited overall dimension, namely, the dual-stator (DS) machines [2]-[4]. For the DS machines, the thermal management and protection issues associated with the PMs tend to be problematic issues with the cantilever cupped rotor. The stator-PM DS machines [4] can well facilitate the PM heat dissipation, but also have a simple and robust rotor which is preferable for high-speed critical-safety operation. Nevertheless, the inner and outer stators in the preceding stator-PM DS structures are structurally duplicated, the geometric conflicts between the PM excitations and windings on the stator still exist similar to those single stator counterparts. Therefore, this paper aims to propose novel DS biased PM machines (DS-BPMM) only having biased PM excitations in the inner stator. Different from the existing DS machines having two identical stators, the developed DS-BPMMs combines the advantages of the design concept of “partitioned stator (PS) [5]” and the conventional DS machines. In the perspective of the geometry, the proposed machines can be considered as the synergies of an outer-rotor stator PM machine plus a separate outer stator similar to traditional fractional-slot machines. As a result, the space tradeoff between PM and copper areas, as well as severe magnetic saturation are significantly alleviated compared to the traditional DS counterparts. In this paper, the electromagnetic characteristics of the DS-BPMMs with different PM arrangements in the inner stator are investigated and compared. The machine topology and operating principle based on interior PM (IPM) and surface-mounted PM (SPM) structures will be addressed. Finally, an IPM-DS-BPMM prototype is manufactured and tested to verify the theoretical analyses. II. MACHINE TOPOLOGIES AND STATOR/ROTOR POLE COMBINATION Figs. 1 (a) and (b) show the proposed machine topologies, which can be regarded as IPM and SPM types, respectively. It should be noted that the total PM usage, outer stator, stack length, and rated current are kept the same for the two designs to offer a fair comparison. Meanwhile, the two machines are both characterized by a 6/11/6 outer-stator-pole/rotor-segment/inner-stator-pole configuration. Since the two machines comply with the variable reluctance principle, their stator/rotor pole combinations can be governed by [6] $N_s/\text{GCD}(N_s, N_r)=km$ (1) where GCD signifies the Greatest Common Divisor between the stator pole number N_s and rotor pole number N_r , m is the number of phases, and k is a positive integer. It should be emphasized that the outer stator pole number is identical to that of the inner stator pole in these two machines. Besides, the flux linkage of single-coil is bipolar for SF machine, while unipolar for VR machine. However, the resultant phase flux linkage of VR topology is bipolar, which is mainly attributed to the opposite connection of armature windings in the same phase, as evidenced by the coil and phase flux linkages in the outer stator windings in Figs. 1 and (c) and (d), respectively. III. ELECTROMAGNETIC PERFORMANCE COMPARISON The open-circuit back-EMFs of the two machines are shown in Fig. 2(a). The significantly high EMF magnitudes can be observed in the IPM case. This is mainly attributed to the higher resultant phase flux linkage of the IPM machine due to its bipolar coil flux linkage. Accordingly, the SPM machine exhibits relatively lower torque capability compared to the IPM counterpart as reflected in the rated-load steady torque in Fig. 2(b). Meanwhile, it can be observed that the IPM one shows ~higher torque ripple ratio than the SPM one, which is undesired for the applications requiring smooth torque performance. IV. EXPERIMENTAL VALIDATION Based on the analysis above-mentioned, the IPM configuration is selected and manufactured as shown in Fig. 2(c). The finite element (FE) and measured back-EMF waveforms are shown in Fig. 2(d), in which the good agreement between FE predictions and

test results are achieved. The detailed characteristics analysis, comparison results, and experimental validation will be presented in the full paper.

[1] G. A. Capolino and A. Cavagnino, “New trends in electrical machines technology,” *IEEE Trans. Ind. Electron.*, vol. 61, no. 8, pp. 4281-4285, Aug. 2014. [2] M. Abbasian, M. Moallem, and B. Fahimi, “Double-stator switched reluctance machines (DSSRM): fundamentals and magnetic force analysis,” *IEEE Trans. Energy Convers.*, vol. 25, no. 3, pp. 589-597, Sep. 2010. [3] S. Niu, K. T. Chau, J. Z. Jiang, and C. Liu, “Design and control of a new double-stator cup-rotor permanent-magnet machine for wind power generation,” *IEEE Trans. Magn.*, vol. 43, no. 6, pp. 2501-2503, Jun. 2007. [4] D. Kim, H. Hwang, S. Bae, and C. Lee, “Analysis and design of a double-stator flux-switching permanent magnet machine using ferrite magnet in hybrid electric vehicles,” *IEEE Trans. Magn.*, vol. 52, no. 7, pp. 1-4, Jul. 2016. [5] D. Evans and Z. Q. Zhu, “Novel partitioned stator switched flux permanent magnet machines,” *IEEE Trans. Magn.*, vol. 51, no. 1, Art. no. 8100114, Jan. 2015. [6] J. T. Chen, and Z. Q. Zhu, “Winding configurations and optimal stator and rotor pole combination of flux-switching PM brushless AC machines,” *IEEE Trans. Energy Convers.*, vol. 25, no. 2, pp. 293 - 302, Jun. 2010.

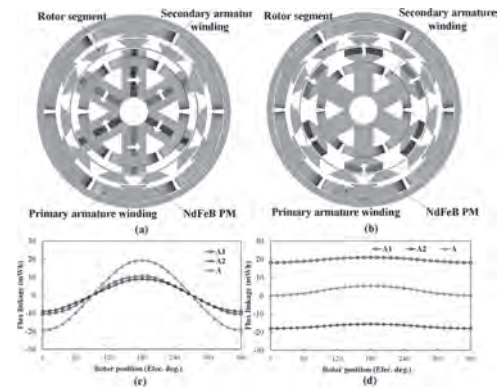


Fig. 1. Topologies and flux linkage waveforms of the DS-BPMMs.

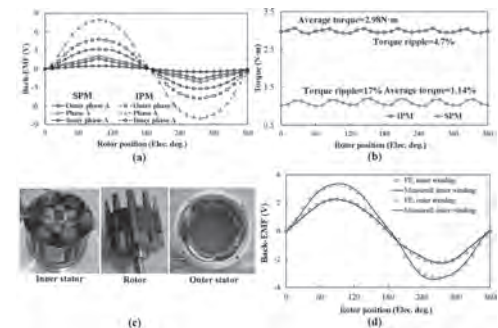


Fig. 2. Electromagnetic performance comparison and test result. (a) Back-EMFs. (b) Rated-load steady torque waveforms. (c) Prototype. (d). FE predicted and measured phase EMF waveforms.

Session BV
WOUND ROTOR, AXIAL FLUX AND MEMORY MOTORS
(Poster Session)

Mi-Ching Tsai, Co-Chair
National Cheng Kung University, Tainan, Taiwan
Jen-Yuan (James) Chang, Co-Chair
National Tsing Hua University, Hsinchu, Taiwan

BV-01. Analysis of Inter-Turn Short-Circuit Faults of Axial Split Phase Permanent Magnet Synchronous Motors.

F. Chai¹ and L. Geng¹

1. Harbin Institute of Technology, Harbin, China

I. Introduction The inter-turn short-circuit (ITSC) faults can cause excessively high short-circuit current in PM motors. This elevated current level will increase the temperature of the faulty windings and further melt the insulation of the nearby turns. As a result, some more serious faults can be induced, such as the interphase short-circuit fault, phase-to-ground short-circuit fault, and PM demagnetization [1]. The axial split phase permanent magnet synchronous motor (ASP-PMSM) has better isolation performance between phases compared to traditional circumferential split phase permanent magnet synchronous motor (CSP-PMSM) [2], which is benefit in preventing the spread of fault between phases. In this paper the behavior difference of ITSC fault between ASP-PMSM and CSP-PMSM has been investigated. Through theoretical analysis, finite element analysis (FEA) and experimental verification, it is found that compared to the CSP-PMSM, the ASP-PMSM has inherently advantages in mitigating the severity of ITSC fault. II. Modeling And Analysis of ITSC Fault *A. Topology and advantages.*

As shown in Fig.1 (a), the phase-stators of ASP-PMSM are independently distributed along axial direction, which realized excellent magnetic, physical and thermal isolation between phases. These features are benefit in preventing the spread of fault between phases. There is only one phase in the circumferential direction of ASP-PMSM, and therefore the number of turn in series per phase of the ASP-PMSM is closed to three times that of CSP-PMSM. *B. The behavior of fault current.* This section build the electrical model of PMSM with ITSC fault, as is shown in Fig.1(b). For an incipient fault, the contact resistance is not ideal zero. Therefore, the contact resistor r_f is included in this model to consider the degradation process of insulation materials. Based on this model, the expression of fault current i_f is derived. $|i_f| = |V_f| / (R_f + R_s + j\omega L_a N_s / N_1)$ $V_f = e_a - R_f i_f + j\omega L_a (N_1 - N_s) / N_1 i_a$ $R_f = N_r / N_s$. In above equation, N , N_1 and N_s represent number of turns in series, number of turns per coil and number of shorted turns; respectively; and represent the phase back-EMF vector and current vector, respectively; L_a represents the self-inductance of phase A; R_s represents the phase resistance. The vector diagram of V_f for CSP-PMSM and ASP-PMSM is shown in Fig.1 (c) and (d), respectively, the blue line and black line represents the vector at low speed and high speed, respectively. Because the number of turns in series of ASP-PMSM is triple that of CSP-PMSM, therefore the R_f for ASP-PMSM is triple that of CSP-PMSM. At low speed, the amplitude of vector V_{f-ls} in Fig 1(d) is three times larger than that in Fig.1 (c). Thus the fault current of ASP-PMSM is larger than that of CSP-PMSM. However, for an incipient fault, the fault current of ASP-PMSM and CSP-PMSM are both small at low speed. At high speed, the amplitude of vector V_{f-hs} in Fig.1 (d) is smaller than that in Fig.1 (c). Thus the fault current of ASP-PMSM is smaller than that of CSP-PMSM. It can also be seen from Fig.1 (c) and (d) that the higher the fault resistance, the higher the speed to obtain the minimum short circuit current, that is, for an incipient fault, the ASP-PMSM can obtain lower fault current than CSP-PMSM at relative high operating speed. III. Simulation Analysis The fault current of ASP-PMSM and CSP-PMSM at different contact resistance and operating speed combinations is calculated by FEA and shown in Fig.1 (e) and (f). It can be seen that when the fault resistance is relatively large, the fault current of ASP-PMSM is small in the full speed range. This point is very benefit in limiting the further deterioration of fault and expanding the span life of the faulty motor. The simulation results are consistent with the theoretical analysis results in section II. The variation of fault current with the number of shorted turns at different contact resistance conditions is also investigated. The losses of two types of motors under healthy and different fault conditions are compared. It is verified that the copper loss of ASP-PMSM at different ITSC fault conditions is much lower than that of CSP-PMSM, which proved that the ASP-PMSM itself can mitigating the fault severity of ITSC fault compared to that of CSP-PMSM. IV. Experimental Test A 6.3kW prototype is manufactured, and the test platform is shown in Fig.2(a). The variation of one-turn short-circuit current with the operating speed at different contact resistance conditions is tested, and shown in Fig.2(b) and (c), which proved the accuracy of the above analysis. V. Conclusion 1) For an incipient fault, the ASP-PMSM can achieve small

fault current at much wider speed range than that of CSP-PMSM, and the ASP-PMSM investigated in this paper has realized low fault current within full speed range. This is very useful to limit the further deterioration of fault and expanding the span life of the faulty motor. 2) With the same number of shorted turns, the loss of ASP-PMSM are much smaller than that of CSP-PMSM, it is proved that the ASP-PMSM itself can mitigating the fault severity of ITSC compared to that of CSP-PMSM. 3) The experimental test verified the accuracy of the theoretical analysis and the FEA.

[1] N. Leboeuf, T. Boileau, B. Nahid-Mobarakeh, F. Meibody-Tabar, and G. Clerc, "Real-time detection of inter-turn faults in PM drives using back EMF estimation and residual analysis," IEEE Trans. Industry Applications, vol. 47, no. 6, pp. 2402-2412, 2011. [2] Feng Chai, Lina Geng, Yulong Pei, "A novel fault tolerant motor with integral slot non-overlapping concentrated Winding," IEEE Access, vol.7, PP. 99462 – 99469, Jul. 2019.

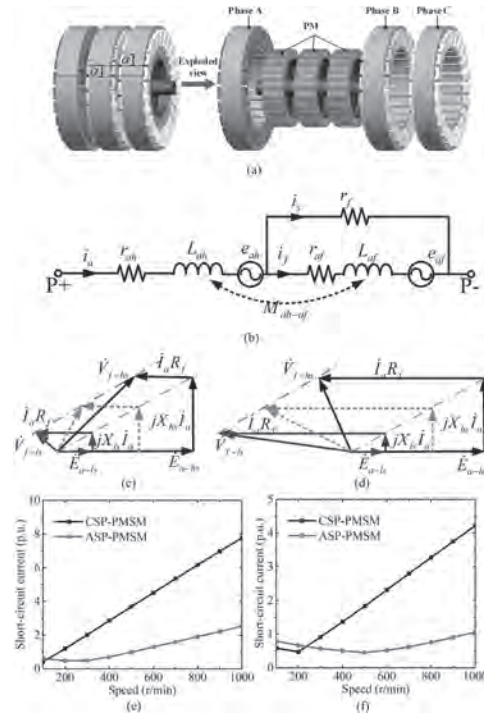


Fig. 1 (a) Motor topology (b) Electrical circuit model. Vector diagram of (c) CSP-PMSM and (d) ASP-PMSM at different speed. The one-turn fault current varies with speed when r_f is (e) 5mΩ and (f) 10mΩ.

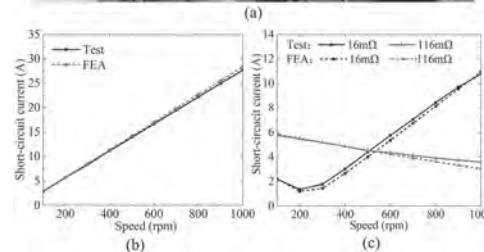
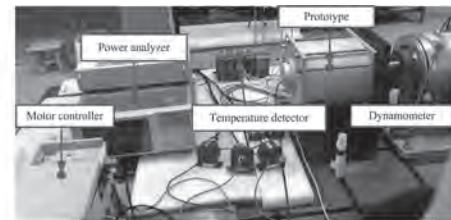


Fig.2 (a) The test platform. The one-turn ITSC fault current varies with speed at (b) zero contact resistance condition and (b) non-zero contact resistance condition.

BV-02. A Hybrid Excitation Axial Flux Permanent Magnet Generator for Direct Drive Wave Energy Conversion.

Y. Li¹, L. Huang¹, M. Chen¹, P. Tan¹, Y. Liu¹ and M. Hu¹

1. Department of Electrical Engineering, Southeast University, Nanjing, China

I. Introduction Direct drive wave energy conversion (DDWEC) device using permanent magnet linear generator (PMLG) eliminates the inefficient transmission device and achieves simpler mechanical structure. However, due to the direct connection between buoy and translator, the low-speed linear reciprocating wave motion will be directly transmitted to the translator. So PMLG needs to adopt a low-speed design [1]. It is necessary to increase the number of pole pairs of the generator or use power electronic devices to increase the output voltage and power density. But this will increase the loss and reduce the efficiency of the whole system. The linear-rotating axial flux permanent magnet generator (AFPMG) is proposed to improve the output voltage and power density of the DDWEC. By employing the magnet screw (MS) and AFPMG, it combines the merits of MS and AFPMG and realizes the soft connection between the buoy and generator rotor. The nut and screw of MS are directly connected to the buoy and generator rotor, respectively. When approximately 0.5m/s reciprocating wave motion comes, the movement can be accelerated by MS and magnetic field modulation and finally the speed of the rotor will reach 1200 rpm/min, which can improve the output voltage and power density consequently. While this structure brings advantages, at the same time, due to the use of a large number of rare-earth PMs, it will increase power generation costs and reduce practical competitiveness. Therefore, a hybrid excitation axial flux permanent magnet generator (HE-AFPMG) is proposed to reduce the amount of PMs and become a candidate for DDWEC. Not only that, because the wave conditions (typically 3-20s) are constantly changing, the corresponding wave excitation forces of the same buoy vary widely. By using hybrid excitation, the excitation current can easily adjusted to regulate the magnetic field of the air gap [2], which make generator suitable for different working conditions in wave energy conversion. II. Machine Configuration and Operation Principle In the proposed topology, as shown in Fig. 1, the armature winding and field winding are placed in upper stator and lower stator of AFPMG, respectively. PMs are placed at the slots of the upper stator and work as parallel excitation source. There is no risk of irreversible demagnetization in PMs with this configuration, meanwhile, it can reduce flux linkage and back electromotive force (EMF) harmonics. The operation principle of AFPMG based on modulation effect is similar to a magnetic gear and a magnetically geared machine when the rotor is consists of modulation teeth. The magnetic field will be accelerated due to the magnetic gear effect, when the excitation magnetic field passes through the air gap and modulation teeth. Eventually, potentials are induced in the armature windings. The number of pole pairs and speed of armature magnetic field are expressed as follow: $p_{av} = |p_{fv} \pm p_{mt}|$, $\Omega_{av} = (p_{fv}\Omega_{fv} \pm p_{mt}\Omega_{mt}) / (p_{fv} \pm p_{mt})$ where p_{av} , Ω_{av} , p_{fv} , Ω_{fv} are the number of pole pairs and rotational speed of magnetic field in armature winding and field winding, respectively. p_{mt} and Ω_{mt} are the number and rotational speed of modulation teeth, respectively. In proposed AFPMG, the upper stator pole number $N_{us} = 12$, hence the number of pole pairs of magnetic field in armature winding $p_{av} = 2$ or $p_{av} = 1$ when the number of modulation teeth satisfies $p_{mt} = N_{us} \pm 2$ or $p_{mt} = N_{us} \pm 1$. Fig.1 III. Results Fig.2 The output power versus excitation current in proposed HE-AFPMG with armature winding having different load current is shown in Fig.2. IV. Conclusion The application of hybrid excitation in AFPMG used in DDWEC can eliminate risk of irreversible demagnetization in PMs and reduce flux linkage and back electromotive force harmonics. Meanwhile, it can adjust the air gap magnetic field to suit different sea conditions.

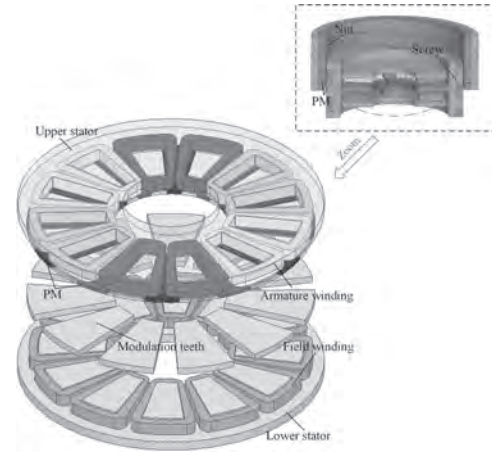


Fig. 1

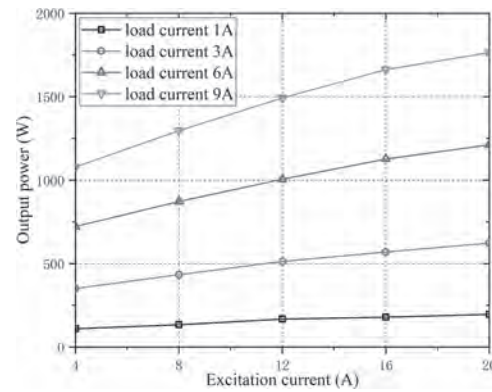


Fig. 2

[1] W. Li, K. T. Chau and J. Z. Jiang, "Application of Linear Magnetic Gears for Pseudo-Direct-Drive Oceanic Wave Energy Harvesting," in *IEEE Transactions on Magnetics*, vol. 47, no. 10, pp. 2624-2627, Oct. 2011. [2] C. Ye, Y. Du, J. Yang, X. Liang, F. Xiong and W. Xu, "Research of an Axial Flux Stator Partition Hybrid Excitation Brushless Synchronous Generator," in *IEEE Transactions on Magnetics*, vol. 54, no. 11, pp. 1-4, Nov. 2018.

BV-03. Axial-Flux Permanent Magnet Machine Application Research With Strap-Wire Technique and Difference Analysis of Rotor Eddy-Current Loss Between Simulation and Test.

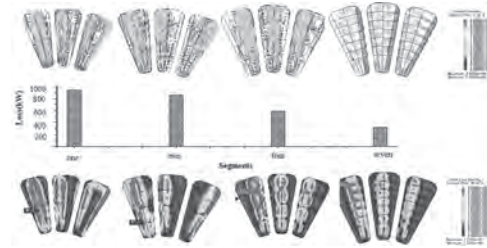
R. Pei¹ and H. Zhang¹

1. Electrical Engineering, Shenyang University of Technology, Shenyang, China

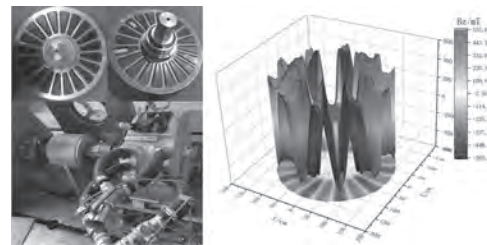
Due to the widespread concern of the greenhouse effect, people's requirements for energy saving and emission reduction of drive systems are becoming higher. The electrification of drive systems seems to be an irresistible trend. As the core of electric drive system, electric motor has been widely mentioned. The Permanent Magnet Synchronous Machine (PMSM) proved to be better in energy conversion which efficiency is higher than conventional Induction Machines [1-2]. In the application field of commercial logistics vehicles, the trend of electrification is increasing and the space occupied by the electric drive system is limited. As a result, a higher demand for density is required. Conventional electric motors applied in this platform are mainly Radial Flux Permanent Machines (RFPM). In particular, the application of the logistics EV traction motor requires low maximum speed but high output torque. The conventional design developed on this platform is a PMSM using traditional round copper wire as winding part and the rotor adopts "delta" shape topology. The "flux barrier" structure was added to increase the reluctance torque ratio, which was aimed to increase torque density of the whole system. However, due to the further reduction in already limited space, it will be difficult to meet the requirements using RFPM. Since the topological structure of the disc motor was proposed in last 70s [3-4], many researches have been done, especially on AFPM's topological structures. Among them, some classic structures are: the TORUS (double-rotor-one-stator) structure, whose stator part is composed of copper winding and iron core, and the rotor part is composed of the surface mounted PMs and back iron; the AFIR (double-stator-one-rotor) structure, whose stator part is the same, but rotor part is composed only of the fan-shaped PMs [5-6]. As there is no back iron structure in the rotor part for AFIR, its rotational inertia is quite low and resulting the starting torque is low [7-8]. This advantage attracts us because the size requirements are more stringent for our platform. Based on this consideration, the optimal structure of the traction motor is selected as the AFIR structure with two stators and one rotor. In AFPM design, the rotor Permanent Magnets (PM) are directly in contact with the air gap, and the complex magnetic field has rich harmonic content, resulting in a higher proportion of eddy current losses in rotor PMs. Which can cause higher temperature rise in the rotor of an AFIR structure AFPM. Reducing PM eddy current loss is significantly important to the PM topology design, rotor temperature rise and overall performance. The AFPM in this paper adopts an AFIR 24s/20p design. The rotor PMs are segmented with identical radial distance, in order to reduce the length of the eddy current path in each PM and reduce the eddy-current loss, thereby reducing the risk of PM demagnetization caused by high temperature. In this paper the main body is divided in three parts, in part II, the design problems will be presented, which mainly includes: 1) Stator and rotor design, 2) The influence of the rotor support material on the motor, 3) The magnetic field measurement on the surface of the segmented magnet, 4) difference analysis between simulation and test. Part III will mainly introduce the problems encountered and the corresponding solutions during the manufacturing process, which includes: 1) assembly problem due to strong magnetic force, 2) air-gap width balance before and after test and in part IV we conclude. This application research is aimed to have a positive guiding significance for the AFPM production. We hope that our description of prototype developing process and the solutions we took to deal with the manufacturing problems can have a positive influence for future research.

[1] Edward, Iman, Said Wahsh, and M. A. Badr. "Analysis of PMSM drives for electric vehicles." Proceedings of the 37th SICE Annual Conference. International Session Papers. IEEE, 1998. [2] Situ, Lixin. "Electric vehicle development: the past, present & future." 2009 3rd International Conference on Power Electronics Systems and Applications (PESA). IEEE, 2009. [3] P. Campbell, "Principles of a permanent-magnet axial-field d.c. machine," in *Proceedings of the Institution of Electrical Engineers*, vol. 121, no. 12, pp. 1489-1494, December 1974. [4] P. Campbell, "The magnetic circuit of an

axial-field DC electrical machine", *IEEE Transactions on Magnetics*, Vol. Mag11, No.5, Sept. 1975, pp.1541-1543. [5] E. Spooner and B. J. Chalmers, "TORUS, a slotless, toroidal stator, permanent magnet generator", *Proc. IEE, Part-B*, Vol.139, No. 6, Nov. 1992, pp. 497-506. [6] F. Caricchi, F. Crescimbeni and E. Santini, "Basic principles and design criteria of axial-flux PM machines having counterrotating rotors", *IEEE Transactions on Industry Applications*, Vol.31, No. 5, Sept/Oct 1995, pp.1062-1068. [7] Aydin, M, Huang, S and Lipo, T.A. (2004). Axial flux permanent magnet disc machines: A review. *Conf. Record of SPEEDAM*. [8] Akatsu, K. and Wakui, S., "A comparison between axial and radial flux PM motor by optimum design method from the required output NT characteristics", in *international journal for computation and mathematics in electrical and electronic engineering*, Vol. 25 No. 2, pp. 496-509.



Impact of PM Segment Number on Rotor PM Eddy Current Loss



Rotor magnetic flux density distribution

BV-04. Electromagnetic Analysis and Efficiency Improvement of Axial-Flux Permanent Magnet Motor With Yokeless Stator by Using Grain-Oriented Silicon Steel Material.

J. Hou¹, W. Geng¹, Q. Li¹ and Z. Zhang²

1. College of Automation Engineering, Nanjing University of Science and Technology, Nanjing, China; 2. College of Automation Engineering, Nanjing University of Aeronautics and Astronautics, Nanjing, China

I. INTRODUCTION With the increasingly serious problems of energy shortage and environmental pollution, the development of electric vehicles has become the focus of the world. Electric motors and their drive systems are one of the largest electrical energy consumptions, consuming more than twice as much as lighting, the next largest end-use, accounting for about between 43% and 46% of all global electricity consumption [1]. Therefore, it is necessary to further improve the overall efficiency of electric motors, especially for New European Driving Cycle (NEDC). More and more scholars improve motor efficiency by changing motor materials [2-6]. Grain-Oriented electrical steel materials (GO materials) are mainly used in the core manufacturing of transformers, reactors and large generators. In recent years, GO materials are gradually introduced into motors. Compared with the non-oriented electrical steel materials (NO materials) commonly used in motors, the GO material has the advantages of lower core loss characteristic and higher saturation magnetic flux density. However, the GO material has different permeability and core loss in different directions, so it is difficult to design an axial-flux permanent magnet (AFPM) motor with yoke to take advantage of the GO material. The main flux of the AFPM motor with yokeless stator studied in this paper only passes through the stator in one direction, eliminating the disadvantages of AFPM motor with stator yoke. This paper discusses the application of GO materials in AFPM motors with yokeless stator, compares the basic characteristics of the GO material and NO material used in AFPM motor, analyses the difference between two axial-flux topologies in the use of materials and verifies through finite-element analysis (FEA). **II. DESCRIPTION OF THE AFPM MACHINE AND GRAIN-ORIENTED ELECTRICAL STEEL SHEET** The GO material has electromagnetic anisotropy: the electromagnetic properties in different directions are different, as is shown in Fig.1(a). In the easy magnetization direction of GO material, it can be seen from Fig.1(b-e) that it is easier to magnetize than NO material, with higher saturation point and lower core loss. However, in the direction of hard magnetization, the GO material is harder to magnetize and has higher core loss. So reasonable use of the easy magnetization direction can provide better torque output ability and less core loss for motors. The explosive view of the AFPM machine investigated in the paper with 48-slot /8-pole is shown in Fig.2, which belongs to the axial-flux topology with a single-stator double-rotor. Main parameters of the motor are shown in Tab. I. Due to the arrangement of the PMs, the main magnetic flux paths only pass through the stator in one direction, which can be set as easy magnetization direction, without passing through the stator yoke tangentially, as shown in Fig.3. **III. FEA AND PERFORMANCE** Due to AFPM machine's particular 3-D configuration, 3-D FEA is carried out. Fig.4 shows the stator flux distributions and flux density under no load, showing that the main flux paths go through the easy magnetization direction. It should be noted that even if the GO material is easier to magnetize, the air-gap flux density and back-EMF are not greatly improved under no-load condition due to the large air-gap and PM reluctance. With the increase of armature current, the advantages of GO material are gradually manifested. The torque output capacity of the AFPM machine with GO material and NO material obtained by 3-D FEA is shown in Fig.5, reflecting that the motor with GO material has better torque output capacity than that of NO material. Taking $I_{ms}=530A$ as an example, the torque of GO material is about 15 N.m higher than that of NO material, increased by about 3%. Fig.6 shows the efficiency map of the motor with different materials. The GO material not only improves the torque, but also improves the efficiency. Tab. II compares torque, core loss and efficiency of motors with yokeless stator using different materials under typical working conditions. Similarly, this paper also tried the application of GO material in AFPM machine with stator yoke. As is shown in Fig.7, since a tangential magnetic circuit passes the stator yoke, it is hard to avoid the different magnetization direction when using the easy magnetization direction. Tab. III compares the torque and efficiency of the AFPM machine with yoke

under several working conditions. With the stator using GO material, the torque output capacity is lower than that with NO material, and core loss is also increased. Hence, it is not recommended to use GO material in this AFPM topology. **IV. CONCLUSION** By introducing GO material to yokeless stator, an attempt is made in this paper to use its electromagnetic anisotropy to make the main magnetic flux paths of the motor passing through its easy magnetization direction, without crossing hard magnetization direction, so as to improve torque performance and reduce core loss as well as efficiency. Base on the 3-D FEA model of 48-slot /8-pole AFPM machine, the field distributions, flux density, torque output capacity and efficiency map have been compared between GO and NO material. Benefitting from GO material and yokeless structure, the torque output capacity of AFPM machine is increased by about 5%, the core loss is also reduced by 10%, and the efficiency is improved by 2%. Furthermore, the inapplicability of GO material in the AFPM with stator yoke is also discussed and verified in this paper.

[1] P. Waide and C. U. Brunner, "Energy-efficiency policy opportunities for electric motor-driven systems," *International Energy Agency (IEA)*, 2011. [2] W. Geng, Z. Zhang and Q. Li, "High Torque Density Fractional-Slot Concentrated-Winding Axial-Flux Permanent-Magnet Machine With Modular SMC Stator," *IEEE Transactions on Industry Applications*, vol. 56, no. 4, pp. 3691-3699, July-Aug. 2020. [3] D. Kowal, P. Sergeant, L. Dupre and A. Van den Bossche, "Comparison of Nonoriented and Grain-Oriented Material in an Axial Flux Permanent-Magnet Machine," *IEEE Transactions on Magnetics*, vol. 46, no. 2, pp. 279-285, Feb. 2010. [4] J. Ma et al., "Optimal Design of an Axial-Flux Switched Reluctance Motor With Grain-Oriented Electrical Steel," *IEEE Transactions on Industry Applications*, vol. 53, no. 6, pp. 5327-5337, Nov.-Dec. 2017. [5] Y. Tsuchiya and K. Akatsu, "A Study of the Switched Reluctance Motor using Grain-Oriented Electrical Steel Sheets," 2020 *IEEE Energy Conversion Congress and Exposition (ECCE)*, Detroit, MI, USA, 2020, pp. 3623-3628. [6] S. Javadi, M. Mirsalim and J. Sabzivand, "3-D FEM analysis of a novel structure for axial-flux homopolar generators using a grain-oriented silicon steel stator core," 2008 *International Conference on Electrical Machines and Systems*, Wuhan, 2008, pp. 3640-3643.

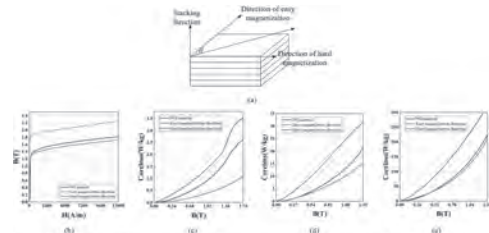


Fig. 1. Description and characteristics of GO material: (a) Magnetization characteristics; (b) B-H curve; (c) B-H curve (NO); (d) P core loss (GO); (e) P core loss (NO).

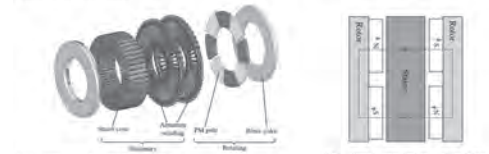


Fig. 2. Exploded view of the AFPM machine.

Fig. 3. Main magnetic flux paths of the AFPM motor with yokeless stator.

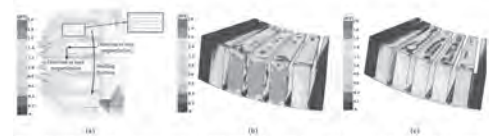


Fig. 4. Field distributions and flux density under no load: (a) Field distribution; (b) Flux density of GO material; (c) Flux density of NO material.

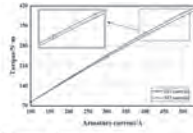


TABLE I
MAIN PARAMETERS OF AFPM MOTOR WITH WORKING STATUS

Parameters	Value
Stator Pole-pair diameter	200 mm
Stator Pole-pair diameter	150 mm
Pole-pair	6-33
Armature length	60 mm
Armature length	1.5 mm
PM thickness	8 mm
PM material	34C20
DC voltage	550 V
Rated current	250 A
Peak current	330 A

Fig. 2. Comparison of torque output capacity.

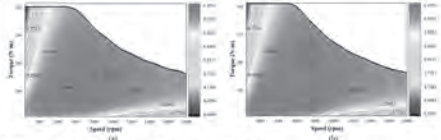


Fig. 6. Efficiency map with different stator materials. (a) M0 material, (b) M90 material.

TABLE II
COMPARISON OF TORQUE, CORE LOSS AND EFFICIENCY OF MOTORS WITH VARIOUS SLA FOR USING DIFFERENT MATERIALS UNDER TYPICAL WORKING CONDITIONS

Speed (rpm)	Current (A)	Angle (deg)	M0 material			M90 material		
			Torque (N.m)	Core loss (W)	Efficiency (%)	Torque (N.m)	Core loss (W)	Efficiency (%)
4500	500	45	179.36	11.7	0.87990	177.21	7.18	0.88104
7500	600	65	226.99	30.1	0.947211	241.88	99.6	0.961177
13500	350	75	173.33	1.763	0.981271	171.53	7450	0.977003
18000	350	90	148.87	2.783	0.971667	141.17	7872	0.97253



Fig. 7. Another AFPM motor topology with star-type. (a) Main magnetic flux paths of the AFPM machine. (b) Field distribution.

TABLE III
COMPARISON OF TORQUE, CORE LOSS AND EFFICIENCY OF MOTORS WITH VARIOUS SLA FOR USING DIFFERENT MATERIALS UNDER TYPICAL WORKING CONDITIONS

Speed (rpm)	Current (A)	Angle (deg)	M0 material			M90 material		
			Torque (N.m)	Core loss (W)	Efficiency (%)	Torque (N.m)	Core loss (W)	Efficiency (%)
4500	500	45	179.10	9.68	0.91144	180.26	1.01	0.92994
7500	600	65	217.17	13.26	0.951626	213.08	2627	0.951168
13500	350	75	148.53	2.531	0.959391	146.52	2.026	0.955827
18000	350	90	145.10	3.039	0.951421	144.77	2913	0.95431

BV-05. Quantitative Comparison of Magnetic-Differential Double-Rotor Stator-Permanent-Magnet Motors for Electric Vehicles.

T. Yang¹, K. Chau¹, T. Ching², L. Cao¹ and H. Wang¹

1. *Electrical & Electronic Engineering, The University of Hong Kong, Hong Kong*; 2. *Faculty of Science and Technology, University of Macau, Taipa, Macao*

INTRODUCTION The world is witnessing growing popularity for electric vehicles (EVs), which is believed as a mitigation to climate change [1]. With the prevailing of EVs, electric machine, especially permanent magnet (PM) machine, has gained significant achievements recently [2]. Compared with the rotor-PM machine that locates PM materials in the rotor, the stator-PM machine exhibits the merits of better PM cooling and rigidity for its stator-fixed PM configuration [3]. As a core part of the EV propulsion system, the vehicle differential system is updated frequently over time. Traditional mechanical differential (MechD) system shows overall low efficiency for its bulky and lossy differential gear [4]. By driving and providing differential action directly to the wheels, the electronic differential (ElecD) system is then proposed to obtain higher efficiency in EVs [5]. Nevertheless, due to the electronic system, serious errors might occur because of system faults, e.g. motor or feedback faults. To maintain high efficiency and compactness as well as to achieve high reliability and robustness, the magnetic differential (MagD) system is proposed in [5]. By simply integrating a set of magnetic coupling (MC) windings in an axial-field double-rotor (AF-DR) flux switching PM (FSPM) motor, the MagD system meets the needs of high reliability, efficiency, and power density. However, in general, there are three types of stator-PM motors, i.e. doubly salient PM (DSPM) motor, flux reversal PM (FRPM) motor, and FSPM motor [6], and each of them possesses unique advantages over their counterparts. The analysis of the other two types of stator-PM motors from the perspective of MagD system is absent in the literature. Therefore, the purpose of this paper is to quantitatively analyze and compare the performance of three types of magnetic-differential AF-DR stator-PM motors, and a prototype of the motor with overall better performance is fabricated to verify the analysis. **METHODOLOGY** To illustrate the operation principles of three motors, motor topologies plus magnetic flux distributions with different rotor positions are depicted in Fig. 1. Each motor takes on the classical stator/rotor-pole number combination, namely 12 stator-slot and 8 rotor-pole (12 s/8 p) for DSPM motor, 12 s/10 p for FSPM motor, and 12 s/16 p for FRPM motor [6-8]. As is shown in Fig. 1, MC windings locate in the middle of the stator concerning the DSPM and FSPM motors cases, whereas they are split into two parts and placed on two ends of the stator in FRPM motor to avoid the short-circuit of the MC flux. When no cornering action is required, there is only PM flux in the motor, as its distribution is shown in Fig. 1; When the vehicle is in the curvilinear movement, the MC windings will be injected with DC current, MC flux thereafter is generated. As depicted in Fig. 1, on one side, the MC flux strengthens the overall flux, while on the other side the flux is weakened. Consequently, the torque produced from each side will be differentiated, leading to different speeds of two rotors. As a result of cornering, two rotors will be in unalignment positions. However, it can be found in Fig. 1 (b) that the MC flux can still regulate the flux correctly to create differential torque to rotors. The quantitative comparison is conducted by simulation using JMAG. All three motors are optimized in the same practice, aiming at providing reasonably large torque and low torque ripple under the same constraints, viz. outer diameter of 420 mm for both stator and rotor, 0.6 mm of air gap length, and 186.4 mm of stack length. The overall motor performance comparison is listed in Table I. For a fair comparison, all these motors adopt the same rotating speed of 900 r/min. It turns out that with the same 0.4 split ratio, FRPM motor has the smallest volume and also consumes the least PM materials over three optimized motors. FSPM motor shows a more sinusoidal waveform and larger no-load back electromotive force (EMF) amplitude than its two counterparts due to its exquisite structure, therefore FSPM motor adopts brushless (BL) AC control strategy whereas BLDC for the rest. It is seen that FSPM motor provides the largest torque while maintaining the lowest torque ripple and loss. FRPM motor shows the largest loss due to its highest operating frequency. Nevertheless, as for the torque per PM volume, FRPM motor excels 3.5 times and 2.5 times that of DSPM and FSPM motor, which is attractive to cost-sensitive cases. **CONCLUSION**

In this paper, quantitative analysis and comparison are made among three types of magnetic-differential AF-DR stator-PM motors for EVs based on finite element analysis. It can be seen that all three motors can function as the differential in MagD system, and within the given size, FSPM motor provides the largest torque while the lowest torque ripple and power loss, thus highest efficiency. However, FRPM motor is attention-worthy for the rather high production of torque per PM consumption. An FSPM motor for MagD system is manufactured to verify the analysis, which will be further elaborated in the full paper. Acknowledgment This work was supported by a grant (Project No. 17205518) from the Hong Kong Research Grants Council, Hong Kong Special Administrative Region, China.

[1] W. Liu, K. T. Chau and C. H. T. Lee, "A switched-capacitorless energy-encrypted transmitter for roadway-charging electric vehicles," *IEEE Trans. Magn.*, vol. 54, no. 11, pp. 1-6, Nov. 2018. [2] C. Liu, K. T. Chau and J. Z. Jiang, "Comparison of stator-permanent-magnet brushless machines," *IEEE Trans. Magn.*, vol. 44, no. 11, pp. 4405-4408, Nov. 2008. [3] B. Gaussens *et al.*, "Analytical armature reaction field prediction in field-excited flux-switching machines using an exact relative permeance function," *IEEE Trans. Magn.*, vol. 49, no. 1, pp. 628-641, Jan. 2013. [4] K. T. Chau, *Electric vehicle machines and drives: Design, analysis and application*, Hoboken, NJ, USA: Wiley, 2015. [5] L. Cao, K. T. Chau and C. H. T. Lee, "A double-rotor flux-switching permanent-magnet motor for electric vehicles with magnetic differential," *IEEE Trans. Ind. Electron.*, vol. 68, no. 2, pp. 1004-1015, Feb. 2021. [6] M. Cheng, W. Hua and J. Zhang, "Overview of stator-permanent magnet brushless machines," *IEEE Trans. Ind. Electron.*, vol. 58, no. 11, pp. 5087-5101, Nov. 2011. [7] H. Fan, K. T. Chau and C. Liu, "Doubly salient dual-PM linear machines for regenerative shock absorbers," *IEEE Trans. Magn.*, vol. 53, no. 11, pp. 1-5, Nov. 2017. [8] J. Yu, C. Liu and H. Zhao, "Design and optimization procedure of a mechanical-offset complementary-stator flux-reversal permanent-magnet machine," *IEEE Trans. Magn.*, vol. 55, no. 7, pp. 1-7, July 2019.



Fig. 1. Topologies and operation principles of AF-DR stator-PM motors with rotors under: (a) Aligned position: (i) DSPM motor. (ii) FRPM motor. (iii) FSPM motor. (b) Unaligned position: (i) DSPM motor. (ii) FRPM motor. (iii) FSPM motor

Characteristics	Motor types		
	DSPM	FRPM	FSPM
Volume (dm ³)	15.75	13.12	13.77
PM Volume (dm ³)	1.37	0.47	1.75
Back-EMF Amplitude (V)	150.2	165.5	298.7
EMF Range with MC Flux (One Side)	-24% ~ +13%	-24% ~ +13%	-64% ~ +10%
Total Torque (N·m)	526.6	628.2	950.1
Torque ripple	63.3%	18.2%	7.8%
Total Torque/Volume (N·m/dm ³)	33.43	47.88	69.00
Total Torque/PM Volume (N·m/dm ³)	384.4	1336.6	542.9
Torque Range with MC Flux (One Side)	-24% ~ +13%	-16% ~ +13%	-87% ~ +13%
Output Power (kW)	19.62	39.21	89.54
Loss (kW)	5.81	10.57	4.39
Efficiency	89.9%	84.9%	95.4%

Table I Motor performance

BV-06. A Novel Wound Field Switched Flux Machine With Zero-Sequence Field Current Excitation.

X. Zhang³, H. Yang^{1,2} and S. Niu²

1. Electrical Engineering, Southeast University, Nanjing, China; 2. Electrical Engineering, The Hong Kong Polytechnic University, Kowloon, Hong Kong; 3. Henzhen In Drive Ampere Co. Ltd., Shenzhen, China

I. INTRODUCTION Due to the absence of neither permanent magnets (PMs) nor windings on the rotor, stator wound-field synchronous (SWFS) machines [1]-[5] were presented for potential applications to domestic appliances and more-electric aircraft, and renewable energy, etc. SWFS machines have the advantages of the eliminations of brushes and slip rings, low cost, fault tolerance, simple as well as a robust double salient structure similar to switched reluctance machines (SRMs) [6], which are suitable for critical-safety applications. Besides, the demerits of high torque ripple, acoustic noise, and vibration in SRM are alleviated with the SWFS machines which can be fed by a standard three-phase full-bridge inverter. Nevertheless, the existence of additional DC windings makes SWFS machines suffer from restricted torque density and redundant DC power source. Thus, the variable flux reluctance machines (VFRMs) [5] [7] with integrated DC bias and AC current excitations were developed by using an open-winding winding configuration to offer DC excitations. However, the inherently unipolar coil flux linkage in VFRMs still results in a relatively low torque density. Therefore, this paper attempts to propose a novel wound field switched flux (WFSF) machine with a zero-sequence field current excitation. An open-winding circuit is employed to generate a zero-sequence current to offer DC excitation. Moreover, the SF working principle will be employed to improve the torque capability compared to the VFRM. In this paper, the machine topology, operating principle, and design considerations will be described, respectively. Then the major electromagnetic performance will be analyzed and compared with the conventional WFSF counterpart, which confirms the superiority of the proposed design. **II. MACHINE TOPOLOGIES AND OPERATING PRINCIPLE** Figs. 1 (a) and (b) show the WFSF machines with conventional separate and integrated DC and AC excitations. It demonstrates that the two machines are with identical stator/rotor doubly salient structure and single-layer overlapping winding layout. The main difference lies in the winding functions of the two sets of windings in the two WFSF machines. In the conventional WFSF machine [2]-[4], one set of winding serves as continuous DC excitation while another works as the armature winding. On the other hand, two sets of windings are both injected with integrated AC plus DC bias currents in the WFSF machine with zero-sequence field current excitation. As a result, more copper area is available for the armature windings in the proposed WFSF machine with integrated "AC+DC" current excitations. The control circuit is illustrated in Fig. 1(c), in which the open-winding-based dual three-phase inverter with a single voltage source is utilized [7], and the output terminals of two inverters are connected to both ends of the stator windings. This method is the utilization of the constant zero-sequence current acting as the field current, while two three-phase currents are controlled by two inverters. The operating principle of the proposed WFSF machine is shown in Fig. 1(d). For each group armature windings, such as A1 and B2, when A1 is injected with continuous DC current, and the sinusoidal flux linkage will be induced in B2, and vice versa. As a result, when an AC sinusoidal current with a DC bias is applied to both two coils A1 and B2, the effective electromagnetic energy conversion will be achieved similar to those conventional WFSF counterparts [2]-[4]. **III. ELECTROMAGNETIC PERFORMANCE AND COMPARISON** Fig. 2(a) shows the open-circuit coil and phase flux linkage waveforms, it can be the DC biases in two individual coils are canceled, and a bipolar and sinusoidal phase flux linkage can be obtained. Besides, the open-circuit phase back-EMF waveforms at 400 r/min are shown in Fig. 2(b). It can be observed that the back-EMF is symmetric and sinusoidal in the WSFC machine with zero-sequence field excitation, while asymmetric non-sinusoidal for the conventional case. This is mainly attributed to the fact that the dual three-phase winding arrangement in the proposed machine allows the even-order harmonic cancellation within one phase. Besides, the steady torque and torque versus current characteristics of the two machines are compared as shown in Figs. (c) and (d), respectively. It should be noted that the winding turns of the two machines are designed as the same for a fair comparison. As

a result, it demonstrates the WSFC machine with zero-sequence field excitation exhibits 68% higher magnitudes of steady torque, together with 30.4% lower torque ripple than the conventional case. Meanwhile, it demonstrates that the average torques of the proposed machine exceed that of the conventional counterpart regardless of the armature current excitations. Thus, better electromagnetic performance can be obtained with the proposed design with zero sequence field excitation. The detailed characteristics analysis, comparison results, and experimental verification will be presented in the full paper.

[1] Z. Q. Zhu, Y. J. Zhou, J. T. Chen and J. E. Green, "Investigation of nonoverlapping stator wound-field synchronous machines." *IEEE Trans. Energy Convers.*, vol. 30 no. 4, pp. 1420-1427, May. 2015. [2] H. Pollock, C. Pollock, R. T. Walter, and B. V. Gorti, "Low cost, high power density, flux switching machines, and drives for power tools," in *Conf. Rec. 38th IEEE IAS Annu. Meeting*, Oct. 2003, vol. 3, pp. 1451-1457. [3] Y. Tang, J. J. H. Paulides, T. E. Motoasca, and E. A. Lomonova, "Flux switching machine with DC excitation," *IEEE Trans. Magn.*, vol. 48, no. 11, pp. 3583-3585, Nov. 2012. [4] B. Gaussens, E. Hoang, O. Barriere, J. Saint-Michel, and M. Gabsi, "Analytical approach for air-gap modeling of field-excited flux-switching machine: No-load operation," *IEEE Trans. Magn.*, vol. 48, no. 9, pp. 2505-2517, Sep. 2012. [5] X. Liu and Z. Q. Zhu, "Electromagnetic performance of novel variable flux reluctance machines with dc-field coil in stator," *IEEE Trans. Magn.*, vol. 49, no. 6, pp. 3020-3028, Jun. 2013. [6] K. Vijayakumar, R. Karthikeyan, S. Paramasivam, R. Arumugam, and K. N. Srinivas, "Switched reluctance motor modeling, design, simulation, and analysis: a comprehensive review," *IEEE Trans. Magn.*, vol. 44, no. 12, pp. 4605-4617, Dec. 2008. [7] Z. Q. Zhu, B. Lee, and X. Liu, "Integrated field and armature current control strategy for variable flux reluctance machine using open winding," *IEEE Trans. Ind. Appl.*, vol. 52, no. 2, pp. 1519-1529, Mar./Apr. 2016.

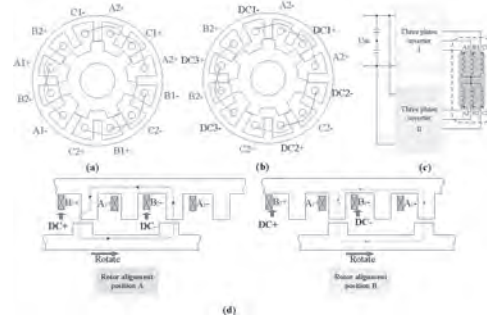


Fig. 1. Topologies of the WFSF machines (a) with zero-sequence field current excitation and (b) conventional separate AC and DC windings. (c) Control circuit. (d) Operating principle.

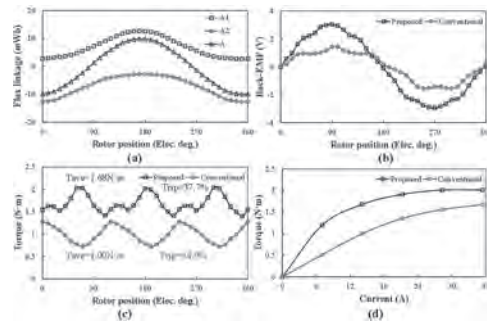


Fig. 2. Electromagnetic characteristics comparison. (a) Flux linkages in the proposed machine. (b) Back-EMFs. (c) Steady-state torque. (d). Torque versus current characteristics.

BV-07. Prediction of Power Generation Performance of Wound Rotor Synchronous Generator Using Nonlinear Magnetic Equivalent Circuit Method.

D. Kwon¹, C. Kim¹, K. Shin² and J. Choi¹

1. Chungnam National University, Daejeon, The Republic of Korea;

2. Chonnam National University, Gwangju, The Republic of Korea

Wound rotor synchronous machines are widely used because of their advantages, such as simple control, cost efficiency, and stable operation [1]. Because of these advantages, the wound rotor synchronous generator (WRSG) is used in large factories, aircraft, ships, and hydroelectric power generation that require a large power supply [2]. The WRSG does not have a rare earth magnet, and it forms a magnetic field through the rotor winding, as shown in Fig. 1(a). A magnetic field is formed by applying current to the rotor windings through an exciter, and the magnetic flux density can be controlled using the exciter to increase the power density. The core of many electrical machines is made of electrical steel with nonlinear characteristics, and the magnetic flux density must be adjusted to a level where the core is unsaturated to satisfy the user's desired output power, efficiency, and voltage. Therefore, it is necessary to evaluate the electromagnetic characteristics through electromagnetic analysis during the initial design. Finite element analysis (FEA) software is commercially available because it can obtain accurate analysis results that reflect nonlinearity. However, FEA consumes significant analysis time in the initial design, in which the design parameters change frequently [3]. Therefore, in this study, we propose a nonlinear magnetic equivalent circuit (MEC) to predict the electromagnetic and power generation characteristics of the WRSG. The magnetic equivalent area was divided according to the magnetic path of the WRSM (Fig. 1(b)). The paths through which the magnetic flux passes are divided into stator, rotor, air-gap, and interpolar regions. The magnetic flux inside the circuit could be calculated using the magnetomotive force(MMF) and reluctance, and the flux density in air gap could be calculated using the magnetic flux. Fig. 2(a) shows a comparison of the air gap flux density derived through the MEC and FEA when a field current is applied. The air flux density derived for the MEC represented the flux density waveform when the rotor position rotated, which could be used to derive the stator flux linkage waveform according to the rotor position. The derived flux linkage induced a back electromotive force (EMF) at no load (Fig. 2(b)). In the initial position, the rotor was positioned such that the flux linkage to the windings of one phase was maximized, and the back EMF through the flux that varied according to the rotation of one slot pitch was derived. The back EMF was influenced by the MMF of the rotor winding, and beyond the linearly increasing region, it became saturated because of the nonlinearity of the core material. The back EMF derived from the nonlinear MEC increased linearly and then nonlinearly, owing to saturation beyond a certain field current (Fig. 2(c)). The back EMF obtained using the nonlinear MEC was compared with those obtained through FEA and experimental measurements; the comparison validates the nonlinear MEC proposed in this study. It is necessary to determine the values of the back EMF, inductance, and phase resistance, which are equivalent circuit parameters, to predict the power generation characteristics of a WRSG. A MEC based on the rotor position must be constructed to reflect the inductance that varies with the rotor position, owing to the salient structure of the WRSG. Fig. 2(d) shows the prediction results of power generation characteristics using the inductance derived through the MEC, back EMF, and phase resistance. The FEA results indicated the power generation characteristics in the low-voltage regulation rate region, and the MEC results were in good agreement with the FEA results. Even when the rotational speed of the WRSG changed, the MEC results were in good agreement with the FEA results. By predicting power generation characteristics, the speed and power required by the designer can be predicted, which is useful in the initial design. The nonlinear MEC and analysis results of the WRSG will be presented in further detail in the main paper.

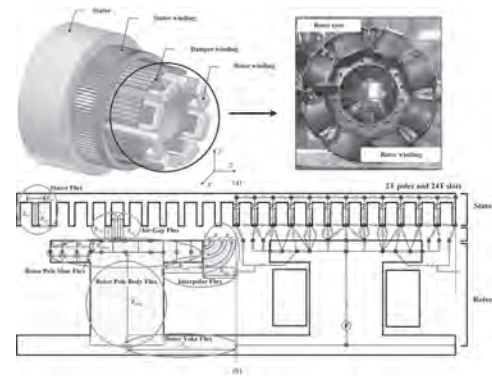


Fig 1. (a) WRSG analysis model and rotor core experimental model; (b) Construction of nonlinear MEC

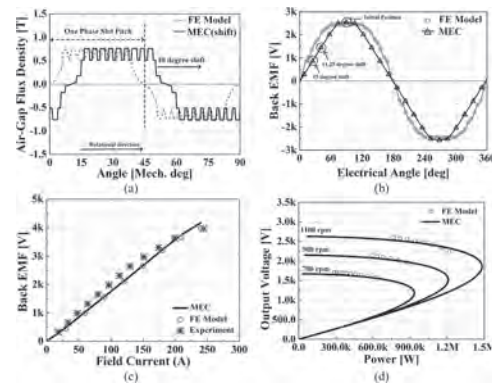


Fig 2. Comparison of electromagnetic characteristics obtained using the FEA, MEC, and experimental methods: (a) Comparison of air-gap flux density obtained using FEA and MEC methods; (b) Waveform of back EMF at rated speed of 900 rpm; (c) Variation of back EMF with field current; (d) Power-voltage curve

[1] S. Nuzzo, M. Degano, M. Galea, et al, *IEEE Trans. Ind. Electron.*, vol. 64, no. 3, pp. 1958–1970, Mar. 2017. [2] A. Griffio, D. Drury, T. Sawata, et al, *IEEE Trans. Ind. Electron.*, vol. 59, no. 9, pp. 3579–3587, Sep. 2012. [3] H.W. derbas, J.M. Williams, A.C. Koenig, et al, *IEEE Trans. Energy Convers.*, vol. 24, no. 2, pp. 388–396, Jun. 2009.

BV-08. Research on Optimal Design of Commutation Performance of Starter-Generator Used in Aero-Engine.

R. Sun¹, H. Peng¹, G. Huang¹, D. Shi¹ and L. Zhuo^{1,2}

1. National Engineering Research Center for Small and Special Precision Motors, Guizhou Aerospace Linquan Motor Co., Ltd, Guiyang, China;

2. Department of Electrical Engineering, Harbin Institute of Technology, Harbin, China

Abstract: Compared with the conventional motors used on the ground, the DC starter-generators (DCSGs) for aero-engines have higher electrical, thermal, magnetic and mechanical loads. Excessive electrical loads will increase the armature response of the (DCSGs) and worsen the commutation, thus shortening the lifetime and reducing the reliability of the (DCSGs). In order to improve the lifetime and reliability of the (DCSGs), this paper studied the effects of commutator structure, compensation windings, commutating poles and brush sizes on commutation effect of DCSGs based theory analysis combined with numerical analysis. Then effective measures to improve the commutation performance of this type of DCSGs are proposed, and the commutation spark observation test of a certain type of DCSGs verifies the effectiveness of the optimization design measures proposed in this paper. **Index Terms :** DC starter-generators (DCSGs); Brush; Commutation; Optimal design. I. Introduction The DC starter-generators (DCSGs) used in aero-engine is installed on the engine accessory box. When the aero-engine starts, it acts as a starter motor to drive the engine to ignite. After the engine ignites, it acts as a generator to supply power to the aircraft network. Due to the special application environment of the DCSG, it has the characteristics of low voltage and high current compared with the motor used on the ground. The commutation process is extremely bad, and it may produce larger commutation sparks or even ring fire, shortening the lifetime of the brush and reducing the operational reliability of DCSGs [1][2][3][4]. This paper optimizes the design of parameters such as commutator structure, commutating pole winding and brush size, and studies the influence of parameter changes on the commutation performance of DCSGs under the conditions of low voltage and high current, and discusses the effectiveness of improving the commutation performance of this type of DCSGs. The method provides a reference for commutation spark suppression in commutation of the same type of DCSGs. II. Large Current Commutation Modeling The electromotive force and current in the armature winding of the DCSG form an AC-DC voltage and current conversion through the cooperation of the commutator and the brush. This conversion process is called commutation. There is a complicated electromagnetic process in the commutation process, and reactance electromotive force is generated in the commutation element. By reducing the armature reaction and adjusting the brush width to reduce the reactive electromotive force, the commutation spark can be reduced and the commutation performance can be improved. III. Optimal Design Take a 9kW, 6250rpm~12000rpm DCSG as an example to study the influence of commutator structure selection, compensation winding, commutating pole and brush size on DCSG commutation performance. Finite element analysis model of the DCSG is shown in Fig.1. IV. Experimental Verification A start-up test was carried out on the simulated engine load characteristics of a 9kW a DCSG. The test bench is shown in Fig.2. No visible commutation sparks were observed in the test, which verified that the effectiveness of the commutation performance optimization design method proposed in this paper. V. Conclusion This paper studies the optimization design of DCSG to improve its commutation performance. Based theory analysis combined with numerical analysis, the influence of different commutator types, compensation windings, commutating pole windings and brush parameters on the commutation performance of the DCSG is analyzed. The prototype is tested for starting and generating performance. The experimental results verify the effectiveness of the optimized design method in improving the commutation performance, which can provide a reference for improving the commutation performance of the same type of DCSG, and is useful for improving the operating reliability and lifetime of the DCSGs.

[1] Takashi, Fukutsuka and Yasunobu. "Arc discharge during commutation process in DC motor immersed in ethanol: approach to contact state of brush on commutator segment", IEEJ Transactions on Power and Energy, Vol. 139, pp.293-301,2019. [2] H. Kim, H. Kim and W. Moon. "Design

optimization of brush permanent magnet DC motors using response surface method", Journal of Magnetics, vol. 25, pp. 355-362, 2020. [3] K. Sawa, M. Isato and T. Ueno. "Commutation characteristics and brush wear of DC motor at high rotation speed," 2017 IEEE Holm Conference on Electrical Contacts, pp. 176-181, 2017. [4] Z. Qingliang, Takahiro and Ueno. "The new commutation theory to the optimization technique of the large DC machine commutation design", IEEJ Transactions on Industry Applications, Vol. 131, pp. 654-666, 2011.

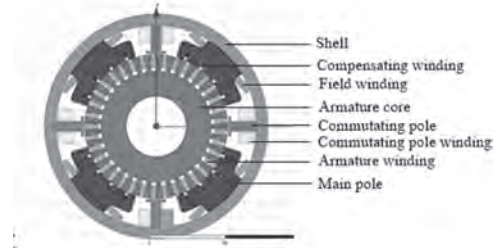


Fig.1. Finite element analysis model of the DCSG.

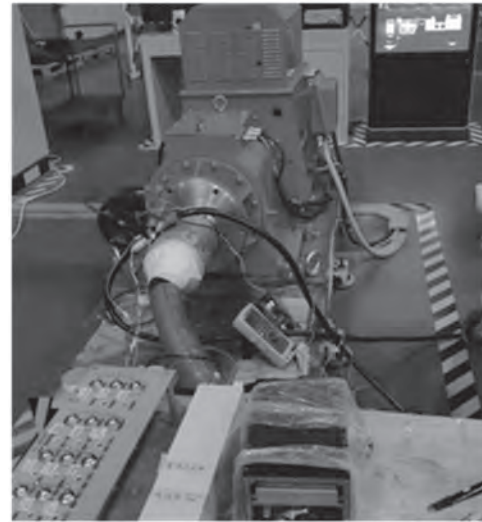


Fig.2. Test bench of DCSG.

BV-09. Comparative Study of MW Class Superconducting Machines According to Shielding and Electromagnetic Structures Based on Analytical Method.

K. Shin¹, T. Bang², H. Cho² and J. Choi²

1. Chonnam National University, Yeosu, The Republic of Korea; 2. Chonnam National University, Daejeon, The Republic of Korea

The concept of an electric aircraft and ship implies the development of an entirely new electric propulsion system. Among the key technologies of these systems, electric motors and generators are required for high performances such as high efficiency and high specific power. However, the conventional electric machine (such as a permanent magnet machine and induction machine) has a limitation in increasing the specific power due to the limitations of material technology. The application of superconducting (SC) technology with high power and low losses has emerged as a suitable alternative to next-generation technologies for electrical systems such as electric propulsion aircraft, ships, and more [1], [2]. These advantages make it possible to reduce the size and weight of the electric machine with MW class and achieve high energy efficiency in the electrical system. The structure of the SC machine with the high performance is a fully SC machine with a superconductor in both armature coils and field coils. This fully SC machine can utilize both high electrical loading and high magnetic loading. However, due to the feasibility and limitations of the design technology of a fully SC machine, it is reasonable to develop a design technology for a partially SC machine that applies a superconductor to field coils [3], [4]. It is relatively easy to manufacture and has technical accessibility and economic feasibility compared to a fully SC machine. Also, under the DC condition, the SC materials have almost no electromagnetic losses, but under the AC condition, the loss according to the current magnitude and harmonic order increases. Therefore, in this paper, a study on the electromagnetic design of the MW class SC machine with a superconductor in the field and copper in the armature was carried out. As shown in Fig. 1(a), the structure of a partially SC machine has a three-phase armature coil (copper) on the inner rotor and a SC field coil on the outer stator. To improve the power density, the weight of the system, and the shielding capability, the electromagnetic field analysis of SC machine with the core material of the rotor and the shielding of the field coil are very important in the design stage. For the electromagnetic design of the SC machine, the finite element (FE) method, which is an analysis method that considers the complex structure and non-linear material properties, and an analytical method that provides insights between machine performance and design variables and allows fast analysis is mainly used. The FE method requires a long time to analyze the electromagnetic field, and it is difficult to predict the relationship between design variables and performance. To overcome these problems, an analytical method considering shielding conditions and type of armature core as shown in Fig. 1(b) was proposed. The proposed analytical method is to calculate the analytical solution by deriving the governing equation and general solution for each domain based on Maxwell's equation and electromagnetic field theory and applying appropriate boundary conditions. In the proposed model, it is possible to analyze the electromagnetic performance according to the type of rotor core and shielding conditions by considering the permeability and current density conditions in regions II and VII. The magnetic permeability of the air core is the same as that of the vacuum, and the magnetic permeability of the electrical steel core can be calculated using the iteration method based on magnetic field analysis. In addition, the active shield and the passive shield were selected to have the same magnetic field at the outermost shell. To verify the validity of the electromagnetic analysis results of the proposed method, the two-dimensional FE model (ANSYS Electronics Desktop 2020 R3) according to the type of rotor core and shielding conditions is shown in Figs. 1(c) and 1(d). Based on the derived analytical solution, electromagnetic performances can be predicted as shown in Fig. 2. The magnetic field and the electromagnetic performance obtained using the analytical method were compared with those obtained using FE analysis, and the validity of the analytical method presented in this paper was verified through comparison of the analysis results. The FE model requires each analysis model according to the shielding condition and the type of core, but the proposed model can derive the analysis results for the current condition and material characteristics in one model. Using the proposed analytical method, it is possible

to derive an optimal design for MW class SC machine by comparing the weight, power density, and efficiency of the system under the same electromagnetic performance conditions. The analytical modeling, analysis results, performance rating, and discussion according to the core type and shielding conditions of SC machines will be presented in the full paper.

[1] K. S. Haran, T. O. Deppen, and L. Zheng, "Actively Shielded High-Field Air-Core Superconducting Machines," IEEE Trans. Appl. Supercond. vol. 26, no. 2, Mar. 2016, Art. no. 5202508. [2] Y. Terao, W. Kong, H. Ohsaki, H. Oyori, and N. Morioka, "Electromagnetic design of superconducting synchronous motors for electric aircraft propulsion," IEEE Trans. Appl. Supercond., vol. 28, no. 4, Jun. 2018, Art. no. 5208005. [3] P. N. Barnes, M. D. Sumption, and G. L. Rhoads, "Review of high power density superconducting generators: Present state and prospects for incorporating YBCO windings," Cryogenics, vol. 45, pp. 670–686, 2005. [4] F. Lin, R. Qu, D. Li, Y. Cheng, and J. Sun, "Electromagnetic design of 13.2 MW fully superconducting machine," IEEE Trans. Appl. Supercond., vol. 28, no. 3, Apr. 2018, Art. no. 5205905.

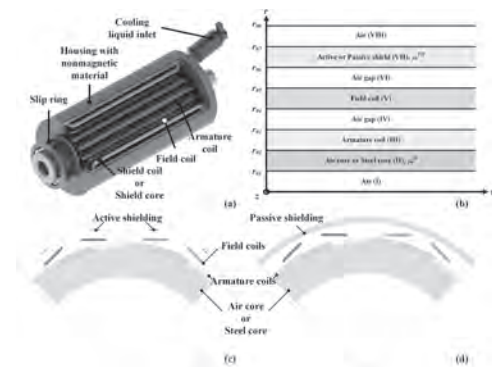


Fig. 1. SC machine: (a) structure, (b) analytical model, (c) actively shielded SC machine, and (d) passively shielded SC machine according to core materials.

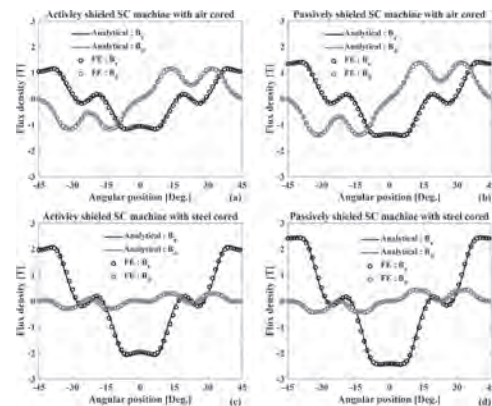


Fig. 2. Comparison of the flux density at the center of the armature coil by analytical and FE analysis: (a) actively shielded and coreless SC machine, (b) passively shielded and coreless SC machine, (c) actively shielded and cored SC machine, and (d) passively shielded and cored SC machine.

BV-10. A Novel Asymmetric-PM Variable Flux Memory Machine With Anti-Demagnetization Barrier Design.

W. Liu¹, H. Yang¹ and H. Lin¹

¹. Southeast University, Nanjing, China

I. Introduction Permanent magnet synchronous machine (PMSM) is widely recognized as a competent candidate for automotive propulsion [1], which offer the merits of high power density and high efficiency. Nevertheless, due to the inverter voltage and current limitations, the air-gap flux of the conventional PMSM is difficult to adjust even though a continuous negative d -axis current is injected for flux-weakening under high-speed operation [2]. As a result, how to realize effective air-gap flux adjustment, and further extend the speed range as well as high efficiency operation is regarded as a major challenge for the conventional PMSMs. Fortunately, the concept of variable flux memory machine (VFMM) is proposed to address the above issues [3]-[4]. The low coercive force (LCF) PM can be varied via a magnetizing or demagnetizing current pulse, in which the air-gap flux density can be flexibly adjusted. Generally, high coercive force (HCF) and LCF PMs are simultaneously employed in VFMM to realize high torque density and excellent flux adjustability [5]-[6]. Due to the magnetization state (MS) stabilization effect of HCF PMs on LCF PMs in series magnetic circuit VFMM, the unintentional on-load demagnetization issue can be avoided. Nevertheless, it also brings the problems of limited flux regulation range and higher required current pulse level for full remagnetization, which are undesirable for practical applications [7]. Therefore, this paper proposes a novel asymmetric-PM VFMM (APM-VFMM) with anti-demagnetization barrier design to realize wide flux regulation range and excellent on-load demagnetization withstand capability. The topology and features of the proposed APM-VFMM are introduced, respectively. The electromagnetic characteristics under different MSs are evaluated and compared. The efficiency maps are investigated to verify the advantages of the proposed design in terms of excellent flux regulation range and high efficiency operation over a wide speed range. II. Machine Configuration The topology evolution of the proposed APM-VFMM is shown in Fig. 1, in which the magnetic barrier is designed to resist the on-load unintentional demagnetization of the LCF magnet. The “U”-shaped magnetic barrier is added to the conventional series magnetic circuit VFMM, thereby forming into the anti-demagnetization barrier design. Then, the LCF magnet can be a substituted for the HCF magnet on one sided portion of the barrier design to form an asymmetric-PM configuration. The corresponding cross section of the proposed machine is shown in Fig. 2, which are characterized by a dual-layer PM structure [7]. The “U”-shaped magnetic barrier of the first PM layer can be employed to protect the working point stability of LCF PMs. For the second PM layer, asymmetric spoke-type hybrid PM arrangement is located on the d -axis, which can reduce magnetic saturation and enlarge flux regulation range. Each LCF magnet has an adjacent spoke-type HCF magnet to form a series magnetic circuit, achieving excellent demagnetization withstand capability. III. Electromagnetic Performance The open-circuit air-gap flux density waveforms of the proposed APM-VFMM under different MSs are plotted in Fig. 2(a) and (b), in which the flux-enhanced and flux-weakened states refer to the cases that the LCF magnets forward or reverse magnetized by twice the rated current considering inverter capacity, respectively. It demonstrates that the magnetic field in the flux-weakened state is significantly lower than flux-enhanced state, which implies that an expected flux-weakening effect can be achieved. Furthermore, the torque characteristics of the proposed machine are plotted in Fig. 2(c) and (d). It can be observed that the proposed machine in flux-enhanced state provides higher output torque than that of the flux-weakened state. Finally, the efficiency maps of the proposed machine under different MSs are shown in Fig. 2(e) and (f), which confirm that the proposed machine can achieve high efficiency maintaining by selecting appropriate MS under different operating regions.

[1] I. Boldea, L. N. Tutelea, L. Parsa, and D. Dorrell, *IEEE Trans. Ind. Electron.*, vol. 61, no. 10, pp. 5696-5711, Oct.2014. [2] W. L. Soong and T. J. E. Miller, *IEE Proc. Electr. Power Appl.*, vol. 141, no. 6, pp. 331-340, Nov. 1994. [3] V. Ostovic, *IEEE Ind. Appl. Mag.*, vol. 9, no. 1, pp. 52-61, Jan./Feb. 2003. [4] H. Hua, Z. Q. Zhu, A. Pride, R. P. Deodhar, and T. Sasaki, *IEEE Trans. Ind. Appl.*, vol. 53, no. 5, pp. 4396-4405, Sept./Oct.

2017. [5] A. Athavale, K. Sasaki, B. S. Gagag, T. Kato, and R. D. Lorenz, *IEEE Trans. Ind. Appl.*, vol. 53, no. 5, pp. 4318- 4326, Sep./Oct. 2017. [6] H. Yang, S. Lyu, H. Lin, Z. Q. Zhu, H. Zheng, and T. Wang, *IEEE Trans. Ind. Electron.*, vol. 67, no. 7, pp. 5258-5268, July 2020. [7] H. Yang, H. Lin, Z. Q. Zhu, S. Lyu, and H. Wang, in *Proc. Energy Convers. Congr. Expo (ECCE 2018)*, Portland, OR, Sept. 23-27, 2018.

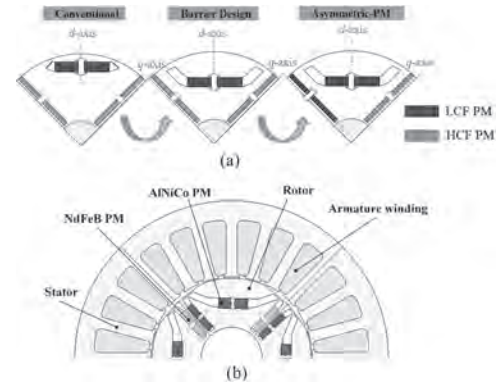


Fig. 1. Machine topology. (a) Topology evolution. (b) Cross section of the proposed APM-VFMM.

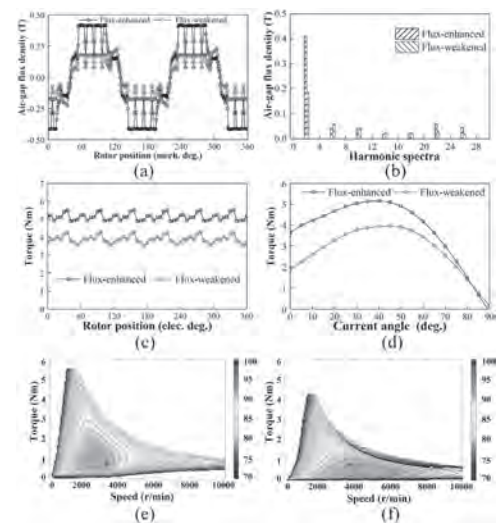


Fig. 2. Electromagnetic characteristics. (a) Open-circuit air-gap radial flux densities. (b) Harmonic spectra. (c) Steady-state torque waveforms. (d) Torque-angle waveforms. (e) Efficiency maps under flux-enhanced state. (f) Efficiency maps under Flux-weakened state.

Session BW

DESIGN AND CONTROL OF RELUCTANCE MACHINES AND INDUCTION MACHINES

(Poster Session)

Duc-Kien Ngo, Co-Chair

Vinh University of Technology Education, Vinh, Vietnam

Po-Wei Huang, Co-Chair

National Cheng Kung University, Tainan City, Taiwan

BW-01. Withdrawn

BW-02. Torque Ripple Optimization for Synchronous Reluctance Motors Based on a Virtual Permanent Magnet Harmonic Machine.

Y. Xu¹, C. Di¹, X. Bao¹ and D. Xu¹

1. Hefei University of Technology, Hefei, China

Introduction: The torque ripple can hardly be avoided for synchronous reluctance motors (SynRMs) in load conditions. It is generated by the interaction of the stator and rotor electromagnetic field harmonics, which have the same number of pole pairs but different rotating angular frequencies. In the air gap, the flux density is equal to the magnetomotive force (MMF) times the permeance. In [1], the air-gap field was analyzed, and a method for designing low-torque-ripple SynRMs was proposed. However, it did not consider the rotor permeance distribution and was limited to a relatively symmetrical rotor topology. In [2], it was verified that the torque ripple is highly affected by the position of the flux-barrier ends. The introduction of non-uniform flux barriers is capable of reducing the torque ripple. Based on the recent air-gap field modulation theory [3], the SynRM rotor with multi-layer flux guides, or flux barriers, can modulate extra harmonics in the air gap, whose frequencies are different from the primitive MMF. It is considered that the topology of the SynRM rotor is usually asymmetric, especially when a rotor with non-uniform flux barriers is adopted, and a series of permeance harmonics are produced. However, it is quite difficult to calculate the rotor permeance by analytical methods when the flux-barrier ends distribute along the rotor surface non-uniformly. This study proposes a method to analyze the effects that the rotor topology has on the rotor permeance harmonics by a virtual permanent magnet harmonic machine (VPMHM). By adjusting the rotor topology, certain permeance harmonics resulting in tremendous torque ripple can be avoided. Instead of simulating the output torque waveform directly, the proposed method can accelerate the optimization process and save much time. Analysis model: In [4], the concept of a VPMHM was introduced to generate harmonics with sinusoidal magnetization. Fig. 1(a) shows the model of the VPMHM, and Fig. 1(b) shows the implementation of the VPMHM in the optimization process for SynRMs in this study. The VPMHM has two parts, an ideal stator yoke whose permeability is infinite and an annular permanent magnet (PM) with the sinusoidal magnetization. The VPMHM is capable of generating sinusoidal distributed flux density in the air gap. Once an actual rotor is put in, the flux density waveform is no longer the pure sinusoid because of the modulation of the flux guides. The harmonics can be regarded as the effects of the rotor permeance. In this article, a 36-slot, 4-pole SynRM model is taken as an example to investigate the effects of the rotor permeance and perform the finite-element based optimization. The rated phase current is 130 Arms, and the motor is controlled by the maximum torque per ampere (MTPA) strategy. Results: An initial rotor was fast established based on some specific rules. The rotor permeance is mainly determined by the positions of the flux-barrier ends. With the help of the VPMHM, there is no need to analyze the entire dynamic process. A large-scale enumeration calculation is carried out for the air-gap electromagnetic field under different positions of the flux-barrier ends. The rotor that can create the minimum harmonics, whose orders are the same as the stator harmonics is preferred. Compared with the absolute values, per unit values are used to describe the magnitude which makes the comparison easier and more straightforward during the optimization process. Fig. 2(a) shows the fast Fourier transform (FFT) results of the air-gap flux density harmonics before and after the optimization. Though both of them contain considerable 21st and 23rd order harmonics, the effects on torque ripple are minor because the magnitudes of the corresponding stator harmonics are relatively small. The 17th and 19th order harmonics are evidently suppressed, which have the same number of pole pairs as the stator slot harmonics. Hence, the torque ripple caused by the slot harmonics can be mitigated. The fifth and seventh order harmonics slightly increase, but the influences of them are not severe as that of the stator slot harmonics when a short-pitched double-layer winding is adopted. For validation, Fig. 2(b) shows the results of the output torque waveform as a function of time at the nominal load. Compared with the initial rotor, it is salient that the torque ripple is effectively suppressed after optimization.

[1] A. Vagati, M. Pastorelli, G. Francheschini, IEEE Transactions on Industry Applications, vol. 34, no. 4, pp. 758-765, July-Aug. 1998, doi:

10.1109/28.703969. [2] N. Bianchi, S. Bolognani, D. Bon and M. Dai Pre, IEEE Transactions on Industry Applications, vol. 45, no. 3, pp. 921-928, May-june 2009, doi: 10.1109/TIA.2009.2018960. [3] M. Cheng, P. Han and W. Hua, IEEE Transactions on Industrial Electronics, vol. 64, no. 8, pp. 6063-6074, Aug. 2017, doi: 10.1109/TIE.2017.2682792. [4] C. Di, I. Petrov and J. J. Pyrhönen, IEEE Transactions on Magnetics, vol. 54, no. 12, pp. 1-12, Dec. 2018, Art no. 8111012, doi: 10.1109/TMAG.2018.2873279.

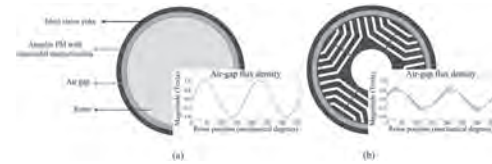


Fig. 1 Concept of the VPMHM and the flux density distribution in the air gap. (a) Model of the VPMHM (b) Implementation of the VPMHM with the actual rotor.

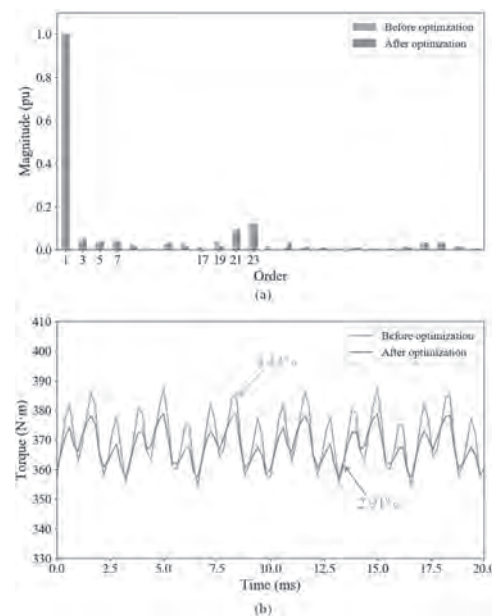


Fig. 2 The results before and after the optimization. (a) Harmonics produced by the SynRM rotor under the excitation of a VPMHM. (b) The output torque waveform as a function of time at the nominal load.

BW-03. Multi-Physic Fields Surrogate-Assisted Optimization of a Permanent Magnet Assisted Synchronous Reluctance Motor.

K. Shuai¹, J. Wang¹, Z. Ling², C. Cheng², J. Zheng², L. Zhou¹ and Y. Ma¹
 1. State Key Laboratory of Advanced Electromagnetic Engineering and Technology, Huazhong University of Science and Technology School of Electrical and Electronic Engineering, Wuhan, China; 2. State Grid Hubei Electric Power Research Institute, Wuhan, China

1. Introduction In recent years, the demand for highly efficient motors is increasing to reduce energy consumption due to the increase in energy cost. Synchronous reluctance motor (SynRM) without magnet on the rotor is regarded as an ideal substitute for permanent magnet synchronous motor to obtain high efficiency, but SynRM has the disadvantages of low power factor and high torque ripple [1]. By insetting PMs within the flux barriers of SynRM, permanent magnet assisted synchronous reluctance motor (PMA SynRM) shows better performance in many aspects including torque, efficiency, and power factor [2]. The main challenge for an optimal design of PMA SynRM is to optimize the multiple design variables while ensuring the reliability of the rotor structure [3]. A novel multi-objective optimization method for PMA SynRM is proposed in this paper to realize high efficiency and low torque ripple. Based on the sensitivity analysis results of design variables, a sequential subspace optimization method (SSOM) [4] is implemented. Meanwhile, artificial neural network (ANN) [5] and multi-objective particle swarm optimization (MOPSO) are used to train surrogate models and perform multi-objective optimization about electromagnetic and structural fields to reduce the required number of the time-consuming finite element analysis (FEA). 2. Winding Configurations and Comparison High torque ripple is a major disadvantage that limits the application of reluctance motors. Fractional-slot windings can obtain the relatively lower torque ripple by reducing the high-order torque harmonics generated by slot harmonics, but PMA SynRM rotors associated with fractional-slot windings cannot maintain the expected reluctance torque contribution since the difference between d -axis and q -axis flux distribution and rotor pole spacing. The windings with an odd number of slots per pole pair are the exception, which can reduce torque ripple while maintaining the saliency ratios of PMA SynRM. Therefore, six typical slot-pole number combinations are compared under the same 4-poles rotor, thermal constraints and main dimensions in this paper to investigate the performance of PMA SynRM. Compared to the integer-slot winding, the fractional-slot winding has more harmonic content, which will result in greater iron loss. At the same time, the high harmonic content also produces a great harmonic leakage that reduces the power factor of the motor. The analysis result is verified by FEA as shown in Tab.1. Fractional-slot concentrated-winding of 6-slot 4-pole can get minimum copper loss but the lowest torque and power factor due to its low winding factor and high harmonics. The efficiency and power factor are improved as the number of slots increases except for the 21-slot 4-pole motor whose harmonic content is the highest among the motors with similar slots. Integer-slot distributed-winding of 36-slot 4-pole motor has a maximum efficiency and power factor, but its torque ripple is quite high. Considering all performances of the motor, the 30-slot 4-pole motor was chosen to be the optimal solution. 3. Multi-objective Optimization It is difficult to get optimal solutions if more than 10 structural variables are optimized simultaneously. To solve multi-parameter optimization problem and reduce the computational cost, a multilevel design optimization method based on sequential subspace is proposed. Firstly, 15 design variables are selected for the optimization. Analysis of variance techniques based on the design of experiment (DOE) method is used to carry out a sensitivity analysis of parameters and the optimization variables are divided into two subspaces: the significant parameter subspace X_1 and the minor parameter subspace X_2 . The specific multilevel optimization flowchart is given in Fig.1. The convergence error is set as 1%. Then, a surrogate model that can replace both the electromagnetic field and structural field FEA of the motor is trained by the ANN to improve optimization efficiency. To further reduce the required number of FEA simulations, the orthogonal experimental design method is adopted to generate a training set for the surrogate model. Ultimately, a multi-objective optimization is performed using the MOPSO algorithm to search for an optimal design that yields high efficiency and low torque ripple. 4. Conclusion The surrogate model successfully converges after three subspace optimizations, and its

results are in good agreement with the FEA. Compared to the initial design, the optimal design yields a much higher efficiency (increased by 1.5%) and lower torque ripple (decreased by 65%) with the same volume, and the maximum stress of the rotor is about 180MPa at rated load condition. The proposed multilevel optimization method can significantly alleviate the computing burden and is suitable for the high-dimensional optimization of the PMA SynRM.

1. N. Bianchi, M. Degano and E. Fomasiero, "Sensitivity Analysis of Torque Ripple Reduction of Synchronous Reluctance and Interior PM Motors", IEEE Transactions on Industry Applications, vol. 51, pp. 187-195(2015).
2. S. Ooi, S. Morimoto and Y. Inoue, "Performance Evaluation of a High-Power-Density PMA SynRM With Ferrite Magnets", IEEE Transactions on Industry Applications, vol. 49, pp. 1308-1315(2013).
3. S. S. R. Bonthu, S. Choi and J. Baek, "Design Optimization With Multiphysics Analysis on External Rotor Permanent Magnet-Assisted Synchronous Reluctance Motors", IEEE Transactions on Energy Conversion, vol. 33, pp. 290-298(2018).
4. G. Lei, C. Liu and Y. Guo, "Techniques for Multilevel Design Optimization of Permanent Magnet Motors", IEEE Transactions on Energy Conversion, vol. 30, pp. 1574-1584(2015).
5. J. Song, F. Dong and L. Wang, "An Efficient Multiobjective Design Optimization Method for a PMSLM Based on an Extreme Learning Machine", IEEE Transactions on Industrial Electronics, vol. 66, pp. 1001-1011(2019).

Table.1 Performance of machines with different slots

Quantity	4p6s	4p18s	4p21s	4p24s	4p30s	4p36s
Copper loss/W	506	683	627	661	697	676
Rotor Iron loss/W	165.1	140.2	155.2	147.7	134.5	128.7
Torque/(Nm)	78.8	91.1	90.0	93.2	95.3	94.3
Torque ripple/%	43.5	19.7	9.34	28.1	14.3	24.4
Power factor	0.743	0.839	0.837	0.840	0.849	0.856
Efficiency/%	93.12	92.94	93.12	93.15	93.14	93.24

Table.1 Performance of machines with different slots

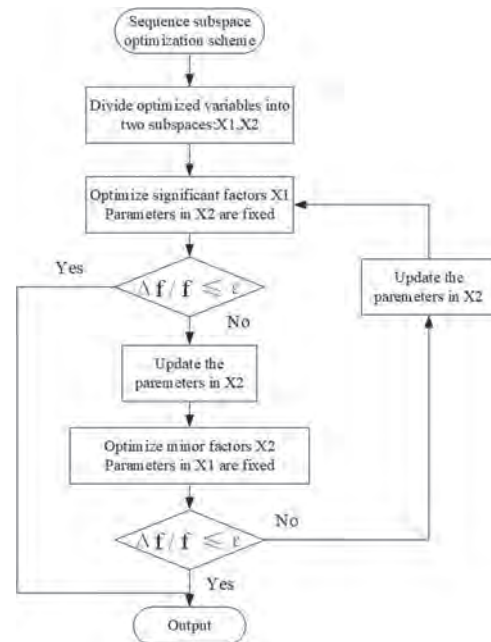


Fig. 1 Multilevel optimization framework for PMA SynRM design

BW-04. Experimental Determination of Equivalent Iron Loss Resistance for Prediction of Iron Losses in a Switched Reluctance Machine.

A. Memon¹, S. Bukhari^{2,3} and J. Ro³

1. Mehran University of Engineering and Technology, Jamshoro, Pakistan;
 2. Sukkur IBA University, Sukkur, Pakistan; 3. Chung-Ang University, Seoul, The Republic of Korea

Switched Reluctance Machine has progressed as a suitable contender in the family of electrical machines for its high starting torque and better performance in different operating conditions. The need of accurate modeling of this machine is therefore dependent on the accurate determination of losses of which iron loss is exigent. This paper aims to determine iron loss from the equivalent circuit of the machine based on the input data tables that are directly obtained from the experiments performed on an existing 4-phase switched reluctance machine. The experimental determination of the iron losses has been compared with those who were predicted under the same operating conditions. Equivalent Circuit of Switched Reluctance Motor The iron losses calculation from the equivalent circuit of the switched reluctance machine (SRM) is presented in [1] that included two ends i.e., unaligned and miss-aligned positions of the machine. Whereas an intermediate position was not taken into consideration. Fig. 1 shows an equivalent circuit in which R represents phase winding resistance, L is self-inductance, and resistive branch 'r' that is dependent on rotor position, change in flux linkage, and frequency of phase switching. This element is connected in parallel to 'L' to represent the iron loss in the core of the machine [1]. The arrangement i.e., the parallel combination of 'r' and 'L' shown in the circuit Fig. 1 [1] describes the flux penetration and eddy current in the magnetic core of the motor. A review on different methods for loss calculations of SRM is given in [2]. Results For purpose of the illustration, the waveforms of currents and in the equivalent circuit are shown in Fig.2 (a). Fig.2 (b) shows the equivalent iron-loss-resistance vs. flux-linkage in the intermediate position of currents and in the equivalent circuit of Fig.1.

1. Corda, J. and Jamil, S.M., 2009. Experimental determination of equivalent-circuit parameters of a tubular switched reluctance machine with solid-steel magnetic core. *IEEE Transactions on Industrial Electronics*, 57(1), pp.304-310. 2. Li, S., Zhang, S., Habetler, T.G., and Harley, R.G., 2019. Modeling, Design Optimization, and Applications of Switched Reluctance Machines—A Review. *IEEE Transactions on Industry Applications*, 55(3), pp.2660-2681.

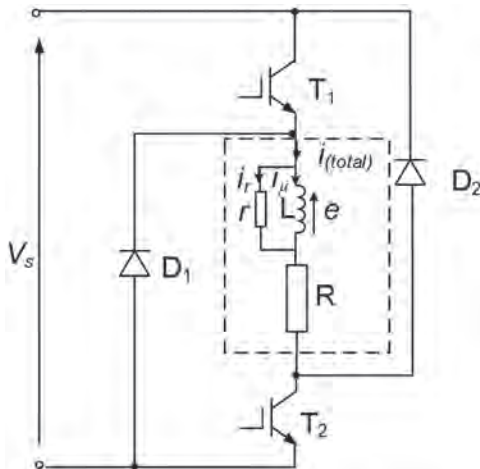


Fig. 1. Equivalent circuit of one phase.

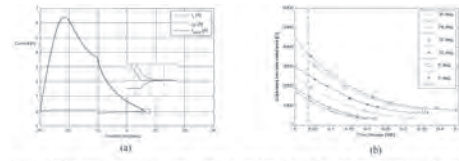


Fig. 2. (a) Waveforms of currents i_r , i_L , and i_s , and (b) Experimental equivalent iron-loss-resistance vs. flux-linkage in intermediate position.

BW-05. Research on Sliding Mode DITC Based on Gray Wolf Optimization Algorithm for SRM.

L. Feng¹, X. Sun¹ and J. Zhu²

1. Jiangsu University, Zhenjiang, China; 2. University of Sydney, Sydney, NSW, Australia

Abstract—In this paper, an improved direct instantaneous torque control (DITC) with sliding mode control and gray wolf optimization algorithm (GWOA) is proposed suppress torque ripple and enhance the anti-interference ability. First, the sliding mode speed controller based on a novel reaching law is designed to reduce torque ripple and startup time. Second, an anti-disturbance sliding mode observer is presented and combined with the SMSC to build up an anti-disturbance composite speed control strategy. Then, the GWOA is employed to automatically tune the parameters including the turn-on angle, turn-off angle, and coefficient in speed controller and observer for better comprehensive performance. Finally, the simulation and experimental results indicate that the proposed control method behaves well in aspects of the dynamic response and robustness, anti-interference ability, and torque ripple suppression. Introduction Due to many inherent features such as robust structure, no windings and PMs on the rotor, wide speed regulating range and high reliability, switched reluctance motors (SRMs) are becoming one potential candidate for hybrid electric vehicle (HEV) applications [1],[2]. However, SRM suffers from high torque ripple owing to the salient structure and nonlinear magnetization characteristics, which limits further development [3]. Direct instantaneous torque control The structure diagram of the DITC system combining speed controller and disturbance observer is shown in Fig. 1. The instantaneous torque obtained by the look-up table method is taken as the control quantity and then sent to torque controller after comparing with reference torque. Design of speed controller Based on conventional reaching law, an improved adaptive law is established as: $ds/dt = -[k_1s/(\delta + (1-\delta)e^{-\alpha|s|}) + k_2|s|\beta] \text{sgn}(s)$, $k_1 > 0$, $k_2 > 0$, $0 < \delta < 1$, $\alpha > 0$, $1 < \beta < 2$. The adaptive law is introduced into the speed controller to further suppress the chattering and increase convergence speed correspondingly. Design of disturbance observer based on modified STA In order to improve the anti-interference ability, the disturbance observer based on modified STA was employed in DITC system. The modified STA is defined as: $du/dt = -\lambda_1|u|^{1/2} \text{sgn}(u) + u_1$, $du_1/dt = -\lambda_2|u|^{2l} \text{sgn}(u)$. Gray wolf optimization algorithm for auto-tuning The GWOA mimics the strict hierarchy and predatory behaviour of gray wolves in nature, which has been widely used in some specific applications. In the social hierarchy, gray wolves are divided into the wolf α , β , δ , and θ from high to low, which represent the best solution, the second-best solution, the third-best solution, and candidate solution, respectively. The mathematical model of the encircling behaviour of gray wolf can be expressed as follows: $D = |CX_p - X|$, $X(t+1) = |X_p - A \times D|$ where t is the current iteration number, D is the distance between the gray wolf and prey, X and X_p represent the position vector of the gray wolf and prey. The coefficient vectors C and A can be calculated as $A = 2a \times r_1 - a$, $C = 2r_2$ where r_1 and r_2 are random vectors in $[0, 1]$, and a is linearly decreased from 2 to 0 over the course of iterations. The mathematical model of the hunting behavior of gray wolf are shown as follows: $D_p = |CX_p - X|$, $X_n = |X_p - A \times D_p|$, $X(t+1) = (X_1 + X_2 + X_3)/3$ where the subscript p denotes α , β and δ , respectively, n denotes 1, 2 and 3, respectively, and X_n is the movement instructions given by α , β and γ , respectively. Compared with other algorithms, the GWOA stands out due to the feature of strong local search capability and high convergence rate. However, GWOA is hard to achieve a satisfactory result in solving complex optimization problems, which is likely to fall into a local solution. Simulation and experimental validation Simulations and experiments using DITC system with conventional PI and proposed sliding mode control method are compared to verify the accuracy and effectiveness. The test devices and platform for the dynamic characteristics is shown in Fig. 2.

[1] X. Sun, K. Diao, G. Lei, Y. Guo, and J. Zhu, "Real-Time HIL Emulation for a Segmented-Rotor Switched Reluctance Motor Using a New Magnetic Equivalent Circuit," *IEEE Transactions on Power Electronics*, vol. 35, no. 4, pp. 3841-3849, 2020. [2] W. Ding, G. Liu, and P. Li, "A Hybrid Control Strategy of Hybrid-Excitation Switched Reluctance Motor for Torque Ripple Reduction and Constant Power Extension," *IEEE Transactions on Industrial Electronics*, 2019. [3] N. Yan, X. Cao, and Z. Deng, "Direct

Torque Control for Switched Reluctance Motor to Obtain High Torque-Ampere Ratio," *IEEE Transactions on Industrial Electronics*, vol. 66, no. 7, pp. 5144-5152, 2019.

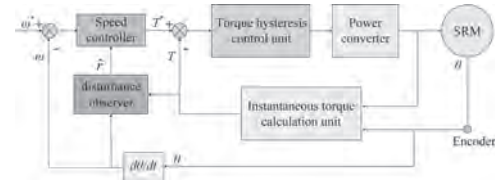


Fig. 1. Block diagram of DITC system.



Fig. 2. Devices and platform for testing dynamic characteristics.

BW-06. Multiphysics and Two-Step Multi-Fidelity Optimization for a Switched Reluctance Motor.

B. Wan¹, X. Sun¹ and J. Zhu²

1. Jiangsu University, Zhenjiang, China; 2. University of Sydney, Sydney, NSW, Australia

Abstract-This paper presents an optimization method considering both electromagnetic and thermal performance, and a novel strategy to construct an approximate model considering multi-fidelity finite element models (FEMs) is proposed. The electromagnetic and thermal FEMs are established in ANSYS/Maxwell and Fluent, respectively. Finally, both simulation and experimental results are given and discussed. Compared with the initial design, the optimal solution exhibits lower housing temperature, higher torque, lower torque ripple and less loss. 1. Introduction Tradition optimization mainly considers electromagnetic performance and the approximate model is constructed only with the 2D FEMs [1]. In the optimization, the multiphysics performance is considered, and the 3D FEMs are predicted by 2D FEMs and the errors between 2D and 3D FEMs. The temperature of the housing, output torque, torque ripple and total loss are taken into consideration. The objective function and constraints can be defined as Function: $\min f_1(TEM_{housing}), f_2(-T_{out}), f_3(T_{ripple}), f_4(P_{loss})$ Constraints: $1.10-T_{out} \leq 0, J_c - 5 \leq 0$ (1) where $TEM_{housing}, T_{out}, T_{ripple}, P_{loss}$ and J_c are housing temperature, output torque, torque ripple, loss, and allowable current density. 2. Electromagnetic and thermal FEA The 2D and 3D electromagnetic FEMs are established in Maxwell, and the 2D and 3D thermal FEMs are established in Fluent. The 2D housing thermal model in Fluent for the initial design is shown in Fig.1. 3. Two-step multi-fidelity strategy The flowchart of this optimization process is presented in Fig.1. In the first step, the initial sample points are generated by the design of experiment (DoE) and the errors between 2D and 3D FEMs are utilized to create response surface (RES). In the second step, additional sample points are generated and radial basis function (RBF) is constructed by 2D models. Then, the result of 3D FEM is predicted by the errors between 2D and 3D FEMs and the results of 2D FEMs. The $\beta_j^{RES}(x)$ and δ_j^{RES} is the ratio and variance between 2D and 3D FEMs 4. Results The proposed method can reduce the computational burden and improve the performance of the motor. The number of 3D and 2D FEMs are 96 and 512, respectively. The computational time duration is about 149h, which is much shorter than only use 3D FEMs. The accuracy of the approximate model in the proposed method is 1.70% and 1.06% for the 3D electromagnetic and thermal FEA, which is much more accurate than the approximate model only constructed by 2D FEMs. For the initial design, the $TEM_{housing}, T_{out}, T_{ripple}$ and P_{loss} is 371.53°C, 0.96 Nm, 0.31 and 227.18W, respectively. After the optimization, the $TEM_{housing}, T_{out}, T_{ripple}$ and P_{loss} is 337.51°C, 1.18 Nm, 0.23 and 207.83 W. 5. Conclusion In this paper, a multiphysics optimization method, which can improve the performance of the switched reluctance motor, is proposed. At the same time, the two-step multi-fidelity strategy can greatly improve the accuracy of the approximate model and reduce the computational cost.

[1] G. Y. Sizov, P. Zhang, D. M. Ionel, N. A. O. Demerdash, and M. Rosu, "Automated Multi-Objective Design Optimization of PM AC Machines Using Computationally Efficient FEA and Differential Evolution," *IEEE Trans. Ind. Appl.*, vol. 49, no. 5, pp. 2086-2096, 2013.

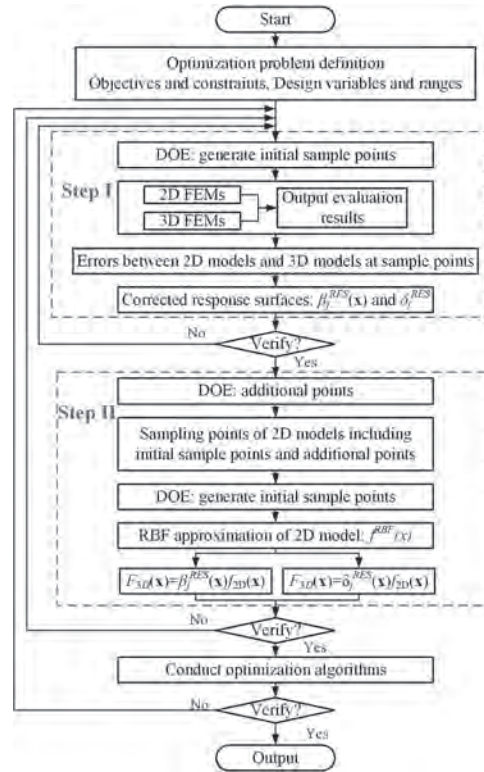


Fig. 1. Flowchart of this optimization.

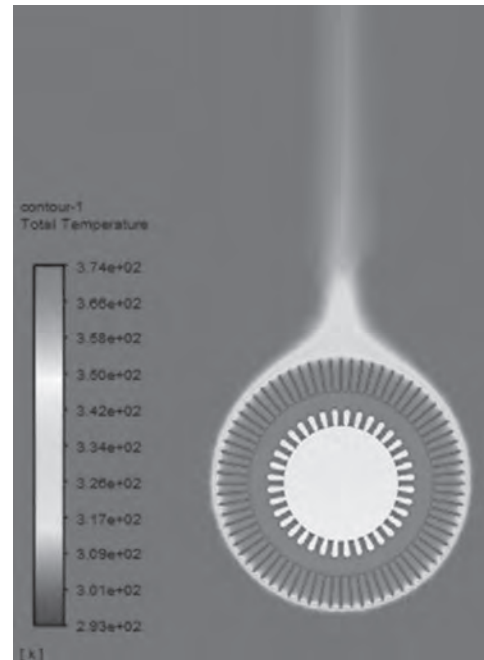


Fig. 2. 2D housing thermal model in fluent for the initial design.

BW-07. System Level Sequential Subspace Design Optimization of Switched Reluctance Motor Drive Systems Based on Space Reduction Strategy.

K. Diao¹, X. Sun¹ and J. Zhu²

1. Jiangsu University, Zhenjiang, China; 2. University of Sydney, Sydney, NSW, Australia

Abstract—In this paper, a novel system level sequential design optimization method is presented for switched reluctance motor (SRM) drive systems. First, the multiobjective optimization problem for the SRM drive systems is defined. Then, all parameters of the drive systems, including the motor level and control level are divided into two subspaces according to their influences on the objectives. Finally, the optimization of each subspace is performed sequentially until a convergence criterion is met. The sensitivity analysis, the approximate models, and the genetic algorithm are employed for the implementation. Besides, the space reduction method is introduced to reduce the computational cost. The step size of each control factor will be halved in the next iterative process. To verify the effectiveness of the proposed method, An SRM drive system with a 12/10 configuration and angle position method, is investigated.

I. Introduction Due to the absence of any windings and magnets in the rotor, the switched reluctance motors (SRMs) provides the best alternatives for the other machines under harsh environments of extremely high temperatures and pressures [1]. The trade-offs to the overall consideration and the implementation of multiobjective optimization are necessary to meet the requirements for different applications. Previous works are mostly on component level rather than the system level [2]. Theoretically, assembling individually optimized components into a system cannot guarantee the optimal system performance as each part is coupled to each other. Thus, the perfect cooperation of motor and control levels should be optimized simultaneously. The main problem in the system level optimization is the computation burden due to the abundant optimization variables. In this paper, the space reduction strategy will be integrated into the system level optimization flowchart.

II. System-Level Sequential Subspace Design Optimization An SRM drive system with a 12/10 configuration and angle position method, will be investigated, as shown in Fig. 1. The optimization flowchart is presented in Fig. 2, and it can be divided into the following steps. *Step 1:* Define the system level optimization model, including objective function, constraints, and design parameters. The optimization problem can be defined as $\min: f(x_s) \text{ s.t. } g_i(x_s) \leq 0, i=1,2,\dots,n$ (1) $x_{sl} \leq x_s \leq x_{su}$ where x_s, f, g_i are the design parameter vector, objective and constraints of motor, respectively, x_s consists of motor parameter vector and control parameter vector, x_{sl} and x_{su} are the lower boundary and upper boundary, respectively. *Step 2:* Divide all the parameters in motor and control aspects into two subspaces. X_1 and X_2 represent the significant and non-significant subspaces, respectively. *Step 3:* Optimize X_1 . Generate samples and simulate their response by using the orthogonal array (OA) [1]. An OA with a higher level with 5 levels can be assigned to X_1 . The Kriging model [2] is developed based on the data. Then, conduct the optimization by using non-dominated sorting genetic algorithm (NSGA) II. The optimal solution is selected for the next subspace. *Step 4:* Optimize X_2 . In this step, an OA with 3 levels is assigned to X_2 . The optimal solution is selected by the same implementation in step 3. *Step 5:* Termination judgement. Compute the motor performance with the obtained optimal design and compare it with the last objective. If the relative error is less than a given value, terminate the optimization process and output the optimal design. Otherwise, go to the next step. *Step 6:* Reduce the design space of the design parameters in X_1 and X_2 , respectively. Assume the initial design space of an optimization variable is $[a, b]$, and the optimal value of this variable is x_0 . For X_1 in which there are 5 levels for each design parameter with a step size $2d$, the next design space and new levels are $[a, a+d, a+2d, a+3d, a+4d]$, $x_0-2d < a$; $[b-4d, b-3d, b-2d, b-d, b]$, $x_0+d > b$; (2) $[x_0-2d, x_0-d, x_0, x_0+d, x_0+2d]$, others For X_2 in which there are 3 levels for each design parameter with a step size $2d$, the next design space and new levels are $[a, a+d, a+2d]$, $x_0-d < a$; $[b-2d, b-d, b]$, $x_0+d > b$; (3) $[x_0-d, x_0, x_0+d]$, others It can be found that the step size is halved during the space reduction.

[1] G. Lei, C. Liu, Y. Li, D. Chen, Y. Guo, and J. Zhu, "Robust Design Optimization of a High-Temperature Superconducting Linear Synchronous Motor Based on Taguchi Method," *IEEE Trans. Appl. Supercond.*,

vol. 29, no. 2, pp. 1-6, 2019. [2] K. Diao, X. Sun, G. Lei, Y. Guo, and J. Zhu, "Multiobjective System Level Optimization Method for Switched Reluctance Motor Drive Systems Using Finite Element Model," *IEEE Trans. Ind. Electron.*, 2020.

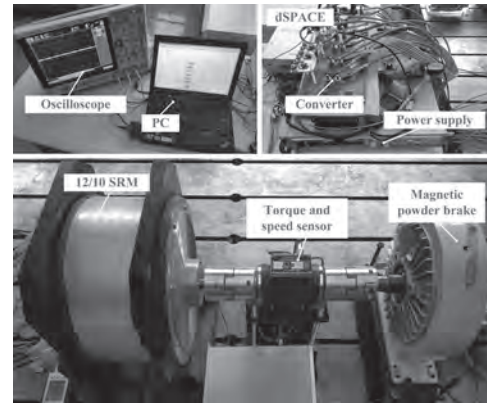


Fig. 1. Experimental platform.

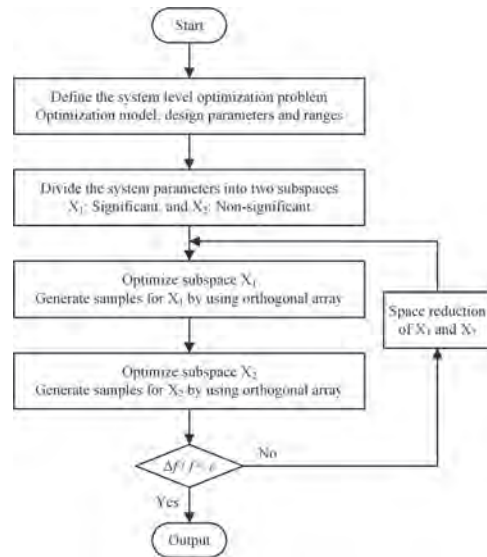


Fig. 2. Flowchart of the optimization strategy.

BW-08. Unified Control for Switched Reluctance Motors for Electric Vehicles.

X. Tang¹, X. Sun¹ and J. Zhu²

1. Jiangsu University, Zhenjiang, China; 2. University of Sydney, Sydney, NSW, Australia

Abstract-This paper proposes a unified control method to improve the ability of switched reluctance motors (SRM) to cope with variable operating conditions. The traditional single control method has obvious defects. The control method proposed in this paper is based on a 12/10 pole SRM. In the three-phase SRM (TSRM) mode, direct instantaneous torque control (DITC) is utilized to reduce torque ripple at low speed. In the six-phase SRM (SSRM) mode, A current-adjusted angular position control is used to increase the speed range and reduce torque ripple in high speed. The principle of dynamic coordinated control is utilized to implement switching between different modes to improve the performance of SRM. 1. Introduction A novel unified control method is proposed, which uses DITC and current control in the overlapped phase area to reduce torque ripple and obtain a wider speed range [1]. Compared with the traditional control method, the method has obvious advantages, but the speed adjustment range needs to be further expanded. Multi-objective optimization function and finite element method (FEA) are used to determine the motor parameters [2]. Experimental results prove that an SRM with 12/10 pole can be used not only as a three-phase motor but also as a six-phase motor. However, the paper does not propose a control method for switching between different modes. A unified control method is proposed for SRM in different modes. 2. The proposed method The multimode switched reluctance motor (MMSRM) is mainly composed of stator, rotor and coils. The electromagnetic performance of the TSRM and SSRM are analyzed via FEA. The flux distribution of the TSRM when one phase is excited is shown in Fig. 1 (a). MMSRM is utilized as a six-phase motor. When phase A is excited, the magnetic flux distribution at the aligned position is shown in Fig. 1(b). Compared with SSRM, TSRM has a higher instantaneous torque [2]. But the torque ripple also increases. In the low-speed range, MMSRM is used as TSRM. The direct instantaneous torque control can effectively reduce torque ripple. At the same time, the load capacity range of SRM is expanded. As the speed increases, the back electromotive force (EMF) voltage of the machine increases, which limits the ability of the controller to adjust the current. SRM enters the single pulse mode, and it is impossible to accurately track the reference current. Current-adjusted angular position control is used to reduce torque ripple in high speed. A paper confirms that the turn-off angle increases with increasing speed [1]. The calculation of the turn-off angle can be expressed as equation (1). $\theta_d = 180^\circ + aI_{actual} + b\omega + cI_{actual}^2 + d\omega I_{actual} + eI_{actual}^3 + f\omega I_{actual}^2$ (1) where $a, b, c, d, e,$ and f are the machine-specific coefficients, I_{actual} is the actual phase, and ω is the operating speed. For switching under different modes, the principle of dynamic coordinated control is utilized. Establishing the corresponding optimization objective function can greatly improve the overall efficiency of the motor. The unified control principle is shown in Fig. 2. The input parameters of the dynamic coordinated control principle are obtained through the input of working condition parameters and SRM state feedback. The unified control principle is shown in Figure 2. The input of the dynamic coordinated control principle is obtained through the input of working condition parameters and SRM state feedback. Equation (2) is used to establish the principle of SRM mode switching. $Q_1 = \{xcx_1 \mid (v < v_s) \text{ and } (\omega = 0)\}$; $Q_1' = \{xcx_1 \mid (v > v_s) \text{ and } (\omega > 0)\}$; $Q_2 = \{xcx_2\}$; $Q_3 = \{xcx_1, xcx_2\}$ (2) where Q, x_1 and x_2 respectively represent the mode judgment code, the trigger condition of TSRM and the trigger condition of SSRM. v, v_s and ω respectively represent the vehicle speed, threshold of vehicle speed and motor speed.

[1] Y. Hu, W. Ding, T. Wang, S. Li, S. Yang, and Z. Yin, "Investigation on a Multimode Switched Reluctance Motor: Design, Optimization, Electromagnetic Analysis, and Experiment," *IEEE Trans. Ind. Electron.*, vol. 64, no. 12, pp. 9886-9895, 2017. [2] T. Husain, A. Elrayyah, Y. Sozer, and I. Husain, "Unified Control for Switched Reluctance Motors for Wide Speed Operation," *IEEE Trans. Ind. Electron.*, vol. 66, no. 5, pp. 3401-3411, 2019.

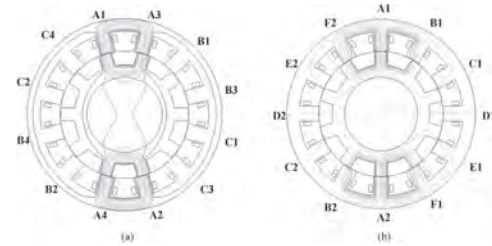


Fig. 1. Topology of the SRM. (a) Excitation state of TSRM. (b) Excitation state of SSRM.

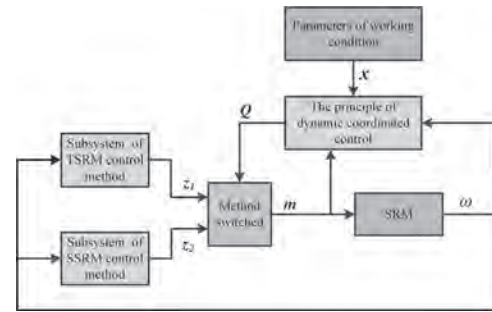


Fig.2. Schematic diagram of the unified control.

BW-09. Development of a Dual-Ferrite-Assisted DC-Saturation-Relieving Hybrid Reluctance Machine for Electric Propulsion.

W. Wang¹, X. Zhao¹ and S. Niu¹

1. Department of Electrical Engineering, The Hong Kong Polytechnic University, Kowloon, Hong Kong

Abstract—Reluctance machines with DC field coil in stator is a competitive candidate for electric vehicle propulsion due to the elimination of rare-earth permanent magnets (PM), robust structures and controllable excitation. But with the increasing of DC field current, it is exposed to the risk of extra DC saturation in stator core. As a consequence, the torque density is constrained. To solve this problem, based on the comprehensive consideration of production cost and torque performance, this paper proposes a new type of hybrid reluctance machine with dual ferrite permanent magnets (PMs) in stator slots. The inner ferrite PM is magnetized tangentially, which can effectively achieve the DC-saturation-relieving (DCSR) effect, while the outer ferrite PM is magnetized radially to increase the motor torque density through flux modulation effect. Based on finite element analysis, machine torque density can be improved by 20% while the efficiency boosts up by 5%, respectively.

Index Terms—hybrid reluctance machine (HRM), ferrite, DC-saturation-relieving (DCSR), flux modulation I. Introduction Permanent magnet (PM) machines are widely used in electrical vehicles and more electric aircraft propulsion systems. However, this rare-earth material is a nonrenewable resource, which is desired to be reduced in the machines. Switched reluctance motor (SRM) can be seen as a potential non-PM solution[1]. However, it can be only operated in the first quadrant of BH curve, and its torque density is poorer than that of PM machine. In addition, the torque ripple is serious because of half-cycle conducting. Doubly-fed doubly salient motor (DF-DSM) and SRM have similar rotor and stator structure. The difference is that the space of the stator slot is shared by DC and AC coils, which allows DF-DSM to be driven by a universal inverter[2], but meanwhile, its torque density is lower than that of SRM. Another structure named as variable flux reluctance machine (VFRM) can be designed with flexible number of the rotor teeth and the stator teeth. With the help of symmetrical magnetic circuit and odd rotor pole pairs design, the even-order flux harmonics are cancelled. Consequently, higher torque density and lower cogging torque can be acquired[3]. Unfortunately, the torque density of VFRM is still lower than that of SRM and quite lower than that of PM machine. In addition, due to the existence of DC field windings, the stator slot is prone to magnetic circuit saturation. This problem is especially obvious under high load conditions, which will seriously affect torque performance and increase core loss. To solve this problem, an innovative DC-saturation-relieving (DCSR) method using tangential PMs embedded in the slots was proposed in a previous study[4]. PMs are applied to create a magnetic field in the opposite direction to weaken the magnetic circuit saturation caused by the DC field windings. This paper conducted a study on HRM using ferrite PMs. To begin with, as a man-made material, ferrite PMs can effectively replace rare-earth PMs and greatly save motor costs[5]. Furthermore, this paper adopts the design of auxiliary excitation of dual ferrite PMs. On the one hand, the inner ferrite PMs are used to release the saturation of the magnetic circuit and do not produce the flux deviation. On the other hand, the magnetic field generated by the outer ferrite PMs and the DC excitation windings can improve through flux modulation effect. The finite element analysis is discussed as follows, and prototype experiments are going to be conducted. II. Configuration of HRM The structure of the proposed HRM is shown in Fig. 1(a). It consists of DC field windings, AC armature windings, outer ferrite PMs, inner ferrite PMs, 12 stator teeth and 11 rotor teeth. It is noticeable that dual ferrite PMs play different roles in this machine. On the one hand, as shown in Fig. 1(b), the inner ferrite PMs are tangentially magnetized to generate a magnetic flux opposite to that of DC field windings, so the saturation of the magnetic circuit can be decreased by the effect of DCSR. It is worth noting that the inner ferrite PMs only adjust the deviation degree of the flux linkage, but have no influence on the phase of the flux linkage. On the other hand, in Fig. 1(c), the outer ferrite PMs, magnetized radially, only affects the magnitude of the flux linkage. The emerging flux modulation principle also contributes to the improvement of torque density and efficiency. III. Performance analysis When the HRM is excited by DC only, the magnetic circuit distribution under no load condition is shown in Fig. 2(a). In the case of high

current density, the magnetic circuit in the rotor teeth is severely saturated, which will seriously affect the torque performance. With the help of dual ferrite PMs, the magnetic circuit saturation in the stator slots and teeth are effectively released by the DCSR effect which can be found in Fig. 2(b). At the same time, as can be seen in Fig. 2(c), the torque density of the motor has been significantly improved by about 20%. Conclusion A dual-ferrite-assisted DCSR hybrid reluctance machine is proposed in this paper. With the help of flux modulation effect and DCSR effect, the torque density and the efficiency can be increased by 20% and 5%, respectively.

[1] Y. Hu, L. Xiao and C. Pan, IEEE Trans. Power Electron., Vol. 35, p. 9563-9573 (2020) [2] Y. Wang, Z. Zhang and R. Liang, IEEE Trans. Ind. Electron., Vol. 63, p. 7434-7443 (2016) [3] Z. Q. Zhu, B. Lee and X. Liu, IEEE Trans. Ind. Appl., vol. 52, p. 1519-1529 (2016) [4] X. Zhao, S. Niu, and X. Zhang, IEEE Trans. Ind. Electron., Vol. 67, p. 9571-9581 (2020) [5] A. Fasolo, L. Alberti and N. Bianchi, IEEE Trans. Ind. Appl., Vol. 50, p. 3708-3716 (2014)

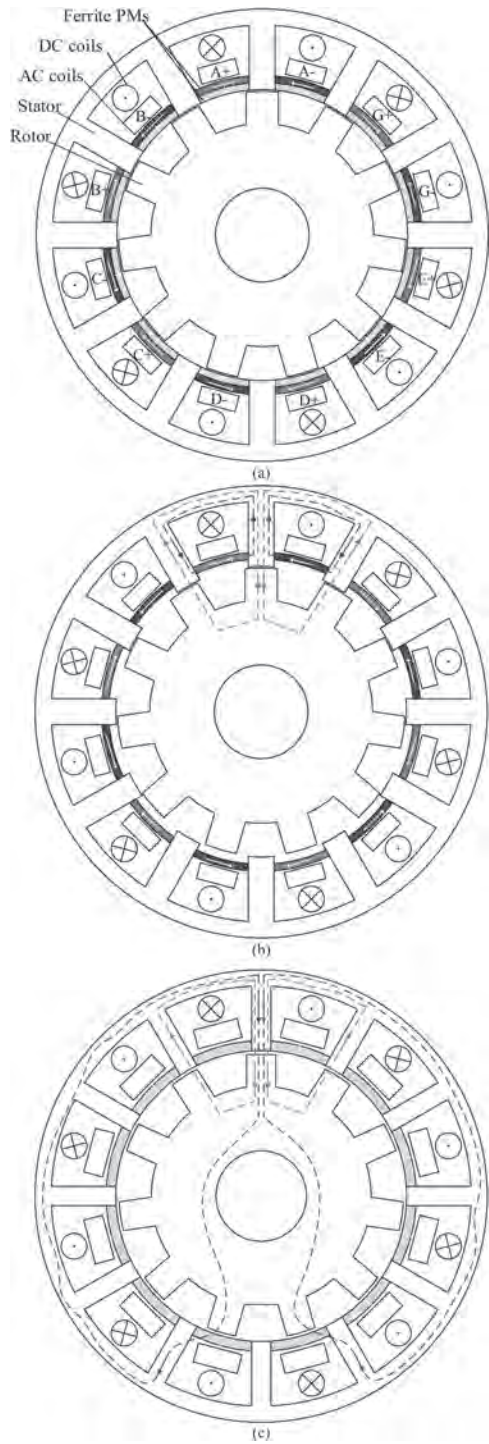


Fig. 1. (a) Configuration of HRM. (b) Flux linkage of inner ferrite PMs. (c) Flux linkage of outer ferrite PMs.

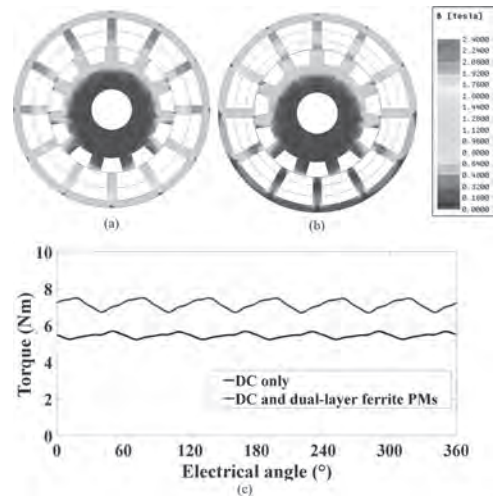


Fig. 2. (a) Magnetic field distribution of DC only. (b) Magnetic field distribution of DC and dual ferrite PMs. (c) Steady torque curves.

BW-10. Optimization of Stator Construction for Weight Reduction of Axial-Field Dual-Rotor Segmented Switched Reluctance Machine.

W. Sun¹, Q. Li¹, L. Sun¹, Y. Wan¹ and X. Jiang¹

1. Department of Electrical Engineering, School of Automation, Nanjing University of Science and Technology, Nanjing, China

I. Introduction Axial-field switched reluctance machine (AFSRM) inherits the advantages of switched reluctance machine (SRM) such as simple and rugged construction, low cost, and fault-tolerant operation [1]. The unique feature of axial-field topology also makes AFSRM suitable for applications with low length-diameter ratio, such as vehicle wheels. In our previous studies, a novel AFSRM, namely axial-field dual-rotor segmented switched reluctance machine (ADS-SRM), is developed and investigated [2], [3]. However, the emphases are laid on its design methodology and torque ripple reduction. For electrical machines in automobile use, it is also necessary to reduce their weights [4]. In this paper, the optimization of stator construction for the weight minimization of ADS-SRM is implemented. After optimization, the weight of whole machine, including iron cores and coils, is reduced by roughly 25%, while the torque production capability is maintained. II. Optimization of Stator Construction Fig. 1(a) shows the discussed three-phase 12/8 ADS-SRM [2]. The motor consists of a single internal stator and two external rotors. The stator consists of twelve excitation poles, the outer and inner flux-conductive rings. The rotor consists of eight rotor segments at each side. Figs. 1(b) and 1(c) show the measuring points and operating points of flux density in the stator of ADS-SRM, respectively. It is observed that the iron-core saturation in the outer and inner flux-conductive rings is much smaller than that in the excitation pole. It is indicated that the utilizations of the iron core in the outer and inner flux-conductive rings are relatively low. To improve their utilizations, the geometries of the outer and inner flux-conductive rings should be modified. In this paper, the proposal is given in Figs. 2(a) and 2(b). As shown in Figs. 2(a) and 2(b), the runway-shaped grooves are considered on the flux-conductive rings. In Figs. 2(a) and 2(b), d is the distance between the upper/lower edge of the groove and the end surface of the flux-conductive ring, S_o and S_i are respectively the cross-sectional areas of each flux path in the outer and inner flux-conductive rings after modification, S_m is the cross-sectional area of the excitation pole, the coefficient k is the ratio between S_m and $S_o(S_i)$. Here, $S_o=S_i$. After the optimization of k and d , the weights of iron core and whole machine are 3.9 kg and 6.4 kg, respectively. The corresponding optimal values of k and d are 9 and 3 mm, respectively. The corresponding optimal values of k and d are 9 and 3 mm, respectively. Fig. 2(c) shows the motor geometry after optimization, and Fig. 2(d) shows the iron-core operating points in the optimized three-phase 12/8 ADS-SRM. Figs. 2(e) and 2(f) show the magnetic field distributions at unaligned and aligned rotor positions, respectively. The static torque characteristics of ADS-SRM before and after optimization are shown in Figs. 2(g) and 2(h), respectively. The modification of the stator construction is thus proved to have significant improvement in the utilization of the iron core, while there is roughly no degradation in the motor's torque-production capability. III. Conclusion This paper addresses the way to improve the utilization of the iron core at the stator part of ADS-SRM. An effective flux-conductive ring shape feature by having runway-shaped grooves is proposed and its optimal design delivered by optimizing the groove parameters shows significant improvement in the iron-core utilization at the stator part. Through the optimization of the groove parameters, the weight of whole machine is reduced by about 25%, from 8.5 kg to 6.4 kg, while there is roughly no degradation in the motor's torque-production capability.

[1] R. Krishnan, "Switched reluctance motor drives: modeling, simulation, analysis, design and applications," Boca Raton, FL: CRC Press, Jun., (2001). [2] W. Sun, Q. Li, L. Sun and L. Li, "Development and investigation of novel axial-field dual-rotor segmented switched reluctance machine," IEEE Transactions on Transportation Electrification, doi: 10.1109/TTE.2020.3033668, (2020). [3] Q. Li, W. Sun, L. Sun and L. Li, "Rotor segment split and its optimization of axial-field dual-rotor segmented switched reluctance machine," Energy Reports, vol. 6, suppl. 9, pp. 1144-1150, (2020). [4] T. Takahashi, M. Takemoto, S. Ogasawara, etc., "Size and weight reduction of an in-wheel axial-gap motor using ferrite permanent magnets for electric commuter cars," IEEE Transactions on Industry Applications, vol. 53, no. 4, pp. 3927-3935, July-Aug., (2017).

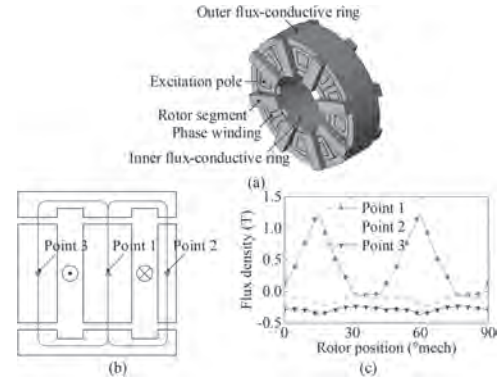


Fig. 1. (a) Motor geometry of three-phase 12/8 ADS-SRM. (b) Measuring points and (c) operating points of flux density in stator.

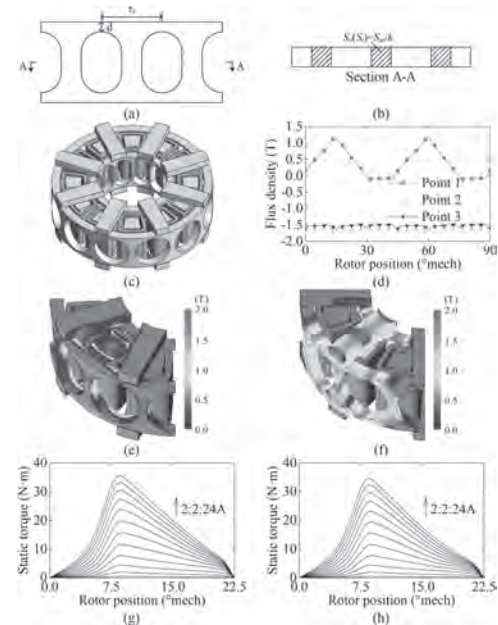


Fig. 2. (a) Front view and (b) section A-A of modified flux-conductive rings. (c) Motor geometry, (d) operating points, and magnetic field distributions at (e) unaligned and (f) aligned rotor positions after optimization. Static torque characteristics (g) before and (h) after optimization.

BW-11. Design and Optimization of Starting Capability of a Line-Start Synchronous Reluctance Motor.

Y. Hu^{1,2}, B. Chen^{1,2}, Y. Xiao², J. Shi², X. Li² and L. Li³

1. State Key Laboratory of Air-conditioning Equipment and System Energy Conservation, Zhuhai, China; 2. Gree Electric Appliances, Inc., Zhuhai, China; 3. Harbin Institute of Technology, Harbin, China

Abstract —The starting characteristics of a three-phase line-start synchronous reluctance motor(LS-SynRM) is introduced, and the main factors that affect the starting capability of the LS-SynRM are analyzed, and the optimization points for improving the starting capacity of the LS-SynRM are summarized. Under the condition that the efficiency of the motor keeps unchanged, a new rotor structure is proposed to improve the starting capacity of the LS-SynRM, and the effectiveness of the proposed rotor structure is verified by finite element analysis (FEA) and experimentation. 1. *Introduction* Compared with three-phase squirrel cage induction motors (SCIMs), three-phase line-start synchronous reluctance motors have the advantages of low cost, high efficiency, and constant speed, and have achieved a good development in recent years. The design method, efficiency optimization, and test method of the LS-SynRMs are studied in [1]-[4], but the research of starting characteristics of LS-SynRMs are few. In this paper, the starting capability of a 1.1kW six-pole LS-SynRM are analyzed and optimized to effectively improve the starting capability of the LS-SynRM. 2. *The starting principle and characteristics* During the starting process of a LS-SynRM, there are asynchronous torque T_a , negative-sequence asynchronous torque T_b , and reluctance pulsating torque T_c . Due to the magnetic field of rotor has serious imbalance($X_d \neq X_q$, X_d and X_q are the dq -axis reactance respectively), the rotor conductor bars induce positive and negative rotating magnetic fields; The positive rotating magnetic field induced by the rotor conductor bars interacts with the rotating magnetic field generated by the stator winding to generate the asynchronous torque T_a . the negative rotating magnetic field induced by the rotor conductor bars interacts with the rotating magnetic field generated by the stator winding to generate the negative-sequence asynchronous torque T_b ; When $s < 0.5$ (s is the slip rate), $T_b < 0$, which acts as a brake and affects the ability of the motor to pull into synchronization. In addition, the interaction of the rotating magnetic fields generated by stator and rotor respectively with different speeds produces a reluctance pulsating torque T_c with an average value of zero. When the inertia is small, the reluctance pulsating torque affects the pull in torque of the LS-SynRM. It can be seen that the starting capability of the LS-SynRM is related to the asynchronous torque T_a , the negative-sequence asynchronous torque T_b , and the reluctance pulsating torque T_c . 3. *Optimization and design of starting capability of LS-SynRM* Starting from three aspects of the asynchronous torque T_a , the negative-sequence asynchronous torque T_b , and the reluctance pulsating torque T_c , the starting capacity of a 1.1kW six-pole LS-SynRM are analyzed and optimized. Fig.1a shows the initial rotor structure of the LS-SynRM. The effects of rotor conductor bars structure, filling rate of conductor bars, flux barrier layers, and rotor inertia on the torque during the starting process are analyzed by finite element simulation, and a new rotor structure is proposed(Fig.1b). Without reducing the efficiency of the motor, the starting capacity of the improved motor has increased by 89%, and the effect is extremely obvious. Fig.2 shows the load torque, torque and speed curves of the initial LS-SynRM and the improved LS-SynRM when starting up with a under load (same inertia). The maximum pull-in torque of the initial LS-SynRM is 6.4Nm, and the maximum pull-in torque of the improved LS-SynRM is 12.1Nm, which is 89% higher than that of the initial LS-SynRM, and the starting capability of the improved LS-SynRM is significantly improved. 4. *Experimental verification* In order to further verify the improvement effect of the starting capability of the improved LS-SynRM, the initial LS-SynRM and the improved LS-SynRM were made and tested. The pull-in torque of the initial LS-SynRM is 6.2Nm, and the pull-in torque of the improved LS-SynRM is 11.8Nm. The pull-in torque of the improved LS-SynRM is 90.3% higher than that of the initial LS-SynRM, and the improvement effect of the improved LS-SynRM is verified. Since the actual temperature of the motor during the test is slightly higher than the temperature given during the simulation, the resistance increases, the pull-in torque of the motor test is slightly smaller than the simulated pull-in torque. 5. *Conclusion* The starting characteristics of a three-phase line-start synchro-

nous reluctance motor is introduced; The starting capacity of a 1.1kW six-pole LS-SynRM are analyzed, and the results show that the asynchronous torque at high speed is small, and the negative sequence asynchronous torque (braking torque) is large, resulting in a small pull-in torque and poor starting ability. For this reason, a new rotor structure is proposed, the simulated pull-in torque of improved LS-SynRM is improved by 89% than that of the initial LS-SynRM; Then the improvement effect of the starting capability of the improved LS-SynRM was further verified by the test for prototype.

[1] H. Liu and J. Lee, "Optimum Design of an IE4 Line-Start Synchronous Reluctance Motor Considering Manufacturing Process Loss Effect," in IEEE Transactions on Industrial Electronics, vol. 65, no. 4, pp. 3104-3114, April 2018. [2] Y. Hu, Y. Xiao, B. Chen and J. Shi, "Effect of Direction and Shape of Rotor Conductor Bars on Parameters of Line-Start Synchronous Reluctance Motor," 2018 21st International Conference on Electrical Machines and Systems (ICEMS), Jeju, 2018, pp. 634-639. [3] S. T. Boroujeni, N. Bianchi and L. Alberti, "Fast Estimation of Line-Start Reluctance Machine Parameters by Finite Element Analysis," in IEEE Transactions on Energy Conversion, vol. 26, no. 1, pp. 1-8, March 2011. [4] H. Kärkkäinen et al., "Direct-On-Line Synchronous Reluctance Motor Efficiency Verification with Calorimetric Measurements," 2018 XIII International Conference on Electrical Machines (ICEM), Alexandroupoli, 2018, pp. 171-177.

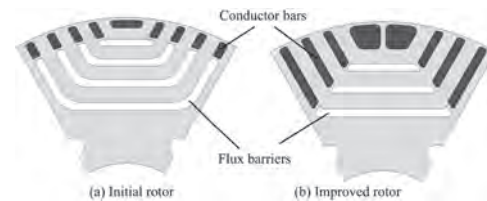


Fig.1. The initial and improved rotors of LS-SynRM

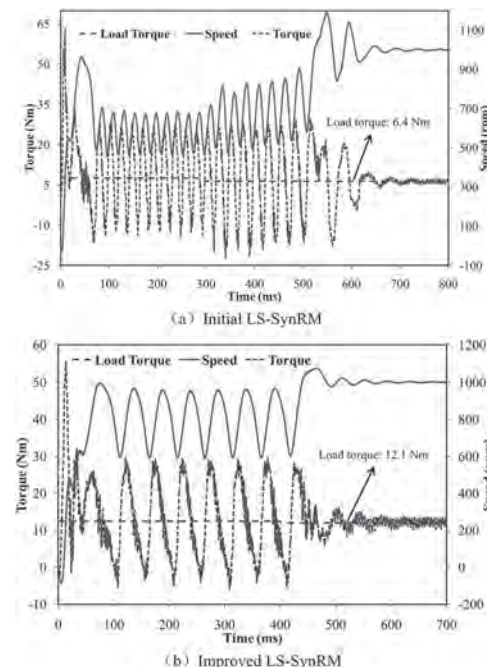


Fig.2. The load torque, torque, and speed curves of the initial and improved LS-SynRM

BW-12. A Study on Analysis and Design of Line-Start Synchronous Reluctance Motor Considering Rotor Slot Opening and Bridges.

H. Kim¹, Y. Park¹, S. Oh¹ and J. Lee¹

1. Electrical Engineering, Hanyang University, Seongdong-gu, The Republic of Korea

1. Abstract According to IEC 60034-1, as the industrial applications, not only efficiency but also power factor are important performance index. As a direct on line motor to replace induction motor (IM), a line-start synchronous reluctance motor (LS-SynRM) have a high efficiency but a low power factor than that of IM. Therefore, in this paper, the optimal design of LS-SynRM is proposed considering the efficiency, power factor, and mechanical stress using rotor slot opening and bridges. Based finite element analysis (FEA), the performances of LS-SynRM are analyzed according to the slot opening and the number of bridges. The initial model is selected considering the efficiency, power factor, and mechanical reliability. Then, based on the initial model, the optimal design is performed to improve the efficiency, power factor, and mechanical stress. Finally, the optimal design result is verified through the manufacture and experiment. 2. Introduction As the consumption of electric energy is increased, the efficiency of electrical motor is important. According to IEC 60034-1, the efficiency of motor is defined from IE1 to IE4. Recently, the industrial motors have been required to satisfy the IE4 class efficiency. A line-start synchronous reluctance motor (LS-SynRM) have been studied as an alternative to induction motor because LS-SynRM can have IE4 class efficiency. However, because of the saliency characteristic, LS-SynRM have a limited power factor [1]. In the industrial motors, the power factor is also an important factor according to IEC 60034-1 [2]. Therefore, the power factor of LS-SynRM must be improve for industrial application. In this paper, the optimal design of LS-SynRM is performed considering the efficiency, power factor and mechanical stress. The efficiency and power factor improve through reduction of leakage flux of the outer rib. In order to reduce the leakage flux, the rotor slot opening of outer rib is used, but the mechanical stress increases. Therefore, the bridges and rotor slot opening are used to improve the efficiency, the power factor, and mechanical reliability. First, based on finite element analysis (FEA), the performances of LS-SynRM are analyzed according to the number of bridges. Considering the performances of LS-SynRM, the initial model is selected. Furthermore, the optimal design is performed to maximize the efficiency, the power factor, and mechanical reliability. To verify FEA result, the optimal model of LS-SynRM is manufactured, and the experiment of LS-SynRM is performed. 3. Design of LS-SynRM LS-SynRM must be operated at synchronous speed. Moreover, LS-SynRM at synchronous speed have same performance with SynRM. Therefore, the performance of LS-SynRM at synchronous speed is as follow Eq. (1). $T_e = P_n(L_d - L_q)$ i_{dq} , $PF = (L_d - L_q) / (L_d + L_q)$ (1) Where T_e is torque, P_n is pole pair, L_d is d-axis inductance, L_q is q-axis inductance, i_d is d-axis current, i_q is q-axis current, and PF is power factor. From Eq. (1), the torque and power factor is function of the dq-axis inductance. In particular, the power factor is determined by the saliency ratio (L_d/L_q). Therefore, to improve power factor, the saliency ratio must be increased. From the relationship of the inductance and magnetic resistance as follows Eq. (2), the power factor is also function of the magnetic resistance ratio (R_q/R_d). $L = N^2/R$ (2) Where L is inductance, N is turn of winding, and R is the magnetic resistance. Therefore, the power factor of LS-SynRM are determined the design parameters design parameters affecting the dq-axis magnetic resistance. Based on the magnetic equivalent circuit [3], the q-axis magnetic resistance is increased by the rotor slot opening, but the mechanical stress of rotor is increased. In order to decrease the mechanical stress, the bridge is applied to the rotor. However, the d-axis magnetic resistance is increased by the bridges. Therefore, the design of rotor slot opening and bridge is relationship of trade off for motor performance. Considering the objective function, the optimal design is performed to improve the efficiency, power factor, and mechanical reliability. Fig. 1 shows the motor performance according to the two design parameters. As a result of the optimal design, the thickness of slot opening and bridge are designed to be 0.5[mm] and 0.5[mm], respectively. Fig. 2 shows the manufactured optimal LS-SynRM to verify FEA result. In the future, the detail the magnetic equivalent circuit will be discussed considering the slot opening and bridges. Furthermore, the optimal design method will be discussed

considering the efficiency, power factor and mechanical stress. 4. Conclusion In this paper, the performances of LS-SynRM are analyzed according to the rotor slot opening and bridges based on the magnetic equivalent circuit and FEA. Furthermore, the optimal design is performed to improve the efficiency, power factor, and the mechanical reliability. As a result, the rotor slot opening and bridges are designed to improve the efficiency and power factor considering the mechanical reliability. In the future, the detail magnetic equivalent circuit will be discussed according to the rotor slot opening and bridges. Moreover, the detail optimal design considering the mechanical reliability will be discussed. Finally, FEA and experiment result of manufactured LS-SynRM will be added to verify the optimal design result.

[1] K.-J. Joo, I.-G. Kim, and J. Lee, IEEE Trans. Magnetics, Vol. 53, Art no. 8102604 (2017) [2] A.T.D. Almeida, F.J.T.E. Ferreira, and A.Q. Duarte, IEEE Trans. Ind. Appl. Vol. 50, pp. 1274-1285 (2014) [3] J.-K. Lee, D.-H. Jung, and J. Lim, IEEE Trans. Magnetics, Vol. 54, Art no. 8103005 (2018)

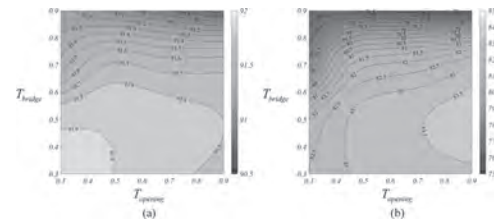


Fig. 1 Performance map of LS-SynRM according to design parameters (a) efficiency (b) power factor

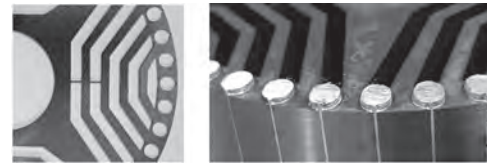


Fig. 2 Manufacture of optimal LS-SynRM

BW-13. Suspension Characteristics for a Novel Three-Pole Bearingless Switched Reluctance Motor.

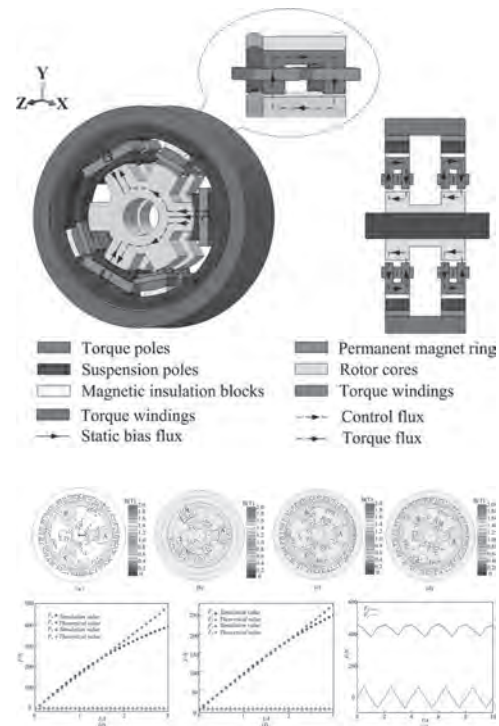
X. Ye¹, Z. Wang¹ and L. Mo¹

1. Huaiyin Institute of Technology, Huai'an, China

I. Introduction Switched reluctance motors (SRMs) inherently have the advantages of simple structure, no mechanical friction, flexible control and long service life so that they have a good application prospect in hybrid electric vehicle, military and rail transit. Bearingless switched reluctance motors (BSRMs) combine the merits of SRMs and magnetic bearings. However, in the traditional BSRMs, double windings are wound on the stator poles to produce suspension force and torque at the same time. It leads to a problem of nonlinear strong coupling between the torque flux and suspension flux. Therefore, a novel three-pole BSRM is presented, which produces torque and radial controllable suspension force. Each torque pole is designed to be two poles in the axial direction, and suspension poles can be designed larger. The torque poles take up less radial space of the stator in order to increase the radial suspension force density. Firstly, the configuration and suspension principle of the novel BSRM are introduced. Then, the mathematical model of radial suspension force calculation is presented by means of equivalent magnetic circuit. Finally, according to the main parameters of the BSRM, the air-gap magnetic fields and radial suspension forces are analyzed by MagNet 3D. The research results verify the performance of the proposed BSRM. II. Configuration and Suspension Principle According to Fig.1, the proposed BSRM consists of two pieces of stator cores with six stator poles, two rotor cores with six rotor poles and two radial magnetized permanent magnets. The stator poles can be divided into torque poles and suspension poles. Different from conventional BSRM, the torque poles are designed to place axially, the width of rotor pole and torque pole is designed to be equal, the width of suspension pole is designed to be larger than that of the rotor pole. Therefore, there is always a rotor pole under the suspension pole when the rotor is rotating. Radial suspension control flux is generated by radial control current, and the bias flux is generated by two permanent magnets, which form a close path through two stator cores and two rotor cores. Torque flux passes through the torque poles, air gaps and rotor poles, which is separated from the control flux. The paths of suspension flux and torque flux are separated. The torque and suspension force are decoupling naturally. Based on the equivalent magnetic circuit analysis, the mathematical models of suspension force are deduced. The radial suspension force can be written as $F_j = F_{pm} + k_{ij} \times ij$ where the subscript "j" denotes A, B and C. F_{pm} is the magnetic attraction force produced by the bias flux at the equilibrium position. k_{ij} is the radial force-current stiffness. F_m and k_{ij} can be given as $F_{pm} = S \times \mu_0 \times F_m \times F_m \div (4g^2)$ $K_{ij} = S \times \mu_0 \times F_m \times N \div (2g^2)$ where μ_0 is vacuum permeability. S is radial magnetic pole area. g is radial air gap length. N is number of radial control coils. III. Models, Design and Analysis To analyze the electromagnetic performance of the proposed three-pole BSRM, including magnetic flux distribution and the force-current relationships, the software MagNet is used to build the finite element model. The simulation results are shown in Fig. 2. Fig. 2(a) shows the bias flux distribution of the proposed BSRM. When the rotor is located in the balance position, the air gap bias flux density under three suspension poles is equal. Fig. 2(b) shows the control flux distribution when the maximum suspension force in the X direction is generated. The reluctant flux distribution is shown in Fig. 2(c) and Fig. 2(d). In Fig. 2(c), it can be seen that the air gap flux density increases under pole A and decreases under pole B and pole C, resulting in a suspension force pointing to the positive X direction. Fig. 2(d) shows another case of the reluctant flux distribution. The air gap density increases under pole B and decreases under pole C. It leads to the suspension force pointed to the positive Y direction. Therefore, the correctness of magnetic circuit and suspension mechanism is proved. The relationship between the control current and radial suspension force F_x and F_y can be calculated. Comparison between the simulation value and theoretical value is shown in Fig. 2(e) and Fig. 2(f). In Fig. 2(e), the suspension force in the X direction is produced, when the current changes from 0 to 3 A. When the control current changes from 0 to 3 A, the force-current relationship is shown in Fig. 2(f). Based on the above analysis, the correctness of the mathematical model is proved. Fig. 2(g) shows the fluctuation suspension force F_x and F_y . It can be seen that the force is stable in the rotating condition. IV. Conclusion This paper presents

a novel three-pole BSRM with independent torque and suspension force magnetic circuit. The theory analysis and simulation results are verified the electromagnetic performance of the proposed BSRM.

[1]J. Ju, H. Zhu and C. Zhao, "Radial Force-Current Characteristic Analysis of Three-Pole Radial-Axial HMB," *2016 IEEE Vehicle Power and Propulsion Conference (VPPC)*, Hangzhou, 2016, pp. 1-6. [2]R. Zhu, W. Xu, C. Ye, J. Zhu, G. Lei and X. Li, "Design Optimization of a Novel Heteropolar Radial Hybrid Magnetic Bearing Using Magnetic Circuit Model," in *IEEE Transactions on Magnetics*, vol. 54, no. 3, pp. 1-5, March 2018, Art no. 8201105.



BW-14. A Wireless Three-Phase Switched Reluctance Motor Using Single Receiver.

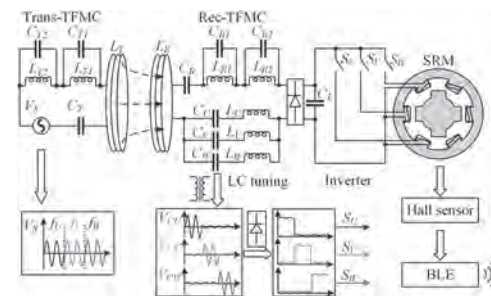
H. Wang¹, K. Chau¹, C. Lee², X. Tian¹ and T. Yang¹

1. Electrical and Electronic Engineering, University of Hong Kong, Hong Kong; 2. Electrical and Electronic Engineering, Nanyang Technological University, Singapore, Singapore

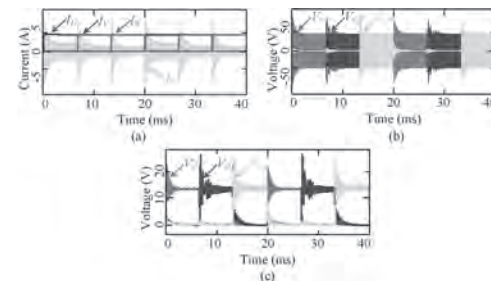
INTRODUCTION Since Nicholas Tesla proposed the concept of wireless power transfer (WPT) in the 1890s, it has been considered as an innovative technology, which offers definite advantages of reliability and electrical isolation [1]. Due to these outstanding advantages, many researchers have applied this emerging technology in the domestic and industrial electronic areas, such as consumer electronics and medical devices [2]. The idea of wireless motor can be traced back to 2016 when Motoki Sato proposed probably the first wireless motor [3], which aims to avoid power cable friction. Although it is favorable in harsh environments, it is ill-suited for isolated environments, because the motor controller is installed in the secondary side, which highly requires regular maintenance. To overcome this problem, wireless switched reluctance (SR) motor [4] is proposed, which adopts a self-drive circuit to replace the motor controller. However, this system needs three receivers to feed three-phase stator windings, and this causes three drawbacks: 1) this topology is bulky and heavy; 2) mutual inductance between receivers will harm system selectability; 3) after commutation, the energy restored in the receiver coil will be discharged by feeding the corresponding stator winding, which extends the commutation time and causes reverse torque. In other words, this topology highly limits motor speed and decreases system efficiency. The purpose of this paper is to propose a new wireless SR motor with single receiver, which takes distinct advantages of compact structure and better dynamic performance. The key is to employ a suitable three-frequency resonating compensation (TFRC) network [5], and a specially designed self-drive inverter. **METHODOLOGY** Fig. 1 depicts the system configuration, where L_T and L_R are the inductance of transmitter and receiver; C_T , C_{T1} , L_{T1} , C_{T2} , and L_{T2} are the resonant inductances and resonant capacitance to constitute the primary TFRC network, while C_R , C_{R1} , L_{R1} , C_{R2} , and L_{R2} constitute the secondary TFRC network; L_U , C_U , L_V , C_V , L_W , and C_W constitute three-phase LC tuning circuits to offer the control signal for secondary inverter; C_L is the filter capacitance of the bridge rectifier; S_U , S_V , and S_W comprise the three-phase inverter; V_S , V_{CU} , V_{CV} and V_{CW} are adopted to represent the voltage of AC power source, C_U , C_V , and C_W , respectively. It should be noted that the TFRC network can fully compensate transmitter and receiver at three frequencies, namely f_U , f_V , and f_W , and the design procedure is described in [5]. Besides, U-phase, V-phase, and W-phase LC tuning circuits are resonant at f_U , f_V , and f_W , respectively. The whole control process can be handle from the primary side by changing the frequency of V_S , and the method of extracting control signal for secondary inverter is basically same as wireless SPIM [6]. Taking U-phase as an example, when the primary side transmits the energy at f_U , the receiver current mainly flows the U-phase LC tuning circuit, so V_{CU} is high while V_{CV} and V_{CW} are almost zero, thus only S_U is switched on while the other switches are off. Therefore, by switching system frequency alternatively, three stator windings can be fed in turns, and rotating stator magnetic field can be acquired. Besides, rotor position can be detected by Hall position sensor, and transmitted to the primary side through Bluetooth. In addition, power balance between three phases is also considered. As the secondary induced voltage is inversely proportional to the transmitting frequency, the effective value of transmitter current should be carefully regulated according to [6]. Circuit simulations are carried out to show the feasibility of the proposed system. The key parameters will be given in the full paper, and the load motor is replaced by 20 Ω resistor, which is the equivalent resistance of SR motor according to [4]. The result is shown in Fig. 2 (a), where three stator windings are fed with I_U , I_V , and I_W in turns, which proves the feasibility of this system. Meanwhile, it can be observed that the value of three-phase current is the same by changing the transmitter current I_T in different phases. Besides, self-drive ability is also analyzed. As shown in Fig. 2(b) and (c), V_{CU} , V_{CV} , and V_{CW} are reliably higher than 7V when the system operates at the corresponding frequencies, and these voltages can be employed to control inverter after isolating and rectifying. **CONCLUSION** In this paper, a novel wireless SR motor system is presented. Compared with [4], the proposed system employed single trans-

mitter and single receiver system to achieve compact structure, and a self-drive inverter is adopted to avoid the freewheeling and the resulting reverse torque. Besides, this system retains the merit of secondary-controller-less, which is favorable for maintenance-free operation. For verification, simulations are conducted and prove system feasibility. Furtherly, the experiment will be given in the full paper. Acknowledgment This work was supported by a grant (Project No. 17207420) from the Hong Kong Research Grants Council, Hong Kong Special Administrative Region, China.

[1] Y. Bu, T. Mizuno, and H. Fujisawa, "Proposal of a wireless power transfer technique for low-power multireceiver applications," *IEEE Transactions on Magnetics*, vol. 51, no. 11 (2015) [2] H. Moon, S. Kim, and H. H. Park, "Design of a resonant reactive shield with double coils and a phase shifter for wireless charging of electric vehicles," *IEEE Transactions on Magnetics*, vol. 53, no. 3 (2015) [3] M. Sato, G. Yamamoto, and D. Gunji, "Development of wireless in-wheel motor using magnetic resonance coupling," *IEEE Transactions on Power Electronics*, vol. 31, no. 7, pp. 5270-5278 (2016) [4] C. Jiang, K. T. Chau, and W. Liu, "An LCC-compensated multiple-frequency wireless motor system," *IEEE Transactions on Industrial Informatics*, vol. 15, no. 11, pp. 6023-6034 (2019) [5] Z. Zhang, X. Li, and H. Pang, "Multiple-frequency resonating compensation for multichannel transmission of wireless power transfer," *IEEE Transactions on Power Electronics*, to be published. [6] H. Wang, K. T. Chau, and C. H. T. Lee, "Design, analysis and implementation of wireless shaded-pole induction motors," *IEEE Transactions on Industrial Electronics*, to be published.



System configuration of wireless SR motor



Simulation results under rated condition. (a) Current of transmitter and load. (b) Voltages of capacitors in LC tuning circuits. (c) Voltages of capacitors in LC tuning circuits after rectification.

BW-15. Coupling Method of Circuit Equation and Magnetic Field Distribution for Characterization of Induction Motors by Coordinate Transformation.

Y. Kim¹

1. Department of Electrical and Electronic Engineering, Joongbu University - Inno-Media Campus, Goyang, The Republic of Korea

I. Introduction In this paper, a new coupling method for efficient and simple analysis of induction motor is presented. The circuit concept is applied to stator winding and each conductor loop of rotor composed of rotor bar and end ring segment. The flux linkage by magnetic field distribution is used instead of inductance matrix. The flux linkage is calculated using air-gap flux density distributions by unit current in stator winding and rotor bars. Once the field distribution by one coil is calculated by FEM, its result is used for total flux linkage by employing a coordinate transformation. Its numerical results show a good agreement with the existing results. Especially the method is very effective in analyzing the effect of the number of rotor bars. This This method can be used for the analysis of both three-phase induction motors and single-phase induction motors. As the classical theory for operating characteristics of induction motor, there are two main theories: the two-motor theory of two rotating fields and the cross field theory. But they cannot deal the coil distribution and accurate magnetic field distribution, so that the effects of the number of rotor bars is not characterized. On the other hand, its full finite element analysis requires massive calculation time and complex modeling techniques for time-stepping eddy current problem and remeshing problem. In this paper, the circuit concept is applied to the stator winding and the rotor conductor loops composed of rotor bar and end ring segment. The flux linkage obtained from FE field analysis is employed instead of inductance matrix. The flux linkage is calculated using the air gap field distribution by a unit current in stator and rotor bars. The total flux linkage of external circuit equation is easily calculated using superposition of each coil field and a coordinate transformation. That is, this method requires only few field analyses of a unit current of stator and rotor conductor. Once the flux parameters are obtained, the overall motor characteristics such as stator current, rotor bar current, torque are easily calculated in both transient state and steady state. The transient characteristics for the all currents are calculated in a recursive form by using finite time difference scheme. II. Coupling Method Circuit and Flux Distribution The circuit equation of stator winding is represented by conventional voltage equation. The flux parameter of magnetic flux linkage is composed of the fields by both the stator winding current and the rotor bar currents. The circuit equation of rotor winding is also expressed by general equation like an Faraday's law. This Faraday formula requires a bar resistance, an endring resistance, and a current of each conductor bars. Also, the distribution of magnetic flux density on the rotor surface is required. Also, the KCL for the rotor bar and end ring is needed. Using the above equation we can calculate output current for the input voltage. The motor torque on the rotor bars can be also calculated from Lorentz force formula by using the resulting currents and magnetic flux density distribution. III. Numerical Applications The proposed algorithm is applied to a single and three phase induction motor. The rotor bar current is obtained as in Fig. 1. The average torque-speed curves according to different rotor bar resistances are shown in Fig. 2. This analysis technique is considered to be very useful to quickly grasp the characteristics in the initial process of designing single-phase and three-phase induction motors.

[1] Gyriil G. Veinott, E. E., D. Eng., *Theory and Design of Small Induction Motors*, McGRAW-HILL, 1959, pp. 184-197. [2] N. Sadowski, R. Carlson, S. R. Arruda, C. A. da Silva and M. Lajoic-Mazenc, "Simulation of Single-phase Induction Motor by a General Method Coupling Field and Circuit Equations," *IEEE Trans. on Magnetics*, Vol. 31, No. 3, 1995. [3] Sheppard J. Salon, *Finite Element Analysis of Electrical Machines*, Kluwer Academic Publisher, 1995. [4] D. Kim and B. Kwon, "A Novel Equivalent Circuit Model of Linear Induction Motor Based on Finite Element Analysis and Its Coupling With External Circuits," in *IEEE Transactions on Magnetics*, vol. 42, no. 10, pp. 3407-3409, Oct. 2006. [5] M. Liu, K. W. Chan, J. Hu, Q. Lin, J. Liu and W. Xu, "Design and Realization of a Coreless and Magnetless Electric Motor Using Magnetic Resonant Coupling Technology," in *IEEE*

Transactions on Energy Conversion, vol. 34, no. 3, pp. 1200-1212, Sept. 2019.

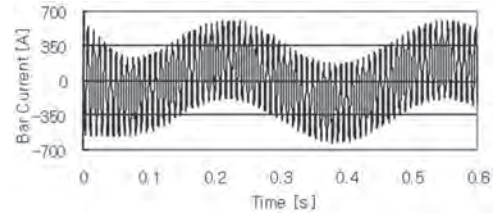


Fig. 1 Calculated Rotor Bar Current

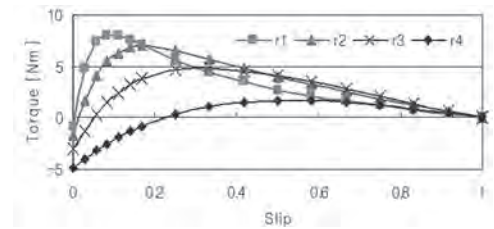


Fig. 2 Torque vs. Speed Characteristic Curve

BW-16. A Primary-Controlled Wireless Single-Phase Induction Motor Using Secondary Self-Drive Half-Bridge Inverter.

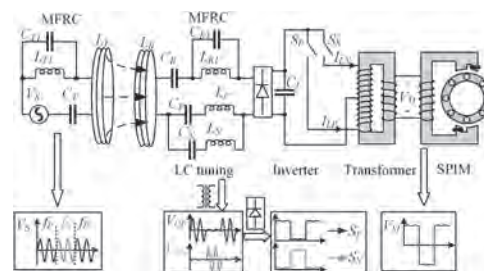
H. Wang¹, K. Chau¹, C. Lee², X. Tian¹ and T. Yang¹

1. *Electrical and Electronic Engineering, University of Hong Kong, Hong Kong*; 2. *Electrical and Electronic Engineering, Nanyang Technological University, Singapore, Singapore*

INTRODUCTION Wireless power transfer (WPT) is increasingly popular in many interdisciplinary areas, such as energy encryption and electric vehicles [1]. As the WPT has unique advantages of higher flexibility and no sparking hazard [2], the WPT changes the conventional usage of energy in industry and domestic applications. Recently, a number of efforts have been made to incorporate WPT into electric motors to achieve wireless motor, which is favorable for harsh and watery environments. [3] can be regarded as a landmark paper for proposing dual controller wireless motor, which cascades the traditional motor system in the receiver side of WPT, thus wire abrasion can be avoided in harsh environments. However, motor controller is fragile and not suitable for isolated environments, so WPT with primary-control systems for DC motor [4], switched reluctance (SR) motor [2], and shaded pole induction motor (SPIM) [5] have been studied, which used self-drive circuit to replace the motor controller. However, DC motor suffers from the fragile carbon brushes and commutator, wireless SR motor needs three receivers, and wireless SPIM needs five controlled switches. To solve these problems, this paper proposed a new wireless system with secondary half-bridge inverter for SPIM, thus the number of controlled switches can be eliminated from five to two, and the key is to employ a three-winding transformer. **METHODOLOGY** Fig. 1 depicts the system configuration, where L_T and L_R are the inductance of transmitter and receiver, while C_T , C_{T1} , and L_{T1} are the resonant inductances and resonant capacitance to constitute the multiple-frequency resonating compensation (MFRC) network [6] at the transmitter side, and C_R , C_{R1} , and L_{R1} constitute the receiver's MFRC network; L_P , C_P , L_N , and C_N constitute the positive and negative LC tuning circuits, which are resonant at f_P and f_N , respectively; C_L is the filter capacitance of the bridge rectifier; S_p and S_n comprise the half-bridge inverter to control two primary transmitter windings, namely, positive and negative windings, respectively, and I_{LP} and I_{LN} are used to represent the current of these two windings; V_S , V_{CP} , V_{CN} , and V_M are adopted to represent the voltage of AC source, C_P , C_N , and load motor, respectively. It should be mentioned that the switched-capacitor array is adopted in [5], but this compensation suffers from high voltage switching stress. Thus, a specially designed MFRC network is employed in this paper (the design method is detailed in [6]), which can seamlessly compensate the receiver and transmitter at two frequencies without any voltage stress. The working principle is almost the same as [5], as the whole control process can be separated into positive and negative half-cycles, and the control signal for S_p and S_n are extracted from V_{CP} , V_{CN} , respectively. Taking positive half-cycle as an example, when the primary side transmits the energy at f_P , the receiver current mainly flows the positive LC tuning circuit, so V_{CP} is high while V_{CN} is almost zero, thus S_p is on, and S_n is off. Therefore, by transmitting at f_P or f_N in turns, the positive and negative windings of the transformer are fed in turns. As the two primary windings of the transformer are reversely wound, AC voltage can be induced in the secondary winding of the transformer. Circuit simulations are carried out to show the feasibility of the proposed system. It should be mentioned that the load motor is replaced by a 120 Ω resistor, which is the equivalent resistance of SPIM in [5], and the other parameters will be given in the full paper. The simulation results are presented in Fig. 2, which depicts the waveforms of power source V_S and load voltage V_M , as well as the inverter output current I_{LP} and I_{LN} at different speeds. It should be noted that the power source should be higher when transmitting at a higher frequency [5], i.e., f_N , in this paper. Consistent with theory analysis, when the system frequency alternatively changes between f_P and f_N , I_{LP} and I_{LN} correspondingly change, and an AC voltage V_M is induced in the secondary side of the transformer to feed the SPIM. Besides, when the system works at rated condition, i.e., the effective value of V_M is 110 V, V_S is 70 V and 97 V at positive and negative half-cycles, respectively; when the system works at 25 Hz, and the effective value of V_M is 55 V, V_S becomes 35 V and 50 V at positive and negative half-cycles, respectively. Thus, it can be calculated that V_S/V_M is around 0.64 and 0.91 at positive and negative half-cycles, respectively. In

other words, both the frequency and voltage of the load can be proportionally controlled from the primary side, thus the speed regulation can be achieved. **CONCLUSION** This paper proposed a novel WPT system for SPIM with a self-drive half-bridge inverter. Compared with former research [5], less controlled switches are applied, thus the proposed system has higher stability and is more suitable for isolated environments. Besides, in order to compensate the transmitter and receiver at two frequencies, a proper MFRC network is employed, which successfully avoids the voltage switching stress. Finally, the simulation results are presented to show system's feasibility and the speed regulation ability, and the experiment will be given in the full paper.

[1] M. H. Mahmud, W. Elmahmoud, and M. R. Barzegaran, "Efficient wireless power charging of electric vehicle by modifying the magnetic characteristics of the transmitting medium," *IEEE Transactions on Magnetics*, vol. 53, no. 6, (2017) [2] C. Jiang, K. T. Chau, and Y. Leung, "Design and analysis of wireless ballastless fluorescent lighting," *IEEE Transactions on Industrial Electronics*, vol. 66, no. 5, pp. 4065-4074 (2019) [3] M. Sato, G. Yamamoto, D. Gunji, T. Imura, and H. Fujimoto, "Development of wireless in-wheel motor using magnetic resonance coupling," *IEEE Transactions on Power Electronics*, vol. 31, no. 7, pp. 5270-5278 (2016) [4] C. Jiang, K. T. Chau, and T. W. Ching, "Time-division multiplexing wireless power transfer for separately excited DC motor drives," *IEEE Transactions on Magnetics*, vol. 53, no. 11 (2017) [5] H. Wang, K. T. Chau, and C. H. T. Lee, "Design, analysis and implementation of wireless shaded-pole induction motors," *IEEE Transactions on Industrial Electronics*, to be published. [6] Z. Zhang, X. Li, and H. Pang, "Multiple-frequency resonating compensation for multichannel transmission of wireless power transfer," *IEEE Transactions on Power Electronics*, to be published.



System topology of wireless SPIM for traditional SPIM

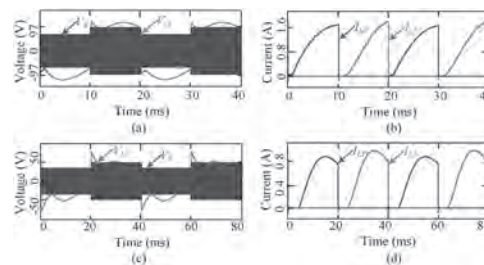


Fig. 2 Circuit simulation results at different frequencies. (a) Voltage at 50 Hz. (b) Current at 50 Hz. (c) Voltage at 25 Hz. (d) Current at 25 Hz.

BW-17. Influence of Driving Mode on Loss of Doubly Salient Brushless DC Motor With Rectangular Wire Winding.

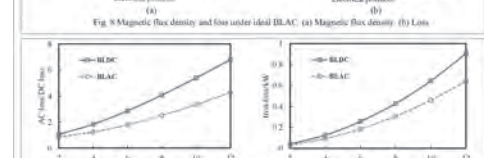
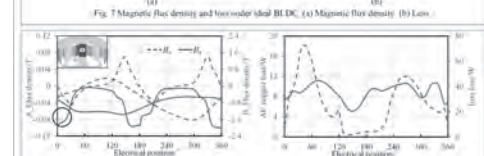
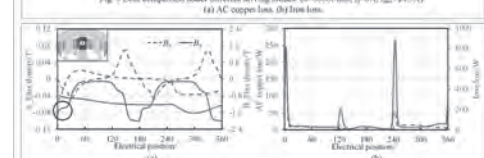
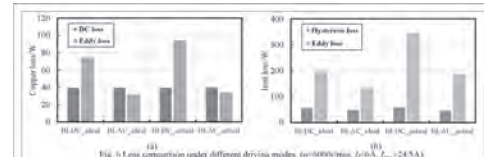
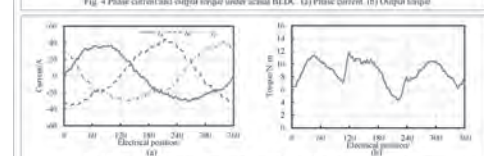
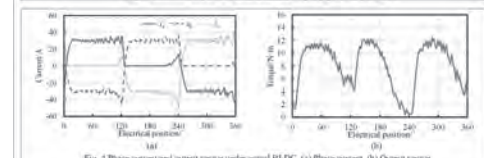
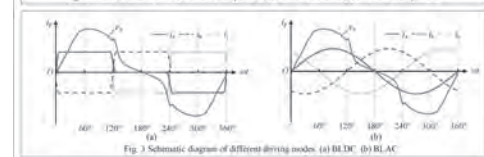
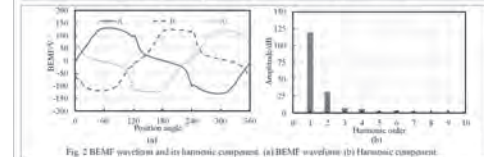
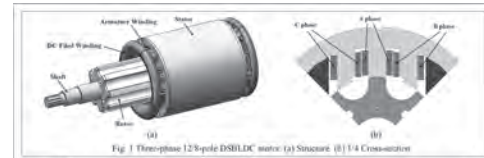
J. Zhang¹, Y. Xia¹, Z. Zhang¹, X. Chen¹ and M. Zhang¹

1. College of Automation Engineering, Nanjing University of Aeronautics and Astronautics, Nanjing, China

I. INTRODUCTION Doubly salient brushless DC (DSBLDC) motor offers the merits of simple structure, low cost, and high reliability because there is no permanent magnet on the rotor. The preformed rectangular wire winding has high filling ratio and excellent heat transfer performance [1], which can greatly improve the performance and fabrication efficiency of DSBLDC motor. Therefore, the DSBLDC motor with rectangular wire winding is applied in harsh operation conditions and low cost applications. The loss of the motor affects both efficiency and the heating of the motor, so the loss analysis is particularly important. At present, the loss analysis of DSBLDC motor mainly focuses on the influence of motor structure and winding form, and the control method is seldom studied. In this paper, the loss of a DSBLDC motor with rectangular wire winding driven by square wave and sinusoidal wave are comparatively studied, and the effect of PWM on motor loss in actual operation is considered. The influence of speed on loss under different driving modes is also studied. The loss of a 4.2kW DSBLDC motor with rectangular wire winding driven by different driving modes has been analyzed. II. MACHINE AND DRIVING MODES Fig. 1(a) shows the configuration of the 12/8-pole DSBLDC motor. The armature winding in the stator adopts rectangular wire winding, as shown in Fig. 1(b). The back electromotive force (BEMF) waveform and its harmonic component of DSBLDC motor are shown in Fig. 2. The BEMF of DSBLDC motor has the second harmonic component, and the BEMF waveform is near-sinusoidal. According to its BEMF characteristic, it can be respectively driven by square wave current or sinusoidal wave current, as shown in Fig. 3. In general, these two driving modes are called BLDC driving mode and BLAC driving mode respectively. Fig. 4 and Fig. 5 show the actual waveforms of phase current and output torque under two driving modes. The influence of pulse-width modulation (PWM) on motor loss should also be considered. By comparing Fig. 4(b) and Fig. 5(b), it can be seen that the output torque characteristic of BLAC mode is obviously better than that of BLDC mode. III. LOSS ANALYSIS AC copper loss and iron loss are the two main parts of the DSBLDC motor loss. AC copper loss consists of DC loss and eddy loss, and iron loss consists of hysteresis loss and eddy loss. Fig. 6 shows the results of loss comparison for the BLDC mode and BLAC mode with ideal and the actual phase current waveform under PWM control. When the effective value of phase current is 24.5A, the DC loss in AC copper loss and the hysteresis loss in iron loss are basically same in each driving mode, while both eddy losses in AC copper loss and iron loss of BLAC mode are less than that of BLDC mode. In addition, the actual PWM control causes high-frequency current ripple, which has more obvious influence on BLDC mode than BLAC mode, making the loss difference between the two driving modes further enlarged. Fig. 7 and Fig. 8 show the curves of the magnetic flux density and loss when the DSBLDC motor is driven by ideal BLDC and BLAC current. AC copper loss and iron loss analysis take point A at the armature winding position and point B at the stator core position as examples respectively. According to the relevant formula, the eddy loss is proportional to the second power of the magnetic density change rate. In BLDC mode, the magnetic flux density changes rapidly during the commutation, resulting in a significant increase of AC copper loss and iron loss. In BLAC mode, the magnetic flux density changes slowly during the whole cycle, so there is no significant increase of loss. The ratio of AC loss to DC loss and iron loss vary with the speed under two driving modes, as shown in Fig. 9. With the increase of the speed, AC copper loss and iron loss in BLDC mode increases faster than that in BLAC mode. IV. CONCLUSION In this paper, the copper loss and iron loss of a DSBLDC motor respectively driven by BLDC and BLAC are analyzed and compared. The output torque characteristic of BLAC mode is better than BLDC mode, and the loss characteristic is also better than BLDC mode. Under the two driving modes, The DC loss in AC copper loss and the hysteresis loss in iron loss are basically the same, but the eddy losses both in AC copper loss and iron loss of the BLAC mode decrease significantly, due to the reduction of magnetic field harmonic content in the motor groove and the iron core. Meanwhile, actual PWM control will relatively increase the loss

of the motor, but the influence on the BLAC mode is obviously less than that of the BLDC mode, making the loss advantage of BLAC mode more obvious. The loss increases with the increase of speed, and the increase is less in BLAC mode than in BLDC mode. The simulation results verify the correctness of the loss analysis.

[1] Y. Zhao, D. W. Li, T. H. Pei and R. H. Qu, "Overview of the rectangular wire windings ac electrical machine," in *CES Transactions on Electrical Machines and Systems*, vol. 3, no. 2, pp.160-169, June, 2019.



Session CA

SPIN CONVERSION EFFICIENCY BY VARIOUS METHODS TOWARDS DEVICE APPLICATIONS

Atsufumi Hirohata, Chair
University of York, York, United Kingdom

INVITED PAPERS**CA-01. Electrical Generation of Spin Currents.**

A.D. Kent¹, C. Safranski², J. Xu¹ and J.Z. Sun²

1. *Center for Quantum Phenomena, Department of Physics, New York University, New York, NY, United States*; 2. *IBM T. J. Watson Research Center, New York, NY, United States*

Spin currents in magnetic random access memory (MRAM) devices being developed by the semiconductor industry are generated by passing an electrical current perpendicular to layers that form a magnetic tunnel junction [1]. However, it is now widely appreciated that current flow in the plane of a layer can generate significant spin currents through spin-orbit coupling, as first reported in heavy non-magnetic metal layers (e.g. Pt, Ta & W). In this case, however, the spin polarization is generally confined to the plane of the layers. An important research goal is to create a spin current with an arbitrary polarization, including one with a significant out-of-plane spin polarization to enable efficient switching and displacement of domain walls in perpendicularly magnetized layers. In this talk we discuss spin-orbit induced charge-to-spin conversion in various materials and nanostructures [2] and with *magnetic materials*. Specifically, we will report our observation of spin torques with a planar Hall effect symmetry from CoNi, with a spin polarization in the magnetization direction of the layer [3]. We found the strength of this effect to be comparable to that of the spin Hall effect in Pt, indicating that the planar Hall effect in ferromagnetic metals holds great promise as a spin current source with a controllable spin polarization direction.

[1] A. D. Kent and D. C. Worledge, *Nature Nanotechnology* 10, 187 (2015)

[2] J-W. Xu and A. D. Kent, *Physical Review Applied* 14, 014012 (2020)

[3] C. Safranski, J. Z. Sun, J-W., Xu and A. D. Kent, *Physical Review Letters* 124, 197204 (2020)

CA-02. Unconventional Spin Currents in Obliquely Magnetized Magnetic Films.

B. Hillebrands^{1,2}, D. Bozhko³, H. Musiienko-Shmarova^{1,2}, V. Tyberkevych⁴, A.N. Slavin⁴, I. Syvorotka⁵ and A.A. Serga^{1,2}
 1. Physics, Technische Universitat Kaiserslautern, Kaiserslautern, Germany; 2. Research Center OPTIMAS, Kaiserslautern, Germany; 3. Physics, Colorado State University, Fort Collins, CO, United States; 4. Physics, Oakland University, Rochester, MI, United States; 5. Department of Crystal Physics and Technology, Scientific Research Company "Carat", Lviv, Ukraine

A spin current - a flow of spin angular momentum - can be carried either by spin-polarized free electrons or by magnons, the quanta of spin waves. Traditionally, it was assumed that a spin wave in a magnetic film with spin-sink-free surfaces could transfer energy and angular momentum only along its propagation direction. In this talk, using the data of Brillouin light scattering (BLS) spectroscopy in combination with an extended theory of dipole-exchange spin-wave spectra, I show that in obliquely magnetized magnetic films, the in-plane propagation of spin waves is accompanied by a transverse spin current without any corresponding transverse transport of energy [1]. It is found that in the case of oblique magnetization, the transverse profiles of in-plane-propagating dipole-exchange spin waves are formed by two co-propagating partial waves with opposite group velocities. Their superposition results in a traveling wave pattern, which carries angular momentum and can be treated as a transversal spin current. Its existence is evidenced by the behavior of thermal spectra of magnons in a yttrium iron garnet film measured in a wide range of wavenumbers using our novel wavevector-resolved BLS setup. In the case of an external excitation of the spin-wave modes carrying the transversal spin current, the angular momentum conservation law would lead to mechanical deformations or/and to the rotation of the magnetic film as a whole, which could be detected using the existing methods of spin mechatronics [2]. Furthermore, the presence of the unconventional spin current may be directly electrically detected [1, 3]. We believe that these non-trivial properties of spin-wave modes may be used in the future to control the effects of spin pumping or/and to generate spin currents in nano-scale spintronic signal processing and signal-generating devices. Funding by the Deutsche Forschungsgemeinschaft (DFG, German Research Foundation) within the Research Unit TRR 173-268565370 "Spin+X" (projects B01 and B04), as well as financial support by the European Research Council within the AdG SuperMagnonics, is gratefully acknowledged. The work was also supported in part by the US National Science Foundation, by the US Air Force Office of Scientific Research, and by the Oakland University Foundation.

[1] D. A. Bozhko, H. Yu. Musiienko-Shmarova, V. S. Tyberkevich, A. N. Slavin, I. I. Syvorotka, B. Hillebrands, and A.A. Serga, *Unconventional spin currents in magnetic films*, Phys. Rev. Research 2, 023324 (2020). [2] M. Matsuo, E. Saitoh, and S. Maekawa, *Spin-mechatronics*, J. Phys. Soc. Jpn. 86, 011011 (2017). [3] P. M. Gunnink, R. A. Duine, and A. Rückriegel, *Electrical Detection of Unconventional Transverse Spin Currents in Obliquely Magnetized Thin Films*, Phys. Rev. B 101, 220407 (2020).

CA-03. Spin Current Generation Driven by Ferromagnetic Resonance.*T. Mewes¹ and C. Mewes¹**1. Physics & Astronomy, The University of Alabama System, Tuscaloosa, AL, United States*

Conservation of angular momentum couples spin-currents present in a system with the magnetization dynamics of the ferromagnet. Injecting spin-currents into ferromagnets thereby enables the control of the magnetic state [1]. This forms the basis for many spintronic device applications including spin-transfer torque random access memory [2] and spin torque oscillators [3]. However, the inverse effect where the magnetization generates a spin current also takes place. This can be achieved very efficiently by driving the precession resonantly using an electromagnetic field at GHz frequencies. The same approach has been employed in ferromagnetic resonance spectroscopy experiments for over a hundred years now. Historically ferromagnetic resonance spectroscopy has extensively been used to determine the gyromagnetic ratio, magnetic anisotropies, and exchange stiffness of materials. In recent years the focus has shifted to utilizing broadband ferromagnetic resonance spectroscopy to determine the mechanisms responsible for magnetic damping [4]. In this context the observation that the precession of the magnetization can drive a spin-current into adjacent layers, is known as spin-pumping [5]. In ferromagnetic resonance spectroscopy spin pumping leads to a non-local contribution to the damping in the ferromagnet. This also enables the generation of pure spin currents by exciting the precession of a ferromagnet enabling new functionalities of spintronic devices. Based on this, ferromagnetic resonance spectroscopy can also be used to quantify the relevant parameters governing the spin current generation in these systems, including the interfacial spin mixing conductance [6] and the spin diffusion length [7]. In multilayer systems the spin currents generated at the ferromagnetic resonance frequently also result in the generation of a DC voltage most notably via the inverse spin Hall effect [8]. This has led to the ability to electrically detect ferromagnetic resonance with high sensitivity in small sample volumes, triggering a renewed interest in ferromagnetic resonance spectroscopy. We expect this to continue to enable new insights into the mechanisms foundational to the generation and detection of spin-currents driven by ferromagnetic resonance.

[1] J.C. Slonczewski, Current-driven excitation of magnetic multilayers, *J. Magn. Magn. Mater.* 159, L1 (1996). [2] E. Chen, D. Apalkov, A. Driskill-Smith, et al., Progress and Prospects of Spin Transfer Torque Random Access Memory, *IEEE Trans. Magn.* 48, 3025 (2012). [3] R. K. Dumas; S. R. Sani; S. M. Mohseni et al., Recent Advances in Nanocontact Spin-Torque Oscillators, *IEEE Trans. Magn.* 50, 1 (2014). [4] C. K. Mewes, T. Mewes, Relaxation in Magnetic Materials for Spintronics, *Handbook of Nanomagnetism*, Pan Stanford Publishing, Singapore, p. 71 (2015). Stanford Publishing, Singapore, 2015) p. 71. [5] Y. Tserkovnyak, A. Brataas, G.E.W. Bauer, Enhanced Gilbert Damping in Thin Ferromagnetic Films, *Phys. Rev. Lett.* 88, 117601 (2002). [6] M. Weiler, M. Althammer, M. Schreier et al., Experimental Test of the Spin Mixing Interface Conductivity Concept, *Phys. Rev. Lett.* 111, 176601 (2013). [7] A. J. Berger, E. R. J. Edwards, H. T. Nembach et al, Determination of the spin Hall effect and the spin diffusion length of Pt from self-consistent fitting of damping enhancement and inverse spin-orbit torque measurements, *Phys. Rev. B* 98, 024402 (2018). [8] E. Saitoh, M. Ueda, H. Miyajima, G. Tatara, Conversion of spin current into charge current at room temperature: Inverse spin-Hall effect, *Applied Physics Letters* 88(18), 182509 (2006).

CA-04. Transverse Thermoelectric Conversion Based on Spin Caloritronics.*K. Uchida*¹*1. Research Center for Magnetic and Spintronic Materials, National Institute for Materials Science, Tsukuba, Japan*

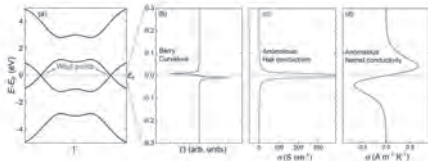
The interconversion between spin, charge, and heat currents is actively studied from the viewpoints of fundamental physics and thermoelectric applications in the field of spin caloritronics. This field is a branch of spintronics, which has developed rapidly since the discovery of the thermo-spin conversion phenomenon called the spin Seebeck effect. In spin caloritronics, various thermo-spin conversion phenomena have subsequently been discovered and magneto-thermoelectric effects, thermoelectric effects unique to magnetic materials, have received renewed attention with the advances in physical understanding and thermal/thermoelectric measurement techniques. The transverse thermoelectric conversion is one of the central topics in spin caloritronics, which is usually realized by the anomalous Nernst effect (ANE) and the anomalous Ettingshausen effect (AEE) in magnetic materials. In ANE (AEE), a heat (charge) current induces a transverse charge (heat) current in the direction perpendicular to the magnetization direction. Based on this symmetry, ANE/AEE exhibits a convenient scaling law that is entirely different from that of conventional thermoelectric effects. Furthermore, the thermoelectric output of ANE/AEE can be actively controlled through the manipulation of magnetization. Thus, ANE (AEE) has the potential to realize simple and versatile thermal energy harvesting or heat-current sensing (thermal energy management) applications. In this talk, we mainly report our recent experimental progress on ANE and AEE [1-5]. We also show a novel approach for transverse thermoelectric generation that exhibits a similar symmetry to ANE but is driven by a different mechanism [6].

[1] T. Seki, R. Iguchi, K. Takanashi, and K. Uchida, *Appl. Phys. Lett.* 112, 152403 (2018). [2] S. Ota *et al.*, *Sci. Rep.* 9, 13197 (2019). [3] H. Nakayama *et al.*, *Appl. Phys. Express* 12, 123003 (2019). [4] J. Wang, Y. K. Takahashi, and K. Uchida, *Nature Commun.* 11, 2 (2020). [5] A. Miura *et al.*, *Appl. Phys. Lett.* 115, 222403 (2019), *Appl. Phys. Lett.* 117, 082408 (2020), *Phys. Rev. Mater.* 4, 034409 (2020). [6] W. Zhou *et al.*, *Nature Mater.* (in press).

CA-05. Berry Curvature and Semimetals.C. Felser¹, Y. Sun¹ and C. Shekhar¹¹. *Chemical Physics of Solids, Max-Planck-Gesellschaft, Dresden, Germany*

Topology, a mathematical concept, recently became a hot and truly trans-disciplinary topic in condensed matter physics, solid state chemistry and materials science. Since there is a direct connection between real space: atoms, valence electrons, bonds and orbitals, and reciprocal space: bands, Fermi surfaces and Berry curvature, a simple classification of topological materials in a single particle picture should be possible [1]. A new class of topological phases that have Weyl points was also predicted in the family that includes NbP, NbAs, TaP, MoP and WP₂. [3-5]. Beyond Weyl and Dirac, new fermions can be identified in compounds that have linear and quadratic 3-, 6- and 8- band crossings that are stabilized by space group symmetries [2]. Crystals of chiral topological materials CoSi, AlPt and RhSi were investigated by angle resolved photoemission and show giant unusual helicoid Fermi arcs with topological charges of ± 2 [6,7]. In agreement with the chiral crystal structure two different chiral surface states are observed. As a consequence, the magnetic Heusler compounds have already been identified as Weyl semimetals: for example, Co₂YZ [8-11], and Co₃Sn₂S₂ [12-15]. In all these materials the Berry curvature and the classical anomalous Hall (AHE) and spin Hall effect (SHE) are enhanced and interesting for potential applications.

[1] Bradlyn et al., Nature 547 298, (2017), Vergniory, et al., Nature 566 480 (2019), [2] Bradlyn, et al., Science 353, aaf5037A (2016). [3] Shekhar, et al., Nat. Phys. 11, 645 (2015) [4] Liu, et al., Nat. Mat. 15, 27 (2016) [5] Gooth et al., Nature 547, 324 (2017) [6] Schröter, et al., Nature Physics 15, 759 (2019) preprint arXiv: 1812.03310 [7] Sanchez, et al., Nature 567, 500 (2019) [8] Kübler and Felser, EPL 114, 47005 (2016) [9] Wang, et al. Phys. Rev. Lett. 117, 236401 (2016) [10] Chang et al., Scientific Reports 6, 38839 (2016) [11] Belopolski, et al., Science 365, 1278 (2019) [12] Liu, et al. Nature Physics 14, 1125 (2018) [13] Liu, et al. Nat. Phys. Nature Physics 14, 1125 (2018) [14] Liu, et al., Science 365, 1282 (2019) [15] Morali, et al., Science 365, 1286 (2019)



CA-06. Spin Transport Driven by Emergent Magnetic Fields.*M. Matsuo*¹*1. Kavli Institute for Theoretical Sciences, University of Chinese Academy of Sciences, Beijing, China*

Spin current is a key concept in spintronics. In nonmagnetic metals, the spin-orbit coupling has been utilized for the spin current generation. Recently, an alternative scheme using emergent magnetic fields in moving media is demonstrated [1-5]. In this talk, we will present our recent results on spin transport in nonmagnetic metals driven by a variety of emergent magnetic fields originating from: 1. Liquid metal flow [2,3]. 2. Elastic motion [2,4]. 3. Rigid rotation [1,5]. 4. Non-uniform conductivity of gradient material [6]. 5. Surface plasmon polaritons [7,8]. Firstly, we consider the spin-current generation in moving media. In a moving media, such as elastic materials with the Rayleigh type surface acoustic wave is excited or a pipe flow of liquid metal, the vorticity field couples to conduction electron spin. As a result, the mechanical angular momentum of the moving media is converted into spin angular momentum. In particular, a spin current is generated along the vorticity gradient [2,3,4]. It should be noted that the mechanism using the spin-vorticity coupling is free from the strength of the spin-orbit coupling, and thus, weak spin-orbit coupling materials such as Cu can be utilized for the spin-current source [4]. In a rigid rotating metal, the conventional spin-orbit coupling is augmented due to the emergent magnetic field originating from mechanical rotation [1]. The mechanically induced spin-orbit coupling leads to the spin Hall effect [1]. We introduce a theory of the mechanical analog of the spin Hall effect and an experimental demonstration using magneto-optical detection of spin accumulation under the influence of mechanical rotation [5]. Next, we will discuss our recent experimentally demonstration of the nonreciprocal generation of spin current in a surface-oxidized copper film [6]. This nonreciprocity relies on the transfer of angular momentum from the velocity field of conduction electrons' collective motion. Finally, we consider a mechanism of angular momentum conversion from a transverse optical spin in surface plasmon polaritons (SPPs) to conduction electron spin. Conduction electrons in the metal follow the SPP's SPP's transversally spinning electric field, and the resulting orbital motions create inhomogeneous static magnetization in the metal. We will also present an experimental demonstration of the SPPs-induced spin current generation [8]. Such conversion from light to a spin current can be used as a coupler in next-generation spintronic computing with optical data transfer or storage.

[1] M. Matsuo et al., Phys. Rev. Lett 106, 076601 (2011) [2] M. Matsuo et al., Phys. Rev. B 87, 180402(R)(2013); Phys. Rev. B 96,020401(R) (2017). [3] R. Takahashi et al., Nat. Phys. 12, 52 (2016); Nat. Comm. 11, 3009 (2020). [4] D. Kobayashi et al., Phys. Rev. Lett. 119, 077202 (2017). [5] A. Hirohata et al., Sci.Rept. 8, 1974 (2018). [6] G. Okano et al., Phys. Rev. Lett. 122, 217701 (2019). [7] D. Oue and M. Matsuo, Phys. Rev. B 101, 161404(R) (2020). [8] T.J. Wijaya et al., arXiv:2004.12348

Session CB

SPIN INJECTION AND SPIN TRANSFER TORQUES

Tao Wang, Chair

Huazhong University of Science and Technology, Wuhan, China

CONTRIBUTED PAPER

CB-01. Local Control of the Exchange Bias by Current in a Pt/Co/NiO Structure.

M. Stebliy¹, A. Kolesnikov¹, M. Bazrov¹, A. Ognev¹, A. Davydenko¹, E. Stebliy¹, X. Wang², C. Wan², C. Fang², M. Zhao², X. Han² and A.S. Samardak¹

1. School of Natural Sciences, Far Eastern Federal University, Vladivostok, Russian Federation; 2. Institute of Physics, Chinese Academy of Sciences, Beijing, China

Recent theoretical and experimental studies of current-induced manipulation of spin ordering in ferro- (FM) and antiferromagnets (AFM) open up prospects for the development of modern devices for spintronics [1-3]. Antiferromagnets have a number of advantages over ferromagnets that make it possible to fabricate devices with a higher recording density, stability and speed of operation. Thanks to these features, a novel direction of antiferromagnetic spintronics is being actively developing [4,5]. However, the complexity of the experimental study of pure antiferromagnets forces us to seek alternative methods to control and register the Néel ordering. One of the ways is a study of advanced composite materials based on FM/AFM thin films, where the exchange bias (EB) effect at the interface between different magnetic phases opens an additional degree of freedom for modification and measuring the spin structure inside the AFM [6,7]. We present experimental possibility for manipulation of the exchange bias field in the Pt/Co/NiO structure by means of electric current [8]. Our experimental study revealed the mechanism of current-induced transformation in the magnitude and direction of the exchange bias field in this advanced structure. The orientation of the magnetization in FM layer plays a decisive role on direction of exchange bias and the effect of the current is reduced by heating in the investigated structure. Combination of domain structure in FM and influence of current with certain amplitude allows making different distributions of the exchange bias field strength inside the structure. For example, an EB field profile of “Min-Max-Min” type is shown in Fig. 1(c). A domain structure of FM for this case was obtained in the coercive force during remagnetization (see Fig. 1(a)). Hysteresis loops for the regions with Max and Min exchange bias fields are presented in Fig. 1(c). Another interesting EB distribution is shown in Fig. 1(e). The corresponding EB field profile of “Zero-Max-Zero” type could be used to control the nucleation centers of bubble skyrmions and pinning of domain walls. The presented results are useful not only for condensed matter physics in general, but also, for various practical applications in spintronics. Authors acknowledge the financial support of the Russian Ministry of Education and Science under the state task (0657-2020-0013), the Russian Foundation for Basic Research (grant 19-02-00530) and RSF-NSFC grant 21-42-00041. A.G. Kolesnikov thanks the scholarship of President of the Russian Federation for young scientists and graduate students (SP-350.2019.1). Xiufeng Han and Caihua Wan appreciate supports from the National Natural Science Foundation of China [NSFC, Grant No. 51831012, 51620105004, 11974398 and 12061131012] and Beijing Natural Science Foundation (Grant No. Z201100004220006).

[1] A. Hirohata, K. Yamada, Y. Nakatani, I.-L. Prejbeanu, B. Diény, P. Pirro, B. Hillebrands, *Journal of Magnetism and Magnetic Materials* 2020, 509, 166711. [2] S. A. Wolf, A. Y. Chtchelkanova, D. M. Treger, *IBM Journal of Research and Development* 2006, 50, 101. [3] X. Li, J. Yang, *National Science Review* 2016, 3, 365. [4] T. Jungwirth, X. Marti, P. Wadley, J. Wunderlich, *Nature Nanotechnology* 2016, 11, 231. [5] V. Baltz, A. Manchon, M. Tsoi, T. Moriyama, T. Ono, Y. Tserkovnyak, *Reviews of Modern Physics* 2018, 90, 015005. [6] J. Nogués, I. K. Schuller, *Journal of Magnetism and Magnetic Materials* 1999, 192, 203. [7] P.-H. Lin, B.-Y. Yang, M.-H. Tsai, P.-C. Chen, K.-F. Huang, H.-H. Lin, C.-H. Lai, *Nature Materials* 2019, 18, 335. [8] M.E. Stebliy, A.G. Kolesnikov, M.A. Bazrov, M.E. Letushev, A.V. Ognev et al., *Applied Physics Letters* 2021, 10.1063/5.0035667.

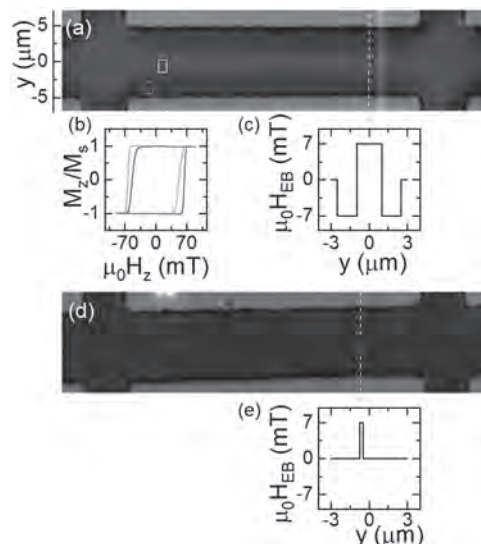


Fig. 1. (a) Illustration of the magnetic structure of the Hall bar, divided into three domains, using a Kerr microscope. (b) The graph shows the magnetic hysteresis loops recorded from the corresponding regions after passing a 30 mA pulse through the structure. (c) The exchange bias field profile. (d) Magnetic structure containing multiple isolated domains selected in the process of magnetization reversal. (e) The graph shows the profile of the exchange bias field after passing the current pulse.

INVITED PAPER

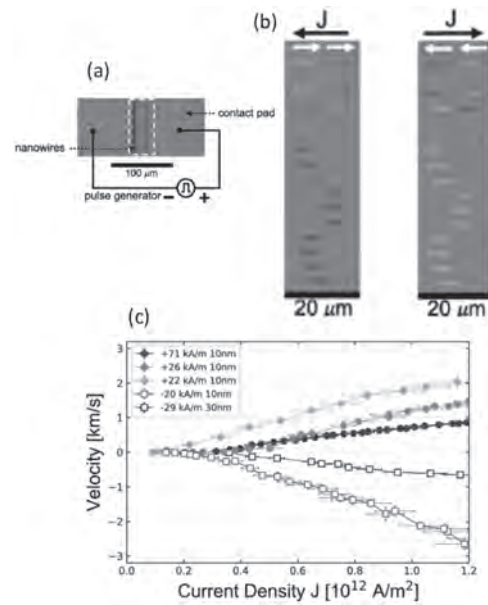
CB-02. Very Large Domain Wall Velocities Driven by Spin Transfer Torque in Ferrimagnetic Mn_4N Compounds INVITED.

S. Ghosh¹, T. Komori², A. Hallal¹, J.A. Peña Garcia³, T. Gushi², T. Hirose², H. Mitarai², H. Okuno⁴, J. Vogel³, M. Chshiev¹, J. Attané¹, L. Vila¹, T. Suemasu² and S. Pizzini³

1. SPINTEC, UGA-CNRS-CEA, Grenoble, France; 2. University of Tsukuba, Tsukuba, Japan; 3. Institut Néel, UGA-CNRS, Grenoble, France; 4. IRIG-MEM, CEA, Grenoble, France

Spin-transfer torque (STT) and spin-orbit torque (SOT) are spintronic mechanisms allowing magnetization manipulation using electrical currents. Beyond their fundamental interest, they allow envisaging applications to new classes of magnetic memories and logic devices, in particular based on domain wall motion. In the last 10 years the interest of the spintronic community has focused on thin ferromagnetic films deposited on a heavy metal, in which the interfacial Dzyaloshinskii-Moriya interaction (DMI) stabilises chiral Néel walls which can be moved by spin orbit torques associated to the spin Hall effect (SHE-SOT). Studies on systems in which domain walls are moved by STT are now rare, mainly because there are practically no reports of efficient STT in thin films with perpendicular magnetisation. A growing interest towards ferrimagnets appeared recently, as the efficiency of the torques is enhanced in the vicinity of magnetization compensation point. In this work, we report the study of current-driven domain wall (DW) dynamics in ferrimagnetic manganese nickel nitride ($Mn_{4-x}Ni_xN$) films with perpendicular magnetic anisotropy (PMA). The films are deposited on $SrTiO_3(001)$ substrates and crystallize in an anti-perovskite structure with two types of Mn atoms: Mn(I) located at the corners and Mn(II) located at the face centered sites. The two magnetic sublattices are antiferromagnetically coupled, with the net magnetization parallel to the Mn(I) moment. In the Mn_4N films, neither bulk nor interfacial DMI are present; domain walls have then Bloch internal structure and are driven by the “classical” spin-transfer torque (STT). Our Kerr microscopy measurements showed that, thanks to the large spin polarization of conduction electrons and to the ferrimagnetic structure leading to low spontaneous magnetisation, domain walls in Mn_4N can be moved by STT with an unprecedented efficiency [1]. More recently, DW dynamics was also studied in Ni-doped Mn_4N films ($Mn_{4-x}Ni_xN$). Since the Ni moment aligns antiparallel to the net magnetization in Mn_4N , the film composition can be finely adjusted to give a magnetisation compensation close to room temperature [2,3]. Films with compositions above and below the compensation composition and net magnetization parallel and antiparallel to that of Mn_4N were grown. Close to the compensation point, the reduced angular momentum strongly enhances the spin-transfer torque so that domain wall velocities approaching 3000 m/s were measured for a current density of 1.2×10^{12} A/m². These speeds are comparable with the largest reported for ferrimagnetic films deposited on a heavy metal, where SHE-SOT is the driving mechanism. In addition, while below the compensation point the DWs move in the direction of the electron flow, a reversal of the domain wall motion direction is observed when the magnetic compensation composition is crossed (Figure 1). This striking feature, related to the change of direction of the spin polarization with respect to that of the angular momentum, is in agreement with 1D analytical model and explained using *ab initio* calculations. Our material, composed of abundant elements, and free of critical elements such as cobalt, rare earths and heavy metals, is a promising candidate for the development of sustainable spintronics applications.

[1] T. Gushi et al. Nano Letters 19, 8716 (2019). [2] T. Komori, J. Appl. Phys. 125, 213902 (2019). [3] T. Komori et al. J. Appl. Phys. 127, 043903 (2019).



(a) Sketch of the device used for domain wall dynamics measurements; (b) Differential polar magneto-optical Kerr microscopy images, showing the displacement of domain walls during the application of a negative (left) and positive (right) current pulses, for a sample with composition below the compensation point. The white arrows indicate the direction of motion of the DWs; (c) domain wall speed versus current density for several $Mn_{4-x}Ni_xN$ compositions below (positive speeds, parallel to electron flow) and above (negative speeds, antiparallel to electron flow) the compensation composition.

CONTRIBUTED PAPERS

CB-03. Optically Detected Spin-Orbit Torque Ferromagnetic Resonance in an in-Plane Magnetized Ellipse.

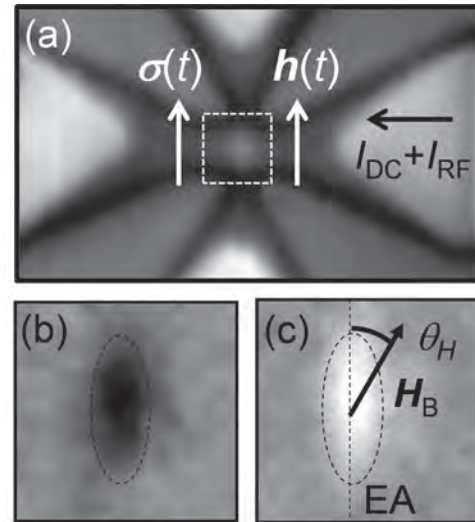
P.S. Keatley¹, K. Chatzimpaloglou¹, T. Manago^{1,2}, P. Androvitsaneas¹, T. Loughran¹, R.J. Hicken¹, G. Mihajlović³, L. Wan³, Y. Choi³ and J. Katine³

1. Department of Physics and Astronomy, University of Exeter College of Engineering Mathematics and Physical Sciences, Exeter, United Kingdom;
2. Department of Applied Physics, Fukuoka University, Fukuoka, Japan;
3. San Jose Research Center, Western Digital Corp, San Jose, CA, United States

Spin-orbit torque (SOT) is currently the subject of intense research activity due to its potential for switching storage elements in magnetic random access memory[1], generating microwave frequency spin wave auto-oscillations in spin Hall nano-oscillators (SHNOs)[2], and manipulating magnetic textures, e.g. skyrmions[3] in magnetic logic devices. Device operation is underpinned by the spin Hall effect, in which a spin current can be efficiently generated at the interface between a ferromagnetic metal (FM) and a current carrying heavy metal (HM) underlayer due to strong spin-orbit coupling in the HM. The spin current may then exert a SOT on the magnetization of the FM, exciting magnetization dynamics central to device function. A recent study of nano-contacted SHNOs[2] revealed a spatial dependence of the SOTs due to the current distribution within the HM of the device. Moreover, micron and sub-micron scale ferromagnetic elements are known to support non-uniform equilibrium states resulting from strong demagnetizing fields[4]. Since the in-plane (Slonczewski) spin-torque term of the Landau-Lifshitz equation of motion depends upon the relative local orientation of the magnetization and the injected spin polarization, the resulting SOT can be spatially dependent. At the same time the Oersted (Oe) field generated by the DC and RF currents (I_{DC} , I_{RF}) in the HM will also lead to a spatially dependent DC deflection and RF excitation of the magnetization respectively. Therefore, to explore the influence of non-uniform SOTs at the nanoscale, a spatially resolved probe of the resulting magnetization dynamics is required. In this work time-resolved scanning Kerr microscopy (TRSKM) was used to acquire spatiotemporally resolved SOT ferromagnetic resonance (FMR) spectra from an in-plane magnetized $\text{Co}_{40}\text{Fe}_{40}\text{B}_{20}$ (2 nm) ellipse of size $2 \times 0.8 \mu\text{m}^2$ positioned at the centre of a Pt(6 nm) Hall cross[5]. DC and RF currents were combined using a bias tee and passed through the $2 \mu\text{m}$ wide Pt lead perpendicular to the long axis of the ellipse, such that the resulting spin polarisation ($\sigma(t)$) and Oe-fields ($h(t)$) were parallel to the long axis of the ellipse, Figure 1(a). Preliminary time-resolved polar Kerr measurements in response to a broadband current pulse allowed the resonance frequency (~ 2.7 GHz) to be determined for an in-plane bias magnetic field (H_B) of 200 Oe, while the time-resolved measurements at $H_B = 200$ Oe in response to an RF current with frequency (f_{RF}) of 2.72 GHz allowed the time delay of node and antinodes of precession at resonance to be determined. Sweeping the magnetic field with the time delay set to a node or an antinode allowed the real or imaginary components of the dynamic susceptibility to be probed respectively. Time-resolved polar Kerr images, Figs. 1(b) and 1(c) revealed that the dynamics at resonance were quasi-uniform at the center of the ellipse, while weaker signal at the edge was consistent with the spatial resolution of ~ 400 nm. SOT-FMR spectra were therefore acquired from the center of the ellipse for a range of field angles θ_B and I_{DC} , while f_{RF} was set to 3.2 GHz so that the resonance field was well separated from the field at which switching of the equilibrium magnetization occurred. Optically-detected SOT-FMR spectra acquired with H_B applied along the HA ($\theta_B = 90^\circ$), and $I_{DC} = 0$ mA showed negligible influence of SOT, i.e. symmetric FMR peaks with respect to field with no broadening or narrowing when magnetized in opposite HA directions. A macrospin calculation reproduced the peaks and a damping parameter α of 0.03 was extracted, similar to the previously reported value for these devices[1]. The coefficient of the in-plane torque term (ST) was assumed to be zero in the HA calculations with $I_{DC} = 0$ mA. The value of I_{DC} was then increased from 1 mA to 10 mA and spectra measured with H_B along the HA, which again showed symmetric FMR peaks. However, when the bias field was applied 30° to either side

of the HA, marked asymmetry in both amplitude and linewidth were observed, in addition to a combined one- and two-fold angular dependence of the resonance field due to the DC Oe-field and shape anisotropy respectively. For a particular field history, the linewidth exhibited a marked crossover from broad to narrow as θ_B was changed from $+30^\circ$ to -30° from the HA. These observations were reproduced by the macrospin calculations, but failed to reproduce the linewidth narrowing/broadening for a single value of ST with $\alpha = 0.03$, while a smaller value of $\alpha = 0.025$ reproduced the linewidth of all FMR peaks with $ST = (6.75 \pm 0.75) \times 10^{-7}$ Oe $\text{A}^{-1} \text{cm}^2$. This work paves the way for spatially resolved characterization of SOT devices at the deep nanoscale, e.g. using near-field magneto-optical techniques[6,7], that is needed to achieve greater understanding of SOT-induced dynamics.

[1] G. Mihajlović, O. Mosendz, L. Wan, *et al.*, Applied Physics Letters, Vol. 109, p. 192404 (2016) [2] T. M. Spicer, P. S. Keatley, T. H. J. Loughran, *et al.*, Physical Review B, Vol. 98, p. 214438 (2018) [3] K. Zeissler, S. Finizio, C. Barton, *et al.*, Nature Communications, Vol. 11, p. 428 (2020) [4] P. S. Keatley, V. V. Kruglyak, A. Neudert, *et al.*, Physical Review B, Vol. 78, p. 214412 (2008) [5] P. S. Keatley, K. Chatzimpaloglou, T. Manago, *et al.*, Under Review, (2021) [6] J. Rudge, H. Xu, J. Kolthammer, *et al.*, Review of Scientific Instruments, Vol. 86, p. 023703 (2015) [7] P. S. Keatley, T. H. J. Loughran, E. Hendry, *et al.* Review of Scientific Instruments, Vol. 88, p. 123708 (2017)



(a) A reflectivity image of the device acquired using the TRSKM with the current, spin polarization, and Oe-field directions overlaid. The ellipse is centered within the dashed white region of interest, which defines the scan range in (b) and (c). (b) and (c) Polar Kerr images acquired at opposite antinodes of precession while the ellipse was at resonance in response to an RF current only. An in-plane bias field of ~ 200 Oe was applied perpendicular to the long, easy axis (EA) of the ellipse ($\theta_B = 90^\circ$). The nominal outline of the $2 \times 0.8 \mu\text{m}^2$ ellipse is shown by the overlaid dashed line.

CB-04. High-Precision Measurement Method of Magnetic Field Induced by Spin- Accumulated Electrons in FeCoB Nanomagnet.

V. Zayets¹

1. Platform Photonics Research Center, National Institute of Advanced Industrial Science and Technology (AIST), Tsukuba, Japan

An electrical current flowing through a nanomagnet can create an accumulation of spin- polarized electrons at nanomagnet boundaries. The magnetic field $H^{(SA)}$, which is originated by the accumulated spins, causes a torque, which may reverse the magnetization direction of the nanomagnet. This effect is called the Spin-orbit torque (SOT). The effect is used as a writing mechanism in magnetic Random Access Memory (MRAM). We report high-precision measurements of $H^{(SA)}$ in a FeCoB nanomagnet. A conventional measurement method of SOT is the method of the second harmonic¹⁻³, in which the current in the nanomagnet is modulated at a low frequency (~ 1 kHz) and the second harmonic of the Hall voltage is measured by the lock-in technique. In this method the second harmonic is generated due to the modulation of the magnetization direction by the current. The electrical current creates the spin accumulation due to the Spin Hall effect. The magnetic field $H^{(SA)}$ of the spin accumulation turns the magnetization direction from its easy axis. The Hall voltage is linearly proportional to the current and to the perpendicular component of the magnetization and they both are modulated. The frequency beating creates the second harmonic, which is proportional to the induced magnetic field $H^{(SA)}$ and therefore to the spin accumulation. This measurement method of $H^{(SA)}$ is indirect and contains several non-linear contributions, which makes the result interpretation difficult. For the same reason, it is difficult to identify a systematical error within this measurement method; the method suffers from a poor measurement precision and a poor reproducibility. The abstract describes a new method to measure magnetic field $H^{(SA)}$, which is induced by the spin accumulation in a nanomagnet. The proposed measurement is a direct measurement of $H^{(SA)}$. The merits of proposed method are a high precision (~1 Oe), a high- reproducibility and repeatability. A measurement of a magnetic field, which is induced by a tiny nanomagnet, is a challenging task. Additional measurement challenge is that the measured magnetic field $H^{(SA)}$ is very small. In the proposed method, the magnetic field $H^{(SA)}$ is measured by scanning external magnetic field H_{ext} perpendicularly to the magnetization direction and a DC measurement of the Hall voltage. The $H^{(SA)}$ is evaluated from the symmetry of the scan with respect to the reversal of the H_{ext} direction. The measurement of $H^{(SA)}$ in a nanomagnet is based on the fact that the nanomagnet magnetization is turned towards the $H^{(SA)}$ or towards any other magnetic field applied perpendicularly to the magnetization easy axis. The turning angle is symmetrical with respect to a reversal of direction of the applied magnetic field. The $H^{(SA)}$ is small (about of a few Oe) and therefore the magnetization turning angle is small (~0.1°) and difficult to measure. In the proposed method, a larger external magnetic field H is applied and scanned from negative to positive polarity. The $H^{(SA)}$ slightly shifts symmetry point of the scan from the point $H=0$. The fitting of the positive part of the scan to the negative part gives $H^{(SA)}$ with a high precision. The magnetic field $H^{(SA)}$ induced by the spin accumulation is measured in a FeCoB (thickness is 1.1 nm) fabricated on top of a Ta (thickness is 2.5 nm) nanowire contacted by a pair of Hall probes. The magnetization of the nanomagnet is perpendicular-to-plane. About 100 nanomagnets, which sizes vary between 50 x 50 nm to 3000 x 3000 nm, were measured. The external in-plane magnetic field is scanned either along or perpendicular to the current for an individual measurement of each component of $H^{(SA)}$. Additionally, a perpendicular- to- plane magnetic field H_z is applied in order to verify the dependency of the $H^{(SA)}$ on the Perpendicular Magnetic Anisotropy (PMA)⁴. Figure 1 shows measured $H^{(SA)}$ as a function of H_z and the current density for a 3000 x 3000 nm nanomagnet. The $H^{(SA)}$ depends substantially on both H_z and current density and both dependencies are related to each other. The component of $H^{(SA)}$, which is induced by the current, is always perpendicular to the component of $H^{(SA)}$, which is induced by perpendicular magnetic field H_z . Since H_z modulates the PMA strength⁴, the observed dependence implies that the current- induced $H^{(SA)}$ is substantially influenced by the PMA effect. It was suggested² that the second harmonic method measures two different types of torques. The field-like (FL) torque is measured, when the magnetization is inclined along the current. The damp-like (DL) torque is measured, when the magnetiza-

tion is inclined perpendicularly to the current. The suggestion was based on the symmetry of $H^{(SA)}$ with respect to the magnetization reversal. We have observed the same symmetry (Fig.1). However, our measurements can be explained more clearly by assuming that instead of two independent objects (FL and DL torques) there is only one independent object: the magnetic field $H^{(SA)}$, which is monotonically changing its direction and magnitude influenced by H_z and current. There are clear tendencies for observed direction and magnitude of $H^{(SA)}$. The direction of $H^{(SA)}$ is about 45° with respect to current for a larger nanomagnet (size > 800 nm) and nearly parallel to current for a smaller nanomagnet.

[1] U. H. Pi *et al.*, APL Vol. 97, p.162507 (2010). [2] K. Garello *et al.*, Nat. Nanotechnol. Vol. 8, p. 587 (2013). [3] J. Kim *et al.*, Nat. Mater. Vol. 12, p. 240 (2013). [4] V.Zayets MMM 2020, N4-03.

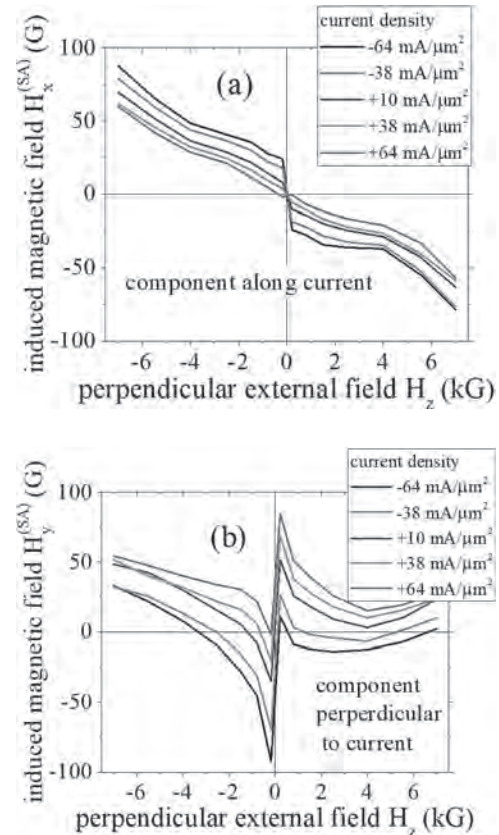


Fig.1 Measured in-plane magnetic field $H^{(SA)}$ induced by the spin accumulation as a function of a perpendicular-to- plane magnetic field and current density in a FeCoB nanomagnet. Measured component of $H^{(SA)}$ (a) along current (b) perpendicular to current.

INVITED PAPER

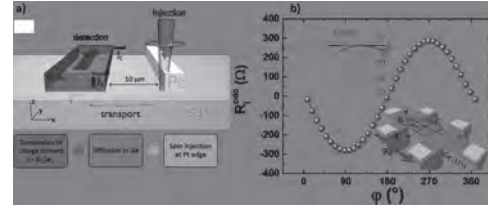
CB-05. Tuning the Spin-Orbit Interaction in Germanium for Spin Generation, Detection and Manipulation INVITED.

T. Guillet¹, C. Zucchetti², A. Marchionni², A. Hallal³, A. Marty³, C. Vergnaud³, G. Isella², H. Jaffrès⁴, N. Reyren⁴, J. George⁴, M. Chshiev³, M. Finazzi², A. Masseboeuf³, H. Okuno⁵, F. Bottegoni², A. Fert⁴ and M. Jamet³

1. Institut Catala de Nanociencia i Nanotecnologia, Bellaterra, Spain;
2. Physics, Politecnico di Milano, Milano, Italy; 3. IRIG-SPINTEC, CEA Grenoble, Grenoble, France; 4. UMR CNRS Thales, Palaiseau, France;
5. IRIG-MEM, CEA Grenoble, Grenoble, France

One of the main goals of spintronics is to achieve the spin transistor operation and for this purpose, one has to successfully implement a platform where spin currents can be easily injected, detected and manipulated at room temperature. In this sense, our work shows that Germanium is a very good candidate thanks to its unique spin and optical properties as well as its compatibility with Silicon-based nanotechnology. Throughout the years, several spin injection and detection schemes were achieved in Ge but the electrical manipulation of the spin orientation is still a missing part.[1,2] Recently we focused on two approaches in order to tune the spin-orbit interaction (SOI) in a Ge-based platform. Both rely on the structural inversion asymmetry and the spin-orbit coupling at surfaces and interfaces with germanium (111). First, we performed the epitaxial growth of the topological insulator (TI) Bi₂Se₃ on Ge(111). After characterizing the structural and electrical properties of the Bi₂Se₃/Ge heterostructure [3], we developed an original method to probe the spin-to-charge conversion at the interface between Bi₂Se₃ and Ge by taking advantage of the Ge optical properties. The results showed that the hybridization between the Ge and TI surface states could pave the way for implementing an efficient spin manipulation architecture.[4] The latter approach is to exploit the intrinsic SOI of Ge(111). By investigating the electrical properties of a thin Ge(111) film epitaxially grown on Si(111), we found a large unidirectional Rashba magnetoresistance, which we ascribe to the interplay between the externally applied magnetic field and the current-induced pseudo-magnetic field in the spin-split subsurface states of Ge(111).[5] The unusual strength and tunability of this UMR effect open the door towards spin manipulation with electric fields in an all-semiconductor technology platform. By further depositing an ultrathin Fe film on Ge(111), we could measure simultaneously the magnetoresistance contribution from the ferromagnetic Fe layer and the UMR from the Rashba gas at the Fe/Ge(111) interface.[6] Although the amplitude of the UMR is lower than for pure Ge(111), its temperature decay is slower, which indicates that the Rashba spin-orbit coupling has been reinforced. In a last step, we integrated perpendicularly magnetized (Co/Pt) multilayers-based magnetic tunnel junctions on the Ge (111) platform. We took advantages of the properties of the magnetic film and the semiconducting substrate to develop a second original electro-optical hybrid technique to detect electrically the magnetic circular dichroism in (Co/Pt) and perform magnetic imaging.[7] Then, these MTJs were then used to perform spin injection and detection in a lateral spin valve device. The perpendicular magnetic anisotropy (PMA) allowed to generate spin currents with the spin oriented perpendicular to the sample plane.

[1] C. Zucchetti et al., Phys. Rev. B 96, 014403 (2017) [2] F. Rortais et al., Appl. Phys. Lett. 18, 182401 (2017) [3] T. Guillet et al., AIP Advances 8, 115125 (2018) [4] T. Guillet et al., Phys. Rev. Lett. 124, 027201 (2020) [5] T. Guillet et al., Phys. Rev. B 101, 184406 (2020) [6] T. Guillet et al., ArXiv 2011.00351 (2020) [7] T. Guillet et al., Phys. Rev. Applied 15, 014002 (2021)



a) Illustration of the microdevice used for optical spin orientation. The scattering of circularly polarized light on the right (left) edge of a Pt stripe will create a pure spin current in germanium with in-plane orientation pointing to the right (left) respectively. The spin current is then absorbed and converted into a charge current in the Bi₂Se₃ bar by inverse Rashba-Edelstein effect. b) Experimental evidence of the UMR, the insets represent the measurement geometry, as well as a schematic picture of the electronic band structure of Ge. The subsurface states splitted by Rashba spin-orbit coupling are highlighted and lie in the bandgap above the valence band.

CONTRIBUTED PAPER

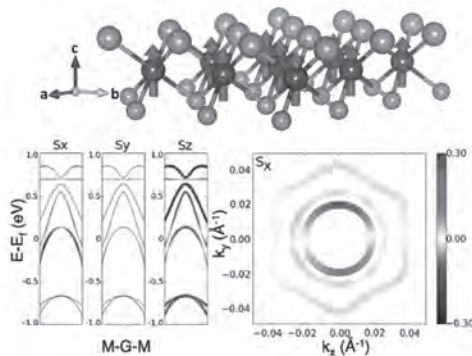
CB-06. Theory of Spin-Orbit Torque and Dzyaloshinskii-Moriya Interaction in van der Waals Magnets.

A. Manchon¹, S. Laref², I. Smaili², J.H. Garcia³, K. Kim⁴,
U. Schwingenschlogl² and S. Roche³

1. Aix-Marseille Université, Marseille, France; 2. King Abdullah University of Science and Technology, Thuwal, Saudi Arabia; 3. Institut Català de Nanociència i Nanotecnologia, Bellaterra, Spain; 4. Korea Institute of Science and Technology, Seongbuk-gu, The Republic of Korea

Two-dimensional magnets based on van der Waals materials are currently fostering great expectations for the advancement of spin-orbitronics, which aims to exploit the spin-orbit coupling in non-centrosymmetric magnetic heterostructures to enable current-driven magnetic torques and stabilize homochiral magnetic textures. Van der Waals magnets are particularly appealing for this purpose as their properties can be tuned by surface engineering at the atomic level. In this talk, I will present our investigation of the spin-orbitronics properties of selected highly promising van der Waals candidates, both in pristine and Janus configurations, from first principles and effective tight-binding models. I will first discuss the spin-orbit torque that emerges from inversion symmetry breaking in magnetic transition metal dichalcogenide monolayers [1] and demonstrate that sizable torques can be obtained, whose magnitude is controlled by the electric dipole due to the chalcogen elements. Most importantly, I will show the existence of a unique spin-orbit torque component that allows for field-free current-driven switching, of highest interest for applications. Then, I will discuss the nature of Dzyaloshinskii-Moriya interaction in these systems, and how they can stabilize magnetic skyrmions, but also magnetic bimerons depending on the magnetic anisotropy properties [2]. Finally, I will discuss the spin-orbitronics properties of $\text{Fe}_3\text{Ge}_2\text{Te}_2$ and show that in spite of its high symmetry, its inherent mirror symmetry breaking enables the onset of an in-plane Dzyaloshinskii-Moriya interaction that can stabilize planar chiral textures [3].

[1] I. Smaili, S. Laref, J. H. Garcia, U. Schwingenschlogl, S., A. Manchon arXiv:2007.07579 [2] S. Laref, V. M. L. D. P. Goli, I. Smaili, U. Schwingenschlogl, A. Manchon, arXiv:2011.07813 [3] S. Laref, K.-W. Kim, A. Manchon, Physical Review B 102, 060402(R) (2020)



(Top) Vanadium-based transition metal dichalcogenide monolayer with Janus structure. (Bottom left) Spin-projected band structure displaying the Rashba-like antisymmetric spin texture in momentum space. (Bottom right) Corresponding spin texture at Fermi level in (k_x, k_y) plane. This spin texture gives rise to spin-orbit torque.

Session CC**SPIN ORBIT TORQUES**

Shiheng Liang, Co-Chair
Hubei University, Wuhan, China

Kaiming Cai, Co-Chair
IMEC, Leuven, Belgium

INVITED PAPER

CC-01. Spin-Orbit Magnetic State Readout in Scaled Ferromagnetic/ Heavy Metal Nanostructures INVITED.

V. Pham^{1,3}, I. Groen¹, S. Manipatruni², W. Choi¹, D.E. Nikonov², E. Sagasta¹, C. Lin², T. Gosavi², A. Marty³, L. Hueso¹, I.A. Young² and F. Casanova¹

1. CIC nanoGUNE, San Sebastian, Spain; 2. Components Research, Intel Corp., Hillsboro, OR, United States; 3. Spintec, CEA-CNRS, Grenoble, France

Fast, high-density and energy-efficient computations are highly expected in the new generation of the nanodevices based on spintronic effects but it is challenged to bring them to microelectronic industry [1]. Recently, based on inverse spin-orbit effects, a new concept of magneto-electric spin-orbit (MESO) logic proposed [2] promises an advance in energy efficiency beyond CMOS technology [2, 3]. Spin to charge conversion is one key for building such devices. Particularly, inverse spin Hall effect (SHE) [4] / inverse Edelstein effects [5] are used for magnetic reading which can generate an electromotive-force with the advantage of cascading for the next elements of logic circuits and magnetoelectric effect which can reuse the spin-orbit-produced current/voltage for the magnetic writing so that allows saving energy. In this talk, our results on the electrical detection of direct/inverse SHE in the ferromagnet/spin-orbit material nanostructure [6-8] are firstly presented. Besides dedicating a promising tool for the metrology of spin-orbit materials, the studies on spin-charge conversion lay the groundwork for achieving the spin-orbit magnetic state readout operation [9], which is a big step on the route approaching the realization of MESO logic. Then, we report the favourable scaling law for such detection of an in-plane magnetic state of a magnet by using the inverse SHE in CoFe/Pt nanostructures [Fig. 1]. By reducing the dimensions of the device, a large inverse spin Hall signal of 0.3 Ω at room temperature [Fig. 2] is obtained and an effective spin-charge conversion rate for the ferromagnetic/heavy metal system is quantified. Adding a tunnelling barrier, 3.4 Ω spin Hall signal amplitude has been produced by replacing Pt by highly resistive amorphous Ta. This work also predicts that this spin-charge conversion nanostructure could be properly used to drive spin logic circuits [2, 3].

[1] B. Dieny, I. L. Prejbeanu, K. Garello, P. Gambardella, P. Freitas, R. Lehnendorff, W. Raberg, U. Ebels, S. O. Demokritov, J. Akerman et al., *Nat. Electron.*, Vol. 3, 446 (2020). [2] S. Manipatruni, D. E. Nikonov, C.-C. Lin, T.A. Gosavi, H. Liu, B. Prasad, Y.-L. Huang, E. Bonturim, R. Ramesh, I. A. Young, *Nature*, Vol. 565, 35 (2019) [3] S. Manipatruni, D. E. Nikonov, I. A. Young, *Nature Phys.*, Vol. 14, p.338–343 (2018). [4] M. I. Dyakonov and V. I. Perel, *JETP Lett.*, Vol. 13, p.467 (1971); [5] J.-C. Rojas-Sánchez, S. Oyarzún, Y. Fu, A. Marty, C. Vergnaud, S. Gambarelli, L. Vila, M. Jamet, Y. Ohtsubo, A. Taleb-Ibrahimi, P. Le Fèvre, F. Bertran, N. Reyren, J.-M. George, and A. Fert, *Phys. Rev. Lett.*, Vol.116, p.096602 (2016). [6] V. T. Pham, L. Vila, G. Zahnd, A. Marty, W. Savero-Torres, M. Jamet, and J.-P. Attané, *Nano Lett.*, Vol 16, p 6755 (2016) [7] V. T. Pham, L. Vila, G. Zahnd, A. Marty, W. Savero-Torres, M. Jamet, and J.-P. Attané, *Appl. Phys. Lett.*, Vol. 114, p.222401 (2019). [8] V.T. Pham, M. Cosset-Cheneau, A. Brenac, O. Boulle, A. Marty, J.-P. Attané, L. Vila arXiv:2011.12207 (2020) [9] V. T. Pham, I. Groen, S. Manipatruni, W. Y. Choi, D. E. Nikonov, E. Sagasta, C.-C. Lin, T. A. Gosavi, A. Marty, L. E. Hueso, I. A. Young and F. Casanova, *Nat. Electron.*, Vol. 3, 309 (2020)

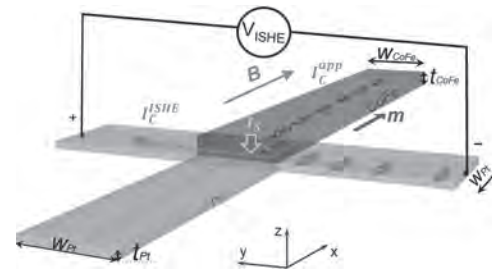


Fig. 1. Sketch of the spin-to-charge conversion nanostructure for detecting in-plane magnetic state detection. CoFe electrode (grey) is patterned on top of a Pt T-shaped nanostructure (red). The magnetization (m) of the CoFe electrode (red arrow) is controlled by a magnetic field B (gold arrow). A charge current I_C^{app} (dashed blue arrow) is used to inject a spin-polarized current I_S along the z -direction (yellow arrow) from CoFe into Pt. I_S is converted into a charge current I_C^{ISHE} (solid blue arrow) in the y -direction by the ISHE in Pt, which is measured as a voltage (V_{ISHE}) in the open circuit condition. The sign of the voltage is changed by m reversal. Note that the spin-polarized current I_S is simplified as a subtraction between flows of the majority and the minority spins.

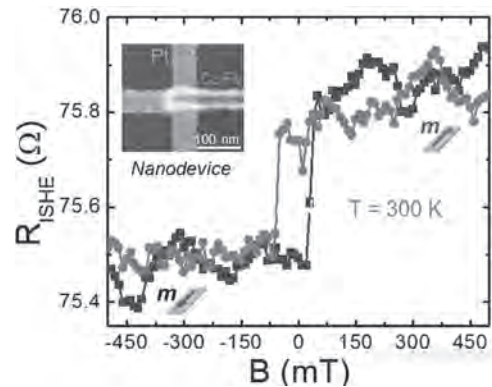


Fig. 2. An inverse spin Hall signal for spin-orbit magnetic state readout. The transverse resistance R_{ISHE} what is the normalized value from the measured ISHE voltage by applied charge current ($R_{ISHE} = V_{ISHE} / I_C^{app}$) as a function of the magnetic field B measured for the nanodevice (inset) at 300 K with the ISHE configurations as shown in Fig. 1. The two magnetization orientations are indicated. Blue squares correspond to trace and red circles to retrace of the magnetic field.

CONTRIBUTED PAPERS

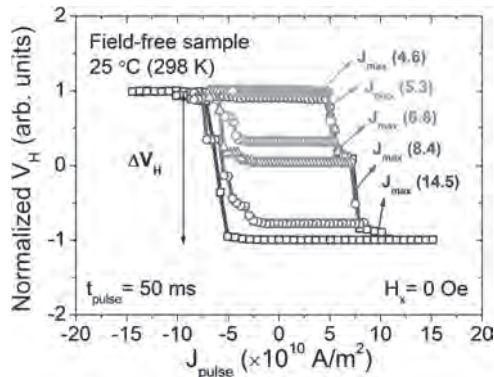
CC-02. Pulse-Width and Thermal Effects on Field-Free Memristive Spin-Orbit Torque Switching.

W. Liao¹, T. Chen¹, Y. Hsiao¹ and C. Pai^{1,2}

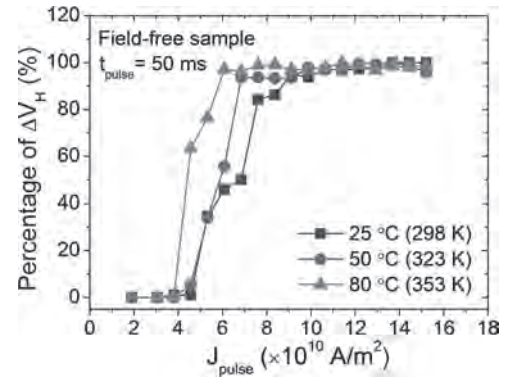
1. Materials Science and Engineering, National Taiwan University, Taipei, Taiwan; 2. Center of Atomic Initiative for New Materials, National Taiwan University, Taipei, Taiwan

Spin-orbit torque (SOT) has been demonstrated to manipulate the magnetization in various types of heterostructures. Besides the conventional current-induced SOT switching with the assistance of in-plane bias field, field-free SOT switching and memristive SOT switching have also drawn lots of interests due to the possible applications in commercial magnetic random access memory (MRAM) and neuromorphic computing devices. To further decrease power consumption in such devices, most works commit to enhance the SOT efficiency. However, the thermal stability of device is also essential for reliable applications. Especially when SOT devices are integrated with CMOS that the thermal dissipations from transistors can cause significant increase of ambient temperature. In this work, we systematically investigate the SOT efficiencies, thermal stability factors (Δ), and memristive SOT switching behaviors of a standard W/CoFeB/MgO device and a field-free CoFeB/W/CoFeB/MgO device. In both samples, the SOT efficacies are characterized to be constant from 25 °C (298 K) to 80 °C (353 K), where the thermal stability factors (Δ) are slightly degraded as increasing the temperature. The memristive SOT switching behaviors in both systems with various pulse-widths and temperatures are also examined.¹ The memristive switching windows are found to shrink at elevated temperatures, which poses the potential challenge of employing SOT devices in realistic neuromorphic applications. Our results suggest that, although the SOT efficacy is robust against thermal effects, the reduction of Δ at elevated temperatures could be detrimental to standard memory as well as neuromorphic (memristive) device applications.²

[1] S. Z. Rahaman, I. Wang, T. Chen, C. Pai, D. Wang, J. Wei, H. Lee, Y. Hsin, Y. Chang, S. Yang, Y. Kuo, Y. Su, Y. Chen, K. Huang, C. Wu, and D. Deng, IEEE Electron Device Lett. 39, 1306 (2018). [2] W.-B. Liao, T.-Y. Chen, Y.-C. Hsiao, and C.-F. Pai, Appl. Phys. Lett. 117, 182402 (2020).



The memristive current-induced switching of a field-free device with various J_{\max} .



Switching percentages as functions of the applied J_{\max} for temperature-dependent measurement.

CC-03. Modulation of Thermal Stability and Spin-Orbit Torque in IrMn/CoFeB/MgO Structures Through Atom Thick W Insertion.

D. Xiong¹, S. Peng¹, J. Lu¹, W. Li¹, H. Wu², Z. Li¹, H. Cheng¹, Y. Wang¹, C.H. Back³, K. Wang² and W. Zhao¹

1. Beihang University, Beijing, China; 2. University of California Los Angeles, Los Angeles, CA, United States; 3. Technische Universität München, München, Germany

Spin-orbit-torque- (SOT-) driven switching of ferromagnets (FM) with perpendicular magnetic anisotropy (PMA) has attracted extensive attention as it allows for lower-power and faster magnetization switching compared with the conventional spin-transfer torques.[1] However, the requirement of a static magnetic field collinear with the current to achieve deterministic switching poses a challenge to the SOT device application. By introducing antiferromagnets (AFM), recent studies have shown that the in-plane exchange-bias field generated at the AFM/FM interface enables field-free switching of perpendicular magnetization, which makes AFM/FM structure a promising candidate for future spintronic devices.[2,3] On the other hand, CoFeB/MgO-based magnetic tunnel junctions are attractive in achieving the state-of-the-art tunnel magnetoresistance (TMR) ratio, which is important for the development of advanced nonvolatile spintronics memories and logics.[4] Therefore, field-free magnetization switching in AFM/CoFeB/MgO structures has been drawing intense attention.[5] In these structures, however, the PMA was not strong enough to guarantee the long-term data storage for magnetoresistive random-access memory and was reported to be deteriorated upon annealing at temperatures above $\sim 200^\circ\text{C}$ due to the diffusion of Mn.[6] Besides, the spin-orbit torque of these AFM/CoFeB/MgO systems was not strong enough to implement low-power consumption for magnetization control. All the mentioned bottlenecks hinder the development of these structures in SOT devices. In this work[7], we investigated the modulation of thermal stability and SOT in IrMn/CoFeB/MgO structures through atom thick W insertion. The films consisting of Ta(2 nm)/IrMn(5 nm)/W(t_W)/Co₄₀Fe₄₀B₂₀(1 nm)/MgO(2.5 nm)/Ta(3 nm) were deposited on thermally oxidized Si substrate by magnetron sputtering, followed by annealing at 300°C for 30 minutes under an in-plane magnetic field of 1.5T. Subsequently, the films were patterned into Hall bar devices with the longitudinal channel and transverse channel width of 5 μm and 3 μm , respectively. Figure 1(b) presents magneto optical Kerr effect (MOKE) measurements, which shows that samples with W insertion exhibit sharp PMA signals while the magnetic signal of reference sample without W insertion vanished. This W layer serves as a thermal barrier to prevent the diffusion of Mn during annealing, which is confirmed by the results of spherical aberration corrected transmission electron microscope (ACTEM) and atomic-resolution electron energy-loss spectroscopy (EELS). Figure 1(d) shows field-dependent Hall resistance (R_{Hall}) measurements with in-plane applied magnetic fields $\mu_0 H_x$. The magnetization could not be fully pulled into the in-plane direction with magnetic field even up to 1000 mT, indicating the strong PMA of the samples with W insertion which is much larger than that in our previous report without W insertion, the PMA field of which is only ~ 300 mT.[6] Figure 2(b) presents W layer thickness dependence of SOT effective fields. Both damping-like effective field $\Delta\mu_0 H_x$, and field-like effective field $\Delta\mu_0 H_y$, are tuned by W layer thickness. Focusing on the variation trend of effective fields with W layer thickness, we find that the changes in SOT fields and PMA fields (Fig. 2a) track each other fairly closely. In order to investigate visually this relation, we plot SOT fields as a function of PMA fields in Fig. 2c. SOT fields scale roughly linearly with PMA fields, which is in consistence with theoretical calculations and experimental demonstration in other systems.[8] That is, the existence of interfacial spin-orbit coupling (ISOC) at heavy metal/FM interfaces quantified by PMA fields would reduce, in a linear manner, the effective SOT exerted on the FM layer. Finally, field-free magnetization switching was implemented in the sample with W insertion, and the obtained exchange bias field of 1.5 mT is comparable to that shown in our previous work without W insertion [6]. In summary, we have demonstrated that the thermal stability and PMA fields in IrMn/CoFeB/MgO heterostructures can be effectively enhanced by incorporating a thin W layer at the IrMn/CoFeB interface via suppressing the diffusion of Mn during annealing. Moreover, SOT fields scaling linearly with ISOC in IrMn/W/CoFeB quantified by PMA fields indicates that efficient

SOT could be achieved by minimizing the ISOC via the tuning of insertion W layer thickness. Finally, field-free switching of perpendicular magnetization is achieved when a thin W layer is inserted. This work demonstrates an efficient scheme for thermally robust technological application based on AFM spintronics.[7]

[1] S. Peng, D. Zhu, and J. Zhou, Adv. Electron. Mater., Vol. 5, p. 1900134 (2019). [2] S. Fukami, C. Zhang, and S. Duttapudua, Nat. Mater., Vol. 15, p. 535 (2016). [3] S. Peng, D. Zhu, and W. Li, Nat. Electron., Vol. 3, p. 757 (2020). [4] L. M. Loong, W. Lee, and X. Qiu, Adv. Mater., Vol. 28, p. 4983 (2016). [5] S. Peng, J. Lu, and W. Li, in International Electron Devices Meeting (IEDM 2019), p. 661 (2019). [6] J. Jeong, Y. Ferrante, and S. V. Faleev, Nat. Commun., Vol. 7, p. 10276 (2016). [7] D. Xiong, S. Peng, and J. Lu, Appl. Phys. Lett., Vol. 117, p. 212401 (2020). [8] L. Zhu, D. C. Ralph, and R. A. Buhrman, Phys. Rev. Lett., Vol. 122, p. 077201 (2019).

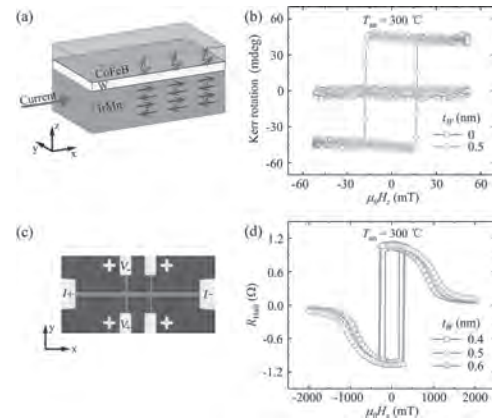


FIG. 1. (a) Schematic of deposited IrMn/W/CoFeB stacks. (b) MOKE measurements of film samples with and without W insertion under perpendicular magnetic fields. (c) Micrograph of the fabricated Hall bar device and illustration of the setup for Hall bar measurements. (d) Hall resistance (R_{Hall}) of samples annealed at 300°C with different W layer thickness under in-plane magnetic fields.

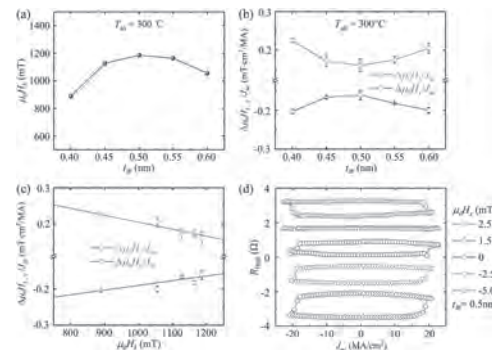


FIG. 2. (a) W layer thickness dependence of effective PMA fields. (b) W layer thickness dependence of damping-like fields (purple square) and field-like fields (blue circle). (c) Scaling of damping-like fields (purple square) and field-like fields (blue circle) with PMA fields. (d) SOT-driven magnetization switching under various in-plane magnetic fields for the sample with 0.5 nm W insertion layer.

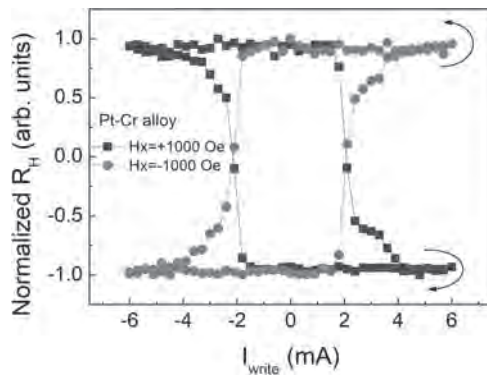
CC-04. Benchmarking of Spin-Orbit Torque Switching Efficiency in PtCu Alloys.

C. Hu¹ and C. Pai¹

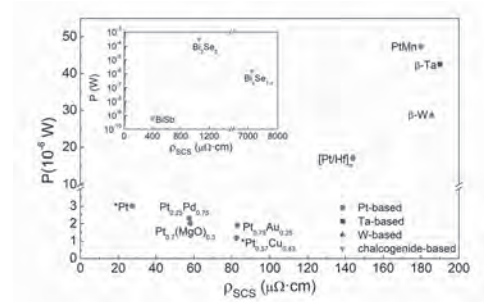
1. Materials Science and Engineering, National Taiwan University, Taipei, Taiwan

To satisfy the requirements for fast, energy-efficient, and robust spin-orbit torque magnetic random-access memories (SOT-MRAM), it is of significance to develop a spin current source (SCS)/ferromagnet (FM) magnetic heterostructures possessing large damping-like spin-orbit torque (DL-SOT) efficiency, good thermal stability, and low power consumption. In this study [1], we systematically investigate $Pt_xCu_{1-x}/Co/MgO$ magnetic heterostructure with perpendicular magnetic anisotropy (PMA) and report a tremendous improvement on spin-orbit torque switching efficiency of Pt-Cu alloy. The largest damping-like spin-orbit torque (DL-SOT) efficiency of the Pt-Cu alloy, characterized by anomalous Hall hysteresis loop shift measurements [2], is about 0.44. It's almost three times than its counterpart (pure Pt). This large DL-SOT efficiency can be explained by raising resistivity with alloying under the premise of preserving intrinsic Pt properties. Moreover, current-induced magnetization switching measurement [3, 4] is performed, and we confirm a larger DL-SOT efficiency of Pt-Cu alloy and ensure the thermal stability can be preserved under alloying. The lowest critical switching current density in Pt-Cu alloy layer is about 2.37×10^6 A/cm², which is significantly lower than 3.42×10^7 A/cm² of pure Pt in our control experiments. This improvement results from the simultaneous enhancement of spin-orbit torque efficiency and reduction of coercivity of the Co layer. Furthermore, combining large DL-SOT efficiency and moderate resistivity of Pt-Cu alloy, the power consumption excluding current shunting and Joule heating reduces from 1.61×10^{13} mW/cm³ (pure Pt) to 4.64×10^{11} mW/cm³ (Pt-Cu alloy). This performance is also competitive with other reported materials systems. According to its large DL-SOT efficiency and capability to achieve lower power consumption and to preserve good thermal stability in $Pt_xCu_{1-x}/Co/MgO$ magnetic heterostructure, Pt-Cu alloy is suggested to be an attractive candidate for future SOT-MRAM applications.

[1] Hu, C.-Y. and Pai, C.-F., *Advanced Quantum Technologies*, Vol. 3, 2000024 (2020). [2] Pai, C.-F., Mann, M., Tan, A. J., et al., *Physical Review B*, Vol. 93, 1440189 (2016). [3] Miron, I. M., Garello, K., Gaudin, G., et al., *Nature*, Vol. 476, 189-193 (2011). [4] Liu, L.Q., Lee, O. J., Gudmundsen, T. J., et al., *Physical Review Letters*, Vol. 109, 096602 (2012).



Representative SOT switching loops of Pt-Cu(5)/Co(1)/MgO(2) structure under $H_x = \pm 600$ Oe.



Summary of calculated power consumption based on a SCS(5)/CoFeB(1) prototype device.

CC-05. Characterization of Spin-Orbit Torque Efficiency in Magnetic Heterostructures With Perpendicular Magnetic Anisotropy via Spin Torque Ferromagnetic Resonance.

J. Wei¹, C. He¹, X. Wang¹, H. Xu¹, Y. Liu¹, Y. Guang¹, C. Wan¹, J. Feng¹, G. Yu¹ and X. Han¹

1. Institute of Physics, Beijing, China

We report a spin Hall magnetoresistance (SMR)-based spin-torque ferromagnetic resonance (ST-FMR) study of SOT efficiency in perpendicularly magnetized W/CoFeB/MgO structures, as shown in Fig. 1(a). A full analysis of the ST-FMR spectrum is developed for the PMA sample. The typical ST-FMR spectrum of PMA system shows two resonance modes, i.e., in-plane and out-of-plane magnetization precession modes, as shown in Fig.1(b). The damping-like torque efficiency of -0.31 is obtained from the angular dependence of symmetric and antisymmetric components of the out-of-plane resonance mode, as shown in Fig1(d-f), in which the significant contribution of spin-pumping-induced inverse spin Hall effect (ISHE) is carefully considered. The SOT efficiencies for the samples without PMA are also determined as reference values ($\xi_{DL} = -0.35$ and $\xi_{FL} = -0.05$) by analyzing the FM thickness dependence of SOT efficiency. By performing the modulation of damping measurement for the in-plane mode, the damping-like torque efficiency is determined to be -0.38 , which is consistent with the reference value. The obtained values of damping-like torque efficiency by different means are consistent with each other. The present work provides useful insights to determine the damping-like torque efficiency of the PMA sample via ST-FMR measurements.

[1] L. Q. Liu, Chi-Feng Pai, Y. Li, et al., Science 336, 555 (2012). [2] C. He, G. Yu, C. Grezes, et al., Phys. Rev. Appl. 10, 034067 (2018).

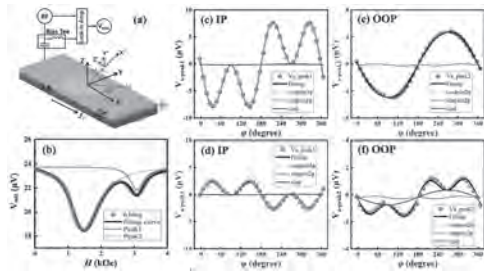


FIG. 1. (a) The schematic of ST-FMR measurements setup including a bias tee, a microwave signal generator and a lock-in amplifier. The J_c denotes the charge current undergoing the sample, and the J_s denotes the spin current along the normal direction of films. The external field H is applied in the plane at angle ϕ with respect to the X axis. **(b)** Experimental ST-FMR spectra for the perpendicular magnetized sample with $t_{FM} = 1.0$ nm measured at the angle $\phi = 63^\circ$. The angular dependence of symmetric (c), (e) and antisymmetric (d), (f) components of the IP and OOP mode, respectively.

CC-06. A two-Terminal Planar Memory Device Controlled by Spin-Orbit Torques.

C. Avci¹, C. Lambert¹ and P. Gambardella¹

¹. Department of Materials, ETH Zurich, Zurich, Switzerland

Spin-orbit torques (SOTs) have emerged as a versatile tool to manipulate the magnetization in magnetic heterostructures [1]. They typically occur in normal metal/ferromagnetic (NM/FM) bilayers where the bulk spin Hall and interfacial spin galvanic effects convert the injected charge current into pure spin currents [2]. The elimination of an FM polarizer to generate spin currents, in contrast to the conventional spin-transfer torque schemes, offers great flexibility in device design, architecture, and functionality [3]. One such device is the three-terminal magnetic tunnel junction (MTJ), where the magnetization of the free FM layer (i.e., the magnetic state of the device) is controlled by a planar current injection generating SOTs, and the magnetization state is probed by a vertical current injection through the oxide barrier via tunnel magnetoresistance [4]. Three-terminal MTJs are considered for scalable, low-power, and high speed magnetic random-access memory applications [5]. The development of three-terminal MTJs for memory applications is already at an advanced stage [6]. Additionally, SOTs allow for the realization of even simpler memory devices, which could simplify the MRAM production process and diversify the circuit design, material spectrum, and related physical phenomena. In this work, we report a new two-terminal device where the magnetic state is controlled and probed by currents sent through the same planar path. This simple device is made of a hard FM (TbCo) and a soft FM (Co) layer, each possessing perpendicular magnetic anisotropy, separated by a Pt layer that acts as a SOT generator. Current injection in the presence of a static in-plane field switches the magnetization of Co between up and down states as in the standard SOT switching scheme. However, unlike in the typical SOT devices, the magnetization state is not probed by the Hall effect but rather by the longitudinal resistance, which has two distinct levels for parallel and antiparallel orientations of TbCo and Co. This magnetoresistive phenomenon stems from the current-in-plane giant magnetoresistance, albeit much smaller in amplitude (<0.1%). This device offers a new pathway to a highly scalable, all-electrical, two-terminal memory that can be produced with low fabrication efforts.

[1] Miron et al., *Nature* 476, 189 (2011) [2] Manchon et al., *Rev. Mod. Phys.* 91, 035004 (2019) [3] Song et al., *Prog. Mater. Sci.*, <https://doi.org/10.1016/j.pmatsci.2020.100761> [4] Cubukcu et al., *Appl. Phys. Lett.* 104, 042406 (2014) [5] Diény et al., *Nature Electron.* 3, 446 (2020) [6] Garello et al., *Proc. Symp. VLSI Circuits*, pp. T194-T195 (2019)

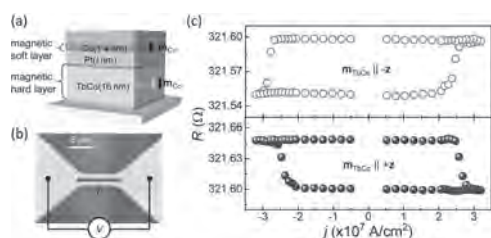


Figure 1 - (a,b) Layer and device structure used in this study. (c) Current-induced magnetization switching in the top Co layer detected by longitudinal resistance measurements in devices similar to the one shown in (b).

CC-07. Spin-Orbit Torque Switching of Synthetic Antiferromagnetic Layer by Metallic Bilayers With Opposite Spin Hall Angles.

D. Zhang¹, H. Li² and J. Wang¹

1. *Electrical and Computer Engineering, University of Minnesota Twin Cities, Minneapolis, MN, United States*; 2. *Chemical Engineering and Materials Science, University of Minnesota Twin Cities, Minneapolis, MN, United States*

Spin-orbit torque (SOT) switching of perpendicular magnetic tunnel junctions (p-MTJs) has been attracted considerable interest recently for spin memory applications due to the fast magnetization switching speed (1~4). Recently, the synthetic antiferromagnetic (SAF) free layer provides lots of benefits for MTJ performance, such as very small stray field, ultrafast switching speed, and large thermal stability (5~6). In this presentation, we will show our experimental results about the SOT switching of the SAF free layer via the bilayer spin Hall channel. The SAF stack of the [Co/Pd]/Co/Ru/Ta/CFB with perpendicular magnetic anisotropy (PMA) was developed on Ta/Pd seed layers which also serve as the spin Hall channel for spin-orbit torque (SOT) switching. First of all, the antiferromagnetic coupling behavior of the SAF layers was verified under a sweeping magnetic field with VSM and AHE measurements. Then, the Second Harmonic Hall measurement was conducted to characterize the SOTs generated by the Ta/Pd bilayers. The results are plotted in Fig. 1(a). We can find that the spin-torque efficiency of the Ta/Pd bilayer increases as increasing of the thickness of the Pd layer. With the thinner Pd layer, the spin torque efficiency cancels each other because of the opposite spin Hall angle. When the thickness of the Pd layer increases, the spin torque efficacy is dominant by the Pd layer. Furthermore, the current switching of the SAF layers with SOT was then demonstrated as shown in Fig. 1(b). In addition, magnetic field-free SOT switching of the SAF layer with PMA was also realized at a certain configuration of the Ta/Pd bilayer structure.

1. I. M. Miron, K. Garello, G. Gaudin, P.-J. Zermatten, M. V. Costache, S. Auffret, S. Bandiera, B. Rodmacq, A. Schuhl and P. Gambardella, *Nature* 476, 189–193 (2011) 2. L. Liu, C. F. Pai, Y. Li, H. W. Tseng, D. C. Ralph, R. A. Buhrman, *Science* 336, 555-558 (2012) 3. A. Manchon, J. Zelezny, I. M. Miron, T. Jungwirth, J. Sinova, A. Thiaville, et al., *Rev. Mod. Phys.* 91, 035004 (2019). 4. E. Grimaldi, V. Krizakova, G. Sala, F. Yasin, S. Couet, G. S. Kar, K. Garello, and P. Gambardella, *Nat. Nanotech.* 15, 111–117(2020) 5. C. Yoshida, T. Takenaga, Y. Iba, Y. Yamazaki, H. Uehara, H. Noshiro, K. Tsunoda, A. Hatada, M. Nakabayashi, A. Takahashi, M. Aoki, and T. Sugii, *IEDM13-68*, 3.4.1 6. A. Bergman, B. Skubic, J. Hellsvik, L. Nordström, A. Delin, and O. Eriksson, *Phys. Rev. B* 83, 224429 (2011)

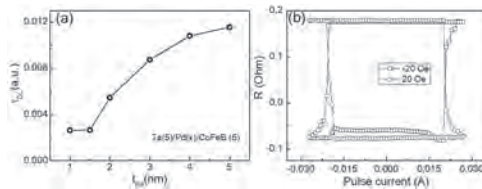


FIG. 1. (a) the damping-like spin Hall efficiency (τ_{DL}) as a function of the thickness of the Pd layer (t_{Pd}). (b) SOT switching of SAF layer through the bilayer spin Hall channel.

CC-08. Second Harmonic Study of the Self-Spin-Orbit Torques in Ferrimagnetic Materials.

H. Damas¹, D. Céspedes-Berrocal^{1,5}, D. Maccariello³, A.Y. Arriola Córdova⁵, E. Martin¹, J. Bello¹, P. Tang⁴, P. Vallobra¹, Y. Xu¹, S. Migot¹, J. Ghanbaja¹, S.F. Zhang⁴, S. Mangin¹, C. Panagopoulos², V. Cros³, M. Hehn¹, S. Petit-Watelot¹, A. Fert³ and J. Rojas-Sanchez¹

1. Institut Jean Lamour, Université de Lorraine, Nancy, France;

2. Nanyang Technological University School of Physical and Mathematical Sciences Division of Physics and Applied Physics, Singapore, Singapore;

3. Unite Mixte de Physique CNRS/Thales, Palaiseau, France;

4. Department of Physics, University of Arizona, Tucson, AZ, United States;

5. Universidad Nacional de Ingeniería, Lima, Peru

In order to address the high demand for data in information technology, spintronics proposes attractive solutions. The most recent are based on the exploitation of the spin-orbit coupling of non-magnetic heavy metals to use the spin-orbit torque (SOT) exerted on the magnetic layer attached to the heavy metal [1,2]. However, magnetic material can be a source of spin current as well. We studied GdFeCo alloys in which the 5d band of Gd induces large spin-orbit couplings. In GdFeCo, we can identify spin currents of two different symmetries, SAHE-like [3,4] and SHE-like [5] corresponding respectively to the Spin Anomalous Hall Effect and Spin Hall Effect symmetries [6]. Only the second one can generate torques on the magnetic layer. In this work [6], we present a detailed study of different systems to account for the *self-torque* in GdFeCo/Cu. The characterization of the *self-torque* is carried out by means of harmonic Hall voltage measurements in samples where the GdFeCo layer exhibits out of plane magnetization. The samples were grown by magnetron sputtering and standard optical lithography was used to micro fabricate the Hall bar devices. We focus first on the temperature dependence of the effective fields associated to the *self-torque* in GdFeCo/Cu. As shown in Fig. 1, the amplitude of the damping-like (DL) effective field increases when the temperature approaches the magnetization compensation temperature T_{CM} and changes sign when crossing the last. The field-like (FL) effective field shows the same behavior. Even far from T_{CM} , the efficiency $H_{DL}/J_{GdFeCo} = 2.10^{-10}$ Oe/(A/m²) is in the order of magnitude or higher than with the use of most of the heavy metals [1]. However, the associated DL and FL torques do not increase as the effective fields when approaching T_{CM} but do change sign. Furthermore, in a second set of experiments, we compare the *self-torque* in GdFeCo/Cu with torques in GdFeCo/Cu/Pt and GdFeCo/Cu/Ta structures. The supplementary heavy metal allows an additional torque generation on the magnetization via the SHE and, in addition, acts as a spin-sink of the spin current emitted by GdFeCo. The improvement of the GdFeCo-emitted-spin-current absorption allowed by this extra layer is the source of a magnified DL *self-torque*. We found that the efficiency associated to the *self-torque* is increased by a factor of 4 in the GdFeCo/Cu/Ta structure and a factor of 7 in the GdFeCo/Cu/Pt structure compared to the *self-torque* in GdFeCo/Cu as shown in Fig. 2. Therefore, we conclude that sizeable spin-orbit effects can arise from quasi-isolated magnetic layer with strong spin-orbit coupling such as GdFeCo. These effects give rise to large self-induced effective fields enhanced near the magnetization compensation temperature. The addition of a heavy metal, which improves the spin-current absorption outside the ferrimagnetic layer, enhances the DL *self-torque*. This paves the way for new architectures to achieve and exploit SOT switching as well as free heavy metal SOT switching and skyrmions manipulation.

[1] A. Manchon, J. Zelezny, IM. Miron, Rev. Mod. Phys., Vol. 91, p.035004 (2019) [2] TH. Pham, SG. Je, P. Vallobra, Phys. Rev. Appl., Vol. 9, p.064032 (2018) [3] T. Taniguchi, J. Grollier, and MD. Stiles, Phys. Rev. Appl., Vol. 3, p.044001 (2015) [4] S. Lihama, T. Taniguchi, K. Yakushiji, Nat. Electron., Vol. 1, p.120 (2018) [5] VP. Amin, PM. Haney, and MD. Stiles, J. Appl. Phys., Vol. 128, p.151101 (2020) [6] D. Céspedes-Berrocal, H. Damas, S. Petit-Watelot, Adv. Materials (2021) <https://doi.org/10.1002/adma.202007047> ArXiv: 2010.09137

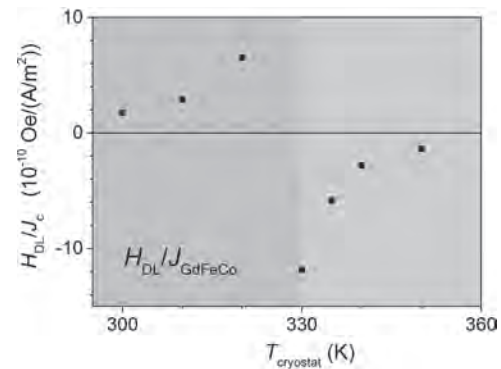


Fig. 1 : Temperature dependence of the damping-like efficiency in Gd₂₇Fe_{50.9}Co_{10.2}(10nm)/Cu(2nm)/AlO_x(2.5nm). The magnetization compensation temperature T_{CM} is depicted by the background change of color. The DL effective field diverges near T_{CM} as the magnetization is zero and its sign is reversed above T_{CM} .

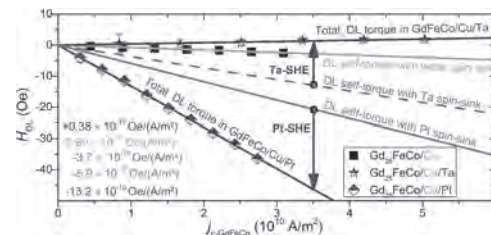


Fig. 2 : DL total effective field for Gd₂₅Fe_{65.6}Co_{9.4}(10nm)/Cu(6nm), Gd₂₅Fe_{65.6}Co_{9.4}(10nm)/Cu(6nm)/Ta(5nm), and Gd₂₅Fe_{65.6}Co_{9.4}(10nm)/Cu(6nm)/Pt(5nm) as a function of the current density in the GdFeCo layer. There is only a small H_{DL} in GdFeCo/Cu (orange line) in which the spin absorption in Cu is small. H_{DL} in GdFeCo/Cu/Pt (blue diamonds) and GdFeCo/Cu/Ta (violet stars) corresponds to the addition of the SHE contribution from Pt (Ta) to the self-torque enhanced by the spin absorption outside GdFeCo by the spin-sink Pt or Ta.

CC-09. Spin-Orbit Torque in Naturally Oxidized Ta-O/Co-Fe-B/Mg-O/Ta Structures.

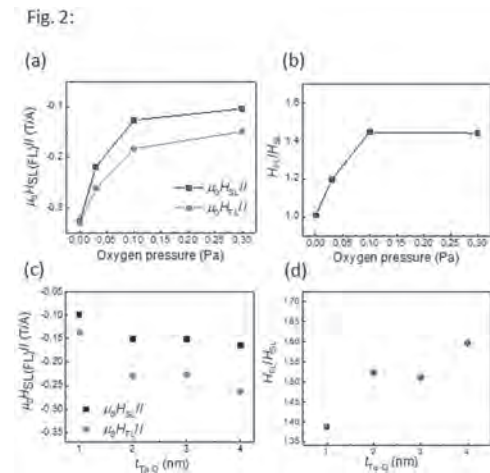
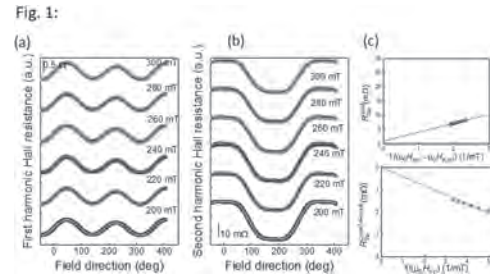
T. Nguyen^{1,2}, S. DuttaGupta^{1,3}, Y. Saito⁴, V. De Zoysa Karunathilaka³, S. Fukami^{1,3}, S. Ikeda^{1,4}, T. Endoh^{1,4} and Y. Endo^{1,5}

1. Center for Science and Innovation Spintronics (Core Research Cluster), Tohoku University, Sendai, Japan; 2. Center for Spintronics Research Network, Tohoku University, Sendai, Japan; 3. Research Institute of Electrical Communication, Tohoku University, Sendai, Japan; 4. Center for Innovative Integrated Electronic Systems, Tohoku University, Sendai, Japan; 5. Graduate School of Engineering, Tohoku University, Sendai, Japan

Spin-orbit torque (SOT)-induced magnetization switching in heavy metal/ferromagnetic (HM/FM) heterostructures has attracted immense interest owing to its potential for the development of high-performance spintronics devices [1-4]. The SOT has been induced by two orthogonal components: the Slonczewski-like field (H_{SL}) and the field-like field (H_{FL}) which are equally capable of magnetization reversal [5,6]. Conventionally, H_{SL} is considered to originate from the bulk spin Hall effect (SHE) induced by the strong spin-orbit coupling of bulk HM [1], and H_{FL} is related to the interfacial Rashba Edelstein effect (REE) originating from the broken inversion symmetry [7]. While H_{FL} was weaker than H_{SL} in many HM-based SOT structures, obscuring the physics of H_{FL} , a sizable value of H_{FL} was reported in Ta-based SOT structures [8]. However, the detailed investigation of H_{FL} has not been performed, and the further manipulation of H_{SL} and H_{FL} has not been reported. Herein, to investigate more details on the contribution of H_{SL} and H_{FL} to the SOT efficiency, we choose Ta/Co-Fe-B system and study the change in H_{SL} and H_{FL} by oxygen incorporation into Ta-layer. Furthermore, the SOT origin in these structures is also discussed. The in-plane magnetized Ta-O (t_{Ta-O} nm)/Co₂₀Fe₆₀B₂₀ (1.2 nm)/MgO (1.3 nm)/Ta (1.0 nm) stacks with different Ta-O layer thickness (t_{Ta-O}) were fabricated on thermally oxidized Si substrates by RF sputtering. Ta-O underlayer (UL) was formed by in-situ natural oxidation of Ta layer at 0.3; 0.1; 0.03 Pa for 30 minutes. A stack with a 1 nm-Ta UL was also prepared as a reference sample for comparison. H_{SL} and H_{FL} were evaluated using an extended harmonic Hall measurement for Hall bar devices, which enables the exclusion of the thermoelectric effects. An in-plane external magnetic field with various strengths (H_{ext}) was rotated in the film plane, whose direction was represented by the azimuthal angle θ . 10 Hz AC current was applied to the channel and the first and second harmonic Hall voltages were measured by a lock-in amplifier. Figures 1 (a) and (b) show the in-plane magnetic field angle θ dependence of the first ($R\omega$) and second ($R_2\omega$) harmonic Hall resistance at different H_{ext} . $R\omega$ component for the in-plane magnetized sample is dominated by the planar Hall resistance, following the equation: $R_1\omega=R_{PHE}\sin2\theta$ (1), where R_{PHE} is the planar Hall resistance coefficient. From $R_2\omega$ component, H_{SL} and H_{FL} can be obtained as follows: $R_2\omega = -\{R_{AHE}[H_{SL}/(H_{ext}-H_{k,eff})+R_T]\}\times\cos\theta + [2R_{PHE}(H_{FL}+H_{OE})/H_{ext}]\times(2\cos^3\theta-\cos\theta)$ (2), where R_T is the second harmonic Hall resistance coefficient due to the thermoelectric voltage, H_{OE} is the current-induced Oersted field. R_{AHE} is the anomalous Hall effect (AHE) resistance and $H_{k,eff}$ is the effective anisotropy field, evaluated from the AHE measurement in the perpendicular magnetic field direction. From the $\cos\theta$ contribution of $R_2\omega$ as a function of $1/(\mu_0H_{ext}-\mu_0H_{k,eff})$ (upper panel of Fig. 1 (c)); and the $(2\cos^3\theta - \cos\theta)$ contribution of $R_2\omega$ as a function of $1/(\mu_0H_{ext})$ (lower panel of Fig. 1 (c)), H_{SL} and H_{FL} were evaluated. Figures 2 (a) and (b) show the oxygen pressure (P_{Oxygen}) dependence of μ_0H_{SL}/I , μ_0H_{FL}/I , and H_{FL}/H_{SL} for samples with Ta-O UL of 1 nm, in comparison with the reference sample (dots at $P_{Oxygen} = 0$ Pa). Herein, I is the total current applying to the device. The sign and magnitude of μ_0H_{SL}/I and μ_0H_{FL}/I are consistent with those in the previous work [8]. For all samples, the values of μ_0H_{SL}/I and μ_0H_{FL}/I are in the same order, implying their equal contribution to the total SOT in both Ta and Ta-O UL systems. As P_{Oxygen} increases, the magnitude of μ_0H_{SL}/I decrease, which might be attributed to the low oxygen-incorporating in the system. However, H_{FL}/H_{SL} increases with the increase of P_{Oxygen} meaning that this ratio would be enhanced by oxidation [9]. Figures 2 (c) and (d) show the t_{Ta-O} dependence of μ_0H_{SL}/I , μ_0H_{FL}/I , and H_{FL}/H_{SL} for stack with Ta-O UL oxidized at 0.3 Pa. The absolute values of μ_0H_{SL}/I , μ_0H_{FL}/I increase and converge to a certain value as t_{Ta-O} increases, suggesting the coexistence of bulk and interface effects originating from SHE, and REE [6].

The absolute value of μ_0H_{FL}/I is higher than that of μ_0H_{SL}/I suggesting the stronger interfacial REE-related origin than bulk SHE-related origin, which also can be observed in Fig. 2 (d) with the increase of H_{FL}/H_{SL} ratio as t_{Ta-O} increases. These results are of importance to understand the SOT induced magnetization switching, as well as to design the spintronic devices using oxidized HM/FM systems. The authors acknowledge the Core Research Cluster program of Tohoku University, Japan. This work was supported by JSPS KAKENHI Grant Number 19K23583, 19H00844, and by CSRN, and Cooperative Research Project from CSIS, Tohoku University, Japan. This research has been partly carried out at the Laboratory for Nanoelectronics and Spintronics, RIEC, Tohoku University. Fig. 1: Field direction dependence of $R\omega$ (a) and $R_2\omega$ (b) at different magnetic field strength. The black curves are fitting data with eqs. (1), (2). (c) The $\cos\theta$ contribution of $R_2\omega$ as a function of $1/(\mu_0H_{ext}-\mu_0H_{k,eff})$ (upper); and the $(2\cos^3\theta - \cos\theta)$ contribution of $R_2\omega$ as a function of $1/(\mu_0H_{ext})$ (lower). Fig. 2: Oxygen pressure dependence of μ_0H_{SL}/I (a) and H_{FL}/H_{SL} (b) for samples with 1 nm thick UL. t_{Ta-O} dependence of μ_0H_{SL}/I (c) and H_{FL}/H_{SL} (d) for samples with Ta-O UL oxidized at 0.3 Pa.

[1] L. Liu et al., Science 336, 555, (2012). [2] S. Fukami et al., in Symp. VLSI Technol. Dig. Tech. Papers, pp. 60–61, (2016). [3] H. Honjo et al., IEDM Technical Digest 28.5, (2019). [4] M. Natsui et al., in Symp. VLSI Technol. Dig. Tech. Papers, CM2.2, (2020). [5] C. Zhang et al., Appl. Phys. Lett. 107, 012401, (2015). [6] Y. Du et al, Phys. Rev. Appl. 13, 054014, (2020). [7] V. M. Edelstein, Solid State Commun. 73, 233, (1990). [8] C. Zhang et al., Appl. Phys. Lett. 103, 262407, (2013). [9] H. An et al., Sci. Adv. 4, eaar2250, (2018).



CC-10. Efficient Spin-Orbit Torque Generation in Semiconducting WTe₂ With Hopping Transport.

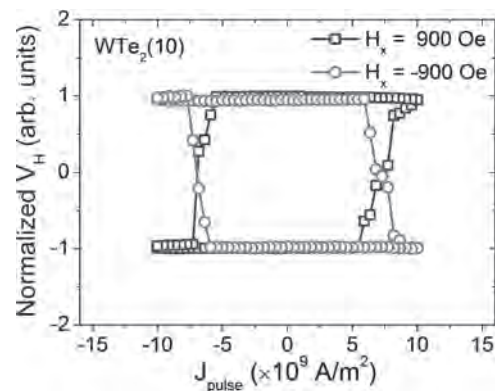
C. Peng¹, W. Liao¹, T. Chen¹ and C. Pai^{1,2}

1. *Materials Science and Engineering, National Taiwan University, Taipei, Taiwan*; 2. *Center of Atomic Initiative for New Materials, National Taiwan University, Taipei, Taiwan*

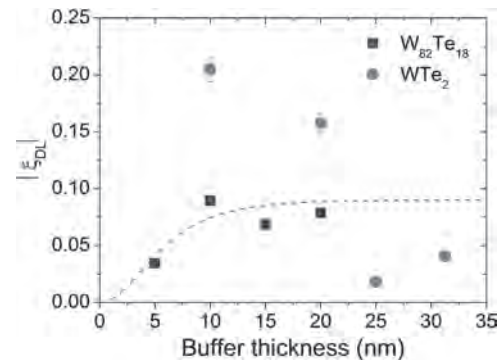
Spin-orbit torques (SOTs) originated from the spin-orbit interactions in various types of materials systems and magnetic heterostructures have been shown to be an effective mechanism to manipulate and switch the magnetization in contemporary magnetic memory devices. When it comes to materials with sizable efficiency of generating spin current from charge current, 5d transition metals such as Pt [1], Ta [2], and W [3] are the representative candidates due to the sizable spin Hall effect (SHE). More recently, topological insulators (TIs) are reported to possess high SOT efficiency from spin momentum locking of the topologically-protected surface states (TSSs) [4]. Another family of emergent materials, transition metal dichalcogenides (TMDs), have also gained lots of attention due to not only the strong SOC but also their unconventional SOT features from the lack of inversion symmetry. Particularly, for exfoliated WTe₂, it is proposed to exhibit anomalous spin torques and extremely large damping-like (DL) SOT efficiency [5, 6]. However, most of the previously studied crystalline WTe₂ are prepared by mechanical exfoliation, which limits their potentials for industrial application. It is therefore crucial to explore the possibilities of employing WTe₂ layers prepared by conventional materials growth approaches, such as magnetron sputter deposition, to see their spin transport properties as compared to the exfoliated cases. In this work, we report the DL-SOT efficiencies from both stoichiometric WTe₂ and co-sputtered W_{100-x}Te_x-based magnetic heterostructures prepared by high vacuum sputter depositions. Both series of deposited multilayer stacks are amorphous. We first quantify the damping constant of WTe₂/CoFeB devices with in-plane magnetic anisotropy (IMA) through ST-FMR measurements, from which the damping constant is determined to be $\alpha_{\text{WTe}_2/\text{CoFeB}}=0.009\pm 0.001$, smaller than those obtained from control samples with classical spin Hall transition metals, namely Pt/CoFeB ($\alpha_{\text{Pt/CoFeB}}=0.033\pm 0.003$) and W/CoFeB ($\alpha_{\text{W/CoFeB}}=0.014\pm 0.002$). The largest DL-SOT efficiency from the stoichiometric WTe₂/CoTb devices with perpendicular magnetic anisotropy (PMA) is further estimated to be $\xi_{\text{DL}}^{\text{WTe}_2}\sim 0.20$ by current-induced hysteresis loop shift measurement, which are greater than those of the W-based control sample ($\xi_{\text{DL}}^{\text{W}}\sim 0.04$). To give further evidence of the sizable DL-SOT efficiency in WTe₂, we perform the current-induced magnetization switching measurement from WTe₂/CoTb devices. As shown in Fig. 1, the switching polarities depend on the applied H_x , which is consistent with the SOT-driven switching mechanism. More importantly, the critical switching current density J_c of WTe₂/CoTb structure is further demonstrated to be $J_c\sim 7.05\times 10^9$ (A/m²), which is much lower than those from the 5d transition metal-based heterostructures ($J_c\sim 10^{11}$ A/m²). Note that this value is of the same order as the exfoliated 80 nm-thick-WTe₂ case reported by Shi. S *et al.* ($J_c\sim 3\times 10^9$ A/m²) [6]. All of the advantages mentioned above indicate that the amorphous sputtered WTe₂ is a competitive SOT source in the emergent chalcogenide materials category. To explore the possible origins of SOT in the amorphous WTe₂ heterostructures, we turn to compare the stoichiometric WTe₂ with co-sputtered W₈₂Te₁₈ samples. Fig. 2 shows the SOC layer thickness dependence of $|\xi_{\text{DL}}|$ from both type of samples. For the co-sputtered case, the thickness dependence of efficiency can be well fitted by the spin diffusion model, which suggests that the SOC within W₈₂Te₁₈ is of bulk origin (such as the SHE). In contrast, for WTe₂, $|\xi_{\text{DL}}^{\text{WTe}_2}|$ decays with increasing the stoichiometric layer thickness, which indicates the possible existence of interfacial contributions of SOC besides the bulk effect. We speculate that interfacial effects could play crucial roles on the SOT generation in the Te-rich (stoichiometric) regime, even if the TMD layer is amorphous. Further studies are required to elucidate the SOC and SOT generation mechanisms in these amorphous TMD systems. Lastly, we turn our focus on the electrical transport properties of amorphous WTe₂. Most of the previous works claimed that the textured WTe₂ is one kind of Weyl semimetal, while our sample is predominately amorphous and therefore should not fall into this category. To get insight into the electron transport behavior behind, we investigate the temperature dependence of resistivity from the amorphous

WTe₂. The amorphous WTe₂ is inclined to behave as semiconductor rather than metal or semimetal. Within the absence of periodic lattices and band structure, the hopping mechanism such as the small polaron hopping (SPH) model is more suitable to describe the phenomenon [7]. In high temperature regime (323-423K), the resistivity of WTe₂ can be well fitted by the SPH model, which indicates that thermally-activated hopping polarons from electron-lattice interaction dominate the transport mechanism behind, and therefore suggests that the sputtered amorphous WTe₂ is semiconducting with hopping transport property.

- [1] I. M. Miron, K. Garello, G. Gaudin, *Nature*, Vol. 476, p.189-193 (2011)
 [2] L. Liu, C.-F. Pai, Y. Li, *Science*, Vol. 336, p.555 (2012) [3] C.-F. Pai, L. Liu, Y. Li, H. W. Tseng, *Appl. Phys. Lett.*, Vol. 101, 122404 (2012) [4] A. R. Mellnik, J. S. Lee, A. Richardella, *Nature*, Vol. 511, p.449-451 (2014)
 [5] D. MacNeill, G. M. Stiehl, M. H. D. Guimaraes, *Nat. Phys.*, Vol. 13, p.300-305 (2017) [6] S. Shi, S. Liang, Z. Zhu, K. Cai, *Nat. Nanotechnol.*, Vol. 14, p.945-949 (2019) [7] N. F. Mott, E. A. Davis, Clarendon press: Oxford (1979)



Current-induced magnetization switching from a WTe₂(10)/CoTb(6)/Ta(2) device with applied bias fields $H_x = \pm 900$ Oe.



Buffer layer thickness dependence of $|\xi_{\text{DL}}|$ for W₈₂Te₁₈-based and WTe₂-based devices. The blue dashed line represents the fitting of the $|\xi_{\text{DL}}(t_{\text{W82Te18}})|$ data to a spin diffusion model with spin diffusion length $\lambda_s^{\text{W}_{82}\text{Te}_{18}}\sim 4.1$ nm.

CC-11. Magnetic Layer Thickness Dependence of Spin-Orbit Torques in Pt / Co / Al / (Pt | Ta) Skyrmion Magnetic Multilayers.

S. Krishnia¹, F. Ajejas¹, Y. Sassi¹, N. Reyren¹, S. Collin¹, J. George¹, H. Jaffrès¹, V. Cros¹ and A. Fert¹

1. Unité Mixte de Physique, CNRS, Thales, Université Paris-Saclay, Palaiseau, France

Current-induced spin-orbit torques (SOTs) provide a unique mechanism to manipulate the magnetization of diverse class of magnetic multilayers and devices. The core of the phenomenon is charge to spin-current conversion in ferromagnetic/heavy-metal heterostructures which is governed by spin-orbit interactions mainly through spin Hall effect in heavy metals or Rashba effect at interface with broken inversion asymmetry¹. The non-equilibrium spin-current (of spin σ) interacts with local magnetic moments (m) via exchange interaction and creates two different components of spin-transfer torques: damping-like and field-like, where H_{DL} and H_{FL} are damping-like and field-like effective fields². In the macrospin approach of spin-orbit torque induced dynamics, the magnetization reversal in systems with perpendicular magnetic anisotropy is governed by damping-like torque and Dzyaloshinskii-Moriya interaction³. However, recent micromagnetic studies predict a unique reversal path which is determined by interplay between damping-like and field-like torques⁴. In this work, we will show how the ratio of field-like torque to damping-like torque is affected by the thickness of magnetic layer. A series of samples Pt 8|Co x |Al 1.4|Pt 3 with $x = 0.7, 0.9, 1.2, 1.4$ (numbers are thicknesses in nm) is deposited using magnetron sputtering. 5- μm -wide Hall bar structures were fabricated using optical lithography and Ar ion-milling technique. All the devices show perpendicular magnetic anisotropy. We used AC harmonic Hall voltage measurement technique to quantify current-induced effective fields. This technique exploits a sinusoidal current (I_{AC}) of frequency 727 Hz and simultaneous measurement of the first and second harmonics of the Hall voltage as a function of an in-plane field (H) applied along or transverse to the current direction ($H \parallel I_{AC}$ and $H \perp I_{AC}$), and extract H_{DL} or H_{FL} effective fields. The measured H_{DL} and H_{FL} increase linearly with the current for all the Co thicknesses as shown in Figure 1(a) and 1(b), respectively. Furthermore, the H_{DL} ($= m \times \sigma$) changes sign with magnetization direction whereas H_{FL} ($= \sigma$) is independent of magnetization direction, in agreement with literature². Figure 2 shows the H_{DL} and H_{FL} for an estimated current density $J_{Pt}=10^{11}$ A/m² in seed Pt layer as a function of Co thickness. The measured H_{DL} and H_{FL} increase with decreasing the Co thickness. The observed behavior confirms the interfacial nature of spin-orbit torques⁵. Interestingly, here we observe a clear increase in the ratio of H_{FL}/H_{DL} with decreasing the Co thickness. To corroborate the phenomenon, we next quantify the SOTs in Pt 8|Co x |Al 1.4|Ta 5 series and the similar increasing trend in H_{FL}/H_{DL} is observed when the Co thickness is decreased. The results suggest for additional mechanisms of spin-current generation which will be discussed in details during the conference. Acknowledgement-French ANR grant TOPSKY (ANR-17-CE24-0025), DARPA TEE program grant (MIPR#HR0011831554) and EU grant SKYTOP (H2020 FET Proactive 824123) are acknowledged for their financial support.

1. Garello, K. *et al. Nat. Nanotechnol.* 8, 587–593 (2013). 2. Hayashi, M., Kim, J., Yamanouchi, M. & Ohno, H. *Phys. Rev. B* 89, 1–15 (2014). 3. Lee, O. J. *et al. Phys. Rev. B* 89, 1–8 (2014). 4. Baumgartner, M. *et al. Nat. Nanotechnol.* 12, 980–986 (2017). 5. Park, Y. K. *et al. NPG Asia Mater.* 12, (2020).

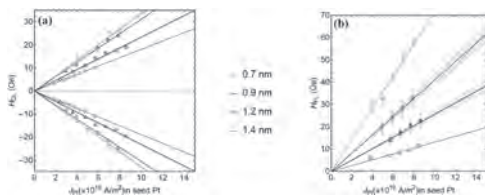


Figure 1. Current-induced SOT effective fields (a) H_{DL} and (b) H_{FL} as a function of current density in seed Pt layer for various Co thicknesses.

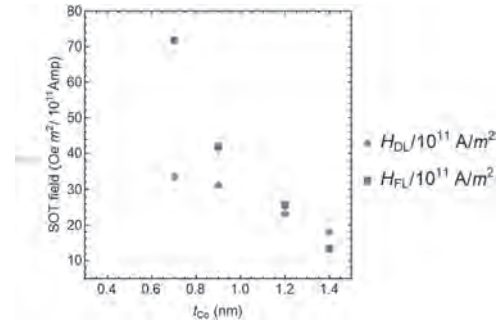


Figure 2. Plot of H_{DL} and H_{FL} per 10^{11} A/m² current density in seed Pt layer with respect to the Co thickness.

CC-12. Detection of Spin-Orbit Torques for in-Plane Magnetized Heterostructures by Utilizing Spin Hall Effective Field.

Y. Liu¹, T. Chen¹, T. Lo¹, T. Tsai¹, S. Yang², Y. Chang², J. Wei² and C. Pai^{1,3}

1. Materials Science and Engineering, National Taiwan University, Taipei, Taiwan; 2. Electronic and Optoelectronic System Research Laboratories, Industrial Technology Research Institute, Hsinchu, Taiwan; 3. Center of Atomic Initiative for New Materials, National Taiwan University, Taipei, Taiwan

The spin current generated from the spin Hall effect of the heavy metal layer can exert spin orbit torques (SOTs) on the adjacent ferromagnetic layer and further produce current-induced SOT-driven magnetization switching. However, for the ferromagnetic layer with in-plane magnetic anisotropy (IMA), probing such switching phenomenon typically relies on tunneling magnetoresistance of three-terminal devices[1-3], differential planar Hall resistance in Hall-bar devices[4], or Kerr effect imaging approach[5]. In this work, we provide a reliable and all-electrical scheme to characterize both the damping-like SOT (DL-SOT) and field-like SOT (FL-SOT) in micron-sized heterostructures with IMA. Firstly, for magnetic heterostructures containing heavy metals, there exist current-induced in-plane spin Hall effective fields (H_{eff}^y) and unidirectional magnetoresistance (UMR) that will modify their anisotropic magnetoresistance (AMR) behavior (Fig.1). The electrical detection of SOT-driven magnetization switching (Fig.2 (b) and (d)) in W/CoFeB heterostructures is demonstrated by means of AMR measurement under such influences. Through switching measurements with various pulse widths, the effective DL-SOT efficiency ($|\xi_{\text{DL}}| \approx 0.32$) can be extracted for Hall-bar devices with $2.0 \text{ nm} \leq t_{\text{Co-Fe-B}} \leq 3.5 \text{ nm}$, which is fairly consistent with the values for thin W layer obtained by other approaches[3, 6-8]. The effective FL-SOT efficiency ($|\xi_{\text{FL}}| \leq 0.05$) can be obtained by AMR loops shift measurements and is found to be slightly enhanced by inserting a MgO layer on top of CoFeB. Moreover, we demonstrate that for a micro-sized device with a well-defined easy axis (along y -direction), as prepared from an 8-inch CMOS-compatible fabrication facility, the detection of SOT switching can also be achieved by the UMR readouts. Our studies suggest that this pump (DL-SOT) -probe (SHF-modified AMR or UMR) approach allows for characterizing key parameters of SOT switching from IMA heterostructures without lengthy device fabrication processes and complicated measurement protocols.

[1] M. Cubukcu, O. Boulle, M. Drouard, et al., Appl. Phys. Lett., Vol. 104, 042406 (2014). [2] L. Liu, C.-F. Pai, Y. Li, et al., Science, Vol. 336, 555 (2012). [3] C.-F. Pai, L. Liu, Y. Li, et al., Appl. Phys. Lett., Vol. 101, 122404 (2012). [4] G. Mihajlović, O. Mosendz, L. Wan, et al., Appl. Phys. Lett., Vol. 109, 192404 (2016). [5] S. Shi, S. Liang, Z. Zhu, et al., Nat. Nanotechnol., Vol. 14, 945-949 (2019). [6] R. Bansal, G. Nirala, A. Kumar, et al., Spin, Vol. 08, 1850018 (2019). [7] Q. Hao, G. Xiao, Phys. Rev. Appl., Vol. 3, 034009 (2015). [8] S. Mondal, S. Choudhury, N. Jha, et al., Phys. Rev. B, Vol. 96, 054414 (2017).

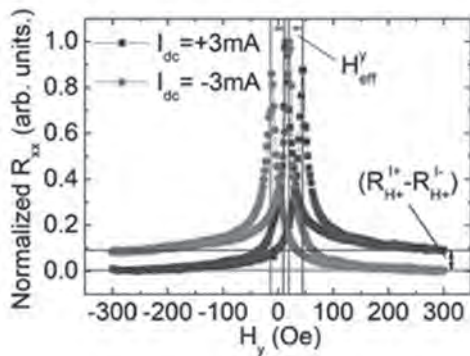


Fig. 1. Representative shifted AMR loops measured from a W(3)/CoFeB(1.8) sample with dc currents $I_{\text{dc}} = \pm 3 \text{ mA}$.

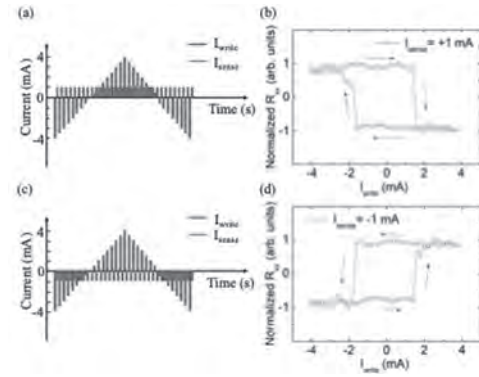


Fig. 2. (a, c) Measurement sequence for the switching experiment and (b, d) current-induced SOT switching results of a W(3)/Co₄₀Fe₄₀B₂₀(1.8) Hall-bar sample with opposite sense currents $I_{\text{sense}} = +1 \text{ mA}$ and $I_{\text{sense}} = -1 \text{ mA}$.

CC-13. Engineering the Spin-Orbit Torques and Interfacial Dzyaloshinskii-Moriya Interaction by Stacking Order in Tb/Co Ferrimagnetic Multilayers.

M. Martini^{1,2}, C. Avci², S. Tacchi³, C. Lambert² and P. Gambardella²
 1. Leibniz-Institut für Festkörper- und Werkstoffforschung Dresden eV, Dresden, Germany; 2. Department of Materials, ETH Zurich, Zurich, Switzerland; 3. Istituto Officina dei Materiali del CNR (CNR-IOM), Perugia, Italy

We characterized the spin-orbit torques (SOTs), current-induced switching, domain wall (DW) motion and interfacial Dzyaloshinskii-Moriya interaction (DMI) in synthetic ferrimagnets consisting of Co/Tb layers with differing stacking order grown on a Pt underlayer. We find that the magnetotransport properties and magnetization switching of these systems are highly sensitive to the stacking order of the Co and Tb layers and to the element in contact with Pt. Our study shows that Tb is an efficient SOT generator when in contact with Co, and its position in the stack can be adjusted to generate torques additive to those generated by the Pt layer and the Pt/Co interface. With optimal stacking and layer thickness, the damping-like SOT efficiency (the effective spin Hall angle) reaches up to 0.3, well beyond that expected from the Pt/Co bilayer. Moreover, the magnetization can be easily switched by the injection of pulses with current density of about 10^7 A/cm² despite the extremely high perpendicular magnetic anisotropy barrier (up to 3.5 T). Efficient switching is due to the combination of large SOTs and low saturation magnetization owing to the ferrimagnetic character of the multilayers. We observed current-driven DW motion in the absence of an external field, which is indicative of homochiral Néel-type DWs stabilized by the interfacial DMI. Characterization of the DMI in separate multilayers by Brillouin light scattering reveals that the position of the Tb layer plays a critical role also for the amplitude of the DMI. The largest DMI is obtained in layers where Co is sandwiched between Pt and Tb, similarly to the stack where large SOTs are observed. These results show that the stacking order in transition metal/rare-earth synthetic ferrimagnets plays a major role in determining the magnetotransport properties relevant for spintronic applications.

- [1] Avci, C. O., Beach, G. S., & Gambardella, P. (2019). Effects of transition metal spacers on spin-orbit torques, spin Hall magnetoresistance, and magnetic anisotropy of Pt/Co bilayers. *Physical Review B*, 100(23), 235454.
- [2] Emori, S., Bauer, U., ... & Beach, G. S. (2013). Current-driven dynamics of chiral ferromagnetic domain walls. *Nature materials*, 12(7), 611-616.
- [3] Avci, C. O., Rosenberg, E., ... & Beach, G. S. (2019). Interface-driven chiral magnetism and current-driven domain walls in insulating magnetic garnets. *Nature nanotechnology*, 14(6), 561-566.
- [4] Schulz, T., Lee, K., ... & Kläui, M. (2017). Effective field analysis using the full angular spin-orbit torque magnetometry dependence. *Physical Review B*, 95(22), 224409.

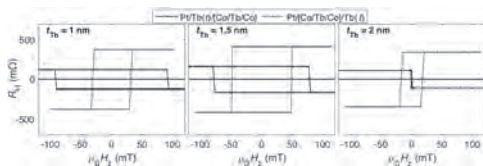


Fig.1 Room-temperature Hall resistance with an out-of-plane field sweep in Pt(4)/Tb(t)[Co(0.5)/Tb(0.65)/Co(0.5)] and Pt(4)/[Co(0.5)/Tb(0.65)/Co(0.5)]/Tb(t) with perpendicular magnetic anisotropy (numbers indicate thicknesses in nm.). The anomalous Hall effect (AHE) is positive and large in the Pt/[Co/Tb/Co]/Tb multilayers as opposed to the Pt/Tb/[Co/Tb/Co] multilayers where the AHE is negative and relatively small. This means that, i) at room temperature the total magnetization is dominated by the Co (Tb) sublattice for the layers with the Pt/Co (Pt/Tb) interface, i.e., the magnetization compensation temperature sits below (above) room temperature; ii) the Pt/Co interface has a significant contribution to the AHE as was recently evidenced in Ref. [1], which is presumably the reason for the large reported here. This set of data clearly shows the crucial role of the stacking order in the magnetic compensation as well as the AHE features, as is the case for the other magnetic properties.

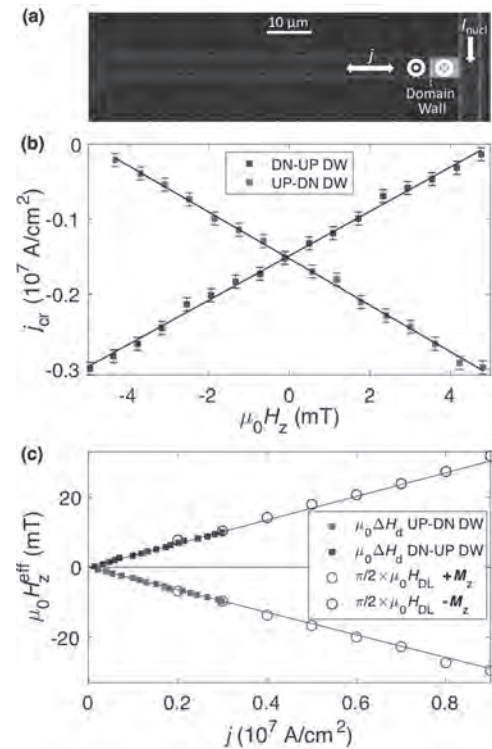


Fig.2 (a) Kerr image after the nucleation of a magnetic domain (white region). The red dotted line indicates the current line, whereas the blue one refers to the gold nucleation line. (b) Critical current density to depin the up-down and down-up DWs as a function of the out-of-plane magnetic field in Pt/[Co/Tb/Co]/Tb(1). The linear variation of $j_{cr}(H_z)$ shows that the current induces a DL-SOT that acts as an effective magnetic field along $\pm z$, assisting or hindering the effect of H_z , which changes the depinning field H_{dep} [2,3]. (c) Change in depinning field ΔH_d and rescaled damping-like effective field $\pi/2 \times H_{DL}$ versus current density for both DWs and magnetic states respectively, in Pt/[Co/Tb/Co]/Tb(1). The two measurements are in excellent agreement meaning that the DWs are of purely homochiral Néel-type [4].

CC-14. Spin Hall Magnetoresistance and Spin Orbit Torque Efficiency in (Pt,Ta)/FeCoB Bilayers.

M. Kuepferling¹, A. Magni¹, A. Sola¹, V. Basso¹, G. Soares¹, W. Skowronski², S. Lazarski², K. Grochot², M.V. Khanjani³ and J. Langer³
 1. Istituto Nazionale di Ricerca Metrologica, Torino, Italy; 2. AGH University of Science and Technology, Krakow, Poland; 3. Singulus Technologies AG, Kahl am Main, Germany

The current induced spin-orbit-torque (SOT) [1-4] is the key physical parameter describing the generation of magnetization dynamics in bilayers composed by a heavy metal (HM) layer and a ferromagnetic (FM) layer. Such bilayers, especially when associated with a magnetic tunnel junction at the FM layer (then forming the so called 3-terminal device), are considered as promising elements to be applied in novel magnetic memories, microwave generators and even bio-inspired types of computing [1]. Therefore, the robust and accurate determination of the SOT in HM/FM bilayers is of high relevance for optimizing future applications. In HM/FM bilayers the SOT is mainly caused by the spin Hall effect (SHE) of the HM layer, by which a spin current is injected into the FM layer. 3-terminal devices with application as magnetic memories adopt mainly FM films with perpendicular magnetic anisotropy, while for sensor applications also the configuration with in-plane magnetic anisotropy is of interest. The determination and quantification of the SOT can be performed in both cases by different techniques. While in a 3-terminal device the magnetization dynamics of observed via the tunnel magnetoresistance effect, in HM/FM bilayers other methods can be employed, such as the SOT-ferromagnetic resonance (FMR), the harmonic Hall voltage measurement and the spin Hall magnetoresistance (SMR). The SMR is a straightforward method when the FM layer is an insulator, while with metallic FM, in which the testing electric current is not confined in the HM layer only, it is accompanied by additional effects, such as the anisotropic magnetoresistance or the anomalous Nernst effect [5]. Therefore, it is important to analyse the measurement results by accurate models taking into account all aspects. The dominant theoretical approach for SHE-SOT is the drift-diffusion model considering spin accumulation at the interface between the FM and HM by introducing a spin mixing conductance. However, the agreement with experiments may be poor if spin dissipation at the interface (spin memory loss, spin dependent scattering, etc.) is disregarded [2]. In this paper we analyze transport measurements on FM/HM bilayers as a function of the HM thickness by employing a non-equilibrium thermodynamic approach to SHE-SOT [6] with the aim to reach a semi-quantitative agreement. The study was performed on HM/FM bilayers with HM=Pt (wedge 4-19nm), Ta (wedge 4-19nm), and FM=Fe₆₀Co₂₀B₂₀ (2nm) prepared at Singulus Technologies AG. All samples were annealed for 2h at 310°C in a magnetic field of 1T in order to develop an in-plane magnetic anisotropy (y axis). For the transport measurements the films were patterned into μm-size Hall bars/crosses (along x axis) by optical lithography and ion beam etching with Ti/Au contact pads. Magneto-optic Kerr effect (MOKE) and SMR measurements were performed following the protocol of [5], while SOT-FMR and harmonic Hall voltage measurements and analysis were based on references [3,4]. Fig.1 shows the comparison between MOKE loops and the SMR signal. The loop along the y axis is more rectangular and indicates the magnetic easy anisotropy axis. The SMR signal is much more pronounced with the field along the x axis, while it shows a small peak close to the coercivity when the field is along the y axis. With MOKE the anisotropy was determined and a dependence on HM thickness was observed. Fig.2 presents the summary of the SOT-FMR and harmonic Hall voltage measurements for HM/FM bilayers with different thickness of HM. FMR analysis enabled determination of effective magnetization and magnetization damping ($\alpha = 0.015$ for Pt and 0.0075 for Ta), while anomalous Hall effect and harmonic Hall measurements resulted in SOT efficiencies dependence vs. HM thickness. While damping-like SOT efficiency for Ta reaches $\xi_{DL-Ta} = -0.35$ and $\xi_{DL-Pt} = 0.15$ for Pt, with high resistivity difference ($\rho_{Ta} > 200 \mu\Omega\text{cm}$ and $24 < \rho_{Pt} < 52 \mu\Omega\text{cm}$) taken into account, the spin Hall conductivity for Pt of $\sigma_{SH-Pt} = 2.9 (10^5 \text{ S/m})$ exceeds the one for Ta $\sigma_{SH-Ta} = 1.7 (10^5 \text{ S/m})$ and is among the highest values reported [8]. The HM thickness dependence of the SMR is analyzed by considering both the finite conductance at the interface [7] (an approach valid for small thicknesses) and thermodynamic approach [6] (valid for larger thicknesses). The results are compared with the

harmonic Hall voltage measurements the SOT and the SOT efficiency and discussed in relation to the key parameters as the spin Hall angle and the spin diffusion length. Acknowledgements: WS acknowledges National Science Centre Grant No. UMO-2015/17/D/ST3/00500, Poland. Microfabrication was performed at the Academic Centre for Materials and Nanotechnology of AGH.

[1] B. Dieny et al. Nature Electronics 3, 446 (2020) [2] A. Manchon et al., Rev. Mod. Phys. 91, 035004 (2019) [3] M. H. Nguyen et al., Phys. Rev. Lett., 116, 126601 (2016) [4] C. F. Pai et al. Phys. Rev. B., 92, 064426 (2015) [5] Y.-T. Liu et al Phys. Rev. Applied 13, 044032 (2020) [6] H. Nakayama et al., Phys. Rev. Lett. 110, 206601 (2013) [7] V. Basso et al., J.Phys.D: Appl.Phys., 51, 214006 (2018) [8] L. Zhu et al. Phys. Rev. Applied 10, 031001 (2018)

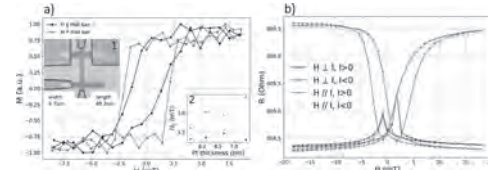


Fig. 1. a) MOKE loop on Hall bar device with Pt thickness $t_{Pt}=6.12$ nm, under applied field parallel (black) or perpendicular (red) to the Hall bar. Inset 1: Hall bar. Inset 2: variation of the MOKE loop's coercive field with different Pt thickness. b) SMR measurement on the same $t_{Pt}=6.12$ nm device, with applied field parallel (darkgreen, lightgreen) and perpendicular (blue, red) to the Hall bar, with opposite electric current flows.

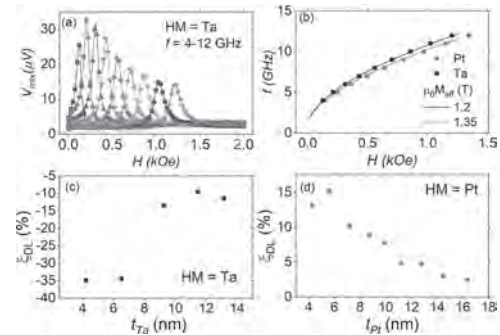


Fig. 2. Magneto-transport measurement results of HM/FM bilayers: (a) SOT-FMR for $t_{Ta} = 4.4$ nm buffer with different excitation frequency (f) symmetric shape of the signal indicate dominance of the damping-like SOT, (b) f vs. in-plane magnetic field (H) for different HM with $t_{HM} \approx 5$ nm, fitting based on Kittel formula enables effective magnetization calculation, (c)-(d) damping-like SOT efficiency dependence on t_{HM} .

Session CD

SPIN HALL EFFECTS

Yi Wang, Chair

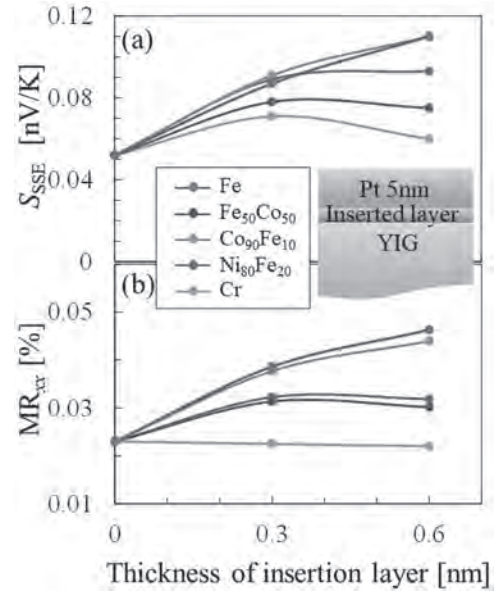
Dalian University of Technology, Dalian, China

INVITED PAPERS

CD-01. Spin Current Enhancement by Inserting Ultra-Thin Magnetic Layer at Interface Between YIG and Pt INVITED.H. Yuasa¹*1. Kyushu University, Fukuoka, Japan*

Spin current control has attracted increasing attention from the viewpoint of fundamental research and application owing to their attractive performances; zero Joule heating, nano scale devices, and expansion of dimension. As typical phenomena we investigated the spin Seebeck effect (SSE) and the spin Hall magnetoresistance (SMR) in the bilayer consisting of a magnetic insulator Y3Fe5O12 (YIG) and a heavy metal (Pt). Since the spin current is originated from the diffusion phenomenon, the signals, that is, spin Seebeck coefficient and MR_{xx} of SMR, are generally small. Therefore, it is important to increase the efficiencies of spin current generation and propagation for practical use. We observed significant enhancement of SSE and SMR values by inserting 0.3nm or 0.6 nm layers of magnetic materials with different composition (Cr, Ni80Fe20, Co90Fe10, Fe50Co50, and Fe) at the YIG/Pt interface [1]. The SSE and SMR showed the mostly same dependences on the insertion layer composition and thickness as shown in Fig. 1, indicating that there is the common reason of SSE and SMR enhancement. To find the reason, we investigated the magnetism of Pt on the insertion layers and the insertion layers themselves. It is known that the magnetization is induced in the Pt layer when Pt contacts the ferromagnetic metals including Fe or Co. However, it has not been clarified whether Pt on the sub-nm-thick magnetic layer is magnetized. In order to investigate the Pt magnetic property, we carried out X-ray magnetic circular dichroism (XMCD) at the BL39XU of SPring-8. The Pt thickness was decreased to 1 nm in order to emphasize the signal from Pt near the interface with the insertion layers. As a result, it was confirmed that there is merely negligible moment in Pt for all samples with and without insertion layers by XMCD. Next, we investigated the magnetism of the sub-nm insertion layers by generalized magneto-optical ellipsometry (GME). Although the magnetic materials with sub-nm thickness does not show magnetization at room temperature in general, there is the possibility that magnetization is induced when ultra-thin magnetic layer is deposited on the ferrimagnetic YIG. However, it is difficult to measure the magnetization of sub-nm insertion layers deposited on the YIG by using macroscopic measurement such as VSM or SQUID because the magnetization signal of the insertion layers is hidden by that of YIG. Compared to this, the surface magnetic information can be extracted by GME analysis. It was found that the magnetic insertion layers of 0.3 nm and 0.6 nm did not exhibit a measurable magnetization. On the contrary, when the thickness of insertion layers is increased to 1 nm, the magnetization becomes obvious and SSE and SMR were decreased. Taking it into consideration, the state of losing magnetic order in the insertion layers seems to increase the spin current propagation from YIG to Pt. In summary, the SSE and SMR was enhanced by the insertion of thin magnetic material layers, which did not result from a net interface magnetization in Pt and the insertion layers. On the contrary, the paramagnetic state is considered to have an important role to enhance the spin current related phenomena.

[1] T. Niimura et al., Phys. Rev. B 102 094411 (2020).



Spin Seebeck coefficient S_{SSE} (a) and MR_{xx} of SMR (b) for YIG/insertion layer/Pt where the insertion layer material is Cr, Ni80Fe20, Co90Fe10, Fe50Co50, or Fe.

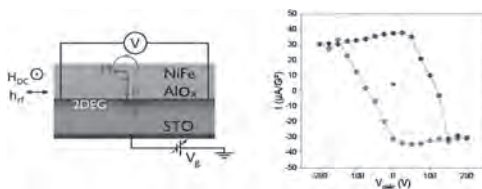
CD-02. Spin to Charge Conversion in the Topological Insulator HgTe and in STO-Based two-Dimensional Electron gas INVITED.

J. Attané¹

¹. Spintec, University Grenoble Alpes, Grenoble, France

While classical spintronics has traditionally relied on ferromagnetic metals as spin generators and spin detectors, a new approach called spin-orbitronics exploits the interplay between charge and spin currents enabled by the spin-orbit coupling in non-magnetic systems, in particular using the spin Hall effect. However, the interconversion efficiency of the direct and inverse spin Hall effect is a bulk property that rarely exceeds ten percent, and does not take advantage of interfacial and low-dimensional effects otherwise ubiquitous in spintronics. In this contribution, we report the observation of spin-to-charge current conversion in strained mercury telluride, using spin pumping experiments at room temperature. We show that a HgCdTe barrier can be used to protect the HgTe topological surface states, leading to high conversion rates, with inverse Edelstein lengths up to 2.0 ± 0.5 nm. These measurements, associated with the temperature dependence of the resistivity, suggest that these high conversion rates are due to the spin momentum locking property of HgTe surface states [1]. We then focus on the SrTiO₃ (STO)-based 2D electron system, presenting experiments performed on NiFe/Al/STO heterostructures. We investigate the nature of the spin-to-charge conversion through a combination of spin pumping, magnetotransport, spectroscopy and gating experiments, finding a very highly efficient spin-to-charge conversion, with inverse Edelstein lengths beyond 20 nm. More importantly, we demonstrate that the conversion rate can be tuned in amplitude and rate by a gate voltage. We then discuss the amplitude of the effect and its gate dependence on the basis of the electronic structure of the 2DES and highlight the importance of a long scattering time to achieve efficient spin-to-charge interconversion. Finally, we harness the electric-field-induced ferroelectric-like state of SrTiO₃ to manipulate the spin-orbit properties of the two-dimensional electron gas. Using spin pumping techniques and a back-gate voltage (cf. figure), we efficiently convert spin currents into positive or negative charge currents, depending on the polarization direction [3]. This non-volatile effect opens the way to the electric-field control of spin currents and to ultralow-power spintronics, in which non-volatility would be provided by ferroelectricity rather than by ferromagnetism.

[1] P. Noël *et al.*, Phys. Rev. Lett. 120, 167201 (2018) [2] D. C. Vaz *et al.*, Nature Materials 1-7 (2019) [3] P. Noël *et al.*, Nature, 580(7804), 483-486 (2020)



Left: Scheme of the spin-pumping technique. A *rf* field is used to induce magnetization precession in the NiFe layer. This leads to the injection of a pure spin current J_s into the 2D electron gas at the surface of STO. This spin current is then converted into a charge current J_c , which can be detected using a voltmeter. The back gate is used to pole the STO. **Right:** For a given spin current, the produced charge current depends in a non-volatile way of the gate voltage.

CONTRIBUTED PAPERS

CD-03. Spin Hall Conductivity Enhancement of Tungsten by Copper Alloying.B. Coester¹, G.D. Wong¹, X. Zhan^{1,2}, J. Tang², W. Gan¹ and W. Lew¹

1. School of Physical & Mathematical Sciences, Nanyang Technological University College of Science, Singapore, Singapore; 2. MIT Key Laboratory of Advanced Metallic and Intermetallic Materials Technology, School of Materials Science and Engineering, Nanjing University of Science and Technology, Nanjing, China

Spin currents generated by the spin Hall effect in e.g. heavy metals like tungsten (W) are interesting candidates for next generation information storage applications. The spin Hall effect has intrinsic and extrinsic contributions of which the latter can be controlled by adding impurities into the material. This enhances the spin Hall angle (SHA) θ_{SH} , which is the ratio of charge to spin current density [1]. When considering energy efficient spin current generation, it is necessary to also consider the spin Hall conductivity, which is the SHA divided by the charge resistivity. While W in its high resistive phase (β -W) has the highest spin Hall angle among pure heavy metals, it has a relatively low spin Hall conductivity (SHC). In contrast, α -W is a low resistivity phase with a low SHA but high SHC [2]. In this work, we investigated the changes in SHA and SHC in α -W with copper (Cu) impurities. We chose to measure the SHA with spin-torque ferromagnetic resonance (ST-FMR), as it also provides information about the ferromagnetic effective damping α_{eff} . The effective damping parameter is essential when optimizing the stack for energy efficient applications because it is inversely proportional to the critical switching current density. Multilayer stacks of Ti(2)|Fe(5)|Cu_{100-x}W_x(5)|Ti(10) were fabricated with the Cu_{100-x}W_x layers deposited via co-sputtering of Cu and W at different RF and DC-powers to obtain alloys of different concentrations. The ST-FMR measurements were carried out for 6 different frequencies (10-15 GHz) and at each frequency the field was swept from 0 to 5 kOe. The measured DC voltage contains a symmetric and anti-symmetric Lorentzian function, whose prefactors can be used to obtain the spin Hall angle. We found that the SHA increases with increasing W concentration until it reaches a maximum at around 60% W. The SHA changes from 0.054 ± 0.004 to 0.20 ± 0.02 , which corresponds to an enhancement of 270%. For the SHC, the trend is similar, with an increase of 120%. Results are shown in Fig 1 (a) and (b), respectively. As the resistivity also increases with impurity content, the SHC shows a smaller enhancement than the SHA. The large SHA at 60% W could be attributed to a high crystallinity as revealed by XRD measurements. As ST-FMR offers the determination of the effective damping, we can determine the ratio of α_{eff}/θ_{SH} , which is proportional to the critical magnetization switching current density [3]. We find that it increases only slightly with increasing W concentration (Fig 2 (a)). At 60% W, α_{eff}/θ_{SH} decreases by a factor of 4 as compared to pure W. The ratio of α_{eff}/θ_{SH} almost follows the inverse of the SHA (Fig 2 (b)), suggesting that the change in damping affects the ratio less than changes in SHA. Our findings here reveal that the Cu₄₀W₆₀ alloy has excellent spin-orbit torque switching characteristics, allowing it to be utilized in energy-efficient spintronic devices.

[1] G.D.H. Wong et al., Scientific Reports., 10(1), p. 9631 (2020) [2] W.-B. Liao et al., physica status solidi (RRL) – Rapid Research Letters., Vol. 13(11), p. 1900408 (2019) [3] K.-S. Lee et al., Applied Physics Letters., Vol. 102(11), p. 112410 (2013)

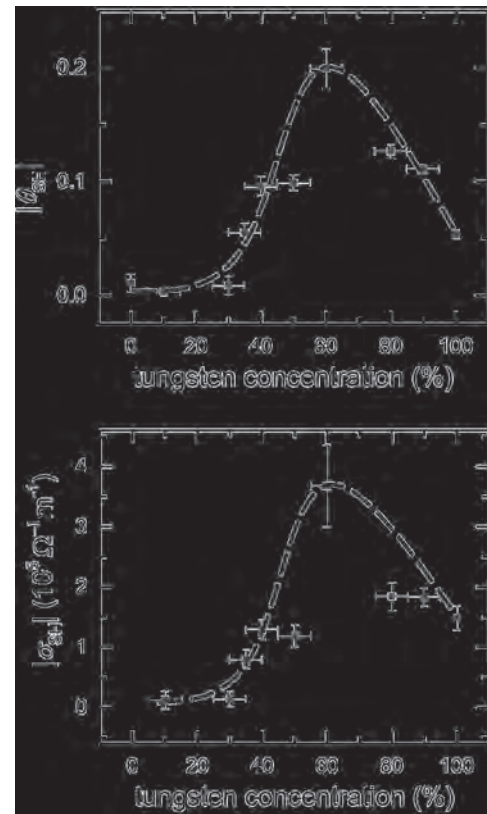


Fig.1: (a) spin Hall angle and (b) spin Hall conductivity for different W concentration. Dashed lines serve as guide-to-the-eye.

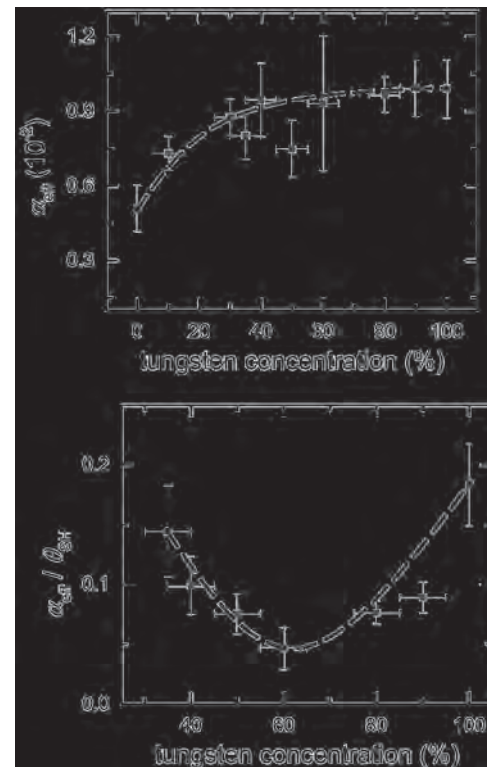


Fig.2: (a) effective damping (b) ratio of effective damping and spin Hall angle, which gives information about the qualitative behaviour of the critical switching current for in-plane magnetization. Dashed lines serve as guide-to-the-eye.

CD-04. High-Throughput Techniques for Measuring the Spin Hall Effect.

M. Meinert⁸, B. Gliniors¹, O. Gueckstock^{2,5}, T. Seifert^{2,5}, L. Liensberger^{3,6}, M. Weiler^{7,3}, S. Wimmer⁴, H. Ebert⁴ and T. Kampfrath^{2,5}

1. Faculty of Physics, Universitat Bielefeld, Bielefeld, Germany;

2. Department of Physics, Freie Universitat Berlin, Berlin, Germany;

3. Walther-Meissner-Institut fur Tieftemperaturforschung, Garching, Germany;

4. Department Chemie, Ludwig-Maximilians-Universitat Munchen, Munchen, Germany;

5. Fritz-Haber-Institut der Max-Planck-Gesellschaft, Berlin, Germany;

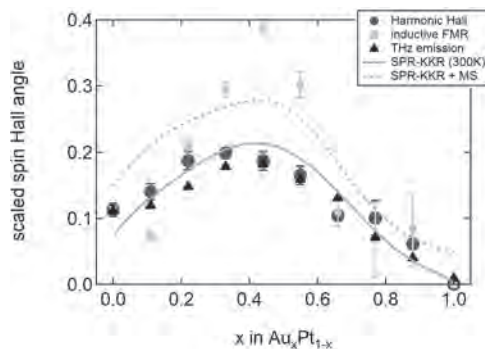
6. Physik-Department, Technische Universitat Munchen, Munchen, Germany;

7. Fachbereich Physik, Technische Universitat Kaiserslautern, Kaiserslautern, Germany;

8. Department of Electrical Engineering and Information Technology, Technische Universitat Darmstadt, Darmstadt, Germany

The spin Hall effect in heavy-metal thin films is routinely employed to convert charge currents into transverse spin currents and can be used to exert torque on adjacent ferromagnets. Conversely, the inverse spin Hall effect is frequently used to detect spin currents by charge currents in spintronic devices up to the terahertz frequency range. Numerous techniques to measure the spin Hall effect or its inverse were introduced, most of which require extensive sample preparation by multi-step lithography. To enable rapid screening of materials in terms of charge-to-spin conversion, suitable high-throughput methods for measuring the spin Hall angle are required. Here [1], we compare two lithography-free techniques, terahertz emission spectroscopy [2] and broadband ferromagnetic resonance [3], to standard harmonic Hall measurements [4] and theoretical predictions [5] using the binary-alloy series $\text{Au}_x\text{Pt}_{1-x}$ as benchmark system. Despite being highly complementary, we find that all three techniques yield a spin Hall angle with approximately the same x -dependence, which is also consistent with first-principles calculations. Quantitative discrepancies are discussed in terms of magnetization orientation and interfacial spin-memory loss.

[1] M. Meinert, B. Gliniors, O. Gueckstock et al., Phys. Rev. Appl., Vol. 14, p.064011 (2020). [2] T. Seifert, S. Jaiswal, U. Martens et al., Nat. Photonics, Vol. 10, p.483 (2016). [3] A. J. Berger, E. R. J. Edwards, H. T. Nembach et al., Phys. Rev. B, Vol. 97, p.094407 (2018). [4] K. Fritz, S. Wimmer, H. Ebert et al., Phys. Rev. B, Vol. 98, p.094433 (2018). [5] M. Obstbaum, M. Decker, A. K. Greitner et al., Phys. Rev. Lett., Vol. 117, p.167204 (2016).



CD-05. Magnetization-Dependent Inverse Spin Hall Effect at Perpendicular Magnetized Tb-Co/Pt Interface.

A. Yagmur¹, H. Awano¹ and K. Tanabe¹

¹ Toyota Technological Institute, Nagoya, Japan

Recently, it has been investigated that spin-orbit coupling at magnetic/nonmagnetic interface induces a spin-to-charge current conversion with different symmetry from the conventional inverse spin Hall effect (c-ISHE) [1,2]. Here, the orientation of spin current polarization can be manipulated by the direction of perpendicular magnetized material (figure) [3]. In this study, we investigate the magnetization-dependent inverse spin Hall effect (md-ISHE) in SiN(10 nm cap)/Tb_xCo_{100-x}(19 nm)/Pt(1 nm)/YIG(167 nm)/SiO₂ (substrate) devices due to spin Seebeck effect. We clearly observe voltage signals due to the c-ISHE and md-ISHE in our devices, which the md-ISHE polarity depends on the magnetization direction of the spin-converter layer. Moreover, the magnitude of induced charge current due to md-ISHE is observed to be almost insensitive for all Tb_xCo_{100-x} samples, whereas the c-ISHE significantly depends on the composition ratio. This work was partially supported by a Grant-in-Aid for Scientific Research (C) (Grant No. 20K05307) from JSPS and the Tokai Foundation of Technology.

[1] A. M. Humphries, T. Wang, E. R. J. Edwards, S. R. Allen, J. M. Shaw, H. T. Nembach, J. Q. Xiao, T. J. Silva, and X. Fan, Observation of spin-orbit effects with spin rotation symmetry, Nature Communications 8, 911 (2017).

[2] S. C. Baek, V. P. Amin, Y.-W. Oh, G. Go, S.-J. Lee, G.-H. Lee, K.-J. Kim, M. D. Stiles, B.-G. Park, and K.-J. Lee, Spin currents and spin-orbit torques in ferromagnetic trilayers, Nature Materials 17, 509 (2018). [3] T. C. Chuang, D. Qu, S. Y. Huang, and S. F. Lee, Magnetization-dependent spin Hall effect in a perpendicular magnetized film, Phys. Rev. Research 2, 032053 (2020).

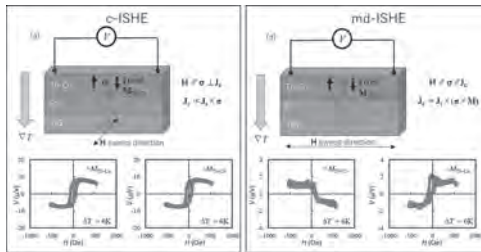


Figure (a) Schematic illustrations and results of (a) c-ISHE and (b) md-ISHE.

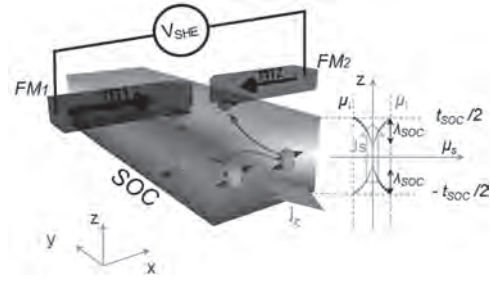
CD-06. Role of the Interfacial Asymmetric Spin Scattering at Ferromagnet-Pt Interfaces.

V. Pham¹, M. Cosset-Cheneau¹, A. Brenac¹, O. Boulle¹, A. Marty¹, J. Attané¹ and L. Vila¹

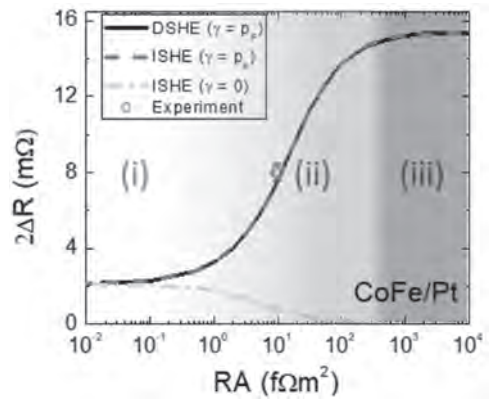
1. SPINtronique et Technologie des Composants, Grenoble, France

The spin to charge interconversion arising from spin-orbit effects is an important tool for spin manipulation. The charge current to spin current conversion has attracted lots of attention as it can be used to write information through the spin orbit torque. The reciprocal mechanism, the spin to charge conversion, has also been found to be essential, in particular as it enables the reading process of magneto-electric spin-orbit devices [1, 2]. Whereas the efficiency of the interconversion is a crucial issue for applications, a consensus on the measured values seems to remain elusive, even for standard materials. The spin to charge interconversion can be for instance obtained by the Spin Hall Effect in platinum. The bulk contribution of platinum to the interconversion efficiency has been widely studied, and the interfacial contributions to the interconversion, such as the spin memory loss at the ferromagnet-platinum interface [3] and spin backflow [4], have been identified as key factors in the measurement of the spin to charge interconversion. These two contributions indeed decrease the amount of spin current flowing through the interface, possibly leading to a wrong estimation of the interconversion efficiency. Here, we will focus on the estimation of the interface resistance of the spin-orbit material/ferromagnetic interface, and of its exact role on spin to charge interconversion, showing that it has up to now been frequently wrongly overlooked. In this contribution, we measured electrically the inverse and direct spin to charge interconversion in ferromagnet/Pt nanostructures (Fig. 1) for different ferromagnetic materials. We find that the amplitude of the Spin Hall signal depends drastically on the magnetic material (CoFe, Co, or NiFe) used for the injection and the detection of the spin current. We show that the use of a conventional analysis, neglecting the interface resistance at the ferromagnet-Pt interface, gives effective spin Hall angle for Pt which are actually strongly dependent on the used ferromagnetic material. By using cross geometry measurement and finite element simulations, we succeeded in extract the interface resistance between Pt and the ferromagnetic materials. Using these resistance values, we show that in order to obtain a consistent spin to charge interconversion efficiency value in the different systems, an interfacial spin scattering asymmetry must be taken into account. This parameter, despite being frequently overlooked in spin-orbitronics experiment, appears to be essential for a proper extraction of the spin to charge interconversion efficiency. Finally, it show that an important interface resistance can, contrarily with what could be expected, enhance the spin Hall signal in electrical measurements (Fig. 2). These results thus provide guidelines for the optimization of the optimization of the write and read processes using spin to charge interconversion in materials with strong spin orbit coupling.

[1] S. Maniapatruni et al. Nature Phys. 14, 338 (2018) [2] V. T. Pham, M. Cosset-Cheneau et al, arXiv:2011.12207 (2020) [3] J.-C. Rojas-Sanchez et al, Phys. Rev. Lett. 112, 106602 (2014) [4] W. Zhang et al, Nature Phys. 11, 496–502 (2015)



Sketches presenting the measurement using the ferromagnet (FM)/ spin-orbit coupling (SOC) nanostructure. The ferromagnetic electrodes allows to probe the spin accumulation and the charge-spin interconversion, and can reciprocally be used to inject a spin current in the SOC material to study the spin-charge interconversion. The studied SOC material is Pt.



Evolution of the interconversion signal when changing the interface resistance RA. The parameter γ represents the amplitude of the spin scattering asymmetry.

CD-07. Effect of Ta Crystallite Size on Spin-Mixing Conductance of Ta/Ni₈₀Fe₂₀ Bilayer Structure.

S. K¹, M. Talluri¹, B. Paikaray¹, J. Pala¹ and C. Murapaka¹

¹. Materials Science and Metallurgical Engineering, Indian Institute of Technology Hyderabad, Hyderabad, India

Spintronic devices explore spin degree of freedom in addition to charge of an electron. The success of spin-based electronics devices depends on the injection, manipulation and detection of spin currents¹. Recently, ferromagnet (FM) and heavy metal (HM) bilayer structures have received great interest due to its spin-charge interconversion. A pure spin current can be generated at the interface between FM/NM via spin pumping. In general, ferromagnetic resonance (FMR) technique is employed in spin pumping to generate pure spin currents through magnetization precession in FM layer which will be injected in to NM layer through the interface. The efficiency of the spin injection is quantitatively measured as spin-mixing conductance($g_{\uparrow\downarrow}$) which estimates the amount of spin current injected into the NM layer. The spin-mixing conductance depends on several parameters such as interface roughness, crystalline phase and quality of the NM layer². The influence of crystalline phase³ and roughness⁴ on spin-mixing conductance have been investigated but the studies on the effect of crystallite size and quality of NM layer on $g_{\uparrow\downarrow}$ are limited. In this work, we have investigated the effect of crystallite size of Tantalum on $g_{\uparrow\downarrow}$ in Ta (18 nm)/Ni₈₀Fe₂₀ (16 nm) bilayers. The bilayer structures are deposited using magnetron sputtering technique. The crystallite size is varied by tuning the growth rate during sputtering deposition by varying the sputtering power from 60 to 120 watt as shown in figure 1(a). Grazing incidence X-Ray diffraction (GI-XRD) technique is used to study the phase of Ta. The Ta films that are deposited at different deposition rates in our study have exhibited BCC (α -Ta) crystal structure as shown in figure 1(b). Crystallite size was calculated by Scherrer formula and observed that with growth rate crystallite size is improved up to 120 watts. The thickness and surface morphology of the Ta films were measured using atomic force microscopy (AFM). The measured average rms roughness for all samples is found to be below 0.6 nm. The Ta/Ni₈₀Fe₂₀ bilayer structures are fabricated to investigate the spin-pumping mechanism at the interface. The FMR technique is used for spin pumping in Ta/Ni₈₀Fe₂₀ in the range of 4 -16 GHz while sweeping magnetic field from 0 – 3000 Oe. From the FMR spectrum shown in figure 2(a) we obtained linewidth and resonance field to determine the change in damping parameter which in turn reveals the spin-mixing conductance. We have quantitatively estimated $g_{\uparrow\downarrow}$ of our bilayer structure and observed that it is in the order of 10^{18} m^{-2} . Interestingly, increase in the crystallite size of Ta in Ta/Ni₈₀Fe₂₀ bilayer film enhances the spin-mixing conductance as shown in the figure 2(b). It shows a better spin pumping at Ta/ Ni₈₀Fe₂₀ interface with larger crystallite size. Enhancement of $g_{\uparrow\downarrow}$ with Ta crystallite size is potentially due to the less scattering in Ta layer thus reducing the spin-back flow.

1. Fabian, J., Sarma, S. Das & Igor Zutic, Jaroslav Fabian, S. D. S. Spintronics: Fundamentals and applications. *Rev. Mod. Phys.* 76, (2004). 2. Tserkovnyak, Y., Brataas, A. & Bauer, G. E. W. Enhanced Gilbert Damping in Thin Ferromagnetic Films. *Phys. Rev. Lett.* 88, 4 (2002). 3. Kumar, A., Bansal, R., Chaudhary, S. & Muduli, P. K. Large spin current generation by the spin Hall effect in mixed crystalline phase Ta thin films. *Phys. Rev. B* 98, 1–6 (2018). 4. Pham, T. K. H. *et al.* Interface morphology effect on the spin mixing conductance of Pt/Fe₃O₄ bilayers. *Sci. Rep.* 8, 1–8 (2018).

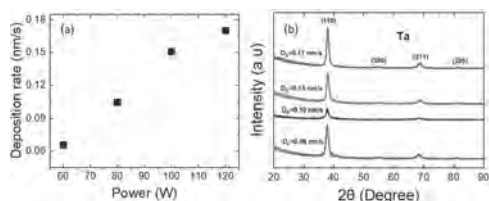


Figure.1: (a) Deposition rate vs Power, (b) X-ray diffraction of Ta at varied deposition rate.

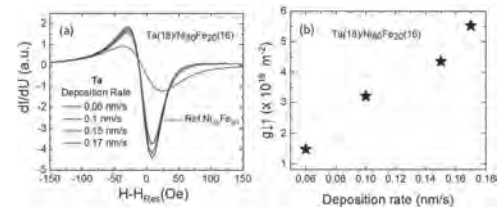


Figure.2: (a) Ferromagnetic response of Ta/Ni₈₀Fe₂₀ and reference Ni₈₀Fe₂₀ at 9 GHz, (b) spin-mixing conductance vs deposition rate of all bilayer structure

CD-08. Spin to Charge Conversion at LaAlO₃/SrTiO₃ Interface States.

A. El Hamdi¹, M. Boselli², J. Chauleau¹, S. Gariglio², J. Triscone² and M. Viret¹

1. SPEC, CEA, CNRS, Université Paris-Saclay, CEA Saclay, Gif-sur-Yvette, France; 2. Département de Physique de la Matière Quantique, University of Geneva, Geneva, Switzerland

Creating a dissipation-less pure spin current and being able to detect it, have been one of the biggest challenges that held the spintronics community for decades. In the beginning of 1970's, Dyakonov et al.¹, made a big break through in this aspect by discovering the Spin Hall Effect (SHE), that made it possible to create a pure spin current by sending an electrical current in non-magnetic heavy metals like Platinum (Pt), this effect relies on the Spin-Orbit Coupling (SOC) interaction which links the spin degree of freedom to the orbital degree of freedom resulting in a preferential directional scattering for electrons of different spins. Recently another type of SOC have been discovered, which relies on the Rashba interaction^{2,3}, this effect stems for a joint action of the SOC and an electrical built-in potential in two-dimensional electrons systems (2 DES) existing at interfaces of two different materials. A promising system to study the spin to charge conversion is the interface between two band gap insulators like the interface between LaAlO₃/SrTiO₃ (LAO/STO), where a 2DES is created due a polar discontinuity at the interface^{4,5}. This 2 DES at the interface of LAO/STO shows a very strong Rashba spin-orbit interaction raising from the breaking of the inversion symmetry. It appears that due to the high dielectric constant in STO below 30K⁶, we are able to tune our Rashba splitting using an electric field⁷. In this work we showed that the Rashba splitting in LAO/STO depends on the angular dependence of the injected spins, so we are able to retrieve an important information regarding the symmetry of the orbitals that are participating in the conversion signal⁸.

¹ M. I. Dyakonov International Journal of Modern Physics B Vol. 23, No. 12n13, pp. 2556-2565 (2009). ² E I Rashba 1959 Fiz. Tverd. Tela 1 407 (E I Rashba 1959 Sov. Phys.-Solid State 1 368). ³ Linding Yuan et al., Nature Communications volume 10, Article number: 906 (2019). ⁴ Thiel S, Hammerl G, Schmehl A, Schneider C W and Mannhart J Science 313 1942 (2006). ⁵ Cantoni C et al Adv. Mater. 24 3952 (2012) ⁶ H. E. Weaver 7 J. Phys. Chem. Solids Pergamon Press. Vol. 11. pp. 274-277 (1959). ⁷ A. D. Caviglia et al., Phys. Rev. Lett. 104, 126803 – Published 26 March (2010). ⁸ J.-Y. Chauleau et al., EPL, vol 116, num 1 (2016)

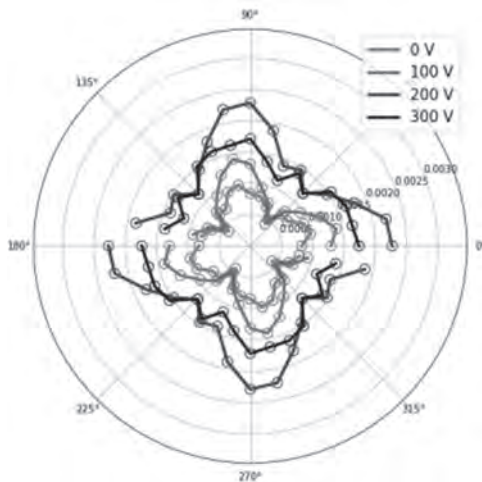


Fig: Angular dependence of the DC IEE conversion signal for a 5-monolayer-thick LAO, for different positive back gate voltages.

CD-09. Non-Conventional Spin Hall Effect in YPt Alloy.

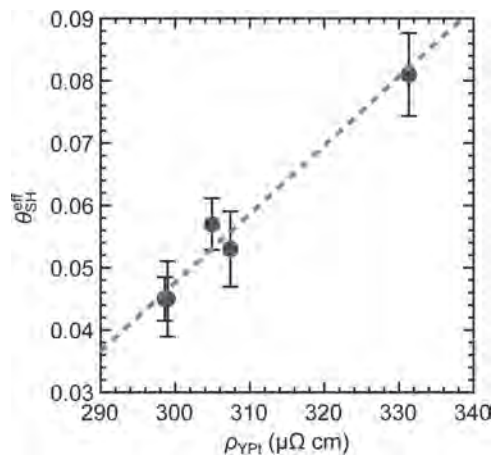
T. Shirokura¹, K. Fujiwara¹ and P.N. Hai^{1,2}

1. Tokyo Institute of Technology, Tokyo, Japan; 2. Tokyo University, Tokyo, Japan

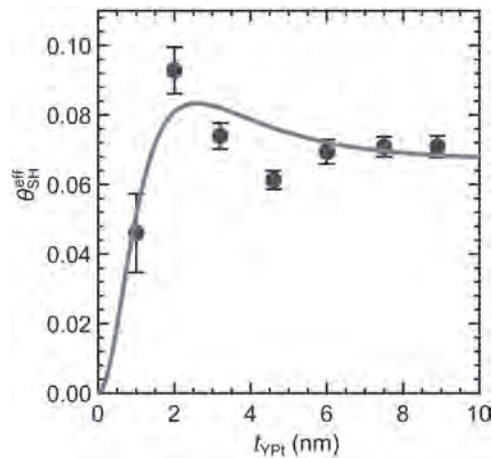
When the spin Hall effect (SHE) is dominated by the intrinsic (Berry phase) mechanism, the spin Hall angle θ_{SH} is proportional to resistivity [1]. Thus, alloying is a promising technique to improve θ_{SH} via resistivity control. Platinum (Pt)-based alloys have been studied intensively in particular, and large θ_{SH} were demonstrated [2]. In Pt-based alloys, dilute doping or alloying with metals with the face-centered-cubic (fcc) crystal structure is utilized to maintain the fcc long range ordering of Pt atoms. However, little work has been done on heavy doping or alloying that completely changes the Pt crystal and band structure. Here, we focused on a Pt-based alloy with orthorhombic crystal structure, YPt [3], to investigate the effect of the crystal structure change on the SHE from those of other fcc Pt-based alloys. We prepared MgAl₂O₄ (2.0)/YPt (t_{YPt})/CoPt (2) on oxidized Si substrates by magnetron sputtering with stoichiometric YPt target, where t_{YPt} is the YPt layer thickness (the unit is nanometer). Here, the CoPt (2) layer has a laminated structure of [Pt (0.4)/Co (0.4)]₂/Pt (0.4). Because the thickness of Pt layers are few times thinner than typical spin diffusion length λ_S of Pt and the laminated structure of CoPt is symmetric, the SHE from the Pt layers were cancelled out and negligible. We fabricated 25×50 μm^2 Hall bars for second harmonics spin-orbit torque measurements [4]. We also fabricated four-terminal 60×100 μm^2 Hall bars to evaluate the sample resistivity by the four-probe technique. To investigate the physical origins of the SHE in YPt, we prepared a series of samples MgAl₂O₄ (2.0)/YPt (11.0 - 14.5) /CoPt (2) with different Ar pressure of 0.3, 0.5, 0.7, 1.0, and 2.0 Pa during YPt sputtering deposition to control the resistivity of YPt layer ρ_{YPt} (referred as series A). The corresponding YPt thickness t_{YPt} is 14.5, 12.8, 12.3, 13.0 and 11.0 nm, respectively. ρ_{YPt} gradually decreased from 331 to 299 $\mu\Omega\text{cm}$ with an increase in Ar pressure from 0.3 to 2.0 Pa. These values are 1.5 - 10 times larger than those of other Pt-based alloys [2,5], indicating a dramatic change of the band structure of YPt from that of Pt. The effective spin Hall angle θ_{SH}^{eff} of these samples were evaluated by the second harmonic technique with alternating currents at 259.68 Hz and large in-plane external magnetic fields H_{ext} parallel with the currents, where the amplitude of the current was changed from 1 to 6 mA, and the sweeping range of H_{ext} was between ± 8.5 kOe. Fig. 1 shows θ_{SH}^{eff} for series A with various YPt deposited at different Ar pressure, as a function of their ρ_{YPt} , where blue dots are experimental data and the red dashed line is an approximation line. A linear dependence of θ_{SH}^{eff} on ρ_{YPt} indicates that the intrinsic and/or the extrinsic side-jump mechanisms dominate the SHE in YPt films. However, the change of θ_{SH}^{eff} for YPt film from 0.045 to 0.081 was nearly doubled when ρ_{YPt} increased only by 10% from 299 to 331 $\mu\Omega\text{cm}$, hence, θ_{SH}^{eff} cannot be explained by only the intrinsic mechanism, which requires a constant value of the effective spin Hall conductivity $\sigma_{SH}^{eff} = \theta_{SH}^{eff} \rho_{YPt}^{-1}$. To deconvolute the contribution of each mechanism, we fit σ_{SH}^{eff} by $\alpha_{ext} \rho_{YPt}^{-2} + \sigma_{SH}^{int}$ [6], where α_{ext} is a coefficient originated from the extrinsic side-jump mechanism, and σ_{SH}^{int} is the intrinsic spin Hall conductivity. We obtained $\alpha_{ext} = (-5 \pm 1) \times 10^{-5} \Omega\text{cm}$ and $\sigma_{SH}^{int} = 700 \pm 100 \Omega^{-1}\text{cm}^{-1}$. The opposite polarity of the extrinsic and intrinsic mechanisms explains the strong sensitivity of θ_{SH}^{eff} to ρ_{YPt} , which is a unique feature of YPt from other conventional Pt-based alloys. Next, we investigated the spin diffusion length in YPt. We prepared another series of samples with different t_{YPt} ranging from 1.0 to 8.9 nm deposited with Ar pressure of 0.3 Pa (referred as series B). Similar to previous reports on heavy metals, ρ_{YPt} tends to increase from 330 to 384 $\mu\Omega\text{cm}$ with a decrease in t_{YPt} from 8.9 to 1.0 nm. The blue dots in Fig. 2 show θ_{SH}^{eff} as a function of t_{YPt} . θ_{SH}^{eff} was ~ 0.07 for thick t_{YPt} but increased up to ~ 0.09 at 2 nm, then dropped to ~ 0.04 at 1 nm. This behavior is originated from the tradeoff between improvement of θ_{SH}^{eff} due to increase in ρ_{YPt} and suppression of θ_{SH}^{eff} due to diffusion of opposite spins from the rear side at small t_{YPt} , similar to Pt films on Ta buffers with strong thickness dependence of resistivity [7]. In our case, although ρ_{YPt} increased only 17% at small t_{YPt} , the high sensitivity of θ_{SH}^{eff} to ρ_{YPt} results in the peak at 2 nm. We fit the experimental data by $\theta_{SH}^{eff} = \theta_{SH0}(\rho_{YPt})[1 - \text{sech}(t_{YPt}/\lambda_S)]$, where the resistivity dependence of $\theta_{SH0}(\rho_{YPt})$ is given by the fitting result of σ_{SH}^{eff} . The red solid line in Fig. 2 shows the best fit curve with $\lambda_S = 0.9$ nm. In Pt-based alloys with the fcc structure, λ_S can

be calculated from their resistivity and λ_S of Pt assuming the Elliott-Yafet mechanism [2]. However, the estimated value of λ_S using the Pt-based alloy model is 0.3 nm [8], which is smaller than the obtained value of 0.9 nm for YPt. Our results show that SHE physics in YPt cannot be explained by extrapolating from conventional fcc Pt-based alloys, indicating the important influence of the band structure change on the SHE of YPt.

[1] E. Sagasta, Y. Omori and M. Isasa, Phys. Rev. B, Vol. 94, p.060412 (2016). [2] L. Zhu, L. Zhu and M. Sui, Sci. Adv., Vol. 5, p.eaav8025 (2019). [3] N. H. Krikorian, J. Less-Common Met., Vol. 23, p.271 (1971). [4] M. Hayashi, J. Kim and M. Yamanouchi, Phys Rev. B, Vol. 89, p.144425 (2014). [5] C. Hong, L. Jin and H. Zhang, Adv. Electron. Mater., Vol. 4, p.1700632 (2018). [6] Y. Tian, L. Ye and X. Jin, Phys. Rev. Lett., Vol. 103, p.087206 (2009). [7] M.-H. Nguyen, D. C. Ralph and R. A. Buhrman, Phys. Rev. Lett., Vol. 116, p.126601 (2016). [8] Y. Wang, P. Deorani and X. Qiu, Appl. Phys. Lett., Vol. 105, p.152412 (2014).



θ_{SH}^{eff} of series A with various YPt deposited at different Ar pressure, as a function of their ρ_{YPt} . Dashed line is an approximation line.



θ_{SH}^{eff} of series B deposited at 0.3 Pa as a function of the YPt layer thickness. Solid line is a fitting curve.

CD-10. Charge-to-Spin Conversion in Perpendicularly Magnetized Ferromagnetic Materials.

Y. Hibino¹, T. Taniguchi¹, K. Yakushiji¹, A. Fukushima¹, H. Kubota¹ and S. Yuasa¹

1. Research Center for Emerging Computing Technologies, National Institute of Advanced Industrial Science and Technology (AIST), Tsukuba, Japan

Introduction: Spin current driven by charge current is one of the key technologies for spin-based memory device. Among them, spin current generated transverse to the charge current has been attracting a great deal of attentions. This is because this spin current generates spin-orbit torques (SOTs) to the adjacent ferromagnet, which could be a promising writing method with high endurance and fast operation. The underlying physics of this charge-to-spin conversion is a spin-orbit coupling related phenomena such as spin Hall effect in non-magnetic materials [3]. Recently, it has been revealed that not only non-magnetic materials but also ferromagnetic materials (FMs) can generate transverse spin current [4-8]. Moreover, FM has a great potential as a spin source for SOT because of the breaking of time reversal symmetry due to the magnetization. This leads to an additional magnetization-dependent transverse spin current generation which can be used as field-free SOT switching [5]. Although the existence of the charge-to-spin conversion phenomena has been mainly studied on in-plane magnetized ferromagnets [5,6], there are few reports on the perpendicularly magnetized case [7]. Here, we focused on the perpendicularly magnetized ferromagnet as a spin current source and quantitatively investigated the charge-to-spin conversion phenomena [8]. Experimental Results: We prepared the following tri-layer base structure; buffer-layer / PML / Cu (3.0 nm) / Fe₇₅B₂₅ (1.3 nm)/ MgO (see Fig. 1a). In this structure, in-plane magnetized highly resistive Fe₇₅B₂₅ layer acts as a detecting layer, and perpendicularly magnetized layer (PML) acts as a spin source material. The PML used here is a Co/Ni multilayer, which is a typical structure for obtaining strong perpendicular magnetic anisotropy. Charge-to-spin conversion in PML is quantitatively investigated by measuring the spin-torque ferromagnetic resonance of the Fe₇₅B₂₅ layer with DC bias current application [8]. We found that the resonance linewidth W is linearly modulated by DC current injection indicating spin injection from PML (Fig. 1b). The efficiency of W modulation significantly changes with the magnetization reversal of PML (+ M_{PML} and - M_{PML} state respectively), indicating the presence of magnetization-dependent charge-to-spin conversion. The spin current generated from PML is further investigated by angular dependence (Fig. 2a). From the angular dependence, we revealed that two types of spin current with different spin polarization are generated from PML as shown in Fig. 2b, and they are polarized along $j_e \times z$ and $m \times (j_e \times z)$ direction respectively (m stands for magnetization of PML) [8]. Furthermore, we investigated the reciprocal process of the charge-to-spin conversion, *i.e.*, spin-to-charge conversion, using a spin-pumping method to inject pure spin current to PML [9]. As a result, we revealed that the spin pumping-induced electromotive force is well explained by the inverse process of charge-to-spin conversion in PML. Conclusion: We reveal that two charge-to-spin conversion mechanisms with different spin polarization coexist in single ferromagnetic material. In addition to this, we observed an inverse process of the charge-to-spin conversion via spin pumping method. Our findings contribute to the deeper understanding of the spin current generation in ferromagnetic materials and will promote the development of SOT-based applications. Acknowledgement: This work was partly supported by JSPS KAKENHI (Grant No. 19J01643), JST CREST (Grant No. JPMJCR18T3), Japan. Part of this work was conducted at the AIST Nano-Processing Facility, supported by the Nanotechnology Platform Program of the Ministry of Education, Culture, Sports, Science and Technology (MEXT), Japan.

[1] A. Manchon *et al.*, Rev. Mod. Phys., Vol. 91, 035004 (2019) [2] L. Liu *et al.*, Science, Vol. 336, 555 (2012) [3] J. Sinova, Rev. Mod. Phys., Vol. 87, 1213 (2015) [4] A. Davidson *et al.*, Phys. Lett. A, Vol. 384, 126228 (2020) [5] S. Iihama *et al.*, Nat. Electro., Vol. 1, 120 (2018) [6] S. C. Baek *et al.*, Nat. Mater., Vol. 17, 509 (2018) [7] A. Humphries *et al.*, Nat. Comm., Vol. 8, 911 (2017) [8] Y. Hibino *et al.*, Phys. Rev. B, Vol. 101, 174441 (2020) [9] K. Ando *et al.*, J. Appl. Phys., Vol. 109, 103913 (2011).

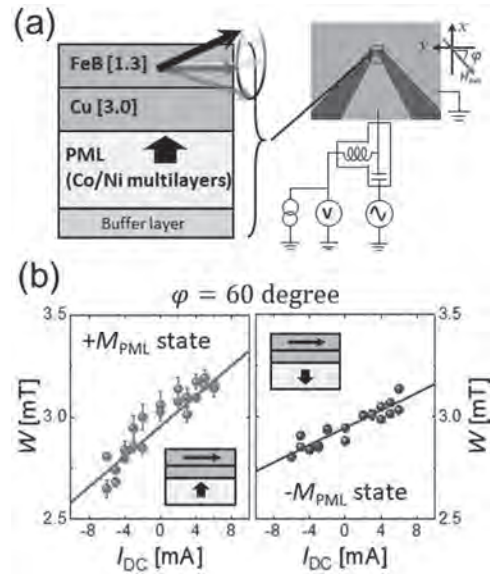


Fig. 1: (a) Schematic of tri-layer based structure (left) and measurement setup of the spin-torque ferromagnetic resonance (right). (b) Resonance linewidth W as a function of applied DC bias current I_{DC} under $+M_{PML}$ (left) and $-M_{PML}$ (right) respectively. The inset schematic shows the magnetization configuration of each measurement.

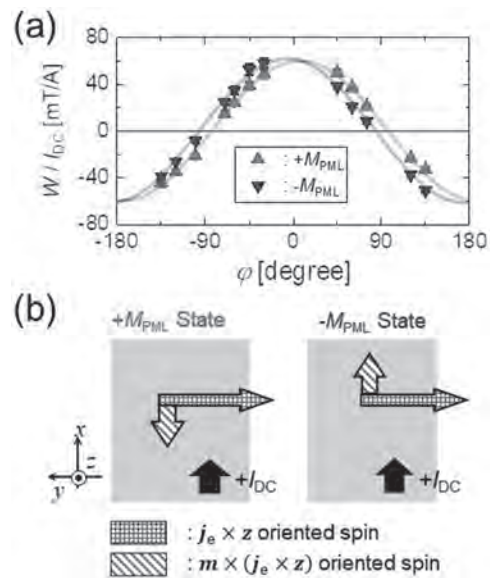


Fig. 2: (a) Angular dependence of efficiency of W modulation via I_{DC} . Upper (downer) triangle shows the measurement under $+M_{PML}$ ($-M_{PML}$) state, and solid curve shows the best fitting curve. (b) Schematic of two components of spin current flowing towards out-of-plane direction ($+z$ direction) under $+M_{PML}$ and $-M_{PML}$ state (left and right respectively) obtained from the fitting.

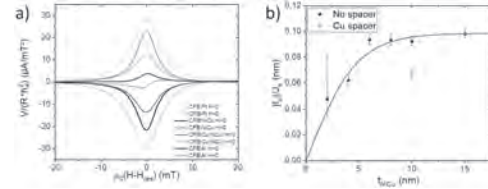
CD-11. Independence of the Inverse Spin Hall Effect With the Magnetic Phase in Thin NiCu Films.

P. Noël¹, S. Varotto^{2,3}, M. Cosset-Cheneau², C. Grezes², Y. Fu², F. Binda¹, C. Murer¹, C. Avci¹, C. Lambert¹, P. Warin², A. Brenac², C. Rinaldi³, J. Jacquot⁴, S. Gambarelli⁴, V. Baltz², L. Vila², J. Attané² and P. Gambardella¹

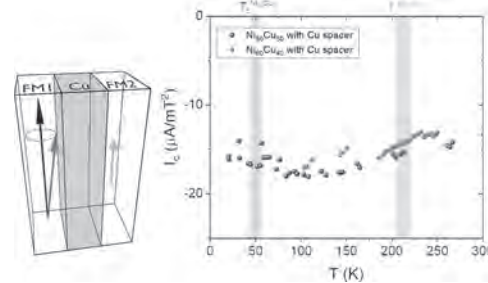
1. DMAT, ETH Zurich, Zurich, Switzerland; 2. SPINtronique et Technologie des Composants, Grenoble, France; 3. Politecnico di Milano Dipartimento di Fisica, Milano, Italy; 4. CEA SYMMES, Grenoble, France

The spin Hall effect (SHE) is closely related to the spin-orbit coupling. Therefore, heavy metals are usually considered as materials of choice to obtain large spin Hall angles. Among these materials, some 5d transition metals such as Pt, Ta or W offer the largest spin-charge interconversion efficiency for spin current detections through the inverse spin Hall effect or to obtain efficient current induced magnetization switching in SOT-MRAM devices [1]. Despite a weaker spin orbit coupling, spin Hall angles comparable to that of the best 5d materials has also been obtained in 3d ferromagnetic metals such as Co [2] or Ni [3]. More recently nonmagnetic alloys containing Nickel atoms such as NiCu [4] and CoNiB [5] attracted great interest for their large spin Hall angles and their potential for spintronic applications. Using the spin pumping by ferromagnetic resonance technique we could compare the spin to charge current conversion in Ni₆₀Cu₄₀ to the one of Pt. As can be seen in figure 1 a) the normalized spin pumping signal obtained in CFB/NiCu is comparable to that of CFB/Pt. We performed a thickness dependence shown in figure 1 b) to extract the spin Hall angle (θ_{SHE}) and spin diffusion length (λ_s) and obtained results comparable to the one of 5d metals using similar method with $\lambda_s = 2.4 \pm 0.3$ nm and $\theta_{\text{SHE}} = 4.1 \pm 0.5$ % [6]. Keller and coworkers [4] noticed similarities in the bandstructure of paramagnetic Nickel and Platinum possibly explaining the origin of the effect. The calculated band structure of ferromagnetic Nickel does not resemble that of Platinum and the origin of the large spin Hall effect observed in ferromagnetic Ni [3] could thus be different. The interplay between the spin-orbit coupling and magnetism is known to be at the origin of specific transport properties such as the anomalous magnetoresistance and the anomalous Hall effect. However, the link between the SHE and the magnetic order is complex and still unexplored [7]. In order to study the effect of the phase transition we performed spin pumping as a function of temperature in Ni₆₀Cu₄₀ and Ni₅₀Cu₅₀ alloys above and below the Curie temperature. To avoid direct contact between the ferromagnetic spin injector CFB and the magnetic NiCu alloy that would modify CFB resonance properties due to the direct coupling [8] we used a 5 nm thick Cu interlayer. The spin pumping measurements performed in CFB/Cu/Ni₆₀Cu₄₀ and CFB/Cu/Ni₅₀Cu₅₀ shown in figure 2 indicate that in NiCu the SHE is insensitive to the magnetic order [6]. A large variety of alloys composed of Ni, Co or Fe in the ferromagnetic or paramagnetic phase could be explored as spin current generators and detectors, extending the number of possible light metal systems with a large SHE. In particular, the large spin Hall effect in NiCu shows that it is a promising alternative to obtain large spin orbit torque without heavy metals.

1] M. Cubukcu *et al.*, Appl. Phys. Lett. 104, 042406 (2014) 2] D. Tian *et al.*, Phys. Rev. B 94, 020403(R) (2016) 3] C. Du *et al.*, Phys. Rev. B 90, 140407(R) (2014) 4] M.W. Keller *et al.*, Phys. Rev. B 99, 214411 (2019) 5] Y. Hibino *et al.*, Phys. Rev. Applied 14, 064056 (2020) 6] S. Varotto, M. Cosset-Chéneau, [...], P. Noël *et al.*, Phys. Rev. Lett. 125, 267204 (2020) 7] V. P. Amin *et al.*, Phys. Rev. B 99, 220405(R) (2019) 8] J. Lindner and K. Baberschke, J. Phys. Condens. Matter 15, R193 (2003)



a) Normalized spin pumping signals in CFB(15)\Pt(15), CFB(15)\Ni₆₀Cu₄₀(10), CFB(15)\Cu(5)\Ni₆₀Cu₄₀(10) and in the CFB(15)\Al(3) reference sample. The spin pumping signals in the light metal alloy NiCu are comparable to the one of Pt. (b) Thickness dependence of the absolute value of the charge current production divided by the injected spin current at resonance.



The normalized spin pumping signal as a function of temperature in the trilayers CFB(15)\Cu(5)\Ni₆₀Cu₄₀(10) and CFB(15)\Cu(5)\Ni₅₀Cu₅₀(10) with different Curie temperatures. For both alloys the inverse spin Hall effect is not affected by the phase transition.

CD-12. Interface Optical Spin Generation in a Ferromagnet/Heavy Metal Heterostructure.

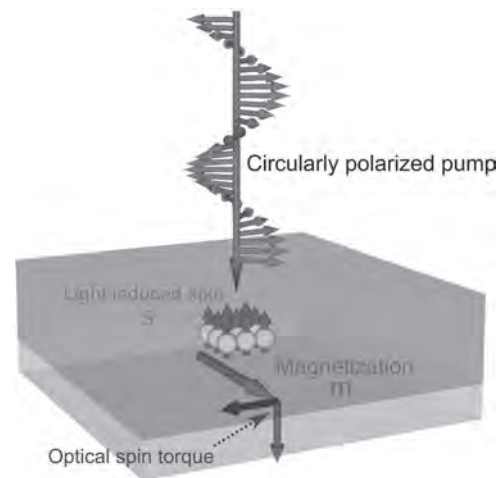
S. Iihama^{1,2}, K. Ishibashi^{3,4} and S. Mizukami^{4,2}

1. Frontier Research Institute for Interdisciplinary Sciences (FRIS), Tohoku University, Sendai, Japan; 2. Center for Spintronics Research Network (CSRN), Tohoku University, Sendai, Japan; 3. Department of Applied Physics, Tohoku University, Sendai, Japan; 4. Advanced Institute for Materials Research (AIMR), Tohoku University, Sendai, Japan

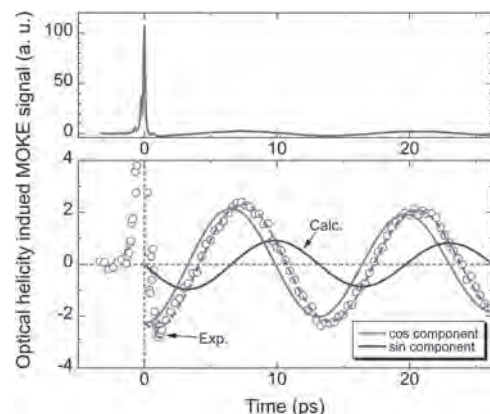
An efficient electrical switching of thin film metallic nanomagnets has been demonstrated by using ferromagnet/heavy metal thin film heterostructures [1][2]. The spin-Hall effect in the heavy metal layer and/or the Rashba-Edelstein effect at the interface have been used to control the nanomagnets efficiently by electrical means. On the other hand, optically induced switching of nanomagnets might be useful for optically-switchable magnetic memories, promising candidate for future fast and low power consumption information processing system using photonic integrated circuits [3]. An increase of optical spin generation efficiency in the materials is crucial for such photo-spintronics devices. Recently, optical helicity induced torque on magnetization in metallic thin films [Fig. 1], termed as *optical spin torque*, has been reported. It was demonstrated that the optical spin torque is induced by the inverse Faraday effect in ferromagnetic metals and the optical orientation effect in nonmagnetic heavy metal layers [4][5]. Both the inverse Faraday effect and the optical orientation effect can be considered as bulk effects in the ferromagnetic layers and the heavy metal layers, respectively. However, interfacial nature of the optical spin generation such as the optical Rashba-Edelstein effect [6] has not been addressed so far. In this study, optical spin torque vectors in the ferromagnet/heavy metal heterostructure with different thicknesses and symmetry of stacking structures were investigated to gain insight into the interfacial nature of optical spin generation [7]. Thin film samples were fabricated by using magnetron sputtering technique. The stacking structure is as follows, Si/SiO₂ sub./ MgO(10) / Fe₅₀Co₅₀ (*d*_{FeCo}) / Pt (*d*_{Pt}) (thickness is in nm). FeCo (Pt) thickness *d*_{FeCo} (*d*_{Pt}) was varied from 1 (2) nm to 4 (10) nm. To study the effect of symmetries for the stacking structure, samples with following stacking structure were also made, Si/SiO₂ sub./ Pt(3) / Co(2) / Pt(3), Si/SiO₂ sub./ Pt(3) / Co(2) / Ta(2), Si/SiO₂ sub./ Co(2) / Pt(3). The optically induced spin was detected by using all-optical time-resolved magneto-optical Kerr effect (TRMOKE). The wavelength and pulse duration were 800 nm and 120 fs, respectively. The pump beam is irradiated on the film at an angle of 10 deg. measured from film normal. Polar MOKE signals were detected to measure normal component of magnetization. In-plane magnetic field up to 2 T was applied. Right circularly polarized (RCP) and left circularly polarized (LCP) pump pulses were irradiated on the ferromagnet/heavy metal heterostructure films. A change in the phase of magnetization precession was observed when the pump laser pulses with different optical helicities were irradiated, indicating the magnetization precession was excited by the optical spin torque. Figure 2 shows optical helicity induced TRMOKE signals where signals are obtained by taking differences between the signals with RCP and LCP pump pulses. Large peak at around delay zero is due to the so-called specular inverse Faraday effect, which is used to define the time when the pump pulse arrives at the film surface. Oscillation signals were fitted by the sinusoidal decayed function, as shown with broken curves in Fig. 2 bottom. The optical helicity induced TRMOKE signals were decomposed into sine and cosine components, as shown with red and blue solid curves in Fig. 2, respectively. This phase analysis was used to evaluate optical spin torque vectors in the heterostructures. The cosine signal indicates that magnetization precession is excited by out-of-plane optical spin torques, which can be explained by the optical orientation effect in the heavy metal Pt layer. In addition, remarkable sine signals was observed. The in-plane field-like optical spin torque evaluated from the sine signal was found to be increased with decreasing FeCo thickness. This increase cannot be explained by the inverse Faraday effect in the ferromagnetic FeCo layer [7]. A possible explanation is that the remarkable in-plane field-like optical spin torque is attributed to the interface spin generated by the optical Rashba-Edelstein effect. Interfacial in-plane torques can be induced by exchange coupling between generated spins and magnetization, which is analogous to the electrical manipulation of magnetization

via the Rashba-Edelstein effect. To validate the optical spin torque induced by the optical Rashba-Edelstein effect, we measured the optical spin torque with changing stacking structure symmetry. It was found that the in-plane optical spin torque was enhanced when Co was sandwiched by SiO₂ and Pt layer, *i.e.*, asymmetric heterostructure [7]. This result supports the optical spin torque induced by the interfacial Rashba spin-orbit coupling owing to the structural inversion symmetry breaking. In conclusion, we studied optical spin torque vectors in the ferromagnet/heavy metal heterostructure. By changing the thickness and the stacking structure symmetry of the heterostructure, we found new type of the interface optical spin generation, optical Rashba-Edelstein effect. This work will lead to efficient optical manipulation of thin film nanomagnets.

[1] I. M. Miron, K. Garello, G. Gaudin *et al.*, Nature, Vol. 475, p. 189 (2011) [2] L. Liu, C. -F. Pai, Y. Li *et al.*, Science, Vol. 336, p. 555 (2012) [3] H. Becker, C. J. Krücker, D. V. Thourhout *et al.*, IEEE J. Sel. Top. Quant., Vol. 26, p. 8300408 (2020) [4] G. -M. Choi, A. Schleife, D. G. Cahill, Nat. Commun. Vol. 8, p. 15085 (2017) [5] G. -M. Choi, J. H. Oh, D. -K. Lee *et al.*, Nat. Commun. Vol. 11, p. 1482 (2020) [6] V. M. Edelstein, Phys. Rev. Lett. Vol. 80, p. 5766 (1998) [7] S. Iihama, K. Ishibashi, S. Mizukami, Nanophotonics, 20200571 (2020)



Schematic illustration of the optical spin torque in a ferromagnet/heavy metal heterostructure.



Optical helicity induced TRMOKE signal obtained by taking differences between signals with RCP and LCP pump pulses for a FeCo(2) / Pt(3) thin film. The optical helicity induced signals at around *t* = 0 [top] and magnetization precession due to the optical spin torque [bottom].

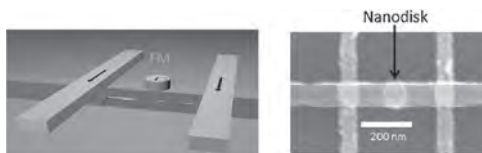
CD-13. Measurement of the Spin Absorption Anisotropy in Lateral Spin Valves.

M. Cosset-Cheneau¹, L. Vila¹, G. Zahnd¹, D. Gusakova¹, V. Pham¹,
C. Grezes¹, X. Waintal², A. Marty¹, H. Jaffrès³ and J. Attané¹

1. SPINtronique et Technologie des Composants, Grenoble, France;
2. Pheliqs, Grenoble, France; 3. CNRS-THALES, Palaiseau, France

The relaxation of a spin current into a ferromagnetic material occurs through different processes depending on the spin currents' polarization orientation. For a polarization collinear with the material magnetization, the relaxation occurs through diffusive processes controlled by the spin diffusion length [1]. When the polarization is transverse with the magnetization, the relaxation is driven by ballistic processes due to band structure mismatch and non-coherent spin precession [2]. Despite being a key ingredient for the understanding of phenomena like Spin Transfer Torque, this anisotropy has never been directly observed so far. In this presentation, we report the observation of the spin relaxation anisotropy on a single device by using a spin absorption method in Lateral Spin Valves (LSVs) [3]. Using a magnetic field, we control the relative orientation between the spin current polarization and the magnetization of a nanodisk-shaped ferromagnetic absorber (fig. 1). We observed that the efficiency of the spin current absorption increases when this polarization and the absorber magnetization have transverse directions. We will present a device that allows the study of spin transport in a LSV with non-collinear ferromagnetic component. By demonstrating a good control over its magnetic states, we will show that we indeed observed the spin current relaxation anisotropy in a single device. We carried out an analysis by introducing bulk characteristic lengths of the transverse spin relaxation, and the spin mixing conductance describing transverse interfacial spin relaxation processes. This data analysis points out the role of both interfacial and bulk contribution in the non-collinear spin current relaxation, and allows the electrical measurement of the spin mixing conductance at 3d ferromagnets-Cu interfaces [3].

[1] T. Valet and A. Fert, Phys. Rev. B 48, 7099 (1993) [2] C. Petitjean et al., Phys. Rev. Lett. 109, 117204 (2012) [3] G. Zahnd et al., Phys. Rev. B 98, 175514 (2018) [3] M. Cosset-Cheneau et al, arXiv:2007.14058 (2020), accepted in Physical Review Letters



Drawing and SEM picture of the device used for the absorption anisotropy measurement. The nanodisk absorbs the spin current that flows between the ferromagnetic electrodes. Its isotropic shape allows to change its magnetization orientation by using a weak external magnetic field.

Session CE

SPIN CURRENTS

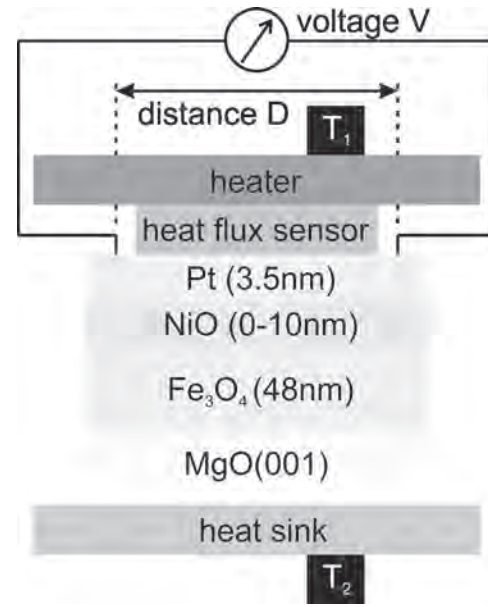
Dushyant Kumar, Chair
National University of Singapore, Singapore

INVITED PAPERS

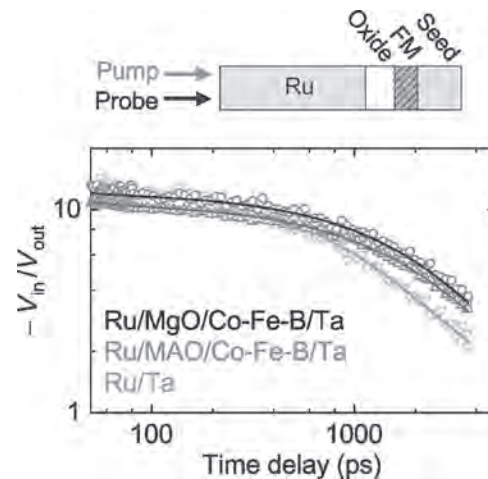
CE-01. Impact of Thermal Conductivity in Insulators on Thermally Induced Spin Currents INVITED.T. Kuschel¹¹ Physics, Universitat Bielefeld, Bielefeld, Germany

Spin currents generated from thermal gradients in magnetic tunnel junctions (MTJs) via the tunnel magneto-Seebeck effect (TMS) [1] or in ferromagnetic insulators via the spin Seebeck effect (SSE) [2,3] have high potential for future nano-electronic devices [4]. The TMS effect can be enhanced by proper choice of barrier [5] and electrode [6] materials. In addition, recent reports highlight the enhancement of thermally induced spin currents by the insertion of antiferromagnetic insulating layers [7] and assign this effect to the improved spin transport properties of the antiferromagnetic oxide layer. However, quantitative determination and comparison of the TMS or SSE coefficients require accurate knowledge of the temperature drop across the insulating tunnel barrier or antiferromagnetic insulating layer. As a promising alternative, the detected thermovoltages are related to the heat flux that passes the insulating material. Unknown properties of the thermal connection between sample and setup make the temperature difference a less reliable quantity compared to the heat flux detection [8-10]. The key property here is the thermal conductivity, which determines both temperature drop and heat flux, and which is needed, e.g., to compare SSE coefficients scaled to the heat flux with literature values. However, the thermal conductivity of oxide materials is experimentally difficult to access. In my talk, I will introduce two spin calorific devices that include an oxide interlayer, and discuss the role of the thermal conductivity of these layers. In particular, these will be the oxide tunnel barrier of an MTJ in a TMS device and the inserted antiferromagnetic oxide layer in an SSE stack (see Fig. 1). Additionally, I will present several experimental approaches to obtain quantitative values for the thermal conductivity in insulators utilizing laser-induced TMS in combination with finite element modeling [11] as well as time-domain thermoreflectance (see Fig. 2) and time-resolved magnetooptic Kerr effect thermometry [12]. Here, we extract values of the thermal conductivity for MgAl_2O_4 and MgO barrier materials in half-MTJ stacks with Co-Fe-B electrode. The results are in nice agreement with theoretical predictions for ultra-thin oxide barriers [13]. Furthermore, we experimentally found that the thermal conductivity does not significantly change when an antiferromagnetic insulating layer, such as NiO, is inserted into SSE devices. Therefore, the temperature profile of the SSE stack does not change as well and cannot explain the enhanced thermal spin current due to the insertion of an antiferromagnetic oxide layer. Thus, we confirm the enhanced spin conductivity induced by the insertion of an antiferromagnetic insulating layer.

[1] T. Kuschel *et al.*, *J. Phys. D: Appl. Phys.* 52, 133001 (2019) [2] K. Uchida *et al.*, *Appl. Phys. Lett.* 97, 172505 (2010) [3] J. Kimling, TK *et al.*, *Phys. Rev. Lett.* 118, 057201 (2017) [4] U. Martens, TK *et al.*, *Commun. Phys.* 1, 65 (2018) [5] T. Huebner, TK *et al.*, *Phys. Rev. B* 96, 214435 (2017) [6] A. Boehnke, TK *et al.*, *Nat. Commun.* 8, 1626 (2017) [7] W. Lin *et al.*, *Phys. Rev. Lett.* 116, 186601 (2016) [8] A. Sola, TK *et al.*, *Sci. Rep.* 7, 46752 (2017) [9] P. Bougiatioti, TK *et al.*, *Phys. Rev. Lett.* 119, 227205 (2017) [10] A. Rastogi, TK *et al.*, *Phys. Rev. Appl.* 14, 014014 (2020) [11] T. Huebner, TK *et al.*, *J. Phys. D: Appl. Phys.* 51, 224006 (2018) [12] H. Jang, TK *et al.*, *Phys. Rev. Appl.* 13, 024007 (2020) [13] J. Zhang *et al.*, *Phys. Rev. Lett.* 115, 037203 (2015)



Investigated SSE systems which contain antiferromagnetic NiO interlayers of various thicknesses on top of Fe_3O_4 . The heater generates the temperature gradient that induces the spin current detected by the orthogonal inverse spin Hall effect voltage in Pt. The obtained electric field V/D is related to the temperature difference T_1-T_2 and to the heat flux which are detected by thermocouples and by a heat flux sensor, respectively.



Time-domain thermoreflectance measurements (open symbols) on the half-MTJ samples with Co-Fe-B electrode and MgO as well as MgAl_2O_4 barrier material. In addition, the reference sample with just the seed layer Ta has been studied. The thick Ru layer absorbs the pump pulse and passes on the heat towards the half MTJ. This reduces the reflected intensity of the probe beam on a 100-1000 ps time scale. The solid lines are fits based on a model that includes the Ru layer, the substrate and an intermediate thermal conductance containing all intermediate layers and interfaces. Figure taken from Ref. [10].

CE-02. Controlling Spin Current Polarization Through non-Collinear Antiferromagnetism INVITED.

T. Nan¹

1. Institute of Microelectronics, Tsinghua University, Beijing, China

Current-induced spin-orbit torque enables highly efficient manipulation of magnetization for spintronic applications. The anti-damping torque is responsible for efficient magnetization manipulation when the torque is collinear with the magnetization leading to a directly change of the effective magnetic damping. But as the anti-damping torque is restricted to lie along an in-plane direction, it is efficient for manipulating only samples with magnetic anisotropy along the in-plane y axis not that along the out-of-plane (z axis) or collinear with the current (x axis). To efficiently and deterministically drive, for example, perpendicularly-magnetized devices that are preferred for high-density memories, an out-of-plane anti-damping torque is required. Such an out-of-plane spin-torque can originate from spin-orbit scattering from ferromagnetic interfaces(1–3), or can arise at the interface in systems with reduced symmetry, such as in bilayers of the non-magnetic transition-metal dichalcogenide and ferromagnetic metals(4); however these effects based on interface or heterostructure engineering have not been demonstrated strong enough for practical anti-damping switching. Here we demonstrate an alternative strategy to achieve unconventional spin-orbit torques, based on long-range non-collinear magnetic order within the *bulk* of the spin-source layer(5). In particular, we use the spin-Hall effect in epitaxial thin films of Mn_3GaN , a metallic antiferromagnet that has a 120° triangular spin texture, which reduces the symmetry sufficiently to allow spin current generation with different spin polarization directions to generate unconventional spin-torques. In heterostructures of epitaxial $\text{Mn}_3\text{GaN}/\text{Cu}/\text{permalloy}$, we observe not only the out-of-plane anti-damping torque, but also the anti-damping torque corresponding to a Dresselhaus-like spin polarization, besides the conventional Rashba-like symmetry. When the non-collinear spin texture is eliminated by heating above the Néel temperature of Mn_3GaN (345 K), the unconventional spin-torques go to zero. Such a control of the spin polarizations is coincident with our symmetry analysis and theory calculation upon the magnetic space groups across the Néel transition. Our results demonstrate an approach based on spin-structure design for controlling spin-orbit torque, enabling high efficient manipulation of magnetization for antiferromagnetic spintronics. The presenter thanks C. X. Quintela, J. Irwin, G. Gurung, D. F. Shao, J. Gibbons, N. Campbell, K. Song, S. Y. Choi, L. Guo, R. D. Johnson, P. Manuel, R. V. Chopdekar, I. Hallsteinsen, T. Tybell, P. J. Ryan, J. W. Kim, Y. S. Choi, P. G. Radaelli, D. C. Ralph, E. Y. Tsymbal, M. S. Rzchowski, C. B. Eom for their contributions in this research.

1. V. P. Amin, M. D. Stiles, Spin transport at interfaces with spin-orbit coupling: Phenomenology. *Phys. Rev. B*, 94, 104420 (2016). 2. S. H. C. Baek, V. P. Amin, Y. W. Oh, G. Go, S. J. Lee, G. H. Lee, K. J. Kim, M. D. Stiles, B. G. Park, K. J. Lee, Spin currents and spin-orbit torques in ferromagnetic trilayers. *Nat. Mater.* 17, 509–513 (2018). 3. A. M. Humphries, T. Wang, E. R. J. Edwards, S. R. Allen, J. M. Shaw, H. T. Nembach, J. Q. Xiao, T. J. Silva, X. Fan, Observation of spin-orbit effects with spin rotation symmetry. *Nat. Commun.* 8, 911 (2017). 4. D. MacNeill, G. M. Stiehl, M. H. D. Guimaraes, R. A. Buhrman, J. Park, D. C. Ralph, Control of spin-orbit torques through crystal symmetry in $\text{WTe}_2/\text{ferromagnet}$ bilayers. *Nat. Phys.* 13, 300–305 (2016). 5. T. Nan, C. X. Quintela, J. Irwin, G. Gurung, D. F. Shao, J. Gibbons, N. Campbell, K. Song, S. Y. Choi, L. Guo, R. D. Johnson, P. Manuel, R. V. Chopdekar, I. Hallsteinsen, T. Tybell, P. J. Ryan, J. W. Kim, Y. Choi, P. G. Radaelli, D. C. Ralph, E. Y. Tsymbal, M. S. Rzchowski, C. B. Eom, Controlling spin current polarization through non-collinear antiferromagnetism. *Nat. Commun.* 11, 4671 (2020).

CONTRIBUTED PAPERS

CE-03. Spin Current Induced by a Surface Plasmon Polariton.

T. Wijaya¹, D. Oue², M. Matsuo³, Y. Ito³, K. Elphick⁵, D. Lloyd⁴,
H. Uchida³, M. Inoue³ and A. Hirohata⁵

1. Graduate School of Engineering, The University of Tokyo, Bunkyo-ku, Japan; 2. Imperial College London, London, United Kingdom; 3. Toyohashi University of Technology, Toyohashi, Japan; 4. Chinese Academy of Sciences, Beijing, China; 5. University of York, York, United Kingdom

Spintronics has been expanding its fields to cover not only electronics and magnetism but also photonics, caloritronics and mechanics in recent years. Among them, photoexcitation using circularly polarised light has been commonly used to generate a spin polarised electrical current mainly in a semiconductor [1]. However, the linkage between a spin current and a propagating surface plasmon polariton (SPP) has not been well investigated theoretically until recently [2]. SPPs are generated in a PHz regime in a non-magnetic metal, which can generate a magnetisation gradient and a resulting spin current. In this study, we have experimentally measured the SPP generated spin current using an inverse spin Hall effect and confirmed it agrees with the above theoretical prediction. A high vacuum sputtering system (PlasmaQuest, HiTUS) was used to deposit 20 nm thick Ag films on a thermally oxidised Si substrate. The films were also patterned into a Hall bar with the width of 1.2 mm and the length of 11 mm. By placing a prism (ThorLab, N-BK7) on the surface of the Hall bar, the Kretschmann arrangement was achieved for SPP introduction by a semiconductor laser (Thorlabs, LDM635 with the wavelength of 635 nm and the power of 0.4 mW). As shown in Fig. 1, a linear polariser and a half-wave plate (Thorlabs, SM05 mounted zero-order 633 nm) were used to generate both *s*- and *p*-polarisations. The spot size of the incident beam was then controlled using a pair of objective and a convex lens. The measured laser spot size was 1.73 mm². The incident angle q of the beam to the prism was controlled by a mirror. The generated spin current was detected using an inverse spin Hall effect as schematically shown in Fig. 3. The source meter (Keithley, 2400) was used to detect the spin Hall voltage by connecting electrical contacts at the diagonal corners of the continuous film and the ends of the Hall bars. The incident angle q was adjusted to show the largest Hall voltage. The measurements were carried out with 600–1,000 repetitions with 0.1 ms interval, providing an average value with a standard deviation. A source current was set to be 0.0 and 0.1 mA for the Hall voltage and resistance measurements, respectively. The continuous films were measured to demonstrate the spin current generation by SPP as shown in Fig. 1a. Ag, Pt and W films were used for the inverse spin Hall measurement with and without a prism. In order to subtract any parasitic effects, *e.g.*, spin caloritronic and photovoltaic effects induced by the laser introduction, a spin current generated by the electro-motive force I_{emf} was first estimated by subtracting the current generated by the electro-motive force with and without the prism. The spin current generated by SPP I_{SPP} was then estimated by taking the difference between those generated by *s*- and *p*-polarisations since only the *p*-polarised light generates SPP. By solving the wave-number matching condition between the laser and SPP, the plasma frequency of Ag is estimated to be 2.18 PHz. I_{SPP} is estimated to be (2.128 ± 0.281) and (6.650 ± 0.169) μ A for the Ag continuous film and Hall bar, respectively, confirming the SPP-induced spin currents. Such a new linkage between spintronics and photonics and lead to a new coupler to convert optical data signals into spin currents for processing and storage and *vice versa*.

[1] A. Hirohata, "Optically Induced and Detected Spin Current," in *Spin Current* S. Maekawa, S. O. Valenzuela, E. Saitoh and T. Kimura (Eds.) (Oxford University Press, Oxford, UK, 2012) p. 49-64. [2] D. Oue and M. Matsuo, *New J. Phys.* 22, 033040 (2020).

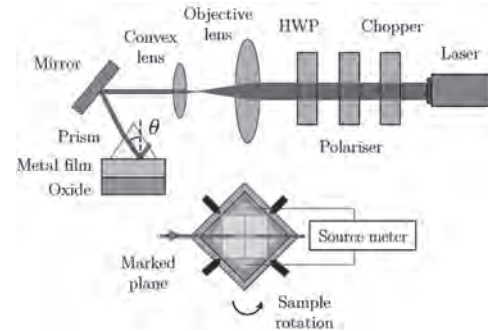


Fig. 1 Schematic diagram of the spin current generation by SPP.

CE-04. Injection, Transport, Detection, and Modulation of Magnon Spin Currents in Magnetic Insulators.

S. Vélez¹, J. Gao¹, J. Gomez-Perez², C. Lambert¹, L. Hueso², M. Fiebig¹, F. Casanova² and P. Gambardella¹

1. Department of Materials, ETH Zurich, Zurich, Switzerland; 2. CIC nanoGUNE, Donostia-San Sebastian, Spain

Recent demonstration of efficient transport and manipulation of spin information by magnon currents has opened exciting prospects for processing information in devices. Magnon currents can be excited in magnetic insulators by applying charge currents in an adjacent metal layer. Here, by implementing a non-local device scheme, we study the magnon diffusion length (MDL) for electrically and thermally excited magnon currents in $Y_3Fe_5O_{12}$ (YIG) and $Tm_3Fe_5O_{12}$ (TmIG) [1,2]. In contrast to earlier reports, our temperature and thickness-dependence studies reveal that the MDL depends on the way the magnon currents are generated, evidencing that magnons of different energies are excited (*sub-thermal* and *thermal* for electrically- and thermally-driven magnon currents, respectively) [1]. At room temperature, the MDL in YIG is $\sim 9 \mu m$ for thermally excited magnons, which is almost twice the value extracted from those excited electrically. This difference gradually decreases as temperature decreases, which is consistent with the expected convergence of the excited magnon distributions at low temperatures. Moreover, we demonstrate that the MDL of thermally induced magnons in YIG is the same regardless of the film thickness and growth conditions, evidencing the robustness of the measurement method to reliably extract the intrinsic MDL. We find the MDL of perpendicularly magnetized TmIG films to be $\sim 300 nm$ [2]. The shorter diffusion length of TmIG compared to YIG is attributed to the larger Gilbert damping of TmIG ($\alpha \sim 0.01$) and the vertical confinement of the magnon modes for ultrathin films. Besides, we investigate the magnetic field dependence of the MDL and analyse it in terms of a modified magnon diffusion equation considering a linear with field enhancement of the magnon damping. We also demonstrate that the non-local thermal signals are dominated by diverse thermoelectric effects of magnetic and spin origin occurring at the detector electrode, and provide a guide on how to disentangle thermally-induced diffusive magnon transport signals from those originated by thermoelectric effects. Finally, by employing a third gate electrode, we demonstrate current-induced modulation of the magnon conductivity in TmIG. The possibility of combining magnon transport in perpendicularly magnetized layers with other device functionalities such as current-induced switching and wall motion [3] open prospects for novel spintronic devices concepts.

[1] J. M. Gomez-Perez, S. Vélez, L. E. Hueso, and F. Casanova, Phys. Rev. B 101, 184420 (2020). [2] J. Gao, S. Vélez et al., *submitted*. [3] S. Vélez et al., Nature Communications 10, 4750 (2019).

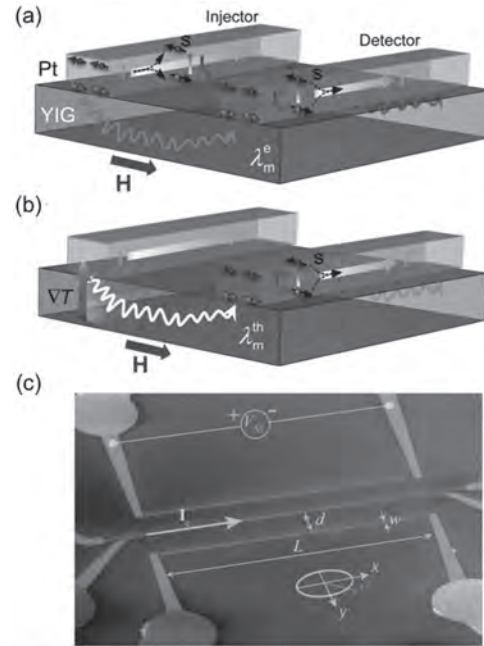


FIG. 1. (a), (b) Schematic representation of the creation, transport, and detection of electrically-induced and thermally-induced magnon currents in nonlocal devices. I_s represent the spin current generated by I , s the vector spin, I^e (I^{th}) and I^c (I^{th}) the spin and charge currents generated at the detector, λ^e (λ^{th}) the magnon diffusion length, and ∇T the thermal gradient. (c) Scanning electron microscopy image of a representative non-local device with $d = 6 \mu m$.

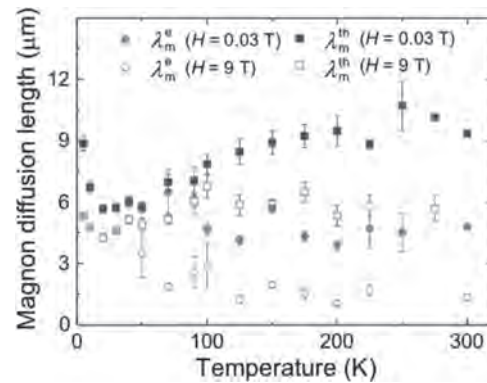


FIG. 2. Temperature dependence of the MDL for electrically- and thermally-driven magnon currents at two different magnetic fields.

CE-05. Magnon Transport in Three-Terminal YIG/Pt Nanostructures Studied by dc and ac Detection Techniques.

J. Gückelhorn^{1,2}, T. Wimmer^{1,2}, S. Geprägs¹, H. Huebl^{1,2}, R. Gross^{1,2} and M. Althammer^{1,2}

1. Magnetism and Spintronics, Walther-Meißner-Institut für Tieftemperaturforschung, Garching, Germany; 2. Physik Department, Technische Universität München, München, Germany

In the field of spintronics, pure spin currents are discussed for spin transport and spin-based information processing at low dissipation levels. Here, magnetically ordered insulators (MOIs) take an exceptional role, as magnon transport can be investigated in an isolated fashion. In addition, its properties can be measured by all-electrical means combining heavy metals (HM) and MOIs in heterostructures. In nanopatterned devices, this allows to excite, control, and detect incoherent magnons and investigate their transport properties. In our experiments, we deposit three electrically isolated platinum (Pt) strips on top of an 11 nm thick yttrium iron garnet (YIG) thin film to realize three-terminal devices [1], as shown in Fig. 1. Driving a charge current through the first Pt strip acting as the injector, a pure spin accumulation is created in the YIG via the spin Hall effect (SHE) and Joule heating. The excited magnons diffuse and can be detected at the detector Pt strip via the inverse SHE. A constant dc charge current I^{mod} applied to the modulator strip placed between the two outer Pt strips allows to manipulate the magnon transport from injector to detector via a SHE induced spin accumulation and Joule heating effects [1]. The magnon diffusion between injector and detector can be modeled as magnon conductivity, which changes in a nonlinear fashion with increasing modulator current and exhibits a threshold behavior. Above threshold, the enhanced magnon conductivity is attributed to a zero effective damping state via SHE induced damping-like spin-orbit torque underneath the modulator [2]. Here, we quantitatively compare two measurement schemes: (i) a dc-technique and (ii) an ac-technique. We demonstrate that both schemes allow to investigate the magnon transport in three-terminal devices and can efficiently distinguish between electrically and thermally injected magnons [3]. In the first case, we apply a varying dc charge current to the injector and measure the detector voltage V_{dc} , utilizing the current reversal method to distinguish between the electrically and thermally injected magnons. For the ac-technique, an ac-current is applied to the injector, while the detector voltage V_{ac} is measured via lock-in detection. We develop a model to compare the SHE contributions resulting in the measured values of V_{dc} and V_{ac} . Both are expected to give identical values if we focus on the linear regime. We experimentally corroborate this model by performing an angle-dependent measurement, where we find a quantitative agreement of the dc and ac voltages, as depicted in Fig. 2(a) and 2(b), respectively. A more detailed comparison of the extracted detector signal amplitudes A_{dc} and A_{ac} of the SHE induced magnons shows that both schemes yield identical results in the low modulator charge current regime. However, we find clear differences above a certain threshold current, as shown in Fig. 2(c), where the ratio $A_{\text{ac}}/A_{\text{dc}}$ exhibits a clear deviation from 1 for $I^{\text{mod}} > 0.55$ mA. This indicates contributions of higher orders to the detector voltage originating from the injector current. Our findings shed new light onto nonlinear effects on the magnon conductance, contributing to the understanding of the manipulation of magnon currents using a three-terminal device, which is crucial for implementing a logic based on incoherent magnons. We gratefully acknowledge financial support by the German Research Foundation via Germany's Excellence Strategy (Grant No. EXC-2111-390814868) and project AL 2110/2-1.

[1] L. J. Cornelissen *et al.*, Physical Review Letters 120, 097702 (2018).
 [2] T. Wimmer *et al.*, Physical Review Letters 123, 257201 (2019). [3] J. Gückelhorn *et al.*, Applied Physics Letters 117, 182401 (2020).

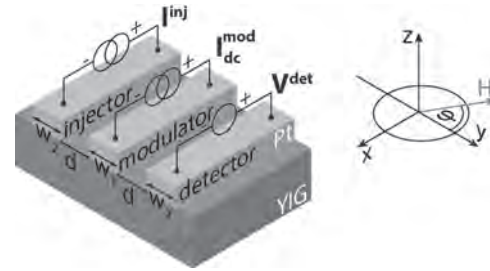


Fig. 1 Sketch of the sample configuration and the experimental external magnetic field geometry.

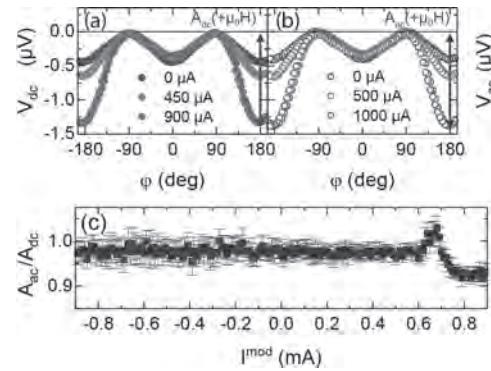


Fig. 2 Detector signals (b) V_{dc} and (c) V_{ac} of the SHE induced magnons plotted as a function of the magnetic field orientation with constant magnitude $\mu_0 H = 50$ mT for positive modulator currents I^{mod} at 280 K. The detector signals induced by SHE magnon transport are in perfect agreement. (c) Ratio of the extracted amplitudes A_{dc} and A_{ac} of the SHE injected magnons for $\mu_0 H = 60$ mT. For large modulator current values, the ratio clearly deviates from 1.

CE-06. Ultra-low Power Domain Wall Device for Spin-Based Neuromorphic Computing.

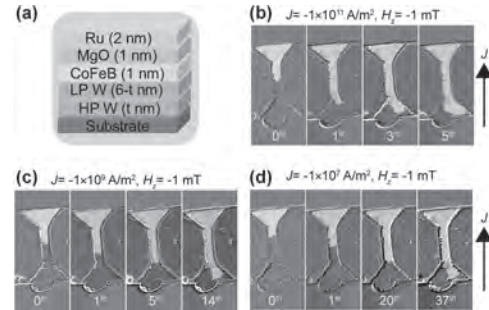
D. Kumar¹, H. Chung², J. Chan¹, T. Jin¹, C. Poh¹, S. Lim², R. Sbiaa³ and S. Piramanayagam¹

1. School of Physical and Mathematical Sciences, Nanyang Technological University, Singapore, Singapore; 2. Agency for Science Technology and Research, Singapore, Singapore; 3. Physics, Sultan Qaboos University, Muscat, Oman

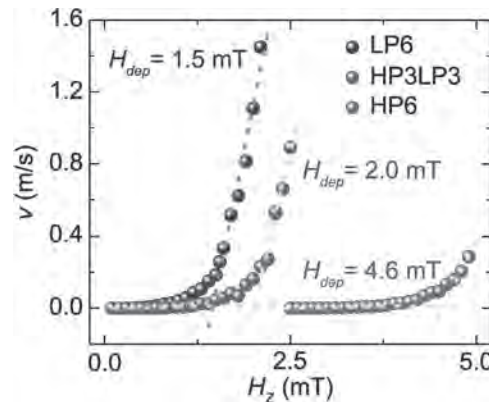
Artificial intelligence (AI) is gaining acceptance in a variety of applications. In order to develop an energy-efficient architecture for AI, neuromorphic computing, which draws inspiration from the human brain, is being investigated. This architecture is a complex interconnection of numerous synthetic neurons and synapses, which are the processing and memory units, respectively. To realize neuromorphic architecture, one needs to fabricate artificial neurons as well as synapses. Several charge and spin-based material systems are being studied towards developing neuromorphic architecture. However, magnetic domain wall (DW) devices are one of the most energy-efficient contenders¹. Besides, utilizing spin-orbit torque to drive DWs provides more degrees of freedom in achieving higher energy efficiency. Therefore, in the present study, we are studying spin-orbit torque for driving the DWs in the proposed novel material engineering to further reduce energy consumption. In SOT driven DW motion, the power can further be reduced either by increasing spin Hall angle or by reducing pinning field while keeping spin Hall angle at optimized values. Since W in β phase results in the highest spin Hall angle (θ_{SH})², we decided to study β -W-based spin Hall layer. However, β -W is obtained by depositing the W films at low power and high Ar gas pressure (HP). These depositions conditions result in granular W films, which in turn results in (a) more defects, (b) higher critical current, (c) larger power, and (d) lower TMR^{2,3}. To resolve these, we have proposed the concept of the dual W layer, where a low-pressure (LP) W, which is expected to be smoother (lesser grains), is deposited between β -W and ferromagnetic layers. The studied stack involves dual W spin Hall layer (SHL) (6 nm)/ CoFeB (1 nm)/ MgO (~1 nm)/ Ru (2 nm). The studied stack is schematically illustrated in figure 1 (a). Firstly, we characterized the thin film samples and observed that the HP3LP3 (this means SOT layer consists of high pressure deposited W (3 nm)/ low pressure deposited W (3 nm)) dual-layer sample exhibits the best structural, magnetic, and electrical characteristics. Therefore, we fabricated DW devices from the HP3LP3 sample. Moreover, we prepared DW devices from single LP6 and HP6 spin Hall layers for comparison purposes. The details of the measurements at the thin film level will be presented in detail during the conference. Subsequently, we studied the DW dynamics in our samples using Kerr microscopy. First, we saturated the DW devices with a large magnetic field. Then, we applied a reversed magnetic field to insert DW in the DW devices. Once the DW is inserted into the devices, we applied current pulses of various amplitudes and observed the DW motion. When current pulses were applied the DW moves in a direction opposite to the current (please refer to figure 1 (b-d)). Moreover, as the amplitude of the current decreases the DW velocity decreases. Most importantly, the DW moves at the current density as small as 10^7 A/m², as shown in figure 1 (d). The detailed measurements revealed that the DW can be moved to a minimum current density of 10^6 A/m². Note, a small OOP magnetic field of -1 mT, which is approximately one-third of the coercivity of the devices, was applied during these measurements. On contrary, we observed that devices with a single spin Hall layer do not show the DW motion. Further harmonic Hall measurements and pinning field measurements showed that ultra-low pinning field (figure 2) in addition to the optimum value of spin Hall angle results in DW motion at such low currents in our dual-layer devices. We have also compared the energy consumption in our devices with respect to the current state-of-art and found a significant reduction in energy consumption in our devices^{4,6}. In addition, we have proposed the design of DW-based neuron and synaptic devices. Moreover, we have proposed and studied the synaptic functions in meander wire, in which two neighboring segments meet at a small offset of “ d ”. We also demonstrated the working stochastic, which is for $d=15\%$, and non-stochastic, which is for $d=50\%$, type synapses in our dual-layer meander devices. In conclusion, the observation of such energy-efficient DW motion

is a significant contribution to the field of neuromorphic computing. The results in detail will be presented during the conference.

P. Chenyun & A. Naemi. IEEE J. Explor. Solid-State Comput. Devices Circuits 3, 101-110 (2017). C. Zhang, S. Fukami, K. Watanabe et al. Applied Physics Letters 109, 192405 (2016). K. Demasius, T. Phung, W. Zhang et al. Nature communications 7, 10644 (2016). S. DuttaGupta, S. Fukami, C. Zhang et al., Nature Physics, 12, 333-336 (2016). K. Fritz, L. Neumann, and M. Meinert, arXiv:1910.13837 (2019). K. Cai, Z. Zhu, J. Lee et al., Nature Electronics, 3, 37-42 (2020).



(a) Schematic illustration of the studied dual-layer stack. DW motion in our dual-layer devices at a current density of (b) 10^{11} A/m², (c) 10^9 A/m², and (d) 10^7 A/m².



The DW velocity vs out-of-plane (OOP) magnetic field curves. A linear fitting of these curves provides information about the pinning field of the studied samples.

CE-07. Spin-Injection-Generated Shock Waves and Solitons in a Ferromagnetic Nanowire.

M. Hu¹, E. Iacocca² and M. Hofer¹

1. Applied Mathematics, University of Colorado Boulder, Boulder, CO, United States; 2. Department of Mathematics, Physics, and Electrical Engineering, Northumbria University, Newcastle upon Tyne, United Kingdom

A promising means for long-distance transport of angular momentum is spin superfluidity [1-4]. In this work, the unsteady nonlinear dynamics of spin transport in an easy-plane, thin-film, one-dimensional ferromagnetic channel is studied analytically. We formulate an initial-boundary value problem (IVBP) for the Landau-Lifshitz equation subject to spin injection into a static, uniformly magnetized nanowire. The long-time steady-state configuration in such channels with zero applied field has been identified as either a dissipative exchange flow (DEF) or a contact soliton DEF (CS-DEF) [5], depending on the strength of the injection. Here, we study the injection-induced highly nonlinear, transient magnetization dynamics that occur prior to the damping-dominated steady-state is reached and include a constant applied field. In particular, we focus on the 1 ns timescale where damping is weak, and the spin dynamics are dominated by spin injection, applied field, exchange interaction, and demagnetizing fields. In our analysis, we recast the Landau-Lifshitz equation into its dispersive hydrodynamic (DH) form [6], in terms of the longitudinal spin density and a magnetic analog of the fluid velocity that is proportional to the spin current. The spin injection is characterized by a nonzero fluid velocity at one end of the channel, hence can be viewed as a spin hydrodynamic “piston”. The DH form captures two important effects in the ferromagnetic system: nonlinearity and dispersion, which are inherited from anisotropy and exchange, respectively. These effects lead to the generation of unsteady nonlinear waves when large gradients occur. A rapid rise in the fluid velocity due to spin injection leads to large gradients that result in a new kind of spin shock wave that is an example of a dispersive shock wave (DSW). DSWs are expanding, highly oscillatory, nonlinear excitations that realize a coherent transition between two states in a variety of dispersive media [7]. Spin wave envelope DSWs have been observed in a Yttrium Iron Garnet feedback ring [8]. We provide a full analytical classification of nonlinear wave solutions to this IVBP in terms of the applied field and injection strength, using the Whitham modulation theory [9]. The solution components are rarefaction waves (RWs), DSWs, and solitons (see Fig. 1). Both RWs and DSWs have been identified as solutions to a pure initial value problem (the Riemann problem) in a two-component Bose-Einstein condensate [10], whose governing equations are equivalent to the DH form of the Landau-Lifshitz equation we study here. In contrast, we show that the injection boundary plays a prominent role in the dynamics. Depending on the interplay between the spin injection intensity and the applied magnetic field magnitude, different types and combinations of RWs, DSWs, and solitons arise. The generation of a soliton is a distinct feature due to the boundary and is identified with an important concept [10]: the magnetic sonic condition. Solitons only occur at the spin injection end and only in the supersonic injection regime. Our analytical solutions are confirmed by micromagnetic simulations.

[1] E. Sonin, Spin currents and spin superfluidity, *Advances in Physics* Vol. 59, p.181 (2010). [2] S. Takei and Y. Tserkovnyak, Superfluid spin transport through easy-plane ferromagnetic insulators, *Physical Review Letters* Vol. 112, p.227201 (2014). [3] H. Skarsvåg, C. Holmqvist, and A. Brataas, Spin superfluidity and long-range transport in thin-film ferromagnets, *Physical Review Letters* Vol. 115, p.237201 (2015). [4] M. Evers and U. Nowak, Transport properties of spin superfluids: Comparing easy-plane ferromagnets and antiferromagnets, *Physical Review B* Vol. 101, p.184415 (2020). [5] E. Iacocca and M. A. Hofer, Hydrodynamic description of long-distance spin transport through noncollinear magnetization states: Role of dispersion, nonlinearity, and damping, *Physical Review B* Vol. 99, p.184402 (2019). [6] B. Halperin and P. Hohenberg, Hydrodynamic theory of spin waves, *Physical Review* Vol. 188, p.898 (1969). [7] G. El and M. Hofer, Dispersive shock waves and modulation theory, *Physica D: Nonlinear Phenomena* Vol. 333, p.11 (2016). [8] P. A. P. Janantha et al., Observation of self-cavitating envelope dispersive shock waves in Yttrium

Iron Garnet thin films, *Physical Review Letters* Vol. 119, p.024101 (2017). [9] G. B. Whitham, *Linear and nonlinear waves*, Vol. 42 (John Wiley & Sons, 2011). [10] S. K. Ivanov et al., Solution of the Riemann problem for polarization waves in a two-component Bose-Einstein condensate, *Physical Review E* Vol. 96, p.062202 (2017). [11] E. Iacocca, T. Silva, and M. A. Hofer, Breaking of Galilean Invariance in the Hydrodynamic Formulation of Ferromagnetic Thin Films, *Physical Review Letters* Vol. 118, p.017203 (2017).

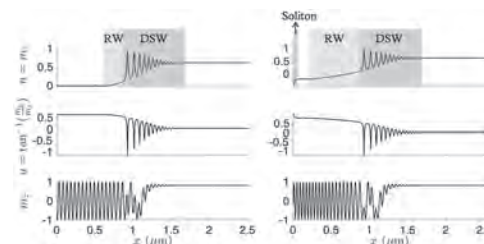


Fig. 1: Example simulations of (top to bottom) the spin density n , the magnetic fluid velocity u , and an in-plane magnetization component m_x , at $t = 1$ ns in (left) the subsonic regime and (right) the supersonic regime.

CE-08. Magnetic and Spintronic Properties of Scandium Substituted Terbium Iron Garnet Thin Films.

B. Khurana¹, J. Bauer¹ and C. Ross¹

1. Materials Science and Engineering, Massachusetts Institute of Technology, Cambridge, MA, United States

Rare earth iron garnet (REIG) thin films have attracted a great deal of attention for spintronic applications over the past few years. Properties of REIG|Pt heterostructures have also been extensively studied. However, effects of nonmagnetic ion substitution on iron sublattice of REIG thin films have not been investigated so far. We report growth, structural, magnetic and spintronic properties of epitaxial scandium substituted terbium iron garnet (TbScIG) thin films on gadolinium gallium garnet (GGG, (111) orientation) substrate. Reciprocal space mapping shows that films are lattice matched to substrate without strain relaxation up to thickness of 66 nm. All the deposited films with varying scandium content have been found to have perpendicular magnetic anisotropy (PMA) due to magnetoelastic anisotropy contribution arising from lattice strain. Their compositions have been determined using wavelength dispersive spectroscopy (WDS) to be $Tb_{2.8}Fe_{5.2}O_{12}$, $Tb_{2.8}Sc_{0.3}Fe_{4.9}O_{12}$, $Tb_{2.9}Sc_{0.5}Fe_{4.6}O_{12}$ and $Tb_{2.8}Sc_{0.8}Fe_{4.4}O_{12}$. Thickness of these films have been determined to vary within 63-73 nm by fitting Laue fringes observed in symmetric high-resolution x-ray diffraction (HRXRD) scans around the GGG (444) peak. Compensation temperatures of TbScIG thin films have been found to decrease with increasing scandium content which is in agreement with larger Sc^{3+} ions occupying octahedral sublattice as reported in past for bulk yttrium iron garnet. Increasing scandium content has been found to be accompanied by increase in room temperature saturation magnetization from 37 emu/cm^3 for $Tb_{2.8}Fe_{5.2}O_{12}$ to 59 emu/cm^3 for $Tb_{2.8}Sc_{0.8}Fe_{4.4}O_{12}$. Anomalous Hall effect (AHE) like spin-Hall magnetoresistance (SMR) measurements have been performed to determine the effect of scandium content on spin mixing conductance of TbScIG|Pt interface. Ferromagnetic resonance (FMR) measurements have been performed to determine the Gilbert damping parameter of these thin films.

1. Rosenberg, E. R. et al. Phys. Rev. Mater. 2, 094405 (2018).
2. Chen, Y.-T. et al. Phys. Rev. B 87, 144411 (2013).
3. Geller, S. J. Appl. Phys. 37, 1408–1415 (1966).
4. Espinosa, G. P. J. Chem. Phys. 37, 2344–2347 (1962).
5. Geller, S. & Gilleo, M. A. J. Phys. Chem. Solids 3, 30–36 (1957).

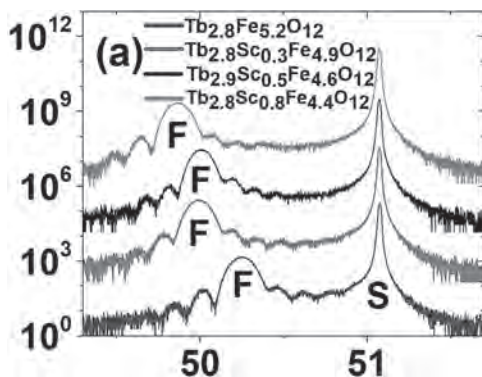


Fig. 1 High-resolution XRD scans of TbScIG/GGG thin films with varying Sc content (vertically offset for clarity with film and substrate peaks labeled F and S respectively)

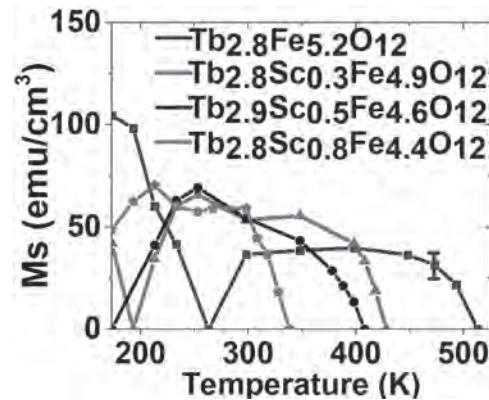


Fig. 2 Magnetic moment versus temperature for TbScIG/GGG thin films with varying Sc content. A typical error bar is attached.

CE-09. Seebeck-Driven Colossal Transverse Thermoelectric Generation.

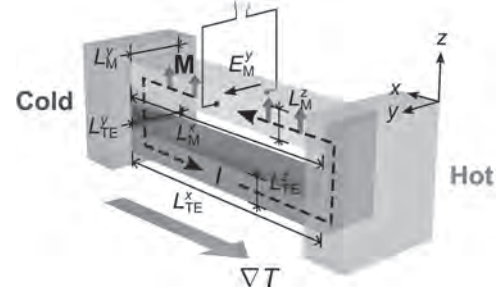
W. Zhou¹, K. Yamamoto¹, A. Miura¹, R. Iguchi¹, Y. Miura¹, K. Uchida^{1,2} and Y. Sakuraba^{1,3}

1. National Institute for Materials Science, Tsukuba, Japan; 2. Institute for Materials Research, Tohoku University, Sendai, Japan; 3. Japan Science & Technology Agency, PRESTO, Kawaguchi, Japan

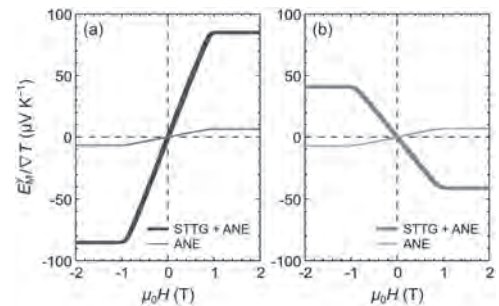
The transverse electric field generated by anomalous Nernst effect (ANE) in a magnetic material is perpendicular to both the temperature gradient (∇T) and its magnetization (M), different from the parallel relationship between the generated electric field and ∇T emerges from Seebeck effect (SE). This allows different design principles for thermoelectric power generation and heat flux sensing devices, which could be advantageous in creating a simple and flexible device with better integratability and scalability.[1-3] However, the practical application of ANE is hampered by the fact that the thermopower of ANE (S_{ANE}) is still orders of magnitude smaller compared to that of SE (S_{SE}), and there has been increasing studies in order to find magnetic materials with large S_{ANE} in recent years. S_{ANE} can be separated into two components as $S_{ANE} = \rho_{xx}\alpha_{xy} - \rho_{AHE}\alpha_{xx}$, where ρ_{xx} is the longitudinal resistivity, ρ_{AHE} is the anomalous Hall resistivity, and α_{xx} and α_{xy} are the diagonal and off-diagonal components of the Peltier tensor, respectively. The first term on the right hand side ($\rho_{xx}\alpha_{xy}$) is considered the intrinsic term of ANE, as α_{xy} directly converts ∇T into a transverse electrical current. The $L2_1$ -ordered Co_2MnGa Heusler alloys have shown large values of α_{xy} originated from their topological band structures, which lead to record high values of S_{ANE} .[4-7] The second term on the right hand side ($-\rho_{xx}\alpha_{xx}$) can be rewritten as $-S_{SE} \times \rho_{AHE} / \rho_{xx}$, indicating it originates from the anomalous Hall effect (AHE) of the longitudinal carrier flow induced by SE. Here, inspired by the second term, we propose a different approach for transverse thermoelectric generation. We considered a hybrid system comprising a thermoelectric material and a magnetic material. The electric field generated by SE of the thermoelectric material was converted to transverse thermoelectric generation by AHE of the magnetic material, which showed a similar symmetry to ANE, but surprisingly, more than one order of magnitude enhancement in thermopower. This is referred to as the Seebeck-driven transverse thermoelectric generation (STTG).[8] To model STTG and derive an expression for its transverse thermopower, we consider a system that consists of a thermoelectric material and a magnetic material electrically connected at both ends along the ∇T direction to form a closed circuit, as shown in Fig. 1. Both materials have a rectangular shape, with L_{TE}^x , L_{TE}^y , and L_{TE}^z (L_M^x , L_M^y , and L_M^z) respectively being the length along x , y , and z directions for the thermoelectric (magnetic) material. The magnetic material has the Seebeck coefficient S_M , anomalous Nernst coefficient S_{ANE} , resistivity ρ_M , and anomalous Hall resistivity ρ_{AHE} . The thermoelectric material has the Seebeck coefficient S_{TE} , and resistivity ρ_{TE} . By solving the linear-response transport equations for the hybrid system, we derived the total transverse thermopower as $S_{tot}^y = (E_M^y / -\nabla T) = S_{ANE} - \rho_{AHE} (S_{TE} - S_M) / ((\rho_{TE} / r) + \rho_M)$, where E_M^y is the transverse electric field along the y direction in the magnetic material and $r = (L_M^x / L_{TE}^x) \times (L_{TE}^y L_{TE}^z / L_M^y L_M^z)$ is the size ratio between the thermoelectric and magnetic materials. In addition to ANE from the magnetic material, S_{tot}^y includes the contribution from the artificial hybridization of SE of the thermoelectric material through S_{TE} and AHE of the magnetic material through ρ_{AHE} (the second term on the right hand side), which is STTG. For the proof-of-concept demonstration of STTG, we deposited a 50-nm-thick $L2_1$ -ordered Co_2MnGa thin film on a single-crystalline MgO (100) substrate and used it as the magnetic material. The MgO substrate was then cut into a rectangular shape and bonded onto a rectangular-shaped 0.5-mm-thick Si substrate, which was used as the thermoelectric material. The Co_2MnGa film and Si substrate were electrically connected to each other through Ohmic contacts and bonding wires near the ends to form the closed circuit. E_M^y in the Co_2MnGa layer was measured while the magnetic field (H) was swept in the direction perpendicular to the sample plane. The same measurement was also carried out without the Co_2MnGa -Si connection. Figure 2 shows the H dependence of E_M^y divided by ∇T for the samples using whether an n-type Si ($S_{TE} = -1.3 \times 10^3 \mu\text{V K}^{-1}$) or a p-type Si ($S_{TE} = 1.3 \times 10^3 \mu\text{V K}^{-1}$) as the thermoelectric material. Without the Co_2MnGa -Si connection, only the ANE contribution from the Co_2MnGa layer was measured, which showed $S_{ANE} \sim$

$6.2 \mu\text{V K}^{-1}$, consistent with previous reports.[4-7] With the Co_2MnGa -Si connection, however, the total transverse thermopower S_{tot}^y increased by one order of magnitude to $82.3 \mu\text{V K}^{-1}$ for using n-type Si; while S_{tot}^y changed sign to $-41.0 \mu\text{V K}^{-1}$ for using p-type Si. The experimentally obtained S_{tot}^y is consistent with the predicted values made using the equation and the properties of the Co_2MnGa and Si, which is $77.2 (-45.3) \mu\text{V K}^{-1}$ for $\text{Co}_2\text{MnGa}/\text{n(p)}$ -type-Si system. Our result indicates that STTG can make significant enhancement from ANE in the transverse thermopower by optimizing transport properties and dimensions of the materials, which would provide great flexibility for designing future thermoelectric power generation and heat flux sensing devices.

[1] K. Uchida, H. Adachi, T. Kikkawa *et al.*, *Proc. IEEE*, Vol. 104, p.1946 (2016). [2] Y. Sakuraba, *Scr. Mater.*, Vol. 111, p.29 (2016). [3] W. Zhou, and Y. Sakuraba, *Appl. Phys. Express*, Vol. 13, p.043001 (2020). [4] A. Sakai, Y. P. Mizuta, A. A. Nugroho *et al.*, *Nat. Phys.*, Vol. 14, p.1119 (2018). [5] S. N. Guin, K. Manna, J. Noky *et al.*, *NPG Asia Mater.*, Vol. 11, p.16 (2019). [6] L. Xu, X. Li, L. Ding *et al.*, *Phys. Rev. B*, Vol. 101, p.180404(R) (2020). [7] K. Sumida, Y. Sakuraba, K. Masuda *et al.*, *Commun. Mater.*, Vol. 1, p.89 (2020). [8] W. Zhou, K. Yamamoto, A. Miura *et al.*, *Nat. Mater.* (2021), DOI: 10.1038/s41563-020-00884-2.



Schematic illustration of the model system for Seebeck-driven transverse thermoelectric generation.



(a) H dependence of the transverse electric field E_M^y divided by ∇T in the Co_2MnGa layer of the $\text{Co}_2\text{MnGa}/\text{n-type-Si}$ sample and (b) $\text{Co}_2\text{MnGa}/\text{p-type-Si}$ sample with (STTG + ANE) and without (ANE) the Co_2MnGa -Si connection.

CE-10. Relaxation Process of Spin-Polarized Quasiparticles in a Superconducting Nb Wire.

T. Iwahori¹, K. Mizokami¹, R. Matsuda¹, K. Ohnishi¹ and T. Kimura¹
1. Physics, Kyushu University, Fukuoka, Japan

Spintronics combining with superconductor electronics is of exciting and challenging subject because of its intriguing and amazing properties. Spin-polarized current injected from the ferromagnetic metal can be carried by quasi-particles in a superconductor. The injected quasiparticles diffusively flow and gradually convert the Cooper pairs within a few micron length scale. Since a conventional Cooper pair consists of a pair of up- and down-spin electrons, the spin-polarized current is expected to take longer time to be transformed to the supercurrent. To investigate the relaxation processes of spin-polarized current in superconductor, we developed a Nb-based multi-terminal device with a ferromagnetic CoFeAl spin injector as schematically shown in Fig. 1. The injected quasiparticles relax with decaying electrochemical potentials. In the probe configuration shown in Fig. 1, the decreasing non-local quasiparticles electrochemical potentials can be detected as non-local resistances. Moreover, by changing the injector from Cu to CoFeAl, we can compare the relaxation lengths for non-polarized and polarized quasiparticles. Figure 2 shows non-local resistances measured with nonmagnetic injectors with changing the distance from 0 to 3000 nm. Non-local resistance depends mainly on a charge imbalance which are a nonequilibrium phenomenon that arises from the conversion of quasiparticle current in the normal metal to supercurrent in the superconductor [1]. From the electrodes-distance dependence of non-local resistances, we estimated the relaxation length of non-polarized quasiparticles is $950 \pm 30\text{nm}$, while that of polarized quasiparticles is $1240 \pm 130\text{nm}$. This difference can be explained by the spin diffusion length at the vicinity of superconducting transition temperature which is longer than that in a normal conducting state.

[1] P. Cadden-Zimansky and V. Chandrasekhar, Phys. Rev. Lett. 97, 237003 (2006).

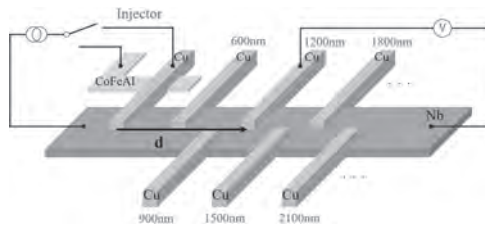


Fig.1 Multi-electrode mesoscopic device

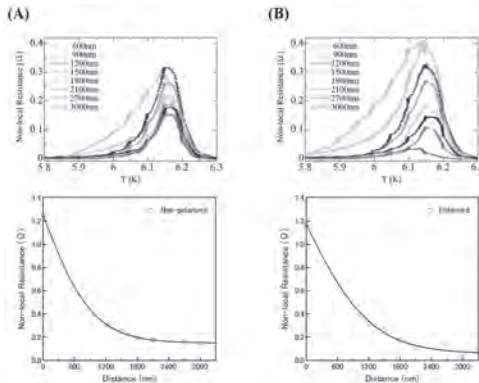


Fig. 2 Temperature dependence of non-local resistances with various distances between an injector and detectors (top), and the electrodes-distance dependence of the maximum values of non-local resistances (bottom) for (A) Non spin polarized quasiparticles and (B) Spin polarized quasiparticles.

CE-11. Theoretical Study on Four-Fold Symmetric Anisotropic Magnetoresistance Effect in Cubic Single-Crystal Ferromagnetic Model.

Y. Yahagi¹, D. Miura¹ and A. Sakuma¹

1. Applied Physics, Graduate School of Engineering, Tohoku University, Sendai, Japan

We theoretically investigated the four-fold symmetric term of the anisotropic magnetoresistance (AMR) effect in cubic ferromagnetic metals (FMs), which has recently been observed experimentally for certain metals, by using fourth-order perturbation theory with respect to the spin-orbit interaction (SOI). The AMR effect is a magnetoresistance effect specific to magnetic metals in which the charge conductivity changes depending on the direction of magnetization in FMs [1], and attracted much attention in the field of spintronics to apply for evaluation of half-metallicity [2] or spin-orbit torque generation [3]. Usually, in experiments on bulk polycrystalline FMs, the longitudinal conductivity is proportional to the $\cos(2\theta)$ where θ is the relative angle between the current direction and the magnetization direction, that is, the AMR effect has two-fold symmetry under the magnetization rotation. Theoretically, this two-fold AMR effect is caused by the SOIs and has been successfully explained by Campbell's model, an s-d impurity scattering model with considering the second-order perturbation in terms of the SOIs [4]. In single-crystal FMs such as Fe4N, however, the AMR measurements exhibited not only the conventional two-fold component but also the unconventional four-fold component proportional to $\cos(4\theta)$ [5]. While this four-fold AMR effect is expected to stem from the symmetry of the cubic crystal, the microscopic origin is not so straightforward because the magnetization direction dependence of the conduction band is too small to explain this effect. Recently, a possible mechanism of the four-fold AMR effect is theoretically proposed by Kokado [6], wherein the s-d scattering coupled with the SOIs and "tetragonal" symmetric crystal fields is responsible for this effect. This theory is an extension of Campbell's model in polycrystalline FMs to the single crystal FM model by taking into account the energy level splitting due to the tetragonal crystal fields on the d-states (Fig. 1). Since it is argued that the splitting among d-states is significant for the presence of a four-fold component, this theory requires the extra assumption of existing the tetragonal (uniaxial or planar) distortion to apply to the cubic crystals including the Fe4N. However, the experiment is confronted with the fact that the four-fold component appears even though the sample is almost cubic crystal and has little distortion. The microscopic origin is still controversial; therefore, it is worthwhile to explore a possible mechanism of the four-fold AMR effect in the cubic symmetric single-crystal FMs without tetragonal distortion. In this work, we show the presence of the four-fold AMR effect in cubic single crystal FMs from a microscopic viewpoint [7]. Our main finding is that the higher-order perturbation terms of SOI can also be responsible for the four-fold AMR effect in cubic FMs, instead of the second-order SOI with tetragonal distortion as mentioned in Kokado's theory. Inspired by the Kokado model, we use the s-d impurity scattering model expressed by an impurity Anderson Hamiltonian with cubic crystal fields and SOI. The conductivity is represented on the basis of the Kubo-Greenwood formula. This approach enables us to consider the non-perturbative role of SOIs on the AMR effects. Firstly, to overlook a physical aspect of this effect, we carried out perturbative analysis with respect to the SOIs. The results indicate that the fourth-order terms of SOI can give rise to the four-fold AMR effect. Furthermore, we extract the two important roles of the SOI: first, to couple the electron's momentum and magnetization, and second, to induce the orbital splitting among d-states instead of the tetragonal crystal field. Secondly, we performed numerical calculations to evaluate the non-perturbative behavior of the AMR effects. As the results, we successfully obtained both the two-fold and four-fold components of the AMR effect without assuming the tetragonal distortion, which is consistent with the perturbative analysis (Fig. 2). Other parameter dependencies will be presented at the conference.

A. Fert, and O. Jaoul, *J. Phys. C*, Vol. 3, p.S95 (1970). [5] M. Tsunoda, H. Takahashi, S. Kokado, Y. Komasaki, A. Sakuma, and M. Takahashi, *Appl. Phys. Express*, Vol. 3, p.113003 (2010). [6] S. Kokado and M. Tsunoda, *J. Phys. Soc. Jpn.*, Vol. 84, p.094710 (2015). [7] Yuta Yahagi, Daisuke Miura, and Akimasa Sakuma, *J. Phys. Soc. Jpn.*, Vol. 89, p.044714 (2020)

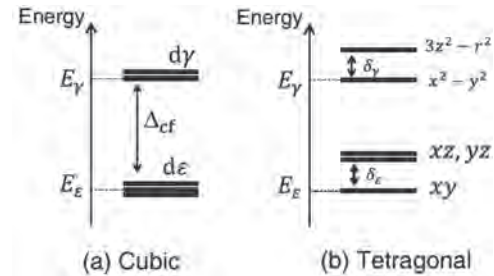


Fig.1: Schematics of the energy level of the d-states under (a) a cubic symmetric and (b) a tetragonal symmetric crystal-field, respectively.

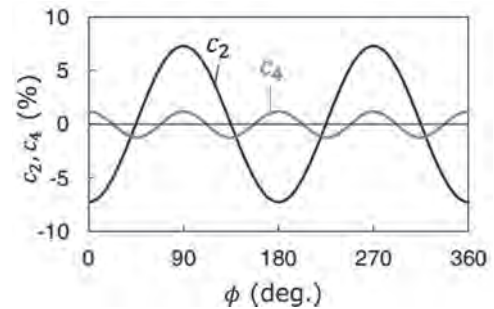


Fig.2: Two-fold (c_2) and four-fold (c_4) components of the AMR ratio.

[1] T. McGuire and R. Potter, *IEEE Trans. Magn.*, Vol. 11, p.1018 (1975).

[2] S. Kokado, M. Tsunoda, K. Harigaya, and A. Sakuma, *J. Phys. Soc. Jpn.*, Vol. 81, p.024705 (2012).

[3] T. Taniguchi, J. Grollier, and M. D. Stiles, *Phys. Rev. Applied*, Vol. 3, p.044001 (2015).

[4] I. A. Campbell,

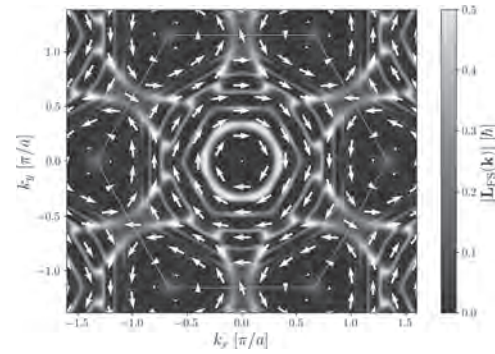
CE-12. Strong Enhancement of the Orbital Rashba Effect in Cu Film by Surface Oxidation.

D. Go^{2,3}, D. Jo¹, T. Gao^{4,5}, K. Ando^{4,5}, S. Blügel², H. Lee¹ and Y. Mokrousov^{2,3}

1. Department of Physics, Pohang University of Science and Technology, Pohang, The Republic of Korea; 2. Peter Grünberg Institut and Institute for Advanced Simulation, Forschungszentrum Jülich GmbH, Jülich, Germany; 3. Institute of Physics, Johannes Gutenberg Universität Mainz, Mainz, Germany; 4. Department of Applied Physics and Physico-Informatics, Keio University, Yokohama, Japan; 5. Keio Institute of Pure and Applied Sciences (KiPAS), Keio University, Yokohama, Japan

In spintronics, Cu is often considered as a passive material which cannot generate spin current by itself due to negligible spin-orbit coupling (SOC). However, recent experiments reported observation of gigantic current-induced spin-orbit torque in surface oxidized Cu/ferromagnet structures [1-5], whose magnitude is comparable to material systems with large SOC such as Co/Pt. These experimental results cannot be explained neither by spin Hall effect nor by Rashba-Edelstein effect since these mechanisms assume strong SOC. On the other hand, electric generation of the orbital angular momentum does not require SOC at all, which can be achieved via orbital Hall effect [6] or orbital Rashba-Edelstein effect [7]. Furthermore, according to a recent theory, injection of orbital angular momentum to a ferromagnet can generate torque on the magnetization, which is called orbital torque (OT) [8]. Thus, it has been proposed that a microscopic mechanism responsible for the torque generation in surface oxidized Cu/ferromagnet is OT, originating in the orbital Rashba effect (ORE) at oxidized region of Cu film. The OT mechanism qualitatively explains anomalous features observed in experiments such as strong suppression of the torque by intermixing of atoms at the interface [3], sign change of the torque for depending on ferromagnets [4], and gigantic enhancement of the torque efficiency by insertion of an ultrathin Pt layer [5]. However, to our best knowledge, there is no direct evidence of the ORE nor theoretical investigation of the electronic structure of Cu film under influence of surface oxidization. In this contribution, we present our recent theoretical results showing that surface oxidization of a Cu film leads to strong enhancement of the ORE [9], which is assessed from first-principles calculations based on density functional theory. We find that microscopic origin of the ORE is the resonant hybridization between O *p*-orbitals and Cu *d*-orbitals. We investigate various stacking geometries (fcc hollow, hcp hollow, bridge, on-top structures) and find that the ORE emerges in a robust manner. The ORE leads to a pronounced orbital texture at the Fermi surface (Fig. 1), where the magnitude of the orbital polarization reaches as much as 0.5 \hbar per state. Because of the orbital texture, application of an external electric field leads to a generation of orbital Hall current, which by far exceeds the magnitude of the spin current of heavy elements. This implies that the OT mechanism can be significant in surface oxidized Cu/ferromagnet structures. Our theoretical results also encourage experimental verification of the orbital texture, i.e. by angle-resolved photoemission spectroscopy or momentum microscopy.

[1] An *et al.* Spin-torque generator engineered by natural oxidization of Cu, Nat. Commun. 7, 13069 (2016). [2] Otano *et al.* Nonreciprocal Spin Current Generation in Surface-Oxidized Copper Films, Phys. Rev. Lett. 122, 217701 (2019). [3] Kim *et al.* Non-trivial charge-to-spin conversion in ferromagnetic metal/Cu/Al₂O₃ by orbital transport, Phys. Rev. B, in press. [4] Tazaki *et al.* Current-induced torque originating from orbital current, arXiv:2004.09165. [5] Ding *et al.* Harnessing Orbital-to-Spin Conversion of Interfacial Orbital Currents for Efficient Spin-Orbit Torques, Phys. Rev. Lett. 125, 177201 (2020). [6] D. Go, D. Jo, C. Kim, and H.-W. Lee, Intrinsic Spin and Orbital Hall Effects from Orbital Texture, Phys. Rev. Lett. 121, 086602 (2018). [7] Go *et al.* Toward surface orbitronics: giant orbital magnetism from the orbital Rashba effect at the surface of sp-metals, Sci. Rep. 7, 46742 (2017). [8] D. Go and H.-W. Lee, Orbital torque: Torque generation by orbital current injection, Phys. Rev. Res. 2, 013177 (2020). [9] Go *et al.* Orbital Rashba effect in surface oxidized Cu film, arXiv:2011.08601.



Orbital angular momentum texture of the surface oxidized Cu film at the Fermi surface. The colormap represents the magnitude and the arrow indicates direction of the angular momentum at each k-point.

Session CF
CONVENTIONAL STT-MRAM MATERIALS, DEVICES AND TECHNOLOGY
Guohan Hu, Chair
IBM, Yorktown Heights, NY, United States

INVITED PAPERS

CF-01. Reliable High Density STT-MRAM Products INVITED.

G. Shimon¹, H.K. Lee¹, S. Ikegawa¹, S. Aggarwal¹, B. Hughes¹, F.B. Mancoff¹, J. Janesky¹, J. Sun¹, K. Nagel¹ and M. DeHerrera¹
 1. Technology R&D, Everspin Technologies Inc, Chandler, AZ, United States

Magneto resistive random-access memory (MRAM) holds the potential to be a universal memory with its non-volatility, high speed, robust endurance, and system power savings capability. In the semiconductor memory and storage space, MRAM is poised to deliver the performance of working memory with the persistence of storage. The pioneer generation of MRAM product dubbed Toggle MRAM was first launched in 2006 and was based on magnetic field switching. Driven by continuous demand for lower power and higher density, spin transfer torque MRAM (STT-MRAM) was introduced into the market. In its commercialization, standalone STT-MRAM product saw rapid evolution toward higher density in which the memory density quadrupled every 2 years between 2015-2019 [1]. The successful scaling of STT-MRAM product is attributed to a concerted effort in materials engineering and the use of advanced process technologies. Most recently in 2019-2020, we saw two momentous events in MRAM development: Everspin launched a milestone 1Gb product [2], and 3 major foundries and 2 other companies announced their STT-MRAM product offerings [1]. In this talk, we will review the fundamental aspects of STT-MRAM with a focus on read and write distributions of MRAM arrays. In order to achieve reliable high density STT-MRAM products it is critical to understand the contributions to these distributions and minimize the variation across the array. For instance, minimizing array write error rate (WER) relies much upon reducing the population of extrinsic magnetic tunnel junction (MTJ) bits in an array. A method was developed to quantify the population of extrinsic bits by calculating the switching failure rate upon doing N repeat of read-write sequence, which we call soft fail count. Figure 1(a) shows example of soft fail improvement by combining MTJ film engineering and process improvement. The soft fail count improvement is seen from both the reduction of outlier bits and tightening of main bits population to reach below the desired requirement. Figure 1(b) shows the median soft fail count plotted against wafer radius from center to edge. Such plot further elucidated the distinct contribution from MTJ film and process changes implemented. Detailed analysis shows that the MTJ film improvement reduces the extrinsic population and improved the switching reliability on the die level, while the process improvement extends the die uniformity across the wafer. These approaches were found to be additive when combined. A low operating voltage coupled with reliable switching (measured as distributions) is critical to integrating MTJ bits on silicon. Figure 2 shows the plots of normalized array operating voltage (V_{op}) and its sigma corresponding to the MTJ film and process improvement shown in Figure 1. Initial MTJ film change from A to B improved the V_{op} by 14% and significantly reduced the sigma by a factor 2.6x. Switching from process A to B using the improved film B improved the V_{op} by a further 3.3% with a comparable sigma level to process A. Finally, combining MTJ film C with Process B produced slight improvement in V_{op} and further reduction in sigma by 20%. This observation corroborated the reduction in bit error soft fail count shown in Figure 1. The improvement in bit-to-bit distribution is critical to enable reliable high density STT-MRAM products. In the talk, we will discuss the impact of these distributions on other key aspects such as data retention, switching pulse widths and endurance.

References: [1] S. Ikegawa, F. B. Mancoff, J. Janesky, and S. Aggarwal, "Magnetoresistive Random Access Memory: Present and Future", IEEE Trans. Elec. Dev. 67(4), 1407 (2020); doi: 10.1109/TED.2020.2965403. [2] S. Aggarwal, H. Almasi, M. DeHerrera, B. Hughes, S. Ikegawa, J. Janesky, H. K. Lee, H. Lu, F. B. Mancoff, K. Nagel, G. Shimon, J. J. Sun, T. Andre, and S. M. Alam, "Demonstration of a reliable 1 Gb standalone spin-transfer torque MRAM for industrial applications," in IEDM Tech. Dig., 2019, No. 2.1.

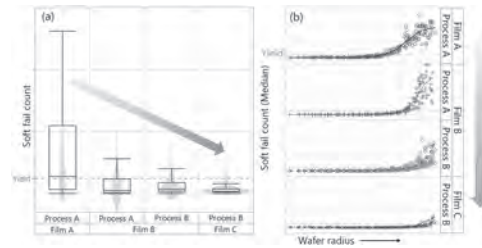


Figure 1. (a) Soft fail count improvement with combinations of MTJ film and process changes, (b) median soft fail count plotted against wafer radius from center to edge showing improvement in bits distribution within die and across wafer uniformity.

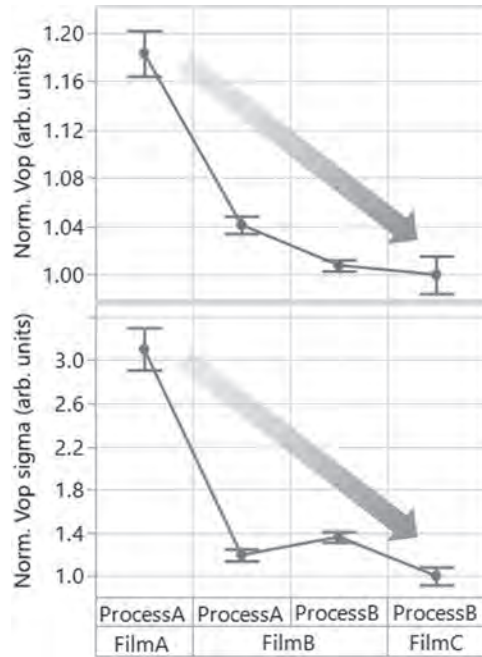


Figure 2. Improvement in operating voltage (V_{op}) and its sigma with combinations of MTJ film and process changes

CF-02. Embedded STT-MRAM for 14nm CMOS Node Cache Applications INVITED.

M. Rizzolo¹

1. IBM, Albany, NY, United States

STT-MRAM materials and technology have recently matured to the point of moving from “lab to fab” for 28nm-22nm node standalone and eNVM applications. Prior work has mostly placed MTJ devices above M2 or even higher in the BEOL stack, depending on the application and integration constraints [1-4]. However, optimizing MRAM for mobile or last-level cache applications requires significant improvements in write speed, write current, endurance, and density of both the MRAM cell in addition to the CMOS [5]. In this work, we present the first Embedded Spin-Transfer-Torque MRAM (eMRAM) technology in a 14 nm CMOS node. Using a 2 Mb eMRAM macro, we achieve an integration at tight MTJ pitch (0.0273 μm^2 cell size), which is aggressively placed between M1 and M2. We demonstrate read and write functionality, including write performance down to 4 ns, and show that the eMRAM process module can be added while obeying the existing CMOS logic BEOL design rules and reliability requirements. Several unit process innovations enabled this integration, including a novel sub-lithographic microstud (μ -stud) bottom electrode (BEL), fine profile control of the MTJ patterning and dielectric films, optimized BEL/MTJ metallization, and optimized post-MTJ low-k planarization across array and logic areas. The result preserves the minimum 3 added mask levels (2 critical for μ -stud and MTJ; 1 non-critical for MTJ alignment marks), without mask-adders for low-k planarization or top electrode (TEL). A shrink patterning process ensures that the μ -stud top CD is always smaller than the MTJ bottom CD, for MTJ sizes down to below 35 nm. This minimizes shunting by eliminating the BEL resputtering onto the MTJ sidewalls during patterning, and increases etch budget. The μ -stud BEL module re-uses current manufacturing processes. Figure 1 shows a TEM cross section of 41nm MTJ devices with a sub-lithographic μ -stud underneath. The alternating MTJ pitch presented a challenge for IBE overetch/cleanup without excessive dielectric gouge. Additional tests were completed showing good device scalability to 35nm, with magnetic property degradation at smaller sizes due to edge damage that could be improved with further etch optimization. Cache applications require writing at high speed with high cycling endurance, but data retention performance can be relaxed (e.g. using ECC and data scrubbing). Figure 2 shows the eMRAM write performance. The array was written to the 1 state, then to the 0 state, versus write pulse voltage and width. The curves show the write voltage for passing median bits vs. write pulse width, from 4 ns - 20 ns. Stack B incorporated materials optimizations to reduce write voltage and time for suitability towards the last level cache. We performed a series of retention bakes at 85°C on arrays of target and smaller sized devices, demonstrating projected fail rates well below 1 ppm for retention times of ≤ 1 min. at nominal 43 nm CD. Results also include endurance cycling tests on 128 kb arrays up to 5×10^6 cycles, and single MTJs up to 10^{10} cycles. No dielectric breakdown or resistance drift was observed in either case. Finally, an early BEOL reliability assessment of electromigration and time-dependent dielectric breakdown supports our eMRAM embeddability for high-performance logic applications.

[1] S. Aggarwal, *et al.*, *IEEE IEDM*, San Francisco, pp. 2.1.1-2.1.4, 2019. [2] K. Lee, *et al.*, *IEEE IEDM*, San Francisco, pp. 2.1.1-2.1.4, 2019. [3] W. J. Gallagher, *et al.*, *Symposium on VLSI Technology*, Kyoto, pp. T190-T191, 2019. [4] J. G. Alzate *et al.*, *IEEE IEDM*, San Francisco, pp. 2.4.1-2.4.4, 2019. [5] S. Sakhare *et al.*, *IEEE IEDM*, San Francisco, pp. 18.3.1-18.3.4.2018.

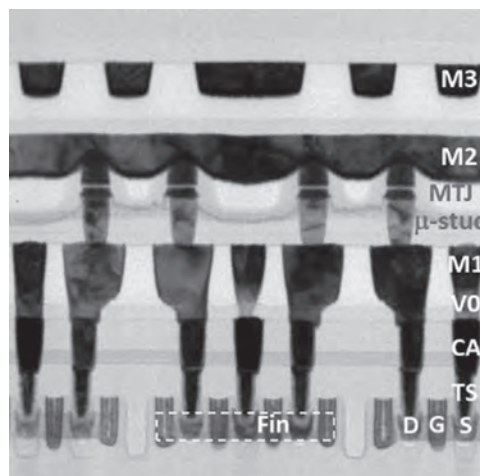


Figure 1: TEM cross section of 41nm MTJ devices inserted between the 14nm node M1 and M2 levels. The μ stud enabled sufficient overetch & cleanup during MTJ patterning.

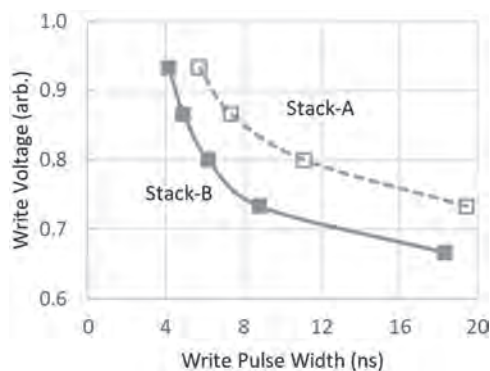


Figure 2: Passing median bit write voltage vs write pulse width for both W0 and W1 operation. Stack B improvements to the free layer enabled higher speed 4ns switching.

CONTRIBUTED PAPERS

CF-03. Perpendicular Magnetic Tunnel Junctions With Reference Layer Based on Four Anti-Ferromagnetically Coupled Co/Pt Layers.

H. Honjo¹, S. Miura¹, K. Nishioka¹, H. Nagauma^{1,3}, T. Watanabe¹, y. Noguchi¹, T. Nguyen^{1,3}, M. Yasuhira¹, S. Ikeda^{1,4} and T. Endoh^{1,2}
 1. Center for Innovative Integrated Electronic Systems, Tohoku University, Sendai, Japan; 2. Graduate School of Engineering, Tohoku University, Sendai, Japan; 3. Center for Spintronics Research Network, Tohoku University, Sendai, Japan; 4. Center for Science and Innovation in Spintronics, Tohoku University, Sendai, Japan

CoFeB–MgO-based magnetic tunnel junctions (MTJs) with perpendicular easy axis have emerged as critical components to develop spin transfer torque magnetoresistance random access memories (STT-MRAMs) [1–6]. To develop a large capacity STT-MRAM, a high tunnel magnetoresistance (TMR) ratio, high thermal stability, and low switching current must simultaneously be realized under a thermal tolerance of 400 °C to ensure CMOS back-end-of-line compatibility. To satisfy these requirements, we have developed high performance MTJ stack structures through physical vapor deposition process development [7–9]. As the size of the MTJs decreases, a more stable reference layer is required to achieve reliable write operations. Furthermore, the magnitude of the stray magnetic field from the reference layer must be minimized. This magnitude significantly increases with a decrease in the MTJ size, resulting in an asymmetrical thermal stability factor between the parallel and antiparallel states [9]. Co/Pt-based synthetic anti-ferro (SyF) magnetically coupled layers with an Ru coupling layer have been widely used as a reference layer to reduce the stray magnetic field. Although the exchange coupling field (H_{ex}) is maximized at a 1st-peak Ru thickness of about 0.4 nm, H_{ex} degrades significantly after 400 °C annealing [10]. Therefore, 0.9 nm-thick Ru (2nd peak) layer is often used in SyF reference layer owing to their high thermal tolerance. Nevertheless, the SyF reference layer with 2nd peak Ru exhibits insufficient stability against the magnetic field and write voltage to realize smaller MTJs. To overcome these issues, we developed a reference layer with four SyF magnetically coupled layers (Quad-SyF). In the Quad-SyF, H_{ex} is determined by the middle SyF layer sandwiched between the top and bottom SyF layers [11]. Moreover, a small stray magnetic field can be realized because each ferromagnetic layer in the Quad-SyF, especially the top layer, can be thinner than those in a conventional SyF. These aspects can help achieve reliable write operations with a high thermal tolerance. We prepared five types of stacks (A–E) as shown in the schematics in Fig. 1 (a) and Fig. 2(a). Stack A corresponds to the MTJ with conventional Co/Pt-based SyF reference layers having a 0.4 nm-thick Ru coupling layer (so-called “2L-1st”), and Stacks B and D correspond to those having a 0.9 nm thick Ru coupling layer (so-called “2L-2nd”). Stack C and E corresponds to an MTJ with Quad-SyF consisting of four anti-ferro magnetically coupled Co/Pt layers and three 0.9 nm-thick Ru coupling layers (so-called “4L-2nd”). All the MTJ stacks were deposited on a 300 mmΦ thermally oxidized Si wafer using a DC/RF magnetron sputtering system. Stack A, B and C were annealed at 300, 350, and 400 °C for 1 h. After annealing at 400 °C for 1 h, Stacks D and E were patterned into the MTJs with diameters ranging from 50–120 nm by using ArF immersion lithography and reactive ion etching techniques. The areal magnetic moment versus magnetic field ($m-H$) curves and TMR ratio were measured using a vibrating sample magnetometer and CIPT, respectively. Figure 1 (b) shows the out-of-plane major $m-H$ curves for the MTJs after annealing at 400 °C for 1 h. The inset shows the minor $m-H$ curves. In the case of the MTJ with 2L-1st, two magnetic reversals corresponding to the free and reference layers occurred. In the case of the MTJ with 2L-2nd, three magnetic reversals corresponding to the free layer, reference layer, and spin-flop of the SyF were observed. In the MTJ with 4L-2nd, four magnetic reversals corresponding to the free layer, reference layer, and spin-flop of the SyF were observed. H_{ex} of the MTJ with 4L-2nd showed a larger value than those of the MTJs with 2L-1st and 2L-2nd. A distinct magnetization plateau region around zero magnetic field was observed in the 2L-2nd and 4L-2nd, whereas the plateau region was not observed in the 2L-1st because of the degradation of the anti-ferro magnetic coupling of the SyF. Figure 1 (c)

shows the dependence of the TMR ratio on the annealing temperature for Stacks A, B, and C. For Stacks B and C, the TMR ratio increased as the annealing temperature increased up to 400 °C. In contrast, for Stack A, the TMR ratio degraded at an annealing temperature of more than 350 °C, as an ideal anti-ferromagnetic configuration could not be realized as mentioned above. Figure 2 shows the MTJ size dependence of the shift magnetic field (H_{shift}). The error bars indicate the standard deviations. H_{shift} of the MTJ with 4L-2nd showed a small value of less than 3 mT when the number of repetitions of the top, 2nd, 3rd and bottom Co/Pt layers set 1, 4, 1, and 2, respectively. The variation in H_{shift} and the MTJ size dependence of H_{shift} for the MTJ with 4L-2nd were smaller than those for the MTJ with 2L-2nd. The employment of Quad-SyF (4L-2nd) can achieve a large H_{ex} , a small shift magnetic field, and high thermal tolerance of the reference layer. This work was supported by CIES’s Industrial Affiliation on STT-MRAM program, CIES Consortium, JST-OPERA, and CAO-SIP.

[1] S. Ikeda et al., Nat. Mater. 9, 721 (2010). [2] H. Sato et al., Appl. Phys. Lett. 101, 022414 (2012). [3] H. Sato et al., IEEE Trans. Magn. 49, 4437 (2013). [4] Y. J. Song et al., IEDM 2018. [5] K. Lee et al., IEDM 2018. [6] Y.-C. Shih et al., VLSI 2018. [7] H. Sato et al., IEDM 2018. [8] H. Honjo et al., VLSI 2015. [9] H. Honjo et al., AIP Adv. 7, 055913 (2017). [10] K. Yakushiji et al., Appl. Phys. Express 8, 083003 (2015). [11] T. Suzuki et al., VLSI Tech. Dig., T188, 2005.

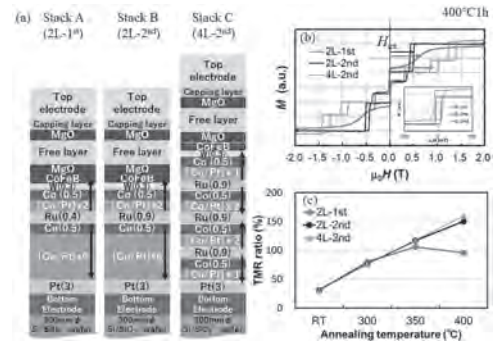


Fig. 1 (a) Schematic of stack structures of the MTJs. The nominal thickness for each layer in nanometers is represented by the numbers in the parentheses. **(b)** Out-of-plane major areal magnetic moment versus magnetic field ($m-H$) curves for the MTJ stacks. Inset is the minor $m-H$ curves. **(c)** Annealing temperature dependence of TMR ratio.

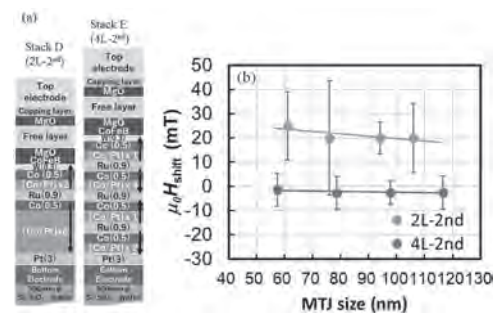


Fig. 2 (a) Schematic of the stack structures of the MTJs. **(b)** MTJ size dependence of the shift field H_{shift} for the MTJs with 2L-2nd and 4L-2nd reference layers.

CF-04. Giant Perpendicular Magnetic Anisotropy Enhancement in MgO-Based Magnetic Tunnel Junction by Using Co/Fe Composite Layer.

L. Vojáček^{1,2*}, F. Ibrahim¹, A. Hallal¹, B. Dieny¹ and M. Chshiev^{1,3}

1. SPINtronique et Technologie des Composants, Grenoble, France;

2. Stredoevropsky Technologicky Institut, Brno, Czechia; 3. Institut Universitaire de France, Paris, France

Magnetic tunnel junctions (MTJ) with perpendicular magnetic anisotropy (PMA) [1] form the basis of the spin-transfer torque magnetic random-access memory (STT-MRAM), which is non-volatile, fast, dense, and has quasi-infinite write endurance and low power consumption. In the usual CoFeB|MgO-based MTJ, the cell diameter must be kept above ~ 30 nm [2], otherwise, the bit becomes thermally unstable due to insufficient PMA. Being able to increase the PMA of the storage layer opens a way to further downsize scaling. In magnetic recording media, this is typically done by introducing heavy metals like Pt or Pd [3], which increases the spin-orbit coupling parameter. However, in the context of STT-MRAM, this would increase the storage layer Gilbert damping and therefore the switching current [4]. To avoid this, multilayers exhibiting bulk PMA based on purely 3d metallic elements were developed [5,6] such as (Fe/Ni) or (Co/Ni) based multilayers. However, these structures are intrinsically complex to fabricate to get large PMA and often do not withstand the required annealing temperature $\sim 400^\circ\text{C}$. Based on density functional theory (DFT) calculations, we propose a rather simple design of MTJ with greatly enhanced PMA up to several mJ/m^2 in the form $\text{Fe}(n)\text{Co}(m)\text{Fe}(n)|\text{MgO}$ [Fig. 1]. This design leverages the well-known interfacial PMA of Fe|MgO along with a strain-induced bulk PMA discovered within bcc Co [plot in Fig. 1]. This strain in bcc Co is induced by the underlying layer. The storage layer can be several nm thick and still exhibit perpendicular magnetization. We perform DFT calculations of the effective PMA (the sum of magnetocrystalline energy E_{MCA} and demagnetizing energy E_{dd}) for different Fe and Co thicknesses and compare with the case of pure Fe, as shown in Fig. 2(a). Unlike in Fe, where the effective PMA decreases with Fe thickness and becomes negative for thicknesses above 11 MLs, in the proposed structure, we see a steady increase of PMA vs. Co thickness. The tunneling magnetoresistance (TMR) estimated from the extended Julliere model is around 300%, comparable with that of the pure Fe|MgO case. After studying the electronic structure of strained bcc Co, we can explain why the large PMA emerges. Calculations based on the second-order perturbation theory [7] reveal that strain leads in bcc Co to a significant shift in the energies of d_{yz} and d_{z^2} minority-spin bands further away from the Fermi level. This is shown to cause an overall increase in PMA. Replacing the middle Fe layers with Co also decreases the negative demagnetizing energy [the magnetocrystalline and demagnetizing energies separately are shown in Fig. 2(b)]. The PMA enhancement can result in a possible downscaling of the cell area by 200% to 300% if an atomically sharp Fe/Co interface can be fabricated. In the case of interfacial mixing, the PMA is reduced by a few 10%. The impact is excessive only in the thinnest $\text{Fe}2\text{Co}3\text{Fe}2|\text{MgO}$ structure, where the drop is about 70%. The thicker structures are far more robust against interdiffusion: in $\text{Fe}3\text{Co}4\text{Fe}3|\text{MgO}$, the drop is only 22%. In conclusion, we propose bcc $\text{Fe}(3\text{ML})\text{Co}(4\text{ML})\text{Fe}(3\text{ML})$ as a storage layer for MgO-based double-barrier MTJ with greatly enhanced perpendicular magnetic anisotropy.

[1] B. Dieny and M. Chshiev, Rev. Mod. Phys., Vol. 89, p.025008 (2017)

[2] S. Ikeda, K. Miura and H. Yamamoto, Nat. Mater., Vol. 9, p.721 (2010)

[3] P. F. Carcia, A. D. Meinhaldt, and A. Suna, Appl. Phys. Lett., Vol. 47,

p.178 (1985) [4] S. Mizukami, E. P. Sajitha and D. Watanabe, Appl. Phys.

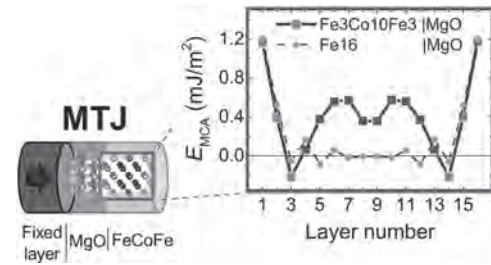
Lett., Vol. 96, p.152502 (2010) [5] K. Hotta, K. Nakamura and T. Akiyama,

Phys. Rev. Lett., Vol. 110, p.267206 (2013) [6] K. Nakamura, Y. Ikeura

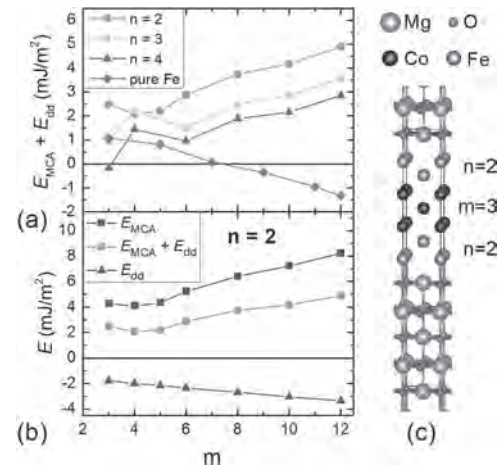
and T. Akiyama, J. Appl. Phys., Vol. 117, p.17C731 (2015) [7] Y. Miura,

S. Ozaki and Y. Kuwahara, J. Phys. Condens. Matter, Vol. 25, p.106005

(2013)



The proposed MTJ with enhanced PMA. FeCoFe trilayer is used as the storage layer. Replacing the middle Fe layers with Co provides a high positive contribution to perpendicular magnetocrystalline anisotropy, as shown in the plot.



(a) Effective PMA ($E_{\text{MCA}} + E_{\text{dd}}$) of the proposed $\text{Fe}(n)\text{Co}(m)\text{Fe}(n)|\text{MgO}$ MTJ with different Fe and Co thicknesses. In $\text{Fe}(n)\text{Co}(m)\text{Fe}(n)|\text{MgO}$, the perpendicular anisotropy is preserved, while in pure Fe/MgO , it would turn in-plane above certain thickness (the Fe thickness is $m+4$ MLs). (b) The magnetocrystalline (E_{MCA}) and demagnetizing energy (E_{dd}) shown separately for structures with $n=2$. (c) Example of the proposed MTJ storage layer with enhanced PMA.

CF-05. Effect of Magnetic Coupling Between two CoFeB Layers on Thermal Stability in Perpendicular Magnetic Tunnel Junctions With MgO/CoFeB/Insertion Layer/CoFeB/MgO Free Layer.

K. Nishioka¹, S. Miura¹, H. Honjo¹, H. Nagauma^{1,3}, T. Nguyen^{1,3}, S. Ikeda^{1,3} and T. Endoh^{1,2}

1. Center for Innovative Integrated Electronic Systems, Tohoku University, Sendai, Japan; 2. Graduate School of Engineering, Tohoku University, Sendai, Japan; 3. Center for Science and Innovation in Spintronics, Tohoku University, Sendai, Japan

Over the past decades, there has been a significant development in spin-transfer-torque magneto-resistive random-access memory (STT-MRAM). The development was brought by CoFeB/MgO-based magnetic tunnel junctions (MTJs) with interfacial perpendicular magnetic anisotropy (IPMA) [1]. Because thermal stability factor (Δ) is proportional to effective PMA constant and the volume of the free layer in a coherent magnetic rotation model [2] and proportional to square root of effective PMA constant and the diameter of the free layer in a domain propagation model [3], Δ decreases with the decrease of MTJ diameter. To achieve great enough Δ value in a smaller MTJ, increasing the number of CoFeB/MgO interfaces has been proposed to increase PMA [4-6]. In double interface MTJ with MgO/CoFeB/insertion layer/CoFeB/MgO free layer, thin non-magnetic layer such as Ta, W or Mo was used as the insertion layer to obtain higher PMA and tunnel magnetoresistance (TMR) ratio [4,7]. When the insertion layer is too thick, the two CoFeB layers in the free layer behave magnetically independent, resulting in no benefits on Δ despite the double interface because effective free-layer volume does not increase. To obtain a benefit of double CoFeB / MgO interfaces on Δ , a great enough magnetic coupling between the two CoFeB layers is required. It is important to clarify the effect of magnetic coupling (the energy constant of unit area: J_{cpl}) on Δ . However, it is not clear how the magnitude of J_{cpl} affects the increase in Δ , although we achieved a strong J_{cpl} in the double interface MTJs [8]. In this study, we propose a method to calculate critical J_{cpl} value to maximize Δ for free layers of MgO/CoFeB/insertion layer/CoFeB/MgO in the double interface MTJs with various MTJ diameters. We introduced magnetic coupling energy between two magnetic layers in the free layer based on magnetic domain propagation model (Model A) and magnetization coherent rotation model (Model B) as shown in Fig.1. When d was larger than the critical diameter d_c ($= 16/\pi [A_s / K_{eff}]^{1/2}$), Model A was applied, in which a blue-colored domain with downward magnetization nucleates from an edge and propagates in each FL1 and FL2. The domain nucleation and propagation behavior from edge region assumed in this model is consistent with the results of micromagnetic simulations of the MTJs with CoFeB / MgO interfaces [9,10]. The nucleated domain area Ω_1 in FL1 and Ω_2 in FL2 were decided by angles ϕ_1 and ϕ_2 . A magnetic energy $E(\phi_1, \phi_2)$ in Model A was calculated as follows. $E(\phi_1, \phi_2) = A(\phi_1) t_1 \sigma_{w1} + A(\phi_2) t_2 \sigma_{w2} + 2J_{cpl} |\Omega(\phi_1) - \Omega(\phi_2)| - (1) \sigma_{w1} = 4(A_s K_{eff1})^{1/2}$, $\sigma_{w2} = 4(A_s K_{eff2})^{1/2}$ ---(2) $A(\phi_i) = d(\pi/2 - \phi_i) \tan \phi_i$, ($i = 1, 2$) ---(3) $\Omega(\phi_i) = d^2 \phi_i/4 + d^2/4 \{ (\pi/2 - \phi_i) \tan^2 \phi_i - \tan \phi_i \}$, ($i = 1, 2$) ---(4) The 1st and 2nd terms in the equation (1) express magnetic domain wall energies of FL1 and FL2, respectively. The third term expresses magnetic coupling energy between FL1 and FL2. A is wall length and σ_w is wall energy per unit area. A_s is stiffness constant of the free layer. When d is smaller than the critical diameter d_c , coherent rotation model (Model B) was applied, in which $E(\phi_1, \phi_2)$ was calculated as follows. The 1st and 2nd terms in the equation (5) express PMA energies of FL1 and FL2. The third term expresses magnetic coupling energy between FL1 and FL2. $E(\phi_1, \phi_2) = \pi d^2/4 \{ K_{eff1} t_1 (1 - \cos^2 \phi_1) + K_{eff2} t_2 (1 - \cos^2 \phi_2) + J_{cpl} (1 - \cos(\phi_1 - \phi_2)) \}$ ---(5) Fig. 2 shows J_{cpl} dependence on Δ for the MTJs with various diameters. We used $K_{eff1} = K_{eff2} = K_{eff, film} + (1 - N_{z-x}) M_s^2 / (2\mu_0)$. $K_{eff, film} = 2.25 \times 10^5$ J/m³, $t_1 = t_2 = 1.2$ nm, $M_s = 0.97$ T and $A_s = 5.4$ pJ/m, which were experimental values in the double interface MTJ [8]. The calculated critical diameter d_c was 23 nm. With increasing J_{cpl} , Δ increases and saturates over a critical J_{cpl} value ($J_{cpl,c}$). The saturated Δ is twice as great as that of $J_{cpl} = 0$. When $J_{cpl} \leq J_{cpl,c}$, energy barrier is minimized in the paths where the magnetizations of FL1 (M_{FL1}) and FL2 (M_{FL2}) separately reverse (not shown in Figures). On the other hand, when the $J_{cpl} \geq J_{cpl,c}$, energy barrier is minimized in the path where M_{FL1} and M_{FL2} reverse simultaneously, resulting in maximum Δ . $J_{cpl,c}$ value rapidly increases with the decrease of the MTJ diameter in Model A ($d \geq d_c$), and

gradually increases in Model B ($d \leq d_c$). $J_{cpl,c}$ value, which is equivalent with $K_{eff} t_1 (= K_{eff, film} t_1 + (1 - N_{z-x}) M_s^2 / (2\mu_0) t_1)$ when $d \leq d_c$, increases with the decrease of the demagnetic field coefficient N_{z-x} . We have reported that J_{cpl} of the blanket film of the double interface MTJ with a W insertion layer thickness of 0.2 nm reaches 0.44 mJ/m² [8]. Therefore, all the $J_{cpl,c}$ values obtained for various diameters based on these models are experimentally achievable. Consequently, we successfully established a method to predict critical J_{cpl} values to maximize Δ for double interface MTJ elements. This work is supported by CIES's Industrial Affiliation on STT-MRAM program, CIES Consortium, JST-OPERA, and CAO-SIP.

- [1] S. Ikeda et al., Nat. Mater. 9, 721 (2010). [2] M. P. Sharrock, IEEE Trans. Magn. 26, 193 (1990). [3] G. D. Chaves-O'Flynn et al. Phys. Rev. Applied 4, 024010 (2015). [4] H. Sato et al. Appl. Phys. Lett. 101, 022414 (2012). [5] K. Nishioka et al., IEEE Trans. Electron Devices 67, 995 (2020). [6] S. Miura et al., IEEE Trans. Electron Devices 67, 5368 (2020). [7] J. H. Kim et al., Sci. Rep. 5, 16903 (2015). [8] K. Nishioka et al., MMM 2020 conference, O2-06. [9] I. Volvach et al., MMM 2020 conference, O2-07. [10] I. Volvach et al., Appl. Phys. Lett. 116, 192408 (2020).

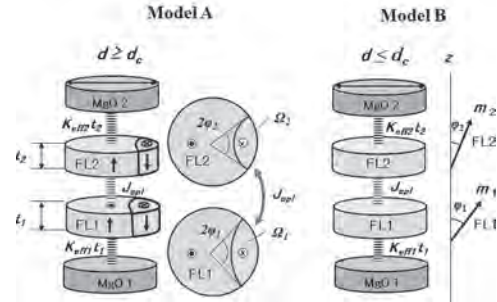


Fig.1 Models to calculate magnetic energy surfaces of the free layer with double-interface MTJs. Model A is a magnetic domain propagation model and Model B is a magnetic coherent rotation model, introducing magnetic coupling energy between two FLs. $K_{eff1} t_1$ and $K_{eff2} t_2$ are effective perpendicular magnetic anisotropy const per unit area which MgO layers give rise to FL1 and FL2, respectively.

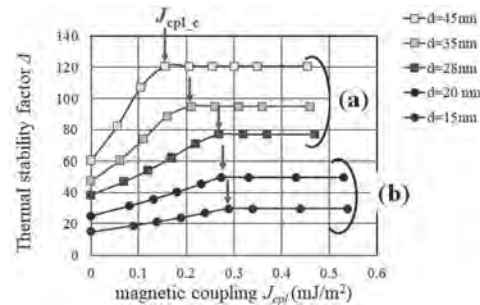


Fig.2 J_{cpl} dependence on Δ for MTJs with various diameters. $J_{cpl,c}$ is a J_{cpl} value which saturates Δ for a MTJ diameter d . (a) Model A is applied when $d \geq d_c = 23$ nm. (b) Model B is applied when $d < d_c = 23$ nm.

CF-06. Towards Spintronic Memory Without Platinum Group Metals (PGMs) for Improved Sustainability.

A. Palomino¹, J. Marty², S. Auffret¹, I. Joumard¹, R. Sousa¹, I. Prejbeanu¹, B. Ageron² and B. Dieny¹

1. Univ. Grenoble Alpes, CEA, CNRS, Grenoble INP, IRIG-SPINTEC, Grenoble, France; 2. Laboratoire CERAG, Univ. Grenoble Alpes, Saint Martin d'Hères, France

Spin transfer-torque Magnetic Random Access Memory (STT-MRAM) is expected to play a major role in the future development of information and communication technologies. One of the drivers of the technology is the non-volatile character of this type of memory that allows to reduce the energy consumption compared to SRAM or DRAM. [1] Globally, we are seeking to develop technologies that help reduce carbon emissions. However, the nature of the materials involved in such technologies is also a concern both in terms of environmental impact and supply risk. [2,3] MRAM contains several materials classified as critical raw materials, in particular by the European Union (EU), being of high importance to the EU economy and whose supply is classified of high risk. [4] In order to improve the stability of the reference layer whose magnetic configuration has to remain fixed during the lifetime of the memory, a synthetic antiferromagnet (SAF) is typically used. This SAF structure is normally based on Co/Pt or Co/Pd multilayers antiferromagnetically coupled through a thin Ru layer. Platinum Group Metals (PGMs) have been classified as critical materials with high supply risk. In addition, obtaining these metals in their refined form requires extensive amounts of energy and CO₂ emissions due to the low initial ore concentration. In this work, an assessment of the impact of the substitution of the Pt required in STT-MRAM for the SAF layer has been made. Alternative solutions can be envisaged such as the use of multilayers based on Co/Ni exhibiting perpendicular anisotropy [5]. A second more challenging approach based on the use of perpendicular shape anisotropy (PSA) does not rely on the use of PGMs. However, this PSA based approach is more challenging from technological point of view due to the requirement of a strict control of the cell diameter at sub-20nm dimensions during the etching process. The possibility of using Co/Ni multilayers for the SAF of MRAM has been already demonstrated [6,7]. We have observed how similar properties to Co/Pt SAF can be obtained by using Co/Ni multilayers (Figure 1). Our study has the added advantage of using a seed layer free of Hf, used in some previous studies to promote the required (111) texture for the Co/Ni multilayers growth [6,7]. Hf is also a material classified as critical and whose production is strongly concentrated in two countries, France and USA. In our study a Cu seed layer is used allowing for more diverse production sources. An evaluation of the environmental (energy and global warming potential) and economic impact of the substitution has been performed. Strong improvements in both economic and environmental aspects can be achieved by the substitution. However due to the tiny amounts of PGM materials used in STT-MRAM, in comparison to the mass of the silicon wafer itself, the environmental impact and price of the silicon wafer on which these memory devices are grown is much higher as shown in Figure 2. Our conclusion is that more attention should be focused on the process of fabrication of silicon wafers or find a substitution to this type of wafers whenever possible. Nevertheless, the high supply concentration of Pt as four mining companies represent the 80% of the global production [8] makes the presence of these alternatives a key aspect to ensure the survival of the technology in case of supply disruptions.

1. B. Dieny and I. L. Prejbeanu, 'Magnetic Random-Access Memory', in Introduction to Magnetic Random-Access Memory, John Wiley & Sons, Ltd, pp. 101–164. (2017) doi:10.1002/9781119079415 2. European Commission. Critical materials for strategic technologies and sectors in the EU - a foresight study. (2020) doi: 10.2873/58081 3. Ku, A. Y. Sustainable Materials and Technologies, 15, 27-32. (2018) doi:10.1016/j.susmat.2017.10.001 4. European Commission. Study on the Review of the List of Critical Raw Materials - Critical Raw Materials Factsheets European Commission. (2017) doi: 10.2873/398823 5. Nuss P, Eckelman MJ. PLoS ONE 9(7): e101298. (2014) doi: 10.1371/journal.pone.0101298 6. Kar, G. S., Kim, W., Tahmasebi, T. et al., IEEE International Electron Devices Meeting. (2014) doi:10.1109/iedm.2014.7047080 7. Tomczak, Y., Lin,

T., Swerts, J., et al. IEEE Transactions on Magnetics, 52(7), 1-4. (2016) doi:10.1109/tmag.2016.2515109 8. Sinsalo, Pia, and Mari Lundström. Metals, vol. 8, no. 4, p. 203. (2018) doi:10.3390/met8040203.

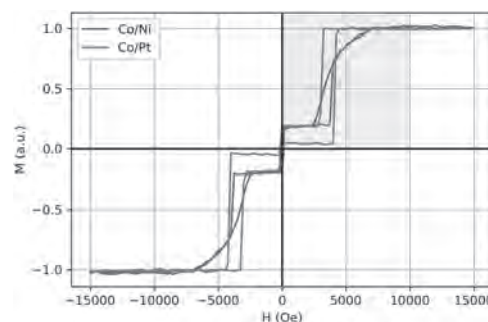


Fig 1. VSM measurements on a MTJ with conventional SAF based on Co/Pt multilayers (red) versus a MTJ with SAF comprising Co/Ni multilayers (green) after annealing at 300°C for 10 minutes. Sample based on Co/Pt SAF has the following composition (thickness in nm) : Ta3/Pt25/[Co0.5/Pt0.25]6/Co0.5/Ru0.9/[Co0.5/Pt0.25]3/ Co0.5/Ta0.2/FeCoB1.2/MgO0.7/Ox/MgO0.5/FeCoB1.5/Ta3/Pt5. Sample based on (Co/Ni) multilayers is Pt-free and has the following composition Ta22/FeCoB0.8/Ta3/Cu3/[Co0.2/Ni0.4]6/Co0.5/Ru0.9/Co0.5/[Co0.2/Ni0.4]3/Ta0.2/FeCoB1.2/MgO0.7/Ox/MgO0.5/FeCoB1.5/Ta3/Al2.

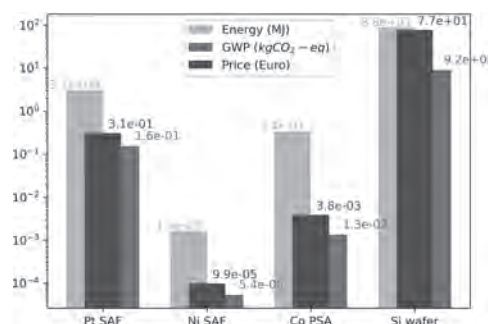


Fig 2. Energy per 300mm wafer, global warming potential (GWP) and price in log scale required to obtain the amount of Pt comprised in a conventional SAF, of Co in the PSA based substitution, of Ni in the case of (Co/Ni) based SAF alternative and for the production of a 300mm bare Si wafer.

CF-07. SAF Based on Co/Ni Multilayers With Improved Annealing Tolerance for Sustainable Pt-Free Reference Layer of STT-MRAM.

A. Palomino¹, M. Mansueto¹, S. Auffret¹, I. Joumard¹, L. Vila¹, R. Sousa¹, I. Prejbeanu¹ and B. Dieny¹

1. Univ. Grenoble Alpes, CEA, CNRS, Grenoble INP, IRIG-SPINTEC, Grenoble, France

Due to the reduced switching current and easier scalability to smaller technology nodes than its in plane magnetized counterpart, Perpendicular Spin transfer-torque Magnetic Random Access Memory (p-STT-MRAM) had a quick industrial development in the last few years. The thermal energy barrier required to meet industrial data retention requirements is provided by a large interfacial anisotropy. For the free layer, this large perpendicular magnetic anisotropy (PMA) is induced at the interface of the ferromagnetic electrode and the oxide barrier. [1] The reference layer must have a thermal stability well above that of the free layer so that the free layer can change its magnetic configuration while the reference layer remains stable. Nowadays, this is typically achieved by coupling a synthetic antiferromagnet structure (SAF) as reference layer. The high thermal stability of the SAF comes from the interfacial magnetic anisotropy provided by magnetic multilayers such as Co/Pt or Co/Pd and the antiferromagnetic RKKY interaction between the two oppositely magnetized components of the SAF. However, the use of critical metals such as Pt is often undesired due to the high price, scarcity or the high supply risk associated to its highly concentrated production. [2,3] Therefore, alternatives based on more common materials such as Ni could help mitigate possible disruptions that might appear on more precious metals and reduce the vulnerability of STT-MRAM to such disruptions. A key factor to achieve a high perpendicular magnetic anisotropy (PMA) in Co/Ni multilayers is to induce a good (111) texture [4,5]. In this study, a smooth buffer layer has been developed first wherein reduced roughness was obtained thanks to the insertion of an amorphous FeCoB layer. Then a Cu seed layer has been used to induce the desired (111) texture with the added advantage of Cu being a very common non-critical metal. A low roughness value of 0.25nm could be obtained for a 5nm Cu seed, sufficiently thick to provide the required (111) texture. The coercive field of the Co/Ni SAF increases with the thickness of the Cu seed layer correlatively with the improved (111) texture, in agreement with previous results on Co/Ni multilayers [5] and SAF [6]. However, further increasing the Cu thickness yields a roughness increase at the tunnel barrier that can be detrimental to the optimal properties of the MTJ. Therefore, a tradeoff must be found on the Cu buffer thickness. Thin film measurements of the coercive field of the MTJ with Co/Ni SAF annealed at 300°C for 10 minutes show a switching field of 3.8 kOe, sufficiently high to meet the typical reference layer requirements. In nanopatterned devices, the reference layer is stable in both parallel and antiparallel magnetic configuration. However, during annealing at 400°C, the coercive field of the reference layer drastically decreases. This decrease of reference layer coercive field has already been observed when annealing Co/Ni Ultrathin SAF p-MTJ at high temperatures [7]. Increasing the Cu seed layer thickness, thus improving the (111) texture increases the switching field of the reference layer (Fig. 1a) but can be detrimental as previously mention due to an increased roughness at the barrier level. In this study, we show that increasing the thickness of the Ta layer, used as a boron getter, separating the top part of the Co/Ni SAF from the FeCoB reference layer allows to keep higher coercive field of the (Co/Ni) SAF layer even after annealing at 400°C (Fig. 1b). However, if this Ta layer is too thick (as in Fig. 1b), the reference and SAF become insufficiently coupled. To circumvent this problem, we proposed here to replace the single Ta layer by a double Ta layer of composition (Ta 0.3nm/Co 1.8nm/ Ta0.45nm). Such composite layer ensures a strong magnetic coupling while providing the benefit of a thicker diffusion barrier. As a result, a higher switching field of the reference layer of 5kOe after annealing at 400°C could be obtained (Figure 2) for an improved stability of the reference layer.

1. Dieny, B., Prejbeanu, I.L., Garello, K. et al. Nat Electron 3, 446–459 (2020). doi : 10.1038/s41928-020-0461-5 2. European Commission. Study on the Review of the List of Critical Raw Materials - Critical Raw Materials Factsheets European Commission. (2017) doi: 10.2873/398823 3. Ku, A. Y. Sustainable Materials and Technologies, 15, 27-32. (2018) doi:10.1016/j.susmat.2017.10.001 4. Enlong Liu, J. Swerts, T. Devolder et al. Journal

of Applied Physics 121, 043905 (2017); doi : 10.1063/1.4974885 5. Justin M. Shaw, Hans T. Nembach, and T. J. Silva. Journal of Applied Physics 108, 093922 (2010); doi : 10.1063/1.3506688 6. Arora, M., Lee-Hone, N. R., Mckinnon, T. et al. J. Phys. D: Appl. Phys. 50 505003 (11pp). (2017) doi:10.1088/1361-6463/aa97fa 7. Tomczak, Y., Lin, T., Swerts, J. et al. IEEE Transactions on Magnetics, 52(7), 1-4. (2016) doi:10.1109/mag.2016.2515109

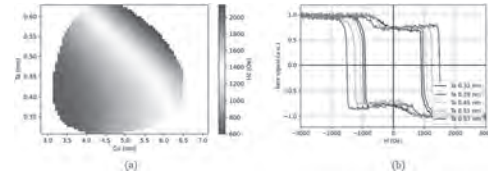


Figure 1. Coercive field (H_c) of the SAF structure increases with both Cu seed layer thickness and Ta getter thickness after annealing at 400°C for 10 minutes (a). MOKE results display the H_c dependence on the Ta getter thickness shown in (a) for a fixed 5nm Cu seed layer thickness (b). The full structure in nm: Ta 22/FeCoB 0.8/Ta 3/ Cu x /6x [Co 0.18/ Ni 0.55] /Co 0.5 / Ru 0.9 / Co 0.5 / 3x [Ni 0.55/ Co 0.18] / Ta Y / FeCoB 1.2 / MgO 1.2/ FeCoB 0.4 / Ta 3 / Pt 5.

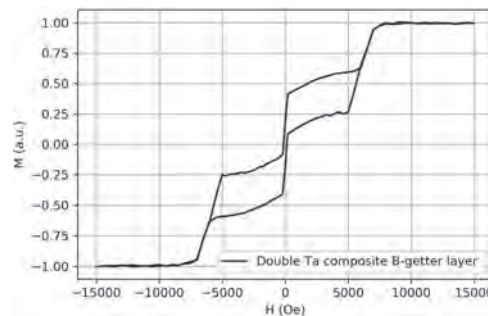


Figure 2. Vibrating sample magnetometer (VSM) measurement of a full MTJ with double Ta composite B-getter layer (Ta 0.3nm/Co 1.8nm/ Ta0.45nm) displaying the SAF switching at field as high as 5kOe. The full structure is in nm: Ta 22/FeCoB 0.8/Ta 3/ Cu 5 /6x [Co 0.18/ Ni 0.55] / Co 0.5 / Ru 0.9 / Co 0.5 / 3x [Ni 0.55/ Co 0.18] / double Ta composite B-getter layer /FeCoB 1.2 / MgO 1.2/ FeCoB 1 / Ta 0.2 /FeCoB 0.8/ MgO 1.2 / FeCoB 0.4/Ta 3 / Pt 5.

CF-08. Correlation of Interfacial Perpendicular Magnetic Anisotropy and Interlayer Exchange Coupling in CoFe/W/CoFe Structures.

J. Chen^{1,2}, S. Peng^{1,2}, D. Xiong^{1,2}, H. Cheng^{1,2}, H. Zhou^{1,2}, Y. Jiang^{1,2}, J. Lu^{1,2}, W. Li^{1,2} and W. Zhao^{1,2}

1. Fert Beijing Institute, BDBC, Beihang University, Beijing, China;

2. School of Integrated Circuit Science and Engineering, Beihang University, Beijing, China

As core device of spin-transfer torque magnetic random-access memory (STT-MRAM) and some other spintronics devices [1], the magnetic tunnel junction (MTJ) has been widely studied to improve performances such as endurance, scalability, read reliability and power consumption. The interfacial perpendicular magnetic anisotropy (PMA) in the CoFeB/MgO/CoFeB structure with a tunnel magnetoresistance (TMR) ratio of over 120% [2] proves that PMA can be used to build high-performance out-of-plane MTJ for STT-MRAM cells. Latter research found that the heavy metal (HM)/ferromagnet interface made great contribution to PMA [3]. First-principles investigations agree that both the MgO/CoFe interface and the CoFe/HM interface attribute to magnetic anisotropy energy (MAE) in the MgO/CoFe/HM structures [4, 5]. Moreover, the MgO/CoFeB/Ta/CoFeB/MgO double-interface structure was demonstrated to improve thermal stability by a factor of 1.9 while keeping comparable critical switching current with the single-interface structure Ta/CoFeB/MgO [6]. The MgO/CoFeB/W/CoFeB/MgO structure was demonstrated to possess strong PMA and large TMR ratio (249%) after annealing at a high temperature [7]. To investigate the MAE in the W-based structure, it is necessary to research the interaction within CoFeB/W/CoFeB layers on MAE. CoFeB/W/CoFeB sandwich may form ferromagnetic or antiferromagnetic coupling (FMC or AFMC), which is expressed as interlayer exchange coupling (IEC). However, it remains unclear about the interactions between MAE and IEC in the perpendicularly magnetized CoFeB/W/CoFeB structure, making the way to enhance PMA in double-interface structure not straight forward. In this work, we first investigated the MAE and IEC of the MgO/CoFe/W/CoFe/MgO structures as a function of W thickness with first-principles calculations as shown in Fig. 1 [8]. Clear oscillation of IEC can be observed in Fig. 1(a). The long and short period of IEC oscillations are 4.8 monolayers (MLs) and 3.2 MLs, respectively, according to simulation. Figure 1(b) shows the MAEs of MgO/CoFe/W/CoFe/MgO structures for FMC and for the arrangement corresponding to IEC are calculated for all thicknesses of W layers. Moreover, for the structure with W thickness of 7 MLs, a strong FMC as well as a strong PMA can be obtained simultaneously, which is promising for high-density STT-MRAM applications with strong thermal stability. Also, we observe a clear oscillation of MAE in ferromagnetically coupled MgO/CoFe/W/CoFe/MgO structure related to the thickness of W layer. To further study the effect of interface interactions on MAE, we calculate the k -space-resolved MAE according to force theorem [8]. Figure 1(c-f) shows the k -resolved MAEs of the ferromagnetically coupled CoFe/W/CoFe structures with the thickness of W layer varies from 1 ML to 4 MLs. The spin-orbit coupling (SOC) breaks the symmetry of 2D-Brillouin-zone slightly making MAE at the points around $[k_x, k_y] = [0.457, 0.257]$ possessing the largest PMA in Fig. 2(c-f). These points that make huge contributions to MAE ferromagnetically coupled are called critical points. The electron states near the Fermi surface have a large influence on MAE. Therefore, we consider spin-resolved bands at critical points. The bands near Fermi energy for spin-up and spin-down states are different, which can be explained by exchange splitting. To explore the properties of the specific electron states, the band-decomposed charge densities of these specific electron states near Fermi energy are shown in Fig. 2(a-d). We can see that only spin-up electron states occupy W layers and that the alternating oscillation of the charge densities at center of W layers: antinode at 1 ML and 3 MLs W layer, while node at 2 MLs and 4 MLs W layers. It is reported that the electron wavefunction confined in thin film is modulated by an envelope function in reference [8]. For a given energy, as the thickness of the W layer in CoFe/W/CoFe structure varies, the center of film layers within the quantum well shows the alternation of node and antinode, shown in Fig. 2(a-d), indicating the presence of QWSs in W layers. The oscillation of IEC in CoFe/W/CoFe originates from QWSs [8]. Thus, these results clearly show that the QWSs correlate the oscillation of IEC and MAE in W-based double-interface structures. In summary, we investigated the MAE

and IEC of the MgO/CoFe/W/CoFe/MgO structures as a function of W thickness with first-principles calculations. The oscillations of both IEC and MAE with the change of W thickness were observed in this structure. QWSs in the W layer are demonstrated to be critical for the oscillations of MAE, leading to significant enhancement of PMA by properly tuning W thickness.

[1] S. Peng *et al.*, *Nature Electronics*, vol. 3, no. 12, pp. 757-764, 2020/12/01 2020, doi: 10.1038/s41928-020-00504-6. [2] S. Ikeda *et al.*, *Nature materials*, vol. 9, no. 9, p. 721, 2010. [3] S. Peng *et al.*, *Advanced Electronic Materials*, vol. 5, no. 8, p. 1900134, 2019. [4] S. Peng *et al.*, *Appl. Phys. Lett.*, vol. 110, no. 7, p. 072403, 2017. [5] C.-H. Chang, K.-P. Dou, G.-Y. Guo, and C.-C. Kaun, *NPG Asia Materials*, vol. 9, no. 8, p. e424, 2017. [6] H. Sato, M. Yamanouchi, S. Ikeda, and H. Ohno, *IEEE Trans. Magn.*, vol. 49, no. 7, pp. 4437-4440, 2013. [7] M. Wang *et al.*, *Nature communications*, vol. 9, no. 1, p. 671, 2018. [8] J. Chen *et al.*, *J. Phys. D: Appl. Phys.*, 2020.

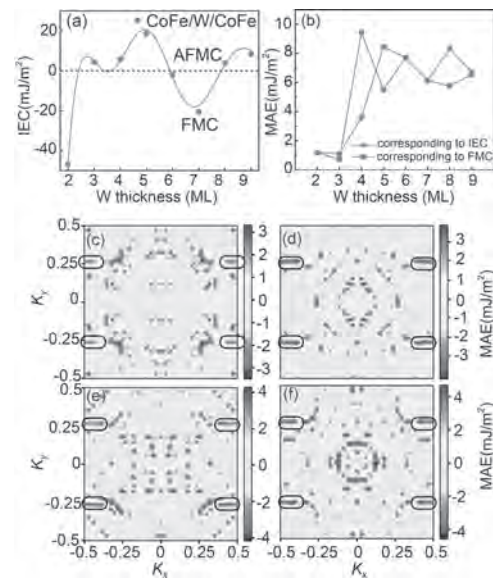


Fig. 1. (a) Interlayer exchange coupling (IEC) of the CoFe/W/CoFe structures as a function of the thickness of W monolayers (MLs). **(b)** Calculated magnetic anisotropy energy (MAE) of the MgO/CoFe/W/CoFe/MgO structures as a function of the thickness of W MLs for the ferromagnetic coupling (FMC) and for the arrangement corresponding to calculated IEC. The k -resolved MAE of (c) CoFe/W 1ML/CoFe, (d) CoFe/W 2MLs/CoFe, (e) CoFe/W 3MLs/CoFe, (f) CoFe/W 4MLs/CoFe structures in 2D-Brillouin-zone. Critical k points are labeled by black rectangles.

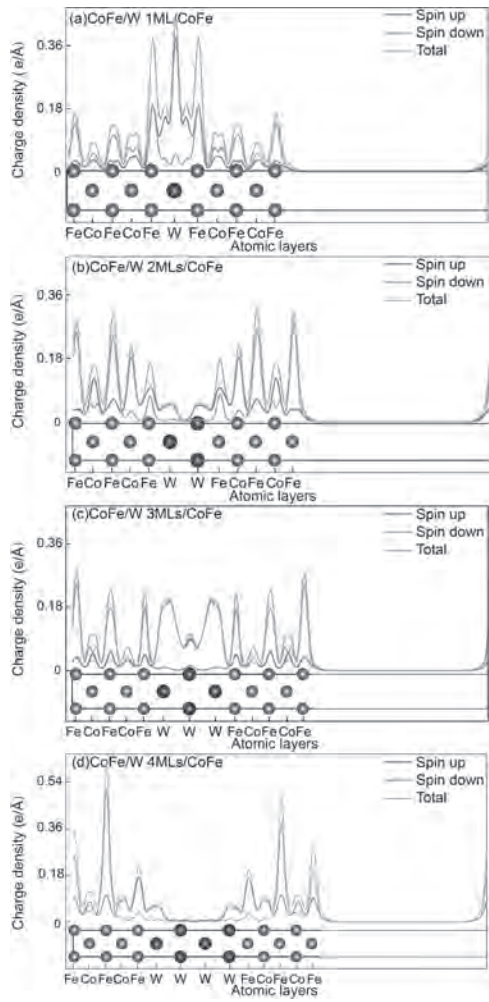


Fig. 2. Charge densities of bands near Fermi energy of (a)CoFe/W 1ML/CoFe, (b)CoFe/W 2MLs/CoFe, (c)CoFe/W 3MLs/CoFe, (d)CoFe/W 4MLs/CoFe. The charge density of spin-up electrons of these bands at the center of structures switch within node and antinode as a function of the number of W layers.

CF-09. Spin Torque Switching of Perpendicular Magnetic Tunnel Junction Nanopillars at Cryogenic Temperatures.

L. Rehm¹, G. Wolf², B. Kardasz², E. Cogulu¹, Y. Chen¹, M. Pinarbasi² and A.D. Kent¹

1. Physics, New York University, New York, NY, United States;

2. Spin Memory Inc, Fremont, CA, United States

The semiconductor industry is actively developing high-density, non-volatile random access memories based on perpendicular magnetic tunnel junction (pMTJ) nanopillars for consumer electronics and thus operation between room temperature and ~ 150 °C [1]. Such devices are also of interest for cryogenic computing systems (4 K) where a persistent, fast, low-energy consuming, and nanometer scale device is needed. It is known that thermal fluctuations play an important role in spin torque switching of magnetic tunnel junctions causing magnetization fluctuations that decrease the switching voltage but also introduce switching errors. Here we explore the effect of temperature on the spin-transfer torque switching probability of state-of-the-art perpendicular magnetic tunnel junction nanopillars (40 to 60 nm in diameter) from room temperature down to 4 K, sampling up to a million switching events (see Fig. 1). We measure both the read disturb rate (as shown in Fig. 1) and the switching voltage versus pulse duration to determine the thermal stability factor Δ , the energy barrier to magnetization reversal E_b , divided by the thermal energy $k_B T$ [2]. For both methods, the junction temperature at the switching voltage—obtained from the thermally assisted spin torque switching model—is found to saturate at temperatures below about 75 K (see Fig. 2). This shows that junction heating is significant below 75 K and that spin-transfer torque switching remains stochastic down to 4 K. This will be discussed along with three-dimensional finite-element simulations (COMSOL) which capture aspects of this behavior and show that this effect is associated with the reduced thermal conductivity and heat capacity of the metals in the junction. These results are important to furthering the understanding the role of temperature in spin torque switching dynamics of pMTJs and their applications as cryogenic memory. Acknowledgements This research was supported by Spin Memory Inc.

[1] A. D. Kent and D. C. Worledge, Nature Nanotechnology 10, 187 (2015).

[2] R. Heindl *et al.*, Journal of Applied Physics 109, 073910 (2011). [3] G.

D. Chaves-O’Flynn *et al.*, Physical Review Applied 4, 024010 (2015). [4]

L. Rehm *et al.*, Appl. Phys. Lett. 115, 182404 (2019). [5] L. Rehm *et al.*, arXiv:2009.01743.

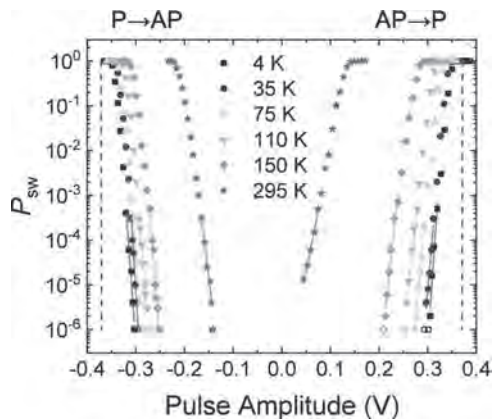


Fig. 1: Switching probability (P_{sw}) in the low-voltage (read disturb, RDR) limit as a function of voltage pulse amplitudes of a 40 nm diameter pMTJ at various bath temperatures and zero field. The pulse duration for this measurement was fixed at 10 μ s. The straight lines represent fits to the data. The empty data points at 10^6 events stand for no errors and were therefore excluded from the fit. The dashed lines indicate the behavior expected for a device temperature of 4 K.

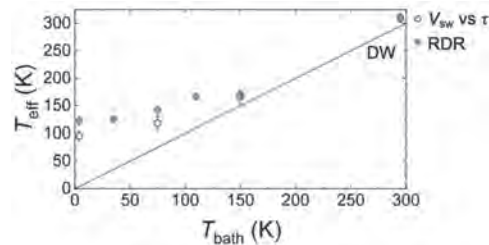


Fig 2: Effective sample temperature T_{eff} from the pulsed voltage ramps and RDR measurements at various temperatures between 4 and 295 K. The dotted black lines represent the expected behavior for a thermally assisted spin torque switching model based on domain wall (DW) reversal [3] with material parameters extracted from VSM and FMR measurements.

CF-10. The Effect of Reduced Exchange Interactions on Switching of Perpendicular Magnetic Tunnel Junctions.

J. Beik Mohammadi¹ and A.D. Kent²

1. Loyola University New Orleans, New Orleans, LA, United States;
 2. New York University, New York, NY, United States

Perpendicular magnetic tunnel junctions, pMTJs, with a composite free layer have been developed and utilized in embedded memories and magnetic sensors. Such applications rely on fast current-induced switching of the free layer. Investigating the switching dynamics of the pMTJ free layer allows researchers to predict and optimize their switching speed. Experimental and micromagnetic simulation studies have been conducted toward this goal [1-3]. However, there continue to be challenges to overcome that are significant for technological applications. One major challenge in prediction and understating the spin transfer torque switching of the free layer is that its magnetic properties, such as magnetic anisotropy and magnetic exchange interaction, depends strongly on the details of the fabrication process and the materials involved. Recent studies suggest that the composite free layer, where a non-magnetic interlayer is inserted to enhance the perpendicular magnetic anisotropy and thermal stability of the free layer, the magnetic exchange constant is significantly lower than the bulk values [1]. The question is how does the reduced exchange interaction affect the spin torque switching dynamics and the switching speed of the free layer? Here we have investigated the effect of reduced exchange interaction on the spin torque switching dynamics and switching speed of the free layer of disk-shaped pMTJs. Our results show that when undergoing spin-transfer torque switching, the exchange interaction plays an important role in determining the switching path[4]: 1) the sequence of the micromagnetic events depends on the exchange interaction strength (see figure 1), and 2) the switching speed is greatly reduced when for lower exchange constants (see figure 2). Figure 1: A 30-nm pMTJ free layer undergoes a spin-torque switching when a long duration current pulse is applied to it (current is 1.6 times the critical current for switching). Material parameters are those mentioned in reference [1]. When exchange interaction is large ($A=19$ pJ/m), the switching is domain wall mediated [4]. For the same size element, when the exchange constant is smaller ($A=8.5$ pJ/m), the center of the element switches first, and this switched region moves to and hits the edge of the disk, and a domain wall is created across the element. By further reduced the exchange interaction ($A=4$ pJ/m), a droplet is formed at the center of the disk (fully reversed cells at the center), then this droplet hits the edge, and one or more domain walls form across the element. If the diameter of the disk is below a critical value [5], $d_c=16/\pi \sqrt{(A/K_{eff})}$ where A is the exchange constant, and K_{eff} is the uniaxial anisotropy that includes demagnetization energy and uniaxial perpendicular anisotropy, spin-torque switching of the free layer is expected to be a uniform macrospin model like switching. When the diameter of the disc is greater than d_c , one or more domain walls (where the magnetization on one side of the wall is reversed and the other side is in the initial magnetic state) can form across the element, and dynamics are more complex. The structure of this domain wall and the magnetization profile of the free layer is very complex and gets even more complex for elements with smaller exchange interaction. In this presentation, I will present our results on how the reduced exchange interaction results in different (and more complex) dynamics that lead to a delayed switching [6]. I will also show that increasing the current does not necessarily make switching more coherent. ACKNOWLEDGEMENTS This research supported by Spin Memory Inc.

1. J. B. Mohammadi, B. Kardasz and A. D. Kent, ACS Applied Electronic Materials 1, 2025 (2019) 2. C. Hahn, G. Wolf and A. D. Kent, Phys. Rev. B94, 214432(2016) 3. Devolder, A. Le Goff and V. Nikitin, Phys. Rev. B93, 224432 (2016) 4. J. Beik Mohammadi and A. D. Kent, arXiv:2003.13875, 2020 (2020) 5. G. D. Chaves-O'Flynn, G. Wolf and A. D. Kent, Phys. Rev. Applied4, 024010 (2015) 6. N. Statuto, J. B. Mohammadi and A. D. Kent, Phys. Rev. B 103, 014409 (2021)

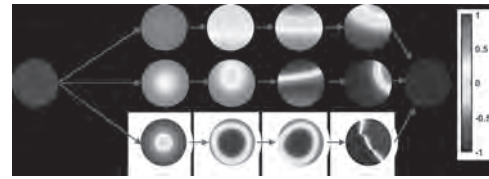


Figure 1: A 30-nm pMTJ free layer undergoes a spin-torque switching when a long duration current pulse is applied to it (current is 1.6 times the critical current for switching). Material parameters are those mentioned in reference [1]. When exchange interaction is large ($A=19$ pJ/m), the switching is domain wall mediated [4]. For the same size element, when the exchange constant is smaller ($A=8.5$ pJ/m), the center of the element switches first, and this switched region moves to and hits the edge of the disk, and a domain wall is created across the element. By further reduced the exchange interaction ($A=4$ pJ/m), a droplet is formed at the center of the disk (fully reversed cells at the center), then this droplet hits the edge, and one or more domain walls form across the element.

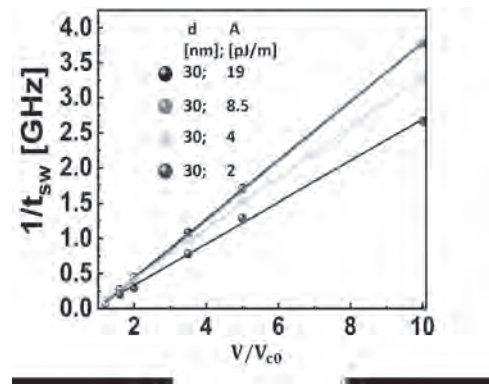


Figure 2: Switching speed of a 30-nm pMTJ free layer vs. overdrive (that is applied voltage divided by the critical/minimum voltage required to switch the free layer). Different color symbols represent the simulated data for different exchange constant, and the solid lines are linear fit to each data set. As seen in this figure, the switching speed is greatly reduced as the exchange interaction is reduced. One interesting result is that although the switching speed vs. overdrive for each exchange constant value is fairly linear, as macrospin model suggests, the slope of the line is greatly reduced for elements with reduced exchange interaction (For example, compare the slope of the red line, that is for $A=8.5$ pJ/m, with the slope of the purple line, that represents the data with $A=2$ pJ/m).

CF-11. Modelling and Optimization of Double Magnetic Tunnel Junctions With Switchable Assistance Layer for High Performance STT-MRAM Applications.

D. Sanchez Hazen^{1,2}, S. Auffret¹, I. Joumard¹, L. Vila¹, L.D. Buda-Prejbeanu^{1,2}, R. Sousa¹, I. Prejbeanu¹ and B. Dieny¹

1. SPINtronique et Technologie des Composants, Grenoble, France;
2. Institut Polytechnique de Grenoble, Grenoble, France

Perpendicular Double Magnetic tunnel junctions (p-DMTJ) are developed for high-performance STT-MRAM applications. In these devices, the thermal stability factor (Δ) of the storage layer (SL) magnetization is increased by sandwiching the SL between two MgO barriers thus benefiting from the interfacial perpendicular anisotropy from the two SL/MgO interfaces [1][2][3]. The critical current to switch the storage layer magnetization is reduced when using above and below the MgO/SL/MgO sandwich two antiparallel polarizers. This provides two spin-transfer torque contributions acting simultaneously on the SL. In such p-DMTJ, the two polarizers are usually pinned by exchange coupling with a synthetic antiferromagnetic structure, increasing the complexity of the stack and its patterning. Alternatively, a simplified DMTJ structure comprising a switchable assistance layer (ASL) that acts as a second polarizer was proposed [4]. It is expected to present the same enhancement in performance as traditional p-DMTJ. For these devices to work, a balance between the energy barriers of the storage layer and of the switchable assistance layer must be fulfilled. Due to the particular voltage driven dynamics, the magnetization of the switchable assistance layer should switch before that of the Storage layer. Thus, it can be set antiparallel to that of the reference layer, generating cumulative STT contributions from the ASL and reference layer. Figure 1.(a) shows a comparison of the structures of a conventional p-DMTJ versus a simplified DMTJ with ASL, as well as the layers switching sequences. Upon write, when starting from the reference (REF) up/ Storage layer down/ Assistance layer down configuration (Figure 1.(b)), in order to switch the magnetization of the SL layer in the up configuration, the electrons have to flow from the REF layer to the ASL layer (positive V pulse). Since in this configuration the REF and ASL layer are in antiparallel configuration, the critical current for switching the SL magnetization is reduced. As a result the SL magnetization switches first followed by the switching of the ASL layer due to their parallel coupling and STT from the SL. When starting from the REF up/ SL up/ASL up configuration (Figure 1.(c)), in order to switch the magnetization of the SL layer in the down configuration, the electrons have to flow from the ASL layer to the REF layer (negative V pulse). Since the ASL energy barrier is lower than the SL one, the critical current to switch the ASL magnetization in this configuration is lower than that to switch the SL magnetization. As a result, the ASL magnetization first switches antiparallel to the REF. This increases the STT efficiency on the SL magnetization, which then switches downwards ending up antiparallel to the REF. In standby conditions, the two free layers will always end up parallel, reinforcing the overall thermal stability of the device by their mutual dipolar coupling. In this work, we report the first experimental observation of the working principal of this type of devices. By comparison with a structure without the Assistance layer, the simplified double magnetic tunnel junction presents an averaged 5-fold increase of the figure of merit (D/Ic) (Figure 2). Secondly, we qualitatively interpreted the experimental observations in these devices by macrospin simulations taking into account heating effect occurring during write cycle. In fact, as a result of the presence of two MgO barriers, Joule heating plays a significant role in the write process [5]. From our model, we have been able to identify that the free layers (SL and ASL) blocking temperature can affect dramatically the performance of these devices. If the ASL's blocking temperature is lower than that of the SL, the temperature rise during the application of the writing pulse can set the ASL in a paramagnetic regime. This suppresses any additional STT or dipolar coupling from this layer and causes an asymmetry on the critical voltage to switch from P to AP and from AP to P. Finally, thanks to an optimization of the structure of our simplified double magnetic tunnel junction, this issue have been solved.

[1] B. Rodmacq et al, patent US8513944B2 (2008) [2] Daniel C. Worledge et al, IEEE MAGNETICS LETTERS, Vol 8, (2017) [3] S. Rao et al, BEOL-compatible double magnetic tunnel junction pSTT-MRAM devices for IoT

and edge computing, IEDM 2020 [4] A. V. Khvalkovskiy et al, Journal of Applied Physics 124, 133902 (2018) [5] N. Strelkov et al, Physical Review B: Condensed Matter and Materials Physics, American Physical Society, 2017, 95, pp.184409 (2017)

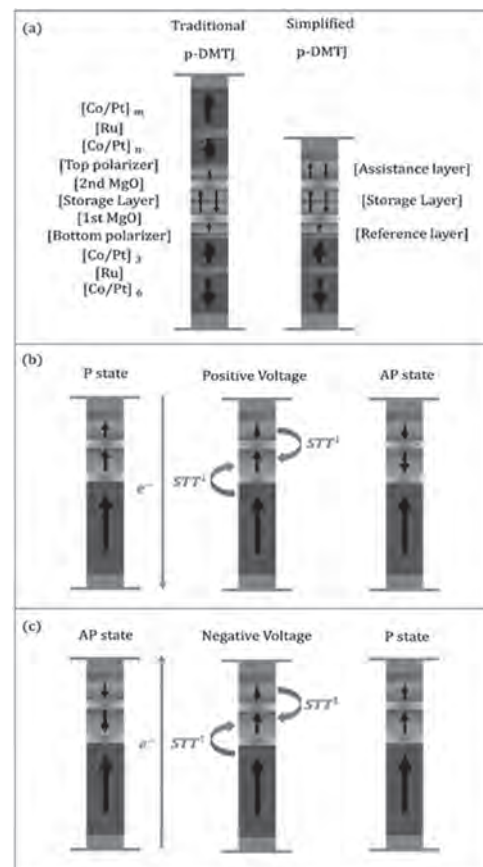


Figure 1. (a) Conventional and simplified double magnetic tunnel junctions comparison. (b) Assistance layer – Storage layer switching dynamics for P to AP states. (c) Assistance layer – Storage layer switching dynamics for AP to P states.

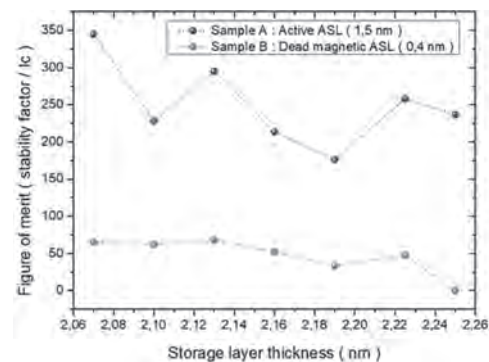


Figure 2. Figure of merit comparison (Thermal stability / Critical switching current density) between Sample A with 1.5 nm of assistance layer and sample B without assistance layer as a function of Storage layer thickness.

CF-12. Demonstration of BEOL-Compatible Double Magnetic Tunnel Junction PSTT-MRAM Devices for low Power Computing.

S. Rao¹, R. Carpenter¹, S. Couet¹, S. Van Beek¹, M. Perumkunnil¹, N. Jossart¹, B. O’ Sullivan¹, S. Kundu¹, W. Kim¹, K. Garello², L. Souriau¹, F. Yasin¹, S. Houshmand Sharifi¹, L. Goux¹, D. Crotti¹ and G.S. Kar¹

1. IMEC, Leuven, Belgium; 2. SPINtronique et Technologie des Composants, Grenoble, France

Rapid advancements in embedded memory technologies have opened the market to a wide range of low power computing applications, such as MCUs and Internet-of-Things (IoT). Innovative solutions, such as *Edge computing*, where data is stored and processed close to the application, have been proposed as a cost and energy-effective solution. STT-MRAM technology is an attractive candidate for edge computing memory owing to its high endurance ($> 10^{12}$ cycles), negligible leakage and non-volatility [1-2]. To enable adoption of eMRAM in low power applications, low active power consumption at operating frequencies ≤ 50 MHz is desirable. Reduction in the write power consumption is possible by materials engineering the free and reference layers in conventional MTJ stacks to improve switching characteristics [3, 4] and RA engineering to reduce switching voltages (V_{sw}) [3]. Unfortunately, J_{sw} improvement has often come at the cost of a lower Δ , which is unsuitable for the targeted application. An alternative approach to minimizing J_{sw} is to incorporate two reference layers (RLs) and MgO barriers on either side of the free layer (FL), also known as Double-MTJ (DMTJ) STT-MRAM [4] (Fig. 1a). A critical requirement is the anti-parallel alignment of the RLs which leads to a ‘doubling’ of the total spin torque. However, this approach suffers challenges in processing (two setting fields), TMR performance, RA control, stray field control, degraded retention times and back-end-of-line (BEOL) compatibility [5]. Thus, to demonstrate the feasibility of DMTJ STT-MRAM the following challenges must be addressed: Δ improvement, offset control ($\mu_0 H_{offset} < 0.1 * \mu_0 H_c$), read/write optimization (TMR $>100\%$, $J_{sw} < 3$ MA/cm²), and BEOL compatibility. In this work, we demonstrate device-level performance with full stray field compensation, best-in-class switching (J_{sw}) and retention (Δ) exceeding 10 years. To achieve BEOL compatibility and compensated stray fields, a 400 °C SAF-SAF design was enabled. Both the bottom-pinned and top-pinned halves of the DMTJ stack employed a synthetic antiferromagnet (SAF) design on either side of the FL. Figure 1(a, b) illustrates the stack design alongside a blanket M-H loop. The challenges involved in the design and demonstration of a 400 °C-compatible top-pinned SAF will be discussed in this work. This includes optimization of the SAF material stack design for annealing and stray field control. The successful demonstration of the SAF-SAF design is shown in the device R-H loops of CD = 80 nm devices where $\mu_0 H_{offset} \sim 0$ mT (Fig. 2a). Figure 2b shows the switching current density (J_{sw}) trends from 125 devices as a function of pulse-width. An average $J_{sw} = 2.7$ MA/cm² at 50 ns is observed on devices with $\Delta = 82$ k_BT and TMR $\sim 100\%$. In addition, WER curves demonstrating 1ppm error-free switching, and a wide switching-breakdown margin of ~ 0.7 V_{DC} will also be presented. These performance metrics clearly exhibit the importance of the SAF-SAF design in achieving manufacturable DMTJ STT-MRAM devices, thus making it ready for implementation in low power applications.

[1] K. Lee et. al, *IEEE IEDM*, pp. 2.2.1-2.2.4 (2019). [2] J. G. Alzate et. al, *IEEE IEDM*, pp. 2.4.1-2.4.4 (2019). [3] L. Thomas et. al., *IEEE IEDM*, pp 18.612-18.615 (2018) [4] G. Hu et al., *IEEE IEDM*, pp 19.38 – 19.41 (2019) [5] G. Hu et al., *IEEE IEDM*, pp. 26.3.1-26.3.4 (2015)

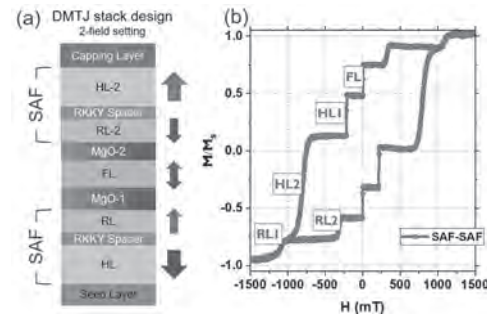


Figure 1: (a) Schematic representation of a double magnetic tunnel junction stack with the SAF-SAF design. Two magnetic field setting steps are required to enable anti-parallel alignment in the two reference layers (RL). The stack was annealed at 400 °C prior to patterning into devices of varying sizes. **(b)** Corresponding M-H loop obtained from blanket film stacks by polar MOKE measurements.

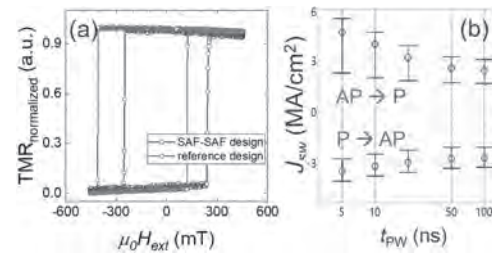


Figure 2: (a) Normalized TMR loops of 80 nm-sized devices comparing the optimized SAF-SAF stack design to the reference DMTJ stack, elucidating full compensation of stray fields. **(b)** Switching current density (J_{sw}) trends in a sample set of 125 devices (CD = 80 nm) measured as a function of pulse-width. Each device was switched 100 times in both directions.

Session CG**EXPLORATORY STT/SOT MRAM MATERIALS, DEVICES AND TECHNOLOGY**

Shunsuke Fukami, Co-Chair
Tohoku University, Sendai, Japan

Lin Xue, Co-Chair
Applied Materials Inc, Santa Clara, CA, United States

INVITED PAPER

CG-01. Ultra-Small Shape-Anisotropy Magnetic Tunnel Junctions Below 10 nm - Material, Device Engineering, and Performance INVITED.

B. Jinnai¹, J. Igarashi¹, S. Fukami¹ and H. Ohno¹
 1. Tohoku University, Sendai, Japan

Spin-transfer torque magnetoresistive random access memories (STT-MRAMs) have been successfully introduced into integrated circuits owing to their non-volatility, high endurance, high-speed operation, and scalability. Since the discovery of a perpendicular easy-axis in a CoFeB/MgO material system [1], which has become the standard material system for magnetic tunnel junction (MTJ), a core building block of STT-MRAM, MTJ scaling has been accelerated while improving device performance in data retention by engineering MTJ device structure (Table 1) [2]. Here we review the MTJ scaling technology and discuss our recent results on ultra-small shape-anisotropy MTJs. Maintaining high data-retention performance, represented by thermal stability factor Δ , is essential for nonvolatile applications. Δ is proportional to total magnetic anisotropy energy density and a volume of a nanomagnet. Hence, magnetic anisotropy energy densities arising from the bulk, interface, and shape are needed to be enhanced to achieve high thermal stability as the MTJ size is scaled. Following the first demonstration of the perpendicular MTJs using a single CoFeB/MgO interface [1], those using double CoFeB/MgO interfaces were invented to enhance the interfacial anisotropy [2], resulting in high thermal stability [2] and thereby high-performance STT-MRAMs using MTJs with tens of nm in diameter for production. Once the MTJs are scaled beyond 2X nm, however, interfacial anisotropy, which is proportional to the MTJ area, becomes insufficient to achieve high thermal stability [4]. To overcome the limitation, the MTJ using quad interfaces was proposed to further enhance interfacial anisotropy for scaling down to 1X nm [5]. Still, scaling of those interfacial-anisotropy MTJs while achieving high performance is challenging for scaling beyond 10 nm. Shape anisotropy, which negatively impacts the total magnetic anisotropy in the interfacial-anisotropy MTJs, was shown to work positively in these dimensions [6]. By making a nanomagnet cylindrical with its thickness larger than its diameter, shape anisotropy turns the easy axis to the perpendicular direction instead of the in-plane easy-axis. In this way, both interfacial and shape anisotropy positively contribute to the total magnetic anisotropy, allowing one to scale MTJs beyond 10 nm. We made the MTJs with a 15-nm-thick FeB layer and achieved the MTJ scaling down to single-digit nanometers (X nm) while maintaining high Δ , yet observing STT switching [6]. Moreover, to understand the physics governing the temperature dependence of the properties of the shape-anisotropy MTJs, we studied the scaling relationship between the energy barrier E between parallel and anti-parallel states and spontaneous magnetization with respect to the temperature and compared it with that of the conventional interfacial-anisotropy MTJs. We found that E of the shape-anisotropy MTJs is less sensitive to temperature and that the shape-anisotropy MTJs have the potential to be used for wide-temperature applications at an X-nm scale [7]. The shape-anisotropy MTJ is proved to be promising for scaling down beyond 10 nm, but several challenges in the shape-anisotropy MTJ remain: (1) switching current is needed to be further reduced at short pulse and (2) an upper limit of a nanomagnetic thickness for coherent switching exists. These challenges are arising from a large volume (thickness) of a nanomagnet meeting high Δ . To address the challenges, we recently proposed the shape-anisotropy MTJ using multilayered ferromagnets, instead of a single ferromagnet [8]. The newly proposed shape-anisotropy MTJs have multilayered ferromagnets separated by MgO layer(s) so that the total ferromagnetic layer thickness can be reduced owing to the enhancement of total interfacial anisotropy. With the multilayered ferromagnet, we showed that a 5-nm-thickness reduction is achieved while obtaining the same Δ as the single ferromagnet and that the MTJs are scaled down to 2.3 nm. In addition, we demonstrated high performance in the X-nm shape-anisotropy MTJs with the multilayered ferromagnets: (1) stable switching (Fig. 1a) and high thermal stability (Fig. 1b) at high temperatures, (2) switching efficiency

improvement (Fig. 1c), and (3) high-speed switching down to 10 ns with the voltage below 1 V (Fig. 1d). The shape-anisotropy MTJs in our studies use the CoFeB/MgO material system without introducing any new material. This means that the device structure can be readily employed in the existing MTJ technology by making a taller and smaller nanomagnet. Note that, not limited to the CoFeB/MgO material system, the concept of the shape-anisotropy MTJs can be adopted to other material systems; indeed, the concept was proved in Co or NiFe material systems [9]. Having the results and the versatility of the concept, the shape-anisotropy MTJs holds promise in the era of the ultimate scaling. This work was supported in part by JST-OPERA JPMJOP1611, JSAP KAKENHI JP19K04486 and JP19J12926, Cooperative Research Projects of RIEC, and DIARE of Tohoku University. J.I. acknowledges financial support from GP-Spin of Tohoku University and JST-OPERA.

[1] S. Ikeda *et al.*, Nat. Mater. 9, 721 (2010). [2] B. Jinnai *et al.*, Appl. Phys. Lett. 116, 160501 (2020). [3] H. Sato *et al.*, Appl. Phys. Lett. 101, 022414 (2012). [4] H. Sato *et al.*, Appl. Phys. Lett. 105, 062403 (2014). [5] K. Nishioka *et al.*, VLSI Symp., T120 (2019). [6] K. Watanabe *et al.*, Nat. Commun. 9, 663 (2018). [7] J. Igarashi *et al.*, Appl. Phys. Lett., to be published (2021). [8] B. Jinnai *et al.*, IEEE IEDM, 24.6 (2020). [9] N. Perrissin *et al.*, Nanoscale 10, 12187 (2018).

Magnetic anisotropy	Interfacial-anisotropy MTJ			Shape-anisotropy MTJ	
	Single interface <small>(Sato et al., Nat. Mater. (2012))</small>	Double interfaces <small>(Jinnai et al., APPL. (2012))</small>	Quad interfaces <small>(Nishioka et al., VLSI Symp.)</small>	Single ferromagnet <small>(Watanabe et al., Nat. Commun. (2018))</small>	Multilayered ferromagnets <small>(Jinnai et al., IEEE IEDM (2020))</small>
Bulk	-0	-0	-0	-0	-0
Interface	$\times 1$	$\times 2$	$\times 4$	$\times 2$	$\times 4, \times 6, \dots$
Shape	In-plane	In-plane	In-plane	Perpendicular	Perpendicular
Scaling to	tens nm	2X nm	1X nm	X nm	X nm

Table 1. Evolution of (Co)FeB/MgO-based MTJ structures with a perpendicular easy-axis.

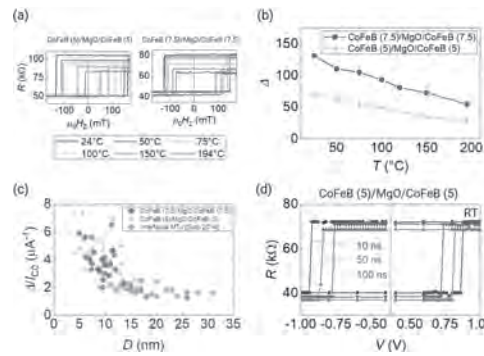


Figure 1. (a) R-H curves at various temperatures [left panel: CoFeB (5)/MgO/CoFeB (5) at $D = 7.1$ nm; right panel: CoFeB (7.5)/MgO/CoFeB (7.5) at $D = 7.6$ nm]. (b) Temperature dependence of Δ in the respective MTJs. (c) Switching efficiency Δ/I_{C0} with respect to D . (d) R-V curves at various pulse widths down to 10 ns with $D = 7.6$ nm.

CONTRIBUTED PAPERS

CG-02. Crossover of Magnetization Reversal Mode With Thickness and Diameter in Shape-Anisotropy Magnetic Tunnel Junctions.J. Igarashi¹, B. Jinnai², K. Watanabe¹, S. Fukami^{1,3} and H. Ohno^{1,3}¹. Laboratory for Nanoelectronics and Spintronics, Research Institute of Electrical Communication, Tohoku University, Sendai, Japan;². WPI Advanced Institute for Materials Research, Tohoku University,Sendai, Japan; ³. Center for Science and Innovation in Spintronics, Tohoku University, Sendai, Japan

Shape-anisotropy magnetic tunnel junction (MTJ) [1], having a cylindrical free layer, is promising for deeply scaled spin-transfer torque magnetoresistive random access memory (STT-MRAM). In shape-anisotropy MTJs, positively utilizing the shape anisotropy as well as the interfacial anisotropy allows one to reduce the MTJ diameter D below 10 nm while simultaneously keeping the thermal stability factor Δ high and capability of STT switching [1-4]. Of particular interest in the shape-anisotropy MTJs is the magnetization reversal mode, which is critical in quantifying Δ with high accuracy. In the conventional interfacial-anisotropy MTJs with such a small size ($D < 30$ nm), magnetization dynamics of the free layer can be reasonably described by a single-domain (coherent reversal) model. On the other hand, in shape-anisotropy MTJs, micromagnetic simulation in previous studies suggests that magnetization reversal mode depends not only on D but also on the thickness t ; the MTJs with too-thick a free layer ($t > \sim 30$ nm) switch incoherently, imposing an upper limit of Δ and also causing a switching delay [2,5]. In this study, we experimentally study the magnetization reversal mode in shape-anisotropy MTJs with various free layer thicknesses and diameters to reveal the crossover of coherent/incoherent reversal. A stack structure of, from the substrate side, Ta (5)/Ru (10)/Ta (15)/synthetic ferrimagnetic reference layer/MgO/(Co_{0.25}Fe_{0.75})₇₅B₂₅ ($t = 15, 30,$ and 50) /MgO/Ru (5) is deposited by dc/rf magnetron sputtering on a thermally oxidized Si substrate. The numbers in parentheses are nominal thicknesses in nm and t represents the free-layer CoFeB layer thickness. For some samples with $t = 50$ nm, Ta (5) capping layer is used instead of MgO, which is confirmed to have little impact on the findings described below. The stacks are processed into circular MTJs with various D by electron beam lithography, reactive ion etching, and multistep Ar ion milling [1]. To study the magnetization reversal mode, we evaluate astroid curves by measuring the magnetic-field-angle dependence of switching fields [6,7]. We also investigate the thickness range in which the coherent reversal model is applicable by comparing Δ values experimentally determined under an assumption of the coherent reversal and those expected from the calculation. Figure 1 shows the magnetic-field-angle dependence of a switching field in a cartesian coordinate, the so-called astroid curve, for the shape-anisotropy MTJs with t of 15 nm and 50 nm. The solid curve is the best fit based on the coherent reversal model as used in [6]. As can be seen, the fitting degree is different for each t . For $t = 15$ nm, the experimental result is well explained by the fit, indicating a coherent reversal, which is consistent with the previous result on a FeB-based shape-anisotropy MTJ with the same free-layer thickness [5]. On the other hand, for the $t = 50$ nm case, the fit is poor; the switching field along the easy-axis ($\mu_0 H_x = 0$ mT, where μ_0 is the permeability in vacuum) is smaller compared with the other angles ($|\mu_0 H_x| > 0$). Such a distortion is also seen for $t = 30$ nm with $D > \sim 15$ nm. Similar behavior was reported in a Py nanowire, and was explained by a buckling mode [9]. The similarity suggests that magnetic moments in the shape anisotropy MTJs with a thicker and larger-diameter free layer is reversed incoherently via an oscillatory buckling along the thickness direction. Next, we measure the switching probability using a pulsed magnetic field and evaluate Δ with a coherent reversal model [10]. The obtained Δ is plotted as a function of D in Fig. 2. The solid curves represent the calculation based on the coherent reversal model, where the whole volume contributes to the energy barrier. For $D < \sim 15$ nm, the measured Δ value agrees well with the calculated one, whereas $D > \sim 15$ nm is much smaller, backing up interpretation of the difference observed in the astroid-curve measurement as crossover of the magnetization reversal mode. In summary, we investigate the magnetization reversal mode and thermal stability factor in shape-an-

isotropy MTJs with various free-layer thicknesses and diameters. We reveal that the magnetization reversal in the MTJs with thicker and larger-diameter free layer proceeds incoherently, affecting the retention property. This study provides a key understanding of the magnetization reversal in the shape-anisotropy MTJs. This work was supported in part by JST-OPERA, JSPS KAKENHI (JP19J12926 and JP19K04486), and DIARE. J.I. and K.W. acknowledge financial support from GP-Spin and JST-OPERA.

[1] K. Watanabe *et al.*, Nature Commun. 9, 663 (2018). [2] N. Perrissin *et al.*, Nanoscale 10 12187 (2018). [3] J. Igarashi *et al.*, Appl. Phys. Lett., to be published (2021). [4] B. Jinnai *et al.*, IEEE IEDM, 24.6.1 (2020). [5] K. Watanabe *et al.*, International Conference on Magnetism 2018, F6-01 (2018). [6] N. Kikuchi *et al.*, IEEE Trans. Magn. 41, 3613 (2005). [7] R. Dittrich *et al.*, J. Appl. Phys. 97, 10J705 (2005). [8] J. Igarashi *et al.*, Appl. Phys. Lett. 111, 132407 (2017). [9] A. B. Oliveria *et al.*, Phys. Rev. B 78, 024423 (2008). [10] Z. Li *et al.*, Phys. Rev. B 69, 134416 (2004).

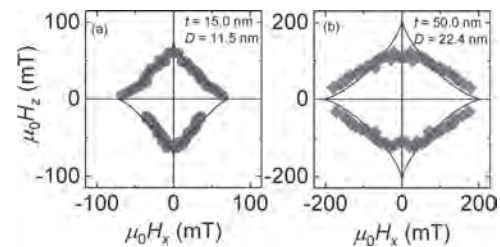


Figure 1 Experimental results of magnetic-field-angle dependence of switching field in the shape-anisotropy MTJs for the thickness of (a) 15 nm and (b) 50 nm with MgO capping layer. The lines correspond to the best fitting based on the coherent reversal model.

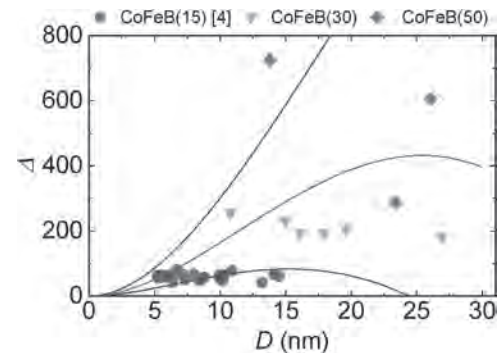


Figure 2. Thermal stability factor Δ as a function of D in the shape-anisotropy MTJs for the thickness of 15 [4], 30, and 50 nm. For the samples with $t = 50$ nm, Ta (5) capping layer is used. The curves correspond to the calculation based on the coherent reversal model.

CG-03. Magnetization Reversal Driven by Spin-Transfer-Torque in sub-20 nm Perpendicular Shape Anisotropy Magnetic Tunnel Junctions.

N. Caçoilo¹, S. Lequeux¹, A. Palomino¹, N. Strelkov¹, B. Dieny¹, R. Sousa¹, O. Fruchart¹, I.L. Prejbeanu¹ and L.D. Buda-Prejbeanu¹
 1. Univ. Grenoble Alpes, CEA, CNRS, Grenoble INP, SPINTEC, Grenoble, France

The perpendicular Spin-Transfer-Torque Magnetic Random Access Memory (p-STT-MRAM) is one of the most promising emerging non-volatile memory technologies. As these devices are limited by their thermal stability factor at technological nodes smaller than 20 nm, their downsize capability is compromised. Indeed, as the device shrinks, there is a decrease in thermal stability due to a decrease in the total interfacial perpendicular anisotropy energy proportionally to the cell area. This decrease significantly reduces the retention time of the memory [1-3]. A promising solution to this problem relies on taking advantage of the shape anisotropy of the storage layer by increasing its thickness to values larger than its diameter. The shape anisotropy becomes out-of-plane, with strength proportional to the large volume of the thick cell, bringing an additional robust and tunable source of perpendicular anisotropy on top of the interfacial perpendicular anisotropy. These two sources of anisotropy allow to extend the downsize scalability of STT-MRAM towards sub-20 nm technological nodes [4, 5]. However, the storage layer thickness also affects the writing operation of the cell and should be examined. In this work, the magnetization reversal mechanism of the PSA-STT-MRAM induced by STT was numerically studied. Micromagnetic simulations were carried out (with and without the effect of thermal fluctuations), enabling the identification of different modes of magnetization reversal in this memory. An initial study comprises pillars with aspect-ratios (AR) between 0.8 and 3, with a fixed diameter of 20 nm. It was shown that, for an AR smaller than 1, the mechanism of reversal follows a macrospin-like reversal. When increasing the AR, a non-coherent reversal develops, which evolves from a buckling-like reversal to a transverse-domain wall nucleation-propagation at higher aspect ratios. This latter mode of reversal is associated with the slowing down of the switching dynamics, an effect which worsens as the layer thickness is increased [Fig. 1]. The inverse of the switching time follows a linear relationship with the applied voltage, a law conserved when considering thermal fluctuations. This demonstrates that, even though the nucleation process is assisted by thermal fluctuations, the reversal is controlled by the STT. Changing both the diameter and the thickness but maintaining a thermal stability factor of around 80 it is observed that the minimum voltage to reverse the storage layer increases [Fig. 2]. We interpret as the weakening influence of the strong interfacial STT of tunnelling electrons. This comes along with a transition from a macrospin-like reversal to a buckling-like reversal when AR is increased, despite the thermal stability value is in the same range. This study shows the possibility to obtain a macrospin-like reversal at low applied voltages at sub-20 nm magnetic tunnel junctions. With their switching time of the order of tens of ns, these PSA-STT-MRAM are not fast-enough memories suitable for Cache application but should be functional for dense DRAM type of applications. Also, the junction Resistance x Area product must be lowered compared to conventional STT-MRAM to maintain the write voltage significantly below the barrier breakdown voltage.

[1] C. Yoshida *et al*, Jpn. J. Appl. Phys. 58, SB3B05 (2019). [2] H. Sato *et al*, Jpn. J. Appl. Phys. 58, 0802A6 (2017). [3] L. Thomas *et al*, J. Appl. Phys. 115, 172615 (2014). [4] N. Perrissin *et al*, Nanoscale 10, 12187-12195 (2018) [5] K. Watanabe *et al*, Nat. Com. 9, 663 (2018).

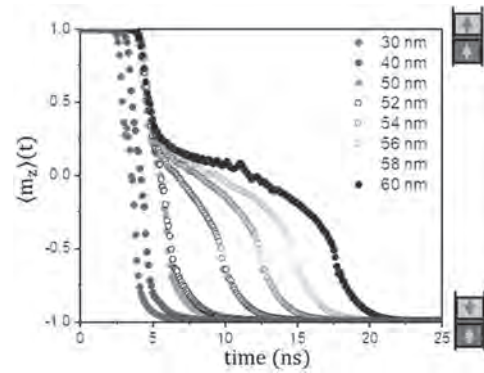


Fig 1: Time traces of the mean reduced magnetization $\langle m_z \rangle$ for different pillar thicknesses for an applied voltage of -3 V.

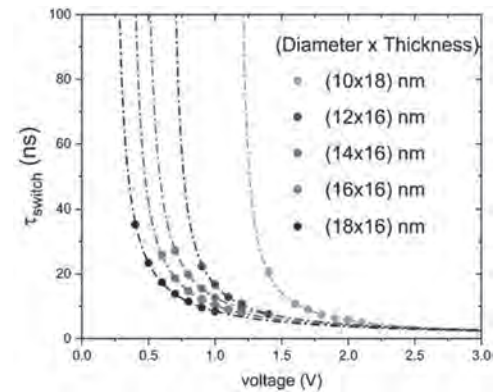


Fig 2: Voltage dependence of the time to reverse 50% of the magnetic layer (switching time - τ_{switch}) for different pillar sizes.

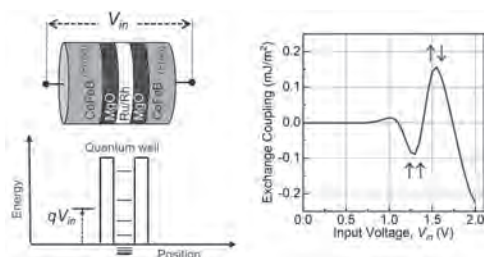
CG-04. Resonance-Enhanced Exchange Coupling for Voltage-Controlled Magnetization Switching.

S. Sayed^{1,2}, C. Hsu¹, N. Roschewsky¹, S. Yang³ and S. Salahuddin^{1,2}

1. *Electrical Engineering and Computer Sciences, University of California Berkeley, Berkeley, CA, United States*; 2. *Materials Sciences Division, E O Lawrence Berkeley National Laboratory, Berkeley, CA, United States*; 3. *IBM Almaden Research Center, San Jose, CA, United States*

Voltage-controlled magnetization switching is of great interest for high density, low energy, fast, and non-volatile memory applications. We propose a new type of two-terminal voltage-controlled magnetic tunnel junction (MTJ) that uses a resonant tunnel barrier (see figure), unlike a conventional MTJ that uses a thin oxide tunnel barrier. The resonant tunnel barrier consists of two oxide layers sandwiching a non-magnetic spacer layer known to exhibit a large interlayer exchange coupling, e.g., Ru, Rh, Ir, etc. A voltage across the structure can control the transmission coefficient between the fixed and the free magnets via the discrete energy states within the resonant tunnel barrier. A resonance-enhanced transmission coefficient leads to an interlayer exchange coupling between the two magnets, the strength of which is determined by the properties of the non-magnetic spacer material. The resonance-enhanced coupling (REC) energy exhibits a voltage-dependent oscillation in sign and the peak equivalent exchange field is strong enough to switch typical ferromagnets used in scaled magnetic memory devices. The free magnet switches to become either antiparallel or parallel to the fixed magnet, if the coupling energy sign is positive or negative, respectively. After the switching, the configuration is retained as the equilibrium interlayer exchange coupling is negligible, suppressed by the large barriers. This mechanism allows us to achieve a bidirectional switching with the same voltage polarity, unlike conventional magnetic devices, where a bidirectional current or a magnetic field is necessary. The threshold exchange coupling energy for switching is determined by only the equivalent anisotropy energy of the free magnet. Based on non-equilibrium Green's function-based calculations, we show that the device current can be significantly low at switching, in the order of $\leq 10^4$ A/cm², in a structure made with existing materials, e.g., CoFeB/MgO/Ru/MgO/CoFeB. The proposed device can provide a few fJ switching energy and ≤ 1 ns switching speed. The switching threshold is decoupled from the speed due to the conservative nature of the exerted torque, unlike the conventional spin-torque devices that exhibit a trade-off due to the nonconservative nature of the switching torque. This feature is very attractive to achieve a magnetoresistive random access memory (MRAM) technology, REC-MRAM, with a significantly low energy-delay product. The magnetization state of the free magnet can be read out with magnetoresistance of the two-terminal device, which is $\sim 30\%$ for the materials combination under consideration. In this new mechanism, the magnetoresistance is higher for smaller voltages, while the exchange field is higher for larger voltages—this is promising for efficient read and write operations in potential memory applications. This work is in part supported by ASCENT, one of six centers in JUMP, a SRC program sponsored by DARPA and in part by the Center for Energy Efficient Electronics Science (E3S), NSF Award 0939514.

[1] S. Sayed et al., Phys. Rev. Applied 14, 034070, 2020.



A new kind of magnetic tunnel junction with a resonant tunnel barrier. A voltage across the structure can tune the transmission coefficient, which in turn induces a large oscillatory interlayer exchange coupling that can switch the free layer in both directions depending on the coupling energy sign.

CG-05. Magnetic Reversal and Critical Current Transparency of CoFeB Superconductor-Ferromagnet-Superconductor Heterostructures.

M. Loving¹, T. Ambrose¹, E. Din¹, S. Keebaugh¹, D. Miller¹, R. Pownall¹, N. Rizzo¹, A. Sidorov¹ and N. Siwak¹
 1. Northrop Grumman Mission Systems, Linthicum, MD, United States

The rising demand for high efficiency computing has driven development pursuits to identify a “beyond-CMOS” dimensionally scalable logic technology. Superconducting technologies (such as reciprocal quantum logic) offer a solution to this growing challenge; however, these systems require a compatible low temperature memory solution that is power efficient, dense, and fast. To meet this need, Josephson magnetic random access memory (JM RAM) is being pursued. [1-4] In its simplest form, JM RAM combines superconducting electrodes (S) with a ferromagnetic (F) spin valve to form magnetic barrier Josephson Junctions (MJJs). JM RAM optimization requires that magnetic layers exhibit single domain switching with abrupt magnetization reversal and low switching fields, at cryogenic temperatures. JM RAM requirements are further complicated as materials selection and thicknesses must allow MJJs to carry a sufficient critical current (I_c), consistent with low error rate operation, at 4K. In this work, we show fundamental low temperature (T) magnetic and I_c responses of a model S/F/S system – Nb/CoFeB/Nb – and relate this to roughness effects that arise in ultra-thin film systems. Ultra-thin CoFeB films (6-13 Å) deposited onto 1500 Å Nb/50 Å Cu and 1500 Å Nb/ML (ML = (10 Å Cu/5 Å Nb)₆/10 Å Cu) and capped with 50 Å Cu/500 Å Nb have been examined structurally, magnetically and electrically. Prior work has shown improved magnetic switching and decreased surface roughness with the incorporation of the ML structure as a buffer under the ferromagnetic layer. [4] The film thicknesses and amorphous structure were confirmed with x-ray reflectivity and diffraction. The magnetic character was probed at 300 K and compared to the 10 K response. MJJ I_c was measured at 4 K. Here, CoFeB films exhibit low reversal fields at 300 K (Fig 1a), analogous to MRAM devices that utilize CoFeB as a soft ferromagnet with a M_s value ~ 1525kA/m. Patterned films, measured at 10 K, show an expansion of the magnetic hysteresis (Fig 1b). Incorporation of the ML buffer shows reduced coercivity (Fig. 1a, T = 300 K) and improved squareness (Fig. 1b, T = 10 K). In electrical devices, the I_c through the CoFeB layer decays exponentially with increasing CoFeB thickness and shows a dip in I_c at 8 Å (Fig 2), characteristic of a change in the equilibrium Josephson phase in an S/F/S structure, the “0 – π ” thickness. While the ultimate objective of these efforts is to achieve a cryogenic memory solution, the work described here probes the fundamental properties of low T magnetics and S/F/S character of a candidate material for this emerging technology.

[1] IM Dayton, MG Loving et al. “Experimental Demonstration of a Josephson Magnetic Memory Cell With a Programmable pi-Junction” IEEE Magnetics Letters 9, 1 (2018) [2] A. Herr and Q. Herr “Josephson Magnetic Random Access Memory System and Method”. US Patent US20110267878 A1, 30 April 2010. [3] MG Loving, TF Ambrose, Ferrimagnetic/ferromagnetic exchange bilayers for use as a fixed magnetic layer in a superconducting-based memory device, US Patent App. 16/256,547, 2020 [4] TF Ambrose, MG Loving, Repeating alternating multilayer buffer layer, US Patent No: 10879447 B2, 29 December 2020

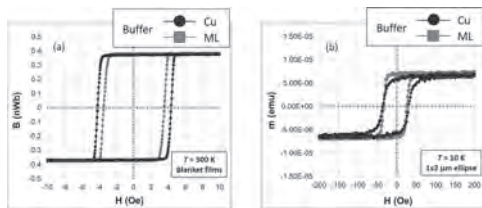


Fig 1: Comparison of a) room temperature (T = 300 K) blanket film measurements and b) low temperature (T = 10 K) patterned array magnetic switching. Both data sets show improved magnetic performance with the ML buffer.

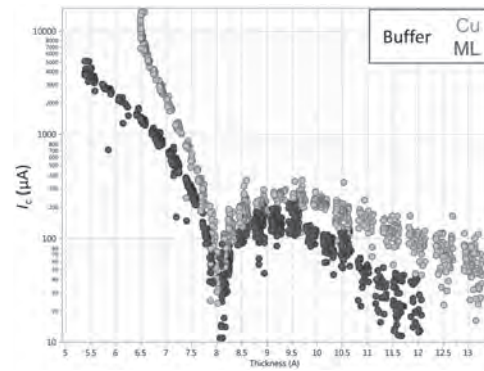


Fig. 2: Comparison of the buffer layer impact on I_c vs. CoFeB thickness, in Angstroms

CG-06. Current-Induced Crystallisation in Heusler Alloy Films.

W. Frost¹, K. Elphick¹, M. Samiepour¹ and A. Hirohata¹

¹ University of York, York, United Kingdom

The current information technology has been relied on von Neumann type computation [1]. In order to manage the recent digital universe and big data, it is essential to investigate alternative technologies to sustain the development in computation. Among them, neuromorphic computation has been attracting intensive studies using the current complementary metal oxide semiconductor (CMOS) architecture and beyond in the last decade to mimic the functionality and operation of a synapse in a brain. A promising synapses operation has been demonstrated via the stochastic operation of a magnetic tunnel junction (MTJ) [2]. However another important feature of a synapse, memory potentiation, has been overlooked to date. In this study we have demonstrated memory functionality via current-induced annealing in a giant magnetoresistive (GMR) junction with ferromagnetic Heusler alloy films. A GMR junction consisting of Cr (3)/W (10)/Co₂FeAl_{0.5}Si_{0.5} (CFAS) (10)/Ag (3)/CFAS (2.5)/Ru (3) (thickness in nm) was fabricated as an artificial synapse with achieving a low resistance-area product for low power consumption. Here we recently reported the reduction in the crystallisation temperature by promoting layer-by-layer growth on a (110) surface [3], of which is comparable with Joule heating induced by a controlled current introduction. The multilayered stack was grown on a thermally oxidised Si substrate using a high target utilisation sputtering system (PlasmaQuest, HiTUS) at room temperature. The stack was patterned into a nanopillar junction using a combination of electron-beam lithography and Ar-ion milling. The seed layer, Cr/W, was patterned into a bottom electrode with a width of 100-200 nm. Just above the bottom Heusler-alloy layer was patterned into a nanopillar with a diameter between 80 and 200 nm, followed by the patterning of a top electrode with Ti/Au. The fabricated nanopillars were measured using a probe station (HiSOL, HMP-400 SMS) with a conventional four-terminal method with a constant current source (Keithley, 2400) and a nanovoltmeter (Keithley, 2182a). The resistance changes were measured after a series of current pulse applications of 500 μ A up to 5 mA for 100 μ s up to 500 μ s. Little change was observed at 500 μ A, which was used for GMR measurements, while monotonic resistance change was measured above 1 mA with the repetition of 100 μ s pulse introduction, confirming the current-induced crystallisation of CFAS(110) and the associated change in the resistivity. The Heusler-alloy crystallisation was then observed using transmission electron microscope (TEM; JEOL, JEM-2200FS) by thinning with focused ion beam (FIB, FEI, Nova 200 Dual Beam). The crystallinity of the CoFeAl_{0.5}Si_{0.5} has been confirmed using nanobeam, which shows some CFAS(220) diffraction spots within polycrystalline ring feature. TEM imaging confirmed CFAS was partially crystallised with maintaining a smooth interface of < 1 nm roughness in the GMR junction. Due to the nature of a simple electrical current introduction employed in this study, the GMR junction does not require post-annealing processes but it can stores the operation cycle permanently as the change in the resistivity. Hence such current-induced crystallisation can be used in a neuromorphic node network, which can revolutionalise solid state memory.

[1] B. V. Benjamin, P. Gao, E. McQuinn, S. Choudhary, A. R. Chandrasekaran, J.-M. Bussat, R. Alvarez-Icaza, J. V. Arthur, P. A. Merolla and K. Boahen, K. Neurogrid *Proc. IEEE*, vol. 102, p. 699 (2014). [2] J. Grollier, D. Querlioz, and M. D. Stiles, *Proc. IEEE*, vol. 104, p. 2024 (2016). [3] J. Sagar, L. R. Fleet, M. Walsh, L. Lari, E. D. Boyes, O. Whear, T. Huminiuc, A. Vick and A. Hirohata, *Appl. Phys. Lett.*, vol. 105, p. 032401 (2014).

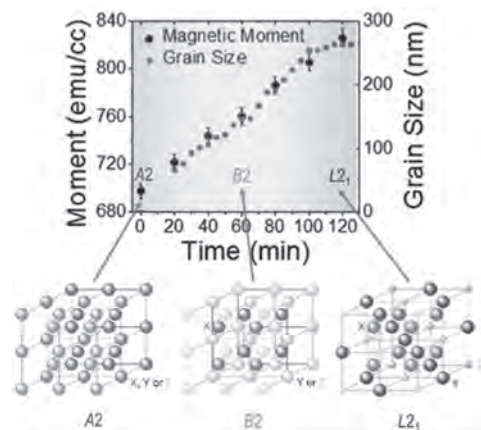


Fig. 1 Evolution of magnetic moment and grain size of the Heusler alloy films and their corresponding crystalline structures.

INVITED PAPER

CG-07. Advanced MTJ and SOT Technology for AI and Automobile Applications INVITED.

T. Endoh^{1,2}

1. Center for Innovative Integrated Electronic Systems, Tohoku University, Sendai, Japan; 2. Graduate School of Engineering, Tohoku University, Sendai, Japan

Introduction: Double CoFeB/MgO interface perpendicular MTJ has become the de facto standard technology of current STT-MRAM. However, there are still issues for high density memory application and high reliable application including Automobile applications. Furthermore, achievement of high speed and high endurance features, in the other words, high speed SRAM replacement is still challenging for STT-MRAM, because of its tradeoff relationship among the retention, endurance, and operational speed. Recently, Spin Orbit Torque (SOT) devices have been intensively researched and developed because SOT devices have the potential to achieve high speed and high endurance. To realize the practical use of SOT-MRAM for LSI applications, these issues must be addressed. This invited paper reviews our recent progresses in STT-MRAM, SOT-MRAM and Nonvolatile AI processors with CMOS/MTJ hybrid technology. The STT-MRAM and SOT-MRAM as NV working memory and AI processors as these applications are particularly suitable for future IoT / AI systems that require ultra-low-power and high-performance computing at the same time. 128Mb STT-MRAM and Quad interface MTJ technology: We developed novel damage control integration process technologies including new low-damage MgO deposition process, low-damage RIE process, and low temperature SiN-cap process. By applying the developed damage control integration process technologies to double interface p-MTJ fabrication, TMR ratio, thermal stability factor, and switching efficiency of Double p-MTJ were successfully improved. Moreover, it was shown that despite the significant increase in thermal stability factor, the endurance of the fabricated Double p MTJs was over 1010. Finally, with our double-interface p-MTJ technology and novel damage control integration process technologies, fabricated 128Mb STT-MRAMs successfully achieved 14ns/7ns write speed at V_{dd} of 1.2V/1.8V, respectively. Next, for further scaling of STT-MRAM, we proposed novel Quad-interface p-MTJ technology which brings forth an increase of thermal stability factor compared with conventional Double-interface p-MTJ technology. We successfully fabricated the quad-interface MTJ using 300mm process based on the damage control integration process. The fabricated Quad p-MTJs achieved an enhancement of switching efficiency in addition to an approximately two times larger thermal stability factor without degradation of TMR ratio. The developed Quad p-MTJ technology will become an essential technology for the scaling of the STT-MRAM beyond 20nm without changing material and process sets from mass-production STT-MRAM. Moreover, the high reliable Quad p-MTJ technology with enough thermal stability factor is suitable for Automobile applications that require high temperature operation such as 150°C. Field-free canted SOT-Device with 350ps write speed and its SOT-MRAM: To realize practical use of SOT-MRAM for LSI applications, we demonstrated 55 nm-CMOS/SOT-device hybrid MRAM cell with magnetic field free writing for the first time. For field free writing, we developed canted SOT device under 300 mm BEOL process with 400°C thermal tolerance. In addition, we developed its advanced process as follows; PVD process of SOT channel layer for high spin Hall angle under 400°C thermal tolerance, low damage RIE technology for high TMR/thermal stability factor, and ultra-smooth surface metal via process under SOT device to reduce contact resistance. By using the developed technologies, our canted SOT devices achieved fast write speed of 0.35 ns without magnetic field, an enough thermal stability factor of 70 for non-volatile memory (over 10 years retention), and a high TMR ratio of 167%, simultaneously. Moreover, we fabricated a field free canted SOT-MRAM cell with 55 nm CMOS technology and demonstrated its write/read performance. These technologies will open to high speed write non-volatile memory such as 1 level cache application of many kinds of application processors. CMOS/MTJ hybrid AI Processor for low power application: Focusing on the indispensable nearest

neighbor search (NNS) function of the brain, we developed a nonvolatile object recognition processor with NSS full-adaptive to any data format, employing nonvolatile memories base on our p-MTJ. The developed object recognition processor was fabricated under 90nm-CMOS/70nm-MTJ hybrid process on 300mm-wafer. The 4-Transistors & 2-MTJs type memory cells were adopted to completely eliminate standby power. Moreover, we successfully developed a self-directed power-gating technique leveraging the non-volatility, high access speed and unlimited endurance features of the p-MTJs. This developed self directed power-gating technique was employed to shut down idle circuit blocks during not only the standby periods but also the full operation periods. The measured peak operation power consumption of the prototype chip was only 130μW and can be further optimized corresponding to the format of reference data. Compared to the latest conventional researches, the significant improvements of both power performance (about 2-3 order reduction) and circuit density (about 2 order improvement) were achieved.

[1] S. Ikeda et al., Nat. Mater. 9, 721 (2010). [2] T. Endoh et al., 2011 International Electron Device Meeting (IEDM), 2011. 34 [3] H. Sato et al., Appl. Phys. Lett. 101, 022414 (2014). [4] T. Saito et al., IEEE T-Magn. 54, 3400505 (2018). [5] H. Sato et al., IEDM 2018, p. 608. [6] K. Lee et al., IEDM 2018, p. 604. [7] Y. J. Song et al., IEDM 2018, p. 416. [8] C. Park et al., VLSI 2018, p. 185. [9] O. Golonzka et al., IEDM 2018, p. 412. [10] C. Park et al., VLSI 2018, p. 185. [11] T. Endoh, IEEE ISPASS2018. (Invited) [12] K. Nishioka et al., VLSI 2019, T11-4; IEEE T-ED 67, 995 (2020). [13] S. Fukami et al., VLSI 2016, T61. 10 [14] H. Honjo et al, IEDM 2019, 28.5.1. [15] T. Endoh, MRAM Development Day 2019 (Invited) [16] T. Endoh, 2020 International Solid-State Circuits Conference (ISSCC) (Invited) [17] T. Endoh et al, VLSI Symp. 2020 (Invited) [18] T. Endoh, Tutorial of IEDM2020 (Invited)

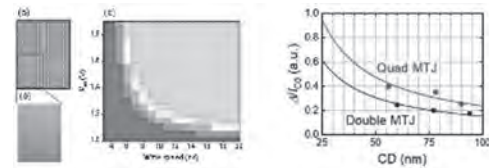


Fig. 1: (a) developed 128Mb STT-MRAM. (b) photograph of its subarray. (c) Shmoo plot of subarray in 128Mb STT-MRAM. (d) Switching efficiency as a function of CD for the Quad- and Double-interface MTJs.

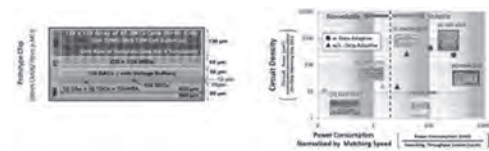


Fig. 2: (a) Developed AI object recognition processor with 90nm-CMOS/70nm-MTJ. (b) Further performance comparisons of the operation power efficiency and circuit density.

CONTRIBUTED PAPERS

CG-08. Effect of Insertion Layer on Reducing Switching Current Density in Spin-Orbit Torque Magnetic Tunnel Junction.

L. Huang¹, J. Lourebam¹, D.M. Repaka¹, J. Qiu¹, S. Yap¹, Y. Toh¹ and S. Lim¹

1. Institute of Materials Research and Engineering, Singapore, Singapore

As the crucial device element for next-generation cache and edge computing technologies, the magnetic tunnel junction (MTJ) has been widely studied with recent focus towards using spin-orbit torque (SOT) to switch the free layer magnetization. Writing the MTJ using SOT approach is attractive, because it can increase the junction endurance as switching current path does not go through the tunneling barrier. In this work, we aim to enhance the SOT switching efficiency in the MTJ through various interlayer insertion designs in the free layer. Our study is carried out using in-plane MTJ (IP-MTJ), which has been demonstrated that no external magnetic field is required for SOT switching [1]. We fabricated W underlayer-based IP-MTJs, and investigate how the insertion layer between the W and CoFeB free layer affects the switching current density of the MTJ. Interestingly, with the insertion of ultra-thin layers such as MgO, Ru and TiW, the switching current drops significantly with the MgO insertion offering ~70% of reduction. Here, standalone 3-terminal IP-MTJ devices of elliptical sizes 300 nm x 600 nm are fabricated using Canon X5 stepper lithography on 8 inch Si wafers. We measure the pulse current switching loops with our home-built probe station [2]. Without insertion layer, the switching current is ~11.9 mA, equivalent to $\sim 1.9 \times 10^{11}$ A/cm². The large value of switching current density is because of the dramatic reduction in the spin Hall angle (SHA) of W underlayer after annealing at 330°C, which also leads to a structural phase change to α -W. While the introduction of an insertion layer universally reduces the current density. The MgO interlayer reduces it by more than 3 times making it superior for insertion layer selection. To understand it better, we performed spin-torque ferromagnetic resonance (ST-FMR) measurement [3] to determine the damping constant, spin Hall angle, and effective saturation magnetization ($M_{s, \text{eff}}$). A representative example of ST-FMR spectra for MgO insertion layer is shown in Fig. 1. We found the thin insertion layer has little influence on the damping constant, but some modifications in $M_{s, \text{eff}}$ and SHA are found, which can be correlated with the switching current reduction results. Further investigations on the role of insertion layer thickness are ongoing and are expected to reveal the optimal insertion layer for SOT current reduction.

[1] L. Liu, C.F. Pai, Y. Li *et al.*, Science, Vol. 336, p.555 (2012) [2] J. Lourebam, J. Huang, S.T. Lim *et al.*, AIP Adv., Vol. 8, p.055915 (2017) [3] L.S. Huang, S.K. He, Q.J. Yap *et al.*, Appl. Phys. Lett., Vol. 113, p.022404 (2018)

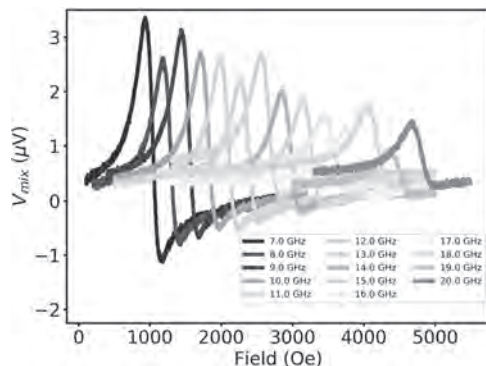


Fig. 1 Field sweep ST-FMR spectra of W/MgO/CoFeB/MgO film. The RF frequency varies from 7 to 20 GHz.

CG-09. Spin Orbit Torque Driven Multi-Level Switching in He⁺ Irradiated W-CoFeB-MgO Hall Bars With Perpendicular Anisotropy.

X. Zhao^{1,2}, M. Sall³, J. Langer⁴, B. Ocker⁴, G. Jakob⁵, M. Klau⁵, W. Zhao¹ and D. Ravelosona^{2,3}

1. Beihang University, Beijing, China; 2. Centre National de la Recherche Scientifique, Paris, France; 3. Spin-Ion Technologies, Palaiseau, France; 4. Singulus, Kahl am Main, Germany; 5. Johannes Gutenberg Universitat Mainz, Mainz, Germany

Spin-orbit torque (SOT) induced magnetic switching has attracted an extensive interest due to its potential high efficiency in terms of switching time and power consumption [1]. Chiral domain wall (DW) motion driven by SOT in nanowires in the presence of Dzyaloshinskii–Moriya Interaction (DMI) at interfaces between HM and FM layers has shown a great potential for applications to racetrack memory devices [2]. One potential advantage of DW driven switching is that multi-level states can be obtained by controlling the position of the DW across a nanostructure such as wires or dots. As such, domain wall Memristors and the possibility to use DWs motion as synapses [3] have been recently demonstrated. Here, we study SOT driven multi-level states in Hall bars based on W-CoFeB-MgO structures by reducing locally the perpendicular magnetic anisotropy through He⁺ ion irradiation across a mask [4]. The structure of the investigated samples is W (4 nm)/Co₂₀Fe₆₀B₂₀ (0.6 nm)/MgO (2 nm)/Ta (3 nm). The films were then patterned into Hall bars consisting in 20 μm wide and 140 μm long wires including 2 Hall crosses with 5 μm wide pads. As shown in previous studies [6], light He⁺ ion irradiation induced interface intermixing can be used to finely tune M_s, interface anisotropy and DMI in CoFeB-MgO structures. One of the Hall cross was then subsequently irradiated through a mask by He⁺ ions with an energy of 15 keV at a fluence of 1×10¹⁹ ions/m² to reduce locally the perpendicular anisotropy K_{eff}. Anomalous Hall Effect measurements combined with Kerr microscopy indicate that the SOT switching process is dominated by domain wall nucleation in the irradiated region followed by rapid domain propagation to switch the irradiated area (figure 1). The reduction of K_{eff} by 20% under ion irradiation is accompanied by a large reduction of the switching current from 4.07 to 1.68 MA/cm² under an in-plane 50 mT field; The switching current is determined by the threshold current to induce DW nucleation as checked by Kerr microscopy. As K_{eff} is lowered in the irradiated Hall bar, the energy barrier to induce DW nucleation by SOT is also reduced. Due to the strong pinning of the DW at the transition between the irradiated and the non-irradiated region as evidenced by Kerr microscopy, we observe an intermediate Hall resistance state between the 2 saturated states (Figure 2). The possibility to increase the number of intermediate states by designing different value of perpendicular anisotropy through He⁺ ion irradiation paves the way towards efficient neuromorphic and memristor devices where the nucleation, motion and pinning can be tailored.

- [1] M. Cubukcu, et al, IEEE Transactions on Magnetics 54, 9300204 (2018)
- [2] K. S. Ryu et al, Nat. Nanotechnol. 8, 527 (2013) [3] S. Lequeux, et al, Scientific Reports 6, 31510 (2016) [4] X.Zhao, Appl. Phys. Lett 116, 242401 (2020)

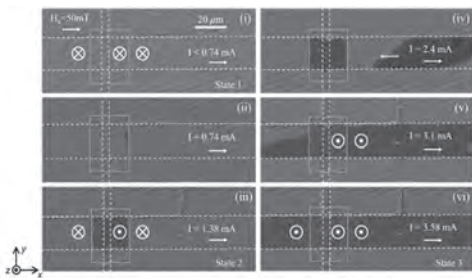


Figure 1. Kerr images showing the SOT induced magnetization switching process of the Hall bar for an increasing current under a 50 mT in-plane magnetic field. The white dashed lines indicate the longitudinal wire and the transverse Hall voltage pads. The gray box corresponds to the irradiated area. The yellow arrow in (iv) shows the direction of domain wall motion.

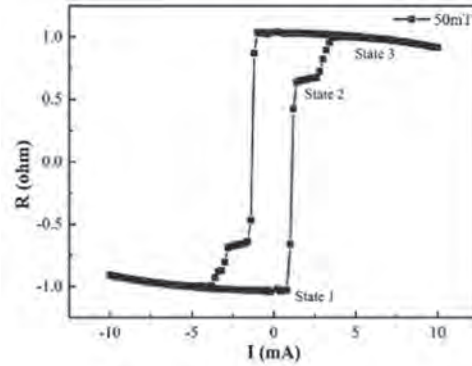


Figure 2. SOT switching curve for an irradiated Hall cross measured under 50 mT. States 1, 2, 3 correspond to down magnetization, intermediate state and up magnetization respectively

CG-10. All-Electrical Manipulation of Magnetization in Magnetic Tunnel Junction via Spin–Orbit Torque.

W. Kong¹, C. Wan¹, X. Wang¹ and X. Han¹

1. Chinese Academy of Sciences Institute of Physics, Beijing, China

In the last decade, spin-orbit torque (SOT) [1-3] has enabled us to electrically control spins of magnetic materials, which provides an idea manner to develop magnetic random-access memory (SOT-MRAM). One crucial step toward the SOT-MRAM is realization of magnetic tunnel junctions (MTJ) whose magnetic states can be switched by SOT at zero applied field. In our previous paper [4], we have realized field-free SOT switching of a perpendicular CoFeB film which coupled with another CoFeB film with in-plane magnetization via a Ta spacer. This structure composed by the perpendicular CoFeB, the in-plane CoFeB and the spacer Ta is entitled as the “T-Type” magnetic structure. Here, by using an in-plane CoFeB/Ta/perpendicular CoFeB T-type magnetic structure as a free layer, we have realized a MTJ switchable by SOT at the field-free condition (Fig. 1) [5]. The spacer layer Ta plays three roles. Besides of absorbing the B element during annealing process to improve TMR ratio, it also mediates exchange coupling and finally generates large enough SOT to drive sharp switching between the parallel and antiparallel states of the MTJ without any applied fields. This work could provide a useful stack with the T-type structure to realize field-free SOT-MRAM or logic devices.

[1] I. M. Miron, K. Garello, G. Gaudin, P.-J. Zermatten, M. V. Costache, S. Auffret, S. Bandiera, B. Rodmacq, A. Schuhl, and P. Gambardella, *Nature*, 476, 189 (2011). [2] L. Liu, C. F. Pai, Y. Li, H. W. Tseng, D. C. Ralph, and R. A. Buhrman, *Science*, 336, 555–558 (2012) [3] L. Liu, O. J. Lee, T. J. Gudmundsen, D. C. Ralph, and R. A. Buhrman, *Phys. Rev. Lett.* 109, 096602 (2012) [4] W. J. Kong, C. H. Wan, X. Wang, B. S. Tao, L. Huang, C. Fang, C. Y. Guo, Y. Guang, M. Irfan, and X. F. Han, *Nat. Commun.* 10, 233 (2019) [5] W. J. Kong, C. H. Wan, C. Y. Guo, C. Fang, B. S. Tao, X. Wang, and X. F. Han, *Appl. Phys. Lett.* 116, 162401 (2020).

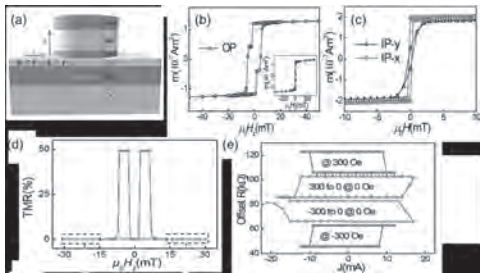


Fig.1 (a) Schematics of a MTJ with the T-type magnetic structure as its synthetic free layer. (b) Out-of-plane and (c) in-plane hysteresis loops of the stack Sub//Ta(8)/Co₄₀Fe₄₀B₂₀(2)/Ta(1.3)/Co₄₀Fe₄₀B₂₀(0.6)/MgO(2.5)/Co₄₀Fe₄₀B₂₀(1.2)/Ta(5)/Ru(5 nm) to show a perpendicular layer and an in-plane layer in it. (d) The TMR ratio as a function of the H_z field and (e) Current-driven magnetization switching at +/-300 Oe and 0 field. The switching direction at zero field depends on the history of reducing field.

CG-11. Evaluation of Read Disturbance Reduction Effect by SOT-MRAM Bi-Directional Read on Device Size Dependence.

Y. Kishi¹, A. Yamada¹, M. Ke¹ and T. Kawahara¹

1. Department of Electrical Engineering, Faculty of Engineering, Tokyo University of Science, Shinjuku-ku, Japan

Spin-orbit torque magnetic RAM (SOT-MRAM) is affected by read disturbances due to spin current in the heavy metal layer that arises from spin-orbit interaction at the time of reading [1]. To resolve this issue, we have proposed a stabilized structure with a bi-directional read path, based on the idea that spin currents flowing in opposite directions on either side of the heavy metal layer cancel each other's effects, that improves the read reliability of SOT-MRAM. We have already reported that this structure reduces the read disturbance [2]. In this study, we evaluated the movement of the magnetization of the free layer at the time of reading in a bi-directional read SOT-MRAM by using an LLG simulator. It was found that the read disturbance caused by SOT is removed in the free layer, as shown in Fig. 1 (a). In other words, the spin currents generated in opposite directions in the heavy metal layer directly affect the magnetization of the free layer, and the free layer functions as if it were two ferromagnets, whose balanced magnetizations cancel the read disturbance. To clarify this mechanism, Fig. 1 (b) shows the simulated magnetization for only the free layer at extremely large currents. The free layer is a ferromagnet magnetized in two opposite directions due to the central vortex magnetization, and the magnetization does not reverse to either side. (That is, it is not a mechanism in which the spin currents cancel themselves in both directions in the heavy metal layer.) Toward the realization of this bidirectional read SOT-MRAM structure, we evaluated the effect on the read disturbance of the size of the direction in which current flows through the heavy metal layer of an SOT structure. The device structure had a magnetic tunnel junction (MTJ) with two ferromagnets (cobalt), in which a pinned layer with a thickness of 3.5 nm and a free layer with a thickness of 1.5 nm sandwiched an insulating layer with a thickness of 1.0 nm, and a heavy metal layer (tungsten) with a thickness of 2.0 nm under the free layer. The magnetization of the two ferromagnetic layers directed toward the short side direction of the device, and the current passed from the pinned layer to both ends in the long side direction of the heavy metal layer. The width in the short side direction was uniformly 30 nm, and there were four device widths for the long side direction, i.e., 30 nm, 60 nm, 120 nm, and 180 nm. We evaluated the magnetization reversal probability of a conventional SOT-MRAM structure and the stabilized SOT-MRAM structure for a read time of 5 ns. Fig. 2 shows that the stabilized SOT-MRAM was about 6 to 10 times more effective than the conventional structure. In the conventional SOT-MRAM, the threshold current was proportional to the width of the device, whereas in the stabilized SOT-MRAM, the threshold current decreased as the width of device increased. The magnetization reversal of the conventional SOT-MRAM was strongly affected by the SOT disturbance due to the spin Hall effect, and the difference in thermal stability depending on the device size also had an influence. On the other hand, in the stabilized SOT-MRAM, the disturbance was canceled out at the free layer and only spin transfer torque in MTJ affected the magnetization reversal. Thus, we expected that the relationship between thermal stability and device size would have a large effect on magnetization reversal, but the result was contrary to that. These results indicate that the force exerted by the spin Hall effect on the magnetization of the free layer is relatively large and easy to act when the device is small. Therefore, a small device of the conventional SOT-MRAM tend to easily occur magnetization reversal, whereas in a smaller device of the stabilized SOT-MRAM, the effect on the magnetization of the free layer is strong enough to cancel the SOT disturbance and the magnetization reversal becomes more difficult. Acknowledgments This work was partly supported by a Grant-in-Aid for Scientific Research (19K04536) from Japan Society for the Promotion of Science.

[1] H. Kazama and T. Kawahara, "Spin-Orbit Torque MRAM Read Reliability", 2017 IEEE International Magnetism Conference (Intermag2017), DOI: 10.1109/INTMAG.2017.8007571, 2017. [2] Y. Kishi, K. Tabata, M. Ke, and T. Kawahara, "Evaluation of Read Disturbance Reduction Effect by Bi-directional Read on Ferromagnetic Material Properties of SOT-MRAM",

ABSTRACT of IEEE/AIP 2020 Magnetism and Magnetic Materials Conference (MMM2020), O2-14, pp.434-435, 2020.

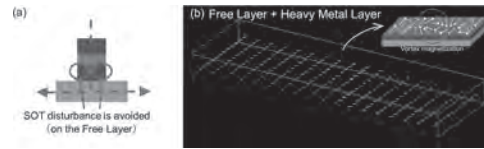


Fig. 1 (a) Stabilized structure (bi-directional read) of SOT-MRAM device [1]. The blue arrows indicate the current directions. Two red circles in the free layer canceled the SOT disturbance. (b) Example of simulation results showing the movement of the magnetization in the free layer of the stabilized structure. We simulated with a two-layer structure consisting of a free layer and a heavy metal layer. A vortex magnetization is created in the middle, dividing the free layer. The two split ferromagnets are magnetized in opposite directions.

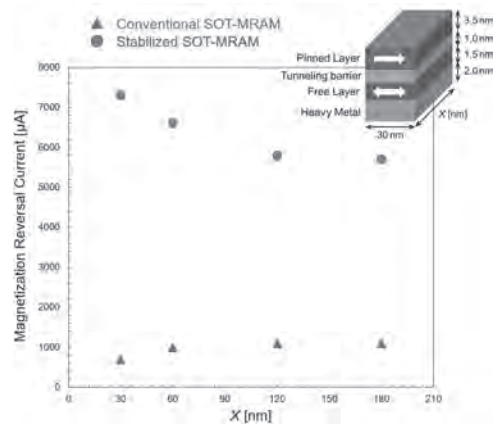


Fig. 2 Comparison of conventional and stabilized (bi-directional read) SOT-MRAM threshold currents for different X sizes of SOT structure for a read times of 5ns. In the SOT structure, two ferromagnetic layers (cobalt) sandwich an insulator, and a heavy metal layer (tungsten) is under the free layer; the current flows from the pinned layer to the long side of the heavy metal layer. The magnetization of the ferromagnetic layers are basically in the short-side direction, but the magnetization of the free layer is in any direction.

CG-12. Multi-bit Spin-Orbit Torque Device for High Density MRAM.

R. Mishra^{1,3}, T. Kim², J. Park² and H. Yang³

1. Centre for Applied Research in Electronics, Indian Institute of Technology Delhi, New Delhi, India; 2. Department of Electrical Engineering, Korea University, Seoul, Korea (the Democratic People's Republic of); 3. Department of Electrical and Computer Engineering, National University of Singapore, Singapore

Spin-orbit torque (SOT) devices¹ are promising candidates for the future magnetic memory landscape as they promise a low read disturbance, high endurance and low read error, in comparison to the spin-transfer torque devices. However, SOT memories are area intensive due to the requirement of two access transistors per bit². Here, we report a SOT memory cell which has multiple bits sharing a common write channel. This enables twice the memory density compared to the conventional SOT-MRAM design. The shared write channel (SWC) design is shown in Fig. 1. Multiple bits share a common write path thereby reducing the need for two access transistors for every bit. With a single pulse of current, different combination of digital information can be written on all the bits on the shared path. SPICE circuit simulations were performed and the area per bit of the 32x32 SWC memory is found to be 0.0414 μm^2 while that of the normal 2 transistor (T)-SOT memory is around 93% larger at 0.0801 mm^2 . However, an essential design requirement for SWC memory is programmable SOT device for which the direction of SOT can be toggled dynamically. With different polarities of SOTs for individual bits on a shared path, information such as '0101..' and '1001..' can be written. A SWC device with 2-bits is demonstrated using a Pt/Co device with a GdO_x gate oxide (Fig. 2(a)). The direction/polarity of SOT in such a device can be toggled by modulating the oxygen content at the Pt/Co interface^{3,4}. This can be achieved by the application of gate voltage through the GdO_x gate. As shown in Fig. 2(b), the multi-bit device can be programmed in different states so that all combination of digital information can be written using an unidirectional current pulse. Our prototype device paves a way towards a high density SOT MRAM architecture.

1. I. Mihai Miron, G. Gaudin, S. Auffret, et al. *Nature Materials* Vol. 9, p. 230 (2010). 2. R. Bishnoi, M. Ebrahimi, F. Oboril et al. in 2014 19th Asia and South Pacific Design Automation Conference (ASP-DAC) p. 700 (2014). 3. R. Mishra, F. Mahfouzi, D. Kumar et al. *Nature Communications* Vol. 10, p. 248 (2019). 4. X. Qiu, K. Narayanapillai, Y. Wu, et al. Spin-orbit-torque engineering via oxygen manipulation. *Nature Nanotechnology* Vol. 10, p. 333 (2015).

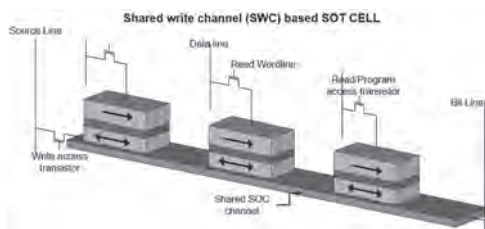


Figure 1. A shared write channel based SOT design. Multiple bits share a common write channel, thereby reducing the need for dedicate write transistor for individual bits.

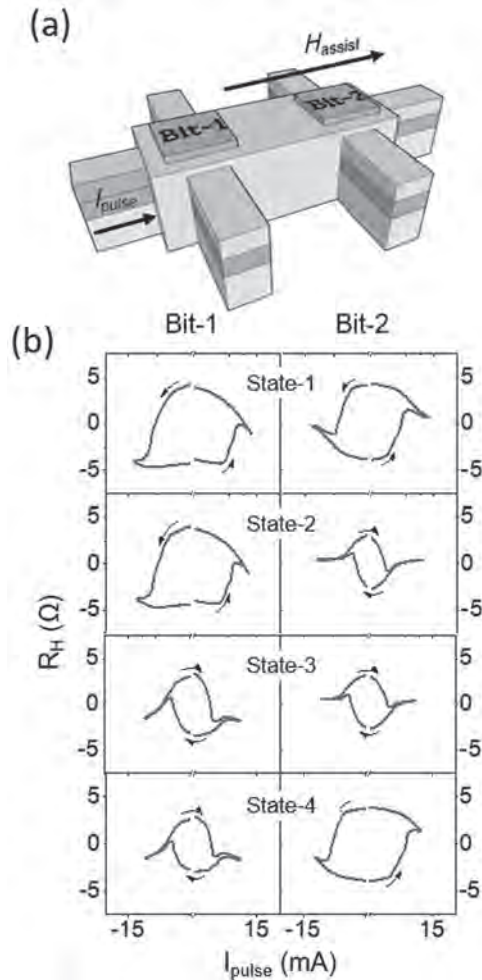


Figure 2. (a) A Pt/Co/ GdO_x based 2-bit memory cell in which SOT polarity of individual bit can be programmed independently. (b) The two bits can be switched independently in different directions depending on the programmed SOT state. The blue switching curve represents normal SOT switching for a Pt device. The red switching curve is obtained after the application of negative gate voltage on the bit, which increases the oxygen content at the Pt/Co interface thereby changing SOT polarity to negative.

INVITED PAPER

CG-13. Voltage-Gate Assisted Spin-Orbit Torque MRAM for High-Density and Low Power Embedded Applications INVITED.

Y. Wu¹, K. Garello², W. Kim¹, M. Gupta¹, M. Perumkunnil¹, S. Van Beek¹, R. Carpenter¹, S. Rao¹, F. Yasin¹, K.K. Vudya Sethu^{1,3}, V. Kateel^{1,3}, D. Crotti¹, S. Couet¹ and G.S. Kar¹

1. IMEC, Leuven, Belgium; 2. SPINtronique et Technologie des Composants, Grenoble, France; 3. ESAT, KU Leuven, Leuven, Belgium

Magnetic random access memory (MRAM) with its inherent non-volatility is believed to address the large stand-by energy issues in the present memory hierarchy [1]. In recent years, the spin-transfer torque (STT)-MRAM has gradually matured and started to appear in the market. Typically, STT writing of perpendicular magnetic tunnel junction (pMTJ) is limited to a few nanoseconds. This is because STT is collinear and competing with the intrinsic damping of the free-layer (FL), resulting in a long incubation delay [2] and large energy consumption. To mitigate STT limitations, spin-orbit torque (SOT) and voltage control of magnetic anisotropy (VCMA) were proposed as alternative MRAM writing mechanisms. SOT is able to switch the FL of a pMTJ by injecting an in-plane current in an adjacent SOT layer, which enables a three-terminal cell structure with energy-efficient and reliable sub-ns writing capabilities [3]. On the other hand, VCMA promises significant advances toward low-power MRAM. The electronic-based VCMA effect can instantly modify the perpendicular magnetic anisotropy (PMA) of the FL to induce precessional switching at GHz rates and ultra-low energy consumption (fJ) [4]. However, both mechanisms also present technological challenges. The challenges for SOT are currently related to the density and write efficiency: the 2-transistor 1-MTJ cell structure limits the array density, and the SOT write current remains larger than for STT-MRAM, which imposes a large selector transistor to accommodate its write current. For VCMA, the write margin is small, and is subject to the variations in VCMA coefficient and field amplitudes, making write control difficult in dense arrays. Further, a large VCMA effect (>1000fJ/Vm) is mandatory to avoid compromising retention in sub-30nm pMTJ, which remains as a major challenge as typical values in pMTJs are 30-60 fJ/Vm at device level [5]. To overcome the above-cited limitations and to combine the best of these two approaches, voltage-gate assisted spin-orbit torque (VGSOT)-MRAM concept [Fig. 1(a)] has been proposed [6]. In this work, we report on VGSOT switching properties in pMTJ, integrated with our 300nm SOT-MRAM platform [3]. The stack is composed of W(3.5nm)/CoFeB(1nm)/MgO(1.7nm, RA ~ 5kΩμm²)/RL/SAF, where the thick MgO ensures pure VCMA gate control without STT contribution. We use an electrical scheme that allows for individual control over SOT/gate pulse amplitudes (V_{SOT}/V_g), and variable pulse duration (t_p). Fig. 1(b) shows exemplary SOT switching probability (P_{sw}) curves under different V_g , at $t_p = 0.4$ ns. We observe a clear decrease (increase) in V_{SOT} under V_g of 1V (-1V) for both AP-P and P-AP transitions. The critical switching voltage, defined at $P_{sw} = 50\%$, is converted into the critical switching current (I_c) and plotted as a function of $1/t_p$ in Fig. 1(c). It shows a typical linear scaling, i.e. $I_c = I_{c0} + q/t_p$ in the sub-ns regime for all gate values [7], where I_{c0} is the intrinsic critical current and q indicates the nucleation energy for magnetization reversal. The linear dependences of I_{c0} and q on V_g [Fig. 1(d)] reflect the direct modification of PMA upon V_g applications and the change of nucleation energy, respectively. We report here a 25% reduction in I_c under $V_g = 1$ V, which corresponds to a 45% reduction in total switching energy to 30fJ at 0.4ns. We further demonstrate that VGSOT offers reliable sub-ns switching with a low write error rate (<10⁻⁵) and that VGOST-pMTJ is highly durable against large read/write stresses (>10¹²) Finally, we benchmark the VGSOT performance at the 5nm technology node against other embedded memory technologies to highlight the VGSOT benefits. It reveals that VGSOT-4MTJ design can reduce the effective cell area to <0.5x of the high-density SRAM at minimal performance degradation. Meanwhile, the constrain of achieving challenging material parameters for VCMA-MTJ ($\xi > 1000$ fJ/Vm) and SOT-MTJ ($\theta_{SH} > 1.5$) can be relaxed to reasonable values: $\xi = 300$ fJ/Vm and $\theta_{SH} = 0.45$. Our study

shows the great potential of this VGSOT approach for fast, dense and low power embedded memory applications.

[1] B. Dieny et al., Nat. Electron. 3, pp. 446–459 (2020) [2] T. Devolder et al., Phys. Rev. Lett. 100, 057206 (2008) [3] K. Garello et al., IEEE VLSI Circ., pp. 81-82 (2018) [4] Y. C. Wu et al., IEEE VLSI Tech., TMFS.4 (2020) [5] C. Grezes et al., IEEE Magn. Lett. 8, 3102705 (2017) [6] H. Yoda et al., IEEE IEDM, pp. 27.6.1-27.6.4 (2016) [7] K. Garello et al., Appl. Phys. Lett. 105, 212402 (2014)

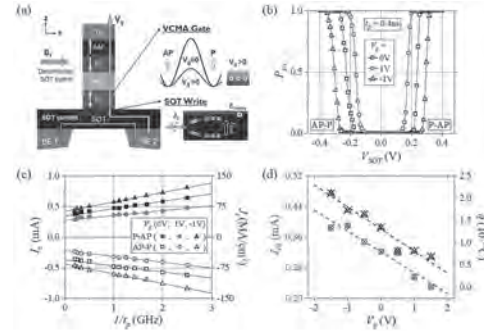


Fig. 1. (a) Illustration of the VGSOT writing scheme. (b) SOT switching probability (P_{sw}) as a function of V_{SOT} under different V_g at $t_p = 0.4$ ns. (c) Critical SOT switching current and current density at $P_{sw} = 50\%$ as a function of $1/t_p$, showing typical linear scaling for all V_g . (d) I_{c0} and q as a function of V_g .

Session CP
SPINTRONICS FUNDAMENTALS
(Poster Session)

Xin Fan, Co-Chair

University of Denver Division of Natural Sciences and Mathematics, Denver, CO, United States

Shuyuan Shi, Co-Chair

Beihang University, Beijing, China

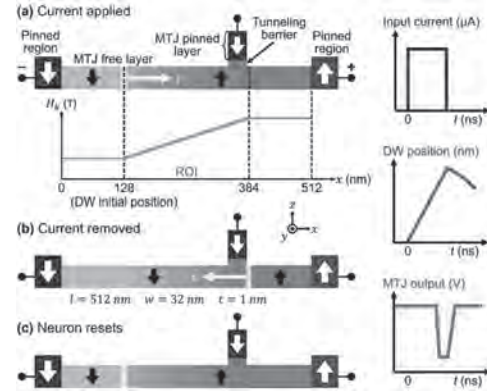
CP-01. Domain Wall Device With a Graded Anisotropy Field as Artificial Neuron for Neuromorphic Computing.

W. Mah¹, T. Jin¹, D. Kumar¹ and S. Piramanayagam¹

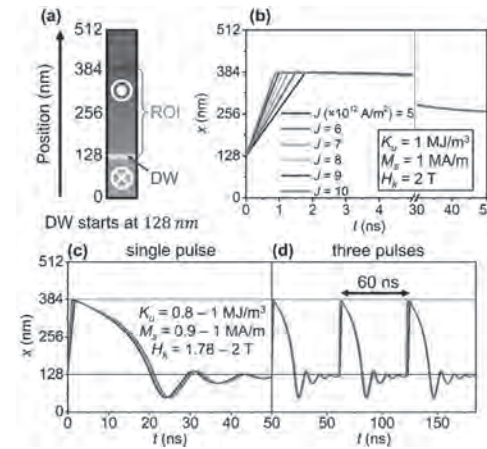
1. SPMS, Nanyang Technological University, Singapore, Singapore

Demand for Artificial Intelligence (AI) has been growing due to their usefulness in commercial electronics as well as tackling global issues, such as a pandemic [1]. Current devices that perform AI rely on the conventional von Neumann architecture, which requires extensive programming and power [2]. Therefore, significant attention is dedicated to the brain-inspired neuromorphic computing (NC) as an alternative that is more power-efficient and a more suitable platform for AI [3]. Neuromorphic architecture consists of a network of interconnected synapses and neurons that mimic their biological counterparts [4]. Sengupta *et al.* have proposed a neuron design based on a domain wall device that uses a magnetic tunnel junction (MTJ) [5] at one end. The tunneling magnetoresistance (TMR) depends on the position of the DW. A current is required to move the domain wall forward or backward (integrate or leak functions respectively). In this work, we place emphasis on designing a domain wall (DW) based artificial neuron, which displays the leaky function without the requirement for a driving current. To achieve leaky function and self-reset process of neuron, we propose a domain wall device, which has an anisotropy field (H_k) gradient in the region of interest (ROI), as shown in Fig. 1(a). This anisotropy gradient is crucial in inducing the automatic returning motion of DW in the absence of current. The design is simulated using Mumax3, and the DW in the free layer nanowire (NW) is driven by spin-transfer-torque (STT). As shown in Fig. 1, current is first applied to propagate the DW towards the threshold position to “fire” the neuron device; current is subsequently removed and DW motion is observed. The micromagnetic parameters used here represent the magnetic properties of CoFeB film with a perpendicular magnetic anisotropy. The magnetic anisotropy constant (K_u) and saturation magnetization (M_s) are graded in ROI, so that H_k gradient is achieved. Some results are presented in Fig. 2(b), showing DW position vs time graph of the reference NW, without any gradient. One may notice that the DW does not return towards the initial position in these devices. Fig. 2(c) corresponds to a device with an H_k gradient. We can notice that the device enables natural return of the domain wall towards the starting position in the absence of current. This suggests that the device displays the leakage function, as well as the ability to reset after the neuron has fired. Fig. 2(d) corresponds to the same device as that of Fig. 2(c), except in this case, three current pulses are consecutively applied with a time interval of 60 ns. These results indicate that the neurons can function with a reset time of about 60 ns. The proposed design has potential applications for DW-based artificial neuron since it displays the integration and leakage functions, while the firing function can be achieved with the utilization of MTJ during the fabrication process.

[1] Z. Hu, Q. Ge, S. Li, L. Jin, and M. Xiong, “Artificial Intelligence Forecasting of Covid-19 in China,” Feb. 2020, Accessed: Jun. 25, 2020. [Online]. Available: <http://arxiv.org/abs/2002.07112>. [2] R. A. Nawrocki, R. M. Voyles, and S. E. Shaheen, “A Mini Review of Neuromorphic Architectures and Implementations,” *IEEE Trans. Electron Devices*, vol. 63, no. 10, pp. 3819–3829, 2016, doi: 10.1109/TED.2016.2598413. [3] H. Farkhani, M. Tohidi, S. Farkhani, J. K. Madsen, and F. Moradi, “A Low-Power High-Speed Spintronics-Based Neuromorphic Computing System Using Real-Time Tracking Method,” *IEEE J. Emerg. Sel. Top. Circuits Syst.*, vol. 8, no. 3, pp. 627–638, Sep. 2018, doi: 10.1109/JETCAS.2018.2813389. [4] J. Grollier, D. Querlioz, K. Y. Camsari, K. Everschor-Sitte, S. Fukami, and M. D. Stiles, “Neuromorphic spintronics,” *Nat. Electron.*, 2020, doi: 10.1038/s41928-019-0360-9. [5] A. Sengupta, P. Panda, P. Wijesinghe, Y. Kim, and K. Roy, “Magnetic tunnel junction mimics stochastic cortical spiking neurons,” *Sci. Rep.*, vol. 6, no. July, pp. 1–9, 2016, doi: 10.1038/srep30039.



The proposed 3T-MTJ device. Magnetizations of the pinned layers are fixed while that of the MTJ free layer NW can be manipulated by applying electrical current. Conduction electrons are polarized by a pinned layer and push the DW by STT. Neuronal firing happens when the DW propagates past the MTJ device, i.e. when parallel configuration of the MTJ is achieved.



(a) Schematic of the NW with the ROI labelled. (b and c) DW position vs time graphs for the reference NW and the result where DWs returned and stabilized around the initial position after neuronal firing. (d) is the case with three pulses sequentially applied. The interval is the same between each pulse, sufficient for DWs to stabilize around the initial position.

CP-02. Study on the Critical State of Two-Dimensional Resonators Topological Insulator.

W. Wang^{1,2}, W. Mo^{1,2}, F. Jin^{1,2}, K. Dong^{1,2}, J. Song^{1,2} and Y. Hui^{1,2}

1. School of Automation, China University of Geosciences, Wuhan, China;
2. Hubei Key Laboratory of Advanced Control and Intelligent Automation for Complex Systems, Wuhan, China

Topological insulator is a material that is conductive on the surface and internally insulated [1]. The unique topological protection characteristics of topological insulators showing robustness to inherent and introduced disorder have attracted widespread attention. Inspired by topological insulators, scientists have tried to extend the magical properties of topological insulators to optical systems, and proposed different systems of optical topological insulators in succession. Recently, Two-dimensional coupled resonant optical waveguide (CROW) has become an advantageous tool for studying optical topological insulators due to their unique structure and compatibility with traditional photonic integrated circuits [2]. This paper mainly studies the coupling strength k range between adjacent rings of two-dimensional micro-ring arrays (as shown in Fig.1) forming optical topological insulators. First, using the transfer matrix method analyzed the transmission relationship and energy band of the micro-ring array to determine the range of appropriate coupling strength. Then we simulated the energy band diagram of the proposed structure under different coupling strengths to verify its topological state. Finally, we explored the influence of the coupling strength on the spectral transmission in the topological state. Based on the above analysis, we obtain the critical value of the coupling strength k to form the optical topological insulator. When the coupling strength is greater than 0.649, the two-dimensional micro-ring topological array becomes an optical topological insulator. Within this coupling strength range, the change of coupling strength will also affect the spectral transmission, as shown in Fig.2. When the k satisfies the condition of the edge state, the spectral transmission is maintained at a relatively high level. In addition, when k is 0.775 in Fig.2(c), the spectral transmission of the system behaves more stable and power value is maintained above 0.9 during the spectrum of 1.557 μm -1.562 μm . Whereas, in other condition such as shown in Fig 7(a), (b) and (d), the spectral transmission fluctuates at a certain value. The coupling coefficient k is farther away from the value of 0.775, the fluctuations are even stronger. The simulation results reveal that there is the optimal coupling coefficient to ensure a flat spectral response in the topological edge state. This research will be helpful for investigating the application of photonic communications based on optical topological insulators in the future works.

[1] M. Hasan, and C. Kane, Colloquium: Topological insulators, Rev. Mod. Phys. 82(4) (2010): 3045-3067. [2] M. Hafezi, E. A. Demler, M. D. Lukin, and J. M. Taylor, Robust optical delay lines with topological protection, Nature Physics 7(11) (2011): 907-912.

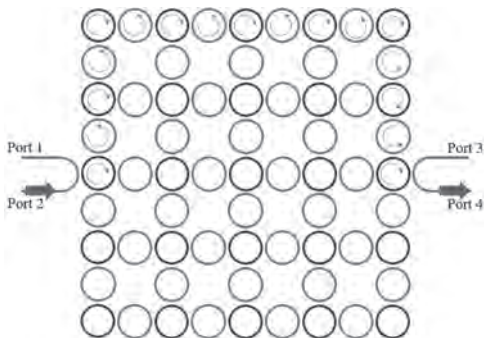


Fig. 1 Schematic diagram of two-dimensional resonators topological insulator.

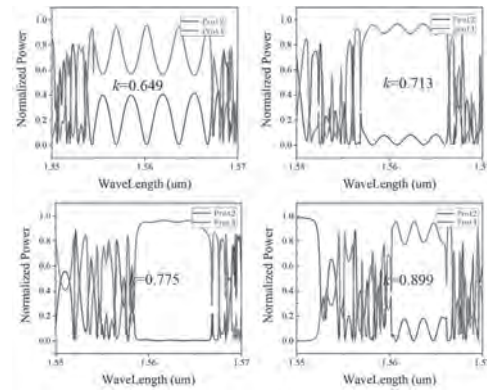


Fig. 2 Transmission characteristic curve of a 5x5 site ring array system, during different coupling coefficient k .

CP-03. Large Spin-Orbit Torque Efficiency in Epitaxial $L1_2$ $PtMn_3$ / Py Heterostructures.

L. Yu¹, M. Oogane^{1,3}, M. Tsunoda^{2,3} and Y. Ando^{1,3}

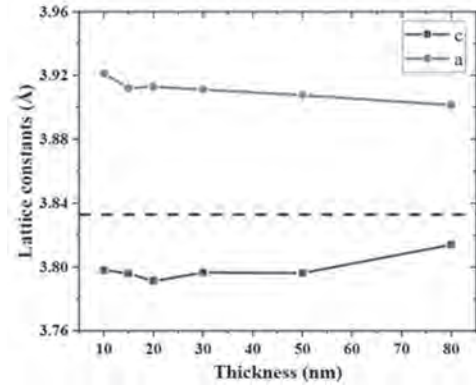
1. Department of Applied Physics, Tohoku University, Sendai, Japan;

2. Department of Electrical Engineering, Tohoku University, Sendai,

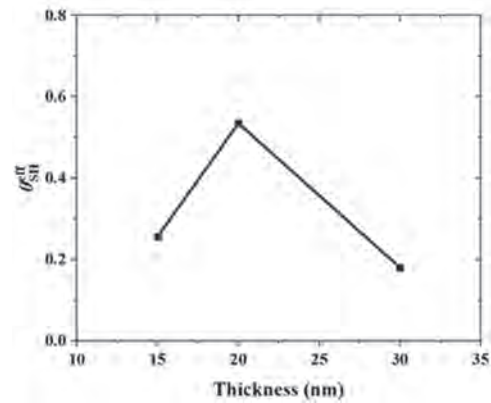
Japan; 3. Center for Spintronics Research Network, Tohoku University, Sendai, Japan

The utilization of current-induced spin-orbit torques (SOTs) in magnetic heterostructures has been devoted lots of research attention as it shows promise for future ultrafast and power conservation magnetic memories [1]. Features of three-terminal non-volatile magnetic memories utilizing SOT-induced magnetization switching promote us to develop kinds of materials in which the SOTs with desiring polarization and orientation are able to be generated efficiently [2]. Comparing to conventional heavy metals like Pt, W, Ta, etc., Mn-based $L1_2$ type antiferromagnets (AFM) XMn_3 (X=Ir, Pt, etc.) are of significant interest due to the high charge current to spin current conversion efficiency, i.e., large spin Hall angle (SHA) they show [3], as well as the potential of controlling SHA and SOTs orientation by tuning the spin texture [4], crystal structure [5], facet orientation [6], etc. they possess. Since recent research showed that the generation of spin current in Mn-based AFM strongly related to magnetic structure [7], it is necessary to fabricate high quality Mn-based AFM single crystal films with known magnetic structure to analysis the SHA features. In this work, we report the fabrication of $L1_2$ $PtMn_3$ single crystal epitaxial films which the magnetic structure is known as kagome-type lattice on a (111) plane, and the $PtMn_3$ thickness dependence of effective SHA θ_{SH}^{eff} . All the samples were prepared by magnetron sputtering system. The stack structure was $MgO(001)$ sub. / $PtMn_3$ (*t*) / Py (4) / $MgAl_2O_4$ (2) / Pt (3) in nm. $PtMn_3$ layer was deposited at substrate temperature (T_s) of 450°C, while other layers were prepared at $T_s = R.T.$ θ_{SH}^{eff} were estimated by Spin-Torque ferromagnetic resonance (ST-FMR) measurement with lock-in amplifier. Fig. 1 shows lattice constant of a-axis and c-axis of $PtMn_3$ films as function of thickness. Since the lattice constant of MgO substrate and $L1_2$ $PtMn_3$ is 4.22Å, 3.833Å respectively, $PtMn_3$ epitaxial films thus under tensile strain which is induced by MgO substrate. With the decreasing of $PtMn_3$ thickness, a-axis became larger while c-axis became smaller, which corresponds to the epitaxial relation. We note that a similar phenomenon also had been observed in previous work [8]. Fig. 2 shows the thickness dependence of measured θ_{SH}^{eff} . We found that the calculated θ_{SH}^{eff} exhibits little variation as a function of the RF excitation frequency, therefore we plotted the θ_{SH}^{eff} as a function of $PtMn_3$ thickness at 6 GHz. θ_{SH}^{eff} of 15nm and 30nm $PtMn_3$ were estimated as 0.27 and 0.19 respectively, which are comparable to that found in $IrMn_3$ single crystal film. We observed a significant increasement of θ_{SH}^{eff} , reaches 0.55, for 20nm $PtMn_3$. We speculate that such a dramatic variation of θ_{SH}^{eff} originates from the change of magnetic structure of $PtMn_3$, which a similar tendency of anomalous Hall conductivity v.s. thickness also reported by previous work [8]. We will show more detail in the conference. This work was supported in part by GP-spin program of Tohoku University.

[1] R. Ramaswamy, J. M. Lee, K. Cai, and H. Yang, Appl. Phys. Rev. 5, 031107 (2018). [2] A. Manchon, J. Zelezny, I. M. Miron, T. Jungwirth, J. Sinova, A. Thiaville, K. Garello, and P. Gambardella, Rev. Mod. Phys. 91 (2019). [3] W. Zhang, M. B. Jungfleisch, W. Jiang, J. E. Pearson, A. Hoffmann, F. Freimuth, and Y. Mokrousov, Phys. Rev. Lett. 113, 196602 (2014). [4] J. Zhou *et al.*, Sci. Adv. 5, eaau6696 (2019). [5] W. Zhang, M. B. Jungfleisch, F. Freimuth, W. Jiang, J. Sklenar, J. E. Pearson, J. B. Ketterson, Y. Mokrousov, and A. Hoffmann, Phys. Rev. B 92, 144405 (2015). [6] W. Zhang, W. Han, S.-H. Yang, Y. Sun, Y. Zhang, B. Yan, and S. S. Parkin, Sci. Adv. 2, e1600759 (2016). [7] M. Kimata *et al.*, Nature 565, 627 (2019). [8] Z. Liu *et al.*, Nat. Electron. 1, 172 (2018).



Lattice constants of a, c-axis as functions of thickness. Dotted line indicates the bulk value of lattice constants for both a-axis and c-axis



Thickness dependence of effective SHA θ_{SH}^{eff}

CP-04. Unconventional Magnetoresistance Induced by Spermagnetism of GdFeCo.

J. Park¹, Y. Hirata², J. Kang¹, S. Lee¹, S. Kim³, C. Phuoc⁴, J. Jeong⁴, J. Park⁵, S. Park⁵, Y. Jo⁵, A. Tsukamoto⁶, T. Ono^{2,7}, S. Kim¹ and K. Kim¹
 1. Department of Physics, Korea Advanced Institute of Science and Technology, Daejeon, The Republic of Korea; 2. Institute for Chemical Research, Kyoto University, Kyoto, Japan; 3. Department of Physics, University of Ulsan, Ulsan, The Republic of Korea; 4. Department of Science and Engineering, Chungnam National University, Daejeon, The Republic of Korea; 5. Center for Scientific Instrumentation, Korea Basic Science Institute, Daejeon, The Republic of Korea; 6. College of Science and Technology, Nihon University, Funabashi, Japan; 7. Center for Spintronics Research Network (CSRN), Graduate school of Engineering Science, Osaka University, Osaka, Japan

Rare earth (RE) - transition metal (TM) ferrimagnetic alloys have been attracting much attentions due to the unconventional spin dynamics phenomena occurring at two critical temperatures, one is called magnetization compensation temperature, T_M , and the other one is called angular momentum compensation temperature, T_A . For examples, a fast domain-wall motion was detected near the T_A of a GdFeCo alloy [1], the skyrmion Hall effect disappeared at T_A of a GdFeCo alloy [2] and a highly efficient spin-orbit torque was measured near the T_M of CoTb alloy [3]. These reports make ferrimagnets more promising candidates for spintronic applications. However, the transports of RE-TM ferrimagnets have not been updated for decades. Especially, one of the most significant questions still remain is whether the transport of RE-TM ferrimagnets are solely associated with either the RE sub-moment or the TM sub-moment, or with both sub-moments. There were some controversies on assigning a dominant role to one of the two sub-moments [4, 5] or both sub-moments [6] in the early studies, but most of recent works have assumed that the TM plays a dominant role in the transport of ferrimagnets [7]. However, there has been no universally accepted consensus on this issue, mainly because of lack of experimental scheme to identify the transport of RE-TM ferrimagnets. In this work, we provide a supporting analysis on the opinion that both submoments are significantly involved to the transport by exploring longitudinal and transverse resistivities of GdFeCo. The longitudinal resistivity, ρ_{xx} , which reflects the change of anisotropic magnetoresistance (AMR), is found to depend on the magnetic field, B , and temperature, T , in a distinct way: the ρ_{xx} increases with increasing B for $T < T_M$, while it decreases for $T > T_M$, and the slope of $\rho_{xx} - B$ curve increases as the temperature decreases. On the other hand, the transverse resistivity, ρ_{xy} , which exhibits conventional anomalous Hall effect (AHE), has little dependence on the external magnetic field. The observed field-and temperature-dependence of the magnetoresistance of GdFeCo qualitatively differ from those of ferromagnetic transition metals caused by the electron-magnon scattering mechanism. These unconventional longitudinal and transverse magnetoresistances can be explained by the antiferromagnetic nature of the magnetic coupling and the ensuing spermagnetism of GdFeCo. Fe and Gd moments in GdFeCo are coupled antiferromagnetically but their directions are spatially dispersed due to the weak exchange interactions [8] (Fig. 1(a)). When a magnetic field is applied to spermagnetic GdFeCo, the cone angle of each sub-moment either increases or decreases depending on the relative direction between the sub-magnetic moment and the external field (Fig. 1(b)). This field-induced opposite change of the two cone angles can explain the observed magnetoresistances as shown in Fig 2. Our results suggest that the unconventional resistance change of GdFeCo is, contrary to the recent reports [6, 7], caused by both the RE and the TM sub-moments.

[1] K. J. Kim, S. K. Kim and Y. Hirata, Nat. Mater. 16, 1187 (2017) [2] Y. Hirata, D. H. Kim and S. K. Kim, Nat. Nanotechnol. 14, 232 (2019) [3] S. G. Je, J. C. Rojas-Sánchez and T. H. Pham, Appl. Phys. Lett. 112, 062401 (2018) [4] A. Ogawa, T. Katayama and M. Hirano, Jpn. J. Appl. Phys. 15, 87 (1976) [5] Y. Mimura, N. Imamura, and Y. Koshiro, J. Appl. Phys. 47, 3371 (1976) [6] T. R. McGuire, R. J. Gambino and R. C. Taylor, J. Appl. Phys. 48, 2965 (1977) [7] T. Okuno, K. J. Kim and T. Tono, Appl. Phys. Express 9, 073001 (2016) [8] M. Mansuripur and M. F. Ruane, IEEE Trans. Magn. MAG-22, 33 (1986)

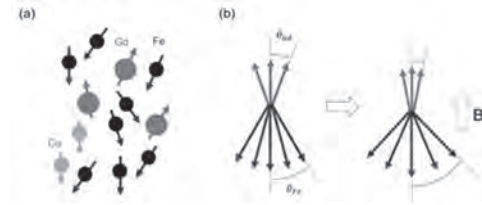


Fig. 1 (a) Spermagnetism of GdFeCo. (b) Cone angles of Fe(θ_{Fe}) and Gd(θ_{Gd}) submoments and their opposite behavior on external B-field.

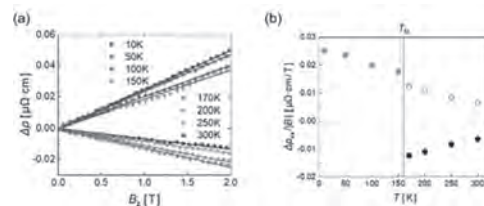


Fig. 2 (a) External B-field dependent change of longitudinal resistivity, $\Delta\rho = \rho_{xx}(B) - \rho_{xx}(0)$, at various temperatures. (b) The slope of the longitudinal resistivity change at various temperatures in (a). The white dots are representing the absolute value of black ones.

CP-05. Large Low Magnetic Field Magnetocapacitance Effect and Spin Accumulation in Graphene Oxide.

S. Singh¹, M. R¹, B. Hiremath¹, B. Kori¹, S. Kumar¹, Y. Bitla² and R.S. Joshi¹

1. Physics, Central University of Karnataka, Gulbarga, India;

2. Physics, Central University of Rajasthan, Ajmer, India

Magnetocapacitance (MC) is the change in capacitance of a solid with applied magnetic field. This change in capacitance is due to spin accumulation which coexists with geometric capacitance [1]. The effect is explained using the formation of spin channels in solids due to selective spin scattering either at interface [2] or by magnetic ions [3]. The MC is observed in magnetoelectrically coupled solids or interfaces as well. It is used as a tool to evaluate the magnetoelectric effect [4]. Spin accumulation in 2-D materials is one of interesting areas of investigation because of its device applications, studied with the help of magnetocapacitance effect. Hence Graphene and related materials have been studied extensively for spin transport [5]. Graphene oxide (GO) is a unique material and has a monomolecular layered structure similar to that of graphene with various oxygen containing functional groups which make the atomic thick layers' defect reach [6]. Delocalized π electrons in aromatic ring structures induce diamagnetism in Graphene like compounds, but in GO π electrons develop ferromagnetism due to its unique structural properties. It has been proven that GO exhibits ferromagnetism with the presence of epoxy groups and it is a soft ferromagnetic material with shaped M-H curve [7]. In the present work we investigate spin dependent capacitance in GO with different frequencies and estimate the spin accumulation length. The magnetic interaction and the origin of magnetocapacitance in these was interpreted with sign of MC and AC magnetoresistance study. The results of GO are compared to reduced GO (rGO) to depict the spin accumulation capacity. For spin accumulation study GO was prepared by modified Hummer's method from graphitic powder and it was further reduced to form rGO using hydrazine hydrate. This method is expected to yield GO with large defect densities. The formed GO was subjected to AFM (inset of Figure 1) and Raman spectroscopic study (Figure 1) confirming the formation of flakes like GO. The magnetism in GO was investigated using a vibrating sample magnetometer showing soft ferromagnetism at room temperature. The GO and rGO were compressed to form parallel plate capacitors to study spin accumulation in them. The AC magnetoresistance (MR) and MC were studied from 100 Hz to 5 MHz at room temperature (Figure 2a). The change in capacitance with frequency was modelled with the Havriliak-Negami relaxation process (inset of Figure 2a). The change in asymmetry parameter showed contribution of defects in the relaxation process. The relaxation time was found to change with applied magnetic field supporting strong magnetic field dependent scattering in GO. We observed positive MC of 20 % at around 200 Hz and 100 Oe, where capacitive coupling is higher and 2.2 % at 1.1 MHz (Figure 2b) which is due to predominant inductive coupling. The positive sign of MC indicates the interface mediated spin accumulation process in GO [1]. This low field MC is very important for device development. The spin diffusion length calculated, equivalent to capacitance change was of the order of 56nm. MR in GO was observed to change sign from negative to positive indicating the increase of interface mediated effects with higher magnetic fields. In contrast to GO, rGO showed no spin accumulation effects except significant change in impedance, attributed to surface permeability change. The report projects GO as a significant spin accumulation material useful in different spintronic device applications.

1. Y. H. Zhu, X. X. Zhang, J. Liu and P. S. He *J. Appl. Phys.* Vol. 122, p. 043902 (2017). 2. G. Catalan, *Appl. Phys. Lett.* Vol. 88, p.1-4(2006). 3. K. T. McCarthy, A. F. Hebard and S. B. Arnason *Phys. Rev. Lett.* Vol. 90(11), p.1172015-8 (2002). 4. K. Manna, R. S. Joshi, S. Elizabeth and P. S. Anil Kumar, *Appl. Phys. Lett.* Vol.104 p.2-6(2014). 5. E. C Ahn *npj 2D Materials and Applications* Vol. 4, p.17 (2020). 6. A. Stergiou, et al.. *J. Nanotechnol.* 5, p.1580-1589 (2014). 7. L. Dongwook, S.Jiwon, *Appl. Phys. Lett.* 106, p.172402 (2015).

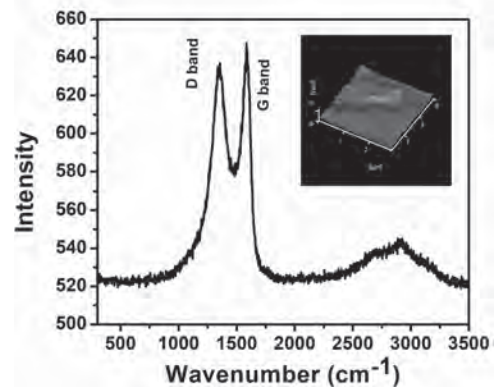


Figure 1: Raman spectra for GO (Inset shows AFM image of as prepared GO grafted on SiO₂ substrate)

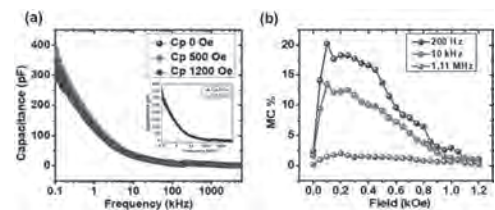


Figure 2 (a). Variation of capacitance with respect to frequency for different applied magnetic fields in GO (inset shows fit of Havriliak-Negami relaxation model to the data) (b) MC in graphene with applied magnetic field for different frequencies.

CP-06. Magnetotransport Phenomena in Topological Insulator / Superconductor $\text{Bi}_2\text{Te}_3/\text{Nb}$ Bilayer and Trilayer Thin Films.

A. Pilidi¹, T. Speliotis¹ and G. Litsardakis²

1. Institute of Nanoscience and Nanotechnology, National Centre for Scientific Research "Demokritos", Athens, Greece; 2. Electrical & Computer Engineering, Aristotle University of Thessaloniki, Thessaloniki, Greece

The topological insulator (TI) and superconductor (SC) condensed matter states are different at the fundamental level. Superconductors spontaneously break gauge symmetry, while topological insulators are defined by a topological invariant of their band structure. Theoretical work by Fu and Kane in 2008 proposed a novel way to engineer an exotic superconducting system using the proximity effect, to combine the electronic properties of these two distinct systems [1]. They showed that the resulting system was a spinless superconductor, which does not break the time reversal symmetry. A proximity coupled topological insulator / superconductor (TI/SC) bilayer system is suitable to realize topological superconductivity [2]. $\text{Bi}_2\text{Te}_3/\text{Nb}$ thin films constitute a simple proximity system of a topological insulator and an s-wave superconductor to study magnetotransport phenomena in topological superconductors, working toward coupling superconductivity and other spin states. In the present work we report studies on the structural and magnetotransport properties of $\text{Bi}_2\text{Te}_3/\text{Nb}$ bilayer and $\text{Bi}_2\text{Te}_3/\text{Nb}/\text{Bi}_2\text{Te}_3$ trilayer samples, as well as reference single layer samples of Bi_2Te_3 and Nb. Samples were fabricated through DC magnetron sputtering process with base pressure 10^{-8} Torr, without breaking the vacuum to ascertain a perfect interface between Bi_2Te_3 and Nb for optimum proximity coupling. The Ar deposition pressure was fixed at 3 mTorr and the substrate's temperature was held constant at 300 °C. Both systems, the $\text{Si}(111)/\text{Bi}_2\text{Te}_3(100\text{nm})/\text{Nb}(100\text{nm})$ bilayer and the trilayer $\text{Si}(111)/\text{Bi}_2\text{Te}_3(100\text{nm})/\text{Nb}(100\text{nm})/\text{Bi}_2\text{Te}_3(100\text{nm})$ trilayer exhibited large pyramid-like structures of Bi_2Te_3 as observed with Field-Emission Scanning-Electron-Microscopy (FESEM) and Atomic Force Microscopy (AFM). The crystal structure of the topological insulator layer is consistent with the rhombohedral space group for Bi_2Te_3 , and reveals a predominant texture with planes oriented along the (00 l) direction as can be inferred from (006) and (00-15) peaks. The coherence diffraction domain size, estimated using Scherrer's formula and considered as average crystallite size is 23 nm for the Bi_2Te_3 layer. The average crystallite size for the superconductor layer of Nb, which is cubic, was extracted from the (101) peak and is equal to 21 nm. For the magnetotransport measurements Hall bar shaped samples were prepared using a Hall stencil mask with current channel length 2.5 mm and width 0.4 mm, aligned in a $7 \times 7 \text{ mm}^2$ $\text{Si}(111)$ substrate. A second mask was then aligned to make pads of Cr/Au and eventually the ohmic contacts were made using a wire bonder. The magnetotransport measurements were performed in a 9 T QD-PPMS and for temperatures varying from 2.5 K to 300 K. The temperature dependence of longitudinal resistance, R_{xx} , confirmed that the 100 nm Nb films present a superconducting transition at 8.7 K which decreases with decreasing film thickness, due mostly to dimensionality and increasing disorder. The magnetoconductivity, $\Delta\sigma_{xx}(B)$, curves of the 100 nm thick Bi_2Te_3 reference sample, which are shown in Figure 1 in the low field region ($B < 0.2$ T), were calculated from the magnetotransport data. Observation of a logarithmic variation of magnetoconductance at fields close to zero is an indication of weak antilocalization (WAL) effects that have been widely described in materials with strong spin-orbit coupling, such as topological insulators [3]. The parameters from fitting magnetoconductivity data to Hikami-Larkin-Nagaoka equation at low temperatures have been extracted. The phase coherence length, l_ϕ , is approximately 300 nm and decreases as temperature is raised. The value of coefficient α that indicates the number of independent conducting channels in the system and the type of localization, is equal to 1 at 2.5 K (WAL in a perfect system with two surface conducting channels, each contributing to the pre-factor with a value of 0.5) and decreases to 0.5 at 15 K. Figure 2 presents low temperature magneto-transport measurements probing the nature of the SC in bilayers of $\text{Bi}_2\text{Te}_3/\text{Nb}$. The onset of superconductivity of Nb layer adjacent to the topological insulator destroys the WAL phenomena and topological properties of Bi_2Te_3 that at the single layer Bi_2Te_3 reference sample dominate in the low field regime at temperatures up to 20 K. At $T=3$ K the switching between the normal and superconducting state is found to occur at magnetic field

value $|B|=1.5$ T, with an excitation current $I = 2$ mA. Magnetoconductance and differential magnetoresistance data are examined to show evidence of proximity effect and topological superconductivity.

[1] Liang Fu and C.L. Kane, Superconducting proximity effect and Majorana Fermions at the Surface of a Topological Insulator, Phys. Rev. Lett. 100 096407 (2008) [2] Gad Koren, Proximity effects at the interface of a superconductor and a topological insulator in $\text{NbN}-\text{Bi}_2\text{Se}_3$ thin film bilayers, Supercond. Sci. Technol. 28 025003 (2015) [3] J.J. Cha et al. Weak antilocalization in $\text{Bi}_2(\text{Se}_x\text{Te}_{1-x})_3$ nanoribbons and nanoplates, Nano Lett. 12 1107–1111 (2012)

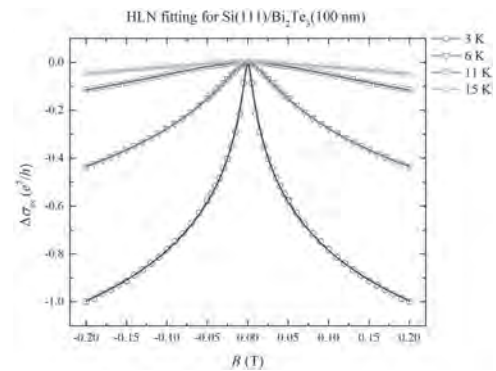


Figure 1: Magnetoconductivity data for the Bi_2Te_3 reference sample, with magnetic field perpendicular to film plane.

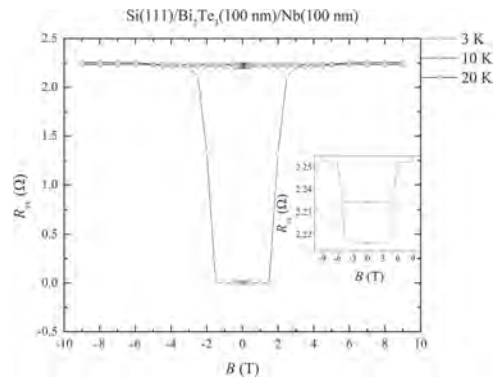


Figure 2: Longitudinal resistance data for the $\text{Bi}_2\text{Te}_3/\text{Nb}$ bilayer film, with the magnetic field perpendicular to film plane.

CP-07. Evidence of Magnetization Switching by Anomalous Spin Hall Torque in NiFe.

T. Ma¹, C. Wan¹, X. Wang¹, W. Yang¹, C. Guo¹, C. Fang¹, M. Zhao¹, J. Dong¹, Y. Zhang¹ and X. Han¹

1. Institute of Physics, Chinese Academy of Sciences, Beijing, China

Recently the anomalous Hall effect was predicted as a possible mechanism to produce magnetization-dependent spin current. Here we have applied NiFe/Ru/perpendicular magnetic multilayers and a specific geometry to demonstrate magnetization switching driven by anomalous spin-orbit torque resulting from the bulk anomalous Hall effect. The anomalous spin Hall torque of NiFe is strong enough not only to switch the magnetization of perpendicular Co but also leads to opposite switching chirality compared with the ordinary spin Hall torque. This work confirmed the existence of a strong anomalous spin Hall torque due to anomalous Hall effect, which may lay a foundation to develop spin-orbit torque devices free of heavy metals. Spin current can be obtained in magnetic materials. Besides the ordinary geometry-constrained spin current, magnetic materials can also give birth to magnetization-dependent spin current components with high efficiency, which grants us a flexible manner to produce polarization-tunable SOT. In theory, the anomalous Hall effect (AHE) and planar Hall effect (PHE) [1] inside magnetic materials or interfacial spin-related scattering [2] on the interface of magnetic materials with nonmagnetic materials can produce spin current. Specifically, AHE, though discovered one century ago, is just recently predicted as a probable spin current source [1,3]. In this paper [4], we also used a core structure of NiFe/Ru/perpendicular ferromagnetic trilayer but a specific geometry to verify the bulk ASHE torque. In this geometry, pinned magnetization of NiFe (M_{NiFe}) by exchange bias, applied current parallel with M_{NiFe} , and applied field H_x transverse to M_{NiFe} was critical to achieve our targeted goal as discussed below. Our results demonstrated that the ASHE torque of NiFe could be not only strong enough to switch magnetization but also lead to opposite switching chirality with ordinary SHE-torque switching. Therefore, this work experimentally verified the newly predicted ASHE torque due to the century-old AHE mechanism not only exists but is also strong, which might lay a foundation for the development of heavy-metal-free SOT devices.

[1] T. Taniguchi, J. Grollier, and M. D. Stiles, *Phys. Rev. Appl.* 3, 044001 (2015). [2] V. P. Amin and M. D. Stiles, *Phys. Rev. B* 94, 104419 (2016). [3] S. Iihama, T. Taniguchi, K. Yakushiji, A. Fukushima, Y. Shiota, S. Tsunegi, R. Hiramatsu, S. Yuasa, Y. Suzuki, and H. Kubota, *Nat. Electron.* 1, 120 (2018). [4] T. Y. Ma, C. H. Wan and X. F. Han*, et al., *Phys. Rev. B* 101, 134417 (2020).

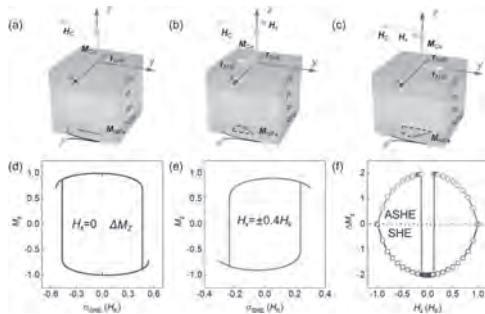


FIG. 1. Schematic diagrams of SOT switching driven by (a) the ordinary SHE and by interplay of the ordinary and anomalous SHE under (b) a small negative or (c) a small positive H_x . Calculated dependence of M_z on current or torque in units of H_K with (d) $H_x=0$ and (e) $H_x = \pm 0.4H_K$. (f) ΔM_z (torque=0) chirality as a function of H_x . Note that after anomalous SHE is taken into account, the switching chirality can be switched from -1 (CW) to $+1$ (CCW). Otherwise, ordinary SHE can only produce the -1 chirality. Calculation was based on the following parameters $H_C = 0.05H_K$ and $H_{EB} = 0.3H_K$.

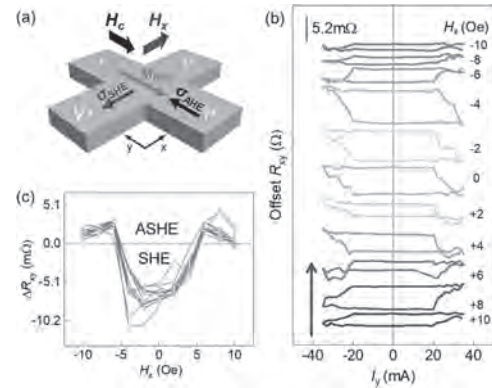


FIG. 2. (a) Measurement setup as applying I_y and H_x . Directions of M_{NiFe} , H_C , σ_{SHE} , and σ_{AHE} are schematically marked. This subfigure depicts a case of small H_x so that M_{NiFe} is nearly aligned along the y axis. (b) Switching behaviors as I_y and H_x applied. (c) H_x dependence of ΔR_{xy} repeated by 10 times. The dotted line separates regions with CW (-1) and CCW ($+1$) switching chirality.

CP-08. Enhancement of the Spin Hall Magnetoresistance in Ta/Pt/ $\text{Ni}_{80}\text{Fe}_{20}$ /MgO(100) Heterostructures by Competing Spin Currents.

H. Jiang¹, K. Wang¹, Y. Hui¹, K. Dong¹, W. Mo¹, J. Song¹ and F. Jin¹

1. China University of Geosciences School of Automation, Wuhan, China

The generation, detection, and manipulation of pure spin currents have attracted considerable attention in the field of spintronics owing to their rich physical phenomena and potential applications [1-2]. The most convenient method for generating and detecting the pure spin currents is to utilize the spin Hall magnetoresistance (SMR) [3-4]. In this letter, a novel structure consisting of two heavy metals that delivers competing spin currents of opposite spin indices is presented. We studied spin Hall effect in Ta-Pt alloys with various Ta composition for Ta/Pt/ $\text{Ni}_{80}\text{Fe}_{20}$ /MgO (001) heterostructures by means of SMR. To determine the relative contributions of Pt and Ta, we measured a series of samples of Ta($t_{\text{Ta}}=0-3\text{nm}$)/Pt(3nm)/ $\text{Ni}_{80}\text{Fe}_{20}$ /MgO (001) with a constant Pt (3) layer and various thicknesses of the Ta layer. Low resistivity, flat, and highly (111)-textured Pt-Ta alloy films are synthesized. It is found the SMR ratio is enhanced with a Ta capping layer at an optimum composition of x between 0.5nm to 1nm. The spin accumulation enhancement at the Pt/ $\text{Ni}_{80}\text{Fe}_{20}$ interface after capping with a Ta layer, which functions as a spin sink at small thickness, is responsible for the SMR ratio enhancement, even though Ta and Pt have opposite spin Hall angles. Our results not only demonstrate a viable scheme for multiple spin currents, but also expand a new avenue for switching a perpendicular ferromagnetic layer by competing spin currents.

[1] Q. L. Ma, Y. F. Li, D. B. Gopman, Y. P. Kabanov, Phys. Rev. Lett., 120, 117703 (2018). [2] Z. Z. Luan, L. F. Zhou, P. Wang, Phys. Rev. B, 99, 174406 (2019). [3] Y. J. Xu, Y. M. Yang, H. Xie, Appl. Phys. Lett., 115, 182406 (2019). [4] P. Yang, Q. M. Shao, G. Q. Yu, Appl. Phys. Lett., 117, 082409 (2020).

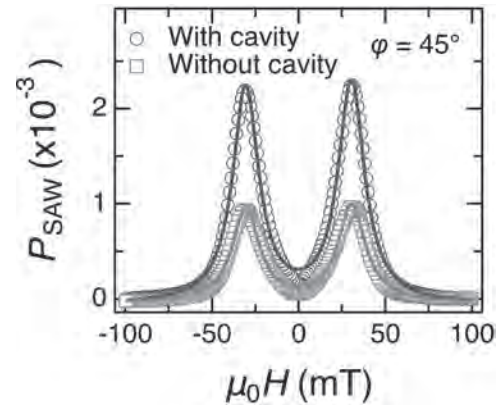
CP-09. Enhancement of Acoustic Spin Pumping by Acoustic Distributed Bragg Reflector Cavity.

Y. Hwang¹, J. Puebla², M. Xu¹, A. Lagarrigue², K. Kondou² and Y. Otani^{1,2}
 1. Institute of Solid State Physics, Tokyo University, Kashiva, Japan;
 2. RIKEN Center for Emergent Physical Characteristics, Wako, Japan

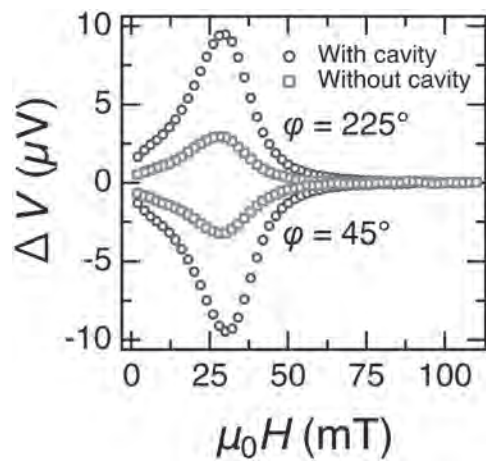
Surface acoustic waves (SAWs) in the GHz frequency range passing through a ferromagnetic layer can excite magnon–phonon dynamics, i.e., a precessional magnetization motion mediated by the magnetoelastic effect [1-3]. This process is known as acoustic ferromagnetic resonance (A-FMR) [4-7]. The A-FMR driven by SAWs can generate spin currents diffusing into adjacent non-magnetic metal layers via the spin pumping effect [8]. This coupled magnon–phonon dynamics can thus be used as a spin current generation method [9] named as acoustic spin pumping (ASP) [10,11]. The generated spin currents can be detected by the inverse spin Hall effect (ISHE) [9,12], or the inverse Edelstein effect (IEE) [6,13]. In SAW driven A-FMR devices, interdigital transducers (IDT) are used for the generation and detection of SAWs [2–7,9,14]. Since the SAWs propagate on both sides of the IDT, at least half of the phonon energy is lost. To reduce the loss and enhance the spin current generation via ASP, we employ acoustic cavity structures. An acoustic cavity (resonator) consists of a pair of acoustic wave reflector gratings, analogous to the distributed Bragg reflector for light [15]. In this presentation, we demonstrate the enhancement of A-FMR and ASP in the presence of acoustic cavities. By applying an external magnetic field, SAWs passing a Ni film induce A-FMR. When the A-FMR occurs, SAW power is attenuated due to the energy conservation, thus the SAW power absorption P_{SAW} is proportional to the induced A-FMR intensity. The measured SAW power absorption in Fig.1 shows the A-FMR signal fitted with a Lorentzian curve. We confirmed an enhancement of 2.04 ± 0.02 times A-FMR on the sample with acoustic cavity. The A-FMR in the Ni layer generates spin current into the Cu layer by the ASP. The generated spin current is converted to a charge current at the interface between Cu and Bi_2O_3 via IEE. We detect the generated electric voltage via IEE at the maximum A-FMR field angles $\phi = 45^\circ$ and 225° , as shown in Fig.2. We define ΔV_{ASP} as the amplitude of the symmetric Lorentzian fitting of DV. The detected electric voltage from the ASP is caused by the charge current, derived from an electric field E induced by the IEE, which is proportional to the flow direction of the spin current density J_s and its spin polarization σ ; $E \propto J_s \times \sigma$ [16]. The converted charge current density J_c is described as $J_c = \lambda_{IEE} J_s$, where λ_{IEE} is the IEE length [17]. Since the Ni/Cu/ Bi_2O_3 trilayers of all samples are fabricated at the same time and the applied external magnetic field angle is the same, thus, $\Delta V_{ASP} \propto J_s$. The enhancement factor of ΔV_{ASP} is 2.96 ± 0.02 at the low-power range, and 1.6 ± 0.7 at the high-power range. However, the power dependence of ΔV_{ASP} has non-linear behavior in the range from 25 mW to 126 mW. This non-linearity in the power dependence is not fully understood. Since this behavior is similar to the case of FMR experiments at the high input radio-frequency (rf) power [21,22] we assume it is from the saturation of magnetic precessional cone angle [23] or multi-magnon scattering [24,25]. We observe a more significant enhancement factor of ASP in the low-power range than the enhancement of A-FMR. In contrast, we find a similar enhancement factor of ASP in the high-power range with that enhancement of A-FMR. The enhancement factor in the high-power range is well described by the multi-magnon scattering in Ref. [26]. However, as far as the author knowledge goes the origin of the higher enhancement factor in the low-power range has not been observed and further understanding is required. In summary, we have demonstrated the enhancement of A-FMR and the spin current generation by using acoustic cavities. Enhancement of 2.04 ± 0.02 times of A-FMR and enhancements of spin current generation from 1.6 ± 0.7 (at a high input rf power) to 2.96 ± 0.02 (at a low input rf power) times were achieved. All the measurements in the present study were carried out at room temperature. At lower temperatures, the SAW confinement can be strengthened by minimizing the interaction with thermal phonons. Minimization of phonon energy losses by further engineering of the acoustic cavities, as well as minimization of magnon energy losses by appropriate selection of materials may lead to magnon–phonon studies in the strong coupling regime.

[1] A. K. Ganguly, K. L. Davis, D. C. Webb, and C. Vittoria, J. Appl. Phys. 47, 2696 (1976). [2] I. A. Feng, M. Tachiki, C. Krischer, and M. Levy,

J. Appl. Phys. 53, 177 (1982). [3] R. F. Wiegert and M. Levy, J. Appl. Phys. 61, 4270 (1987). [4] M. Weiler, L. Dreher, C. Heeg, H. Huebl, R. Gross, M. S. Brandt, and S. T. B. Goennenwein, Phys. Rev. Lett. 106, 117601 (2011). [5] S. L. Dreher, M. Weiler, M. Pernpeintner, H. Huebl, R. Gross, M. S. Brandt, and S. T. B. Goennenwein, Phys. Rev. B 86, 134415 (2012). [6] M. Xu, J. Puebla, F. Auvray, B. Rana, K. Kondou, and Y. Otani, Phys. Rev. B 97, 180301(R) (2018). [7] J. Puebla, M. Xu, B. Rana, K. Yamamoto, S. Maekawa, and Y. Otani, J. Phys. D 53, 264002 (2020). [8] Y. Tserkovnyak, A. Brataas, and G. E. W. Bauer, Phys.Rev.B 66, 224403 (2002). [9] M. Weiler, H. Huebl, F. Goerg, F. Czeschka, R. Gross, and S. T. B. Goennenwein, Phys. Rev. Lett. 108, 176601 (2012). [10] K. Uchida, H. Adachi, T. An, T. Ota, M. Toda, B. Hillebrands, S. Maekawa, and E. Saitoh, Nat. Mater. 10, 737 (2011). [11] K. Uchida, H. Adachi, T. An, H. Nakayama, M. Toda, B. Hillebrands, S. Maekawa, and E. Saitoh, J. Appl. Phys. 111, 053903 (2012). [12] E. Saitoh, M. Ueda, H. Miyajima, and G. Tatara, Appl. Phys. Lett. 88, 182509 (2006). [13] J. C. Rojas Sanchez, L. Vila, G. Desfonds, S. Gambarelli, J. Attane, J. M. De Teresa, C. Magen, and A. Fert, Nat. Commun. 4, 2944 (2013). [14] I. S. Camara, J. Y. Duquesne, A. Lemaitre, C. Gourdon, and L. Thevenard, Phys. Rev. Appl. 11, 014045 (2019). [15] D. T. Bell and R. C. M. Li, Proc. IEEE 64(5), 711 (1976). [16] S. Karube, K. Kondou, and Y. Otani, Appl. Phys. Express 9, 033001 (2016). [17] H. Tsai, S. Karube, K. Kondou, N. Yamaguchi, F. Ishii, and Y. Otani, Sci. Rep. 8, 5564 (2018). [18] R. Manenti, A. F. Kockum, A. Patterson, T. Behrle, J. Rahamim, G. Tancredi, F. Nori, and P. J. Leek, Nat. Commun. 8, 975 (2017). [19] A. Azevedo, L. Vilela-Leao, R. Rodriguez-Suarez, A. Lacerda Santos, and S. Rezende, Phys. Rev. B 83, 144402 (2011). [20] W. Zhang, B. Peng, F. Han, Q. Wang, W. Soh, C. Ong, and W. Zhang, Appl. Phys. Lett. 108, 102405 (2016). [21] V. Castel, N. Vlietstra, B. J. Van Wees, and J. B. Youssef, Phys. Rev. B 86, 134419 (2012). [22] M. B. Jungfleisch, A. V. Chumak, A. Kehlberger, V. Lauer, D. H. Kim, M. C. Onbasli, C. A. Ross, M. Kléau, and B. Hillebrands, Phys.Rev.B 91, 134407 (2015). [23] B. Rana, Y. Fukuma, K. Miura, H. Takahashi, and Y. Otani, Sci. Rep. 7, 2318 (2017). [24] M. B. Jungfleisch, A. V. Chumak, V. I. Vasyuchka, A. A. Serga, B. Obyedkov, H. Schultheiss, P. A. Beck, A. D. Karenowska, E. Saitoh, and B. Hillebrands, Appl. Phys. Lett. 99, 182512 (2011). [25] A. V. Chumak, A. A. Serga, M. B. Jungfleisch, R. Neb, D. A. Bozhko, V. S. Tiberkevich, and B. Hillebrands, Appl. Phys. Lett. 100, 082405 (2012). [26] T. Tashiro, S. Matsuura, A. Nomura, S. Watanabe, K. Kang, H. Siringhaus, and K. Ando, Sci. Rep. 5, 15158 (2015).



Power absorption P_{SAW} at the in-plane magnetic field $\phi = 45^\circ$ at the SAW resonance peak of samples with (blue circles) and without (red squares) acoustic cavity. 10 mW of input rf power is used. Solid curves exhibit Lorentzian fitting curves from the experimental data.



Detected electric voltage when a 10 mW of rf power is applied to an IDT and an external in-plane magnetic field $\phi = 45^\circ$ and 225° is applied. Data are taken from samples with acoustic cavity (blue circles) and without (red squares) acoustic cavity. The detected voltage is normalized with the voltage value at $\mu_0 H = 100$ mT ($\Delta V = V - V_{100mT}$).

CP-10. Influence of the Spin Pumping Induced Inverse Spin Hall Effect on Spin-Torque Ferromagnetic Resonance Measurements.

Q. Liu¹, Y. Zhang³, L. Sun^{1,2}, B. Miao^{1,2}, X. Wang³ and H. Ding^{1,2}

1. Physics, Nanjing University, Nanjing, China; 2. Collaboration

Innovation Center of Advanced Microstructures, Nanjing, China;

3. Physics, Hong Kong University of Science and Technology School of Science, Hong Kong, China

Spin-torque ferromagnetic resonance (ST-FMR) has been widely used to determine the spin-orbit torque (SOT) efficiency in ferromagnet/heavy-metal bilayer systems [1]. When a radio frequency (rf) current flows within the HM, the spin Hall effect (SHE) induced SOT and Oersted field act on the FM layer. When the frequency of the rf current and the applied external magnetic field satisfies the ferromagnetic resonance (FMR) condition, the magnetization of the FM layer oscillates with relatively large amplitude around the equilibrium state. This results in a non-negligible resistance oscillation due to the anisotropic magnetoresistance (AMR) of the FM layer. Consequently, a rectified dc voltage is generated as a result of the interplay of the oscillating current and resistance. Importantly, the lineshape of voltage curve due to the damping-like torque is Lorentzian symmetric, while that from the field-like torque (both SHE and Oersted field origin) is anti-symmetric. Thus, one can obtain the SOT efficiency from lineshape analysis of ST-FMR voltage curve. However, the precession of FM moments also acts as the source for an angular momentum flow, which pumps a pure spin current into its neighboring HM [2]. Wherein, an additional contribution to the dc voltage arises from the inverse spin Hall effect (ISHE) [3] which has Lorentzian symmetric lineshape. In this work, we develop a new method to quantitatively separate the SP-ISHE signal from the ST-FMR signal without tedious symmetry analysis. With the precession angles obtained in both setups via the microwave photoresistance measurements [4], we directly obtain the SP-ISHE contribution in the ST-FMR. Our method does not rely on many unknown parameters such as the spin diffusion length, spin Hall angle of HM, and the effective spin-mixing conductance of FM-HM interface etc. Interestingly, we find that the SP-ISHE is in the opposite sign to the symmetric component of ST-FMR for Py(Ni₈₀Fe₂₀)/Pt bilayer layer. Through the Py thickness dependent measurements, we further estimate both the SHE-induced damping-like-torque efficiency and field-like-torque efficiency for Py/Pt bilayer system.

[1] L. Liu, T. Moriyama, D. C. Ralph, and R. A. Buhrman, Phys. Rev. Lett. Vol. 106, p. 036601 (2011). [2] Y. Tserkovnyak, A. Brataas, and G. E. W. Bauer, Phys. Rev. B Vol. 66, p. 224403 (2002). [3] O. Mosendz, V. Vlaminck, J. E. Pearson, et al. Phys. Rev. B Vol. 82, p. 214403 (2010). [4] N. Mecking, Y. S. Gui, and C. M. Hu, Phys. Rev. B Vol. 76, p. 224430 (2007).

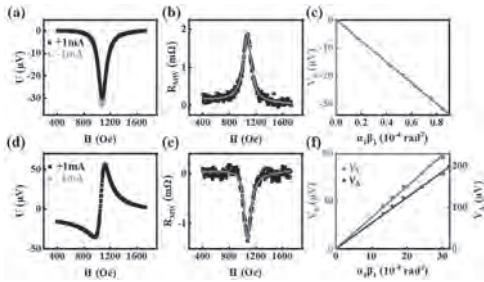


FIG. 1. (a), (b), (c) are the measurements with SP-ISHE configuration at $\phi=90^\circ, f=9$ GHz and (d), (e), (f) are the measurements with ST-FMR configuration at $\phi=10^\circ, f=9$ GHz. (a) and (d) are the magnetic field-dependent voltages of the Py(6 nm)/Pt(6 nm) sample with dc current $+I_0$ (+1 mA, black curve) and $-I_0$ (-1 mA, orange curve). (b) and (e) are the magnetic field-dependent microwave photoresistance. (c) and (f) are the relationship between the measured corresponding amplitudes and the product of the in-plane and out-of-plane precession angles.

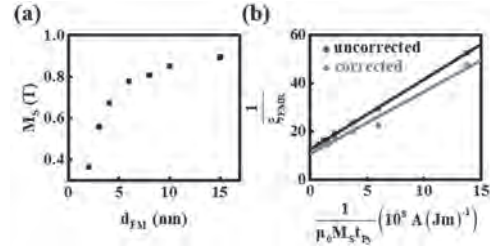


FIG. 2. (a) t_{Py} dependent saturation magnetic moment M_S of Py. (b) Corrected (red) and uncorrected (black) $1/\xi_{FMR}$ versus $1/(\mu_0 M_S t_{Py})$, the lines are fittings with Eq. (4).

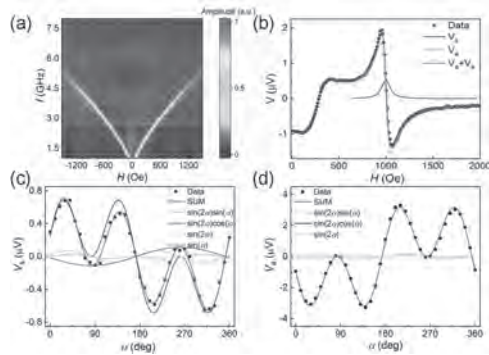
CP-11. Determination of Spin Torque Efficiency in Ferromagnetic Metals via Spin-Torque Ferromagnetic Resonance.

W. Yang¹, J. Wei¹, C. Wan¹, Y. Xing¹, Z. Yan¹, X. Wang¹, C. Fang¹,
C. Guo¹, G. Yu¹ and X. Han¹

1. Chinese Academy of Sciences, Institute of Physics, University of Chinese Academy of Sciences, BeiJing, China

In order to unambiguously demonstrate the transverse M -independent spin current generated by the SHE in FM and eliminate interference from AHE. In this work, we employed spin-torque ferromagnetic resonance (ST-FMR) technique to study the SHE in the ferrimagnetic insulator/ ferromagnetic metals (FMI/FM) systems with FMI being $Y_3Fe_5O_{12}$ and FM being NiFe and CoFeB. The key of this experiment relies on different FMR frequencies of the YIG and the FM film at the same field. Thus at the FMR mode of the YIG driven by spin torque due to SHE, a dc rectification voltage can be detected due to spin Hall magnetoresistance (SMR) while (1) spin current induced by AHE cannot contribute to the dc voltage due to the vanishing $m_{YIG} \times m_{NiFe}$ (2) the anisotropic magnetoresistance (AMR) of FM has no contribution to the measured V_{dc} signal because FM is not in its the precession state. We have indeed obtained large SHE in FM without contamination from AHE. The measured spin torque efficiency ξ of NiFe was 0.009, 25% as large as that of Pt. These results indicate that the spin Hall effect of FM should also be taken into account when investigating the FM/HM heterostructures and furthermore this effect can also benefit the development of spin-orbit torque devices.

[1] V. P. Amin, J. Li, M. D. Stiles, and P. M. Haney, *Phys. Rev. B* 99, 2019, 220405. [2] D. Tian, Y. Li, D. Qu, S. Y. Huang, X. Jin, and C. L. Chien, *Phys. Rev. B* 94, 2016, 020403. [3] K. S. Das, W. Y. Schoemaker, B. J. van Wees, and I. J. Vera-Marun, *Phys. Rev. B* 96, 2017, 220408. [4] W. Wang, T. Wang, V. P. Amin, Y. Wang, A. Radhakrishnan, X. Fan *et al*, *Nature Nanotech.* 14, 2019, 819. [5] H. Wu, S. A. Razavi, Q. Shao, X. Li, K. L. Wang, Y. Liu, G. Yin, and K. L. Wang, *Phys. Rev. B* 99, 2019, 184403.



CP-12. Quantitative Estimation of Thermoelectric Contributions in Spin Pumping Signals Through Microwave Photoresistance Measurements.

J. Cheng¹, K. He¹, M. Yang¹, Q. Liu¹, R. Yu¹, L. Sun^{1,2}, J. Ding³, B. Miao^{1,2}, M. Wu³ and H. Ding^{1,2}

1. Nanjing University, Nanjing, China; 2. Collaborative Innovation Center of Advanced Microstructures, Nanjing, China; 3. Colorado State University, Fort Collins, CO, United States

Spin pumping is a technique widely used to generate pure spin current and characterize the spin-charge conversion efficiency of heavy metals, which utilizes a microwave to excite the precession of the magnetic moments. However, the microwave irradiation may also bring possible thermoelectric artifacts. Both the eddy currents in conductors and magnon-phonon scattering in ferromagnet could heat the samples [1]. Typically, for devices with a thin film deposited on a thick substrate, the temperature increase might establish a perpendicular temperature gradient, which gives rise to thermoelectric signals such as the longitudinal spin Seebeck effect (LSSE) [2] and the anomalous Nernst effect (ANE) [3]. Therefore, the spin pumping signals are potentially contaminated with thermoelectric contributions [4]. The separation of the LSSE and ANE contributions from the spin pumping signal is not straightforward. Under an out-of-plane (perpendicular) temperature gradient, the LSSE and ANE produce thermoelectric signal with $E_{th} \propto \nabla_z T \times M$, where M represents the magnetization direction of ferromagnet. One can readily find that the spin pumping, LSSE, and ANE voltages all share the same symmetry with the same angular dependence, hence inseparable and additive. Furthermore, if the thermoelectric contributions are dominating, the measured signal in the ferromagnet/heavy metal structure may even fail to denote the spin Hall angle sign of the heavy metal [5]. Therefore, it is important to develop a quantitative method to separate thermoelectric contributions in the spin pumping experiments. In this work, we present a universal and quantitative method to obtain the thermoelectric contributions in spin pumping voltage via the assistance of the microwave-photoresistance measurements. We apply this method on two typical systems, i.e., Py(Ni₈₀Fe₂₀)/Pt and YIG(Y₃Fe₅O₁₂)/Pt bilayers, and find that the microwave radiation indeed can raise the sample temperatures and create a perpendicular temperature gradient. This vertical temperature gradient induces a sizable thermal voltage due to the LSSE and the ANE near zero magnetic field, which acts as a background for spin pumping signals at higher fields. However, the additional heat dissipation due to magnon-phonon scattering at the ferromagnetic resonance condition is negligibly small, in consistent with previous findings [6]. This conclusion is further supported by the field-dependent microwave absorption measurement using a vector network analyzer. Therefore, we conclude that the thermoelectric contributions are little, if any, as compared with the spin pumping signal in our measurement geometry.

[1] N. Yoshikawa and T. Kato, J. Phys. D: Appl. Phys. Vol. 43, p. 425403 (2010). [2] K. Uchida, H. Adachi and E. Saitoh, Appl. Phys. Lett. Vol. 97, p. 172505 (2010). [3] T. Miyasato, N. Abe and Y. Tokura, Phys. Rev. Lett. Vol. 99, p. 086602 (2007). [4] Y. Huo, F. L. Zeng and Y. Z. Wu, Phys. Rev. Appl. Vol. 8, p. 014022 (2017). [5] W. W. Lin and C. L. Chien, arXiv:1804.01392(2018). [6] P. Noel, M. Cosset-Cheneau and J. P. Attane, J. Appl. Phys. Vol. 127, p. 163907 (2020).

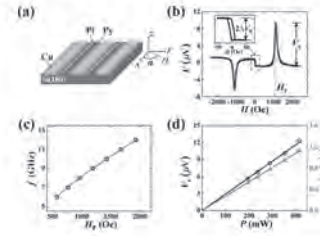


Fig. 1 (a) Schematic illustration of the experimental setup for spin pumping measurements of Py/Pt bilayer. (b) Field-dependent voltage for a Py(6 nm)/Pt(3 nm) bilayer stripe with 8.5 GHz microwave irradiation, where the magnetic field is applied along the y-direction. The black symbols represent the experimental data, and the red lines are the Lorentz line fittings. The inset presents the zoomed-in feature near zero magnetic field. $2\Delta V_0$ denotes the difference of the voltage background for the positive and negative fields. (c) Microwave frequency f dependent resonance field H_r . Black circles are the experimental data, and the red line is the fitting with Kittel equation. (d) Microwave input power dependent V_r (black hexagon, left scale) and ΔV_0 (red triangle, right scale). The lines are linear fittings.

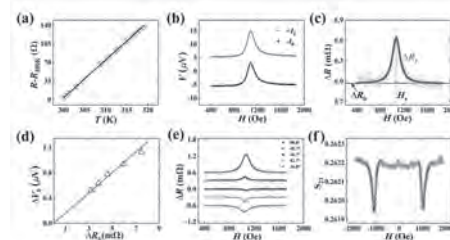


Fig. 2 (a) R - T curve of a Py(6 nm)/Pt(3 nm) bilayer near room temperature, with a slope of $7.12(\pm 0.02) \Omega/K$. $R_{300K} = 8.86 \text{ k}\Omega$. (b) Magnetic field-dependent voltages with dc current $+I_0$ ($+0.9 \text{ mA}$, red curve) and $-I_0$ (-0.9 mA , black curve) for the Py/Pt sample, respectively. (c) The resistance difference ΔR of the Py/Pt bilayer between microwave on and off states. (d) Linear relation between the thermoelectric ground ΔV_0 and the resistance difference background ΔR_b . (e) Magnetic field dependent ΔR for different α . The curves are shifted for clarity. (f) Magnetic field-dependent S_{21} parameter data for a “7 mm×7 mm” Py(6 nm)/Pt(3 nm) film.

CP-13. Qualitative Evaluation of the Temperature Dependence of Dynamical Spin Injection in CoFeB/Pt/CoFeB Trilayer Thin Films.

S. Obinata¹, R. Iimori¹ and T. Kimura¹

1. Physics, Kyushu University, Fukuoka, Japan

Dynamical spin injection based on ferromagnetic resonance (FMR) has been intensively investigated owing to its simple structure with variable applications [1]. When the FMR is excited in ferromagnetic-metal (FM)/nonmagnetic-metal (NM) bilayer thin films, the spin current flows from the FM layer into the NM layer. Although the mechanism of the dynamical spin injection is mainly explained by spin pumping, FMR-heating could be a possible reason for the dynamical spin injection [2]. To investigate the dominant contribution for the dynamical spin injection, we measured the temperature dependence of the inverse spin Hall signal in a CoFeB/Pt/CoFeB trilayer structure. Fig.1 shows the schematic illustration of the measurement system. Here, the bottom Cu layer acts as the coplanar wave guide for generating a high frequency magnetic field, resulting in the efficient excitation of the FMR of the trilayer structure. In addition, since the Cu layer with sufficiently low electrical resistivity is directly connected to the trilayer, we are able to purely observe inverse spin Hall signal in the Pt due to the dynamical spin injection with eliminate the spurious signals such as the rectified anisotropic magnetoresistance and anomalous Nernst effects.[3] The observed inverse spin Hall signals at room temperature (297K) and low temperature(77K) are shown in Fig.2. It should be emphasized that the sign of the inverse spin Hall signal at 77 K is opposite from that at 297 K. This can be explained by the change of the thermal gradient in CoFeB/Pt/CoFeB/Cu/Sub, indicating that the FMR heating is a dominant mechanism for the dynamical spin injection.

[1] Ryo Iguchi and Eiji Saitoh JPSJ 86. 011003(2017) [2] Kazuto Yamanoi et al, APL107, 182410(2017) [3] Sora Obinata et al. MMM Conference November2-6, 2020; virtual

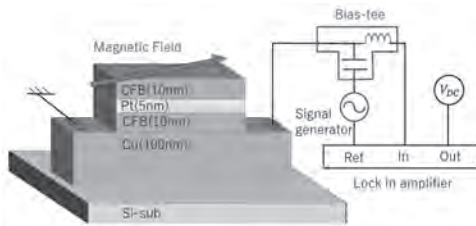


Fig.1 Schematic illustration of measurement setup

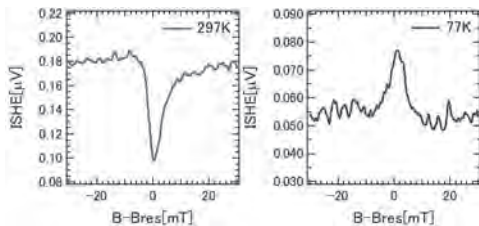


Fig.2 ISHE signals measured at 297K and 77K

CP-14. Direct Magneto-Optical Observation of Current-Induced Spin Accumulation in InAs two-Dimensional Electron gas (2DEG) Structure.

W. Lee¹, S. Kim^{2,3}, K. Lee¹, H. Koo^{2,3} and G. Choi⁴

1. Department of Physics, Korea Advanced Institute of Science and Technology, Daejeon, The Republic of Korea; 2. KU-KIST Graduate School of Converging Science and Technology, Seongbuk-gu, The Republic of Korea; 3. Korea Institute of Science and Technology, Seongbuk-gu, The Republic of Korea; 4. Department of Energy Science, Sungkyunkwan University College of Natural Science, Suwon, The Republic of Korea

Spin-orbit coupling (SOC) is one of the most important parts of spintronics. The momentum and spin of electrons are coupled by spin-orbit interaction. Two of the representative phenomena that originated from SOC are Rashba-Edelstein effect (REE) [1] and spin Hall effect (SHE) [2, 3]. There are numerous studies on REE and SHE, but direct observation of those effects has been elusive. Concerning the spin Hall effect, a current-induced spin accumulation has been directly observed using the magneto-optic Kerr effect (MOKE). [4, 5] However, there has been no direct observation of spin accumulation induced by the Rashba-Edelstein effect. In this study, we investigated the current-induced spin accumulation in InAs two-dimensional electron gas (2DEG) channel directly by using the MOKE. As a result, the in-plane spin accumulation throughout the channel by REE and the out-of-plane spin accumulation at the edges of the 2DEG channel by SHE were directly observed. Our result is of importance because it exhibits both spin accumulation components originating from REE and SHE in the same structure and they are unambiguously separated. Moreover, we determined the current-induced magneto-optic constant of InAs 2DEG, which is essential for further optical studies on this structure.

[1] V. M. Edelstein, Spin polarization of conduction electrons induced by electric current in two-dimensional asymmetric electron systems. *Solid State Communications* 73, 233-235. (1990) [2] M. I. D'yakonov, and V. I. Perel, Current-induced spin orientation of electrons in semiconductors. *Phys. Lett.* 35A, 459 (1971) [3] M. I. D'yakonov, and V. I. Perel, Possibility of Orienting Electron Spins with Current. *Sov. Phys. JETP Lett.* 13, 467 (1971) [4] Y. K. Kato, R. C. Myers, A. C. Gossard, and D. D. Awschalom, Observation of the spin Hall effect in semiconductors. *Science* 306, 1910-1913. (2004) [5] C. Stamm, C. Murer, M. Berritta, J. Feng, M. Gabureac, P. M. Oppeneer, and P. Gambardella, Magneto-Optical Detection of the Spin Hall Effect in Pt and W Thin Films. *Phys. Rev. Lett* 119, 087203. (2017)

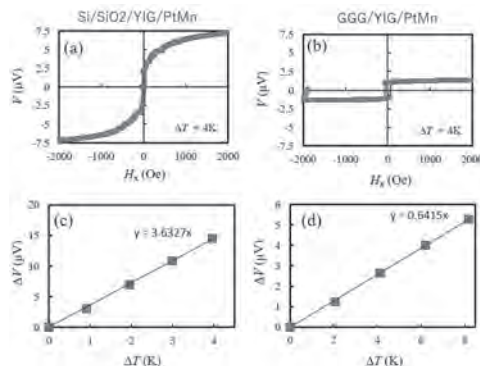
CP-15. Spin Seebeck Effect in Antiferromagnetic PtMn/YIG(Yttrium Iron Garnet) Thin Films.

S. Ranjbar¹, A. Yagmur¹, M. Al-Mahdawi³, M. Oogane^{2,3}, Y. Ando^{2,3}, K. Tanabe¹ and H. Awano¹

1. Toyota Technological Institute, Nagoya, Japan; 2. Tohoku University - Aobayama Campus, Sendai, Japan; 3. Center for Science and Innovation in Spintronics (Core Research Cluster), Organization for Advanced Studies, Tohoku University, Sendai, Japan

The generation and detection of spin currents are key a role in investigating basic physics phenomena and for applications in the field of spintronics. One method of generating spin current is the spin Seebeck effect (SSE) via applying a heat current along with the magnetic materials. The spin current can be converted to an electrical voltage in large spin-orbit coupling materials due to the inverse spin Hall effect (ISHE). Recently, many reports have been shown that paramagnetic, ferrimagnetic, and antiferromagnetic materials reveal large spin-to-charge current conversion [1-4]. In this work, we investigate the SSE in thin-film the antiferromagnetic PtMn on top of sputtered YIG films. We prepared the following film stacks using rf and dc magnetron sputtering: substrate/buffer/Y₃Fe₅O₁₂ (100 nm)/800 C/Pt_{0.35}Mn_{0.65} (10 nm)/MgO (2 nm)/Ta (1 nm)/375 C, where the temperatures are the post-annealing temperatures, and the films are grown at the room temperature. We used four substrate/buffer combinations: Gd₃Ga₅O₁₂ (GGG) sub., Si/SiO₂ sub., Si/SiO₂/Ta (5 nm), and Si/SiO₂/Ta (5 nm)/Pt (5 nm). We optimized the YIG's sputtering growth condition for stoichiometry, high saturation magnetization, low ferromagnetic resonance damping constant, and low surface roughness. The PtMn is made with rich Mn composition having an fcc phase. Subsequently, we measured the SSE. We applied a thermal gradient across the thickness direction of the substrate, and measured the conversion of generated spin current to electric voltage by means of ISHE in PtMn. Figure 1(a-b) shows our measurement result in the Si/SiO₂/YIG/PtMn and GGG/YIG/PtMn samples as a function of applied magnetic field H_x at $\Delta T = 4$ K. We observed that SSE voltage V_{SSE} is revealed in both samples. Moreover, the magnitude of V_{SSE} is proportional to ΔT as shown in Fig. 1(c-d). Even though our films are antiferromagnetic and have a Mn-rich composition, the magnitude of V_{SSE} in our samples is comparable to what is found in YIG/Pt systems [4]. Further data and discussion will be presented. This work was supported by the Center for Science and Innovation in Spintronics (CSIS), Center for Spintronics Research Network (CSRN), Tohoku University, and by JSPS KAKENHI Grant Number JP19K15429. JP20H02185

[1] Nakata et al., "Spin Seebeck voltage enhancement by Mn system metals insertion at the interface between YIG and nonmagnetic layer." *Japanese Journal of Applied Physics* 58, no. SB (2019): SBBI04. [2] Seki et al., "Observation of inverse spin Hall effect in ferromagnetic FePt alloys using spin Seebeck effect." *Applied Physics Letters* 107, no. 9 (2015): 092401. [3] Kikkawa et al. "Longitudinal spin Seebeck effect free from the proximity Nernst effect." *Physical review letters* 110, no. 6 (2013): 067207. [4] Mendes et al., "Large inverse spin Hall effect in the antiferromagnetic metal Ir 20 Mn 80." *Physical Review B* 89, no. 14 (2014): 140406



(a-b) Field dependence of SSE voltage in the PtMn at $\Delta T=4$ K, (c-d) ΔV as a function of ΔT .

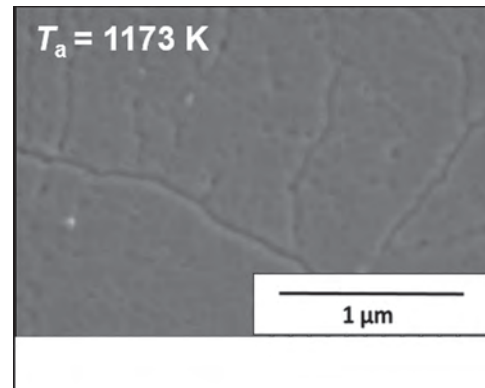
CP-16. Annealing Temperature Dependence of Longitudinal Spin Seebeck Voltage in YIG Films Prepared by sol-gel Spin Coating Method.

K. Yamada¹, S. Masaki¹ and M. Shima¹

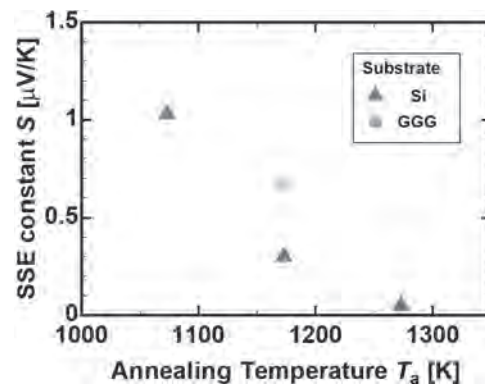
1. Chemistry and Biomolecular Science, Gifu University, Gifu, Japan

Thermoelectric conversion elements using the spin Seebeck effect (SSE) have attracted much attention owing to their unique physical properties as well as the industrial applications in a relatively simple structure [1-3]. Many studies using $\text{Y}_3\text{Fe}_5\text{O}_{12}$ (YIG) have been reported as a magnetic insulator for SSE measurements. Since YIG is an insulator with high Curie temperature that allows magnons to propagate over a long distance, it is suitable for SSE observation. SSE measurements are often carried out using YIG prepared in a sintered bulk or a film grown by a physical vapor deposition method, SSE has also been studied using YIG films prepared by metal-organic decomposition (MOD) which is a simple process used for surface coating [3]. We have previously observed SSE in YIG films prepared on a Si substrate by co-precipitation, which consist of densely packed YIG nanoparticles [4]. In order to enhance the SSE voltage, the YIG films are required to have a flat film surface made by a different chemical process, which enables magnons to coherently propagate. In this paper, we report on the longitudinal SSE (LSSE) voltage in YIG films prepared on a Si or gadolinium gallium garnet (GGG) substrate by sol-gel spin-coating to investigate the annealing-temperature dependence of LSSE voltage in the samples. YIG film samples were synthesized by sol-gel and subsequent spin-coating processes, followed by annealing at $T_a = 1073\text{-}1273$ K for 0.5 hour in air. From the XRD spectra of the YIG films, diffraction peaks associated with the garnet phase are readily observed in the spectra of all the annealed samples, proving that they are polycrystalline YIG. Figure 1 shows a surface morphological SEM image from a YIG film made on a Si substrate annealed at 1173 K. The average surface roughness measured by SPM is ~ 10 nm or less, which is 30% smaller than that of YIG films prepared by co-precipitation. The areal fraction of voids estimated in the film surface by SEM imaging is $\sim 10\%$, which is 75% smaller than those of YIG films prepared by co-precipitation. The obtained results indicate that the YIG films with a flatter surface can be made by the sol-gel method. To conduct SSE voltage measurements, a 5 nm Pt metal was sputtered on the YIG films. A temperature gradient ΔT was applied between the top of each sample (Pt side) and the bottom of the substrate to measure the voltage induced by LSSE. Figure 2 shows the variation of the SSE constant S with the annealing temperature T_a . The values of S in each sample are calculated from the ΔT dependence of the saturation SSE voltage $V_{\text{SSE}}^{\text{Sat}}$. The value of S for YIG/Pt films made on a Si substrate decreases with increasing T_a , showing the same trend as those observed for co-precipitated YIG films, which is attributable to the microstructural evolution of the nanocrystalline YIG films upon annealing. Besides, the magnitude of S is at least 30% smaller than that of co-precipitated YIG films. It is speculated that the observed decrease in the magnitude of S is owing to the increase in the interfacial area between densely packed nanoparticles as the increase in the coercive force of YIG films prepared by sol-gel is observed according to their magnetic measurements by VSM. The values of S in the YIG/Pt films synthesized on a GGG substrate annealed at 1173 K are larger than those made on a Si substrate presumably because a single crystal YIG film is formed on the GGG substrate which yields a high efficiency of magnon excitation.

[1] K. Uchida et al, Nature, Vol. 455, p. 778 (2008) [2] K. Uchida et al, Nat. Mater. Vol. 9, p. 894 (2010) [3] A. Kirihara et al, Nat. Mater. Vol. 11, p. 686 (2012) [4] K. Yamada et al, IEEE Trans. Magn. Vol. 55, p. 4500104 (2019)



SEM surface image of a YIG film annealed at 1173 K.



SSE constants S of Pt(5 nm)/YIG films on a Si or GGG substrate plotted as a function of T_a .

Session CQ
NOVEL IMAGING AND MEASUREMENT TECHNIQUES I
(Poster Session)

Jose R. L. Mardegan, Chair
DESY, Hamburg, Germany

CQ-01. Calibration of a Coil Array Geometry Using an X-ray Computed Tomography.

D. Oyama¹, Y. Adachi¹, M. Higuchi¹ and G. Uehara¹
 1. Applied Electronics Laboratory, Kanazawa Institute of Technology,
 Kanazawa, Japan

Introduction: Biomagnetic measurement systems, such as a magnetoencephalography (MEG), are commonly composed of multi-channel magnetic sensor array more than 100. It is very important to know the positions, orientations, and sensitivities of the magnetic sensors precisely to accurately estimate the neuronal activity. So far, a calibration technique is employed to measure the sensor geometry and sensitivity after assembling or cooling the sensor arrays [1]. This calibration technique is performed by estimating the geometry and sensitivity of the sensors from the measured magnetic field distribution generated by a multi-coil array. However, there is no discussion about the accuracy of the estimation because the coil array itself has not been calibrated and its accuracy has not been evaluated. Therefore, we propose the calibration technique for the coil array based on the three-dimensional (3D) measurement using an X-ray computed tomography (CT). In this paper, we present a calibration result of the coil array and a comparison of the accuracy of the MEG source localization between using the designed and calibrated coil array geometries to measure positions, orientations, and sensitivities of MEG sensors. We fabricated a 18-channel coil array. This coil array was composed of 6 coil modules that have concentric 3 coils orthogonal to each other. The diameter and the distance between each coil were designed 30 mm and about 70 mm, respectively. (1) 3D measurement using X-ray CT The 3D measurement was performed using an X-ray CT machine (inspeXio SMX-225CT FPR HR, Shimadzu Corporation). The center position, the orientation of the normal vector, and the radius of each coil were obtained by fitting a circle equation to the 3D data. We call this process “calibration of the coil array”. (2) Measurement of the MEG sensor geometries In this study, we used a whole-head MEG system, which was installed at the Kanazawa Institute of Technology [2]. This MEG system consisted of 160 arrayed SQUID (superconducting quantum interference device) sensors, which had the first-order axial gradiometers. The coil array was placed at the center of the helmet of the MEG cryostat, and the magnetic signals were generated by applying sinusoidal current waveform (80 Hz) to each coil. After measuring the magnetic signals, we estimated the sensor array layout (position, orientation, and sensitivity of each sensor). The sensor array layouts were obtained by solving the inverse problem using (A) designed and (B) 3D measured coil array geometry. (3) MEG source localization In order to confirm that the performance of the MEG system can be improved by employing the 3D-measured coil array geometry, we compared the source localization accuracy using the sensor layouts between (A) and (B). An MEG phantom, which emulates the neuronal activity in human brain as equivalent current dipoles (ECDs) [3], was used to provide the signal sources. The magnetic signals from the ECDs were measured by the MEG sensors, then the sources were localized using the sensor layouts (A) and (B). Results and Discussions: (1) 3D measurement using X-ray CT Figure 1 shows the results of the 3D measurement of the coil array using the X-ray CT. Figure 1 (a) is the entire polygon data converted from the X-ray CT image, and Fig.1 (b) shows the designed geometries of the coils in the module 1 (blue) and the obtained circles based on the X-ray CT measurement (red). The differences between designed and the 3D-measured coil geometries were 0.6 ± 0.3 mm, 0.7 ± 0.4 degrees, and 0.3 ± 0.1 mm (mean \pm standard deviation of 18 coils) in the center position, the orientation of the normal vector, and the radius, respectively. (2) Measurement of the MEG sensor geometries The sensor array layouts were estimated using the designed and the 3D-measured coil array geometries. The differences of the estimated layouts were 1.2 ± 0.9 mm, 1.0 ± 0.6 degrees, and 0.7 ± 1.9 % (mean \pm standard deviation of 160 sensors) in position, orientation, and sensitivity, respectively. (3) MEG source localization Figure 2 shows the differences between true value and localized values of the sources in position and orientation, respectively. Both displacements in position and orientation decreased by using the 3D-measured coil array geometry. It was demonstrated that the source localization accuracy was improved by defining the sensor layout using the calibrated coil array geometry. Conclusion: We demonstrated the calibration method of the coil array based on the 3D measurement using the X-ray CT machine. Although

the coil array was fabricated precisely, the calibration of the coil array is necessary to bring the best out of the MEG system.

[1] T. Yoshida, et al., “Calibration system for multichannel SQUID magnetometer,” in *Proc. 16th Annu. Int. Conf. IEEE Eng. Adv. New Opportunities Biomed. Eng.*, pp.171-172 (1994). [2] H. Kado, et al., “Magnetoencephalogram systems developed at KIT,” *IEEE Trans. Appl. Supercond.*, vol. 9 (2), pp. 4057-4062 (1999). [3] D. Oyama, et al., “Dry phantom for magnetoencephalography – Configuration, calibration, and contribution,” *J. Neurosci. Methods*, vol. 251, pp. 24-36 (2015).

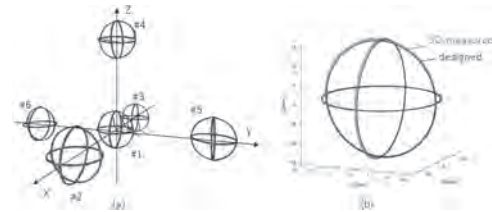


Fig. 1 Results of X-ray CT measurements of the coil array. (a) entire polygon data, (b) designed and 3D-measured geometries of the coils in the module 1.

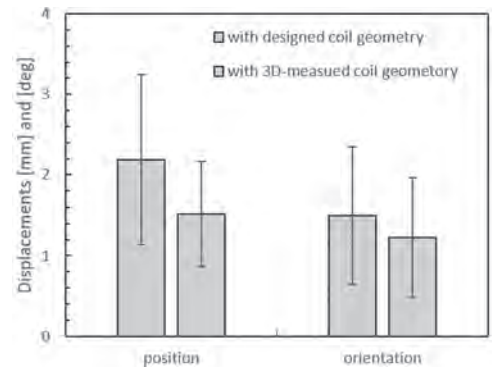


Fig. 2 Results of the source localization experiment. This graph shows the differences between the true value and the localized values of the signal sources in position and orientation. The lengths of the squares and the error bars indicate the mean and the standard deviation of 49 signal sources).

CQ-02. Residual Flux Density Measurement Method of the Single-Phase Transformer Based on Phase Difference.*Y. Ren*^{1,2}*1. Hebei University of Technology State Key Laboratory of Reliability and Intelligence of Electrical Equipment, Tianjin, China; 2. Hebei University of Technology, Tianjin, China*

Inrush current is the reason why large power transformers cannot close without load^[1]. Controlling the closing phase of circuit breaker can effectively reduce the inrush current when the circuit breaker is closed. However, it is necessary to know the value and direction of residual flux in the transformer core to control the closing phase angle. Therefore, the accurate detection of residual flux has important reference significance for the protection of power transformer. This paper proposes a method of measuring residual flux density in single-phase transformers based on the phase difference between the test voltage and the transient current, and establishes the relationship between the phase difference and residual flux based on the magnetic properties of the iron core. The finite element method is used to model and analyze the measured square transformer core, and the fitting relationship between residual flux and phase difference is obtained according to the calculation result. The experimental results show that the relative error between the finite element calculation results and the experimental results is within 5.93%, which verifies the feasibility of the proposed method and the accuracy of the relation obtained by the finite element calculation. The relationship between different residual flux and phase difference is obtained, which provides effective information for controlling the closing phase of circuit breaker.

[1] Y. Wang, Z. Liu and H. Chen, "Research on Residual Flux Prediction of the Transformer," *IEEE Transactions on Magnetics*, Vol. 53, no. 6, pp. 1-4, June 2017.

CQ-03. Three-Dimensional Magnetic Field Gradient Imaging of Permanent Magnet by Alternating Magnetic Force Microscopy: Transformation of Measuring Magnetic Field Direction Based on MFM tip Transfer Function.

H. Saito¹, S. Wada¹ and T. Matsumura¹

1. Graduate School of Engineering Science, Akita University, Akita, Japan

I. Introduction Observation and analysis of magnetic domain structure of magnetic materials with high spatial resolution are essential for understanding and improving the magnetic properties of the materials. In this regards, magnetic force microscopy (MFM) is widely used to observe the magnetic domain structure with high spatial resolution. MFM detects the gradient of magnetic field of which direction is the same as that of MFM tip magnetization. The control of the measuring direction is important to analyze the magnetic domain structure precisely. However, the measuring direction control is not easy especially for hard magnetic materials because the tip magnetization often varies by the strong sample magnetic field at the measuring position. In recent years, we have developed new novel MFM, which enables to fix the measuring field direction on DC magnetic field imaging, based on our developed alternating magnetic force microscopy (A-MFM) [1] and highly sensitive Co-GdO_x superparamagnetic tip (SP tip) [2] of which magnetization direction is parallel to the applied magnetic field. A-MFM detects magnetic force gradient near the sample surface with high spatial resolution by using the frequency modulation of cantilever oscillation caused by off-resonant alternating magnetic force [1]. For the imaging of hard magnetic materials, the SP tip, which is magnetized normal to the sample surface by homogeneous AC magnetic field, is used and the SP tip detects the alternating magnetic force between AC tip magnetization and DC magnetic field from the sample and measure the gradient of magnetic field normal to the sample surface [3]. We successfully observed the magnetic domain structure of a very rough fractured Sr ferrite magnet without topographic crosstalk by fixing the measuring direction of DC magnetic field normal to the sample surface [3]. In this study, by using an observed A-MFM image of NdFeB sintered magnet of which measuring direction of magnetic field is normal to the sample surface, we demonstrate three-dimensional magnetic field gradient imaging by measuring field direction transformation, which is based on MFM tip transfer function [4]. A-MFM images, which were measured by SP tip, satisfy the necessary condition of the proposed three-dimensional imaging that the measuring detection of magnetic field for the observed image is fixed. II. Principle of three-dimensional magnetic field gradient imaging Generally, MFM signal of $\partial F_z/\partial z$ can be expressed by $m_x(\partial^2 H_x/\partial z^2) + m_y(\partial^2 H_y/\partial z^2) + m_z(\partial^2 H_z/\partial z^2)$, where the z direction is normal to the sample surface and $m=(m_x, m_y, m_z)$ and $H=(H_x, H_y, H_z)$ are the tip magnetization and the magnetic field from the sample, respectively. Here our used Co-GdO_x SP tip is composed of magnetically separated magnetic nanoparticles of which diameter is less than 7 nm and each nanoparticle is thought to behave as a magnetic dipole m . The magnetic field gradient component can be expressed by the transfer function G for sample's magnetic charge ρ_m , which is the source of magnetic fields [4]. For examples, gradient of perpendicular magnetic field ($\partial^2 H_z/\partial z^2$) is expressed by the following in wave number k space. $(\partial^2 H_z/\partial z^2)(k_x, k_y, z) = G[\partial^2 H_z/\partial z^2](k_x, k_y, z-z_0)\rho_m(k_x, k_y, z_0)$, where the $z-z_0$ is the tip-sample distance. In the case of obtaining the $(\partial^2 H_x/\partial z^2)$ image from $(\partial^2 H_z/\partial z^2)$ image, the measuring direction transformation filter $G[\partial^2 H_x/\partial z^2]/G[\partial^2 H_z/\partial z^2]$ is used in the following. $(\partial^2 H_x/\partial z^2)(k_x, k_y, z) = G[\partial^2 H_x/\partial z^2](k_x, k_y, z-z_0)\rho_m(k_x, k_y, z_0) = G[\partial^2 H_x/\partial z^2]/G\partial^2 H_z/\partial z^2(k_x, k_y, z)$. The $\partial^2 H_y/\partial z^2$ image can be obtained in the similar way. The proposed method enables to obtain three magnetic field gradient components from only one component. Various images, such as the amplitude and direction of magnetic field gradient also can be obtained by using these three components. III. Experimental procedure Our A-MFM system was based on a magnetic force microscope with an electromagnet to apply AC magnetic field to the tip for generating off-resonant alternating magnetic force between the AC tip magnetization and DC magnetic field from the sample. A-MFM image was observed at room temperature in air atmosphere using home-made high susceptibility superparamagnetic Co-GdO_x granular alloy film [2] coated Si tip. The film thickness was 100 nm. The amplitude and the frequency of the AC magnetic field were 200 Oe and 89 Hz, respectively. A sample of demagnetized NdFeB anisotropic sintered magnet with

c-plane was placed over the electromagnet. IV. Results Fig.1(a) shows the $\partial^2 H_z/\partial z^2$ image of NdFeB demagnetized sintered magnet. Fig(b) and (c) show the transformed $\partial^2 H_x/\partial z^2$ and $\partial^2 H_y/\partial z^2$ image from the $\partial^2 H_z/\partial z^2$ image, respectively. Fig(d), (e) and (f) show the images of the intensity of magnetic field gradient $|\partial^2 H/\partial z^2|$, polar angle θ and azimuthal angle Φ of the magnetic field gradient, respectively. As seen in these figures, magnetic field distribution is clearly observed. This method needs only one MFM image of which the measuring detection of magnetic field is fixed, while most methods of three-dimensional magnetic field imaging needs three magnetic field sensors for each three-dimensional direction. The proposed imaging is thought to be useful to obtain the precise information of magnetic field distribution and analyze the magnetic domain structure.

- [1] H. Saito, H. Ikeya, G. Egawa, S. Ishio, S. Yoshimura, J. Appl. Phys., Vol. 105, p.07D524(2009), [2] Y. Cao, P. Kumar, Y. Zhao, Y. Suzuki, S. Yoshimura, H. Saito, J. Magn. Magn. Mater., Vol. 462, p.119 (2018), [3] Y. Cao, Y. Zhao, P. Kumar, S. Yoshimura, H. Saito, J. Appl. Phys., Vol. 123, p.224503 (2018), [4] H. Saito, J. Chen, S. Ishio, J. Magn. Magn. Mater., Vol. 191, p.153 (1999)

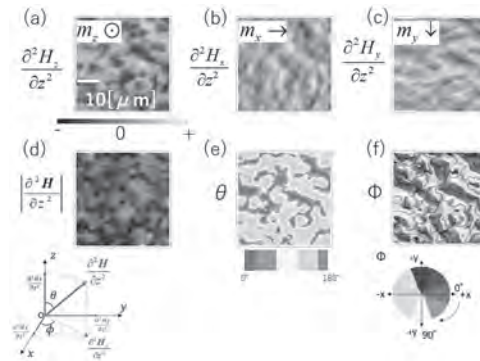


Fig.1 (a) Measured perpendicular magnetic field gradient image $\partial^2 H_z/\partial z^2$ and its signal transformed images [(b) $\partial^2 H_x/\partial z^2$, (c) $\partial^2 H_y/\partial z^2$, (d) $|\partial^2 H/\partial z^2|$, (e) polar angle θ and (f) azimuthal angle Φ] for a NdFeB sintered magnet.

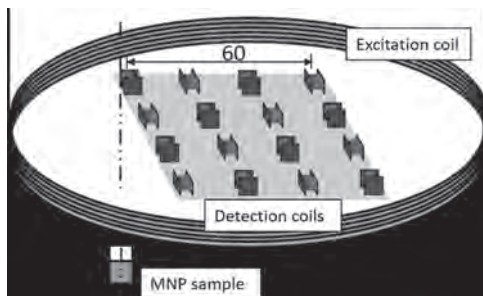
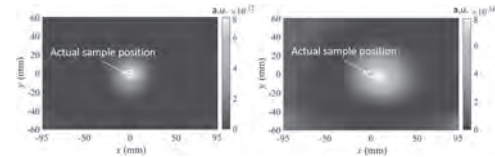
CQ-04. Inverse Problem Analysis in Magnetic Nanoparticle Tomography With Minimum Variance Spatial Filter.

N. Okamura¹, T. Sasayama¹ and T. Yoshida¹

¹. Kyushu University, Fukuoka, Japan

INTRODUCTION In recent years, imaging of magnetic nanoparticles (MNPs) has attracted attention as a new diagnostic imaging technique for the imaging of certain targets, such as cancer cells [1]. We previously proposed an MNP imaging method, “magnetic nanoparticle tomography” (MNT), that uses multiple magnetic sensors [2], [3]. In the previous study, an inverse problem analysis was performed to estimate the position of MNPs using the non-negative least squares method (NNLS), which is often used for magnetic particle imaging (MPI). The NNLS method achieves high sensitivity and spatial resolution. However, due to the existence of measurement noise and high sensitivity of NNLS, some MNPs are incorrectly estimated, that is, some artefacts appear. In this study, we apply the minimum variance spatial filter (MV-SF), which is often used in magnetoencephalography (MEG) inverse problem analysis [4], to reduce the artefacts. **METHODS** The experimental setup is presented in Fig. 1. The Resovist MNP sample was arranged in a sinusoidal magnetic field, which was generated using an excitation coil. The third harmonic magnetic field from MNPs was detected using 16 detection coils. To improve the sensitivity, a cancellation circuit for the fundamental magnetic field was employed. The two-dimensional concentration map of the MNP sample was subsequently obtained by the application of the MV-SF. The distance between the MNP sample and the imaging system (excitation coil and detection coils) was set from 25 mm to 40 mm at intervals of 5 mm. We used two samples with different concentrations of 100 $\mu\text{g-Fe}$ and 500 $\mu\text{g-Fe}$ and estimated the positions for each of them. **RESULTS** The result of the reconstructed map when the MNP sample was set at are shown in Fig. 2. The white circle in the figure represents the actual sample position. Fig. 2 (a) depicts the result for a sample containing 500 $\mu\text{g-Fe}$. This result reveals that a sharp signal peak position is observed in the vicinity of the sample position. Fig. 2 (b) exhibits the result for a sample containing 100 $\mu\text{g-Fe}$. This result indicates that the error between a sharp signal peak position and the actual sample position is within 10 mm. No artefacts appear in both results, contrary to the results using NNLS [3]. From these results, we can conclude that MV-SF is useful for reducing the artefact and estimating the positions of MNPs in magnetic nanoparticle tomography. **ACKNOWLEDGMENTS** This work was supported by the Japan Society for the Promotion of Science (JSPS) Grant-in-Aid for Young Scientists [grant number JP19K14996], and by a research grant from the Mazda Foundation.

[1] T. Knopp and T. M. Buzug, “Magnetic Particle Imaging—An Introduction to Imaging Principles and Scanner Instrumentation,” Springer, 2012. [2] T. Sasayama, T. Yoshida, K. Enpuku, “Two-Dimensional Magnetic Nanoparticle Imaging Using Multiple Magnetic Sensors Based on Amplitude Modulation,” *Journal of Magnetism and Magnetic Materials*, Vol. 505, 2020, Art. no. 166765. [3] T. Sasayama, N. Okamura, and T. Yoshida, “Sensitivity Improvement of Magnetic Nanoparticle Imaging by Compensation with Digital-to-Analog Converter,” *IEEE Trans. Magn.* In press. DOI: 10.1109/TMAG.2020.3014375. [4] K. Sekihara and S. S. Nagarajan, “Adaptive Spatial Filters for Electromagnetic Brain Imaging,” New York, USA: Springer-Verlag, 2008.



CQ-05. Estimation of Magnetocardiography Current Sources Using Multiple Spatial Filters.

K. Kobayashi¹, M. Iwai¹, Y. Ono¹ and W. Sun²

1. Iwate University, Morioka, Japan; 2. Kindai University, Hiroshima, Japan

Introduction Magnetocardiography (MCG) is a noninvasive technique that detects the magnetic field generated by the electrical activity of the heart [1]. The estimation of MCG current sources is useful technics for clinical application [2]. Exact low resolution brain electromagnetic tomography (eLORETA) [3] spatial filter is used for visualizing brain activity, as it is a genuine inverse solution with exact, zero error localization in the presence of measurement and structured biological noise. However, it tends to reconstruct a large spatial extension for deep sources due to the decreasing sensitivity of the sensors. In this study, we aim to reduce the influence of the source depth in the reconstructed current sources using multiple spatial filters. **Method** In order to solve the problem of the large spatial extension for deep sources, in addition to the conventional measurement at the front (chest) of the body, the back is also measured. It is possible to improve the estimation accuracy for a deep signal source. Estimation of MCG current sources was used eLORETA spatial filter. We examined two types of spatial filters for two-side measurement. The first method (128ch method), a spatial filter (128ch) was produced by a read-field matrix using two 64ch sensors as one 128ch sensor. In this method, the regularization parameter λ which determines noise immunity has the same value on the front side and the back side. The second method (2×64 ch method), two spatial filters (64ch) were separately calculated then one spatial filter (2×64 ch) was produced from the two spatial filters (64ch). In this method, different λ can be determined on the front side and the back side, and the optimum noise immunity can be given to each. In this study, a spatial filter was created by setting λ as 1% of the maximum eigenvalue in 128ch method, 1% of the maximum eigenvalue on the front side and 5% on the back side in 2×64 ch method. We estimate MCG current sources within a $175 \text{ mm} \times 175 \text{ mm} \times 995 \text{ mm}$ volume. Three thousand two hundred and forty voxels were divided with the size of each voxel being $10 \text{ mm} \times 10 \text{ mm} \times 10 \text{ mm}$. For the forward problem, we calculate the lead-field matrix K using the Biot-Savart Law. For each current source location, K includes two columns that represent X component and Y component, respectively. **Results and Discussions** We estimated MCG sources at R peak, which indicates the activities of ventricle. Fig.1 (a), (b), and (c) show the estimation results by the conventional 64ch spatial filter, the proposed 128ch spatial filter, and the 2×64 ch spatial filter, respectively. The upper side is a front view of the heart, and the lower side is a below view of the heart. Each frame represents an analytic space. The estimation result shows voxels with a threshold of 90% or more of the strongest point of the estimated source. Compared to Fig. (a), the estimated sources of Fig. (b) and Fig. (c) are able to suppress the spatial extension of the estimated sources due to the effect of providing the measurement surface on the back side. Moreover, the estimated source of Fig. (b) is not estimated correctly because it appears not only in the ventricle but also in the vicinity of the atrium. It is considered that the estimation is incorrect due to the influence of noise because λ is constant. On the other hand, in Fig. (c), the estimated source appears at the ventricular position, and it is thought that the active position of the heart can be estimated more accurately. **Conclusion** We proposed two types of spatial filter produced method of eLORETA by two-side measurements of the front and back of the body. By using the back side in addition to the front side, the spatial extension of the estimated source could be suppressed. Among them, the signal source could be estimated at the correct position by produced using a 2×64 ch spatial filter that can determine the regularization parameter λ on the front side and the back side respectively.

[1] D. Cohen, E.A. Edelsack, J.E. Zimmerman, "Magnetocardiograms taken inside a shielded room with a superconducting point-contact magnetometer", *Applied Physics Letter*, Vol. 16, pp. 278-280, 1970. [2] J. S. W. Kwong, B. Leithäuser, J.-W. Park, C.-M. Yu, "Diagnostic value of magnetocardiography in coronary artery disease and cardiac arrhythmias: A review of clinical data," *Int. J. Cardiol.*, vol. 167, pp. 1835-1842, Sep. 2013. [3] R.D. Pascual-Marqui, "Discrete, 3D distributed, linear imaging

methods of electric neuronal activity. Part 1: exact, zero error localization", *Mathematical Physics*, arXiv: 0710. 3341, 2007.

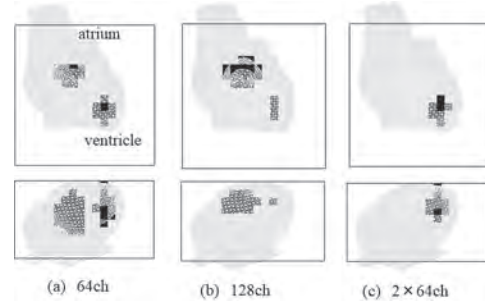
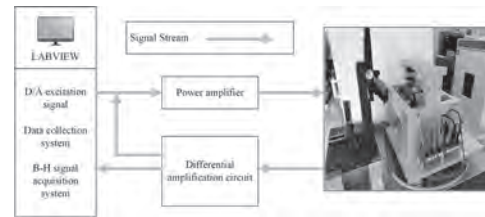


Fig. 1. The estimation results by (a) the conventional 64ch spatial filter, (b) the proposed 128ch spatial filter, (c) the 2×64 ch spatial filter. The upper side is a front view of the heart, the lower side is a below view of the heart. Each frame represents an analytic space. The voxel is the estimated source with a threshold of 90% or more of the strongest source.

CQ-06. Magnetic Properties Measurement and Analysis of Electrical Steel Sheet Under Cutting Influence.

Y. Li¹, Y. Fu¹, Y. Dou¹, C. Zhang¹ and K. Zhang¹
 1. Hebei University of Technology, Tianjin, China

Magnetic cores of electrical machines and power transformers are often affected by different manufacturing steps such as punching, bending, cutting, stacking or welding during the production process. By comparing and evaluating the effects of different manufacturing processes on the deterioration of the magnetic properties, it comes out that the cutting influence is the most harmful. A large number of studies have shown that the material will produce mechanical stress during the cutting process, which determines the increasing in total loss and the decreasing in permeability. For practical aspects, knowing the extent of these effects accurately is of great significance to the efficiency improvement of the electrical equipment. Different cutting methods have different effects on the internal structure and magnetic properties of electrical steel sheets^[1]. Laser cutting will produce thermal stress during processing, while mechanical cutting will produce plastic deformation near the cutting edge, which both lead to deterioration in the magnetic properties of the material. Studying the effect of different cutting techniques on magnetic properties is of great significance to accurately simulate and predict the iron losses of electrical equipment. The existing research methods cut the same sample into the different number of strips along the rolling direction, and these methods conclude that the magnetic performance deteriorates more obviously with the number of cuts increases. But they cannot systematically compare the differences in magnetic properties and degraded depth of the cutting technologies.^[2-5] Some scholars cut the electrical steel sheet from the middle position and studied the effect of cutting in different areas.^[6] However, the samples have to be punched to wind the B coil, which will also affect the magnetic properties of the silicon steel sheet. Therefore, the measurement of the magnetic properties affected by cutting is difficult. Different cutting has different effects on the permeability and loss of different silicon steel sheets, which is also a subject that needs to be analyzed and compared. In this paper, the influence of cutting methods, such as wire cutting and laser cutting on the local magnetic properties of the silicon steel sheet is studied and analyzed. The magnetic properties measurement system is shown in Fig. 1. A mobile B - H sensing structure is designed to sense the distribution of local magnetic properties near the cutting edges. Magnetic properties of the non-oriented (NO) silicon steel samples B35A270 and 50JN470 are measured and characterized with the variation of distance from cutting edges. The results demonstrate that the magnetic properties deterioration depends on the cutting methods and the material characteristics. Wire cutting has little effect on magnetic performance and the effect can be observed near the cutting edge. As a contrast, the decrease of the relative magnetic permeability can be observed in a deeper width of the steel strips cutting by laser. The multiple trends of laser cutting loss which vary with cutting depth are also compared and discussed. Moreover, a mathematical model used to simulate the cutting edge effect by the finite element simulation can also better describe the magnetization curve of the electrical steel sheet damage trend, thus providing a model basis for the application of electrical equipment under actual working conditions. Fig. 1 The magnetic properties measurement system



- [1] G. Loisos, A. J. Moses, Journal of Materials Processing Tech. vol.161, p.151-155 (2004). [2] A. Saleem, N. Alatawneh¹, R. R.Chromik¹, IEEE Trans. vol.52, p.1-1 (2016). [3] H. M. S. Harstick, M. Ritter, and A. Plath, Metallogr. Microstruct. Anal. vol.3, p.244-251 (2014). [4] R. Siebert, J. Schneider, and E. Beyer, IEEE Trans. Magn. vol.50, p.1-4 (2014). [5] R. Sundaria, A. Hemeida, and A. Arkkio. IECON 2019 - 45th Annual Conference of the IEEE Industrial Electronics Society. IEEE, (2019). [6] R. Rygal, A.J Moses, and N. Derebasi. Journal of Magnetism and Magnetic Materials (2000).

CQ-07. Localized Magnetic Properties Measurement of Interlocking Core Laminations.

Y. Li¹, K. Zhang¹, Y. Dou¹, Y. Fu¹ and C. Zhang¹

1. State Key Laboratory of Reliability and Intelligence of Electrical Equipment, Hebei University of Technology, Tianjin, China

In rotational ac machines, interlocking is a commonly used manufacturing method to fix the silicon steel laminations. To analyze the range of degraded magnetic properties caused by the interlocking process more accurately, the distribution of magnetic properties around the interlock was investigated and the areas damaged to varying degrees was quantified. This work is meaningful for the accurate modeling and simulation of machines.

I. Introduction Electrical steel sheets are usually assembled into core laminations through interlocking, welding or gluing. In comparison, interlocking is suitable for batch production and become the main method of fixing among electrical steel sheets currently. However, the deterioration of the magnetic properties caused by interlocking cannot be ignored. The formation of interlocks is always accompanied by plastic deformation and generation of residual stress, which will change the movement of magnetic domain under magnetization, and the hysteresis characteristics will be significantly influenced. Furthermore, the interlocking process destroys the insulation, resulting in inter-lamination short circuits. At high frequencies, the interlaminar eddy current loss even contributes more to the deterioration of magnetic properties. There have been several magnetic measurements of interlocks on lamination ring cores with primary winding and secondary winding before, and they have investigate the effect of the interlocks number, sizes, and shapes on the overall magnetic properties of lamination ring cores^[1-3]. However, the overall magnetic properties of ring cores cannot be served for accurate simulation of the interlocking process. Some preliminary attempts for interlocking localized magnetic measurements are also in progress, but they mainly focus on interlocks with a single size and a single magnetization direction^[4]. Therefore, a more comprehensive localized magnetic properties measurement is necessary.

II. Experimental and Results A localized magnetic measurement sensor with two B-needle probes and a H-coil have been manufactured. The distance between the B-needle probes is 3.5 mm and the size of the H-coil is 3 mm×3 mm. As is shown in Fig. 1(a), the sensor was connected to a three-axis precision positioning table, and the displacement accuracy of the sensor is 0.1 mm. Then four hollow square shaped samples with interlocks were wound by the exciting coils. The detailed information of samples and interlocks was shown in Fig 1(b). More than three hundred measurement points are taken on the concave and convex surfaces around each interlock to achieve higher resolution measurements of the local vector magnetic properties. Due to the length limitation of the abstract, Fig. 2 shows part of measured results at 50 Hz with 0.5 T sinusoidal excitation. The white rectangle represents the the upper part of the interlocking position. For the single sheet, it can be seen that the loss increases and the magnetic permeability decreases near the interlock. This is attributed to the generation of residual stress during the formation of the interlocks. For the ten-layer laminate, in addition to the residual stress, the insulation between laminations is destroyed near the interlocks and interlaminar short circuits is formed, which will produce extra eddy current loss. The ratio of loss increment and the ratio of permeability decrement of the three interlocks at 50Hz and 0.5T magnetic density will be provided in the whole paper. The damaged areas of varying degrees was quantified. Besides, the size of the interlocks can also cause different influence on the magnetic properties near the interlocks. The measurement were performed with Sample 2 and Sample 4, and the results show that the magnetic properties deterioration area around larger interlocks is bigger. The deterioration area hardly change with different magnetic flux. III. Conclusions In this paper, we concluded the influence of interlocks on the magnetic properties as follows: 1) The size of the interlock and the degree of localized magnetic degradation are positively but not linearly correlated. The requirements for fastened strength should be taken into consideration when selecting a appropriate size. 2) The local magnetic degradation caused by interlocking in the rolling direction is much lower than that in the transverse direction. 3) On the basis of planar distribution of magnetic degradation, different levels of magnetic degradation caused by interlocking can be quatified. Applying these results to the electrical machines can contribute to the improvement in simulations of them.

[1] J. Shen, G. Zhou, S. Jin and H. Hao, 2015 International Conference on Sustainable Mobility Applications, Renewables and Technology (SMART) IEEE., p.1-4(2015). [2] K. Senda, H. Toda, and M. Kawano, Ieej Journal of Industry Applications., Vol. 4, p.496-502(2015). [3] S. Imamori, S. Steentjes and K. Hameyer. IEEE Transactions on Magnetics., Vol. 53,(2017). [4] S. Imamori, S. Aihara and H. Shimoji, et al. Journal of Magnetism and Magnetic Materials., Vol. 500, (2020).

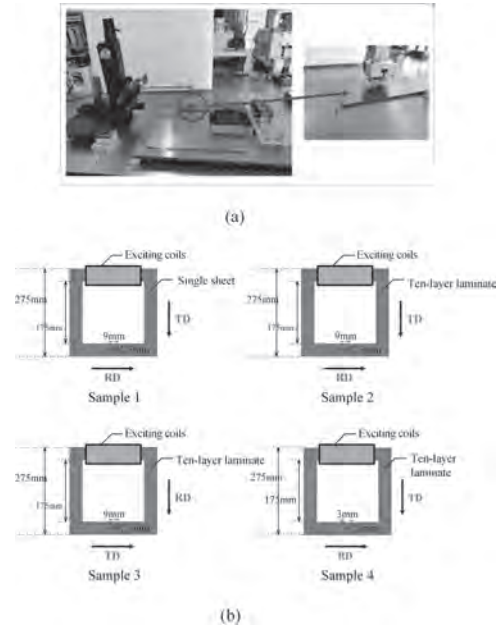


Fig 1. (a)The measuring device.(b) The detailed information of samples and interlocks.

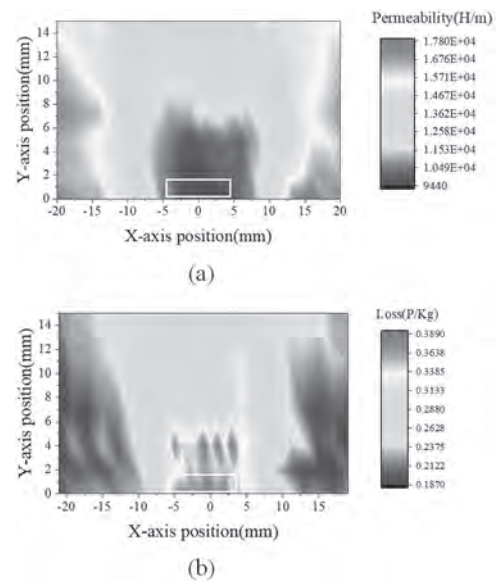


Fig2. Part of the experimentally measured planar distribution of magnetic properties at 50Hz and 0.5T magnetic density. (a) Upper part of the permeability around the interlock on the convex surfaces of Sample 1. (b) Upper part of the loss around the interlock on the concave surface on the Sample 2.

CQ-08. 3D Magnetic Structure of Domain Walls in Soft Magnetic Racetracks by MFM and X-ray Microscopy.

J. Hermosa^{1,2}, A. Hierro Rodriguez^{1,2}, J. Martín^{1,2}, A. Sorrentino³,
M. Velez^{1,2}, E. Pereiro³, C. Quiros^{1,2} and S. Ferrer³

1. Physics Dept., Universidad de Oviedo, Oviedo, Spain; 2. Centro de Investigación en Nanomateriales y Nanotecnología, El Entrego, Spain; 3. ALBA Synchrotron, Cerdanyola del Vallès, Spain

In plane magnetization stripes of soft magnetic alloys have been proposed as magnetic information storage devices. In these kind of systems, regions of uniform magnetization with opposite senses are separated by domain walls (DW), known as head-to-head or tail-to-tail walls, that may have different structures depending on the width and thickness of the stripes. Usually, two types of DW are expected, known as transverse or vortex, depending on stripe width and thickness. The work by Nguyen et al [1] has shown that in stripes thicker than 60 nm, a third type of head-to-head DW may exist, the so called Landau wall, with a significant out-of-plane magnetization core that is not homogenous across the film thickness. These walls have three internal degrees of freedom: chirality, determined by the sense of rotation of the in-plane circulation of the magnetization; polarity, defined by the upwards or downwards normal magnetization; and the sense of the Neel caps. This can result in richer topological configurations than the standard vortex and transverse walls. In particular, the Neel caps modify the shape and position of top and bottom vortices, leading to non-trivial magnetic textures and singularities with possible interest in magnetic transport applications. In this work, we have grown 80 nm -150 nm thick permalloy racetracks by sputtering on Si substrates and on 50 nm thick Si-N membranes in order to study their 3D internal structure by a combination of Magnetic Force Microscopy (MFM), X ray magnetic transmission microscopy (MTXM) and magnetic X-ray tomography [2] at the Mistral Beamline of Alba Synchrotron. Briefly, curved permalloy stripes have been defined by e-beam lithography and lift-off with width in the 200 nm - 5000 nm range and several microns length with different degrees of curvature. These structures have been characterized at remanence after saturating them with an in-plane magnetic field transverse to the average stripe orientation in order to nucleate domain walls and inhomogeneous domain structures. Figure 1(a) shows the MFM image of a 140 nm thick permalloy stripe showing a central domain wall bounded by two half vortex structures, together with a rhomboid transverse domain (diamond state) close to the stripe end. Magnetic transmission X-ray microscopy images (Fig. 1(b)) reveal polarity reversals within the core of the central domain wall and the development of a transverse structure near the right end of the permalloy stripe. Micromagnetic simulations, as shown in Fig. 2 confirm that these walls have indeed a complex 3D magnetic structure across the thickness and can display polarity reversals along their length related with the presence of magnetic singularities such as Bloch points and magnetic antivortices. These 3D magnetic configurations will be resolved in more detail with the aid of angular tilt series of MTXM images around different rotation axes which are the basis for a recently developed magnetic X-ray tomography method. Work supported by Spanish MINECO under grant PID2019-104604RB/AEI/10.13039/501100011033.

[1] V. D. Nguyen et al., "Third type of domain Wall in soft magnetic nanostrips"; Scientific Reports 5 (2015) 12417 [2] A. Hierro-Rodriguez et al. "Revealing 3D magnetization of thin films with soft X-ray tomography: magnetic singularities and topological charges" Nature Communications 11, 6382 (2020).

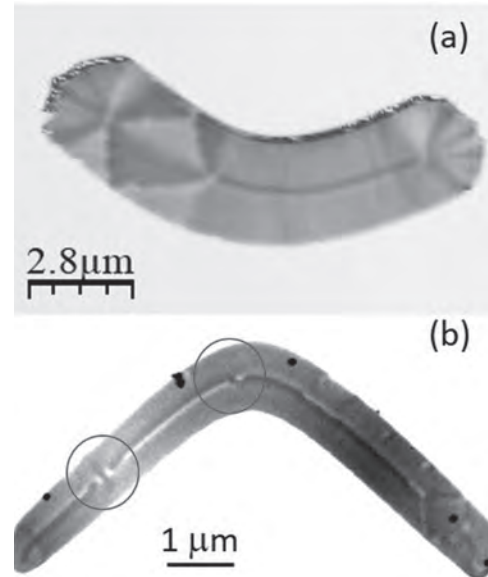


Fig. 1. (a) MFM image of 140 nm thick permalloy stripe at transverse remanence. (b) MTXM image at normal incidence of permalloy stripe. Note the polarity reversals at domain wall core. Black dots in this image correspond to 100 nm Au nanoparticles used for alignment.

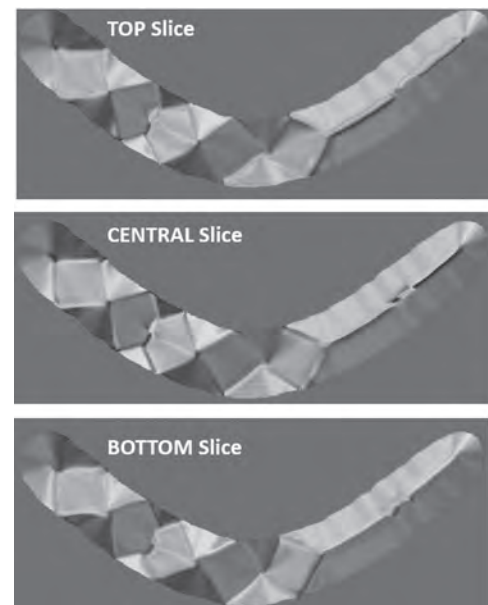


Fig. 2. Micromagnetic simulations of the magnetic configuration of thick permalloy stripes at different sample depths (top/central/bottom slices). Note the subtle changes in magnetization orientation at domain wall cores related with the 3D domain wall configuration.

CQ-09. Research on Mid-Distance High-Efficiency Wireless Power Transmission System Using Class E Amplifier.

N. Zhang¹, Y. Zhang¹, S. Ning², S. Wang¹, B. Lai³ and T. Zhu¹

1. School of Electrical Engineering, Xi'an Jiaotong University, Xi'an, China; 2. School of Electronic Information and Artificial Intelligence, Shaanxi University of Science and Technology, Xi'an, China; 3. Quanzhou Experimental Middle School, Quanzhou, China

I. Introduction Wireless power transfer (WPT) system can effectively make up for the shortcomings of traditional electric energy transmission and has a wide range of application prospects in the fields of electric vehicles, biomedicine, and portable equipment [1-3]. There are several ways to realize WPT, among which the WPT based on magnetic coupling resonance has many advantages, such as long transmission distance, high efficiency, simple implementation, and so on, which can meet the requirements of most scenarios. The WPT system needs a stable and efficient high-frequency power supply. The Class E Amplifier, with only one switch component, can realize soft-switching by matching the appropriate bypass capacitor and then get a high efficiency (close to 100%) in MHz [4]. Hence, the Class E Amplifier is extremely suitable for a high-frequency WPT system. At present, the scholars' research generally focuses on the short-range and high-efficiency WPT systems within 20cm, whose transmission distance is insufficient [5-6]. Silicon MOSFET can not meet the needs of the high-frequency power supplies, GaN components can work at a higher frequency and higher efficiency [7]. Herein, a mid-range high-efficiency wireless power transfer system based on class E power amplifier and Gan components is proposed. This paper optimizes the coupling coil and load in theory and simulation and gives the system parameter design method of ZVS (Zero Voltage Switching) operation of the class E power amplifier. Finally, the Wide Band-gap Semiconductor GaN component is used to build the physical model to verify the accuracy of the design. More detailed results and discussion will be presented in the extended paper. II. Double coil wireless power transmission system based on the class E power amplifier The wireless power transmission system mainly includes three subsystems, class E power amplifier, coupling coil, and load. And the topology is shown in Figure 1. According to the circuit model, the factors that affect the transmission efficiency and power of the system are analyzed, and it is concluded that the mutual inductance of the coils, the load, and the AC resistance of the coils have a great influence on the transmission characteristics. III. Design and optimization of the flat spiral coils for the WPT system The parameters of the coupling coils are closely related to the performance of the WPT system. The design and optimization are carried out through theory and simulation, and the comparison is carried out through experimental measurement. a. Calculation of coil self-inductance and mutual-inductance According to Neumann's formula [8], the mutual inductance calculation method of the flat spiral coil is derived. The self-inductance and mutual-inductance of the coil are calculated by theory and COMSOL electromagnetic field simulation tool. b. Calculation of the coil AC resistance and determination on the spacing between coil turns To reduce the coil AC resistance as much as possible, the relationship between coil AC resistance and turn spacing is analyzed by COMSOL Multiphysics. And then determines the spacing between coil turns is 2mm. The theoretical calculation, finite element simulation, and experimental measurement results are compared and analyzed, and the results are quite consistent. IV. System circuit simulation calculation and experimental verification Powered by a 24V DC power supply, the optimal load resistance is 10Ω and set the transmission distance to 40cm, then we determine the parameters of the system components. a. Circuit simulation using PSIM Build the system simulation model in PSIM, the circuit realizes soft switching, and the simulation results are shown in Figure 2. The output power of the load is 26.85W and the transmission efficiency is 87.89%. b. System experiment verification In particular, in view of the low on-resistance and small parasitic capacitance of GAN devices, which enable them to maintain high efficiency during high-frequency operation, GaN devices are introduced as switching devices in the experiment. According to the design parameters, we build the experimental model and carry out the relevant measurement. The experimental results are in good agreement with the simulation results. When the distance between coils is 40cm, the output power of the load is 25.99W and the transmission efficiency is 87.34%. V. Conclusions Aiming at the problem of low

efficiency of medium and long-distance wireless power transmission, this paper conducts comprehensive efficiency optimization from coil parameter optimization, load, and class E power amplifier. Using new GaN devices, a wireless power transmission system that takes into account the characteristics of mid-range and high efficiency has been developed.

[1] Y. Bu, S. Endo, T. Mizuno, IEEE Transactions on Magnetics, vol. 54, pp. 1(2018) [2] F. Benassi, D. Masotti, A. Costanzo, 2019 IEEE International Conference on RFID Technology and Applications (RFID-TA), pp. 306(2019) [3] N. Hasegawa, S. Yoshida, S. Furuta, et al., 2014 IEEE Wireless Power Transfer Conference, pp. 21(2014) [4] F. Tamjid, A. Ghahremani, M. Richardson, et al., 2017 IEEE Topical Conference on RF/Microwave Power Amplifiers for Radio and Wireless Applications (PAWR), pp. 25(2017) [5] L. Kou, J. Lu, P. Di Maso, 2019 IEEE 7th Workshop on Wide Bandgap Power Devices and Applications (WiPDA), pp. 205(2019) [6] H. Li, J. Li, K. Wang, W. Chen, et al., IEEE Transactions on Power Electronics, vol. 30, pp. 3998(2014) [7] J. Song, M. Liu, C. Ma, IEEE Transactions on Industrial Electronics, vol. 67, pp. 8281(2019) [8] H. A. Wheeler, Proceedings of the Institute of Radio Engineers, vol. 16, pp. 1398(1928) [9] H. L. Chan, K. W. E. Cheng, D. Sutanto, 2000 Eighth International Conference on Power Electronics and Variable Speed Drives, pp. 69(2000)

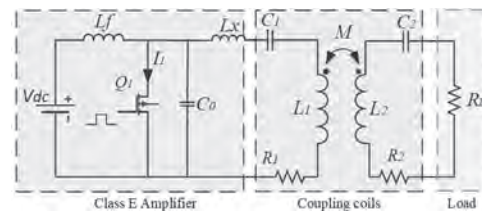


Fig. 1 Topology of the WPT system

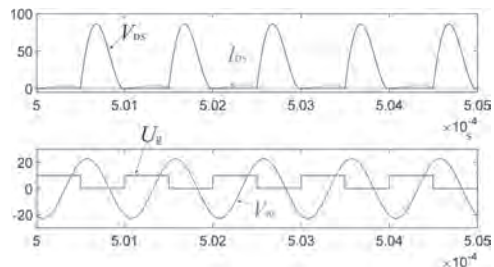


Fig. 2 System circuit simulation results using PSIM

CQ-10. Estimation of the Focality of Coils and Quality of Stimulation of Biological Tissues During Transcranial Magnetic Stimulation.

I.C. Carmona¹, O.F. Afuwape², D.C. Jiles² and R.L. Hadimani^{1,3}
 1. Dept. of Mechanical and Nuclear Engineering, Virginia Commonwealth University, Richmond, VA, United States; 2. Dept. of Electrical & Computer Engineering, Iowa State University, Ames, IA, United States; 3. Dept. of Biomedical Engineering, Virginia Commonwealth University, Richmond, VA, United States

As one of the emerging neurostimulation techniques, the Transcranial Magnetic Stimulation (TMS) regulates the synaptic activity of neurons to treat several psychiatric conditions and neurological disorders. During TMS, E-fields are induced within the brain through the application of time-varying magnetic fields, using coils located outside the head [1-4]. Different definitions are proposed in the literature to measure the focality of the E-field in the brain and estimate the stimulated area during TMS. However, most of them differ in measurement methodologies, showing lack of homogeneity and diverse criteria toward a unique conception, without evaluating possible scenarios of under or overstimulation of the biological tissue. Another common fact in the field is the use of definitions of “focality” without reference to a target area and/or focal distance, parameters intrinsically related and required for comparison between coils. Furthermore, to evaluate the degree of stimulation, a criterion indicating how well the stimulated area overlaps the targeted area is required. This work proposes a generalized function and methodology for the focality quantification in TMS coils, considering target area, focal distance, maximum magnitude and stimulation threshold. New definitions such as “specific focality (*sf*)” and “focality form factor (*d_n*)” are introduced, seeking to describe the suitability of coils for specific stimulation applications. The proposed definitions also offer a general framework to compare coils using homogeneous methodology, parameters and nomenclature, with potential impact in the industry on the standardization of TMS measurement methods. We have performed finite element simulations over an anatomically accurate human head model, including three of the common TMS coils in the literature (single circular coil, figure of eight coil and quadruple butterfly coil [5]). The head model was built based on MRI of an adult healthy subject and defined by layer including the scalp, skull, cerebrospinal fluid, gray matter and white matter. All the layers were assigned typical electromagnetic properties reported in the literature. Magnetic flux densities and electric fields were obtained in the surface of the primary motor cortex (M1) using the head model, over the subregion that controls the first dorsal interosseous (FDI) muscle. Then, the introduced “specific focality” measure was used. This is defined as the normalized dimensionless focality based on new proposed mathematical functions. The functions designed are called *Adjusted Even Symmetry Error Function Complement (AES-erfc)* and *Corrected-Adjusted Even Symmetry Error Function Complement (CAES-erfc)*. They define the focality as a quantity between zero and one (interchangeable to a percentage notation), as a function of the defined “focality form factor” (*d_n*), a normalized ratio between the stimulated area and the targeted area. The result is a measurement system that identifies different scenarios of focal stimulation (*d_n*=0), overstimulation (*d_n*≥0), understimulation (*d_n*≤ 0) or no stimulation (*d_n*=-1 in CAES-erf) [see Fig.1]. The calculated results of the specific focality over target areas and volumes were compared with other pre-existing measures in the literature, such as the *area of the half-value (A_{E1/2})* [6] and *area of the half-energy (AE_E)* [67], for the surface specific focality [Fig.2, table 1], and *area of the half-value (A_{V1/2})* and tangential fields spread (*S_T*) [6-7], for the volumetric specific focality [Fig.2, table 2]. Our study shows -consistently with other currently used measures- that the QBC is the coil with highest focality for the defined target, followed by the F8C. The proposed specific focality measure assigns a dimensionless value to each coil compared to results in surface units of existing definitions. With this new parameter definition, it becomes easier to evaluate the focality of a TMS coils in the context of a specific target area -or volume- and focal distance, as well as to identify scenarios of stimulation that is focal and with either understimulation or overstimulation with respect to the target size.

[1] M. T. Wilson, A. D. Tang, K. Iyer, H. McKee, J. Waas, and J. Rodger, “The challenges of producing effective small coils for transcranial

magnetic stimulation of mice,” Biomed. Phys. Eng. Express, vol. 4, no. 3, Apr. 2018, doi: 10.1088/2057-1976/aab525. [2] P. Rastogi, E. G. Lee, R. L. Hadimani, and D. C. Jiles, “Transcranial Magnetic Stimulation-coil design with improved focality,” AIP Adv., vol. 7, no. 5, May 2017, doi: 10.1063/1.4973604. [3] Z.-D. Deng, S. H. Lisanby, and A. V. Peterchev, “Electric field depth-focality tradeoff in transcranial magnetic stimulation: simulation comparison of 50 coil designs,” Brain Stimul., [4] I. P. de Sousa, C. R. H. Barbosa, and E. C. Monteiro, “Safe exposure distances for transcranial magnetic stimulation based on computer simulations,” PeerJ, vol. 2018, no. 6, 2018. [5] P. Rastogi, Y. Tang, B. Zhang, E. G. Lee, R. L. Hadimani, and D. C. Jiles, “Quadruple Butterfly Coil with Passive Magnetic Shielding for Focused Transcranial Magnetic Stimulation,” IEEE Trans. Magn., vol. 53, no. 11, Nov. 2017, doi: 10.1109/TMAG.2017.2711962. [6] Z. De Deng, S. H. Lisanby, and A. V. Peterchev, “Electric field depth-focality tradeoff in transcranial magnetic stimulation: simulation comparison of 50 coil designs,” Brain Stimul., vol. 6, no. 1, pp. 1–13, Jan. 2013, doi: 10.1016/j.brs.2012.02.005. [7] L. M. Koponen, J. O. Nieminen, and R. J. Ilmoniemi, “Minimum-energy coils for transcranial magnetic stimulation: Application to focal stimulation,” Brain Stimul., vol. 8, no. 1, pp. 124–134, Jan. 2015, doi: 10.1016/j.brs.2014.10.002.

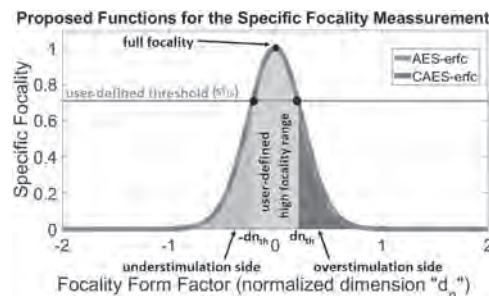


Fig.1. Proposed AES-erfc and CAES-erfc functions for the focality assesment.

Table 1 – Results of *sf_s* along with existing definitions

Coil	<i>A_{E1/2}</i>	<i>sf_s</i>	Condition	<i>A_{E_E}</i>	<i>sf_v</i>	Condition
QBC	151 mm ²	0.9736 (97.36%)	Highly focal. Minimal overstimulation outside	132 mm ²	0.9556 (95.56%)	Very focal. Low overstimulation outside
F8C	189 mm ²	0.4437 (44.37%)	Poorly focal. Moderate overstimulation outside	165 mm ²	0.8254 (82.54%)	Focal. Low overstimulation outside
SCC	716 mm ²	4.176E-05 (0.00%)	Non focal. High overstimulation outside	625 mm ²	4.176E-05 (0.00%)	Non focal. High overstimulation outside

Table 2 – Results of *sf_v* along with existing definitions

Coil	<i>A_V</i>	<i>S_T</i>	<i>sf_v</i>	Condition
QBC	75.5 mm ²	100.96 mm ²	0.8226 (82.26%)	Moderately focal. Low overstimulation outside
F8C	94.5 mm ²	126.20 mm ²	0.4708 (47.08%)	Poorly focal. High overstimulation outside
SCC	358 mm ²	477.12 mm ²	6.2854E-04 (0.00%)	Non-focal. Very high overstimulation outside

Fig.2. Tables 1 and 2.

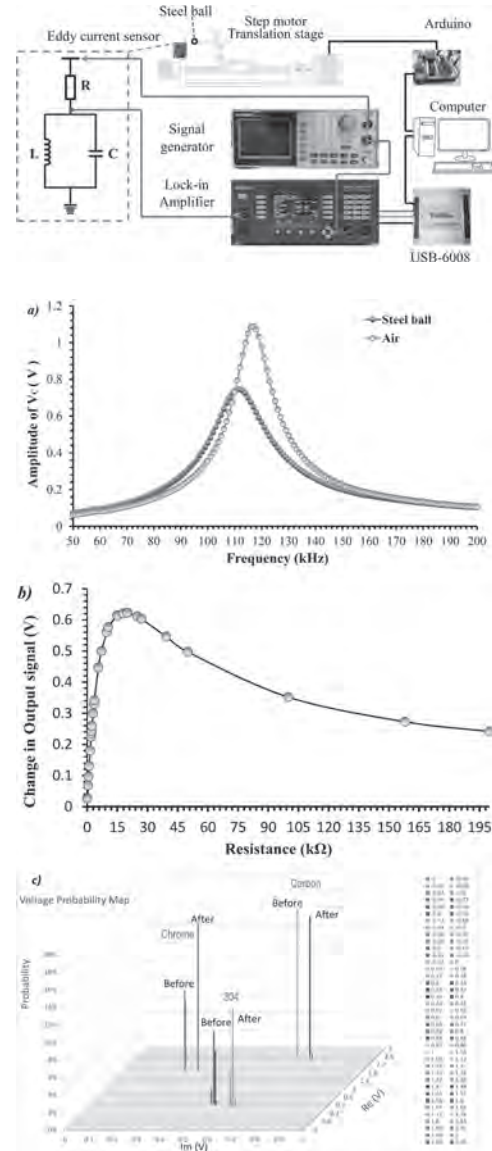
CQ-11. Steel Ball Sorting Based on Electromagnetic Induction Using Eddy Current Technique.

D. Dao¹, J. Jeng¹, C. Dinh¹, V. Doan¹, T. Pham¹ and H. Nguyen¹

1. Department of Mechanical Engineering, National Kaohsiung University of Science and Technology, Kaohsiung, Taiwan

There were many machine failures caused by the damage of the rolling bearing, for which the main reason was the quality of the steel ball [1]. Many works have been reported on assessing the geometric quality of steel balls, such as shape, size, and surface defects. In contrast, testing the material properties of steel balls is rarely mentioned [2]. As the quality and working life of the bearing depend primarily on the material properties of the steel ball, it is necessary to unambiguously classify the properties of steel balls in making bearings and other applications to ensure the reliability of the mechanical machine system. In this digest, we report on the eddy-current technique for the classification of steel balls based on the amplitude and phase of the eddy-current signal. Three types of 4-mm steel balls, including carbon, chrome, and stainless 304 steel balls, were tested to determine if it had undergone the surface hardening process. Fig. 1 shows the components of the RLC-resonance eddy-current system, which was designed to convert the electromagnetic induction of the steel ball into the phase-sensitive voltage output signals. The pickup coil is mounted statically to detect the eddy-current signal when the steel ball moves back and forth through the pickup coil by the stepping motor translation stage. A microcontroller (Arduino Uno) is used as the main unit to gather and process the data of the stage, such as the position and velocity. The micro-step determined on the driver is set to be 1/32. Fig. 1. The experimental eddy-current system for steel ball sorting. To detect the signal, the reference waveform for the lock-amplifier is synchronized to the excitation signal of the eddy current sensor. The lock-in amplifier receives the output signal from the sensor and generates the analog output voltages in proportion to the in-phase (real) and quadrature-phase (imaginary) components of the signal. The voltages are digitized by the data acquisition (DAQ) device NI USB 6008 from the National Instruments. The translation stage and the DAQ device are both controlled by the computer with the graphic user interface software designed using the Visual Studio C# programming language. The real and imaginary voltage components of the recorded eddy-current signals are subsequently converted into the probability map to show whether the steel balls can be classified by eddy-current sensors. The change in the detected signal should be due to the difference in the electromagnetic properties of the steel balls since the ball diameters are all 4 mm with an error less than 10 μm. Fig. 2. Eddy-current classification of steel balls: (a) determining the resonant frequency, (b) finding out the optimal resistance, and (c) voltage probability map of the steel balls before and after the surface hardening process. The impedance of the pickup coil can be calculated according to Dodd and Deeds method [3]: $Z_c = [(2\pi\omega\mu n^2 r_m^2)/(l_2 - l_1)^2 (r_2 - r_1)^2] [l^2 [(r_2, r_1)/\alpha^2] \{(l_2 - l_1)(1 + e^{-\alpha/\alpha}) - 1/\alpha\} d\alpha$ (1) where Z_c is the impedance of the coil (Ohm), μ is the permeability (Henry/meter), I is the applied current (ampere), α is the separation constant (meter⁻¹), r_2 is the outer radius of the coil (meter), r_1 is the inner radius of the coil (meter), r_m is the average radius of the coil, ω is the angular frequency (rad/second), l_2 is the distance from metal testing to top of the coil (meter), l_1 is the distance from metal testing to bottom of the coil (meter), n is the number of turns (turns), respectively. Fig. 2(a) shows the voltage amplitude measured at the output terminal when the driving frequency varies from 50 kHz to 200 kHz. The output response is maximized at the resonant frequency of 116 kHz for the RLC circuit. To achieve the higher response, the voltage outputs with various resistors are measured, as shown in Fig.2(b), where the optimal resistance is found to be 20 kΩ. The demodulated eddy-current signals were collected and repeated 100 times for each type of ball, and the result is converted into the voltage probability map in Fig. 2(c). It is found that the steel balls before and after the surface hardening treatment can be classified based on the difference in the eddy-current signal caused by the variation in electrical conductivity and permeability. The result indicates that the proposed method is feasible for application in sorting the material quality of steel balls, which plays a crucial role in mechanical systems. The authors would like to thank Tan Kong Precision Tech Co. Ltd. for providing the steel ball samples. This work is supported by the Ministry of Science and Technology of Taiwan under Grant No. MOST108-2221-E992-083MY2.

[1]. H. K. D. H. Bhadeshia, “Steels for bearings”, *Progress in materials Science*, 57(2) 268-435 (2012). [2]. D. Rifai, A. N. Abdalla and K. Ali, “Giant magneto-resistance sensors: A review on structures and non-destructive eddy current testing applications”, *Sensors*, 16(3) 298 (2016). [3]. C. V. Dodd, and W. E. Deeds, “Analytical solutions to eddy-current probe-coil problems”, *Journal of applied physics*, 39(6) 2829-2838 (1968).



Session CR
NOVEL IMAGING AND MEASUREMENT TECHNIQUES II
(Poster Session)

Chuanpu Liu, Chair
Colorado State University, Boulder, CO, United States

CR-01. Study on Sensor and Analysis Area in the Signal Source Estimation by Spatial Filter for Magnetocardiogram.

M. Iwai¹, S. Narita¹, W. Sun² and K. Kobayashi¹

1. Iwate University, Morioka, Japan; 2. Kinki University, Higashiosaka, Japan

Background Magnetocardiograms (MCGs) have become increasingly relevant for clinical research, due to its potential to detect early stages of heart disease. Especially, establishment of technology that can detail specify lesion parts of heart disease is expected. The estimation result by the current spatial filter method contains errors (eLORETA^[1], and so on ...). It cannot be said to be sufficient estimation accuracy for clinical application. If the current spatial filter method is used for magnetocardiography, the estimated solution of the signal source at the deep position tends to be wider than the estimated solution of the signal source at the shallow position. Factors include the fact that the number of sensors in the signal source estimation is very small compared to the unknown number, and that the magnetic field provided by the signal source is greatly attenuated according to the distance from the sensor. To solve these problems, improvement of the measurement system such as increasing the number of sensors is being considered^[2], but the increase in equipment and cost becomes an obstacle. Therefore, in this study, we proposed a method focusing on the relationship between the analysis area of signal source estimation and the sensor plane. **Methods** Conventionally, the sensor plane is bigger than the analysis area at size in the xy plane, because the analysis area is designed the same size of the heart, on the other hand, the sensor plane is designed the sufficiently larger than the heart size. However, in that case, the information of the sensors located at the ends could not be utilized, and the amount of information that affects the estimation result was different for each sensor, which was a cause of deriving a biased estimated solution. Therefore, in this research, we consider that the amount of information of each sensor can be used equally by setting an analysis area larger than the sensor area, and propose a new environment setting method for signal source estimation. **Simulation** We carried out a simulation to consider which size of the analysis area is the best. We performed the source signal estimation by eLORETA using the R-wave peak averaging data that the actual MCGs that the xiphoid process of the subject was adjusted to the 51ch sensor. We compared the following three sizes of the analysis area. Analysis area (a) is (x=120 mm, y=120 mm, z=80 mm), (b) is (x=176 mm, y=176 mm, z=80 mm), (c) is (x=224 mm, y=224 mm, z=80 mm). Other simulation conditions are shown in Fig. 1. **Simulation Results** Fig. 2 shows the signal source estimation result of each analysis area at R-wave peak. Red frame indicate sensor plane, blue frame indicate each analysis area, green frame indicate analysis area (a). Since the signals of the heart are originally considered to be single block, it is desirable that the estimated solution is a single block. Shown in Fig. 2, It was estimated as a single block except for the analysis area (a), which is the conventional method. In addition, the position and size of the estimated solution shown in Fig. 2 are very similar to the area of the heart obtained from CT images. Furthermore, we evaluated three analysis area using GOF (Goodness of fit) that is evaluation method that indicate the degree of agreement between the magnetocardiogram created by the estimated signal source and the measured magnetocardiogram. As a result, the GOF of each analysis area was about 0.996, which was not a big difference. **Summary** We examined the relationship of the sensor plane and analysis area using the actual MCG data in order to apply the spatial filter method MCG proposed a new analysis setting. By changing the size of the analysis area, the division of the estimated solution was suppressed and the shape of the heart could be roughly estimated. It found that the estimated result by using analysis area (b) and (c) are very similar to the area of the heart obtained from CT images. From these results, it was shown that it is possible to visualize the movement of the myocardium by estimating the time-series waveform of the magnetocardiogram.

References [1] R.D. Pascual-Marqui. Discrete, "3D distributed, linear imaging methods of electric neuronal activity. Part 1: exact, zero error localization.", arXiv :0710.3341 [math-ph], 2007. [2] W. Sun and K. Kobayashi. "Simulation of Extended Source Localization using sLORETA Method for Magnetocardiography". Journal of the Magnetics Society of Japan, vol. 41, pp. 75-80, 2017.

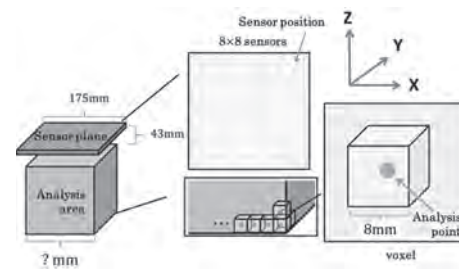


Fig. 1 Simulation conditions.

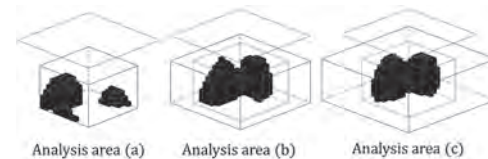


Fig. 2 the result of each analysis area's signal source estimation at R-wave peak.

CR-02. Influence of the Earth's Magnetic Field on the Diagnosis of Steel Rope With the use of MFAM Technology.

P. Mazurek¹

1. Department of Machinery Engineering and Transport, AGH University of Science and Technology, Krakow, Poland

Steel wire ropes used in roped transport devices like lifts, hoists, cableways, winches, are subjected to bending fatigue. Many parameters affect bending fatigue lifetime, such as tensile load, sheave diameter, and rope composition. According to the application area, steel wire ropes are often exposed to atmospheric influences, and the impact of corrosion is inevitable [1]. Non-destructive damage detection is a critical way to assess damage states to guarantee wire ropes reliability and safety. With intelligent sensors, signal processing, and pattern recognition technology developing rapidly, this field has made significant progress. Microelectromechanical systems (MEMS) have allowed magnetic field sensors with potential applications such as automotive industry, navigation systems telecommunications, and non-destructive testing [2]. Optically-pumped magnetometers (OPMs) have been developed since the 1960s. OPMs have generated renewed interest over the last 15 years, in part due to their increased sensitivity, when operated in the spin-exchange relaxation free (SERF) regime. Micro-Fabricated Atomic Magnetometer (MFAM) is a magnetometer system which can be used for land, airborne or even marine survey applications [3]. The Geometrics' MFAM is a laser pumped cesium magnetometer module that measures the total magnetic field strength. It uses cesium atoms contained in a small, evacuated glass vapour cell as the sensing element. The cesium is solid at room temperature. Hence, the cell is heated to increase the vapour pressure and the number density, of the cesium atoms in the cell. The cell is also filled with nitrogen buffer gas. The photon's angular momentum in the pump beam is transferred to the atom in the excitation process. As the atom decays non-radiatively through a quenching pathway provided by the nitrogen buffer gas, it loses random amount of angular momentum. As the spin polarization precesses, the intensity of the probe light transmitted through the cell is modulated at the Larmor frequency. The probe light is detected with a photodiode and the photocurrent amplified to generate the oscillating probe signal. The resultant Larmor spin precession can be detected with near-resonant light and serves as a measure of the ambient magnetic field. A schematic of the sensor is shown in Fig. 1 [4], [5]. The paper presents one of the first applications of MFAM sensors for diagnostics steel wire ropes. The module features two sensors that can be used independently or as an intrinsic gradiometer. The miniature scalar Optical Atomic Magnetometer [OAM] sensor used here, measures only 2.5cm x 2.5 cm x 3 cm. The Bell-Bloom type atomic magnetometer measures the Larmor precession of cesium atoms through non-resonant absorption of a probe beam. The examined cable is the 7x7+7x19W+IWRC steel wire rope type of 6,5 mm diameter, coated, with a metallic central core strand and crossed to the right. Cable construction is robust and widely used in the industrial field, mainly, in lifting applications. The examination aims to check the influence of the Earth's magnetic field on the diagnosis of steel rope using MFAM Technology. The rope permanently attached to the device shown in Fig 2. Under the rope, at a distance of 80mm, an MFAM Magnetometer (2 sensors: M1 and M2) was attached, which with the use of appropriate software could move at a constant speed of 3 mm/s. I recorded the measurement of the magnetic field around the rope over a measuring length of 380 mm. Then I increased the distance between the rope and the sensors to 120mm and 160mm. Each measurement was carried out three times by moving back and forth. I concluded MFAM technology's future on the non-destructive damage detection methods for steel wire ropes based on the research. The MFAM method is future-proof but requires further investigation. It is crucial to choose the appropriate distance from the tested object (the Earth's magnetic field's influence is a significant factor). In practical applications, the biggest challenge in using MFAM sensors is the stability of the vapour cell's operating temperature and need to separate the Earth's magnetic field. A promising avenue for research is to combine various methods to characterize and detect damages from multiple dimensions. For example, the combination of the electromagnetic and optical methods can grasp the size of the effective cross-sectional area of wire ropes. The types of damages are real-time and intuitively master its surface morphology characteristics to provide more valuable steel wire

rope health evaluation parameters. Although there are many issues and challenges, as new technologies and algorithms are introduced, it is believed that MFAM technology will realize evident and accurate non-destructive diagnostics of steel wire ropes.

[1] M. Al-Shaibah *et al.*, 'Characterization of a Resonant Lorentz Force MEMS Magnetometer', in *2020 Symposium on Design, Test, Integration Packaging of MEMS and MOEMS (DTIP)*, Jun. 2020, pp. 1–2 [2] Z. Guo, X. Xu, and T. Zhang, 'Research on the calibrated method for MEMS magnetometer arrays', Feb. 2020 [3] G. Oelsner *et al.*, 'Integrated optically pumped magnetometer for measurements within Earth's magnetic field', *arXiv:2008.01570 [physics]*, Aug. 2020, Accessed: Dec. 09, 2020. [Online] [4] R. Zhang *et al.*, 'Active Magnetic-Field Stabilization with Atomic Magnetometer', *Sensors*, vol. 20, no. 15, Art. no. 15, Jan. 2020 [5] R. Zhang, K. Smith, and R. Mhaskar, 'Highly sensitive miniature scalar optical gradiometer', *2016 IEEE SENSORS*, 2016

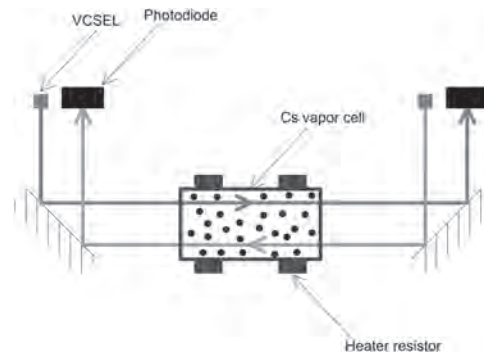


Fig.1. Schematics showing the internal structure of the sensor



Fig.2. Measuring device

CR-03. Adaptive Suppression of Mode Mixing in CEEMD Based on Genetic Algorithm for Motor Bearing Fault Diagnosis.

Z. Ke¹, C. Di¹ and X. Bao¹

1. School of Electrical Engineering and Automation, Hefei University of Technology, Hefei, China

Introduction: Analyzing and processing the non-linear and non-stationary vibration signals is a critical issue in the motor bearing fault diagnosis. In order to solve this problem, Empirical Mode Decomposition (EMD) was proposed, which decomposes the signal in Intrinsic Mode Functions (IMFs) [1]. However, the EMD has the drawback of the so called “mode mixing” phenomenon, which means that the signal components with different amplitudes in one IMF, or the signal components with a similar amplitude in different IMFs. To address this issue, an effective solution was proposed, which suppresses the mode mixing by adding the Gaussian white noise in the original signal, named as “Ensemble Empirical Mode Decomposition (EEMD)” [2-3]. But it brings in some new harmonics in IMFs. To overcome these problems, the Complete Ensemble Empirical Mode Decomposition (CEEMD) was put forward, which adds the opposite Gaussian white noise in the original signal for the EMD respectively [4]. However, the amplitude of the Gaussian white noise is usually estimated by the practical experience rather than calculating by equations. Besides, the inappropriate Gaussian white noise could not mitigate the mode mixing effectively. The essence of mode mixing is the coupling between IMFs, and IMFs are not orthogonal to each other. This paper focuses on the mode mixing, and optimizes the amplitude of the white noise by the genetic algorithm (GA) to minimize the orthogonality among IMFs. Optimization Method: Mutual information is an indicator which symbolizes the correlation between the data. The mutual information between IMFs obtained by the CEEMD will be affected and changed, when the amplitude of the white noise varies. Therefore, the white noise amplitude (All of these values are multiples of the standard deviation of the signal) is used as the input function, and the minimum mean of the mutual information between IMFs is used as the objective function in the GA. As a consequence, it can suppress the mode mixing phenomenon theoretically, when the amplitude of white noise is the minimum mean of the mutual information. Results: The bearing vibration fault signal used in this paper comes from the Case Western Reserve University [5]. In Fig.1, the values in the bar denote the mean of mutual information of IMFs corresponding to different white noise amplitudes, where 0.1103 is the white noise amplitude selected by GA and 0.1 to 0.4 are the values selected by the experience. The mean of mutual information is 0.5728 when the amplitude of the white noise is 0.1103, which is smaller than the amplitudes of 0.1, 0.2, 0.3 and 0.4 that the mean of mutual information is 0.705, 0.6230, 0.6998 and 0.7093, respectively. Fig.2 shows the amplitude of IMFs in figure Fig.2 (a) and the spectrum diagram of IMFs in figure Fig.2 (b) decomposed by the CEEMD with the optimized white noise. It can be seen from the figure Fig.2 (b) that the main components of each IMF are distributed at different frequencies. Meanwhile, it shows in the spectrum of IMF3 that the five times frequency (539.1 Hz) component of the bearing outer race fault. It proves the effectiveness of the proposed method in motor bearing fault diagnosis. Detailed results and discussion will be given in the full paper.

[1] N. E. Huang, Z. Shen, S. R. Long, et al., *Proc. R. Soc. Lond. A Math. Phys. Sci.*, vol. 454, p. 903-995, (1998). [2] Z. WU and N. E. Huang, *Adv. Adapt. Data Anal.*, vol. 01, p. 1-41, (2008). [3] P. Flandrin, G. Rilling and P. Gonçalvès, *IEEE Signal Process. Lett.*, vol. 11, p. 112-114, Feb. (2004). [4] F. Liu, J. Gao and H. Liu, *IEEE Access*, vol. 8, p. 19810-19819, (2020). [5] C. W. R. University, “<https://csegroups.case.edu/bearingdatacenter/pages/12k-drive-end-bearing-fault-data>,” (2014).

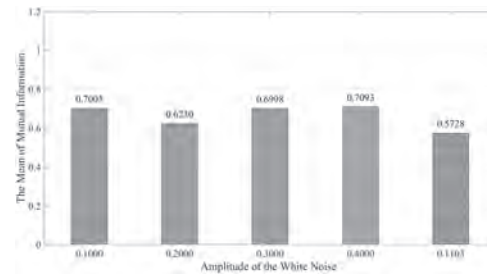


Fig. 1 The mean mutual information of different amplitude of the white noise.

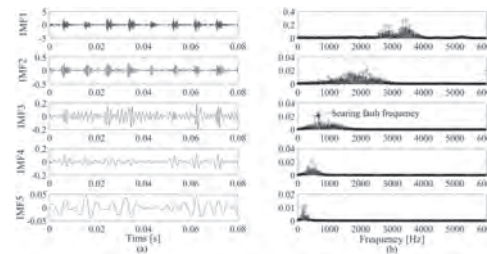


Fig. 2 IMFs decomposed by the CEEMD with the optimized white noise. (a) Amplitude of IMFs. (b) Spectrum diagram of IMFs.

CR-04. Diamagnetic Susceptibility of a Single Particle Detected From its Parabolic Movement Caused by Magnetic Field Gradient and Terrestrial Gravity.

K. Hisayoshi¹, S. Jinnouchi¹, C. Uyeda¹ and K. Terada¹

1. Earth & Space Science, Osaka University, Toyonaka, Japan

In a standard measurement of diamagnetic susceptibility χ_{DIA} (per unit mass), it is necessary to prepare a bulk sample that weigh more than ~ 0.5 mg. In the present report, we show that χ_{DIA} of a small particle is determined from its parabolic movement that is induced by a field gradient generated by a Niobium magnetic circuit, without the necessity of knowing mass m of particle. This principle of measuring χ_{DIA} is based on a recent finding that acceleration of a translating particle induced in an area of magnetic field gradient is independent to m ; it is uniquely determined by intrinsic χ_{DIA} value of material [1][2]. This characteristic derives from a well-known fact that a magnetic body force induced in a particle is proportional to m . The observed results overturn a common recognition that ordinary diamagnetic particles are magnetically inert unless a strong field is applied in the experiment [3]; the result indicate that most solid particles composed of diamagnetic or weak paramagnetic materials may potentially show translation at a low field produced by a permanent magnet, which is usable in practical applications. It was proposed that material identification of a particle is possible[4], by collating the obtained χ_{DIA} value with a compiled list of published data [5]; unlike many conventional methods of chemical analysis, the identification is conducted without consuming the small sample. In the present experiment, field-induced parabolic translations were observed in three diamagnetic materials, namely graphite, bismuth and diamond. The particles were released at an initial position as shown in Fig.1 with negligibly small initial velocity, and the particles translated in an area with magnetic field gradient in normal gravity. Fig 2 shows the example of the trajectory observed for a graphite particle and a bismuth particle which proceeded in the xz -plane of Fig.1; they were observed by a high-speed camera (CASIO EX-F1, Japan). The χ_{DIA} value of each particles were determined from a relationship between velocity of particle $v(x,z)$ and field intensity $B(x,z)$; the theoretical equation used in the calculation was deduced from an assumption that the variance of potential energy (i.e., magnetic & gravitational) of a particle between two arbitrary positions in the trajectory was completely converted to kinetic energy. The χ_{DIA} values obtained in this manner was consistent with the published values [5]. The accuracy of the χ_{DIA} values obtained by the present apparatus was significantly improved compared to that obtained in the previous research [3]; the improvement was achieved by optimizing the field distribution of the magnetic circuit, thus decreasing the fluctuation of $v(x)$ values. The accuracy was also increased by precisely identifying the initial position of sample improving the observation using the hi-vision camera. Accordingly, accuracy of χ_{DIA} obtained for a submillimetre-particle was improved to a level of $\sim 4 \times 10^{-7}$ emu/g, and variance of χ_{DIA} between different materials can be distinguished by the proposed method; in previous studies, the accuracy remained at a level of $\sim 10 \times 10^{-6}$ emu/g [1][2] [4]. The experimental techniques achieved in this study will be a milestone in reducing the measurable size of the sample to micrometre scale. According to recent measurements, the velocities of ferro- (ferri-)magnetic particles [6] and paramagnetic particles [2] during their field-induced translation were also independent to m . Hence, similar motions as reported in the present study is generally expected to occur in all categories of magnetic material by a relatively low magnitude of field-gradient. It is expected from the results shown in Fig.2 that an ensemble of heterogeneous particles can be separated into fractions of different materials [2][4] by releasing the ensemble from the initial position in Fig. 1. By improving the compact system, a non-destructive chemical analysis can be conducted shortly after collecting the heterogeneous particles at the site of material explorations in various research fields; such method of pre-treatment will improve the efficiency of reaching a target sample in the research.

[1] C. Uyeda, K. Hisayoshi and S. Kano, J. Phys. Soc. Jpn. Vol.79, p.064709 (2010). [2] K. Hisayoshi, C. Uyeda and K. Terada, Sci. Rep. vol.6, p.38431 (2016) [3] G. Maret and K. Dransfield, Adv. Appl. Phys. Vol.46, p.143 (1985) [4] C. Uyeda, K. Hisayoshi and K. Terada, Sci. Rep. Vol.9, p.3971 (2019). [5] R. Gupta, Landolt Bornstein. New Series II, Vol.46

“Diamagnetism”, p.445 (19830 [6] C. Uyeda, K. Kuwada and K. Hisayoshi, J. Jpn. Soc. Powder Metall. Vol.61, p.S78 (2014)

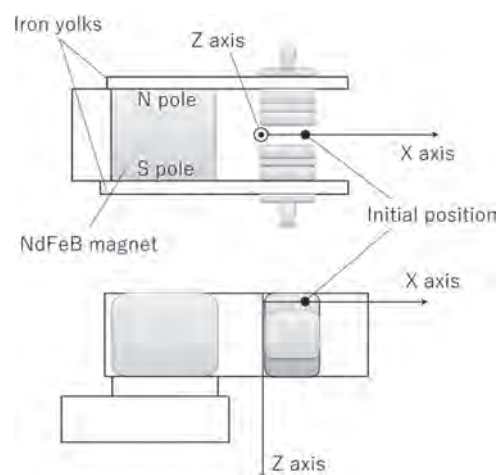


Fig.1 A top view (above) and a side view (below) of a NdFeB magnetic circuit developed in the present study to observe parabolic translation of a diamagnetic particle in terrestrial gravity.

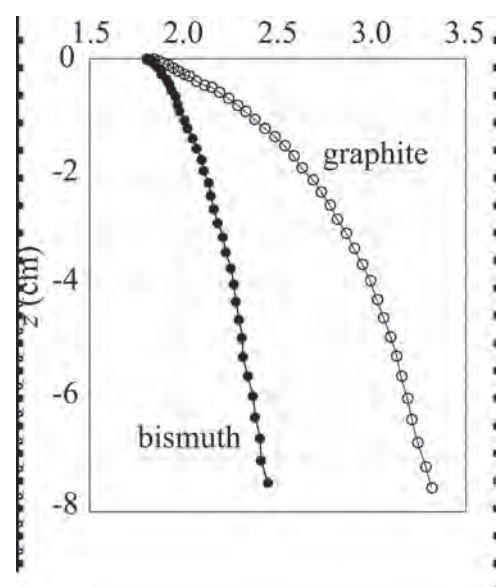


Fig.2 Trajectories of a graphite particle and a bismuth particle that translated from the initial position described in Fig.1. The particles translated in the xz plane in the figure. The χ values obtained from the trajectories was 49×10^{-7} emu/g for graphite and was 11×10^{-7} emu/g for bismuth; the values were both consistent with the published values [4].

CR-05. “ULMAG – Ultimate Magnetic Characterization,” a Novel Experimental Setup for the Beamline ID12 at the European Synchrotron Radiation Facility (ESRF).

A. Aubert¹, K. Skokov¹, G. Gomez², I. Radulov¹, F. Wilhelm³, A. Rogalev³, H. Wende², O. Gutfleisch¹ and K. Ollefs²

1. Technische Universität Darmstadt, Darmstadt, Germany; 2. Universität Duisburg-Essen, Duisburg, Germany; 3. ESRF, Grenoble, France

With the increasing demand for new high-tech and energy-efficient devices, multi-stimuli functional materials with strong interplay between their structural, magnetic, and electronic subsystem appear at the forefront of research in material science [1,2]. They form a new family of promising materials for applications in different technological areas, like heat-assisted magnetic recording (HAMR), thermal energy storage, novel spintronic devices, and magnetic refrigeration. In a first-order phase transition (FOPT) material [3], the changes caused by external stimuli not only impact one subsystem of the solid (e.g., change of magnetization induced by a magnetic field), but also give rise to significant transformations occurring in other subsystems (e.g., expansion of the crystal lattice, change in electrical resistivity, heating of the sample, etc.). However, the contributions of the different subsystems are usually characterized independently and in different samples, environment, or even laboratories. This makes difficult to assemble scattered pieces of a puzzle into one coherent picture, and this is probably a reason why the mechanisms of magneto-structural coupling remain till now poorly understood. Therefore, it is important to change the existing paradigm and to develop a novel experimental approach allowing the characterization of the magnetic materials exhibiting a FOPT by combining various experimental techniques, including: • field/temperature dependencies of magnetization both macroscopically (magnetometry) and in the element selective manner (XMCD) • changes occurring in the crystal lattice (X-ray diffraction) and in the sample as whole (dilatometry) • thermal response of the material (calorimetry). The key point is that all these measurements should be performed simultaneously on the same sample and under strictly identical experimental conditions. Such an experimental setup is to be implemented at the beamline ID12 at the European Synchrotron Radiation Facility (ESRF) in Grenoble (France) in the framework of the project ULMAG – Ultimate MAGnetic characterization. It will serve as a versatile tool for combined macroscopic and microscopic characterization of magnetic materials open to all users. In our presentation, we describe the ULMAG setup, which is inspired from a previously purpose-built device “MaRS” at TU Darmstadt [4]. The MaRS is based on a commercial VSM option of QD-PPMS [4]. However, in ULMAG, the sample must remain static for the experiments with x-rays at the beamline, impeding the VSM possibility. Thus, the magnetic measurements are performed by means of a GaAs Hall probe situated as close as possible to the sample. This allows to estimate the stray-field produced by the surface of the sample, mirroring the surface magnetization of the sample. The dilatometry and calorimetric properties are measured by means of strain gauges and thermometer, respectively, as described in our previous study [4]. A first prototype was built based on the commercial resistivity option of the QD-PPMS. The sensors are connected to external instruments controlled by the MultiVu software implemented in the QD-PPMS. This prototype serves as a proof of concept and the general scheme of the sample with the different sensors are presented in Fig. 1. At the ESRF, we are building a similar prototype which will have in addition the X-Ray beam (see Fig. 1). With the current ULMAG setup, we can probe under the same conditions and simultaneously the (i) magnetic, (ii) magneto-volumetric and (iii) caloric changes as function of the magnetic field (up to 8 T) and temperature (4-350 K). Preliminary experiments are performed on a quasi-equiatom FeRh sample with the antiferromagnetic (AFM) to ferromagnetic (FM) transition occurring around 300 K (see Fig. 2). Results show that contrary to what is usually assumed, magnetic and magneto-volumetric changes (parallel and perpendicular) do not evolve hand in hand but rather occur at different fields (or temperatures for temperature induced transition, not shown here). Such peculiarities were also observed in other samples (La-Fe-Si and FeRh) measured with the MaRS [4-6]. The combination of XMCD with the macroscopic properties reported above is planned to be performed in early 2021 at the beamline ID12 of the ESRF. This will be a first achievement to complete a new way of characterizing magneto-

caloric materials. In the future, the use of this set-up will be extended to study other types of magnetic compounds like magnetostrictive materials or permanent magnets and beyond. Acknowledgements: This work was funded by the Federal Ministry of Education and Research (BMBF) under the grant number BMBF-Projekt05K19RD2.

- [1] O. Gutfleisch, et al, *Magnetic materials and devices for the 21st century: stronger, lighter, and more energy efficient*. Adv Mater, vol. 23, p. 821 (2011). [2] O. Gutfleisch, et al., Mastering hysteresis in magnetocaloric materials, Phil. Trans. R. Soc. A, vol. 374, p. 20150308 (2016). [3] J. Y. Law, et al., *A quantitative criterion for determining the order of magnetic phase transitions using the magnetocaloric effect*. Nat Commun, vol. 9, p. 2680 (2018). [4] D. Yu. Karpenkov et al. *Pressure Dependence of Magnetic Properties in La(Fe,Si)13: Multistimulus Responsiveness of Caloric Effects by Modeling and Experiment* Phys. Rev. Applied, vol. 13, p. 034014 (2020) [5] K. Skokov et al, to be published [6] K. Skokov et al, to be published

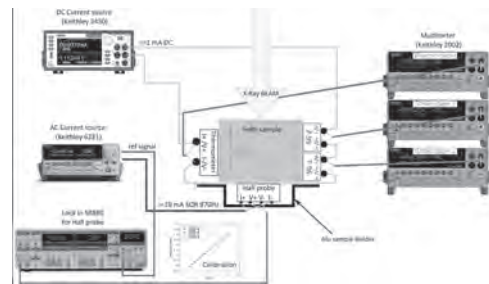


Fig.1: Schematic of the ULMAG setup for simultaneous measurements of magnetic stray field, magnetovolume change, caloric change and XMCD/XRD, expected to be implemented at ID12 at ESRF (Grenoble, France).

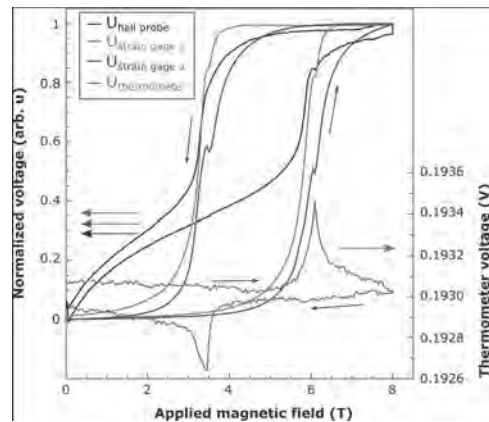


Fig. 2: Simultaneous measurements of the stray field (hall probe), the magnetostriction (strain gage // and ⊥), and the calorimetry (thermometer); showing a magnetic field induced AFM—FM transition at 245 K for a quasi-equiatom FeRh.

CR-06. Magnetic Anisotropy Detected in a Small Crystal by Observing its Rotational Oscillation Caused by a Ferrite Magnetic Circuit.

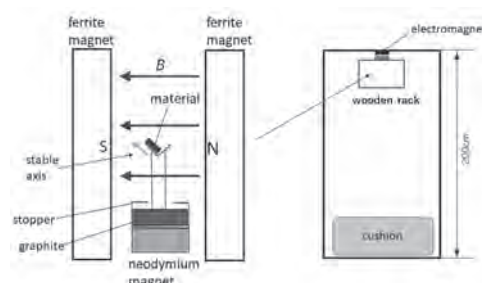
C. Uyeda², S. Sugiura², K. Hisayoshi¹ and K. Terada¹

1. Osaka University, Suita, Japan; 2. Osaka University, Osaka, Japan

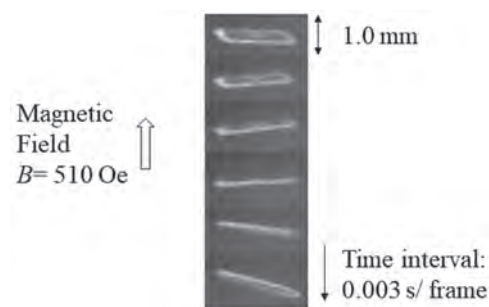
An apparatus to obtain magnetic anisotropy $\Delta\chi$ (per unit mass) of a diamagnetic or a paramagnetic crystal is newly designed and operated in microgravity (μg) condition. In this experiment, rotational harmonic oscillation of a millimeter size crystal was observed, which was caused by a magnetic anisotropy energy $-\frac{1}{2}m\Delta\chi B^2$ of the crystal with mass m ; here oscillation was induced by a homogeneous field B produced in area of μg [1][2]. The period of this oscillation τ is described as $\tau = 2\pi (l/m)^{1/2} \Delta\chi^{-1/2} B^{-1}$, in condition that angle of amplitude is small. Note that τ is independent to m in the above equation, and if oscillation is observable, $\Delta\chi$ can be obtained by measuring τ , l/m and B no matter how small crystal particle may be [1]-[3]. Using a standard commercial apparatus, detection of $\Delta\chi$ is prevented in a small sample due to the background signal from the sample holder, and also due to the difficulty in measuring m . Hence in using the conventional methods, it is necessary to prepare a single crystal with a millimeter-size to obtain an accurate $\Delta\chi$ value. It is noted that the obtainable size of a single crystal is below sub-millimeter level in many materials, and it is presently difficult to obtain reliable $\Delta\chi$ values in these materials. As described in Fig.1, a pair of ferrite magnetic plate (10cm x 5cm x 1cm) was introduced in the present study to generate B ($B = 0.051\text{T}$). By introducing these plates, area of homogeneous field was enhanced to a spherical space of $\phi \sim 3$ cm, and the mm-size sample released in μg area could remain inside the homogeneous area of during the τ measurement. Note that a solid particle released in μg space tends to freely translate, and in previous researches [3], the sample frequently moved away from the small homogeneous space of $\phi \sim 1.0\text{cm}$ during the τ measurement. Due to this disturbance, success rate of $\Delta\chi$ measurement was less than 20%. In the present experiment, $\Delta\chi$ values were obtained in millimetre size crystals of paramagnetic chrorite and a diamagnetic graphite following the aforementioned procedure. The millimetre-size sample used in the experiment was separated from the bulk single crystal using a wire saw and a titanium knife to avoid ferromagnetic contaminations. The sample was placed on a sample stage that was located at the the field center as shown in Fig 1. A short microgravity condition (duration $< 0.5\text{s}$) was supplied by conducting a free fall of the apparatus which was installed in a wooden rack [3]. Shortly after the beginning of the free fall, the sample stage was slightly lifted from its initial position, which was effective in inducing a smooth release of the small sample in a diffuse area. The rotational-oscillation of the samples were observed by a high-speed camera (ZWO ASI290MC), which could observe and preserve the sample motions with a spatial resolution of 0.004 cm and a time resolution of 0.033 fps. Fig.2 shows a time dependent image of a graphite crystal showing that field-induced rotational oscillation occurs at a low field intensity produced by the ferrite plates; it was generally considered that dynamic motion of diamagnetic and paramagnetic material were realized by a existence of ultra high magnetic field [4]. The experimental values of τ and l are obtained from the images, and are used in the calculation of $\Delta\chi$ according to the aforementioned procedure. The values obtained in this manner are $+(7.7 \pm 0.8) \times 10^{-6} \text{emu/g}$ and $-(2.2 \pm 0.6) \times 10^{-5} \text{emu/g}$ for chrorite and graphite, respectively; these values are consistent with the published data measured by the conventional torque methods [5]. According to the aforementioned principle of the proposed $\Delta\chi$ measurement, further improvement of sensitivity is possible, specifically by increasing the magnitude of B and/or τ ; improvement is also possible by decreasing the value of l/m . The experimental techniques achieved in the present study will be a milestone in reducing the measurable size of the sample down to micrometre scale. Diamagnetic anisotropy originate from the 3-dimensional distribution of localized electrons that compose a material. In case of organic materials, origin of $\Delta\chi$ were explained in terms of a molecular-orbital method; consistency of this method was examined by comparing theoretical and experimental values of $\Delta\chi$ [5]. Similar investigation was not performed in other types of solid materials because the number of experimental $\Delta\chi$ values were limited due to the difficulty of detecting the small $\Delta\chi$ values. By improving the method proposed in the present report, $\Delta\chi$ having a magnitude below $1 \times 10^{-9} \text{emu/g}$ can be obtained for oxides with high crystal symmetry. The improvement of $\Delta\chi$ sensitivity will increase the number of reliable data to

clarify the relationship between diamagnetic anisotropy and spatial electron distribution assigned to individual diamagnetic crystals [2][5].

[1] C. Uyeda, Phys. Chem. Mineral 20, 77–81(1993) [2] C. Uyeda, K. Hisatoshi, T. Tanaka, Appl. Phys. Lett. 28, 094103 (2005). [3] C. Uyeda et al., J. Phys. Soc. Jpn. 79, 064709 (2010). [3] (2011) [4] G. Maret & K. Dransfield, Adv. Appl. Phys. 46, 143 (1985). [5] R. Gupta, Landolt Bornstein. New Series II, 46 “Diamagnetism”, p 445 (1983).



An apparatus developed to detect magnetic anisotropy $\Delta\chi$ in a small crystal by observing its field-induced translation in a short μg condition, which is supplied by a compact drop shaft shown in the right portion of figure.



Time dependent image of a graphite crystal showing field-induced rotational oscillation by a field produced by a ferrite magnetic circuit. The c-axis of graphite is normal to the sample plane showing oscillation with respect to B . Period of oscillation τ is obtained from these images, and is used to calculate $\Delta\chi$ of the crystal.

CR-07. Design of Transcranial Magnetic Stimulation Coils for Mouse With Improved Stimulus Focus and Intensity.

H. Yu¹, B. Du¹, G. Xu¹ and L. Guo¹

1. Hebei University of Technology, Tianjin, China

Abstract: Transcranial magnetic stimulation (TMS) is a non-invasive and painless treatment for brain disorders. Rodent models of TMS provide a possibility to reveal the mechanism of TMS at cellular and molecular level. However, their application has been hampered by lack of stimulating coils with appropriate focus and intensity. In this study, we analyzed various types of coils and proposed conductive shield and iron core materials to improve the coil performance. The results showed that combination of Halo coil and figure of eight coil with shield and iron core could generate better stimulus focus (29.2 mm²) and intensity (87.6 V/m). Keywords: Transcranial magnetic stimulation; Coils; Focus; Mouse model I. Introduction At present, most commercial animal coils generally cannot meet the requirements of stimulus depth, stimulus intensity and stimulus focus simultaneously. Therefore, it is necessary to further develop a special TMS coil for small animals [1, 2]. II. Method In this study, a mouse model was constructed with three-compartment body-skull-brain model of conductivities 0.3344, 0.0203 and 0.106 S/m. The mouse and coil models were shown in Fig.1. The shield conductor (Cu) with a thickness of 1 mm had a window in the middle. The iron core was made of sheets of silicon steel. All the coils were kept at a distance of 5 mm from the highest point of the mouse head. The stimulus intensity is defined as the max of the electric field (E_{max}), and the focus was defined as the half power region (HPR). III. Results The results showed that Halo coil, shield and iron core could complement each other well. The combination of Halo coil and figure of eight coil with shield, iron core could get a better stimulus focus (29.2 mm²) and a higher stimulus intensity (87.6 V/m), which had increased about 79% and 54% respectively compared to the general commercial coil, as shown in Fig.2. IV. Conclusion Our results suggested that the combination of Halo coil and figure of eight coil with shield and iron core could improve TMS coil performance. We provided an alternative method to deliver TMS to small animals by constructing a coils with better stimulus intensity and stimulus focus.

[1] Meng Q, Jing L, Badjo J P, et al. A novel transcranial magnetic stimulator for focal stimulation of rodent brain [J]. Brain Stimulation, 2018, 11(3): 663-665. [2] Alekseichuk I, Mantell K, Shirinpour S, et al. Comparative modeling of transcranial magnetic and electric stimulation in mouse, monkey, and human [J]. Neuroimage, 2019, 194: 136-148.



Fig.1 Mouse and coil models of this study

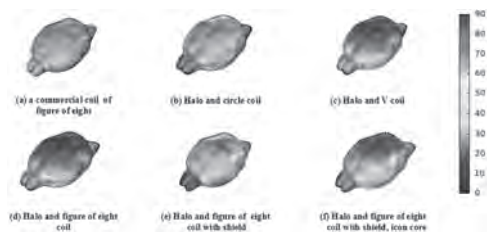


Fig.2 Electric field induced in the brain of the mouse

CR-08. Study on the Multi-Coil Data Fusion Based on Planar Eddy Current Coil in Non-Destructive Testing.

N. Zhang¹, Z. Ma¹, S. Ning², S. Wang¹, X. Xu¹, Y. Zhang¹, Y. Du¹ and H. Qiu¹

1. School of Electrical Engineering, Xi'an Jiaotong University, Xi'an, China; 2. School of Electronic Information and Artificial Intelligence, Shaanxi University of Science and Technology, Xi'an, China

I. Introduction Non-destructive testing (NDT) is a large group of analysis techniques widely used in science and industry to evaluate the properties of material, component, or system without causing damage. In the last decades, eddy current testing becomes a significant branch of NDT. An eddy current testing system for NDT needs a signal generator, an excitation coil, a receiver coil, and a microprocessor. To optimize the accuracy of the eddy current testing, a method focused on excitation signal and testing coils has been given more and more attention [1]. Due to the skin effect, the excitation signal with the high frequency is more sensitive to the defects on the surface, and the low-frequency is more sensitive to the defects deep inside of the specimen. Although quite a lot of design for NDT system has been worked out, there have been no solutions considering both excitation signal and coils [2-5]. In this paper, a planar coil with multi-frequency stimulations was applied to an eddy current non-destructive testing. By numerical calculation, the distribution of the magnetic flux density of the coil was analyzed. With the multi-frequency excitation current signal, the cracks can be identified in detail. A simulation model was established to calculate the distribution of the electric field induced by excitation coils. The calculation was also verified by measurement. More details will be presented in the extended paper. II. Design of The Eddy Current Testing System The excitation current plays a significant role in eddy current testing. As mentioned in section I, the excitation current with both low and high frequencies can detect not only the surface defects but also the defects deep inside of the specimen. A signal generator was proposed to generate the square waveform. The signal generator was composed of an oscillating circuit, a frequency divider, and an H-type circuit. The IR2110 was adopted in an H-type circuit to control the power MOSFET. As the key point of an eddy current testing system, the excitation coil made a significant contribution to the sensitivity of the testing system. According to Biot-Savart's law, the turn number of the excitation coil is proportional to the testing linearity, and the thickness of the coil is inversely proportional to the testing sensitivity. A solenoid is widely used in standard eddy current testing system. However, the volume is large, the cost is high, and the magnetic field intensity decays rapidly outside the solenoid. To avoid these disadvantages, the excitation coil was designed in planar type. The planar coil is small in volume, is easily manufactured, has excellent repeatability, and remarkably lower cost. If the inductance of the coil is inappropriate, the output of the coil does not respond sensitively to the change of specimen. Because of the low inductance of the receive coil, the eddy current sensor with an excitation coil and receive coil could be more sensitive. In this research, as shown in Fig. 1, the eddy current sensor is composed of an excitation coil and a receive coil array on both sides of a printed circuit board. III. Simulations and Experiments The frequency of the excitation signal is set up to 100 kHz by many experiments. According to the frequency of the excitation current, the planar excitation coil is designed by FEM simulation. The inductance and resistance of the coil calculated by Ansoft are 365.2 μH and 23.0 Ω . The excitation voltage is set as 28 V. The maximum magnetic flux density of the planar excitation coil is 1.25 mT, and the magnetic flux density measured by a Gauss meter is 1.3 mT. Moreover, the magnitude of the induced electric field, the maximum induced electric field strength from 1 mm above the center of the excitation coil is about 8.43 V/m. As shown in Fig. 2, the excitation coil induces eddy current on the iron plate is verified by FEM calculation. The directions of the induced current on the iron plate are simulated. Due to the eddy current on an iron plate, the output of the induced voltage of receiver coils carries the details of the specimen. The experiment was carried out on an iron plate. The excitation coil and receiver coils were set on one side of the iron plate over 1 mm, and were installed on a power-slipway. The coils moved from the left of the first line to the right and then changed to the next line. When the coils were moving, the signal sampling and processing module check the voltage of the receiver coils then process the data. The interior defects and surface

defects were judged by Fast Fourier Transform (FFT). After the FFT, the signals from the coil array were fused by parameter weight, and the system identified each block by comparing the fused value with a regular value. If the value was higher than the threshold, the testing system would mark the block as a defect. At last, the testing system outputted the result in coordinate value. Then the PC could visualize the coordinate value. IV. Conclusions In this work, based on a numerical calculation of field distribution, a planar eddy current excitation coil and an array of planar eddy current receive coil were proposed. With the multi-frequency excitation signal, the defects on both surface and interior were detected. By proper design, the defects of the specimen could recognize by the non-destructive testing system.

[1] Teterko, A. Ya, V. M. Uchanin, and V. I. Hutnyk., *Materials Science*, vol. 49, no. 6, pp. 857-865(2014). [2] Zeng, Wei Qin, Wei Min Zhang, and Shu Hao Wang., *Applied Mechanics and Materials*. Vol. 345. (2013). [3] Sasayama, Teruyoshi, et al., *IEEE Transactions on Applied Superconductivity*, Vol. 26, no. 5(2016). [4] Wang, Hongbo, Wei Li, and Zhihua Feng., *IEEE Transactions on Magnetics* Vol. 51, no. 9(2015) [5] Zhou, H. T., et al., *Procedia Engineering* Vol. 130, pp. 1649-1657(2015).

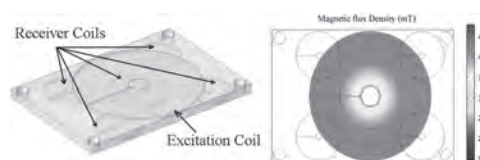


Fig. 1 The distribution of Magnetic flux density of excitation coil

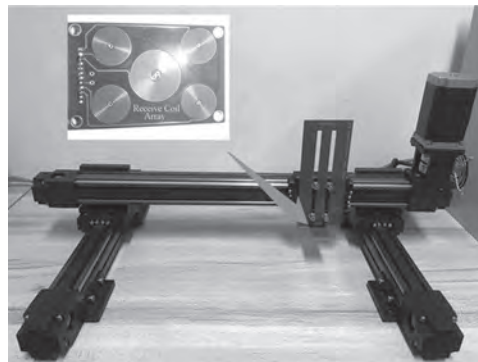


Fig.2 The testing platform based on planar eddy current coil and power-slipway

CR-09. Magnetization Measurement System With Giant Magnetoresistance Zero-Field Detector.

V. Doan¹, J. Jeng¹, H. Nguyen¹, C. Dinh¹, D. Dao¹ and T. Pham¹
 1. Department of Mechanical Engineering, National Kaohsiung University of Science and Technology, Kaohsiung City 807618, Taiwan

Magnetic hysteresis loop measurement [1]-[4] is crucial for the development of advanced magnetic materials. From the magnetization versus magnetizing field (M - H) curve, one can extract the useful magnetic properties, which are important for applications in sensors, transformers, actuators, and miscellaneous electrical devices. The M - H measurements were usually done by using the vibrating sample magnetometer [1] or the SQUID magnetometer [2], for which the magnetizing field are virtually static during the measurement. The induction-coil-based hysteresis loop and susceptibility measurement systems [3], [4] are rapid and low-cost devices capable of determining the alternating-current (AC) magnetic properties, which is important for inferring the frequency-dependent features such as the energy loss due to eddy currents in conducting materials. The convention hysteresis loop measurement device [3] is designed for the magnetic induction versus field (B - H) measurement of toroidal samples. The alternating susceptibility measurement system (AC susceptometer) is capable of determining the frequency dependent initial magnetization and susceptibility. But the induction coil can't detect the environmental direct-current (DC) field. For the soft magnetic materials, the non-zero environmental magnetic field can significantly alter the measured result, which must be compensated by using a magnetic sensor to detect the unwanted magnetic interference. To achieve higher accuracy in the M - H measurement, we proposed a M - H measurement system combining the signal processing method of B - H measurement and the coil design of the AC susceptometer. The interference from the environmental magnetic field is eliminated by using a giant magnetoresistance (GMR) sensor as the zero field detector, as shown in Fig. 1. The system consists of solenoidal magnetization and pickup coils. The pickup coil consists of reference and sensing coils symmetrically positioned with respect to the excitation coil. The sensing coil detects the magnetization of the sample, whereas the reference coil is wound in the opposite direction to null out the magnetizing signal. The signal output of the integrator is proportional to the magnetization of the sample. The current in the magnetization coil is directly proportional to the magnetizing field strength H . However, the DC level of the magnetizing field at the sample is usually shifted by the environmental field, which can't be observed by monitoring the current in the coil. To solve the problem, the GMR sensor, which is the GF708 spin-valve sensor [5] from Sensitec GmbH, is used for the zero field detector. The sensor has a very high sensitivity but the dynamic range less than 2 Oe. The output of GMR is used as the trigger for taking the M - H curve to eliminate the disturbance from the environmental DC field, as shown in Fig. 2. The 1-Hz sinusoidal current signal measured by a resistor shows a peak-to-peak amplitude of 0.96 A, corresponding the magnetizing field amplitude of 6.7 mT. When the environmental DC field was completely eliminated in the pickup coil, the observed output signal of the GMR has a zero-field-crossing point defined by the trigger level, shown as in Fig. 2. The trigger point to activate the M - H measurement is at the intersection of the trigger level line and the GMR signal curve for "No external field". When the DC field (of about 0.77 mT) was applied, the trigger point shifted by 40 ms in comparison with the zero-field curve, while the current waveform in the coil remained unchanged. The new trigger point to activate the M - H measurement is at the intersection between the trigger level line and the GMR signal curve with "External field". The coercivity and the asymmetry pinning field of the GMR sensor induces a constant time shift in the trigger point, which can be corrected by employing a calibration procedure provided that the sweeping magnetizing field always saturates the output of GMR on both field polarities. With the GMR zero-field detector to set the trigger point, the high-quality M - H curve can be obtained by taking averaging for multiple cycles of the sweeping magnetizing field. In this way, the accuracy of the M - H curve measurement for the soft magnetic materials is successfully improved by eliminating the interference from the environmental field without using a costly magnetic shield chamber. This work is supported by the Ministry of Science and Technology of Taiwan under Grant No. MOST108-2221-E992-083MY2.

[1] S. Foner, "Vibrating sample magnetometer", *Review of Scientific Instruments*, 27(7), 548-548 (1956). [2] R. Nagendran, N. Thirumurugan, N. Chinnasamy, M. P. Janawadkar, & C. S. Sundar, "Development of high field SQUID magnetometer for magnetization studies up to 7 T and temperatures in the range from 4.2 to 300 K", *Review of Scientific Instruments*, 82(1), 015109 (2011). [3] V. Munoz, M. C. Martinez, & V. Such, "Improved systems for the measurement of hysteresis loops: DC and AC characterization", *Journal of Physics E: Scientific Instruments*, 20(7), 861 (1987). [4] R. B. Goldfarb & J. V. Minervini, "Calibration of ac susceptometer for cylindrical specimens", *Review of scientific instruments*, 55(5), 761-764 (1984). [5] C. Reig, S. Cardoso, & S. C. Mukhopadhyay, "Giant magnetoresistance (GMR) sensors", In *Smart Sensors, Measurement and Instrumentation*, 6(1), pp.1-301 (2013).

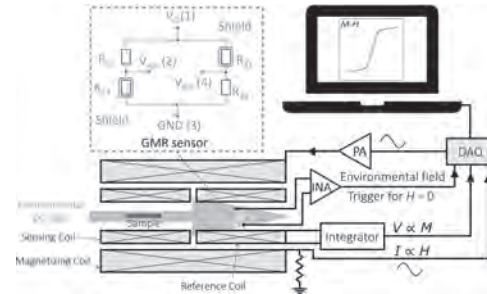


Fig. 1. Schematics of the magnetization measurement system with GMR zero-field detector

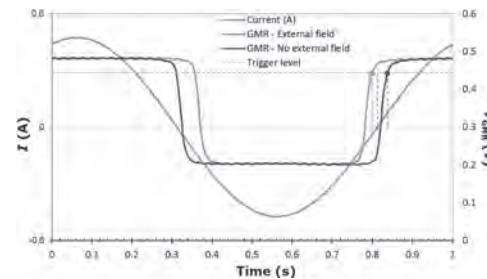


Fig. 2. The trigger points of the GMR zero-field detector for the M - H measurement system

CR-10. A Matching Method for Magnetic Anomaly Signals Under Low Signal-to-Noise.

J. Qiu¹ and J. Ou¹

1. College of Optoelectronic Engineering, Chongqing University, Chongqing, China

Many scholars have found that magnetic anomaly signals can reflect the characteristics of magnetic target, such as distance, speed, magnetic moment and other related information [1-3]. This provides a new idea for target recognition by matching magnetic anomaly signals. However, the magnetic anomaly signals in the detection environment are weak and easily disturbed by the strong background noise of the geomagnetic field, resulting in a low signal-to-noise ratio (SNR) of the signals output by the magnetic sensor [4], which brings great challenges to the traditional signal matching method. In this paper, a method combining OBF (Orthogonal Basis Function) decomposition and EDR (Edit Distance on Real sequence) is proposed to match magnetic anomaly signals under low SNR. The calculation process of OBF-EDR method is divided into three steps (Fig. 1). Step 1: The OBF method is used to decompose the magnetic anomaly signals. According to the characteristics that the background noise is not correlated with the basis function, three sets of discrete basis function coefficient sequences with higher SNR can be obtained [5]. Step 2: The sequences of discrete basis function coefficient are taken as the calculation object, and the EDR method with strong anti-noise ability is used to measure and get their similarity results. Step 3: The matching result of the magnetic anomaly signals is calculated through the similarity results of the three sets of discrete basis function coefficient sequences by the weight method. The simulation shows that the curves of matching accuracy of OBF-EDR and EDR method have the same changing trend with the change of signals' SNR, but the curve of matching accuracy of OBF-EDR method moves to the direction of lower SNR compared with that of EDR (Fig. 2). It indicates that the OBF-EDR method can match the magnetic anomaly signals correctly at a lower SNR than the EDR method. What's more, when the matching accuracy of OBF-EDR reaches 0.9, the required signal's SNR is -2dB, which is 7dB lower than that of EDR method. The above conclusions prove the advantage of the OBF-EDR method to matching magnetic signals under low SNR.

[1] Y. Shen, J. Wang, and J. Shi, *J. Magn. Magn. Mater.*, 484, 164-171, (2019). [2] Y. Shen, D. Hasanyan, and J. Gao, *Smart Mater. Struct.*, 22, 095007, (2013). [3] J. Wang, Y. Shen, and R. Zhao, *J. Magn. Magn. Mater.*, 505, 166761, (2020). [4] O. Faggioni, M. Soldani, and A. Gabellone, *J. Appl. Geophys.* 72, 46-56, (2010). [5] B. Ginzburg, L. Frumkis, and B. Kaplan, *Sens. Actuator A-phys.*, 102, 67-75, (2002).

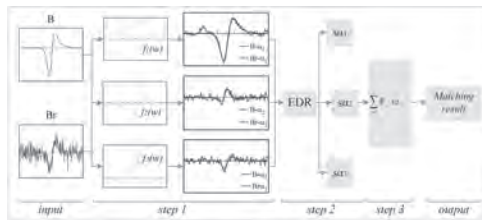


Fig.1. OBF-EDR method calculation process.

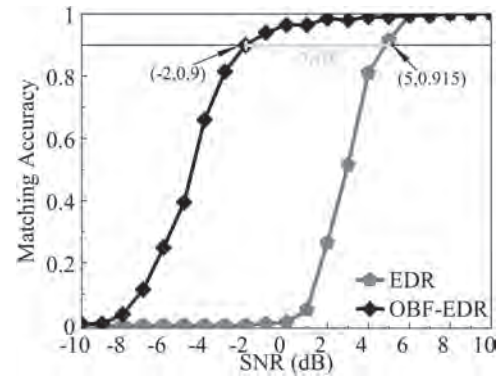


Fig.2. Matching accuracy of OBF-EDR and EDR method to match the magnetic anomaly signals under different SNR.

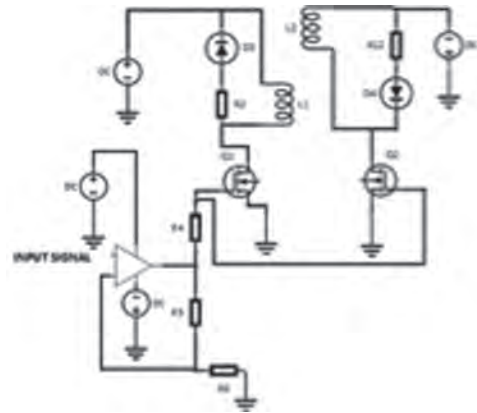
CR-11. Design of Stable Biphasic Pulsed Magnetic Fields for Portable Diagnostic Applications.

N. Prabhu Gaunkar¹, W. Theh¹, N. Bouda¹ and M. Mina¹

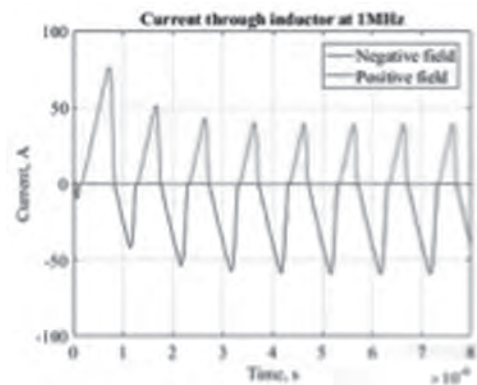
¹. Electrical and Computer Engineering, Iowa State University, Ames, IA, United States

Biphasic or monophasic pulsed magnetic fields are commonly used in non-invasive stimulation of biological systems [1]. Biphasic systems bring the advantage of using both the positive and negative pulsed fields, thereby leading to twice the amount of signal obtained by using monophasic pulsed field systems [2]. With a focus on medical applications, biphasic pulses have been used in transcranial magnetic stimulation applications [2, 3] for neuronal excitation and in magnetic resonance applications for inducing proton transitions [4, 5]. Typically, commercial field generator systems with sophisticated data acquisition and processing mechanisms are used for such medical applications. However, with the recent trends towards portable diagnostics, a redesign of the pulsed field generator systems for improved portability is required. In this work, design and challenges of creating biphasic low-pulsed magnetic fields, which may be utilized for portable NMR applications, is discussed. Since portable solutions rely on permanent magnet geometries, the strength of static field is low and correspondingly, the strength of the pulsed field is typically low (less than 0.1T). Prior portable pulsed field generators have been designed to obtain repetitive pulses at both high (up to 0.5T) [2,3] and low-field strengths (0.05T) [4]. However, obtaining high-frequency (1-10MHz) pulsed sinusoidal fields (both monophasic or biphasic) is a challenge for most portable systems. The monophasic pulse generators are useful in obtaining higher pulsed fields and amplitudes with limits on the number of nuclear spins that may be excited during an excitation cycle. Meanwhile, biphasic pulses can provide uniform excitation but have lower field amplitudes. Both the techniques are equally valuable and appropriate pulse sequencing techniques can be designed to make such pulsed field generators valuable additions in pulsed NMR applications. This work highlights the design parameters and challenges of both techniques and details the design of a biphasic portable pulsed field generator operational between 0.5 – 2 MHz. The primary challenge of biphasic pulsed generators is the rapid switching between the different phases. The designed biphasic pulse generator (Figure 1) includes two switching devices and intertwined inductors connected to a common terminal and pulsed with a 180 degree offset. The two switches operate such that only one inductor is active at a particular time. The biphasic generator is designed to obtain a maximum of +/- 15A through the inductor (Figure 2) at an operational frequency of 1MHz. Synchronizing the phase offset between the two switching devices ensures simultaneous operations. In summary, different aspects of the switching device, load, operational frequency and phase synchronization needed to obtain stable biphasic pulsed magnetic fields will be highlighted in this paper.

[1]. N. M. Shupak, F. S. Prato and A. W. Thomas, "Therapeutic uses of pulsed magnetic-field exposure: A review," in *URSI Radio Science Bulletin*, vol. 2003, no. 307, pp. 9-32, Dec. 2003. [2]. J. Selvaraj, P. Rastogi, N. Prabhu Gaunkar, R. L. Hadimani and M. Mina, "Transcranial Magnetic Stimulation: Design of a Stimulator and a Focused Coil for the Application of Small Animals," in *IEEE Transactions on Magnetics*, vol. 54, no. 11, pp. 1-5, Nov. 2018, Art no. 5200405. [3]. N. R. Bouda, M. Mina and R. J. Weber, "High-Current Magnetic Field Generator for Transcranial Magnetic Stimulation Applications," in *IEEE Transactions on Magnetics*, vol. 50, no. 11, pp. 1-4, Nov. 2014, Art no. 5400204. [4]. N. Prabhu Gaunkar, J. Selvaraj, L. Bauer, M. Mina, R. Weber and D. Jiles, "Design and Experimental Implementation of a Low Frequency Pulsed Magnetic Field Generator," in *IEEE Transactions on Magnetics*, vol. 53, no. 11, pp. 1-4, Nov. 2017, Art no. 6501004. [5]. N. Prabhu Gaunkar, "Developments in static and pulsed magnetic field systems for detection of magnetic resonance in non-uniform magnetic fields" (2018). *Graduate Theses and Dissertations, Iowa State University*, 17291.



Schematic of biphasic pulsed field generator



Current through inductor at a frequency of 1MHz (estimated from current sense resistor)

Session CS
MAGNETIC MODELLING
(Poster Session)

Benjamin Ducharne, Chair
Institut National des Sciences Appliquees de Lyon, Villeurbanne, France

CS-01. Dynamical Rearrangements of 3D Vortex Structures in Moving Domain Walls in Continuous and Antidot Patterned Permalloy Films.

V.V. Zverev^{1,2} and I. Izmozherov²

1. Department of Theoretical Physics and Applied Mathematics, Ural Federal University, Ekaterinburg, Russian Federation; 2. M.N. Mikheev Institute of Metal Physics of the Ural Branch of the Russian Academy of Sciences, Ekaterinburg, Russian Federation

Progress in the development of nanomagnetism has forced the scientific community to pay close attention to 3D magnetic nanostructures [1]. Currently, the use of X-ray nanotomography makes it possible to determine temporal evolution of the magnetization [2, 3]. Since both spatial and temporal resolution of experimental methods is limited, it is natural to compare the experimental results with the computer simulation predictions. This approach allows resolve both the fine spatial structure of vortex aggregates and the fast processes of topological rearrangements. In our simulations, we take advantage of instability of a domain wall motion in a magnetic field above a certain threshold value. In continuous films this instability generates various dynamic vortex structures and spin waves [4, 5]. In the case of antidot films, new types of vortex-induced topological rearrangements of magnetization can be observed in the region of the array of holes. We simulate the process of magnetization reversal in a permalloy cuboid with the dimensions $X = 800$ nm, $Y = 200$ nm (the film thickness), $Z = 400$ nm, with periodic boundary conditions along the z axis. This axis is the easy magnetization axis in the film plane and the y axis is perpendicular to the film plane. We have considered a single rectangular hole with size d as well as arrays with three or nine such holes, where $d = 25, 50$, or 100 nm. Micro-magnetic simulations of magnetic dynamics were performed by solving the Landau-Lifshitz-Gilbert (LLG) equation using *mumax3* solver [6]. We used a 3D orthogonal uniform mesh of size $a = 3.125$ nm. To visualize the magnetization topological structure we employed an approach based on the calculation of topological charges of two types [4, 5]. They satisfy the laws of conservation and we have classified permissible transformations of the magnetization distributions at the film boundaries. When a domain wall moves in a sample with holes, various scenarios of transformations of vortex structures are realized. We have specified the initial distribution of magnetization as a specially formed configuration containing a C-shaped (vortex) domain wall (DW) near the boundary of the sample. The axis of the DW (the z axis) is in the plane of the sample. To the right (left) of the DW, the magnetization is directed against (along) the direction of the z axis. After turning on the DC magnetic field $H = 200$ Oe along the z axis, the DW begins to move, becoming the S-shaped one. Further movement of the DW is accompanied by the generation of vortex structures leading to the complex dynamics of magnetization reversal in the antidot array. (a) In the case of large holes ($d = 100$ nm), after the DW reaches the antidot array boundary, the vortex structures disappear and the process of magnetization reversal stops. The final steady-state configuration of the magnetization in the three-hole array is as follows: when traversing the contours of the boundaries of the holes clockwise, the magnetization makes a full turn clockwise (counterclockwise) for the middle (lower) hole. This means that the holes are carriers of topological charges and are topologically equivalent to local vortex and antivortex. (b) In the case of medium-sized holes ($d = 50$ nm), the displacement of the magnetization reversal region is accompanied by the appearance of vortices near the holes. Some vortices connect the lateral boundary surfaces of adjacent holes. (c) In the case of small holes, in the regions between the holes, emerging magnetization distributions look like fragments of DWs. The appearance of vortex filaments similar to the vortex core of C-shaped DWs is typical. Evolution of the 3D magnetization distribution leads to a number of peculiar instant topological configurations. (a) Two vortex filaments connect the boundary surfaces of the film and two other filaments connect the lateral boundaries of the hole with the boundaries of the film (Fig 1a). At the upper boundary of the film, there are two local vortices and one local antivortex (ends of vortex filaments on the surface, Fig. 1b). Additionally, there is an antivortex-like configuration around the hole. At the lower boundary, there is one local vortex, two local antivortices, and a vortex-like configuration around the hole (Fig. 1c). (b) One vortex filament connects the boundary surfaces, the other filament connects the intra-film boundary of the hole and the boundary of the film. There is a local vortex and an antivortex-like hole

at the upper boundary, and a vortex-antivortex pair at the lower boundary. (c) A fully antivortex-like hole is combined with a local vortex at the upper boundary and vortex-like hole at the lower boundary.

[1] A. Fernández-Pacheco, R. Streubel, O. Fruchart, et al. Nature Comm. Vol. 8, 15756 (2017). [2] C. Donnelly, S. Finizio, S. Gliga, et al. Nat. Nanotechnol. Vol. 15, p. 356 (2020). [3] C. Donnelly, K. L. Metlov, V. Scagnoli, et al. Nat. Physics Lett. <https://doi.org/10.1038/s41567-020-01057-3> (2020). [4] V. V. Zverev, E. Zh. Baykenov, I. M. Izmozherov. Phys. Met. Metallogr. Vol. 120, p. 1299 (2019). [5] V. V. Zverev, E. Zh. Baykenov, I. M. Izmozherov. Phys. Solid State, Vol. 61, p. 2041 (2019). [6] A. Vansteenkiste, J. Leliaert, M. Dvornik et al. AIP Advances, Vol. 4, 107133 (2014).

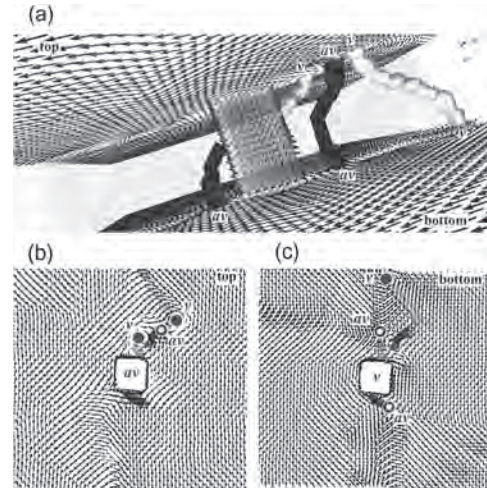


Fig. 1. A snapshot of the vortex structure (a) inside the film, (b) at the upper boundary (top), (c) at the lower boundary (bottom).

CS-02. Numerical Simulation of the Structure and Dynamics of Magnetic Vortices and Solitons in Multilayer Ferromagnetic Nanostructures.

K. Samsonov¹, S. Stepanov², G. Antonov², A. Ekomasov², R. Kudryavtsev³, A. Gumerov², K. Zvezdin⁴ and E.G. Ekomasov^{1,2}

1. *Department of Physical Processes and Systems Modeling, University of Tyumen, Tyumen, Russian Federation*; 2. *Department of Theoretical Physics, Bashkir State University, Ufa, Russian Federation*; 3. *Institute of Molecule and Crystal Physics UFIC RAS, Ufa, Russian Federation*; 4. *A. M. Prohorova Institute of General Physics, RAN, Moscow, Russian Federation*

The structure and dynamics of magnetization in a vortex spin-transfer nanooscillator, which is a three-layer spin-valve magnetic nanopillar with a small diameter, is studied during the passage of a spin-polarized current and the presence of an external magnetic field. Using micromagnetic simulation [1,2], we studied the dynamic change in the vortices structure, the formation of the C-structure vortex state and edge vortices, the trajectory of movement and the time it takes to reach different dynamic modes. The time needed for the vortices to reach different dynamic modes was found. The possibility of the dynamic generation of radial edge vortices without the presence of a Dzyaloshinsky field or an external inhomogeneous magnetic field is shown. We demonstrate that a vortex in a thick magnetic layer can be a generator of spin waves in a thin magnetic layer with an adjustable oscillation frequency. We consider also multilayer magnetic structures, which are periodically alternating layers of two materials with different physical properties. In such systems it is possible to generate localized magnetization waves (LMW) of the magnetic solitons and breathers type [3]. Special interest in magnetic solitons and breathers is currently associated with the appearance of new experimental techniques that allow to study formation and propagation of localized magnetization waves of nanometer dimensions and their interaction with domain walls (DW). The possibility of controlling the structure and dynamic parameters of magnetic solitons and breathers using an external magnetic field is shown [4]. Dependences of the center of the DW and amplitudes of the LMW on time are constructed and analyzed in the presence of three, five and seven layers. It is shown that the LMW vibrations for the case of five layers can be described by the model with two harmonic oscillators, and for the case of seven layers, three harmonic oscillators. This work was supported by RFBR, project No 20-31-90048.

1. A.E.Ekomasov et al., *Journal of Magnetism and Magnetic Materials*, 471, 2019, 513-520; 2. E.G. Ekomasov et al., *Chelyabinsk Physical and Mathematical Journal*. 2020. Vol. 5, iss. 2. P. 161–173; 3. A.M. Gumerov et al., *Journal of Physics: Conference Series. VII Euro-Asian Symposium “Trends in Magnetism”*. 2019. V. 1389. p. 012004: 1–6; 4. E. G. Ekomasov et al., *Letters on Materials* 10 (2), 2020 pp. 141-146.

CS-03. Angular Remanence and Anisotropy Orientation Distribution in Nickel Films on LiNbO₃.

S.A. Mathews¹ and N. Charipar¹

1. Materials Science and Technology Division, US Naval Research Laboratory, Washington, DC, United States

Nickel thin films (100 nm) deposited on 128° Y-cut: LiNbO₃ exhibit a well-defined magnetic anisotropy upon annealing at 325° C [1]. Simulating the magnetization of these films using a temperature dependent Stoner-Wohlfarth model indicates that the films have a very narrow angular distribution of anisotropy axes [2]. Here we report a direct measurement of the angular distribution of anisotropy axes by the angular remanence technique [3]. The angular range over which the easy axis remanence drop significantly is a measure of the angular distribution of the anisotropy axes. For annealed nickel thin films on 128° Y-cut: LiNbO₃ the FWHM of the remanence as a function of angle (α) is approximately 0.44°.

[1] S.A. Mathews, N.S. Bingham, R.J. Suess, K.M. Charipar, R.C.Y. Auyeung, H. Kim, and N.A. Charipar, *IEEE Trans. Mag.*, Vol. 55, Issue 2, (2019) [2] S.A. Mathews, A. Ehrlich, and N. A. Charipar, "Hysteresis branch crossing and the Stoner-Wohlfarth model", *Scientific Reports*, 10:15141 (2020). [3] H.J. Richter and H. Hibst, *Jour. Mag. Mag. Mat.*, 95, 118-122 (1991).

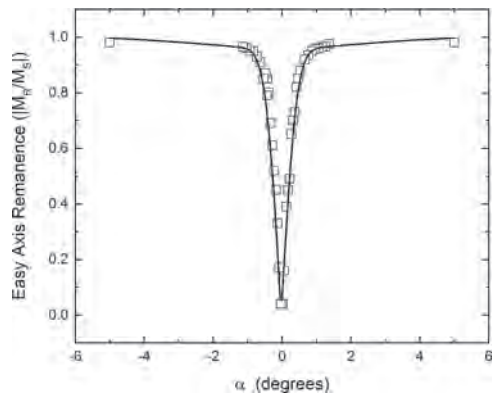


Figure 1: Absolute value of easy axis remanence as a function of α (angle between the hard axis and the saturating field). Open squares represent measured data. The solid line represents the model, assuming an ensemble of Stoner-Wohlfarth particles with two normal (Gaussian) distributions of anisotropy orientation.

CS-04. Transverse Susceptibility of Nickel Thin Films With Uniaxial Anisotropy.

S.A. Mathews¹, C. Musi² and N. Charipar¹

1. *Materials Science and Technology Division, US Naval Research Laboratory, Washington, DC, United States*; 2. *Nova Research Inc, Alexandria, VA, United States*

In this work, we report transverse susceptibility (TS) measurements performed on nickel thin films, deposited on 128° Y-cut LiNbO₃ substrates and annealed at low temperature. The films exhibit a strong uniaxial anisotropy [1] and hysteresis branch crossing (HBC) [2]. The results are compared to numeric solutions to the Stoner-Wohlfarth (SW) model [3] using a finite temperature approximation [4] and a distributed anisotropy. The experimentally observed TS-curves, measured with applied field close to the hard axis, are shown to be in excellent agreement with the SW-model, confirming that the magnetization in these samples occurs via coherent rotation. As predicted by Aharoni [5], the TS curves show three peaks or cusps: two reversible peaks associated with anisotropy field, and one irreversible peak associated with the discontinuity in the transverse magnetization.

[1] S.A. Mathews, N.S. Bingham, R.J. Suess, K.M. Charipar, R.C.Y. Auyeung, H. Kim, and N.A. Charipar, *IEEE Trans. Mag.*, Vol. 55, Issue 2, (2019) [2] S.A. Mathews, A.C. Ehrlich, and N.A. Charipar, *Scientific Reports*, 10:15141 (2020) [3] Stoner, E.C. and Wohlfarth, E.P., *Phil. Trans. Roy. Soc. of London Series A*, 240, no. 826, pp.599-624 (1948). [4] L. Lanci and D. Kent, *J. Geophys. Res.*, Vol. 108, No. B3, 2142 (2003). [5] A. Aharoni, E. M. Frei, S. Shtrikman, and D. Treves, *Bull. Res. Council. Isr.*, Sect. F 6A, 215 (1957).

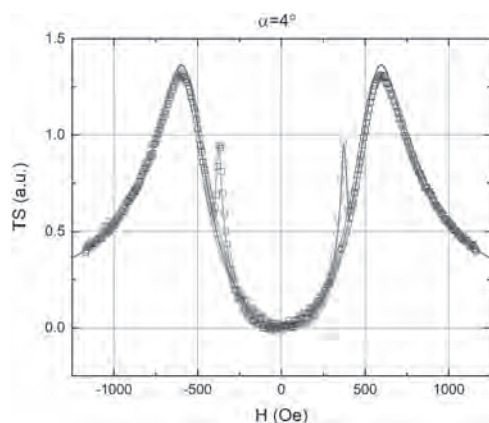


Figure 1: Measured (open squares) and simulated (solid lines) transverse susceptibility of a nickel thin film on LiNbO₃. The field is applied at an angle $\alpha=4^\circ$ from the hard axis. The ascending and descending curves are shown in red and blue, respectively.

CS-05. Application of an Improved Interpolating Element-Free Galerkin Method in Magnetic Field Calculation.

F. Yang¹ and C. Gu¹

1. Huazhong University of Science and Technology School of Electrical and Electronic Engineering, Wuhan, China

Abstract-In this paper, an improved interpolating element-free Galerkin method (IIEFGM) with nonsingular weight function is introduced to calculate the magnetic field distribution of electrical machine. Since the shape function satisfied the property of Kronecker-delta function, the IIEFGM can impose the boundary conditions directly. Meanwhile, the IIEFGM adopts nonsingular weight function, which means the weight function of the conventional element-free Galerkin method (EFGM) can be used. To demonstrate the effectiveness of IIEFGM, the magnetic field distribution of a permanent magnet coreless disc machine is analyzed. The selection of weight function and the nodes distribution are discussed, the comparison with Finite element method (FEM) shows the IIEFGM has high computational accuracy. I. Introduction Meshless methods are the important supplement to the finite element method in solving boundary problems, and element-free Galerkin method is the most widely used method. The mainly difference between the EFGM and the FEM is the construction method of the shape function, however, since the shape function of EFGM does not satisfy the property of Kronecker-delta function, the imposition of boundary conditions required additional methods, such as penalty method. To solve this problem, reference [1] proposed an interpolating element-free Galerkin method (IEFGM), however, the method adopt singular weight, which makes the computation difficult. Reference [2] proposed IIEFGM with nonsingular weight function, which has the advantages of both the FEM and the IEFGM. In this paper, a permanent magnet coreless disc machine (PMCDM) is taken as an example [3] the IIEFGM is introduced to calculate the magnetic field distribution of the PMCDM, and the comparison with the FEM validated the effectiveness of the IIEFGM. II The foundation of the IIEFGM In conventional EFGM, the basis function is defined as: $p_1=1$, $p_2=x$, $p_3=y$ ($m=3$), and the trial function is $u^h(x)=p^T(x)a(x)$. The coefficients $a(x)$ can be obtained by minimizing the weighted least-square function, then the shape function $N(x)$ can be derived. To make the shape function satisfied the property of the Kronecker-delta function, the IIEFGM modified the basis function. Then the boundary conditions can be imposed directly, and the negative exponential function is selected as the weight function. III Magnetic field calculation of the PMCDM Fig.1 shows the magnetic field distribution of the PMCDM by using IIEFGM, the problem domain is divided into the radial part and the circular part. Fig.2 depicts the main flux density on the airgap center line. It can be seen that the calculated results obtained by IIEFGM are in excellent agreement with the results with the FEM. IV Conclusion This paper introduced an improved interpolating element-free Galerkin method. The Galerkin weak form and the discretized equation are derived, the flow of the algorithm is optimized, and a weight function with higher accuracy is given. Based on IIEFGM, the magnetic field distribution of a PMCDM is analyzed, numerical results verified the effectiveness of the IIEFGM. The study results provide references for the application of IIEFGM.

[1] Ren H, Cheng Y, "The interpolating element-free Galerkin (IEFG) method for two-dimensional potential problems," *Engineering Analysis with Boundary Elements*, Vol. 36(5), p.873-880, 2012. [2]Wang J F, Sun F X, Cheng Y M, "An improved interpolating element-free Galerkin method with a nonsingular weight function for two-dimensional potential problems," *Chinese Physics B*, Vol. 21, No.9, 2012. [3]Gu C L, Wu W, Shao K R, "Magnetic field analysis and optimal design of DC permanent magnet coreless disc machine," *IEEE Transactions on Magnetics*, Vol. 30(5), p. 3668-3671, 1994.



Fig.1 Magnetic field distribution. (a) circular direction, (b) radial direction

Fig.1 Magnetic field distribution. (a) circular direction. (b) radial direction

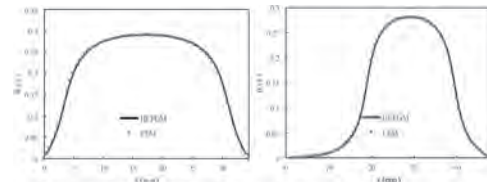


Fig.2 Main flux density on airgap center line. (a) circular direction. (b) radial direction

Fig.2 Main flux density on airgap center line. (a) circular direction. (b) radial direction

CS-06. An Improved Hysteresis Model Based on Bouc-Wen Model Under Quasi-Static and Dynamic Magnetizations.

Y. Li¹, Y. Li¹, Z. Lin¹, Z. Cheng² and Y. Tian¹

1. State Key Laboratory of Reliability and Intelligence of Electrical Equipment, Hebei University of Technology, Tianjin, China;

2. R&D Center, Baoding Tianwei Group Co., Ltd, Baoding, China

Introduction Hysteresis of magnetic materials is a complicated physical phenomenon. The appropriate mathematical expression which can describe the hysteresis mechanism is desired in the design of electromagnetic devices, such as transformers and reactors. It could enable researchers to model the hysteresis accurately, and hence improve the performance and efficiency of the devices. This paper modifies the Bouc-Wen model to model the hysteresis of magnetic materials, and accords the parameters of the model with physical meaning. At present, the magnetic hysteresis models are classified as mathematical models and physical models. The Preisach model, as a mathematical model, can describe the hysteresis phenomenon, but it cannot describe the magnetization process of the materials[1]. The domain structure model, which has a clear physical meaning and takes into account of energies related to the growth of the domain, can describe the hysteresis well, but it only studies in microscopic range, and is complicated to be employed in engineering applications[2]. To model the magnetic properties efficiently and accurately, a practical model which can correlate model parameters describing magnetization process with the hysteresis phenomenon responsible to the applied magnetic field is needed. The model proposed in this paper has the feature to simulate the magnetization process in general by adjusting the parameters according to the materials characteristic in applied magnetic fields. Theorem Ferromagnetism reveals that the internal mechanism of hysteresis is very complicated. The magnetization process mainly includes motion of the domain wall and rotation of the spontaneous magnetization of domain [3]. The process of wall motion is very similar to the kinetic process of viscous friction, such as nonlinear hysteretic mechanics Bouc-Wen model, so that the kinetics model is exploited to describe the domain wall motion. However, it cannot characterize the rotation of the domain magnetization[4]. The model is modified by introducing a term which can characterize the rotation process. The improved model includes the four resistances encountered when the domain wall moves and the domain magnetization rotates during the magnetization process: i) the resistance caused by the increasing energy of the domain wall, which is linearly related to the displacement of the domain wall; ii) the resistance caused by the local eddy current, which is proportional to the moving velocity of the domain wall; iii) the resistance caused by the rotation of the domain magnetization; and iv) the hysteretic restoring force caused by material defects, which is proportional to the hysteretic displacement. The hysteretic displacement which describes the inelastic behavior of domain wall motion is calculated by the differential equation of the Bouc-Wen model. The improved model can be used to calculate the magnetic hysteresis under high and low magnetic field strengths. The parameters of the model representing the damping coefficients of each resistance are identified by the particle swarm algorithm. It is found that the damping coefficient is a function of the strength of the applied field under quasi-static magnetization, and the shape parameters of the model are constants. Since eddy current will cause the reactive force during the motion of domain wall and rotation of domain magnetization under dynamic excitation, the model must be modified to take the account of dynamic excitation into damping coefficients. A function of damping coefficients related to applied field strength and frequency is discussed in detail in the full paper. Experiment In order to simulate magnetization process using the improved model, the oriented silicon steel B27R090 with relatively simple domain structure is used. The Single Sheet Test is used as the experimental platform to measure the magnetic properties of the sample under quasi-static and dynamic magnetizations. Fig. 1 and Fig.2 show the measured hysteresis loops and the predicted hysteresis loops under sinusoidal excitation at 5 Hz and 50 Hz. The predicted hysteresis loops calculated by the improved Bouc-Wen model are in good agreement with the measured loops when the flux density is between 0.3 T and 1.4 T. The calculated total losses using the improved Bouc-Wen model is also in good agreement with the the measurement results. The full paper will discuss the results in detail.

[1] Mayergoz I D, IEEE Transactions on Magnetics., Vol. 22, p. 603-608(1986) [2] Sudo M, Mifune T and Matsuo T, IEEE Transactions on Magnetics., Vol. 49, p. 1829-1832 (2013) [3] Bertotti G, IEEE Transactions on Magnetics., Vol. 24, p. 621-630 (2002) [4] Ikhouane F, José Rodellar, Nonlinear Dynamics., Vol. 42, p. 63-78 (2005)

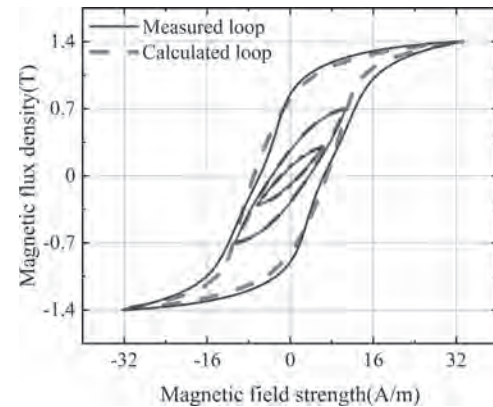


Fig.1 Measured (solid lines) and calculated (dashed lines) hysteresis loops under sinusoidal excitation with amplitudes of flux density of 0.3 T, 0.7 T, and 1.4 T at frequencies of 5 Hz

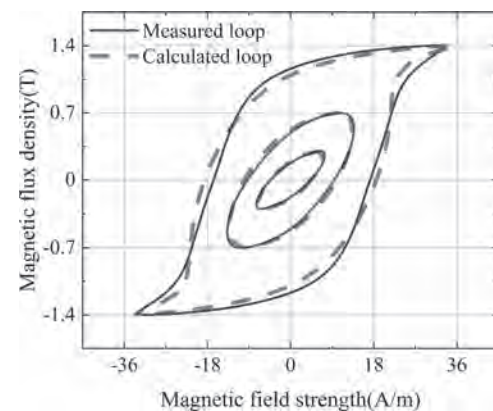


Fig.2 Measured (solid lines) and calculated (dashed lines) hysteresis loops under sinusoidal excitation with amplitudes of flux density of 0.3 T, 0.7 T, and 1.4 T at frequencies of 50 Hz

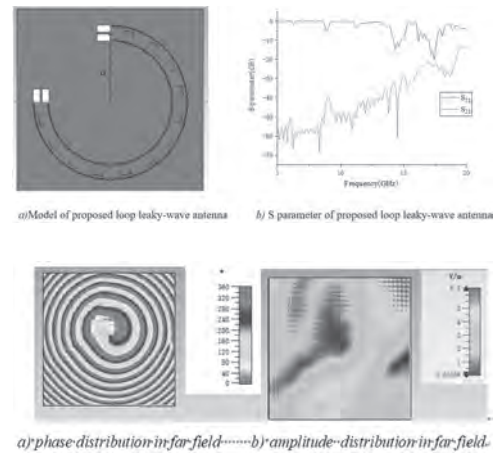
CS-07. Circular Polarized Vortex Beam Generating Based on Leaky-Wave Antenna With Substrate Integrated Waveguide.

Q. Zhang¹, W. Chen¹, Y. Zhao¹ and J. Fu¹

1. Harbin Institute of Technology, Harbin, China

Abstract—A circular polarized vortex beam generating based on leaky-wave antenna with substrate integrated waveguide(SIW) is proposed in this paper. Comparing with phased array antenna, the leaky-wave antenna is working without complicated feeding network and phase shifter. Then the unit is designed to realize circular polarization. Finally The loop leaky-wave antenna with SIW is designed to generate vortex beam and works at 14.5 GHz. The simulated gain reaches 11.4 dBi with generating -1 mode orbital angular momentum(OAM) of vortex beam. Vortex electromagnetic wave are electromagnetic waves with orbital angular momentum Wave. The most important characteristic of orbital angular momentum is its orthogonality in different modes. The degree of freedom of electromagnetic wave includes frequency and polarization. It is amazing that the orthogonality of vortex electromagnetic wave provides extra freedom for electromagnetic wave. Therefore, vortex electromagnetic wave has the potential to be used in communication and imaging systems[1]-[3]. In this paper, A circular polarized vortex beam generating based on leaky-wave antenna with substrate integrated waveguide(SIW) is proposed. Because the leaky-wave antenna is working without complicated feeding network and phase shifter. And the unit is designed to realize circular polarization. Then the radiation pattern of loop leaky-wave antenna is derived from the leaky-wave unit. Finally The loop leaky-wave antenna with SIW is proved to radiate -1 mode vortex electromagnetic wave with circular polarization in the simulation of CST Studio. The simulation model is showed as Fig. 1 a), the reason the loop leaky-wave antenna is three-quarter circle is that CST Studio limits the wave port should be put at the coordinate axis. And from [4], we know a part of circle to radiating is enough to radiate vortex beam. The microstrip line is designed for impedance matching to transmit microwave to the loop leaky-wave antenna. The S_{11} and S_{21} is showed in Fig. 1 b). It is showed the S_{11} is lower than -10dB and S_{21} is also low, because the most energy is radiated to open space. Fig. 2 a) is the phase distribution in far field at 14.5GHz. As we can see, the phase distribution is -1 mode vortex beam form. The radius of loop antenna determines the phase difference between adjacent unit, and in this paper, the radius is 52mm to make the OAM mode is -1. Fig. 2 b) shows the amplitude distribution in far field. The distribution is not uniform, which is caused by deletion of loop leaky-wave antenna. If the loop leaky-wave antenna is complete circle, the distribution will be improved. A circular polarized vortex beam generating based on leaky-wave antenna with substrate integrated waveguide (SIW) is proposed in this paper. Comparing with phased array antenna, the leaky-wave antenna is working without complicated feeding network and phase shifter. We proof linear polarized unit can radiate circular polarized beam but the beam is not clean, so we design unit with circular polarized radiation. Finally, the loop leaky-wave antenna with SIW is designed to transmit vortex beam and works at 14.5 GHz. The simulated gain reaches 11.4 dBi with generating -1 mode vortex beam.

[1] Yan, Y., Xie, G., Lavery, M. P. J. "High-capacity millimetre-wave communications with orbital angular momentum multiplexing." *Nature Communications* vol. 5, pp. 4876, 2014. [2] Shilie, Zheng, Xiaonan, et al. "Orbital angular momentum mode-demultiplexing scheme with partial angular receiving aperture." *Optics express*. vol. 23, no. 9, pp.12251-12257, 2015. [3] Bai, Q., A. Tennant, and B. Allen. "Experimental circular phased array for generating OAM radio beams." *Electronics Letters* 50.20:1414-1415, 2014. [4] Xiong, Xiaowen, et al. "Direct Generation of OAM Mode-Group and Its Application in LoS-MIMO System." *IEEE Communications Letters* PP.99(2020):1-1.



CS-08. Field Computation in Media Exhibiting Hysteresis Using Hopfield Neural Networks.

A. Adly² and S. Abd-El-Hafiz¹

1. Engineering Mathematics and Physics Dept., Cairo University, Giza, Egypt; 2. Elect. Power Engineering Dept., Cairo University, Giza, Egypt

It is known that the assessment of local magnetization in objects exhibiting hysteresis is crucial to the accurate design and/or performance estimation of a wide range of electromagnetic devices. Among the widely used approaches to carry out the afore-mentioned assessment tasks, the integral equations approach has been widely adopted (See, for instance [1]). In the past, it was demonstrated that an elementary hysteresis operator may be constructed using a two-node Hopfield Neural Network (HNN) having step activation functions and positive inter-node feedback [2]. The approach was further extended in [3] to construct a 2D vector hysteresis operator using a tri-node Hopfield Neural Network (HNN) having orientation-dependent inter-node feedback values. Utilization of this extension was previously partially utilized in 2D field computations by coupling the proposed approach with time consuming iterative integral equation methodologies [4]. The purpose of this paper is to offer a novel 2D field computation approach in media exhibiting hysteresis that solely utilizes HNNs. The approach is based on the novel incorporation of domain-domain interaction in the overall HNN energy formulation. Consequently, 2D field computation may be accomplished by employing typical HNN automated energy minimization algorithms. Consider a HNN comprised of N clusters of tri-node HNNs. The total applied field H_t at any node u in HNN $\#i$ having a triangular median given by (x_i, y_i) may be given by: $H_{t_{iu}} = (H + \sum_{j=1, N} h_{ji}) \bullet e_{iu} + \sum_{v=1, 3} f_{iv} k_{copl} | e_{iv} \bullet e_{iv} |$, (1) $h_{ij} = -\nabla \cdot (\sum_{s=1, 3} (f_{is} e_{is} \bullet R_{jp}) / (4\pi | R_{jp} |^3)) |_{(x_i, y_i)}$, $R_{jp} = (x - x_j) e_x + (y - y_j) e_y$, (2) where H is the external applied field, e_{ab} is the unit vector denoting the orientation of node $\#b$ in HNN $\#a$, k_{copl} is the internal tri-node coupling factor using which the switching value of the elementary operator may be tuned, while f represent the HNN step activation function given by: $f(H_t) = \{+1 \text{ if } H_t > 0, -1 \text{ if } H_t < 0, \text{ Unchanged if } H_t = 0\}$. (3) It should be mentioned here that, in HNN terminology, all coupling factors between any two nodes in the overall HNN may be deduced from (1) and (2). The proposed implementation yields node outputs corresponding to, an automatically achieved, minimized value of the HNN energy E (in line with the magnetostatic energy) given by: $E = -\sum_{i=1, N} (\sum_{u=1, 3} [(H + \sum_{j=1, N} h_{ji}) \bullet f_{iu} e_{iu} + 1/2 \sum_{v=1, 3} f_{iv} k_{copl} | e_{iv} \bullet e_{iv} |])$. (4) Local magnetization values of any tri-node HNN, denoted by HNN $\#i$, representing a triangular subdivision may be deduced from: $M_i(H) = \sum_{u=1, 3} f_{iu} e_{iu}$. (5) Hence, total output of the overall HNN representing the magnetization of the magnetized body under consideration may thus be expressed using superposition in the form: $M(H) = \sum_{i=1, N} M_i(H)$. (6) In order to demonstrate the proposed methodology, consider the case of a pair of tri-node HNN (i.e., $N=2$) as shown in Fig. 1.a. Sample results for this particular case are given in Figs. 1 and 2 for the two tri-node HNNs representing triangular subdivisions whose vertices have the coordinates $(1.0, 0.5)$, $(-0.5, 0.5)$, $(-0.5, -0.5)$ and $(1.0, 0.5)$, $(1.0, -0.5)$, $(-0.5, -0.5)$, respectively. In Figs. 1.b and 1.c results corresponding to x-axis cyclic and rotational applied inputs are demonstrated when the two triangles join to form a rectangular shape. Variations of the x-axis cyclic input-output curves resulting from the change in the vertical spacing Dy and/or horizontal spacing Dx between both triangular subdivisions are further demonstrated in Fig. 2. Results clearly highlight the impact of the incorporation of domain-domain interaction in the introduced field computation approach. It should be mentioned that using such an approach HNN modules, which are widely available in a number of mathematical simulation tools, may be utilized in 2D field computation in media exhibiting hysteresis. More details of the approach for arbitrary 2D objects, demonstration of local magnetization vector plots, simulations and comparisons with finite element analysis tools will be presented in the full paper.

[1] A.A. Adly, I.D. Mayergoyz and R.D. Gomez, IEEE Transactions on Magnetics, Vol. 29, p. 2380 (1993). [2] A.A. Adly and S.K. Abd-El-Hafiz, Journal of Magnetism and Magnetic Materials, Vol. 263, No.3, p. 301 (2003). [3] A.A. Adly and S.K. Abd-El-Hafiz, Proceedings of ECTICON, Paper No. 1067, p. 1 (2016). [4] A.A. Adly and S.K. Abd-El-Hafiz, Journal of Magnetism and Magnetic Materials, Vol. 434, p. 151 (2017).

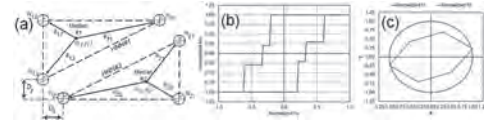


Fig. 1. (a) Two identical tri-node HNNs having different orientations, (b) Superposition of the HNN outputs for $Dx=Dy=0$ corresponding to a cyclic input along the x-direction, and (c) Superposition of the HNN outputs for $Dx=Dy=0$ corresponding to a rotational input.

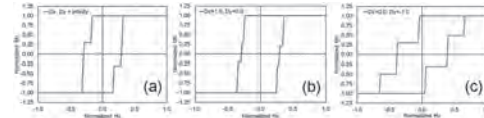


Fig. 2. Superposition of the HNN outputs corresponding to a cyclic input along the x-direction for; (a) $Dx=Dy=\infty$ (i.e., no interaction), (b) $Dx=1.0, Dy=0$, and (c) $Dx=0.0, Dy=-1.0$.

CS-09. Magnetic Properties and Moment Field Motion Determined by the Shape of the Magnetic Nanowire.

Y. Chen¹ and B. Stadler²

1. CEMS, University of Minnesota, Minneapolis, MN, United States;

2. ECE, University of Minnesota, Minneapolis, MN, United States

Magnetic nanowires (MNWs) are increasingly important for applications in memory [1], biolabels [2], and nanowarming of cryopreserved organs [3]. Object Oriented Micromagnetic Framework (OOMMF) was used to visualize moments inside MNWs. The magnetic properties of MNWs, such as coercivity, remanence, and reversal mechanism were investigated as a function of nanowire shape. Experimental measurements of magnetic nanowires (MNW) often reveal features that are difficult to explain due to statistical shearing of features and interaction fields in large arrays [4]. Measurements of individual nanowires can be used to remove interaction field effects [5], and other measurements such as first-order reversal curves (FORC) [6] and the projection method [7] often attempt to statistically separate bulk effects. For nickel MNWs with fixed length of 3 μm , the coercivity and the remanence are negatively correlated to the diameter of the wire, (Fig.1). This is in consistent with the theory that expresses the coercivity field of the infinite long cylinder as: $h_{ci} = 1.08D_0^2/D^2$, $D_0 = 2A^{0.5}/M_s$, where h_{ci} is the reduced coercivity field of the cylinder with high aspect ratio, D_0 is the fundamental unit length defined by the exchange constant A and saturation magnetization M_s of the material (Ni in this case) used to make MNWs. When the diameter is increased to 200 nm, in addition to a continued reduction in coercivity and remanence, a ‘wasp waist’ appeared in the hysteresis loop, Fig.2. (solid line) The reversal can be divided into three different parts showing three types of magnetic moment behaviors in the MNW. In the first part, since there is a large area for curling in 200nm-diameter nanowires, the magnetic moments at the tips of the MNW fall from pointing along z-axis to aligning in the xy-plane and in the form of vortex. Next, when the external field is further reduced, the outer shell of moments turns from in-plane to the negative z-axis. Finally, the axial core of the MNW switches to the negative z-axis and the wire is fully saturated in the negative z-direction. Interestingly, at H_c ($M = 0$), the two vortex walls converged in the center of the MNW and a three-dimensional vortex(hedgehog) [8] was observed using a 2D cross-sectional view, Fig.2 (b). Next, with all other parameters unchanged, flat-tipped cylinders were replaced with ellipsoids so that the tips of wire had infinitesimally small areas where vortex was no longer supported. With this shape, the coercivity of the nanowires significantly increased (Fig.1 and 2, dashed line) to $H_c = 180, 160, 50, 11$ mT from 140, 90, 30, 5 mT for the MNWs with 30, 50, 100, 200nm diameters, respectively. This increase in coercivity occurs because the field to nucleate a vortex at the tips is lower than to nucleate vortex in the center of the wire which is the case for ellipsoidal MNWs. For these ellipsoids, increasingly negative applied fields cause the vortex to expand to include the coherent curling of the whole nanowire. In conclusion, the coercivity of the nanowire depends on the geometry of the wire in two ways. First, with the length of the wire fixed, the coercivity is reduced by increasing the diameter of the wire. Second, when the tip of the wire is engineered so that the nanowires are ellipsoidal rather than cylindrical, the coercivity is increased and the moment switching begins at the center of the wire instead of the end.

[1] Maqableh, Mazin M., et al. *Nano letters* 12.8 (2012): 4102-4109. [2] Sharma, Anirudh, et al. *Nanotechnology* 26.13 (2015): 135102. [3] Shore, Daniel, et al. *Nanoscale* 11.31 (2019): 14607-14615. [4] Madhukar Reddy, Sai, et al. *Journal of Applied Physics* 111.7 (2012): 07A920. [5] Jin Park, Jung, et al. *Journal of Applied Physics* 113.17 (2013): 17A331. [6] Dobrotă, Costin-Ionut, et al. *Journal of applied physics* 113.4 (2013): 043928. [7] Kouhpanji, Mohammad Reza Zamani, et al. *RSC Advances* 10.22 (2020): 13286-13292. [8] Charilaou, Michalis, et al. *Physical review letters* 121.9 (2018): 097202.

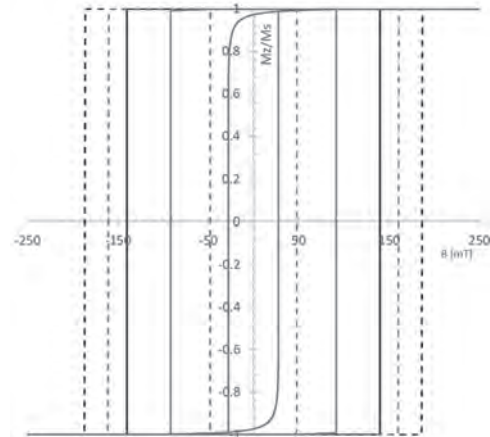


Fig.1 Hysteresis loops generated via OOMMF for nickel MNWs with diameter of 30 nm(black), 50 nm(red) and 100 nm(blue) in cylinder shape (solid line) and ellipsoid shape (dashed line).

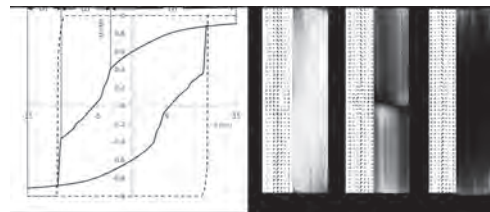


Fig.2 (a) Hysteresis loop generated via OOMMF for 200 nm nickel MNWs with cylinder shape (solid line) and ellipsoid shape (dashed line). Numbered regions indicate the distinct periods where the domain walls exhibit different types of motion. (b) The corresponding moment state of the cylindrical wire is labelled at three different applied field in the form of 2D vector field and 3D heat map.

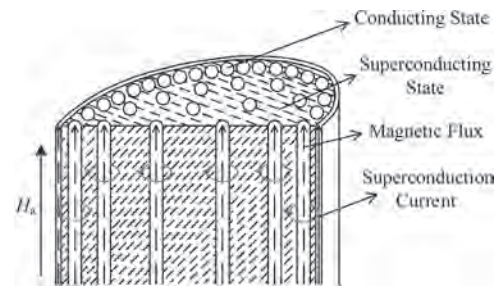
CS-10. Magnetic Characteristic Analysis of High Temperature Superconductors by the Elemental Operator Model.

W. Xu¹, N. Duan², S. Wang² and J. Zhu³

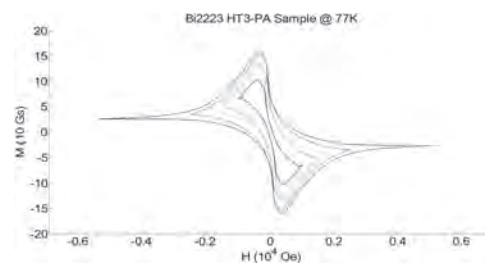
1. State Grid Shaanxi Electric Power Company Construction Branch, Xi'an, China; 2. Xi'an Jiaotong University, Xi'an, China; 3. University of Sydney, Sydney, NSW, Australia

Abstract — In this paper, to accurately analysis the magnetic properties of high temperature superconductor, the elemental operator model is proposed. The calculated and measured results of silver-sheathed Bi2223 superconducting tape samples under external magnetic field are compared to show the effectiveness and accuracy of the proposed method. I. Introduction The hysteresis phenomenon of high temperature superconductor (HTS) is caused by the pinning of magnetic flux due to various defects, as illustrated in Fig.1, such as voids, normal inclusions, grain boundaries, and compositional variations. The consequence of flux-pinning is that the flux remains constant in the interior of the HTS until a new flux is applied. This phenomenon constitutes a memory in the HTS, which can be well described by Bean's critical-state model. Based on the mechanisms of superconductor, the HTS magnetic characteristic can be described via an infinite set of antimagnetic operators and magnetic operators. The property of antimagnetic operator and magnetic operator can be obtained by the antimagnetic curves and elementary hysteresis loops of different switching values of magnetic field, respectively[1,2]. In this paper, in the framework of the elemental operator and wind-rose method, as mentioned in [3], the underlying principle, experimental verification, and the error analysis of the elemental operator have been introduced. II. Elemental Operator Method In the proposed model, based on the mechanisms of HTS, it is assumed that lots of interacting magnetic elemental operators and antimagnetic operators. The magnetic elemental operators, which possesses its own biaxial anisotropy and anisotropy coefficient are enclosed in the HTS material. The interacting elemental operator which possesses its own biaxial anisotropy and anisotropy coefficient. Then, the magnetization direction of each biaxial elemental operator is determined from the various energy contributions of the material anisotropy and applied field. Similar to the determination method of Stoner-Wohlfarth (S-W) particle, the stable orientation of the magnetization in the HTS structure can be obtained by minimizing the energy of the elemental operator. With this wind-rose curve, graphical interpretation can be given for the magnetization process of this biaxial elemental operator. In this H_x - H_y plane, four regions can be separated by the wind-rose curve, and different region corresponding to different number of the energy minima exists. The energy barrier of elemental operator under different magnetic field can decide the position of energy minima, which means the stable orientation of the magnetization. Besides, the determination of the actual energy minimum is related to the magnetization history. Based on the energy barrier diagrams of the elemental operator, the number of energy minimum and the stable orientation of the magnetization can be obtained. When the magnetic field applies inside the wind-rose curve, with the increase of magnetic field, four, three and two energy minima may exist corresponding to different magnetic field magnitudes. When the magnetic field applies outside the wind-rose curve, the magnetization only has one stable orientation as there is only one energy minimum. For the bulk magnetic hysteresis, a collection of biaxial elemental operators can be considered with different easy axis orientations and weights associated to each operator. To simulate the magnetic properties of different HTS materials by this model, the different distribution functions and parameters are needed. Each HTS has an optimal distribution function and parameters, which deliver the best results. With different parameters of the distribution function, this model can be employed to predict the magnetic characteristic of different HTS materials. III. Experimental verification The experiment was carried out on a Bi-2223 multi-filamentary tape with an external magnetic field parallel to a wide surface of the specimen and perpendicular to the long axis of filaments, and the magnetization versus the applied magnetic field, M - H , over the HTS sample at the temperature of 77.3 K was recorded, as shown in Fig.2. The magnetization curves measured and simulated by the presented method, respectively. The comparison illustrated that the elemental operator model that we have proposed agrees accurately with the experimental results for both the limiting hysteresis loop and major loops.

[1] N. N. Duan, W. J. Xu, S. H. Wang, et al., Journal of Applied Physics, vol. 117, no. 17, p. 17A718 (2015). [2] N. N. Duan, W. J. Xu, S. H. Wang, et al., IEEE Transactions on Magnetics, vol. 51, no. 3, p. 7300904(2015). [3] W. J. Xu, N. N. Duan, S. H. Wang, et al., IEEE Transactions on Industrial Electronics, vol. 64, no.3, pp. 2459-2467(2017).



Different state of HTS under external magnetic field



Hysteresis loops of Bi2223 HT3-PA sample at 77K

CS-11. Iron Loss Calculation of non-Oriented Silicon Steel Considering Hysteresis Using Fourier Series Expansion.

H. Zhao¹, Y. Gao¹, W. Guan², K. Muramatsu³ and H. Hamzeshbahmani⁴
 1. Oita University, Oita, Japan; 2. Wuhan University, Wuhan, China;
 3. Saga University, Saga, Japan; 4. Durham University, Durham, United Kingdom

1. Introduction Iron loss calculation is important for efficiency prediction of electric machines. To establish a general iron loss model which is applicable to a wide range of magnetization and frequency, the physical phenomena such as micro-eddy currents, pinning effect, etc. during the dynamic domain wall motion should be one option [1]. The authors have proposed a dynamic iron loss modeling method considering the pinning effect macroscopically and the calculation accuracy is confirmed to be improved [2]. However, in the electromagnetic field analysis, the static hysteresis phenomenon was not considered. In [3], a method considering the static hysteresis phenomenon in the electromagnetic field analysis by introducing the reactive magnetic field H_{hys} is proposed. In this paper, we applied this method and proposed a method to calculate H_{hys} simply by using the Fourier series expansion. The iron losses and the dynamic hysteresis loops under different frequencies are obtained and compared with the measured ones. 2. Analysis model and method The analysis model is one non-oriented silicon steel (JIS C 2550-1986: 50A470, thickness: 0.5mm). Only half region is analyzed due to symmetry. Sinusoidal flux are imposed by using the Dirichlet boundary conditions. The nonlinear eddy current analysis with $A-\Phi$ (A : magnetic vector potential and Φ : electrical scalar potential) method is carried out to obtain the flux distribution and eddy current distribution. The static hysteresis phenomenon is considered by using the reactive magnetic field H_{hys} expressed by a Fourier series. The $B-H$ hysteresis loops due to the static hysteresis phenomenon and eddy currents are calculated using the obtained flux distribution. B of each time step is calculated by averaging all the flux density in the steel region and H is calculated by averaging all the flux density in the coating region then divided by the permeability in the vacuum. 3. Results and Discussions The obtained iron losses are shown in Fig. 1 and compared with the measured ones. It shows that the iron loss calculation accuracy is much improved by considering the static hysteresis phenomenon. The obtained dynamic hysteresis loops under different frequencies are shown in Fig. 2 and compared with the measured ones. It shows that by considering the static hysteresis phenomenon in the electromagnetic field analysis, the accuracy of dynamic hysteresis loops are much improved. More investigation will be given in the full paper.

[1] Y. Gao, Y. Matsuo, and K. Muramatsu, "Investigation on simple numeric modeling of anomalous eddy current loss in steel plate using modified conductivity," *IEEE Trans. on Magn.*, vol. 48, no. 2, pp. 635-638, 2012. [2] W. Guan, H. Qian, F. Fang, Y. Luo, J. Yang, B. Chen, Y. Gao, and K. Muramatsu, "Numerical modeling of excess loss in SiFe sheet considering pinning effect," *IEEE Trans. on Applied Superconductivity*, vol. 26, no. 7, Art. no. 0608804, 2016. [3] K. Yamazaki and Y. Sakamoto, "Electromagnetic field analysis considering reaction field caused by eddy currents and hysteresis phenomenon in laminated cores," *IEEE Trans. on Magn.*, vol. 54, no. 3, Art. no. 1300204, 2018.

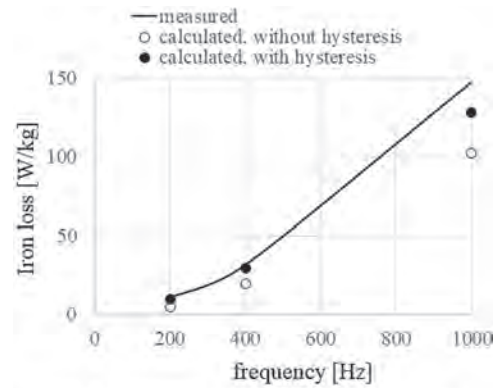


Fig. 1 Comparison of iron losses under 1T.

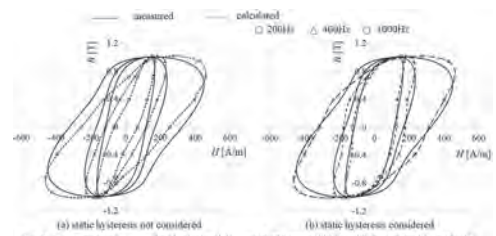


Fig. 2 Comparison of measured and calculated dynamic $B-H$ loops at 200Hz, 400Hz, and 1000Hz under 1T.

CS-12. 3D Simulations of Domain Wall Structure and Hysteresis in Cobalt Films With Columnar Defects.

V.V. Zverev^{1,2} and I. Izmozherov²

1. Department of Theoretical Physics and Applied Mathematics, Ural Federal University, Ekaterinburg, Russian Federation; 2. M.N. Mikheev Institute of Metal Physics of the Ural Branch of the Russian Academy of Sciences, Ekaterinburg, Russian Federation

Magnetic films with perpendicular magnetic anisotropy (PMA) are an important subject of research, as they are used in nonvolatile memory devices and sensors. Moreover, they are also interesting as ferromagnetic systems with nontrivial configurations of magnetization. This is due to the fact that in PMA materials the influence of magnetocrystalline anisotropy and magnetostatic self-interaction are opposite to each other. Being projected onto the film plane, the emerging magnetization distribution can look like a stripe or bubble domain state, or as a labyrinth domain structure [1]. Along with this, the magnetization near the film boundaries differs from the magnetization inside the film, and the domain walls (DWs) have a vortex structure [2]. As shown in [3, 4], this system may contain a large number of vertical and horizontal Bloch lines (VBLs and HBLs), as well as Bloch points (BPs). In this work, we numerically investigate the process of magnetization reversal in a Co(001) PMA film containing an antidot array [5] (a system of columnar defects). In our case, these defects are square holes. We show that these holes can lead to appearance of stable HBLs located on the DWs and pinned to adjacent holes. The formation of HBLs and VBLs is accompanied by the transfer of the topological charge. We numerically calculated the distribution of magnetization in a 180° DW located between two holes. For this, we have minimized the total magnetic energy in a cuboid with dimensions $X = 150$ nm, $Y = 200$ nm, $Z = 800$ nm, using the *mumax3* [6] solver (Y is the film thickness). Periodic boundary conditions were imposed along the z axis. To visualize HBLs and VBLs, we numerically calculated the density of the gyrotropic vector [3]. The topological charges of BPs were calculated by integrating the gyrotropic vector over closed surfaces. The following magnetization distributions were found: (a) two VBLs without BPs, (b) the HBL connecting holes and containing a BP, (c) the HBL connecting holes and not containing a BP. The domain structure in a cuboid with dimensions $X = 1024$ nm, $Y = 1024$ nm and $Z = 200$ nm, containing an antidot array was also simulated (Z is the film thickness). The period of the rectangular array was chosen to be 100 nm or 200 nm. Hysteresis loops were calculated by minimizing the total energy including the Zeeman energy. The magnetic field step was chosen to be 250 Oe. The initial condition for each step was chosen as the result of the previous energy minimization. The simulation results are shown in Figs. 1, 2. The static domain structure in Fig. 1 was obtained for the period of the array 100 nm. We can see that the complex configuration of magnetization within the antidot array entails a nontrivial distribution of HBLs and BPs. In Fig. 2 the hysteresis loops are shown for the case of continuous film and for antidot arrays with periods 100 nm and 200 nm (the magnetic field is perpendicular to the film surface).

[1] L. Fallarino, O. Hovorka and A. Berger. Phys. Rev. B, Vol. 94, 064408 (2016). [2] M. Kisielewski, A. Maziewski, V. Zablotskii. JMMM Vol. 316, p. 277 (2007). [3] E. Zh. Baykenov, I. M. Izmozherov, V. V. Zverev. Bull. Russ. Acad. Sci.: Phys. Vol. 83, p. 809 (2019). [4] I. M. Izmozherov, E. Zh. Baykenov, V. V. Zverev. Phys. Met. Metallogr. Vol. 122, No. 3 (2021) (in print). [5] T. Schneider, M. Langer, J. Alekhina, et al. Sci. Rep. Vol. 7, 41157 (2017). [6] A. Vansteenkiste, J. Leliaert, M. Dvornik, et al. AIP Advances. Vol. 4, 107133 (2014).

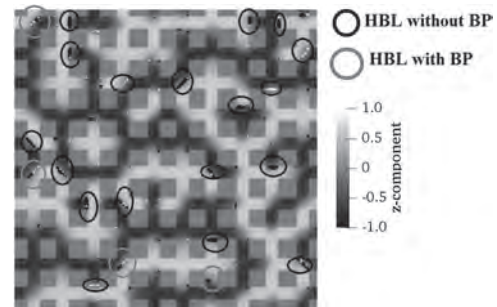


Fig.1. Domain structure in an antidot Co film. The HBLs are marked.

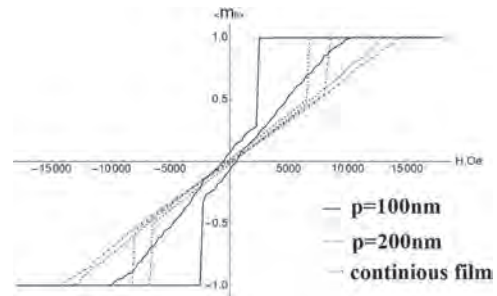


Fig.2. Hysteresis loops for the case of continuous film and for antidot arrays with periods 100 nm and 200 nm.

CS-13. Quantitative Analysis of Buried Pipeline Corrosion Under Dynamic Electromagnetic Interference in DC-Subway.

Z. Cai¹, X. Liu¹ and x. Zhang¹

1. School of Electrical and Automation Engineering, East China JiaoTong University, Nanchang, China

There is electromagnetic interference in the DC power supply system of metro, which will produce electrochemical corrosion to the adjacent metal structure of rail. Buried metal pipeline is one of the main objects of electrochemical corrosion. Due to the characteristics of buried pipeline laying and the randomness of electromagnetic leakage, it is difficult to directly and effectively analyze the corrosion law of buried pipeline under electromagnetic interference. In addition, due to the lack of corrosion detection, it is easy to cause metro operation accidents.

1. Introduction In recent years, many scholars have indirectly evaluated the electromagnetic interference degree and electrochemical corrosion of buried metal by the pipe-to-soil voltage [1-2]. Due to the characteristics of buried pipeline laying and the randomness of electromagnetic distribution, it is difficult to directly and effectively analyze the corrosion law. Some scholars have tried to investigate the electromagnetic interference of buried pipelines from the perspective of electrochemical corrosion mechanism [3-4]. However, the existing research is mainly focused on the static corrosion problem, which is lack of considering the operation of metro vehicles, so there is no direct basis for quantitative analysis of the corrosion area of buried pipelines. In this paper, the model and verification platform for dynamic electromagnetic interference are established, and the impact of metro vehicle operation state on corrosion area is analyzed quantitatively, as well as the cumulative effect of electrochemical corrosion under weak electromagnetic interference.

2. Simulation experiment This research set up an experimental platform for simulating stray current corrosion under the motion of subway vehicles as shown in Fig.1. Based on the corrosion experiment and simulation of buried pipeline, the dynamic corrosion process and law of buried pipeline metal are studied under the action of Variable electromagnetic interference. The graphite electrode (positive) indicates a moving metro vehicle, and its movement is realized by a slider block controlled by a stepper motor. The movement process of the slider block simulates the actual movement of the subway vehicle. The programmable DC power supply provides dynamic current that leaks during the movement of the graphite electrode (positive). The leakage current of the positive graphite electrode forms an electrochemical corrosion environment in the simulated soil solution, and finally flows back through two graphite electrodes (negative), and the buried pipeline specimen was placed in a simulated soil solution. The above process truly simulates the double side power supply system of metro. The finite element simulation model was used to simulate the entire process of buried pipeline corrosion under the dynamic electromagnetic interference. Finally, the experimental results and simulation results were compared and analyzed.

3. Results When the graphite electrode (positive electrode) moves to the 40th second, the corrosion current density distribution of buried pipeline is shown in Figure 2 (a). When the corrosion current value is negative, it indicates the current density of the outgoing pipeline, and when the corrosion current value is positive, it indicates the current density of the incoming pipeline. Therefore, the corresponding anode area and cathode area are divided on the buried pipeline. The metal of buried pipeline in anode area is corroded by electronic loss caused by corrosion current. The pipeline metal in anode area is corroded by the electronic loss caused by corrosion current. The closer the anode area of the buried pipeline is, the greater the corrosion current density of the outgoing pipeline is. Obviously, the metal surface of both ends of the buried pipeline is seriously corroded. With the frequent start and stop of metro vehicles, the anode area of buried pipeline is constantly changing.

4. Conclusions The results show that under the dynamic electromagnetic interference, the metal of buried pipeline is bipolar, and the anode area (corrosion area) changes with the running state of metro vehicles. Therefore, in the case of no excavation detection of buried pipelines, the corrosion area caused by electromagnetic interference can be quantitatively identified by analyzing the operation of metro vehicles. And the cumulative effect of stray current cannot be neglect under the condition of uniform speed of metro vehicles.

1. Zakowski, W. Sokólski, Corrosion Science., Vol.41, p.2213(1999). 2. S. R. Allahkaram, M. Isakhani-Zakaria, Journal of Natural Gas Science and Engineering., Vol.26, p.453(2015). 3. K. Tang, Materials Today Communications., Vol.20, p.100564(2019). 4. S. Qian, Y. F. Cheng, Construction and Building Materials., Vol.148, p.675(2017).

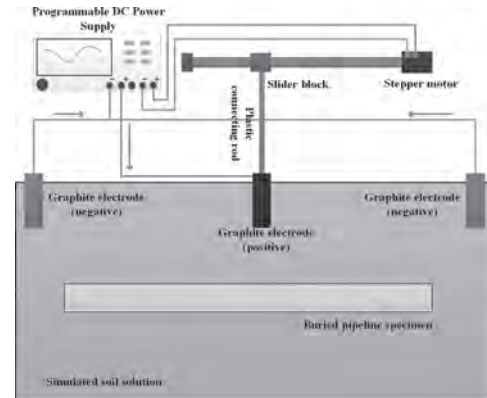


Fig.1 Corrosion experiment device for buried pipelines under stray current

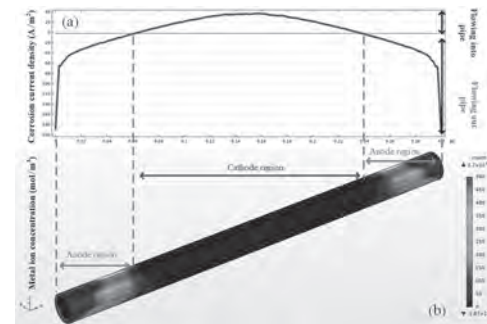


Fig.2 Comparative analysis of stray current corrosion of buried pipelines under electromagnetic interference

CS-14. Precision Improvement by Superconvergent Patch Recovery Method on Intensity Calculation of Electromagnetic Field.

N. Zhang¹, P. Song¹, S. Ning², S. Wang¹, X. Xu¹, Z. Ma¹, Y. Zhang¹ and H. Qiu¹

1. School of Electrical Engineering, Xi'an Jiaotong University, Xi'an, China; 2. School of Electronic Information and Artificial Intelligence, Shaanxi University of Science and Technology, Xi'an, China

I. Introduction In the preprocessing of the finite elements, the triangular unit is the easiest one to fit the complex boundary. However, since the field intensity is obtained by differential operation of the bit function, the calculation accuracy is reduced by the first order. If the field intensity at any point in the triangle line element is considered to be the same, it will obviously lead to a significant error, especially in the areas with large gradients of field intensity. In the superconvergence theory, if the region is meshed by normal segmentation, the triangular Gaussian integration point has superconvergence (the triangular Gaussian integration point is the center of gravity of the triangle) [1]. The field intensity calculation accuracy of the superconvergence point is the highest. Based on the triangle line element method, the error of calculated field intensity is minimal only at its center of gravity. Therefore, the field intensity of the triangular element is an approximate exact solution at the superconvergence point. It is obtained not only the field intensity on the triangle node through the interpolation method, which has the same precision as the superconvergence point, but also the field intensity at any point in the area, and then increasing the calculation precision of the field intensity. In this paper, based on the super-convergence element stress recovery method, an improved superconvergent patch recovery (SPR) method is proposed for the problem of low precision of field intensity in electromagnetic field numerical calculation. The proposed method not only retains the advantages of the triangular three-node finite element method such as time-saving, convenient and memory-saving, but also improves the calculation precision of the electric field intensity, and the method can also be adapted to the calculation of the magnetic field intensity. II. Applications of superconvergent patch recovery method based on superconvergence The SPR method utilizes the stress on the superconvergence point in the element and builds smoothing stress with superconvergence properties according to two interpolations [2~4]. In this research, take the electric field intensity as an example. Firstly, the inner node is defined as a node that associated with another unit. The unit slice includes the entire unit around the inner node. Then, the approximate true solution E_p is defined in equation (1), where P is an L-order interpolation expansion; A is the undetermined coefficient. Define the least-squares fitting formula in equation (2), where E_h is the numerical solution; $n=mk$, m is the number of units included in each unit slices, k is the number of superconvergence points in each unit. In the three nodes of the triangle, the center of gravity of this triangle is the superconvergence point ($k=1$). Determine the minimum value of $F(a)$ by equation (3). Then the undetermined coefficient A could be obtained. Take the coefficient A into equation (1), the high-precision electric field intensity including the units slice could be determined. III. The smooth processing method of boundary nodes for field intensity calculation a. Electric field intensity calculation of nodes on the smooth media interface By numerical calculation, the electric field intensity E_i at each superconvergence point on the unit slice associated with point p can be obtained by equation (4) and (5). b. Electric field intensity calculation of nodes on the boundary of a smooth field The point p is located at the boundary of the field, which is different from the inner node. The point p is not surrounded by units. If the point p is on the first-class boundaries, the electric field equals to zero. After decomposing the electric field intensity of the superconvergence point on the unit, the electric field intensity at that point could be calculated by interpolation. c. Electric field intensity calculation of nodes on the unsmooth medium interface and field boundary In this type of medium interface, the normal direction and tangential direction of the point p is uncertain. The electric field intensity of the superconvergence point on the unit associated with the point p into a component parallel to the coordinate axis should be decomposed. Then the interpolation calculation could be carried out to obtain the field intensity. IV. Method verifications To verify the proposed method, the calculation of the electric field intensity of the grounding metallic groove was carried out. As shown in Fig. 2, compared with the analytical method,

low-rank FEM, and high-rank FEM, the improved SPR method achieves the highest precision. Due to the local interpolation of an improved SPR method, the memory cost is much less than that of high-rank FEM. In addition, the improved SPR method has the lower order equations leads to a lower time cost. V. Conclusions In this paper, in order to improve the precision in field calculation by finite element method with triangular elements, the superconvergent patch recovery method is introduced to solve electromagnetic problems. By interpolation of the field intensity at superconvergent nodes, the electric field intensity at any point can be derived more accurate. For multi-media interface characters and various boundary conditions, the interpolation methods are presented. The proposed method is verified by calculating the field distribution of a grounding metallic groove. More detail will be presented in the extended paper.

[1]M. Kasper, J. Franz, IEEE transactions on magnetics, Vol. 31, pp. 1424(1995). [2]Q. Lin, J. Li, Mathematics of Computation, Vol. 77, pp. 757(2008) [3]J. Zhu, O.C. Zienkiewicz, International Journal for Numerical Methods in Engineering, Vol. 30, pp. 1321(1990) [4]Y. Huang, J. Li, Q. Lin, Numerical Methods for Partial Differential Equations, Vol. 28, pp. 1794,(2012)

$$E_p = Pa \tag{1}$$

$$F(a) = \sum_{i=1}^n [E_h(x_i, y_i) - E_p(x_i, y_i)]^2 = \sum_{i=1}^n [E_h(x_i, y_i) - P(x_i, y_i)a]^2 \tag{2}$$

$$\sum_{i=1}^n [P^T(x_i, y_i)P(x_i, y_i)a] = \sum_{i=1}^n [P^T(x_i, y_i)E_h(x_i, y_i)] \tag{3}$$

$$E_i = E(x_p, y_p)e_x + \frac{D_x(x_p, y_p)}{\varepsilon_1} e_y \tag{4}$$

$$E_p = E(x_p, y_p)e_x + \frac{D_x(x_p, y_p)}{\varepsilon_0} e_y \tag{5}$$

Fig. 1 Equations

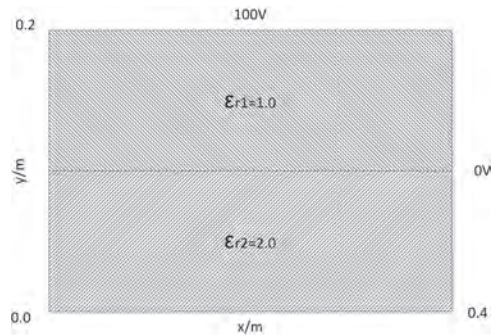


Fig. 2 Details of grounding metallic groove.

WEDNESDAY, 28 APRIL 2021

LIVE Q&A SESSIONS, 2:00 AM EUROPE CEST

Session DA
2D MATERIALS FOR SPINTRONICS
Hyunsoo Yang, Chair
National University of Singapore, Singapore

INVITED PAPERS

DA-01. Ultra-Thin Heusler Films and Lamellae That Host non-Collinear Spin Textures.

S. Parkin^{1,2}

1. NISE, Max Planck Institute for Microstructure Physics, Halle (Saale), Germany; 2. Martin-Luther-Universität Halle-Wittenberg, Halle, Germany

The recent discovery of anti-skyrmions[1] and elliptical block skyrmions[2] in lamellae formed from single crystals of inverse tetragonal ternary Heusler compounds makes these compounds extremely interesting. Related binary compounds host chiral domain walls whose current induced motion in films that are only 1 unit cell thick has recently been observed. These films were prepared using a novel method of chemical templating[3]. We show that strain can dramatically affect the current induced domain wall motion in such films, changing both its magnitude and, remarkably, even its direction. Anti-skyrmions are extremely interesting objects that have high stability[4] and whose size can be tuned by more than an order of magnitude [5] by varying the thickness of the host lamella. These properties derive from the symmetry of the bulk Dzyaloshinskii-Moriya vector exchange interaction that stabilizes them that itself is derived from their underlying crystal structure. We have found similar properties in other materials with related symmetries[6]. The current induced motion of anti-skyrmions has not yet been realized but theoretical models suggest that the skyrmion Hall angle will vary strongly with current direction and, for certain crystal directions, will be zero. Whilst we have found no evidence, to date, for current induced motion of such objects from volume spin-transfer torques, models show that spin-orbit torques should give rise to their motion. For this purpose, ultra-thin 2D layers are needed that can be coupled to heavy metal layers in which spin currents can be generated. In this talk we discuss progress in preparing high quality, epitaxial, ultra-thin films of ternary inverse tetragonal Heusler compounds that are only 1 to 2 unit cells thick and the exploration of non collinear spin textures in these films as well as their current induced motion. Finally, we discuss the first observation of fractional anti-skyrmions and Block skyrmions in nano-stripes formed from inverse tetragonal ternary Heusler compounds.

[1] Nayak, A.K., et al., *Magnetic antiskyrmions above room temperature in tetragonal Heusler materials*. Nature, 2017. 548(7669): p. 561-566. [2] Jena, J., et al., *Elliptical Bloch skyrmion chiral twins in an antiskyrmion system*. Nat. Commun., 2020. 11: p. 1115. [3] Filippou, P.C., et al., *Chiral domain wall motion in unit-cell thick perpendicularly magnetized Heusler films prepared by chemical templating*. Nat. Commun., 2018. 9: p. 4653. [4] Saha, R., et al., *Intrinsic stability of magnetic anti-skyrmions in the tetragonal inverse Heusler compound $Mn_{1.4}Pt_{0.9}Pd_{0.1}Sn$* Nat. Commun., 2019. 10: p. 5305. [5] Ma, T., et al., *Tunable Magnetic Antiskyrmion Size and Helical Period from Nanometers to Micrometers in a D_{2d} Heusler Compound*. Adv. Mater., 2020: p. 2002043. [6] Srivastava, A.K., et al., *Observation of Robust Néel Skyrmions in Metallic PtMnGa*. Adv. Mater., 2020. 32: p. 1904327.

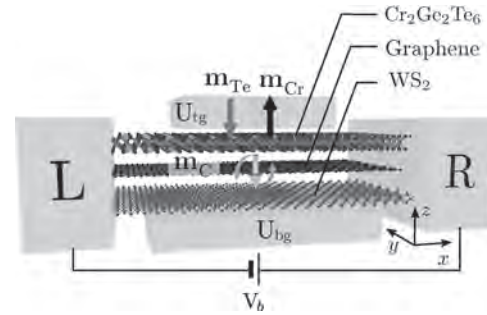
DA-02. Spin-Orbit Torque in van der Waals Heterostructures of Magnetic Two-Dimensional Materials.

B. Nikolić¹

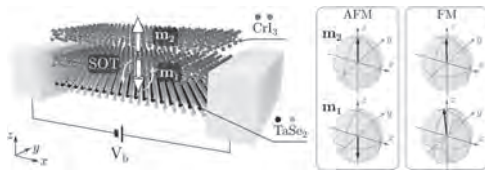
1. University of Delaware, Newark, DE, United States

The bilayer heterostructures composed of an ultrathin ferromagnetic metal (FM) and a nonmagnetic material hosting strong spin-orbit coupling (SOC) are a principal resource for spin-orbit torque (SOT) [1] and spin-to-charge conversion [2] effects in next generation spintronics. The key to understand these effect is current-driven nonequilibrium spin density [3]. For example, it generates SOT when it is noncollinear to the direction of local magnetization and it can arise due to variety of microscopic mechanisms, including the spin Hall effect, spin-orbit proximity effect and different interfacial scattering mechanisms. The recently discovered two-dimensional (2D) magnetic materials [4] offer new avenue for highly efficient and gate- or disorder-tunable SOT in van der Waals (vdW) heterostructures composed of few monolayers of atomically thin materials where the spin Hall effect from the bulk is absent. Using first-principles quantum transport calculations, which combine nonequilibrium Green functions with noncollinear density functional theory [1], we predicted [5] that injecting unpolarized charge current parallel to the interface of bilayer-CrI₃/monolayer-TaSe₂ vdW heterostructure will induce SOT-driven dynamics of magnetization on the first monolayer of CrI₃ that is in direct contact with metallic transition metal dichalcogenide (TMD) TaSe₂. By combining calculated complex angular dependence of SOT with the Landau-Lifshitz-Gilbert equation for classical dynamics of magnetization, we find that this can reverse the direction of magnetization on the first monolayer to become parallel to that of the second monolayer, thereby converting bilayer CrI₃ from antiferromagnet to ferromagnet which can be detected by passing vertical current and is of potentially great interest to magnetic memory applications since it does not require any external magnetic field. We explain the mechanism of such *current-driven nonequilibrium phase transition* by showing that first monolayer of CrI₃ becomes conducting due to doping by evanescent wavefunctions injected by metallic TaSe₂, while concurrently acquiring strong SOC via this proximity effect. Another vdW heterostructure exhibiting SOT is *doubly proximitized* graphene, which is neither magnetic nor hosts SOC in its isolated form, but proximity induced magnetic moments will exhibit SOT in Cr₂Ge₂Te₆/graphene/WS₂ vdW heterostructure which can be tuned by two orders of magnitude via the gate voltage [6].

- [1] B. K. Nikolić, K. Dolui, M. Petrović, P. Plecháč, T. Markussen, and K. Stokbro, in W. Andreoni and S. Yip (eds.), Handbook of Materials Modeling (Springer, Chan, 2018); arXiv:1801.05793. [2] F. Mahfouzi, N. Nagaosa, and B. K. Nikolić, Phys. Rev. B 90, 115432 (2014). [3] P.-H. Chang, T. Markussen, S. Smidstrup, K. Stokbro, and B. K. Nikolić, Phys. Rev. B 92, 201406(R) (2015). [4] M. Gibertini, M. Koperski, A. F. Morpurgo, and K. S. Novoselov, Nat. Nanotech. 14, 408 (2019). [5] K. Dolui, M. D. Petrović, K. Zollner, P. Plecháč, J. Fabian, and B. K. Nikolić, Nano Lett. 20, 2288 (2020). [6] K. Zollner, M. D. Petrović, K. Dolui, P. Plecháč, B. K. Nikolić, and J. Fabian, Phys. Rev. Res. 2, 043057 (2020).



Spin-orbit-torque-operated van der Waals heterostructures from Ref. [6].



Spin-orbit-torque-operated van der Waals heterostructures from Ref. [5].

DA-03. Spin-Orbit Proximity Phenomena in Van der Waals Heterostructures.

L.A. Benítez², W. Savero Torres², J.F. Sierra², M.V. Costache², J.H. Garcia², S. Roche^{1,2} and S.O. Valenzuela^{1,2}

1. *Institucio Catalana de Recerca i Estudis Avancats, Barcelona, Spain;*

2. *Institut Catala de Nanociencia i Nanotecnologia, Bellaterra, Spain*

The isolation of a large variety of two-dimensional materials (2DM) and their co-integration in van der Waals heterostructures has opened new avenues for innovative material design and engineering. In particular, the structural interface quality in the atomically smooth 2DMs has led to alternative and versatile strategies beyond simply combining materials functionalities. Indeed, properties of interest can be imprinted in a chosen 2DM by proximity-induced effects. Such an approach is compelling for spintronic devices, which harness their functionality from thin layers of magnetic and non-magnetic materials and their interfaces. In this talk, I will present recent experiments in which we investigate the spin dynamics in graphene-transition metal dichalcogenides heterostructures. I will show that the spin-orbit coupling in graphene can be strongly enhanced by proximity effects. As a consequence, the spin relaxation becomes highly anisotropic, with spin lifetimes that are markedly different depending on the spin orientation [1,2]. I will further demonstrate that the proximity-induced spin-orbit coupling leads to strongly enhanced spin-to-charge interconversion [3]. By performing spin precession experiments in appropriately designed Hall bars (Fig. 1), we are able to separate the contributions of the spin Hall and the spin galvanic effects. Remarkably, their corresponding conversion efficiencies can be tailored by electrostatic gating in magnitude and sign, peaking near the graphene charge neutrality point and having a large magnitude even at room temperature (Fig. 2).

[1] L. A. Benítez, J. F. Sierra, W. Savero Torres, et al., *Nature Phys.* 14 (2018) [2] L. A. Benítez, J. F. Sierra, W. Savero Torres, et al., *APL Materials* 7, 120701 (2019) [3] L. A. Benítez, W. Savero Torres, J. F. Sierra, et al., *Nature Mater.* 19, 170 (2020)

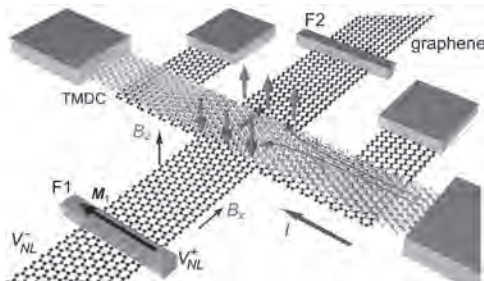


Fig. 1. Spin-to-charge interconversion (SCI) in graphene by proximity of a TMDC. A current I generates a transverse spin current owing to the SHE (red arrows) and an in-plane spin density due to the inverse SGE (blue arrow).

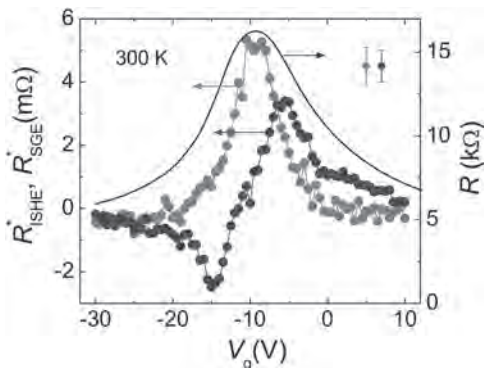


Fig. 2. Tunable SCI as a function of carrier density, modulated by the gate voltage V_g .

DA-04. Optimization of Spin to Charge Transduction Efficiency for Magnetic State Readout.

T. Gosavi¹, E.S. Walker¹, K. Oguz¹, C. Lin¹, J. Plombon¹, H. Li¹,
D.E. Nikonov¹, S. Clendenning¹ and I.A. Young¹

1. Components Research, Intel Corp, Hillsboro, OR, United States

Spintronic beyond CMOS devices need a charge/voltage readout of their magnetic state for efficient and direct integration with other electronic components [1]. The magnetoresistance readout, though efficient for a memory system, is limiting in logic technology as it does not generate an electromotive force to drive other circuit elements [2]. We propose a readout mechanism, using local spin injection devices, that uses large spin-orbit coupling effects to generate charge current/voltage as an output [3,4]. We show that the inverse spin Hall effect in Ta can generate an output voltage of 0.32 mV in a local spin injection device and, we demonstrate the favorable dimensional scaling of this novel readout mechanism [5]. Layered 2D materials that have large inverse Edelstein effect lengths, long scattering time constants and high in-plane resistivity can increase the output voltage of spin injection devices beyond heavy metals. In this talk, we will discuss our experimental work in Bi₂Te₃, Sb₂Te₃, and BiSb₂Te₃ to optimize spin to charge transduction efficiency.

[1] Nikonov, D. E. & Young, I. A., Benchmarking of beyond-CMOS exploratory devices for logic integrated circuits. *IEEE J. Explor. Solid-State Computat. Devices Circuits* 1, 3–11 (2015) [2] Manipatruni, S., Nikonov, D. E. & Young, I. A. Beyond CMOS computing with spin and polarization. *Nat. Phys.* 14, 338 (2018). [3] Manipatruni, S., Nikonov, D.E., Lin, C.C. *et al.* Scalable energy-efficient magnetoelectric spin-orbit logic. *Nature* 565, 35–42 (2019). [4] Pham, V.T., Groen, I., Manipatruni, S. *et al.* Spin-orbit magnetic state readout in scaled ferromagnetic/heavy metal nanostructures. *Nat Electron* 3, 309–315 (2020). [5] C. Lin *et al.*, “Experimental demonstration of integrated magneto-electric and spin-orbit building blocks implementing energy-efficient logic,” *2019 IEEE International Electron Devices Meeting (IEDM)*.

DA-05. Significant Dzyaloshinskii-Moriya Interaction in Two-Dimensional Janus Structures and its Electrically Control in 2D Magnetoelectric Multiferroics.*H. Yang*¹*1. Ningbo Institute of Materials Technology and Engineering, Chinese Academy of Sciences, Ningbo 315201, China*

The Dzyaloshinskii-Moriya interaction (DMI) plays a tremendous role for fast domain wall motion and allows creation of magnetic skyrmions which are very promising for spintronic devices. A standard ingredient in such devices is an interface between ferromagnetic metal and heavy nonmagnetic metal (HM), where the HM provides large spin orbit coupling as the energy source to obtain strong DMI[1]; or using Rashba effect at interface between a light element and ferromagnetic metal [2]. However, using a single two-dimensional (2D) magnet to obtain DMI and create skyrmions is rare even though the discoveries of truly 2D magnets such as Cr₂Ge₂Te₆, CrI₃, VSe₂, MnSe₂ and Fe₃GeTe₂ etc. have opened up new opportunities for spintronic technology. We demonstrate that significant DMI can be obtained in a series of Janus monolayers of manganese dichalcogenides MnXY (X/Y = S, Se, Te, X ≠ Y) in which the difference between X and Y on the opposite sides of Mn breaks the inversion symmetry. In particular, the DMI amplitudes of MnSeTe and MnSTe are comparable to those of state-of-the-art ferromagnet/heavy metal (FM/HM) heterostructures. In addition, by performing Monte Carlo simulations, we unveil that at low temperatures the ground states of the MnSeTe and MnSTe monolayers can transform from ferromagnetic states with worm-like magnetic domains into the skyrmion states by applying an external magnetic field. At increasing temperature, the skyrmion states start fluctuating above 50 K before evolution to a completely disordered structure at higher temperature. The present results pave the way for new device concepts utilizing chiral magnetic structures in specially designed 2D ferromagnetic materials[3]. Moreover, we unveil that topological magnetism and its electric control can both be achieved in the two-dimensional (2D) magnetoelectric multiferroics. We verify that significant DMI can promote the stabilization of sub-10 nm skyrmion in 2D multiferroics with perpendicular magnetic anisotropy such as CrN monolayer. [4]

[1] *Hongxin Yang*, André Thiaville, Stanislas Rohart, Albert Fert, Mairbek Chshiev, *Physical Review Letters* 115, 267210(2015) [2] *Hongxin Yang*, Gong Chen, Alexandre AC Cotta, Sergey A Nikolaev, Edmar A Soares, Waldemar AA Macedo, Kai Liu, Andreas K Schmid, Albert Fert, Mairbek Chshiev *Nature Materials* 17, 605 (2018) [3] Jinghua Liang, Weiwei Wang, Haifeng Du, Ali Hallal, Karin Garcia, Mairbek Chshiev, Albert Fert, *Hongxin Yang Phys. Rev. B* 101, 184401 (2020) Editors' suggestion [4] Jinghua Liang, Qirui Cui, *Hongxin Yang*, *Physical Review B* 102, 220409 (2020) (R)

DA-06. Electrical and Chemical Control of Magnetism in Layered Ferromagnetic Semiconductors.*G. Eda*¹*1. National University of Singapore, Singapore*

Recent discoveries of gate-tunable magnetism in ferromagnetic two-dimensional (2D) materials such as CrI_3 and Fe_3GeTe_2 highlight the unique potential of this class of materials for novel spintronic devices. Understanding the interplay between magnetic order, free electron density, and electric field in the 2D limit is essential for uncovering the full potential of these materials. In this talk, we will first discuss electrical control of magnetism in $\text{Cr}_2\text{Ge}_2\text{Te}_6$ (CGT), a van der Waals ferromagnetic semiconductor, in an electric double-layer transistor (EDLT) geometry. We show that degenerately electron-doped CGT exhibits enhanced Curie temperature of up to 200 K, and rotation of its easy axis from out-of-plane to in-plane orientation. We demonstrate that similar changes in Curie temperature and easy axis can be induced by Na intercalation, which is accompanied by heavy electron doping of the host. We will further discuss our exploration of magnetism in other van der Waals materials such as NbFeTe_2 and magnetically doped transition metal dichalcogenides.

Session DB

SPINS IN GRAPHENE OTHER 2D MATERIALS

Ivan Vera-Marun, Chair

The University of Manchester, Manchester, United Kingdom

CONTRIBUTED PAPERS

DB-01. Magnetic Nano/Microfibres With Highly Oriented van der Waals CrI₃ Inclusions by Electrospinning.

V. Bayzi Isfahani¹, J. Filipe Horto Belo da Silva², L. Boddapati³, A. Gomes Rolo¹, R. Maria Ferreira Baptista¹, F. Leonard Deepak³, J. Pedro Esteves de Araújo², E. de Matos Gomes¹ and B. Gonçalves Almeida¹

1. Centro de Física das Universidades do Minho e Porto, Departamento de Física, Universidade do Minho, Braga, Portugal; 2. FIMUP - Instituto de Física de Materiais avançados, Nanotecnologia e Fotónica, Universidade do Porto, Universidade do Porto, Porto, Portugal; 3. Nanostructured Materials Group, International Iberian Nanotechnology Laboratory (INL), International Iberian Nanotechnology Laboratory, Braga, Portugal

Low-dimensional 2D semiconductor magnetic materials have been attracting much attention, due to their potential applicability in a wide range of technologies, such as data storage, sensing, spintronic devices or in biomedical applications. In this respect, materials composed by 2D layers bonded to one another through weak van der Waals interactions present enormous potential for several of these applications. They often exhibit strongly anisotropic behaviour and can be cleaved into very thin specimens, frequently monolayer crystals. In this regard, chromium triiodide (CrI₃) is a Van der Waals material with an intrinsic ferromagnetic nature, with a relatively high Curie temperature of about 61 K in its bulk form. Previous research on CrI₃ shows that although this material has been of great interest to researchers in recent years, its synthesis by alternative methods has not been considered. In other words, in most of the reported research, a bulk sample has been prepared by the chemical vapour transport (CVT) method and CrI₃ monolayer, bilayer or multi-layer samples are then, typically, made by mechanical exfoliation methods. This is a cumbersome sample preparation procedure and the resultant samples are prone to light, air and moisture induced degradation. To prevent the latter, new and efficient synthetic strategies and storage methods are required. Additionally, in order to design efficiently aligned 2D magnetic material devices, it is very important to control their morphology and magnetization orientation, to take advantage of the CrI₃ anisotropic magnetic properties. In this regard, the electrospinning technique is a relatively simple and low-cost technique, which has been significantly developed in recent years. Electrospinning is based on the extrusion of a thin fibre from an electrically charged polymer precursor solution, mixed with the active functionalizing inclusions, provoked by a strong applied DC electric field. The solution is loaded into a syringe with its needle connected to a high voltage source. At the threshold voltage, when the electrostatic forces overcome the surface tension of the precursor solution, a jet is continuously emitted that dries in-flight, forming the fibres. They are then collected as a mesh on a grounded collector plate. Electrospinning is a very powerful tool for controlling the morphology and molecular orientation of the polymer chains along the fibres. The fibre diameters can vary from several nanometers up to several micrometres, depending on the parameters of the process, while their lengths can reach several meters. This method is, then, very effective for creating oriented inclusions encapsulated in the polymer matrix, allowing the production of functionalized fibre arrays with anisotropic properties. As such, in this work, we demonstrate the implementation of this approach for synthesising highly oriented chromium triiodide (CrI₃) magnetic inclusions inside nano/microfibres with a polyethylene oxide matrix (PEO) by the electrospinning technique. The samples are identified as PC_x in which x represents the mass amount of CrI₃ as the precursor. The structural, microstructural, and spectroscopic analysis shows uniformly dispersed CrI₃ nanosized inclusions inside the fibres, as seen in HAADF-STEM images (Figure 1). The inclusions present a C2/m monoclinic structure [1] at room temperature, where their c-axis is perpendicular to the fibre mat plane and the ab layers are in-plane. Analysis of the magnetic properties show that the samples have a ferromagnetic - paramagnetic phase transition at ~ 55-56 K, lower than that of bulk CrI₃ [2,3]. Noticeably, a field-driven metamagnetic transition is observed below ~ 45 K, from M vs. H curves, when the applied magnetic field is perpendicular to the fibre mat plane (H[⊥]ab), while it is strongly reduced when the field is in-plane (H[∥]ab) (Figure 2). This metamagnetic transition occurs at around a transition field (H*) of 19 kOe at 5 K

and shifts to lower fields by increasing the temperature (inset of Figure 2). This anisotropic behaviour is attributed to the field-induced changes from antiferromagnetic to ferromagnetic interlayer magnetic moment alignment along the CrI₃ c-axis stacked layers [4], induced by the perpendicular applied magnetic field. These CrI₃ electrospun fibres then show an efficient cost-effective route to synthesize magnetic composite fibres with highly oriented van der Waals inclusions, for spintronic applications, taking advantage of their anisotropic 2D layered materials properties.

[1] M-A. McGuire et al., Chemistry of Materials, Vol. 27, p. 612-620 (2015)

[2] Y. Liu et al., Scientific reports, Vol. 9, p. 1-8 (2019) [3] S. Mondal et al.,

Physical. Review B, Vol. 99 p. 180407 (2019) [4] V. Bayzi Isfahani et al.,

Nanotechnology (2021), <https://doi.org/10.1088/1361-6528/abd4a3>

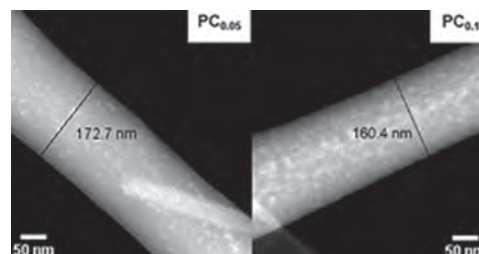


Figure 1. HAADF-STEM images showing the nanosized CrI₃ inclusions inside the fibres.

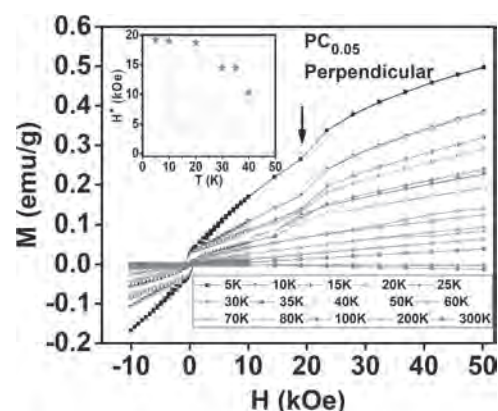


Figure 2. M vs. H hysteresis curves obtained with the applied magnetic field perpendicular to the fiber mat plane. Inset: Variation of metamagnetic transition field (H*) with temperature.

DB-02. Spin Filtering Manipulation in WS₂-Based Magnetic Tunnel Junctions.

V. Zatko¹, J. Peiro¹, M. Galbiati¹, S.M. Dubois², P. Brus³, B. Servet³, J. Charlier², M. Och⁴, C. Mattevi⁴, F. Godel¹, A. Vecchiola¹, K. Bouzehouane¹, S. Collin¹, F. Petroff¹, A. Fert¹, B. Dlubak¹ and P. Seneor¹

1. *Unite Mixte de Physique CNRS/Thales, Palaiseau, France*; 2. *Universite catholique de Louvain, Louvain-la-Neuve, Belgium*; 3. *Thales Research and Technology France, Palaiseau, France*; 4. *Imperial College London, London, United Kingdom*

While very recent, the introduction of 2D materials in Magnetic Tunnel Junctions (MTJs) has already shown some promising properties (atomic thickness control, diffusion barrier, spin filtering...)[1]. Graphene and the 2D insulator h-BN have been the first 2D materials to show strong impact on spin transport in MTJs. It was shown that strong spin filtering occurred with the creation of an insulating spin channel in metallic graphene and metallic channel in insulating h-BN[2][3]. The recent advent of the wide Transition Metal Dichalcogenides (TMD) family of 2D semiconductors (MoS₂, WS₂...) opened new opportunities for further tailoring of spintronics properties. Preliminary results highlighted that maintaining interfaces and materials quality (such as preventing ferromagnets oxidation) remains a crucial issue. Here, we will present results on band filtering in WS₂ based spin valves. We will detail a protocol to fabricate spin valves based on CVD grown WS₂, with step-by-step characterizations in support (Raman spectroscopy, photoluminescence, AFM measurements...) which aims at preserving interfaces spin properties by avoiding oxidations and degradations. The WS₂ layers are integrated in Co/Al₂O₃/WS₂/Co magnetic tunnel junctions acting as hybrid spin valve structures (Figure 1). We make use of a tunnel Co/Al₂O₃ spin analyzer to probe the extracted spin-polarized current from the WS₂/Co interface. The fabrication process is further validated by the measurements of magnetoresistance spin signals above state of the art for 2D semiconductors based MTJs. For monolayer based junctions, the spin polarization extracted from the WS₂/Co interface is measured to be positive. Interestingly, for bi- and tri-layers WS₂, the observed spin signal is reversed, which indicates a switch in the mechanism of interfacial spin extraction (Figure 2). This unusual thickness dependent property will be explained in light of the peculiar thickness band-structure evolution of WS₂, with Density Functional Theory calculations in support. This allows us to unravel a model of band filtering enabling spin selection and sign inversion through a selective K-Q transition in the band structure. Our work thus demonstrates the potential of WS₂ for K-Q band filtering and its tailoring in MTJs. As this band structure evolution is common to many other TMDs, our work also opens the way to the integration of members of this very large 2D materials family, in order to reveal their spin transport properties in Magnetic Tunnel Junctions [4].

[1] Piquemal-Banci *et al.* J. Phys. D: Appl. Phys. 50, 203002 (2017). [2] Piquemal-Banci *et al.* ACS Nano 12, 4712 (2018). [3] Piquemal-Banci *et al.* Nature Communications 11, 5670 (2020) [4] Zatko *et al.* ACS Nano 12, 14468 (2019)

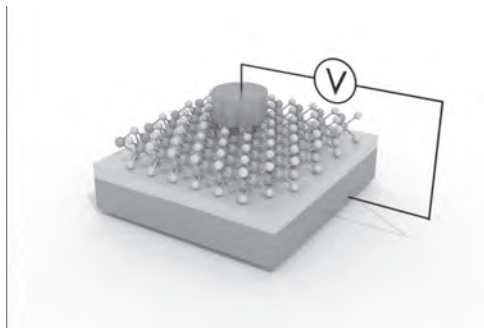


Fig.1: Schematic of the Co/Al₂O₃/WS₂/Co Magnetic Tunnel Junction.

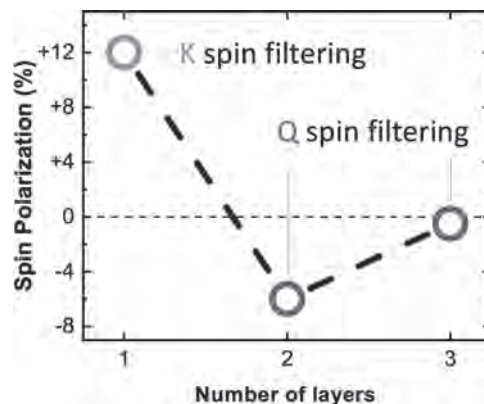


Fig. 2: Spin Polarization of Co/WS₂ versus the number of WS₂ layers.

DB-03. Spin Valves With Exfoliated 2D Materials: MoS₂.

M. Galbiati^{1,2}, F. Godel², A. Vecchiola², V. Zatkan², S. Tatay¹, R. Galceran², S. Mañas-Valero¹, M. Piquemal-Banci², M. Martin², A. Forment-Aliaga¹, E. Coronado¹, B. Dlubak² and P. Seneor²

1. Universitat de Valencia Institut de Ciència Molecular, Paterna, Spain;

2. Unite Mixte de Physique CNRS/Thales, Palaiseau, France

In the last years 2D materials have attracted a huge attention thanks to the amazing properties that arise when thickness approaches the single layer level and thanks to the large number of functionalities that they offer. Recently, they started to appear as high potential candidates for spintronics devices since, thanks to their intrinsic two-dimensional nature, they create thin, tuneable and free of defects barriers with sharp interfaces. Despite this potential, investigation of 2D materials for spintronics is still at the beginning. Only very recently few works started to appear using other 2D materials beyond graphene [1,2,3]. In particular, concerning the family of transition metal dichalcogenides (TMDCs), promising theoretical calculations were first reported predicting an extremely large magnetoresistance (MR) signal up to 300% in Fe/MoS₂/Fe MTJs [4]. However, experimental results are still far from these expectations. Indeed, most of experimental works have to face the main technological issue of avoiding bottom FM electrode oxidation during fabrication process, limiting in turn MR signals. Here we will show an in-situ fabrication approach to avoid oxidation of the FM electrodes during the device fabrication process that tackles this fundamental problem. This allowed the successful fabrication of NiFe/MoS₂/Co MTJs with multilayer MoS₂ mechanically exfoliated flakes (Fig. 1) showing the highest results reported so far for MoS₂-based spin valve devices (Fig. 2) [5] and confirming that our in situ fabrication protocol allows maintaining high quality non-oxidized interfaces between the ferromagnetic electrodes and the 2D layer. Beyond interfaces and material quality, we suggest that an overlooked more fundamental physics issue related to spin-current depolarization could explain the limited MR observed so far in MoS₂-based magnetic tunnel junctions [5,6]. This points to a path towards the observation of larger spin signals in line with theoretical predictions above 100%. We envision the impact of our work to be beyond MoS₂ and its broader transition-metal dichalcogenides family by opening the way to an accelerated screening of other 2D materials that are yet to be explored for spintronics.

[1] W. Wang, A. Narayan, L. Tang et al, Nano Lett., Vol. 15, p. 5261–5267, (2015). [2] A. Dankert, P. Pashaei, M. Venkata Kamalakar et al., ACS Nano, Vol. 11, p. 6389–6395, (2017). [3] W.C. Wong, S. M. Ng, H. F. Wong et al., IEEE Trans. Magn., Vol. 53, p.1600205 (2017). [4] K. Dolui et al., Phys. Rev. B, Vol. 90, p. 041401(R), (2014). [5] M. Galbiati et al., Phys. Rev. Appl. Vol. 12, p. 044022, (2019). [6] M. Galbiati et al., ACS Appl. Mater. Interfaces, 10, 30017 (2018).

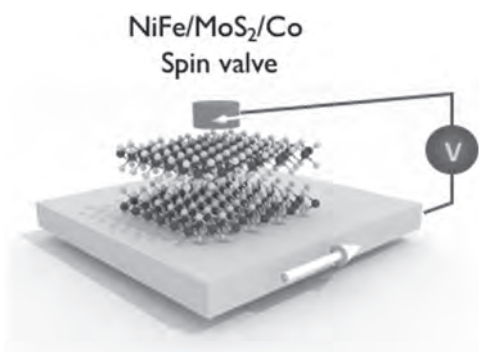


Fig 1: Schematic of the NiFe/MoS₂/Co spin valve.

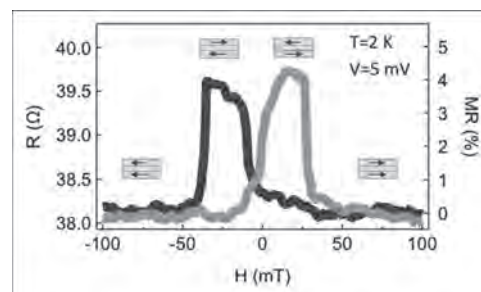


Fig. 2: Magnetoresistance signal measured in this NiFe/MoS₂/Co spin valve.

DB-04. Intrinsic 2DXY Ferromagnetism in a van der Waals Monolayer Grown by Molecular Beam Epitaxy.

A. Bedoya Pinto¹, J. Ji¹, A. Pandeya¹, P. Gargiani², M. Valvidares², P. Sessi¹, F. Radu³, K. Chang^{1,4} and S. Parkin¹

1. Max-Planck-Institut für Mikrostrukturphysik, Halle, Germany;
2. Consorcio para la Construcción Equipamiento y Explotación del Laboratorio de Luz Síncrotron, Barcelona, Spain; 3. Helmholtz-Zentrum Berlin für Materialien und Energie GmbH, Berlin, Germany; 4. Beijing Academy of Quantum Information Sciences, Beijing, China

Long before the recent fascination with two-dimensional materials, the critical behaviour and universality scaling of phase transitions in low-dimensional systems has been a topic of great interest. Particularly intriguing is the case of long-range magnetic order in two dimensions, once considered to be excluded in systems with continuous symmetry by the Mermin-Wagner theorem, but later revisited from the viewpoints of topological vortex order, symmetry breaking fields and finite size effects. Recent experiments on van der Waals monolayer systems [1] show that a sizable out-of-plane magnetic anisotropy is able to stabilize 2D long-range ferromagnetic order, as demonstrated in CrI_3 , CrBr_3 and Fe_3GeTe_2 , while a spontaneous magnetic ordering has remained elusive for an in-plane 2D magnetic system in the monolayer limit. In this work, we construct a large-area, nearly ideal easy-plane system, a CrCl_3 monolayer on Graphene/6H-SiC (0001) grown by molecular-beam epitaxy (Figs. 1a and 1b), which exhibits ferromagnetic ordering as unambiguously determined by element-specific X-ray magnetic dichroism [2]. Hysteretic behaviour of the field-dependent magnetization is sustained up to a temperature of 10 K (Fig. 1c), and angular dependent measurements evidence a clear in-plane easy axis, unlike all other van der Waals monolayer magnets reported to date. Moreover, the analysis of the critical exponents of the temperature-dependent magnetization show a scaling behaviour that is characteristic of a 2D-XY system (Fig. 1d). These observations suggest the first realization of a finite-size Berezinskii-Kosterlitz-Thouless (BKT) phase transition in a quasi-freestanding monolayer magnet with a XY universality class; accessible through the bottom-up growth of a van der Waals layer with an in-plane hexagonal crystal symmetry and negligible substrate interaction. The realization of XY magnetism in two dimensions opens the door to explore exotic physics such as spin superfluidity [3], and further constitutes an ideal platform to stabilize truly 2D topological spin textures, such as merons [4]. Apart from the novel physics discovered herein, the ability to grow homogeneous monolayer magnets by molecular beam epitaxy adds versatility and scalability to integrate 2D magnets in devices and large-area functional heterostructures. The strategies to achieve a high Curie temperature in the truly 2D limit will be also discussed in view of applications.

[1] K. S. Burch, D. Mandrus, J. G. Park, Magnetism in two-dimensional van der Waals materials. *Nature* 563, 47–52 (2018). [2] A. Bedoya-Pinto et al., Intrinsic 2D-XY ferromagnetism in a van der Waals monolayer. <https://arxiv.org/abs/2006.07605> (2020) [3] S. Kim, et al., Transport signature of the BKT transition in 2D easy-plane magnets. <https://arxiv.org/abs/2003.08956> (2020) [4] X. Lu, R. Fei, L. Zhu, L. Yang, Meron-like topological spin defects in monolayer CrCl_3 . *Nat. Commun.* 11, 4724 (2020).

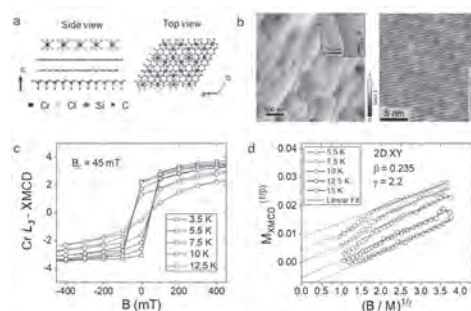


Figure 1. (a) Schematic crystal structure of $\text{CrCl}_3/\text{Graphene}/6\text{H-SiC}$ layers in top view and cross-section configurations. (b) Scanning tunneling microscopy images of the CrCl_3 layer grown on $\text{Graphene}/6\text{H-SiC}$ (0001). The overview image reveals that both Graphene and CrCl_3 follow the SiC topography with atomic terraces. The atom resolved image features a moiré pattern, which results from the superposition of the hexagonal unit cell of CrCl_3 and graphene . (c) Hysteresis loops of the XMCD signal at the Cr L_3 edge, as a function of temperature, indicating clear ferromagnetic behaviour. Remanence and coercive field vanish at 12.5K. (d) Modified Arrott-Plots for the temperature-and field dependent XMCD data. A consistent set of critical exponents is inferred ($\beta=0.235$, $\gamma=2.2$), matching with the predictions of the 2DXY model. The XMCD data in Figures 3c and 3d were acquired at the VekMaG beamline in BESSY, Berlin.

DB-05. High Spin Hall Conductivity in Large-Area Type-II Dirac Semimetal PtTe₂.

H. Xu¹, J. Wei¹, X. Han¹ and G. Yu¹

¹. Beijing National Laboratory for Condensed Matter Physics, Chinese Academy of Sciences, Beijing, China

Recently, two-dimensional transition metal dichalcogenides (TMDs) emerge as intriguing platforms for spintronics study because of their controllability in structure, stacking order, conductivity, non-trivial energy band topology and interplay between spin and pseudospin [1,2]. With strong spin-orbit coupling [3], TMDs also show great potentials in manipulation of magnetic moment by using of spin-orbit torque (SOT), however, most of the present study is restricted to the mechanically exfoliated samples with small sizes and relatively low conductivities [4,5]. Therefore, the efficiency of magnetization switching in TMD/FM bilayer might not be comparable with conventional HM/FM bilayer and not suitable for large-scale application. Here, we develop a manufacturable recipe to fabricate large-area thin films of PtTe₂, a type-II Dirac semimetal, to study their capability of generating SOT [6]. PtTe₂/Py bilayer was fabricated and characterized by spin-torque Ferromagnetic resonance (ST-FMR) technology. Large SOT efficiency together with high conductivity results in a giant spin Hall conductivity ($0.2\text{-}2 \times 10^5 \text{ h}/2e (\Omega\text{m})^{-1}$) of PtTe₂ thin films, which is one of the largest values among the presently reported TMDs. We further demonstrate that the SOT from PtTe₂ layer can switch a perpendicularly magnetized CoTb layer efficiently. This work paves the way for employing PtTe₂-like TMDs for wafer-scale spintronic device applications.

[1] K. Deng, G. L. Wan, and S. Y. Zhou et al., *Nat. Phys.* 12, 1105 (2016)

[2] X. Xu, W. Yao, D. Xiao and T. F. Heinz, et al., *Nat. Phys.* 10, 343 (2014)

[3] H. T. Yuan, M. S. Bahramy, and N. Nagaosa et al., *Nat. Phys.* 9, 563 (2013)

[4] Q. M. Shao, G. Q. Yu, et al., *Nano Lett.* 16, 7514 (2016)

[5] D. MacNeill, G. M. Stiehl, and D. C. Ralph et al., *Nat. Phys.* 13, 300 (2017)

[6] H.J. Xu, G.Q. Yu, and X.F. Han et al., *Adv. Mater.* 32, 2000513 (2020)

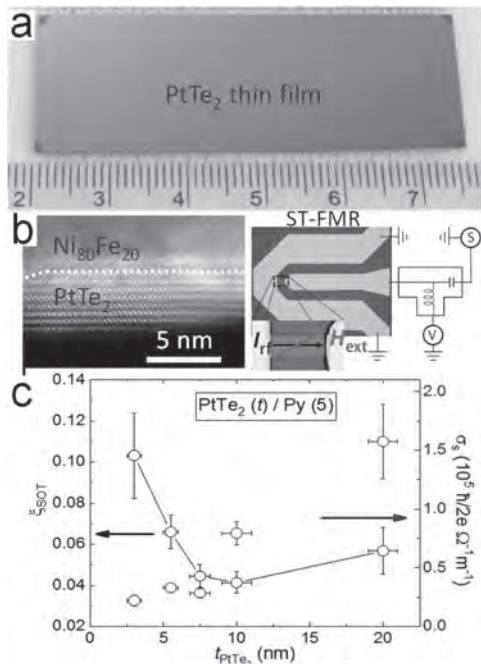


Figure 1 (a) Wafer-scale PtTe₂ thin films with thicknesses of ~10 nm. (b) left, Cross-sectional HAADF-STEM image of a PtTe₂/Py stack, where the interface is indicated by the white dashed lines; right, the layout of ST-FMR device with GSG connection. (c) Thickness dependence of efficiency of SOT (ξ_{SOT}) and spin Hall conductivity σ_s .

DB-06. Coexistence of Topological and Rashba States in Ferroelectric SnTe.

L. Nessi⁵, A. Novati⁵, M. Cantoni⁵, S. Cecchi¹, G. Vinai², D. Mondal², J. Fujii², I. Vobornik², R. Calarco³, R. Bertacco³, S. Picozzi⁴ and C. Rinaldi⁵

1. Epitaxy, Paul-Drude-Institut für Festkörperelektronik, Berlin, Germany; 2. IOM-CNR, Istituto Officina dei Materiali Consiglio Nazionale delle Ricerche, Trieste, Italy; 3. CNR-IMM, Consiglio Nazionale delle Ricerche, Roma, Italy; 4. CNR-SPIN, Consigli Nazionale delle Ricerche, Chieti, Italy; 5. Physics, Politecnico di Milano, Milano, Italy

The chalcogenides GeTe [1] and SnTe [2] are the prototypes of ferroelectric Rashba semiconductors (FERSC), a class of materials in which ferroelectricity is coupled to the Rashba spin texture, enabling the non-volatile ferroelectric control of spin-to-charge conversion [3]. While the properties of GeTe as FERSC have been widely investigated [4, 5], SnTe is mostly known as topological material, probably due to the low Curie temperature (100 K) as bulk ferroelectric. However, attempts to bring the critical temperature of ferroelectric SnTe to room temperature [6] are motivated by the prediction of giant intrinsic spin Hall conductivity in its Rashba phase [7], with the possibility of controlling the spin-to-charge conversion ferroelectrically. Here we propose to identify some conditions leading to stable ferroelectric SnTe at room temperature by exploiting the dipolar interaction with ferroelectric GeTe. First, we study the growth of epitaxial thin SnTe(111) films on GeTe(111)/Si(111) by molecular beam epitaxy. Then, by spin and angular photoemission spectroscopy experiments, we access the band dispersion of the SnTe in such heterostructure as a function of temperature. The work shows the coexistence of topological and Rashba states in SnTe(111), suggesting that the ferroelectric distortion of SnTe on GeTe survives up at room temperature, possibly thanks to the dipolar interaction with the ferroelectric GeTe underneath. We find a nice agreement with density functional theory calculations [2] which also predict the tunability of topological and Rashba bands with the orientation of the ferroelectric polarization. These preliminary results open the way to the investigation of SnTe/GeTe for reconfigurable spin-based transistors based on the ferroelectric control of the spin transport. Acknowledgements. C.R. and S.P. acknowledges the project TWEET, grant no. 2017YCTB59 by MIUR.

[1] D. Di Sante *et al.*, *Adv. Mater.*, Vol. 25, p. 509 (2013). [2] E. Plekhanov, S. Picozzi *et al.*, *Phys. Rev. B*, Vol. 90, p. 161108(R) (2014) [3] Paul Noël *et al.*, *Nature*, Vol. 580, p. 483-486 (2020) [4] C. Rinaldi *et al.*, *Nano Letters*, Vol. 18, p. 2751 (2018). [5] C. Rinaldi *et al.*, *APL Mater.*, Vol. 4, p. 032501 (2016). [6] K. Chang *et al.*, *Science*, Vol. 353, p. 274 (2016) [7] H. Wang *et al.*, *npj Comput. Mater.*, Vol. 6, p. 7 (2020)

DB-07. Bulk-Like Magnetic Moments in Epitaxial Two-Dimensional Superlattices.

J. Sun¹, S. Liu^{2,3}, F. Xiu^{2,3} and W. Liu¹

1. *Electronic Engineering, Royal Holloway University of London, Egham, United Kingdom*; 2. *State Key Laboratory of Surface Physics and Department of Physics, Fudan University, Shanghai, China*; 3. *Institute for Nanoelectronic Devices and Quantum Computing, Fudan University, Shanghai, China*

The family of two dimensional (2D) magnets has been expanded with tremendous speed since the two pioneering 2D magnetic insulators, Cr₂Ge₂Te₆ [1] and CrI₃ [2], were isolated in 2017, and has exhibited great potential in developing spintronic devices for next generation data storage [3]. Over the past four years, the magnetism of 2D magnets has been extensively studied by the full arsenal of probing techniques. Due to their sensitivity to external stimuli, various modulations, such as electron gating [4]–[6], have been taken to manipulate the magnetic properties of van der Waals (vdWs) systems. Such 2D magnets can be incorporated to form heterostructures with clean and sharp interfaces, which gives rise to exotic phenomena as a result of the interfacial proximity effect. Very recently, we have demonstrated the first inch-scale epitaxial two-dimensional ferromagnetic superlattices (Fe₃GeTe₂/CrSb)_n, in which Fe shows a significantly reduced moment (1.05 μ_B/atom) [7] comparing to bulk Fe₃GeTe₂ [8]. Here we report a detailed x-ray magnetic circular dichroism (XMCD) study of the spin and orbital moments of this system. Fig. 1a shows the schematic diagram of the (4-layer Fe₃GeTe₂/CrSb)₆ superlattices. These were grown in a Perkin Elmer 430 MBE on sapphire(0001) with a base vacuum of 10⁻⁹ Torr. The Fe₃GeTe₂ layers were grown at the substrate temperature of ~310 °C, with the source temperatures of Fe (99.99%), Ge (99.999%) and Te (99.999%) at 1165 °C, 1020 °C and 285 °C, respectively, co-evaporated from Knudsen cells. The substrate temperature was changed to 280 °C when growing CrSb films with Cr (99.99%) and Sb (99.999%) cell temperatures of 1180 °C and 400 °C, respectively. The synchrotron-based x-ray magnetic circular dichroism (XMCD) technique was performed to unambiguously determine the spin and orbital moments of the superlattices. Oppositely circular polarized x-rays with 100% degree of polarization were used successively to resolve XMCD signals from each of the magnetic elements. The light-helicity was switched in a fixed magnetic field (5 T), which was applied in normal incidence with respect to the film plane and in parallel with the beam, as shown in Fig. 1b. The XMCD was obtained by subtracting the two x-ray absorption spectra (XAS), (σ⁻ - σ⁺), with different helicity. Fig. 1c and 1d show typical pairs of XAS and XMCD spectra of the (Fe₃GeTe₂/CrSb)₆ superlattices obtained at 3 K in total electron yield (TEY). The XAS of Fe L_{2,3} edges well resembles that of bulk Fe₃GeTe₂ [8], whilst that of Cr show multiple structures for both spin-orbit split core levels. The strongly dichroic spectra of Fe and Cr clearly indicate the ferromagnetic coupling between the Fe₃GeTe₂ and the CrSb layers in the superlattices. By applying sum rules, we obtained m_s = 1.58 ± 0.1 μ_B/atom and m_l = 0.22 ± 0.02 μ_B/atom for the Fe and m_s = 0.94 ± 0.09 μ_B/atom and m_l = 0.29 ± 0.03 μ_B/atom for the Cr, respectively. Unlike the reduced moment of the Fe₃GeTe₂ in (Fe₃GeTe₂/CrSb)₃ [7], that in (Fe₃GeTe₂/CrSb)₆ shows a bulk-like moment [8]. Future work to explore the tuning of the spin polarized band structure of both the 2D ferromagnetic superlattices via the interface engineering will be of great interest and have strong implications for both fundamental physics and the emerging spintronics technology.

[1] C. Gong *et al.*, “Discovery of intrinsic ferromagnetism in two-dimensional van der Waals crystals,” *Nature*, vol. 546, no. 7657, pp. 265–269, 2017. [2] B. Huang *et al.*, “Layer-dependent ferromagnetism in a van der Waals crystal down to the monolayer limit,” *Nature*, vol. 546, no. 7657, pp. 270–273, 2017. [3] X. Lin, W. Yang, K. L. Wang, and W. Zhao, “Two-dimensional spintronics for low-power electronics,” *Nat. Electron.*, vol. 2, no. July, pp. 22–24, 2019. [4] Y. Deng *et al.*, “Gate-tunable room-temperature ferromagnetism in two-dimensional Fe₃GeTe₂,” *Nature*, vol. 563, no. 7729, pp. 94–99, Nov. 2018. [5] B. Huang *et al.*, “Electrical control of 2D magnetism in bilayer CrI₃,” *Nat. Nanotechnol.*, vol. 13, no. 7, pp. 544–548, 2018. [6] I. A. Verzhbitskiy *et al.*, “Controlling the magnetic anisotropy in Cr₂Ge₂Te₆ by electrostatic gating,” *Nat. Electron.*, pp. 1–6,

Jun. 2020. [7] S. Liu *et al.*, “Two-dimensional ferromagnetic superlattices,” *Natl. Sci. Rev.*, vol. 7, no. 4, pp. 745–754, Apr. 2020. [8] J. X. Zhu *et al.*, “Electronic correlation and magnetism in the ferromagnetic metal Fe₃GeTe₂,” *Phys. Rev. B*, vol. 93, no. 14, p. 144404, 2016.

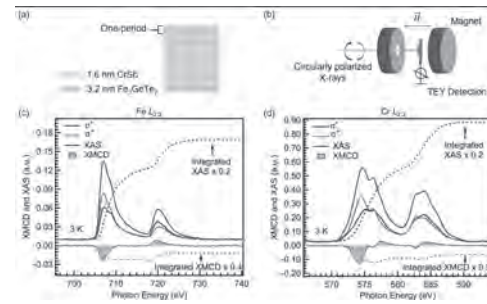


Figure 1. Element-specific magnetic states measured by XAS and XMCD of (Fe₃GeTe₂/CrSb)₆ superlattice. (a) Schematic of (Fe₃GeTe₂/CrSb)₆ superlattices, including the 4-layer Fe₃GeTe₂ (~ 3.2 nm) and CrSb (~ 1.6 nm). (b) Schematic of experimental setup of XMCD measurement. (c) Typical pair of XAS and XMCD spectra at Fe L_{2,3} edge obtained using TEY mode at 3 K and 5 T. (d) Typical pair of XAS and XMCD spectra at Cr L_{2,3} edge obtained using TEY mode at 3 K and 5 T. (XAS spectra are offset vertically for clarity).

DB-08. Critical Fluctuations Induced g-Factor Anisotropy in the Two-Dimensional Ferromagnetic Insulators CrXTe₃ (X=Si, Ge).

Z. Li^{1,2}, D. Xu^{1,2}, X. Li^{1,2}, H. Liao^{1,3}, X. Xi¹, Y. Yu^{1,4} and W. Wang^{1,3}

1. Beijing National Laboratory for Condensed Matter Physics, Institute of Physics, Chinese Academy of Sciences, Beijing, China; 2. University of Chinese Academy of Sciences Education Foundation, Beijing, China; 3. Songshan Lake Library, Dongguan, China; 4. Wuhan Institute of Physics and Mathematics Chinese Academy of Sciences, Wuhan, China

Recent discoveries of magnetic van der Waals (vdW) materials provide the ideal platform for exploring intrinsic two-dimensional (2D) magnetism down to the 2D limit and potential opportunities for new spin-related applications. However, according to Ginzburg criterion, 2D magnetism is associated with strong intrinsic magnetization fluctuations, which will break down the approximation of mean field theory in the neighborhoods of critical points [1]. In this talk, we will show the evidence for the magnetization-fluctuation-induced effective g factor anisotropy in the 2D ferromagnetic insulators CrXTe₃ (X = Si, Ge) by means of ferromagnetic resonance (FMR). After deriving the classical and quantum models of magnetic resonance [2, 3], we confirm the dramatic anisotropic shift of the measured g factor to originate from fluctuations with anisotropic interactions. The deduction of the g factor behind the fluctuations is consistent with the spin-only state ($g \approx 2.050(10)$ for CrSiTe₃ and 2.039(10) for CrGeTe₃). In addition, we will show that the abnormal enhancement of g shift, supplemented by specific heat and magnetometry measurements. We believe the results presented in this talk strongly suggest that CrSiTe₃ exhibits a more typical two-dimensional nature than CrGeTe₃ and may be closer to the quantum critical point.

[1] B. Zappoli, D. Beysens, and Y. Garrabos, The ginzburg criterion, in Heat Transfers and Related Effects in Supercritical Fluids (Springer Netherlands, Dordrecht, 2015) pp. 371-372. [2] H. Beljers and J. Smit, Phil. Res. Rep 10 (1955). [3] K. Nagata, I. Yamamoto, H. Takano, and Y. Yokozawa, J. Phys. Soc. Jpn. 43, 857 (1977).

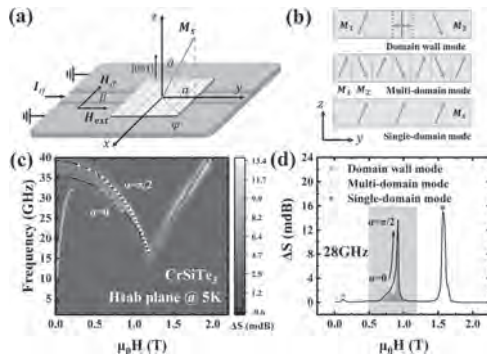


FIG. 1. (a) Coplanar waveguide with a rectangular single crystal placed parallel to the ab plane. The domain wall is represented by a blue solid line. (b) Illustration of three different resonant modes from the side view. (c) Frequency- and field-dependent FMR spectra (in-plane, $\beta = \pi/2$) for CrSiTe₃ at 5 K. The solid lines represent fitting for the single domain mode and multi-domain mode. (d) Typical microwave transmission at 28 GHz sliced from (c). The resonant peak of the multidomain mode is formed by the superposition of a series of peaks with different angles α .

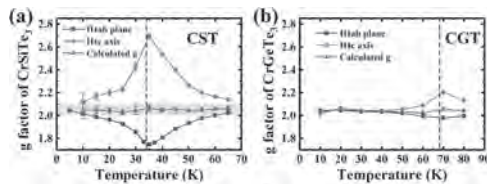


FIG. 3. (a,b) Temperature dependence of the effective g factor with the field applied both in-plane and out-of-plane for CST and CGT. The real g factor is calculated with $g = 1/3g_{ab} + 2/3g_c$.

DB-09. Spin-Orbit Driven Effects in Graphene-FM Systems.

A. Gudín Holgado^{1,2}, J.M. Diez^{1,2}, P. Ollerros-Rodríguez¹, F. Ajejas¹,
A. Anadón¹, I. Armay¹, R. Guerrero¹, J. Camarero^{1,2}, R. Miranda^{1,2} and
P. Perna¹

1. Nanoscience, Instituto Madrileño de Estudios Avanzados, Madrid,
Spain; 2. Instituto Nicolás Cabrera & IFIMAC, Universidad Autónoma de
Madrid, Madrid, Spain

The development of room temperature magnetic devices exploiting Spin Orbit effects is at the forefront of actual research. A major challenge for future spintronics is to develop suitable spin transport channels with superior properties such as long spin lifetime and propagation length. Graphene can meet these requirements, even at room temperature [1]. However, the development of all-graphene spintronic devices requires that, in addition to its passive capability to transmit spins over long distances, other active properties are incorporated to graphene. The generation of long-range magnetic order and spin filtering in graphene have been recently achieved by molecular functionalization [2] as well as by the introduction of giant spin-orbit coupling (SOC) in the electronic bands of graphene [3]. On the other side, taking advantage of the fast motion of perpendicular magnetic anisotropy (PMA) chiral spin textures, i.e., Néel-type domain walls (DWs) and magnetic skyrmions, can satisfy the demands for high-density data storage, low power consumption and high processing speed [4], while the presence of graphene enables the possibility to electrically tune the magnetic properties [5]. Here, we report on high quality, epitaxial graphene/Co(111)/HM(111) stacks grown on (111)-oriented insulating oxide crystals, characterized by STM, LEED, STEM, Kerr Magnetometry and Microscopy, XAS-XMCD, XMRS and SP-ARPES, which exhibit enhanced PMA for Co layers up to 4 nm thick and left-handed Néel-type chiral DWs stabilized by interfacial Dzyaloshinskii-Moriya interaction (DMI) localized at both graphene/Co and Co/HM interfaces with opposite sign [6,7]. While the DMI at Co/HM side is due to the intrinsic SOC [8], the sizeable DMI experimentally found at the Gr/Co interface has Rashba origin [6]. The active magnetic texture is protected by the graphene monolayer and stable at 300 K in air, and, since it is grown on an insulating substrate, amenable to be controlled electrically [5].

[1] W. Han, R.K. Kawakami, M. Gmitra and J. Fabian, *Graphene Spintronics*, Nat. Nanotech. 9, 794 (2014). [2] D. Maccariello, *et al.*, *Spatially resolved, site-dependent charge transfer and induced magnetic moment in TCNQ adsorbed on graphene*, Chemistry of Materials 26 (9), 2883-2890 (2014). [3] F. Calleja *et al.*, *Spatial variation of a giant spin-orbit effect induces electron confinement in graphene on Pb islands*, Nature Physics 11, 43-47 (2015). [4] A. Fert, V. Cros and J. Sampaio, *Skyrmions on the track*, Nat. Nanotech. 8, 152-156 (2013). [5] JTC2019 SOgraphMEM project <https://nanociencia.imdea.org/sographmem/> [6] F. Ajejas, *et al.*, *Unravelling Dzyaloshinskii-Moriya interaction and chiral nature of Graphene/Cobalt interface*, Nano Lett. 18(9), 5364-5372 (2018). [7] F. Ajejas, *et al.*, *Thermally Activated Processes for Ferromagnet Intercalation in Graphene-Heavy Metal Interfaces*, ACS Applied Materials and Interfaces, 12 (3), pp. 4088-4096 (2020). [8] F. Ajejas, *et al.*, *Tuning domain wall velocity with Dzyaloshinskii-Moriya interaction*, Appl. Phys. Lett. 111, 202402 (2017).

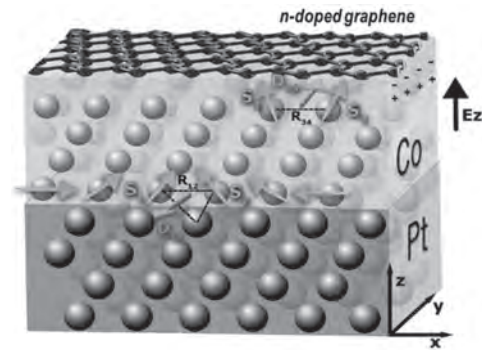


Figure 1. Sketch of the interplay between Spin-Orbit Coupling-induced Dzyaloshinskii-Moriya Interaction (DMI) at the Co/Pt and opposite Rashba-type DMI at the gr/Co interfaces [6].

DB-10. Room-Temperature Ferromagnetism in 2D vdW Fe₃GeTe₂ and its Potential Application.T. Nie¹¹. Beihang University, Beijing, China

Since the discovery of single-layer graphene in 2004, two-dimensional (2D) van der Waals (vdW) materials represented by it have demonstrated excellent electrical, magnetic, mechanical and optical physical properties under the structure of one or several layers of atomic thickness¹. Based on these superior properties, 2D-layered vdW ferromagnetic materials have become the basis for constructing low-dimensional spintronics devices², in which Fe₃GeTe₂ (FGT)³, Cr₂Ge₂Te₆⁴ and CrI₃⁵ as the main representative materials exhibit strong perpendicular magnetic anisotropy and other important characteristics in single layer. However, the Curie temperature (T_c) of above materials has not reached room temperature yet, which has greatly hindered the subsequent development for device application. Therefore, recently researchers have been committed to explore 2D vdW ferromagnetic materials for room-temperature T_c in both theory and experiment. Here, we report that the interfacial engineering effect could effectively increase the T_c of the 2D vdW ferromagnetic material FGT from 230 K to 400 K, through heteroepitaxy with topological insulator of Bi₂Te₃. A theoretical calculation was further carried out to describe the magnetic properties by using first-principles calculations and the self-consistent Hubbard U approach (DFT+Uscf) together with the Monte Carlo (MC) simulations. After combination with Bi₂Te₃, the intralayer interactions in FGT was calculated to dramatically increase compared to that in pure FGT, well explaining the T_c enhancement. Our results may open up a new door to benefit the magnetic order in the 2D limit and realize spintronic devices based on 2D-layered vdW ferromagnetic materials with room temperature performances towards industrialization.

1. Geim, A. K.; Novoselov, K. S. The Rise of Graphene. *Nat. Mater.* 2007, 6 (3), 183–191. 2. Lin, X.; Yang, W.; Wang, K. L.; Zhao, W. Two-Dimensional Spintronics for Low-Power Electronics. *Nat. Electron.* 2019, 2 (7), 274–283. 3. Liu, S.; Yuan, X.; Zou, Y.; Sheng, Y.; Huang, C.; Zhang, E.; Ling, J.; Liu, Y.; Wang, W.; Zhang, C.; Zou, J.; Wang, K.; Xiu, F. Wafer-Scale Two-Dimensional Ferromagnetic Fe₃GeTe₂ Thin Films Grown by Molecular Beam Epitaxy. *npj 2D Mater. Appl.* 2017, 1 (1), 30. 4. Gong, C.; Li, L.; Li, Z.; Ji, H.; Stern, A.; Xia, Y.; Cao, T.; Bao, W.; Wang, C.; Wang, Y.; Qiu, Z. Q.; Cava, R. J.; Louie, S. G.; Xia, J.; Zhang, X. Discovery of Intrinsic Ferromagnetism in Two-Dimensional van Der Waals Crystals. *Nature* 2017, 546 (7657), 265–269. 5. Huang, B.; Clark, G.; Navarro-Moratalla, E.; Klein, D. R.; Cheng, R.; Seyler, K. L.; Zhong, D.; Schmidgall, E.; McGuire, M. A.; Cobden, D. H.; Yao, W.; Xiao, D.; Jarillo-Herrero, P.; Xu, X. Layer-Dependent Ferromagnetism in a van Der Waals Crystal down to the Monolayer Limit. *Nature* 2017, 546 (7657), 270–273.

DB-11. Electrical Resistivity, Galvanomagnetic and Optical Properties of WTe_2 Single Crystal.

A. Domozhirova¹, S. Naumov¹, A. Makhnev¹, E. Shreder¹, S. Podgornykh¹, E. Marchenkova¹, V. Chistyakov¹, J. Huang² and V. Marchenkov^{1,3}
 1. M.N. Mikheev Institute of Metal Physics, UB RAS, Ekaterinburg, Russian Federation; 2. National Cheng Kung University, Tainan, Taiwan; 3. Ural Federal University, Ekaterinburg, Russian Federation

Transition metal dichalcohedides (TMDs) are a group of compounds with the chemical formula MX_2 , where M is a transition metal (e.g. Mo, W), X is a chalcogen (Te, Se, S, etc.). Such materials have a layered structure, where metal atom sheets are sandwiched between two chalcogen sheets. The atomic bonding within the X - M - X layer is covalent, while the interlayer coupling is realized due to the van der Waals interaction. Therefore, such materials are considered structurally and electronically two-dimensional. In addition, TMDs attract attention for their promising electronic properties [1, 2]. TMD WTe_2 , MoTe_2 and $\text{Mo}_x\text{W}_{1-x}\text{Te}_2$ are known to exhibit the topological Weyl semimetal (TWS) features when crystalized in an orthorhombic structure [3, 4]. Such materials have promising prospects for use in spintronics and micro- and nanoelectronics due to unusual electronic and magnetic properties (e.g. extremely large magnetoresistance, high charge carrier mobility, spin-polarized transport) owing to their nontrivial topology of the electronic band structure. Since TWSs were discovered relatively recently, at present such materials have not yet been extensively studied and are a hot research direction. Therefore, the purpose of this work is a comprehensive study of the electrical, galvanomagnetic and optical properties of the WTe_2 single crystal. WTe_2 single crystals were grown by the chemical vapour transport method as described in [5]. XRD analysis revealed that WTe_2 have an orthorhombic structure with the lattice parameters $a = 3.435(8) \text{ \AA}$, $b = 6.312(7) \text{ \AA}$ and $c = 14.070(4) \text{ \AA}$. The chemical composition of the samples was confirmed by X-ray microanalysis using a FEI Inspect F scanning electron microscope equipped with an EDAX attachment. The temperature dependences of the electrical resistivity $\rho(T)$ and galvanomagnetic properties (magnetoresistivity and Hall Effect) were measured by the standard four-probe method in the temperature range from 1.8 to 300 K in magnetic fields of up to 9 T. An electric current flowed in the $(00l)$ plane of the sample, and the magnetic field vector was directed perpendicular to the $(00l)$ plane. The optical properties were measured using the Beattie method with one reflection from the $(00l)$ plane of the samples in the spectral range of 0.17–5.0 eV at room temperature. The studies carried out showed that the temperature dependence of the electrical resistivity $\rho(T)$ has a “metallic” behaviour and ρ monotonically increases with temperature from 20 to 860 $\mu\text{Ohm}\times\text{cm}$ according to a quadratic law at $T < 60 \text{ K}$, reaches a linear dependence with a tendency to saturation at higher temperatures. T^2 – dependence of ρ at low temperatures is known to be explained by several mechanisms, in particular, strong electron-electron scattering. In addition, in [6, 7], it is shown that the electron–phonon–surface interference scattering mechanism can lead to $\rho \sim T^2$ in pure metals. Since the WTe_2 single crystal has a layered structure, interface scattering of current carriers can cause $\rho \sim T^2$. The magnetoresistivity $\Delta\rho_{xx}/\rho$ of the WTe_2 single crystal is found to reach 1700% at $T = 1.8 \text{ K}$ in a magnetic field of 9 T. The field dependence $\Delta\rho_{xx}/\rho(B)$ changes according to a law close to quadratic in the investigated range of fields. This behaviour of the magnetoresistivity is inherent in compensated conductors with a closed Fermi surface in the region of high effective magnetic fields [8]. The state of electron-hole compensation leads to a high mobility of current carriers, which is also characteristic of TWSs. The Hall Effect data obtained allow us to conclude that the majority charge carriers are electrons with the concentration $n \sim 10^{19} \text{ cm}^{-3}$ and the mobility $\mu \approx 7500 \text{ cm}^2/\text{V}\times\text{s}$ at $T = 1.8 \text{ K}$. Optical studies show that, in the investigated spectral region, the optical conductivity spectrum $\sigma(E)$ is one broad band centered at 3.4 eV, formed by interband transitions. In the infrared region of the spectrum, low values of the imaginary part ϵ_2 and positive values of the real part of ϵ_l of the complex permittivity are observed, which gives grounds to conclude that there is no contribution from free carriers of up to the boundary of the investigated spectral region. The revealed features, such as the large magnetoresistivity, high mobility of charge carriers, along with their relatively low concentration, insignificant contribution from free carriers to optical conductivity, are apparently the manifestation of the

topological nature of the material, however, to clarify it, further studies are required. The research was carried out within the state assignment of the Ministry of Education and Science of the Russian Federation (theme “Spin”, No. AAAA-A18-118020290104-2), supported in part by RFBR (project No. 20-32-90069) and the Government of Russian Federation (Decree No. 211, Contract No. 02. A03.21.0006).

1. J. A. Wilson and A. D. Yoffe, *Adv. Phys.*, Vol. 18, p. 193 (1969). 2. P. K. Das, D. D. Sante, F. Cilento et al., *Electron. Struct.*, Vol. 1, p. 014003 (2019). 3. Y. Wu, D. Mou, N. H. Jo et al., *Phys. Rev. B*, Vol. 95, p. 121113(R) (2016). 4. I. Belopolski, D. S. Sanchez, Y. Ishida et al., *Nat. Commun.*, Vol. 7, p. 13643 (2016). 5. A. N. Domozhirova, S. V. Naumov, S. M. Podgornykh et al., Accepted for publication in *Journal of Physics: Conference Series* (2021). 6. V. E. Startsev, V. P. D'yakina, V. I. Cherepanov et al., *Zh. Eksp. Teor. Fiz.*, Vol. 79, p. 1335 (1980). 7. V. V. Marchenkov, *Low Temp. Phys.*, Vol. 37, p. 852 (2011). 8. I. M. Lifshitz, M. Ya. Azbel and M. I. Kaganov, *Electronic Theory of Metals* (Moscow: Nauka) (1971).

Session DC
SPINS IN TOPOLOGICAL INSULATORS AND 2D MATERIALS
Claudia Felser, Chair
Max-Planck-Gesellschaft, Dresden, Germany

CONTRIBUTED PAPERS

DC-01. Magnetotransport and ARPES Studies of Large-Area Sb₂Te₃ and Bi₂Te₃ Topological Insulators Grown by MOCVD on Si.

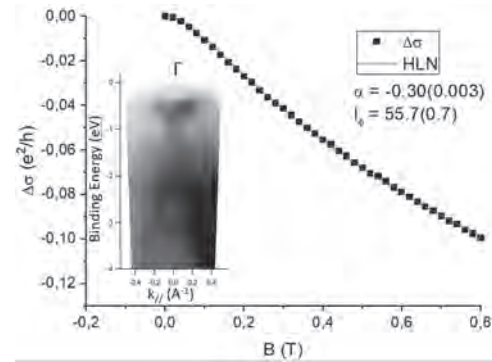
L. Locatelli^{1,2}, A. Kumar¹, R. Cecchini¹, E. Longo^{1,2}, M. Rimoldi¹, P. Tsipas³, A. Dimoulas³, M. Longo¹ and R. Mantovan¹

1. Material science, Consiglio Nazionale delle Ricerche, Agrate Brianza, Italy; 2. Material science, Università degli Studi di Milano-Bicocca, Milano, Italy; 3. Material science, Ethniko Kentro Ereunas Physikon Epistemon Demokritos, Athena, Greece

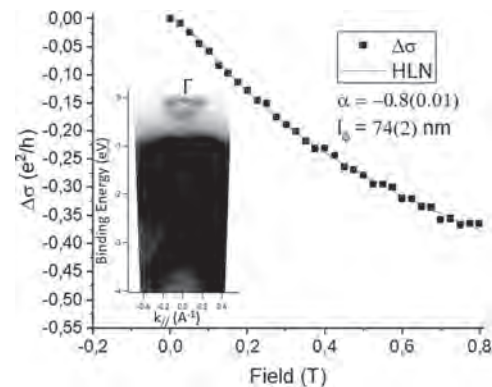
Chalcogenide thin films have become of interest in energy conversion, as thermoelectric materials, and for spintronic applications. Amongst them, antimony telluride (Sb₂Te₃) and bismuth telluride (Bi₂Te₃) have gained attention as Topological Insulators (TI) [1,2]. In order to make a step toward technology transfer, it is of major importance to achieve epitaxial quality-TI on large area, Si-based substrates. We have recently developed Metal Organic Chemical Vapor Deposition (MOCVD) processes to grow Bi₂Te₃ and Sb₂Te₃ thin films on top of 4" Si(111) substrates [1,3]. In this contribution we report clear evidence of the existence of topologically-protected surface states (TSS) in both ~90 nm-thick Bi₂Te₃ and ~30 nm-thick Sb₂Te₃ films by making use of magnetotransport (MR) and angle resolved photoemission spectroscopy (ARPES) studies. MR measurements were performed in the Van der Pauw configuration on ~1 x 1 cm² samples without any processing or capping layers, in the 5-295 K temperature range. Following MR, samples were analysed by *ex situ* ARPES. In order to make this possible, prior to ARPES, the samples were cleaned under vacuum by 1.5 keV Ar ion sputtering for about 15 sec at 10⁻⁵ mbar. The sputtering cycles were repeated as many times as necessary to obtain a clean surface free of C and O contaminants, as verified by *in situ* X-ray photoelectron spectroscopy. As a final step, annealing under vacuum was performed at 290 °C for ~10 min, in order to recover the damage induced by Ar⁺ sputtering. Finally, flat and well-ordered surfaces were obtained, as checked by streaky reflection high-energy electron diffraction patterns. ARPES spectra were acquired at room temperature with a 100 mm hemispherical electron analyzer equipped with a 2D CCD detector (SPECS). The He I (21.22 eV) resonant line was used to excite photoelectrons and the energy resolution of the system was greater than 40 meV. Both Sb₂Te₃ and Bi₂Te₃ films exhibited a metallic behaviour, reaching a resistivity of 0.83 mΩ cm and 1.4 mΩ cm at 5 K, respectively. From Hall measurements, we identified the carrier type, being holes in Sb₂Te₃ and electrons in Bi₂Te₃, as expected. The evolution of the carrier density with the lowering of the temperature turned out to be different for the two samples: an increasing of the hole density for the Sb₂Te₃ and a decreasing of the electron density for the Bi₂Te₃ were observed. The corresponding mobilities displayed a maximum at 5 K, suggesting a suppression of bulk conduction at low temperature with a potentially higher contribution from the TSS. Quite interestingly, at 5 K, we detected a 430% increase of electron mobility in Bi₂Te₃, to be compared with a marginal 6% increase of hole mobility in the case of Sb₂Te₃. In both Sb₂Te₃ and Bi₂Te₃, MR measurements highlighted the presence of clear weak antilocalization (WAL) at low temperature, as shown in figures 1 and 2. WAL was interpreted in the framework of the Hikami-Larkin-Nagaoka (HLN) model as a first proof of the existence of 2D-conduction channels connected to TSS [4]. The two HLN parameters α (being connected to the number of conducting channels) and the coherence length ($l\phi$) were extracted by fitting the magnetoconductance values (MC). The α values were 0.3 and 0.8 for Sb₂Te₃ and Bi₂Te₃ respectively, meaning that in Bi₂Te₃ the 2D-conduction is highly dominating when compared to Sb₂Te₃, in agreement with the corresponding temperature behaviour of electron and hole mobilities. At 5.5 K, the $l\phi$ reached the value of 74 nm in Bi₂Te₃ and 55 nm in Sb₂Te₃, again indicating a more favourable TSS-connected transport in Bi₂Te₃ than in Sb₂Te₃. Comparing the obtained α and $l\phi$ values with those reported in the literature for Bi₂Te₃ grown by MBE [5], we observe a very similar value for α and a slightly lower coherence length for our material. For what concerns Sb₂Te₃, the obtained α and $l\phi$ values are still lower than those previously reported for Sb₂Te₃ grown by MBE [6]. As clearly shown in the insets of figures 1 and 2, ARPES measurements evidenced the typical Dirac-like band structure represented

by a linear dispersion relation in both Sb₂Te₃ and Bi₂Te₃ (Fermi level E_F is placed at 0 eV). ARPES showed that for both Sb₂Te₃ and Bi₂Te₃, the Dirac point is not exactly at E_F, cutting the valence band in Sb₂Te₃ and the conduction band in Bi₂Te₃, in accordance with Hall measurements. ARPES data were in nice agreement with the partial overlap between TSS and bulk conduction observed at low T in transport measurements. This is most likely the explanation why, for both materials, we did not reach the ideal $\alpha=1$ value expected for a pure TSS conduction. Our results showed that the TI properties of Bi₂Te₃ and Sb₂Te₃ grown by MOCVD on large areas Si substrates, are approaching those obtained by state-of-the-art methods, such as MBE, thus making a fundamental step toward potential technology transfer of TI. On the other hand, to enhance the TSS contribution in the MOCVD-grown TIs and, therefore, their functionalities, the Fermi level must be moved in the bulk band gap, closer to the Dirac point. [7]

[1] R. Cecchini, R. Mantovan,... and M. Longo, Phys. Status Solidi PRL, Vol 12(8), 1800155 (2018) [2] Y. L. Chen, J. G. Analytis,... and Z. X. Shen, Science 325, 178-181 (2009) [3] M. Rimoldi, R. Cecchini,... and R. Mantovan, RSC Advances, Vol 10(34), 19936-19942 (2020) [4] S. Hikami, A. I. Larkin, Y. Nagaoka, Prog. Theor. Phys., Vol 63(2), 707-710 (1980) [5] A. Roy, S. Guchhait, ... and S. K. Banerjee, Apl, Phys. Lett., 102(16) 163118, (2013) [6] Y. Takagaki, A. Giussani, & R. Calarco, J. Phys.: Condens. Matter 25(34), 345801 (2013) [7] C. Chang, P. Tang,... & Q. Xue, Phys. Rev. Lett. 115(13) 136801 (2015)



1) HLN fit of the magnetoconductance and ARPES analysis of a Sb₂Te₃ film.



2) HLN fit of the magnetoconductance and ARPES analysis of a Bi₂Te₃ film.

DC-02. Role of Ising Superconductivity in the Transition-State Enhancement of Magnon Spin to Quasiparticle Charge Conversion Efficiency.

K. Jeon¹, K. Cho¹, A. Chakraborty¹, J. Jeon¹, J. Yoon¹, H. Han¹ and S. Parkin¹

1. Max Planck Institute of Microstructure Physics, Halle / Saale, Germany

Superconductors (SCs) with Ising spin-orbit coupling (SOC), which internally pin electron spins to out-of-plane (OOP) directions such that OOP Cooper pairing can be stabilized against both orbital and paramagnetic effects of in-plane (IP) applied magnetic fields [1-3], have been of particular focus as a central ingredient for the topological protection of spin-triplet Cooper pairs and Majorana fermions [4,5]. Here, we experimentally examine how this so-called Ising superconductivity [1-3] affects the conversion efficiency of magnon spin to quasiparticle charge in a superconducting flake of 2-H NbSe₂, transferred on top of Y₃Fe₅O₁₂-based non-local magnon devices [6]. Comparing with a reference device composed of a spin-singlet superconducting Nb thin film [7], we show that the Y₃Fe₅O₁₂-induced IP exchange spin-splitting in the NbSe flake is hindered by its inherent OOP SO-field, which in turn limits the transition-state enhancement of spin-to-charge conversion efficiency. Our results may have implications for proximity-controlled equal-spin triplet pairing [8] via tuning of IP exchange and OOP SO fields in Ising SC/insulating ferromagnet bilayers.

[1] J. M. Lu, O. Zeliuk, I. Leermakers, N. F. Q. Yuan, U. Zeitler, K. T. Law, and J. T. Ye, *Science* 350, 1353 (2015). [2] Y. Saito *et al.*, *Nature Phys.* 12, 144 (2016). [3] X. Xi, Z. Wang, W. Zhao, J. Park, K. T. Law, H. Berger, L. Forro, J. Shan, and K. F. Mak, *Nat. Phys.* 12, 139 (2016). [4] S. M. Frolov, M. J. Manfra, and J. D. Sau, *Nat. Phys.* 16, 718 (2020). [5] Benjamin T. Zhou, Noah F. Q. Yuan, Hong-Liang Jiang, and K. T. Law, *Phys. Rev. B* 93, 180501(R) (2016). [6] A. V. Chumak, V. I. Vasyuchka, A. A. Serga, and B. Hillebrands, *Nat. Phys.* 11, 453 (2015). [7] K.-R. Jeon, J.-C. Jeon, X. Zhou, A. Migliorini, J. Yoon, and S. S. P. Parkin, *ACS Nano* 14, 15874 (2020). [8] J. Linder and J. W. A. Robinson, *Nat. Phys.* 11, 307 (2015).

DC-03. Room Temperature Nonlinear Hall Effect and Wireless RF Rectification in Weyl Semimetal TaIrTe₄.

D. Kumar¹, C. Hsu¹, R. Sharma¹, T. Chang^{2,3}, P. Yu⁴, J. Wang^{5,6}, G. Eda^{5,6}, G. Liang¹ and H. Yang¹

1. Department of Electrical and Computer Engineering, National University of Singapore, Singapore; 2. National Cheng Kung University, Tainan, Taiwan; 3. Center for Quantum Frontiers of Research & Technology (QFort), National Cheng Kung University, Tainan, Taiwan; 4. State Key Laboratory of Optoelectronic Materials and Technologies, School of Materials Science and Engineering, Sun Yat-Sen University, Guangzhou, China; 5. Centre for Advanced 2D Materials, National University of Singapore, Singapore; 6. Department of Physics, National University of Singapore, Singapore

In contrast to the Hall effect, the nonlinear Hall effect (NLHE) can produce a transverse voltage in zero magnetic field [1]. The NLHE is a second-order phenomenon, which exhibits two components; one is the voltage oscillating at twice the frequency 2ω of the driving alternating current and the other is a d.c. component that is generated due to the rectification effect. Therefore, the NLHE can be utilized in applications requiring frequency doubling or rectification such as energy harvesting, wireless communications and IR detectors [2,3]. However, it requires NLHE to be detected at room temperature. Despite of several studies of NLHE in topological materials and 2D materials, the room-temperature NLHE has not yet been achieved [4,5]. In this work, we report the room-temperature NLHE in a type-II Weyl semimetal TaIrTe₄, which hosts a robust NLHE due to broken inversion symmetry and large band overlapping at the Fermi level. The NLHE is present only when the electric field is applied along the axis of the mirror plane (a-axis of the crystal). We also observe a temperature-induced sign inversion of NLHE in TaIrTe₄. Our theoretical calculations suggest that the observed sign inversion is a result of temperature-induced shift in the chemical potential indicating a direct correlation of NLHE with the electronic structure at the Fermi surface. Finally, based on the observed room-temperature NLHE in TaIrTe₄ we demonstrate the wireless RF rectification with zero external bias and magnetic field. As shown in Fig. 1(b), an incident electric field along a-axis (E_a) generates a rectified voltage along b-axis (V_b), whereas, there is no rectification when the incident electric field is along b-axis (E_b) in consistent with the symmetry constraints of NLHE. This work opens a door to realizing room temperature applications based on the NLHE in Weyl semimetals.

[1] I. Sodemann and L. Fu, Phys. Rev. Lett., 115, p.216806 (2015) [2] H. Isobe, S.-Y. Xu, and L. Fu, Sci. Adv., 6, p.eaay2497 (2020) [3] G. Pacchioni, Nat. Rev. Mater., 4, p.514 (2019) [4] Q. Ma, S.-Y. Xu, H. Shen, Nature, 565, p.337 (2019) [5] K. Kang, T. Li, E. Sohn, Nat. Mater., 18, p.324 (2019)

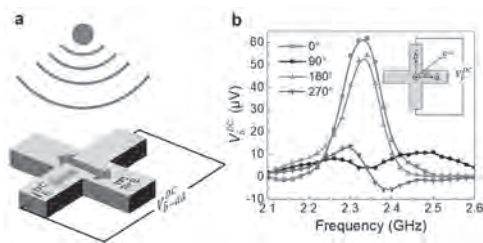


Fig. 1. (a) Schematic of the rectifier fabricated on TaIrTe₄. Patch antenna with a high directivity and gain of 3 dBi at ~2.4 GHz is used for electromagnetic radiation. The Hall bar device, utilizing the room-temperature NLHE in TaIrTe₄, rectifies the incident electric field along a-axis (E_a) and generates a d.c. along the transverse direction b-axis (I_b). (b) The rectified d.c. voltage measured along b-axis (V_b) as a function of frequency while aligning the incident electric field at four different angles ($\theta = 0^\circ, 90^\circ, 180^\circ, \text{ and } 270^\circ$) relative to a-axis as shown in the inset.

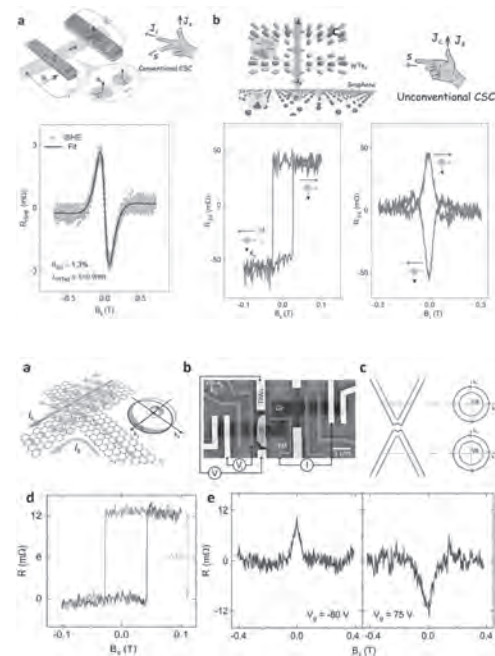
INVITED PAPER

DC-04. Charge Spin Conversion in Topological Materials and Heterostructures INVITED.S.P. Dash¹*1. Microtechnology and Nanoscience, Chalmers University of Technology, Gothenburg, Sweden*

An outstanding feature of topological quantum materials is their unique spin topology in the electronic band structures with novel charge to spin conversion effects. Here, I will present the novel charge to spin conversion phenomenon in topological insulators, Weyl semimetals, and its van der Waals heterostructures with graphene. The discovery of topological Weyl semimetals has revealed opportunities to realize several extraordinary physical phenomena in condensed matter physics. Weyl semimetals with strong spin orbit coupling, broken inversion symmetry, and novel spin textures are predicted to exhibit a charge to spin conversion effect that can efficiently convert the charge current to a spin current. We report a direct experimental observation of charge-spin conversion and its inverse effect in semimetal WTe₂ at room temperature as shown in Fig. 1 (Ref. 1). We also observe an evolution of the charge to spin conversion signals from WTe₂ and graphene hybrid device with a geometrical design (Ref. 2). The spin precession measurements of the signal at different gate voltages and ferromagnet magnetization show the robustness of the charge to spin conversion in WTe₂ at room temperature. These results can be useful for designing heterostructure devices and in the architectures of 2D spintronic circuits. We could also detect an unconventional charge to spin conversion in WTe₂, which is different from the conventional spin Hall and Rashba Edelstein effects (Ref. 3). Such a large and unconventional spin polarization can be possible in WTe₂ due to a reduced crystal symmetry combined with its large spin Berry curvature, spin orbit interaction with a novel spin texture in the Fermi states. A robust and practical method is demonstrated for electrical creation and detection of such a spin polarization in WTe₂ using both charge to spin conversion and its inverse phenomenon and utilized it for efficient spin injection and detection in the graphene channel up to room temperature. These findings open opportunities for utilizing Weyl materials WTe₂ as nonmagnetic spin sources in all electrical van der Waals spintronic circuits and high performance nonvolatile spintronic technologies. Unique electronic spin textures in topological insulators are promising for emerging spin-orbit driven memory and logic technologies. However, there are several challenges related to enhancing their performance, electrical gate tunability, interference from trivial bulk states, and heterostructure interfaces. We address some challenges by integrating 2D graphene with a 3D topological insulator (TI) in van der Waals heterostructures to take advantage of their remarkable spintronic properties and engineer proximity induced spin orbit phenomena (Ref. 4). In these heterostructures, we experimentally demonstrate a gate tunable spin galvanic effect (SGE) at room temperature, allowing for efficient conversion of a nonequilibrium spin polarization into a transverse charge current (Ref. 5). Systematic measurements of SGE in various device geometries via a spin switch, spin precession, and magnetization rotation experiments establish the robustness of spin to charge conversion in the graphene and TI heterostructures. Importantly, using a gate voltage, we reveal a strong electric field tunability of both amplitude and sign of the spin galvanic signal. These findings provide an efficient route for realizing all electrical and gate tunable spin orbit technology using TIs and graphene in heterostructures. Fig. 1. Charge to spin conversion in WTe₂ at room temperature. a. Device geometry and Hanle measurement of conventional charge to spin conversion in WTe₂ (Ref. 1). B. Measurement of unconventional charge to spin conversion in WTe₂. The measurement of spin valve and Hanle signals both in parallel and antiparallel configurations at room temperature show the unconventional nature of charge to spin conversion (Ref 3). Fig. 2. Spin galvanic effect in graphene and topological insulator heterostructure at room temperature. a. A schematic representing the spin galvanic effect, where spin polarized carriers diffuse in the graphene and TI heterostructure, acquire a transverse momentum and produce a charge current. b. A scanning electron microscopy picture of a graphene and TI

hybrid device and measurement scheme. c. Schematics of band structures of proximitized graphene develop Rashba spin split bands in the valence and conduction bands. d. The SGE signal R measured with the inplane magnetic field B_x. e. The SGE was detected via spin precession with the out of plane field B_z at different gate voltages in the valence and conduction band of proximitized graphene (Ref 5).

1. Observation of charge to spin conversion in Weyl semimetal at room temperature. B Zhao, D Khokhriakov, Y Zhang, H Fu, B Karpiak, AM Hoque, X Xu, Y Jiang, B Yan, SP Dash. *Phys. Rev. Res.* 2 (1), 013286 (2020).
2. Charge-spin conversion signal in WTe₂ van der Waals hybrid devices with a geometrical design. B. Zhao, A. Md. Hoque, D. Khokhriakov, B. Karpiak, S.P. Dash. *Appl. Phys. Lett.* 117, 242401 (2020).
3. Unconventional charge-to-spin conversion Weyl Semimetal WTe₂. B Zhao, B Karpiak, D Khokhriakov, A Johansson, AM Hoque, X Xu, Y Jiang, I Mertig, SP Dash. *Advanced Materials*, 2000818 (2020).
4. Tailoring emergent spin phenomena in Dirac material heterostructures. D Khokhriakov, A. W. Cummings, K Song, M Vila, B Karpiak, A Dankert, S Roche and SP. Dash. *Science Advances*, 4, 9, eaat9349 (2018).
5. Gate-tunable Spin-Galvanic Effect in Graphene - Topological insulator van der Waals Heterostructures at Room Temperature. D Khokhriakov, AM Hoque, B Karpiak, SP Dash. *Nature Communication* 11, 3657 (2020).



CONTRIBUTED PAPERS

DC-05. Strain-Tailored Magnetic Anisotropy and Dzyaloshinskii-Moriya Interaction at MoS₂/Fe₄N(111) Interface.

J. Jiang¹ and W. Mi¹

1. Department of Applied Physics, Tianjin University, Tianjin, China

Topological chiral spin textures, such as chiral domain walls and magnetic skyrmions, offer a unique opportunity to bring topology into room-temperature spintronic devices [1]. The stability of chiral spin textures is defined by the competition of Heisenberg exchange coupling, magnetic anisotropy and interfacial Dzyaloshinskii-Moriya interaction (DMI) [2], which can be engineered by the customized magnetic interfaces. Fe₄N has been considered as a promising material in spintronic devices thanks to the high saturation magnetization, high Curie temperature and high spin polarization [3]. However, low magnetocrystalline anisotropy seriously prevents it from being an ideal candidate for magnetic information storage. The traditional approach for perpendicular magnetic anisotropy (PMA) and interfacial DMI engineering is to use ferromagnet (FM)/oxide interfaces [4], multilayer structures comprising FM/nonmagnetic metal (NM) interfaces [5], or graphene/FM interfaces [6]. Recent theoretical prediction and experimental evidence have triggered interest in the hybrid interfaces between 3d FMs and two-dimensional transition-metal dichalcogenides (2D TMDs) [7,8]. The potentials of 2D TMDs in pushing magnetic information storage to the atomic thin limit, the ability to form hybrid interfaces without the need for lattice matching, as well as the attractive semiconducting electronic band structures, provide advantages for magnetization manipulation at atomic-scale interfaces. For 2D TMDs, The lack of inversion center in the crystal structure provides significant advantage, which is already used to obtain unconventional PMA at 2D TMDs/FM interfaces. In addition, 2D TMDs are very promising to enhance the DMI parameter at 2D TMDs/FM interfaces owing to their intrinsic spin-orbit coupling (SOC). In this work, the magnetic anisotropy and DMI of MoS₂/Fe₄N(111) interfaces are investigated via first-principles calculations. It is found that the large PMA and anticlockwise chiral DMI appear at the MoS₂/Fe₄N(111) interface. Strong variations of the PMA and DMI parameters are demonstrated by applying in-plane biaxial strain of the interfaces. The variations of PMA and DMI under strain can be attributed to the hybridization of in-plane and out-of-plane *d* orbitals in interfacial Fe atom layer, respectively. These results show the possibility of stabilizing chiral spin textures in the 2D TMDs/FM systems. Further, the method of strain controlling PMA and DMI at MoS₂/Fe₄N interface opens another pathway for the development of spintronic devices using 2D TMDs. This work is supported by National Natural Science Foundation of China (51871161 and 52071233).

[1] A. Fert, N. Reyren and V. Cros, *Nat. Rev. Mater.* 2, 17031 (2017). [2] A. Fert and P. M. Levy, *Phys. Rev. Lett.* 44, 1538 (1980). [3] W.B. Mi, Z.B. Guo, X.P. Feng, et al, *Acta Mater.* 61, 6387 (2013). [4] S. Ikeda, K. Miura, H. Yamamoto, et al, *Nat. Mater.* 9, 721 (2010). [5] H. Yang, A. Thiaville, S. Rohart, et al, *Phys. Rev. Lett.* 115, 267210 (2015). [6] H. Yang, G. Chen, A. A. C. Cotta, et al, *Nat. Mater.* 17, 605 (2018). [7] B. Peng, Q. Li, X. Liang, et al, *ACS Nano* 11, 12257 (2017). [8] A. Kumar, A. K. Chaurasiya, N. Chowdhury, et al, *Appl. Phys. Lett.* 116, 232405 (2020).

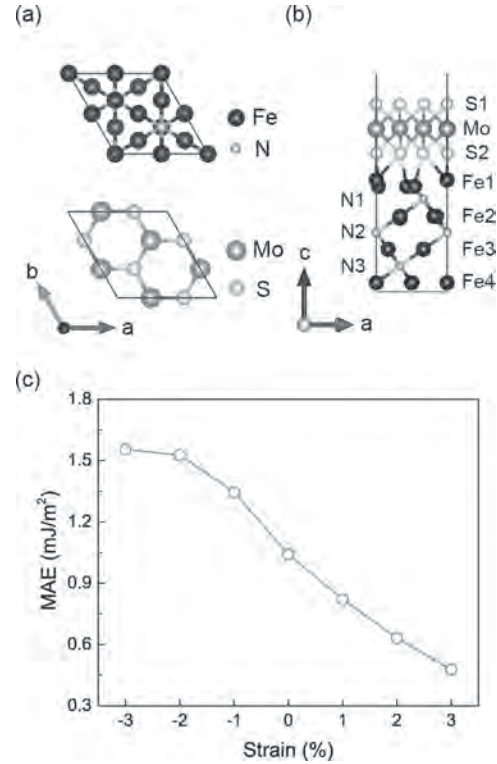


Figure 1. Top views of Fe₄N(111)-1×1 and MoS₂-√3×√3. (b) Side view of optimized MoS₂/Fe₄N interface. (a) Magnetic anisotropy energy as a function of strain at the MoS₂/Fe₄N interface

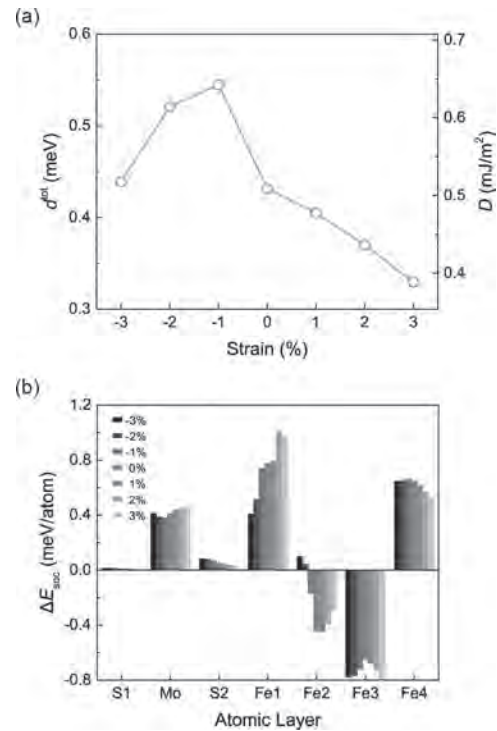


Figure 2. (a) Total DMI strength *d*^{tot} and micromagnetic DMI parameter *D* as a function of strain at the MoS₂/Fe₄N interface. (b) Layer resolved SOC energy differences associated DMI under strains

DC-06. Anomalous Transport in Magnetic Topological Materials.

Y. Sun¹, E. Liu^{1,2}, J. Noky¹, Q. Xu¹, L. Muechler³, K. Manna¹, S. Guin¹, J. Brink⁴ and C. Felser¹

1. *Max-Planck-Institut für Chemische Physik fester Stoffe, Dresden, Germany*; 2. *Chinese Academy of Sciences Institute of Physics, Beijing, China*; 3. *The Flatiron Institute, New York, NY, United States*; 4. *Leibniz-Institut für Festkörper- und Werkstofforschung Dresden eV, Dresden, Germany*

The interplay between symmetry breaking and topological electronic structure is crucial to design anomalous transport properties in materials. Materials with strong or quantum electromagnetic responses have an extensive impact on the development of data storage, information processing, energy conversion, etc. In magnetic materials, the anomalous transport of anomalous Hall effect, anomalous Nernst effect, and magneto-optical effect et al. can be understood from the Berry curvature of the electronic band structures. Two typical band structures of Weyl points and nodal line band structures host strong local Berry curvature. Since the Berry curvature is time-reversal symmetry odd, such strong Berry curvatures can lead to strongly enhanced anomalous transport signals. With this guiding principle, we studied the anomalous Hall effect in magnetic Weyl semimetal $\text{Co}_3\text{Sn}_2\text{S}_2$ [1-3] and magnetic nodal line semimetal in Heusler compound $\text{Co}_2\text{Mn}(\text{Ga}/\text{Al})$ [4]. With a mirror symmetry, the inverted band structure forms a nodal loop in the absence of spin-orbital coupling. This nodal line can be broken by spin-orbital coupling and a bandgap opens, which generates non-zero Berry curvature in the bandgap and forms a hot loop, see Figure 1a-b. Such strong Berry curvature in the magnetic system can lead to a strongly enhance or even quantized anomalous Hall effect. We applied this idea to real materials of magnetic Heusler compounds $\text{Co}_2\text{Mn}(\text{Ga}/\text{Al})$. Protected by mirror symmetries the band inversion between the bands with opposite mirror eigenvalue forms three gapless nodal lines in the $k_x=0$, $k_y=0$, and $k_z=0$ mirror planes, respectively. With spin-orbital coupling, the symmetry of the system is reduced. Taking magnetic along z , the mirror symmetries in $k_x=0$ and $k_y=0$ planes are broken, which leads to band anti-crossings with strong local Berry curvature locating in the opened bandgap around original nodal lines, see Figure 1d. Integral of the Berry curvature in the whole k -space gives a large intrinsic anomalous Hall conductivity reaching ~ 1500 to ~ 2000 S/cm [4]. Weyl points is another typical band structure and present as the Berry curvature monopole, and therefore naturally results in a strong anomalous Hall effect. In ideal models with only one pair of Weyl points locating at the Fermi level, the intrinsic anomalous Hall conductivity can be presented as the combination distance of Weyl points and the quantized anomalous Hall conductance. Inspired by these excellent relations, we studied the anomalous Hall effect in $\text{Co}_3\text{Sn}_2\text{S}_2$, and a new record of three-dimensional anomalous Hall angle ($\sim 20\%$) was observed, which offers the 1st three-dimensional material with both strong anomalous Hall conductivity and anomalous Hall angle [1]. It indeed shows as a Weyl semimetal from electronic band structure analysis. One crucial symmetry in $\text{Co}_3\text{Sn}_2\text{S}_2$ is the three mirror planes parallel to the c direction, which results in three pairs of nodal lines connected by a c_{3z} rotation symmetry. Because the magnetization is aligned along the z -direction, the mirror symmetries are broken by spin-orbital coupling. Meanwhile, one pair of Weyl points with opposite chirality remains along each of the former nodal lines, leading to the so large anomalous Hall effect. Though the strong anomalous Hall effect provides a promising signature for the existence of Weyl and nodal line band structure. Our transport work about $\text{Co}_3\text{Sn}_2\text{S}_2$ and $\text{Co}_2\text{MnGa}/\text{Al}$ inspired the direct band structure detection by ARPES and STM [5-7], and they are in turn became the 1st experimentally verified magnetic Weyl semimetal and nodal line semimetal, respectively. Applying temperature gradient instead of the electrical field, the Weyl points and nodal lines induced Berry curvature can also lead to strongly enhanced anomalous Nernst effect. From our theoretical calculations and experimental measurements, the anomalous Nernst conductivity can reach around 3 and 6 A/(m-K) in $\text{Co}_3\text{Sn}_2\text{S}_2$ [8] and Co_2MnGa [9], respectively, with Co_2MnGa keeping the record. Owing to the large anisotropy, $\text{Co}_3\text{Sn}_2\text{S}_2$ is, so far, the only material with a large anomalous Nernst effect with zero magnetic fields. In addition, very recently, a giant magneto-optical response was observed in $\text{Co}_3\text{Sn}_2\text{S}_2$ with the applied field from polarized light [10]. Very recently, a strong interest in antifer-

romagnets is rising. In an antiferromagnet without such kind of joint TO symmetry to reverse Berry curvature, it allows the existence of anomalous Hall effect, anomalous Nernst effect, magneto-optical responses, and special spin current, etc. The nonzero anomalous Hall effect in antiferromagnets was proposed as early as 2001 in distorted non-linear magnetic structures [11]. However, its experimental realization was not successful until 2015 [12-16]. This understanding can be further expanded into collinear antiferromagnets. Different from non-linear antiferromagnets, the collinear antiferromagnetic structure can be usually understood from two sublattices connected by translation of inversion operation. Therefore, there are mainly two ways to break the joint symmetry, to replace the magnetic atoms connected by the joint TO symmetry, or change the the nonmagnetic sites. With this understanding, we predicted the anomalous Hall and Nernst effect in anti-Heusler Weyl semimetal Ti_2MnAl [17-18].

[1] Enke Liu, Yan Sun, Nitesh Kumar, et al. *Nat. Phys.*, 14, 1125 (2018) [2] Qiunan Xu, Enke Liu, Wujun Shi, et al. *Phys. Rev. B* 97, 235416 (2018) [3] Lukas Muechler, Enke Liu, Jacob Gayles, et al. *Phys. Rev. B* 101, 115106 (2020) [4] Kaustuv Manna, Lukas Muechler, Ting-Hui Kao et al. *Phys. Rev. X* 8, 041045 (2018) [5] D. F. Liu, et al. *Science* 365, 1282 (2019) [6] Noam Morali, et al. *Science* 365, 1286 (2019) [7] Ilya Belopolski et al. *Science* 365, 1278 (2019) [8] Satya N. Guin, Praveen Vir, Yang Zhang et al. *Adv. Mater.* 31, 1806622 (2019) [9] M. Ikhlas, T. Tomita, and T. Koretsune, et al. *Nat. Phys.* 13, 1085 (2017) [10] Y. Okamura, S. Minami, Y. Kato et al. *Nat. Comm.* 11, 4619 (2020) [11] R. Shindou, and N. Nagaosa, *Phys. Rev. Lett.* 87, 116801 (2001) [12] H. Chen, H., Q. Niu, and A. H. MacDonald, A., *Phys. Rev. Lett.* 112, 017205 (2014) [13] J. Kübler, and C. Felser, *Europhys. Lett.* 108, 67001 (2014) [14] S. Nakatsuji, N. Kiyohara, and T. Higo, *Nature* 527, 212–215 (2015) [15] A. Nayak, et al. *Sci. Adv.* 2, e1501870 (2016). [16] Z. Q. Liu¹, H. Chen, J. M. Wang, et al. *Nat. Elec.* 1, 172 (2018) [17] Wujun Shi, Lukas Muechler, Kaustuv Manna, et al. *Phys. Rev. B* 97, 060406(R) (2018) [18] Jonathan Noky, Jacob Gayles, Claudia Felser, and Yan Sun, *Phys. Rev. B* 97, 220405(R) (2018)

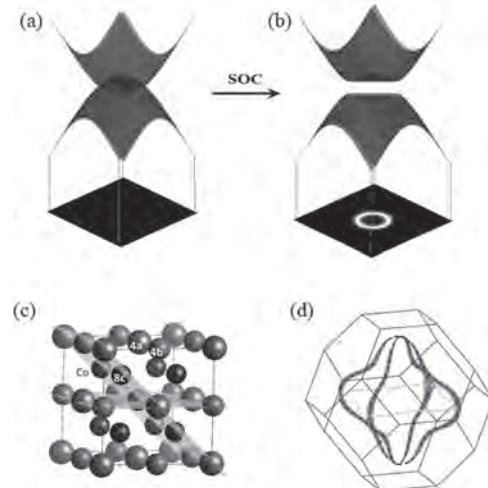


Figure 1 (a-b) Nodal line band structure generated and non-zero Berry curvature hot ring located in the bandgap. (c-d) Crystal structure and Berry curvature distribution for Co_2MnGa . [Ref.4]

DC-07. Nonlinear Anomalous Hall Effect in van der Waals Ferromagnet.

J. Zhou¹ and J. Charlier¹

1. Institute of Condensed Matter and Nanosciences, Universite catholique de Louvain, Louvain-la-Neuve, Belgium

The interplay of symmetry and magnetism can determine the tensors of intrinsic anomalous Hall effect (AHE) [1]. In the past decades, AHE has been extensively researched in cubic crystals such as Fe ferromagnet [2], in which AHE σ_{xy} exists only when the magnetization has a component along the direction of $\mathbf{J}_x \times \mathbf{E}_y$, where \mathbf{J}_x is the Hall current and \mathbf{E}_y is the electric field. The van der Waals ferromagnets provide opportunities to break this strict rule thanks to the low-symmetry structure. Here, we employed the VSe₂ ferromagnet to study the tensor of intrinsic AHE with varying magnetization in different planes. The VSe₂ monolayer, with the space group P-3m1 (No.164), can exhibit in-plane magnetic anisotropy and ferromagnetism at room temperature [3]. Using *ab-initio* calculations, we have verified that in the VSe₂ monolayer, the AHE σ_{xy} can be preserved with the absence of z-direction magnetization, and present a period of $2\pi/3$. Moreover, for any plane, σ_{xy} exhibit nonlinear anisotropy with respect to magnetization, and xz-plane magnetization σ_{xy} slightly different from the yz-plane one. The symmetry analysis produces the AHE formulae, which fit well with *ab-initio* data due to the higher-order terms. Our findings pave a new route to the emerging field of nonlinear spintronic phenomena.

[1] R. R. Birss, Symmetry and Magnetism, North-Holland (1964) [2] Y. Yao *et al.*, *Phys. Rev. Lett.* Vol. 92, p. 037204 (2004) [3] M. Bonilla *et al.*, *Nat. Nanotechnol.* Vol. 13, p. 289 (2018)

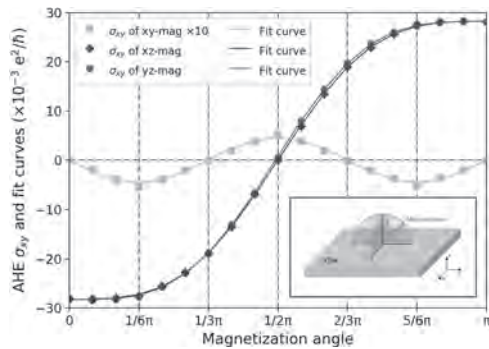


Fig.1 Evolution of the AHE σ_{xy} when magnetization varies in different planes. Inset: Diagram of the variation of magnetization.

DC-08. Tunable Electronic and Magnetic Properties of Two-Dimensional Janus Magnetic Materials.

R. Li¹, H. Bai¹ and W. Mi¹

1. Department of Applied Physics, Tianjin University, Tianjin, China

Two-dimensional magnetic materials have attracted much attention since they provide new opportunities for the development of multifunctional devices.¹⁻² Half-metal materials with 100% spin polarization are highly desired in spin-based devices. Because they are not only the ideal electrode materials for the magnetic tunneling junctions (MTJ),³ but also can realize high efficient spin injection to the semiconductors.⁴ Janus magnetic materials have broken the time and space symmetries simultaneously, which may show novel physical properties comparing with their counterparts.⁵⁻⁶ However, the electronic and magnetic properties of Janus half-metal materials are still unclear, so we selected the half-metal, 1T-FeCl₂ monolayer,⁷⁻⁸ as the prototype to study the electronic and magnetic properties of its Janus structures, and the strains are applied to tunable their properties in this work. The FeXY ($X, Y = \text{Cl, Br and I}$) monolayers are half-metals and their ferromagnetism stem from the super-exchange interaction according to the GKA theory. The Curie temperature (T_c) of Janus FeClBr, FeClI and FeBrI are 28, 21 and 29 K, respectively (Figure 1 (a)). In the meantime, the T_c under biaxial strains is investigated and the T_c are 54, 42 and 61 K at $e = -6\%$, increasing about 100% comparing with the unstrained FeXY monolayer. Besides, the MAE of FeXY strongly relies on the angle of magnetization and increases considerably under compressive strain. The MAE of FeBrI as an example is shown in Fig. 1 (c), the unstrained FeBrI is IMA, but translating from IMA to PMA when $e < 0$ and $e > 2\%$, this will help to increase the density of storage. And the absolute value of MAE enhances one order magnitude when the $e = -6\%$. It is demonstrated that the compressive strains effectively enhance the ferromagnetism of FeXY. The atom-resolved MAE shows that the main contributions of MAE come from Fe and I atoms. Additionally, the MAE of I atom translates from IMA to PAM when $e < -2\%$ which induce the translation of total MAE. To further explicate the change of MAE, the orbital-resolved MAE of FeBrI is calculated and the results plotted in Figure 2. The I atom is IMA at $e = 0\%$, because the matrix element differences between p_x and p_y orbitals are negative and the absolute value is larger than the p_y and p_z orbitals. However, the p_x and p_y orbitals hybridization translate to the positive at $e = -6\%$, which make the magnetic anisotropy translate from IMA to PMA. Our studies provide an example of the 2D Janus half-metal materials and enrich the 2D magnetic material library. This work is supported by National Natural Science Foundation of China (51871161 and 52071233).

[1] B. Huang, G. Clark, E. N. Moratalla, et al, Nature, 546, 270-273 (2017). [2] C. Gong, L. Li, Z. Li, et al, Nature, 546, 265-269 (2017). [3] K. I. Kobayashi, T. Kimura, H. Sawada, et al, Nature, 395, 677-680 (1998). [4] S. Sugahara and M. Tanaka, Appl. Phys. Lett., 84, 2307-2309 (2004). [5] Q. F. Yao, J. Cai, W. Y. Tong, S. J. et al, Phys. Rev. B, 95, 165401 (2017). [6] A. Y. Lu, H. Zhu, J. Xiao, et al, Nat. Nanotechnol., 12, 744-749, (2017). [7] E. Torun, H. Sahin, S. K. Singh et al, Appl. Phys. Lett., 106, 192404 (2015). [8] M. Ashton, D. Gluhovic, S. B. Sinnott, et al, Nano Lett., 17, 5251-5257 (2017)

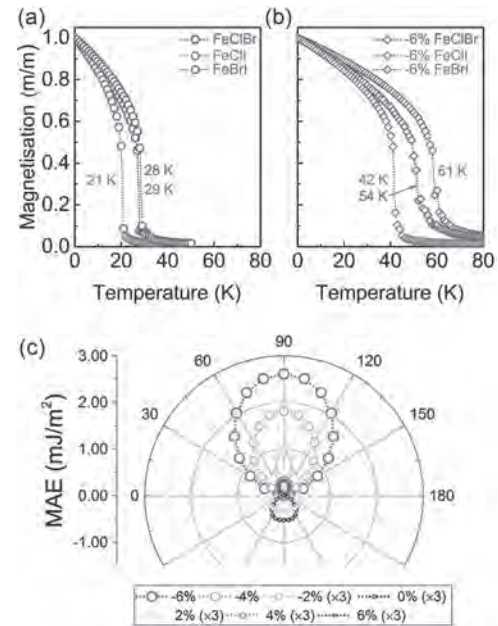


Figure 1. The Curie temperature of Janus FeXY ($X, Y = \text{Cl, Br and I}$) monolayers as a function of temperature at $e=0$ (a) and -6% (b). Angular dependence MAE of FeBrI monolayer under different strain (c)

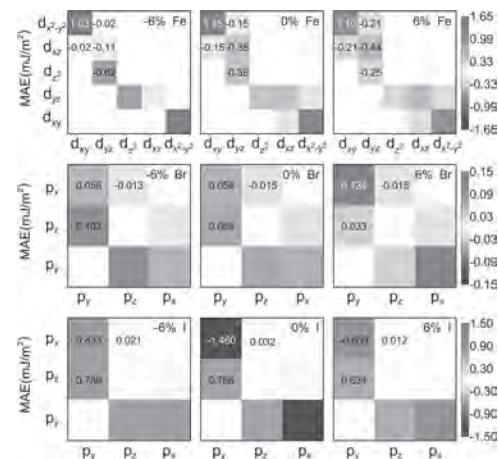


Figure 2. Orbital-resolved MAE of FeBrI monolayer under $e = -6\%$, 0% and 6% .

DC-09. Correlation of Magnetic Properties of van der Waals Itinerant Magnet Fe₃GeTe₂ Using Magnetometry and Raman Spectroscopy.

D. Sagkovi^{1,2}, M. Cubukcu^{1,3}, T. Vincent^{1,4}, S. Khan^{2,3}, H. Kurebayashi^{2,3} and O. Kazakova¹

1. National Physical Laboratory, Teddington, United Kingdom; 2. London Centre for Nanotechnology, London, United Kingdom; 3. University College London, London, United Kingdom; 4. Royal Holloway University of London, Egham, United Kingdom

Two-dimensional magnetic (2DM) van der Waals (vdW) materials have attracted significant attention over the last few years, after the first experimental demonstration of ferromagnetism persisting down to the monolayer limit [1]. Since then, new vdW 2DM materials emerge frequently, covering a broad spectrum of diverse properties also found in other 3D counterpart systems – ferro/antiferromagnetism (FM/AFM), metallic/semiconducting behaviour and many non-trivial electronic phases. Out of this expanding pool of 2DM, one category that stands out is FMs with strong out-of-plane anisotropy, which present superior qualities desirable for magnetic random-access memory and other spintronic applications. Fe₃GeTe₂ (FGT) is a prominent member of this family that features a lot of interesting properties, such as a relatively high, thickness-dependent T_c (150 K – 220 K) that can be tuned to room temperature by doping, high spin-orbit coupling originating from a strongly correlated electronic system, application in spin valves, topological phases and Kondo behaviour, amongst others [2]. FGT is a quasi-2D itinerant ferromagnetic metal, and its structure consists of Fe₃Ge layers sandwiched by single-atom layers of Te. Among the FGT layers, Te atoms are bonded together by vdW forces, allowing for exfoliation of the material in ultra-thin flakes with the scotch-tape exfoliation technique. Despite the considerable efforts that have already taken place in order to determine the underlying micromagnetic structure and behaviour of FGT, its highly anisotropic and non-trivial nature has not yet allowed for a consensus in the relevant scientific community. Our work therefore aims to shed light for the case of quasi-bulk FGT, by combining magnetic susceptibility measurements and Raman spectroscopy [3]. Our magnetometry study picks up the main point of controversy around FGT, which is a kink found below the Curie temperature, roughly at 150 K. This possible magnetic transition has been shown to represent a FM to AFM interlayer coupling between the vdW bonded layers [5], however it has been argued that this can be due to different reasons, such as domain wall pinning effects. A temperature dependent Raman study can provide further insight by indirectly detecting a phase change – electronic reconfiguration leads to a qualitative change in the Raman signal, and that is what our results suggest (Fig. 1). The separation between the Raman peaks is a possible sign of this magnetic transition, a signature that often accompanies other 2D material related properties and transitions however rarely related to magnetic properties. Additionally, it has been shown that variations in the sample history, i.e. temperature and applied magnetic field (as well as number of atomic layers), result in different magnetic phases, such as labyrinth and stripe domains, bubble-like lattice and possibly skyrmion phases [4]. Our systematic magnetometry study provides insight regarding the formation of these different magnetic states, following three different magnetization protocols, namely: zero-field cooling (ZFC), field cooling (FC) and field warming (FW) methods (Fig. 2). The magnetometry results are correlated to Raman responses, examined up to 2nd order. Particular interest arises from a prominent feature (a 2nd kink below 150 K) that has not been observed before – suggesting the existence of possibly another magnetic phase. Our results advance the understanding of the underlying mechanisms of Fe₃GeTe₂, an important 2DM that is often incorporated in spintronic vdW heterostructures and devices.

C. Gong, L. Li and X. Zhang, Nature, Vol 546, p. 265-269 (2017) Y. Deng, Y. Yu and Y. Zhang, Nature, Vol 563, p. 94-99 (2018) L. Du, J. Tang and Z. Sun, Adv. Funct. Mat., Vol 29 (2019) H. Wang, C. Wang and J. Li, APL, Vol 116 (2020) J. Yi, H. Zhuang and Z. Gai, 2D Materials, Vol 4 (2020)

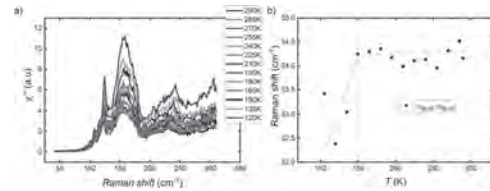


Fig. 1: Temperature-dependent Raman response: a) 2nd order Raman susceptibility. b) Temperature dependent separation of the peaks @150 and @120 cm⁻¹

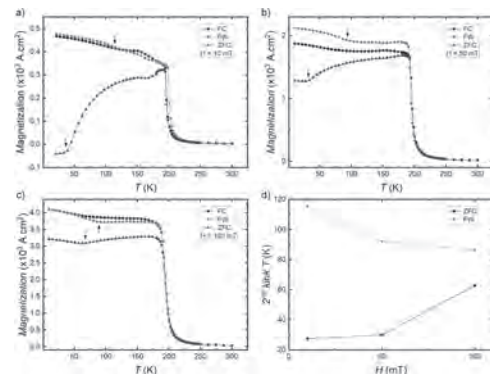


Fig. 2: Magnetization measurements of quasi-bulk FGT: FC, FW and ZFC protocols obtained under different applied magnetic fields. a) H_{appl.} = 10 mT, b) H_{appl.} = 50 mT, c) H_{appl.} = 100 mT, d) a magnetometry feature (kink) position in temperature under varied applied H field (arrows in a, b, c)

DC-10. Direct Observation of Tunable Magnetic Domains in Noncentrosymmetric Ferromagnetic Weyl Semimetal CeAlSi.

B. Xu¹, J.D. Franklin¹, A. Jayacody¹, H. Yang², F. Tafti² and I. Sochnikov¹
 1. Physics, University of Connecticut, Storrs, CT, United States;
 2. Physics, Boston College, Chestnut Hill, MA, United States

Magnetic domain walls (DWs) in a Weyl semimetal can induce localized charges and be treated as local axial gauge fields.[1] Dynamics and textures of magnetic DWs may largely alter the electronic behaviors in a Weyl semimetal system.[2] In this work, we imaged the spontaneous magnetization and magnetic susceptibility of a ferromagnetic (FM) Weyl semimetal candidate CeAlSi using scanning SQUID microscopy [3], [4]. We observed the ferromagnetic DWs lined-up with [100] direction (or other degenerate directions) and the coexistence of stable and metastable domain phases, which arise likely due to the magnetoelastic and magnetostriction effects and are highly tunable with small strains. The temperature evolution of the FM domains shows that stable domains shrink while metastable domains grow and eventually collapse to narrow domain-wall-like features as temperature rises towards $T_c \sim 8.3\text{K}$ (fig.1) We applied in-plane external field as the CeAlSi sample was cooled down to $\sim 8\text{K}$, showing that the pattern of FM domains is strongly correlated with both the amplitude and the orientation of the external field. The area of stable domains increases with field (fig.2) and reaches maximum when the field is parallel to the easy axis of the CeAlSi crystal. Our results suggest these heterogeneous phases can be manipulated and therefore provide a practical way to study the interplay between magnetism and electronic properties in Weyl system.

[1] Y. Araki, A. Yoshida, and K. Nomura, *Phys Rev B*, vol. 98, no. 4, p. 045302, Jul. 2018 [2] J. D. Hannukainen, Y. Ferreira, A. Cortijo, and J. H. Bardarson, *Phys. Rev. B*, vol. 102, no. 24, p. 241401, Dec. 2020 [3] H.-Y. Yang *et al.*, *ArXiv200607943 Cond-Mat*, Jun. 2020 [4] B. Xu, J. Franklin, H.-Y. Yang, F. Tafti, and I. Sochnikov, *ArXiv201106168 Cond-Mat*, Nov. 2020

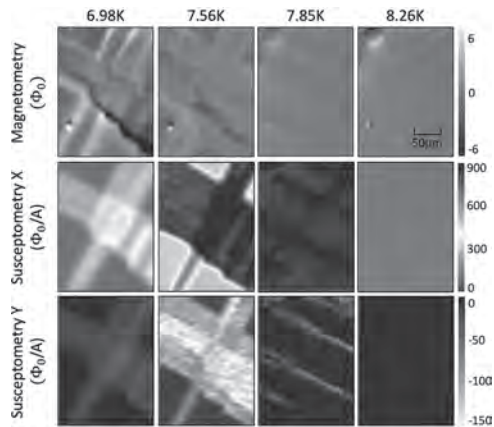


Figure 1. The temperature evolution of the magnetic domains in the CeAlSi crystal. Upper row: dc magnetizations in flux units. Middle and lower rows are the in-phase component and the out-of-phase component of the ac susceptibility. Dark green and dark marine areas in the in-phase and out-of-phase components, respectively, are stable in-plane domains. Light green and light marine areas in the in-phase and out-of-phase components, respectively, are metastable domains. The stable domains shrink, while the metastable grow towards the transition, and eventually collapse to narrow features reminiscent of the domain boundaries roughly lined up with the crystallographic $\langle 1\ 0\ 0 \rangle$ direction. The dc magnetization contrast reduces towards the transition, while the amplitude of the in-phase and out-of-phase signals grow. The metastable regions show enhanced signals. Immediately above the transition temperature, all signals collapse to small values, and no domains persist.

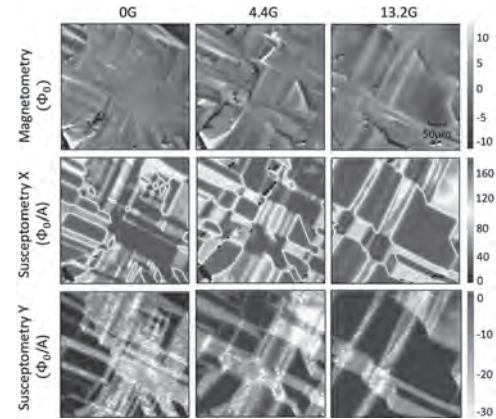


Figure 2. The growth of domains with magnetic field in a CeAlSi crystal that was as-cooled through the transition at $\sim 8\text{K}$. The stable and metastable domains in the in-phase and out-of-phase components are represented the same way as in fig 1.

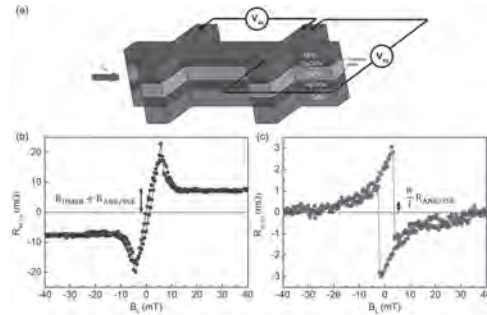
DC-11. Unidirectional Spin-Hall Magnetoresistance in HgTe Topological Insulator - Ferromagnet Heterostructures.

C. Grezes¹, J. Papin², M. Cosset-Cheneau¹, P. Noël^{1,3}, Y. Fu¹, A. Brenac¹, P. Ballet⁴, T. Meunier², J. Attané¹ and L. Vila¹

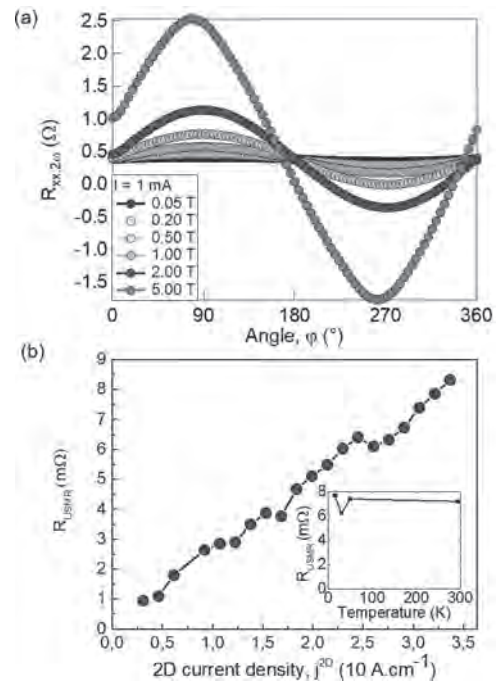
1. CEA Grenoble, SPINtronique et Technologie des Composants, Grenoble, France; 2. Institut NEEL, Grenoble, France; 3. ETH Zurich, Zurich, Switzerland; 4. CEA Grenoble, LETI, Grenoble, France

The surface states of three-dimensional topological insulators (TIs) exhibit a large spin-orbit coupling leading to spin-momentum locking, the electron spin being locked perpendicularly to the electron momentum. This property is promising for spintronic applications, as the Rashba Edelstein effect can create, from a charge current at the conducting surface of a TI, a spin accumulation. Reciprocally, the injection of a spin current creates a net charge current by inverse Edelstein effect. Recently, we have demonstrated a large spin-to-charge conversion efficiency in strained mercury telluride (HgTe) TI at room temperature [1], with conversion rates one order of magnitude higher compared to conventional materials. Achieving the mirror charge-to-spin conversion would be of great interest for memory and logic applications, with two effects in particular that could be exploited. First, the spin-orbit torques (SOT), in which the spin accumulation induces a torque on the magnetization [2], which can be used as a switching mechanism in a magnetoresistive random access memories (SOT-MRAM). Second, the unidirectional spin-hall magnetoresistance (USMR), in which depending on the relative directions between the spin accumulation and the magnetization, the system holds high or low resistance state [3]. While conventional SOT devices suffer from a three-terminal geometry, this USMR effect has potential to be used as a new reading mechanism for developing a novel type of SOT-MRAM with a two-terminal geometry and smaller footprint. Here we report unidirectional spin-Hall magnetoresistance in HgTe topological insulator-ferromagnet heterostructures up to room temperature. Results are shown from a 3 μm wide Hall bar device made of a NiFe ferromagnetic layer with in-plane magnetization on top of a HgTe layer with a thin HgCdTe insertion to protect the TI surface state (Figure 1). Harmonic measurements of the longitudinal and Hall resistance are performed to investigate both USMR and spin-orbit torque effects. A change in the nonlinear magnetoresistance upon switching the magnetization from +y to -y direction is demonstrated (Figure 1b), corresponding to the signature of the USMR driven by Edelstein effect. Anomalous Nernst and spin Seebeck effects are measured from the nonlinear magnetoresistance in the x direction, showing negligible contributions. The results show USMR efficiency of 2.6 ppm A cm⁻¹ at 10K, three times higher than in ferromagnet-normal bilayer and on the same order of low temperature Bismuth Selenide TI. USMR signal is seen to increase linearly with the current density, confirming the unidirectional nature of USMR in HgTe (Figure 2). Experimental results at room temperature further show comparable USMR efficiency, bringing HgTe compatible for room temperature applications. Ongoing material engineering is discussed to improve further the USMR efficiency on HgTe system, the high efficiency observed in this first demonstration constituting an important step towards SOT-MRAM with two-terminal geometry at room temperature.

[1] P. Noel et al., Phys. Rev. Lett. 120, 167201 (2018). [2] I. M. Miron et al., Nature 476, 189–193 (2011). [3] C. O. Avci et al., Nature Physics 11, 570–575 (2015).



Sample layout and nonlinear magnetoresistance (a) Structure of the sample and measurement geometry. (b) Second harmonic longitudinal resistance as a function of the magnetic field along the y direction. (c) Second harmonic Hall resistance as a function of the magnetic field along the x direction. All measurement were performed with a current density of $j^{2D} = 3.3 \text{ A cm}^{-1}$ at a temperature of 10K.



XY angular dependence and extraction of USMR efficiency. (a) Angular dependence of the second harmonic longitudinal resistance when the magnetic field is rotated in the xy plane. (b) Current dependence of the USMR resistance at 10K. Inset shows USMR as a function of the temperature.

DC-12. Evolution of the THz Emission Signal as a Function of the Interface Quality Between Fe and Large-Area Topological Insulator Sb_2Te_3 on Si.

L. Locatelli^{1,2}, G. Bierhance³, O. Gueckstock³, A. Kumar¹, E. Longo^{1,2}, M. Alia¹, R. Cecchini¹, M. Longo¹, T. Kampfrath³ and R. Mantovan¹

1. IMM Unit of Agrate Brianza, Consiglio Nazionale delle Ricerche, Agrate Brianza (MB), Italy; 2. Material Science, Università degli Studi di Milano-Bicocca, Milano, Italy; 3. Physical Chemistry, Fritz-Haber-Institut der Max-Planck-Gesellschaft, Berlin, Germany

Topological insulators (TI) are gaining attention from a technological point of view due to their foreseen highly efficient capability to control adjacent magnetic media through spin to charge (S2C) conversion [1]. However, in order to make a decisive step toward technology transfer, it is necessary to develop fabrication methods suitable to guarantee their large-scale production. We developed a Metal Organic Chemical Vapour Deposition technique (MOCVD) process to grow epitaxial-quality antimony telluride (Sb_2Te_3) topological insulator (TI) on 4" Si(111) substrates [2]. When compared to granular- Sb_2Te_3 grown on SiO_2 [3], the epitaxial- Sb_2Te_3 on top of Si(111), shows improved magnetoconductance (MC) performances, especially upon proper annealing, as described in [2]. Figure 1 displays the MC signal emerging from the epitaxial (annealed) Sb_2Te_3 on Si(111), at 5.5 K. Clearly, the MC displays a non-parabolic shape, which we attribute to weak antilocalization. In the framework of the Hikami-Larkin-Nagaoka (HLN) model [3], we extract the parameters α (being connected to the number of conducting channels), and coherence length (l_ϕ), as depicted in the inset of Figure 1. The values of α and l_ϕ for the annealed sample are 0.3 and 55 nm, respectively, thus indicating a 2D-type of conduction due to the existence of topologically-protected surface states (TSS). The as-deposited sample shows a much smaller MC signal, and the extracted α and l_ϕ are comparable with those previously obtained for granular- Sb_2Te_3 on SiO_2 [3]. Following the MC studies, both the as-deposited and epitaxial Sb_2Te_3 samples have been covered with evaporated ^{57}Fe (5nm) and subsequently *in situ* capped with Au(5nm) to prevent Fe oxidation. To investigate the potential role of the Sb_2Te_3 preparation on S2C efficiency, terahertz (THz) emission spectroscopy has been conducted on both samples. The Fe layer is saturated by an external in-plane magnetic field. The multilayer system is excited using femtosecond laser pulses, which launch a longitudinal spin-polarized electron current. Through S2C conversion, the spin current is converted into a transverse charge current concomitantly ejecting a THz pulse which we record in the time domain via electro-optic (EO) detection (see Figure 2) [4,5]. Our results show a considerable impact of Sb_2Te_3 annealing on the THz signal amplitude suggesting a S2C conversion contribution from the Fe/ Sb_2Te_3 interface. Conversion-electron Mössbauer spectroscopy (CEMS) has been conducted on the same samples studied by THz emission spectroscopy. The Fe/as-deposited- Sb_2Te_3 spectrum resembles those previously reported for the Fe/granular- Sb_2Te_3 system [6], and CEMS reports that a large fraction of Fe atoms ($\leq 60\%$) coordinates paramagnetically with Te in a "FeTe" type of bonding. Surprisingly, this fraction collapses to $\leq 10\%$ at the interface with annealed (epitaxial) Sb_2Te_3 , with a CEM-spectrum mostly dominated by pure Fe, reflecting a remarkable improvement of the chemical-structural-magnetic quality of the Fe/annealed- Sb_2Te_3 interface. We propose the suppression of the "FeTe"-type of bonding at the interface as being the main source for the enhancement of the S2C conversion as observed by THz emission spectroscopy. To conclude, the annealed epitaxial Sb_2Te_3 develops TSS-connected conduction as shown by MC (Figure 1), which turns out in an enhancement of the THz signal in Fe/ Sb_2Te_3 heterostructures as due to S2C conversion (Figure 2). By means of CEMS, the evolution of the S2C efficiency with the Sb_2Te_3 annealing is attributed to a remarkable suppression of intermixing occurring at the Fe/ Sb_2Te_3 interface, when Fe is deposited in direct contact on top of annealed and epitaxial Sb_2Te_3 .

[1] A. Soumyanarayanan, N. Reyren, A. Fert *et al.*, Nature 539, 509 (2016)
 [2] M. Rimoldi, R. Cecchini, C. Wiemer *et al.*, RSC Advances 10(34), 19936 (2020) [3] R. Cecchini, R. Mantovan, C. Wiemer *et al.*, Phys. Status Solidi RRL 12, 1800155 (2018) [4] T. Seifert, S. Jaiswal, U. Martens *et al.*, Nat. Photonics, 10, 483 (2016) [5] T. Seifert, S. Jaiswal, J. Barker *et al.*, Nat

Commun 9, 2899 (2018). [6] E. Longo, C. Wiemer, R. Cecchini *et al.*, Adv. Mater. Interfaces 7, 2000 (2020)

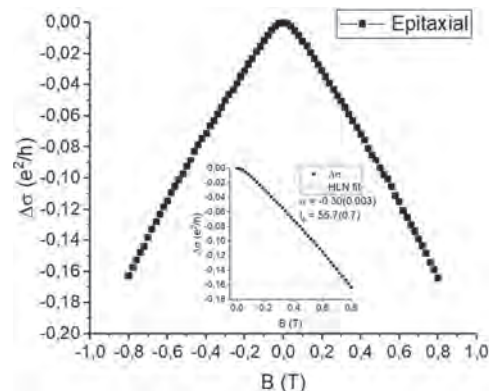


Fig.1. Magnetoconductance signal of the epitaxial (annealed) Sb_2Te_3 on Si(111), at 5.5 K. The inset shows the fit in the framework of the Hikami-Larkin-Nagaoka model, from which the α and l_ϕ parameters are extracted.

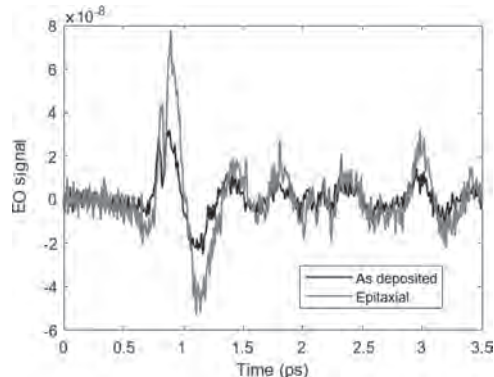


Fig.2. THz emission signals of the Au/Fe/as-deposited- Sb_2Te_3 (black curve) and Au/Fe/epitaxial- Sb_2Te_3 (red curve) heterostructures.

**DC-13. 2D Magnetic Crystals: Can we Probe Magnetic Order?
Theoretical Study of vdW Layered MnPS₃ Crystals Exhibiting Large
Exciton Binding Energy.**

M. Birowska¹, P.E. Faria Junior² and J. Fabian²

1. University of Warsaw, Uniwersytet Warszawski, Warszawa, PL,
academic, Warsaw, Poland; 2. Universitat Regensburg, Regensburg,
Germany

Atomically thin, magnetic materials have gained a lot of attention since 2017, when the first 2D ferromagnet was reported [1]. This breakthrough has triggered research on 2D magnetic materials [2]. They are not only important from a fundamental point of view -to understand the theory of magnetism in reduced dimensions-, but also for technological applications. However, probing the magnetic order of the 2D systems by conventional magnetic experimental setups is very challenging. On the other hand, it is well known, that even in the single layer limit, semiconducting two-dimensional materials strongly absorb light. Therefore, optical spectroscopy is a good method for their characterization. Here we present the results of the comprehensive theoretical investigation of the binding energy of the 2D magnetic crystal MnPS₃ based on the density functional theory and versatile formalism of the Bethe-Salpeter equation. The MnPS₃ is one important example from the large family of transition metal phosphorus trisulfide (MPS₃) [3]. We demonstrate that the large binding energy of the exciton equal to more than 1 eV and obtained for monolayer of MnPS₃ [4], is two times greater than in the case of transition metal dichalcogenides. We also highlight the role of the magnetic orderings in electronic and optical properties. In particular, the strong impact of the magnetic ordering on the binding energy of excitons in the monolayer limit is demonstrated, as well as its substantial influence on effective mass of the carriers. In addition, we have shown that the magnetic state of the monolayer samples is sensitive to the polarization of light. Aforementioned results indicate the possibility of indirect probing of magnetic properties via optical or transport measurements. The study was accomplished thanks to the funds allotted by the National Science Centre, Poland within the framework of the research project ‘SONATA12’ no. UMO-2016/23/D/ST3/03446. Financial support from the Deutsche Forschungsgemeinschaft (DFG, German Research Foundation) under Project-ID 314695032 (SFB1277) is acknowledged by P.E.F.J. and J.F. and under Project-ID 317551441 by J.K. Access to computing facilities of TU Dresden ZIH for the project ‘TransPheMat’, PL-Grid Polish Infrastructure for Supporting Computational Science in the European Research Space, and of the Interdisciplinary Center of Modeling (ICM), University of Warsaw are gratefully acknowledged.

[1] B. Huan *et al.*, Nature, Vol. 546, p. 270-273 (2017) [2] M. Gibertini *et al.*, Nature Nanotechnology, Vol. 14, p. 408 (2019). [3] R. Brec, Solid State Ionics vol. 22, p. 3-30 (1986). [4] M. Birowska, Paulo E. Faria Junior, J. Fabian, J. Kunstmann, <http://arxiv.org/abs/2009.05030>.

Session DD

MAGNETISM IN CURVILINEAR AND CYLINDRICAL GEOMETRIES

Oksana Chubykalo-Fesenko, Chair
Instituto de Ciencia de Materiales de Madrid, CSIC, Madrid, Spain

INVITED PAPER**DD-01. Curvilinear Magnetism INVITED.***D.D. Sheka¹**1. Faculty of Radiophysics, Electronics and Computer Systems, Taras Shevchenko National University of Kyiv, Kyiv, Ukraine*

Curvilinear magnetism is a rapidly developing research area of modern magnetism which deals with curved magnetic wires and curved magnetic films [1]. By extending planar geometries into three dimensional space, there appear new, sometimes, unexpected physical effects, stemming from mutual interplay between the geometrical properties of the underlying substrate and the magnetic order parameter. By tailoring curvature and topology of the conventional magnetic materials there appears a possibility to control material response leading to modification or even launching new functionalities [2, 3]. This is granted by complementary expertise and advances of fundamental researched, materials sciences and technologies. This talk focuses on the peculiarities emerging from geometrically curved magnetic objects, including 3D bent and twisted curved wires and films. The curvilinear geometry manifests itself in emergent anisotropy and chiral interactions. These curvature-induced interactions can be local stemming from the exchange energy [4, 5], but also can be nonlocal due to magnetostatics [6]. As a consequence, family of novel curvature-driven effects emerge, which include magnetochiral effects and topological patterning, resulting in theoretically predicted unlimited domain wall velocities, chirality symmetry breaking etc. Current and future challenges of the curvilinear magnetism will be discussed.

[1] E. Y. Vedmedenko, R. K. Kawakami, D. D. Sheka et al, *JPhysD*, vol. 53, p.453001 (2020) [2] R. Streubel, P. Fischer, F. Kronast et al, *JphysD*, vol. 49, p.363001 (2016) [3] P. Fischer P, D. Sanz-Hernández, R. Streubel et al, *APL Materials*, vol. 8, p. 010701 (2020) [4] Y. Gaididei, V. P. Kravchuk and D. D. Sheka, *PRL*, vol. 112, p. 257203 (2014) [5] D. D. Sheka, V. P. Kravchuk and Y. Gaididei, *JPhysA*, vol. 48, p.125202 (2015) [6] D. D. Sheka, O. V. Pylypovskyi, P. Landeros et al, *Communications Physics*, vol. 3, p. 128 (2020)

CONTRIBUTED PAPERS

DD-02. Micromagnetic Description of Symmetry-Breaking Effects in Curvilinear Ferromagnetic Shells.

D.D. Sheka¹, O. Pylypovskiy^{2,3}, P. Landeros^{4,5}, A. Kakay² and D. Makarov²
 1. *Taras Shevchenko National University of Kyiv, Kyiv, Ukraine;*
 2. *Helmholtz-Zentrum Dresden-Rossendorf, Dresden, Germany;*
 3. *Kyiv Academic University, Kyiv, Ukraine;* 4. *Universidad Tecnica Federico Santa Maria, Valparaiso, Chile;* 5. *Center for the Development of Nanoscience and Nanotechnology (CEDENNA), Santiago, Chile*

The behaviour of any physical system is governed by the order parameter, determined by the geometry of the physical space of the object, namely their dimensionality and curvature. Usually, the effects of curvature are described using local interactions only, e.g. local spin-orbit- or curvature-induced Rashba and Dzyaloshinskii-Moriya interactions (DMI). In the specific case of ferromagnetism, until recently, there was no analytical framework, which was treating curvature effects stemming from local [1] and non-local [2] interactions on the same footing. The lack of a proper theoretical foundation impedes the description of essential micromagnetic textures like magnetic domains, skyrmion-bubbles and vortices. Here, we present a micromagnetic theory of curvilinear ferromagnetic shells, which allows to describe the geometry-driven effects stemming from exchange and magnetostatics within the same framework [3]. A general description of magnetic curvilinear shells can be done using tangential derivatives of the unit magnetization vector. Tangential derivatives are represented by the covariant derivatives of in-surface components and the regular derivative of the normal magnetization component, normalized by the square root of the corresponding metric tensor coefficient. This allows to separate the explicit effects of curvature and spurious effects of the reference frame. The shape of a given thin shell can be determined by two principal curvatures k_1 and k_2 , which are functions of coordinate. The respective classification of curvilinear surfaces operates with (i) developable surfaces, where one of the principal curvatures equals to zero; (ii) minimal ones, where the mean curvature $k_1 + k_2 = 0$; and (iii) the general case. The local geometry-driven energy contributions are represented by the DMI and anisotropy, whose coefficients are determined by powers of the principal curvatures. This allows to cancel the influence of one of the DMI terms for the developable surfaces for any magnetic texture. The magnetostatic interaction is a source of new chiral effects, which are essentially non-local in contrast to the conventional DMI. The physical origin is the non-zero mean curvature of a shell and the non-equivalence between the top and bottom surfaces of the shell. We demonstrate that the analysis of non-local effects in curvilinear thin shells can become more straightforward when introducing three magnetostatic charges. In this respect, in contrast to the classical approach by Brown [4], we split a conventional volume magnetostatic charge into two terms: (i) magnetostatic charge, governed by the tangent to the sample's surface, and (ii) geometrical charge, given by the normal component of magnetization and the mean curvature. In addition to the shape anisotropy (local effect), there appear four additional non-local terms, determined by the surface curvature. Three of them are zero for any magnetic texture in shells with the geometry of minimal surfaces. The fourth term is determined by the non-equivalence of the top and bottom surfaces of the shell and becomes zero only for the special symmetries of magnetic textures. The discovered non-local magnetochiral effects introduce handedness in an intrinsically achiral material and enables the design of magneto-electric and ferro-toroidic responses. This will stimulate to rethink the origin of chiral effects in different systems, e.g. in fundamentally appealing and technologically relevant skyrmionic systems, and further theoretical investigations in the field of curvilinear magnetism as well as experimental validation of these theoretical predictions. These developments will pave the way towards new device ideas relying on curvature effects in magnetic nanostructures. The impact of effects predicted in this work goes well beyond the magnetism community. Our description of the vector field behaviour can be applied to different emergent field of studies of curvature effects. The prospective applications include curved superconductors [5], twisted graphene bilayers [6], flexible ferroelectrics [7], curved liquid crystals [8].

[1] Yu. Gaididei, V. P. Kravchuk, D. D. Sheka, *Phys. Rev. Lett.*, 112, 257203 (2014); D. D. Sheka, V. P. Kravchuk, Yu. Gaididei, *J. Phys. A: Math. Theor.*, 48, 125202 (2015); O. V. Pylypovskiy, V. P. Kravchuk, D. D. Sheka et al, *Phys. Rev. Lett.*, 114, 197204 (2015); V. P. Kravchuk, D. D. Sheka, A. Kakay et al, *Phys. Rev. Lett.*, 120, 067201 (2018) [2] P. Landeros, A. S. Nunez, *J. Appl. Phys.* Vol. 108, p. 033917 (2010); J. A. Otalora, M. Yan, H. Schultheiss et al, *Phys. Rev. Lett.*, 117, 227203 (2016); J. A. Otalora, M. Yan, H. Schultheiss et al, *Phys. Rev. B*, 95, 184415 (2017) [3] D. D. Sheka, O. V. Pylypovskiy, P. Landeros et al., *Comm. Phys.* 3, 128 (2020) [4] W. F. Brown Jr. *Micromagnetics* (Wiley, New York, 1963) [5] V. Vitelly, A. M. Turner, *Phys. Rev. Lett.*, 93, 215301 (2004) [6] W. Yan, W.-Y. He, Z.-D. Chu et al, *Nat. Comm.*, 4, 2159 (2013) [7] M. Owczarek, K. A. Hujak, D. P. Ferris et al, *Nat. Comm.*, 7, 13108 (2016) [8] G. Napoli, L. Vergori, *Phys. Rev. Lett.*, 108, 207803 (2012)

DD-03. Magnetic Phase Diagrams and Helicity Control of Reversal Modes in Ferromagnetic Nanotubes.

H. Salinas¹, J. Restrepo¹ and O. Iglesias^{2,3}

1. Instituto de Física, Universidad de Antioquia, Medellín, Colombia;

2. Condensed Matter Physics, Universitat de Barcelona, Barcelona, Spain;

3. IN2UB, Barcelona, Spain

We investigate the effects of the competition between exchange (J) and dipolar (D) interactions on the magnetization reversal mechanisms of ferromagnetic nanotubes. Using atomistic Monte Carlo simulations for a model with Heisenberg spins on a cylindrical surface, we study how the competition between both interactions influences the low temperature magnetic order of the nanotubes as well as the thermal-driven transitions involved, showing that helical (H) states become stable for a range of intermediate values of $\gamma=D/J$ and establishing phase diagrams for the stability of FM, H and vortex states as a function of the radius R and length L of the nanotube, see Fig. 1 [1]. We also study the reversal behavior under application of a magnetic field, showing that for which helical (H) states are energetically favorable at zero applied field, we show that the hysteresis loops can occur in four different classes that are combinations of two reversal modes with well-differentiated coercivities with probabilities that depend on R and L . This variety in the reversal modes is found to be linked to the metastability of the H states during the reversal that induces different paths followed along the energy landscape as the field is changed. We further demonstrate that reversal by either of the two modes can be induced by tailoring the nanotube initial state so circular states with equal or contrary chirality are formed at the ends (Fig. 2), thus achieving low or high coercive fields at will without changing γ . Finally, the results of additional micromagnetic simulations performed on tubes with a similar aspect ratio show that dual switching modes and its tailoring can also be observed in tubes of microscopic dimensions [2]. Acknowledgements: Work supported by Spanish MINECO (PGC2018-097789-B-I00), Catalan DURSI (2017SGR0598) and EU FEDER funds (Una manera de hacer Europa), Colciencias Beca de Doctorados Nacionales, ConvocatoriaNo. 727, Project No. CODIUdeA 2017-16253, also CSUC for supercomputer facilities.

[1] H. D. Salinas, J. Restrepo, Óscar Iglesias, *Sci. Rep.* 8, 10275 (2018). [2] H. D. Salinas, J. Restrepo, Óscar Iglesias, *Phys. Rev. B* 101, 054419 (2020).

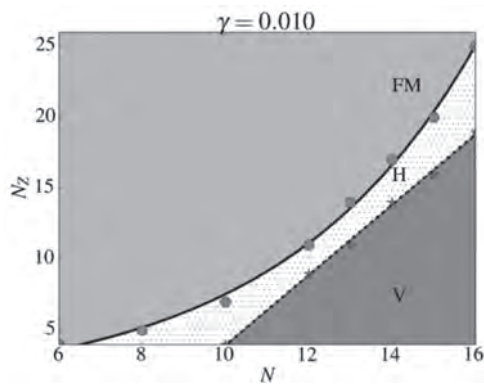


Fig. 1: Typical phase diagram.

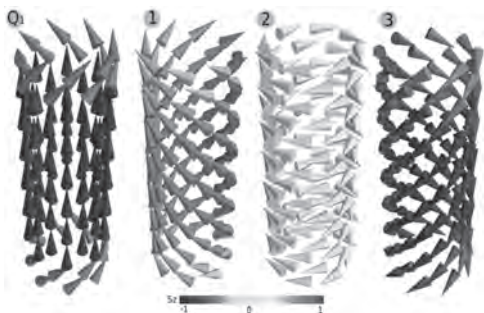
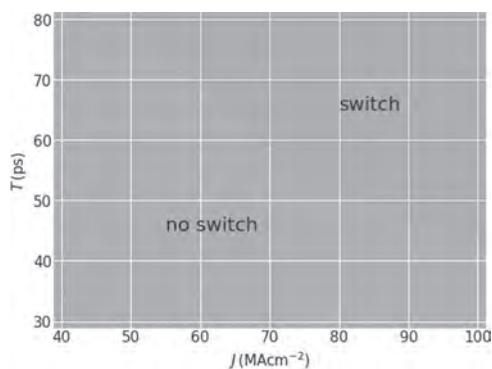


Fig. 2: Snapshots of spin configurations during a reversal mode.

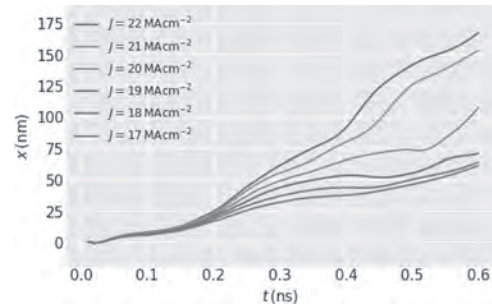
DD-04. Spin-Polarised Current Bloch Point Manipulation.M. Beg¹, M. Lang¹ and H. Fangohr^{2,1}¹. Faculty of Engineering and Physical Sciences, University of Southampton, Southampton, United Kingdom; ². Max Planck Institute for the Structure and Dynamics of Matter, Hamburg, Germany

Recently, it was demonstrated that confined helimagnetic nanostructures, composed of grains of different chirality (and consequently, a different sign of Dzyaloshinskii-Moriya energy constant), can host stable Bloch points [1]. In addition, it was shown that Bloch points undergo hysteretic behaviour and that their type can be changed using an external magnetic field. In this work, using Ubermag [2] micromagnetic simulations with OOMMF [3] as a computational backend, we explore if Bloch point magnetisation states can be manipulated using spin-polarized currents in nano-disk and nano-strip FeGe samples. We start by showing that a zero-field stable Bloch point emerges not only in thin-film disk samples [1] but also in an extensive range of planar geometries, including nanostrips. We then explore whether Bloch point's type can be switched using spin-polarized current pulses. We simulate a FeGe [4] nanodisk with 150 nm diameter, 20 nm thickness of the bottom layer with $D < 0$ and 10 nm thickness of the top layer with $D > 0$. We begin by relaxing a uniform $+z$ magnetisation state, which results in a head-to-head Bloch point. To a relaxed head-to-head Bloch point, we apply a spin-polarised current pulse with current density J and duration T , polarised in the negative z -direction. We vary current density J and pulse duration T and observe whether the type of Bloch point changes. In Fig. 1 we show a diagram depicting J - T regions for which Bloch point type switching occurs from head-to-head to tail-to-tail. In the second part of our work, we simulate nanostrips with 450 nm length and 90 nm width. Similar to nanodisks previously simulated, the thickness of the bottom layer with negative Dzyaloshinskii-Moriya constant is 20 nm and the thickness of the top layer with positive DM constant is 10 nm. We apply current polarised in $-y$ -direction and track both x and y positions of the Bloch point. In Fig. 2, we show how Bloch point moves in the x -direction for different current densities J . Our findings demonstrate that Bloch points can be manipulated using spin-polarized currents. Using current pulses polarised in $-z$ -direction, we were able to switch the Bloch point's type, whereas, with currents polarised in the negative y -direction, we managed to move Bloch point in the x -direction. Our results, in addition to being of interest to fundamental physics, bring Bloch points one step closer to being potential candidates for future data storage and information processing devices.

[1] M. Beg *et al.* Stable and manipulable Bloch point. *Scientific Reports* 5, 17137 (2015). [2] M. Beg *et al.* User interfaces for computational science: A domain-specific language for OOMMF embedded in Python. *AIP Advances*, 7, 056025 (2017). [3] M. J. Donahue and D. G. Porter, OOMMF User's Guide, Version 1.0, Interag. Rep. NISTIR 6376, Natl. Inst. Stand. Technol. Gaithersburg, MD, 1999. [4] M. Beg *et al.* Ground state search, hysteretic behaviour, and reversal mechanism of skyrmionic textures in confined helimagnetic nanostructures. *Scientific Reports*, 5, 17137 (2015).



Switching diagram of a head-to-head Bloch point in a 150 nm FeGe diameter disk using current pulse polarised in negative z -direction, with current density J and pulse duration T .



Bloch point's x -coordinate as a function of time for different current densities J polarised in the negative y -direction.

DD-05. Time Resolved Imaging of Oersted Field Induced Magnetization Dynamics in Cylindrical Magnetic Nanowires.

M. Schöbitz^{1,2}, S. Finizio³, A. De Riz¹, J. Hurst¹, J. Toussaint⁴, C. Thirion⁴, D. Gusakova¹, J. Bachmann², J. Raabe³ and O. Fruchart¹
 1. SPINtronique et Technologie des Composants, Grenoble, France;
 2. Inorganic Chemistry, Friedrich-Alexander-Universität Erlangen-Nürnberg, Erlangen, Germany; 3. Paul Scherrer Institut, Villigen, Switzerland; 4. Institut NEEL, Grenoble, France

Understanding magnetization dynamics in nanosized systems is a key condition not only to realize innovative new applications, but also to further expand our comprehension of the underlying fundamental physics. Only recently has it been possible to image magnetic objects such as domain walls (DWs) with high temporal and spatial resolution and versatile environments or excitations, using, for example time resolved x-ray magnetic circular dichroism with scanning transmission x-ray microscopy (XMCD STXM). Continuous developments of this technique have allowed for a shift of interest from simple systems such as flat nanostrips, that lend themselves more readily to magnetic imaging, to more intricate systems such as three dimensional nanostructures, with added complexity from the volume [1,2]. A textbook case for such an investigation is provided by cylindrical magnetic nanowires (NWs) featuring a novel type of DW, the Bloch-point wall (BPW) [3] which exhibits azimuthal curling of magnetic moments around a Bloch-point on the NW axis. The dynamics of these walls stand out compared to DWs in flat nanostrips due to fascinating theoretical predictions of fast, stable speeds and the controlled emission of spin waves [4]. Recent experiments in NWs indicate that the Oersted field induced by nanosecond pulses of current plays a key role in stabilising walls exclusively of the BPW type and further switches the azimuthal circulation to be parallel to the field [5]. This allows controlling the wall structure and enables fast DW motion with speeds > 600 m/s and an absence of Walker breakdown. The importance of the Oersted field in NWs was further studied with simulations to determine a strong radial dependence, scaling as one-over radius cubed, and a complex mechanism of the BPW switching process, involving nucleation and annihilation of pairs of Bloch-points [6]. In the case of longitudinally magnetised domains, the peripheral magnetic moments also tend to align with the Oersted field with the degree of tilt related to a competition between magnetic exchange and Zeeman energy. It is clear that the Oersted field has a major influence on magnetization dynamics in NWs, yet few predictions have been confirmed experimentally due to the complexity of such experiments. Further, without time resolved measurements, no quantitative comparisons of *eg.* tilt angles in magnetization may be made with the simulations. Verifications of these effects are therefore strongly required in order to control the system and employ it in possible future applications. Here, we make use of time resolved XMCD STXM to image the magnetization dynamics in NWs subjected to nanosecond pulses of electrical current. Time resolved images were acquired with a temporal resolution of 200 ps, to image the effect of positive and negative polarity 3 ns duration voltage pulses of chosen amplitude applied to magnetically soft Co₃₀Ni₇₀ NWs with diameters 93, 97 and 101 nm. We first observed the tilting of magnetization towards the applied Oersted field direction in longitudinally magnetized domains (Fig. 1a) and created a model based on the absorptivity of x-rays and a description of the magnetization in a NW cross section to accurately reproduce the observed magnetic contrast and extract quantitative information. We find that the degree of tilt on the surface of these NW samples is of the order of 18±8° per 10¹² A/m² applied (Fig. 1b), which is in agreement with theoretical predictions from ref. [6]. We then observe the expansion (Fig. 2b,d) and compression (Fig. 2a,c) of the BPW width due to the application of a parallel and antiparallel Oersted field, respectively. This effect, previously predicted by simulations, occurs when the applied current density is insufficiently strong to induce the BPW circulation switching. The magnetic contrast of the phenomenon is again reproduced with our simple model giving quantitative information about this “breathing” of the BPW. We expect that this work lays the foundation for and provides an incentive to further studying complex magnetisation dynamics in NWs. With increased control of the NW materials, the predicted ultrafast DW motion and associated spin wave emissions [4] may be visualized using this technique. Further, the quantitative analysis provided herein shows the depth of information obtainable with time resolved XMCD STXM

and that a direct comparison of the observed dynamics to *ie.* simulations and theory is possible. This type of direct collaboration will significantly grow the understanding of three dimensional magnetic nanosized systems and enable better control over them.

[1] C. Donnelly *et al.*, Time-resolved imaging of three-dimensional nanoscale magnetization dynamics. Nat. Nanotech. 15 p.356-360 (2020)
 [2] A. Fernández-Pacheco *et al.*, Three-dimensional nanomagnetism. Nat. Comm. 8 p.15756 (2017) [3] S. Da Col *et al.*, Observation of Bloch-point domain walls in cylindrical magnetic nanowires. Phys. Rev. B. 89 p.180405 (2014) [4] R. Wieser *et al.*, Current-driven domain wall motion in cylindrical nanowires. Phys. Rev. B. 82, p.1-7 (2010) [5] M. Schöbitz *et al.* Fast Domain Wall Motion Governed by Topology and Oersted Fields in Cylindrical Magnetic Nanowires. Phys. Rev. Lett. 123 p.217201 (2019) [6] A. De Riz *et al.* Mechanism of current-assisted Bloch-point wall stabilization for ultra fast dynamics. arxiv: 2011.14869v1

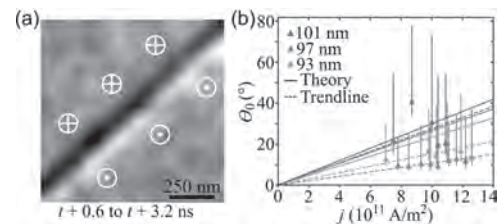


Figure 1: (a) Time resolved imaging of the tilting of magnetization in cylindrical NWs due to an applied Oersted field with white arrows indicating the direction of the Oersted field. (b) Tilt angle calculated from the magnetic images for three different NW diameters and compared with theoretical predictions.

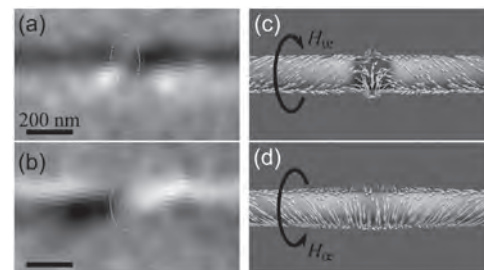


Figure 2: (a) Time resolved images of the compression (a) and expansion (b) of a Bloch-point DW in cylindrical NWs due to an applied Oersted field. Illustrations of the compressed (c) and expanded (d) DW from (a,b) with the Oersted field direction indicated.

DD-06. Mechanism of Current-Assisted Bloch-Point Wall Stabilization for Ultra Fast Dynamics.

A. De Riz¹, J. Hurst¹, M. Schöbitz^{1,2}, C. Thirion³, J. Bachmann^{2,4},
J. Toussaint³, O. Fruchart¹ and D. Guskova¹

1. Univ. Grenoble Alpes, CNRS, CEA, IRIG-SPINTEC, Grenoble, France;

2. Friedrich-Alexander-Universität Erlangen-Nürnberg, Erlangen,

Germany; 3. Neel Institute, Univ. Grenoble Alpes, CNRS, Grenoble,

France; 4. Institute of Chemistry, St. Petersburg State University, St. Petersburg, Russian Federation

Current-driven domain wall dynamics in circular cross-section nanowires is a key phenomenon to be studied with a view to designing three-dimensional magnetic memory devices. The information stored in this type of device would be encoded by magnetic domains separated by magnetic domain walls. Two types of domain walls exist in magnetically soft cylindrical nanowires: the transverse-vortex wall (TVW) and the Bloch-point wall (BPW). The latter has a distinct topology and exhibits azimuthal curling of magnetic moments (also called circulation) around a Bloch point – a micromagnetic singularity. This micromagnetic object is expected to prevent the usual Walker breakdown, and thus enable high domain wall speed. The Walker breakdown is expected to not occur in the case of the Bloch-point wall, as it would require a too large energy of dipolar origin with a head-on magnetization configuration along all three directions. We showed recently [1] that the previously overlooked Oersted field associated with an electric current is a key in experiments to stabilize the BPW and reach speed above 600m/s with spin-transfer. Here we use micromagnetic simulations, analytical modeling and topological arguments to understand in detail and quantitatively the underlying phenomena, in particular the switching from negative to positive circulation of the BPW, with respect to the applied current [2]. The switching of the azimuthal circulation of the BPW to match that of the Oersted field occurs above a threshold current which we quantify as a function of geometry and material parameters. The key result is a $1/R^3$ dependence of the switching threshold, with R the wire radius, with the effect of the Oersted field becoming predominant for wire radius above typically 30nm. To the contrary, the speed of walls remains largely determined by spin-transfer alone, in a below-Walker regime. Thanks to a generalized micromagnetic scaling of lengths and densities of current, the present result can be applied to wires made of any magnetically soft material. We also highlight the complexity of BPW transformation involving the nucleation and/or annihilation of the topological objects at the surface (vortex/antivortex pairs) and in the volume (Bloch points) [Fig.1].

[1] M. Schöbitz, A. de Riz, S. Martin *et al.*, Phys. Rev. Lett. 123, 217201 (2019) [2] A. De Riz, J. Hurst, M. Schöbitz, C. Thirion, J. Bachmann, J. C.

Toussaint, O. Fruchart, D. Guskova, arXiv:2011.14869 (2020)

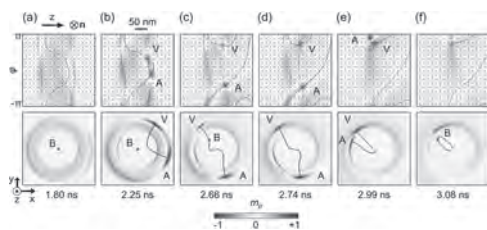


Figure 1: Snapshots illustrating the switching mechanism of BPW circulation in a permalloy wire under applied current. Top row: unrolled maps of radial magnetization, wire axis along z , periphery along ϕ . Bottom row: same surface maps of radial magnetization seen from inside of the wire as a 3D view. A, V and B labels highlight surface vortex and antivortex as well as Bloch point.

DD-07. Micromagnetics of Chemical Barriers Inserted Within Permalloy Cylindrical Nanowires: Towards the Control of Domain Wall Motion.

L. Álvaro Gómez^{1,2}, M. Schöbitz¹, C. Fernández González^{2,3}, S. Ruiz Gómez⁶, I. Andersen⁷, N. Mille⁵, J. Hurst¹, M. Foerster⁶, L. Aballe⁶, R. Belkhou⁵, J. Toussaint⁴, L. Cagnon⁴, C. Thirion⁴, A. Masseboeuf¹, D. Gusakova¹, L. Pérez García^{3,2} and O. Fruchart¹

1. SPINtronique et Technologie des Composants, Grenoble, France; 2. Fundacion IMDEA Nanociencia, Madrid, Spain; 3. Física de Materiales, Universidad Complutense de Madrid, Madrid, Spain; 4. Institut NEEL, Grenoble, France; 5. Synchrotron SOLEIL, Gif-sur-Yvette, France; 6. Sincrotron ALBA, Barcelona, Spain; 7. Centre d'Elaboration de Materiaux et d'Etudes Structurales, Toulouse, France

Cylindrical magnetic nanowires are a three-dimensional system in which magnetization may be manipulated by spin-polarized currents in order to controllably nucleate, move and pin magnetic domain walls (DWs). Such control makes them excellent candidates for three-dimensional storage devices such as in the well-known concept of Racetrack memories [1]. Due to their geometry, cylindrical nanowires can host a DW with curling magnetization not subject to the Walker breakdown limitation [2], and thus that can reach velocities over 1 km/s. This kind of DW is known as the Bloch-Point wall (BPW) [3] [4] and it was experimentally reported under static conditions for the first time in 2014 [5]. Recently, velocities above 600 m/s driven by spin-transfer torques have been also reported [6]. In order to achieve the desired control of DW motion, effective pinning sites need to be set along the wire's axis. Here, we propose a system based on cylindrical Permalloy ($\text{Fe}_{20}\text{Ni}_{80}$) nanowires with evenly spaced chemical barriers: Fe-rich segments ($\text{Fe}_{80}\text{Ni}_{20}$) of length ranging from 20 to 100 nm and 1 μm separation. We present an overview of their static micromagnetic configuration as well as their response to applied field and nano-second electric current pulses. This is a prerequisite to investigating and understanding the interplay of DWs with chemical modulations. Quantitative understanding is achieved combining magnetic imaging by means of X-ray Magnetic Circular Dichroism (XMCD) coupled to PhotoEmission Electron Microscopy (PEEM), Scanning Transmission X-ray Microscopy (STXM) or X-ray ptychography with <15 nm spatial resolution (Figure 1), and micromagnetic simulations with mumax3 and feeLLGood codes, as well analytical modeling. In addition, Transmission Electron Microscopy (TEM) combined with electron holography was used to extract valuable qualitative and quantitative information on the local magnetic behavior. The Fe-rich barriers have a spontaneous magnetization of 1.4 T whereas the Permalloy segments of 0.8 T. Such magnetization change at the interface generates volume charges and thus a dipolar energy increase. This energy cost can be overcome with a vortex state at the chemical barrier where the magnetization remains axial at the core and curling at the shell. The XMCD images indeed show a curling magnetic state at the chemical barriers (Figure 2). In addition, magnetic images are supported by a quantitative post processing code that simulates the magnetic contrast coming from XMCD-PEEM technique for a specific three dimensional magnetization texture, allowing us to extract the curling angle of the magnetization with respect to the wire's axis. The strength of curling increases with both the modulation length and wire diameter, with a clear analogy with the vortex state in flat magnetic disks. The strength of curling was assessed by imaging under large axial magnetic field. The chirality of curling is random at rest but can be switched deterministically by means of the Oersted field of nanosecond current pulses, showing again a clear correlation between the strength of curling and the geometry of the modulations.

[1] S. S. P. Parkin *et al.*, *Science*, vol. 320, no. 5873, p. 190 (2008). [2] R. Hertel, *Journal of Physics: Condensed Matter*, vol. 28, no. 48, p. 483002 (2016). [3] H. Forster *et al.*, *Journal of Applied Physics*, vol. 91, no. 10, pp. 6914–6919 (2002). [4] A. Thiaville and Y. Nakatani, 'Spin dynamics in confined magnetic structures III', vol. 101 pp. 161–205 (2006). [5] S. Da Col *et al.*, *Phys. Rev. B*, vol. 89, no. 18, p. 180405 (2014). [6] M. Schöbitz *et al.*, *Phys. Rev. Lett.*, vol. 123, no. 21, p. 217201 (2019).

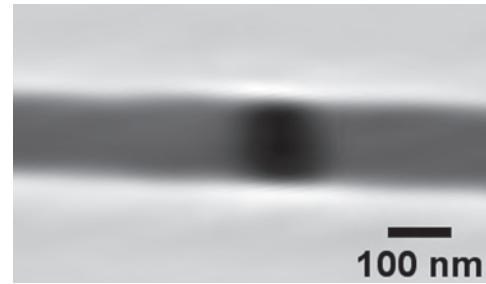


Figure 1: Reconstructed amplitude ptychographic XAS image at Fe L3 edge of a permalloy cylindrical nanowire of 140 nm of diameter with a Fe-rich chemical barrier ($\text{Fe}_{80}\text{Ni}_{20}$) of 100 nm in length (dark region).

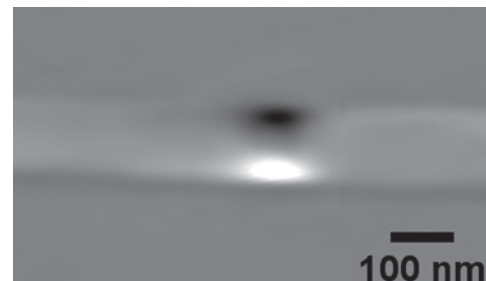


Figure 2: Reconstructed XMCD ptychographic image of the chemical barrier shown in Fig. 1. The curling magnetization is indicated by the dark and light bipolar contrasts.

DD-08. Theoretical Study of Current Induced Domain Wall Motion in Magnetic Nanotubes With Azimuthal Magnetization.

J. Hurst¹, A. De Riz¹, M. Stano², J. Toussaint³, O. Fruchart¹ and D. Gusakova¹

1. SPINtronique et Technologie des Composants, Grenoble, France;

2. Stredoevropsky technologicky institut, Brno, Czechia; 3. Institut NEEL, Grenoble, France

Nanowires and nanotubes are one-dimensional conduits, providing an ideal playground to investigate the fundamentals of domain-wall motion and spin-wave propagation. While simulations have been dominating for two decades, the first experiments are emerging. In particular, a peculiar class of domains were observed recently in nanotubes – domains with azimuthal (flux-closure) magnetization [1] (CoNiB, 400nm diameter). Azimuthal magnetization relates to the curvature-induced magnetic anisotropy resulting from the anisotropy of the granular structure, combined with inverse magnetostriction and/or inter-grain interface anisotropy. Interestingly, besides the conventional spin-transfer torques, a significant Oersted field directly coupled to the azimuthal magnetization through Zeeman energy may exist in a tubular geometry. This opens new possibilities for the manipulation of the domain walls in such geometries. Curvature-induced anisotropy together with Oersted field effects suggest that according to the domain wall type their dynamical features may be very different from the case of thin flat strips, now well established theoretically and experimentally. Given that, we report a theoretical overview [2] of the magnetic domain wall behavior under an electric current in infinitely long nanotubes with azimuthal magnetization, combining the one-dimensional analytic model and micromagnetic simulations. We derive a phase diagram predicting the stable azimuthal domains versus the anisotropy strength and the tube geometry, see Fig. 1. In addition, we predict the types of stable walls, either Néel or Bloch, pictured in Fig. 2, resulting from the competition between the curvature induced exchange energy, the demagnetization energy and the anisotropy energy. We also draw the panorama of the impact of the Oersted field on wall motion in tubes with azimuthal domains, pointing at curiosities such as opposite directions of motion below and above the Walker current and dramatic contrast between Néel and Bloch walls. In particular, we show the existence of spin-transfer torque and/or Oersted dominated regime for both domain wall structures and we predict large domain wall speeds reaching potentially 800 m/s, before the occurrence of a so-called Walker breakdown, see Fig. 2. We show how the domain wall speed and the walker field depend on the anisotropy and the geometrical parameter of the magnetic tubes and highlight the most suitable parameters to achieve high domain wall speed. Our study may guide the experimental realization of magnetic tubes, targeting the optimal parameters to get the desired properties.

[1] M.Stano, O. Fruchart, Magnetic Nanowires and Nanotubes, Handbook of Magnetic Materials, Elsevier, v. 27, pp.155-267, (2018). [2] J. Hurst, A. De Riz, M. Stano, J.-C. Toussaint, O. Fruchart, D. Gusakova, arXiv:2010.01966, (2020) [Accepted for publication in PRB].

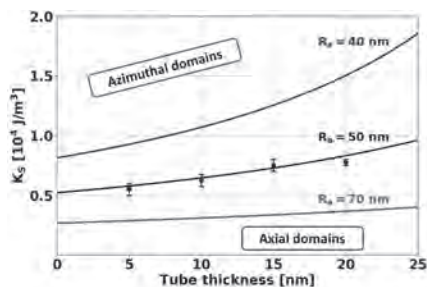


Fig. 1 : Threshold values of the anisotropy strength separating axial monodomain (below the curve) from azimuthal monodomain (above the curve) as a function of the tube thickness for three different external tube radius. The markers indicate an estimation of the threshold anisotropy value obtained with feelLGood simulations [2].

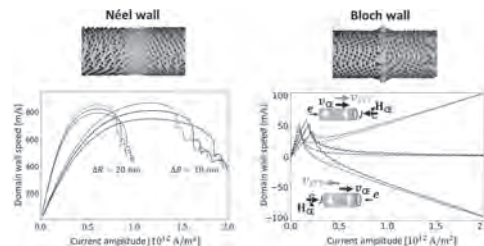


Fig. 2 : Time-averaged domain wall speed for a Néel wall (left panel) and a Bloch wall (right panel) versus the applied current density for two nanotube thicknesses: $\Delta R=10$ nm (full lines) and $\Delta R=20$ nm (dashed lines). Three different configurations are considered: disconsidering spin-transfer torques~(black curves), with spin-transfer torque and Oersted field cooperating~(red curve), and with spin-transfer torque and Oersted competing~(blue curve).

DD-09. Dynamic State Transitions in Vortex-Based Magnetic Tunnel Junctions for High Frequency Data Transmission.

A. Jenkins¹, L. San Emeterio Alvarez¹, L. Benetti¹, L. Martins¹, P.P. Freitas¹ and R. Ferreira¹

1. Spintronics, International Iberian Nanotechnology Laboratory, Braga, Portugal

Vortex-based spin torque nano-oscillators (STNOs) are nanoscale tunable multifunctional radio-frequency devices which have been proposed for a diverse variety of applications, ranging from novel wireless communications paradigms [1, 2], random number generators [3] and more recently the building blocks of novel bio-inspired computing architectures for neuromorphic computing [4]. The competitiveness of STNOs as an emerging technology lies in several key characteristics relative to conventional electronics, including tunability, multi-functionality, scalability and radiation hardness. Vortex-based STNOs have been shown to demonstrate superior performance parameters in terms of output power emission and signal linewidth to other STNO-based radio frequency devices, operating in the 50 MHz to 1 GHz regime. By harnessing the rich dynamics associated with non-homogeneous magnetisation configurations in confined nanostructures, the free layer of a magnetic tunnel junction (MTJ) can be forced, via a localised magnetic field, to transition between two magnetic states: the quasi-uniform and vortex states. In this report we demonstrate that such transitions can be driven back and forth to a dynamic equilibrium by exciting an MTJ with alternating magnetic fields close to the resonant modes of the magnetic vortex. The induced magnetic state transitions leads to a strong dependence of the resistance of the MTJ to the incoming signal, resulting in nominally identical devices which can act as both high frequency sources and detectors. In this presentation we will show how this dynamic behaviour can have exciting potential for future emerging paradigms, such as novel analogue wideband communication, integrated rf source/sensors and the building blocks for neuromorphic computing architectures.

- [1] - A. S. Jenkins, L. San Emeterio Alvarez, R. Dutra, R. L. Sommer, P. P. Freitas, and R. Ferreira, "Wideband High-Resolution Frequency-to-Resistance Converter Based on Nonhomogeneous Magnetic-State Transitions," *Phys. Rev. Appl.*, vol. 13, no. 1, p. 014046, Jan. 2020. [2] - A. S. Jenkins, L. San Emeterio Alvarez, P. P. Freitas, and R. Ferreira, "Digital and analogue modulation and demodulation scheme using vortex-based spin torque nano-oscillators", *Scientific Reports*, vol. 10, 11181 (2020) [3] - A. S. Jenkins, L. S. E. Alvarez, P. P. Freitas, and R. Ferreira, "Nanoscale true random bit generator based on magnetic state transitions in magnetic tunnel junctions," *Sci. Rep.*, vol. 9, no. 1, p. 15661, Dec. 2019. [4] - H. Farkhani, T. Boehnert, M. Tarequzzaman, J. D. Costa, A. Jenkins, R. Ferreira, J. Madsen, F. Moradi, "LAO-NCS: Laser Assisted Spin Torque Nano Oscillator-Based Neuromorphic Computing System," *Front. Neurosci.*, vol. 13, Jan. 2020.

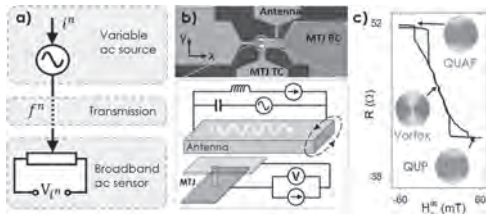


Figure 1 – (a) Schematic representation of the modulation and demodulation scheme and (b) single device schematic and (c) transfer curve showing possible magnetisation states of the free layer, (insets are micromagnetic simulations).

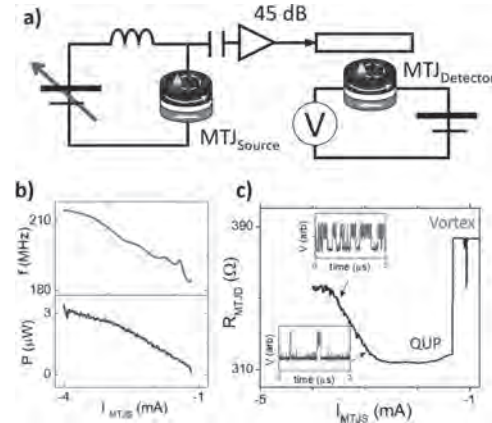


Figure 2- (a) schematic circuit showing how the signal created by MTJ_{source} is fed into the antenna of MTJ_{detector}. The (b) spectral properties of MTJ_{source} alongside the (c) resultant resistance response of MTJ_{detector} as a function of the current applied to the MTJ_{source} (I_{MTJS}). The insets in (c) show example time traces, where the free layer is transitioning between the vortex (green) and QUP (blue) states.

DD-10. Heusler-Compound Nanocontact Vortex Oscillators.

J. Létang¹, C. de Melo^{2,3}, C. Guillemard^{2,4}, A. Vecchiola⁵,
S. Petit-Watelot², M. Yoo¹, T. Devolder¹, K. Bouzouane⁵, V. Cros⁵,
S. Andrieu² and J. Kim¹

1. Centre de Nanosciences et de Nanotechnologies, Orsay, France;

2. Institut Jean Lamour, Nancy, France; 3. Laboratoire Matériaux
Optiques Photonique et Systemes, Metz, France; 4. Synchrotron SOLEIL,
Gif-sur-Yvette, France; 5. Unite Mixte de Physique CNRS/Thales,
Palaiseau, France

Spin-torque nano-oscillators (STNO) are nanoscale spintronic devices in which applied currents drive self-sustained magnetization oscillations. Heusler compounds are promising materials for spintronics as they exhibit low Gilbert damping for magnetization dynamics and large spin polarizations due to their (almost) half-metallic nature [1,2]. As such, they are ideal for devices such as spin-torque nano-oscillators, where critical currents can be reduced by the lower damping values and output signals enhanced by stronger magnetoresistances. This idea has been explored in vortex-based systems involving $\text{Co}_2\text{Fe}_x\text{Mn}_{1-x}\text{Si}$ where large output powers and large quality factors have been reported [3]. A unique feature of nanocontact vortex oscillators is the onset of periodic core reversal above a critical current [4-6]. This reversal occurs concurrently with the steady-state gyration around the nanocontact, giving rise to various behaviors we have previously studied: chaotic core reversal [4,5], phase-locking or modulation phenomena [6] in permalloy-based spin valves. These dynamics are driven primarily by currents flowing in the film plane (CIP), resulting in spin-transfer torques of the Zhang-Li form, rather than the Slonczewski torques associated with currents perpendicular to the film plane in nanopillar geometries. Here, we will discuss how the dynamics changes when all Heusler spin valves are used instead. We fabricated 20-nm nanocontacts on $\text{Co}_2\text{MnGe}/\text{Au}/\text{Co}_2\text{MnGe}$ films grown by molecular beam epitaxy, with a nano-indentation technique [7]. We investigated the vortex dynamics in the time and frequency domain at room temperature. An example of the measured current-dependence of the power spectral density is given in Fig. 1. We observe a rich harmonic content with oscillations that persist down to 4.5 mA, which is lower than previous cases [4-6]. Moreover, the power spectra comprise broad bands that are reminiscent of a chirped signal. Other frequency domains measurements show single frequency signal, broad spectral lines or extinction of the signal over current intervals. Time domain measurements enable us to observe other behavior, such as mode hopping, which can be seen on Fig. 2 for different currents. Other measurements have exhibit other behaviors, such as mode coexistence, intermittent signal or signal fluctuations. We attribute the rich dynamics to the coupled motion of vortices in the free and reference layers. This hypothesis is supported by some simulations.

[1] T. Graf *et al.*, IEEE Trans. on Magn., 47, 367-373 (2011) [2] C. Guillemard *et al.*, Phys. Rev. Appl., 11, 064009 (2019) [3] T. Yamamoto *et al.*, Phys. Rev. B 94, 094419 (2016) [4] S. Petit-Watelot *et al.*, Nat. Phys., 8, 682-687 (2012) [5] T. Devolder *et al.*, Phys. Rev. Lett. 123, 147701 (2019) [6] J. Létang *et al.*, Phys. Rev. B 100, 144414 (2019) [7] J. Létang *et al.*, arXiv:1906.08492 (2019)

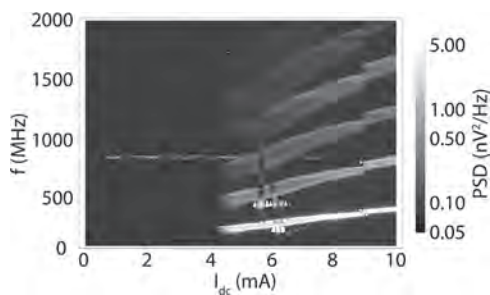


Figure 1: Power spectral density of vortex oscillations with applied dc current. The frequency bands are suggestive of a chirped signal.

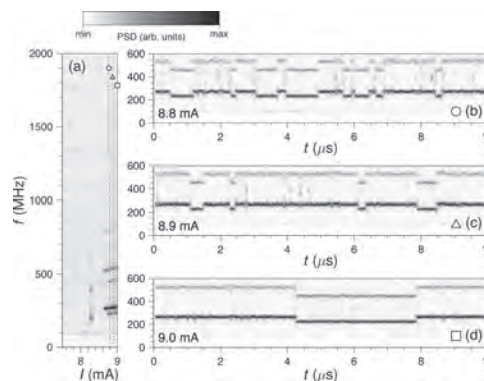


Figure 2: (a) Power spectral density computed from time-domain measurements. (b-d) Time-domain measurements for different dc current. Mode hopping between two frequencies is visible.

Session DE
MULTIFERROICS AND MAGNETOELECTRIC MATERIALS

Julius de Rojas, Chair
Universitat Autònoma de Barcelona, Barcelona, Spain

CONTRIBUTED PAPERS

DE-01. The Crucial Role of Stoichiometry to get Ultra-low Magnetic Damping in Heusler Compounds.S. Andrieu¹, C. Guillemard^{1,2}, S. Petit-Watelot¹ and F. Bertran³

1. Institut Jean Lamour, universite de lorraine, Nancy, France;

2. ALBA synchrotron, Barcelona, Spain; 3. SOLEIL synchrotron, Saint Aubin, France

Heusler magnetic compounds offer a wide variety of electronic properties very promising for spintronics and magnonics. Some of them exhibit a spin gap in their band structure at the Fermi energy. This peculiar electronic property was denominated as Half-Metal Magnetic (HMM) behavior [1]. This leads to two very interesting properties for spintronics, i.e. fully polarized current together with ultra-low magnetic damping, two key-points for spin-transfer-torque based devices. The full polarization was experimentally reported in Co_2MnSi [2,3], and we measured a magnetic damping in the 10^{-4} range on this compounds. Recently, we reported magnetic damping in the same range for other Heusler compounds [4]. In this talk, we show that a key experimental point to get ultra-low magnetic damping (in the 10^{-4} range) is to control the compound stoichiometry as best as possible. Single-crystalline Co_2MnZ thin films with $Z=\text{Al, Si, Ga, Ge, Sn}$ and Sb were grown by using Molecular Beam Epitaxy [4]. We developed a process to control the Co, Mn and Z fluxes with accuracy lower than 1% [5]. The electronic properties of these Co_2MnZ compounds were examined by using in situ techniques like electron diffraction during the growth, and spin resolved photoemission (SR-PES performed at SOLEIL synchrotron), and ex situ techniques like x-ray diffraction, transmission electron microscopy and ferromagnetic resonance. Electron diffraction during the growth (RHEED) allowed us to verify the stoichiometry after fluxes calibration [5]. This consists in recording diffracted intensity during deposition : if the growth is 2-dimensional, intensity oscillations are observed (called RHEED oscillations) due to interferences between electron scattered by the n^{th} grown atomic plane, and $(n+1)^{\text{th}}$ plane that is growing (fig.1). We observed this behavior for the Co_2MnZ series grown at 250C on a V or Cr buffer layers. Interestingly, a bilayer by bilayer growth mode was observed. Bilayer growth mode is well-known for MBE-grown semiconductors and is associated to the growth of basic blocks of the zinc blend or diamond structures. Similarly, the basic block for Co_2MnZ Heusler compounds is a cube with Co atoms at its 8 corners, and Mn or Z in the center of the cube. These Heusler compounds thus want to develop these basic blocks during the growth, leading to bilayer growth. This is a clear experimental proof of chemical ordering during the growth [5]. Finally, the excellent agreement between the delay to complete 2 atomic planes measured by RHEED and the time deduced from fluxes calibration allows us to confirm stoichiometry accuracy around 1% for each element. The spin (half-) gaps obtained by SR-PES on $\text{Co}_2\text{Mn-Si, -Ge}$ and $-\text{Sn}$ were found to be in very good agreement with *ab initio* calculations. The lowest magnetic damping values were obtained for these former HMM compounds, and are greater for $\text{Co}_2\text{Mn - Al}$ and Ga where no spin gap was observed (Table I). The control of the stoichiometry also offered us a robust experimental demonstration of the correlation between the spin polarization and the magnetic damping in $\text{Co}_2\text{MnSi}_x\text{Al}_{1-x}$ epitaxial thin films [6]. Finally, we show that single crystalline thin films are not mandatory, since we observed spin gap and magnetic damping values as low as 10^{-3} in polycrystalline $\text{Co}_2\text{Mn-Si}$ and $-\text{Ge}$ grown on glass [7]. This highlights the key role of the stoichiometry control for getting low damping, more importantly than structural defects like grain boundaries for instance.

[1] *New Class of Materials: Half-Metallic Ferromagnets*, R. A. de Groot et al, *Phys. Rev. Lett.* 50, 2024 (1983) [2] *Direct observation of half-metallicity in the Heusler compound Co_2MnSi* , M. Jourdan et al., *Nat. Commun.* 5, 3974 (2014) [3] *Direct evidence for minority spin gap in the Co_2MnSi Heusler compound*, S. Andrieu et al, *Phys. Rev. B* 93, 094417 (2016) [4] *Ultra-low magnetic damping in Co_2Mn -based Heusler compounds promising materials for spintronic*, C. Guillemard et al, *Phys. Rev. Appl.* 11, 064009 (2019) [5] *Issues in growing Heusler compounds in thin films for spintronic applications*, C. Guillemard et al, Invited Tutorial, *J.Appl. Phys.*, 128,

241102 (2020) [6] *Engineering $\text{Co}_2\text{MnAl}_x\text{Si}_{1-x}$ Heusler compounds as a model system to correlate spin polarization, intrinsic Gilbert damping and ultrafast demagnetization*, C. Guillemard et al, *Adv. Mat.* 1908357 (2020) [7] *Polycrystalline Co_2Mn -based Heusler thin films with high spin polarization and low magnetic damping*, C. Guillemard et al, *Appl. Phys. Lett.* 115, 172401 (2019)

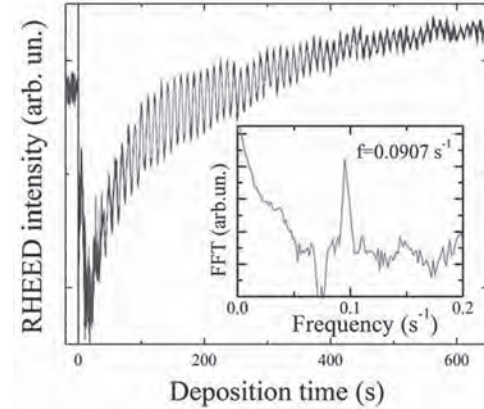


Fig.1 : Electron Diffraction Intensity oscillations during the growth of Co_2MnGa on a V(001) buffer layer. The oscillations correspond to a bilayer by bilayer growth mode [5].

	HRTEM structure	Spin polarization (%)	Spin gap (eV)	FMR		
				$\mu_0 M_{\text{eff}}$ (T) / (μ_0)	g	α ($\times 10^{-3}$) / ΔH_{eff} (mT)
Single-crystalline Co_2MnZ films						
Co_2MnAl	B2	63	no	1.07 / 4.3	2.02	1.10 / 12
Co_2MnSi	L2 ₁	100	0.7	1.31 / 5.1	2.01	0.46 / 14
Co_2MnGa	L2 ₁	100 *	-0	1.33 / 5.4	1.96	2.10 / 102
Co_2MnGe	L2 ₁	100	0.5	1.22 / 5.0	1.99	0.53 / 24
Co_2MnSn	X+L2 ₁	81	0.25	1.20 / 5.3	2.00	0.91 / 16
Co_2MnSb	?	36	?	1.14 / 5.1	2.02	0.96 / 133
Polycrystalline Co_2MnZ films						
Co_2MnSi	B2+L2 ₁	100	0.7	1.32 / 5.1	1.99	1.6 / 7
Co_2MnGe	?	90	0.5	1.22 / 5.0	2.00	1.5 / 13
Co_2MnGa	?	55	no	1.23 / 4.9	1.95	4.6 / 121

Table I : review of the structural and electronic properties observed on the Co_2MnZ series. The crystalline structures were determined using transmission electron microscopy, spin polarization and gap using spin-resolved photoemission, and magnetic properties using ferromagnetic resonance (FMR) [5].

DE-02. Electronic Transport Properties of Antiperovskite Mn₄N Epitaxial Films.

Z. Zhang¹ and W. Mi¹

1. Department of Applied Physics, Tianjin University, Tianjin, China

The control of magnetization by electric current plays an important role in the applications of magnetic recording, nonvolatile memories, etc. As a key way to realize the manipulation of magnetization efficiently, the application of spin transfer torque (STT) and spin-orbit torques (SOT) requires materials with high spin polarization in electron transport.¹⁻³ Besides, magnetic materials with low magnetization could reduce the critical switching current effectively due to the switching current is proportional to the saturation magnetization.⁴ Antiperovskite type Mn₄N films have attracted a lot of attention due to the perpendicular magnetic anisotropy (PMA) and low saturation magnetization.^{5,6} However, the details about electronic transport properties in Mn₄N films are not yet clear. Thus, the electronic transport properties of the Mn₄N films with different thicknesses on MgO substrates have been investigated systematically. Fig. 1(a) presents the $\rho_{xx}(T)/\rho_{xx}(300\text{ K})$ of Mn₄N films with different thicknesses on MgO(001) substrates. It is obvious that the resistivity continuously increases as the temperature increases in most films, showing a metallic conduction mechanism for the Mn₄N films. However, there is an abnormal trend in the 4.7-nm-thick Mn₄N films whose resistivity decreases as the temperature increases. In order to evaluate the purity and integrity of the Mn₄N films, the residual resistivity ρ_{xx0} at 0 K originated from impurity scattering is extracted from the $\rho_{xx}-T$ curves.⁷ Fig. 1(b) shows the $\rho_{xx}-T$ and fitting curve of the 78.8-nm-thick Mn₄N film. The ρ_{xx0} is obtained by fitting the $\rho_{xx}-T$ at low temperatures using the expression as $\rho_{xx}(T) = \rho_{xx0} + \alpha T^\beta$, where ρ_{xx0} and T are the residual resistivity and temperature, and the coefficient α and β will change with the scattering model. The calculated ρ_{xx0} of the 78.8-nm-thick Mn₄N film is 30.56 $\mu\Omega\text{ cm}$, which is slightly less than $\rho_{xx}(2\text{ K}) = 30.95\ \mu\Omega\text{ cm}$. The calculated β is 2.014 below 85 K, which is closely proportional to 2 for the ferromagnets. And the ρ_{xx0} of other thicknesses were obtained by fitting the $\rho_{xx}-T$ curves with the thickness from 7.8 to 47.3 nm in the same way. The thickness-dependent $\rho_{xx0}(t)$ curve is shown in the inset of Fig. 1(b). It is obvious that the ρ_{xx0} increases with the decrease of the film thickness, which imply the enhancement of the electron-electron interaction effects and interfacial scattering.⁸ Anomalous Hall effect of the Mn₄N films were measured in the temperature range of 5-300K and in magnetic fields to 7 T. The Hall bars were used for measuring the Hall resistivity ρ_{xy} of Mn₄N films with the thickness of 4.7-78.8 nm. The AHE is analyzed by the expression as $\rho_{xy} = \rho_{OH} + \rho_{AH} = R_0 H + R_s M$, where R_0 and R_s are ordinary and anomalous Hall coefficients, respectively. Fig. 2(a)-(h) shows the hysteretic property of the Hall resistivity ρ_{xy} for the different thickness as a function of applied magnetic field H at the temperatures of 5-300 K. The hysteretic property of ρ_{xy} due to the AHE caused by quantum mechanical spin-orbit interaction, and the linear property at the high-field regions due to the ordinary Hall effect (OHE) originated from the Lorentz force.⁹ The definition of MR is $[\rho_{xx}(H) - \rho_{xx}(0)]/\rho_{xx}(0) \times 100\%$, where $\rho_{xx}(0)$ is the resistivity of the film at 0 T. MR of the Mn₄N film displays a negative signal and butterfly shape. The films with the thickness of 47.3 nm and 23.6 nm show a sudden lift as the magnetic field increases from 0 to 0.5 T, and the sign of MR is positive. Then, MR gradually decreases and sign turns negative with the increasing magnetic field above 0.5 T. The MR of 11.0 nm and 7.8 nm thick films shows the same trend except for the turning point at about 1 T. The upturn of MR in the low fields is mainly due to the Lorentz force effect, which causes a decline of mean free paths and a rise of the scattering rates.¹⁰ And the downturn of MR at high fields could be attributed to the enhancement of ferrimagnetic order and the reduction of electron scattering by spin-wave excitations and local magnetic anisotropy.¹¹ At a certain temperature, MR of the Mn₄N films increases with the increase of film thickness. These results provide experimental basis for application of SOT devices. This work is supported by National Natural Science Foundation of China (51871161 and 52071233).

[1] S. Picozzi, A. Continenza, and A. J. Freeman, Phys. Rev. B 66, 094421 (2002). [2] Y. Takahashi, A. Srinivasan, B. Varaprasad, et al, Appl. Phys. Lett. 98, 152501 (2011). [3] A. Schmehl, V. Vaithyanathan, A. Herrnberger, S. Thiel, et al, Nature Mater. 6, 882-887 (2007). [4] K. Yamada, K. Oomaru,

S. Nakamura, et al, Appl. Phys. Lett. 106, 042402 (2015). [5] Y. Yasutomi, K. Ito, T. Sanai, K. Toko, et al, J. Appl. Phys. 115, 17A935 (2014). [6] K. Ito, Y. Yasutomi, K. Kabara, et al, AIP Adv. 6, 056201 (2016). [7] G. Su, Y. Li, D. Hou, et al, Phys. Rev. B 90, 214410 (2014). [8] A. Cotter, Thin Solid Films 1, 297-307 (1968). [9] S. Onoda, N. Sugimoto, and N. Nagaosa, Phys. Rev. B 77, 165103 (2008). [10] X. Feng, W. Mi, and H. Bai, J. Appl. Phys. 110, 053911 (2011). [11] B. Raquet, M. Viret, E. Sondergard, O. Cespedes, and R. Mamy, Phys. Rev. B 66, 024433 (2002).

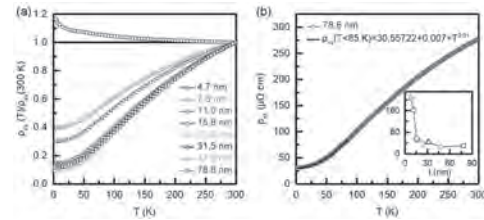


Figure 1. (a) Temperature-dependent $\rho_{xx}(T)/\rho_{xx}(300\text{ K})$ of Mn₄N films with different thicknesses on MgO substrates. (b) The longitudinal resistivity $\rho_{xx}(T)$ of the 78.8-nm-thick Mn₄N film and the fitting curve obtained below 85 K (blue line). The inset shows the thickness-dependent ρ_{xx0}

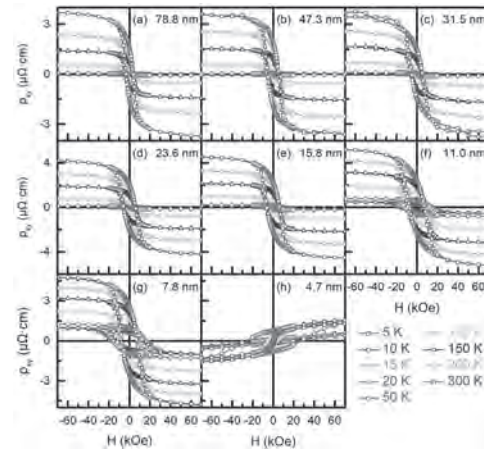


Figure 2. Magnetic field-dependent Hall resistivity $\rho_{xy}(H)$ of the (a) 78.8 nm, (b) 47.3 nm, (c) 31.5 nm, (d) 23.6 nm, (e) 15.8 nm, (f) 11.0 nm and (g) 7.8 nm and (h) 4.7 nm thick Mn₄N films at different temperatures

DE-03. Transport Properties of Co_2MnSi Heusler Compounds.

C. de Melo^{1,2}, C. Guillemard^{1,3}, V. Palin¹, J. Rojas-Sanchez¹, S. Petit-Watelot¹ and S. Andrieu¹

1. Institut Jean Lamour, Nancy, France; 2. Laboratoire Matériaux Optiques Photonique et Systemes, Metz, France; 3. Synchrotron SOLEIL, Gif-sur-Yvette, France

Co-based Heusler compounds are promising candidates for many emerging spintronic applications regarding the potential full spin polarization and ultra-low magnetic damping, together with their high Curie temperature (900 – 1000 K) and tunable electronic properties [1]. In particular, the existence of a minority spin gap and 100% spin polarization has been demonstrated by spin-resolved photoemission spectroscopy (SR-PES) for Co_2MnSi thin films, and an ultra-low magnetic damping coefficient of 4.6×10^{-4} was obtained for this compound, which is the lowest value reported so far for a conductive material [2]. Tunnel magnetoresistance (TMR) ratios as high as 1995 % and 354 % has been reported for epitaxial $\text{Co}_2\text{MnSi}/\text{MgO}/\text{Co}_2\text{MnSi}$ magnetic tunnel junctions at low and room temperature, respectively [3]. Large magnetoresistance ratios over 30%, at room temperature, and over 60 %, at low temperatures, have been also reported for current perpendicular-to-plane giant magnetoresistance (CPP-GMR) devices, with Co_2MnSi as ferromagnetic electrode [15]. However, the electronic properties and the half-metallicity seem to be very sensitive to the structure and composition of the films [1], which can negatively impact the physical properties and the performance of these films when implemented into GMR or TMR magnetoresistive devices. In this work, we report on the transport properties of Co_2MnSi Heusler compounds fabricated by molecular beam epitaxy, and patterned into Hall bars by standard UV-photolithography. The formation of the chemically-ordered $L2_1$ phase was verified by X-ray diffraction, reflection high-energy electron diffraction (RHEED) and high-angle annular dark-field scanning transmission electron microscopy (HAADF-STEM) (see Figure 1). A considerable increase in the resistivity of the films was observed with the decrease of thickness as a result of the increase in the inelastic electron scattering at the film surface. Fitting the film's resistivity versus thickness using Fuchs and Sondheimer model allows us to estimate the electron mean free path for Co_2MnSi equal to 13 ± 5 nm, a key parameter to consider when employing these alloys for current-in-plane (CIP) magnetoresistive devices. Furthermore, by fitting the resistivity of the films versus temperature, we access to the distance between the Fermi energy and the minority spin conduction band minimum ($k_B \cdot \Delta$), as shown in Figure 2. These values in combination with spin-resolved photoemission spectroscopy (SR-PES) measurements, performed to a 20-nm Co_2MnSi film, permit to estimate the spin gap of Co_2MnSi between 0.55 - 0.7 eV, in good agreement with *ab initio* calculations [6]. A negative anisotropy magnetoresistance (AMR) ratio was measured for all the samples, which is a signature of the Half-metallicity of the Co_2MnSi films. Moreover, AMR values ranging from -0.15 to -0.24 were obtained, which are in good agreement with the highest values reported in the literature for Co_2MnSi . The carrier's concentration and carrier's mobility of the films and their dependency with temperature was determined from Hall effect measurements. Finally, the evolution of films resistivity with thickness and temperature provided the ideal scenario to study the scaling of Hall resistivity with longitudinal resistivity. The linear trend observed indicates that screw scattering is the dominant temperature-dependent scattering mechanism taking place in Co_2MnSi . The electrical parameter obtained here were measured on high-quality Co_2MnSi films, with ultra-low magnetic damping and 100% spin polarization, which can be very useful in views of the implementation of Co_2MnSi films in magnetoresistive devices. Moreover, we demonstrate the feasibility of the electrical transport measurements as a mean to verify the half-metallicity of Heusler compounds, and to estimate their spin gap, as a complement to SR-PES measurements.

[1] C. Guillemard, S. Petit-Watelot, S. Andrieu *et al.*, J. Appl. Phys., Vol. 128, p.241102 (2020) [2] C. Guillemard, S. Petit-Watelot, S. Andrieu *et al.*, Phys. Rev. Appl., Vol. 11, p.064009 (2019) [3] H. Liu, Y. Honda, T. Taira *et al.*, Appl. Phys. Lett., Vol. 101, p.132418 (2012) [4] Y. Sakuraba, K. Izumi, T. Iwase *et al.*, Phys. Rev. B., Vol. 82, p.094444 (2010) [6] S. Picozzi, A. Continenza, and A.J. Freeman, Phys. Rev. B., Vol. 66, p.094421 (2002)

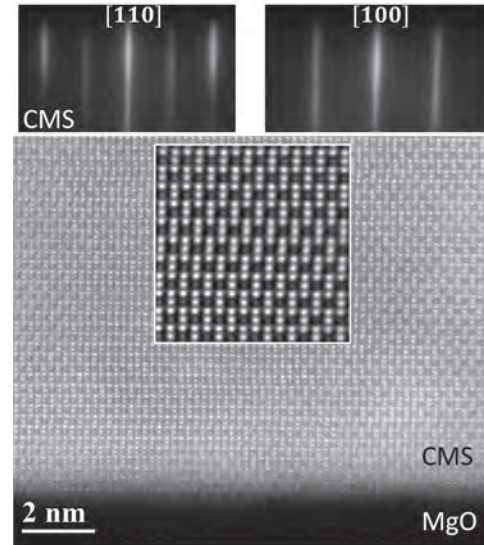


Fig. 1. Reflection high-energy electron diffraction (RHEED) patterns for a 15-nm Co_2MnSi film (noted CMS) along the [110] (left column) and [100] (right column) azimuths (top). High-angle annular dark-field scanning transmission electron microscopy (HAADF-STEM) micrograph of the CMS layer along the [110] zone axis (bottom).

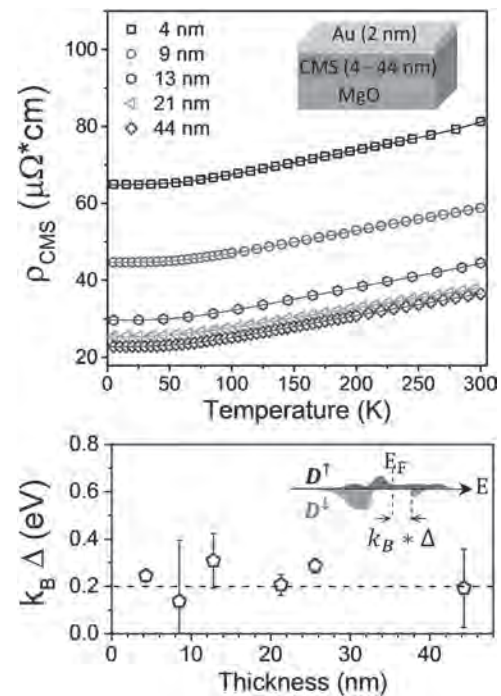


Fig. 2. Resistivity of the Co_2MnSi films versus temperature from 300 to 5 K (top). Distance between the Fermi energy and the bottom of the minority spin band ($k_B \cdot \Delta$) versus films thickness (bottom).

DE-04. Enhancement of the Anomalous Nernst Effect in Polycrystalline Co₂MnGa/AlN Multilayers.

J. Wang^{1,2}, Y. Lau^{1,2}, W. Zhou³, T. Seki^{1,2}, Y. Sakuraba^{3,4}, T. Kubota^{1,2}, K. Ito^{1,2} and K. Takanashi^{1,2}

1. Institute for Materials Research, Tohoku University, Sendai, Japan; 2. CSRN, Tohoku University, Sendai, Japan; 3. Research Center for Magnetic and Spintronic Materials, National Institute for Materials Science, Tsukuba, Japan; 4. PRESTO, Japan Science and Technology Agency, Tokyo, Japan

I. INTRODUCTION Thermoelectric generators (TEG) that convert waste heat to electricity is regarded as alternative and environment-friendly technology for harvesting and recovering heat [1]. Although the conventional thermoelectric devices based on the Seebeck effect (SE) are promising, SE-based TEGs suffer from the high fabrication cost due to their complex structure and the usage of toxic, rare, and expensive elements. Furthermore, the one-dimensional relationship between the heat and carrier transports defined in SE makes it very challenging to achieve a high energy conversion efficiency and be only limited to a flat heat source surface [1, 2]. Recently its counterpart, the anomalous Nernst effect (ANE) in ferromagnetic materials, has gained increasing interests with its potential merits to further improve the figure-of-merit, ZT , simplify a thermopile structure with low-cost materials, and be applicable for a non-flat surface [2, 3]. However, to date, the reported thermoelectric conversion efficiency of the ANE is too small compared with the SE, which hampers its application as TEG. Thus, it is quite meaningful to explore valid approaches to achieve larger ANE output. In this study, we focus on the multilayer structure with full Heusler alloy Co₂MnGa which is a famous ferromagnet exhibiting the large ANE thanks to its characteristic electronic band structure [3, 4]. In addition to the ANE originating from the bulk property of Co₂MnGa, we expect the enhancement of ANE in the multilayer structures as reported previously [5, 6]. Here, polycrystalline Co₂MnGa/AlN multilayer films were prepared on the amorphous substrates, the layer thickness dependence of ANE was investigated. We found that the large anomalous Nernst thermopower (S^{ANE}) of $4.9 \pm 0.4 \mu\text{V K}^{-1}$ can be obtained even for the polycrystalline Co₂MnGa. **II. EXPERIMENTAL METHOD** The film stacking structure is Si/SiO₂/AlN(20)/[Co₂MnGa(t)/AlN(5)]_{2.5/ t} ($t = 2.5, 5.0, 12.5, \text{ and } 25.0$, thickness in nm), which was fabricated by DC magnetron sputtering at room temperature. Then all the films were post-annealed at 500 °C for 3 hours. For the ANE measurement, the thin films were first patterned into Hall-cross shapes through the use of photolithography and Ar ion milling. After milling, the on-chip thermometers made of the 100-nm-thick sputtered Pt were prepared by the lift-off process. The in-plane temperature gradient was generated by an on-chip heater, and the temperature on the cold and hot sides of the sample was monitored by two Pt on-chip thermometers. An external magnetic field (± 2 T) was applied perpendicular to the sample plane. **III. RESULT AND DISCUSSION** The structural characterization was carried out using the x-ray diffraction. For all samples, the Co₂MnGa layers showed the (110)-oriented textures on the SiO₂ substrate. The 25-nm-thick Co₂MnGa film (single layer) exhibited the weak Co₂MnGa 220 peak. On the other hand, [Co₂MnGa (12.5)/AlN (5)]₂ multilayer film (multilayer) with the Co₂MnGa layers sandwiched by dielectric AlN layers shows a much stronger (110) texture. Moreover, the satellite peaks were observed around $2\theta = 44.6^\circ$ of the multilayer sample, indicating shape and abrupt Co₂MnGa/AlN interfaces. Furthermore, the largest S^{ANE} of $4.9 \pm 0.1 \mu\text{V K}^{-1}$ was achieved for the multilayer film while the value of S^{ANE} was $3.8 \pm 0.4 \mu\text{V K}^{-1}$ for the single layer film. Although the present S^{ANE} of $4.9 \pm 0.1 \mu\text{V K}^{-1}$ is smaller than the record-high value of S^{ANE} which is $\sim 8.0 \mu\text{V K}^{-1}$ for single crystal Co₂MnGa bulk [7], it is still promising one order of magnitude larger than those for other ferromagnets with similar magnetizations [8]. The results indicate that the large ANE output can be obtained even for the polycrystalline Co₂MnGa which quite meaningful for practical application. This fact also implies that multilayers and/or superlattices with low dimension and sharp interfaces are promising platform/candidates to achieve large ANE. The present results provide new insight into the correlation between microstructure and ANE. We consider that the size and interface effect are the primary origins for the enhancement of ANE in the proposed Co₂MnGa/AlN multilayer films. There are three possible scenarios for explaining the enhancement of ANE in the multilayer samples. First, the

distinct thermal expansion coefficient, elastic modulus, and lattice mismatch between metals (Here Co₂MnGa) and ceramics (here AlN) would introduce tremendous interface stress during the annealing, *i.e.* heating and cooling processes. The interface stress in the Co₂MnGa layer may be a driving force to promote the chemical ordering of Co₂MnGa. Second, the lattice distortion in Co₂MnGa due to the interface stress will modify its electronic band structures. Third, the composition variation in the Co₂MnGa layers may occur via the interdiffusion through the interface. The detailed structural analyses will be addressed in the presentation. This work successfully demonstrated a way to achieve giant ANE thermopower for the polycrystalline Co₂MnGa layer on the amorphous substrate by exploiting the dielectric AlN layers. This is an important finding for practical applications. This work was supported by KAKENHI (18H05246) and CSRN.

[1] S. Twaha, *et al.*, *Renew Sustain Energy Rev*, 65, 698 (2016) [2] Y. Sakuraba, *Scr. Mater.* 111, 29 (2016) [3] A. Sakai, *et al.*, *Nat Phys.* 14, 1119 (2018) [4] K. Sumida *et al.*, *Commun Mater* 1, 89 (2020) [5] K. Uchida *et al.*, *Phys. Rev. B* 92, 094414 (2015) [6] C. Fang *et al.*, *Phys. Rev. B* 93, 054420 (2016) [7] Xu, L. *et al.*, *Phys. Rev. B* 101, 180404 (R) (2020) [8] S. N. Guin *et al.*, *NPG Asia Mater.* 11, 16 (2019)

DE-05. Enhancement of $L2_1$ -Atomic Order and Spin-Polarization in Co_2MnZ ($Z = \text{Ge}, \text{Sn}$) Heusler Thin Films by low-Temperature Annealing Process.

*V.K. Kushwaha*¹, *Y. Sakuraba*¹, *T. Nakatani*¹, *T. Sasaki*¹, *I. Kurniawan*¹ and *K. Hono*¹

1. Research Center for Magnetic and Spintronic Materials, National Institute for Material Science, Tsukuba, Japan

Half-metallic ferromagnets (HMFs) have attracted much interest as promising materials in spintronics devices since they generate highly spin-polarized current due to the absence of one spin-channel at the Fermi level (E_F). Among the known HMFs, the use of Co_2 -based Heusler alloys enables enhancing the giant-magnetoresistance, tunnel-magnetoresistance, and spin-accumulation effects, thereby improving the performance of spintronic devices [1-3]. Despite the large magnetoresistance (MR) ratio observed in Heusler based devices, the structural disorder is still one of the remaining issues which lower the P . Therefore, it is essential to have a highly ordered Heusler structure to realize the half-metallicity. The structural order ($B2 \rightarrow L2_1$) of the Heusler alloys e.g., Co_2MnSi [4] and $\text{Co}_2\text{FeGe}_{0.5}\text{Ga}_{0.5}$ [1] have been promoted by annealing at high temperatures ($>500^\circ\text{C}$) resulting in an enhanced MR ratio. However, for various applications, the permissible maximum annealing temperature is restricted, e.g., for a magnetic read head in a hard disk drive (HDD) the annealing temperature is limited to 300°C because of the temperature tolerance of the NiFe shield. Therefore, it is desirable to search for other Heusler alloys that crystallize in $L2_1$ -order below 300°C . The present work is motivated by Okubo *et al.* [5]'s report, where the $L2_1$ to $B2$ -order transition temperature of Co_2MnZ ($Z = \text{Ge}, \text{Sn}$) Heusler alloys is very high ($>1500\text{K}$) suggesting high energetical stability of $L2_1$ -structure; and hence $L2_1$ -order is expected to appear even in the as-deposited state or by low-temperature annealing. Co_2MnZ ($Z = \text{Ge}, \text{Sn}$) and reference $\text{Co}_2\text{FeGe}_{0.5}\text{Ga}_{0.5}$ films were deposited on MgO (001) single crystal substrate using an ultra-high vacuum magnetron sputter system at room temperature and then post-annealed *in-situ* at $T_{\text{ann}} = 200\text{-}700^\circ\text{C}$ to induce the atomic-ordering. Here, $\text{Co}_{50}\text{Fe}_{50}$ (3nm) was used as a buffer layer to deposit Co_2MnZ films to suppress a phase separation. Co_2MnSn films with two different compositions $\text{Co}:\text{Mn}:\text{Sn} = 53.4:29.3:17.3$ and $47.4:25.5:27.1$ were deposited, which we refer to as Sn-poor and Sn-rich films, respectively. The crystal structure of the films was analyzed using a high-resolution X-ray diffractometer with $\text{Cu-K}\alpha$ radiation. Finally, to quantify the P of the conduction electron in the bulk region, Co_2MnZ and $\text{Co}_2\text{FeGe}_{0.5}\text{Ga}_{0.5}$ films were microfabricated into a non-local spin valve (NLSV) device using electron-beam lithography, Ar-ion milling, and the lift-off techniques. X-ray diffraction revealed that Co_2MnZ and $\text{Co}_2\text{FeGe}_{0.5}\text{Ga}_{0.5}$ films are epitaxially grown along (001) direction. The degree of $L2_1$ -ordering (S_{L2_1}) as a function of T_{ann} of Co_2MnZ , $\text{Co}_2\text{FeGe}_{0.5}\text{Ga}_{0.5}$, and Co_2MnSi [4] films are shown in Fig.1(a). In the case of $\text{Co}_2\text{FeGe}_{0.5}\text{Ga}_{0.5}$ and Co_2MnSi , $L2_1$ -ordering was observed above 500°C . Interestingly, in Co_2MnZ films, $L2_1$ -ordering appeared even in the as-deposited state and it enhances systematically with increasing T_{ann} . Figure 2(a) shows a scanning electron microscopy (SEM) image of a typical NLSV device using Co_2MnGe and Cu and the schematic of non-local measurement. We observed a clear spin-accumulation signal (ΔR_S) in all our NLSV devices, which decays with increasing the gap-length (d); as Fig.2(b) shows a representative ΔR_S - d curve of Co_2MnGe film ($T_{\text{ann}} = 300^\circ\text{C}$). To evaluate P , the measured ΔR_S in the Cu channel was analyzed by one-dimensional spin diffusion model [6]. The evaluated P of the films are displayed in Fig.1(b), which varies systematically with increasing T_{ann} . The spin-polarization P of Co_2MnGe at $T_{\text{ann}} = 300^\circ\text{C}$ is higher (~ 0.65) than that of Co_2MnSn and $\text{Co}_2\text{FeGe}_{0.5}\text{Ga}_{0.5}$ due to a higher S_{L2_1} , suggesting that Co_2MnGe is a promising material for various practical applications. For Co_2MnSn , however, low P was found in both compositions, despite high S_{L2_1} . Because first-principle calculations predict highly spin-polarized electronic structure in the Sn-rich composition, it is desirable to check the microstructure by transmission-electron microscopy to understand the origin of low P . In conclusion, we elucidated that Co_2MnGe is a promising material to obtain high atomic order and large P in the sputtered film without high-temperature annealing. Since the present Co_2MnGe film has a slightly Co-rich composition which is not suitable to obtain high P due

to the formation of the Co antisite disorder, optimization of the composition ratio is expected to lead to higher P .

[1] S. Li *et al.*, Appl. Phys. Lett. 103, 042405 (2013). [2] H. Liu *et al.*, Appl. Phys. Lett. 101, 132418 (2012). [3] Ikhtiar *et al.*, J. Appl. Phys. 115, 173912 (2014). [4] Y. Sakuraba *et al.*, Phys. Rev. B 82, 094444 (2010). [5] A. Okubo *et al.*, Appl. Phys. Lett. 96, 222507 (2010). [6] S. Takahashi and S. Maekawa, Phys. Rev. B 67, 052409 (2003).

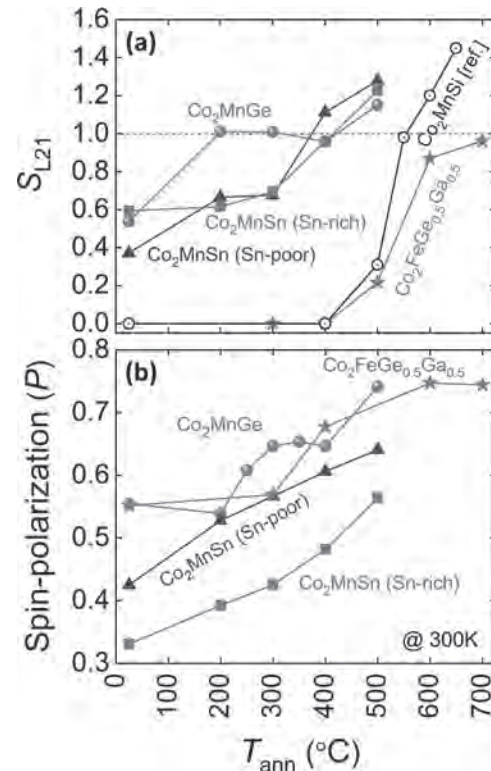


Fig.1. T_{ann} dependence of (a). S_{L2_1} , and (b). bulk spin-polarization P measured in NLSV devices. S_{L2_1} exceeding 1 is expected to be caused by off-stoichiometry in the films.

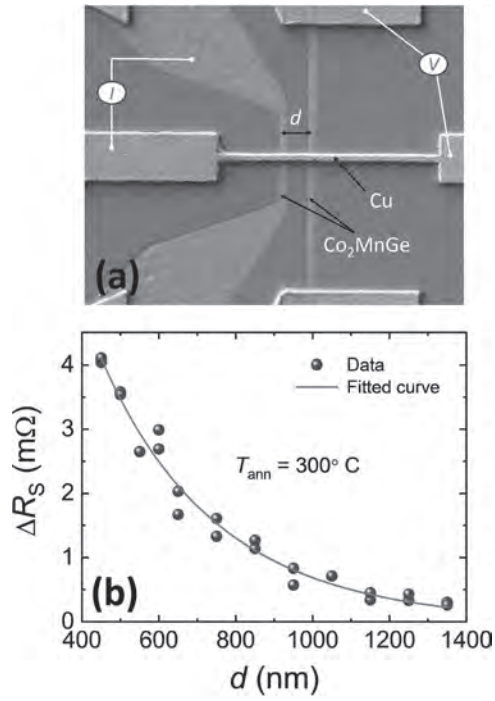


Fig.2. (a). An SEM image of a typical NLSV device using Co_2MnGe and Cu, and the schematic of non-local measurement. (b). The gap-length (d) dependence of ΔR_S of NLSV based on Co_2MnGe film ($T_{\text{ann}} = 300^\circ\text{C}$). The solid line indicates the fitting curve using one-dimensional spin diffusion model [6].

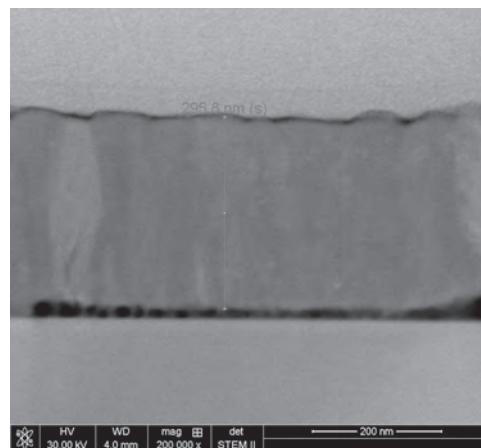
DE-06. Growth of Ruddlesden–Popper (CaO)(CaMnO₃)_n Thin Films by Laser Ablation Deposition.

B. Machado da Silva¹, J. Oliveira¹, T. Rebelo^{1,3}, P. Rocha-Rodrigues², P. Lekshmi², A.L. Lopes², J. Pedro Esteves de Araújo², F. Leonard Deepak³ and B. Gonçalves Almeida¹

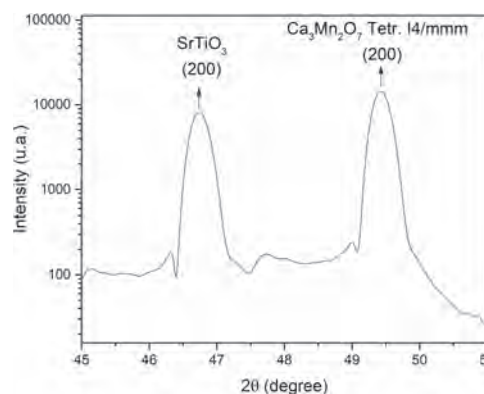
1. Centro de Física da Universidade do Minho e o Centro de Física da Universidade do Porto, Universidade do Minho, Braga, Portugal; 2. Dep. Física e Astronomia, Universidade do Porto Instituto de Física dos Materiais Instituto de Nanociencia e Nanotecnologia, Porto, Portugal; 3. International Iberian Nanotechnology Laboratory, Braga, Portugal

Room temperature magnetoelectric (ME) compounds are rare and high-quality artificially multilayered ones are in general difficult and costly to produce. In this respect, magnetic Naturally Layered Perovskite structures (NLP) with improper ferroelectricity [1, 2], such as the Ruddlesden-Popper (RP) calcium manganite compound Ca₃Mn₂O₇ [2], offer an alternative route to achieve non-expensive and high-performance room temperature MEs for information storage, sensors, and actuators or low power energy-efficient electronics. They allow exploring oxygen octahedra nonpolar rotations and cation site displacement to attain non-centrosymmetry. Additionally, due to their high sensitivity to lattice-distortions, their preparation in thin film form over crystalline substrates allows the manipulation of acentricity and enables the tuning of lattice, electric and magnetic interactions. However, crystallizing the desired layer with RP structure is challenging. Thus, the preparation conditions to obtain the envisaged Ca_{n+1}Mn_nO_{3n+1} phases, with different n, need to be optimized. The objective of this study is to identify the deposition conditions that lead to different phases of (CaO)(CaMnO₃)_n with n = 2 (improper ferroelectric Ca₃Mn₂O₇) and/or with n = ∞ (CaMnO₃). Here we adopted the Laser ablation deposition method for developing (CaO)(CaMnO₃)_n thin films. As such, thin films of calcium manganate have been prepared over SrTiO₃ substrates using Ca₃Mn₂O₇ target by laser ablation. Polycrystalline Ca₃Mn₂O₇ was synthesized using a conventional high-temperature ceramic route. The phase purity of the target was checked using XRD. The deposition parameters were studied, specifically oxygen partial pressures (from 10⁻³ to 10⁻¹ mbar), laser fluences (10⁻⁵ J/cm²), substrate temperatures (from room temperature to 730 °C) and post-annealing influence. Further, a detailed structural study using X-ray diffraction (XRD), microstructural analysis by scanning electron microscopy (SEM), quantification of composition with energy-dispersive X-ray spectroscopy (EDS), magnetic property using SQUID magnetometer, and dielectric analysis by impedance analyzer were carried out. The XRD results show that for oxygen pressures in the range 10⁻² - 10⁻¹ mbar, deposition temperatures of 600 °C to 730 °C and laser fluences from 1.7 J/cm² to 2.9 J/cm², the films are polycrystalline, stabilizing in the CaMnO₃ orthorhombic Pnma phase. The SEM measurements show dense films with smooth surfaces (Fig.1). The corresponding EDS measurements indicate a 1:1 atomic proportion in these samples. On the other hand, by decreasing the oxygen pressure, increasing the temperature and increasing the laser fluence, the Ca/Mn proportion increases, so that for films prepared on SrTiO₃, at 730 °C, with 4 J/cm² laser fluence, ~10⁻³ mbar oxygen pressure and with a post-annealing process, the Ca₂Mn₃O₇ (n = 2) phase is stabilized, as confirmed by XRD (Fig.2). The corresponding EDS analysis further gives a Ca/Mn atomic ratio of ~1.5:1, consistent with the presence of this phase. The corresponding magnetic properties of the films, that are correlated with the stabilized phases and preparation conditions, will be present as well as the dielectric properties that were characterized by impedance spectroscopy.

[1] Ghosez, P., Triscone, J.-M., Coupling of three lattice instabilities: Multiferroics, Nature Materials, vol. 10, n. 4, 2011, 269–270. [2] Rocha-Rodrigues, P., Santos, S. S. M., Miranda, I. P., Oliveira, G. N. P., Correia, J. G., Assali, L. V. C., Petrilli, H. M., Araújo, J. P., Lopes, A. M. L., Ca₃Mn₂O₇ structural path unraveled by atomic-scale properties: A combined experimental and ab initio study, Physical Review B, 101, 064103, 2020.



The cross-section image from SEM shows a dense film with a thickness of about 300 nm.



The XRD diffractogram confirms the stabilization of the Ca₂Mn₃O₇ phase (n = 2).

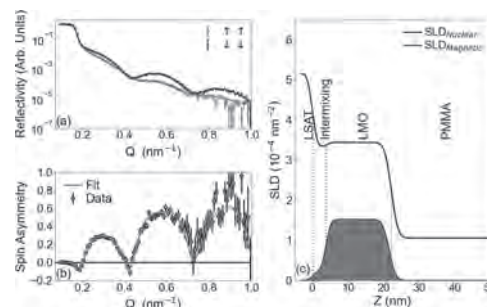
DE-07. Interfacial Corrugation and Magnetism of Freestanding $\text{LaMnO}_{3+\delta}$ Thin Films.

Q. Lu¹, P.P. Balakrishnan², A. Grutter² and X. Zhai³

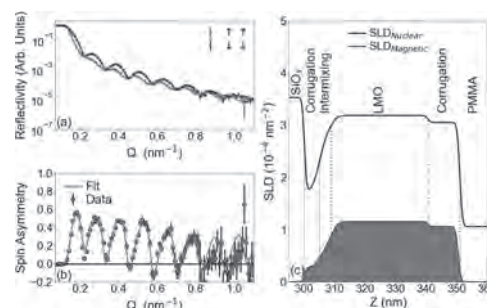
1. University of Science and Technology of China Hefei National Laboratory for Physical Sciences at the Microscale, Hefei, China;
2. NIST Center for Neutron Research, Gaithersburg, MD, United States;
3. ShanghaiTech University School of Physical Science and Technology, Shanghai, China

Complex oxide thin films have highly tunable magnetic properties, not only due to the correlated degrees of freedom within these materials, but also due to the constraints imposed by choice of substrate material. For example, the magnetic properties of manganite materials depend heavily on the bond lengths and angles, resulting in a dead layer at the substrate/film interface [1,2,3]. Recently, techniques have been developed to separate oxide thin films from the substrate after growth, decoupling structural and chemical degrees of freedom at the interface [4]. This technique therefore may allow us to reduce dead layers at the interface of manganite thin films. Thin films of (001)-oriented $\text{LaMnO}_{3+\delta}$ (LMO) were grown using pulsed laser deposition on a water-soluble $\text{Sr}_3\text{Al}_2\text{O}_6$ (SAO) film on top of a (001) SrTiO_3 substrate. After coating the film with a $1\mu\text{m}$ thick support layer of PMMA polymer, the SAO was dissolved in water, allowing the film to be separated from the substrate; this freestanding film could then be transferred to a different substrate, in this case, oxidized Si or LSAT. X-ray diffraction measurements show that freestanding films remain highly crystalline and oriented, but are no longer strained to the substrate. Magnetometry measurements indicate very similar T_C , magnetic anisotropy, and saturation magnetization for both freestanding and epitaxial films, and cannot discern any difference in dead layer. Therefore, polarized neutron reflectometry (PNR) was performed at multiple temperatures to understand the depth profile of both the nuclear and magnetic structure of these freestanding films. As shown in Fig. 1, the film transferred onto the LSAT substrate is very smooth and has an expected structure. Between the substrate and freestanding film is a region with slightly lower nuclear scattering length density (SLD); from STEM and EELS, we find that this region is caused by intermixing with or residue from the water-soluble layer. In contrast, the film transferred onto silicon has a much more complicated structure, as shown in Fig. 2. The PNR data can only be explained with a long-range corrugation or rumpling of the film when placed on the Si substrate, with water incorporated into the interfacial region. After chemical removal of the PMMA support, this corrugation remains. Regardless of the substrate material, the magnetic profile within the freestanding manganite film is uniform, and there is no evidence of the magnetically dead layers at the substrate/film interface seen in epitaxial films. Thus, although choice of substrate can still affect freestanding films through chemical effects – which may have implications for the integration of these freestanding films with silicon-based devices – removing the structural constraints imposed by epitaxial growth is a promising avenue to reduce the dead layer in manganites.

- [1] Zhai, X., Cheng, L., Liu, Y., *et al.* Nat. Commun. 5, 4283 (2014). [2] Moon, E. J., Balachandran, P. V., *et al.* Nano Lett. 14, 2509-2514 (2014). [3] Liao, Z., Zhang, J. Appl. Sci. 9, 144 (2019). [4] Lu, D., Baek, D. J., Hong, S. S., *et al.* Nat. Mater. 15, 1255–1260 (2016).



(a) PNR data and (b) spin asymmetry of a 20 nm LMO freestanding film transferred onto an LSAT substrate, taken at 50K in an in-plane magnetic field of 3T. (c) The nuclear and magnetic depth-profile used to generate the best-fit model.



(a) PNR data and (b) spin asymmetry of a 40 nm LMO freestanding film transferred onto a Si/SiO_x substrate, taken at 7K in an in-plane magnetic field of 1.5T. (c) The nuclear and magnetic depth-profile used to generate the best-fit model.

DE-08. Ferromagnetism in C-Doped ZnO Powder: the Role of Oxygen Vacancies and Carbon Defects.

S. Akbar^{1,2}, S. S. K. Hasanain^{3,5}, M. Jamil³, G. Jaffari³, S. Shah⁴ and P. Rudolf²

1. Katholieke Universiteit Leuven, Leuven, Belgium; 2. Rijksuniversiteit Groningen Faculty of Science and Engineering, Groningen, Netherlands; 3. Physics department, Qaid-i-Azam University, Islamabad, Pakistan; 4. Department of Physics and Astronomy, University of Delaware, Newark, DE, United States; 5. COMSTECH Secretariat, Islamabad, Pakistan

We elucidate the role of defects in C-doped ZnO powders as a source of ferromagnetism. Samples prepared by standard solid-state reaction were sintered in either reducing (95 % Ar + 5 % H) or nitrogen atmosphere. For the samples sintered in a reducing atmosphere X-ray diffraction and X-ray photoelectron spectroscopy data gave evidence for C substitution at Zn sites (C_{Zn}) and carbon in interstitial sites (C_i). X-ray photoelectron and Auger spectroscopy studies demonstrated the presence of oxygen vacancies, zinc interstitials and defect complexes involving C-C bonds. Magnetization studies showed room temperature ferromagnetism in these powder samples, with the saturation magnetization being largest for compositions with a high concentration of carbon defect complexes with (C-C) bonds and with high Zn_i concentration. We relate the zinc interstitials and the defect complexes with C-C bonds to the formation and stabilization of Zn vacancies and thus support the prediction that ferromagnetism in ZnO type oxides is associated with cation (zinc) vacancies. Samples sintered in nitrogen, an atmosphere that favours hole doping, showed instead diamagnetic behaviour.

DE-09. Electronic Properties and Electronic Structure of Co_2YSi ($Y = \text{Ti, V, Cr, Mn, Fe, Co, Ni}$) Heusler Alloys.

A. Semiannikova¹, Y. Perevozchikova¹, A. Lukoyanov^{1,2}, E. Shreder¹,
A. Makhnev¹, P. Korenistov¹ and V. Marchenkov^{1,2}

1. Graduate School of Engineering, Nagoya University, Nagoya, Japan;

2. Ural Federal University, Ekaterinburg, Russian Federation

Energy gap parameters can vary significantly in X_2YZ Heusler alloys [1], where Y -elements are 3d-transition metals and Z -components are s - and p -elements. Therefore, changes in different physical properties, especially, in electronic and optical characteristics are observed. Some features may indicate conditions close to half-metallic ferromagnets (HMFs) [2] and spin gapless semiconductors (SGSs) [3]. Such compounds are promising materials for spintronics because they can possess almost 100% spin polarization of charge carriers. HMFs hold an energy gap near the Fermi level for the current carriers with spin down, while its absence for current carriers with spin up. In turn, SGSs are like HMFs for the spin projection down, however, for the opposite spin direction, the gap is being zero [2, 3]. Thus, the aim of the work is to follow the changes in the electronic transport, optical properties of the Co_2YSi ($Y = \text{Ti, V, Cr, Mn, Fe, Co, Ni}$) Heusler alloys system experimentally, and to compare the results obtained with the electronic band structure calculation, to establish their interconnection and suggest possible proximity to HMF- and/or SGS-states in the Co_2YSi system. According to the data of X-ray structural analysis, all compounds are found to be ordered in the $L2_1$ structure. The electrical resistivity was measured in a wide temperature range using a PPMS setup. The field and the temperature dependences of the magnetic properties being studied too on the SQUID magnetometer. The coefficients of the normal and anomalous Hall Effect were found. The values of current carrier concentration and their mobility were estimated. Results of optical measurements showed good agreement with electronic band structure calculation. Besides, the correlation between the changes in these electronic, optical characteristics, and the coefficient of the current carrier spin polarization depending on the number of valence electrons are observed, which may point to the possible states of the HMF or SGS in this system of Heusler alloys. The work was performed within the framework of the state assignment of the Ministry of Science and High Education of Russia (the themes "Spin", No. AAAA-A18-118020290104-2-2 and "Electron" No. AAAA-A18-118020190098-5) with partial support from the RFBR (project No. 20-32-90065), and the Government of the Russian Federation (Decree No. 211, Contract No. 02. A03.21.0006).

[1] T. Graf, C. Felser, and S.S.P. Parkin, Prog. Solid State Chem., Vol. 39, p. 1 (2011) [2] M.I. Katsnelson, V.Yu. Irkhin, L. Chioncel et al., Rev. Mod. Phys., Vol. 80, p. 315 (2008). [3] X.L. Wang, Phys. Rev. Lett. Vol. 100, p. 156404 (2008).

Session DF
MULTIFERROICS AND MAGNETOELECTRIC PHENOMENA
Pan He, Chair
Fudan University, Shanghai, China

CONTRIBUTED PAPERS

DF-01. Domain Walls in Antiferromagnetic Samples With non-Trivial Surface Topography.

O. Pylypovskiy^{1,2}, N. Hedrich³, K. Wagner³, A.V. Tomilo⁴, B.J. Shields³, T. Kosub¹, D.D. Sheka⁴, D. Makarov¹ and P. Maletinsky³

1. Helmholtz-Zentrum Dresden-Rossendorf, Dresden, Germany; 2. Kyiv Academic University, Kyiv, Ukraine; 3. Universitat Basel, Basel, Switzerland; 4. Taras Shevchenko National University of Kyiv, Kyiv, Ukraine

Antiferromagnets (AFMs) have regained strong attention from the magnetism community especially with the advent of antiferromagnetic spintronics [1]. The key operational element of spintronic devices is represented by information carriers, such as domain walls (DWs) and skyrmions. The simplest AFM DW separates two regions with the opposite orientation of the Neel order parameter. Although highly relevant, the experimental studies of AFM DWs (visualization, dynamics, mechanics) are challenging because of strict requirements on measurement techniques to access their properties. Here, we overcome these limitations and conduct detailed, quantitative studies of the mechanics and the nanoscale properties of individual, antiferromagnetic DWs in a single crystal Cr_2O_3 – a room-temperature, magneto-electric, insulating AFM [2]. Our results reveal a remarkably pristine DW behaviour, which is governed by DW energy minimization and boundary conditions, but largely unaffected by pinning or disorder – a “textbook example” of antiferromagnetic DW physics. In our experiment, the crystal’s (0001) surface is patterned by a grid of mesas with mean thickness and width $t=166$ nm and $w=2400$ nm, respectively. The DW is nucleated by means of magnetoelectric field cooling by inverting the electric bias field over opposite halves of the sample. The DW may also be dragged through the mesa pattern by a focused laser spot. The magnetic texture is imaged using Nitrogen Vacancy (NV) magnetometry [3]. We find that the DW mimics an elastic surface with specific mechanical properties, determined by the interaction with the topographic features of the sample where the DW is (i) deflected from the straight plane crossing the mesa; (ii) bent around mesa corners. To address the DW behaviour theoretically, we perform large-scale spin-lattice simulations with GPU speed-up [4]. The analytical Ansatz is developed based on the numerically-obtained, three-dimensional DW profile. All main features of the DW behaviour can be determined taking into account the nearest-neighbour exchange and uniaxial anisotropy for a general model of a bipartite AFM. Crossing the mesa, the DW experiences an S-shaped distortion observed at the mesa surface, which is the result of exchange-driven boundary conditions at the side faces of the mesa, see Fig. 1. Below the top surface, the DW possesses a twist to match this distortion with the straight plane far below the sample’s surface. We find that the DW surface is deflected from the plane over a characteristic depth of $0.34w$. Comparison of the equilibrium DW direction in bulk and at the mesa’s top surface allows us to derive an effective Snell’s law for the DW behaviour at the sample’s surface with the given incidence and refraction angles θ_1 and θ_2 . The effective refraction coefficient is determined by the analytical energy minimization and reads $n_{\text{eff}} = 1 + 3.1t/w + O(\theta_1)$. Controlled manipulation via laser not only enables DW dragging through the mesa, but also pinning at mesa corners. The shape of the DW surface is governed by its intrinsic elasticity. In terms of mechanics of an elastic ribbon, the corresponding tension coefficient is determined by the temperature-dependent exchange stiffness and anisotropy coefficient. This allows for curved DW states in which it is pinned at the opposite mesa sides. Using mesas as bistable pinning sites, we propose a potential DW-based AFM memory concept. Here, the memory state “0” or “1” is associated with the direction of the Neel order parameter at the mesa surface. We have realized such pinning sites experimentally and have shown manipulation of the state via laser dragging. In summary, we realize engineered DW potentials and control over DW trajectories by topographic structuring and manipulation of the DW position by means. The physics of AFM DWs in a single crystal with non-trivial surface topography is described theoretically by means of spin-lattice simulations and analytical model. A novel nanoscale AFM memory architecture is suggested.

[1] T. Jungwirth, J. Sinova, A. Manchon et al, Nat. Phys. Vol. 14, p. 200 (2018); T. Jungwirth, X. Marti, P. Wadley et al, Nat. Nano. Vol. 11, p. 231 (2016); V. Baltz, A. Manchon, M. Tsoi et al, Rev. Mod. Phys. Vol. 90, p. 015005 (2018); O. V. Pylypovskiy, D. Y. Kononenko, K. V. Yershov et al, Nano Lett. Vol. 20, p. 8157 (2020) [2] N. Hedrich, K. Wagner, O. V. Pylypovskiy et al, arXiv:2009.08086 [3] L. Rondin, J.-P. Tetienne, T. Hingant et al, Rep. Prog. Phys. Vol. 77, p. 056503 (2014); N. Hedrich, D. Rohner, M. Batzer et al, Phys. Rev. Applied, Vol. 14, p. 064007 (2020) [4] SLasi simulation package, <http://slasi.knu.ua>; O. V. Pylypovskiy, D. D. Sheka, Book of Abstracts, EUROPT Workshop, p. 11 (2013)

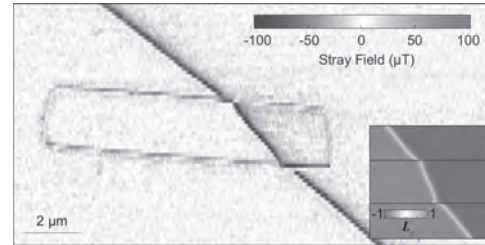


Fig. 1. The deflection of the DW from the straight path and distortion at the mesa surface shown by the stray magnetic field image taken using Nitrogen Vacancy microscopy. Inset shows the DW trajectory in spin-lattice simulations.



Fig. 2. Concept of DW-based AFM memory with bits defined by the direction of the Neel order parameter at the mesa top surface (red or blue color, respectively).

DF-02. Oxygen vs. Nitrogen Magneto-Ionics.

J. de Rojas¹, A. Quintana², A. Lopeandía¹, J. Salguero³, B. Muñiz³, F. Ibrahim⁴, M. Chshiev^{4,5}, A. Nicolenco¹, M. Liedke⁶, M. Butterling⁶, A. Wagner⁶, L. Henderick⁷, J. Dendooven⁷, C. Detavernier⁷, V. Sireus¹, L. Abad⁸, C.J. Jensen², K. Liu², J. Nogues^{9,10}, J. Costa-Krämer³, E. Menéndez¹ and J. Sort^{1,10}

1. Physics, Universitat Autònoma de Barcelona, Barcelona, Spain; 2. Physics, Georgetown University, Washington, DC, United States; 3. Instituto de Micro y Nanotecnología (CNM-CSIC), Tres Cantos, Spain; 4. Univ. Grenoble Alpes, CEA, CNRS, Spintec, Grenoble, France; 5. Institut Universitaire de France, Paris, France; 6. Helmholtz-Zentrum Dresden-Rossendorf, Dresden, Germany; 7. Solid State Sciences, Universiteit Gent, Gent, Belgium; 8. Institut de Microelectrònica de Barcelona, (CNM-CSIC), Bellaterra, Spain; 9. Institut Català de Nanociència i Nanotecnologia, Bellaterra, Spain; 10. Institutio Catalana de Recerca i Estudis Avançats, Barcelona, Spain

Voltage-controlled magnetism, where magnetic properties are controlled via an applied electric field instead of current, could represent a significant increase in energy savings in future magnetically actuated devices. Practically, however, this approach faces several important obstacles, such as thickness limitations in electrically charged metallic films, mechanical failure in strain-mediated piezoelectric/magnetostrictive devices, and a lack of room-temperature multiferroics. Voltage-driven ionic motion (magneto-ionics) may provide a path forward by avoiding many of these drawbacks. Nevertheless, translating magneto-ionics into real world devices requires significant improvements in magneto-ionic rates, cyclability, and magnetization. Here, we report on the development of magneto-ionics in single-layer, semiconducting transition metal oxides and nitrides, and the subsequent enhancements in their performance. We first present electrolyte-gated and defect-mediated O transport in single-layer, paramagnetic Co_3O_4 at room temperature (i.e. without thermal assistance), which allows voltage-controlled magnetic switching (referred to here as ON-OFF ferromagnetism: Fig. 1) via internal reduction/oxidation processes^[1]. Negative bias partially reduces Co_3O_4 to Co, resulting in films with Co- and O-rich areas (ferromagnetism: ON). Positive bias re-oxidizes Co back to Co_3O_4 (paramagnetism: OFF). We show that the bias-induced motion of O is caused by mixed vacancy clusters, with O motion promoted at grain boundaries and assisted by the development of O-rich diffusion channels. The generated ferromagnetism is shown to be stable, and easily erased by sufficient positive bias. This voltage-induced process is demonstrated to be compositionally, structurally, and magnetically reversible and self-contained. We then show that room-temperature magneto-ionic effects in electrolyte-gated paramagnetic Co_3O_4 films can be significantly increased, both in terms of generated magnetization (6 times larger) and speed (35 times faster), if the electric field is applied using an electrochemical capacitor configuration (utilizing an underlying conducting buffer layer: Fig. 2) instead of electric-double-layer transistor-like configuration (placing the electric contacts at the side of the semiconductor)^[2]. In addition to gains in speed, magnetization measurements show a marked increase in the squareness ratio and a decrease in the switching field distribution of the hysteresis loops in Co_3O_4 biased in the capacitor configuration, the result of the formation of more uniform ferromagnetic regions. These results are attributed to the uniform electric field applied throughout the film, as confirmed by COMSOL simulations. As the measured films are quite thick, further miniaturization promises even greater magneto-ionic rates. We then demonstrate room-temperature voltage-driven nitrogen magneto-ionics (i.e., N transport) by electrolyte-gating of a CoN film^[3]. Nitrogen magneto-ionics in CoN is compared to oxygen magneto-ionics in Co_3O_4 , in films using an electrochemical capacitor configuration. Both materials are shown to be nanocrystalline (face-centered cubic structure), and show reversible voltage-driven ON-OFF ferromagnetism (Fig. 1). Nitrogen transport is found to occur uniformly throughout the film, creating a plane-wave-like migration front, without assistance of diffusion channels. Nitrogen magneto-ionics also requires lower threshold voltages and exhibits enhanced rates and cyclability, due to the combination of a lower critical electric field required to overcome the energy barrier for ion diffusion and the lower electronegativity of nitrogen with respect to oxygen, consistent with *ab initio* calculations contrasting N vs. O motion in cobalt stacks. These

results place nitrogen magneto-ionics as a robust alternative for efficient voltage-driven effects and, along with oxygen magneto-ionics, may enable the use of magneto-ionics in devices that require endurance and moderate speeds of operation, such as brain-inspired/stochastic computing or magnetic micro-electro-mechanical systems.

[1] A. Quintana, E. Menéndez, M. O. Liedke et al., ACS Nano, Vol. 12, p. 10291 (2018) [2] J. de Rojas, A. Quintana, A. Lopeandía et al., Advanced Functional Materials, Vol. 30, p. 2003704 (2020) [3] J. de Rojas, A. Quintana, A. Lopeandía et al., Nature Communications, Vol. 11, p. 5871 (2020)

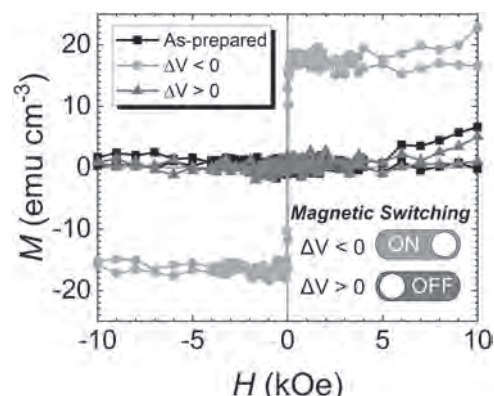


Fig. 1. Hysteresis loops (M vs. H) of as-prepared, negatively-biased, and positively-biased CoN films at magneto-ionic activation voltages.

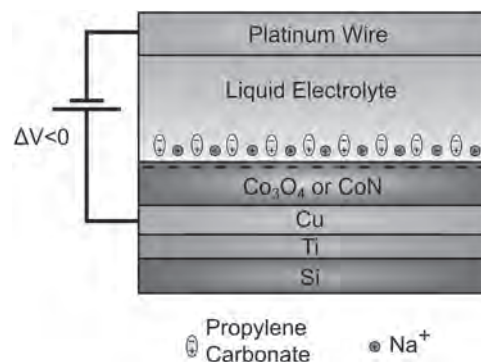


Fig. 2. A schematic of the electrochemical capacitor configuration used to bias cobalt-oxide (Co_3O_4) and cobalt-nitride (CoN) films.

DF-03. Magneto-Ionic Effect in Iron Triad Nanostructures With Different Shapes and Composition.

M. Kutuzau¹, M. Nichterwitz^{1,2}, S. Honnali¹, D. Wolf³, S. Schneider³, K. Nielsch^{1,4} and K. Leistner¹

1. Leibniz-Institut für Festkörper- und Werkstofforschung Dresden eV, Dresden, Germany; 2. Physical Chemistry, Technische Universität Dresden, Dresden, Germany; 3. Dresden Center for Nanoanalysis, Technische Universität Dresden, Dresden, Germany; 4. Institute of Material Science, Technische Universität Dresden, Dresden, Germany

Interfacial electrochemical effects on magnetism, often also named magneto-ionic effects, are an emerging room-temperature and low-voltage approach in the research area of voltage control of magnetism [1]. In magneto-ionic systems, the magnetic layer is gated via a solid or liquid electrolyte and the applied voltage triggers ion migration and interfacial redox reactions, which impact the magnetic properties. In contrast to multiferroic systems and capacitive electronic charging, magneto-ionic concepts make significant magnetic property changes possible at room temperature and without the need for strain mediation [2], [3]. Since the mechanism is based on electrochemical charge transfer at the electrode/electrolyte interface, the morphology and the composition may be key to the magneto-ionic efficiency. We report magneto-ionic manipulation of ultrathin films in extended and stripe geometry and 3D nanoplatelet structures. In situ magnetic transport measurements are used in this study to determine and analyze the magneto-ionic effect. For FeOOH nanoplatelets, the application of a low voltage via liquid electrolyte gating yields an ON switching of magnetization (deduced from changes of the anomalous Hall resistance, see Figure 1a) [4]. The transformation proceeds via voltage-induced dissolution/redeposition, with the initially paramagnetic FeOOH structure as iron ion reservoir. The time-dependency of the reduction reaction enables the non-volatile setting of magnetic layers with different total magnetic moments. A large reversible magneto-ionic change of magnetization of up to 15% is achieved in the resulting iron films, which is explained by the enhanced roughness of the iron films obtained from the nanoplatelet structure. For thin Fe₃O₄/Fe films in stripe geometry, we achieved a tunable magnetoresistance by electrolytic gating (Figure 1b) [5]. Here, the tuning mechanism relies on voltage-triggered redox reactions, which locally affect the Fe₃O₄ regions. In the low-magnetic-field region (<1 T), a crossover from positive to negative magnetoresistance is achieved by a voltage change of only 1.72 V. We will further present first results on the impact of the composition in iron triad magneto-ionic systems on magnetic properties by going beyond iron structures. The proposed approach is promising for the development of energy-efficient magnetic switches, sensors, and magnetic actuation, and may offer new avenues in magnetoelectronic devices.

[1] K. Leistner, Current Opinion in Electrochemistry Vol. 25, p. 100636 (2021) [2] C. Navarro-Senent et al., APL Materials, Vol. 7, p. 030701 (2019) [3] K. Duschek et al., J. Mater. Chem. C, Vol. 6, p. 8411 (2018) [4] M. Nichterwitz et al., J. Phys. D: Appl. Phys., Vol. 53, p. 084001 (2020) [5] M. Nichterwitz et al., ACS Appl. Electron. Mater., Vol. 2, p. 2543 (2020)

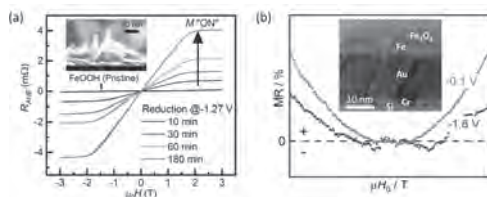


Fig. 1 (a) electric “ON” switching of magnetism via electrolytic gating of FeOOH nanoplatelets. Magnetization curves as measured by anomalous Hall effect (AHE) after reduction at -1.27 V for different reduction times. The inset shows the cross-sectional REM image of a FeOOH pristine sample. (Adapted from [4]). (b) Voltage-control of the magnitude and the sign of magnetoresistance (MR) of FeO_x/Fe nanocomposite thin films by electrolytic gating in LiOH. The inset shows a cross-sectional HR-TEM image of the pristine iron oxide-iron nanocomposite film. (Adapted from [5]).

DF-04. The Impact of Stress on the Magnetoelectric Coupling Between a Multilayered Ferromagnet and a Ferroelectric Single Crystal.L. Garten¹, K. Bussmann¹, P. Finkel¹ and M. Staruch¹*1. US Naval Research Laboratory, Washington, DC, United States*

Heterostructured artificial multiferroics have opened up the possibility for novel applications like multi-state memory or magnetic field sensors, as well as enhance performance of energy harvesters or tunable antennae or phase shifters. Magnetic thin films have been grown under strain with the goal of utilizing the large strain generated with a stress-induced interferroelectric phase transition in single crystal $\text{Pb}(\text{In}_{1/2}\text{Nb}_{1/2})\text{O}_3\text{-Pb}(\text{Mg}_{1/3}\text{Nb}_{2/3})\text{O}_3\text{-PbTiO}_3$ (PIN-PMN-PT) [1] to optimized the magnetoelectric (ME) coupling. It was previously observed that for magnetostrictive phases laminated under zero stress, this phase transitional stress did not result in any ME coupling [2]. In this work, FeCo/Ag multilayered films were grown on (011) PIN-PMN-PT single crystals using sputter deposition. The FeCo/Ag multilayers were deposited onto two substrates: One with zero stress, while another was grown simultaneously with the substrate under an in-situ strain of $\sim 1400 \mu\epsilon$ along the [001] direction using a home-built stress fixture. The magnetic easy axes varied significant between the two films after the strain had been released due to the difference in the stresses in the film. The sample grown under zero strain showed a 90° rotation of the magnetic easy axis under the collective effect of tensile and compressive stresses in-plane imposed by the piezocrystal. The change in magnetization with applied voltage was large at zero stress but decreases with increased external stress applied to the sample, which is expected resulting from a stress-induced change in magnetic anisotropy that limits the effects of magnetoelastic-imposed stresses. In contrast, the magnetization loops for the sample grown in the stress fixture was unchanged with application of stress during the measurements, and zero magnetoelectric effect was observed. The possibility of high stresses beyond the plastic limit of FeCo due to both applied pre-stress and the intrinsic stress from sputter deposition are investigated, and the results will be compared.

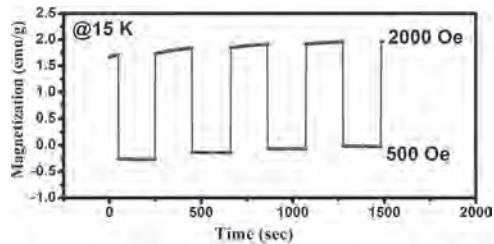
[1] P. Finkel, M. Staruch A. Amin, M. Ahart, and S.E. Lofland, *Scientific Reports* 5, 13770 (2015). [2] M. Staruch, J.F. Li, Y. Wang, D. Viehland, and P. Finkel, *Appl. Phys. Lett.* 105, 152902 (2014).

DF-05. Structural Transformation, Magnetization Reversal Along With Magnetic Switching Effect in Cr Doped GdMnO₃ Perovskite.

P. Tiwari¹ and C. Rath¹

1. Materials Science, Indian Institute of Technology BHU Varanasi, Varanasi, India

Due to their enthralling fundamental physics along with potential application in the field of multiferrocity, rare earth manganites have received a lot of attention within research communities. Here we have investigated the effect of Cr in structural as well as in different magnetic transitions in GdMnO₃. In 50 % Cr doped sample, we have observed a O type concentration from Rietveld refinement of X-ray diffraction patterns. The structural transformation is accompanied with a considerable decrease in the Jahn–Teller distortion factor also confirmed from XRD. An enhancement in Neel temperature (T_N) from ~ 42 K to ~ 140 K is confessed from Magnetic measurement. Along with increase in T_N , interestingly, we inspect magnetization reversal (MR) with spin reorientation (T_{SR}) for Cr doped sample. On the basis of competition between Mn, Cr and Gd the mechanism for such a magnetic behavior is discussed. The incorporation of Cr not only constructively modifies the crystal structure but also evokes the magnetic reversal phenomenon. The promising structure and magnetic properties of Cr doped GdMnO₃ offer potential pathways for spintronics and magnetic switching devices.



DF-06. *in-Situ* Single Crystal Synchrotron X-ray Diffraction Study on the Structure of Multiferroic Antiferromagnet $\text{Ba}_2\text{MnGe}_2\text{O}_7$ From low- to High-Temperature.

R. Dutta¹, H. Thoma², D. Vadim³, D. Chernyshov³, B. Nafrađi⁴, T. Masuda⁵ and V. Hutanu¹

1. Institute of Crystallography, RWTH Aachen University and Julich Centre for Neutron Science (JCNS) at Heinz Maier-Leibnitz Zentrum (MLZ), 85748, Garching, Germany; 2. Julich Centre for Neutron Science (JCNS) at Heinz Maier-Leibnitz Zentrum (MLZ), 85748, Garching, Germany; 3. Swiss-Norwegian Beam Lines at ESRF, rue Jules Horowitz, FR-38042, Grenoble Cedex 9, France; 4. Ecole Polytechnique Federale de Lausanne, Laboratory of Nanostructures and Novel Electronic Materials, 1015 Lausanne, Swaziland; 5. International Graduate School of Arts and Sciences, Yokohama City University, Yokohama, Kanagawa 236-0027, Japan

Melilite-type multiferroic oxides such as $\text{Ba}_2\text{MGe}_2\text{O}_7$ ($\text{M} = \text{Cu}, \text{Mn}, \text{Co}$) are the potential candidates for studying exotic quantum phenomena including low-energy magnetic, electronic and structural properties along with the magnetoelectric effect. Spontaneous electric polarization in $\text{Ba}_2\text{MnGe}_2\text{O}_7$ arises due to the spin-dependent d - p hybridization mechanism between the transition metal $3d$ and ligand p orbitals like its sister compounds $\text{Ba}_2\text{CoGe}_2\text{O}_7$ and $\text{Ba}_2\text{CuGe}_2\text{O}_7$ [1-3]. While all the three compounds exhibit similar non-centrosymmetric tetragonal nuclear structure with space group P-42₁m (n.113) below the corresponding Néel temperatures (T_N), they differ from each other mainly by their local spin microstructure [1, 4-6]. But there is no single report on any structural phase transition if exists in these materials from high-T to below T_N . This is crucial to investigate in detail the structural evolution with temperature as the spin-dependent d - p hybridization mechanism involving the coupling between transition metal ions and ligand oxygen atoms strongly depends on the corresponding bond-length inside the MO_4 tetrahedron. Here we report a systematic structural study of the magnetoelectric $\text{Ba}_2\text{MnGe}_2\text{O}_7$ under varying temperature from RT to 673 K and cooling from 673 K to 110 K using single crystal synchrotron radiation diffraction at BM01, ESRF. Within this entire temperature range the structure was described in the same crystallographic space group P-42₁m with slight change in lattice parameters. From the reconstructed 2D reciprocal map obtained at the all temperatures we have observed no appearance of extra reflection or any extra symmetry extinction compared to RT phase (sg:P-42₁m), therefore no phase transition has been detected from 673 K down to 110 K. Interestingly, the forbidden reflections, which arise from multiple diffraction so called “Renninger effect” [7], observed at all temperatures. However, the structural parameters e.g. bond-lengths in the MnO_4 tetrahedron, anisotropic displacement parameters (ADP) and lattice constant changes with temperature continuously. We have refined the structures in the space group P-42₁m using JANA2006 [8] and the results are presented in the Fig. 1. Lattice parameters were refined before the data reduction using CrysAlisPro [9] which give nice agreements with the reported values e.g. $a = b = 8.4847(3)$ Å and $c = 5.5162(4)$ Å at RT. ADP ellipsoids of oxygen atoms at 673 K are enlarged due to high temperature effects while after cooling back to RT resemble well the starting value before heating. While cooling at 110 K, ADP ellipsoids of O3 atoms are flattened in one directions. Local arrangements of MnO_4 tetrahedron and the electron density distributions are slightly different for those different temperatures. This feature could have a direct consequences to the observed dielectric relaxation (dipole relaxation) in $\text{Ba}_2\text{MnGe}_2\text{O}_7$ around 150 – 210 K [10], which was suggested to be results of changeable valence state of Mn transition metal ions though be observed in ceramic material. Changeable valence state of Mn atoms in $\text{Ba}_2\text{MnGe}_2\text{O}_7$ is more likely not the case, rather high-spin ($S = 5/2$) or low-spin ($S = 1/2$) magnetic ground state is possible in the d - p hybridization process [6]. Figure 2 shows the reconstructed (0KL) planes obtained at RT (starting phase), 673 K and 110 K. It is immediately noticeable that all the allowed structural Bragg reflections did not change with temperature except the intensity. In this space group forbidden reflections are found at $(h00)$ and $(0k0) = 2n+1$ which are marked as yellow circle. The evolution of the intensity of the main Bragg peak shown in fig. 2(d) is completely reversible while cooling from 673 K, whereas the change in intensity of the forbidden reflections are quite dramatic only during heating. In summary, our first systematic temperature

dependent structural study on $\text{Ba}_2\text{MnGe}_2\text{O}_7$ single crystal using synchrotron radiation diffraction indicates that no structural phase transition take place in the large temperature range from 673 to 110 K. The observed forbidden peaks of weak intensity are of purely parasitic nature (Renninger scattering). Their intensity ratio to the main Bragg peaks in the range of RT to 110 K are well consistent with our previous neutron diffraction study at 10 K and RT only. Detailed investigation of the structural parameters, especially the flattened electron density of O3 atoms in the MnO_4 tetrahedral at 110 K, could relate the reported dielectric properties at low temperature region [10]. This study may sheds lights on the structural dependent d - p hybridization mechanism when a finite electric polarization exist under the external magnetic field [1] far above the antiferromagnetic ordering temperature ($T_N \sim 4$ K). In our opinion this is the advanced and novel study in these Melilite multiferroic oxides where the knowledge of such structural information are crucial in the field of magnetoelectric coupling based device applications and important to have beforehand for studying magnetic structure, strongly correlated electronic properties and the temperature dependent crystal-electric-field (CEF) excitations.

[1] H. Murakawa et al., Phys. Rev. B 85, 174106 (2012). [2] S. Miyahara et al., Journal of the Physical Society of Japan 80, 073708 (2011). [3] H. Murakawa et al., Phys. Rev. Lett. 105, 137202 (2010). [4] A. Zheludev et al., Phys. Rev. B 54, 15163 (1996). [5] A. Zheludev et al., Phys. Rev. B 68, 024428 (2003). [6] T. Masuda et al., Phys. Rev. B 81, 100402(R) (2010). [7] A. Sazonov et al., Inorg. Chem., 57, 5089–5095 (2018). [8] V. Petricek et al., Z. Kristallogr. 229 (5), 345-352 (2014). [9] CrysAlisPRO v.46, (2018), Oxford Diffraction /Agilent Technologies, England. [10] J. Su et al., (ISAF/ECAPD/PFM), 2012, vol. 1–3, pp. 9–13, doi: <http://dx.doi.org/10.1109/ISAF.2012.6297818>.

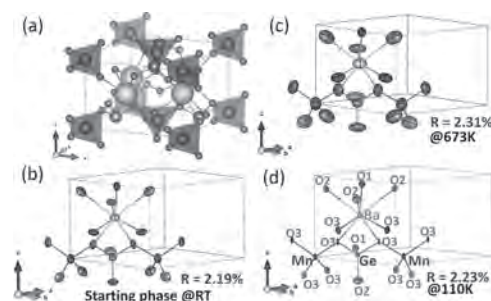


Figure 1: (a) Chemical unit cell of $\text{Ba}_2\text{MnGe}_2\text{O}_7$ structure at RT. (b-d) Refined ADPs of all atoms in the unit cell at RT, 673 and 110 K where “R” denotes the refinement R-factor.

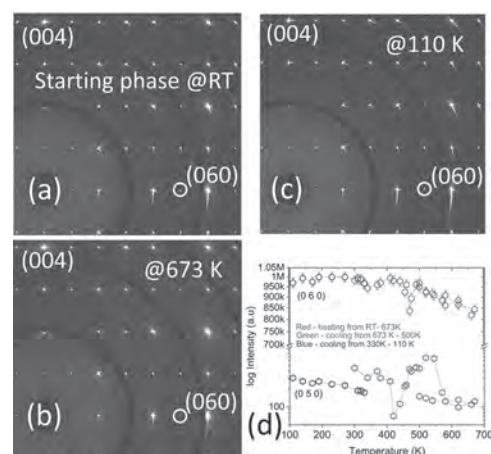


Figure 2: (a-c) reconstructed (0KL) reciprocal maps. (d) Intensity vs. temperature plot for main Bragg reflection (060) and forbidden reflection (050).

DF-07. Magnetoelectric Excitations in the Polar Antiferromagnets Ni-Based Tellurates $a_{3-x}B_xTeO_6$ ($a, B = Ni, Mn, Co, x=1-2$).

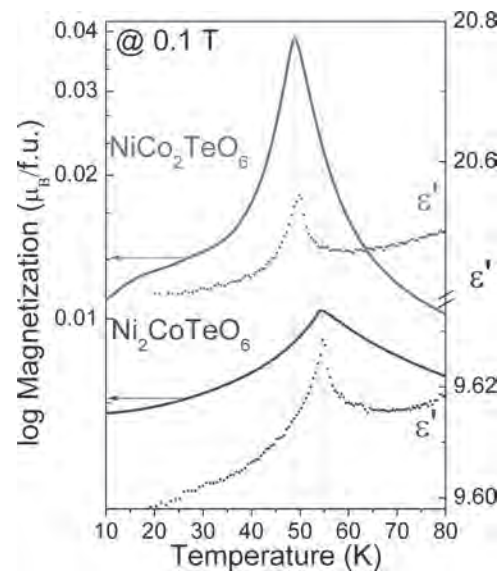
S. Skiadopoulou^{1,2}, M. Retuerto³, F. Borodavka², C. Kadlec², F. Kadlec², M. Greenblatt³ and S. Kamba²

1. School of Physics, CRANN, Trinity College Dublin Faculty of Engineering Mathematics and Science, Dublin, Ireland; 2. Dielectrics, Institute of Physics of the Czech Academy of Science, Praha, Czechia; 3. Chemistry and Chemical Biology, Rutgers The State University of New Jersey, New Brunswick, NJ, United States

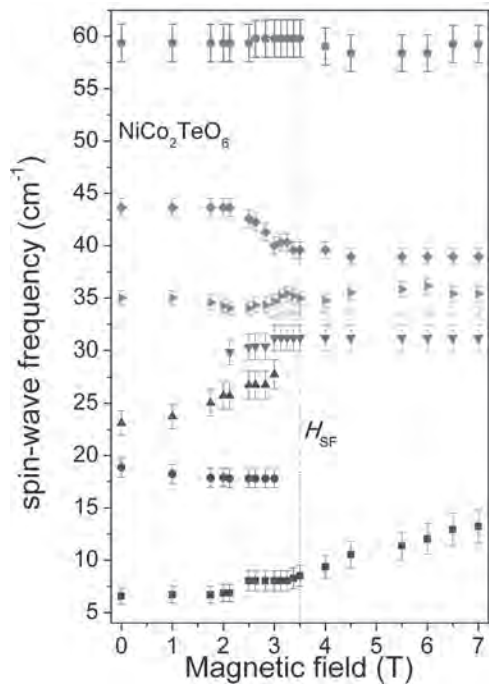
Multiferroics (MFs) are materials that can combine at least two primary ferroic properties: ferromagnetism, ferroelectricity and ferroelasticity.[1] In the case of magnetoelectric (ME) MFs, coupling between ferroelectricity and ferromagnetism occurs. Throughout the history of MFs, the *static ME coupling* has peaked the interest of the MF community. However, there is great significance in what happens away from the static regime in MF systems; hence the popular movement toward the exploration of the *dynamical ME effect* in recent years.[2] Both cases share the same quantum-level microscopic mechanisms, but in the latter case the magnetization and polarization order parameters are not static, but oscillatory. This oscillating behaviour of polarization and magnetization manifests in the hybrid elementary excitations known as *electromagnons*, which very often lie in the terahertz (THz) or far infrared (IR) region of the spectrum. As the very word indicates, the electromagnons are *electro-active magnons*,[3] namely collective spin and lattice excitations that couple the dielectric and magnetic properties. Therefore, both the electric and magnetic component of the electromagnetic radiation can be brought into play to excite and detect such dynamical behaviour. The polar antiferromagnet Ni_3TeO_6 transcends the ME performance of most single-phase MFs, exhibiting non-hysteretic colossal ME coupling.[4] A collinear antiferromagnetic (AFM) order appears below $T_N = 53$ K, inducing a tremendous increase in the existing - but negligible - polarization of the R3 polar structure (up to $3,280 \mu C m^{-2}$ at 2 K). The highest ME coupling value occurs at the spin-flop transition at 8 T. The presence of dynamical ME coupling in Ni_3TeO_6 was reported in 2017 by Skiadopoulou *et al.*[5] Two spin excitations were observed simultaneously in Raman and time-domain THz spectra below the Néel temperature $T_N=53$ K. These magnons showed high tunability in external magnetic field. Due to symmetry considerations, these excitations were assigned to *electromagnons*. Since Ni_3TeO_6 presents a collinear AFM spin structure, the symmetric exchange striction is most probably responsible for the emergent dynamical ME effect. The quest for compounds with enhanced ME coupling led to the investigation of a series of compounds of the form $A_{3-x}B_xTeO_6$ ($A, B = Ni, Mn, Co, x=1-2$), inspired by the highly praised ME behaviour of Ni_3TeO_6 . In Ni_2MnTeO_6 , although the spin order and magnon spectra closely resemble Ni_3TeO_6 ,[6] partial substitution of Ni by Mn shows increased T_N by 20 K, while preserving the non-centrosymmetric structure R3.[6],[7] In addition, the spin-flop transition takes place at an external magnetic field of 5 T, which is 3 T lower than in Ni_3TeO_6 . The increase in Neel temperature and decrease of the critical magnetic field which may trigger a colossal ME effect are in favour of possible ME applications. More recently, Ni_2CoTeO_6 and $NiCo_2TeO_6$ compounds were synthesised for the first time, in the form of single crystals and ceramics.[8] The ME properties are preserved by Co-substitution. The non-centrosymmetric R3 space group is maintained at least up to RT for both Ni_2CoTeO_6 and $NiCo_2TeO_6$. The AFM ordering appears at $T_N = 54$ and 49 K for Ni_2CoTeO_6 and $NiCo_2TeO_6$, respectively (Fig. 1). As anticipated, both compounds evidence an interplay of magnetic and dielectric properties, indicated by the dielectric anomaly seen at T_N (Fig. 1). In contrast to the magnetic ordering in the previously studied Ni_3TeO_6 and Ni_2MnTeO_6 , which are collinear along the *c*-axis, both Co-based compounds present a helical non-collinear structure with the spins in the *ab*-plane. The magnetic structures of both compounds are quite similar, with a small difference between the magnetic propagation vectors: $k_1=(0, 0, 1.299(4))$ and $k_2=(0, 0, 1.2109(1))$, for Ni_2CoTeO_6 and $NiCo_2TeO_6$, respectively. Hysteretic spin-flop transitions were observed near 8 T (Ni_2CoTeO_6) and 4 T ($NiCo_2TeO_6$), unlike Ni_3TeO_6 and Ni_2MnTeO_6 , which did not show any hysteretic behavior. Below T_N both compounds demonstrate numerous spin-excitations in the THz range, which are considerably influenced by external magnetic field, with clear modifications at the spin-flop transition

of ~ 4 T for the case of $NiCo_2TeO_6$ (Fig. 2). Six magnons strongly dependent on magnetic field are present in the THz spectra of the Co-richer compound $NiCo_2TeO_6$. Both compounds present at least one magnetic excitation simultaneously seen by Raman spectroscopy, possibly revealing the magnetoelectric character of the magnon.

[1] H. Schmid, *Ferroelectrics* Vol. 162, p.317 (1994). [2] Y. Tokura, S. Shinichiro, and N. Naoto, *Reports Prog. Phys.*, Vol. 77, p.76501 (2014). [3] M. Bibes, J.E. Villegas, and A. Barthélémy, *Adv. Phys.*, Vol. 60, p.5 (2011). [4] Y.S. Oh, S. Artyukhin, J.J. Yang, et al., *Nat Commun*, Vol. 5, p.3201 (2014). [5] S. Skiadopoulou, F. Borodavka, C. Kadlec, et al., *Phys. Rev. B*, Vol. 95, p.184435 (2017). [6] M. Retuerto, S. Skiadopoulou, F. Borodavka, et al., *Phys. Rev. B*, Vol. 97, p.144418 (2018) [7] R. Mathieu, S.A. Ivanov, P. Nordblad, et al., *Eur. Phys. J. B*, Vol. 86, p.1 (2013). [8] S. Skiadopoulou, M. Retuerto, F. Borodavka, et al. *Phys. Rev. B*, Vol. 101, p.14429 (2020)



Temperature dependences of magnetization (at 0.1 T) and permittivity (at 0.1 MHz) for Ni_2CoTeO_6 and $NiCo_2TeO_6$ ceramics, presenting AFM phase transition at 54 and 49 K, respectively. The dielectric anomalies also appear at the same temperatures for each compound.



Magnetic field dependence of spin-wave frequencies in the THz range for $\text{NiCo}_2\text{TeO}_6$, at 5 K. The spin-flop transition is clearly seen at approximately 3 T (dotted line), by the steps on the magnon branches, as well as both the appearance of new modes and extinction of ones present in the low-field phase.

DF-08. New Insight About the Magnetic Order in Peculiar Multiferroic Ba₂CoGe₂O₇ by Revealing the Sign of the Dzyaloshinskii-Moriya Interaction by Polarized Neutron Diffraction.

H. Thoma¹ and V. Hutanu^{1,2}

1. Jülich Centre for Neutron Science (JCNS) at Heinz Maier-Leibnitz Zentrum (MLZ), Forschungszentrum Jülich GmbH, Garching, Germany;
 2. Institute of Crystallography, Rheinisch-Westfälische Technische Hochschule Aachen, Aachen, Germany

The antiferromagnetic Ba₂CoGe₂O₇ has aroused great interest in current condensed matter research over the last decade, starting in 2008 when the appearance of ferroelectricity below the magnetic ordering temperature and a strong in-plane anisotropy were first reported [1]. Since the observed unique behaviour of the electric polarization with changing magnetic field in Ba₂CoGe₂O₇ could not be explained by existing models, they accounted these effects to the presence of Dzyaloshinskii-Moriya interaction (DMI) [2,3], which is allowed by its non-centrosymmetric space group P-4₂m. Subsequently, to better explain this unconventional phenomena, a novel spin-dependent p-d hybridization mechanism of multiferroicity [4] and a spontaneous toroidal effect mechanism [5] were proposed. Also spin-nematic interactions were suggested as origin for the experimentally observed peculiar behaviour of the induced polarization [6]. This large variety of new models instigated further detailed studies of Ba₂CoGe₂O₇, including a detailed determination of the crystal structure [7] and a theoretical symmetry analysis, identifying most of the observed peculiar effects as symmetry-forced results of the weak ferromagnetic (WF) canting, resulting from DMI [8]. This further endorses the DMI as a fundamental basis for the emergence and understanding of the unconventional multiferroic behavior observed in Ba₂CoGe₂O₇. Therefore, not only the magnitude of the DMI exchange constant, but also its sign is of particular interest. In general, polarized neutron diffraction (PND) was proposed as one of the most suitable methods to determine this absolute DMI-sign in WF materials [9]. PND provides a direct access to the scattering contribution from nuclear-magnetic interference and thus reveals the phase difference between the nuclear and magnetic structure. This permits to determine the absolute direction of the individual magnetic moments with respect to the atomic arrangement, distinguishing between two equivalent AFM arrangements. In our study we performed PND measurements on a high quality Ba₂CoGe₂O₇ single crystal at the polarized diffractometer VIP at the Orphée reactor of LLB (Saclay, France) [10]. The crystal was placed in a high magnetic field of 6 T along the [100] direction to obtain a single domain state with the WF moments aligned along and the AFM structure perpendicular to the applied field direction. The asymmetry values $A = (I^- - I^+) / (I^- + I^+)$ for 545 Bragg reflections were measured. Here, I_{\pm} is the measured intensity for the two antiparallel spin orientations of the incoming neutron beam. Using these values and the crystal structure reported previously [7], we could refine the precise orientation of the AFM moments in Ba₂CoGe₂O₇ at 2 K (Fig. 1). Overall, we observed a good fit agreement between the calculated and experimentally measured asymmetry values (Fig. 2). The resulting magnetic moment value of around 2.6 μ_B/Co^{2+} is in good agreement with previous non-polarized neutron and macroscopic studies [11]. Performing a detailed symmetry analysis of the magnetic structure, including the symmetry averaging of the DMI vector, we deduced its restriction along the z-axis. Depending on the absolute sign of the D_z component, two symmetry-equivalent AFM spin configurations could be realized. By comparison with the experimentally observed magnetic moment directions in regard to the quantization field (Fig. 1), we can finally and unambiguously determine the negative sign of D_z in Ba₂CoGe₂O₇. To further emphasize the power of the presented PND method, we additionally relate the D_z -sign to the expected asymmetry-sign of the single exemplary (210) reflection. By evaluating the nuclear and magnetic scattering factors, we obtain an opposite signed asymmetry value $A_{(210)}$ and m_b (the AFM moment in b-direction for the central Co atom in Fig. 1). Moreover, utilizing the general equation for the DMI energy, the sign of D_z must be opposite to m_b to be energetically favored, leading finally to same signed $A_{(210)}$ and D_z values. Thus, the experimentally determined negative asymmetry value for just one reflection allows one to conclude about the negative sign of D_z in the whole compound. In fact, all the asymmetry points shown in Fig. 2 within the two white areas support the negative sign of D_z , whereas asymmetry points in

the gray areas would support an inverted sign. All experimental asymmetries lie in the white areas proving that PND allows to determine such a fundamental information as the sign of the DMI from the measurement of a single reflection. This is especially powerful for difficult samples or/and technically challenging experiments (e.g. high pressure) where the collection of large datasets is impossible. Within this study, we could for the first time experimentally determine the absolute sign of the DMI in the peculiar non-centrosymmetric multiferroic Ba₂CoGe₂O₇. The precise spin arrangement and its evolution with applied in-plane magnetic field up to 6 T could be established. On one side, our results provide new input for theoretical modeling on this intriguing material. On the other side, they demonstrate the capability of PND to straightforwardly determine the DMI-sign in the large class of WF materials with zero propagation vector.

[1] H. T. Yi, Y. J. Choi, S. Lee et al., *Appl. Phys. Lett.* 92(21), 212904 (2008), [2] I. E. Dzyaloshinskii, *Sov. Phys. - JETP* 5, 1259 (1957), [3] T. Moriya, *Phys. Rev.* 120, 91 (1960), [4] H. Murakawa, Y. Onose, S. Miyahara et al., *Phys. Rev. Lett.* 105(13), 137202 (2010), [5] P. Toledano, D. D. Khalyavin, L. C. Chapon, *Phys. Rev. B* 84, 094421 (2011), [6] M. Soda, M. Matsumoto, M. Månsson et al., *Phys. Rev. Lett.* 112(12), 127205 (2014), [7] V. Hutanu, A. Sazonov, H. Murakawa et al., *Phys. Rev. B* 84, 212101 (2011), [8] J. M. Perez-Mato, J. L. Ribeiro, *Acta Crystallogr., Sect. A: Found. Crystallogr.* 67(3), 264–268 (2011), [9] V. E. Dmitrienko, E. N. Ovchinnikova, S. P. Collins et al., *Nat. Phys.* 10, 202 (2014), [10] A. Gukasov, S. Rodrigues, J.-L. Meunier et al., *Physics Procedia* 42, 150 (2013), [11] V. Hutanu, A. Sazonov, M. Meven et al., *Phys. Rev. B* 86, 104401 (2012)

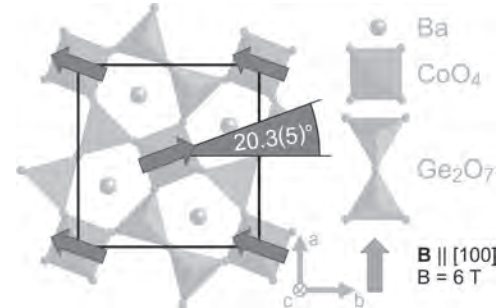


Fig. 1: Refined magnetic moment arrangement in Ba₂CoGe₂O₇ in the WF phase at 2 K with applied magnetic field of 6 T along the a-axis as results from PND data.

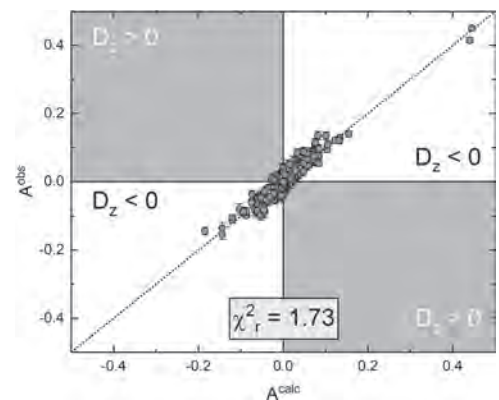


Fig. 2: Comparison between the calculated and observed asymmetry values for the refinement of the magnetic structure shown in Fig. 1.

DF-09. Magnetic Phases and Chirality Control in Magnetic Multiferroics $\text{Nd}_{0.8}\text{Tb}_{0.2}\text{Mn}_2\text{O}_5$ by the Neutron Scattering.

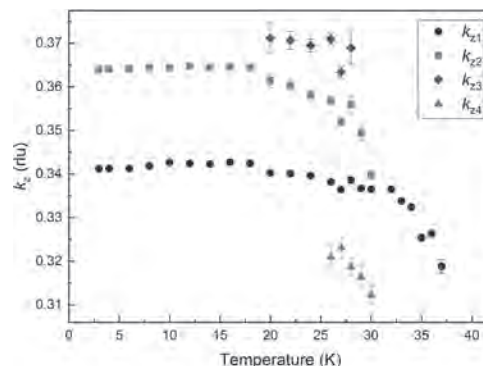
I. Zobkalo¹, S. Gavrilov¹, A. Matveeva¹, A. Sazonov^{2,4}, S. Barilo³ and V. Hutanu^{2,4}

1. Condensed Matter Research Department, FGBU Petersburg Nuclear Physics Institute named after B P Konstantinov, Gatchina, Russian Federation; 2. Institute of Crystallography, RWTH Aachen University, Aachen, Germany; 3. Scientific-Practical Materials Research Centre NAS of Belarus, Minsk, Belarus; 4. Jülich Centre for Neutron Science at Heinz Maier-Leibnitz Zentrum, Garching, Germany

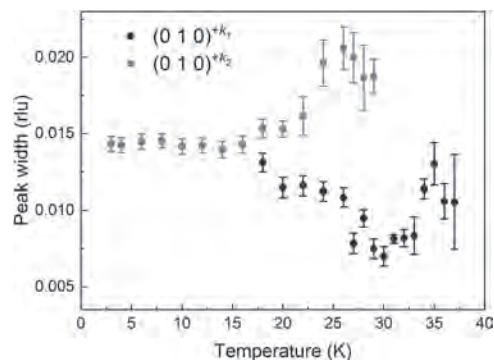
Manganite oxides family RMn_2O_5 (R – rare-earth element) represents example of a multiferroics with extremely interesting and close relationship between magnetism and ferroelectricity [1-3]. The particularities of the magnetic alignment seems to play the decisive role in this M-E coupling. In order to go deep in the understanding in explicit the microscopic mechanisms responsible for spin-driven ferroelectricity in these compounds the investigations of the magnetic ordering in the $\text{Nd}_{0.8}\text{Tb}_{0.2}\text{Mn}_2\text{O}_5$ single crystal were performed. The magnetic phase diagram in both parent compounds is rather complicate, and is different for them. TbMn_2O_5 is characterized by several successive phases - high-temperature incommensurate, at $T_{\text{CP}} < T < T_{\text{N}}$ ($T_{\text{CP}} = 35 \div 37$ K, $T_{\text{N}} = 45$ K), commensurate at $T_{\text{LTIC}} < T < T_{\text{CP}}$ ($T_{\text{LTIC}} = 20 \div 24$ K) and low-temperature incommensurate, at $T < T_{\text{LTIC}}$ [4]. The ferroelectric ordering in TbMn_2O_5 can also be represented as successive ferroelectric phases in the same temperature ranges. In TbMn_2O_5 , chiral scattering was detected in all magnetically ordered phases [4]. In contrast to TbMn_2O_5 , chiral scattering was observed in multiferroic NdMn_2O_5 , only below the temperature $T \sim 20$ K, i.e., below this temperature, the transition from a incommensurate non-chiral magnetic phase to a chiral one occurs [5]. The temperature of this chiral transition corresponds to the temperature of the ferroelectric transition T_{CE} [6], while the value of the ferroelectric polarization is extremely small. The temperature and electric field dependences of magnetic ordering in single crystal $\text{Nd}_{0.8}\text{Tb}_{0.2}\text{Mn}_2\text{O}_5$ were investigated using diffraction of unpolarized and polarized neutrons. The temperature dependence of the propagation vectors of the observed magnetic phases is shown at Fig. 1. Our results demonstrate that two magnetic phases coexist in a broad temperature range, indicating magnetic phase separation. One of them bears features of TbMn_2O_5 , another – of NdMn_2O_5 . Thus, phase 1 or “Tb-phase” has higher temperature of alignment $T_{\text{N}} \approx 37$ K, but it is still lower than that of TbMn_2O_5 . The propagation vector $k_1 = (0.5 \ 0 \ k_{z1})$ is commensurate along a -axis and incommensurate along c -axis at all temperatures of alignment, while for TbMn_2O_5 propagation vector $k = (\frac{1}{2}-\delta_x, 0, \frac{1}{4}+\delta_z)$ is non-commensurate in both a and c directions in two incommensurate phases – HTIC and LTIC. It was possible to change the ratio of “right” and “left” spirals in $\text{Nd}_{0.8}\text{Tb}_{0.2}\text{Mn}_2\text{O}_5$ crystals by an external electric field. The features of phase 2 – “Nd-phase” – are close to those of magnetic order at NdMn_2O_5 . It has transition temperature the same as $T_{\text{N}} = 30$ K in NdMn_2O_5 , the propagation vector $k_2 = (0.5 \ 0 \ k_{z2})$ has the same component along a^* and k_{z2} value is close to that of NdMn_2O_5 . It is difficult to say whether this “Nd-phase” is chiral in whole temperature range of existence or it is chiral below some definite temperature T_{Ch} , which takes place in NdMn_2O_5 , with its $T_{\text{Ch}} = 20$ K. Compared to NdMn_2O_5 , the system $\text{Nd}_{0.8}\text{Tb}_{0.2}\text{Mn}_2\text{O}_5$ exhibits even greater ability to generate ordered magnetic phases of the same type. This leads to the fact that, in the narrow temperature range of 20 K – 30 K two more magnetic incommensurate phases were observed. Such phenomena were observed in the compounds of this family like TbMn_2O_5 in narrow temperature range [7, 8], in NdMn_2O_5 – in a broad temperature range [5, 9]. This feature should be connected with the magnetic inhomogeneity of the system. This inhomogeneity could follow from the non-rigidity of the Mn^{3+} - Mn^{4+} bonding at RMn_2O_5 family. From another side, at RMn_2O_5 series the bond lengths and angles in the Mn^{3+} and Mn^{4+} polyhedra are in the critical position for the superexchange interactions or close to it [10]. The small deviation in the geometrical arrangement of Mn^{3+} - Mn^{4+} bonding provide different magnetic interaction strength. The coexistence of two rare earth ions with different types of ground state: Kramers-like Nd^{3+} and non-Kramers one Tb^{3+} , could lead to different types of site anisotropies. The system energy lowers by phase separation state for two main phases with their characteristic resembling those of phases of pure compounds. The broadening of the

incommensurate reflections at low temperature (Fig.2) could be connected with the existence of several propagation vectors, distributed around the two main values $k_{1,2}$. At the temperature region 22 K – 30 K, the competing interactions lead to more phases with similar vectors $k_{3,4}$. Approximately at the same temperature region competing interactions stabilize the commensurate structure in TbMn_2O_5 . The studied system $\text{Nd}_{0.8}\text{Tb}_{0.2}\text{Mn}_2\text{O}_5$ at this temperature range corresponds to the least homogeneous state, when the energy minimum achieved by the separation on three and four magnetic phases. This fact can be one more indication that CM phase in RMn_2O_5 is not really commensurate. Propagation vector component k_z in this phase could be not precisely commensurate and it arises as not very stable result of interplay of different interaction. Recent work [8] witnesses in favor of that where k_z component of propagation vector in TbMn_2O_5 changed value in magnetic field from 0.25 to 0.32. As another argument can be the “reverse” transition from CM to LTIC phase. The work was supported by the Russian Foundation for Basic Research grant # 19-52-12047, and DFG grant # SA 3688/1-1.

1. N. Hur, S. Park, P. A. Sharma, et al. Nature 429, 392 (2004).
2. Y. Noda, H. Kimura, M. Fukunaga, et al. J. Phys.: Condens. Matter 20, 434206 (2008).
3. G. R. Blake, L. C. Chapon, P. G. Radaelli, et al. Phys. Rev. B 71, 214402 (2005).
4. I.A. Zobkalo, S.V. Gavrilov, A. Sazonov, et al. J. Phys.: Condens. Matter 30, 205804 (2018).
5. I.A. Zobkalo, A.N. Matveeva, A. Sazonov, et al. Phys. Rev. B 101, 064425 (2020).
6. S. Chattopadhyay, V. Baledent, et al., Phys. Rev. B 93, 104406 (2016).
7. I.A. Zobkalo, S.V. Gavrilov, V.A. Sanina, et al. Physics of the Solid State 56, 51 (2014).
8. T. Chatterji, P. J. Brown. J. Appl. Phys. 116, 203904 (2014).
9. I. A. Zobkalo, S. V. Gavrilov, et al., J. Magn. Magn. Mater. 354, 85 (2014).
10. L. M. Volkova, D. V. Marinin. J. Phys.: Condens. Matter 21, 015903 (2009).



Temperature dependence of propagation vectors for four magnetic phases in heating mode



Temperature dependence of peak width of satellites $(0 \ 1 \ 0)^{+k_1}$ and $(0 \ 1 \ 0)^{+k_2}$ in heating mode

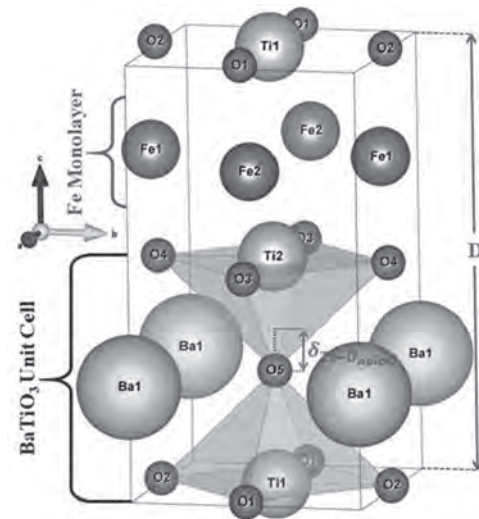
DF-10. Enhanced Strain-Induced Magnetoelectric Coupling in Polarization-Free Fe/BaTiO₃ Heterostructures.

C. Amorim¹, J.S. Amaral¹ and V.S. Amaral¹

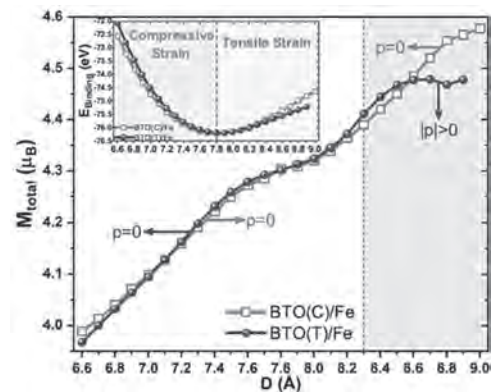
¹. Universidade de Aveiro CICECO, Aveiro, Portugal

Magnetolectrics (ME), materials which possess a coupling between their magnetic and electric orders, are the most studied type of multiferroic (MF) materials due to their obvious potential in technological applications such as: ultralow power logic-memory devices, magnetic sensors, energy harvesting/conversion devices, spintronic devices, among others [1-4]. Still, the ME effect presents an inherent obstacle which is related to the apparent necessity of empty d orbitals (d^0) for Ferroelectrics against semi-filled d orbitals (d^n) for magnetic order [4-5]. Therefore, the search for magnetolectric materials typically revolves around the struggle to simultaneously coexist magnetic and ferroelectric orders in the same material, either using an intrinsic or extrinsic/composite approach. In fact, due this paradoxical limitation when having an electric and magnetic order in a single phase, extrinsic MF have been showing the most promising results, managing to achieve substantial ME couplings even at temperatures close to room temperature [4,6-8]. Via *ab initio* calculations of a prototypical Fe/BaTiO₃ interface, we predict that it is possible to tune the magnitude of the individual magnetic moments, even for non-polar BaTiO₃ (BTO), through a uniaxial strain in cubic and tetragonal Fe/BTO heterostructures. By comparing polar and non-polar Fe/BTO heterostructures, we show that the Fe, Ti and equatorial O atomic magnetic moments are induced and enhanced as a result of their local crystal field. The crystal field may be controlled solely by the manipulation of the inter-atomic distances of their neighboring atoms (which will affect their electrostatic fields and orbital hybridizations), or by the BTO electric dipole moments, working as a local polarization. Contrary to conventional assumptions, a Fe/BTO interface does not require electrical polarization to be able to tune its magnetic moment. In fact, by applying strain, the sensitivity of the non-polar region is higher than that of its polar equivalent. Additionally, comparing the tensile region of the cubic and tetragonal supercells, it is clear that the non-polar cubic supercell reaches higher total magnetizations than its polar tetragonal counterpart. When the polarization is present, it dominates the crystal field contributions, thus constraining the effects of other perturbations such as strain. The results of our work reiterate the extrinsic magnetolectric potentialities and reduces the requirements for an electric control of magnetism. Therefore, we should rethink the conventional search and optimization of ME materials, without the limitations which come with magnetic ferroelectrics.

[1] Dong, S.; Liu, J.-M.; Cheong, S.-W.; Ren, Z. Multiferroic materials and magnetolectric physics: symmetry, entanglement, excitation, and topology. *Advances in Physics* 2015, 64, 519–626. [2] Fiebig, M. *et al*, The evolution of multiferroics. *Nature Reviews Materials* 2016, 1, 16046. [3] Song, C.; Cui, B.; Li, F.; Zhou, X.; Pan, F. Recent progress in voltage control of magnetism: Materials, mechanisms, and performance. *Progress in Materials Science* 2017, 87, 33–82. [4] Spaldin, N. A.; Ramesh, R. *Advances in magnetolectric multiferroics*. *Nature materials* 2019, 18, 203. [5] Hill, N. A. Why are there so few magnetic ferroelectrics? *J. Phys. Chem. B* 2000, 104, 6694–6709. [6] Vaz, C. A.; Hoffman, J.; Ahn, C. H.; Ramesh, R. Magnetolectric coupling effects in multiferroic complex oxide composite structures. *Advanced Materials* 2010, 22, 2900–2918. [7] Cherifi, R. O. *et al*, M. Electric-Field Control of Magnetic Order Above Room Temperature. *Nat. Mater.* 2014, 13, 345–351. [8] Mundy, J. A. *et al*, Atomically engineered ferroic layers yield a room-temperature magnetolectric multiferroic. *Nature* 2016, 537, 523–527.



Fe₂/BaTiO₃ supercell composed of a Fe monolayer on top of a BaTiO₃ unit cell.



Total magnetization of the Fe₂/BaTiO₃ heterostructure as a function of D (the supercell total height), for the supercells containing the cubic and tetragonal BTO unit cells. The inset shows the binding energy in the same range of D.

DF-11. Magnetoelectric Coupling and Spin-Canting in FeCr_2O_4 Ferrimagnet.

K. Vasin¹ and M. Eremin¹

1. Department of Quantum Electronics and Radiospectroscopy, Kazan Federal University Institute for Physics, Kazan, Russian Federation

Multiferroics are attracting increased attention in modern research. As a novel class of multifunctional material, they find wide variety of applications and are also of interest for fundamental scientific research since the microscopic theory of the magnetoelectric coupling are not yet entirely clear [1, 2]. Among a vast class of materials, spinel-type ferrimagnets have a few other unusual features like orbital ordering [3], spin-ice [4], besides multiferroicity. The authors of the work [5] mentioned, there are evidences that the orbital degeneracy of the Jahn-Teller active Fe^{2+} -ions ($3d^6$, $S = 2$) in tetrahedral environment plays a crucial role in magnetoelectric coupling of FeCr_2O_4 . The spontaneous polarization arises at $\sim 100\text{K}$ [5], while ferrimagnetic order appears below 70K . The compound also exhibits orbital ordering of Fe^{2+} ions at $135\text{-}141\text{K}$ due to the cooperative Jahn-Teller effect [6, 7]. Within the framework of the quantum mechanical approach, we found two the most effective, in our opinion, mechanisms of magnetoelectric coupling caused by the combined action of the odd crystal field from the tetrahedral environment of the iron ions, the spin-orbit interaction and the exchange field acting on the 3d iron electrons from the chromium spins. Estimated macroscopic polarization projection to c-axis P_c in the magnetically and orbitally ordered phase depends on the angle φ of Fe spin projection at ab-plane, while other two P_a and P_b are also determined by the canting angle between Fe and Cr magnetic sublattices like in the inverse DM mechanism [1]. We estimated $P_c = -700 \sin(2\varphi) \mu\text{C}/\text{m}^2$ and $P_a = \pm 100 \sin(\varphi) \mu\text{C}/\text{m}^2$, $P_b = \pm(-1)100 \cos(\varphi) \mu\text{C}/\text{m}^2$ taking $\sim 50^\circ$ as the canting angle. There is no in-plane (ab) polarization if the Fe and Cr spins are collinear. The existing data on polarization measurements reports average value of $\sim 34 \mu\text{C}/\text{m}^2$ observed on FeCr_2O_4 powder. According to the measurements of the hyperfine field on ^{51}Fe in Mossbauer study [8], down to the $\sim 40\text{K}$ spins of Fe ions tend to rotate towards the a-axis, which means the domination of P_a , P_b components, i.e. $\varphi \rightarrow 0$ or 90° . The magnitudes of P_a and P_b agree to the measured one by the order of the magnitude at this phase. There are actually two types of FeO_4 tetrahedrons in FeCr_2O_4 , which are rotated along the c-axis by 90° with respect to each other. The vector P has an opposite sign in the front for the second type of tetrahedron. It puzzles us, because the simple collinear spin structure leads to zero polarization in total. Moreover, the possible canting angle between Fe and Cr spins seem to be different from site to site in order to get non-zero P_a , P_b components. The neutron scattering has not been measured yet, but it reports spin-ice structure for the relative compound FeV_2O_4 with a large canting angles $\sim 55^\circ$ [4]. The existence of polarization above Curie temperature we connects with the short-range magnetic order. The super-exchange interaction of the ground state of chromium ions with excited states of the iron ion differs from the isotropic exchange spin coupling, which induces the DM interaction. The operator is derived in the second order of perturbation theory with simultaneous accounting of the spin-orbit interaction operator and the superexchange interaction operator acts between ground (θ) and excited (η) orbital states of Fe^{2+} as illustrated in Fig. 1. The exact scheme we used to derive the second mechanism of magnetoelectric coupling, which induces in-plane (ab) spontaneous polarization. The estimated canting angle between Fe and Cr spins does not exceed 2° . We suggest another mechanism of non-collinearity between Fe and Cr sublattices, leading to much larger canting angles. The canting of the magnetic sublattices may result from the minima of the sum of the magnetic anisotropy energy and the Jahn-Teller coupling on the iron sites, and the molecular (exchange) isotropic field, acting from the chromium ions. We performed numerical diagonalization of model Hamiltonian and it yielded to the maximal canting angle $\gamma \sim 50^\circ$ in ac-plane (see Fig. 2) and $\sim 5^\circ$ in ab-plane. The obtained results may be overestimated, because we take into account only the energy of Fe sites due to the relatively weak magnetic anisotropy of Cr spins. Nevertheless, we believe that this scenario is relevant for the nature of non collinear spins ordering in FeV_2O_4 [4] (Fe-V canting is $\sim 69^\circ$), and FeCr_2S_4 [9] (Fe-Cr $\sim 10^\circ$). We hope that our investigations will stimulate the researchers to carry out further developments of magnetoelectric coupling theory.

A. P. Pyatakov, A. K. Zvezdin, Phys. Usp., Vol. 55, p. 557–581 (2012) Y. Tokura, S. Seki, and N. Nagaosa, Rep. Prog. Phys., Vol. 77 (2014) K. Tsuda, D. Morikawa, Y. Watanabe, S. Ohtani, and T. Arima, Phys. Rev. B, Vol. 81 (2010) G. J. MacDougall, V. O. Garlea, A. A. Aczel et al., Phys. Rev. B, Vol. 86 (2012) K. Singh, A. Maignan, Ch. Simon et al., Appl. Phys. Lett., Vol. 99 (2011) S. Ohtani, Y. Watanabe, M. Saito et al., J. Phys.: Condens. Matter, Vol. 22 (2010) K. V. Vasin, M. V. Eremin, Journal of Experimental and Theoretical Physics, Vol. 129, p. 1029-1035 (2019) S. Nakamura, A. Fuwa, Physics Procedia, Vol. 75, p. 747-754 (2015) A. Strinic, S. Reschke, K. V. Vasin et al., Phys. Rev. B, Vol. 102 (2020)

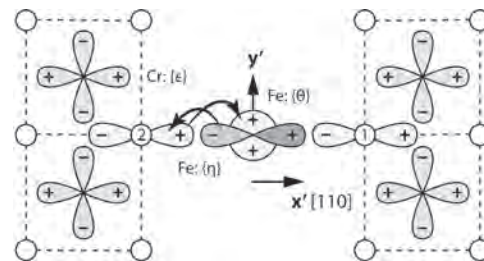


Fig 1. The spatial distribution of the relevant single-electron orbitals of the chromium and iron ions.

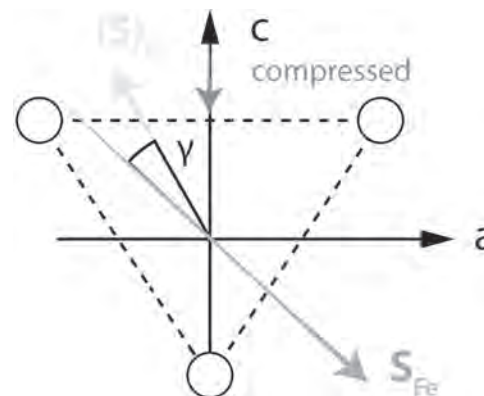


Fig 2. Projections of the tetrahedron and Fe, Cr spins onto the ac-plane.

DF-12. Development and Analysis of Highly-Efficient Magnetolectric Cobalt Ferrite/Barium Titanate Composites Using a Scalable Synthesis Technique.

F. Safi Samghabadi¹, L. Chang^{2,3}, M. Khodadadi^{1,3} and D. Litvinov^{2,3}

1. Materials science and engineering, University of Houston System, Houston, TX, United States; 2. Department of Electrical & Computer Engineering, University of Houston System, Houston, TX, United States; 3. Center for Integrated Bio & Nano Systems, University of Houston System, Houston, TX, United States

Direct magnetolectric (ME) coupling in single-phase multiferroic materials is limited to high magnetic fields and/or cryogenic temperatures. More robust ME behavior has been achieved in multi-phase composites that combine magnetostrictive and piezoelectric materials in a matrix 1–3. The ME effect in such composites is due to the induced stresses within the magnetostrictive or piezoelectric phases controlled by the application of external magnetic or electric fields, which transfer through the interface to the piezoelectric or magnetostrictive phases, respectively 4. Therefore, two factors play a crucial role in the effectiveness of the ferroic phases conjugation: resistivity of the ceramic, which directly governs the electrical poling effectiveness of the ferroelectric phase, and the interface of the two materials, which influences the strain transfer 5. Wide choice of materials, volume fraction, and microstructure in multi-phase composites allow addressing these challenges 1,3. There are multiple applications for magnetolectric (ME) materials in sensors, energy harvesting, magnetolectric random access memory, antennas, drug delivery, etc 2. The implementation of ME materials in some of these applications demands the use of nano-multiferroic samples. Although, the characterization methods to study the ME coupling in bulk materials are well-developed; however, the measurement of ME coupling at the nanoscale is still challenging 6. In this work, high magnetolectric coupling coefficient CoFe₂O₄-BaTiO₃ composites were developed using commercial CoFe₂O₄ and BaTiO₃ powders as precursors. The bulk magnetolectric coefficient in the optimized CoFe₂O₄-BaTiO₃ composite where individual CoFe₂O₄ grains are fully enclosed by the BaTiO₃ matrix was found to be comparable with the numbers reported for the composites based on core-shell structures 7, 8. This presentation will detail the physical (magnetic, electric, magnetolectric, and magneto-mechanical) and microstructural properties of the developed composites, offer the analysis of the observed behaviors, and outline the routes for further improvements. The composites were produced by dry ball-milling of precursor powders followed by annealing at 1200 °C. Properties of the composite as a function of synthesis precursor choice and precursor mixture composition were explored. The microstructural characterization (focused ion-beam depth profiling of pellet composites etched in hydrochloric acid to selectively remove CoFe₂O₄ and piezo-force microscopy of polished pellets) of the synthesized CoFe₂O₄-BaTiO₃ composited clearly revealed a dramatic dependence on the size and phase (cubic vs. tetragonal) of BaTiO₃ precursor. This dependence has translated into a dramatic difference between magnetolectric coupling coefficients observed in the composites synthesized with cubic and tetragonal BaTiO₃ precursors. Utilizing 50 nm cubic BaTiO₃ precursor powder results in a material, in which relatively large individual CoFe₂O₄ grains are fully embedded into and well-insulated by a BaTiO₃ matrix. This microstructure enhances the strain-mediated coupling between CoFe₂O₄ and BaTiO₃ grain. Furthermore, it leads to higher electrical resistivity, which, in turn, enables effective electrical poling. The highest magnetolectric coupling coefficient is exhibited in CoFe₂O₄-BaTiO₃: 20-80% composites that utilize a 50 nm cubic BaTiO₃ powder as precursor with a value as high as 4.3 mV/Oe.cm. The dependence of magnetolectric coupling coefficient on the value of the external DC magnetic field for different compositions of CoFe₂O₄-BaTiO₃ composites is shown in Fig. 1 and, as will be shown in this presentation, correlates well with magnetic and magnetostrictive properties and is in agreement with theoretical analysis. In addition to the detailed characterization of bulk properties, the dependence of the local surface potential on the magnitude of external DC magnetic fields was studied using Kelvin Probe Force Microscopy (KPFM). The line profile of the surface potential for the (CoFe₂O₄-BaTiO₃ (50 nm cubic):30-70%) sample for different values of external magnetic field is shown in Fig. 2.

1 J.S. Andrew, J.D. Starr, and M.A.K. Budi, Scripta Materialia 74, 38 (2014). 2 Y. Cheng, B. Peng, Z. Hu, Z. Zhou, and M. Liu, Physics Letters A 382, 3018 (2018). 3 N. Ortega, A. Kumar, J.F. Scott, and R.S. Katiyar, Journal of Physics: Condensed Matter 27, 504002 (2015). 4 J. Ma, J. Hu, Z. Li, and C.-W. Nan, Advanced Materials 23, 1061 (2011). 5 M. Fiebig, ChemInform 36, (2005). 6 G. Caruntu, A. Yourdkhani, M. Vopsariou, and G. Srinivasan, Nanoscale 4, 3218 (2012). 7 G.V. Duong and R. Groessinger, Journal of Magnetism and Magnetic Materials 316, e624 (2007). 8 G.V. Duong, R. Sato Turtelli, and R. Groessinger, Journal of Magnetism and Magnetic Materials 322, 1581 (2010).

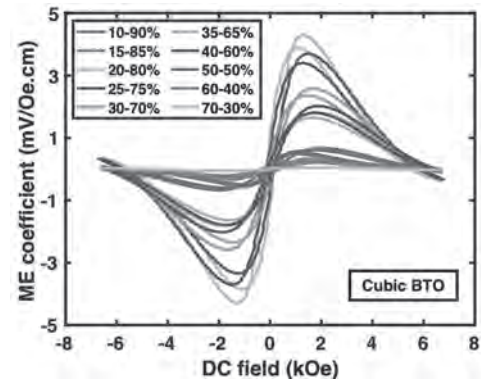


Fig. 1. ME coefficient vs DC magnetic field for different CoFe₂O₄-BaTiO₃ compositions prepared with 50 nm cubic BaTiO₃ precursor

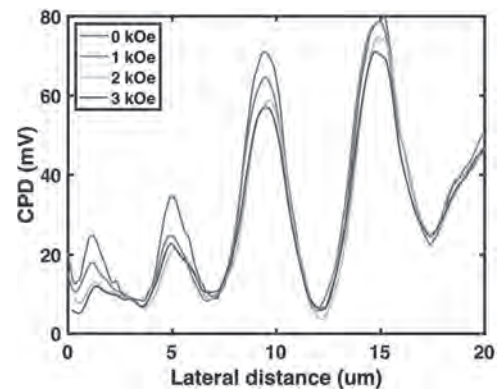


Fig. 2. Contact Potential Difference (CPD) measured for CoFe₂O₄-BaTiO₃ (50 nm cubic):30-70% using KPFM at different external magnetic fields.

Session DG

SPIN LIQUIDS AND NOVEL SPIN SYSTEMS

Shawn Pollard, Chair

The University of Memphis, Memphis, TN, United States

CONTRIBUTED PAPERS

DG-01. Micromagnetic Simulations of Magnetization Reversal in Kagome Artificial Spin Ice.

B.M. Cecchi¹, M.F. Velo¹ and K. Pirota¹

1. Universidade Estadual de Campinas Instituto de Física Gleb Wataghin, Campinas, Brazil

Artificial spin ice (ASI) is a magnetic metamaterial designed to exhibit frustration [1]. It consists of an array of magnetostatically interacting nanomagnets arranged in a geometry that prevents these interactions to be all satisfied simultaneously. They were originally conceived to replicate, in an artificial manner, interesting frustration induced phenomena found in natural frustrated magnets known as spin ices [2]. One of those most remarkable phenomena is the emergence of quasiparticles similar to magnetic monopoles when such materials are excited above the ground state [3]. In ASI, this behavior is experimentally reproduced by subjecting the system to a magnetization cycle [4]. The magnetization reversal proceeds by creation of one-dimensional strings of flipped nanomagnets, referred as Dirac strings, that host the magnetic monopoles at their ends. This reversal mechanism has been already reproduced by Monte Carlo-based simulations, where the nanomagnets are treated as Ising variables and a phenomenological random switching field distribution is employed [5]. In this work, we reproduced the same behavior using a more fundamental approach, that was lacking in literature, based on micromagnetic simulations, applied particularly to a large scale (more than a thousand magnets) kagome lattice arrangement of ASI [6]. We regarded a more realistic description of the shape of each nanomagnet, including its finite size and roughness at the edges, in such a way that no *a priori* switching field distribution was required but that came out naturally. Furthermore, our simulations predict a critical angle between the applied field and the direction of a sublattice that separates different reversal regimes: the process is mostly 2D for angles above the critical value, and it is 1D (i.e., via Dirac strings and monopoles) otherwise.

[1] S. H. Skjærvø, C. H. Marrows and R. L. Stamps, *Nature Review Physics*, Vol. 2, p. 13–28 (2020) [2] R. F. Wang, C. Nisoli and R. S. Freitas, *Nature*, Vol. 439, pp. 303–306 (2006) [3] C. Castelnovo, R. Moessner and S. L. Sondhi, *Nature*, Vol. 451, p. 42–45 (2008) [4] E. Mengotti, L. J. Heyderman and A. F. Rodríguez, *Nature Physics*, Vol. 7, p. 68–74 (2011) [5] R. V. Hügli G., G. Duff and B. O’Conchuir, *Philos. Trans. R. Soc. A Math. Phys. Eng. Sci.*, Vol. 370, p. 5767–5782 (2012) [6] M. F. Velo, B. M. Cecchi, and K. R. Pirota, *Physical Review B*, Vol. 102, p. 224420 (2020)

DG-02. Withdrawn

DG-03. The Impact of the Intralayer and Interlayer Magnetism on the Electronic Properties of vdW Heterostructure NiPS₃/FePS₃ – a Theoretical Approach.

K. Kotur¹ and M. Birowska¹

1. University of Warsaw, Uniwersytet Warszawski, Warszawa, PL, academic, Warsaw, Poland

The vertical stacking of the 2D materials into the vdW heterostructures has attracted much attention during last years [1], mostly due to a new phenomena that can be observed in such heterostructures. Just recently the 2D magnetic crystals have been experimentally reported [2], opening the possibility to study the vdW layered magnets, exhibiting different magnetic phases [3,4]. Proximity between magnetic 2D crystals might serve as sensitive tool to examine details of the magnetic structure. Here, we present a comprehensive *ab initio* study of the prototypical example of vdW magnetic system NiPS₃/FePS₃. The individual layers are the members of large family of transition metal phosphorus trichalcogenides MPX₃ [5], which are anti-ferromagnets. The impact of the intralayer and interlayer magnetism on the electronic properties of the heterobilayer is examined in the framework of the density functional theory. In particular, the band alignments, band offsets and band gaps are investigated and compared with isolated layers. Our results have demonstrated the moderate influence of intralayer magnetism on the electronic and energetic properties of the system along with negligible impact of interlayer magnetism on these properties. In addition, spatial separation of charges at the band edges are demonstrated, implying the existence of the interlayer excitons in NiPS₃/FePS₃ structure. The study was accomplished thanks to the funds allotted by the National Science Centre, Poland within the framework of the research project ‘SONATA12’ no. UMO-2016/23/D/ST3/03446. Access to computing facilities of TU Dresden ZIH for the project ‘TransPheMat’, PL-Grid Polish Infrastructure for Supporting Computational Science in the European Research Space, and of the Interdisciplinary Center of Modeling (ICM), University of Warsaw are gratefully acknowledged.

[1] D. L. Duong *et al.*, ACS Nano 2017, Vol. 11, p. 11803–11830. [2] B. Huan *et al.*, Nature, Vol. 546, p. 270-273 (2017). [3] D. Zhong *et al.* Science Advances, Vol. 3, p. 1-6 (2017). [4] M. Birowska *et al.* <http://arxiv.org/abs/2009.05030>. [5] R. Brec, Solid State Ionics, Vol. 22, p. 3-30 (1986).

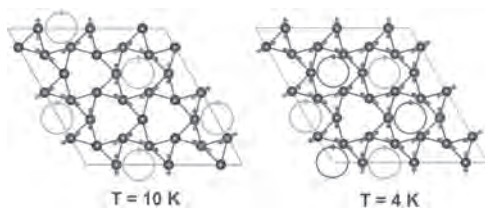
DG-04. Neutron Scattering Revealing Kagome Spin Ice in a Frustrated Intermetallic Compound.

H. Deng¹, K. Zhao², H. Chen³, K. Ross³, V. Petricek⁴, G. Guenther⁵, M. Russina⁵, V. Hutanu¹ and P. Gegenwart²

1. Institute of Crystallography, RWTH Aachen University and Jülich Centre for Neutron Science (JCNS) at Heinz Maier-Leibnitz Zentrum (MLZ), Garching, Germany; 2. Experimentalphysik VI, Center for Electronic Correlations and Magnetism, Universität Augsburg, Augsburg, Germany; 3. Department of Physics, Colorado State University, Fort Collins, CO, United States; 4. Institute of Physics, Czech National Academy of Science, Praha, Czechia; 5. Helmholtz-Zentrum Berlin für Materialien und Energie GmbH, Berlin, Germany

Frustrated magnetic structures hold configurations wherein localized magnetic moments or spins interact through competing exchange interactions, rendering macroscopic degeneracy of exotic ground states like spin ice and providing an excellent platform for discovering novel states and properties. One example is the pyrochlore spin ice, in which four nearest-neighbor Ising-like spins on the vertices of the corner-sharing tetrahedra are forced to form the local “2-in-2-out” configuration for each tetrahedron, which forms spin ice in analogy to the water ice[1]. In two dimensions (2D), ice rules can be similarly defined for in-plane Ising like classical spins residing on the kagome lattice, which require “2-in-1-out” or “1-in-2-out” local arrangements of the spins on its triangles[2]. A $\sqrt{3}\times\sqrt{3}$ ground state can be selected by further neighbor exchange couplings or the long-range dipolar interaction. As a result, kagome spin ices show a characteristic multi-stage ordering behavior under changing temperature. Experimentally, kagome spin ices have only been realized in artificial spin ice systems formed by nanorods of ferromagnets organized into honeycomb networks[3-5]. However, the large magnetic energy scales and system sizes make it challenging to explore the rich phase diagram of spin ices in the thermodynamic limit. Neutron scattering, though measuring the energy and momentum of in-coming and out-going neutrons, offers one of the most powerful tools in the study of magnetic structures and dynamics of magnets. Through neutron scattering and other experimental and theoretical approaches, we discover that the intermetallic compound HoAgGe is a naturally existing kagome spin ice that exhibits a fully ordered ground state[6]. The multi-stage ordering behavior was confirmed by Single-crystal neutron diffraction: below 11.6 K the Ho spins enter a partially ordered state with one-third of them still fluctuating, while below ~ 7 K, all spins order into the $\sqrt{3}\times\sqrt{3}$ ground state of the kagome ice with crystalized magnetic monopoles. All these observations are in good agreement with Monte Carlo simulations of a classical spin model including both dipolar interactions and up to 4th nearest-neighbor exchange couplings on the noncentrosymmetric kagome lattice of HoAgGe.

[1] Bramwell, S. T., and Gingras, M. J. P. *Science* 294, 1495–1501 (2001)
 [2] Chern, G.-W. et al. *Phys. Rev. Lett.* 106, 207202 (2011) [3] A. S. Wills, R. Ballou and C. Lacroix, *Phys. Rev. B* 66, 144407 (2002) [4] G. Möller, R. Moessner, *Phys. Rev. B* 80, 140409 (2009) [5] G.-W. Chern, P. Mellado and O. Tchernyshyov, *Phys. Rev. Lett.* 106, 207202 (2011) [6] Zhao, K., Deng, H., Chen, H. et al. *Science* 367, 1218–1223 (2020)



The refined magnetic structures of HoAgGe at 10K and 4K

DG-05. Withdrawn

DG-06. Numerical Studies of Spin Glasses in the Frame of Edwards-Anderson Model.

A. Rybin^{1,2}, A.O. Korol^{1,2}, D. Kapitan^{1,2}, E. Vasiliev^{1,2}, M. Padalko^{1,2}, K. Soldatov^{1,2}, Y. Shevchenko^{1,2}, A. Makarov^{1,2} and V.Y. Kapitan^{1,2}

1. Far Eastern Federal University, Vladivostok, Russian Federation;

2. Far Eastern Post, Russian Academy of Sciences, Vladivostok, Russian Federation

A particular interest to the behavior of magnetic frustrated spin systems is explained that the problem of finding a ground state, i.e., the state with the lowest energy is a very difficult task due to the macroscopic degeneracy and frustrations that are present in most realistic spin glass models. This problem is fundamentally difficult to solve since it often requires the search for potential solutions over huge spaces of possible states. Among conventional methods which are using in statistical physics, one of the most powerful approaches is the Monte Carlo simulation, consisting of stochastic sampling over a state space and an evaluation of estimators for physical quantities. However, the ability of modern machine learning techniques to classify, identify, or interpret massive data sets provides a complementary paradigm to the above approach in statistical physics to analyze the exponentially large number of states. The main research object is the two-dimensional Edwards-Anderson model, with the exchange integral J as a random function and the average value of J is zero in a system. In such the system, one half of the spins' interaction is ferromagnetic, and the other is antiferromagnetic. It is well known that critical phenomena occur in condensed matter under certain conditions, when an abrupt change in its properties occurs. Near the critical points, various phenomena may arise. The critical region can be described by a set of state parameters (order parameters), which allow one to obtain information about the anomalous behavior of thermodynamic averages, internal processes, and the nature of the objects of study. The first research direction related to the fact, that the temperature behavior of the average magnetization modulus equals to zero for the Edwards-Anderson model. Because of this, we calculated an average size of the percolation cluster, which is defined as the relative size of maximum cluster, which include spins in the ground state, to the total number of spins. The average size of the percolation was chosen as an order parameter. This order parameter, in contrast to other thermodynamic characteristics, makes it possible to describe the behavior of the system with a change in temperature. Using this parameter, we calculated main critical exponents of these two models: correlation length, magnetization, specific heat and susceptibility. The second research direction was about the problem of finding a ground state for the Edwards-Anderson model. In present work, for simulation we used a combination of our Hybrid Multispin Method (HMM) and the Restricted Boltzmann Machine (RBM) to predict the ground states for the Edwards-Anderson spin glass model. The problem of spin glass simulation is determined by the high complexity of obtaining configurations with the lowest possible energy level (ground state). At the moment, no universal algorithm exists to directly generate the ground state. To predict the GS, we used the data of the HMM to train our neural network and to predict spin glass state with a lower energy level than in the training data sets. We used small spin systems (4×4 and 6×6) to verify our results and compare them with those of the exact solution calculated by a brute-force method (BFM). Our research has shown that the ground states of spin glass systems can be predicted using a neural network. However, given the absence of an exact solution to determine the number of degenerations at the ground energy level for big systems, it is impossible to check whether our algorithms reach the global energy minimum. Nonetheless, machine-learning algorithms can make a significant contribution to solving NP-complete problems in the future. This work was supported by the state task of the MSHE of Russia No. 075-00400-19-01.

S. Edwards, P. Anderson, Phys. F: Metal Phys., Vol. 5 (5), p. 965 (1975)
 A. Patashinski, V. Pokrovskii, Pergamon Press (1979) A.G. Makarov et al., JETP Letters., Vol. 110 (10), pp. 702-706 (2019) R. Salakhutdinov, A. Mnih, G. Hinton, Restricted Boltzmann machines for collaborative filtering // Proceedings of the 24th international conference on Machine learning, pp. 791-798 (2007)

DG-07. Two Magnetic Compensation Compositions in $Mn_{4-x}Co_xN$ Epitaxial Films at Room Temperature Proved by X-ray Magnetic Circular Dichroism.

H. Mitarai¹, T. Komori¹, T. Hirose¹, K. Ito^{2,3}, K. Toko¹, L. Vila⁴, J. Attané⁴, K. Amemiya⁵ and T. Suemasu¹
 1. Inst. of Appl. Phys., Univ. of Tsukuba, Tsukuba, Japan; 2. IMR, Tohoku Univ., Sendai, Japan; 3. CSRN, Tohoku Univ., Sendai, Japan; 4. Univ. Grenoble Alpes, CEA, CNRS, Spintec, Grenoble, France; 5. IMSS, KEK, Tsukuba, Japan

In our information society, the importance of energy conservation is increasing year by year. To tackle this issue, the transition from volatile memory to non-volatile memory can be a solution. One of the candidates for non-volatile memories is a racetrack memory^[1], driven by current-induced domain wall motion (CIDWM). For practical use, faster CIDWM and lower threshold current density are key factors. In order to reach this goal, we have been focusing on and investigating Mn_4N as a promising material. Mn_4N film is an antiperovskite ferrimagnet without rare-earth elements, which is advantageous in fast magnetization reversal due to its perpendicular magnetic anisotropy ($K_u \sim 1.1 \times 10^5$ J/m³) and a small saturation magnetization ($M_S \sim 80$ kA/m)^[2]. Previous study on 1-2- μ m-wide Mn_4N strips showed the fastest spin-transfer-torque-driven domain wall motion ($v_{DW} \sim 900$ m/s at 1.3×10^{12} A/m²) at room temperature (RT)^[2], comparable to those reported in the system including rare-earth 4f magnets or heavy metals. To achieve faster v_{DW} , Mn_4N based mixed crystals have been studied in pursuit of the use of magnetic and/or angular momentum compensation for more efficient CIDWM thanks to diverged damping constants. Recently, $Mn_{4-x}Ni_xN$ films have been suggested to have a magnetic compensation (MC) point between $x = 0.1$ and 0.25 at RT^[3]. We found that $Mn_{4-x}Co_xN$ films have a compensation point between $x = 0$ and 0.8 from x-ray magnetic circular dichroism (XMCD) measurements^[4]. However, there is a lack of information about the magnetic behavior of $Mn_{4-x}Co_xN$ at values x much smaller or larger than 0.8. Considering that the compensation in $Mn_{4-x}Ni_xN$ takes place in a small range of composition x , further compensation points can be found when x is far from 0.8. In this work, we performed XMCD measurements on $Mn_{4-x}Co_xN$ epitaxial films at $x = 0.2$ and 1.3 and investigated the change in magnetic structures by composition ratio to verify MC at RT. 20-30 nm-thick $Mn_{4-x}Co_xN$ films with $x = 0-1.3$ were epitaxially grown on SrTiO₃(001) substrates by molecular beam epitaxy. SiO₂ or Ta capping layers were sputtered *in-situ* on the surface to prevent oxidation. X-ray absorption spectroscopy (XAS) and XMCD measurements were performed at BL-16A of KEK-PF for $x = 0.2$ and 1.3. In these measurements, we applied an external magnetic field of 5 T perpendicular to sample surfaces. The incidence angle of the circularly polarized x-ray was 54.7°(magic angle) to the plane in order to simplify the sum rule calculation. For $x = 0.8$, the XMCD measurements were carried out at BL23SU of SPring-8^[4]. Figures 1(a)-1(c) show the XAS and XMCD spectra of Mn in $Mn_{4-x}Co_xN$ at $x = 0.2, 0.8$ ^[4], and 1.3, respectively. In these figures, the sharp peak near 640 eV comes from Mn atoms at corner sites (I sites), and the broad peak near 643 eV originates from those at face-centered sites (II sites)^[4]. We observed the sign reversals of XMCD signals between $x = 0.2$ and 0.8, and also between $x = 0.8$ and 1.3. Similar sign reversals were also observed in the XMCD signals of Co atoms. These results indicate that MC occurs twice in the range of $x = 0-1.3$ in $Mn_{4-x}Co_xN$. Besides, the XAS spectra of Co indicate that Co preferentially occupied the corner sites. We also calculated the mean magnetic moment of Co by using the sum rule analysis. Figure 2 shows the expected magnetic structures derived from the XMCD measurements. Around $x = 0.2$, Co atoms preferentially replaced Mn(I) and thus the total magnetic moment of I site and that of face-centered site (II site) became closer. With further increasing x , the total magnetic moment became zero. In this manner, the first MC occurred between $x = 0.2$ and 0.8. After the first MC, the total magnetic moment of II sites became larger and this led to the reversal of magnetic moments of all atoms in order to minimize the Zeeman energy. Above $x = 0.8$, Co atoms gradually got to occupy II sites and thus the second MC occurs. As far as we investigated, $Mn_{4-x}Co_xN$ is the only material which has two MC points at RT. This property can be useful for spintronic devices, for example, the use of compensation in a wide range of composition. The XMCD experiment

for $x = 0.2$ and 1.3 was performed with the approval of the Photon Factory Program Advisory Committee (Proposal No. 2019G574).

[1] S. Parkin and S. Yang, Nat. Nanotechnol., Vol.10, p.195 (2015) [2] T. Gushi *et al.*, Nano Lett., Vol.19, p.8716 (2019) [3] T. Komori *et al.*, JAP, Vol.127, p.043903 (2020) [4] K. Ito *et al.*, Phys. Rev. B, Vol.101, p104401 (2020)

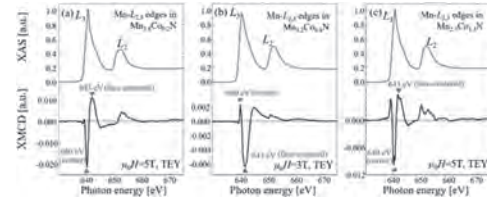


Fig. 1 XAS (blue) and XMCD (black) spectra in (a) $Mn_{3.8}Co_{0.2}N$, (b) $Mn_{3.2}Co_{0.8}N$ ^[3], and (c) $Mn_{2.7}Co_{1.3}N$ films at the Mn $L_{2,3}$ absorption edges.

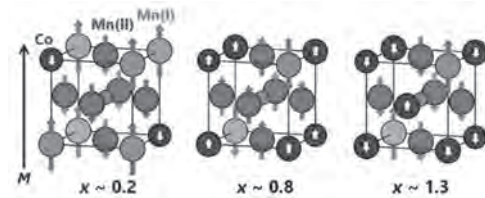


Fig. 2 Schematic of the expected magnetic structures of $Mn_{4-x}Co_xN$.

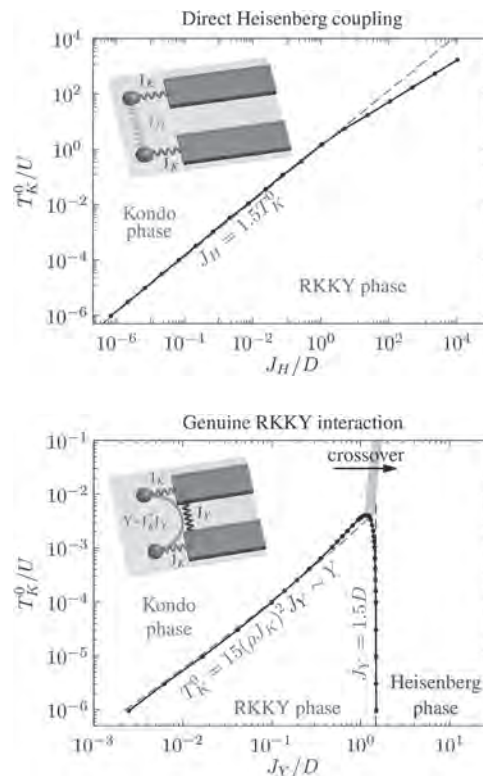
DG-08. Surprises in the Phase Diagram of two Impurities on Flat-Band Hosts Coupled by Genuine RKKY Interaction.

K.P. Wójcik^{1,2} and J. Kroha¹

1. *Physikalisches Institut, Rheinische Friedrich-Wilhelms-Universität Bonn, Bonn, Germany*; 2. *Institute for Molecular Physics, Polish Academy of Sciences, Poznan, Poland*

Since the seminal papers of Jones and Varma [1,2], the Ruderman-Kittel-Kasuya-Yosida (RKKY) interaction Y between two Kondo impurities is often modeled by a Heisenberg coupling term J_H . It gives rise to a quantum phase transition between the Kondo and the RKKY phases in the two-impurity Kondo model for arbitrarily large Kondo couplings, even in the presence of charge fluctuations (the relevant phase diagram, obtained with a numerical renormalization group technique is shown in Figure 1 for a comparison with further results). However, the significance of this result is still controversial. Firstly, the transition is fragile to particle-hole asymmetry, smearing the critical point into a crossover in its presence [3,4]. This has led to the common belief that it cannot be realized in a realistic 2-impurity system and has made its relevance for lattice models debatable. Moreover, in this model the Y and the Kondo exchange J_K are considered independent, although Y is genuinely generated from J_K , and the Kondo temperature depends on Y , as has been shown experimentally [5] and theoretically [6]. Recently, it has been shown that the quantum phase transition can be restored for weaker particle-hole symmetry by parameter fine-tuning [7]. We revisit the problem by considering a geometry of two impurities, where each one is coupled to a different host as in [5], and the RKKY interaction is induced solely by J_K and an inter-host exchange coupling J_Y . We show by numerical renormalization group (NRG) calculations that, for a properly symmetric case, this causes a transition, if the Kondo coupling is not too strong. Moreover, another phase transition occurs then at very strong J_Y (of the order of the bandwidth D), which is not present in the Jones-Varma model [1,2], and drives the system to yet another phase, with non-universal impurity spectral density. The two phase transition lines meet for increasing J_K and, hence, are replaced by a single crossover above a critical value of J_K . The corresponding phase diagram is presented in Figure 2. The phase diagram can be understood by analyzing the relevant quasiparticle pictures. In the Kondo regime, the relevant quasi-particles are spatially somewhat extended objects, and their effective bandwidth is given by the width of the Abrikosov-Suhl resonance, which is of the order of the Kondo temperature T_K . Therefore, the first transition (as recognized by Jones and Varma [2]) happens at the RKKY interaction strength of the order of T_K . In the RKKY phase the Kondo quasiparticles are destroyed and the conduction electron states alone comprise the relevant quasiparticles. The second phase transition then happens when the inter-host coupling becomes of the order of the bandwidth D . For inter-host couplings exceeding the second critical value, the band electrons become irrelevant again and the effective quasiparticles (which we call Heisenberg quasi-particles) are somewhat analogous to the Kondo quasi-particles, in that the two hosts mutually spin-screen each other. The latter observation also explains why a continuous crossover is possible between the Kondo phase and the Heisenberg one. The two transitions present for genuine RKKY interaction can be recognized in the NRG results as abrupt changes of the local density of states of electrons localized at impurities and of conduction band electrons at the impurity sites, as well as from the divergence of corresponding staggered magnetic susceptibilities. This may make them detectable despite the fact that all static spin-spin correlation functions are continuous through both transitions (like in the Jones-Varma model). As the inter-host exchange must be of the order of the width of the conduction band for the second transition to be observed, the phenomenon seems relevant to narrow-bandwidth materials, such as twisted bilayer graphene or other flat-band Moirés [8].

- [1] B. A. Jones and C. M. Varma, *Phys. Rev. Lett.*, vol. 58, p. 843 (1987).
 [2] B. A. Jones, C. M. Varma, and J. W. Wilkins, *Phys. Rev. Lett.*, vol. 61, p. 125 (1988). [3] R. M. Fye, *Phys. Rev. Lett.*, vol. 72, p. 916 (1994). [4] I. Affleck, A. W. W. Ludwig, and B. A. Jones, *Phys. Rev. B*, vol. 52, p. 9528 (1995). [5] J. Bork *et al.*, *Nat. Phys.*, vol. 7, p. 901 (2011). [6] A. Nejati, K. Ballmann, J. Kroha, *Phys. Rev. Lett.*, vol. 118, p. 117204 (2017). [7] F. Eickhoff, B. Lechtenberg, F. Anders, *Phys. Rev. B*, vol. 98, 115103 (2018). [8] L. Balents *et al.*, *Nat. Phys.*, vol. 16, p. 725 (2020).



DG-09. Anomalous Electronic and Magnetic Properties of Noncentrosymmetric YbCoC₂.

D. Salamatın¹, N. Martin², V. Sidorov¹, N. Chitchełkatchev¹, M. Magnitskaya¹, J. Guo³, C. Huang³, L. Sun³ and A. Tsveyashchenko¹
 1. Institute for High Pressure Physics RAS, Troitsk, Russian Federation;
 2. Commissariat a l'energie atomique et aux energies alternatives Siege administratif, Gif-sur-Yvette, France; 3. Chinese Academy of Sciences Institute of Physics, Beijing, China

The dual nature of the 5 f and 4 f electrons, i.e., the coexistence of localized and itinerant states in a variety of actinide and rare-earth (RE) heavy-fermion systems (e.g., UPt₃, UPd₂Al₃ [1], UGe₂ [2–4], PuCoGa₅ [5], YbRh₂Si₂ [6], YbAl₃ [7]) is the subject of an intense discussion. The standard model for 4f electrons in RE metals and their compounds is that an integral number of 4f electrons are assumed being localized at each RE ion site. This applies to both “normal” REs, where a single 4f configuration of given occupation is stable, and to mixed-valent cases, where fluctuations between states with different integral 4f occupations take place. The nature of magnetism (itinerant or localized) and the competition between ordered and disordered ground states in these mixed-valent (“abnormal”) RE elements (Ce, Eu, and Yb), remain a major challenge in condensed matter physics. In this context, the Kondo effect and the Ruderman-Kittel-Kasuya-Yosida (RKKY) interaction arising between itinerant and localized 4f electrons play essential roles. The noncentrosymmetric carbide YbCoC₂, first synthesized more than 30 years ago, represents an interesting platform for studying such physics. Here, we report on the study of its bulk magnetic and transport properties at ambient and elevated pressure, complemented by neutron diffraction measurements and ab initio calculations. We show that YbCoC₂ is a heavy-fermion compound with an amplitude modulated incommensurate magnetic order. Its Néel temperature is the highest among Yb³⁺-based systems, exceeding the previous record value belonging to β-YbAlB₄. Taken together, our experimental and numerical results indicate that the dual nature of the 4f electrons is essential for understanding the magnetic and transport properties of YbCoC₂. A wealth of experimental and numerical results presented in this study unambiguously establishes that the noncentrosymmetric YbCoC₂ is an unusual heavy-fermion system, displaying incommensurate antiferromagnetic ordering with the transition temperature reaching 33 K under pressure. The nature of its magnetic structure is surprising in itself, since the isostructural compounds RCoC₂ (where R = Gd-Tm) display FM ordering. This fact is well captured by our ab initio calculations, which also reproduce the direction of the Yb magnetic moments and, quantitatively, their amplitude. As a key result, we reveal a strong hybridization between the 4f states of Yb and the 3d orbitals of Co. We believe that this feature is instrumental in explaining the robustness of the magnetic order and its enhancement under applied external pressure. Another appealing finding concerns the evolution of the magnetic structure with pressure. Indeed, a fine-tuning of the tight competition between RKKY and Kondo interactions is a well-proven route towards the observation of quantum criticality, exotic forms of superconductivity, and novel strange metallic states [8]. This work is supported by Russian Science Foundation (17-12-01050 and 18-12-00438).

[1] T. Takahashi, N. Sato, T. Yokoya, A. Chainani, et al, J. Phys. Soc. Jpn. 65, 156 (1996). [2] R. Troc, Z. Gajek, and A. Pikul, Phys. Rev. B 86, 224403 (2012). [3] A. Yaouanc, P. Dalmas de Réotier, P. C. M. Gubbens, et al, Phys. Rev. Lett. 89, 147001 (2002). [4] F. Haslbeck, S. Säubert, M. Seifert, et al, Phys. Rev. B 99, 014429 (2019). [5] C. Booth, Y. Jiang, D. Wang, et al, Proc. Natl. Acad. Sci. USA 109, 10205 (2012). [6] S. Danzenbächer, D. V. Vyalikh, K. Kummer, et al, Phys. Rev. Lett. 107, 267601 (2011). [7] T. Ebihara, Y. Inada, M. Murakawa, et al, J. Phys. Soc. Jpn. 69, 895 (2000). [8] D. A. Salamatın, N. Martin, V. A. Sidorov, et al, Phys. Rev. B 101, 100406(R) (2020)

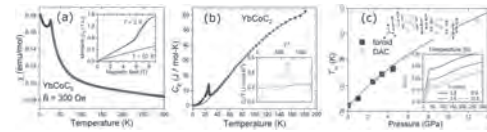


Fig.1 (a) T-dependence of magnetic susceptibility, measured in the external magnetic field B=300 Oe (blue points). The red line is the fit of a modified Curie-Weiss law to the T=28–300 K data. Inset: isothermal magnetization measured in the B=0–9 T field range at T=2 and 50 K. (b) Temperature dependence of the heat capacity Cp (blue points). The red line is the fit of two Debye laws to the high-temperature data, extrapolated down to T→0. Inset: the low-temperature part of Cp/T vs T². The red line is the linear approximation of Cp/T vs T² extended down to 0 K. (c) Pressure dependence of the magnetic transition temperature T_m (blue squares and light-blue circles, respectively). The red line is the approximation with the function f(P–P_{c0})^α, where f=18.6 K/GPa^{1/5}, P_{c0}=5.7 GPa, and α=1/5. Inset: temperature dependence of the isobaric electrical resistance, measured at P=2.8–12.9 GPa.

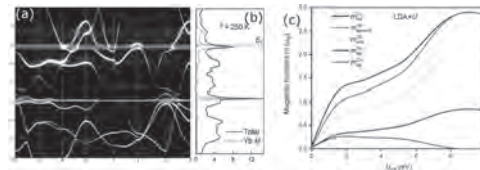


Fig.2 The DMFT band structure (a) and DOS (b) at T = 250 K. The DOS is in arb. units and the Fermi energy are set to zero. (c) The LDA+U calculations: the magnetic moment per formula unit and its partial contributions as functions of U_{eff}. The green line is the spin moment of Co, the violet line is the spin moment of Yb, the cyan line is the orbital moment of Yb, the red line is the total moment of Yb, and the blue line is the total magnetic moment.

DG-10. The Influence of Electron-Withdrawing Groups on the Relaxation Time of Field-Induced Er(III) Single Molecule Magnets.

I.A. Kühne², K. Esien¹, C. Pauly², H. Müller-Bunz², S. Felton¹ and G.G. Morgan²

1. School of Mathematics and Physics, Queen's University Belfast, Belfast, United Kingdom; 2. University College Dublin College of Science, Dublin, Ireland

Single molecule magnetism (SMM) presents a novel avenue for the pursuit of a bottom up approach to the design of next generation magnets, their molecular origin of magnetism and sensitivity to their chemical environment allows SMMs to be designed and exploited at the molecular level¹. Applications include proposals for SMMs to be used as qubits and components in spintronic devices^{2,3}. Here we present the synthesis and magnetic properties of mononuclear Ln(III) complexes, where two Er(III) complexes exhibit SMM behavior and blocking temperatures of around 40K.⁴ We used a synthetic approach and ligand fine-tuning where the ligand field is favorable for the Er(III) compounds to exhibit SMM properties. Single crystal structure analysis was carried out to obtain structural information on all the presented complexes. The field dependence of the magnetization for both Er(III) compounds were measured at 2, 3 and 5 K; the magnetization curves did not saturate at high fields indicating the presence of significant magnetic anisotropy and/or low-lying excited states. In order to investigate the potential presence of slow relaxation of the magnetization caused by SMM behavior, ac magnetic susceptibility measurements were performed, in applied dc-fields from 0 to 3000 Oe, in attempts to suppress any quantum tunneling of the magnetization (QTM). For both compounds the in-phase and out-of-phase ac susceptibility show field-dependent signals; the optimum field was found to be 500 Oe and this was used for further ac measurements. In both cases, the ac measurements reveal temperature dependent in- and out-of-phase signals with clear maxima up to 3.5 K. The maxima of the frequency dependent out-of-phase susceptibility curves were used to extract the relaxation time as a function of temperature.

[1] B. M. Day, F.-S. Guo, R. A. Layfield, *Acc. Chem. Res.* 51,1880–1889 (2018). [2] M. Shiddiq et al., *Nature* 531, 348–351 (2016). [3] S. Thiele et al., *Science* 344, 1135–1138 (2014). [4] I.A. Kühne, et al., *Dalton Trans* 48, 15679 (2019)

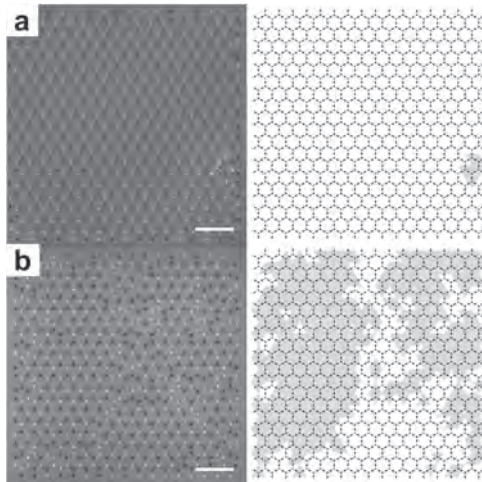
DG-11. Dynamical Freezing in an Artificial Kagome ice Magnet.

N. Rougemaille¹, V. Schanilec¹ and B. Canals¹

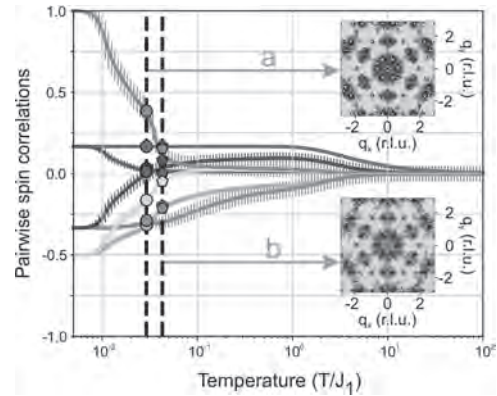
1. Institut NEEL, Grenoble, France

Two-dimensional arrays of interacting magnetic nanostructures allow the exploration of the many body physics associated with highly frustrated magnets in a convenient manner. Based on a lab-on-chip approach, artificially made structures can be viewed as experimental simulators of frustrated magnetism, complementing what can be done with chemically synthesized compounds. For example, collective magnetic phenomena such as emergent charge crystallization, magnetic moment fragmentation, and Coulomb phase physics have been recently evidenced in artificial systems. If the initial motivation was to realize an artificial ice magnet, a wide range of systems have been now investigated, including structures that have no counterparts in bulk materials. Whether they are chemically synthesized or nanofabricated, the spin dynamics of frustrated magnets generally freezes before magnetic ordering eventually sets in at very low temperature. Here, we will show how dynamical freezing can be bypassed in an artificial kagome ice to access low-energy states [1]. More specifically, we will demonstrate that the a priori dynamically inaccessible ordered ground state and fragmented spin liquid configurations can be obtained reproducibly, imaged in real space at room temperature, and studied conveniently (Figs.1 and 2). We will then identify the mechanism by which dynamical freezing occurs in the dipolar kagome ice. Besides, although artificially made structures were initially designed to address the physics of frustrated spin models, they can be used to investigate vertex models as well. Experimental strategy to fabricate artificial vertex models will be also briefly discussed [2].

[1] V. Schanilec et al., Phys. Rev. Lett. 125, 057203 (2020). [2] Y. Perrin et al., Phys. Rev. B 99, 224434 (2019).



Real space magnetic images with their associated spin-charge representations in an artificial kagome ice trapped within a fragmented spin state. Scale bar is 6 μm .



Analysis of the pairwise spin correlations.

Session DP

**MULTIFERROICS AND MAGNETOELECTRICS: PHENOMENA, MATERIALS AND TRANSPORT
(Poster Session)**

Stella Skiadopoulou, Chair
The University of Dublin Trinity College, Dublin, Ireland

DP-01. Effect of Mixing the Low-Valent Transition Metal Atoms Y = Sc, Ti, V, Cr, Mn and Fe on the Properties of Quaternary Heusler Compounds $\text{Co}_{2-x}\text{Y}_x\text{FeSi}$ ($0 \leq x \leq 1$).

R. Mahat¹, S. KC¹, U. Karki¹, J. Law², V. Franco², I. Galanakis³, A. Gupta⁴ and P. LeClair¹

1. *Physics and Astronomy, The University of Alabama, Tuscaloosa, AL, United States*; 2. *Dpto. Física de la Materia Condensada ICMSE-CSIC, Universidad de Sevilla, Sevilla, Spain*; 3. *Department of Materials Science, University of Patras, Patras, Greece*; 4. *Department of Chemistry and Biochemistry, The University of Alabama, Tuscaloosa, AL, United States*

The realization of physical systems whose electronic and magnetic properties can be easily manipulated by playing with valence electrons are very promising from both the fundamental and applied perspectives. Half-metallic ferromagnets are ideal candidates for spintronic applications because of their high spin polarization of charge carriers at the Fermi level [1,2]. High Curie temperature is one of the important precondition of the half-metallic ferromagnets from the application point of view. Co_2 -based intermetallic Heusler alloys (L_2 structure, space group $Fm-3m$, # 225) are among the most attractive half-metallic systems due to their high Curie temperatures, high spin polarization and the structural similarity to binary semiconductors [1,2]. The Co_2FeSi (CFS) system is one such candidate of interest for spintronic applications due to its high Curie temperature crystallizing in the L_2 structure but Fermi level falls on the edge of the minority conduction band (in both generalized gradient approximation (GGA) and GGA+U approach) making the system shy from being robust half metallic. High $T_c = 1100\text{K}$ and large magnetic moment of $6.00 \mu_B/\text{f.u.}$ is reported in Ref [3]. If one of the Co atom in CFS is replaced by low valence transition metal atom Y = Sc, Ti, V, Cr, Mn, and Fe, alloys with rich and useful properties can be tailored. The quaternary Heusler alloy CoFeMnSi [4] is observed theoretically and experimentally to be spin gapless semiconductor, CoFeCrSi [5] is reported to be half-metallic with some structural disorder, CoFeVSi and CoFeTiSi are reported theoretically to be nearly half-metallic and half-metallic respectively, but both are observed experimentally to show multi-phase behavior in bulk form. The Fermi level lies on the edge of the minority valence band in all Y substituted quaternary Heusler alloys, leading to an unstable half-metallicity. So, as we go from CFS to CoFeYSi , Fermi level is shifted from lower edge of conduction band to upper edge of valence band in minority spin channel which is in accordance to Ref. [2,6]. They have suggested that an expansion of the lattice should shift the Fermi level deeper in energy and the contraction should shift it higher in energy. Therefore, one can expect robust half metallicity with Fermi level exactly at the middle of the band gap for some intermediate Y concentrations in CFS due to the expansion of the lattice when Y with larger atomic radius substitutes for Co. The substitution of Y to Co may be also seen as d-electron deficiency. In this work, we have introduced the substitution of all low valence transition metal atoms Y = Sc, Ti, V, Cr, Mn, and Fe to Co atoms in the parent CFS system, and examined the structural, electronic, magnetic, and mechanical properties of quaternary Heusler compounds $\text{Co}_{2-x}\text{Y}_x\text{FeSi}$ ($0 \leq x \leq 1$) to get a global overview of the electronic, magnetic and mechanical properties, promising candidates for spintronics applications. All single phase alloys exhibit face centered cubic crystal structure with a strong tendency towards L_2 ordering, as corroborated by X-ray diffraction. The low-temperature saturation magnetic moments agree fairly well with our theoretical results and also obey the Slater-Pauling rule, a prerequisite for half metallicity. Fig. 1 shows the linear decrease of the spontaneous magnetizations measured at 2K with the valence electron counts per formula units with element Y = Ti, V, Cr, Mn, Fe, and Co in $\text{Co}_{2-x}\text{Y}_x\text{FeSi}$ ($x = 0.50$). All alloys are soft ferromagnets with high Curie temperatures, ranging from 700K to 1100K, allowing for applications at room temperature and above. The Curie temperatures are observed to vary almost linearly with the saturation magnetic moment which is also expected in half-metallic systems. First-principles calculations also predicted finite band gap in the minority spin channel for most of the alloys in $\text{Co}_{2-x}\text{Y}_x\text{FeSi}$ series. Fig. 2 shows the calculated density of states (DOS) plots using GGA approach for majority and minority spin channels of $\text{Co}_{2-x}\text{Mn}_x\text{FeSi}$ ($0 \leq x \leq 1$) alloys, where the Fermi level is represented by the zero energy. It can be seen clearly that the system exhibits half-metallic behavior after Mn substitution. In the case of parent compound CFS, there is significant amount of DOS at

the Fermi level on both the spin channels. After Mn substitution, the Fermi level is observed to shift deeper in energy-levels and falls at the middle of the energy gap on spin down channel for $x = 0.50$. Further increase of Mn content shifts the Fermi level towards the lower edge of energy gap due to lattice expansion. But, still Fermi level lies within energy gap making the system Half-metallic. In addition, conduction band and valence band in majority spin channel touch each other at Fermi level in $x = 1$, making the system spin gapless semiconductor. The energy gap is observed to increase with the increase of Mn content. Although, the calculated minority spin gap is the highest for $x = 1$, the half-metallic gap is greater for $x = 0.50$. Relatively high mechanical hardness values among the reported Heusler alloys are also observed, approaching 16 GPa for the most Ti-rich material [6-8].

1. C. Felser, G. H. Fecher, and B. Balke, *Angewandte Chemie International Edition*, 46, 668 (2007). 2. I. Galanakis, P. Dederichs and N. Papanikolaou, *Physical Review B*, 66, 174429 (2002). 3. E. Fischer, J. Karel and S. Fabbrici, *Physical Review B*, 94, 024418 (2016). 4. L. Bainsla, A.I. Mallick and M.M. Raja, *Physical Review B*, 91, 104408 (2015). 5. Y. Jin, P. Kharel and P. Lukashev, *Journal of Applied Physics*, 120, 053903 (2016). 6. R. Mahat, S. KC and U. Karki, *Physical Review B*, Submitted (2021). 7. R. Mahat, S. KC and D. Wines, *Journal of Alloys and Compounds*, 830, 154403 (2020). 8. R. Mahat, S. KC and D. Wines, *Journal of Magnetism and Magnetic Materials*, 521, 167398 (2021).

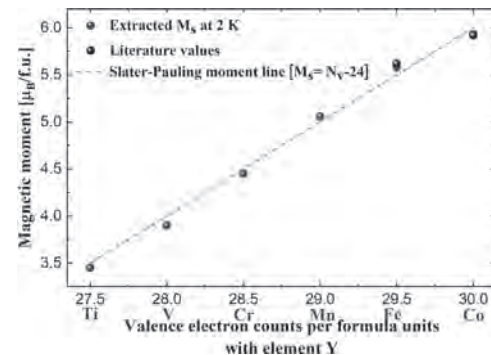


Fig. 1. The saturation magnetic moment versus valence electron counts per formula units with element Y = Ti, V, Cr, Mn, Fe, and Co in $\text{Co}_{2-x}\text{Y}_x\text{FeSi}$ ($x = 0.50$), both experimental and expected from Slater Pauling rule for half metals. The black data points represent reported literature values [3].

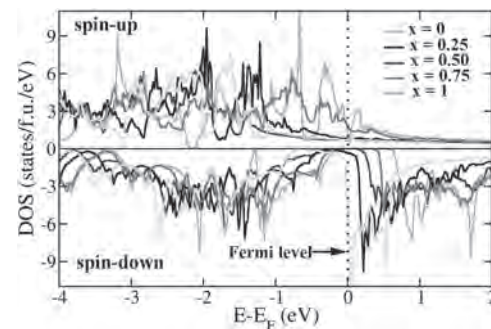


Fig. 2. Spin polarized total DOS for $\text{Co}_{2-x}\text{Y}_x\text{FeSi}$ (Y = Mn, $0 \leq x \leq 1$). Number of states is scaled with respect to one formula unit.

DP-02. Observation of Room-Temperature Magnetoresistance in Graphene/CoFe₂O₄ Nanocomposite.

S. Roy^{2,1}, I. Sivakumar², F. Francis², V. G. V.² and A. Subramanian¹
 1. Manipal Academy of Higher Education, Manipal, India; 2. Centre for Nano and Soft Matter Sciences, Bangalore, India

The magnetic field dependent electrical properties, such as magnetoresistance (MR) and magnetocapacitance (MC) effects, are nowadays promising for their application in data storage, magnetic sensor, and spintronic devices [1, 2]. For MR based applications, it is essential to have better magneto-crystalline anisotropy and control over the magnetic field induced charge transport. It has been observed that many ferrite nanoparticles (MFe₂O₄, M = Mg, Mn, Fe, Co, Ni, etc.) are having very good magnetic anisotropy even at room temperature, which is suitable for spintronics based applications [3]. However, the electronic charge transport through these materials is hindered by their higher resistivity. Therefore, the incorporation of conducting matrix with the ferromagnetic nanoparticles can give rise to an efficient system for MR based applications. In particular, the addition of 2D material like graphene with the ferromagnetic nanoparticles has been found to enhance the MR by many orders [4]. The longer spin diffusion length and the possibility of charge transfer between the d-orbital of transition metal to the p-orbital graphene make this material suitable for preparing composite with ferrites for better spintronics applications [5]. Here, we report an observation of room-temperature magnetoresistance properties of reduced graphene oxide (rGO) / cobalt ferrite (CFO) nanocomposite, which were synthesized by chemical methods followed by mixing in different ratios. The CFO nanoparticles are prepared by the coprecipitation method followed by annealing at 600 °C for three hours. On the other hand, graphene oxide was prepared using modified Hummer's method followed by reduction to rGO using hydrothermal method. The composite between the CFO nanoparticles and rGO was prepared by mixing in different mass ratios (1:1, 2:1, and 3:1). The crystal structure of the samples has been investigated from the x-ray diffraction study, which confirms the formation of rGO as well as cubic CFO nanocrystals. The Raman spectra confirmed various vibrational modes of CoFe₂O₄ nanoparticles, as well as the D and G peaks of rGO. The morphology and size distribution of the CFO nanoparticles has been studied from TEM images. The magnetic hysteresis (MH) curve shown in figure 1 (a) at 300 and 10 K shows the ferromagnetic nature of the CFO nanoparticles. The room temperature MR study of CFO – rGO nanocomposites are shown in figure 1 (b). Maximum negative MR of - 1.4 % was observed for the 1:1 ratio of CFO and rGO, whereas the MR was decreased to - 1% with the increase of CFO content in 2:1 and 3:1 ratio. In the presence of an external magnetic field, the parallel alignment of the ferromagnetic moments of CFO reduces the electron – spin scattering and increases the tunneling probability of the charge carrier through the particles, which can effectively reduce the resistance [6]. However, the charge transport through the grains of oxide nanoparticles are largely dominated by the grain – grain boundary induced scattering of charge carriers, which results in higher resistance of the material. Therefore, to reduce the inter grain charge scattering, it is very crucial to introduce a conducting matrix in between the grains of the nanoparticles. It has been observed that the addition of carbon-based conducting materials like graphite or graphene has enhanced the MR of many magnetic oxides [7]. In our study, the highest MR value observed in the 1:1 ratio can be understood from the better connectivity of the CFO nanoparticles through the conducting rGO matrix, which improves the charge transfer between the d-orbital of the transition metal and the p-orbital of rGO at the interface. However, the higher amount of CFO in the samples of 2:1 and 3:1 ratio leads to the less fraction of nanoparticles surrounded by the rGO matrix. Hence, the CFO-rGO interfacial charge transport, as well as the interparticle connectivity, reduces. The reduced interparticle connectivity gives rise to higher resistivity, and the grain – grain boundary induced scattering plays a major role in the charge conduction. To understand the grain – grain boundary induced effects, we have studied the frequency-dependent capacitance of the CFO nanoparticles with and without magnetic field. Figure 1 (c) shows the variation of capacitance with the increase of frequency from 100 Hz to 1 MHz under 0 and 0.5 T applied fields. The capacitance value decreases under the magnetic field, representing a negative MC effect. The MC value of nearly – 2.4 % was observed at 100 Hz, whereas with the increase

of frequency to 1 MHz, the MC value was reduced to nearly – 1.5 %. At lower frequency, the major contribution to the capacitance comes from the collective response of space charge polarization, defects, and the grain – grain boundary induced effects [8]. However, with the increase of frequency, the contribution from the grain boundary and the space charge polarization decreases gradually, and the bulk polarization originates from dipolar effects.

[1] M.-H. Phan and H.-X. Peng, Progress in Materials Science 53, 323 (2008). [2] J. F. Scott, Journal of Materials Chemistry 22, 4567 (2012). [3] Kebede K. Kefeni, Titus A.M. Msagati, Bhekhe B. Mamba, Materials Science and Engineering B 215, 37 (2017). [4] G. Abellán, H. Prima-Garcia, and E. Coronado, J. Mater. Chem. C, 4, 2252 (2016). [4] Xiaojie Liu, C. Z. Wang, Y. X. Yao, W. C. Lu, M. Hupalo, M. C. Tringides, and K. M. Ho, Phys. Rev. B 83, 235411 (2011). [5] T. Prakash, G. V. M. Williams, J. Kennedy, and S. Rubanov, Journal of Applied Physics 120, 123905 (2016). [6] S. Bhattacharya, R. Maiti, M. Baskey Sen, S. K. Saha and D. Chakravorty, J. Phys. D: Appl. Phys. 48, 435002 (2015). [7] S. Roy, R. Katoch, and S. Angappane, IEEE Transactions on Magnetics, 55 (2), 1-4 (2019).

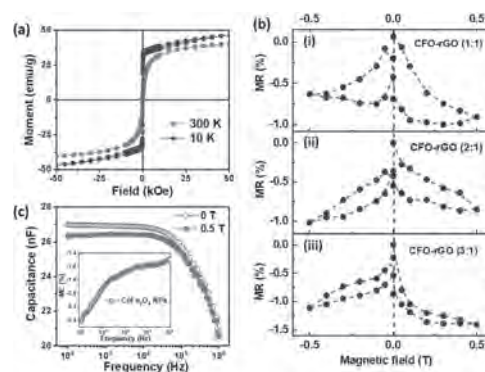


Figure 1. (a) Magnetic hysteresis (MH) curves at 300 and 10 K of CoFe₂O₄ nanoparticles. (b) Room temperature magnetoresistance of CFO-rGO nanocomposite of various ratios (i-iii). (c) Variation of the capacitance of CoFe₂O₄ nanoparticles with frequency under the magnetic fields 0 and 0.5 T. Inset shows the magnetocapacitance effect in the frequency range of 100 Hz to 1 MHz.

DP-03. Highly Nonlinear Magnetoelectric Effect in Buckled Honeycomb Antiferromagnetic $\text{Co}_4\text{Ta}_2\text{O}_9$.

N. Lee¹, D. Oh¹, S. Choi^{2,3}, J. Moon¹, J. Kim¹, H. Shin¹, K. Son⁴, J. Nuss², V. Kiryukhin³ and Y. Choi¹

1. Department of Physics, Yonsei University, Seodaemun-gu, The Republic of Korea; 2. Max Planck Institute for Solid State Research, Stuttgart, Germany; 3. Department of Physics and Astronomy, Rutgers The State University of New Jersey, New Brunswick, NJ, United States; 4. Max-Planck-Institut für Intelligente Systeme, Stuttgart, Germany

Strongly correlated materials with multiple order parameters provide unique insights into the fundamental interactions in condensed matter systems and present opportunities for innovative technological applications. A class of antiferromagnetic honeycomb lattices compounds, $\text{A}_4\text{B}_2\text{O}_9$ (A = Co, Fe, Mn; B = Nb, Ta), have been explored owing to the occurrence of linear magnetolectricity. From our investigation of magnetolectricity on single crystalline $\text{Co}_4\text{Ta}_2\text{O}_9$, we discovered strongly nonlinear and antisymmetric magnetolectric behavior above the spin-flop transition for magnetic fields applied along two orthogonal in-plane directions. This observation suggests that two types of inequivalent Co^{2+} sublattices generate magnetic-field-dependent ferroelectric polarization with opposite signs. The results motivate fundamental and applied research on the intriguing magnetolectric characteristics of these buckled-honeycomb lattice materials.

[1] N. Lee, D. G. Oh and Y. J. Choi, Scientific Reports, vol. 10, 12362 (2020)

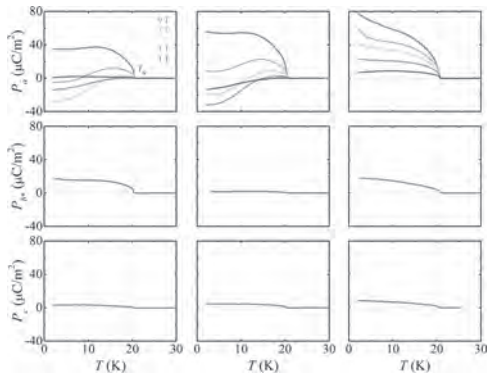


Fig. 1 Temperature dependence of the anisotropic ferroelectric polarization. (a–c) T dependence of P_a obtained by integrating the pyroelectric current after poling from 100 to 2 K in at H_a , H_{b^*} , and H_c , respectively. P_a was measured at $H = 1, 3, 5, 7$ and 9 T. (d–f) T dependence of P_{b^*} measured at $H_a = 9$ T, H_{b^*} , and H_c , respectively. (g–i) T dependence of P_c measured at $H_a = 9$ T, H_{b^*} , and H_c , respectively.

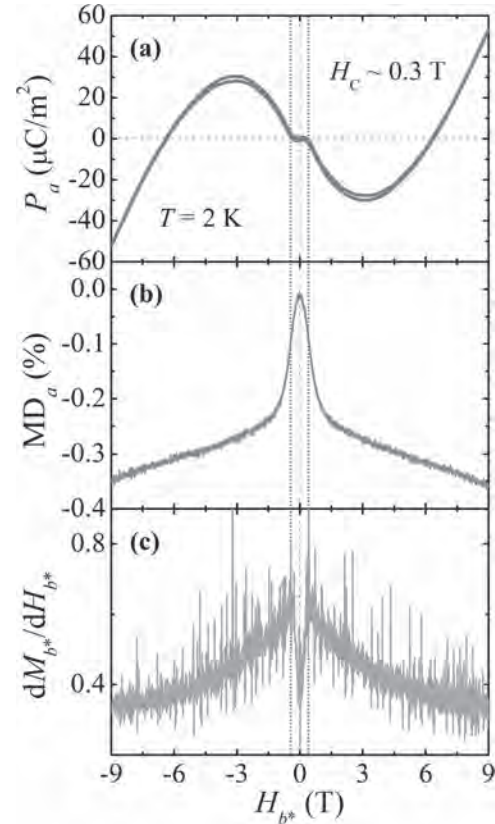


Fig. 2 Comparison of electric and magnetic properties. (a) H_{b^*} dependence of P_a at $T = 2$ K. (b) H_{b^*} dependence of the magnetodielectric effect along the a axis, $\text{MD}_a (\%) = \{\epsilon'(H) - \epsilon'(0T)\} / \epsilon'(0T) \times 100$, measured with AC excitation of $E_a = 1$ V at $f = 100$ kHz and $T = 2$ K. (c) H_{b^*} derivative of M_{b^*} at 2 K.

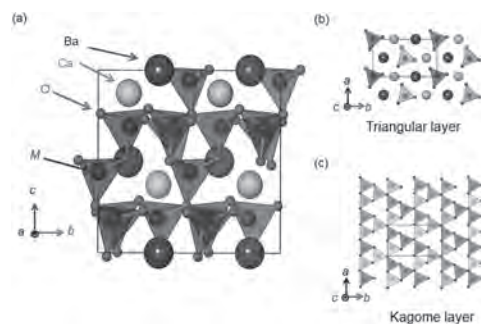
DP-04. Polarity Dependence of Change in Electric Polarization (Magnetization) Induced by Magnetic (Electric) Fields in CaBaM_4O_7 ($M=\text{Co}, \text{Fe}$) Single Crystals.

T. Shirasaki¹, H. Endo¹, M. Noda¹, M. Akaki², H. Kuroe¹ and H. Kuwahara¹

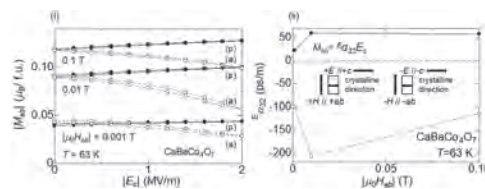
1. Phys.Div., Jochi University, Chiyoda-ku, Japan; 2. Molecular Photo-science Reserch Center, Kobe University, Kobe, Japan

Introduction Multiferroic materials have been attracting much attention because they have multiple ordered (ferroelastic, ferroelectric, and ferromagnetic) states. In particular, magnetic and ferroelectric material has a property that magnetization M (electric polarization P) can be controlled by electric E (magnetic H) field. Such property is called “magnetoelectric (ME) effect”. In magnetic and ferroelectric material, there is also a possibility of observing an optical response that the rate of absorption is different between the cases that light enters from one direction and the opposite direction. Such a large nonreciprocal response in the visible light region was discovered in CuB_2O_4 [1]. The observed nonreciprocal response in light is thought to be originated from dynamical AC ME response. The present compounds, CaBaM_4O_7 ($M=\text{Co}, \text{Fe}$), have been attracting interest for their nontrivial magnetism because of the geometrically frustrated crystal structure consisting of triangular and Kagome layers. From the viewpoints of the studies of multiferroics, we have expected that the magnetic ordering couples with the spontaneous electric polarization P due to the crystal structure with a polar point-group of $mm2$. Indeed, we have observed the change of P_c induced by the weak ferromagnetic ordering in $\text{CaBaCo}_4\text{O}_7$ [2]. Then the magnetic-field H_{ab} -induced giant variation in P_c was reported and the magnetostriction mechanism was proposed to explain the observed giant ME effect [3]. Also in the case of $\text{CaBaFe}_4\text{O}_7$, the ME coefficient $^H\alpha_{cc}$ defined as $\Delta P_c = ^H\alpha_{cc} H_c$ with a maximum value of 39 ps/m was reported for the measurements of H_c -induced change of P_c at 80 K below the ferrimagnetic transition temperature of 275 K [4]. In this work, we have systematically investigated nonreciprocal DC ME response, i.e., crystalline (polar) direction dependence of ME coefficients for CaBaM_4O_7 ($M=\text{Co}, \text{Fe}$) single crystals. Especially, we focused on the electric-field (E_c)-induced magnetization (M_{ab} or M_c) in CaBaM_4O_7 ($M=\text{Co}, \text{Fe}$), which had almost not yet been performed. Results and Discussion Figure 1 shows the Schematic crystal structure of CaBaM_4O_7 ($M = \text{Co}, \text{Fe}$). The space group of $\text{CaBaCo}_4\text{O}_7$ at room temperature is orthorhombic $Pbn2_1$, which is distorted and lowered symmetry from the higher one of hexagonal $P6_3mc$. Its (magnetic) point group is ($m'm2'$) $mm2$. Those of $\text{CaBaFe}_4\text{O}_7$ are $Pbn2_1$ and $mm2$, which are the same as $\text{CaBaCo}_4\text{O}_7$ [2,4]. Its magnetic point group is unknown yet. Both materials have quasi-triangular lattices and quasi-Kagome ones stacked along the c -axis direction. There exists multidomain structure within the orthorhombic ab plane in spite of no such one in the c axis. A spontaneous electric polarization along the c axis (P_c) is expected from the polar point group of $mm2$. Figure 2(i) shows the electric field dependence of the magnetization of $\text{CaBaCo}_4\text{O}_7$ in constant magnetic fields. The magnetic field (H_{ab}) was applied within the magnetic easy ab plane perpendicular to the c axis, and the electric field (E_c) was applied along the c axis which is the direction of spontaneous electric polarization (P_c). The configuration among the external magnetic field, electric field, and crystalline direction (spontaneous electric polarization) is presented in the inset of Fig. 2(ii). When the electric field is applied in the parallel direction (p) to the crystalline direction, the magnetization increases as the electric field increases. Such trends can be clearly seen as solid symbols in Fig. 2(i). Conversely, in the antiparallel (a) case, the magnetization decreases with electric field (See open symbols). Figure 2(ii) shows the magnetic field dependence of $^E\alpha_{32}$ which is a component of linear ME tensor and defined as $M_{ab} = ^E\alpha_{32} E_c$. Depending on the configurations between the electric field and the crystal direction, $^E\alpha_{32}$ shows opposite signs. The observed crystalline-direction (polarity) dependence of change in magnetization can be regarded as a DC nonreciprocal response. As is well known for the diode, nonreciprocal response is indispensable in device applications. Therefore, we explore the novel nonreciprocal phenomena as mentioned above in the present polar magnetic compounds, CaBaM_4O_7 ($M = \text{Co}, \text{Fe}$), for the future application such as “thermal diode”.

[1] M. Saito *et al.*, J. Phys. Soc. Jpn. 77, 013705 (2008). [2] H. Iwamoto *et al.*, J. Phys. Conf. Ser. 400, 032031 (2012). [3] V. Caignaert *et al.*, Phys. Rev. B 88, 174403 (2013). [4] V. Kocsis *et al.*, Phys. Rev. B 93, 014444 (2016).



Schematic crystal structure of CaBaM_4O_7 ($M = \text{Co}, \text{Fe}$) projected onto the bc plane (a). Its quasi-triangular (b) and quasi-Kagome layers (c) are projected onto the ab plane. The rectangular boxes represent the boundaries of unit cell [2].



(i) Electric field dependence of magnetization in $\text{CaBaCo}_4\text{O}_7$. Solid symbols correspond to the parallel configuration between the electric field and the crystalline (polar) direction, and open ones to the antiparallel configuration. (ii) Magnetic field dependence of $^E\alpha_{32}$ ($\equiv M_{ab}/E_c$) deduced from the data shown in (i). The inset is a schematic diagram of the configuration among the external magnetic/electric fields and the crystal direction.

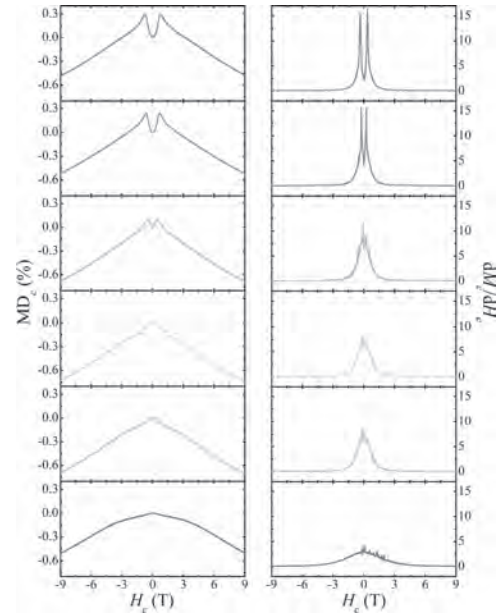
DP-05. Anisotropic and Nonlinear Magnetodielectric Effects in Orthoferrite ErFeO₃ Single Crystals.

H. Shin¹, D. Oh¹, J. Kim¹, Y. Choi¹ and N. Lee¹

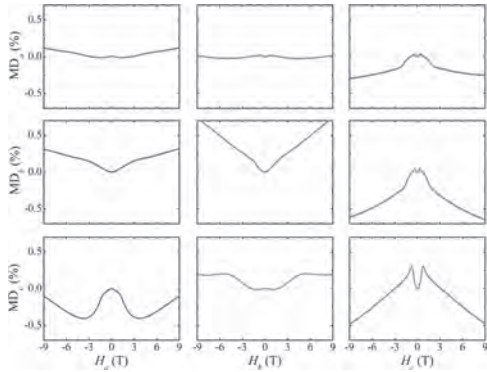
1. Physics, Yonsei University, Seodaemun-gu, The Republic of Korea

In rare-earth orthoferrites, strongly correlated order parameters have been thoroughly investigated, which aims to find multiple functionalities such as multiferroic or magnetoelectric properties. We have discovered highly anisotropic and nonlinear magnetodielectric effect from detailed measurements of magnetoelectric properties in single-crystalline orthoferrite, ErFeO₃. Isothermal dielectric constant varies in shapes and signs depending on the relative orientations between the external electric and magnetic fields, which may be ascribed to the spin-phonon couplings. In addition, a dielectric constant with both electric and magnetic fields along the c axis exhibits two symmetric sharp anomalies, which are closely relevant to the spin-flop transition, below the ordering temperature of Er³⁺ spins, $T_{Er} = 3.4$ K. We speculate that the magnetostriction from the exchange couplings between Er³⁺ and Fe³⁺ magnetic moments would be responsible for this relationship between electric and magnetic properties. Our results present significant characteristics of the orthoferrite compounds and offer a crucial guide for exploring suitable materials for magnetoelectric functional applications.

[1] H. J. Shin, Y.J. Choi and N. Lee, Scientific Reports., 10:11825 (2020)



Temperature evolution of magnetodielectric effect along the c axis. (a)–(f) H_c dependence of MD_c at $T = 2, 2.5, 3, 3.5, 5$ and 10 K. (g)–(l) H_c derivative of M_c and dM_c/dH_c measured at $T = 2, 2.5, 3, 3.5, 5$ and 10 K.



Magnetodielectric effect of ErFeO₃. Magnetodielectric (MD) effect defined as $MD (\%) = (\epsilon'(H) - \epsilon'(0T)) / \epsilon'(0T) \times 100$ for (a)–(c) a (MD_a), (d)–(f) b (MD_b), and (g)–(i) c (MD_c) axes, respectively, at $H_a, H_b,$ and H_c up to ± 9 T and $T = 2$ K.

DP-06. Structural and Electromagnetic Characteristics of La-Sr Manganite With Paired Substitution of Zn and Ti for Manganese Depending on Oxygen Content.

V. Karpasyuk¹, A. Badelin¹, Z. Datskaya¹, I. Derzhavin¹ and S. Estemirova^{2,1}

1. Astrakhan State University, Astrakhan, Russian Federation;

2. Institute for metallurgy UrO RAN, Ekaterinburg, Russian Federation

The aim of this work is to establish the influence of deviation from oxygen stoichiometry on the properties of La-Sr manganites with manganese-substituting combination of divalent and quadrivalent ions having different electron configuration: $Zn^{2+}(3d^{10})$ and $Ti^{4+}(3p^6)$. Polycrystalline manganites of $La_{0.7}Sr_{0.3}Mn_{0.9}(Zn^{2+}_{0.5}Ti^{4+}_{0.5})_{0.1}O_{3+\gamma}$ compositions were prepared by ceramic processing. The sintering step was performed in air at 1473 K for 10 h. Obtained samples were then divided into three groups, which were exposed to heat treatments at 1223 K for 96 h at a partial pressure of oxygen in the gas phase of $P_{O_2} = 10^{-1}$ Pa, 10^{-8} Pa, and 101.3 kPa. All synthesized manganites were rhombohedral. Oxygen non-stoichiometry index (γ) of the samples of above-mentioned groups was calculated from the data on unit cell volume (V) according to algorithm proposed earlier [1] with the allowance for concentrations of Mn^{4+} and Mn^{3+} ions, anion and cation vacancies. As follows from Fig. 1, unit cell volume decreases as a function of γ , and specific magnetization (σ) shows a tendency to increase almost within the measurement error. Temperature dependences of $d\mu(T)/dT$, where $\mu(T)$ is magnetic permeability as a function of temperature T , are presented on Fig. 2. Curie point defined as the temperature corresponding to the maximum of $|d\mu(T)/dT|$, is equal to 219, 226, 229 K for manganites with values of $\gamma = -0.008, 0.000, 0.009$, respectively. One can see that temperature interval of “ferromagnetic-paramagnetic” transition is sufficiently wide (from 8 to 15 K), especially in stoichiometric manganite. Broadening of the transition interval can be associated with the formation of clusters, segregations, and magnetic inhomogeneities with various magnetization and transition temperature [2]. Manganite annealed in oxygen has the narrower transition interval than those annealed in vacuum, due to vacancy mechanism of cation diffusion, which smooths out spatial variations of the composition. Scanning electron microscopy studies have revealed the existence of micro-inhomogeneities having various configurations, including modulated structures. Manganite annealed at $P_{O_2} = 10^{-8}$ Pa has the highest absolute value of magnetoresistance: $|MR| = 60\%$ in the field of 9.2 kOe at 120 K. Magnetostriiction constant (λ) is maximal for a sintered sample having the oxygen non-stoichiometry index of $\gamma = 0.004$. At $T = 140$ K, it reaches gigantic value of $\lambda = 7 \times 10^{-3}$ and drops to 10^{-4} at 293 K. Interpretation of established regularities is discussed in terms of mechanisms of charge compensation with the allowance for formation of singly charged oxygen ions [3,4], diffusion processes, electron configuration and radii of substituents, double-exchange and Coulomb interactions.

1. D. Merkulov, A. Badelin and V. Karpasyuk, Acta Physica Polonica A, Vol. 127, p.248 (2015) 2. V. Karpasyuk, A. Badelin, and I. Derzhavin, Journal of magnetism and magnetic materials, Vol. 476, p.371 (2019) 3. J. Mizusaki, N. Mori and H. Takai, Solid State Ionics, Vol. 129, p.163 (2000) 4. V. Karpasyuk, A. Badelin and D. Merkulov, Journal of Physics: Conference Series, Vol. 1347, p.012036 (2019)

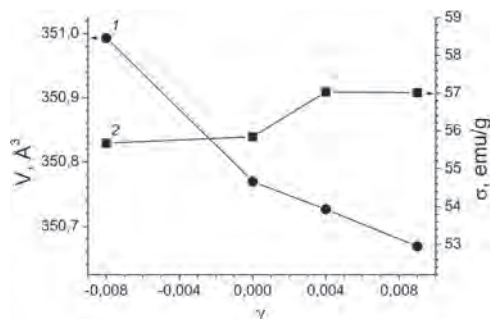


Fig.1. Dependencies of unit cell volume (1) and magnetization (2) on non-stoichiometry index

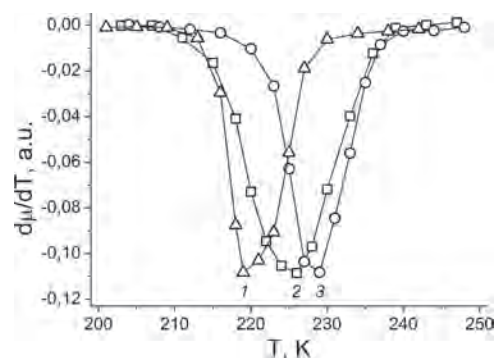


Fig.2. Temperature dependences of $d\mu(T)/dT$ for manganites with $\gamma = -0.008$ (1); 0.000 (2); 0.009 (3)

DP-07. Withdrawn

DP-08. High-Temperature Martensitic Transformation in Pr-Sr Manganites.

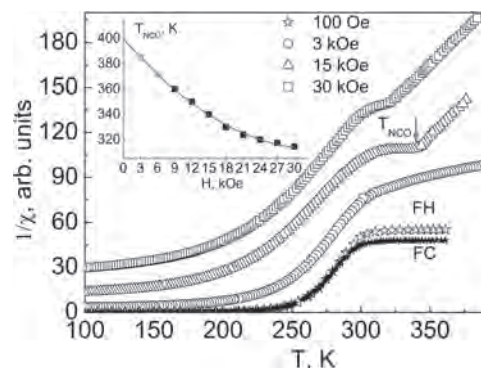
Y.E. Samoshkina¹, M.V. Rautskii¹, D.S. Neznakhin², E. Stepanova², N. Andreev³ and V. Chichkov³

1. Federal Research Center KSC SB RAS, Kirensky Institute of Physics, Krasnoyarsk, Russian Federation; 2. Ural Federal University, Institute of Natural Sciences and Mathematics, Yekaterinburg, Russian Federation; 3. National Research Technological University "MISIS", Moscow, Russian Federation

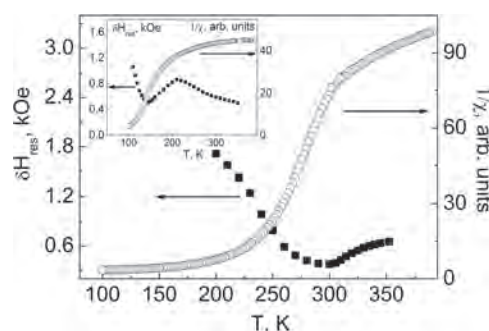
A strong coupling between spin, orbital, charge, and lattice degrees of freedom determines the unique properties of mixed valence manganites [1]. A phase separation phenomenon plays an important role in the physics of these materials [1, 2]. However, mechanisms of spontaneous phase separation are still not fully understood that does not permit to control the process by means of the external factors such as temperature, magnetic field, and pressure. The charge ordering (CO), which is the spatial ordering of the Mn^{3+} and Mn^{4+} ions, is closely related to the phase separation and is one of the most interesting phenomena observed in the mixed valence manganites. Herewith, the CO state is observed in the different materials with the $R^{3+}_{1-x}A^{2+}_xMnO_3$ general formula [3, 4]. There are studies that indicate the martensitic nature of the charge ordering state in the mixed valence manganites [5, 6]. In this work, the polycrystalline films $Pr_{1-x}Sr_xMnO_3$ with $x=0.2$ and 0.4 were investigated in the temperature range of 100-390 K using the electron magnetic resonance (EMR) spectroscopy in the X-band and the magnetic susceptibility measurements. The films thickness is 100-130 nm. Single-crystal zirconium oxide stabilized by yttrium (YSZ) was used as the substrate. The samples were prepared by dc magnetron sputtering with the "facing-target" scheme that allows transferring elements from a target to a substrate without changes in the composition. The magnetic susceptibility data showed that the Curie temperature (T_C) of the films is 115 K for $x = 0.2$ and 215 K for $x = 0.4$. These values are significantly lower than for the single crystals of the same composition (150 K and 300 K, respectively). This situation implies the presence of the phase separation in the films and the detection of possible magnetic correlations above T_C . The presence of the Griffiths-like phase in the films above their T_C was previously established using analysis of the EMR spectra [7]. This phase represents the short-range ferromagnetic correlations in the paramagnetic region. The Griffiths temperature (T_G) is 145 K for $x = 0.2$ and 295 K for $x = 0.4$ and corresponds to T_C of the single crystals of the same composition. New research shows the presence of the CO state in the films above their T_G . Temperature dependents of the inverse magnetic susceptibility measured for the samples in the external magnetic fields of $H = 0.1 - 30$ kOe demonstrate a pronounced shoulder in the wide temperature range up to values above room temperature. The example is shown in the Fig. 1 for the film with $x = 0.4$. It is should note that the pronounced shoulder above T_G was also observed on the temperature dependence of the inverse residual magnetization of the films magnetized in the field of $H = 500$ Oe. In the case of the film with $x = 0.4$, the shoulder width as well as the temperature near the charge-ordering transition (T_{NCO}) decreases with the growth of the applied magnetic field. The T_{NCO} dependence on the applied magnetic field was traced. Inset in the Fig. 1 shows the $T_{NCO}(H)$ dependence for the film with $x = 0.4$. In the case of the film with $x = 0.2$, the inverse magnetic susceptibility above T_G exhibits an ambiguous behavior in the high magnetic fields. For materials in the ferromagnetic region, the resonance line expands with decreasing temperature. The resonance line broadening observed for manganites above their T_C (or T_G) with increasing temperature is usually explained by the presence of spin-lattice relaxation and magnetic polarons. The temperature dependence of the resonance linewidth for the film with $x = 0.2$ indicates the presence of the charge ordering in the range of $T = 200-350$ K (Inset in the Fig. 2). For the film with $x = 0.4$, a maximum of about 350 K is also assumed (Fig. 2). The temperature hysteresis of the inverse magnetic susceptibility of the films is observed in the weak magnetic field above their T_G . The example is shown in the Fig. 1 for the film with $x = 0.4$. This behavior is a direct evidence of the martensitic nature of the CO state [8]. The high-temperature charge ordering ($T_{NCO} = 600$ K) was previously observed in the Bi-Sr manganite with $x = 0.25$ [3]. This behavior was explained by the exclusive role of the $6s^2$ electrons of Bi^{3+} . The role of the $6s^2$ electrons of Pr^{3+} and the effect

of intrinsic strains in the samples other than strains associated with grain boundaries or substrate lattice mismatch in films are discussed.

1. E. Dagotto, T. Hotta, A. Moreo, Phys. Rep., Vol. 344, p. 1 (2001) 2. A. Krichene, W. Boujelben, S. Mukherjee, et al., Acta Materialia, Vol. 131, p. 491 (2017) 3. J.L. Garcia-Munoz, C. Frontera, M.A.G. Aranda, et al., J. Solid State Chem., Vol. 171, p. 84 (2003) 4. D.M. Polishchuk, A.I. Tovstolytkin, E.L. Fertman, et al., J. Magn. Magn. Mat., Vol. 410, p. 109 (2016) 5. V. Podzorov, B.G. Kim, V. Kiryukhin, et al., Phys. Rev. B, Vol. 64, p. 140406 (2001) 6. S. Dhieb, A. Krichene, N. Chniba Boudjada, et al., J. Phys. Chem. C, Vol. 124, p.17762 (2020) 7. Yu.E. Samoshkina, M.V. Rautskii, E.A. Stepanova, et al., J. Exp. Theor. Phys., Vol. 125, p. 1090 (2017) 8. X. Liang, J. Bai, J. Gu, et al., J. Mater. Sci. Technol., Vol. 44, p. 31 (2020)



Temperature dependences of the inverse magnetic susceptibility for the film with $x = 0.4$. The curves were measurement in two modes at $H = 100$ Oe: cooling (FC) and heating (FH). Inset: dependence of the temperature near the charge-ordering transition (T_{NCO}) on the applied magnetic field. The squares are the experimental points, the line is the fit and approximation.



Temperature dependence of the inverse magnetic susceptibility at $H = 3$ kOe and the resonance linewidth in the X-band for the film with $x = 0.4$. Inset: temperature dependence of the inverse magnetic susceptibility at $H = 3$ kOe and the resonance linewidth for the film with $x = 0.2$.

DP-09. Effects of a Molecular C₆₀ Interfaces on the Spin Hall Magnetoresistance of YIG/PtMn.

S. Alotibi¹, B. Hickey¹, M. Ali¹ and O. Céspedes¹
 1. University of Leeds, Leeds, United Kingdom

5d metals are used in electronic architectures because of their high spin-orbit coupling (SOC) leading to efficient spin ↔ electric conversion and strong magnetic interactions. When C₆₀ is grown on a metal, the electronic structure is altered due to hybridisation and charge transfer. Previously, it has been shown that this can lead to the emergence of spin ordering [1]. This interfacial effect is also critical in spin filtering and spin transport effects [2]. We have studied the spin Hall magnetoresistance (SHMR) for YIG/Pt/C₆₀ and YIG/Ta/C₆₀. [3]. The SHMR at room temperature are up to a factor 6 higher than for the pristine metals, with the spin Hall angle increased by 20-60%. Here we studied YIG/PtMn with without C₆₀. PtMn is an antiferromagnet that has been shown to have a strong spin Hall effect [4]. This will allow us to determine if the molecular orientation can play a role in the enhanced SOC observed in Pt. We aim to: investigate the mechanisms that generate spin orbit scattering at the hybrid conducting interface and maximise the effect. By fitting the SHMR data, we can extract the spin Hall angle which is significantly higher with the molecular overlayer. The SHMR saturates once the applied field saturates the magnetisation out-of-plane, at 0.1-0.15 T for a YIG film, and no higher than 0.5 T for any measured condition. However, above this field range, other contributions such as Koehler MR, localisation and the Hanle effect can result in significant linear contributions to the MR that would artificially enhance the SHMR ratio and spin hall angle [Fig1]. Thus, the spin Hall angle Θ_{SH} is bigger for PtMn/C₆₀ than PtMn, which we attribute to an enhancement of the spin orbit coupling (SOC) by the C₆₀. Figure 2 shows the maximum SHMR measured as a function of the PtMn thickness for both pure metal and PtMn covered on molecules. Also, the PtMn/C₆₀ SHMR value is increased after annealing the sample at 200 C.

References 1. F. Al ma'mari, *et al.*, Nature. 524, 69—73 (2015) 2. M. Cinchetti, *et al.*, Nature materials. 16, 507 (2017) 3. S. Alotibi, *et al.*, arXiv preprint: 1912. 02712, 2020. 4. Y. Ou, Phys. Rev. B 93, 220405(R) (2016).

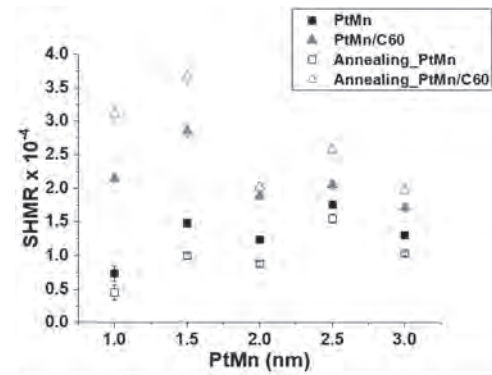


Figure 2 shows the maximum SHMR measured in PtMn and PtMn/C₆₀ before and after the annealing.

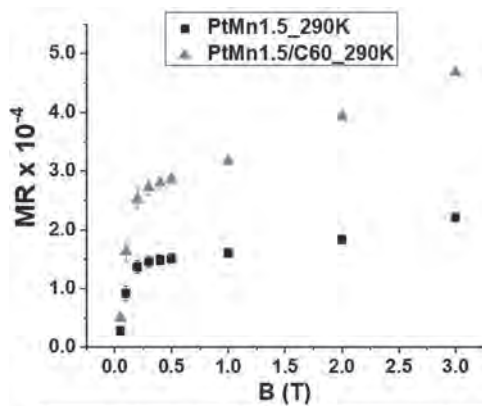


Figure 1 shows the change in the measured MR as a function of the applied magnetic field.

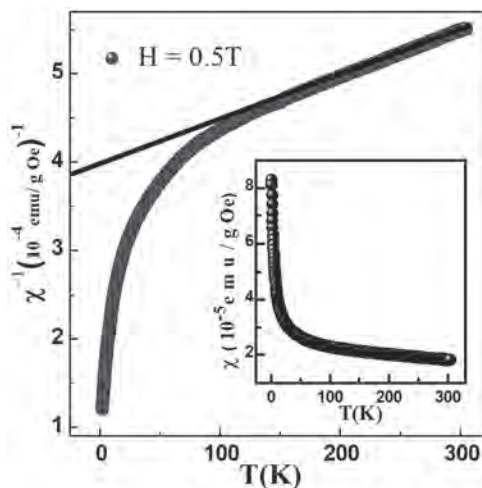
DP-10. Magneto-Transport Study on Topological Chiral Semimetal CoSi.

S. Monga¹, R. Rawat¹ and R.K. Gopal¹

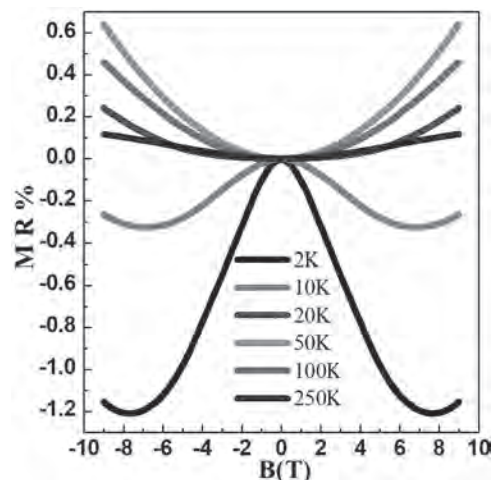
¹. Indian Institute of Science Education and Research Mohali, Mohali, India

Topological chiral semi-metal CoSi exhibit unusual quasi-particles excitations near the band crossing point, which have spin-1 and charge-2 chiral charge [1]. Like Dirac and Weyl semimetals, these semimetals also show some unusual electrical transport behavior, such as large magneto-resistance, mobility, and anomalous Hall effects. Therefore, we have performed temperature and magnetic field dependent electrical transport measurements on the topological chiral semimetal CoSi poly-crystals. We observed that while χ versus T indicates the paramagnetic nature of poly-crystals (inset of image1), $1/\chi$ versus T behavior indicates that there is the presence of some weak antiferromagnetic exchange interaction at low temperature [2]. These poly-crystals show anomalous behavior in resistivity versus temperature measurements in the vicinity of such magnetic exchange interaction. The temperature and angle-dependent magneto-resistance (MR) measurements show negative behavior at low temperature, which is in contrast to the single crystal counterpart of CoSi, probably due to the presence of weak exchange interaction [3,4].

1. D. Takane, and T. Sato, Phys. Rev. Lett. 122, 076402, (2019). 2. Banik, S. et al. Phys. Rev. B 77, 224417 (2008). 3. X. Xu and S. Jia, Phys. Rev. B 100, 045104 (2019). 4. S.S Samatham, D Venkateshwarlu, and V Ganesan, Mater. Res. Express 1 026503, (2014).



Temperature dependence of $1/\chi$ showing the presence of exchange interaction at low temperature. Inset shows the temperature dependence of χ



Temperature-dependent magneto-resistance(MR) showing a change in MR from negative to positive as the temperature is increased

DP-11. Explore the Large Bohr-Magneton on a Half-Heusler BeMnN.

R. Zhang¹, Y. Zeng², X. She¹, Y. Zou¹, R. Huang¹ and C. Fong³

1. Nanjing University, Nanjing, China; 2. Hangzhou Dianzi University, Nanjing, China; 3. University of California Davis, Davis, CA, United States

Since the prediction of half-metallic properties in the half-Heusler NiMnSb by de Groot *et al.* [1], much attention has been paid to explore more half-Heusler alloys due to the potential for spintronic device applications [2]. In half-metals, a unique physical property for them is that one of the spin channels is metallic while the other exhibits insulating behavior. Thus, the spin polarization of the current for a half-metal at the Fermi level is contributed entirely by one spin channel and can reach 100%. In this work, we designed the half-Heusler alloys BeMnN and investigated their electronic properties based on the first-principles calculations. It is shown that the alloy of BeMnN arises a value of $6 \mu_B$ /unit-cell at the lattice constant 7.11 \AA when the atoms are arranged in α configuration. Meanwhile, this Be-based half Heusler alloy is a half metal. Generally, half Heusler alloys composed of one 3-d transition metal elements, the magnetic moments/unit-cell predicted by first-principles calculations are equal and less than the maximum value of $5 \mu_B$ /unit-cell which is the largest atomic magnetic moment for a 3-d transition metal element. The physical origin of this large magnetic moment in the alloy of BeMnN is presented based on the charge density distributions. Compared to the lattice constant of InSb (6.47 \AA), the calculated value of the BeMnN is 0.64 \AA larger. Our calculation suggests a way to achieve large magnetic moments for half Heusler alloys.

[1] R. A. de Groot, F. M. Mueller, P. G. van Engen, and K. H. J. Buschow, Phys. Rev. Lett. 50, 2024 (1983). [2] C. Felser and B. Hillebrands, J. Phys. D: Appl. Phys. 40 (2007).

DP-12. Strain Modulated Structure Distortion and Magnetic Properties of Orthorhombic LuMnO₃ Thin Films.

A. Zhang¹, H. Cao¹, Y. Tang¹ and X. Wu²

1. Hohai University, Nanjing, China; 2. Nanjing Univeristy, Nanjing, China

Epitaxial orthorhombic LuMnO₃ films were prepared on (001)-LaAlO₃ substrates by pulsed laser deposition (PLD). The results of structural investigation reveal that the out-of-plane parameter c slowly decreases with increasing thickness of films and the out of plane tensile strain exists in the films. Analysis of Raman spectra shows that the lengths of in-plane Mn-O bonds expand with the increasing thickness of the films. The temperature dependence on magnetization $M(T)$ curves prove that the antiferromagnetic transition temperatures T_N obviously increases with increasing thickness of the films, which can be attributed to the enhanced super-exchange interaction between surfaces caused by the stretching of in-plane Mn-O bonds. The magnetic measurements also reveal that FM and AFM phases coexist in the films. The FM phase exists in the thin layer near to the interface under in-plane tensile strain, while AFM structure is stable in the region near the surface with strain relaxed. These results show that the magnetic properties of LuMnO₃ films can be sensitively manipulated by the strain of the films.

Session DQ
INTERACTIONS IN COMPLEX MAGNETS
(Poster Session)

Hao Deng, Chair

Rheinisch-Westfälische Technische Hochschule Aachen, Garching, Germany

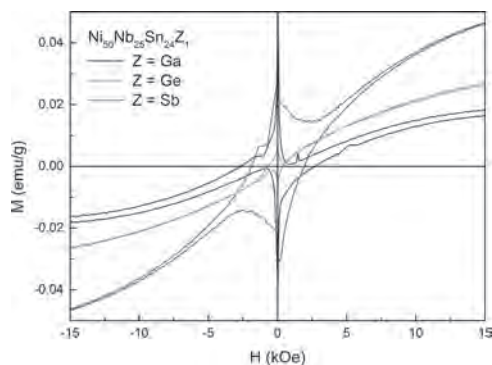
DQ-01. Effect of Doping on Ferromagnetic and Superconducting Properties of Ni_2NbSnZ ($Z = Ga, Ge, \text{ and } Sb$) Heusler Alloy.

S. Nalevanko^{1,2}, L. Galdun^{2,3}, M. Varga², A. Dzubinska², M. Reiffers⁴, J. Kačmarčík⁵ and R. Varga^{2,3}

1. Institute of Physics, Univerzita Pavla Jozefa Safarika v Kosiciach, Kosice, Slovakia; 2. CPM - TIP, Univerzita Pavla Jozefa Safarika v Kosiciach, Kosice, Slovakia; 3. RVmagnetics, a. s., Kosice, Slovakia; 4. Fac. Hum. and Nat. Sci., Presovska univerzita v Presove, Presov, Slovakia; 5. Centre of Low Temperature Physics, Institute for Experimental Physics, Slovak Academy of Science, Kosice, Slovakia

Heusler alloys are materials with the composition X_2YZ , where X and Y are transition metals and Z is the p-element. By the change of an element in the composition, new properties, e. g. the magnetocaloric effect, spin-polarization, or coexistence of ferromagnetism and superconductivity can be achieved. Those properties can be combined to achieve multifunctional Heusler alloys. Nowadays, new superconducting materials are being explored, such as HTC superconductors, superconducting magnets, and also as mentioned, ferromagnetic superconductors. Heusler alloy Ni_2NbSn represents the superconductor with the ferromagnetic behaviour under the critical temperature of superconductivity. It would be difficult for the alloy Ni_2NbSn to find practical usage since the critical temperature is 3.4 K at zero external magnetic field. One of the possibilities to increase the critical temperature can be the doping with various p-elements, to modify the lattice constant. In this topic, we decided to study the doped series of alloys $Ni_{50}Nb_{25}Sn_{25-x}Z_x$, where Z is $Ga, Ge, \text{ or } Sb$ and $x = 1, 2$. Their structural, magnetic, and electric properties were analyzed to show the effect of modifying the lattice constant on the critical temperature of the Ni_2NbSn Heusler alloy. This research was supported by the projects APVV-16-0079 and Slovak VEGA grant. No. 1/0053/19.

T. Graf, C. Felser and S. S.P. Parkin, Progress in Solid State Chemistry, Vol. 39, p.1-50 (2011) T. Klimczuk, C. H. Wang and K. Gofryk, PHYSICAL REVIEW B, Vol. 85, p.174505 (2012)



Hysteresis loops of alloys with 1% doping.

DQ-02. Non Magnetic-Magnetic Transition in Cr₃A (A=As,Ga) and Thier Transition Metal Doped Compounds.

H.K. Krarcha¹ and A. Ferroudj²

1. *Earth Sciences and Universe Institute, Universite Batna 2, Fesdis, Algeria;* 2. *Department of physics, Universite Batna 2, Fesdis, Algeria*

Crystallographic structure and mail parameters of Cr₃A and thier transition metal doped ternary compounds CrM₂A (A=As, Ga & M=Rh, Mo, Fe, Co, and Ni) have been precisely ditermined. Non magnetic – magnetic transi-tion was predicted on Cr₃A compounds by substitution of transition metal elements M=Rh, Mo, Fe, Co, and Ni. We used First-principle calculations using Density functional theory (DFT) within generalized gradient approx-imation (GGA) pseudo-potentials and plane waves basis VASP (Vienna ab initio Software Package) [1,2]. Cr₃As no magnetic but by doping it with low ferromagnetic transition element are transformed to a high ferromagnetic alloy with magnetic moment of range 4 to 5μ_B. Electronic and mechan-ical proprieties has been computed and showed that these compounds have the strongest alloying ability and structural stability. In the abscence of the theoretical or experimental results for CrM₂A, future experimental work will testify our calculated results

1-G. Kresse, J. Furthmu□ller, Efcieny of ab-initio total energy calcula345 tions for metals and semiconductors using a plane-wave basis set, Com346 putational materials science 6 (1) (1996). 2- G. Kresse, J. Furthmu□ller, E□cient iterative schemes for ab initio total energy calculations using a plane-wave basis set, Physical review B 54 (16) (1996) 11169.

DQ-03. Phase States and Critical Properties of a Dilute Magnet With Frustration.

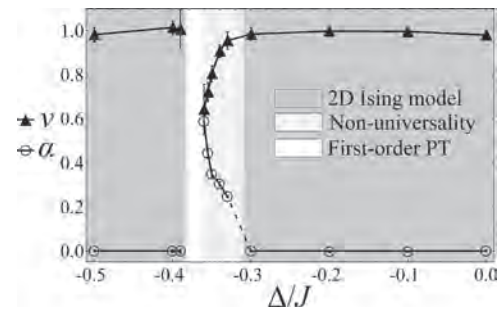
D. Yasinskaya¹, V. Ulitko¹, Y. Panov¹ and A. Moskvina¹

¹. Institute of Natural Sciences and Mathematics, Ural Federal University, Ekaterinburg, Russian Federation

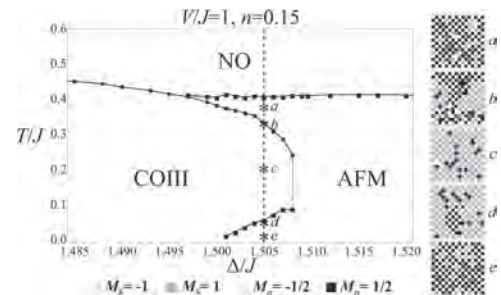
Frustrated systems with two or more competing interactions have a wide variety of phases with unconventional properties and complex symmetry. The pseudospin formalism is a powerful method to study complex magnetic systems with various degrees of freedom. Pseudospin models of anisotropic magnets are widely used to describe the properties of binary alloys, classical and quantum liquids, dilute magnets, superconductors, and many other physical systems [1]. In addition, disorder caused by introduction of impurities and defects into the system significantly affects the critical behavior and phase states of magnets [2]. This work is devoted to modelling and theoretical description of phase and critical properties of a low-dimensional site-dilute magnet with frustration caused by the competitive charge and spin orders. We consider the Blume-Emery-Griffiths-type spin-pseudospin model, which was initially proposed [3] to consider the competition between spin and charge orders in underdoped high- T_c cuprates like $\text{La}_{2-x}\text{Sr}_x\text{CuO}_4$ in the normal state. The model considers the CuO_2 planes as a system of charge triplets consisting of three many-electron mixed-valence centers $[\text{CuO}_4]^{7-6-5-}$ (corresponding nominally to the copper ion states $\text{Cu}^{1+;2+;3+}$). Two charge states $\text{Cu}^{1+;3+}$ are associated with two components of the pseudospin $S=1$ triplet with $M_S=\pm 1$. The Cu^{2+} state associated with the $M_S=0$ component is magnetic and has a conventional spin $\sigma=1/2$. Within this pseudospin formalism, the Hamiltonian of the static spin-pseudospin model includes Ising spin exchange coupling (J), on-site (Δ) and inter-site (V) density-density correlations, which have the form of single-ion pseudospin anisotropy and Ising exchange coupling in the language of pseudospin operators. The chemical potential μ is necessary to take into account the constant charge density doped in the CuO_2 plane, which gives the concentration of doped charged impurities n . The properties of the spin-pseudospin model in the ground state were studied with the mean-field approximation [3,4], and the temperature phase diagrams were obtained with the Bethe approximation [5]. We performed a computer simulation of a spin-pseudospin model using the classical Monte Carlo method and a modified Metropolis algorithm on a 2D square lattice with periodic boundary conditions. Phase transitions and critical properties of a dilute magnet with frustration were investigated in the framework of the theory of finite-size scaling. The system demonstrates the 2D Ising universality class as it is far from frustration, while as the system approaches the frustrated state, significant changes are observed in the critical behavior of the system: spin (charge) metastable phase states are formed, first-order phase transitions occur, and the critical exponents for second-order phase transitions depend on the parameters of the model, i.e. the critical behavior of the system becomes non-universal (for example, see Fig. 1) [6]. Also, the critical behavior becomes non-universal with an increase in the density of the doped charge n in the non-frustrated state. In addition, temperature and ground state phase diagrams were obtained, and the features of the formation of phase states with an increase in the density of doped impurities in frustration were revealed. There is a wide variety of phase states with different properties in the ground state. If the spin exchange coupling is greater than the one for pseudospin ($V/J \leq 1$), there are actually two phases in the ground state, namely the charge order (CO) and the antiferromagnetic (AFM) order, which is unstable with respect to the phase separation into charge and spin subsystems that behave like immiscible quantum liquids. Various configurations of phase separation are formed depending on the value of n , viz., a charge/AFM droplet or a charge/AFM stripe. There are 5 phases in the ground state for $V/J > 1$: AFM and “ferromagnetic” orders, and three types of CO. Analysis of the system in frustration has shown that the ground state of the system turns out to be degenerate not at one specific point, but in a whole range of parameters. Under identical calculation conditions, both AFM order and CO can form with a certain probability. Charge doping in a frustrated state leads to unusual effects. When the spin exchange coupling is strong ($V/J \leq 1$), AFM order changes to CO with decreasing temperature (or vice versa, depending on the value of n), as well as reentrant order-order phase transitions [7] occur, which is shown in Fig. 2. Thus, the competition between charge and magnetic orders, leading to frustration of

the system, as well as charged impurities, significantly affect the properties of a two-dimensional Ising magnet. This work was prepared with the financial support of Competitiveness Enhancement Program - CEP 3.1.1.1-20.

[1] Hovhannisyants V. V. et al., Physical Review E., Vol. 96, p. 062103 (2017) [2] Giacomini G., Springer, Vol. 2025 (2011) [3] Y. D. Panov et al., J. Supercond. Novel Magn., Vol. 29, p. 1077 (2016). [4] Y. D. Panov et al., J. Low Temp. Phys, Vol. 187, p. 646 (2017). [5] Y. D. Panov et al., JMMM, Vol. 477, p. 162 (2019). [6] D. N. Yasinskaya et al., Acta Phys. Pol. A., Vol. 137, p. 979 (2020) [7] D. N. Yasinskaya, V. A. Ulitko, Y. D. Panov, Phys. Solid State, Vol. 62, p. 1713 (2020)



Dependence of critical exponents for heat capacity and susceptibility on single-ion anisotropy Δ/J for $V/J=0.2$, $n=0$. Dark gray corresponds to the universality class of the 2D Ising model, light gray corresponds to non-universal critical behavior. White color corresponds to first-order phase transitions



Temperature phase diagram for $n = 0.15$, $V/J=1$ near the frustration. The order type changes twice when the temperature decreases, i.e. the reentrant phase transition to AFM takes place

DQ-04. Specific Heat of $\text{YbMn}_6\text{Ge}_{6-x}\text{Sn}_x$ Compounds.

*P. Haraux*¹, *L. Eichenberger*¹, *L. Diop*¹ and *T. Mazet*¹

1. Institut Jean Lamour, Nancy, France

The study of quantum critical effects and more generally of the physical properties of “strange metals” is currently of high interest in condensed-matter physics [1]. In rare-earth based intermetallics, heavy-fermion behaviors and quantum criticality are mainly investigated in materials where Ce or Yb are alloyed with non-magnetic elements [2]. Quantum critical effects are then generally perceived at low temperature near the magnetic instability of almost trivalent $4f$ element. Recently, we showed that the situation is somewhat different in $\text{YbMn}_6\text{Ge}_{6-x}\text{Sn}_x$ where intermediate valent Yb is alloyed with a ferromagnetic Mn sublattice. In this series of compounds, several very unusual phenomena have been evidenced using magnetic measurements, neutron diffraction and electronic spectroscopies [3-6]. That includes an abnormal thermal variation of the Yb valence [3,4], a record value for the Yb magnetic ordering temperature (up to $T_{\text{Yb}} = 125$ K [4,5]), a Yb magnetic instability occurring for far from trivalent Yb ($v \sim 2.73$) and signatures of quantum criticality up to room temperature [6]. These unusual phenomena have been tentatively ascribed to the strong Mn-Yb exchange interactions. For a further understanding of the $\text{YbMn}_6\text{Ge}_{6-x}\text{Sn}_x$ series of compounds ($x \geq 4.0$), we have performed specific heat (C_p) measurements. Our results indicate that these alloys are heavy-fermion materials ($\gamma > 50$ mJ.mol⁻¹.K⁻²) and that the electronic specific heat coefficient reaches a maximum value $\gamma \sim 280$ mJ.mol⁻¹.K⁻² for compositions close to the Yb magnetic instability near $x \sim 5.20$ (Figure 1). Details about the analysis of the data will be presented on the poster together with a discussion of the results.

[1] H. Zhao, et al., *Nat. Phys.* 15, 1261-1266 (2019). [2] H. V. Löhneysen, et al., *Rev. Mod. Phys.* 79, 1015 (2007). [3] T. Mazet, et al., *Phys. Rev. Lett.* 11, 096402 (2013). [4] T. Mazet, et al., *Phys. Rev. B* 92, 075105 (2015). [5] L. Eichenberger, et al., *Phys. Rev. B* 96, 155129 (2017). [6] L. Eichenberger, et al., *Phys. Rev. B* 101, 020408 (R) (2020).

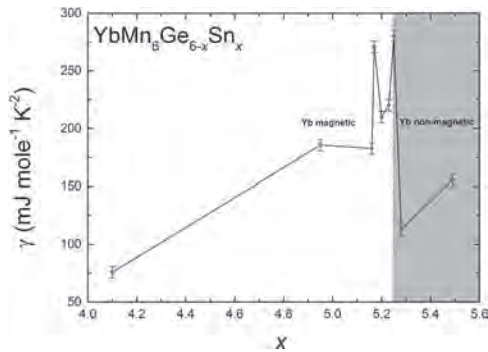


Fig. 1: Composition dependence of the electronic specific heat coefficient γ in $\text{YbMn}_6\text{Ge}_{6-x}\text{Sn}_x$ ($x \geq 4.0$)

DQ-05. Exact Spin Dynamics of High Spin Nanoscale Molecular Magnetic Clusters.*O. Ciftja*¹*1. Physics, Prairie View A&M University, Prairie View, TX, United States*

A common feature of many organic-based molecular magnets is that inter-molecular magnetic interactions are extremely weak compared to intra-molecular ones. As a result a bulk sample can be described in terms of independent individual molecular magnets made up of a finite cluster of coupled magnetic spins. Because of the large value of individual spins of several molecular magnetic compounds it turns out that such systems can be described to very high accuracy, at sufficiently high temperatures, by a classical Heisenberg spin model. Only for sufficiently low temperatures need one incorporate the quantum character of the spins. In this work we focus on the exact spin dynamics of small nanoscale molecular magnetic clusters of classical Heisenberg spins. The present study permits us to obtain analytical solutions for the time-dependent spin-spin autocorrelation function for certain clusters of classical Heisenberg spins coupled through exchange interaction. This study underscores the potential utility of a classical spin treatment of nanoscale magnetic clusters and provides results useful to interpret data obtained from neutron scattering experiments.

DQ-06. Structural and Magnetic Properties of Cathode Materials Substituted With Transition Metal Based on NaFeO₂.

S. Jung¹, H. Choi¹ and C. Kim¹

¹. Department of physics, Kookmin University, Seongbuk-gu, The Republic of Korea

INTRODUCTION The development of cathode materials for sodium iron batteries (SIBs) that have improved the cost problem is being actively studied. It has been reported that NaFeO₂, a representative oxide of Fe²⁺/Fe³⁺ redox reactions, has a capacity problem due to structural changes caused by the movement of iron during charging and discharging [1]. However, layered oxides substituted by other transition metals at the iron position can inhibit the migration of iron and oxides such as O3 type-NaFe_{1/2}Co_{1/2}O₂, and P2 type-NaFe_{1/2}Mn_{1/2}O₂ are attracting attention. These layered compounds are high-capacity cathode materials, showing high speed performance and good stability [2]. In this study, structural and magnetic properties of O3-NaFe_{1/2}Co_{1/2}O₂, and P2-NaFe_{1/2}Mn_{1/2}O₂, which are materials substituted with transition metals of O3-NaFeO₂, were analyzed to study the effects and properties on performance. **EXPERIMENT PROCEDURES** O3-NaFeO₂ was prepared through a conventional solid state reaction method. The starting materials Na₂CO₃ and Fe₃O₄ were mixed according to the chemical molar ratio, and the mixture was calcined at 300 °C for 5 h in air. The powder is ground for 30 min, compression molded, and sintered at 650 °C for 10 h in air. The starting materials are Na₂CO₃, Fe₃O₄, and Co₃O₄ for O3-NaFe_{1/2}Co_{1/2}O₂ and Na₂CO₃, Fe₃O₄, and Mn₃O₄ for P2-NaFe_{1/2}Mn_{1/2}O₂ respectively. The mixtures are sintered at 900 °C for 10 h in air. Other manufacturing methods are the same as above. The structural properties of the samples were observed through X-ray diffraction (XRD) using CuK α radiation in the 2 θ range of 10-80°. The analysis result of crystal structure was obtained based on the Rietveld method. To observe the magnetic properties, a vibrating sample magnetometer (VSM) was used to measure the temperature dependence of field cooled (FC) and zero field cooled (ZFC) curves in the temperature range of 4.2-295 K and 1000 Oe magnetic field. Through the ⁵⁷Fe Mössbauer spectrometer, we observed the behavior of the iron valence state and the electric quadrupole interaction of the sample. The Mössbauer measurements were carried out over a wide temperature range of 4.2-295 K in transmission geometry with a 50 mCi ⁵⁷Co in Rh matrix. **RESULTS AND DISCUSSION** The XRD patterns through Rietveld refinement analysis show that NaFeO₂ and NaFe_{1/2}Co_{1/2}O₂ have an octahedral hexagonal crystal structure with R-3m space group and NaFe_{1/2}Mn_{1/2}O₂ has a prismatic hexagonal crystal structure with P6₃/mmc space group. In the case of the P2 type, it was difficult to obtain a sample in which Na ions were perfectly located in the octahedron at the Miller index value (003) and it was found to be Na_xFe_{1/2}Mn_{1/2}O₂ by the stoichiometric equation. The temperature-dependent magnetization values were measured ZFC, and FC for NaFeO₂, NaFe_{1/2}Mn_{1/2}O₂, and NaFe_{1/2}Co_{1/2}O₂ in a 1000 Oe magnetic field over a wide temperature range of 4.2-295 K. From the tendency of the ZFC-FC curve to increase rapidly below the Néel temperature (T_N), it was found that antiferromagnetic behavior was observed at temperatures under T_N and paramagnetic behavior was observed at temperatures above T_N. In addition, As the antiferromagnetic behavior was weakened by the substitution of Mn and Co in the Fe ion site. The Mössbauer spectra of each compound were measured 4.2-295 K at various temperatures. The Mössbauer data of NaFeO₂, NaFe_{1/2}Mn_{1/2}O₂, and NaFe_{1/2}Co_{1/2}O₂ were analyzed as 6 lines of resonance absorption at 4.2 K and doublet above T_N temperature. (Fig. 1) The isomer shift (δ) and electric quadrupole splitting (ΔE_Q) values of NaFeO₂, and NaFe_{1/2}Co_{1/2}O₂ are 0.24, 0.22 mm/s and 0.48, 0.58 mm/s, and it can be seen that they have Fe³⁺ ions. Also, it was found that NaFe_{1/2}Mn_{1/2}O₂ has Fe³⁺/Fe⁴⁺ ions with δ = 0.22, 0.03 mm/s and ΔE_Q = 0.72, 0.69 mm/s.

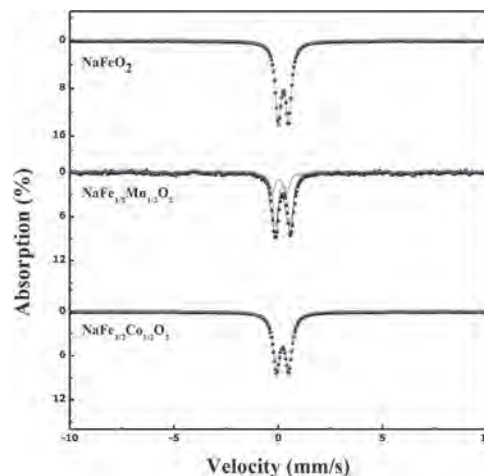


Fig. 1 Mössbauer spectra of NaFeO₂, NaFe_{1/2}Mn_{1/2}O₂, and NaFe_{1/2}Co_{1/2}O₂ at room temperature.

[1] Dieky Susanto, Min Kyung Cho, and Ghylam Ali, *Chem.Mater.*, Vol. 31, p. 3644 (2019). [2] Joon-ki park, Geun-gyung Park, Hunho H.kwak, *ACS Omega*, Vol. 3, p. 361 (2018).

DQ-07. Synthesis, Structural, and Mössbauer Studies of Tavorite LiFePO_4F Cathode Material.

H. Choi¹, S. Jung¹ and C. Kim¹

¹. Department of Physics, Kookmin University, Seoul, The Republic of Korea

INTRODUCTION Phosphate fluoride-based cathode material is attracting great interest in secondary batteries due to its superior properties compared to phosphate-based cathode [1, 2]. The theoretical discharge capacity and redox voltage of LiFePO_4F are 152 mAh/g and 2.75 V. In the case of LiFePO_4F , unlike other intercalation cathode materials, starts in a state of charge and then discharge to form $\text{Li}_2\text{FePO}_4\text{F}$. In this paper, we synthesized the tavorite-structured LiFePO_4F by two-step solid state reaction method with different molar ratios of LiF. We report on the structural and magnetic properties of LiFePO_4F , especially as studied by Mössbauer spectroscopy.

EXPERIMENT PROCEDURES The tavorite LiFePO_4F cathode was synthesized by two-step solid state reaction method. First, the FePO_4 was obtained using stoichiometric mixture of Fe_2O_3 and $(\text{NH}_4)_2\text{HPO}_4$ as starting materials. The mixture was calcined at 300 °C for 7 h in air and sintered at 870 °C for 8 h in air. After that, the obtained FePO_4 and LiF were mixed at different mole ratios of 1:1, 1:1.05, and 1:1.1, respectively. The mixture pressed into pellets and sintered at 625 °C for 1.5 h. The crystal structure of sample was determined with X-ray diffraction measurements (XRD) using Rigaku Ultima IV using $\text{Cu}/\text{K}\alpha$ radiation. The magnetic properties of sample was measured by using a vibrating sample magnetometer (VSM) at various temperature. Mössbauer spectra were recorded from 4.2 and 295 K using a in transmission geometry employing a ^{57}Co source and fitted by a least square fit programmed assuming Lorentzian line shapes.

RESULTS AND DISCUSSION The XRD patterns of FePO_4 , which was pre-synthesized to make LiFePO_4F , were confirmed the formation of hexagonal structure with P3_121 . The XRD patterns of LiFePO_4F synthesized from above FePO_4 and excess LiF were measured. Secondary phases from XRD patterns were found in the sample synthesized with LiF mole ratios of 1 and 1.1. The crystal structure of the refined LiFePO_4F (LiF-excess 5 %) was determined to be triclinic with P space group and the lattice constants were $a = 5.2973$ Å, $b = 7.2539$ Å, $c = 5.1506$ Å, $\alpha = 107.92^\circ$, $\beta = 98.52^\circ$, and $\gamma = 107.36^\circ$ (Fig. 1). The temperature dependent zero-field-cooled (ZFC) and field-cooled (FC) magnetization susceptibility $\chi(T)$ curves were measured at 100 Oe in the temperature range from 4.2 to 295 K. From ZFC-FC curve, the magnetic property of LiFePO_4F showed antiferromagnetic behavior below the Néel temperature. The Mössbauer spectra of the LiFePO_4F were obtained at various temperatures ranging from 4.2 to 295 K. The Mössbauer spectrum at 295 K was analyzed symmetric doublet with the electric quadrupole splitting of 1.10 mm/s and the isomer shift of 0.31 mm/s and, which is Fe^{3+} state (Fig. 2). Since LiFePO_4F has two crystallographically unique Fe sites, Mössbauer for each temperature was measured to investigate detailed magnetic properties. The spectrum at 4.2 K were confirmed had two set of eight asymmetric line indicating that they have both magnetic dipole interaction and electric quadrupole interaction. The value of isomer shift at all temperature was analyzed as Fe^{3+} ions.

[1] Y. Zhang, Q. Liang, C. Huang, et al., J. Solid State Electr., Vol. 22, p.1995 (2018). [2] N. Goubard-Bretesché, E. Kemnitz, and Nicola Pinna, Chem. Eur. J., Vol. 25, p.6189 (2019).

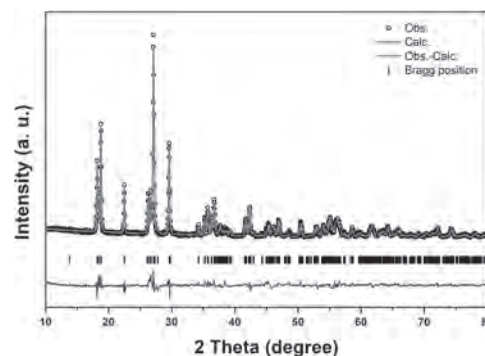


Fig. 1. Refined XRD patterns of tavorite LiFePO_4F .

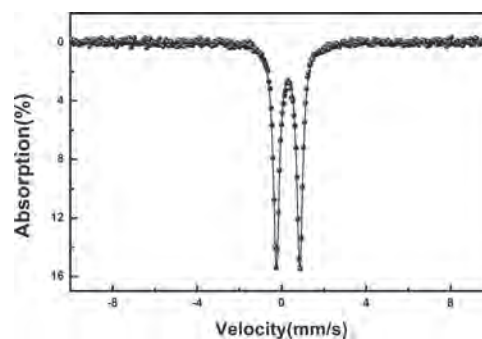


Fig. 2. Mössbauer spectrum of tavorite LiFePO_4F at 295 K.

DQ-08. Magnetic Properties of Quasi-Two-Dimensional Oxyborates $(\text{Ni,Cu})_2\text{MnBO}_5$ With Ludwigite Structure.

S.N. Sofronova¹, E. Moshkina¹, E. Eremin¹ and M. Molokeev¹

1. L. V. Kirensky Institute of Physics SB RAS, Krasnoyarsk, Russian Federation

At present, the study of physical properties of magnetic quasi-low-dimensional compounds intensively developed. Oxyborates with ludwigite structure are the members of such type of compounds due to the presence of quasi-two-dimensional elements in their structure. The unit cell of ludwigites includes 4 non-equivalent positions which can be occupied by magnetic cations. The magnetization reversal is occur in $(\text{Ni,Mn})_3\text{BO}_5$ [1]. The exchange bias effects is occur in $\text{Ni}_5\text{GeB}_2\text{O}_{10}$ [2]. In this work, single crystals of $(\text{Ni,Cu})_2\text{MnBO}_5$ with ludwigite structures were synthesized by flux method, using the fluxes based on bismuth trimolybdat. Structural and magnetic characterization of the samples was carried out. Magnetic transition occurs at the temperature at around 75 K (Fig. 1). M-H curves measured at 10 K are presented on Figure 2. Indirect exchange interactions calculation was held for the compound $(\text{Ni,Cu})_2\text{MnBO}_5$ in frameworks of the Anderson-Zavatskiy indirect exchange interactions model. Calculation results showed that ferromagnetic and antiferromagnetic interaction competition presents between ions in plane and ions connected planes. Acknowledgments The research was funded by RFBR, Krasnoyarsk Territory and Krasnoyarsk Regional Fund of Science, project number 20-42-240011

[1] L.N. Bezmaternykh, E.M. Kolesnikova, E.V. Eremin, et al. J. Magn. Magn. Mater. 364,55 (2014) [2] S.N. Sofronova, L.N. Bezmaternykh, E.V. Eremin, et al. J. Magn. Magn. Mater. 401, 217 (2016)

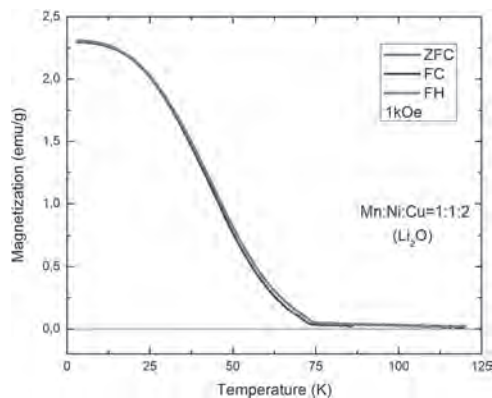


Fig.1. The magnetization in the zero-field-cooled (ZFC), field-cooled (FC), and field-cooled-heating (FH) conditions measured at $H=1$ kOe.

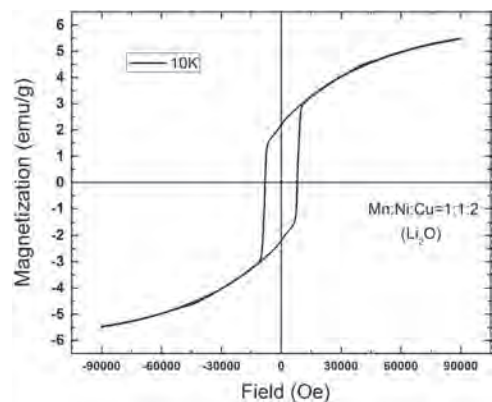


Fig. 2. M-H hysteresis loops measured at 10 K.

DQ-09. Signatures of Long Range Dipolar Interactions in Artificial Square ice.

O. Brunn^{1,2}, Y. Perrin¹, B. Canals¹ and N. Rougemaille¹

1. Institut NEEL, Grenoble, France; 2. Institute for Scientific Instruments, Czech Academy of Science, Brno, Czechia

Analyzing the magnetic structure factor of a field demagnetized artificial square ice, qualitative deviations from what would predict the square ice model are observed. Combining micromagnetic and Monte Carlo simulations, we demonstrate that these deviations signal the presence of interactions between nanomagnets that extend beyond nearest neighbors. Including further neighbor, dipolar-like couplings in the square ice model, we find that the first seven or eight coupling strengths are needed to reproduce semi-quantitatively the main features of the magnetic structure factor measured experimentally. An alternative, more realistic numerical scenario is also proposed in which the ice condition is slightly detuned. In that case as well, the features evidenced in the experimental magnetic structure factor are only well-described when further neighbor couplings are taken into account. Our results show that long range dipolar interactions are not totally washed out in a field demagnetized artificial square ice, and cannot be neglected as they impact the magnetic correlations within the ice manifold.

DQ-10. Estimation of Exchange Interaction in a Kondo Lattice System.S. Pandey¹, V. Siruguri¹ and R. Rawat¹¹. University Grants Commission Department of Atomic Energy Consortium for Scientific Research, Mumbai, India

Abstract: The Compressible Kondo Lattice model is applied to describe the result of energy scale of Co substituted CeRu₂Ge₂ compounds in terms of the on-site Kondo exchange interaction J and the electron density of states at the Fermi level $N(E_F)$. The value of $JN(E_F)$ is obtained from the experimental results and the Doniach diagram is constructed. Introduction: Amongst the systems displaying strong electron correlations, one of the most studied family is Ce based ternary intermetallic system: CeT₂X₂ (T = transition element and X = Si or Ge). This system has attracted continuous attention as it shows exotic physical properties such as unconventional superconductivity, Kondo effect, heavy fermion, and non-Fermi liquid behaviour. Investigating the physical properties of these ternary systems under the presence of external parameters has been a focus for past few years. One such series studied in this context is CeRu_{2-x}Co_xGe₂ ($x=0-2$), where the ferromagnetic ground state changes into the paramagnetic state through an intermediate antiferromagnetic phase with increase in Co concentration [1]. For the Co rich compounds in this series, the $\rho(T)$ behaviour is typical of a Kondo lattice system, showing incoherent Kondo scattering at higher temperatures ($\ln T$ dependence) and a coherent Kondo scattering at lower temperatures characterized by a well-defined peak at T_{\max} [2]. It was also observed for this system, that the Kondo temperature (T_K) increases with the chemical compression of the lattice as x increases. Therefore, we can study its experimental results on the basis of the compressible Kondo lattice (CKL) model. The aim of the present work is to study the volume dependence of T_K (obtained from the magnetization and electrical resistivity) and to determine the value of the product $JN(E_F)$ (where J is the exchange interaction between the conduction electrons and localized $4f$ electrons and $N(E_F)$ is the density of states at Fermi level), for Co substituted CeRu₂Ge₂ compounds. Results and Discussion: The most important energy scale that describes the heavy fermion systems is Kondo temperature (T_K), which can be estimated from the resistivity maximum (T_{\max}). With the application of the CKL model, we have estimated the value of $|JN(E_F)|$ for the present system using the volume dependence of T_{\max} as described by the Doniach theory [3]. For the Kondo lattice systems, the T_{\max} and T_K are closely related and exponentially proportional to $JN(E_F)$, $T_{\max} \propto T_K \propto \exp(-1/|JN(E_F)|)$ (1) The CKL model describes the volume dependence of $JN(E_F)$ as, $|JN(E_F)| = |JN(E_F)|_0 \exp[-q(V-V_0)/V_0]$ (2) where, $|JN(E_F)|_0$ is the value at the initial volume V_0 , while $|JN(E_F)|$ corresponds to the volume V . and q is the Grüneisen parameter of $|JN(E_F)|$ which varies between the value 6 and 8. Combining Eq. (1) and (2) yields the volume dependence of T_{\max} : $T_{\max}(V) = T_{\max}(V_0) \exp[-q\Delta V/V_0]$ (3) We apply Eq. (2) and (3) to our experimental results of CeRu_{2-x}Co_xGe₂ [1, 2], shown in Fig.1(a). The solid lines are the least square fits of the data to the Eq. (3) which gives the value of $|JN(E_F)|_0 = 0.097$. For heavy fermion materials the value of $JN(E_F)$ should be of the order of 0.1 and our value of $|JN(E_F)|_0$ is comparable to the other heavy fermion compounds such as CeCu₆ ($|JN(E_F)|_0 = 0.09$) [4] and CeInCu₂ ($|JN(E_F)|_0 = 0.081$) [5]. Further, we have calculated the value of $|JN(E_F)|$ for the other compounds of the series using Eq. (2) and the obtained values are used to construct the Doniach phase diagram as shown in Fig. 1(b). Here for comparison, we have also included the values of $|JN(E_F)|$ for other heavy fermion compounds studied under hydrostatic pressure. The solid curve in the Fig. 1(b) shows the least square fit to the relation: $T_K = D|JN(E_F)|^{1/2} \exp(-1/|JN(E_F)|)$ (4) The estimated value of the coefficient D is 3000 K. It can be observed from the Fig. 1(b) that the order of magnitude of $|JN(E_F)|$ for the present series is in fair agreement with the values obtained independently for the pressure studies on the other heavy fermion compounds. Conclusion: Application of Compressible Kondo Lattice model for the CeRu_{2-x}Co_xGe₂ compounds yields the value of $|JN(E_F)|_0 = 0.097$. The value of $|JN(E_F)|$ obtained for the present series using this model is used to construct Doniach diagram and is in line with the other Kondo compounds studied using hydrostatic pressure. The results indicate the volume effects to be mainly responsible for the hybridization in the CeRu_{2-x}Co_xGe₂ compounds.

[1] R. Rawat and V. G. Sathe, *J. Phys. Cond. Mater.* 17, 313 (2005) [2] S. Pandey, V. Siruguri, and R. Rawat, *Phys. Rev. B* 98, 155129 (2018) [3] S. Doniach, *Physica B* 91, 231 (1977) [4] T. Kagayama and G Oomi, *Transport and Thermal Properties of f-Electron Systems* (New York: Plenum) p 155 (1993) [5] T. Kagayama, G. Oomi, H. Takahashi, et al., *Phys. Rev. B* 44, 7690 (1991) [6] K. Umeo, H. Kadomatsu, and T. Takabatake, *Phys. Rev. B* 54, 1194 (1996) [7] E. Bauer, R. Hauser, E. Gratz, et al., *Phys. Rev. B* 48, 15873 (1993) [8] D. Huo, J. Sakurai, T. Kuwai, et al., *J. Appl. Phys.* 89, 7634 (2001)

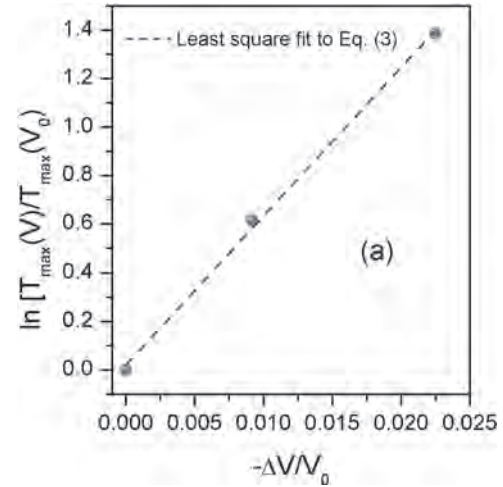


Fig. 1: (a) Plot of $\ln [T_{\max}(V)/T_{\max}(V_0)]$ as a function of $(-\Delta V/V_0)$. The dashed line is the least square fit to the data against a theoretical expression based of CKL model.

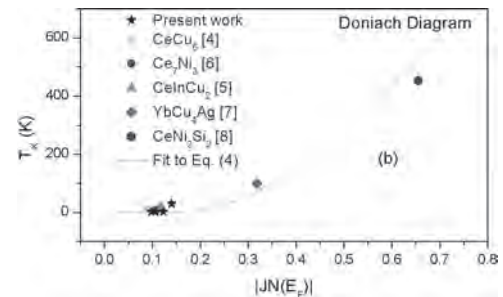


Fig 1: (b) Doniach diagram constructed using the $|JN(E_F)|$ values obtained from the present work and is compared with the other systems as well studied using hydrostatic pressure.

DQ-11. Are Field Demagnetized, Athermal, Artificial Square ice Magnets Stochastic Systems?

O. Brunn^{1,2}, *B. Canals*¹ and *N. Rougemaille*¹

1. Institut NEEL, Grenoble, France; 2. Institute for Scientific Instruments, Czech Academy of Science, Brno, Czechia

Field demagnetization protocols may be employed to bring athermal, artificial spin systems into an arrested, low-energy magnetic configuration. Such protocols, applied to systems in which thermal fluctuations are absent, are intrinsically deterministic: if the field history and the sample properties were known, the final configuration would be completely determined. Here, we study the response of a given athermal, artificial square ice submitted to successive, albeit similar, field demagnetization protocols. We show that each resulting arrested state differs from the previous one. Analyzing these magnetic states, we demonstrate that our artificial ice magnet behaves as a stochastic system. We propose a mechanism by which stochasticity can be induced.

WEDNESDAY, 28 APRIL 2021

LIVE Q&A SESSIONS, 2:30 PM EUROPE CEST

Session ZA

IEEE MAGNETICS SOCIETY AWARD CEREMONY

Bernard Dieny, Co-Chair
Spintec, Grenoble, France

Juergen Fassbender, Co-Chair
HZDR, Dresden, Germany

Session ZA
PLENARY SESSION
Bernard Diény, Chair
Spintec, Grenoble, France

INVITED PAPERS**ZA-01. Antiferromagnetism: Celebrating 50 Years Since the Nobel Prize.**

*I.K. Schuller*¹

1. Center for Memory and Recording Research (CMRR); Center for Advanced Nanoscience (CAN), University of California San Diego, La Jolla, CA, United States

Antiferromagnetism, discovered by Louis Néel, is a very interesting and complex physical phenomenon which has led to much new physics and important applications. Many antiferromagnetic materials were found since its discovery. Recent development of novel bulk and thin film synthesis techniques and materials genomic computational methods have accelerated and broadened considerably the plethora of antiferromagnetic materials. Antiferromagnets become particularly interesting when incorporated into inhomogeneous hetero- and/or nano-structures. This has led to interesting phenomena such as Exchange Bias and important recent applications in the field of Spintronics. I will describe the main features of antiferromagnetism, the interesting physical phenomena, unique devices and the principal open research issues. The research at UCSD was supported by the Office of Basic Energy Science, U.S. Department of Energy, BES-DMS funded by the Department of Energy's Office of Basic Energy Science, DMR under grant DE FG02 87ER-45332.

ZA-02. From Spin-Resolved Atomic-Resolution Imaging to Magnetic Materials and Devices by Design.

R. Wiesendanger¹

1. Dept. of Physics, Universität Hamburg, Hamburg, Germany

Being able to observe atomic-scale spin structures and to probe magnetic properties atom-by-atom is decisive for the discovery of new magnetic phenomena, the optimization of magnetic materials as well as the development of nano- or even atomic-scale spintronic devices. Spin-Polarized Scanning Tunneling Microscopy (SP-STM) [1] being based on the observation of vacuum tunneling of spin-polarized electrons between a highly spin-polarized and atomically sharp probe tip and a sample under investigation [2] allows for atomic-scale studies of magnetic order of ferro- [3], antiferro- [4] and ferrimagnetic [5] materials, including the internal structure of magnetic domain walls down to the atomic level [6,7]. By combining SP-STM with energy-resolved tunneling spectroscopy, the powerful method of Spin-Polarized Scanning Tunneling Spectroscopy (SP-STs) evolved providing access to spin-resolved electronic states of ferro- [8] and antiferromagnetic [9] or even molecular [10,11] materials with atomic-scale spatial resolution. Magnetic field-dependent SP-STM studies led to the development of nano-scale [12] or even single-atom magnetometry [13] allowing the probing of single-atom magnetization in metallic [14] or diluted magnetic semiconductor systems [15]. A very important issue for SP-STM studies is the appropriate choice of a highly spin-polarized and atomically sharp probe tip with a minimum magnetic stray field in order to avoid disturbances of the magnetic state of atomic-scale systems. Half-metallic ferromagnetic CrO₂ thin film probe tips were used in the very early studies in order to achieve an almost 100% spin polarization [2]. However, these tips exhibit a non-negligible stray field, so that they were only useful in applications to antiferromagnetic materials. On the other hand, magnetic stray fields can be avoided by making use of antiferromagnetic probe tips, e.g. Cr thin film [16] or bulk [17] tips, which have proven to be very useful for imaging magnetic domain walls [16] or magnetic vortex states [18] in ferromagnetic nanostructures. However, Cr tips usually offer a spin polarization of around 20% only, thereby the spin contrast is not as high as it could be. Recently, we were able to prepare atomically sharp SP-STM tips offering both, a very high spin polarization and a negligible magnetic stray field: By picking up a single magnetic atom from a sample surface with a superconducting STM tip, we created a magnetic bound state within the superconducting energy gap, a so-called Yu-Shiba-Rusinov state, being 100% spin-polarized [19], and subsequently made use of that state to probe the magnetic structure of artificially created spin chains made up of manganese atoms on a niobium substrate [20]. Thanks to the capability of SP-STM to combine real-space atomic resolution with spin sensitivity, numerous discoveries could be made in magnetic thin films and nanostructures, such as the first experimental observations of chiral domain walls [21-23], spin spirals [24] and skyrmionic lattice states [25,26] due to interfacial Dzyaloshinskii-Moriya (DM) interactions. Moreover, SP-STM allowed the first observation of the internal spin structure of individual chiral magnetic skyrmions [27, 28] as well as their local manipulation, i.e. creation and annihilation, by local (vertical) spin current injection [27] and local electrical fields [29] which is an important prerequisite for any application of magnetic skyrmions in magnetic data storage or logic devices [30]. It has been realized in recent years that complex magnetic states in thin film systems can arise from the competition of various magnetic interactions, including isotropic and anisotropic as well as higher-order exchange interactions. It is extremely important to probe the nature of these interactions down to the atomic scale in order to be able to design novel types of magnetic materials and devices based on that knowledge. SP-STM has allowed probing the distance and directional dependencies of RKKY interactions directly in real space at the atomic level [31], yielding important information about the distance regimes for which maximum ferro- or antiferromagnetic coupling between individual magnetic atoms is achieved. Based on this kind of insight, artificial magnets [14] and even prototype atomic-scale spin logic devices [32] could be fabricated. Moreover, the stabilization of spin systems via symmetrically tailored RKKY interactions [33] could be demonstrated recently. Similarly, SP-STM has recently been applied to study the distance dependence of interfacial DM interactions [34] which subsequently allowed tailoring non-collinear chiral spin structures at the atomic level [35]. Chiral

spin chains are of considerable interest for realizing information transfer by vector spin chirality in finite magnetic chains [36]. Moreover, when combined with superconducting substrates, atomic-scale model systems for topological superconductivity and Majorana bound states can be realized [37, 38] offering great potential for topological quantum computation. Finally, time-resolved SP-STM measurements have provided novel insight into the dynamics of nano-scale classical [39] or even quantum magnetic systems [40]. Local spin-current injection from a highly spin-polarized tip into nano-scale magnetic systems [41] has proven to be a very valuable method to induce and manipulate the spin dynamics of small clusters or even single magnetic atoms on surfaces [40]. Studying the influence of the dynamical states of chiral spin chains on superconducting substrates on the dynamics of Majorana states is one of the exciting directions of ongoing research activities.

[1] R. Wiesendanger, *Rev. Mod. Phys.* 81, 1495 (2009): "Spin mapping at the nanoscale and atomic scale". [2] R. Wiesendanger, H.-J. Güntherodt, G. Güntherodt, R.J. Gambino, and R. Ruf, *Phys. Rev. Lett.* 65, 247 (1990): "Observation of vacuum tunneling of spin-polarized electrons with the scanning tunneling microscope". [3] O. Pietzsch, A. Kubetzka, M. Bode, and R. Wiesendanger, *Phys. Rev. Lett.* 84, 5212 (2000): "Real-Space Observation of Dipolar Antiferromagnetism in Magnetic Nanowires by Spin-Polarized Scanning Tunneling Spectroscopy". [4] S. Heinze, M. Bode, A. Kubetzka, O. Pietzsch, X. Nie, S. Blügel, and R. Wiesendanger, *Science* 288, 1805 (2000): "Real-space imaging of two-dimensional antiferromagnetism on the atomic scale". [5] R. Wiesendanger, I.V. Shvets, D. Bürgler, G. Tarrach, H.-J. Güntherodt, J.M.D. Coey, and S. Gräser, *Science* 255, 583 (1992): "Topographic and magnetic-sensitive scanning tunneling microscopy study of magnetite". [6] M. Pratzer, H. J. Elmers, M. Bode, O. Pietzsch, A. Kubetzka, and R. Wiesendanger, *Phys. Rev. Lett.* 87, 127201 (2001): "Atomic-scale magnetic domain walls in quasi-one-dimensional Fe nanostripes". [7] M. Bode, E. Y. Vedmedenko, K. von Bergmann, A. Kubetzka, P. Ferriani, S. Heinze, and R. Wiesendanger, *Nature Materials* 5, 477 (2006): "Atomic spin structure of antiferromagnetic domain walls". [8] M. Bode, M. Getzlaff, and R. Wiesendanger, *Phys. Rev. Lett.* 81, 4256 (1998): "Spin-Polarized Vacuum Tunneling into the Exchange-split Surface State of Gd(0001)". [9] M. Kleiber, M. Bode, R. Ravlić, and R. Wiesendanger, *Phys. Rev. Lett.* 85, 4606 (2000): "Topology-induced spin frustrations at the Cr(001) surface studied by spin-polarized scanning tunneling spectroscopy". [10] J. Brede, N. Atodiresi, S. Kuck, P. Lazic, V. Caciuc, Y. Morikawa, G. Hoffmann, S. Blügel, and R. Wiesendanger, *Phys. Rev. Lett.* 105, 047204 (2010): "Spin- and energy-dependent tunneling through a single molecule with intramolecular spatial resolution". [11] J. Schwöbel, Y. Fu, J. Brede, A. Dilullo, G. Hoffmann, S. Klyatskaya, M. Ruben, and R. Wiesendanger, *Nature Communications* 3, 953 (2012): "Real-space observation of spin-split molecular orbitals of adsorbed single-molecule magnets". [12] O. Pietzsch, A. Kubetzka, M. Bode, and R. Wiesendanger, *Science* 292, 2053 (2001): "Observation of magnetic hysteresis at the nanometer scale by spin-polarized scanning tunneling spectroscopy". [13] F. Meier, L. Zhou, J. Wiebe, and R. Wiesendanger, *Science* 320, 82 (2008): "Revealing magnetic interactions from single-atom magnetization curves". [14] A. A. Khajetoorians, J. Wiebe, B. Chilian, S. Lounis, S. Blügel, and R. Wiesendanger, *Nature Physics* 8, 497 (2012): "Atom-by-atom engineering and magnetometry of tailored nanomagnets". [15] A. A. Khajetoorians, B. Chilian, J. Wiebe, S. Schuwalow, F. Lechermann, and R. Wiesendanger, *Nature* 467, 1084 (2010): "Detecting excitation and magnetization of individual dopants in a semiconductor". [16] A. Kubetzka, M. Bode, O. Pietzsch, and R. Wiesendanger, *Phys. Rev. Lett.* 88, 057201 (2002): "Spin-Polarized Scanning Tunneling Microscopy with Antiferromagnetic Probe Tips". [17] A. Schlenhoff, S. Krause, G. Herzog, and R. Wiesendanger, *Appl. Phys. Lett.* 97, 083104 (2010): "Bulk Cr tips with full spatial magnetic sensitivity for spin-polarized scanning tunneling microscopy". [18] A. Wachowiak, J. Wiebe, M. Bode, O. Pietzsch, M. Morgenstern, and R. Wiesendanger, *Science* 298, 577 (2002): "Direct Observation of Internal Spin-Structure of Magnetic Vortex Cores". [19] L. Cornils, A. Kamlapure, L. Zhou, S. Pradhan, A. A. Khajetoorians, J. Fransson, J. Wiebe, and R. Wiesendanger, *Phys. Rev. Lett.* 119, 197002 (2017): "Spin-polarization of the Yu-Shiba-

- Rusinov state of an individual atom". [20] L. Schneider, Ph. Beck, J. Wiebe, and R. Wiesendanger, *Science Advances* 7, eabd7302 (2021): "Atomic-scale spin-polarization maps using functionalized superconducting probes". [21] A. Kubetzka, O. Pietzsch, M. Bode, and R. Wiesendanger, *Phys. Rev. B* 67, 020401 (2003): "Spin-polarized scanning tunneling microscopy study of 360° walls in an external magnetic field". [22] E. Y. Vedmedenko, L. Udvardi, P. Weinberger, and R. Wiesendanger, *Phys. Rev. B* 75, 104431 (2007): "Chiral magnetic ordering in two-dimensional ferromagnets with competing Dzyaloshinsky-Moriya interactions". [23] S. Meckler, N. Mikuszeit, A. Pressler, E. Vedmedenko, O. Pietzsch, and R. Wiesendanger, *Phys. Rev. Lett.* 103, 157201 (2009): "Real-space observation of a right-handed inhomogeneous cycloidal spin spiral by spin-polarized scanning tunneling microscopy in a triple axes vector magnet". [24] M. Bode, M. Heide, K. von Bergmann, P. Ferriani, S. Heinze, G. Bihlmayer, A. Kubetzka, O. Pietzsch, S. Blügel, and R. Wiesendanger, *Nature* 447, 190 (2007): "Chiral magnetic order at surfaces driven by inversion asymmetry". [25] K. von Bergmann, S. Heinze, M. Bode, E. Y. Vedmedenko, G. Bihlmayer, S. Blügel, and R. Wiesendanger, *Phys. Rev. Lett.* 96, 167203 (2006): "Observation of a complex nano-scale magnetic structure in a hexagonal Fe monolayer". [26] S. Heinze, K. von Bergmann, M. Menzel, J. Brede, A. Kubetzka, R. Wiesendanger, G. Bihlmayer, and S. Blügel, *Nature Physics* 7, 713 (2011): "Spontaneous atomic-scale magnetic skyrmion lattice in two dimensions". [27] N. Romming, Ch. Hanneken, M. Menzel, J. E. Bickel, B. Wolter, K. von Bergmann, A. Kubetzka, and R. Wiesendanger, *Science* 341, 636 (2013): "Writing and deleting single magnetic skyrmions". [28] N. Romming, A. Kubetzka, Ch. Hanneken, K. von Bergmann, and R. Wiesendanger, *Phys. Rev. Lett.* 114, 177203 (2015): "Field-dependent size and shape of single magnetic skyrmions". [29] P.-J. Hsu, A. Kubetzka, A. Finco, N. Romming, K. von Bergmann, and R. Wiesendanger, *Nature Nanotechnology* 12, 123 (2017): "Electric-field-driven switching of individual magnetic skyrmions". [30] R. Wiesendanger, *Nature Reviews Materials* 1, 16044 (2016): "Nanoscale magnetic skyrmions in metallic films and multilayers: a new twist for spintronics". [31] L. Zhou, J. Wiebe, S. Lounis, E. Vedmedenko, F. Meier, S. Blügel, P. H. Dederichs, and R. Wiesendanger, *Nature Physics* 6, 187 (2010): "Strength and directionality of surface RKKY-interaction mapped on the atomic scale". [32] A. A. Khajetoorians, J. Wiebe, B. Chilian, and R. Wiesendanger, *Science* 332, 1062 (2011): "Realizing all-spin based logic operations atom by atom". [33] J. Hermenau, S. Brinker, M. Marciani, M. Steinbrecher, M. dos Santos Dias, R. Wiesendanger, S. Lounis, and J. Wiebe, *Nature Commun.* 10, 2565 (2019): "Stabilizing spin systems via symmetrically tailored RKKY interactions". [34] A. A. Khajetoorians, M. Steinbrecher, M. Ternes, M. Bouhassoune, S. Lounis, M. dos Santos Dias, J. Wiebe, and R. Wiesendanger, *Nature Commun.* 7, 10620 (2016): "Tailoring the chiral magnetic interaction between two individual atoms". [35] M. Steinbrecher, R. Rausch, K. T. Ton, J. Hermenau, A. A. Khajetoorians, M. Potthoff, R. Wiesendanger, and J. Wiebe, *Nature Commun.* 9, 2853 (2018): "Non-collinear spin states in bottom-up fabricated atomic chains". [36] M. Menzel, Y. Mokrousov, R. Wieser, J. E. Bickel, E. Vedmedenko, S. Blügel, S. Heinze, K. von Bergmann, A. Kubetzka, and R. Wiesendanger, *Phys. Rev. Lett.* 108, 197204 (2012): "Information transfer by vector spin chirality in finite magnetic chains". [37] H. Kim, A. Palacio-Morales, T. Posske, L. Rózsa, K. Palotas, L. Szunyogh, M. Thorwart, and R. Wiesendanger, *Science Advances* 4, eaar5251 (2018): "Towards tailoring Majorana bound states in artificially constructed magnetic atom chains on elemental superconductors". [38] L. Schneider, S. Brinker, M. Steinbrecher, J. Hermenau, T. Posske, M. dos Santos Dias, S. Lounis, R. Wiesendanger, and J. Wiebe, *Nature Commun.* 11, 4707 (2020): "Controlling in-gap end states by linking nonmagnetic atoms and artificially-constructed spin chains on superconductors". [39] M. Bode, O. Pietzsch, A. Kubetzka, and R. Wiesendanger, *Phys. Rev. Lett.* 92, 067201 (2004): "Shape dependent Thermal Switching Behavior of Superparamagnetic Nanoislands". [40] A. A. Khajetoorians, B. Baxevanis, Ch. Hübner, T. Schlenk, S. Krause, T. Wehling, S. Lounis, A. Lichtenstein, D. Pfannkuche, J. Wiebe, and R. Wiesendanger, *Science* 339, 55 (2013): "Current-driven spin dynamics of artificially constructed quantum magnets". [41] S. Krause, L. Berbil-Bautista, G. Herzog, M. Bode, and R. Wiesendanger, *Science* 317, 1537 (2007): "Current-induced magnetization switching with a Spin-Polarized Scanning Tunneling Microscope".

Session EA

SPIN ANGULAR MOMENTUM TRANSPORT: SPIN WAVES PUSHING NEW FRONTIERS

Timo Kuschel, Co-Chair

Bielefeld University, Bielefeld, Germany

Matthias Althammer, Co-Chair

Walther-Meißner-Institut, Garching, Germany

INVITED PAPERS

EA-01. Non-Stationary Thickness Profiles of Spin Wave Modes Propagating in Obliquely Magnetized Magnetic Films.

C. Trevillian¹, V. Tyberkevych¹ and A.N. Slavin¹

1. Physics, Oakland University, Rochester, MI, United States

The dynamics of spin waves propagating in thin magnetic films has been studied intensively for several decades, and is relatively well-understood [1,2]. However, investigations have been mainly focused on the cases of either perpendicular or in-plane magnetization, where forward volume, backward volume, and surface magnetostatic (or dipolar) long-wavelength wave modes have been identified [1]. A more general dipole-exchange theory of the spin wave spectrum in magnetic films applicable also to the short-wavelength spin waves has been later developed by the research group of B.A. Kalinikos [2]. The conventional theory led to the understanding that a spin wave in a magnetic film with spin-sink-free surfaces is a non-uniform travelling wave having a stationary distribution of the variable magnetization along the film thickness, and can transfer energy and angular momentum only along the in-plane direction of the spin wave propagation. It turned out, that the situation becomes substantially more complicated in the case when the magnetic film is magnetized obliquely (see Fig.1), and short-wavelength dipole-exchange spin waves are considered. The results of recent experiments [3], performed using Brillouin light-scattering spectroscopy, in combination with the numerical results, based on the theory of dipole-exchange spin-wave spectra [2], have shown two effects: (i) thickness profiles of the propagating spin waves (both in in-plane and obliquely magnetized films) are strongly dependent on the in-plane wavenumber k due to the strong dipolar hybridization between the modes having different thickness profiles, and demonstrate “dipolar pinning” [4] with the increase on the in-plane wavenumber (see Fig.2, top panel); (ii) transverse (thickness) profiles of the spin waves propagating in the film plane in an *obliquely* magnetized film are *non-stationary*, i.e. are changing with time in the process of the wave propagation (see Fig.2, bottom panel). This last phenomenon might mean that there could be a transverse (along the film thickness) transfer of spin angular momentum without corresponding transverse transfer of energy. In the end, this issue of transverse spin transport is related to the boundary conditions at the surfaces of the magnetic film. In our simple system Fig. 1, we consider a magnetic film with spin-sink-free surfaces. However, if there is a spin-sink formed by a layer of a heavy metal, such as Pt, present at the film surface, it may be possible to experimentally detect the transfer of spin angular momentum along the film thickness in an obliquely magnetized magnetic film supporting the unidirectional spin wave propagation in the film plane. Further experimental studies are necessary to clarify the issue of possible transverse spin angular momentum transfer in obliquely magnetized magnetic films.

[1] R. Damon and J. Eshbach, J. Phys. Chem. Solids, vol. 19, p.308 (1960). [2] B. Kalinikos and A. Slavin, J. Phys. C, vol. 19, p.7013 (1986). [3] D. Bozhko, H. Musiienko-Shmarova, V. Tiberkevich, et al., Phys. Rev. Research, vol. 2, p.023324 (2020). [4] K.Yu. Guslienko, S.O. Demokritov, B. Hillebrands, and A.N. Slavin, Phys. Rev. B, vol.66, 132402 (2002).

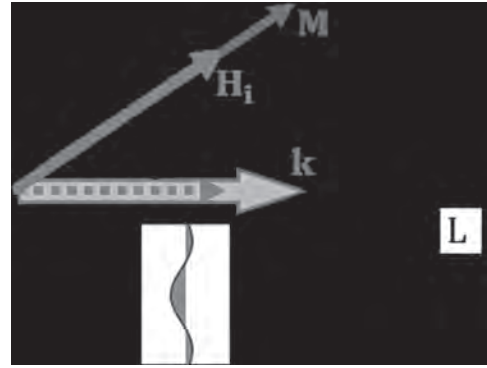


Fig. 1. Geometry of an obliquely magnetized (by an internal magnetic field H_i directed at an angle θ to the surface) spin-sink-free magnetic film of the thickness L carrying a propagating spin wave having a wavenumber k . An example of a transverse profile of the dynamic magnetization in a propagating spin wave is shown along the film thickness.

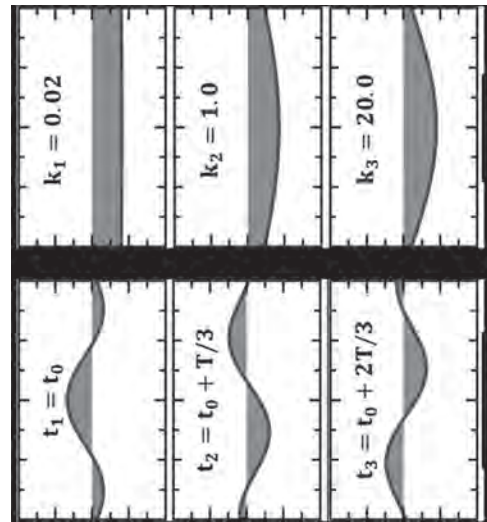


Fig. 2. Numerically calculated transverse dynamic magnetization profiles of spin wave modes propagating in a $5.6 \mu\text{m}$ thick yttrium-iron garnet (YIG) film. Top panel: profiles in an in-plane magnetized ($\theta = 0$) film, corresponding to three different values of the in-plane wavenumber, and demonstrating the effect of “dipolar pinning”. Bottom panel: profiles of the wave having in-plane wavenumber $k = 1 \text{ rad } \mu\text{m}^{-1}$ in an obliquely magnetized ($\theta = \pi/4$) film at three different time moments, demonstrating that the transverse spin wave profile is non-stationary. T - is the period of the spin wave frequency.

EA-02. Spin Waves and Spin Currents.

S. Demokritov¹, B. Divinskiy¹, I. Borisenko¹, V.E. Demidov¹ and S. Urazhdin²

1. *Institute for Applied Physics, Westfälische Wilhelms-Universität Munster, Munster, Germany*; 2. *Emory University, Atlanta, GA, United States*

The concept of spin current, introduced analogously to the charge current, has gained a great significance in spintronic and magnonic systems. Two distinct types of spin transport mechanisms can be identified. The first one is associated with diffusion of spin-polarized conduction electrons from one part of the system to another, followed by their spin relaxation mainly due to the exchange interaction with the localized electrons. The second mechanism is mediated by the transfer of spin between localized magnetic moments due to their mutual interaction. The latter can be also described as spin transport by propagating spin waves. Interplay between these two phenomena enables generation of propagating spin waves by spin currents carried by conduction electrons. Reciprocally, spin waves can produce spin currents carried by spin-polarized electrons, which is known as spin pumping. In my talk I will discuss several phenomena involving interplay between spin waves and electron spin currents, including the excitation of propagating spin waves by spin polarized electric current [1] and the spin-Hall effect (SHE) [2]. In the first case a simplified model considering only the exchange interaction provides an adequate description of the observed phenomena, based on the conservation of angular momentum in the spin subsystem. However, the physical origin of SHE is the relativistic spin-orbit coupling, which mixes the angular momentum of spin subsystem with that of the lattice. Surprisingly, the same is valid for the magnetic dipole interaction. I will illustrate the importance of mixing between spin and orbital degrees of freedom with the examples of spin-wave pumping experiments [3] and the dynamics of Bose-Einstein condensate of magnons [4].

[1] S. Urazhdin et al. *Nature Nanotech.* 9 509 (2014) [2] B. Divinskiy et al. *Adv. Mater.* 1802837 (2018) [3] H. Kurebayashi et al., *Nature Mat.* 10, 660 (2011). [4] I.V. Borisenko et al., *Nature Comm.* 11, 1691443 (2020).

EA-03. Pure Spin Current and Spin Hall Effect in Antiferromagnetic Insulators.*K. Shen*¹*1. Department of Physics, Beijing Normal University, Beijing, China*

Magnons in an easy-axis antiferromagnet with uniaxial anisotropy have two circularly polarized modes, which, very similar to the spin states of electrons, carry opposite angular momentum. Spin transport mediated by these antiferromagnetic magnons has attracted much attention recently. In this talk, we will discuss explicitly the role of different microscopic mechanisms behind. Specifically, we will show that the exchange interaction can lead to strong mode splitting and confluence processes, which change the magnon number but conserve the total angular momentum. Such processes can drive the two oppositely polarized magnon species to opposite chemical potentials, resulting in a pure magnon spin current, i.e., a counterflow of the two species without net magnon current [1]. The dipole-dipole interaction, on the other hand, is demonstrated to be able to introduce an effective magnon spin-orbit coupling, which then gives rise to electron-like spin-orbit phenomena, such as an intrinsic magnon spin Hall effect and D'yakonov-Perel'-type magnon spin relaxation [2]. Moreover, we show that the dipole-dipole interaction is able to generate Damon-Eshbach-type magnon surface modes [3]. In contrast to the nonreciprocity of the conventional Damon-Eshbach mode in ferromagnets, the surface modes in antiferromagnets experience a spin-momentum locking, just like the surface modes in an electronic topological insulator. Our work suggests that the antiferromagnetic insulators could be a suitable platform for exploring electron-like spin dynamics in insulators and designing novel spintronic devices.

[1] Ka Shen, Phys. Rev. B 100, 094423 (2019). [2] Ka Shen, Phys. Rev. Lett. 124, 077201 (2020). [3] Jie Liu, Lin Wang, and Ka Shen, Phys. Rev. Research 2, 023282 (2020)

EA-04. Long Range Coupling of Magnetic Bilayers by Coherent Phonons.

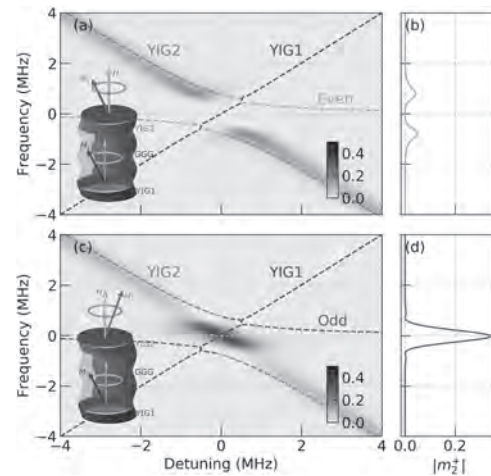
K. An¹, A. Litvinenko¹, R. Kohno¹, A. Fuad¹, R. Lopes Seeger¹, V.v. Naletov^{1,2}, L. Vila¹, U. Ebels¹, G. de Loubens³, H. Hurdequint³, N. Beaulieu⁴, J. Ben Youssef⁴, N. Vukadinovic⁵, G.E. Bauer⁶, A.N. Slavin⁷, V. Tyberkevych⁷ and O. Klein¹

1. Université Grenoble Alpes, CEA, CNRS, Grenoble INP, Spintec, Grenoble, France; 2. Institute of Physics, Kazan Federal University, Kazan, Russian Federation; 3. Service de Physique de l'Etat Condense, Gif/Sur Yvette, France; 4. Laboratoire des Sciences et Techniques de l'Information de la Communication et de la Connaissance, Brest, France; 5. Dassault Aviation, Saint-Cloud, France; 6. Institute for Materials Research and WPI-ALMR and CSRN, Tohoku University, Tohoku, Japan; 7. Oakland University, Rochester, MI, United States

Recent progresses in quantum information technologies have demonstrated the benefits of leveraging coherence effects such as collective spin precession in ferromagnets in order to process information more efficiently. This coherent transfer between different waveforms is an important ingredient of the quantum information processing as it allows transport of quantum states without loss of frequency or phase. An efficient hybridization process requires to reach a strong coupling regime, where the interaction rate between two collective states becomes larger than their relaxation rates. While increasing the overlap integral between two spatio-temporal patterns is primarily a design issue, diminishing the internal friction inside an object is a much more complex task, which requires know-how in material research and growth technology. In spintronics, this has revived interest for insulating materials and in particular garnets, which are the magnetic materials benefiting from the lowest magnetic damping. The sound wave attenuation coefficient in garnets is also exceptional, i.e. up to an order of magnitude lower than that in single crystalline quartz. In addition to the low damping of magnetic and sound waves, a strong coupling can be established between spin-waves (magnons) and lattice vibrations (phonons) through the magnetic anisotropy and strain dependence of the magnetocrystalline energy in magnetic garnets. The magnetoelasticity leads to new hybrid quasiparticles ("magnon polarons") when spin wave and acoustic wave dispersions cross [1]. This coupling has been exploited in the past to produce microwave acoustic transducers [2]. The adiabatic conversion between magnons and phonons in magnetic field gradients proves their strong coupling in yttrium iron garnet (YIG) [3]. Here we first demonstrate that the spin waves can be strongly coupled to coherent transverse sound waves that have very long characteristic decay length and propagate ballistically over millimetric distances. The experiment was performed at room temperature with a magnetic field applied perpendicular to the film. Our sample consists of two 200 nm thick YIG layers deposited on both sides of a 0.5 mm thick gadolinium gallium garnet (GGG) substrate. The circularly polarized standing sound waves couple to the magnetization oscillations in both layers. An interference pattern is observed and it is explained as the strong coupling of the magnetization dynamics of the two YIG layers either in phase or out of phase by the standing transverse sound waves [4]. This long range coherent transport of spin by phononic angular momentum can add new functionalities to insulator spintronic circuits and devices. Furthermore, such mediation of coherent spins could induce a novel dynamic exchange coupling in a spin-valve system when the magnetic resonances of two layers are brought within the strength of the magnetoelastic coupling. To detect such coupling, a Pt strip electrode was deposited on one YIG layer to monitor its dynamics through the inverse spin Hall effect (ISHE). This improves the measurement sensitivity of the phonon mediated spin transfer. In our sample, the two YIG layers have initially different spontaneous magnetizations. We tune the difference between two magnetic resonances either i) by varying the polar angle of an external magnetic field or ii) by applying a temperature gradient along the stack direction. The existence of the novel dynamic coupling is evidenced by an emergence of the "bright" and "dark" collective states in both measurements. Our observation of such collective modes resembles the level attraction/repulsion behavior between two hybridized modes [5]. This feature is similar to the coupling control via microwave phase [6]. We show that the observed behavior is in agreement with theoretical predictions. Finally we discuss the detection of heat carried by coherent phonons. We

measure thermal voltages across Pt in YIG|GGG|Pt system, where no ISHE voltage should be present. The signal appears only at the acoustic phonon resonances indicating that the heat can be efficiently carried by circularly polarized coherent phonons excited by magnons. When the magnetic field direction is tilted away from the film normal direction, the signal vanishes, suggesting that the heat carried by acoustic phonons becomes less coherent. We perform several control experiments, which shows the universality of the signal and possible enhancement schemes.

[1] T. Kikkawa, K. Shen, B. Flebus et al., Phys. Rev. Lett. 117, 207203 (2016) [2] M. Pomerantz, Phys. Rev. Lett. 7, 312 (1961) [3] J. Holanda, D. S. Maior, A. Azevedo et al., Nat. Phys. 14, 500 (2018) [4] K. An, A.N. Litvinenko, R. Kohno et al., Phys. Rev. B 101, 060407(R) (2020) [5] M. Harder, Y. Yang, B. M. Yao et al., Phys. Rev. Lett. 121, 137203 (2018) [6] I. Boventer, C. Dörflinger, T. Wolz et al., Phys. Rev. Research 2, 013154 (2020)



Theoretical calculation of (a,b) the dark and (c,d) bright states formation. The insets show the magnetic precession states of both layers when (a) even or (c) odd phonon mode mediates the coupling between two magnetic layers. The dashed lines show the calculated eigenvalues. The linecuts in (b) and (d) are along the zero detuning case.

EA-05. Spin Waves in YIG-Semiconductor Heterostructures.

S. Nikitov^{1,2} and M. Morozova^{2,3}

1. *Kotelnikov Institute of Radioengineering and Electronics of the Russian Academy of Sciences, Moscow, Russian Federation;* 2. *Moscow Institute of Physics and Technology National Research University, Dolgoprudnyj, Russian Federation;* 3. *N. G. Chernyshevskogo Saratov National State Research University, Saratov, Russian Federation*

The most important parameters of complementary CMOS electronics, such as high speed information processing, small size of transistors, rather small energy consumption and low thermal radiation have fundamental restrictions. Magnonics - is one of the alternative conceptual solutions to overcome these restrictions [1-3]. Basically, the main idea of this is to combine magnonics with conventional CMOS technologies [4,5]. Interaction of magnons (spin waves) in micron- or nanosized ferromagnetic films with transport of electrons in semiconductors adjacent to these films permits to develop novel component base of the microwave or THz nanoelectronics with unique characteristics. The most suitable materials for combination in spintronics (magnonics) and electronics beyond CMOS are yttrium-iron-garnet (YIG) and Si. YIG possess very low damping for spin waves propagation. Si has very high mobility of current carriers and wide band gap. Novel technologies in YIG - semiconductor materials in which Si and GaAs are used as substrates for YIG films show possibilities for their integration in beyond CMOS electronics [6]. In this work we study spin waves propagation in a heterostructure consisting of corrugated YIG film grown on gallium-gadolinium-garnet (GGG) substrate attached to Si wafer. By using electric and magnetic control of wave propagation we are able to study linear and nonlinear effects accompanying spin waves propagation. Fig. 1 shows the layout of the investigated structure. The heterostructure was made on the base of YIG film with a thickness of $\approx 10 \mu\text{m}$ and saturation magnetization G grown on GGG substrate. On the surface of the YIG film, the periodic structure was created with the period $L = 200 \mu\text{m}$ in the form of grooves with the depth of $1 \mu\text{m}$ and the width of $100 \mu\text{m}$ (1D magnonic crystal (MC)). To form an MC/SC (semiconductor) type structure on the MC surface, the n -type doped silicon semiconductor wafer (with electrons carrier density $N = 3 \cdot 10^{11} \text{ cm}^{-3}$ and conductivity $\approx 10 \cdot 10^{-5} \text{ Ohm}^{-1} \text{ m}^{-1}$) was placed. The thickness of SC layer = $500 \mu\text{m}$, the length 3 mm, and the width is equal the width of MC = 4 mm. Copper contacts with chromium adhesive layer were deposited on the SC surface at the distance 2.5 mm relative to each other. When a control voltage U is applied to the contacts, a directional drift of charges in the SC (EC) takes place. For the excitation and receiving of the magnetostatic spin wave, $30 \mu\text{m}$ -wide microstrip transducers were used. The transducers were placed on the MC surface at a distance of 9.5 mm relative to each other. An external constant magnetic field was applied parallel to the microstrip transducers, and the magnetostatic surface waves (MSSW) was excited in the MC. In Fig. 2 the amplitude-frequency characteristic (AFC) curves for surface spin waves in MC/SC structure are shown at the input power $P_0 = 23 \text{ dBm}$ and various voltages applied to SC. The strongly pronounced minima in AFC curves respect to frequency band gaps of magnonic crystals (Bragg frequencies): at the absence of the voltage (at $U=0 \text{ V}$ the central frequency of band gap (BG) - $f_{nl} = 4.11 \text{ GHz}$), at the applied voltage $U=20 \text{ V}$ the central frequency of band gap - $\approx 4.08 \text{ GHz}$. At the voltage increase the BG central frequency moves to lower values. In Fig. 2 the band gap central frequency is marked $f_l = 4.12 \text{ GHz}$ for linear case ($P_0 = 11 \text{ dBm}$) at $U=0 \text{ V}$. It can be seen that for $f_l > f_{nl}$, thus at the increase of the input power the band gap in nonlinearly shifted. We also considered the features of spin wave pulses propagation through the MC/SC structure depending on the electric voltage variation. The nonlinear shift of the band gap permits to form conditions for band gap solitons. We developed the adequate nonlinear theory for such wave propagation. The theoretical results are obtained using the coupled waves method for forward wave and wave reflected from the spatial non-uniformities of periodic structure. The microwave method for measuring amplitude versus frequency data of propagating spin waves was applied. The parameters of these solitons further can be governed by the double electric and magnetic control. In particular, the exciting number of solitons, their threshold appearance and propagation velocity can be controlled by the electric current applied to the semiconductor. We have further discovered the effect of the nonlinear switching at which the YIG film with periodic

structure can transmit the wave signal through it at the frequencies of the band gap due to high power signal wave. In this case the heterostructure demonstrates the bistability properties and hysteresis appearance at the wave power increase. The obtained results permit to consider heterostructures based on magnonic crystals and semiconductor layers as the possible candidates for integration of magnonics component base into semiconductor electronics architecture. The work was supported by the grant from the Government of the Russian Federation for state support of academic research conducted under the guidance of leading scientists (project no. 075- 15-2019-1874), by the Russian Foundation for Basic Research (grant 19-29-03049) and by the State Task No. 0030-2019-0013.

1. V. Chumak, V. I. Vasyuchka, A. A. Serga et al., *Nature Physics*, VOL. 11, p. 453 (2015).
2. S. A. Nikitov, D. V. Kalyabin, I. V. Lisenkov et al., *Phys. Usp.* VOL.58, p. 1002 (2015).
3. S. A. Nikitov, A.R. Safin, D. V. Kalyabin, et al., *Phys. Usp.* VOL.63, p. 945 (2020).
4. C. Felser and G. Fecher, eds., *Spintronics: From materials to devices* (Springer Netherlands, 2013).
5. A. Sidorenko, ed., *Functional Nanostructures and Metamaterials* (Springer International Publ., New York, 2018).
6. A.V. Sadovnikov, E.N. Beginin et al., *Phys. Rev. B*, VOL. 99, p.054424 (2019)

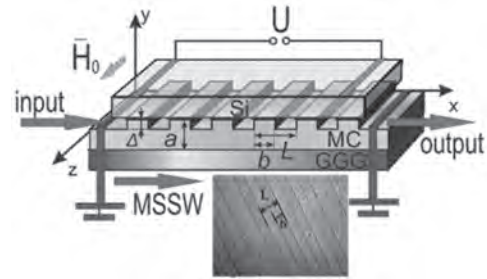


Fig. 1. Experimental layout of the MC/SC structure.

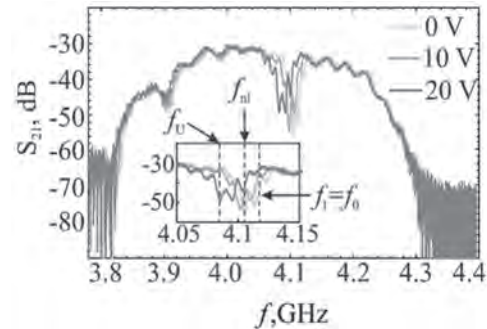


Fig. 2. The amplitude-frequency characteristics for MSSW in the MC/SC structure and application of voltage $U= 0 \text{ kV/cm}$ (green curve), $U= 10 \text{ V}$ (orange), $U= 20 \text{ V}$ (red).

EA-06. 3D Imaging of Topologically Stabilized Spin Textures in Nanostructured Materials – Towards Ultrafast Imaging of Spin Transport.

*E. Catting-Subramanian*¹, *A. Rana*², *Y. Lo*², *C. Liao*¹, *C. Bevis*¹, *X. Lu*², *P. Johnsen*¹, *S. Ryan*¹, *J. Miao*², *H. Kapteyn*¹ and *M. Murnane*¹

1. *JILA, University of Colorado Boulder, Boulder, CO, United States;*

2. *University of California Los Angeles, Los Angeles, CA, United States*

The advent of materials with complex, topologically-stabilized magnetic textures, such as skyrmions, stemming from careful tuning of the Dzyaloshinskii–Moriya interaction, direct light-induced manipulation of spins, or geometric frustration [1], has opened up exciting avenues of research. Understanding the structure and dynamics of, and achieving control over, spin on the scale of the magnetic exchange interaction is both a question of fundamental physics and at the forefront of developing quantum technologies like spintronics and low-energy data transport and memory [2]. Because of the small size of these intricate nanoscale magnetic textures, few to hundreds of nm, and their low contrast, it is quite challenging to image them in 3D directly without prior knowledge of the sample or extensive simulation. Their dynamics of such systems can also prove challenging to capture, as some magnetic processes occur on the timescale of twenty femtoseconds or less [3]. To fully understand the static and dynamic electronic, magnetic, and structural properties of complex samples we combine complementary nanoscale imaging and spectroscopy techniques: resonant x-ray magnetic circular dichroism (MCD) provides element-specific magnetic sensitivity; ptychography yields diffraction-limited images with phase contrast, ideal for low-contrast materials; and time-resolved extreme ultraviolet (EUV) spectroscopies can capture atto-to-nanosecond dynamics. By integrating soft x-ray MCD imaging with scalar ptycho-tomography [4, 5] we demonstrate a technique capable of directly imaging the 3D magnetic field within a Ni metalattice material, with no need for prior knowledge or simulation, that is applicable to a wide range of magnetic nanostructured samples.

[1] J. E. Han and V. H. Crespi, *Phys. Rev. Lett.*, Vol. 89, p. 197203 (2002)

[2] P. Fischer, *IEEE Trans. Magn.*, Vol. 51, p. 0800131 (2015) [3] W. You,

P. Tengdin, C. Chen, *et al.*, *Phys. Rev. Lett.*, Vol. 121, p. 77204 (2018) [4]

C. Donnelly, M. Guizar-Sicairos, V. Scagnoli, *et al.*, *Nature*, Vol. 547, p.

328 (2017) [5] A. Pryor, Y. Yang, A. Rana, *et al.*, *Scientific Reports*, Vol.

7, p. 10409 (2017)

Session EB
FUNDAMENTAL MAGNONIC PHENOMENA
Benjamin Jungfleisch, Chair
University of Delaware, Newark, DE, United States

INVITED PAPER

EB-01. Curvilinear Antiferromagnetism: Current State and Perspectives INVITED.O. Pylypovskiy^{1,2}1. Helmholtz-Zentrum Dresden-Rossendorf, Dresden, Germany;
2. Kyiv Academic University, Kyiv, Ukraine

Antiferromagnets (AFMs) emerged as a versatile material science platform, which enabled numerous fundamental discoveries including the observation of monopole quasiparticles in frustrated systems and collective quantum effects, such as spin superfluidity and Bose–Einstein condensation of magnetic excitations [1]. Primary advantages of antiferromagnets are their terahertz operating frequencies, the absence of stray fields, magnetic field robustness, all of which result in numerous advantages including those in spintronics and spinorbitronics [2]. The key enabler of those applications is the presence of the Dzyaloshinskii-Moriya interaction (DMI). This, in turn, put stringent requirements on the magnetic symmetry of AFM, which should support weak ferromagnetism and chiral helimagnetism. This makes the portfolio of material systems available for these studies very limited that renders the progress in AFM-related fundamental and technological research to depend on time-consuming material screening and optimization of intrinsic chiral properties of AFMs. The field of curvilinear magnetism is well explored for ferromagnets, where magnetic responses are tailored by local curvatures [3]. By contrast, the topic of curvilinear AFMs is at its infancy [4–9]. The energy landscape of ring AFM and geometrically frustrated chains at non-zero temperature is characterized by a large number of metastable states including long-living noncollinear textures if anisotropy is strong enough [6]. In experiment, curvilinear AFMs are mainly represented by the molecular magnets [7] and metalized DNA molecules [8]. The shape anisotropy stemming from magnetostriction plays the major role in the ordering of the Neel vector in perovskite zig-zag stripes and nanodots determining the easy direction as the parallel or perpendicular to the boundary [9]. In this presentation, we will demonstrate that chiral responses of AFMs can be tailored by a geometrical curvature without the need to adjust material parameters. In a general case, an intrinsically achiral one-dimensional curvilinear AFM spin chain behaves as a chiral helimagnet with geometrically tunable DMI, orientation of the Neel vector and the helimagnetic phase transition, see Fig. 1 [4]. The helix-shaped spin chain possesses two ground states: the so-called homogeneous and periodic ones with respect to the motion along the chain. The energetically favorable state is determined by the direction of the geometry-driven DMI vector. In contrast to ferromagnets, there is no easy axis anisotropy competing with the geometry-driven one. Furthermore, the curvature-induced DMI results in the hybridization of spin wave modes. The low-frequency branch is gapless for straight chains and possesses the gap for any finite curvature. In addition, the DMI enables a geometrically-driven local minimum of the low frequency branch which increases for larger curvature and torsion, see Fig. 2. This opens exciting perspectives to study long-lived collective magnon states in AFMs. These findings position curvilinear 1D antiferromagnets as a novel platform for the realization of geometrically tunable chiral antiferromagnets for antiferromagnetic spinorbitronics and fundamental discoveries in the formation of coherent magnon condensates in the momentum space. The proposed description of vector fields living at curvilinear geometries can be applied for other systems with complex order parameters, such as ferroelectrics [10] or liquid crystals [11].

[1] C. Castelnovo, R. Moessner, S. L. Sondhi, *Nature*, Vol. 451, p. 42 (2008); N. Nagaosa, Y. Tokura, *Phys. Scr.* Vol. T146, p. 014020 (2012); A. A. Zvyagin, *Low Temp. Phys.* Vol. 39, p. 901 (2013) [2] T. Jungwirth, J. Sinova, A. Manchon et al, *Nat. Phys.* Vol. 14, p. 200 (2018); V. Baltz, A. Manchon, M. Tsoi et al, *Rev. Mod. Phys.* Vol. 90, p. 015005 (2018) [3] R. Streubel, P. Fischer, F. Kronast et al, *J. Phys. D: Appl. Phys.* Vol. 49, p. 363001 (2016); A. Fernandez-Pacheco, R. Streubel, O. Fruchart et al, *Nat. Comm.* Vol. 8, p. 15756 (2016); D. D. Sheka, O. V. Pylypovskiy, P. Landeros et al., *Comm. Phys.* 3, 128 (2020) [4] O. V. Pylypovskiy, D. Y. Kononenko, K. V. Yershov et al, *Nano Lett.* Vol. 20, p. 8157 (2020) [5]

K. K. Nanda, A. W. Addison, E. Sinn et al, *Inorg. Chem.* Vol 35, p. 5966 (1996); O. Cador, D. Gatteschi, R. Sessoli et al, *Ang. Chem. Int. Ed.* vol 43, p. 5196 (2004); M. Grzelczak, M. Correa-Duarte, V. Salgueirino-Maceira et al, *Ang. Chem. Int. Ed.* Vol. 46, p. 7026 (2007); T. Guidi, B. Gillon, S. A. Mason et al, *Nat. Comm.* Vol. 6, p. 7061 (2015) [6] S. Castillo-Sepulveda, R. A. Escobar, D. Altbir et al, *Phys. Rev. B*, Vol. 96, p. 024426 (2017) [7] S. J. Blundell, F. L. Pratt, *J. Phys.: Cond. Matt.* Vol. 16, p. R71 (2004) [8] K. Mizoguchi, S. Tanaka, M. Ojima et al, *J. Phys. Soc. Jap.* Vol. 76, p. 043801 (2007) [9] A. D. Bang, I. Hallsteinsen, R. V. Chopdekar et al, *Appl. Phys. Lett.* Vol. 115, p. 112403 (2019); M. S. Lee, P. Lyu, R. V. Chopdekar et al, *J. Appl. Phys.* Vol. 127, p. 203901 (2020) [10] M. Owczarek, K. A. Hujsak, D. P. Ferris et al, *Nat. Comm.* Vol. 7, p. 13108 (2016) [11] G. Napoli, L. Vergori, *Phys. Rev. Lett.* Vol. 108, p. 207803 (2012)

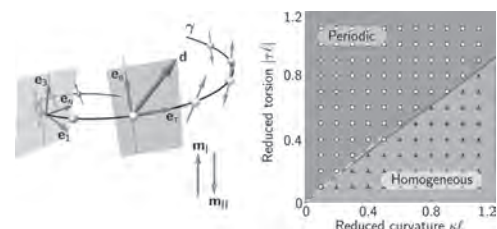


Fig. 1. A general AFM spin chain and the helimagnetic phase transition of helix-shaped spin chain. The curvature-driven DMI and anisotropy modify the magnetic response as follows. The DMI is represented by vector \mathbf{d} , while the equilibrium hard and easy axes for the Neel vectors are shown by \mathbf{e}_1 and \mathbf{e}_3 , respectively. Adapted with permission from [4]. Copyright (2020) American Chemical Society.

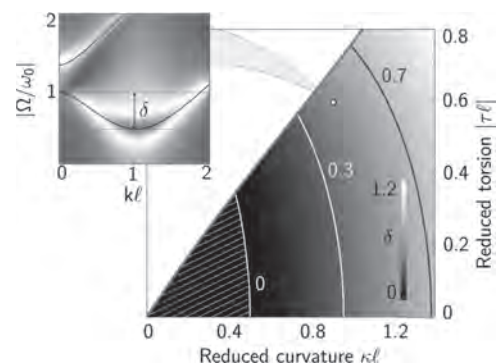


Fig. 2. The spin wave dispersion of the helix-shaped AFM spin chain and the respective depth δ of the local minimum at the dispersion curve. Adapted with permission from [4]. Copyright (2020) American Chemical Society.

CONTRIBUTED PAPERS

EB-02. Strongly Nonlinear Ferromagnetic Resonance of Bi-Doped YIG Nanodisks.

I. Ngouagnia Yemeli¹, D. Gouéré², H. Merbouche², T. Srivastava^{2,1}, H. Hurdequint¹, V. Cros², M. Muñoz³, S. Sangiao⁴, J. De Teresa⁴, O. Klein⁵, A. Anane² and G. de Loubens¹

1. Service de Physique de l'Etat Condense, Gif Sur Yvette, France; 2. Unite Mixte de Physique CNRS/Thales, Palaiseau, France; 3. Instituto de Micro y Nanotecnología (CNM-CSIC), Madrid, Spain; 4. Universidad de Zaragoza Departamento de Física de la Materia Condensada, Zaragoza, Spain; 5. SPINtronique et Technologie des Composants, Grenoble, France

One current goal of spintronics is the development of a sustainable information technology based on the transport of pure spin currents. One promising way to do this is to use spin waves (SWs), the elementary excitations of magnetically ordered materials: by collective precession of magnetic moments, they can transport angular momentum. SW information processing also offers interesting alternatives to conventional microelectronics [1]. For this, yttrium iron garnet (YIG), an insulating ferrimagnet, is the ideal material because it has the lowest magnetic damping. Furthermore, thanks to the spin orbit torque (SOT), it is possible to control the relaxation time of SWs in YIG by an electric current injected into an adjacent platinum layer [2]. However, such metal/insulator hybrid devices presently have certain limitations, as a sudden drop in the amplitude of the main mode beyond a certain excitation threshold, which originates from nonlinear coupling with other SW modes [2]. Different strategies can be considered to overcome these issues. In nanopatterned samples the available SW modes become quantized, which severely limits the available nonlinear processes. As a result, nonlinear saturation thresholds are postponed, which allows to reach much higher amplitudes of single mode dynamics [3]. The perpendicular magnetic anisotropy (PMA) can also be used to control the sign of the nonlinear frequency shift. Recently, the growth of ultra-thin films of Bismuth doped YIG (BiYIG) with tunable PMA has been achieved while preserving a high dynamic quality [4]. It was shown that the emission characteristics of SWs emitted by SOT in thin BiYIG films where PMA compensates the in-plane shape anisotropy are greatly improved [5]. Here, we study the magnetization dynamics in individual nanodisks patterned from such a 30 nm thick BiYIG film, with diameters ranging from 1 μm down to 200 nm. The static magnetic field is applied perpendicularly to the sample plane. To excite the ferromagnetic resonance (FMR) of the BiYIG nanodisks, we use the spatially uniform in-plane microwave field produced by an antenna integrated on top. To detect it, we employ a magnetic resonance force microscope [6] in which a cobalt nanosphere grown at the tip of a soft cantilever [7] is dipolarly coupled to the longitudinal component of the magnetization of the nanodisk positioned underneath (Fig. 1). By studying the SW spectra of these BiYIG nanodisks in the linear regime, we find that their effective anisotropy field is weakly dependent of the diameter and negative, about -10 mT, which means that the PMA slightly overcompensates the shape anisotropy. The damping parameter is found to increase as the diameter is decreased and lies in the high 10^{-4} – low 10^{-3} range for all disks. We then perform measurement of the main resonance line, corresponding to the quasi-uniform mode, as a function of the microwave power injected into the antenna, which is varied by up to four orders of magnitude (excitation field ranging from 0.03 mT to 3 mT at 5 GHz). For all the disks, we observe a distortion of the resonance line at intermediate excitation power, corresponding to the onset of foldover. As expected, due to the negative effective anisotropy field, the resonance line shifts towards higher magnetic field as the precession angle increases, which is opposite to the behavior reported on undoped YIG nanodisks [3]. For the largest BiYIG disks, the dynamics witnessed at higher power is quite more complex and interesting, as shown in Fig. 2 for the 700 nm diameter nanodisk. We observe a rapid saturation of the peak amplitude, corresponding to average precession angles of the order of 10° to 20° , accompanied with a broadening of the line towards both lower and higher magnetic field. To understand this behavior, we perform extensive micromagnetic simulations. Using the magnetic parameters extracted in the linear regime and the nominal geometry of the nanodisks, these simulations

reproduce the main characteristics of the measured FMR lines in the strongly nonlinear regime. They reveal that a dynamic instability is responsible of the observed behavior: as the amplitude of the quasi-uniform mode increases with the driving field, its precession profile gets more and more localized at the center of the disk, which eventually leads to the formation of a dynamic soliton similar to a wave bullet [8]. Moreover, this soliton is not stable over time, resulting in a rich temporal dynamics, which, depending on the exact driving conditions, can be quasi-periodic or intermittent. To experimentally access this complex temporal dynamics, we use the method introduced in [3], which consists in applying a second, much weaker excitation field of varying frequency, in addition to the main driving field at high power. The obtained frequency modulation spectra indeed reflect the existence of rich low-frequency temporal variations in the dynamics of the magnetization, as suggested by the simulations.

[1] A. Chumak et al. Nat. Phys. 11, 453 (2015) [2] A. Hamadeh et al. Phys. Rev. Lett. 113, 197203 (2014); M. Evelt et al. Appl. Phys. Lett. 108, 172406 (2016) [3] Y. Li et al. Phys. Rev. X 9, 041036 (2019) [4] L. Soumah et al. Nat. Commun. 9, 3355 (2018) [5] M. Evelt et al. Phys. Rev. Appl. 10, 041002 (2018) [6] O. Klein et al. Phys. Rev. B 78, 144410 (2008) [7] S. Sangiao et al. Beilstein J. Nanotechnol. 8, 2106 (2017) [8] A. Slavin and V. Tiberkevich, Phys. Rev. Lett. 95, 237201 (2005)

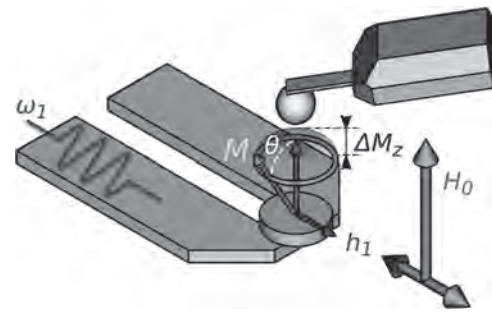


Fig.1 - Schematics of the experiment. The microwave field supplied by the antenna drives the magnetization of a BiYIG nanodisk into FMR, opening a precession angle around the perpendicularly applied field, which is detected by the cantilever of a magnetic resonance force microscope.

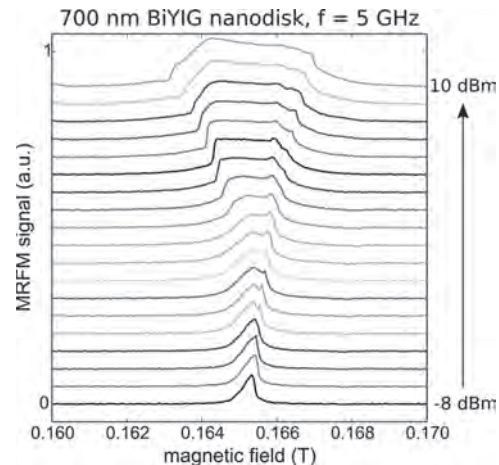


Fig.2 - Main resonance line of the 700 nm diameter nanodisk recorded at 5 GHz as a function of the driving power, increased by step of 1 dB from -8 dBm to 10 dBm. The spectra have been vertically offset for clarity.

EB-03. Observation of Higgs and Goldstone Spin-Wave Modes in Weak Magnetic Stripes.

M. Grassi¹, M. Geilen², K. Ait Oukaci³, Y. Henry¹, D. Lacour³, D. Stoeffler¹, M. Hehn³, P. Pirro² and M. Bailleul¹

1. Institut de Physique et Chimie des Matériaux de Strasbourg, CNRS, Université de Strasbourg, Strasbourg, France; 2. Fachbereich Physik and Landesforschungszentrum OPTIMAS, Technische Universität Kaiserslautern, Kaiserslautern, Germany; 3. Institut Jean Lamour, CNRS, Université de Lorraine, Nancy, France

Spontaneous symmetry breaking is an ubiquitous ingredient in physics. It governs second order phase transitions whose statics are well described within the universal Ginzburg-Landau (GL) theory, as confirmed by a number of observations. However, the picture for the corresponding dynamics is less clear. Indeed, in the ordered phase, GL theory predicts two different low-energy excitations: the zero frequency Goldstone mode, corresponding to an oscillation of the phase of the order parameter, and the non-zero-frequency Higgs mode, corresponding to an oscillation of its amplitude.[1] In practice, the amplitude mode has remained very difficult to observe in condensed matter, either because it does not couple to the experimental probes or because it decays too fast into other types of excitations.[1] In this communication, we show that an archetypal micromagnetic texture, the so-called weak magnetic stripes,[2] constitutes an ideal platform to investigate such dynamics. Combining Brillouin light scattering with micromagnetic simulations and analytical modeling, we evidence spin wave features that can be directly identified to Goldstone/Higgs modes. The system is a 180nm thick amorphous CoFeB ferromagnetic magnetic film exhibiting a small perpendicular magnetic anisotropy K . [3] Under a strong enough in-plane magnetic field H , the film is homogeneously saturated. However, its spin-wave spectrum already displays a characteristic feature precursor of the nucleation of an inhomogeneous magnetic texture. This is shown in figure 1b, which displays a color plot of the spin-wave dispersion simulated in the Damon Eshbach configuration (wave-vector $k_{\perp}H$). One recognizes a low frequency branch with a minimum around $k_c=21$ rad/ μm . Upon reducing the field, this minimum shifts to lower frequency and eventually reaches the horizontal axis (Fig. 1c), which is the behavior expected in the GL description: Upon approaching the critical field H_c , the curvature of the magnetic energy along a certain direction in the configuration space decreases to zero, which is associated to the softening of the corresponding normal mode. The mode profile at this point is shown in Fig. 1d: one recognizes an undulation of the vertical component of the magnetization in the middle of the film, together with quadrature undulations of the in-plane component of the magnetization on the top and bottom surfaces insuring magnetic flux closure. This pattern, and the critical fields and wavelength, correspond precisely to the weak magnetic stripes observed in this system. [3]. Indeed, upon further decreasing the field, the nucleation proceeds as a freeze of the soft spin-wave mode in a state with a given phase (or equivalently a given lateral position within the period), which constitutes the broken symmetry. Concomitantly, the characteristic cusp of the spin wave spectrum splits in two: One branch remains soft and a second one emerges with a gradual increase of its minimum frequency (Fig. 2a,b). Inspecting the spatial profile of these two modes (Fig. 2c,d) allows one to recognize them unambiguously as a Goldstone mode (rigid lateral oscillation of the stripe texture) and a Higgs mode (oscillation of the amplitude of the texture around its equilibrium value), respectively. We probe these modes experimentally using Brillouin light scattering onto thermally excited spin waves. The symbols in Fig. 1b,c and Fig. 2b show the position of the measured peaks. Although the limited wave-vector / frequency range accessible (<20 rad/ μm , >2 GHz) does not allow to cover all the way down to the cusp, the agreement with the simulations is good. In particular, the measured dispersions display the very characteristic features predicted, namely the negative slopes (in the $k_{\perp}H$ configuration this can only happen due to the perpendicular anisotropy), the critical softening and the subsequent splitting in the broken symmetry phase. These essential features are visible around H_c and k_c , which explains why they have been largely overlooked by the magnetism community, as previous dynamic studies of stripe domains had focused onto the $k \approx 0$ (ferromagnetic resonance) and/or deep supercritical (near remanence) regimes. [4,5] To support this identification, we shall present a Ginzburg Landau

theory of weak stripe statics based on a stray-field-free ansatz [2,6] and extend it to the dynamics using the dipole-exchange spin wave formalism. [7] We shall also discuss the observability of these characteristic spin-wave modes for different measurements and compare them with Higgs/Goldstone modes occurring in other condensed-matter systems at completely different length/energy scales.[1,8]

[1] D. Pekker and C.M. Varma, Annu. Rev. Condens. Matter Phys. 6, 269 (2015) [2] A. Hubert and R. Schäfer, Magnetic Domains, Springer (1998) [3] K. Ait Oukaci et al., Phys. Rev. Appl. 14, 024083 (2020) [4] N. Vukadinovic et al., Phys. Rev. Lett. 85, 2819 (2000) [5] C. Banerjee et al., Phys. Rev. B 96, 024421 (2017) [6] A. Hubert, Phys. Stat. Sol. 32, 519 (1969) [7] M. Grassi et al., Phys. Rev. Appl. 14, 024047 (2020) [8] Matsumoto M., J. Phys.: Conf. Ser. 592, 012123 (2015)

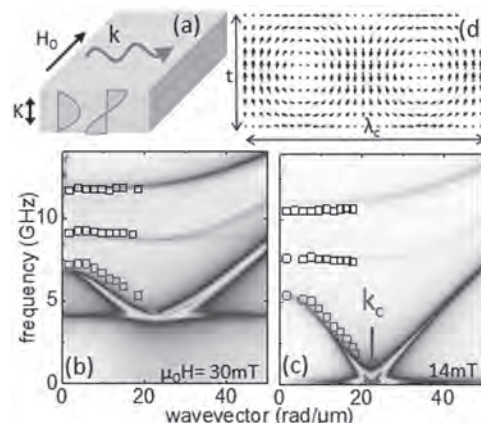


Figure 1: Spin wave dispersions above H_c . (a) Geometry of the system. (b) Color plot: amplitude spectral density simulated for a 180nm thick CoFeB film in the Damon-Eshbach configuration ($k_{\perp}H$) under a saturating in-plane field $\mu_0H=30\text{mT}$. Symbols: measured dispersion. (c) Idem at the critical field $\mu_0H_c=14\text{mT}$. (d) Vector plot of the dynamic magnetization distribution at the softening point $(k_c, 0)$ in panel c]. The first order magnetic anisotropy constant, saturation magnetization and exchange constant are $K=36\text{kJ/m}^3$, $\mu_0M_s=1.67\text{T}$ and $A=16\text{pJ/m}$, respectively.

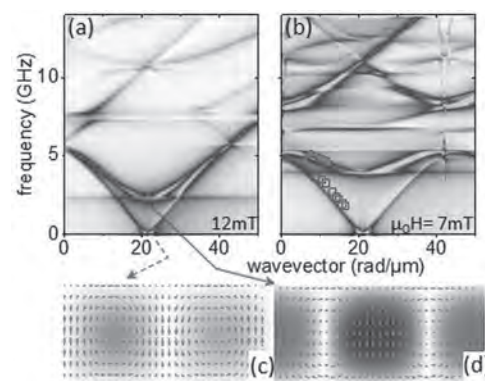


Figure 2: Spin-wave dispersion below H_c . (a) Simulated amplitude spectral density at $\mu_0H=12\text{mT}$. (b) Idem at $\mu_0H=7\text{mT}$. The symbols show the measured dispersions. (c) Color plot of the vertical component of the dynamic magnetization for the Goldstone mode superimposed onto the nucleated weak stripe texture. (g) Same for the Higgs mode.

EB-04. Space-Quasiperiodic and Time-Chaotic Parametric Patterns in a Magnonic Quasicrystal Active Ring Resonator.

S.V. Grishin¹, O.I. Moskalenko¹, A.N. Pavlov¹, D.V. Romanenko¹, A.V. Sadovnikov¹, Y.P. Sharaevskii¹, I.V. Sysoev¹, T.M. Medvedeva², E.P. Seleznev³ and S. Nikitov⁴

1. N. G. Chernysevskogo Saratov National State Research University, Saratov, Russian Federation; 2. Institute of Higher Nervous Activity and Neurophysiology, Moscow, Russian Federation; 3. V. A. Kotelnikova Institute of radiotechnology and electronics of the Russian Academy of Science in Saratov, Saratov, Russian Federation; 4. V. A. Kotelnikova Institute of radiotechnology and electronics of the Russian Academy of Science in Moscow, Moscow, Russian Federation

The spatio-temporal patterns and chaos are the most common natural phenomena that are observed in the open, highly nonequilibrium systems related to the various fields of science. Both phenomena are the traditional objects of the research in synergetics [1]. In dissipative systems with energy inflow from outside and outflow (dissipation), the dissipative solitons are formed due to a balance between gain and loss [2]. The solitons are asymptotically stable states of a dynamical system, while dynamic chaos is a result of the development of Lyapunov instability. In nonlinear magnonics, the chaotic solitons [3,4] and chaotic multisoliton complexes [5,6] were discovered in the time domain. Besides the chaotic temporal patterns, the quasiperiodic solitons were observed in an optical Fibonacci superlattice [7]. It was shown that in such structure, the quasiperiodic spatial solitons were formed through three-wave parametric interaction and had quasiperiodic spatial localization at both a signal wave and a second harmonic frequencies. Both parametric spatial patterns were the conservative solitons and did not have chaotic temporal dynamics. In the paper, we demonstrate a new type of the spatio-temporal parametric patterns that have both chaotic temporal and quasiperiodic spatial localizations at the magnetostatic surface spin wave (MSSW) and parametrically excited spin wave (SW) frequencies. Such dissipative patterns are formed, when a magnonic quasicrystal (MQC) with Fibonacci-type structure is used in a feedback loop of an active ring resonator. We know of only one paper [8] in which SW localization in a MQC consisting of dipolar coupled permalloy nanowires was investigated. But, here SW localization was studied in the linear case. The MQC is a quasiperiodic sequence of crests and grooves that are formed on a surface of an yttrium iron garnet (YIG) film by the etching technique. The MQC is both a multiresonant and nonlinear element. The density of its forbidden bands is much greater than for a magnonic crystal with similar dimensions of the crests and grooves. It leads both to a narrowing of the passbands located between the forbidden bands. The narrower passbands of the MQC make possible to perform frequency selection of the eigenmodes of an active ring resonator, when the MQC is used in its feedback loop. The MQC can support three-wave parametric decay instability of the MSSW that provides a self-generation of the sequences of the relaxation-type pulses. The MQC controls their amplitude and phase profiles through own frequency-selective properties. Thus, the MQC is able to perform simultaneously the frequency selection of the ring eigenmodes and to form the sequences of the parametric pulses with amplitude and phase profiles similar to the ones of the dissipative solitons. In Fig. 1, the scheme of an active ring resonator containing the MQC with Fibonacci-type structure, an amplifier and a variable attenuator is presented. The wideband amplifier operates in 2-4 GHz frequency band. An external microwave (MW) pulse generator forms the external MW pulses that are used both to synchronize the operation of the MQC active ring resonator with an interferometer included in the Brillouin light scattering setup and to realize the time filtration of the self-generated dissipative solitons. The variable attenuator controls a ring gain. Fig.2 demonstrates the spatial and temporal distributions of the light radiation intensity, that are proportional to the square of the magnetization amplitude. These distributions are measured at both the MSSW and SW frequencies. The spatial map of the MSSW magnetization distribution measured at the frequency f_{osc1} (see Fig.5a-i) corresponds to the superposition of the MSSW odd (first and third) width modes propagating in a ferromagnetic waveguide. This spatial distribution has clear maxima localized only in the grooves of the MQC. Besides, as follows from Fig.5b-i, the SW excitation at a frequency $f_{osc1}/2$ is also observed in the region of the existence of the MSSW first and third width

modes. However, in contrast to the MSSWs, the maxima of the SW magnetization amplitude are localized only in the crests of the MQC. As follows from Fig.2, the packets of the MSSW and SW pulses are formed at each spatial point of the crests and grooves. Each packet consists of four pulses, one of which (the first pulse) has the largest amplitude. For the MSSW pulses (see Fig.5a-ii,a-iii), their amplitudes are maximum in grooves and minimum in crests. For the SW pulses (see Fig.5b-ii,b-iii), the situation is exactly the opposite. The amplitudes of the SW pulses are maximum in crests and minimum in grooves. The chaotic nature of the generated dissipative solitons is evidenced by the estimates of the highest Lyapunov exponent from the experimental time series. The work was supported by the Russian Foundation for Basic Research (Project No.19-02-00075).

1. H. Haken, Advanced Synergetics (Springer, Berlin, Heidelberg, 1985).
2. N. Akhmediev and A. Ankiewicz, Dissipative Solitons: From Optics to Biology and Medicine (Springer-Verlag, Berlin, 2008).
3. E.N. Beginin, S.V. Grishin, and Y.P. Sharaevsky, JETP Lett., Vol.88, p.647 (2008).
4. Z. Wang, A. Hagerstrom, J.Q. Anderson, and et al., Phys. Rev. Lett., Vol.107, p.114102 (2011).
5. S.V. Grishin, B.S. Dmitriev, O.I. Moskalenko, and et al., Phys. Rev. E, Vol.98, p.022209 (2018).
6. A.S. Bir, S.V. Grishin, O.I. Moskalenko, and et al., Phys. Rev. Lett., Vol.125, p.083903 (2020).
7. C.B. Clausen, Y.S. Kivshar, O. Bang, and P. L. Christiansen, Phys. Rev. Lett., Vol.83, p.4740 (1999).
8. F. Liseicki, J. Rychly, P. Kuswik, and et al., Phys. Rev. Appl. Vol.11, p.054061 (2019).

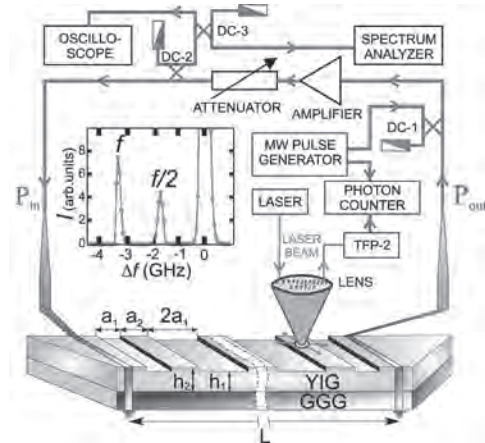


Fig.1 The scheme of a MQC active ring resonator.

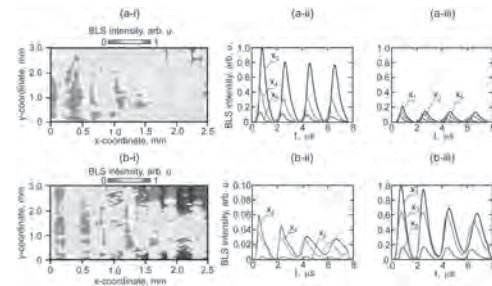


Fig.2 The spatial (a-i), (b-i) and temporal (a-ii), (a-iii), (b-ii), (b-iii) distributions of the square of the magnetization amplitude measured (a) at the MSSW frequency $f_{osc1}=3241.3$ MHz and (b) at the SW frequency $f_{osc1}/2$. In both cases, the temporal distributions are obtained for grooves (a-ii), (b-ii) and crests (a-iii), (b-iii). The symbols x_1-x_6 correspond to six values of the spatial coordinate: $x_1=0.2$ mm, $x_2=0.4$ mm, $x_3=0.65$ mm, $x_4=0.75$ mm, $x_5=1.9$ mm, $x_6=2.15$ mm. Even symbols correspond to the grooves, and odd symbols correspond to the crests.

EB-05. Phase Noise Considerations in Magnon Based Parametric Excitations.

A. Venugopal¹ and R. Victora¹

¹. Department of Electrical Engineering and Computer Science, University of Minnesota, Minneapolis, MN, United States

The significance of phase noise lies in the fact that most if not all devices based on magnons employ the nonlinearity of the magnetic system in order to realize their functionalities. An important entity in such parametrically excited systems is the *phase* of the magnons, which plays a crucial role in governing the nonlinear physics and hence the physical properties of interest of such devices. It is due to this importance of phase that in the recent past, many devices have been proposed and/or demonstrated that directly employ the magnon phase for the realization of important applications. The analytical theory developed is supported using rigorous GPU-based micromagnetic simulations [1]. A 5.1 μm thick sample of yttrium iron garnet (YIG) with saturation magnetization, 145 emu/cm^3 , and exchange constant, 3.77×10^{-7} erg/cm is used. Demagnetization-, exchange-, and thermal-fields are included in addition to the applied-fields. A primary microwave signal of 6 GHz is used at a bias-field of .200 Oe. In our previous study [2], we had provided an accurate theoretical prediction of the increase in the threshold-field when an additional secondary signal is introduced. The secondary signal modifies the phase-relationship between the magnons and the primary microwave signal. While the importance of the phase as a fundamental entity has increased, studies on the implications of the phase-noise are few. This is due primarily to the difficulties in accessing, manipulating, and analyzing the phase accurately. Previous studies of noise mainly consider thermal-noise and often make use of the macrospin approximation. In magnonics, noise studies exist largely only for spin-torque oscillators. In the radio frequency (RF) applications, noise is usually modeled at a circuit level [3], and a microscopic study of phase-noise remains to be done. Ours is a more general treatment of phase-noise implications and, consequently, applicable across all magnon-based nonlinear applications. We have used analytical techniques drawn from hydrodynamics to evaluate the effects of phase-noise. Moreover, the simulations performed are based on state-of-art GPUs, using software optimized to study the magnon based physics specifically. Such simulations would not have been computationally possible in the past. Hence, this is a timely study of an important entity. (1) At first, we introduce a Gaussian phase-noise of zero mean and standard-deviation, σ , to understand its impact on the nonlinearity threshold. For a *temporal-noise*, we find that the threshold-field scales as $e^{(\sigma^{2/2})}$, but the growth rate of the magnons that partly determines the transient-time scales as $e^{-(\sigma^{2/2})}$ (Fig. 1). We have demonstrated these results analytically as well as using micromagnetic simulations. The results are of particular importance for RF devices like Frequency Selective Limiters (FSLs), Signal to Noise-ratio Enhancers, etc., that are often employed in noisy environments and are therefore subjected to temporal phase-noise. As mentioned earlier, few studies of phase-noise at the magnonic scale exists for such conventional RF devices despite the nonlinear behavior being a crucial part of device-functionality. (2) We find that similar changes as above are seen in the threshold-field and the growth-rate when a *spatial* phase-noise of similar mean and standard-deviation is employed. As can be observed from Fig. 2, the simulation data-points are nearly identical to those obtained in the case of temporal noise. For magnonic applications [4], this points to the importance of process variations and microstructural quality during the production of magnetic samples that can give rise to spatial-noise conditions. (3) Compared with phase-noise, we find that frequency-noise leads to only trivial variations in the threshold-field. Frequency noise alters the amplitude of the spin-waves. Therefore, information when encoded into the spin-wave amplitude, is more likely to suffer distortion under frequency noise when compared with phase noise. Apart from lowering the signal to noise ratio, frequency noise increases the magnon frequency deviation. Some of the proposed magnonic logic schemes [5] employ a combination of amplitude-, phase- and frequency- encoding to realize beyond-Neumann architectures where the above considerations would be crucial. Likewise, these results also play an important role in conventional communication systems that employ a combination of modulation techniques. Our studies, thus, allow phase noise considerations to be included in the design and/or operation of nonlinear magnetic devices. These results are important for both

the traditional and novel magnon-based applications since device performance characteristics often strongly depend on the threshold-field as well as the transient-time. This is evident, e.g., in the ongoing efforts to miniaturize nonlinear magnetic rf device -FSL- especially for autonomous automobile applications [6]. Also, our results are independent of the mode of pumping (parallel or perpendicular) and the magnetic-material (applies to insulators, e.g., YIG as well as metals, e.g., NiFe). The results, in general, could be used to understand the nonlinear properties of other parametric systems that involve three-particle processes.

1. A. Venugopal, T. Qu, and R. H. Victora, *IEEE Trans. Microwave Theory Tech.*, vol. 68, no. 2, pp. 602–610 (2020).
2. A. Venugopal, T. Qu, and R. H. Victora, *Appl. Phys. Lett.*, vol. 117, no. 152404 (2020).
3. M. Shukla, M. Y. Koledintseva, M. Geiler, *et al.*, “Adaptive Interference Mitigation Using Frequency-Selective Limiters over GPS Band for Automotive Applications,” 2020 IEEE International Symposium on Electromagnetic Compatibility & Signal/Power Integrity (EMCSI), Reno, NV, USA, pp. 614-618 (2020).
4. A. A. Serga, A. V. Chumak and B. Hillebrands, *J. Phys. D: Appl. Phys.* vol. 43, no. 264002, (2010).
5. A. Khitun, M. Bao and K. L. Wang, *J. Phys. D: Appl. Phys.*, vol. 43, no. 264005 (10pp), (2010).
6. A. O. Boryszenko, S. M. Gillette, M. Y. Koledintseva, *IEEE Trans. Microwave Theory Tech.*, vol. 67, no. 12, pp. 4871-4880 (2019).

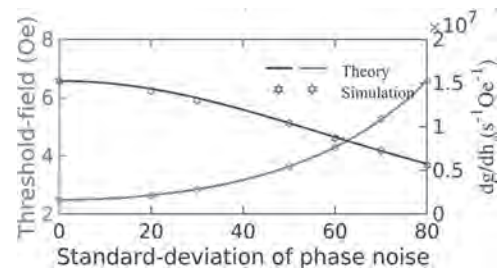


Fig. 1. Comparison of simulated data and theoretical prediction of threshold-fields and the slope of growth rate w.r.t microwave field intensity.

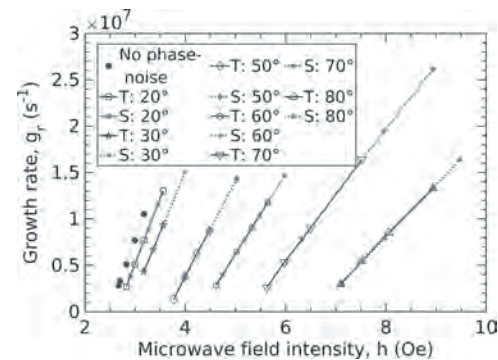


Fig. 2. Growth rate of magnons vs the primary rf field intensity for various phase-noise standard deviations. ‘T’ refers to temporal noise, ‘S’ to spatial noise.

EB-06. Bosonic Bott Index and Disorder-Induced Topological Transitions of Magnons.

X. Wang¹, A. Brataas² and R. Troncoso²

1. Hunan University, Changsha, China; 2. Norwegian Technical and Natural Sciences University, Trondheim, Norway

We investigate the role of disorder on the various topological magnonic phases present in deformed honeycomb ferromagnets. To this end, we introduce a bosonic Bott index to characterize the topology of magnon spectra in finite, disordered systems. The consistency between the Bott index and Chern number is numerically established in the clean limit. We demonstrate that topologically protected magnon edge states are robust to moderate disorder and, as anticipated, localized in the strong regime. We predict a disorder-driven topological phase transition, a magnonic analog of the “topological Anderson insulator” in electronic systems, where the disorder is responsible for the emergence of the nontrivial topology. Combining the results for the Bott index and transport properties, we show that bulk-boundary correspondence holds for disordered topological magnons. Our results open the door for research on topological magnonics as well as other bosonic excitations in finite and disordered systems [1]. We start from a ferromagnetic honeycomb layer [Fig. 1(a), (c)]. The honeycombs can be distorted, controlled by the bond angle θ , as shown in Fig. 1. We consider nearest-neighbor (NN) ferromagnetic exchange energy, NN pseudodipolar interaction [2], and on-site anisotropy energy. For strong enough perpendicular easy-axis anisotropy, the out-of-plane ferromagnetic state is an equilibrium state. We then calculate the spin wave spectra upon this state using the standard methods. Because of the bosonic commutation relation, we result in a non-Hermitian generalized eigenvalue problem $\eta H T = T \eta E$, where H is the Hermitian Hamiltonian, E is the diagonal matrix of eigenvalues, η is a metric due to the bosonic commutation relation, and T is the Bogoljubov transformation matrix diagonalizing the Hamiltonian. We define a bosonic Bott index, which takes the same form as the electronic Bott index [3] but with a modified projector $P = T \eta \Gamma T^\dagger \eta$, where Γ is a matrix selecting certain states. We first consider the clean limit. Figure 1(b) and (d) show spin wave spectra for infinite system, 100-wide zigzag strip, and 40×40 finite flake (from left to right) for normal and squeezed honeycomb lattices, respectively. Gapped bulk spectra in infinite and periodic systems and gapless (crossing) edge states for an open strip can be observed, indicating a nontrivial topology. A topological transition happens at $\theta = \pi/2$. When $\theta > \pi/2$ such as Fig. 1(a) ($\theta = 2\pi/3$), the upper (lower) band has Chern number $+1$ (-1), and the Bott indices for the finite flake give the same values as the Chern numbers. For $\theta < \pi/2$ such as Fig. 1(c) ($\theta = 5\pi/12$), the signs of Chern numbers as well as Bott indices flip. The system can also be tuned to be topologically trivial by staggered anisotropy. The Bott indices are still consistent with Chern numbers during this process. Then we add a non-correlated random anisotropy ranged $[-W, W]$ onto each spin in the normal honeycomb lattice to study the effect of disorder. In this non-periodic system, the k -space Chern number cannot be directly used, and the Bott index becomes powerful. When the system is nontrivial in clean limit (Bott index is 1 for the upper band), for moderate disorder, the Bott index is still one, meaning that the system keeps nontrivial. When the disorder is strong enough, a topological transition occurs and the system becomes topologically trivial [Fig. 2(a)]. This phenomenon is consistent with the common wisdom that the topology is quite robust since very strong disorder is needed to break the topology. A more remarkable phenomenon occurs when the disorder affects a topologically trivial system [Fig. 2(b)]. For a trivial system in clean limit (the band structure of a strip near the gap in the clean limit is shown in the inset), there are no gapless edge states inside the bulk gap. Surprisingly, as the disorder strength increases, the Bott index increases from zero and reaches a plateau of $B=1$ and then drops to zero large disorder. This finding indicates that there exists a disorder-induced topological phase, similar to the topological Anderson insulator phase in electronic systems [4]. We further demonstrate the bulk-boundary correspondence in our topological magnon model by studying the transport properties. We calculate the total transmission of magnons at the mid-gap energy across a disordered sample sandwiched by two clean leads, and compare them with the Bott index results in Fig. 2(a) and (b). The agreement is quite good, demonstrating the fact that when the Bott index is nontrivial, there exists robust edge channel inside the bulk band gap, which is the common

wisdom of bulk-boundary correspondence. The existence of edge states in strongly disordered magnets is further confirmed by the calculation of the real-space wave functions. Eigenstates whose energies are closest to the mid-gap energy for a certain disorder configuration are calculated, and the expectation values $\langle S_x \rangle$, $\langle S_y \rangle$ are plotted in Fig. 2(c) and (d), corresponding to the circled data points in (a) and (b), respectively.

- [1] X. S. Wang, A. Brataas, and R. E. Troncoso, Phys. Rev. Lett. 125, 217202 (2020). [2] G. Jackeli and G. Khaliullin, Phys. Rev. Lett. 102, 017205 (2009). [3] H. Huang and F. Liu, Phys. Rev. Lett. 121, 126401 (2018). [4] J. Li, R.-L. Chu, J. K. Jain, and S.-Q. Shen, Phys. Rev. Lett. 102, 136806 (2009).

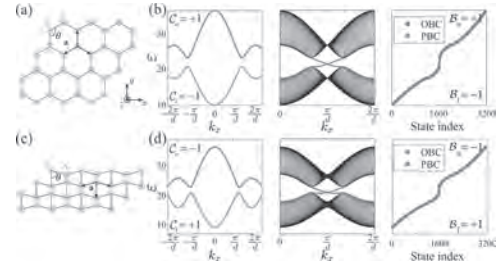


Fig. 1. (a) Schematic of a normal honeycomb magnet. (b) From left to right: the spin-wave spectra for infinite samples, zigzag strips of width 100 along rows, and 40×40 finite samples. (c) Schematic of a squeezed honeycomb magnet of $\theta = 5\pi/12$. (d) Spin-wave spectra for (c).

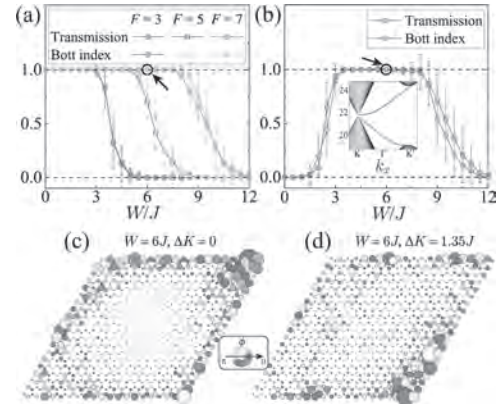


Fig. 2. Comparison between the Bott index and the total transmission for (a) topologically nontrivial and (b) trivial systems. (c) and (d) plot $\langle S_x \rangle$, $\langle S_y \rangle$ of eigenstates. The size of the circles indicates the amplitude, and the color encodes the azimuthal angle.

EB-07. Inelastic Scattering of Spin Wave Beam at the Edge Localized Spin Waves and Second Harmonic Generation of Spin Waves.

P. Gruszecki¹, K. Guslienko^{2,3}, I. Lyubchanskii^{4,5} and M. Krawczyk¹

1. Faculty of Physics, Adam Mickiewicz University in Poznan, Poznan, Poland; 2. Depto. Física de Materiales, Universidad del País Vasco UPV/EHU, San Sebastian, Spain; 3. IKERBASQUE, The Basque Foundation for Science, Bilbao, Spain; 4. Donetsk Institute for Physics and Engineering (branch in Kharkiv) of the National Academy of Sciences of Ukraine, Kharkiv, Ukraine; 5. Faculty of Physics, V. N. Karazin Kharkiv National University, Kharkiv, Ukraine

Spin waves (SWs) are precessional magnetization disturbances propagating in magnetic media in the form of waves at microwave frequencies [1] that are the most commonly used frequencies range for wireless communication. Wavelengths of SWs are several orders of magnitude shorter than the lengths of electromagnetic waves of corresponding frequencies. The dynamics of SWs even in uniformly magnetized films is extraordinarily rich. It is easy to obtain effects difficult to be achieved for other type of waves, such as nonreciprocity, excitation caustic-beam that are characteristic for hyperbolic media, easy external control over propagation (e.g., by inhomogeneous magnetic field) [2]. Non-linear phenomena are also easily available [1,3]. All these make SWs to be a promising candidate for information carriers, especially in the context of beyond-CMOS applications [4]. SWs may be confined to certain areas of the thin film, e.g., in a potential well created by an inhomogeneity of the static demagnetizing field in the vicinity of film's edge. Such localized modes are called edge SWs (E-SWs). Usually, the frequencies of E-SWs are downshifted with respect to bulk-type SWs (B-SWs), i.e., SWs propagating far from the edge where the static effective field is practically homogenous. Here, we theoretically study by means of micromagnetic simulations [5] and analytical modelling the dynamics of the E-SWs localized at the edge of thin permalloy film and their interaction with B-SWs. Firstly, we focus on the utilization of the E-SWs to excite short B-SWs propagating in the form of plane waves. Secondly, we study the inelastic non-linear scattering of B-SW beam by the E-SWs. We consider propagation of the E-SW along the edge of 10 nm thick permalloy film that is uniformly magnetized by the external field of value 300 mT directed perpendicularly to the film's edge (see Fig. 1a, where the system is presented along with exemplary result of a simulation). The E-SW is excited by the point-source-like microwave field of frequency 12 GHz located at the film's edge. There are visible two prominent peaks in the simulated spectrum (Fig. 1b). The first one corresponds to the frequency of the microwave field (12 GHz) and propagation of the E-SWs, whereas the second peak has doubled frequency (24 GHz) and corresponds to the B-SWs propagating obliquely outwards the edge in the form of plane waves. It indicates excitation of the B-SWs by the propagating E-SWs in the process of second harmonic generation. Noteworthy, the wavelength of the B-SWs is over twice shorter than the wavelength of the E-SWs shown in Fig. 1a. The B-SW of wavelength equal to 78 nm is excited by the 285 nm long E-SW. For the same sample, we analytically and numerically analyze the interaction of an obliquely incident B-SW beam (at frequency f) with an E-SWs at frequency n . We find that due to the inelastic scattering the secondary B-SW beams with up- and down-shifted frequency ($f-n$, $f+n$) can be excited. In Fig. 2 an exemplary result of simulation for a B-SW beam incident at the films edge where E-SW propagates and the resulting secondary scattered beam with frequency $(f+v)=42$ GHz are shown. Moreover, we observe angular shifts between the primary incident and the scattered beams with shifted frequencies and analyze the efficiency of the scattering process. Finally, we present an application of this effect for SW demultiplexing. *Acknowledgments.* The research was supported by the National Science Centre of Poland, project no. 2019/35/D/ST3/03729 (P.G. and M.K.); COST action under project CA17123 MAGNETOFON (I.L.); the Spanish MCIU grant PID2019-108075RB-C3-3 (K.G.). K.G. acknowledges support by IKERBASQUE (the Basque Foundation for Science). The simulations were performed at the Poznan Supercomputing and Networking Center (Grant No. 398).

[1] A. Gurevich and G. Melkov, *Magnetization oscillations and waves* (CRC Press, Boca Raton, 1996). [2] A. Barman et al., *J. Appl. Phys.* 128, 170901 (2020). [3] A. V. Chumak et al., *Nat. Phys.* 11, 453 (2015). [4] B.

Murmann, B. Hoefflinger, "IRDS—International Roadmap for Devices and Systems, Rebooting Computing, S3S" in *NANO-CHIPS 2030* (Springer, Cham, 2020). [5] A. Vansteenkiste et al., *AIP Advances* 4, 107133 (2014).

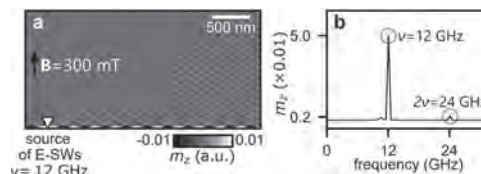


Fig. 1. (a) System under consideration with the snapshot of the out-of-plane magnetization component (m_z) in the steady state with E-SW excitation at 12 GHz. The source of E-SWs is located in the area indicated by the white triangle. (b) Simulated SW frequency spectrum.



Fig. 2. Scheme of the system under investigation with the result of micromagnetic simulation performed for B-SW beam at frequency $f = 30$ GHz incident under the angle 60° and scattered on an E-SW at $v = 12$ GHz. Red (at the edge), yellow and blue (beams) corresponds to presence of the SWs of frequencies v , f , and $f+v$, respectively. The white color denotes areas, where at least two frequencies are mixed.

EB-08. Evolution of Room-Temperature Magnon gas Toward Coherent Bose-Einstein Condensate.

T.B. Noack¹, V.I. Vasyuchka¹, A. Pomyalov², V.S. L'vov², A.A. Serga¹ and B. Hillebrands¹

1. *Fachbereich Physik and Landesforschungszentrum OPTIMAS, Technische Universität Kaiserslautern, Kaiserslautern, Germany;*

2. *Department of Chemical and Biological Physics, Weizmann Institute of Science, Rehovot, Israel*

Nowadays a lot of effort is put into the creation of a practical quantum computer. For this ambitious aim different research fields propose and investigate new materials and technologies. One of such promising systems, a magnon Bose-Einstein condensate (BEC) in magnetic crystals, may allow the creation of magnon-BEC-based qubit at room temperature. A prerequisite for such a qubit is the appearance of spontaneous coherence in magnon BEC. Also, the presence of coherence of the magnon Bose-Einstein condensate is essential for understanding such fundamental properties of it as the possibility of a dissipative magnon supercurrent [1], excitation of Josephson oscillations [2], and propagation of Bogoliubov waves [3]. In most of the previous studies in this field, the magnon BEC is investigated by means of Brillouin light scattering (BLS) spectroscopy [4,5] delivering information about the spectral density of a magnon gas. Unfortunately, due to the limited frequency resolution of the optical Fabry-Pérot interferometers used in BLS facilities, the conventional BLS technique does not allow one to prove the coherence of a magnon BEC directly. The insufficient frequency resolution makes it impossible to separate the relaxation dynamics of condensed and thermal magnons. Moreover, the possible outflow of the condensate from a spatially localized probing light spot complicates the interpretation of the obtained experimental results (see [6] and the corresponding discussion in [7]). For all these reasons only indirect indications of the coherency, obtained on the magnon BEC in magnetic crystals, could be provided yet. Up to this day, a decisive proof of the full coherence magnon BEC remained elusive. In our work, we report a first direct experimental observation of the evolution of magnon BEC towards full coherence, whose degree is limited only by the natural processes of the magnon relaxation into the crystal lattice. To achieve this, we use a novel concept that enhances the coupling of the parametrically-driven magnon system with the probing electromagnetic field. The obtained electric signal was investigated time-resolved by a spectrum analyzer to reach the required frequency resolution necessary for the proper display of the magnon BEC state. A pulsed electromagnetic parametric pumping was used to inject magnons, increase, thus the chemical potential of the magnon gas, and trigger the BEC formation process. It is found that the radiation spectrum picked up after the termination of a pump pulse is narrowed by two orders of magnitude, compared to the broad-band spectrum obtained during the process of parametric pumping. The resulting spectrum width is only limited by the magnon relaxation frequency. We study this spectrum evolution in many details and identify the conditions for BEC creation. We believe that this direct demonstration of the coherence of the magnon BEC brings the implementation of the room temperature BEC-based computing closer. This research was funded by the European Research Council within the Advanced Grant No. 694709 "Super-Magnonics" and by the Deutsche Forschungsgemeinschaft (DFG, German Research Foundation) within the Transregional Collaborative Research Center – TRR 173 – 268565370 "Spin+X" (project B01). The authors are grateful to G. A. Melkov and H. Yu. Musiienko-Shmarova for the fruitful discussions.

[1] D. A. Bozhko, A. A. Serga, P. Clausen, V. I. Vasyuchka, F. Heussner, G. A. Melkov, A. Pomyalov, V. S. L'vov, and B. Hillebrands, Supercurrent in a room-temperature Bose-Einstein magnon condensate, *Nat. Phys.* 12, 1027 (2016). [2] A. J. E. Kreil, A. Pomyalov, V. S. L'vov, H. Yu. Musiienko-Shmarova, G. A. Melkov, A. A. Serga, and B. Hillebrands, Josephson oscillations in a room-temperature Bose-Einstein magnon condensate, arXiv:1911.07802. [3] D. A. Bozhko, A. J. E. Kreil, H. Yu. Musiienko-Shmarova, A. A. Serga, A. Pomyalov, V. S. L'vov, and B. Hillebrands, Bogoliubov waves and distant transport of magnon condensate at room temperature, *Nat. Commun.* 10, 2460 (2019). [4] S. O. Demokritov, V. E. Demidov, O. Dzyapko, G. A. Melkov, A. A. Serga, B. Hillebrands, and

A. N. Slavin, Bose-Einstein condensation of quasi-equilibrium magnons at room temperature under pumping, *Nature* 443, 430–433 (2006). [5] A. A. Serga, V. S. Tiberkevich, C. W. Sandweg, V. I. Vasyuchka, D. A. Bozhko, A. V. Chumak, T. Neumann, B. Obry, G. A. Melkov, A. N. Slavin, and B. Hillebrands, Bose-Einstein condensation in an ultra-hot gas of pumped magnons, *Nat. Commun.* 5, 3452 (2014). [6] V. E. Demidov, O. Dzyapko, S. O. Demokritov, G. A. Melkov, and A. N. Slavin, Observation of spontaneous coherence in Bose-Einstein condensate of magnons, *Phys. Rev. Lett.* 100, 047205 (2008). [7] A. J. E. Kreil, H. Y. Musiienko-Shmarova, S. Eggert, A. A. Serga, B. Hillebrands, D. A. Bozhko, A. Pomyalov, and V. S. L'vov, Tunable space-time crystal in room-temperature magnetodielectrics, *Phys. Rev. B* 100, 020406(R) (2019).

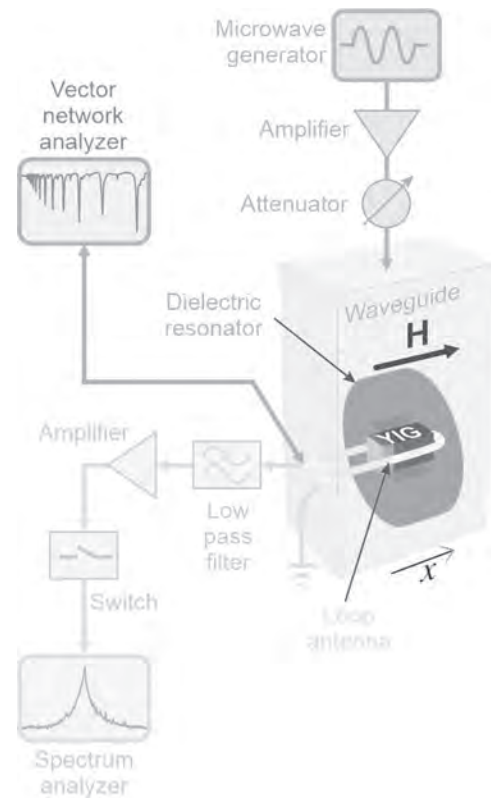


Fig. 1 Sketch of the experimental setup. The sample holder section shows an open waveguide with an internally mounted dielectric resonator. A bulk YIG sample is placed in an opening of the resonator together with a large detection loop to detect the radiated signals from the whole sample volume.

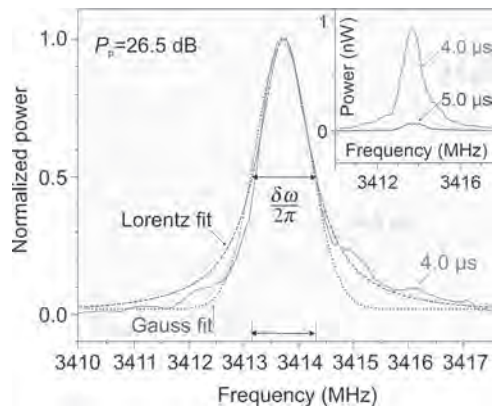


Fig. 2 Radiated signal of the magnon BEC measured for different times during the free decay of the system. The signals demonstrate a lorentz shape with a FWHM bandwidth of approx. 1 MHz. In normalized view it is visible that the BEC signal demonstrates an unchanged singel-state profile for a long observation period.

EB-09. Investigation of Caustic Spin Wave Beams in Soft Thin Films.

A. Wartelle¹, T. Taniguchi¹ and C.H. Back¹

1. Technische Universität München, München, Germany

In thin-films-based experiments, spin waves (SWs) are often investigated in confined geometries or as plane waves in full films. There are exceptions, such as SW channeling along domain walls [1], which are appealing in terms of SW steering. However, this approach relies on the preparation of a specific magnetic texture and transferring the SW out of it, back into the domains, seems challenging. An alternative route towards the steering of strong, channeled SWs exists, namely caustic SW beams (CSWBs). Caustic phenomena in anisotropic wave propagation correspond to sharply-defined lines/surfaces with large intensities [2]. They have been investigated in a variety of fields [2], and can be expected in micromagnetism. In thin films, caustics can arise due to the marked anisotropy of the SW dispersion relation (DR), illustrated in Fig.1. From such a plot, the direction θ_v of the group velocity $v_g = \nabla_k \omega$ can be determined from the local normal to the curve. It can be seen in Fig.1 that a portion of the red curve (at 8.5 GHz) is almost straight, leading to a stationary θ_v around a value θ_{vc} for this range of wavefront angles ϕ . Thus, an excitation of SWs with a broad wave vector spectrum would lead to strong emission in the direction θ_{vc} . The corresponding anisotropic enhancement defines a CSWB. Such beams have so far been studied notably upon scattering of a confined SW into a wide film [4,5,6]. In the present work, we tackle theoretically the emission of CSWBs in full, soft thin films; the latter could be stimulated by the tip of a microstrip antenna. We restrict ourselves to applied fields below ferromagnetic resonance (FMR). After dimensionless rewriting of the DR, only three free parameters are left: the ratio of dipolar-exchange length to film thickness $\eta = l_{ex}/d$, the normalized SW frequency $v = \omega/(\gamma^* J_s)$ (J_s : saturation induction), and the reduced applied field $h = B_a/J_s$. We then investigate the properties of caustic points numerically and analytically, using suitable approximations. An experimental situation corresponds to fixed film thickness; we therefore record the caustic wavenumbers (WNS) $k_c^* d$, beam directions θ_{vc} and wavefront directions ϕ_c as a function of v and h , at fixed η . As the example in Fig.2 shows, caustic points can exhibit a rich behaviour. Starting with the caustic WNS, one can see a low-frequency, low-field pocket in the dipolar-dominated regime. Above its sharp boundary, a relatively wide band appears, corresponding to $k_c^* d$ varying slowly in the dipolar-exchange regime. A final transition brings $k_c^* d$ into the exchange-dominated regime; the latter has an upper boundary above which no caustic point exists (blue region in Fig.2). The map of $\phi_c(h, v)$ displays a similar aspect. In the bottom pocket, the caustic wavefront angle is almost constant, with a numerically found limit of about 54.7° . Our analytical approximation yields a value of $\arccos(1/\sqrt{3}) \approx 54.7^\circ$, in excellent agreement. The corresponding limit for θ_{vc} is numerically 109° and 103° from analytics. In the dipolar-exchange band, by contrast with $k_c^* d$, ϕ_c varies significantly and saturates at 90° in the exchange-dominated region. This saturation is in stark correlation to that of the caustic beam direction θ_{vc} , which also goes to 90° . All the above properties can be understood from the geometrical evolution of the DR curve when v increases, as illustrated in Fig.1. The markers on the curves correspond to their caustic point (2.5 GHz omitted for clarity). At the bottom pocket's boundary, the tangent to the DR at $k_c^* d$ passes close to the origin: hence, $\partial k_c / \partial \phi_c$ is large. In the exchange-dominated regime, the curve flattens near $\phi = \pi/2$. This accelerates the increase of $k_c^* d$ (cf. curves at 16 and 18.5 GHz) while bringing θ_{vc} and ϕ_c to $\pi/2$ at a certain threshold frequency. Beyond the latter, the curve rounds more and more: θ_v can no longer be stationary, thus, no caustic point exist. From this investigation, we can thus predict two very different types of CSWBs. At the low- k_c pocket's upper boundary, due to the very straight and oblique DR curve, the CSWB should feature a broad wavelength spectrum. By contrast, at the upper boundary of the caustic band, the CSWB's wavelength spectrum should be much narrower. Indeed, the DR at $k_c^* d$ is tangent to a circle $k^* d = \text{const}$. In addition, since this CSWB consists of two beams with overlapping directions, its amplitude should be correspondingly larger. This phenomenon has been studied theoretically by Kim et al. [7]. The first type of CSWB should be invisible in magneto-optical microscopy, but Brillouin light scattering should reveal the broadband SW beam. The second type of CSWB would require time-resolved Scanning Transmission X-ray Microscopy due to the higher k_c .

[1] V. Sluka, T. Schneider, R. A. Gallardo *et al.*, Nature Nanotechnology, Vol.14, 4, pp.328-333 (2019) [2] Y. A. Kravtsov and Y. I. Orlov, "Caustic, Catastrophes and Wave Fields", Springer-Verlag 1993 [3] B. A. Kalinikos and A. N. Slavin, Journal of Physics C: Solid State Physics, Vol.19, 7013, pp.7013-7033 (1986) [4] V. E. Demidov, S. O. Demokritov, D. Birt *et al.*, Physical Review B, Vol.80, 014429 (2009) [5] T. Schneider, A. A. Serga, A. V. Chumak *et al.*, Physical Review Letters, Vol.104, 197203 (2010) [6] F. Heussner, A. A. Serga, T. Brächer *et al.*, Applied Physics Letters, Vol.111, 122401 (2017) [7] J.-V. Kim, R. L. Stamps and R. E. Camley, Physical Review Letters, Vol.117, 197204 (2016)

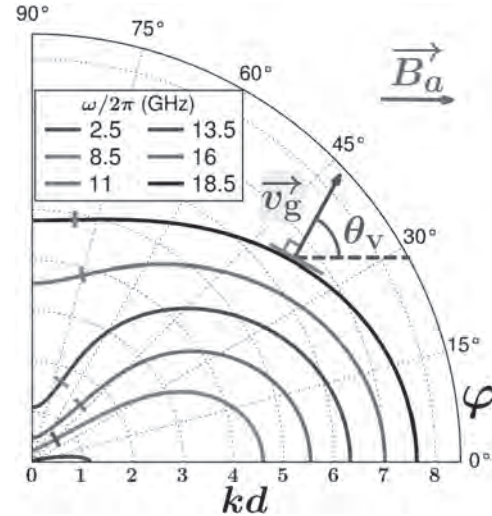


Fig.1: Polar plot of the normalized SW wave number $k^* d$ (d : film thickness) as a function of the angle ϕ from the applied field to the wave vector. The DRs are calculated from the model by Kalinikos and Slavin [3], for an applied induction B_a of 20 mT, frequencies $\omega/(2\pi)$ of 2.5, 8.5, 11, 13.5, 16 and 18.5 GHz, a reduced gyromagnetic ratio $\gamma/(2\pi) = 29.3$ GHz/T, saturation induction $J_s = \mu_0 \cdot M_s = 0.92$ T, film thickness 60 nm and dipolar-exchange length $l_{ex} = 6.2$ nm. Owing to the DR's symmetries, the curves shown here generates the whole polar plots by line symmetry around the quadrant boundaries.

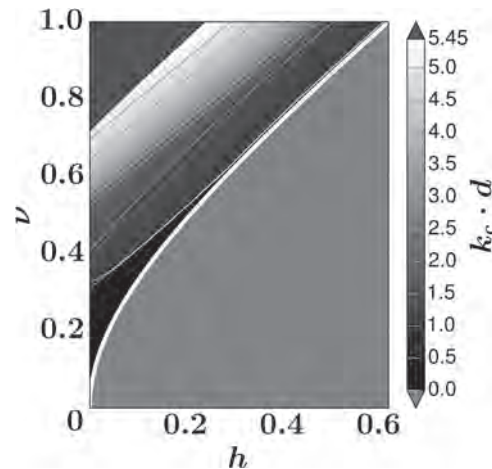


Fig.2: Gray-level map of the normalized caustic wave number $k_c^* d$ as a function of h and v , for $\eta = 0.10355$. The yellow curve corresponds to FMR; the red filled region below is not considered here. In the top left corner's blue filled region, no caustic points exist.

EB-10. A Model for Description of Linear Properties and Stability of Bose-Einstein Condensate of Magnons at Room Temperature.

P. Artemchuk¹, V. Tyberkevych¹ and A.N. Slavin¹

¹. Department of Physics, Oakland University, Rochester, MI, United States

Bose-Einstein condensate is a collective phenomenon which takes place when many bosons – particles having integer value of spin – experience transition to the same single quantum state. The famous example is formation of Cooper pairs of electrons, responsible for the superconducting properties of some materials at extremely low temperatures. Magnons – quasi-particles corresponding to spin waves propagating in magnetic media – are bosons as well. Hence, if we describe oscillation of magnetization as a set of magnons, the phenomenon like Bose-Einstein condensation should also exist in this case. Indeed, the Bose-Einstein condensation of magnons at room temperature has been observed under parametric pumping in thick ferrite films [1], and, recently, by rapid cooling in ultra- thin films [2]. The stability of Bose-Einstein condensate of magnons (mBEC) is determined by the nonlinear interaction between magnons. This includes both interaction between magnons in the same spectral minimum (self-interaction), and the interaction between magnons belonging to two different spectral minima (cross-interaction). mBEC can be stable if the coefficient of nonlinear interaction is positive, i.e. if the interaction is repulsive [3]. It is well known that the self-interaction between magnons in relatively thick films is attractive [3]. However, mBEC has been experimentally proven to be stable [1, 2, 4]. It was shown in [5] that coefficient of nonlinear interaction in mBEC is negative, but rather small, so relatively strong repulsive interaction between magnons in different spectral minima may provide stability to mBEC. Recently, it has been also shown [6] that it is possible to separate mBEC in two parts, each containing magnons from *only one spectral minimum*, which means that mBEC in each of the minima is stable, and this stability is independent of the strong cross-interaction of magnons from different minima. Thus, the theory developed in [5] cannot be used to explain stability of separated mBEC. Also, the theory [5] assumes a uniform profile of a magnon mode across the film thickness, and infinite in-plane sizes of the magnetic film sample. Both these simplifications are, generally, incorrect. Due to the long-range nature of the dipolar interaction, finite-size effects may have a significant impact on the nonlinear interactions of magnons [4]. Here, we present a simple, but rather accurate model of the nonlinear interactions in mBEC that takes into account the finite-size effects. Using Landau-Lifshits equation and vector Hamiltonian approach [7], we derived approximate analytical expressions for the linear dispersion characteristics and nonlinear interaction coefficients of magnons near the minima of the magnon spectrum (i.e. in the mBEC region). We showed that magnons undergoing mBEC can be described as a gas of weakly-interacting bosonic particles in an infinite potential well formed by a ferromagnetic film. The rest energy of the magnons in mBEC is determined by the dipolar interaction inside a film sample. This leads to a strong anisotropy of the effective mass of magnons in the magnetic film. In the direction along the applied in-plane magnetic field, the effective mass is $m_{\parallel} = \hbar M_s / (32\pi\gamma A)$ (where M_s is the saturation magnetization, \hbar is the Planck constant, γ is the gyromagnetic ratio, and A is the exchange stiffness). For yttrium-iron garnet (YIG), this “longitudinal” mass is $m_{\parallel} \approx 1.5 \times 10^{-30} \text{ kg} \approx 1.6 m_e$ (m_e is the electron mass). In the directions perpendicular to the applied field magnons are described by the “perpendicular” mass $m_{\perp} = (18\lambda/d)m_{\parallel}$, which depends on the ratio of the exchange length $\lambda = (2A/\mu_0 M_s^2)^{1/2}$ to the thickness of the film d . For typical experimental conditions $m_{\perp} \ll m_{\parallel}$; for example, $m_{\perp} \approx 0.06 m_{\parallel}$ in a YIG film of the thickness $d = 5 \mu\text{m}$. The huge anisotropy of the effective mass leads to the anisotropy of the dynamical mBEC properties. In particular, the speed of the Bogolyubov waves [8] depends strongly on the direction of the wave propagation. Since the perpendicular mass m_{\perp} depends on the thickness of the film, it is possible to achieve the inverse mass relation $m_{\perp} > m_{\parallel}$ in ultra-thin YIG films with $d < 300 \text{ nm}$. Under the assumption of totally pinned spins, which is an accurate approximation in the mBEC region, we derived approximate analytical expressions for the nonlinear frequency shift due to the self- and cross- interactions in mBEC: $\Delta f = (F_{\text{self}} + 2F_{\text{cross}})n$; $F_{\text{self}} = F_0 (2N_d - 3\pi\lambda/d\sqrt{2})$; $F_{\text{cross}} = F_0$. Here $F_0 = \gamma^2 \mu_0 \hbar / 4\pi^2$ is the normalisation constant, n is the magnon density, N_d is the component of the demagnetization

tensor $N = \text{diag}(N_x, N_y, N_z)$ corresponding to the direction along the applied in-plane magnetic field. These expressions show that the nonlinear cross-interaction stays large and positive independently of the confinement of the sample in the applied field direction, while the self-interaction coefficient changes its sign when N_d become greater than the critical value N_{cr} : $N_{\text{cr}} = (3\pi/2\sqrt{2})(\lambda/d)$. The result explains possibility to separate mBEC into two stable components corresponding to the different minima of the mBEC spectrum [4, 6]. The developed model allows one to make simple and accurate predictions about the stability of the mBEC depending on the shape of the sample used, and to describe dynamics of fluctuations and waves of magnon density in the mBEC. Also, it makes possible to directly apply theoretical methods developed to describe condensates of atoms to study the mBEC dynamics, and, therefore, it might be very useful in further investigations of coherent magnonic phenomena.

[1] S. O. Demokritov, V. E. Demidov, O. Dzyapko et al., *Nature*, vol. 443, pp. 430-433, 2006. [2] M. Schneider, T. Brächer, D. Breitbach et al., *Nat. Nanotechnol.*, vol. 15, pp. 457–461, 2020. [3] V. S. L’vov, *Wave turbulence under parametric excitation*, Springer Series in Nonlinear Dynamics (Springer, Berlin, 1994). [4] I. V. Borisenko, B. Divinskiy, V. E. Demidov et al., *Nat. Commun.*, vol. 11, no. 1691, 2020. [5] O. Dzyapko, I. Lisenkov, P. Nowik-Boltyk et al., *Phys. Rev. B*, vol. 96, no. 064438, 2017. [6] I. V. Borisenko, V. E. Demidov, V. L. Pokrovsky et al., *Sci. Rep.*, vol. 10, no. 14881, 2020. [7] V. Tyberkevych, A. Slavin, P. Artemchuk, et al., arXiv:2011.13562 (2020). [8] D. A. Bozhko, A. J. E. Kreil, H. Yu. Musiienko-Shmarova et al., *Nat. Commun.*, vol 10, no. 2460, 2019.

EB-11. Effect of the Local Exchange Invariance on the Magnetization Dynamics in a Ferromagnet.

P. Ansalone¹, S. Perna², C. Serpico², M. d'Aquino², V. Scalera² and V. Basso¹

1. Istituto Nazionale di Ricerca Metrologica, Torino, Italy; 2. Università degli Studi di Napoli Federico II, Napoli, Italy

The magnetism in curved geometries is attracting attention because of several theoretical predictions with possible potential applications, such as a curvature induced effective *Dzyaloshinskii-Moriya* like interaction [1]. Within this setting, analogously to a geometric curvature, a curvature induced by a gauge field [2] is a fruitful aspect to consider in the interaction of the magnetization with an applied static electric field. In a quantum description of the motion of a magnetic moment, an electric field does not modify the energy but it rather modifies the linear momentum, therefore introducing an additional phase for the corresponding *Schrödinger* wave function, an effect which is known as the *Aharonov-Casher's* effect [3]. The classical analog is the spin wave of a ferromagnet. It has been shown that a spin wave, which is carrying a magnetic moment, will acquire a phase when the system is subjected to an electric field [4]. This effect, even if rather small, can be experimentally observed [5]. It is therefore of interest to extend this idea to a general micromagnetic description of the problem. The aim of this research is to pose the problem of the micromagnetics under the effect of an electric field by using the so-called gauge invariance. Briefly the spin-waves, which are small oscillations, deviate from the uniform magnetization with respect to a local reference frame and around the e_z direction. They interact with an applied electric field E Fig.(1) modifying the spin wave dispersion relation. Therefore, according to the so-called local exchange invariance [6], we propose a phase shift model, in the exchange spin waves regime, in order to possibly describe and interpret the data shown in [5]. More in details the local gauge symmetry is approximately a local invariance property (because of its thermodynamic origin), of the lagrangian density of the magnetization $m(x, t)$ of a ferromagnet. It is known that it is invariant with respect to the $SO(3)$ global symmetry [7]. In our case this symmetry reduces to a unitary representation of the $SO(2)$ group, (*i.e.*, $U(1)$). Due to the reason that this symmetry has to be local (*i.e.*, to be position dependent) the invariance of the lagrangian density is broken unless introducing a gauge field able to solve the technical problem of the parallel transport of the magnetization vector. Therefore we show that a particular orientation of a reference frame has no physical relevance. In fact, gauge invariance should occur whenever one can define non-collinear, local reference frames. In our model, the orientation of the local non-coordinate reference frames cannot be uniquely defined because of the presence of an electric field. Summarizing in our invariant gauge formulation the reference frames' orientation is unspecified with respect to a local phase which defines an invariance property of the exchange interaction terms in the lagrangian density of the magnetization $m(x, t)$. The Lagrangian density of a ferromagnet, interacting with an electric field, is transformed into a new Lagrangian density upon a formal redefinition of the standard partial derivative. Moreover the transformation group, which expresses this invariance, imposes definite restrictions on the dispersion relation that at the first order in a *Taylor* expansion was previously found to be $\omega = \omega(k_y) - \gamma_L c^2 \partial \omega / \partial k_y E_x$ [4], with γ_L the gyromagnetic ratio and c the speed of light. Therefore our findings point to a more advanced theoretical interpretation with respect to previous discoveries [4] in order to drive experiments in manipulating spin waves and developing electrically tunable magnonic devices.

[1] R. Streubel et al., J. Phys. D: Appl. Phys. 49, 363001 (2016). [2] S.G. Tan, et al., Physics Reports, Volume 882, Pages 1-36, (2020). [3] Y. Aharonov and A. Casher, Phys. Rev. Lett. 53, 319, (1984). [4] V. Basso and P. Ansalone, EPL, Vol. 130, Number 1, Article 17008, (2020). [5] X. Zhang, T.Liu, M.E. Flatté and H.X. Tang Phys. Rev. Lett. 113, (2014). [6] I.E. Dzyaloshinskii and G.E.Volovik, J.Physique, 39, 693, (1978). [7] W. F. Brown, Magnetoelastic interactions, pp. 26 and 79, (Vol. 9), Berlin: Springer, (1966).

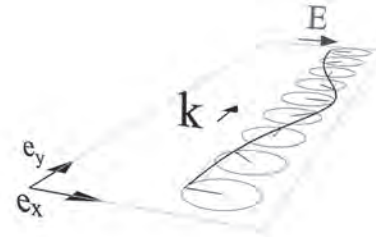


Fig. 1 The system under study is a two dimensional infinite ferromagnetic layer with primary magnetization along the direction e_z , an external electric field is applied perpendicularly to both the magnetization and k spin-wave vector.

EB-12. Stationary State of Bose-Einstein Condensate of Magnons: Theory and Experiment.

G. Li¹, H. Jia¹ and V. Pokrovsky¹

1. Department of Physics and Astronomy, Texas A&M University System, College Station, TX, United States

Two recent reports of the Münster University experimental team led by S.O. Demokritov [Borisenko et al., Nat. Comm. 2020, Borisenko et al., Sci. Rep. 10, 14881 (2020)] displayed several important facts contradicting to the existing theories of the Bose-Einstein condensate of magnons (BECM) [Tupitsyn et al. 2008, Rezende 2009, F. Li et al. 2013]. We present simplified theoretical arguments to determine what are properties of the uniform stationary BECM established under the action of permanent parametric pumping that follows from the experimental facts. We point out that the complete equilibrium was not established in the magnon system because the inter-condensates relaxation time is much longer than the lifetime of condensate magnons. Since the magnons repulse each other, the uniform stationary state of the condensate does not collapse. If the inter-condensates relaxation processes are negligible, then the stationary state of the condensate must be symmetric since the processes of parametric pumping and those responsible for finite magnons lifetime are identical for the two condensates. The weak inter-condensates relaxation processes lead to a weak spontaneous violation of the use of reflection symmetry. This prediction agrees with the inter-condensate interference structure of the condensate discovered by Novik-Boltyk et al. [Novik- Boltyk 2012]

Borisenko, I., Divinskiy, B., Demidov, V. *et al.* Direct evidence of spatial stability of Bose-Einstein condensate of magnons. *Nat Commun* 11, 1691 (2020). Borisenko, I.V., Demidov, V.E., Pokrovsky, V.L. *et al.* Spatial separation of degenerate components of magnon Bose-Einstein condensate by using a local acceleration potential. *Sci Rep* 10, 14881 (2020) Tupitsyn, I. S., Stamp, P. C. E. & Burin, A. L. Stability of Bose-Einstein condensates of hot magnons in yttrium iron garnet films. *Phys. Rev. Lett.* 100, 257202 (2008). Rezende, S. M. Theory of coherence in Bose-Einstein condensation phenomena in a microwave-driven interacting magnon gas. *Phys. Rev. B* 79, 174411 (2009) Li, F., Saslow, W. M. & Pokrovsky, V. L. Phase diagram for magnon condensate in yttrium iron garnet film. *Sci. Rep.* 3, 1372 (2013) Nowik-Boltyk, P., Dzyapko, O., Demidov, V. E., Berloff, N. G. & Demokritov, S. O. Spatially non-uniform ground state and quantized vortices in a two-component Bose-Einstein condensate of magnons. *Sci. Rep.* 2, 482 (2012)

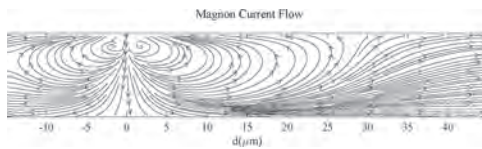
EB-13. Novel Transport Properties of Viscous-Fluid Type Magnon in Magnetic Thin Film.

Y. Li¹, Y. Wang¹ and J. Zhang¹

1. School of Physics, Tongji University, Shanghai, China

Due to low transport dissipation property, magnon was considered as a candidate of next-generation carrier of spintronic industry. In 2016, the van Wees group[1] found an interesting difference between electrically and thermally excited magnons on the nonlocal transport in a very short range. Unlike electrically excited magnons, thermally excited magnons showed a sign-reversal in less than about 300 nm distance between heat injector and magnons detector. Some people developed a bulk SSE theory to explain this phenomenon. According to this theory, a heat flow J_q in YIG will excite a thermal magnon flow $J_{m,q}$ along with it, A diffusive magnon flow is induced to balance the thermal magnon flow, until the system reaches a steady-state. The sign-reversal derived from a competition of these two magnon flow. While in our point of view, this theory may not reach the nature of transmission properties of thermally excited magnons. To clarify the physical essence and gain complete information in the reciprocal space of this process, we adapted mesoscopic Boltzmann method to study magnon transports[2]. In the method, like phonon, we introduced a special scattering process named “Normal Scattering”, which prevents magnons’ momenta during scattering process. When normal scattering is dominant, magnons turned to a uniform velocity. This uniform velocity makes magnons flux acting as a viscous fluid. Based on Boltzmann method, we developed a new diffusion method of magnons viscous fluid to simplify the calculation and found its nonlinear property. Two-dimensional figures of magnon flux showed the viscosity of magnon fluid created two eddies near the heat source. And the numerical result could fit Experimental data precisely. Our results show magnon flow may be controlled like a viscous fluid by applied magnetic field, which has promising applications in nanoscale magnon-based spintronic devices.

1, J. Shan, L. Cornelissen, N. Vlietstra, J. Youssef, T. Kuschel, R. Duine, and B. van Wees, Phys. Rev. B 94, 174437 (2016) 2, T. Liu, W. Wang & J. Zhang, Phys. Rev. B, 99, 214407 (2019).



EB-14. Oscillating Behavior of Inverse Faraday Effect in YFeO₃.A.A. Voronov^{1,2}, D. Ignatyeva^{1,3}, A. Zvezdin^{2,4} and V.I. Belotelov^{1,2}

1. Faculty of Physics, Lomonosov Moscow State University, Moscow, Russian Federation; 2. Russian Quantum Center, Moscow, Russian Federation; 3. Physics and Technology Institute, V.I. Vernadsky Crimean Federal University, Simferopol, Russian Federation; 4. Prokhorov General Physics Institute of the Russian Academy of Sciences, Moscow, Russian Federation

Studying spin system dynamics concerns different rapidly growing fields of technology such as developing new types of information transfer systems [1], quantum computing [2, 3], new approaches for magnetic recording and reading [4]. The most common way to excite spin oscillations is by using the inverse Faraday effect (IFE). It is based on a Raman-like coherent optical scattering process and does not require absorption of light. This gives us two main advantages of this effect: it is instantaneous and non-thermal [5]. IFE results in magnetization induced by high-power laser radiation according to the following formula: $M_{in} = \chi/16\pi [E \times E^*]$, (1) where χ is magneto-optical susceptibility, E is the electric field of the incident light, and E^* is its complex conjugate. The cross product in formula (1) is zero for linearly polarized incident light and is maximum for circularly polarized light. The excitation of high order spin waves requires the nonuniform distribution of the electromagnetic field in the medium. It is commonly achieved by using the nanostructured materials in which the resonant phenomena can occur breaking the uniformity of the field. For example, in work [6] the all-dielectric 1D grating was used to generate spin waves due to the excitation of propagating waveguide modes. Another way to excite spin waves is the utilization of anisotropic materials in which the polarization conversion of the incident light occurs. Such a transformation leads to the spatial dependency of magnetization induced via IFE. This nonuniformity of the magnetic torque allows one to excite the spin waves of a high order. Let us consider the case of biaxial crystals the influence on the incident light polarization of which is described by the permittivity tensor ϵ_{ij} . The diagonal components of this tensor are assumed not to be equal $\epsilon_{11} \neq \epsilon_{22} \neq \epsilon_{33}$ and connected with cartesian coordinates x , y , and z respectively. Let the light fall under the normal incidence to the plane of the material and propagate along the z -axis. Placing the material under study in an external magnetic field along the z -axis leads to the appearance of additional off-diagonal components which are $\epsilon_{12} = -i \times g$ and $\epsilon_{21} = i \times g$. Polarization of the light propagating in such a medium transforms due to the anisotropy and Faraday effect. This process is described theoretically in [7]. To be more specific, consider the YFeO₃ crystal with an orthorhombic cell. Its crystallographic axes a , b , and c are oriented along x , y , and z axes respectively. The main refractive indices of such material are $n_1 = 2.365$, $n_2 = 2.4$, $n_3 = 2.337$ at the wavelength of 633 nm (ϵ'' is assumed to be zero). The transformation of the incident light with circular polarization when it passes through anisotropic medium results in oscillations of the magnetization induced via IFE (blue line on Fig. 1). It worth noting that oscillations of magnetization occur for linearly polarized light. The maximum value of cross-product in formula (1) can be achieved for the polarization of incident light at an angle of 45° to the a crystal axis (green line on Fig. 1). In this case, the material behaves as a quarter-wave plate fully transforming the initial linear polarization to circular. One can observe the oscillations even for light polarized linearly along the crystal axis but their maximum value is two times smaller compared to the previous scenarios (Fig. 2). In this situation, the polarization transformation due to birefringence must disappear but the Faraday effect slightly rotates the polarization off the axis allowing the anisotropy to take its place. The oscillations of IFE due to the birefringent properties of the material under study have been theoretically demonstrated. Such a behavior of the induced magnetization is important for generating spin waves of a high order allowing one to avoid additional nanostructuring of the material. This work was supported by the Ministry of Science and Higher Education of the Russian Federation (mega-grant no. 075-15-2019-1934).

[1] S. Neusser and D. Grundler, *Advanced Materials*, Vol. 21 p. 2927 (2009)
 [2] K. Ganzhorn, S. Klingler, T. Wimmer, et al, *Applied Physics Letters*, Vol. 109, p. 022405 (2016) [3] D. Lachance-Quirion, Y. Tabuchi, A. Glorpe, et al, *Applied Physics Express*, Vol. 12, p. 070101 (2019) [4] D.O. Ignatyeva,

C.S. Davies, D.A. Sylgachev, et al, *Nature Communications*, Vol. 10, p. 1 (2019) [5] A.V. Kimel, A. Kirilyuk, P.A. Usachev, et al, *Nature*, Vol. 435, p. 655 (2005) [6] A.I. Chernov, M.A. Kozhaev, D.O. Ignatyeva, et al, *Nano Letters*, Vol. 20, p. 5259 (2020) [7] A.K. Zvezdin, V.A. Kotov, *Modern magneto-optics and magneto-optical materials*, CRC Press (1997)

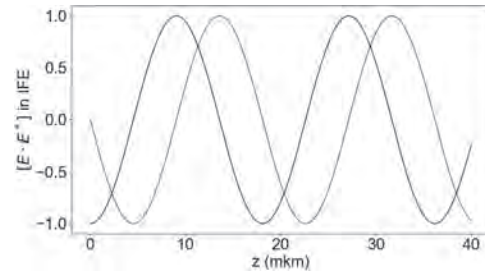


Fig. 1. Cross product of electric field and its complex conjugate depending on the propagation length for circularly (blue line) and linearly polarized at an angle of 45° to the crystal axis (green line) incident light.

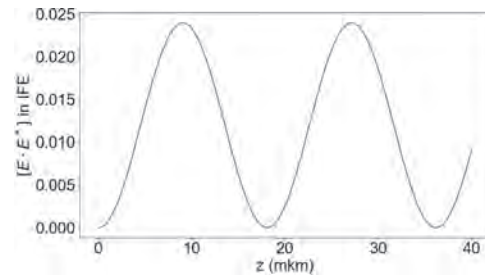


Fig. 2. Cross product of electric field and its complex conjugate depending on the propagation length for incident light polarized along the a crystal axis.

Session EC

HYBRID MAGNONIC STRUCTURES

Mathias Weiler, Chair

Technische Universität Kaiserslautern, Kaiserslautern, Germany

INVITED PAPERS

EC-01. Nonreciprocity and Unconventional Singularities in Cavity Magnonics INVITED.

Y. Wang^{2,1}, Y. Yang¹, J. Rao¹, Y. Gui¹ and C. Hu¹

1. University of Manitoba, Winnipeg, MB, Canada; 2. Zhejiang University, Hangzhou, China

Cavity magnonics built on strongly coupled cavity photons and magnons has gradually demonstrated its unique advantages in fundamental and applied research in the past few years. It has several advantages, including flexible turnability, excellent controllability, and high compatibility. Furthermore, a versatile platform based on coherently coupled microwave photons, magnons, phonons, superconducting qubits, and optical photons has begun to take shape. The hybrid system is expected to be applied in quantum information processing, transfer, and storage. Before 2018, all experiments were carried out in the case of coherent coupling between cavity photons and magnons. In 2018, an intriguing dissipative coupling between cavity photon and magnon was observed for the first time, which originated from the cooperative dissipation of the cavity mode and magnon mode. Unlike the coherent coupling case, where the spectrum is shown as an anti-crossing between cavity mode and magnon mode, the spectrum is shown as a level attraction in the case of dissipative coupling. The revelation of dissipative coupling greatly enhances the richness and functionality of the cavity magnonics and stimulates some fundamental research. We will introduce this trend with two recent works from our group. After revealing the dissipative coupling mechanism, we first realized nonreciprocity and unidirectional invisibility in cavity magnonics by utilizing the interference effect between the coherent and dissipative couplings. The isolation ratio can be relatively large with optimized small insertion loss. With the dissipative coupling mechanism and magnon mode linewidth engineering technique, we construct an anti-parity-time (APT) symmetric cavity magnonics system. Besides the dissipative coupling, the APT symmetric system also needs (i) the cavity mode and magnon mode have the opposite frequency, which can be effectively realized with a detuned cavity magnonics system in the rotating frame, (ii) the same damping or gain rates of the cavity mode and magnon mode, which can be engineered by adjusting the damping rate of the magnon mode to match that of the cavity mode. Further, we observed the exceptional points in this APT symmetric cavity magnonics system, which are the transition points between the PT-symmetry-preserved and PT-symmetry-broken phases. Between two EPs, the maximal coherent superposition of photon and magnon states is robustly sustained by the preserved APT symmetry. Moreover, we observed another kind of singularity, arising from the dissipative coupling of two antiresonances, is an unconventional bound state in the continuum (BIC). At the settings of BICs, the coupled system exhibits infinite discontinuities in the group delay. We find that both singularities coexist at the equator of the eigenvector mapped Bloch sphere, revealing a unique hybrid state that simultaneously exhibits the maximal coherent superposition and slow light capability. We expect to explore more interesting physics and applications based on the dissipative coupling in cavity magnonics.

1. H. Huebl, et al, Phys. Rev. Lett. 111, 127003 (2013). 2. Y. Tabuchi, et al, Phys. Rev. Lett. 113, 083603 (2014). 3. X. Zhang, et al, Phys. Rev. Lett. 113, 156401 (2014). 4. M. Goryachev, et al, Phys. Rev. Applied 2, 054002 (2014). 5. L. Bai, et al, Phys. Rev. Lett. 114, 227201 (2015). 6. Y.-P. Wang, Phys. Rev. Lett. 123, 127202 (2019). 7. Y. Yang, Phys. Rev. Lett. 125, 147202 (2020).

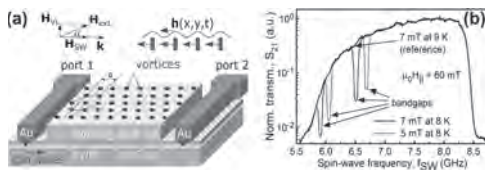
EC-02. Magnon Fluxonics INVITED.

O. Dobrovolskiy¹

1. Universitat Wien, Wien, Austria

The field of magnonics considers the operations with data carried by spin waves and their quanta, magnons [1]. Traditionally, magnonics has been a room-temperature research discipline. Nowadays, the new direction of cryogenic magnonics attracts increasing attention. The decrease in temperature, in particular, results in the reduction of thermal population n of magnons below 1 opening access to single-magnon quantum physics [2]. Moreover, cryogenic temperatures allow for combining magnonics with superconductivity [3-5]. Ferromagnetism and superconductivity are fundamental cooperative phenomena in condensed matter physics. Entailing opposite spin orders, they share an essential conceptual similarity: Disturbances in magnetic ordering in magnetic materials can propagate in the form of spin waves (magnons) while magnetic fields penetrate the majority of technologically relevant (type II) superconductors as a lattice of magnetic flux quanta (fluxons, Abrikosov vortices). Despite a rich choice of wave and quantum phenomena predicted, magnon-fluxon coupling has lacked experimental scrutiny so far. In this talk, a selection of our recent results [5] on the interaction of spin waves with the flux lattice in ferromagnet/superconductor Py/Nb bilayers will be presented - see Fig. 1. In this system we found the magnon frequency spectrum to exhibit a Bloch-like band structure (as shown in Fig. 1(b)) which can be tuned by the biasing magnetic field. Furthermore, the frequency spectra of spin waves scattered on the flux lattice moving under the action of a transport current in the superconductor exhibit Doppler shifts. The resonance absorption of spin waves is explained by their inelastic scattering on the vortex lattice constituting a reconfigurable magnonic crystal [6]. The observed Doppler shifts arise due to the modified dispersion relation for spin waves scattered on the moving vortex lattice constituting a moving Bragg grating. In addition, manipulation of spin waves and tailoring of their transmission spectra in Py will be exemplified by using adjacent Nb layers with nanofabricated pinning potential landscapes. A special attention will be devoted to direct-write hybrid superconductor-based systems with fast relaxation of non-equilibrium effects and supporting ultra-fast vortex motion at $>10\text{km/s}$ velocities [7]. Research leading to these results was done in collaboration with R. Sachser, T. Brächer, T. Böttcher, V. Kruglyak, R. Vovk, V. Shklovskij, M. Huth, B. Hillebrands and A. Chumak.

[1] A. V. Chumak, V. I. Vasyuchka, A. A. Serga, et al., Nat. Phys. 11 (2015) 453 [2] D. Lachance-Quirion, S. P. Wolski, Y. Tabuchi, et al., Science 367 (2020) 425 [3] I. A. Golovchanskiy, N. N. Abramov, V. S. Stolyarov, et al., Adv. Func. Mater. 28 (2018) 1802375 [4] A. A. Bespalov, A. S. Mel'nikov, and A.I. Buzdin, Phys. Rev. B 89 (2014) 054516 [5] O. V. Dobrovolskiy, R. Sachser, T. Brächer, et al., Nat. Phys. 15 (2019) 477 [6] A. V. Chumak, A. A. Serga, and B. Hillebrands, J. Phys. D: Appl. Phys. 50 (2017) 244001 [7] O. V. Dobrovolskiy, D. Yu. Vodolazov, F. Porrati, et al., Nat. Commun. 11 (2020) 3291



(a) Sketch of the experimental system. (b) Fluxon-induced reconfigurable magnonic crystal: Bandgaps in the spin-wave transmission spectra in Py are observed when the Nb layer contains an array of Abrikosov vortices.

CONTRIBUTED PAPERS

EC-03. Magneto-Rotation Coupling Inducing Nonreciprocal Surface Acoustic Waves.

M. Xu^{1,3}, K. Yamamoto^{2,3}, J. Puebla³, K. Baumgaertl⁴, B. Rana³, K. Miura⁶, H. Takahashi⁶, D. Grundler^{4,5}, S. Maekawa^{3,2} and Y. Otani^{1,3}

1. Tokyo University Institute for Solid State Physics, Ibaraki, Japan; 2. Japan Atomic Energy Agency, Naka-gun, Japan; 3. RIKEN Institute for Physical and Chemical Research, Wako, Japan; 4. Institute of Materials (IMX), School of Engineering, Ecole Polytechnique Fédérale de Lausanne (EPFL), Lausanne, Switzerland; 5. Institute of Microengineering (IMT), School of Engineering, Ecole Polytechnique Fédérale de Lausanne (EPFL), Lausanne, Switzerland; 6. Research and Development Group, Hitachi Ltd, Tokyo, Japan

Acoustic wave has been widely integrated into modern electronics to enable various functions, including sensing, communication, signal filtering, etc. Conventionally, acoustic waves propagate equally forward and backward. Here, we employ a fundamentally new mechanism, magneto-rotation coupling[1], to break the symmetry of the propagation, and consequently induces an unprecedented rectification ratio to 100% at the optimized condition, in accordance with the theoretical prediction. As a unique feature of surface acoustic waves, individual lattice point undergoes a rotation motion, which changes its sign according to the wave propagation direction (see the blue and red oriented circles in figure 1(a)). More than 40 years ago, Maekawa and Tachiki developed a theoretical framework [1], proposing the coupling between the lattice rotation and the magnetization via magnetic anisotropy, namely magneto-rotation coupling. Thus, to break the symmetry of the propagation, here, we employ magneto-rotation coupling to capture the chirality of the acoustic waves in a perpendicularly anisotropic ultra-thin film Ta/CoFeB(1.6 nm)/MgO (see figure 1(b)), achieving a giant nonreciprocal acoustic wave attenuation (see figure 1(c)) with a rectification ratio up to 77% [2].

[1] S. Maekawa and M. Tachiki, Surface acoustic attenuation due to surface spin wave in ferro and antiferromagnets, AIP Conf. Proc. 29, 542 (1976).

[2] M. Xu, K. Yamamoto, J. Puebla, K. Baumgaertl, B. Rana, K. Miura, H. Takahashi, D. Grundler, S. Maekawa, and Y. Otani, Nonreciprocal surface acoustic wave propagation via magneto-rotation coupling, Vol. 6, no. 32, eabb1724 (2020).

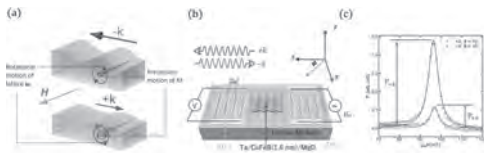


Fig. 1. (a) Schematic of the nonreciprocity mechanism. (b) Illustration of the experimental setup. (c) Attenuation of acoustic waves, $P_{\pm k}$, near a spin-wave resonance condition for surface acoustic wavenumbers $+k$ and $-k$.

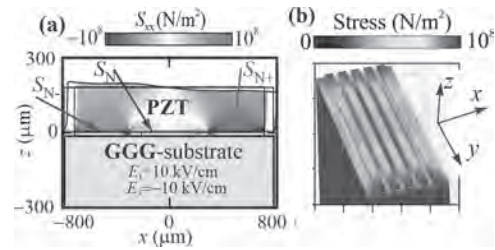
EC-04. Strain Mediated Tunable Spin-Wave Transport in Magnonic Crystal YIG/PZT and YIG/GaAs Structures.

A.V. Sadovnikov¹, E. Beginin¹, A. Grachev¹, A. Stognijj¹, S.E. Sheshukova¹ and S. Nikitov¹

1. Magnonics, N. G. Chernyshevskogo National Research University in Saratov, Saratov, Russian Federation

Recently a lot of research has been directed towards the use of spin waves in ferro- and antiferromagnetic structured films for signal processing at microwave and terahertz frequencies due to the possibility to carry the information signal without the transmission of a charge current [1,2,3]. Recent theoretical and experimental studies suggest that strain can be used to engineer energy-efficient complicated 2D and 3D piezoelectric material and heterostructures [3,4]. The combination of strain tuning and spin-wave coupling can underlie a new branch of functional magnonics- magnon straintronics [5]. Thus, the voltage-driven spin-wave operation can be potentially used for low-dissipation spin-wave-based logic circuits and memory elements. One of the alternative methods of control over nonreciprocal features of spin waves can consist in the combination of a double-layer magnetic structure with semiconductor substrate and light-induced variation of the GaAs semiconductor substrate properties[6]. We demonstrate the voltage-driven and laser-induced nonreciprocity of spin waves in the ferromagnetic-semiconductor and ferromagnetic-piezoelectric structure. Surface spin waves in yttrium iron garnet film grown at the top of n-type gallium arsenide (GaAs) and PZT (lead zirconate titanate) substrate were studied by means of Brillouin light-scattering (BLS) spectroscopy and microwave spectroscopy techniques. We demonstrate the experimental observations of the strain-mediated spin-wave coupling phenomena in different magnonic structures based on the asymmetric adjacent magnonic crystals, adjacent magnetic yttrium iron garnet stripes and array of magnetic stripes, which demonstrates the collective spin-wave phenomena. The device for voltage-controlled spin-wave transport along bilateral magnonic stripes and magnonic crystals was demonstrated (Fig.1). The model describing the spin-wave transmission response and predicting its value is proposed based on the self-consistent equations [5]. It was shown, that the strainmediated spin-wave channels can be used to route the magnonic information signal and thus the composite magnon-straintronic structure could provide to fabricating magnonic platforms for energy-efficient signal processing. The three-channel isolator-based directional coupler (Fig.1) distinguishes itself as an ideal platform for magnonics in three key aspects: first, dual tunability with both the magnetic and electric field; second, it supports large spin-wave propagation distances, which is appropriate for spin-wave interference in magnonic logic applications; and third, its versatile magnonic component with the voltage-controlled frequency-selective characteristics. We show that the spin-wave dispersion can be modified in a controlled manner by illumination of the semiconductor substrate with the infrared laser radiation (Fig.2). Thus, the advantage of ferromagnetic/semiconductor structures as compared to conventional YIG based units is the light control over the spin-wave dispersion and nonreciprocity. This may be the first experimental step in integrated semiconductor magnonics on the base of YIG/GaAs structures. This work was supported partly by the grant of Russian Science Foundation (#20-79-10191). S.E.S. acknowledges support from the Scholarship and Grant of the President of the RF (No. SP-949.2021.5, No. MK-1870.2020.9)

1. V. V. Kruglyak, S. O. Demokritov, and D. Grundler, *J. Phys. D* 43, p. 264001 (2010). 2. D. Sander, S.O. Valenzuela, D. Makarov et al, *J. of Phys.D: Appl. Phys.* Vol. 50, p. 363001 (2017) 3. A. V. Chumak, et.al. *Nat. Phys.* 11, p. 453 (2015). 4. Y. K. Fetisov and G. Srinivasan, *Appl. Phys. Lett.* 88, p. 143503 (2006). 5. A. V. Sadovnikov, *Phys. Rev. Lett.* 120, p. 257203 (2018) 6. A. V. Sadovnikov, et. al., *Phys. Rev. B* 99, p. 054424 (2019)



EC-05. Reconfigurable Spin-Wave Propagation in Magnetic Stripe Domains in Hybrid System.

K. Szulc¹, S. Tacchi², P. Gruszecki¹, F. Valdes Bango³, C. Quiros^{3,4}, A. Hierro Rodriguez³, J. Diaz^{3,4}, J. Martín^{3,4}, M. Velez^{3,4}, G. Carlotti⁵, M. Krawczyk¹ and L. Alvarez Prado^{3,4}

1. Faculty of Physics, Uniwersytet im Adama Mickiewicza w Poznaniu, Poznan, Poland; 2. Sede Secondaria di Perugia, Istituto Officina dei Materiali Consiglio Nazionale delle Ricerche, Perugia, Italy; 3. Departamento de Fisica, Universidad de Oviedo, Oviedo, Spain; 4. Centro de Investigacion en Nanomateriales y Nanotecnología (CIINN), Consejo Superior de Investigaciones Científicas, Oviedo, Spain; 5. Dipartimento di Fisica e Geologia, Università di Perugia, Perugia, Italy

Very recently magnetic stripe domains, characterized by alternating up and down out-of-plane orientation of the magnetization, have received great interest due to the possibility to use stripe patterns to manipulate spin-wave (SW) propagation as in artificial magnonic crystals [1]. In this work, we demonstrate the control of the SW propagation by using reconfigurable regular stripe-pattern domain structure in the hybrid system. The investigated system consists of 64-nm-thick NdCo layer and 10-nm-thick NiFe layer, coupled through an Al layer of different thicknesses. Magnetic force microscopy (MFM) measurements show that, due to the perpendicular magnetic anisotropy of the NdCo film, the system develops stripe domains aligned with the last in-plane saturation direction [2]. The domain pattern is found to have a period of about 140 nm, which is almost independent on the thickness of the Al layer. The magnetization reversal of the trilayer system was investigated by vibrating sample magnetometer, showing that the hysteresis loop is characterized by a two-step process, due to the different coercivity of the NiFe and NdCo films. Detailed analysis of the hysteresis loops along with micromagnetic simulations indicates that the stray magnetic field coming from the NdCo layer induces a regular domain structure also in the NiFe layer, which is tuned by the thickness of Al spacer. In addition, upon reversing the applied magnetic field, an antiparallel state, characterized by an antiparallel alignment of the magnetization component parallel to the domain axis in the NdCo and NiFe stripes, is formed. Then, Brillouin light scattering spectroscopy has been used to measure the spectra of the SWs propagating in the direction perpendicular to stripe domains for the parallel and the antiparallel state. For both configurations, the dispersion relation shows a strongly nonreciprocal mode (Figs. 1-2). However, in the parallel state SWs propagating with positive and negative wavevector are both characterized by a positive dispersion, while in the reversed state SWs propagating with negative wavevector show a negative dispersion. The above experimental results have been satisfactorily reproduced by numerical simulations. The latter show that the detected SW mode is mainly localized in the NiFe layer and its frequency nonreciprocity can be ascribed to the static magnetization configuration as well as to the interaction with the NdCo induced by the SWs via the dynamic stray field.

[1] C. Banerjee et al., Phys. Rev. B 96, 024421 (2017) [2] D. Markó et al., Appl. Phys. Lett. 115, 082401 (2019)

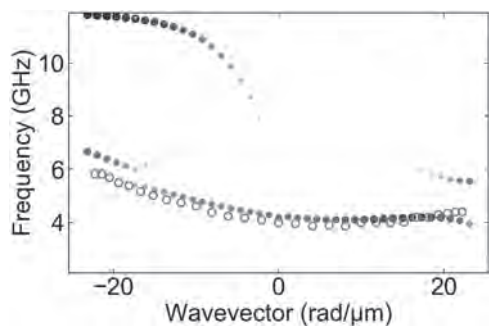


Fig. 1. Dispersion relation in the NdCo(64 nm)/Al(5)/NiFe(10) in the parallel state. Empty and full dots mark the results of Brillouin light scattering measurements and simulations, respectively. Size and color intensity of the numerical results indicate the predicted intensity in the measurements.

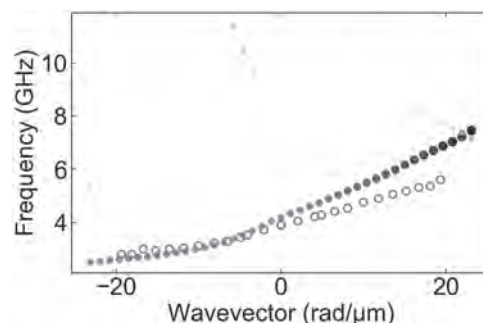


Fig. 2. Dispersion relation in the NdCo(64 nm)/Al(5)/NiFe(10) in the antiparallel state.

EC-06. Velocity Modulation of Surface Acoustic Waves via Einstein-de Haas Effect.

S. Tateno¹, Y. Kurimune¹, M. Matsuo^{2,4}, K. Yamonoi¹ and Y. Nozaki^{1,3}
 1. Dept. of Physics, Keio University, Yokohama, Japan; 2. Kavli Institute for Theoretical Sciences, University of Chinese Academy of Sciences, Beijing, China; 3. Center for Spintronics Research Network, Keio University, Yokohama, Japan; 4. Advanced Science Research Center, Japan Atomic Energy Agency, Tokai, Japan

Einstein-de Haas (EdH) effect is the fundamental phenomenon that the microscopic spin angular momentum is converted to the angular momentum of mechanical rotation. A mechanical torque due to the EdH effect, the magnitude of which is proportional to the time derivative of the magnetization, is difficult to be detected, which keeps its practical application away. However, recent development of microfabrication technology has enabled to sensitively detect the tiny EdH torque using micro-fabricated mechanical resonators [1,2]. These findings show that the EdH effect can be utilized for the new principle of the mechanical torque generation in sub-micron scale device. Moreover, it was demonstrated that the ultrafast demagnetization due to the laser heating excited the transverse strain wave in a Fe film due to the EdH effect, where the timescale and conversion efficiency of the angular momentum transfer were quantitatively estimated [3]. Rayleigh-type surface acoustic waves (RSAWs), the displacement of which oscillates elliptically, have been widely used to excite the spin waves in a ferromagnetic thin film via the magnetoelastic interaction [4]. Recently, as the phenomena based on the angular momentum conversion from the lattice rotation to the magnetization or electron spin, the gyromagnetic spin-wave excitation [5] and the spin current generation in a nonmagnetic metal with a weak spin-orbit coupling [6] were demonstrated. In this study, we demonstrate both acceleration and deceleration of RSAW velocity in the ferromagnetic (FM) film based on the EdH effect. When the spin-wave is gyromagnetically excited by RSAW propagation through the FM film, the EdH torque is generated in the FM lattice as the back action of the spin-wave resonance (SWR) (Fig. 1(a)). As shown in Fig. 1(a), the direction of EdH torque is opposite to the time derivative of the magnetization. We theoretically expect that the transverse velocity of RSAW can be modulated by the EdH torque, resulting in the phase change of RSAW propagation. In the experiment, we successfully observed the phase change of RSAW propagation, whose magnitude and variation were consistent with our analytical prediction. Figure 1(b) shows the schematic experimental setup for measuring the phase change of RSAW. A pair of inter-digital transducers (IDTs) consisting of Ti(3)/Au(30) is fabricated on a piezoelectric LiNbO₃ substrate by the electron beam evaporation. The numbers in the parentheses indicate the layer thickness in nanometers. The width and space of the electrode of IDT are 550 nm. The Ni₈₁Fe₁₉ (NiFe) film with a lateral size of 400×400 μm² is sputtered between a pair of IDTs. By applying a microwave with the fundamental frequency of RSAW excitation into one of IDTs, RSAWs are excited via the piezoelectric effect. The RSAWs propagating through the NiFe film are electrically detected by the other of IDTs using a vector network analyzer (VNA) as the inverse process of the RSAW excitation. Figures 2(a) and 2(b) show the reduced RSAW energy dissipation ΔP_{norm} and phase difference $\Delta\theta$, respectively, as a function of external magnetic field swept in the direction parallel to the RSAW wave vector at the RSAW frequency of 1.75 GHz. Steep peaks appear at 4.6 and -4.0 mT in Fig. 2(a), showing that the spin-wave is excited because the values of the resonant field and resonant frequency are matched with the spin wave dispersion of a 20-nm-thick NiFe film. A bipolar change of $\Delta\theta$ is observed in the vicinity of the resonance field of spin-waves. From the angle between the applied external field and RSAW wave vector, it can be seen that the spin-wave is excited via gyromagnetic effect, not the magnetoelastic coupling [5]. The increase and decrease in $\Delta\theta$ can be explained by our analytical model consisting of the elastic motion equation with the EdH torque term. The maximum value of phase change $\Delta\theta_{\text{max}}$ is -0.035 rad at 5.0 mT. This value is as large as that in case using the magnetoelastic coupling in a single Ni film [7]. In addition, the order of $\Delta\theta_{\text{max}}$ is comparative to the value analytically obtained by assuming a loss-less conversion of the angular momentum. The consistency in $\Delta\theta_{\text{max}}$ suggests that the EdH effect is robust in the angular translation from the magnetization to the lattice in the gigahertz regime.

[1] K. Harii, et. al., Nat. Commun. 10, 2616 (2019). [2] K. Mori, et. al., Phys. Rev. B 102, 054415 (2020). [3] C. Dornes, et. al., Nature 565, 209 (2019). [4] M. Weiler, et. al., Phys. Rev. Lett. 106, 117601 (2011). [5] Y. Kurimune, et. al., Phys. Rev. Lett. 124, 217205 (2020). [6] D. Kobayashi, et. al., Phys. Rev. Lett. 119, 077202 (2017). [7] R. Sasaki, et. al., Phys. Rev. B 95, 020407 (R) (2017). [8] S. Tateno, et.al., submitted.

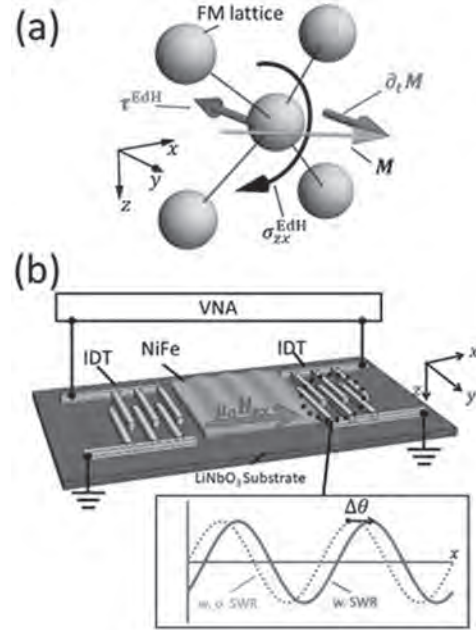


Fig. 1 (a) Schematic of the stress based on EdH effect σ^{EdH}_{zx} and the EdH torque τ^{EdH} in the Ni-Fe lattice. The direction of the EdH torque is opposite to the time derivative of the magnetization. (b) Experimental setup for measuring the phase change $\Delta\theta$ of RSAW using a VNA. The external field is applied along the RSAW propagation direction.

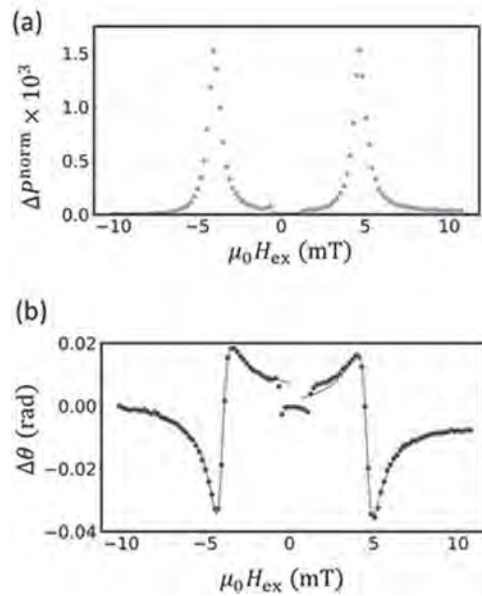


Fig. 2 The field dependence of (a) ΔP_{norm} and (b) $\Delta\theta$ at the fundamental frequency of RSAW excitation, respectively. The red solid line in (b) shows the result of the best fit using our analytical model.

EC-07. Confined Magnetoelastic Waves in Thin Waveguides.

F. Vanderveken^{1,2}, J. Mulkers³, J. Leliaert³, B. Van Waeyenberge³,

B. Soree^{1,2}, O. Zografos¹, F. Ciubotaru¹ and C. Adelmann¹

1. IMEC, Leuven, Belgium; 2. Katholieke Universiteit Leuven, Leuven, Belgium; 3. Universiteit Gent, Gent, Belgium

In recent years, the coupling between the elastic and magnetic domain in magnetostrictive materials has gained strong interest [1]. The magnetoelastic coupling in these materials results in elastic response originating from magnetic excitations and vice versa. At microwave frequencies, this mutual interaction leads to coupling between elastic and magnetic waves, forming magnetoelastic waves. Whereas plane magnetoelastic waves are already studied in bulk materials some decades ago [2-4], the magnetoelastic waves in thin magnetostrictive films gained attention only recently [5,6]. By contrast, many recent spin-wave-based information processing applications employ nanoscale waveguides for information transfer and computation [7]. At these nanoscales, confinement of both the elastic and magnetic waves leads to multiple modes each of which with a specific mode profile and consequently also to confined magnetoelastic waves. The shape of the magnetoelastic field depends on the displacement profile and the shape of the magnetoelastic body force depends on the magnetization profile. As a consequence, it is expected that every mode experiences different magnetoelastic coupling strength. This presents a rather complex multiphysics problem where analytical methods are hard or even impossible, and thus numerical approaches are preferred. Therefore, in this work, we present the development of a novel mumax3 extension that allows the numerical calculation of magnetoelastic waves in scaled waveguides [8]. Furthermore, we present results of magnetoelastic waves in a nanoscale waveguide with static magnetization along the wave propagation direction. The studied system consists of a thin CoFeB waveguide with width of 200 nm and thickness of 20 nm. A weak external field of 5 mT is applied in the longitudinal direction of the waveguide to initiate the static magnetization along this direction. The resonant modes in the structure are numerically found by applying a 5 ps excitation pulses and performing a two-dimensional fast Fourier transform. By comparing the numerical result with the analytical uncoupled dispersion relations of confined elastic and magnetic waves, all modes were identified. The uncoupled resonant waves of this structure consist of confined magnetic spin waves, antisymmetric and symmetric lamb waves and out-of-plane shear elastic waves. Fig. 1a shows the numerically obtained dispersion relations and Fig. 1b shows the overlay with the analytically calculated dispersion relations for uncoupled elastic and magnetic waves. The magnetoelastic coupling leads to the formation of anti-crossings near the reciprocal point where the uncoupled elastic and magnetic dispersion relations would intersect with each other. These anti-crossings identify regions of strong interaction between the elastic and magnetic domain and correspond to pure magnetoelastic waves. The magnetoelastic waves are shown to have different behavior as compared to the pure elastic or magnetic waves. The magnetoelastic wave group velocity is rather unaffected in the quasi-magnetic or quasi-elastic regime whereas it strongly differs close to the anti-crossing. Furthermore, the magnetization and displacement value are shown to take both high values close to the anti-crossing. However, when approaching the quasi-elastic regime there is a very strong decay of the magnetization component of the magnetoelastic wave and vice versa for the displacement component and the quasi-magnetic regime. Lastly, careful analysis of the dispersion relations also shows reciprocal points with weak or even without anti-crossing. The frequency gap formed by the anti-crossing is a good measure of the magnetoelastic coupling strength and thus provides much information. The variation in amplitude of this frequency gap is attributed to the wave confinement and their mode profiles. Every elastic and magnetic mode has its own mode profile and thus also its own magnetoelastic body force and field. Considering these mode dependent body forces and fields together with the mode's overlap integral allows to identify the strength of the coupling between the different elastic and magnetic waves. The strongest coupling is shown to exist between the odd magnetic modes and symmetric lamb modes and even magnetic modes and anti-symmetric lamb modes. This work has been partially funded by the European Union's Horizon 2020 research and innovation programme within the FET-OPEN project CHIRON under grant agreement No. 801055. FV acknowledge the

financial support from Fonds voor Wetenschappelijk Onderzoek (FWO) under the grant No. 1S05719N.

[1] A. D. Kent and D. C. Worledge, *Nature Nanotechnol.* Vol. 10, p. 187 (2015) [2] C. Kittel, *Phys. Rev.* Vol. 110, p. 836 (1958). [3] E. Schlomann and R. I. Joseph, *J. Appl. Phys.* Vol. 35, p. 2382 (1964). [4] P. A. Fedders, *Phys. Rev. B.* Vol. 9, p. 3835 (1974). [5] Y. Nozaki and S. Yanagisawa, *Electr. Eng. Jpn.* Vol. 204, p. 3 (2018). [6] S. Bhuktare, A. Bose, H. Singh, and A. A. Tulapurkar, *Sci. Rep.* Vol. 7, p. 840 (2017). [7] A. Khitun and K. L. Wang, *J. Appl. Phys.* Vol. 110, p. 34306 (2011). [8] F. Vanderveken, et al., https://github.com/Fredericvdv/Magnetoelasticity_MuMax3.

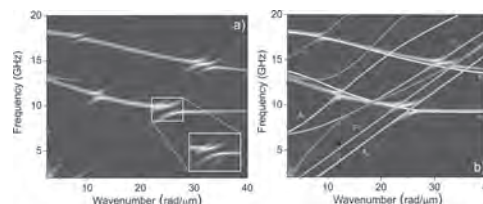


Figure 1: Dispersion relations of magnetoelastic waves in a 200 nm wide and 20 nm thick CoFeB waveguide. (a) Numerically calculated dispersion relations. The inset shows a magnification of a region near a magnetoelastic gap. (b) Analytically calculated dispersion relations of uncoupled elastic and spin waves superimposed to the numerically obtained results.

EC-08. The Interaction Between Surface Acoustic Waves and Spin Waves: the Role of Anisotropy and Spatial Profiles of the Modes.

N.K. Babu¹, A. Trzaskowska¹, P. Graczyk², G. Centala¹, S. Mieszczak¹, H. Glowinski², M. Zdunek¹, S. Mielcarek¹ and J.W. Klos¹

1. ISQI, Faculty of Physics, Adam Mickiewicz University in Poznan, Poznan, Poland; 2. Institute of Molecular Physics, Polish Academy of Sciences, Poznan, Poland

The interaction between different types of wave excitation in hybrid systems is usually anisotropic. Magnetoelastic coupling between surface acoustic waves and spin waves strongly depends on the direction of the external magnetic field. However, in the present study we observe that even if the orientation of the field is supportive for the coupling, the magnetoelastic interaction can be significantly reduced for surface acoustic waves with a particular profile in the dirR/S-SAWection normal to the surface at distances much smaller than the wavelength. We use Brillouin light scattering to investigate thermally excited phonons and magnons in a magnetostrictive CoFeB/Au multilayer deposited on a Si substrate – see Fig.1. The experimental data interpretation is based on a linearized model of interaction and finite element method computations[1]. For propagating waves, the coupling requires matching both the frequencies and the wavelengths[2]. This condition can be fulfilled for spin waves (SWs) and surface acoustic waves (SAWs) existing in the same range of frequencies and wave vectors. However, the strength of the magnetoelastic interaction depends on the orientation of the wave vector with respect to the direction of the static magnetic field[3]. Moreover, this interaction is different for different types of SAWs, specifically, Rayleigh-SAWs (R-SAW) and Love-SAWs (L-SAW)[1,4] – see Fig.2. Thus, the coupling is strongly anisotropic and cannot be observed for arbitrary SAWs and SWs, even if their frequencies and wave vectors match. Our study reveals an additional factor limiting the interaction between SAWs and SWs. The SAW/SW coupling proves to require an appropriate profile of the elastic wave near the surface of the magnetostrictive structure, at distances much smaller than the wavelength. For R-SAWs the tangential component of displacement u_x can have nodes within the magnetic layer, resulting in a reduction of the net strength of magnetoelastic interaction even if the strain ϵ_{xx} is locally significant. In an L-SAW the displacement u_y does not have any nodes (u_x changes monotonously in the normal direction). The location of R-SAW nodes depends on elastic properties of the system, specifically, the elastic material parameters of the multilayer and the substrate, and the thickness of the multilayer. We have shown that this additional factor plays a role for some types of surface acoustic waves (R-SAW), while other types (L-SAW) are insensitive to it. We believe that the studies on magnon-phonon interaction in confined geometries (surfaces, cavities) are very promising and can reveal unusual interaction mechanisms. *Sample* We used naturally oxidized (001) silicon as a substrate supporting the studied $[\text{Co}_{20}\text{Fe}_{80}\text{B}_{20}/\text{Au}]_{20}$ multilayers deposited on top of a 4 nm titanium (Ti) and a 15 nm gold (Au) buffer layers. The multilayers were deposited by magnetron sputtering in argon atmosphere. *Method* We studied the dispersion relations of thermally excited SAWs and magnetostatic SWs using a six-pass tandem Brillouin spectrometer (Scientific Instruments©TFP2-HC), which ensures a contrast of 10^{15} . A frequency-stabilized diode-pumped solid-state laser (Coherent©VERDI V5) operating at $\lambda_0 = 532$ nm was used as a source of incident light. The measurements were performed in the 180° backscattering geometry with crossed (p-s)polarization of incident and scattered light for SWs and non-crossed (p-p) polarization for SAWs. Using the finite element method in COMSOL Multiphysics®, we solve numerically the coupled equations of motion for mechanic displacement and magnetization. The CoFeB/Au multilayer is treated as a 60-nm-thick effective magnetic layer, and the CoFeB/Au multilayer together with the Ti/Au buffer as an 80-nm-thick effective acoustic layer on a Si substrate. *Acknowledgement* The research leading to these results has received funding, hereby gratefully acknowledged, from the National Science Centre, Poland, project No. UMO-2016/21/B/ST3/00452. S. Mies. would like to additionally acknowledge the financial support from the National Science Centre, Poland, project No. UMO-2020/36/T/ST3/00542.

[1] N. K. P. Babu, A. Trzaskowska, P. Graczyk, et al., Nano Lett. (2020) https://doi.org/10.1021/acs.nanolett.0c03692 [2] Y. Hashimoto, D. Bossini,

T. H. Johansen, et al., Phys. Rev., Vol. 97, 14040 (2016) [3] L. Dreher, M. Weiler, M. Pernpeintner, et al., Phys. Rev. B 86, 134415 (2012) [4] M. Geilen, F. Kohl, A. Nicoloiu, et al., Appl. Phys. Lett. Vol. 117, 213501 (2020) [5] N.E. Khokhlov, P.I. Gerevenkov, L.A. Shelukhin, et al., Phys. Rev. Applied Vol. 12, 044044 (2019)

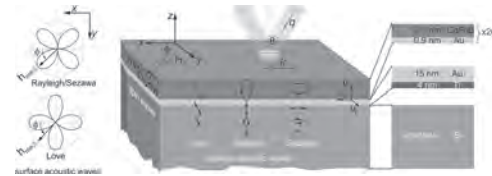


Fig.1 In the studied system acoustic waves propagate along the surface of the silicon substrate and are mostly concentrated in the CoFeB/Au multilayer cover. The multilayer can be regarded as an effective magnetostrictive medium where surface acoustic waves can interact with spin waves. The anisotropy of magnetoelastic interaction (i.e. the dependence on the orientation Φ of magnetic field) is different for Love and Rayleigh/Sezawa acoustic waves (L-SAW, R/S-SAW); presented on the left are the respective polar plots of the in-plane component of magneto elastic field.

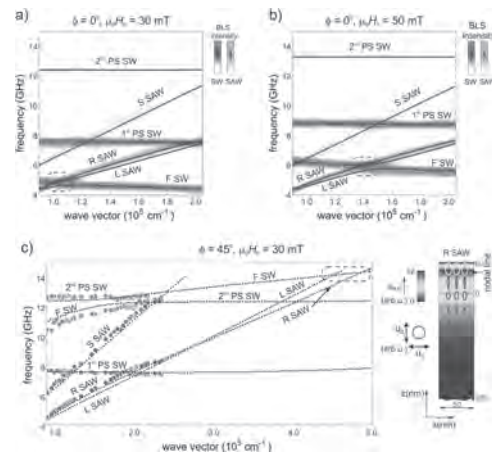


Fig.2 The BLS experimental magnetoelastic dispersion relation measured for magnons (redlines) and phonons (blue lines) with an in-plane applied magnetic field of (a) 30 mT and (b) 50 mT for $\Phi=0$ deg. The dashed shows the regions where the frequencies of fundamental spin wave fundamental mode (F-SW) and L-SAW or R-SAW are agreed. The interactions is seen for L-SAW only. (c) For $\Phi=45$ deg observe the lack of R-SAW/F-SW interaction, which cannot be explained based on the interaction anisotropy (see $h_{me,i}(\Phi)$ for R-SAW in Fig.1). The R-SAW/F-SW interaction is suppressed to zero due to the presence of a nodal line for the ϵ_{xx} component of the strain tensor, which averages to zero the magnetoelastic coupling.

EC-09. Analytical Model for Unitary Magnon-Mediated Quantum Gates in Hybrid Magnon-Photon Systems.

C. Trevillian¹ and V. Tyberkevych¹

1. Physics, Oakland University, Rochester, MI, United States

Modern quantum computing architectures are built to provide low-error environments within which to perform the unitary operations that form the bases of quantum computations. These low-error environments necessary for successful quantum computation require use of complex structures that make large-scale implementation difficult, leading to the investigation of coupled magnon-photon systems [1-6] that can achieve strong coupling rates (> 100 MHz) as a potential platform for hybrid quantum computing architectures. Such coupled magnon-photon systems benefit from the magnetic field tunability of the resonant magnon frequency, where *dynamic tuning* of resonant magnon frequencies with a pulsed magnetic field at rates comparable to or less than the order of the magnon-photon energy exchange time can realize unique operations not possible with static tuning [7-8]. Previously, we analyzed this problem numerically and found that a parabolically shaped pulsed magnetic field profile can realize the coherent exchange of quantum data and the generation of entanglement by changing the curvature λ and maximum frequency Δ of the parabolic profile [8]. That is, in the same physical structure, depending on the shape of the pulsed magnetic field, different *unitary magnon-mediated quantum gates* can be realized [8]. Here, we consider an analytical approach to study this system. Namely, we consider a hybrid magnon-photon system, consisting of two photonic resonators having degenerate frequencies ω_p and one magnonic resonator with a dynamically-tuned resonance frequency $\omega_m(t)$. The photonic resonators are not directly coupled with each other but are both coupled with the magnonic mode with the coupling rate κ . We consider a simple analytically-solvable interaction protocol in this hybrid system, which can be experimentally realized with rectangular magnetic field pulses of sufficiently large magnitude. We assume that initially ($t < 0$) the frequency difference $|\omega_m - \omega_p| \gg \kappa$ and interaction between the subsystems can be ignored. At $t = 0$ the magnonic mode frequency $\omega_m(t)$ is brought within the efficient interaction interval $\Delta = \omega_m - \omega_p \sim \kappa$ and is held constant for the duration T . After $t = T$, the magnonic frequency is once again moved out of the photonic resonance region and any interaction between the subsystems stops. Depending on the control pulse parameters Δ and T , different behaviors of the hybrid system can be realized. Of particular interest is the situation, in which the magnonic and photonic subsystems stay completely decoupled after the action of the control pulse. Such a case corresponds to a unitary operation on the photonic modes, realized through the indirect magnon-mediated coupling, and is of great importance for practical applications of magnonic resonators in quantum computing systems. Using our model, we derived a simple analytical condition of realizing unitary magnon-mediated operations, namely, for each detuning Δ there exist an infinite series of pulse durations $T_n(\Delta) = 2n\pi / (8\kappa^2 + \Delta^2)^{1/2}$ providing unitary conditions (here, n is a positive integer). The resulting effect of the magnon interaction on the photonic subsystem, in this case, can be described by 2×2 unitary matrix $U_n = U e^{i(n\pi^2 - T_n(\Delta)\Delta/4)}$ relating photonic states before and after the pulse, which has components: $U_{11} = e^{i2\pi\cos(\theta_n)}$, $U_{12} = e^{i\pi^2\sin(\theta_n)}$, $U_{21} = -e^{-i\pi^2\sin(\theta_n)}$, $U_{22} = e^{-i2\pi\cos(\theta_n)}$. Here $\theta_n = n\pi/2 - T_n(\Delta)\Delta/4$ has the meaning of inter-mode energy exchange angle. For example, for $\theta_n = \pi/2 + m\pi$ (m is an integer number) a complete exchange of two photonic states is achieved, while $\theta_n = \pi/4 + m\pi$ describes 50% mixing behavior that allows one to entangle the two photonic modes. The obtained results allow one to select pulse parameters realizing the desired unitary operation and, also, to analyze the limitations on the performance of the proposed magnon-mediated gates. Thus, it is clear that the simple rectangular pulse cannot realize all possible unitary gates since the matrix U_n depends only on one continuous parameter (θ_n), while the general 2×2 unitary matrix has 4 independent parameters. On the other hand, this pulse profile is sufficient to achieve an arbitrary exchange angle θ_n . The shortest pulse duration for which a complete exchange ($\theta_n = \pi/2$) is possible is $T_{min} = \pi / (\kappa\sqrt{2})$ and is realized at exact resonance $\Delta = 0$. Our results, also, show a possibility to realize magnon-mediated unitary gates working in off-resonance conditions $|\Delta| \geq \kappa$. For example, $\theta_n = \pi/2$ gate can be realized with $\Delta = 18(2/19)^{1/2}\kappa$ and $T_{10} = (19/2)^{1/2}\pi/\kappa$. While such off-resonance operations require longer interaction times, their advantage in comparison to

resonance-type operations is that the magnonic and photonic subsystems remain only weakly coupled throughout the whole process. This may lead to weaker decoherence of the quantum photonic subsystem caused by spin-lattice relaxation processes in the magnonic resonator. In general, n -th unitary branch $T_n(\Delta)$ has n different detuning values Δ , for which a given exchange angle θ_n (up to multiples of π) is achieved, which leaves a lot of space for optimization of practical magnon-mediated unitary gates. In summary, we proposed a simple model of magnon-mediated interaction in dynamically-tuned hybrid magnon-photon quantum systems. We derived analytically the conditions under which such interaction results in a unitary operation on the photonic subsystem and obtained expressions for the parameters of the control pulse necessary for achieving the desired operation. Our results can be used for estimation and optimization of performance parameters of practical hybrid magnon-photon systems.

[1] H. Huebl, C. W. Zollitsch, J. Lotze, et al., Phys. Rev. Lett., vol. 111, no. 127003, 2013. [2] Y. Tabuchi, S. Ishino, T. Ishikawa, et al., Phys. Rev. Lett, vol. 113, no. 083603, 2014. [3] X. Zhang, C.-L. Zou, L. Jiang, et al., Phys. Rev. Lett., vol. 113, no. 156401, 2014. [4] Y. Tabuchi, S. Ishino, A. Noguchi, et al., Science, vol. 349, no. 6246, pp. 405-408, 2015. [5] Y. Li, T. Polakovic, Y.-L. Wang, et al., Phys. Rev. Lett., vol. 123, no. 107701, 2019. [6] J. Hou and L. Liu, Phys. Rev. Lett., vol. 123, no. 107702, 2019. [7] C. Trevillian and V. Tyberkevych, FE-09, Digests of the Intermag Conference, 2020. [8] C. Trevillian and V. Tyberkevych, Q2-07, Abstracts of the 65th Annual Conference on Magnetism and Magnetic Materials, 2020.

EC-10. Topological Magnon-Polaron in a two-Dimensional Ferromagnet.

G. Go¹, S. Kim² and K. Lee²

1. Korea University, Seongbuk-gu, The Republic of Korea; 2. Korea Advanced Institute of Science and Technology, Daejeon, The Republic of Korea

We theoretically investigate the topological aspects of the magnon-phonon hybrid excitation in a simple two-dimensional (2D) square-lattice ferromagnet with perpendicular magnetic anisotropy [1]. Several distinguishing features of our model are as follows. Our model is optimized for atomically thin magnetic crystals, i.e., 2D magnets. The recent discovery of magnetism in 2D van der Waals materials opens huge opportunities for investigating unexplored rich physics and future spintronic devices in reduced dimensions [2,3]. In our 2D model, we ignore the nonlocal dipolar interaction, which is not a precondition for a finite Berry curvature in 2D magnets. Moreover, the Berry curvature we find requires neither a special spin asymmetry such as the Dzyaloshinskii-Moriya interaction (DMI) nor a special lattice symmetry: Our 2D model description is applicable for general thin-film ferromagnets. Therefore, we show that even without such long-range dipolar interaction, DMI, or special lattice symmetry, the nontrivial topology of a magnon-phonon hybrid can emerge by taking account of the well-known magnetoelastic interaction originates from the magnetocrystalline anisotropy. Because the magnetocrystalline anisotropy is ubiquitous in ferromagnetic thin-film structures, our result does not rely on specific preconditions and thus is quite generic. Furthermore, we show that the topological structures of the magnon-polaron bands can be manipulated by effective magnetic fields via topological phase transition. We uncover the origin of the nontrivial topological bands by mapping our model to the well-known two-band model for topological insulators [4], where the Chern numbers are read by counting the number of topological textures, called skyrmions, of a certain vector in momentum space. In this picture, the magnon-phonon hybridization induces the chiral texture of the momentum space vector. As an experimental probe for our theory, we propose the thermal Hall conductivity [Fig. 2].

[1] G. Go et al., Topological Magnon-Phonon Hybrid Excitations in Two-Dimensional Ferromagnets with Tunable Chern Numbers, Phys. Rev. Lett. 123, 237207 (2019). [2] C. Gong et al., Discovery of intrinsic ferromagnetism in two-dimensional van der Waals crystals, Nature (London) 546, 265 (2017). [3] B. Huang et al., Layer-dependent ferromagnetism in a van der Waals crystal down to the monolayer limit, Nature (London) 546, 270 (2017). [4] B. A. Bernevig, T. L. Hughes, and S.-C. Zhang, Quantum spin Hall effect and topological phase transition in HgTe quantum wells, Science 314, 1757 (2006).

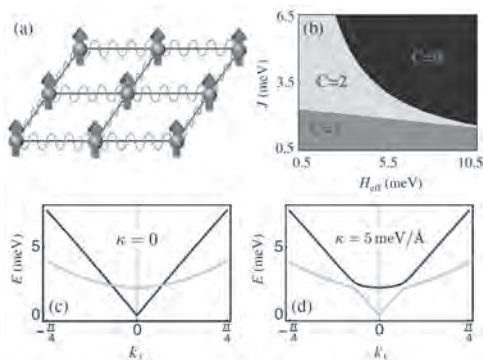


Fig. 1. (a) The schematic illustration of the magnon and phonon system. The ground state of the magnetization is given by the uniform spin state along the z-axis (red arrow). (b) The Chern number of our magnon-phonon hybrid system. H represents the effective magnetic field including the anisotropy field and the external magnetic field. Band dispersion (c) without the magnon-phonon interaction and (d) with the magnon-phonon interaction.

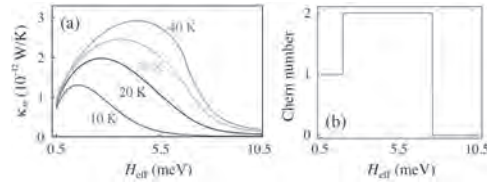


FIG. 2. (a) Dependence of thermal Hall conductivity on the effective magnetic field H_{eff} and with different temperatures T using the parameters in the main text. (b) Dependence of the Chern number on the effective magnetic field H_{eff} using the parameters in the main text.

EC-11. Focused SAWs Enhance Nonlinearity in ADFMR.

D.A. Bas¹, P. Shah¹ and M. Page¹

¹. Air Force Research Laboratory, Wright-Patterson AFB, OH, United States

Acoustically-driven ferromagnetic resonance (ADFMR) gained interest in 2012 as Dreher *et al.* (1) developed it as a powerful and versatile method of examining complex magnetoacoustic interactions. While initial studies established the technique, the physical mechanisms behind the coupling must be thoroughly understood if ADFMR is to be exploited in next-generation microwave communications devices. In particular, the nonlinearity of ADFMR driven at high powers (2) is not well characterized, which may result in unwanted or unpredicted behavior when devices become optimized. To address this aspect, we produce ADFMR devices using curved interdigitated transducers (IDTs), in contrast to the straight IDTs that are typically used. Like an optical lens, these IDTs are engineered to focus acoustic energy towards a region smaller than the IDTs themselves. In this way, acoustic and magnetic amplitudes in a small region in the center of the device may be driven much higher than was previously possible, allowing examination of nonlinear processes such as Suhl instabilities. This may also produce an avenue for improved magnetoacoustic coupling, as well as further device miniaturization. Our devices are produced in much the same way as previously described (2), using aluminum split-finger IDTs and a 20-nm thin-film nickel layer grown on a y-cut lithium niobate (LiNbO₃) substrate. We examine a device using a scanning acoustic-wave imaging interferometer similar to that used in Ref. (3). A 785-nm laser is split into signal and reference paths using an acousto-optic modulator operated at 40 MHz. The signal component is focused onto the device with a 10X objective lens. The beams are then recombined and the interference between them is recorded using a lock-in amplifier. Meanwhile, the ADFMR device is driven at its fundamental frequency 284 MHz or a higher odd harmonic. The DC photodiode signal is simultaneously recorded as a reference image (Fig. 1a), and follows the reflectivity of the scanned spot, showing the exact positions of the metallic nickel and aluminum surfaces. The vibration of the probed spot, downmixed to the range of the lock-in, is shown in Fig. 1b. Here, the gaussian-like curve of the focused SAWs is clearly visible as they converge to a high-amplitude region near the center of the device. Extracting a longitudinal segment of this signal allows us to see the oscillatory behavior in Fig. 1c. These oscillations indicate a standing wave with wavelength $v/f = 12 \mu\text{m}$ ($v = 3488 \text{ m/s}$ is the Rayleigh velocity of SAWs in the LiNbO₃ and $f = 284 \text{ MHz}$ is the driving frequency), as the output of the device is reflected back towards the input. To quantify the power convergence, transverse slices were taken near the center and fitted with the lorentzians shown in Fig. 1d, using the fitting parameters in Fig. 1e. Near the center ($X \approx 20.7 \text{ mm}$), the amplitude reaches a value of nearly 5 times greater than it is near the IDTs, as the width shrinks to a minimum of $22 \mu\text{m}$, demonstrating that the focused IDTs significantly increase the energy density in a small region. ADFMR measurements on a focused IDT device show extremely power-dependent behavior. The linear regime is accessed with a -15 dBm driving field (Fig. 2a), where the shape is independent of power. However, with only +15 dBm of input power (Fig. 2b) the absorption lobes begin to shift towards lower field, and with a weaker maximum absorption. At +25 dBm of input power (Fig. 2c) the lobes shift even further and are much weaker in comparison. These results are a clear indication that a nonlinear power regime is accessed with modest input powers with the assistance of the curved IDTs, dramatically concentrating acoustic energy density. *This material is based on work supported by the Air Force Office of Scientific Research under project number FA9550-20RXCOR074

1. L. Dreher, M. Weiler, M. Pernpeintner, H. Huebl, R. Gross, M. S. Brandt, and S. T. B. Goennenwein, "Surface acoustic wave driven ferromagnetic resonance in nickel thin films: Theory and experiment," *Physical Review B*, vol. 86, no. 13, p. 134415, 2012. 2. D. Bas, P. Shah, M. McConney and M. Page, "Optimization of acoustically-driven ferromagnetic resonance devices," *Journal of Applied Physics*, vol. 126, no. 11, p. 114501, 2019. 3. Z. Shen, X. Han, C. L. Zou, and H. X. Tang "Phase sensitive imaging of 10 GHz vibrations in an AlN microdisk resonator," *Review of Scientific Instruments*, vol. 88, No. 12, p. 123709, 2017.

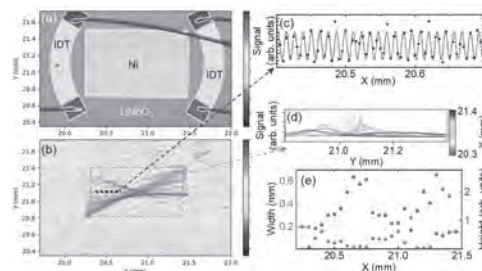


Figure 1. Interferometric imaging of microwave surface acoustic waves on a device. (a) Reflectivity map of the device in arbitrary units, scanned with 5- μm steps, highlighting the curved interdigitated transducers (IDTs), thin film of nickel (Ni), and substrate of lithium niobate (LiNbO₃). (b) Interferometric acoustic wave imaging showing the amplitude of surface vibrations in arbitrary units, demodulated at the fundamental frequency of the IDTs (284 MHz) after downmixing. (c) Line scan indicated by the blue dashed line in (b), fitted with a sinusoid of period 12 μm , which corresponds to the period of standing waves in LiNbO₃ at 284 MHz. (d) A series of lorentzian fits along the Y-direction for the data indicated by the dashed orange box in (b). (e) Fitting parameters width and height for the curves in (d).

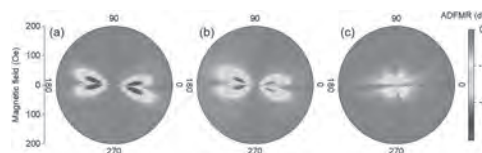


Figure 2. Normalized ADFMR signal in a focused IDT device. Driving field is (a) -15 dBm, (b) +15 dBm, and (c) +25 dBm at 864 MHz.

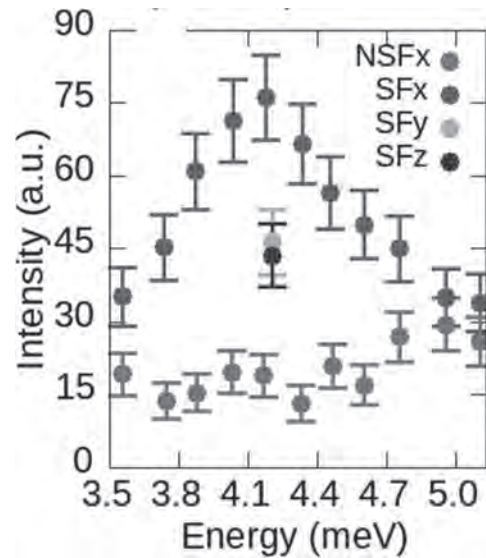
EC-12. Study of a new Type of Excitation in the Multiferroic Magnetolectric Compound $GdMn_2O_5$, the Electromagnon.

A. Vaunat¹, V. Balédent¹, P. Roy², S. Petit³, M. Lepetit⁴ and P. Foury¹
 1. *Laboratoire de Physique des Solides, Laboratoire de Physique des Solides, Orsay, Île-de-France, FR, academic/physics, Orsay, France;*
 2. *Synchrotron SOLEIL, Gif-sur-Yvette, France;* 3. *Laboratoire Leon Brillouin, Gif-sur-Yvette, France;* 4. *Institut NEEL, Grenoble, France*

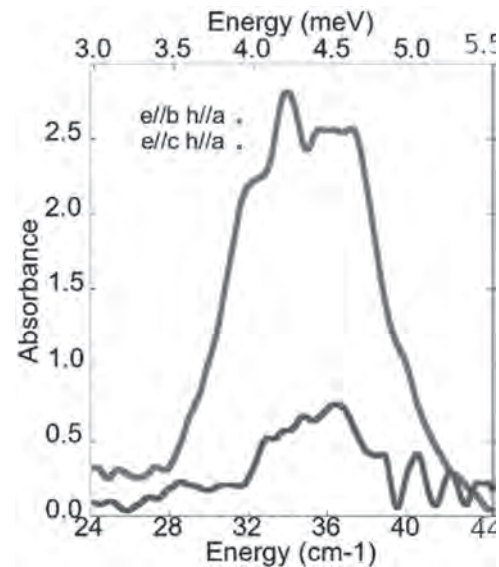
Magnetolectric multiferroics, which simultaneously stabilize magnetic and polar static orders, have been predicted to present unusual dynamical magnetolectric effects (ME). The relatively large magnitude of this dynamical ME response as well as its strong interaction with light is extremely attractive for potential applications among others are multifunctional spin-based memories or optical switches. The dynamical ME effects under consideration in this presentation, are characterized by the existence of an electro-active magnetic excitation called electromagnon. The electroactivity of electromagnons was first observed in type II multiferroics, where ferroelectricity is magnetically induced. In orthorhombic $RMnO_3$ and RMn_2O_5 ($R=Tb, Y$) families, both THz [1] and Raman [2] spectroscopies showed that this mode can be excited by means of the electric field of the light. The demonstration of the complementary magnetic nature of this excitation has been the prerogative of inelastic neutron scattering (INS) [3]. Sincethen, electromagnons have also been reported in Type I multiferroics hexagonal $RMnO_3$ [4], in $BiFeO_3$ and even in a paraelectric compound $Ba_2Mg_2Fe_{12}O_{22}$. To describe this unusual property, different mechanisms were proposed, in particular for the manganites families. These models basically rely on the very same magnetolectric coupling which accounts for the static properties: lattice vibrations alter the exchange couplings or anisotropies which in turn affect the magnon spectrum. In helical magnetic systems for instance, where the multiferroicity originates from Dzyaloshinskii-Moriya Interaction (DMI), the same DMI has been proposed to explain the origin of the electromagnon [5]. Although later refuted in $DyMnO_3$, such DMI based scenario seems to be at play in CuO . Other propositions are based on Exchange-Striction (ES) [6], and couple a polar lattice mode to the magnon spectrum [1]. So far, these models have been consistent with experimental results in $TbMn_2O_5$ [3]. These interpretations tend to reduce the definition of the electromagnon to a hybrid magnon-phonon mode, or, as proposed in $ErMnO_3$, to a mixing between a magnon and an electro-active rareearth crystal field transition [4]. In this presentation we question this issue and support the idea that electroactivity can be a purely electronic phenomenon. The RMn_2O_5 multiferroic compounds crystallize in the polar Pm space group [7] but present quasi-symmetries of the paraelectric $Pbam$ space group. Along the c direction, the structure is composed of chains of $Mn^{4+}O_6$ octahedra, separated by layers of R^{3+} or Mn^{3+} ions. In the (a,b) plane, zig-zag chains of $Mn^{4+}O_6$ octahedra and $Mn^{3+}O_5$ square-pyramids run along the a axis and are stacked along b . $GdMn_2O_5$, like the other members of the family, shows an Incommensurate Magnetic ordering (ICM) below $T_N=38$ K, with a magnetic propagation wave vector $k_1=(\frac{1}{2},0,0.28)$. Then, below $T_c=32$ K, the magnetic order becomes commensurate with a propagation wave vector $k_2=(\frac{1}{2},0,0)$, accompanied by the largest electric polarization known in type II multiferroics [8]. This strong electric polarization has been ascribed to two cooperative ES mechanisms [6]. As all members of the series, the electric polarization is mainly oriented along the b axis [8] even if few studies have recently suggested the existence of small additional components along the a and even the c directions. The dynamical properties of this compound have been studied by means of IR and INS on high quality single crystals. In this presentation, we will mainly focus on the demonstration and characterization of an electromagnon present in the compound $GdMn_2O_5$. More precisely, the IR measurements allowed us to demonstrate the existence of an excitation below the T_N , at an energy of 35cm^{-1} at 5K, which is electroactive because it is sensitive to the direction of the electric field of light (see fig. 1). The temperature tracking shows that this excitation disappears above the T_N , which shows the magnetic origin of this excitation. Moreover, INS measurements have allowed us to measure the excitation in the center of the magnetic zone $(\frac{1}{2},0,0)$ (see fig. 2), but also to measure its dispersion, which we have been able to interpret through simulations based on the «Holstein-Primakov» representation, which shows that this excitation is an electroactive spin wave, and thus an electromagnon. Polarized INS measurements (see fig. 2) allowed us to discriminate between

the nuclear and magnetic contributions, and to show that this excitation is purely magnetic, thus excluding the hypothesis of a coupling with a phonon. Finally, the presence of a crystalline field level was excluded by both INS and IR measurements, and by ab-initio calculations. Consequently, the electroactivity of this electromagnon is of a different nature than those observed in the past, and seems to have a purely electronic origin.

a[1] A. B. Sushkov, R. V. Aguilar and S. W. Cheong, Phys. Rev. L 98, 3 (2007) [2] P. Rovillain, Cazayous and A. Sacuto, Phys. Rev. B 86, 014437 (2012) [3] S. Petit, V. Balédent and P. Foury-Leylekian, Phys. Rev. B 87, 1 (2013) [4] L. Chaix P. Roy and V. Simonet, Phys. Rev. L 112, 1 (2014) [5] H. Katsura, A. V. Balatsky and N. Nagaosa, Phys. Rev. L 98, 1 (2007) [6] V. Balédent, M. B. Lepetit, and P. Foury-Leylekian, Phys. Rev. B 97, 5 (2018) [7] V. Balédent, S. Chattopadhyay and P. Foury-Leylekian, Phys. Rev. L 114, 117601 (2015) [8] B. Khannanov, E. I. Golovenchits and V. A. Sanina, J.Phys.: Conf. Series 572, 12046 (2014)



Inelastic polarized neutron scattering at $Q=(3/2,0,0)$ performed at THALES@ILL for 15 K. NSFx, SFx SFy and SFz stands for Non-Spin-Flip, Spin-flip with polarisation parallel to a, c and b crystallographic axis respectively.



Absorbance at 5 K with a reference at 40 K in Gd for $e//a$ $h//b$ & $e//b$ & $h//a$ (electric and magnetic field of the light) with respect to crystallographic axis.

EC-13. Magnetodynamic Properties of FeGaB/Al₂O₃ Multilayer Thin Film Stack for Microwave Applications.

Y. Karampuri¹, W. Yuxi¹ and W. Tao¹

¹. ShanghaiTech University, Shanghai, China

Integrated magnetic devices show great potential for applications of radio-frequency and microwave integrated circuits, such as chip-scale magnetic inductors, bandpass filters, phase shifters, etc. [1, 2]. Recently, many researchers have been vastly concentrating on ferromagnetic/insulator sandwich structure for high-frequency applications. This thin film stack reduces the eddy-current as well as the out-of-plane anisotropy [3, 4], reducing the energy dissipation in form of heat. The FeGaB has soft magnetic nature, a large magnetostriction coefficient, and saturated at lower magnetic fields. Due to the low loss property of Al₂O₃ in microwave frequency, we have attempted to obtain low damping (α) and narrow linewidth through the FeGaB/Al₂O₃ thin film stack and characterize the ferromagnetic resonance (FMR) by utilizing Cryo-FMR. In this article, Ta (5)/ [FeGaB (15)/ Al₂O₃ (3)] n /Ta (3) / Al₂O₃ (2) thin-film stack are deposited by DC and RF sputtering on Si substrate, where n indicates the number of multilayer ($n=1, 5,$ and 10) and parenthesis indicates thickness in nanometers. Fig.1 (a) shows normalized magnetic loop of the thin film stack, which reveals that the magnetic saturation moment has increased for increasing layer thickness. The coercive field (H_c) has a low value below 3 Oe as indicated in Fig.1 (b). The dynamical magnetic properties have been studied using NanoOsc Instruments Cryo-FMR in VersaLab system with temperature variation 300-100 K and exciting frequency from 2 to 20 GHz. The ferromagnetic absorption spectrum is shown in Fig.2 (a). The absorption spectrum contains the perpendicular standing spin wave (PSSW) modes for $n=5$ and $n=10$ in addition to FMR mode. The linewidth of absorption spectrum is fitted with $dH = dH_0 + \alpha f/\gamma$, ($d = \Delta$) to obtain damping factor (α), and inhomogeneous line width (dH_0) [5]. The thin film stack with $n=1$ has a narrow linewidth and a low damping factor compared to other two thin film stacks, as shown in Fig.2 (b). When the temperature decreases, the damping factor has decreased for $n=1$, but increased for $n=5$ and $n=10$ due to defects arise for lowering the temperature. The Fig.2 (c) shows temperature dependent inhomogeneous linewidth for thin film stacks. As the temperature lowering to 100 K, the dH_0 has increased for $n=1$ and $n=10$ thin film stacks, whereas decreased for $n=5$. The dH_0 is lower for $n=1$ and larger value for $n=5$. The frequency dependence of FMR fields (H_{res}) plot provides effective magnetization (M_{eff}) and magnetic anisotropy, when the plot has fitted to the Kittel equation. The M_{eff} has a lower value for $n=10$ than other two stacks. The M_{eff} has increased in all thin film stack as the temperature decreases. Since the absorption of the spectrum shows the PSSW modes in addition to FMR mode, the exchange magnetic fields (H_{ex}) have been calculated by the subtraction method [6]. The plot of H_{ex} and number of PSSW mode has provided the spin-wave exchange stiffness (A), saturation magnetization of thin film stack has multiplied with the exchange stiffness. At 300K, the A values are 7.1108, and 5.3213 pJ/m, respectively. In summary, we have deposited multilayer film stack of Ta (5)/ [FeGaB (15)/ Al₂O₃ (3)] n /Ta (3) / Al₂O₃ (2) onto Si substrates, and studied magnetodynamic (ferromagnetic resonance) properties with multilayer thickness and temperature dependence. The magnetic properties of thin film stack reveal that saturation magnetic moment has enhanced for increasing thickness of thin film stack, and H_c has obtained below 3 Oe. Therefore, the multilayer thin film stacks have the most significant for microwave applications. The dynamic magnetic properties suggest that the lowest damping and narrow linewidth are obtained for $n=1$ thin film stack compared to other thin film stacks. The FMR absorption spectrum of thin film stack with $n=5$, and $n=10$ show the PSSW modes in addition to the FMR mode. Consequently, the spin-wave exchange stiffness has been extracted. The temperature-dependent stiffness has followed the T^2 model, which provides the strong presence of electron-magnon interaction in materials. The constant of spin-wave exchange stiffness has calculated with help of saturation magnetic moment

and the exchange stiffness. Hence, the multilayer thin film stacks can be employed for microwave device applications.

- [1] Y. He, et.al, " *IEEE Trans. on Magn.*, vol. 54, no. 9, pp. 1-4, 2018.
 [2] T. Wu, et.al, *IEEE Magn. Lett.*, vol. 2, pp. 6000104-6000104, 2011.
 [3] X. Xing, et.al, *IEEE Trans. on Magn.*, vol. 47, no. 10, pp. 3104-3107, 2011. [4] T. Wu, et.al, *Appl. Phys. Lett.*, vol. 98, no. 1, pp. 012504, 2011.
 [5] K. Yadagiri, & T. Wu, *J. Magn. Magn Mater.*, vol. 515, pp. 167277, 2020/12/01/, 2020. [6] K. Yadagiri, et.al, *IEEE Trans. on Magn.*, vol. 57, no. 1, pp. 1-7, 2021.

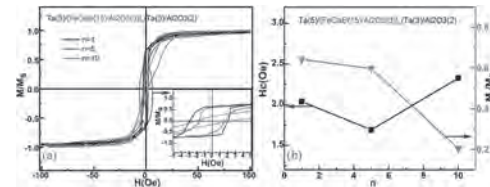


Fig.1 (a) Normalized M-H loop for Ta (5)/ [FeGaB (15)/ Al₂O₃ (3)] n /Ta (3) / Al₂O₃ (2); $n=1, n=5$ and $n=10$, inset of Fig.1 (a) shows the H_c of thin film stacks, (b) coercive field H_c (Oe) and M_r/M_s as a function of number of multilayer (n).

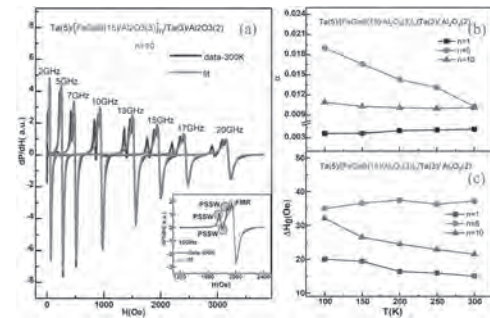


Fig.2 (a) The absorption spectra of Ta (5)/ [FeGaB (15)/ Al₂O₃ (3)] n /Ta (3) / Al₂O₃ (2); $n=10$ at 300 K with exciting frequencies 2-20 GHz; inset of figure shows absorption spectra at 15 GHz with FMR mode and PSSW modes, (b) the damping factor (α) versus temperature for thin film stack, and (c) the inhomogeneous linewidth (ΔH_0) as a function of temperature for Ta (5)/ [FeGaB (15)/ Al₂O₃ (3)] n /Ta (3) / Al₂O₃ (2).

Session ED

MAGNON SPINTRONICS

Satoshi Iihama, Co-Chair

Tohoku University, Sendai, Japan

Sergiu Ruta, Co-Chair

University of York, York, United Kingdom

INVITED PAPER

ED-01. Reconfigurable Magnonics Using Self-Biased Reprogrammable Nanomagnetic Structures INVITED.A. Haldar¹ and A.O. Adeyeye²¹. Physics, Indian Institute of Technology Hyderabad, Hyderabad, India;². Physics, Durham University, Durham, United Kingdom

Magnetic materials are at the hearts of billions of high frequency communication devices and on-chip integration of magnetic microwave devices is of paramount importance for efficient utilization of the huge electromagnetic (EM) spectrum beyond 5G. Magnonics – a sub-field of spintronics – employs magnetic waves and oscillations in magnetic thin films and patterned nanostructures for processing GHz to sub-THz EM signal [1-2]. Magnetic ferrites are conventionally used in such magnetic microwave devices. However, due to the need for external bias magnetic field and incompatibility with complementary metal oxide semiconductor (CMOS) process, ferrites are not suitable for miniaturized microwave components. On the other hand, metallic magnetic thin films and nanostructures have great potential for efficient engineering of microwaves. Although, the need for bias field remains a bottleneck. We have been working on solutions where the requirement of the bias-field is absent. We have successfully demonstrated several strategies for achieving such device architecture by utilizing self-biased nanomagnets with reprogrammable remanent states which are associated with distinct magnetization dynamics [2-11]. To illustrate reconfigurable microwave properties, we have shown in Fig 1 as an example, a pair of dipolarly coupled rhomboid nanomagnets (RNMs). Two different remanent states ($\uparrow\uparrow$ and $\uparrow\downarrow$) are obtained by utilizing a simple field initialization (H_i) scheme: applying a saturating field along short and long axes of the RNMs with subsequent removal of the field (Fig. 1(a)). Due to different distributions of the stray fields for the two remanent states, the effective fields (Fig. 1(b)) are different which manifest in the shift of the microwave spectra for the two remanent states. Measurement of microwave properties from a single isolated nanomagnetic pair was obtained by using micro-focused Brillouin light scattering (micro-BLS) experiment (Fig. 1(c)) and the micro-BLS spectra are shown in Fig. 1(d). This strategy for reconfigurable magnonic responses is expanded to 2D arrays of the RNMs for different magnetic configurations: antiferromagnetic-type and ferrimagnetic-type artificial magnonic crystals. The maximum amount of the shift in the microwave responses is achieved by using multilayer isolated as well as dipolar-coupled networks of RNMs. Beyond, RNM shape, we have also demonstrated reconfigurable microwave operation based on other strategic shapes with multiple remanent states, such as arrow-, C-, L- and S-type nanomagnets and zigzag nanowires. Furthermore, we emphasize that such self-biased nanomagnets are also suitable for magnonic device applications where the propagation and gating of magnons – quanta for spin waves – are of primary interest. Conventionally, a large bias magnetic field is used in order to satisfy an orthogonal orientation between spin wave propagation and magnetization direction for efficient transmission characteristics (known as surface geometry or Damon-Eshbach mode). The need of such bias field hinders device integration on-chip for magnonic waveguides. Therefore, we have proposed and demonstrated a self-biased magnonic waveguide based on dipolar-coupled but physically separated chain of RNMs (Fig. 2). A prototype of such magnonic devices is shown in Fig. 2(a) where a microwave antenna (input) excites the spin waves and the spin waves are detected using micro-BLS technique with a focused laser spot (output). In order to gate the spin wave propagation, we have flipped a RNM in the waveguide and it is marked as ‘gate’ in the scanning electron microscopy (SEM) image (Fig. 2(b)). Such waveguide design enables one to have two different remanent states: ferromagnetically ordered (FO) and FO with a defect (FO*) when field initialized (same scheme as mentioned above) along the width and the length of the waveguide, respectively. FO and FO* remanent magnetic states are shown in Fig. 2(b) using magnetic force microscopy (MFM) images. Gating of the spin wave propagation has been shown by plotting 2D spatial profiles of the spin wave intensities using micro-BLS technique which clearly indicate gated magnon flow for the FO* state in comparison to the FO state. Thus, one can also achieve binary gating

of output signal amplitude using such self-biased nanomagnetic waveguide which is remarkable as it also eliminates the need for bias field. In this presentation, we would like to emphasize the need for bias-free reconfigurable magnonics along with recent developments and future roadmap.

[1] A. Haldar, C. Tian and A. O. Adeyeye, *Sci. Adv.* 3, e1700638 (2017). [2] A. Haldar, D. Kumar and A. O. Adeyeye, *Nat. Nanotech.* 11, 437 (2016). [3] A. Haldar and A. O. Adeyeye, *ACS Nano.* 10, 1690 (2016). [4] A. Haldar and A. O. Adeyeye, *Appl. Phys. Lett.* 108, 192404 (2016). [5] A. Haldar and A. O. Adeyeye, *Appl. Phys. Lett.* 108, 022405 (2016). [6] A. Haldar and A. O. Adeyeye, *J. Appl. Phys.* 123, 243901 (2018). [7] K. Begari and A. Haldar, *J. Phys. D: Appl. Phys.* 51, 275004 (2018). [8] K. Begari and A. Haldar, *J. Phys. D: Appl. Phys.* 52, 335003 (2019). [9] K. Begari and A. Haldar, *J. Phys. D: Appl. Phys.* 53, 455005 (2020). [10] A. Haldar and A. O. Adeyeye, *Appl. Phys. Lett.* 116, 162403 (2020). [11] A. Haldar and A. O. Adeyeye, *J. Appl. Phys.* 128, 240902 (2020).

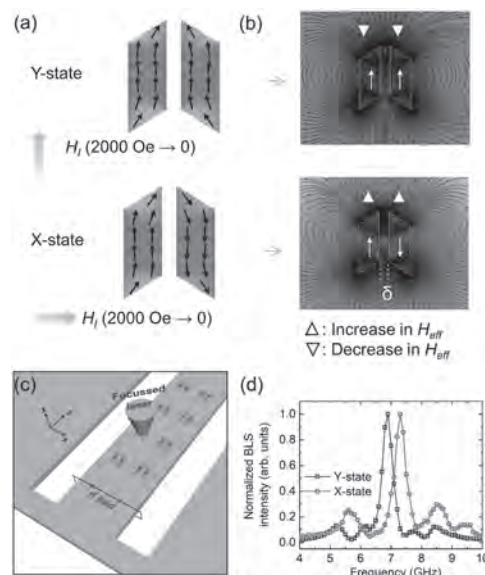


Figure 1: (a) Reprogrammable remanent states (X- and Y-state) of a RNM network. (b) Stray field distributions showing difference in the effective field for the two remanent states. (c) Measurement scheme from a single RNM network using micro-BLS technique. (d) Reconfigurable microwave responses for the two different remanent states.

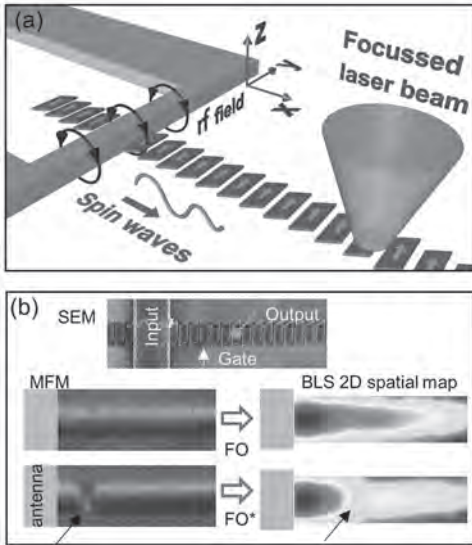


Figure 2: (a) Propagating spin wave measurement scheme from a RNM chain using micro-BLS technique. (b) Logic device based on dipolar coupled RNM chain is shown in the SEM image. MFM images show the two different magnetic states (FO and FO*). Logic operation is demonstrated by using 2D spatial maps of the spin wave propagation for the FO and FO* states.

CONTRIBUTED PAPERS

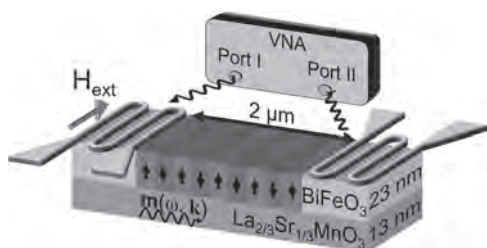
ED-02. Voltage-Controlled Magnonic Crystal at the Sub-Micron Scale.

H. Merbouche¹, I. Boventer¹, V. Haspot¹, S. Fusil¹, V. Garcia¹, D. Gouéré¹, C. Carrétéro¹, A. Vecchiola¹, R. Lebrun¹, P. Bortolotti¹, L. Vila², M. Bibes¹, A. Barthélémy¹ and A. Anane¹

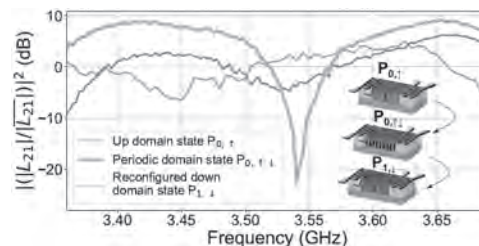
1. *Unite Mixte de Physique CNRS/Thales, Palaiseau, France*; 2. *CEA, CNRS Grenoble INP, Spintec, Université Grenoble Alpes, Grenoble, France*

Magnonics where magnons, the associated quasiparticles of spin waves are used to perform advanced logical or analogue functions represents a promising paradigm for new means of information processing for beyond complementary metal oxide semiconductor (CMOS) based architectures. Furthermore, in view of the emerging nano-magnonics which can eventually lead to a large-scale integration of magnonic devices new approaches for a compact, reconfigurable operation of magnonic device are required. Although such a reconfigurability is key to any efficient application such as magnonic filters, it has hitherto only theoretically [1] but not experimentally been shown on a sub-micron scale. On the other hand, multiferroics inherently offer compact means to implement voltage-control and reconfigurability in such microscopic magnonic systems [2]. In this work, we combine multiferroics with ferromagnets by employing a fully epitaxial heterostructure to achieve such voltage-controlled and reconfigurable magnonic system. Frequency filtering is most often based on magnonic crystals (MC) where a periodic modulation of the spin wave's energy landscape results in frequency bandgaps in the magnon spectrum [3,4]. Here, we employ a thin-film multiferroic bismuth ferrite BiFeO₃ (BFO)- lanthanum strontium manganite La_{2/3}Sr_{1/3}MnO₃ (LSMO) heterostructure with a low Gilbert damping $\sim 6 \times 10^{-3}$ for the LSMO layer. Instead of modulating the sample shape, we create a MC by imprinting a periodic remnant electrical polarization in the multiferroic BFO layer which modulates the effective magnetic field in the ferromagnetic layer. We characterize the spin wave propagation spectra in this artificial, voltage-induced magnonic crystal and demonstrate the occurrence of a robust magnonic bandgap with >20 dB rejection, i.e. filtering. The imprinted ferroelectric domains can be reconfigured repeatedly and are long-lived. Our results open a new path for the transduction and configurable filtering of spin waves within a single magnonic device. In general, bridging between the scientific fields of functional oxides and magnonics, it opens new perspectives for the development of beyond CMOS based technologies [5].

[1] Q. Wang, A. V. Chumak, L. Jin *et al.*, *Phys. Rev. B* 95, 134433 (2017) [2] N. Spaldin and R. Ramesh, *Nat. Mat.* 18, 203-212 (2019) [3] P. Frey, A.A. Nikitin, D. Bozhko *et al.*, *Commun Phys* 3, 17 (2020) [4] A. V. Chumak, A. A. Serga and B. Hillebrands, *J. Phys. D: Appl. Phys.* 50, 244001 (2017) [5] H. Merbouche, I. Boventer, V. Haspot *et al.*, submitted



Schematics of the experimental setup shown for the periodic ferroelectric domain state for the BFO layer.



Evidence for the bandgap for the BFO/LSMO heterostructure with periodic domains in the BFO in the amplitude representation in logarithmic scale. The data is normalized by the mean amplitude. At the bandgap frequency, the amplitude is dropping by >20 dB. A reconfiguration of the periodic domain state to the uniform down state erases the gap and reconstitutes the initial uniform state's response. P_{n,m} label the different domain states where n is the cycle number (1 cycle : down (virgin)-> up-> periodic->) and m the direction of the ferroelectric polarization.

ED-03. Micromagnetic Simulations of Spin Waves Propagation by SOT in a Bi-YIG Waveguide.

A. El Kanj¹, H. Merbouche¹, D. Gouéré¹, I. Boventer¹, R. Lebrun¹, P. Bortolotti¹, V. Cros¹ and A. Anane¹

1. Unite Mixte de Physique CNRS/Thales, Palaiseau, France

In the last decades, the investigation of microwave spin waves (SW) in thin magnetic films has been an attractive field of research due to their very short wavelength reaching down to nanometers at GHz frequencies. SW also have a rich dispersion relation, that depends on their propagation direction with respect to a magnetic field. Hence, SW -based devices are promising candidates for microwave information processing, and eventually for overcoming the limitations encountered with CMOS-devices such as power consumption. In magnonic devices, a key challenge is to achieve long propagation distances of the spin waves. This requires to work with magnetic materials with small magnetic damping such as Yttrium Iron Garnet (YIG). (YIG), has by far the lowest magnetic damping which allows the spin waves propagation to be spread over millimeter-scale distances making it a reference material for spin-wave dynamics studies. Kajiwara and al. [1] confirmed that an electric current injection in a YIG film can be converted into spin-waves. In fact, when placing a non-magnetic metal with a high spin orbit coupling such as platinum on top of a magnetic insulator such as YIG, flow of charge current in the metal leads to its conversion into a pure spin current (via the Spin Hall Effect), which is then injected in the magnetic insulator where it adds up as an additional torque on the YIG's magnetization. The above-mentioned mechanism of STT generation originating from pure spin-current obtained through the spin-orbit interaction of a heavy metal is called spin orbit torque (SOT). Recent studies [2], [3] with Platinum stripes placed on top of a 20 nm thick YIG waveguide (Pt/YIG) showed that SOT could generate a full compensation of the damping, leading to auto-oscillations of the magnetization above a critical injected current density. When excited with a microwave field, spin waves propagation length was increased by a factor of 10 in the bilayer. However, the possibility to achieve an amplification of propagating spin-waves was not observed yet, due to the onset of nonlinear dissipative processes above the critical current. More recently, materials having perpendicular magnetic anisotropy have demonstrated a full damping compensation along with SW emission, such behavior is accomplished by substituting Bismuth in YIG [4]. Here, we report on a study of SW propagation driven by SOT in a Pt/Bi-YIG waveguide where SW are detected using micro-focused Brillouin Light Scattering spectroscopy (BLS). The 20 nm thick and 21 μm long Bi-YIG waveguide is covered with 7 nm of Platinum. The experiments show the lossless propagation of a pulse of spin-waves excited by an rf-field generated by an antenna placed on top of the waveguide, under zero or positive damping during the course of 200 ns. Here, we show the full scale micromagnetic simulations done to emulate this experiment. The result shows a verification of the lossless propagation of SWs as seen in the experiment. By including a realistic Gilbert damping parameter and the Slonczewski torque to the Bi-YIG structure to compensate the magnetic losses, the results reproduce not only the steady state dynamics but also transitional dynamics when the rf-excitation is turned on and off at the ns time-scale. In summary, the inclusion of STT in the micromagnetic simulations showed an accordance with the experimental results, which verifies the ability to obtain a lossless propagation of SWs in the Bi-YIG waveguide and their non-suppression even after a hundred of nanoseconds after cutting off the excitation field.

[1] Y. Kajiwara *et al.*, "Transmission of electrical signals by spin-wave interconversion in a magnetic insulator," *Nature*, vol. 464, no. 7286, Art. no. 7286, Mar. 2010 [2] M. Collet *et al.*, "Generation of coherent spin-wave modes in yttrium iron garnet microdisks by spin-orbit torque," *Nat. Commun.*, vol. 7, no. 1, Art. no. 1, Jan. 2016 [3] M. Evelt *et al.*, "High-efficiency control of spin-wave propagation in ultra-thin yttrium iron garnet by the spin-orbit torque," *Appl. Phys. Lett.*, vol. 108, no. 17, p. 172406, Apr. 2016 [4] L. Soumah *et al.*, "Ultra-low damping insulating magnetic thin films get perpendicular," *Nat. Commun.*, vol. 9, no. 1, Art. no. 1, Aug. 2018

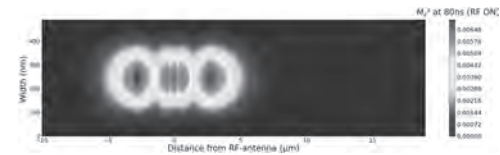


Fig.1: Two dimensional colormap showing the spin waves intensity in the simulated Bi-YIG waveguide after 80 ns from turning the rf-excitation on.

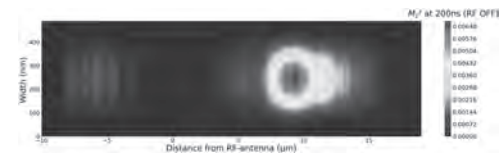


Fig.2: Two dimensional colormap showing a lossless propagation of the SW intensity under SOT amplification, 100 ns after emission. The extracted group velocity is 55 m/s. The intensity of z-component of the magnetization is identical to that of Fig.1 recorded at a timestamp of 80 ns.

ED-04. Short-Range Thermal Magnon Diffusion in Magnetic Garnet.

K. An¹, R. Kohno¹, N. Thiery¹, D. Reitz⁵, L. Vila¹, V.v. Naletov^{1,2}, N. Beaulieu³, J. Ben Youssef³, G. de Loubens⁴, Y. Tserkovnyak⁵ and O. Klein¹

1. CEA, CNRS, Spintec, Universite Grenoble Alpes, Grenoble, France;

2. Institute of Physics, Kazan Federal University, Kazan, Russian Federation;

3. LabSTICC, CNRS, Universite de Bretagne Occidentale, Brest, France;

4. SPEC, CEA-Saclay, CNRS, Universite Paris-Saclay, Gif-sur-Yvette, France;

5. Department of Physics and Astronomy, University of California Los Angeles, Los Angeles, CA, United States

Conversion of heat into spin current has recently drawn a lot of attention due to its potential usage on heat recovery via the spin Seebeck effect (SSE) [1] as well as fundamental interests including generation of spin super currents [2] and Bose-Einstein condensation of magnons [3]. The underlying mechanism for SSE is understood as a combination of interfacial and bulk (intrinsic) contribution. The interfacial SSE is driven by the temperature drop at the interface between metal and magnetic layer while the bulk SSE is driven by diffusive thermal magnons. In the nonlocal spin transport measurements, the long range exponential decay of thermally generated spin signal was explained solely by the intrinsic SSE [4] while there are several studies showing that there is another decay mechanism in subhundred nanometer scale [5-7]. Here, we study the spatial decay of thermally excited magnon currents inside a thin magnetic insulator by focusing on the short-range behavior in the nonlocal geometry. We compare SSE signal ($\Delta_{1,2}$) on the same device before and after adding a nonmagnetic Al capping layer. The Al capping alters the thermal profile significantly near the heat source, which results in that the nonequilibrium thermal magnon profile deviates from an exponential decay and shows two sign reversals within 1 μm from the heat source. From simulated temperature profiles, we find the vertical temperature gradient also reverses twice within the same length scale in the Al deposited case. The correlation suggests that thermal magnons behave locally at this length scale. Using a phenomenological spin transport model, we calculate the spatial profile of nonequilibrium spin density. The observed short-range behavior can be accounted if the relevant decay length is on the order of subhundred nanometers. Our result shows the existence of the shorter decay length in the nonlocal magnon transport experiments. This suggests that the long-range SSE signal in previous measurements should be attributed to magnons with lower energy.

[1] S. R. Boona, R. C. Myers, and J. P. Heremans, *Energy & Environmental Science*, 7, 885 (2014). [2] D. A. Bozhko, A. A. Serga, P. Clausen, et al., *Nature Physics*, 12, 1057 (2016). [3] Y. Tserkovnyak, S. A. Bender, R. A. Duine, et al., *Physical Review B*, 93, 100402. (2016). [4] L. J. Cornelissen, J. Liu, R. A. Duine, et al., *Nature Physics*, 11, 1022 (2015). [5] A. Kehlberger, U. Ritzmann, D. Hinzke, et al., *Physical Review Letters*, 115, 096602. (2015). [6] A. Prakash, B. Flebus, J. Brangham, et al., *Physical Review B*, 97, 020408. (2018). [7] J. S. Jamison, Z. Yang, B. L. Giles, et al., *Physical Review B*, 100, 134402. (2019).

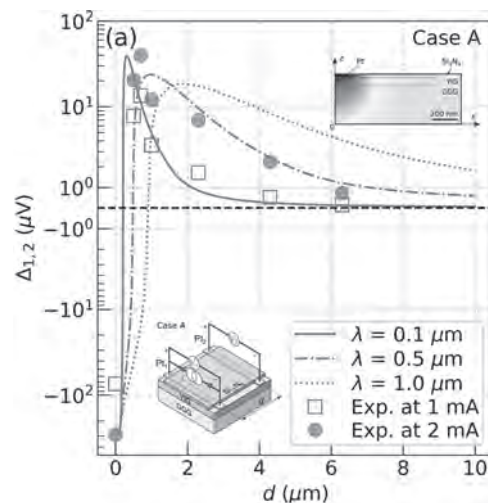


Fig.1: Comparison of the experimentally measured local and non-local SSE signals ($\Delta_{1,2}$) at 1 and 2 mA injection and the numerically calculated chemical potential profiles with different input values of decay length λ for YIG/Pt/Si₃N₄ (case A) on a symmetric log scale. The insets show the schematic of the sample structure (bottom left) and temperature profile (top right).

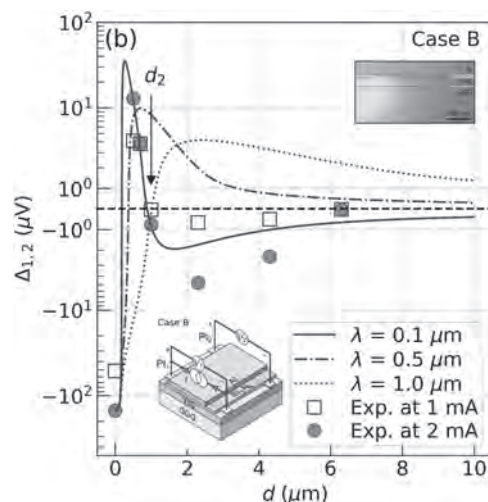


Fig.2: Same plots as Fig.1 for YIG/Pt/Si₃N₄/Al (case B). The result with $\lambda = 0.1 \mu\text{m}$ reproduces the measured double crossing as shown, revealing the short range thermal magnon diffusion. The second crossing does not appear anymore when increasing λ to 0.5 or 1 μm . The insets show the schematic of the sample structure (bottom left) and temperature profile (top right).

ED-05. Spin-Wave Emission From Vortex Cores Under Static Magnetic Bias Fields.

S. Mayr^{1,2}, L. Flajšman^{3,4}, S. Finizio¹, A. Hrabec^{1,2}, M. Weigand⁵, J. Förster⁶, H. Stoll⁶, L. Heyderman^{1,2}, M. Urbánek³, S. Wintz^{1,6} and J. Raabe¹

1. Paul Scherrer Institut, Villigen, Switzerland; 2. Department of Materials, ETH Zurich, Zurich, Switzerland; 3. CEITEC BUT, Brno University of Technology, Brno, Czechia; 4. Department of Applied Physics, Aalto University, Aalto, Finland; 5. Helmholtz-Zentrum Berlin für Materialien und Energie GmbH, Berlin, Germany; 6. Max-Planck-Institute Stuttgart, Stuttgart, Germany

Spin waves are collective excitations of a spin system, where the magnetic moments precess with a spatially periodic phase shift that determines the wavelength [1]. From a technological point of view, the use of spin waves as signal carriers in future spintronic logic and memory devices has the advantages of a potentially lower power consumption and improved miniaturization prospects compared to the present charge-based CMOS technology [2]. For achieving nanoscale integration, topological spin textures such as magnetic vortex cores can be driven by alternating magnetic fields to excite coherent spin waves with short, sub-micrometer wavelengths, as shown recently for both synthetic ferrimagnetic systems and single ferromagnetic layers [3, 4]. In this contribution, we will demonstrate the versatility of this excitation mechanism by showing that the application of a static magnetic bias field makes the vortex core a manipulable spin-wave source that can be continuously translated in space without altering the resulting spin-wave dispersion relation [5]. We employ time-resolved scanning transmission x-ray microscopy (TR-STXM) to directly image vortex-core spin textures as well as the emission and propagation of spin waves from them. By applying a static in-plane magnetic bias field, we can continuously displace the vortex core from its equilibrium position in the center of a structured element. For a synthetic ferrimagnet (Co/Ru/Ni₈₁Fe₁₉), it is possible to shift the core relatively close to the edge while maintaining a radial, isotropic spin-wave emission pattern (see Figure 1). The wavelengths of the excited spin waves are not noticeably changed by the applied magnetic bias field, but remain tunable by the driving frequency in the same way as without bias field. For a single Ni₈₁Fe₁₉ layer with a thickness of the order of 100 nm, we observe a similar behavior for relatively small magnetic bias fields but when the vortex core approaches the edge of the disk, it also expands (see Figure 2). This expansion can be seen as a transformation from a zero-dimensional point source to a one-dimensional curved object where its shape and extent is controlled by the magnitude of the applied magnetic bias field. Such an expansion leads to a directional emission of the spin waves that propagate away from the core in mainly two opposite directions rather than radially as observed for non-expanded cores. For certain combinations of magnetic bias fields and driving frequencies, focusing effects appear. Such effects provide promising means for a controlled and directional propagation of spin waves without the need for additional patterning or waveguides.

[1] A.G. Gurevich and G.A. Melkov, *Magnetization Oscillations and Waves*. Vol. 1, CRC Press (1996) [2] A.V. Chumak *et al.*, *Nat. Phys.* Vol.11, p.453-461 (2015) [3] S. Wintz *et al.* *Nat. Nanotechnol.* Vol.11, p.948-953 (2016) [4] G. Dieterle *et al.*, *Phys. Rev. Lett.* Vol.122, p.117202 (2019) [5] S. Mayr *et al.*, *Nano Lett.* accepted (2021)

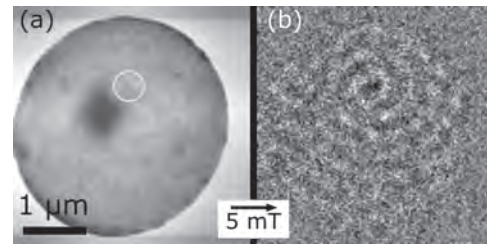


Fig. 1: TR-STXM snapshots of a synthetic ferrimagnet, taken with out-of-plane magnetic sensitivity at the Fe L₃ edge at a magnetic bias field of 5 mT. (a) Absolute absorption image showing the black vortex core shifted from the center of the structure (green circle). (b) Normalized contrast displaying the radial spin-wave emission from the core for a 1 GHz alternating field excitation.

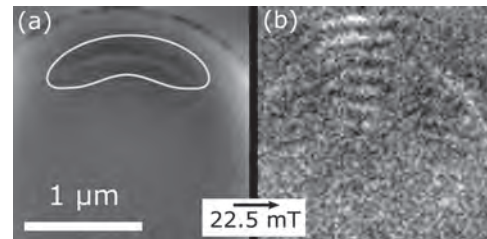


Fig. 2: TR-STXM images with out-of-plane sensitivity displaying the response of the vortex in a Ni₈₁Fe₁₉ layer to a magnetic bias field of 22.5 mT. (a) Absolute absorption image showing the expansion of the vortex core (encircled in green). (b) Normalized image displaying only the temporal changes with respect to the average magnetization, showing the spin waves emitted from the expanded vortex core in two directions for an excitation frequency of 8.6 GHz.

ED-06. Parity-Controlled Spin-Wave Excitations in Synthetic Antiferromagnets.

A. Sud^{1,2}, Y. Koike³, S. Iihama³, C.W. Zollitsch², S. Mizukami³ and H. Kurebayashi^{1,2}

1. Electronic and Electrical Engineering, University College London, London, United Kingdom; 2. London Centre for Nanotechnology, London, United Kingdom; 3. Tohoku National University, Sendai, Japan

Synthetic antiferromagnets (SyAFs) are an excellent platform to explore novel spintronic and magnonic concepts with coupled magnetic moments[1,2]. Unlike a homogeneously magnetised single-layer ferromagnet, coupled magnetic layers are able to offer rich magnetic states where the competition between interlayer exchange coupling, external-field-induced Zeeman interaction as well as other magnetic anisotropy terms plays a role. This can expand into their dynamic regimes as the coupled moment nature inherently provides two eigenmodes, acoustic and optical modes[3-7], where time-dependent components of two coupled moments are oscillating in-phase (acoustic) and out-of-phase (optical) in a spin-flop (canted) regime. When we excite spin-waves by oscillating magnetic fields, the spatial symmetry/profile of microwave excitation determines which spin-wave modes are excited. In the simplest case, a uniform distribution of microwave excitation fields across a magnet can excite the uniform spin-wave mode (wavevector $k = 0$) as well as higher-order spin-wave resonance modes ($k > 0$) with odd index numbers since the spatial profile of the microwave excitation and spin-wave mode amplitude (with phase) matches to each other in terms of symmetry. This in turn suggests that it should be possible to control the selection rules of spin-wave excitations by designing the spatial profile of excitation fields. Accessing hidden spin-wave states as well as tailoring spin-wave excitation efficiency by this approach has not been much explored in the past. We report in this work the current-induced-torque excitation of acoustic and optical modes in Ta/NiFe/Ru/NiFe/Ta synthetic antiferromagnet stacks grown on SiO₂/Si substrates (Fig 1(a)). The two Ta layers serve as spin torque sources with the opposite polarisations both in spin currents and Oersted fields acting on their adjacent NiFe layers. This can create the odd symmetry of spatial spin torque distribution across the growth direction, allowing us to observe different spinwave excitation efficiency from synthetic antiferromagnets excited by homogeneous torques. We analyse the torque symmetry by in-plane angular dependence of symmetric and anti-symmetric lineshape amplitudes for their resonance (as shown in Fig 2(a-b)) and confirm that the parallel (perpendicular) pumping nature for the acoustic (optical) modes in our devices, which is in stark difference from the modes excited by spatially homogeneous torques. The terms parallel (perpendicular) pumping here signify that the torque (hence spin-wave excitation efficiency) is maximised when the oscillating fields and dc magnetic field are collinear (perpendicular) to each other respectively. This is evident from Fig 2(c-d) that strongly suggests the torque symmetry for the acoustic (optical) mode excitation being of form $\sin \Phi$ ($\cos \Phi$). We also generalize macrospin model for this particular spin-torque excitation geometry, which excellently supports our experimental observation. Our results offer capability of controlling spin-wave excitations by local spin-torque sources and we can explore further spin-wave control schemes based on this concept. We envisage that the control of spin-wave excitations in STT nanodevices will be useful for future spintronic and magnonic nano-devices.

[1] R. A. Duine, K.-J. Lee, S. S. P. Parkin, and M. D. Stiles, Nat. Phys. 14, 217 (2018). [2] A. V. Chumak, V. I. Vasyuchka, A. A. Serga, and B. Hillebrands, Nat. Phys. 11, 453461 (2015). [3] F. Keffer and C. Kittel, Phys. Rev. 85, 329 (1952). [4] J. J. Krebs, P. Lubitz, A. Chaiken, and G. A. Prinz, J. Appl. Phys. 67, 5920 (1990). [5] S. M. Rezende, A. Azevedo, and R. L. Rodriguez-Surez, J. Appl. Phys. 126, 151101 (2019). [6] A. Sud, Y. Koike, S. Iihama, C. Zollitsch, S. Mizukami, H. Kurebayashi, arXiv:2012.12999. [7] A. Sud, C. W. Zollitsch, A. Kamimaki, T. Dion, S. Khan, S. Iihama, S. Mizukami, and H. Kurebayashi, Phys. Rev. B 102, 100403(R) (2020).

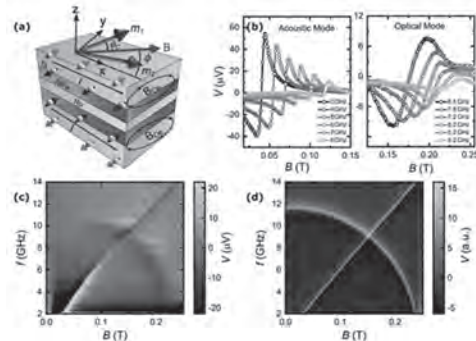


FIG. 1: (a) A schematic of the sample geometry used for STT-FMR measurements in our study. (b) V obtained at different frequencies for acoustic and optical modes in our device for $\Phi = 55^\circ$ (the values for some frequencies have been scaled to show them properly). (c) A 2D colorplot of V as a function of applied field and frequency, measured for $\Phi = 55^\circ$. (d) Numerical results calculated for the experimental conditions as in (c).

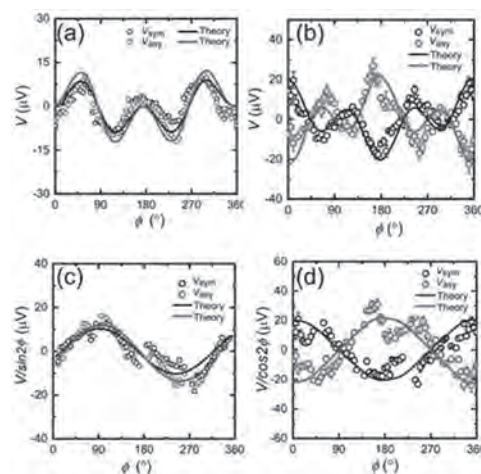


FIG. 2: (a-b) Angular dependence of symmetric (V_{sym}) and antisymmetric (V_{asy}) components of voltage for (a) acoustic mode measured at 8 GHz and (b) optical mode measured at 8.5 GHz. The solid curves are obtained using theoretical model. (c-d) The symmetry of torques obtained by dividing the Voltage by (c) $\sin 2\Phi$ for acoustic mode and (d) $\cos 2\Phi$ for optical mode. The dominant $\sin \Phi$ ($\cos \Phi$) dependence of torques confirms the parallel (perpendicular) pumping configuration.

ED-07. Insight on the Effect of SOT on Propagating Magnons: Spin-Wave Amplification and Frequency Dependent Efficiency.

H. Merbouche¹, B. Divinskiy², D. Gouéré¹, C. Calo³, P. Bortolotti⁴, V. Cros¹, A. Anane¹, V.E. Demidov² and S. Demokritov²

1. *Unite Mixte de Physique CNRS/Thales, Palaiseau, France;*
 2. *Westfälische Wilhelms-Universität Munster, Munster, Germany;* 3. *III-V Lab, Palaiseau, France;* 4. *Thales Research and Technology France, Palaiseau, France*

Spin wave (SW) based computing i.e. magnonics relies on propagating SW as information carriers. Being quasiparticles, magnons (the SW quanta) have a finite lifetime characterizing the exponential decay of the magnons population. Consequently, up to now, all magnonic devices operate within a short time-window and on short propagation distances. Finding a SW amplification paradigm is hence a prerequisite for the development of magnonics as a credible CMOS alternative. Two schemes are currently envisioned for SW amplification: Parametric pumping¹ and spin-orbit-torque amplification (SOT)². Here we will discuss SOT amplification in BiYIG/Pt bilayer³ (Fig.1). Using micro Brillouin light scattering spectroscopy (μ -BLS) on a 500 nm wide Pt/BiYIG waveguides, we take advantage of the strong BLS signal of BiYIG (nearly two orders of magnitude the one of YIG³) to extensively study the influence of SOT on coherent propagating magnon modes. By passing current in the Pt layer, the spin accumulation resulting from the spin-Hall effect induces a positive torque that compensates the Gilbert damping of BiYIG when the magnetic field orientation is perpendicular to the waveguide axis. At subcritical values, the current has a linear effect that lowers the effective damping, thus significantly increasing the decay length of the propagating magnons, similar to what was observed previously in a YIG/Pt waveguide⁴. However, by increasing the excitation frequency of these propagating magnons for a constant external field, we observe a gradual but strong decrease of the modulation efficiency of their lifetime in our BiYIG/Pt waveguide. Once the current in the Pt layer reaches a threshold value, the vanishing effective damping allows for the onset of the auto-oscillation regime⁵ where the thermal magnons get incoherently amplified and the magnetization auto-oscillates in the main uniform mode. However, coherent propagating magnons strongly interact with the auto-oscillations⁶, preventing the observation of their propagation at continuous supercritical current. To circumvent these non-linear interactions, we study the auto-oscillation transient regime for the first time by performing time-resolved μ -BLS measurements. When the SOT is switched on, the uniform auto-oscillation grows exponentially, in agreement with the Slavin & Tiberkevitch non-linear auto-oscillator model⁷ in the linear regime limit. The onset of non-linearities only occurs when the auto-oscillation reaches its stable orbital, after few hundreds of nanoseconds typically. Using a rf and DC pulse scheme, we propagate rf-excited magnons before the onset of non-linearities at supercritical currents and observe the amplification of propagating magnons (Fig. 2-a). Similarly to what was observed in the continuous regime at subcritical currents, the modulation efficiency of the propagating magnons lifetime strongly decreases with frequency (Fig. 2-b). This experiment sheds new light on the influence of SOT on propagating magnons and pave the way toward a magnonic spin-wave amplifier using DC current.

¹ T. Brächer, P. Pirro, and B. Hillebrands, *Phys. Rep.* 699, 1 (2017). ² V.E. Demidov, S. Urazhdin, A. Anane, V. Cros, and S.O. Demokritov, *J. Appl. Phys.* 127, 170901 (2020). ³ L. Soumah, N. Beaulieu, J. Ben Youssef, and A. Anane, *Nat. Commun.* 9, 3355 (2018). ⁴ M. Evelt, V.E. Demidov, and A. Anane, *Appl. Phys. Lett.* 108, 172406 (2016). ⁵ M. Collet, V. Cros, A. Anane, G. de Loubens, and O. Klein, *Nat. Commun.* 7, 10377 (2016). ⁶ B. Divinskiy, S. Urazhdin, S.O. Demokritov, and V.E. Demidov, *Nat. Commun.* 10, 5211 (2019). ⁷ A. Slavin and V. Tiberkevitch, *IEEE Trans. Magn.* 45, 1875 (2009).

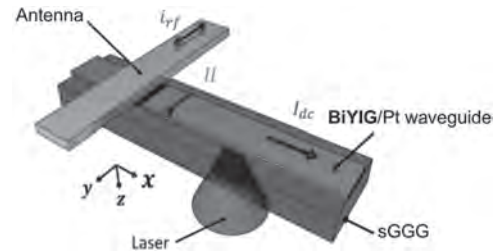


Fig. 1 : Schematic representation of the 0.5 μ m-wide BiYIG/Pt waveguide. The DC current is applied in the Pt along the waveguide axis and a 300nm-wide strip rf-antenna is used to excite propagating magnons. The μ -BLS laser spot is focused from the back of the sample.

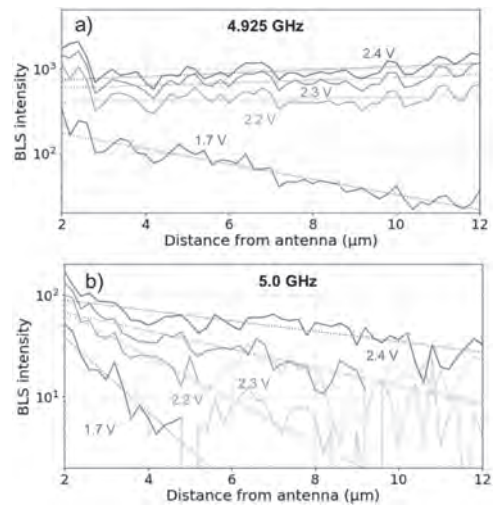


Fig. 2 : Spin-wave intensity as a function of the distance to the antenna. The experimental curves (solid lines) are linearly fitted (dotted lines) in log scale for 4 frequencies (only 2 shown here) 4.925 GHz (a), 4.95 GHz, 4.975 GHz and 5.0 GHz (b) and 4 DC voltages corresponding to one subcritical current (1.7V) and three supercritical currents (2.2, 2.3 and 2.4V). The FMR is constant during the pulse with value 4.885 ± 0.01 GHz. The positive slope at supercritical currents at 4.925 GHz indicates an amplification of the propagating spin-waves (negative effective damping) due to SOT. The damping compensation efficiency gradually decreases as the frequency is increased, and the spin-waves are no longer amplified at 5.0 GHz for the applied voltages.

ED-08. Antiferromagnetic Artificial Neural Networks With Symmetric Coupling.

H. Bradley¹, S. Louis¹ and V. Tyberkevych¹

¹ Physics, Oakland University, Rochester, MI, United States

Artificial neural networks (NN) running on traditional computing hardware tend to be relatively slow and power-hungry. One possible solution to this issue is to create hardware with neurons that spike in a manner similar to biological neurons. For example, Intel [1] and IBM [2] have recently fabricated neuromorphic chips based on spiking NN. Still, neurons in these chips are fabricated with multiple silicon transistors, which limits power efficiency of such an approach. The development of neuromorphic chips would benefit from a nanoscale, single element synthetic neuron that behaves in a manner that closely resembles a biological neuron. Such a synthetic neuron can be fabricated with nanometer dimensions from an antiferromagnetic (AFM) material mounted on platinum [3]. These “AFM neurons” are spin Hall oscillators driven by a sub-threshold spin current that can produce ultra-short (~ 5 ps) spikes in response to a weak external stimulus. In traditional spiking NN, synapses that connect artificial neurons are formed by complex active circuits. A much simpler approach would be to use passive memristors as artificial synapses [4]. However, memristors create *symmetric coupling* between neurons, which allows a spike produced by one neuron to travel to all neighboring neurons, both forwards and backwards. Unfortunately, this bi-directional signal propagation makes use of standard machine learning algorithms impossible. Therefore, it would be interesting to design NN in which unidirectional spike propagation is possible even with symmetrically coupled neurons. Here, we demonstrate that the unidirectional signal propagation is realizable in symmetrically-coupled NNs based on AFM neurons. This regime is possible due to an effective inertia that originates from exchange coupling between the two magnetic sublattices [3] and creates a relatively long refractory period - an interval of time after a neuron fires when it is unable to fire again. We show, that it is possible to adjust synapse weights such that each neuron is still in its refractory period when it receives a backward propagating signal from its neighbors. Then, a simple chain of neurons receiving an input at one end carry the signal to the opposite end without any reflections. However, for such a simple chain of AFM neurons, an input can occur at either end, and thus spikes would be able to travel in both directions. It would be beneficial to create an ‘isolator’ neuromorphic circuit, which would allow the propagation of spikes in only one direction. Figure 1 depicts the schematic of a possible ‘isolator’ circuit composed of AFM neurons. This figure uses circles to represent AFM neurons. The isolator is composed of neurons 4, 5, and 6. In the figure, double arrows represent symmetrical synapses with arrow width proportional to the coupling strength. This isolator allows spikes to be carried “forwards” from neuron 1 to 9, but stops signals carried “backwards” from neuron 9 to 1, as illustrated by the results of numerical simulations shown in Fig. 2. The isolator functions as follows. When the spike is initiated in neuron 1 (Fig. 2(a)), it travels along the chain to neuron 4. Then, the spike generated by neuron 4 travels to both neuron 5 and neuron 6. Neuron 5 also generates a spike, which is carried to neuron 6. The synaptic weights connecting to neuron 6 are small enough that a single input is not sufficient to induce a spike in the AFM neuron. However, when both spikes combine at neuron 6, they provide enough stimulus for neuron 6 to fire. The spike can then continue to propagate from neuron 6 to 9. When traveling backwards (Fig. 2(b)), a spike begins at neuron 9 and travels unidirectionally to neuron 6. Neuron 6 will generate a spike, but the synaptic weights from neuron 6 to 4/5 are insufficient to induce an additional spike. This, in effect, prevents the backward travel of spikes through the isolator. Using the proposed isolator NN, it is possible to design a number of other neuromorphic circuits supporting unidirectional information propagation, for example, neuromorphic combiners and unidirectional memory rings. The creation of such circuits with symmetric synapses shows hope for AFM neurons to be used to create more realistic spiking NN. The delay caused by the exchange inertia in the AFM neurons plays a key role in any neuromorphic circuit constructed with these neurons. These physically realistic neurons will increase the possibility for more functional spiking neural network hardware.

[1] M. Davies et al., *Loihi: A Neuromorphic Manycore Processor with On-Chip Learning*, in *IEEE Micro*, vol. 38, no. 1, pp. 82-99, January/February 2018, doi: 10.1109/MM.2018.112130359. [2] M. V. DeBole et al., *TrueNorth: Accelerating From Zero to 64 Million Neurons in 10 Years*, in *Computer*, vol. 52, no. 5, pp. 20-29, May 2019, doi: 10.1109/MC.2019.2903009. [3] R. Khymyn, I. Lisenkov, J. Voorheis, O. Sulymenko, O. Prokopenko, V. Tiberkevich, J. Akerman, and A. Slavin, *Ultra-fast artificial neuron: generation of picosecond-duration spikes in a current-driven antiferromagnetic auto-oscillator*, *Scientific Reports* 8, 15727 (2018). [4] Sung Hyun Jo, Ting Chang, Idongesit Ebong, Bhavitavya B. Bhadviya, Pinaki Mazumder, and Wei Lu *Nanoscale Memristor Device as Synapse in Neuromorphic System*, *Nano Lett.* 2010, 10, 4, 1297-1301

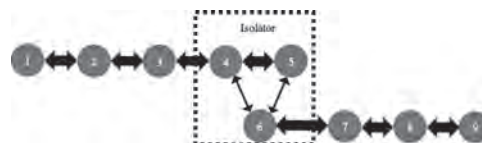


Fig 1: Chain of spiking neurons, configured as an isolator circuit. Gray circles represent neurons, and black arrows represent coupling between neurons. Thick black arrows represent symmetric synaptic weight tuned such that a spike cannot flow backwards. Thin black double arrows represent symmetric synaptic weight weak coupling.

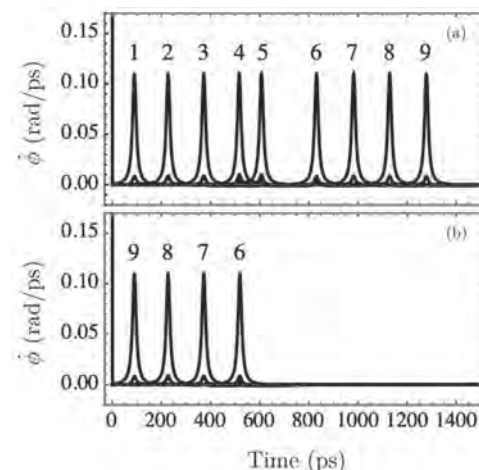


Fig 2: Results of simulation of AFM neurons configured as an isolator circuit. (a) Initial spike is in neuron 1. The spike travels through the chain, to neuron 9. (b) The initial spike is at neuron 9. The spike travels to neuron 6, then is unable to continue.

ED-09. Amplifying Spin Waves Along Néel Domain Wall by Spin-Orbit Torque.*Y. Zhou*¹*1. School of Science and Engineering, The Chinese University of Hong Kong, Hong Kong*

Traveling spin waves in magnonic waveguides undergo severe attenuation, which tends to result in a finite propagation length of spin waves, even in magnetic materials with the accessible lowest damping constant, heavily restricting the development of magnonic devices. Compared with the spin waves in traditional waveguides, propagating spin waves along strip domain wall are expected to exhibit enhanced transmission. Here, we demonstrate, theoretically and through micromagnetic simulations, that spin-orbit torque associated with a ferromagnet/heavy metal bilayer can efficiently control the attenuation of spin waves along a Néel-type strip domain wall, despite the complexity in the ground-state magnetization configuration. The direction of the electric current applied to the heavy-metal layer determines whether these spin waves are amplified or further attenuated otherwise. Remarkably, our simulations reveal that the effective current densities required to efficiently tune the decay of such spin waves are just $\sim 10^{10}$ Am⁻², roughly an order smaller than those required in conventional spin waveguides. Our results will enrich the toolset for magnonic technologies.

1. X. Xing and Y. Zhou, *NPG Asia Mater.* 8, e246 (2016). 2. X. Xing, P. W. T. Pong, J. Åkerman, and Y. Zhou, *Phys. Rev. Appl.* 7, 054016 (2017). 3. X. Xing, J. Åkerman, and Y. Zhou, *Phys. Rev. B* 101, 214432 (2020)

ED-10. Mutual Synchronization of an Array of Spin-Torque Oscillators With Perpendicular Polarizer.

M. Castro^{2,1}, D. Mancilla², A. Litvinenko¹, M. Ibarra Gomez¹, B. Dieny¹, S. Allende², L.D. Buda-Prejbeanu¹ and U. Ebels¹
 1. Univ. Grenoble Alpes, CEA, CNRS, Grenoble INP, SPINTEC, 38000, Grenoble, France; 2. Universidad de Santiago de Chile, Cedenna, Santiago, Chile

The mutual synchronization of spin-torque nano-oscillators (STNOs) arranged in a large array improves the individual properties of each STNO, increasing the output-power and reducing the linewidth of the emitted signal. These improvements are required to implement STNOs in wireless communication schemes [1] and furthermore open applications for different oscillator based neuromorphic computing schemes [2]. Many theoretical and experimental studies considered single STNO devices [3], while experimentally the synchronization of a large number of STNOs remains a challenging task [4]. This is because the synchronized state and the phase-locking depend on the geometry, device resistance, input signals, coupling mechanism, among others [5]. As a first step to guide experiments on the synchronization behavior of STNO arrays, we have undertaken a theoretical study, combining numerical and analytical approaches based on the spin-wave formalism [3]. The STNO devices considered here are of circular cross-section (100nm in diameter) with a perpendicular polarizer and an in-plane magnetized free layer under a strong out-of-plane field. This field is larger than the saturation field. The free layer magnetization is orientated out-of-plane leading to an out-of-plane precession mode that is advantageous to induce strong dipolar coupling between STNOs, which is the coupling mechanism considered here. We derived analytically the coupled equations of amplitudes and phases where the latter are similar to the Kuramoto-phase equation, but limited to a finite number of devices. Solving for the stationary states, this model provides analytical expressions for the locking-range, the stationary amplitudes, and the frequency of oscillations of the synchronized state. These solutions depend on the array geometry, number N of STNOs in the array, separation between STNOs, distribution of the DC current, as well as the different magnetic material parameters, and the external magnetic field. In this work, we investigate the solution of these equations for two specific array geometries: a straight line and a ring structure ($N=3,6$ and 10), shown in figure 1b. Our results show that the locking-range depends on the separation among the STNOs (because this scales the coupling strength), but it is independent of the angle among them. Furthermore, we show that the locking-range is larger when the STNOs are placed in a ring structure (or triangle for $N=3$) as compared to a straight-line structure. Finally, the most interesting result is that for the ring structure, we identify two dynamic modes that represent a standing wave for the STNO phases along the ring structure (observed for $N>5$). These two dynamics modes are shown in Fig. 2 and are called here (a) the in-phase mode, with identical phases for all STNOs, and (b) the out-of-phase mode, where the phase difference between two adjacent STNOs is $2\pi/N$. We study how these states and their existence range are modified upon variation of the current density through the different STNOs (identical and non-identical currents), the STNO separation, and the number of STNOs in the ring. The analytical results are in good agreement to the numerical solutions of the Landau-Lifshitz-Gilbert (LLG) equation, as long as the separation among the STNOs is above a certain critical value. For smaller separations, the dipolar interactions become too strong and non-linear effects would require to go beyond the first-order approximations used to solve the amplitude and phase equations. The results reported here represent a first step to validate the phase equations and to define their limitations, and can be used to address now the Kuramoto equations to find solutions for large scale structures (N very large). We acknowledge financial support in Chile from FONDECYT 1200867, and Financiamiento Basal para Centros Científicos y Tecnológicos de Excelencia AFB 180001. D. M.-A. acknowledges Postdoctorado FONDECYT 2018, 3180416. M. A. Castro acknowledges Conicyt-PCHA/Doctorado Nacional/2017-21171016. The project was supported in part by ERC Advanced Grant MAGICAL No. 669204

[1] T. Chen, et al., Proceedings of the IEEE., 104, 1919-1945(2016).
 [2] J. Grollier, et al., Nat. Electron. 3, 360 (2020). [3] A. Slavin and V.,

Tiberkevich, IEEE Trans. Magn., 45,1875(2009). [4] S. Tsunegi, et al., Scientific Reports., 8, 13475(2018). [5] R. Lebrun, et al., Nat. Commun. 8, 15825 (2017).

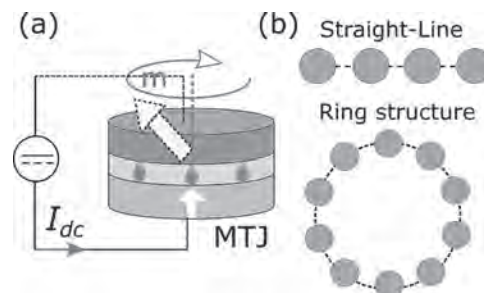


Fig.1: (a) Schematics of an STNO device and (b) two configurations for a coupled STNO array.

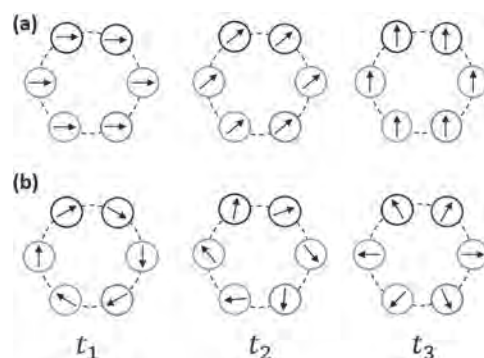


Fig. 2: Schematics of the two dynamic modes obtained for the ring structure. The snapshots show the instantaneous distribution of the x- and y- components of the magnetization in three consecutive time steps $t_1 < t_2 < t_3$, for (a) the in-phase and (b) the out-of-phase modes.

ED-11. The Interplay Between the Rapid Cooling-Induced BEC and SHE-STT-Driven Bullet Mode.

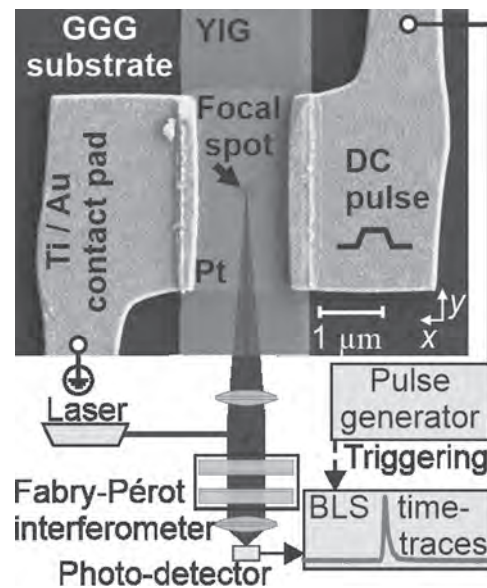
M. Schneider¹, D. Breitbach¹, R. Serha¹, Q. Wang², A.A. Serga¹, A.N. Slavin³, V. Tyberkevich³, B. Heinz¹, B. Lägell¹, C. Dubs⁴, T. Brächer¹, S. Knauer², O. Dobrovolskiy², P. Pirro¹, B. Hillebrands¹ and A. Chumak²

1. *Fachbereich Physik, Technische Universität Kaiserslautern, Kaiserslautern, Germany*; 2. *Faculty of Physics, Universität Wien, Wien, Austria*; 3. *Department of Physics, Oakland University, Rochester, MI, United States*; 4. *Innovent eV Technologieentwicklung Jena, Jena, Germany*

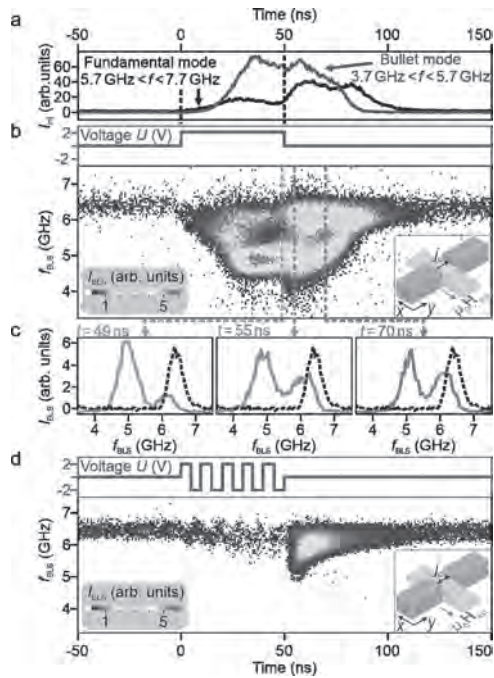
It has been shown that a rapid cooling of Yttrium-Iron-Garnet (YIG)/Pt nanostructures preheated by a DC electric current pulse sent through the Pt layer leads to an overpopulation of a magnon gas and to the subsequent Bose-Einstein condensation (BEC) of magnons [1]. Hereby, the application of a sufficiently-long DC heating pulse was used to generate a high population of magnons being in equilibrium with the phononic system. The subsequent rapid decrease in the temperature resulted in the break of the equilibrium, in the over-population of magnons over the whole magnon spectrum, and, in the following, in a redistribution of magnons from higher to lower energies. Finally, if the elevated temperature was high enough, and the cooling process fast enough, the chemical potential reached the minimal energy of the system and the BEC was triggered [1]. In these experiments, a Pt or Al layer was used to heat the YIG nanostructure. For a Pt heater, in addition to the Ohmic heating effects, one expects the generation of a spin-polarized current transverse to the YIG/Pt interface due to the spin Hall effect (SHE) [2]. The spin current, consequently, is known to act on the magnetization dynamics in the YIG via spin-transfer torque (STT). Whereas in our previous studies the induced disequilibrium was found to be mainly given by the temperature increase and subsequent rapid cooling, we observe a significant contribution of the spin Hall effect (SHE) in a new set of samples. The larger effect of the SHE-STT was reached by a modification of the structures (see Fig. 1) with respect to those in the original study [1], i.e. by a decrease in the YIG thickness, and via using a sputtered Pt layer instead of an epitaxially grown Pt layer studies to enhance the spin Hall angle [3]. It was found that SHE-induced STT enhances the BEC formation at the bottom of the magnon spectrum – in the minimum frequency of the fundamental spin-wave mode, and excites a nonlinear magnon mode – the spin-wave bullet, located below the linear magnon spectrum [4]. We investigated the dynamics of these magnon states employing Brillouin light scattering (BLS) spectroscopy. A sketch of the experimental setup and SEM images of the investigated structure is depicted in Fig. 1. The application of a 50-ns-long DC-pulse to a 7-nm-thin Pt layer on top of a 34-nm-thin and 2- μm -wide YIG strip results in the SHE-STT. At sufficiently large amplitudes of the DC-pulse applied, the bullet mode is formed during the DC pulse at a frequency around 1.8 GHz below the frequency of the fundamental mode, see Fig. 2b. The pronounced magnon density peak in the left panel in Fig. 2c (solid orange line), measured at the time just before the current pulse is switched off, clearly demonstrates the bullet mode formation. The SHE-STT nature of the mode is confirmed by the variation of the magnetisation orientation with respect to the current direction. The consequent switching of the DC pulse off results in the rapid cooling-induced BEC of magnons at the frequency around 6 GHz - see Fig. 2c. The results of the control experiment with no SHE-STT contribution under periodically changing polarity of the applied current (Fig. 2d) are in agreement with the original findings presented in Ref. [1]. The interplay between the magnon condensate and the SHE-STT bullet mode, after the current pulse was gone, attracts special attention. Initially, in the rapid cooling phase of the process, thermally-induced excess magnons populate both the bullet mode and the condensate, see Fig. 2a. Further, both modes decay slower than expected from their lifetime indicating that they are still pumped from the gas. Finally, about 30 ns after the DC pulse is turned off, a qualitatively new process begins, resulting in the redistribution of magnons from the bullet mode to the condensate. This phenomenon manifests itself in an elevation of the condensate density accompanied by an increased decay of the bullet mode, and apparently occurs when the chemical potential of the magnon gas [1] decreases below the bullet mode frequency. The results

suggest a path towards the application of macroscopic quantum states in spintronic devices.

[1] M. Schneider, T. Brächer, D. Breitbach, V. Lauer, P. Pirro, D. A. Bozhko, H. Y. Musiienko-Shmarova, B. Heinz, Q. Wang, T. Meyer, F. Heussner, S. Keller, E. T. Papaioannou, B. Lägell, T. Löber, C. Dubs, A. N. Slavin, V. S. Tiberkevich, A. A. Serga, B. Hillebrands, and A. V. Chumak, Bose-Einstein condensation of quasiparticles by rapid cooling, *Nature Nanotechnology* 15, 457 (2020). [2] L. J. Cornelissen, K. J. H. Peters, G. E. W. Bauer, R. A. Duine, and B. J. van Wees, Magnon spin transport driven by the magnon chemical potential in a magnetic insulator, *Phys. Rev. B* 94, 014412 (2016). [3] E. Sagasta, Y. Omori, M. Isasa, M. Gradhand, L. E. Hueso, Y. Niimi, Y. Otani, and F. Casanova, Tuning the spin hall effect of pt from the moderately dirty to the superclean regime, *Phys. Rev. B* 94, 060412 (2016). [4] A. Slavin and V. Tiberkevich, Spin wave mode excited by spin-polarized current in a magnetic nanocontact is a standing self-localized wave bullet, *Phys. Rev. Lett.* 95, 237201 (2005).



Colored SEM images of the investigated structures and sketch of the experimental setup. The structures consists of a 2- μm -wide and 34-nm-thick YIG strip. A 3- μm -long Platinum-heater (7 nm) on top is contacted by Ti/Au leads. The magnon intensity below the Pt-covered region is measured using time-resolved BLS spectroscopy. The shape of the Ti/Au contact pads attached to the Pt injector results in a DC current parallel to the short axis of the strip. Qualitatively the same results were obtained for another set of samples with a DC current flowing parallel to the short axis of the strip.



(a) Integrated BLS intensity from (b) as a function of the time within the two indicated frequency ranges. (b) BLS intensity color-coded as a function of time and the BLS frequency. During the pulse ($0 \text{ ns} < t < 50 \text{ ns}$ and $U = 2.0 \text{ V}$) the formation of a bullet mode is visible. The inset shows a sketch of the structure. (c) BLS intensity as a function of the BLS frequency at three different time steps, indicated by the dashed lines in (b). The black dashed lines depict the thermal BLS spectrum without a DC pulse present. (d) Integrated BLS intensity color coded as a function of time and the BLS frequency. In contrast to (b), the current polarity is alternating during the pulse, effectively switching off the contribution of the SHE-STT while keeping the heating constant.

ED-12. Chiral Spin-Wave Velocities Induced by All-Garnet Interfacial Dzyaloshinskii-Moriya Interaction in Ultrathin Yttrium Iron Garnet Films.

H. Wang¹, J. Chen^{1,3}, T. Liu², J. Zhang¹, K. Baumgaertl³, C. Guo⁴, Y. Li^{5,6}, C. Liu^{1,2}, P. Che³, S. Tu¹, S. Liu⁷, P. Gao^{5,6}, X. Han⁴, D. Yu⁷, M. Wu², D. Grundler^{3,8} and H. Yu¹

1. School of Integrated Circuit Science and Engineering, Beihang University, Beijing, China; 2. Department of Physics, Colorado State University, Fort Collins, CO, United States; 3. School of Engineering, Ecole Polytechnique Federale de Lausanne, Lausanne, Switzerland; 4. Beijing National Laboratory for Condensed Matter Physics, Institute of Physics, Chinese Academy of Sciences, Beijing, China; 5. Electron Microscopy Laboratory, School of Physics, Peking University, Beijing, China; 6. International Center for Quantum Materials, School of Physics, Peking University, Beijing, China; 7. Shenzhen Institute for Quantum Science and Engineering (SIQSE), and Department of Physics, Southern University of Science and Technology, Shenzhen, China; 8. Institute of Microengineering (IMT), School of Engineering, Ecole Polytechnique Federale de Lausanne, Lausanne, Switzerland

Spin waves can probe the Dzyaloshinskii-Moriya interaction (DMI), which gives rise to topological spin textures, such as skyrmions. However, the DMI has not yet been reported in yttrium iron garnet (YIG) with arguably the lowest damping for spin waves. In this work, we experimentally evidence the interfacial DMI in a 7-nm-thick YIG film by measuring the nonreciprocal spin-wave propagation in terms of frequency, amplitude, and most importantly group velocities using all electrical spin-wave spectroscopy. The velocities of propagating spin waves show chirality among three vectors, i.e., the film normal direction, applied field, and spin-wave wave vector. By measuring the asymmetric group velocities, we extract a DMI constant of $16 \mu\text{J}/\text{m}^2$, which we independently confirm by Brillouin light scattering. Thickness-dependent measurements reveal that the DMI originates from the oxide interface between the YIG and garnet substrate. The interfacial DMI discovered in the ultrathin YIG films is of key importance for functional chiral magnonics as ultralow spin-wave damping can be achieved.

[1]. H. C. Wang, J. L. Chen, T. Liu, J. Y. Zhang, K. Baumgaertl, C. Y. Guo, Y. H. Li, C. P. Liu, P. Che, S. Tu, S. Liu, P. Gao, X. F. Han, D. P. Yu, M. Z. Wu, D. Grundler, and H. M. Yu*, Chiral Spin-Wave Velocities Induced by All-Garnet Interfacial Dzyaloshinskii-Moriya Interaction in Ultrathin Yttrium Iron Garnet Films, *Phys. Rev. Lett.* 124, 027203 (2020).

ED-13. Modulation of Magnon-Magnon Coupling by Inherent Symmetry Breaking in Synthetic Antiferromagnets.

A. Sud^{1,2}, C.W. Zollitsch², M. Tam¹, A. Kamimaki³, Y. Koike⁴, S. Iihama⁴, S. Mizukami⁴ and H. Kurebayashi^{1,2}

1. Electronic and Electrical Engineering, University College London, London, United Kingdom; 2. London Centre for Nanotechnology, London, United Kingdom; 3. Research Center for Emerging Computing Technologies (RCECT), National Institute of Advanced Industrial Science and Technology (AIST), Tokyo, Japan; 4. Tohoku National University, Sendai, Japan

Quantum magnonics is a rapidly growing field offering myriad of potential applications[1,2] particularly in the realm of coherent information processing. Magnons which are the collective excitations of spins offer exotic functionalities such as the ability to couple to various dynamic systems. Realisation of strong coupling, owing to large spin densities, which is tunable into the ultrastrong coupling regime makes them suitable for coherent information exchange at much faster speeds. Apart from this the easily accessible gigahertz frequency range, simple fabrication and miniaturization provides an ideal platform for incorporation in various microwave electronic circuits. Recently[3,4,5], Synthetic Antiferromagnets(SyAF) have attracted prodigious interest due to the controllable exchange coupling in the GHz regime making them a test bed for various magnonic applications[6]. Moreover, the substantially large mode volume overlapping gives them an advantage over light-matter interactions in attaining higher a coupling strength. A SyAF consists of two ferromagnetic thin films (FM) with an antiferromagnetic exchange coupling separated by a non-magnetic spacer (NM). When the two FMs are symmetric, a mode crossing occurs between symmetry protected in-phase and out-of-phase resonance precessions via in-plane external magnetic field tuning. This is reminiscent of degeneracy between even and odd parity magnons. This degeneracy and subsequent mode crossing can be lifted by breaking the symmetry either extrinsically or intrinsically. Extrinsic symmetry breaking (SB) can be exerted by tilting the external magnetic field out-of-plane which shifts the rotational symmetry axis from the SyAF plane, and the system is no longer symmetric under two-fold rotation. This leads to hybridization of the two modes and an anticrossing gap is generated. Additionally, a coupling gap can be induced by dynamic dipolar interaction[3]. The strength of the coupling between two magnon modes is determined by the size of the gap. Maximizing the coupling efficiency is thus easily attainable by the controllability of the coupling gap by external magnetic field orientation. Apart from an extrinsic control of coupling strength the symmetry of the system can be broken intrinsically by using either two different FMs or the same FMs with different thickness. This would lead to a coupling gap even for the external applied fields applied in-plane, owing to a change of magnetization under two-fold rotation. In this work we demonstrate the control of magnon-magnon coupling in SyAFs via intrinsic and extrinsic SB. The schematic of the two modes in SyAF system is shown in Fig 1(a). We first consider a symmetrical SyAF structure CoFeB/Ru/CoFeB as in Fig 2(a). The apparent mode crossing results from a degeneracy of two non-interacting modes which is protected by a two-fold rotational symmetry. By tilting the external field (see Fig 2(b)) we break this symmetry and an anticrossing gap appears. This demonstrates the extrinsic SB. When two FMs with different thickness are considered an inherent SB exists in the system which opens a gap even for an in-plane field as in Fig 2(c). Further, breaking the symmetry as in 2(d) by tilting the field leads to an increase of the gap and thus the coupling strength. This effect can be further enhanced when using two FMs of different materials, exhibiting a large coupling gap for an in-plane field as in Fig 2(e). Here, the coupling strength far exceeds the losses, described by the frequency half-width at half maximum of the individual modes. The absolute coupling strength reaches 30% of the mode frequencies, indicating the onset of the ultrastrong coupling regime. By calculating the coupling gap as a function of external field tilt angle we can putatively claim that both intrinsic and extrinsic SB can realise strong magnon-magnon coupling in SyAFs. Further, the strong coupling leads to an entanglement between even and odd parity modes, making it attractive for quantum information applications. We generalize a theoretical model in the macro spin limit by solving the two coupled LLG(Landau Lifshitz Gilbert) equations to describe the microwave absorption spectroscopy for the SB

induced coupling in SyAFs. This study should shed light on the potential of SyAFs for studying and controlling magnon-magnon coherent coupling at room temperature. Moreover large tunable coupling strengths in this system will provide a novel platform for increased control of quantum systems.

[1] G. Kurizki, P. Bertet, Y. Kubo, K. Mølmer, D. Petrosyan, P. Rabl, and J. Schmiedmayer, Proc. Natl. Acad. Sci. U.S.A. 112, 3866 (2015). [2] M. Ruggenthaler, N. Tancogne-Dejean, J. Flick, H. Appel, and A. Rubio, *Nature Reviews Chemistry*, 2(3), pp.1-16 (2018). [3] Y. Shiota, T. Taniguchi, M. Ishibashi, T. Moriyama, and Teruo Ono, Phys. Rev. Lett. 125, 017203 (2020). [4] A. Sud, C. W. Zollitsch, A. Kamimaki, T. Dion, S. Khan, S. Iihama, S. Mizukami, and H. Kurebayashi, Phys. Rev. B 102, 100403(R) (2020). [5] M. Ishibashi, Y. Shiota, T. Li, S. Funada, T. Moriyama, and T. Ono, Sci. Adv. 6, eaaz6931 (2020). [6] A. Guedes, M. J. Mendes, P. P. Freitas, and J. L. Martins, Journal of applied physics 99,08B703 (2006).

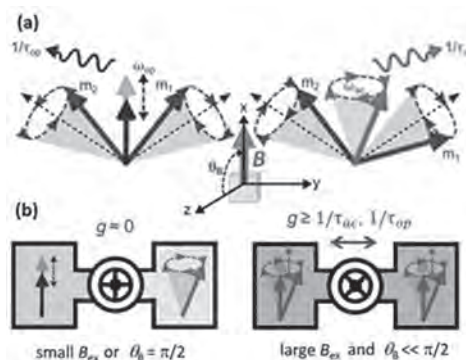


Fig 1. (a) Schematic of resonance modes in SyAFs. Two moments (m_1 and m_2) are coupled antiferromagnetically and canted at equilibrium. Under microwave irradiation, they precess in-phase (acoustic mode) and out-of-phase (optical mode) at different angular frequencies ω_{ac} and ω_{op} respectively. We define θ_B as in the figure. (b) Schematics of the magnon-magnon coupling phenomena. When the exchange field (B_{ex}) is small or two moments are within the film plane, the coupling strength (g) is zero and we can valve g by tuning B_{ex} and θ_B .

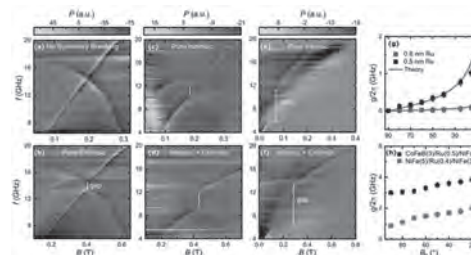


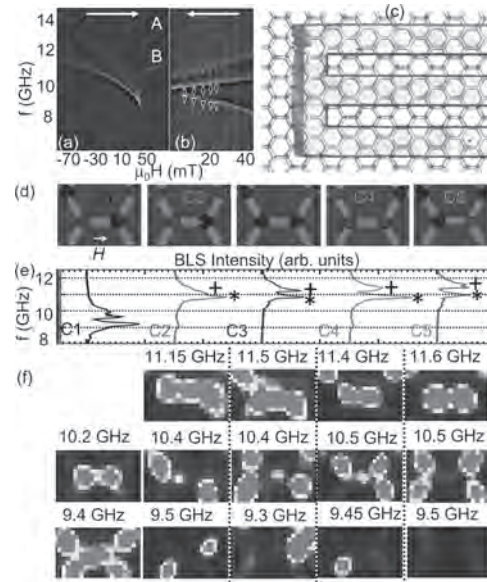
Fig 2. Microwave transmission as a function of frequency.(a) For CoFeB(5)/Ru(0.5)/CoFeB(5) at $\theta_B = 90^\circ$, the two modes show mode crossing (b) At $\theta_B = 25^\circ$ a gap appears. (c) In NiFe(5)/Ru(0.4)/NiFe(3) intrinsic SB occurs and the gap is seen for $\theta_B = 90^\circ$ which increases as in (d) for $\theta_B = 30^\circ$. (e) CoFeB(3)/Ru(0.5)/NiFe(3) showing large gap at (e) $\theta_B = 90^\circ$ and (f) $\theta_B = 20^\circ$. (g-h) Coupling strength $g/2\pi$ as a function of θ_B which increases as the tilt angle is increased.* The numbers in brackets are the thickness of the FM layer in nm.

ED-14. Direct Observation of Magnon Modes in Kagome Artificial Spin Ice With Topological Defects.

V. Bhat^{2,1}, S. Watanabe¹, K. Baumgaertl¹ and D. Grundler^{1,3}
 1. *Institute of Materials, Laboratory of Nanoscale Magnetic Materials and Magnonics, School of Engineering, Ecole Polytechnique Federale de Lausanne, Lausanne, Switzerland;* 2. *International Research Centre MagTop, Institute of Physics, Polish Academy of Sciences, Warsaw, Poland;* 3. *Institute of Microengineering, Laboratory of Nanoscale Magnetic Materials and Magnonics, School of Engineering, Ecole Polytechnique Federale de Lausanne, Lausanne, Switzerland*

Kagome artificial spin ice (KASI) is a network of Ising type nanobars on a kagome lattice [1,2]. Great progress has been made in understanding defects including disordered states in KASI via quasistatic imaging techniques [1,3]. However, the magnetodynamic study of disordered states has been confined to global magnetodynamic (e.g. broadband spin wave spectroscopy) and micromagnetic simulations [4]. Furthermore, the simulation study on KASI has shown the presence of novel magnetodynamic microstates that offer excellent insights into the KASI's disordered regime [4]. From the fundamental physics side, dynamically controlled microstates may offer a way to create Dirac strings via microwave-assisted switching interior to the KASI lattice in a controlled manner and study the disordered regime systematically. From the magnonic application perspective, experimental studies of microstates in KASIs are key towards their usage as a new type of microwave filter [5] and reprogrammable magnonic crystal [6]. We investigate spin dynamics of a KASI consisting of $\text{Ni}_{81}\text{Fe}_{19}$ nanomagnets arranged on an interconnected kagome lattice using broadband spin wave spectroscopy (Fig. a,b), magnetic force microscopy (MFM) (Fig. c), and micro-focus Brillouin light scattering (BLS) microscopy (Fig. e-f). Micro-focus BLS performed on magnetically disordered states exhibit a series of magnon resonances that depend on topological defect configurations that we image by magnetic force microscopy. Nanomagnets on a Dirac string and between a monopole-antimonopole pair show pronounced modifications in magnon frequencies. Our work is key for the creation and annihilation of Dirac strings via microwave-assisted switching and reprogrammable magnonics based on ASIs.

1) S. Ladak, D. Read, G. Perkins, L. Cohen, and W. Branford, *Nature Physics* 6, 359 (2010). 2) R. Wang, C. Nisoli, R. Freitas, J. Li, W. McConville, B. Cooley, M. Lund, N. Samarth, C. Leighton, V. Crespi, *et al.*, *Nature* 439, 303 (2006). 3) E. Mengotti, L. J. Heyderman, A. F. Rodriguez, F. Nolting, R. V. Hugli, and H.-B. Braun, *Nat. Phys.* 7, 68 (2011). 4) V. Bhat, F. Heimbach, I. Stasinopoulos, and D. Grundler, *Physical Review B* 93, 140401 (2016). 5) X. Zhou, G.-L. Chua, N. Singh, and A. O. Adeyeye, *Advanced Functional Materials* 26, 1437 (2016). 6) M. Krawczyk and D. Grundler, *J. Phys.: Condens. Matter* 26, 123202 (2014).



Grayscale AESWS spectra map of KASI for a field protocol of (a) -90 mT → +90 mT and (b) -90 mT → 45 mT → 0 mT. (c) Magnetic force microscopy images of KASI after a field protocol of -100 mT → +44 mT → 0 mT. Stray fields detected by MFM are colored in blue and red consistent with charges $Q = +q$ and $Q = -q$, respectively. (d) Sketches of charge configurations (blue and red spheres) and magnetization vectors M (arrows) for configurations C1 to C5. (e) BLS intensities measured at the central position on horizontal nanobars belonging to the configurations displayed above the spectra at $\mu_0 H = 25$ mT. (f) Spatially resolved BLS intensity maps at 25 mT for fixed frequencies in configurations C1 to C5 displayed above.

ED-15. Dependence of Spin Wave Modes on the Geometry of Nanomagnets in Square Artificial Spin Ice Vertices.

N. Arora¹ and P. Das¹

¹. Department of Physics, Indian Institute of Technology Delhi, New Delhi, India

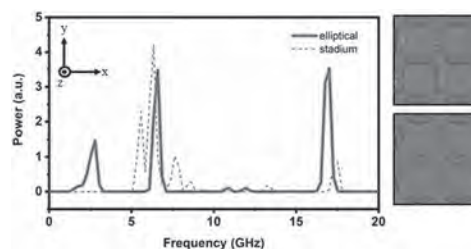
In this work, we report our micromagnetic simulation results on the correlation between spin wave modes and emergent microstates in square artificial spin ice (S-ASI), consisting of elliptical and stadium shape magnetic nanoislands. S-ASI¹ is a lithographically patterned engineered dipolar coupled nanostructure array, consisting of orthogonal square sublattices of highly shape anisotropic nanoislands. These islands behave as a macrospin due to high shape anisotropy where each macrospin, according to the dumb-bell model, can be considered as a magnetic dipole of charge separated by the length of the nanoisland. Recently, there is a growing interest in the low-energy collective spin excitation of magnetic nanostructures of vastly different shapes resulting in the development of the field of magnonics. These excitations or spin waves are the magnetic analogs of electromagnetic waves, phonons, and plasmons which can be treated as a perturbation in terms of phase-coherent precession of magnetization vector that propagates in coupled magnetic media. The field of magnonics offers new functionalities in modern technological devices e.g., magnonics logic, phase shifters, microwave antenna, directional coupler, SW-based multiplexer, grating, and neuromorphic computing, etc. S-ASI exhibit geometrical frustration and therefore, it shows ground state degeneracy. The microstates in S-ASI enable the possibility of tunability of associated spin-wave modes and alter the spin-wave band gap without structural deformation. This key feature of S-ASI makes it a potential candidate for reconfigurable magnonics². The interesting dynamic behavior of ASI suggests that it can be perceived as magnonic crystals with potential applications in logic devices³, data storage⁴, microwave filter⁵, spin logic gate³, etc. Hence, detailed investigation^{6,7} of spin wave dynamics and evolution of modes in ASI systems involving highly shape anisotropic nanoislands of different shapes is very important. The question of the correlation between underlying magnetic states of dipolar coupled nanoislands of shapes such as ellipse and stadium, etc., and the spin wave modes is far from properly understood. In this work, we have performed a detailed study of the dynamical behavior of emergent microstates in S-ASI, using micromagnetic simulations. For these studies, we have considered S-ASI to be consisting of four square ring-type structures with elliptical and stadium shaped nanoislands of permalloy with dimensions $300 \text{ nm} \times 100 \text{ nm} \times 25 \text{ nm}$ and lattice constant 150 nm (edge-to-edge distance of nanoislands). The magnetization reversal behavior of stadium-shaped magnetic nanoislands in S-ASI geometry involves the formation of vortices, antivortices, etc. whereas for the case of elliptical nanoislands the reversal involves sharp switching of spins. In order to investigate the dependence of the behavior of spin wave dynamics on local magnetic behavior in the S-ASI of two different shapes, we have investigated the spin wave modes and emergent microstates in both the shapes as a function of a number of square-type rings (i.e., single ring, double ring, triple ring, and quadruple ring e.g., S-ASI) of nanoislands. For S-ASI involving elliptical nanoislands, our studies reveal that emergent microstates at remanence with net local magnetic charges at the junction of the nanoislands for head-to-head or tail-to-tail configuration enhances spin wave generation in the proximity islands up-to ~95% as compared to islands in the proximity of zero local charges (in head-to-tail or tail-to-head configuration). Thus, we observe that the power profiles in remanence map the local charges present in the S-ASI or ring-type structures. We observe the presence of ubiquitous switching identifier mode at ~ 18 GHz (saturation) in nanoislands with an easy axis along the external bias field. This mode shows marked power variation in the switched nanoislands with respect to un-switched nanoislands. Our simulation results show that observed spin wave spectra and calculated mode profiles remain consistent as a function of rings. Our studies of S-ASI involving stadium shaped nanoislands further show that the spin wave spectra are significantly different than for the elliptical case (see Fig. 1). In the case of stadium-shaped nanoislands, the demagnetization field is inhomogeneous which creates variation in the local field within the nanoislands whereas, in the case of elliptical nanoisland, demagnetization field variation is observed near the edges. However, for a similar magnetization configuration, we have observed several new

spin-wave modes with complex mode profiles in the case of stadium shape nanoislands (Fig. 2). Thus, our study gives new insight in understanding the origin of spin wave mode behavior in terms of the evolved microstates and demonstrate spin wave modes as a tool to investigate magnetization reversal and local magnetic charges in artificial spin ice system.

(1) S. T. Bramwell *et al.*, Science 294, 1495–1501 (2001). (2) E. Iacocca *et al.*, Phys. Rev. B 93, 134420 (2016). (3) H. Arava *et al.*, Nanotech. 29, 265205 (2018). (4) Y.-L. Wang *et al.*, Science 352, 962–966 (2016). (5) I. Huynen *et al.*, IEEE Microw. Guided W. 9, 401–403 (1999). (6) S. Gliga *et al.*, Phys. Rev. Lett. 110, 117205 (2013). (7) E. Iacocca *et al.*, Phys. Rev. Appl. 13, 044047 (2020).



The power profile of the spin wave mode excited at ~ 6.5 GHz in S-ASI with (left) elliptical and (right) stadium-shape nanoislands at 200mT external field.



(left) Spin wave spectra of S-ASI consisting of stadium shape and elliptical shape nanoislands saturated along the x-axis at 200mT. (right) magnetization configuration of S-ASI with the stadium and elliptical shape nanoislands.

Session EE

NANOSCALE AND APPLIED MAGNONICS

Oleksandr Dobrovolskiy, Co-Chair
University of Vienna, Vienna, Austria

Qi Wang, Co-Chair
Universitat Wien, Vienna, Austria

INVITED PAPER

EE-01. Nanoscale Magnonic Devices: From Conventional to Inverse-Design Magnonics INVITED.Q. Wang¹¹ *Universitat Wien, Wien, Austria*

Spin waves, and their quanta magnons, are of great interest as potential data carriers in future low-energy computing devices [1]. The phase of a spin wave provides an additional degree of freedom, while the scalability of structures and wavelengths down to the nanometer regime [2] are further advantages. Recently, a set of magnonic data processing units was demonstrated. However, the development of each of them requires specialized investigations and, usually, one device design is suitable for one function only. Moreover, an integrated all-magnonic circuit, which is suitable for the cascading of multiple magnonic units, has not yet been demonstrated. In the first half of my talk, I will present briefly the experimental realization of a nanoscale magnonic directional coupler, which consists of two separated single-mode waveguides with a width of 350 nm as shown in Fig. 1a [3]. A U-shaped antenna is used to excite spin waves and space-resolved Brillouin Light Scattering (BLS) spectroscopy is exploited for detection. It is shown that the data is coded into the spin-wave amplitude is guided towards one of its two outputs depending on the signal frequency, magnitude, and on the magnetic field. Using micromagnetic simulations, we also propose an integrated magnonic half-adder that consists of two directional couplers and we investigate its functionality for information processing within the magnon domain. In the second part of the talk, I will present the method of inverse-design magnonics, in which any functionality can be specified first, and a feedback-based computational algorithm is used to obtain the device design [4]. Our proof-of-concept prototype is based on a rectangular ferromagnetic area which can be patterned using square shaped voids as shown in Fig. 1b. To demonstrate the universality of this approach, we explore linear, nonlinear and nonreciprocal magnonic functionalities and use the same algorithm to create a magnonic (de-)multiplexer, a nonlinear switch and a circulator. Thus, inverse-design magnonics can be used to develop highly efficient rf applications as well as Boolean and neuromorphic computing building blocks.

A. V. Chumak, V. I. Vasyuchka, A. A. Serga, & B. Hillebrands, *Nat. Phys.* 11, 453 (2015). Q. Wang, B. Heinz, R. Verba, et al. *Phys. Rev. Lett.* 122, 247202 (2019). Q. Wang, M. Kewenig, M. Schneider, et al. *Nat. Electron.* 3, 765-774 (2020). Q. Wang, P. Pirro, A. V. Chumak, arXiv:2012.04544.

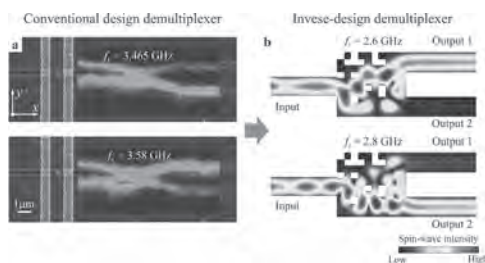


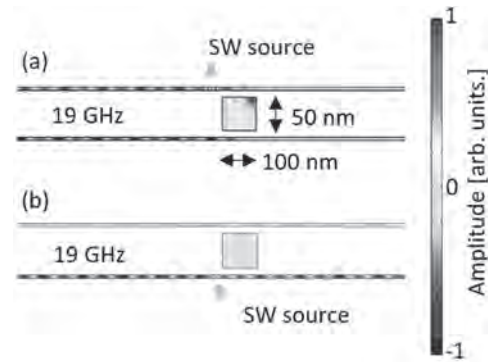
Fig. 1 The evolution from the conventional design (a) to inverse-design (b) magnonic demultiplexers.

CONTRIBUTED PAPERS

EE-02. Spin-Wave Circulation in a Ferromagnetic Resonator With Two Adjacent Layers.K. Szulc¹, M. Krawczyk¹ and P. Roberjot¹*1. Uniwersytet im Adama Mickiewicza w Poznaniu, Poznan, Poland*

The early development of photonic devices [1, 2] is leading the way for their magnonic analogs [3] such as spin-wave (SW) generators [4], couplers [5, 6], and phase shifters [7]. Such basic functional components are necessary for the development of miniaturized and energy-efficient magnetic circuits for processing high-frequency microwave signals. Our study goes along further development of SW devices, to demonstrate circulation [8] and other functionalities using ferromagnetic conduits coupled by resonators in analogy to photonic channel add-drop filters [1]. We investigate the propagation behavior of SW in a cobalt (Co) bi-layer structure separated by a non-magnetic material and coupled with a permalloy (Py) stripe placed between two layers. The layers have a thickness of 5 nm, the separation between the stripe and the layers is of 10 nm and the stripe has a thickness of 50 nm. All elements are saturated in the same in-plane direction, perpendicular to the propagation of SWs. We investigate numerically the SW dynamics governed by the Landau-Lifshitz-Gilbert equation, solved numerically using the software COMSOL Multiphysics. We study the SWs dynamics with two different approaches. In the first approach, we investigate the SW dispersion relation of the system in the frequency domain. The lattice constant of the system is set at 500 nm. To analyze the origin of different type of interactions and possible functionalization we calculate the dispersion relations for two layers, the stripe only, three layers, and finally for the two layers coupled with the Py stripe. The dispersion relations allow to determine propagation properties, the coupling between the modes and their hybridization. We found that the coupling between the elements is strong at some frequencies at which suitable conditions for control of propagating SWs are formed. As a second approach, we used the time-domain simulations to demonstrate functionality of the proposed system. We excite the system with an antenna generating SWs with a single frequency. We found interesting propagation properties for a 19-GHz spin wave. The excitation of a wave in the top layer generates an edge mode in the Py resonator (Fig. 1a) and the SW is fully transmitted to the bottom layer propagating in the left. The excitation in the bottom layer (Fig. 1b) is not transferring to the top layer even if the Py resonator is weakly excited. Due to inversion symmetry with respect to the horizontal mid-plane, the analogous properties are for SW excited on the right side of the resonator. Thus, we demonstrated the functionality of a circulator in the system which is suitable for further miniaturization through decreasing the size of a resonant element. The proposed system composed of two thin-film SW conduits coupled by a ferromagnetic resonator can operate with different functionalities in dependence on the frequency. The next investigations, at other frequencies, positioned at proximity of other Py resonances, offer other functionalities, like magnetostatic screening from the direct coupling between the waveguides. The operation can be further tuned by changing the magnetization characteristics, magnetic field, and by exploring the third dimension. The research leading to these results has received funding from the Polish National Science Centre, project No. UMO-2018/30/Q/ST3/00416.

[1] S. Fan et al. In: *Opt. Exp.* 3 (Aug. 1998), pp. 4-11. [2] S. Fan et al. In: *Phys. Rev. Lett.* 80 (Feb. 1998), pp. 960-963. [3] A. Barman and A. Haldar. In: *Solid State Phys.* 65 (May 2014), pp. 1-108. [4] P. Gruszecki et al. In: *Solid State Phys.* 6 (Mar. 2016), p. 22367. [5] A. Sadovnikov et al. In: *Appl. Phys. Lett.* 107 (Nov. 2015), p. 202405. [6] Q. Wang et al. In: *Nature Electronics* 3 (Dec. 2020), pp. 1-10. [7] Z. Zhang et al. In: *J. Phys. D* 53.10 (Dec. 2019), p. 105002. [8] K. Szulc et al. In: *Phys. Rev. Appl.* 14 (Sept. 2020), p. 12.

**Fig.1**

EE-03. Towards Wave-Based Logic Operation Using Multi-Directional sub-100 nm Magnons.

S. Watanabe¹, V. Bhat², A. Mucchietto¹, S. Shan¹ and D. Grundler^{1,3}

1. *IMX, Ecole Polytechnique Federale de Lausanne, Lausanne, Switzerland*; 2. *Institute of Physics, Polska Akademia Nauk, Warszawa, Poland*; 3. *IMT, Ecole Polytechnique Federale de Lausanne, Lausanne, Switzerland*

Spin waves (SWs) are promising quanta for transmission and processing of information for future communication devices. Excitation and detection of beyond 20 GHz magnons with sub-100 nm wavelength are of key importance [1]. We report on the magnonic grating coupler (MGC) effect [2] for which prepared specific nanopillars. Depending on the type of MGC lattice and nanopillar diameters, magnons are emitted resonantly on the chip in a multitude of directions with different efficiency. We demonstrate the interference effect of short-wave magnons independent of propagation directions. We engineered grating couplers for broadband magnon emission by preparing 100-nm-thick permalloy nanopillars in a periodic square lattice and an aperiodic (Penrose P3) quasicrystalline arrangement [3] on insulating ferrimagnetic yttrium iron garnet (YIG) films. Characteristic lengths amounted 480 nm. Several sub-micron-wide coplanar waveguides (CPWs) with separations of 12 micrometers were integrated on top of the MGC samples to excite/detect SWs by broadband spectroscopy. The MGC sample based on the quasicrystalline arrangement allowed for SW emission omnidirectionally with a broad range of wave vectors. SWs of up to 25.3 GHz were detected in the square lattice-based MGC sample. These parameters were achieved in very small magnetic fields of only a few mT in contrast to previous studies on grating couplers [2]. SWs simultaneously excited by two emitters interfered constructively/destructively at a separate detector antenna depending on the phase difference of the two phase-coherent SWs. Thereby a binary 1/0 output operation could be realized with 70 nm-wavelength magnons over distances of more than 10 micrometers. The applied field direction and specific microwave frequency defined the SW emission direction for the interference experiment. Our study and findings on sub-100 nm magnons are important for future magnonic devices targeting at information processing via wave-logic on the nanoscale. The work was supported by SNSF grant 163016.

[1] A.V. Chumak, V. I. Vasyuchka, A. A. Serga et al., *Nature Physics*, Vol.11, p. 453 (2015) [2] H. Yu, G. Duerr, R. Huber et al., *Nat. Commun.*, Vol. 4, p. 2702 (2013) [3] S. Watanabe, V.S. Bhat, K. Baumgaertl et al., *Adv. Funct. Mater.*, Vol. 30, p. 2001388 (2020)

EE-04. Long-Range Propagation of Spin Waves in Transversely Magnetized Nano-Scaled Yttrium Iron Garnet Conduits.

B. Heinz¹, Q. Wang², M. Schneider¹, E. Weiß², A. Lentfert¹, B. Lägel¹, T. Brächer¹, C. Dubs³, P. Pirro¹ and A. Chumak²

1. Physics, Technische Universität Kaiserslautern, Kaiserslautern, Germany; 2. Physics, Universität Wien Fakultät für Physik, Wien, Austria; 3. Innovent eV Technologieentwicklung Jena, Jena, Germany

Spin-wave based data transport and information processing aims to complement computation technology by exploiting wave logic, with the benefits of potentially reducing the feature size, as well as allowing for data multiplexing and more energy efficient operations [1]. Recent studies provide advanced theoretical models for nano-scaled spin-wave conduits and revealed a reasonably long propagation distance for longitudinally magnetized conduits, thus proving the fundamental feasibility of magnonics at the sub-100nm scale [2]. In contrast, little focus has been put on transversely magnetized nano-conduits. However, these systems are of great interest offering a large group velocity and a potentially protected transport of energy and information caused by the intrinsic chirality of the spin-wave modes [3]. Thus, they promise a significantly enhanced spin-wave decay length. Here, we present a study of propagating spin-wave packets in a transversely magnetized nanoscopic yttrium iron garnet conduit of 50 nm width and 44 nm thickness. Pulsed spin-wave packets are excited using a coplanar waveguide antenna. Space and time-resolved micro-focused Brillouin-light-scattering spectroscopy is employed to measure the spin-wave group velocity and decay length. As shown in Fig. 1A, a long-range spin-wave propagation is observed with a decay length of up to 8 μm , which is multiple times larger than reported values for the corresponding longitudinal magnetized state [2]. In addition, a large spin-wave lifetime of up to 44.7 ns is found, see Fig. 1B. The results are supported with micro-magnetic simulations, revealing a frequency non-reciprocity for counter-propagating spin waves, see Fig. 1C, caused by the trapezoidal cross-section of the studied structure and the associated curved internal field distribution which introduces a spacial symmetry break. The presence of this non-reciprocity is experimentally verified and is particularly interesting for an application in spin-wave devices since it allows for a novel device architecture and low-loss unidirectional data transport.

[1] A. Mahmoud, F. Ciubotaru, F. Vanderveken, A. V. Chumak, S. Hamdioui, C. Adelman and S. Cotozana J. of Appl. Phys. 128, 161101 (2020). [2] B. Heinz, T. Brächer, M. Schneider, Q. Wang, B. Lägel, A. M. Friedel, D. Breitbach, S. Steinert, T. Meyer, M. Kewenig, C. Dubs, P. Pirro, and A. V. Chumak, "Propagation of spin-wave packets in individual nano-sized yttrium iron garnet magnonic conduits," Nano Lett. 20, 4220–4227 (2020). [3] M. Mohseni, R. Verba, T. Brächer, Q. Wang, D. A. Bozhko, B. Hillebrands, and P. Pirro, "Backscattering immunity of dipole-exchange magnetostatic surface spin waves," Phys. Rev. Lett. 122, 197201 (2019).

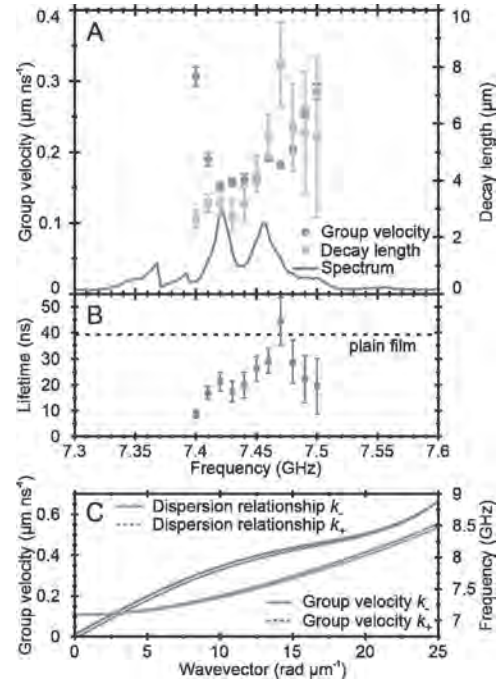


Fig. 1 (A) Group velocity and decay length measured via microfocused BLS spectroscopy. The light gray curve is the associated cw excitation spectrum. Frequency shifted due to a magnetic field difference of 0.2 mT. **(B)** Experimental lifetime derived from the decay length and group velocity. **(C)** Results of the micro-magnetic simulations. A frequency non-reciprocity is observed for counter-propagating spin waves.

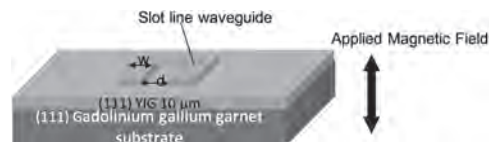
EE-05. Enhancement of Magnetization Dynamics via Spin Waves by Slot Line Waveguide for Perpendicularly Magnetized Yttrium Iron Garnet.

T. Koda¹, S. Muroga² and Y. Endo^{3,4}

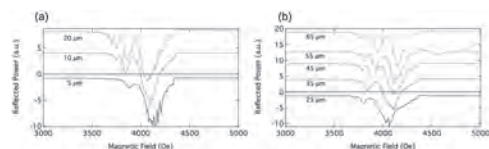
1. Electronic Mechanical Engineering, National Institute of Technology, Oshima College, Suo-Oshima, Japan; 2. Mathematical Science and Electrical-Electronic-Computer Engineering, Akita University, Akita, Japan; 3. Electrical Engineering, Tohoku University, Sendai, Japan; 4. Center for Spintronics Research Network, Tohoku University, Sendai, Japan

A slot line waveguide that consists of two equal-width lines induces local magnetization dynamics around each line. Spin waves emitted from the local magnetization dynamics propagate and interact with the other side of the local magnetization dynamics. We have studied the high frequency waveguide's size dependence of magnetization dynamics to understand the interaction. In our previous study, we reported the interaction for the case of which the magnetic field applied to the film plane [1,2]. We have revealed that the interaction induces the resonantly excited magnetization dynamics, and the excitation condition is determined by the design of lines. In this paper, we study the magnetization dynamics induced by a slot line waveguide with the applied magnetic field perpendicular to the plane. The spin wave mode for our previous study was magnetostatic surface spin waves (MSSW) [3]. When the magnetic field is applied normally to the film plane, forward volume magnetostatic spin waves (FVMSWs) are induced [3]. YIG (111) single crystal thin films with the thickness of 10 μm were epitaxially grown on gadolinium gallium garnet (GGG) (111) single crystal substrates. All the slot line waveguides were fabricated directly on the YIG (111) single crystal thin film using a combination of photolithography, Ar ion milling and sputtering techniques (as) shown in Fig. 1 (a). The line width and the gap between the lines in the waveguides were systematically varied. The high frequency power response was evaluated with a vector network analyzer. The input signal strength was fixed at 0 dBm for all the measurements and the frequency was set at a frequency between 3.0 and 13.0 GHz for each measurement. Figs 2 (a) and (b) show the magnetization dynamics at 7.0 GHz dependent on the line width and the gap, respectively. Multiple peaks were observed for all the measurement conditions. The magnetic field at the peak of magnetization lowered with the increase of the line width. The number of peaks also increased with the line width as well as the distance between lines. It should be noted that the number of peaks is much larger compared to the measurement for in plane [2]. We assume this is caused by the shorter wavelength of spin waves for FVMSW compared to MSSW, which enhances the periodicity of the condition for the same phase between local magnetization dynamics and spin waves. Those experimental results indicate that artificially controlled magnetization dynamics can be effectively induced with the use of FVMSW. We thank GRANOPT Co, Ltd. for their support of YIG single crystal thin films. This work was supported in part by JSPS KAKENHI Grant Number JP18K14114. This work was supported in part by CSRN, Tohoku University. A part of this work was carried out at Nano-Fabrication Support Laboratory, Yamaguchi University supported by "Nanotechnology Platform Project" of the Ministry of Education, Culture, Sports, Science and Technology (MEXT), Japan. A part of this work was carried out at Nano-Fabrication Support Laboratory, Yamaguchi University supported by "Nanotechnology Platform Project" of the Ministry of Education, Culture, Sports, Science and Technology (MEXT), Japan.

[1] Tetsunori Koda, Sho Muroga, and Yasushi Endo. "Artificial control of magnetization dynamics via spin waves by slot line waveguide." in Digests of Intermag 2020, session GE-5, Montreal, Canada, 4-8 May, 2020. [2] Tetsunori Koda, Sho Muroga, and Yasushi Endo, "Synchronized excitation of magnetization dynamics via spin waves in Bi-YIG thin film by slot line waveguide" *Appl. Phys. Lett.* 116, 102403 (2020). [3] A A Serga, A V Chumak, and B Hillebrands. "YIG magnonics" *J. Phys. D: Appl. Phys.* 43 264002 (2010).



Schematic View of measurement set up for magnetization dynamics using a slot line waveguide. Magnetic field is applied to perpendicular to the plane.



Magnetization dynamics measured at 7.0GHz for (a) Line's width dependence and (b) Line's gap dependence.

EE-06. Withdrawn

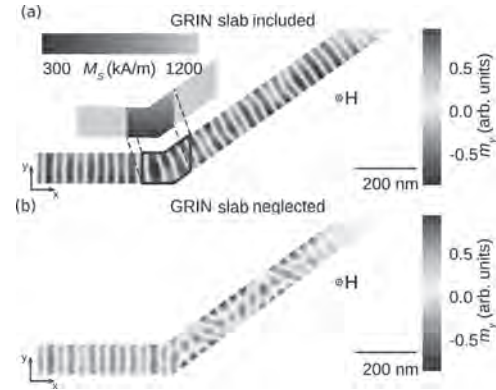
EE-07. Anomalous Refraction of Spin Waves as a Way to Guide Signals in Curved Magnonic Multimode Waveguides.

S. Mieszczak¹, O. Busel², P. Gruszecki¹, A. Kuchko^{2,3}, J.W. Klos¹ and M. Krawczyk¹

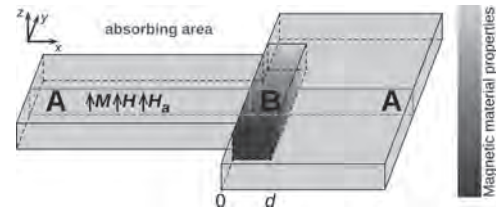
1. Faculty of Physics, Uniwersytet im Adama Mickiewicza w Poznaniu, Poznan, Poland; 2. National Technical University of Ukraine "Igor Sikorsky Kyiv Polytechnic Institute", Kyiv, Ukraine; 3. Institute of Magnetism of NAS of Ukraine, Kyiv, Ukraine

Phase and amplitude are the fundamental characteristics of waves. The processing of any wave relies on the interference effects, which depend on these characteristics. Thus, the control of spin waves' (SWs') phase and amplitude is essential in magnonics to perform both analog and digital SW-based computing [1]. Equally important is the transmission of the information (i.e. guiding and routing of the signal). We present a method for a coherent spin-wave guiding within the narrow magnonic nanostripe. In the magnonic multimode waveguide, scattering between the modes is one of the most important factors for the SW decoherence at the bends. Therefore, the question arises: can we modify the properties of the bending region to block the redistribution of incoming mode into the perpendicularly quantized modes, keeping the transmission as high as possible? Our proposed solution is to fill the bending region with the material of spatially tailored properties, which refract the SW and redirect its propagation strictly along the outgoing section of the waveguide (fig. 1). In other words, we are looking for the particular kind of graded-index (GRIN) element for SWs [2]. To design the GRIN element, we proposed an algorithm which achieving desired properties in a few steps. In the first step, we developed the analytical theory for the scattering of exchange SWs on the homogeneous ferromagnetic slab of finite width embedded in a ferromagnetic layer. Minimizing the total energy, we derived the boundary conditions on the interfaces between the slab and its surroundings. As a results, we obtained the complete relations between the phases and amplitudes of the incident and scattered SWs. Later, we used our findings to demonstrate both analytically and numerically anomalous refraction for the purely exchange SWs incident from a waveguide to a semi-infinite film through a flat magnonic GRIN slab (fig. 2). We treat the GRIN element as an inhomogeneous slab linking the waveguide's input and output branches at the bend. For anomalous refraction, the wavefronts of refracted waves are tilted at a desirable angle with respect to wavefronts of the incident waves. The effect can be observed even at normal incidence. This phenomenon requires a linear change of the transmitted waves phase alongside the interface, where the refraction takes place. To describe it, we used the generalization of Snell's law [3]. From previous step, we knew the phase which is acquired at specific positions so we can conduct analytical calculation of generalized Snell's law and get the refraction angle. In the ultimate step, we could design the magnonic waveguide with the GRIN element at the bend. Knowing the SW bending, we design the properly shaped curved magnonic waveguide with GRIN element and run micromagnetic simulations. Fig. 1 presents a snapshot from simulations, where results are compared to the structure with the neglected GRIN element. We demonstrate that our findings can be used to guide the spin waves smoothly in curved waveguides, even through sharp bends, without reflection and scattering between different waveguide's modes, preserving the phase, the quantity essential for wave computing. *The systems* In all the simulations we consider SW propagation in 5-nm-thick Co-Fe-B film ($M_S = 1200$ kA/m, $A_{ex} = 27$ pJ/m, neglected dumping) in the presence of the out-of-plane magnetic field (applied along the z-axis) of value $\mu_0 H = 0.5$ T. The SW frequency was 25 GHz. The width of the slab had 150 nm. In the considerations, we neglected dipolar interaction, however we checked and discussed the impact of this kind of interaction on the proposed system. In the first step, we considered reduced magnetization saturation in the slab in the range of 300–800 kA/m or additional anisotropy with anisotropy constant in the range of 0–490 kJ/m³. Anomalous refraction was demonstrated for two-dimensional system (fig. 2) composed of three sections. 100 nm wide waveguide, GRIN element with induced The gradient of the magnetic parameters was induced along the y-axis. Saturation magnetization changes in the range of 300–800 kA/m on the distance 100 nm, with direct contact with waveguide. Finally, using the previous step's knowledge, we design a curved waveguide, which supports coherent SW propagation alongside the waveguide [4].

1. G. Csaba, Adam Papp, and W. Porod, Physics Letters A 381, 1471 (2017).
2. C. S. Davies, A. Francis, A. V. Sadovnikov, S. V. Chertopalov, M. T. Bryan, S. V. Grishin, D. A. Allwood, Y. P. Sharaevskii, S. A. Nikitov, and V. V. Kruglyak, Physical Review B 92, 020408 (2015).
3. N. Yu, P. Genevet, M. A. Kats, F. Aieta, J.-P. Tetienne, F. Capasso, and Z. Gaburro, Science 334, 333 (2011).
4. S. Mieszczak, O. Busel, P. Gruszecki, A. N. Kuchko, J. W. Klos and M Krawczyk, Physical Review Applied, 13, 054038 (2020)



Propagation of SWs in the Co-Fe-B waveguide, where the GRIN slab is placed at the bend (a). The color map represents a dynamical component of the magnetization in the y-direction. A snapshot is taken at the moment when a steady state is reached. At the beginning of the horizontal branch of the waveguide, the microwave antenna excites the SWs and at the end of the tilted branch, the SWs are damped to avoid reflections. After taking a turn, the SWs propagate smoothly. (b) SWs' propagation in the waveguide without a gradient of magnetic parameters. After taking a turn, the SWs show a complex behaviour due to interference between different modes of the waveguide.



The geometry of the simulation system with the GRIN element used to demonstrate anomalous refraction. The system consists of the ferromagnetic slab (B) characterized by the gradient of magnetic parameters (e.g., saturation magnetization M_S or anisotropy field H_A) which links the straight section of the waveguide and the semi-infinite plane made of the homogeneous material A. The magnetic parameters in the slab B are changing in the y-direction. At each x-z cross-section, the phase shift of transmitted wave is different, which allows refracting the plane wave propagating initially in the x-direction.

EE-08. Sub-Micrometer Near-Field Focusing of Spin Waves in Ultrathin YIG Films.

B. Divinskiy¹, N. Thiery², L. Vila², O. Klein², N. Beaulieu³, J. Ben Youssef³, S.O. Demokritov¹ and V.E. Demidov¹

1. Institute for Applied Physics, Westfälische Wilhelms-Universität Münster, Münster, Germany; 2. Univ. Grenoble Alpes, Grenoble, France; 3. Université de Bretagne Occidentale, Brest, France

It is now well established that the propagation of spin waves can be controlled by using approaches similar to those used in optics. In recent years particular attention was given to the possibility to controllably focus propagating spin waves. Such focusing can be achieved relatively easily in confined geometries. In the case of extended magnetic films, the implementation of spin-wave focusing appears to be less straightforward. Several approaches have been suggested. However, all of them are rather complex in terms of practical implementation, particularly on the nanoscale. Here, we experimentally demonstrate tight focusing of a spin-wave beam excited in extended nanometer-thick films of YIG by a simple microscopic antenna functioning as a single-slit near-field lens. We show that the focal distance and the minimum transverse width of the focal spot can be controlled in a broad range by varying the frequency/wavelength of spin waves and the antenna geometry. The experimental data are in good agreement with the results of numerical simulations. Our findings provide a simple solution for the implementation of magnonic nanodevices requiring a local concentration of the spin-wave energy.

B. Divinskiy, N. Thiery, L. Vila, O. Klein, N. Beaulieu, J. Ben Youssef, S. O. Demokritov, and V. E. Demidov, Appl. Phys. Lett. 116, 062401 (2020)

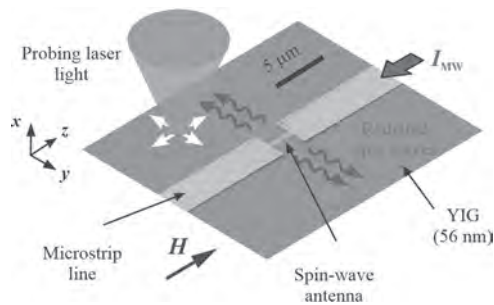


Fig.1 Schematic of the experiment.

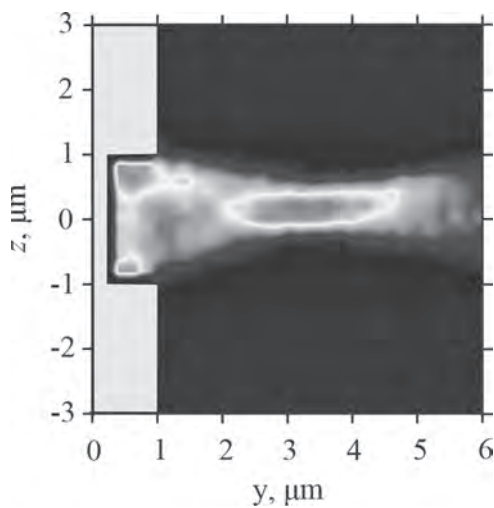


Fig. 2 Measured intensity map of spin waves radiated by the antenna.

EE-09. Low-Loss Magnonic Crystals Based on Nanometer-Thick YIG Films.

H. Qin¹, F. Hermann¹ and S. van Dijken¹

1. NanoSpin, Department of Applied Physics, Aalto-yliopisto, Aalto, Finland

Magnonics utilizing spin waves for information transport, storage, and processing offers an alternative for CMOS-based technology free of detrimental Joule heating at high operation frequency [1]. The realization of magnonic devices requires active control of spin waves and low transmission losses. Magnonic crystals, i.e., metamaterials with periodically modulated magnetic properties, made of yttrium iron garnet (YIG) are promising candidates for performing such tasks because of ultralow magnetic damping [2]. Thus far, several types of micrometer-thick YIG magnonic crystals have been explored including crystals made of periodic shallow airgrooves, metallic stripe arrays on top of a YIG film, and width-modulated YIG structures [2]. On the other hand, programmable control of spin-wave transmission in micrometer-thick YIG films has been demonstrated using current-carrying meander structures [3], optical absorbers [4], and strain coupling to a piezoelectric layer [5]. However, micrometer-thick YIG magnonic crystals with a large number of crystal units are not compatible with miniaturized on-chip device integration. In addition, magnonic crystals based on thick YIG films exhibit small bandgaps in the range 5 MHz – 50 MHz, which limits the manipulation of propagating spin waves. Low-loss nanomagnonics requires smaller YIG magnonic crystals with larger tunable bandgaps [6]. Here, we present the experimental realization of magnonic crystals made of only 2 - 4 discrete 260-nm-thick YIG stripes with robust bandgaps up to 200 MHz for Damon-Eshbach spin waves [7]. The YIG stripes of the magnonic crystal are separated by airgrooves or grooves filled by CoFeB. Compared to micrometer-thick YIG films, the opening of larger bandgaps with less crystal units in arrays of thin YIG stripes is explained by strong Bragg reflection on the individual scatterers. Moreover, efficient dipolar coupling between the YIG stripes via in-plane dynamic fields facilitates low-loss transmission in the allowed bands of the magnonic crystal. The bandgaps of the nanometer-thick YIG magnonic crystals are tunable through a variation of the groove depth, lattice constant, and film thickness [8]. For instance, the bandgaps of a 260-nm-thick YIG crystal widen upon an increase of the groove depth from half to full film thickness. Importantly, low-loss spin-wave transmission in the allowed bands of the magnonic crystal is hardly affected by the patterning of fully discrete YIG stripes. Downscaling of the YIG film thickness to 35 nm decreases the bandgap size through a flattening of the spin-wave dispersion relation. We show that a reduction in the lattice constant effectively compensates for this trend. For 65-nm-thick YIG crystals, we realized 100–200 MHz bandgaps by decreasing the lattice constant from 50 μm to 10 μm . Finally, we show that robust bandgaps up to 220 MHz in combination with low-loss spin-wave transmission at allowed frequencies are attained in a 45-nm-thick YIG crystal with a lattice constant of 2 μm (see Fig. 1). We anticipate that further downscaling of YIG magnonic crystals to the nanoscale is possible through an optimization of the fabrication process and efficient spin-wave excitation over a broad range of wave vectors.

[1] A.V. Chumak et al., Nat. Phys. 11, 453 (2015) [2] A.V. Chumak et al., J. Phys. D: Appl. Phys. 50 244001 (2017) [3] A.V. Chumak et al., Nat. Commun. 1, 141 (2010) [4] M. Vogel et al., Nat. Phys. 11, 487 (2015) [5] A.V. Sadovnikov et al., Phys. Rev. Lett. 120, 257203 (2018) [6] M. Krawczyk et al., J. Phys. Condens. Matter 26 (2014) [7] H.J. Qin et al., Nat. Commun. 9, 5445 (2018) [8] H.J. Qin et al., Appl. Phys. Lett. 116, 202403 (2020)

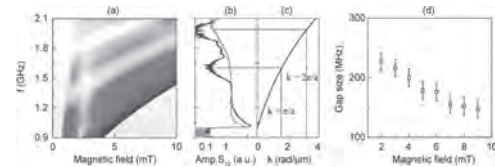


Fig. 1: (a) Contour plot of spin-wave transmission spectra (amplitude of S_{12}) for a YIG magnonic crystal as a function of external magnetic field. The crystal consists of four 0.5- μm -wide airgrooves with a separation of 2 μm . (b) Line profile of spin-wave transmission (blue curve) for an external magnetic field of 5 mT and a reference spectrum (orange curve) measured on an unpatterned part of the same YIG film. (c) Dispersion relation of Damon-Eshbach spin waves in YIG for a magnetic field of 5 mT. The horizontal and vertical dashed lines indicate the bandgap center frequencies and corresponding Bragg scattering wave vectors. (d) Measured gap size of the first bandgap as a function of external magnetic field.

EE-10. Brillouin Light Scattering Study of Spin Waves in CoP Exchange Spring Thin Films.

A. Samanta^{1,2}, G. Gubbiotti³ and S. Roy^{1,2}

1. Micropower Systems and Nanomagnetism Group, Micro-Nano-Systems Center, Tyndall National Institute, Cork, Ireland; 2. Department of Physics, University College Cork, Cork, Ireland; 3. Istituto Officina dei Materiali del Consiglio Nazionale delle Ricerche (CNR-IOM), Sede di Perugia, c/o Dipartimento di Fisica e Geologia, Università degli Studi di Perugia, Perugia, Italy

Brillouin Light Scattering (BLS) [1, 2] experiment has been used to determine the spin waves in Co-rich cobalt phosphorous (CoP) exchange spring [3, 4] thin films prepared by the electrodeposition techniques [5, 6] at room temperature. The static magnetic measurement using hysteresis loop tracer (ShB Instruments, USA) shown in FIG. 1 (a)-(b) reveals the hysteresis loop structures for the electrodeposited thin films – the staircase like exchange spring nature with the presence of two coercivities in the hysteresis loops – composed by the soft and hard magnetic phases in a single material. Contrasted with the conventional single-phase magnetic material having a comparatively low coercivity – such kind of exchange spring nanomagnetic frameworks are promising for cutting edge, forefront magnetic applications due to their relatively higher energy product – the blend of magnetization and permanent magnetic field [7]. The differential of the magnetization shown in FIG. 1 (c)-(d) confirms the presence of two coercivities in the 2.8 μm , 5.7 μm thick thin films, respectively. Utilizing a (3+3)-pass tandem Fabry-Perot interferometer, and considering the backscattering geometry, the BLS spectra of the thermally excited SWs were measured. The BLS Spectra of the 2.8 μm thick CoP thin film shows that the peaks are very broad. The field dependent BLS spectra of 5.7 μm thick CoP thin film electrodeposited for 60 min is shown in FIG. 2(a). The BLS study yields two main modes present in the BLS spectrum: the lowest frequency one is a band of bulk modes (B) while the one at the higher frequency (sharp peak) is the so-called Damon-Eshbach surface spin wave (S) [8]. On the Stokes-side of the spectra, two well resolved peaks (S and B, as mentioned in the figure) are observed while the anti-Stokes side of the spectra shows only one peak (B). The S mode is observed only on one side of the spectrum, depending on the direction of the external magnetic field. This is the consequence of the nonreciprocal character of the S wave and of the micrometer thickness of the investigated films. The external magnetic field dependent BLS spectra shows an almost linear dependence of the mode frequencies vs the magnetic field intensity. The BLS spectra shown in FIG. 2(b) reveals the effect of magnetization reversal at constant polarization which unveils the predicted side change of Damon Eshbach (DE) surface mode. The change in Stokes/anti-Stokes ratio has also been affirmed because of the associated transfer of the S and B mode interaction with this magnetization reversal [8].

[1] G. Gubbiotti, X. Zhou, A. O. Adeyeye, Phys. Rev. B 101, 224431 (2020). [2] S. Tacchi, G. Gubbiotti, M. Madami, J. Phys. Condens. Matter 29, 73001 (2016). [3] E. E. Fullerton, J. S. Jiang, M. Grimsditch, Phys. Rev. B 58, 12193 (1998). [4] F. Magnus, M. E. Brooks-Bartlett, R. Moubah, Nat. Commun. 7, ncomms11931 (2016). [5] P. McCloskey, B. Jamieson, T. O'Donnell, J. Magn. Magn. Mater. 320, 2509 (2008). [6] S. Roy, A. Connell, M. Ludwig, J. Magn. Magn. Mater. 290–291, 1524 (2005). [7] H. Zeng, J. Li, J. P. Liu, Nature 420, 395 (2002). [8] J. R. Sandercock and W. Wetting, J. Appl. Phys. 50, 7784 (1979).

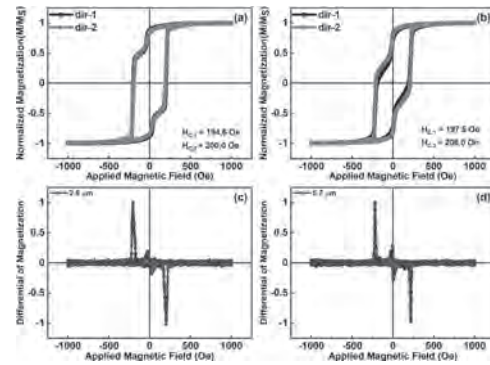


FIG. 1: Hysteresis loop of the electrodeposited CoP thin films measured ShB Hysteresis loop tracer in XY plane, and here, dir-1+90°=dir-2. The thickness of the films is (a) 2.8 μm , (b) 5.7 μm , for the electrodeposited time (a) 30 min, (b) 60 min. (c)-(d) The differential of the magnetization of the (a) 2.8 μm , (b) 5.7 μm thick thin films, respectively.

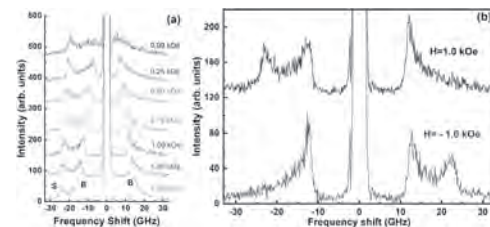


FIG. 2 (a) BLS spectra of the 5.7 thick CoP thin film (electrodeposited for 60 min) at different in-plane bias magnetic fields measured from 1.50 kOe to 0 Oe with the backscattering geometry. (b) BLS Spectra of 5.7 in a bias magnetic field of +1.0 and -1.0 kOe revealing the effect of the reversal of the magnetization on the frequency position of the Damon-Eshbach wave.

EE-11. Design of a Coplanar-Waveguide-Based Microwave-to-Spin-Wave Transducer.

H.O. Aquino¹, G.H. Bernstein¹ and W. Porod¹

¹. Electrical Engineering, University of Notre Dame, Notre Dame, IN, United States

Spin waves (SWs) are emerging as a potential alternative to electrical signals for computing and signal processing. Because SWs have relatively short wavelengths at microwave frequencies, they have the potential for applications in high-speed chip-scale electronics [1]. This work seeks to design and fabricate a spin-wave-based real-time spectrum analyzer that exploits SW interference in analogy to an optical spectrometer [2]. Here, microwave electrical signals are converted into SWs. All processing is then done by the diffraction and interference of SWs as they propagate in a magnetic thin film. After the interference pattern forms, SWs are then converted back into electrical signals. This type of device requires SWs having an isotropic dispersion relation, which, in turn, requires an out-of-plane DC bias field. These spin waves are forward-volume spin waves (FVSW). The focus of the work presented here is to explore the design space of a microwave-to-spin-wave transducer for FVSWs, where the microwave signal is introduced by a coplanar waveguide (CPW). The SW excitation spectrum of an external RF magnetic field acting on a magnetic thin film is the result of the interference between SWs launched from all points of the film that are excited by the magnetic field. For a magnetic field from a CPW, this interference results in a comb-like spatial-frequency response, which is equivalent to the Fourier transform (FT) of the spatial distribution of the magnetic field that acts on the magnetic film [3]. However, because the device described above requires a relatively constant transfer function over the full bandwidth, i.e., without nulls, the comb-like excitation spectrum from a CPW would not be suitable for our applications. Launching spin waves from the edge of the film can be used to improve the spin-wave excitation spectrum for a couple of reasons. First, it has been shown that the edge of a film can be an efficient broadband source of spin-waves [4]. And second, because only part of the CPW's field acts on the magnetic film, the FT of only that part describes the excitation spectrum; the FT of the spatial distribution is more delta-function-like and therefore is more broadband than the previous case. To design the edge-launched SW transducer, micromagnetic simulations were done in Mumax3 [5] using the magnetic field from CPWs simulated in Ansys HFSS. Our simulations (Fig. 1) show the frequency response of this simulated structure with the edge 2 μm away from the CPW. These simulations verify that the transducer's excitation spectrum is improved, i.e., made more uniform, by placing the CPW beside the edge of the film rather than on top of the film. This improved bandwidth comes at the cost of transducer efficiency, since only the field to the side of the CPW acts on the magnetic film. Because the magnetic field decreases rapidly with distance from the CPW, the edge of the film should be as close to the CPW as possible to increase coupling between the CPW and the film. Representative waveforms given in Fig. 2 show that because the small out-of-plane component of the RF magnetic field is parallel to the large DC-bias magnetic field, it contributes very little to the excitation of a SW compared to the in-plane components of the field. The results of the simulations show that for the same magnetic field, raising the bottom of the CPW increases the in-plane component of the field and increases the amplitude of the SW. Yet another configuration would be to place the CPW on the magnetic film and create an edge-launcher by etching a gap in the film to the side of the CPW. Excessively large fields can produce unstable spin-waves with additional unwanted undesirable frequency components [6]. With a gap in the magnetic material, the internal magnetic field crosses the gap at a reduced field strength, removing the unwanted structure and resulting in SWs at the desired wavelength, as well as a smoother frequency response (Fig. 1.). The structure of the previous paragraph was simulated with the properties of an YIG thin film having different thicknesses (30 nm and 243 nm). It is found that increasing the distance between the gap and the CPW increases the amplitude of the resulting SW with diminishing returns, as shown in Fig. 2. With a gap that is 2 μm wide and 6 μm away from the CPW, we find that for the thinner film this structure produces a SW with a smaller amplitude than when the material underneath the CPW is nonmagnetic and the edge is flush with CPW. However, with the thicker film (Fig. 2), the

structure with the magnetic film under the CPW produces a larger SW than the structure without the magnetic material under the CPW.

[1] G. Csaba, Á. Papp and W. Porod, *Physics Letters A*, Vol. 381, no. 17, pp. 1471-1476 (2017) [2] Á. Papp, et al., *Scientific Reports*, vol. 7, no. 1, pp.9245-9245 (2017) [3] S. Maendl, I. Stasinopoulos and D. Grundler, *Applied Physics Letters*, vol. 111, no. 1, p. 012403 (2017) [4] F. Mushenok, et al., *Applied Physics Letters*, Vol. 111, p. 042404 (2017) [5] A. Vansteenkiste, et al., *AIP Advances*, vol. 4, no. 10, p. 107133 (2014) [6] H. Aquino, et al., poster presented at the 78th Device Research Conference

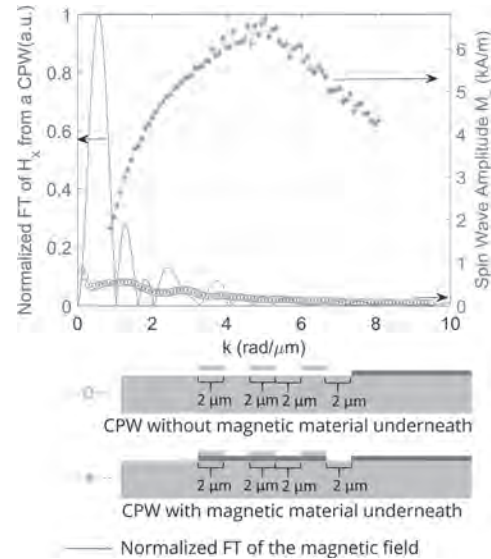


Fig. 1. The spatial frequency response of simulated microwave to SW transducers with the CPW placed to the side of the film with and without magnetic material underneath the CPW. The same magnetic field was used for both transducers. The FT of the field is shown to illustrate the comb-like response of a CPW on the film.

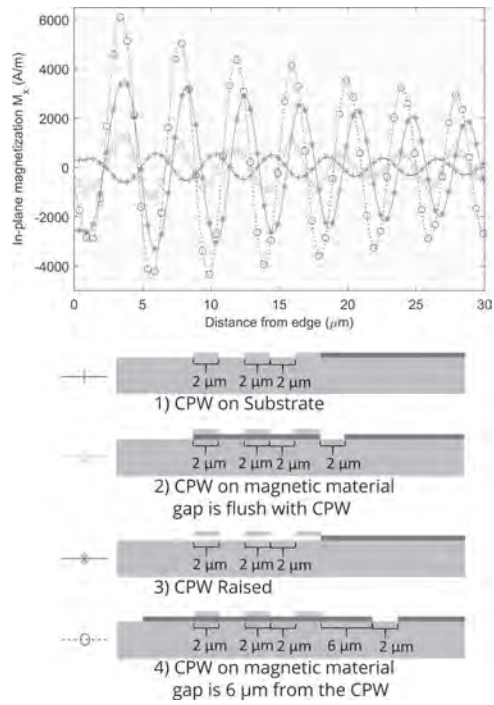


Fig. 2. Simulation results with SWs (in-plane magnetization, M_x) launched from the edge of a 243 nm thick YIG film. All plots begin at the edge of the magnetic film. 1) The edge is flush to the CPW and the bottom of the 300 nm thick CPW is in the same plane as the bottom of the magnetic film; 2) the CPW is on the magnetic film with a $2\ \mu\text{m}$ gap etched to the side of the CPW; 3) the CPW is raised on nonmagnetic material such that the bottom of the CPW is in the same plane as the top of the magnetic film; and 4) the CPW is on the magnetic film with the gap $6\ \mu\text{m}$ to the side.

EE-12. Withdrawn

EE-13. Magnonic Bragg Filter Design for India’s 5G Spectrum.

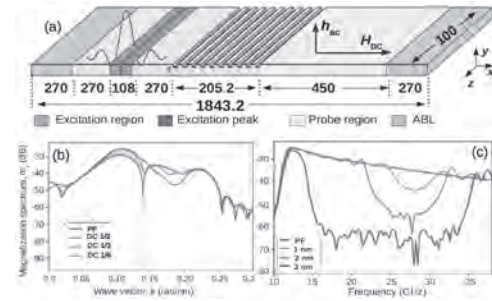
M. Malathi¹, L.P. Nair¹, G. Venkat² and A. Prabhakar¹

1. Electrical Engineering, Indian Institute of Technology Madras, Chennai, India; 2. Materials Science and engineering, The University of Sheffield, Sheffield, United Kingdom

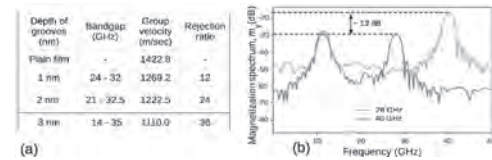
Signal processing, conditioning, filtering and are becoming critical parts of RF communications. We have designed a magnonic Bragg filter with a tailored frequency response. A systematic procedure for arriving at the period of Bragg grating, excitation, probe region etc., has been formulated to simulate the expected spectral response. We simulate and analyze a 1D magnonic Bragg narrow band rejection filter at 28 GHz, the frequency allotted to India, in the 5G spectrum. The magnonic filter with 10 grooves has a pass band from 12 GHz to 50 GHz and a tuneable band gap with attenuation as high as 36 dB. Modulating the depth and the duty cycle of the magnonic crystal, we demonstrate that we could tune parameters like, the bandgap, rejection ratio and group velocity of the spin waves. The rejection efficiency of the filter at the frequency of 28 GHz is 90% higher compared to a signal of 40 GHz, in the pass band. INTRODUCTION 5G mobile telecommunications operate above 24 GHz band and these signals suffer much higher path loss [1]. Magnons, or quanta of spin waves (SW) have been explored as information carriers and for computing [2] with the help of magnonic crystals (MCs). Experimental demonstrations show tuning of bandgaps in MCs, by varying parameters such as the applied magnetic field (H_{DC}), width, thickness [3, 4] etc. With extensive experimental investigations being pursued, we arrive at an optimized set of design procedures to estimate different simulation parameters. A magnonic Bragg filter (MBF) is designed to operate at 28 GHz and simulated using the micromagnetic simulation tool, MuMax³. The tunability of bandgaps, rejection and group velocity with modulations of duty cycle and depth of the gratings are studied extensively to finally realize an optimized and highly efficient 1D MBF. DESIGN PROCEDURE The nonlinear dispersion relation between frequency(ω) and wavenumber(k_{SW}) introduces a constraint in the filter design. We must invert $\omega(k_{SW})$, find k_{SW} for a given excitation geometry, and then pick the Bragg wavelength(Λ). We must also use a broadband excitation to capture the full spectrum. Micromagnetics thus become computationally intensive, and a simple MBF simulation occupies terabytes of storage. Hence, we developed custom Go routines to extract the relevant spatially averaged and temporally sampled data from MuMax³ simulations [5]. For our purposes, we assume a strip of permalloy, with saturation magnetization 800 kA/m, exchange constant 1.3×10^{-11} J/m and damping constant $\alpha = 0.006$ [6]. The backward volume spin waves configuration excites SWs along x , parallel to H_{DC} , as in Fig.1(a). At $\omega=28$ GHz, and with $H_{DC}=54.9$ kA/m (a convenient field value chosen for our future experiments), we obtained $k_{SW} = 0.145$ rad/nm from the dispersion relation [7, Eqn(18)]. This corresponds to a wavelength $\lambda_{SW} = 43.33$ nm, and we choose $\Lambda=21.6$ nm to match this at normal incidence. A broadband small signal excitation of $h_y(x,t)$ with cut off values of $k_c = \pm 0.3$ rad/nm and $f_c = \pm 50$ GHz is applied using sinc pulses in space and time. This yields sinc pulses with a peak centered at 100 ps and spread over 108 nm. In the probe region, the magnetization component m_y is collected for post processing. We chose a probe region $6 \times \lambda_{SW}$ long, and locate it sufficiently far away from gratings to minimize transient interferences. Absorbing boundary regions are defined at either boundaries with a parabolic variation of α from 1 to 0.006 to absorb the reflections from edges[8]. With all these estimated parameters, the dimensions of the MC with 10 grooves on an 8 nm thick permalloy film is $1843.2 \times 8 \times 100$ nm³. DUTY CYCLE & DEPTH MODULATIONS While the grating period decides the reflected k_{SW} , the duty cycle (DC) of the grating affects the bandgap. We simulated gratings with depths of 2 nm and DCs of 50%, 33.3% and 16.7%. 1D spectral plots in Fig.1(b) show sharp dips of the order of 20 dB consistently, at $k_{SW}=0.145$ rad/nm for all MCs except the plain film, indicating that this wavevector is rejected irrespective of the DC variation. We also study the effect of depth modulation for gratings of depths 1 nm, 2 nm and 4 nm, all with a DC of 50%. The 1D-FFT plot in Fig.1(c), shows the occurrence of bandgaps in the designed frequency range. The effective thickness of the film allows propagation of both exchange and dipolar coupled SWs. From Fig.2(a), we observe a narrower bandgap, a reduced group velocity of the SWs, and an increase in frequency rejection ratio with increasing groove depth thickness. Based on these studies, the

MBF is optimized to have 2 nm depth and a DC of 50%. Finally, to confirm the performance, a single frequency sinusoidal excitation at 28 GHz (in the bandgap), is compared with that of 40 GHz (not in bandgap) and observed that the rejection efficiency is about 90% higher at 28 GHz, as in Fig.2(b). CONCLUSION For a given frequency response of a magnonic device, we developed a systematic set of procedures to plan out various simulation parameters. The magnonic Bragg filter is designed and realized to reject frequency of 28 GHz efficiently. This study highlights the effect of variations, in duty cycle and depth, of MCs with sub-micron features, and assists in the fabrication process. We also expect that the outlined design procedure, and the computational routines, will be helpful to the magnonic community.

[1] Jack Browne, <https://www.mwrf.com/technologies/systems/article/21120263/surveying-the-status-of-5g-technology>, (2020) [2] A. Mahmoud, F. Ciubotaru and F. Vanderveken, J. Appl. Phys., Vol. 128, p. 161101 (2020) [3] P. Frey, A. A. Nikitin and D. A. Bozhko, Comm. Phys., Vol. 3, p.17(2020) [4] A. V. Chumak A. A. Serga and S. Wolff, Appl. Phys. Lett, Vol. 94, p.172511 (2009) [5] <https://github.com/LekhaRam/Mumax310AveragedSampling> (2020) [6] Y. Zhao, Q. Song and S. H. Yang, Sci. Rep., Vol. 6, p.22890 (2016) [7] B. A. Kalinikos, IEE Proc.H., Vol. 127, p.4 (1980) [8] G. Venkat and A. Prabhakar, J. Magn. Magn. Mater., Vol. 450, p.34 (2018)



(a) Structure of MBF with dimensions in nm (b) Variation of m_y in k space with DC (c) Spectrum of depth modulated SW



(a) Results of depth modulated MC (b) Sinusoidal excitation at 28 GHz & 40 GHz for the optimized 1D MBF

EE-14. Subwavelength Resonant Control of the Spin-Wave Phase in Thin Ferromagnetic Films.

K. Sobucki¹, W. Smigaj², J.N. Rychly³, M. Krawczyk¹ and P. Gruszecki¹
 1. *Nanomaterials, Uniwersytet im Adama Mickiewicza w Poznaniu, Poznan, Poland*; 2. *Met Office, Exeter, United Kingdom*; 3. *Polska Akademia Nauk Instytut Fizyki Molekularnej, Poznan, Poland*

In contemporary developing world demand for small and less energy-consuming devices rapidly increases. To meet this requirement a new generation of technology has to be developed which overcome problems known from the usage of electronics such as frequency limit and heat dissipation. One possible answer promises spin waves (SW) which have a short wavelength and do not suffer from Joule heating as electrons [1]. To successfully use SWs in widespread devices there is a need to find methods that allow handling this type of low energy consuming information carrier. The usage of metasurfaces consisting of arrays of nano-resonators was an innovative concept in modern optics, as made it possible to design a new class of optical systems with properties unheard in classical optics as for example flat lenses [2]. Such devices become available because metasurfaces enable complete control of electromagnetic wave's phase and amplitude at subwavelength distances. However, such a concept has not been yet widespread in the realm of magnonics, although it would be extremely useful in the design of SW devices [3]. Especially because SW propagation is significantly limited by damping, so requires the usage of technology that works well in the constrain of ultra-short distances. Here, we present extensive theoretical research on the influence of the position and geometry of a ferromagnetic stripe on the reflection and transmission of the SWs from the edge and middle, respectively, of a permalloy film (Fig. 1) [4]. We have focused on how properties of SW change with the resonator width and separation between both elements. Interactions between the stripe and the layer, which depend on the value of separation between the elements and dimensions of the stripe, affect the propagation and reflection of SW. To check the scope of the interactions we use three numerical methods. Namely, finite element method in frequency domain, micromagnetic simulations [5], and finite element modal method. Employing three different methods allowed us to cross-check their results to confirm their correctness. We show that the phase shift as a function of the stripe's width is characterized by intervals of small and steady growth which are separated by narrow areas of resonances in which phase increases linearly (Fig. 1 inset a). In the areas of resonances there is a visible increase of amplitude and resonances appear periodically in function of a stripe width with a period of about 160 nm. Simulations with increasing separation show (Fig.1 inset b) that resonances also occur with changes of separation but then the function is not periodic. Additionally above certain separation resonances do not appear anymore. The behavior of phase changes is explained with analytical model in which the reflection coefficient consists of two terms of different origins. The first one is responsible for a slow increase of phase with increasing width of the resonator and is a result of phase accumulated in the reflection of the long-wavelength mode. The second term has origin in constructive interference of the short-wavelength mode in the bilayer part of the system, playing a role of the resonator. This term gives significant input only at certain widths of the resonator, which can be predicted from Fabry-Pérot resonance conditions [6]. Intervals of rapid phase changes (Fig. 1 inset a) are caused by the presence of the second term. Because of the properties of the second term, the system used in the simulations can be considered as a realization of the Gires-Tournois type magnonic interferometer [7]. Furthermore, we extend the idea of resonance control of SW phase to the transmission mode. Acquired knowledge allows designing a new class of SW devices based on the Gires-Tournois interferometer concept and manipulations of SW with the usage of magnetic elements smaller than the wavelength of SW. Control of the SW phase can be used for the creation of SW-optical elements such as flat lenses and phase shifters. Especially interesting idea is utilization of proposed interferometer in the system to detect magnetic particles in the vicinity of the bilayer part. The research leading to these results has received funding from the Polish National Science Centre projects No. UMO-2015/17/B/ST3/00118, UMO-2019/33/B/ST5/02013, and UMO-2019/35/D/ST3/03729. The simulations were partially performed at the Poznan Supercomputing and Networking Center (Grant No. 398).

[1] M. Krawczyk and D. Grundler, *J. Phys.: Condens. Matter* 26, 123202 (2014) [2] N. Yu, et al., *Nat. Mater.* 13, 139–150 (2014) [3] M. Zelent, et al., *Nanoscale* 11, 9743-9748 (2019) [4] K. Sobucki, et al., arXiv preprint arXiv:2007.15226 (2020) [5] A. Vansteenkiste et al., *AIP Advances* 4, 107133 (2014) [6] F. Fabry, A. Perot, *Ann. Chim. Phys.* 16, 115 (1899) [7] F. Gires, P. Tournois, *R. Acad. Sci. Paris.* 258, 6112–6115 (1964)

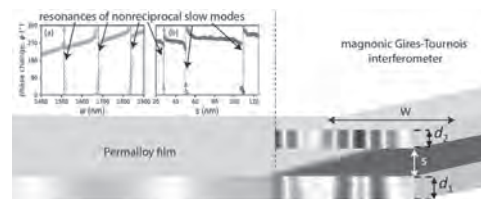


Fig. 1 Geometry of the system used in the simulations. Parameters w and s were manipulated in the simulations, where $d_1 = 5$ nm, $d_2 = 40$ nm and $\mu H_0 = 0.1$ T were kept constant. In simulations frequency of 11 GHz was assumed. Between coordinates $x = 0$ and $x = w$ the bilayered part is regarded as resonator. Inset (a) Phase shift as a function of stripe's width. Resonances appear periodically with increasing stripe's width with period around 160 nm. Inset (b) Phase shift as a function of stripe-film separation.

EE-15. Multifrequency Spin Wave Device for Parallel Data Processing Using Micro Structured Yttrium Iron Garnet Thin Films.

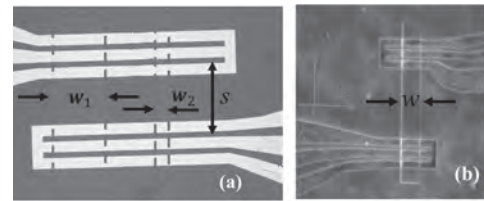
M. Sarker¹, S. Nakamura¹, H. Yamahara¹, M. Seki¹ and H. Tabata¹

1. Electrical Engineering and Information System, The University of Tokyo, Bunkyo-ku, Japan

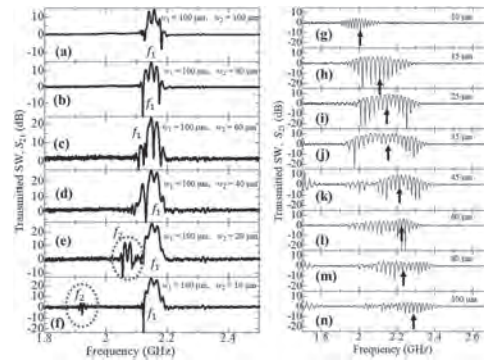
Spin waves (SWs) and their quanta magnons in the magnetic structures offer data transmission and data encoding capability in both amplitude and phase, providing an additional degree of freedom compared to their electronic counterparts. Most of the works in this field are focused on developing novel and energy efficient control mechanisms of SW by different means such as voltage [1], current [2], light [3], heat [4] etc., to use it in logic applications. However, this wave-based computation has the tremendous potential of parallel data processing. A multifrequency magnon network would allow parallel data processing within a single element, which is not possible in conventional transistor-based electronic logic. There are few reports about SW channeling in multiple paths in metallic ferromagnet [5] [6]. In this work, we experimentally demonstrated a novel multifrequency SW device that can operate at multiple frequencies simultaneously using the shape anisotropy of the magnonic film. We have used yttrium iron garnet Y₃Fe₅O₁₂ (YIG) as the magnonic material due to its extraordinarily low damping constant. A 145 nm-thick YIG film was grown on a (111)-oriented single crystalline Gd₃Ga₅O₁₂ (GGG) substrate by pulsed laser deposition technique. Two patterned YIG waveguide with width w_1 and w_2 were fabricated by hot orthophosphoric etching at 160 °C temperature after photolithography as shown in Figure 1(a). w_1 was maintained at 100 μm , whereas w_2 was varied in the steps of 10, 20, 40, 60, 80, and 100 μm to implement a multichannel spin wave device. Subsequently, a system of two co-planner waveguide (CPW) made of 90 nm thick Au was integrated into the YIG film using *dc* magnetron-sputtering. The separation between the center lines of the exciting and detecting antenna (S) was designed as 200 μm . Another series of single channel SW device as shown as Figure 1(b) was fabricated by the similar procedure as Figure 1(a), where the width w of the devices was varied in the step of 10, 15, 25, 35, 45 60, 80, and 100 μm to investigate the contribution of shape anisotropy. For device characterization, we employed the microwave technique using the vector network analyzer (VNA). A *dc*-biased magnetic field ($\mu_0 H_{\text{ext}} = 25\text{mT}$) was applied in the in-plane direction and perpendicular to the SW propagation path, where magnetostatic surface SW (MSSW) was excited in the YIG film. To investigate SW propagation, we followed a similar approach as in the reference [7] The transmitted SW, scattering parameter S_{21} for a multichannel device (Figure 1(a)) has been shown in Figure 2(a)-(f). Figure 2(a) to (d) shows a single mode SW transmission with maximum propagation at $f_1 = 2.15$ GHz. However, Figure 2(e) and (f) shows the appearance of an additional SW propagation mode at $f_2 = 2.06$ GHz and $f_2 = 1.92$ GHz, respectively, along with the first mode at 2.15 GHz. Thus, it indicates that additional mode appears only when the width of the second waveguide has been shrunk beyond 20 μm , and it happens at a lower frequency than the first mode. To investigate the origin of the emergence of the second low frequency SW mode we have performed another set of the experiment where we have done the same measurement for the single channel SW device shown in Figure 1(b). Transmitted SW signals for these devices are shown in 2(g) to (n). We have found that the center frequency (indicated by arrow) of the transmission spectra has been moved from 2.25 GHz to 2.00 GHz when waveguide width has been changed from 100 μm to 10 μm . This frequency shifting can be attributed to the reduction effective magnetic field due to shape anisotropy induced demagnetizing field (H_d). When a magnonic film is micro structured as a bar, an H_d is developed inside the micro structured waveguide [8]. We have calculated this H_d as 3.2, 4.0, 5.3, 8.0, 15 and 32 mT for 100, 80, 60, 40, 20 and 10 μm waveguide respectively from $H_d = t^*4\pi M_s/w$, where t , M_s and w are the thickness, saturation magnetization and width of the waveguide, respectively. We have used $M_s = 140$ kA/m, which is the standard value for YIG film. This demagnetizing field reduces the effective magnetization based on the relation: $H_{\text{eff}} = H_{\text{ext}} - H_d$. According to the Kittel equation, the reduction of will result in the reduction of SW frequency, $f_{\text{FMR}} : f_{\text{FMR}} = \gamma \sqrt{H_{\text{eff}}(H_{\text{eff}} + M_{\text{eff}})}/2\pi$, where γ is the gyromagnetic ratio. As the width of the waveguide gets smaller, the demagnetizing field becomes larger, causing more reduction of H_{eff} and SW frequency. These results provide us with a guideline that even by using same

magnetic material operating under the same magnetic bias field, the resonant frequencies of the individual micron size magnets on a single chip can be tuned by varying the width of the magnet. In this work, combining such two different magnonic channel with the distinguishable anisotropic demagnetizing field has made it possible to make a multifrequency SW device for parallel data processing.

- [1] S. Choudhury, H. Takahashi, A. Barman, *Sci. Adv.* 2020; 6:eaba5457 [2] S. Sarker, H. Yamahara, H. Tabata, *Appl. Phys. Lett.* 117, 152403 (2020) [3] M. Vogel, A. V. Chumak, B. Hillebrands, *Nat. Phys.* 11, 487-491 (2015) [4] V. Castle, G.E.W. Bauer, *Phys. Rev. B* 96, 064407, (2017). [5] F. Heussner, B. Hillebrands, P. Pirro, *Phys. Status Solidi RRL* 2020, 14, 1900695 [6] K. Vogt, F.Y. Fradin, H. Schultheiss, *Nat. Comm.* 5:3727 (2014) [7] S. Sarker, H. Yamahara, H. Tabata, *AIP Advances* 10, 015015 (2020) [8] T. Manago, S. Yakata, T. Kimura, *JJAP* 52 (2013) 053001



(a) Optical image of multichannel SW device (b) Microscopic image of single channel SW device



Transmitted SW signal for in multichannel device for $w_1 = 100 \mu\text{m}$ and (a) $w_2 = 100 \mu\text{m}$ (b) $w_2 = 80 \mu\text{m}$ (c) $w_2 = 60 \mu\text{m}$ (d) $w_2 = 40 \mu\text{m}$ (e) $w_2 = 20 \mu\text{m}$ (f) $w_2 = 10 \mu\text{m}$. Transmitted SW for single channel device for (g) $w = 10 \mu\text{m}$ (h) $w = 15 \mu\text{m}$ (i) $w = 25 \mu\text{m}$ (j) $w = 35 \mu\text{m}$ (k) $w = 45 \mu\text{m}$ (l) $w = 60 \mu\text{m}$ (m) $w = 80 \mu\text{m}$ (n) $w = 100 \mu\text{m}$

Session EP
MAGNONICS I
(Poster Session)

Alexandr V. Sadovnikov, Chair
Saratov State University, Saratov, Russian Federation

EP-01. Standing Spin Wave Resonance Properties of Multiple Spin Wave Modes on Co₂FeAl Magnetic Strip Under Zero Bias Field.

X. Ya¹, K. Kurihara², K. Koki², H. Ogami², Y. Kurokawa², H. Yuasa², T. Tanaka² and K. Matsuyama²

1. IMI, Kyushu University, Fukuoka, Japan; 2. ISEE, Kyushu University, Fukuoka, Japan

Geometrically confined standing spin wave resonance (SSWR) has attracted intense research interests as a fundamental physics and practical applications [1][2]. The magnetostatic surface wave (MSSW) mode has been reported owning larger signal intensity than magnetostatic backward volume wave (MSBVW) mode[3]. These two modes are controlled by bias field continuously applied to magnetic strip, where the bias field is applied in the vertical or parallel directions according to MSSW or MSBVW modes, respectively. In this study, we successfully deposited Co₂FeAl films with 4-fold in-plane anisotropy and studied SSWR properties of the fabricated magnetic strips. Due to the 4-fold anisotropy, we succeeded in generating MSSW and MSBVW modes under zero bias field and confirmed absorption intensity difference between these two modes. Considering MSSW mode as ‘ON’ state and MSBVW mode as ‘OFF’ state, the absorption intensity difference demonstrated a spin wave switch or sensor device. Co₂FeAl films were deposited on MgO (001) substrate at 400°C by sputtering method. The angular dependence of the squareness are plotted in Fig. 1(a), which showed strong 4-fold in-plane anisotropy (an easy axis corresponds to MgO[001]) when film thickness was 60 nm. Co₂FeAl (400) peak at 65 degree of the corresponding XRD translated the 60-nm-thick film was well crystallized. The magnetic strip was fabricated by lithography techniques, where the lateral coordinates were defined to coincide with the anisotropy directions. 100-nm-thick SiO₂ insulating layer was deposited on the strips and Grand-Signal-Grand coplanar waveguide (CPW) was fabricated on the SiO₂ layer (Fig. 1(b)). The transmission characteristics of S₂₁ was measured by VNA under the bias field, H_b, ranged from 600 Oe to 0. The S₂₁ of MSSW and MSBVW at different H_b are shown in Fig. 2(a). The broad absorption dip includes multiple MSSW resonance modes, which are shown by the Lorentzian fitting. The absorption intensity of MSSW mode at various H_b were greater than 0.5 dB, while the absorption intensity of MSBVW mode were less than 0.2 dB. The absorption intensity ratio of MSSW to MSBVW exceed 20 dB when H_b = 600 Oe, which is large enough to distinguish the ON/OFF states. The resonance frequency estimated from the Lorentzian fitting were shown in Fig. 2(b). Micromagnetic simulation explains that the discontinuous H_b dependence of SSWR frequency is reasoned by the absorption intensity balance of multiple modes. The absorption intensity of each order was different and the dominant order changes with the bias field. The dominant order changed from 7th order to 5th order at strong bias field, and from 5th order to 3rd order at weak bias field.

[1] T. Schneider, A. A. Serga, B. Leven, and B. Hillebrands, Appl. Phys. Lett., vol. 92, p. 022505-1-3 (2008) [2] X. Ya, H. Chen, S. Oyabu, B. Peng, H. Otsuki, T. Tanaka, and K. Matsuyama, J. Appl. Phys., vol. 117, p. 17A719-1-3 (2015). [3] Kazuto Yamanoi, Satoshi Yakata, Takashi Kimura, and Takashi Manago, JJAP, vol 52, p. 083001 (2013)

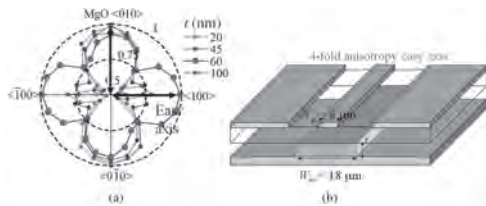


Fig. 1 (a) Squareness for the CoFeAl film deposited at various film thickness. (b) schematic of a CPW on magnetic strip.

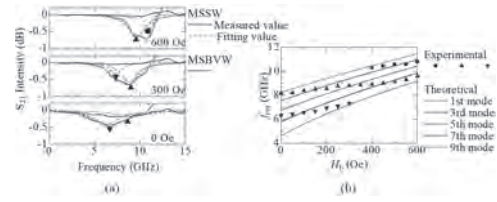


Fig. 2 (a) S₂₁ parameter at different bias field, (b) dependence of resonance frequency on the bias field.

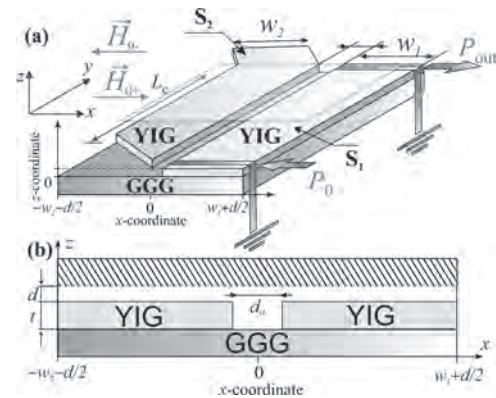
EP-02. Nonreciprocal Spin-Wave Propagation in Lateral Magnonic Stripes.

S. Odintsov¹, A.V. Sadovnikov¹ and F. Ogrin²

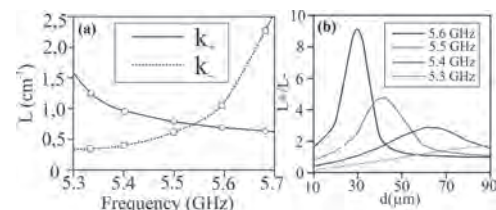
1. N. G. Chernyshevskogo National Research University in Saratov, Saratov, Russian Federation; 2. University of Exeter, Exeter, United Kingdom

Nonreciprocity is a vital, unique, and fundamental signal transmission characteristic widely required in a large number of RF, microwave and millimeter-wave circuit, and module applications, which include communication systems, radar, and measurement equipment. Without any doubts, the nonreciprocal properties are indispensable for the development of emerging circuits and systems such as the highly anticipated in-band full-duplex transceiver systems. The recent development of nanotechnology in combination with the increased interest in the properties of artificial crystals brought back the topic of spin-wave (SW) nonreciprocity and its potential application in functional devices. The surface spin waves (SSWs) propagating in a ferromagnetic film along the direction perpendicular to a tangentially applied magnetic field H_0 (Damon-Eshbach geometry) [1] possess nonreciprocal properties. Recently, of great interest is the study of the properties of spin waves during their propagation in magnetic waveguide structures of micro and nano scale. In this case, the main attention is paid to the use of spin waves (STs) as carriers of information signals, since it is possible to implement a number of signal processing devices based on the principles of magnonics [2], taking into account the possibility of coding the signal using both amplitude and spin phase the waves. As is known, the properties of SW spin waves are determined by the dipole and exchange interactions in magnetic media and can change significantly with changing medium parameters, for example, the magnitude and direction of the magnetization field [3]. In this paper, we consider structures consisting of laterally coupled YIG micro- and nanowaveguides that can be used as basic elements for creating various devices of functional magnonics: waveguides, filters, couplers. It also explores the possibility of controlling the propagation modes of spin waves by adding a metal layer. The structure of a directional coupler with metal layer on it is schematically shown in Fig. 1. Two parallel waveguides with length $L_c = 8$ mm, width $w_1 = w_2 = 200$ μm and thickness $t = 10$ μm are placed laterally parallel with a gap $d_0 = 15$ μm . Metal layer placed above it on distance d . The numerical modelling of this structure is performed using the micromagnetic simulation and finite element method with the following parameters of an Yttrium Iron Garnet (YIG) film: saturation magnetization $M_s = 1.4 \cdot 10^5$ A/m, exchange constant $A = 3.5$ pJ/m and Gilbert damping $\alpha = 2 \cdot 10^{-4}$. A external magnetic field $B_{\text{ext}} = 1200$ Oe is applied along the long axis of the waveguides (x-direction in Fig. 2). The results of numerical simulation by the finite element method are presented on Fig. 2. Figure 2(a) shows the dependence of the coupling length of the MSSW on the frequency in the case of the positive and negative directions of wave propagation along the structure. The wavelength depends on the frequency of the wave, which propagates in the negative direction. The lines show the normalized value of the pumping lengths when the distance between the metal and the surface of the microwave ovens changes from 10 μm to 90 μm . It can be seen that at a distance of $d = 30$ μm at a frequency of 5.6 GHz, the largest difference is observed, about 9 times, between the pumping length of waves propagating oppositely to each other in the structure under study. At the same time, it can be said that at a distance of more than 90 μm , the influence of the metal has practically no force over the entire frequency range of the MSSW wave, which can propagate in this structure under the considered parameters. This work was supported by the Russian Science Foundation (20-79-10191)

1. R. W. Damon and J. R. Eshbach, J. Phys. Chem. Solids 19, 308 (1961).
 2. S.A. Nikitov, A.R. Safin, D.V. Kalyabin, A.V. Sadovnikov, E.N. Beginin, M.V. Logunov, M.A. Morozova, S.A. Odintsov, S.A. Osokin, A.Yu. Sharaevskaya, Yu.P. Sharaevskiy, A.I. Kirilyuk *Phys. Usp.* 63 945–974 (2020)
 3. A. V. Sadovnikov, E. N. Beginin, S. A. Odincov, S. E. Sheshukova, Y. P. Sharaevskii, A. I. Stognij, S. A. Nikitov, Applied Physics Letters 108 (2016).



(a) Schematic view of lateral magnonic stripes with metal layer; (b) view on structure along x-axis (along wave propagation)



(a) Frequency dependence of the coupling length of the MSSW, with opposite directions of wave propagation along x-axis; (b) dependence of normalized coupling length of gap between waveguides and metal layer

EP-03. Unidirectional Spin-Wave Coupler Based on YIG Nonidentical Magnonic Crystals.

V. Gubanov¹, S.E. Sheshukova¹, A.V. Sadovnikov¹ and S. Nikitov²

1. *Nonlinear Processes, N. G. Chernyshevskogo National Research University in Saratov, Saratov, Russian Federation*; 2. *V. A. Kotelnikova Institute for Radiotechnologu and Electronics, Russian Academy of Sciences, Moscow, Russian Federation*

The study of physical principles that determine the possibility of using spin waves (SW) to create information signal processing devices based on magnonics principles is of great interest [1]. Microstructures based on the iron-yttrium garnet (YIG) can be used in the processing of spin-wave signals due to the low attenuation. To control the properties of SW propagating, the method of structuring YIG films and creating irregular micro- and nanoscale waveguides, including structures with broken translational symmetry, can be used [2]. In this work, the numerical simulations and Brillouin light scattering technique results of the unidirectional spin wave propagation in lateral nonidentical magnonic crystals was shown (MC) [3,4]. In Figure 1 present the structure was made up of two MC waveguides (MC1 and MC2) with different width, oriented along the direction of the y axis. Each MC waveguide represents a structure with grooves 1 microns deep, repeating with a period of $D = 200$ microns. The length of sections of microwave structures with a periodic system of grooves is 5 mm. The width of magnon crystals MC1 and MC2 along the z axis were $500 \mu\text{m}$ and $200 \mu\text{m}$, respectively. The value of lateral gap d between MC1 and MC2 was $20 \mu\text{m}$. The structure was placed in an external magnetic field with the magnitude $H_0 = 1300$ Oe directed along the z-axis in order to excite a surface magnetostatic spin wave (SMSW). By the means of Brillouin light scattering technique, we obtained 2-D intensity maps of the spin wave propagating in the structure for case spin wave excitation on MC1. The possibility of unidirectional coupling of SW propagating in MCs near the frequency boundary of the transmission zone is demonstrated. Based on the results of micromagnetic modeling, the mechanism that accompanies the observed mode of intermode coupling in the lateral system of nonidentical MCs is determined, and the spatial-frequency signal separation modes are studied. The proposed device can act as spin-wave unidirectional coupler for planar interconnecting element for magnonic conduits operating in a regime of single mode propagation in one of the MCs. As results we demonstrate the perspective system of nonidentical magnonic crystals as a building block for integrated magnonic circuits for the concept of spin-wave signal processing units for logic gates such as demultiplexer, directional coupler and signal splitter. Experimental structure and was performed by the Russian Foundation for Basic Research (project no. 20-37-90020). Micromagnetic simulation was performed by Grant of the President of RF (No. MK-1870.2020.9).

[1] V. V. Kruglyak, S. O. Demokritov, D. Grundler, *Journal of Physics D: Applied Physics* Vol. 43, P.260301 (2010) [2] A. V. Sadovnikov, C. S. Davies, V. V. Kruglyak, et al., *PHYSICAL REVIEW B*. Vol. 96, P. 060401(R) (2017) [3] A. V. Sadovnikov, V.A. Gubanov, S.E. Sheshukova, et al., *Physical Review Applied*, 9(5) (2018) [4] A. V. Sadovnikov, A. A. Grachev, A. A. Serdobintsev, et al., *IEEE Magnetics Letters*, 1–1 (2019)

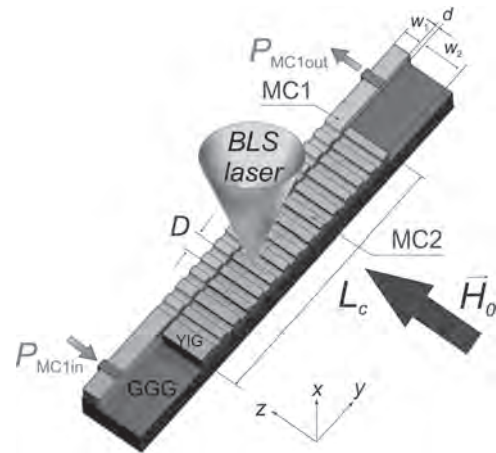


Fig.1 Scheme of the unidirectional spin-wave coupler.

EP-04. Current-Induced Spin-Wave Doppler Shift and Attenuation in Compensated Ferrimagnets.

D. Kim¹, S. Oh¹, D. Lee¹, S. Kim² and K. Lee²

1. Korea University, Seongbuk-gu, The Republic of Korea; 2. Korea Advanced Institute of Science and Technology, Daejeon, The Republic of Korea

For ferromagnets, the adiabatic spin transfer torque (STT) causes current-induced spin-wave (SW) Doppler shift [1] whereas the non-adiabatic STT controls SW attenuation [2,3]. It was predicted [4] that the current-induced SW Doppler shift by the adiabatic STT is also present for antiferromagnets. In addition, a numerical study found a non-negligible non-adiabatic STT for antiferromagnetic domain walls [5], suggesting that electrical currents can control the attenuation of antiferromagnetic SWs. Recently, an experiment on GdFeCo ferrimagnets shows that the adiabatic torque in this material can be large [6]. Thus, the current-induced SW Doppler shift of compensated ferrimagnets is expected to be similar in magnitude to that of ferromagnets. Moreover, the same experiment [6] shows that the non-adiabatic torque in this material is also large. This large non-adiabaticity of spin current in compensated ferrimagnets is attributed to the enhanced spin mistracking [5-7], originating from the weakened spin dephasing in the antiferromagnetically aligned spin moments [8]. This unique STT characteristic of compensated ferrimagnets motivates us to investigate STT effects on ferrimagnetic SWs. In this work, we theoretically and numerically study the STT-controlled ferrimagnetic SW dynamics near the angular momentum compensation point. We show that the ferrimagnetic SW Doppler shift for right-handed SWs is opposite to that for left-handed SWs since they carry opposite spin polarizations. We also find that the SW attenuation is suppressed and the SW amplitude is even amplified when a sufficiently large non-adiabatic torque is exerted. Figures 1(a) and (b) respectively show the current-induced SW Doppler shift of the right- and left-handed SWs at the angular momentum compensation temperature T_A (T_2) when the current density $J_c = \pm 5 \times 10^{12}$ A/m² is applied. Symbols are numerical results and solid lines are theories, which are in good agreement. For the right-handed SW [Fig. 1 (a)] and wave vector $k > 0$, a positive (negative) current decreases (increases) the SW frequency. On the other hand, for the left-handed SW [Fig. 1 (b)] and $k > 0$, a positive (negative) current increases (decreases) the SW frequency. Therefore, the sign of Doppler shift of the right-handed SW is opposite to that of the left-handed SW, which originates from the opposite spin polarizations carried by left- and right-handed SWs. Figure 2(a) and (b) show the SW attenuation length as a function of the current density for $\beta=10\alpha$, where β is the non-adiabaticity and α is the damping constant. The SW frequency ($\omega/2\pi$) is 0.4 THz. Theoretical and numerical results are shown near the T_A and T_1 (T_3) is the temperature which is below (above) T_A . For a positive β , we find that the SW attenuation length of both right- and left-handed SWs increases when electrons move in the same direction with the SW propagation. In addition, when sufficiently large non-adiabatic torque is applied, the SW amplitude exponentially increases from the SW source.

[1] V. Vlaminck, and M. Bailleul, Science 322, 410 (2008). [2] S.-M. Seo, K.-J. Lee, H. Yang et al., Phys. Rev. Lett. 102, 147202 (2009). [3] K. Sekiguchi, K. Yamada, S.-M. Seo et al., Phys. Rev. Lett. 108, 017203 (2012). [4] A. C. Swaving and R. A. Duine, Phys. Rev. B. 83, 054428 (2011). [5] H.-J. Park, Y. Jeong, S.-H. Oh et al., Phys. Rev. B 101, 144431 (2020). [6] T. Okuno, D.-H. Kim, S.-H. Oh et al., Nat. Electron. 2, 389 (2019). [7] J. Xiao, A. Zangwill, and M. D. Stiles, Phys. Rev. B 73, 054428 (2006). [8] J. Yu, D. Bang, R. Mishra et al., Nat. Mater. 18, 29 (2019).

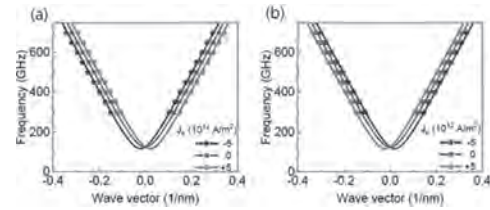


Fig. 1. Current-induced Doppler shift of (a) right- and (b) left-handed SWs in a ferrimagnet at the angular momentum compensation temperature.

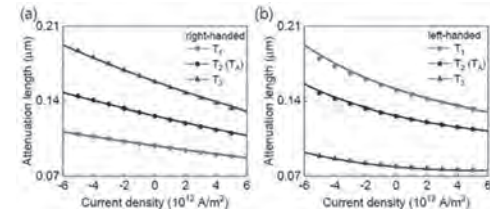


Fig. 2. The SW attenuation length for (a) right- and (b) left-handed SWs as a function of the current density.

EP-05. Magnon Blocking Effect in Antiferromagnet Spaced Magnon Junction.

Z. Yan¹, C. Wan¹ and X. Han¹

¹. Chinese Academy of Sciences, Institute of Physics, University of Chinese Academy of Sciences, Beijing, China

Magnon valve effect (MVE) and magnon junction effect (MJE) which show the spin-dependent magnon transmission through ferromagnetic insulator (FMI) /spacer [S = nonmagnetic metal or antiferromagnetic insulator (AFMI=AFI)]/ferromagnetic insulator (FMI) sandwiches have been experimentally reported by our group [1-3]. It opens a door for promising applications in magnonics. However, the MJE is still not well interpreted, such as its physical origin and the optimized structure of AFMI spacer. It is intuitively regarded that the AFMI spacer would effectively modulate the magnon transmission and a high switching on-off ratio of magnon flow can be expected after a wise choice of the spacer, which would be proven in this work. Here, we study in theory magnon transmission through sandwich structure of FMI|AFI|FMI by atomistic spin model simulation [4]. We reproduced the MJE observed in experiments and proposed a magnon selection rule induced magnon blocking effect (MBE) to explain it. More importantly, following the proposed mechanism, different kinds of AFI spacers were evaluated. It showed that magnon transmission could be remarkably changed by the AFI spacers with various FMI configurations. This works on the MBE can provide significant and meaningful information for both the fundamental physics and the appealing applications of magnon junctions.

[1] H. Wu, and X. F. Han* et al., *Phys. Rev. Lett.* 120, 097205 (2018). [2] C. Y. Guo, C. H. Wan, and X. F. Han* et al., *Phys. Rev. B* 98, 134426 (2018). [3] C. Y. Guo, C. H. Wan, and X. F. Han* et al. *Nat. Electron.* 3, 304–308 (2020). [4] Z. R. Yan, C. H. Wan and X. F. Han*, *Phys. Rev. Appl.* 14, 044053 (2020)

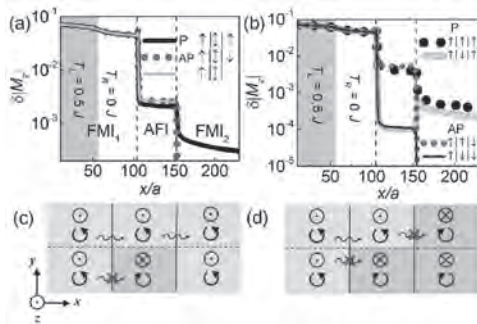


Fig. 1. Magnon junction structure and space dependence of magnon potential. (a) Magnon potential ($|M_x|$) as function of layer (x) of P state (solid line), AP state (short dot) and FMI1|AFI system (green line). **(b)** Separated channel dependent $|M_x|$ from (a): $\uparrow\uparrow\uparrow\uparrow$ (black line), $\uparrow\downarrow\uparrow\uparrow$ (red line), $\uparrow\uparrow\downarrow\downarrow$ (blue line) and $\uparrow\downarrow\downarrow\downarrow$ (green line). **(c)** and **(d)** Schematics of spin dependent magnon blocking of P and AP state respectively. Spin-up (spin-down) lattices can only accommodate right- (left-) circularly polarized magnons. While only right-circularly polarized magnons are favored in FMI with upward magnetization, both left- and right-circular polarizations are permitted in AFMI owing to two spin-opposite lattices. This selection rule thus makes the MBE occur when magnons try to diffuse into a spin lattice, which does not support their polarization.

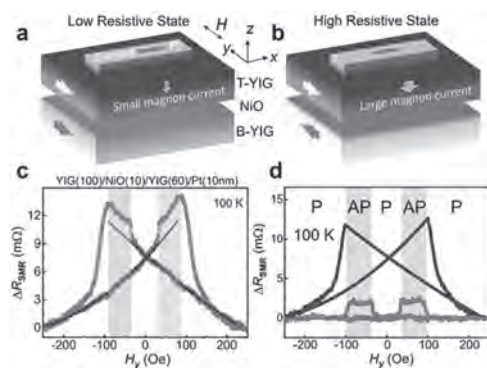
EP-06. A Nonlocal Spin Hall Magnetoresistance in a Pt Layer Deposited on a Magnon Junction.

C. Guo¹, C. Wan¹ and X. Han¹

¹. Chinese Academy of Sciences Institute of Physics, Beijing, China

The spin wave (magnon) have many excellent properties that are unavailable in electron-based spintronic devices, which could drastically reduce the power consumption of spintronic devices^[1-4]. Magnon valves^[3] and magnon junctions (MJs)^[4] based on yttrium iron garnet ($\text{Y}_3\text{Fe}_5\text{O}_{12}$, YIG), with the structures YIG/Au/YIG and YIG/NiO/YIG, respectively, have been fabricated. Here we report a magnetoresistance effect that occurs in a platinum layer deposited on a magnon junction consisting of two insulating magnetic YIG layers separated by an antiferromagnetic nickel oxide spacer layer. The resistance of the platinum layer is found to depend on the magnetization of the YIG layer in direct contact with it (an effect known as the spin Hall magnetoresistance), but also the magnetization of the adjacent YIG layer in the junction; the resistance of the platinum layer is higher when the two YIG layers are aligned antiparallel than when parallel^[5]. We assign this behaviour to a magnonic nonlocal spin-Hall magnetoresistance (MNSMR) in which spin-carrying magnon propagation across the junction affects the spin accumulation at the metal interface and hence modulates the spin Hall magnetoresistance. The effect could be used to develop spintronic/magnonic devices that have spin transport properties controlled by an all-insulating magnon junction and are thus free from Joule heating.

[1] H. Wu, and X. F. Han* et al., *Phys. Rev. B* 93 (2016) 060403(R) [2] C. Y. Guo, C. H. Wan, and X. F. Han* et al., *Appl. Phys. Lett.* 114,192409(2019). [3] H. Wu, and X. F. Han* et al., *Phys. Rev. Lett.* 120(9),097205(2018). [4] C. Y. Guo, C. H. Wan, and X. F. Han* et al., *Phys. Rev. B* 98, 134426 (2018). [5] C. Y. Guo, C. H. Wan, X. F. Han* et al. *Nat. Electron.* 3, 304–308 (2020).



EP-07. Excitation of Short Wavelength Spin Waves in a Ferromagnetic Conduit With a Microwave Pumped Perpendicularly Magnetized Nanodot.

M. Moalic¹, M.K. Zelent¹ and M. Krawczyk¹

1. Physics of Nanostructures Division, Uniwersytet im Adama Mickiewicza w Poznaniu Wydział Fizyki, Poznań, Poland

One of the main research directions in magnonics focuses on the excitation of short wavelength SWs (SWs). Recently, a few approaches have been proposed, but with some limitations like the lack of an efficient source of SWs, which further limits the development of magnonic applications. We propose a system (Fig 1.) that generates a local excitation of SWs in a thin ferromagnetic waveguide with the help of a nanodot that possesses perpendicular magnetic anisotropy. Our idea is to use the confined SW modes in the nanodot pumped by a global microwave magnetic field directed along the magnetization of the waveguide, which will emit propagating SWs due to direct static and dynamic coupling with the waveguide. Two study cases are put against each other: a nanodot inscribed with a skyrmion and a nanodot in a fully saturated state along out-of-plane direction. The system can function with several combinations of magnetic materials. The waveguide has to be ferromagnetic and present a low enough damping so that the SWs can propagate over a significant distance, which is why Permalloy is an ideal candidate having one of the lowest Gilbert damping [1]. The waveguide is magnetically saturated along its length and is separated from the nanodot by a spacer of 1.5 nm. It is 384 nm wide and 4.5 nm thick, and a few micrometers long with absorbing boundary conditions at its edge both extremities to avoid any kind of back-propagating SWs. The nanodot must have a specific geometry and size, as it requires a strong enough interfacial Dzyaloshinskii-Moriya Interaction to allow for the formation of a skyrmion. For this reason, the nanodot is made of Pt/Co/Ir circular layers with a diameter of 300 nm to create a strong shape anisotropy which allows the presence of a metastable state such as a skyrmion in its core. When relaxing this system, an imprint of the skyrmion is created in the waveguide, meaning the magnetization below the nanodot will deviate from their saturated magnetization along the x axis because of the dipolar coupling with the skyrmion. In the same way, the waveguide will influence the magnetization inside the nanodot and affect the shape of the skyrmion. In our example, the skyrmion's core expands and becomes egg shaped under the influence of the waveguide. Confined skyrmions present a wide range of different resonant modes [2] when excited by an external magnetic field. Such modes are also present here and influence the shape of the resulting imprint which will start oscillating along with the skyrmionic modes acting like an antenna. This complex movement of both halves of the imprint, alternating phases and amplitude is what generates the coherent and efficient propagating SWs. Interestingly, only asymmetrical SWs can be created this way, but modifying the material parameters or the geometry will cause the imprint to change shape which allows us to tune the efficiency of the antenna for specific microwave frequencies. In the case of a fully saturated nanodot with the same magnetic parameters as the one with the skyrmion, the created imprint is less visible because of the simpler magnetic texture. It leads to a very inefficient coupling for a narrow range of frequencies compared to the broadband SW excitations (Fig 2.) that a skyrmion can generate. We found that the propagating SWs can be excited in a broad frequency band from a few to a dozen GHz with wavelengths that can be shorter than 100 nm. Furthermore, our studies look for the magnetic parameters and geometry that would be most suitable for an efficient conversion of global electromagnetic radiation to short wavelength SWs. *The work was supported by National Science Centre of Poland, Project SHENG No. UMO-2018/30/Q/ST3/00416.*

[1]: Zhao, Yuelei, et al. Scientific reports 6 (2016): 22890. [2]: Kim, Joo-Von, et al. Physical Review B 90.6 (2014): 064410.

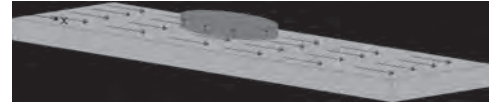


Fig 1. The system used in the micromagnetic simulations: the Permalloy waveguide (12 μm x 384 nm x 4,5 nm) and the Pt/Co/Ir nanodot (300 nm x 1.5 nm), separated by a 1.5 nm thick spacer.

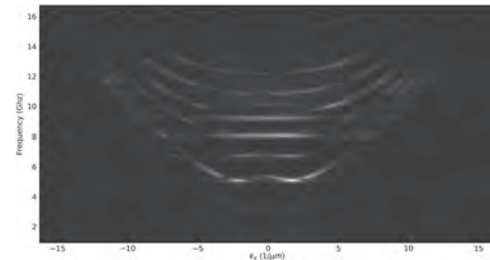


Fig 2. The dispersion relation of the SWs generated by the skyrmion and waveguide system. This was calculated using the Fast Fourier Transform of the time- and space-resolved magnetization of the waveguide under a global magnetic field.

EP-08. Design of Broadband XOR Logic Gate Based on Edge-Mode Type Spin Wave.

L. Zheng¹, D. Zhang¹, L. Jin¹, T. Wen¹, Y. Liao¹, X. Tang¹ and Z. Zhong¹
¹. University of Electronic Science and Technology of China State Key Laboratory of Electronic Thin Films and Integrated Devices, Chengdu, China

Spin wave logic devices are mainly based on the interference effect of spin waves. The phase modulation of spin waves has become the main direction of spin wave logic device design. SWs in Damon-Eshbach configuration in waveguide exhibits two types of mode: edge mode spin waves (E-SWs) and central mode spin waves (C-SWs)^[1-3]. There has been much effort devoted to the development of a good deal of spin wave devices based on C-SWs such as phase shifters, logic gates, transistors, multiplexers, as well as majority gates. However, there are few researches of E-SWs in the waveguide. As well as known, the propagation of C-SWs in the waveguide is usually accompanied by the hybridization of multiple modes, which is not conducive to control the propagation characteristics of the spin waves precisely. Therefore, E-SWs may be more suitable for the design of spin wave devices. In this work, we propose a novel design of spin wave XOR gate based on edge-mode type spin wave, whose schematic is shown in Fig. 1. We perform micromagnetic simulations using the MuMax3 software to study the phase shift characteristics and logic functionality in the structure^[4]. The structure is composed of input waveguide, output waveguide and interference Y-type waveguide. The external field (H_0) of 1000 is applied parallel to the y-axis. The length, width and thickness of the narrow YIG waveguide are $L_1 = 500$ nm, $W_1 = 50$ nm, $T_w = 10$ nm, respectively. The length, width and thickness of the wide YIG waveguide are $L_c = 3000$ nm, $W_2 = 400$ nm, $T_w = 10$ nm, respectively. The distance between the Co element and the input wave guide is $L_c = 500$ nm. The length and thickness of Co element are $L_h = 970$ nm, $T_w = 10$ nm, respectively. The gap between the YIG waveguide and the Co element is $G = 110$ nm. The simulation results are shown in Fig. 2. The wave-numbers of E-SWs on both sides of Phase Shift Zone in YIG waveguide change after placing the Co element with high saturation magnetization on one side of YIG waveguide^[5]. Therefore, π phase shift can be achieved by setting appropriate structural parameters. Based on this feature, this structure can realize the function of a spin-wave XOR logic gate. The local inhomogeneity of the effective field on one side of the YIG waveguide is the main reason for the phase shift. The stray field of the Co element causes this local inhomogeneity. Therefore, this phase shift is controllable by adjusting the stray field of the Co element. It can be changed by fine-tuning the Co magnetization direction through the SOT effect. Therefore, by applying an appropriate current on β -Ta, the operating frequency of the XOR gate can be broadened by utilizing the SOT effect^[6]. In summary, we demonstrated a spin wave XOR gate based on edge mode type spin wave phase shifter. The operating frequency of the proposed XOR gate is a broadband rather than a specific frequency. The input and output signals are all encoded with the amplitude of SWs. The feature of proposed design is that the dipole field generated by Co element is used to shift the phase of the edge mode spin wave on one side of the YIG waveguide, so that the SWs on both sides have a phase difference.

- [1] K. Bernstein, R. K. Cavin, W. Porod. Proceedings of the IEEE, 98 (12), 2169–2184. (2010). [2] S. D. Bader, S. S. P. Parkin. Spintronics. Annu. Rev. Condens. Matter Phys. 1:71–88. (2010). [3] S. Saha, S. Barman, Y. Otani. Nanoscale, 7 (43). (2015). [4] A. Vansteenkiste, J. Leliaert, M. Dvornik. Aip Advances, 4 (10), 107133. (2014). [5] Zhizhi Zhang, M. Vogel, M. B. Jungfleisch. Physical Review B, 100 (17), 174434. (2019). [6] Zhiwei Ren, Shuang Liu, Lichuan Jin. Scientific Reports, 9, 7093. (2019).

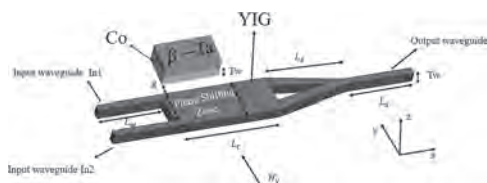


Fig. 1. Schematic of SOT-based broadband spin wave XOR logic gate.

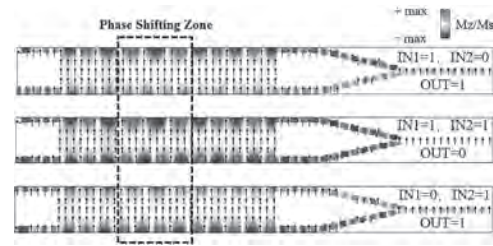


Fig. 2. Diagram of spin wave propagation with current density of at 4.41GHz excitation frequency.

EP-09. Linear and Nonlinear Spin-Wave Propagation in Magnonic Waveguide With Linearly Varying Width.

V. Gubanov¹, E. Beginin¹, A.V. Sadovnikov¹ and S. Nikitov²

1. *Nonlinear Processes, N. G. Chernyshevskogo National Research University in Saratov, Saratov, Russian Federation*; 2. *V. W. Kotelnikova Institute for Radiotechnology and Electronics, Russian Academy of Sciences, Moscow, Russian Federation*

In recently time the study of magnetostatic spin wave (MSW) propagation in ferromagnetic structures is of great interest [1,2]. In this work we experimentally and by micromagnetic simulation studied spin wave (SW) propagation in microwaveguide with linearly varying width, formed from a yttrium iron garnet (YIG) film. The YIG film was grown on the gadolinium gallium garnet (GGG) substrate with a thickness of 500 μm . Magnonic waveguide with linearly varying width [3] was fabricated by the laser scribing technique from the YIG film. The scetch of structure is shown in Fig. 1 consists of segments: I - input waveguide with a length of 5 mm and a width of 2500 μm ; II - waveguide with a smoothly varying width from 2500 μm to 200 μm , with a length of 10 mm; III - output waveguide 5 mm long and 200 μm wide. The thickness of the YIG film corresponded to 10 μm . The SW was excited by supplying a microwave signal to a microstrip antenna 30 μm wide, located in the I segment of the waveguide structure at a distance of 1500 μm from the starting of the waveguide. Studied srtructure was placed in external magnetic field with the magnitude $H_0 = 1200$ Oe directed along the z-axis in order to excite a surface magnetostatic spin wave (MSSW). Micromagnetic modeling was carried out based on the solution of the Landau-Livshitz-Hilbert equation by the finite difference method. Also, when modeling the structure, regions with an increased attenuation parameter were introduced at the ends of the waveguide to get rid of reflections. Transmission and dispersion characteristics of the studied structure were experimentally measured using the microwave network analyzer E8362C PNA. The experimental measurement square of intensity spin wave was performed by the Brillouin light scattering (BLS) technique in backscattering configuration. A laser beam with a wavelength of 532 nm was focused to a spot of a diameter of 25 μm on the surface of magnonic waveguide with linearly varying width. Transformation of the beating pattern of the first and third transverse modes can be explained by mode decomposition from BLS map with amplitude resolution. the results of calculating the distribution of the magnetization of the MSSW in the linear and nonlinear modes, respectively, are shown. In this case, in a narrow region of the waveguide, a nonlinear process of three-magnon MSSW decay is observed. This confirmed by maps of dynamic magnetization distribution at frequencies equal to the frequency of the signal pumping frequency, obtained experimentally by BLS technique. This work was supported by the Russian Science Foundation (project no. 20-79-10191).

[1] V. V. Kruglyak, S. O. Demokritov, D.Grundler, Journal of Physics D: Applied Physics, 43(26), 264001, (2010) [2] D. Sander, S. O. Valenzuela, D. Makarov, et. al., Journal of Physics D: Applied Physics, 50(36), 363001, (2017) [3] D. V. Kalyabin, A. V. Sadovnikov, E. N. Beginin, et. al., Journal of Applied Physics, 126(17), 173907. doi:10.1063/1.5099358, (2019)

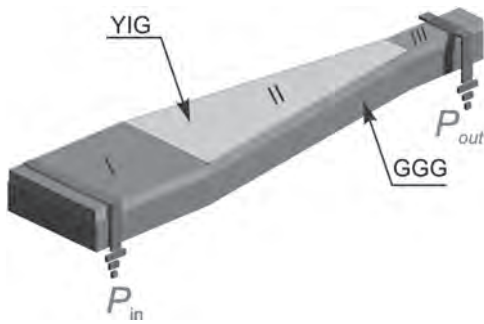


Fig.1 The scetch of studied structure with linearly varying width with marked segments.

Session EQ
MAGNONICS II
(Poster Session)

Jaroslław W Klos, Chair
Uniwersytet im Adama Mickiewicza w Poznaniu, Poznań, Poland

EQ-01. Magnetization Dynamics and Spin Wave Excitation in Strain-Mediated Multiferroic Heterostructures With the Interfacial Dzyaloshinskii-Moriya Interaction.

D. Nian¹, M. Zhu¹, H. Yang¹, Y. Qiu¹, G. Yu¹ and H. Zhou¹

1. Key Laboratory of Electromagnetic Wave Information Technology and Metrology of Zhejiang Province, China Jiliang University, Hangzhou, China

As one type magnetization dynamics excitations in magnetic materials, spin waves are providing a promising candidate as information carriers in the future spintronic logic and computing circuits and systems. Several concepts and building block for spin wave-based devices have been developed in recent years, including magnonic crystals, logic gates, transistor, multiplexers and wake-up receiver. The excitation and manipulation of magnetization dynamics is an essential part of all these spin wave-based devices. Electrical methods of magnetization dynamic excitation are conventionally used the magnetic field induced by a microwave antenna or spin torque oscillation induced by spin-polarized currents. However, these methods are generally introducing high Ohmic energy consumption due to the high current density, which contrary to the requirement for energy efficient spintronic devices. Furthermore, for practical applications, it is very desirable to use devices without permanent magnetic field bias. Motivated by these shortcoming, alternative approaches for the excitation of magnetization dynamics have been explored recently, include the effect of the voltage-controlled magnetic anisotropy, the elastic waves and strain pulse. A more comprehensive investigation of magnetization dynamics and spin wave excitation in nanoscale multiferroic heterostructures with perpendicular anisotropy (PMA) and Dzyaloshinskii-Moriya interaction (i-DMI) has not yet been attempted. In this work, by means of a micromagnetic simulation combined with electromechanical to explore a promising way to excitation spin wave using voltage-controlled strain in a nanoscale multiferroic heterostructures with PMA and i-DMI. In this heterostructure, the excitation area is setting at the center of ferromagnetic nanostrip with an electrode underneath which can easily get a biaxial isotropy in-plane strain (Fig.1(a)). The relaxed profiles of the out-of-plane magnetization components along the center width direction with different DMI coefficient are demonstrated in Fig. 1(b). A SinC strain field pulse is applied locally at the excitation region to excite magnetization dynamics with a wide frequency range. The frequency spectra (Fig.1(c)) clear shown that two distinct resonance peaks around at 4 GHz and 13 GHz. It is worth mentioning, that all the spin dynamics excited by the strain fields are symmetric within the in-plane axis direction, that means only the odd values node are excited. The spin wave frequency spectra in terms of frequency versus propagation distance are obtained by an FFT of δm_x on the time scales. And the spin wave transmission characteristics (Fig.1(d)) are obtained by probing the spectra intensity in x position 200 nm and 1000 nm, respectively. The propagation characteristics of spin wave studied in detail for different frequency, for example, the spin wave profiles generated and transferred by biaxial isotropy in-plane strain at 4 GHz, 4.5 GHz and 13 GHz are shown in Fig. 2(a)-(c). The dynamic magnetization profiles show that the spin wave phases front of these modes are perpendicular to the propagation direction. The dispersion characteristics in terms of the width position along the y direction versus wave vector are obtained by a two-dimensional (2D) FFT of magnetization components δm_x . The results are shown in Fig. 2(d)-(f). At 4 GHz and 4.5 GHz, the width mode $n=1$ with a wave vectors $k_x=0.015$ rad/nm and $k_x=0.037$ rad/nm are present, respectively. Note, the mode $n=0$ with an extremely small amplitude is also observer. At 13 GHz, both $n=1$ and high order $n=3$ modes are present with wave vector $k_x=0.164$ rad/nm and $k_x=0.059$ rad/nm, respectively. To summarize, we analyzed the excitation of magnetization dynamics and spin waves via the magnetoelastic effect by applying locally biaxial isotropy in-plane strains, and we studied their propagation characteristics in non-uniformly magnetized ferromagnet waveguides induced by i-DMI. Our works show the potential of using strain with the presence of i-DMI as perspective for integrating spin waves emitter into future logic or computing devices and hinting at possible technological applications in strain controlled spintronic systems.

1. J. Chen, J. Hu and H. Yu, *iScience*, 23, 101153 (2020). 2. R. Verba, M. Carpentieri and G. Finocchio, et al., *Sci Rep*, 6, 25018 (2016). 3. Q. Wang,

T. Brächer and M. Mohseni, et al., *Appl. Phys. Lett.*, 115, 092401 (2019). 4. A. V. Chumak, P. Pirro and A. A. Serga, et al., *Appl. Phys. Lett.*, 95, 262508 (2009). 5. S. Klingler, P. Pirro and T. Brächer, et al., *Appl. Phys. Lett.*, 106, 212406 (2015). 6. M. á. Kostylev, A. Serga and T. Schneider, et al., *Appl. Phys. Lett.*, 87, 153501 (2005). 7. F. Macia, F. C. Hoppensteadt and A. D. Kent, *Nanotechnology*, 25, 045303 (2014). 8. R. Verba, M. Carpentieri and G. Finocchio, et al, *Phys. Rev. Appl.*, 7 (2017).

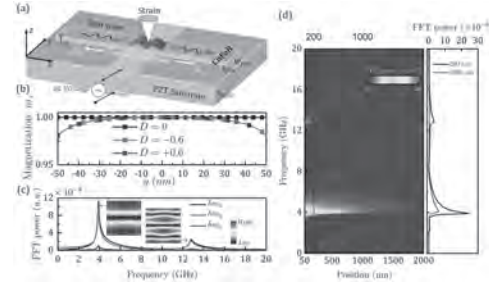


Fig. 1 (a) Schematic view of the investigated multiferroic heterostructures, the yellow color indicates the region where strain field is applied. (b) Equilibrium magnetization components m_z across the width direction of nanostrip. (c) The spin dynamic characteristics obtained by integrating the perturbation over the excitation area. (d) The frequency spectra obtained from an FFT of the temporal evolution of perturbation magnetization in space.

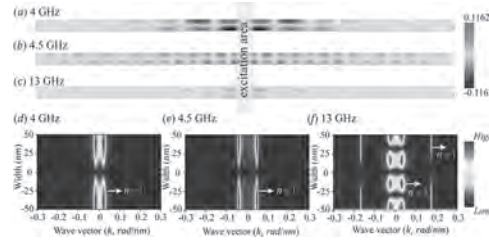


Fig.2 (a)-(c) Snapshots of the magnetization distribution pattern for different excitation frequency: 4 GHz, 4.5 GHz and 13 GHz, respectively. (d)-(e) Spin wave wavenumber distribution across the ferromagnet strip width computed by 2D FFT of the magnetization component δm_x .

4. J. Wang, J. Wang, J. Wang, et al., *Appl. Phys. Lett.*, 100, 122401 (2012). 5. J. Wang, J. Wang, J. Wang, et al., *Appl. Phys. Lett.*, 100, 122401 (2012). 6. J. Wang, J. Wang, J. Wang, et al., *Appl. Phys. Lett.*, 100, 122401 (2012). 7. J. Wang, J. Wang, J. Wang, et al., *Appl. Phys. Lett.*, 100, 122401 (2012). 8. J. Wang, J. Wang, J. Wang, et al., *Appl. Phys. Lett.*, 100, 122401 (2012).

EQ-02. A Novel Approach for Controlling Spin-Wave Dynamics in Magnonic Crystals Using Metal-Insulator Switching of Vanadium Dioxide.

A.A. Nikitin¹, A.A. Nikitin¹, A.E. Komlev¹ and A.B. Ustinov¹

1. Physical Electronics and Technology, St. Petersburg Electrotechnical University, St. Petersburg, Russian Federation

In the last decade, peculiarities of spin-wave (SW) processes in diverse magnetic materials have opened new avenues in the field of magnonics. An increased research activity in this field is due to developing of novel microwave devices for analog signal processing and data transmission. Artificial spatially periodic magnetic media, called magnonic crystals (MCs), constitute one of the most promising building blocks for these applications [1]. In these crystals, the formation of spectral regions, band-gaps, with prohibited wave propagation is caused by Bragg scattering. Further advances in the field were achieved owing to a development of the dynamic MCs [2]. Promising functionalities of these crystals arise from the nonreciprocal behavior and dynamic controllability that provides altering of the band-gaps from full rejection to full transmission. Usually two types of the dynamic MCs are distinguished: the current-controlled and voltage-controlled ones. The first one originates from a spatial variation of a magnetic field induced by an electric current in the metal wires or periodic screens [3]. The mechanisms behind the second one are divided into the two types. These are a voltage-controlled perpendicular magnetic anisotropy in ferromagnetic-dielectric heterostructures [4] and a voltage-controlled variation of the ferroelectric layer permittivity in ferrite-ferroelectric structures [5]. Another way to produce a fully tunable MC is to use a laser radiation, which creates thermal landscapes and results in periodic modulations of the saturation magnetization [6]. Recently, our work [7] shows promising features of the metal-insulator transition (MIT) in the heterogeneous ferrite-vanadium dioxide structures. Such transition is characterized with an abrupt change of the VO₂ conductivity (by four or five orders of magnitude) near the phase transition temperature at ultrafast timescales. Therefore, a combination of ferrite films with materials exhibiting the MIT allows one to exploit novel spin-wave phenomena that are of interest for enhancement of the functionality of the magnonic devices. The aim of the present work is to study the application of the MIT for controlling the microwave SW dynamics in the MC, which is composed of VO₂ and grooved yttrium iron garnet (YIG) films (see Fig. 1a). The ferrite structure was fabricated in the form of the 3-cm-long and 2-mm-wide stripe of the 5.5- μm -thick single-crystal YIG film. This film had a saturation magnetization of 1985 G at room temperature. In order to produce a MC, the thickness of the YIG film was periodically modulated to a depth of 0.8 μm using a wet chemical etching. The periodic pattern consisted of 10 parallel grooves with a width of 65 μm spaced by 265 μm , so that a lattice constant was 330 μm . The film was epitaxially-grown on the gallium gadolinium garnet (GGG) substrates of 500- μm thickness. The films had the ferromagnetic resonance linewidth of 0.5 Oe at 5 GHz. A 0.55- μm -thick VO₂ film was deposited on a silicon dioxide substrate with thickness of 500 μm by a reactive DC magnetron sputtering. This film demonstrates a MIT around 339 K, which manifests itself as a variation of the resistance from 148 k Ω down to 25 Ω with the temperature increase from 327 K to 348 K (see Fig. 1b). The VO₂ sample has in-plane dimensions of 3x3 mm². The composed YIG-VO₂ structure was magnetized by a spatially uniform bias magnetic field of 1566 Oe applied parallel to the antennas providing the conditions for excitation of the surface SWs. To accomplish the measurements, the experimental waveguiding structure was placed in a temperature-controlled probe station providing monitored heating and cooling. The transmission characteristics of the structure were measured for different temperatures by the vector network analyzer. The experimental results are shown in Fig. 2. Near room temperature the resistance of the VO₂ film is high. Therefore, the VO₂ film has a negligible effect on the SW propagation in the YIG-VO₂ bilayer in the experimental frequency range. In particular, at the initial temperature $T = 327$ K, the band-gaps are formed at the frequencies expected from the conventional Bragg analysis (see Fig. 2a). To analyze only the direct MIT impact on the original band structure of the MC, the SW carrier frequency was normalized by the cutoff frequency for the surface SW f_c [8]. This enables one to keep out of sight the frequency shifts of the band-gap positions due to changing of the YIG-film saturation

magnetization. An increase of temperature up to $T = 348$ K provides a sharp drop of the VO₂ resistance down to 25 Ω . It leads to a drastic change in the SW group velocity (see Fig. 2b). Therefore, the frequency bandwidth of the transmission characteristic is narrowed and becomes less than the frequency distance to the first-order band-gap. As a result, the band structure of the proposed MC is fully suppressed. A utilization of this phenomenon is practically beneficial because it enables one to control SW dynamics in the waveguiding structure. In particular, the low and high levels of microwave attenuation in the structures are determined by a high-resistance and low-resistance states of the VO₂, respectively. As a result, the YIG-VO₂ layered structure operates as a switch triggered by the MIT phase transition in the VO₂ film. The reported study was funded by RFBR and JSPS, project # 21-52-50006.

1. G. Csaba, Á. Papp, W. Porod, Phys. Lett. A 381 (17), 1471-1476 (2017).
2. A. V. Chumak, T. Neumann, A. A. Serga, et al., J. Phys. D, 42 (20), 205005 (2009).
3. A. A. Nikitin, A. B. Ustinov, A. A. Semenov, et al., Appl. Phys. Lett., 106 (10), 102405 (2015).
4. B. Rana, Y. Otani, Phys. Rev. Appl. 9 (1), 014033 (2018).
5. A. B. Ustinov, A. V. Drozdovskii, A. A. Nikitin, et al., Commun. Phys., 2, 137 (2019).
6. M. Vogel, A. V. Chumak, E. H. Waller, et al., Nat. Phys., 11 (6), 487 (2015).
7. A. A. Nikitin, A. A. Nikitin, A. B. Ustinov, et al., J. Appl. Phys., 128 (18), 183902 (2020).
8. D. D. Stancil and A. Prabhakar, Spin Waves: Theory and Applications (Springer, New York, 2009).

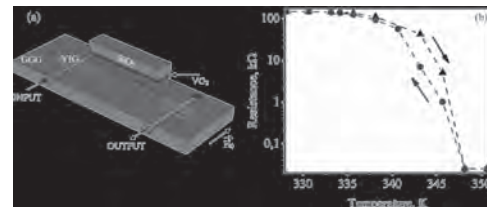


Fig. 1 (a) Sketch of the experimental structure. (b) Resistance-temperature curves of the VO₂ film.

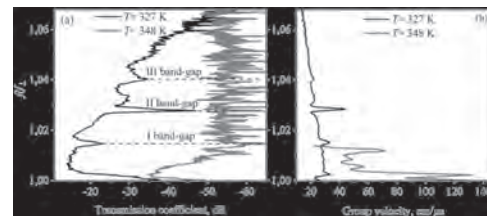


Fig. 2 (a) Transmission characteristics and (b) group velocities of the surface SW.

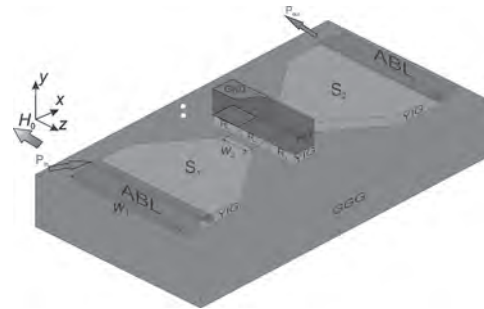
EQ-03. Withdrawn

EQ-04. Voltage-Controlled Fano Resonances in Irregular Magnonic Structure.

A. Grachev¹, E. Beginin¹, I. Fil'chenkov¹ and A.V. Sadovnikov¹
 I. N. G. Chernyshevskogo National Research University in Saratov, Saratov,
 Russian Federation

Fano resonances generally appears in the interaction of subsystems with a continuous (continuum) and discrete spectrum of energy states and also observed in many physical systems: quantum and nanoscale [1], optical and microwave [2], plasmonic [3]. Systems of coupled Fano resonators [4], nonlinear effects [5], bistable and nonreciprocal properties are also being investigated. One of the promising approaches for the generation, transmission and processing of information signals is using spin waves (SW) as information carriers. By analogy with electronics, this area is called “magnonics” [6,7]. SWs characteristics can be modulated (amplitude, phase, frequency) and can propagate in waveguides based on various films of magnetically ordered materials. Currently, yttrium-iron garnet (YIG) is the magnetic material with the lowest losses (the smallest ferromagnetic resonance line width). Potentially, spin-wave excitations, due to their low damping in coupled waveguide-resonator systems, can also exhibit Fano resonances. However, unlike optical systems, systems based on magnetic materials have the following feature: the dependence of the equilibrium state of magnetic moments and, therefore, internal static magnetic fields on the geometric dimensions and shape of magnetic subsystems (waveguides and resonators), the magnitude and direction of the external magnetic field, anisotropy fields, etc. Here we study the characteristics of the Fano resonance in a coupled system of lateral magnonic stripes with piezoelectric layer and resonators depending on the geometric parameters of the systems, the magnitude of the coupling between them, and the electric field of the piezoelectric layer. Using micromagnetic simulation of spin-wave excitations and numerical integration of the coupled wave equation system, the transfer characteristics of the lateral system and the Fano resonance parameters are calculated. Micromagnetic modeling was carried out for the structure (see Fig. 1) based on a YIG film with a thickness of 10 μm and a saturation magnetization of $4\pi M_0 = 1750$ G. The structure consists of two tapered planar magnonic stripes with a widths $w_1 = 2500$ μm and $w_2 = 200$ μm . A system of resonators with a width of “ w_2 ” and a length of 500 μm is located between the stripes. A 200 μm -thick lead zirconate titanate (PZT) is used as a piezoelectric material. A 1 μm -thick titanium electrode is placed (“GND” in Fig. 1) on a top side of PZT, which does not have a significant effect on the propagation of SW in magnetic stripes. On the bottom side of PZT a 100 nm-thick titanium electrode. The entire structure is placed in an external uniform magnetic field, $H_0 = 1200$ Oe, directed along the Z axis, which ensures efficient excitation of magnetostatic surface waves. To reduce parasitic SW reflections from the boundaries of microwave guides, layers ($0 < x < 0.6$ mm and $6.0 < x < 6.6$ mm) with exponentially increasing dissipation parameters (ABL) were introduced. The features of exhibiting constructive and destructive interference of SWs under the conditions of Fano resonance are shown. An effective tuning of the strain of the piezoelectric layer and the effect of magnetostriction in lateral structure. This work was supported by the Russian Science Foundation Grant (#20-79-10191).

[1] A.E. Miroshnichenko, S. Flach, Yu.S. Kivshar, *Rev. Mod. Phys.*, Vol. 82, P. 2257–2298 (2010). [2] M. Galli, S. L. Portalupi, M. Belotti, L.C. Andreani, L. O’Faolain, and T. F. Krauss, *Appl. Phys. Lett.*, Vol. 94, P. 10–13 (2009). [3] R. Ortuno, M. Cortijo, A. Martinez, *J. Opt.*, Vol. 19, P. 025003 (2017). [4] B. Djafari-Rouhani, H. Al-Wahsh, A. Akjouj and L. Dobrzynski, *Journal of Physics: Conference Series*, Vol. 303, P. 012017 (2011). [5] M. Kroner, A. O. Govorov, S. Remi, B. Biedermann, S. Seidl, A. Badolato, P. M. Petroff, W. Zhang, R. Barbour, B. D. Gerardot, R. J. Warburton, K. Karrai, *Nature*, Vol. 451, P. 311–314 (2008). [6] A.A. Grachev, S.E. Sheshukova, S.A. Nikitov, A.V. Sadovnikov, *Journal of Magnetism and Magnetic Materials*, Vol. 515, P. 167302 (2020). [7] A.V. Sadovnikov, A.A. Grachev, A.A. Serdobintsev, S.E. Sheshukova, S.S. Yankin, S.A. Nikitov, *IEEE Magnetics Letters*. Vol. 10. 5506405 (2019).



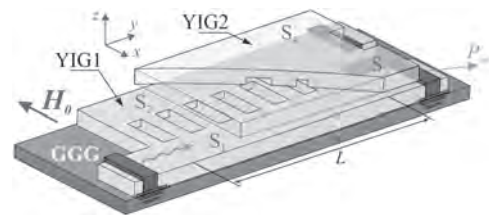
EQ-05. Collimated Spin-Wave Beams in a Three-Dimensional Multi-layer Magnon-Crystal Arrays Near the Bandgap Frequencies.

S. Odintsov¹, S. Sheshukova¹, A.V. Sadovnikov¹ and S. Nikitov²
 1. N. G. Chernyshevskogo National Research University in Saratov, Saratov, Russian Federation; 2. V. A. Kotelnikova Institute of Radiotechnology and Electronics in Saratov, Moscow, Russian Federation

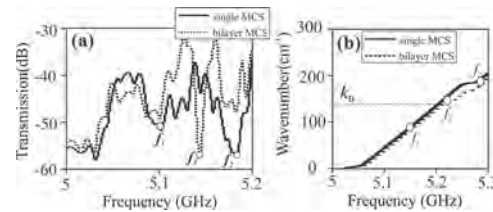
Investigations of the transfer of spin momentum in planar and multilayer magnetic structures make it possible to reveal that spin waves (SW) could potentially be used as data carriers in low energy computing devices [1]. Properties of spin-wave transport in three-dimensional (3D) magnonic networks [2] are determined by the dipole and exchange interactions and can change significantly with a change in the parameters of the medium, such as variation in the direction and magnitude of the equilibrium magnetization caused by elastic deformations, modification of substrate properties by the laser light [3]. The present work is devoted to the development of the ideas of the directed branching of SW in 3D structures. In this work, we propose a magnonic structure with the possibility of spin-wave transport in both the lateral and vertical directions. In this case, the effects of collimation of a spin-wave beam in arrays of magnonic-crystal structures make it possible to use the periodic properties of the medium to control the SW propagation length at frequencies near the non-transmission band of an individual magnonic crystal. For this, a system of lateral spin-waveguide channels separated by a periodic structure was fabricated on the surface of each film. Fig. 1 (a) shows a schematic view from above of each single magnonic crystal structure (YIG₁ and YIG₂) which are placed one above the other. Films of yttrium iron garnet (YIG), which are grown on a gallium-gadolinium garnet (GGG) substrate, were separated by a vertical gap of g in the direction of the z axis. A system of waveguides (S_1, S_2, S_3 and S_4) of equal width $w = 200 \mu\text{m}$ is formed from the YIG film, S_1 and S_2 are oriented parallel to each other, S_3 and S_4 were placed above them in such a way that the resulting structure was two systems of lateral stripes $S_1 - S_2$ and $S_3 - S_4$. The thickness of the YIG films for both structures was $t = 10 \mu\text{m}$. The length of the coupling area is $L = 4 \text{ mm}$ (see Fig.1a). Thus one can consider the single MCS as a lateral array of microwave guides separated by periodic sequence of grooves with a length in y -direction $a = 100 \mu\text{m}$ period of $D = 200 \mu\text{m}$ in the direction of the y axis on the surface of YIG films. The groove width along the x axis is $d = 50 \mu\text{m}$, the groove thickness in the direction of the z axis was $s = 1 \mu\text{m}$. Fig.1(b) shows a schematic diagram of the structure and demonstrates the geometric dimensions including the primitive cell of a magnonic crystal (MC) (on the right part of Fig. 1b). The experimental study was performed, with samples of a magnonic-crystal structure based on thin films of yttrium iron garnet that were made by laser scribing based on a precision laser cutting system based on a fiber laser “MiniMarker2-20A4”. In the input section of the lower film S_1 , there is a microstrip antenna with a width of $30 \mu\text{m}$, to which a microwave signal was applied to efficiently excite the MSSW [34]. The structure was placed in an external magnetic field $H_0 = 1200 \text{ Oe}$, as in the numerical simulation. Input and output transducers are attached to the YIG film (see Fig. 1(a)) at a distance of 4 mm from each other. The uniform static magnetic field $H_0 = 1200 \text{ Oe}$ was applied in the plane of the waveguide along the x -direction for the effective excitation of the guided MSSW. Transmission and dispersion of MSSW were experimentally measured using PNA-X Keysight Vector Network Analyzer(VNA). First, the measurement of the transmission response for the one layer MCS was performed. The solid line in Fig. 5(a) shows the measured MSSW intensity for the MCS. A well pronounced forbidden bands where spin waves are not allowed to propagate is clearly observed for the frequencies of $f_1 = 5.1 \text{ GHz}$ and $f_2 = 5.193 \text{ GHz}$. These two gaps in the magnetostatic surface waves spectra are typical for the system of coupled magnonic crystal, where two gaps are formed at the Bragg resonance condition for the symmetric and anti-symmetric modes. For single MCS structure we use the formalism where we can also consider the two coupled magnonic crystal waveguides separated by the array of grooves. In this case the formation of two gaps in spin-wave spectra can be explained also with the symmetric and antisymmetric modes as in Ref. [4]. Next we measure coupled MCS place one above the other with the gap of $g = 80 \mu\text{m}$. In the present structure we have four eigenmodes and each of them can satisfy the Bragg condition forming the band gaps. The microwave measurement of the fabricated two layer MCS shows that one

more forbidden frequency band has been added to the two bandgaps at the frequency $f_3 = 5.15 \text{ GHz}$ (see Fig. 5(a)). From the experimentally measured phase shift for the MSSW, the dispersion characteristic of MC was obtained (fig.5(b)). The dispersion measurement reveals that the frequency f_3 corresponds to the Bragg wavenumber k_B . This work was supported by the Russian Foundation for Basic Research under Project 19-37-90079

1. V. V. Kruglyak, S. O. Demokritov, D. Grundler, J. Phys. D: Appl. Phys. 43 (2010) 264001.
2. E. Beginin, D. Kalyabin, P. Popov, A. Sadovnikov, A. Sharaevskaya, A. Stognij, S. Nikitov, “3D Magnonic Crystals” In G. Gubbiotti (Eds) “Three-Dimensional Magnonics”, Jenny Stanford Publishing, 2019.
3. A. V. Sadovnikov, E. N. Beginin, S. E. Sheshukova, Y. P. Sharaevskii, A. I. Stognij, N. N. Novitski, V. K. Sakharov, Y. V. Khivintsev, S. A. Nikitov, Route toward semiconductor magnonics: Light-induced spin-wave nonreciprocity in a yig/gaas structure, Phys. Rev. B 99 (2019) 054424.
4. M. Morozova, A. Y. Sharaevskaya, A. Sadovnikov, S. Grishin, D. Romanenko, E. Beginin, Y. Sharaevskii, S. Nikitov, Band gap formation and control in coupled periodic ferromagnetic structures, Journal of Applied Physics 120 (2016) 223901.



(a) Concept of the bilayer magnonic crystal structure;



(a) transmission characteristics, measured with signal network analyzer for one MCS and two layer of MCS;(b)experimentally measured dispersion for one layer MCS and two layer of MC

EQ-06. Surface Spin Wave Propagation in the Orthogonal Vertical Junction of YIG-Based Magnonic Waveguide.

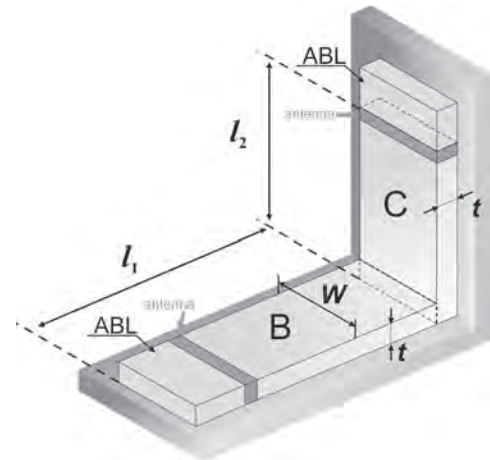
A.A. Martyshkin¹, E. Beginin¹ and A.V. Sadovnikov¹

I. N. G. Chernyshevskogo National Research University in Saratov, Saratov, Russian Federation

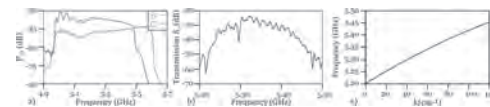
With the development of technologies for the manufacture of magnetic structures, within the framework of the direction of magnonics, the mechanisms and methods of excitation and control of spin waves (SW) in magnetic materials are being actively studied [1, 2]. One of the key problems in the development of spin-wave devices is associated with the damping of spin waves [3]. A record low level of SW attenuation can be achieved when using films of yttrium iron garnet (YIG) [3]. At the same time, in YIG, it is possible to excite and propagate SWs with a wavelength from tens of nanometers to a few millimeters [2]. Improvement of the technological process of manufacturing thin YIG films made it possible to create multilevel micro- and nanostructures for the implementation of magnon networks [4], on the basis of which it is proposed to create an element base for information signal processing devices [5-6]. The use of the effects of spin-wave interference and amplitude-phase coding is a promising way to create a magnon networks for processing information signals in a wide frequency range [7]. The paper proposes and investigates a variant of vertical spin-wave transport based on orthogonally coupled magnetic microwave guides. With the help of numerical and experimental studies, the features of the transmission of the spin-wave signal at orthogonal coupling of the waveguide sections have been revealed. To describe the physical processes causing the propagation of a spin-wave signal in an irregular structure, we used the method of numerical micromagnetic simulations based on a numerical solution of the Landau-Lifshitz-Gilbert equation [8]. Magnetic films are formed from yttrium-iron-garnet (YIG) waveguides (Fig. 1) with thickness of $t = 10 \mu\text{m}$, $l_1 = l_2 = 2500 \mu\text{m}$ and width $w = 500 \mu\text{m}$. The exchange constant of the YIG film was assumed to be equal $A_{\text{ex}} = 3.614 \cdot 10^{-12} \text{ J/m}$ and the saturation magnetization $M_0 = 1.395 \text{ A/m}$. To reduce SW reflections from the boundaries of waveguides in the numerical simulation, regions ABL (absorbing boundary layers) with an exponentially increasing dissipation parameter. Fig.2a shows the results of calculating the spectrum of the spin-wave signal in orthogonal magnonic waveguide. The drop in signal power at the output by 5 dB is associated with attenuation in the YIG. For experimental investigation were fabricated by laser scribing a continuous YIG film epitaxially grown on a substrate of gadolinium gallium garnet (GGG). The waveguides were magnetized by a uniform field $H_0 = 1150 \text{ Oe}$, directed along the short symmetry axis of the waveguides for efficient excitation of a magnetostatic surface spin wave. Spin wave transmission characteristics were acquired using two $30 \mu\text{m}$ wide microstrip antennas positioned on either end of the waveguides. The input antenna's dynamic magnetic field couples to the YIG's magnetization, exciting spin waves propagating along the waveguide. The efficiency of spin wave propagation was measured using a vector-network-analyzer. The results from the characterization of the waveguides are shown in Fig.2b. Fig. 2c shows the result of calculating the effective wavenumbers in the frequency range of the MSSW excitation. It can be seen that the phase incursion and the effective wavenumber begin to increase with increasing frequency, which corresponds to the case of MSSW. Proposed spin-wave transport in orthogonal vertical junction makes it possible to implement functional processing of information signals (frequency filtering and phase correction) during signal transmission in a wide frequency range. This work was supported by the Russian Science Foundation Grant (#20-79-10191).

[1] V.V. Kruglyak, S.O. Demokritov, D. Grundler, *J.Phys. D: Appl. Phys.*, Vol.43, p.264001 (2010) [2] A.V. Chumak, V.I. Vasyuchka, A.A. Serga, *Nature Physics.*, Vol.11, p.453. [3] A.G. Gurevich, G.A. Melkov, *Magnetization Oscillations and Waves*, CRC-Press, London, New York. (1996) [4] A.A. Martyshkin, S.A. Odintsov, A.V. Sadovnikov, *JETP Lett.*, Vol.110, No.8, pp.533-539 (2019) [5] V.E. Demidov, S. Urazhdin, S.O. Demokritov, *J. Appl. Phys.*, Vpl.127, p.170901 (2020) [6] N. Thiery, V.V. Naletov, O. Klein, *Phys. Rev. B*. Vol.97, p.064422 (2018) [7] A.V. Sadovnikov, E.N. Beginin, S.A. Nikitov, *Appl.Phys. Lett.*, Vol.107, p.202405

(2015) [8] A. Vansteenkiste, J. Leliaert, B. Waeyenberge, *AIP Advances*, Vol.4, p.107133 (2014)



Schematic view of the orthogonal magnetic waveguide



Numerical results of transmission spectrum of the input signal (red) and output (blue) (a). Experimental transmission characteristics S_{21} (b). Numerical result of effective wavenumbers (c).

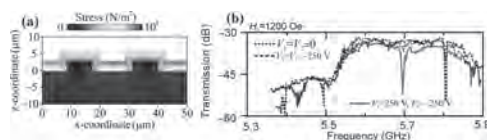
EQ-07. Brillouin Light Scattering Study of Spin-Wave Spectra in YIG/LiNbO₃ Magnonic Crystals.

A.V. Sadovnikov¹, A. Stognijj², A. Serokurova², E. Beginin¹, S.E. Sheshukova¹ and A. Grachev¹

1. Magnonics, Saratov State University named after N. G. Chernyshevsky, Saratov, Russian Federation; 2. Materials Research Center, National Academy of Sciences of Belarus, Belarus, Minsk, Belarus

Recently magnetic micro- and nanostructures are extensively studied due to their potentials as candidates for future magnonic devices [1,2] and beyond-CMOS (complementary metal-oxide semiconductor) technologies, as they are free of Joule heating and, respectively, free of power loss associated with traditional electronics[3]. Magnetostatic spin waves (MSW) propagating in such structures are considered as signal carriers for information processing. In recent years much research has been directed towards the ways of the control of MSW for signal processing at microwave and subterahertz frequencies. The effect of the electric field on the magnetic configuration results from the modification of the effective internal magnetic field. The latter is changed due to inverse magnetostriction (Villary effect) as a result of the local deformation of the magnetic film. Here we report the experimental observation with Brillouin light scattering (BLS) technique of the spin-wave transport in different magnonic structures based on the yttrium iron garnet (YIG) magnonic crystals (MCs) [5] (Fig.1), and 3D array of meander type YIG waveguide [6], which demonstrates the collective spin-wave phenomena and tunable spin-wave transport. With the BLS mapping of the 3D magnonic structure we show, that the combination of frequency and spatial filtering features of the MC and both lateral and vertical spinwave transport leads to the possible concept of the tunable magnonic frequency demultiplexer. We considered the meander-type structures magnetized by in-plane magnetic field oriented at different angles with respect to the meander segments orientations (Fig.2). For the perpendicular orientation of magnetic field the spin-wave propagation regime essentially depends on the total height of the meander and contains three frequency domains formed by forward volume magnetostatic waves, localized modes, and backward volume magnetostatic waves. In the case of longitudinally magnetized structure, scattering of surface magnetostatic waves in the junctions between the vertical and horizontal segments caused the formation of the quasistanding waves. The gradients of inhomogeneous static magnetic fields can lead to the effective generation of short-wavelength dipole-exchange waves whose spatial distribution is non-resonant. The voltage-controlled spin-wave transport along 3D magnonic structures was demonstrated (Fig.2). Obtained results together with the possibility to integrate magnonics and semiconductor electronics on the base of YIG/LiNbO₃ structures[4] can provide the basis for the development of 3D-elements for magnonics and spintronics devices with extended frequency characteristics controlled by the total height of the meander-type structure This work was supported by the grant RFBR (#19-29-03034, 18-29-27026). S.E.S. acknowledges support from the Scholarship and Grant of the President of the RF (No. SP-949.2021.5, No. MK-1870.2020.9).

1. V. V. Kruglyak, S. O. Demokritov, and D. Grundler, *J. Phys. D* 43, p. 264001 (2010). 2. E.N. Beginin, D.V. Kalyabin, P.A. Popov et al In G. Gubbiotti (Eds) “Three-Dimensional Magnonics” CRC Press (Taylor&Francis), Jenny Stanford Publishing, New York (2019) 3. A. V. Sadovnikov, *Phys. Rev. Lett.* 120, p. 257203 (2018) 4. A. V. Sadovnikov, et al., *Phys. Rev. B* 99, p. 054424 (2019) 5. A.V. Sadovnikov et al *IEEE Trans on Magn*, Vol. 53, p. 2801804 (2017). 6. E.N. Beginin, A.V. Sadovnikov, V.K. Sakharov et al, *JMMM*, vol. 492, p. 165647 (2019)



EQ-08. Discrete Breathers and Their Stability in a Finite-Size Monoaxial Chiral Helimagnet.

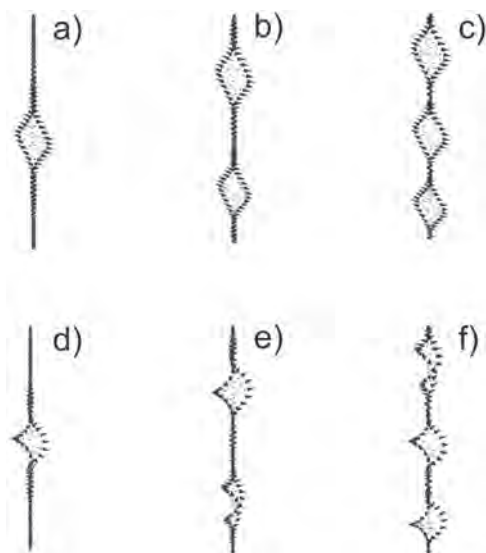
A.S. Ovchinnikov¹, I.G. Bostrem¹, V.E. Sinitsyn¹, E.G. Ekomasov^{2,3} and J. Kishine⁴

1. *Institute of Natural Sciences and Mathematics, Ural Federal University, Ekaterinburg, Russian Federation;* 2. *Bashkir State University, Ufa, Russian Federation;* 3. *South Ural State University, Chelyabinsk, Russian Federation;* 4. *The Open University of Japan, Chiba, Japan*

An existence and stability of discrete breathers in the monoaxial chiral helimagnet with Dzyaloshinskii-Moryia (DM) interaction and easy-plane anisotropy are investigated. We focus on the phase of forced ferromagnetism when the magnetic system is subjected to an external magnetic field directed along the chiral axis. The intrinsic breather modes have high frequencies above the maximum frequency of the spin-wave spectrum and are excited at the Brillouine zone boundary. We modify the numerical algorithm suggested in Ref. [1] to find the nonlinear solutions and show that these localized modes are characterized by a sign-changing ordering of transversal spin components. The discrete breathers in a finite-size system may be categorized by number of embedded kink-antikink pairs forming a regular breather lattice (Fig. 1). The DM interaction suppresses amplitude of these modes and lowers their symmetry by allowing only excitations with an odd envelope function with respect to the center of the system. The energy of the discrete modes demonstrates a linear dependence on number of bound kink-antikink pairs. Floquet stability analysis [2] is employed to examine stability of the breather modes depending on their frequency and external parameters, such as strengths of the external magnetic field and the local anisotropy. The work is supported by the RFFI grant (project 20-02-00213).

[1] S. Rakhmanova and D. L. Mills, Phys. Rev. B, Vol. 54, p. 9225 (1996).

[2] J. M. Khalack, Y. Zolotaryuk, and P. L. Christiansen, Chaos, Vol. 13, p. 683 (2003).



Spatial distribution of spin moments (blue arrows) in a spin chain with different numbers of kink-antikink pairs. Cases without DM interaction: (a) $n = 1$, (b) $n = 2$, (c) $n = 3$; and with an account of the DM interaction: (d) $n = 1$, (e) $n = 2$, (f) $n = 3$.

EQ-09. Cherenkov-Type Radiation of Spin Waves Induced by Interfacial Dzyaloshinskii-Moriya Interaction.

H. Xia¹, H. Chen¹, C. Won², H.B. Zhao³ and Y. Wu¹

1. Department of physics, Fudan University, Shanghai, China; 2. Department of physics, Kyung Hee University, Seoul, The Republic of Korea;

3. Department of Optical Science and Engineering, Fudan University, Shanghai, China

Cherenkov effect is a fundamental physical phenomenon in high-energy particle physics, which refers to the electromagnetic radiation produced by a charged particle passing through a medium faster than the speed of light in the medium. The electromagnetic wave by the Cherenkov effect is analogous to the bow wave caused by a power boat traveling faster than the speed of water waves or to the shock wave produced by an aircraft traveling faster than the speed of sound in air. We investigated the Cherenkov-type radiation of spin waves (SWs)[1,2] in thin film systems with interfacial Dzyaloshinskii-Moriya interaction (DMI) utilizing micromagnetic simulation. The effect of DMI on SW propagation is analogous to the flow of magnetic medium leading to the Doppler effect [3,4], which refers to an effective DMI-induced Doppler velocity $v_{\text{DMI}}=2\gamma D/M_s$, and a spin-polarized current can enhance or suppress it. We demonstrated that, for the Doppler velocity exceeding a critic value, a Cherenkov-type radiation of SWs is excited from a magnetically irregular point where a Mach cones is formed. As shown in Fig. 1 (d), the critic velocity is 1204m/s in our simulation, beyond which the SW group velocity is larger than the phase velocity. As shown in Fig. 1 (a), if the strength of DMI is 1.59mJ/m² the DMI induced Doppler velocity is 700m/s lower than the critic velocity, no SWs are emitted. As shown in Fig. 2 (b) and (c), once the strength of DMI is up to 3.18mJ/m² or 4.55mJ/m², the DMI induced Doppler velocity is up to 1400m/s or 2000m/s, the Cherenkov-type radiation of SWs is excited and the 2D SW Mach cone is observed. Fig. 2 (e) shows the simulated Mach angle as a function of the DMI-induced Doppler velocity, and the simulation result fits well with our theory. Combining the effects of spin polarized current and DMI, the constant Cherenkov radiation of SWs can be achieved in thin film systems experimentally, and can be tuned by the current density. Due to the fundamental interests and potential applications in magnonic devices based on SWs, the predicted Cherenkov-type radiation of SWs in thin film systems deserves further experimental explorations.

[1] M. Yan, C. Andreas and A. Kakay, Appl. Phys. Lett. Vol.99, P.122505 (2011). [2] M. Yan, A. Kakay, and C. Andreas, Phys. Rev. B Vol.88, P.220412 (2013). [3] V. Vlaminck and M. Bailleul, Science Vol.322, P.410 (2008). [4] T. Kikuchi, T. Koretsune, and R. Arita, Phys. Rev. Lett. Vol.116, P.247201 (2016).

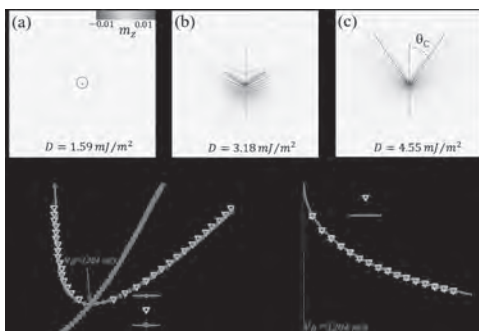


Fig. 1 The excitation of the spin Cherenkov effect. (a-c) The snapshot images of simulated distribution after applying a constant field in the center of the disk with different DMIs. (d) The calculated phase velocity $v_p(k)$ and group velocity $v_g(k)$ of SWs. The red circles for and are extracted from the SW dispersion $w(k)$ with zero DMI. (e) The Mach cone angle θ_c as a function of the Doppler velocity v_{DMI} .

Session ER
MICROWAVE AND MILLIMETER WAVE DEVICES
(Poster Session)

Nian X Sun, Chair
Northeastern University, Boston, MA, United States

ER-01. Direct Current Control of the Chaotic Dark Parametric Solitons in a Magnonic Crystal Active Ring Resonator.

*D.V. Romanenko¹, A.S. Bir¹, S.V. Grishin¹ and S. Nikitov²
 1. N. G. Chernyshevskogo National Research University in Saratov, Saratov, Russian Federation; 2. V. A. Kotelnikova Institute for Radiotechnology and Electronics, Russian Academy of Science, Moscow, Russian Federation*

In the last two decades, the rapid development of broadband communication systems is the cause of the creation of the ultrashort pulse (USP) sources. In optics, there are various methods for USP generation, one of which was given the Nobel Prize in Physics [1]. Nowadays, some optical methods for USP generation start to be used in the microwave range to generate both the USPs of “giant” amplitude [2] and the multisoliton complexes consisting of bright and dark spin-wave envelope solitons [3]. Recently, a new method for the ultrashort dark pulse generation was proposed [4]. It is based on the use of three-wave nonlinear spin-wave interactions and a nonlinear amplification. Using this method, the generation of microwave dark multisoliton complexes was obtained. Each multisoliton complex consists of some dark parametric pulses of submicrosecond duration that contains the trains of dark incoherent spin-wave envelope solitons possessing a subnanosecond duration. The characteristics of such patterns are controlled by a variable attenuator that is managed by the nonlinear loss of a magnetostatic spin wave (MSW), propagating in an irregular magnonic waveguide. Dynamic control of the MSW loss can be realized with the help of direct current (DC) [6,7]. If DC flows in a wire conductor located on the ferromagnet surface, then the internal magnetic field is locally changed in the ferromagnet. This causes a change not only in the MSW dispersion, but also in its linear loss. Dynamic control of the MSW loss by means of DC underlies the operation of a dynamic magnonic crystal (MC) [7]. The dynamic MC is a ferromagnetic medium, the internal magnetic field of which is periodically changed in space by DC. By analogy with photonic crystals, a periodic change in the parameters of the medium is the reason for the forbidden zones (FZs) formation. At FZs frequencies, the MSW linear loss undergo a significant change. Dynamic control of the MSW loss can also be realized for a static MC, if a DC-controlled local inhomogeneity is created on the surface of a periodic structure. This will make it possible to control not only the MSW loss at the frequencies of the FZs, but also the FZ location in the MSW spectrum. In this work, it is demonstrated the dynamic control of the loss and FZs of the static MC due to a local change in the MC internal magnetic field. In addition, the static MC with dynamic control of the loss and FZs is used in a feedback loop of an active ring resonator to manage a duty cycle of the chaotic dark parametric envelope solitons. The parametric wave model with nonlinear amplification is used to explain the experimental results. As shown in Fig.1a, the MC, contained in the feedback loop of the active ring resonator, is a periodic structure of crests and grooves that are formed on the surface of an yttrium-iron garnet film with a thickness of 10 μm. The crests and grooves have the same width of 100 μm. An external bias field $H_0=356$ Oe is applied tangentially to the surface of the MC and directed along to the input and output microstrip lines. Such field configuration supports a magnetostatic surface spin wave (MSSW) propagation. The strength of the bias field is chosen so that three-wave nonlinear spin-wave interactions are allowed for the MC. A wire conductor connected to a DC source is placed along the longitudinal symmetry axis of the MC. Depending on the polarity of the DC, the MC internal magnetic field can either increase or decrease. As shown in Fig.1b, such changes of the internal magnetic field lead to the management of both the linear and nonlinear MSSW loss. In addition to the MC, the generator contains an amplifier stage, consisting of a klystron amplifier and two transistor amplifiers, that are necessary to compensate the loss. The output transistor amplifier of the stage operates in the output power saturation mode, and the other two amplifiers operate in the linear amplification mode. In addition, a resonant frequency of the klystron amplifier is tuned to a frequency located near the center frequency of the MC first FZ. This is necessary in order to realize the amplitude and phase conditions for signal generation. A generated microwave signal is fed through the directional couplers to the inputs of a spectrum analyzer and a real-time oscilloscope for analysis and processing. In Fig.2, the dark parametric soliton modes obtained both experimentally and calculated on the basis of the parametric wave model with nonlinear amplification are presented. The presented in

Fig2a experimental results show that a change in the DC polarity leads to a change in the duty cycle of the generated chaotic dark parametric solitons. A similar effect is observed in a numerical experiment (see Fig2b), if the frequency of the parametrically excited spin waves is detuned from the half value of the MSSW frequency. This work was supported by the Russian Science Foundation (Project No.19-79-20121).

1. D. Strickland and G. Mourou, *Opt. Commun.*, Vol.55, p.447 (1985).
2. N.S. Ginzburg, G.G. Denisov, M.N. Vilkov, and et al., *Phys. Plasmas*, Vol.24, p.023103 (2017).
3. S.V. Grishin, B.S. Dmitriev, O.I. Moskalenko, and et al., *Phys. Rev. E*, Vol.98, p.022209 (2018).
4. A.S. Bir, S.V. Grishin, O.I. Moskalenko, and et al., *Phys. Rev. Lett.*, Vol.125, p.083903 (2020).
5. M. Tsoi, A.G.M. Jansen, J. Bass, and et al., *Phys. Rev. Lett.*, Vol.80, p.4281 (1998).
6. S.O. Demokritov, A.A. Serga, A. Andre, and et al., *Phys. Rev. Lett.*, Vol.93, p.047201 (2004).
7. A.V. Chumak, T. Neumann, A.A. Serga, and et al., *J. Phys. D: Appl. Phys.*, Vol.42, p.205005 (2009).

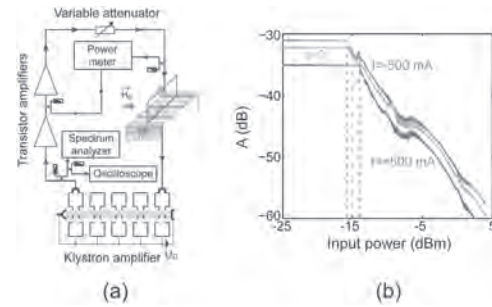


Fig.1 (a) Block diagram of the dark parametric soliton active ring resonator based on direct current-controlled magnonic crystal. (b) Dependences of the MSSW loss on the input power, measured at the MC FZ frequency at various values and polarity of DC.

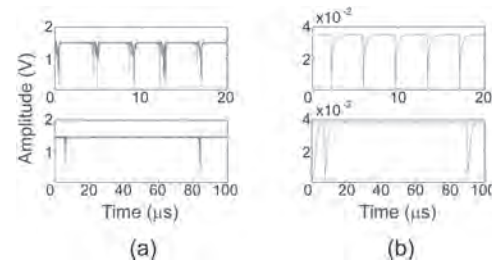


Fig.2 Sequences of the dark parametric envelope solitons obtained (a) experimentally and (b) calculated by the model. In (a), the pulses are obtained for two DC polarities: +320 mA (top panel) and -200 mA (bottom panel). In (b), the pulses are obtained for two values of the SW frequency detuning: 10⁻²⁵ Hz (top panel) and 10⁻³¹⁵ Hz (bottom panel).

ER-02. Spin Current Nano-Oscillator (SCNO) as a Potential Frequency-Based, Ultra-Sensitive Magnetic Biosensor: a Simulation Study.

R. Saha¹, K. Wu¹, D. Su² and J. Wang¹

1. *Electrical & Computer Engineering, University of Minnesota Twin Cities, Minneapolis, MN, United States*; 2. *Chemical Engineering and Material Science, University of Minnesota Twin Cities, Minneapolis, MN, United States*

The ongoing COVID-19 pandemic has pushed the performance requirements of a point-of-care (POC) biosensor by many folds. In this context, magnetic biosensing for POC detection of diseases using magnetoresistance (MR) sensors have been explored intensively [1,2]. Although the attractive part of MR biosensing is that biological samples exhibit zero magnetic background thereby suppressing noise from cellular matrix, its room temperature single molecular sensitivity is significantly affected by high thermal noise. As an alternate to the MR biosensing scheme, the possibility of a frequency-based biosensing scheme shows great promise. However, all studies on frequency-based biosensing are limited to detection of MNPs using magnonic crystals (MCs) [3,4], ferromagnetic nanodots [5] and/or nanodiscs [6]. The advantage of a frequency-based, dynamic approach over the static MR-based sensing is that the device response is linear over a large range of the externally applied magnetic field leading to enhanced accuracy. This frequency is typically of the orders of several GHz, which is way too high as compared to the low frequency $1/f$ noise, and hence devoid of DC voltage-level drift. This work [7] is a micromagnetic simulation-based study on the GHz-frequency ferromagnetic resonances (FMR) for the detection of MNPs using spin current nano-oscillator (SCNO) operating in precession mode. Fig. 1(a) gives a schematic view of the SCNO array with the ferromagnetic (FM) nanopillar of dimensions $160 \text{ nm} \times 80 \text{ nm} \times 5 \text{ nm}$ located $0.5 \mu\text{m}$ apart such that the stray fields of adjacent PMA-FM nanopillars do not influence the device performance. On applying a charge current (J_c , A/m^2) through the heavy metal (HM) layer along $-x$ direction, it causes spin accumulation along $\pm y$ and generation of a spin current along z direction (Fig. 1(b)). When a magnetic field (H_{dc} , Oe) is externally applied along $+y$ direction, the spin current causes the FM nanopillar to operate in precession. The magnetic stray fields from the MNPs in a target antibody-antigen-capture antibody-MNP complex (sandwich structure) on the SCNO surface interact with the FMR frequency of the SCNO device. At the nanoscale, this causes a shift in the peak frequency of the device and generate measurable resonance peak shifts (Fig. 1(c)). As these nano-oscillators are of the dimensions of several nanometers and the size of the antibodies is about 10 nm , extremely precise control over printing of these capture antibodies on the SCNO sensor surface is necessary. This called for a study on the peak frequency shift with respect to different positions of the MNPs on the SCNO biosensor surface and ways to eradicate this effect to further improve bio-sensing. Additionally, a study has been made on how MNPs with different sizes can alter the SCNO device performance. This simulation-based study on the SCNO device shows the feasibility of a frequency-based nano-biosensor with the sensitivity of detecting a single MNP (Fig. 1(c)), even in presence of background noise.

[1] Wu K, Klein T, Krishna V D, Su D *et al.* 2017 *ACS Sens.* 2 1594–601. [2] Ng E, Yao C, Shultz T O *et al.* 2019 *Nanomedicine Nanotechnol. Biol. Med.* 16 10–9. [3] Inoue M, Baryshev A, Takagi H *et al.* 2011 *Appl. Phys. Lett.* 98 132511. [4] Metaxas P J, Sushruth M, Begley R A *et al.* 2015 *Appl. Phys. Lett.* 106 232406. [5] Sushruth M, Ding J, Duczynski J *et al.* 2016 *Phys. Rev. Appl.* 6 044005. [6] Albert M, Beg M, Chernyshenko D *et al.* 2016 *Nanotechnology* 27 455502. [7] Saha R, Wu K, Su D *et al.* 2020 *Nanotechnology* 31 37550.

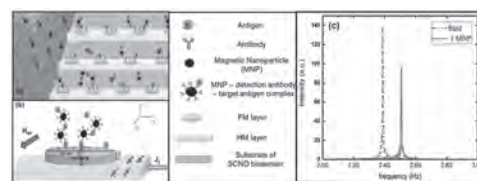


Figure 1. (a) Schematic of the SCNO biosensor array with the sandwich mechanism of target antibody – antigen – capture antibody – MNP complex demonstrated. (b) A single PMA-FM nanopillar of the SCNO biosensor array zoomed in. The black-dashed arrow in the ferromagnetic nanopillar demonstrates precession mode operation. The color and symbol codes for the structures are given in the adjacent column. (c) Comparison between the peak frequency of a bare sensor to that of the sensor with a single MNP on its surface at $i = 15 \text{ mA}$ and $H_{dc} = 1.1 \text{ kOe}$. The simulation results show measurable peak frequency shifts between a bare sensor to that of a single MNP.

ER-03. Estimation of Noise Suppression in MSL With Co-Zr-Nb Films Considering Impedance Matching.

T. Mikami¹, S. Muroga¹ and M. Tanaka¹

1. Graduate School of Engineering Science, Akita University, Akita, Japan

Sheet- and film-type soft magnetic materials have been widely used to suppress unexpected noise in mobile and wearable devices using ferromagnetic resonance (FMR) losses [1][2]. The designs of these magnetic noise suppressors are mainly based on large-scale electromagnetic field simulations and “trial and error” experiences. In previous studies, the effect of the complex permeability of the magnetic sheet and film on circuit parameters of transmission lines was investigated by a simple magnetic circuit analysis using only the cross-sectional size and material parameters [3]. However, the effect on the reflection and the transmission coefficients have not been estimated quantitatively and the design guideline of the noise suppressor has not been clarified. In this paper, the estimation method of the reflection and the transmission coefficients of a transmission line with a noise suppressor is investigated including the effect of the complex permeability. A 95 μm-width microstrip line (MSL) with a Co-Zr-Nb film is discussed as a test bench. The electrical equivalent circuit parameters of the MSL with Co-Zr-Nb film were calculated by the magnetic circuit analysis and the characteristic impedance was estimated. The thickness of the Co-Zr-Nb film was determined considering impedance matching below 1 GHz range, where it was assumed that a signal frequency range, and the conductive noise suppression by the Co-Zr-Nb film at 3 GHz was estimated. Figure 1 illustrates the magnetic circuit in the cross-sectional view of the MSL with the Co-Zr-Nb film. The MSL was fabricated on low-temperature co-fired ceramic (LTCC) substrate with the thickness $h=100\ \mu\text{m}$ and the relative permittivity of 9.8. The width, thickness and length of the signal line are $w_s=95\ \mu\text{m}$, $t_s=3\ \mu\text{m}$, and 10 mm, respectively. The Co-Zr-Nb film was fabricated using radio frequency (RF) sputtering and deposited on a SiO₂ substrate. The film thickness t was obtained by the magnetic circuit analysis and the electromagnetic simulation so that the characteristic impedance of the MSL with and without the film have a same value. The electrical equivalent circuit of the MSL with the Co-Zr-Nb film was obtained to calculate the characteristic impedance. The circuit consists of series impedance $Z = R + j\omega L = (R_m + R_s + R_e) + j\omega L_m$ and parallel conductance $Y = j\omega C$, where R_m and L_m were calculated by the magnetic circuit analysis considering the effect of the complex permeability of the Co-Zr-Nb film. R_s and R_e were the resistance of the signal line including the skin effect and the increase of resistance due to the eddy current loss generated in the film [3], respectively. $C = 2\ \text{pF}$ calculated by experimental value at 0.1 GHz [4]. Figure 2(a) shows the estimated characteristic impedance $Z_0 = (Z/Y)^{0.5}$ with $t = 0.1\text{-}1\ \mu\text{m}$. Below 1 GHz, the impedance is roughly constant and the estimated impedance of the MSL with 1-μm-thick film is almost the same as the measured value of MSL without the film. Therefore, $t = 1\ \mu\text{m}$ was used to calculate the reflection and the transmission coefficient. Figure 2(b) and (c) shows the reflection coefficient $|S_{11}|$, transmission coefficient $|S_{21}|$, and the noise suppression $P_{\text{loss}}/P_{\text{in}} = 1 - (|S_{21}|^2 + |S_{11}|^2)$ of the MSL with 1-μm-thick film obtained by the electrical equivalent circuit analysis. In the case with the film, $|S_{11}|$ and $|S_{21}|$ were almost the same as the measured value within about 8 dB and 0.1 dB below 5 GHz, respectively. $|S_{11}|$ increased up to 8 dB below 1 GHz but the value kept less than -25 dB. On the other hand, $|S_{21}|$ decreased as the frequency increased because of the combination of FMR and Joule losses in each film at 3 GHz. $P_{\text{loss}}/P_{\text{in}}$ is maximized at 3 GHz. In summary, the reflection and the transmission coefficients of a transmission line with a noise suppressor were quantitatively estimated including the effect of the complex permeability using the magnetic circuit analysis using the cross-sectional size and material parameters. The thickness of the Co-Zr-Nb film was determined considering characteristic impedance matching. As a result, the reflection coefficient was lower than -25 dB below 1 GHz, and the conductive noise suppression was obtained at 3 GHz. Those results give a way to clarify the design guideline of the noise suppressors. This work was supported in part by JSPS KAKENHI Grant Number 20K04497. Part of this work was carried out under the Cooperative Research Project Program of the Research Institute of Electrical Communication, Tohoku University.

[1] S. Yoshida et al., IEEE Trans. Magn., Vol.37, No.4, pp.2401-2403 (2001). [2] K. Kondo et al., IEEE Trans. Magn., Vol.45, No.10, pp.4250-4252 (2009). [3] S. Muroga et al., J. Elec. Materi., Vol.48, No.3, pp.1342-1346 (2019). [4] T. Mikami et al., The 44th Annual Conf. Magn. Jpn, 14dD-11 (2020).

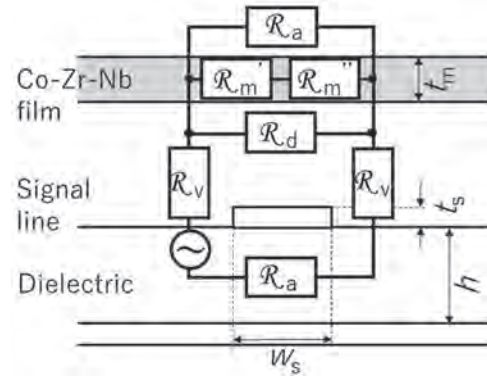
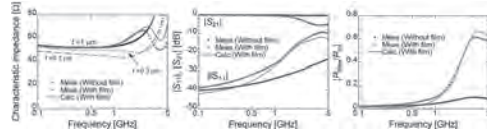


Fig.1 cross-sectional dimensions and magnetic circuit of a one line MSL with Co-Zr-Nb film



(a) Characteristic impedance (b) S parameter (c) Input loss ratio Fig.2 Transmission characteristics

ER-04. Withdrawn

ER-05. High Efficient Wireless Power Transfer Through Metamaterial Coupled Magnetic Resonance.

A.H. Ferreira¹, D.C. Correia², Ú. do Carmo Resende² and R.M. de Souza Batalha¹

1. Graduate Program in Electrical Engineering, Pontifícia Universidade Católica de Minas Gerais, Belo Horizonte, Brazil; 2. Electrical Engineering Department, Centro Federal de Educacao Tecnológica de Minas Gerais, Belo Horizonte, Brazil

Nowadays, the Wireless Power Transfer (WPT) presents itself as a new option to charge batteries, in order to eliminate the respective cables and gain mobility, convenience and ease for the user. One of the WPT techniques uses the Coupled Magnetic Resonance (CMR). This technology is capable of transmitting electromagnetic energy from a power source (transmitter coil) to an electric load (in the receiver coil) through a gap in the air and the variation and oscillation of magnetic fields [1]. Metamaterials (MM's) are typically conductive elements such as copper, gold and silver [2]. They present unnatural magnetic properties, obtained from their internal arrangement, which allow them to obtain a negative refractive index, making them perfect lens. Thus, they are used between the coils to increase the efficiency of WPT. Veselago called the MM's as left-handed materials (LH materials) because the propagation of electromagnetic waves with the electric and magnetic fields and propagation vector forms a left-handed triad when compared to conventional materials. He predicted several behavioral phenomena that occur in LH media such as the reversal of the Doppler effect and the Snell's law and negative refraction [3]. In this work, since the technique chosen was that of strong resonant magnetic coupling, where the magnetic characteristic of the evanescent field prevails, we opted to use a structure with MNG characteristics (Mi-negative Medium, $\epsilon > 0, \mu < 0$), which can be obtained from the Split Ring Resonators (SRR's). If the magnetic field H is perpendicular to the plane of the rings, in order to induce resonant currents in the loop and generate equivalent magnetic dipole moments, this MM exhibits plasmatic permeability as a function of frequency [4]. The main goal is to propose a metamaterial topology that allows a horizontal misalignment between transmitter and receiver coils, resulting in a more efficient system. The system was simulated on CST® Studio software. The transmitter and receiver coils are flat and have 7 loops, width of 2.49 mm, spacing of 1.0 mm, inner radius of 22 mm and outer radius of 47 mm. These coils are in a FR4 substrate with dimensions of 100 x 100 x 1.5 mm. The distance between the coils ranged from 4 cm to 10 cm without misalignment. The transmitter coil has an alternating voltage source (Vmax of 100 V) and the receiver has a resistor of 100 Ω as load. This same system was simulated with a metamaterial slab placed at half way between the coils. The metamaterial slab has the dimensions of 100 x 150 x 1.5 mm, and 12 unit cells arranged in a 4x3 array with two copper Split-ring resonators (SRR's) with height of 0.02 mm, width of 1.63 mm, and spacing of 1.47 mm, and 2 capacitors of 47 nF. The system was designed and computed for a resonance frequency of 1 MHz. The best results were at 4 cm with the MM slab, where there was an increase of 77.32% in the efficiency (12.23% to 23.46%), 24% in the maximum voltage (67.19 V to 83.42 V) and current (671.89 mA to 834.20 mA), 54% in the power (45.14 W to 69.59 W). Figure 2 shows the efficiency of the system, at 4 cm, simulated with a horizontal misalignment between the coils, with and without metamaterial. Although the system is very sensitive to the misalignment, it still presents a better efficiency compared to no MM setup. After introducing the MM slab, there was an increase in the efficiency of 55.63% (13.14% to 20.45%) in 1 cm, 52.72% (10.81% to 16.51%) in 2 cm and 49.41% (7.67% to 11.46%) in 3 cm of misalignment. Even with 2 cm of misalignment, the system with MM is more efficient than the one without it (16.51 to 13.23%). Thus, the MM was able to increase efficiency in wireless power transfer even with horizontal misalignment between coils.

[1] D. C. Corrêa, U. C. Resende and F. S. Bicalho, "Experiments With a Compact Wireless Power Transfer System Using Strongly Coupled Magnetic Resonance and Metamaterials," in IEEE Transactions on Magnetics, vol. 55, no. 8, pp. 1-4, Aug. 2019. [2] X. Wang, Y. Wang, Y. Hu, Y. He and Z. Yan, "Analysis of Wireless Power Transfer Using Superconducting Metamaterials," in IEEE Transactions on Applied Superconductivity, vol. 29, no. 2, pp. 1-5, March 2019. [3] D. Smith, J. B. Pendry; Reversing light

negative refraction. Physics Today, 57, pp. 37-45, 2009. [4] C. Caloz.; T. Itoh; T. Electromagnetic Metamaterials: Transmission Line Theory and Microwave Applications. The Engineering Approach. [s.l.] Wiley, 2006.

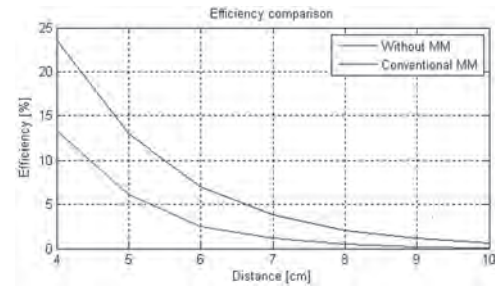


Fig. 1 – Efficiency comparison without misalignment

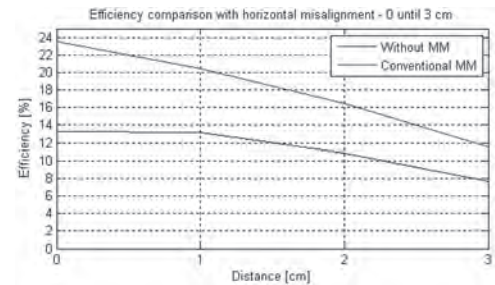


Fig. 2 - Efficiency comparison with misalignment between coils

ER-06. Ultra-Fast Spectrum Analysis at GHz Frequencies Using Spin-Torque Nano-Oscillators.

A. Litvinenko¹, A. Sidi El Valli¹, S. Louis², V. Tyberkevych², L. Vila¹, S. Auffret¹, B. Dieny¹, A.N. Slavin² and U. Ebels¹

1. Univ. Grenoble Alpes, CEA, CNRS, Grenoble INP, SPINTEC, Grenoble, France; 2. Oakland University, Rochester, MI, United States

In modern radar and communication systems it is important to determine the frequency composition of complex external signals on the μs time scale and faster [1]. Common swept-tuned spectrum analyzers (SA) are limited to sweep times of 10-100 ms determined by the characteristic times of macroscopic VCOs and YIG-tuned reference oscillators. In contrast, recent progress in spintronics has led to the development of spin-torque nano-oscillators (STNO) generating in the GHz frequency range, and naturally having time constants of the order of several nanoseconds determined by the intrinsic properties of magnetization dynamics at nano-scale [2]. In [3] it was proposed theoretically and in [4] demonstrated experimentally for a vortex-state configuration that STNOs can be used as a central element of an ultra-fast spectrum analyzer. A fastest sweep rate of $0.67\mu\text{s}$ was achieved for spectral analysis in the range of 25MHz around center frequency of 300MHz. Here we focus on increasing the bandwidth and operational frequency of the STNO SA concept. For this purpose a special uniform-state STNO was nanofabricated. We show that our uniform-state STNO has a very wide frequency-current tuning range and high operational frequency. With such an STNO we pushed the STNO-based SA concept to a central frequency of 9 GHz. The corresponding SA performances sufficiently exceed the results obtained with a vortex-state STNO with a reduced sweep time of $T = 20$ ns, and a record sweep range of 1GHz (limited mostly by STNO power and not by the tuning range capabilities) keeping the RBW (resolution bandwidth) close to the theoretical limit (50 MHz). This GHz-frequency technique of spectrum analysis was implemented as shown in Fig. 1. The STNO was used as a local oscillator whose frequency was sweep-tuned via an additional saw-tooth sweep signal. The STNO output is, then, mixed with the input signal, digitized, and processed with a matched filter, resulting in a narrow output peak whose temporal position corresponds to the input frequency while the width determines the RBW. In the top panel of the inset of Fig. 1 we show a series of peaks obtained with an input signal whose frequency was changing in time in a saw-tooth manner with a period of 500ns. The sweeping rate of the STNO SA was chosen 10 times faster so that the changes of the input signal frequency could be correctly tracked. As can be seen from the spectrogram in the bottom panel of the inset, the shape of the instantaneous input frequency was successfully tracked with sufficient RBW of 34.6MHz. Financial support is acknowledged from the EC program ERC MAGICAL 669204, from the NSF of the USA (Grants # EFMA-1641989 and "ECCS-1708982), and by the US AFOSR (MURI grant # FA9550-19-1-0307).

[1] V.C., Chen and W.J., Miceli, "Time-varying spectral analysis for radar imaging of manoeuvring targets", IEEE Proceedings - Radar, Sonar and Navigation 145, 262-268 (1998). [2] T. Chen, *et al.*, "Spin-Torque and Spin-Hall Nano-Oscillators", IEEE Proceedings, 104, 1919-1945 (2016). [3] S. Louis, *et al.*, "Ultra-fast wide band spectrum analyzer based on a rapidly tuned spin-torque nano-oscillator", *Applied Physics Letters* 113, 112401 (2018). [4] A. Litvinenko, *et al.*, "Ultrafast sweep-tuned spectrum analyzer with temporal resolution based on a spin-torque nano-oscillator," *Nano Letters* 20; 6104-6111 (2020).

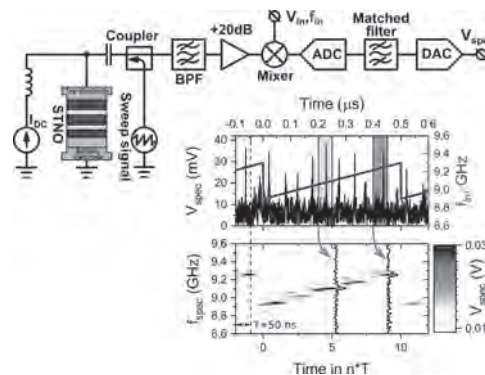


Fig.1. Ultra-fast GHz STNO-based spectrum analyzer. In the inset, top panel, left axis: V_{spec} vs time for 10 consecutive sweeps. Right axis: The time variation of the input signal frequency f_{in} . Bottom panel: f_{spec} vs time in the form of waterfall spectrogram.

ER-07. Two-Dimensional Airy Beam Generation and Manipulation Utilizing Metasurface.

Z. Zhao¹, X. Ding¹, K. Zhang¹, J. Fu¹ and Q. Wu¹
 1. Harbin Institute of Technology, Harbin, China

Two-dimensional Airy beam can be widely used in long distance high-efficiency wireless power transfer and security communication in microwave band. How to excite Airy beams effectively has drawn a lot of attentions in recent years. Wen-Long Guo et al. proposed a metasurface-based one-dimensional Airy beam excitation method [1], which successfully generated the one-dimensional Airy beam. Yongjun Huang et al. successfully generated the two-dimensional Airy beam in the microwave band by using a metasurface composed of a single-layer C-shaped complementary split ring resonators (C-SRR) [2] operating in microwave band. While the manipulation of the deflection of the main lobe has not been achieved in the previous works, and the size of the proposed metasurface is too large to integrate with other devices. In this paper, a novel method to generate and control two-dimensional Airy beam is proposed. By changing the parameters and rotation angles of the unit cell structures, as shown in Fig. 1(a), the amplitude and phase of the transmission coefficient can be adjusted, then the desired two-dimensional Airy beam can be excited by arranging the unit cells to construct the metasurface. In addition, the deflection conditions of the main lobe can be manipulated by changing the attenuation coefficient of the two-dimensional Airy function. The envelope of the two-dimensional Airy beam can be described by equation (1): $U(x,y)=E_{ai}(x)E_{ai}(y)\exp(ax)\exp(ay)$ (1) $E_{ai}(x)=(\int \cos(t^3+3+xt)dt)\div\pi$ (2) Here, a is the attenuation coefficient in the two-dimensional Airy function. In this paper, simplified amplitude modulation method is used, as shown in Fig.1 (b), the main amplitude region of the two-dimensional Airy function is selected to design the desired envelope. As shown in Fig.1 (c), the number of horizontal and vertical elements of the proposed metasurface is 22, which greatly reduces the size of the device that exciting the two-dimensional Airy beam. Fig.1 (d) to (f) show the normalized energy distribution of the two-dimensional Airy beam at different distances along the propagating direction when a equals 0.1. It can be seen that the main lobe moves along the diagonal direction, which shows the self-acceleration phenomenon of the two-dimensional Airy beam. The self-acceleration direction of the two-dimensional Airy beam is the diagonal direction, and the deflection of the main lobe is related to the amplitude distribution in the self-bending direction [3]. By changing the attenuation coefficient, different amplitude distribution of the unit cells on the diagonal of proposed metasurface can be achieved to control the deflection of the main lobe. Fig.2 (a) to (c) show the calculated and simulated results of electric field distribution of the vertical diagonal plane with different attenuation coefficients. The simulated results agree well with the calculated results in the deflection trajectory, which verifies that the deflection conditions of the main lobe can be manipulated effectively.

[1] Wen-Long Guo, Ke Chen, Guang-Ming Wang, Adv. Optical Mater., Vol. 8 (2020) [2] Huang Y, Li J, Xu H X, IEEE Transactions on Antennas and Propagation., pp(99):1-1 (2020) [3] Zhi Li, Hua Cheng, Zhaocheng Liu, Advanced Optical Materials., Vol. 4, pp.1230-1235 (2016) [4] Qingbin Fan, Wenqi Zhu, Yuzhang Liang, Nano Letters., Vol. 19, pp.1158-1165 (2018) [5] X. Ding, F. Monticone, K. Zhang, Advanced materials., Vol. 27, pp.1195 (2015)

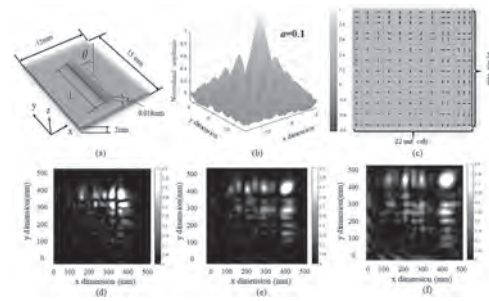


Fig.1. a) Schematic diagram of a unit cell of the proposed single layer metasurface b) Normalized amplitude distribution of two-dimensional Airy function c) Schematic diagram of the entire surface array. The normalized horizontal plane energy distribution when the propagation distance is d) 90mm, e) 180mm, f) 240mm.

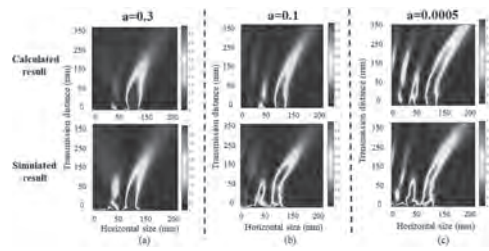


Fig. 2. The energy distribution at the vertical diagonal plane when the attenuation coefficient is a) 0.3, b) 0.1, c) 0.0005.

ER-08. Thresholdless Broadband Spin-Torque Diode Rectification via Spatial Nonuniformity of the Magnetization Distribution.

I. Kindiak^{1,2}, G. Kichin², P. Skirdkov^{2,3}, A. Jenkins⁴, R. Ferreira⁴ and K. Zvezdin^{2,3}

1. *Moscow Institute of Physics and Technology, Dolgoprudny, Russian Federation*; 2. *New Spintronic Technologies, Moscow, Russian Federation*; 3. *Prokhorov General Physics Institute of the Russian Academy of Sciences, Moscow, Russian Federation*; 4. *Nanotechnology Laboratory (INL), Braga, Portugal*

Growing interest for power autonomous nanodevice networks demands new feasible technologies for energy harvesting from ambient sources such as electromagnetic noise. Nanopillar magnetic tunnel junction (MTJ) is a spintronic device that potentially is a viable solution. Recent research has revealed that these devices are capable of converting radio frequency currents to DC voltage via spin-torque diode (STD) rectification effect [1]. STD rectification combines both tunnel magnetoresistance (TMR) and spin transfer torque effects (STT), and thus, when injecting a RF current, an MTJ generates a DC voltage signal, which in general has a resonant behavior. This phenomenon has established a new method for magnetic properties evaluation called ST-FMR as well as offered a promising approach for wireless energy transmission. State-of-the-art spin torque diodes significantly outperform the conventional Schottky diodes in terms of sensitivity at low microwave powers below 1 uW [2-4]. Wide frequency bandwidth is an essential feature for the energy harvesting. Recently, several works have reported non-resonant broadband spin-torque diode rectification regimes. From theoretical [5,6] and experimental [7,8] works, it follows that these regimes require either out-of-plane component of the biased magnetic field, which tilts initially planar magnetization of the free layer, or fine-tuning of perpendicular magnetic anisotropy via magnetic layers thickness adjustments. Here we report an efficient broadband spin-torque diode rectification in circular magnetic tunnel junctions with 200 nm and 250 nm diameters which have intermediate in-plane magnetization distribution between quasi-uniform and magnetic vortex. We show that the STT driven dynamics of spatially nonuniform free layer magnetization distribution provides a wide frequency bandwidth. The rectification is limited at high frequencies by the FMR frequency which is about 3.5 GHz in this work. We demonstrate that this rectification regime can operate at zero threshold power and provides sufficient unbiased sensitivity below 1 uW (up to 200 mV/mW). Finally, we present results of micromagnetic modeling which are consistent with our experimental data and provide an insight into magnetization dynamics of the system. The authors are grateful to Vincent Cros for the discussions and valuable recommendations on this work. The research has been supported by Russian Science Foundation grant 19-12-00432.

[1]Tulapurkar, A. A. et al., *Nature* 438, 339–342 (2005). [2]Miwa, S. et al., *Nat. Mater.* 13, 50–56 (2014). [3]Fang, B. et al., *Nat. Commun.* 7, 11259 (2016). [4]Zhang, L. et al., *Appl. Phys. Lett.* 113, 102401 (2018) [5]Zhang, L. et al. *Appl. Phys. Lett.* 113, 102401 (2018) [6]Prokopenko, O. V. & Slavin, A. N., *Low Temp. Phys.* 41, 353–360 (2015) [7]Fang, B. et al., *Phys. Rev. Appl.* 11, 014022 (2019) [8] Tarequzzaman, M. et al., *Appl. Phys. Lett.* 112, 252401 (2018).

ER-09. Magnetic and Microwave Properties of FeNi Thin Films of Different Thicknesses Deposited Onto Cyclo Olefin Copolymer Flexible Substrates.

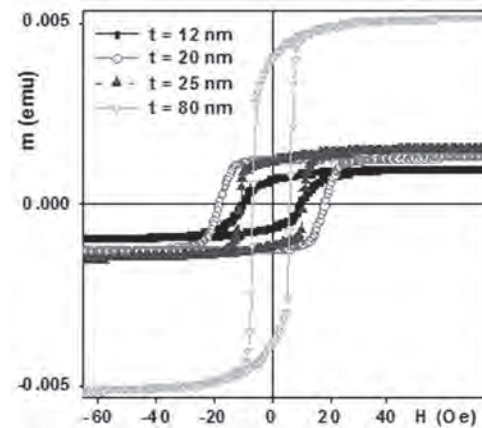
C. Madrid Aguilar¹, A. Svalov², A. Kharlamova³, E. Shalygina³, A. L. Larraga⁴, I. Orue⁴ and G.V. Kurlyandskaya^{1,2}

1. *Electricidad y Electrónica, Universidad del País Vasco Facultad de Ciencia y Tecnología, Leioa, Spain;* 2. *Institute of Natural Sci. and Math., Ural Federal University, Ekaterinburg, Russian Federation;* 3. *Department of Magnetism, M.V. Lomonosov Moscow State University, Moscow, Russian Federation;* 4. *SGIKER, Universidad del País Vasco Facultad de Ciencia y Tecnología, Leioa, Spain*

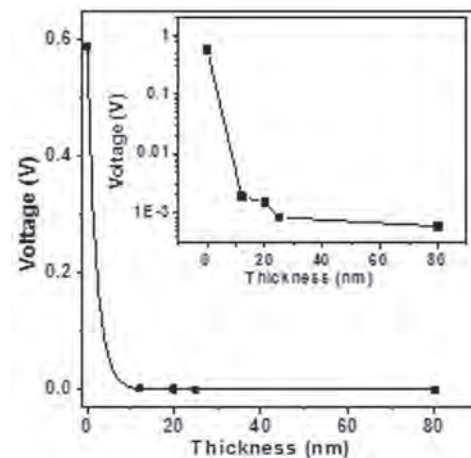
Soft magnetic thin films and multilayered structures deposited onto flexible substrates are attracting more attention for variety of technological applications [1,2]. Flexible electronics and magnetic field sensors require fabrication of complex elements which can operate using different magnetic effects: magnetoelastic effect, magnetoresistance and magnetoimpedance (MI) among others [3,4]. Low weight, high adaptability in multipurpose devices combining more than one functional component may compensate the lower magnetic characteristics of thin films deposited onto flexible in comparison with traditional rigid substrates. One of rapidly developing areas of flexible MI specialized detectors is MI biosensing [5]. It was shown earlier that high sensitivities with respect to applied magnetic field can be achieved for Fe₁₉Ni₈₁/Ti-based sensitive elements fabricated onto cyclo olefin copolymer (COC) flexible transparent substrates widely used in microfluidic systems [3,5]. Transparency is an additional request for microfluidic systems. For successful biosensing weak fields should be detected at the level at least micro Oersteds. This requires special environments without electronic interferences and random magnetic fields. We therefore propose to use COC substrates and the same magnetic material Fe₁₉Ni₈₁ both as functional magnetic layers of sensitive element of MI biosensor and shielding material preventing undesirable electronic interferences. In this work the structure, transparency, static magnetic properties and microwave absorption of Fe₁₉Ni₈₁ thin films deposited onto COC substrates were studied as a function of the permalloy layer thickness. Thin films of the thicknesses of 12, 20, 25 and 80 nm were deposited by magnetron sputtering technique onto COC substrates (Zeonor ZF14 100 μm thick commercial film) at room temperature using alloyed FeNi target for deposition. Background pressure was 3×10⁻⁷ mbar and the argon gas pressure during sputtering was 3.8×10⁻³ mbar. The deposition rate of 28 nm/min for was defined by special calibration of the system. The thicknesses of the films were determined by the deposition time and calculated using the deposition rate. The microstructure was analyzed by XRD technique with a PHILIPSPERT PRO diffractometer (working parameters are 40 kV and 40 mA) employing Cu-Kα radiation (λ = 1.5418 Å). The magnetic hysteresis loops were measured by a vibrating sample magnetometer (VSM). Microwave properties were studied at a fixed frequency. Gunn diode microwave transmitter was employed as a microwave radiation source. It consists of the gun diode in 10.525 GHz cavity, a microwave horn to direct the output and 18 cm stand to reduce reflections. Transmitter provides coherent linearly polarized along the axis of the diode microwave output at a wavelength of 2.85 cm. In order to characterize the properties of FeNi films, the transmission and reflection properties were studied. XRD spectra for FeNi films showed the presence of intensive maximum at 2θ ≈ 44° being (111) reflection. Figure 1 shows the results of the VSM measurements in-plane magnetic hysteresis loops of FeNi thin films with different thickness (t). As to expect the total magnetic moment (m) is increased with the increase of the film thickness. The lowest coercivity close to 6 Oe was observed for the most thick film of 80 nm. This value is consistent with the coercivities of permalloy films obtained for flexible substrates in previous studies. In the other cases, the coercivities were increased (being below 19 Oe) most probably due to special contribution of the surface roughness, which is higher for COC substrate in comparison with standard rigid substrates. As the first step of the microwave studies, the output voltage signal of the receiver was measured for head-to-head aligned configuration of the microwave transmitter and receiver in as a function of the distance (r) between them in two cases. In the first one no intermediate substances between the transmitter and receiver was allowed. In the second case COC 100 μm thick top was covering the horn open plane being

parallel to the axis of the diode. It was confirmed that for the frequency of 10.525 GHz COC substrates contributions to the microwave absorption can be neglected: both output voltages V(1/r) were linear and showing the same slope and regression. As the next step, the power absorption was measured in the same configuration for all thin films deposited onto COC substrates (Figure 2). One can clearly see that 80 nm thin FeNi film, which still has transparency of about 10% insures a complete protection with respect to the component of microwave signal polarized along the diode axis. It worse mentioning that even 12 nm permalloy film is almost as effective as 80 nm film but having much higher transparency. Obtained results indicate that Fe₁₉Ni₈₁ films deposited onto COC substrates can be used as effective shielding materials in complex multipurpose devices. This work was supported by the RSF grant 18-19-00090. Selected measurements were performed at SGIker services UPV-EHU.

[1] C.A. Grimes, IEEE Trans. Magn. 31(6) (1995) 4109. [2] M. Melzer, D. Makarov, A. Calvimontes, D. Karnaushenko, S. Baunack, R. Kaltofen, Y.F. Mei, O.G. Schmid, Nano Lett.11(2011) 2522. [3] E. Fernández, A.V. Svalov, A. García-Arribas, J. Feuchtwanger, J. M. Barandiaran, G.V. Kurlyandskaya, J. Nanosci. Nanotech. 12 (2012) 7496. [4] K. Agra, F. Bohn, T.J.A. Mori, G.L. Callegari, L.S. Dorneles, M.A. Correa, J. Magn. Mater. 420 (2016) 81. [5] A. García-Arribas, F. Martínez, E. Fernández, I. Ozaeta, G.V. Kurlyandskaya, A.V. Svalov, J. Berganzo, J.M. Barandiaran, Sens. Act. A 172 (2011) 103.



VSM hysteresis loops of FeNi films with different thicknesses t deposited onto flexible COC substrates: m is a total magnetic moment of the sample.



Output voltage dependence of the microwave receiver on the thickness of FeNi film deposited onto flexible COC substrates with an exponential decay fit. Inset shows the same output voltages in a logarithmic scale.

ER-10. Metamaterial Based Broadband Absorber Design.

C. De Moro do Carmo¹, L. Ribeiro¹, Ú.d. Resende² and R.M. de Souza Batalha¹

1. *Electrical Engineering, Pontifícia Universidade Católica de Minas Gerais, Belo Horizonte, Brazil;* 2. *Electrical Engineering, Centro Federal de Educacao Tecnológica de Minas Gerais, Belo Horizonte, Brazil*

Metamaterial absorbers (MA) have exhibited great interest from researchers due to the near-perfect absorptive efficiency, as well as wide-angle incidence properties and an almost complete absence of polarization sensitivity [1], [2]. These materials aim to absorb the incident wave to generate a greater intensity of the electric field in the receiver. It implies that all the incident radiation is absorbed in a specific frequency range. These materials can produce resonances for the electrical and magnetic polarizations and autonomously adjust the effective parameters of the medium [1]. Although great efforts have been concentrated in the search for metamaterials with good performance in the THz range, research is still necessary to develop and improve MAs [3], [4]. The design presented in this work combines the materials used in [5] with the design suggested in [6], to produce a simpler design without noble metals. To choose the dimensions and thickness of each layer of the MA, several simulations were carried out to determine the parameters that would result in the maximum absorption of the incident waves for the frequency range under analysis. The MA is presented in Fig.1-a and Fig.1-b, and it is composed of Nickel (Ni) disks resonators arranged in a 4x4 array and a nickel ground plane separated by silicon dioxide (SiO₂) substrate. The choice of materials, such as nickel rather than gold (Au), for the construction of the MA structure, aims to obtain cost-effective and easily producible metamaterials. The size and thicknesses of metals and the dielectric layers are exhibited in the top view at Fig.1-a and the side view at Fig.1-b. Boundary conditions are set as electric on the x-axis, magnetic on the y-axis, and open on the z-axis. The propagation has the direction along the positive z-axis from the open add space wave port with a separation distance to prevent near field effect between EM wave and the MA, as demonstrated in [5]. The study selected visible frequency range, but also investigated infrared and ultraviolet frequency. The dielectric parameters of nickel and silicon dioxide are complex and dependent on frequency. Nickel was chosen because it presents better absorption efficiency than other metals in the visible region and enables high-temperature applications [5]. The results are obtained using the CST Microwave Studio software. The absorption and dispersion of the incident electromagnetic waves are related to the reflected and transmitted radiation at the materials media interfaces through the Scattering Parameters [2], [7]. These parameters can be determined by the absorption capacity (A) through the relation: $A = 1 - R - T$. To reach the maximum absorption level, the reflection coefficient (R), as well as the transmission coefficient (T) should be minimized by using a continuous metallic plane [5]. Then, the MA response will depend only on the reflection values. Sweep simulations were performed varying the unit cell's dimensions, and the best results were presented in Fig.2-a. The proposed design has a high absorption capacity, which is above 96.14% at all frequencies in the visible light region, and the average absorption in all spectrum analyzed is 99.24%. It means that the presented MA can absorb almost all the incident radiation. Hence, the total incident energy can penetrate the structure and be converted into electrical energy. Therefore, the MA can be used in the entire frequency range of the visible light spectrum with better performance compared to the other metals proposed in the literature, such as copper, gold, and aluminium [4], [5], [6]. Furthermore, the MA's absorption behaviour is also examined at infrared and UV frequency regions and are shown in Fig.2-b. For the IR-region, the average absorption percentage is 99.79% between 800 and 1000 THz (300-375 nm). That is a good performance for an infrared detector operating in the mentioned frequency band. For the UV region, the average absorption percentage is 90.11% from 100 up to 350 THz (850-3000 nm). Additionally, the proposed MA has 99.22% of average absorption in all analyzed spectrum. The structure has an absorption value greater than 90% in the entire range of the analyzed spectrum. The reason is that the imaginary part of nickel's dielectric constant is higher than other metals in this frequency range, as shown in [5]. It should be noted that the proposed MA has an extremely wide-bandwidth absorption in a frequency range close to those reported in the current literature. Furthermore,

the presented design has the thinnest thickness compared with the other structures presented in [5], [6], with a simpler design and without noble metals. The MA shown can be considered compatible with several applications, including solar energy harvesting, IR detector, cloaking, shielding for EMC, and sensing. A detailed analysis of the results will be discussed in the full paper. Acknowledgment(s): This work was supported by the Brazilian institutions CAPES, CNPq, and FAPEMIG.

[1] H. Tao et al., *Optics Express*, vol. 16, no. 10, p. 7181 (2008). [2] Y. Wang et al., *IEEE Transactions on Magnetics*, vol. 47, no. 10, p. 2592–2595 (2011). [3] J. Y. Rhee et al., *Journal of Electromagnetic Waves and Applications*, vol. 34, no. 10, p. 1338–1371 (2020). [4] S. K. Patel et al., *Journal of the Optical Society of America B-Optical Physics*, vol. 37, no. 7, p. 2163–2170 (2020). [5] M. Bagmanci et al., *International Journal of Modern Physics B*, vol. 33, no. 8, p. 1950056 (2019). [6] D. Katrodiya, C. Jani, V. Sorathiya, and S. K. Patel, *Optical Materials*, vol. 89, p. 34–41 (2019). [7] C. M. Watts, X. Liu, and W. J. Padilla, *Advanced Materials*, vol. 24, no. 23, p. OP98–OP120 (2012).

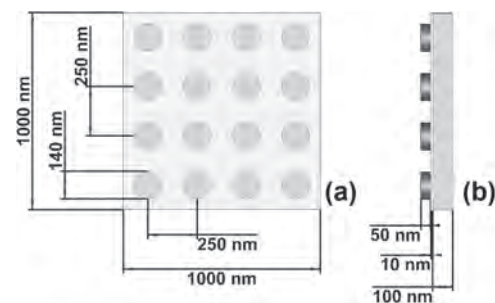


Fig. 1. Unit cell geometry for the designed structure: (a) Top view and; (b) Side view of the MA design.

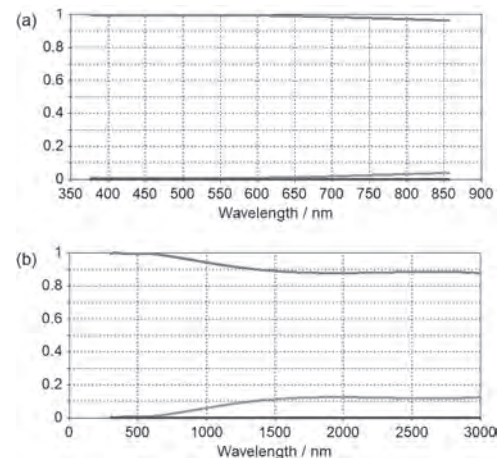


Fig. 2. Absorption (red), Transmission (blue), and Reflection (green) behaviors of the designed structure: (a) visible light region (350 to 800 THz) and; (b) all analyzed spectrum (100 to 1000 THz).

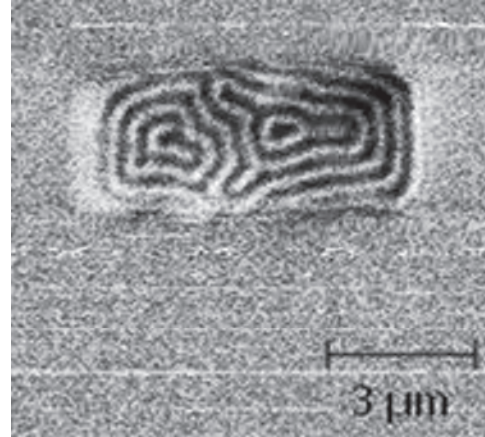
ER-11. Magnetic Shielding of Pillar-Structured Spin-Torque Vortex Oscillators.

G. Büttel¹, M. Qaid², T. Peters³, K. Rott³, I. Sivanesarajah¹, J. Demir³, J. Schmalhorst³, G. Reiss³, G. Schmidt² and U. Hartmann¹

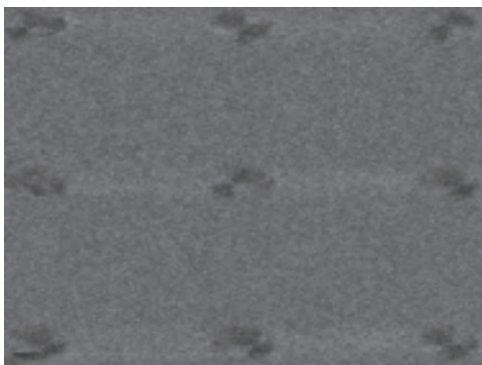
1. Institute of Experimental Physics, Universität des Saarlandes, Saarbrücken, Germany; 2. Institute of Experimental Physics, Martin-Luther-Universität Halle-Wittenberg, Halle, Germany; 3. Department of Physics, Universität Bielefeld, Bielefeld, Germany

Spintronic radiofrequency (rf) emitters and diodes are an interesting class of potential future low-power and nano-sized devices for information technology, energy harvesting, neuromorphic computing and sensor types based on rf circuitry operation and detection [1-3]. In case of pillar-structured spin-torque oscillators/diodes exhibiting a magnetic vortex structure in the free layer, it is known that the emission frequency and quality factor both strongly depend on an external biasing field [4]. For commercialization of spintronic rf devices an operation and performance unimpaired by varying and fluctuating external fields, like the earth magnetic field or field of nearby current lines, is required. We have simulated and experimentally validated several material and geometrical designs enabling a magnetic shielding of such devices in small external in-plane fields up to 100 Oe. Micromagnetic simulations were carried out within the MUMAX framework [5]. The micromagnetic design yields nearly zero variation of the effective field at the pillar exhibiting a vortex structure within a varying external field. The micromagnetically validated design was fabricated by means of common micro- and nanofabrication techniques and by sputtering magnetic layers beyond their critical thickness. The latter enforces stripe domains and a strong anisotropy perpendicular to the thin-film plane of the free layer of the MTJ-pillar and to the external fields. Magnetic force microscopy (MFM) within an external field was employed to investigate the stability of the vortex in the presence of the surrounding shielding structures and to compare the experimental results with the micromagnetic simulations. This work was supported by the German Federal Ministry of Education and Research (BMBF) under grant number 16ES1081K.

[1] Tsunegi, S., Yakushiji, K., Fukushima, *Applied Physics Letters*, 109(25), 252402 (2016) [2] Zhang, L., Fang, B., Cai, *Applied Physics Letters*, 113(10), 102401 (2018) [3] Marković, D., Leroux, N., Mizrahi, *Physical Review Applied*, 13(4), 0442011..2012 (2020) [4] Würft, T., Raberg, W., Prügl, *Applied Physics Letters*, 115(13), 132407 (2019) [5] Vansteenkiste, A., Leliaert, J., Dvornik, *AIP advances*, 4(10), 107133 (2014)



Phase contrast image recorded by MFM of a potential microfabricated magnetic shielding structure with strong perpendicular anisotropy showing stripe domains. The NiFe structure was deposited by sputtering, has a thickness of 300nm well above its critical thickness and can shield several 100 of Oe in-plane and parallel to the free layer of the MTJ before being saturated.



Phase contrast image recorded by MFM of an array of 3x3 MTJ-pillars with a 1400x700nm geometry within zero external field showing mostly a single-vortex domain structure in the top NiFe free layer. The MTJ layer stack consists of the following materials (thickness in nm): Ta5Ru30Ta10Ru5MnIr12CoFe3Ru0.92CoFeB3MgO1.2CoFeB3Ta0.4NiFe30Ta3Ru3

ER-12. Simultaneous Evaluation of Permeability and Permittivity Using a Flexible Microstrip Line-Type Probe up to 67 GHz.

S. Yabukami¹, K. Nozawa¹, C. Iwasaki¹, S. Takahashi¹, K. Okita¹, M. Sato¹ and S. Sugimoto¹

¹ Tohoku University, Sendai, Japan

I INTRODUCTION High frequency permeability and permittivity measurement of electromagnetic material is important for radio wave absorber, noise suppressor and electromagnetic shielding materials of 5th generation or 6th generation. Usually, in order to measure the magnetic permeability and the permittivity simultaneously, the sample had to be processed into a solenoid [1]. Further, when the permittivity and the magnetic permeability are separately measured, it is necessary to process the sample into a thin shape or a needle shape, and the method using the waveguide has problems such as discontinuous frequency. In our previous work, we developed a flexible microstrip line-type probe, and presented broad bandwidth permeability measurements of magnetic thin films [2]. However application of strong DC magnetic field (about 2 T) did not completely saturate samples in calibration, so remnant ferromagnetic resonance over several 10 GHz limited the upper frequency range. In the present study, we have developed a new calibration method that estimates the state of infinite magnetic field application by changing the DC magnetic field step by step, and realized accurate evaluation at 30 GHz or higher. The probe is applied to the simultaneous evaluation of permeability and permittivity of electromagnetic materials without restriction on sample size. **II EXPERIMENTAL PROCEDURE** Fig. 1 shows the schematic view of the microstrip line type probe [2], which is composed of a wrap-around microstrip conductor (10 mm in length, 0.36 mm in width) on a flexible substrate (130 μm in thickness, $\epsilon_r = 2.3$), a ground plane, lead lines, and two connectors. The microstrip line sloped to meet the lead line at either end, and had slopes to maintain a characteristic impedance of around 50 Ω and to allow close contact of a large samples with the probe. An electromagnetic material was in contact with the microstrip conductor via a PET film or directly. In permeability and permittivity measurement, firstly, S_{21} is calibrated without sample. Secondly, the DC magnetic field was increased to 20 kOe in 2 kOe increments, S_{21} was measured. Then $S_{21}^{(\text{sat})}$ under an infinite magnetic field was estimated by exponential approximation. This method can separate magnetic signal from nonmagnetic signal, and can remove the effect of remnant ferromagnetic resonance under finite strong field. Thirdly, $S_{21}^{(\text{sample})}$ is measured by removing the strong dc field, and then the complex permeability is optimized by $S_{21}^{(\text{sample})} - S_{21}^{(\text{sat})}$ using FEM analysis (magnetic field calculation) [2]. Then the complex permittivity also optimized by $S_{21}^{(\text{sat})}$ using FEM analysis (electric field calculation), because magnetic signal was removed in $S_{21}^{(\text{sat})}$, therefore dielectric signal mainly can be obtained. **III Experimental results** Fig. 2 shows the real part of permeability of Fe-Fe₃O₄ in polymer (10 mm x 10 mm, 0.1 mm in thickness)[3] to demonstrate permeability measurement up to 67 GHz when the DC field was changed. Ferromagnetic resonance frequency increased and the permeability decreased as DC field increased, which was reasonable frequency characteristics. The relative permittivity also shows in Fig. 2. The real part of permittivity was about 12 in lower frequency, the absolute value comes from that of the polymer. It was reasonable that the imaginary part of permittivity was negligible small.

[1] <https://www.keysight.com/jp/ja/assets/7018-03896/brochures/5991-2171.pdf> [2] S. Yabukami et al., *IEEE Trans. Magn.* Vol. 56 (2020). [3] M. Sato et al., *Autumn Meeting of the Japan Society of Powder and Powder Metallurgy*, 1-49A(V) (2020).

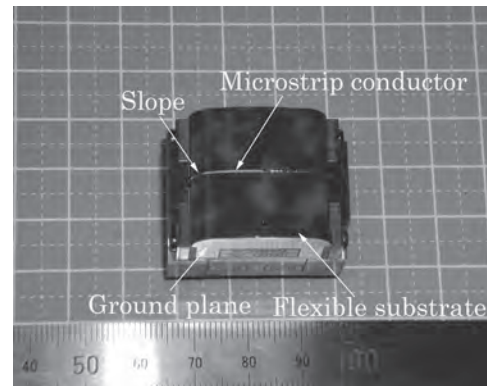


Fig. 1 Schematic view of the probe.

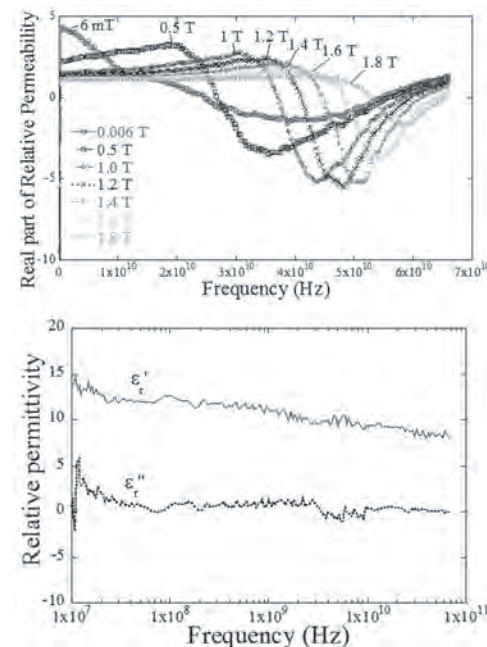


Fig.2 The real part of permeability and permittivity of Fe-Fe₃O₄ in polymer.

ER-13. Experimental Study of Microwave Magnetic Properties of Composites Under Magnetic Bias.

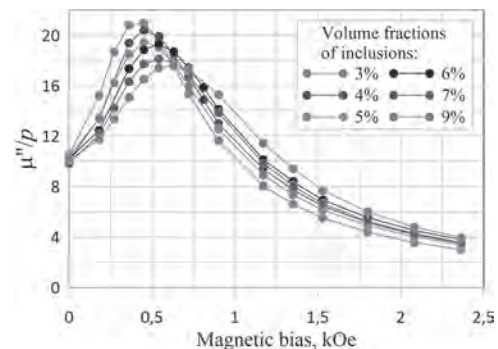
A. Shiryaev¹, K. Rozanov¹, A. Artemova¹, S. Bobrovskii¹, A. Naboko¹, A. Osipov¹, D. Petrov¹ and P. Zezulina¹

1. Institute for Theoretical and Applied Electromagnetics RAS, Moscow, Russian Federation

Composites filled with ferromagnetic inclusions possess a combination of promising magnetic, electrical and mechanical properties. High-frequency magnetic properties of the composites are useful in development of radar absorbers, microwave devices, etc. The effective permeability is a complicated function of frequency, the microstructure of the composite, and the properties of its constituents. Reliable techniques for determining of physical mechanisms resulting in the appearance of magnetic loss peaks at high frequencies are not found in the archived literature. A useful technique for studying microwave magnetic properties involves coaxial measurements of frequency dependence of complex permeability under external magnetic bias [1]. The calibration techniques for the coaxial line have been well established, and an accurate permeability measurement is available in the frequency range of 100 MHz to 20 GHz. The measuring coaxial cell is placed inside a coil that creates magnetic bias parallel to the coaxial axis. Making the measurement under various permanent magnetic fields gives an opportunity for comparing the magnetic characteristics of a sample in both the demagnetized and magnetized states and for determining the physical mechanisms responsible for different peaks of magnetic loss. These data may be of importance for understanding the magnetic structure and dynamic magnetic properties of tiny magnetic particles. The reported research focuses on the intrinsic permeability of magnetic powder particles under external permanent magnetic field. First, the intrinsic permeability of the particle is retrieved with a mixing rule. We selected composites whose permeability satisfies the simplest one, the Wiener mixing rule [2]. According to this mixing rule, the intrinsic permeability is equal to the effective permeability of the composite normalized to the volume fraction of inclusions. The samples under study are composites with a paraffin wax matrix filled with flake-shaped sendust particles [3]. The microwave material parameters of the samples with different fraction of inclusions are measured in a 7/3 coaxial line under external magnetic field up to 2400 Oe. The figure shows measured magnetic loss that is normalized to the volume fraction of inclusions and plotted against the external field at the fixed frequency of 5 GHz. The data for different volume fractions of inclusions are shown by different colors. When the external magnetic bias is nil, normalized loss is the same for different fractions and, therefore, the effective permeability of the composites obeys the Wiener mixing rule. However, an increase in the external field leads to a divergence of the curves. This divergence cannot be eliminated by accounting for the demagnetization on the measured sample. Therefore, the Wiener mixing rule is not valid for the permeability measured under external magnetic field. To search for the reasons of the invalidity of the mixing rule in the external field and to determine the physical mechanisms leading to the appearance of magnetic loss, the measured dependences are fitted by the Lorentzian dispersion law [2] including two Lorentzian terms. The low-frequency Lorentzian peak have a similar behavior for all volume fractions of inclusions in the composites. Namely, an increase in the external field leads to a decrease in the amplitude of the peak, with the frequency of the magnetic loss peak remaining almost unchanged. The high-frequency peak is found only in the presence of an external field. Its amplitude increases up to fields of several hundred Oersteds, then decreases. The relaxation and resonant frequencies of this peak rise with an increase in magnetic bias. It is suggested that this behavior can be attributed to the presence of a domain structure in the powder particles. An increase in the external field leads to a decrease in the amount of different domains in a particle and the amplitude of the main peak decreases with no frequency shift. The presence of a domain structure neutralized the interaction between closely spaced particles and the resonant frequencies are the same for different fraction of inclusions. The Wiener mixing rule is valid for such peaks. Under external bias, the domain structure vanishes that increases the contribution to magnetic loss from the ferromagnetic resonance (FMR), which is responsible for the second peak. In this case, the interaction occurs between the particles and the peak associated with the FMR should be described by other mixing rules. Thus, we propose

a technique for determining the physical mechanisms leading to the appearance of loss peaks. The technique consists in analysis of the data on microwave permeability obtained under external magnetic field. It is shown that the mixing rule, which correctly retrieves the intrinsic permeability in the absence of the external field, is not valid under magnetic bias. Based on the measured data, the physical mechanisms leading to the appearance of loss peaks are determined, and the invalidity of mixing rules under magnetic bias is explained. It is shown that the main peak of magnetic loss is attributed to the presence of domain structure in the particles. An increase in the external field leads to an increase in the FMR contribution to magnetic loss, which may obey other mixing rules. Funding: The reported study was funded by RFBR, project number 19-32-90165.

[1] A.O. Shiryaev, S.Y. Bobrovskii, etc., *J. Magn. Magn. Mater.*, Vol. 477, p.329 (2019) [2] K.N. Rozanov and M.Y. Koledintseva, *J. Appl. Phys.*, Vol. 119, p. 073901 (2016) [3] S.N. Starostenko, K.N. Rozanov, etc., *J. Appl. Phys.*, Vol. 121, p. 245107 (2017)



The measured dependence of the normalized magnetic loss on the external field at the fixed frequency of 5 GHz.

Session FA
TERAHERTZ SPINTRONICS

Alina Deac, Co-Chair
Helmholtz-Zentrum Dresden-Rossendorf, Dresden, Germany
Paul Nutter, Co-Chair
Manchester University, Manchester, United Kingdom

INVITED PAPERS

FA-01. Probing and Driving Ultrafast Spin Transport With Terahertz Electromagnetic Pulses.

T. Kampfrath^{1,2}

1. Department of Physics, Freie Universität Berlin, Berlin, Germany;

2. Department of Physical Chemistry, Fritz-Haber-Institut der Max-Planck-Gesellschaft, Berlin, Germany

To take advantage of the electron spin in future electronics, spin angular momentum needs to be transferred and detected. Heat gradients and electric fields have been shown to efficiently drive spin transport at megahertz and gigahertz frequencies. However, to probe the initial elementary steps that lead to the formation of spin currents, one needs to launch and measure transport on femtosecond time scales. To achieve this goal, we transfer spintronic concepts to the terahertz frequency range by employing both ultrashort optical and terahertz electromagnetic pulses [1]. This experimental strategy provides new insights into central transport phenomena, for instance the spin Seebeck effect [2], the anomalous Hall effect [3] and anisotropic magnetoresistance [4]. Interesting applications such as the efficient generation of ultrashort terahertz electromagnetic pulses [5] and the high-throughput characterization of spin-to-charge conversion in the bulk [6] and at interfaces [7] of spintronic structures emerge.

[1] E.Y. Vedmedenko et al., *The 2020 Magnetism Roadmap*, J. Phys. D: Appl. Phys. 53, 453001 (2020) [2] T.S. Seifert et al., *Femtosecond formation dynamics of the spin Seebeck effect revealed by terahertz spectroscopy*, Nature Commun. 9, Article number: 2899 (2018) [3] T.S. Seifert et al., *Frequency-independent terahertz anomalous Hall effect in DyCo₅, Co₃₂Fe₆₈ and Gd₂₇Fe₇₃ thin films from DC to 40 THz*, Advanced Materials (accepted) (2021) [4] L. Nadvornik et al., *Terahertz anisotropic magnetoresistance reveals strong intrinsic contributions*, arXiv:2010.06280 (2021) [5] J.A. Fülöp et al., *Review: Laser-Driven Strong-Field Terahertz Sources and their Novel Applications*, Adv. Opt. Mat. 1900681 (2019) [6] M. Meinert et al., *High-throughput techniques for measuring the spin Hall effect*, Phys. Rev. Applied 14, 064011 (2020) [7] O. Gueckstock et al., *Terahertz spin-to-charge conversion by interfacial skew scattering in metallic bilayers*, Advanced Materials (accepted) (2021)

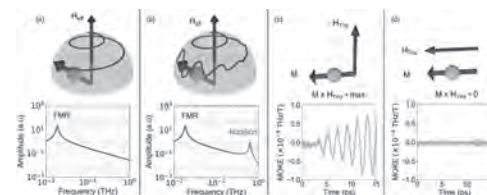
FA-02. Inertial Spin Dynamics in Ferromagnets.

S. Bonetti^{1,2}

1. Stockholms Universitet, Stockholm, Sweden; 2. Universita Ca' Foscari, Venezia, Italy

The vast majority of digital information worldwide is stored in the form of tiny magnetic bits in thin-film materials in the hard-disk drives installed in large-scale data centres. The positions of the north and south magnetic poles with respect to the thin-film plane encodes the logical 'ones' and 'zeros', which are written using strongly localized, intense magnetic fields. The dynamics of the magnetization in the writing process is described by the Landau–Lifshitz–Gilbert (LLG) equation, which correctly models the reversal of a magnetic bit at nanosecond timescales. Until 20 years ago, it was believed that all of the relevant physics of magnetization dynamics could be based solely on it. However, the pioneering experiment of Bigot et al. in 1996 [1] revealed the occurrence of spin dynamics on subpicosecond scales that could not be described by the LLG equation, giving birth to the field of ultrafast magnetism. This field explores some of the currently most investigated and debated topics in condensed matter physics [2], with implications for both our fundamental understanding of magnetism as well as possible applications for faster and more energy-efficient data manipulation. Recently, the LLG equation was reformulated to include a term to obtain a physically correct inertial response [3], which was not present in the original formulation. This term predicts the appearance of spin nutations, similar to the ones of a spinning top, at a frequency much higher (in the terahertz range) than the spin precession described by the conventional LLG equation (typically at gigahertz frequencies), as shown schematically in Fig. 1a,b. However, the lack of intense magnetic field sources at these high frequencies has hampered the experimental observation of such nutation dynamics. In this work, we use intense narrowband terahertz magnetic field transients from a superradiant terahertz source and the femtosecond magneto-optical Kerr effect (MOKE) to detect inertial magnetization effects in ferromagnetic thin films. We find evidence for nutation dynamics with a characteristic frequency of the order of 1 THz, which is damped on timescales of the order of 10 ps. We are able to qualitatively describe the observed magnetization dynamics with a macrospin approximation of the inertial LLG equation and highlight implications for ultrafast magnetism, and magnetic data processing and storage. The basic idea is to perform a forced oscillator experiment as a function of the frequency of the terahertz magnetic field H_{THz} , detecting the amplitude and phase of the response with the femtosecond MOKE in an attempt to observe the signature of a resonance. The response of the magnetization is maximized when H_{THz} and the static magnetization (which is controlled with an external magnetic field) are orthogonal to each other. This is illustrated schematically in the top panels of Fig. 1c,d, with the corresponding experimental measurement in the bottom panels, where we show the detected polar MOKE signal. In this talk, we will present direct experimental evidence of intrinsic inertial spin dynamics in ferromagnetic thin films in the form of a nutation of the magnetization at a frequency of the order of 0.5 THz. This allows us to reveal that the angular momentum relaxation time in ferromagnets is on the order of 10 ps. We anticipate that our results will allow for a better understanding of the fundamental mechanisms of ultrafast demagnetization and reversal, with implications for the realization of faster and more efficient magnetic data-processing and storage devices.

[1] Beaurepaire, E., Merle, J.-C., Daunois, A. & Bigot, J.-Y., *Phys. Rev. Lett.* 76, 4250–4253 (1996). [2] Kirilyuk, A., Kimel, A. V. & Rasing, T., *Rev. Mod. Phys.* 82, 2731–2784 (2010). [3] Ciornei, M.-C., Rubi, J. M. & Wegrowe, *Phys. Rev. B* 83, 020410 (2011).



a) Top: schematic of the magnetization dynamics and relaxation around an effective magnetic field H according to the standard LLG equation. Bottom: LLG-simulated response of a ferromagnetic system to an external a.c. magnetic field of varying frequency. b) Similar to a) but considering the inertial formulation of the LLG equation described in the text. c) Top: the geometrical configuration that maximizes the torque of H_{THz} on the magnetization M (that is, when they are orthogonal). Bottom: measured response from the polycrystalline NiFe sample in the maximum torque configuration and with a driving field centred at around 0.6 THz. d) Similar to c) but when H_{THz} and M are parallel; no torque is exerted on the same sample by the same driving field.

FA-03. Terahertz Spin-Charge Conversion in Magnetic Single and Multiple Layers.

Y. Wu¹, Q. Zhang^{1,2}, Z. Chen² and X. Zhang²

1. Department of Electrical and Computer Engineering, National University of Singapore, Singapore; 2. Department of Electrical & Electronic Engineering, Southern University of Science and Technology, Shenzhen, China

I. INTRODUCTION Femtosecond laser pumping provides a convenient way to generate transient spin or spin-polarized current from ferro-/ferri-/antiferromagnetic materials in the picosecond regime. The subsequent conversion of the transient spin current to charge current gives rise to terahertz (THz) emission. Several spin-to-charge current conversion mechanisms have been proposed to account for the experimental observations which include but are not limited to inverse spin Hall effect (ISHE),^{1,2} inverse Rashba-Edelstein effect (IREE),^{3,4} and anomalous Hall effect (AHE).^{5,6} Since the pioneering work of Kampfrath et al.,¹ many studies have been conducted to enhance the THz emission efficiency through both materials and structure engineering, which have led to the realization of broadband THz sources with magnetically controllable polarization and an efficiency comparable to that of ZnTe-based emitters. Here, we report our recent studies of THz emission based mainly on AHE from different types of structures including single ferromagnetic (FM) layers with both uniform and graded magnetization and synthetic antiferromagnet (SAF). We will also discuss THz emission from multilayers involving AFMs such as Mn₃Sn. II. RESULTS AND DISCUSSION Figure 1 shows the schematics of structures investigated: (a) single FM layer with uniform magnetization, (b) and (c) single FM layer with magnetization gradient, and (d) SAF. Also shown in the figure are magnetization distributions of the four types of structures. We chose (Fe_xMn_{1-x})_yPt_{1-y} as the FM layer as it exhibits much larger AHE as compared to CoFeB or NiFe. In addition, its magnetization can be tailored by varying the Pt composition via co-sputtering of Fe_{0.8}Mn_{0.2} and Pt targets. By setting the Fe₈₀Mn₂₀ and Pt cathode power at 50 W and 15 W, respectively, we obtained (Fe_{0.8}Mn_{0.2})_{0.67}Pt_{0.33} (hereafter FeMnPt) films with $\theta_{AHE} = 0.0269$. An increase of Pt power leads to a decrease of FeMnPt magnetization, and therefore, a magnetization gradient can be readily introduced in the thickness direction by varying the Pt sputtering power. Figure 2a shows the intensity of THz emission from a 9 nm single layer FeMnPt film. The polarization direction changes sign when either the pumping direction or magnetization direction is flipped, suggesting that the emission mechanism is similar to that of FM/heavy metal bilayer emitter, though there is no heavy metal involved in the present case. As illustrated in Fig. 1, when the laser-excited super-diffusive electrons reach the top and bottom surfaces of FeMnPt, they will be reflected back at the two respective interfaces, one with the MgO capping layer and the other with the quartz substrate. The difference in reflectivity between the two interfaces leads to a net spin polarized current $j_1 = j_{11} - j_{12}$ flowing in the thickness direction; the subsequent conversion of j_1 to a transverse charge current via AHE gives rise to the THz emission. As the intensity of THz emission is proportional to $\theta_{AHE} m \times j_1$ with m the magnetization direction and θ_{AHE} the AHE angle, there are two possible ways to enhance the emission efficiency, one is to reduce the magnetization near one of the interfaces as much as possible, and the other is to make the magnetization near the two interfaces have opposite directions. The former can be achieved by introducing a magnetization gradient in the thickness direction and the latter can be realized in an SAF structure. The magnetization gradient introduces an additional contribution to the transverse charge current given by $\theta_{SHE} \sigma s \times \nabla(\mu_s/2e)$, where θ_{SHE} is the spin Hall angle, σ the conductivity, s the net spin polarization direction of non-equilibrium electrons and μ_s the spin chemical potential. Therefore, the magnetization gradient may either enhance or reduce the THz emission, depending on the sign of $\nabla(\mu_s)$ relative to j_1 . Figure 2b and 2c show the THz emission from 9 nm FeMnPt with the magnetization gradient profiles shown in Fig. 1b and 1c, respectively. The THz waveform in Fig. 2b exhibits the same polarity as that of the uniform film in Fig. 2a, but the peak-to-peak amplitude is increased by a factor of 5.4. This means that a positive Pt composition gradient helps to enhance the THz emission. On the other hand, the sample with a negative Pt gradient gives a much smaller THz signal with an opposite polarity. The ratio of the peak-to-peak amplitudes of the three samples is 1:5.4:-2.15. These results

demonstrate that the magnetization gradient is an effective knob to tune THz emission from single layer FM. On the other hand, Fig. 2d compares the THz emission from a FeMnPt(4 nm)/Ru(0.8 nm)/FeMnPt(4 nm) SAF (solid-line: 0 Oe; dashed-line: 200 Oe) with that of a 5 nm single layer FeMnPt (dotted-line). As expected, the THz emission of SAF at zero field is almost twice of that of the single layer sample, whereas its amplitude at 200 Oe, i.e., when the two magnetizations are aligned in the same direction, is the smallest among the three peaks. Detailed field-dependent measurements of the THz polarization showed that the THz emitter is a powerful tool to probe the magnetization states of SAF subjected to an external field. In addition to FM, we have also investigated THz emission from AFM with large AHE such as Mn₃Sn. Our preliminary results showed that there is negligible THz emission from Mn₃Sn.

- [1] T. Kampfrath et al., Nat. Nanotech. 8, 256 (2013). [2] T. Seifert et al., Nat. Photonics. 10, 483 (2016). [3] M. B. Jungfleisch et al., Phys. Rev. Lett. 120, 207207 (2018). [4] C. Zhou et al., Phys. Rev. Lett. 121, 086801 (2018). [5] Q. Zhang et al., Phys. Rev. Appl. 12, 054027 (2019). [6] Q. Zhang et al. Phys. Rev. Appl. 13, 054016 (2020).

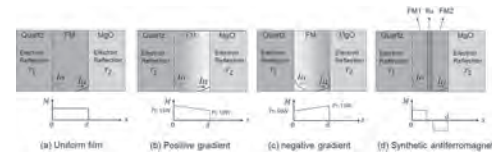


FIG.1 Schematic sample structure and the corresponding magnetization profile.

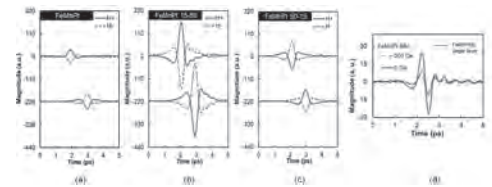


FIG.2 (a)-(c) THz emission from samples corresponding to Fig. 1(a)-(c), respectively. (d) Comparison of THz emission from single layer FM and SAF.

FA-04. Controlling Antiferromagnetic Resonances.

T. Moriyama¹

1. Institute for Chemical Research, Kyoto University, Uji, Japan

In antiferromagnetic spintronics where manipulation of the antiferromagnetic spins is a central technological challenge[1], it is important to understand the dynamic properties, especially their THz spin dynamics and the magnetic damping. While both experimental and theoretical investigations of the antiferromagnetic resonance began in 1950s[2], they have been recently revisited with more advanced experimental techniques [3,4] as well as with more rigorous theoretical treatments[5] in the context of emerging antiferromagnetic spintronics. In the early stage of the investigations, the state-of-art spectroscopy with a rather inefficient and weak far-infrared source[1] was employed to investigate various antiferromagnets, such as NiO, CoO, MnO, and Cr₂O₃. Although their high resonant frequencies have been experimentally confirmed, the experimental technique at the time was not sufficiently sensitive to withstand detail analyses of the spin dynamics and the magnetic damping. However, thanks to the recent development of the THz technologies, frequency-domain THz spectroscopies with much better sensitivity than before has now become accessible and affordable for investigating in more detail the spin dynamics in antiferromagnets. In this work, a frequency domain continuous wave THz spectroscopy system capable of scanning up to $\omega = 2$ THz with the frequency resolution <10 MHz is employed to investigate the antiferromagnetic resonances. NiO-based materials are used to demonstrate controllability of the antiferromagnetic resonance properties, such as resonance frequency and linewidth, or Q-factor. First, we investigated temperature dependence of antiferromagnetic resonance and the damping in poly- and mono-crystalline NiO. The resonant frequency (~ 1 THz at room temperature) was found to decrease with increasing temperature, which was nicely explained by the temperature dependence of the anisotropy with a power of the sublattice magnetization with the exponent $n = 0.72$. We also found the damping parameters to be $\alpha = 5.0 \pm 0.4 \times 10^{-4}$ and $7.4 \pm 0.4 \times 10^{-4}$ for the mono- and poly-crystalline samples, respectively. The remarkable difference in α depending on the crystallinity manifests the significance of the extrinsic damping in antiferromagnet[6]. Second, we investigated the antiferromagnetic resonance in the cation-substituted NiO of Ni_{1-x}M_xO (M = Mn, Li, or Mg). We show the wide range tunability of the resonant frequency as well as the Q-factor by the magnetic doping (Mn²⁺ substitute), the non-magnetic doping (Mg²⁺ substitute), and the hole doping (Li⁺ substitute). We discuss the trends of how those different doping impact the antiferromagnetic resonance properties, which will be appreciated as a design guideline for THz materials adapting to various types of applications such as THz microwave absorbers and filters where the control of resonant frequency and Q-factor is important[7]. Lastly, we investigated the spin pumping enhanced antiferromagnetic damping in the (NiO)_{1-x}HM_x (HM = Pt and Pd) granular systems (Fig. 1 (a)). The spin pumping effect due to antiferromagnetic dynamics at the THz frequency was quantitatively elucidated by characterizing the linewidth $\Delta\omega$ of the (NiO)_{1-x}HM_x granular systems as a function of x (Fig. 1(b) and (c)). The mixing conductance of the NiO/Pt and NiO/Pd interface was found to be $g_{\uparrow\downarrow} = 12 \text{ nm}^{-2}$ and 5 nm^{-2} , respectively. Our experimental results resolved the missing part of the spin interaction physics in antiferromagnets at THz, *i.e.* the spin pumping effect. The experimental manifestation of the value of $g_{\uparrow\downarrow}$ helps understanding various spin current transfer phenomena with antiferromagnets, and would further motivate and promote the antiferromagnetic spintronics[8]. In summary, we explored frequency-domain THz spectroscopies of antiferromagnetic NiO and showed detail quantitative analysis of the antiferromagnetic damping, observation of the THz spin pumping effect in NiO/Pt and NiO/Pd and determination of the spin mixing conductance, and control of the antiferromagnetic resonance properties by various cation substitutions of NiO. These results are important milestone for future THz antiferromagnetic spintronics This work was supported in part by JSPS KAKENHI Grant Numbers 17H04924, 15H05702, 17H04795, 17H05181 (“Nano Spin Conversion Science”), by the Collaborative Research Program of Institute for Chemical Research, Kyoto University (grant # 2018-61 and 2019-87), and by the U.S. Department of Energy, Office of Basic Energy Sciences, Division of Materials Science and Engineering under Award No. DE-SC0012190.

[1] V. Baltz et al., *Rev. Mod. Phys.* 90, 015005 (2018). [2] L. R. Maxwell et al., *Rev. Mod. Phys.* 25, 279 (1953). [3] T. Kampfrath et al., *Nat. Photon.* 5, 31 (2011). [4] T. Satoh et al., *Phys. Rev. Lett.* 105, 77402 (2010). [5] A. Kamra et al., *Phys. Rev. B* 98, 184402 (2018). [6] T. Moriyama et al., *Phys. Rev. Mater.* 3, 051402 (2019). [7] T. Moriyama et al., *Phys. Rev. B* 101, 060402 (2020). [8] T. Moriyama et al., *Phys. Rev. Mater.* 4, 074402 (2020).

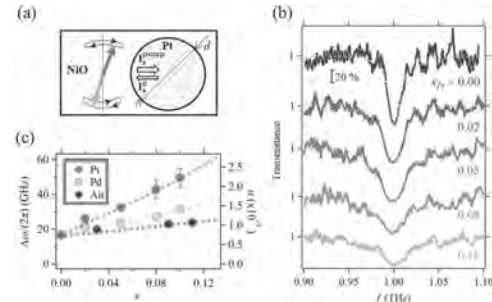


Fig. 1 (a) Schematic illustration of the spin pumping effect with NiO/HM (HM = Pt, Pd) granular system (b) Transmission spectra for (NiO)_{1-x}Pt_x (c) Composition dependence of $\Delta\omega$.

FA-05. Ferrimagnetic Thin Films Systems for Spintronic THz Emitters.

M. Fix², R. Schneider¹, J. Bensmann¹, S. Michaelis De Vasconcellos¹,
R. Bratschitsch¹ and M. Albrecht²

1. *Westfälische Wilhelms-Universität Münster, Münster, Germany;*

2. *Universität Augsburg, Augsburg, Germany*

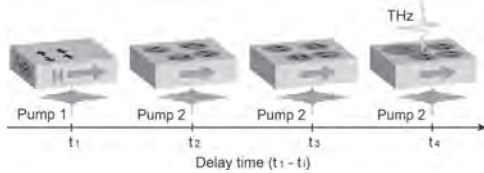
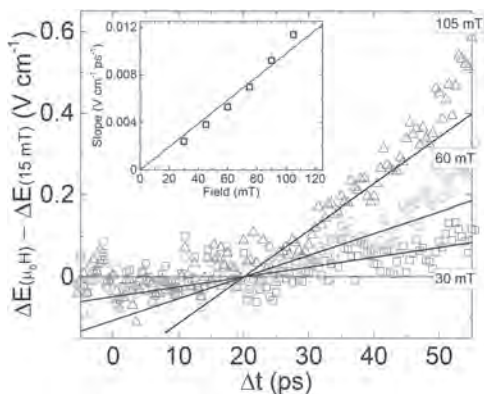
THz radiation in the frequency range from 0.3 to 30 THz bridges the gap between electronic and optical frequencies. It has been used for probing and driving fundamental resonances in gaseous, liquid, and solid materials. However, it is still challenging to generate broadband THz radiation with sufficient power in a convenient way. Recently, a new type of THz emitter has been discovered, which is based on the inverse spin Hall effect [1, 2]. These “spintronic” THz emitters typically consist of ferromagnetic (FM)/nonmagnetic metal bilayers, which are easy to prepare. In previous studies we have shown that bilayers consisting of ferrimagnetic (FI) Tb(Gd)-Fe alloys can be utilized as well as efficient spintronic THz emitters [3,4]. We find that the THz emission amplitude closely follows the in-plane magnetization of the Fe sublattice. In a further study, we have utilized the magnetic compensation temperature of a FI layer to control the THz emission solely by temperature [5]. This is enabled by coupling two ferrimagnetic layers and depending on the relative alignment of the Fe moments in the two layers, the spintronic emitter system can be either in a high- or in a low-amplitude terahertz emitting state. This approach was extended to spin valve systems with a pinned and a free FM Fe layer, decoupled from each other by either a W or a Pt layer. In this case the THz emission amplitude can be controlled by small external magnetic fields [6] and allows for fast switching, which opens a new route for a controllable and efficient type of spintronic terahertz emitter system.

[1] T. Kampfrath *et al.*, Nature Nanotechnology 8, 256 (2013). [2] T. Seifert *et al.*, Nature Photonics 10, 483 (2016). [3] R. Schneider *et al.*, ACS Photonics 5, 3936 (2018). [4] R. Schneider *et al.*, Appl. Phys. Lett. 115, 152401 (2019). [5] M. Fix *et al.*, Appl. Phys. Lett. 116, 012402 (2020). [6] M. Fix *et al.*, Appl. Phys. Lett. 117, 132407 (2020).

FA-06. THz Spintronics of Antiferromagnetic FeRh/Pt.G. Li¹ and A. Kimmel¹*1. Radboud Universiteit, Nijmegen, Netherlands*

Understanding how fast short-range interactions build up long-range order is one of the most intriguing topics in condensed matter physics. FeRh is an example of a material for studying this problem in magnetism, where the microscopic spin-spin exchange interaction is ultimately responsible for either ferro- or antiferromagnetic macroscopic order. Femtosecond laser excitation of antiferromagnetic FeRh induces ferromagnetism and the dynamics of the emergent order on the characteristic time-scale of the exchange interaction has long been a topic of intense debates. The first-order magnetic phase transition in FeRh has attracted considerable attention in material science, magnetocalorics, magnetic recording and spintronics. Aiming to reveal femto-, pico and nanosecond kinetics of the emergent ferromagnetism in FeRh, we employed the concepts of spintronic THz emitter and THz emission spectroscopy. In particular, analyzing THz emission from a FeRh/Pt bilayer excited by a single laser pulse, we reveal the main spin-dependent sources of the laser-induced THz emission [1]. We argue that stroboscopic measurements of first-order phase transitions are hampered by thermodynamically allowed co-existence of two competing phases. In particular, the stroboscopic measurements of THz emission from FeRh may result in the absence of temperature hysteresis and domination of the measured signal not by laser-induced magnetization dynamics in the antiferromagnetic phase, but by the dynamics triggered in co-existing ferromagnetic nuclei. To minimize the influence of the latter we employed double-pump THz emission spectroscopy. We performed a systematic analysis of the emitted radiation from FeRh/Pt bilayer and revealed the experimental conditions for ultrafast magnetometry with the best signal-to-noise ratio. We show that although femtosecond laser pulse launches ultrafast spin dynamics in the antiferromagnet, nuclei generated by femtosecond laser pulse during the first 20 ps of their lifetime do not emit THz, insusceptible to the external magnetic field and, strictly speaking, have not established ferromagnetic spin order yet [2].

[1] R. Medapalli et al, Appl. Phys. Lett. 117, 142406 (2020). [2] G. Li et al, <https://arxiv.org/abs/2001.06799>.

**Principle of double-pump THz emission spectroscopy and its application to FeRh**

Double pump THz emission due to emerging ferromagnetism in antiferromagnetic FeRh/Pt. The solid lines are linear fits emphasizing a linear increase between 20 ps and 40 ps. The inset shows the magnetic field dependence of the slope of the linear fits.

Session FB

SPIN PUMPING, RESONANCE AND THZ DYNAMICS

Kyusup Lee, Co-Chair

National University of Singapore, Singapore

Raghav Sharma, Co-Chair

National University of Singapore, Singapore

INVITED PAPER

FB-01. Efficiency of THz Spintronic Emitters: From Spin-Hall Effect in 3d Metals to Surface States in Topological Insulators INVITED.

E. Rongione^{1,2}, L. Baringthon^{1,3}, J. Hawacker², T. Dang¹, P. Lefèvre³, N. Reyren¹, R. Lebrun¹, J. George¹, S. Dhillon² and H. Jaffrès¹
 1. *Unite Mixte de Physique CNRS/Thales, Palaiseau, France;*
 2. *Laboratoire de Physique de l'ENS, Paris, France;* 3. *Cassiopée beamline, Synchrotron SOLEIL, Saint-Aubin, France*

Abstract THz spintronics emitters represent today novel sources for broadband emission using nanometer-scaled materials. We present and model the THz spintronic emission based on the spin Hall effect in 3d metals and on the inverse Rashba-Edelstein effect in the optimized topological insulator $\text{Bi}_{1-x}\text{Sb}_x$. 1. Introduction Terahertz (THz) spintronic emitters are promising candidates for covering the so-called THz gap as they offer broadband emission going up to 30 THz [1]. Conventionally, they consist in nanometer-thin heterostructures composed by a ferromagnetic layer and a heavy metal from the 3d-5d family which, owing to their high spin-orbit coupling (SOC), allow spin-to-charge conversion (SCC) from a pure transient spin-current coming from the ferromagnetic layer into a transverse transient charge current. Efforts have been made recently to increase the output emission power of such devices by layer thickness engineering in order to optimize spin-to-charge interconversion and to reduce both THz absorption in metallic layers and spin current relaxation in thick ferromagnets. In this study, we evidence the processes timescales at stake in the emission properties of metallic THz spintronic emitters using Finite Domain Time Domain (FDTD) simulations. We evidence the main figure of merit which will permit to optimize the next generation of THz emitters. We then turn towards an alternative type of THz spintronic emitters based on topological insulators. We discuss the role of surface states in the conversion mechanisms and highlight promising THz emission in topological insulator $\text{Bi}_{1-x}\text{Sb}_x$. 2. Optimization of THz metallic spintronic emitters based on FDTD modelling Conventional THz spintronic emitters are based on ferromagnet/heavy metal heterostructures such as Co/Pt, W/CoFeB/Pt or Fe/Pt. Shining infrared femtosecond laser pulses on the heterostructure induces a transient spin current diffusing from the ferromagnet to the heavy metal. Through spin-to-charge conversion due to the inverse spin Hall effect (ISHE), a THz wave is generated. The direction of the THz emission depends on the direction of the magnetization: the polarization can thus be easily tuned by small external magnetic field. The amplitude of the THz emission depends strongly on the amplitude of the interconversion mechanism, which is related to skew-scattering and side-jump effects in heavy metals. In first approximation, the amplitude of the emission is thus given by the spin Hall angle $\theta_{\text{SHE}} = j_c/j_s$, ratio between the incoming spin current and the generated charge current given by $j_c \propto \theta_{\text{SHE}} (j_s \times \sigma)$ where σ is the spin accumulation orientation [2,3]. Here, we provide a comprehensive understanding of the THz emission processes using FDTD modelling, including spin-dependent timescales such as spin-flip rates in heterostructures. We obtain a good agreement between experiments obtained by THz time-domain spectroscopy (THz-TDS) and performed simulations as shown in Fig. 1. We also evidence the crucial role of the interface quality between the heavy metal and the ferromagnet, as spin backflow or interfacial spin-flip may decrease the conversion. We thus propose a figure of merit $\eta \propto g_{\uparrow\downarrow} \sigma_{\text{SHE}} l_{\text{sf}}^{\text{HM}}$ which defines the THz emission strength in metallic heterostructures. This product includes the spin-mixing conductance $g_{\uparrow\downarrow}$ illustrating interface quality, spin-Hall conductivity σ_{SHE} linked to interconversion strength and spin diffusion length in the conversion material $l_{\text{sf}}^{\text{HM}}$ proportional to spin-current relaxation. We believe that our results will help optimizing the next generation of THz spintronic emitters. 3. Towards surface-states mediated THz emission using topological insulators Alongside ISHE-based emitters, topological insulators (TI) are studied here as an alternative source for THz emitters. They present conductive surface-states which allow interfacial interconversion via inverse Rashba-Edelstein effect (IREE). In these systems, strong spin-to-charge conversion is expected owing to *i*) the Fermi velocity of interfacial carriers and *ii*) the insulating behaviour of the material bulk, reducing possible THz absorption in the heterostructure. Such

systems have been proven to show emission in the THz range, for example with topological insulator Bi_2Se_3 [4]. We report in Fig. 2 emission features from $\text{Bi}_{1-x}\text{Sb}_x/\text{Co}$ interface. Experimental data are taken with standard electro optic sampling (EOS) using ZnTe(111) 500 μm thickness. Emission performance of $\text{Bi}_{0.79}\text{Sb}_{0.21}(15)/\text{Co}(4)$ is about the same order of magnitude as Co(2)/Pt(4) single-ISHE conversion state-of-the-art emitter. As recovered on IREE-based emitter, THz emission phase is reversed as applied magnetic field direction is reversed. Topological insulators here illustrated by $\text{Bi}_{1-x}\text{Sb}_x$ are thus suitable candidates for strong output THz emitters.

[1] Seifert, T. et al., “Efficient metallic spintronic emitters of ultrabroadband terahertz radiation”, *Nature Photon* 10, 483–488 (2016). [2] Dang T. H., Rongione E. et al., “Ultrafast spin-currents and charge conversion at 3d-5d interfaces probed by time-domain terahertz spectroscopy”, *Appl. Phys. Rev.* 7 (2020) [3] Hawacker J., Rongione E. et al., “Correlation between spin-mixing-conductance, THz emission and spin-memory-loss at magnetic/heavy metal interfaces”, to be submitted [4] Wang, X. et al., “Ultrafast Spin-to-Charge Conversion at the Surface of Topological Insulator Thin Films”, *Adv. Mater.* 30, 1802356 (2018).

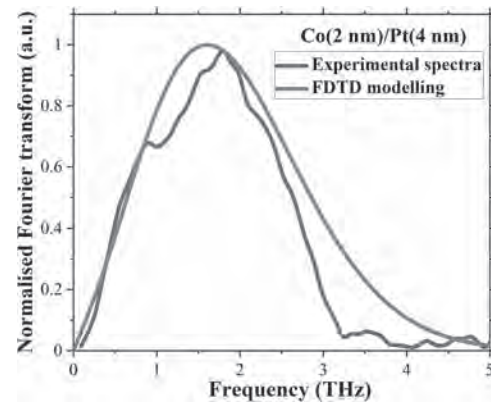


Fig. 1 – Comparison between experimental measurements (blue curve) and FDTD simulations (red curve) for Co(2)/Pt(4) metallic THz emitter considering an infrared excitation pulse duration about 100 fs.

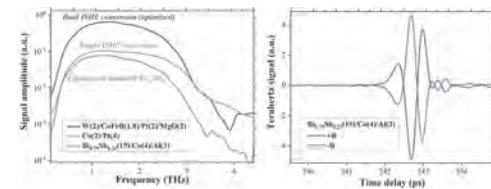


Fig. 2 – $\text{Bi}_{0.79}\text{Sb}_{0.21}/\text{Co}$ emission alongside metallic ISHE-based emitters for comparison (left). Magnetic field dependence of $\text{Bi}_{0.79}\text{Sb}_{0.21}/\text{Co}$ emission: phase reversal with field direction change proves magnetic origin of the emission (right). Thicknesses in brackets are given in nanometers.

CONTRIBUTED PAPERS

FB-02. Spin Pumping in Embedded Lateral Nanostructures in $\text{Fe}_{60}\text{Al}_{40}$.
*T. Strusch¹, R. Meckenstock¹, R. Bali², J. Ehrler², K. Potzger², K. Lenz²,
 J. Lindner², M. Farle¹ and A. Semisalova¹*

*1. Faculty of Physics, Universität Duisburg-Essen, Duisburg, Germany;
 2. Institute of Ion Beam Physics and Materials Research, Helmholtz-Zentrum Dresden-Rossendorf, Dresden, Germany*

We report on ferromagnetic resonance (FMR) detected spin pumping in $\text{Fe}_{60}\text{Al}_{40}/\text{Pd}$ and $\text{Py}/\text{Fe}_{60}\text{Al}_{40}$ bilayer and laterally patterned $\text{Fe}_{60}\text{Al}_{40}$ nanostructures. The magnetic properties of $\text{Fe}_{60}\text{Al}_{40}$ alloy are easily tailorable from paramagnetic to ferromagnetic state by variation of the structure through ion beam irradiation, making a promising material for the fabrication of magnetic landscapes and magnonic crystals [1,2]. Exploiting this easy tunability we show that $\text{Fe}_{60}\text{Al}_{40}$ can be used as well as spin source as spin sink in spin pumping experiments. Using the material with the identical chemical composition leads to a new pathway creating geometries for lateral spin pumping and might lead to an increase in efficiency in spin pumping as the writing of structures using ion beam irradiation allows to realize spin-based binary logic systems. Characteristic quantities to estimate the efficiency of spintronic systems are the spin mixing conductance and the spin diffusion length determined by thickness and frequency dependent FMR measurements [3]. Therefore, two sets of bilayer samples consisting of ferromagnetic (FM) and paramagnetic (PM) layers have been prepared, i.e. FM $\text{Fe}_{60}\text{Al}_{40}$ films of 5 nm thickness capped with Pd of varying thickness as well as Py of 5 nm thickness capped with PM $\text{Fe}_{60}\text{Al}_{40}$ of varying thickness. They were investigated using frequency dependent FMR measurements in a range of 2 to 35 GHz. The FMR linewidth and damping analysis reveal a spin mixing conductance of $g^{\uparrow\downarrow} = (2.092 \pm 0.046) \times 10^{18} \text{ m}^{-2}$ and a spin diffusion length of $\lambda_{\text{FeAl}} = 17.2 \pm 0.86 \text{ nm}$ (see Fig. 1) for paramagnetic $\text{Fe}_{60}\text{Al}_{40}$, and $g^{\uparrow\downarrow} = (4.454 \pm 0.0479) \times 10^{18} \text{ m}^{-2}$ and $\lambda_{\text{Pd}} = 8.513 \pm 1.631 \text{ nm}$ for Pd. Based on a result of the determined efficiency of $\text{Fe}_{60}\text{Al}_{40}$ used as spin source and spin sink, we investigate the spin pumping in laterally patterned $\text{Fe}_{60}\text{Al}_{40}$ nanostructures (see Fig. 2) representing 500 nm wide stripes of FM $\text{Fe}_{60}\text{Al}_{40}$ separated with PM $\text{Fe}_{60}\text{Al}_{40}$ stripes of different width (100-400 nm) produced in 40 nm thick film, which demonstrate a decrease of the damping parameter with increasing width of PM $\text{Fe}_{60}\text{Al}_{40}$ areas.

[1] D. Holzinger et al., J. Appl. Phys. 114, 013908(5) (2013). [2] B. Obry et al., Appl. Phys. Lett. 102, 202403 (2013). [3] J. M. Shaw et al., Phys. Rev. B 85, 054412 (2012)

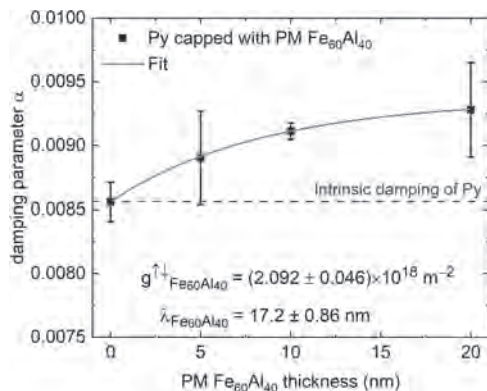


Fig.1: Extracted damping parameter in dependence of the paramagnetic FeAl-layer thickness. The solid red line indicates the fit for extracting the spin mixing conductance and the spin coherence length. The dashed blue line shows the intrinsic damping contribution of the Py thin film.

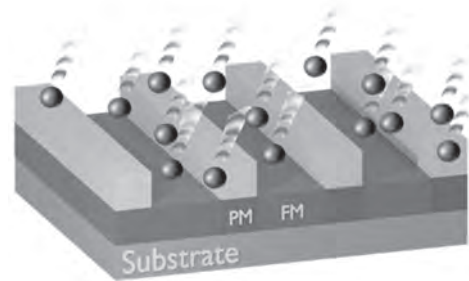


Fig.2: Ion irradiation with Ne^+ of the $\text{Fe}_{60}\text{Al}_{40}$ film with mask. The structural disordering occurs in the unmasked stripes, causing the transition from paramagnetic to ferromagnetic state.

FB-03. Spin Waves and Spin Pumping Driven by Cavity Confined Bulk Hypersonic Waves.

N. Polzikova¹, S. Alekseev¹, S. Dizhur^{1,2}, V. Luzanov³, A. Raevskiy³ and S. Nikitov^{1,2}

1. V. A. Kotelnikova Institute for Radiotechnology and Electronics, Russian Academy of Science, Moscow, Russian Federation; 2. Moscow Institute of Physics and Technology State University, Dolgoprudnyj, Russian Federation; 3. V. A. Kotelnikova Institute of Radiotechnology and Electronics, Russian Academy of Sciences, Fryazino, Russian Federation

In recent years, the magnon-phonon coupling in magnetostrictive materials has gained renewed interest due to emerging spintronic and magnonic applications, such as low power consumption microwave devices. Linear and parametric acoustically driven spin waves (ADSW) were studied in various hybrid magnon-phonon structures containing piezoelectric and ferro (ferri) magnetic layers [1-4]. Previously [5-7], we have demonstrated the piezoelectric excitation of linear and parametric ADSW in the gigahertz frequency range and their detection by the combination of spin pumping and inverse spin Hall effect (ISHE) in the spintronic hybrid High overtone Bulk Acoustic wave Resonator (HBAR) with the structure ZnO – YIG–GGG–YIG – Pt (Fig.1a). Here, the features of phonon-magnon interconversion in the phononic cavity mentioned above are studied in detail. The pump frequency f_p , power P , and magnetic field H dependences of the ISHE voltage U_{ISHE} as well as resonance frequencies f_n are experimentally and theoretically studied. As a result of magnetoelastic interaction, bulk acoustic waves (BAW) cavity modes excite magnons in the YIG films either at frequencies f_n or at half resonance frequencies (when the threshold power is exceeded). When specifying a certain frequency range, depending on the value of the applied magnetic field, either direct excitation of linear ADSWs or parametric excitation (in low magnetic fields) is observed. In the first case the important features of ADSW and acoustic spin pumping are determined by double resonance: the magnetoelastic (MER) in YIG films and BAW resonance of the entire resonator structure. Electrical detection of ADSWs occurs while simultaneously measuring the electrical response of the ZnO transducer and the dc voltage signal on the Pt stripe. The dependences of the resonance frequencies f_n and U_{ISHE} on the field H and the frequency f are correlated with each other (Fig. 1b). The fitting of the theoretical and experimental dependences allows us to determine a number of magnetic and magnetoelastic parameters of YIG and field dependencies of the resonance frequencies: magnetoelastic $f_{\text{MER}}(H)$ and ferromagnetic $f_{\text{FMR}}(H)$. For the frequency range around 2.4 GHz, the magnetic field corresponding to the ferromagnetic resonance is $f_{\text{FMR}} \approx 5340\text{Oe}$. In the second case when the field decreases below H_{FMR} , the HBAR spectrum f_n is practically independent of the magnetic field, but the clearly detectable voltage $U_{\text{ISHE}}(f, H)$ is significantly field dependent. The signal from the parametric ADSW was observed when: (i) the pump frequency coincided with one of the HBAR resonant frequencies, (ii) half of the pump frequency coincided with one of the spin wave frequencies for a given magnetic field (see Fig.2a), and (iii) the pump power exceeded a threshold, depending on the field (see Fig 2b). It can be seen from Fig. 2 the field of the maximum voltage is close to the critical field $H_c = 184\text{Oe}$, at which $f_{\text{FMR}}(H_c) = f_p/2$. It indicates that $U_{\text{ISHE}}(H_c)$ originates from the detection of parametric ADSW with wave number $q = 0$. The voltage signal is observed in the field range below 432 Oe. This field correlates with the value $H_{c1} = f_p/(2\gamma)$ in Fig. 2a. Above this field, the excitation of any parametric spin wave is impossible; therefore, the voltage signal is suppressed. But at the higher fields, the linear excitation of ADSW takes place at the H_{FMR} , at which $f_{\text{FMR}}(H_{\text{FMR}}) = f_p$. In Fig. 2, the field $H_{c2} = H_{c1}/2 = f_p/(4\gamma)$ corresponds to the upper limit on H for the possible decays of parametric magnons with the frequency $f_p/2$ into two secondary parametric ones at a frequency $f_p/4$. Measurements with a smaller field step show that, in some field ranges, the $U_{\text{ISHE}}(H)$ dependence has additional features, which can be explained by parametric excitation of various groups of magnons. For example, in a field near $H_{c3} = 100\text{Oe}$, the nonmonotonic behavior of the $U_{\text{ISHE}}(H)$ dependence is apparently due to the magnon confluence process, for which the condition $f_{\text{FMR}}(H_{c3}) = f_p/3$ is satisfied [8]. For certain ranges of fields and powers, the data of Fig. 2b can be fitted as $U_{\text{ISHE}}(P, H) \sim (P - P_{\text{th}}(H))^{1/2}$, where the fitting parameter $P_{\text{th}}(H) \approx 0.4\text{mW}$ can be interpreted as a threshold power. We explain the low threshold obtained by the high

efficiency of electric power transmission into the acoustic pump confined in the phononic cavity - high-Q hybrid HBAR. This work was carried out in the framework of the State task 0030-2019-0013 ‘‘Spintronics’’ and with partial support of the RFBR (Project No. 20-07-01075).

1. M. Weiler, H. Huebl and F. S. Goerg, Phys. Rev. Lett., Vol.108, p.176601 (2012). 2. P. Chowdhury, A. Jander and P. Dhagat, IEEE Magn. Lett., Vol. 8, p.1 (2017). 3. H. Keshtgar, M. Zareyan and G. E. Bauer, Solid State Commun., Vol.198, p.30 (2014). 4. I. Lisenkov, A. Jander and P. Dhagat, Phys. Rev. B., Vol.99, p.184433 (2019). 5. N. I. Polzikova, S. G. Alekseev, I. I. Pyataikin., AIP Adv., Vol.8, p.056128 (2018). 6. N. Polzikova, S. Alekseev, V. Luzanov, J. Magn. Mater., Vol. 479, p.38 (2019). 7. S. G. Alekseev, S. E. Dizhur and N. I. Polzikova, Appl. Phys. Lett., Vol.117, p.072408 (2020). 8. T. B. Noack, V. I. Vasyuchka and D. A. Bozhko, Phys. Stat. Sol. b, Vol.256, p.1900121(2019).

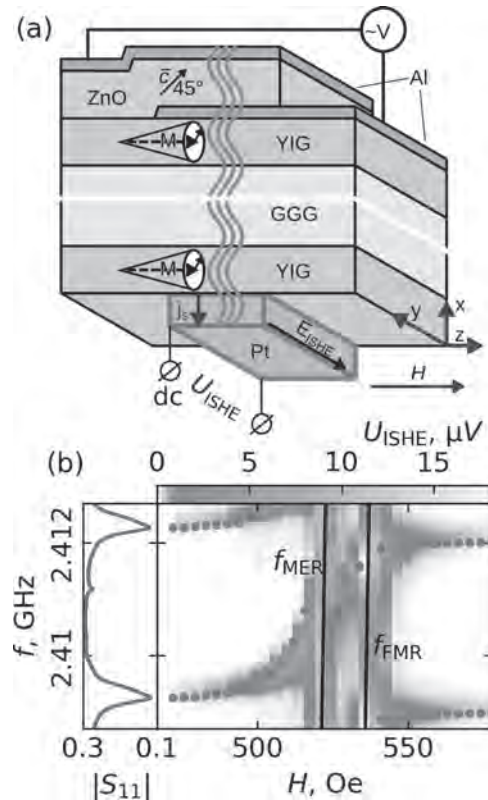


Fig.1 (a) Schematic of hybrid HBAR for ADSW excitation and acoustic spin pumping. The rf voltage V is applied across the piezoelectric transducer sandwiched between thin-film Al electrodes. The transducer launches and detects a bulk shear acoustic waves, which propagate vertically. **(b)** Left panel – the fragment of HBAR spectrum, containing two resonant frequencies f_n and f_{n-1} at zero magnetic field. Right panel – 3D colour plot $U_{\text{ISHE}}(f, H)$. The red points correspond to positions of HBAR resonant frequency f_n positions. The calculated frequencies $f_{\text{MER}}(H)$ and $f_{\text{FMR}}(H)$ are shown by black lines.

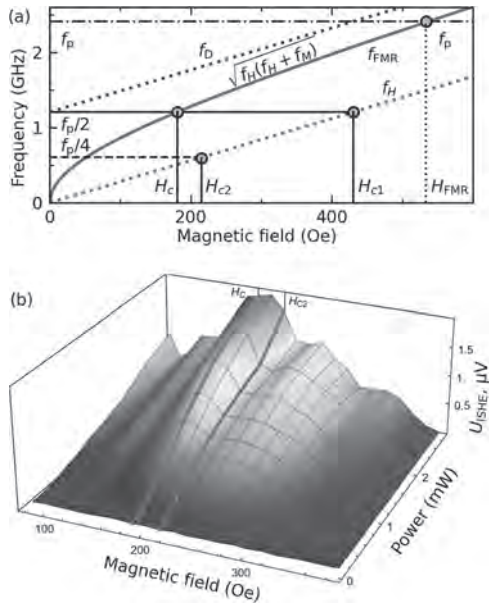


Fig. 2. (a) Dependences of spin wave frequencies at $q = 0$ on the magnetic field: $f = f_H(0)$ at $\theta=0$; $f = f_{FMR}$ at $\theta=90$ deg (θ is the angle between wave vector and magnetic field), $f_D = f_H(0) + f_M / 2$ - upper boundary of dipole (non-exchange) surface magnetostatic waves, $f_p = f_n = 2.412$ GHz. (b) 3D plot represents $U_{ISHE}(H, P)$ measured at $f_p = f_n = 2.412$ GHz. Red lines – power dependences $U_{ISHE}(H_c, P)$ and $U_{ISHE}(H_{c2}, P)$.

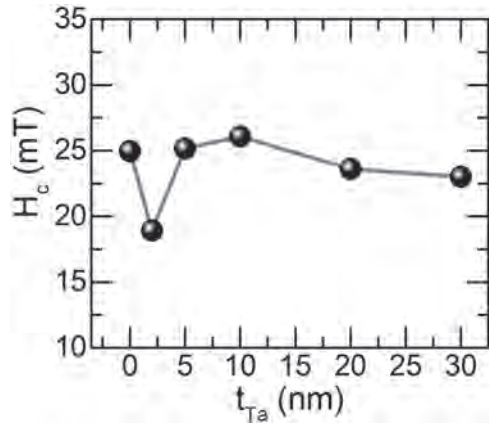
FB-04. Effect of Ta Capping Layer on Damping Properties in Co₅₀Fe₅₀ Thin Films.

B. Panigrahi¹, S.K. Sahoo¹, M.M. Raja², H. Basumatary² and A. Haldar¹
 1. Physics, Indian Institute of Technology Hyderabad, Hyderabad, India;
 2. DRDO Defence Metallurgical Research Laboratory, Hyderabad, India

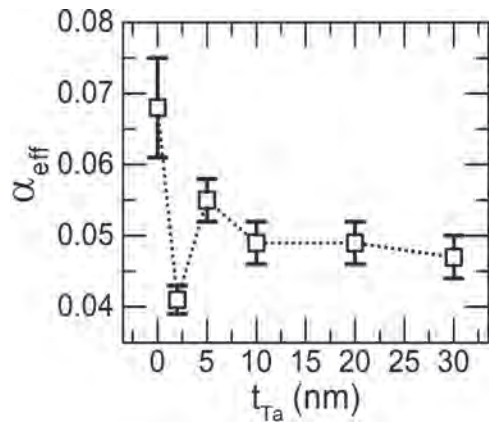
The use of a nonmagnetic (NM) capping layer on top of a ferromagnetic (FM) layer can efficiently increase the Gilbert damping parameter when the choice of the NM layer is a heavy metal (HM)[1][2]. Spin pumping is an efficient method for the generation of spin currents in FM/NM bilayer films where magnetization precession driven by ferromagnetic resonance (FMR) pumps spin current into NM layer via spin angular momentum transfer[3][4]. The saturation magnetization, Gilbert damping and spin mixing conductance are the critical parameters for efficient spin pumping mechanism. An anti-damping torque can be generated by the application of external DC to the NM layer due to the involvement of Rashba spin-orbit interaction [5][6]. Nevertheless, this procedure reduces the efficiency of the device operation [7]. On the other hand, lower damping value can be achieved for the smaller or comparable thickness of heavy metal NM layer to its spin diffusion length in absence of external DC[8]. In this scenario, a non-equilibrium spin accumulation occurs at the interface due to Rashba spin orbit interaction, which does not allow dissipation of spin angular momentum at the interface. As a result, an anti-damping effect can be observed in FM/HM bilayer system. Heavy metals such as Pt, Ta, etc. show high spin-orbit coupling (SOC) and possess short spin diffusion length up to few nm[9] Bilayers such as Permalloy(Py)/Tantalum(Ta) and CoFeB/Ta has been extensively studied in this context[2], [10]. CoFe alloys as a choice of FM layer provides high saturation magnetization and the composition of the CoFe alloy plays a vital role as the concentration of Co and Fe tune the saturation magnetization and coercivity[11], [12]. Therefore, a systematic variation of NM layer thickness and its effect on magnetization dynamics of CoFe alloy offers the possibility of optimization of Gilbert damping parameter and exploration of interfacial phenomena. In this work, we report a comprehensive study of static and dynamic magnetic properties of a series of sample considering Co₅₀Fe₅₀ and Ta as FM and NM layer respectively. A series of Co₅₀Fe₅₀ (20 nm)/Ta (t nm), henceforth CoFe (20)/Ta (t), samples were deposited on Si substrates at a base pressure of 2×10⁻⁷ Torr using UHV magnetron sputtering system. The thickness of the Ta layer was varied as 0, 2, 5, 10, 20, and 30nm. In-plane magnetic hysteresis measurements were carried out using magneto-optical Kerr effect (MOKE) technique with a field variation from -50 mT to 50 mT. A lock-in based FMR technique was used to study the magnetization dynamics where samples were placed on a coplanar waveguide (CPW) in flip-chip configuration. FMR responses were recorded by varying the magnetic field from -300mT to +300mT at a fixed excitation frequency in field sweep mode. The frequency was varied from 2-18 GHz with a step of 1 GHz. MOKE measurements revealed that there were almost negligible variations in coercive fields (H_C) for all samples except for CoFe (20)/Ta (2). Fig.1 shows the variation of H_C as a function of Ta thickness. The H_C for bare CoFe and CoFe (20)/Ta (2) sample was 24 mT and 19 mT respectively. The drop in H_C for CoFe (20)/Ta (2) sample may occur due to various reason such as interface strain, variation of microstructure or oxidation at the surface. FMR measurements were performed to investigate the magnetization dynamics of our samples. The linewidth (ΔH), resonance field (H_{res}), magnetic anisotropy field (H_K), saturation magnetization (4πM_s), effective Gilbert damping (α_{eff}) and spin mixing conductance (g_⊥) were extracted by fitting the experimental spectra to the appropriate fitting equation. H_{res} for our samples were found invariant irrespective of Ta layer thickness, which was clear evidence of negligible extrinsic two magnon scattering contribution to the overall damping [13]–[15]. The minimum and maximum 4πM_s values were obtained as 1756 mT and 1878 mT for CoFe (20)/Ta (2) and CoFe (20)/Ta (30) sample respectively. 1872 mT was obtained for bare CoFe (20) sample. H_K was almost unchanged for all the samples except for CoFe (20)/Ta (2) sample where it was reduced slightly to -105 mT. In-homogenous linewidth broadening (ΔH₀) for our samples was varying in between (70 ~ 90 mT). Fig.2 represents the variation of (α_{eff}) as a function of Ta thickness. FMR measurement revealed that there was a significant reduction in α_{eff} for CoFe (20)/Ta (2) sample i.e. 0.041 as compared to bare CoFe (20) sample i.e. 0.068. The sudden decrease in α_{eff} can be attributed to Rashba spin-orbit

interaction at the interface. The capping layer thickness of Ta in this sample is lower than the spin diffusion length of Ta which is 2.7 nm [9]. Hence, the non-equilibrium spin accumulation at the interface doesn't dissipate their spin angular momentum in the regime of spin diffusion length, which leads to the anti-damping phenomena and ultimately reduces the damping. α_{eff} was further increased to 0.055 for CoFe (20)/Ta (5) sample and saturated to 0.049 for the higher thickness of Ta capping layer. An anomalous trend in α_{eff} was observed due to the absence of DC current in the NM layer and this behaviour is consistent with the earlier report on Py/Ta bilayer [8]. The maximum g_⊥ was obtained as 38.7 × 10¹⁸ m⁻² for CoFe (20)/Ta (2) sample. It is expected due to the enhancement of Δα with the involvement of Rashba spin orbit interaction and higher thickness of FM layer.

[1] S. Azzawi *et al.*, "Evolution of damping in ferromagnetic/nonmagnetic thin film bilayers as a function of nonmagnetic layer thickness," *Phys. Rev. B*, vol. 93, no. 5, pp. 1–6, Feb. (2016). [2] E. Montoya *et al.*, "Spin transport in tantalum studied using magnetic single and double layers," *Phys. Rev. B*, vol. 94, no. 5, p. 054416, Aug. (2016). [3] Y. Tserkovnyak, A. Brataas, and G. E. W. Bauer, "Spin pumping and magnetization dynamics in metallic multilayers," *Phys. Rev. B*, vol. 66, no. 22, p. 224403, Dec. (2002). [4] M. Jamali, A. Klemm, and J.-P. Wang, "Precessional magnetization induced spin current from CoFeB into Ta," *Appl. Phys. Lett.*, vol. 103, no. 25, pp. 1–5, Dec. (2013). [5] A. Manchon, H. C. Koo, J. Nitta, S. M. Frolov, and R. A. Duine, "New perspectives for Rashba spin-orbit coupling," *Nat. Mater.*, vol. 14, no. 9, pp. 871–882, Sep. (2015). [6] G. Allen, S. Manipatruni, D. E. Nikonov, M. Doczy, and I. A. Young, "Experimental demonstration of the coexistence of spin Hall and Rashba effects in β-tantalum/ferromagnet bilayers," *Phys. Rev. B*, vol. 91, no. 14, pp. 1–9, Apr. (2015). [7] S. E. Barnes, J. Ieda, and S. Maekawa, "Rashba Spin-Orbit Anisotropy and the Electric Field Control of Magnetism," *Sci. Rep.*, vol. 4, no. 1, pp. 1–5, May (2015). [8] N. Behera, S. Chaudhary, and D. K. Pandya, "Anomalous anti-damping in sputtered β-Ta/Py bilayer system," *Sci. Rep.*, vol. 6, pp. 1–9, May (2016). [9] M. Morota *et al.*, "Indication of intrinsic spin Hall effect in 4d and 5d transition metals," *Phys. Rev. B - Condens. Matter Mater. Phys.*, vol. 83, pp. 1–5, (2011). [10] V. Lauer, P. Pirro, B. Heinz, M. Geilen, and A. V. Chumak, "The role of the non-magnetic material in spin pumping and magnetization dynamics in NiFe and CoFeB multilayer systems," vol. 163901, pp. 1–9, (2015). [11] A. Melloul and A. Kharmouche, "Synthesis, structure and magnetic properties of CoxFe100-x thin films thermally evaporated onto Si (111) substrate," *J. Mater. Sci. Mater. Electron.*, vol. 30, no. 14, pp. 1–7, Jul. (2019). [12] S.-M. Ahn and G. S. D. Beach, "Crossover between in-plane and perpendicular anisotropy in Ta/Co x Fe 100- x /MgO films as a function of Co composition," *J. Appl. Phys.*, vol. 113, no. 17, pp. 1–3, May (2013). [13] J. Lindner *et al.*, "Non-Gilbert-type damping of the magnetic relaxation in ultrathin ferromagnets: Importance of magnon-magnon scattering," *Phys. Rev. B - Condens. Matter Mater. Phys.*, vol. 68, no. 6, pp. 1–4, (2003). [14] K. Lenz, H. Wende, W. Kuch, K. Baberschke, K. Nagy, and A. Jánossy, "Two-magnon scattering and viscous Gilbert damping in ultrathin ferromagnets," *Phys. Rev. B - Condens. Matter Mater. Phys.*, vol. 73, no. 14, pp. 1–6, (2006). [15] N. Behera, A. Kumar, S. Chaudhary, and D. K. Pandya, "Two magnon scattering and anti-damping behavior in a two-dimensional epitaxial TiN/Py(t Py)/β-Ta(t Ta) system," *RSC Adv.*, vol. 7, no. 14, pp. 8106–8117, (2017).



Variation of H_c values for different thicknesses of Ta.



Effective Gilbert damping (α_{eff}) as a function of Ta thickness.

FB-05. Controlled Nonlinear Magnetic Damping in Spin-Hall Nano-Devices.

B. Divinskiy¹, S. Urazhdin², S.O. Demokritov¹ and V.E. Demidov¹

1. Institute for Applied Physics, Westfälische Wilhelms-Universität Münster, Münster, Germany; 2. Department of Physics, Emory University, Atlanta, GA, United States

Large-amplitude magnetization dynamics is substantially more complex compared to the low-amplitude linear regime, due to the inevitable emergence of nonlinearities. One of the fundamental nonlinear phenomena is the nonlinear damping enhancement. It imposes strict limitations on the operation and efficiency of magnetic nanodevices. In particular, nonlinear damping prevents excitation of coherent magnetization auto-oscillations driven by the injection of spin current into spatially extended magnetic regions. Here, we show experimentally and by micromagnetic simulations that nonlinear damping is determined by the ellipticity of magnetization precession, which is controlled by the magnetic anisotropy. We achieve almost circular precession by tailoring the perpendicular magnetic anisotropy of the magnetic film to compensate the dipolar anisotropy, resulting in suppression of nonlinear damping, and enabling coherent magnetization dynamics driven by spatially extended spin current injection into a microscopic magnetic disk. Our results provide a route for the implementation of efficient active spintronic and magnonic devices driven by spin current.

B. Divinskiy, S. Urazhdin, S. O. Demokritov, and V. E. Demidov, Nature Commun. 10, 5211 (2019)

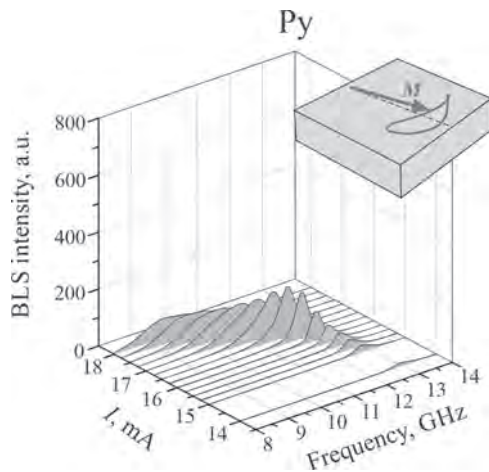


Fig.1 Spectra of magnetic oscillations in Py with elliptical magnetization precession.

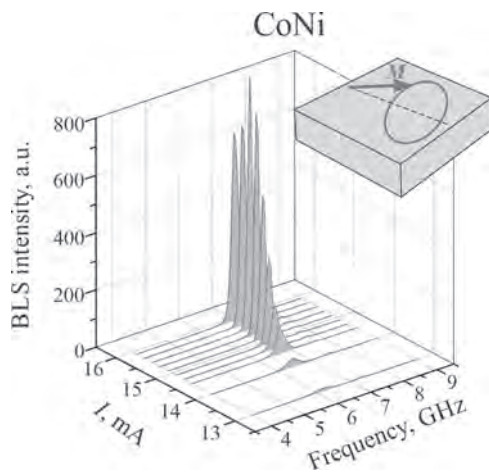


Fig. 2 Spectra of magnetic oscillations in CoNi with circular magnetization precession.

FB-06. Unraveling Relaxation Mechanisms in Ultra-low Damping Fe₈₀Co₂₀ Thin Films.

D. Velázquez Rodríguez¹, J. Gómez¹, G. Alejandro¹, L. Avilés¹, M. van Landeghem², E. Goovaerts² and A. Butera³

1. Resonancias Magnéticas, Centro Atómico Bariloche. Comisión Nacional de Energía Atómica (CNEA). Consejo Nacional de Investigaciones Científicas y Técnicas (CONICET), Bariloche, Argentina; 2. Departement Fysica, Universiteit Antwerpen, Groenenborgerlaan 171, B-2020, Groenenborgerlaan, Belgium; 3. Resonancias Magnéticas, Centro Atómico Bariloche. Comisión Nacional de Energía Atómica (CNEA). Consejo Nacional de Investigaciones Científicas y Técnicas (CONICET). Universidad Nacional de Cuyo (UNCUYO), Bariloche, Argentina

FeCo alloys have been widely studied for decades because of their unique metallic and magnetic properties. In recent years, the search of new systems adequate for spintronic devices promoted the study of bilayers consisting of a ferromagnetic film (FM) in contact with a non-magnetic conductive metal (NM). In these bilayers, when the FM is exposed to microwave radiation it can be driven to its ferromagnetic resonance (FMR) condition to produce the injection of a pure spin current across the FM/NM interface. In this framework, the search for new materials and alloys suitable for the fabrication of FM/NM systems, from which an intense pure spin current could be obtained, is one of the main challenges of today's spintronics. With the purpose of increasing the intensity of the pure spin current density, $J_s^{(sp)}$, which is inversely proportional to the damping parameter (α) of the ferromagnet ($J_s^{(sp)} \sim 1/\alpha^2$) [1] during the spin pumping, the search of materials with low damping constants has been very active during the last years. A recent work by M. Schoen *et al.* [2] reported that Fe_xCo_{100-x} polycrystalline alloys present an ultra-low magnetic damping near $x = 75$ (20 Oe at 10 GHz), which make them promising candidates for the efficient injection of spin currents. Our results highlight the influence of the sputtering conditions (deposition power and temperature) on the magnetic properties of Fe₈₀Co₂₀/Ta bilayers deposited on MgO(001) and Si(001) which have been studied using ferromagnetic resonance and magneto-optic Kerr-effect techniques. We found that for the studied fabrication conditions the samples deposited on MgO(001) presented [100] epitaxial growth with a cubic anisotropy field ~ 300 Oe, while those sputtered on Si(001) grow polycrystalline with a small uniaxial anisotropy. Moreover, the deposited samples on MgO grow with the axis [100] of the Fe₈₀Co₂₀ rotated by 45° from the axis [100] of the MgO substrate (this was verified using XRD techniques). We have found that the optimal growth conditions to obtain a minimum in the damping constant and films with cubic symmetry are 13 - 16 W of sputtering power and single crystal MgO substrates. Substrate heating during sputtering at temperatures of 150 °C also helps to increase the quality of the films. Ferromagnetic resonance measurements at different excitation frequencies (Fig. 1) have determined exceptionally low damping values for ferromagnetic conductors ($\alpha \sim 3 \times 10^{-3}$), which makes the Fe₈₀Co₂₀/Ta system an excellent candidate for future applications in spintronic devices. From the dependence of the FMR linewidth on different excitation frequencies, we also found, different relaxation mechanisms act in easy and hard magnetization directions (Fig. 1). From the analysis of the dependence of the FMR linewidth on the orientation of the applied magnetic field and the excitation frequency, we were able to separate the contribution of the different relaxation mechanisms (Gilbert damping, two magnon scattering and mosaicity) to the linewidth and to explain quantitatively the observed behavior (Fig. 2). We made simulations to estimate the mosaicity and obtained relatively small values, consistent with a good quality of the samples. Finally, we also estimated the strength of the two magnon scattering which agrees with values reported in Fe-rich alloys [3]. The models proposed in this work were corroborated for different excitation frequencies. Our present results are very promising for the development of spintronic devices with improved functionalities. This work was partially supported by Conicet under Grant PIP 201501-00213, ANPCyT Grant PICT 2013-0401, and U.N. Cuyo Grant 06/C556 all from Argentina. We also received financial support through the international cooperation project between Argentina and Belgium MINCYT-FWO FW/15/01-VS.041.16 N.

[1] JE Gómez, B. Zerai Tedlla, NR Álvarez, G. Alejandro, E. Goovaerts y A. Butera Phys. Rev. B 90, 184401 (2014) [2] Martin AW Schoen, Danny

Thonig, Michael L. Schneider, TJ Silva, Hans T. Nembach, Olle Eriksson, Olof Karis y Justin M. Shaw. Nature Physics, 12, 839 (2016) [3] K. Lenz, H. Wende, W. Kuch y K. Baberschke, Phys. Rev. B 73, 144424 (2006)

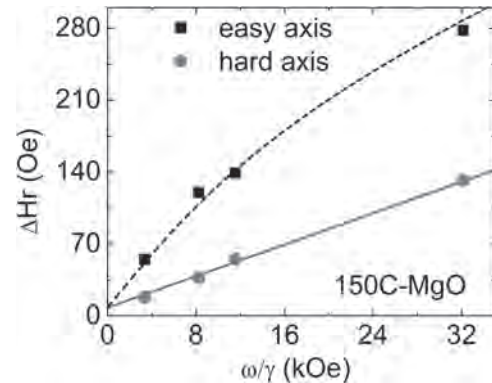


Fig.1 Frequency dependence of the resonance linewidth for the sample grown on MgO and heated at 150 °C, for the easy (solid squares) and hard (solid circles) anisotropy axes. The fit (solid line) was made considering a linear dependence (Gilbert damping), while the dashed line represents the linear contribution for the hard direction with the addition of two magnon scattering term.

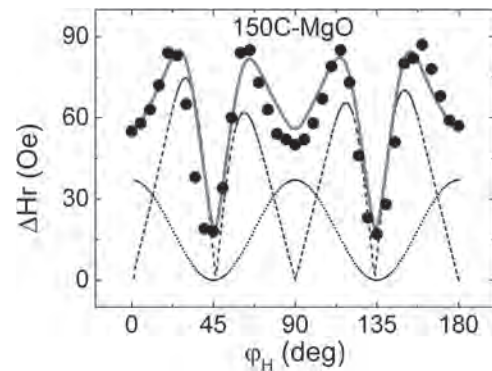


Fig.2 Angular variation of ΔH_r (solid circles) and added contributions of two magnon scattering term and mosaicity (solid lines) for X-band. We also show the individual contribution of two magnon scattering and mosaicity as dotted and dashed lines, respectively.

FB-07. Phonon Pumping by Magnonic Spin Currents: Experiments and Theory.

S.M. Rezende¹, J. Holanda², D. Maior¹, O. Santos¹ and A. Azevedo¹
 1. Física, Universidade Federal de Pernambuco Centro de Ciências Exatas e da Natureza, Recife, Brazil; 2. Física, Universidade Federal do Espírito Santo, Vitória, Brazil

We report the experimental observation of an excitation in a film of the ferrimagnet yttrium iron garnet (YIG), driven by the spin current generated by the giant spin Hall effect in a platinum strip with nanoscopic silver particles adjacent to the YIG film. The excitation, detected by Brillouin light scattering (BLS), has a frequency different from the thermal magnons and phonons in YIG, and does not vary with the applied magnetic field, but changes with film thickness. We interpret the BLS signal as due to phonons excited by the magnonic spin current injected into the YIG film, in a process that is the Onsager reciprocal of the spin pumping by coherent elastic waves. The observations are supported by a theory based on a process where one magnon in the magnonic spin current creates one phonon and another magnon, with conservation of energy and momentum. The theoretical value of the critical current in the metallic strip necessary to drive phonons is in order of magnitude agreement with the value measured experimentally. The experiments were performed with two samples, sample A made is with a 154 nm thick single-crystal YIG film grown by liquid-phase epitaxy onto a 0.5 mm thick [111]-oriented $\text{Gd}_3\text{Ga}_5\text{O}_{12}$ (GGG) substrate, cut in rectangular shape with dimensions 8.0 x 1.0 mm², and sample B made in the same way with a 93 nm thick YIG film. The bilayer samples were prepared by deposition on the YIG film of a metallic layer strip, made of Pt (3 nm)/Ag (9 nm)/Pt (3 nm) of width 150 μm , by means of DC magnetron sputtering. As shown in Ref. [1], with the appropriate deposition conditions, the strip forms nanoscopic particles of Ag in the midplane of a 6 nm thick Pt layer, that exhibits a giant spin Hall effect (SHA). A charge current in the metallic strip is converted into a spin current that flows into the YIG film as a magnonic spin current. The excitations in the YIG films are detected by back-scattering BLS using a (2x3)-pass tandem Fabry-Perot interferometer. Figure 1a shows the BLS spectrum obtained with the YIG (154 nm)/[Pt-Ag] sample, with no current in the NM strip. The spectrum was collected with 6 000 interferometer scans, with the sample under an in-plane magnetic field of 2.0 kOe. The peak denoted by M, with frequency shift of 12.6 GHz, corresponds to the Stokes scattering by thermal magnons. The inset shows the measured frequency shifts for some values of the magnetic field and the solid line represents the calculations with the magnon dispersion relation. The peak at 26 GHz, denoted by TP-GGG, is due to transverse phonons in the GGG substrate. For positive currents in the NM strip with intensity below 23 mA, there is no change in the BLS spectrum of Fig. 1(a). However, for currents above 23 mA, a new peak in the BLS spectrum shows up with frequency 7.55 GHz, with much larger intensity than the thermal peaks. Figure 1b shows the BLS spectra obtained with only 1 000 interferometer scans. The peak intensity increases with increasing current, as in Fig. 1c, and the frequency increases slightly to 7.8 GHz as the current approaches mA. For currents above this value, the BLS peak broadens and its intensity decreases due to heating effects. The thermal magnon peak cannot be seen in Fig. 1b because with 1 000 scans its amplitude is only 5 counts. The nonmagnetic character of the current driven excitation is demonstrated in Fig. 1e showing that the frequency of the excitation does not depend on the magnetic field. A clue to the origin of the observed current-driven excitation is given by measurements in a thinner YIG film. Figure 1e shows data obtained with sample YIG/[Pt-Ag]-B, that has a YIG film with thickness 93 nm and a metallic layer as in the previous sample. By passing a current in the metallic strip of the sample, a peak emerges in the BLS spectrum for currents above a critical value smaller than in YIG/[Pt-Ag]-A, and with larger frequency, 13.5 GHz. Figure 1f shows that the frequency also does not vary with the magnetic field. The facts that the frequency of the BLS peaks increase with decreasing YIG film thickness and do not depend on the magnetic field, strongly suggest that the current driven oscillations originate from phonons. The origin of the phonon pumping observed here lies in the magnon-phonon interaction. Calculations show that the mechanism of the phenomenon reported is the generation of phonons by a magnon-phonon-

magnon splitting process, driven by magnons of the magnonic spin current in the YIG film generated by the spin Hall effect in the metallic layer [2].

[1] O. Alves-Santos, E. F. Silva, M. Gamino, R. O. Cunha, J. B. S. Mendes, R. L. Rodríguez-Suárez, S. M. Rezende, and A. Azevedo, Phys. Rev. B 96, 060408(R) (2017). [2] J. Holanda, D. S. Maior, O. Alves Santos, A. Azevedo, and S. M. Rezende, Appl. Phys. Lett., 118, 022409 (2021).

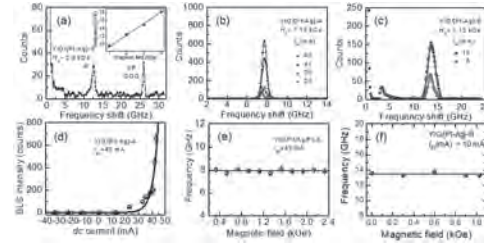


Figure 1. (a) BLS spectrum of YIG (154 nm)/GGG under an in-plane magnetic field of 2.0 kOe, measured with 6 000 interferometer scans. Inset shows the field dependence of the magnon (M) peak. TP-GGG denotes the transverse phonon in GGG. (b) BLS spectra in the YIG (154 nm)/[Pt-Ag] sample under an in-plane magnetic field of 1.13 kOe, with a *dc* current in the [Pt-Ag] layer with intensity as indicated, collected with 1 000 interferometer scans. (c) BLS spectra in the YIG (93 nm)/[Pt-Ag] sample under an in-plane field of 1.13 kOe, with a current in the [Pt-Ag] layer of intensity as indicated, collected with 1 000 interferometer scans. (d) BLS peak intensity versus current in the YIG (154 nm)/[Pt-Ag] sample. (e) Frequency of the BLS peak with current 43 mA versus applied field in the YIG (154 nm)/[Pt-Ag] sample. (f) Frequency of the BLS peak with current 10 mA versus applied field in the YIG (93 nm)/[Pt-Ag] sample.

FB-08. Compositional Effect on Spin-Wave Auto-Oscillation Behavior of Ni_{100-x}Fe_x/Pt Spin Hall Nano-Oscillators.

M. Haidar¹, H. Mazraati², P. Durrenfeld³, H. Fulara³, M. Ranjbar³ and J. Åkerman³

1. American University of Beirut, Beirut, Lebanon; 2. NanOsc AB, Kista 164 40, Sweden, Stockholm, Sweden; 3. Goteborgs Universitet, Goteborg, Sweden

The recent demonstration of pure spin current-induced spin-transfer torque arising from the spin Hall effect (SHE) represents an efficient route to controlling the magnetization dynamics in magnetic nanostructures. In a ferromagnet /heavy metal bilayer, a pure spin current is generated when a longitudinal charge current passes through the HM and induces a transverse spin current due to the strong spin-orbit coupling in the HM [1, 2]. The conversion of the charge current density (J_C) to pure spin current density (J_S) is characterized by the spin Hall angle (θ^{SHA}) in these bilayers. The pure spin current may be sufficient to excite perpetual self-oscillations in the magnetization, which can further induce spin waves in these systems. This is of particular interest for spintronics applications and has led to a new class of microwave devices called spin Hall nano-oscillators (SHNOs) [3,4]. Generating higher spin current densities through a higher θ^{SHA} is necessary to improve the performance of SHNOs and to avoid higher charge current densities. So far, studies have focused on different HMs with various spin-orbit coupling strengths to generate higher spin current---for example, the β -phase of W, Ta, or Ni_xCu_{1-x}. In this work, we demonstrate the compositional effect on the magnetodynamic and auto-oscillations properties of Ni_{100-x}Fe_x/Pt ($x= 10$ to 40) nanoconstriction based spin Hall nano-oscillators [5]. The devices are fabricated from Ni_{100-x}Fe_x(5) /Pt (6) bilayer (thicknesses in nanometers) deposited in a high vacuum magnetron sputtering chamber where Ni-Fe alloys were co-sputtered under the same conditions and from pure Ni and Fe targets, where the composition was established by varying the respective plasma powers. Two kinds of spin Hall devices were fabricated from each film: (1) 8 x 16 μm^2 rectangular stripes and (2) nanoconstriction-based SHNOs with a width of 140 nm. We first discuss the ST-FMR spectra measured on rectangular stripes to determine the variation of the magnetodynamics with the Fe content. We measure an increase in the magnetization ($\mu_0 M_s$) and a decrease in the Gilbert damping. In addition to that, we measure a reduction of the impact of spin-torque on the ST-FMR linewidth with the dc current ($\mu_0 \Delta H / I$) as Fe content increases Fig. 1(a). This is translated into a reduction in the spin Hall angle with the increase of Fe content as shown in Fig. 1(b). The reduction in the spin Hall angle can be correlated primarily to the compositional effect: the spin Hall angle scales inversely proportional with the saturation magnetization. Note that the observed variation of spin Hall angle with increasing Fe content is also qualitatively consistent with the decrease of damping as a function of the Fe content, and can be well explained in terms of the spin transport model Ref. [6]. The suppression of spin pumping due to increased $\mu_0 M_s$ should result in lowering the effective spin mixing conductance and therefore spin-torque efficiency, which can be seen as a monotonic decrease of spin Hall angle with increasing Fe content in Fig. 1(b). Next, we turn to discuss the compositional effect on the characteristics of auto-oscillations in nanoconstriction-based SHNOs. We record the generated microwave power spectral density (PSD) as a function of a direct current (I) under an in-plane magnetic field $\mu_0 H = 0.05$ T using a spectrum analyzer and a low noise amplifier with a +33 dB gain. The spectral characteristics of the auto-oscillations i.e. frequency, power, and linewidth were extracted from the PSD. It is interesting to note that the onset auto-oscillation frequency differs between devices, i.e. the onset frequency shifts up for Fe-rich devices due to higher magnetization. The integrated power varies with the dc current, showing a bell shape of amplitude around 1 pico-watt. A qualitative comparison between the power of devices shows that Fe-rich devices have lower output power. This is understood as the readout of devices depends on AMR and as the AMR drops in Fe-rich devices the power follows. Finally, the measured auto-oscillations have linewidths around 50 MHz. The threshold current for auto-oscillations, (I_{th}), is extracted from plots of p^{-1} vs. I , [7] as shown in the inset of Fig. 1(c). For Fe-rich devices, higher currents are required to excite auto-oscillations. The enhancement in threshold current densities for Fe-rich devices is a direct consequence of the reduction in the spin Hall angle. Our

experimental results show that the dominant compositional effect is from the magnetization that plays a central role in determining the characteristics of the spin Hall devices.

[1] J. E. Hirsch, Phys. Rev. Lett. 83, 1834 (1999). [2] M. I. D'yakonov' et al., J. Exp. Theor. Phys. Lett.13, 467 (1971). [3] V. E. Demidov, et al., Nat. Mater. 3459, 1028 (2012). [4] T. Chen et al., Proc. IEEE 104, 1919 (2016). [5] M. Haidar et al., Appl. Phys. Lett. 118, 012406 (2021). [6] M. W. Keller, et al., Phys. Rev. B 99,214411 (2019). [7] A. Slavin et al., IEEE Transactions on Magnetics 45, 1875 (2009).

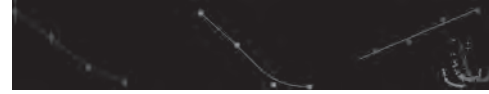


Fig. 1 (a, b) Variation in $|\mu_0 \Delta H / I|$ and the spin Hall angle (θ^{SHA}) as a function of Fe composition extracted from the ST-FMR measurements. (c) Threshold current vs. Fe concentration. Inset shows how the threshold is extracted from a linear fit of p^{-1} vs. I at low currents (dashed line).

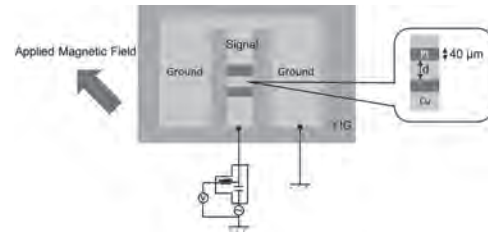
FB-09. Evaluation of Interaction Between Local Magnetization Dynamics and Spin Waves Measured by ST-FMR.

T. Koda¹, S. Muroga², S. Hashi³ and Y. Endo^{4,5}

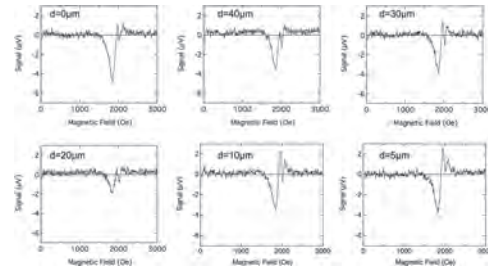
1. *Electronic Mechanical Engineering, National Institute of Technology, Oshima College, Suo-Oshima, Japan;* 2. *Mathematical Science and Electrical-Electronic-Computer Engineering, Akita University, Akita, Japan;* 3. *Research Institute of Electrical Communication, Tohoku University, Sendai, Japan;* 4. *Electrical Engineering, Tohoku University, Sendai, Japan;* 5. *Center for Spintronics Research Network, Tohoku University, Sendai, Japan*

The control of magnetization dynamics is an important issue for the development of high-frequency devices based on spintronics. There are several ways to excite magnetization dynamics. In our previous study, we reported the amplification of magnetization dynamics derived from the interaction between local magnetization dynamics and spin waves by using a slot line waveguide [1]. In this paper, we report the study on the evaluation of the interaction by measuring ST-FMR. The spin orbit torque is caused by the spin current induced by the spin hall effect in ferromagnetic and non-ferromagnetic bilayer system. The ST-FMR is originally used for the estimation of the spin orbit torque via the measurement of the spin hall magneto resistance. We found that the ST-FMR signals for the samples described below delivered information on the interaction between local magnetization dynamics and spin waves. Fig.1 shows the sample structure and measurement set up for the ST-FMR. We used yttrium iron garnet (YIG) as a ferromagnetic layer. Coplanar waveguides were prepared on the YIG film. The signal line consisted of Cu layer (200 nm), and was partially replaced by 10nm thick Pt layer. In the separated Pt areas, additional local magnetization dynamics was excited by the spin orbit torque, emitting spin waves. The distance between Pt areas was systematically varied, leading the change of the strength of the interaction between the local magnetization dynamics and spin waves at the Pt areas. Fig.2 shows the distance between Pt areas dependence of ST-FMR signal measured at 7.0 GHz. The sample with one Pt shows symmetrical peaks. On the other hand, the samples with two Pt areas indicate that the asymmetry of the peaks changes with the distance of Pt areas. The symmetry and asymmetry of the peaks reflect the contribution of torques to the magnetization dynamics from the spin orbit torque and RF magnetic field respectively at Pt areas [2]. It should be noted that the strength of RF magnetic field was fixed for all the samples, meaning that the increase in the asymmetry was caused by an additional torque to the magnetization. Another factor is speculated from the interaction between local magnetization dynamics and spin waves because the direction of the torque for the interaction is considered the same as the direction for the RF Oersted field, leading the asymmetry of the peak for the ST-FMR measurement. The asymmetry of the curve showed strong dependence on the distance between Pt areas, reflecting the strength of the interaction. Those experimental results give a way to design the artificially controlled magnetization dynamics effectively. We thank GRANOPT Co, Ltd. for their support of YIG single crystal thin films. This work was supported in part by JSPS KAKENHI Grant Number JP18K14114. This work was supported in part by CSRN, Tohoku University. Part of this work was carried out under the Cooperative Research Project Program of the Research Institute of Electrical Communication, Tohoku University. A part of this work was carried out at Nano-Fabrication Support Laboratory, Yamaguchi University supported by “Nanotechnology Platform Project” of the Ministry of Education, Culture, Sports, Science and Technology (MEXT), Japan.

[1] Tetsunori Koda, Sho Muroga, and Yasushi Endo, “Synchronized excitation of magnetization dynamics via spin waves in Bi-YIG thin film by slot line waveguide” *Appl. Phys. Lett.* 116, 102403 (2020). [2] Luqiao Liu, Takahiro Moriyama, D. C. Ralph, and R. A. Buhrman, “Spin-Torque Ferromagnetic Resonance Induced by the Spin Hall Effect” *Phys. Rev. Lett.*, 106, 036601 (2011).



Schematic view of measurement set up for ST-FMR measurement. A part of the signal line consists of Pt layer for inducing the spin orbit torque.



Gap of Pt areas dependence of ST-FMR signal measured at 7.0 GHz.

FB-10. Nonsymmetric Spin Pumping in a Multiferroic Heterostructure Using Surface Acoustic Wave.

P. Rovillain^{1,2}, R. Cardoso de Olivero³, M. Marangolo^{1,2} and J. Duquesne^{1,4}
1. Institut des NanoSciences de Paris, Paris, France; 2. Sorbonne
Universite, Paris, France; 3. Universidade Federal do Parana, Curitiba,
Brazil; 4. Centre National de la Recherche Scientifique, Paris, France

Spintronics research concentrated its efforts on handling spin polarization current leading to the success-story of giant magnetic resistance spin valves [1-2]. More recently, pure spin currents, i.e. a spin flux without charge flux, are at the centre of interest since they do not produce Joule heating, reducing power dissipation in spintronics devices, as in STT-MRAM [3]. These applications require an increase in the emission and detection efficiencies via a full understanding of the complex physics behind pure spin currents. Spin current can be detected by inverse spin Hall effect (ISHE) that corresponds to the conversion of a spin current into a detectable charge current by measuring the voltage on a normal metal presenting a strong spin-orbit interaction. Pure spin current emission can be obtained by temperature gradients, by charge currents and by magnetization dynamics. This last mechanism permits to generate pure spin current via ferromagnetic resonance in a ferromagnetic material [4]. We will present acoustic spin pumping experiments in Co/Pt bilayers, using surface acoustic waves (SAW) to induce the magnetization precession in the Co layer taking advantage of resonant magneto-elastic coupling. We will report a peculiar behaviour of SAW-FMR assisted spin pumping in a multiferroic system where Co/Pt bilayer is in contact with a ferroelectric substrate LiNbO₃ [5]. We will show that the substrate on which the bilayer is deposited plays a role in the spin current excitation processes. We will show that the electrical polarization vector affects the ISHE voltage: the inversion of the magnetization and of the SAW propagation vector modifies the spin pumping efficiency. We suggest that this polarization is an important factor in the spin pumping excitation processes. The nature of the coupling with the magnetic polarization may be due to a magnetoelectric coupling at the interface between LiNbO₃ and Co, inducing non equilibrium spin density across the whole thin film [6] and affecting spin pumping efficiency.

[1] M. N. Baibich, J. M. Broto, A. Fert, F. N. Van Dau, F. Petroff, P. Eitenne, G. Creuzet, A. Friederich, and J. Chazelas, *Phys. Rev. Lett.* 61, 2472 (1988). [2] J. M. George, L. G. Pereira, A. Barthelemy, F. Petroff, L. Steren, J. L. Duvail, A. Fert, R. Loloee, P. Holody, and P. A. Schroeder, *Phys. Rev. Lett.* 72, 408 (1994). [3] S. Maekawa, S. O. Valenzuela, E. Saitoh, and T. Kimura, *Spin Current* (Oxford University Press, 2017) pp. 1-520. [4] M. Weiler, H. Huebl, F. S. Goerg, F. D. Czeschka, R. Gross, and S. T. B. Goennenwein, *Phys. Rev. Lett.* 108, 176601 (2012). [5] P. Rovillain, R. Cardoso de Oliveira, M. Marangolo, and J.-Y. Duquesne *Phys. Rev. B* 102, 184409 (2020). [6] C.-L. Jia, T.-L. Wei, C.-J. Jiang, D.-S. Xue, A. Sukhov, and J. Berakdar, *Phys. Rev. B* 90, 054423 (2014).

FB-11. Laser Pulse Induced Ultrafast Spin Current Through the Antiferromagnetic Insulator in Pt/CoO/FeCoB.

Y. Sasaki^{1,2}, G. Li³, T. Moriyama⁴, T. Ono⁴, R.V. Mikhaylovskiy⁵, A. Kimel³ and S. Mizukami²

1. Department of Applied Physics, Tohoku University, Sendai, Japan; 2. WPI Advanced Institute for Materials Research, Tohoku University, Sendai, Japan; 3. Radboud University, Institute for Molecules and Materials, Nijmegen, Netherlands; 4. Institute for Chemical Research, Kyoto University, Uji, Japan; 5. Lancaster University Department of Physics, Lancaster, United Kingdom

Spin current transmission in antiferromagnetic materials is one of the intriguing topics in antiferromagnetic spintronics. The antiferromagnetic order can mediate the transmission of the spin current in the form of propagating magnons. Several groups have reported this phenomenon in varieties of antiferromagnetic materials, such as NiO, CoO, Fe₂O₃, FeMn, and IrMn. Most of the investigations have so far been conducted at frequencies much lower than the resonant frequency of the antiferromagnetic materials. In order to explore the physics of the phenomenon, it is crucial to extend the investigation to the THz range, at which antiferromagnets typically have a good susceptibility to electromagnetic field, because this frequency domain embraces the antiferromagnetic resonant frequencies. A suitable method for investigating antiferromagnetic dynamics could be a relatively recently developed technique, where THz radiation is generated with an ultrashort laser pulse in a heavy metal (HM) / ferromagnetic metal (FM) bilayer structure [1,2]. In this work [3], we investigated laser stimulated THz emission from Pt/CoO/FeCoB and explored the sub-picosecond pulsed spin current transmission through the antiferromagnetic CoO interlayer. We also particularly look into the polarization of the THz electromagnetic wave and reveal that the latter is influenced by the Néel vector in the antiferromagnets. Figure 1 shows the schematic illustration of the measurement set up. Magnetic field of 100 mT was applied to $\langle 110 \rangle$ direction and the CoO Néel vector initially remains in one of the $[100]$ directions, which is an easy axis of CoO. The field cooling process then invokes a twisting of the CoO magnetic moment. The THz electromagnetic wave with x and y components and the polarization angle ϕ was detected by using two wire grid polarizers. The polarization of the emitted THz wave is parallel to the electric field E_c induced in the Pt layer. The polarization of the THz wave essentially tells us the polarization direction of the spin current injected into the HM layer through the antiferromagnetic layer. Figures 2(a) and 2(b) show the y component of the THz wave, E_y^{peak} , and ϕ as a function of temperature. E_y^{peak} decreases with decreasing temperature regardless of CoO layer thickness d_{CoO} , which is associated with the dependence of the sheet conductivity of the films and the inverse spin Hall conductivity of the Pt layer [4]. On the other hand, one can notice that ϕ apparently increases at lower temperature and has an onset at around 200K and 300K for $d_{\text{CoO}}=2.0$ and 5.0 nm, respectively, which coincide with the blocking temperature for these samples. Assuming the polarity of spin density of the ultrafast spin current induced in the FM layer is same direction as magnetization in FeCoB layer, the variations of ϕ for $d_{\text{CoO}}=2.0$ and 5.0 nm below the blocking temperature indicates that the spin current carried by the THz magnon experiences a non-uniform scattering background, which preferentially scatters the spin orthogonal to the Néel vector gradually rotating away from the axis of magnetization in FeCoB layer. This observation is consistent with previous reports on the spin current experiments in exchange biased systems where the spin current impedance was modified by an accommodation of Néel vector twisting [5]. In summary, we found that sub-picosecond pulsed spin current induced by the femtosecond laser pulse can transmit through antiferromagnetic CoO layers. Our results not only demonstrate the picosecond magnon spin current transmission, but also the picosecond interaction of the THz magnons with the Néel vector in the antiferromagnet. This work was partially supported by JSPS KAKENHI Grant (Nos. 17H04924, 17H05181, H1803787, 19K21972, and 26103004), the Center for Spintronics Research Network (CSRN), and the Center for Science and innovation in Spintronics (CSIS). This work was also partly promoted by the Collaborative Research Program of the Institute for Chemical Research, Kyoto University. One of the authors (YS) acknowledges the Graduate Program in Spintronics (GP-Spin) at Tohoku University.

[1] T. Seifert, *et al.*, Nature Photon. 10, 483 (2016). [2] T. Seifert, *et al.*, Nature Communications 9, 2899 (2018). [3] Y. Sasaki, *et al.*, Appl. Phys. Lett. 117, 192403 (2020). [4] M. Matthiesen, *et al.*, Appl. Phys. Lett. 116, 212405 (2020). [5] T. Moriyama, *et al.*, Phys. Rev. Lett. 119, 267204 (2017).

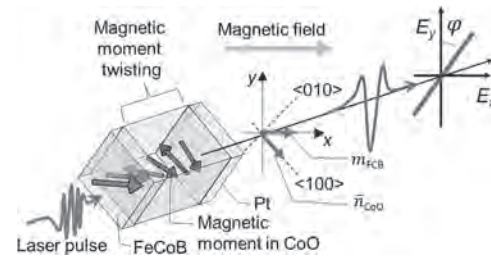


Figure 1. Schematic illustration of the measurement setup.

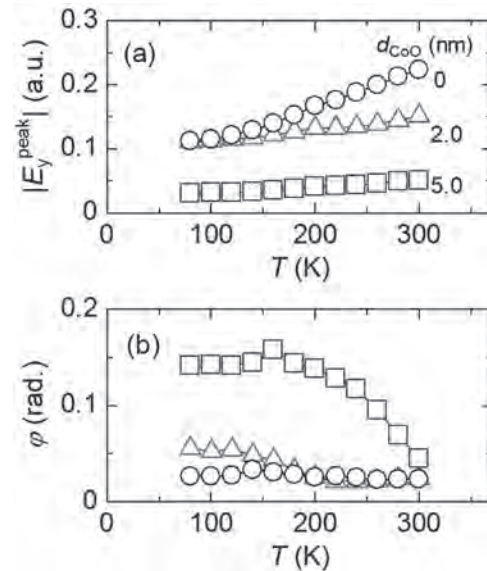


Figure 2. Temperature dependence of (a) the peak intensity of E_y and (b) THz polarization angle ϕ . Open circle, triangle, and square show the data for films with $d_{\text{CoO}}=0, 2.0$ and 5.0 nm, respectively.

FB-12. Tunable Terahertz Wave via Synthesis of Spin and Charge Induced Radiations in Topological Insulator.

H. Wang^{1,3}, X. Chen², H. Zhao¹, C. Fang^{1,3}, T. Nie^{1,3}, X. Wu² and W. Zhao^{1,3}

1. School of Integrated Circuit Science and Engineering and Advanced Innovation Center for Big Data and Brain Computing, Beihang University, Beijing, China; 2. School of Electronic and Information Engineering, Beihang University, Beijing, China; 3. Beihang-Goertek Joint Microelectronics Institute, Beihang University, Qingdao, China

Elliptically or circularly polarized terahertz (THz) radiation plays increasingly important roles in both scientific research and practical applications, such as wireless communication, composition analysis and undamaged imaging¹. Recently, the realization of highly efficient THz radiation in ferromagnetic multilayer via spin-charge conversion (SCC) brings new hope for the emerging spin THz emitter at room temperature². However, achieving an easily-tuned THz emitter with polarization and ellipticity manipulable still be challenging. Topological insulator (TI), with strong spin-orbital coupling and spin-momentum-locked surface states, has been regarded as the most effective spin-charge convertor in spin THz emitter³. In addition, the broken inversion symmetry at surface provides topological insulator numerous fascinating nonlinear optical phenomena, the dominant one is linear photogalvanic effect (LPGE), which could yield a polarization-dependent terahertz radiation in topological insulator⁴. By contrast, the terahertz wave induced by SCC is polarization-independent. This difference in polarization-dependence of two terahertz components makes it possible to control them separately, inspiring a new approach in chirality-tuned terahertz emission by synthesizing the SCC-induced and LPGE-induced terahertz waves only by tailoring the polarization of incident pumping laser. Here we prepared a Bi₂Te₃ (10nm)/Fe (3nm) heterostructure by molecular beam epitaxy (MBE) and measure the terahertz response after illumination by a linear polarized femtosecond laser. The terahertz wave was probed by a terahertz time domain spectroscopy (THz-TDS). As shown in Figure 1a, the amplitude of the terahertz generated in Bi₂Te₃/Fe heterostructure is higher than single Bi₂Te₃ or Fe thin film, almost keeps in the same level with W/CoFeB/Pt trilayer⁵. The latter is usually regarded as a typical spin terahertz emitter and the result proves the high efficiency of Bi₂Te₃/Fe heterostructure in terahertz emission. After further careful examination, we divided the overall terahertz radiation into two components. The first is SCC-induced spin terahertz. Generated from the spin-charge conversion in the Bi₂Te₃/Fe interface, this component is only magnetization-dependent. Meanwhile, an ultrafast photocurrent can also originate in Bi₂Te₃ film due to LPGE in the inversion symmetry breaking surface, leading to a terahertz wave. Notably, the direction of the LPGE-induced terahertz is related with the polarization of incident laser, which provides a simple method to construct orthogonal terahertz components by adjusting the incident polarization. More importantly, a phase difference between these two terahertz components could be observe because of the delayed time between SCC and LPGE. After deliberately tuning the incident laser to promise both terahertz components in the same magnitude, an elliptical polarized terahertz wave appears in Bi₂Te₃/Fe heterostructure. Furthermore, a terahertz wave with arbitrarily tailored chirality and ellipticity could be got by tailoring the pumping laser polarization. Overall, we have demonstrated a highly efficient terahertz emission in Bi₂Te₃/Fe heterostructure. Compared with conventional spintronic terahertz emitter, Bi₂Te₃/Fe can realize terahertz wave with arbitrarily tailored chirality only by adjusting the incident polarization. The engineering of topological insulator and ferromagnet heterostructure may open up a great opportunity to study high-performance TI-based spintronic terahertz devices with easy controllability.

(1) D. M. Mittleman, *Opt. Express.*, Vol. 26, p.9417 (2018) (2) T. Kampfrath; M. Battiato; P. Maldonado, et al., *Nat. Nanotechnol.*, Vol. 8, p.256 (2013) (3) X. Wang; L. Cheng; D. Zhu, et al., *Adv.Mater.*, Vol. 30, p.1 (2018) (4) C. M. Tu; Y. C. Chen; P. Huang, et al., *Phys. Rev. B.*, Vol. 96, p.1 (2017) (5) Y. Wu; M. Elyasi; X. Qiu, et al., *Adv.Mater.*, Vol. 29, p.1 (2017)

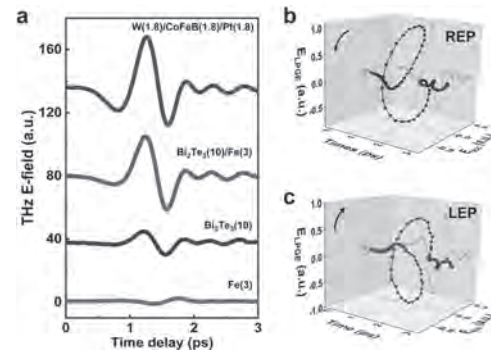


Fig. 1. (a) Typical THz temporal waveforms generated from Fe (3 nm), TI (10 nm), TI (10 nm)/Fe (3 nm) and W (1.8 nm)/CoFeB (1.8 nm)/Pt (1.8 nm), respectively. **(b, c)** Generation right and left-handed elliptical polarized THz waves by tuning incident laser polarization angle.

FB-13. Emission of THz Radiation From $\text{Co}_{20}\text{Fe}_{60}\text{B}_{20}/\text{Pt}$ Spintronic Thin Films With Varying Microstructural Properties.

C. Bull^{1,2}, R. Ji¹, C. Lin¹, S. Hewett¹, T. Thomson², D. Graham^{1,3} and P. Nutter²

1. Photon Science Institute, Dept. of Physics & Astronomy, The University of Manchester, Manchester, United Kingdom; 2. Nano Engineering and Spintronic Technologies Group, Dept. of Computer Science, The University of Manchester, Manchester, United Kingdom; 3. The Cockcroft Institute, Sci-Tech Daresbury, Daresbury, United Kingdom

The ability to generate and control pulses of terahertz (THz) radiation has revolutionised a multitude of critical technologies, from medical imaging [1] to the detection of explosives [2]. Furthermore, sub-picosecond pulses of THz radiation have future application in the ultrafast control of electron spin states [3] and picosecond magnetisation switching in ferromagnets [4], ferrimagnets [5] and antiferromagnets [6]. To exploit the full potential of THz technology, broadband emitters are required which can generate radiation over a spectral range of 1-10 THz [7]. Spintronic emitters, consisting of ferromagnetic (FM)/non-magnetic (NM) heavy metal thin films, have been shown to produce THz pulses with large electric field amplitudes and gapless bandwidths of up to 30 THz [8]. This THz emission is produced when the spintronic structure is excited by femtosecond laser pulses, demonstrating their potential as low-cost sources of broadband radiation. Whilst it has been well established that particular combinations of FM/NM materials, such as $\text{Co}_{20}\text{Fe}_{60}\text{B}_{20}/\text{Pt}$, produce pulses of THz radiation with high electric field amplitudes (300 kV/cm) [8], a detailed understanding of the role that material properties contribute to the generation process of THz radiation has yet to be fully explored in order to inform the future design of optimum performance spintronic emitters. In particular, post deposition annealing of CoFeB based structures has been shown to enhance the emission of THz radiation by up to a factor of 3 [9,10] further increasing the potential utility of these emitters. This enhanced electrical field amplitude has been attributed to two possible effects: 1) diffusion of Boron into the heavy metal layer, leading to an increased number of scattering centres and a reduced hot electron relaxation length, λ_{NM} [9]; or 2) local crystallisation of CoFeB leading to an increase in mean free path of hot electrons travelling through the FM layer [9,10]. In order to explore the electric field enhancement, we present a systematic study which investigates the effects of inducing defects in the NM layer and crystallisation of the FM/NM interface upon the emission of THz radiation from $\text{Co}_{20}\text{Fe}_{60}\text{B}_{20}$ (2.5 nm)/Pt (3 nm) spintronic thin films. The films have been grown onto fused silica substrates using magnetron sputtering where the base pressure was better than 5×10^{-8} Torr. We present results from two series of films. In the first series, the dc sputtering power for Pt was varied between 25 W and 100 W in order to control defects in the Pt layer [11]. In the second series, the films were annealed post deposition between 200°C and 400°C to induce crystallisation at the CoFeB/Pt interface. For all films, the $\text{Co}_{20}\text{Fe}_{60}\text{B}_{20}$ layer was sputtered at 100 W dc power to enable direct comparison. The structural properties of $\text{Co}_{20}\text{Fe}_{60}\text{B}_{20}/\text{Pt}$ films were characterised via X-ray diffraction (Fig. 1a) and atomic force microscopy (Fig. 1b-e), from which the crystalline ordering and the surface roughness of the Pt were observed to change with varying sputtering power (series 1) and annealing temperature (series 2). X-ray reflectivity analysis of $\text{Co}_{20}\text{Fe}_{60}\text{B}_{20}/\text{Pt}$ films (series 2) shows a decrease in density of the Pt layer and increase in interfacial roughness of the CoFeB layer, indicating diffusion at the CoFeB/Pt interface with post deposition annealing above 200°C. We have used terahertz time-domain spectroscopy to measure the electric field amplitude of the emitted THz pulses from $\text{Co}_{20}\text{Fe}_{60}\text{B}_{20}/\text{Pt}$ films (see Fig. 2). Initial analysis shows that interfacial interdiffusion has a significant influence on the THz electric field amplitude. A full analysis of our results will be presented at the conference.

[1] R. M. Woodward et. al., J.Biol.Phys. 29, 257 (2003); [2] K. Kawase et. al., Opt. Express 11, 2549 (2003); [3] S. Baierl et. al., Nat. Photonics 10, 715 (2016); [4] D. Polley et. al., J. Phys. D: Appl. Phys. 51, 084001 (2018); [5] S. Wienholdt et. al. Phys. Rev. Lett. 108, 247207 (2012); [6] T. Kampfrath et. al., Nat. Photonics 5, 31 (2001); [7] M. T. Hibberd et. al., Appl. Phys. Lett. 114, 031101 (2019); [8] T. Seifert et. al., Nat. Photonics 10, 483 (2016); [9] Y. Sasaki et. al., J. Phys. Soc. Jpn. 111, 102401 (2017);

[10] Y. Gao et. al., IRMMW-THz Paris, France, 1-3 (2019) DOI: 10.1109/IRMMW-THz.2019.8874416; [11] S. Mahieu et. al. Thin Solid Films 515, 1229 (2006).

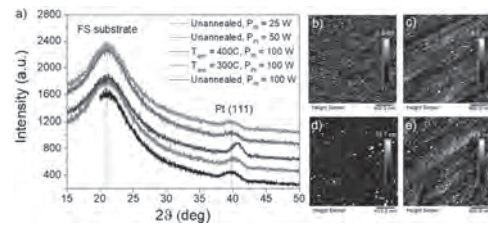


Fig. 1: Structural analysis of $\text{Co}_{20}\text{Fe}_{60}\text{B}_{20}$ (2.5 nm)/Pt (3 nm) thin films deposited onto fused silica substrates. (a) X-ray diffraction spectra for $\text{Co}_{20}\text{Fe}_{60}\text{B}_{20}/\text{Pt}$ films with increasing Pt sputtering power (series 1 = pink - 25 W, and green - 50 W) and annealing temperature (series 2 = black - unannealed, red - $T_{\text{ann}} = 300^\circ\text{C}$ and blue - $T_{\text{ann}} = 400^\circ\text{C}$). (b)-(e) Atomic force microscopy images of (series 2) b) unannealed $\text{Co}_{20}\text{Fe}_{60}\text{B}_{20}/\text{Pt}$ film, and films annealed at c) $T_{\text{ann}} = 200^\circ\text{C}$, d) $T_{\text{ann}} = 300^\circ\text{C}$ and e) $T_{\text{ann}} = 400^\circ\text{C}$. RMS roughness observed to increase with annealing temperature from 0.81 nm (unannealed) to 2.06 nm ($T_{\text{ann}} = 400^\circ\text{C}$).

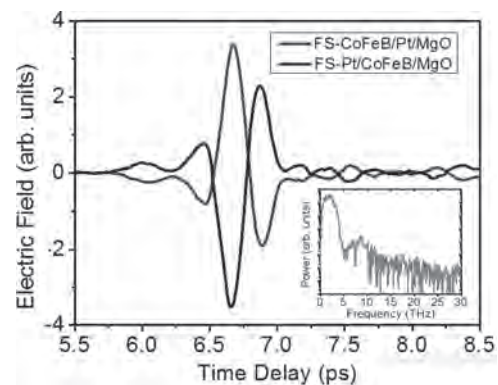


Fig. 2: Example of THz pulses generated from FS-CoFeB/Pt and FS-Pt/CoFeB thin films (capped with MgO), measured using terahertz time-domain spectroscopy. Inset shows the corresponding frequency spectrum for the FS-CoFeB/Pt thin film.

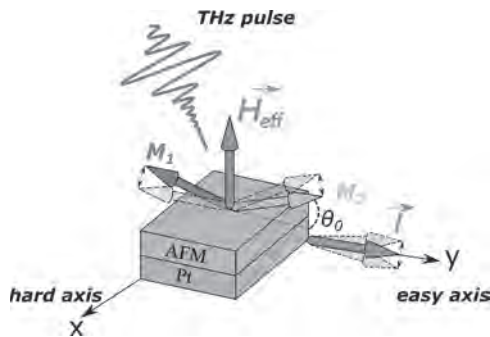
FB-14. Electrically Tunable Detector of THz-Frequency Signals Based on an Antiferromagnet.

P. Stremoukhov^{1,2}, A. Safin^{3,4}, K. Saeedi Ilkhchy¹, C.F. Schippers⁵, R. Lavrijsen⁵ and A. Kirilyuk¹

1. HFML-FELIX Laboratory, Radboud University, Nijmegen, Netherlands; 2. Magnetic Heterostructures and Spintronics Lab, Moscow Institute of Physics and Technology, Moscow, Russian Federation; 3. Kotel'nikov Institute of Radio Engineering and Electronics of RAS, Moscow, Russian Federation; 4. Department of Formation and Processing of Radio Signals, National Research University "Moscow Power Engineering Institute", Moscow, Russian Federation; 5. Department of Applied Physics, Eindhoven University of Technology, Eindhoven, Netherlands

The development of small and simple room-temperature devices capable of generating and/or receiving resonant signals in a "THz-gap" still stands a significant challenge. However antiferromagnetic spintronics promises to be the right direction for the research and development of THz technology. Recently [1], [2], it has been theoretically proposed to use active AFM generators for the detection of external THz-frequency signals via the mechanism of injection-locking of such a signal to the oscillations generated by a DC-current-driven AFM/HM THz generator. An alternative way to develop quasi-passive AFM/HM-based detectors [3] is to use the fact that resonance eigenfrequencies of the AFM dynamic modes (standing AFMR modes) lie in the THz frequency range. It has been shown theoretically in [3], that a dielectric AFM having bi-axial anisotropy, such as NiO, can be used for the resonance quadratic rectification of a linearly-polarized AC spin current of THz-frequency, and could have a sensitivity in the range of 10^2 - 10^3 V/W. In this work [4], we propose the concept of an electrically tunable resonance detector of THz-frequency signals based on an antiferromagnetic/heavy metal bilayer. The conversion of a THz-frequency input signal into DC voltage is done using the inverse spin Hall effect in a bilayer. An additional bias DC current in the HM layer can be used to vary the effective anisotropy of the AFM, and, therefore, to tune the AFMR frequency. The proposed hetero-structure works as a resonance-type quadratic detector which can be tuned by the bias current in the range of at least 10% of the AFMR frequency. In addition, we discuss experimental results obtained during spin-pumping experiments with antiferromagnetic/heavy metal bilayer (NiO/Pt). The results were obtained in the HFML-FELIX laboratory where we have access to intense THz radiation free-electron laser source as well as high DC magnetic fields up to 38T.

[1] O. Gomonay, T. Jungwirth, and J. Sinova. *Physical Review B* 98.10 (2018) [2] R. Khymyn, V. Tiberkevich, and A. Slavin, Book of abstracts "Intermag – 2018", p. 795, (2018) [3] R. Khymyn, V. Tiberkevich, and A. Slavin, *AIP Advances* 7.5 (2017) [4] A. Safin, V. Puliafito, M. Carpentieri, G. Finocchio, S. Nikitov, P. Stremoukhov, A. Kirilyuk, V. Tyberkevych, and A. Slavin *Appl. Phys. Lett.* 117, 222411 (2020)



Schematic view of the THz-frequency resonance detector based on the AFM-Pt structure.

Session FC

GHZ TO THZ PRECESSIONAL MAGNETIZATION DYNAMICS

Matthieu Bailleul, Chair

Universite de Strasbourg, Strasbourg, France

INVITED PAPER

FC-01. High-Frequency Magnetoacoustic Resonance Through Strain-Spin Coupling in Perpendicular Magnetic Multilayers INVITED.

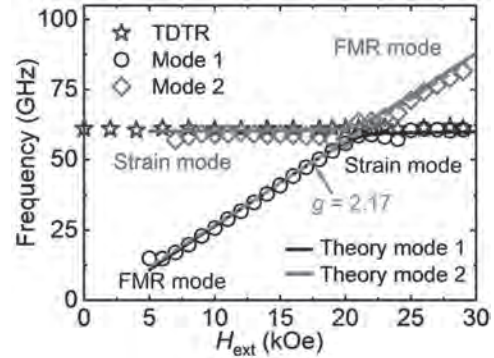
T. Qu¹, D. Lattery², J. Zhu³, D. Zhang¹, J. Wang¹, X. Wang¹ and R. Victora¹

1. University of Minnesota Twin Cities, Minneapolis, MN, United States;
2. Seagate Recording Head Operations, Bloomington, MN, United States;
3. Dalian University of Technology, Dalian, China

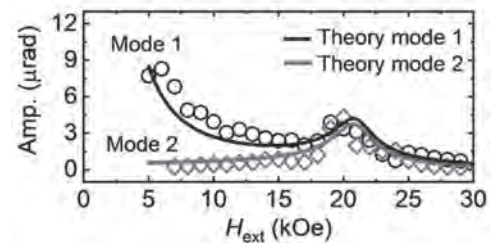
In recent years, magnon-phonon coupling has attracted renewed interest[1] both from the physics and technological perspectives owing to its efficient conversion of energy between magnon and phonon. In particular, the magneto-acoustic resonance, has become a focal point, partly owing to the possibility for rapid switching, which is significant for applications in cloud storage, advanced spin memory, logic, and other spintronic devices. An ultrafast optical approach, specifically femtosecond laser pulses, is a powerful tool to initiate the coupling and its successive detection. The laser pulse simultaneously generates the phonon and magnon, through thermal expansion and fast demagnetization. The thermal expansion produces a local strain or phonon, whose frequency is tunable by both the material composition and geometry. At the same time, the fast demagnetization excites the magnetization out of equilibrium and creates magnons. The femtosecond time scale of the laser pulse benefits the detection of both magnon and phonon, as their dynamics endure longer than the pulse time scale. However, research reported in the literature mostly launch strain electrically in piezoelectric materials, which leads to a different phonon propagation direction. In addition, the literature study of the coupling is confined to materials unsuitable for spintronic applications. These materials, limit the resonance frequency or require low temperature for the magnetoacoustic resonance. To date, direct demonstration of magnon-phonon coupling remains elusive in materials with high perpendicular magnetic anisotropy, which are capable of achieving ultrahigh frequency resonance at room temperature. Here, we report an extremely high frequency magnetoacoustic resonance up to 60 GHz, originating from magnon-phonon coupling in [Co/Pd]_n multilayer with perpendicular magnetic anisotropy. Our theory uncovers the physics of resonance in a coupled system, and is based on the equation of motion for both magnon and phonon, with coupling introduced in the Hamiltonian through the magnetostrictive energy. Owing to the magnon and phonon possessing the same symmetry, the physics at resonance presents an enhanced wave envelope in the time domain, an anticrossing in the frequency domain, and significant hybridization of both magnons and phonons. When the frequencies of magnon and phonon approach each other in the resonance regime, these two modes hybridize into a quasiparticle contributed by both magnon and phonon. This hybridization generates an anticrossing in the dispersion with a frequency gap Δf in Fig. (a), which is quantitatively determined by the coupling coefficient in our model and consistent with our experiment. The amplitudes of both modes increase in the hybridization regime in Fig. (b): the original phonon mode is now highly visible owing to the admixed magnon, the original magnon mode is enhanced owing to the pumping from phonons. In addition, the resonance in the time domain (an enhanced wave envelope) indicates the strain substantially influences the spin dynamics at an ultrafast picosecond time scale. All these physical features are demonstrated in both ultrafast optical measurements and micromagnetic simulations. The ultrafast optical measurements [3] of the time-resolved magneto-optical Kerr effect (TR-MOKE) and time-domain thermoreflectance (TDTR) directly observe the dynamics of magnon and phonon. The frequency and the amplitude of TR-MOKE and TDTR signals are consistent with the modeling, which indicates the transition of the system from hybridization to de-hybridization, controlled by the external applied field. The simulations apply the properties of the [Co/Pd]_n multilayers, whose structures are optimized to achieve a maximum resonance frequency allowable with current experimental settings. All the [Co/Pd]_n multilayers samples were prepared in an ultrahigh vacuum magnetron sputtering system. With an appropriate strain, the simulation predicts that the system is able to undergo a large-angle magnetization precession and achieve a rapid switching. In summary, our work

demonstrates an efficient energy transfer among magnon and phonon at an ultrafast picosecond scale, which paves a potential pathway for enabling an ultrahigh speed strain-assisted magnetization switching in a technologically relevant magnetic system.

[1] A. Kirilyuk, A. V. Kimel, T. Rasing, Ultrafast optical manipulation of magnetic order. *Rev. Mod. Phys.* 82, 2731–2784 (2010). [2] D.-L. Zhang, J. Zhu, T. Qu, D. M. Lattery, R. H. Victora, X. Wang, J.-P. Wang, High frequency magnetoacoustic resonance through strain-spin coupling in perpendicular magnetic multilayers. *Sci. Adv.* 6, eabb4607 (2020) [3] D. B. Huang, D. Lattery, X. Wang, Materials Engineering Enabled by Time-Resolved Magneto-Optical Kerr Effect for Spintronic Applications, *ACS Appl. Electron. Mater.*, 2020 (appears online).



The frequency of the [Co(0.8 nm)/Pd(1.5 nm)]₁₁ multilayers as a function of H_{ext} . Two frequencies of spin precession (mode 1, open black circles; mode 2, open red diamonds) are derived by fitting the experimental data of TR-MOKE. The figure also includes the frequency of acoustic wave measured from TDTR (blue stars). The anticrossing point of mode 1 and mode 2 occur at the resonance field ($H_{ext} \approx 21$ kOe), where the frequencies of modes 1 and 2 split and open a gap Δf . We assign the strain mode as the one with field-independent frequencies that are nearly identical to the acoustic wave frequencies from TDTR. The frequency of the FMR mode increases linearly with H_{ext} .



The individual M_z amplitudes of modes 1 and 2 as a function of H_{ext} for the [Co(0.8nm)/Pd(1.5nm)]₁₁ multilayers. There exists an apparent amplification of both modes due to the coupling between these two modes near the anticrossing point. (Figure is taken from Ref. 2.)

CONTRIBUTED PAPERS

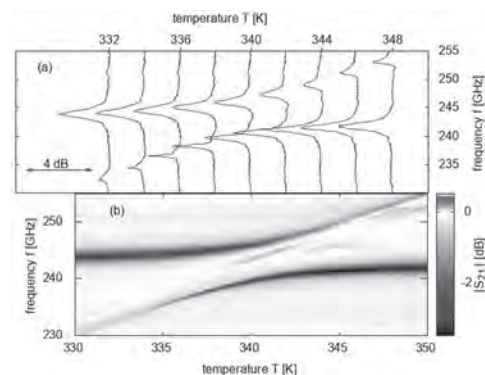
FC-02. Strong Coupling of Antiferromagnetic Resonance With sub-THz Cavity Fields.M. Bialek^{1,2}, J. Zhang², H. Yu² and J. Ansermet¹

1. Ecole Polytechnique Federale de Lausanne, Lausanne, Switzerland;

2. Beihang University, Beijing, China

We study coupling of electromagnetic waves to an antiferromagnetic resonance at THz frequencies [1,2]. In ferromagnetic materials, the Purcell effect and magnon-polaritons were shown [3], allowing single magnon detection [4] or observation of level attraction due to dissipative coupling [5]. Antiferromagnetic materials, in contrast to ferromagnets, are interesting due to their high-frequency dynamics, while they are still characterized by low coupling of spins to the lattice. For applicational reasons their abundance, huge number of existing materials and lack of stray fields are also advantages. However, in the case of antiferromagnets, there are only a few examples of an indirect strong coupling of spin waves with electromagnetic waves [6, 7] or at GHz frequencies [8]. Here, we report a direct and strong magnon-phonon coupling in high-temperature antiferromagnet hematite $\alpha\text{-Fe}_2\text{O}_3$. A cube of hematite (0.2 mm edge length) was placed inside a gold-plated tube (2 mm long, 0.58 mm internal diameter). This cavity has the lowest mode at about 0.24 THz, as predicted by electrodynamic simulations. The cavity was placed inside a double-cone holder that allowed focusing THz beam into the cavity and collecting the transmitted THz beam from it. We measured transmission spectra in the 0.2-0.3 THz frequency band using a continuous wave spectrometer based on extenders to a vector network analyser. This system is characterized by very high dynamic range and very high frequency resolution. We used temperature as a tuning parameter, because the frequency of the antiferromagnetic resonance in hematite rises monotonically with it from room temperature until about 700 K. Our data (Fig. 1) show very clear avoided crossing of the cavity mode and the antiferromagnetic resonance with the minimum splitting of about 6 GHz and the cooperativity factor of about 40. The splitting predicted by a microscopic model [3] is about 15 GHz. The difference is caused by imperfect matching of the cavity magnetic field with the magnetic moment of the antiferromagnetic resonance in the cube, that is confirmed by electrodynamic simulations. We notice that we can tune the coupling between the experimental setup and the cavity that results in different lineshapes of the cavity mode. We fitted observed spectra with a model based on the input-output theory [3]. We also observed coupling with higher order modes of the cavity that is not as clear as with the lowest mode. We acknowledged support by the Sino-Swiss Science and Technology Cooperation (SSSTC) grant no. EG-CN_02_032019, EPFL and the SNF R'Equip under Grant No. 206021_144983.

[1] M. Bialek, J. Zhang, H. Yu et al, arXiv:2012.10910 [2] D. L. Mills and E. Burstein, Rep. Prog. Phys. 37, 817 (1974). [3] H. Huebl, Ch. W. Zollitsch, J. Lotze et al, Phys. Rev. Lett. 111, 127003 (2013). [4] D. Lachance-Quirion, S. P. Wolski, Y. Tabuchi et al, Science 367, 425 (2020). [5] M. Harder, Y. Yang, B. M. Yao et al, Phys. Rev. Lett. 121, 137203 (2018). [6] X. Li, M. Bamba, N. Yuan et al, Science 361, 794 (2018). [7] P. Sivarajah, A. Steinbacher, B. Dastrup et al, J. Appl. Phys. 125, 213103 (2019). [8] J. R. Everts, G. G. G. King, N. J. Lambert et al, Physical Review B 101, 214414 (2020).



(a) Normalized transmission spectra at different temperatures. (b) Normalized transmission spectra in a form of map.

FC-03. Characterizing Interlayer Coupling in Synthetic Ferromagnetic Thin Films.

H.J. Waring¹, Y. Li¹, C. Moutafis¹, I. Vera-Marun² and T. Thomson¹

1. Computer Science, The University of Manchester, Manchester, United Kingdom; 2. Physics and Astronomy, The University of Manchester, Manchester, United Kingdom

The phenomena of interlayer exchange coupling (J_{IEC}) between thin ferromagnetic (FM) layers allows materials with precisely tailored properties to be created, and is key to the future development of spintronics. Synthetic ferromagnets (SFMs) have the same FM/Non-magnetic(NM)/FM structure as the widely studied Synthetic Antiferromagnet (SAF) [1], but describe the case where the magnetisation of the two FM layers are aligned in parallel. The structure of a SFM and its resonant dynamics is shown in Fig.1a. It is known that the formation of a double resonance consisting of an Acoustic Mode (AM) and an Optic Mode (OM) requires a difference in layer magnetisation (M_{Diff}) and a FM J_{IEC} [2] [3]. However, to date, a comprehensive description of the resonant properties as a function of J_{IEC} and difference in layer magnetisation has not been reported despite their widespread use in quasi-static devices [4]. Here, we investigate, both experimentally and via numerical simulations, the hitherto uncharted dependence of the observed double resonance on M_{Diff} and J_{IEC} [5]. The samples were fabricated using magnetron sputtering and characterized by X-ray Reflectivity (XRR) to measure layer thickness, vector Vibrating Sample Magnetometry (VSM) to verify AF coupling and a Vector Network Analyser – Ferromagnetic Resonance (VNA-FMR) setup which allows fundamental dynamic properties to be explored. These SFMs exhibited a J_{IEC} consistent with coupling on the 1st FM RKKY coupling peak and have structure Ta(2 nm)/CoFeB(5 nm)/Ru(t_{Ru})/CoFeB(5 nm)/Pt(4 nm) where t_{Ru} is the thickness of the ruthenium layer, acting as the non-magnetic spacer layer. Our simulations, performed using MuMax³, show that M_{Diff} and J_{IEC} have orthogonal dependencies on the two resonant modes. We further demonstrate that the conventional understanding of the phases of these modes, described as possessing an in-phase or out-of-phase nature for the AM and OM respectively, does not capture fully the intricacy of the resonant dynamics. Comparison between experimental and simulated data allows M_{Diff} , J_{IEC} and the resonant phases of each mode to be accurately determined. These findings are directly applicable to the creation of tailored SFMs for spintronic devices with applications in STT/SOT-MRAM where control of these parameters is paramount [3] [6].

[1] H. J. Waring, N. A. B. Johansson, I. J. Vera-Marun et al., Zero-field Optic Mode beyond 20 GHz in a Synthetic Antiferromagnet, *Phys. Rev. Appl.*, Vol. 13, p. 034035 (2020) [2] B. Heinrich and J. F. Cochran, Ultrathin metallic magnetic films: magnetic anisotropies and exchange interactions, *Adv. Phys.*, Vol. 42, p. 523–639 (1993) [3] T. McKinnon, P. Omelchenko, B. Heinrich et al., FMR study of interlayer exchange coupling in FeCoB|Ta|FeCoB trilayers with in-plane anisotropy, *J. Appl. Phys.*, Vol. 123, p.223903 (2018) [4] T. Devolder, E. Liu, J. Swerts et al., Ferromagnetic resonance study of composite Co/Ni - FeCoB free layers with perpendicular anisotropy, *Appl. Phys. Lett.*, Vol. 109, p.142408 (2016) [5] H. J. Waring, Y. Li, I. J. Vera-Marun et al. *Phys. Rev. Lett.*, Manuscript In Preparation. [6] S. Yakata, H. Kubota, T. Seki et al., Enhancement of thermal stability using ferromagnetically coupled synthetic free layers in MgO-based magnetic tunnel junctions, *IEEE Trans. Magn.*, Vol. 46, p. 2232–2235 (2010)

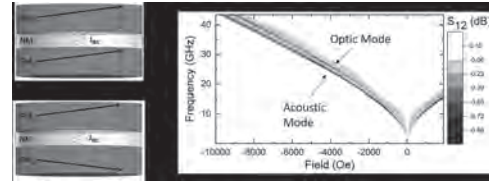


Fig.1 a) The resonant dynamics of a synthetic ferromagnetic (SFM) system with a ferromagnetic (FM₁)/non-magnetic (NM)/FM₂ structure and a FM interlayer exchange coupling J_{IEC} . An optic mode is seen in addition to the acoustic mode only in cases where the layer magnetization of FM₁ ($M_{s,1}$) and FM₂ ($M_{s,2}$) are different. **b)** 2D map of the resonant spectra of a SFM when the NM spacer layer, consisting of Ru, thickness $t_{\text{Ru}} = 1.10\text{nm}$.

FC-04. FMR and Thermal Spin Pumping in Garnets|Pt Bilayers.

L.M. Solís^{1,2}, S. Carreira⁴, M. Aguirre^{2,3}, L. Steren¹, A. Butera⁵, J. Gómez⁵, J. Briático⁴ and C. García⁶

1. Centro Atómico Constituyentes, San Martín, Argentina; 2. Universidad de Zaragoza Instituto de Nanociencia de Aragón, Zaragoza, Spain; 3. Universidad de Zaragoza Departamento de Física de la Materia Condensada, Zaragoza, Spain; 4. Unite Mixte de Physique CNRS/Thales, Palaiseau, France; 5. Centro Atómico Bariloche, Bariloche, Argentina; 6. Universidad Tecnica Federico Santa Maria Departamento de Física, Valparaíso, Chile

The $\text{Y}_3\text{Fe}_5\text{O}_{12}$ (YIG) ferrimagnetic insulator is recognized as a model system for spintronic and magnonic phenomena, including spin pumping, spin Seebeck, proximity effects, and spin wave propagation. In these materials, the spin current is produced by spin-waves or magnons. Magnons can be electrically excited and sensed via the Spin Hall Effect (SHE) and Anomalous Spin Hall Effect (ASHE) or they can be thermally excited through the Spin Seebeck Effect (SSE). To detect the spin current, a thin non-magnetic layer such as Pt is deposited on top of the material of interest. This transforms the spin current into an observable thermoelectric voltage (V_{SSE}) via the Inverse Spin Hall Effect (ISHE). Pt/YIG systems allow efficient spin-charge conversion and pure detection of spin-current effects, respectively, due to their unique magneto-optical and spin dynamic properties [1]. These properties allow a clean detection of the pure spin current thanks to the spin-orbit effects in the Pt/YIG microstructures [2]. Additionally, Rare Earth (RE) garnet films are magnetic and magnetoelastic, and their properties can be manipulated through choice of composition and substrate. When a proportion of bismuth (Bi) is added, the magneto-optical properties of YIG increase according to the concentration of bismuth (Bi) at the yttrium site [3]. But there are few studies on how the spin dynamic properties are modified due to this substitution. In this work we study different parameters in the manufacture of ferrimagnetic/non-magnetic bilayers to raise the thermoelectric spin voltage V_{SSE} . Samples with different thicknesses of pure $\text{Y}_3\text{Fe}_5\text{O}_{12}$ (YIG) films and a 5% Bi substitution, that is, thin films of $\text{BiY}_2\text{Fe}_5\text{O}_{12}$ (BiYIG), were grown on $\text{Gd}_3\text{Ga}_5\text{O}_{12}$ (111) and $\text{Gd}_3\text{Sc}_2\text{Ga}_3\text{O}_{12}$ (111) substrates by pulsed laser deposition (PLD). XRD, HR-TEM / STEM-HAADF and GPA measurements revealed high quality crystalline films as it can be seen in Figure 1. Ferromagnetic resonance (FMR) measurements were performed at room temperature for all heterostructures. A resonance field (H_{res}) and a resonance linewidth (FWHM) were extracted and are shown in Figure 2 as a function of frequency. These values allow the calculation of a Gilbert damping coefficient that is directly correlated with the SSE according to Chang et. Al [4]. In our case, the Gilbert damping coefficient is $(5-14) \times 10^{-4}$ for the YIG//GGG samples and $(18-19) \times 10^{-4}$ for the YIG//SGGG samples. The linewidth of BiYIG samples is much wider. After growth of an 8 nm-Pt coating layer by sputtering, the damping in all the samples increases due to the contribution due to spin pumping from the YIG or BiYIG to the metal film. The difference between the H_{eff} result and the bulk value of $4\pi M_s$ reported (1750 G [5]) demonstrates the existence of a perpendicular anisotropy. With a maximum 20K thermal difference across the entire structure, we measure longitudinal SSE voltages in both YIG and BiYIG samples with sputtered Pt. The YIG//SGGG combination reported to have the best voltage signal from the Inverse spin-Hall effect (V_{ISHE}) and Spin Seebeck Effect (V_{SSE}), along with the co-occurrence of a positive perpendicular anisotropy. In the case of the BiYIG samples, the voltages induced in the BiYIG//SGGG bilayers were lower with respect to YIG//SGGG but higher with respect to YIG//GGG. The samples with the lowest perpendicular magnetic anisotropy showed the highest V_{SSE} in both cases, YIG and BiYIG. This work is funded thanks to the SPICOLST (GA 734187) project framed within ‘‘Horizon 2020 Funding’’ of the European Union with the MARIE SKŁODOWSKA-CURIE - RISE Actions (Research and Innovation Staff Exchanges) program coordinated by the University of Zaragoza.

[1] S. M. Rezende, R. L. Rodríguez-Suárez, and R. O. Cunha, Physical Review B, Vol. 89, p. 014416 (2014) [2] C. Du, H. Wang, and P. C. Hammel, Journal of Applied Physics, Vol. 117, p. 172603 (2015) [3] R. Kumar, B. Samantaray, and Z. Hossain, Journal of Physics: Condensed Matter, Vol. 31, p. 435802 (2019) [4] H. Chang, P. P. Janantha, and J. Ding,

Science advances, Vol. 3, p. e1601614 (2017) [5] Bhoi B., Journal of Alloys and Compounds, Vol. 797, p. 523-528 (2019)

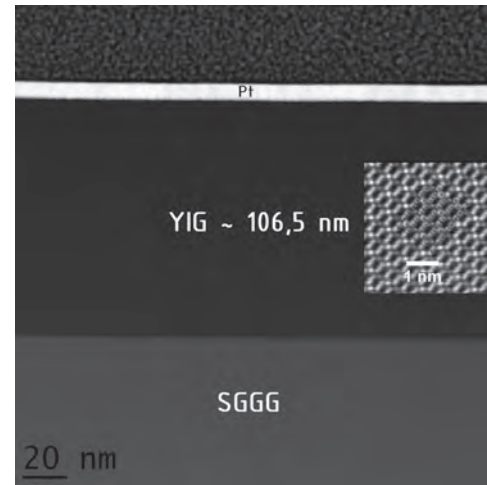


Figure 1: Structural characterization at room temperature of the $\text{Y}_3\text{Fe}_5\text{O}_{12}$ film grown on $\text{Gd}_3\text{Sc}_2\text{Ga}_3\text{O}_{12}$ (111) crystal by PLD with an 8 nm-Pt coating layer grown by sputtering. Measurements were made by HRTEM / STEM-HAADF.

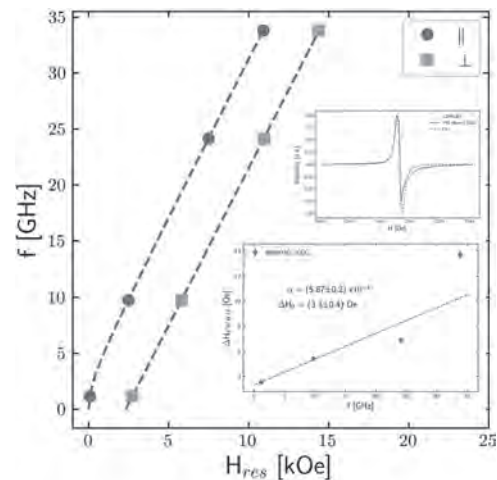


Figure 2: Room temperature ferromagnetic resonance measurements (FMR) of raw 66nm - $\text{Y}_3\text{Fe}_5\text{O}_{12}$ film grown on $\text{Gd}_3\text{Ga}_5\text{O}_{12}$ (111) crystal by PLD. The resulting α value is 5.8 ± 0.2 . The difference between H_{eff} (2335 G) and the bulk value of $4\pi M_s$ reported (1790 G) demonstrates the existence of a perpendicular anisotropy.

FC-05. Time Resolved MOKE Study of the Ta/CoFeB/MgO Films.

Y. Gong¹, X. Lu¹, J. Su², Z. Chen¹, L. Yang¹, Y. Yan¹, X. Ruan¹, J. Du³, J. Cai², J. Wu⁴, L. He¹, R. Zhang¹ and Y. Xu^{1,4}

1. School of Electronic Science and Engineering, Nanjing University, Nanjing, China; 2. Institute of Physics, Chinese Academy of Sciences, Beijing, China; 3. Department of Physics, Nanjing University, Nanjing, China; 4. Department of Electronics and Physics, University of York, York, United Kingdom

CoFeB thin film has been demonstrated to be a promising material for spintronics devices such as Spin-transfer torque magnetic random access memory (STT-MRAM) with high perpendicular magnetic anisotropy (PMA) and low Gilbert damping.¹ In this work, we have investigated the ultrafast laser induced magnetization precession, especially the magnetic damping, of a series of Ta/CoFeB/MgO thin films using the pump-probe time-resolved magneto-optical Kerr effect (TR-MOKE) measurements. A series of samples: Si substrate/MgO(3)/CoFeB(tCoFeB)/Ta(5) with different ferromagnetic layer thickness = 7.3, 3.7, 2.2, 1.3, 1.2, 1.0, 0.9 (numbers are thickness in nanometers) are fabricated by magnetron sputtering. In TR-MOKE measurements, the pump laser pulse with 800 nm wavelength and a fluence varying from 1.4 to 12.7 mJcm² was used to trigger the magnetization dynamics while the probe laser pulse was frequency-doubled to 400 nm wavelength. We found an interesting relationship between pump fluence and damping. In thick samples (tCoFeB ≥ 3.7 nm) α_0 increases continuously with increasing pump fluence, but remains almost unchanged in medium thick samples (1.3 nm ≤ tCoFeB ≤ 2.2 nm). In thin samples (tCoFeB ≤ 1.2 nm), intrinsic damping constant α_0 shows decreasing trends with varying rates. According to our previous investigations, the contributions of α_0 can be classified as two part: the bulk damping term named α_{bulk} and the interfacial damping named α_{inter} , which is related to the spin pumping effect.^{2,3} Our findings provide some insight into the ultrafast laser pulse stimulated dynamic magnetic precession in MgO/CoFeB/Ta structures, which is valuable for the development of high-performance spintronic devices such as STT-MRAM.

1. Liu, T., Zhang, Y., Cai, J.W., Pan, H.Y. Thermally robust Mo/CoFeB/MgO trilayers with strong perpendicular magnetic anisotropy. *Sci. Rep.* 4, 5895 (2014). 2. Liu, B., *et al.* Femtosecond laser-heating effect on the magnetization dynamics in perpendicularly magnetized Ta/CoFeB/MgO film. *New J. Phys.* 21, 053032 (2019). 3. Liu, B., *et al.* Transient enhancement of magnetization damping in CoFeB film via pulsed laser excitation. *Appl. Phys. Lett.* 109, 042401 (2016). 4. Panda, S.N., Mondal, S., Sinha, J., Choudhury, S., Barman, A. All-optical detection of interfacial spin transparency from spin pumping in β -Ta/CoFeB thin films. *Sci. Adv.* 5, eaav7200 (2019).

FC-06. Electric-Field Modulation of Perpendicular Magnetic Anisotropy and Damping Constant in MgO/Co/Pt Trilayers.

A. Sakoguchi¹, T. Kato², D. Oshima² and S. Iwata³

1. Department of Electronics, Nagoya University, Nagoya, Japan;
2. Institute of Materials and Systems for Sustainability, Nagoya University, Nagoya, Japan; 3. Koeki Zaidan Hojin Nagoya Sangyo Kagaku Kenkyujo, Nagoya, Japan

Voltage controlled magnetic anisotropy (VCMA) has attracted much attention, since it can dramatically reduce the power consumption during the writing in magnetic random access memory (MRAM) [1]. The voltage-induced anisotropy change triggers the magnetization precession, and a stable magnetization switching is confirmed by the application of appropriate voltage pulses [1]. It is also reported that the stable switching is significantly influenced by the relaxation time of the magnetization precession [2], and thus the magnetization dynamics under the application of the electric field is an important topic to be understood [2]. In this study, we report the electric-field modulation of perpendicular magnetic anisotropy (PMA) and the magnetization dynamics in MgO/Co/Pt trilayers by using time-resolved magneto-optical Kerr effect (TRMOKE). ITO(20)/MgO(10)/Co(1.2)/Pt(1.6)/Ta(10)/oxidized Si substrate (thickness in nanometer) was prepared by using a magnetron sputtering system. The film was microfabricated into a Hall-bar structure and a gate electrode of ITO(15 nm) was deposited on the junction. Gate voltage was applied from -3 V to 3 V corresponding to the electric field from -0.3 V/nm to 0.3 V/nm. To investigate PMA, we measured anomalous Hall effect (AHE). The magnetization dynamics was measured by TRMOKE using high-power fiber laser with $\lambda=1040$ nm, a pulse width of 500 fs, and a repetition frequency of 100 kHz. During the measurement, an external magnetic field H_{ext} in the range of 5-14 kOe was applied in the direction of 73 deg from the film normal. The measured precession was fitted with the damped oscillation function, $\exp(-t/\tau)\sin(\omega t)$, where τ and ω denote relaxation time and angular frequency of the precession. By fitting the H_{ext} dependence of ω , we estimated effective magnetic anisotropy field H_k and g-factor. Figure 1 shows the electric field E dependence of H_k estimated from AHE and TRMOKE. H_k decreases linearly with increasing the electric field in both measurements. The variation of PMA with the electric field η obtained from AHE and TRMOKE were -32 fJ/Vm and -47 fJ/Vm, respectively. Figure 2 (a) shows the electric field dependence of the inverse of relaxation time $1/\tau$ obtained at $H_{\text{ext}}=14$ kOe. $1/\tau$ is known to consist of four contributions; effective Gilbert damping α_{eff} , anisotropy axis distribution $\Delta\theta_H$, anisotropy distribution ΔH_k and two-magnon scattering (TMS). The four contributions depend on H_{ext} and E , since H_k depends on E , and we fitted H_{ext} and E dependences of $1/\tau$ by assuming material-dependent parameters which are independent of H_{ext} and E . The extracted four contributions at $H_{\text{ext}}=14$ kOe are also shown in Fig. 2 (a). The results indicate a large electric-field modification of $1/\tau$ is caused by the two contributions: effective Gilbert damping and $\Delta\theta_H$, which have the same trend as the electric-field modification of $1/\tau$. Figure 2 (b) shows the electric field dependence of α_{eff} . α_{eff} is found to decrease with increasing electric field with a ratio of -13 % per 1 V/nm. Okada *et al.* reported a ferromagnetic resonance (FMR) study on MgO/CoFeB/Ta trilayers, and they showed PMA variation of $\eta=-60$ fJ/Vm and α modulation of -21 % per 1 V/nm [3]. These results are similar to our results, however their samples have MgO(001)/bcc-CoFe interface. Our study indicates similar PMA and α modulations are found in MgO/Co/Pt trilayers having MgO(111)/fcc-Co interface.

[1] Y. Shiota, *et al.*, Nat. Mater., 11, 39 (2011). [2] R. Matsumoto, *et al.*, Appl. Phys. Express 12, 053003 (2019) [3] A. Okada, *et al.*, Appl. Phys. Lett. 105, 052415 (2014).

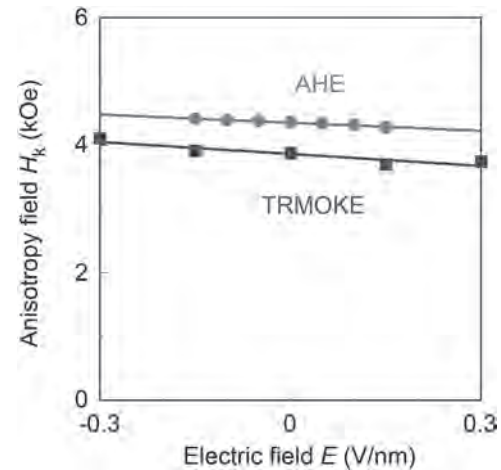


Fig.1 Electric field dependence of effective magnetic anisotropy field H_k of the MgO/Co/Pt trilayers.

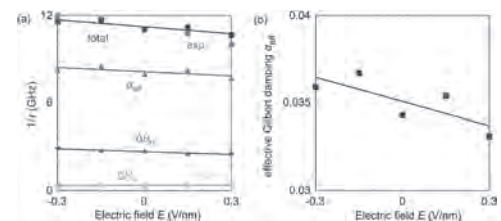


Fig.2 (a) Electric field dependence of the inverse of relaxation time $1/\tau$ at an applied magnetic field $H_{\text{ext}}=14$ kOe. Four contributions to $1/\tau$: effective Gilbert damping α_{eff} , anisotropy axis distribution $\Delta\theta_H$, anisotropy distribution ΔH_k and two-magnon scattering, are extracted by the fitting of H_{ext} and E dependences of $1/\tau$, and are plotted in the same figure. (b) Electric field dependence of the effective damping constant α_{eff} of the MgO/Co/Pt trilayers.

FC-07. Magnetization Dynamics of Ultrathin [CoFeB (t_{CoFeB}) / Pd] $_N$ Films With Perpendicular Magnetic Anisotropy.

A.S. Silva¹, S. Sá¹, S.A. Bunyae¹, C. Garcia², Í.J. Sola³, G.N. Kakazei¹, H. Crespo¹ and D. Navas⁴

1. Institute of Physics for Advanced Materials, Nanotechnology and Photonics (IFIMUP)/Departamento de Física e Astronomia, Universidade do Porto Faculdade de Ciências, Porto, Portugal; 2. Departamento de Física y Centro Científico Tecnológico de Valparaíso-CCTVal, Universidad Tecnica Federico Santa Maria, Valparaiso, Chile; 3. Laser Applications and Photonics group, Applied Physics Department, Universidad de Salamanca, Salamanca, Spain; 4. Instituto de Ciencia de Materiales de Madrid, Madrid, Spain

Thin films with perpendicular magnetic anisotropy (PMA) have been widely studied for perpendicular recording media since the middle of the 1970s when Prof. Iwasaki suggested this approach [1]. Since then, a great effort has been done by the research community for the use of this kind of nanostructures with PMA in other technological applications such as in high-density spin-transfer torque magnetic random access memories (STT-MRAM) [2], skyrmion-based devices [3] or even in synthetic antiferromagnets for biomedical applications [4]. PMA in thin films can be usually achieved through different strategies such as by using materials with large magnetocrystalline anisotropy energy [5] as well as multilayer thin films with high surface anisotropy energy contributions [6]. Regarding the last alternative, Ikeda *et al.* [2] demonstrated in 2010 that amorphous CoFeB ultrathin films can show PMA and it is supported by the CoFeB/MgO interfacial anisotropy contribution. Since then, the development of non-magnetic/ferromagnetic superlattices with PMA, using CoFeB alloys as the ferromagnetic element, has received great attention. In particular, PMA in CoFeB/Pd was first demonstrated in bilayers by Fowley *et al.* [7] as well as in multilayers by Jung *et al.* [8]. Literature has reported that the effective anisotropy energy depends on the thickness of magnetic (t_{CoFeB}) and non-magnetic (t_{Pd}) layers as well as on the number of bilayers (N). In this work, the dynamical response of [CoFeB (t_{CoFeB}) / Pd (10 Å)] $_5$ multilayered ultrathin films ($1 \text{ \AA} \leq t_{CoFeB} \leq 5 \text{ \AA}$) were studied by using two complementary methods: broadband ferromagnetic resonance (Figure 1 a) and time-resolved magneto-optical Kerr effect (Figure 1 b). The perpendicular magnetization was confirmed for multilayers with $t_{CoFeB} \leq 4 \text{ \AA}$, while magnetization became in-plane oriented for $t_{CoFeB} \geq 5 \text{ \AA}$. This behaviour was explained by considering competing contributions from surface and magnetoelastic anisotropies. In addition, we have observed that the effective damping parameter is reduced with increasing t_{CoFeB} (Figure 1 c), and the lower parameter, $\alpha_{eff} \approx (0.019 \pm 0.001)$, was determined for the multilayer with 4 Å CoFeB thickness. We have suggested that for $t_{CoFeB} \geq 4 \text{ \AA}$ the layer is continuous and the main contribution to effective damping is coming from spin-pumping when for lower thicknesses α_{eff} is dominated by two-magnon scattering. Afterwards, we have studied the magnetic behaviour of ultrathin [CoFeB(t_{CoFeB})/Pd(10 Å)] $_N$ films. Intending to ensure that the system shows PMA, t_{CoFeB} (3 or 4 Å) was fixed, while the number of bilayers (N) was ranged from 3 to 15. We observed that our samples show PMA and it is generally improved with N . In addition, we studied the dependence of α_{eff} with the number of CoFeB/Pd repeats (N). Up today, literature in superlattices with PMA reported that α_{eff} is proportional, inversely proportional or even, independent of N [9]. Therefore, the reported relationship between the damping parameter and N in superlattices with PMA is still unclear. We show that the evolution of α_{eff} with N shows a complex behaviour that we have correlated with the magnetization process: larger α_{eff} for samples with square hysteresis loops while α_{eff} is independent of N for samples with bow-tie-shaped hysteresis loops.

1. S. Iwasaki, Y. Nakamura and K. Ouchi, IEEE Trans. Magn., MAG-61, 1456 (1979). 2. S. Ikeda *et al.*, Nat. Mater, 9, 721 (2010). 3. C. Moreau-Luchaire *et al.*, Nature Nanotechnology, 11, 444 (2016). 4. R. Mansell *et al.*, Sci. Rep., 7, 4257 (2017). 5. N. Inaba, Y. Uesaka, and M. Futamoto, IEEE Trans. Magn., 36, 54 (2000). 6. C. J. Tatnall *et al.*, J. Magn. Magn. Mater., 165, 391 (1997). 7. C. Fowley *et al.*, IEEE Trans. Magn., 46, 2116 (2010). 8. J. H. Jung *et al.*, Appl. Phys. Express, 3, 023001 (2010). 9. A. Barman *et al.*, J. Appl. Phys., 101, 09D102 (2007); S. Mizukami *et al.*, Appl. Phys.

Express, 4, 013005 (2011); H.-S. Song *et al.*, Appl. Phys. Lett., 102, 102401 (2013).

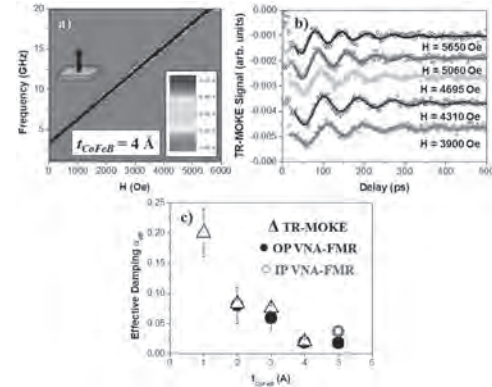


Fig. 1. (a) VNA-FMR spectra of the [CoFeB (4 Å) / Pd (10 Å)] $_5$ multilayer thin film with the external magnetic field applied perpendicularly to the sample plane. (b) Time-resolved magneto-optical Kerr effect (TR-MOKE) signals of a [CoFeB (2 Å) / Pd (10 Å)] $_5$ multilayer thin film under different external applied fields ($H = 5650, 5060, 4695, 4310 \text{ Oe}$ and 3900 Oe) and when H was applied at $\theta_H = 78^\circ$. Theoretical curves (solid curves) are fits to the experimental data (open symbols). Data was moved along the vertical axis for clarity. (c) Evolution of the effective damping (α_{eff}) vs t_{CoFeB} and determined from the TR-MOKE measurements (Δ), the perpendicular VNA-FMR (\bullet) and the in-plane VNA-FMR (\circ) measurements.

FC-08. Control of Static and Dynamic Magnetic Properties of $\text{Ni}_x\text{Fe}_{100-x}$ Alloy Thin Films.

M.R. McMaster¹, W. Hendren¹, J. Scott¹ and R. Bowman¹

¹ Mathematics and Physics, Queen's University Belfast, Belfast, United Kingdom

Tailoring and control of electromagnetic properties of synthetic magnetic structures is advantageous for high frequency applications, such as shielding materials in magnetic recording, where characterisation in the gigahertz frequency range is necessary to determine parameters for simulations and aid component design. In such applications it is desirable to have a high saturation magnetization, low coercivity, high permeability and close to zero magnetostriction. Meeting almost all of these requirements, NiFe is the material of choice for many high frequency applications. We present a systematic study of the effects of process settings, dopants and composition on the ferromagnetic resonance (FMR) and spin wave properties of $\text{Ni}_x\text{Fe}_{100-x}$ alloy thin films fabricated by magnetron sputtering and investigated using a coplanar waveguide, vector network analyser (VNA) [1], vibrating sample magnetometer (VSM) and x-ray diffraction (XRD), with the aim to determine any relation between microstructure and the static and dynamic magnetic properties. It has been found that changes in the NiFe crystal structure and deposition can have significant impact on the magnetic properties, examples of which can be seen in Fig. 1 and 2. This work extends into compositionally modulated superlattice structures to explore further possibilities with respect to material design and optimization [2]. VAMPIRE [3] atomistic simulations have been employed in conjunction with these experiments and to provide parameters for FMR simulations using the micromagnetic model, OOMMF [4].

[1] Y. Ding et al. J. Appl. Phys. 96. (2004) [2] C.B. Hill et al. Meas. Sci. Technol. 24. (2013) [3] R.F.L. Evans et al. J. Phys.: Condens. Matter 26, 103202 (2014) [4] M. J. Donahue and D. G. Porter, "OOMMF User's Guide, Version 1.0," NISTIR 6376, National Institute of Standards and Technology, Gaithersburg, MD (Sept 1999).

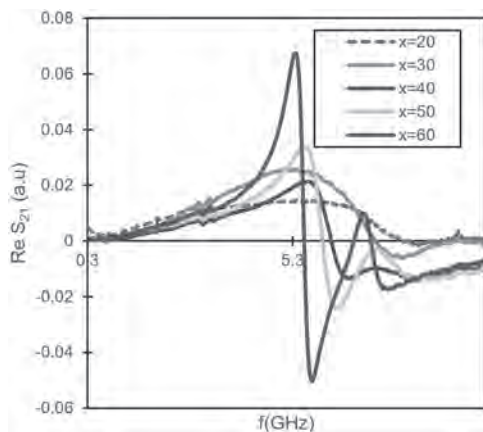


Fig. 1 : FMR spectra at an applied field of 2530e showing the broadening of the FMR and therefore increased damping with increasing Fe content in $\text{Ni}_x\text{Fe}_{100-x}$ thin films. Note particularly the most significant changes occur at $x=40$ which marks the fcc/bcc transition.

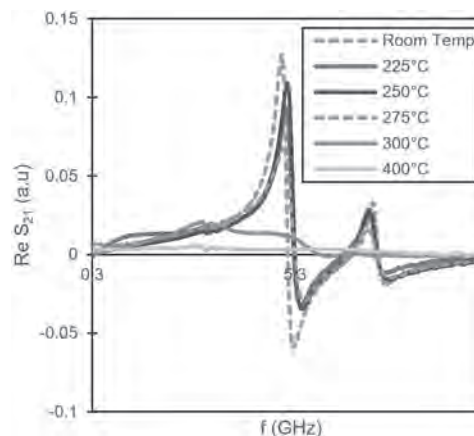


Fig. 2 : FMR spectra at an applied field of 2530e illustrating the effect of increasing substrate temperature during deposition on $\text{Ni}_{80}\text{Fe}_{20}$, where a suppression of the FMR response is seen at 300°C and above.

FC-09. Physical Mechanism Governing Sigmoid Curves of Stochastic Magnetic Tunnel Junctions.

K. Kobayashi¹, W.A. Borders¹, S. Kanai^{1,2}, K. Hayakawa¹, S. Fukami^{1,3} and H. Ohno^{1,4}

1. Laboratory for Nanoelectronics and Spintronics, Research Institute of Electrical Communication, Tohoku University, Sendai, Japan; 2. Division for the Establishment of Frontier Sciences, Organization for Advanced Studies, Tohoku University, Sendai, Japan; 3. Center for Spintronics Research Network, Tohoku University, Sendai, Japan; 4. Center for Science and Innovation in Spintronics, Tohoku University, Sendai, Japan

Unconventional computing utilizing the probabilistic nature of physical systems – probabilistic computing – has recently gathered much attention for its potential to effectively address computationally complex problems [1]. A stochastic magnetic tunnel junction (MTJ) is a promising element to construct a probabilistic bit (p-bit), a fundamental building block of the probabilistic computers, owing to fast fluctuation rate and high controllability as well as the manufacturability based on current spin-transfer torque (STT) magnetoresistive random access memory (MRAM) technology. Recently, a proof of concept of the probabilistic computer using stochastic MTJs was presented, where integer factorization was demonstrated as an illustrative example of a combinatorial optimization problem [2]. Performance of stochastic MTJs is characterized by a time-varying fluctuation of magnetization and time-averaged response to the external field and current, and in this regard, understanding the physical mechanism governing these properties is of high importance. In this research, we investigate the mechanism governing the sigmoid-like time-averaged response to external field and current in stochastic MTJs with various sizes. We use the same stack structure used in the demonstration of integer factorization [2], *i.e.*, Ta(5)/ Pt(5)/ synthetic ferrimagnet/ Ta(0.3)/ Co₁₉Fe₅₆B₂₅(1)/ MgO(1.1)/ Co₁₉Fe₅₆B₂₅(*t*)/ Ta(5)/ Ru(5) (thickness in nm), which is deposited by dc/rf magnetron sputtering on a thermally oxidized Si substrate. Both top and bottom CoFeB layers have perpendicular easy axis. We design the thickness of the free layer *t* so that the thermal stability factor Δ_0 is low enough to show superparamagnetic behavior. All films are processed into MTJs with various junction diameters *D* by electron beam lithography and Ar ion milling. We determine *D* of each device from their electrically measured resistance *R*, with a resistance area product *RA* determined from several MTJs with *D* ~ 80 nm. Typical TMR ratio is 90% and *RA* = 6.3 Ωμm². The measurement circuit for the time-averaged resistance $\langle R \rangle$ is shown in Fig. 1(a). We monitor the magnetization fluctuation of the MTJ by measuring *R* vs. time under dc bias current *I* with various magnitudes using an oscilloscope connected in parallel to the MTJ. The relaxation time τ of the studied MTJ is found to range from 1 ms to 1 s, corresponding to Δ_0 of 14 to 21, by assuming the Néel-Arrhenius law, $\tau = \tau_0 \exp \Delta_0$ with τ_0 being attempt time 1 ns [3]. The $\langle R \rangle$ against external perpendicular magnetic field *H* and *I* for the MTJ with nominal *D* = 50 nm are shown in Figs. 1(b) and (c), respectively. Clear sigmoidal-like characteristics with respect to *H* and *I* are observed as a result of the change of the ratio of τ in parallel (P) and anti-parallel (AP) states τ_p/τ_{AP} . We normalize $\langle R \rangle$ using resistances at P and AP states as $\langle r \rangle \equiv \tau_p/(\tau_p + \tau_{AP})$. The normalized sigmoid curves $\langle r \rangle$ against *H* and *I* are shown in Figs. 1(d) and (e), respectively. In order to characterize the external field and current dependences of stochasticity of MTJs, we derive an analytical expression of the slope of the sigmoidal curve around the center ($\langle r \rangle = 1/2$) [see Figs. 1(d) and (e)]. We define the shift current I_s and the shift field H_s as *I* and *H* to take $\langle r \rangle = 1/2$ (P state probability of 50%), respectively. When MTJs are in P (AP) state, τ is given by $\tau_{P(AP)} = \tau_0 \exp \{ \Delta_0 [1 \pm (I - I_s)/I_{C0}]^{n_t} \}$, where n_t is a switching exponent for *I* and I_{C0} the intrinsic critical current. Here, we assume $n_t = 2$, which was derived by analyzing the Fokker-Planck equation [4]. Then, the partial derivative of $\langle r \rangle$ ($= \tau_p/(\tau_p + \tau_{AP})$) with respect to *I* at $I = I_s$ is derived to be $\partial \langle r \rangle / \partial I|_{I=I_s} = \Delta_0 / I_{C0}$, which has been used as a figure of merit of STT switching in nonvolatile MTJs [5-7]. We apply the same procedure for $\partial \langle r \rangle / \partial H$ and obtain $\partial \langle r \rangle / \partial H|_{H=H_s} = \Delta_0 / H_K^{\text{eff}}$ with H_K^{eff} being the perpendicular effective anisotropy field. Experimentally measured $\partial \langle r \rangle / \mu_0 \partial H|_{H=H_s}$ and $\partial \langle r \rangle / \partial I|_{I=I_s}$ for MTJs with different *t* are plotted as a function of *D* in Figs. 2(a) and (b), respectively. The *H* derivative of sigmoid curve $\partial \langle r \rangle / \partial H|_{H=H_s}$ monotonically increases with increasing *D*. Since the analytical expression of the *H* derivative, $\Delta_0 / H_K^{\text{eff}}$, can be converted to $M_S A_{\text{eff}} / 2k_B T$ (A_{eff} denotes an

effective area for thermal activation), where the spontaneous magnetization M_S , thermal energy $k_B T$, and thickness *t* are independent of *D*, this result indicates that A_{eff} increases with the device size; in other words, relatively coherent magnetization switching takes place in this *D* regime. On the other hand, the *I* derivative, $\partial \langle r \rangle / \partial I|_{I=I_s}$, decreases with increasing *D*. The reason for this behavior is not clear but we note that a similar result is also observed in the size dependence of Δ_0 / I_{C0} in nonvolatile MTJs [5-7]. In conclusion, this work has studied the physical mechanism governing the sigmoid-like response of stochastic MTJs, which strongly affects the performance of probabilistic computing. We derived an analytical expression of the slope of sigmoid curve and experimentally show that the slope varies with the device size. This work is supported in part by JST-CREST JP1082016.

- [1] P. R. Feynman, Int. J. Theor. Phys. 21, 467 (1982). [2] W. A. Borders *et al*, Nature 573, 390 (2019). [3] W. F. Brown Jr., Phys. Rev. 130, 1677 (1963). [4] T. Taniguchi *et al*, Phys. Rev. B 83, 054432 (2011). [5] J. Z. Sun *et al*, Phys. Rev. B 84, 064413 (2011). [6] H. Sato *et al*, Appl. Phys. Lett. 105, 062403 (2014). [7] B. Jinnai *et al*, IEEE IEDM 24.6 (2020).

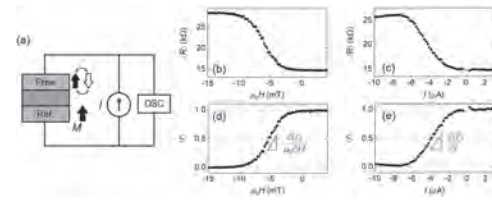


Fig. 1 (a) Measurement circuit and (b),(c) ((d),(e)) time averaged resistance $\langle r \rangle$ (sigmoid curve $\langle r \rangle$) as a function of external perpendicular magnetic field $\mu_0 H$ and bias current *I*, respectively (μ_0 denotes a permeability in vacuum).

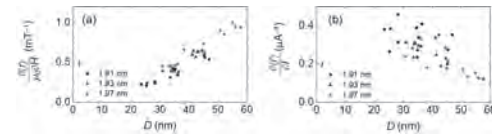


Fig. 2 (a)(b) Slopes of sigmoid curve $\langle r \rangle$ against $\mu_0 H$ and *I*, respectively, as a function of junction diameter *D* measured for the devices with different CoFeB free layer thicknesses *t*.

Session FD

ULTRAFAST MAGNETIZATION DYNAMICS, DAMPING AND NUTATION

Justin Shaw, Chair

National Institute of Standards and Technology, Gaithersburg, MD, United States

INVITED PAPER

FD-01. Engineering Spintronic Devices to Observe Ferromagnetic Layer Switching Induced by a Single-Femto-Second Current Pulse INVITED.

S. Iihama^{1,5}, Q. Remy², J. Igarashi³, G. Malinowski², M. Hehn², J. Gorchon², J. Hohlfeld², S. Fukami⁴, H. Ohno³ and S. Mangin²

1. Center for Spintronics Research Network, Tohoku National University, Sendai, Japan; 2. Institut Jean Lamour, Université de Lorraine, Nancy, France; 3. Research Institute of Electrical Communication, Tohoku National University, Sendai, Japan; 4. Research Institute of Electrical Communication, Tohoku National University, Sendai, Japan; 5. Frontier Research Institute for Interdisciplinary Science, Tohoku National University, Sendai, Japan

The magnetization reversal of a ferromagnetic layer using a single ultrashort optical pulse in a GdFeCo/Cu/[Co/Pt] spin-valve structure was first demonstrated in 2018 [1]. This work has attracted attention for future ultrafast and energy-efficient magnetic storage or memory devices. However, the mechanism and the role of the magnetic properties of the ferromagnet as well as the time scale of the magnetization switching are not fully understood. The single GdFeCo layer demonstrates all-optical helicity-independent switching (AO-HIS). In that case, the magnetization of this Rare-earth – Transition Metal alloy can be switched with one single femto-second pulse whatever light helicity is used. AO_HIS was attributed to the presence of two exchange coupled magnetic sublattices (the Rare Earth and the Transition Metal one) showing different relaxation times after the ultrafast laser excitation [2] in the GdFeCo/Cu/[Co/Pt] spin-valve studied in ref [1]. The switching of the [Co/Pt] ferromagnetic layer is observed after a single femto-second laser pulse. It has been carefully checked that no exchange coupling between the two magnetic layers exist. The [Co/Pt] switching would then result from the combined effect of the spin current generated by the AO-HIS of the GdFeCo layer [3] and the laser-induced heating of the ferromagnet. More recently single-shot all-optical magnetization switching was investigated in a GdFeCo/Cu/[Co_xNi_{1-x}/Pt] spin-valve structure. It was demonstrated that the threshold fluence for switching both the GdFeCo and the ferromagnetic layer depends on the laser pulse duration and the thickness and the Curie temperature of the ferromagnetic layer. We were able to explain most of the experimental results using a phenomenological model. This work provides a way to engineer ferromagnetic materials for energy efficient single-shot all-optical magnetization switching [4,5].

[1] S. Iihama, Y. Xu, M. Deb, G. Malinowski, M. Hehn, J. Gorchon, E.E. Fullerton, S. Mangin, Single-Shot Multi-Level All-Optical Magnetization Switching Mediated by Spin Transport. *Adv. Mater.* 2018, 30 (51), 1804004. <https://doi.org/10.1002/adma.201804004>. [2] Radu, I.; Vahaplar, K.; Stamm, C.; Kachel, T.; Pontius, N.; Dürr, H. A.; Ostler, T. A.; Barker, J.; Evans, R. F. L.; Chantrell, R. W.; Tsukamoto, A.; Itoh, A.; Kirilyuk, A.; Rasing, T.; Kimel, A. V. Transient Ferromagnetic-like State Mediating Ultrafast Reversal of Antiferromagnetically Coupled Spins. *Nature* 2011, 472 (7342), 205–208. <https://doi.org/10.1038/nature09901>. [3] Choi, G.-M.; Min, B.-C. Laser-Driven Spin Generation in the Conduction Bands of Ferrimagnetic Metals. *Phys. Rev. B* 2018, 97 (1), 014410. <https://doi.org/10.1103/PhysRevB.97.014410>. [4] Q. Remy, J. Igarashi, S. Iihama, G. Malinowski, M. Hehn, J. Gorchon, J. Hohlfeld, S. Fukami, H. Ohno and S. Mangin Energy Efficient Control of Ultrafast Spin Polarized Current to Induce Single Femtosecond Pulse Switching of a Ferromagnet *Adv. Sci.* 2001996 (2020) [5] J. Igarasi, Q. Remy, S. Iihama, G. Malinowski, M. Hehn, J. Gorchon, J. Hohlfeld, S. Fukami, H. Ohno, S. Mangin, Engineering single-shot all-optical switching of ferromagnetic materials *Nano Lett* 20, 12, 8654–8660 (2020)



By combining a single femtosecond laser pulse with an ultra-short spin current, generated by the demagnetization of a ferrimagnetic GdFeCo layer, it is possible to reverse the magnetization of a ferromagnetic Co / Pt multilayer. The energy required for this reversal can be controlled by modifying the properties of the different layers

CONTRIBUTED PAPER

FD-02. Micromagnetic Understanding of Switching and Self-Oscillations in Ferrimagnetic Materials.

F. Cutugno¹, L. Sánchez-Tejerina^{2,3}, R. Tomasello⁴, M. Carpentieri¹ and G. Finocchio²

1. Politecnico di Bari Dipartimento di Ingegneria Elettrica e dell'Informazione, Bari, Italy; 2. Department of Mathematical and Computer Sciences, Physical Sciences and Earth Sciences, Università degli Studi di Messina, Messina, Italy; 3. Department of Biomedical, Dental, Morphological and Functional Imaging Sciences, Università degli Studi di Messina, Messina, Italy; 4. Institute of Applied and Computational Mathematics, Foundation for Research and Technology, Heraklion, Greece

Ferrimagnetic materials (FiM) represent a promising direction for the realization of spin-based devices since they can combine the THz ultrafast dynamics typical of antiferromagnets (AFMs) with an easier way to control the magnetic state via well-established optical and electrical methods already applied to FMs, such as the magneto-optical Kerr effect (MOKE)¹ or anomalous Hall effect (AHE)². FiMs can be modeled as AFMs by considering two antiferromagnetically-coupled sublattices³⁻⁵ but, unlike AFMs, the two magnetic sublattices can have a different magnetic moment and angular momentum. Consequently, the net magnetization and angular momentum of FiMs can be varied by changing either the FiM's chemical composition⁶ or temperature⁷ leading to two different compensation points: the magnetic compensation point (MCP), i.e. a zero net magnetization state, and an angular momentum compensation point (AMCP), i.e., a vanishing net angular momentum compensation state. In this work, we micromagnetically analyze, by means of Petaspin micromagnetic solver⁵, the magnetization dynamics of a current-driving transition metal/rare earth ferrimagnet in a spin Hall geometry as a function of the uncompensation parameter of the angular moments of the two sublattices⁸. This approach allows us to show the crucial effect of non-uniform dynamics in the system which cannot be caught by the macrospin approximation. Particularly, we have reported the switching time as a function of the uncompensation parameter (FIG.1) for a current $|J|=1.3$ TA/m². We have shown the switching time diverges at the AMCP, where the only dynamical solution is a self-oscillation state. More interestingly, a finite discontinuity of the switching time appears near the MCP. We show that this discontinuity is related to a change of the switching mechanism, from uniform to non-uniform dynamics with a corresponding increase of the switching time in the latter case. We have additionally analyzed the effect of the interfacial Dzyaloshinskii-Moriya interaction (IDMI) on the switching time and oscillations amplitude. These are relevant characteristics for the design of magnetic memories (switching time) and spin torque nano-oscillators (oscillation amplitude) since they will determine their performances. In FIG.1, we can see the effect on the switching time of the IDMI and how it is beneficial for the use of FiMs as storage devices since it promotes shorter switching times as it advantageously assists the nucleation of new domains. In this work, we also study the self-oscillation frequency and amplitude as a function of the current density. We show that the current thresholds between the changes of dynamical state are well described by the analytical macrospin formula⁸. We observe a linear dependence of the frequency on current independently of the IDMI and compensation point in agreement with the analytical formula⁸. For example, by considering the MCP case (FIG.2), the amplitude of the oscillations decreases non-monotonically as the current increases. For the self-oscillation case, we observe that the effect of IDMI is detrimental for the applicability of FiM as THz sources because it induces a significant reduction of the self-oscillations amplitude at low currents (see Fig. 2). Besides, as we can see in Fig.2, the peak-to-peak amplitude of the oscillations non-monotonically decreases as the current increases. This is due to the non-uniform oscillation mediated by domain walls. For low currents, the domain wall periodicity is larger than the device size and, hence, the whole device oscillates with roughly the same phase. As we increase the current, the periodicity decreases thus averaging the out-of-plane component of the Néel vector over the sample size reduces the value of the peak-to-peak amplitude. Consequently, we obtain the minimum amplitude when the periodicity is close to the device size. By further increasing

the current, the periodicity becomes smaller and the average magnetization value increases. Our results give a better insight into the dynamics excited in FiMs thus paving the way for the design of more performant ferrimagnetic memory and THz nano-oscillator devices.

[1] K. Fleischer, N. Thiagarajah, Y.-C. Lau, et. al., Phys. Rev. B, Vol. 98, 134445 (2018). [2] K. Ueda, M. Mann, C.-F. Pai, A.-J. Tan, and G.S.D. Beach, Appl. Phys. Lett., Vol. 109, 232403 (2016). [3] V. Puliafito, R. Khymyn, M. Carpentieri, et. al., Phys. Rev. B, Vol. 99, 024405 (2019). [4] L. Sánchez-Tejerina, V. Puliafito, P. Khalili Amiri, et. al., Phys. Rev. B, Vol. 101, 14433 (2020). [5] L. Sánchez-Tejerina, R. Tomasello, V. Puliafito, et. al., IEEE Magn. Lett., Vol. 11, 1 (2020). [6] S. Woo, K.M. Song, X. Zhang, et. al., Nat. Commun., Vol. 9, 959 (2018). [7] L. Caretta, M. Mann, F. Büttner, et. al., Nat. Nanotechnol., Vol. 13, 1154 (2018). [8] I. Lisenkov, R. Khymyn, J. Akerman, et. al., Phys. Rev. B, Vol. 100, 100409 (2019).

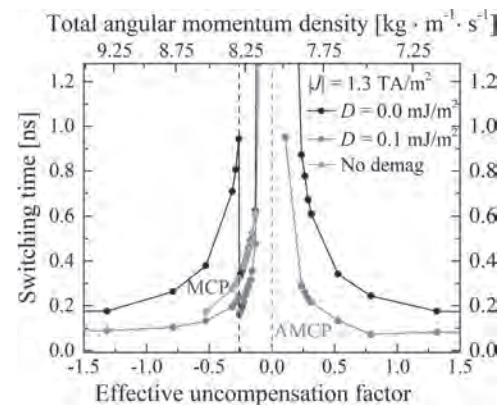


Fig. 1 Switching time as a function of the effective angular momentum uncompensation factor (top axis) of the two sublattices for a current density of $|J|=1.3$ TA/m². The black line corresponds to a dynamics without DMI, while the red line corresponds to a system with non-vanishing DMI. Orange line stands for simulations without demagnetizing field neither DMI. In blue the values of switching time are highlighted for MCP, in magenta there is the line that refers to AMCP.

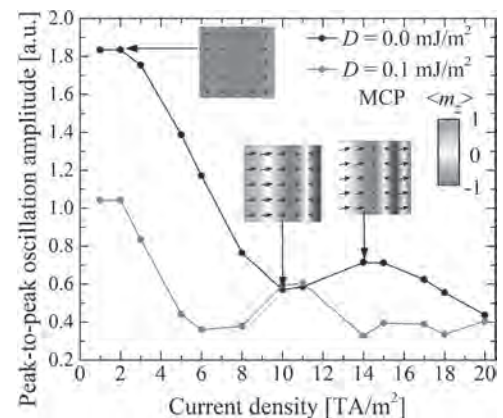


Fig. 2 Amplitude of self-oscillations at the MCP vs applied current for vanishing and non-vanishing IDMI. The snapshots represent the spatial distribution of the 1st-sublattice magnetization at different current densities as indicated by the arrows and arbitrary times. The colors refer to the z-component of the magnetization.

INVITED PAPER

FD-03. Faster Chiral Versus Collinear Magnetic Order Recovery After Optical Excitation Revealed by Femtosecond XUV Scattering INVITED.

N. Kerber^{1,2}, D. Ksenzov³, F. Freimuth⁴, F. Capotondi⁵, E. Pedersoli⁵, I. Lopez-Quintas⁵, B. Seng^{1,6}, J. Cramer^{1,2}, K. Litzius^{1,2}, D. Lacour⁶, H. Zabel⁷, Y. Mokrousov^{1,4}, M. Kläui^{1,2} and C. Gutt³

1. Institut für Physik, Johannes Gutenberg Universität Mainz, Mainz, Germany; 2. Johannes Gutenberg University Mainz Graduate School of Excellence Materials Science in Mainz, Mainz, Germany; 3. Department Physik, Universität Siegen, Siegen, Germany; 4. Forschungszentrum Jülich Peter Grunberg Institut, Jülich, Germany; 5. Elettra Sincrotrone Trieste SCPA, Trieste, Italy; 6. Institut Jean Lamour, Nancy, France; 7. Ruhr-Universität Bochum Fakultät für Physik und Astronomie, Bochum, Germany

In the field of magnetism and spintronics chiral magnetic structures, such as spin spirals, chiral domain walls and skyrmions [1-2], are intensively investigated due to their fascinating properties such as potentially enhanced stability and efficient spin-orbit torque driven dynamics [3-4]. It has been shown that these structures are stabilized by the Dzyaloshinskii-Moriya interaction (DMI) that favours a chiral winding of the magnetisation. While the investigation of static structures and slow (ns) dynamics of chiral magnetic structures has been intensified recently, experimental studies addressing the ultimate fs-ps dynamics of the chirality have been elusive so far as ultrafast pump-probe experiments have so far concentrated on the collinear order in magnetic systems [5-7]. In this work we employ circularly polarized light pulses from an XUV free-electron laser and investigate time-resolved the evolution of the chiral order of domain walls in magnetic thin film samples by an IR pump - X-ray magnetic scattering (XRMS) probe experiment (Fig. 1a) [8]. Using samples with interfacial DMI and perpendicular magnetic anisotropy exhibiting labyrinth-like domain patterns (Fig. 1b), we measure in the same experiment both the (CL+CR) sum signal (Fig. 1d) corresponding to the ferromagnetic order in the domains (average collinear domain magnetisation $m_z^2+m_x^2$) and the difference signal (CL-CR) (Fig. 1e) corresponding to the average chiral order in the domain walls (chiral order correlator $m_z m_x$). In contrast to the (CL+CR) signal, phase information is preserved in the dichroic signal (CL-CR) allowing to determine the domain wall chirality (left/right-handed) and character (Bloch (helical), Néel (cycloidal)) [9-10]. Fig. 1f shows the orthoradial profile of the dichroic signal, which indeed confirms the prevalence of fully right-handed Néel-type domain walls [9-10]. This provides a tool to individually probe the time resolved dynamics of the chiral magnetic order in the domain walls [8]. In a next step we investigated the time evolution of the scattering signals upon IR laser excitation. The key step is the comparison of the collinear ferromagnetic order dynamics and the chiral order dynamics. To ascertain both, we calculated the average intensity for the sum and the difference signal as a function of the wavevector Q_r for different time delays. With this the numerical integration of the radial profiles for each time delay leads to the data shown in Fig. 2a, which demonstrates the evolution of the total intensity of the sum and the difference signal as a function of delay time normalized to the unpumped total intensity. The data shown in Fig. 2b is the result of a second experimental run. We find an ultrafast intensity decrease of both signals in the sub-ps regime with similar time constants. However, a significantly faster recovery of the chiral signal in the sub-ns timescale is observed [8]. In order to explain the key finding of the experimentally observed faster recovery of the chiral signal after laser excitation we can envisage two different mechanisms: (1) a change in the size ratio between domain walls and domains caused by an increase of the domain wall width during the whole investigated time frame or (2) a faster recovery dynamics of the chiral order within the domain walls compared to the ferromagnetic order in the domains leading to a faster build-up of the chiral magnetisation [8]. We subsequently investigate the origin of the faster recovery of the chiral signal by performing numerical simulations of the scattering signal, which reproduce the experimental findings. We conclude from these that the main driver behind our experimental findings is likely

mechanism (2) leading to a faster recovery of the chiral order in the domain walls in comparison to the ferromagnetic order in the domains. In the future further fundamental aspects will be studied in detail e.g. the dependence of the timescales of the chiral order build-up on the absolute strength of the DMI by varying the heavy metal layers. The better control of the DMI and the chirality of spin structures on the ultrafast timescale can finally allow for the controlled ultrafast manipulation of chiral magnetism, e.g. ultrafast writing of chiral topological objects such as skyrmions and pave the path to applications in the field of ultrafast chiral spintronics.

[1] Jiang, W. J. et al. *Phys. Rev.* 704, 1–49 (2017). [2] Everschor-Sitte, K., Masell, J., Reeve, R. M. & Kläui, M. *J. Appl. Phys.* 124, 240901 (2018). [3] Fert, A., Cros, V. & Sampaio, J. *Nat. Nanotech.* 8, 152–156 (2013). [4] Woo, S. et al. *Nat. Mater.* 15, 501–506 (2016). [5] Koopmans, B. et al. *Nat. Mater.* 9, 259–265 (2010). [6] Battiato, M., Carva, K., & Oppeneer, P. M. *Phys. Rev. Lett.* 105, 027203 (2010). [7] Pfau, B. et al. *Nat. Commun.* 3, 1100 (2012). [8] Kerber, N. et al. *Nat. Commun.* 11, 6304 (2020). [9] Zhang, S. L. et al. *Phys. Rev. B* 96, 094401 (2017). [10] Chauleau, J.-Y. et al. *Phys. Rev. Lett.* 120, 037202 (2018).

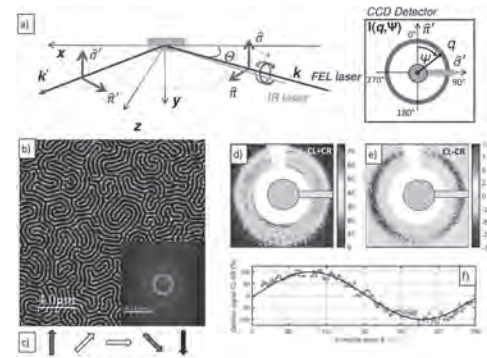


Figure 1: Experimental setup and diffraction images. (a) Measurement geometry: A magnetic thin film sample is pumped by an optical infrared laser pulse and probed by a circularly polarized X-ray FEL pulse. Afterwards an IR-protected CCD detector records the magnetic SAXS pattern. (b) MFM image of a typical labyrinth domain pattern of the $[\text{Ta}(5.3 \text{ nm})/\text{Co}_{20}\text{Fe}_{60}\text{B}_{20}(0.93 \text{ nm})/\text{Ta}(0.08 \text{ nm})/\text{MgO}(2.0 \text{ nm})]_{\times 20}/\text{Ta}(1.6 \text{ nm})$ sample. (d) The resulting sum = CL+CR of the diffraction pattern confirms that the diffraction corresponds to the magnetic domains observed by MFM. (e) The dichroic scattering signal = CL-CR and its azimuthal dependence (f) confirms the presence of (c) right-handed chiral Néel (cycloidal) domain walls [8].

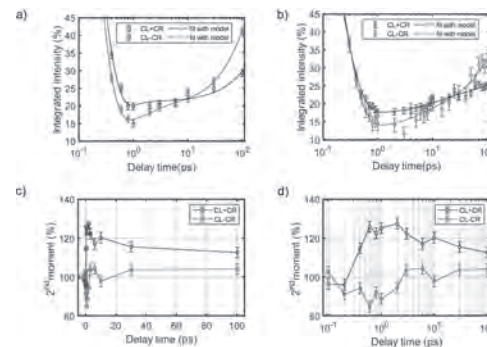


Figure 2: Time dependence of total scattering intensities and second moments. Time evolution of the (a,b) radially integrated intensity from two different experimental runs and (c,d) the 2nd moments of the sum signal (ferromagnetic order) and the difference signal (chiral magnetic order) from the scan shown in (a). The solid lines in (c,d) provide a guide to the eye [8].

CONTRIBUTED PAPERS

FD-04. Ultrafast Electronic Manipulation of Antiferromagnetic Spin Spiral States.S. Ghosh¹, F. Freimuth^{1,2}, O. Gomonay², S. Blügel¹ and Y. Mokrousov^{1,2}¹. Forschungszentrum Julich GmbH, Julich, Germany; ². Johannes

Gutenberg Universität Mainz, Mainz, Germany

Ultrafast optical generation of chiral magnetic structure is one of the most promising and highly sought-after technology for next generation magnetic memory devices. Recent experimental demonstration of generation of skyrmions with ultrafast laser pulse [1] has revealed a new horizon in this field. However, a proper theoretical understanding of the underlying interactions taking place at different timescales as well as main stimulants of the process are still in darkness. Most of the existing studies focus on the magnetic interactions only and completely neglect the interaction between the electric field of the laser and the electronic wavefunction of the material and thus create a huge gap in the complete understanding of the laser assisted magnetization dynamics. We bridge this gap by employing a quantum-classical hybrid method [2] to study the evolution of quantum states as well as the magnetic moments on equal footing and demonstrate that how a stable spin spiral can be generated from a collinear anti-ferromagnetic spin chain with an ultrashort laser pulse [3] (Fig.1,2). We use a minimal tight binding model to define our antiferromagnetic chain with a scalar hopping and onsite magnetic exchange. The laser electric field is modelled as a Gaussian pulse which couples to the hopping. On being hit by the pulse several different mechanisms take place at different timescale starting with an instantaneous change in occupation of states resulting in a gradual buildup of effective torque which leads to the magnetization dynamics. The magnetization dynamics being a slower process compared to the quantum evolution lags by approximately 50fs behind the incident of laser. To initiate this process the initial state must deviate from an ideal collinear state. A stronger deviation shows a faster convergence to the steady state configuration. The mixing of quantum states gives rise to different emergent spin mixing interactions which drives the subsequent dynamics. The system finds its chiral state within a timescale of 1ps. The timeframe of the different steps of the spiralization process is of the same order of the timescales associated with the ultrafast demagnetization which indicates towards the similar underlying physics. After 1ps the dynamics becomes slower and the chain gradually attains a uniform steady chiral structure. We characterize this evolution in terms of the relative angle between adjacent magnetic moment and vector chirality which clearly distinguish different time frames. The relative angle and the induced chirality can be tuned by the strength of the amplitude field. We further show that these effects are fairly robust against thermal fluctuations. Our results thus reveal several salient features of optical manipulation of chirality which has not been revealed in existing literature and thus would be instrumental in their experimental realization.

[1] F. Büttner et.al. Nat. Matter. 20, 30 (2021). [2] A. Ono and S. Ishihara, Phys. Rev. Lett. 119, 207202 (2017). M. D. Petrović, B. S. Popescu, U. Bajpai, P. Plecháč, and B. K. Nikolić, Phys. Rev. Applied 10, 054038 (2018). [3] S. Ghosh, F. Freimuth, O. Gomonay, S. Blügel and Y. Mokrousov, arXiv:2011.01670



Fig. 1: Formation of a spin spiral (solid arrows) from an collinear anti-ferromagnetic (transparent arrows) chain with 32 sites.

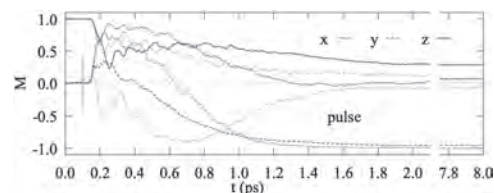


Fig. 2: Time evolution of the components of magnetization over time for 1st (solid) and 17th (transparent) magnetic moment. The yellow line shows the laser pulse.

FD-05. Ultrafast Dynamics in Electronic Band Structure of Optically Excited Epitaxial FeRh: X-ray Absorption Spectroscopy and Density Functional Theory Approach.

N. Agarwal^{1,2}, *L. le Guyader*¹, *J.A. Arregi Uribe*², *R. Carley*¹, *A. Yaroslavtsev*^{1,3}, *I. Vaskivskyi*⁵, *R. Kurta*¹, *M. Izquierdo*¹, *L. Mercadier*¹, *G. Mercurio*¹, *R. Gort*¹, *N. Gerasimova*¹, *J. Schlappa*¹, *B.E. Van Kuiken*¹, *M. Teichmann*¹, *V. Valmispild*², *D. Turenne*³, *S. Molodtsov*¹, *V. Uhlig*⁴, *C.H. Back*⁶, *H. Durr*³, *A. Lichtenstein*² and *A. Scherz*¹

1. *European XFEL GmbH, Schenefeld, Germany*; 2. *Universitat Hamburg, Hamburg, Germany*; 3. *Uppsala Universitet Institutionen for fysik och astronomi, Uppsala, Sweden*; 4. *CEITEC BUT, Brno University of Technology, Brno, Czechia*; 5. *Institut Jozef Stefan, Ljubljana, Slovenia*; 6. *Technische Universitat Munchen, Munchen, Germany*

The observation of ultrafast and coherent control of spins in magnetic materials at room temperature [1-2] has prompted the experimental and theoretical efforts to understand the underlying mechanisms driving such magnetic phenomena. In order to understand the driving mechanisms, in this non-equilibrium regime, it is necessary to disentangle the relevant interactions (exchange, spin-lattice, electron-phonon, coulomb etc.). Stoichiometric B2 ordered epitaxial (001) FeRh undergoes a first order magnetic phase transition from antiferromagnetic (AFM) to ferromagnetic (FM) at $\approx 380\text{K}$. In the AFM phase of FeRh, only Fe has net magnetic moment, whereas in the FM phase both Fe and Rh carry net moments. The phase transition is also accompanied by a $\approx 1\%$ isotropic lattice expansion in the bulk BCC structure, and changes in electronic structure, see [3-5] and refs. therein. Since magnetic and structural dynamics can occur at different timescales, it makes FeRh an ideal candidate for disentangling relevant interaction mechanisms at different timescales. The phase transition has been extensively studied theoretically and experimentally [6-10], in thermal equilibrium (static heating) and at ultrafast time scales (fs- optical excitation), but a precise knowledge of the roles of the electronic, phononic and spin sub-systems remains elusive. We have studied the laser-driven AFM to FM phase transition in FeRh with X-ray absorption spectroscopy (tr-XAS) around the Fe L3 edge. The experiments were performed at the SCS Instrument of the European XFEL. We also performed the density functional theory (DFT) calculations to simulate the XAS spectra at different time delays including magnetic, lattice and temperature changes. Temperature modelling was done using two temperature model (2TM). In this contribution, we will discuss the changes in the electronic band structure of FeRh in the femto- and picosecond timescales, derived from the X-ray absorption spectroscopy measurements at the Fe L3 absorption and compare them with the density functional theory simulations.

[1] E. Beaupaire et al., Phys. Rev. Lett. 76, 4250 (1996) [2] J.-Y. Bigot et al., Nature Physics 5, 515 (2009) [3] J.-U. Thiele et al. Appl. Phys. Lett. 82, 2859 (2003) [4] A.X. Gray et al., Phys. Rev. Lett. 108, 257208 (2012). [5] C. Baldasseroni et al., Appl. Phys. Lett. 100, 262401 (2012). [6] J.-U. Thiele, M. Buess, C.H. Back, Appl. Phys. Lett 85, 2857 (2004). [7] G. Ju et al., Phys. Rev. Lett. 93, 197403 (2004) [8] I. Radu et al., PRB 81, 104415 (2010) [9] S. Mariager et al., Phys. Rev. Lett. 108, 87201 (2012) [10] F. Quirin et al., Phys. Rev. B 85, 020103(R) (2012)

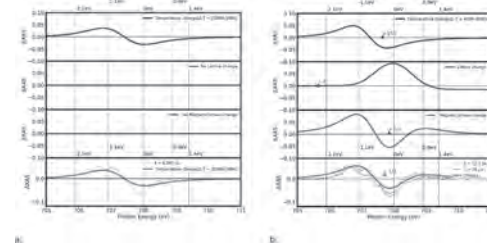


Figure-1: a: X-ray absorption (XAS) changes: (dashed line: experiment) near the Fe L3 edge before and after laser excitation at a fixed time delay of 70 fs, (solid lines: DFT theory) XAS changes corresponding to temperature of 2000K b: X-ray absorption (XAS) changes: (dashed line: experiment) near the Fe L3 edge before and after laser excitation at a fixed time delay of 11.5 ps and 70 us, (solid lines: DFT theory) XAS changes corresponding to net changes including temperature (400K), lattice (0.5 % expansion) and magnetic changes (AFM->FM)

FD-06. Magnon-Phonon Damping Calculations in the Spin-Lattice Dynamics Model.

M.S. Strungaru¹, M.O. Ellis², S. Ruta¹, O. Chubykalo-Fesenko³, R.F. Evans¹ and R.W. Chantrell¹

1. Physics, University of York, York, United Kingdom; 2. Computer Science, The University of Sheffield, Sheffield, United Kingdom; 3. Instituto de Ciencia de Materiales de Madrid, Madrid, Spain

The relaxation of the magnetisation in magnetic materials is of great importance from both an applied and fundamental point of view. Conventional modelling of magnetisation dynamics employs the Landau-Lifshitz-Gilbert (LLG) equation [1], where the damping is included phenomenologically by the Gilbert damping term. This describes the coupling of the magnetic modes (given primarily by the atomic spin) to the non-magnetic modes (lattice vibrations and electron orbits) which are assumed to be in equilibrium. Recent studies of the dynamics induced by THz laser pulses has highlighted the necessity of understanding magnetisation relaxation beyond this assumption. In reality the spin and lattice dynamics mutually influence one another, hence it is necessary to employ a unified model of molecular and spin dynamics [2,3,4], Spin-Lattice dynamics (SLD). In the present work we employ a model where the transfer of energy and angular momentum between the lattice and the spin system (Fig. 1) is realised by the pseudo-dipolar coupling [3,4], which arises from the spin-orbit interaction and can be parameterised by magneto-elastic experiments. The spin system exchange parameters are taken from ab-initio parameterisation for BCC iron [2], while for the phonon system interactions potential we compare the Harmonic and Morse potentials. Our results in Fig. 1 show that equilibration of both sub-systems can be obtained on a sub-nanosecond timescale in both the microcanonical and canonical ensembles, the relaxation time being governed by the energy initially deposited in the system. We also observe that the equilibrium magnetisation is independent of the thermostat and by coupling the spin system only to the lattice vibrations the magnetisation temperature dependence can be reproduced without the need of a phenomenological spin damping [3]. Our model allows the evaluation of the effective magnon-phonon damping (Fig. 2) which agrees well with the values measured in magnetic insulators where they depend predominantly on magnon-phonon coupling rather than on electronic effects. The functional form of the damping variation is quadratic, in accordance with the form of the pseudo-dipolar coupling term. The magnon-phonon damping has been also calculated for an alternate form of the coupling, where the pseudo-dipolar coupling is replaced by an on-site form, i.e a Néel-like anisotropy term. The latter leads to much smaller damping values, as shown in Ref. [3], suggesting that the magnon-phonon damping can clearly have complex behaviour depending on the properties of the system, especially the coupling term. Based on this remark, no universal behaviour of damping as a function of temperature can be deduced for spin lattice models. The model developed in this work [3] opens the possibility to describe the distinct dynamics of spins and phonons, necessary for the understanding of ultrafast magnetisation dynamics experiments and the subsequent angular momentum transfer between the two subsystems. We have demonstrated that the model works well in the absence of a phenomenological Gilbert damping, which consists mainly of electronic contributions, hence the SLD model can be employed to study magnetic insulators, such as YIG, where the principal contribution to damping is via magnon-phonon interactions.

[1] T. L. Gilbert, IEEE Trans. Magn. 40, 3443 (2004). [2] P.-W. Ma et al., Phys. Rev. B, vol. 78, no. 2, p. 024434, Jul. 2008. [3] M. Strungaru et al. arXiv preprint arXiv:2010.00642 (2020) (accepted in Phys. Rev. B) [4] M. Abmann and U. Nowak, J. Magn. Magn. Mater 6 469 (2019): 217-223.

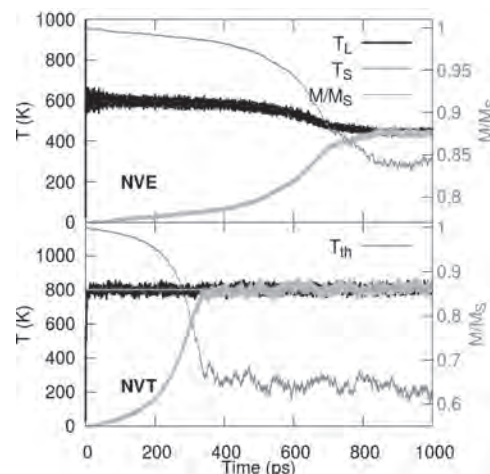


Fig.1: NVE (microcanonical – top panel) and NVT (canonical – bottom panel) simulations for a $10 \times 10 \times 10$ unit cell BCC Fe system. The spin system is initialised at a spin temperature $T_S = 0K$ corresponding to a saturated magnetic state in the z direction, while the lattice velocities are initialised by a Boltzmann distribution at $T_L = 1200 K$ (for NVE) and $T_L = 600 K$ (for NVT). In both cases we obtain equilibration of the two subsystems under 1ns.

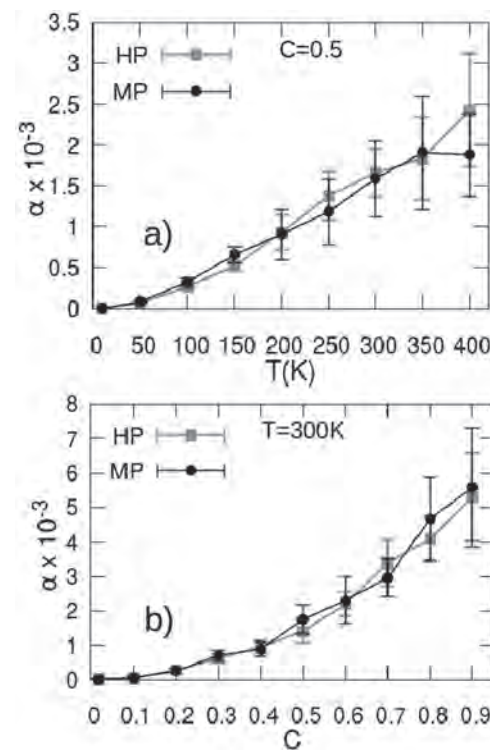


Fig.2 Damping parameter extracted from fitting the z component of the magnetisation for two different choices of potential: HP- Harmonic Potential (green open squares) and MP-Morse Potential (black open circles) as a function of temperature - Panel a) and as a function of the coupling strength - Panel b); The effective damping in Panel a) is calculated for a constant coupling strength of $C = 0.5$, while in Panel b) the damping is calculated for a constant temperature of $T = 300K$. The black and green lines represent the average damping parameter obtained from the simulations using the Morse and the Harmonic Potentials, respectively.

FD-07. Nutation Resonance in Ferromagnets.M. Cherkasskii¹, M. Farle^{2,3} and A. Semisalova²

1. St. Petersburg State University, St. Petersburg, Russian Federation;

2. Universitat Duisburg-Essen, Duisburg, Germany; 3. Kirensky Institute of Physics, Federal Research Center KSC SB RAS, Krasnoyarsk, Russian Federation

Recently, the effects of inertia in the spin dynamics of ferromagnets were reported to cause nutation resonance [1-8] at the frequencies higher than the conventional ferromagnetic resonance. It was shown that spin-orbit induced inertia is responsible for nutation, which should be considered together with magnetization precession in a magnetic field. Recently nutation in ferromagnets was confirmed experimentally [1], since nutation and precession operate at substantially different time scales, and conventional microwave ferromagnetic resonance (FMR) spectroscopy techniques do not easily reach the high-frequency (sub-Terahertz) regime, required to observe the inertia effect which in addition yields much weaker signal. The interest in the ultrafast spin dynamics has inspired various theoretical studies. For instance, a relation between the Gilbert damping constant and the inertial regime characteristic time was elaborated in ref. [2]. The exchange interaction, damping, and moment of inertia can be calculated from the first principles as shown in [3]. In [4], the inertial regime was introduced in the framework of the mesoscopic nonequilibrium thermodynamics theory, and it was shown to be responsible for the nutation superimposed on the precession of magnetization. Wegrowe and Ciornei [5] discussed the equivalence between the inertia in the dynamics of uniform precession and a spinning top within the framework of the Landau-Lifshitz-Gilbert equation generalized to the inertial regime. This equation was studied analytically and numerically in ref. [6, 7]. In this digest we present new results on the frequency dependence of high-frequency magnetic susceptibility in ferromagnets taking inertia effects into account [8]. We performed calculations based on the Landau-Lifshitz-Gilbert equation with the additional inertia term and obtained an analytical solution. These results provide a basis for further studies of magnetocrystalline anisotropy and damping in magnetic materials in the sub-Terahertz range and furthermore a guideline for experimental research. Using circular variables of magnetization and magnetic field we obtained the dependence of the susceptibility on frequency for the right-hand precession, i.e. positive polarization (Fig. 1(a)). Due to the contribution of nutation, the frequency and linewidth of this resonance are slightly different from the ones of usual FMR. In Fig. 1(b) the nutation resonance possessing negative polarization is presented. Note that the polarizations of ferromagnetic and nutation resonances are reversed. In addition, we derived a general analytical expression for the linewidth of nutation resonance in ferromagnets, and will show its dependence on magnetization, the Gilbert damping, the inertial relaxation time and applied magnetic field. We find that the nutation linewidth can be tuned by the applied magnetic field, and this tunability breaks the direct relation between losses and the linewidth.

[1] K. Neeraj, N. Awari, S. Kovalev *et al.*, Nat. Phys. (2020), doi: 10.1038/s41567-020-01040-y [2] M. Fähnle, D. Steiauf, and C. Illg, Phys. Rev. B, Vol. 84, 172403 (2011). [3] S. Bhattacharjee, L. Nordström, and J. Fransson, Phys. Rev. Lett., Vol. 108, 057204 (2012). [4] M.-C. Ciornei, J. M. Rubí, and J.-E. Wegrowe, Phys. Rev. B, Vol. 83, 020410 (2011). [5] J.-E. Wegrowe and M.-C. Ciornei, Am. J. Phys., Vol. 80, p. 607 (2012). [6] E. Olive, Y. Lansac, and J.-E. Wegrowe, Appl. Phys. Lett., Vol. 100, 192407 (2012). [7] E. Olive, Y. Lansac, M. Meyer *et al.*, J. Appl. Phys. 117, 213904 (2015). [8] M. Cherkasskii, M. Farle, and A. Semisalova, Phys. Rev. B 102, 184432 (2020).

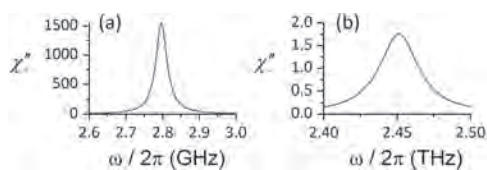


Fig. 1. (a) The FMR peak with nutation. (b) The nutation resonance. The calculation was performed for $\gamma/(2\pi)=28 \text{ GHz T}^{-1}$, $\mu_0 M_0=1 \text{ T}$, $\mu_0 H_0=100 \text{ mT}$, $\alpha=0.0065$ and $\tau = 10^{-11} \text{ s}$.

FD-08. Midpoint Numerical Technique for Inertial Ultra-Fast Landau-Lifshitz-Gilbert Nutation Dynamics.

M. d'Aquino^{2,1}, V. Scalera¹, K. Neeraj³, S. Perna¹, S. Bonetti^{4,3} and C. Serpico¹

1. DIETI, Università degli Studi di Napoli Federico II, Napoli, Italy;

2. Engineering Department, Università degli Studi di Napoli Parthenope, Napoli, Italy; 3. Stockholms Universitet, Stockholm, Sweden; 4. Università Ca' Foscari, Venezia, Italy

The study of magnetization dynamics in nanomagnetic systems is fundamental for applications such as recording, sensing and low power computing, which are ubiquitous in the area of information and communication technologies[1]. Quantitative analysis of magnetization dynamical phenomena is usually addressed by solving the Landau-Lifshitz-Gilbert (LLG) equation, which describes the precessional motion of spins produced by external actions (external field, spin-torques, etc.) and mutual spin-spin interactions. Due to the strongly nonlinear nature of the LLG equation, the possible magnetization regimes exhibit multistability, nonlinear resonance, quasi-periodicity and spatio-temporal chaos. Analytical solutions exist in very special situations, while in generic conditions one has to resort to numerical simulations. In the last decade, the LLG equation has been reformulated[2] including a physically correct inertial response which predicts the appearance of spin nutations, similar to the ones of a spinning top, at a frequency much higher (in the terahertz range) than the spin precession described by the conventional LLG equation, typically at gigahertz frequencies. Nutation-type magnetization motions have been also theoretically predicted to be produced by applying circularly-polarized microwave field to rotationally-symmetric magnetic nanoparticles[3], which triggers the combination of the external microwave frequency with an intrinsic frequency characteristic of the system in the usual gigahertz range. However, the lack of intense magnetic field sources at terahertz frequencies has hampered the experimental observation of ultra-fast nutation dynamics. Very recently, experimental evidence has been found[4] for nutation dynamics with a characteristic frequency of the order of 1 THz which is damped on time scales of the order of 10 picoseconds. From the mathematical modelling point of view, the inclusion of such inertial effects occurs by augmenting the LLG equation with a term proportional to the second derivative of the magnetization vector field, which implies that magnetization evolves in time as the result of a nonlinear dynamical system of order higher than that associated with the classical precessional dynamics. In this paper, we propose an appropriate time-integration scheme, based on the implicit midpoint rule technique[5] for the numerical solution of the inertial LLG (iLLG) equation and the relevant properties of the numerical scheme are discussed. The midpoint rule is an unconditionally stable and second order accurate scheme which preserves the fundamental geometrical properties of the classical precessional LLG dynamics[6]. When inertial effects are considered, the numerical integration of iLLG has to address the issue of the higher order of the dynamical system. This, on one hand, implies a dramatic change of micromagnetic codes and, on the other hand, results in at least doubling the computational cost of the numerical scheme. Here we develop an efficient implementation of the midpoint rule technique for iLLG dynamics, based on suitable multi-step method for the inertial term. The proposed iLLG time-stepping can be built on the top of that associated with classical precessional LLG dynamics retaining a computational cost with the same order of magnitude. This requires the assumption that magnetization evolution starts with zero time derivative, which is reasonable from the practical perspective of experiments driven by ultra-short excitation pulses. Moreover, we show that the mathematical properties of the proposed technique allow to choose the amplitude of the time-step according to accuracy requirements, avoiding the possibility to incur in numerical stability issues, yielding much smaller simulation times than conventional off-the-shelf schemes such as Runge-Kutta or linear multi-steps. The main difficulty related to the implementation of the implicit midpoint time-stepping is the necessity of solving a large system of globally coupled nonlinear equations. This problem has been circumvented by using special and reasonably fast quasi-Newton iterative technique. The proposed technique is validated by computing the broadband frequency response of a ferromagnetic film magnetized along the easy direction and subject to out-of-plane AC field with frequency ranging from gigahertz to terahertz

(see fig. 1). In particular, the numerically computed response is compared with the analytical solution developed by solving the linear magnetization dynamics in the inertial regime. One can see in Fig. 1 that, beside the peak at the ferromagnetic resonance (Kittel) frequency, a secondary peak at about 630 GHz appears, which is associated with ultra-fast nutation dynamics.

[1] B. Dieny, I.L. Prejbeanu, K. Garello, P. Gambardella, P. Freitas, R. Lehdorff, W. Raberg, U. Ebels, S.O Demokritov, J. Akerman, A. Deac, P. Pirro, C. Adelmann, A. Anane, A.V. Chumak, A. Hirohata, S. Mangin, S.O. Valenzuela, M.C. Onbasli, M. d'Aquino, G. Prenat, G. Finocchio, L. Lopez-Diaz, R. Chantrell, O. Chubykalo-Fesenko, P Bortolotti, Nature Electronics 3 (8), 446-459, 2020. [2] Ciornei, M.-C., Rubí, J. & Wegrowe, J.-E. Magnetization dynamics in the inertial regime: Nutation predicted at short time scales. Physical Review B 83, 020410 (2011). [3] C. Serpico, M. d'Aquino, G. Bertotti, and I.D. Mayergoyz, "Quasiperiodic magnetization dynamics in uniformly magnetized particles and films," J. Appl. Phys., vol 95, no. 11, pp. 7052–7054, Jun. 2004. [4] N. Kumar, N. Awari, S. Kovalev, D. Polley, N. Zhou Hagström, Sri Sai Phani Kanth Arekapudi, A. Semisalova, K. Lenz, B. Green, J.-C. Deinert, I. Ilyakov, M. Chen, M. Bowatna, V. Scalera, M. d'Aquino, C. Serpico, O. Hellwig, J.-E. Wegrowe, M. Gensch, S. Bonetti, Nat. Phys. (2020). <https://doi.org/10.1038/s41567-020-01040-y>. [5] M. d'Aquino, C. Serpico, G. Miano, I. D. Mayergoyz, and G. Bertotti, "Numerical integration of landau-lifshitz-gilbert equation based on the midpoint rule," J. Appl. Phys., vol. 97, no. 10, p. 10E319, May 2005. [6] M. d'Aquino, C. Serpico, and G. Miano, "Geometrical integration of Landau-Lifshitz-Gilbert equation based on the midpoint rule," J. Comput. Phys., vol. 209, no. 2, pp. 730–753, 2005.

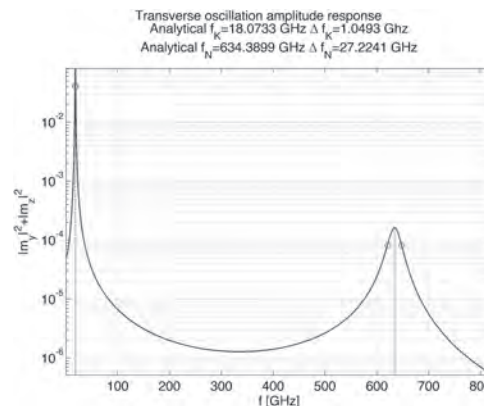


Fig. 1 Frequency response of magnetization oscillation transverse to the easy direction for an infinite ferromagnetic thin-film. The applied DC field bias is 0.35 T, the Gilbert damping constant is 0.023, the time scale of inertial effects is about 11 picoseconds. Peaks associated with usual GHz FMR frequency and ultra-fast nutation in the THz regime are visible.

Session FE
ELECTRIC FIELD EFFECTS AND MAGNETIZATION SWITCHING

Dennis Meier, Chair
Norges teknisk-naturvitenskapelige universitet, Gjøvik, Norway

INVITED PAPER

FE-01. Spin Current-Driven Control and Detection of Magnetization in Ferrimagnetic Insulators INVITED.C. Avci¹*1. Department of Materials, ETH Zurich, Zurich, Switzerland*

Ferrimagnetic insulators (FIs) host an array of attractive properties for spintronics research and potential applications. Some prominent features are tunable saturation magnetization, perpendicular anisotropy, low damping, and highly ordered single crystal structure that could be beneficial for obstacle-free domain wall and skyrmion motion. However, electrically manipulating and detecting the magnetization in FIs, which is a prerequisite for spintronic devices, has been impossible for a long time due to the lack of physical phenomena to do so. Recent advances in spin current generation and detection have provided the relevant tools to detect the magnetization vector of FIs by purely electrical means [1,2]. Consequently, the research into MIs has gained significant momentum in the past decade. In this talk, we will discuss some of the recent efforts in controlling and detecting the magnetization vector via spin currents in FIs with perpendicular magnetic anisotropy. First, we will briefly overview the experiments of current-induced switching and electrical detection of magnetization vector in a FI, thulium iron garnet, with perpendicular anisotropy [3,4]. We will then discuss the emergent interfacial chiral magnetism, and current-driven dynamics of domain walls in rare-earth-based FIs. We will show that chiral magnetic interactions stabilize Néel-type domain walls in ultrathin FIs that can be propelled by spin-orbit torques with velocities ~ 0.8 km/s [5]. Finally, we will discuss a new thermoelectric effect that allows electrical detection of the out-of-plane magnetization component in FIs in a nonlocal device geometry [6]. We will show that, by using an engineered temperature gradient, we can convert a thermally-induced spin current in a FI into an electrical signal across a Pt detector that is proportional to the perpendicular component of the magnetization.

[1] Uchida et al. *Appl. Phys. Lett.* 97, 172505 (2010) [2] Nakayama et al. *Phys. Rev. Lett.* 110, 206601 (2013). [3] Avci et al. *Nat. Mater.* 16, 309 (2017) [4] Avci et al., *Appl. Phys. Lett.* 111, 072406 (2017) [5] Avci et al. *Nat. Nanotech.* 14, 561 (2019) [6] Avci et al. *Phys. Rev. Lett.* 124, 027701 (2020)

CONTRIBUTED PAPERS

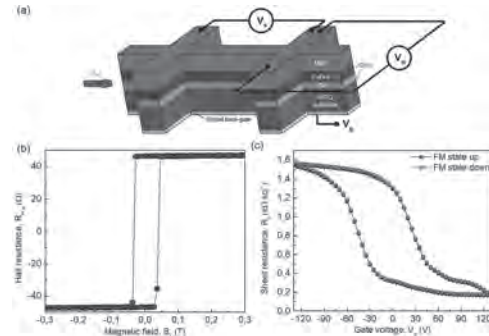
FE-02. Non-Volatile Electric-Field Control of Spin-Orbit Torques in Perpendicular Ferromagnet - SrTiO₃ System.

C. Grezes¹, M. Cosset-Cheneau¹, P. Noël^{1,2}, L.M. Vicente Arche³, F. Trier³, S. Auffret¹, K. Garello¹, M. Bibes³, L. Vila¹ and J. Attané¹

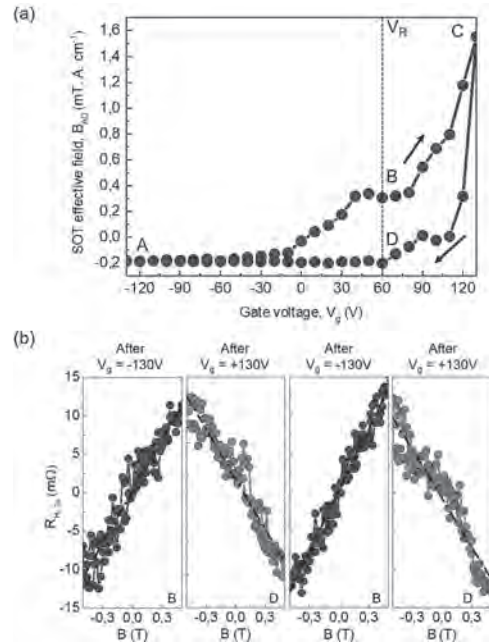
1. CEA Grenoble, SPINtronique et Technologie des Composants, Grenoble, France; 2. ETH Zurich, Zurich, Switzerland; 3. Unite Mixte de Physique CNRS/Thales, Palaiseau, France

While classical spintronics has traditionally relied on ferromagnetic metals as spin generators and spin detectors, spin-orbitronics exploits the interplay between charge and spin currents enabled by the spin-orbit coupling (SOC) in non-magnetic systems. The realization of magnetization switching induced by in-plane current injection in heavy metal/ferromagnetic heterostructures [1] has drawn increasing attention to spin-orbitronics, leading to the advent of spin-orbit torques magnetoresistive random access memories (SOT-MRAM). Compared to heavy metals, oxide 2D electron gases have emerged as alternative spin-orbitronics material systems. They benefit from an efficient spin-charge interconversion through the direct and inverse Edelstein effects, which appear at their interfaces where the broken inversion symmetry induces a Rashba SOC [1]. Recently, we have demonstrated an enhancement of the spin-to-charge conversion efficiency by two orders of magnitude in SrTiO₃-based 2D gas compared to conventional heavy metals [2], along with a non-volatile electric-control of the spin-to-charge conversion [3]. While the sign and efficiency of the SOTs are fixed by the stack of materials in conventional SOT devices, achieving an electric-control of the mirror charge-to-spin conversion would be of great interest for developing reconfigurable SOT-MRAM and logic gates, offering the possibility of active manipulation of the torque by electric field for building new architectures. Here we report electric-field control of spin orbit torques with electrical remanence in a perpendicular ferromagnet - SrTiO₃ system. Results are shown from a 1 μm wide Hall bar device made of a CoFeB ferromagnetic layer with perpendicular magnetization on top of a SrTiO₃ substrate with a thin Ta insertion to protect the 2D electron gas at the interface (Figure 1). The perpendicular magnetization is achieved using an MgO capping layer that ensures high interfacial magnetic anisotropy along with compatibility for integration in magnetic tunnel junctions for SOT-MRAM. To modulate the 2D gas properties, voltage is applied to the devices via a back-gate. Non-volatile electric-field control of the sheet resistance is achieved with 1150% contrast (Figure 1c), with two switchable and remanent high and low resistivity states of the 2D electron gas. Spin-orbit torques effective fields are further measured using second harmonic Hall methods. A remanent electric-field control of the SOT efficiency is demonstrated, with inversion of the sign of the SOT anti-damping-like effective field (Figure 2). Anti-damping-like and field-like torque effective fields per 2D current density of 1.6 and 0.1 mT. A. cm⁻¹ respectively are reached in the 2D gas low resistivity state. These results are consistent with a combination of both intrinsic modulation of the SOT efficiency together with extrinsic modulation due to the non-volatile electric-control of the current injection in the 2D gas. The non-volatile control of the SOT effective field is further evidenced in Figure 2b, which displays reproducible inversion of the SOT torques after initializing with negative or positive voltage pulses of ±130 V, opening the way to reconfigurable spin-orbit torque memory and logic gate architectures.

[1] I. M. Miron et al., Nature 476, 189–193 (2011). [2] E. Lesne et al., Nature Materials, 15, 1261–1266 (2016). [3] D. C. Vaz et al., Nature Materials, 18, 1187–1193(2019). [4] P. Noel et al., Nature 580, 483–86 (2020).



Schematic of the sample and magnetotransport properties. (a) Structure of the sample and measurement geometry. (b) Out-of-plane magnetic field dependence of the anomalous Hall resistance at zero electric field ($V_g = 0$ V). (c) Gate dependence of the sheet resistance at zero magnetic field after initializing the ferromagnet (FM) in the up (blue) and down (red) states. All data have been measured at 10K.



Electric-field control of spin orbit torques with electrical remanence. (a) Spin-orbit torques anti-damping-like effective field as a function of the gate voltage for $j^{2D} = 4$ A.cm⁻¹. (b) Normalized second harmonic Hall resistance at electrical remanence V_R after initializing with negative (blue) or positive (red) voltage pulses of ±130 V. Dashed and dotted lines are linear fits, yielding SOT effective fields $B_{AD} = +0.29, -0.20, +0.32$ and -0.18 mT. A. cm⁻¹, respectively.

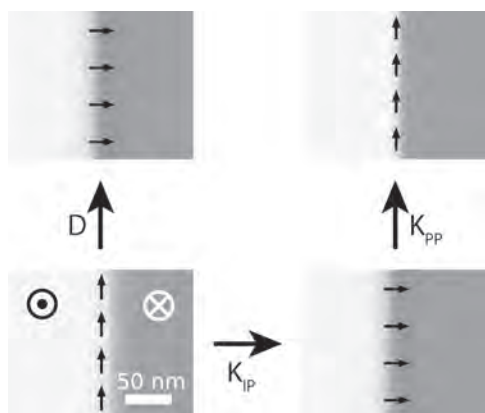
FE-03. Control of Magnetic Domain Wall Type Using Anisotropy Modulations.

K.J. Franke¹, A.K. Schmid² and C. Marrows¹

1. School of Physics and Astronomy, University of Leeds, Leeds, United Kingdom; 2. National Center for Electron Microscopy, Molecular Foundry, E. O. Lawrence Berkeley National Laboratory, Berkeley, CA, United States

The presence of a Dzyaloshinskii-Moriya interaction (DMI) in perpendicular magnetized thin films stabilizes Néel type domain walls of fixed chirality, as opposed to the Bloch walls that are formed in the absence of a DMI [1]. Néel walls of fixed chirality have been shown to be driven efficiently in the same direction by electric currents through spin-orbit torques [2,3]. Later, a large tuning of the DMI with an applied voltage was demonstrated [4], which can be used for example for electric field control of magnetic domain wall motion via the modulation of the DMI [5]. Here, we demonstrate an alternative mechanism for the control of domain wall type: Using micromagnetic simulations and analytical modeling, we show that the presence of a uniaxial in-plane magnetic anisotropy can also lead to the formation of Néel walls in the absence of a DMI. It is possible to abruptly switch between Bloch and Néel walls via a small modulation of both the in-plane, but also the perpendicular magnetic anisotropy [6]. This opens up a route towards efficient electric field control of the domain wall type with tiny applied voltages, as the magnetic anisotropy can be modulated via the direct voltage controlled magnetic anisotropy (VCMA) mechanism [7], or via magnetoelastic anisotropy induced through coupling to a piezoelectric element [8].

1. A. Thiaville, S. Rohart, E. Jué, V. Cros, and A. Fert, EPL (Europhysics Letters) 100, 57002 (2012). 2. K.-S. Ryu, L. Thomas, S.-H. Yang, and S. S. P. Parkin, Nat. Nanotech. 8, 527–533 (2013) 3. S. Emori, U. Bauer, S.-M. Ahn, E. Martinez, and G. S. D. Beach, Nat. Mater., 12, 611–616 (2013) 4. T. Srivastava, et al., Nano Letters 18, 4871 (2018) 5. T. Koyama, Y. Nakatani, J. Ieda, and D. Chiba, Science Advances 4 (2018) 6. K. J. A. Franke, et al., in preparation (2021) 7. T. Maruyama, et al., Nat. Nanotech. 4, 158 (2009). 8. S. Li, et al., J. Appl. Phys. 117, 17D702 (2015)



In a perpendicular magnetized thin film, domain walls (DWs) are generally of Bloch type (bottom left). The presence of a DMI (top left), stabilizes Néel walls. Alternatively, and in-plane magnetic anisotropy can also form Néel walls (bottom right). An increase in the perpendicular magnetic anisotropy switches the DW type back to Bloch (top right).

FE-04. Voltage Control of Néel Domain Wall Interactions and Pinning Sites.

J. Zehner^{1,2*}, I. Soldatov¹, K. Nielsch^{1,2}, R. Schäfer¹ and K. Leistner¹
 1. Institute for Metallic Materials, Leibniz-Institut für Festkörper- und Werkstofforschung Dresden eV, Dresden, Germany; 2. Institute of Material Science, Technische Universität Dresden, Dresden, Germany

Mechanisms for voltage control of magnetism are often based on strain or charge effects. Recently, a new approach based on electrochemical mechanisms was discovered. Due to the ionic reactions involved, it is promising especially for large and non-volatile voltage induced effects on the magnetic properties.^[1,2] In the charge-based or electrochemical approach, the fast majority of publications reports on Co-based thin films with perpendicular anisotropy. In our study, we focus on a distinctly different system, namely FeO_x/Fe thin films with uniaxial in-plane anisotropy. Although films with uniaxial in-plane anisotropy hold great potential for switchable artificial magnetic stray field landscapes for lab-on-a-chip or for giant magnetoresistance sensors, there are no reports of electrochemical voltage control of such films yet. We demonstrate that significant effects on their magnetic properties can be achieved via electrolytic gating. The detailed analysis of the interplay between electrochemical processes and hysteresis, anisotropy and domain changes allow us to reveal an oxygen-based tuning of the Néel wall interactions as the underlying mechanism. The thin films are composed of 3nm FeO_x and 5nm Fe. In-plane angular magnetometry measurements show the presence of a uniaxial anisotropy. Along the easy axis, the shape of the magnetization curve is close to rectangular. Nevertheless, the hysteresis along the hard axis is more rounded and the coercivity (H_C) is comparable with the H_C along the easy axis (red curve in Figure 1 a). This behavior is known to be caused by charged Néel domain wall interactions. These interactions block the rotation of the magnetization and lead to a large hysteresis along the hard axis. Upon voltage application, H_C strongly decreases along every angle. In the vicinity of the hard axis, H_C almost completely vanishes (blue curve in Fig. 1 a). As H_C and anisotropy are strongly correlated, we investigate the anisotropy of the thin film via anhysteretic measurements. We find an increase of the uniaxial anisotropy energy density upon the voltage-triggered oxide-metallic transformation. This is an unusual finding as it is often assumed in voltage control of magnetism that H_C and anisotropy are directly proportional to another. Obviously, this simple model is not applicable here. Instead, changes in the microstructure or the magnetic domain structure dominate over direct anisotropy effects. To evaluate how the magnetic domain structure is affected, we investigated the AC-demagnetized state, which resembles the equilibrium domain state. Upon a low voltage application (1V), and thus transforming the FeO_x to metallic Fe, the domain size significantly increases, see Fig. 1 b and c. In order to understand the domain coarsening, we approximated the change in the surface energy density for the Néel walls. This calculation shows an increase in domain-wall energy of 40% upon the oxide-metal transformation, which could explain the decrease in the number of domain walls and the associated increase in the domain size. In order to propose a consistent mechanism which explains the observed changes, we focused on the specific properties of the magnetically charged Néel walls. The Néel domain wall interactions becomes a significant factor, as soon as their tails overlap which is when the domain width is smaller than two times the tail width. With the extracted domain size from Fig. 1, we calculated strong interactions for the oxidized state. For the oxide to metal transformation, the interactions are significantly decreased. A comparable trend is expected and also observed in the remanent state. As a result, the tails would not overlap and we thus expect significantly fewer interactions between the walls in the reduced state. This is consistent with the observed voltage controlled deblocking. To demonstrate the technological relevance, we demonstrated that our electrochemical based switching mechanism allows for 180° magnetization reversal along the easy axis. Purely magnetic field reversal shows the nucleation and growth of magnetic domains (Fig. 2 (a) red curve and (b)). In comparison, during voltage assisted switching, the magnetization reversal occurs at a lower field within seconds (Fig. 2 (a) blue curve and (c)). Assuming a linear relation between the electrode diameter and the switching energy, we estimate the energy efficiency of this process to be 5fJ for an electrode diameter of 3nm. These value approaches the same range as for the so far

lowest reported switching energies. Interestingly, the domain evolution is similar to the reversal process induced by a magnetic field. This indicates that the nucleation sites and the local distribution of pinning sites that affect the reverse domain growth do not change substantially during the reduction process. However, the E-induced switching proceeds at much lower magnetic field, which points to a substantially reduced pinning strength during the FeO_x to metal Fe transformation. The reversible and low voltage (1V) control of defect sites might be transferrable to other defect-controlled materials, such as type II superconductors or materials with specific mechanical properties.^[3]

[1] C. Navarro-Senent, A. Quintana, E. Menéndez, E. Pellicer, J. Sort, *APL Materials* 2019, 7, 030701. [2] C. Song, B. Cui, F. Li, X. Zhou, F. Pan, *Progress in Materials Science* 2017, 87, 33. [3] J. Zehner, I. Soldatov, S. Schneider, R. Heller, N. B. Khojasteh, S. Schiemenz, S. Fähler, K. Nielsch, R. Schäfer, K. Leistner, *Adv. Electron. Mater.* 2020, 6, 2000406.

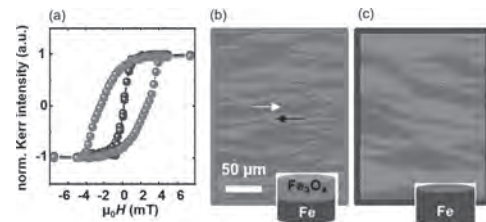


Fig.1: Magnetization curves and magnetic domains in the FeO_x/Fe state (red curve in (a) and domains in (b)) and in the Fe state, blue curve in (a) and domains in (c).

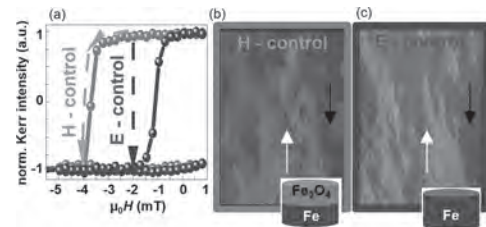


Fig.2: E-induced 180° switching of magnetization (M). (a) pathway for H- and E-induced M-reversal. (b) H-induced and (c) E-induced M-reversal.

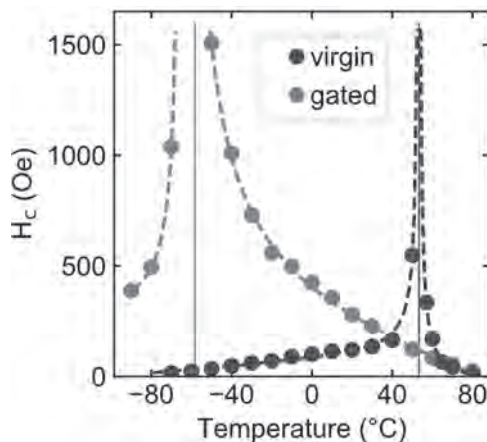
FE-05. Voltage Control of Ferrimagnetic Order and Voltage-Assisted Spin Texture Writing by Solid-State Hydrogen Gating.

M. Huang¹, K. Klyukin¹, L.M. Caretta¹, K. Lee², J. Chang², B. Yildiz^{1,3} and G. Beach¹

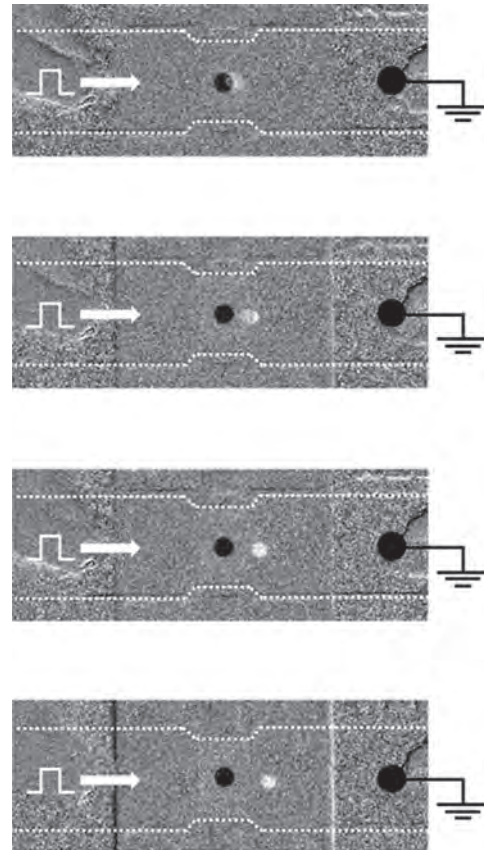
1. Department of Materials Science and Engineering, Massachusetts Institute of Technology, Cambridge, MA, United States; 2. Korea Institute of Science and Technology, Seongbuk-gu, The Republic of Korea; 3. Department of Nuclear Science & Engineering, Massachusetts Institute of Technology, Cambridge, MA, United States

Gate voltage control of magnetic order is desirable for spintronic device applications [1], [2], but 180° magnetization switching is not straightforward since electric fields do not break time-reversal symmetry. Ferrimagnets have two sublattices with opposing magnetic moments, and by changing the relative amplitude of the magnetization of the two sublattices, magnetic reversal can be achieved. Here we show that ferrimagnetic order in rare earth-transition metal thin films can be dynamically controlled by voltage through solid-state hydrogen gating. We focus on GdCo ferrimagnetic structures with perpendicular magnetic anisotropy, and show that the dominant lattice of GdCo ferrimagnetic thin films at room temperature can be reversibly toggled by hydrogen loading/unloading into the material controlled using a solid-state hydrogen pump [3]. The loading/unloading of hydrogen is mediated by a positive gate bias applied to the top electrode generates protons through hydrolysis of ambient moisture in the air, as shown previously [3]. We find that hydrogen injection into the GdCo leads to a significant decrease in the compensation temperature. With a fixed perpendicular bias field, we show that a gate voltage can induce 180° magnetic switching of the sublattices by shifting the magnetic compensation temperature above and below room temperature. The localized nature of the hydrogen gating effect allows for gate-voltage generation of ferrimagnetic spin textures such as chiral domain walls in racetrack devices. The work provides a means to tune ferrimagnetic spin textures and dynamics, and provides a new direction in magnetoionic control of magnetism for data storage and computing.

[1] F. Matsukura, Y. Tokura, and H. Ohno, "Control of magnetism by electric fields," *Nat. Nanotechnol.*, vol. 10, no. 3, pp. 209–220, 2015. [2] E. Y. Tsybal, "Electric toggling of magnets," *Nat. Mater.*, vol. 11, no. 1, pp. 12–13, 2011. [3] A. J. Tan et al., "Magneto-ionic control of magnetism using a solid-state proton pump," *Nat. Mater.*, vol. 18, no. 1, pp. 35–41, 2019.



Coercivity (H_c) versus temperature showing compensation temperature change of GdCo by solid-state ionic gating.



Reversed domain generator based on hydrogen gating: a sequence of wide field MOKE contrast images showing the movement of the generated reversed domain.

FE-06. Exchange Bias Toggling in GdCo/NiO Thin Film System by Solid-State Hydrogen Gating.

M. Hasan¹, J. Zehner², M. Huang¹, K. Leistner² and G. Beach¹

1. Massachusetts Institute of Technology, Cambridge, MA, United States;

2. Leibniz-Institut für Festkörper- und Werkstofforschung Dresden eV, Dresden, Germany

Exchange bias is a well-known and very useful effect that occurs due to an interfacial coupling between adjacent thin films of an antiferromagnet and a ferro(ferri)magnet [1]. Controlling exchange bias in an antiferromagnet/ferro(ferri)magnet thin film system by application of a gate voltage is much sought-after for spintronic applications. However, since the exchange bias effect is related to the ordering of spins in both the antiferromagnet and the ferro(ferri)magnet, and electric fields have little influence over the spin order, electrical control of exchange bias is very hard to achieve practically. Recently, ionic gating of magnetic heterostructures, where a gate voltage is used to drive ions (O^{2-} , H^+ etc.) in or out of the active layers, has yielded very interesting and promising results. Due to the size of the H^+ ion, protonic gating is potentially faster and more reversible compared to gating with other ions and is also able to cause large changes in magnetic properties in the underlying active layers, such as modulation of perpendicular magnetic anisotropy in ultra-thin Co films [2]. The utility of protonic gating was further demonstrated when it was shown that ferrimagnetic order in GdCo metal thin films can be dynamically controlled by this method [3]. GdCo is comprised of two sub-lattices, one made up of Gd atoms and one of Co atoms, and the magnetic moments in each sub-lattice point in opposite directions, hence resulting in ferrimagnetic order. Experimental and theoretical analyses show that the protons being inserted into the GdCo reduce the effective magnetic moment of the Gd atoms, and by starting from a Gd-dominated magnetic state, the overall magnetization can be switched 180 degrees through proton gating. Harnessing this functionality, we have shown, in this work, that exchange bias toggling is possible when we incorporate the GdCo ferrimagnet in an exchange biased heterostructure with NiO serving as the antiferromagnet. Using sputter deposition we have engineered a stack with the structure NiO(33)/Pd(1)/GdCo(10)/Pd(10)/GdO_x(30)/Au(3) on thermalized Si, which has fully shifted loops, i.e. the exchange bias field is larger than the coercive field ($H_{EB} > H_C$), as depicted in Fig. 1(a). When a sufficiently high (>1.5V) positive voltage is applied to the Au top electrode (Pd serves as the bottom electrode), atmospheric water is split and the proton is transported through the GdO_x electrolyte, into the GdCo(10)/Pd(10) layers. Starting from a Gd-dominated state of the GdCo, upon enough insertion of hydron ions after applying +1.8V, the dominant sublattice of GdCo switches from Gd to Co, as expected from previous work, but is now also accompanied by a toggling of the exchange bias direction, as shown in Fig. 1(b). The effect is fully reversible, as shown in Fig. 1(c). We can understand this phenomena when we realize that although the gating does nothing to the relative spin orientation in either the ferrimagnet or the antiferromagnet, the ferrimagnet's magnetization direction depends not only on the spin orientation of the sublattices but also on the relative magnitude. The magnetization direction flips 180 degrees during gating but the relative spin orientation across the interface remains the same. Essentially, if initially the pinned magnetization is $+M_z$ (meaning H_{EB} is -ve) then after gating the pinned magnetization will be $-M_z$ necessarily making $H_{EB} +ve$. To the best of our knowledge, this is the simplest demonstration of exchange bias toggling to date, since our system does not rely on any complex materials or growth processes and works at room temperature, as opposed to some previous works [4,5]. Due to the small size of the proton, our method is highly reversible, and initially we have shown full cycling toggling of the exchange bias up to 10 times, where the hysteresis loop remains fully shifted throughout the process (Fig. 2) as evidenced by H_{EB}/H_C being over 1. We believe our simple but robust method to toggle exchange bias can serve as a platform for demonstrating more functionalities and/or devices and can have broad implications for spintronics in general. This work is supported in part by SMART, one of seven centers of nCORE, a Semiconductor Research Corporation program, sponsored by National Institute of Standards and Technology (NIST).

[1]. Y. Fan et al., Nature Nanotechnology, Vol. 8, p. 438 (2013) [2]. A.J. Tan et al., Nature Materials, Vol. 18, p. 35 (2019) [3]. M. Huang et al.,

manuscript under review [4]. S. Wu et al., Physical Review Letters, Vol. 110, p. 067202 (2013) [5]. X. He et al., Nature Materials, Vol 9, p. 579 (2010)

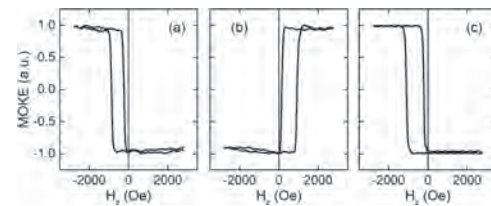


Fig. 1. MOKE hysteresis loops of the structures described in the text in the (a) initial state, (b) after applying +1.8V for 180s and (c) after applying 0V for 80s. The MOKE signal follows the Co magnetic moments, which is why in the Gd dominated state (a) and (c) the loops are inverted

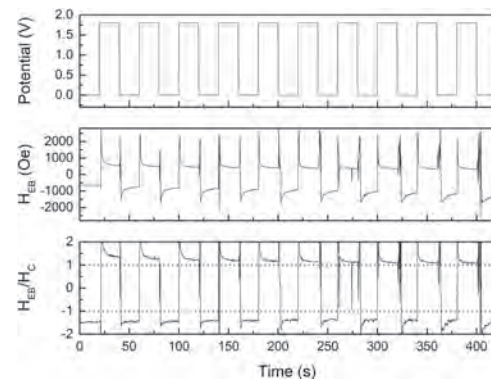


Fig. 2. Reversible toggling of exchange bias in sample with fully shifted loops, where the voltage was toggled between +1.8V and 0V with period of 40s. Note that the erratic oscillations in EB towards the latter cycles are due to noise during measurement of individual hysteresis loops

FE-07. Experimental Demonstration of Voltage-Gated Spin-Orbit Torque Switching in Antiferromagnet/Ferromagnet Structure.

W. Li^{2,4}, S. Peng^{1,4}, J. Lu^{1,4}, H. Wu³, X. Li³, D. Xiong¹, Y. Zhang², Y. Zhang², K. Wang³ and W. Zhao^{1,4}

1. School of Integrated Circuit Science and Engineering, Beihang University, Beijing, China; 2. School of Electronic and Information Engineering, Beihang University, Beijing, China; 3. Department of Electrical Engineering, University of California Los Angeles, Los Angeles, CA, United States; 4. Hefei Innovation Research Institute, Beihang University, Hefei, China

Magnetic random-access memory (MRAM) has recently emerged as a promising way for next generation memory due to its nonvolatility, low power consumption and high density. How to achieve energy-efficient magnetization switching is one of the main challenges for MRAM. Recent studies propose spin orbit torque (SOT) as a promising method for data writing [1]. However, an external magnetic field along current direction is usually needed to realize deterministic switching. It can be overcome by using antiferromagnet/ferromagnet structures in which exchange bias can replace external field [2]. Voltage control of magnetic anisotropy (VCMA) is another candidate method for lowering down the energy height by inducing electron accumulation at the ferromagnet/oxide interface[3]. Combination of VCMA and SOT effect may lead to decrease of power consumption by a gate voltage lowering the energy barrier height. For example, Yoda *et al.* propose a new spintronics-based memory employing the VCMA effect as a bit selecting principle and the SOT effect as a writing principle. [4]. Back *et al.* reported that a gate voltage can be used to manipulate both perpendicular magnetic anisotropy and spin orbit torque[5]. Hence, it is essential to make it clear whether the voltage-controlled spin-orbit effective torques (VCSOT) or voltage controlled magnetic anisotropy causes the decrease of critical current, or both. In this work, we investigate VCSOT effect and VCMA effect in the IrMn/CoFeB/MgO structures. The film structures were thermally oxidized Si substrate/Ta(2)/IrMn(5)/CoFeB(0.94)/MgO(2.5)Al₂O₃(5), (with film thickness in nm in the parentheses). The films were patterned into Hall bar by ion beam etching (IBE) and lithography as shown in Fig. 1(a). Fig. 1(b) shows the micrograph of the Hall bar and the measurement setup. Furthermore, to explore voltage-gated SOT switching, a gate voltage is applied at the top electrode and the switching loops are obtained with no external field applied as shown in Fig. 1(d). Figure 1(f) presents critical current density J_c dependence on voltage applied to MgO (V_{MgO}) with 5 mT field applied. These results indicate that a gate voltage can be used to effectively modulate SOT-driven perpendicular magnetization switching and this is a feasible writing method for low energy consumption. Next, spin-orbit effective fields at the different voltage were measured by using a second harmonic method as shown in Fig. 2 (a). The damping-like torque efficiency decreases with positive voltage increasing, whereas the field-like torque efficiency shows weaker voltage dependence. These results demonstrate that V_{MgO} can modulate spin torques in IrMn/CoFeB/MgO system. The damping-like torque efficiency under V_{MgO} of -0.4 V is 1.5 times larger than that under V_{MgO} of 0.4 V. A larger J_c is required for the magnetization switching under positive voltage due to the reduction of θ_{SHE} . Through VCSOT effect, positive voltage tends to increase J_c , which is reverse to the experimental results in Fig. 1(f). In-plane hysteresis loops at different gate voltages are obtained as shown in Fig. 2(b). The dependence of anisotropy energy $K_{eff}(V_{MgO})$ on gate voltage is shown in Fig.2 (c). By linear fitting, K_{eff} decreases by 55% when V_{MgO} changes from -0.6V to 0.6V. According to theoretical research from Ref.[6], the J_c for SOT switching is proportional to K_{eff} . Therefore, the decrease of K_{eff} will lead to significant reduction of J_c . Figure 2(d) shows the interfacial anisotropy coefficient K_i . We can see that the K_i changes linearly with V_{MgO} due to VCMA effect. From the slope of the linear fitting, the VCMA coefficient ξ of 34.3 fJ/Vm is obtained for IrMn/CoFeB/MgO structure. Therefore, VCSOT effect is not the reason for the reduction of J_c in the voltage-gated SOT switching. The decrease of J_c in the voltage-gate SOT switching is mainly caused by the reduction of PMA due to VCMA effect. In summary, we demonstrate field-free switching in the IrMn/CoFeB/MgO structures and show the critical switching current can be modulated by the control voltage. Moreover, VCSOT effect and VCMA effect are

explored. We measured spin-orbit effective torques under different voltage. We concluded that through VCSOT effect, positive voltage tends to increase J_c , which is reverse to the experimental results. Next, we measured anomalous Hall resistance at different voltage to explore VCMA effect. From quantitative calculation, the critical switching current at different voltage is consistent with experiments. Therefore, we concluded VCSOT effect hindered the reduction of J_c , while the VCMA effect made a main contribution to the J_c reduction. This work provides comprehensive understanding of voltage-gated spin torque switching.

[1] M. Miron, K. Garello and G. Gaudin., *Nature*, vol. 476, no. 7359, pp. 189–193. (2011). [2] S.Z. Peng, D. Q. Zhu and W S Zhao., *Adv. Electron. Mater.* Vol. 5 pp. 1100134. (2019). [3] W.G. Wang, M. Li and C.L. Chien., *Nat.Mater.*, vol. 11, no. 1, pp. 64–68. (2012). [4] H. Yoda, N. Shimomura and A. Kurobe., *IEEE Electron Devices Meet. (IEDM)*, pp. 27.6.1-27.6.1. (2016). [5] L. Chen, M. Gmitra and C.H. Back., *Nat. Electron.*, vol. 1, no. 6, pp. 350–355, (2018). [6] K.S. Lee, S.W. Lee and K.J. Lee., *Appl. Phys. Lett.* vol.102, pp. 112410. (2013).

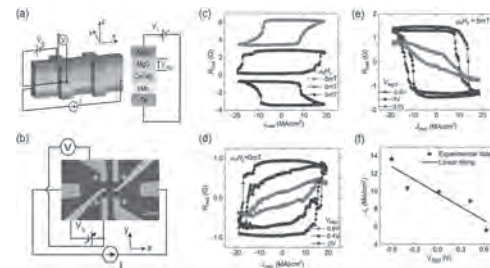


Fig.1 (a) Schematic of IrMn/CoFeB/MgO structures. (b) Micrograph of the Hall bar and the measurement setup. (c) SOT-driven magnetization switching with various in-plane external field. Voltage-gated SOT switching under different gate voltages with (d)no external field and (e)5 mT in-plane external field. (f) Critical current density J_c dependence on voltage applied to MgO (V_{MgO}) with 5 mT field applied.

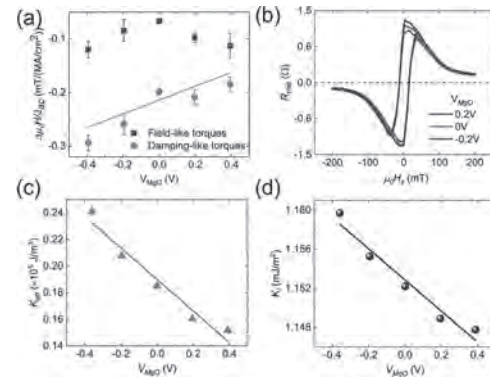


Fig.2 (a) The dependence of spin-orbit effective torques on voltage in MgO layer (V_{MgO}). The error bars are standard deviations. (b) Anomalous Hall resistance (R_{Hall}) under different gate voltages (V_{MgO}) (c) K_{eff} and (d) K_i dependence on V_{MgO} .

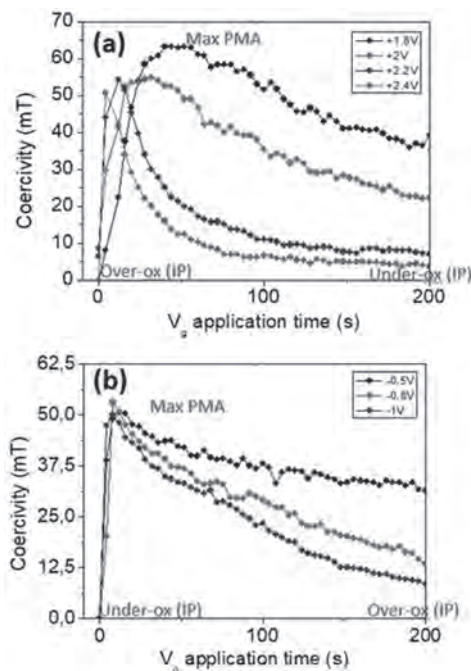
FE-08. Large Reversible Voltage Manipulation of Interfacial Magnetic Anisotropy in Pt/Co/Oxide Multilayers.

A. Fassatoui¹, J.A. Peña Garcia¹, A. Bernand-Mantel², L. Ranno¹, H. Béa³, J. Vogel¹ and S. Pizzini¹

1. UGA-CNRS, Institut NEEL, Grenoble, France; 2. INSA Toulouse, Toulouse, France; 3. UGA-CNRS-CEA, SPINtronique et Technologie des Composants, Grenoble, France

The voltage control of magnetic anisotropy (VCMA) is an active field of research, as it is a promising route towards the realization of low power spintronic devices. Among a few proposed VCMA mechanisms, voltage-induced oxygen migration (i.e., magneto-ionic effect) has demonstrated large modulation of magnetic anisotropy. In this work, we study the voltage control of the interfacial perpendicular magnetic anisotropy (PMA) in a series of Pt/Co/MOx (M=Al and Tb) trilayers [1]. The stacks were patterned by electron beam lithography and ion beam etching into stripes (1 – 50 μm width) then covered with a 10 nm thick ZrO_2 dielectric layer and a 6 nm thick Pt top electrode to form capacitor-like structures. We show a large modification of interfacial magnetic anisotropy ($\beta > 2000 \text{ fJ}/(\text{Vm})$) accompanied by a non-volatile effect at room temperature (RT). This modification is explained in terms of voltage-induced oxygen migration towards/away from the Co/MOx interface. The Co films can be reversibly switched from an under-oxidized state with in-plane anisotropy (IPA) to an optimal oxidized state with maximum PMA, to an over-oxidized state under applied voltage (see figure). The switching time depends on the amplitude of the applied voltage. Here, we demonstrate that the switching time can be reduced from several seconds down to few milliseconds at RT by adjusting the voltage amplitude.

[1] A. Fassatoui, S. Pizzini, Phys. Rev. Appl. 14, 064041 (2020).



Variation of the coercivity of a Pt/Co/TbOx/ZrOx/Pt device during the application of different gate voltages: (a) for positive voltages showing the transition from an over-oxidised state, to max PMA, to under-oxidised state with in-plane anisotropy; (b) transition from under-oxidised to over-oxidised state with negative voltage. In both cases, increasing slightly the voltage gives rise to large acceleration of the electric-field effect.

FE-09. Reversible and Irreversible Magneto-Ionic Regimes in Ta/CoFeB/HfO₂.

R. Pachat¹, D. Ourdani², J.W. van der Jagt³, M.A. Syskaki⁴, A.D. Pietro⁵, M. Belmeguenai², Y. Roussigné², G. Durin⁵, S. Ono⁶, J. Langer⁴, D. Ravelosona^{3,1} and L.H. Diez¹

1. Centre de Nanosciences et de Nanotechnologies, Université Paris-Saclay, Palaiseau, France; 2. Laboratoire des Sciences des Procédés et des Matériaux, Université Sorbonne Paris Nord, Villetaneuse, France; 3. Spintron technologies, Palaiseau, France; 4. Singulus Technologies AG, Kahl am Main, Germany; 5. Istituto Nazionale di Ricerca Metrologica, Torino, Italy; 6. Central Research Institute of Electric Power Industry, Yokosuka, Japan

Controlling magnetic properties of materials with electric fields (EFs) is of remarkable importance in spintronics applications due to its potential for much lower power consumption devices. Much like the power efficiency, two other sought-after features to incorporate are non-volatility and reversibility. This has been demonstrated with magneto-ionics, where EFs induce the migration of mobile ionic-species towards/away from the magnetic interface [1–4]. However, several works conducted in a variety of magneto-ionic materials have revealed important issues like irreversibility, the need of elevated temperatures to recover the initial states and chemical and structural degradation [4–6]. Recent studies have also focused on the differences in magneto-ionic reversibility between various oxides [7], pointing out the importance of the mechanisms governing ionic conduction. In this study, we unravel a higher degree of complexity in an HfO₂ based device and demonstrate the coexistence of two distinct magneto-ionic regimes. For this purpose, we chose amorphous Ta/CoFeB/HfO₂ thin films grown by magnetron sputtering with an ionic-liquid gate. It is shown that a gate voltage drives the anisotropy of the system from an underoxidized state exhibiting in-plane anisotropy (IPA) to an optimum oxidation level resulting in perpendicular anisotropy (PMA) and further into an overoxidized state resulting in IPA in a non-volatile manner. The IPA (underoxidized) to PMA regime is found to be highly irreversible and is significantly faster than the PMA to IPA (overoxidized) regime which is fully reversible under the same gate voltages. In addition, the effective damping parameter also shows a marked dependence with the anisotropy evolution in different regimes; IPA to PMA regime going from 0.029 to 0.012 and only a modest increase to 0.014 in the PMA to IPA regime. The existence of two magneto-ionic regimes has been linked to a difference in the chemical environment of oxygen species added to under/over oxidized layers. Our results show that different magneto-ionic regimes can coexist and that their identification is of great importance for tuning the properties and the design of high performance spintronics devices based on magneto-ionics.

[1] U. Bauer, S. Emori, and G. S. D. Beach, Nat. Nanotech. 8, 411 (2013) [2] U. Bauer, L. Yao, A. J. Tan, and G. S. D. Beach, Nat. Mater. 14, 174 (2015) [3] A. J. Tan, M. Huang, C. O. Avci, and G. S. D. Beach, Nat. Mater. 18, 35 (2019) [4] L. Herrera Diez, Y. Liu, D. Gilbert, M. Belmeguenai, J. Vogel, S. Pizzini, E. Martinez, A. Lamperti, J. Mohammedi, A. Laborieux, et al., Phys. Rev. Appl. 12, 034005 (2019) [5] C. Bi, Y. Liu, T. Newhouse-Illige, M. Xu, M. Rosales, J. W. Freeland, O. Mryasov, S. Zhang, S. G. E. te Velthuis, and W. G. Wang, Phys. Rev. Lett. 113, 267202 (2014) [6] D. A. Gilbert, A. J. Grutter, E. Arenholz, K. Liu, B. J. Kirby, J. A. Borchers, and B. B. Maranville, Nat. Commun. 7, 12264 (2016) [7] A. Fassatoui, Phys. Rev. Appl. 14, 064041 (2020)

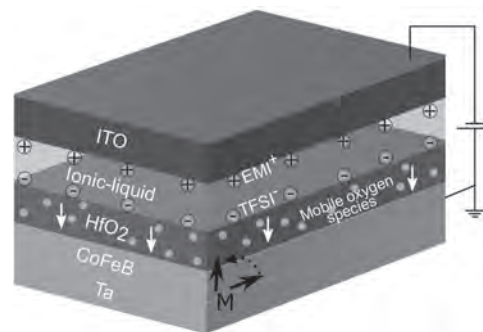


Fig. 1: Graphic representation of the Ta/CoFeB/HfO₂ magneto-ionic stack covered with an [EMI-TFSI] ionic liquid gate. The gate voltage induces motion of oxygen species in HfO₂ that drive anisotropy changes in the CoFeB layer.

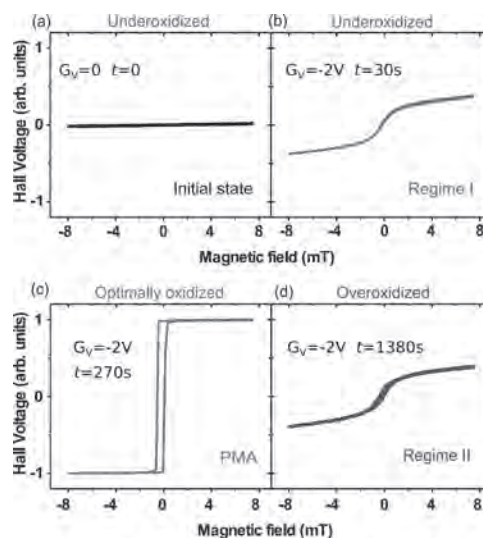


Fig. 2: A progressive oxidation is induced upon exposure to a gate voltage $G_v = -2V$. Different exposure times t drive the system from IPA (a, initial state) through regime I (IPA to PMA) (b) into PMA (c) and back to IPA through regime II (PMA to IPA) (d).

Session FG
ANTIFERROMAGNETIC SPINTRONICS I
Samik DuttaGupta, Chair
Tohoku University, Sendai, Japan

CONTRIBUTED PAPERS

FG-01. Interpretation of the Anomalous Hall Effect as an Effective Topological Hall Effect in Noncollinear Kagome Magnets.O. Busch¹, B. Göbel¹ and I. Mertig¹¹. Institute for Physics, Martin-Luther-Universität Halle-Wittenberg, Halle, Germany

The Hall effect is one of the best known effects in (solid-state) physics. Conventionally, this phenomenon describes the occurrence of charge currents that are perpendicular to an externally applied electric field due to a time-reversal symmetry breaking magnetic field. Besides, in ferromagnetic systems, the net magnetization can break time-reversal symmetry even in the absence of a magnetic field which allows the so-called anomalous Hall effect. This effect originates from extrinsic and intrinsic contributions that are both related to the existence of spin-orbit coupling [1]. Moreover, another contribution to the Hall effect, which is known as the topological Hall effect, can exist even if spin-orbit coupling is negligible. It may occur in certain noncollinear noncoplanar magnetic textures with a nonzero scalar spin chirality like skyrmions [2, 3]. However, recent works [4, 5] reported the occurrence of an anomalous Hall effect in several compensated kagome magnets (cf. Fig. 1). These materials are coplanar antiferromagnets with vanishing net magnetization, and still, a group theoretical analysis allows the existence of the effect. The large conductivities obtained via first-principle calculations have been confirmed in experiments for Mn_3Sn [6] and Mn_3Ge [7]. However, a straightforward microscopic picture for this phenomenon was still missing. In this talk, we present an explanation on a microscopic level based on tight-binding calculations and analytical considerations [8]. For coplanar kagome magnets, we show the equivalence of spin-orbit coupling and an out-of-plane tilting of the magnetic moments. The existence of spin-orbit interaction does not only break a combined time-reversal and mirror symmetry of the Hamiltonian but can be transformed to a magnetic texture that is virtually canted, whereas, the original texture remains coplanar [cf. Fig. 2(a)]. Consequently, the ‘new’ anomalous Hall effect can be interpreted as a combination of an effective anomalous and topological Hall effect due to the net magnetic moment and the net scalar spin chirality of this virtual magnetic texture, respectively. Furthermore, as we demonstrate, a noncoplanar kagome magnet with spin-orbit coupling is able to behave like a system that is virtually coplanar and with compensated spin-orbit coupling [cf. Fig. 2(b)]. In this case, the combination of mirror and time-reversal symmetry of the Hamiltonian that was broken before has been restored. A critical out-of-plane tilting angle of the real texture can be found, where the virtual texture is coplanar and the Hall effect is absent for all energies. As we show in detail, the electronic properties are determined by this virtual texture that is hidden in the Hamiltonian. In consequent investigations, the calculations have been repeated for other transport quantities like the spin Hall effect where charge currents are converted into spin currents. These results can again be related to the virtual spin texture which has, however, different consequences for the spin Hall effect. Besides, in order to simulate the experimental situation, the investigated model was extended from a two-dimensional kagome lattice, as considered here, to a more realistic model including d -orbitals and kagome planes that are stacked along the out-of-plane direction.

[1] N. Nagaosa, J. Sinova, S. Onoda, *et al.* “Anomalous Hall effect”. *Rev. Mod. Phys.* 82, 1539 (2010). [2] P. Bruno, V. K. Dugaev, and M. Taillefumier. “Topological Hall Effect and Berry Phase in Magnetic Nanostructures”. *Phys. Rev. Lett.* 93, 096806 (2004). [3] N. Nagaosa and Y. Tokura. “Topological properties and dynamics of magnetic skyrmions”. *Nat. Nanotechnol.* 8, 899 (2013). [4] H. Chen, Q. Niu, and A. H. MacDonald. “Anomalous Hall Effect Arising from Noncollinear Antiferromagnetism”. *Phys. Rev. Lett.* 112, 017205 (2014). [5] Y. Zhang, Y. Sun, H. Yang, *et al.* “Strong anisotropic anomalous Hall effect and spin Hall effect in the chiral antiferromagnetic compounds Mn_3X ($X=Ge, Sn, Ga, Ir, Rh,$ and Pt)”. *Phys. Rev. B* 95, 075128 (2017). [6] S. Nakatsuji, N. Kiyohara, and T. Higo. “Large anomalous Hall effect in a non-collinear antiferromagnet at room temperature”. *Nature (London)* 527, 212 (2015). [7] A. K. Nayak,

J. E. Fischer, Y. Sun, *et al.* “Large anomalous Hall effect driven by a nonvanishing Berry curvature in the nonlinear antiferromagnet Mn_3Ge ”. *Sci. Adv.* 2, e1501870 (2016). [8] O. Busch, B. Göbel, and I. Mertig. “Microscopic origin of the anomalous Hall effect in noncollinear kagome magnets”. *Phys. Rev. Research* 2, 033112 (2020).

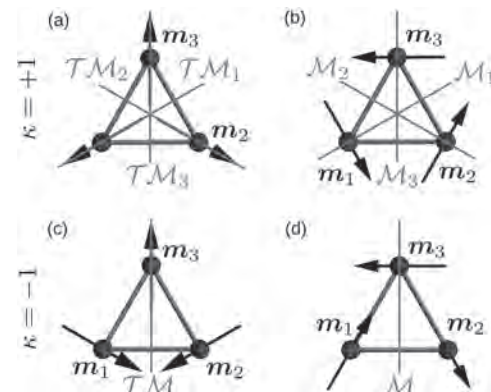


Fig. 1. Overview of the discussed coplanar kagome magnets. The arrows indicate the magnetic moments that are located at the basis atoms of the unit cell. The configurations can be characterized by their vector spin chiralities [(a), (b) positive, and (c), (d) negative]. Besides, each magnetic texture has different symmetry planes (time reversal T, mirror M or a combination of both) as indicated by the red lines.

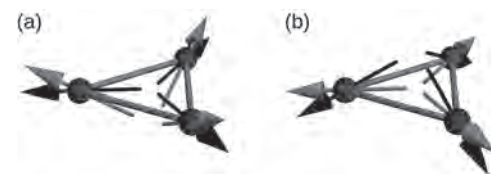


Fig. 2. Within the considered model, spin-orbit coupling gives rise to a virtual magnetic texture (red arrows) that is tilted out of the kagome plane with respect to the original magnetic texture (black arrows). (a) The virtual texture of a coplanar configuration can be noncoplanar resulting in the occurrence of an effective anomalous and topological Hall effect. (b) At a critical out-of-plane canting angle of the real magnetic texture, spin-orbit coupling is compensated and the virtual magnetic texture is coplanar. In this case, the anomalous Hall effect is absent.

FG-02. Temperature-Dependent Magnetic Properties and Domain Wall Width of the Antiferromagnet Mn_2Au .

S. Jenkins¹, R. Rama-Eiroa^{2,3}, A. Naden¹, U. Atxitia⁴, O. Chubykalo-Fesenko⁵, R.M. Otxoa^{2,6}, R.W. Chantrell¹ and R.F. Evans¹

1. Department of Physics, University of York, York, United Kingdom;

2. Donostia International Physics Center, San Sebastian, Spain;

3. Polymers and Advanced Materials Department: Physics, Chemistry, and Technology, University of the Basque country, San Sebastian, Spain;

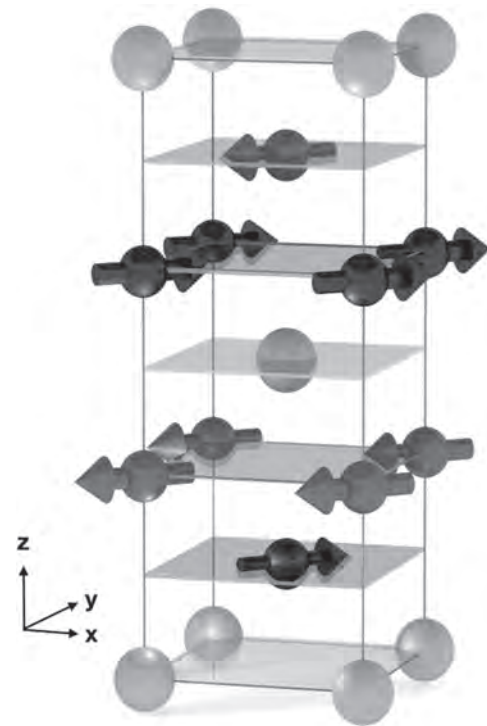
4. Dahlem Center for Complex Quantum Systems and Fachbereich Physik,

Freie Universität Berlin, Berlin, Germany; 5. Instituto de Ciencia de

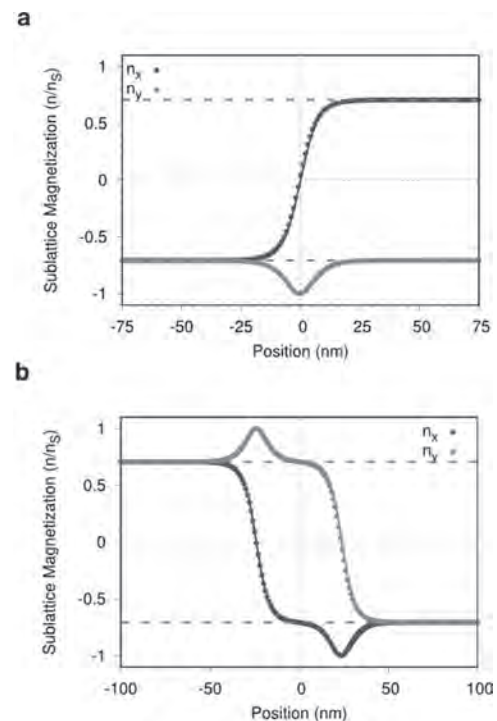
Materiales de Madrid, Madrid, Spain; 6. Hitachi Cambridge Laboratory, Cambridge, United Kingdom

Antiferromagnetic spintronic devices have the potential to greatly outperform their current ferromagnetic counterparts due to their robustness to external fields, ultrafast dynamics and potential for high data density storage. Mn_2Au is one of the most promising materials for antiferromagnetic spintronics due to its very high Néel temperature, moderate in-plane anisotropy and layered two sublattice spin structure [1]. Here we present atomistic spin simulations that allow us to estimate the temperature dependent magnetic properties of Mn_2Au single crystals. We introduce a thermodynamically consistent spin Hamiltonian guided by previous *ab-initio* calculations [3], which includes easy plane and rotational anisotropy terms. Temperature scaling of the anisotropy parameters is crucial for the performance optimization of antiferromagnetic devices, from the scale of magnetic domains to stability under thermal activation [2]. However, scaling in antiferromagnet has been barely studied due to the inherent difficulties to measure antiferromagnetic order parameter, n . We find a scaling of the easy plane anisotropy with the sublattice magnetization of $n^{2.32}$. This is consistent with its two-ion origin [4], whereas the rotational anisotropy presents a n^{10} dependence, consistent with the Callen-Callen scaling in ferromagnets of a 4th order anisotropy. The crystal structure is shown in Fig. 1 showing two distinct Mn sites with a 180 degree relative orientation. We obtain quantitative agreement with experimental measurements of the temperature dependence of the order parameter by using a thermal-bath temperature rescaling, which has been demonstrated to work in ferromagnets. Our model provides a critical temperature (Neel) of 1256 K from the *ab initio* values of the exchange interactions. Due to the presence of four easy directions, the domain wall structure of 90 degrees and 180 degrees are stable in Mn_2Au . We find a narrow domain wall width of 23.13 ± 0.085 nm at zero temperature in both cases as shown in Fig. 2. Applying thermal spin fluctuations yields a domain wall width that increases with temperature, up to 25 ± 2 at 300K and to 53 ± 18 nm at 800K, matching well with experimental results of Sapozhnik *et al*[5]. In the case of a 180 degree wall the two separate 90 degree walls are weakly bound and separate at high temperatures. Further analysis of the domain wall width could provide information about the scaling of the exchange stiffness in antiferromagnets, a pivotal parameter for the construction of hierarchical multiscale models in magnetism, which are missing for antiferromagnets. When an electrical current is applied to the system along the [110] direction a spin orbit torque (SOT) is generated by the flow of electrons through the system interacting with the Au atoms. These SOTs cause the domain wall to move. For a Neel anti-damping SOT field of 0.05 T we find a domain wall velocity of 250 m/s at 0K, which is different to the usually fast dynamics displayed by anti-ferromagnetic materials. This is because the SOT applied is precessional in nature and both sublattices have precessional motion in the same direction. Applying a field-like SOT yields the usual fast motion of the domain walls. The atomistic spin model [6] used here to compute thermal properties of Mn_2Au provide new insights on the temperature dependent magnetic properties – magnetic order and anisotropies and domain wall widths in Mn_2Au . The understanding of the macroscopic parameters is necessary for the developments of multiscale models of Mn_2Au that could greatly help to the development of novel antiferromagnetic spintronic devices.

[1] V. Barthem *et al* Nature communications 4 (2013) [2] L Rózsa, S Selzer, T Birk, U Atxitia, U Nowak Physical Review B 100, 064422 (2019) [3] A. B. Shick *et al*. Phys. Rev. B 81, 212409 (2010) [4] R.F.L. Evans *et al*. Phys. Rev. B 102, 020412(2020) [5] A. A. Sapozhnik, Phys. Rev. B 97, 134429 (2018)



Magnetic unit cell of Mn_2Au . The Mn atoms (atoms with arrows) form two anti-parallel sublattices aligned along the [110] and [-1-10] crystal directions. The gold coloured atoms represent Gold.



90 degree and 180 degree domain wall profiles.

FG-03. Effects of Spin-Orbit Torque on the Ferromagnetic and Exchange Spin-Wave Modes in Ferrimagnetic Co-Gd Alloy.

B. Divinskiy¹, G. Chen², S. Urazhdin², S.O. Demokritov¹ and V.E. Demidov¹

1. Institute for Applied Physics, Westfälische Wilhelms-Universität Münster, Münster, Germany; 2. Department of Physics, Emory University, Atlanta, GA, United States

In recent years, it was demonstrated that spin-orbit torque (SOT) can be utilized to implement efficient magnetic oscillators – SOT oscillators – that can serve as nanoscale sources of microwave signals. SOT oscillators based on ferromagnetic materials operate at frequencies in the range of about 0.1–30 GHz, with the upper limit determined by the practically accessible magnitudes of static magnetic fields. However, one of the most significant challenges in modern microwave technology is the lack of compact and reliable microwave sources capable of generating signals in the frequency range 0.1–10 THz, which is commonly referred to as the “terahertz gap”. It was recently proposed that the operational frequency of SOT oscillators based on antiferromagnetic (AFM) and ferrimagnetic (FiM) materials can be significantly higher than in ferromagnet-based oscillators, owing to the large internal effective exchange fields. The latter can reach magnitudes of dozens of Tesla, enabling terahertz-frequency dynamics even in the absence of external magnetic fields, and paving the way for the implementation of SOT oscillators capable of filling the “terahertz gap.” Among the most attractive FiM systems are transition metal-rare earth (TM-RE) alloys, which exhibit two types of dynamic magnetic modes. In the first mode, the magnetizations of the two sublattices remain antiparallel to each other during precession. The frequency of this mode is determined mainly by the external static magnetic field and the effective gyromagnetic ratio, and typically lies in the gigahertz range. In the second mode, called the exchange mode, the magnetizations of the two sublattices do not remain antiparallel to each other, resulting in a large contribution of exchange interaction to the dynamic mode energy. Consequently, the frequency of this mode is determined by the exchange constant, and typically falls in the terahertz region. Both the ferromagnetic and the exchange modes have been experimentally observed in TM-RE alloys using ferromagnetic resonance and ultrafast optical pump-probe techniques. However, the effects of SOT on these dynamic modes remain unexplored. Here, we report an experimental study of the effects of SOT on the magnetization dynamics in a Co-Gd film, which is a canonical TM-RE alloy. We utilize microfocus Brillouin light spectroscopy (BLS) to detect the ferromagnetic and exchange modes, and study the dependences of their characteristics on the SOT generated by an electric current in the Pt layer adjacent to the Co-Gd film. By analyzing the intensity and the linewidth of these modes, we demonstrate that the effects of SOT are significant only for the ferromagnetic mode, but there is no sizable effect of SOT on the exchange mode. We also show that the frequencies of both modes can be electronically tuned by Joule heating. Our findings are important for the practical implementation of ultrahigh-frequency SOT oscillators based on FiM materials, and are also likely to be relevant to the AFM-based SOT devices.

B. Divinskiy, G. Chen, S. Urazhdin, S. O. Demokritov, and V. E. Demidov, Phys. Rev. Applied 14, 044016 (2020)

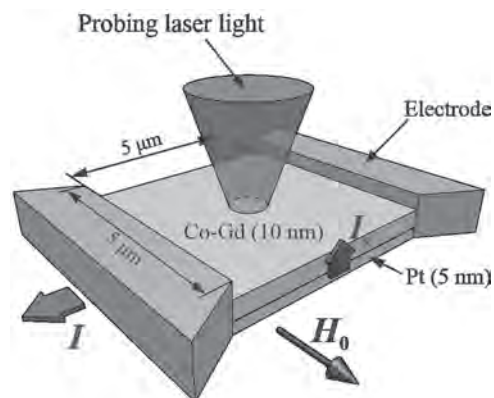


Fig.1 Schematic of the experiment.

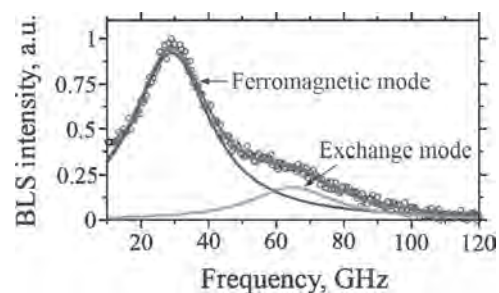


Fig. 2 Representative BLS spectrum. Symbols are experimental data. Curves are the Lorentzian fits for the ferromagnetic and the exchange modes, and their sum.

FG-04. Quantifying Spin Torques in CoO(001)/Pt Bilayers by Comparing Field- and Current-Induced Switching.

L. Baldrati¹, C. Schmitt¹, O. Gomonay¹, R. Lebrun², R. Ramos³, E. Saitoh^{3,4}, J. Sinova¹ and M. Kläui¹

1. Institut für Physik, Johannes Gutenberg-Universität Mainz, Mainz, Germany; 2. Unite Mixte de Physique CNRS/Thales, Palaiseau, France; 3. WPI-Advanced Institute for Materials Research, Tokyo University, Tokyo, Japan; 4. Tokyo University, Tokyo, Japan

Antiferromagnets (AFMs) are promising materials for spintronics, that compared to ferromagnets exhibit faster dynamics, enhanced stability with respect to interfering magnetic fields and higher bit packing density, thanks to the absence of long-range magnetic coupling via stray fields. However, the absence of a net magnetic moment makes manipulation using conventional magnetic fields challenging [1]. For the use of AFMs, one requires efficient electrical writing and reading. Recently, there have been reports on the current-induced switching of the Néel vector orientation [2-5]. In particular, we demonstrated that in the insulating antiferromagnet NiO/heavy metal Pt thin film system there are multiple effects contributing to the electrical signal [6]. These include the switching of the magnetic Néel order, whose mechanism is debated in terms of origin and efficiency [2-6], but also non-magnetic signals possibly related to annealing or electromigration in the Pt layer [7]. While NiO has been intensively studied, key information such as the torque strength is missing so far. Using a different AFM such as CoO, that we study here [8], entails a number of advantages: we first show that, due to the compressive strain by the MgO substrate, a fourfold in-plane magnetic anisotropy of the CoO layer with two easy axes of the Néel order in the (001) plane is favored, and the spin flop field is accessible (around 7 T at 200 K). Such a system with two orthogonal stable states (along the [110] and [-110] directions) is ideal for applications where the orientation of n is read by spin Hall magnetoresistance (SMR) [4, 9, 10]. Furthermore, we achieve electrical switching and probe its symmetry, where the accessible spin flop field allows us to directly compare the effects of fields and currents. By looking at the switching above and below the Néel temperature in the CoO/Pt bilayer, we can show that this switching is of magnetic origin, as the signal related to the antiferromagnetism disappears above the Néel temperature, which in CoO is easily accessible around room temperature. For the switching, 8-arms Hall stars devices are used, made of Pt 2 nm thick, with the pulsing arms orientated along the [110] and [-110] easy axes (Fig.1). Before the pulses, the Néel vector n is aligned along [110]. When current pulses are applied along the orientation given by the contact combination 3-2 (initial state $n||j_{\text{pulse}}$), the transverse resistance drops in a step-like fashion, indicating a current-induced 90° n rotation (Fig. 1a). Performing a MR scan with field along the contact combination 4-1 after the current pulses, shown in Fig. 1b, yields a field-induced spin flop transition of n back to the initial state (along [110]). No background was subtracted to the data in Fig. 1, meaning that at this temperature (200 K), pulse length (1 ms), average current density ($j_{\text{pulse}} = 1.15 \times 10^{12}$ A m⁻²) and in this switching configuration (straight pulses), where the effect of hot corners is not important, the non-magnetic effects are negligible and the electrical signal is dominated by a step-like magnetic contribution. At higher current densities the non-magnetic signal, possibly related to a local annealing process and electromigration in the Pt layer, can be observed and does not disappear above the Néel temperature, in contrast to the magnetic one. Finally, one can see how the threshold and saturation current density of the switching vary as a function of the magnetic field applied during the switching. By doing this, we find a linear relation between the current and the magnetic field and we ascertain a current-field equivalence ratio of value 4×10^{-11} T A⁻¹ m², that is orders of magnitude higher than for ferromagnets. The Néel vector final state ($n_{\perp}j$) in the center of the device and the linear current-field dependence are in line with a thermomagnetoelastic switching mechanism for a negative magnetoelastic constant of the CoO, whose sign is at the moment not known for CoO thin films. With this we show that, for the switching of AFMs, currents are much more efficient than magnetic fields.

[1] V. Baltz et al., Rev. Mod. Phys., Vol. 90, p. 015005 (2018); [2] L. Baldrati et al., Phys. Rev. Lett., Vol. 123, p. 177201 (2019); [3] T. Moriyama et al., Sci. Rep., Vol. 8, p. 14167 (2018); [4] X. Z. Chen et al., Phys. Rev.

Lett., Vol. 120, p. 207204 (2018); [5] H. Meer et al., Nano Lett. 10.1021/acs.nanolett.0c03367, (2020); [6] F. Schreiber et al., Appl. Phys. Lett., Vol. 117, p. 082401 (2020); [7] T. Matalla-Wagner et al., Phys. Rev. Research, Vol. 2, p. 033077 (2020); [8] L. Baldrati et al., Phys. Rev. Lett., Vol. 125, p. 077201 (2020); [9] H. Nakayama et al., Phys. Rev. Lett., Vol. 110, p. 206601 (2013); [10] L. Baldrati et al., Phys. Rev. B, Vol. 98, p. 024422 (2018).

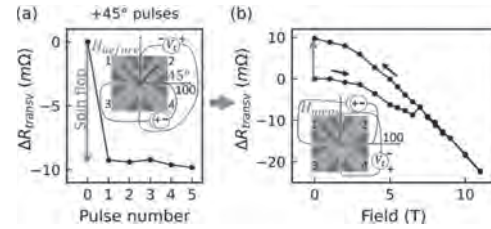


Figure 1: Symmetry of the current-induced switching. (a) Current-induced spin flop transition. (b) Field-induced spin flop, resetting n . Adapted from Ref. [8].

FG-05. Dynamics of Synthetic Antiferromagnetic Skyrmion From Current-Induced Deterministic Motion to Thermally-Activated Diffusive Motion.

T. Dohi^{1,2}, S. DuttaGupta^{1,3}, F. Kammerbauer², N. Kerber^{2,4}, B. Seng^{2,5}, Y. Ge², K. Raab², R. Gruber², M. Brems², J. Rothörl², P. Virnau^{2,4}, S. Fukami^{1,3}, M. Klau^{2,4} and H. Ohno^{1,3}

1. RIEC, Tohoku University, Sendai, Japan; 2. Institute of Physics, Johannes Gutenberg Universität Mainz, Mainz, Germany; 3. CSIS, Tohoku University, Sendai, Japan; 4. Johannes Gutenberg University Mainz Graduate School of Excellence Materials Science in Mainz, Mainz, Germany; 5. Institut Jean Lamour, UMR CNRS 7198, Université de Lorraine, Nancy, France

Magnetic skyrmions, topologically stabilized quasi-particles, have attracted much attention not only from fundamental physics but also from device applications¹. Ferromagnetic skyrmions can be easily stabilized at room temperature by an interfacial Dzyaloshinskii-Moriya interaction (DMI) and can be efficiently controlled electrically through spin-orbit torques (SOT)². However, problems arise from a large gyrotropic force due to the skyrmion Hall effect (SkHE)³, which is a diagonal motion along with current flow direction, that is easily able to surpass repulsive force from device edge. Thus, ferrimagnetic/antiferromagnetic skyrmions, which consist of two skyrmions antiferromagnetically coupled at each sublattice^{4,5}, have received much attention due to a SkHE-free motion. Formation of ferrimagnetic⁶/synthetic antiferromagnetic (SyAFM) skyrmions⁷ has lately been demonstrated. Also, the SkHE-free motion of a half skyrmion is observed in a ferrimagnetic system at a specific temperature where angular momentum is compensated⁸. Earlier theoretical work has also predicted intriguing thermal characteristics of AF skyrmion including topology-dependent diffusive dynamics^{5,9}. Nevertheless, the thermal effect on AF skyrmion is hitherto experimentally unexplored. Our work comprises two parts to comprehensively cover the full dynamics range. The first one is about the current-induced deterministic motion¹⁰, where we show the current-induced motion of skyrmions with suppressed SkHE even at room temperature in a SyAFM system. In the second part, we demonstrate the first observation of thermal diffusive dynamics for SyAFM skyrmions, which allows us to uncover the thermal effect on AF-coupled skyrmions. Ir-based SyAFM system whose ferromagnetic elements are composed of CoFeB is used for this work. The second peak of oscillation of the interlayer exchange coupling is used for maximizing antiferromagnetic exchange coupling as well as stabilizing perpendicular easy axis. Figure 1 shows the current density dependence of average velocity and SkHE for the skyrmion in the FM and SyAFM systems. We find that skyrmions in both systems are driven by current, indicating topological stabilization stemming from the skyrmion spin structure. More importantly, the skyrmions in the SyAFM system are driven by an order-of-magnitude smaller current density than those in the ferromagnetic system at comparable velocities. Based on an extended Thiele's equation with a separately quantified SOT strength, it is shown that the achieved efficient motion of SyAFM skyrmions can be attributed to the enhanced SOTs by Pt, Ir, and W, compensated magnetic moments, and the reduction of effective topological charge. Figure 1 also shows that monotonically increasing SkHE with velocity for the FM skyrmions as in previous studies that consider an effect of pinning and/or field-like torque on SkHE³. Meanwhile, for a SyAFM skyrmion, no noticeable SkHE is observed, even in the depinning and flow regime¹⁰. Such inhibition of SkHE should be primarily caused by a reduction of the effective topological charge due to opposite magnetization at each sub-lattice. The achieved favorable properties are attributed to the employed stack structure which is engineered so that the interlayer exchange coupling, DMI, and SOT act in a concerted way¹⁰. Figure 2 shows the trajectories of SyAFM skyrmion under $|\mu_0 H| = 0.1$ mT at 297.2 K measured for 1 hour. We observe that some of SyAFM skyrmions are displaced from an original position through the trajectory even though there is no bias current. The thermal diffusive dynamics of AF coupled skyrmions have been observed for the first time. We measure mean squared displacement to characterize the diffusion constant as previously conducted for FM skyrmions¹¹. We find that the temperature dependence of diffusion constant of SyAFM skyrmions behaves approximately linear in log scale but more sensitive compared to that of FM skyrmions due to possibly suppressing gyrotropic force which stems from

finite topological charge. Also, large size fluctuation of SyAFM skyrmions is observed with the thermal diffusive dynamics, which is consistent with the observed uneven sizes of skyrmions during the current induced motion. The origin could be intrinsic large thermal fluctuation of spins, relatively small interlayer exchange coupling, and/or differences in the magnetic properties between ferromagnets. In conclusion, we find that SyAFM skyrmions can be efficiently driven by currents with suppressed SkHE at room temperature, which has been a challenge of skyrmion research so far. Also, we show the first observation of the thermal diffusive dynamics of AF coupled skyrmions, which indicates that AF skyrmions would be promising to realize not only deterministic skyrmionic devices such as race-track memory¹² but also unconventional computing e.g. the skyrmion-based token computing^{11,13}. This work was supported in part by JSPS KAKENHI 19H05622.

[1] N. Nagaosa and Y. Tokura, Nat. Nanotechnol. 8, 899 (2013). [2] S. Woo *et al.*, Nat. Mater. 15, 501 (2016). [3] K. Litzius *et al.*, Nat. Electron. 3, 30 (2020). [4] X. Zhang *et al.*, Nat. Commun. 7, 10293 (2016). [5] J. Barker and O. A. Tretiakov, Phys. Rev. Lett. 116, 147203 (2016). [6] S. Woo *et al.*, Nat. Commun. 9, 959 (2018). [7] W. Legrand *et al.*, Nat. Mater. 19, 34 (2020). [8] Y. Hirata *et al.*, Nat. Nanotechnol. 14, 232 (2019). [9] C. Schütte *et al.*, Phys. Rev. B 90, 174434 (2014). [10] T. Dohi *et al.*, Nat. Commun. 10, 5153 (2019). [11] J. Zázvorka *et al.*, Nat. Nanotechnol. 14, 658 (2019). [12] A. Fert *et al.*, Nat. Nanotechnol. 8, 152 (2013). [13] Y. Jibiki *et al.*, Appl. Phys. Lett. 117, 082402 (2020).

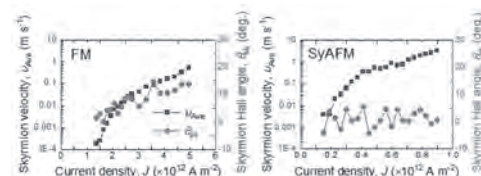


Figure 1 Average velocity of skyrmions (black, rectangle) and skyrmion Hall angle (red, circle) as a function of current density in FM (Left) and SyAFM (Right) system.

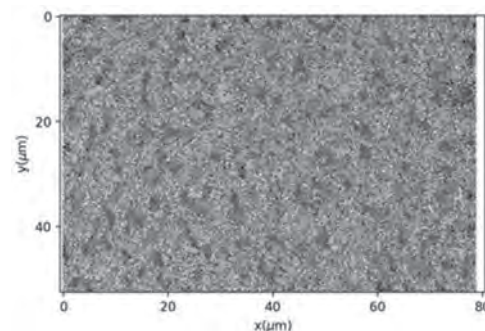


Figure 2 Trajectories of SyAFM skyrmions for 1 hour under $|\mu_0 H| = 0.1$ mT at 297.2 K. Skyrmions have allotted color, respectively. The motion of skyrmions is traced by using trackpy.

FG-06. Identification of Néel Vector Orientation in Antiferromagnetic Domains Switched by Currents in NiO/Pt Thin Films.

C. Schmitt¹, L. Baldrati¹, L. Sanchez-Tejerina², F. Schreiber¹, A. Ross¹, M. Filianina¹, S. Ding¹, F. Fuhrmann¹, R. Ramos³, F. Maccherozzi⁴, D. Backes⁴, E. Saitoh³, G. Finocchio² and M. Kläui¹

1. Johannes Gutenberg Universität Mainz, Mainz, Germany; 2. Università degli Studi di Messina, Messina, Italy; 3. Tohoku University, Sendai, Japan; 4. Diamond Light Source Ltd, Didcot, United Kingdom

Efficient electrical read-out and writing of antiferromagnetic (AFM) insulators is a key prerequisite in view of using this class of materials as active elements in spintronic applications. The understanding of the electrical manipulation of the antiferromagnetic order n is a crucial aspect to exploit the advantages these materials exhibit compared to ferromagnets, such as THz dynamics, enhanced stability with respect to interfering magnetic fields and higher bit packing densities due to the absence of stray fields [1]. The absence of a net magnetic moment in antiferromagnets makes manipulation using conventional magnetic fields challenging. Recently, several reports demonstrated current-induced writing of the Néel order orientation in antiferromagnets and different switching mechanisms have been put forward [2-5]. The mechanisms depend on the type of domains present in AFM thin films. So far, however, it is largely unknown between which types of domains electrical switching occurs and in which direction the Néel vector is pointing. There are reports stating that in MgO//NiO the tensile strain induces a preferential out-of-plane orientation of n with respect to the sample plane [2] and on the other hand the Néel vector switching is detected electrically by spin Hall magnetoresistance (SMR) measurements, sensitive to the in-plane components of n , thus indicating the presence of an in-plane component of the Néel vector [6]. In our work [7] we focus on collinear insulating antiferromagnetic NiO/Pt thin films as a materials platform, and we image reversible electrical switching by photoemission electron microscopy (PEEM) employing the x-ray magnetic linear dichroism (XMLD) effect (Fig.1). By varying the x-ray polarization, energy and sample azimuthal angle, we identify the crystallographic orientation of the domains that can be switched by currents and quantify the Néel vector direction changes, showing that the switching occurs between different T-domains. The Néel vector orientation in these domains shows an enlarged out-of-plane component pointing along $[\pm 1 \pm 1 3.8]$, different from the bulk $\langle 112 \rangle$ directions. The final state of the in-plane component of the Néel vector n after switching in a Hall cross geometry by current pulses j along the $[1 \pm 1 0]$ directions is $n \parallel j$ in the centre of the device.

[1] V. Baltz, et al., Rev. Mod. Phys. 90, 015005 (2018). [2] T. Moriyama, et al., Sci. Rep. 8, 14167 (2018). [3] X. Z. Chen, et al., Phys. Rev. Lett. 120, 207204 (2018). [4] L. Baldrati, et al., Phys. Rev. Lett. 123, 177201 (2019). [5] P. Zhang, et al., Phys. Rev. Lett. 123, 247206 (2019). [6] S. Altieri, et al., Phys. Rev. Lett. 91, 137201 (2003). [7] C. Schmitt, et al., arXiv:2008.08507 (2020)

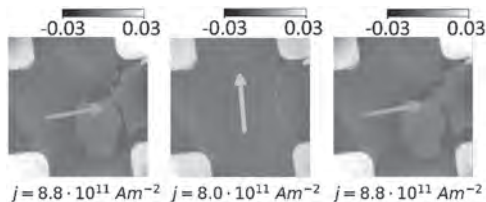


Fig. 1: The application of current pulses alternating between $[100]$ and $[010]$ reveals reversible switching of three different T-domains (Figure adapted from Ref. 7).

FG-07. Exchange Bias Switching in an Antiferromagnet/Ferromagnet Bilayer Driven by Spin-Orbit Torque.

S. Peng^{1,2}, D. Zhu¹, W. Li^{1,2}, H. Wu³, A. Grutter⁴, D. Gilbert^{4,5}, J. Lu^{1,2}, D. Xiong¹, W. Cai¹, P. Shafer⁶, K. Wang³ and W. Zhao^{1,2}

1. Fert Beijing Institute, BDBC, School of Integrated Circuit Science and Engineering, Beihang University, Beijing, China; 2. Hefei Innovation Research Institute, Beihang University, Hefei, China; 3. Department of Electrical Engineering, University of California Los Angeles, Los Angeles, CA, United States; 4. NIST Center for Neutron Research, National Institute of Standards and Technology, Gaithersburg, MD, United States; 5. Materials Science and Engineering, The University of Tennessee Knoxville Tickle College of Engineering, Knoxville, TN, United States; 6. Advanced Light Source, E. O. Lawrence Berkeley National Laboratory, Berkeley, CA, United States

Electrical manipulation of the magnetization and exchange bias in antiferromagnet (AFM)/ferromagnet (FM) heterostructures[1,2] is expected to be of use in several high performance spintronic devices. An efficient method for electrical switching of the FM magnetization is to use the spin-orbit torque (SOT) generated from a heavy metal layer in AFM/FM/heavy metal structures[3]. The in-plane exchange field generated at the AFM/FM interface enables field-free switching of the perpendicular magnetization[4,5]. However, manipulation of the exchange bias is usually achieved by field cooling, which requires an external magnetic field and high temperature, hindering its application in practical devices. It has been demonstrated that the exchange bias field at the AFM/FM interface can be switched by the SOT generated in the Pt layer in a Pt/Co/IrMn structure, passing through the thin Co layer[2]. Strong SOTs can also be generated in certain AFM thin films (such as IrMn and PtMn) due to their giant spin Hall angle[6,7], allowing simpler spintronic devices to be created. Here, we report the current-induced switching of exchange bias field in a perpendicularly magnetized IrMn/CoFeB bilayer structure using a spin-orbit torque generated in the antiferromagnet IrMn layer[8]. By manipulating the current direction and amplitude, independent and repeatable switching of the magnetization and exchange bias field below the blocking temperature can be achieved. Figure 1a illustrates four states for the CoFeB magnetization and the interfacial IrMn spins. By applying a negative pulse current in the presence of an in-plane magnetic field of $\mu_0 H_x = 100$ mT, switching of the magnetization from up to down can be realized, as shown in Fig. 1c. Interestingly, the exchange bias field before the magnetization switching is -1.3 mT (Fig. 1b), but it changes to 1.6 mT after the magnetization switching (Fig. 1d), indicating reversal of the exchange bias field from negative to positive driven by the SOT current. Next, we find that when a relatively small current (e.g. 7 mA) is applied to a sample with D_p state, only the magnetization switches, while the exchange bias field remains unchanged, leading to a transition from D_p to U_{AP} state, as shown in Fig. 1e. Then, when a pulse current with amplitude of 8 mA is applied to the samples with U_{AP} state, the exchange bias field is reversed alone, but the magnetization remains unswitched, resulting in a transition from U_{AP} to U_p state (see Fig. 1f-h). X-ray magnetic circular dichroism (XMCD), polarized neutron reflectometry (PNR) measurements and micromagnetic simulations show that a small net magnetization within the IrMn interface plays a crucial role in these phenomena. Figure 2 illustrates the micromagnetic simulation results of exchange bias and its manipulation by SOT. Figure 2a shows the schematic of the AFM/FM exchange bias system. Initially, a positive exchange bias field is obtained, as shown in Fig. 2b. When we apply a SOT current of $J_{SOT} = 90 \text{ MA}\cdot\text{cm}^{-2}$, the FM magnetization can be switched while the exchange bias field is still positive, as indicated in Fig. 2c. Moreover, Fig. 2c also shows that a large SOT current ($J_{SOT} = 270 \text{ MA}\cdot\text{cm}^{-2}$) can be used to reverse the exchange bias field. Figure 2d and 2e are snapshots of the z component of FM magnetization at selected times upon the application of different SOT currents. Through sweeping the SOT current density, it is clearly shown in Fig. 2f that the critical switching current density for the exchange bias is larger than that for the magnetization. Furthermore, to confirm the different critical current densities for magnetization and exchange bias field, temperature- and thickness-dependent switching are explored. In summary, we have reported current-induced exchange bias switching via the SOT originating from the AFM layer in an IrMn/CoFeB bilayer. The independent switching of magnetization and

exchange bias field in a repeatable manner is demonstrated by manipulating the current direction and amplitude in the presence of an in-plane magnetic field. Experimental results from PNR and XMCD indicate a small net magnetization exists at the IrMn interface, comprised primarily of rotatable uncompensated Mn spins and a much smaller fraction (<10%) of pinned spins. Micromagnetic simulations and temperature-dependent measurements show that the critical current density to switch the interfacial pinned spins, and hence the exchange bias field, is larger than that of magnetization reversal, and this difference allows the FM layer and exchange bias to be individually manipulated by SOT currents, rather than via perpendicular magnetic fields.

[1] D.R. Xiong, S.Z. Peng and W.S. Zhao, *Appl. Phys. Lett.* Vol. 117, no. 21, pp. 212401 (2020). [2] P.H. Lin, B.Y. Yang and C.H. Lai, *Nat. Mater.* Vol. 18, pp. 335–341 (2019). [3] S.Z. Peng, D.Q. Zhu and W.S. Zhao, *Adv. Electron. Mater.* Vol. 5, pp.1900134 (2019). [4] Y.W. Oh, S.C. Baek and B.G. Park, *Nat. Nanotechnol.*, Vol. 11, pp.878–884 (2016). [5] S.Z. Peng, J.Q. Lu and W.S. Zhao, *IEEE Int. Electron Devices Meet. (IEDM)*, p. 28.6.1-28.6.4 (2019). [6] D. Wu, G.Q. Yu and K.L. Wang, *Appl. Phys. Lett.*, Vol. 109, pp.222401 (2016). [7] Y.X. Ou, S.J. Shi and R.A. Buhrman, *Phys. Rev. B*, Vol. 93, pp. 220405(R) (2016). [8] S.Z. Peng, D.Q. Zhu and W.S. Zhao, *Nat. Electron.* Vol. 3, pp. 757–764 (2020).

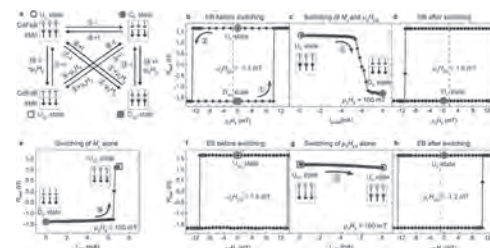


Fig.1 Exchange bias and magnetization switching driven by current-induced SOT. a, Schematic configurations of four states for the CoFeB magnetization and interfacial IrMn spins and transitions among them. b-h, Concurrent switching of the magnetization and exchange bias field (b-d), independent switching of magnetization (e) and independent switching of exchange bias field (f-h) by a pulse current in the presence of an in-plane magnetic field.

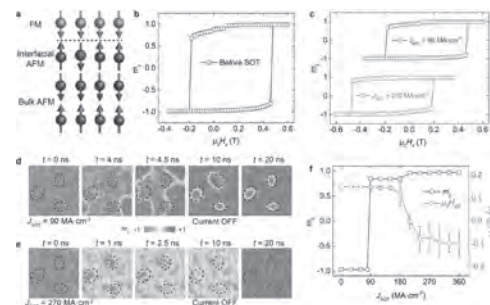


Fig.2 Micromagnetic simulation results of exchange bias and its manipulation by SOT. a, Schematic of the AFM/FM exchange bias system. b, c, Hysteresis loops (b) before and (c) after application of SOT currents. d, e, Snapshots of the z component of the FM magnetization configuration (m_z) at selected times. f, Switching of the exchange bias and magnetization under different SOT current densities.

FG-08. Spontaneous Hall Effect in the Mn_5Si_3 Antiferromagnet, due to Antiferromagnetic Zeeman Spin-Splitting.

R. Lopes Seeger¹, H. Reichlova^{2,3}, R. Gonzalez-Hernandez^{4,5}, I. Kounta⁶, R. Schlitz², D. Kriegner^{2,3}, P. Ritzinger², M. Lammel⁷, M. Leiviska¹, V. Petricek³, P. Dolezal⁸, E. Schmoranzero⁸, A. Badura⁸, A. Tomas^{2,9}, V. Baltz¹, L. Michez⁶, J. Sinova^{5,3}, S.T. Goennenwein^{2,10}, T. Jungwirth^{3,11} and L. Smejkal^{3,5}

1. SPINtronique et Technologie des Composants, Grenoble, France; 2. Technische Universitat Dresden, Dresden, Germany; 3. Czech National Academy of Science, Praha, Czechia; 4. Universidad del Norte, Barranquilla, Colombia; 5. Johannes Gutenberg Universitat Mainz, Mainz, Germany; 6. CINaM, Marseille, France; 7. Institute for Metallic Materials, Leibnitz Institute of Solid State and Materials Science, Dresden, Germany; 8. Univerzita Karlova, Praha, Czechia; 9. Leibniz Institute for Solid State and Materials Research Dresden (IFW Dresden), Dresden, Germany; 10. Universitat Konstanz, Fachbereich Physik, Konstanz, Germany; 11. University of Nottingham School of Physics and Astronomy, Nottingham, United Kingdom

We identified and exploited a novel mechanism in an emerging branch of spintronics based on transport phenomena governed by crystal and magnetic symmetries, and its interplay with the antiferromagnetic order [1]. In this talk, we will focus on the origin of the subsequent experimental observation of a large spontaneous Hall effect in the Mn_5Si_3 antiferromagnet, arising mostly by time-reversal symmetry breaking. These findings could prove essential for the development of robust large effects, vital in new device concepts. More specifically, the Zeeman effect is among the cornerstones of quantum physics that contributed to the development of spintronics. To date, the Zeeman spin-splitting of atomic energy levels or bands in crystals has been associated with the presence of a magnetic dipole. Countering the established physical picture [2-4], we identify an antiferromagnet with a band-structure comprised of separated crystal-momentum valleys with opposite Zeeman spin-splittings, which allows for their probing and exploiting by analogous electron-transport phenomena as used for the Zeeman effect in the presence of the magnetic dipole. In this talk we focus on one of the most prominent consequences of spin splitting – the spontaneous Hall effect. We experimentally demonstrated its presence in Mn_5Si_3 , an antiferromagnet with separated Zeeman spin-split valleys [1]. We carefully disentangled various contributions to the measured transversal signal and we show that the signal is dominated by a robust spontaneous (present at zero magnetic field) Hall contribution with broad coercivity, which can only be attributed to the antiferromagnetic Zeeman effect. We further present structural, magnetization and magneto-transport results in a sample series and discuss the role of epitaxial growth on our results.

[1] H. Reichlova, R. L. Seeger et al, under review. arXiv:2012.15651 [2] L. Néel. Magnetism and Local Molecular Field. Science 174, 985-992 (1971). [3] N. J. Ghimire et al. Large anomalous Hall effect in the chiral-lattice antiferromagnet $CoNb_3S_6$. Nat. Com. 9, 3280 (2018). [4] C. Sürgers, et al. Large topological Hall effect in the non-collinear phase of an antiferromagnet. Nat. Com. 5, 3400 (2014).

FG-09. Switching Experiment of Antiferromagnetic CoO in Different Temperatures.

M. Grzybowski¹, C.F. Schippers¹, K. Rubi², U. Zeitler², M. Bal², B. Koopmans¹ and H. Swagten¹

1. Applied Physics Department, Eindhoven University of Technology, Eindhoven, Netherlands; 2. High Field Magnet Laboratory, Radboud Universiteit, Nijmegen, Netherlands

Antiferromagnets (AF) have many potential applications in spintronics such as data storage or long-range spin transport devices. The control of spins in AF by electrical current is proven to be possible by different mechanisms [1,2] but it remains challenging to verify experimentally [3]. Such detection can be unambiguously performed with the use of magnetic imaging techniques [4]. However, they are typically sensitive to the topmost layer and cannot be applied in more complex structures where the AF is buried far from the top interface. To mitigate this problem, we present a study of electrical signals in switching experiment in various temperatures for CoO. Basing on this temperature dependence of electrical data for AF CoO thin film we extract patterns that do not follow the trend expected for thermal effects but are probably fingerprints of magnetic changes. In characterization experiments for CoO, magnetoresistance studies for CoO reveal clear spin-flop transitions and pronounced antiferromagnetic hysteresis loops due to strong in-plane anisotropy. Magnetoresistance shows abrupt changes in R_{xy} around 7 T (240K) when the magnetic field is aligned along [110] axes (easy axes). They can be attributed to spin-flop transitions observed by means of Spin Hall Magnetoresistance. This behavior is hysteretic and absent when the field is aligned along [100] directions (hard axes) or in $T = 304$ K (above Néel temperature T_N). It confirms the presence of biaxial anisotropy in CoO and easy axes along [110] in agreement with literature [5]. Hysteresis loops in R_{xy} when the magnetic field is rotated with respect to crystalline axes are observed up to the highest tested magnetic fields due to the strong in-plane anisotropy. In the actual switching experiments of CoO (Fig. 1), the temperature dependence of the transverse resistance R_{xy} variations after current pulses applied in alternating directions in a CoO | Pt device is examined. Resistivity variations due to thermal effects (such as asymmetric heating) increase with increasing temperature or current pulse amplitude and persist above T_N of CoO. However, at lower current magnitudes we find a pattern that decreases with increasing temperature and vanishes above T_N suggesting its magnetic origin (Fig. 2). In conclusion, we demonstrate that manipulation of temperature may help to gain more insight into the nature of electrical signals variations in experiments with antiferromagnets. These presented experimental findings can be important for current research activities towards using antiferromagnets in real spintronic devices.

[1] P. Wadley, B. Howells, J. Zelezny et al., Science, 351, 587 (2016). [2] L. Baldrati, O. Gomonay, A. Ross et al., Phys. Rev. Lett., 123, 177201 (2019). [3] C. C. Chiang, S. Y. Huang, D. Qu, et al., Phys. Rev. Lett., 123, 227203 (2019). [4] M. J. Grzybowski, P. Wadley, K. W. Edmonds et al., Phys. Rev. Lett., 118, 057701 (2017). [5] L. Baldrati, C. Schmitt, O. Gomonay et al., Phys. Rev. Lett., 125, 077201 (2020).

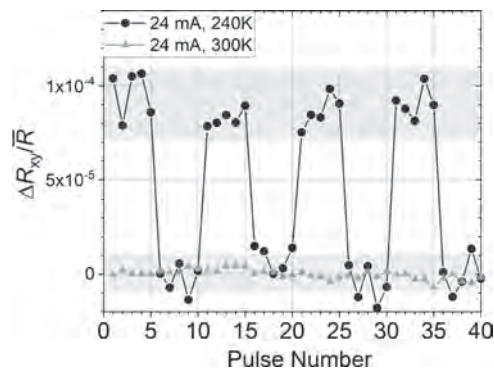


Fig. 1 The switching experiment for CoO (5 nm) | Pt (5 nm) thin films device where the transverse resistivity R_{xy} is measured after each pulse of high current (the direction of the pulsing current is changed to perpendicular one after each 5 pulses). Interestingly, above T_N the pattern visible in 240K is not present.

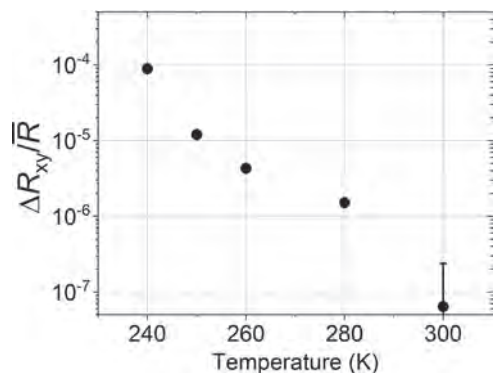


Fig. 2 The magnitude of R_{xy} variations after pulsing in orthogonal directions in CoO for 24 mA current diminishes with increasing temperature and is practically invisible in room temperature (above T_N). This trend is different for higher currents where R_{xy} variations increases with T as expected for thermal effects.

FG-10. Observation of Antiferromagnetic Magnon Pseudospin Dynamics and the Magnon Hanle Effect.

T. Wimmer^{1,2}, A. Kamra³, J. Gückelhorn^{1,2}, M. Opel¹, S. Geprägs¹, R. Gross^{1,2}, H. Huebl^{1,2} and M. Althammer^{1,2}

1. Magnetism and Spintronics, Walther-Meißner-Institute for Cryogenic Research, Garching, Germany; 2. Physik Department, Technische Universität München, München, Germany; 3. Department of Physics, Norwegian Technical and Natural Sciences University, Trondheim, Norway

The spin-1/2 of an electron makes it an archetypal two-level system and inspires the description of other two-level systems using an analogous pseudospin. The quantized spin excitations of an ordered antiferromagnet are such pairs of spin-up and -down magnons and can be characterized by a magnonic pseudospin. The similarity between electronic spin and magnonic pseudospin has triggered the prediction of exciting phenomena like emergent spin-orbit coupling and topological states in antiferromagnetic magnonics. An experimental observation of the associated dynamics of antiferromagnetic pseudospin, however, has eluded experiments thus far. As a first step we will introduce the concept of magnon pseudospin and the description of magnon pseudospin dynamics, as well as briefly discuss similarities to electron spin transport [1]. In the second part, we show our recent experiments demonstrating control of magnon spin transport and pseudospin dynamics in a 15 nm thin film of the antiferromagnetic insulator hematite (α -Fe₂O₃) utilizing two Pt strips for all-electrical magnon injection and detection [2] (c.f. Fig. 1 (a)). We observe an oscillation in polarity of the magnon spin signal at the detector as a function of the externally applied magnetic field (see Fig. 1 (b)), which we quantitatively explain in terms of diffusive magnon transport. In particular, we observe a coherent precession of the magnon pseudospin caused by the easy-plane anisotropy and the Dzyaloshinskii-Moriya interaction. This observation can be viewed as the magnonic analogue of the electronic Hanle effect and the Datta-Das transistor, unlocking the high potential of antiferromagnetic magnonics towards the realization of electronics-inspired phenomena. Financial support from the Deutsche Forschungsgemeinschaft (DFG, German Research Foundation) under Germany's Excellence Strategy - EXC-2111 - 390814868 and project AL2110/2-1, and the Research Council of Norway through its Centers of Excellence funding scheme, project 262633, "QuSpin" is gratefully acknowledged.

[1] A. Kamra et al., Physical Review B 102, 174445 (2020) [2] T. Wimmer et al., Physical Review Letters 125, 247204 (2020)

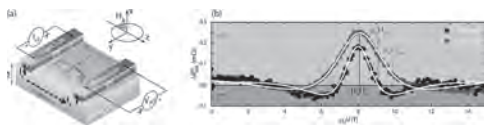


Fig. 1: (a) Sketch of the device geometry, the electrical wiring, and the coordinate system. The canting of the magnetic sublattices m_1 and m_2 and the corresponding net moment m_{net} as well as the Néel order parameter n are illustrated. Upon applying a charge current I_{inj} to the injector, a spin current I_s with spin polarization s is generated via the SHE and injected into the hematite (α -Fe₂O₃) with thickness $t = 15$ nm. The emerging antiferromagnetic magnon current is then detected via the inverse SHE induced current at the detector by measuring the electrical voltage drop $V_{\text{el}}^{\text{det}}$. (b) Magnon transport signal $V_{\text{el}}^{\text{det}}$ as a function of the external magnetic field magnitude. The signal oscillates between positive and negative values. The qualitative behaviour is very similar to the electronic Hanle effect.

FG-11. Antiferromagnetic Textures in Presence of Inhomogeneous Strain Field.

O. Gomonay¹

1. Johannes Gutenberg Universitat Mainz, Mainz, Germany

Antiferromagnets are considered as prospective materials for spintronic applications as they could be effectively manipulated with the electrical and optical pulses, and also show magnetic dynamics and low susceptibility to the external magnetic field. The mechanisms involved into control and manipulation of antiferromagnetic states were usually related with the current- or laser-induced spin-torques. However, recent experiments [1,2] demonstrated that heating and heat-induced strains that follow current and laser pulses can produce similar or even stronger effects on the magnetic dynamics. In this paper we consider dynamics of an antiferromagnetic texture in presence of the inhomogeneous distribution of strains. These strains via magnetoelastic interactions contribute into magnetic anisotropy and set preferable directions for the Neel vector. We use NiO as a model system for an easy-plane collinear antiferromagnet with strong magnetoelastic coupling and nontrivial domain structure, which includes domains of S- (spin) and T- (twin) types. First, we calculated antiferromagnetic textures that appear in response to the strain distribution for two different, experimentally relevant situations: i) strains induced by the temperature gradients; ii) strains induced by the sample patterning. We found that those components of the strain tensor that are symmetry related with the spontaneous magnetostrictive strains, affect orientation and width of the domain wall, and control the morphology of the magnetic domains. The other components of the strain tensor affect distribution of the Neel vector inside the domain wall and could influence the domain wall chirality. Strains are also responsible for stabilization of 180 domain walls otherwise unstable in easy-plane antiferromagnets. Strong correlations between strains and distribution of the Neel vector opens a way for manipulation of the magnetic textures by strain and, vice versa, for visualization of strain distribution via magnetic ordering. Next, to study the response of an antiferromagnetic texture to the optical and current pulses we further calculated the magnon spectra of an antiferromagnetic texture that appears on top of two neighboring domains. We considered two different cases corresponding to the S-type and T-type domains correspondingly. Expectedly, we found that the domain wall is pinned by the spontaneous strains. This effect shows up in a localised magnon mode that corresponds to oscillations of the domain wall separating two S domains. The frequency of oscillations falls in the gap of the magnon spectra and lays below the low-frequency branch (see Fig. 1). Its value scales with the strength of magnetoelastic coupling. Polarization of the localised mode in this case coincides with the polarization of low-frequency magnons and corresponds to in-plane oscillations. In case of the domain wall separating two different T domains we found much richer behaviour. First, when compared with homogenous case, the magnon modes of a multidomain sample are hybridised, so that the Neel vector oscillates both in-plane and out-of-plane. This results in a birefringe effect when the magnon flux with the out-of-plane polarization splits into two beams with in- and out-of plane polarization after passing through the domain wall. Second, low-frequency eigen modes are seen as a superposition of a propagating mode with the in-plane polarization and a localised mode whose polarization has both in-plane and out-of-plane components (see Fig. 2). In other words, oscillations of the domain wall are mixed with propagation modes and the eigen-frequencies of the localised modes are distributed over the wide range of values. Thus, oscillations of the domain walls could be induced by magnon fluxes with the generic polarization and frequency. Moreover, due to nonlinearity of magnetic interactions such oscillations can result in parametric up- or down-conversion. Hence, a magnetic response of the multidomain sample involves the magnonic modes that would be absent in case of a single domain antiferromagnet. To conclude, we believe that our findings can be used for tailoring antiferromagnetic textures for the efficient current- and/or optical induced switching.

1. Wörnle, M. S., Welter, P., Kašpar, Z., et al, arxiv.1912.05287(2019)
2. Meer, H., Schreiber, F., Schmitt, C., et al, *Nano Letters*, acs.nanolett.0c03367,(2020).

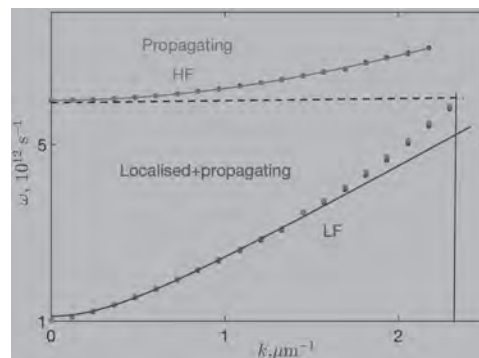


Fig.1 Spin-wave spectra (symbols) calculated for antiferromagnetic texture consisting of two different T domains. Solid lines show magnon spectra in a homogenous sample.

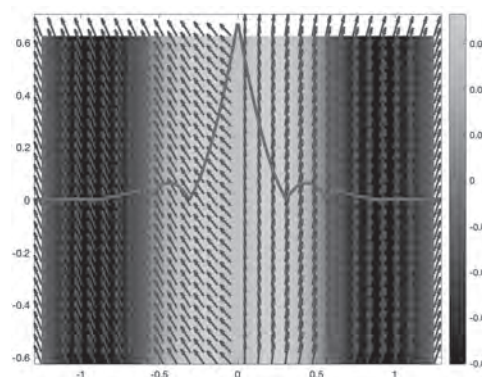


Fig.2 Low-frequency eigen-mode in the vicinity of the domain wall between two T-domains. Arrows show orientation of the Neel vector in equilibrium. Color code and solid line show distribution of the in-plane and out-of-plane components of excitation.

INVITED PAPER**FG-12. Ultrafast Spin Current Generated From an Antiferromagnet
INVITED.***D. Wu*¹*1. Nanjing University, Nanjing, China*

Antiferromagnets (AFMs) have the potential to push spintronic devices from the static or gigahertz frequency range to the terahertz (THz) range for the sake of the high-speed processing. However, the insensitivity of AFMs to magnetic fields also makes it hard to manipulate spin currents. While the ultrafast generation of the spin current in ferromagnet/heavy metal (FM/HM) structures has received a lot of attention in recent years, it is still unknown as to whether a similar scenario can be observed in an AFM/HM system. Here we show the optical generation of ultrafast spin current in an AFM/HM heterostructure at zero external magnetic field and at room temperature by detecting the associated THz emission [1]. We believe this is a common phenomenon in antiferromagnets with strong nonlinear optical effects. Our results open an avenue of fundamental research into antiferromagnetism and a route to AFM spintronic devices.

[1] H. Qiu, et al., *Nature Physics* (<https://doi.org/10.1038/s41567-020-01061-7>).

CONTRIBUTED PAPERS

FG-13. Anomalous Nernst Effect in Compensated Ferrimagnetic Mn_2Ru_xGa .Y. Lau^{1,2}, J. Wang^{1,2}, T. Kubota^{1,2} and K. Takahashi^{1,2}

1. Institute for Materials Research, Tohoku University, Sendai, Japan;

2. Center for Spintronics Research Network, Tohoku University, Sendai, Japan

Introduction: Compensated ferrimagnets possess two or more inequivalent, antiferromagnetically-coupled sublattices such that the net magnetization is zero. The detailed compensation conditions can be typically tuned by varying the temperature, chemical composition or strain. These materials do not only possess the advantages of an antiferromagnet, i.e. faster switching, higher storage density and being immune to external field perturbation, but also, they are compatible with the commonly employed reading and writing schemes for conventional ferromagnets. A prototypal compensated ferrimagnet is Mn_2Ru_xGa which was first identified as a half metallic compensated ferrimagnet in 2014 [1]. Mn_2Ru_xGa crystallizes in the inverse Heusler structure (Space group No. 216), where Mn atoms occupy $4a$ and $4c$ sites of distinct chemical environment. Compensation is achieved when the moments from the two antiferromagnetically coupled Mn sites cancel each other. Ru of composition x then act as a knob for tuning the compensation temperature T_{comp} . Previous works have demonstrated high spin polarization [1], large anomalous Hall effect (AHE) [2], finite tunnel magnetoresistance [3], efficient spin-orbit torque switching [4] and all-optical toggle switching [5] in nearly compensated Mn_2Ru_xGa . Here we unveil the potential of exploiting Mn_2Ru_xGa with perpendicular magnetic anisotropy for spontaneous thermoelectric generation at room temperature via anomalous Nernst effect (ANE) with no stray field coupling to the surrounding. Experimental Methods and Results: Epitaxial Mn_2Ru_xGa (001) films with thicknesses ~ 27 nm and x ranging from 0.26 to 0.73 were grown on MgO (001) substrates at a substrate temperature of $\sim 350^\circ C$ by magnetron co-sputtering Mn_2Ga and Ru targets. The unit cell of Mn_2Ru_xGa makes a 45-degree rotation with respect to that of MgO such that the in-plane epitaxial relationship is MgO [100] // Mn_2Ru_xGa [110]. The substrate induced in-plane biaxial compressive strain leads to $\sim 1\%$ of the tetragonal distortion along the out-of-plane c -axis, which defines the easy axis of the magnetization. Millimeter-scale Hall bar devices were fabricated for characterizing the transport and thermoelectric response of Mn_2Ru_xGa films with varying x . An electrical current or a heat current was applied along the long axis of the Hall bar, along the [110] axis of Mn_2Ru_xGa . The in-plane temperature gradient was monitored by measuring the resistance change of two on-chip Pt wires. Vibrating sample magnetometry at room temperature shows that adding Ru from $x = 0.26$ to $x = 0.60$ reduces monotonically the saturation magnetization M_s from ~ 90 kA/m to below 5 kA/m, followed by a slight upturn of M_s upon further increasing x to 0.73. This reflects the magnetic compensation of Mn_2Ru_xGa is achieved at room temperature for $x \sim 0.6$. We also found that the AHE signal for films with $x = 0.51$ and $x = 0.73$ are of opposite sign whereas for $x = 0.60$ the coercivity diverges, which corroborates this interpretation. Concerning the thermoelectric properties of Mn_2Ru_xGa at room temperature, both the Seebeck coefficient S_{xx} and the anomalous Nernst coefficient S_{xy} change sign across the compensation. $|S_{xx}|$ for all the samples are relatively small ($< 1 \mu V/K$) whereas their transverse counterpart $|S_{xy}|$ are around $0.3 \mu V/K$, which is comparable to many $3d$ ferromagnets but with orders of magnitude smaller M_s for Mn_2Ru_xGa . The small $|S_{xx}|$ also leads to relatively large anomalous Nernst angle $|S_{xy}/S_{xx}|$ of the order of 0.5. S_{xy} can be expressed as $S_{xy} = \rho_{xx}\alpha_{xy} + S_{xx}\rho_{xy}/\rho_{xx}$ where α_{xy} denotes the transverse thermoelectric conductivity. We found the second term, referring to the collective contribution of AHE and Seebeck effect, is negligible. ANE in Mn_2Ru_xGa is therefore governed by the first term, i.e. the direct conversion from a thermal gradient to a transverse charge current. We obtain $\alpha_{xy} = +0.12$ A/(K \bullet m) for $x = 0.26$ which reduces to $\alpha_{xy} = +0.07$ A/(K \bullet m) and $\alpha_{xy} = -0.07$ A/(K \bullet m) for $x = 0.51$ and $x = 0.73$, respectively. α_{xy} reverses its sign across the compensation suggesting that it depends on the magnetization direction of a Mn sublattice and not on the net moment, in analogy with ρ_{xy} of AHE. Finally, it is worth noting that $|\alpha_{xy}|$ and $|S_{xy}|$ of Mn_2Ru_xGa near the compensation are comparable to

those of the chiral antiferromagnetic Mn_3Sn [6] with an additional advantage of high tunability. We expect further enhancement of the thermoelectric performance of compensated Heusler compounds by improving the chemical ordering and/or by tuning the Fermi level via substitutional alloying [7]. This work was partly supported by JSPS KAKENHI (No. JP20K15156, JP20K05296).

[1] H. Kurt *et al.*, Phys. Rev. Lett. 112, 027201 (2014) [2] N. Thiyagarajah *et al.*, Appl. Phys. Lett. 106, 122402 (2015) [3] K. Borisov *et al.*, Appl. Phys. Lett. 108, 192407 (2016) [4] J. Finley *et al.*, Adv. Mater. 31, 1805361 (2019) [5] C. Banerjee *et al.*, Nat. Commun. 11, 4444 (2020) [6] M. Ikhlas *et al.*, Nat. Phys. 13, 1085 (2017) [7] Y. Sakuraba *et al.*, Phys. Rev. B 101, 134407 (2020)

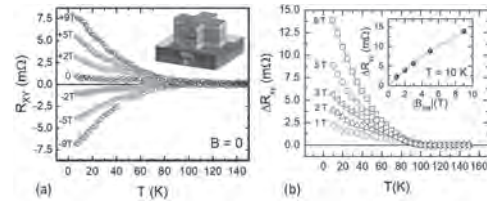
FG-14. Electrical Readout of the Antiferromagnetic State of IrMn Through Anomalous Hall Effect.

M. Asa¹, C. Rinaldi^{1,2}, R. Pazzocco¹, L. Nessi¹ and M. Cantoni¹

1. Physics, Politecnico di Milano, Milano, Italy; 2. IFN, Consiglio Nazionale delle Ricerche, Roma, Italy

Antiferromagnetic spintronics is on the rise as it could provide advantages over ferromagnetic-based conventional spintronics in terms of scalability, reliability and speed, opening the route to extend the working frequency of memory and logic devices from the current GHz range up to THz [1]. The electrical read-out of the magnetic state in antiferromagnetic materials, however, presents additional challenges due to the lack of a net magnetization which prevents the use of the typical detection schemes employed for ferromagnets. The possibility to access the magnetic configuration state in antiferromagnets by electrical methods would then provide a versatile characterization tool and is fundamental for the development of spintronic devices. At variance with ferromagnets, only few antiferromagnetic conductors have been demonstrated to show anisotropic magnetoresistance [2,3] allowing for a direct electric detection of the magnetic configuration by resistive measurements. In IrMn, the most widely used metallic antiferromagnet in applications, a small anisotropic magnetoresistance [4] has been demonstrated, whereas tunneling anisotropic magnetoresistance has been used to infer its magnetic state [5]. Here we follow a different approach exploiting interfacial effects between the antiferromagnet and a suitable neighboring metal layer. This approach, already employed for the insulating antiferromagnet Cr₂O₃ [6,7], underlines the critical role of interfaces in the determination of the transport properties related to the antiferromagnetic state. In this contribution we report the electrical detection of the antiferromagnetic state of IrMn through anomalous Hall measurements in Ta/IrMn heterostructures, grown by DC magnetron sputtering on a SiO₂/Si substrate. The magnetic state is set in the antiferromagnet through out-of-plane field cooling and detected electrically by transverse resistance measurements in Hall bar structures, without the need of any ferromagnetic layer. An offset compensation system has been used to isolate the transverse resistance from spurious contributions (longitudinal resistance and magnetoresistance) [8]. The signal goes to zero at the Néel temperature of the antiferromagnet (T_N), above which the system becomes paramagnetic. T_N is found out to be 110 K for our 4 nm thick IrMn film, smaller than in the bulk (650 K) because of the finite thickness. The amplitude of the signal increases with the magnetic field applied during the cooling (whereas the value of T_N is not affected) and is enhanced by the proximal interface with the Ta layer. We ascribe this enhancement to spin Hall magnetoresistance at room temperature and above, and to magnetic proximity which is the leading term at lower temperatures. From the temperature dependence of the effect and the comparison between Ta/IrMn and Ru/IrMn interfaces, we propose an explanation of such readout based on the simultaneous occurrence of spin-Hall magnetoresistance and magnetic proximity effect in Ta. These findings highlight how interface effects could be generally employed for the investigation of antiferromagnetic materials as well as for the electrical readout of the antiferromagnetic state.

[1] T. Jungwirth, J. Sinova, A. Manchon et al, Nat. Phys, Vol. 14, p. 200 (2018) [2] S.Y. Bodnar, L. Smejkal, I. Turek et al, Nat. Commun., Vol. 9, p. 348 (2018) [3] P. Wadley, B. Howells, J. Zelezny et al, Science, Vol. 351, p. 587 (2016) [4] T. Kosub, M. Kopte, F. Radu et al, Phys. Rev. Lett., Vol. 115, p. 097201 (2015) [5] D. Petti, E. Albisetti, H. Reichlová et al, Appl. Phys. Lett., Vol. 102, p. 192404 (2013) [6] J.M. Taylor, E. Lesne, A. Markou et al, Appl. Phys. Lett., Vol. 115, p. 062403 (2019) [7] M. Asa, C. Autieri, R. Pazzocco, et al., Phys. Rev. Research, vol. 2, p. 043394 (2020) [8] M. Asa, C. Rinaldi, R. Pazzocco, et al., J. Appl. Phys., Vol. 128, p. 053904 (2020)



(a) Transverse resistance (R_{XY}) in Ta (2 nm)/IrMn (4 nm) /Ta (2 nm) Hall cross at remanence resulting from different field cooling processes. In the inset a sketch of the sample is reported. (b) Anomalous Hall resistance difference (ΔR_{XY}) at remanence between states set with upward ($+B_{set}$) and downward ($-B_{set}$) field cooling. The value of B_{set} is reported beside each curve. The inset reports the value of ΔR_{XY} at 10 K as function of the absolute value of the writing field B_{set} . The red line is a guide for the eye.

FG-15. X-Ray Magnetic Linear Dichroism Studies of Electrical Switching of Antiferromagnetic Order in α -Fe₂O₃ Epitaxial Films.

E. Cogulu¹, N.N. Statuto¹, Y. Cheng², F. Yang², R. Chopdekar³, H. Ohldag³ and A. Kent¹

1. Department of Physics, New York University, New York, NY, United States; 2. Department of Physics, The Ohio State University, Columbus, OH, United States; 3. Advanced Light Source, E O Lawrence Berkeley National Laboratory, Berkeley, CA, United States

Recently, manipulation of antiferromagnetic (AFM) order has been gaining the attention of the spintronics community. Magnetic switching of AFM spin axis has been reported in thin films based on electronic transport methods, which provide only spatially averaged information on AFM states. Other techniques, such as x-ray magnetic linear dichroism (XMLD), can provide local information on AFM domains. In this study, we report direct observation of spin reorientation in response to current pulses in (0001) α -Fe₂O₃/Pt heterostructures. Our experiment combines the application of current pulses and spatially resolved photoemission electron microscopy (PEEM) with XMLD to detect AFM contrast. Pulses were applied in two different configurations A and B (Fig. 1a), and XMLD images were interleaved with current pulse sequences to reveal changes in the AFM domains in the center of the cross (Fig. 1c). Our polarization dependent analysis reveals that the Néel vector of our α -Fe₂O₃ films have an out-of-plane component in their equilibrium state, contrary to what previous work indicate. Finally, we show clear evidence of AFM domains reorientation outside of the current path, which leads us to the conclusion that spin-orbit torque may not be the only driven effect in the electrical switching process.

E. Cogulu, N. Statuto and A. D. Kent, "X-ray Magnetic Linear Dichroism Studies of Electrical Switching of Antiferromagnetic Order in α -Fe₂O₃ Epitaxial Films" (2020), arXiv:2012.04127 [cond-mat.mes-hall].

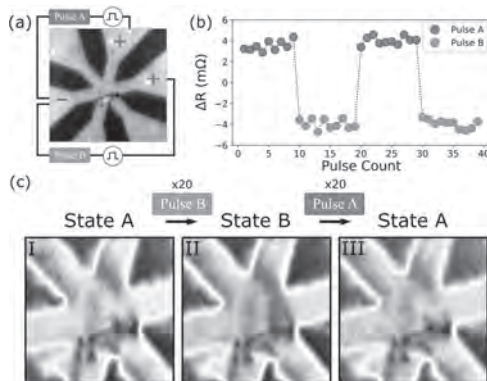


FIG1. (a) PEEM image of the 6-legged Hall cross with schematic representation of the circuit. Dark regions correspond to α -Fe₂O₃ (30 nm thickness) and bright region correspond to Pt (2 nm thickness). The Pt leads are aligned with the 3 easy axes of Fe₂O₃. Plus and minus signs represent the connections to the two pulse generator outputs, where the minus sign indicates a connection to ground. (b) Resistance data showing switching between two states after sequential current pulses applied along both current paths showed at panel a. (c) XMLD-PEEM images (4 μ m field of view) before and after a 4 mA current pulse along the pulse A & B configurations.

Session FH
ANTIFERROMAGNETIC SPINTRONICS II
Vito Puliafito, Chair
Universita degli Studi di Messina, Messina, Italy

INVITED PAPER**FH-01. New Aspects of Magnetoelectric Responses in Chiral Antiferromagnets INVITED.***H. Chen*^{1,2}*1. Department of Physics, Colorado State University, Fort Collins, CO, United States; 2. School of Advanced Materials Discovery, Colorado State University, Fort Collins, CO, United States*

Antiferromagnets have always been overshadowed by ferromagnets in real-life applications based on magnetism or spintronics. This is primarily due to that antiferromagnet order parameters, in contrast to the ferromagnetic magnetization, are only weakly coupled to magnetic fields, and are hence difficult, in conventional view, to be manipulated. I will discuss several recent theoretical and experimental developments that counter this conventional wisdom, in a class of antiferromagnets that have stable noncollinear magnetic order. I will first explain a theory for the time-reversal-symmetry-breaking counterparts of the conventional SHE and ISHE in the noncollinear antiferromagnet Mn₃Sn, which are named as the magnetic spin Hall effect (MSHE) and the magnetic inverse spin Hall effect (MISHE), respectively [1]. I will then discuss the concept of spin density polarization, and how to use it to describe spin-Hall effects in a magnetic insulator as bulk effects, without using the spin current language [2]. I will finally present an exploration on the nontrivial orbital coupling between chiral antiferromagnets and external magnetic fields [3,4], and the potential detection of the elusive itinerant orbital magnetization by magnetic neutron scattering.

[1] M. Kimata, H. Chen, et al. *Nature* 565, 627 (2019). [2] H. Chen, Q. Niu, and A. H. MacDonald, arXiv:1803.01294 [3] H. Chen et al., *PRB* 101, 104418 (2020). [4] X. Li, A. H. MacDonald, and H. Chen, arXiv:1902.10650

CONTRIBUTED PAPERS

FH-02. Penetration Depth of Cooper Pairs in the IrMn Antiferromagnet.

R. Lopes Seeger¹, G. Forestier¹, O. Gladii¹, M. Leiviska¹, S. Auffret¹, I. Joumard¹, C. Gomez², M. Rubio-Roy¹, A. Buzdin^{3,4}, M. Houzet⁵ and V. Baltz¹

1. SPINtronique et Technologie des Composants, Grenoble, France; 2. Grenoble INP, CIME Nanotech, Grenoble, France; 3. Univ. Bordeaux, CNRS, LOMA, Talence, France; 4. Dept. Mat. Sci. & Met, Univ. Cambridge, Cambridge, United Kingdom; 5. Univ. Grenoble Alpes, CNRS, CEA, PHELIQS, Grenoble, France

Suppression of superconductivity due to proximity effects between a superconductor and a ferromagnet can be partially lifted when different directions of the short-range exchange field are sampled simultaneously by a Cooper pair. Partial recovery of the superconducting critical temperature, ΔT_C , is therefore expected when the ferromagnet is set in a multi-domain state compared to a single domain state [1-3]. Here, we discuss series of experimental results for ferromagnet(Pt/Co)/spacer(IrMn)/superconductor(NbN) heterostructures [4]. By tuning the various parameters into play, e.g. superconducting coherence length-to-thicknesses ratio, and domain sizes, we obtained a recovery of the superconducting critical temperature $\Delta T_C/T_C$ as large as 10% (Fig. 1(a,b)). Such a large scale of $\Delta T_C/T_C$ opened the pathway for novel investigations. In particular, from the spacer thickness-dependence of $\Delta T_C/T_C$, characteristic length for Cooper pair penetration ($\xi_{\text{IrMn}} \sim 6.7$ nm) (Fig. 1(c)) was deduced in the IrMn antiferromagnet [4]. It is a crucial information for electronic transport, which are currently difficult to access experimentally for antiferromagnets [5].

[1] A. I. Buzdin, Rev. Mod. Phys. 77, 935 (2005). [2] M. Houzet and A. I. Buzdin, Phy. Rev. B 74, 214507 (2006). [3] L. Y. Zhu, T. Y. Chen, and C. L. Chien, Phys. Rev. Lett. 101, 017004 (2008). [4] R. L. Seeger et al, in preparation. [5] V. Baltz et al, Rev. Mod. Phys. 90, 015005 (2018).

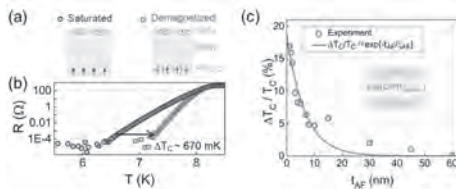


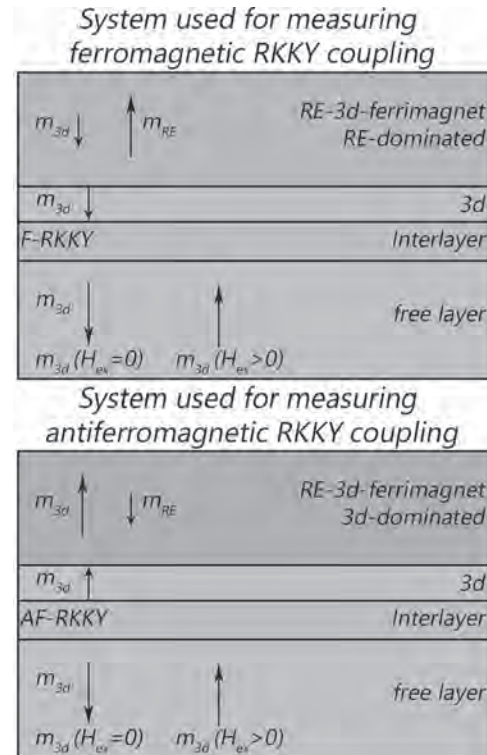
Fig. 1 (a) Schematics of the saturated (circle) and demagnetized (square) states in a (Pt/Co)_n/IrMn/NbN stack. Those states are accessed by performing two procedures involving field-cycling and cooling. (b) Representative data showing the temperature (T)-dependence of the stack's resistance (R) for the two states represented in (a). ΔT_C represents the difference in superconducting critical temperature of the NbN layer between the saturated and demagnetized states of the (Pt/Co) ferromagnet: $\Delta T_C = \Delta T_{C,demag} - \Delta T_{C,sat}$. (c) Spacer thickness dependence of $\Delta T_C/T_C$, for the case of the IrMn antiferromagnetic (AF) spacer. The line is a fit to the data.

FH-03. The Effect of RKKY Exchange Coupling Through Heavy Metal Interlayers on Future Skyrmionic Devices.

P. Mirzadeh Vaghehfi¹, A. Mandru¹, O. Yildirim¹, T. Dutta¹ and H.J. Hug^{1,2}
 1. Empa, Swiss Federal Laboratories for Materials Science and Technology, Dübendorf, Switzerland; 2. Universität Basel Departement Physik, Basel, Switzerland

Room temperature skyrmions have been the focus of research for development of skyrmionic devices based on thin film multilayers (MLs) with perpendicular anisotropy (PMA) and interfacial Dzyaloshinskii-Moriya interaction (iDMI)¹. The skyrmion spin texture is governed by several competing energies: iDMI, exchange energy, anisotropy energy, and magnetostatic energy. It has been shown that the skyrmion wall type and chirality determine the strength of the stray field above and below the thin film structure². Moreover, knowing the type and strength of the interlayer coupling is a prerequisite for designing future skyrmionic devices³. Recent studies⁴ showed that the spin texture of the skyrmion in each ferromagnetic (F) layer depends on its position within the ferromagnet/heavy metal ML. The dependence of the skyrmion wall on the vertical position inside the multilayer was attributed to the minimization of the total energy, which included the formation of a flux-closure structure to reduce the magnetostatic energy. However, the existence of even a weak Ruderman–Kittel–Kasuya–Yosida (RKKY) interlayer exchange could significantly alter this scenario by dominating magnetostatic energy contributions. Neglecting the RKKY exchange in modelling work stems from the fact that it has not been thoroughly studied in structures supporting skyrmion formation. Therefore, it is important to investigate the role of RKKY coupling in such multilayered structures in combination with the other energies present in these systems. Here, we report on multilayered systems that allow the assessment of interlayer RKKY interaction relevant for systems with iDMI, thus providing the required input for the design of multilayer systems with well-defined uniform skyrmion spin textures throughout the multilayer system. Note that a similar concept has been already used to measure RKKY interactions⁵, but for systems with a magnetic in-plane anisotropy without iDMI. Also, because the coercivity of the pinned layer was very small, only antiferromagnetic (AF) exchange coupling could be measured. Here we are interested in systems with PMA with iDMI supporting skyrmions, with ferromagnetic layers that can be coupled either by ferromagnetic or antiferromagnetic RKKY exchange. To assess RKKY interactions in such systems, a rare-earth ferrimagnet based multilayered system is proposed. The magnetically hard rare-earth amorphous ferrimagnet consisting of a Tb_xFe_{1-x} alloy is exchange-coupled to a thin Co layer. The magnetization of the latter remains pinned up to reasonably high fields by the magnetically hard ferrimagnet layer. This bi-layer system is then separated from a “free” magnetic layer by an interlayer consisting of the typical noble metal used in systems with iDMI. In the simplest case the “free” layer is a 1.5nm-thick Co layer deposited on a Pt substrate to obtain PMA. The net magnetic moment of the rare-earth based ferrimagnet layer is governed by the composition of rare-earth and transition metal (Tb_xFe_{1-x} with $15 < x < 30$), such that either the magnetic moment of the rare-earth or transition metal element aligns parallel to the direction of an applied test-field H_{ex} . Consequently, the adjacent Co layer aligns antiparallel or parallel to H_{ex} , which permits the measurement of a ferromagnetic or antiferromagnetic RKKY exchange coupling, respectively, occurring between the “pinned” and “free” Co layers through the interlayer. The RKKY coupling energy density can be obtained from magnetometry using $E = M_{free\ layer} \cdot t \cdot H_{ex}$. The situation however becomes more challenging if the “free” Co layer has asymmetric interfaces, hence the material at the top (e.g. Ir) is different from that at the bottom (Pt). In such a case the remanence of the “free” layer is suppressed by the formation of skyrmions or chiral domains arising from the net DMI generated by the asymmetric interfaces. To overcome this problem, we designed the free layer as a multilayer system with symmetric interfaces suppressing the net DMI. The proposed multilayer design permits to reliably measure the RKKY interactions occurring in all typical magnetic multilayer systems exhibiting iDMI, which provides the so-far missing input for micromagnetic simulations of such systems relevant for the design of future skyrmionic devices.

1. M. Bacani, M. A. Marioni, J. Schwenk, H. J. Hug, *Scientific Reports* 9, 3114 (2019).
2. M. A. Marioni, M. Penedo, M. Bacani, J. Schwenk, H. J. Hug, *Nano Letters* 18, 4, 2263-2267 (2018).
3. D. Suess, C. Vogler, F. Brückner, P. Heistracher, C. Abert, *Aip Advances* 8, 11 (2018).
4. W. Legrand, J. Y. Chauleau, D. Maccariello, N. Reyren, S. Collin, K. Bouzehouane, N. Jaouen, V. Cros, A. Fert, *Science Advances* 4, 7 (2018).
5. S. S. P. Parkin, *Physical Review Letters* 67 (25), 3598-3601 (1991).



FH-04. Mechanism of Current-Induced Magnetotransport in Epitaxial Antiferromagnetic α -Fe₂O₃.

A. Churikova¹, D. Bono¹, A. Wittmann¹, L. Scipioni², A. Shepard², T. Newhouse-Illige², J.A. Greer², N.O. Birge³ and G. Beach¹

1. *Materials Science and Engineering, Massachusetts Institute of Technology, Cambridge, MA, United States*; 2. *PVD Products, Inc, Wilmington, MA, United States*; 3. *Department of Physics and Astronomy, Michigan State University, East Lansing, MI, United States*

Antiferromagnets (AFs) are promising candidates for next generation spintronic devices. Hematite (α -Fe₂O₃), an easy-plane AF insulator with triaxial anisotropy, is one of the materials at the forefront of this effort, spurring discoveries of magnon-mediated long-distance spin transport and unambiguous control of the AF order by electrical current [1]. Contrary to ferromagnets, where domain structure is governed by long-range demagnetizing fields, the domain structure in AFs is controlled by destressing fields of magnetoelastic origin [2]. The electrical control of domains has been studied in AFs with an adjacent heavy metal as a source of interfacial anti-damping-like spin-orbit torque (SOT). But, AF switching has been shown to at least partially result from thermo-magnetoelastic torques, generated by current-induced temperature gradients [3,4]. The competition of a thermo-magnetoelastic torque and SOT complicates the fundamental understanding of the origin of domain re-distribution. In our work, we develop a method for discerning the two effects by heating a Pt device on α -Fe₂O₃ independently of the applied current. Implementing a combination of angle-dependent spin-Hall magnetoresistance (SMR) and current pulsing, we probe, respectively, the full and partial re-orientation of AF domains in epitaxial α -Fe₂O₃/Pt bilayers. We find that the origin of the current-induced switching signal, which results from domain re-orientation, is primarily of SOT origin in α -Fe₂O₃. The remanent switching amplitude (~5% of the expected signal amplitude) and a temperature-dependent study of key switching signatures reveals the existence of pinning barriers to domain wall motion. This study advances the understanding of current-induced effects in AF materials with low anisotropy and high magnetostriction, where magnetoelastic effects are thought to dominate.

[1] Y. Cheng, S. Yu, M. Zhu, J. Hwang, and F. Yang, *Phys. Rev. Lett.* 124, 027202 (2020). [2] J. Fischer, O. Gomonay, R. Schlitz, K. Ganzhorn, N. Vlietstra, M. Althammer, H. Huebl, M. Opel, R. Gross, S. T. B. Goennenwein, and S. Geprägs, *Phys. Rev. B* 97, 014417 (2018). [3] H. Meer, F. Schreiber, C. Schmitt, R. Ramos, E. Saitoh, O. Gomonay, J. Sinova, L. Baldrati, and M. Kläui, *Nano Lett.* [acs.nanolett.0c03367](https://doi.org/10.1021/acs.nanolett.0c03367) (2020). [4] L. Baldrati, C. Schmitt, O. Gomonay, R. Lebrun, R. Ramos, E. Saitoh, J. Sinova, and M. Kläui, *Phys. Rev. Lett.* 125, 077201 (2020).

FH-05. Observation of the Magnetic Cluster Octupole Domain Evolution in Antiferromagnet Mn_3Ge .

M. Wu^{1,2}, H. Isshiki², T. Chen³, T. Higo³, S. Nakatsuji^{3,2} and Y. Otani^{1,2}
 1. Center for Emergent Matter Science, Rikagaku Kenkyujo, Wako, Japan; 2. The University of Tokyo Bussei Kenkyujo, Kashiwa, Japan; 3. Department of Physics, The University of Tokyo, Bunkyo-ku, Japan

Antiferromagnetic (AFM) spintronics is an emerging subject where one tries to exploit the indispensable properties of AFMs for spintronics such as negligible stray fields and terahertz resonance frequencies. Unfavorably, small electric, and magnetic responses make it difficult to write and read the information in AFM spintronic devices. Thus, from the applied perspective, it is crucial to search the AFM materials having manipulable AFM order. Mn_3Ge and Mn_3Sn are novel functional AFMs that exhibit magnetic responses comparable to FMs^{1,2}. The magnetic states characterized by magnetic cluster octupoles (MCOs) are tunable under a small external magnetic field. Thus, data writing and reading can be realized by inductively using a recording head, likewise FMs. A recent numerical simulation predicts an antiferromagnetic domain wall (AFDW) velocity up to 2 km/s without a walker break down³. A pulse current could drive such AFDW under the threshold current density of 10^9 A/m², two or three orders of magnitude smaller than in FMs⁴. Thus, it could open a new avenue for racetrack memory applications to overcome the shortcomings of low velocity and high energy consumption of ferromagnetic domain walls. Besides, the multistate of MCOs could generate multilevel magnetic responses rather than conventional two-level memory responses. It may provide a new idea for three-dimensional memory without vertical multilayer architecture. Therefore, the understanding of AFDW structure and dynamics in Mn_3Sn and Mn_3Ge is indispensable for the memory application. We put our focus on Mn_3Ge in this study because it has the native advantages of strong chemical stability in air and robustly retaining the MCO structure down to 0.3 K over the Mn_3Sn . We grew Mn_3Ge single crystal using the bismuth flux method⁵. The obtained single crystal sample is a perfect hexagonal column, reflecting the hexagonal crystal structure. We performed polar and longitudinal MOKE measurements at room temperature. Figure 1a shows a polar hysteresis loop measured by laser scanning MOKE microscope. The positive and negative signs of the MOKE signal correspond respectively to oppositely aligned MCOs with the order parameters of α_{\pm} , as shown in the inset of Fig 1a. Figure 1(b) shows the angular dependence of longitudinal MOKE measurement at room temperature. The intensity of decreased from 5.6 mdeg to 0 deg with increasing from 0° to 90°. Domain observation was furtherly performed by using high-resolution CCD MOKE microscope. Firstly, a magnetic field, up to -100 Oe downwards, which is larger than the saturation field according to the MOKE hysteresis loop in Fig. 1b, was applied to reset the magnetization in the crystal. We subtracted the image background at this state; then, we captured MCO domain images continuously while sweeping the magnetic field from -20 Oe down to 30 Oe with a sweep rate of 2.5 Oe/s, as shown in Fig. 2a. The exposure time of the CCD camera was 50 ms. Firstly, the droplet of the tilted MCO domain appears at 2 Oe. Here, the gray at -100 Oe and the white areas at 25 Oe represent the oppositely polarized MCO domains. The droplet occurs at the surface center due to the nearly zero magnetization in Mn_3Ge . Noticeably, the color contrast gradually changes from gray to white within a narrow magnetic field range of about 2 Oe. As the grayscale in the CCD camera is proportional to the out-of-plane component of MCO moment M_z . We can obtain the tilting angle ϕ of the MCO moment where $\cos\phi = M_z/M$, as shown in Fig. 2b. In this way, we can understand how the magnetic octupole evolves during the domain nucleation process. The six-fold symmetry in the kagome plane may offer the possibility of a multilevel MCO memory application. The droplet of the switched domain emerges in the magnetic field range from $H_1 = 1.875$ Oe to $H_2 = 3$ Oe, as shown in Fig. 2c. The decrease in magnetic potential energy compensates for the energy consumed by AFDW. Thus, we have: $-\mu_0(MH_2 - MH_1) \times \Delta V - \sigma \times \Delta S = 0$ where M and, σ denote the MCO moment (7 $\mu\text{B}/\text{Mn}$) and the 180° AFDW energy density, respectively. ΔV is the volume of the switched MCO domain, and ΔS is the area of nucleated AFDW. We estimated the and by assuming the hemi-ellipsoidal MCO domain beneath the surface, as illustrated in Fig. 2c. The obtained σ is 0.0198 erg/cm². In conclusion, we have obtained the large MOKE signal, including the polar and longitudinal MOKE. The sizeable

MOKE signals enable us visualize the MCO domain optically. Thereby, we systematically studied MCO domain evolution and estimated the AFDW propagation in a single crystal Mn_3Ge . Our work provides important insights for the study on the exploitation of the AFDW based memory devices.

1. S. Nakatsuji, N. Kiyohara & T. Higo. *Nature* 527, 212–215 (2015). 2. N. Kiyohara, T. Tomita & S. Nakatsuji. *Phys. Rev. Appl.* 5, 064009 (2016). 3. T. Nomoto & R. Arita. *Phys. Rev. Res.* 2, 012045 (2020). 4. S. Sugimoto, Y. Nakatani, Y. Yamane, *et al. Commun. Phys.* 3, 1–9 (2020). 5. M. Wu, H. Isshiki, T. Chen, *et al. Appl. Phys. Lett.* 116, 132408 (2020).

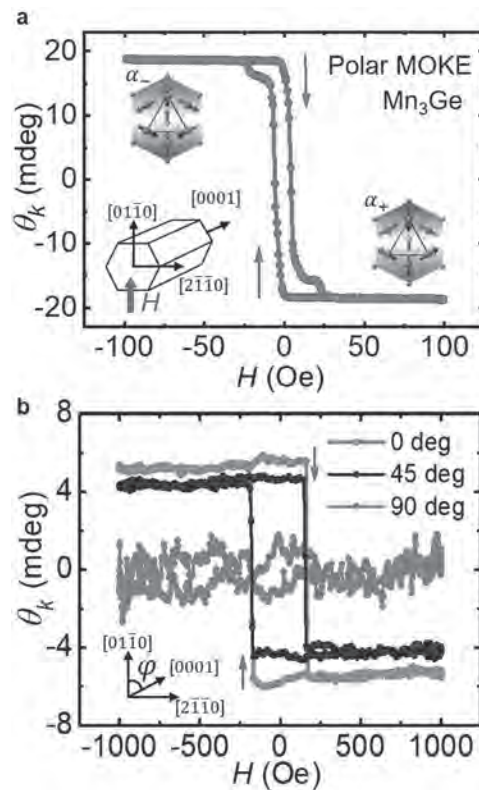


Fig.1 Polar and longitudinal MOKE signals in Mn_3Ge (a) Field dependence of the polar MOKE. (b) Field dependence of θ_k under the longitudinal set-up at various values of ϕ .

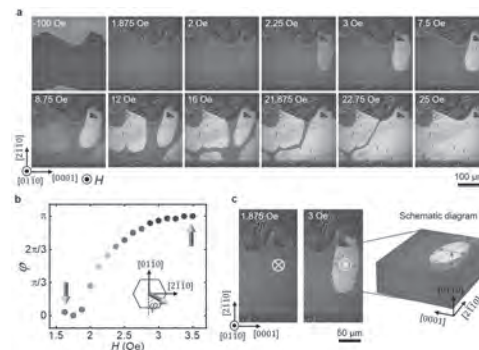


Fig.2 MCO domain evolution on Mn_3Ge surface observed by CCD MOKE microscope. a, MCO domain evolution process under the sweeping magnetic field. b, Tilting angle ϕ of the MCO moment with respect to the magnetic field during the MCO domain nucleation process. c, The left image shows first droplet of nucleated MCO domains and the right image is the schematic diagram of hemi-ellipsoidal MCO domain shape beneath the surface.

FH-06. Direct Observation of Spin-Orbit Torques, Dzyaloshinskii-Moriya Interaction and Chiral Spin Textures in Single Layer Ferrimagnets.

S. Krishna^{1,3}, E. Haltz^{1,4}, L. Berges¹, L. Aballe², M. Foerster², L. Bocher¹, R. Weil¹, A. Thiaville¹, J. Sampaio¹ and A. Mougin¹

1. Université Paris-Saclay, CNRS, Laboratoire de Physique des Solides, Orsay, France; 2. Alba Synchrotron Light Facility, CELLS, Barcelona, Spain; 3. Unité Mixte de Physique, CNRS, Thales, Université Paris-Saclay, Palaiseau, France; 4. University of Leeds School of Physics and Astronomy, Leeds, United Kingdom

Magnetic layers interfaced with materials with strong spin-orbit coupling (SOC) (such as Pt, Ta) manifest several fascinating phenomena when the inversion symmetry is broken¹. One direct consequence of SOC is the interplay between charge and spin transport via spin Hall effect (SHE) in heavy metals, which leads to non-equilibrium spin accumulation at the surfaces². Another mechanism, the Rashba effect, arises when the electrical carriers move in an interfacial electric field and experience the resultant magnetic field that couples with their spins³. Both mechanisms give rise to spin-orbit torques (SOTs) in the magnetic layer, with damping-like and field-like components⁴. The SOTs are an efficient way to manipulate chiral magnetic textures, such as Néel domain walls (DWs)^{5,6} and skyrmions, whose chirality is induced by another product of SOC, the Dzyaloshinskii-Moriya interaction (DMI)⁷. However, up to now, the SOC was mainly studied in 3d-transition-metals (TM) (Co, Ni, Fe)/5d-heavy-metal (Pt). Very recently, interfacial DMI has been observed in TmIG/Pt and TbIG/Pt garnets thin films grown on Gd₃Ga₅O₁₂ (GGG) substrates, which was attributed to the orbital moment in rare-earth (RE) material⁸. On the other hand, experiments on [Co/Tb]n multilayers did not show any SOT contribution from the RE⁹. The underlying origin of SOC and role of RE (specially Gd, which has no atomic orbital momentum) on SOC in ferrimagnets hence remain to be understood and need to be addressed by sophisticated experimental evidence. Here, we demonstrate that the effects of SOC can be obtained without any need of additional nonmagnetic heavy metal in a single layer GdFeCo ferrimagnet (RE-TM alloy). For this study, a Si/SiOx(100nm)/GdFeCo(5nm)/Al(5nm) film was grown by co-evaporation in ultra-high vacuum with a controlled stoichiometry. The ferrimagnet is composed of two sub-lattices of Gd (RE) and FeCo (TM) which are coupled antiferromagnetically. At the magnetic compensation temperature, $T_M \approx 275$ K for this sample, the net magnetization vanishes (M_S) and the anisotropy and the coercive fields diverge. To investigate the existence of SOC inside the ferrimagnetic layer, first we quantify the two components of current-induced effective fields, damping-like (H_{DL}) and field-like (H_{FL}) by using second harmonic Hall voltage measurement technique. The temperature dependence of H_{DL} and H_{FL} per current density in GdFeCo layer are shown in Figure 1(a) and 1(b). Both H_{DL}/J and H_{FL}/J diverge at, showing the expected scaling with $1/M_S$. Another phenomenon induced by SOC is the DMI, which favours chiral magnetic textures. In the single layer GdFeCo ferrimagnet, we observed chiral Néel domain wall structures of width (Δ) = 20 ± 10 nm, using photoemission electron microscopy combined with X-ray magnetic circular dichroism (XMCD-PEEM) as shown in Figure 2(a), which further indicate the presence of internal DMI or SOC in GdFeCo. The DMI is quantified using Brillouin light scattering (BLS) technique in Damon-Eshbach geometry and the DMI constant (is obtained from the slop of frequency shifts (Δf) of nonreciprocal spin waves vs wave vector (figure 2(c)). Though the DMI amplitude is much smaller in GdFeCo if compared with Pt/Co and Ta/Co systems, the chiral DWs are stabilised due to lower net magnetization of GdFeCo, as the threshold D_c for Néel DW stabilisation is proportional to M_s . The occurrence of these phenomena also requires a broken inversion symmetry. Electron Energy-Loss Spectroscopy (EELS) studies in a scanning transmission electron microscopy (STEM) reveal an inhomogeneity in Gd concentration along the film thickness. This elemental inhomogeneity breaks the spatial inversion symmetry and the combination of broken inversion asymmetry and electronic hybridization of RE-5d and TM-3d electrons favors the emergence of net SOC effects (SOTs, DMI and chiral Néel DWs) inside the GdFeCo layer. These results show that phenomena that can only exist in systems with broken inversion symmetry and strong SOC -- spin-orbit torques, chiral textures, and DMI -- can occur in a ferrimagnetic thin layer without a heavy

metal adjacent layer. This should be taken into account when analysing these phenomena even in bi-layers, and may be very useful for applications as it may allow removing the requirement for a heavy-metal layer and improving the efficiency of SOT-driven magnetisation switching.

1. Soumyanarayanan, A. *et al. Nature* 539, 509–517 (2016).
2. Stamm, C. *et al. Phys. Rev. Lett.* 119, 087203 (2017).
3. Sánchez, J. C. R. *et al. Nat. Commun.* 4, 1–7 (2013).
4. Garello, K. *et al. Nat. Nanotechnol.* 8, 587–593 (2013).
5. Emori, S. *et al. Nat. Mater.* 12, 611–616 (2013).
6. Ryu, K.-S. *et al. Nat. Nanotechnol.* 8, 527–533 (2013).
7. Thiaville, A. *et al. Epl* 100, (2012).
8. Caretta, L. *et al. Nat. Commun.* 11, 1–9 (2020).
9. Yu, J. *et al. Nat. Mater.* 18, 29–34 (2019).

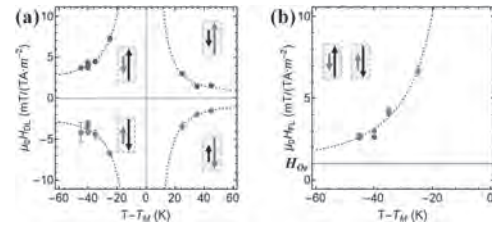


Figure 1. (a) H_{DL} and (b) H_{FL} effective fields per current density as a function of temperature. Purple points correspond to an up saturated film state and khaki to down one. The diagrams represent the direction and magnitude of Gd (black) and FeCo (red) magnetic moments. The dotted lines are guides to the eyes.

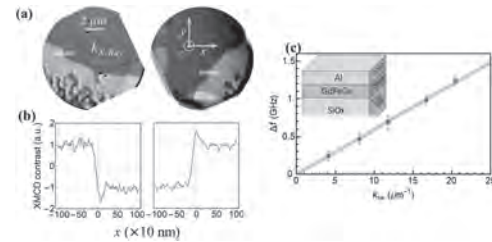


Figure 2. (a) Multidomain XMCD-PEEM images at the Gd $M_{4,5}$ edge (1178.7 eV) at $T = 230$ K. The green arrow shows the direction of the X-ray beam at a grazing angle of 16° . The dark (bright) contrast corresponds to a down (up) magnetic domain. (b) Intensity profiles (black lines) averaged over the yellow regions in (a). The thick yellow line is a fit to the experimental data using the theoretical profile. The presence of a peak or a dip in the line scan is an evidence of chiral Néel DWs. (c) The DMI induced frequency shifts (Δf) of nonreciprocal spin waves vs wave vector magnitudes $|k_{sw}|$ for GdFeCo thin film

FH-07. Roles of Destressing, Pinning, and Weak Ferromagnetism for Magnetic Reversal in α -Fe₂O₃.

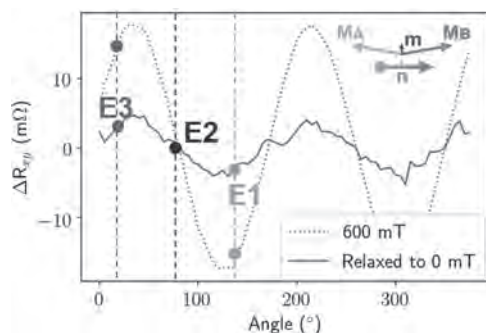
A. Wittmann¹, A. Churikova¹, L. Scipioni², A. Shepard², T. Newhouse-Illige², J.A. Greer², N.O. Birge³ and G. Beach¹

1. Massachusetts Institute of Technology, Cambridge, MA, United States;

2. PVD Products, Wilmington, MA, United States; 3. Michigan State University, East Lansing, MI, United States

We study the magnetic reversal of the canted antiferromagnet α -Fe₂O₃. At room temperature, the Dzyaloshinskii-Moriya interaction (DMI) induces canting of the two magnetic sublattices M_A and M_B giving rise to a weak ferromagnetic (FM) moment m . We employ spin Hall magnetoresistance (SMR) measurements to study electrical and magnetic field control of the Néel order in α -Fe₂O₃/Pt bilayers. The angle-dependent magnetoresistance (ADMR) shows the characteristic saturated negative SMR signal of AFMs (dotted curve in figure 1) in agreement with previous findings¹⁻⁴. We note that the FM moment lifts the degeneracy of the sublattices and consequently the orientation of the Néel vector with respect to the applied magnetic field. The solid blue curve in figure 1 shows the remanent resistance as a function of the angle of the preceding saturating magnetic field. The data show a simple scaling between the saturated ADMR signal and the remanent resistance by a factor of 5. The lack of signatures of anisotropy in the remanent signal implies that the relaxation of the SMR signal is dominated by destressing effects favoring an equilibrium state with multiple domains distributing the orientation of the Néel vector along random directions. Furthermore, we observe hysteresis in the SMR signal. The irreversibility upon switching the direction of the magnetic field in combination with investigating the transient effects of current-induced changes in the domain structure allows us to study the nature and formation of antiferromagnetic as well as ferromagnetic domain walls at low magnetic fields. Our work emphasizes the importance of the FM moment induced by DMI and the relaxation effects for the equilibrium domain structure in α -Fe₂O₃.

1. Lebrun, R. *et al.* Anisotropies and magnetic phase transitions in insulating antiferromagnets determined by a Spin-Hall magnetoresistance probe. *Commun. Phys.* 2, 50 (2019). 2. Cheng, Y., Yu, S., Zhu, M., Hwang, J. & Yang, F. Electrical Switching of Tristate Antiferromagnetic Néel Order in α -Fe₂O₃ Epitaxial Films. *Phys. Rev. Lett.* 124, 027202 (2020). 3. Fischer, J. *et al.* Large Spin Hall Magnetoresistance in Antiferromagnetic α -Fe₂O₃/Pt Heterostructures. *Phys. Rev. Appl.* 13, 014019 (2020). 4. Zhang, P., Finley, J., Safi, T. & Liu, L. Quantitative Study on Current-Induced Effect in an Antiferromagnet Insulator/Pt Bilayer Film. *Phys. Rev. Lett.* 123, 247206 (2019).



Transverse resistance (solid blue line) after H has been reduced from a saturated state (dotted blue line) to zero field as a function of angle of the applied magnetic field. The inset in the top right corner shows a schematic of the canting of the sublattice magnetization M_A and M_B due to DMI giving rise to the ferromagnetic moment m .

FH-08. Symmetry of Transversal Conductivity Signal in Antiferromagnetic Mn₅Si₃.

A. Badura¹, H. Reichlova^{2,7}, R. Schlitz², D. Kriegner^{2,7}, R. Lopes Seeger³, I. Kounta⁴, L. Michez⁴, E. Schmoranzarová¹, V. Baltz³, S.T. Goennenwein^{2,5} and L. Smejkal^{6,7}

1. Department of Chemical Physics and Optics, Univerzita Karlova Matematicko-fyzikalni fakulta, Praha, Czechia; 2. Institute for Solid State and Materials Physics, Technische Universitat Dresden, Dresden, Germany; 3. SPINtronique et Technologie des Composants, Grenoble, France; 4. Centre Interdisciplinaire de Nanoscience de Marseille, Marseille, France; 5. Fachbereich Physik, Universitat Konstanz, Konstanz, Germany; 6. Institut für Physik, Johannes Gutenberg Universität Mainz, Mainz, Germany; 7. Physics, Czech Academy of Science, Praha, Czechia

The Hall effect family is of fundamental importance among the magne-to-transport phenomena, as it represents a way to dissipationless transport. [1] Hall effects manifest as a transverse component to conductivity, perpendicular to the direction of the electrical current. Apart from the long-known ordinary Hall effect that is present in all conductive materials, the anomalous Hall effect was a long time thought to be exclusive to ferromagnetic systems. In the last years, the Hall effect family has been explored in materials with zero net magnetic moment. Both anomalous Hall effect [2] and topological Hall effect were detected [3] also in non-collinear antiferromagnets (AFM). Very recently, a novel type of spontaneous Hall effect was reported also in the collinear phases of antiferromagnetic Mn₅Si₃ [4] and RuO₂ [5]. All the above-mentioned Hall effects rely on detection of transversal voltage which is expected to be odd in magnetic field. Any even contribution to the transversal voltage is often considered as an artefact related to misalignment of the Hall cross and, consequently, only antisymmetrized transversal voltage data are presented. However, it has been theoretically shown [6] that for certain low-symmetry magnetic systems, even components would be present in the transverse voltage data. In our presentation, we aim to experimentally demonstrate the presence of the even contribution to transversal resistance in a low-symmetry antiferromagnetic phase of Mn₅Si₃ indicating that the symmetry of the signal could serve as a probe of the degree of spin symmetry of the material. The ratio between odd and even contributions in various samples will be shown and the role of the crystal quality will be discussed Mn₅Si₃ is a compensated antiferromagnet that can order both collinearly and non-collinearly in different temperature regimes, with the two phase transitions at T_{N1} ≈ 70 K and T_{N2} ≈ 200 K in thin-film layers [4]. Our samples are 20 nm thick epilayers, prepared by molecular beam epitaxy on Si(111) substrate, which results in the c-axis of Mn₅Si₃ to be oriented perpendicular to the sample plane. The layers were patterned to Hall bar devices with a channel width of 10 μm using standard laser lithography and Ar+ milling. Both longitudinal (ρ_{xx}) and transverse (ρ_{xy}) resistivities were measured simultaneously as a function of external magnetic field B_z applied in the out-of-plane direction. The longitudinal and transverse signals measured at two different temperatures corresponding to the collinear (180 K) and non-collinear (40 K) antiferromagnetic phase of Mn₅Si₃, are shown in Fig. 1(a) and (b), respectively. Note that all the curves presented in Fig. 1 were shifted for clarity, and the ordinary Hall resistance was removed from ρ_{xy} by subtracting the signal linear in B_z. The longitudinal signal Δρ_{xx} (see Fig.1(a)) corresponds to the magnetoresistance (MR). The strong magne-toresistance observed at 40 K is significantly suppressed in the collinear phase at 180 K in accord with the expected behaviour [5]. In contrast, the transverse resistivity persists even in the collinear phase (see Fig 1(b)), with a clear hysteretic behaviour and coercive field of 2 T. This spontaneous Hall response has recently been attributed to a novel antiferromagnetic Zeeman effect [4]. As for the case of any Hall effect, generated transverse voltage is expected to be odd in the inducing magnetic field. However, the data in Fig. 1 (b) clearly contain both odd and even component. This feature is highlighted in Fig. 2, where the corresponding hysteresis curves are split into symmetric (a) and antisymmetric (b) parts. Notably, the symmetrical component that reflects signals even B_z is comparable in magnitude to the antisymmetrical one at 40 K, but disappears entirely at 180 K. To exclude the possible origin in MR-related artefacts, we compare the shapes of the ρ_{xx} and even ρ_{xy} by subtraction the normalized curves, i.e. Δρ(B_z) = ρ_{xx}(B_z) / ρ_{xx}(0) - Δρ^(sym)_{xy}(B_z) / ρ^(sym)_{xy}(0). The resulting non-trivial curve, shown in Fig. 2(c),

demonstrates the difference in shapes of MR and even transverse voltage. The comparison is, however, possible only in the low-temperature regime, as the transverse detected at 180 K do not display any sizable even component. This observation is in agreement with the assumed lowering of the symmetry in the non-collinear phase of Mn₅Si₃. As shown in [6], the shape of the linear response tensor can be extended to deal with more complex situations, such as the low magnetic symmetry of the Mn₅Si₃. The transversal voltage does not need to show purely antisymmetric elements.

[1] N. Nagaose et al., Rev. Mod. Phys. 82, 1539 (2010) [2] S. Nakatsuji, N. Kiyohara, and T. Higo, Nature 527, 212-215 (2015) [3] Ch. Surges et al., Nat. Comm. 5, 3400 (2015) [4] H. Reichlova et al., arXiv:2012.15651v1 (2020) [5] https://arxiv.org/abs/2002.08712 [6] M. Seeman et al., Phys. Rev. B 92, 155138 (2015)

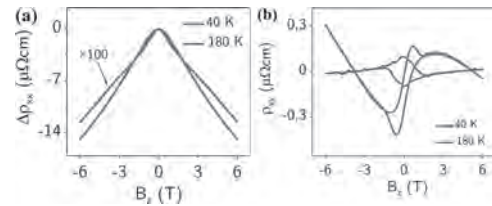


Fig. 1. (a) Longitudinal and (b) transverse resistivity measured as a function of the out-of-plane magnetic field B_z at two different temperatures, corresponding to the collinear (180 K) and non-collinear (40 K) phase of Mn₅Si₃.

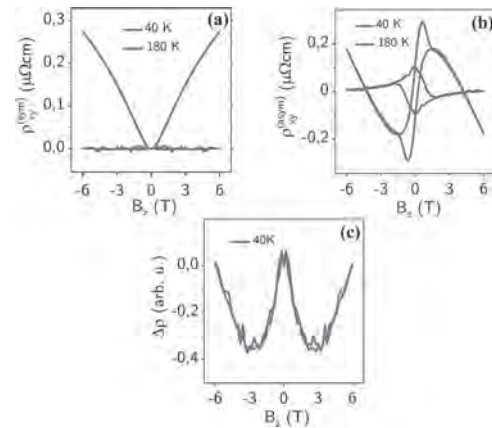


Fig. 2. (a) symmetrized and (b) antisymmetrized components of transverse resistance data in Mn₅Si₃ measured at 40 K and 180 K, respectively. Panel (c) demonstrates the difference in shape by subtracting normalized curves for ρ_{xx}(B_z) and ρ^(sym)_{xy}(B_z).

FH-09. Reversible Interlayer Exchange Coupling Regulation Induced by Phase Change of Atomically Thin VO₂.

X. Fan¹, G. Wei¹, X. Lin¹ and W. Zhao¹

¹. Beihang University, Beijing, China

Regulation of electronic properties in spintronic interfaces (spinterfaces) can give rise to the optimization and even emergence of abundant spintronic effects. However, a proof-of-concept demonstration of such a strategy has rarely been achieved. Here, we experimentally demonstrate a reversible switching from antiferromagnetic coupling through insulating spinterface to ferromagnetic coupling through metallic spinterface in [Pt/Co]₂/VO₂/[Co/Pt]₂ heterostructure, where atomically VO₂ is considered as a controllable spinterface via its reversible metal-to-insulator transition. Furthermore, we attribute such an evolution to two distinct coupling mechanisms of spin-dependent tunneling and Ruderman-Kittel-Kasuya-Yosida interaction determined by the electronic states of VO₂. The effect of VO₂-tailored interlayer exchange coupling highlights the great potential of spinterface as a magic building block in beyond-CMOS electronic devices. **1. Preparation and characterization of atomically thin VO₂ and heterostructures** Both atomically thin VO₂ and [Pt/Co]₂/VO₂/[Co/Pt]₂ heterostructure are deposited by sputtering. Ultrathin VO₂ is chosen as an electrically-controllable spacer to regulate the interlayer exchange coupling via its metal-insulating transition around 340K¹. First, the phase change of atomically thin VO₂ lies at the heart of whole works. XPS result in Fig. 1a is displayed to check the valence state of vanadium of VO₂ thin film from which we can see that the proportion of VO₂ reaches 97%. Meanwhile electrical transport with a junction device of Au/VO₂/Au is also performed to confirm the phase change of VO₂. From It is clearly in Fig. 1b that the I-V curve changes from tunneling (300K) to linear (340K) suggesting a transition from insulating state to metallic state of VO₂. We also show the dependence of resistance ratio of ultrathin VO₂ (2nm) on temperature comparing with a bulk sample (40 nm) (Fig. 1c). Based on such an atomically thin VO₂, we prepare the heterostructure of [Pt/Co]₂/VO₂/[Co/Pt]₂ (Fig. 1d). To prove the good quality and continuity of heterostructure, high-resolution transmission electron microscopy measurement is required profiled in Fig. 1e. In addition, PMA of heterostructure is also measure by p-MOKE in Fig. 1f. **2. Interlayer exchange coupling switching via phase change** The change on electronic state of spinterface induced by phase change will arise the interlayer exchange coupling switching. In order to investigate the coupling change, we measure the hysteresis loops of heterostructure with various thicknesses of VO₂ as temperature rises to trigger the phase change. The loops change from double spin flips to single flip (Fig. 2a) that indicates a transition from antiferromagnetic coupling at low temperature to ferromagnetic coupling at high temperature. Besides such a dynamic process of coupling switching, we extract the exchange coupling field of different samples with temperature increasing (Fig. 2b left). To further verify the reliability of the experimental data, we compare the coupling strength value calculated by experimental data with that calculated by theoretical fitting at room temperature with various thicknesses of VO₂ (Fig. 2b right). As for theoretical fitting, due to different electronic state of VO₂, spin-dependent tunneling model² is applied at insulating VO₂ while RKKY interaction model³ is used at metallic VO₂. In the final, to confirm reversibility of such a promising interlayer exchange coupling regulation, we also show the hysteresis loop after the temperature decrease back to the low temperature (Fig. 2c).

1. Morin, F. J. Oxides Which Show a Metal-to-Insulator Transition at the Neel Temperature. *Phys. Rev. Lett.* 3, 34–36 (1959). 2. Faure-Vincent, J. *et al.* Interlayer Magnetic Coupling Interactions of Two Ferromagnetic Layers by Spin Polarized Tunneling. *Phys. Rev. Lett.* 89, 107206 (2002). 3. Parkin, S. S. P. & Mauri, D. Spin engineering: Direct determination of the Ruderman-Kittel-Kasuya-Yosida far-field range function in ruthenium. *Phys. Rev. B* 44, 7131–7134 (1991).

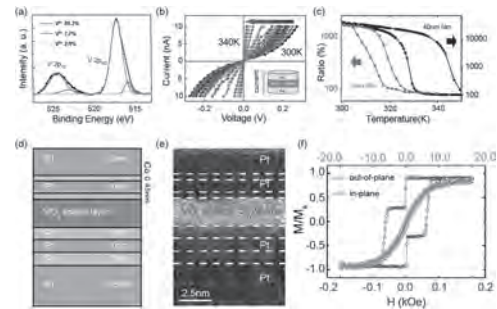


Figure 1. Atomically Thin VO₂ and Magnetic Heterostructures

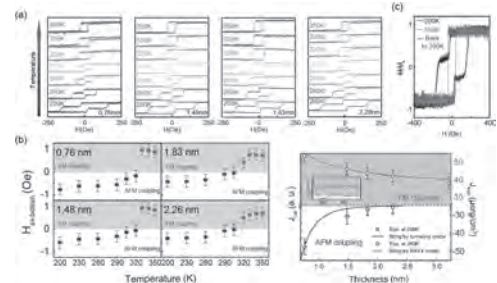


Figure 2. Interlayer exchange coupling switching

FH-10. The Chiral Hall Effect in Canted Ferromagnets and Antiferromagnets.

J. Kipp^{1,2}, *K. Samanta*¹, *F. Lux*^{1,2}, *M. Merte*^{1,2}, *D. Go*^{1,3}, *J. Hanke*¹, *M. Redies*^{1,2}, *F. Freimuth*¹, *S. Blügel*¹, *M. Lezaic*¹ and *Y. Mokrousov*^{1,3}
1. *PGI-1/IAS-1, Forschungszentrum Julich GmbH, Julich, Germany;*
2. *Physics, Rheinisch-Westfälische Technische Hochschule Aachen, Aachen, Germany;* 3. *Physics, Johannes Gutenberg Universität Mainz, Mainz, Germany*

The anomalous Hall effect (AHE) reflects the immense diversity of mechanisms for intrinsic or extrinsic current generation that can be found in the world of magnets. This world offers numerous exciting classes of antiferromagnets, where the anomalous and recently discovered crystal Hall [1] effect as well as the topological Hall effect in non-coplanar antiferromagnets [2] have been studied in the past decades. In this work, we uncover a novel type of Hall effect emerging in generic canted spin systems. Identifying a clear fingerprint of this chiral Hall effect (CHE) in discrete tight-binding models as well as ab-initio calculations is central in establishing a solid understanding of this new phenomenon closely tied to real space topology of magnetic textures. In this study, we provide robust numerical evidence for the CHE in a honeycomb lattice of canted spins and present a material candidate, SrRuO₃. We uncover contributions to the Hall conductivity sensitive to the canting angle between neighboring spins which can be directly related to the imprinted vector chirality. Exploring the symmetry properties of the CHE we demonstrate the complex interplay of symmetry, topology and chirality in canted spin systems.

[1] L. Smejkal, R. Gonzalez-Hernandez, T. Jungwirth, J. Sinova, *Science Advances* 6 (2020) [2] L. Smejkal, Y. Mokrousov, B. Yan, A. H. MacDonald, *Nature Physics* 14, 242–251 (2018) [3] J. Kipp et al., arXiv:2007.01529 (2020)

FH-11. Imprinting the Domain Structure of a Metallic Antiferromagnet on Thin Ferromagnetic Layers.

S. Bommanaboyena¹, D. Schoenke¹, R. Reeve¹, M. Klau¹ and M. Jourdan¹
 1. Physics, Johannes Gutenberg Universitat Mainz, Mainz, Germany

The theoretical prediction of Néel order manipulation in antiferromagnetic (AFM) Mn_2Au by current induced bulk spin-orbit torques [1] and subsequent experimental realization of the same [2, 3] have led to a surge of interest in the study of this material for spintronics applications. However, the absence of a net magnetic moment in antiferromagnets poses a major challenge to the visualization of antiferromagnetic domains and it is usually resolved by complex synchrotron-based microscopy methods such as X-ray magnetic linear dichroism - photoemission electron microscopy (XMLD-PEEM) [4, 5]. In this work we present an alternative technique to image antiferromagnetic domains in-house by imprinting them on thin ferromagnetic overlayers via interfacial exchange coupling. The domains of the Mn_2Au /ferromagnet bi-layer system were first observed using X-ray magnetic linear/circular dichroism - photoelectron emission microscopy for the antiferromagnetic and ferromagnetic layers, respectively. The ferromagnet was found to mimic the underlying Mn_2Au domain pattern, thereby enabling us to indirectly image the AFM domains of Mn_2Au using an in-house scanning electron microscope with polarization analysis (SEMPA) (Figure 1). Furthermore, superconducting quantum interference device (SQUID) magnetometry measurements were carried out to quantify the pinning field acting upon the ferromagnet and an unusually large exchange coupling was revealed at the Mn_2Au /ferromagnet interface. Our results unlock novel possibilities for in-house study of antiferromagnets and take us a step further towards the realization of next generation spintronics devices based on this remarkable material. This project is funded by the Deutsche Forschungsgemeinschaft (DFG, German Research Foundation) TRR 173 268565370 (projects A01 & A05).

[1] J. Zelezny et al., *Phys. Rev. Lett.*, 113, 157201 (2014). [2] S. Yu. Bodnar et al., *Nat. Commun.*, 9, 348 (2018). [3] M. Meinert et al., *Phys. Rev. Appl.*, 9, 064040 (2018). [4] A. A. Sapozhnik et al., *Phys. Rev. B*, 97, 134429 (2018). [5] S. Yu. Bodnar et al., *Phys. Rev. B*, 99, 140409(R) (2019).

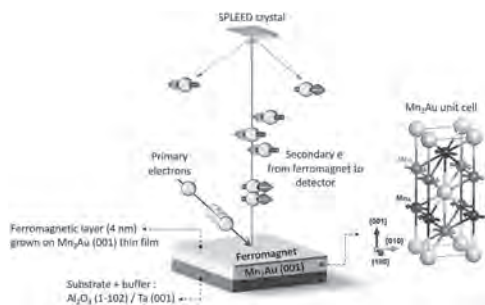


Figure 1. Scanning electron microscopy with polarization analysis to study the domain structure of Mn_2Au imprinted on the ferromagnetic overlayer. The SEMPA resolves in-plane magnetization into horizontal and vertical components.

FH-12. Cavity Magnon Polaritons and Inverse Spin Hall Effect in Easy-Axis Antiferromagnets.

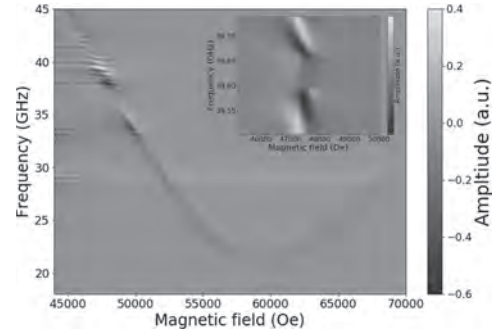
I. Boverter¹, H.T. Simensen⁴, A. Anane¹, M. Kläui^{2,3}, A. Brataas⁴ and R. Lebrun¹

1. *Unite Mixte de Physique CNRS/Thales, Palaiseau, France*; 2. *Johannes Gutenberg Universität Mainz, Mainz, Germany*; 3. *Johannes Gutenberg University Mainz Graduate School of Excellence Materials Science in Mainz, Mainz, Germany*; 4. *Center for Quantum Spintronics, Department of Physics, Norwegian Technical and Natural Sciences University, Trondheim, Norway*

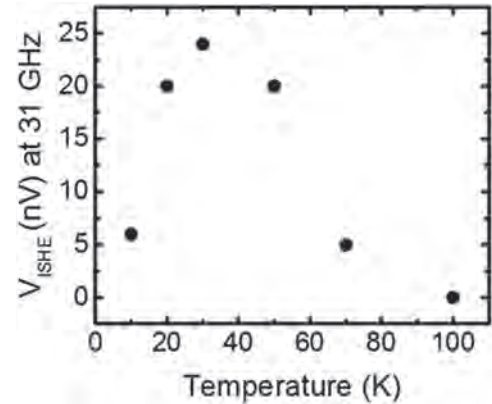
Contemporary spintronics, utilizing the electronic spin for information processing and microelectronics, is mostly based on ferromagnetic device architectures. In view of long term perspectives to enable enhanced data processing speeds and downscaling for on-chip information processing, spintronics with antiferromagnets is a promising avenue [1]. Antiferromagnets exhibit the key advantage over ferromagnets that their resonance frequency is enhanced by the exchange coupling of the sublattices, and thus generally in the terahertz regime. In compensated antiferromagnets, the absence of a net moment however strongly impedes simple access to their ultrafast dynamics, especially in thin films, and the development of ultra-fast antiferromagnet-based devices [2]. Experimental access to the spin dynamics can be facilitated by spin-to charge conversion mechanisms such as the spin pumping effect [3,4] or by probing the light-matter interaction of the spin system via a coupling to cavity resonator photons [5]. The spin pumping effect generates alternating (AC) and continuous (DC) spin currents in an adjacent conductor which can be electrically detected, for instance, by the inverse spin hall effect (ISHE) [6]. On the other hand, light-matter interaction is also at the heart of cavity spintronics which describes the generation and manipulation of cavity-magnon polaritons (CMP) for a general understanding of these interactions and applications for information processing and spintronics. The CMP is the associated quasiparticle to the hybridization of cavity resonator photons and collective spin excitations, i.e. magnon modes and the hallmark for a coherent information transfer in the strong coupling regime [5]. Such coherent information transfer is key for the implementation of microwave-to-optics transducers or quantum-based information processing schemes such as quantum memories [7]. Probing the spin dynamics electrically by spin-to-charge mechanisms or via the light-matter interaction of a strongly coupled photon-magnon system allows to study the physics of spin dynamics from different perspectives as it is at the crossroads of spintronics, magnonics and photonics. In this work, we access the spin dynamics of a collinear (easy axis) antiferromagnetic system by using a bulk chromium oxide (Cr₂O₃) sample as a model system. We both investigate the hybridization between the spin precession in the low frequency left-handed mode with cavity resonator photons and its temperature dependence via recording the corresponding ISHE voltages. We measure a CMP in Cr₂O₃ at 150 K and we observe several, small couplings to resonator modes below the spin flop field at 6 T. For instance, for a resonator mode ~39.6 GHz, we find a coupling strength of approximately 50 MHz. For the spin pumping experiment, we find a non-monotonous temperature dependence of the ISHE voltage signal with a peak at 30 K of the low frequency left-handed mode. The opposite signs of the ISHE voltages between the left-handed mode of Cr₂O₃ and the right-handed mode of ferrimagnetic YIG confirm the mode polarity. We compare our findings to the work of J.Li et al., who studied the temperature dependence of the high frequency right-handed mode of Cr₂O₃ [8]. We find qualitatively the same temperature dependence towards higher signals with the signal vanishing above 100 K as the net spin current polarization decreases to higher temperatures [8]. Hence, we study the spin dynamics of our model system Cr₂O₃ for GHz frequencies based on electrical detection and light matter interaction. Notably, establishing antiferromagnets in cavity spintronics could bridge frequency regimes from the GHz to the optical range. Further, the demonstration of a coupling and, eventually, coherent information exchange is a promising way towards quantum information processing schemes with antiferromagnets [9].

[1] V. Baltz, A. Manchon, M. Tsoi et al., *Rev. Mod. Phys.* 90, 015005 (2018).
 [2] T. Kampfrath, A. Sell, G. Klatt et al., *Nat. Photonics* 5, 31 (2011). [3] Y. Tserkovnyak, A. Brataas, and G. E. W. Bauer, *Phys. Rev. B* 66, 224403

(2002). [4] M. V. Costache, M. Sladkov, S. M. Watts et al., *Phys. Rev. Lett.* 97, 216603 (2006). [5] M. Harder and C. M. Hu, *Solid State Physics*, 69, 47 - 121 (2018). [6] E. Saitoh, M. Ueda, H. Miyajima et al., *Appl. Phys. Lett.* 88, 182509 (2006). [7] D. Lachance-Quirion, Y. Tabuchi, A. Gloppe et al., *Appl. Phys. Expr.* 12, 070101 (2019). [8] J. Li, C. B. Wilson, R. Cheng et al., *Nature* 578, 7793 (2020).



Dispersion relation of the CMP for a bulk chromium oxide sample (Cr₂O₃) at 150 K with several couplings for higher frequencies across the spin flop field at ~6 T. Inset displays the gradient calculated from the amplitude spectrum in the main. It shows exemplarily a zoom on one clearly separated anticrossing at 39.6 GHz with a coupling strength of ~50 MHz.



Temperature dependence of the ISHE voltage from spin pumping with the same crystal up to 100 K.

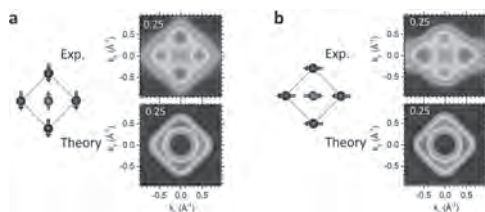
FH-13. Néel Vector Alignment Induced Symmetry Breaking in the Electronic Band Structure of the Antiferromagnet Mn_2Au .

M. Jourdan¹, S.V. Chernov¹, S. D'Souza², S. Bommanaboyena¹, S. Bodnar¹, K. Medjanik¹, S. Babenkov¹, O. Fedchenko¹, D. Vasilyev¹, S. Agustsson¹, C. Schlueter³, A. Gloskovskii³, Y. Matveyev³, V. Strocov⁴, Y. Skourski⁵, L. Smejkal¹, J. Sinova¹, J. Minar², M. Klau¹, G. Schoenense¹ and H. Elmers¹

1. Institute of Physics, Johannes Gutenberg Universitat Mainz, Mainz, Germany; 2. New Technologies-Research Centre, Zapadoceska univerzita v Plzni, Plzen, Czechia; 3. Deutsches Elektronen-Synchrotron, Hamburg, Germany; 4. Paul Scherrer Institut, Villigen, Switzerland; 5. Helmholtz-Zentrum Dresden-Rossendorf, Dresden, Germany

In the paramagnetic space group of Mn_2Au , the two Mn atoms are connected by inversion symmetry. However, in the antiferromagnetically (AFM) ordered state the inversion symmetry is broken. Our ab-initio calculated energy bands show the corresponding coupling of the energy bands to the Néel vector direction [Elm20], which is significant due to the strong spin-orbit interaction in Mn_2Au . Here, we focus on the experimental investigation of the Néel vector alignment induced anisotropies in the electronic band structure by angular resolved photoemission spectroscopy (ARPES). We investigate epitaxial $\text{Mn}_2\text{Au}(001)$ thin films [Jou15, Bom20], with photon energies in the vacuum-ultraviolet, soft, and hard X-ray range [Elm20]. Our samples consist in the as grown state of AFM domains with the Néel vector equally distributed parallel to both magnetic easy axes [110] and [1-10] of the tetragonal crystal structure. To enable the observation of Néel vector orientation induced symmetry breaking, we align the staggered magnetization by a 50 T magnetic field pulse via a spin-flop transition parallel to one of the two easy axis [Sap18]. Thus, in the ARPES experiments, we see the effect of averaging over AFM domains with antiparallel Néel vector, resulting in a 2-fold symmetry of the electronic states within the ab-plan of the tetragonal crystal structure. We observed a maximum asymmetry of $\approx 10\%$ probed by bulk-sensitive hard X-ray photoemission spectroscopy (probing depth ≈ 5 nm) at a binding energy of 0.25 eV (see Fig. 1), which is reduced to $\approx 5\%$, if probing with more surface sensitive soft X-rays (probing depth ≈ 1 nm). Additionally, probing uncapped samples even more surface sensitive with vacuum-ultraviolet light reveals a maximum spin-orbit interaction induced band splitting of ≈ 100 meV. These anisotropies can lead to large magnetoresistance, transport and topological effects [Elm20].

[Bom20] S. P. Bommanaboyena et al., J. Appl. Phys. 127, 243901 (2020). [Elm20] H.-J. Elmers et al., ACS Nano, 14, 17554 (2020). [Jou15] M. Jourdan et al., J. Phys. D: Appl. Phys. 48, 385001 (2015). [Sap18] A. A. Sapozhnik et al., Phys. Rev. B 97, 134429 (2018).



Experimental photoemission results (upper panels) for two epitaxial Mn_2Au sample halves with the staggered magnetization aligned vertically (a) and horizontally (b) as indicated on the real space unit cells. The intensities are represented as constant energy sections $I(E_B, k_x, k_y)$ at a binding energy of 0.25 eV. The photon energy is 5230 eV. The lower panels show corresponding calculations of the spectral function densities, averaging over two antiparallel directions of the Néel vector.

FH-14. Theoretical Study of Hybrid Vortex and Dynamical Phase Transitions in an Antiferromagnetic Nanostripe.

R. Tomasello¹ and S. Komineas^{2,1}

1. Institute of Applied and Computational Mathematics, Foundation for Research and Technology, Heraklion, Greece;

2. Department of Mathematics and Applied Mathematics, University of Crete, Heraklion, Greece

Antiferromagnets (AFMs) exhibit features, such as low magnetic susceptibility, robustness against external fields and lack of stray fields, that are favorable for the building blocks of spintronic devices [1]. This opens the way for a number of potential applications including storage with picosecond switching [2], THz oscillators [3], racetrack memory based on magnetic solitons such as domain walls (DWs) [4] or skyrmions [5]. AFM materials can be characterized by an easy-plane anisotropy which promotes the formation of vortices as well as spiral phases [6]. Vortices have been discussed theoretically in infinite films [7] and observed experimentally by imprinting techniques [8], but they have received less attention than other magnetic solitons. On the other hand, two spiral phases can be obtained statically in an easy-plane AFM with Dzyaloshinskii-Moriya interaction (DMI). For weak DMI constant, $\lambda < \lambda_{NF}$, the Néel state is the ground state. For $\lambda = \lambda_{NF}$, an intermediate phase is obtained in the form of a nonflat spiral. This spiral presents a continuous rotation of the Néel vector \mathbf{n} in the x - z plane, while its y -component oscillates around a nonzero value. At $\lambda > \lambda_F$, a flat spiral is obtained with \mathbf{n} fully rotating on the x - z plane. In this work, we theoretically study vortices in easy- plane AFMs with an interfacial DMI. We consider a stripe geometry, infinite long in the x -direction and confined in the y -direction, as this is the most suitable for applications involving shifting of magnetic information, while it will also give rise to interesting effects on the magnetic structure. We firstly calculate the magnetic ground state, which we find to be uniform (y -direction) and perpendicular to the boundaries. Then we numerically study the stabilization of a single vortex. We observe that this vortex is Néel close to its core and it gradually becomes Bloch as we go away from the core thus exhibiting a hybrid character. For this reason, we refer to it as *hybrid vortex*. The Néel chirality is a consequence of the interfacial DMI, while the Bloch character is due to the boundary conditions which force the Néel vector to be oriented primarily along the y -axis in the far field. The increase of λ leads an increase of the vortex core width and a faster rotation of the Néel vector towards the y -axis. We further analyze the hybrid vortex dynamics by propagating it along the x -direction at a velocity v . Figure 1(a) depicts that a propagating vortex is contracted along the x -direction, similarly to DWs [4] and it is elongated along the y -direction, similarly to skyrmions [5]. Figure 2(b) shows the width L_x of the propagating vortex in the x -axis as a function of velocity for various values of λ . We define the width of the vortex core as the distance between the positions where the z -component is 0.5. The width L_x , in the direction of propagation, closely follows the law of Lorentz-type contraction $L_x = 1/\sqrt{1 - v^2}$ (red solid line) despite that the model is not Lorentz invariant. For each λ , the vortex achieves a maximum velocity. Therefore, there is a minimum achievable vortex width which decreases with decreasing λ . When the velocity exceeds the maximum value, the hybrid vortex becomes unstable to periodic configurations, thus giving rise successively to a nonflat spiral at a critical velocity v_{NF} , a vortex chain and a flat spiral at a critical velocity v_F . We wish to stress that these are dynamical phase transitions, in contrast to the previously-mentioned static transitions. While the spiral phases are anticipated by a study of the 1D model [8], the vortex chain is a feature of the stripe geometry. In addition, no vortex lattice has been found in this system in an infinite film [8]. A theoretical explanation for the dynamical behavior is obtained and it leads to the general result that the velocity of localized excitations in chiral magnets cannot reach the spin wave velocity. Our results provide an understanding of the statics and dynamics of vortices in chiral AFMs and could be useful for the design of antiferromagnetic devices based on magnetic solitons. This work was supported by the project “ThunderSKY,” funded by the Hellenic Foundation for Research and Innovation (HFRI) and the General Secretariat for Research and Technology (GSRT), under grant agreement No. 871.

[1] V. Baltz et al. Rev. Mod. Phys. 90, 015005 (2018). [2] V. Lopez-Dominguez et al. Phys. Rev. Appl. 11, 024019 (2019). [3] R. Khymyn et

al. Sci. Rep. 7, 43705 (2017); V. Puliafito et al., Phys. Rev. B 99, 024405 (2019). [4] T. Shiino et al., Phys. Rev. Lett. 117, 087203 (2016); L. Sánchez-Tejerina et al. Phys. Rev. B 101, 014433 (2020). [5] A. Salimath et al. Phys. Rev. B 101, 024429 (2020); S. Komineas et al., SciPost Phys. 8, 086 (2020). [6] J. Chovan et al. Phys. Rev. B 65, 064433 (2002). [7] S. Komineas and N. Papanicolaou, Nonlinearity 11, 265 (1998). [8] J. Wu et al., Nat. Phys. 7, 303 (2011); F. P. Chmiel et al., Nat. Mater. 17, 581 (2018).

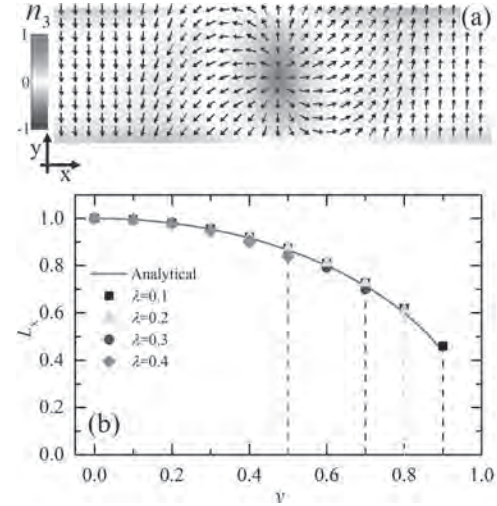


Figure 1: (a) Vector plot for $\lambda = 0.4$ for the propagating hybrid vortex with velocity $v = 0.60$. (b) Vortex core width L_x in the direction of propagation for a propagating hybrid vortex as a function of velocity v , for various values of λ , normalized to the width of a static vortex. The red solid line shows the expected result for Lorentz-type contraction. The dashed lines mark the maximum obtained velocities for the respective λ values.

[1] V. Baltz et al. Rev. Mod. Phys. 90, 015005 (2018). [2] V. Lopez-Dominguez et al. Phys. Rev. Appl. 11, 024019 (2019). [3] R. Khymyn et

Session FP
MAGNETIZATION DYNAMICS, DAMPING AND ULTRAFAST SWITCHING
(Poster Session)

Vijaysankar Kalappattil, Chair
Colorado State University, Fort Collins, CO, United States

FP-01. Independent Relationship Between Ultrafast Demagnetization and Anisotropic Gilbert Damping in Single Crystal $\text{Co}_{50}\text{Fe}_{50}$ Films.

H. Xia¹, Y. Wu¹ and H.B. Zhao²

1. Department of physics, Fudan University, Shanghai, China;

2. Department of Optical Science and Engineering, Fudan University, Shanghai, China

A giant anisotropic Gilbert damping of single crystal $\text{Co}_{50}\text{Fe}_{50}$ films grown on $\text{MgO}(100)$ substrate has been reported and was attributed to the anisotropic spin-orbit coupling (SOC) [1]. However, the anisotropy of Gilbert damping was measured only up to 30 GHz, which still leaves a puzzle whether the two-magnon scattering can contribute to the observed damping anisotropy. We performed a time resolved magneto-optical Kerr effect (TR-MOKE) measurement which can determine the damping constant up to 55 GHz, thus the contribution on the Gilbert damping measurement from the two-magnon scattering is suppressed. Our TR-MOKE measurement shows that the damping constant for M along [100] is about 330% of that for M along [110] (Fig. 1(b)), which further demonstrates that the anisotropic Gilbert damping is an intrinsic property of the $\text{Co}_{50}\text{Fe}_{50}$ films. As a contrast, the anisotropy of the Gilbert damping is very weak in the single crystal $\text{Fe}/\text{MgO}(100)$ film. The correlation between the fs-laser induced ultrafast demagnetization and Gilbert damping is one important issue in understanding the ultrafast spin dynamics. In the past researches[2-5], in order to study how the ultrafast demagnetization depends on the Gilbert damping, the alloy systems with different compositions were introduced to vary the Gilbert damping constant, but the other effects related to the composition variation may also influenced the demagnetization process. Here, the magnetization-orientation dependent Gilbert damping in CoFe alloy provides one clean system to investigate the correlation between Gilbert damping and ultrafast demagnetization in one same sample. Our results in Fig. 1(c) show that the demagnetization is independent of the magnetization orientation, indicating the absent correlation between Gilbert damping and ultrafast demagnetization, in contrast with the previous studies [2-5]. These incomprehensible experimental results will promote the theoretical development of the ultrafast dynamics.

[1] Y. Li, F. L. Zeng and S. S. L. Zhang, Phys. Rev. Lett. Vol.122, p.117203 (2019). [2] Y. Ren, Y. L. Zuo and M. S. Si, IEEE Trans. Magn. Vol.49, p.3159 (2013). [3] W. Zhang, W. He and X. Q. Zhang, Phys. Rev. B Vol.96, p.220415 (2017). [4] W. Zhang, Q. Liu and Z. Yuan, Phys. Rev. B Vol.100, p.104412 (2019). [5] H.S. Song, K.D. Lee, and J.W. Sohn, Appl. Phys. Lett. Vol.103, p.022406 (2013).

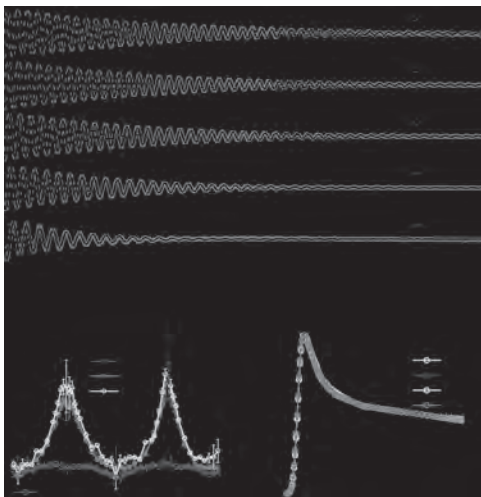


Fig.1 Gilbert damping and ultrafast demagnetization measured by TR-MOKE. (a) The normalized MOKE signals after background subtraction. (b) Gilbert damping varies with the magnetization angle. (c) The real ultrafast demagnetization curves when is along different crystalline.

FP-02. Magnetic Nanowires as a Source of Irradiation of THz Frequency.

I. Doludenko¹, D. Zagorsky¹, S. Chigarev² and E. Vilkov²

1. *Institute for Crystallography and Photonics, Russian Academy of Science, Moscow, Russian Federation*; 2. *Kotelnikov Institute of Radioengineering and Electronics of Russian Academy of Sciences, Moscow, Russian Federation*

Among nanomaterials, metal nanowires (NWs), consisting of alternating layers of various compositions (layered NWs), are of particular interest. Such structures can be obtained by the method of matrix synthesis - filling of nanosized pores in a special matrix. Layered NWs can have various applications, for example, as optically active surfaces (SERS). Another practically important property is giant magnetoresistance (GMR). According to preliminary estimates, NWs consisting of alternating layers of various magnetic metals can also be used to generate electromagnetic radiation. It is known that when current passes through the magnetic layer, its spin polarization occurs. When this current flows through subsequent layers, a change in the energy state of the electrons is possible. Relaxation of this state can lead to the generation of electromagnetic radiation, in particular, terahertz frequency. In this work, NWs arrays consists of several (three) layers (for example- Ni/Co/Ni) were grown from aqueous solutions of corresponding metal salts, using "two-bath" electrochemical approach. A track membrane with a pore diameter of 100 nm was used as a matrix. Particular attention was paid to the method of bringing contacts to the resulting array of layered NWs. When passing a current through such arrays, a signal with a frequency of 15-25 THz was detected. The measurements were carried out on a Golay cell and a Bruker spectrometer. It was found that with the standard method of making the contacts (a thin flat layer over the entire surface), the generated signal is not stable. Local burnout of a thin conductive layer occurs. To solve this problem, a method was proposed for forming contacts in the form of discontinuous periodic stripes. This method also made it possible to change the total effective electrical resistance of the array. An example of the obtained sample with contact strips is shown in Fig. 1. An SEM image of an array of layered NW is also shown. Fig. 1. SEM image of the sample surface with separate strips-current leads (left); SEM image of an array of layered NW between two contact layers (right). Figure 2 shows the generation signal and its dependence on time (for the NWs array and the GLOBAR (heat source)). Fig. 2. Left- Signal intensity versus time: 1- NWs array, 2- heat source-GLOBAR; On the right, the figure shows the nature of the angular distribution of the signal intensity. Comparison of the dependence of the signal intensity on time for the NWs array and for the heat source shows a sharp increase of the signal in the first case. This proves the nonthermal nature of the signal that arises when current flows through an array of NWs with magnetic transitions. The paper also provides a theoretical assessment of the possibility of using such an NWs array to solve the inverse problem, namely, to obtain a THz radiation detector.

FP-03. Spin-Torque Oscillation Modes of a Composite Synthetic Antiferromagnetic Free Layer in Dual Magnetic Tunnel Junctions.

X. Chao¹, Y. Zhang¹ and J. Wang¹

1. University of Minnesota, Minneapolis, MN, United States

Spin-torque oscillators (STOs) have been extensively studied due to their potential applications in hardware neural networks [1]. For future practical STO devices, multiple magnetic tunnel junctions in series are demanded. Because it will involve a complicated stack structure, there are very limited experimental attempts so far. In this work, the spin-torque oscillation modes of a composite synthetic antiferromagnetic free layer in dual magnetic tunnel junctions with MgO barriers are studied experimentally by analyzing its field- and current-dependent power spectra. Two oscillation modes are observed under different magnetic fields and bias currents due to the unique layer structure as follows: seed layer/PtMn/Co₇₀Fe₃₀/Ru/Co₆₀Fe₂₀B₂₀/MgO/Co₂₀Fe₆₀B₂₀/Ru/Co₂₀Fe₆₀B₂₀/MgO/Co₆₀Fe₂₀B₂₀/Ru/Co₇₀Fe₃₀/PtMn/capping layer. With increasing field, the first mode shows a frequency reduction at low magnetic fields followed by an increasing frequency at high magnetic fields, while the second mode reveals a frequency increase at both low and high magnetic fields (Fig. 1(b)). The current-dependent power spectra of these two modes are also different. With increasing current, the frequency of the first mode drops at low magnetic fields (Fig. 2(a)) and rises at high magnetic fields (Fig. 2(c)), while the other decreases at low and high magnetic fields. These two modes could be tentatively understood by considering the coupling, the bias asymmetry of the spin torque, and the different thicknesses of Co₂₀Fe₆₀B₂₀ in the composite synthetic antiferromagnetic free layer.

[1] M. Romera, P. Talatchian, S. Tsunegi *et al.*, *Nature*, Vol. 563, p. 230, (2018).

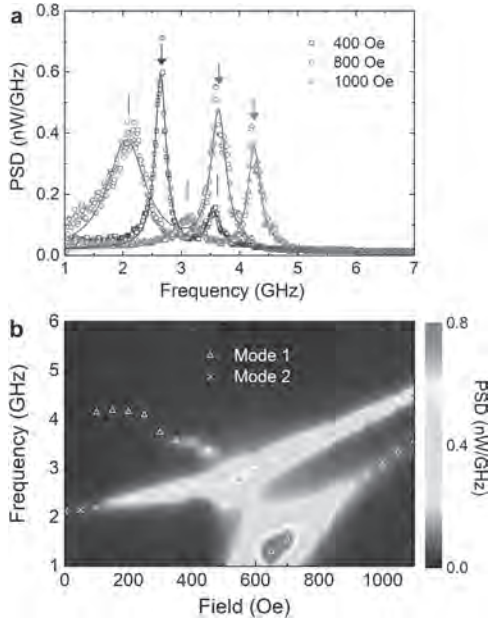


Fig. 1 (a) The power spectral density of the free layer measured at the current of 0.3 mA and the bias fields of 400, 800, and 1000 Oe. The hollow signs are experimental results. The solid curves are Lorentzian fittings. (b) The power spectral density of the free layer as a function of magnetic field from 0 to 1100 Oe. The triangles and the crosses correspond to the frequencies of the two modes.

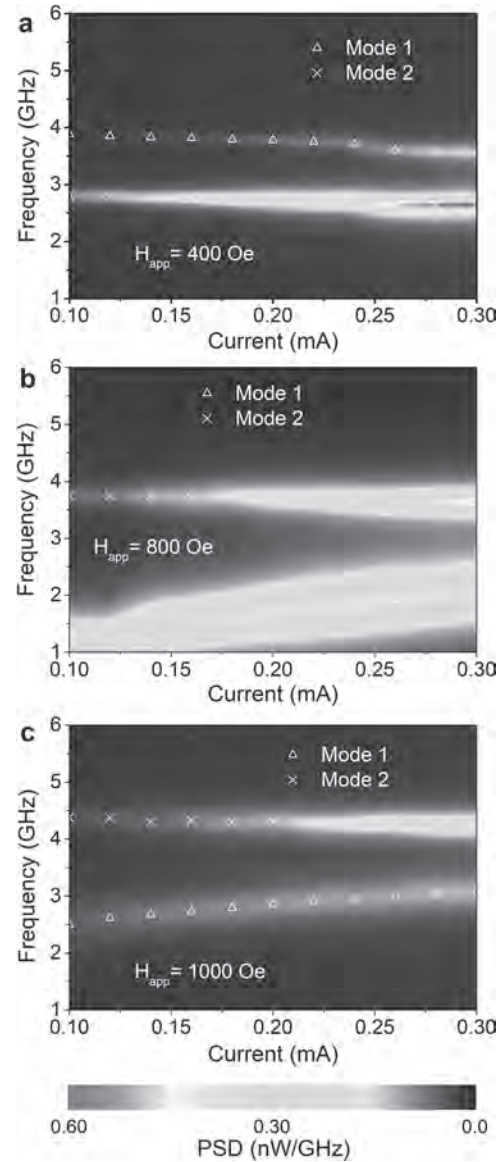


Fig. 2 The current-dependent power spectral density of the two modes measured at the magnetic fields of (a) 400 Oe, (b) 800 Oe, and (c) 1000 Oe. The triangles are the frequencies of the first mode, and the crosses are the frequencies of the second mode.

FP-04. Chirped Photonic Crystals With GdFeCo for Layer-Selective Magnetization Control.

O. Borovkova¹, D. Ignatyeva^{1,2}, A. Kalish^{1,2} and V.I. Belotelov^{1,2}

1. *M. V. Lomonosov Physics Faculty, Moscow State University, Moscow, Russian Federation*; 2. *Russian Quantum Center, Moscow, Russian Federation*

Up-to-date technologies require modern information devices to process large amounts of data at high rates. Methods of the ultrafast magnetism are very promising in this respect since they allow controlling the magnetization of a magnetic material by the femtosecond laser pulses at a picosecond time scales. Ferrimagnetic alloy of gadolinium-iron-cobalt (GdFeCo) is one of the most promising materials for further development of the information storage devices, since it allows to perform a single-shot all-optical magnetization switching during a few picoseconds in the area of pulse action on the GdFeCo film. A mechanism of all-optical switching originates from the ultrafast spin dynamics of the exchange-coupled Gd and FeCo sublattices which are thrown out of balance due to the light-induced thermal heating of the spin sublattices. If the delivered energy exceeds the threshold, the magnetizations of the two sublattices are reversed at the picosecond timescales due to the difference of the relaxation times for these sublattices. Thus, ultrafast all-optical magnetization switching depends on the amount of energy delivered by the optical pulse and is characterized by a threshold femtosecond pulse intensity required for the magnetization switching. Nowadays many efforts are put to study how to control the process of all-optical switching via tailoring the properties of the femtosecond pulse and via the additional patterning of the magnetic structure. In this work we propose a design of photonic nanostructure where the parameters of the dielectric layers determine the spatial light distribution and the resonances of the absorption in the GdFeCo layers. We propose to use the magnetophotonic crystal (MPC) structures, that were shown to perform tunable localization of light at the resonant frequencies enabling the enhancement of the optomagnetic interaction in a magnetic material. The proposed magnetophotonic crystal with thin smooth or patterned layers of GdFeCo ferrimagnetic alloy provides the local magnetization control and targeted remagnetization of the single layers of the multilayer structure. By the frequency tuning of the input femtosecond laser pulses one can select the magnetic layer of GdFeCo in which the energy of the laser pulse is mostly concentrated and exceeds the magnetization reversal threshold, while in others it is 1.5-2 times lower. In other words, the proposed MPC allows to 'turn on' one certain magnetic layer of the structure and leave all other layers 'turned off'. As GdFeCo material is perspective for data storage applications allowing a significant increase of the writing speed, the proposed structure can be implemented for the purposes of the record density increase in such a device. Usually, the magnetic bit cells are arranged in the plane of a single magnetic layer. Using the proposed MPC, bit cells can be arranged in several magnetic layers separated by the submicron dielectric spacers and addressed individually. This configuration is quite simple for fabrication and doesn't require a precise positioning of the laser pulse. Besides that, another configuration of the chirped MPC structure with the patterned GdFeCo layers is addressed. For the higher density of the information recording the magnetic layer can be nanostructured to separate bit cells in the lateral direction. The patterning of the magnetic layer can be implemented along both axes in the plane of the structure layers. In our work we limited ourselves by one-dimensional patterning for the sake of the modelling simplicity. It should be stressed that the patterned chirped MPC allows combining two approaches instantaneously, the bit cells arranged in plane and the bit cells arranged in different layers. It opens up the ample opportunities for the significant increase of the information recording density. We also provide the method of an all-optical single-wavelength information reading in this multilayered structure. Thus, the designed MPC with GdFeCo layers could serve as a basis of 3D information storage devices. To sum up, a design of the MPC structure providing a selective magnetization switching in the different magnetic layers at different frequencies is proposed. The MPC contains the thin layers of GdFeCo as magnetic counterparts. By illuminating the MPC by femtosecond laser pulses at the certain frequencies we create the conditions for the highest concentration of the electromagnetic field in the necessary layer of the structure while in the other GdFeCo layers the intensity is at least 1.5 times smaller. Thus, one can

achieve selective all-optical magnetization reversal in a single layer of the multilayered stack determined by the laser frequency without any impact on the other layers. The magnetic layers of the MPC are separated from each other by the non-magnetic layers, and can be patterned, so, they can serve as the unit cells for information storage. We also provide a mechanism of single-wavelength reading of the information stored in such a multilayered stack. The approach was demonstrated for the 4 layers of SiO₂, TiO₂ and GdFeCo for the sake of simplicity, however it could be extended to the larger number of layers by the proper design of the chirped photonic crystal. The work was supported by Russian Science Foundation, grant No. 19-72-10139.

A. Kirilyuk, A.V. Kimel, T. Rasing. *Rev. Mod. Phys.* Vol. 82, p. 2731 (2010). A.V. Kimel, A. Kirilyuk, P.A. Usachev, et al. *Nature* Vol. 435, p. 655 (2005). J.Y. Bigot, M. Vomir, E. Beaurepaire. *Nature Physics* Vol. 5, p. 515 (2009). A.I. Chernov, M.A. Kozhaev, D.O. Ignatyeva, et al. *Nano Letters* Vol. 20, p. 5259 (2020). U. Atxitia, T.A. Ostler. *Appl. Phys. Lett.* Vol. 113, p. 062402 (2018). M. Inoue, et al. *J. Phys. D: Appl. Phys.* Vol. 39, p. R151 (2006).

FP-05. Magnetization-Orientation Dependent Terahertz Emission From the Fe/Pt (110) Single-Crystal Film.

C. Liu¹, W. Lu², Z. Wei³, H. Xia^{1,4}, H.B. Zhao⁴, Y. Wu¹, Z. Yuan² and J. Qi³

1. Department of Physics, Fudan University, Shanghai, China; 2. The Center for Advanced Quantum Studies and Department of Physics, Beijing Normal University, Beijing, China; 3. State Key Laboratory of Electronic Thin Films and Integrated Devices, University of Electronic Science and Technology of China, Chengdu, China; 4. Shanghai Ultra-precision Optical Manufacturing Engineering Research Center, and Key Laboratory of Micro and Nano Photonic Structures (Ministry of Education), Department of Optical Science and Engineering, Fudan University, Shanghai, China

The ferromagnetic (FM)/heavy metal (HM) heterostructure has been demonstrated to be an efficient and broadband Terahertz (THz) source, which has attracted much attentions in the ultrafast spintronics field [1,2]. The THz polarization from the spintronics THz emitter is easy to be manipulated by rotating the magnetic field, but in all the previous studies, the THz intensity was expected to be independent of the magnetization orientation. However, the spin-orbit coupling in the film system with lower in-plane symmetry may depend on the crystalline orientation, which can induce the magnetization (M) orientation dependent THz emission. In this contribution, we systematically investigated THz emission from the Fe(211)/Pt(110) crystalline bilayer grown on MgO(110), and demonstrate for the first time that the intensity of the emitted THz wave depends on the M-orientation. The measured THz field is 11% stronger for M//Pt than that for M//Pt[001] (Fig.1). Experimental measurements and first-principle calculations combined with the superdiffusive spin transport model indicate that both spin current generation and the following spin current injecting into the Pt layer are independent of the M-orientation, but the spin-to-charge conversion efficiency in the Pt layer and the following THz wave radiation can be strongly influenced by the M-orientation due to the anisotropic spin Hall effect and longitudinal conductance in Fe/Pt bilayer, which give rise to the anisotropic THz emission. The theoretical calculation clarifies that the emergent anisotropic THz emission is mainly attributed to the lattice distortion in the film induced by the epitaxial strain. The calculated anisotropy of THz wave well agrees with the experimental results. Our studies provide a new route to modify the THz emission utilizing the intrinsic crystalline structure degree of freedom.

¹T. Kampfrath, M. Battiato, and P. Maldonado, Nature Nanotechnology 8, 256 (2013). ²T. Seifert, S. Jaiswal, and U. Martens, Nature Photonics 10, 483 (2016).

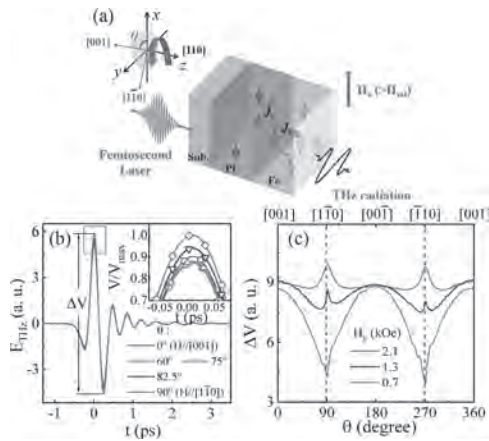


Fig. 1. (a). Schematic drawing of THz emission geometry from Fe/Pt heterostructure. (b). Typical time-domain THz signals with different sample angles. (c). Peak-to-valley amplitude ΔV as a function of sample angle with the external magnetic field of 0.7, 1.3 and 2.1 kOe, respectively.

FP-06. Cavity-FMR Studies of LPE Epitaxial YIG Films.

H. Hurdequint¹, G. de Loubens¹, J. Ben Youssef², N. Beaulieu² and N. Vukadinovic³

1. SPEC, CEA-Saclay, Université Paris-Saclay, Gif-sur-Yvette 91191, France; 2. LabSTICC, CNRS, Université de Bretagne Occidentale, 29238 Brest, France; 3. Dassault Aviation, 92552 Saint-Cloud, France

The recent development of techniques (various methods of deposition have been used), enabling the elaboration of very thin epitaxial YIG films has brought a renewed interest for exploiting the resonance properties of such films. When the thin YIG film is coated with a heavy metal (such as Pt), a non local extra damping of the microwave magnetization is observed [associated to the (YIG/Pt) interfacial coupling]. Different techniques [1,2] of microwave absorption measurements have been used to characterize the resonance properties of such films. We highlight here basic results we have obtained in our *cavity-FMR studies* at X-band (9.725 GHz) on the 5 films whose characteristics are given below. These films correspond to (111) oriented YIG layers deposited by LPE [3] on GGG substrates. We have: F1 [YIG58], F2 [YIG44], F3 [YIG15], with thicknesses in nm, corresponding to the virgin YIG layers. Films F4 [YIG15/Pt3] and F5 [YIG58/Pt3] refer, respectively, to films F3 and F4 which have been coated by a Pt (3nm) over layer deposited by evaporation. We performed a detailed study of the angular variation of the resonance spectrum (angle θ_H of the dc field with the film normal) and we exploit the main characteristics of the observed resonance lines. A basic observation in these YIG films is that the resonance spectrum corresponds indeed to the superposition of individual resonances (arising from different parts of the film, weakly coupled by the dipolar interactions). We summarize below the results obtained for the main characteristics (Hres, linewidth ΔH) of the *principal resonance*. *Angular variation of Hres* : results and analysis In perpendicular (PER) geometry, the resonance condition reads [4, 5]: $(\omega/\gamma) = H_{PER} - H_{eff}$ (Eq.1), where $H_{eff} = 4\pi M - H_A - 2/3 H_{an}$, with $H_A = 2K/M$ a uniaxial perpendicular anisotropy (spin-orbit origin) and $H_{an} = 2K_1/M$ the YIG cubic anisotropy. Taking the measured value for $4\pi M$ and the bulk value for H_{an} (- 87 Oe), we get for the 3 virgin YIG films: F1: $(- H_A) = 37$ Oe (easy plane); F2: $H_A = 48$ Oe (easy axis); F3: $H_A = 130$ Oe (easy axis). One observes thus that the uniaxial perpendicular anisotropy changes sign versus the YIG thickness. *Linewidth ΔH of the principal resonance* : angular variation and analysis The linewidth ΔH of the principal resonance is the sum of two different contributions: $\Delta H = \Delta + \Delta H_{inh}$. The first one (Δ) corresponds to the relaxation rate of the magnetization vector (proportional to the *intrinsic damping* parameter α). The second one is an inhomogeneous width corresponding to a distribution ΔH_{res} . The basic observation for the virgin YIG layers is that ΔH displays a *sharp minimum* at a specific field orientation θ_H where it reduces to the *intrinsic width* Δ . This behavior is well accounted for theoretically [ref 4], where the inhomogeneous contribution induced by a distribution $P(H_i)$ has been discussed (where $H_i = 4\pi M - H_A$). Thus for F2 we find $\Delta = 0.8$ Oe [leading to $\alpha = 2 \times 10^{-4}$]. Intrinsic width for the films F4 and F5 coated by a Pt(3nm) overlayer : Δ may be decomposed as: $\Delta = \Delta_0 + \Delta_S$, where the second term corresponds to the increment of the damping induced by the (YIG/Pt) interfacial coupling. We find $\Delta_S(F5) = 1.57$ Oe and $\Delta_S(F4) = 5.25$ Oe varying approximately as $(1/t)$ with the YIG thickness t . *Characteristics of the resonance spectra* : remarkable phenomena observed A) For the virgin thick (58nm)YIG layer (filmF1), in a broad range of field orientations, the FMR spectrum displays a *fine structure*: on superposition of the principal resonance, a series of regularly spaced narrow (0.8 Oe) resonance lines are observed. We ascribe them to standing elastic waves, excited in the YIG layer through the *magneto-elastic coupling* [6], which develop across the whole sample [500 μ m thick GGG substrate +YIG layer]. Taking into account the transverse sound velocity in such a medium, the estimated frequency splitting (3.5 MHz) between two successive waves is well consistent with the observed field splitting (~ 1.2 Oe) between the individual resonance lines. B) For the two thin (15 nm) YIG layers (films F3 and F4), besides the principal resonance, two standing spin waves (we label SW1 and SW2) are observed in the resonance spectrum. These spin waves are collective modes associated to the *non-uniform exchange* in the YIG films. Such standing spin waves are here observed since the YIG layer thickness is comparable to the YIG exchange length (18nm). The resolved spin wave spectrum is observed continuously

from the PAR to the PER geometry, except for a specific orientation (31 deg for F2) where it collapses to the *uniform mode*.

[1] Y. Sun et al, Phys.Rev.Lett.111, 106601 (2013). [2] C. Du et al, Phys. Rev. Applied. 1, 044004 (2014). [3] N. Beaulieu et al, IEEE Magn. Letter.9, 3706005 (2018). [4] H. Hurdequint, J. Magn.Magn.Mater. 242-245, 521 (2002). [5] H. Makino and Y. Hidaka, Mat.Res.Bull. Vol16, pp 957-966 (1981). [6] A. Gurevich and G. Melkov, Magnetization oscillations and Waves, CRC Press (1996).

FP-07. Optically Induced Spin Wave Excitation in one-Dimensional Iron-Garnet Nanostripes.

D. Krichevsky^{1,4}, D. Ignatyeva^{3,4}, D. Karki⁵, P. Zimnyakova³, M. Levy⁵ and V.I. Belotelov^{3,2}

1. Moscow Institute for Physics and Technology State University, Dolgoprudnyj, Russian Federation; 2. Russian Quantum Center, Moscow, Russian Federation; 3. Moscow State University M. V. Lomonosova Physics Faculty, Moscow, Russian Federation; 4. V. I. Vernadskogo Crimean State University, Simferopol', Ukraine; 5. Michigan Technological University, Houghton, MI, United States

Spin control in magnetic materials is a fundamental basis of the most current energy efficient devices, such as magnetic memory, Boolean and quantum logical elements [1]. In the last few decades, femtosecond laser systems opened up opportunities for ultrafast spin control in various magnetic materials such as ferromagnetic metals, iron garnets, and even antiferromagnetic dielectric oxides [2]. Special attention is paid to nonthermal spin wave control via inverse magneto-optical effects, such as inverse Faraday, inverse transverse magneto-optical Kerr, or inverse Voigt effects. Moreover, recent advances in fabrication techniques provide capabilities for light localization at the nanoscale regions together with optical modes excitation in the nanostructures [3,4]. The aforementioned advances of the nanostructures increase the efficiency of light-matter interaction and bring new horizons to all-optical spin control in magnetic materials. Here we report on spin wave amplitude enhancement in all-dielectric iron garnet nanostructure based on one-dimensional iron garnet grating. The grating consists of solitary strips of 400 nm width on gadolinium gallium garnet substrate placed with subwavelength period (600 nm). The height of the nanostructure was 225 nm. For spin wave launch pump-probe technique is utilized in Voigt configuration [2]. For pumping a circularly polarized pulse of ~200 fs duration at 600 nm and normal incidence was used. Probe pulse of 200 fs duration at 820 nm (transparency region of the structure) was linearly polarized. The probe angle of incidence was ~30 deg. The external magnetic field was equal to 100 mT. The nanostructure support propagation of waveguiding modes that are well defined in transmittance spectra at ~600 nm (Figure 1). The electromagnetic field localization and enhancement inside the nanostraps due to waveguiding mode excitation result in spin wave amplitude enhancement (up to 2 times). Moreover, as can be noted from figure 2 there is a shift in spin wave frequency between pure film and nanostructure. The effect can be associated with the existence of additional boundaries between magnetic strips and external media. This work was financially supported by the Russian Ministry of Education and Science, Megagrant project N 075-15-2019-1934

1. A. V. Chumak et. al. Nature Physics, Vol. 11(6), p. 453, (2015) 2. A. Kirilyuk et. al. Reviews of Modern Physics, Vol. 82(3), p. 2731, (2010). 3. A. I. Chernov et. al. Nano Letters, Vol. 20(7), p. 5259, (2020). 4. A. L. Chekhov et. al. Nano letters, Vol. 18(5), p. 2970, (2018).

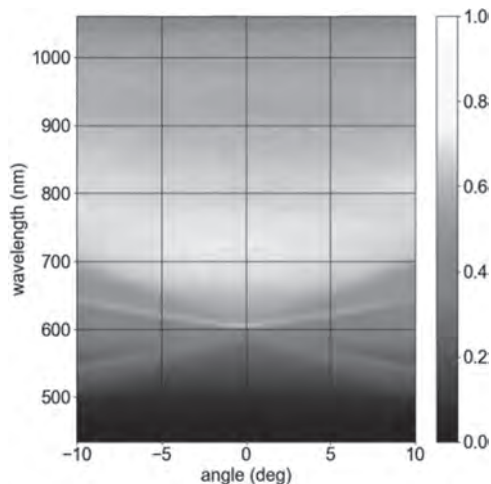


Figure 1 Transmission of the nanostructure as a function of incident angle and wavelength

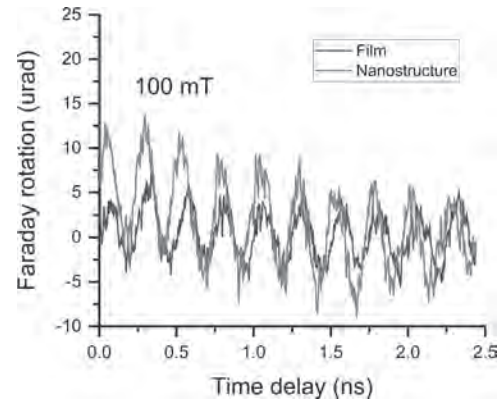


Figure 2 Spin wave precession for a pristine garnet film of 225 nm thickness (black) and nanostructure (red)

FP-08. Measurement of Dynamic Properties in Ta/NiFe Microstrip Using Frequency Sweep Technique.

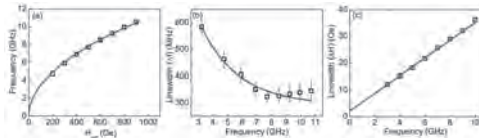
D. Tiwari^{1,2}

1. SPINtronic et Technologie des Composants, Grenoble, France;

2. Indian Institute of Technology Delhi, New Delhi, India

The ability of spin polarized current and pure spin current to manipulate the magnetization of the ferromagnet has opened huge opportunities in metallic spintronics. Prime interest to study the interconversion from charge current to spin current has led to the search of new material with large spin orbit coupling such as Pt, Ta, W, and Pd, also known as heavy metals. Thus, the separation of the components of spin polarized electrons (i.e. up spin and down spin electrons) when a charge current is applied to heavy metal via spin orbit coupling is called spin Hall effect (SHE). The conversion efficiency from the applied charge current density J_c to spin current density J_s is given by spin Hall angle, $\theta_{SH} = J_s/J_c$. Numerous techniques have been developed to measure SHE. Electrically driven ferromagnetic resonance (FMR) commonly known as spin-torque FMR, can excite magnetization dynamics in metallic ferromagnets and allows tuning of magnetic damping. In this work, we have investigated Ta/NiFe thin films using spin-torque FMR frequency sweep technique and the obtained value of α agrees with FMR field sweep method. The low value of α and ΔH_0 relate to the good quality of thin films and patterning of the device into microstrip does not increase the damping in the system. We showed the variation in Gilbert damping parameter with I_{dc} which indicates the presence of current induced damping like torque in the system. The calculated value of transparency is high and can be enhanced further by matching the electronic properties of the NM and FM materials. The low value of α and high transparency in Ta/NiFe bilayers can be superior candidates for future spintronic devices

[1] T. Kimura, Y. Otani, T. Sato, S. Takahashi, and S. Maekawa, "Room-temperature reversible spin Hall effect," Physical Review Letters, vol. 98, p. 156601, 2007. [2] L. Liu, T. Moriyama, D. C. Ralph, and R. A. Buhrman, "Spin-torque ferromagnetic resonance induced by the spin hall effect," Phys. Rev. Lett., vol. 106, p. 036601, 2011 [3] S.S. Kalarickal, P. Krivosik, M. Wu, C.E. Patton, L. Michael, P. Kabos, T.J. Silva, and J.P. Nibarger, "Ferromagnetic resonance linewidth in metallic thin films: Comparison of measurement methods," Journal of Applied Physics, vol. 99, p. 093909, 2006



(a) FMR resonance frequency as a function of the external field H_{ext} . The solid line is a fit using Kittel formula. (b) Frequency (f) vs. linewidth (Δf) variation. (c) Plot of linewidth with frequency measured using field sweep FMR technique.

FP-09. Ferromagnetic Resonance Linewidth Broadening Induced by a Tunable Inhomogeneity Effect.

Y. Xing¹, Z. Yan¹, J. Wei¹, C. Wan¹, G. Yu¹ and X. Han¹

1. Chinese Academy of Sciences Institute of Physics, Beijing, China

A phenomenon of $Y_3Fe_5O_{12}$ (YIG)-ferromagnetic-resonance (FMR) linewidth broadening in magnetically coupled YIG-Co films is reported. The broadened linewidth cannot be attributed to previous effects [1-3] which only depend on the crystalline quality of YIG. Through micromagnetic simulation, the origin of this broadened linewidth was found to be a new type of inhomogeneity effect induced by the inhomogeneous dipolar field of Co layer. Furthermore, it shows that the extent of the linewidth broadening depends on the magnetization state of Co. The broadening is remarkable when the Co domains are random. The influence of Co on YIG-FMR linewidth still exists when the spacer between YIG and Co is 315 nm, indicating it is a long-range effect due to the dipolar origin. Our experiment results reveal that the influence of the dipolar interaction on FMR is remarkable in magnetically coupled heterostructures. Researchers should pay more attention to the dipolar interaction while investigating these systems.

[1] L. Chen and C. H. Back* et al., *Nature Physics* 14, 490–494 (2018). [2] Kh. Zakeri* and J. Lindner et al., *Phys. Rev. B* 76, 104416 (2007). [3] Hiroto Sakimura and Kazuya Ando* et al. *Phys. Rev. Research* 1, 013013 (2019).

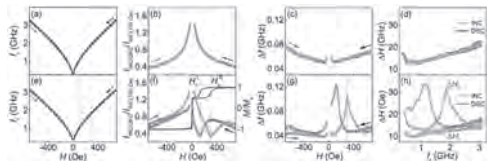


Figure 1 YIG-FMR properties of Sample 1 and Sample 2. The structures of Sample 1 and 2 are YIG (100 nm) and YIG(100)/MgO(15)/Co(3)/IrMn(10)/Ru(2 nm). (a)-(c) and (e)-(g) are H dependence of resonance frequency f_r , intensity I and full width at half maximum (FWHM) Δf of Sample 1 and 2, respectively. (d) and (h) are f_r dependence of ΔH converted from (c) and (g). Black (red) curves represent the sweep direction is decreasing (increasing) in (a)-(h). The left (right) black dashed lines in (e)-(g) represent the field where $M_{co}=0$ as H decreases (increases). In (b) and (f), all the intensity I has been normalized to $I_{INC(100\text{ Oe})}$. In (f), the blue curves represent M/M_s - H loop of Sample 2.

FP-10. Tunable Microwave Properties of Zigzag Nanowires.

K. Begari¹ and A. Haldar¹

¹. Physics Department, Indian Institute of Technology Hyderabad, Hyderabad, India

I. Introduction Tunable magnetization dynamic properties having frequencies in the GHz range have great potential in a variety of reprogrammable microwave technologies [1]. Magnetic nanostructures and their arrays are found to be promising for microwave devices that operate in sub-20 GHz frequency regime [2]. Microwave properties can be tuned by controlling the magnetization orientations and magnetic interactions in nanostructures or multilayers. In general, tunable microwave properties are driven by an external bias field which hinders device integration. Therefore, a bias-field-free operation is of great interest. Previously, we have shown such operations based on rhomboid-shaped nanomagnet [3-5]. Here, we have proposed a new zigzag magnetic nanowire for reprogrammable magnetic and microwave properties in the absence of any external bias field using micromagnetic simulations [6]. II. Initialization of remanent magnetic states: We have designed zigzag nanowire based on number of crests (Z_n), example Z_5 having the five crests as shown in fig. 1(a). Figure 1(a) indicates schematic of the zigzag nanowire have the dimensions are width (w) = 100 nm, arm length (L) = 300 nm, thickness (t) = 20 nm, slanted edge angle (ϕ) = 45 degree and zigzag angle (θ) = 90 degree. We have obtained two different remanent magnetic states in zigzag nanowire by using a simple field initialization process. When the field initialized from 2000 to 0 Oe along y, we have observed tail to tail or head to head magnetic configuration in a remanent magnetic state and it is referred as Y-state. On the other hand, such kind of domain walls are not exist when the field initialized along x and which is known as X-state. The magnetic configuration of X- and Y-states as shown in figure 1(b). Shape anisotropy of the zigzag nanowire is a major role to get two distinct remanent magnetic states. These two distinct remanent states having two different magnetic dynamic responses. III. Ferromagnetic resonance: The dynamics responses of the remanent magnetic states obtained by applying the *Sinc* pulse along the x axis. The *sinc* pulse is denoted by H_S and it is defined as, where H_{S0} = amplitude (50 Oe), f_c = cut-off frequency which is less than the Nyquist frequency (f_N), i.e. ($f_c < f_N$) and = simulation time. The time dependent magnetization recorded up to 4 ns in step of 10 ps. The Fourier transforms are performed on time dependent magnetization to obtain the ferromagnetic resonance (FMR) spectra in frequency domain. Figure 1(c) shows the FMR spectra for X and Y-states of the zigzag magnetic nanowire (Z_5) at $H_{ext} = 0$. The frequency responses are found in 3-15 GHz range. The FMR modes observed at 7.8 and 9.6 GHz for the X-state. On the other hand, the frequency absorption appeared at 4.5, 6.4 and 8.4 GHz for the Y-state. IV. 2D spatial profiles: The location of the FMR modes are identify based on detail investigation of the 2D spatial profiles of X- and Y -states as shown in figure 2 (a & b). We have observed 7.8 GHz mode at near the bend and 9.6 GHz mode at the central of the zigzag nanowire for the X-state. We have labelled the modes are e-type (7.8 GHz) at near bend and c_0 type (9.6 GHz) at the center. On the other hand, two e modes (e_1 and e_2) and c_0 mode observed for the Y-state. We have investigated the frequency shift of these two distinct modes between the X-state and Y-state. The frequency shift found $\Delta f = 1.2$ GHz for the c-type mode and $\Delta f = 1.4$ GHz for the e type mode (e_1). The large frequency shift can be clearly distinguishing the distinct states. The frequency responses are in GHz range and have good potential to use in microwave device operation. Also, Zigzag magnetic nanowire applicable for flexible microwave devices.

1. A. V. Chumak, V. I. Vasyuchka, A. A. Serga, and B. Hillebrands, Nat. Phys. 11, 453 (2015). 2. M. Krawczyk and D. Grundler, J. Phys.: Condens. Matter 26, 123202 (2014). 3. A. Haldar and A. O. Adeyeye, ACS Nano 10, 1690 (2016). 4. A. Haldar and A. O. Adeyeye, Appl. Phys. Lett. 108, 022405 (2016). 5. K. Begari and A. Haldar, J. Phys. D: Appl. Phys. 51, 275004 (2018). 6. M. J. Donahue and D. G. Porter, Interagency Report No. NISTIR 6376, National Institute of Standards and Technology, Gaithersburg, MD, 1999.

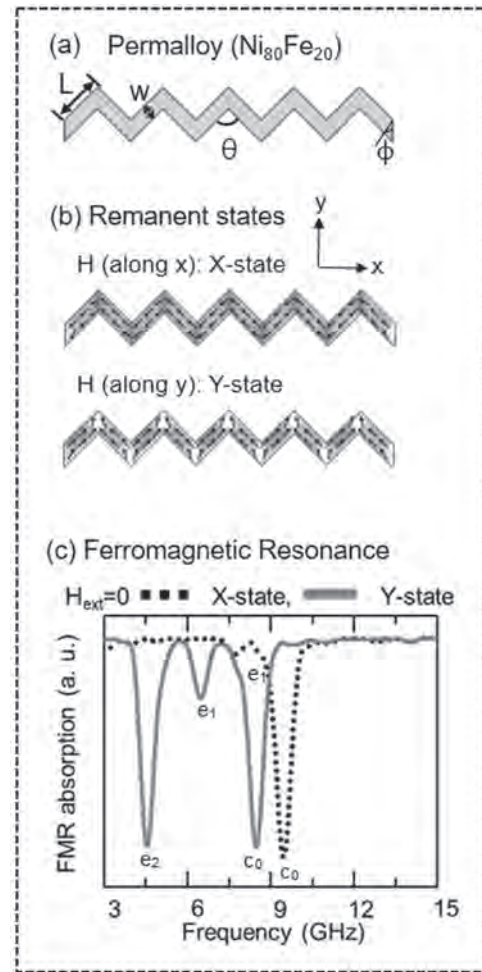


Figure 1 : (a) Schematic diagram of zigzag nanowire (b) remanent states and (c) ferromagnetic resonance spectra at $H_{ext} = 0$.

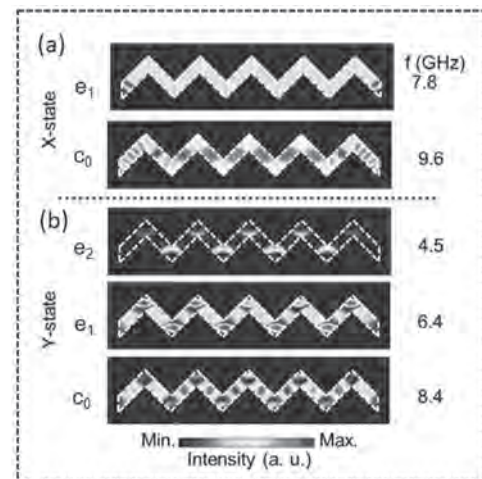


Figure 2: 2D spatial profiles for the (a) X-State and (b) Y-State.

FP-11. Study on Comparison Between in-Plane and out-of-Plane Dynamic Magnetic Properties for Fe-M Binary Alloy Thin Films.

Y. Endo¹, T. Nguyen² and T. Miyazaki³

1. Graduate School of Engineering, Tohoku University, Sendai, Japan;

2. Center for Science and Innovation in Spintronics, Tohoku University,

Sendai, Japan; 3. Technical Division, School of Engineering, Tohoku University, Sendai, Japan

I. INTRODUCTION Ferromagnetic resonance (FMR) measurement technique is well known to be one of the important methods to evaluate the dynamic magnetic properties such as the effective saturation magnetization, damping constant, and so on, of magnetic thin film materials [1]. Recently, a broadband FMR (B-FMR) measurement technique with a coplanar waveguide (CPW) and a vector network analyzer (VNA) has been widely used to investigate them [2]-[4]. The reason for this is that the films are excited in a very wide range of RF frequency changing external magnetic field intensity and its high sensitivity allows for downsizing of the samples to the micro-scale, which provide detailed information on very thin films subjected to practical use under a variety of circumstances. In general, for FMR measurement technique, it is pointed out that the non-uniform magnetization precession mode occurs by the applied direction of external magnetic field. However, for the B-FMR measurement technique, this problem still remains an open question. Herein, we chose Fe-M binary alloys as magnetic thin film materials, investigated the in-plane and out-of-plane dynamic magnetic properties of Fe-M binary alloy thin films using the B-FMR measurement technique, and further discussed the difference between these properties in their films by the applied direction of external magnetic field in detail. II. EXPERIMENTAL PROCEDURES 10-nm thick Fe-M (M=Ni, Si, Co, and Ga) binary alloy thin films were fabricated by DC magnetron sputtering onto glass substrates. These film compositions were determined by energy dispersive x-ray spectroscopy (EDX), while the crystallographic structure of these films was performed using the high-angle XRD analysis and TEM observation, indicating that all film structures are polycrystalline and bcc phase. As for the dynamic magnetic properties of these films, the in-plane and out-of-plane effective saturation magnetization ($4\pi M_{s,eff, //}$, $4\pi M_{s,eff, \perp}$) and the in-plane and out-of-plane effective damping constants ($\alpha_{//}$, α_{\perp}) were evaluated by the B-FMR measurement technique. The external magnetic field was applied parallel to the CPW plane and swept between -0.01–0.3 T at various resonance frequencies. On the other hand, $4\pi M_{s,eff, \perp}$ and α_{\perp} of the films were determined in an external magnetic field applied perpendicular to the CPW plane swept between 1.4–3.3 T at various resonance frequencies. These measurements were performed at room temperature. The other magnetic properties of these films were already described in [4], [5] in detail. III. RESULTS AND DISCUSSION $4\pi M_{s,eff, //}$, $4\pi M_{s,eff, \perp}$, $\alpha_{//}$, and α_{\perp} of 10-nm thick Fe-M (M=Ni, Si, Co, and Ga) thin films are summarized in Table 1 and 2. As be noticed in Table 1, $4\pi M_{s,eff, //}$ values of these films became higher or lower than those of saturation magnetization ($4\pi M_s$) evaluated by VSM, which might be attributed to the appearance of negative or positive surface anisotropy. On the other hand, $4\pi M_{s,eff, \perp}$ of these films almost agreed with those of $4\pi M_s$ evaluated by VSM, meaning that the easy magnetization direction of every film is in the film plane. As for the effective damping constant (Table 2), in case of M=Ni, $\alpha_{//}$ value was almost equal to that of α_{\perp} , indicating that the intrinsic damping can be obtained regardless of the external magnetic field direction. On the other hand, in case of M=Si, Co, and Ga, these damping depend on the external field direction, and these $\alpha_{//}$ values were higher than those of α_{\perp} . The reason for these differences might be that the non-uniform magnetization precession mode appears by magnetic inhomogeneities such as the two-magnon scattering, the anisotropy dispersion, and so on when the external magnetic field is applied in the film plane. On the basis of these results, it is suggested that the external magnetic field direction must be seriously selected by the kind of magnetic materials as their effective damping constants are evaluated by the B-FMR measurement technique. ACKNOWLEDGEMENT The authors thank Prof. Satoshi Okamoto, and Associate Prof. Nobuaki Kikuchi at Tohoku University for performing the photo lithography and measuring XRD diffraction patterns. This work was supported in part by KAKENHI (JP17H03226) from MEXT, Japan. This work was supported in part by CSIS, CSRN, and CIES, Tohoku University. This work was also supported in part by the ASRC in Japan.

[1] J. H. E. Griffiths, Nature 148, 670 (1946)., [2] G. Council et al., J. Appl. Phys. 95, 5646 (2004). [3] M. Toda et al., J. Magn. Soc. Jpn. 31, 435 (2007). [4] Y. Endo et al., J. Appl. Phys. 109, 07D336 (2011). [5] Y. Kawabe et al., Trans. Magn. Soc. Jpn. 3, 34 (2019).

Materials (Fe-M)	Fe-Ni (Fe ₂₂ Ni ₇₈) (M=Ni)	Fe-Si (Fe ₂₇ Si ₇₃) (M=Si)	Fe-Co (Fe ₅₀ Co ₅₀) (M=Co)	Fe-Ga (Fe ₅₀ Ga ₅₀) (M=Ga)
$4\pi M_{s,eff, //}$ in case of external magnetic field // film plane	12.64 kG	13.40 kG	17.36 kG	21.18 kG
$4\pi M_{s, \perp}$ in case of external magnetic field \perp film plane	10.04 kG	15.04 kG	23.24 kG	13.93 kG
$4\pi M_s$ by VSM	10.38 kG	15.05 kG	19.86 kG	14.61 kG

Table 1. Comparison between the in-plane and out-of-plane effective saturation magnetization ($4\pi M_{s,eff, //}$, $4\pi M_{s,eff, \perp}$) for Fe-M binary alloy thin films.

Materials (Fe-M)	Fe-Ni (Fe ₂₂ Ni ₇₈) (M=Ni)	Fe-Si (Fe ₂₇ Si ₇₃) (M=Si)	Fe-Co (Fe ₅₀ Co ₅₀) (M=Co)	Fe-Ga (Fe ₅₀ Ga ₅₀) (M=Ga)
In-plane damping ($\alpha_{//}$) in case of external magnetic field // film plane	0.00626	0.01082	0.03471	0.02600
Out-of-plane damping (α_{\perp}) in case of external magnetic field \perp film plane	0.00641	0.00545	0.00722	0.00741

Table 2. Comparison between the in-plane and out-of-plane effective damping constants ($\alpha_{//}$ and α_{\perp}) for Fe-M binary alloy thin films.

FP-12. Theory of Spin-Torque Ferrimagnetic Resonance.

S. Kim¹, D. Lee², S. Oh³, H. Koo^{1,4} and K. Lee⁵

1. KU-KIST Graduate School of Converging Science and Technology, Korea University, Seongbuk-gu, The Republic of Korea; 2. Department of Materials Science & Engineering, Korea University, Seongbuk-gu, The Republic of Korea; 3. Department of Nano-Semiconductor and Engineering, Korea University, Seongbuk-gu, The Republic of Korea; 4. Center for Spintronics, Korea Institute of Science and Technology, Seongbuk-gu, The Republic of Korea; 5. Department of Physics, Korea Advanced Institute of Science and Technology, Daejeon, The Republic of Korea

Compensated ferrimagnets show both ferromagnetic and antiferromagnetic dynamics, i.e., fast magnetization dynamics [1-5] and vanishing Skyrmion Hall effect [6] with finite magnetization. As the dynamics of ferrimagnets can be driven with current-induced spin torques [7, 8], it is important to find a way of quantifying spin torques in ferrimagnetic materials. One of the main methods to quantify the spin torque in ferromagnets is the spin torque ferromagnetic resonance (ST-FMR) technique [9, 10]. For ferromagnets, the damping-like (DL) and field-like (FL) torque components are separately determined through ST-FMR line-shape analysis. However, it is unclear if this line-shape analysis is valid even for ferrimagnets. In this work, we report a theory of spin torque ferrimagnetic resonance (ST-FiMR) in ferrimagnet/heavy metal bilayer structures. We investigated ST-FiMR for two cases. (i) Identical DL and FL torque efficiencies of two sublattices in a ferrimagnet, and (ii) Different DL and FL torque efficiencies of two sublattices, considering different spin polarization between rare-earth and transition metal elements [11]. For both cases, the mixing voltage originating from the DL torque is linearly proportional to the effective net spin density of the system, resulting in sign reversal at the angular momentum compensation condition. In addition, at the compensation condition, the line-shape can be anti-symmetric, in contrast to entirely symmetric signals for ferromagnets. Our result suggests that the line-shape analysis established for ferromagnets is invalid for ferrimagnets especially near the compensation condition so that the proposed theory must be implemented to analyze the spin torque ferrimagnetic resonance.

[1] K.-J. Kim et al., Nat. Mater. 16, 1187 (2017). [2] S.-H. Oh et al., Phys. Rev. B 96, 100407(R) (2017). [3] L. Caretta et al., Nat. Nanotechnol. 13, 1154 (2018). [4] S. A. Siddiqui et al., Phys. Rev. Lett. 121, 057701 (2018). [5] S.-H. Oh and K.-J. Lee, J. Magn. 23, 196 (2018). [6] Y. Hirata et al., Nat. Nanotechnol. 14, 232 (2019). [7] J. Yu et al., Nat. Mater. 18, 29 (2019). [8] T. Okuno et al., Nat. Electron. 2, 389 (2019). [9] A. A. Tulapurkar et al., Nature 438, 339 (2005). [10] J. C. Sankey et al., Phys. Rev. Lett. 96, 227601 (2006). [11] C. Kaiser et al., Phys. Rev. Lett. 95, 047202 (2005).

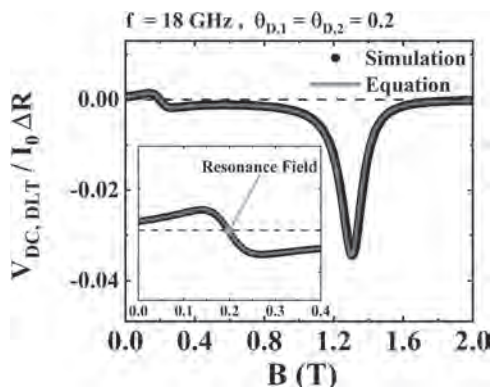


Fig. 1. Spin torque ferrimagnetic resonance signal only with damping-like torque (DLT).

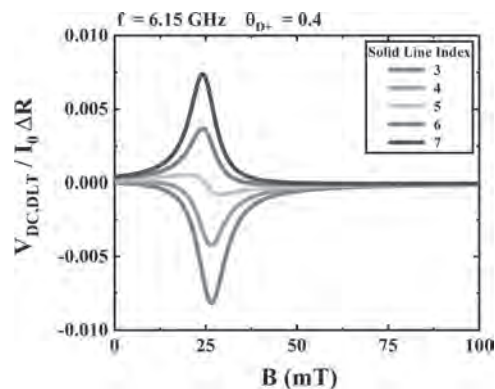


Fig. 2. Sign reversal of spin torque ferrimagnetic resonance near angular momentum compensation condition.

FP-13. Spin Transfer Torque Oscillation in Orthogonal Magnetization Disks.

L. Chuhan¹, H. Naoki¹, H. Shu¹, Y. Kurokawa¹ and H. Yuasa¹
 1. Kyushu University, Fukuoka, Japan

The orthogonal magnetization multilayer has the in-plane and perpendicular anisotropy magnetic layers, which has been proposed for the fast magnetization switching by spin transfer torque [1]. On the other hand, it is difficult to obtain the stable spin transfer torque oscillation (STO) in the orthogonal magnetization since the switching occurs too easily. In this study, we introduced the 90 degree magnetic coupling to obtain the STO in the orthogonal configuration. In typical, the 90 degree coupling between two magnetic layers is described by the bilinear coefficient A_{12} and biquadratic coefficient B_{12} , and obtained under the conditions of $A_{12} < |B_{12}|$ and $B_{12} < 0$ by using suitable layer as a spacer. [2] In our model, the multilayer consists of three layers with thickness of 2 nm; a top layer with the in-plane magnetic anisotropy, a nonmagnetic spacer, and a bottom layer with the perpendicular magnetic anisotropy sequentially. Figure 1 shows the calculated magnetization map in the top layer (a) and the side views of the magnetization configuration of the top and bottom layers (b) when the top layer is CoFe with M_s of 1450 emu/cc, H_k of 35 Oe, and a damping constant of 0.01, and the bottom layer is Fe/Pt with M_s of 800 emu/cc and H_k of 15000 Oe. The top and bottom layer has the vortex magnetization and the perpendicular magnetization, respectively, when a current density is zero. By increasing the current density, the magnetization of the top layer oscillates with frequency 35 GHz while the bottom layer maintains the perpendicular magnetization. This stable STO is due to the 90 degree coupling. Figure 2 shows the STO frequency as a function of the current density for various conditions. First, let us focus on the relation between the STO frequency and magnitude of 90 degree coupling. The STO frequency of the CoFe top layer was increased by decreasing B_{12} from -0.3 to -0.6 , that is, increasing the 90 degree coupling. Next, we compared the STO performances by changing the top layer material from CoFe to NiFe and Ni with small M_s and small damping constant. As a result, the frequency achieved 45 GHz and the necessary current density was reduced to 6×10^7 A/cm². In summary, it was found that the STO was stably realized in the orthogonal configuration by introducing 90 degree magnetic coupling, and the STO frequency was increased by enhancement of 90 degree coupling. Additionally, our calculation indicates that it is possible to increase the frequency and necessary current density by material selection.

[1] H. Liu et al., Appl. Phys. Lett. 97, 242510 (2010). [2] G. Nagashima., et al, J. Appl. Phys. 126, 093901 (2019)

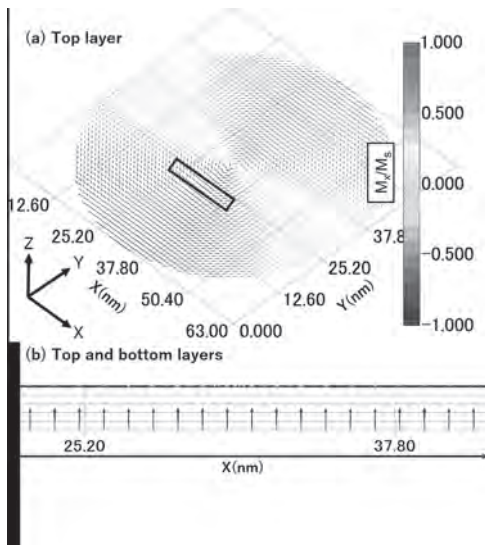


Fig. 1 (a) Magnetization configuration in the top layer. (b) Side views of magnetization configuration in the top and bottom layers. The shown magnetization corresponds to the enclosed area in (a).

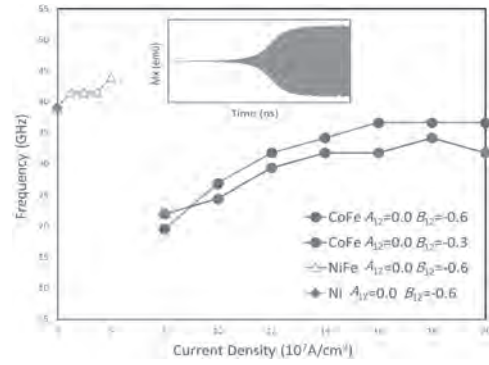


Fig. 2 STO frequency as a function of the current density for various conditions; $B_{12}=-0.3$ and $B_{12}=-0.6$ for CoFe top layer, and $B_{12}=-0.6$ for CoFe, NiFe, and Ni top layers.

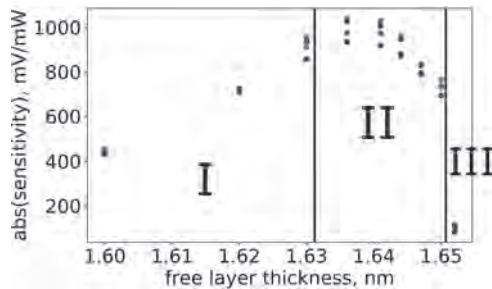
FP-14. Sensitivity Optimization of Spin-Torque Diode With Perpendicular Anisotropy Through Free Layer Thickness Tuning.

A. Buzdakov^{1,2}, P. Skirdkov^{1,3} and K. Zvezdin^{1,3}

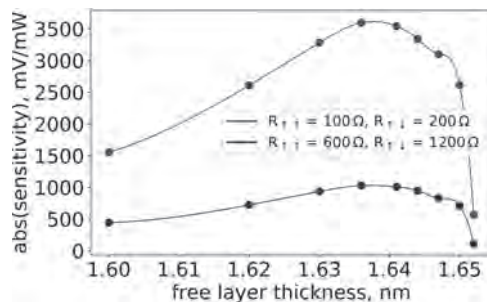
1. New Spintronic Technologies, Russian Quantum Center, Moscow, Russian Federation; 2. Moscow Institute of Physics and Technology, Engineering Center, Dolgoprudnyj, Russian Federation;

3. A. M. Prohorova Institute of General Physics, RAN, Moscow, Russian Federation

Spin-torque diode is one of the emerging novel technology in spintronics. Based on the spin-torque diode effect, it could be used for effective RF detection and harvesting, as its sensitivity significantly overcomes the sensitivity of commonly used Schottky diodes. Usage of perpendicular magnetic anisotropy (PMA) in the free layer appears to be one of the most promising designs for spin-torque diodes. We report an efficient design rule to develop spin-torque diodes with PMA with record microwave sensitivity. We study the impact of the free layer magnetization tilt on the sensitivity of the spin-torque diode. This magnetization tilt can be effectively engineered by choosing the ratio of the shape and surface anisotropy and interlayer magnetostatic interactions. With the help of micromagnetic modeling over a broad range of input powers and free layer thicknesses, we demonstrate a significant role of non-linearity and inhomogeneous magnetization dynamics in achieving high sensitivity levels (see Fig.1). Our modeling for typical state-of-the-art parameters of magnetic tunneling junction demonstrates a possibility to reach a record-breaking unbiased microwave sensitivity of 3500 mV/mW (see Fig.2), which is far beyond the parameters of commercial Schottky diodes. We also analyze the impact of direct current bias on sensitivity both in case of current is lower than the critical one and in case of current is higher than the critical one and injection locking occurs. These results can be very important for the development of efficient spintronic ambient energy harvesters. Financial support by the Russian Science Foundation (Project No. 19-12-00432) is gratefully acknowledged.



Unbiased spin-torque diode sensitivity as a function of free layer thickness derived from micromagnetic modeling. Color refer to input power: red – 2 nW, blue – 20 nW, green – 100 nW, brown – 1000 nW.



Unbiased diode sensitivity dependences on the thickness for $R_p = 600\Omega$, $R_{ap} = 1200\Omega$ (red) and $R_p = 100\Omega$, $R_{ap} = 200\Omega$ (blue) in case of 20 nW incident power.

THURSDAY, 29 APRIL 2021

LIVE Q&A SESSIONS, 3:00 PM EUROPE CEST

Session GA
SPINTRONICS FOR PROBABILISTIC COMPUTING
Olga Kazakova, Chair
National Physical Laboratory, Teddington, United Kingdom

INVITED PAPERS

GA-01. Tuneable Stochastic Domain-Wall Trajectories in a Magnetic Galton Board.

*D. Sanz Hernandez*¹, *M. Massouras*², *N. Reyren*¹, *N. Rougemaille*³,
V. Schánilec^{3,4}, *K. Bouzouane*¹, *M. Hehn*², *B. Canals*³, *D. Querlioz*⁵,
*J. Grollier*¹, *F. Montaigne*² and *D. Lacour*²

1. Unite Mixte de Physique CNRS/Thales, Palaiseau, France;

2. Institut Jean Lamour, Nancy, France; 3. Institut NEEL, Grenoble, France; 4. CEITEC, Brno, Czechia; 5. Centre de Nanosciences et de Nanotechnologies, Orsay, France

We present our recent realisation of a nanomagnetic Galton board [1], a nanoscale recreation of the paradigmatic experiment in which balls travel through an array of pegs, designed by Sir Francis Galton to demonstrate the emergence of order from randomness. In our nanoscale experiment, balls are substituted by magnetic domain-walls, a honeycomb nanowire lattice recreates the peg array, and an externally applied magnetic field takes the role of gravity (Figure 1). Using high-resolution immersion Kerr microscopy, we image domain wall propagation through this nanoscale system a very large number of times (Figure 2), and demonstrate that complex domain wall dynamics can be employed to generate high-quality stochasticity suitable for computing applications. By varying the direction of the externally applied field, we were also able to demonstrate the continuous tuneability of the stochastic domain-wall decision process, a critical step to the realisation of functional computing systems. To conclude, we will discuss the technical advances that enabled this study, in which millions of domain-wall trajectories were imaged and analysed. These will be of great interest to those performing stochasticity studies in spintronics, as being able to acquire and deal with large datasets is an important experimental challenge in the field. The results demonstrated open promising paths in the design and development of spintronic devices in which the intrinsic stochasticity of domain-wall dynamics is exploited using new computing architectures.

[1] Sanz-Hernández, Dédalo, et al. “Tunable Stochasticity in an Artificial Spin Network”, DOI: 10.1002/adma.2020081

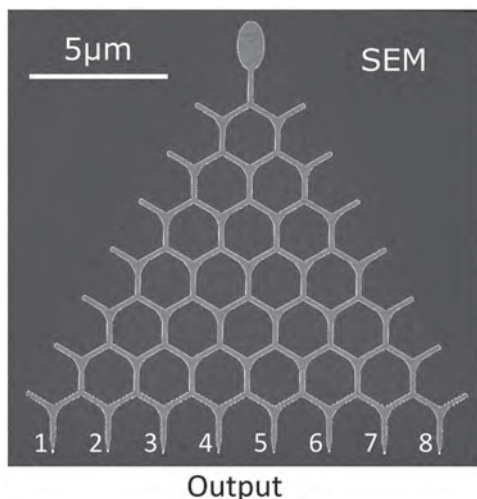


Figure 1. Nanoscale magnetic Galton board formed by an elliptical domain-wall injection pad (top) and a bifurcating nanowire network.

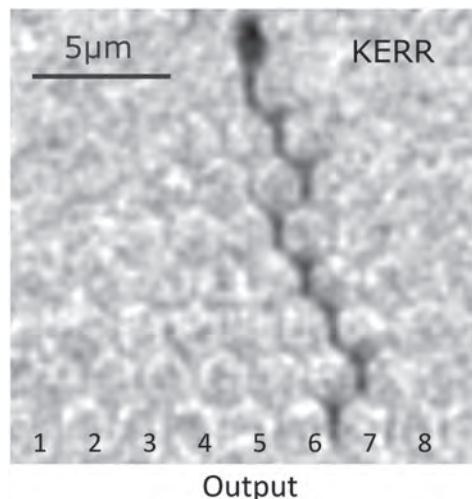


Figure 2. Oil-immersion longitudinal Kerr microscopy image of the board presented in Figure 1, after the injection of a domain-wall in the system. The trajectory followed by the wall is observed as a dark trace.

GA-02. From Stochasticity to Functionality: Harnessing Magnetic Domain Walls for Probabilistic and Neuromorphic Computing.

T. Hayward¹, I.T. Vidamour^{1,2}, M.O. Ellis², A. Welbourne¹, R. Dawidek¹, T.J. Broomhall¹, M. Chambard¹, M. Drouhin¹, A.M. Keogh¹, A. Mullen¹, S. Kyle¹, M. Al Mamoori¹, P. Fry³, N. Steinke⁴, J.F. Cooper⁵, F. Maccherozzi⁶, S. Dhési⁶, L. Aballe⁷, M. Foerster⁷, J. Prat⁷, E. Vasilaki² and D. Allwood¹

1. Department of Materials Science and Engineering, The University of Sheffield, Sheffield, United Kingdom; 2. Department of Computer Science, The University of Sheffield, Sheffield, United Kingdom; 3. Nanoscience and Technology Centre, The University of Sheffield, Sheffield, United Kingdom; 4. Institut Laue-Langevin, Grenoble, France; 5. ISIS Neutron and Muon Source, Rutherford Appleton Laboratory, Didcot, United Kingdom; 6. Diamond Light Source Ltd, Didcot, United Kingdom; 7. ALBA Synchrotron Light Facility, Barcelona, Spain

Domain walls (DWs) in magnetic nanowires are a topic of intense interest due to proposals to use them as data carriers in non-volatile logic and memory devices. However, despite their apparent technological potential such devices are challenging to realise, in part because DWs pinning and propagation is highly stochastic, making digital devices unreliable [1]. While materials engineering approaches can be used to suppress stochasticity [2], it is also interesting to consider whether alternative computer paradigms could prove more resistant to, or even benefit from, stochasticity. In this talk we will present three examples of how embracing DW stochasticity as a functional, rather than technologically inhibiting feature can facilitate novel computational devices. Figure 1(a) presents results that illustrate typical stochastic DW behaviours in a 400 nm wide $\text{Ni}_{80}\text{Fe}_{20}$ nanowire device, as characterised by focused magneto-optic Kerr effect (FMOKE) magnetometry. DWs were injected from the pad to a patterned defect in the nanowire's middle and the distributions of magnetic fields required to propagate them through the defect characterised. The depinning field histogram shows both fractional pinning probabilities and multimode depinning field distributions, both characteristic features of stochasticity induced by complex DW dynamics [3]. However, while individual reversals of such a device are highly stochastic, average properties are well-defined, and more importantly, highly tuneable. Figure 1(b) illustrates how applying modest magnetic fields orthogonal to a similar nanowire/defect combination allows DWs pinning probabilities to be tuned between 0 and 1. Thus, stochastic pinning can be used to create random bit-streams with tuneable average values. In our first example of the utility of these effects we use stochastic DW pinning to realise the stochastic computing paradigm in DW logic networks. In stochastic computing, floating point numbers are encoded in the average value of random binary bit-streams, and single conventional logic gates perform complex mathematical operations that would usually require extended logic networks to perform. For example, an AND gate performs a multiplication operation. Figure 2(a) presents the results of FMOKE magnetometry, illustrating how the output of a DW AND gate with stochastic input produces output bitstreams consistent with those expected. In our second example we use the stochastic pinning of DWs to facilitate two neuromorphic computing approaches: a feed-forward neural network and a Boltzman machine. In the feed-forward network, nanowires act as binary stochastic synapses, with the probability of DW propagation taking the role of a synaptic weight. Simulations of network behaviour allow us to demonstrate that such a device can perform machine learning tasks including written digit recognition. In the Boltzman machine, where stochasticity is used to sample a defined, or trained, probability distribution, the nanowires take the role of stochastic neurons. We apply this approach to an integer factorisation problem where network is defined so that the binary representation of the integer factors are the most probable states for the neurons. In our final example, we show how DWs driven by rotating magnetic fields within an interconnected nanoring array, can be used to perform reservoir computing [4]. We characterise a ring array's behaviour using a combination of MOKE, polarised neutron reflectivity and photoemission electron microscopy, and show how emergent behaviour arises from stochastic interactions between DWs at the array's junctions (Figure 2(b)). Using the magnitude of the rotating applied field as an input we then demonstrate how this allows the array to be used as a

reservoir and perform a range of time series analysis tasks including speech recognition and chaotic series prediction.

[1] T.J. Hayward and K.A. Omari, Beyond the quasi-particle: stochastic domain wall dynamics in soft ferromagnetic nanowires, *Journal of Physics D: Applied Physics* 50, 8, 084006 (2017). [2] T.J. Broomhall, A.W. Rushforth, M.C. Rosamond, E.H. Linfield, and T.J. Hayward, *Physical Review Applied* 13, 024039 (2020). [3] T.J. Hayward, *Scientific Reports* 5, 13279 (2015). [4] R. W. Dawidek, T. J. Hayward, I. T. Vidamour, T. J. Broomhall, M. Al Mamoori, A. Mullen, S. J. Kyle, P. W. Fry, N. J. Steinke, J. F. K. Cooper, F. Maccherozzi, S. S.Dhesi, L. Aballe, M. Foerster, J. Prat, E. Vasilaki, M. O. A. Ellis, D. A. Allwood, submitted to *Advanced Functional Materials* (2020).

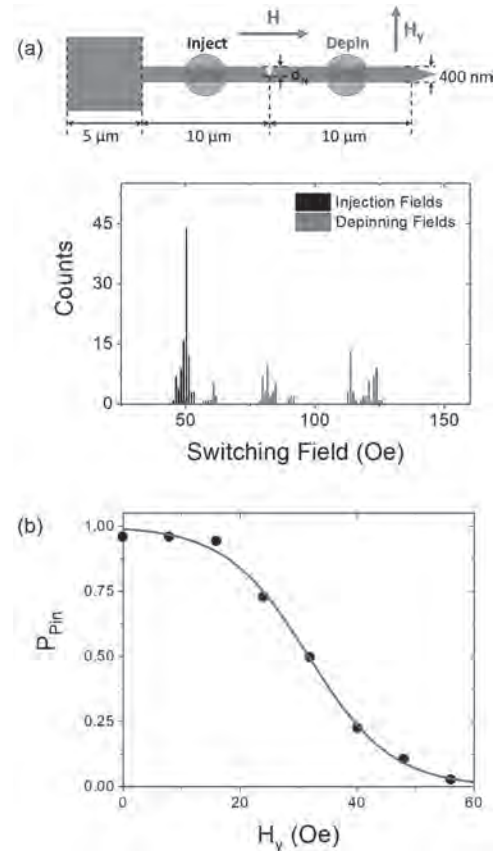


Figure 1: (a) Characterisation of stochastic DW pinning at a $d_N = 80$ nm notch in a 400 nm wide, 25 nm thick $\text{Ni}_{80}\text{Fe}_{20}$ nanowire. The experimental geometry is shown at the top of the figure with green circles representing where injection and depinning field histograms were measured. (b) Illustration of how the pinning probability of DWs in similar system were tuned by applying magnetic fields (H_y) orthogonal to the nanowire.

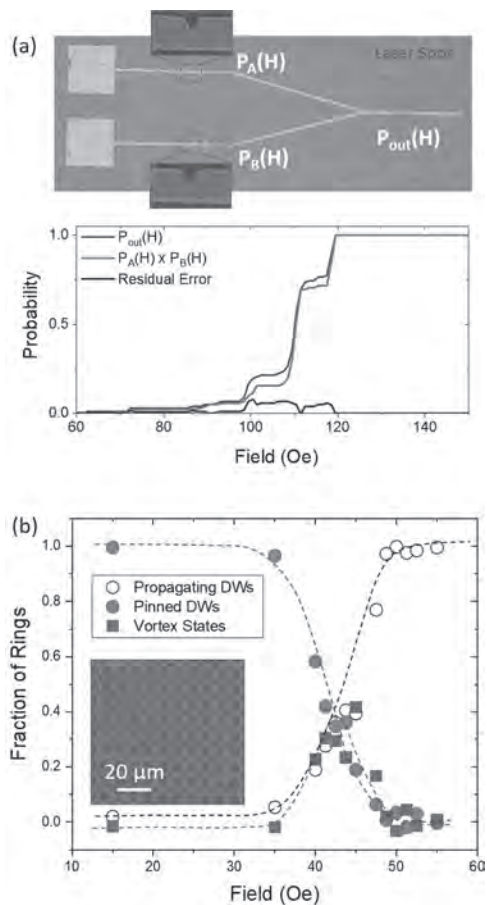


Figure 2: (a) Stochastic computing with a DW AND gate. An SEM of the measured device is shown at the top of the figure, with green circles indicating where FMOKE measurements were made to measure the probability of DWs passing through the input nanowires (P_A and P_B) and output nanowire (P_{out}). The plot shows $P_A \times P_B$ and P_{out} as a function of applied field; the close tracking of these curves shows that AND gate performed a multiplication operation on the input bit-streams. (b) Behaviour of an interconnected nanoring array as a function of rotating applied field amplitude. The number of rings with propagating DWs, pinned DWs and in vortex states are shown at each applied field value.

GA-03. Hidden Skyrmion Diffusion and Brownian Computing.

Y. Suzuki^{1,2}, S. Miki¹, E. Tamura¹, M. Goto^{1,2}, R. Ishikawa⁴, T. Nozaki³, Y. Tanaka¹ and H. Nomura^{1,2}

1. Graduate School of Engineering Science, Osaka University, Toyonaka, Japan; 2. Center for Spintronics Research Network, Osaka University, Toyonaka, Japan; 3. Research Center for Emerging Computing Technologies, AIST, National Institute of Advanced Industrial Science and Technology, Tsukuba, Japan; 4. Osaka University Joint research Laboratory for future technology, ULVAC, Toyonaka, Japan

Magnetic Skyrmion is a particle-like magnetic excitation in ferromagnetic material similar to the Dirac-monopole in the spin-ice systems. Since the magnetic Skyrmion is topologically protected [1], it can survive under thermal agitation and shows Brownian motion. The skyrmion system can be an ideal platform to design stochastic computer [2] and/or in Brownian computer [3], since magnetic Skyrmion is a special particle that may show Brownian motion in all-solid-state devices. Therefore, investigation of the Brownian motion of the magnetic Skyrmion is now the subject of scientific and technical interest. The dynamics of the Skyrmions in a two-dimensionally extended film at finite temperature is described by the Thiele equation [4]. According to the equation, the Skyrmion may pose a velocity perpendicular to the force's direction and tend to turn right or left depending on its chirality determined by the Skyrmion number. This gyro-motion reduces the (diagonal element of the) diffusion constant [5]. Naïvely thinking, we may suppose that the diffusion flow may pose a component perpendicular to the gradient of the skyrmion density because of the gyro-motion. The component should be proportional to the gradient of the Skyrmion density and newly defined "gyro-diffusion constant" (off-diagonal element of the diffusion constant) [6]. However, such flow is divergence-less and does not appear in the equation of diffusion. According to this context, we mention the gyro-diffusion constant as "the hidden diffusion constant". In this talk, we show evidence of gyro-motion in diffusion and discuss the observation of the gyro-diffusion constant. Then, we mention recent progress to implement "Brownian computer" by use of Skyrmions. In our experiments, the magnetic Skyrmions are bubble-shaped magnetic domains generated in a ferromagnetic thin film having spontaneous magnetization perpendicular to the film surface. The Skyrmions have their diameter adjusted to 1 μm to allow the observation by an optical microscope with polarization analysis (MOKE microscope). To create the Skyrmions, Ta/CoFeB/Ta sandwiched films [7] possessing perpendicular magnetic anisotropy and the interfacial-Dzyaloshinskii-Moriya interaction (*i*-DMI) were fabricated. Changing the upper and lower Ta film thicknesses independently, the ratio of the *i*-DMI energy to the magnetic anisotropy energy was adjusted. Besides, by eliminating the annealing process, the generation of grain boundaries was suppressed. The annealing free process enhanced the diffusion coefficient of skyrmions by a factor of more than 10 compared to the previous study [2] and comparable to the recent observations [7,8]. Firstly, we have developed the Skyrmion channel by a slight modification of the SiO₂ passivation layer thickness. By this method we could make degradation and dipole-field free channels. With this method the Skyrmions show free Brownian motion even in a complicated Skyrmion circuit like Hub (Y-cross) [7]. Secondly, we put a Skyrmion in one-dimensional channels to interfere with its gyro-motion. As a result, a significant increase in the diagonal diffusion constant was observed. This is clear evidence of the role of gyro-motion in the diffusion process. Thirdly, we have observed the diffusion of a Skyrmion in uniformly extended ferromagnetic films. In the uniform film, Skyrmions show free diffusion as it is shown in Fig. 1. The analysis of the simultaneous position-position correlation function $\langle X(t) \cdot X(t) \rangle$, which is a half of the mean square displacement (MSD), results that $\langle X(t) \cdot X(t) \rangle$ is proportional to the elapsed time providing the diagonal diffusion constant as its slope. On the other hand $\langle X(t) \cdot Y(t) \rangle$ is zero as it is expected from the symmetry. While, we have found that simultaneous velocity-position correlation functions ($\langle V_x(t) \cdot X(t) \rangle$ and $\langle V_x(t) \cdot Y(t) \rangle$) are non-zero. From the theory, $\langle V_x(t) \cdot Y(t) \rangle$ corresponds to the gyro-diffusion constant. The size of the observed gyro-diffusion constant is about 1/10 of the diagonal diffusion constant, and non-negligible. However, the sign of the observed gyro-diffusion constant is opposite to that expected from a sense of gyro-motion. Since the sense of the gyro-motion is determined by the sign of the

Skyrmion number, it should not be changed easily. The change of the sign in the gyro-diffusion constant will be discussed in terms of the diffusion in a potential. Finally, essential devices to construct a Brownian computing circuit, i.e. hub, ratchet, and c-join [3], were tested. By now, ratchet and c-join need a control using MOKE observation and manual feedback. To overcome this difficulty, we are now developing autonomous devices using voltage control [9, 10] of the Skyrmion (Fig. 2). Acknowledgments The authors acknowledge Mr. Y. Jibiki of Osaka University, Dr. S. Auffret, Dr. C. Baraduc, and Dr. Hélène Béa of Spintech, France for their initial contributions. The authors also acknowledge Dr. M. Oogane for his FMR measurements. This research and development work was supported by the ULVAC, Inc., the Ministry of Internal Affairs and Communications, Basic research S (20H05666) of JSPS, and CREST (Non-classical Spin project) of JST.

[1] N. Nagaosa et al., *Nat. Nanotech.* 8, 899-911 (2013). [2] J. Zazvorka et al., *Nat. Nanotech.* 14, 658 (2019). [3] F. Peper et al., *ACM J. Emerg. Technol. Comput. Syst.* 9, 1, Article 3 (2013). [4] A. Thiele et al., *Phys. Rev. Lett.* 30, 230 (1973). [5] C. Schuette et al., *Phys. Rev. B* 90, 174434 (2014) [6] E. Tamura et al. <https://arxiv.org/abs/2005.04860>. [7] Y. Jibiki et al., *Appl. Phys. Lett.* 117, 082402 (2020). [8] L. Zhao et al., *Phys. Rev. Lett.* 125, 027206 (2020). [9] T. Nozaki et al., *Appl. Phys. Lett.* 114, 012402 (2019). [10] M. Scott et al., *Nano Lett.* 17, 3006 (2017).

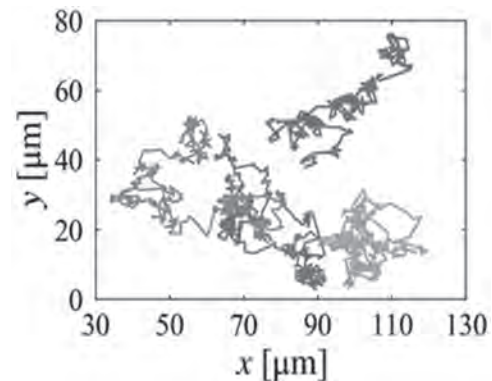


Fig. 1 Trajectories of magnetic skyrmions observed at 316 K using a MOKE microscope.

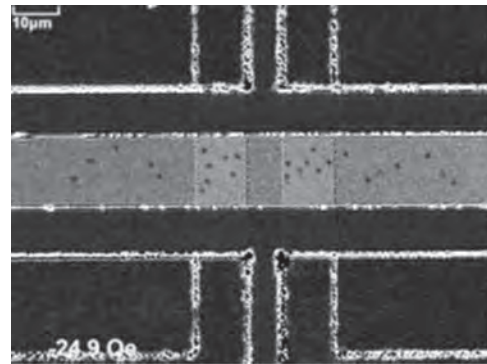


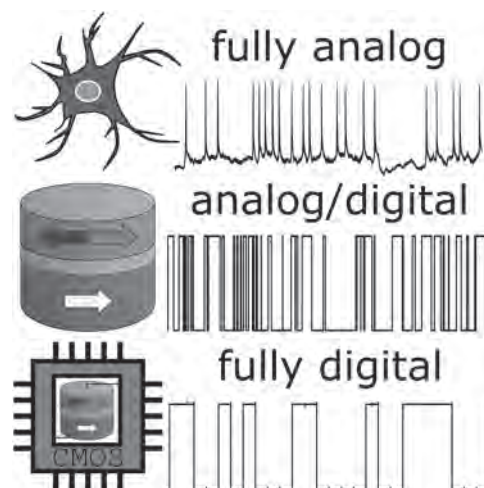
Fig. 2 Voltage/current controlled Skyrmion ratchet (test device).

GA-04. Running Deep Neural Networks on Superparamagnetic Fluctuations.

M. Daniels¹, A. Madhavan^{1,2}, P. Talatchian⁵, A. Mizrahi^{3,4} and M. Stiles¹
 1. Physical Measurement Laboratory, National Institute of Standards and Technology, Gaithersburg, MD, United States; 2. IREAP, University of Maryland at College Park, College Park, MD, United States; 3. Centre National de la Recherche Scientifique, Paris, France; 4. Thales Defence, La Defense, France; 5. Commissariat a l'energie atomique et aux energies alternatives, Paris, France

Magnetic tunnel junctions offer significant and near-term improvements to new computer chips, most immediately from non-volatile memory applications [1]. These devices consist of two magnetic layers whose relative alignment – parallel or antiparallel – determine the device's two-terminal resistance. When the energy barrier between these two states is sufficiently small, thermal fluctuations can cause the device to exhibit random telegraph noise in its resistive state. In this case, the device is called a superparamagnetic tunnel junction [2]. Computing with random telegraph noise can offer favorable properties such as noise-tolerance, massive parallelism, and – for certain operations – low power and area footprints. The field of stochastic computing addresses questions of engineering such systems but has mostly been restricted to the use of low-quality pseudorandom number generators. The low periodicity and high cross-correlations between these devices have restricted traditional stochastic computing by forcing frequent regeneration of stochastic bitstreams. Crossing in and out of the stochastic domain can incur significant energy penalties [3]. In our work [4], we introduce a low-energy circuit for extracting programmable randomness from superparamagnetic tunnel junctions. The required probability is determined via a digital input signal, rather than an analog current, so ohmic losses are minimized (Figure 1). Using detailed analog circuit simulation, we find that our device requires only half the energy of the traditional all-CMOS solution, while also offering infinite-period truly random bitstreams. To demonstrate the value of truly random bitstreams, we designed a deep neural network modeled after LeNet5 [5], a famous convolutional neural network used for handwriting recognition. Traditional neural networks multiply neuron outputs by a synaptic weight, add these products together at the input of another neuron, and then apply a nonlinear operation to that input sum. In our implementation, the values passed between neurons are encoded in the expected value of the voltage on any given wire. To multiply two signals together, we need only use a Boolean AND gate to construct the joint distribution of the wires. Feeding many wires into a Boolean OR gate generates a polynomial function which looks like linear addition near the origin, but acquires high-order nonlinear corrections when the inputs are strong. However, the OR gate only functions in this way because the inputs can be regarded as statistically independent, which would be impossible with pseudorandom number generators absent an unacceptable increase in energy consumption. We implement LeNet5 using superparamagnetic tunnel junctions together with these simple logic gates and train a simulation of this deep neural network. We are able to achieve 97 % accuracy on handwritten digit recognition using only 150 nJ per inference. This energy efficiency represents a factor of 1.4 to 7.7 improvement over comparable proposals that do not use tunnel junctions. However, after systematic optimization, the best CMOS-only solution is able to achieve 99.1 % accuracy [6]. Questions about the best way to train OR-gate neurons for optimal performance is a question for future research. Nevertheless, our demonstration shows that taking a digital approach to utilizing SMTJ fluctuations can unlock extremely energy-efficient circuit designs with the potential for offering stochastic neural networks computing in near-term application specific integrated circuits.

[1] Apalkov, Dieny, and Slaughter, Proc. IEEE 104, 1796 (2016) [2] Camsari, Faria, Sutton, and Datta, Phys. Rev. X 7, 031014 (2017) [3] Manohar, IEEE Comp. Arch. Lett. 14, 119 (2015) [4] Daniels, Madhavan, Talatchian, *et al.*, Phys. Rev. App. 13, 034016 (2020) [5] LeCun, Bottou, Bengio, *et al.*, Proc. IEEE 86, 2278 (1998) [6] Li, Ji, Ren, *et al.*, IEEE Trans. Comp. Aid. Des. Int. Circ. Sys. 38, 1543 (2019)



Neurons in the brain have analog outputs in analog time; superparamagnetic tunnel junctions have digital states in analog time. To use digital circuitry to discretize the time variable, removing the need for steady state currents and the associated ohmic losses.

GA-05. Magnetic Defect-Driven Dynamics in Artificial Spin ice.

R. Puttock^{2,3}, C. Gatel¹, M. Rosamond⁴, A. Fernandez Scarioni⁵, V. Antonov³, E. Snoeck¹, A. Manzin⁶, V. Neu⁷, F. Garcia-Sanchez^{6,8}, H.W. Schumacher⁵ and O. Kazakova²

1. Centre d'Elaboration de Matériaux et d'Etudes Structurales, Toulouse, France; 2. Quantum Materials and Sensors, National Physical Laboratory, Teddington, United Kingdom; 3. Department of Physics, Royal Holloway University of London, Egham, United Kingdom; 4. School of Electronic and Electrical Engineering, University of Leeds, Leeds, United Kingdom; 5. Physikalisch-Technische Bundesanstalt, Braunschweig, Germany; 6. Istituto Nazionale di Ricerca Metrologica, Torino, Italy; 7. Leibniz-Institut für Festkörper- und Werkstofforschung Dresden eV, Dresden, Germany; 8. Universidad de Salamanca, Salamanca, Spain

Despite attempts to design correlated systems to influence the properties of a physical system, it is often those inspired by nature that yield the best results. Artificial spin ice (ASI) are lithographically defined 2D projections of geometrically frustrated materials that are often used for experimentally model more complex atomistic systems [1-2]. In addition, ASI exhibit interesting physics, including collective dynamics [3-4] and emergent monopole stabilisation [5], that can be applied to probabilistic computing, signal propagation, and logic devices [6-7]. The capacity to design an almost infinite number of topologies to induce novel effects, and the ability to probe these characteristics optically, electrically and by scanning probe techniques have made ASI an exciting candidate for probabilistic computing [8]. Here, two custom ASI systems are shown to exhibit interesting defect behaviours from the inherent array design. The first design models the influence of a ferromagnetic defect in the centre of the structured array. Defects in crystal systems can have bountiful effects on the local physical properties. These effects in-turn can often be exploited for novel applications. For example, defects in transition-metal dichalcogenides have applications in quantum information processing as single photon point-sources due to highly localised excitons bound to the defect-site [9]. Alternatively, nitrogen vacancies in diamond exhibit spin-dependent fluorescent rates required for high resolution magnetometry [10]. The magnetic defect in the ASI system acts as a source of emergent monopoles at lower energy-barriers than a pristine lattice. Recent results of the delicate interplay between defect and lattice states are studied in the context of signal propagation applications by magnetic imaging techniques, including magnetic force microscopy (MFM); Lorentz TEM; and electron holography. We reveal how the magnetic defect affects the surrounding structure compared to those formed independently from the defect, e.g., from discontinuous lattice-edges. The second presented system is a quasi-hexagonal ASI lattice, which is arranged to encompass competing interactions from both ferromagnetic/antiferromagnetic coupling between parallel islands and geometric frustration (Fig. 1a) [11]. By including parallel islands along just one axis, the lattice exhibits an additional shape anisotropy under field directions (Fig 1b-c). We demonstrate that the inclusion of these coupled islands promotes the non-uniform break-down of Ising “macrospins” in the islands under a specified field protocol (Fig. 1d). Through MFM and micromagnetic modelling, we investigate the disrupted periodicity of the energy states across the lattice and the predictability of non-Ising state formation. Control over the local coupling effects have application in programmable logic, e.g. non-Boolean or probabilistic computing [12].

[1] R. F. Wang *et al.*, *Nature*, vol. 439, no. 7074, pp. 303–306, Jan. 2006. [2] M. Tanaka *et al.*, *Phys. Rev. B - Condens. Matter Mater. Phys.*, vol. 73, no. 5, pp. 3–6, 2006. [3] M. B. Jungfleisch *et al.*, *Phys. Rev. Appl.*, vol. 8, no. 6, pp. 1–7, 2017. [4] A. Farhan *et al.*, *Phys. Rev. B*, vol. 96, no. 6, p. 064409, Aug. 2017. [5] S. Ladak *et al.*, *Nat. Phys.*, vol. 6, no. 5, pp. 359–363, May 2010. [6] S. H. Skjærvø *et al.*, *Nat. Rev. Phys.*, vol. 2, no. 1, pp. 13–28, Jan. 2020. [7] S. Gliga, E. Iacocca, and O. G. Heinonen, *APL Mater.*, vol. 8, no. 4, p. 040911, Apr. 2020. [8] H. Arava *et al.*, *Nanotechnology*, vol. 29, no. 26, 2018. [9] A. Srivastava *et al.*, *Nat. Nanotechnol.*, vol. 10, no. 6, pp. 491–496, Jun. 2015. [10] G. Balasubramanian *et al.*, *Nature*, vol. 455, no. 7213, pp. 648–651, 2008. [11] R. Puttock *et al.*, *Small*, vol. 2003141, pp. 1–8, Sep. 2020. [12] Project supported by the UK government department for Business, Energy and Industrial Strategy through NMS funding (Low Loss Electronics). LTEM and EH was available through funding from the

European Union’s Horizon 2020 research and innovation programme under grant agreement No 823717 – ESTEEM3.

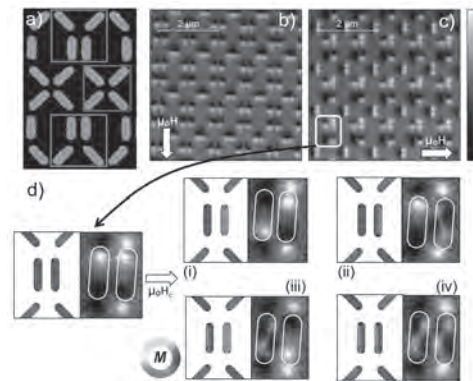


Figure 1. (a) AFM image of four primitive cells of the quasi-hexagonal ASI lattice where three vertex-shapes are outlined. MFM images of unimodal (b) and bimodal (c) configurations favourable when the field is aligned along y- and x-axes, respectively. (d) Four possible magnetic configurations in parallel islands upon application of a critical field.

GA-06. An Atomic-Scale Boltzmann Machine Capable of Self-Adaption.*A.A. Khajetoorians¹**1. Institute for Molecules and Materials, Radboud Universiteit, Nijmegen, Netherlands*

There is a growing pursuit to create neuromorphic devices that are able to perform machine learning tasks, both in an energy efficient manner and compatible with CMOS architecture. These approaches are based on taking the complex response of materials and mimicking aspects of a given machine learning model. Typically, what cannot be mimicked directly in a material, such as learning, is supplemented by other devices, circuitry, or external computers. These various approaches often face a number of bottlenecks, related to scaling, functionality independent of computers, and energy efficient operation. Ultimately constructing autonomous materials, namely individual materials that independently adapt their physical properties based on input data, requires deeper fundamental research linking physical processes to machine learning concepts. In this way, it is necessary to link quantum phenomena in materials to concepts like plasticity, memory, and learning. In this way, new types of quantum materials can be designed for autonomous recognition, as well as new functionalities can be explored, such as quantum machine learning. Energy-based models, like the Boltzmann machine, provide a natural link between physics and machine learning functionality via the Ising model and the physics of multi-well potentials and glasses (1, 2). I will discuss a new model system, based on the recently developed concept of orbital memory (3), which mimics the behavior of a Boltzmann machine directly in its stochastic dynamics and in one elemental material, down to the atomic-scale (4). Using scanning tunneling microscopy (STM) to fabricate nano-scale arrays of cobalt atoms on semiconducting black phosphorus, we observe stochastic noise described by the tunable multi-well landscapes seen in stochastic energy-based models. Utilizing a concept based on separation of time scales and the anisotropic behavior of black phosphorus (5), I will show that these multi-well landscapes are adaptive and exhibit inherently coupled neural and synaptic dynamics, at the atomic-scale. I will discuss perspectives of learning in these systems, and how such model systems provide fundamental insight into the future design of quantum-based brain-like devices. This work was done in collaboration with H.J. Kappen, Brian Kiraly, Elze J. Knol, and Werner M.J. van Weerdenburg. This work was funded by NWO-Vidi Manipulating the interplay between superconductivity and chiral magnetism at the single-atom level² with project number 680-47-534. This project has received funding from the European Research Council (ERC) under the European Union's Horizon 2020 research and innovation programme (grant agreement No 818399).

1. A. Kolmus, M. I. Katsnelson, A. A. Khajetoorians and H. J. Kappen, *New J. Phys.* 22 (2), 023038 (2020). 2. U. Kamber, A. Bergman, A. Eich, D. Iusan, M. Steinbrecher, N. Hauptmann, L. Nordström, M. I. Katsnelson, D. Wegner, O. Eriksson and A. A. Khajetoorians, *Science* 368 (6494), eaay6757 (2020). 3. B. Kiraly, A. N. Rudenko, W. M. J. van Weerdenburg, D. Wegner, M. I. Katsnelson and A. A. Khajetoorians, *Nat. Commun.* 9 (1), 3904 (2018). 4. B. Kiraly, E. J. Knol, H. J. Kappen and A. A. Khajetoorians, *arXiv*, 2005.01547 (2020). 5. B. Kiraly, E. J. Knol, K. Volckaert, D. Biswas, A. N. Rudenko, D. A. Prishchenko, V. G. Mazurenko, M. I. Katsnelson, P. Hofmann, D. Wegner and A. A. Khajetoorians, *Phys. Rev. Lett.* 123 (21), 216403 (2019).

Session GB

NEUROMORPHIC COMPUTING

Alice Mizrahi, Co-Chair

Unite Mixte de Physique CNRS/Thales, Palaiseau, France

Dedalo Sanz Hernandez, Co-Chair

Unite Mixte de Physique CNRS/Thales, Palaiseau, France

CONTRIBUTED PAPERS

GB-01. Ferrimagnetic Co-Gd-Bilayer-Based Fast and Energy-Efficient Synaptic Devices for Neuromorphic Computing.U. Sahu¹, N. Sisodia², J. Sharda¹, P.K. Muduli² and D. Bhowmik¹¹. Electrical Engineering, Indian Institute of Technology Delhi, New Delhi, India; ². Physics, Indian Institute of Technology Delhi, New Delhi, India

Ferromagnetic devices, where current pulses flowing through the heavy metal layer below the ferromagnetic layer move the ferromagnetic domain wall through spin-orbit torque, have been proposed and experimentally demonstrated as synapses for neuromorphic computing [1–3]. But since ferrimagnets are known to exhibit faster domain wall motion compared to ferromagnets, the potential for ferrimagnetic synapses also needs to be explored [4]. Here, we first carry out micromagnetic simulations of current-induced domain wall motion in a ferromagnetic device as well as a ferrimagnetic Co/Gd-bilayer-based device. The working principle of the ferrimagnetic synapse is just the same as the ferromagnetic synapse: current flowing through the underlying heavy metal layer moves the domain wall in the ferrimagnetic bi-layer just like it moves it in the ferromagnetic layer (Fig. 1a) [4]. Motion of the domain wall leads to a change in conductance and hence an update in the weight stored in the synapse [1, 2]. In our simulation, the spin Hall angle of the heavy metal (Pt), current flow through which generates the necessary spin-orbit torque for domain wall motion, is considered to be 0.13 [4]. For the ferrimagnetic system, dynamics of the magnetic moments of both the Co and Gd layers, exchange-coupled with each other (coupling strength = -0.9 mJ/m²), has been modeled in ‘mumax3’ [4]. The temperature-dependent variation of the Co and Gd magnetic moments is also considered. From our simulations (Fig. 1b), we observe that in the ferrimagnetic system, the domain wall velocity is highest at the angular-momentum-compensation temperature, $T=165$ K, at which moment in Gd layer (m_{Gd}) = 0.9 times moment in Co layer (m_{Co}). This is consistent with the experimental observation and corresponding one-dimensional-domain-wall calculations reported by Blasing *et al* [4]. Fig. 2a shows that across a wide range of current density through the heavy metal layer, domain wall velocity in the ferrimagnetic system at the angular-momentum-compensation temperature (165 K) is 2X–2.5X higher than that in the ferromagnetic system at room temperature. Next, we carry out system-level simulations with the device characteristic in Fig. 2a to compare the performance of the ferromagnetic and the ferrimagnetic devices as synapses in a crossbar-array-based neuromorphic system that mimics a Fully Connected Neural Network (FCNN) with a hidden layer. Synaptic weights are updated in both the ferromagnet-synapse and ferrimagnet-synapse crossbars using the thresholding algorithm, proposed by Kaushik *et al.* [5], to achieve on-chip learning in the crossbars on Iris data set of flowers and MNIST data set of handwritten digits. Using this thresholding algorithm, for Iris data set, we obtain train accuracy of 100% and test accuracy of 96%, and for MNIST, we obtain train accuracy of 98% and test accuracy of 92%. We obtain these same accuracy numbers for both ferromagnetic and ferrimagnetic synapse crossbars because we allow the same number of conductance states for both these types of synapses (50). According to this thresholding algorithm, for each synapse in the FCNN, the synaptic weight/conductance is either increased or decreased by a fixed amount or kept the same at any particular iteration [5]. Thus training can be achieved only by applying current pulses of fixed magnitude and duration to the ferrimagnetic or ferromagnetic synapses — positive polarity of current for weight increase and negative polarity for weight decrease (Fig. 1a). A shorter duration pulse needs the domain wall to move with a higher velocity compared to a longer duration pulse to cause the same weight update. Hence, a shorter pulse needs to be of higher current magnitude and will consume more energy. Fig. 2b shows how energy consumed by a pulse increases with a decrease in duration of the pulse, both in the case of the ferrimagnetic system and the ferromagnetic system. We do observe that for the same duration of current pulse, energy consumed is 4X lower for the ferrimagnetic system than for the ferromagnetic system. Similarly, if the energy consumption per pulse is kept constant, pulses of time duration 4X lower can be used for the ferrimagnet compared to the ferromagnet. As a result, when we compare the energy

consumption and time taken for on-chip learning in the two aforementioned crossbar systems, we observe that for the same net energy consumption in the system, the ferrimagnetic crossbar can be trained 4X faster than the ferromagnetic crossbar. Similarly, for the same speed across the two crossbars, the ferrimagnetic crossbar can be trained at 4X lower energy than the ferromagnetic crossbar. Thus, our study shows that ferrimagnetic-bilayer-based systems can pave the way for fast and energy-efficient neuromorphic computing in the future.

[1] A. Sengupta and K. Roy, IEEE Trans. Biomed. Circuits Syst., vol. 10, no. 6 (2016) [2] D. Kaushik, U. Singh, U. Sahu, I. Sreedevi, and D. Bhowmik. AIP Adv. vol. 10, no. 025111 (2020) [3] R. Blasing, T. Ma, S-H. Yang *et al.* Nature Communications, vol. 9, no. 4984 (2018) [4] T. Jin, W. Gan, F. Tan *et al.*, J. Phys. D: Appl. Phys., vol. 52, no. 445001 (2019) [5] D. Kaushik, J. Sharda, and D. Bhowmik. Nanotechnology vol. 31, no. 364004 (2020)

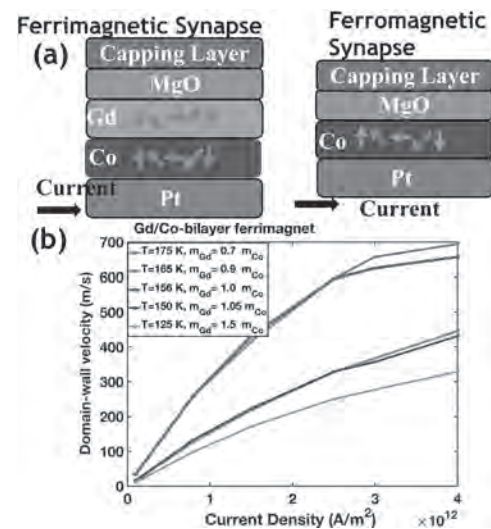


Fig. 1 (a) Schematics of ferrimagnetic (Co/Gd-bilayer-based) and ferromagnetic (Co-based) synaptic devices. The domain wall is shown through rotating green arrows, which correspond to magnetic moments. (b) Domain-wall velocity vs current density flowing through the heavy metal layer (Pt), for different values of temperature, which correspond to different ratios of Gd’s magnetic moment (m_{Gd}) to Co’s magnetic moment (m_{Co}).

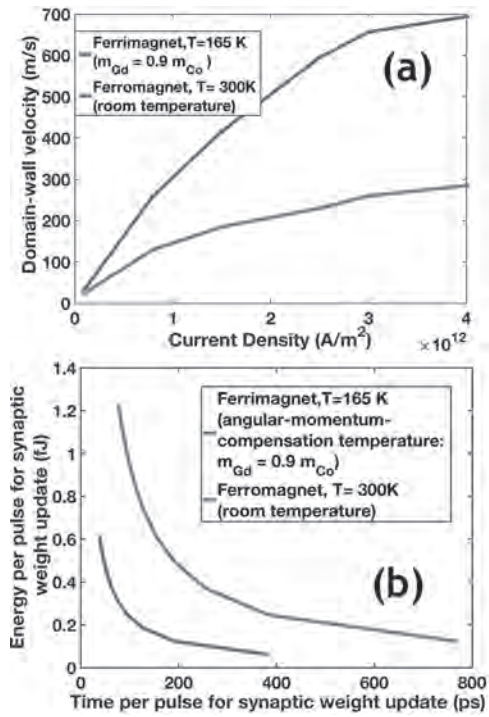


Fig. 2. Comparison of (a) domain-wall velocity vs current density characteristic and (b) energy per synaptic-weight-update pulse vs time duration of such a pulse for ferrimagnetic synapses (at angular-momentum compensation temperature, when domain-wall velocity is highest) and ferromagnetic synapses (at room temperature).

GB-02. Domain Wall-Magnetic Tunnel Junction Spin Orbit Torque Devices for in-Memory Computing.

T. Leonard¹, M. Alamdar¹, C. Cui¹, B.P. Rimal¹, L. Xue², O.G. Akinola¹, T.P. Xiao³, J.S. Friedman⁴, C.H. Bennett³, M.J. Marinella³ and J.C. Incorvia¹

1. The University of Texas at Austin, Austin, TX, United States; 2. Applied Materials Inc, Santa Clara, CA, United States; 3. Sandia National Laboratories, Albuquerque, NM, United States; 4. The University of Texas at Dallas, Richardson, TX, United States

There are many potential applications for spintronics including in-memory, neuromorphic, and radiation hard computing. In-memory computing offers a solution to the memory wall bottleneck that hinders traditional architectures. Neuromorphic computing has the potential to revolutionize how data-intensive tasks, such as image recognition, are computed by emulating how a biological brain operates. Radiation hard computing is useful for certain situations, mainly space applications, where the Earth's atmosphere does not protect sensitive CMOS hardware. All of these applications can be achieved using domain wall motion-based devices. The domain wall magnetic tunnel junction (DW-MTJ) device architecture is explored in this work as shown in figure 1. DW-MTJ devices operate by sending a current pulse along a ferromagnetic wire to propagate a domain wall from the input to the output of the device. As the domain wall passes under the MTJ, the magnetization state of the bottom layer of the CoFeB/MgO/CoFeB junction changes. By controlling where the domain wall is, the MTJ can have programmable resistance. We use current driven domain wall motion to electrically switch the devices. It has been shown that spin logic requires high tunneling magnetoresistance, low switching voltages, and high stability. These hurdles have been overcome in this work by utilizing perpendicular anisotropy, spin orbit torque switching, and optimized fabrication. Incorvia et al. in 2015 demonstrated that information could be encoded in a magnetic wire by moving a domain wall, but the TMR of those devices was 12% [1]. Here, we develop a process that maintains as much TMR as possible, achieving TMR > 150%, as well as no reduction in resistance-area (RA) product after device fabrication. There were several improvements made to the previous fabrication process. The main change was to remove the reactive ion etch step to contact the MTJ. Incorvia et al. opened a via in polymethylmethacrylate (PMMA) and then used a CF₄ reactive ion etch through a hydrogen silsesquioxane (HSQ) layer to expose the MTJ and wire contacts. In our new process, we replaced this step with a negative tone resist and encapsulation step to achieve the same result of an open via to the MTJ and domain wall track without exposing the sensitive layers to a reactive etch. This way the MTJ is never directly exposed: during all etches and encapsulation, the MgO is protected by negative resist. Furthermore, the encapsulation was performed at relatively low temperatures of 100 °C to prevent any additional loss of TMR, and silicon nitride was used instead of silicon oxide to reduce oxidation. These factors allowed our devices to maintain their high TMR post-processing. The TMR is shown in the field loops of four devices in figure 2. The average achieved was 164±17%, compared to the unpatterned film TMR of 168±6%. Before fabrication, the film had RA = 35±2 Ω·μm² and the devices have RA = 31±3 Ω·μm². This indicates that our fabrication process had little to no negative impact on the magnetic integrity of our material. These devices utilize electrical initialization of domain walls rather than an external magnetic field, so they can be fabricated as straight wires rather than curved. This allows for increased density if this technology becomes industrialized. Previous iterations of these devices were curved to allow an external magnetic field to nucleate a domain wall at an initial position. Here, we opted for an electrical approach by implementing an oersted field line near the left contact of each device. A short pulse is sent through this line which nucleates a domain wall in the ferromagnetic track [2]. This is one step closer towards all electric operation of the memory-in-logic devices. These oersted field lines increased stability and repeatability by nucleating the domain wall in the same position each time, rather than an unpredictable location via external magnetic field nucleation. Calculating the variability based on the switching voltage range over 10 cycles with both nucleation methods showed an improvement from external magnetic field (105%) variability to the oersted field line (7%) variability. We show in simulation that these improvements bring the variability of the technology within the regime

for large circuit function such as a 32-bit full adder [3]. *Partial funding from Sandia National Lab (SNL). SNL is managed and operated by NTESS under DOE NNSA contract DE-NA0003525.*

¹J. A. Currivan-Incorvia, S. Siddiqui, S. Dutta, E. R. Evarts, C. A. Ross & M. A. Baldo. 2015 IEEE Int. Electron Devices Meet. 32–36 (2015) ²G. Zahnd, V. T. Pham, A. Marty, M. Jamet, C. Beigné, L. Notin, C. Vergnaud, F. Rortais, L. Vila & J. P. Attané. J. Magn. Magn. Mater. Vol. 406, p. 166–170 (2016) ³T. Patrick Xiao, M. J. Marinella, C. H. Bennett, X. Hu, B. Feinberg, R. Jacobs-Gedrim, S. Agarwal, J. S. Brunhaver, J. S. Friedman & J. A. C. Incorvia. IEEE J. Explor. Solid-State Comput. Devices Circuits., Vol. 5, p. 188-196 (2019)

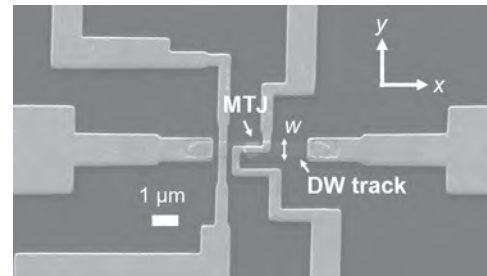


Fig.1: Top-down SEM image of a DW-MTJ device. Patterned domain wall track (labeled DW track) and magnetic tunnel junction (labeled MTJ) identified. Device width (labeled w) is 450 nm. Widths down to 250 nm were patterned and tested.

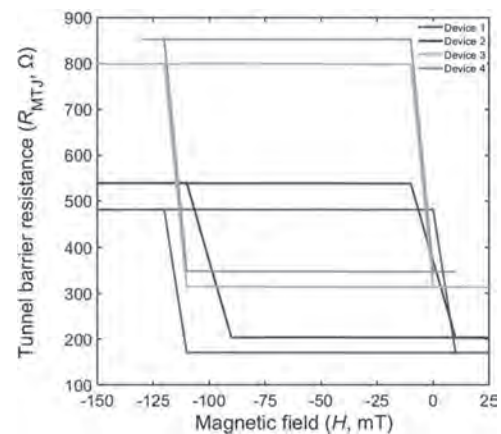


Fig. 2: Field loop for devices in this work. R_{MTJ} is the measured resistance through the tunnel junction. Spin-orbit torque current switching was also performed and will be presented.

GB-03. Imaging the Emergent Behaviour in Nanoring Assemblies for Reservoir Computing Applications.

G. Venkat¹, R. Dawidek¹, T. Hayward¹, A. Mullen¹, S. Kyle¹, P. Fry², F. Maccherozzi³, S. Dhési³, L. Aballe⁴, M. Foerster⁴, J. Pratt⁴ and D. Allwood¹

1. Materials Science and Engineering, The University of Sheffield, Sheffield, United Kingdom; 2. Nanoscience and Technology Centre, The University of Sheffield, Sheffield, United Kingdom; 3. Diamond Light Source Ltd, Didcot, United Kingdom; 4. ALBA Synchrotron Light Facility, Consorcio para la Construcción Equipamiento y Explotación del Laboratorio de Luz Sincrotron, Barcelona, Spain

Stochastic behaviour has traditionally been a limiting factor in the development of nanomagnetic technology. However, it can also give rise to rich physical behaviours. For example, in artificial spin ice (ASI) arrays [1,2] stochastic effects give rise to emergent behaviour that can help us to understand phenomena in frustrated systems. In particular, this emergent behaviour is useful for a novel form of neuromorphic computing called ‘reservoir computing’ which is highly efficient for time domain processing of signals [3]. One such system that exhibits probabilistic, emergent behaviour with complexity is an array of interconnected nanowire rings of $\text{Ni}_{80}\text{Fe}_{20}$ [4-5]. Here we characterise the emergent behaviour of domain wall (DW) states in a nanoring array using X-ray imaging under the application of rotating fields of different amplitudes in order to better understand the array’s magnetic response and ascertain its suitability for reservoir computing. Fig. 1 (A) shows an SEM micrograph of a representative rectangular $\text{Ni}_{80}\text{Fe}_{20}$ ring array of which we have obtained the magnetic response by applying an in-plane rotating magnetic field. Magneto-optic Kerr effect (MOKE) measurements show a strongly nonlinear magnetisation variation with field amplitude (Fig. 1 (B)) - an essential response for reservoir computing. We have shown this system to be a promising candidate for reservoir computing using various macroscopic measurement techniques [5-6]. It is clear that these complex dynamics are due to the interplay of pinned and propagating DWs (Fig. 1 (B)) and different magnetic states in the array. We used X-ray Photo Emission Electron Microscopy (X-PEEM) to image the magnetic states across a ring array with rings of radius 2 microns and width of 500 nm with an $\text{Ni}_{80}\text{Fe}_{20}$ thickness of 10 nm and with a 2nm Al layer to prevent oxidation. X-PEEM images were obtained with an Elmitec SPELEEM-III microscope on the I06 beamline at the Diamond Light Source using XMCD at the Fe-L₃ edge. Samples were mounted on cartridges with a quadrupole magnet, to provide an in-plane magnetic field with arbitrary direction, designed and built at the CIRCE XPEEM beamline at the ALBA Synchrotron. Samples were subject to an initialisation field pulse of 160 Oe followed by 30 rotations of an in-plane magnetic field of various strengths. A representative X-PEEM image of the array (Fig. 2 (A)) obtained with a rotating field strength of 30 Oe at a frequency of 8 Hz shows multiple magnetisation states. The allowed magnetic configurations are shown schematically in Fig. 2 (B). There are four types of ‘onion’ states (two DWs separated by 180°), two ‘vortex’ states (zero DWs) and eight ‘three-quarter’ states (two DWs separated by 90°) possible. A dedicated Python code was used to analyse the magnetisation states in the X-PEEM image (Fig. 2 (A)). The rings were mapped to circles using the Hough transform available in the OpenCV library [7] and the color of each quarter was recorded. Then the color scheme of an entire circle was assigned to a magnetic configuration. The population of various states at different amplitudes of the rotating field was extracted and is shown in Fig. 2 (C). We can see that ‘onion’ states (at lower fields) give way to ‘vortex’ and ‘three-quarter’ states and at higher fields ‘onion’ states dominate again. This is consistent with the previous MOKE measurements that were attributed to static onion states at low field magnitudes, due to DW pinning, and dynamic onion states at high fields (as shown in Fig. 1 (B)) when DWs readily overcome the pinning potentials presented by ring junctions. Note that this behaviour leads to the emergent dynamics which the ring assembly shows under the influence of a rotating magnetic field. The variation in the magnetic states population also indicates ‘fading memory’ as the state population at a given field is independent of the population at a previous field. This is another desirable property for a system to function as a reservoir. The normalised magnetisation response of the array can be extracted from the state population (Fig. 2 (D)) and

in order to measure the array’s response to field strength. This is similar to that obtained from previous MOKE measurements but highlights the significance of dynamic local variation in magnetic structure. We have thus imaged the emergent DW dynamics in nanoring arrays using X-PEEM and have obtained their magnetic response to show their suitability for reservoir computing applications. The different complex magnetic states in the array, which give rise to their emergent magnetic behaviour, provide insights into the evolution of these states. We hope that this study will pave the way for further investigations into the suitability and implementation of these systems for advanced computing purposes.

[1] Wang et al., Nature 439, 303 (2006) [2] Branford et al., Science 335, 1597 (2012) [3] Jensen et al., ALIFE 2018: The 2018 Conference on Artificial Life (July 2018) pp.15-22 [4] Negoita et al., J. Appl. Phys. 114, 013904 (2013) [5] R. Dawidek et al., Adv. Funct. Mater. 2021, 2008389 [6] I. Vidamour et al. presented at MMM-2020 [7] Bradski, Dr. Dobb’s Journal of Software Tools 2236121 (2000)

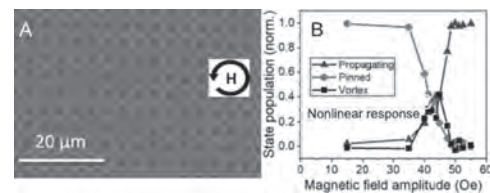


Fig. 1: (A) An SEM image of a fabricated ring array. (B) MOKE measurements of the array showing the ‘nonlinear response’ of its magnetization and the different dynamic states in the system.

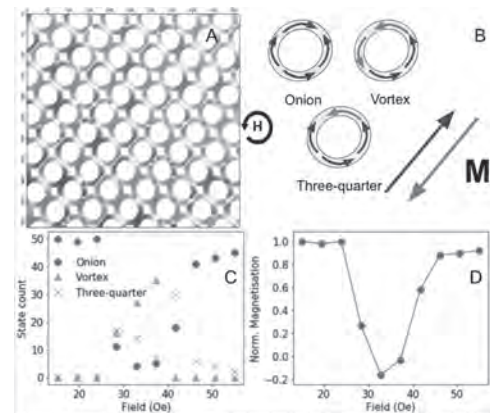


Fig. 2: (A) A representative X-PEEM image of a ring array. (B) A schematic showing the different types of magnetic states possible in the array. The arrows show the magnetisation direction which the measurement was sensitive to. (C) The variation of the magnetisation states in the array with rotating field amplitude and (D) the normalised magnetisation derived from the magnetisation states.

GB-04. Voltage-Controlled, Thermally Driven Superparamagnetic Ensembles for Tuneable Timescale Reservoir Computing.

A. Welbourne¹, A. Levy², M.O. Ellis³, H. Chen¹, E. Vasilaki³, D. Allwood¹ and T. Hayward¹

1. Materials Science, The University of Sheffield, Sheffield, United Kingdom; 2. Physics, École Polytechnique, Paris, France; 3. Computer Science, The University of Sheffield, Sheffield, United Kingdom

Reservoir computing has been gaining traction as a bio-inspired, machine-learning approach for solving computationally hard problems, such as speech recognition and prediction of chaotic time series, that are becoming fundamental to modern technology [1]. By making use of a complex, fixed reservoir with a single output layer, the approach minimises expensive training steps. Magnetic systems are well positioned to fulfill the requirements of the reservoir, providing non-linearity, fading memory, and reproducible responses. In particular, magnetic systems subject to a temporal input sequence can perform the entire role of the reservoir, replacing complex networks of transistors whilst only requiring a single input and output [2]. This offers the potential for compact devices, with reduced energy costs for computation. Here, we propose strain-mediated, voltage controlled superparamagnetic ensembles as an ideal candidate for an ultra-low-energy reservoir. Single superparamagnetic nano-dots with uniaxial anisotropy exhibit stochastic behavior, switching between states with a characteristic timescale set by their energy barriers. Micromagnetic simulations (Fig. 1a) demonstrate this telegraphing behavior for CoFeB nano-dots, where the auto-correlation time has been verified to be below 5 ns and the strain-induced anisotropy can compete with the intrinsic anisotropy [3-6]. Borders et al. [7] have shown how tuning such telegraph noise in magnetic tunnel junctions can be used for integer factorization. Here, however, we make use of the collective behavior of extended ensembles of nano-dots such that the average magnetisation becomes predictable; thus, showing the reproducible response required for reservoir computing. Input is provided by addition of a strain-mediated anisotropy (Fig. 1b)—a technique that is predicted to achieve ultra-low-power consumption [8]. This acts to rotate the intrinsic anisotropy axis, biasing dwell time in one state over the other [9]. Whilst the internal system dynamics are driven by thermal noise, the average magnetisation obeys simple rules that, when subject to a temporally varying input, produce a complex non-linear response with fading memory (Fig. 1c). Using an analytical model of the response of the superparamagnetic ensemble [10], we simulate the physical reservoir. By inputting a temporal sequence and training a single layer of weights from the output, we can perform standard machine learning benchmarks with competitive performance over a range of input timescales. Fig. 2 presents the performance for spoken digit recognition on the TI-46 dataset and chaotic time series prediction on the NARMA10 task. In both cases the performance approaches that of competing reservoirs [1,2], despite the relative simplicity of the system. The intrinsic timescale of the system (τ) is controlled by the ratio of energy barrier (anisotropy, KV) to the thermal energy ($K_B T$ at 300 K). Fig. 2a demonstrates that by tuning the input rate and strength (relative to the intrinsic timescale and anisotropy respectively), optimal performance of 95 % recognition of the spoken digits 0-9 with five female speakers can be achieved. This is realised for $\tau \sim 50$ ns ($KV/K_B T = 20$) and $\tau \sim 1$ ms ($KV/K_B T = 50$). For the NARMA10 task (Fig. 2b), the highest performance is achieved across this entire timescale range by tuning the strength of a feedback term (i.e. the output is fed back into the input stream with a given weight). Robust performance on timescales ranging from hundreds of nanoseconds up to seconds would allow a physical realisation of such a reservoir to be tuned to provide computation in real time for a wide range of possible physical inputs: from decision-making in driverless cars (fast) to speech recognition (slow). The simplicity of the system and the ease of manufacture, coupled with the low energy consumption expected for such a, thermally driven, device makes it an ideal candidate for edge computing where high performance is needed at very low latency and power.

[1] L. Appeltant et al., Nat Commun. 2, 468 (2011). [2] J. Torrejon et al., Nature. 547, 428–431 (2017). [3] A. Vansteenkiste et al., AIP Advances. 107133 (2014). [4] J. Leliaert et al., AIP Advances. 7, 125010 (2017). [5] S. Zhang et al., Scientific Reports. 4, 3727 (2014). [6] C. Saffranski et al., arXiv:2010.14393[cond-mat] (2020). [7] W. A. Borders et al., Nature. 573,

390–393 (2019). [8] K. Roy, S. Bandyopadhyay and J. Atulasimha, Applied Physics Letters. 99 (2011). [9] Z. Guo et al., Appl. Phys. Lett. 112, 052904 (2018). [10] O. Hovorka et al., Appl. Phys. Lett. 97, 062504 (2010).

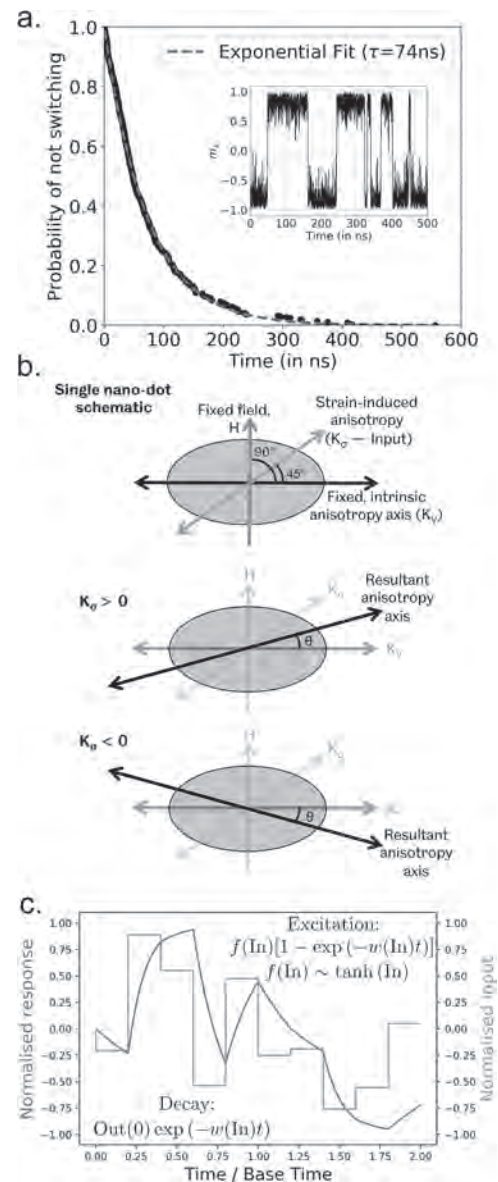


Fig. 1: a. Telegraphing behaviour of a single superparamagnetic nano-dot. Micromagnetic simulation for a 40 nm diameter, 4 nm thick CoFeB cylinder with 8.2 KJ/m³ uniaxial anisotropy at 300 K. b. Rotation of the intrinsic anisotropy axis in a nano-dot via strain anisotropy. The rotation biases the dwell time in one magnetic state (left/right pointing) versus the other. c. Analytical response of an ensemble of superparamagnetic nano-dots to a global input via strain. A temporal input sequence produces the non-linear response with fading memory required for reservoir computing.

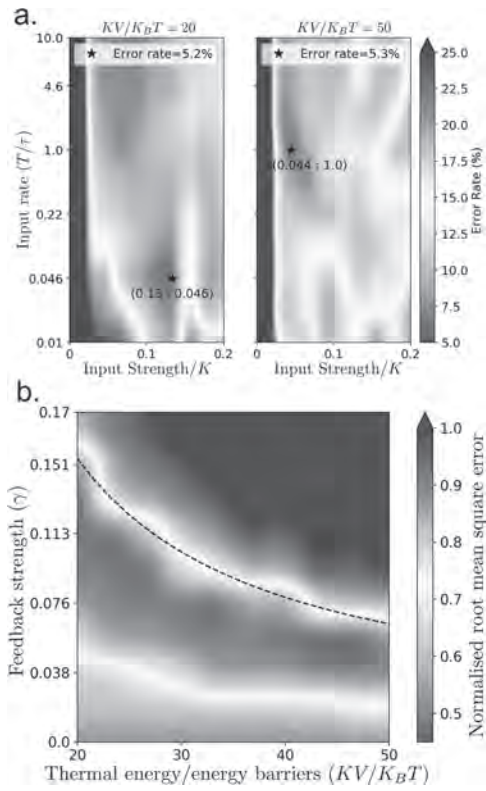


Fig 2: a. Performance on a spoken-digit recognition test using the TI-46 dataset. Performance is tuned by the input rate (relative to the intrinsic timescale) and strength. Optimal performance (95 % recognition accuracy) is achieved for intrinsic timescales of 50 ns ($KV/K_B T = 20$, left) and 1 ms ($KV/K_B T = 50$, right) and approaches that of competing reservoirs [2]. **b.** Performance on a chaotic time series prediction task (NARMA10). Performance is maintained across the entire timescale range by tuning a feedback parameter.

GB-05. Hardware Implementation of a Magnetic Tunnel Junction Based Bitstream Generator for Stochastic Computing.

E. Becele¹, L. Anghel¹, G. Prenat¹ and I. Prejbeanu¹

1. SPINtronique et Technologie des Composants, Grenoble, France

Stochastic computing has recently gain attention mainly due to its low cost, fast and energy efficient circuit level implementations. In addition, it is rather fault-tolerant and noise resilient. The success of stochastic computing is due to the fact that complex functions are extremely difficult to be implemented by conventional binary logic design while they can be effectively approximated by stochastic computing. Stochastic computing uses probabilistic representation of real-valued numbers. It represents and processes numbers thanks to bitstreams. Such a stream represents the number p if the proportion of digit 1 in the stream is equal to p [1]. One of the major requirements for accurate stochastic computation is to use non-repeating and uncorrelated random number generators to produce the bitstreams. In pure digital conventional circuits, such randomness arises from Linear Feedback Shift Register (LFSR) based Random Number Generator (RNG). They output a bitstream that represents the quantity 0.5, and is then processed to represent whatever number [1]. However, LFSRs are made of CMOS logic gates and flip-flops. The produced bitstream is totally predictable, requires an important amount of energy along with a high silicon area. Recently, nanoscale devices such as Magnetic Tunnel Junctions (MTJ) have been considered for bitstream generators due to their inner randomness [2]. The so-designed circuits produce pure random bitstreams (the sequence is not deterministic), and they operate in a very energy efficient way. The MTJ is a structure in which a binary information is stored as the relative direction of the magnetization of a magnet with respect to a reference one. The behaviour of this magnetization depends in part on thermal fluctuations [2], which can be leveraged as a source of stochasticity. Two types of schemes have been proposed for an MTJ based bitstream generator. First, a MTJ based RNG [3-5]: a sequence of bits '0' and '1' with a proportion of 50% each is generated, then processed to produce the bitstream. Second, a programmable circuit tunes the MTJ in such way that it generates directly the required bitstream, without the need of any post-processing [6]. Its implementation implies less hardware cost. However, full circuit implementation of the second scheme has not been proposed so far. In this work, we designed a bitstream generator composed of a single MTJ, a writing circuit, a reading circuit and a feedback loop. The operating principle, schematically represented in Figure 1, is the following: a current passes through the writing path of the MTJ (that has been previously set in the logic state "0") during a short period with a specific amplitude. This brings about a probability (denoted p) that the magnetization experiences a switching. After repeating the process N times, the resulting bitstream is composed of an average of Np bit seen as "1". The obtained bitstream then represents the number p in its stochastic representation. The reading circuit, similar to the latch-type voltage-mode sense amplifier published in [7], designed and optimized to allow asynchronous operations for low power operation, has the advantage that the static currents required to measure the resistance of the MTJ last a very short time, allowing for important energy saving. The inner CMOS based latch decorrelates the output of the reading circuit to the MTJ so that the state of the read MTJ is stored and remains available after the reading process, while the MTJ can be used again. The feedback loop, connected to the output of the reading circuit extracts the number that is represented by determining the ratio of bits at "1" and "0". It determines the gap between the number that is computed with respect to the one that is to be represented. In the case of a large gap, the writing current is modified accordingly. This current is increased if there are too many "0"s, and reversely it is decreased when there are too many "1"s. The writing unit is connected in series to the writing path of the MTJ. It aims at imposing a current through the writing path that is determined by the feedback loop. It is made of several transistors in parallel, acting like independent current sources. This configuration allows the circuit to find the proper writing current required for a given bitstream. This also allows handling temperature dependence of the writing current. Indeed, with temperature variation the writing current may vary in time. In our proposed circuit, the real-time tracking of the optimal writing current by the proposed feedback loop handles this problem. In conclusion, we propose an innovative single MTJ based bitstream generator leveraging the unique stochastic

properties of the magnetization of the storage layer. The critical issue of PVT variations and noise are solved by our system thanks to the feedback loop and to the versatility of the writing circuit that allow for the generation of a relevant writing current that can be generalized to any bitstream computation. This study opens the way to the design of fast and energy efficient stochastic computing based circuit.

[1] A. Alaghi and J. P. Hayes, ACM Trans. Embed. Comput. Syst [2] W. Brown, Phys. Rev. 130 (1963) 1677-1685 [3] Akio Fukushima et al 2014 Appl. Phys. Express 7 083001 [4] F. Ouattara, A. Nejat and L. Torres, IEEE Access, vol. 7, pp. 59271-59277, 2019 [5] S. Oosawa, T. Konishi and N. Onizawa, IEEE 13th International New Circuits and Systems Conference (NEWCAS), Grenoble, 2015, pp. 1-4 [6] LA de Barros Naviner et al., 13th IEEE International New Circuits and Systems Conference (NEWCAS), 2015 [7] H. Zhang, W. Kang and, IEEE Access, vol. 6, pp. 64250-64260

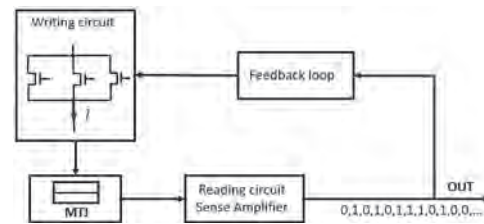


Fig.1 : Schematic of the bitstream generator

GB-06. Domain Wall Motion Based Neuromorphic Computing With Voltage Controlled Spin Neuron and Stochastic Magnetic Tunnel Junction Synapse.

A.H. Lone¹, S. Amara¹ and H. Fariborzi¹

1. CEMSE (Integrated Circuits and Systems Group), King Abdullah University of Science and Technology, Thuwal, Saudi Arabia

The spintronic devices such as the domain wall and skyrmion based devices are being explored for their applications in neuromorphic computing [1-3], due to their non-volatile behaviour, stochastic switching and energy efficiency. The electric field control of these devices has attracted extensive attention and has further gained popularity both in memory and logic applications as it provides an efficient way to improve the data storage density [4-8]. Neuromorphic computing has been shown to be a superior alternative in terms of speed and energy, when compared to training on a conventional computing unit. A magnetic tunnel junction (MTJ), which constitutes the building block of a magnetic random-access memory (MRAM), is a competitive candidate for the next generation memory devices because it is non-volatile and exhibits high endurance, low power consumption, high operation speed and integration capability [8-9]. The present work discusses the proposal of a spintronic neuromorphic system with spin orbit torque driven domain wall motion-based neuron and synapse. The domain wall motion in the neuron is controlled by the electric field at the gate generated by voltage signals from pre-neurons as shown in Fig. 1(a). The application of voltage as input and output variable helps in reducing power consumption, as pinning site can be turned ON/OFF only when required. Further it provides better fanout as post-neuron output from first stage can act as infinite number of pre-neurons to next stage, which is going to play an important role in realization of system level neuromorphic architectures. For the implementation of the synaptic weight, we propose 3-terminal MTJ with stochastic domain wall motion in the free layer. The edge roughness results in intrinsic pinning of domain wall and this adds to the stochastic behaviour of domain wall motion in presence of spin transfer torque and/or spin orbit torque [10]. We have incorporated these intrinsic pinning effects by creating triangular notches on the sides of free layer as shown in Fig. 1(b). The complete neuromorphic circuit containing neurons, synapses and control circuitry implementation of spike time dependent plasticity is shown in Fig. 1(a). The sensing unit consists of a voltage comparator which provides high positive or zero voltage feedback pulse to the weight-updating unit. The weight updating unit takes this signal and the pre-neuron signal to decide the sign of the synaptic weight update pulse based upon spike timing correlation between the pre- and post-neuron. For modelling the micromagnetics and spin transport in both synapse and neuron, we developed a micromagnetic Non-Equilibrium Green's Function (*MuMag-NEGF*) coupled model. In Fig. 2(a), we show that in the presence of the gate voltage the uniaxial anisotropy for a 20 nm-wide region is varied slightly which results in the pinning of domain wall at 40 nm from the centre. In the absence of gate voltage uniaxial anisotropy is uniform and the domain wall moves more than 100 nm right in 10 ns, where it is sensed by the MTJ as post neuron spike. Also, the reduction of domain wall velocity is shown in Fig. 2(b). The thermal effects result in the stochastic domain wall motion but stochasticity is tuned by the external current in the form of spin orbit torque. Fig. 2 (c) shows the stochastic magnetization switching in MTJ synapse and stochasticity is tuned in either direction with application of positive and negative current pulses. In the presence of more positive pulses, the MTJ gradually moves into low resistance state, while in the presence of more negative pulses it moves into high resistance state, as shown in Fig. 2(d). When a current pulse is applied, the probability of domain wall moving increases. The dynamic pattern recognition capabilities of the circuit are tested on 9x9 cross-bar architecture, consisting of 9 pre-neurons, 9 post-neurons and 81 synapses. In summary, here we have successfully designed and demonstrated the on-chip stochastic dynamic learning by adopting the spike time dependent plasticity as the learning algorithm. At the end of training phase, we demonstrated that all pattern synapses stochastically evolve into low resistance state (high weight) while the remaining background synapses are in high resistance state (low weight).

[1]. Deming Zhang, Weisheng Zhao et. al, "All spin neural networks based on compound spintronic synapses and neurons," *IEEE Advances in Biomedical Circuits and Systems*, vol. 10, no.4, August-2016. [2]. Otitoaleke Akinola, Jean Anne C Incorvia et.al, "Three terminal magnetic tunnel junction circuits showing spike timing-dependent plasticity," *J. Phys. D: Appl. Phys.* 52 (2019) 49LT01 (11pp). [3]. Yangqi Huang, Weisheng Zhao et.al, "Magnetic-skyrmion based synaptic device," *IOP Nanotechnology*, 28 08LT02, 2017 [4]. Jiang Nan, Weisheng Zhao et.al, "Efficient Magnetic Domain Nucleation and Domain Wall Motion with Voltage Control Magnetic Anisotropy Effect and Antiferromagnetic/Ferromagnetic Coupling," *IEEE TRANSACTIONS ON MAGNETICS*, Vol. 55, No. 7, JULY 2019. [5]. Jialin Cai et.al, "Voltage-Controlled Spintronic Stochastic Neuron Based on a Magnetic Tunnel Junction," *Phys. Rev. Applied* 11, 034015, 6 March 2019.[6]. M. Bauer, R. Alexis, G. Atwood, B. Baltar, A. Fazio, K. Frary, M. Hensel, M. Ishac, J. Javanifard, M. Landgraf, D. Leak, K. Loe, D. Mills, P. Ruby, R. Rozman, S. Sweha, S. Talreja, and K. Wojciechowski, in *IEEE International Solid-State Circuits Conference Digest of Technical Papers* (1995), p. 132. [7]. T. S. Jung, Y. J. Choi, K. D. Suh, B. H. Suh, J. K. Kim, Y. H. Lim, Y. N. Koh, J. W. Park, K. J. Lee, J. H. Park, K. T. Park, J. R. Kim, J. H. Yi, and H. K. Lim, *IEEE J. Solid-State Circuits* 31, 1575 (1996). [8]. X. H. Lou, Z. Gao, D. V. Dimitrov, and M. X. Tang, *Appl. Phys. Lett.* 93, 242502 (2008). [9]. N. Locatelli, V. Cros, and J. Grollier, *Nat. Mater.* 13, 11 (2014). [10]. F. N. Tan et.al, "High Velocity Domain wall propagation using voltage control magnetic anisotropy," *Scientific Reports*, 2019) 9:7369.

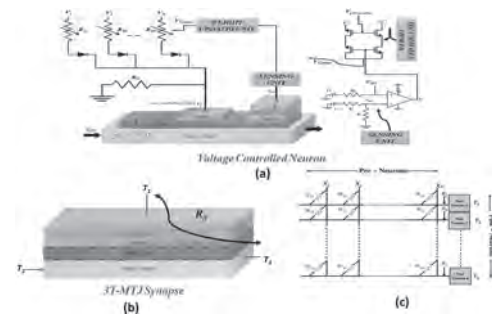


Fig. 1: (a) Neuromorphic circuit implementation of spike time dependent plasticity-based pattern recognition. The circuit consists of voltage-controlled magnetic anisotropy post neuron and stochastic 3T-MTJ synapse with domain wall driven by SOT. (b) 3T-MTJ stochastic synapse schematic with small notches. (c) Cross-bar architecture implementation of the circuit.

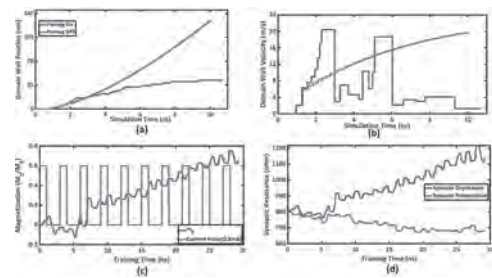


Fig. 2: (a) Domain wall position in neuron for pinning ON and pinning OFF controlled by gate voltage. (b) Domain wall velocity for the pinning and non-pinning case. (c) Magnetization in the free layer MTJ synapse showing stochastic behavior with a positive current pulse. (d) MuMAG – NEGF coupled computed resistance evolution of the synapse.

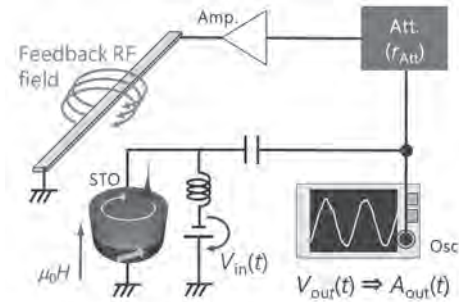
GB-07. Enhanced Computational Ability of Spin Torque Oscillator With Delayed-Feedback Circuit for Physical Reservoir Computing.

A. Kamimaki¹, S. Tsunegi¹, K. Nakajima², K. Yakushiji¹, A. Fukushima¹, S. Yuasa¹ and H. Kubota¹

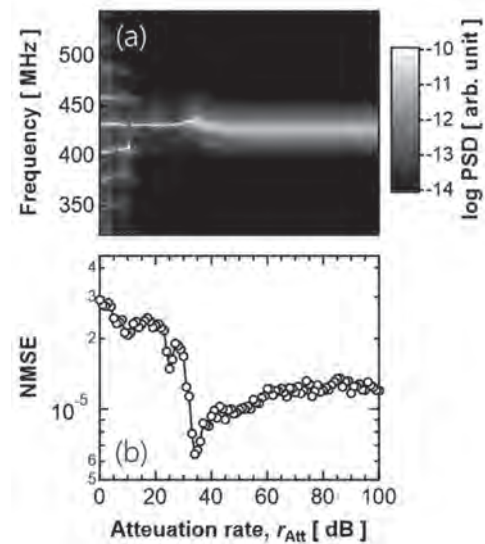
1. Research Center for Emerging Computing Technologies (RCECT), AIST, Tsukuba, Japan; 2. Department of Mechano-Informatics, Univ. of Tokyo, Tokyo, Japan

Physical reservoir computing using spin-torque oscillator (STO) has been attracting much attention after the demonstration of highly accurate human voice recognition [1]. To enhance the computational ability of STOs, there are two approaches: an array of STOs, and delayed feedback system. In the STO array, theoretical study was performed on 10-1000 STOs with interaction to obtain highly nonlinear dynamics, resulting in enhancement of computational ability that is competitive to quantum reservoir [4]. A similar highly nonlinear dynamics can be generated by using the feedback system, where outputted power from STO was reinjected in the form of electrical current or magnetic field to induce additional torque. By tuning the additional torque, complex magnetization dynamics such as amplitude modulation [5] and chaos [6,7] can be induced. These nonlinear dynamics are expected to enhance the computational ability even without interactions between STOs. Recent study showed that tunable nonlinear dynamics and delayed response by the feedback effect are adaptable for specific temporal pattern recognition task [7]. However, quantitative comparison of computational ability between the array system and the feedback system has not been investigated. In this work, we quantitatively evaluate the computational ability of STO with delayed-feedback circuit by performing a general task. The computational ability was evaluated by performing second order nonlinear autoregressive moving average (NARMA2) task [3,4]. The NARMA2 task aims to reproduce target outputs, defined by nonlinear transformation of the random inputs, from the amplitude of the STO. Figure 1 is a schematic illustration of vortex-type STO [2] with a delayed feedback circuit. To excite an auto-oscillation of the vortex core, perpendicular magnetic field of about 0.5 T and bias voltage of 350 mV were applied. In addition, we superposed random-pulse voltage with the width of 25 ns on the bias voltage. The random pulse was based on the uniform random number in the range of [-1,1] with the magnitude of 75 mV; therefore, the total input voltage varied from 275 to 425 mV. The outputted signal of the STO was amplified and converted to the RF magnetic field, which was applied to the STO with time delay of about 30 ns. The strength of the feedback signal was controlled by a tunable attenuator. Figure 2(a) shows power spectral density of the STO with delayed feedback as a function of attenuation. In the large attenuation region, the power spectra show a broad peak. With decreasing the attenuation, sharp multiple peaks appeared in the spectra below 30 dB. Such a split of spectrum is often observed when the feedback effect induces the amplitude modulation [5,6]. Figure 2(b) summarizes the dependence of normalized mean square error (NMSE) of NARMA2 task on the attenuation. It is clearly shown that NMSE can be minimized at an attenuation of 34 dB, below which the sharp multi peak structure appeared in the spectra. The observed minimum NMSE (6.4×10^{-6}) is comparable to that theoretically obtained in the array of 16-coupled STOs [3]. This result indicates that single STO with delayed-feedback circuit can compete with the STO array. This work is supported by NEDO.

[1] J. Torrey et al., Nature 547, 428 (2017). [2] S. Tsunegi et al., Jpn. J. Appl. Phys. 57, 120307 (2018). [3] T. Kanao et al., Phys. Rev. Applied 12, 024052 (2019). [4] K. Fujii et al., Phys. Rev. Applied 8, 024030 (2017). [5] D. Kumar et al., Sci. Rep. 6, 30747 (2016). [6] T. Taniguchi et al., Phys. Rev. B 100, 174425 (2019). [7] J. Williams et al., Appl. Phys. Lett. 114, 232405 (2019). [8] M. Riou et al., Phys. Rev. Applied 12, 024049 (2019).



Schematic illustration of spin-torque oscillator (STO) with delayed-feedback circuit. Auto-oscillation is driven by random pulse voltage $V_{in}(t)$. Power of the feedback is controlled by the rate of attenuator r_{Att} . Reservoir computing is performed using time-series amplitude $A_{out}(t)$ obtained by the Hilbert transformation of output voltage $V_{out}(t)$.



(a) Power spectral density (PSD) of STO with the delayed feedback circuit as a function of attenuation rate r_{Att} . (b) Normalized mean-squared error (NMSE) of second order nonlinear autoregressive moving average (NARMA2) task against attenuation rate. NMSE shows a minimum value (6.4×10^{-6}) at $r_{Att} = 34$ dB.

GB-08. In-MRAM Processing Elements With Single-Step Convolution for Binary Neural Network.

Z. Bian¹, J. Chen¹ and H. Cai¹

1. Southeast University, Nanjing, China

Recent research on deep learning shows that Binary Neural Network (BNN) is able to significantly reduce computation and memory cost with small precision loss [1][2]. By binarizing inputs and weights to +1 or -1 in BNNs, multiply-and-accumulate (MAC) operations can be replaced by XNOR operation in memory. Nonvolatile memory for BNN such as resistive random access memory (RRAM) and magnetic random access memory (MRAM) was reported in [3]-[6]. In this paper, we use spin-torque transfer magnetic random access memory (STT-MRAM) to complete XNOR and single-step convolution in memory. The main contributions include: (1) A STT-MRAM based structure with four transistors and two magnetic tunnel junctions (MTJ) (4T-2M) is proposed for binary convolution and fully connection operations using current mode sense amplifier. (2) The impact of different tunnel magnetoresistance ratio (TMR) and different size of MTJ on accumulating in memory has been explored. (3) By quantizing sensing yield into model, the trade-off between energy and performance is investigated. As shown in Fig. 1 (a), a 4T-2M bit-cell structure represents one synaptic weight, ‘-1’ is represented by two MTJs as parallel (P) and anti-parallel state (AP). The opposite combination is used to represent ‘1’. Two encoded word lines (WLs) represent one input value. To complete the XNOR operation, an offset-canceling current-sampling sense amplifier (OCCS SA) [7] is used (see Fig. 1(b)) to compare the current difference between source line (SL) and SLB. Fig.1 (c) shows the structure of the proposed STT-MRAM block. For convolution operation, the row decoder decodes by appropriate timing decodes the multiple WLs to input parallel, and output through path <1> as the result of convolution. For fully connected operation, the row decoder activates the WLs row by row, and output through path <2> with bit-counting as the result of one fully connected. We implement 9 bits XNOR and accumulation to perform 3 × 3 convolution. Fig. 1(d) lists all the combinations in the convolution. The worst case is four ‘-1’ and five ‘1’ accumulation or its opposite combination, which causes the minimum current difference between “5I_{AP}+4I_P” and “5I_P+4I_{AP}”. Fig. 1(e) illustrates the circuit realization of BNN. When one group of WLs is simultaneously activated, I_{SL} and I_{SLB} will be different depending on the resistance of MTJs on two SLs. A CSA is implemented to generate high level when weighted sum is positive, and low level when weighted sum is negative. The output of the CSA represents the output of the neuron. SPICE-level simulation is performed using a Verilog-A model of STT MTJ and an industrial 28-nm CMOS process. Fig.2 (a) shows the simulation results that the sensing yield in different TMR and MTJ critical dimension (CD) can up to 99.8%. The sensing yield is positively correlated with TMR and negatively correlated with MTJ CD. As Fig.2(b) indicated, smaller MTJ CD leads to higher sensing margin [8]. As shown in Fig. 2(c), a BNN model consisting of two convolutional stages and one fully connected layer as the classifier is designed. Validation results on MNIST handwritten digit dataset is shown in Fig. 2(d). Sensing yield is quantized into model when sensing processes is failed, the results of convolution will be flipped. Lower TMR and larger MTJ CD result in a lower sensing yield and a dramatic decrease in accuracy. When TMR is greater than 2 with 40nm MTJ or TMR is greater than 1.5 with MTJ smaller than 35nm, the accuracy could achieve >95% (<1.8% loss). Fig. 2(e) illustrates the energy saving of single-step convolution can achieve 51.2% compared with that of row by row with a slight decrease in accuracy.

[1] M. Courbariaux, et al., arXiv: 1602.02830, 2016. [2] M. Rastegari, et al., arXiv: 1603.05279, 2016. [3] Z. Dong et al., IEEE Transactions on Electron Devices, vol. 66, no. 1, pp. 793-801(2019) [4] L. Chang et al., IEEE Transactions on Very Large Scale Integration (VLSI) Systems, vol. 27, no. 11, pp. 2668-2679(2019) [5] Y. Pan et al., IEEE Transactions on Magnetics, vol. 54, no. 11, pp. 1-5(2018) [6] Y. Zhang et al., IEEE Transactions on Electron Devices, vol. 67, no. 2, pp. 469-473, Feb. 2020. [7] T. Na et al., IEEE Journal of Solid-State Circuits, vol. 52, no. 2, pp. 496-504, Feb. 2017. [8] Zhao, W. S., et al. Microelectronics Reliability, vol. 52, no. 9–10, Sept. 2012.

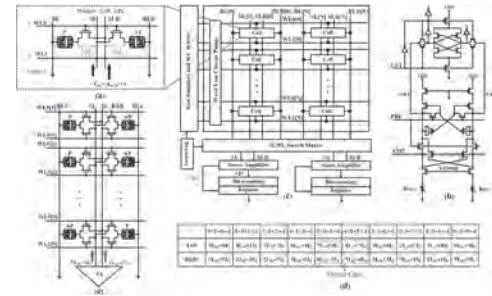


Fig.1 (a) Cell configurations to represent one weight using two MTJs and four transistors. (b) Schematic of OCCS SA. (c) 4T2M based array to complete convolution and fully connection, <1> indicates path 1 and <2> indicates path 2. (d)The list of all the combinations in the convolution. (e) Schematic of the XNOR and accumulate operation as convolution in memory.

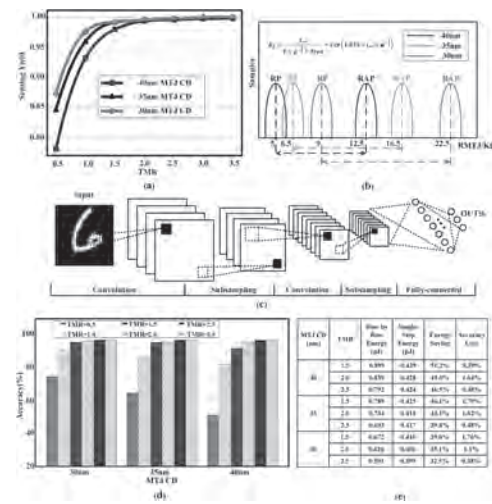


Fig.2 (a) The sensing yield in different TMR with different MTJ CDs. (b) The resistance distribution of different MTJ CDs. (c) Diagram of the BNN topology used for evaluation with MNIST. (d) The performance of binary neural network with different MTJ CDs and different TMR. (e) Trade-off between energy saving and accuracy loss.

GB-09. Neuromorphic Computation With a Single Magnetic Domain Wall.

R.V. Ababei¹, M.O. Ellis², I.T. Vidamour¹, E. Vasilaki², D. Allwood¹ and T. Hayward¹

1. Materials Science, The University of Sheffield, Sheffield, United Kingdom; 2. Computer Science, The University of Sheffield, Sheffield, United Kingdom

Classifying or predicting complex time-dependent signals (e.g. speech, financial data, the weather) is a challenging computational task. Reservoir computing (RC) is an efficient neuromorphic computing approach that is ideally suited to such tasks and is typically implemented in software using a recurrent neural network (RNN) with fixed synaptic weights (the reservoir) connected to a single, trainable readout layer. However, more efficient implementations of RC are possible if the software RNN reservoir is substituted with a physical system with the correct properties, such as non-linear response to input signals and inherent memory, leading to a readily deployable, hardware-based neuromorphic computing platform [1]. In this work, we propose a novel approach to RC where the dynamics of a single magnetic domain wall (DW) trapped between two defect sites in a nanostrip acts as a hardware-based reservoir. We demonstrate how such a device, with dimensions smaller than $1\ \mu\text{m}$, is capable of performing complex data analysis tasks, such as speech recognition. We have modelled a Ni nanowire with two anti-notches (shown in the inset of Fig. 1(a)) using both a simple 1D model[2] and micromagnetic simulations. Both models show the DW exhibit complex oscillatory dynamics similar to the Duffing oscillator, thus giving highly non-linear responses to applied magnetic fields (Fig. 1(a)). We exploit the DW dynamics for RC by using an applied field to inject time-multiplexed input signals into the reservoir and show how this approach allows the device to perform classification tasks. We have explored how the regime of applied fields affects the accuracy of sine and square wave classification, showing that the best recognition rate is obtained at the edge of a chaotic regime of oscillation (Fig. 1(b)). We have also demonstrated that the same approach can be used for more complex tasks, such as spoken digit recognition and handwritten digits recognition. Our work opens a new perspective for neuromorphic computing in nanomagnetic hardware.

[1] M. Riou et al., Phys. Review Applied, 2019 [2] A. Pivano et al., Phys Review B, 2016

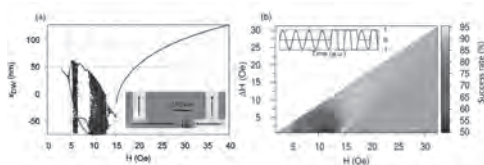


Fig. 1: Simulations of Ni nanostrip at 500 MHz. Figure (a) shows a typical bifurcation diagram computed with 1D model at 500MHz and the inset of Fig. 1(a) illustrates the typical geometry of a Ni nano-strip with two anti-notches separated by 350 nm. Figure (b) shows the recognition rate for the sine and square task computed with 1D model of a domain wall in a Ni nanostrip. The input field is oscillatory comprising two terms: H -the constant offset of the field and ΔH -the amplitude of the stimulus. The inset shows a sequence of inputs and its corresponding output calculated during the classification process using 1D model.

GB-10. Superiority of in-Plane Easy-Axis Stochastic Nanomagnet for Shorter Relaxation Time.

S. Kanai^{1,2}, K. Hayakawa¹, T. Funatsu¹, W.A. Borders¹, J. Igarashi¹, B. Jinnai³, H. Ohno^{1,4} and S. Fukami^{1,5}

1. Laboratory for Nanoelectronics and Spintronics, Research Institute of Electrical Communication, Tohoku University, Sendai, Japan; 2. Division for the Establishment of Frontier Sciences, Organization for Advanced Studies, Tohoku University, Sendai, Japan; 3. WPI-Advanced Institute for Materials Research, Tohoku University, Sendai, Japan; 4. Center for Science and Innovation in Spintronics, Tohoku University, Sendai, Japan; 5. Center for Spintronics Research Network, Tohoku University, Sendai, Japan

Unconventional computing utilizing stochastic behavior to effectively solve complex problems, *i.e.*, “probabilistic computing,” has gathered much attention [1]. Stochastic magnetic tunnel junction (MTJ) is a promising device to compose the probabilistic bit, a fundamental unit of the probabilistic computer, with efficient as well as individual control of its stochasticity. The average duration of MTJ dwelling in each state, *i.e.*, relaxation time τ , determines the critical indices of the computer’s performance, *e.g.*, accuracy and computing time. As a proof of concept, integer factorization has been demonstrated with stochastic MTJs with a perpendicular easy axis (p-MTJs) [2], whose typical τ is on the order of milliseconds. Meanwhile, τ of MTJs with an in-plane magnetic easy axis (i-MTJs) is reported down to sub-microseconds [3]. Here we experimentally and theoretically address the τ of nanomagnets in low-thermal-stability MTJs and elucidate the physical mechanism causing the different fluctuation timescale between p- and i-MTJs. A stack structure, Ta (5.0)/PtMn (20)/Co (2.6)/Ru (0.90)/CoFeB (2.4)/MgO/CoFeB (2.1)/Ta (5.0)/Ru (5.0) (thickness in nm), is deposited on a thermally oxidized Si substrate by dc/rf magnetron sputtering. Both bottom (reference) and top (free) CoFeB layers have an in-plane easy axis. Effective perpendicular anisotropy field $\mu_0 H_K^{\text{eff}}$ of the top CoFeB layer is -0.46 T (negative sign indicates in-plane easy axis). The stack is processed into elliptic MTJs with geometry averaged diameter D of 55 nm. Typical TMR ratio is 110% and $RA = 32 \Omega\mu\text{m}^2$. Figure 1(a) shows the measurement circuit and Fig. 1(b) shows time-averaged $\langle R \rangle$ as a function of in-plane magnetic field H along a long axis of MTJs, indicating superparamagnetic behavior with zero coercivity. Figure 1(c) shows a measured random telegraph noise (RTN) at $\mu_0 H = -7.9$ mT. τ averaged for P and AP states $\tau_{\text{ave}} = (\tau_P \tau_{\text{AP}})^{0.5}$, where τ_P (τ_{AP}) is the τ to stay at P (AP) state, which is about two orders shorter than that ever reported in MTJs [3]. We then numerically calculate τ of p- and i-MTJs based on a stochastic Landau-Lifshitz-Gilbert (LLG) equation including a thermal field [4]. We define magnetic energy with H_K^{eff} and in-plane anisotropy field $H_{K,\text{in}}$ as $E = M_S v (H_K^{\text{eff}} + H_{K,\text{in}} \sin^2 \varphi) \sin^2 \theta / 2$, with M_S , v , θ , and φ being the spontaneous magnetization, the volume of nanomagnet, the polar angle, and the azimuthal angle, respectively. We set the same Δ for both systems; $\mu_0 H_K^{\text{eff}} = 10$ mT, $\alpha = 0.02$, and thermal stability factor $\Delta = H_K^{\text{eff}} M_S v / 2k_B T = 3.8$ ($k_B T$ is thermal energy) are assumed for the p-MTJ, and $\mu_0 H_K^{\text{eff}} = -0.46$ T, $\mu_0 H_{K,\text{in}} = 10$ mT, $\alpha = 0.02$, and $\Delta = H_{K,\text{in}} M_S v / 2k_B T = 3.8$ for the i-MTJ. Figures 2(a) and 2(d) show the directions of magnetization, a torque from perpendicular magnetic anisotropy, that by damping, and that by the thermal fluctuation calculated by E and LLG equation for p- and i-MTJs, respectively. In the p-MTJs, the torque from H_K^{eff} directs in the azimuthal direction, and the only torque directing in the polar direction to induce magnetization switching is the thermal fluctuation field. Accordingly, the magnetization precesses with perpendicular anisotropy field and switches from one energy stable direction to the other with a random fluctuation field, as shown in the magnetization trajectory in Fig. 2(b). In this case, τ is found to be well described by the random-walk under damping [4,5] as $\tau = \pi^{0.5} \Delta^{-0.5} (2\alpha\gamma\mu_0 H_K^{\text{eff}})^{-1} \exp(\Delta)$. τ in this condition is calculated as ≈ 0.8 ns, which is consistent with the calculated RTN shown in Fig. 2(c). On the other hand, as shown in Figs. 2(d) and 2(e), the directions of the torques in i-MTJs are different from those in the perpendicular system due to the difference in the landscape of energy potential. τ is calculated to be 20 ns [Fig. 2(f)], which is close to the experimentally obtained τ , and several tens of times shorter than that calculated for the perpendicular system even with the same Δ . We numerically simulate τ as a function of Δ and clarify that the values are well described by $\tau = \pi(\alpha\gamma\mu_0\Delta)^{-1} [H_K^{\text{eff}}(H_K^{\text{eff}} + H_{K,\text{in}})]^{-0.5} \exp(\Delta)$, which is analyt-

ically derived with Fokker-Planck equation [4,6] under $\Delta \gg 1$ and $-H_K^{\text{eff}} \gg H_{K,\text{in}}$. In conventional understanding, a decrease of H_K^{eff} decreases Δ , leading to shorter τ for p-MTJs. However, our analysis indicates that it *increases* the prefactor of $\exp(\Delta)$, in proportion to $H_K^{\text{eff}-1.5}$. This dilemma determines a lower limit of τ as $\tau_{\text{min}} = M_S v \ln 2 (\alpha\gamma\mu_0 k_B T)^{-1}$, at which magnetization dynamics is dictated by the thermal fluctuation. For example, τ_{min} is 151 ns for a p-MTJ with $D = 60$ nm, thickness of 1 nm, $M_S = 1.4$ T, and $\alpha = 0.02$ at room temperature. For i-MTJs, one can be free from the dilemma because the prefactor is mainly determined by H_K^{eff} whereas $\exp(\Delta)$ is determined by $H_{K,\text{in}}$, leading to $(\pi\Delta)^{-0.5} M_S |H_K^{\text{eff}}| v / 4k_B T$ times shorter τ than that with p-MTJs for the same Δ . This ratio reasonably explains the different τ observed for p-MTJs and i-MTJs, indicating i-MTJs with $\mu_0 |H_K^{\text{eff}}| \sim 1$ T can achieve τ down to nanoseconds. This work is in part supported by JST-CREST No. JP1082016, and JSPS Nos. 19J12206, 19J12926, 19H05622, 20H02178, and 19KK0130.

[1] P. R. Feynman, Int. J. Theor. Phys. Vol. 21, p.467-488 (1982) [2] W. A. Borders, A. Z. Pervaiz, S. Fukami, *et al.*, Nature Vol. 573, p.390-393 (2019) [3] B. Parks, A. Abdelgawad, T. Wong, *et al.*, Phys. Rev. Appl. Vol. 13, p.014063 (2020) [4] W. F. Brown Jr., Phys. Rev. Vol. 130, p.1677-1686 (1963) [5] T. Taniguchi, and H. Imamura, Phys. Rev. B Vol. 85, p.184403 (2012) [6] T. Taniguchi, Y. Utsumi, and H. Imamura, Phys. Rev. B Vol. 88, p.214414 (2013)

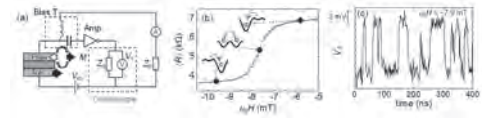


Fig. 1 (a) Measurement circuit for time-averaged resistance $\langle R \rangle$ and random telegraph noise (RTN). (b) In-plane magnetic field $\mu_0 H$ vs. $\langle R \rangle$. (c) RTN signal measured as transmitted voltage V_T .

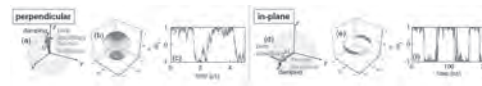


Fig. 2 (a)(d) Directions of the torques. (b)(e) Calculated magnetization trajectories and (c)(f) time vs. their easy axis component. The conditions for (a)-(c) perpendicular and (d)-(f) in-plane easy axes are shown.

GB-11. Machine Learning With Stochastic Magnetic Domain Wall Based Neurons and Synapses.

M.O. Ellis¹, A. Welbourne², S. Kyle², T. Hayward², D. Allwood² and E. Vasilaki¹

1. Department of Computer Science, The University of Sheffield, Sheffield, United Kingdom; 2. Department of Material Science and Engineering, The University of Sheffield, Sheffield, United Kingdom

The bottleneck between data storage and processing on conventional computing hardware is seen as a significant limitation to many forms of machine learning algorithms [1]. One route to solve this issue is to employ physical devices that can naturally mimic brain-like behaviour, known as neuromorphic computing. Magnetic materials are already widely used for long-term data storage, but ongoing work seeks to make use of their potential as both working memory and computing architectures. Particularly, devices based on magnetic domain walls (DWs) can perform logic operations [2] and can readily store information [3]. However, the stochasticity of DW pinning limits the feasibility of creating technologically viable devices. Here, we demonstrate how stochasticity can be changed from a technologically inhibitive behaviour into an integral property of machine learning algorithms that could be used in specialised neuromorphic devices. We first present experimental measurements that demonstrate the feasibility of tuning stochastic processes by applying external stimuli. Focused magneto-optic Kerr effect measurements were used to probe the pinning of DWs at notch-shaped defect sites in 400 nm wide Permalloy nanowires (Fig. 1(a)). DWs were injected into the nanowires and propagated to the defect sites using a field parallel to the nanowire (H_x). The probability of the DWs being pinned at the defect sites was found to depend sigmoidally on the magnitude of a field transverse to the nanowire length (H_y), (Fig. 1(b)). We apply this stochastic behaviour in two possible contexts, as a stochastic neuron for a binary network or as a stochastic synapse for feed forward network, where we model the pinning behaviour based on the experimental results. In the first case, we have modelled these DW wires as neurons in a Boltzmann machine, which exploits their randomness in order to sample a defined, or trained, probability distribution. We apply this to the task of integer factorisation [4], where the connectivity of the neurons is defined so that the binary representation of the integer factors are the most probable states. Such a device inherently exploits the tunable stochasticity of the system to solve complex problems. In the second case, we have explored the properties of feedforward artificial neural networks where the nanowires acted as binary stochastic synapses (BSS). These synapses are individually random but the output can be improved by repeatedly sampling the network to include redundancy. We have developed both mean-field and stochastic based learning methods, where for low repeats of the synapse the stochastic learning is seen to outperform the mean-field based method. It is found that for a single cycle of the network it can be trained to recognise handwritten digits with error rate of 17%. Repeated sampling of the network decreased the error rate to 8% for 128 cycles - close to mean field performance (Fig. 2). Following this we have expanded our network to become a multi-layer perceptron with both inhibitory and excitatory synapses. The additional layer increases the pathways through the network thus reducing the impact of the stochasticity on the classification. For the same classification test the error rate is seen to reduce to 5.5% with a hidden layer of 500 neurons. In conclusion, the pinning of DWs in nanowires can be tuned by applying a magnetic field transverse to the wire and the resultant pinning probability has been used as both stochastic neurons and synapses. As a neuron, we have demonstrated its ability to perform integer factorisation as part of a Boltzmann machine. While as a stochastic synapse, we have been able to train single and multi-layer networks to classify handwritten digits with close to digital network performance. Our work illustrates how the intrinsic stochasticity of DW devices can be harnessed to provide tunable bespoke hardware for machine learning tasks.

[1] M. M. Sabry Aly *et al.*, *Proceedings of the IEEE*, Vol. 107, no. 1, p. 19 (2019) [2] D. A. Allwood *et al.*, *Science*, Vol. 309, Issue 5741, p. 1688 (2005) [3] R. L. Stamps *et al.*, *J. Phys. D: Appl. Phys.*, Vol. 47, p. 333001 (2014) [4] W. A. Borders *et al.*, *Nature*, Vol. 573, p. 390 (2019)

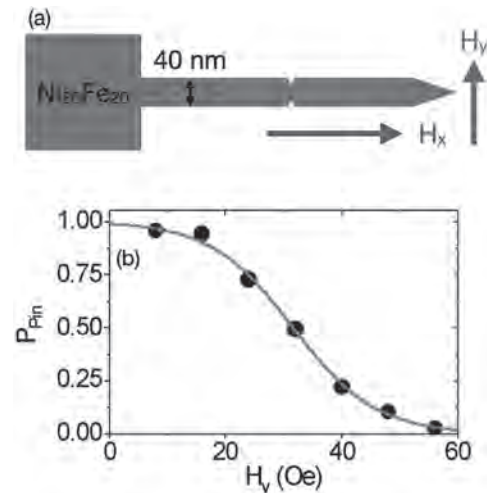


Fig. 1: (a) Schematic of a notched magnetic nanowire for use as a synapse with a parallel driving field (H_x) and a tunable transverse depinning field (H_y). (b) Pinning probability as a function of transverse field, showing a sigmoidal dependence.

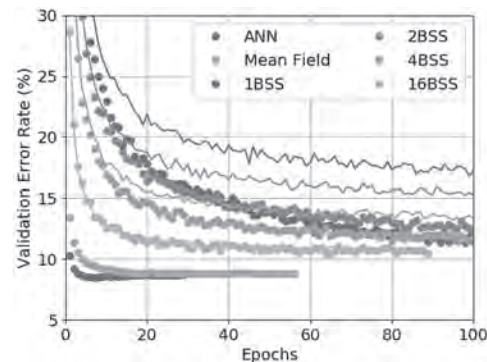


Fig. 2: The validation error rate of handwritten digits using a single layer network with binary stochastic synapses (BSS) for varying number of cycles of the network. Lines and points show the training using the mean-field or stochastic methods respectively.

GB-12. Mutually Coupled Superparamagnetic Tunnel Junctions.

P. Talatchian^{1,3}, M. Daniels², A. Madhavan^{3,2}, E. Jue⁴, M.R. Pufall⁴, W.H. Rippard⁴, J.J. McClelland² and M. Stiles²

1. Univ. Grenoble Alpes, CEA, CNRS, SPINTEC, Commissariat à l'énergie atomique et aux énergies alternatives Siège administratif, Grenoble, France; 2. Alternative Computing Group, Physical Measurement Laboratory, National Institute of Standards and Technology, Gaithersburg, MD, United States; 3. Institute for Research in Electronics and Applied Physics, University of Maryland at College Park, College Park, MD, United States; 4. Physical Measurement Laboratory, National Institute of Standards and Technology, Boulder, CO, United States

Magnetic tunnel junctions consist of two ferromagnetic layers separated by a thin insulating layer. The relative orientation of the two layers' magnetization has two stable configurations: parallel or antiparallel (P or AP). For use as a binary non-volatile memory in magnetic random access memory (MRAM), the retention time in each of the two configurations needs to be on the order of several years. This corresponds to energy barriers larger than $40 kT$ (k is the Boltzmann constant, and $T=300$ K is room temperature). If the energy barrier becomes smaller than $12 kT$, thermal fluctuations induce random switching of the magnetization between the P and the AP states with a mean timescale between $10 \mu\text{s}$ and 1 ms. Such fluctuating, low-energy-barrier tunnel junctions are referred to as superparamagnetic tunnel junctions [1]. Recently, superparamagnetic tunnel junctions have become attractive as compact and energy-efficient devices for applications that require truly random variables [2,3], including innovative computing schemes [4,5,6,7,8]. Through adapted circuit co-design approaches, we previously showed that those devices are promising for implementing artificial neural networks with reduced energy consumption [9]. In cognitive computing, these superparamagnetic tunnel junctions can be used to emulate biological neurons [10, 11]. Here, we investigate simple ways of coupling these devices to extend these innovative computing schemes. To mimic neuron-like interconnections, it is important to develop simple schemes to couple such devices. Significant work has been done to develop coupling strategies for magnetic systems such as harmonic spin-torque nano-oscillators, which are useful for cognitive computing [12,13,14,15], but there is no equivalent scheme for superparamagnetic tunnel junctions. In this work, we experimentally demonstrate a simple electrical coupling method between two superparamagnetic tunnel junctions. We couple two stochastic magnetic junctions by placing them in parallel in a simple electrical circuit. We use the fact that their switching rate can be controlled deterministically by the applied current. They couple because their stochastic electrical transitions change the current flowing through the other device, changing its switching rate. In our circuit, the total applied current in each nanojunction is shared and depends on the joint resistance states of the nanojunctions. Depending on the current state of the system, transitions to certain joint states are favored while others are less probable. This coupling mechanism leads to non-zero cross-correlation between the stochastic switching events of the two fluctuating tunnel junctions, demonstrating their mutual coupling. We show experimentally that the cross-correlation becomes large when the switching time scales of the two superparamagnetic tunnel junctions are such that they both have roughly a 50 % probability to be in the parallel or antiparallel state. We also demonstrate that the cross-correlation increases when the total current applied to the system increases. We reach 18 % for the largest Pearson correlation value measured in the system. We find good agreements between numerical simulations of a comparable four-state Markov state process and our experiments. As we do not use sophisticated circuits for the coupling purpose, our approach opens new paths to compact and energy-efficient implementations of scaled-up arrays of coupled superparamagnetic tunnel junctions for new cognitive computing schemes.

[1] W. H. Rippard et. al. PRB, Vol 84, 064439 (2011). [2] B. Parks et. al. AIP Advances, Vol 8, 055903 (2018). [3] D. Vodenicarevic et. al. Phys. Rev. Appl, Vol 8, 054045 (2020). [4] A. Mizrahi et. al. Nature Communications, Vol 9, 1533 (2018). [5] K. Camsari et. al. Appl. Phys. Rev, Vol 6, 011305 (2019). [6] K. Camsari et. al. Phys. Rev. X, Vol 7, 031014 (2017). [7] A. Sengupta et. al. IEEE Trans. on Electron Devices, Vol 63, 2963 (2016). [8] W. A. Borders et. al. Nature, Vol 573, 390 (2019). [9] M. W. Daniels, et al.

Phys. Rev. Appl, Vol 13, 034016 (2020). [10] W. Gerstner et. al. Neuronal Dynamics, Cambridge Univ. Press (2014). [11] J. Grollier et. al. Nature Electronics, Vol 3, 360 (2020). [12] W. H. Rippard et. al. PRL, Vol 95, 067203 (2005). [13] S. Kaka et. al. Nature, Vol 437, 389 (2005). [14] A. A. Awad, Nat. Phys, Vol 13, 292 (2017). [15] M. Romera†, P. Talatchian† et al. Nature, Vol 563, 230-234 (2018).

GB-13. Nanomagnetic Self-Organizing Logic Gates.

P. Gypens^{1*}, J. Leliaert¹, M. Di Ventra², B. Van Waeyenberge¹ and D. Pinna^{3,4}

1. Dept. of Solid State Sciences, Universiteit Gent, Gent, Belgium;
 2. Department of Physics, University of California San Diego, La Jolla, CA, United States; 3. Dept. of Physics, Johannes Gutenberg Universitat Mainz, Mainz, Germany; 4. Forschungszentrum Julich Peter Grunberg Institut, Julich, Germany

The end of Moore’s Law for complementary metal-oxide semiconductor (CMOS) technology has prompted the search for low-power computing, resulting in several promising proposals based on magnetic logic. One approach aims at tailoring arrays of nanomagnetic islands in which the magnetostatic interactions constrain the equilibrium orientation of the magnetization to embed logical functionalities [1]. Despite the realization of several proofs of concepts of such nanomagnetic logic, it is still unclear what the advantages are compared to the widespread CMOS designs, due to their need for clocking and/or thermal annealing for which fast convergence to the ground state is not guaranteed. In fact, it seems increasingly evident that “beyond CMOS” technology will require a fundamental rethinking of our computing paradigm. In this respect, digital memcomputing machines have been proposed [2]. These machines consist of *self-organizing logic gates* (SOLGs) which are able to dynamically “self-organize” into their logically correct states irrespective of whether the signal is applied to the traditional input terminals, or the traditional output terminals. This type of terminal-agnostic logic thus allows for reversed computing. Here [3], we introduce a novel concept of SOLGs that employs stray-field coupled nanomagnetic islands to perform terminal-agnostic logic: nanomagnetic self-organizing logic gates. We thereby focus on the design of a functionally complete NAND gate with which any Boolean circuit can be constructed in a bottom-up approach. Our strategy to build such a nanomagnetic SO-NAND gate relies on two main properties: *balancedness* and *dynamic error suppression* (DES) – see Figure 1. For reversible logic to work, the logically correct states should be occupied equally in thermodynamical equilibrium (and not only after a relaxation process into the ground states, as balancedness was originally defined [4]). This contrasts the balanced NAND gate proposed in Ref. [5]. To allow for larger circuits, the probability of being in a logically incorrect state should be suppressed. To this end, our DES scheme periodically checks the logical correctness of the gate/coupling and applies additional fields on each island of the gate/coupling if necessary. Our DES scheme is thus based on *local* information, i.e. the magnetization state of a single gate or coupling. This locality is in sharp contrast to the biasing used in p-bit logic inversion, for which the logical behavior of a collection of super-paramagnetic tunnel junctions (SMTJ) is fully imposed by *globally*-determined time-varying spin currents [6]. Owing to its locality, our approach does not suffer from scaling issues. To show the usefulness of our SO-NAND gate, we use it as a building block to construct a self-organizing two-bit multiplier – see Figure 2. Our SO-2BM is capable of decomposing *any* output number into its (prime)factors, finding each possible decomposition without clearly favoring nor penalizing any solution. This fact indicates that the balancedness remains largely conserved throughout the whole system, which allows the extension to larger systems in order to solve more complex problems.

[1] A. Imre, G. Csaba, L. Ji *et al.*, Science, Vol. 311, p. 205-208 (2006).
 [2] F. Traversa and M. Di Ventra, Chaos, Vol. 27, p. 023107 (2017). [3] P. Gypens, J. Leliaert, M. Di Ventra *et al.*, arXiv preprint arXiv:2012.12721 (2020). [4] J. Lust and B. Dixon, Inf. Sci., Vol. 113, p. 193-204 (1999). [5] P. Gypens, J. Leliaert and B. Van Waeyenberge, Phys. Rev. Appl., Vol. 9, p. 034004 (2018). [6] W. Borders, A. Pervaiz, S. Fukami *et al.*, Nature, Vol. 573, p. 390-393 (2019). [7] J. Leliaert, A. Vansteenkiste, A. Coene *et al.*, Med. Biol. Eng. Comput., Vol. 53, p. 309-317 (2015).

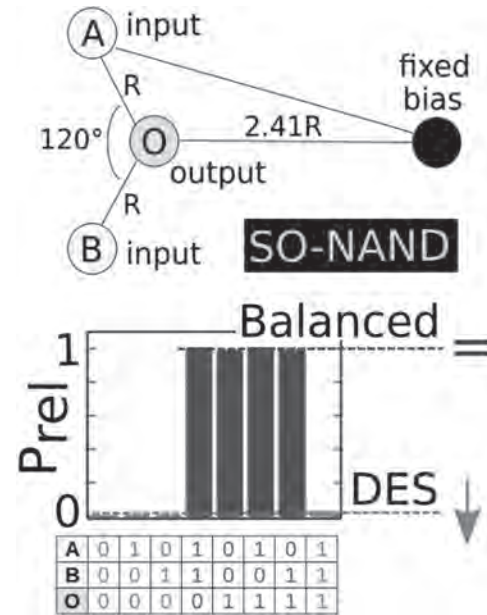


Fig. 1: Schematic representation of a self-organizing NAND gate consisting of four nanomagnetic islands with perpendicular anisotropy. The probability distribution is obtained with the macrospin simulation tool Vinamax [7] which numerically solves the Landau-Lifshitz-Gilbert equation taking thermal fluctuations into account. Logically incorrect states are suppressed by a dynamic error suppression (DES) scheme, while still preserving the balancedness of the gate. P_{rel} is the probability relative to the most likely logical state.

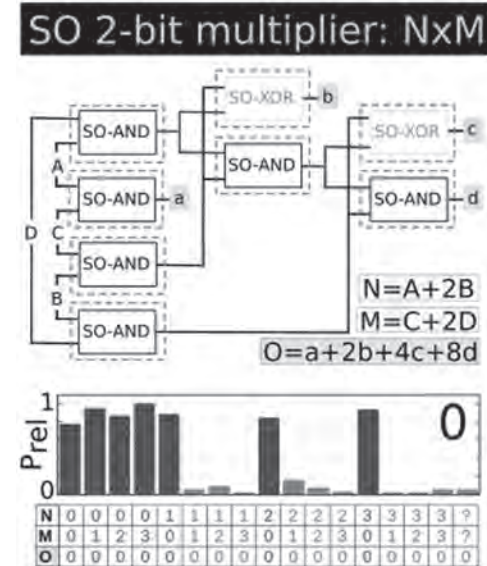


Fig. 2: Schematic representation of a self-organizing two-bit multiplier and the relative probability distribution obtained with Vinamax for an output fixed to 0. P_{rel} is the probability relative to the most likely logical state. The four output islands of the SO-2BM, labeled from a to d, are fixed such that they represent a certain number (0, 1, 2, 3, 4, 6, or 9) and the system is allowed to explore its state space. The magnetization of the input islands, corresponding to the solution of the computation, are labeled from A to D. All states of which one of the inputs is logically inconsistent are aggregated into the “??”-state.

Session GC
NEW APPROACHES IN COMPUTATIONAL MAGNETISM
Dieter Suess, Chair
Vienna University of Technology, Vienna, Austria

INVITED PAPER

GC-01. Entropic Effects and Solitons in Thermally Activated Magnetic Transitions INVITED.

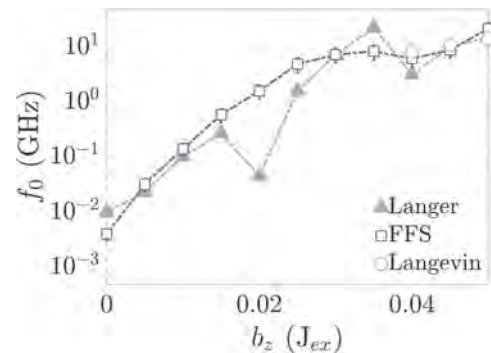
L. Desplat^{1,2}, C. Vogler³, D. Suess³, R. Stamps⁴ and J. Kim¹

1. Centre de Nanosciences et de Nanotechnologies, Palaiseau, France;
 2. Institut de Physique et Chimie des Matériaux de Strasbourg, Strasbourg, France; 3. Universitat Wien, Wien, Austria; 4. University of Manitoba, Winnipeg, MB, Canada

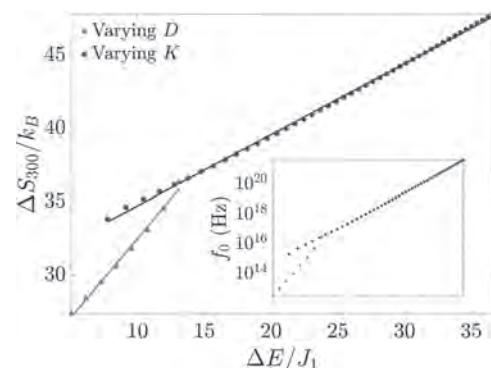
The rate of thermally activated transitions can generally be described by the Arrhenius law, as $k=f_0 \exp(-\Delta E/k_B T)$. In the previous expression, ΔE is the internal energy barrier, and f_0 is a prefactor that encompasses both dynamical and entropic contributions. In this work, we show how the activation entropy can play a crucial role in thermally activated magnetic transitions. To that end, we study two types of transitions involving solitons either as the stable state or the transition state, namely, skyrmion annihilation, and domain-wall mediated magnetization reversal in nanodisks. The aforementioned transitions pertain to the class of rare events, i.e., they are unlikely to arise in the course of a Langevin simulation, because the mean waiting time between events is much larger than the integration timestep. In this case, one possible approach is to use a form of reaction rate theory to calculate the energy barrier and the Arrhenius prefactor. To this end, we apply Langer's theory [1], which is an extension of the Kramers method to many dimensions. Alternatively, one may use a path sampling method such as forward flux sampling [2] in order to sample the transition path ensemble from the system's dynamics and extract a transition rate. In this work, we employ both methods in conjunction to study the thermal stability of magnetic skyrmions and nanodisks, for which the two methods show a good agreement. Magnetic skyrmions are particle-like, two-dimensional, non-collinear solitonic spin textures with a nontrivial topology. In ultrathin films and multilayers, small skyrmions are stabilized by an interfacial form of the Dzyaloshinskii-Moriya interaction (DMI). Skyrmion-based designs currently appear very promising for novel spintronics devices, e.g., for racetrack memories and logic gates, reservoir computing, or probabilistic computing [3]. Isolated skyrmions exist as metastable excitations of the collinear magnetic ground state and can be long-lived. For applications, a stability of up to 10 years at room temperature is a technological requirement, and the ability to accurately predict that stability is therefore crucial. We find that skyrmions can be stabilized not only by an internal energy barrier, but also by a large activation entropy. This stems from the fact that the metastable skyrmion state possesses a large entropy compared to the transition state, because skyrmions exhibit stable internal modes of deformation [4]. When applying a destabilizing magnetic field perpendicular to the skyrmion core, the skyrmion lifetime decreases quickly with the field amplitude. This results from a shrinking of the skyrmion, which simultaneously reduces the energy barrier, as well as the activation entropy through the suppression of the stable internal modes (Fig. 1) [5]. Next, we compute the mean waiting times between thermally activated domain-wall mediated magnetization reversals in a perpendicularly magnetized nanodisk. We use parameters that resemble that of a free CoFeB layer, as typically used in magnetoresistive random access memories [6]. By varying the perpendicular anisotropy and the interfacial DMI, we find that the Arrhenius prefactor can take extreme, seemingly non-physical values up to 10^{21} Hz, which is orders of magnitude beyond the typically assumed value of 10^9 Hz, and vary drastically as a function of material parameters. We show that the prefactor behaves like an exponential of the energy barrier, which stems from a linear variation of the activation entropy with the energy barrier (Fig. 2) [7]. This phenomenon, known as the Meyer-Neldel rule, or entropy-enthalpy compensation, has been reported across diverse fields of the natural sciences for over a century—in semiconductors, chemical reactions, biological death rates, etc [8]. In magnetism, it was only recently observed in the decay of the skyrmion lattice [9]. This result implies that the transition state, which, in the case of the magnetization reversal, is a domain wall found in the center of the disk, tend to possess a very large entropy compared to the collinear ground state. This is verified by the existence of gapless, low energy modes propagating along domain walls [10]. These

findings suggest that the Arrhenius prefactor, which is typically taken as an attempt frequency within the characteristic timescale of a magnetic system's dynamics, may in some cases contain a very large entropic contribution which should not be neglected. This seems to be particularly true in magnetic transitions involving solitons.

[1] J. S. Langer, Annals of Physics, Vol. 54, p.258 (1969) [2] R. J. Allen, P. B. Warren, and P. R. ten Wolde, Phys. Rev. Lett., Vol. 94, p.018104 (2005) [3] A. Fert et al., Nat. Nanotechnol., Vol. 3, p.152 (2013) ; Prychynenko et al., Phys. Rev. Appl., Vol. 9, p.014034 (2018) ; D. Pinna et al, Phys. Rev. Appl., Vol. 9, p.064018 (2018) [4] L. Desplat, D. Suess, J.-V. Kim et al., Phys. Rev. B, Vol. 98, p.134407 (2018) [5] L. Desplat, C. Vogler, D. Suess et al., Phys. Rev. B, Vol. 101, p.060403(R) (2020) [6] J. Sampaio, A. Khvalkovskiy, M. Kuteifan et al., Appl. Phys. Lett., Vol. 108, p.112403 (2016) [7] L. Desplat and J.-V. Kim, Phys. Rev. Lett., Vol. 125, p.107201 (2020) ; L. Desplat and J.-V. Kim, Phys. Rev. Appl., Vol. 14, p.064064 (2020) [8] A. Yelon, B. Movaghar, and R. Crandall, Rep. Prog. Phys., Vol. 69, p.1145 (2006) [9] J. Wild, T. N. Meier, S. Pollath et al., Sci. Adv., Vol. 3, p.e1701704 (2017) [10] F. Garcia-Sanchez, P. Borys, R. Soucaille, et al., Phys. Rev. Lett., Vol. 114, p.247206 (2015)



Arrhenius prefactor for skyrmion collapse as a function of the perpendicular external magnetic field in units of the exchange coupling constant, J_{ex} . The prefactor is computed through Langer's theory, forward flux sampling (FFS), and direct Langevin simulations.



Activation entropy for domain-wall mediated magnetization reversal in a nanodisk at $T = 300$ K as a function of the activation energy normalized by the exchange constant, A , and the disk thickness d , for variations of the DMI, D , and of the anisotropy, K . The inset shows the corresponding variation of the Arrhenius prefactor, f_0 .

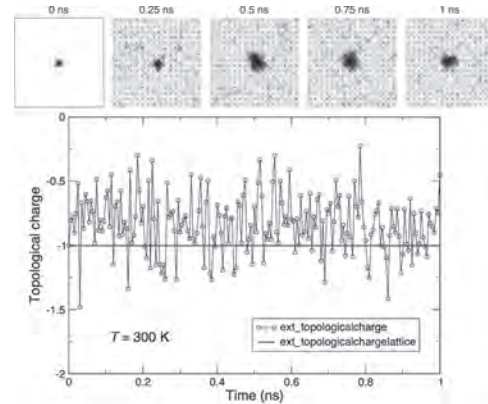
CONTRIBUTED PAPERS

GC-02. On Quantifying the Topological Charge in Micromagnetics Using a Lattice-Based Approach.J. Kim¹ and J. Mulkers²

1. Centre for Nanoscience and Nanotechnology (C2N), CNRS, Université Paris-Saclay, Palaiseau, France; 2. Department of Solid State Sciences, Universiteit Gent, Gent, Belgium

The topological charge or skyrmion number Q is a useful measure to characterize the topology of spin textures such as vortices and skyrmions in two-dimensional systems. When the magnetization field $m(r)$ is projected onto the unit sphere, Q measures the number of times the magnetic moments wrap around this sphere. For vortices and merons, $Q = \pm 1/2$, while for skyrmions, $Q = \pm 1$. Higher-order half- and full-integer charges are also possible. In numerical micromagnetism, a common approach involves solving the equations of motions for $m(r)$ that is discretized on a regular grid. The underlying assumption is that cell-to-cell variations in m are sufficiently small such that the exchange energy, proportional to the square of the magnetization gradient, remains meaningful. However, issues can arise under certain conditions, such as in the nucleation and annihilation of vortices and skyrmions, or in the stochastic dynamics under random fields, where large cell-to-cell variations in the magnetization can reduce the accuracy of the finite-difference approximations of the spatial derivatives used to estimate Q , which can result in spurious deviations from half- and full-integer values of Q . Here, we will describe a lattice-based implementation for the open source micromagnetics code MuMax3 [1] that allows an accurate determination of Q , particularly under Langevin dynamics used to model finite temperatures and in nucleation and annihilation processes [2]. The implementation is based on the approach of Berg and Lüscher [3], which involves summing over the solid angle subtended by three spins, forming elementary signed triangles, that are constructed from the finite difference cells. The implementation accounts for both periodic boundary conditions and finite-sized systems. A comparison between the finite-difference and lattice-based approaches is given in Fig. 1, where the time variation of the total topological charge is shown for a system hosting a single skyrmion under a temperature of 300 K. The blue circles represent the Q computed using finite-difference derivatives, which exhibit large fluctuations about the expected value of $Q = -1$ that are about as large as Q itself. Moreover, the time-averaged mean Q does not coincide with -1 . The solid red line represents the result of the lattice-based approach, which remains constant near the expected value of -1 . More precisely, the result is limited primarily by the single-precision of the floating-point arithmetic used, e.g., we find $Q = -1.0000001, -1.0000004, -1.0000008, -1.0000002,$ and -0.9999996 over 20-ns intervals at 400 K. We also show how the lattice-based approach is vastly superior to the finite-difference approximation in other test cases, which involve skyrmion-antiskyrmion pair nucleation due to spin-transfer torques and skyrmion fluctuations in finite dots. While the results do not necessarily call into question the validity of published work (since the topological charge is often only used as a proxy for magnetization gradients), they do highlight the care with which noninteger values of Q should be interpreted, particularly when processes such as nucleation, annihilation, and thermal fluctuations are at play. This work was partially supported by the Agence Nationale de la Recherche under contract no. ANR-17-CE24-0025 (TOPSKY) and Fonds Wetenschappelijk Onderzoek (FWO-Vlaanderen) through Project No. G098917N.

[1] A. Vansteenkiste, J. Leliaert, M. Dvornik et al., *AIP Adv* 4, 107133 (2014). [2] J.-V. Kim and J. Mulkers, *IOP SciNotes* 1, 025211 (2020). [3] B. Berg and M. Lüscher, *Nucl Phys* 190, 412 (1981).



Topological charge, Q , as a function of time for a skyrmion in a 1-nm thick film with periodic boundary conditions at 300 K. Blue circles represent the calculation based on a finite-difference approximation to spatial derivatives, as provided by the package `ext_topologicalcharge` in MuMax3, while the solid red line represents the calculation with the lattice-based approach, which is provided by the package `ext_topologicalchargelattice`. The top inset illustrates snapshots of the micromagnetic state.

GC-03. Theoretical Study of TheTransport of Skyrmions at Room Temperature in Granular Racetracks.

*J. Castell-Queralt¹, L. González-Gómez¹, N. Del-Valle¹ and C. Navau¹
1. Physics, Universitat Autònoma de Barcelona, Barcelona, Spain*

Magnetic skyrmions are whirling magnetic structures that can be found on certain magnetic materials [1]. They are promising candidates to become the next generation of information carriers as well as basic elements in ultra-dense magnetic memories, logic devices or computational systems due to their small size and high mobility. Skyrmions can be stabilized in ferromagnetic ultrathin films with the aid of interfacial Dzyaloshinskii-Moriya (iDM) interaction with a heavy-metal substrate. The same mechanism allows the formation of skyrmions in multilayers with alternate ferromagnets and heavy-metals. The experimental finding of room-temperature skyrmions has boosted the potentiality of skyrmions for applications and, in consequence, the study of their current-driving dynamics at non-zero temperatures. Skyrmionic racetracks are considered one of the most reliable systems to transport skyrmions using the spin-orbit torque produced by a spin-polarized current fed in a heavy-metal substrate. The racetrack borders create a confining potential whose intensity determines the limit speed that a skyrmion can achieve inside a track without being annihilated at the border. As temperature increases, the topological protection of skyrmions is reduced, however, in some systems it is possible to stabilize and transport them. Apart from compromising stability, temperature can turn skyrmion dynamics into stochastic. As temperature increases the dispersion of the skyrmions position becomes larger, behaving like a Brownian particle. This stochastic motion sets new conditions and restrictions on the applicability of racetracks. In particular some binary questions like: Will the skyrmion be annihilated at the edge of the racetrack?, now become probabilistic questions: Which is the probability of a skyrmion to be annihilated at the edge of the racetrack? To address this kind of questions, a deterministic approach has been developed to study the dynamics of skyrmions at non-zero temperatures [2]. By solving the Fokker-Planck equation (FPE) for a skyrmion we can directly determine the probability of finding a skyrmion for a given time and position. In [2], the dynamics of a skyrmion when approaching a pinning potential and when driven along a racetrack was studied. In this work we present a natural continuation to that study: the granularity of the ferromagnet is taken into account while the skyrmion is moving along a racetrack. When nanomagnetic systems are studied from a theoretical point of view, usually we do not consider the granularity of the ferromagnetic materials that form the system, neglecting the influence of the polycrystalline structure and the presence of defects. However, in experiments we cannot avoid them. The granularity and defects difficult the motion of skyrmions at low velocities setting an unpinning velocity, adding an additional ingredient to the transport of skyrmions: they can be pinned in some point of the track [3]. We simulate the granularity of the material setting a random array of pinning potentials with random (within a range) intensities. We study how the probability of a skyrmion to reach the end of track of length without being trapped or annihilated (success probability) changes as we vary the density of pinning potentials, which is proportional to the density of crystal grains, and the intensity of the pinning potentials, which is proportional to the difference of the magnetic properties between grains. In Fig. 1 and Fig. 2 we show different snapshots for the density of probability of a skyrmion being on a given position, in a simulation where 100 pin potentials are placed randomly. In Fig. 2 the average intensity of the pinning potentials is higher than in Fig. 1. We can observe in Fig. 1 that the probability of success is close to 1, indicating that the skyrmion will survive to its travel along the track without getting pinned. However, in Fig. 2 we observe that there is a considerable probability that the skyrmion gets pinned and does not reach the end of the track. In order to build real devices, we need to ensure that the probability of success is as close to 1 as possible. We study how this success probability depends on the skyrmion speed, and granularity of the track at room temperature, finding that the granularity can even help in some cases.

[1] Albert Fert, Vincent Cros, João Sampaio, Nat. Nanotechnology, 8, 152–156(2013) [2] Josep Castell-Queralt, Leonardo González-Gómez, Carles Navau, Phys. Rev. B 101, 140404(R) (2020) [3] Barton L. Brown, Uwe C. Täuber, and Michel Pleimling, Phys. Rev. B, 100, 024410 (2019)



Snapshots of the time evolution of the probability density of finding a skyrmion at a certain position. The corresponding snapshot times are, from left to right, 1.5/4.5/7.8/13.5 ns. The track length is 1 mm. There are 100 pinning sites randomly distributed on the track with moderate intensity. The success probability is close to 1 (higher than when we have no granularity), with a small probability of being annihilated at the edge of the track or being trapped.



Snapshots of the time evolution of the probability density of finding a skyrmion at a certain position. The corresponding snapshot times are, from left to right, 0.6/1.8/3.9/9/15 ns. The track length is 1 mm. There are 100 pinning sites randomly distributed on the track with high intensity. The success probability is close to 0 since the trapping probability of the skyrmion is close to 1 (the skyrmion would be most likely trapped at some pinning site).

GC-04. Numerical Solution of the Fokker-Planck Equation by Spectral Collocation and FEM Methods for Stochastic Magnetization Dynamics.

V. Scalerà¹, P. Ansalone², S. Perna¹, C. Serpico¹ and M. d’Aquino¹

1. Department of Electrical Engineering and ICT, Università degli Studi di Napoli Federico II, Napoli, Italy; 2. Istituto Nazionale di Ricerca Metrologica, Torino, Italy

During the last decade, the increasing demand of energy efficiency for low power electronics oriented a considerable progress in optimizing nanomagnetic and spintronic devices [1]. In this framework, magnetization switching is a fundamental process to investigate, in order to obtain a compromise between energy efficiency and speed in magnetic recording technology. In particular, magnetic random access memories (MRAMs) have proved to represent a valid alternative solution with respect to conventional non volatile electronic memories in terms of speed, scalability and low operation power [2-3]. Concerning the latter aspect, a significantly important issue is the design of memory cells with low enough operation power (e.g. within the IoT paradigm) but capable of reliable switching within a prescribed delay time, which may vary depending on applications (from fractions of ns to seconds and beyond). This means, in terms of nanomagnet physics, that magnetization switching for low energy barriers compared to the energy of thermal fluctuations, in the presence of a small/moderate external excitation (magnetic field/spin-polarized current) becomes a central issue to investigate. This occurs because, when the external current/field pulse is applied, the energy barrier which guarantees the required data retention at zero excitation (usually $> 60 k_B T$) is lowered, and thermal fluctuations may trigger and drive the magnetization reversal process. The analysis of stochastic magnetization dynamics [4] is usually performed by using two approaches which are complementary. On one hand, one can use the so-called *Langevin* dynamics approach, where the magnetization switching process of a large number of nanomagnet replicas is numerically studied via the stochastic *Landau-Lifshitz-Gilbert* (LLG) equation and the relevant information are extracted from the ensemble statistics [5-6]. On the other hand, the second approach exploits the fact that the stochastic LLG equation is associated with a drift-diffusion equation, referred to as *Fokker-Planck* (FP) equation, which describes the time evolution of the magnetization transition probability density function (pdf). In this paper, we numerically solve the FP equation on the unit sphere without any symmetry assumption on the particle. To this end, we have developed two methods: the spectral-collocation (SM) [7] and the FEM [8] methods, respectively. We show that both methods accurately predict the dominant relaxation time by comparing the numerical results with the asymptotic analytical theory [5] valid for large energy barriers ΔG with respect to the thermal energy $k_B T$. The first method consists in choosing a grid of points and expanding the solution using a set of smooth basis functions. The grid on the unit sphere is constructed by using as coordinates the component of magnetization along the z-axis and the azimuthal angle associated to the rotation around the z-axis itself. The grid points are equispaced in the azimuth angle and are distributed as *Chebyshev* nodes in the z variable. For the FEM, a triangulated unit sphere is considered and it is obtained recursively bisecting the edges starting from a tetrahedral polyhedron [10]. The mesh has vertices $p_i, i=1, \dots, N_p$, which are the nodes where the unknown pdf is located. The results were tested for different triangulations with an increasing number of points in order to verify the convergence of the numerical FEM method. The computational approaches are validated comparing the slowest thermal relaxation time constant for an ensemble of magnetic particles, and the approximate analytical expression given in [5], as shown in Fig.(1). This time constant is of interest because it determines the thermal stability of a magnetic memory. We verify the FEM code in the following conditions: $N_p=(8194, 65536, 131074)$ until reaching the desired convergence with respect to the analytical results in the limit of large energy barriers. The SM method shows a high accuracy from small to intermediate energy barriers, whereas for higher energy barriers the method requires an increasing number of grid points, on the unit sphere, limiting the possibility to compute the relaxation time to slightly above $26 k_B T$, after which the numerical results deviate from the analytical prediction. Conversely the method is accurate for low energy barriers and it achieves machine precision in the limit case of zero energy barrier (pure diffusion on the unit sphere).

The FEM method exhibits a lower accuracy in the relaxation time computation, one can see that it covers a broader range of energy barriers up to $35 k_B T$. The numerical tests presented here run on a PC using MATLAB. In conclusion, the developed methods allow accurate analysis of thermal switching processes for generic particles under different operating conditions depending on the moderately large or small amplitude of the energy barrier in the presence of external excitation. It is possible to show (not reported here due to limited space) that they allow to straightforwardly determine the switching times distributions [9], instrumental to assess the write-error rates of MRAM cells [11], in the intermediate regime between thermal and ballistic switching which is of great interest for applications.

[1] B. Dieny et al., *Nature Electronics* 3 (8), 446-459, (2020). [2] D. Apalkov et al., *Proceedings of the IEEE*, Vol. 104, No. 10, (2016). [3] S. Bhatti et al., *Materials Today*, Volume 20, Number 9, (2017). [4] G. Bertotti, I.D. Mayergoyz, C. Serpico, *Nonlinear Dynamics in Nanosystems*, Elsevier, (2009). [5] W.F. Brown, *Physical Review*, vol. 130, no. 5, (1963). [6] D.B. Reeves, J.B. Weaver, *Applied Physics Letters*, vol. 107, issue 22, (2019). [7] D. P. Ansalone, C. Ragusa, M. d’Aquino, C. Serpico and G. Bertotti, *IEEE Transactions on Magnetics*, vol. 45, (2009). [8] N.V. Peskov, *Physica B: Condensed Matter*, vol. 599, (2020). [9] M. d’Aquino et al., *Journal of Magnetism and Magnetic Materials* 475, 652-661, (2019). [10] S. Maddali S. Maddali, *SphereMesh*, <https://github.com/siddharth-maddali/SphereMesh>, (2021). [11] M. d’Aquino, S. Perna, C. Serpico, *Physica B: Condensed Matter*, Volume 577, (2020).

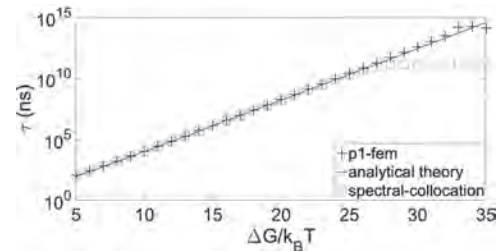


Fig. 1. Comparison between numerical results and analytical approximated values, for the following parameters values: $T=300K$, $\alpha=0.01$ and $k_{eff}=0.3569$ takes into account shape and crystalline anisotropy, $M_s=8 \cdot 10^5$ A/m and no applied field. The number of unknowns are $N_p=131074$ for the FEM and $N_p=21632$ for SC methods.

GC-05. Towards Reproducible Micromagnetic Workflows Using Ubermag.

M. Beg¹, M. Lang¹, R. Pepper¹ and H. Fangohr^{2,1}

1. Faculty of Engineering and Physical Sciences, University of Southampton, Southampton, United Kingdom; 2. Max Planck Institute for the Structure and Dynamics of Matter, Hamburg, Germany

Micromagnetics complements theoretical and experimental methods to support research in magnetism. The Object-Oriented MicroMagnetic Framework (OOMMF) [1] is a micromagnetic simulation tool solving non-linear time-dependent partial differential equations using the finite-difference method. It is probably the most widely used simulation tool in the micromagnetics community. It was written in C++, wrapped with Tcl, and driven through configuration files that follow the Tcl syntax. The typical computational workflow the user must follow to simulate a particular problem is to write a configuration file. After that, the user runs OOMMF by providing the configuration file to the OOMMF executable. When the OOMMF run is complete, results are saved in OOMMF-specific file formats. Finally, the user analyzes the result files. One of the specific goals of a computational micromagnetic study is parameter-space exploration. More precisely, the user repeats the simulation for different values of input parameters by changing them in the configuration file. It is often difficult to automate this, and it is challenging for the user to keep a log of all steps performed in the entire micromagnetic study. Besides, postprocessing and analysis of results is performed outside OOMMF, using techniques and scripts that are mostly developed by the user, or carried out manually. Consequently, it is hard to track, record, and convey the exact simulation procedure. Without this information, resulting publications are generally not reproducible. To address this situation, we developed a Python interface to the OOMMF executable to expose OOMMF to a general-purpose programming language supported by Jupyter. This allows us to conduct micromagnetic simulations from within the Jupyter notebook [2] to capitalize on the benefits of this environment. We developed a set of Python libraries we refer to as Ubermag, which expose the computational capabilities of OOMMF so that it can be controlled from Python. These Python libraries provide a domain-specific language to define a micromagnetic problem. A micromagnetic model, defined using the domain-specific language, is not aware of the particular simulation tool that will perform the actual micromagnetic simulation, and it is only used to describe the model. When a simulation is required, the model is translated into the OOMMF configuration file, the OOMMF executable is called, and the output files are read. By exposing the micromagnetic simulation capabilities to Python and driving the research from Jupyter Notebook, we have available all the benefits of the Jupyter research environment and all tools from Python's scientific stack are readily available. Ubermag and the Jupyter environment simplify the efforts to make micromagnetics publications reproducible. For each figure in the publication, one notebook can be provided. Using Binder [3], the community can inspect and re-run all the calculations in the cloud and make the publication reproducible.

[1] M. J. Donahue and D. G. Porter, OOMMF User's Guide, Version 1.0, Interag. Rep. NISTIR 6376, Natl. Inst. Stand. Technol. Gaithersburg, MD, 1999. [2] T. Kluyver *et al.* Jupyter Notebooks - a publishing format for reproducible computational workflows. *Positioning and Power in Academic Publishing: Players, Agents and Agendas*, 87-90, 2016. [3] <https://mybinder.org/>

GC-06. Machine Learning Methods for the Prediction of Micromagnetic Magnetization Dynamics.

L. Exl^{1,2}, N.J. Mauser^{1,2}, S. Schaffer^{1,2}, T. Schrefl^{3,1} and D. Suess^{1,4}
 1. Research Platform MMM Mathematics - Magnetism - Materials, Universitat Wien, Wien, Austria; 2. Wolfgang Pauli Institute, Vienna, Austria; 3. Department of Integrated Sensor Systems, Donau-Universitat Krems, Krems, Austria; 4. Faculty of Physics, Universitat Wien, Wien, Austria

Machine learning (ML) entered the field of computational micromagnetics only recently [1,2,3]. The main objective of these new approaches is the automatization of solutions of parameter-dependent problems in micromagnetism such as fast respond curve estimation modeled by the Landau-Lifschitz-Gilbert (LLG) equation. Data-driven models for the prediction of solutions of time- and parameter-dependent partial differential equations require high dimensional training data-structures. ML in this case is by no means a straight-forward trivial task, it needs algorithmic and mathematical innovation. Our work [4] introduces theoretical and computational conceptions of certain kernel-based dimensionality reduction approaches for efficient machine learning of the solution trajectories of LLG via the notion of low-dimensional feature space integration, Fig.1. We will mainly concentrate on computational aspects, specifically, kernel methods will be studied with focus on numerically stable and efficient implementation of kernel ridge regression and kernel principal component analysis via low-rank treatment of certain dense operations. A second line follows neural network auto-encoders as dimensional reduction for the training data with focus on smooth latent space variable description suitable for the feature space integration scheme. This will be doable due to a certain modification of contractive regularization that maintains feasibility despite the typically large computational demands coming with such approaches. We verify and compare numerically by means of a NIST standard problem, Fig.2.

[1] A. Kovacs, J. Fischbacher, H. Oezelt, M. Gusenbauer, L. Exl, F. Bruckner, D. Suess, T. Schrefl. Learning magnetization dynamics, *Journal of Magnetism and Magnetic Materials* 491 (2019): 165548. doi: <http://10.1016/j.jmmm.2019.165548> [2] L. Exl, N.J. Mauser, T. Schrefl, D. Suess. *Learning time-stepping by nonlinear dimensionality reduction to predict magnetization dynamics*, *Communications in Nonlinear Science and Numerical Simulation* 84 (2020): 105205. doi: 10.1016/j.cnsns.2020.105205 [3] L. Exl, J. Fischbacher, A. Kovacs, H. Oezelt, M. Gusenbauer, K. Yokota, T. Shoji, G. Hrkac, and T. Schrefl, *Magnetic microstructure machine learning analysis*, *Journal of Physics: Materials*, 2 (2019): 014001. doi: 10.1088/25157639/aaf26d [4] Exl, L., Mauser, N. J., Schaffer, S., Schrefl, T., & Suess, D. (2020). Prediction of magnetization dynamics in a reduced dimensional feature space setting utilizing a low-rank kernel method. *arXiv preprint arXiv:2008.05986*. <https://arxiv.org/pdf/2008.05986.pdf>

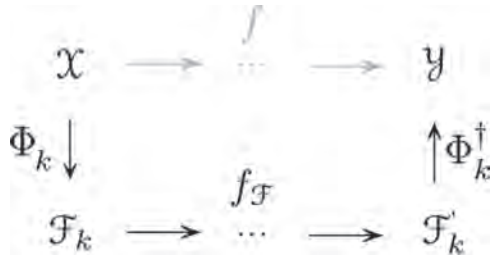


Fig.1: Time-integration scheme in low-dimensional feature space.

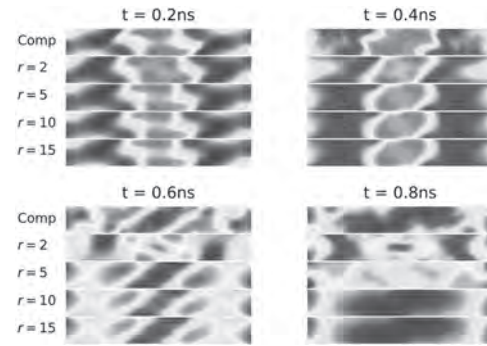


Fig.2: Snapshots for comparison of simulated and predicted magnetization states for varying ranks r.

GC-07. Combined Micromagnetic Simulation and Machine Learning Approach to Analysis of Polycrystalline Bilayer System With Exchange Bias.

N. Kulesh¹, N. Permyakov¹, V. Zverev¹, A. Koshelev¹, A. Bolyachkin¹ and V. Vas'kovskiy¹

1. B. N. Yeltsin Federal University of the Urals, Ekaterinburg, Russian Federation

The exchange interaction between two magnetic materials may lead to a symmetry breaking manifesting itself as a unidirectional anisotropy induced in one layer (usually ferromagnetic material F) by another one less susceptible to an external magnetic field (usually antiferromagnetic material AF). The unidirectional anisotropy in the F layer leads to a hysteresis loop shifted along the magnetic field axis and the phenomenon is called exchange bias (EB). Despite its seeming simplicity, the EB has an intricate microscopic mechanism, which has been approached by many models of different complexity dealing with perfect or imperfect interface, polycrystalline structure of F and AF, and bulk spin configuration in the AF layer [1]. For real-life applications e.g. sensors, memory cells or spintronic devices, the number of significant parameters affecting coercivity and EB field of the F layer could become too large to be accounted by simplified models, so computer simulation becomes a method of choice. The increasing complexity leads to more realistic and universal models but makes it difficult to evaluate their performance and limitations, study interconnections between model's parameters, and make a fast prediction on how the system with a given set of parameters would behave. In this study we approach this problem by applying methods of machine learning to a dataset obtained by a micromagnetic model representing a polycrystalline bilayer film consisting of F and AF layers. As AF state cannot be readily set in the continuous media approach, we adopted the model described in [2] by substituting AF with F material, for which contributions to Zeeman and magnetostatic energies were disabled. The example of the simulated hysteresis loop along with the geometry is shown in Fig. 1. Micromagnetic simulation was performed using MuMax3 software with GPU acceleration [3]. As an income several material and structural parameters have been chosen including saturation magnetization (same for F and AF), uniaxial magnetic anisotropy constants of F and AF, exchange constants in F and AF, attenuation coefficient of exchange constant between F and AF, thickness of the F layer, and average crystallites size (8 variables in total). As a result of approximately 1800 hysteresis loops simulations, for each configuration (each parameter has been varied randomly within a realistic range) two outcome parameters have been extracted: coercivity and EB field. The model has been validated with a smaller set of simulations where single parameter has been varied while fixing others at realistic values typical for a popular FeNi/FeMn system. Principal component analysis (PCA) allowed identifying readily input parameters having the strongest positive and negative correlations with the output parameters. Correlation coefficients for saturation magnetization, the thickness of the F layer, and the attenuation coefficient were significant for both coercivity and EB field, whereas the coefficient for AF anisotropy constant was among the largest only for EB field. Both PCA and T-SNE (t-distributed stochastic neighbor embedding) data visualizations suggested the possibility of building a data approximator. As EB field and coercivity are known to have complex nonlinear dependencies on some parameters, we chose the gradient boosting, which is a suitable algorithm for the current task. In this work Catboost open source library based on decision trees was used. The dataset was split into two parts for training the model and testing it using the root mean square error (RMSE) metric. The trained model could predict EB field for a test set of 500 examples rather well with RMSE = 0.04, whereas higher RMSE = 0.13 was achieved for coercivity, which could also be considered a good result. To demonstrate the applicability of the model for fast search of optimal coercivity and EB field, we employed Broyden-Fletcher-Goldfarb-Shanno and differential evolution algorithms realized in SciPy library to find sets of input parameters giving the largest values of output parameters. This approach allowed us to identify several areas of the highest coercivity and EB field values exceeding those in the training set, which were confirmed by additional micromagnetic simulations. Although the RMSE was large, the model can be further improved by including more examples of computer simulation to resolve the areas of interest. In conclu-

sion, machine learning algorithms were successfully used for in-depth analysis of a bilayer micromagnetic model with exchange bias. The model capable of predicting values of coercivity and exchange bias using material and structural parameters as an input was successfully created and trained. The proposed approach was demonstrated to be suitable for building optimization algorithms allowing to find areas of interest in multidimensional space of income parameters giving the desired values coercivity and EB field. The demonstrated approach can be useful for the analysis of computer models as well as real systems with exchange bias. This work was supported by the Russian Science Foundation (project No 19-72-00141).

[1] F. Hellman, A. Hoffmann, Y. Tserkovnyak et al., *Rev. Mod. Phys.* Vol. 89, a.n. 025006 (2017) [2] J. De Clercq, A. Vansteenkiste, M. Abes et al., *J. Phys. D: Appl. Phys.*, Vol. 49, a.n. 435001 (2016) [3] A. Vansteenkiste, J. Leliaert, M. Dvornik et al. *AIP Advances*, Vol. 4, a.n. 107133 (2014)

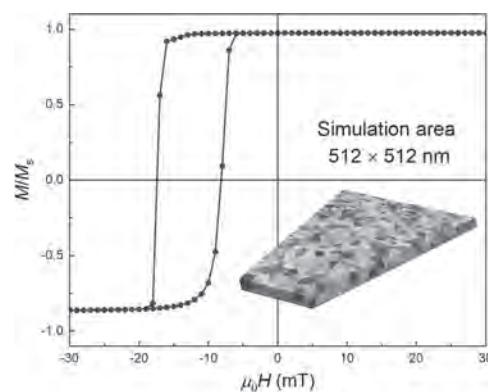


Figure 1. Hysteresis loop simulated using a micromagnetic model of a bilayer with exchange bias consisting of F and AF layers. In the inset a slice of the geometry with Voronoi tessellation is shown. The colors are given to differentiate the crystallites.

GC-08. Multiclass Permanent Magnets Superstructure for Indoor Localization Using Artificial Intelligence.

A. Ivry¹, E. Fisher², R. Alimi², I. Mosseri² and K. Nahir²

1. *Electrical Engineering, Technion Israel Institute of Technology, Haifa, Israel;* 2. *Technology Division, Soreq Nuclear Research Center, Yavne, Israel*

Smartphone-based indoor localization methods draw increased interest and are frequently employed for position estimation of users inside enclosures like malls, conference halls, and crowded venues. Magnetic sensing has recently attracted considerable attention due to its pervasiveness and autonomy, introducing two main positioning approaches utilizing magnetic sensors. The first approach is identifying the magnetic field characteristics of the surrounding infrastructure as signatures, thus creating a specific magnetic fingerprint. This scheme does not require additional hardware deployment, while interferences and anomalies from indoor infrastructure and objects greatly improve magnetic field discernibility. Yet, this approach requires knowledge of magnetic maps or computationally expensive calculations for applying simultaneous localization and mapping (SLAM). Furthermore, some environments may cause strong electromagnetic interference that differs from the underline magnetic fingerprint, leading to localization errors. The second approach uses active magnetic flux transmitters as markers, which is energy consuming and requires expensive transmitter units. In our recent work, we introduced the Permanent Magnets Superstructure for Indoor Localization method (PMSIL). This approach allows simple, low-power, and robust smartphone localization in unknown-magnetic-fingerprint locations by deploying permanent magnets in pre-known locations. Practically, we embed small-volume-large-moment permanent magnets in given locations inside the building and arrange them in a single specific geometric configuration. This results in a supervised super-structure magnetic signature pattern, constituting unambiguous magnetic environments. The localization algorithm learned this unique pattern during the training stage using artificial intelligence (AI) methods and detected it in ongoing data streams during real-time localization by applying binary classification. Thus, localization is based on smartphone motion rather than on the static positioning of the magnetometer. In this study, we propose an extended version of the PMSIL method, called Multiclass-PMSIL (M-PMSIL), in which magnets are arranged in a variety of configurations in pre-known locations. These constellations generate a bank of distinct patterns that are learned by the multiclass AI-based algorithms during training and recognized on-the-fly during localization. This extension permits covering a broader area in which the user can be localized. As M-PMSIL is landmark-based, we draw comparisons to three competing state-of-the-art approaches for indoor localization with landmark-based magnetism mechanisms. We also refer to localization methods based either on spatial-temporal sequence matching or on fusion with motion. The database is recorded by a user strolling back and forth with a hand-held smartphone across a 100 m long and 3 m wide in-door corridor. Along this corridor, three neodymium magnets with different magnetic moment norms are positioned in a row, with 3 m separating between them. During the experiment, these magnets are permuted in all 6 possible combinations and every new combination is relocated along the corridor, creating 6 distinct magnetic patterns. For the sake of generalization, recordings are made in different walking paces between 0.5 to 1.5 m/s, and different crossing distances from the magnets of 0.5 m, 1m, and 1.5 m. A snippet of data recorded by the smartphone indoor can be seen in Fig. 1, including 2 of the 6 magnet constellations used in this study. The training set includes 40 minutes of randomly selected recorded data that contains 10 passes across each of 6 different magnetic patterns, while the test set contains 20 minutes of data. The 6 classes, i.e., magnetic permutations to be localized, are balanced for both disjoint sets. In this study, 6 AI-based architectures are used for localization. Their performance is compared in Fig. 2 using the receiving operating characteristic (ROC) curve, allowing analysis of the trade-off between true positive rate (TPR) and false-positive rate (FPR) in various operation points. We may observe that the long short-term memory (LSTM) network produced the best classification results, followed by the gated recurrent unit (GRU) and recurrent neural network (RNN) models. The least performant methods are the fully connected deep neural network (DNN), and support vector machine (SVM), with and without prin-

cipal component analysis (PCA). To quantify the multiclass classification accuracy of the methods, we derive the maximal sum of TPR and FPR from the ROC curve. LSTM shows 95% accuracy, while GRU and RNN reach 90% and 87%, respectively. DNN shows 82%, SVM-PCA method reaches 80%, and SVM produces 75% accuracy. Our approach achieves mean localization error (MLE) lower than 1 m, supersedes competing landmark-based methods, as UnLoc and MapCraft achieved MLE between 1-2 m. The IODetector was able to obtain classification accuracy as high as 82% indoor, which falls short to the 95% obtained by the LSTM. Additional methods, rooted in spatial-temporal sequence matching or on fusion with motion, also show lower MLE and classification accuracy compared to our study.

[1] S. He and K. Shin, *ACM Comput. Surv.*, Vol. 50, p.1-37 (2017) [2] K. Watanabe, K., Hiroi, K., Kamiyama, et al., *Journal of Information Processing.*, Vol. 27, p.10–24, (2019) [3] E. Weiss and R. Alimi, *Low-Power and High-Sensitivity Magnetic Sensors and Systems*. Artech House, (2018) [4] T. N. Sainath, O. Vinyals, A. Senior, et al., *IEEE International Conference on Acoustics, Speech and Signal Processing (ICASSP)*, pp.4580–4584, (2015) [5] J. N. Mandrekar, *J. Thorac. Oncol.*, vol. 5, pp. 1315–1316, (2010)

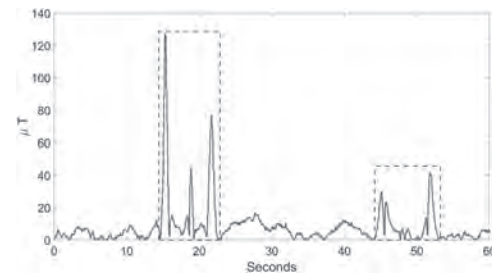


Fig 1: Norm value of three-axial magnetic signals recorded with a smartphone. Rectangles confine measurements of three magnets positioned in a row, in two distinct magnet constellations.

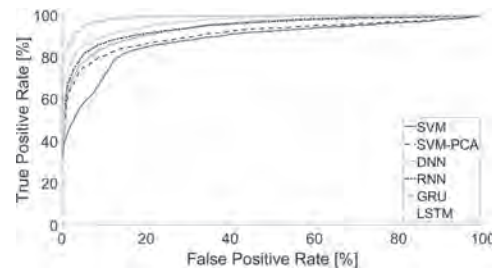


Fig 2: Multiclass classification performance of six AI methods.

GC-09. Simulating Sintered Magnets Using the Full Demagnetization Tensor With MagTense.

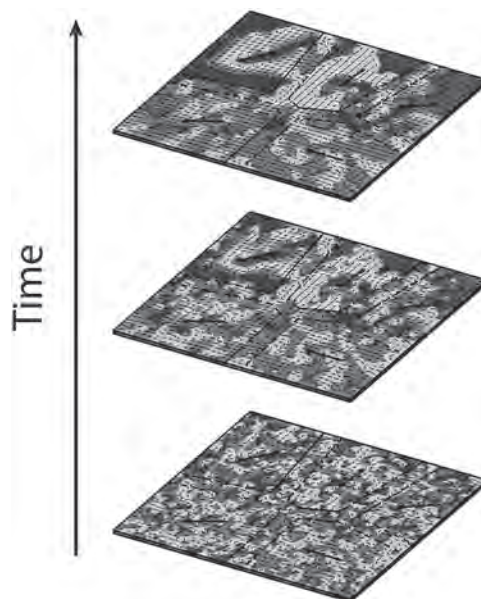
A.R. Insinga¹ and R. Bjørk¹

1. Department of Energy Conversion and Storage, Danmarks Tekniske Universitet, Lyngby, Denmark

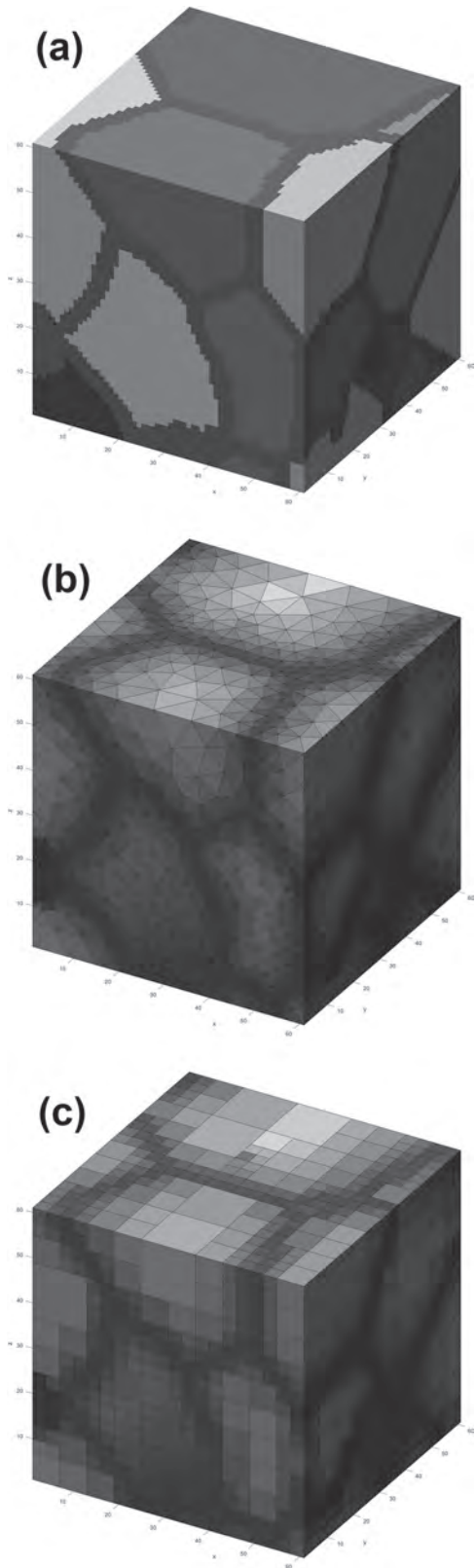
At the microscopic scale, magnetic systems can be described by the formalism of micromagnetics, which is used for e.g. micromagnetics of rare-earth efficient permanent magnets [1]. In a micromagnetic model, the governing equations must be discretized and represented by a number of interactions taking place between the discretized moments in the system. These interactions can be described by different magnetic fields, such as an exchange- and an anisotropy field. Of these, it is the calculation of the demagnetization field that is the most time consuming part [2]. There are in general three methods that have been applied to calculate the demagnetization field: finite difference-based fast Fourier transform methods, tensor-grid methods and finite-element methods. All methods have inherent advantages and shortcomings, e.g. the finite difference Fourier-based approaches are extremely fast but unfortunately require that the magnetic moments lie on a regular grid [3], while the finite element method allows easy meshing of complex geometries but also requires that an environment outside the object of interest is modelled. Here we present a novel open-source micromagnetism framework called MagTense that uses an analytically exact approach to calculate the full demagnetization tensor in real space for computations [4]. This ensures that the calculated magnetic field is correct, and at the same time allows for easy meshing of complex geometries. In MagTense the discretization approach used subdivides the region Ω into N “tiles”, adjacent to each other. The magnetization field is then represented by a vector of $3N$ components, three for each tile. The demagnetization field generated by each tile is computed analytically by assuming that the tile is uniformly magnetized. The analytical expression of the demagnetization tensor is known for many different tiles, such as the rectangular cuboid (rectangular prism) [5] and the tetrahedron [6], thus allowing great flexibility to build meshes for any geometry. The total demagnetization field at any point is obtained by summing the individual contributions from all the tiles in the magnet domain Ω . Besides the calculation of the demagnetization field, the other components of the effective field must also be calculated, i.e. the exchange-, external- and anisotropy field. For the case of a Cartesian mesh of rectangular cuboids the exchange interaction field can easily be computed by applying standard finite difference schemes. However, methods are also available for the case of unstructured polyhedral meshes. Using MagTense we have calculated the solution to the μmag standard micromagnetic problems 2, 3 and 4 and find that the MagTense framework accurately predicts the solution to each of these [7]. For example for standard problem 3, we get side length at the crossover energy between the vortex and flower state of 8.477, which is in line with two of the published μmag results. We have also implemented the MagTense framework to support both CPU and GPU calculations, where in the latter the demagnetization calculations are performed on the GPU using the CUDA framework. On μmag standard problem 4, we see a decrease in total simulation time of a factor of 100 for the GPU implementation. To demonstrate the use of MagTense on a sample with multiple grains we show in Fig. 1 the magnetization evolution of a thin slice of a multi-grain material starting from a random state. The structure has been generated using a centroidal Voronoi tessellation. The hard magnetic phase in the five grains is characterized by a strong anisotropy, corresponding to the direction indicated by the thick black arrows, while the grain-boundary is soft-phase with isotropic properties. Inside the grains we observe the emergence of magnetic domains aligned to the easy axis, while at the grain-boundary we see the formation of magnetic vortices. To simulate realistic grain samples, we have also utilized a sintering modeling framework based on kinetic Monte Carlo [8] to generate fully realistic microstructures of sintered powder compacts. We then subdivide these grain structures into magnetic tiles for simulating the magnetic properties of the complete sample. Shown in Fig. 2 (a) is an example of multi-grain sample generated using the sintering modeling framework. The colours indicate different grains, gray corresponding to the grain boundary soft-phase. The thickness of the grain boundary phase can be specified as an input parameter. Fig. 2 (b) and 2(c) show the tetrahedral and Cartesian meshes, respectively, applied to this geometry. The colours

indicate the distance of a point from the nearest grain boundary, which in both cases was used to control the resolution of the mesh. In this way the mesh is finer at the boundary between grains which is where the nucleation is expected to occur during a field-reversal process.

[1] J. Fischbacher, A. Kovacs, M. Gusenbauer, H. Oezelt, L. Exl, S. Bance, and T. Schrefl., *J. Phys. D: Appl. Phys.*, 51(19):193002, (2018). [2] C. Abert, L. Exl, G. Selke, A. Drews, T. Schrefl, *Journal of Magnetism and Magnetic Materials*, 326:176–185, (2013). [3] A. Vansteenkiste, Ben Van de Wiele, *Journal of Magnetism and Magnetic Materials*, 323(21):2585–2591, (2011). [4] R. Bjørk and K. K. Nielsen, *Magtense - a micromagnetism and magnetostatic framework*, doi.org/10.11581/DTU:00000071, <https://www.magtense.org>, (2019). [5] R. Bjørk, E. B. Poulsen, K. K. Nielsen, A. R. Insinga, “MagTense: a micromagnetic framework using the analytical demagnetization tensor”, submitted, (2021). [6] A. Smith, K. K. Nielsen, D. V. Christensen, C. R. H. Bahl, R. Bjørk, J. Hattel. *Journal of Applied Physics*, 107(10):103910, (2010). [7] K. K. Nielsen, A. R. Insinga, R. Bjørk, *IEEE Magnetics Letters*, 10:8918242, (2019). [8] V. Tikare, M. Braginsky, D. Bouvard, A. Vagnon, *Comp. Mat. Sci.*, 48:317-25, (2010).



Spontaneous evolution of magnetic domains in a multi-grain structure. The color indicate the local direction of magnetization.



Simulated sintered powder sample and corresponding adaptive meshes.

GC-10. Magnetostatic Field Computation in Thin Films Based on k-Space Fast Convolution With Truncated Green's Function.

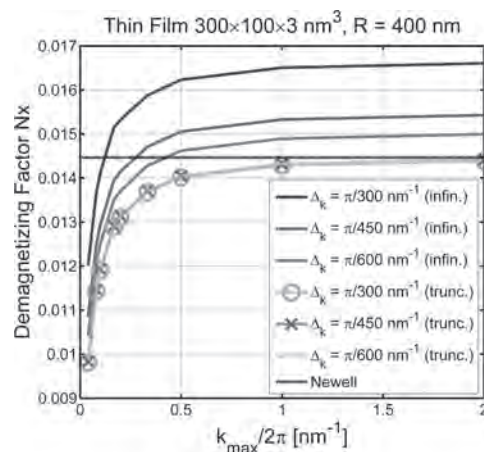
S. Perna¹, V. Scalera¹, M. d'Aquino², N. Iserna¹, F. Villone¹ and C. Serpico¹

1. *Universita degli Studi di Napoli Federico II, Napoli, Italy*; 2. *Universita degli Studi di Napoli Parthenope Dipartimento di Ingegneria, Napoli, Italy*

The numerical studies of magnetization dynamics in micromagnetic systems with spatially distributed magnetization crucially rely on the computation of magnetostatic fields generated by the ferromagnet. The solution of the magnetostatic problem can be written as convolution of an appropriate Green's function with the magnetization vector field. Since the Green's function is long-range, after discretization of the problem in N cells, the direct numerical computation of the convolution integral has a computational cost scaling as N^2 . In this work, we use, as it is often done in micromagnetics, the Fast Fourier Transform (FFT) method to reduce the computational cost scaling to $N \log N$. We consider micromagnetic systems with thin-film geometry where the magnetization can be considered constant across the thickness of the magnet. In these situations, only the field averaged across the thickness is relevant to the magnetostatic interactions and both the magnetization and the averaged field inside the magnet depend only on two spatial variables. The usual approach to deal with this type of problem is to use FFT to compute the discretized version of the convolution integral relating the field and the magnetization [1]. The dual approach to the usual one, is based on the discretization of the integral relation between the field (averaged across the thickness) and the magnetization in the reciprocal space (k -space). The connection in the k -space is given by the Fourier transform of Green function of the magnetostatic problem which, in case of infinite thin-films, can be written in a special form taking into account the thin-film geometry [2]. The analysis in the k -space has been extensively used in connection with linear spin wave dynamics in thin films working as magnonic waveguide, where all the relation of practical use (e.g dispersion relations), are easily obtained by algebraic manipulations. When the dimensions of the thin film are finite, the reconstruction of the magnetostatic field with the infinite film Green's function, is altered by the presence of replicas of the thin film in the ordinary space due to the sampling operation in the k -space. This effect is usually smoothed by using zero-padding, which increases the distance between two interacting replicas weakening their coupling. In this work, a fast convolution algorithm in the k -space able to remove the influence of replicas in the reconstruction of the magnetostatic field in thin films of finite size, is proposed and applied to study linear spin wave dynamics. It is based on the use of the Fourier transform of truncated Green function, which has been recently used to compute volume potentials defined on free-space in a finite (truncated) domain [3]. Such method, guarantees a regularization of the Green function by cutting off the interaction in physical space beyond the domain of interest and this in turn produces spectral accuracy [5] for the Fourier transform evaluation by FFT algorithm. The accuracy of the proposed method is studied by comparing the results with analytical calculations and with those obtained by fast convolution with the infinite thin film Green's function as a function of mesh size. For example, in the figure, the computation of the demagnetizing factor along the x direction for a thin film of dimensions $L_x = 300\text{nm}$, $L_y = 100\text{nm}$ and $L_z = 3\text{nm}$ as a function of the mesh dimension ($k_{x\text{max}} = k_{y\text{max}} = k_{\text{max}}$) and discretization step-size ($\Delta_{kx} = \Delta_{ky} = \Delta_k$) in the k -space is considered. With solid lines, the curves in the infinite film approximation (infin.) are indicated, while curves with symbols results from the proposed approach (trunc.). The horizontal dotted line, represents the analytical value of the demagnetizing factor evaluated with Newell's formula [6]. Computation with $\Delta_k < \pi/300\text{nm}^{-1}$, for the duality property of the Fourier transform, are equivalent to use zero padding in the ordinary space. This produces a substantial improving of estimation accuracy with respect to the analytical value, in case of infinite film approximation. As a benchmark of the proposed approach, it results that the curves computed with the truncated Green function, show a weak dependence from Δ_k for $\Delta_k > \pi/R$ and collapse into the same one for $\Delta_k < \pi/R$, where R is the radius of a disk region which defines the compact support of the truncated Green function. This, as a confirmation of the fact, that when the region that exceeds the support of the truncated Green's function is zero padded, there is no effect on the computation of the magnetostatic field. Moreover, for sufficient value of

k_{max} the asymptotic value tends towards analytical one, since when $\Delta_k < \pi/R$ the influence of replicas on the magnetostatic field computation is removed.

[1] R.D. McMichael, M.J. Donahue, D.G. Porter, J. Eicke, *Journal of Applied Physics*, vol. 85, pp. 5816-5818, (1999). [2] V. Scalera et al., *IEEE Transactions on Magnetics*, doi: 10.1109/TMAG.2020.3014383. [3] F. Vico, L. Greengard, M. Ferrando, *Journal of Computational Physics*, Vol. 323, p. 191-203 (2016). [4] B.A. Kalinikos, A.N. Slavin, *J. Phys. C: Solid State Phys.* Vol. 19, p.7013-7033 (1986). [5] L.N. Trefethen, SIAM, Philadelphia, (2000). [6] A.J. Newell, W. Williams, D.J. Dunlop, *J. Geophysical Research*, Vol. 98, pp. 9551-9555 (1993).



Comparison of the demagnetizing factor computed analytically with Newell's formula [6] and numerically with k -space FFT convolution with the infinite film Green's function (infin.) and with the truncated Green's function (trunc.), for different mesh dimension k_{max} and step-size Δ_k in the k -space.

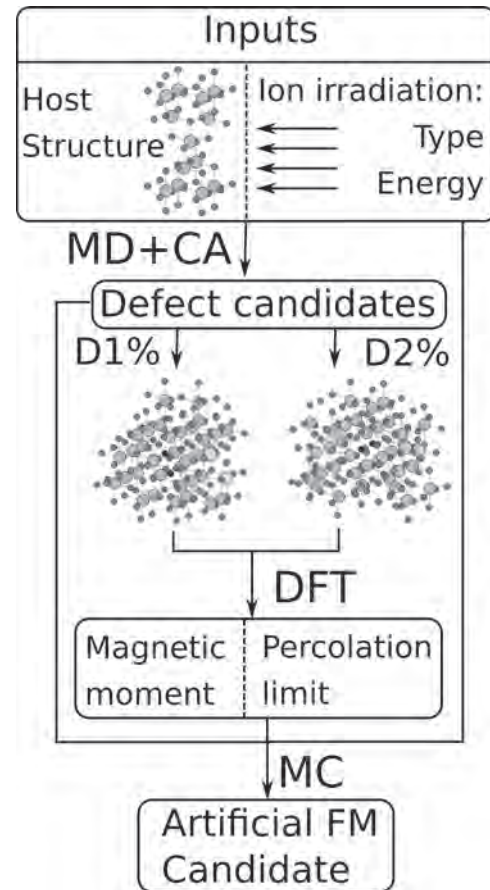
GC-11. Toward a Systematic Discovery of Artificial Functional Magnetic Materials.

L. Botsch¹ and P.D. Esquinazi¹

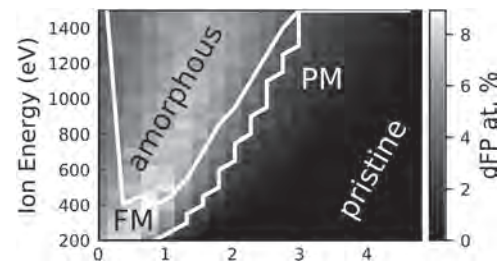
¹. Universität Leipzig, Leipzig, Germany

Magnetic materials play a major role in many spintronic and other technological applications such as magnetic storage, logic devices, magnetic field sensors and magnetic random access memory. Materials with strong intrinsic ferromagnetic (FM) order above room temperature, such as the transition metals Fe, Ni or Co and their alloys, are rather unusual among the magnetic materials known today and there is still the need for new functional materials with magnetic order above room temperature. In the past two decades, a method of creating artificial ferromagnetic materials has emerged and a multitude of so-called defect-induced ferromagnets were reported. Since the first prediction of an artificial ferromagnetic material with transition temperature above 300-K, based on Mn doped ZnO appeared twenty years ago, the field has substantially evolved. First, it was realized that doping with magnetic impurities was not at all necessary in order to induce a robust FM order in the non-magnetic host matrix, rather all kinds of lattice defects were at the origin of the measured magnetic signals. This realization promised great possibilities to construct new functional magnetic materials, as any non-magnetic material could potentially host a certain kind of defect, turning it into an artificial ferromagnet. The hunt was on and the result was a plethora of reports ranging from oxide, nitride, carbon-based, 2D van der Waals and many more materials showing signals of ferromagnetism upon introducing all kinds of nominally non-magnetic defects. One of the most promising and versatile methods for introducing these defects is the irradiation with non-magnetic ions, owing to the availability of ion sources ranging over the whole periodic table and energies from few eV to hundreds of MeV. Although many experiments were accompanied by theoretical studies, such as electronic structure calculations based on density functional theory (DFT), the search was mostly guided by blind trial and error and a brute force approach. It is therefore not very surprising that most of the reported materials only showed very tiny magnetic signals, which soon led to debates about the nature of the effect and raised the question of whether this route could eventually lead to a robust magnetic order above room temperature, comparable with intrinsic ferromagnets. Furthermore, the measurement of the magnetization of such artificial ferromagnetic samples turns out to be quite difficult due to the inherent uncertainty of the magnetic volume, leading to largely underestimated values in the literature. Considering the enormous amount of host material candidates and lattice defects, a more systematic search method and better selection criteria are highly needed. In this presentation, a computational scheme for the systematic discovery of candidate artificial magnetic materials that can be created by ion irradiation is introduced. The scheme is based on first principle calculations, guided by experimental constraints, automatically restricting the potential defects to those accessible experimentally and can readily be implemented for high throughput material discovery. We further provide a method to determine the defect distribution created within the host lattices, allowing to obtain accurate magnetization values. We demonstrate the predictive power of the scheme by comparing systematic experimental investigations to the calculations and provide corrections to the magnetization, that reach values as high as those of typical intrinsic ferromagnets. We show that the method is applicable to a wide range of host materials and ion irradiation parameters (100 eV - 200 MeV) and yields artificial functional magnetic materials, e.g. in TiO₂, SiC and CeO₂ hosts, in a controllable way, ranging from thin magnetic films down to 2D magnetic monolayers. The artificial magnetic materials can be tailored to application requirements, exhibiting properties like, e.g., strong perpendicular magnetic anisotropy.

L. Botsch, P. D. Esquinazi, C. Bundesmann et al., Under review (2021) P. D. Esquinazi, W. Hergert, M. Stiller et al., *Physica Status Solidi B*, Vol. 257, p. 1900623 (2020) M. Stiller, A. T. N'Diaye, H. Ohldag et al., *Physical Review B*, Vol. 101, p. 014412 (2020)



Computational scheme for the discovery of artificial magnetic materials



Magnetic phase diagram of an artificial 2D ferromagnetic phase emerging in a TiO₂ host by low energy ion irradiation, calculated using the scheme (Figure 1) and realized experimentally.

Session GD

NOVEL RECORDING AND DOMAIN WALL DEVICES

See-Hun Yang, Chair

International Business Machines Corp, Yorktown Heights, NY, United States

CONTRIBUTED PAPERS

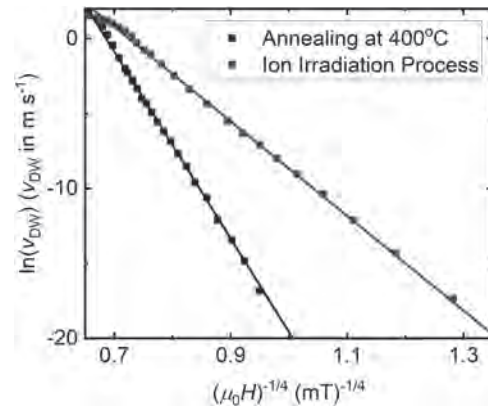
GD-01. Enhancing Domain Wall Motion in W/CoFeB/MgO Ultrathin Films Through He⁺-Irradiation-Induced Crystallization.

J.W. van der Jagt¹, M. Sall¹, N. Vernier², D. Mailly², M. Belmeguenai³, Y. Roussigné³, L. Herrera Diez², R. Juge¹ and D. Ravelosona^{1,2}

1. Spin-Ion Technologies, Palaiseau, France; 2. Centre de Nanosciences et de Nanotechnologies, Palaiseau, France; 3. Laboratoire des Sciences des Procédés et des Matériaux, Villeneuve, France

Devices based on magnetic domain wall (DW) motion are among the most promising candidates for future spintronic data storage, logic, and neuro-morphic devices. One critical issue that hinders DW motion is the presence of structural inhomogeneities such as interface intermixing, interface roughness, or crystalline texture, that cause a distribution of magnetic properties in the material. As a result, domain walls undergo local pinning leading to the so-called creep regime at low driving forces. Even beyond this creep regime, the DW motion remains affected by defects. Thus, to achieve fast and efficient DW motion, good control over the intrinsic defects in the material must be obtained. Ultra-thin CoFeB/MgO-based structures with perpendicular magnetic anisotropy are considered the most promising candidates for the future generation of Magnetic Random Access Memory (MRAM) devices. These films are usually annealed at high temperatures (300-400°C) to crystallize the CoFeB layer and get high Tunneling Magnetoresistance (TMR). This treatment at high temperatures results in the presence of undesirable intrinsic defects. To address this issue, we have developed a very promising process solution based on post-growth He⁺ ion irradiation to tailor the structural properties of ultrathin magnetic films at the atomic level and improve their performances [1-4]. The utilization of light ions provides the precise control of inter-atomic displacements through the low energy transfer. The key feature of the technology is the post-growth control of structural properties and the related magnetic properties. To perform these irradiation techniques, we have used a compact ion-irradiation facility (Helium-S® from Spin-Ion Technologies), capable of ultra-fast He⁺ ion irradiation on 1-inch wafers with energies ranging between 5-30 keV [5]. Here, we have studied the influence of two different processes of crystallization in W-CoFeB-MgO structure on domain wall dynamics. The first process is based on the combination of He⁺ ion irradiation at low fluences (10¹⁴ ions/cm² to 10¹⁵ ions/cm²) with annealing. The second process consists of pure thermal annealing. For both processes, annealing temperatures ranging from RT to 400°C have been used. Our results first demonstrate that ion irradiation can induce full crystallization of the CoFeB-MgO materials at much lower temperatures (<250°C) than the pure annealing process (>350°C). In addition, higher anisotropy values can be obtained, which is consistent with sharper interfaces. Domain wall dynamics measured by Kerr microscopy have been compared for both processes. Strong differences have been evidenced in both the creep (few nm/s) and flow regime (few m/s). In particular, the ion-irradiation-induced crystallization process results in higher domain wall velocities as shown in Figure 1 for the creep regime where structural defects have a strong influence. This is consistent with a much lower density of structural inhomogeneities in the material crystallized by ion irradiation. Finally, we will discuss the crystallization process under ion irradiation and show preliminary results of DW motion in magnetic wires where local ion irradiation can also be used to minimize edge defects. Our results show that He⁺ ion irradiation is a very versatile tool to enhance magnetic materials and devices.

[1] J. Fassbender, D. Ravelosona, and Y. Samson, *J. of Phys. D.: Appl. Phys.*, Vol. 37, no. 16 (2004) [2] T. Devolder, I. Barisic, S. Eimer et al., *J. of Appl. Phys.*, Vol. 113, no. 20, p. 203912 (2013) [3] L. Herrera Diez, F. Garcia-Sanchez, J.-P. Adam et al., *Appl. Phys. Lett.*, vol 107, p. 032401 (2015) [4] X. Zhao, B. Zhang, N. Vernier et al., *Appl. Phys. Lett.*, vol. 115, p.122404 (2019) [5] www.spin-ion.com



Domain wall velocity as a function of the applied out-of-plane magnetic field in the creep regime for the regular annealing process (400°C, 1h) and the process based on He⁺ irradiation at lower annealing temperatures.

GD-02. Exploration of Magnetic Nanotubes as new Spintronic Building Block.

D. Tiwari¹, M. Jaber¹, M. Scheuerlein², M. Schöbitz¹, J. Hurst¹,
A. Masseboeuf¹, L. Vila¹, J. Attané¹, W. Ensinger², M. Rioult³, R. Belkhou³,
D. Gusakova¹ and O. Fruchart¹

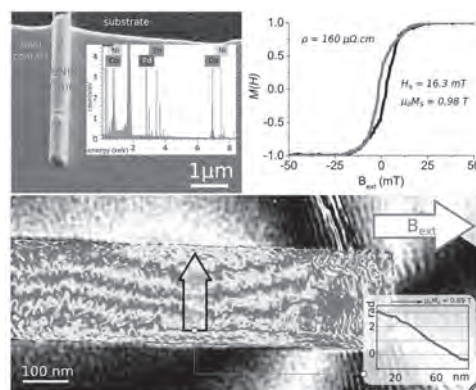
1. *SPINtronique et Technologie des Composants, Grenoble, France;*

2. *Technical University of Darmstadt, Darmstadt, Germany;*

3. *Synchrotron SOLEIL, Gif-sur-Yvette, France*

Ferromagnetic one-dimensional conduits carry the promises of future high-density and low consumption memories as well as new logic gate paradigms. These systems are indeed ideal for domain walls propagation and spin waves generation, and have also been proposed as field sensor [1]. The emergence of curvilinear magnetism [2] came up with the possibility in dealing with tridimensional consideration of such 1D-conduits (being also of fundamental academic interest as new magnetic textures) : ferromagnetic nanotubes are merging on a single structure the micromagnetism consideration of domain walls and the multi-layered stack needed for spintronic (core-shell structures). Unexpectedly, but technologically ideal, an azimuthal curling of magnetization was initially observed in electroless Co-rich CoNi nanotubes [2], that we attributed to curvature-induced magneto-elastic anisotropy. We report here detailed magnetic and structural information to quantify the effect of anisotropy, and better identify its microscopic origin by analyzing different parameter of tube structure and chemistry as well as using new tools for tube magnetic investigation. CoNiB-based ferromagnetic nanotubes were fabricated by electroless plating in polycarbonate templates with diameters ranging from 160 to 450 nm, wall thicknesses from 20 to 65 nm, and several tens of μm in length. Following template dissolution and dispersion, nanotubes were either contacted using laser lithography for AMR (Anisotropic Magneto-Resistance) measurements, dispersed on suitable TEM (Transmission Electron Microscopy) grids or prepared by means of FIB (Focused Ion Beam) for cross-section analysis. Structural analysis revealed a relative homogeneity in critical parameters such as diameter and tube thickness along the whole object, with expected slight variations towards tubes extremities. We noticed a segregation of Nickel towards the tube surfaces that could be associated to an inhomogeneity of magnetic properties across the tube wall (radial direction) already observed in thin films [4]. This inhomogeneity would imply inverse-magnetostriction (magnetoelastic) related anisotropy, even in the case of an alloy with no expected magnetostriction nor magnetocrystalline anisotropy from the nominal composition. Magneto-transport measurements were carried out at varying temperature, applied field magnitude and direction, and showed a material resistivity (at 300K) below $200 \mu\Omega\cdot\text{cm}$, still one order of magnitude higher than in the bulk. This has been related to the nanocrystalline nature of the tubes (induced by grain boundaries) and is considered with non curvilinear system (electrodeposited thin films) for magnetostriction investigation. From $R(B_{\text{ext}})$ loops with a magnetic field applied along the tube axis, we confirmed the azimuthal magnetic curling at remanence, inferred the magnetization process and thereby extracted the anisotropy field of the order of $K_{\text{eff}} = 7.5 \text{ kJ}\cdot\text{m}^{-3}$. Such reversal has been then scrutinized through Electron Holography to locally map and quantify the magnetic flux (see Figure) during a magnetic loop. We extended these measurements to various tube parameters to propose a general picture of the curvature-induced anisotropy. These on-going experiments are of fundamental importance to infer for the capacities of such system to experimentally confirm high domain wall velocities (as well as spin wave propagation) that could offer technological solution for racetrack memories.

[1] M. Stano & O. Fruchart. Magnetic nanowires and nanotubes, *Handbook of magnetic materials* vol.27, Ed. Ekkes Brück, North Holland (2018). [2] Fernández-Pacheco, A. *et al.* Three-dimensional nanomagnetism. *Nature Communications* 8,15756 (2017). [3] Michal Stano *et al.* Flux-closure domains in high aspect ratio electroless-deposited CoNiB nanotubes. *SciPost Physics* 5, 38 (2018) [4] Hertel, R. Ultrafast domain wall dynamics in magnetic nanotubes and nanowires. *Journal of Physics: Condensed Matter* 28, 483002 (2016).



(Top Left) SEM view of a contacted Nanotube for magneto-transport measurements. Inset display an EDX spectra of the tube for Co/Ni composition. (Top right) Single tube hysteresis loop reconstructed from resistance measurement under applied field along the tube axis (two senses) and associated anisotropy field and saturated magnetization. (Bottom) Cosine of phase image obtained by Electron holography on a magnetized tube extremity: the black and white lines display the magnetic flux. The phase profile (inset) enables to quantify the local saturated magnetization (phase derivative) knowing the sample thickness.

GD-03. Innovative Use of Functional Segments in the Construction of a 3D Racetrack Memory Based on Cylindrical Nanowire Arrays.

J. Rial¹ and M.P. Proenca^{1,2}

1. IFIMUP—Institute of Physics for Advanced Materials, Nanotechnology and Photonics, Department of Physics and Astronomy, Universidade do Porto Faculdade de Ciências, Porto, Portugal; 2. Universidad Politecnica de Madrid Instituto de Sistemas Optoelectronicos y Microtecnología, Madrid, Spain

The huge amount of new data generated every day has caused the need to search for new systems to store all this information in the smallest possible areas. S. Parkin proposed a new storage device called racetrack memory, in which magnetic domains are used to store the information in ferromagnetic stripes along its length [1]. In this novel system, the domain walls (DWs) are pinned at artificial defects created along the stripe, and the depinning is achieved by the application of spin-polarized current pulses. These pulses initiate the DWs movement, transporting the bits along the stripe reaching the read/write heads, increasing the speed of reading/writing data. In particular, 3D racetrack memories, made of arrays of vertically aligned nanowires, allow us to greatly increase the information density stored on a device. However, this potential new storage device still has some limitations that prevent its use. One of the biggest drawbacks is the unwanted overheating of the system caused by the current pulses in the physical notches in the stripe, which are required to pin the DWs. This issue could be solved using chemical constraints, which would allow to pin the DWs maintaining the diameter constant along the wire. Considering this idea, a novel configuration based on cylindrical nanowires (NWs) with chemical constraints is proposed in this work. The choice of cylindrical NWs instead of stripes with rectangular section allows, in addition to the use of chemical constraints, to avoid the Walker breakdown thus enabling a faster propagation of information along the device [2]. Furthermore, the manufacturing method of NWs is cheaper than the stripes fabrication method, making the NWs more scalable [3]. In this work, we propose a novel design of a racetrack memory using two functional segments along the NW: a “writing section” and a “storage section” (Fig. 1). The introduction, for the first time, of a “writing section” along the NW eases to write the information directly in the NW, without the need of an external writing head. The writing section design in the nanowire is made of two magnetic segments with different coercive fields, isolated from the “storage section” by a non-magnetic constraint. The magnetic simulations performed have proved how one can switch the magnetization (bit information) of the “writing section” without modifying the bit recorded in the rest of the NW [4]. The information written in this first section can then be recorded into the racetrack memory wire by applying a spin-polarized current through the device. The magnetic simulations show a successful depinning of the DWs from the chemical constraints achieved by the application of a spin current pulse through the NW, thus moving the magnetic bits in the whole NW without any loss of information (Fig. 2). The success of this novel design has been proved by the design of three different configurations of “writing sections”, obtaining in all three cases a successful recording and bit movement [4]. Arrays of 3 and 7 NWs (hexagonal array) were also simulated to investigate the effect of neighboring magnetic wires in the bit movement of the central wire. These novel NWs can be easily fabricated by the electrodeposition method, a well-known process where it is possible to tune the properties of the nanowires. The subsequent characterization of their properties, as well as their effectiveness to record a new bit, can then be measured by fast domain wall injection [5], a process where it is possible to characterize the nanowires individually. The improvements achieved in the use of cylindrical magnetic NWs as racetrack memories will help to develop a faster magnetic storage device with greater capacity and reliability, fabricated with low-cost and scalable methods. This work was financially supported by projects POCI-01-0145-FEDER-028676 and UIDB/04968/2020 from Portuguese FCT and COMPETE 2020 (FEDER).

[1] S. P. Parkin, M. Hayashi, and L. Thomas, *Science*, vol. 320, p. 90-194 (2008) [2] N. Biziere et al., *Nano Letters* vol. 13, p.2053 (2013) [3] C. T. Sousa et al., *Applied Physics Reviews*, vol. 1, p. 031102 (2014) [4] J. Rial and M. P. Proenca, *Nanomaterials* vol.10, p.2403 (2020) [5] J.L. Prieto, M. Muñoz, and E. Martínez, *Physical Review B*, vol. 83, p.104425 (2011)

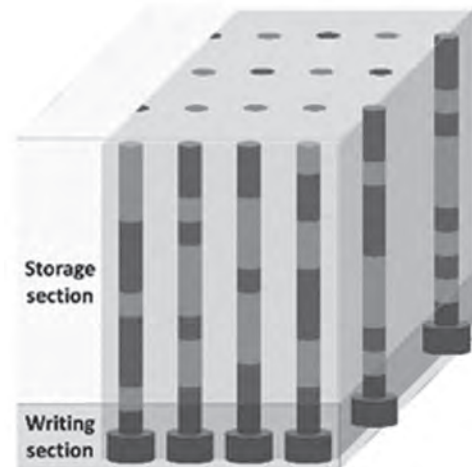


Figure 1. Schematic representation of a 3D racetrack memory device using arrays of cylindrical magnetic nanowires, illustrating the writing and storage sections.

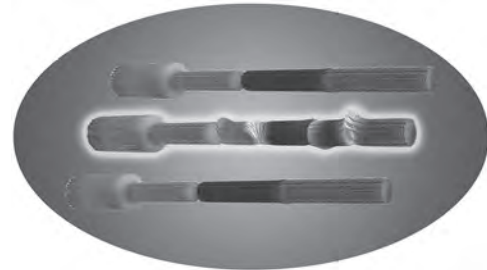


Figure 2. Domain wall movement along the central nanowire under the application of a spin-polarized current.

GD-04. Domain Wall Damping in Ultrathin Nanostripes With Dzyaloshinskii-Moriya Interaction.

O.M. Volkov¹, O. Pylypovskiy¹, F. Kronast², C. Abert³, E. Oliveros Mata¹, P. Makushko¹, M. Mawass², V. Kravchuk⁴, D.D. Sheka⁵, J. Fassbender¹ and D. Makarov¹

1. Institute of Ion Beam Physics and Materials Research, Helmholtz-Zentrum Dresden-Rossendorf, Dresden, Germany; 2. Helmholtz-Zentrum Berlin für Materialien und Energie GmbH, Berlin, Germany; 3. Faculty of Physics, Universität Wien Fakultät für Physik, Wien, Austria; 4. Institut für Theoretische Festkörperphysik, Karlsruhe Institut für Technologie, Karlsruhe, Germany; 5. Tarasa Shevchenko National University of Kyiv, Kyiv, Ukraine

Structural inversion symmetry breaking in low-dimensional magnetic systems determines their electronic and magnetic properties at interfaces [1,2]. Asymmetrically sandwiched magnetic films can provide strong perpendicular magnetic anisotropy and Dzyaloshinskii-Moriya interactions (DMI), which is necessary for prospective memory and logic devices based on chiral non-collinear magnetic textures, e.g. skyrmions [3,4], skyrmion bubbles and chiral domain walls (DWs) [5]. The device performance is determined by the static and dynamic micromagnetic parameters [6,7]. In particular, the speed of a DW-based racetrack memory is defined by both the strength of the external driving, e.g. magnetic field or spin-polarized current, and internal magnetic parameters, e.g. the DMI constant and damping parameter [6,7]. The necessity of having a strong DMI in asymmetrically sandwiched magnetic structures requires the utilization of ultrathin (in the range of 1 nm) magnetic films, which implies the polycrystallinity and compromised structural quality of the layer stack. Structural imperfections in addition to the spin-pumping mechanism [8,9], that arises due to the proximity of a ferromagnetic material with a heavy-metal, lead to a substantial enhancement of the magnetic damping parameter of ultrathin films compared to bulk. Accessing this parameter typically requires dynamic experiments on the motion of DWs in confined geometries, which are usually done in the creep regime due to the pronounced pinning. Here, we demonstrate both experimentally and theoretically the presence of tilted DWs in statics in perpendicularly magnetized asymmetric //CrO_x/Co/Pt layer stacks with surface-induced DMI, Fig. 1. We show that in such systems there are two possible theoretical mechanism for the appearance of titled DWs: (I) A unidirectional tilt could appear in equilibrium as a result of the competition between the DMI and additional in-plane easy-axis anisotropy, which breaks the symmetry of the magnetic texture and introduce tilts [10]. (II) A static DW tilt could appear due to the spatial variation of magnetic parameters, which introduce pinning centers for DWs. A moving DW can be trapped in a tilted state after the external driving field is off. Based on these theoretical approaches, we perform a statistical analysis of the DW tilt angles obtained in statics after the external magnetic field used for the sample demagnetization was off. We found that the second approach corresponds better to the experimental observations and allows to determine self-consistently the range of DW damping parameters and DMI constants for the particular layer stack. Using two reference fields, which provide two characteristic tilt angles, allow us to retrieve the range of DMI strength $D \geq 0.8$ mJ/m² and DW damping parameters $\alpha \geq 0.1$. The upper limit for the DMI constant agrees with an independent transport-based measurement giving $D = 0.90 \pm 0.13$ mJ/m², which further refines our estimate of the damping parameter $\alpha = 0.13 \pm 0.02$. This value lies in a typical DW damping range for the Co-based asymmetrical layer stacks, that are obtained from dynamic experiments [11,12]. Thus, the combination of the proposed method with standard metrological techniques opens up opportunities for the quantification of both static and dynamic micromagnetic parameters based on static measurements of the DW morphology.

[1] A. Fert, N. Reyren, and V. Cros, Nature Reviews Materials 2, 17031 (2017). [2] R. Wiesendanger, Nature Reviews Materials 1, 16044 (2016). [3] A. N. Bogdanov and D. A. Yablonskii, Zh. Eksp. Teor. Fiz. 95, 178 (1989). [4] S. Woo, K. Litzius, B. Krüger, et al., Nature Materials 15, 501 (2016). [5] S. Emori, U. Bauer, S.-M. Ahn, et al., Nature Materials 12, 611 (2013). [6] C. Garg, S.-H. Yang, T. Phung, et al., Science Advances 3, e1602804 (2017). [7] S. Parkin and S.-H. Yang, Nature Nanotechnology 10,

195 (2015). [8] Y. Tserkovnyak, A. Brataas, G. E. W. Bauer, et al., Reviews of Modern Physics 77, 1375 (2005). [9] A. Brataas, Y. Tserkovnyak, and G. E. W. Bauer, Physical Review Letters 101, 037207 (2008). [10] O. V. Pylypovskiy, V. P. Kravchuk, O. M. Volkov, et al., Journal of Physics D: Applied Physics 53, 395003 (2020). [11] J.-M. L. Beaujour, J. H. Lee, A. D. Kent, et al., Physical Review B 74 (2006). [12] A. J. Schellekens, L. Deen, D. Wang, et al., Applied Physics Letters 102, 082405 (2013).

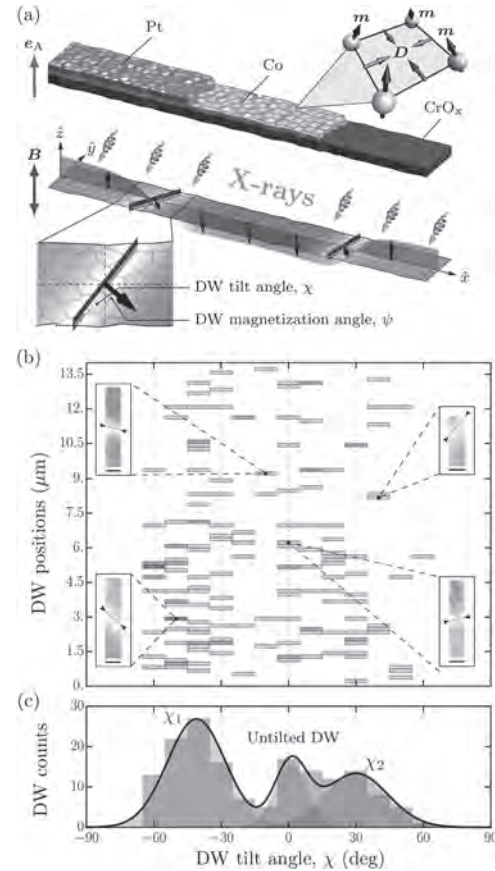


Fig. 1. (a) Schematic illustration of a //CrO_x/Co/Pt asymmetric multi-layer nanostripe and the corresponding magnetic contrast with two tilted DWs. The angle between the DW plane and the y-axis is the DW mechanical tilt angle, χ , while the magnetization inside the DW is canted by the angle, ψ with respect to y-axis. **(b)** Phase diagram of equilibrium DW morphologies for a ferromagnetic stripe with the width 200 nm extracted from X-ray magnetic circular dichroism photoelectron emission microscopy images after the AC demagnetization. **(c)** The corresponding distribution of DW counts vs. the tilt angle χ .

GD-05. Magnetic Nano-Horns for Measurement of the Interfacial Dzyaloshinskii-Moriya Interaction.

T. Wong¹ and V.M. Sokalski²

1. Department of Physics, Carnegie Mellon University, Pittsburgh, PA, United States; 2. Department of Materials Science and Engineering, Carnegie Mellon University, Pittsburgh, PA, United States

The interfacial Dzyaloshinskii-Moriya Interaction is a critical property of magnetic thin films for the stabilization of chiral magnetic objects, including skyrmions, for use in future spintronic applications.[1] However, direct measurement of the strength of this interaction remains an experimental challenge.[2] Here, we present a technique for direct extraction of the interfacial Dzyaloshinskii-Moriya Interaction using a tapered c-shape (herein referred to as a nanohorn). A schematic of this idea is shown in figure 1. The nanohorn is designed to provide a driving force for the DW to propagate in the counter-clockwise direction driven by a reduction in the overall length of the DW itself. An in-plane magnetic field coupled with the interfacial DMI provides a driving force for propagation in the clockwise direction. This is due to the Zeeman energy associated with the DW's internal magnetization and the magnetic field. The balance of these forces results in an energy minimum in wall position that depends directly on the strength of iDMI. In short, the rest position of the DW can be read like the needle of an analog meter to determine the strength of DMI. A series of micromagnetic calculations using Mumax3 were performed using the gradient descent approach to determine the energy of the DW as a function of its position along the nanohorn radius. Here, we use material parameters $A = 15\text{pJ/m}$, $K_{\text{eff}} = 598\text{kJ/m}^3$, $M_s = 800\text{kA/m}$ for a film thickness of 2nm. The width of the magnetic nanohorn ranges from $\sim 100\text{-}200\text{nm}$ although larger dimensions are not expected to significantly impact the results. The sides of this horn follow the two polar equations $r = a+b-c\theta$, $r = a-b+c\theta$. This produces a shape with a circular arc of radius a along its center and radial width increasing symmetrically from this arc in a linear rate $2c$. We note that there are a range of parameters where there is no energy minima, which is not useful experimentally. However, the degree of horn tapering can be designed to work for material systems with different strengths of DMI. In the presentation, comparison with semi-analytical calculations will be presented, which show minimal differences in the equilibrium wall position likely due to dipolar interactions and slight tilting of the DW. Challenges associated with experimental realization of this technique will be discussed along with ways to mitigate them as evidenced by additional micromagnetic modeling. Most notably, there are dynamic limitations with driving the wall to its equilibrium, which can be addressed through increased statistics (simultaneously examining many nanohorns of different dimensions) and exciting the DW with AC magnetic fields to overcome edge pinning. Prospects for the experimental use of this technique for different materials systems will be discussed.

[1] Thiaville, A., Rohart, S., Jué, É., Cros, V. and Fert, A., 2012. Dynamics of Dzyaloshinskii domain walls in ultrathin magnetic films. *EPL (Europhysics Letters)*, 100(5), p.57002. [2] Lau, D., Pellegren, J.P., Nembach, H.T., Shaw, J.M. and Sokalski, V., 2018. Disentangling factors governing Dzyaloshinskii domain-wall creep in Co/Ni thin films using Pt x Ir 1-x seed layers. *Physical Review B*, 98(18), p.184410.

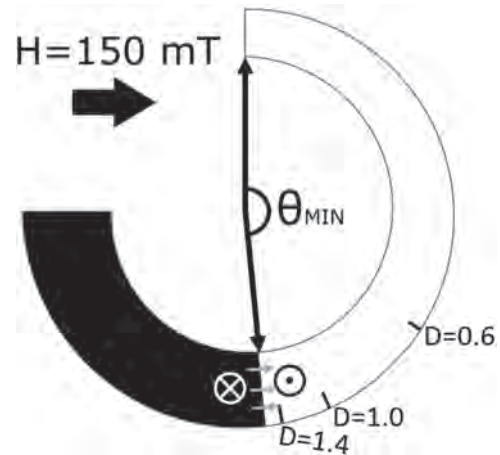


Figure 1: Schematic of the coordinate system and example micromagnetic output for a nanohorn with $D = 1.6\text{ mJ/m}^2$ and $\mu_0 H_x = 150\text{mT}$. Orange arrows show the DW internal magnetization direction. Tick marks along the circumference indicate the equilibrium position (θ_{MIN}) of the domain wall for a range of other DMI strengths.

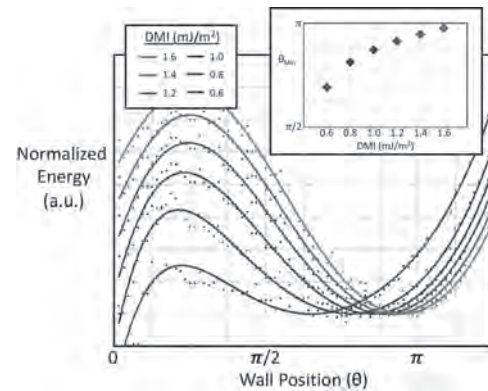


Figure 2: Domain wall energy vs wall position (θ) normalized to the energy minima for varying DMI strengths. The lines shown are empirical fits to the micromagnetic energy output. Inset: Equilibrium wall position (θ_{MIN}) vs DMI strength.

GD-06. Consequences of Pt/Co vs Co/Pt Deposition Order on Interfacial Magnetic Properties in Pt-Co-Ni Based Asymmetric Superlattices.

N. Pandey¹, M.P. Li¹, H. Nembach^{2,3}, J. Shaw², M. De Graef¹ and V.M. Sokalski¹

1. Department of Materials Science and Engineering, Carnegie Mellon University, Pittsburgh, PA, United States; 2. Quantum Electromagnetics Division, National Institute of Standards and Technology, Boulder, CO, United States; 3. Department of Physics, University of Colorado Boulder, Boulder, CO, United States

The Pt-Co-Ni multi-layer system has shown promising tunability of its interfacial magnetic properties (including Dzyaloshinskii-Moriya interaction (DMI) and magnetic anisotropy) for the development of future chiral spintronic devices. Previous work has shown that the system supports stabilization of Néel Skyrmions [1] and efficient movement of Dzyaloshinskii domain walls (DW) [2]. However, the vast majority of the work has focused on the case of a Pt/Co deposition order (from substrate side) leading to predominantly left-handed chiral Neel domain walls. Moreover, it is expected that there will be interesting properties that could result from combining left and right-handed domain walls in more complicated heterostructures [3]. Here, we leverage the Pt-Co/Ni multi-layer system to compare the role of the Pt/Co interface when on the bottom vs top of the asymmetric repeat unit. The film stacks under consideration are $[\text{Pt}/(\text{Co}/\text{Ni})_M]_N$ or $[\text{Pt}/(\text{Ni}/\text{Co})_M]_N$ and were deposited by DC magnetron sputtering in an argon plasma with pressure fixed at bar (2.5 mTorr). Film stacks were grown on oxidized Si substrates with a Ta/Pt seed layer to induce FCC (111) texture. $\text{Pt}/(\text{Co}/\text{Ni})_M]_N$ multi-layers show strong perpendicular magnetic anisotropy (figure 1a) with a pinched perpendicular MH loop characteristic for bubble materials. Lorentz Transmission Electron Microscopy (LTEM) shows contrast only in the tilted orientation confirming the presence of Néel-type Skyrmions and domain walls, which suggests a significant interfacial DMI strength. This is likely due to differences in the DMI associated with Pt/Co and Ni/Pt interfaces. For these samples, Brillouin Light Scattering (BLS) spectroscopy shows a shift in the spin wave spectra corresponding to $|D|=0.21$ mJ/m², which is sufficient to stabilize the Néel configuration. For the $[\text{Pt}/(\text{Ni}/\text{Co})_M]_N$ sample with all deposition conditions otherwise identical, there is a marked drop in perpendicular magnetic anisotropy with a less clearly defined pinch in the MH loop (Figure 2 a). Lorentz TEM shows only Bloch type domain walls with no preferred chirality (Figure 2 b). Furthermore, application of a perpendicular field stabilizes achiral Bloch bubbles along with a large number of topologically trivial bubbles (or type 2 bubbles) with two vertical Bloch lines inside. It is reasonable to expect that the reduction in magnetic anisotropy is related to the Pt/Co interface quality, which would in turn impact the DMI strength explaining the absence of Neel DWs. It has previously been proposed that the origin of the deposition order effect is due to intermixing between the Pt and Co [4]. It is possible that higher adatom energy of Pt results in a higher degree of intermixing at the interface when deposited onto Co, which will be discussed along with possible steps to mitigate the problem experimentally. As a secondary note, although it has a relatively small DMI, this system can serve as a playground for evaluating the role of topology on the annihilation field of the magnetic bubbles. In-situ Lorentz TEM images show an appreciably larger annihilation field for the non-trivial bubbles (i.e. Bloch Skyrmions) than for the trivial bubbles. Statistics on the annihilation field will be presented in detail in this paper.

1. D.Lau et al., *Physical Review B*, vol. 9. P. 184410 (2018) 2. S. Parkin, et al., *Science*, vol. 320, no. 5873, p. 190–194. (2008) 3. N. Pandey, et al., *AIP Advances*, vol. 10, no. 1, p. 015233. (2020) 4. R. Lavrijsen et al, *Physical review B*, vol 91.10, p. 104414. (2015)

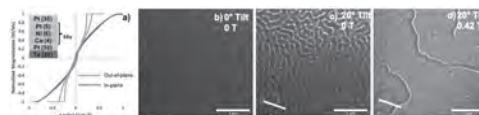


Fig 1: a) M-H loop of $[\text{Pt}(5\text{\AA})/\text{Co}(4\text{\AA})/\text{Ni}(6\text{\AA})]_{\times 50}$ multilayer structure. Fresnel mode LTEM with: b) 0° tilt and 0 T OOP field showing no DW contrast. c) 20° tilt and 0 T OOP field showing Néel wall contrast. d) 20° tilt and 0.42 T OOP field showing formation of Néel Skyrmions.

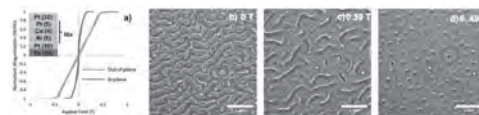


Figure 2: a) M-H loop of $[\text{Pt}(5\text{\AA})/\text{Ni}(6\text{\AA})/\text{Co}(4\text{\AA})]_{\times 50}$ multilayer structure. Fresnel mode LTEM with: b) 0 T OOP field showing labyrinth-like DW contrast. c) 0.39 T OOP field showing growth of bubbles from Bloch domain walls. d) 0.49 T OOP field showing a mixed bubble system; red and green circles – achiral Bloch bubbles, blue circle – topologically trivial bubbles (type II).

GD-07. Origin and Optical Switching of Perpendicular Magnetization for $\text{Co}_{100-x}\text{Gd}_x/\text{Pt}$ Multilayers.

T. Seki^{1,2}, J. Wang¹, Y. Lau¹, Y. Takahashi² and K. Takanashi¹

1. Institute for Materials Research, Tohoku University, Sendai, Japan;

2. National Institute for Materials Science, Tsukuba, Japan

Introduction: Magnetization manipulation on ultrashort timescales is one of the major issues for developing high speed spintronic devices. All-optical switching (AOS) of magnetization by femtosecond laser pulses has attracted much attention as a route for ultrafast magnetization manipulation. Following the pioneering demonstrations of all-optical helicity dependent switching (AO-HDS) [Refs.1,2], another type of AOS was reported in Gd-Fe-Co [Ref.3], which is called AO helicity independent switching (AO-HIS). The AO-HIS is observed for the limited materials such as Gd-Fe-Co [Ref.3] and Co/Gd multilayer [Ref.4]. On the other hand, recent studies demonstrated that the AO-HDS was achieved for several ferromagnetic alloys, ferrimagnetic alloys and multilayers [Refs.5,6], suggesting that exploiting a variety of materials is beneficial to elucidate the underlying mechanism of AOS. The perpendicularly magnetized Gd-based alloys are representative materials not only for the AOS study, but also for the research of antiferromagnetic spintronics. However, the origin of perpendicular magnetic anisotropy (PMA) has not been fully understood yet. For example, in the case of Co-Gd, the thick Co-Gd single layer film sometimes exhibits the PMA [Ref.7] whereas the thin Co-Gd single layer often shows the in-plane magnetization [Ref.8], and the condition to obtain the PMA is not clear. Nevertheless, many spintronics and AOS studies exploited the combination of Gd-based alloy and Pt without addressing the origin of PMA. In addition, although a magnetic moment may be induced in Pt due to the proximity effect, the role of interface magnetism on the magneto-optical response has not been elucidated yet. These facts make the combination of Gd-based alloy and Pt a unique platform to investigate the correlation between the fundamental magnetic properties and the AOS behavior, which will provide knowledge to gain insight into the AOS. In this study, we paid attention to the combination of Co-Gd and Pt. The origin of PMA and the role of induced magnetic moment were first investigated for the Co-Gd/Pt multilayers with various Co-Gd layer thicknesses (t) and alloy compositions ($\text{Co}_{100-x}\text{Gd}_x$). Then, the AOS experiments were carried out in order to find the composition dependence of AOS probability. Experimental Results: Thin films with the stacking structure of $[\text{Pt}(2.0)/\text{Co}_{100-x}\text{Gd}_x(t)]_3/\text{Pt}(2.0)$ (in nanometer) were prepared on sapphire (11-20) substrates using an ultrahigh vacuum compatible magnetron sputtering system. All the layers were deposited at room temperature. By tuning the sputtering powers of Co and Gd targets, the Gd concentration x at. % was widely varied in the range from $x = 12$ to 37 at. %. The alloy compositions were determined by the electron probe x-ray microanalysis. The film structures were characterized using x-ray reflectivity (XRR) and reflection high energy electron diffraction. Magnetic properties were measured using a superconducting quantum interference device magnetometer, a vibrating sample magnetometer and a polar magneto-optical Kerr effect set-up. The AOS experiment was carried out at room temperature with right and left circularly polarized laser pulses (center wavelength of 514 nm, pulse duration of ~200 fs, and repetition rate of 10 kHz) under zero magnetic field. The typical laser power was ~2.8 mW and the corresponding laser fluence applied was 0.9~2.1 mJ/cm². A single laser pulse with a diameter of ~30 nm was illuminated on the surface of films (demonstration of helicity dependence) and/or the center of the microfabricated Hall cross (quantification of AOS probability). The XRR profiles were well fitted for all the samples with the assumption of the $[\text{Pt}/\text{Co-Gd}]_3/\text{Pt}$ layer stack, meaning that the designed layered structures were successfully prepared. From the thickness and composition dependences of magnetization and magnetic anisotropy energy, we found that the magnetic anisotropy coming from the Co-Gd/Pt interface plays the major role for obtaining PMA while the contribution from the bulk properties of Co-Gd is negligibly small. This is of different origin for Gd-Fe-Co, in which the bulk magnetic anisotropy leads to the PMA. The proximity-induced magnetic moment in Pt remarkably appeared for the thin Co-Gd layers, which coupled with the Co magnetic moment in parallel. It is noted that the proximity-induced Pt moment largely affected the condition for the magnetization compensation of Co-Gd. The Co-Gd/Pt multilayers clearly exhibited the single laser pulse AO-HIS in the wide

Co-Gd composition range, and the maximum AOS probability was obtained around the compensation composition of Co-Gd. The above findings are useful to improve the performance of AOS-based device.

[1] C. D. Stanciu *et al.*, Phys. Rev. Lett. 99, 047601 (2007). [2] K. Vahaplar *et al.*, Phys. Rev. Lett. 103, 117201 (2009). [3] T. A. Ostler *et al.*, Nat. Commun. 3, 666 (2012). [4] M. L. M. Laliou *et al.*, Phys. Rev. B 96, 220411(R) (2017). [5] S. Mangin *et al.*, Nat. Mater. 13, 286 (2014). [6] C.-H. Lambert *et al.*, Science 345, 1337 (2014). [7] M. Binder *et al.*, Phys. Rev. B 74, 134404 (2006). [8] W. Zhou *et al.*, Phys. Rev. Mater. 2, 094404-1-7 (2018).

GD-08. RKKY Exchange Coupling Mediated Ultrafast all-Optical Switching of a Ferromagnet.

J. Chatterjee¹, D. Polley¹, H. Jang¹, A. Pattabi¹, S. Salahuddin¹ and J. Bokor¹

1. Department of Electrical Engineering and Computer Sciences, University of California Berkeley, Berkeley, CA, United States

Ultrafast helicity-independent all-optical switching (HI-AOS)¹ as well as ps current-pulse driven magnetization reversal² of ferrimagnetic GdFeCo suggest the pathway of realizing ultrafast magnetization reversal of a MTJ based memory element. Previously, MTJ devices were reported using GdFeCo as a free layer³. However, due to the low spin polarization of GdFeCo and lack of thermal treatment, the TMR was too small (0.6 %) for a practical memory device. Therefore, it is of much interest to switch a ferromagnet, which is known to have higher spin-polarization, with ultrafast excitation. More recently, two routes of HI-AOS switching of a ferromagnet have been demonstrated. Firstly by exploiting ballistic spin polarized current injection, which is shown in a GdFeCo/Cu/[Co/Pt] spin-valve structure⁴. In this structure, the spin current, generated due to the switching of GdFeCo under optical excitation, is responsible for the switching of Co/Pt multilayers. A second route is RKKY exchange coupling of HI-AOS of GdFeCo to a ferromagnet^{5,6}. On this particular platform, 7 ps switching speed of Co/Pt multilayers has been demonstrated when ferromagnetically coupled with a GdFeCo ferrimagnet. However, GdFeCo does not hold PMA for a patterned dot with a diameter less than about one nm⁷. Hence, GdFeCo is not desirable for building a coupled ferromagnet-ferrimagnet heterostructure as a storage layer of a nano-patterned memory cell. On the other hand, CoGd ferromagnetic alloy has been shown to maintain its PMA, as well as exhibit HI-AOS when it is patterned down to at least 200 nm diameter⁷. Therefore, in this work, we investigated the static magnetic properties, all-optical switching and time-resolved magnetization dynamics of a CoGd/Pt spacer (1 to 4 nm)/[Co/Pt] multilayer heterostructure. We demonstrate that the strength and type of indirect RKKY exchange coupling between the CoGd-ferrimagnet and Co/Pt MLs-ferrimagnet depends on the Pt spacers thickness. Irrespective of the type of RKKY coupling, optical toggle switching of both the Co/Pt multilayers and CoGd alloy has been observed. Only for decoupled case (Pt spacer 4 nm), the magnetization of Co/Pt multilayer is not reversed. Figure 1(a) shows that, for 4 nm spacer, although the magnetization of CoGd is reversed after 1.5 ps, the Co/Pt multilayer is only partially demagnetized followed by a slow recovery to its initial magnetization direction. In contrast to the decoupled sample, a ferromagnetically coupled sample (Pt spacer 1 nm) exhibits switching of both the CoGd alloy and Co/Pt multilayer, as shown in Fig. 1(b). The CoGd reverses its magnetization after ~1.5 ps. The Co/Pt multilayer on the other hand, although has slightly higher demagnetization rate, stays demagnetized then switching at 3 ps. To the best of our knowledge, this is the fastest switching of a ferromagnet ever reported. In order to qualitatively understand the microscopic mechanism of magnetization reversal of Co/Pt MLs and both sublattices of the CoGd alloy, we performed theoretical calculations extending the microscopic three temperature model proposed by Beens et al⁸. Considering inter-sublattice, intra-sublattice and indirect RKKY exchange scattering, we explain the magnetization reversal dynamics of different magnetic components of ferromagnetically and anti-ferromagnetically coupled as well as decoupled ferromagnet-ferrimagnet heterostructures. The calculated values of switching times are in agreement with the experimental observations. These results represent a significant step towards ultrafast, nanoscale spintronic memory technologies.

¹ I. Radu, K. Vahaplar, C. Stamm et al Nature 472, 205 (2011). ² Y. Yang, R.B. Wilson, J. Gorchon, C.-H. Lambert et al. Sci. Adv. 3, e1603117 (2017). ³ J.Y. Chen, L. He, J.P. Wang, and M. Li, Phys. Rev. Appl. 7, 021001 (2017). ⁴ S. Iihama, Y. Xu, M. Deb, et al. Adv. Mater. 30, 1 (2018). ⁵ J. Gorchon, C.H. Lambert, Y. Yang, et al., Appl. Phys. Lett. 111, 042401 (2017). ⁶ L. Avilés-Félix, L. Álvaro-Gómez, G. Li, et al. AIP Adv. 9,125328, (2019). ⁷ A. El-Ghazaly, B. Tran, A. Ceballos, et al. Appl. Phys. Lett. 114, 232407 (2019). ⁸ M. Beens, M.L.M. Laliou, A.J.M. Deenen, et al., Phys. Rev. B 100, 220409R (2019).

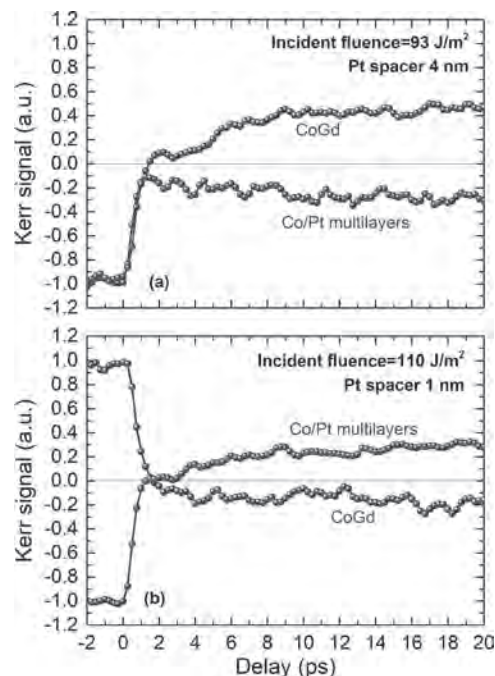


Fig. 1. Depth resolved time resolved magnetization dynamics of (a) decoupled ([Co/Pt]₃/Co/Pt 4 nm/CoGd/cap) and (b) ferromagnetically ([Co/Pt]₃/Co/Pt 1 nm/CoGd/cap) coupled stacks.

GD-09. All-Electrical Control of Nanoscale Domain Wall Devices Using Magnetic Tunnel Junction Read and Write INVITED.

E. Raymenants^{1,2}, D. Wan¹, K. Garello^{3,1}, I. Asselberghs¹, I. Radu¹, S. Couet¹ and V. Nguyen¹

1. IMEC, Leuven, Belgium; 2. Katholieke Universiteit Leuven, Leuven, Belgium; 3. SPINtronique et Technologie des Composants, Grenoble, France

Fast domain wall (DW) motion in magnetic nanostructures is crucial for future spintronic devices, such as racetrack memory [1], spin logic [2] and neuromorphic computing [3]. The discovery of fast DW transport governed by spin-orbit torque (SOT) and the Dzyaloshinskii-Moriya interaction (DMI) in ultrathin magnetic layers on heavy metals was a breakthrough in the development of low energy devices based on DW motion. However, a lack of all-electrical control of DWs in nanoscale devices impedes to bring these advanced materials to practical applications. Therefore, finding energy-efficient ways to electrically write, read and transport DWs is a necessity. As demonstrated in STT-MRAM technology, the magnetic tunnel junction (MTJ) based on a CoFeB/MgO free layer (FL) [4], which offers efficient spin-transfer torque (STT) write and a high tunneling magnetoresistance (TMR) readout signal, could be a potential solution to electrically operate a full functional DW device. However, such an MTJ stack poses significant challenges to realize a DW device, which particularly relate to low DW speed and poor manufacturability of a CoFeB/MgO based DW conduit using industrial integration platforms [5]. Here, we propose and develop a new type of MTJ stack that incorporates typical high DW velocity materials (*i.e.*, Pt/Co) as the second FL into a conventional MTJ with a CoFeB/MgO based FL. We firstly demonstrate that the fundamental properties of a standard MTJ device are not compromised by the integration of DW conduit materials. Complete functional DW devices, consisting of multiple MTJ pillars connected by a common FL, have been fully integrated using such novel MTJ stack, Figure 1 (a). We then demonstrate that all-electrical control of a DW in a nanoscale device, *i.e.*, STT write, TMR read and SOT driven DW motion, can be achieved. As an example, figure 1 (b) presents field-driven domain expansion from P2 through the whole track, after the domain was nucleated by STT in P2. Figure 1 (c) demonstrates the current-driven DW transport from P2 to P1, with small field assistance. No change in resistance was observed in P3, as expected from directional current-driven DW motion. Finally, we show that these DW devices can be used to investigate the SOT driven DW dynamics in nanoscale devices where conventional magnetic imaging techniques become ineffective. Our DW devices show good TMR read-out and efficient STT writing, comparable to current STT-MRAM devices. The devices are fabricated in imec's 300 mm CMOS fab on full wafers which clears the path for large scale integration. This proof-of-concept thus offers potential solutions for high performance and low-power DW-based devices for logic and neuromorphic applications [5,6].

1. Parkin et al., Science 320, 190 (2008) 2. Zhaochu., et al., Nature 579, 214 (2020) 3. Siddiqui., et al., Nano Lett. 20, 1033 (2019) 4. Ikeda, et al., Nat. Mater. 9, 721 (2010) 5. Raymenants, et al., 2018 IEDM, 36.4 6. Raymenants, et al., 2020 IEDM, 21.5

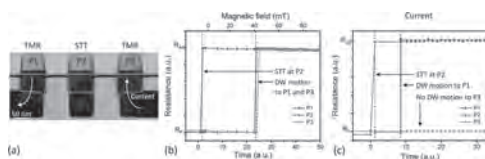


Figure 1 | (a) TEM image of a DW device. The figure highlights how current can flow through the FL track, transporting DWs from pillar to pillar. (b) Domain was nucleated in P2 by STT, after which external field expanded it to the outer pillars, P1 and P3. (c) A domain was nucleated in P2 by STT, after which directional DW transport was achieved from P2 to P1 when driven by SOT and a small assist field. No DW propagation was observed to P3 as expected [6].

Session GP
MRAM AND NEUROMORPHIC COMPUTING
(Poster Session)

Shouzhong Peng, Chair
Beihang University, Beijing, China

GP-01. Modeling of Single-Digit Nanometer Perpendicular Shape Anisotropy Magnetic Tunnel Junction Driven by Spin-Transfer-Torque.

M. Wang¹ and Y. Jiang¹
 1. Jiangnan University, Wuxi, China

Spin Transfer Torque Magnetic Random Access Memory (STT-MRAM) has become one of the leading candidates for next generation memory applications, for which a key challenge is the simultaneous achievement of low switching current, high thermal stability and large TMR. Low switching current can be achieved with small device size; however, the thermal stability of perpendicular magnetic tunnel junction is extremely reduced at ultrafine scales. A new approach has been recently proposed by revisiting the shape anisotropy [1, 2]. The concept of Perpendicular Shape Anisotropy (PSA) MTJ is developed with a thicker free layer to keep its thermal stability in single-digit nanometers. Due to the PSA emerges as the main source of perpendicular anisotropy, high thermal stability can be achieved even down to sub-10-nm. The device shows possible application in the nanometer scale and is compatible with the developed CMOS technology. In this manner, the SPICE model of the device is highly required since its operation principle is different from the incumbent STT-MTJ device. In this paper, a dynamic model of the PSA-MTJ is developed, including its micromagnetic simulation using LLG equation. In the nanometer scale, the stochastic term is also included. By analyzing the instantaneous magnetization vector, the switching time is extracted. The impacts of write current scaling on the switching time, the energy consumption and the write failure rate of PSA-MTJ are studied. Based on the model, both the static and dynamic behaviors can be captured. The scale effect of the PMA region with different diameters is studied based on the developed model. Finally, hybrid MTJ/CMOS simulation is performed to validate the developed model for circuit designs and simulations in the single-digit nanometer scale. Figure 1 (a) shows the thermal stability factor Δ as a function of free layer thickness t and diameter D . Figure 1 (b) shows the region achieving both high thermal stability and low critical voltage V_{C0} . Figure 2 shows the dynamic properties of z-component of normalized magnetization with different device sizes, applied current is 70 uA with 15 ns width. The switching time can be extracted from the 90% magnetization reversal point.

[1] K. Watanabe, B. Jinnai, S. Fukami, H. Sato, and H. Ohno, Nat Commun., Vol. 9, no. 1, p. 663 (2018). [2] N. Perrissin et al., Nanoscale., Vol. 10, no. 25, pp. 12187-12195 (2018).

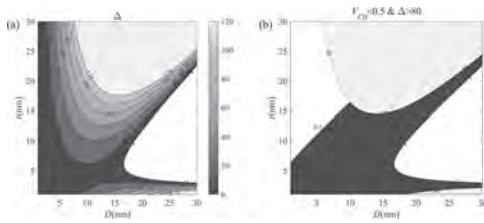


Fig. 1 (a) as function of t and D . (b) Regions satisfying $\Delta > 80$ and $V_{C0} < 0.5$ V.

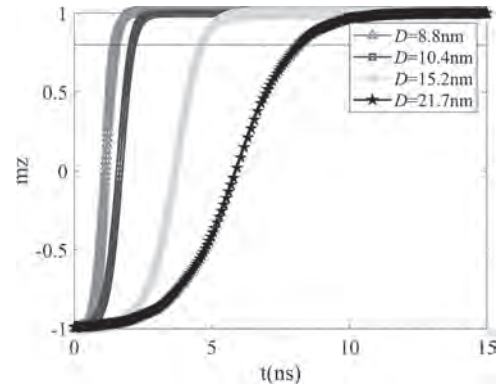


Fig.2 The z-component of magnetization with different D ($t = 15$ ns).

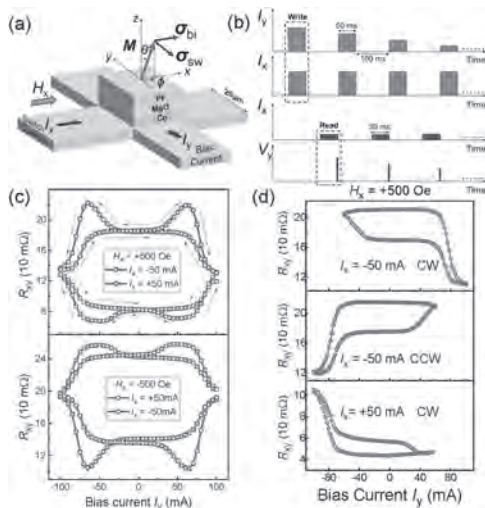
GP-02. Chirality-Reversible Multistate Switching via Bi-SOT in a Perpendicularly Magnetized System.

W. Yang¹, C. Wan¹, Z. Yan¹, X. Zhang¹, M. Stebliy², X. Wang¹, C. Fang¹, C. Guo¹, Y. Xing¹, T. Ma¹, A. Ognev², A.S. Samardak², M. Tung³, G. Yu¹ and X. Han¹

1. Institute of Physics, University of Chinese Academy of Sciences, Beijing, China; 2. School of Natural Sciences, Far Eastern Federal University, Vladivostok, Russian Federation; 3. Material and Chemical Engineering Laboratory, Industrial Technology Research Institute, Hsinchu, Taiwan

Spin-orbit torque (SOT) offers a fast and efficient way to control magnetization, making this technique bear exciting prospect both in magnetic random access memories (SOT-MRAM) and data processing, especially in the fields of neural computing and spin logics. Conventionally, only spin-up and spin-down states of a magnetic system are utilized to encode binary data. Meanwhile, spin torques including spin-orbit torque and spin-transfer torque (STT) can switch magnetization between the two states and thus write digits 0 or 1 into the magnetic system. In this work, a bi-SOT strategy (two orthogonal SOTs provided by two vertical in-plane currents) can switch a perpendicular system (Pt/Co/MgO) from the spin-up/spin-down states to a random state with zero averaged m_z , which makes three-state storage or ternary computing physically potential. Furthermore, we can use the newly-introduced random state by electric method to reverse chirality (clockwise or counterclockwise direction) of the SOT switching which used to be realized by a direction-reversible magnetic field. The multistate nature and the flexible chirality offered by this bi-SOT technique may find matched applications in ternary computing, neural computing and spin logics.

[1] X. Zhang C. H. Wan, Z. H. Yuan, C. Fang, W. J. Kong, H. Wu, Q. T. Zhang, B. S. Tao, X. F. Han, *J. Mag. Mag. Mater.* 428, 2017, 401-405 [2] C. Wan, X. Zhang, Z. H. Yuan, C. Fang, W. J. Kong, Q. T. Zhang, H. Wu, U. Khan, X. F. Han, *Adv. Electron. Mater.* 3, 2017, 1600282 [3] X. Wang, C. H. Wan, W. J. Kong, X. Zhang, Y. W. Xing, C. Fang, B. S. Tao, W. L. Yang, L. Huang, H. Wu, M. Irfan and X. F. Han et al. *Adv. Mater.* 30, 2018, 1801318. [4] W. J. Kong, C. H. Wan, X. Wang, B. S. Tao, L. Huang, C. Fang, C. Y. Guo, Y. Guang, M. Irfan, and X. F. Han, *Nature Commun.* 10, 2019, 233.



GP-03. Increasing the Correlation Time of Spin Torque Oscillators Synchronised by Magnetostatic Interactions.

S. Greaves¹

¹ RIEC, Tohoku University, Sendai, Japan

Introduction Spin torque oscillators (STOs) and MRAM devices can exhibit non-linear behaviour which can be exploited to carry out tasks which would otherwise take a long time or require a huge amount of processing power when using conventional, von Neumann computing architecture. Arrays of phase-locked STOs can be used to measure the degree of matching between a test value and a reference value, and this can be used for applications such as image recognition. STOs which are sufficiently close together can be synchronised via the magnetostatic interactions between the devices. The strength of the magnetostatic interactions depends upon the relative location of the STOs, their shape and their magnetic properties. This work examines the requirements for STO synchronisation and ways to extend the correlation time (the time during which the STO magnetisation is phase-locked). The model Arrays of STOs were modelled using micromagnetic simulations. Each STO had a cylindrical shape with a diameter, D , of 60 nm and consisted of a 5 nm thick spin injection layer (SIL) and a 10 nm thick free layer (FL), separated by a 2.5 nm non-magnetic interlayer. The saturation magnetisation, M_s , of the SIL and FL was 637 and 1591 emu/cm³, respectively, with uniaxial anisotropy, K_u , of 8×10^6 erg/cm³ and zero, respectively. The SIL easy axis was along the z , or vertical axis. An electric current flowing through the STOs exerted a spin torque on the magnetisation, causing the free layer magnetisation to rotate in the x - y plane. In this work the STO diameter was sufficiently small that the free layer magnetisation was largely uniform and no vortices were formed. Results The average free layer magnetisation correlation, $\langle M_1 \cdot M_2 \rangle$, was calculated for two STOs as a function of their separation and the temperature; the results are shown in fig. 1. When the STOs were very close together ($dx < 140$ nm) the magnetostatic field was so strong that the electric current could not induce oscillation. As the STO separation increased, the magnetostatic field from one STO acting on the other decayed rapidly, limiting the range of separations over which the magnetisation was synchronised. Increasing the temperature decreased the degree of correlation between the magnetisation. Even when the value of $\langle M_1 \cdot M_2 \rangle$ was high, there were occasions when the magnetisation of the STOs slipped out of phase, i.e. the phase difference exceeded 180°. Such events are referred to as phase slips and the time interval between phase slips is denoted here as the correlation time. For practical applications the magnetisation should remain phase-locked for 1000 - 10000 oscillations, equivalent to correlation times of 200 - 2000 ns in the case of the STOs described here, which had an oscillation frequency of about 5 GHz. The correlation time decreased as the number of STOs in the array increased. Fig. 2 shows the average correlation time for an array of nine STOs in which the angle between the STOs, θ , was varied from zero (STOs arranged in a straight line along the x axis) to 60°. The correlation time was calculated using the magnetisation of the STOs at either end of the array. When the STOs were in a straight line ($\theta = 0^\circ$) the maximum correlation time was about 30 ns for STOs with a separation of 180 nm. Introducing an angle between the STOs increased the correlation time. When $\theta = 60^\circ$ the correlation time was increased by more than an order of magnitude compared to $\theta = 0^\circ$. When $dx = 180$ nm and $\theta = 60^\circ$ the correlation time exceeded the maximum simulation time of 10 μ s, and for $dx = 220$ nm the correlation time was about 300 ns. The reason for the increase in correlation time with θ can be understood by plotting the magnetostatic field in the fifth (central STO) as a function of θ for the case when the FL magnetisation was perpendicular to the array of STOs, i.e. along the y axis, as shown in the inset to fig. 2. When $\theta = 0^\circ$ the component of H_d along the y axis was negative and the magnetostatic energy favoured an anti-parallel alignment of the magnetisation in adjacent STOs, increasing the probability of a phase slip. As the angle between STOs was increased the magnetostatic field approached zero and became positive for $44^\circ < \theta < 61^\circ$, i.e. the magnetostatic energy favoured parallel alignment of the FL magnetisation over this range of θ and the correlation time was increased. The total output power of arrays of STOs also increased when an angle was introduced between the STOs. The effect of STO size and position distributions will also be discussed.

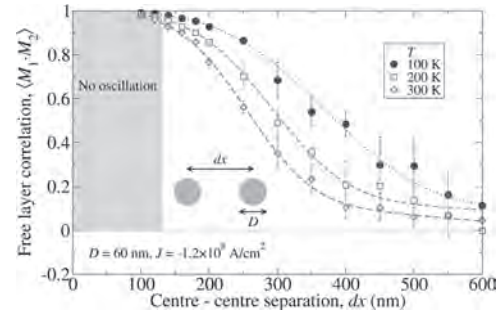


Fig. 1 Correlation of free layer magnetisation of two STOs as a function of separation and temperature.

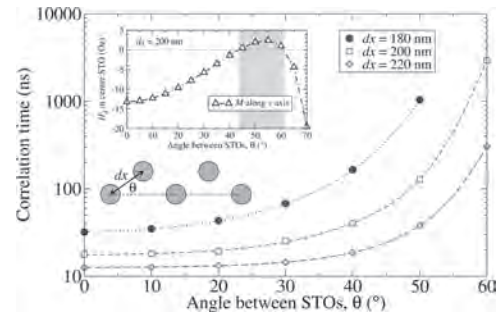


Fig. 2 Correlation time of STO magnetisation for arrays of nine STOs. $T = 300$ K. Inset: H_d in centre STO vs. angle between STOs for $dx = 200$ nm.

GP-04. Room Temperature Emulation of Synaptic Plasticity in Permalloy - Based Synaptic Transistor for Neuromorphic Computing.

M. Peda¹, A.K. P.S.¹, W. Renshaw^{2,3} and S. Piramanayagam²

1. Department of Physics, Indian Institute of Science, Bangalore, India;

2. Division of Physics and Applied Physics, Nanyang Technological University, Singapore, Singapore; 3. School of Electrical and Electronic Engineering, Nanyang Technological University, Singapore, Singapore

Human brain-inspired neuromorphic computing (NC), which emulates neural activities, is considered for the low-power implementation of artificial intelligence. It gives the benefit of parallel processing, ultralow power consumption, self-learning, and fault tolerance. The realization of hardware elements, such as artificial synaptic devices, which are the basic building blocks of neuromorphic computing systems, is an essential path towards this goal. Two terminal artificial synaptic devices have been studied using resistive random-access memory and memristors and have emulated the synaptic functions. However, in these two-terminal devices, both learning and signal transmission cannot occur concurrently, which leads to an incomplete emulation of a synapse. On the other hand, in a three-terminal synaptic device, signal transmission and learning occur independently through the channel and external gate respectively, leading to complete emulation of a synapse. Much progress has been made in three-terminal devices based on oxides [1], organic materials [2,3], and 2D materials [4]. Electrolyte gating has been widely used for conductance modulation by massive carrier injections at a very low gate voltage. However, studies based on metallic ferromagnetic systems remain highly unexplored. Additionally, a synaptic device based on magnetic metal has a spin degree of freedom that can be tuned along with. In this work, we have demonstrated a three-terminal coplanar synaptic transistor based on permalloy by electrolyte gating. The channel consists of a stack of Ta (3 nm)/NiFe (3 nm)/Ta (1 nm) on the silicon substrate. EMIM-TFSI ionic liquid was used as the gate dielectric. Fig. 1(a) shows the transfer curve measured at different sweeping rates. A giant anticlockwise loop opening in the transfer curve shows a non-volatile and reversible change of channel conductance suitable for emulating synaptic functions. We have obtained the highest room temperature conductance modulation of 11 % for a metal at the slowest sweeping rate, as shown in Fig. 1(b). The transistor's working principle is based on the formation of an electric double layer (EDL) at the interface of ionic liquid and channel and by intercalation/extraction of oxygen ions. Multilevel non-volatile states are a prerequisite for realizing analog computing. We have obtained gating controlled multilevel, non-volatile, reversible conducting states by applying positive gate pulses of different amplitude shown in Fig. 1(c). The channel conductance remained constant at zero gating showing the non-volatile nature of the state. Furthermore, the channel conductance can be brought back to the initial state by applying negative gate pulses. The retention of conducting states is checked separately, which shows retention of up to a few hours or more. In this permalloy based artificial synapse, the gate pulses act as the external stimuli, and the channel conductance act as the synaptic weight. We have emulated the essential synaptic functions at room temperature. A basic form of short-term plasticity like excitatory postsynaptic conductance (EPSC) and paired-pulse facilitation (PPF) has been emulated, as shown in Fig. 2(a) and Fig. 2(b), respectively. Moreover, we have shown a transition from short-term memory (STM) to long-term memory (LTM) by varying the gate pulse amplitude, duration, and number shown in Fig. 2(c). The change in channel conductance is more significant at higher amplitude, duration, and number due to the intercalation/extraction of more oxygen ions into the channel. Long-term plasticity behavior like long-term potentiation (LTP) and multiple potentiation and depression cycles have been demonstrated in Fig. 2(d-f). The writing and reading energy per synaptic event are calculated at different gate amplitude and duration showing a linear escalation. The lowest writing energy consumed in our device is 0.6 nJ, and can be further reduced by reducing the channel dimension and the pulse width. The variation of magnetic transport properties of the device with gating is also studied. Along with the emulation of synaptic functions, the device showed dynamic filtering behavior and can act as a high-pass filter. These results provide an insight into the potential application of ferromagnetic metal-based synaptic transistor for large-scale, low power consuming, silicon compatible neuromorphic computing network.

¹J.T. Yang, C. Ge, J.Y. Du, H.Y. Huang, M. He, C. Wang, H. Bin Lu, G.Z. Yang, and K.J. Jin, *Adv. Mater.* 30, 1 (2018). ²W. Xu, S.Y. Min, H. Hwang, and T.W. Lee, *Sci. Adv.* 2, 1 (2016). ³Y. Van De Burgt, E. Lubberman, E.J. Fuller, S.T. Keene, G.C. Faria, S. Agarwal, M.J. Marinella, A. Alec Talin, and A. Salleo, *Nat. Mater.* 16, 414 (2017). ⁴C.J. Wan, Y.H. Liu, P. Feng, W. Wang, L.Q. Zhu, Z.P. Liu, Y. Shi, and Q. Wan, *Adv. Mater.* 28, 5878 (2016).

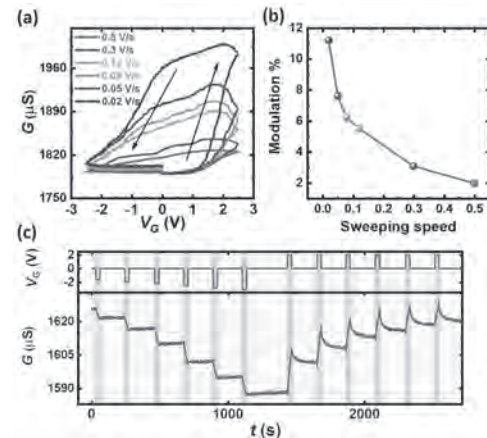


Fig. 1 (a) Transfer curve measured at a different sweeping rate, $I_{SD} = 10 \mu A$, channel conductance shown as a function of gate voltage. (b) The conductance modulation with the sweeping rate. (c) Multilevel, non-volatile, reversible conducting states realized by applying 30 s gate pulses of different amplitude and brought back to the initial state by applying a negative pulse.

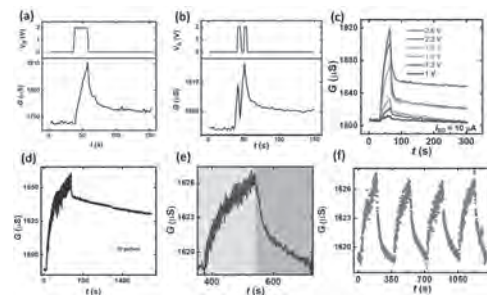


Fig. 2 (a) Excitatory postsynaptic conductance (EPSC) triggered by positive presynaptic spike, (2 V, 20 s), $I_{SD} = 10 \mu A$ (b) Paired pulse facilitation (PPF) by applying pair of pulses (2 V, 5 s), 3s apart (c) EPSC triggered by presynaptic spikes of different amplitude ($\Delta t = 30$ s) showing the transition from STM to LTM (d) Long term potentiation (LTP) triggered by 50 consecutive presynaptic spikes (2 V, 3 s) (e) Biological potentiation and depression in series with 20 positive and negative pulses, $V_G = \pm 1$ V (f) Cycles of potentiation and depression showing repeatability of emulation of synaptic function.

GP-05. Current Induced Magnetization Switching in $L1_0$ FePt and Ta/FePt Films With Large Perpendicular Magnetic Anisotropy Through Spin-Orbit Torque.

Y. Tao^{1,2}, C. Sun^{1,2}, Y. Jiao^{1,2}, X. Hu^{1,2} and K. Dong^{1,2}

1. School of Automation, China University of Geosciences, Wuhan, Wuhan, China; 2. Hubei Key Laboratory of Advanced Control and Intelligent Automation for Complex Systems, Wuhan, China

Over the last decade, magnetization manipulation based on spin-orbit torque has attracted wide research attention as it shows tremendous potential for the next generation ultrafast and power efficient nonvolatile memories. Very recently, centrosymmetric $L1_0$ FePt is reported to achieve the room temperature SOT switching in single layer and a new type of inversion asymmetry called composition gradient is responsible for the observed SOT. Due to its inherent superior perpendicular magnetic anisotropy (PMA), the FePt in $L1_0$ phase enables high thermal stability when device size reduced to nanoscale, which may provide a simple structure towards industry application. In this work, current-induced perpendicular magnetization switching is obtained in 6 nm thick $L1_0$ FePt single layer and in Ta/6nm FePt bilayer, respectively. The switching ratio of $L1_0$ FePt single-layer (Figure 1 (e)) in the optimum applied magnetic field (500Oe) is relatively small, about 3.3%. However, the Ta/FePt bilayers have a slightly larger switching ratio (about 4.3%) than the $L1_0$ FePt single-layer. In addition, the stability of the switching loop of the Ta/FePt bilayers film is relatively better and the critical current density is reduced in the case of a Ta/FePt bilayer. Moreover, we found that the SOT effective fields become smaller in FePt/Ta bilayer compared to that in single FePt layer by measuring the harmonic Hall voltages, which may attribute to the combined effect of the opposite spin current generated by Ta HM layer and the smaller perpendicular anisotropy. The SOT efficiency β_{DL} of the Ta/FePt bilayers is 3.2×10^{-10} Oe $m^2 A^{-1}$, which is several times of the traditional Ta/CoFeB/MgO structure reported before. The results indicate a new scheme of current-induced magnetization switching for high PMA and high coercive materials, which is expected to be applied to spintronics devices with high thermal stability and ultra-high storage density in the future.

Fukami S, Zhang C, DuttaGupta S, et al, Nature materials, 2016, 15(5): 535-541. Liu L, Yu J, Gonzalez-Hernandez R, et al, Physical Review B, 2020, 101(22): 220402. Manchon A, Zelezny J, Miron I M, et al., Reviews of Modern Physics, 2019, 91(3): 035004. Tang M, Shen K, Xu S, et al, Advanced Materials, 2020, 32(31): 2002607. R. Ramaswamy, J. M. Lee, K. Cai, et al, Appl. Phys. Rev. 5, 031107(2018).

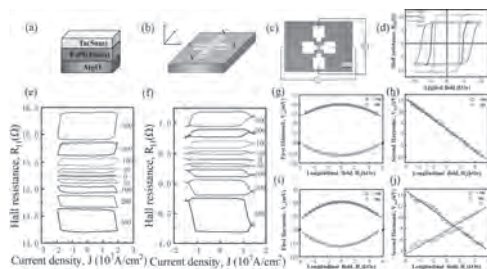


Fig.1 (a) A schematic of Ta/FePt bilayer structure.(b) Schematic of Hall bar structure (c)Schematic illustration of Hall device together with the measurement circuit.(d) R-H hysteresis characteristic measured by AHE. Positive R_{AHE} corresponds to“upward” magnetization, whereas negative R_{AHE} corresponds to “downward” magnetization.(e)and (f) SOT switching loops obtained under varying H_x for (e) 6-nm FePt single layer and (f) 5-nm Ta/ 6-nm FePt bilayer. (g)-(j) Field dependence of first and second-harmonic signals for 6-nm FePt film ($I_{ac} = 6mA$).

Session HA

NEW TRENDS IN SKYRMIONICS: MATERIALS, DYNAMICS AND DETECTION TECHNIQUES

Riccardo Tomasello, Chair

Foundation for Research and Technology - Hellas, Heraklion, Greece

INVITED PAPERS

HA-01. Skyrmions in Chiral Magnetic Multilayers.

K. Zeissler¹, S. Finizio², K. Shahbazi¹, J. Massey¹, F. Al Ma'mari¹, A. Huxtable¹, D. Bracher², A. Kleibert², S. Wintz^{2,3}, S. Mayr^{2,4}, T. Weßels⁵, A.V. Sadovnikov⁶, M. Rosamond¹, E. Linfield¹, T. Moore¹, J. Raabe², G. Burnell¹ and C. Marrows¹

1. University of Leeds, Leeds, United Kingdom; 2. Paul Scherrer Institut, Villigen, Switzerland; 3. Helmholtz-Zentrum Dresden-Rossendorf, Dresden, Germany; 4. ETH Zurich, Zurich, Switzerland; 5. Forschungszentrum Julich GmbH, Julich, Germany; 6. N. G. Chernyshevskogo National Research University in Saratov, Saratov, Russian Federation

Magnetic skyrmions are topologically-nontrivial spin textures with particle-like properties [1]. Their size, topological stability, and mobility suggest their use in future generations of spintronic devices, the prototype of which is the skyrmion racetrack [2]. To realise a racetrack requires three basic operations: the nucleation (writing), propagation (manipulation), and detection (reading) of a skyrmion, all by electrical means. Here we show that all three are experimentally feasible at room temperature in Pt/Co/Ir or Pt/CoB/Ir multilayers in which the different heavy metals above and below the magnetic layer break inversion symmetry and induce chirality by means of the Dzyaloshinskii-Moriya interaction, defining the structure of Néel skyrmion spin textures [3]. We show deterministic nucleation on nanosecond timescales using an electrical point contact on top of the multilayer [4] (Figure 1), current-driven propagation along a wire in which the skyrmions are channelled by defects in the multilayer [5], and their detection by means of the Hall effect (Figure 2) that reveals an unexpectedly large contribution to the Hall signal that correlates with the topological winding number [6].

[1] N. Nagaosa & Y. Tokura, *Nat. Nanotech.* 8, 899 (2013). [2] A. Fert et al. *Nature Nanotech.* 8, 152 (2013). [3] K. Zeissler et al. *Sci. Rep.* 7, 15125 (2017). [4] S. Finizio et al., *Nano Lett.* 19, 7246 (2019). [5] K. Zeissler et al., *Nature Comm.* 11, 428 (2020) [6] K. Zeissler et al. *Nature Nanotech.* 13, 1161 (2018).

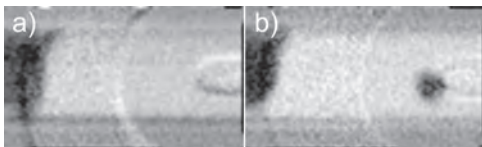


Figure 1. STXM images (a) before and (b) after electrical nucleation of a skyrmion at a 500 nm wide injector contact to a Pt/CoB/Ir multilayer.

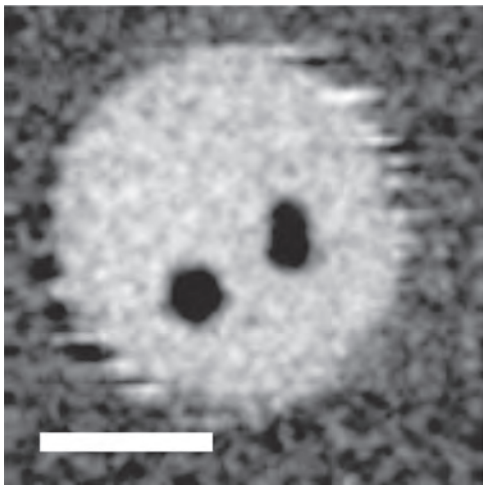


Figure 2. STXM image of two skyrmions in an electrically-connected 1 μm diameter Pt/Co/Ir multilayer dot. 500 nm scale bar.

CONTRIBUTED PAPERS

HA-02. Electrical and optical nucleation of magnetic skyrmions.

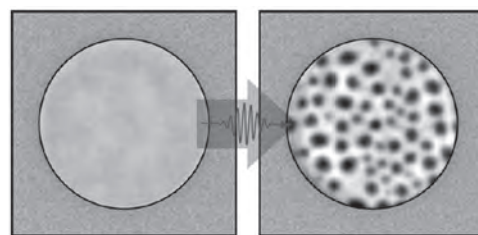
F. Büttner^{1,2}, B. Pfau³, M. Böttcher⁴, M. Schneider³, G. Mercurio⁵, C.M. Günther⁶, A. Wittmann², K. Gerlinger³, L. Kern³, C. von Korff Schmising³, D. Engel³, J. Gaida⁷, M. Moeller⁷, T. Harvey⁷, K. Bagschik⁸, A. Scherz⁵, J. Sinova⁴, C. Ropers⁷, J. Mentink⁹, B. Dupé⁴, G. Beach² and S. Eisebitt³

1. Helmholtz-Zentrum Berlin für Materialien und Energie GmbH, Berlin, Germany; 2. Massachusetts Institute of Technology, Cambridge, MA, United States; 3. Max-Born-Institut für Nichtlineare Optik und Kurzzeitspektroskopie, Berlin, Germany; 4. Johannes Gutenberg Universität Mainz, Mainz, Germany; 5. European XFEL GmbH, Schenefeld, Germany; 6. Technische Universität Berlin, Berlin, Germany; 7. Georg-August-Universität Göttingen, Göttingen, Germany; 8. Deutsches Elektronen-Synchrotron, Hamburg, Germany; 9. Radboud Universiteit, Nijmegen, Netherlands

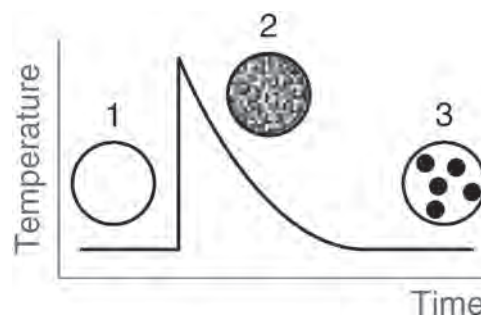
Magnetic skyrmions are long-lived topological excitations in a small subset of magnetic materials, including some heavy-metal / ferromagnet multilayers with strong interfacial spin-orbit interactions. Skyrmions are a rare example of a compact, unbound, and switchable topological state of matter. Here, “compact” means that each skyrmion is confined to a very small area of the sample. Thanks to this property, even micrometer-sized samples can host a very large number of such topological objects and thereby acquire a very large topological charge. “Unbound” means that skyrmions, unlike vortices or hedgehogs, can exist without their topological counterpart, the antiskyrmion. In fact, skyrmions are often found in pure form, such as ordered (crystalline) or disordered (amorphous) arrays. These dense skyrmion states can be considered a topological phase, with the order parameter being the topological charge. Finally, “switchable” means that, due to the discrete nature of the lattice, skyrmions can be nucleated and annihilated, leading to a change of the global topological charge. Switching from a topological trivial state to a skyrmion state is a topological phase transition. Such a phase transition requires the overcoming of strong energy barriers—the same energy barriers that also allow skyrmions to exist at room temperature [1]. Topological phase transitions are therefore expected to be of first order, with a transition dynamic characterized by slow and heterogeneous nucleation, as known, e.g., from the freezing of water. In fact, heterogeneous nucleation is the underlying principle of electrical skyrmion nucleation, which crucially relies on material defects to break the translational symmetry [2]. Surprisingly, however, we find picosecond homogeneous nucleation of an extended topological phase, comprising a dense array of nanometer-scale magnetic skyrmions, after a single femtosecond laser pulse in metallic ferromagnetic multilayers. Lorentz transmission electron microscopy and skyrmion Hall effect measurements confirm that only skyrmions, and not antiskyrmions, are nucleated by the light pulse, even in an achiral Pt/Co/Pt material. This presentation will focus on the nucleation dynamics of this all-optical topological phase transition, which we were able to follow in real time during the early user operation of beamline SCS at the European XFEL [3]. Using time-resolved small angle x-ray scattering, we discovered that rapid, homogeneous nucleation of the skyrmion phase is mediated by a previously undisclosed transient fluctuation state. This state, which is characterized by high spatial frequency magnetic fluctuations, persists for approximately 100 ps after exciting our magnetic multilayer with a femtosecond, infrared laser pulse. The topological phase emerges from these fluctuations by nucleation and coalescence, a mechanism that goes beyond existing theories of topological phase transitions such as the Kibble–Zurek mechanism and the Berezinskii–Kosterlitz–Thouless transition. The process is completed on a time scale of 300 ps. Using atomistic spin dynamics simulations, we confirm that the fluctuation state is key to the ultrafast increase of the global topological charge, enabled by an almost complete elimination of the topological energy barrier in this transient state of matter.

[1] F. Büttner, I. Limesh, and G. S. D. Beach, Theory of isolated magnetic skyrmions: From fundamentals to room temperature applications. *Scientific Reports* 8, 4464 (2018). [2] F. Büttner, I. Limesh, M. Schneider, B. Pfau,

C. M. Günther, P. Hessing, J. Geilhufe, L. Caretta, D. Engel, B. Krüger, J. Viehhaus, S. Eisebitt, and G. S. D. Beach, Field-free deterministic ultrafast creation of magnetic skyrmions by spin-orbit torques. *Nature Nanotechnology* 12, 1040 (2017). [3] F. Büttner, B. Pfau, M. Böttcher, M. Schneider, G. Mercurio, C. M. Günther, P. Hessing, C. Klose, A. Wittmann, K. Gerlinger, L.-M. Kern, C. Strüber, C. von Korff Schmising, J. Fuchs, D. Engel, A. Churikova, S. Huang, D. Suzuki, I. Limesh, M. Huang, L. Caretta, D. Weder, J. H. Gaida, M. Möller, T. R. Harvey, S. Zayko, K. Bagschik, R. Carley, L. Mercadier, J. Schlappa, A. Yaroslavtsev, L. Le Guyader, N. Gerasimova, A. Scherz, C. Deiter, R. Gort, D. Hickin, J. Zhu, M. Turcato, D. Lomidze, F. Erdinger, A. Castoldi, S. Maffessanti, M. Porro, A. Samartsev, J. Sinova, C. Ropers, J. H. Mentink, B. Dupé, G. S. D. Beach, and S. Eisebitt, Observation of fluctuation-mediated picosecond nucleation of a topological phase. *Nature Materials* 20, 30 (2021).



Magnetic state of the sample before (left) and after (right) exposure with a single fs laser pulse. The circle (1.5 μm diameter) indicates our field of view. Black (white) indicates magnetization pointing up (down).



Schematic of the process of all-optical topological switching. Starting with a uniform state (1), the sample is heated to a transient fluctuations state (2) by the laser. The fluctuations remove the topological energy barrier and allow skyrmion seeds to nucleate. The final state (3) is a skyrmion state obtained after coalescence and growth of the skyrmion nuclei.

HA-03. Coexistence of Distinct Skyrmion Phases Observed in Hybrid Ferromagnetic/Ferrimagnetic Multilayers.

A. Mandru¹, O. Yildirim¹, R. Tomasello⁴, P.T. Heistracher³, M. Penedo¹, A. Giordano⁵, D. Suess³, G. Finocchio⁵ and H.J. Hug^{1,2}

1. *Empa, Swiss Federal Laboratories for Materials Science and Technology, Dübendorf, Switzerland*; 2. *Department of Physics, University of Basel, Basel, Switzerland*; 3. *Faculty of Physics, University of Vienna, Vienna, Austria*; 4. *Institute of Applied and Computational Mathematics, Heraklion, Greece*; 5. *Department of Mathematical and Computer Sciences, University of Messina, Messina, Italy*

Systems in which magnetic skyrmions occur at room temperature could enable new computing architectures as well as compact and energetically-efficient storage such as racetrack memories. There are two fundamental problems that prevent the successful implementation of skyrmions in a racetrack device. A first problem is not being able to restrict the skyrmion motion along straight paths and one solution is the use of antiferromagnetically-coupled skyrmions [1]. The second problem is not having stable inter-skyrmion distances, which translates into fluctuating distances among bits. A potential solution was revealed with the first experimental observation of coexisting skyrmions and chiral bobbars [2], opening the possibility that a chain of binary data bits could be encoded by two different solitons. However, this has only been observed in B20-type single crystalline materials and at low temperatures. With our work, we present a ferro-/ferri-/ferromagnetic multilayer system that can host two distinct skyrmion phases at room temperature. The two phases represent a tubular (strong contrast) and a partial (weak contrast) skyrmion (see Figure 1), as revealed from quantitative magnetic force microscopy data complemented by micromagnetic simulations. Furthermore, the tubular skyrmion can be converted into a partial skyrmion. Given its high tunability, this hybrid system serves as a promising platform for future skyrmionic devices.

[1] W. Legrand et al., *Nat. Mater.* 19, 34–42 (2020) [2] F. Zheng et al., *Nat. Nanotechnol.* 13, 1–7 (2018)

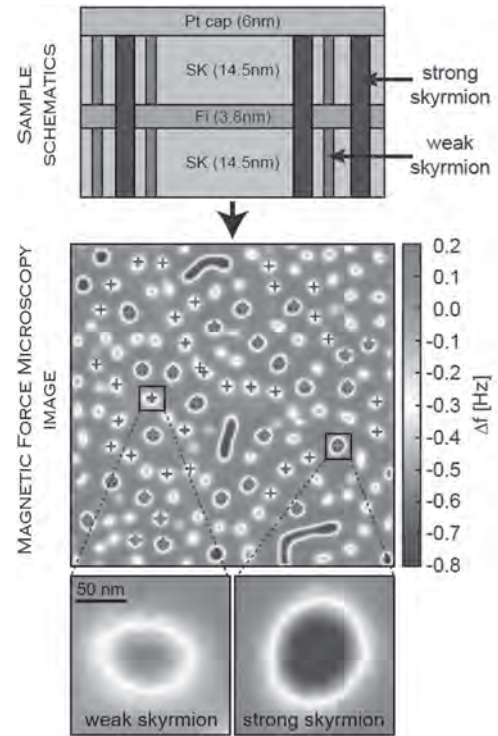


Fig. 1 Upper: Schematics of the trilayer sample consisting of two ferromagnetic skyrmion (SK) layers separated by a 3.8-nm thick ferrimagnetic (Fi) layer; SK = [Ir(1nm)/Fe(0.3nm)/Co(0.6nm)/Pt(1nm)]₅ and Fi = [TbGd(0.2m)/Co(0.4nm)]₆/TbGd(0.2nm). The weak skyrmions are depicted by the vertical pale blue rectangles penetrating through the SK layers only. The strong skyrmions are indicated by wider dark blue rectangles penetrating through all layers. Lower: $2 \times 2 \mu\text{m}^2$ magnetic force microscopy image taken in a magnetic field of about 133 mT, highlighting a weak and a strong skyrmion in the lower two panels.

HA-04. A Close Look at Skyrmions in Ultrathin Films and Synthetic Antiferromagnets.*L. Aballe*¹*1. Experiments Division, ALBA Synchrotron Light Facility, Cerdanyola del Vallès, Spain*

Thanks to its extreme surface sensitivity and element specificity, X-ray photoemission electron microscopy permits imaging magnetic nanostructures with sub-nanometer thickness and even fully compensated synthetic antiferromagnets. In addition, XPEEM is sensitive to both in plane and out of plane magnetization components, so it can unambiguously determine the character and chirality of domain walls. Several skyrmionic systems have been measured at the ALBA Synchrotron Light Source XPEEM, profiting the functional sample environments that allow applying small magnetic fields and/or current pulses in order to study skyrmion nucleation and propagation and the effect, for example, of disorder or of targeted modulations of the magnetic anisotropy. I will give an overview of the strenghts and limits of the technique, the experiments carried out in DMI systems over the past few years, and an outlook for the near future including instrumental upgrades in development.

Olivier Boulle et al., Room temperature chiral magnetic skyrmion in ultrathin magnetic nanostructures, *Nature Nanotechnology* 11, 449 (2016)
Michael Foerster et al., Custom sample environments at the ALBA XPEEM, *Ultramicroscopy* 171, 63 (2016)
Roméo Juge et al., Magnetic skyrmions in confined geometries: Effect of the magnetic field and the disorder, *Journal of Magnetism and Magnetic Materials* 455, 3 (2018)
Lucia Aballe et al., Pulse picking in synchrotron-based XPEEM, *Ultramicroscopy* 202, 10 (2019)
Roméo Juge et al., Current-Driven Skyrmion Dynamics and Drive-Dependent Skyrmion Hall Effect in an Ultrathin Film, *Physical Review Applied*, 12, 044007 (2019)
Anna Mandziak et al., Combining high temperature sample preparation and in-situ magnetic fields in XPEEM, *Ultramicroscopy* 214, 113010 (2020)
Sachin Krishnia et al., Making spin-orbit coupling visible in single layer ferrimagnets: direct observation of spin-orbit torques and chiral spin textures, submitted
Teng Xu et al., Ferrimagnetic Néel skyrmions stabilized on top of noncollinear antiferromagnetic Mn₃Sn, submitted
Kumari Gaurav Rana et al., Room temperature skyrmions in an exchange biased antiferromagnet, submitted

HA-05. Thermal Generation, Manipulation and Thermoelectric Detection of Skyrmions.

Z. Wang^{1,11}, M. Guo^{1,2}, H. Zhou^{1,11}, L. Zhao^{1,11}, T. Xu^{1,11}, R. Tomasello³, H. Bai^{1,11}, Y. Dong^{1,11}, S. Je⁴, W. Chao⁴, H. Han⁵, S. Lee⁵, K. Lee⁵, Y. Yao⁶, W. Han⁶, C. Song⁷, H. Wu², M. Carpentieri⁸, G. Finocchio⁹, M. Im⁴, S. Lin¹⁰ and W. Jiang^{1,11}

1. State Key Laboratory of Low-Dimensional Quantum Physics and Department of Physics, Tsinghua University, Beijing, China; 2. Institute of Microelectronics, Tsinghua University, Beijing, China; 3. Institute of Applied and Computational Mathematics, Foundation for Technological Research, Heraklion, Greece; 4. Center for X-ray Optics, E O Lawrence Berkeley National Laboratory, Berkeley, CA, United States; 5. School of Materials Science and Engineering, Ulsan National Institute of Science and Technology, Ulsan, The Republic of Korea; 6. School of Physics, Peking University, Beijing, China; 7. School of Materials Science and Engineering, Tsinghua University, Beijing, China; 8. Department of Electrical and Information Engineering, Politecnico di Bari, Bari, Italy; 9. Department of Mathematical and Computer Sciences, Universita degli Studi di Messina, Messina, Italy; 10. Theoretical Division, Los Alamos National Laboratory, Los Alamos, NM, United States; 11. Frontier Science Center for Quantum Information, Tsinghua University, Beijing, China

The magnetic skyrmion is a particle-like topologically stable spin texture that has been observed in chiral bulk magnets and asymmetric magnetic multilayers. Skyrmions can be generated and driven through the spin-polarized electric currents in the presence of an external magnetic field. Our early results show that the skyrmions can be thermally activated and behave like Brownian particles [1], which motivates us to explore the thermal control of skyrmion dynamics. Through using on-chip heaters, we are able to thermally generate, manipulate and thermoelectrically detect skyrmions [2]. Figure 1 shows that the skyrmion nucleation from the edge of the microstructured [Ta/CoFeB/MgO]₁₅ multilayer, upon applying an electric current pulse to the upper heater on the side that generates local joule heating. The local creation of joule heating can facilitate a domain morphological transition and nucleate skyrmions by overcoming the low energy barrier. As the temperature of the heater is increased, more skyrmions are generated, which is accompanied by a unidirectional diffusion motion from the hot to the cold regions. This is due to the interplay among the repulsive forces between skyrmions, thermal spin-orbit torques, magnonic spin torques, and entropic forces. The ability to generate and manipulate skyrmions using heat opens another avenue of exploiting skyrmions in insulating and metallic materials. Moreover, by utilizing the anomalous Nernst effect in the same device, we can obtain the Nernst voltage which develops in the presence of a thermal gradient and magnetization perpendicular to each other. Since the magnetization can be varied by the change in the total number of skyrmions. We observed several discretized steps in the time evolution of Nernst voltages, as shown in Fig. 2. Each step is 90 ± 10 nV which is attributed to the annihilation of a single skyrmion. The thermoelectric detection of skyrmion is important because the electrical detection of skyrmions is still challenging in many materials systems, but it is key to enabling spintronic applications.

[1] L. Zhao, Z. Wang and W. Jiang, PRL, 125, 027206 (2020). [2] Z. Wang, M. Guo and W. Jiang, Nat. Electron., 3, 672 (2020).

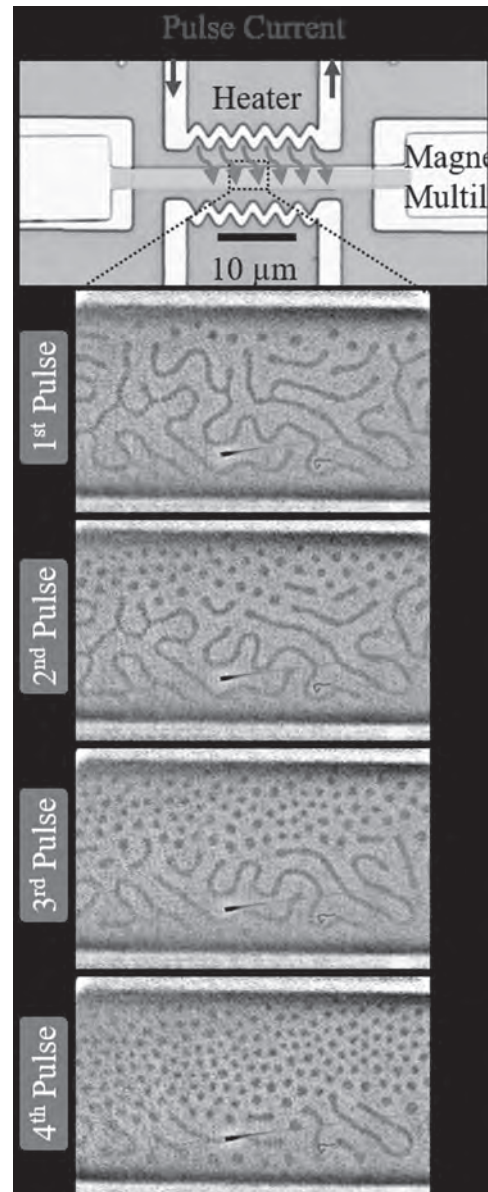


Fig. 1 Optical image of the microstructured magnetic multilayer with two Ta/Pt heaters on top of a 100-nm-thick Si₃N₄ membrane and the consecutive X-ray images acquired from the multilayer sample after applying pulse voltages to the upper heater.

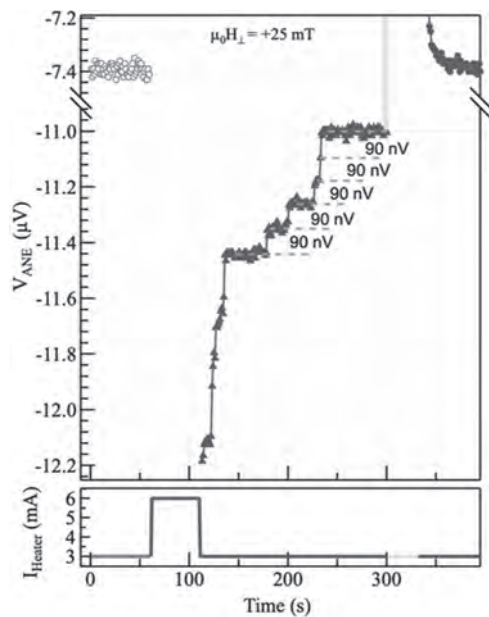


Fig. 2 'Discretized' steps of the Nernst voltage difference $\Delta V_{ANE} = 90 \pm 10$ nV are detected after switching off the 6 mA current and applying a small current of 3 mA.

HA-06. Nonlinear and Stochastic Dynamics of Skyrmions in Frustrated Magnets.

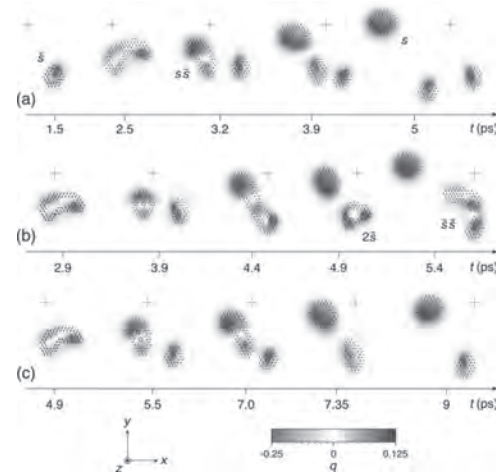
U. Ritzmann¹, L. Desplat^{2,3}, R.E. Camley⁴, B. Dupé⁵ and J. Kim²

1. Department of Physics, Freie Universität Berlin, Berlin, Germany; 2. Centre de Nanosciences et de Nanotechnologies, CNRS, Université Paris-Saclay, Palaiseau, France; 3. Institut de Physique et Chimie des Matériaux de Strasbourg, CNRS, Université de Strasbourg, Strasbourg, France; 4. Department of Physics and Energy Science, University of Colorado at Colorado Springs, Colorado Springs, CO, United States; 5. Nanomat/Q-mat/CESAM, Université de Liege, Liege, Belgium

Competing interactions can give rise to a variety of interesting noncollinear magnetization states. An interesting model system in which such states can be explored is the bilayer PdFe/Ir (111), which exhibits frustrated exchange and a sizeable Dzyaloshinskii-Moriya interaction (DMI). In particular, such systems can simultaneously support skyrmions and antiskyrmions – their antiparticle counterpart [1-5]. This provides an interesting testbed to investigate how opposite topological charges respond to drive forces such as spin-orbit torques (SOTs). In this talk, we will describe results from atomistic spin dynamics simulations in which we studied skyrmion and antiskyrmion dynamics under spin-orbit torques in PdFe/Ir (111), where the Hamiltonian parameters have been extracted from first-principles calculations. In the single particle limit, a divergence between the skyrmion and antiskyrmion motion appears above a current threshold, whereby antiskyrmions are found to deviate from rectilinear motion and execute instead trochoidal trajectories in the film plane [6]. This behavior represents the transition to the Walker regime, whereby helicity oscillations drive the trochoidal motion, much like the large-angle magnetization precession above Walker breakdown in domain wall dynamics in which the wall profile oscillates continuously between Bloch and Néel states. Through an extended Thiele model in which a deformation amplitude and helicity are elevated to dynamical variables, we show that simulated antiskyrmion trajectories can be reproduced by accounting for the helicity dependence of the DMI. For a range of strong damping-like SOTs, the single-particle dynamics gives way to pair-production, whereby a single antiskyrmion initial state can result in a gas of skyrmions and antiskyrmions. This occurs in an analogous fashion to magnetic vortex core reversal, whereby strong deformations in the antiskyrmion motion results in the formation of an additional skyrmion-antiskyrmion pair, which then separates because the opposite charges move in different ways. We have identified three main scattering mechanisms by which this occurs, which are either elastic, result in antiskyrmion bound states, or annihilation of a generated antiskyrmion – see Fig. 1 [7]. Together, these processes can drive a proliferation of particles whose growth rate and production asymmetry depends on the strength of the chiral interactions and the damping-like SOT. Interestingly, we can draw close parallels with conditions for baryogenesis in high-energy physics, which describes the prevalences of matter over antimatter in the observable universe. The generation processes also raise the question of energy barriers and minimum-energy paths towards antiskyrmion merging and annihilation. Through geodesic nudged elastic band calculations, we find that both processes involve similar energy barriers and depend on the relative helicities of the scattering particles. Annihilation is found to occur via intermediate meron-antimeron states, as seen in previous work [8]. We will also discuss the Langevin dynamics of such skyrmion and antiskyrmion states. This work was partially supported by the Agence Nationale de la Recherche under Contract No. ANR-17-CE240025 (TOPSKY), the Deutsche Forschungsgemeinschaft via TRR 227, and the University of Strasbourg Institute for Advanced Study (USIAS) via a fellowship, within the French national program “Investment for the Future” (IdEx-Unistra).

[1] B. Dupé, C. N. Kruse, T. Dornheim, and S. Heinze, *New J. Phys.* *18*, 055015 (2016). [2] S.-Z. Lin and S. Hayami, *Phys. Rev. B* *93*, 064430 (2016). [3] L. Rózsa et al., *Phys. Rev. B* *95*, 094423 (2017). [4] X. Zhang et al., *Nat. Commun.* *8*, 1717 (2017). [5] A. O. Leonov and M. Mostovoy, *Nat. Commun.* *8*, 14394 (2017). [6] U. Ritzmann, S. von Malottki, J.-V. Kim, S. Heinze, J. Sinova, and B. Dupé, *Nat. Electron.* *1*, 451 (2018). [7] U. Ritzmann, L. Desplat, B. Dupé, R. E. Camley, and J.-V. Kim, *Phys. Rev. B*

102, 174409 (2020). [8] L. Desplat, J.-V. Kim, and R. L. Stamps, *Phys. Rev. B* *99*, 174409 (2019).



Main scattering processes involving antiskyrmions: (a) elastic; (b) bound-state; (c) annihilation.

Session HB
SKYRMIONS: CONTROL AND MANIPULATION
Guoqiang Yu, Chair
Chinese Academy of Sciences, Beijing, China

INVITED PAPER

HB-01. Spin–Orbit Torque Switching of a Ferromagnet With Picosecond Electrical Pulses INVITED.

K. Jhuria¹, J. Hohlfeld¹, A. Pattabi², E. Martin¹, A.Y. Arriola Córdova^{1,3}, X. Shi⁴, R. Lo Conte², S. Petit-Watelot¹, J. Rojas-Sanchez¹, G. Malinowski¹, S. Mangin¹, A. Lemaître⁵, M. Hehn¹, J. Bokor^{2,6}, R.B. Wilson⁴ and J. Gorchon¹

1. Institut Jean Lamour, Nancy, France; 2. University of California Berkeley Department of Electrical Engineering and Computer Sciences, Berkeley, CA, United States; 3. Universidad Nacional de Ingeniería, Lima, Peru; 4. Department of Mechanical Engineering and Materials Science and Engineering Program, University of California Riverside, Riverside, CA, United States; 5. Centre de Nanosciences et de Nanotechnologies, Orsay, France; 6. E O Lawrence Berkeley National Laboratory, Berkeley, CA, United States

The development of approaches that can efficiently control the magnetization of magnetic materials is central to the creation of fast and low-power spintronic devices. Spin transfer torque can be used to electrically manipulate magnetic order in devices, but is typically limited to nanosecond timescales. Alternatively, spin–orbit torque can be employed, and switching with current pulses down to about 200 ps has been demonstrated [1,2]. However, the upper limit to magnetization switching speed remains unestablished. In this talk I will present our recent results [3], where we show that photoconductive switches can be used to apply 6-ps-wide electrical pulses and deterministically switch the out-of-plane magnetization of a common thin cobalt film via spin–orbit torque. We probe the ultrafast magnetization dynamics due to spin-orbit torques with sub-picosecond resolution using the time-resolved magneto-optical Kerr effect (MOKE). We also estimate that the magnetization switching consumes less than 50 pJ in micrometre-sized devices.

[1] Garelo, K. et al. Ultrafast magnetization switching by spin–orbit torques. *Appl. Phys. Lett.* 105, 212402 (2014) [2] Grimaldi, E. et al. Single-shot dynamics of spin–orbit torque and spin–transfer torque switching in three-terminal magnetic tunnel junctions. *Nat. Nanotechnol.* 15, 111–117 (2020) [3] Jhuria, K. et al. Spin–orbit torque switching of a ferromagnet with picosecond electrical pulses. *Nat. Electronics.* 3, 680–686 (2020)

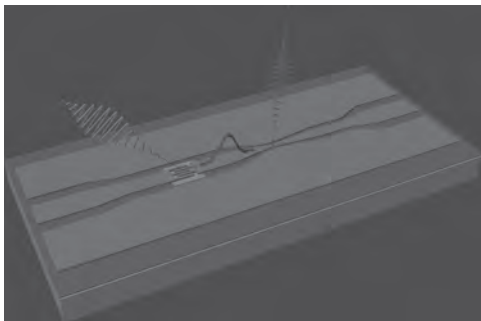


Fig 1. Schematic of time-resolved picosecond spin-orbit torque experiments. A femtosecond-wide optical pump is used to trigger a picosecond-wide electrical pulse via the excitation of an Auston photo-switch. A second optical probe beam is used to detect the induced dynamics on the magnetization with sub-picosecond resolution.

HB-03. Nucleation of Metastable Skyrmion Lattices Following a Non-Equilibrium Laser-Induced Heating Path.

P. Ollerós-Rodríguez¹, M.S. Strungaru², S. Ruta², P.I. Gavriloaea², P. Perna¹, R.W. Chantrell² and O. Chubykalo-Fesenko³

1. *Fundacion IMDEA Nanociencia, Madrid, Spain;* 2. *University of York Department of Physics, York, United Kingdom;* 3. *Instituto de Ciencia de Materiales de Madrid, Madrid, Spain*

Magnetic Skyrmions are nanometer-sized spin textures with a defined chirality induced by the Dzyaloshinskii-Moriya interaction. Due to their specific configuration and chirality, magnetic skyrmions are said to be topologically protected and they show a well-defined behaviour under the effect of external excitations such as spin-polarized currents. Because of their properties, magnetic Skyrmions are considered promising candidates for their implementation in next-generation spintronic devices[1]. However, the usage of Skyrmions in technological applications is constrained by the ability to nucleate, stabilize and manipulate them. The main drawback related to the nucleation of magnetic skyrmions arises from the fact that they are usually metastable magnetic configurations, so special protocols must be designed in order to access these skyrmionic states. In many different scientific fields and due to their interesting properties, the study of metastable phases and the dynamical paths needed to reach them are of great interest. In this sense, it is usually necessary to supply and/or remove a substantial amount of energy to the system in a short timescale, so the system evolves towards a far-from-equilibrium path in the configuration space. In the recent years, the study of the light-induced magnetization-dynamics has gained relevance due to its ultrafast and localized character. Particularly, recent experiments have shown the feasibility of the laser-induced nucleation of skyrmions by means of ultrafast magnetization dynamics[2,3]. In these experiments the nucleation takes place under external magnetic fields which are known to transform skyrmionic states from metastable to stable ground states of the system. In the present work we explore the nucleation of magnetic skyrmions in realistically parametrised[4,5] Pt/Co/Heavy-Metal magnetic trilayers via atomistic spin dynamics (ASD) simulations using the software package Vampire[6]. Quasi-static simulations by increasing temperature above the Curie one and cooling down the system in a timescale of few nanoseconds produce a stable ground state in the form of stripe domains, as is usually found in these kind of systems. Next, we model the dynamics under ultrafast non-polarized femtosecond laser pulse varying the pulse duration and intensity. We present phase diagrams of the magnetic states after the laser pulse action revealing the possibility of accessing final metastable skyrmionic states for a proper window of laser parameters. The same protocols have been studied adding external static fields pointing both, parallel and antiparallel to the initial magnetization. Under these conditions, slow field-cooling processes now leads to stable ground states in the form of skyrmion lattices. As a result, the window of laser parameters leading to final skyrmionic states is substantially increased. Interestingly, the results show that applying a laser pulse and under the effect of external fields it is possible to access both, metastable and stable skyrmionic states, being even possible to nucleate skyrmion lattices with different polarizations. Our results unambiguously demonstrate the necessity of following a highly non-equilibrium dynamical path in order to reach a final metastable skyrmion lattice in the absence of external fields.

[1] A. Fert, N. Reyren and V. Cros, *Nature Reviews Materials*, Vol. 2, p.17031 (2017) [2] S.-G. Je, P. Vallobra, T. Srivastava et al., *Nano Letters*, Vol. 18(11), p.7362-7371 (2018) [3] F. Büttner, B. Pfau, M. Böttcher et al., *Nature Materials*, Vol. 20, p. 30-37 (2021) [4] R. Moreno, R. Evans, S. Khmelevskiy et al., *Physical Review B*, Vol. 94, p. 104433 (2016). [5] H. Yang, A. Thiaville, S. Rohart et al., *Physical Review Letters*, Vol. 115, p. 267210 (2015). [6] R. F. Evans, W. J. Fan, P. Chureemart et al., *Journal of Physics: Condensed Matter*, Vol. 26, p. 103202 (2014).

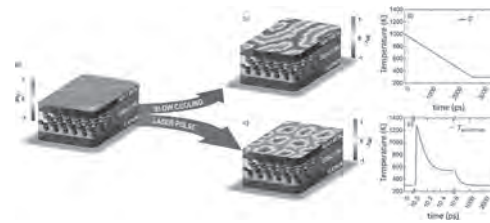


Fig.1 Light-induced nucleation of metastable skyrmion lattices. a) Initial saturated state. b) Ground state of the system obtained after a slow zero-field cooling process. c) Nucleated metastable skyrmion lattice obtained after applying an ultrafast laser pulse. d) Temperature profile following a slow zero-field cooling process. e) Temperature profile of the laser-induced nucleation of skyrmion lattice.

HB-04. Skyrmion Density Modulation via Current-Induced Skyrmion-to-Stripe Transformation.

C.C. Ang¹, W. Gan¹, G.D. Wong¹ and W. Lew¹

1. Physics & Applied Physics, Nanyang Technological University School of Physical and Mathematical Sciences Division of Physics and Applied Physics, Singapore, Singapore

Electrical current remains one of the simplest and most accessible tools for the control of magnetic skyrmions. However, it can be challenging to only perform the intended operation among all the possible current-induced effects such as deformation, nucleation, and propagation [1-3]. While current-induced skyrmion nucleation has been demonstrated [1,2], its equally important complementary operation of current-induced skyrmion annihilation remains elusive. Our investigation on the current-induced skyrmion effects revealed an additional regime at low current densities where skyrmion annihilation can be performed via skyrmion-stripe transformation [4]. In this work, an experimental study of current-induced skyrmion-stripe transformation in a Pt/Co/Fe/Ir magnetic bilayer was performed. Using a Hall cross device shown in Fig. 1(a), a slow evolution of the magnetization after current injection was observed and showed distinct features in the high and low current density regimes. High current density injection induced a sharp negative change in magnetization followed by a continuous decay back to equilibrium while low current density induced a gradual positive change in magnetization from equilibrium before decaying back to equilibrium forming a peak as shown in Fig. 1(b). In situ observation under magneto-optical Kerr (MOKE) imaging showed that at high current densities, additional magnetic skyrmions were nucleated as shown in Fig. 2(e-h). In contrast, at low current densities, skyrmions expanded into stripes. The resulting competition for space annihilates skyrmions. Eventually the stripes contract into skyrmions with a lower overall density as shown in Fig. 2(a-d). The mechanism for the skyrmion-to-stripe transformation was further investigated by analyzing the MOKE images of the stripe domains over many runs. The stripe domains were found to nucleate at predictable spots on the wire which can be attributed to pinning sites. Together with the additional requirement of a long current pulse duration of several milliseconds for the transformation to occur, the transformation was concluded to be occurring as the result of a skyrmion-pinning site interaction and creep motion. A skyrmion at a pinning site undergoes slow creep elongation into a stripe due to the weak propagative being insufficient to fully depin the skyrmion. By utilizing the combination of skyrmion nucleation at high current density and skyrmion annihilation at low current density, skyrmion density control was demonstrated purely by current density modulation. In addition, the volatile nature of these current-induced stripes offers interesting possibilities for neuromorphic computing applications such as artificial leaky-integrate fire neurons which requires a continuous decaying property after an excitation, and artificial synapses with short-term plasticity which requires a temporary retention of state after excitation. In conclusion, our work revealed additional current-induced magnetic texture transformations which can be exploited for skyrmion density control using solely current modulation. In addition, our findings establish an additional requirement of a minimum operating current density in the design of skyrmionic devices to avoid unintended skyrmion deletion.

[1] W. Jiang, P. Upadhyaya, W. Zhang, *Science* 349, 283 (2015). [2] F. Büttner, I. Lemesh, M. Schneider, *Nat. Nanotech.* 12, 1040 (2017). [3] W. Legrand, D. Maccariello, N. Reyren, *Nano Lett.* 17, 2703 (2017). [4] C. C. I. Ang, W. Gan, G. D. H. Wong, and W. S. Lew, *Phys. Rev. Appl.* 14, 054048 (2020).

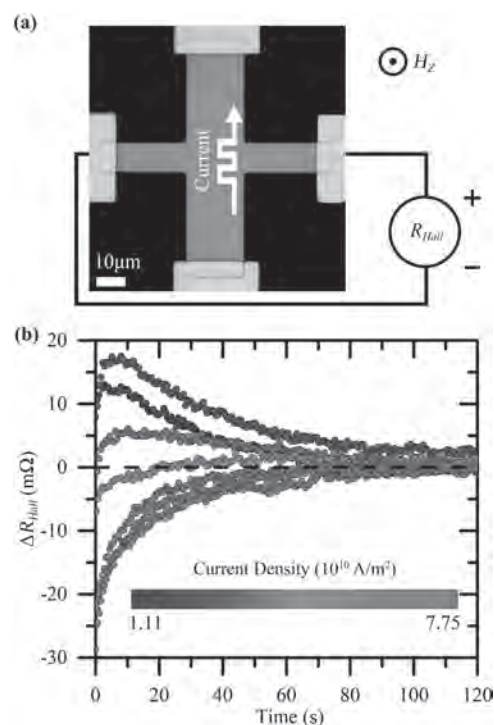


Fig. 1 (a) Measurement setup consisting of a Hall cross with widths of 20 and 10 μm . (b) Time evolution of Hall resistance change ΔR_{Hall} after 30 current pulses of 10 ms are injected for a range of current densities. Error bars are omitted for the graph for clarity, and the data have a standard deviation of 6ms or less.

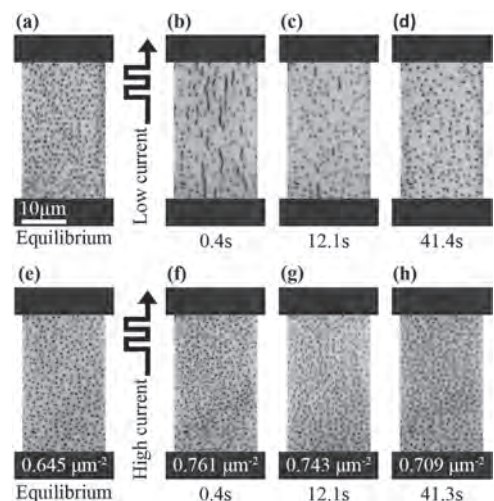


Fig. 2 MOKE images of current-induced magnetic states and their relaxation process back to equilibrium. (a) Magnetization state at equilibrium. Magnetization state at (b) $t = 0.4$ s, (c) $t = 12.1$ s, and (d) $t = 41.4$ s after injection of 2.21×10^{10} A/m^2 current pulses. (e) Magnetization state at equilibrium with skyrmion density of $0.645 \mu\text{m}^{-2}$. Magnetization state at (f) $t = 0.4$ s, (g) $t = 12.1$ s and (h) $t = 41.3$ s after injection of 7.20×10^{10} A/m^2 current pulses. Skyrmion density are stated below the respective MOKE images.

HB-05. X-Ray and Electron Beam Lithography of Zero-Field Magnetic Skyrmions.

Y. Guang¹, Y. Liu³, I. Bykova², Z. Yan¹, G. Yu¹, X. Han¹ and G. Schütz²
 1. Building M, Chinese Academy of Sciences Institute of Physics, Beijing, China; 2. Max-Planck-Institut für Intelligente Systeme, Stuttgart, Germany; 3. Riken Center for Emergent Matter Science, Wako, Japan

Magnetic skyrmions [1,2], with their small size, topological stability and low driving-current density, hold promises for high-density and energy-efficient information storage devices [3,4]. Here, we demonstrate the creation of individual skyrmions at zero-field in an exchange-biased magnetic multilayer with exposure to soft X-rays. In particular, a single skyrmion with 100-nm size can be created at the desired position using a focused X-ray spot of sub-50-nm size. This single skyrmion creation is driven by the X-ray-induced modification of the antiferromagnetic order and the corresponding exchange bias. And artificial skyrmion lattices with various arrangements can be patterned using X-ray [5]. Furthermore, by exploiting the fact that the antiferromagnetic order can also be reconfigured by local thermal excitations, a focused electron beam with a graphic pattern generator to “print” skyrmions is used, which is referred to as skyrmion lithography [6]. These works provide a route to design arbitrary skyrmion patterns, thereby establishing the foundation for further exploration of topological magnetism.

[1] S. Mühlbauer, B. Binz and C. Pfleiderer, et al., *Science* 323, 915 (2009).
 [2] X. Z. Yu, N. Nagaosa, and Y. Tokura, et al., *Nature*. 465, 901 (2010).
 [3] N. Romming, J. E. Bickel and K. V. Bergmann, et al., *Science* 341, 636 (2013). [4] A. Fert, N. R. Ren, V. Cros. *Nat. Rev. Mater.* 2, 17031 (2017).
 [5] Y. Guang, L. Bykova, Y. Z. Liu, G. Q. Yu* and X. F. Han, et al., *Nat. Commun.* 11, 949 (2020). [6] Y. Guang, Y. Peng, Z. R. Yan, G. Q. Yu* and X. F. Han, et al., *Adv. Mater.* 32, 20003003 (2020).

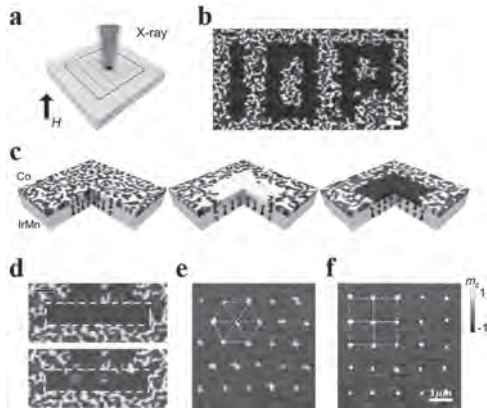


Fig. 1 (a) Sketch of X-rays measurement. (b) Single domain with IOP pattern. (c) Initial magnetic domain pattern imaged by STXM at zero field, and zero-field magnetic domain after scanning the central area (dashed lines) using circular X-ray under magnetic field of 2000 Oe and -2000 Oe. (d) Creating single skyrmion. (e)-(f) Triangular and Square skyrmion lattice.

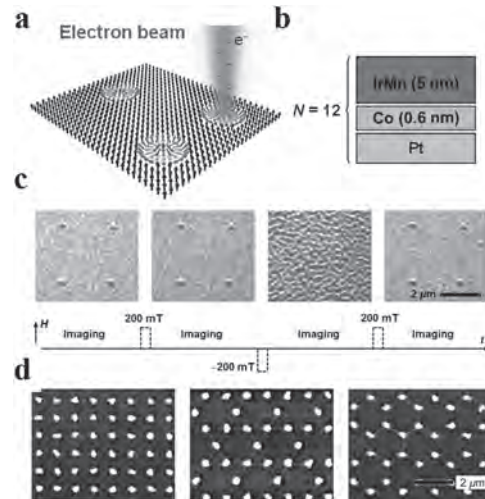


Fig. 2 (a) Sketch of electron beam measurement. (b) A schematic of sample structures. (c) Demonstration of the created antiferromagnetic domain with time sequence of applying the magnetic field and imaging process. (d) MFM images of EBL-patterned artificial skyrmion lattices with square, kagome, and honeycomb configuration.

HB-06. Real-Time Detection of Hall Effects: Measuring Current-Induced Magnetization Switching in the Time Domain.

G. Sala¹, V. Krizakova¹, E. Grimaldi¹, C. Lambert¹, T. Devolder² and P. Gambardella¹

1. D-MATL, ETH Zurich, Zurich, Switzerland; 2. Centre de Nanosciences et de Nanotechnologies, Orsay, France

The broad family of Hall effects comprises phenomena of ordinary, anomalous, planar, topological, and quantum origin. These effects are ubiquitous in electronic systems and are essential tools for studying the physics of condensed-matter systems and spintronic devices. The anomalous Hall effect [1], for instance, allows for probing the appearance of magnetically-ordered phases, field- and current-induced magnetization reversal, domain wall motion, and spin-orbit torques [2]. The planar Hall effect and the spin Hall magnetoresistance can also be used to track the response of antiferromagnets and magnetic insulators to applied magnetic fields, currents, and heat [3]. Despite the fundamental and technological importance of the Hall effects, their detection has been limited so far to the low frequency regime by their inherent small magnitude. There exist only few examples of time-resolved measurements of the magnetization dynamics using the Hall effect [4]. In contrast, measurements of the GHz dynamics associated with other magnetoresistance effects, such as the tunnel magnetoresistance, have become a common routine [5]. Extending this capability to Hall effects would provide an important tool to investigate a vast range of electronic and magnetic systems. Here we present a novel concept to perform all-electrical time-resolved measurements of any kind of Hall magnetoresistance [6]. Our approach removes the large non-magnetic potential that originates from the current leakage into the transverse arms of the Hall cross (see Fig. 1a). Since this background is much larger than the Hall voltage, it saturates the acquisition range of the measuring instrument (an oscilloscope) and impedes high-frequency measurements of transverse signals. The key idea to suppress the spurious contribution consists of delivering to the Hall cross two counter-propagating electric pulses of opposite polarity. Their synchronous arrival at the device center forces a local virtual ground that hinders the transverse current shunting (see Fig. 1b). Since the current does flow along the longitudinal direction, the Hall voltage is not removed, differently from the non-magnetic transverse potential. The vertical resolution of the oscilloscope can be thus fully exploited to acquire the background-free Hall voltage and sense the associated dynamics. Our approach is simple and, as compared to traditional Hall measurements, requires only an additional component, namely, the balun divider that generates the electric signals of opposite polarity (Fig. 1c). Importantly, the amplitude, duration, and waveform of the electrical excitation can be arbitrarily chosen. Moreover, RF and DC components can be combined in a single setup to perform both low and high frequency measurements. Overall, our technique achieves the signal quality necessary for the single-shot acquisition and, hence, for the detection of stochastic events with a resolution <50 ps. This capability is unique to our technique and is an advantage over standard non-electrical pump-probe schemes that can sense only the reproducible dynamics. We benchmarked our technique by studying the magnetization switching of ferrimagnetic GdFeCo caused by electric pulses with duration ranging between 0.3 and 20 ns. Our time-resolved measurements of the anomalous Hall effect show that the spin-orbit-torque-induced dynamics comprises a fast reversal (equivalent domain wall speed >1 km/s), as typical of ferrimagnets [7,8], and a long, unexpected incubation delay (Fig. 2). We associate this phase with the time required to nucleate a reversed domain assisted by Joule heating. In addition, the single-shot anomalous-Hall traces reveal the existence of broad distributions of the nucleation and reversal times and disclose the stochastic character of the dynamics triggered by the spin-orbit torques.

[1] Nagaosa N. et al., Rev. Mod. Phys. 82, 1539–1592 (2010) [2] A. Manchon et al., Rev. Mod. Phys. 91, 035004 (2019) [3] Wadley P. et al., Science (80-.) 351, 587–590 (2016) [4] Yoshimura Y. et al., Nat. Phys. 12, 157–161 (2016) [5] Grimaldi E. et al., Nat. Nano. 15, 111–117 (2020). [6] Sala G. et al., Nat. Comm (in press) [7] Caretta L. et al., Nat. Nano. 13, 1154–1160 (2018) [8] Cai K. et al., Nat. Electr. 3, 37–42 (2020)

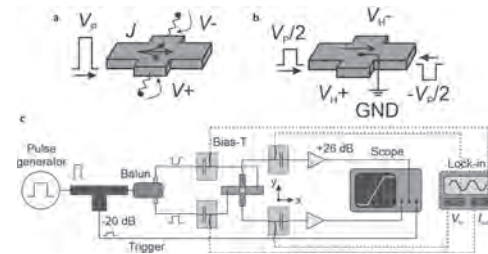


Figure 1. Experimental setup for time-resolved Hall effect measurements. a, The current J produced by a pulse V_p leaks through the transverse arms of the Hall cross and builds up spurious potential V_+ and V_- . b, When the two pulses with opposite polarity meet at the center of the Hall cross, they impose a virtual ground and force the current to propagate along the longitudinal direction. The background-free Hall potential V_H can thus be acquired with improved sensitivity. c, Schematics of the RF setup. The initial pulse is fed to a balun divider, which splits the signal into two half pulses with opposite polarity that reach the device at the same instant. The current-induced transverse Hall potentials V_H are amplified and detected by the oscilloscope, triggered by an attenuated portion of the initial pulse. The lock-in amplifier and the bias-Ts form the DC sub-network (dashed lines).

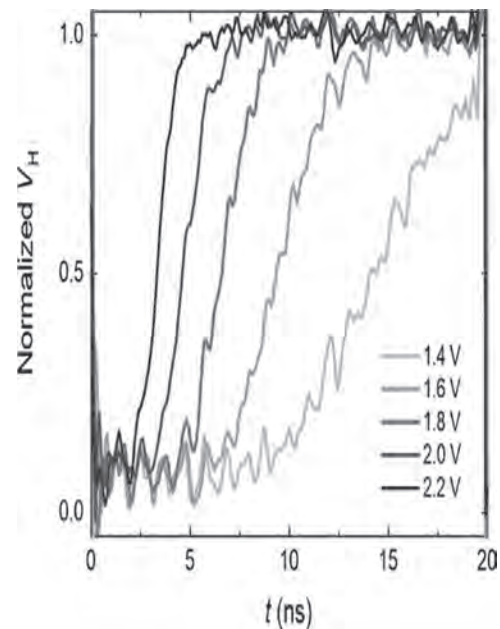


Figure 2. Spin-orbit torque magnetization switching of GdFeCo measured by time-resolved Hall effect. Normalized anomalous Hall voltage V_H measured during the application of 20-ns-long electric pulses. The duration of the initial quiescent phase and reversal are determined by the pulse amplitude.

HB-07. Voltage-Controlled Skyrmion Chirality Switch.

C. Fillion¹, R. Kumar^{1,3}, A. Fassatoui², S. Pizzini², L. Ranno², S. Auffret¹, I. Joumard¹, O. Boulle¹, G. Gaudin¹, L.D. Buda-Prejbeanu¹, C. Baraduc¹ and H. Béa¹

1. SPINTEC, Grenoble, France; 2. Institut NEEL, Grenoble, France;
3. Antaios, Meylan, France

In Heavy-Metal/Ferromagnet/Metal-Oxide (HM/FM/MOx) magnetic trilayers, the Structural Inversion Asymmetry (SIA) together with the Spin-orbit Coupling (SoC) is at the origin of an additional exchange interaction, the interfacial Dzyaloshinskii-Moriya Interaction (iDMI) [1]. In thin films with Perpendicular Magnetic Anisotropy, this additional exchange, together with the dipolar interaction, stabilizes non-collinear chiral magnetic spin textures such as Néel Domain Walls (DWs) with a given chirality and interestingly, magnetic skyrmion bubbles [2]. The control of iDMI amplitude and sign is thus of great importance, as it determines the DW internal structure and chirality, and their direction of motion driven by Spin-orbit Torques [3]. In most of the existing studies, the iDMI has been controlled by tuning the deposition parameters, such as the FM thickness, the nature of the bottom HM and top oxide or, as recently found, the oxidation state at the top interface [4,5]. Contrary to these approaches, voltage control of the interfacial magnetic properties enables a local and dynamical tuning of iDMI. In Srivastava et al. [6] we have shown that a 130% variation of the iDMI amplitude in Ta/CoFeB/TaOx can be obtained by biasing the sample with a gate voltage [6]. However, a voltage control of skyrmion chirality is still much awaited, since it would enable highly-controllable magnetic skyrmions. In this study, we report on the observation of voltage-controlled chirality switch of magnetic skyrmion bubbles in a Ta/FeCoB/TaOx trilayer heterostructure. The use of polar-Magneto-Optical Kerr-Effect (p-MOKE) microscope through a transparent Indium Tin Oxide (ITO) electrode allowed us to directly observe the current-induced motion of the spin textures and its inversion under or after the application of a gate voltage (see Fig. 1). In addition to skyrmion bubbles, we also demonstrate the voltage-effect on the chirality of magnetic labyrinthine domains. We show that successive voltage pulses of opposite sign reverse the DW chirality back and forth by tuning the oxidation state at the top FeCoB/TaOx interface. Micromagnetic simulations show that such a chirality reversal is also feasible on nanometer scale magnetic skyrmions without their annihilation. This local and dynamical control of the chirality paves the way to an efficient control of magnetic skyrmions enabling new functionalities for spintronic logic devices and memories.

[1] I. E. Dzyaloshinskii, J. Exptl. Theoret. Phys., (U.S.S.R.), vol. 46, p 960 (1964) [2] A. Fert, N. Reyren and V. Cros, Nature Review Materials, vol. 46, p. 6 (2017) [3] A. Thiaville et al., EPL (Europhysics Letters), vol. 100, p. 57002 (2012) [4] R. Kumar et al., Arxiv, 2009.13136, p. 11 (2020) [5] M. Arora, J. M. Shaw, and H. T. Nembach, Physical Review B, vol. 101, p. 4 (2020) [6] T. Srivastava et al., Nano Letters, vol. 18, p. 4871 (2018)

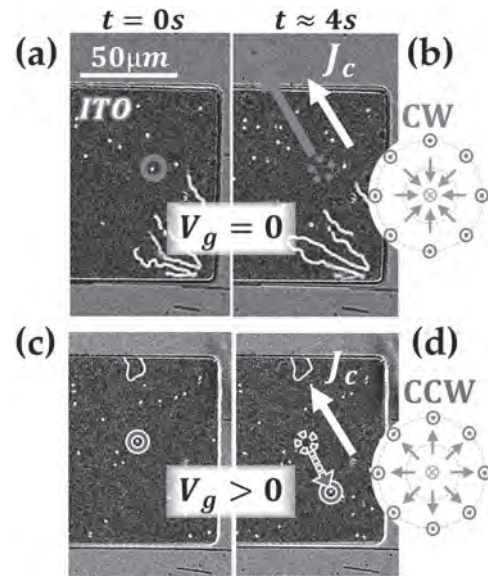


Fig. 1 : Voltage induced chirality switch on magnetic skyrmion bubbles measured through their current-induced motion under p-MOKE microscope. The dark rectangular region corresponds to the ITO transparent electrode below which voltage is applied. Under the ITO (resp. around it), black (resp. grey) regions correspond to magnetization pointing up, and white (resp. black) regions to magnetization pointing down. The current density (white arrow) is the same on (b) and (d). (a)-(b) Initially, the skyrmion bubbles are moving along the current density as depicted by the solid red arrow, consistent with a ClockWise (CW) chirality, schematically represented in the inset of (b). (c)-(d) Under the application of a positive gate voltage on ITO, an inversion of the skyrmion bubbles motion occurs below it, consistent with a CounterClockWise (CCW) chirality, as schematically represented in the inset of (d).

HB-08. Stabilization and Switching of Magnetic Merons in AuPt/Co/W(110) Epitaxial Thin Films.

J.A. Peña García¹, L. Camosi², A. Fassatoui¹, S. Pizzini¹, O. Fruchart³, A. Thiaville⁴, S. Rohart⁴, F. Genuzio⁵, T. Mendes⁵, A. Locatelli⁵ and J. Vogel¹

1. CNRS Institut Neel, Grenoble, France; 2. Institut Catala de Nanociencia i Nanotecnologia, Bellaterra, Spain; 3. SPINtronique et Technologie des Composants, Grenoble, France; 4. Laboratoire de Physique des Solides, Orsay, France; 5. Elettra Sincrotrone Trieste SCpA, Trieste, Italy

Topological magnetic textures such as skyrmions have been extensively studied during the last decade due to their potential application in spintronics devices. In ultrathin films systems, a key parameter to stabilize chiral topological magnetic textures is the Dzyaloshinskii-Moriya interaction (DMI), obtained at the interfaces between ferromagnetic layers and heavy-metals, promoting a unique chirality of the magnetic texture. We focus on an ultrathin epitaxial $\text{Au}_{1-x}\text{Pt}_x/\text{Co}(0.6-0.8\text{nm})/\text{W}(110)$ trilayer, a model system exhibiting perpendicular magnetic anisotropy (PMA) and interface DMI. The epitaxial growth of Co (0001) on W(110) gives rise to a C_{2v} crystal symmetry at the Co/W(110) interface. This symmetry results into a biaxial magnetic anisotropy, with an in-plane easy axis along the W[1-10] direction, and into an anisotropic DMI [1]. In this work, we have used Brillouin light spectroscopy to show the effect of the Pt-to-Au composition on the PMA and DMI of the trilayer. The balance between the different magnetic interactions, give rise to the stabilization in circular nanodots of different magnetic textures such as elliptical skyrmions [2] or magnetic merons [3], which have been observed with X-ray magnetic circular dichroism photoemission electron microscopy (XMCD-PEEM). In this presentation, we will focus on the stabilization of magnetic merons which are radial chiral textures with a topological charge $Q=1/2$ and topologically equivalent to a circular vortex. We will discuss the stabilization of magnetic merons, and how the topological charge can be switched under the application of an external perpendicular magnetic field as shown with XMCD-PEEM (Figure 1)

[1] Camosi, L., et al., Physical Review B, 95(21), 214422. 2017 [2] Camosi, L., Pena Garcia, J. New Journal of Physics, 2021 (accepted) [3] Pena Garcia, J., Camosi, L., et al. (in preparation)



Magnetic merons stabilized in a circular nanodot observed with XMCD-PEEM when the x-rays are along the W [1-10]. Under a perpendicular magnetic field, the topological charge has switched from $Q=+1/2$ to $Q=-1/2$.

HB-09. Observation of Magnetic Skyrmion Bubbles in a van der Waals Ferromagnet Fe_3GeTe_2 .

B. Ding¹, Z. Li¹, H. Li¹, Y. Yao¹ and W. Wang¹

1. Chinese Academy of Sciences Institute of Physics, Beijing, China

Two-dimensional (2D) van der Waals (vdW) materials are a family of quantum materials that have attracted great research attention in the past decade as they possess a diverse range of novel phenomena which are promising for technological applications. Among these materials, Fe_3GeTe_2 (FGT) is only ferromagnetic metal, exhibiting a strong out-of-plane uniaxial magnetic anisotropy down to atomic-layer thicknesses,^[1-4] which is very critical for spintronic applications, typically, magnetic-tunneling-junctions and magnetic random-access-memory devices. In this talk, we will show that a Bloch-type magnetic skyrmion bubble can indeed be realized in the single crystals of 2D vdW FGT. A high-density hexagonally-packed lattice of skyrmion bubbles emerges by a simple field-cooling process and keeps stable after turning off the magnetic field.^[5] Besides, we will show that the density of field free skyrmion lattice was tuned by changing the value of the cooling magnetic field. The highest-density skyrmion bubble was obtained when the field was applied at $H = 500$ Oe. As the value of the magnetic field is increasing, the size of the skyrmion is increasing but the density of skyrmion is decreasing. When the field is higher than 800 Oe, only stripe domain is observed. Finally, we will show the results from the micromagnetic simulations. We found that total energy of the skyrmion lattice is higher than that of the stripe domain, which indicates that the field free skyrmions is a metastable state compared with the ferromagnetic state. We believe the results presented in this talk could be useful for understanding the topological spin textures physics in 2D vdW materials.

[1] Y. Deng, Y. Yu, Y. Song, et al, *Nature* 563, 94 (2018). [2] Z. Fei, B. Huang, P. Malinowski, et al, *Nat. Mater.* 17, 778 (2018). [3] D. R. Klein, D. MacNeill, J. L. Lado, et al, *Science* 360, 1218 (2018). [4] V. Y. Verchenko, A. A. Tsirlin, A. V. Sobolev, et al, *Inorg. Chem.* 54, 8598 (2015). [5] B. Ding, Z. Li, G. Xu, et al, *Nano Lett.* 20, 868 (2020).

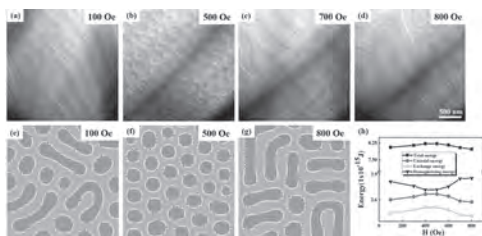


Figure 1 L-TEM images demonstrating the skyrmion generation and sustainability via fielding cooling manipulation in Fe_3GeTe_2 . L-TEM images acquired at 93K after a magnetic field cooling at (a) 100 Oe, (b) 500 Oe, (c) 700 Oe, and (d) 800 Oe. The corresponding simulation of the field free skyrmion lattice is obtained at (e) 100 Oe, (f) 500 Oe, (g) 800 Oe. (g) The cooling field dependence of the energy terms in the simulations.

HB-10. Non-Linear Magnetic Response at Topological Defects in Helimagnetic FeGe.

M. Stepanova^{1,2}, E. Lysne^{1,2}, P. Schoenherr^{9,3}, J. Masell⁴, L. Köhler⁵, A. Rosch⁶, N. Kanazawa⁷, Y. Tokura^{4,7}, A. Qaiumzadeh², A. Brataas², M. Garst^{5,8} and D. Meier^{1,2}

1. Department of Materials Science and Engineering, Norwegian University of Science and Technology, Trondheim, Norway; 2. Center for Quantum Spintronics, Norwegian University of Science and Technology, Trondheim, Norway; 3. University of New South Wales, Sydney, NSW, Australia; 4. RIKEN, Wako, Japan; 5. Technische Universität Dresden, Dresden, Germany; 6. Universität zu Köln, Köln, Germany; 7. The University of Tokyo, Bunkyo-ku, Japan; 8. Karlsruher Institut für Technologie, Karlsruhe, Germany; 9. ETH, Zurich, Switzerland

The lamellar morphology of chiral spin textures is analogous to liquid crystals and biological systems. Similar to cholesteric liquid crystals, chiral magnets possess a periodic layered structure and form a wide variety of non-trivial topological defects[1,2]. Using magnetic force microscopy (MFM), we resolve 1D and 2D topological defects in the near-room temperature helimagnet FeGe, including disclinations and dislocations with nonzero topological winding number, as well as three fundamental types of helimagnetic domain walls. Interestingly, in addition to their non-trivial structure, all topological defects in FeGe exhibit a pronounced non-linear magnetic response in MFM, which is not observed in regions with perfect lamellar-like order. This magnetic signature is reminiscent of the so-called “lines of flare” in cholesteric liquid crystals, suggesting local variations in magnetic susceptibility. We investigate the origin of the magnetic signature of the topological defects and discuss the possibilities to utilize the anomalous local response as read-out signal in spintronics devices.

1. A. Dussaux, P. Schoenherr, K. Koumpouras, J. Chico, K. Chang, L. Lorenzelli, N. Kanazawa, Y. Tokura, M. Garst, A. Bergman, C. L. Degen, and D. Meier, *Nature Communications*, Vol. 7, p.12430 (2016). 2. P. Schoenherr, J. Müller, L. Köhler, A. Rosch, N. Kanazawa, Y. Tokura, M. Garst, and D. Meier, *Nature Physics*, Vol. 14, p.465 (2018).

HB-11. Enhancement of Skyrmion Density Achieved via Interface Engineering.

S. Bhatti^{1*}, H. Tan², V.Z. Li³, M. Sall⁴, R. Juge⁴, R. Mahendiran⁵, A. Soumyanarayanan^{2,5}, D. Ravelosona^{4,6}, S. Lim² and S. Piramanayagam¹
 1. School of Physical and Mathematical Sciences, Nanyang Technological University, Singapore, Singapore; 2. Institute of Materials Research and Engineering, Agency for Science Technology and Research, Singapore, Singapore; 3. Wuhan University, Wuhan, China; 4. Spin-Ion Technologies, Paris, France; 5. Department of Physics, National University of Singapore, Singapore; 6. University of Paris-Saclay/CNRS, Paris, France

Skyrmions are chiral spin textures, which have gained considerable interest due to their promising applications in memory and synaptic devices [1]. These textures can exist in a low-density state or in a high-density state [2]. A high density skyrmion state is more favourable for high-density memory devices. However, formation of the high density state requires a subtle balance of magnetic properties. One of the key requirements needed for the high density state is a relatively high value of Dzyaloshinskii-Moriya interaction (DMI) as compared to the effective magnetic anisotropy (K_{eff}) and exchange coupling energy (A_{ex}) [3]. DMI is an anti-symmetric exchange interaction induced by spin-orbit coupling in the presence of broken inversion symmetry [4]. In a specific thin material system, DMI can be tuned by either changing the thickness of ferromagnet or by varying its stoichiometry. Former has been reported for materials like Pt/Co/AlO_x, Pt/CoFeB/AlO_x, and Ta/FeCoB/TaO_x [5, 6]. In these studies, decreasing the thickness of ferromagnet results in a higher DMI. However, a decrease in thickness also results in an enhanced value of K_{eff} , which limits the skyrmion density to a certain number. In the latter report, which was carried out on Ir/Fe/Co/Pt structures, the thickness and composition of the ferromagnetic layers was varied to modulate skyrmion size and density [7]. However the used material system, because of polycrystalline nature of FM resulting in grains, is inadequate for an unhindered skyrmion motion. Here, we report a reduction of effective anisotropy energy density K_{eff} by using post growth 20 keV He⁺ ions induced interface intermixing, without compromising DMI. We have used Pt/CoFeB/MgO stacks to study the effect of varying ion irradiation dose and carried out Monte Carlo simulations to get the probability of the ions' distributions and the intermixing in the sample [8]. The displacement of ferromagnetic layer atoms increases linearly with increasing dose (inset of Fig. 1a). To study the effect of such intermixing on magnetic properties, we have used a vibrating sample magnetometer. We have found that K_{eff} is reduced as atomic intermixing at interfaces between the ferromagnetic and non magnetic layers increase, which corroborates the behaviour of K_{eff} from previous reports [9]. Interestingly, even at high dose, K_{eff} still remained positive, indicating an out-of-plane magnetization. (Fig. 1a). Moreover, we have observed an increase in the saturation magnetisation (M_s) (fig 2a), due to increased polarization of the ferromagnetic component. The increase in polarization is caused by formation of CoPt alloy at the Co-Pt interface, which results in the increase of the spin moment at interface up to ~17% [10]. Furthermore, we speculate the increase in magnetisation also includes contribution from the migration of B atoms at interstitial sites between Co and Fe atoms. Besides, we have measured the interfacial Dzyaloshinskii-Moriya interaction (DMI) by the Brillouin light scattering spectroscopy. We have noticed an increase in the DMI values of the irradiated samples. Considering a possibility of change in the effective thickness of FM, we have calculated surface M_s and hence, interface DMI (Fig. 2a inset and 1c). We find that the interface DMI increases under intermixing. Moreover, we have used micromagnetic simulations to estimate the exchange coupling energy (A_{ex}) by assessing the periodicity of equilibrium state achieved at zero field (Fig. 1d). Noticeably, both DMI (interface DMI) and A_{ex} follows a similar trend as M_s . To probe the change in magnetization dynamics due to the modification of the magnetic properties, we have carried out magnetic force microscopy (MFM) as shown in Fig. 2a and 2b. We notice the zero-field periodicity of labyrinthine textures is reduced by ~50 nm, depicting a higher density of striped domains after processing the sample (Fig. 2c). The skyrmion density is increased up to six folds as compared to the pristine sample (Fig. 2d). We speculate that the increase in skyrmion density and reduction in periodicity is due to the reduction of domain wall energy. Furthermore, we have also measured the skyrmion size and we observe a reduction by

~50 nm, down to 75 nm for large intermixing (Fig. 2d). Besides, we have carried out a comparatively low energy treatment (annealing) of deposited stack to explain the physical phenomena of skyrmion density enhancement. Our study demonstrates that post growth He⁺ irradiation can achieve a high density skyrmion state, which is promising for memory, logic and neuro-morphic applications.

[1] A. Fert, N. Reyren, and V. Cros, Nature Review Materials., Vol. 2, p.1 (2017) [2] X. Yu, Y. Onose, and N. Kanazawa, Nature., Vol. 465, p.901 (2010) [3] A. Bogdanov and A. Hubert, Journal of magnetism and magnetic materials., Vol. 138, p.255 (1994) [4] A. Fert, Materials Science Forum (Trans Tech Publ), p.439 (1990) [5] J. Cho, Nam-Hui Kim, and Sukmook Lee, Nature communications, Vol. 6, p.1 (2015) [6] T. Srivastava, W. Lim and I. Joumard, Physical Review B., Vol 100, p.220401 (2019) [7] A. Soumyanarayanan M Raju and AL Gonzalez Oyarce, Nature materials., Vol. 16, p.898 (2017) [8] M. Bonder, N. Telling and P. Grundy, Journal of Applied Physics., Vol. 93, p.7226 (2003) [9] M. S. El Hadri, M. Hehn and G. Malinowski, Journal of Physics D: Applied Physics., Vol. 51, p.215004 (2018) [10] B. Zimmermann, W. Legrand and D. Maccariello, Applied Physics Letters., Vol. 113, p.232403 (2018)

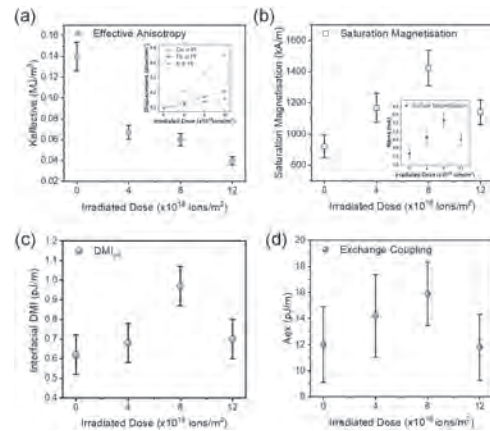


Fig.1 Effect of He⁺ irradiation induced interface intermixing on magnetic properties of CoFeB. Variation in (a) $K_{effective}$, (b) Saturation Magnetization (M_s), (c) Interface DMI (DMI_{int}) and (d) Exchange coupling (A_{ex}) energy due to varying dose of He ions. Inset of (a) shows a linear relation of atoms intermixing and varying dose. Inset of (b) shows varying surface magnetization due to the irradiation dose. The trend of M_s influences the DMI_{int} and A_{ex} .

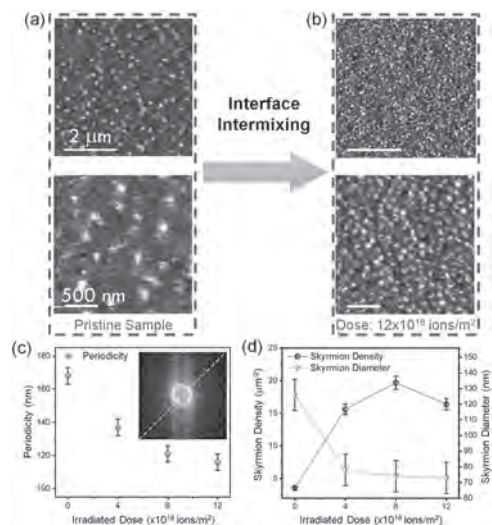


Fig.2 Effect of interface intermixing on magnetization dynamics of CoFeB. (a) and (b) MFM images depicting change in skyrmion density (top image) and size (bottom image) due to the interface intermixing. (c) Periodicity of magnetic textures as function of irradiated dose. Inset shows 2D FFT of pristine sample, used to calculate the periodicity. (d) Variation of skyrmion density (up to six folds) and reduction of skyrmion size (up to ~50 nm) due to varying dose.

HB-12. Thermal Evolution of Magnetic Skyrmion Formation Mechanism in Chiral Multilayers.

X. Chen¹, E. Chue², J. Kong³, H. Tan¹, H. Tan¹ and A. Soumyanarayanan^{2,1}
 1. Institute of Materials Research and Engineering, Singapore, Singapore;
 2. Department of Physics, National University of Singapore, Singapore;
 3. Institute of High Performance Computing, Singapore, Singapore

Magnetic skyrmions are nanoscale topological spin structures stabilized by chiral interactions and they are promising candidates for realizing brain-inspired computing devices [1,2]. One important prerequisite of such applications is the controlled formation of skyrmions. Skyrmions could form via one of two pathways - nucleation from uniform magnetization or evolution from magnetic stripes. The latter can be further divided into two distinct mechanisms – the reversible shrinking of a stripe into a skyrmion or the irreversible fission of a stripe into multiple skyrmions [3]. In this work, Ir/Fe/Co/Pt chiral multilayers were characterized with first-order reversal curve (FORC) magnetometry in conjunction with Lorentz transmission electron microscopy (LTEM) over the temperature range of 100 - 350 K. With both techniques, we observed a marked increase in stripe-to-skyrmion fission tendency with increasing temperature. FORC magnetometry consists of measuring a series of minor hysteresis loops (M(H,Hr)) and computing the quantity ρ ($= -1/2 \text{ dM(H,Hr)}/\text{dHdHr}$) which represents the degree of irreversibility of a magnetic process [4,5]. The fission of stripes into skyrmions at intermediate fields and the annihilation of skyrmions at high fields are two processes that are revealed by FORC as $\rho \neq 0$ features [3]. The annihilation-fission separation (AFS, indicated by red arrows in Fig. 1e-h) could be used as a proxy of the favourability of the fission process. In Fig. 1i, one can observe the rise of AFS with temperature. LTEM microscopy captures the real-space evolution of magnetic textures as the field is swept. By tallying the stripe and skyrmion densities and tracking their field dependence, we estimate the average number of skyrmions generated by a stripe, η , using the ratio of the maximum skyrmion to stripe densities. As shown in Fig. 2, η increases 3-fold: from ~ 1 at 100K to ~ 3 at 350K. We interpret our results as the consequence of temperature-dependent magnetic interactions such as direct exchange, Dzyaloshinskii–Moriya interaction (DMI), and anisotropy. The relative strengths of these competing interactions will determine the energy barrier of the fission process. With theoretical modeling from geodesic nudged elastic band (GNEB) calculations [6], we found that the barrier height is greatly reduced with increasing temperature. These findings establish temperature as an important tuning parameter and provide insights into skyrmion formation, which is crucial to the realization of skyrmionic devices.

1. Fert, A. *et al. Nat. Rev. Mater.* 2, natrevmats201731 (2017). 2. Soumyanarayanan, A. *et al. Nat. Mater.* 16, nmat4934 (2017). 3. Tan, A. K. C. *et al. Phys. Rev. Mater.* 4, 114419 (2020). 4. Pike, C. R. *et al. J. Appl. Phys.* 85, 6660 (1999). 5. Davies, J. E. *et al. Phys. Rev. B* 70, 224434 (2004). 6. Bessarab, P. F. *et al. Comput. Phys. Commun.* 196, 335–347 (2015).

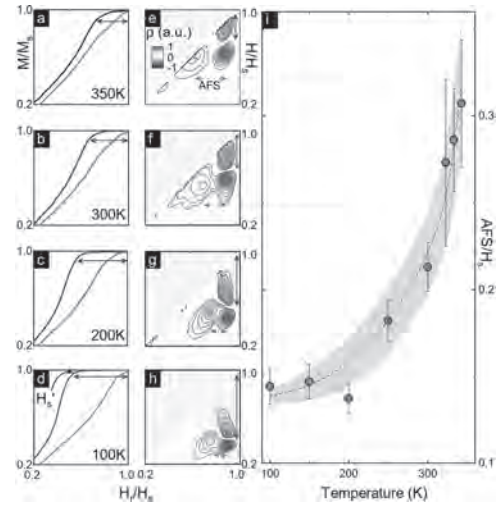


Fig. 1: Temperature dependence of annihilation-fission separation (AFS). (a-d) Out-of-plane (OP) hysteresis loops of a multilayer sample from 100K to 350K. (e-h) Irreversibility ρ (H,Hr) derived from FORC magnetometry at the same temperatures. Hr, the reversal field, is the starting point of each minor loop. AFS are indicated by red arrows. (i) AFS plotted against temperature, showing a remarkable temperature dependence.

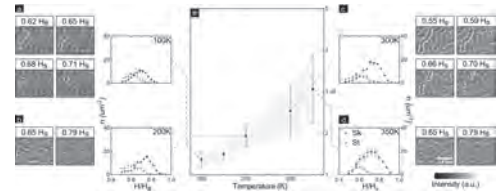


Fig. 2: Texture density evolution imaged by LTEM. (a-d) Field evolution of stripe (St) and skyrmion (Sk) densities of a multilayer sample from 100 K to 350 K. While the stripe densities remained relatively constant, the skyrmion densities appreciated significantly with temperature. Accompanying LTEM images show the field evolution of stripes into skyrmions over selected fields. White dot lines enclose a typical magnetic domain for 100K and 300K. (e) η , estimated by ratio of maximum skyrmion to stripe densities, increases with temperature.

HB-13. Stable Zero-Field Skyrmions in Magnetic Bilayers.S. Mallick¹, G. Pradhan^{1,2} and S. Rohart¹*1. University Paris Saclay, Laboratoire de Physique des Solides, Orsay, France; 2. National Institute of Science Education and Research, Bhubaneswar, India*

Magnetic skyrmions are quasiparticle-like chiral textures that appears in materials with broken inversion symmetry. Implementation of skyrmions in data storage technologies requires the ability of stabilizing them at room temperature and efficiently driving the textures under spin-orbit torque (SOT). Skyrmion stabilization at zero field, as per the requirement of application, can be realized by controlling the interplay between the anisotropy energy, Dzyaloshinski-Moriya interaction (DMI), exchange interaction, and dipolar coupling [1]. Here we show the formation of stable magnetic skyrmions at remanence following the application of an external perpendicular field. We also control the size and density of the skyrmions by manipulating the strength of the applied magnetic field. Further, we observe motion of the skyrmions in nanotrack under the influence of SOT. We chose asymmetric superimposition of two magnetic layers with appropriate combination of materials and thicknesses to satisfy the energy requirements to constrict skyrmions. When the thickness of the ferromagnetic layer is near the spin-reorientation transition (SRT), the effective anisotropy vanishes and the ferromagnetic ground state is the stripe phase [1]. In order to stabilize skyrmion phase in absence of any bias field, we increase the stability of the homogeneous state using a reduced ferromagnet thickness to enhance the anisotropy of the system. Hence we chose the following thin film heterostructure: Si/SiO₂/Ta(3 nm)/Pt(5 nm)/Co(1.4 nm)/Au(1 nm)/Pt(5 nm)/Co(1.4 nm)/Au(2.5 nm), where the SRT of Co is ~ 1.6 nm. FIG 1 (a) shows the PMOKE hysteresis with minor loops for the sample. While major loops show a 100% remanence, minor loop show the possibility to demagnetize the sample, through the creation of textures. As shown by magnetic force microscopy in FIG 1 (b) and (c) at remanence after application of perpendicular magnetic field of 48, and 31 mT, the resulting magnetic state strongly depend on the maximum applied field. The larger the maximum field, the smaller the textures and their density. Therefore, after the application of sufficiently large magnetic field, skyrmions are stable even at remanence. The longevity of the magnetic textures has been confirmed by performing MFM imaging at different times after application of the external field. We have observed MOTION of these skyrmions in a patterned nanotrack under the influence of SOT by applying 10 ns wide pulses with a current density of $\sim 6 \times 10^{11}$ A/m², which opens a perspective toward skyrmionic spintronics devices at zero field.

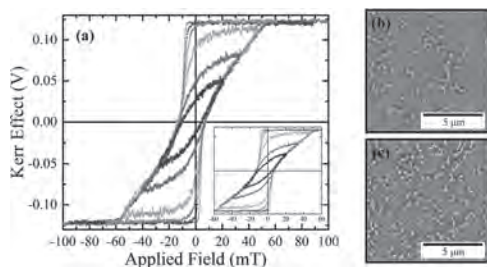
[1] A. Hrabec *et al*, *Nat. Comm.* 8, 15765 (2017)

FIG 1: (a) Polar magneto-optic Kerr effect (PMOKE) Hysteresis with minor loops in the asymmetric bilayer sample. MFM images of the same sample at remanence after application of perpendicular magnetic field of: 48 mT (b), and 31 mT (c), respectively.

Session HC

SKYRMIONS: DMI AND DYNAMICS

Chun-Yeol You, Chair

Daegu Gyeongbuk Institute of Science and Technology, Daegu, The Republic of Korea

INVITED PAPER

HC-01. Chirality Control in Ferromagnetic Multilayers Through Intra- and Interlayer DMI INVITED.*S. Pollard*¹*1. Physics and Materials Science, The University of Memphis, Memphis, TN, United States*

The Dzyaloshinskii-Moriya interaction (DMI) plays a key role in the formation and motion of chiral domain walls and magnetic skyrmions. Traditionally, DMI has been generalized to two forms - bulk-like DMI in single crystal chiral magnets lacking inversion symmetry, and interfacial DMI, formed as a result of inversion symmetry breaking at the interface of bilayer and multilayer systems, such as the extensively studied ferromagnet/heavy metal heterostructures. In these bi- and multilayer structures, it is widely believed that interfacial DMI is limited to asymmetric structures and will result solely in a Néel chirality, imposing challenges, such as a significant skyrmion Hall effect, for further development of spintronic devices. Here, we present our recent results in Co/Pd multilayers which challenge this understanding [1,2,3]. Systematic observations of domain structure and response to externally applied magnetic fields was performed using in-situ Lorentz transmission electron microscopy. For samples with a total magnetic thickness less than 6.7 nm, a pure Néel spin structure was observed [1]. However, in thicker samples, the competing demagnetization energy results in a mixed chiral Néel/achiral Bloch domain boundary. By comparing the observed Lorentz intensity to image simulations and micromagnetic modeling, key material parameters such as the exchange stiffness and domain mixing angle, found to be between 55 and 60 degrees, are measured and an interfacial DMI of nominally 1.0 mJ/m² is extracted from a sample consisting of 10 x Co(0.7 nm)/Pd(0.5 nm) layers [2]. These results are agreement with values extracted from Kerr microscopy on lower repetition samples, indicating a saturation of DMI with increasing layer repetition. For a larger net magnetic thickness we observe a large asymmetry in the chirality of the Bloch component of these domain walls. For the largest thicknesses, only clockwise Bloch chiralities are observed, indicating a complete asymmetry. Further, as samples are relaxed from saturation with a magnetic field applied at an angle to the film normal, domain nucleation and expansion is characterized by propagation of the domain wall along the in-plane field component with the internal domain wall spin structure oriented along the magnetic field. These 360-degree domains are characterized by one clockwise and one counterclockwise Bloch domain wall. During the relaxation process, these domains may also expand via branching. This branching occurs predominantly through expansion of the clockwise wall, with little branching along the counterclockwise region. This is in disagreement with expected behavior, wherein branching from either side would be equally probable. We term this behavior chiral branching. We develop a model accounting for an interlayer contribution to the Dzyaloshinskii-Moriya interaction which, in combination with a large demagnetization field, can break the degeneracy between Bloch chiralities, showing qualitative agreement with a systematic investigation across a range of repetitions and layer thicknesses [3]. These results open a new avenue in which to modulate the internal domain wall spin texture and new means in which to control the skyrmion Hall angle, and add to recent results finding that interlayer DMI plays a key role in determining spin structure and dynamics in magnetic multilayers.

[1] J. A. Garlow, et al., *Phy. Rev. Lett* 122, 237201 (2019). [2] S. D. Pollard, et al., *Nat. Comm.* 8, 14761 (2017). [3] S. D. Pollard, et al., *Phys. Rev. Lett* 125, 227203 (2020)

CONTRIBUTED PAPERS

HC-02. Experimental Correlation of Interfacial Dzyaloshinskii-Moriya Interaction Amplitude and Work Function in Magnetic Multilayers and its Relation With Rashba Effect at Metallic Interfaces.

F. Ajejas¹, W. Legrand¹, Y. Sassi¹, S. Collin¹, A. Vecchiola¹, K. Bouzheouane¹, S. Pizzini², N. Reyren¹, V. Cros¹ and A. Fert¹

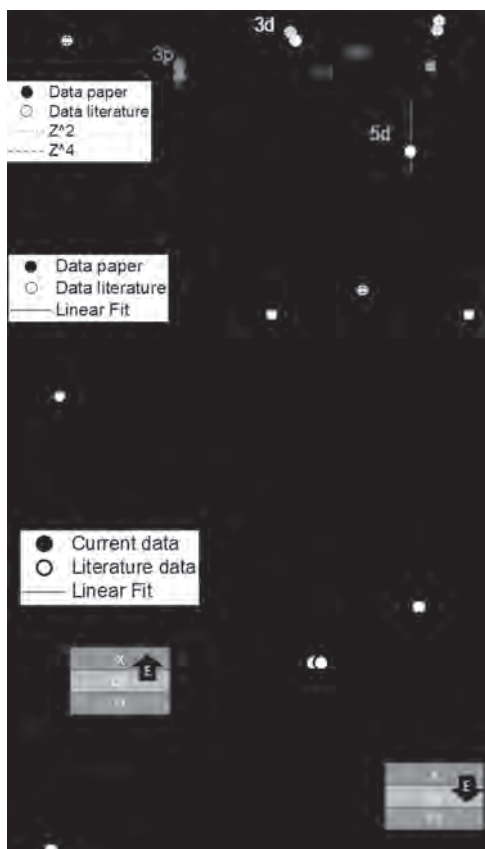
1. *Unite Mixte de Physique CNRS/Thales, Palaiseau, France*; 2. *Institut NEEL, Grenoble, France*

Magnetic multilayers (MML) with large perpendicular magnetic anisotropy (PMA) and Dzyaloshinskii-Moriya interaction (DMI) have attracted great attention in recent years owing to the possibility of stabilizing non-collinear magnetic textures such as chiral domain walls (DW) [1], spin spirals [2] or skyrmions [3-4] with chiral Neel magnetization rotation. The latter are promising candidates as carriers of information for next-generation race-track magnetic memories or logic devices. The accurate experimental determination of the DMI is an important challenge as it is necessary to tailor the properties of future devices. The determination of the effective DMI amplitude D is still a current subject of active research since the origin of the DMI is not well known. Beyond the three-sites Fert-Levy model [5], first principle calculations for the common Pt|Co|M systems were carried out [6], aiming at finding a simple relation between the DMI and the intrinsic properties of the metallic element that would be easily accessible to the experimentalist, providing guidance to design systems with a required D value. In this study, we perform thorough measurements to determine DMI strength by asymmetric expansion of domains in the presence of an in-plane magnetic field, using Kerr microscopy [7-8]. Results are shown in Figure 1 for all the different materials selected to build asymmetric trilayers with the general structure is Pt|Co|M, with $M = \text{Ni, Pd, Ru, Al, Al|Ta and MoSi}$. The symmetric (asymmetric) expansion of Néel-type bubble without (under the presence of) an external in-plane magnetic field of Pt|Co|Al trilayer is displayed in panel (a). In panels b-g are plotted the expansion velocities of the up and down domain branches as function of the in-plane field for all the studied systems. The minima of the plotted curves correspond to the field which compensates H_{DMI} , which is related to D by, is the DW parameter. From the D , we estimate the effective interfacial DMI (summing Pt and M contributions), $D_s = D * t$, with t the Co thickness. We look for correlation between D_s and three material properties in Fig. 2. In Fig. 2a is presented in log-log scale the absolute value of D_s as function of atomic number (Z). As DMI is proportional to spin-orbit coupling, Z scales with different power laws *e.g.* Z^2 and Z^4 for $3d$ and $4d$ elements, becoming more complex for the heaviest elements. Fig. 2b shows D_s as function of Pauling electronegativity (χ) [6]. Here we found a linear correlation in good agreement with theoretical calculations (Pearson- r dispersion index of 0.74). Finally, in panel c is presented D_s as a function of the work function difference ($\Delta\Phi$) [9] at the Co|M interfaces. We find a striking linear relationship between D_s and $\Delta\Phi$ (Pearson- r dispersion index of 0.93). This strong correlation points to Rashba-like interfacial fields, leading to the modulation of the effective interfacial DMI.

[1] A. Thiaville *et al.* EuroPhys. Lett, 100, 57002 (2012) [2] P. Ferriani *et al.* Phys. Rev. Lett. 101, 27201 (2008). [3] A. Fert, N. Reyren, V. Cros, Nat. Rev. Mat. 2, 17031 (2017). [4] C. Moreau-Luchaire *et al.* Nat. Nano. 11, 444 (2016); O. Boulle *et al.*, Nat. Nano 11 (5), 449 [5] A. Fert and P.M. Levy, Phys. Rev. Lett., 44,1538 (1980) [6] H. Jia *et al.* Phys. Rev. M 4, 024405 (2020) [7] F. Ajejas *et al.* Appl. Phys. Lett. 111, 202402 (2017); [8] T. Ha Pham *et al* EPL 113 67001 (2016) [9] Y.-K. Park *et al.* NPG Asia Materials 10, 995 (2018)



a) Expansion of Néel-type bubble in Pt|Co|Al trilayer for different external in-plane magnetic field B_x , b-g) Domain wall velocity vs. B_x for up/down and down/up DWs.



Parameter relationships. D_s as function of, a) Atomic Number (Z); b) Electronegativity (χ); and c) work function difference ($\Delta\Phi$), for Pt|Co|M samples with different M values, as denoted in the figure.

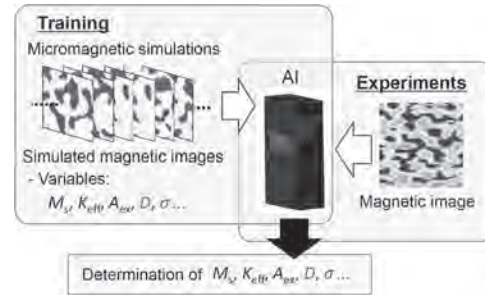
HC-03. Determination of the Dzyaloshinskii-Moriya Interaction From a Single Magnetic Domain Image Using Machine Learning.

K. Tanabe¹, M. Kawaguchi², K. Yamada³, T. Sawa¹, S. Hasegawa², M. Hayashi² and Y. Nakatani⁴

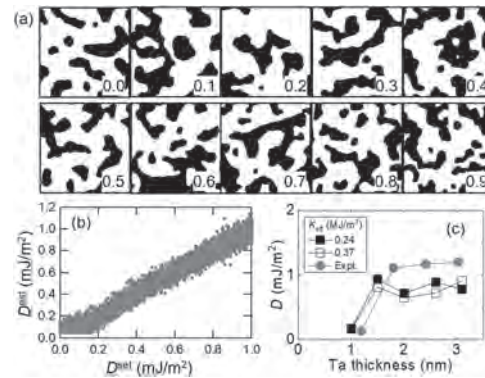
1. Toyota Technological Institute, Nagoya, Japan; 2. The University of Tokyo, Bunkyo-ku, Japan; 3. Gifu University, Gifu, Japan; 4. Denki Tsushin University, Chofu, Japan

Recently, the Dzyaloshinskii-Moriya (DM) interaction, which emerges at the interface of ferromagnetic layer and non-magnetic layer with strong spin-orbit interaction, has attracted much attention in spintronics. To evaluate the strength of the DM interaction (the DM exchange constant), a number of approaches have been proposed. As many of the approaches make use of the dynamics of the magnetic system, for example, current- or field-induced motion of domain walls, propagation of spin waves, and current/field dependence of the magnetization reversal processes, there are difficulties in accurately extracting the DM exchange constant. In this study, we present that the DM exchange constant can be simply extracted from a magnetic domain image using machine learning[1]. Magnetic domain structure is determined by minimization of magnetic energy of the system, which typically includes magneto-static, magneto-elastic, anisotropy, Heisenberg exchange, and DM exchange energies. The pattern of the magnetic domain structure, therefore, includes information of the DM exchange constant. A convolutional neural network is used to characterize the magnetic domain pattern with high sensitivity. To train the neural network, a large number of images with different patterns that derive from a magnetic system with fixed material parameters are required. As such image acquisition using existing experimental setup is typically cumbersome, here we use micromagnetic simulations to generate the images for supervised learning. We use the trained system to estimate the DM exchange constant from experimentally obtained magnetic domain images in Fig. 1. The training data set is generated using a homemade micromagnetic simulation code. We first generate training images where parameters other than the DM exchange constant are fixed. The DM exchange constant (D) is varied from 0 to 1.00 mJ/m². The initial condition and the pattern of magnetic-anisotropy distribution are varied to generate 100,000 images of the equilibrium magnetic state for a given parameter set with various values of D. Exemplary images of the equilibrium magnetic state with different D are shown in Fig. 2(a). Model validation is performed with 10,000 testing images with different values of D created using the same code. D^{set} corresponds to D used in the simulations to generate the testing images. The testing images are studied by the trained system: the estimated D returned from the system is denoted as D^{est}. The relation of D^{set} vs. D^{est} is shown in Fig. 2(b). When D^{set} is larger than ~0.05 mJ/m², we find a linear relation between D^{set} vs. D^{est} with a root mean square error of ~0.046 mJ/m². We next use the trained system to estimate D from experimentally obtained magnetic domain images. The film stacking of the samples used is: Si sub./Ta (d)/Pt (2.6 nm)/Co (0.9 nm)/MgO (2 nm)/Ta (1 nm). The thickness of the Ta seed layer (d) is varied to change D of the films via modification of the (111) texture of the Pt layer. The DM exchange constant is estimated using magnetic field induced switching of magnetization[2]. A Hall bar is patterned from the films using conventional optical lithography. We use the Hall voltage to probe the magnetization via the anomalous Hall effect. The magnetic domain images of the films are acquired using a magnetic microscope equipped with a magnetic tunnel junction sensor. The value of D the trained system returned for each image is plotted against d in Fig. 2(c). Interestingly the d dependence of the estimated D is consistent with that of the experiments (red circles in Fig. 2(c)). Note that the magnitude of K_{eff} does not significantly influence estimation of D. In summary, we have demonstrated that machine learning can be applied to extract the DM exchange constant (D) from a single magnetic domain image. The accuracy of the supervised learning in estimating D is found to be ~0.05 mJ/m², which is significantly better than conventional experimental approaches. This approach can be extended to estimate all relevant material parameters at once from a single magnetic domain image, which will significantly simplify materials research for magnetic memory and storage technologies. Acknowledgements: This work was partly supported by JSPS Grant-in-Aid and the Center of Spintronics Research Network of Japan.

[1] M. Kawaguchi, K. Tanabe, K. Yamada et al., npj Computational Material, in press. [2] S. Kim, P.-H. Jang, D.-H. Kim et al., Phys. Rev. B., Vol. 95, p.220402(R) (2017).



Concept of the study. Micromagnetic simulations are used to generate thousands of training images. There are five relevant material parameters: M_s , K_{eff} , A_{ex} , D , and σ . Here we vary D and σ in the simulations so that the system can learn domain patterns with different D and σ . After the supervised training, we feed the system with an experimentally obtained image of magnetic domains to extract D and σ . Images taken from Ref. [1].



D obtained from pattern recognition and machine learning. (a) Typical magnetic domain images calculated using micromagnetic simulations. Dark and bright contrast represents the magnetization direction along the film normal. The DM exchange constant is varied from 0 to 0.90 mJ/m²: the corresponding value is indicated at the bottom right corner of each image. (b) The DM exchange constant (D^{est}) estimated from the testing images are plotted as a function of D set in the simulations (D^{set}). (c) DM exchange constant (D) estimated from the measured domain images using the trained system. Two different values of K_{eff} are used in the simulations to generate the training images: the estimated values obtained from the two trained systems are denoted using open and solid squares. Images taken from Ref. [1].

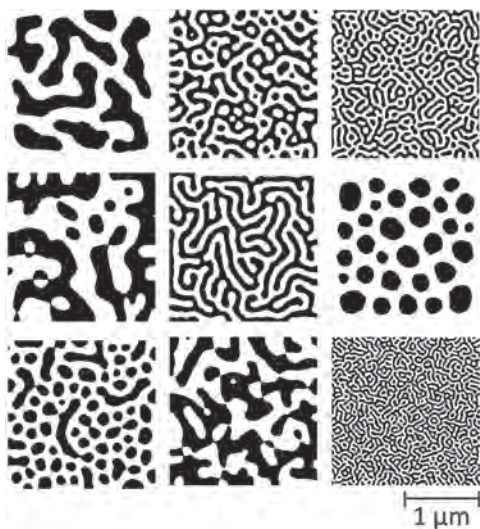
HC-04. Estimation of Magnetic Parameters From Domain Images With Convolutional Neural Networks in Chiral Multilayers.

J. Kong¹, Y. Ren², X. Chen³, N. Tey^{4,3}, P. Ho³, C. Ciprian¹, N. Ng¹, K. Khoo¹ and A. Soumyanarayanan^{2,3}

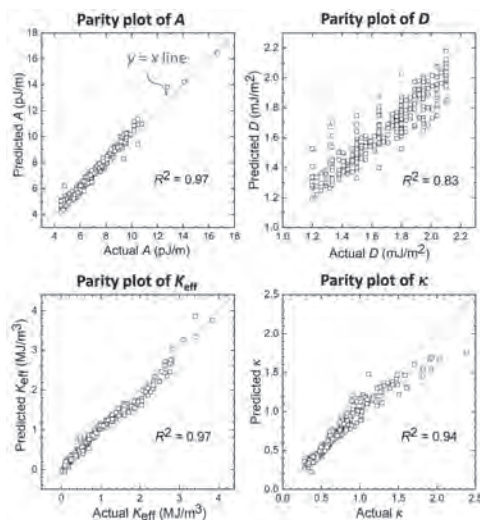
1. Institute of High Performance Computing, Singapore, Singapore;
2. Physics, National University of Singapore, Singapore, Singapore;
3. Institute of Materials Research and Engineering, Singapore, Singapore;
4. Department of Materials, Imperial College London, London, United Kingdom

Magnetic multilayer films are known to host a variety of novel magnetic configurations such as topological magnetic skyrmions with potential nano-electronic applications. However, characterizing these material systems at film and device-level typically involves a combination of several magnetometry, microscopy, and spectroscopy experiments. Some of these techniques can be time-consuming and expensive, or even inaccessible to materials scientists. Therefore, to rapidly characterize these material systems, it is crucial to maximize the information extracted from results of experiments that are more accessible, such as domain images obtained from magnetic force microscopy (MFM). We show that deep convolutional neural networks are able to extract magnetic parameters, in particular the exchange interaction (A), Dzyaloshinskii-Moriya interaction (D), effective anisotropy (K_{eff}), and the thermodynamic stability (κ), from images of domain configurations. Experimentally realistic training and validation input images, as shown in Fig. 1, were generated through micromagnetic simulations with MuMax3 [1]. The magnetic parameters and structures used in the simulations are based on Ir/Fe/Co/Pt multilayers with tunable magnetic properties [2, 3]. The neural network architecture, implemented with the Keras package [3], consists of multiple convolutional layers followed by a fully connected network with 4 outputs corresponding to the magnetic parameters of interest. The trained models were consistently able to reach R^2 values greater than 0.9 on validation data, as shown in Fig. 2. By inspecting the intermediate feature maps of the neural network, we find that the network is able to learn features such as domain boundaries. Notably, testing the models on experimentally obtained MFM images yield magnetic parameters that were consistent with our knowledge of the material systems. Our work thus demonstrates the utility of developing machine models trained on simulation data as a means to accelerate the characterization of magnetic systems.

[1] A. Vansteenkiste, J. Leliaert, M. Dvornik et al, *AIP Advances* 4, 107133 (2014). [2] A. Soumyanarayanan, M. Raju, A. L. Gonzalez Oyarce et al., *Natural Materials* 16, 898-904 (2017). [3] A. K. C. Tan, J. Lourebam, X. Chen et al., *Phys. Rev. Materials* 4, 114419 (2020). [4] F. Chollet et al., <https://keras.io> (2015)



Representative micromagnetic images used as input for the training and validation of neural networks.



Parity plots showing the predicted micromagnetic magnetic parameters (exchange stiffness A , Dzyaloshinskii-Moriya interaction D , effective anisotropy K_{eff} , and thermodynamic stability κ) vs the actual parameters on the validation data.

INVITED PAPER

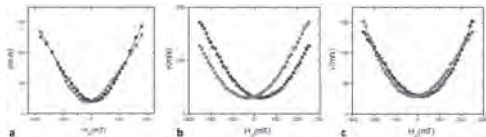
HC-05. Effect of Chiral Damping on the Dynamics of Chiral Domain Walls and Skyrmions INVITED.

C. Safeer^{1,2}, M. Nsibi¹, J. Nath¹, H. Yang¹, I. Joumard¹, S. Auffret¹, G. Gaudin¹ and I. Miron¹

1. SPINtronique et Technologie des Composants, Grenoble, France; 2. CIC nanoGUNE, San Sebastian, Spain

While for many years magnetic domain walls (DWs) were considered to be Bloch type in ultra-thin magnetic layers with perpendicular anisotropy and particularly in stacks lacking inversion symmetry, the observation of the Dzyaloshinskii Morya interaction (DMI) in these stacks combined with the use of advanced imaging techniques have shown that these DWs were in fact of the Neel type and that they also had a precise chirality. These discoveries have led to significant advances in understanding the mechanisms governing the current induced motion of these DWs and to the reinterpretation of many past experimental results. These discoveries and reinterpretation have also allowed the demonstration of skyrmionic bubbles (Sk) and the development of their current induced dynamics. By analogy with DMI, which is a chirality dependent energy, we have demonstrated the existence of a chirality dependent dissipation: the chiral damping (α_c)^{1,2}. As their chirality is altered, the induced variations of the damping parameter modify the DWs and Sk dynamics. Nevertheless, as this phenomenon shares with DMI the same origins, spin-orbit interaction and symmetry breaking, and as their effects and consequences are often confused, the influence of chiral damping on the dynamics of Sk and chiral DW has remained elusive so far, even though the understanding of this influence is crucial both for the understanding of chiral phenomena in the field of magnetism but also with the aim of developing innovative memory, logic or neuromorphic devices based on these chiral magnetic objects. In this study, we clearly separate the effects of DMI and α_c in Sk and DW dynamics and, by focusing on the flow regime, which is both simpler to unambiguously interpret the experimental results and more relevant for the application objectives, we show that the effects of chiral dissipation are ubiquitous: they occur in all possible types of DW and SK motion: *i*) field-driven DW motion, *ii*) current induced DW motion, *iii*) current induced dynamics of skyrmionic bubbles. For each of these experiments, the observed asymmetries cannot be explained by considering either only DMI or only α_c . A simple numerical modelling including these two mechanisms and using a single set of parameters makes it possible to reproduce the relevant features of these experimental results (Figure). Finally, these numerical simulations allow us to show the importance of α_c for the stability and dynamics of skyrmionic bubbles in the regime of high spin-orbit torques and strong DMI sought for the applications: when they are distorted under the action of an electric current, α_c can increase or decrease these distortions. These results show the importance of the chiral damping in the dynamics and stability of DW and Sk and the need to understand and control it in the objectives of applications using these chiral magnetic objects.

1. Jué, E. *et al.*, Nat. Materials, 15, 272–277 (2016). 2. Akosa, C. A., Miron, I. M., Gaudin, G. & Manchon, A. Phys. Rev. B, 93, 1–5 (2016).



a. Measured DW velocity vs. H_{ip} (red for down/up DW, blue for up/down DW) at constant $H_z = -82$ mT. **b.** When only DMI is considered, numerical simulations cannot reproduce the crossing of curves: the up-down DW velocity is always higher than that of down-up DW for positive in-plane fields. **c.** When DMI and α_c are taken into account, experimental results are well reproduced by numerical simulations.

CONTRIBUTED PAPERS

HC-06. Tailoring Interfacial Effect in Thin Films With DMI by He Irradiation.

A. Sud¹, D. Sagkovits^{1,2}, C. Barton², M. Sall³, L. Herrera Diez⁴, D. Ravelosona^{3,4}, S. Zhang⁵, X. Zhang⁵, G. Carlotti⁶, S. Tacchi⁷, H. Kurebayashi¹, O. Kazakova² and M. Cubukcu^{1,2}

1. London Centre for Nanotechnology, University College London, London, United Kingdom; 2. National Physical Laboratory, Teddington, United Kingdom; 3. Spin-Ion Technologies, Palaiseau, France; 4. Centre de Nanosciences et de Nanotechnologies, Orsay, France; 5. King Abdullah University of Science and Technology Physical Sciences and Engineering Division, Thuwal, Saudi Arabia; 6. Università degli Studi di Perugia Dipartimento di Fisica e Geologia, Perugia, Italy; 7. Dipartimento di Fisica e Geologia-Univ. Perugia, CNR, Istituto Officina dei Materiali-Perugia, Perugia, Italy

Recently, an ever-growing interest of the community of solid-state physics has been captured by the promising potentials of the magnetic skyrmions [1]. The skyrmion chiral property is generally driven by an additional anti-symmetric term in the exchange energy, namely the Dzyaloshinskii-Moriya interaction (DMI), induced by the lack of structural inversion symmetry and the spin-orbit coupling. As they have a high stability, small size and they can be moved by very small currents densities, skyrmions are considered as the ultimate magnetic storage bit for a new generation of devices of ultra-dense information storage and low power consuming spintronic logic and neuromorphic computing devices [2]. One of the major advantages of using interfacial DMI in thin films is that several materials parameters, that define not only the existence of skyrmions but also their dimensions, can be experimentally tuned, such as the magnetic anisotropy, or the DMI strength, which can be efficiently tailored. Here, we show a novel method to control interfacial effect in thin films with DMI using He irradiation. We compare SQUID, Ferromagnetic resonance (FMR), Magnetic force microscopy (MFM) as well as Brillouin light scattering (BLS) results on Ta(4.7 nm)/Pt(4nm)/Co(1.4nm)/Ta(1.9nm)₂₀ stacks as a function of He irradiation dose to study the behaviour of the magnetic properties and interfacial effect of the stacks, such as magnetic anisotropy, intrinsic damping, effective magnetization, exchange stiffness as well as DMI. Our results show clear evidence of *i*) tailoring interface *ii*) different magnetic properties in thin film with different irradiation dose. These results can open novel way to manipulate skyrmions, as well as control of interface of spin-orbit torque devices and spin injection into a thin film, for example using spin pumping. Figure 1 (a) shows typical magnetization measurements while sweeping the external magnetic field in the direction perpendicular (out-of-plane) and parallel (in-plane) to the substrate at room temperature. Figure 1 (b) shows anisotropy energy density K and anisotropy field H_k with different Helium irradiation dose IR . As IR is increased further, a significant IR dependent diminishment of K and H_k occurs that is explained by the tailoring interface of the samples via IR . Figure 2 (a) show typical two-dimensional color plots of microwave absorption as a function of microwave frequency f and perpendicular magnetic field B . We determined the effective magnetization M_{eff} from out-of-plane fits of the resonance H_{res} as different frequency using frait equation [3]. We show that M_{eff} decrease with increasing IR (Fig. 2 (c)). The linear dependence of FMR linewidth ΔH on frequency f (Fig. 2(b)) allows the computation of the Gilbert-type damping constant α [4]. We see the clear enhancement of α with IR (Fig. 2(d)), suggesting of high rates of spin injection in the non-magnetic layers by spin pumping. Funding from the EMPIR project TOPS "Metrology for topological spin structures" (#17FUN08) is acknowledged.

[1] A. Fert *et al.* Nat. Nanotech. 8, 152 (2013) [2] J. Grollier *et al.* Nat. Electronics, 3, 360–370(2020) [3] S Klingler *et al.* J. Phys. D: Appl. Phys. 48 015001 (2015) [4] J.-C. Rojas-Sanchez, M. Cubukcu *et al.* Phys. Rev. B. 88, 064403 (2013)

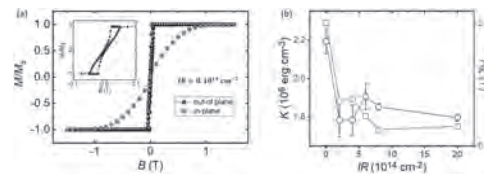


Figure 1. SQUID measurements. (a) Normalized magnetization M/M_s versus applied magnetic field B plots for out-of-plane and in-plane configurations for sample with He irradiation dose $IR=8.10^{14} \text{ cm}^{-2}$. (b) Anisotropy energy density K and anisotropy field H_k plots as a function of He irradiation dose IR .

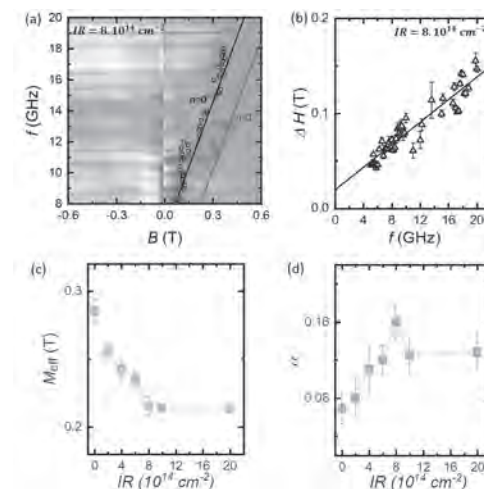


Figure 2. FMR measurements. (a) Two-dimensional colour plots of microwave absorption as a function of microwave frequency f and magnetic field B for the out-of-plane configuration for sample with $IR=8.10^{14} \text{ cm}^{-2}$. We can clearly identify two modes; $n=0$ FMR uniform mode and $n=1$ spin wave mode. The solid line is fit to deduce the M_{eff} . (b) FMR linewidth ΔH as a function of frequency f for the out-of-plane configuration for sample with $IR=8.10^{14} \text{ cm}^{-2}$. The solid line is fit to deduce the Gilbert damping constant α . M_{eff} (c) and damping α (d) as a function of IR .

HC-07. Spin Dynamics of Skyrmion Lattices in a Chiral Magnet Resolved by Micro-Focus Brillouin Light Scattering.

P. Che¹, T. Schönenberger², A. Magrez³, H. Berger³, H.M. Ronnow² and D. Grundler^{1,4}

1. *Laboratory of Nanoscale Magnetic Materials and Magnonics, Institute of Materials, Ecole Polytechnique Federale de Lausanne, Lausanne, Switzerland;* 2. *Laboratory for Quantum Magnetism, Institute of Physics, Ecole Polytechnique Federale de Lausanne, Lausanne, Switzerland;* 3. *Crystal Growth Facility, Institute of Physique, Ecole Polytechnique Federale de Lausanne, Lausanne, Switzerland;* 4. *Institute of Microengineering, Ecole Polytechnique Federale de Lausanne, Lausanne, Switzerland*

Chiral magnets hosting non-collinear spin textures such as skyrmion lattices (SkL) [1] provide novel functionality in magnonics because of the formation of bandgaps in the magnon band structure and asymmetric magnon dispersion relations [2]. Multiple SkL phases were observed in the bulk chiral magnet Cu_2OSeO_3 , e.g. high temperature SkL near T_C , low temperature SkLs when the magnetic field was applied along an easy axis and metastable SkL when Cu_2OSeO_3 was quenched by fast cooling down [3-5]. Their dynamic modes are hard to be discriminated in large bulk samples because they coexist with conical and helical phases. Conventionally detected spin excitations (magnons) show complex spectra with a multitude of resonances due to multiple domains of different phases and boundary conditions. It is challenging to understand the one-to-one correspondence between an individual SkL phase and its magnon spectra. Here we report the local spectroscopy of magnons by scanning Brillouin light scattering (BLS) microscopy on Cu_2OSeO_3 in SkL phases. Thanks to the high sensitivity of BLS, we resolved the dynamic behavior of all reported SkL phases. Clockwise, counterclockwise and breathing modes of hexagonal SkL were detected by BLS proving simultaneous thermal excitation of all three modes which exhibit different polarization characteristics. Using the magnon modes, we were able to locate SkL phases and investigate the stabilization mechanism of non-collinear multi-domains. Our observations of locally excited thermal magnons in Cu_2OSeO_3 deepen the understanding of the SkL dynamics in chiral magnet. They pave the way for further design of magnonic devices based on chiral magnets. We acknowledge the financial support from Swiss National Science Foundation (SNSF) via Sinergia Network NanoSkyrmionics CRSII5 171003.

[1] S. Mühlbauer, B. Binz and F. Jonietz, etc. *Science*, 323, 915 (2009). [2] M. Garst, J. Waizner and D. Grundler, *J. Phys. D: Appl. Phys.*, 50, 293002 (2017). [3] A. Chacon, L. Heinen, M. Halder, etc. *Nat. Phys.* 14, 936-941 (2018). [4] F. Qian, L.J. Bannenberg, H. Wilhelm, etc. *Sci. Adv.* 4, eaat7323 (2018). [5] R. Takagi, Y. Yamasaki, T. Yokouchi, etc. *Nat. Commun.*, 11, 5685 (2020).

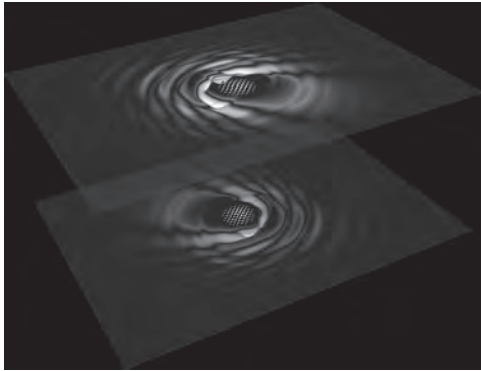
HC-08. Spin Wave Radiation by a Topological Charge Dipole.

S.A. Diaz¹, T. Hirose², D. Loss³ and C. Psaroudaki^{4,5}

1. Johannes Gutenberg Universität Mainz, Mainz, Germany; 2. University of Tokyo, Tokyo, Japan; 3. Universität Basel, Basel, Switzerland; 4. California Institute of Technology, Pasadena, CA, United States; 5. Universität zu Köln, Köln, Germany

The use of spin waves (SWs) as data carriers in spintronic and magnonic logic devices offers operation at low power consumption, free of Joule heating. Nevertheless, the controlled emission and propagation of SWs in magnetic materials remains a significant challenge. Here, we propose that skyrmion–antiskyrmion bilayers form topological charge dipoles and act as efficient sub-100 nm SW emitters when excited by in-plane ac magnetic fields. The propagating SWs have a preferred radiation direction, with clear dipole signatures in their radiation pattern, suggesting that the bilayer forms a SW antenna. Bilayers with the same topological charge radiate SWs with spiral and antispiral spatial profiles, enlarging the class of SW patterns. We demonstrate that the characteristics of the emitted SWs are linked to the topology of the source, allowing for full control of the SW features, including their amplitude, preferred direction of propagation, and wavelength.

[1] S. A. Diaz, T. Hirose, D. Loss, and C. Psaroudaki, *Nano Letters* 20, 6556 (2020).



Skyrmion-antiskyrmion bilayers form topological charge dipoles and act as efficient sub-100 nm spin wave emitters when excited by in-plane ac magnetic fields.

HC-09. Ferromagnetic Resonance of Skyrmions in Thin Film Multilayers.

T. Srivastava^{1,2}, Y. Sassi¹, I. Ngouagna Yemeli², F. Ajejas¹, A. Vecchiola¹, K. Bouzehouane¹, N. Reyren¹, V. Cros¹, J. Kim³, T. Devolder³ and G. de Loubens²

1. *Unite Mixte de Physique CNRS/Thales, Palaiseau, France*; 2. *Service de Physique de l'Etat Condense, Gif Sur Yvette, France*; 3. *Centre de Nanosciences et de Nanotechnologies, Orsay, France*

Magnetic skyrmions are chiral whirling textures of magnetization with a non-trivial topology. Their nanometric size and particle-like behavior has engendered huge interest for their potential applications in memory and logic devices. The observation of magnetic skyrmions at room temperature has triggered extensive research to decipher their various static and dynamic properties which is crucial for their eventual implementation in spintronic devices [1]. In the case of ultra-thin multilayer films consisting of heavy metal (HM)/ferromagnet (FM)/insulator (I), skyrmions are primarily stabilized by interfacial Dzyaloshinskii-Moriya interaction (iDMI) in combination with perpendicular anisotropy, dipolar, exchange and Zeeman energies, where each of these contributions can be finely tuned [2]. The non-trivial skyrmion topology and its emergent electro-dynamics is at the heart of phenomena like the skyrmion Hall effect and the topological Hall effect. Another interesting consequence of the skyrmions topology is reflected in their unique spectral signatures given by the gyrotropic rotational modes [3] (clockwise and counter-clockwise) and the breathing mode [4], when excited by an in-plane or an out-of-plane rf magnetic field. These unique dynamics open up new prospects for skyrmion-based microwave detectors [5] and nano-oscillators [6]. However, the experimental observation of skyrmion resonance dynamics remains limited. So far, skyrmion eigen modes have been mainly observed at low temperature in bulk systems [7]. Only few studies have been carried out in thin films, but with zero iDMI [8]. The experimental observation of the excitation modes of homochiral skyrmions stabilized by iDMI at room temperature remains elusive and challenging owing to usually elevated damping parameter and material inhomogeneities in HM/FM/I systems. Here, we study the magnetization dynamics in a [Pt/CoFeB/AIOx] \times 20 multilayer deposited by sputtering. First, the system is optimized by tuning the Pt and CoFeB thicknesses to host magnetic skyrmions at room temperature, along with a minimized damping parameter $\alpha \sim 0.02$, measured by ferromagnetic resonance (FMR). The quasi-static magnetic domain configuration is observed by magnetic force microscopy (MFM) where on sweeping an out-of-plane (OP) magnetic field from saturation to zero, random skyrmion nucleation occurs, forming a lattice structure which then breaks into a mixture of skyrmions and stripes at lower fields; finally transforming into labyrinthine domains as shown in Fig. 1. The dynamic response of the system is measured by Vector Network Analyser (VNA) FMR with an rf field applied in-plane and varied over a frequency (f) range of 0.1-20 GHz, and an OP dc magnetic field swept from -0.55 T to +0.55 T. The frequency-field dispersions indicated in Fig. 2 (a) show several resonant modes corresponding to the domain configurations observed by MFM at the respective applied fields. At fields above the saturation, the well-known Kittel mode is observed, pertaining to uniform precession. Below saturation, distinct modes arise in the resonance spectrum with both positive and negative dispersions at low ($f < 2$ GHz), medium ($2 < f < 7$ GHz) and high frequencies ($f > 7$). The low frequency mode is observed on increasing the field towards saturation as can be seen on comparing Fig. 2 (a) and (b). Micromagnetic simulations further give an insight into the mechanisms involved in the subsequent dynamic behavior of the skyrmions. We observe that the low frequency mode (LFM) is due to the excitations localized at the skyrmion edges, corresponding to the breathing dynamics. The medium frequency mode (MM), on the other hand, arises due to the localized excitations in the inter-skyrmion region, *i.e.* the non-reversed magnetic zone, and has a negative dispersion. The origin of the high frequency mode (HFM) lies in the excitations across the skyrmion lattice and corresponds to the spin waves travelling across both the reversed and non-reversed regions. These latter modes (MM and HFM) are hence attributed to the magnonic crystal modes of the skyrmion lattice. This observation opens up new possibilities of creating and designing dynamically modulable skyrmion-based magnonic crystals at room temperature.

[1] A. Fert *et al.*, Nat. Rev. Mater. 2, 17031 (2017) [2] W. Legrand *et al.*, Sci Adv 4, 7, (2018) [3] M. Garst *et al.* J. Phys. D: Appl. Phys. 50, 293002 (2017) [4] J.-V. Kim, *et al.*, Phys. Rev. B 90, 064410 (2014) [5] G. Finocchio *et al.*, Appl. Phys. Lett. 107, 262401 (2015) [6] F. Garcia-Sanchez *et al.*, New J. Phys. 18, 075011 (2016) [7] Onose *et al.* Phys. Rev. Lett. 109, 037603 (2012) [8] S. A. Montoya *et al.* Phys. Rev. B 95, 224405 (2017)

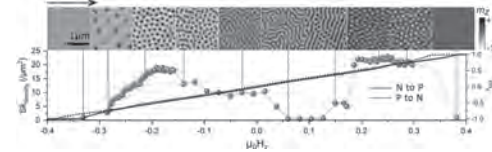


Fig. 1. Magnetic domain configurations: randomly distributed skyrmions, skyrmion lattice, skyrmion-stripe mix, and labyrinthine domains, measured by MFM under the application of OP magnetic field swept from negative to positive values. The OP hysteresis curve in blue is plotted below. The solid blue curve corresponds to the OP field sweep from negative to positive (NtoP) values and the dashed curve from positive to negative (PtoN). The corresponding skyrmion density (red spheres) determined from the MFM images is also plotted. A dense skyrmion lattice is seen to be stable between 0.18T and 0.32T. The dashed grey line indicates the possible extrapolation of the observed skyrmion density at higher field values in accordance with the OP hysteresis curve (NtoP).

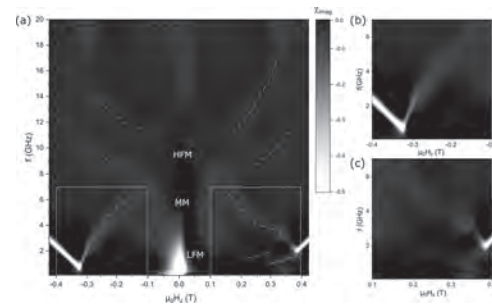


Fig. 2. (a) Frequency-field dispersion map (with dashed curves at HFM as a guide to the eye) measured by VNA-FMR by scanning over a frequency range of 0.1 GHz to 20 GHz with an applied OP field swept from -0.55 T to +0.55 T. (b) and (c) Zoom of the areas indicated by white squares in (a).

HC-10. Skyrmion Diffusion in a Confined System.

S. Chengkun^{1,2}, N. Kerber^{2,3}, J. Rothl², Y. Ge², K. Raab², B. Seng^{2,4}, M. Brems², F. Dittrich², R. Gruber², J. Zázvorka², F. Kammerbauer², T. Dohi², J. Wang¹, Q. Liu¹, P. Virnau^{2,3} and M. Klau^{2,3}

1. Key Laboratory for Magnetism and Magnetic Materials of the Ministry of Education, Lanzhou University, Lanzhou, China; 2. Institute of Physics, Johannes Gutenberg Universität Mainz, Mainz, Germany; 3. Johannes Gutenberg University Mainz Graduate School of Excellence Materials Science in Mainz, Mainz, Germany; 4. Institut Jean Lamour, UMR CNRS 7198, Université de Lorraine, Nancy, France

Magnetic skyrmions are magnetic quasi-particles with a number of interesting properties for possible future applications in, memory storage devices, or non-conventional computing [1-7]. We have shown that in low energetic landscapes of thin film magnetic multilayers, skyrmions show Brownian-like diffusion [7], which can be influenced by magnetic fields, temperature, and the magnetic properties of the pinning site [8,9]. While the diffusive dynamics have experimentally been studied in the continuous film [7,8,10], the device application requires a fabrication process in general, which means that skyrmions move rather in confined geometry. Here we show that the diffusive dynamics of skyrmions can be significantly modified for the geometry of the confined system and the skyrmion density. It is experimentally shown that the critical factor to unravel the underlying physics is the commensurability effect which is corroborated with Molecular dynamics simulations, as well as the pinning effect. The combination of experiment and analysis enables us to reveal the intriguing behavior that pinning sites for magnetic skyrmion depends on the magnetic field strength of the order of μT . Our findings could pave the way to control the thermal dynamics of skyrmions and the pinning effect to realize novel skyrmionic device applications. Stable skyrmions are nucleated by applying a magnetic out-of-plane (OOP) field while pulsing once an in-plane field [10]. We study the skyrmion diffusion in confined geometries varying both the symmetry of the geometry as well as the number of skyrmions from a sparse population to a fully lattice-like situation [11]. Basic geometries like triangles and circles are used. By measuring the mean squared displacement (MSD) of the trajectories of the skyrmions in the structures, the diffusion coefficient is calculated. Figure 1 shows the thermal behavior of skyrmions as a function of the skyrmion density in triangular geometry [11]. As can be seen in Fig. 1(a), The number of skyrmions can be precisely controlled by varying the OOP field to allow us to investigate the skyrmion density dependence of the skyrmion diffusion in confined geometries. Figure 1(b) presents the time-averaged configurations over 9600 Kerr images, where some configurations exhibit blur skyrmions which move with arbitrary time scale. It is shown that the diffusion qualitatively depends on the commensurability of the skyrmion number. Also, we find that the states for skyrmion numbers of 1, 3, 6, and 10 commensurate with the geometry and lead to a saturation of the MSDs as a function of time. The MSDs for an incommensurate state exhibit a non-monotonic relation and do not saturate over the experimental timescale. As shown in Fig. 1(c), molecular simulations agree qualitatively with the experimental findings that corroborating the basic dependence of skyrmion numbers on the motion in triangular confinement [11]. The quantitative difference from the simulation could be related to the pinning effect on the magnetic skyrmion. To explore the behavior closely, we investigate the magnetic field dependence of the skyrmion diffusion under a simplified environment. Figure 2 shows the OOP magnetic field dependence of histograms of skyrmion center positions in the circular geometry. For eliminating the commensurability effect, and the symmetry breaking of magnetic potential, we nucleate a single skyrmion in a circular geometry. We can see not only the modification of the depth of the pinning potential but also the pinning site transition with a small magnetic field of the order of μT , where the size of the skyrmion is modified. More intriguingly, the behavior shows hysteresis to a magnetic field, on the other hand, the reproducibility confirmed after applying a large magnetic field of 8 T suggests that the pinning sites themselves are not linked with the magnetic origin of pinned spins. Thus, the possible origin could arise from the topological spin texture itself. In conclusion, we reveal that the skyrmion diffusion is governed by the commensurability in confined geometry, as well as the magnetic field-dependent skyrmion pinning. The results show that for any potential skyrmi-

onic device based on thin magnetic layers the numbers of skyrmions in the structured geometry as well as the geometry itself influence not only the arrangement but also the thermal diffusive motion of the skyrmions. Also, the pinning effect remains significant however, our findings indicate that magnetic skyrmions could be a new useful tool for experimentally exploring the pinning effect, which is a critical factor for any magnetic objects, and the possibility that the pinning sites are able to be tailored even after film deposition and fabrication process.

[1] A. Fert *et al.*, Nat. Nanotechnol.8, 152 (2013). [2] X. Zhang *et al.*, Sci. Rep. 5, 7643 (2015). [3] X. Zhang *et al.*, Sci. Rep. 5, 9400 (2015). [4] F. Garcia-Sanchez *et al.*, New J. Phys. 18, 075011 (2016). [5] S. Zhang *et al.*, New J. Phys. 17, 023061 (2015). [6] D. Prychynenko *et al.*, Phys. Rev. Appl. 9, 014034 (2018). [7] J. Zázvorka *et al.*, Nat. Nanotechnol. 14, 658 (2019). [8] T. Nozaki *et al.*, Appl. Phys. Lett. 114, 012402 (2019). [9] N. Kerber *et al.*, preprint arXiv:2004.07976 (2020). [10] J. Zázvorka *et al.*, Adv. Funct. Mater. 30, 2004037 (2020). [11] C. Song *et al.*, preprint arXiv:2009.03995 (2020).

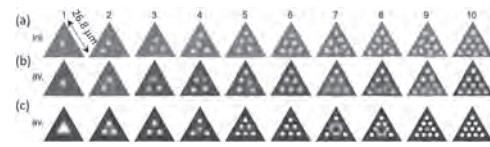


Fig. 1 Thermal behavior of skyrmions as a function of the skyrmion density in triangular geometry. (a) The initial state of the skyrmion configurations. (b) The time-averaged configurations over 9600 Kerr images. (c) Simulations of the histograms of skyrmion center positions for configurations of 1 to 10 skyrmions inside the triangle containing positions from 1 million independent frames.

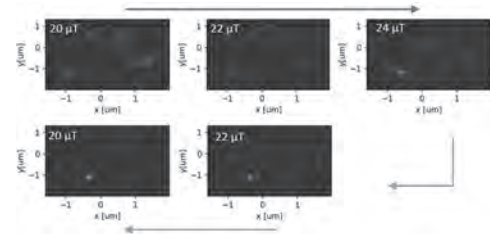


Fig. 2 The OOP magnetic field dependence of histograms of skyrmion center positions at 341.5 K in the circular geometry, where we plot and integrate the position where skyrmion exists at each frame in a 60 minutes video (57600 frames) on a two-dimensional map. A brighter contrast means that the skyrmion dwell time is longer at these points corresponding to an energy minimum.

HC-11. Micromagnetic Study of Thermal Gradient-Driven Skyrmion Motion in Magnetic Multilayers.

E. Raimondo¹, A. Giordano¹, M. Carpentieri³, W. Jiang², R. Tomasello⁴ and G. Finocchio¹

1. Department of Mathematical and Computer Sciences, Physical Sciences and Earth Sciences, Università degli Studi di Messina, Messina, Italy; 2. State Key Laboratory of Low-Dimensional Quantum Physics and Department of Physics, Tsinghua University, Beijing, China; 3. Department of Electrical and Information Engineering, Politecnico di Bari, Bari, Italy; 4. Institute of Applied and Computational Mathematics, Idryma Technologias kai Ereunas, Heraklion, Greece

Magnetic skyrmions are topologically-protected magnetization textures characterized by a non-trivial topology [1]. They have been observed in bulk materials [2] and asymmetric multilayers [3,4] in presence of a finite Dzyaloshinskii-Moriya interaction (DMI). The manipulation (nucleation, shifting, and detection) of skyrmions usually occurs via electrical currents [3], however, thermal effects have been also used to reshuffle skyrmions for low-power unconventional applications [5]. Recently, thermal gradients have been applied to magnetic multilayers where thermally-generated skyrmions unidirectionally diffuse from hot regions to cold regions [6]. This observation has been explained through the combination of repulsive forces between skyrmions, thermal spin-orbit torques, magnonic spin torques as well as entropic forces. Here, inspired by Ref. [6], we study, by means of micromagnetic simulations, the effect of thermal gradients on skyrmion motion from a fundamental point of view. We have previously demonstrated [7] that temperature induces a variation of the magnetic parameters (exchange, interfacial DMI, perpendicular anisotropy constants) which reduce with temperature following atomistically-computed scaling relations. The set of scaled values of those parameters can be used to deterministically simulate the effect of thermal fluctuations instead of a stochastic thermal field [7]. With this in mind, we consider a linear thermal gradient applied along the x-axis (Fig. 1) with the hot and cold regions placed on the left and right side, respectively. We firstly study a 1-repetition ferromagnetic sample with a number of cells $N_{cx}=300$, $N_{cy}=300$, and $N_{cz}=1$ where a Néel skyrmion is initially placed at the center of the sample. We analyze the effect of a linear gradient of only one parameter at time. The skyrmion exhibits two velocity components that follow the generalized Thiele equation [8], where the component parallel to the gradient direction depends on the parameter varied. In particular, the perpendicular anisotropy and exchange gradients move the skyrmion from the cold to the hot region, therefore to the region where those parameters are smaller. On the contrary, the saturation magnetization (magnetostatic field) and the DMI shift the skyrmion from the hot to the cold region, thus towards the region where those parameters are larger. Afterward, we study the effect of the gradients all at once, observing an overall skyrmion motion from the cold to the hot region (Fig. 1). Furthermore, we study the effect of the skyrmion profile on the thermal gradient-driven skyrmion motion. In magnetic multilayers, the skyrmion is characterized by a thickness-dependent profile which gives rise to the so-called *hybrid skyrmion* [4]. Therefore, we study the effect of the thermal gradients on a single hybrid skyrmion as a function of the number of ferromagnetic repetitions. Fig.1 shows a comparison of the skyrmion trajectories, where a dependence on the number of repetitions is observed. Our results can be useful for a deeper understanding of the effect of thermal gradients and therefore for the design of low-power thermally-driven skyrmion applications. This work was supported by the project “ThunderSKY,” funded by the Hellenic Foundation for Research and Innovation (HFRI) and the General Secretariat for Research and Technology (GSRT), under grant agreement No. 871.

[1] G. Finocchio et al., J. Phys. D: Appl. Phys. 49, 423001 (2016). [2] X. Z. Yu et al., Nature 465, 901 (2010). [3] S. Woo et al., Nat. Mater. 15, 501 (2016). [4] W. Li et al., Adv. Mater. 1807683, 1 (2019). [5] J. Zázvorka et al., Nat. Nanotech. 14, 658 (2019). [6] Z. Wang et al., Nat. Electron. 3, 672 (2020). [7] R. Tomasello et al. Phys. Rev. B 97, 060402 (2018). [8] R. Tomasello et al. Phys. Rev. B 98, 024421 (2018).

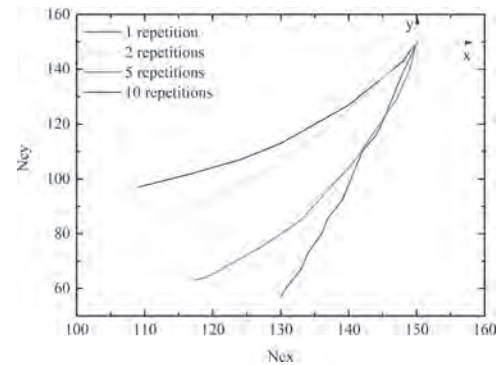


Figure 1: skyrmion trajectory under a thermal gradient (gradients of the parameters all at once) in a magnetic multilayer for different ferromagnetic repetitions, as obtained by micromagnetic simulations. The hot and cold regions are located on the left and right side, respectively.

Session HD

SKYRMIONS: POTENTIAL APPLICATIONS

Sebastian Alejandro Diaz, Chair
Johannes Gutenberg Universitat Mainz, Mainz, Germany

INVITED PAPER

HD-01. Advanced Cognitive Computing Using Adaptive Spintronic Materials INVITED.

P. Jadaun^{1,2}, C. Cui¹ and J.C. Inorvia¹

1. *Electrical and Computer Engineering, The University of Texas at Austin, Austin, TX, United States;* 2. *IMEC, Leuven, Belgium*

The second-generation of Artificial intelligence (AI) has experienced intense growth due to its excellence in big-data applications. However, state-of-the-art AI lacks the advanced cognitive abilities seen in the brain, including the abilities to adapt to the environment, to understand context and to build coherent representations of the outside world. In addition, the implementation of second-generation AI with conventional CMOS uses large amounts of energy and area [1]. Spintronic nanodevices are particularly attractive for neuromorphic implementation of AI due to their small footprint, high endurance and low power consumption [2]. While these devices can implement ultra-low-power AI [3], they have yet to mimic the more rich, adaptive and computationally powerful behavior seen in the brain which forms the basis for advanced cognition. Here, we show the proof-of concept of a self-adaptive artificial neuron that utilizes adaptive spintronic materials that alter their structure and properties in response to external stimuli, in order to realize advanced cognitive abilities such as context-awareness and feature binding. The self-adaptive neuron is constructed from an artificial skyrmion lattice with five skyrmions hosted in a bilayer of thulium iron garnet (TmIG) and platinum (Pt). We report micromagnetic simulation results that show the neuron, when excited by an oscillating magnetic field, produces spin waves originating from skyrmion oscillations with a multi-frequency spectrum. The spectrum consists of four distinct resonant modes, identified as gyration, breathing, and hybridizations of both. Since each resonant frequency can represent one bit of information, the multi-frequent spectrum enables a large basis of information representation. Crucially, we show that both the amplitude and frequency of these resonant modes can be modulated by re-arranging the skyrmions in the lattice. This ability of the lattice to regulate its oscillatory dynamics in response to external input mimics a critical neural property called neuromodulation which plays a key role in advanced cognitive processes, including information transfer, decision-making, memory, object representation, consciousness etc. As a result of neuromodulation, the self-adaptive neuron demonstrates bio-plausible properties such as bursting and cross-frequency coupling [7], as well as advanced cognitive processes, namely context-awareness and feature binding. Context-awareness allows the neuron to make complex, high-level decisions while accounting for multiple factors to develop a deeper understanding of its circumstance. To implement context-awareness, the neuron receives a human spoken command and contextual information about the color of a box. Integrating both inputs, the neuron decides to open the box if and only if the human being gives the command to open and the box is not red in color. In addition, feature binding allows the neuron to correctly combine different segments of information (say, 'red' color and 'circular' shape) and construct a coherent percept ('red circle'). To implement feature binding, a network of neurons receives visual information about two objects and processes information about their color and shape separately. The network then correctly binds together the two features (color and shape) to obtain coherent percepts of the original object. These results realize context-aware AI and the fusion of information from different sensory streams, which can have significant impact on human-machine collaboration, bio-medicine, smart energy, advanced manufacturing, agriculture and education. Adaptive materials can thus help realize neuromorphic circuits with advanced cognitive abilities for third generation AI, one that understands and adapts to a complex and ever-changing environment, learns without supervision from small datasets and better collaborates with human beings.

[1] Cisco, Cisco Global Cloud Index: Forecast and methodology 2016–2021, 1513879861264127, (2018). [2] S. Singh, A. Sarma, N. Jao et al., ACM/IEEE 47th Annual International Symposium on Computer Architecture (ISCA), Valencia, Spain (2020). [3] P. A. Merolla, et al., *Science*, vol. 345, pp. 668-673 (2014). [4] E. Marder, *Advances in Neural Information*

Processing Systems 6 (NIPS) (1993). [5] L. Gao, P.-Y. Chen and S. Yu, *Appl. Phys. Lett.*, vol. 111, p. 103503, (2017). [6] T. Jackson, S. Pagliarini and L. Pileggi, 28 nm CMOS, IEEE International Conference on Rebooting Computing (2018). [7] R. F. Helfrich and R. T. Knight, *Trends in Cognitive Sciences*, vol. 20, p. 916, (2016).

CONTRIBUTED PAPERS

HD-02. Magnetic Skyrmions as Information Entropy Carriers.R. Zivieri¹*1. Istituto Nazionale di Alta Matematica Francesco Severi, Roma, Italy*

Recently, magnetic skyrmions have been employed as information carriers via the digital encoding of bits of information to perform information storage and computing (see e.g. [1]). In this work, it is proposed a simple scheme to use Néel skyrmions hosted in ferromagnetic materials as information entropy carriers. To show that, we start from the definition of entropy noting that the Boltzmann's configurational entropy of magnetic skyrmions [2] has a complete identification with Jaynes's information entropy [3], the continuous limit of Shannon's entropy. The information entropy can be regarded as the average value of the information (or information content) produced by a stochastic source of data measuring the unpredictability of the state. The more the probability is lower, the more the information content is higher and the more the information entropy is higher. In the 1D case Jaynes's continuous information entropy takes the form [4]: $\int_X p(x) \log_2(p(x)/m(x)) dx$ (1) where $p(x)$ is the probability density function referred to the continuous variable x , the function $m(x)$, called the "invariant measure", makes part of the definition of the limit of the density of a set of N discrete points $\{x_i\}$ as $N \rightarrow \infty$ and $X = \{x_1, x_2, x_N\}$ is a random variable. The key message contained in Jaynes's information entropy is the following: a low-probability event carries more information than a high probability event. In other words, if an event is less probable, due to its high degree of unpredictability, is more interesting than a high-probability event. If this concept is applied to the configurational statistical entropy of a skyrmions population, that is defined as $S = -k_B \langle \ln f_0 \rangle$ (k_B is the Boltzmann constant) in terms of the statistical average $\langle \dots \rangle$ of $\ln f_0$ with f_0 the Gaussian probability distribution, the information is contained in $\ln f_0$. As for the case of Jaynes's information entropy, the amount of information carried out by each of the different events is a random variable represented by the skyrmion size at a given T and instant of time whose expectation value is the information entropy determined at each temperature. Let us suppose having a distribution of skyrmion diameters obtained taking pictures of the skyrmions at different instants of time having the same average energy. The event (message) occurring at the instant of time t_1 when the skyrmion area $A_{\text{sky}}^{\text{mp}}$ corresponds to the most probable skyrmion diameter $D_{\text{sky}}^{\text{mp}}$ carries less information than all the events occurring at different instants of time corresponding to skyrmion diameters D_{sky} such that $A_{\text{sky}} \neq A_{\text{sky}}^{\text{mp}}$ with A_{sky} the generic skyrmion area. The more D_{sky} is far away from $D_{\text{sky}}^{\text{mp}}$, the less is its probability and the more the corresponding event carries information. In other words, the more A_{sky} differs from $A_{\text{sky}}^{\text{mp}}$, the more the event is unpredictable and the more it encodes bits of information. It has been found that the effect of temperature is the broadening of the distributions of the skyrmion diameters at every external bias field H_{ext} [2]. Hence, with increasing temperature the interval of diameters belonging to the distribution increases leading to a higher number of events carrying more information and to a higher entropy that encapsulate more information. On the other hand, the effect of H_{ext} is opposite: at fixed temperature there is the narrowing of the distributions of diameters with increasing H_{ext} leading to a lower number of events carrying more information and to a lower entropy encapsulating less information. Hence, via the analogy between Jaynes's entropy and the configurational thermodynamic entropy, the following conclusions can be drawn: (1) room temperature magnetic skyrmions carry more information entropy than the ones at low temperature and (2) at fixed T , in the region of metastability, magnetic skyrmions that are not perturbed by H_{ext} encapsulate more information entropy than the ones subjected to H_{ext} . Owing to the above considerations, a simple entropy data communication system based on the employment of ferromagnetic materials hosting magnetic skyrmions at a given T may be suggested and employed in future spintronic devices. Data communication systems consists of: (1) a data source, (2) a communication channel and (3) a receiver. The receiver should interpret the data that come from the source collecting them. The proposed data communication system is schematically shown in Fig.1. The data source of entropy information can be regarded as a thermal bath at a given T in thermodynamic equilibrium with the ferromagnetic material (e.g.,

cylindrical dot) hosting the magnetic skyrmion. The thermal bath excites the thermal breathing mode that acts as a source of entropy. The communication channel can be thought of the ferromagnetic material itself hosting the magnetic skyrmion able to collect the entropy information bits (message) coming from the magnetic skyrmion. The receiver could be a special device able to identify and collect the bits of entropy. It can be ideally supposed that the amount of entropy is less than the capacity of the communication channel leading to the communication and to the storage of all the data to the receiver. In this way, magnetic skyrmions may be employed as novel temperature and magnetic field dependent information entropy carriers via the transmission of bits of entropy.

[1] J. Müller, New J. Phys., Vol. 19, p. 025002 (2017) [2] R. Zivieri, R. Tomasello, O. Chubykalo-Fesenko et al., Phys. Rev. B, Vol. 99, p. 174440 (2019) [3] E.T. Jaynes, IEEE Trans. Syst. Sci. Cybern., Vol. SSC-4, p. 227 (1968) [4] R. Zivieri, Appl. Sci., Vol. 10, p. 52 (2020)

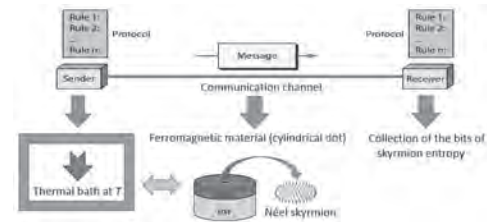


Fig.1. Scheme of the entropy data communication system. FM: ferromagnet, HM: heavy metal.

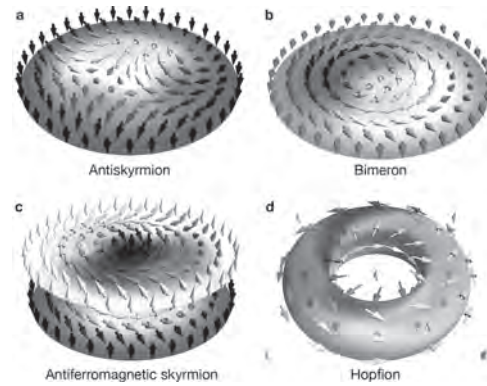
HD-03. Going Beyond Skyrmions: Alternative Magnetic Nano-Objects for Spintronics.

B. Göbel^{1,2}, J. Jena², O. Tretiakov³, S. Parkin² and I. Mertig¹

1. Martin-Luther-Universität Halle-Wittenberg, Halle, Germany; 2. Max-Planck-Institut für Mikrostrukturphysik, Halle, Germany; 3. University of New South Wales, Sydney, NSW, Australia

Magnetic skyrmions have attracted enormous research interest since their discovery a decade ago. Especially the non-trivial real-space topology of these nano-whirls leads to fundamentally interesting and technologically relevant effects – the skyrmion Hall effect of the texture and the topological Hall effect of the electrons. Furthermore, it grants skyrmions in a ferromagnetic surrounding great stability even at small sizes, making skyrmions aspirants to become the carriers of information in the future. Still, the utilization of skyrmions in spintronic devices has not been achieved yet, among other reasons, due to shortcomings in their current-driven motion. In this talk, we present our recent advances in the field of topological spin textures that go beyond skyrmions [1]. The majority of the discussed objects can be considered the combination of multiple skyrmions or the skyrmion analogues in different magnetic surroundings, as well as three-dimensional generalizations. We classify the alternative magnetic quasiparticles – some of them observed experimentally, others theoretical predictions – and present the most relevant and auspicious advantages of this emerging field. A special focus is on magnetic antiskyrmions [2,3,4], bimerons [5], antiferromagnetic skyrmions [6] and hopfions [7]. These objects (shown in Fig. 1) exhibit advantageous emergent electrodynamic effects compared to conventional skyrmions, either due to their lower symmetry or due to a compensated topological charge. As we will show, all four of these objects can be driven parallel to the current, without a skyrmion Hall effect which makes them the ideal bits in data storage devices. Furthermore, we show that the antiferromagnetic skyrmions exhibit a topological version of the spin Hall effect which could help their detection. For bimerons and hopfions we show that the topologically induced Hall response can be distinguished much more easily from the anomalous and conventional Hall effect. This is because their emergent field is perpendicular to the net magnetization and the stabilizing magnetic field; all three quantities are (anti)parallel for skyrmions and most other magnetic nano-objects. Also, we show that some of these objects can even coexist, allowing for an advanced version of the racetrack memory data storage, where a bit sequence could, for example, be encoded by a sequence of skyrmions ('1' bit) and antiskyrmions ('0' bit); cf. Fig. 2. This concept would be more reliable than conventional racetracks: When the information is encoded by the presence or absence of a single type of topological object, the information is susceptible to thermal motion and interactions between the carriers of information. An unintended change in the bit sequence would lead to a loss of the stored information. Only when the information is encoded by at least two distinct carriers, the bit sequence can become irregular without any harm to the stored data.

[1] B. Göbel, I. Mertig, O. Tretiakov. "Beyond skyrmions: Review and perspectives of alternative magnetic quasiparticles". *Physics Reports* in press (2020), arXiv preprint: 2005.01390 [2] J. Jena*, B. Göbel*, S. Parkin. *et al.* "Elliptical Bloch skyrmion chiral twins in an antiskyrmion system". *Nature Communications* 11, 1115 (2020). [3] J. Jena*, B. Göbel*, S. Parkin. *et al.* "Evolution and competition between chiral spin textures in nanostripes with D_{2d} symmetry". *Science Advances* 6, eabc0723 (2020). [4] P. Sivakumar, B. Göbel, S. Parkin. *et al.* "Topological Hall Signatures of Two Chiral Spin Textures Hosted in a Single Tetragonal Inverse Heusler Thin Film". *ACS Nano* 14, 13463 (2020). [5] B. Göbel, I. Mertig, O. Tretiakov. *et al.* "Magnetic bimerons as skyrmion analogues in in-plane magnets". *Phys. Rev. B.* 99, 060407(R) (2019). [6] B. Göbel, A. Mook, J. Henk, I. Mertig. "Antiferromagnetic skyrmion crystals: Generation, topological Hall, and topological spin Hall effect". *Phys. Rev. B.* 96, 060406(R) (2017). [7] B. Göbel, C. Akosa, G. Tatara, I. Mertig. "Topological Hall signatures of magnetic hopfions". *Phys. Rev. Research* 2, 013315 (2020).



Overview of the discussed magnetic nano-objects. (a) Magnetic antiskyrmion, (b) magnetic bimeron, (c) antiferromagnetic skyrmion, (d) magnetic hopfion. The arrows correspond to magnetic moments whose color is determined by their orientation.



In Heusler materials the anisotropic DMI stabilizes antiskyrmions (red) and elliptically deformed skyrmions (blue). These coexisting types of topologically distinct objects may encode data as '0' and '1' bits, respectively.

HD-04. Ion-Irradiated Skyrmion Racetracks for Current Induced Skyrmion Guiding at Room Temperature.

R. Juge^{1,2}, K. Bairagi¹, K. Rana¹, M. Sall², D. Mailly³, V. Pham¹, Q. Zhang¹, N. Sisodia¹, M. Foerster⁴, L. Aballe⁴, M. Belmeguenai⁵, Y. Roussigné⁵, S. Auffret¹, L.D. Buda-Prejbeanu¹, D. Ravelosona², G. Gaudin¹ and O. Boulle¹

1. Université Grenoble Alpes, Saint-Martin-d'Heres, France; 2. Spin-Ion Technologies, Palaiseau, France; 3. Centre de Nanosciences et de Nanotechnologies, Orsay, France; 4. ALBA Synchrotron Light Facility, Barcelona, Spain; 5. CNRS, Laboratoire des Sciences des Procédés et des Matériaux, CNRS, Paris, France

Magnetic skyrmions are localized chiral whirling of magnetization that hold great promise as nanoscale information carrier. Skyrmion racetrack memory and logic devices have recently been proposed where trains of skyrmions in tracks are manipulated by electrical current [1]. These devices require the controlled nucleation and current driven motion of skyrmions in narrow tracks. In particular, the skyrmion Hall effect (i.e. the skyrmion motion towards the track edge), is a critical issue as it can lead to the skyrmion annihilation [2–5]. Here, we report on the controlled nucleation and current induced guiding of magnetic skyrmions along tracks defined by local He⁺ ion irradiation on an ultrathin sputtered magnetic film at room temperature. A He⁺ focused ion beam was used to define 150 nm wide tracks (red areas, Fig.1a) within a sputtered ultrathin Pt/Co/MgO film patterned into 3- μ m-wide tracks [5,6]. Magnetometry and Brillouin Light Scattering measurements show that the He⁺ ion irradiation results in a decrease of the perpendicular magnetic anisotropy as well as the Dzyaloshinskii-Moriya interaction. Under a small perpendicular magnetic field, this leads to the nucleation of skyrmion race-track (Fig.1b), whose size and density can be tuned by the field amplitude. Experiments of current induced skyrmion motion, show that the skyrmions move along the He⁺ ion defined tracks (Fig.2 a-f) for two different angles of the current injection. The track acts as a local potential well that guides the skyrmion trajectory, which allows to suppress the skyrmion Hall effect and also it helps in gaining the velocity along the track line. These results are in line with micromagnetic simulations using experimentally derived magnetic and transport parameters (Fig.2 g-h). A deeper insight into the dynamics of the moving skyrmions using micromagnetic simulations show that the steady-state velocity of the skyrmions can be enhanced by tuning the magnetic damping parameter and the height of the ion-defined potential well. These results open a new path to nucleate and guide skyrmions in race-track memory and logic devices.

[1] A. Fert, V. Cros and J. Sampaio, Nat. Nanotechnol. 8, 152 (2013). [2] J. Sampaio, V. Cros, S. Rohart et al., Nat. Nanotechnol. 8, 839 (2013). [3] W. Jiang, X. Zhang, G. Yu et al., Nat. Phys. 13, 162 (2017). [4] S. Woo, K. Litzius, B. Kruger et al., Nat. Mater. 15, 501 (2016). [5] R. Juge, S-G Je, D-S Chaves et al., Phys. Rev. Appl. 12, 044007 (2019). [6] O. Boulle, J. Vogel, H. Yang et al., Nat. Nanotechnol. 11, 449 (2016).

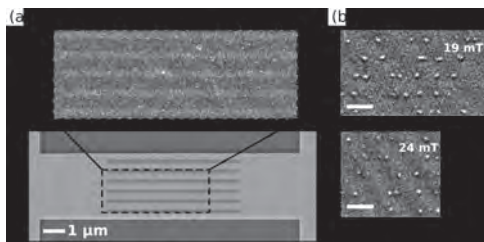


Fig. 1: a) Bottom: SEM image of a 3- μ m-wide Pt/Co/MgO track. The red lines indicate the irradiated patterns (6000 \times 150 nm²). Top: AFM image after irradiation (Dose = 6 ion/nm²). b) MFM images showing the skyrmions along the track for $\mu_0 H = 19$ mT and 24 mT (scale bar is 500 nm for both).

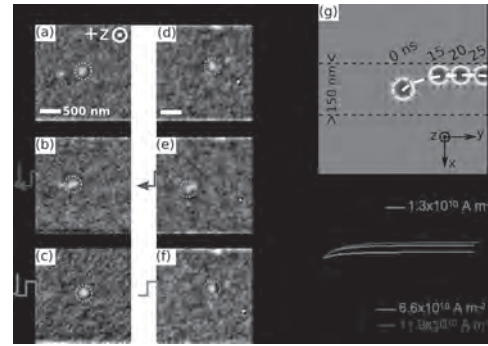


Fig. 2: Sequence of XMCD-PEEM images showing the current-driven motion of skyrmions in He⁺-ion-irradiated tracks (red shaded area) at an angle (a-c) 0° and (d-f) 22.5° with respect to the current direction ($J = 6.6 \times 10^{10}$ A.m⁻², pulse width 11 ns, $\mu_0 H = 10$ mT). (g) Micromagnetic simulations showing the current driven skyrmion motion in a 150-nm-wide irradiated track (region between the dashed line). The current flows along y ($J = 6.6 \times 10^{10}$ A.m⁻²) and applied OOP field $\mu_0 H = 33$ mT. (h) Skyrmion trajectories recorded at different current densities.

HD-05. Positional Stability of Skyrmions via Pinning Sites in a Racetrack Memory.

M. Morshed¹, H. Vakili² and A. Ghosh^{1,2}

1. Department of Electrical and Computer Engineering, University of Virginia, Charlottesville, VA, United States; 2. Department of Physics, University of Virginia, Charlottesville, VA, United States

Magnetic skyrmions are topologically protected chiral spin textures stabilized by the Dzyaloshinskii–Moriya interactions (DMI) in systems lacking inversion symmetry. The attractive features of skyrmions, such as ultra-small size, solitonic nature, and easy mobility with small electrical currents, make them promising as information-carrying bits in low power high-density memory and logic applications [1, 2]. In a skyrmion-based boolean racetrack memory, information can be encoded by the presence (bit “1”) and absence (bit “0”) of skyrmions at a particular position in the track. For an unconventional use of skyrmion racetrack, such as for native temporal memory [1], the information is encoded into the spatial coordinates of the skyrmions, which then can be translated into the timing information needed for race logic operations. The thermal stability of skyrmions is a critical issue for both of these applications, as a randomly displaced skyrmion can alter the sequence of the “0” and “1” bits in a Boolean memory application. Similarly, for race logic applications, the displacement of skyrmions would change the spatial coordinates of the skyrmion and hence the encoded analog timings. For reliable information extraction, it is essential to guarantee the positional stability of skyrmions for a certain amount of time. For example, for a long-term memory application it would require positional stability of years, while for cache memory, hours would be sufficient. In an ideal racetrack, skyrmions are susceptible to thermal fluctuations and exhibit Brownian motion that leads to the diffusive displacement of skyrmions [3]. Moreover, skyrmions show inertia driven drift shortly after a current pulse is removed, rather than stopping immediately. One way to control such undesirable motion is by engineering confinement barriers such as point defects with a different anisotropy, or notches etched into the racetrack (missing materials), which ensure the pinning of skyrmions. If the required unpinning current is too large, it will destabilize the skyrmions, which can cause annihilation of the skyrmions. In addition, high currents have been shown to randomly nucleate unwanted skyrmions as well [4]. This would mean that the energy barrier needs to be optimized in such a way that it can hold the skyrmions for a long enough time and yet requires a modest current to unpin them. Using micromagnetic simulations [5], we present a quantitative analysis of racetrack geometries with different types of notches to calculate the minimum energy barriers associated with them. To calculate the energy barrier, we use the string method to find the minimum energy path (MEP) for the skyrmion to go over the notch [6]. We vary material parameters, specifically, the DMI, anisotropy ratio between the pinning sites and the rest of the magnetic material, and the geometry of the notches, in order to get the optimal barrier height. Furthermore, we investigate the effects of topology in the unpinning process by comparing the unpinning behavior of a ferrimagnetic vs a ferromagnetic skyrmion. We find a range of energy barriers (up to $\sim 45 k_B T$) that can provide a long enough positional lifetime (years) of skyrmions for long-term memory applications while requiring a moderate amount of current ($\sim 10^{10} - 10^{11} A/m^2$) to move the skyrmions. Our results open up possibilities to design practical skyrmion-based racetrack geometries for spintronic applications.

[1]. H. Vakili, M. N. Sakib, and A. W. Ghosh, IEEE J. Explor. Solid-State Comput. Devices Circuits, 1 (2020). [2]. H. Vakili, Y. Xie, and A. W. Ghosh, Phys. Rev. B, 102, 174420 (2020). [3]. L. Zhao, Z. Wang, and W. Jiang, Phys. Rev. Lett., 125, 027206 (2020). [4]. F. Büttner, I. Lemesch, and G. S. D. Beach, Nat. Nanotechnol., 12, 1040-1044 (2017). [5]. A. Vansteenkiste, J. Leliaert, and B. V. Waeyenberge, AIP Adv., 4, 107133 (2014). [6]. W. E. W. Ren, and E. Vanden-Eijnden, J. Chem. Phys., 126, 164103 (2007)

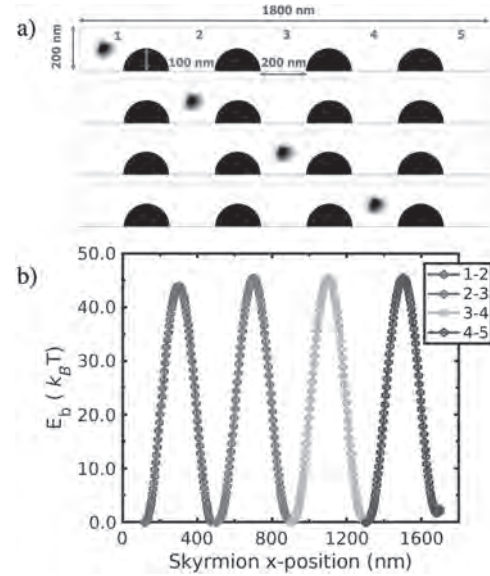


Fig. 1: a) The racetrack geometry with four identical semicircular notches (radius 100 nm) separated by 200 nm from each other. The space between notches would be the places where the skyrmions would be positioned. b) Calculated minimum energy path for skyrmion passing a notch. The used material parameters are $M_s=100$ kA/m, $A_{ex}=12$ pJ/m, $K_u = 50$ kJ/m³, $D=0.80$ mJ/m², 200 nm racetrack width, and 5 nm thickness. A barrier height of $\sim 45 k_B T$ for a skyrmion with a radius ~ 30 nm is found that can give a positional lifetime of \sim years for the skyrmion, which can be driven with a moderate current. The minimum unpinning current is calculated to be a 4 ns current pulse of 1.4×10^{11} A/m². Skyrmions can be localized in the racetrack with lifetime long enough even for long term memory, the racetrack will be digitized.

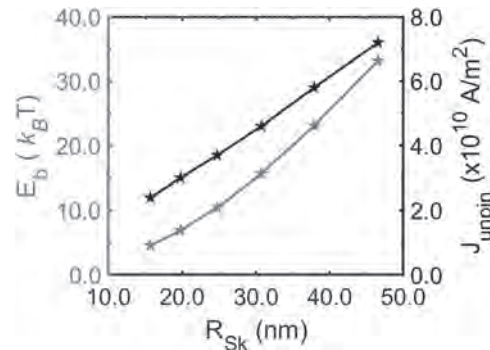


Fig. 2: The energy barrier (red) and the corresponding minimum unpinning current (black) for a racetrack having a semicircular notch (radius 75 nm) as a function of skyrmion size. The used material parameters are $M_s=100$ kA/m, $A_{ex}=12$ pJ/m, $K_u = 50$ kJ/m³, $D=0.65 - 0.90$ mJ/m², 200 nm racetrack width, and 3 nm thickness. It shows low unpinning current with large enough energy barrier. The energy barrier increases faster with radius than the unpinning current which would help to get a large enough barrier and small enough unpinning current.

HD-06. Interplay of Skyrmion Interactions With Current-Driven Dynamics in Multilayer Wire Devices.

M. Sim^{1,2}, A.K. Tan³, D. Thian², H. Tan², N.C. Lim², S. Yap², P. Ho² and A. Soumyanarayanan^{2,1}

1. Department of Physics, National University of Singapore, Singapore;
2. Institute of Materials Research and Engineering (IMRE), Agency for Science Technology and Research, Singapore, Singapore; 3. Data Storage Institute (DSI), Agency for Science Technology and Research, Singapore, Singapore

Magnetic skyrmions are topologically protected two-dimensional spin structures stabilized by interfacial Dzyaloshinskii-Moriya interactions in thin film multilayers [1]. Their stability in nanowire devices coupled with ease of electrical manipulation and detection suggests a range of applications, especially for memory and novel computing architectures. Planar charge currents in multilayer nanowires exert a spin-orbit torque, which can be used to move skyrmions longitudinally, i.e., along the current direction. Meanwhile, skyrmions also experience a Magnus force which results in a transverse deflection known as the Skyrmion Hall effect (SkHE). Notably, the size of a skyrmion is expected to play a key role in determining its velocity, SkHE deflection, and interaction with disorder [2]. These facets have been examined extensively within simulations, and recently in experimental works [2,3]. In this work, we investigate the converse effect – wherein skyrmion dynamics affects their physical properties. To this end, we examine the dynamics of skyrmions in configurations with densities ≈ 10 skyrmions/ μm^2 in Pt/Co/MgO multilayer nanowires with an in situ external magnetic field. A series of unidirectional current pulses ($J \sim 4 - 5 \times 10^{11}$ A/m²) were applied through the nanowire. This was followed by imaging of intermediate skyrmion positions on the nanowires by magnetic force microscopy (MFM) and image analysis to track skyrmion trajectories. While skyrmion motion was initially consistent with the flow regime with size-independent velocity, they were found to gradually aggregate at the nanowire edge due to SkHE. This congregation of skyrmions results in a population difference of about 1/3 along the transverse of the nanowire. Intriguingly, clustering of skyrmions appear to have a steric effect, affecting skyrmion sizes (see Fig. 1). Within the cluster, skyrmions are quantifiably smaller ($> 20\%$) than the skyrmions on the periphery and are also found to move slower than the peripheral skyrmions. Next, we studied the effect of clustering induced local changes of skyrmion properties within the nanowires (Fig. 2). Evident differences in behaviour of larger (periphery) and smaller (clustered) skyrmions were observed. At length scales of approximately 1.5 times the skyrmion size, skyrmions get compressed by up to 30% as they approach other skyrmions – likely due to skyrmion-skyrmion interactions. Conversely, skyrmion sizes were also found to increase as they moved away from the clustered region. Interactions between pinned and moving skyrmions in relation to their spatial positions in the cluster were also studied. Our results suggest that skyrmion interactions may play a key role in influencing their dynamics in dense device configurations. Furthermore, it highlights possibilities for the dynamic engineering of current induced skyrmion behaviour along a nanowire with strategic size manipulation.

1. A. Fert *et al.*, *Nat. Rev. mater.* 2, 17031 (2017). 2. Litzius, K. *et al. Nat. Phys.* 13, (2017). 3. Zeissler, K. *et al. Nat. Commun.* 11, 1–11 (2020).

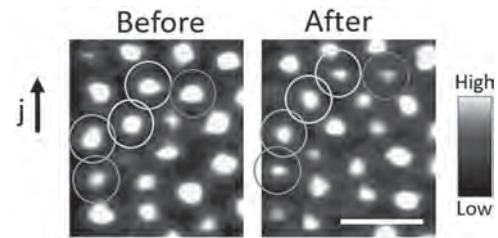


Fig. 1: MFM images of regional skyrmion clustering in the nanowires, depicting skyrmion motion and size changes before (left) and after (right) a current pulse, j , is applied to the wire device. Selected skyrmions are colour coded to depict size changes. Skyrmion size analysis yields size reductions of 12% (red), 31% (green), 10% (blue), 20% (purple), and 28% (orange). The scalebar represents $0.5 \mu\text{m}$.

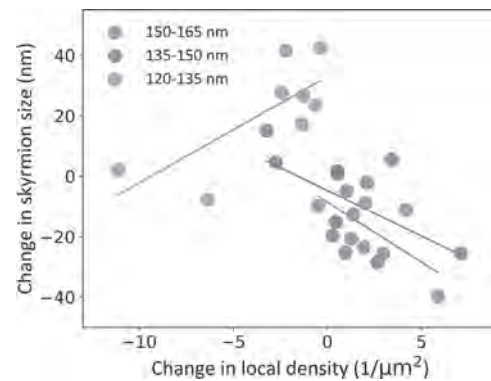


Fig. 2: Change in skyrmion size with local density for skyrmions of varying sizes. Skyrmion sizes decreases at higher densities for larger skyrmions (red, purple) due to skyrmion-skyrmion interactions, while the trend for smaller skyrmions (green) includes the effects of skyrmion-nanowire edge interactions as these skyrmions are adjacent to the edge.

HD-07. Static Structures and Dynamics of Frustrated Topological Spin Textures.

X. Zhang¹, J. Xia^{2,8}, M. Ezawa³, O. Tretiakov⁴, H.T. Diep⁵, Z. Hou⁶, W. Wang⁷, G. Zhao⁸, Y. Zhou² and X. Liu¹

1. Department of Electrical and Computer Engineering, Shinshu University, Nagano, Japan; 2. School of Science and Engineering, The Chinese University of Hong Kong, Shenzhen, Shenzhen, China; 3. Department of Applied Physics, The University of Tokyo, Tokyo, Japan; 4. School of Physics, The University of New South Wales, Sydney, NSW, Australia; 5. Laboratoire de Physique Théorique et Modélisation, Université de Cergy-Pontoise, Cergy-Pontoise, France; 6. South China Academy of Advanced Optoelectronics, South China Normal University, Guangzhou, China; 7. Institute of Physics, Chinese Academy of Sciences, Beijing, China; 8. College of Physics and Electronic Engineering, Sichuan Normal University, Chengdu, China

The magnetic spin textures with non-trivial topology has been an important topic in the fields of magnetism and spintronics for the last few years [1]. For example, the magnetic skyrmion is a promising topological spin texture, which exists in perpendicularly magnetized systems and can be used as a spintronic information carrier. On the other hand, magnetic bimeron is a topological counterpart of skyrmions in in-plane magnets, which can also be used to carry information. In this talk, we will show the static properties of skyrmions and bimerons with different topological structures in a frustrated ferromagnetic monolayer [2], where the topological spin textures are characterized by the vorticity Q_v and helicity η . We will also talk about the dynamics of frustrated skyrmions and bimerons driven by the spin-orbit torques, which depend on the strength of the damping-like and field-like torques. We find that these particle-like topological spin textures with $Q_v = \pm 1$ can be driven into linear or elliptical motion, which depends on the direction of spin polarization. We numerically reveal the damping dependence of the skyrmion/bimeron Hall angle driven by the damping-like torque. Besides, we will show that the isolated bimeron with $Q_v = \pm 1$ can be driven into self-rotation by the damping-like torque at certain conditions. The rotation frequency is proportional to the driving current density. In addition, we will computationally demonstrate the possibility of creating a bimeron state with a higher or lower topological charge by the current-driven collision and merging of bimeron states with different Q_v . Finally, we will give an outlook on other possible topological spin textures in frustrated magnetic systems, such as the skyrmionium and bimeronium. We believe the results presented in this talk could be useful for understanding the topological spin textures physics in frustrated magnetic systems.

[1] Nat. Rev. Phys. 2, 492 (2020); J. Phys. D: Appl. Phys. 53, 363001 (2020); J. Phys.: Condens. Matter 32, 143001 (2020); J. Appl. Phys. 124, 240901 (2018); Nat. Rev. Mats. 2, 17031 (2017); Adv. Mater. 29, 1603227 (2017); Phys. Rep. 704, 1 (2017); J. Phys. D: Appl. Phys. 49, 423001 (2016); Proc. IEEE 104, 2040 (2016); Nat. Rev. Mats. 1, 16044 (2016); J. Phys.: Condens. Matter 27, 503001 (2015); Nat. Nanotech. 8, 899 (2013). [2] Phys. Rev. B 101, 144435 (2020); Appl. Phys. Lett. 117, 012403 (2020); Phys. Rev. Appl. 11, 044046 (2019); Nat. Commun. 8, 1717 (2017).

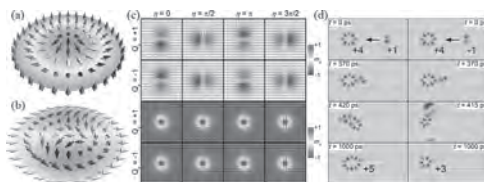


Fig. 1. (a) Illustration of a skyrmion with $Q_v = 1$. (b) Illustration of a bimeron with $Q_v = 1$. (c) Top view of simulated static bimeron solutions with different Q_v and η . (d) Current-induced collision and merging of an isolated bimeron and a cluster-like bimeron state.

HD-08. Spin Orbit Torque Dynamics of Magnetic Skyrmions in GdCo Ferrimagnetic Thin-Films.

L. Berges¹, E. Haltz¹, R. Weil¹, J. Sampaio¹ and A. Mougin¹
 1. Laboratoire de Physique des Solides, Orsay, France

Magnetic skyrmions are a peculiar kind of chiral magnetic textures stabilized by chiral interactions like the Dzyaloshinskii-Moriya interaction (DMI) [1]. Their topological properties offer interesting robustness qualities but, as a counterpart, add a complexity to their dynamics. Since their first observation in a bulk chiral magnet in 2009 [2], rapid experimental advances demonstrated their stability at room temperature without any magnetic field in ferromagnet/heavy metal bilayers and multi-stacks [3]. The experimental demonstrations of smaller and smaller skyrmions at room temperature (down to few 10s of nm) suggest that they are the perfect candidates for information storage and logic devices. Before building such devices, we first need to master skyrmions' static and dynamical properties, namely the nucleation and stabilization of small skyrmions that can move at high speed inside tracks. One significant issue with skyrmion dynamics is the topological deflection. Also known as Skyrmion Hall effect, it is caused by the topological charge of skyrmion and consists in a deflecting force proportional and perpendicular to the skyrmion velocity. Deflection can lead to the expulsion of skyrmions from the tracks that contain them, and thus imposes a limit to the skyrmion velocity. Experiments and calculations found that the deflection angle varies with skyrmion velocity and diameter probably due to its interaction with pinning disorder [4]. It has been suggested that antiferromagnetically-coupled systems, such as antiferromagnets, synthetic antiferromagnets (SAFs) or ferrimagnets, may be used to overcome these issues. The low net magnetization of these systems reduces the size of the skyrmions, and their low angular momentum density should suppress the troublesome topological deflection. Ferrimagnetic Rare-Earth/Transition Metal alloys possess two anti-parallel sublattices whose relative magnetic moments can be changed by temperature or alloy composition. Ferrimagnets share properties from ferromagnets and antiferromagnets (at the magnetic compensation) with which they present many similarities. They are perfect systems to study the advantages of antiferromagnetically-coupled materials, while preserving the effects that have already been used to stabilize and drive skyrmions in ferromagnets. Recent results on SAF showed the promising advantages of using multi-lattices coupled antiferromagnetically [5], and in 2018 a huge breakthrough was achieved in Rare-Earth/Transition Metal ferrimagnets where the smallest skyrmions were observed (10-30nm) [6] as well as a reduced topological deflection [7]. Using co-evaporation in Ultra-High-Vacuum [8], we grew ferrimagnetic thin film of Ta(1nm)/Pt(5nm)/Gd_{0.3}Co_{0.7}(5nm)/Ta(5nm) with an amorphous structure that decreases pinning of skyrmions. By optimizing the material stack and the process conditions, we were able to strengthen the interfacial DMI while keeping a balanced interfacial anisotropy to obtain out of plane magnetized samples (around room temperature) that can host skyrmions. We then observed the skyrmions by Magneto-Kerr Microscopy with sizes smaller than the technique's resolution limit (around 500 nm) (Fig. 1). After saturating the sample, we were able to nucleate skyrmions in the tracks and to tune their overall density by applying magnetic fields. Skyrmions were also nucleated on the edges of the track by nanosecond-long current pulses. Thanks to the tunability of the magnetic properties of the ferrimagnet, we studied the sample in a range of magnetic field and temperature (0–40 mT, and 295–320 K). We observed different regimes: saturated magnetic textures, skyrmions with different densities, and stripes textures. Skyrmions were observed between ~295-310 K. The field necessary for nucleating skyrmions increased with temperature (8 mT at 295 K, 15 mT at 305 K), probably due to a decreasing M_s (as the compensation temperature of this sample is above the tested range). We also observed their dynamics under the application of nanosecond current pulses. The current going through the adjacent Pt layer generates a spin orbit torque (SOT) due to the spin Hall effect, which drives the skyrmions. We observed speeds higher than 150 m/s (for ~10 GA/m²) in a denser skyrmion regime and up to 40 m/s in the most diluted regime (Fig. 2), limited for higher current density by edge nucleations. The speed seems to follow a linear dependence with current. In the conditions of higher density, the velocity was higher and the depinning current lower, probably due to a change of the skyrmion diameter. We also studied the evolution of the deflection angle of the skyr-

mions, which increased from 40° at low current to finally saturate around 60°. This work shows that ferrimagnetic skyrmions can be nucleated, stabilized and propagated by SOT in amorphous rare earth/transition metal thin films. In these results, we stabilized skyrmions far away from the magnetic compensation of the sample (also far away from the angular compensation). We have since prepared new samples with accessible magnetic and angular compensation in order to study the dynamical properties of our sub-micron skyrmions in these very peculiar regimes.

[1] – A. Fert et al., Nature Nanotechnology, Vol 8, p 152–156 (2013) [2] – X. Z. Yu et al. Nature, Vol 465, p 901–904 (2010) [3] – A. Hrabec et al., Nature Com. Vol 8, 15765 (2017) [4] – Joo-Von Kim et al. Appl. Phys. Lett., Vol 110, 132404 (2017) [5] – W. Legrand et al., Nature Materials, Vol 19, p 34–42 (2020) [6] – L. Caretta et al., Nature Nanotechnology, Vol 13, p 1154–1160 (2018) [7] – S. Woo et al. Nature Communications Vol 9, 959 (2018) [8] – E. Haltz et al. Physical Rev. Materials Vol 2, 104410 (2018)

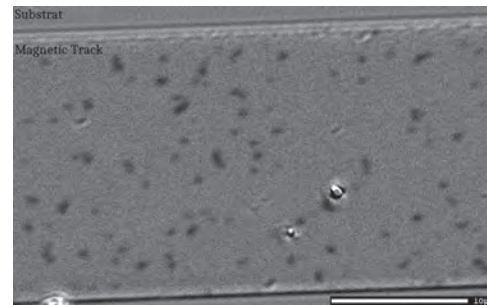


Fig.1 : Magneto-Kerr Microscopy image of skyrmions in GdCo micro-structured sample.

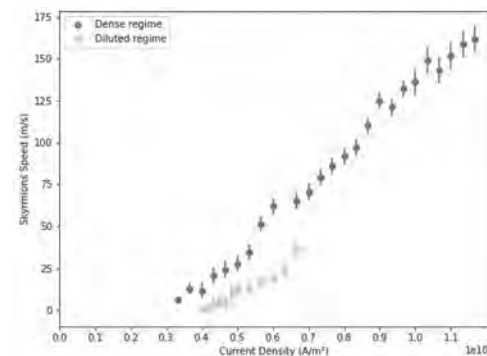


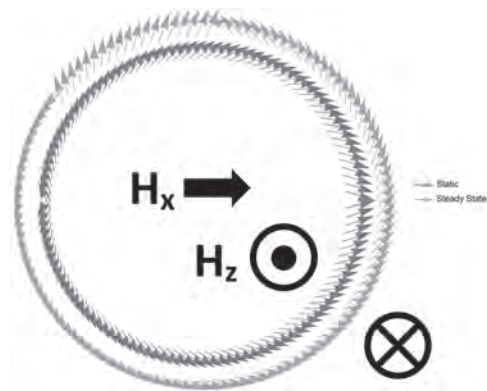
Fig. 2 : SOT-driven velocity at room temperature in diluted and denser regime.

HD-09. Impacts of Steady-State Domain Wall Configuration on Domain Wall Stiffness and Directional Domain Propagation in the Creep Regime.

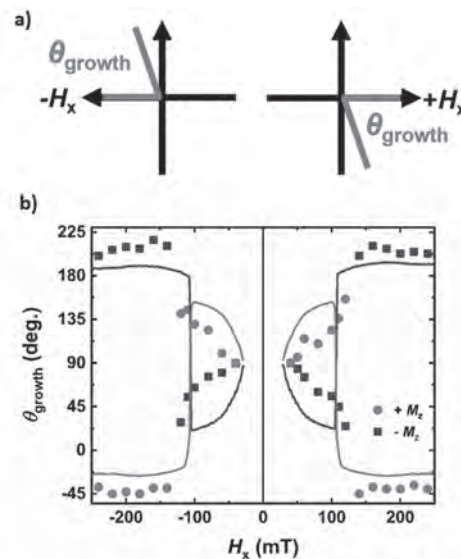
M.D. Kitcher¹, J. Brock², R. Medapalli², E. Fullerton² and V.M. Sokalski¹
 1. *Materials Science & Engineering, Carnegie Mellon University, Pittsburgh, PA, United States*; 2. *Center for Memory and Recording Research, University of California San Diego, La Jolla, CA, United States*

Typically, stabilizing small, robust skyrmions requires a strong Dzyaloshinskii-Moriya Interaction (DMI). Accurately measuring the strength of DMI in prospective skyrmion host materials is therefore crucial to realizing proposed skyrmion-based devices for racetrack memory and neuromorphic computing.[1–2] In the creep regime, the velocity of a domain wall is governed by an Arrhenius law and is inversely proportional to its elastic energy.[3] Early work on the impact of DMI on domain walls showed that the resting energy of a wall is modulated by the DMI’s effective field and that the presence of an in-plane field results in asymmetric domain growth due to the (mis)alignment of the two fields.[4] Subsequent studies have proposed creep models that reflect the intricacies of the relevant velocity and elastic energy scales.[5–6] As such, the sign and strength of the Rashba DMI found in thin film systems has been deduced from the asymmetric creep expansion of domains when an in-plane field is present; wall segments with core magnetizations parallel to the in-plane field have reduced energies, resulting in enhanced velocities—and vice-versa.[5–6] However, Brock et al., recently reported experimental results that deviate remarkably from the above-mentioned creep models. Observations made in [Co(0.7 nm)/Ni(0.5 nm)/Pt(0.7 nm)]_{N>3} films include highly asymmetric dendritic domain growth perpendicular to the in-plane field for low fields and sharp variations of the growth direction with the strength of the in-plane field.[7–8] While one study focused on the apparent preference of Bloch walls of a specific handedness and attributed most of the phenomena to interlayer DMI [8], further investigation of the findings in [7] revealed that the trends that clearly defy the symmetries expected from an intrinsically favored wall chirality with H_z. [7] In this work, we address these peculiarities by considering the impact of the driving field on the domain wall magnetization, dispersive stiffness, and creep velocity. We show that even in the creep regime, the core magnetization of a domain wall, as per the Landau-Lifshitz-Gilbert equation, can be driven to a steady-state equilibrium that deviates significantly from the static case. We find that for material parameters comparable to those reported in [7], a bubble domain in the presence of an in-plane field can exhibit sharp discontinuities in its steady-state wall magnetization profile. Similar to the findings reported in [10], such a point represents a sudden reorientation of the magnetizations along the domain wall due to the nuanced competition between the effective DMI field, the domain wall anisotropy field, the in-plane field, the driving field and Gilbert damping. Consequently, the domain wall energy and stiffness landscapes can be equally complex, highly sensitive to the in-plane field and significantly different from the static case. Incorporating a steady-state treatment of domain wall profiles into the dispersive stiffness framework developed in [5], we compute the steady-state stiffness and creep velocity profiles of an expanding domain for the scenarios reported in [7]. As seen in Figure 2., our modelling of the N=3 film shows remarkable agreement with the observed dendritic growth directionalities as a function of the strength of the in-plane field: first propagating uniformly for very weak fields, then at 90° from the field direction, then gradually reducing to ≈20°, and then abruptly reversing direction to ≈200°. Moreover, the model reproduces the curious observation that that the propagation direction is constant for both driving field directions; switching the domain polarization switches the directions of both the DMI and applied field torques, leaving the Bloch chirality at steady state unchanged. Comparing the magnetization profiles to the propagation directions and stiffness values reveals that segments with the lowest elastic energy (and thus the highest velocity) occur close to reorientation positions in the magnetic profile. The sudden emergence of such points is also responsible for the drastic changes in the growth direction. In light of these insights, we discuss the impact of steady-state profiles on DMI values obtained via bubble expansion experiments. Finally, we consider how our steady-state stiffness model could be used in tandem with these growth experiments to more easily determine the value of Gilbert damping in thin films.

1. R. Tomasello, E. Martinez, R. Zivieri et al., Scientific Reports., Vol. 4, (2014) 2. G. Bourianoff, D. Pinna, M. Sitte and K. Everschor-Sitte, AIP Advances., Vol. 8, p. 055602 (2018) 3. P. J. Metaxas, J. P. Jamet, A. Mougin, Physical Review Letters., Vol. 99, p. 217208 (2007) 4. S. Je, D. Kim, S. Yoo et. al., Physical Review B., Vol. 88, p. 214401 (2013) 5. J.P. Pellegren, D. Lau, and V. Sokalski. Physical Review Letters., Vol. 119, p. 027203 (2017) 6. D. Lau, J. P. Pellegren, H. T. Nembach et al., Physical Review B., Vol. 98, p. 184410 (2018) 7. J. Brock, R. Medapalli and E.E. Fullerton, Bulletin of the American Physical Society. (2020) 8. S.D. Pollard, J. A. Garlow, K. Kim, et al., Physical Review Letters., Vol. 125, p. 227203 (2020) 9. L. Sánchez-Tejerina, O. Alejosa, and E. Martínez, Journal of Magnetism and Magnetic Materials., Vol. 423, p. 405–410 (2017)



Simulated static (blue/dark) and steady-state (yellow/light) equilibrium wall magnetization profiles for an expanding bubble domain similar to those observed in [7].



(a) Conventions used for defining the growth direction of a domain in the presence of an in-plane field. (b) Experimental (markers) and semi-analytically computed (lines) plots of domain growth direction against in-plane field for the [Co(0.7 nm)/Ni(0.5 nm)/Pt(0.7 nm)]₃ sample referenced in [7].

Session HP
SKYRMIONS
(Poster Session)

Soong-Geun Je, Chair
Chonnam National University, Gwangju, The Republic of Korea

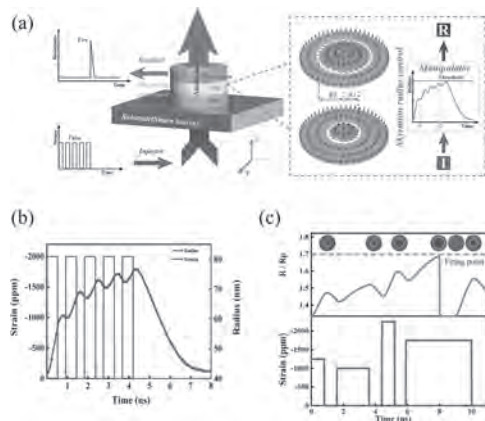
HP-01. Voltage-Controllable Magnetic Skyrmion Dynamics for Spiking Neuron Device Applications.

M. Zhu¹, S. Cui¹, Y. Qiu¹, H. Yang¹, G. Yu¹ and H. Zhou¹

¹. China Jiliang University, Hangzhou, China

The spintronics devices have been considered as promising candidates for future artificial neural networks by mimicking the functionality of biological neurons with nonvolatile control, which can enable effective reduction of energy consumption and heat generation during the information processing and transmission. Among them, voltage-controlled magnetic skyrmions have attracted special attentions because that they will satisfy the demands of well-controlled, high efficient, and energy-saving for future skyrmion-based neuron device applications. In this work, we propose a compact leaky-integrate-fire (LIF) spiking neuron device by deploying the voltage-driven skyrmion dynamics in a multiferroic nanodisk structure. The relationship between the skyrmion dynamics and the characteristics of voltage induced piezostrains have been investigated, where the skyrmion radius can be effectively modulated by the applied piezostrain pulses. Similar to the biological neuron, the proposed skyrmionic neuron will accumulate a membrane potential as skyrmion radius varying by inputting the continuous piezostrain spikes, and the skyrmion radius will return to the initial state in the absence of stimulus. Therefore, this skyrmion radius based membrane potential will reach a definite threshold value by the strain stimuli and then reset by removing the stimuli. The skyrmion size variation can be transformed to resistance detection signal by the magnetoresistance effect, which means that the skyrmionic neuron could fire an output resistance spike with controlling the input strain pulses. Such LIF neuronal functionality and behaviors of the proposed skyrmionic neuron device are elucidated through the comprehensive micromagnetic and theoretical studies. Our results provide a new route for realizing voltage-controllable skyrmionic neuron in future energy-efficient and tunable neuromorphic computing hardware.

1. P. A. Merolla, J. V. Arthur, and D. S. Modha, *Science*, Vol. 345, p. 668 (2014). 2. X. Liang, G. Zhao, and Y. Zhou, *Applied Physics Letters*, Vol. 116, p. 122402 (2020). 3. X. Chen, Y. Zhou, and W. Zhao, *Nanoscale*, Vol. 10, p. 6139 (2018).



(a) Schematic of the proposed spiking neuron and demonstration of the LIF behaviors of the skyrmion-based artificial neuron. (b) Skyrmion radius varying with the spiking strain signals under the homogeneous square wave with the frequency of 1.09 GHz. (c) The creation of LIF functionality based on the Resistance-Strain characteristic by magnetoresistance effect of the skyrmionic neuron device.

HP-02. Evolution and Competition Between Chiral Spin Textures in Nano-Stripes With D_{2d} Symmetry.

J. Jena³, B. Göbel¹, V. Kumar², I. Mertig¹, C. Felser² and S. Parkin³

1. Institute of Physics, Martin Luther University, Halle, Germany; 2. Max Planck Institute for Chemical Physics of Solids, Dresden, Germany; 3. Max Planck Institute of Microstructure Physics, Halle, Germany

Magnetic skyrmions (Sks) and antiskyrmions (aSks) are topologically protected non-trivial spin textures^{1,2}. Those objects can be used as magnetic bits in spintronics devices^{3,4}. However, the presence of the skyrmion Hall effect in the Sk always hinders its movement along the straight path, and the transverse deflection of it will cause a problem on reading data in devices. The unwanted Hall effect can be eliminated in aSk host systems^{2,5} such that it can be moved in a straight path along the current direction⁶. Therefore, it is highly desired to prepare nano-stripes along specific crystallographic directions of the aSk host compound. Here we stabilize a single-chain of aSks in nano-stripes of $Mn_{1.4}Pt_{0.9}Pd_{0.1}Sn$ prepared along different crystallographic directions within the tetragonal basal plane⁷. We observe the enhanced stability of aSks compared to bulk systems without providing in-plane magnetic field components. Additionally, the presence of dipole-dipole interactions with the anisotropic Dzyaloshinskii-Moriya exchange interaction (DMI) in the Heusler compound $Mn_{1.4}Pt_{0.9}Pd_{0.1}Sn$ allows the stability of distinct spin textures called elliptical Bloch skyrmions^{7,8}. The co-existence of elliptical skyrmions (eSks) and aSks is found in nano-stripes at room temperature⁷. The simultaneous existence of different spin textures in a racetrack has great advantages. It is not needed to write the distances between the magnetic bits anymore, unlike the racetrack of only single type magnetic objects. Our results provide a gateway for the remaining steps towards realizing an advanced version of racetrack storage devices based on magnetic aSks and eSks.

1. Mühlbauer et. al., *Science* 323, 915 (2009). 2. Nayak et. al., *Nature* 548, 561 (2017). 3. Parkin et. al., *Science* 320, 190 (2008). 4. Fert et. al., *Nat. Nanotechnol.* 8, 152 (2013). 5. Jena et. al., *Nano Lett.* 20, 59 (2019). 6. Huang et. al., *Phys. Rev. B* 96, 144412 (2017). 7. Jena et. al., *Sci. Adv.* 6, 49, eabc 0723 (2020). 8. Jena et. al., *Nat. Commun.* 11, 1115 (2020).

HP-03. Dynamic Property of Ferromagnetic Skyrmion in an in-Plane Magnetic Field.

J. Guo¹, J. Xia², X. Zhang², P. Pong^{3,1} and Y. Zhou²

1. University of Hong Kong, Hong Kong; 2. The Chinese University of Hong Kong, Shenzhen, Shenzhen, China; 3. New Jersey Institute of Technology, Newark, NJ, United States

1. Introduction As quasiparticle-like swirling topological spin textures in nanostructures¹, magnetic skyrmions are expected to be widely used in future spintronic applications². The creation and transmission of an isolated skyrmion in magnetic films are important for skyrmionic applications, which utilize skyrmions as information carriers³. An exemplary application is the racetrack-type storage memory⁴. Recently, it has been reported that spin-polarized current, spin wave, magnetic field, and temperature gradients, can effectively modulate the dynamics of skyrmions⁵. As the most widely used method, the magnetic field has been used to manipulate magnetic spin textures in studies⁶. Slonczewski and Berger first proposed theoretically spin transfer torque (STT)⁷ can be induced when spin polarized current passes through the magnetic layer/non-magnetic layer. STT is an effect in which the orientation of a magnetic layer in a spin valve can be modified by applying a spin-polarized current. On the other hand, in magnetic multilayered structures, metallic ferromagnets in contact with heavy metals exhibit strong effects due to spin-orbit coupling. Such spin-orbit coupling effects give rise to spin-orbit torque (SOT)⁸ on the ferromagnetic (FM) materials. In this work, we demonstrate that a skyrmion guide on the nanotrack under both in-plane magnetic field and spin-transfer torque or spin-orbit torques driven. In applying both in-plane magnetic field and STT conditions, we focus on spatially sinusoidal-varying Gilbert damping coefficients and non-adiabatic STT coefficients with in-plane magnetic field. For in-plane magnetic field and SOT conditions, we discuss the effect on damping-like torque, field-like torque with in-plane magnetic field. The results provide a guide for designing and developing the skyrmion transporting nanotrack channel in spintronic devices based on the manipulation of skyrmions. 2. Simulation Methods The skyrmion dynamics guide is based on an ultrathin FM nanotrack structure. All simulations are processed by using the Object Oriented Micromagnetic Framework (OOMMF). The time-dependent magnetization dynamics are governed by the LLG equation including STT (adiabatic and non-adiabatic) and SOT (field-like and damping-like). Note that we consider the effect of both in-plane magnetic field and STT or SOT driven. In the first part, the magnetization dynamics is based on the Landau-Lifshitz-Gilbert (LLG) equation augmented with in-plane magnetic field, adiabatic and non-adiabatic STT: $dm/dt = -\gamma m \times H_{\text{eff}} + \alpha(m \times dm/dt) + u(m \times dm/dt \times m) - \beta u(m \times dm/dt)$ where m represents the reduced magnetization, M/MS . γ and α are the gyromagnetic ratios and Gilbert damping constant, respectively. β is the strength of the non-adiabatic STT coefficient and u represents the adiabatic STT coefficient. The Gilbert damping coefficient α and the non-adiabatic STT coefficient β are defined as functions of the longitudinal coordinate x as follows: $\alpha(x) = \alpha_{\text{amp}} \{1 + \sin[2\pi(x/\lambda)\alpha]\}$; $\beta(x) = \beta_{\text{amp}} \{1 + \sin[2\pi(x/\lambda)\beta - \theta]\}$ where α_{amp} is the amplitude of α function and β_{amp} represents the amplitude of β function, respectively. $\lambda\beta$ and θ denote the wavelength and phase of β function. In the second part, the magnetization dynamics is based on the Landau-Lifshitz-Gilbert (LLG) equation augmented with in-plane magnetic field, and spin-orbit torque (SOT): $dm/dt = -\gamma |m| m \times H_{\text{eff}} + \alpha(m \times dm/dt) + \zeta_{\text{DLT}} m \times (m_p \times m) - \zeta_{\text{FLT}} m \times m_p$, where ζ_{SOT} , ζ_{DLT} , and ζ_{FLT} stand for the spin-orbit torque, damping-like torque and field-like torque, respectively. 3. Results and Discussion The effects of varying damping coefficient α and non-adiabatic coefficient β on velocity in both x and y direction, and skyrmion hall angle ϕ are illustrated in Fig. 1, by fixing external magnetic field as 800 mT. We set α_{amp} and β_{amp} from 0.1 to 0.5 in our simulation to obtain the discipline, by fixing β_{amp} and α_{amp} in Fig. 1(a)-(c) and Fig. 1(d)-(f), respectively. The contour lines in Fig. 1(g)-(i) result from the combinations of α_{amp} and β_{amp} . The results show that the damping coefficient α exhibits declining effect on velocity, while non-adiabatic STT coefficient β exhibits increasing influence. The polarization rate is fixed at 0.4 and the value of field-like torque is modified to change the ratio of $K = \zeta_{\text{FLT}}/\zeta_{\text{DLT}}$. Applying both magnetic field and SOT to drive skyrmion simultaneously at magnetic field $H = 800$ mT. The ratio of field-like torque and damping-like torque K and damping-like torque ζ_{DLT} both indicates increasing effect on skyrmion velocity, as shown in Fig.

2(a)-(b). However, damping-like torque ζ_{DLT} provides more contribution on skyrmion motion.

1. X. Zhang, Y. Zhou, K. M. Song, T.-E. Park, J. Xia, M. Ezawa, X. Liu, W. Zhao, G. Zhao and S. Woo, J. Phys. Condens. Matter 32 (14), 143001 (2020).
2. A. Fert, N. Reyren and V. Cros, Nat. Rev. Mater. 2 (7), 1-15 (2017).
3. W. Kang, X. Chen, D. Zhu, S. Li, Y. Huang, Y. Zhang and W. Zhao, presented at the 2018 Design, Automation & Test in Europe Conference & Exhibition (DATE) (unpublished).
4. C. Song, C. Jin, J. Wang, H. Xia, J. Wang and Q. Liu, Appl. Phys. Lett. 111 (19), 192413 (2017).
5. C. Schütte, J. Iwasaki, A. Rosch and N. Nagaosa, Phys. Rev. B 90 (17), 174434 (2014).
6. J. Müller, New J. Phys. 19 (2), 025002 (2017).
7. M. D. Stiles and A. Zangwill, Phys. Rev. B 66 (1), 014407 (2002).
8. Y. Li, K. W. Edmonds, X. Liu, H. Zheng and K. Wang, Adv. Quantum Technol. 2 (1-2), 1800052 (2019).

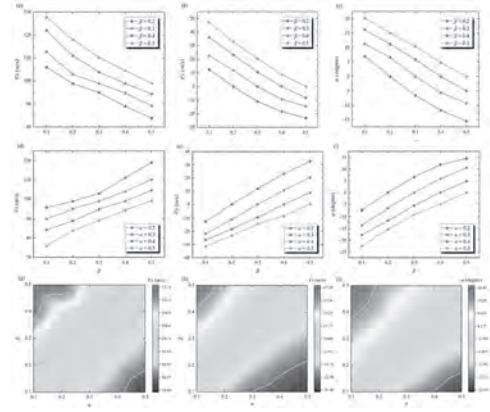


Figure 1. Both magnetic field and STT driven skyrmion are applied to study the effect of damping coefficient α on velocity in both x and y direction, and skyrmion hall angle ϕ : (a) The V_x as a function of α at a fixed $\beta = 0.2-0.5$. (b) The V_y as a function of α at a fixed $\beta = 0.2-0.5$. (c) The ϕ as a function of α at a fixed $\beta = 0.2-0.5$. The effect of non-adiabatic β on velocity in both x and y direction, and skyrmion hall angle ϕ . (d) The V_x as a function of β at a fixed $\alpha = 0.2-0.5$. (e) The V_x as a function of β at a fixed $\alpha = 0.2-0.5$. (f) The V_x as a function of β at a fixed $\alpha = 0.2-0.5$. (g) V_x , (h) V_y , and (i) skyrmion hall angle ϕ at magnetic field $H = 800$ mT.

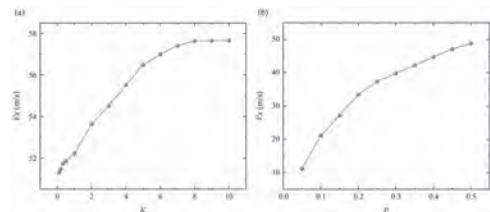


Figure 2. Applying both magnetic field and SOT to drive skyrmion at magnetic field $H = 800$ mT: (a) V_x as the function of the ratio of field-like torque and damping-like torque from 0.1 to 10. (b) V_x as the function of damping-like torque, which indicates the polarization.

HP-04. Static and Dynamic Behaviour of Double Skyrmions in Pt/Co/MgO Trilayer.

F. Nasr¹, C. Fillion¹, O. Boulle¹, C. Baraduc¹, H. Béa¹ and L.D. Buda-Prejbeanu¹

1. SPINtronique et Technologie des Composants, Grenoble, France

Topological non-trivial whirling spin textures such as magnetic skyrmions have recently triggered a lot of interest by virtue of their potential nanosized solitonic nature, stability and tunability. All these attributes, if combined with the efficient current-induced motion via spin orbit (SO) torque, make them attractive to build elementary units of digital information for spintronic logic devices and memories. In ultra-thin ferromagnetic films with Perpendicular Magnetic Anisotropy (PMA) sandwiched between a heavy metal with strong SO and an insulator (i.e. HM/FM/I), the chirality of this spin arrangements is ascribable to an antisymmetric exchange, Interfacial Dzyaloshinskii-Moriya Interaction (iDMI) [1,2]. Among the possible topological magnetic quasi-particles, which can be stabilised in such peculiar trilayer systems, a lower dimension (1D) non-trivial magnetic texture, named Domain Wall Skyrmion (DWSk), has been newly reported and experimentally observed using Lorentz Transmission Electron Microscopy [3]. The DWSk is a 1D topological excitation sharing the same integer topological charge, noted Q , as conventional 2D skyrmions ($Q = 1$). It is describable as a localized 2π rotation of the In-Plane (IP) component of magnetization within a Néel domain wall which stands between two perpendicular magnetic domains. It can be intuitively viewed as the counterpart of a 2π -vertical Bloch lines coming about in Bloch instead of Néel domain walls. Skyrmions with chiral kinks inside the otherwise homochiral domain wall, hereinafter called Double Skyrmion (DSk), have been numerically predicted as a soliton solution [4,5]. In our work, we investigated the stability and the spin-driven dynamics of the DSk in a sample of the type Pt/Co(0.9nm)/MgO [6] using micromagnetic simulations [7]. Interestingly, as shown in Fig.1a, we are able to stabilise simultaneously various spin-textures including skyrmion (Sk, $Q=1$), double skyrmion (DSk, $Q=2$) and domain wall skyrmion (DWSk, $Q=1$). It is found that such magnetization pattern is robust against both thermal fluctuations and normally distributed anisotropy, for different grain-like region sizes. We also proved the resilience of double skyrmion to material parameters variation (DMI, anisotropy) and applied field. The static analysis is complemented with the investigation of the dynamic regime of motion under electrical current. Fig.1b shows the trajectory of the double skyrmion induced by spin-orbit torque. In the limit of moderate injected current the skyrmion and the double skyrmion behave similarly (Fig.1c). However, depending on the geometry of the injected current the double skyrmion can be annihilated or splits in two skyrmions, opening the path to conceive logical devices.

[1] I.E. Dzyaloshinskii Sov. Phys. JETP 5, (1957), J. Phys. Chem Solids, 4, 241 (1958) [2] T. Moriya Phys. Rev Lett., 4, 228, (1960), Phys. Rev. 120, 91, (1960) [3] Li et al., <https://arxiv.org/abs/2004.07888> (2020) [4] Kuchkin et al., Phys. Rev. B 102, 144422 (2020) doi.org/10.1103/PhysRevB.102.144422 [5] S.-G. Je Current Applied Physics 21, 175 (2021) doi.org/10.1016/j.cap.2020.10.021 [6] Juge et al., Phys. Rev. Applied 12, 044007 (2019) doi.org/10.1103/PhysRevApplied.12.044007 [7] Vansteenkiste et al. AIP Adv. 4, 107133 (2014). doi/10.1063/1.4899186

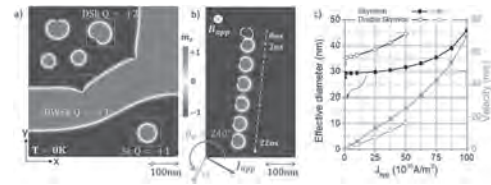


Fig. 1: a) Multidomain equilibrium state of $0.5\mu\text{m} \times 0.5\mu\text{m}$ ideal Pt/Co(0.9nm)/MgO dot at 0K and no applied magnetic field. The color scale is associated to the perpendicular component of magnetization. b) Sequence of micromagnetic simulation snapshots illustrating the current-induced SOT driven DSK dynamics at 0K with $J_{\text{app}} = 50 \times 10^{10} \text{ A/m}^2$. The skyrmion Hall angle of DSk is 64° . c) Comparison of DSk and Sk velocities (orange) and effective diameters (black) as a function of injected current density.

HP-05. Tunable Microwave Properties of a Skyrmion in an Antidot Nanodisk Structure.

A. Joseph¹, C. Murapaka¹, A. Haldar² and B. Paikaray¹

1. Department of Materials Science and Metallurgical Engineering, Indian Institute of Technology Hyderabad, Hyderabad, India; 2. Department of Physics, Indian Institute of Technology Hyderabad, Hyderabad, India

Chiral interactions between magnetic moments in ferromagnetic systems with broken inversion symmetry has attracted lots of attention in the recent years. Dzyaloshinskii-Moriya interaction[1] (DMI) present in these systems leads to an ordering of the spins that forms various exotic spin configurations such as chiral domain walls[2] and skyrmion[3]. DMI is an anti-exchange interaction which prefers to cant the neighbouring spins orthogonal to each other that forms whirling structures such as skyrmions. A magnetic skyrmion is a topological object having particle-spin like configuration, which can be stabilized in ferromagnetic systems with DMI. Recently magnetic skyrmions are proposed as promising candidates for non-volatile memory and logic applications due to their nanoscale size, high stability, high density and small driving currents required for their motion. Besides memory applications, skyrmions also hold great potential in the emerging area of magnonics where collective spin excitations (magnons) are used as a medium of information processing. In addition, observation of skyrmions on low Gilbert damping materials may allow the use of the skyrmions for manipulations of magnon transport. Recently skyrmion generation at an antidot is demonstrated using micromagnetic simulations[4]. In this work, we present the various routes for obtaining giant tunability in microwave properties based on skyrmion dynamic via micromagnetic simulations using Mumax3. We have investigated microwave properties of magnetic skyrmions in a circular nanodisk having antidot at the centre. An in-plane ac magnetic field excites gyrotropic dynamics with a clockwise and a counter-clockwise mode. We have systematically investigated skyrmion resonant modes as a function of DMI and perpendicular magnetic anisotropy (K). Large variation of resonant modes as a function of small out-of-plane bias magnetic field has been demonstrated. Simulated microwave spectrum of this Néel type skyrmion in an antidot nanodisk has been shown in figure 1(a) and it is compared with an antidot nanodisk having uniform OOP magnetization without any skyrmions. It is to be noted that there is no external bias field applied for these results in fig 1(a). Microwave responses are found in 13-22 GHz frequency range. The most prominent modes are found at 13 GHz and 17 GHz for the disk with a skyrmion and no skyrmion, respectively. Therefore, the modes at 13.1 GHz can be associated to the skyrmion resonances whereas the other higher frequency modes arise from the bulk magnetization (OOP) of the disk. Next, we demonstrate the tunability of the skyrmion resonance modes by applying a small bias field (H_{ext}) along the OOP direction of the nanodisk with a single skyrmion. We have varied the polarity and the magnitude of the OOP field. The results are shown in fig 1(b) where the microwave resonance spectra are shown at different external fields: 0 to 35 mT. A relatively large frequency shift of 3.3 GHz has been observed for a change of 35 mT bias field. To further explore the functionalities, we have investigated skyrmion stabilization with various combinations of the parameters, DMI and K. Néel skyrmion is found to be stabilized at $K = 0.25 \times 10^6 \text{ J/m}^3$ and $\text{DMI} = 1.8 \times 10^{-3} \text{ J/m}^2$. Next, we have varied the K from 0.22 to 0.34 ($\times 10^6$) J/m^3 for a fixed value of $\text{DMI} = 1.8 \text{ mJ/m}^2$ and we have varied the parameter DMI from 1.6 mJ/m^2 to 1.9 mJ/m^2 , for a fixed value of $K = 0.25 \times 10^6 \text{ J/m}^3$ shown in fig 2(a & b) respectively. Furthermore, a broad microwave tunability of 9.8 GHz has been shown with a variation of magnetic anisotropy of $1 \times 10^5 \text{ J/m}^3$. The manifestation of inertial mass of the skyrmion, its dependence on the resonance responses and the size of the skyrmion are explained by using Thiele's equation. The inertial mass of the skyrmion is estimated to be in the order of 10^{-23} kg . We believe these results will have potential implications in the area of skyrmion based nano-scale reconfigurable microwave devices.

[1] Dzyaloshinsky 1958 A Thermodynamic Theory of Gadolinium Molybdate *J. phys.chem.solids* 46 763–72 [2] DeJong M D and Livesey K L 2017 Domain walls in finite-width nanowires with interfacial Dzyaloshinskii-Moriya interaction *Phys. Rev. B* 95 054424 [3] Fert A, Reyren N and Cros V 2017 Magnetic skyrmions: Advances in physics and potential applications *Nat. Rev. Mater.* 2 17031 [4] Kumar Behera A,

Murapaka C, Mallick S, Bhusan Singh B and Bedanta S 2021 Skyrmion racetrack memory with an antidot *J. Phys. D: Appl. Phys.* 54

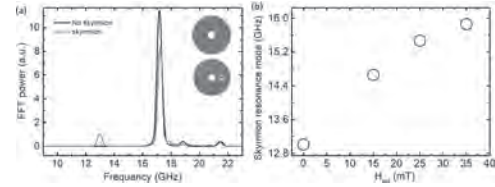


Fig 1. (a) Dynamic responses of a disk with a skyrmion and without a skyrmion in an antidot and (b) Skyrmion resonance modes for different OOP bias magnetic field ranging from 0-35 mT.

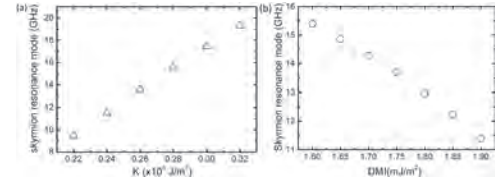


Fig 2. (a) Variations of the gyrotropic modes of skyrmion as a function of K for a fixed DMI = 1.8 mJ/m² and (b) variations of the gyrotropic modes of skyrmion as a function of DMI for a fixed K = 0.25×10⁶ J/m³.

HP-06. Potential Well Inducing the Motion of Skyrmion and Sensing Distance.

F. Jin^{1,2}, L. Yang^{1,2}, W. Mo^{1,2}, J. Song^{1,2}, K. Dong^{1,2}, Y. Hui^{1,2}, L. Liu^{1,2}, H. Wang^{1,2}, Y. Wei^{1,2} and Y. Liu^{1,2}

1. China University of Geosciences School of Automation, Wuhan, China;
 2. Hubei key Laboratory of Advanced Control and Intelligent Automation for Complex Systems, China University of Geosciences, Wuhan, China

Magnetic skyrmions are topologically protected spin texture with diameters in the nanometer length scale. Thus, skyrmions possess profound applications for next-generation spintronics, such as racetrack memory and logic gates. In order to be used in devices, it is necessary to consider how to manipulate magnetic skyrmions. By reading literature, we learned that skyrmion has two driving methods, one is current drive and the other is voltage-controlled magnetic anisotropy (VCMA) drive. The method of using the potential well generated by the VCMA can induce the motion of the skyrmion, which can not only avoid the Joule heating caused by the current-induced methods, but also simplify the existing complex structure. Therefore, studying the movement properties of skyrmion induced by potential wells generated by VCMA alone is necessary. First we study the possibility of the potential well induced skyrmion movement within a certain distance. Then, the relevant factors that affect the distance of skyrmion induction, such as the D value of DMI, the perpendicular magnetic anisotropy (PMA) constant K_u , the external magnetic field H, and the relation between the size of skyrmion and the inductive distance, are studied. The simulation result is shown in Fig.1. All the parameters that cause the radius of skyrmion to change will affect the maximum sensing distance of skyrmion. Finally, the continuous motion scheme of skyrmion induced only through the potential well generated by VCMA explored in Fig.2. In the picture, the green area represent the voltage-controlled potential well and 1, 2 are two sets of potential energy wells driven by inverted square wave voltage signals. In this way, setting a spaced potential well with alternating voltage control on a long track could enable the skyrmion to achieve continuous motion on the track. Overall, the method of using the potential well generated by the VCMA can realize the drive control of skyrmion continuous movement. This work provide guidance for the design of low energy consumption voltage-driven skyrmion driving method and a new concept for track memory.

[1] Wang, X. *et al.* Efficient skyrmion transport mediated by a voltage controlled magnetic anisotropy gradient. *Nanoscale* 10, 733-740, doi:10.1039/c7nr06482a (2018). [2] Zhang, X., Ezawa, M. & Zhou, Y. Magnetic skyrmion logic gates: conversion, duplication and merging of skyrmions. *Scientific Reports* 5, doi:10.1038/srep09400 (2015).

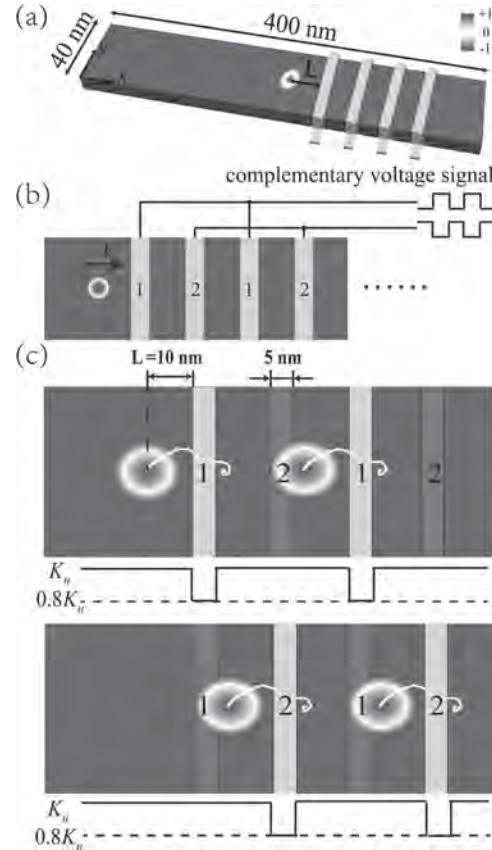


Fig.2

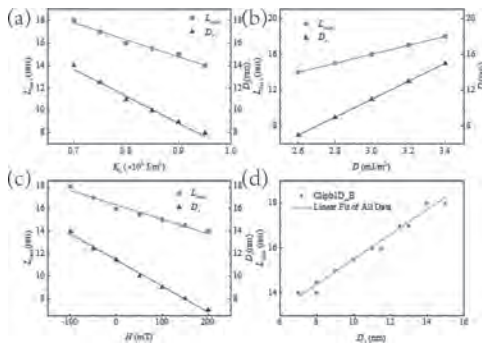


Fig.1

HP-07. Nucleation, Annihilation and Stability of Skyrmions in Ultra-thin Ir/Co/Pt Dots With Stochastic Fluctuations.

F. Tejo¹, D. Cortés², J. Escrig³ and O. Chubykalo-Fesenko¹

1. Instituto de Ciencia de Materiales de Madrid, Madrid, Spain; 2. Universiteit Utrecht, Utrecht, Netherlands; 3. Universidad de Santiago de Chile, Santiago de Chile, Chile

Magnetic skyrmions have been intensively investigated during the last because they exhibit novel properties that make them candidates for the development of future generations of spintronic devices, such as race-track-like memories[1], logic devices[2], or nano-oscillators[3]. Due to their solitonic nature, skyrmions behave like quasi-particles, and therefore their dynamics and stability can be studied. Furthermore, its topological protection promises high long-term stability[4]. In this work, we have investigated the nucleation, stability and annihilation process of skyrmions with current and magnetic fields and at non-zero temperatures in ultrathin magnetic dots using micromagnetic simulations. In our study, we have considered a circular Cobalt nanodisk, with perpendicular anisotropy and Dzyaloshinski-Moriya interaction with parameters corresponding to a three-layer Ir/Co/Pt system[5]. We study the influence of spin-transfer torques, particularly the role of field-like torque and the magnetic field in the nucleation, annihilation, and stability process of skyrmions. Our results show that, for some values of current densities, the field-like torque plays a fundamental role in stabilization of various magnetic states, such as isolated skyrmions, skyrmions clusters, and target skyrmions. Additionally, this torque allows controlling the size of the skyrmions because it acts as an effective perpendicular to the plane field. On the other hand, we have observed that the nucleation and annihilation processes strongly depend on temperature. At zero temperatures skyrmions created by spin-polarized current are (meta) stable states which exist when the current is switched off. However, in the presence of temperature these skyrmions only exist in the presence of current. When the current is switched off, their dynamics is largely influenced by thermal fluctuations (see Fig.1). Particularly, the skyrmions move around the disc in a diffusion matter, breathe and can be additionally nucleated, deformed or annihilated. Our results provide relevant information on the skyrmions dynamics in presence of temperature, which is an important additional factor in understanding skyrmion-based applications.

[1] S. Zhang, A. Baker, S. Komineas, and T. Hesjedal, Sci. Rep. 5, 15773 (2015). [2] X. Zhang, M. Ezawa, and Y. Zhou, Sci. Rep. 5, 9400 (2015). [3] F. Garcia-Sanchez, J. Sampaio, N. Reyren, V. Cros, and J.-V. Kim, New J. Phys. 18, 075011 (2016). [4] S. Rohart, J. Miltat, and A. Thiaville. Phys. Rev. B 93, 214412 [5] C. Moreau-Luchaire et al. Nat. Nanotechnol. 11, 444–448(2016)

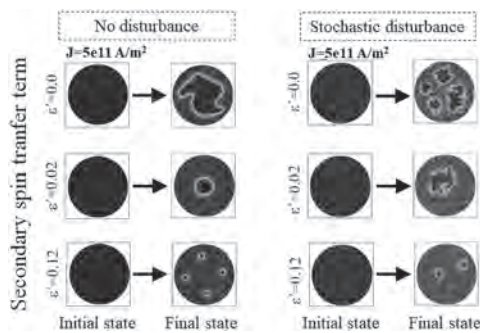


Figure 1: Temporal evolution of magnetization as a function of the secondary spin-transfer term when a current density of $J=5e11$ A/m² is applied perpendicular to the sample in a) absence and b) presence of stochastic disturbance.

HP-08. Thermal Gradient Driven Dynamics of Neel Skyrmions in a Nanoracetrack.

Y. Kumar¹, H. Saren¹ and P. Das¹

¹ Physics, Indian Institute of Technology Delhi, New Delhi, India

Magnetic skyrmion is a non-trivial topological object which originates due to the interplay among various types of interactions such as magneto-static, anisotropy, dipolar, exchange interaction, and Dzyaloshinskii-Moriya interaction (DMI). In magnetic thin films, skyrmions originate through the competition between interfacial DMI and exchange interaction¹. Patterned nanostructures provides a pathway to predictably stabilize and thus allow understanding their behavior in presence of different important parameters in a more controlled way (ref.). Moreover, due to the potential application of skyrmions in spintronic devices such as race-track memory etc., several studies of their creation, stability, and dynamics in nano wires have been reported¹. Skyrmions in nanostructures can be dynamically controlled by magnetic field gradient³ and spin-polarized current¹. In case of high-speed skyrmion-based magnetic storage devices, large spin-polarized current density is required to control skyrmion dynamics. This in turn causes Joule heating and skyrmion Hall effect⁴ which limits the efficiency of skyrmion-based devices. These issues can be resolved by employing magnon spin current as a tool to control skyrmion propagation. However, very few studies have so far reported dynamics of skyrmions in presence of temperature gradient in a nanotrack⁵. L. Kong *et al.* reported the systematic investigation of the dynamics of Bloch skyrmions in presence of the temperature gradient. Skyrmions are found to move from region of lower to higher temperature. Moreover, the velocity of skyrmions is found to increase with the increase of thermal gradient⁵. Magnon spin current generated due to thermal gradient diffuses from hot to the cold region. This magnon spin current applies a negative torque on the skyrmion resulting in movement of skyrmion cold to hot region⁴. This study also reports that the skyrmion Hall component is absent or very small with the magnon spin current. A few other studies report the role of temperature on the current induced dynamics which demonstrate the velocity of skyrmion for the constant current density increases with the temperature⁷. Although the dynamical behavior of Bloch skyrmions in presence of a temperature gradient has been reported in literature, there is no comprehensive studies performed to understand the dynamics of Neel skyrmion in presence of temperature gradient. In this work, we performed micromagnetic simulations to investigate the dynamics of Néel skyrmions in a race track of Co/Pt in presence of the temperature gradient. We considered a Co/Pt track with dimensions of 100 nm x 40 nm x 1nm. Individual skyrmions were stabilized due to the i-DMI of ~ 3 mJ/m² in the nanotrack and thereafter, their dynamics in presence of a temperature gradient^{7,8} was studied. Our studies reveal that similar to Bloch skyrmions, the temperature gradient plays a significant role on the velocity of Neel skyrmions in the nanotrack. The skyrmions move from cold to the hotter region and the velocity increases as the temperature gradient is increased (Fig. 1(b)). Furthermore, we have also investigated the role of Gilbert damping constant on the skyrmion velocity in presence of thermal gradient on the track. Our results show that the velocity is inversely proportional to the values damping constant. The details of these results are discussed in this work.

¹ J. Iwasaki, *et al.* Nat. Nanotechnol. 8, 742 (2013). ² A. Casiraghi, *et al.* Nat. Commun Phys. 2, 145 (2019). ³ J. J. Liang *et al.* New J. Phys. 20, 053037 (2018). ⁴ G. Chen, *et al.* Nat. Phys 13, 112–113 (2017). ⁵ L. Kong *et al.* Phys. Rev. Lett. 111, 067203, (2013). ⁶ M T Islam *et al.* J. Phys.: Condens. Matter 31, 455701 (2019). ⁷ Litzius, K. *et al.* Nat Electron 3, 30–36 (2020). ⁸ Everschor, K. *et al.* Phys. Rev. B 86, 054432 (2012).

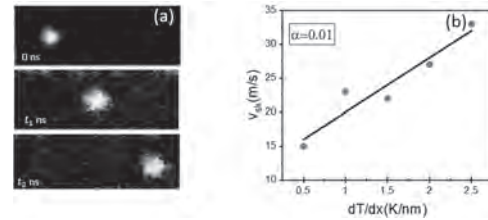


Fig.1.(a) Position of a skyrmion in a nanotrack in presence of temperature gradient at three different times. **(b)** The velocity of Skyrmion as a function of the temperature gradient in K/nm.

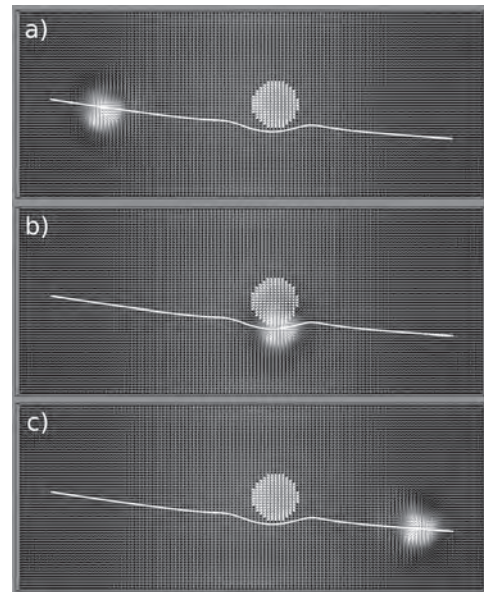
HP-09. Simulations of Magnetoresistive Detection of Skyrmions.H. Chen¹, W. Bouckaert^{1,2} and S. Majetich¹

1. Physics, Carnegie Mellon University, Pittsburgh, PA, United States;

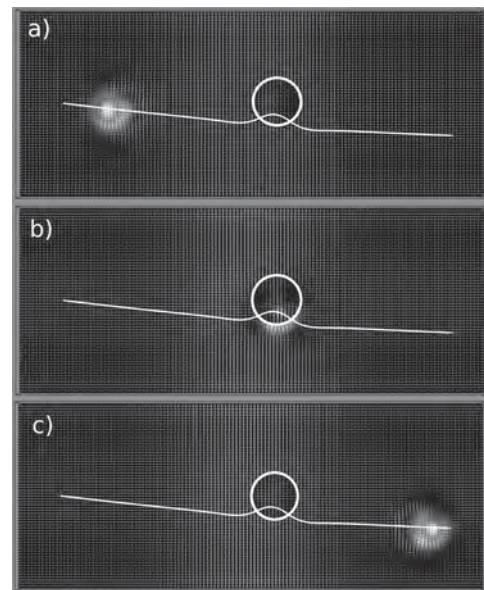
2. Physics, EPFL, Pittsburgh, PA, United States

Skyrmions have been proposed for racetrack memory [1], but there are still many questions about the best way to detect them electronically. The most promising approaches so far have used the transverse voltage due to the skyrmion Hall effect, but the signal is still very weak [2, 3]. Here we use simulations consider alternative vertical detection methods using magnetoresistance. A spin polarized current is used to move a Néel skyrmion down a racetrack that contains a circular magnetic dot above it. When the dot is flush with the racetrack, exchange interactions dominate, while when it is separated by a 1 nm thick tunnel barrier, the interactions are mainly magnetostatic. The trajectory of the skyrmion over a period of ~ 4 ns is calculated using mumax² micromagnetics simulation software. Results for different dot and skyrmion core magnetization directions are used as a guide to predict the magnetoresistance as a function of time, which would be used to detect individual skyrmions. For these model studies, a saturation magnetization of 5.8×10^5 A/m, exchange stiffness 1.5×10^{-12} J/m, anisotropy 8×10^5 J/m³, and damping parameter 0.1 were used for both the racetrack and 20 nm diameter detection dot. In addition, to stabilize 20 nm diameter skyrmions, the racetrack also had a Dzyaloshinskii-Moriya Interaction strength of 3×10^{-3} J/m². A current density of 1×10^{12} A/m² with spin polarization 0.4 was used to move the skyrmions. In all cases there was a transverse deflection due to the skyrmion Hall effect. When the dot is flush with the racetrack, exchange coupling to the skyrmion spin texture background can be treated as an effective magnetic field with an antiskyrmion texture [4]. When there is a 1 nm MgO tunnel barrier separating the dot and racetrack, magnetostatic effects dominate and the magnitude of the interaction field is much smaller. However, simulations show that the vertical tunnel current is dominated by the volume directly below the dot. There will be a transient change in the magnetoresistance as a skyrmion passes by the dot detector. With magnetostatic coupling both the trajectory and skyrmion size as a function of time differ, depending on whether the dot and skyrmion core magnetizations are parallel or antiparallel. When they are parallel (Figure 1), the skyrmion diameter grows slightly as it approaches the dot, since the dipolar field tends to orient misaligned spins. The spatial field gradient due to the dot causes a repulsive deflection around the dot. When the skyrmion core and dot magnetization are antiparallel (Figure 2), the skyrmion slightly shrinks in diameter as it approaches the dot, and there is an attractive interaction. The magnitudes of the deflection depend on the dot and skyrmion stack diameters and thicknesses, but as long as part of the skyrmion passes under the dot, it should also be possible to differentiate core up and core down skyrmions. For Figure 1 there would be a transient drop in resistance, and for Figure 2 a transient rise. If in-plane magnetization dot detectors were used, there would also be characteristic magnetoresistance transients that are sensitive to the in-plane component of the skyrmion spins. This could enable Néel and Bloch skyrmions to be differentiated, if magnetized along the racetrack axis, and chirality detection of Bloch skyrmions, if magnetized perpendicular to the racetrack axis.

1. A. Fert, V. Cros, J. Sampaio, Nat. Nanotech. 8 152 (2013). 2. D. Macciarollo, et al., Nat. Nanotech. 13, 233 (2018). 3. K. Zeissler, et al., Nat. Commun, 11, 428 (2020). 4. K. Hamamoto, M. Ezawa, and N. Nagaosa, Phys. Rev. B 92, 115417 (2015).



20 nm Néel skyrmion trajectory along a 200 nm x 80 nm racetrack, passing by a 20 nm diameter dot separated by a 1 nm tunnel junction barrier. The skyrmion core and dot have parallel magnetizations. a) at beginning, b) repulsion near the dot, and c) at the end of the racetrack.



Similar conditions to those of Figure 1 except that the dot magnetization direction has been reversed, so that it is antiparallel to that of the skyrmion core. Here the interaction near the dot is attractive.

HP-10. Second Harmonic Detection of Chiral Spin Structures in a Magnetic Multilayer.

Y. Wang¹ and J.Q. Xiao¹

¹ University of Delaware, Newark, DE, United States

Second harmonic Hall voltage (SHV) method [1] has been widely used to measure spin-orbit torques (SOTs) in heavy metal/ferromagnet (HM/FM) bilayers. It is typically applied for the single domain regime while the signals in multi-domain regimes are almost always ignored due to the complication from domain structures. In this study, we analyze the SHV data taken in a magnetic multilayer made of W/Pt/Co/SiO₂. First harmonic planar Hall effect (PHE) and anomalous Hall effect (AHE) measurements reveal weak in-plane anisotropy of the Co layer. At low temperatures, the PHE loops become asymmetric, which indicate sizable Dzyaloshinskii-Moriya interaction (DMI) at the Pt/Co interface due to inversion symmetry breaking and strong spin-orbit coupling [2]. Typical sheared hysteresis for labyrinth domains is observed in AHE measurements. Interestingly, the second harmonic Hall voltage loops show “humps” in the intermediate field range where DMI-induced topological Hall effect and magnetic bubbles are typically observed. We explain such enhancement in SHV as a result of chiral Néel wall formation and efficient SOT driven domain wall motion [3]. Our results demonstrate that second harmonic voltage measurement can be utilized to detect chiral spin structures in magnetic multilayers.

[1] M. Hayashi *et al*, Phys. Rev. B 89, 144425 (2014). [2] M. Heide *et al*, Phys. Rev. B 78, 140403(R) (2008). [3] A. V. Khvalkovskiy *et al*, Phys. Rev. B 87, 020402(R) (2013).

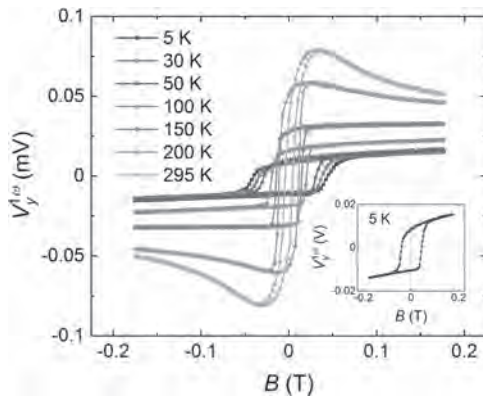


Fig.1 Planar Hall effect measurement under in-plane field results for a W(3)/Pt(1)/Co(1.2)/SiO₂(5) device.

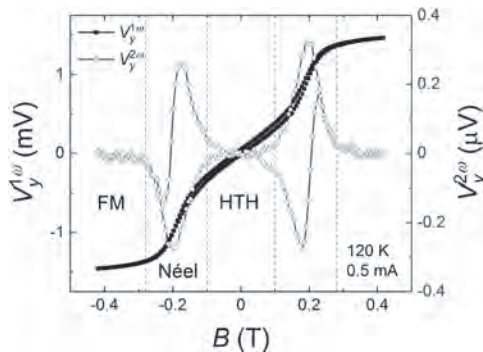


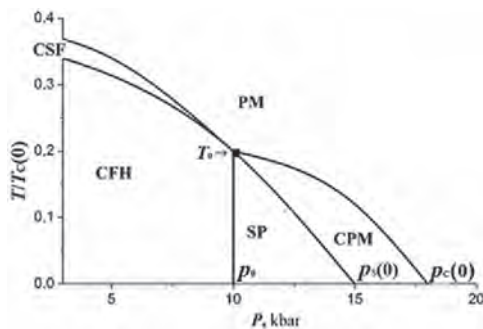
Fig.2 First and second harmonic Hall voltages under a nearly out-of-plane field scan. FM, Néel, and HTH denote ferromagnet, Néel domain wall, and head-to-head domain wall, respectively.

HP-11. Quantum Phase Transitions Under Pressure in a Chiral Itinerant Ferromagnet MnSi.

A. Povzner¹, S. Bessonov¹ and A. Volkov¹

¹. Physic, U, Ekaterinburg, Russian Federation

In the chiral ferromagnets with the Dzyaloshinskii-Moriya (DM) spin-orbit interaction, vortex spin microstructures arise, which are considered as a unit of information for computer memory. In strongly correlated itinerant ferromagnets, these spin structures arise due to the first-order thermodynamic phase transitions, in which an intermediate phase of the chiral spin liquid is realized. However, the experiments indicate the realization of a more complex and still unexplained picture of spin microstructures, which depends not only on temperature and external magnetic field, but also on pressure. In this communication, we investigate the conditions for the occurrence of such spin microstructures in the framework of the spin-fluctuation theory of strongly correlated band ferromagnets with the DM-interaction. We consider the Hubbard model and DM-interaction, which, due to the small relativism, is considered in the mean-field approximation. The resulting expression for the free energy functional contains pressure-dependent magnetic, electronic, and spin-fluctuation terms, which are self-consistent with each other. The conditions for the minimum of free energy and electroneutrality are considered at various pressures in the model of the electronic structure of MnSi obtained from the LDA+U+SO calculations. The effect of pressure on the DOS determined by LDA+U+SO-calculation will be considered in the model of corresponding states. The initial state is chiral ferromagnetic helicoidal spin spiral (CFH) phase. An increase in temperature and pressure leads to thermodynamic and quantum transitions, which are responsible for the formation of the MnSi phase diagram (see fig.). A crossover of a first-order thermodynamic and quantum phase transition is obtained, which leads to the appearance of a chiral spin fluid (CSF). An increase in pressure suppresses local DOS minimum and zero-point spin fluctuations. This leads to the disappearance of the crossover of quantum and thermodynamic phase transitions at the multicritical boundary point (T_0, p_0) . Below the temperature T_0 , at $p=p_0$, a quantum transition to the state of phase segregation (SP) occurs. This transition is accompanied by an increase in the DOS at the Fermi level and leads to the appearance of a ferromagnetic state. In this state, due to the DM-interaction and fluctuating exchange fields, skyrmions of the left and right spin chirality appear. Moreover, in the SP-region baric magneto-volumetric effect is realized, which is observed experimentally. An increase in pressure at $T < T_0$ and $p > p_0$ leads to the crossing of the DOS maximum by the chemical potential and a quantum transition to a paramagnetic state with a nonzero local magnetization (CPM). In the CPM-region ($p > p_s(T)$), the spin chirality fluctuations are realized. An increase in the amplitude of spin fluctuations with increasing pressure in this phase ensures the disappearance of local magnetization. As a result, at $p=p_c(T)$, a second-order phase transition to the paramagnetic phase (PM) without spin chirality occurs. The $(p-T)$ -diagram of MnSi, calculated in the framework of the developed spin-fluctuation approach using the LDA+U+SO spectrum, is consistent with experiment.



Session IA

MAGNETIC RECORDING: ENERGY-ASSISTED, MEDIA, HEAD, MODELS

Simon Greaves, Chair
Tohoku University, Sendai, Japan

CONTRIBUTED PAPERS

IA-01. Characterizing the Oscillation Frequency of a Spin-Torque Oscillator (STO) by Measuring the Change of dc Resistance Upon Injection Locking to an External RF Magnetic Field.

N. Asam¹, H. Suto², S. Tamaru³, H. Sepehri-Amin¹, T. Nakatani¹, W. Zhou¹, H. Kubota³ and Y. Sakuraba¹

1. Research Center for Magnetic and Spintronics Materials, National Institute for Materials Science, Tsukuba, Japan; 2. Corporate Research and Development Center, Toshiba Corporation, Kawasaki, Japan; 3. Research Center for Emerging Computing Technologies, National Institute of Advanced Industrial Science and Technology, Tsukuba, Japan

Microwave-assisted magnetic recording (MAMR) is a new technology where a microwave magnetic field having a frequency of few tens of GHz can assist switching of the magnetic domains in the recording media[1]. This microwave magnetic field is generated by using a spin-torque oscillator (STO) under the influence of the magnetic field from the write pole of the recording head and an applied dc bias current. When certain conditions for bias current and magnetic field are met, spin-transfer torque causes the field generating layer (FGL) of the STO to precess, generating an oscillating magnetic field. Although the oscillation frequency of the magnetic field generated by the STO is a key parameter in MAMR, its conventional measurement using the radio-frequency (RF) electrical signal arising from the magnetoresistance (MR) of STO has the following concerns: the RF electrical signal is sometimes very weak and contains several frequency components that do not correspond to the frequency of the actual magnetic field generated by the STO because of the complex magnetization dynamics of the ferromagnetic layers inside STO; the RF signal attenuates heavily in the write head-STO assembly. Therefore, it is strongly desired to find a way to characterize the oscillation frequency of the STO which is already a part of the write head assembly. In this study, we have proposed and successfully demonstrated a new technique to characterize the actual frequency of the magnetization precession in an STO using injection locking from externally applied radio-frequency (RF) magnetic field. Using our method, there is no need to electrically connect the STO to a spectrum analyzer via an RF-compatible electrical circuit. Injection locking is a phenomenon occurring when an oscillator (in this case, an STO) is forced to couple and synchronize with an external oscillating signal (in this case, oscillating magnetic field at GHz frequency range)[2]. When the FGL of an STO is precessing at a given frequency (f_{FGL}), it can undergo injection locking to an externally applied magnetic field whose frequency(f_{ext}) is close to the f_{FGL} which changes the trajectory of magnetization precession. Since the dc resistance of the STO depends on the trajectory of precession, the effect of injection locking is reflected in the dc resistance of the STO. We can use this phenomenon to detect the f_{FGL} without measuring conventional RF output signal from STO. To demonstrate this experimentally, we used the design of all-in-plane STO which was shown previously as suitable to the MAMR application[3]. We fabricated an STO pillar of around 40nm in diameter and also a co-planar waveguide on top of it to act as an RF antenna that generates an oscillating magnetic field, electrically separated by SiO₂. As shown in fig. 1, a bias current and magnetic field were applied to the STO as usual, and the STO underwent oscillation at the suitable values of bias current and magnetic field. Then, we applied a pulsed RF electrical excitation to the co-planar waveguide from a signal generator, with frequency f_{ext} and pulsed at 1MHz, and monitored the change of dc resistance between off and on parts of the pulse (ΔR) by using a lock-in amplifier with the pulse frequency as reference. Note that although we measured the resistance oscillation of the STO at a frequency of 1 MHz, the measurement result reflected the dc resistance. Because 1 MHz is much smaller than the STO oscillation frequency of few tens of GHz, the RF resistance change due to the STO oscillation is averaged over several precession cycles of the magnetization. Fig. 2 shows an example of such measurement. Fig. 2(a) shows a typical spectrum of the RF output signal with a tiny peak at 32GHz from STO under dc bias voltage (V_{dc}) = 50mV and applied magnetic field (H_{ext}) = 1200mT, from which we could not identify whether or not the frequency of this peak corresponds to the actual magnetization precession. Fig. 2(b) shows the value of ΔR as a function of

f_{ext} for the same values of V_{dc} and H_{ext} . We clearly detected the change in ΔR as a function of f_{ext} , corresponding to injection locking. This informs us of the actual frequency of magnetization precession without measuring the RF output signal. In conclusion, we demonstrated that the dc resistance of the STO changes measurably upon injection locking to an externally applied magnetic field. This can be used to characterize the oscillation frequency of the magnetic field generated by the STO which is already a part of the write head assembly. This will be beneficial for developing an STO-based microwave magnetic field generator for MAMR.

[1] J. G. Zhu, X. Zhu, and Y. Tang, *IEEE Trans. Magn.*, vol. 44, no. 1, pp. 125–131, (2008) [2] S. Urazhdin, *et al.*, *Phys. Rev. Lett.*, vol. 105, no. 10, p. 104101, (2010) [3] H. Sepehri-Amin *et al.*, *J. Magn. Magn. Mater.*, vol. 476, pp. 361–370, (2019)

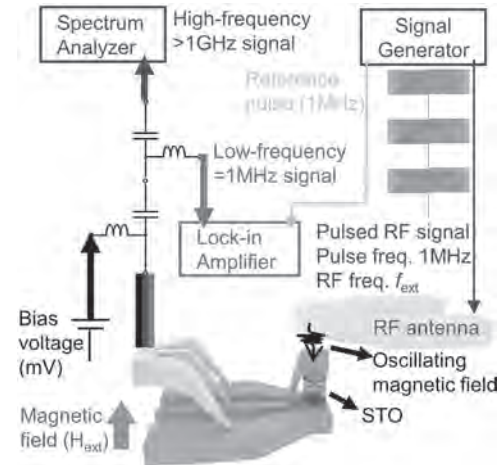


Fig. 1 A schematic of our measurement. The STO is connected to a bias tee setup which allows a mix of dc voltage input (V_{dc}), a high-frequency component and a low-frequency component. The high-frequency component is not to be used in our newly proposed method

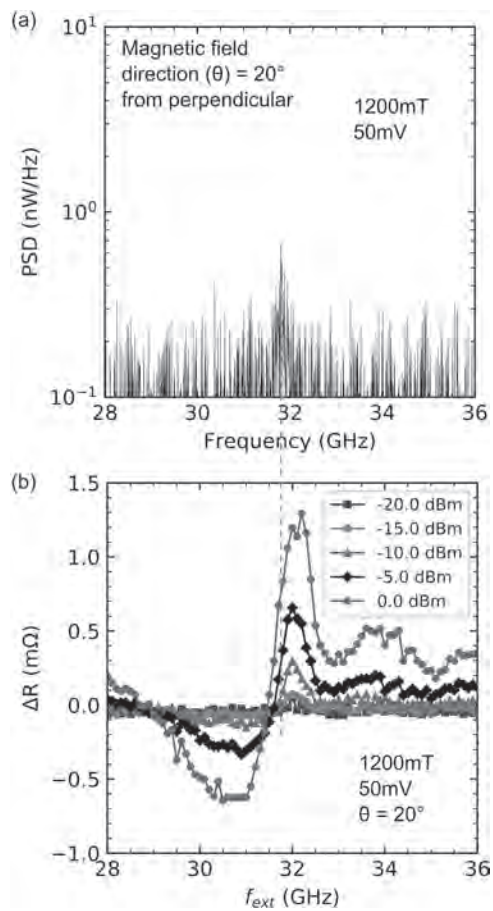


Fig. 2 (a) PSD of the RF electrical signal from the STO (b) Change of resistance ΔR as a function of externally applied RF field frequency f_{ext} under the same bias conditions

IA-02. Double Magnet Master Media for Magnetic Printing Onto Energy-Assisted Magnetic Recording Media.

T. Komine¹

¹. Graduate School of Science and Engineering, Ibaraki University, Hitachi, Japan

Recently, the problem of information storage becomes more serious due to the information explosion. It is widely known that future advances in the areal density of hard disk drives (HDDs) are essentially limited by the magnetic recording trilemma arising from the conflicting requirements between signal-to-noise ratio, writeability, and stability[1]. Energy-assisted magnetic recording (EAMR) such as heat-assisted magnetic recording[2] and microwave-assisted magnetic recording[3] is thought to solve the trilemma by improving writability and enhancing areal recording density. Two-dimensional magnetic recording with shingled writing[4] has also been proposed for increasing track density, which is enabled by partial overlapping of recorded tracks. EAMR combined with SMR is expected to be achieved for the next generation recording schemes of HDDs. On the other hand, servo signal writing is one of serious problems for high areal recording density in hard disks. The self-servo track writing technology, which regenerated from previous written servo patterns, has been adopted during head-disk assembly. However, since the servo signal writing in the present hard disks takes more than a few days per one drives on manufacturing process, and the supply of HDDs can not keep up with the social demand. Magnetic printing with perpendicularly magnetized patterns is a strong candidate for servo track writing with extremely high speed and low cost[5]. However, the recording field strength by utilizing the conventional magnetic printing master medium is not enough to write servo-signals on HDDs with large coercivity for EAMR, and it becomes much weaker as the pattern size or the track pitch decreases. The decrease in the recording field or the field gradient deteriorates the signal-to-noise ratio of servo-signals, and this problem becomes more serious in HDDs which has narrower track width. In order to accurately write servo-signals on HDDs for EAMR combined with SMR, it is essential to enhance the recording field. I propose a new master structure, herein called double magnet master (DMM) medium[6], for magnetic printing technique to improve recording characteristics. Figure 1 shows the schematic illustration of double magnet master medium and recording layer. The DMM medium consists of two magnetic materials with different coercivity. Both materials have perpendicular magnetic anisotropy but exchange interaction between both materials does not act. One material has a coercivity higher than the coercivity of the recording layer, while the other has a lower coercivity. During application of printing field H_p , the magnetization of low coercivity parts (magnet 1) orients to the direction of printing field while high coercivity parts (magnet 2) is not subject to magnetization reversal. As a result, the recording field can be enhanced. The recording field distributions of L/S patterns with pattern length of 10 nm, which corresponds to bit length, were calculated by micromagnetic simulation for conventional perpendicular master (CPM)[5] and DMM media. The magnetic spacing is 2 nm in this case. The printing field H_p was varied from 5 kOe to 50 kOe. In CPM, the recording field H_r consists of the magnetostatic field generated from only the magnet 1, while in DMM, the recording field H_r consists of the magnetostatic fields generated from both magnets 1 and 2. The recording field difference ΔH_r of about 11 kOe for DMM is twice as that for CPM in various printing field. It was clearly found that the recording field can be enhanced by DMM. Since the magnetostatic field generated from double magnets is effective when the magnetization in the harder magnet does not reverse, the printing field is less than the coercivity of the harder magnet, which is about 73kOe by using $L1_0$ -FePt patterns as magnet 2. In order to evaluate printing characteristics of CPM and DMM, the printed magnetization distributions of ECC-type EAMR media [7] with the coercivities of 15kOe and 22kOe were calculated. Figure 2 shows printing performance [8] as a function of printing field H_p . The printing performance of 1 means the perfect printing. The optimum printing fields are slightly less than those of the coercivity of recording layer. The printing performances of DMM were dramatically improved comparing with CPM printing characteristics. It was clearly confirmed that the printing performances of DMM are superior to that of CPM. Therefore, the magnetic printing by utilizing DMM

is a promising way to realized high-speed servo-track writing for EAMR combined with SMR.

[1] H. J. Richter, A. Y. Dobin, *J. Magn. Magn. Mater.* 287 (2005) 4150. [2] M. H. Kryder, E. C. Gage, T. W. McDaniel, W. A. Challener, R. E. Rottmayer, G. Ju, Y. T. Hsia, M. F. Erden, *Proc. IEEE* 96 (2008) 1810-1835. [3] J.-G. Zhu, X. Zhu, Y. Tang, *IEEE Trans. Magn.* 44 Iss. 1 (2008) 125-131. [4] A. Amer, J. Holliday, D. D. E. Long, E. L. Miller, J.-F. Paris, T. Schwarz, *IEEE Trans. Magn.* 47, Iss. 10 (2011) 3691-3697. [5] N. Sheeda, M. Nakazawa, H. Konishi, T. Komine, and R. Sugita, *IEEE Trans. Magn.* 45 (2009) 3676-3678. [6] T. Komine, submitted to *J. Magn. Magn. Mater.* 2021. [7] T. Tanaka, S. Kashiwagi, Y. Kanai, K. Matsuyama, *J. Magn. Magn. Mater.* 416 (2016) 188-193. [8] T. Komine, T. Murata, Y. Sakaguchi, R. Sugita, *IEEE Trans. Magn.* 44 Iss. 11 (2008) 3416-3418.

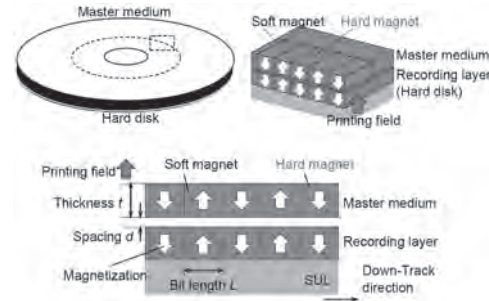


Fig.1 Schematic illustration of magnetic printing process by utilizing double magnet master medium.

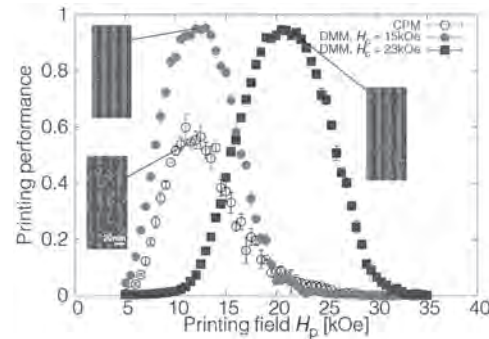


Fig.2 Printed magnetization distribution of recording layer and printing performance as a function of printing field.

IA-03. Depth Selective Magnetic Phase Coexistence in FeRh Thin Films.

W. Griggs¹, B. Eggert², M. Liedke³, M. Butterling³, A. Wagner³, U. Kentsch³, E. Hirschmann³, M. Grimes^{1,4}, A. Caruana⁵, C. Kinane⁵, H. Wende², R. Bali³ and T. Thomson¹

1. The University of Manchester, Manchester, United Kingdom; 2. Universität Duisburg-Essen, Duisburg, Germany; 3. Helmholtz-Zentrum Dresden-Rossendorf, Dresden, Germany; 4. Paul Scherrer Institut, Villigen, Switzerland; 5. ISIS, Rutherford Appleton Laboratory, Didcot, United Kingdom

The ability to engineer magnetic phase distributions over nanometer length scales is invaluable in the development of spintronic and data storage technologies with enhanced efficiency. Equiatomic FeRh with B2 crystallography is a useful material for local manipulation of magnetic phases, owing to its unusual first-order metamagnetic phase transition (MPT) from antiferromagnetic (AF) to ferromagnetic (FM) ordering, which occurs at ~ 100 °C [1]. It has been shown that in addition to the thermally driven MPT, there is a disorder-induced MPT from AF to FM ordering, and that with further disordering a second MPT to PM behaviour can be induced [2]. Bennett et al. [3] have demonstrated that by irradiating FeRh with noble gas ions, the disorder-induced MPTs can be exploited to produce a rich variation in the magnetism as a function of depth. In the present work [4], we combine several non-destructive experimental techniques with extensive simulations to identify a direct correspondence between the nature and concentration of induced defects and the resulting modification of the magnetic depth profile in 40 nm FeRh thin films as the fluence of 25 keV Ne⁺ ions increases. Polarised neutron reflectometry (PNR) was used to determine the magnetisation depth profiles for a range of sample temperatures under an applied field of 1 kOe. The data were fitted to dynamical simulations of the nuclear and magnetic scattering length density (n/mSLD) profiles (Figure 1), which are proportional to the density and in-plane magnetisation, M_x , respectively. The data demonstrate that it is possible to produce a uniform and thermally stable magnetisation with a single-step irradiation, as in Figure 1(b), or to produce a simple bilayer phase structures, as in Figure 1(c) and (d). To elucidate the interplay between the magnetisation depth distributions, the coexistence of magnetic phases, and the ion-induced damage profiles, conversion electron Mössbauer spectroscopy (CEMS) and Doppler broadening variable energy positron annihilation spectroscopy (DB-VEPAS) were performed on each sample. DB-VEPAS allows relative changes of defect concentration to be determined via the line broadening of gamma photons produced from the annihilation of positrons with varying energy E_p . By fitting the DB-VEPAS data, the mean positron diffusion length as a function of increasing fluence is obtained, which is inversely proportional to the concentration of open volume defects. Thus, we demonstrate that the defect concentration monotonically increases with the irradiating fluence. To complement the DB-VEPAS measurements, variable energy positron annihilation lifetime spectroscopy (VEPALS) measurements were also performed on each sample. Here, variations in positron lifetime with increasing fluence signify changes to the size of open volumes; thus, changes in the concentration and the type of defects are determined. By comparing the measured data to theoretical lifetime values calculated using density functional theory (DFT), we identify the predominant defect type for each irradiation condition with depth sensitivity. The PNR, CEMS, and positron data allow the effect of increasing fluence to be explained as shown schematically in Figure 2, wherein the onset of FM and PM phases are associated with the emergence of static disorder and monovacancy defects respectively. In the as-grown case, there is a substantial concentration of monovacancy defects. At the lowest value of the fluence (7.5×10^{13} ions cm⁻²), the defect concentration increases and sub-unit cell atomic displacements begin to dominate. The generation of static disorder continues as the fluence is increased to 3×10^{14} ions cm⁻², with no change to the predominant defect type. On increasing the fluence to 6×10^{14} ions cm⁻², atomic displacements give way to monovacancies, with some static disorder remaining at the substrate interface. For all samples, our data are well described assuming AF, FM, and PM phases only, and do not present evidence for states such as spin glasses or magnetic dead layers. This feature, coupled to the fact that the mSLD profiles of the irradiated samples comprise relatively few sublayers with discrete magnetisations which are stable with

respect to increasing temperature, highlights the effectiveness of sensitive and controlled disordering of ordered alloy precursors for producing technologically useful magnetic configurations. Our results provide the basis for the patterning of single layer or multilayer structures that incorporate FeRh to create devices on sub-100 nm length scales with AF and FM order in close physical proximity.

[1] M. Fallot, Ann. Phys., vol. 10, pp. 291–332 (1938) [2] A. Iwase et al., Nucl. Instrum. Methods Phys. Res., vol. 256, pp. 429–433 (2007) [3] S. P. Bennett et al., Mater. Res. Lett., vol. 6, pp. 106–112 (2018) [4] W. Griggs et al., APL Mater., vol. 8, p. 121103 (2020)

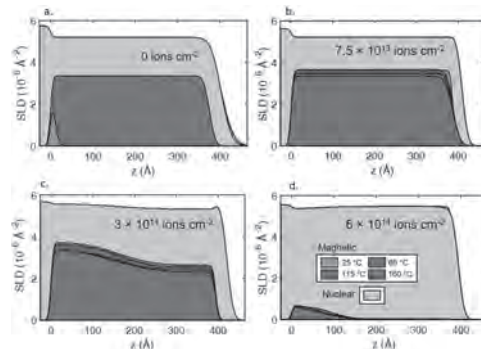


Fig. 1. (a)–(d) Magnetic (coloured) and nuclear (grey) scattering length density (mSLD and nSLD) profiles corresponding to the fitted PNR data for each sample across the range of measured temperatures.

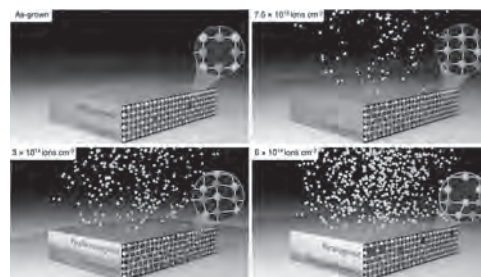


Fig. 2. The effect of increasing the irradiating fluence on the depth-dependent magnetisation, magnetic phase fractions, and concentration and type of structural defects is illustrated.

IA-04. Fabrication of FePt-BN/FePt-SiO_x Dual-Layer Structure for HAMR Media on Corning Lotus™ NXT Glass Substrate.

B. Zhou¹, B. Varaprasad¹, C. Xu¹, M. Huang², D.E. Laughlin¹ and J. Zhu¹
 1. Data Storage Systems Center, Carnegie Mellon University, Pittsburgh, PA, United States; 2. Corning Research and Development Corporation, Corning Inc, Corning, NY, United States

As the current recording media for the heat assisted magnetic recording (HAMR), the granular L1₀-FePt thin film needs to have uniform grain size with small pitch distance and well-defined grain boundaries. To achieve the targeted microstructure with proper L1₀ ordering using sputtering techniques, FePt along with grain boundary materials (segregants) are co-deposited on MgO underlayers at elevated temperature. The columnar growth of FePt is desired to have sufficient grain volume without grain size expansion. The fabrication of grains at small grain pitch with well-defined grain boundaries has been proven to be challenging.[1] Over the past decade, segregant materials, such as carbon, have attracted extensive attention for producing isolated FePt grains with well-defined grain boundaries but has experienced difficulty at reducing grain pitch distance and making grains with large aspect ratio. Though the columnar growth of FePt can be achieved by using some oxide segregant materials, such as TaO_x[2] and TiO_x[3], the resulting films always show poor L1₀ ordering and poor magnetic properties. Proper ordering of FePt can be achieved with SiO_x[4], but the resulting microstructure tends to be maze-like. Therefore, exploiting multilayer deposition is a promising strategy to achieve the desired microstructure with proper ordering and magnetic properties. In this study, we utilize a dual-layer strategy of FePt-BN/FePt-SiO_x on polycrystalline MgO underlayer in order to obtain the desired media microstructure with good L1₀ ordering and magnetic properties. The film stack of Ta(5)|Cr(40)|MgO(6)|Media(6.5) was deposited on Lotus NXT glass substrate with the numbers in parentheses in nm. Lotus NXT glass is one of the promising glass substrates for high-temperature deposition of HAMR media. The Ta and Cr layers were DC sputtered at room temperature and 280°C, respectively. The samples were subsequently annealed at 650°C for 1 hour in order to promote the texture and grain size of Cr buffer layer. The MgO underlayer was RF deposited on Cr buffer layer after the sample cooled down to room temperature. There are two magnetic layers in the media layer, where FePt was co-sputtered with BN and SiO_x, respectively, for the first (M1) and the second (M2) magnetic layer. The deposition temperatures of the M1 layer and the M2 layer were fixed at 700°C and 550°C, respectively. From the microstructural point of view, the main objective of the M1 layer is to obtain well-isolated FePt grains to set the grain center-to-center pitch distance, whereas the M2 layer aims to suppress the lateral growth and to promote the columnar growth of the FePt grains. Fig. 1 (a) shows the in-plane HAADF image of the film stack Lotus NXT glass [Ta(5)|Cr(40)|MgO(6)|Media(6.5) with its (b) grain size distribution profile and (c) grain center-to-center pitch distance distribution profile. The figure demonstrates well-isolated FePt grains with mean grain size of 6.3 nm and mean pitch distance of 8.3 nm. As shown in the XRD pattern of this media in Fig. 1 (d), there are only (001) and (002) peaks from FePt, indicating the c-axis of FePt grains are predominantly perpendicular to the film plane. The broad peak at around 23.5° corresponds to the amorphous peak from Lotus NXT glass substrate. The order parameter (S) considering the relative integrated intensity ratio between (001) and (002), I₀₀₁/I₀₀₂, with the absorption factor and Lorentz factor is 0.7, suggesting good chemical ordering in FePt grains. Fig. 1 (e) shows the perpendicular and in-plane hysteresis loops of this media. The perpendicular coercivity (H_{c⊥}) is 26 kOe. The in-plane loop shows a small opening with the coercivity (H_{c∥}) of 2.9 kOe and the normalized remanence magnetization (M_{r∥}⁰) of 0.08. The remanent ratio, which is M_{r∥}⁰/M_{T⊥}, is 0.09, suggesting a minor in-plane component of FePt grains in the sample. By exploiting the dual-layer structure of FePt-BN/FePt-SiO_x, we have demonstrated well-isolated columnar FePt grains with small mean pitch distance of 8.3 nm. The XRD pattern shows that the grains are well-textured and highly ordered. As a result, the perpendicular coercivity reaches 26 kOe. The utilization of multilayer deposition strategy with segregants BN and SiO_x provides a promising technique to achieve desired HAMR media microstructure without sacrificing FePt chemical ordering and magnetic properties.

[1] Y. Kubota *et al.*, *IEEE Trans. Magn.*, vol. 54, no. 11, p. 3201206, 2018
 [2] B. Lim *et al.*, *J. Appl. Phys.*, vol. 105, no. 7, p. 07A730, 2009 [3] B. S. D. C. S. Varaprasad *et al.*, *IEEE Trans. Magn.*, vol. 49, no. 2, p. 718–722, 2013
 [4] H. Ho *et al.*, *Appl. Phys. Lett.*, vol. 102, no. 11, p. 112411, 2013

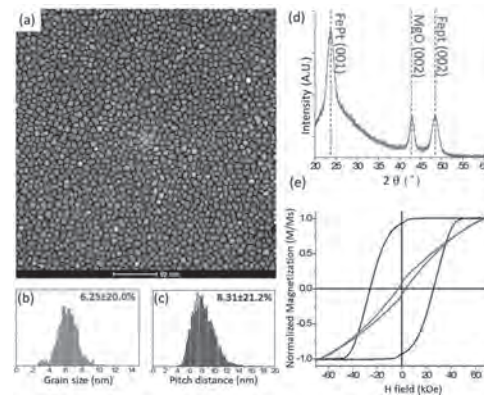


Fig. 1 (a) In-plane HAADF image of the film stack Lotus NXT glass [Ta(5)|Cr(40)|MgO(6)|FePt-38vol.% BN(2)|FePt-35vol.%SiO_x with its corresponding (b) grain size distribution and (c) grain center-to-center pitch distance. Its XRD pattern and magnetic properties are in (d) and (e) respectively.

IA-05. Union Bound Analysis for Spin-Torque Transfer Magnetic Random Access Memory With Channel Quantization.

X. Zhong¹, K. Cai¹ and G. Song¹

1. Singapore University of Technology and Design, Singapore, Singapore

I. INTRODUCTION In recent years, spin-torque transfer magnetic random access memory (STT-MRAM) has received tremendous attention due to its low switching energy, fast read/write speed, and high scalability [1]. However, thermal fluctuation and process variation have a detrimental effect on the data recovery of STT-MRAM, leading to both read errors and write errors [2]. Error correction codes (ECCs), such as the Hamming codes and Bose-Chaudhuri-Hoquenghem (BCH) codes have been employed to improve the reliability of STT-MRAM [2, 3]. Meanwhile, the channel quantizer that quantizes the signal read back from the STT-MRAM cell is critical to support the above ECCs, since high-precision analog-to-digital converters (ADCs) are not applicable for STT-MRAM. Various criteria have been proposed for designing the quantizer for STT-MRAM, including the Maximizing-Mutual-Information (MMI) criterion, the Maximizing-Cut-off-Rate (MCR) criterion, and the Optimizing- Polyanskiy-Poor-Verdu -Bound (PPVB) criterion [4]. However, the final choice of the quantization scheme is still relying on the decoding error rate performance of ECCs. It is typically evaluated by using computer simulations, which are too slow to reach the target error rate level of 10^{-12} or below of data storage systems. In this work, we propose a union bound analysis which can accurately predict the word error rates (WERs) of ECCs with maximum-likelihood (ML) decoding over the quantized STT-MRAM channel. The derived bound provides a theoretical tool for comparing different quantization schemes at the targeted low error rate levels of data storage systems. Moreover, we also present a new criterion to design the quantizer by minimizing the WERs of ECC decoding that are obtained from the union bound analysis. Numerical results show that the union bound optimized quantizer can achieve better WER performance than the state-of-art quantizers for STT-MRAM. II. UNION BOUND ANALYSIS AND CHANNEL QUANTIZATION The union bound analysis is a theoretical technique that is used for bounding the error rate of ML decoding of ECCs. It was mainly developed for codes over symmetric channels [5]. In [6] and [7], more sophisticated union bound techniques were proposed for simple asymmetric channels, *i.e.* the Z-channel and the general binary asymmetric channel (BAC). In this work, we consider the quantized STT-MRAM channel with both write errors and read errors, which can be modelled as a concatenation of a BAC and a binary-input multiple-output discrete memoryless channel. Our proposed union bound analysis first utilizes a function of a predefined multi-dimensional distance between two codewords to calculate the pairwise error probability (PEP) [7] of the quantized STT-MRAM channel. Note that this is different from the cases of the symmetric channels where the PEP is uniquely determined by the Hamming distance of the code. Based on the PEP, we can derive a union bound of the WER of ML decoding as a function of the weight distributions of ECC. Next, we further propose to use the WER obtained from the above union bound analysis as the criterion to design the channel quantizer of STT-MRAM. We also develop effective differential evolution algorithm to determine the optimum quantization boundaries for the multi-bit quantizers. Since our proposed union bound optimized quantizer takes into consideration the weight spectrum of ECC, it can achieve better error rate performance than the prior-art quantizers. III. NUMERICAL AND SIMULATION RESULTS The system parameters of STT-MRAM are taken from [2]. In the quantized STT-MRAM channel model, we assume the write error rate of 10^{-5} , and vary the mean normalized resistance spreads $\sigma_0/\mu_0 = \sigma_1/\mu_1$ of the low and high resistances to account for the influence of different process variations. The (72,64) extended Hamming code [3] is adopted to validate our analysis, and the simulated ML decoding performance is obtained using the Bahl, Cocke, Jelinek and Raviv (BCJR) decoder [5]. In Fig. 1, we compare the decoding WERs provided by the union bound with those achieved by the BCJR decoder through simulations, with the proposed union bound optimized quantizer with different number of quantization bits q . Observe that there is a noticeable gap between the union bound and simulated WERs for the case of $q=1$. However, with two or more quantization bits, the performance gap becomes negligible, and when the WER is less than 10^{-6} , the union bound is almost identical to the simulated WER. In Fig. 2, we fix the

quantization bit to be $q=2$, and compare the WER performance with different types of quantizers. A nice agreement is observed again between the WERs predicted by the union bound and those obtained from simulations, for the various types of quantizers. Moreover, our proposed union bound optimized quantizer outperforms all the other quantizers. There is a larger performance improvement over the MMI quantizer, which is most widely adopted in the literature. This demonstrates the potential of our proposed union bound analysis in predicting the decoding error rate performance and in guiding the design of channel quantizer for STT-MRAM. Acknowledgement: This work is supported by RIE2020 Advanced Manufacturing and Engineering (AME) programmatic grant A18A6b0057 and Singapore MOE Tier 2 fund MOE2019-T2-2-123.

[1] M. Marinella, "The future of memory," in *Proc. Aerospace Conf. Big Sky, MN, USA*, Mar. 2012, pp. 1–11. [2] K. Cai, and K. A. S. Immink, "Cascaded channel modeling, analysis, and hybrid decoding for spin-torque transfer magnetic random access memory (STT-MRAM)," *IEEE Trans. Magn.*, vol. 53, no. 11, pp. 1–11, 2017. [3] K. Cai, Z. Qin, and B. Chen, "Channel capacity and soft-decision decoding of LDPC codes for spin-torque transfer magnetic random access memory (STT-MRAM)," in *Proc. Int. Conf. Comput., Netw., Commun. (ICNC), San Diego, CA, USA*, Jan. 2013, pp. 550–554. [4] Z. Mei, K. Cai and L. Shi, "Information Theoretic Bounds Based Channel Quantization Design for Emerging Memories," in *Proc. IEEE Information Theory Workshop (ITW), Guang Zhou, China*, Nov. 2018, pp. 1–5. [5] W. E. Ryan and S. Lin, *Channel Codes: Classical and Modern*, Cambridge, Cambridge University Press, 2009. [6] A. Barbero, P. Ellingsen, S. Spinsante, and O. Ytrehus, "Maximum likelihood decoding of codes on the Z-channel," in *Proc. IEEE International Conference on Communications (ICC), Istanbul, Turkey*, Jun. 2006, pp. 1–5. [7] G. Song, K. Cai and J. Cheng, "A union bound analysis for codes over binary asymmetric channels," in *Proc. IEEE International Conference on Communications (ICC), Paris, France*, May. 2017, pp. 1–5.

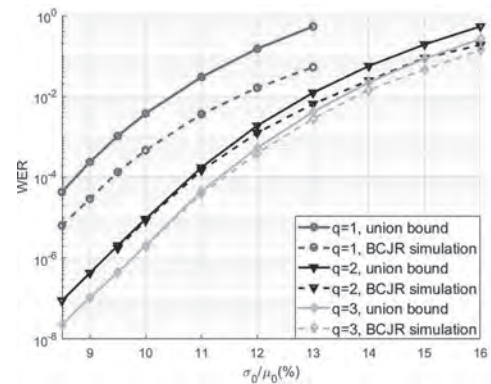


Fig. 1. Comparison between analytical and simulation WERs, with union bound optimized quantizer with $q=1,2,3$.

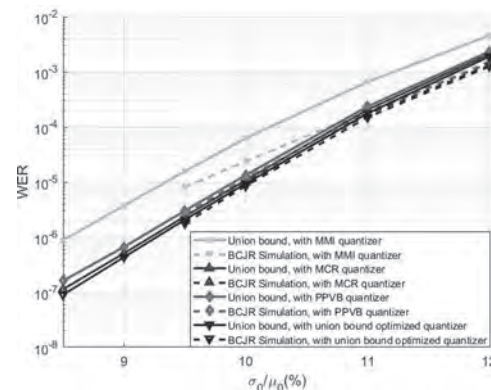


Fig. 2. Comparison between analytical and simulation WERs with different types of quantizers, for $q=2$.

IA-06. Enable TDMR Gain With Convolution Neural Network Based Machine Learning Algorithm.

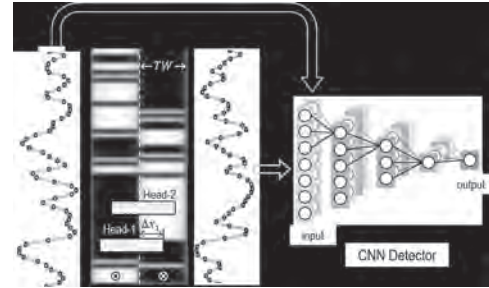
Y. Qin¹ and J. Zhu¹

1. Electrical and Computer Engineering, Carnegie Mellon University, Pittsburgh, PA, United States

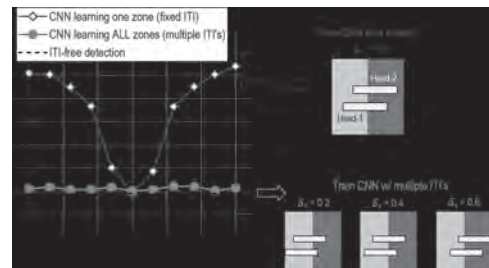
Two-dimensional magnetic recording (TDMR) with laterally-displaced multiple read heads has been developed to alleviate the impact of inter-track interference (ITI) and track edge effects. However, the cross-track (XT) position of the displaced 2nd head varies significantly with the skew angle of head assembly from ID to OD across disk radius [1]. As a result, each disk platter is divided into hundreds of groups of sectors, or zones, to accommodate the skew angle variations. The 2-dimensional equalization technique used in conventional data detection channels requires different channel parameters at different skew angles/zones for channel optimization, and the number of different channel parameter sets across the disk platter are in hundreds. Furthermore, resulting performance gain is further diminished by random fluctuations such as non-repeatable disk runout. In this situation, if we employ machine learning technique on TDMR data detection, one could imagine the possibility of achieving optimal performance in resolving ITI and track edge effects across the entire disk surface while using “learning” to replace relatively complex parameterization of physical modeling. In our previous work, we have developed deep neural network (DNN) for disk drive data detection channels with performance (detection error-rate vs. signal-to-noise ratio) slightly more superior than the state-of-the-art disk drive channels [2,3]. In the work presented here, we train a convolution neural network (CNN) in TDMR system to detect data under a wide range of ITI from different head skew angles. We demonstrate that in the medium noise dominant situation, CNN can learn all ITI in the training dataset and completely recover ITI-free BER without any physical modeling. Our eventual goal is to explore if we can train a single CNN detector to learn and optimize for all head skew angles/zones automatically, thereby lifting the complexity of designing different channel parameter sets at each head skew angle. The recorded tracks and CNN detection scheme are shown in Fig. 1. Two adjacent data tracks are written with random data and arbitrary phase. The width of the track is denoted TW , and no erase-band nor transition curvature is included. Two XT overlapped heads of width greater than TW are used. Here we simplify the modeling and assume each head only captures signals under its XT coverage. Since the relative positions of head-1 and head-2 are locked, we characterize ITI of the reader array with a single variable: the ratio between head-1 coverage of Track-II (Δx_1) versus the track width (TW): $\delta_1 = \Delta x_1 / TW$. Here we assume the ITI stays fixed within each zone, and different zones will have different ITI. In this work, we only investigate the medium noise dominated situation: the jitter noise is modeled as the uncertainty of the transition locations following a Gaussian distribution. Since both heads “see” the same magnetic patterns from the two tracks, the jitter noise is correlated noise. A CNN is used as the data detector in this work. It receives signals from both heads as input, and we only train it to detect data for Track-I. The rest of the parameters are listed in Fig. 1 caption. To simulate reading data at different skew angles, we evaluate the CNN detection BER with signals of 11 different ITI from $\delta_1=0.2$ to 0.8 as in Fig. 2. The black dashed line benchmarks the ITI-free BER. For the blue curve, the CNN detector is trained using signals from one skew angle/zone with a fixed ITI, $\delta_1=0.5$. In this case, CNN can only eliminate the trained ITI, and the detection accuracy degrades significantly whenever the testing ITI is different. In contrast, the red curve plots the BER when we train the CNN using signals with mixed ITI same as the testing dataset. This time CNN can successfully eliminate ITI for all testing head skew angles/zones. Our results suggest that CNN has the capacity to learn very complicated correlations and is solely data-driven. With the learning process, the CNN-based ML channel presented here is capable of resolving the interference from ITI infested signals, automatically rejecting them, and arriving at correct detection. This approach is fundamentally different from the conventional channel design that relies on sophisticated physical modeling and channel parameterization. In addition, the fact that a single CNN can learn a wide range of ITI states that it can optimize the channel performance for head skew angles using a single CNN eliminating the need to use multiple channel parameter sets. Not only this machine learning channel can eliminate the complex physical char-

acterization process required for conventional approach, more importantly, the TDMR performance gain can be fully realized without compromising. The potential of fully eliminating ITI also presents the possibility to have reader width wider than track width which could be critically important as track pitches in HDDs continue to decrease.

[1] Suzuto R, Nakamura Y, Osawa H, et al. Effect of reader sensitivity rotation in TDMR with head skew. IEEE Transactions on Magnetics, 2016, 52(7): 1-4. [2] Qin Y, Zhu J G. Deep Neural Network: Data Detection Channel for Hard Disk Drives by Learning. IEEE Transactions on Magnetics, 2020, 56(2): 1-8. [3] Qin Y, Zhu J G. Automatically Resolving Inter-Track Interference with Convolution Neural Network Detection Channel in TDMR. IEEE Transactions on Magnetics, 2020.



CNN detector in TDMR. The heads have DT sensitivity of $PW50/\text{bit-length} = 2.5$. The green(yellow) signals are from head-1(head-2), and they are sampled 1 bit/period. The jitter width is assumed 1.4nm in this work. The CNN channel has 3 hidden layers (blue) with 50 filters each. The kernel sizes are 3-3-3-1. $ReLU$ is used as the non-linear activation function, and cross-entropy is the loss function.



Detection BER at different zone/ITI. Black dashed curve: ITI-free detection BER. Blue: CNN is only trained with signals of fixed ITI $\delta_1=0.5$. Red: CNN is trained with signals with 11 different ITI (same as the testing dataset).

IA-07. Multilayer Perceptron Based Method for Track Misregistration Correcting in Dual-Reader Two-Track Reading BPMR Systems.

K. Kanhuthod¹ and C. Warisarn¹

1. King Mongkut's Institute of Technology Ladkrabang College of Advanced Manufacturing Innovation, Bangkok, Thailand

I. Introduction Track misregistration (TMR) and two-dimensional (2-D) interference that consists of an inter-track interference (ITI) and inter-symbol interference (ISI) are the significant problems in an ultra-high bit-patterned media recording system (BPMR) which easily degrade the bit-error-rate (BER) performance of the system, because of the extremely narrow distance between bit-islands. It very challenges to control the reader to fly above the center of the desired track. Normally the TMR effect can be controlled by servomechanism [1] which required extra area to store the redundancy bits for tracking the data track. Instead, several works use only readback signals to estimate and correct the TMR effect [2-4]. For example, we proposed a TMR prediction method by using the energy ratio of readback signals, and then the TMR effect can be dealt with utilizing the appropriate 2-D equalizers together with the use of soft-information adjustment (SIA) technique [5]. II. Proposed Methods To improve the TMR estimation accuracy and BER performances of BPMR system; therefore, we propose to use the neural network models called a multi-layer perceptron (MLP) in both TMR level prediction and TMR effect correction processes. We consider the dual-reader two-track reading under BPMR media at an areal density (AD) of 3.0 Tbits/in², which track-pitch, T_t and bit-period, T_b are set to be 14.5 nm. In the reading process, 2 readers simultaneously read the medium of upper- and lower-tracks, while the sidetracks located above and below two main tracks will be also read, which denoted as $r_{-1,k}$, $r_{0,k}$, $r_{1,k}$ and $r_{2,k}$. Then, 4 readback signals are equalized by 1-D (one-dimensional) equalizers which are designed according to signal with no TMR effect. The equalized data sequences will then be multiplied with their absolute value for each data sample to extend their amplitude before sending them to the TMR level prediction and TMR effect correction processes, respectively. In TMR level prediction, four modified readback signals, $u_{-1,k}$, $u_{0,k}$, $u_{1,k}$ and $u_{2,k}$ with the size of $4 \times 32,760$ bits will then be grouped into 4×3 bits in each group before sending to the TMR level prediction process. That means each considered group consists of 12 data bits and so there are 10,920 groups in one set of readback sequence, the number group represented by $j \in \{1, 2, 3, \dots, 10920\}$. Fig. 1(a) shows the structure of the MLP TMR estimator which consists of 1 input layer and 12 input nodes, 5 hidden layers consist of 100 hidden nodes, and 1 output layer with a single node. This MLP TMR estimator receives a group of readback signals at a time for predicting the estimated TMR level, TMR'_j of the j th group. Then, the estimated TMR levels of all groups were averaged to obtain the estimated TMR level, TMR' of the entire sequence. Here, the accuracy percentage of TMR' is measured as accuracy (%) = $100 - (|TMR' - TMR| / TMR \times 100)$ [5]. we also propose to use the MLP data detector which may be employed instead of the conventional detectors-based PRML system. Fig. 1(b) shows the structure of the MLP data detector, which is identical to MLP TMR estimator except for the number of input and output nodes. The MLP data detector receives a group of modified readbacks similar to the MLP TMR estimator, but it also receives an additional estimated TMR level, TMR' that was produced from MLP TMR estimator. Here, it is fixed as one of the input data of the MLP data detector. Finally, we can obtain the estimated user bits of both upper- and lower-tracks, i.e., $a'_{0,k}$ and $a'_{1,k}$ in the size of 2×3 bits for all 10,920 groups. In this study, the leaky rectified linear unit (ReLU) is used as an activation function for the hidden nodes and linear function in the output nodes for both MLP models. The linear regressions are then adopted for calculating their outputs. The Adam algorithm is used to optimize the weights and bias of both MLP models. III. Results and Discussion In this study, we start with the consideration of an accuracy percentage of TMR level estimation in various TMR and SNR levels where the position jitter is given to be 0%. The TMR level is varied from 0% to 15% of a track pitch as mentioned above. The signal-to-noise ratio (SNR) that is defined as $10 \log_{10}(1/\sigma^2)$, where σ is a standard deviation of electronics noise, is first considered at 10, 15, 20, and 25 dBs. We found that the proposed MLP TMR estimator can provide an accuracy percentage higher than 80% for all 4 considered SNRs and all considered TMR levels. Especially, at the higher SNR, e.g., 15, 20, and 25 dBs, we can get more than

90% accuracy for all TMR levels. Moreover, we also investigate the BER of our proposed MLP detector, which is compared with the conventional partial response maximum likelihood (PRML) system that performs based on 2-D equalizers and 2-D Viterbi detectors together with the SIA technique [5] where it is represented with "conventional". As shown in Fig. 2, it seems that at higher SNR, our proposed system can provide better performances for all TMR levels. For example, at BER = 10^{-4} and TMR level is 0%, our proposed system can provide more than 5 dB over the conventional system. The system performance implies that it is possible to use the MLP neural networks for signal processing in BPMR system.

[1] Y. B. Chang, D. K. Park, and N. C. Park, IEEE Trans. Magn., Vol. 38, no. 2, p. 1441 (2002) [2] C. Warisarn, IEEE Trans. on Magn., Vol. 55, no. 7, p. 1 (2019) [3] W. Busyatras, C. Warisarn, and Y. Okamoto, AIP Adv., Vol. 7, p. 056501 (2016) [4] S. Han, G. Kong, and S. Choi, IEEE Transactions on Magnetics, Vol. 55, no. 7, p. 1 (2019) [5] K. Kankhuthod, W. Busyatras, and C. Warisarn, 17th ECTI-CON., p. 735 (2020)

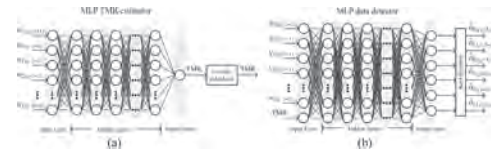


Fig. 1: MLP structures of the TMR level estimator and TMR detector.

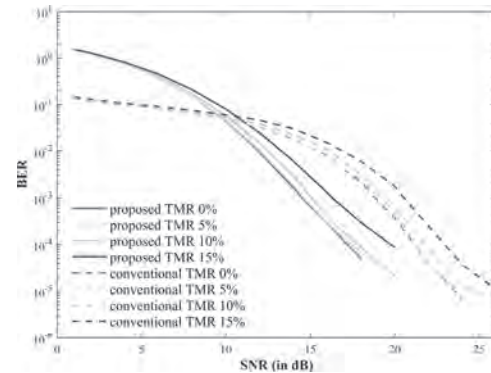


Fig. 2: BER performance comparison between the proposed MLP based TMR correction method versus the conventional method at the AD of 3.0 Tbits/in², here the position jitter is fixed to be 0%.

IA-08. Effect of Lubricant Thickness on the Nanoscale Heat Transfer at the Head-Disk Interface.

Q. Cheng¹, S. Rajauria², E. Schreck², R. Smith², Q. Dai² and D. Bogy¹
 1. Mechanical Engineering, University of California Berkeley, Berkeley, CA, United States; 2. Western Digital Corp, San Jose, CA, United States

I. INTRODUCTION In the head-disk interface (HDI) of heat-assisted magnetic recording (HAMR), a laser is employed over the read/write area to locally heat the recording media to its Curie temperature to facilitate data writing. During this process, the lubricant on the disk undergoes harsh cyclic thermal processes so that the lubricant is partially depleted by the laser [1]. Thus, the lubricant thickness is locally reduced during the writing, but afterwards it recovers gradually due to lubricant reflow [2]. In this study, the effect of the lubricant thickness on the nanoscale heat transfer across the HDI is studied using a thermal fly-height control (TFC) heater and an embedded contact sensor (ECS). The dR/dP , the rate of change in the ECS resistance with respect to the TFC power, was measured to indicate the HDI heat transfer coefficient [3]. It is demonstrated that the ECS is a good thermal sensor for the lubricant thickness through the contact cooling effect. II. EXPERIMENT SETUP Experiments were performed on a component-level spin-stand stage. When flying over the HAMR disks with the lubricant thickness from 8.0 Å to 12.5 Å, the TFC heater was energized until head-disk touchdown occurred. During the touchdown process, the ECS, biased with a constant DC current, was used to monitor the head temperature. An acoustic emission (AE) sensor was used to detect the head-disk contact. The ECS resistance versus the TFC power relation (R-P) was measured. Then the R-P curve's derivative, dR/dP , was obtained to indicate the head-disk nanoscale heat transfer. III. RESULTS AND DISCUSSION Fig. 1 shows the results of dR/dP versus backoff TFC power using different ECS bias currents, where zero backoff power is the TFC power at the head-disk contact onset detected by the AE sensor. The figure presents the contact cooling effect around +1 mW backoff TFC power, which appears as the local minimum. It is seen from the figure that the cooling effect is stronger with a higher ECS bias current, since the hotter ECS undergoes a larger temperature drop when touching the rotating disk surface. Thus, the ECS biased with a higher current delivers better sensitivity for the experiments. Fig. 2 shows the dR/dP curves for the disks with the lubricant thickness varying from 8.0 Å to 12.5 Å. As the lubricant thickness increases, the dR/dP local minimum rises and hence the contact cooling effect weakens. Therefore, the lubricant behaves as a thermal barrier to the head-disk heat transfer and its effect can be quantified by the ECS. IV. CONCLUSIONS In this digest, touchdown experiments are introduced to quantify the effect of the lubricant on the nanoscale heat transfer at the head-disk interface. The experimental results show that a higher ECS bias current ensures a better sensitivity for the experiments and that the lubricant layer weakens the head-disk heat transfer. Taking advantage of this effect, the ECS can be further used to measure the local lubricant thickness depletion and reflow during HAMR operations.

[1] M. Kryder, E. Gage, T. McDaniel, Proc. IEEE, 96(11), 1810-1835 (2008). [2] H. Wu, A. Mendez, S. Xiong, J. Appl. Phys., 117(17), 17E310 (2015). [3] N. Zuckerman, J. Kiely, M. Anaya-Dufresne, IEEE Trans. Magn., 55(3), 1-5 (2018).

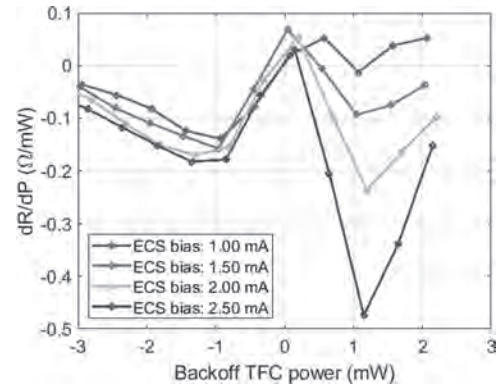


Fig. 1. The dR/dP versus backoff TFC power using different ECS bias currents.

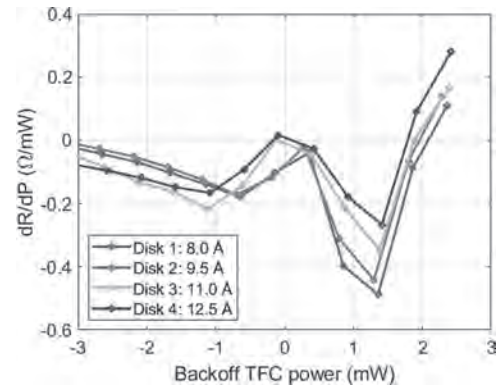


Fig. 2. The dR/dP versus backoff TFC power using different lubricant thicknesses (ECS bias: 2.50 mA).

INVITED PAPERS

IA-09. 317 Gb/in² Recording Areal Density on Strontium Ferrite Tape INVITED.

S. Furrer¹, P. Ebermann¹, M. Lantz¹, H. Rothuizen¹, W. Haeberle¹, G. Cherubini¹, R.D. Cideciyan¹, S. Tsujimoto², Y. Sawayashiki², N. Imaoka², Y. Murata², T. Ueyama², Y. Akano², T. Kaneko², H. Suzuki², M. Shirata², K. Naoi², T. Koike² and H. Doshita²
 1. IBM Research, Rueschlikon, Switzerland; 2. Recording Media Research Laboratories, FUJIFILM Corporation, Odawara, Japan

The current exponential growth in data in combination with the slow-down in areal density and cost scaling of hard disk drives (HDDs) is fueling demand for cost effective storage technology. Magnetic tape storage has a very low total cost of ownership and is suited for the storage of less frequently accessed data where tape's higher access latency is an acceptable trade-off for the reduced cost. Today's best of breed tape drives provide a 20 TB native cartridge capacity at an areal density of 11.7 Gbit/in². This is about two orders of magnitude lower than the areal density of state-of-the-art HDDs and implies that tape has significant potential for continued scaling. This is in line with the projections of the Information Storage Industry Consortium (INSIC) Tape Roadmap that projects a 34% annual growth in tape areal density leading to a predicted 278 Gb/in² in 2029 [1]. In this work we describe a tape areal density demonstration using a prototype perpendicularly oriented strontium ferrite (SrFe) tape that shows the potential of recording at 317 Gbit/in². Key properties of the media include: a particle volume of 950 nm³, a particle coercivity of $H_c=208$ kA/m, a perpendicular squareness ratio of 0.87, a surface roughness $R_a=1.1$ nm and $R_z=17$ nm measured by AFM, and a tape thickness of 4.3 μ m. We investigated the recording potential of the SrFe media by writing repeating 255-bit pseudo-random binary sequences (PRBS) at linear densities ranging from 500 to 768 kbp. The data was read back using a 29 nm side shielded tunneling magneto resistive (TMR) reader from an HDD and the captured readback signal was processed offline using a software read channel. Fig. 1(a) shows the average SNR of the captured data measured at the input of an EPR4 detector and plotted versus linear density. Fig. 1(b) plots the byte-error rate (BER) versus linear density, obtained by processing the data using three detection algorithms: 1) 8-state EPR4 detection, 2) adaptive 16-state noise-predictive maximum-likelihood (NPML) detection and 3) extended 64-state data-dependent NPML detection that tracks the first and second order statistics of the data-dependent noise (D3-NPML). Each data point results from processing about five million bits. To set a target threshold for the BER at the output of the detector, we analyzed the performance of the Reed-Solomon product code used in state-of-the-art tape drives combined with the iterative decoding scheme described in [2]. This analysis indicates a post-error-correction-coding byte-error rate (UBER) of less than $1e-20$, equivalent to that of an enterprise class tape drive, can be achieved with two full decoding iterations if the BER at the output of the detector is $< 4.5e-2$. Hence, we take a $BER < 4.5e-2$ as the target threshold. The D3-NPML detector provides significantly better performance than the NPML detector and crosses the BER threshold of $4.5e-2$ at a linear density of 750 kbp. At a linear density of 702 kbp the D3-NPML detector provides a BER of $2.8e-2$ and the NPML detector also has a BER performance below the target threshold. The average SNR at 750 kbp and 702 kbp are 9.9 dB and 10.6 dB, respectively. Thus, the D3-NPML detector achieves our target $1e-20$ UBER at an operating point of 702 kbp with an SNR margin of about 0.7 dB. In the area of track following, we made a set of advances to enable the rapid track-density scaling projections of the INSIC roadmap. First, we developed a new timing-based servo pattern that is shown in Fig. 2(a). Second, we developed a field programmable gate array prototyping board that implements four servo channels and a quad channel averaging scheme where the tape head position is calculated by combining position estimates from the readback signals of four servo patterns, see Fig. 2(b). Third, we enhanced the tape transport described in [2] with two 20 mm diameter air bearing tape guides and a prototype track-following actuator that enables a lower spacing between the tape guides adjacent to the head. This decreased tape guide spacing reduces compressional wave disturbances

that can degrade the track-following performance. Fourth, we developed a low friction tape head that reduces friction by about 75% compared to the heads used in our previous work [2],[3] and further reduces compressional wave disturbances. Finally, we used the H-infinity framework to design a set of tape velocity optimized track-following controllers. Combining these technologies, we achieved a position error signal (PES) characterized by its standard deviation of $\sigma_{PES} \leq 3.18$ nm over the tape velocity range of 1.2 to 4.1 m/s as shown in Fig. 2(c). We estimate the minimum reliable track width supported by this tracking accuracy with the INSIC model used in our previous work [2], [3], i.e.: track width = $2 \times (2)^{0.5} \times 3\sigma_{PES} + \text{reader width}$. Taking the 29nm width of the reader used for the recording experiments and a worst case $\sigma_{PES} = 3.2$ nm results in a 56.2 nm track width and a track density of 451.9 ktpi. Combined with the linear density of 702 kbp demonstrated with the 29 nm reader enables a potential areal recording density of 317 Gb/in².

[1] Information Storage Industry Consortium (INSIC) 2019-2029 Tape Roadmap, <http://www.insic.org/wp-content/uploads/2019/07/INSIC-Technology-Roadmap-2019.pdf> [2] S. Furrer et al., "85.9 Gb/in² recording areal density on barium ferrite tape", *IEEE Trans. Magn.*, vol. 51, no. 4, Apr. 2015, Art. ID 3100207. [3] M. A. Lantz et al., "123 Gb/in² recording areal density on barium ferrite tape", *IEEE Trans. Magn.*, vol. 51, no. 11, Nov. 2015, Art. ID 3101304.

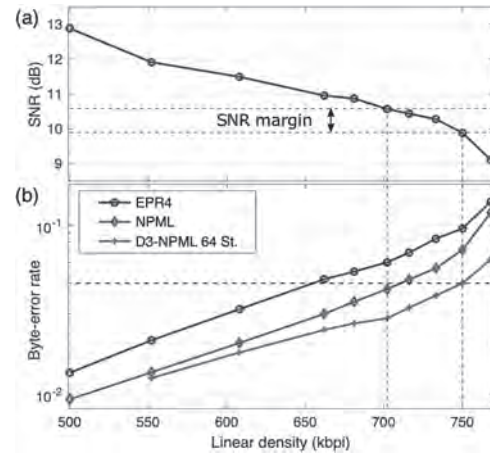


Fig 1. (a) SNR vs. linear density, (b) BER vs. linear density for three detectors. The dashed line in the BER plot indicates the $4.5e-2$ target byte-error rate threshold.

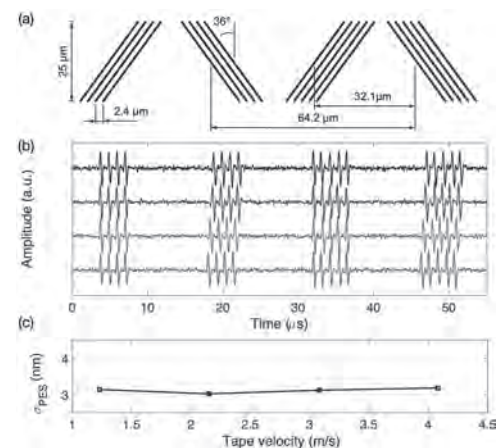


Fig 2. (a) Geometry of the new servo pattern, (b) Read back signals from four servo tracks formatted with the new servo pattern, at 2.15m/s tape velocity, (c) Standard deviation of the PES versus tape velocity.

IA-10. HDD Reader Technology Roadmap to an Areal Density of 4 Tbps and Beyond INVITED.

G. Albuquerque¹, S. Hernandez², M.T. Kief² and L. Wang¹

1. Western Digital Corp Fremont Office, Fremont, CA, United States;
2. Seagate Recording Head Operations, Bloomington, MN, United States

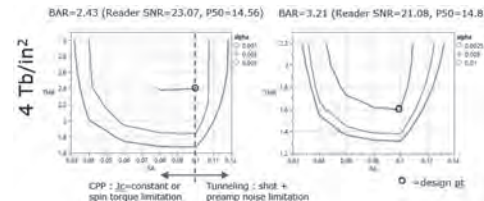
Introduction and Background 60 Zettabytes (ZB or 10^{21} Bytes) will be created in 2021 and grow to 160 ZB by 2025.(1) To store this data, Hard Disk Drives (HDD) areal density must continue to increase from current products near 1.1Tbps (2) to the demonstrated AD of 2.77Tbps (3) and beyond. To support this growth, reader technology must also advance to higher AD with manufacturable solutions. Remarkably, HDD reader technology still utilizes the Spin Valve reader concept that was first introduced in 1997 at ~ 1 Gbps. This 1000x increase in reader AD capability has been achieved by scaling of critical dimensions, the introduction of TMR, advances in stack materials/ processing and utilization of multiple read sensors. The extendibility of the SV TMR design and supporting innovations has been remarkable - but likely not without limits. The HDD industry’s Advanced Storage Research Consortium (ASRC, <http://asrc.idema.org/>) has sought to understand and address read sensor requirements for HDD Areal Densities (AD) up to 4Tbps and higher. In this paper we release the ASRC reader roadmap. We identify critical challenges and key gaps for the SV TMR type reader to support 4Tbps. We then outline what may be required for > 4Tbps and explore how to proceed. Approach and Methods We begin by seeking to understand the potential extendibility of the Reader Spin Valve design with TMR stack. We partition the problem between Resolution and SNR. Multiple reader design geometries are considered. (Figure 1.) The reader design resolution capabilities were determined using a new 2D micromagnetic reciprocity approach. The Bottom SV and derivative Recessed AFM design appear to be sufficient for 4Tbps. To understand the reader SNR requirements, one must begin with the recorded data that one needs to readback. A top-down system level approach and bottom-up micromagnetic modeling approach are combined and iterated to identify the suitable reader requirements. A RSS model is used to estimate reader requirements between 2 and 6 Tbps.(4) A combined finite difference micromagnetic model and analytical reader signal-noise model is used to perform DOE’s to determine the closest fit solutions. Results and Discussion The results of this study show that reader widths must shrink to near 10nm and shield-to-shield spacing approach 15nm to provide cross-track and down-track resolution to support track densities near 1130 kTPI and linear densities > 3600 kFCI for ~ 4Tbps. Meeting these targets will demand improved process capabilities and new innovations in device designs. SNR requirements are used to project TMR reader stack magnetoresistance (MR) and resistance-area (RA) product targets. Within reasonable assumptions for sensor bias, stability and material properties, we show stack requirements are well in excess of 100% MR at 0.10 uOhm-cm RA. (Figure 2) This requirement is significantly more challenging than previously projected and exceeds best reports to date for TMR readers (5). In addition to seeking high signal, it is also vital to understand and manage the noise components. We show thermal magnetic noise is a growing concern but we further show that other contributions such as preamp noise could dominate as reader dimensions shrink and resistance grows. Roadmap Challenges and Gaps An overall reader spec is provided with proposed geometric, magnetic, and electronic targets. We also explore potential future designs to meet requirements > 4Tbps. A summary of key issues, possible solutions and important research topics is reviewed. We hope this study can illuminate and motivate critical research into these key reader technologies. Meeting these challenges will be critical to continued HDD AD growth to 4Tbps and beyond.

1) Data Age 2025, Dec 2018 <https://www.seagate.com/our-story/data-age-2025/> 2) Forbes, July 2020 <https://www.forbes.com/sites/tomcoughlin/2020/07/08/western-digital-data-center-16-20-tb-hdds/?sh=4f56c3f87ba9> 3) TMRC 2020, Paper A7, S. Grantz et al, “Heat Assisted Magnetic Recording Dependence on Reader for Conventional and Shingled Magnetic Recording” see <https://blog.seagate.com/enterprises/energy-assisted-magnetic-recording-will-solve-the-need-for-capacity/> 4) S. Hernandez, et. al, “Geometrical Scaling Limits of Heat-Assisted Magnetic Recording”, IEEE Trans. Magn., 2020 (accepted). 5) Nakatani et al, “Read

sensor technology for ultrahigh density magnetic recording” MRS Bulletin 2018.



A range of reader designs were considered to satisfy the down-track and cross-track resolution requirements. The Bottom SV and derivative Recessed AFM design may be sufficient near 4Tbps.



Reader stack requirements at 4Tbps for BAR 2.4 (left) and 3.2 (right). MR requirement varies with free layer damping constant alpha as illustrated. The best fit is shown by design point circle on graph.

Read

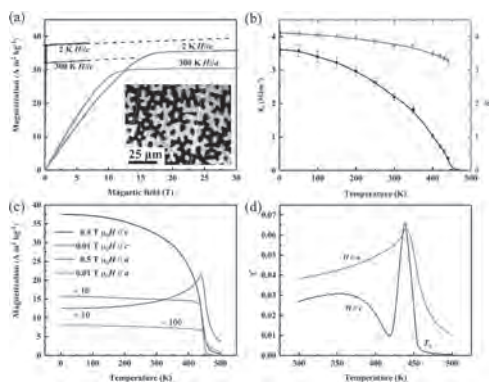
IA-11. New Highly-Anisotropic Rh-Based Heusler Compound for Magnetic Recording

Y. He¹, G. Fecher¹ and C. Felser¹

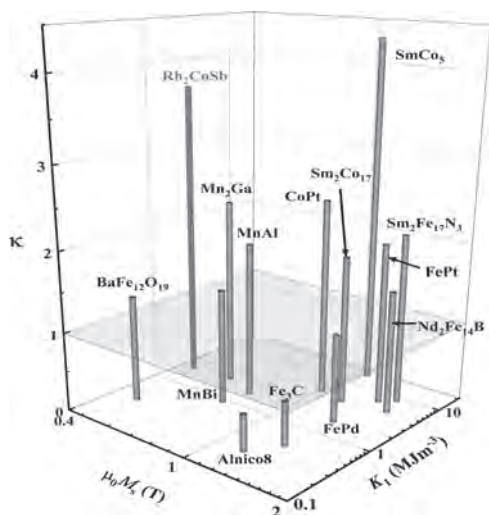
1. Max-Planck-Institut für Chemische Physik fester Stoffe, Dresden, Germany

The development of high-density magnetic recording media is limited by the superparamagnetism in very small ferromagnetic crystals. Hard magnetic materials with strong perpendicular anisotropy offer stability and high recording density. To overcome the difficulty of writing media with a large coercivity, heat assisted magnetic recording (HAMR) has been developed, rapidly heating the media to the Curie temperature T_c before writing, followed by rapid cooling. Requirements are a suitable T_c , coupled with anisotropic thermal conductivity and hard magnetic properties. Here we introduce Rh_2CoSb as a new hard magnet with potential for thin film magnetic recording. A magnetocrystalline anisotropy of 3.6 MJm^{-3} is combined with a saturation magnetization of $\mu_0 M_s = 0.52 \text{ T}$ at 2 K (2.2 MJm^{-3} and 0.44 T at room-temperature). The magnetic hardness parameter of 3.7 at room temperature is the highest observed for any rare-earth free hard magnet. The anisotropy is related to an unquenched orbital moment of $0.42 \mu_B$ on Co, which is hybridized with neighbouring Rh atoms with a large spin-orbit interaction. Moreover, the pronounced temperature-dependence of the anisotropy that follows from its T_c of 450 K, together with a high thermal conductivity of $20 \text{ Wm}^{-1}\text{K}^{-1}$, makes Rh_2CoSb a candidate for development for heat assisted writing with a recording density in excess of 10 Tb/in^2 .

Adv. Mater. 2020, 32, 2004331



Magnetic properties of Rh_2CoSb .



Comparison of the magnetic hardness parameter κ with other hard magnets.

Session IB

MAGNETIC FIELD SENSORS I

Paulo P Freitas, Chair

International Iberian Nanotechnology Laboratory, Braga, Portugal

INVITED PAPER

IB-01. Mechanically Shapeable Magnetic Field Sensor Technologies INVITED.G. Canon Bermudez¹*1. Helmholtz-Zentrum Dresden-Rossendorf, Dresden, Germany*

Magnetic field sensors in a rigid format have been typically associated with recording heads, hard disk drives and the automotive industry. Unlocking new application scenarios requires changing the intrinsic properties of these sensors to make them adaptable to new challenges. One way to accomplish this goal, is to allow these sensors to change shape and be flexible, stretchable or solution-processable, what we call shapeable magnetoelectronics [1]. This technology relies on the smart combination of inorganic thin films prepared directly on flexible or elastomeric substrates. Shapeable magnetoelectronics resulted from the cooperative effort of fundamental and application-oriented communities in the field of curvilinear magnetism [2], and the involvement of fabrication methods for flexible electronics [3], [4]. The combination of these research fields has resulted in a variety of flexible [5], [6], printable [7]–[9], stretchable [10]–[12] and imperceptible [13]–[17] magnetic field sensing elements. Stemming from these developments, various applications like automotive [19], consumer electronics and point of care [6], [13], [14], and virtual reality [15]–[17], have emerged. For automotive purposes, shapeable magnetic sensors can be useful to monitor the magnetic field profile the nonplanar and narrow gaps inside electrical motors, to minimize losses and improve the overall efficiency [5]. In point-of-care applications, they can enable fast biosensing methods for wearable health monitoring based on magnetofluidics [6], [13]. For virtual reality they allow a whole new set of touchless interaction possibilities using the ambient magnetic fields as input stimuli [15]–[17]. One example of this application is an on-skin sensor, which can dim the intensity of a virtual lightbulb based on the relative angle between the sensor and the magnetic field of a permanent magnet [16]. This idea was further improved to remove the need for permanent magnets and instead use the earth's magnetic field as input stimulus. Reaching this level of sensitivity required the use of barber pole [18] modified anisotropic magnetoresistive (AMR) sensors, which allowed detecting magnetic fields of μT with a flexible on-skin patch. Aside from enable artificial magnetoception, the patch can be used as an interactive device for virtual reality which only uses the geomagnetic field [15] (Fig. 1). Further works have improved the sensitivity to about 200 nT, which could have applications for highly sensitive point-of-care devices [14]. In recent works, we have demonstrated shapeable magnetoelectronics which are multimodal, so that they transduce and discriminate both tactile (via mechanical pressure) and touchless (via magnetic field) stimuli in real time [17]. Such a feat is attained by fabricating a magnetic microelectromechanical platform (m-MEMS), which combines flexible magnets based on polymer composites and mechanically compliant magnetic sensors. These m-MEMS e-skins enable complex interactions with magnetically functionalized objects in the real world, which supplement the content data appearing in virtual reality. For example, an augmented reality menu with multiple layers of interaction can be operated with one single sensor using its embedded multi-dimensional touch (Fig. 2, top). A challenging aspect for shapeable magnetoelectronics is the fact that output signals are usually amplified by rigid components outside the flexible supports. This readout scheme can introduce substantial noise through the cabling which is then amplified together with the signals. Eliminating this noise requires including amplifying elements directly on the flexible support, which implies using intrinsically flexible, thin-film transistor technologies. We have demonstrated such an approach, by combining highly sensitive magnetic field sensorics with high performance InGaZnO based readout electronics, on the same flexible support [19] (Fig. 2, bottom). Although entirely flexible, this platform outperforms commercial rigid magnetic sensor systems in responsivity by at least one order of magnitude. This noteworthy performance is achieved by designing a giant magnetoresistive sensor bridge connected to a cascade of differential and power amplifiers acting as readout circuitry. Combining all these features in robust on-skin devices will propel this field beyond exploratory research

and towards full-fledged applications, where shapeable magnetic sensors can be crucial for maximizing device performance.

- [1] D. Makarov, M. Melzer, D. Karnaushenko, and O. G. Schmidt, "Shapeable magnetoelectronics," *Applied Physics Reviews*, vol. 3, no. 1, p. 011101, Mar. 2016, doi: 10.1063/1.4938497. [2] R. Streubel *et al.*, "Magnetism in curved geometries," *J. Phys. D: Appl. Phys.*, vol. 49, no. 36, p. 363001, Aug. 2016, doi: 10.1088/1751-8113/48/12/125202. [3] S. Huang, Y. Liu, Y. Zhao, Z. Ren, and C. F. Guo, "Flexible Electronics: Stretchable Electrodes and Their Future," *Advanced Functional Materials*, vol. 29, no. 6, p. 1805924, 2019, doi: <https://doi.org/10.1002/adfm.201805924>. [4] Y. Liu, M. Pharr, and G. A. Salvatore, "Lab-on-Skin: A Review of Flexible and Stretchable Electronics for Wearable Health Monitoring," *ACS Nano*, vol. 11, no. 10, pp. 9614–9635, Oct. 2017, doi: 10.1021/acsnano.7b04898. [5] M. Melzer *et al.*, "Wearable Magnetic Field Sensors for Flexible Electronics," *Advanced Materials*, vol. 27, no. 7, pp. 1274–1280, Feb. 2015, doi: 10.1002/adma.201405027. [6] G. Lin, D. Makarov, M. Melzer, W. Si, C. Yan, and O. G. Schmidt, "A highly flexible and compact magnetoresistive analytic device," *Lab Chip*, vol. 14, no. 20, pp. 4050–4058, 2014, doi: 10.1039/C4LC00751D. [7] D. Karnaushenko, D. Makarov, C. Yan, R. Streubel, and O. G. Schmidt, "Printable Giant Magnetoresistive Devices," *Advanced Materials*, vol. 24, no. 33, pp. 4518–4522, Aug. 2012, doi: 10.1002/adma.201201190. [8] D. Karnaushenko, D. Makarov, M. Stöber, D. D. Karnaushenko, S. Baunack, and O. G. Schmidt, "High-Performance Magnetic Sensorics for Printable and Flexible Electronics," *Adv. Mater.*, vol. 27, no. 5, pp. 880–885, Feb. 2015, doi: 10.1002/adma.201403907. [9] D. Makarov, D. Karnaushenko, and O. G. Schmidt, "Printable Magnetoelectronics," *ChemPhysChem*, vol. 14, no. 9, pp. 1771–1776, 2013, doi: 10.1002/cphc.201300162. [10] M. Melzer *et al.*, "Stretchable Magnetoelectronics," *Nano Letters*, vol. 11, no. 6, pp. 2522–2526, Jun. 2011, doi: 10.1021/nl201108b. [11] M. Melzer, D. Karnaushenko, G. Lin, S. Baunack, D. Makarov, and O. G. Schmidt, "Direct Transfer of Magnetic Sensor Devices to Elastomeric Supports for Stretchable Electronics," *Advanced Materials*, vol. 27, no. 8, pp. 1333–1338, Feb. 2015, doi: 10.1002/adma.201403998. [12] M. Melzer, D. Makarov, and O. G. Schmidt, "A review on stretchable magnetic field sensorics," *J. Phys. D: Appl. Phys.*, vol. 53, no. 8, p. 083002, Feb. 2020, doi: 10.1088/1361-6463/ab52cf. [13] G. Lin, D. Makarov, and O. G. Schmidt, "Magnetic sensing platform technologies for biomedical applications," *Lab Chip*, vol. 17, no. 11, pp. 1884–1912, May 2017, doi: 10.1039/C7LC00026J. [14] P. N. Granell *et al.*, "Highly compliant planar Hall effect sensor with sub 200 nT sensitivity," *npj Flexible Electronics*, vol. 3, no. 1, p. 3, Feb. 2019, doi: 10.1038/s41528-018-0046-9. [15] G. S. Cañón Bermúdez, H. Fuchs, L. Bischoff, J. Fassbender, and D. Makarov, "Electronic-skin compasses for geomagnetic field-driven artificial magnetoreception and interactive electronics," *Nature Electronics*, vol. 1, no. 11, p. 589, Nov. 2018, doi: 10.1038/s41928-018-0161-6. [16] G. S. Cañón Bermúdez *et al.*, "Magnetosensitive e-skins with directional perception for augmented reality," *Science Advances*, vol. 4, no. 1, p. eaao2623, Jan. 2018, doi: 10.1126/sciadv.aao2623. [17] J. Ge *et al.*, "A bimodal soft electronic skin for tactile and touchless interaction in real time," *Nat Commun*, vol. 10, no. 1, p. 4405, Dec. 2019, doi: 10.1038/s41467-019-12303-5. [18] K. Kuijk, W. van Gestel, and F. Gorter, "The barber pole, a linear magnetoresistive head," *IEEE Transactions on Magnetics*, vol. 11, no. 5, pp. 1215–1217, Sep. 1975, doi: 10.1109/TMAG.1975.1058886. [19] N. Münzenrieder *et al.*, "Entirely Flexible On-Site Conditioned Magnetic Sensorics," *Advanced Electronic Materials*, vol. 2, no. 8, p. 1600188, Aug. 2016, doi: 10.1002/aelm.201600188.

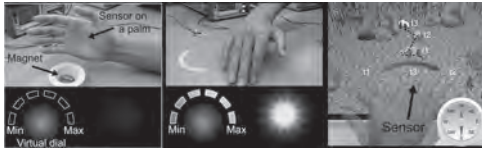


Fig. 1 Shapeable magnetic sensors as touchless interactive devices for virtual reality. (left) Human hand wearing the on-skin magnetic sensor and approaching a permanent magnet. (center) As the user turns it hands over the magnet, the intensity of virtual lightbulb is dimmed. This two panels are adapted from reference [18]. (right) Applying the same concept but changing the sensing principle allows controlling a virtual character on screen using only the earth's magnetic field. This panel is adapted from reference [17]

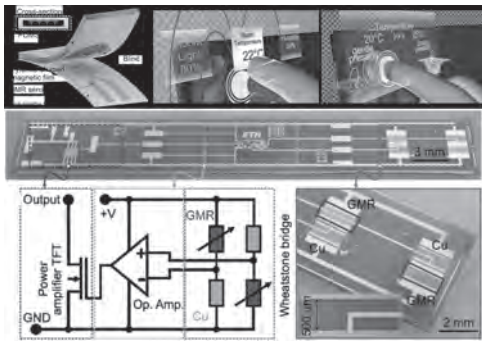


Fig. 2 Multimodal shapeable magneto-electronics and fully flexible conditioning electronics. (top left) Schematic of a m-MEMS. (top center) Approaching an object using the touchless mode of the m-MEMS activates the first layer of interaction. (top right) Touching the object activates a second layer of interaction and opening a new menu. (center) Entirely flexible and on-site conditioned magnetic field sensing platform containing a power amplifying cascade (bottom left) and a giant magneto-resistive sensor Wheatstone bridge (bottom right).

CONTRIBUTED PAPERS

IB-02. ΔE -Effect Magnetic Field Sensors.

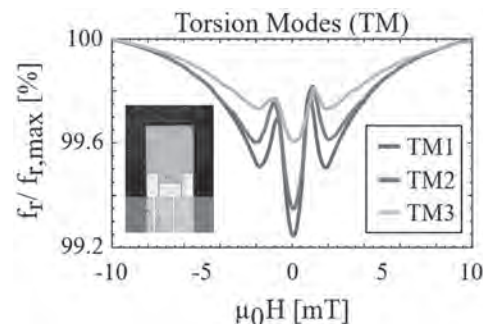
B. Spetzler¹, E. Golubeva¹, J. Su², P. Wiegand³, C. Bald³, J. Schmalz³, C. Kirchhof¹, F. Niekietl², D. Meyners¹, M. Gerken³, G. Schmidt³, R. Rieger³, F. Lofink², J. McCord¹ and F. Faupel¹

1. Institute for Materials Science, Christian-Albrechts-Universität zu Kiel, Kiel, Germany; 2. Fraunhofer-Institut für Siliziumtechnologie ISIT, Izehoe, Germany; 3. Institute for Electrical Engineering and Information Engineering, Christian-Albrechts-Universität zu Kiel, Kiel, Germany

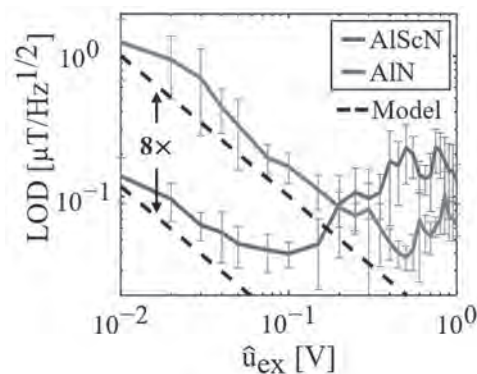
In recent years, magnetoelectric ΔE -effect sensors have been investigated for the detection of small amplitude and low-frequency magnetic fields that typically occur in many biomedical and diagnostic applications. Such sensors are based on magnetoelectric composite resonators, which consist of mechanically coupled magnetostrictive and piezoelectric materials. They can be processed on a large scale by microelectromechanical system (MEMS) technology with dimensions of a few millimeters down to a few micrometers and are compatible with complementary metal-oxide-semiconductor (CMOS) electronics. Furthermore, they can be operated at room temperature with a broad-bandwidth and a large dynamic range and are robust against microphony and mechanical noise. Such sensors utilize the ΔE -effect of the magnetostrictive material, i.e. the change of the mechanical stiffness tensor with magnetization and hence, with an applied magnetic field. Since our first publication of this sensor concept in 2011 [1], much progress has been made in understanding the complex interplay of magnetic, mechanical, and electrical properties and their influence on signal and noise of the sensor system. This holds for different designs of magnetoelectric MEMS cantilevers, but also for surface acoustic wave devices [2]. Here, we present recent experimental and theoretical results on the ΔE -effect, the sensitivity, and the noise of magnetoelectric ΔE -effect sensors. The sensors consist of magnetoelectric MEMS resonators with sputter-deposited AlN or Al₇₃Sc₂₇N as a piezoelectric material and soft-magnetic (Fe₉₀Co₁₀)₇₈Si₁₂B₁₀-based single or multilayers. A magnetoelastic macrospin model of the ΔE -effect in all stiffness tensor components is presented and combined with a finite element electro-mechanical model of the resonator. First and higher order torsion (Fig. 1) and bending modes are compared and analyzed regarding the sensitivity and the ΔE -effect [3]. Measurements and simulations reveal the dependency of the sensitivity on the mode number, caused by the geometry, mode shape, and the ΔE -effect in different stiffness tensor components. Specific rules for the resonator design are derived as a result. Besides the geometric and magnetic material properties, we find that the resonator loss and the piezoelectric material have a decisive impact on signal and noise. The influence of the quality factor Q [4] and the piezoelectric material [5] on signal and noise are investigated experimentally and explained by combining the previous model with a signal-and-noise equivalent circuit model (Fig. 2). Both quantities, Q and the piezoelectric material show the promising potential of significantly increasing the sensitivity and improving the limit of detection (LOD). Yet, an improvement in the LOD is currently limited by magnetic noise that becomes dominant at large operating voltage amplitudes [6]. Hence, understanding the specific origins of magnetic noise in such magnetostrictive resonant structures is crucial for sensor improvement in the future. A physical magnetic noise model is presented to identify the origin of stress-amplified, thermal-magnetic noise. It combines large scale finite differences micromagnetism with the mechanical equations of motion to capture magnetostrictive self-energy and frequency effects. Including the piezoelectric constitutive relation and the operating electronics the sensor's output voltage noise density can be estimated. With the model, we evaluate and discuss experimental results and explain the dependency of magnetic noise on the excitation amplitude and the magnetic bias field. The model provides detailed insights into general noise limits, which arise from using the ΔE -effect as the sensing principle. Finally, we briefly present first applications in cell imaging [7] and show that small signal measurements with simultaneous localization are enabled by a dual-mode operation scheme with compact self-biased ΔE -effect sensors [8]. This is of particular interest for typical biomedical inverse solution problems where the precise knowledge of the sensor's position and orientation is essential. Such applications

could benefit from sensor arrays that provide many measurements with a high spatial resolution. The noise equivalent model is extended to arrays of parallel sensor elements and compared with measurements. Implications and prospects for sensor developments in the future are discussed in a conclusion.

[1] B. Gojdka, R. Jahns, K. Meurisch, et al., APL Vol. 99, p.1-4 (2011); Nature Vol. 480, p.150 (2011) [2] J. Schmalz, A. Kittmann, P. Durdaut, et al., Sensors, Vol. 20, p.1–17 (2020) [3] B. Spetzler, C. Kirchhof, E. Quandt, et al., Phys. Rev. Appl., Vol. 12, p.1-13 (2019) [4] B. Spetzler, C. Kirchhof, J. Reermann, et al, APL., Vol. 114, p.183504 (2019) [5] B. Spetzler, J. Su, R.-M. Friedrich, et al., APL Materials., invited, submitted (2021) [6] P. Durdaut, E. Rubiola, J. Friedt, et al., J. Microelectromech. Syst., Vol. 29, p.1347 - 1361 (2020) [7] N. Lukat, R. M. Friedrich, B. Spetzler, et al., Sensors Actuators A Phys., Vol. 309, 1–8 (2020) [8] B. Spetzler, C. Bald, P. Durdaut, et al., Sci. Rep., accepted, (2021)



Normalized resonance frequencies $f_r/f_{r,max}$ of the first three torsion modes (TM1-3) as functions of the magnetic flux density $\mu_0 H$ applied along the long axis of the cantilever; inset: top photograph of the MEMS cantilever with visible electrodes. A soft magnetic FeCoSiB-Cr multilayer is sputter deposited on the other side.



Measured and simulated limit of detection (LOD) of two sensors of identical design that differs only in the piezoelectric material, which is AlN and AlScN, respectively. At large excitation voltage amplitudes \hat{u}_{ex} magnetic noise impairs the LOD.

IB-03. Directional Magnetic Field Response of FeCo/AlN Heterostructure Magnetoelastic Resonators.

T.R. Mion¹, B. Lefler², S.P. Bennett¹, M. Staruch¹, K. Bussmann¹, S. Lofland³ and P. Finkel¹

1. Material Science & Technology, US Naval Research Laboratory, Washington, DC, United States; 2. Drexel University, Philadelphia, PA, United States; 3. Rowan University, Glassboro, NJ, United States

Compact, ultra-low power magnetic field sensors are desirable for applications in multiple fields from biomedical engineering to military sensors [1,2,3]. Through direct coupling of magnetostrictive and piezoelectric strain, an on-chip sensor can be designed by exploiting the interface between thin films which can generate a charge when under an external magnetic field bias that depends not only on the magnitude of the measured field, but also the magnetic field direction enabling vector sensing capabilities. Magneto-electric MEMS-scale heterostructures deposited in layers on silicon wafers and etched to create beams and cantilevers operating at the electromechanical resonance were shown to work in a stress reconfigurable mode [4,5]. In this work we demonstrate magnetic field and directional response of FeC/AlN MEMS double-clamped heterostructure resonators. Through coupled strain engineering we are able to exploit the magnetic anisotropy and create a preferred axial response along the easy axis length of the suspended heterostructure beam. Resonant frequency response to the external magnetic field produces a sensitive measure of the angular dependence depending on the field vector components along the long and short axes. Figure 1a illustrates the heterostructure design of the double clamped ME MEMS structure and Figure 1b depicts a set of beams fabricated in a rosette pattern between Helmholtz coils used to apply a magnetic field to study the resonance response. The resonant peak shift with applied external magnetic field can be seen in Figure 2a where the butterfly loop has a linear slope df/dH near coercive field at 100G of 35 Hz/mT or 47 Hz/mT depending on the loop leg denoting the best bias response working point for this sensor. Polar plot of the resonance peak vs field at 15° increments can be seen in Figure 2b showing the directional response of the double clamped ME MEMS structures. Limit of detection measurements and further resonant peak angular dependence will be presented and deposition conditions will be discussed to illustrate the necessary conditions required to optimize creation of a high-quality MEMS sensor.

[1] M. Hämäläinen, R. Hari, R.J. Ilmonemi, and O. V. Lounasmaa, Reviews of Modern Physics 65, 413–497 (1993), DOI: 10.1103/RevModPhys.65.413 [2] J. W. Mooney, S. Ghasemi-Roudsari, E. Reade Banham, and B. T. H. Varcoe; Biomed. Phys. Eng. Express 3 (2017) 015008, DOI: 10.1088/2057-1976/3/1/015008 [3] T. R. Clem, Naval Engineers Journal 110, 139–149 (1998), DOI: 10.1111/j.1559-3584.1998.tb02393.x [4] S. P. Bennett, J. W. Baldwin, M. Staruch, and P. Finkel; Applied Physics Letters 111, 252903 (2017), DOI: 10.1063/1.5011728 [5] M. Staruch, et al.; Physical Review Applied 11, 034028 (2019); DOI:10.1103/PhysRevApplied.11.034028

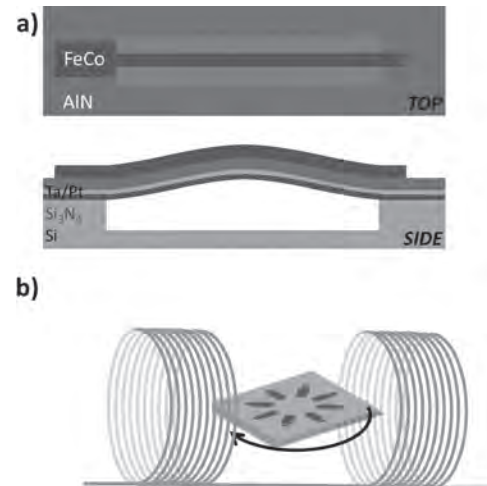


Figure 1: (a) A top view and side view of magnetoelastic arched beam resonator, consisting of a layered film stack on a silicon wafer consisting of Si₃N₄ support, Pt back electrode with Ta adhesion layer, AlN piezoelectric layer, and Fe_{0.7}Co_{0.3} top electrode and magnetostrictive layer. (b) Rosette pattern of beams fabricated on a silicon chip between Helmholtz coils, with rotation for angular dependence measurements.

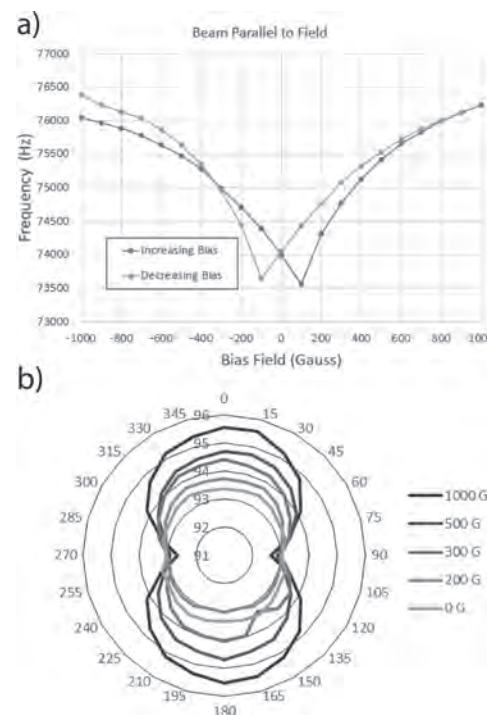


Figure 2: (a) Frequency shift of resonance peak vs bias magnetic field applied parallel to long axis of the beam. (b) Polar plot of the magnetic field response at 15° intervals for 0, 200, 300, 500, and 1000 Gauss.

IB-04. Spin-Torque Dynamics for Noise Reduction in Vortex-Based Sensors.

M. Jotta Garcia¹, J. Moulin², S. Wittrock¹, S. Tsunegi³, K. Yakushiji³, A. Fukushima³, H. Kubota³, S. Yuasa³, U. Ebels⁴, M. Pannetier-Lecoœur², C. Fermon², R. Lebrun¹, P. Bortolotti¹, A. Solignac² and V. Cros¹

1. *Unité Mixte de Physique, CNRS, Thales, Université Paris-Saclay, 91767 Palaiseau, France*; 2. *SPEC, CEA-Saclay, CNRS, Université Paris-Saclay, 91191 Gif-sur-Yvette, France*; 3. *National Institute of Advanced Industrial Science and Technology, Research Center for Emerging Computing Technologies, Tsukuba, Ibaraki 305-8568, Japan*; 4. *Univ. Grenoble Alpes, CEA, CNRS, GINP, SPINTEC, 38054 Grenoble, France*

Magnetoresistive field sensors have a wide range of uses, such as in biomedical applications, in the automotive industry, robotics, or smart city technologies. Figures of merit like sensitivity, detectivity and spatial resolution are used to evaluate the performance of such sensors [1]. At low frequencies, the $1/f$ noise component is dominant and is in fact responsible for hindering the device's detectivity, and, consequently, its performance. There is an active research effort to reduce this noise component and tackle this limitation [2]. Vortex-based devices, in which the free layer exhibits a vortex magnetization distribution in its equilibrium state, are promising magnetic field sensors due to their large linear detection range [3] and the fact that they show practically no hysteresis in this range. Besides, these devices are often considered as model systems for the study of magnetization dynamics. In this study, we focus on the analysis of the $1/f$ noise in a particular type of magnetic sensor based on a vortex magnetic configuration integrated in a magnetic tunnel junction (MTJ) spin torque nano-oscillator. These devices present excellent rf characteristics for future radio-frequency devices and applications, such as rf generation [4], detection [5] or neuromorphic computing [6]. While the use of vortex-based spin-torque nano-oscillators for applications such as these mentioned here has been largely studied, they are newcomers in the magnetic field sensing landscape. In this work, we analyse the $1/f$ low-frequency noise in vortex-based spin-torque nano-oscillators by determining the Hooge parameter in different conditions. The Hooge parameter is typically used to characterize and compare sensor's noise properties. Firstly, we find that in the uniform states the Hooge parameter of the studied device is comparable to that measured in state-of-the-art TMR sensors with similar RA product, $\alpha = 10^{-11} - 10^{-10} \mu\text{m}^2$. In the vortex state, the measured noise level is around one order of magnitude greater than in the parallel (and anti-parallel) state, see Fig. 1a. This is due to the increased probability of pinning of the vortex core into defects or inhomogeneities of the free layer. Secondly, we determine that the dynamics of the vortex core strongly influence the noise level of the device. For a current above a certain threshold, the spin transfer torque surpasses the intrinsic damping of the free layer resulting in self-sustained oscillations of the vortex core [7]. In the self-sustained oscillations' regime, the noise decreases to a level close to that of the antiparallel state, see Fig. 1b. Furthermore, we present a novel strategy for reducing the $1/f$ low-frequency magnetic noise, through the application of an in-plane rf field or injection of an rf current [8]. By using this approach while the device is operating in the self-sustained regime, we are capable of further decreasing the measured noise level to values close to the minimum attainable, see Fig. 2. We find that this noise reduction is non-resonant, see Fig. 2a. As such, we can have a vortex-based STNO with relevant noise properties, comparable to those of state-of-the-art TMR field sensors. At the same time, we profit from the specific advantages of vortex-based spin-torque nano-oscillators for sensing applications: large linear detection range, virtually no hysteresis and high spatial resolution. This noise reduction technique based on the spin-torque dynamics of the vortex can have an impact on the sensors' industry, which may profit from the advantages of the vortex configuration. The work is supported by the French ANR project "SPINNET" ANR-18-CE24-0012.

[1] D. C. Leitão et al., *Nanotechnology* 27, 045501 (2015) [2] L. Huang et al., *Journal of Applied Physics* 122, 113903 (2017); J. Moulin et al., *Appl. Phys. Lett.* 115, 122406 (2019) [3] D. Suess et al., *Nat. Electronics* 1, pages 362–370 (2018) [4] S. Wittrock et al., *Phys. Rev. B* 99, 235135 (2019) [5] A. S. Jenkins et al., *Nat. Nanotech.* 11, 360 (2016); D. Marković et al., *Phys. Rev. Applied* 13, 044050 (2020) [6] M. Romera et al., *Nature* 563, 230–234 (2018); J. Torreyon et al., *Nature* 547, 428–431 (2017) [7] A. Dussaux et al.,

Nat. Comm. 1, 8 (2010) [8] M. Jotta Garcia et al., arXiv:2012.09616 [cond-mat.mes-hall] (2020)

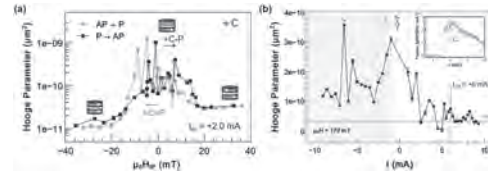


Fig.1 a) Hooge parameter as a function of an in-plane magnetic field that is swept from the parallel to the anti-parallel state and back. b) Evolution of the Hooge parameter with the applied bias current. The inset shows the oscillation power of the rf emission due to the emerging vortex dynamics. The red dotted line represents the Hooge parameter measured in the AP state.

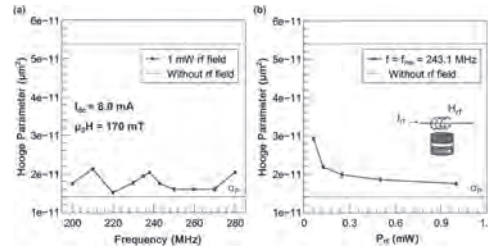


Fig. 2 a) Hooge parameter as a function of the frequency of the applied oscillating field, with $P_{\text{rf}} = 1$ mW. The red line indicates the value measured in the absence of this field. b) Hooge parameter as a function of the power amplitude of the rf field at a fixed frequency, $f = f_{\text{res}} = 243.1$ MHz. The green dotted lines represent the Hooge parameter measured in the P state.

IB-05. Sub-nT Resolution of Single Layer Sensors Based on the AMR Effect in Single Layer $\text{La}_{2/3}\text{Sr}_{1/3}\text{MnO}_3$ Thin Films.

L. Enger¹, S. Flament¹, I. Bhatti¹, B. Guillet¹, M. Lam Chok Sing¹, V. Pierron¹, S. Lebargy¹, T. Gonzalez², J. Camarero², R. Miranda², P. Perna² and L. Méchin¹

1. *Ensicaen, CNRS UMR6072, Ensicaen, Unicaen, Caen, France;*
 2. *IMDEA Nanociencia, Campus de Cantoblanco, Madrid, Spain*

The final goal of our project is to develop a device that acts as a bypass for restoring neuronal signals in regions with spinal cord injuries¹. To detect such signals, a magnetic field sensor can be employed, placed near the spinal cord. This in turn sets several constraints for the sensor itself. It must be of reduced size, operate at zero or very small external biasing field and achieve low detectivity at low frequency, while operating at body temperature (310K). The detectivity of a magnetic sensor is determined both by its sensitivity and its intrinsic noise. If the target signal is in the low frequency region, which is the case for biomedical applications, Anisotropic Magnetoresistance (AMR) sensors become competitive when compared to Tunnelling Magnetoresistance (TMR) and Giant Magnetoresistance (GMR) technologies, due to its low 1/f noise, even if they do not reach same sensitivity values. Additionally, AMR sensors can be of much simpler fabrication, not requiring the stacking of several thin films. We will present results obtained with AMR sensors made of 30 to 60 nm thick epitaxial $\text{La}_{2/3}\text{Sr}_{1/3}\text{MnO}_3$ thin films, which present low intrinsic noise², deposited on 4°, 6° or 8° vicinal SrTiO_3 (STO) substrates and etched in a Wheatstone Bridge design. This design is also referenced in literature as Planar Hall Effect Bridge³ (PHEB). Pulsed Laser Deposition (PLD), photolithography and Ion Beam Etching (IBE) were used for in-lab samples fabrication. The use of a vicinal substrate, which presents a surface miscut angle regarding the crystallographic plane, was selected so as to induce uniaxial anisotropy and an easy magnetic axis along the step edges⁴. The measured AMR curves can be compared to the expected behaviour when considering the Stoner-Wohlfarth model for coherent magnetization reversal. This coherent magnetization reversal process was checked by Magneto-optical Kerr imaging (see figure 1). In order to achieve a higher sensitivity, thus lower detectivity, PLD deposition was performed at different temperatures, which leads to a change in thin film Curie temperature T_c and therefore affects the anisotropy field H_a . A clear reduction in H_a can be seen when changing the deposition temperature from 730° C to 680° C. The anisotropy field depends also on the angle of vicinality, the smaller the angle the smaller the anisotropy field. For vicinal angles ranging from 4° to 8°, the uniaxial anisotropy of the film is preserved. Changing the temperature deposition or the vicinality does not degrade the 1/f noise of the films. The so far achieved detectivity @ 310K is as low as 1nT/Hz^{1/2} at 1 Hz and 300 pT/Hz^{1/2} at 1 kHz in a single-layer sensor (see figure 2) without using performance enhancing techniques such as focusers.

1 <http://www.byaxon-project.eu/> FET Open 2017-2020 2 L Méchin et al, J. Phys. D: Appl. Phys.46, 202001 (2013), <https://doi.org/10.1088/0022-3727/46/20/202001> 3 A.D. Henriksen et al, Appl. Phys. Lett. 97, 013507 (2010), <https://doi.org/10.1063/1.3460290> 4 P Perna et al Adv. Funct. Mater., 27, 1700664 (2017), <https://doi.org/10.1002/adfm.201700664>

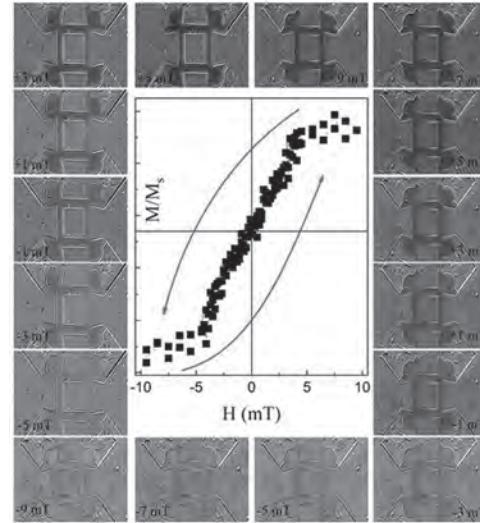


Figure 1: MOKE Imaging of the magnetization reversal process in the AMR Wheatstone bridge sensor and local magnetization loop

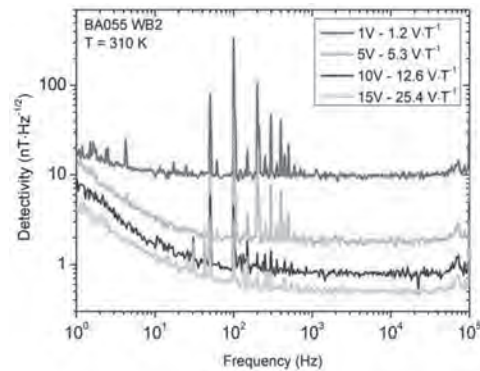


Figure2: Detectivity spectrum at 310K as a function of the polarization of the AMR Wheatstone bridge

IB-06. Sensitivity and Noise of Multiwire Parallel Fluxgate Sensors.P. Ripka¹, D. Hrakova¹, V. Grim¹ and M. Mirzaei¹*1. Electrical Engineering, Czech Technical University in Prague, Prague, Czechia*

Some of the early parallel fluxgate sensors had cores made of magnetic wires and this design is still used in many devices, including gradiometers and low-cost sensor arrays in magnetoelastic torque meters [1]. Wire and also multiwire cores are also being used in transverse fluxgates [2]. Despite their larger noise and lower temperature stability compared to ring-core fluxgates, wire-core parallel fluxgates have several advantages [3]: 1. their sensing direction is precisely defined by the direction of the sensor core 2. they have excellent spatial selectivity which is important for the detection of magnetic particles [4] 3. High sensitivity allows decreasing the core length 4. The large shape anisotropy gives them low crossfield error [5]. The sensitivity of ring-core and race-track fluxgate sensors is well understood and described in the literature [6,7], while such study on wire-cored sensors is missing. We offer it in this paper for the case of voltage output. We calculate the sensitivity as a function of core and pickup coil geometry and configuration of wire core by Finite-element modeling and compare these results with the measurements. We analyze both existing configurations (single-core, Foerster and Vacquier) and propose multiwire fluxgates of two types: with collective excitation and pickup coils and with individual pickup coils. This paper is based on model cores made of 36 mm long, 0.2 mm diameter Permalloy wires with chemical composition $\text{Ni}_{78}\text{Fe}_{15}\text{Cu}_4\text{Mo}_3$. The wires were annealed for 3 hours in a dry hydrogen atmosphere at 1080 °C to obtain near-zero magnetostriction. Our simulation models were based on constant permeability and also on the magnetization curve estimated from the measurement on the wire. Sensitivity and noise properties were measured for sensors containing 2 to 12 wires with different distances between the wires. The model can be upscaled for magnetic rods and downscaled for bundles of microwires and arrays of nanowires. However, the results strongly depend on the aspect ratio of the used wires. Fig. 1 shows examples of the measured fluxgates. The multiwire type has a 3D printed honeycomb bobbin which allows insertion of different configurations of wires in glass or ceramic capillaries. For each configuration, we found the optimum working point (excitation frequency and amplitude) to maximize the sensitivity and minimize the noise. In order to simplify the problem, we did not use the parametric amplification of the output voltage. We studied the effect of pickup coil geometry by FEM modeling and verified the results experimentally: the optimum coil length is 80 % of the core length and the coil diameter should be minimized as the sensitivity is inversely proportional to the pickup coil diameter as shown in Fig.2. In this regard's fluxgate behaves differently from induction sensors without excitation, which shows the increase of sensitivity with the pickup coil diameter. This dependence does not change with the wire permeability. This decrease of the sensitivity is the reason, why multiwire fluxgate with large common pickup coil has larger noise (0.7 to 14 nT/ $\sqrt{\text{Hz}}$ at 1 Hz, depending on configuration) than single-core (180 pT/ $\sqrt{\text{Hz}}$ @1Hz) and Vacquier type (51 pT/ $\sqrt{\text{Hz}}$ @1Hz) sensors. The effective solution to this problem is to use an individual pickup coil for each wire instead of a collective coil common for all wires. The sensitivity of the multiwire fluxgate is increasing with the wire pitch and the noise is inversely proportional to the wire pitch. This is caused by two factors: 1. With increasing wire distance their magnetostatic interaction is decreasing, which results in lower demagnetization 2. With increasing distance the noise correlation between wires is decreasing and the total noise is reduced by the averaging effect, which is stronger for independent noise sources This study was limited to the initial selection of optimum geometry of the wire core and pickup coil of the voltage-output parallel fluxgate. Further increase of sensitivity and noise reduction can be achieved by tuning the pickup coil by the parallel capacitor to the mode of parametric amplification at second harmonics. This study was supported by the Grant Agency of the Czech Republic within the Nanofluxgate project (GACR GA20-27150S).

[1] P. Ripka, Magnetic sensors and magnetometers, Artech House, 2001 [2] M. Butta, M. Vazquez, R. P. del Real et al., AIP Advances Vol. 10, (2020) [3] M. Janosek, "Parallel fluxgate magnetometers," in *High Sensitivity magnetometers*, Springer, 2017 [4] J. Lei, T. Wang, C. Lei et al. Applied

Phys. Lett. Vol. 102, 022413 (2013) [5] P. Ripka, W. Billingsley, Sens. Act. A Vol. 81, p. 176-179 (2000) [6] C. Hinrichs, J. Stahl, K. Kuchenbrandt et al., IEEE Trans. Magn. Vol. 37, p. 1983 (2001) [7] L. Perez, I. Lucas, C. Aroca et al., Sens. Act. A Vol. 130, p. 142 (2006)

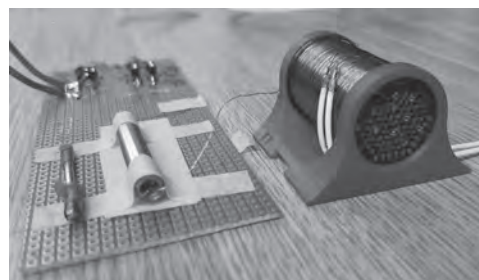


Figure 1 Experimental fluxgate sensors: a) single core, b) Vacquier, c) multiwire

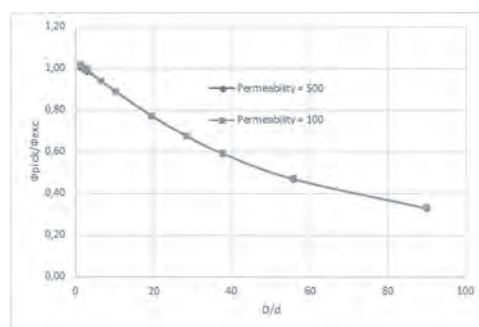


Figure 2 Relative flux of the 36 mm long pickup coil with diameter D as a function of its relative diameter D/d – values calculated by 2D FEM for 36 mm long, d = 0.2 mm diameter magnetic wire core

IB-07. Control of Chirality and Hysteresis in Asymmetric Vortex-Based TMR Sensors.

S. Dounia¹, S. Teresi², J. Alvarez-Hérault¹, L. Lombard¹, J.R. Childress¹, I. Prejbeanu² and C. Baraduc²

1. *Crocus Technology Grenoble, Grenoble, France*; 2. *SPINtronique et Technologie des Composants, Grenoble, France*

In the context of miniaturization, energy conservation, smart devices and IOT, magnetic field sensors based on magnetic tunnel junctions (MTJ) constitute an attractive choice, with small size, very high intrinsic sensitivity and low power consumption. The specific sensor response curve is determined by the magnetization configuration and hysteresis loop behavior of the soft (sensing) layer of the MTJ. A possible implementation is the vortex-based sensor, in which the junction sensing layer magnetization is in a vortex configuration at zero field, consisting of a small central core with out-of-plane magnetization and an in-plane magnetization rotating around the core with a specific chirality (clockwise or counterclockwise). Depending on the geometry, the vortex can be the natural stable micromagnetic configuration of the sensor, with the lowest energy at remanent state. This is the case for circular dots of soft ferromagnetic materials with sufficient thickness [1]. Circular vortex-state sensors typically exhibit much lower sensitivity compared to uniform-magnetization sensors, but are naturally linear and exhibit low hysteresis in a limited field range [2]. Here we use micro-magnetic simulations to study the effect of geometrical asymmetry [3] on the vortex properties, in particular on the vortex nucleation, chirality and magnetization cycle. We explore different modifications of the magnetic dot shape that ensure the control of the vortex chirality. We specifically study magnetic disk or ellipse with a cut on one side of different size and shape. Then we determine the geometrical parameters (in particular the position and size of the cut) that also allow a large nucleation field, thus leading to a quasi-linear response on a large field range. However, due to the asymmetric shape, the control of the vortex chirality is obtained at the cost of a small hysteresis: in general, the magnetization is not exactly zero at remanence. In order to reduce this hysteresis, we study magnetization at remanence for different dots with cut by varying the geometrical parameters and show that certain combination of parameters give zero magnetization at remanence. An analytical model also describes this result, obtained by micromagnetic simulations. Finally, another route to reduce hysteresis is to take advantage of magneto-static interaction between magnetic dots within a 2D array [4]. The stray field of neighboring dots influences the vortex core position and may thus reduce the magnetization at remanence. This effect is explored for pairs of asymmetric dots at different distance and position. Our results show various means to reduce and even cancel the hysteresis.

[1] R. Cowburn, D. Koltsov and D. Tricker, *Physical Review Letters*, Vol. 83, p.1042 (1999) [2] D. Suess, A. Bachleitner-Hofmann and H. Brückl, *Nature Electronics*, Vol. 1, p. 362 (2018) [3] S. Agramunt-Puig, N. Del-Valle, and A. Sanchez, *Applied Physics Letters*, Vol. 104, p. 012407 (2014) [4] O. Sukhostavets, J. Gonzalez and K. Guslienko, *Physical Review B*, Vol. 87, p. 094402 (2013)

IB-08. Magnetic Viscosity in High Precision Magnetoresistive Field Sensors.

J.D. Watts¹, J. Davies¹, J. Novotny¹, D. Huang¹ and P. Eames¹

¹. Advanced Technology Group, NVE Corp, Eden Prairie, MN, United States

Magnetic viscosity, the long time-scale magnetization drift in response to changes in applied field, can directly impact the accuracy of high sensitivity tunneling magnetoresistance (TMR) based field sensors operating with large dynamic field ranges or utilizing long time scales. Recent studies have demonstrated benefits arising from an understanding of magnetic viscosity in the context of field sensing; for instance, as a source of spurious signals from buried ferrite during landmine detection by induction sensors [1], as a tool providing insight into magnetization dynamics [2-5], and even as a novel immunoassay characterization technique for biochemical detection through so-called magnetorelaxometry [6,7]. Although the mechanism of magnetic viscosity has been well described [8,9], quantifying the impacts of the effect in sensor applications and establishing relationships between those impacts and tunable material properties has remained under explored. Therefore, in this work we characterize the magnetic viscosity in a variety of commercial and custom magnetic tunnel junction (MTJ) based sensors, as well as explore the potential impacts of integration with flux concentrator shielding. Utilizing accessible electrical measurements of the TMR or sensor output, a wide range of viscosity behavior is revealed. The results in commercial sensors demonstrate order-of-magnitude differences ranging from 0.2 – 2 μT in the effective sensor output field viscosities, with accuracy implications due to the hysteric nature of the viscous drift in the sensor output. To elucidate underlying differences in the selected commercial sensors, we fabricate and compare custom MTJs with variable free layer thicknesses t_{FL} as well as patterned devices utilizing a variety of flux concentration shielding (with up to 30x flux concentration factors). Fig. 1(a) presents an illustrative case of the magnetoresistance vs applied field for one of the custom MTJs where $t_{\text{FL}} = 4 \text{ nm}$ for a biased sensing layer. For each measurement, the device is first initialized in a saturating field $\mu_0 H_0$ of approximately 30 mT. The field is then abruptly reduced to the measurement field $\mu_0 H_a$, ranging from -25 to 25 mT. The time-dependent rate of change of the MTJ's resistance for such a measurement with the specified value of H_a is shown in Fig. 1(b), illustrating that the observed drift of the device resistance is logarithmic in time and strongly field dependent as expected. These measurements are then used to extract the magnetoresistance's viscosity parameter. The patterned MTJs studied show a 3x increase in sensitivity between $t_{\text{FL}} = 4$ to 20 nm but a corresponding 43% decrease in the magnetic viscosity parameter [Fig. 2(a-b)]. Relationships between the viscosity, magnetic active volumes, and anisotropy will be discussed. These results highlight simple design pathways useful to consider when attempting to enhance or mitigate viscous output effects in high sensitivity MTJs. In addition, the viscosity parameter in certain fabricated MTJs is found to exhibit a strong asymmetric field dependence that is not observed in the sensitivity [Fig. 2(a-b)], highlighting complexities of the reversal mechanism, as well as the deeper insight into magnetization dynamics gained from viscosity characterization.

[1] Y. Das, *IEEE Trans. Geosci. Remote Sens.* 44, 1444 (2006). [2] B. Dolgin *et al.*, *J. Phys. Condens. Matter* 25, 076004 (2013). [3] A. Lisfi *et al.*, *AIP Adv.* 8, 056438 (2018). [4] S.J. Collocott and V. Neu, *J. Phys. D: Appl. Phys.* 45, 035002 (2012). [5] C. Leighton and I.K. Schuller, *Phys. Rev. B* 63, 174419 (2001). [6] F. Wiekhorst, U. Steinhoff, D. Eberbeck, and L. Trahms, *Pharm. Res.* 29, 1189 (2012). [7] C.C. Huang, X. Zhou, and D.A. Hall, *Sci. Rep.* 7, 1 (2017). [8] R. Street and J.C. Woolley, *Proc. Phys. Soc. Sect. A* 62, 562 (1949). [9] E.P. Wohlfarth, *J. Phys. F Met. Phys.* 14, L155 (1984).

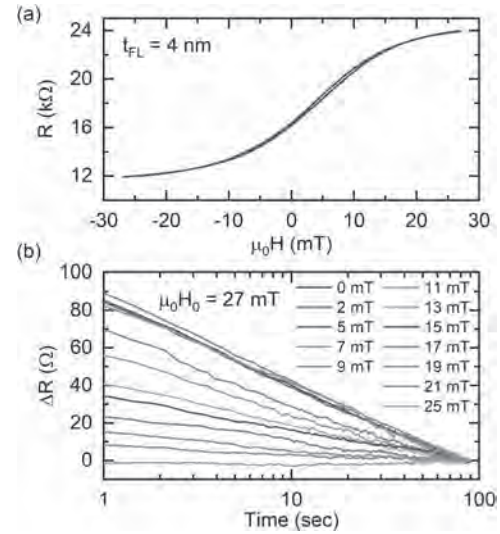


Fig. 1. (a) Resistance vs applied field for patterned MTJ bit strings with free layer thickness $t_{\text{FL}} = 4 \text{ nm}$. (b) Viscosity measurement of the change in resistance ΔR (relative to measured resistance at time $t = 90 \text{ sec}$) for specified $\mu_0 H_a$ between 25 and 0 mT. Saturating initial field $\mu_0 H_0 = 27 \text{ mT}$.

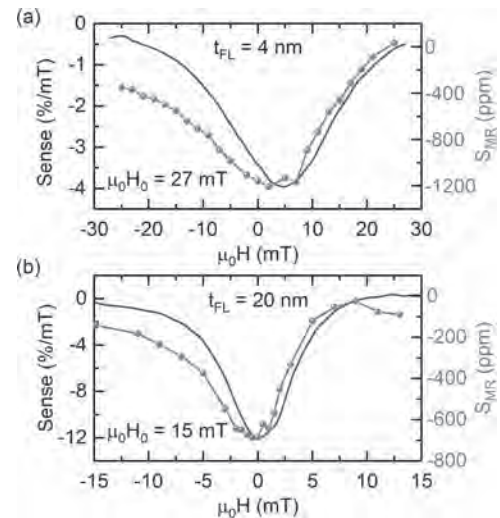


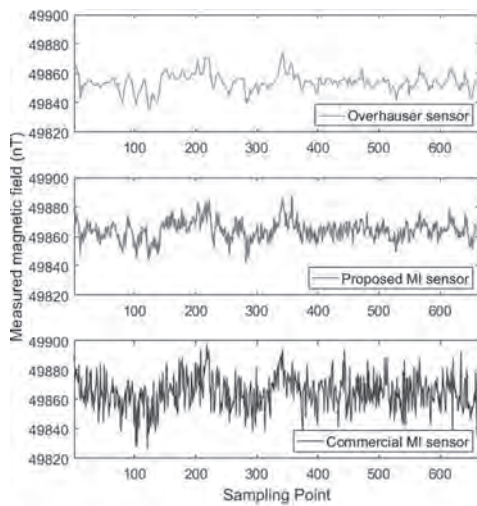
Fig. 2. Sensitivity (black) and magnetoresistance viscosity parameter S_{MVR} (red) as a function of applied field for MTJs with free layer thickness of either (a) 4 nm, or (b) 20 nm. The initial saturating field $\mu_0 H_0 = 27$ or 15 mT as specified. S_{MVR} is shown in parts per million, normalized to the resistance at zero-field.

IB-09. Investigation of a Magneto-Inductive Sensor for Vector Magnetic Field Measurements.

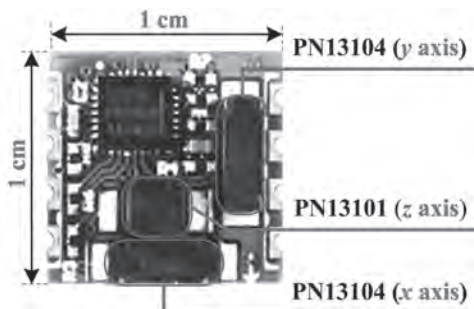
H. Liu¹, X. Wang¹, C. Zhao¹, J. Zhu¹, J. Ge¹, H. Dong¹ and Z. Liu²

1. China University of Geosciences, Wuhan, China; 2. The University of British Columbia, Vancouver, BC, Canada

The low magnetic field measurement has been utilized since ancient times in order to find economic resources, to detect magnetic anomalies, etc. In this case, the vector magnetic survey can simultaneously obtain the modulus and direction information of the magnetic field, which can contribute to obtaining more precise information and characteristics of magnetic field resources. This paper is concerned with the possibility of vector magnetic field measurement with a magneto-inductive (MI) magnetic sensor. To evaluate the capability of the MI sensor, a test platform is set up and its performance including the noise floor, the resolution, the sensitivity, etc., are comprehensively characterized. The laboratory testing results demonstrate that the proposed MI sensor can detect a low magnetic field strength as low as 8.28 nT when the sampling rate is 10 Hz, the typical noise floor is about $0.235 \text{ nT/Hz}^{\{1/2\}}$ at 1 Hz, the sensitivity is about 13 nT, and the non-linearity is no more than 3%. Further, a comparative geomagnetic observation and magnetic anomaly detection among the proposed MI sensor, a high-precision Overhauser sensor, and a commonly used and accepted commercial MI sensor are conducted. The experimental results identify the capability of the proposed MI sensor in weak magnetic detection.



Contrast geomagnetic observation among the commercial Overhauser magnetometer, the proposed MI sensor, and the commercial MI sensor.



The proposed three-axis MI hybrid sensor.

IB-10. Tunnel Magnetoresistance Sensors With CoFeBTa Amorphous Soft-Magnetic Sensing Layer.

T. Nakatani¹, M. Rasly¹, J. Li¹, H. Sepehri-Amin¹, H. Sukegawa¹ and Y. Sakuraba¹

1. National Institute for Materials Science, Tsukuba, Japan

Tunnel magnetoresistance (TMR) magnetic sensors using CoFeB/MgO/CoFeB magnetic tunnel junction (MTJ) are promising for detection of magnetic field with various magnitude and frequency. The soft-magnetic property of the free layer (sensing layer) influences the sensing performance, which is particularly important for detection of small magnetic field such as biomagnetic field. NiFe (permalloy) is frequently used as a soft-magnetic sensing layer of TMR sensors. However, the large film roughness and the fcc 111-texture of the NiFe polycrystalline film tend to lower the TMR ratio. Amorphous ferromagnets such as CoFeSiB [1] have been developed as alternative materials for the sensing layer of TMR sensors. However, the soft-magnetic nature of CoFeSiB is prone to be degraded due to crystallization by annealing at > 300 °C [2], which is the typical annealing temperature for TMR sensors. In this work, we demonstrate an amorphous CoFeBTa material, whose crystallization temperature is ~ 500 °C [3], to the TMR sensing layer and investigated the magnetic, magnetoresistive and low-frequency noise properties. A top-pinned spin-valve structure of bottom lead / Ta(5) / CoFeBTa(20) / Ta(0.3) / CoFeB(3) / MgO(1.8) / CoFeB(2.5) / CoFeBTa(0.6) / CoFe(0.5) / Ru(0.8) / CoFe(3) / IrMn(8) / Ru(8) capping layer (nm in unit) was sputter-deposited [4]. The spin-valve film was annealed twice (two-step annealing) under magnetic fields in two directions that were orthogonal each other. The first annealing at 350 °C induces a uniaxial magnetic anisotropy in the CoFeBTa/Ta/CoFeB free layer in e.g. y -direction and the second annealing at 200 °C defines the pinning direction in the orthogonal direction (x -direction). The patterned TMR devices by photolithography were characterized by dc 4-probe method. Figure 1(a) shows the resistance (R)-magnetic field in x -direction (H_x) curve of a single TMR device (MTJ diameter: 50 μm). The TMR ratio was 160% and the resistance-area product was 40 $\text{k}\Omega \mu\text{m}^2$. A linear R - H transfer curve with a small hysteresis was realized in the intermediate magnetization state after the two-step annealing process. The maximum sensitivity ($1/R_{\min} dR/dH$) of ~ 70 %/mT was obtained at $H_x = 1$ mT. Figure 1(b) shows the noise voltage density ($\sqrt{S_V}$) spectra of the TMR device at various magnetization states. For the noise measurements, bias voltage (V_b) was supplied using a 1.5 V dry cell battery and a ballast resistor. The magnitude of the noise at the intermediate magnetization state ($H_x = 1$ mT) was larger than those of the parallel and anti-parallel magnetization states, indicating that the $1/f$ noise is dominated by some distinct magnetic origins. The noise voltage density increased with increasing V_b , and the Hooge's noise parameter α_H was determined to be $\sim 4 \times 10^{-8} \mu\text{m}^2$ at $H_x = 1$ mT. The minimum detectivity (field-equivalent noise) defined by $\sqrt{S_V}/(1/R_{\min} dR/dH V_b)$ was 2.2 nT/ $\sqrt{\text{Hz}}$ at 10 Hz at $H_x = 1$ mT. For comparison, we fabricated a similar TMR sensor device with a NiFe(20 nm) soft-magnetic layer instead of CoFeBTa. The NiFe sensor showed larger detectivity of 4.5 nT/ $\sqrt{\text{Hz}}$ at 10 Hz than that of the CoFeBTa sensor mainly due to its larger $1/f$ noise. Thus, the CoFeBTa amorphous soft-magnetic layer has a clear advantage over the NiFe one for magnetic sensor applications. We also fabricated a full-bridge magnetic sensor using the CoFeBTa-based TMR devices. Each leg of the full-bridge is composed of 50 TMR devices connected in series as shown in Fig. 2(a). Figure 2(b) shows the output voltage (V_{out}) vs. H curve under various V_b . The non-linearity and hysteresis in the V_{out} - H curve can be attributed to variation of the R - H curve shape of the individual TMR devices of the array, which should be improved in the future. The bridge sensor showed an improved detectivity of 0.5 nT/ $\sqrt{\text{Hz}}$ at 10 Hz independent of V_b .

[1] Kato, Oogane, Fujiwara et al., Appl. Phys. Express Vol. 6, p. 103004 (2014). [2] Jimbo, Fujiwara and Shimizu, J. Appl. Phys. Vol. 117 p. 17A313 (2015). [3] Choi, Nakatani, Read et al., Appl. Phys. Express Vol. 10 p. 013006 (2017). [4] Rasly, Nakatani, Li et al. J. Phys. D: Appl. Phys. Vol. 54, p. 095002 (2021).

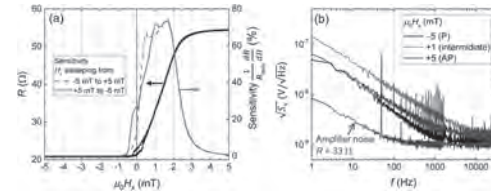


Fig. 1(a) R - H curve and (b) noise spectra of the TMR sensor.

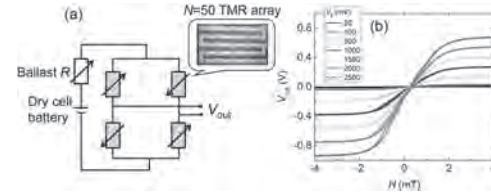


Fig. 2(a) Schematic of full-bridge sensor and (b) output voltage vs. magnetic field.

IB-11. Development of Opposing Current Type GSR Sensor Element to Reduce Induced EMFs in Zero Magnetic Field.

S. Honkura¹ and Y. Honkura²

1. Nanocoil Corporation, Nagoya, Japan; 2. Magnedesign Corporation, Nagoya, Japan

The GSR sensor is a highly sensitive magnetic sensor that utilizes GHz pulses and amorphous wire. The detection principle is that a GHz pulse is applied to an amorphous wire, and makes the rotation of the spins near the surface and the resulting magnetization rotation are detected by the detection coil. In order to achieve higher performance, it is necessary to solve the problem of the induced EMFs in Zero Magnetic field and non-linearity due to the residual twisting stress in the wire. In this study, we report the results that those problems have been solved by using an opposing-current type element. The opposing-current type element has the feature that the current is passed from the center of the element to both ends, and the electromotive force detected by the two identical coils placed on the left and right sides is added and output. Fig.1 shows that when the direction of the current is reversed in the single coil type element, the electromotive force generated by the pulse current energization becomes positive and negative, and is canceled when added. Based on the result, we experimented with the counter-current type element and confirmed that in the case of falling detection, the induced electromotive force in the case of magnetic field $H=0A/m$ almost disappears and only the electromotive force dependent on the magnetic field is generated. This result means that the coil voltage signal can be amplified significantly to give the improved detection power. Furthermore, as shown in Fig. 2, the output was found to be subject to the positive and negative magnetic fields, resulting in a clean sinusoidal function. This means that the linearity of the output can be greatly improved. The development of the counter-current device is expected to improve the sensitivity and linearity of GSR sensors.

1)Y.Honkura, S.Honkura;JMMM,513(2020)167240

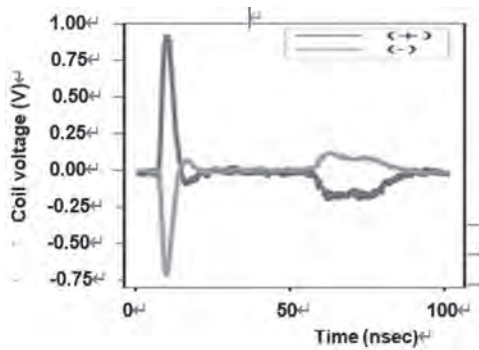


Fig. 1 Effect of current direction on induced electromotive force in zero magnetic field

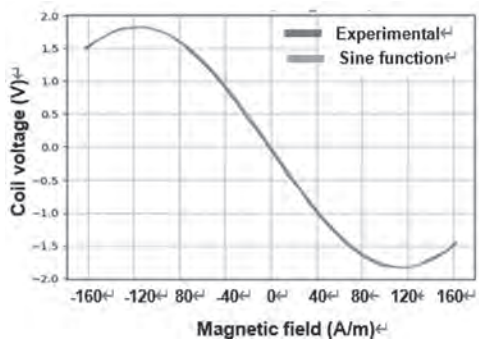


Fig. 2 Sinusoidal output characteristics of the opposing current type GSR element

IB-12. Magnetic Flux Synchronous Motion Modulation for Improving the Low-Frequency Magnetic Field Detection Limit of Magneto-resistive Sensor Using MEMS Resonators.

Z. Liu^{1,2}, J. Chen^{1,2} and X. Zou^{1,2}

1. State Key Laboratory of Transducer Technology, Aerospace Information Research Institute, CAS, Beijing, China; 2. School of Electronic, Electrical and Communication Engineering, University of Chinese Academy of Sciences, Beijing, China

Introduction Magneto-resistive (MR) sensors increase explosively and are used widely in many fields due to its small weight, low power consumption, and high sensitivity, whereas the $1/f$ noise is larger in the low-frequency region and degrades the low-frequency magnetic field detection limit [1]. To reduce the impact of $1/f$ noise, MEMS-based magnetic flux concentrators (MFCs) are utilized to modulate the low-frequency field to a high-frequency region where the $1/f$ noise vanishes and improve the detection limit. MEMS-based MFCs consist of MEMS resonators vibrating with a high frequency and the high relative permeability magnetic film deposited on the surface of MEMS resonators, the combinations of them have been already tested and reported for high-frequency magnetic field modulation, resonance frequency detection, and $1/f$ noise of MR sensor cancellation [2-5]. When the MR sensor is integrated with MEMS-based MFCs and modulating the low-frequency magnetic field to the high-frequency region, the larger the modulation efficiency, the lower the detection limit. However, the modulation efficiency of existing modulation ways is not high, and the low-frequency magnetic field detection limit is low. To improve the low-frequency detection limit of the MR sensor, a new modulation way called synchronous motion modulation (SMM) is proposed. Theory of SMM SMM is evolved from gap-change modulation (GCM) [2] and vertical motion modulation (VMM) [3] with the highest modulation efficiency in the existing literature, as shown in Fig. 1. For GCM, the magnetic film deposited on the bottom of the piezoelectric cantilever resonator is static, and the MFCs deposited on the comb-driven resonator vibrate horizontally. But for VMM, the MFCs are static, and the magnetic film deposited on the bottom of the piezoelectric cantilever vibrates vertically. When the MFCs vibrate horizontally and the piezoelectric cantilever vibrates vertically, this is SMM, which modulates the magnetic flux in the position of the MR sensor to the high-frequency region. In this case, the direct current (DC) magnetic field will be modulated to an alternating current (AC) field and be measured by the MR sensor and bridge circuit. To compare the modulation efficiency of these three modulation ways, the vibration amplitude of comb-driven resonator is the same in SMM and GCM, the vibration amplitude of piezoelectric cantilever resonator is the same in SMM and VMM. The theoretical analyses show that the modulation efficiency of VMM increases with increasing amplitude and decreasing the initial height of magnetic film, but the modulation efficiency of GCM increases with increasing amplitude and decreasing the initial gap of MFCs. Additionally, the modulation efficiency of SMM is the sum of the modulation efficiency of VMM and GCM when two resonators have the same frequency and their phase difference is 180 degree. Validation and results To demonstrate the theoretical analysis above, the finite element method (FEM) simulation is done. Assuming that the magnetic film and MFC with the same frequency of 10 kHz, the same amplitude of 10 μm , and the phase difference of 180 degree, the results are shown in Fig. 2 (a). It is found that the DC magnetic field, 1 μT , is modulated into a high-frequency magnetic field, and the modulated magnetic field waveform is a slightly distorted high-frequency sine wave. The reason is that the modulated magnetic field has many harmonic components, but the amplitude of the first-order component and DC component is much larger than other components. The peak-peak amplitude of the modulated magnetic field of SMM is larger than that of GCM and VMM, the modulation efficiency of VMM, GCM, and SMM is 38.55%, 66.82%, and 100.31%, respectively, and the modulation efficiency of SMM is nearly equal to the sum of modulation efficiency of VMM and GCM. Additionally, the situations when the MEMS resonators vibrate from 1 μm to 10 μm with the step of 1 μm are investigated, as shown in Fig. 2 (b). The results show that the modulation efficiency increases linearly with increasing the amplitude, and the SMM has the maximum modulation efficiency among three modulation ways. What's more, the theoretical values are coincident well with the simulated results, which demonstrates the utility of the theory.

Conclusion Therefore, we can conclude that SMM can significantly improve the modulation efficiency of the MEMS-based MR sensor and improve the low-frequency magnetic field detection limit, and the amplitude of MEMS resonator as large as possible is desired. Of course, fabricating two MEMS resonators as like in this paper and synchronizing them are not easy, the current feasible method is to use MEMS bonding technology and an interface circuit based on a phase-locked loop.

[1] Z. Q. Lei, G. J. Li, W. F. Egelhoff, P. T. Lai, and P. W. T. Pong, "Review of Noise Sources in Magnetic Tunnel Junction Sensors," *IEEE Transactions on Magnetics*, vol. 47, no. 3, pp. 602-612, 2011. [2] A. S. Edelstein, G. A. Fischer, M. Pedersen, E. R. Nowak, S. F. Cheng, and C. A. Nordman, "Progress toward a thousandfold reduction in $1/f$ noise in magnetic sensors using an ac microelectromechanical system flux concentrator (invited)," *Journal of Applied Physics*, vol. 99, no. 8, p. 08B317, 2006. [3] J. Hu, M. Pan, W. Tian, D. Chen, and J. Zhao, "Magnetostatic detection using magneto-resistive sensors with vertical motion flux modulation," *Rev Sci Instrum*, vol. 83, no. 5, p. 055009, May 2012. [4] A. Guedes, R. Macedo, G. Jaramillo, S. Cardoso, P. P. Freitas, and D. A. Horsley, "Hybrid GMR Sensor Detecting 950 pT/sqrt(Hz) at 1 Hz and Room Temperature," *Sensors (Basel)*, vol. 18, no. 3, Mar 6 2018. [5] Q. Du *et al.*, "High Efficiency Magnetic Flux Modulation Structure for Magnetoresistance Sensor," *IEEE Electron Device Letters*, vol. 40, no. 11, pp. 1824-1827, 2019.

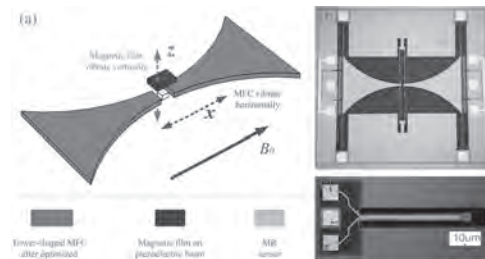


Fig.1 synchronous motion modulation (SMM). (a) The simplified schematic of SMM. The brown part is Tower-shaped MFC deposited on the surface of comb-driven resonator. The blue part is the magnetic film deposited on the bottom of the end of the piezoelectric cantilever resonator. The yellow part is the MR sensor that is used to sense the AC magnetic field; (b) fabricated comb-driven resonator; (c) fabricated piezoelectric cantilever resonator.

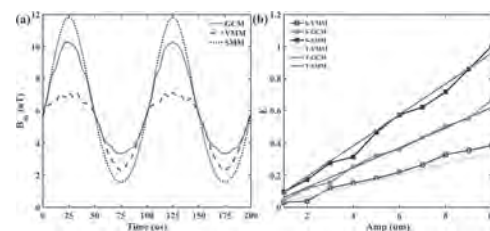


Fig. 2 The comparison of three modulation ways. (a) The time-domain curves of the modulated magnetic field in two periods; (b) the theoretical and simulated modulation efficiency of three modulation ways versus vibration amplitude of two resonators. 'T' and 'S' represent the theoretical results and simulated results.

IB-13. Influence of Preparation Conditions on Long-Term Stability of Magneto-resistive Properties of Nanostructured La-Sr-Mn-Co-O Films Grown by PI MOCVD.

N. Zuraskiene^{1,2}, V. Rudokas¹, M. Vagner^{1,3}, K. Motiejaitis³, M. Koliada¹, V. Stankevicius^{1,2}, S. Kersulis¹, D. Pavilonis¹ and V. Plausinaitiene^{1,3}

1. Functional Materials and Electronics, Center for Physical Sciences and Technology, Vilnius, Lithuania; 2. Faculty of Electronics, Vilnius Gediminas Technical University, Vilnius, Lithuania; 3. Faculty of Chemistry and Geosciences, Vilnius University, Vilnius, Lithuania

It has been demonstrated that perovskite oxides with the general formula ABO_3 (A - lanthanides, alkaline-earth metals, B - transition metal cations) exhibit the colossal magnetoresistance (CMR) phenomenon and can be used for various spintronics applications [1]. Many efforts were made in structural and chemical engineering of such materials in order to tune their functional properties along a wide range of temperatures and magnetic fields. It was found that epitaxial films exhibit high magnetoresistance (MR) values only in the vicinity of phase transition temperature, while polycrystalline films exhibit significant MR in a wide range of temperatures. Engineering of lanthanum manganites with special nanocrystalline (polycrystalline with nanosize grains) structure enabled to develop so-called CMR-B-scalar sensors, which are capable to measure the magnitude of pulsed magnetic fields in very small volumes independently on field direction [2]. Such sensors have been used in advanced scientific equipment to measure magnetic field dynamics [3-4]. It is worth to note, that in the past decades the most extensive research was performed on A-site doped manganites. This doping results in a mixed valance state of the manganese ions (Mn^{3+} and Mn^{4+}) giving rise to the ferromagnetic (FM) double exchange (DE) interaction, which determines transport and magnetic properties of these materials. On the other hand, it was proposed that the B-site doping with $3d$ ions (Co, etc.) would destroy the long-range FM ordering of the $Mn^{3+}-O^{2-}-Mn^{4+}$ network resulting in a complex glassy state which arises from the competition of FM and antiferromagnetic (AFM) interactions. Therefore, significant change of the magnetic and electrical properties of manganites is expected. It was demonstrated, that substitution of Co for Mn in $La_{1-x}Sr_xMnO_3$ results in increased room temperature MR [5]. A variety of competing magnetic interactions in Co-doped manganites [6] still remains unclear, especially in nanostructured films, therefore, their investigations are of great interest. In addition, the long-term stability [7] of magneto-resistive properties of such films is very important for magnetic field sensors applications. In this study, the resistivity ρ and MR of nanostructured Co-doped manganite films deposited at different growth rate was investigated in magnetic fields up to 20 T at room and cryogenic temperatures. The change of these parameters were studied during the long-term storage of the films and accelerated ageing by annealing the films at O_2 and Ar atmosphere. The $La_{0.81}Sr_{0.19}Mn_{1.09}Co_{0.06}O_3$ films (LSMCO) with a thickness of 360 nm were deposited by using a Pulsed-Injection Metal-Organic Chemical Vapor Deposition (PI MOCVD) technique onto a polycrystalline Al_2O_3 substrate at 600 °C temperature keeping different growth rates (9 nm/min, 13 nm/min, and 27 nm/min). The Ag electrodes of the samples were thermally deposited on a Cr sublayer and post annealed at 450°C for 1 h. The ρ dependence on temperature was measured in the temperature range of (5–310) K. The MR measurements were performed in permanent (0-0.8) T magnetic field at (25–290) K and pulsed fields up to 20 T at (80–290) K temperatures. The ρ and MR of films deposited at different growth rates was investigated after such preparation steps: 1) formation of electrodes and post annealing at 450°C for 1 h in Ar or O_2 atmosphere; 2) long-term storage at room temperature for 6 months; 3) accelerated ageing procedure: additional annealing at 100 °C for 8 h in Ar or O_2 . It was found that electrode formation conditions and the long-term storage significantly changes the properties of the films (see Fig.1). After 6 months the resistivity maximum ρ_m of all films significantly increased and the metal-insulator transition temperature T_m shifted to lower temperatures. The annealing at 100 °C for 8 h in O_2 decreased the ρ due to oxygen saturation of the films. The resistivity of nanostructured films mostly depends on the quality of grain boundary material, therefore, the largest changes were obtained for LSMCO film grown at the highest rate (27 nm/min). The annealing in Ar only slightly affected the ρ values. The low-field (0.7 T) MR (Fig.2) changed insignificantly in all temperature range (25-290) K. This is

probably related with the change of a number of charge carriers' hopping centers $Mn^{3+}-O^{2-}-Mn^{4+}$, which depends on the oxygen saturation level. Therefore, despite the resistivity changes, the $MR=100\% \times [\rho(B)/\rho(0)-1]$ was only slightly affected. At 20 T the MR also insignificantly depended on preparation conditions and was $\sim(65-70)\%$ at 80 K and $(55-60)\%$ at 290 K. It was concluded, that for magnetic field sensors application the LSMCO films grown at lower rate (9 nm/min) and annealed at Ar atmosphere are preferable due more stable parameters.

[1] D. Pla, C. Jimenez, M. Burriel, *Advanced Materials Interfaces*, Vol. 4, p. 1600974 (2017) [2] T. Stankevicius, L. Medisaukas, V. Stankevicius et al., *Rev. Sci. Instrum.*, Vol. 85, p. 044704 (2014) [3] T. L. Haran, R. B. Hoffman, S. E. Lane, *IEEE Trans. Plasma Sci.*, Vol. 41, p. 1526 (2013) [4] V. Stankevicius, J. Lueg-Althoff, M. Hahn et al., *Sensors*, Vol. 20, p. 5925 (2020) [5] J. Hu, H. Qin, J. Chen et al., *J. Appl. Phys.*, Vol. 91, p. 8912 (2002) [6] H. Zhao, X. G. Chen, J. Z. Wei et al., *IEEE Trans. Magn.*, Vol. 51, p. 1200205 (2015) [7] M. Egilmez, M.M. Sabera, M. Abdelhadi et al., *Phys. Lett. A*, Vol. 375, p. 4049 (2011)

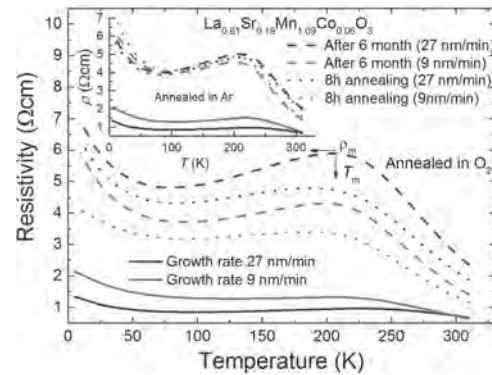


Fig.1. Resistivity vs. temperature dependences of LSMCO films grown at different growth rates and annealed in O_2 or Ar (inset) atmosphere. Solid curves – after formation of electrodes; dashed curves – after long-term storage at room temperature during 6 months; dotted curves – after annealing for 8 h at 100 °C.

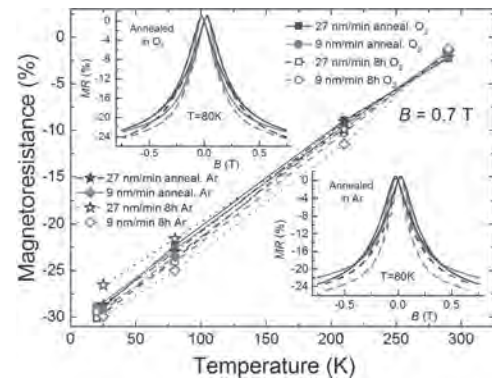


Fig.2. Magnetoresistance vs. temperature dependences of LSMCO films grown at different growth rates and annealed in O_2 or Ar atmosphere. Symbols show MR values measured at $B=0.7$ T. The insets present $MR(B)$ dependences: solid curves – after formation of electrodes; dashed curves – after annealing for 8 h at 100 °C.

Session IC
NON-DESTRUCTIVE EVALUATION & OTHER SENSORS I
Gui Yun Tian, Chair
Newcastle University, Newcastle, United Kingdom

CONTRIBUTED PAPERS

IC-01. A Low-Frequency Eddy Current Probe Based on Miniature Fluxgate Array for Defect Evaluation in Steel Components.M. Saari^{1,2}, N. Nadzri¹, M. Zaini¹, M. Sulaiman¹ and K. Tsukada³

1. Faculty of Electrical & Electronic Engineering Technology, Universiti Malaysia Pahang, Pekan, Malaysia; 2. Automotive Engineering Centre, Universiti Malaysia Pahang, Pekan, Malaysia; 3. Graduate School of Interdisciplinary Science and Engineering in Health System, Okayama University, Okayama, Japan

Monitoring the occurrence of defects in steel structures of crucial applications such as pipelines, aircraft, bridges, etc. is necessary to prevent any fatal accidents from happening in the future. Particularly for cracks, their early detection can be difficult to be achieved as their progression may start at micrometer in size [1]–[3]. To enable detection of these micrometer-sized defects occurred in high permeability materials such as mild steel components, it is important to increase the eddy current signal against the magnetization signal of the material so that the eddy current variation due to the defects will not completely be buried within the strong magnetization signal [2], [4]. Here, the detection area plays an important role where a small detection area will result in a higher ratio of the eddy current signal to the magnetization signal. Compared to the conventional sensing technique using detection coils, in this work, we utilized miniature fluxgates to sense the variation of the eddy current at a high degree of locality while benefiting from their high sensitivity at a low-frequency region for sub-surface defect detection. It also can be expected that the sensitivity of the fluxgates will enable the evaluation of sub-surface defects in a high magnetic permeability material such as mild steels, owing to the increase of the eddy current's penetration depth at the low-frequency region. By using miniature fluxgates (DRV 425, Texas Instruments), we configured the fluxgates and their circuits on a custom-made printed circuit board as shown in Fig. 1 (a). Furthermore, to increase the eddy current intensity within a small area, the generated excitation field was concentrated by using small unshielded ferrite inductors. The inductors were arranged uniformly in two layers so that the eddy current induced between the two layers will flow in the same direction as the layers. Each of the inductors had an inductance of 10 mH and a DC resistance of 30.5 Ohm. Moreover, the fluxgates were also arrayed in 2 layers and fixed equidistantly between the layers of the inductors. This arrangement was expected to enable the construction of the eddy current components in x - and y - directions by taking the differential of the z -component field B_z in y - and x - directions, respectively [1]. This probe is also intended for a mobile application, i.e., low current consumption, where a 20-mA AC current source was used to drive the inductors. We first evaluate the magnetic noise characteristic of the fluxgate where it was measured in a tri-layer magnetic shield. The sensor showed a magnetic noise lower than 10 nT/sqrt(Hz) from 3 Hz until 1 kHz. The fluxgate exhibited a sensitivity of 5V/mT when it was shunted with a 200-Ohm resistor and operated within a region from -0.5 mT to 0.5 mT. Using the developed probe, we measured the magnetic responses B_z induced from 5 artificial slits, whose depth ranges from 2 to 10 mm. The artificial slits were engraved on a mild-steel plate with a thickness of 12 mm, as shown by the schematic drawing of the steel plates in Fig. 2 (a). All of the slits had the same width and length, which were 1 mm and 30 mm, and they were arranged in a parallel direction, separated by a 30-mm distance. The magnetic response B_z of the slits was evaluated by mapping the B_z distribution over the slit area, and it was measured on the top surface with a 1-mm lift-off. A set of frequencies was selected for the excitation field, which is from 10 Hz to 310 Hz, in order to investigate the effect of skin depth penetration. The signal from the sensor was sampled by a data acquisition card (NI-USB 6210) at a 20-kHz sampling frequency and processed using a digital lock-in technique, implemented in Labview. In order to determine a suitable reference signal of the lock-in technique, we implemented a dynamic referencing technique where one of the sensor outputs of the fluxgates was used as the reference signal [4]. Using this referencing technique, we were able to separate the strong magnetization signal from the detected signal, in which the separated signal is mostly dominated by the phase information of the induced signal, i.e., the eddy current signal.

The result for the eddy current distribution at the 30-Hz excitation frequency is shown in Fig. 2 (b). The positions of the slits were located at $y = 29$ mm (10-mm slit), 59 mm (8-mm slit), 89 mm (6-mm slit), 119 mm (4-mm slit), and 149 mm (2-mm slit), respectively. The signal change due to the existence of the slits could be clearly observed from the constructed eddy current distribution. It could be observed that the eddy current was reduced at the location of the slits where the reduction intensity was proportional to the slit depth. The developed probe shows a promising characteristic in assessing steel defects at a high detection sensitivity. Acknowledgments This work was supported by the Ministry of Higher Education of Malaysia under the grant number of FRGS/1/2019/TK04/UMP/02/4 (RDU1901154) and the Research Management Center of Universiti Malaysia Pahang under the grant number of RDU1903100.

[1] M. M. Saari *et al.*, “Design of Eddy Current Testing Probe for Surface Defect Evaluation,” *Int. J. Automot. Mech. Eng.*, vol. 16, no. 1, pp. 6357–6367, 2019, doi: <https://doi.org/10.15282/ijame.16.1.2019.19.0481>. [2] K. Tsukada, M. Hayashi, Y. Nakamura, K. Sakai, and T. Kiwa, “Small Eddy Current Testing Sensor Probe Using a Tunneling Magnetoresistance Sensor to Detect Cracks in Steel Structures,” *IEEE Trans. Magn.*, vol. 54, no. 11, pp. 1–5, 2018, doi: 10.1109/TMAG.2018.2845864. [3] P. A. Petcher and S. Dixon, “Weld defect detection using PPM EMAT generated shear horizontal ultrasound,” *NDT E Int.*, vol. 74, pp. 58–65, 2015, doi: 10.1016/j.ndteint.2015.05.005. [4] M. A. Hadi Putera Zaini, M. Mawardi Saari, N. A. Nadzri, A. Mohd Halil, and K. Tsukada, “An MFL Probe using Shiftable Magnetization Angle for Front and Back Side Crack Evaluation,” *Proc. - 2019 IEEE 15th Int. Colloq. Signal Process. its Appl. CSPA 2019*, no. March, pp. 157–161, 2019, doi: 10.1109/CSPA.2019.8696064.

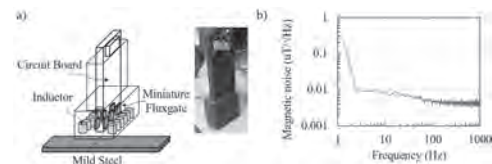


Fig. 1. a) Arrangement of inductors and miniature fluxgate DRV425. b) Magnetic noise characteristic of the miniature fluxgate.

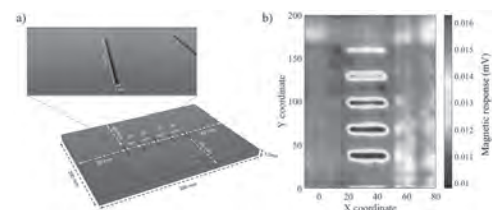


Fig. 2. a) 5 artificial slits with different depths from 2 mm to 10 mm on a 12-mm mild steel plate. b) Distribution of the eddy current component in the x -direction detected by the proposed probe using a 30-Hz and 20-mA excitation current.

IC-02. Examination of Insertion Type Electromagnetic Inspection for Outer Side Defect on Ferromagnetic Steel Tube by Speed Effect Using Only Static Magnetic Field.

M. Tohara¹ and Y. Gotoh²

1. Technical Development Department, Toa Non-Destructive Inspection Co., Ltd, Kitakyushu, Japan; 2. Division of Mechatronics, Department of Innovative Engineering, Oita University, Oita, Japan

Introduction When an electromagnetic sensor composed of a static excitation coil and a detection coil is moved in a steel tube at high speed, an eddy current is generated in the steel tube. If a defect is present in the steel tube, the defect may be detected by the change in the eddy current. Generally, the heat transfer tubes with ferromagnetism in power plants or oil plants are inspected for defects by moving an internally inserted electromagnetic sensor at a high speed of about 1 m/s [1]. In this research, an inner-type electromagnetic sensor using the static magnetic field that moves inside these steel tubes at high speed and detects on the outer side defect in the steel tubes is proposed. The generated eddy current inside the steel tube by constant velocity movement of the static magnetic field is analyzed by the 3-D nonlinear eddy current FEM analysis using step-by-step method. In addition, verification experiment is also conducted. **Inspection Model and Electromagnetic Conditions** Fig.1 shows the proposed electromagnetic sensor using only the static magnetic field and an inspection steel tube (STB340SC). This sensor is composed of two static excitation coils in series, a pair of differential detection coils, and a magnetic yoke of permendur material. The direct current of 1 A is passed through two excitation coils in series so that the plus z -direction of the sensor is the S-pole and the minus z -direction is the N-pole. The permendur material is an alloy of iron and cobalt. The two excitation coils and the differential detection coil are 220 turns \times 2 and 100 turns \times 2, respectively. The outer diameter, length, and thickness of this inspection steel tube are ϕ 19 mm, 460 mm, and 2 mm, respectively. The proposed sensor is inserted in the steel tube at a speed of 1 m/s for minus z -direction. The distance (lift-off: L_o) between the sensor and the steel tube is equal to 0.5 mm. **Analysis and Experimental Results** Fig.2 shows the distribution of only one layer in the y -direction of eddy current density inside the steel tube when the sensor is moved in the minus z -direction of the steel tube without defect at 1m/s. This figure denotes that the directions of the eddy currents generated on the upper side and the lower side of the steel tube are opposite. Since the lower part of the sensor in the moving direction is the N-pole, the eddy current is generated inside the steel tube near the lower part of the sensor in the direction of canceling the N-pole magnetic field. On the other hand, since the upper part of this sensor is the S pole, an eddy current is generated inside the steel tube near it in the direction of canceling the S-pole magnetic field. In addition, Fig.2 denotes that both the upper and lower eddy currents in the thickness of the steel tube are concentrated on the inner surface of the steel tube by skin effect. Fig.3 shows the distribution of the flux density inside the steel tube when the sensor is moved in the minus z -direction of the steel tube without defect at 1m/s. This figure denotes the flux density inside the steel tube near the lower side of the sensor is distributed in the plus z -direction, since the eddy current is generated inside the steel tube in the direction of canceling the N-pole magnetic field. On the other hand, the flux density on the inner surface of the steel tube near the upper side of the sensor is offset because the eddy current is generated in the opposite direction to when the N-pole of lower side of the sensor passed. However, the distribution of flux density in the steel tube near the central region of the sensor is almost uniform. Fig.4 shows comparison results of analysis and experiment of the steel tube with an outer slit defect in the circumferential direction. The width for the z -direction and the depth for the x -direction of the defect are 10 mm and 0.5 mm, respectively. The horizontal axis of the figure indicates the moving position of the sensor, and the vertical axis indicates the differential voltage output by the pair of detection coils in the sensor. This figure shows that an electromagnetic sensor using only a static magnetic field is detected the outer side defect on the steel tube. Moreover, this figure denotes that the calculated result is in agreement with measurement.

[1] M. Zec, R. P. Uhlig, M. Ziolkowski, and H. Brauer, "Finite Element Analysis of Nondestructive Testing Eddy Current Problems with Moving Parts", *IEEE Transactions on Magnetics* vol.44, no.8, pp.4785-4794 (2013).

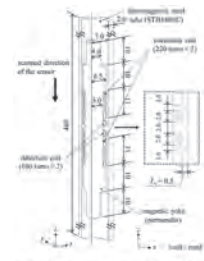


Fig. 1. Inspection model of the steel tube without the defect (1/4 domain).

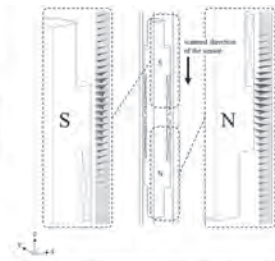


Fig. 2. Distribution of eddy current density in the steel tube (sensor speeds: 1 m/s).

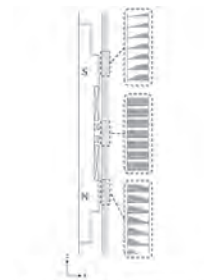


Fig. 3. Distribution of flux density in the steel tube (sensor speeds: 1000 min/s).

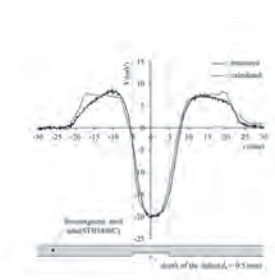


Fig. 4. Comparison results of analysis and experiment.

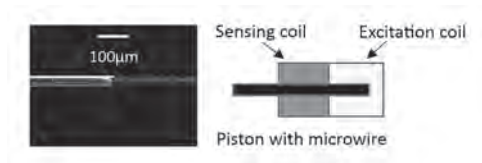
IC-03. Linear Position Sensor Using Magnetically Bistable Microwire.

R. Jurc^{1,3}, P. Jacko^{1,4}, L. Galdun^{1,2}, L. Hvizdos¹, J. Gamcova¹ and R. Varga^{1,2}

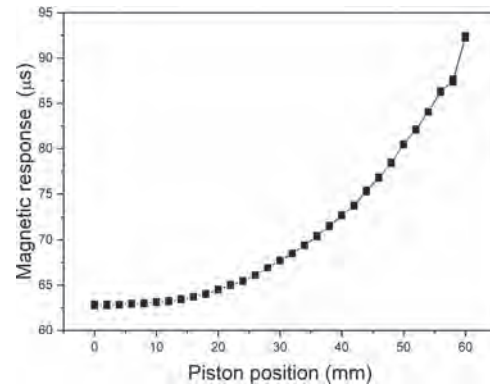
1. RVmagnetics a.s., Kosice, Slovakia; 2. CPM TIP UPJS, Kosice, Slovakia; 3. Faculty of Aeronautics, TUKE, Kosice, Slovakia; 4. Faculty of Electrical Engineering and Informatics, TUKE, Kosice, Slovakia

Linear variable differential transformer (LVDT) sensors offers many advantages in low power consumption, high sensitivity, low hysteresis, etc. These features allow them to be used in wide range of possible applications in critical environments [1]. However, they suffer from some disadvantages like temperature dependence of output, sensitivity to stray magnetic fields and others. Most of the disadvantages arises from the fact that LVDT sensors sense variation of permeability of magnetic core to external stimuli like magnetic field or temperature. Some of the problems can be solved using glass-coated magnetically bistable microwire as a variable core for linear position sensor. Glass-coated amorphous microwires are composite materials having metallic nucleus covered by glass-coating [2]. They are produced by Taylor-Ulitovski method applying drawing and quenching of molten metal that fills glassy capillary. Having positive magnetostriction, they show magnetic bistability (only two oppose saturation magnetic states are allowed in static state) and switching between the two states appears through the single Barkhausen jump. This gives us possibility to separate contribution of external magnetic field, temperature, stress or position [3]. Apart from the above mentioned feature, they offer advantages in small size, glass-coating that provides insulation from chemically aggressive environment, or simple, fast and cheap production of large amount of microwire (up to kilometre of wire can be produced from few grams of master alloy). In the given contribution, we show the linear position sensors similar to LVDT based on magnetically bistable microwire. It consists of two coils (excitation and sensing) having single microwire coaxially placed on linearly moving piston. In contrary to classical LVDT sensors, where position defines the amplitude of the signal measured on the sensing coil, we detect the switching field that is proportional to the position. Application of triangular shape of excitation field allows us to measure switching time that is proportional to the switching field. Using fluxgate like sensing system and measuring the positive and negative switching time, we are able to avoid stray fields dependence of linear position piston sensing. We show, how temperature independence of sensing can be solved by proper chemical composition. Such a sensors show no hysteresis and requires quite small power consumption. Proper design allows to obtain sensitivity down to 20 μm within the range 0-6 cm (see fig. 2). However, sensitivity and range can be adjusted by properly selecting the shape of excitation coil. This work was partially supported by Slovak Grant Agencies VEGA 1/0053/19 and APVV-16-0079.

[1] D. S. Nyce, Linear Position Sensors: Theory and Application, John Wiley & Sons, Inc. (2004) [2] M. Vázquez: Advanced magnetic microwires. In: Kronmüller, H., Parkin, S. S. P. (eds.) Handbook of Magnetism and Advanced Magnetic Materials, Wiley, Chichester, West Sussex, England (2007) [3] R. Jurc, L. Frolova, D. Kozejova et al. Sensoric application of glass-coated magnetic microwires in Magnetic Nano- and Microwires, Second edition, ed. by M. Vázquez, Woodhead Publishing, (2020), ISBN: 9780081028322.



SEM figure of glass-coated microwire (left), Schematic view of linear position sensor with bistable microwire (right)



Dependence of magnetic response of linear position sensor on piston position

IC-04. Effect of Magnetic Circuit on Pulse Voltage Generated by Wiegand Sensor in a Linear Positioning System.

H. Lien¹ and J. Chang¹

¹. Power Mechanical Engineering, National Tsing Hua University, Hsinchu, Taiwan

A Wiegand sensor is composed of a strip of Wiegand wire and a pickup coil. From literature, the Wiegand wire was initially made of NiFe alloy [1-2]. However, it was reported that the wire made of FeCoV alloy offered the optimum performance in generating the Wiegand effect [3]. Diameter of the Wiegand wire is about 0.25 mm. Heat treatment such as quenching and annealing are applied to the wire in order to change grain size of the alloy. After heat-treatment, cold-treatment such as stretching and twisting are then introduced to the wire to make exhibition of different coercivity in its surface region and center region, respectively [1-6]. When external magnetic field passing through axial direction of the wire with different coercivity reaches a certain threshold, the “soft layer” with relatively low coercivity of the wire can fast reverse its direction of magnetization. The fast magnetization reversal of the soft layer leads to generation of large Barkhausen jump, resulting in changes of magnetic flux in the pick-up coil such that the pulse voltage is induced with 10 μ s pulse width and up to 8 V peak voltage [5]. This pulse voltage is also called Wiegand pulse. The peak voltage and pulse width of the pulse is reported to be independent of driving frequency, so it can be used as a zero-speed sensor. Reported in [3], the Wiegand sensor was able to generate electrical power of 600 nJ, which could be used for energy harvesting driving small power components. The material of the Wiegand sensor is stable and cheap, and the pulse energy did not reduce after million times of switching. Advantaged by the above features, the Wiegand sensors have been used in rotary speed measurement [7], Batteryless hall sensors [3], and multi-turn absolute encoders [8]. In this study, we apply Wiegand sensor to linear positioning system so that Wiegand impulse can be used as batteryless limiting switch or reference mark. The focus of this work is placed on the design of the system’s magnetic circuits so that the Wiegand pulse can be triggered effectively. In our experiments, data acquisition NI USB-6216 with up to 400 Ks/s sampling rate and 16-bit resolution to measure Wiegand pulse in different magnetic circuits are employed. The relationship between different magnetic circuits and pulse peak were investigated and obtained in this study. To design the magnetic circuits for the Wiegand sensor, generation of Wiegand pulse if of primary importance. In previous work [1][6], it was reported that to be able to repeatedly generate Weigand pulse, external magnetic field should pass through the wire’s axial axis. To be able to reach this objective, appropriate strength of external magnetic field should be first applied through the axial axis of Wiegand wire so as to magnetize the wire, followed by decreasing external magnetic field to let Wiegand wire have remanence (Br). Lastly, opposite direction of external magnetic field should be applied to the Wiegand wire so that the wire’s soft layer can suddenly reverse its polarity to yield Wiegand pulse. Based on the Wiegand effect mentioned above, we use single magnet to produce external magnetic field. The direction of magnetic field around both sides of the magnet is opposite to that around center of the magnet. The placements of the Wiegand sensor and the magnet are shown and depicted in Fig. 1(a) and Fig. 1(b), respectively. The linear motor carrying the magnet is set to move back and forth at a speed of 30 mm/s along Y-axis, from which the mean value of the pulse peak is computed every 50 runs. The relationship between the mean value of peak voltage and the Flying height (H) is shown in Fig. 2(a), whereas the relationship between pulse signal and time is shown in Fig. 2(b). From measurement results, it was observed that when H is lower than 3.5 mm, the triggering of the pulse signal was limited. As the linear motor moved from left to right, it was observed that the Weigand sensor first generated small pulse signal under 0.1 V first, followed by generation of relatively large pulse signal with magnitude over 0.3 V. This phenomenon was investigated through finite-element simulation. When the magnet moving from left to right, the simulated magnetic flux density in the soft layer of the wire is depicted in Fig. 2(c) showing unsymmetrical hysteresis loop according to the change of magnetic flux density. Based on this unsymmetrical hysteresis loop, one can see that the Br values at state 2 and state 4 are significant different, leading to generation of relatively small pulse signal first at state 2 then relatively large pulse signal at state 4. From Fig. 2(b), it was found that

when H is below 3.5 mm, the Wiegand pulse could not be triggered. As illustrated in the comparison in Fig. 2(d), when H=1 mm, the whole soft layer can’t perform fast magnetization reversal at the same time as the case when H=5 mm. Through this study, we conclude that should one need to effectively trigger Wiegand pulse, appropriate strength of external magnetic field should be applied and whole soft layer of Wiegand wire not fast reversing at the same time should be avoided.

[1] J. R. Wiegand, “Switchable magnetic device,” *U.S. Patent* No 4,247,601, 1981. [2] J. R. Wiegand, “Method of manufacturing bistable magnetic device,” *U.S. Patent* No 3,892,118, 1975. [3] Y. Takemura et al., “Batteryless hall sensor operated by energy harvesting from a single Wiegand pulse,” *IEEE Transactions on Magnetics*, 53.11: 1-6, 2017. [4] S. Abe, A. Matsushita, and M. Naoe, “Annealing and torsion stress effect on magnetic anisotropy and magnetostriction of Vicalloy fine wire,” *IEEE Transactions on Magnetics*, 33.5: 3916-3918, 1997. [5] S. Abe, A. Matsushita, and M. Naoe, “Dependence of large Barkhausen jump on length of a vicalloy fine wire with torsion stress.” *IEEE Transactions on Magnetics*, 34.4: 1318-1320, 1998. [6] X. Sun, T. Yamada, and Y. Takemura, “Output characteristics and circuit modeling of Wiegand sensor,” *Sensors*, 19.13: 2991, 2019. [7] E. Zabler and P. Hauler, “Level amplitude output rotary speed transducer,” *U.S. Patent* No 4,150,314, 1979. [8] W. Mehnert and T. Theil, “Absolute high resolution segment or revolution counter,” *U.S. Patent* No 8,655,615, 2014.

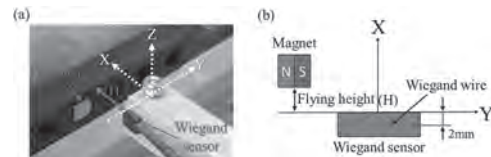


Fig. 1 (a) isometric and (b) top views of placement of Wiegand sensor and magnet.

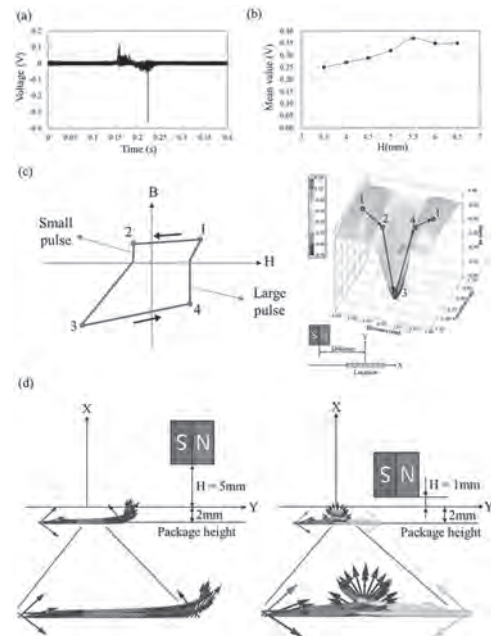


Fig. 2 Measured and simulated results of (a) pulse voltage obtained from the Wiegand sensor, (b) mean value of peak voltage in different H. Magnetic flux density in different location and hysteresis loop of Wiegand wire is shown in (c) exemplified by magnetization direction of soft layer when H=1 mm and 5 mm, respectively in (d).

IC-05. A Magnetization System for Spindle Axial Thermal Elongation Measurements.

K. Peng¹ and J. Chang¹

1. Power Mechanical Engineering, National Tsing Hua University, Hsinchu, Taiwan

Linear and rotary types of positioning systems have been research and development focus in particular to facilitate precision manufacturing with machine tools. Encoders inside the positioning systems are commonly classified into two types, namely optical and magnetic types. The optical type uses light source reflection to target for position in between, whereas the magnetic type uses a magnetic field to measure position of the target. Although optical encoders may have a greater resolution, magnetic encoders have better performance in harsh environments and dust resistance. Moreover, comparing with the same level of product specifications, magnetic encoders have lower cost and fewer components. These advantages make magnetic encoders more commonly used in machine tools [1]. A magnetic encoder usually consists of a sensor head and a magnetic medium, where the medium is composed of a substrate, and a ferromagnetic material covering on its surface, to generate different alternating polarity pattern by magnetizing the ferrite-magnetic medium under an external magnetic field. Even when the external magnetic field is removed, the magnetization polarity could be still maintained [2]. These patterns are not only used in linear positioning systems, but are also used to obtained spindle shaft angular position by assembling a rotary magnetic encoder in robotics joints or rotating machines. Because of its accuracy performance directly affects the work-piece appearance, factors affecting accuracy of the rotating machines play a significant role in the machining process. In the process, an inevitable thermal expansion cannot be ignored under high-speed machining, particularly for the axial elongation of the machine's spindle shaft. This axial elongation can lead to catastrophic failure in the rotating machine if it is not adequately monitored. Therefore, the magnetizer in this paper aims to present a different pattern arrangement, which was conceived by Shih and Hsiao [3] to verify elongation of the spindle shaft in axial direction. In the present study, the aforementioned alternating polarity pattern is magnetized on CoMnP ferromagnetic material on the magnetic ring in the way as illustrate in Fig.1(a). A NdFeB35 permanent magnet serves as an external magnetization source, and special magnetization head shape are utilized to concentrate the magnetic flux to create the designed magnetic pattern. The magnetic ring is concentrically attached to the spindle shaft accompanied with a magnetoresistive (MR) sensor to establish a measurement system along the shaft's axial direction as shown in Fig.1(a). This MR sensor is composed of two Wheatstone bridges, each bridge consisting solely of 4 equally arranged MR elements placed above the magnetic ring. The MR elements can read out a sinusoidal or cosinusoidal voltage signal caused by changes in magnetic field when relative displacement occurs between the medium ring and the sensor. However, the angle between the magnetization vector and the element's current can be altered as the magnetic field signals are affected subsequently due to assembly errors between the sensor and the ring. These problems result in a high position error. In this paper, finite element studies and experiments are adopted to investigate the effect of assembly errors, including flying height, pitch, yaw, and roll errors between the MR sensor head and the magnetic patterns on the ring as illustrated in Fig.1(b) [4]. We aim to reduce position error by optimizing the sensor's installation. From the studies, the optimized flying height is found to be 0.6 to 0.7 mm from the MR element or equivalently 0.1 to 0.2 mm when package dimensions of the sensor head are considered. It is observed that with this optimal flying height, an optimal signal performance can be achieved in which frequency multiplication can be reduced in the measured magnetic signals. As depicted in Fig.2(a), when the sensor head rotates in pitch and yaw directions from 0° to 1.16° with 0.29° and 0.2° steps, respectively, the error percentage is strictly increased by 81.4% and 29.6%, respectively. Moreover, in error percentage of the sensor increases only 3.8% when it rolls from 0° to 1°, implying that sensor assembly in the roll direction possesses more mounting tolerance than other directions. On the other hand, in order to make the measurement system reach to application level for the spindle shaft axial thermal elongation measurement in a high-speed motor (24,000 rpm), a system with a built-in field-programmable gate array to improve firm-

ware sampling rate to 2 kHz is instrumented so that the measured magnetic signals can accurately reflect spindle shaft's actual elongation from unreal or distorted signal waveform due to insufficient sampling rates. As shown in Fig.2(b), along with temperature measurement, the spindle shaft's axial displacements measured by the aforementioned system are compared with commercially available eddy current sensor when the spindle rotates from 1,000 to 24,000 rpm. It can be seen that not only the trends are the same, the difference between the two are neglectable. This suggests that the proposed method and system can instantly measure the spindle's axial thermal elongation in response to the change of temperature in the machine tools.

[1] K. Miyashita, T. Takahashi and M. Yamanaka, "Features of a magnetic rotary encoder." *IEEE Transactions on Magnetics*, vol. 23, no. 5 pp. 2182-2184, Sep.1987. [2] Y.-J. Luo, E.-T. Hwang, and S.-M. Huang, "Multi-pole magnetization of high resolution magnetic encoder." *Proceedings of Electrical/Electronics Insulation Conference*. IEEE, Oct.1993. [3] S.-W. Shih, H.-S. Hsiao, J.-Y. Chang, "The magnetic encoder apparatus and measuring the displacement of the rotation axis." *Taiwan Patent 1662255*, July. 2018. [4] K.-Y. Peng and J.-Y. Chang, "Effects of assembly errors on axial positioning accuracy for rotating machinery with magnetoresistance-based magnetic encoders" *Microsystem Technologies*, January, 2021.

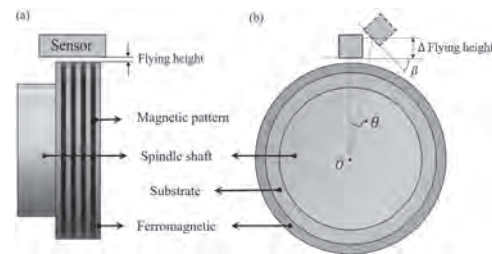


Fig. 1 Schematics of (a) magnetic ring with alternative polarities pattern attached to spindle shaft with (b) sensor assembly errors.

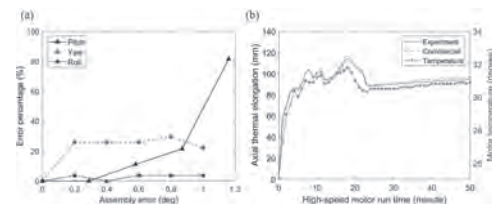


Fig. 2 (a) error percentage at different angles and (b) comparison of the shaft's measured axial thermal elongation.

IC-06. A Simplified 2D Equivalent Model for Magnetic Wire Array.

M. Mirzaei¹, P. Ripka¹ and V. Grim¹

1. Czech Technical University in Prague, Prague, Czechia

The calculation of demagnetization factor and apparent permeability of magnetic core is essential in induction and fluxgate sensors design [1]. The calculations and analyses of demagnetization factors for ellipsoidal and non-ellipsoidal shapes of single element were studied in detail in various publications [1]-[8]. For instance, demagnetization factor for sphere can be analytically calculated and it is 1/3 [2]. Demagnetization factor for single ellipsoidal has closed-form equation [1], but the apparent permeability depends on material permeability (only for very high permeability it depends only on geometry). Demagnetization factor for non-ellipsoidal shape of single element, for example solid cylindrical wire and hollow cylinder, cannot be described in single closed-form formula, however approximations using curve fitting were used [1], [4] and [6]. Magnetic permeability of wire has high impact on the demagnetization [7]-[8]. Using finite element method (FEM) or complex analytical modeling are common methods to take into account magnetic permeability effects on the demagnetization. However, effects of finite relative magnetic permeability can be taken into account using curve fitting [4] and [6] in the closed form equation of the demagnetization factor. The demagnetization factors are categorized to two cases: Fluxmetric (ballistic or central) and magnetometric; magnetometric demagnetization factor is of main interest for sensors applications. We have calculated demagnetization factor and corresponding apparent permeability for multiwire arrays using magnetostatic 3D FEM in [1]. The effect of distance between magnetic wires on the demagnetization factor and apparent magnetic permeability was studied at different relative magnetic permeability. We also compared the simulations with experimental results up to 91 wires. Unfortunately the complexity of the 3D model is increasing fast with the number of wires and 3D FEM simulations of large wire arrays are impossible. This is why we propose novel simplified equivalent 2D model for wire arrays in this paper. The simplified model consists of hollow cylinders and it is axisymmetrical. The basic geometry of the 2D equivalent model is shown in Fig. 1. The model was derived for hexagonal arrays, but similar models can be made for other lattices. The mean diameter of each hollow cylinder is calculated by the average of the circumdiameter (maximal diameter) and the innerdiameter (minimal diameter) of the hexagon. The thickness of each hollow cylinder is obtained assuming the same volume as the volume of wires on the circumference of the corresponding hexagon. The validity and the accuracy of our model is tested by the calculations shown in Fig. 2, with relative material permeability of $m_{r-max} = 500$. The first calculation shows the magnetometric (using volume integral of the flux density B) and fluxmetric (using surface integral of B in the midplane) apparent permeability of the central wire in the array of n wires as a function of n . The results of our simplified 2D model fit very well the full 3D FEM simulations. We have studied apparent permeability and magnetometric demagnetization factors of arrays up to 2000 wires as a function of wire aspect ratio, wire distances and material properties. Two different hexagonal and square arrangements for wires will be considered in the full paper. Increasing wire distance increases apparent permeability and decreases demagnetization factor, which is similar to comparison between solid cylinder and hollow cylinder for demagnetization factor [3]. We will also show the results of the verification measurements on array of Permalloy wires. The simulation results are also valid for the arrays of microwires and even large arrays of nanowires, as for the practically achievable distances the wire interaction is mainly magnetostatic. This study was supported by the Grant Agency of the Czech Republic within the Nanofluxgate project (GACR GA20-27150S).

[1] P. Ripka, V. Grim, M. Mirzaei, acc. for publ. in JMMM, 2021 [2] M. Stafi, *Electrodynamics of Electrical Machines*, Publisher: Iliffe, 1st March 1968 [3] S. G. Sandomirskii, *Russian Electrical Engineering*, vol. 80, pp. 109-112, 2009 [4] S. G. Sandomirskii, *Russian Electr. Eng.* 84, pp. 376-381, 2013 [5] V. F. Matyuk, A. A. Osipov, and A. V. Strelyukhin, *Russian Journal of Nondestructive Testing*, vol. 43, no. 3, pp. 154-162, 2007 [6] M. Nirei, S. Suzuki, K. Tashiro, and H. Wakiwaka, *Journal of the Japan Society of Applied Electromagnetics and Mechanics*, vol. 17, no. 3, pp. 449-452, 2009 [7] D.-X. Chen, J. A. Brug, and R. B. Goldfarb, IEEE Trans. on Magn.

27, pp. 3601-3619, 1991 [8] D.-X. Chen, E. Pardo, A. Sanchez, "Fluxmetric and magnetometric demagnetizing factors for cylinders," *JMMM* 306, pp. 135-146, 2006

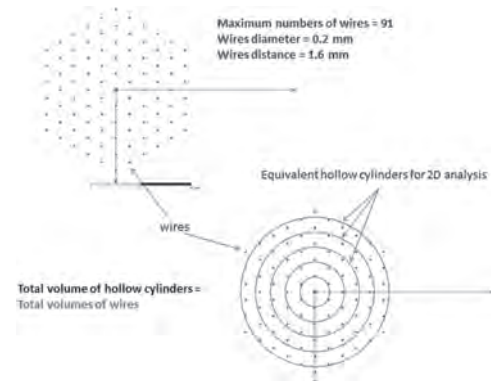


Fig. 1 The wire array and its equivalent 2D model based on the hollow cylinders

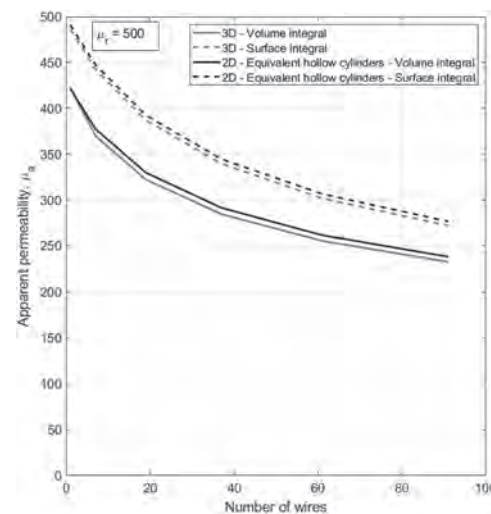


Fig. 2 Apparent permeability (magnetometric using volume integral and fluxmetric using surface integral) of the wire array as a function of the number of wires, n . Calculated by 3D FEM and by the 2D equivalent model

IC-07. A Geometry-Independent Moment Correction Method for the MPMS3 SQUID-VSM Magnetometer.

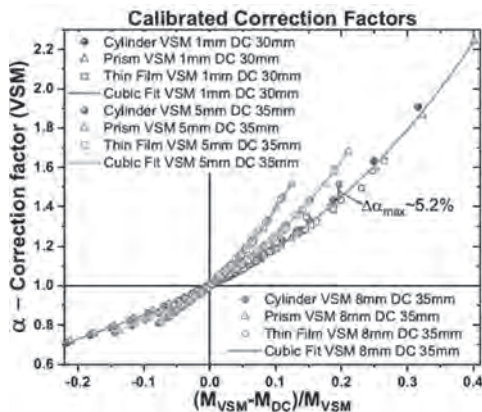
C. Amorim¹, F. Mohseni¹, R.K. Dumas², V.S. Amaral¹ and J.S. Amaral¹
 1. Universidade de Aveiro CICECO, Aveiro, Portugal; 2. Quantum Design Inc, San Diego, CA, United States

The sensitivity and automation capabilities of modern superconducting quantum interference device magnetometers are currently unmatched [1]. The measured moment values are, however, prone to deviations from their actual value due to geometric effects, namely sample size, shape, and radial offset [2,3]. A knowledgeable operator will correct measured moment values taking these effects into account. The current procedure for the MPMS3 magnetometer is based on an available simulation tool, valid for both SQUID-VSM and DC-scan methods [4]. Still, determining the correction factor requires samples with well-defined geometric shapes together with accurate sample dimensions and the usually difficult to determine radial offset [5]. There is no current solution to correct geometry effects of irregular shaped samples. Via an extensive use of the available Sample Geometry Simulator tool [4], in all available geometries, with sample dimensions and radial offset values limited only by the sample chamber volume, we find a systematic relation between the difference of SQUID-VSM and DC-scan measurements and the corresponding geometric correction factors of the MPMS3 SQUID-VSM device. This relation follows a clear trend, independent of sample size, shape, or radial offset, for a given pair of DC-scan length and SQUID-VSM amplitude values. Exploiting this trend, a geometry-independent correction method is presented and validated by measurements of two different geometries of the same Al piece, two different radial offsets of a Ni square, and metallic Fe powder using a far from optimal sample mounting. In this last case, we improved the initial maximum observed deviations from about 35% to better than 3%, by following the proposed correction method, as shown in Table 1. While the presented methodology requires both DC-scan and SQUID-VSM data, its ease of use on correcting magnetization measurements of irregular shaped samples and unknown radial offset values, can be of wide application by the magnetism/ magnetometry community.

[1] M. Buchner, K. Höfler, B. Henne, V. Ney, A. Ney, J. Appl. Phys. Vol. 124, p. 161101 (2018) [2] P. Stamenov, and J. M. D. Coey, Rev. Sci. Instrum. Vol. 77, p. 015106 (2006) [3] Quantum Design MPMS Application Note 1500-015 (2010) [4] Quantum Design MPMS Application Note 1500-020 (2014) [5] G. Morrison, and H-C zur Loye, J. Solid State Chem. Vol. 221, p. 334 (2015)

mass (± 0.001 mg)	M _{sat} (VSM) (emu/g)	Experimental deviation	M _{sat} (DC) (emu/g)	M _{DC} -M _{VSM} (%)	n	Corrected M _{sat} (emu/g)	Corrected deviation
1.800	284.9	+32.7%	216.0	14.9%	1.31	274.1	+2.8%
0.823	351.1	+17.0%	299.0	16.3%	1.100	212.8	-3.6%
0.770	286.1	+11.3%	212.0	15.5%	1.32	215.9	-1.0%
31.614	871.8	+21.6%	715.8	15.1%	1.286	216.8	-1.7%

Measured saturation magnetization and respective corrected values of several Fe powder samples. The measurements were performed using a 1mm SQUID-VSM amplitude and a 30mm DC-scan length.



Simulated correction factors as a function of the relative difference $x = (M_{VSM} - M_{DC}) / M_{VSM}$ for three different pairs of DC-scan lengths and SQUID-VSM amplitudes.

Session ID

MAGNETICS FOR IOT & EMERGING APPLICATIONS

Galina V. Kuryandskaya, Chair
Universidad del Pais Vasco - Campus Bizkaia, Leioa, Spain

INVITED PAPERS

ID-01. MAGNETIQUE and the Virtual Daum, two out-Reach Activities Carried out in a Research Laboratory: What About Researchers' Engagement in Knowledge Sharing? INVITED.

H. Fischer¹, S. Andrieu¹, C. Bellouard¹, C. Bonnet¹, C. Chatelain⁴, K. Dumesnil¹, J. Gorchon¹, T. Hauet¹, M. Hehn¹, D. Hennequin³, S. Heuraux¹, D. Lacour¹, G. Lengaigne¹, S. Mangin¹, P. Molho², F. Montaigne¹, S. Petit-Watelot¹, D. Pierre¹, J. Rojas-Sanchez¹, C. Schlauder¹ and P. Schmitt¹

1. Institut Jean Lamour, Nancy, Grand Est., Nancy, France; 2. Institut NEEL, Grenoble, France; 3. Laboratoire de Physique des Lasers Atomes et Molécules, Villeneuve-d'Ascq, France; 4. Laboratoire de Physique et Chimie Théoriques, Nancy, France

MAGNETIQUE is an itinerant scientific exhibition for the general public with three different levels of reading, presented at the *Palais de la Découverte* in Paris in 2019-20. Through experiments, manipulations and observations, MAGNETIQUE invites the public to discover principles and effects of this omnipresent but unknown phenomenon. Its goal is to share "science in the making" (cf. Jean Perrin) and the scientific process with public: it brings visitors into the researcher's creativity and imagination. MAGNETIQUE includes some sixty interactive experiments specially designed for this exhibition and completed by many videos on touchscreens. Pedagogical experiments are shown to explain the origin of magnetic properties and everyday-life applications. They are essential to explain some of the recent research results. Do-it-yourself experiments invite visitors to be curious and answer many questions about the use of magnetism in computers and data storage. The exhibition is thus organized in a logical and progressive way around 5 thematic blocks: Block 1: Magnetism, where can it be observed? Visitors can test attraction - repulsion between two magnets. They also discover different kind of magnets, some of their fundamental properties, and the principles of the compass. Some experiments with iron powder or ferrofluids are exhibited to visualize the magnetic field produced by a permanent magnet. Visitors can then observe the various behavior of matters under magnetic field, or discover the magnetic field produced by an electric current and test its applications to waste-sorting. This block ends with the exploration of Earth magnetism. Block 2: Magnetism, how can it be explained? This block is devoted to the explanation of the origin of magnetism. Different experiments show characteristics of various magnetic states (diamagnetism, paramagnetism, hard or soft ferromagnetism). Block 3: Magnetism, how can it be useful? This block shows interactions between current and magnetic field. Visitors discover Laplace's force, and its use in loudspeakers or electric motors. Later, they observe induction's phenomenon and its applications to produce electricity in bicycle lighting systems or wind turbines. Two experiments demonstrate the existence of eddy currents and their use in truck breaks. The other experiments concern alternative currents: one illustrates the principle of electromagnetic levitation and its application for ultra-fast trains, other ones shed light on the application for induction heating, electrical transformer, *Witricity* used in wireless chargers, as well as RFID system used in anti-theft devices. Block 4: Magnetism, where to find it in computer? This block only deals with computers: its goal is to show how omnipresent magnetism is in data storage. After having learnt about binary coding, visitors discover how to write and read a byte on a magnetic media thanks to a giant experiment illustrating the principle of data storage. Then, visitors discover magnetic codes hidden in a credit card or a metro ticket, as well as Halbach networks hidden in a magnet. The end of this block is devoted to the explanation of the giant magnetoresistance phenomenon, and its applications in hard disk read heads. Recent research carried out to develop denser, faster and less energy-intensive information storage are discussed through two examples: writing by ultrashort laser pulses and coding in four states. Block 5: Magnetism, what research is being done? This block shows the experimental universe of a research laboratory, the *Jean Lamour Institute* (IJL), whose facilities allow the development of new nanomaterials with new magnetic properties. Visitors can therefore observe a 3D model of the Depositing and Analyzing

nanomaterials under Ultra-high Vacuum (DAUM) platform. An old spectroscopic analysis chamber used in research is also exhibited. Models show crystal growth under ultra-high vacuum, structural and magnetic characterizations of samples and lithography to make three-dimensional nanometric objects. This bloc ends with experiments illustrating applied research topics: innovative sensors with giant magnetoresistance used in ABS, and magnetography as a secure printing technique useful for legal and banking services. The 5th block is completed by a virtual and interactive immersive approach of the IJL's DAUM platform developed with the collaboration of the company Com par l'image. The objective of this application is to invite public inside a virtual laboratory to share a growth layers deposition experience in order to produce materials with new properties. The scenario takes the sequence of real experiments in the laboratory: atomic deposition under ultra-high vacuum, characterization of in-situ surfaces, lithography ... Visitors are then invited to realize by themselves a magnetoresistive virtual sensor used as position sensor in drones. MAGNETIQUE and the VIRTUAL DAUM are two achievements resulting from the commitment of a research laboratory to support out-reach activities in order to establish the difficult link between fundamental research and the general public. Why get involved in this type of mission? Is it a mission for a research laboratory? What about the mission of researchers in the public life? These are some of the questions that will be addressed in this presentation. MAGNETIQUE is available for rental. Contact: helene.fischer@univ-lorraine.fr

- Hélène Fischer, *Reflets de la Physique*, Vol. 57, p. 32 (2018). - Hélène Fischer, *Gazette du vide*, Vol. 36, p. 04 (2020). - Hélène Fischer, Stéphane Mangin, *Découverte*, Vol. 430, p. 44 (2020). - Hélène Fischer, Stéphane Mangin, *Découverte*, Vol 431, p. 24 (2020).



Fig.1 : MAGNETIQUE at the Palais de la découverte, copyright Ph. Levy-EPPDCSI



The Virtual DAUM

ID-02. Magnetolectric Nanowires and Their Applications INVITED.M. Bauer¹, D. Arnold² and J. Andrew¹

1. *Materials Science & Eng., University of Florida, Gainesville, FL, United States*; 2. *Electrical & Computer Engineering, University of Florida, Gainesville, FL, United States*

Composite multiferroic materials represent a novel class of functional materials where multiple types of ferroic ordering coexist. Further, coupling between different types of ferroic materials can result in additional ordering, which can be leveraged to fabricate new multifunctional devices.^{1,2} One-dimensional composite magnetolectric nanofibers, free of substrate-based constraints provide an ideal platform for achieving magnetolectric coefficients that are orders of magnitude greater than those in ideal thin films.³ Here, we will present the synthesis of one-dimensional magnetolectric nanofibers via electrospinning followed by device assembly. Electrospinning can be used to fabricate composite nanowires in a range of configurations by varying the orientation of the piezoelectric and magnetolectric phases, including random, core-shell, or Janus. Here, we will focus on the synthesis and assembly of bi-phasic magnetolectric Janus nanofibers, this structure retains external access to each phase as well as to the interface, making them well suited to form modular structures (Figure 1). As-electrospun fibers are amorphous and form a continuous fiber network, requiring subsequent processing steps to both crystallize the nanofibers while also taking advantage of thermal stresses to break the nanofibers into shorter nanowires for device applications. The final nanowire length can be controlled by the electrospinning parameters (e.g., applied voltage) as well as the calcination ramp rate. Shorter nanowires (<10 mm) result from as-spun nanofibers with a smaller initial diameter, and/or faster calcination ramp rates. Aligned arrays of the nanowires can then be assembled into device architectures via dielectrophoresis (Figure 1b-d). The efficiency of nanowire assembly via dielectrophoresis can be enhanced solvent choice as well as the frequency of the applied voltage. We found optimum assembly using butanol and an applied voltage of 42 volts peak to peak at a frequency of 5kHz. Additionally, prior to assembly it may be necessary to perform an acid rinse of the nanofibers to remove any undesired carbonate phases that may hinder assembly. This method results in a linear density of assembled nanowires of ~20 nanowires/mm. The assembled arrays of magnetolectric nanowires can then be used for a variety of devices, including zero-power magnetic field and current sensors.⁴ Figure 2 shows the magnetolectric coefficients of BaTiO₃/CoFe₂O₄ nanowire arrays. These nanowire arrays have a magnetolectric coefficient of 514±27 mV cm⁻¹ Oe⁻¹ at 1 kHz, considerably larger than bulk values 104 mV cm⁻¹ Oe⁻¹. Figure 2 also shows corresponding device sensitivities. Magnetolectric nanowires can be assembled into arrays for low power sensors, including magnetic field and current sensors and they can also be developed for biomedical applications where the remote delivery of electric fields is desired, such as for neural modulation.⁵ Here, we will demonstrate the versatility of magnetolectric nanowires, their synthesis, and applications. This work opens new opportunities and applications for magnetolectric materials. This work was support by the NSF I/UCRC on Multi-functional Integrated System Technology (MIST Center) IIP-1439644. The authors acknowledge the use of the Major Analytical Instrumentation Center (MAIC) and Nanoscale Research Facility (NRF) at the University of Florida.

1. Spaldin, N. A., *Proc. R. Soc. A* 2020, 476 (2233), 20190542. 2. Nan, C.-W.; Dong, S.; Viehland, D.; Srinivasan, G., *Journal of Applied Physics* 2008, 103 (3), 031101. 3. Xie, S.-H.; Liu, Y.-Y.; Li, J.-Y., *Front. Phys.* 2012, 7 (4), 399-407. 4. Bauer, M. J.; Wen, X.; Tiwari, P.; Arnold, D. P.; Andrew, J. S., *Microsystems & Nanoengineering* 2018, 4 (1), 37. 5. Ferson, N. D.; Uhl, A. M.; Andrew, J. S., P. *IEEE Transactions on Ultrasonics, Ferroelectrics, and Frequency Control* 2020.

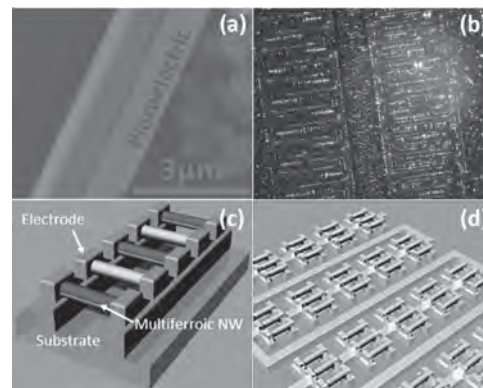


Figure 1. (a) scanning electron microscope image of a biphasic magnetolectric nanowire suspended across an electrode gap (b) optical microscope image of an electrical assembly (c) a schematic magnetolectric voltage source consisting of composite magnetolectric nanowires and (d) a schematic of a possible architecture suitable if the density of the assembled nanowires is found to be generally uniform.

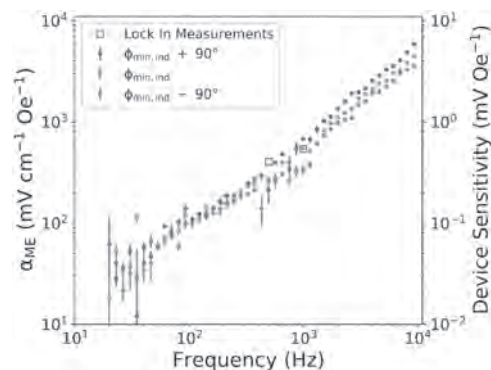


Figure 2. Magnetolectric coefficients and corresponding device sensitivities of BaTiO₃/CoFe₂O₄ nanowire arrays as a function of frequency measured at angles of approximately no inductive effects, the angle of maximum constructive induction, and maximum destructive induction.

CONTRIBUTED PAPERS

ID-03. Evaluation of Magnetoimpedance in Narrow NiFe/Al/NiFe Thin Films for Secured Packaging.

T. Sohier¹, J. Michel¹, S. Borel¹, J. Souriau¹, G. Simon¹ and A. Tria¹

1. CEA, Commissariat à l'énergie atomique et aux énergies alternatives, Grenoble, France

Giant MagnetoImpedance (GMI) is a magnetic phenomenon present in materials or structures with high magnetic permeability - like soft ferromagnetic conductors - that provides a large change of their impedance $Z=R+jX$ when submitted to an external magnetic field H [1]. This effect is under investigation from many years moving promptly from fundamental studies to applicative domains. Indeed, more and more sensors based on this effect, such as magnetic or current sensors are largely deployed. The number and plurality of applications never stop growing up like target detection, high-density information storage, automotive and so on [2]. Up to now, it seems that GMI has never been used for cyber security purposes even though it is a major challenge to be taken up in the coming years, as the number of connected objects is constantly sprouting up [3]. Security and privacy are threatened by the increasing use of insufficiently protected electronic devices that manage, store and share personal or confidential data [4]. Indeed, software protections can be bypassed by attacks aimed at recovering a secret key by physical means (fig. 1) such as fault injection or side channel [5]. Countermeasures [6-7] must be necessarily implemented to prevent hackers from accessing or modifying these components; they must also provide an intrusion alert so that the integrated circuit (IC) can take appropriate action to protect sensitive information. The use of GMI as a hardware-based security offers several advantages in terms of technology (low additional cost, simple process flow, etc.) and cyber security (high sensitivity to the electromagnetic environment, significant Z impedance variation, etc). While the GMI sensor appears to have some very interesting cyber security properties, it also presents some challenges such as the negative impact of film's width reduction [8]. For all these reasons, GMI structure as an active countermeasure (antiprobing layer embedded inside the packaging) will be evaluated in this article. A set of magnetic striplines with different widths from $2\mu\text{m}$ to $20\mu\text{m}$ were fabricated on 200 mm silicon wafers. The soft ferromagnetic/conductor $\text{Ni}_{80}\text{Fe}_{20}/\text{Al}/\text{Ni}_{80}\text{Fe}_{20}$ tri-layer with thicknesses of $100\text{nm}/200\text{nm}/100\text{nm}$ was deposited by dynamic sputtering under a linear magnetic field and patterned. Each device was characterized directly on wafer for both transversal (T) and longitudinal (L) deposition anisotropy between 1 MHz and 10 GHz by using a vector network analyzer. An internal DC current that generates a transversal magnetic field on the studied tri-layer was used as a polarization bias. The experimental procedure reveals that the $6\mu\text{m}$ wide film with transversal (T) deposition anisotropy corresponds to the best tradeoff between GMI response and cybersecurity requisites. The film exhibits magneto-inductive effect higher than 100% on a wide frequency range (5MHz-700MHz). At 60MHz, a significant change of inductance of more than 300 % was observed providing a strong DC current variation sensitivity of $2\text{nH}/\text{mA}$ between 4mA and 9mA (fig 2). The resistive variation appears with increasing frequency of the AC current in the film with respect to the skin effect and ferromagnetic resonance. Moreover, the experiment highlights a strong influence of shape anisotropy on GMI's answer for the films with transversal deposition anisotropy. This effect has to be taken into account in further studies. Nevertheless, the addition of the internal DC current polarization method and the outstanding magneto impedance effect of the $6\mu\text{m}$ wide GMI film makes it a suitable candidate as an antiprobing layer material. In case of an intrusion, the hacker will inevitably modify the design of at least one GMI mesh but also the general magnetic field distribution in the secured packaging due to the unusual polarization method. These first observations are encouraging for the development of a GMI countermeasure against physical attacks.

Tanjidur Rahman, Q.Shi and S.Tajik, IEEE 3rd International Verification and Security Workshop, p.93 (2018) [6] A. Lecavelier, M. Brizoux and A. Grivon, IMAPS MiNaPAD (2017) [7] S. Borel, L. Duperrex and E. Deschaseaux, Proceedings of IEEE 68th Electronic Components and Technology Conference, p.515 (2018) [8] L.V. Panina, D.P. Makhnovskiy, and D.J.Mapps, Journal of Applied Physics, Vol.89, p.7221 (2001)

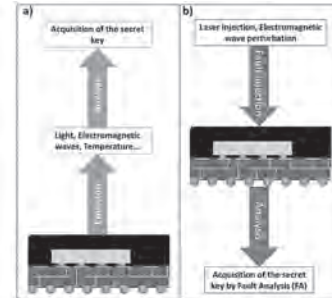


Fig 1: Different physical attacks against a chip. (a) Side channel. (b) Fault injection.

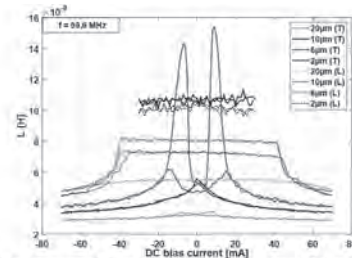


Fig 2: Inductive response of different GMI films polarized by an internal DC bias (frequency 59.6MHz).

[1] M. Knobel and K. Pirota, Journal of magnetism and magnetic materials, Vol. 242-245, p.33 (2002) [2] M. H. Phan and H. X. Peng, Progress in Materials Science, Vol.53, p.323 (2008) [3] M. Semeria, IEEE 62nd International Electron Devices Meeting, p.9 (2016) [4] S. Bhunia, S. Ray and S. Sur-Kolay, "Fundamentals of IP and SoC Security" (2016) [5] M.

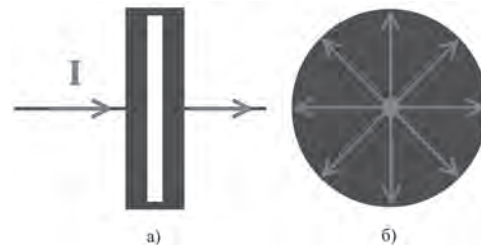
ID-04. Impedance of Planar Structures With Radial Current Distribution.

N.S. Perov¹, I.A. Alekhina¹, N.A. Buznikov² and L.A. Shendrikova¹

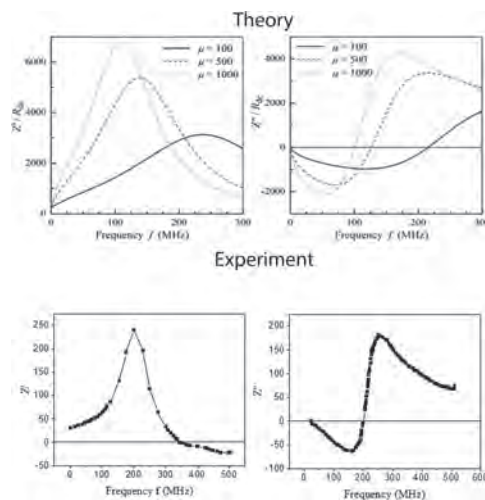
1. Magnetism, Lomonosov MSU, Moscow, Russian Federation; 2. Gazprom VNIIGAZ, Razvilka, Russian Federation

Magnetic sensors play an important role in modern life. They are actively used in many areas of science and technology from navigation systems and high-density data recording to security systems and biomedicine. The magnetoimpedance effect - the dependence of the material's impedance on the applied magnetic field - became the working principle basis of some sensors. For advanced efficiency, large values of permeability were required. The discovery of the giant magnetoimpedance effect in amorphous materials [1] allowed the design of the new type of highly sensitive field detectors. Their pronounced soft magnetic properties make it possible to build magnetic field sensors for geomagnetic applications [2-3], as well as mechanical stress and temperature [4-5]. The GMI effect also allows the detection of bioelectrical activity [6]. The modified construction of the GMI sensor may help to avoid the appearance of parasitic effects caused by the intrinsic magnetic field of the detector. In this work, we consider the planar structure with a radial current distribution with GMI effect for sensor applications. The considered structure consists of two identical ferromagnetic disks separated by a dielectric layer and connected at the periphery by a continuous contact (Fig. 1), the contribution to the inductance of which can be neglected. This system is excited with alternating current $I = I_0 \exp(-i\omega t)$ from the outer plane of the disks. The contact area between the disk and the driving current lead can also be neglected, since it is small compared to the disk area. To determine theoretically the impedance of the disk, it is necessary to consider the distribution of fields in it. The cylindrical coordinate system (ρ, φ, z) was used for the impedance calculation. The expression for the impedance of the disk with radius a was obtained from the surface impedance which depends on the current frequency. Both real and imaginary part of the impedance were taken into account with the expression $Z = Z' + iZ''$. The impedance of the system was considered as the impedance of the oscillatory circuit, in which the inductance $L = 2L_d$ with resistance $R = 2R_d$ (factor 2 takes into account two disks) and the capacitor formed by the interlayer between the disks are connected in parallel. The component of impedance of such system $Z'(f)$ and $Z''(f)$ were calculated for the different permeability (Figure 2, theory). The experimental investigations were carried out using the samples, which prepared from $\text{Fe}_{70}\text{Co}_{24.5}\text{Si}_{2.9}\text{B}_{3.1}$, and $\text{Co}_{72}\text{Ni}_{12.2}\text{Fe}_{5.7}\text{Si}_{6.5}\text{B}_{3.6}$ amorphous ribbons with thicknesses 0.025 and 0.02 mm, respectively. Two disks were cut from every ribbon. Copper leading wires were soldered to the center of the disk. The polyethylene film was used as a dielectric interlayer. Periphery parts of the disks were glued with a silver-based conductive glue. Impedance measurements were carried out using vector network analyzer Agilent FieldFox 9923A in the frequency range 2 MHz-1 GHz. The frequency dependences of real and imaginary impedance part obtained via calculations and in the experiment show similar resonant behavior. The described structure demonstrates resonant frequency dependences of the impedance and thus provides high sensitivity of the sensor. Using sputtering techniques the small-scaled structures can be manufactured for implementation into complex devices.

- [1] L.V. Panina et al. Appl. Phys. – 1994. - v. 76, N 10. - pp. 6198-6203.
 [2] A. Zhukov et al. Journal of Alloys and Compounds. – 2014. – Vol.586. - S279–S286. [3] J. Olivera et al. Sensors Actuators A. Phys. – 2011. - Vol.168. - pp.90–94. [4] M. Nowicki et al. Materials. – 2019. – Vol.12. – 2110. [5] J. Nabias et al. Sensors and Actuators, A: Physical. - 2019. – Vol. 289. – pp.50-56. [6] Z. Wang et al. IEEE ICMA 2016, 7558909, pp.2209-2214.



Planar structure with radial current distribution – section by plane perpendicular to the sensor surface (left), radial current distribution (right).



Theoretical and experimental frequency dependences of the real and imaginary impedance parts.

ID-05. Oxidized Permalloy Films as a Sensitive Element for Magneto-Optical Hydrogen Gas Detection.

D. Kulikova^{1,2}, K. Afanasyev^{1,3}, I. Bykov^{1,3} and A. Baryshev¹

1. All-Russian Research Institute of Automation, Moscow, Russian Federation; 2. Lomonosov Moscow State University, Moscow, Russian Federation; 3. Institute of Theoretical and Applied Electrodynamics of RAS, Moscow, Russian Federation

Hydrogen sensing is one of the most important technology for nowadays and future industries since H₂ is a candidate for the replacement of fossil fuels. It is worth noting that this gas is highly explosive—it is become dangerous if its concentration in air reaches a limit of 4 %. Hence, the development of highly sensitive and selective hydrogen sensors with a quick response is necessary for ensuring safety [1]. Optical methods of hydrogen detection have been actively developed in recent years [2-3]. They are based on changes in the optical absorption and refractive indices of gasochromic materials caused by the presence of a test gas. Palladium and platinum are known catalysts for the decomposition of molecular hydrogen into atomic. Thus, to increase the rate of dissolution of H atoms in, for example, tungsten trioxide Pd or Pt are usually used as a top layer covering it [4]. Magnetic materials can change their magnetic properties under hydrogen exposure too. For example, Pd-rich alloys [5] and Pd-included bi-layers [6] demonstrate transformation of the Kerr rotation angle upon H₂ absorption. Magneto-optical methods of gas detection are of interest for gas sensors development due to possibility for monitoring the phase change (polarization rotation) instead of amplitude. In perspective, this feature can provide much more high sensitivity and selectivity to a target gas in a complex gas mixture. In our work, we studied oxidized permalloy nanofilms. Initial 20 nm-thick permalloy nanofilms were deposited on glass substrates by magnetron sputtering and then annealed in air in a temperature range of 300-475 °C for one hour at the heating rate 750 °C/h. Microscopy methods were used to investigate structural properties of as-deposited and annealed nanofilms, and a double-beam spectrophotometer Shimadzu UV-3600 Plus—to measure the transmission spectra of the samples. Magneto-optical spectra were obtained by a home-made setup based on J.A. Woollam V-VASE ellipsometer and electromagnet generating magnetic fields up to H=±5 kOe. Ellipsometer provides the ellipsometric parameters Ψ and Δ that represent the complex ratio of the reflection coefficients of the p- and s-polarized waves and illustrate a change in polarization; Ψ stands for rotation of the polarization plane (or the main axis of the polarization ellipsis) and Δ—for evolution of the polarization state. This is why the angle of Faraday rotation (θ_F) can be determined as (Ψ(+H)-Ψ(-H))/2. We found that during annealing a disordered array of nanopillars was grown on initially smooth surface (RMS = 1 nm) of as-deposited film (Fig.1a) [7]. The study of optical and magneto-optical spectra revealed the rise of transmission of fabricated permalloy nanofilms with the annealing temperature, and, in addition, the increase of their Faraday rotation in the near-infrared range of spectrum. The observed rise of transmittance and Faraday rotation is responsible for the increase of known characteristic of MO materials FOM=θ_F/K=θ_F√T, where θ_F is an angle of the Faraday rotation, K—absorbance coefficient, T—transmittance of the film. The sample annealed at 425 °C showed the highest value of FOM (Fig.1b). The magneto-optical response of 475 °C-annealed sample was about zero. We suppose that this effect is due to formation of Fe₃O₄ (to Fe²⁺ ions in octahedral site) at 425 °C followed by oxidation up to Fe₂O₃ at higher temperatures [8]. Fig. 1. (a) AFM image of a 20-nm thick annealed at 425 °C permalloy nanofilm. (b) Collected at H=3.8 kOe spectra of as-deposited and annealed at different temperatures permalloy samples. To study nanofilms sensitivity to hydrogen as-deposited and annealed at 425 °C samples were covered by a Pt layer with a thickness of about 5 nm by an e-beam deposition technique. To demonstrate the caused by H₂ change of their magneto-optical properties nanofilms were placed in a non-magnetic cell and fed with a gas mixture of N₂, O₂ and H₂ prepared by mass flow controllers (Bronkhorst). Measurements were carried out at room temperature at a constant gas flow. Faraday rotation spectra of studied samples in flow of artificial air (20% O₂ + 80% N₂) and in flow of 0.5% hydrogen in N₂ are presented in Fig.2. It can be seen well that magneto-optical response of 425 °C-annealed nanofilm significantly changed under 0.5% H₂ exposure—the maximum change was about 0.05 deg at a wavelength of 1 μm. Note that the Faraday rotation of

as-deposited permalloy nanofilm was not altered at the same conditions. Fig. 2. Faraday rotation angle for Pt-covered oxidized at 425 °C permalloy nanofilm in artificial air and under 0.5% H₂ exposure. This result indicates that hydrogenation of formed during annealing different metal oxides (NiO, Fe₃O₄, Fe₂O₃)—the hydrogen and oxygen diffusion around metal ion—define the observed change of the magneto-optical response. The detection of low hydrogen concentrations by measuring the Faraday rotation make it very perspective for further magneto-optical gas sensor development due accumulation of polarization rotation in the multipass regime.

[1] T. Hübert, L. Boon-Brett, G. Black, et al, Sens.&Actuators B: Chem., Vol. 157(2), pp. 329-352 (2011) [2] A. Mirzaei, J.-H. Kim, H.W. Kim, et al, Appl. Sci. Vol. 9, p. 1775 (2019) [3] D.P. Kulikova, A.A. Dobronosova, V.V. Kornienko, et al, Opt. Express., Vol. 28, pp. 32049-32060 (2020) [4] A. Georg, W. Graf, V. Wittwer, Electrochim. Acta, Vol. 46(13-14), pp. 2001-2005 (2001) [5] P.-C. Chang, Y.-Y. Chang, W.-H. Wang, et al, Commun. Chem., Vol. 2:89 (2019) [6] D. Lederman, Y. Wang, E. H. Morales, et al, Appl. Phys. Lett., Vol. 85, p. 615 (2004) [7] D.P. Kulikova, K.N. Afanasyev, I.V. Bykov, et al, Opt. Mat., Vol. 107, p. 110067 (2020) [8] T. Tepper, F. Ilievski, C.A. Ross, et al, J. Appl. Phys., Vol. 93, p. 6948 (2003)

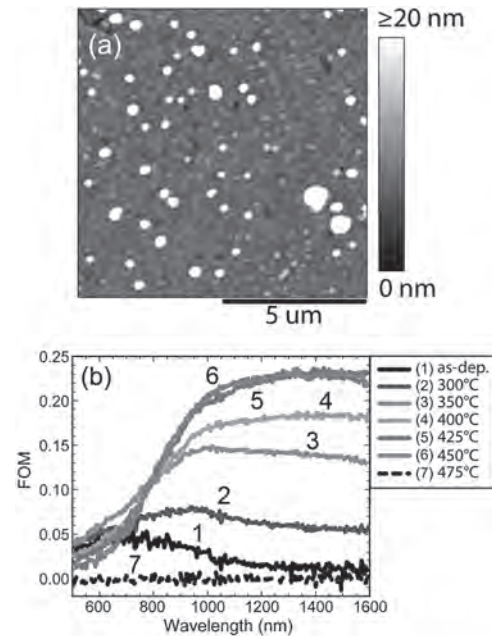


Figure 1

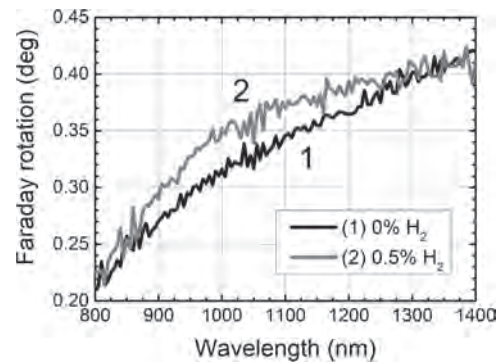


Figure 2

ID-06. Development of High-Sensitivity SI Sensors Using Flexible SI Devices.

M. Hikishima¹, S. Honkura², J. Tanabe¹, K. Kudo², E. Kikuchi¹ and Y. Honkura¹

1. Magnedesign corporation, Nagoya, Japan; 2. Nanocoil corporation, Nagoya, Japan

Strain gauges are sensors that measure a strain generated by a stress applied to an object, metal and semiconductor gauges are widely used. The sensitivity of strain gauges is expressed using the gauge factor, which is about 2 for metal gauges and about 200 for semiconductor gauges. Recently, the SI (stress-impedance) sensor using an amorphous alloy with a gauge factor reaching 1260 has been developed, but it has not been put to practical use due to problems of handling and the influence of external magnetic fields [Shen et al., 1997]. In this paper, we report on the development of a flexible SI sensor element with a magnetic shield to suppress the influence of external magnetic fields. We use the SI element, which is a negative magnetostrictive amorphous wire (FeCoSiB) with a wire length of 2 mm and a diameter of 13 μm , and a flexible film substrate. The amorphous wire is placed on the film and is connected to the electrodes via lead wires from both ends of the wire using gold deposition technique. We manufacture the SI device with a magnetic shield. The shielded SI element uses permalloy plating around the amorphous wire. Figure 1 shows the results of measuring the impedance change by applying a stress to the element. The 18% impedance change was obtained when a tensile stress of 45 MPa was applied, which corresponds to a gage factor of 354. As shown in Figure 2, the effect of the magnetic shield was affected by an external magnetic field of 20 μT without the shield, but with the shield, the rate of change of the impedance of the SI element was reduced to less than 2% even at 100 μT . In this study, the SI element was miniaturized and mass-produced by placing a 2 mm long amorphous wire on a flexible film for use as a contact sensor. In addition, we have developed a SI device that can reduce the influence of the Earth's magnetic field by applying a magnetic shield. In the future, we plan to investigate the response to stress.

K. Mohri, T. Kohsawa, K. Kawashima, H. Yoshida and L.V. Panina, Magneto-inductive effect (MI effect) in amorphous wires. IEEE Transactions on Magnetics, 28(5), pp.3150-3152, (1992). L.P. Shen, T. Uchiyama, K. Mohri, E. Kita and K. Bushida, Sensitive stress-impedance micro sensor using amorphous magnetostrictive wire, IEEE Transactions on Magnetics, 33(5), pp. 3355-3357, doi: 10.1109 / 20.617942 (1997).

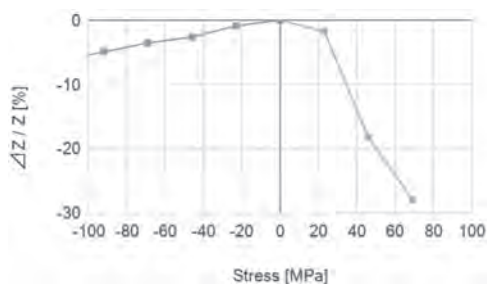


Fig. 1: Effect of stress on impedance change.

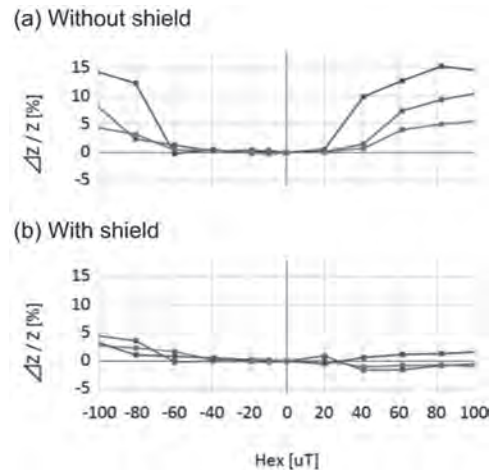


Fig. 2: Shielding effect.

ID-07. Broadband RF Detection and GHz Modulation Rates Enabled by Joule Heating in Perpendicular Anisotropy Magnetic Tunnel Junctions.

A. Sidi El Valli¹, V. Iurchuk¹, A. Litvinenko¹, I. Bendjeddou^{2,3}, N. Lamard¹, J. Langer⁴, J. Wrona⁴, L. Vila¹, R. Sousa¹, I.L. Prejbeanu¹, B. Dieny¹ and U. Ebels¹

1. Univ. Grenoble Alpes, CEA, CNRS, Grenoble INP, Spintec, Grenoble, France; 2. Grenoble Images Parole Signal Automatique, Saint Martin d'Herès, France; 3. Commissariat à l'énergie atomique et aux énergies alternatives Laboratoire d'électronique et de technologies de l'information, Grenoble, France; 4. Singulus Technologies AG, Kahl am Main, Germany

Perpendicular magnetic tunnel junctions (pMTJs) constitute the basic element for magnetic random access memories [1], thanks to their non-volatility, high density, and low power consumption. Their multifunctional properties make it possible to operate also as magnetic field sensors, spin torque nano-oscillators (STNO) or microwave signal detectors [2]. However, quite generally their interfacial perpendicular anisotropy (iPMA) is very sensitive to temperature, and thus to Joule heating when an electric current is passed through them [3]. The induced heating decreases the perpendicular anisotropy and thereby reduces the thermal stability and the potential for memory applications of pMTJs. Nevertheless, here we demonstrate that Joule heating induced modifications of iPMA can be of advantage for radio-frequency (RF) signal generation and detection, that will find applications within wireless communication systems used for the Internet of things (IoT). Quite generally, one can distinguish two different RF dynamical regimes and excitations. The first one is the RF signal generation, where upon injection of a DC current, the spin transfer torque (STT) induces steady state oscillations. The second is the RF signal detection, where an injected RF voltage, (in absence or presence of an additional DC current), excites resonantly via STT the magnetization, which results in a rectified DC voltage in the output. Both regimes have been demonstrated in numerous experiments and are promising for RF applications such as wireless communications [4] or ultra-fast spectrum analysis [5], as well as for neuromorphic computation [6]. A major advantage of MTJ structures is their GHz operational frequency, their high frequency tunability, the possibility to sweep-tune the frequency on short time scales as well as their high sensitivity to low RF power signals [7]. Here we report on the Joule heating effects in pMTJs for both: STT induced RF signal generation and active (RF + DC) RF signal detection. Results are presented for two types of pMTJs, one for which the free layer (FL) thickness is $t = 1.4$ nm and one with $t = 1.8$ nm. This FL thickness determines the orientation of the FL magnetization (in-plane for $t=1.8$ nm, out-of-plane for $t=1.4$ nm) due to the competition between the iPMA and the demagnetizing energy. For pMTJs with FL thickness of $t = 1.8$ nm (in-plane FL), under in plane and/or out of plane bias fields, only damped oscillations have been detected when injecting a DC current. The most interesting result here is a very large frequency shift with DC current characterized by a slope of -4 GHz/mA that occurs for both current signs. We attribute this current-sign-independent frequency shift to the changes in the iPMA due to Joule heating. However, the STT effect is noticeable in the power of the excitations, see Fig. 1a. This will be important for the RF signal detection, where for one current sign it enhances the output voltage by a factor of 4, and strongly reduces it for the opposite sign. The frequency tuning via current will be of interest for the RF signal detection because it allows one to easily tune the detection frequency band in a relatively large range, as illustrated in Fig. 1b, without the need of an external applied field. We emphasize that this tuning is attributed to the Joule heating and not to the STT that does not lead to strong frequency shifts in the damped regime. However, a similarly high frequency tuning has also been observed in the steady state oscillation regime for devices with FL thickness $t = 1.4$ nm (out-of-plane FL) under DC current and out-of-plane field. The corresponding frequency tuning is close to -3 GHz/mA (frequency redshift) with a minimum linewidth of 30 MHz. In view of applications, we tested the frequency modulation using sinusoidal rf signals. Modulation was observed for modulation frequencies larger than 1 GHz, which greatly exceeds the amplitude relaxation frequency given by Γ_p (~200 MHz) of the uniform STNO. Analysis of the phase noise indicates that there are two cut-off frequencies one due to the amplitude relaxation and one due to the heating. To conclude, this work demonstrates how Joule

heating in pMTJs can be exploited to add functionalities to RF signal generation and detection. The authors acknowledge partial funding from ERC MAGICAL No 669204, the Nanoscience Foundation (Grenoble, France) and the EU Horizon 2020 project GREAT No 687973.

[1] IKEDA, S., MIURA, K., YAMAMOTO, H., *et al. Nature materials*, 2010, vol. 9, no 9, p. 721-724. [2] CHAVENT, A., IURCHUK, V., TILLIE, L., *et al. Journal of Magnetism and Magnetic Materials*, 2020, vol. 505, p. 166647. [3] STRELKOV, N., CHAVENT, A., TIMOPHEEV, A., *et al. Physical Review B*, 2018, vol. 98, no 21, p. 214410. [4] JENKINS, Alex S., ALVAREZ, Lara San Emeterio, FREITAS, Paulo P., *et al. Scientific reports*, 2020, vol. 10, no 1, p. 1-7. [5] LITVINENKO, Artem, IURCHUK, Vadym, SETHI, Pankaj, *et al. Nano letters*, 2020, vol. 20, no 8, p. 6104-6111. [6] GROLLIER, Julie, QUERLIOZ, Damien, CAMSARI, K. Y., *et al. Nature electronics*, 2020, vol. 3, no 7, p. 360-370. [7] FANG, Bin, CARPENTIERI, Mario, HAO, Xiaojie, *et al. Nature communications*, 2016, vol. 7, no 1, p. 1-7.

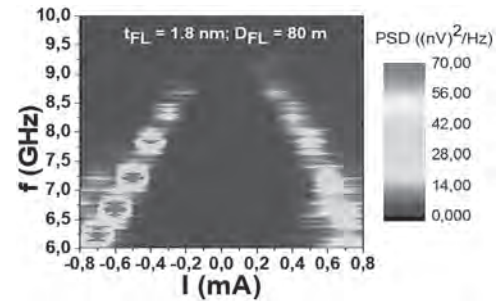


Fig.1 : Frequency tuning of damped oscillations observed for both current signs, measurement carried out under an 800 Oe in-plane bias field.

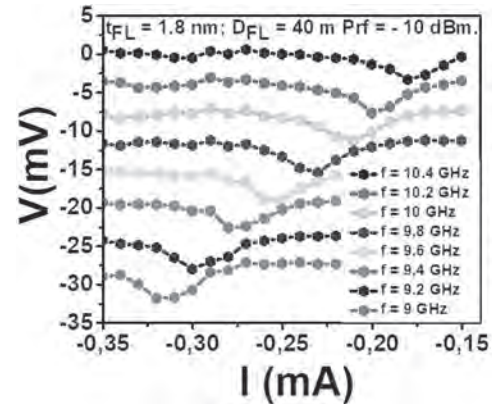


Fig.2 : RF rectification voltage vs DC current, for input signals of different frequencies: 10.4 GHz to 9 GHz.

ID-08. Compact Model of a Spintronic Resonator for Rectifying Purposes in Wireless Sensor Network Applications.

I. Bendjeddou^{1,2}, M. Jotta Garcia³, A. Sidi El Valli⁴, A. Litvinenko⁴, Y. Le-Guenec⁶, S. Bourdel², E. Pistono², D. Morche¹, A. Jenkins⁵, R. Ferreira⁵, P. Bortolotti³, R. Lebrun³, V. Cros³, U. Ebels⁴ and F. Podevin²
 1. Commissariat à l'énergie atomique et aux énergies alternatives Laboratoire d'électronique et de technologies de l'information, Grenoble, France; 2. RFIC-Lab - Univ. Grenoble Alpes, Grenoble INP, Grenoble, France; 3. Unité Mixte de Physique, CNRS, Thales, Université Paris-Saclay, Unité Mixte de Physique CNRS/Thales, Palaiseau, France; 4. Univ. Grenoble Alpes, CEA, CNRS, Grenoble INP, SPINTEC, SPINtronique et Technologie des Composants, Grenoble, France; 5. International Iberian Nanotechnology Laboratory, Braga, Portugal; 6. GIPSA-lab - Univ. Grenoble Alpes, CNRS, Grenoble, Grenoble Images Parole Signal Automatique, Saint Martin d'Heres, France

Wireless sensor networks (WSN) are part of our daily lives and their applications are growing years after years, especially with the advent of the Internet of Things. The price to pay is an increase in energy demand. Hence, the development of autonomous, adaptive, and energy-efficient communicating sensor solutions is a topic of intense research. One way to drastically reduce energy consumption is to wake up the main radio receiver of a WSN for communication only when needed. For that purpose, a wake-up receiver (WuRx) is used, which itself should operate with ultra-low power consumption and provide immunity to parasitic radio signals. Spintronic Resonators (SR) based on Magnetic Tunnel Junctions (MTJ) offer a promising solution to be incorporated in integrated wake-up radio circuits since they are extremely compact and can serve as passive RF-DC converters [1]. Another significant advantage of these spintronic devices is that they provide RF filtering capability, responding in a narrow frequency band around their resonance frequency making it possible to demodulate amplitude or frequency modulated signals with high sensitivity [1, 2]. To achieve this, there is a need for an electrical model of MTJs used as RF-to-DC converters, to offer the possibility to investigate their potentialities once integrated in an actual radio receiver (sensitivity, energy consumption) and facilitate the choice for a modulation scheme in order to optimize the communication power efficiency. The model must be compact, include the physical equations, be generic (can be extended to other types of spintronic junctions), and easy to implement. As a preamble to this model extraction, we have explored the characteristics of one type of SR device, based on the vortex configuration (V-SR), for the case of passive detection and zero DC current biasing. Under zero external magnetic field, V-SRs are working in the 150-400 MHz range [2]. The observed characteristics concern i) RF-DC conversion efficiency ii) V-SRs input impedance matching, iii) demodulation capabilities. All these criteria will contribute to the final sensitivity of the V-SR based WuRx. The equivalent model is then proposed by considering the MTJ-based SR as an RF power controlled DC voltage source with internal resistance. To investigate input impedance matching, the RF equivalent circuit is derived, as illustrated in Fig. 1. This model has been developed on the basis of RF reflection coefficient measurements (S-parameters obtained through a vector network analysis), I(V) measurements, and the physical equations of the ferromagnetic resonance frequency and the rectification DC voltage. In order to evaluate the parasitic parameters external to the junction, an additional measurement is performed on an Open circuit, consisting of the same feeding accesses as in Fig. 1 but without including the V-SRs. Hence, S-Parameters measurements enable to extract the internal parasitic elements of the junction itself (junction capacitance and inductive effect of the magnetic layers due to their high permeability). Also, I(V) DC measurements reveal the non-linear behavior of the V-SRs, enabling to determine the coefficients of the polynomial characteristic, outside resonance [3]. Indeed, the model must consider the effect of the ferromagnetic resonance, the center of interest for the RF-DC conversion. Physical equations from [2] enable to determine the value of the ferromagnetic resonance pulsation and the DC rectification voltage from the geometry of the junction, the RF power, and the DC current injected into the junction. Finally, the behavioral model gathers all equations considering parasitic effects (junction and feeding lines), the non-linear junction resistance through the I(V) characteristics, and the ferromagnetic

resonance response in order to predict the rectifying effect of the V-SR in the whole frequency band of interest. Thirdly, the V-SR model derived from RF and DC measurements is implemented using an electronic design automation software system (ADS) by implementing symbolically defined devices (SDD) [4]. The necessary variables for DC rectification are embedded in the SDD component and rectification is observed through harmonic balance (HB) simulations. Simulation results of the DC rectification voltage are presented in Fig. 2 and compared with the measurement results. Finally, in order to test the demodulation capabilities, the input RF carrier frequency is fixed at the ferromagnetic resonance in order to benefit from the maximum rectified DC voltage and then modulated with an On-Off Keying (OOK) modulation scheme. We obtain for V-SRs data rates up to 20 Mbit/s for an input RF power of -15 dBm leading to a signal to noise ratio of more than 14 dB, which guarantees a bit error rate as low as 10^{-6} . It has to be noticed that 20 Mbit/s is within a comfortable margin regarding the typical data rates reported for existing WuRx in the literature [5]. Based on this performance, a complete RF wake-up system will be designed and tested. Future studies will extend the developed model to other MTJ devices such as described in Ref. [6] that allow for operation at higher frequencies (1-10GHz). Authors acknowledge financial support from ANR-SPINNET ANR-18-CE24-0012.

[1] B. Fang et al., Phys. Rev. Applied, vol. 11, p. 014022 (2019) [2] A.S. Jenkins, et al. Nature Nanotech, vol. 11, p. 360 (2016) [3] H. Simon, K. Wu. IEEE, vol. 102, p. 11 (2014) [4] J. Wood, D. E. Root, et N. B. Tufillaro, IEEE, vol. 52, p. 2274 (2004) [5] H. Bello, al., Sensors 2019, vol. 19, p. 3078 (2019) [6] A. Chavent, al., doi.org/10.1016/j.jmmm.2020.166647

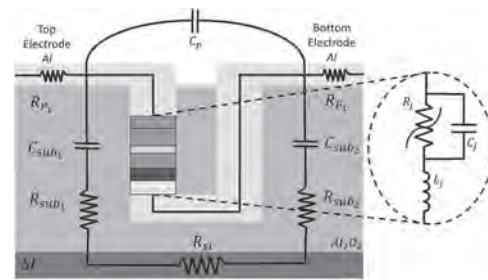


Fig. 1 : RF equivalent electrical model of MTJ:

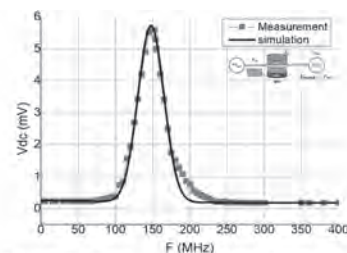


Fig. 2 DC rectified voltage V_{dc} vs frequency of the input signal. Black line: results from simulation as described in the text; Red points: results from experiments on V-SRs measured under zero magnetic external field and zero DC current biasing (passive detection), at $P_{in} = -15$ dBm (diameter $D = 370$ nm, DC resistance $R_{dc} = 35 \Omega$, TMR = 100%)

ID-09. THz Periodic Array Sensor Design.

A. Eroglu¹ and B. Chowdhury¹

1. Electrical and Computer Engineering, North Carolina Agricultural and Technical State University, Greensboro, NC, United States

Abstract Periodic array sensor structures on metamaterials operating at THz ranges are developed and presented. In the proposed formulation, the mutual inductance effects between unit cells and the periodic structures are taken into account with the network synthesis method. The resonant characteristics of THz periodic arrays have been investigated and presented. The analytical results are verified with simulation results for several different cases. Prototypes have then been built and tested. It is confirmed that the proposed method can be used to design and develop THz sensors on metamaterials and implemented for several applications including biomedical. *Main Body* Metamaterial properties can be obtained by implementation of split-ring resonators (SRRs) [1]. SRRs are reported to be used in the design of biosensors at terahertz (THz) ranges in recent years. Terahertz thin-film sensors, plasmonic thin-film sensors, wireless strain sensors are designed with SRRs [2] to be used in biomedical applications. There are several advantages of using periodic structures due to their higher symmetry property than the unit cells [3]. Two of the other essential features of the periodic structures are their passband-stopband characteristics and the ability to support phase velocities which are much less than the light speed [4]. In this paper, closed-form relations for periodic arrays taking into account of complete effects of mutual inductances in the structure are developed with the network synthesis method from microwave frequencies to THz ranges. The step-by step design procedure from development of unit cell to formation of periodic arrays is detailed. The electromagnetic mutual inductance effects that take place between unit cells in the array and substrate are taken into account in the closed form relations for the first time according to the authors' knowledge for periodic arrays. The accuracy of the formulations and models for THz operation are verified with 3D EM simulator and ADS circuit simulator. The proposed method have been implemented for 2x3 until cell as shown in Fig. 1 and the agreement between the simulation and analytical results are illustrated in Fig. 2. Several prototypes have been built and measured. All the analytical, simulation and measurement results are compared, and close agreement is confirmed for all cases.

REFERENCES D. R. Smith, W. J. Padilla, D. Vier, S. C. Nemat-Nasser, and S. Schultz, "Composite medium with simultaneously negative permeability and permittivity," *Physical review letters*, vol. 84, no. 18, p. 4184, 2000. H. K. Kim, D. Lee, and S. Lim, "A fluidically tunable metasurface absorber for flexible large-scale wireless ethanol sensor applications," *Sensors*, vol. 16, no. 8, p. 1246, 2016. F. Bayatur, "Metamaterial-Inspired Frequency Selective Surfaces", PhD Dissertation, 2009. R. Collin, "Foundation of Microwave Engineering", *McGraw-Hill Book Co*, New York, 1966.

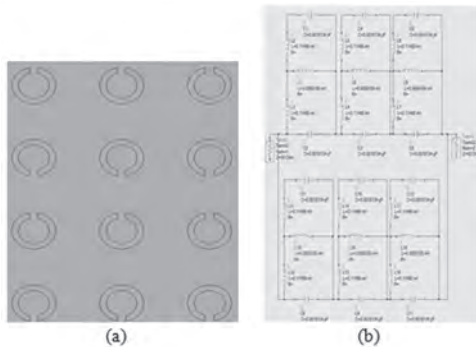


Fig. 1 – 2x3 THz metamaterial periodic array sensor (a) EM Simulation (b) ADS Circuit Simulation

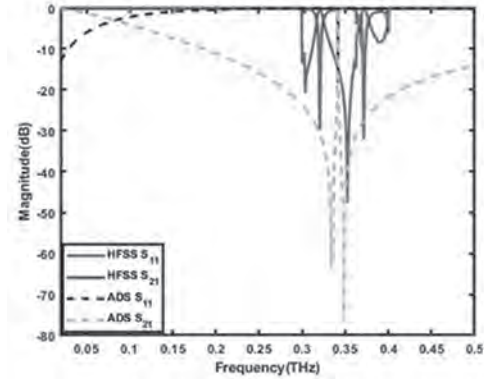


Fig. 2- Comparison of analytical and simulation results

ID-10. Electromagnetic Wave Generation in a Ferromagnet due to Transitions Between Spin Subbands.*E. Karashtin*¹*1. Institute for Physics of Microstructures RAS, Niznij Novgorod, Russian Federation*

We theoretically consider a possibility of generation of electromagnetic radiation due to transitions of electrons between spin subbands in a ferromagnet. It is known that such electro-dipole transitions are forbidden if a uniform ferromagnet is considered in a Vonsovsky s-d exchange model. One possible way to remove this limitation is to suggest that the exchange constant depends on the conduction electron momentum. This mechanism was suggested in [1]. At first, it seems to be fully exchange. However the dependence of the exchange constant on the electron momentum may appear only due to spin-orbit interaction in the subsystem of localized d- or f- electrons which are responsible for magnetization of the medium in this model, and not in the conduction electron subsystem. In the present work, we consider several different mechanisms of electron transitions between spin subbands with photon emission. The most simple mechanism is the magneto-dipole electron transitions which exist due to the magnetic field of the wave. The effects governed by this mechanism are usually very small. Another mechanism appears due to the spin-orbit interaction which exists in the conduction electron subsystem. In our model calculations, we take the Rashba spin-orbit coupling that exists at the medium surfaces. Finally, a fully exchange mechanism of intersubband electron transitions that exists in magnetic medium with non-collinear magnetization distribution is investigated. An example of non-collinear ferromagnet that allows intersubband electro-dipole electron transitions is a magnetic helicoid which may be realized either in natural (holmium, MnSi, FeGe at low temperature) or artificial (magnetic spring structures) materials. For all suggested mechanisms, probabilities of electron transitions between spin subbands are found and estimations are made for realistic parameters. We show that both spin-orbit coupling and exchange coupling in a non-collinear magnetic medium may give reasonable values of electron transition probabilities. Finally, a possibility to create devices based on the investigated mechanisms is discussed. This work was supported by the Russian Science Foundation (Grant #19-72-00130).

[1] A. Kadigrobov, Z. Ivanov, T. Claesson, et al., *Europhys. Lett.* 67, 948 (2004)

ID-11. Cavity Backed Spiral Antenna With Improved Gain.

R. Durbha¹ and M. Afsar¹

1. Electrical and Computer Engineering, Tufts University, Medford, MA, United States

Systems deploying circularly polarized antennas have significant advantage in terms of reflectivity, absorption, minimizing multipath effects, line-of-sight and phasing issues. Advancements in technology development of antennas are no exceptional. Various antenna structures have been developed to meet wideband application criteria. One such antenna which operates over multi-octave bandwidth is a cavity backed spiral antenna. Spiral antennas are described by self-complementing structure which makes them compact, wide beam and broadband. These antennas find applications in wide-band communications, frequency spectrum monitoring, and direction of arrival estimation among many other applications. To meet the system requirements antennas employed are miniaturized by implementing the concept of SWAP. The concept of SWAP is reduction in Size, Weight and Power with minimal/ no degradation of electrical performance of the system. The restriction on the size of antenna is defined by the platform on which it is installed. This constraint limits frequency of operation and effects electrical parameters such as gain, polarization, axial ratio etc. needed to achieve particular figure of merit. The gain of antenna varies proportionally with respect to physical size of aperture. It has significant impact on the receiver performance in terms of sensitivity and dynamic range. To compensate for system performance degradation significant changes in the receiver architecture and complex signal processing techniques have to be implemented. The gain of cavity backed spiral antenna can be improved by minimizing secondary radiation effects caused by unradiated currents. The proposed paper deals with design of a modified cavity backed spiral antenna which integrates techniques such as optimizing the cavity dimensions, shape and size of magnetic material loaded and modifying spiral antenna architecture to improve boresight gain at lower end of frequency spectrum. Such an antenna design overcomes performance constraints set by platform on which it is installed without effecting other antenna performance parameters while trying to retain minimum possible size.

Antenna Systems and Electronic Warfare, Richard A. Poisel, Artech House, 2012. R. Bawer, J.J Wolfe, "The Spiral Antenna", IRE Int. Convention Record, Vol 8, 1960. Bradley Allen Kramer, "Spiral Antenna Miniaturization with High-contrast Dielectrics", Master's Thesis, Ohio State University, 2004.

Session IE
MAGNETORESISTANCE

Xia Hong, Chair
University of Nebraska-Lincoln, Lincoln, NE, United States

INVITED PAPER

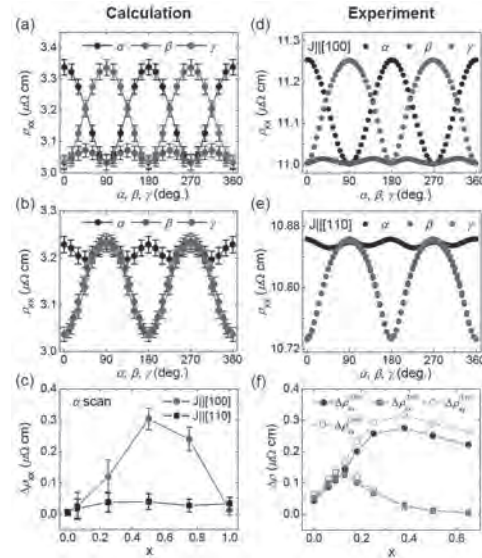
IE-01. Intrinsic Mechanism for Anisotropic Magnetoresistance and Experimental Confirmation in CoFe Alloys INVITED.

Z. Yuan¹

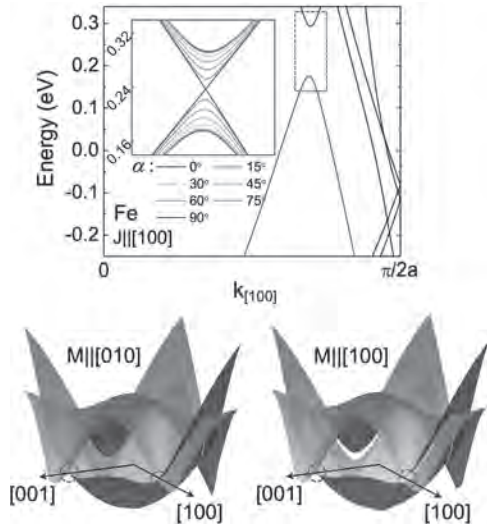
1. Department of Physics, Beijing Normal University, Beijing, China

Anisotropic magnetoresistance (AMR) refers to an electrical phenomenon that the resistivity in a metallic ferromagnet depends on the mutual angle of the magnetization and electric current, which was first discovered by William Thomson in 1857 and is nowadays widely applied in magnetic sensors. Despite of a long history of study, AMR is usually explained vaguely as a complicated relativistic interaction of local magnetic moments and itinerant electrons. Nevertheless, the quantitative description of AMR for a particular magnetic material usually requires some tunable parameters that are determined by experimental measurement. Using first-principles transport calculations, we predict that the AMR of single-crystal CoFe alloys is strongly dependent on the current orientation and alloy concentration. An intrinsic mechanism for AMR is found to arise from the band crossing due to magnetization-dependent symmetry protection [1]. These special k points can be shifted towards or away from the Fermi energy by varying the alloy composition and hence the exchange splitting, thus allowing AMR tunability. The prediction is confirmed by delicate transport measurements, which further reveal a reciprocal relationship of the longitudinal and transverse resistivities along different crystal axes.

[1] F. L. Zeng, Z. Y. Ren, Y. Li, J. Y. Zeng, M. W. Jia, J. Miao, A. Hoffmann, W. Zhang, Y. Z. Wu, and Z. Yuan, Physical Review Letters Vol. 125, p.097201 (2020).



Calculated and experimental resistivity of CoFe alloy for different magnetization and current orientations, as well as the dependence on the alloy concentration.



Upper panel: Calculated band structure using the effective potentials of Fe in $\text{Co}_{0.5}\text{Fe}_{0.5}$ with the magnetization along [100]. The band gap at 0.25 eV above the Fermi level gradually shrinks when the magnetization is rotated towards [010], as shown in the inset. Lower panel: the nodal line formed by two energy bands in the (010) plane at $M||[010]$ (left) and a gap opening up at $M||[100]$ (right).

CONTRIBUTED PAPERS

IE-02. Strain-Free Magnetic Tunnel Junction With Metastable bcc $\text{Co}_x\text{Mn}_{100-x}$ (001) Ferromagnetic Layers.

K. Elphick¹, K. Yoshida², T. Roy², T. Ichinose², K. Kunimatsu², T. Tsuchiya², M. Tsujikawa², Y. Nagai², S. Mizukami², M. Shirai² and A. Hirohata¹

1. University of York, York, United Kingdom; 2. Tohoku University, Sendai, Japan

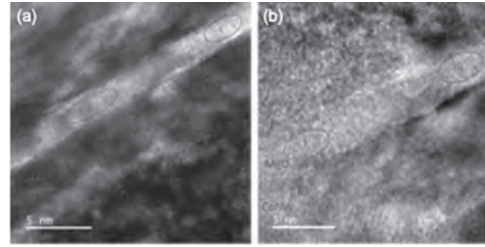


Fig. 1 HRTEM images taken on the $x =$ (a) 75 and (b) 86 sample.

In spintronics, one of the long standing questions is why the MgO barrier is almost the only option to achieve a large tunnelling magnetoresistance (TMR) ratio at room temperature (RT) but not as large as the theoretical prediction [1]. This can be due to the spin fluctuation at the ferromagnet/MgO tunnel barrier interfaces and/or spin-independent hopping within the barrier in a magnetic tunnel junction (MTJ) [2]. One of the approaches to overcome these issues is to employ the lattice softening of the ferromagnetic layers in MTJ. Recently a metastable body-centred cubic (bcc) $\text{Co}_x\text{Mn}_{100-x}$ (CoMn) ferromagnetic films have been reported to exhibit the enhancement of their magnetic moments with an ideal lattice matching with MgO [3], which can be an ideal candidate for the TMR enhancement in MTJ. MTJ stacks were grown using conventional magnetron sputtering on MgO(001) substrates with the structure of Cr (40)/ $\text{Co}_x\text{Mn}_{100-x}$ (10)/MgO (2.4)/ $\text{Co}_x\text{Mn}_{100-x}$ (4)/ $\text{Co}_3\text{Fe}(1.5)/\text{IrMn}$ (10)/Ru (5) (thickness in nm) [4]. For CoMn, four different compositions of $x = 66, 75, 83$ and 86 were used, allowing to control the CoMn lattice constants. To promote the crystallisation of the seed and CoMn layers, *in-situ* annealing was performed after the deposition of the Cr seed layer and $\text{Co}_x\text{Mn}_{100-x}$ layers at 700°C and 200°C , respectively. MTJs were then post-annealed at 325°C for their crystallisation after patterned into pillars with Ti/Au electrodes by photolithography. TMR measurements were carried out using the conventional four-terminal setup with elevating temperature, showing two distinctive TMR ratios of 229% and 142% at room temperature for $x = 75$ and 86 , respectively. The corresponding atomic structures were imaged by cross-sectional transmission electron microscopy (TEM, JEOL JEM-2100 Plus) at 600k magnification. Figure 1(a) shows a cross-sectional high-resolution (HR) TEM image of the MTJ with $x = 75$ showing the larger TMR ratio. Fully epitaxial growth of the entire MTJ is confirmed with some dislocations, of which period is calculated to be (11.4 ± 0.3) nm. This indicates that the $\text{Co}_{75}\text{Mn}_{25}$ layer may induce plastic deformation rather than elastic deformation with inducing dislocations at the boundaries between crystals. The $x = 86$ sample, on the other hand, shows dark black regions at the CoMn/MgO interfaces indicating CoMn/MgO is not fully crystallised within the CoMn layer [see Fig. 1(b)]. These features are found to be induced by dislocations formed at the CoMn/MgO/CoMn interface with the period of (8.9 ± 0.3) nm. These dislocations may be the origin of the interfacial spin fluctuation. In the MgO layer for $x = 75$, two distinctive crystallographic phases are observed as shown as the regions (i) and (ii), which are crystallised along MgO[001] and [100] directions, respectively, as similarly reported in previous reports [5]. For $x = 86$, an additional partially crystallised MgO grains are found, which induces spin-independent hopping to reduce the corresponding TMR ratio. By measuring the lattice constants of CoMn and MgO in the HRTEM images, the top CoMn lattice constants are almost constant across MTJs apart from $x = 86$, confirming the lattice softening of these layers with forming almost strain-free MTJ. These results were compared with *ab initio* calculations on the lattice stability of the CoMn alloys. Calculations confirm the crystalline deformation stability across a broad compositional range in CoMn, proving a strain-free interface for larger TMR ratios. Further optimisation of the CoMn-based MTJs can achieve $> 1,000\%$ TMR ratio at RT.

- [1] A. Hirohata *et al.*, *J. Magn. Magn. Mater.*, vol. 509, p. 166711 (2020).
 [2] C. H. Shang *et al.*, *Phys. Rev. B*, vol. 58, p. R2917 (1998). [3] R.J. Snow *et al.*, *J. Magn. Magn. Mater.*, vol. 419, p. 490 (2016). [4] K. Kunimatsu *et al.*, *Appl. Phys. Exp.*, vol. 13, p. 083007 (2020). [5] G. X. Miao *et al.*, *Appl. Phys. Lett.*, vol. 93, p. 142511 (2008).

IE-03. Large Magnetoresistance in Symmetry-Filtering Scandium Nitride Junctions Using First Principles.

V.C. Rogers¹, S. Karki¹, P. Jadaun¹, D.S. Marshall^{2,3} and J.C. Inorvia¹
 1. Electrical and Computer Engineering Department, The University of Texas at Austin, Austin, TX, United States; 2. TAE Technologies Inc, Foothill Ranch, CA, United States; 3. SEMTE Dept., Arizona State University, Tempe, AZ, United States

Magnetic tunnel junctions (MTJs) show great promise for implementation in high-performance spin transfer torque magnetic random-access memory (STT-MRAM) [1] and novel computing regimes such as magnetic domain wall logic [2] and neuromorphic computing [3]. MTJs consist of an insulating thin film tunneling barrier sandwiched between two ferromagnet electrodes. By altering the magnetization of the electrodes, the rate of tunneling across the barrier can be varied. This provides a mechanism to convert nonvolatile magnetic information to electrical information via modifying the resistivity of the device, achieving on/off tunnel magnetoresistance ratios (TMR) of over 600% at room temperature in state-of-the-art CoFeB/MgO/CoFeB MTJs [4]. Unfortunately, a handful of material setbacks stand in the way of the widespread adoption of even leading MgO MTJs over other emerging technologies, such as Resistive-RAM junctions, in next-generation architectures. MgO's wide bandgap (7.8 eV) is associated with a high junction resistance-area (RA) product, greatly increasing power-draw and necessitating high operating voltages, which leads to device variability challenges and dielectric breakdown [5]. Additionally, MgO creates magnetic dead layers through the oxidation of interfacial Fe atoms and requires ultrathin barrier layers that are difficult to fabricate and may contain pinholes [6]. These setbacks result in a reduction of the effective TMR and an increase in the RA-product, which motivates the search for new barrier materials. Here, we explore the properties of rock-salt structured Scandium Nitride (ScN) magnetoresistive junctions and find it a promising barrier material given its novel electron symmetry filtering properties, high TMR, and low RA-product. Fe/ScN/Fe MTJ supercells were constructed for 3,5,6,7 and 8 atomic layers of ScN, with the ScN lattice rotated by 45 degrees such that the N anions rest over the interfacial Fe, analogous to the Fe/MgO interface. Using the plane-wave basis density functional theory (DFT) package VASP [9], the MTJ supercells were converged and exported to Quantum Espresso [10] to calculate the complex bands, symmetry properties, and to perform spin-polarized electron transport calculations under the Landauer-Büttiker formalism as implemented in PWCOND [9]. A Hubbard +U correction of 4.5 eV was applied to Sc's 3d orbital to correct the electronic band gaps using the PBE-GGA pseudopotentials. In this manner, the indirect Γ -X gap of the ScN was matched near to experimental values [7] at 1.31 eV. The conductance calculations find TMR ratios exceeding 1900% for sufficiently thick systems (> 6 atomic layers of ScN), with spin-dependent transport dominated by unique Δ_2' band filtering through Sc's 3d orbital in the 6-layer system analysed [12]. This mechanism is different from the spin filtering in Fe/MgO/Fe MTJs, where MgO selects for the half-metallic Δ_1 band present in bcc Fe or CoFe electrodes [8]. Instead, ScN selects for Fe's Δ_2' electrons with large crystal momentum, which is only provided in the majority spin of the Fe band structure at the fermi energy. Even with the high TMR and symmetry filtering in ScN, the layer-dependent calculations predict that the devices remain highly conductive with respect to barrier thickness, unlike in MgO systems where the dominant Δ_1 electron wavefunctions decay rapidly across the barrier [8]. Fabricated in a system with minimal symmetry mixing and atomic dislocations, magnetoresistive ScN junctions could operate with a fraction of the power of MgO MTJs, while allowing for thicker barriers with more lenient manufacturing tolerances and maintaining high TMRs characteristic of MgO MTJs. *Partial funding from Sandia National Lab (SNL). SNL is managed and operated by NTESS under DOE NNSA contract DE-NA0003525*

[1] H. Noguchi, K. Ikegami, S. Takaya, ISSCC 132, (2016) [2] J. A. Currivan-Incorvia, S. Siddiqui, S. Dutta, Nat. Comms. 7, 3 (2016). [3] N. Hassan, X. Hu, L. Jiang-Wei, J. Appl. Phys. 124, (2018). [4] S. Ikeda, J. Hayakawa, Appl. Phys. Lett. 93, 1 (2008) [5] L. Xue, A. Kontos, IEEE Trans. Magn. 51, 1 (2015). [6] W. S. Zhao, Y. Zhang, T. Devolder, Microelectron. Reliab. 52, 1848 (2012). [7] D. Gall, M. Stadele, Phys. Rev.

B - Condens. Matter Mater. Phys. 63, 1251191 (2001). [8] W. H. Butler, STAM, 9(1), 014106. (2008) [9] G. Kresse and J. Furthmüller, Phys. Rev. B, 54:11169, (1996) [10] Giannozzi, P., Baroni, S., Bonini, N. Journal of Physics: Condensed Matter, 21(39), 395502 (2009) [11] A. Smogunov, A. Dal Corso, E. Tosatti, Phys. Rev. B 70, 045417 (2004) [12] S. Karki, V. Rogers, (under review) arXiv 2008.12770 (2020)

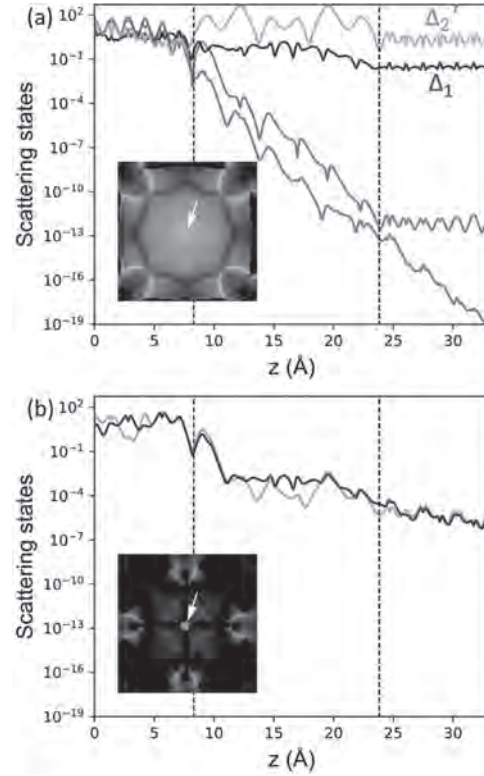


Fig. 1 Scattering states of parallel-magnetized Fe/6ScN/Fe majority spin (a) and minority spin (b) sampled at a high-transmission spike at $k_x = 0.02 (2\pi/a)$ and $k_y = 0.05 (2\pi/a)$.

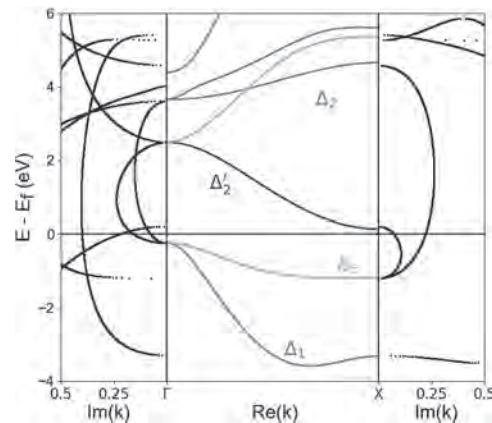


Fig. 2 Complex bands of Scandium Nitride sampled at the Γ and X point, with the symmetry-resolved real bands set in between. A small Hubbard +U bandgap correction is applied.

IE-04. Giant Tunnel Magnetoresistance up to 417% at Room Temperature Using Fe/MgO/Fe Magnetic Tunnel Junctions.

T. Scheike¹, Q. Xiang¹, Z. Wen¹, H. Sukegawa¹, T. Ohkubo¹, K. Hono¹ and S. Mitani¹

1. Research Center for Magnetic and Spintronic Materials, National Institute for Materials Science, Tsukuba, Japan

Magnetic tunnel junctions (MTJs) are a key element for various spintronic devices such as magnetic random-access memories including novel ones, i.e., brain-morphic devices and magnetic logic circuits. For future applications, room temperature (RT) TMR ratios of 1000% are targeted [1]. However, fabricating MTJs with a TMR ratio much larger than 200% is difficult because the spin-polarized tunneling current strongly depends on the ferromagnet (FM)/oxide interfaces quality. MTJs suffer from imperfect interfaces due to dislocations, formation of unfavorable oxide layers at the electrode/barrier interfaces or oxygen vacancies [2,3]. Especially, the fabrication of high-quality FM electrodes on the oxide barrier is difficult due to their different chemical properties which is challenging for fabrication of sharp interfaces. Such imperfections disturb highly spin polarized electron tunneling and lead to reduced TMR ratios experimentally. In fact, the TMR ratio of well-studied Fe/MgO/Fe merely exceed 200% at RT even though theoretical calculations predicted >1000% TMR ratios [2]. Here, we report giant enhancement in RT-TMR ratios of Fe/MgO/Fe by tuning the growth condition of each layer and optimization of barrier interfaces: maximum 417% at RT and 914% at 5 K in a single-crystal, spin-valve-type Fe/MgO/Fe MTJ [4]. Exchange-spin-valve MTJ structures were fabricated in an ultrahigh vacuum magnetron sputtering system (base pressure: 4×10^{-7} Pa) with the structure: MgO(001) substrate/Cr (60)/Fe (30 or 50)/CoFe (0 or 2.24)/Mg (0.5)/wedge-shaped MgO ($d_{\text{MgO}} = 0.5 - 2.5$)/Fe (5)/IrMn (10)/Ru (20) (number in brackets in nm). The MgO barrier was deposited using electron-beam evaporation method and a linear shutter for the wedge-shaped barrier. *In-situ* post-annealing was performed for each layer. After deposition, the wafers were *ex-situ* annealed in a 0.7 T magnetic field at 200°C and subsequently, the TMR ratio and resistance area product (*RA*) was measured using current in-plane tunneling (CIPT) method. The TMR ratio is defined as $\text{TMR} = (R_{\text{AP}} - R_{\text{P}})/R_{\text{P}} \times 100\%$, where R_{P} (R_{AP}) are the resistance for the parallel (antiparallel) state. Thereafter, the wafers were patterned into micrometer scale MTJs using photo- and EB-lithography. The transport properties were investigated using a standard dc 4-probe method. In Fig. 1 (a) and (b), *RA* and TMR ratio vs. d_{MgO} for the MTJ with a 30 nm and 50 nm bottom-Fe is shown, respectively, for the patterned MTJs (dc 4-probe). For the MTJ with 30 nm bottom-Fe the unpatterned wafer (CIPT) results are also shown. As expected, a linear relationship between $\log(RA)$ and d_{MgO} in a wide d_{MgO} range was observed, suggesting good MgO barrier formation. For $d_{\text{MgO}} < 1$ nm, the MgO barrier may be discontinuous. For $d_{\text{MgO}} > 1$ nm, the TMR ratio increases with d_{MgO} and it finally reaches >400%. The inset of Fig. 1 (b) shows the MR loop of the Fe (50 nm)/MgO/Fe MTJ with a maximum 417% TMR ratio which almost doubles previously reported values of Fe/MgO/Fe. Improved Fe/MgO interfaces and well-controlled (001)-orientation of our Fe/MgO/Fe resulted in this significant enhancement of the TMR ratio. In addition, it shows significant oscillatory behavior with d_{MgO} . The oscillation period is 0.31 nm, which agrees with the previous Fe/MgO/Fe report [2]. The oscillation is clearly observed in both the patterned and unpatterned cases, which excludes possible errors of our measurements. The peak-to-valley difference of the oscillation reaches ~80%, which is ~7 times larger than the previous report [2]. The *RA* curves also possess an oscillatory component as seen in Fig. 1 (a). Furthermore, the TMR ratio was increased to 497% at RT by using a Fe/CoFe/MgO/Fe structure (red square in Fig. 1 and MR loop in inset of Fig. 1(b)). This value is larger than other ones of exchange-spin-valve MTJs such as Co/MgO/Co (410%) [5] and $\text{Co}_2(\text{FeMn})\text{Si}/\text{MgO}/\text{Co}_2(\text{FeMn})\text{Si}$ (429%) [6]. In Fig. 2, the temperature dependence of the TMR ratio for an Fe (30 nm)/MgO/Fe MTJ is shown. The TMR ratio is 386% at RT and increases to 914% at 3 K. The respective MR loops are displayed in the inset of Fig. 2. The low temperature (LT) value is around three times larger as compared to other reported values of Fe/MgO/Fe MTJs (250-370%) [2,7]. Our Fe/MgO/Fe MTJ exhibits a giant TMR ratio close to 1,000% at LT, which is often referred as a theoretical value of Fe/MgO/Fe. The study demonstrated that there is more room for improving TMR ratios

of Fe/MgO/Fe MTJs by the optimization of each layer and interface. Further improvement in TMR ratios using the technology in the present study can be expected as demonstrated by the CoFe insertion result. This work was partly supported by the ImPACT Program of the Council for Science, Technology and Innovation (Cabinet Office, Government of Japan), JSPS KAKENHI Grant No. 16H06332, TIA collaborative research program “Kakehashi”, and JPNP16007, commissioned by the New Energy and Industrial Technology Development Organization (NEDO).

[1] D. Ielmini and S. Ambrogio, *Nanotechnology*, Vol. 31, p. 092001 (2020). [2] S. Yuasa *et al.*, *Nat. Mater.*, Vol. 3, p. 868 (2004). [3] X.-G. Zhang, *et al.*, *Phys. Rev. B*, Vol. 68, p. 092402 (2003). [4] T. Scheike *et al.*, *Appl. Phys. Lett.*, in press; arXiv: 2011.08739. [5] S. Yuasa *et al.*, *Appl. Phys. Lett.*, Vol. 89, p. 042505 (2006). [6] H.-x. Liu, *et al.*, *J. Phys. D: Appl. Phys.*, Vol. 48, p. 164001 (2015). [7] S. G. Wang, *et al.*, *Phys. Rev. B*, Vol. 78, p. 180411(R) (2008).

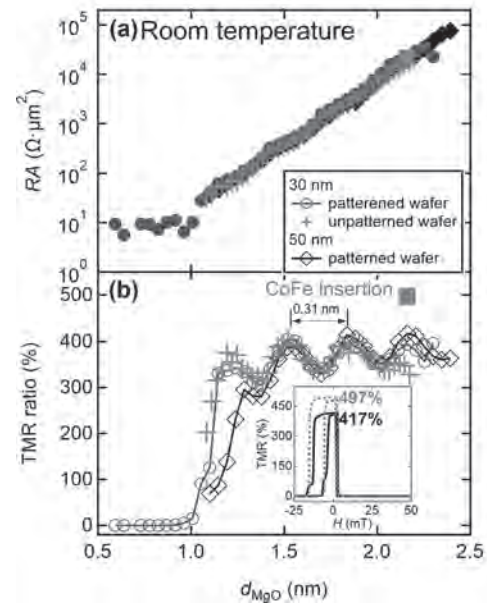


Fig. 1 *RA* (a) and TMR ratio (b) vs. d_{MgO} for Fe/MgO/Fe MTJs with 30 nm (circle and cross) and 50 nm (diamond) bottom-Fe and Fe(50 nm)/CoFe(2.24 nm)/MgO/Fe (square) MTJ. Inset: MR loops of both MTJs at their maximum TMR ratios.

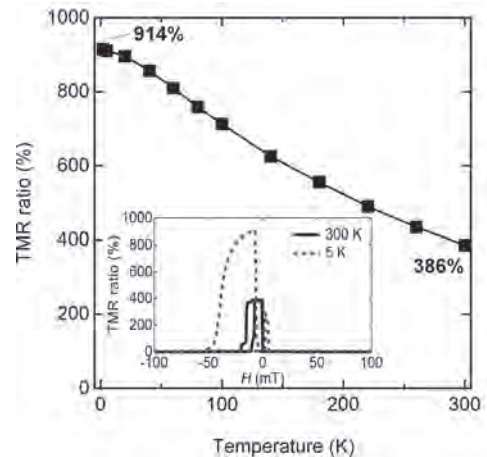


Fig. 2 TMR ratio vs. temperature of a Fe(30 nm)/MgO/Fe MTJ. Inset: MR loops at 300 K and 5 K.

IE-05. High Tunnel Magnetoresistance in Ultrathin MnGa-Based Perpendicular Magnetic Tunnel Junctions Utilizing Ferromagnetic bcc-CoMn Interlayers.

K. Suzuki¹, T. Ichinose¹, R. Monma¹ and S. Mizukami¹
 1. AIMR, Tohoku University, Sendai, Japan

Perpendicular magnetic tunnel junctions (p-MTJs) utilizing tetragonal Mn-based alloy films attracts attention as key devices for magnetic random access memory and THz frequency devices¹. There were many past studies demonstrating those devices, whereas their TMR ratios were much smaller than those predicted by first-principles calculations². Interlayers between the Mn-based alloy and the barrier effectively enhance those TMR ratio, and the TMR ratio of 60% was reported in MnGa/MgO MTJs with FeCo interlayer³. It is crucial to find new interlayer materials to further enhance the TMR ratio for realizing Mn-based p-MTJs for practical applications. Recently, we have reported in-plane type MTJs using bcc-Co₇₅Mn₂₅ electrodes. Bcc-Co₇₅Mn₂₅ is known for its metastable bcc-phase and for ferromagnetism having high Curie temperature⁴. Those MTJs showed a high TMR ratio of over 200%, which may be due to highly spin-polarized $\Delta 1$ band in bcc-Co₇₅Mn₂₅⁵. Here we demonstrate high TMR ratio in ultrathin MnGa-based p-MTJs with the bcc-Co₃Mn alloy interlayer. The result indicates that bcc-CoMn alloy is one of the promising interlayer materials for obtaining high TMR ratio in Mn-based p-MTJs^{6,7}. The samples were prepared using a magnetron sputtering system. The stacking structure of the samples was MgO(001) substrate/Cr(40)/Co₅₅Ga₄₅(30)/ Mn₆₁Ga₃₉(3)/ Co_xMn_{100-x}(0.8) /Mg(0.4)/ MgO(2)/Fe₆₀Co₂₀B₂₀(1.2)/Ta(3)/Ru(5) (thickness is in nanometers) Here, the Co_xMn_{100-x} interlayer was deposited using a co-sputtering technique with Co and Mn targets. All the layers were deposited at room temperature, and the deposition process for the buffer and seed layers was adopted from a previous study⁶. Micro-fabrication of MTJs was performed by standard ultraviolet photolithography, and Ar ion milling etching. After microfabrication, the MTJs were annealed at 250 °C in a vacuum furnace. TMR measurements were performed by a physical property measurement system (PPMS, Quantum Design) using a standard four-probe method at a bias voltage of 1 mV. Figure 1 shows the TMR curves of the MTJs with/without Co₇₅Mn₂₅ interlayer measured at 300 K. The Co₇₅Mn₂₅ interlayer shows the TMR ratio up of approximately 80%, which is much enhanced as compared with that for MnGa-MTJs, ~ 10 %. Meanwhile, the shape of the TMR curve and the increase of coercivity indicate that Co₇₅Mn₂₅ interlayer strongly and antiferromagnetically couples with perpendicularly-magnetized MnGa layer. Figure 2 shows the composition x dependence of the TMR ratio for the MTJs with 0.8-nm-thick Co_xMn_{100-x} interlayer. The TMR ratio for the $x=0$ MTJ is 70% (145%) at 300 K (10K), which is larger than the value expected from Julliere's relation with spin-polarization of fcc-Co and CoFe(B). Moreover, the TMR ratio increases by up to 85% (209%) at 300 K(10 K) for the case of $x=0.8$. Those high TMR ratio would originate from coherent tunneling between highly spin-polarized $\Delta 1$ bands in bcc-Co (Co-Mn) and CoFe(B) electrodes, even though the Co-Mn interlayer thickness is very small, 0.8 nm. This may be also consistent with the temperature dependence of resistance or conductance in these MTJs, which was similar to those observed in Fe/MgO/Fe MTJs. Acknowledgement We would like to thank Y. Kondo for his technical assistance. This work was partially supported by JST CREST (No. JPMJCR17J5).

[1] S. Mizukami *et al.*, Scripta Materialia 118, 70 (2016). [2] J. Jeong *et al.*, Nat. Commun., 7, 10276 (2016). [3] Q. L. Ma *et al.*, Phys. Rev. Lett. 112, 157202 (2014). [4] R. J. Snow *et al.*, J. Magn. Magn. Mater. 419, 490 (2016). [5] K. Kunimatsu *et al.*, Appl. Phys. Express 13, 083007 (2020). [6] K. Z. Suzuki *et al.*, Sci. Rep. 6, 30249 (2016). [7] K. Z. Suzuki *et al.*, submitted.

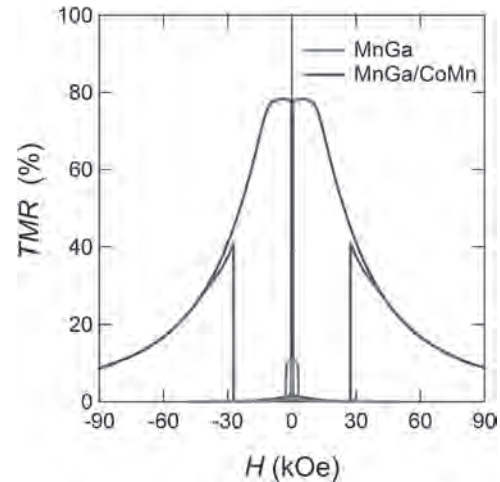


Figure1 TMR curves measured at 300 K for the MnGa-based p-MTJs with/without Co₇₅Mn₂₅ interlayer.

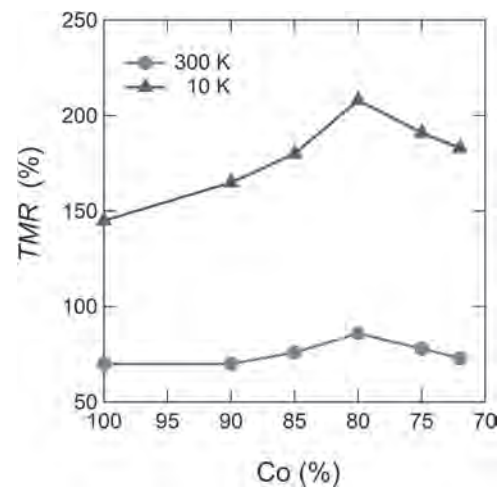


Figure 2 The Co composition dependence of the TMR ratio in MnGa-based p-MTJs with Co_xMn_{100-x} interlayer at 300 and 10 K.

Session IF

MAGNETORESISTANCE, MAGNETOIMPEDANCE AND HALL EFFECTS IN HOMOGENEOUS MATERIALS

Yong-Chang Lau, Chair
Tohoku University, Sendai, Japan

INVITED PAPER

IF-01. Nonlinear Spintronics in Quantum Materials With Inversion Symmetry Breaking INVITED.

P. He¹, S. Zhang², G. Vignale³ and H. Yang⁴

1. Institute for Nanoelectronic devices and Quantum computing, Fudan University, Shanghai, China; 2. Department of Physics, Case Western Reserve University, Cleveland, OH, United States; 3. Department of Physics and Astronomy, University of Missouri, Columbia, MO, United States; 4. Department of Electrical and Computer Engineering, National University of Singapore, Singapore

Spin-orbitronics, which takes advantage of spin-orbit coupling (SOC), has expanded the research objects of spintronics to nonmagnetic materials. Here, we report the emerging nonlinear spintronic phenomena in the inversion-asymmetric nonmagnetic quantum materials with SOC. For instance, the surface state of three-dimensional topological insulator (TI) owns helical spin textures with the spin and momentum perpendicularly locked. We show the observation of a nonlinear magnetoresistance (called bilinear magneto-electric resistance, BMER) [1] and nonlinear Hall effect [2] in a prototypical TI Bi_2Se_3 , which scale linearly with both the applied electric and magnetic fields. We further reveal that these effects are originated from the conversion of a nonlinear spin current to charge current under the application of an external magnetic field. A close link between the BMER and the spin texture was established in TI surface states, which enables a novel transport probe of spin textures. We further extended the observation of BMER effect to the d -orbital two-dimensional electron gas (2DEG) at a SrTiO_3 (STO) (111) surface [3]. The BMER probes a three-fold out-of-plane spin texture, in addition to an in-plane one at the STO (111) surface 2DEG. This novel spin texture is in contrast to the conventional one induced by the Rashba effect. By performing tight-binding supercell calculations, we find that this 3D spin texture is fully described by the confinement effects of the STO t_{2g} conduction band in the (111) plane. We recently reported the observation a sign reversal of nonlinear magnetoresistance with temperature in a semi-metal WTe_2 [4]. Theoretical calculations revealed the critical role of Fermi surface topology and convexity on the nonlinear magneto-response. These findings open a new branch in spintronics, which discusses the nonlinear transport effects in spin-polarized quantum materials, and is therefore referred as nonlinear spintronics.

[1] Pan He, et al. Nature Physics 14, 495 (2018) [2] Pan He, et al. Phys. Rev. Lett. 123, 016801 (2019) [3] Pan He, et al. Phys. Rev. Lett. 120, 266802 (2018) [4] Pan He, et al. Nature commun., 10, 1290 (2019)

CONTRIBUTED PAPERS

IF-02. Magneto-Transport Properties in $Mn_{4-x}Ni_xN$ Films With Large Current Induced Domain Wall Mobility and Investigation in Their Large Anomalous Hall Effect.

T. Komori¹, H. Mitarai¹, K. Toko¹ and T. Suemasu¹

¹. Institute of Applied Physics, Tsukuba University, Tsukuba, Japan

Nowadays, our lives are greatly enriched by information society. Meanwhile, energy resource issue is becoming a serious problem, leading to the demand for devices with lower power consumption. When we focus on the memory, the spread of non-volatile memory, represented by the racetrack memory [1] based on current induced domain wall motion (CIDWM), has been longed for. To realize this, our groups have been investigating anti-perovskite Mn_4N films as candidate materials for the racetrack memory. They show a small saturation magnetization (M_S) of 80 kA m⁻¹ and clear perpendicular magnetic anisotropy (PMA) [2], contributing to high velocity and low threshold current density, respectively. We experimentally demonstrated the domain wall velocity (v_{DW}) of 900 ms⁻¹ at 1.3×10^{12} Am⁻² only by spin-transfer torque (STT) [2]. Note that we achieved this record by rare-earth free material unlikely other reports. Our recent work also pays attention to $Mn_{4-x}Ni_xN$ films because they have compensation point at $x \sim 0.15$ where v_{DW} takes its maximum value [3]. In $Mn_{3.85}Ni_{0.15}N$, we recorded v_{DW} of 2000 m/s at 1.16×10^{12} Am⁻², the fastest purely STT-driven CIDWM [4]. Despite of these amazing performances, large parts of magneto-transport properties in $Mn_{4-x}Ni_xN$ films are still unknown although they are deeply linked to the relationship between conduction electrons and localized ones. Interestingly, we confirmed large anomalous Hall effect (AHE) with a relatively large anomalous Hall angle ($\theta_{AHE} = \rho_{AHE}/\rho_{xx}$) of 2% in Mn_4N films although they don't contain any heavy metal with large spin-orbit coupling [2]. There were attempts to discover the origin of such large AHE, however, it has not been proved by now. In this work, we performed AHE and conductivity measurements at temperatures in the range of 5-300 K, and we plotted σ_{AHE} against σ_{xx} to find out the origin of AHE [6]. Also, we performed anisotropic magnetoresistance (AMR) measurements for the better understanding of spin-dependent scattering in these materials. $Mn_{4-x}Ni_xN$ films (30 nm) were fabricated onto SrTiO₃ (STO)(001) substrates by molecular beam epitaxy. Epitaxial growth was confirmed by X-ray diffraction, and the thickness of each layer was examined by X-ray reflectivity. AHE and AMR measurements were performed by physical properties measurement system. Before measurements, film samples were processed into Hall bars with a width of 200 nm by Ar ion milling. During AMR measurements, DC current was set to flow in the [100] azimuth and a magnetic field of 9 T was applied parallel to the plane. Figure 1 shows the σ_{xx} dependence of σ_{AHE} in $Mn_{4-x}Ni_xN$ /STO in the temperature range of 5-300 K. Note that σ_{xx} became larger at lower temperatures, a typical behavior in metals. The region of $\sigma_{xx} < 10^4 \Omega^{-1}cm^{-1}$ is called "Bad metal regime", where σ_{AHE} is proportional to $\sigma_{xx}\alpha$ ($\alpha \sim 1.8$) in many 3d transition metals [5]. $Mn_{4-x}Ni_xN$ films ($x > 0$) also followed this trend, while Mn_4N showed rather constant σ_{AHE} relative to σ_{xx} . On the other hand, the region of $\sigma_{xx} > 10^4 \Omega^{-1}cm^{-1}$ is called "Good metal regime", where σ_{AHE} did not change so much against σ_{xx} . In $Mn_{4-x}Ni_xN$ at small x ($x = 0$ and 0.05), however, σ_{AHE} decreased with increasing σ_{xx} , thereby, with decreasing temperature. It's also remarkable that σ_{AHE} remained almost unchanged when $x = 0.15$ and 0.2. This discrepancy can be explained in the following. Figure 2 shows the Fourier coefficients C_2 ($\cos 2\theta$) and C_4 ($\cos 4\theta$) of AMR curves of $Mn_{4-x}Ni_xN$ /STO. θ is the angle made by the current and magnetization. C_2 and C_4 components derive from cubic and tetragonal crystalline fields, respectively [6]. Thus, large C_4 components at temperatures lower than 100 K at $x = 0$ and 0.05 originate from tetragonal one although they have cubic structures. Note that C_4 component was very small at $x = 0.15$, and AMR was barely observed at $x > 0.2$. In 3d transition metals, intrinsic AHE comes from hopping of electrons between electronic states d_{yz} and d_{zx} [7]. However, these states rise under the tetragonal crystalline field due to the resolution of degeneracy, leading to smaller number of electrons related to the origin of AHE. Therefore, reflecting our experimental results, unexpected decrease in σ_{AHE} at low temperatures in $Mn_{4-x}Ni_xN$ ($x = 0, 0.05$) can be explained by the emergence of tetragonal field. On the basis of these discus-

sions, we conclude that large AHE in $Mn_{4-x}Ni_xN$ originates from intrinsic AHE at low temperatures. Although we have not fully revealed the case at room temperature due to a limited number of reports on AHE in "Bad metal regime", we suggest that it originates from intrinsic AHE and extrinsic AHE such as phonon-scattering. We believe this work opens the interest in the band structure of $Mn_{4-x}Ni_xN$ films.

[1] S. Parkin and S.-H. Yang, Nat. Nanotechnol. Vol.10, p.195 (2015). [2] T. Gushi, L. Vila and T. Suemasu *et al.*, Nano. Lett. Vol.19, p.8716 (2019). [3] T. Komori, K. Amemiya and T. Suemasu *et al.*, J. Appl. Phys. Vol.127, p.043903 (2020). [4] S. Ghosh, T. Komori and L. Vila *et al.*, IEEE MMM Virtual Conference, R1-11, Nov. (2020). [5] N. Nagaosa, S. Onoda and N. P. Ong *et al.*, Rev. Mod. Phys. Vol.82, p.1539 (2010). [6] S. Kokado and M. Tsunoda, Mater. Today Proceedings Vol.33, p.1864 (2020). [7] H. Kotani, T. Tanaka, K. Yamada Phys. Rev. B Vol.75, p.184416 (2007).

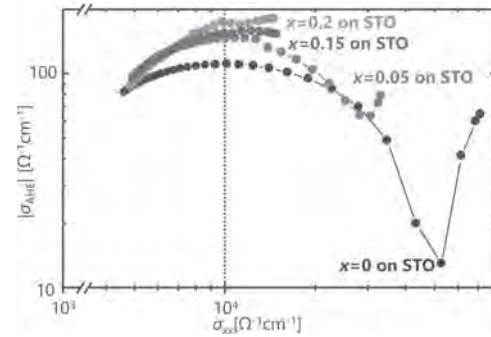


Fig. 1 σ_{xx} dependence of σ_{AHE} in $Mn_{4-x}Ni_xN$ at temperatures (5-300 K). A dashed line indicates the border of Good metal and Bad metal regime.

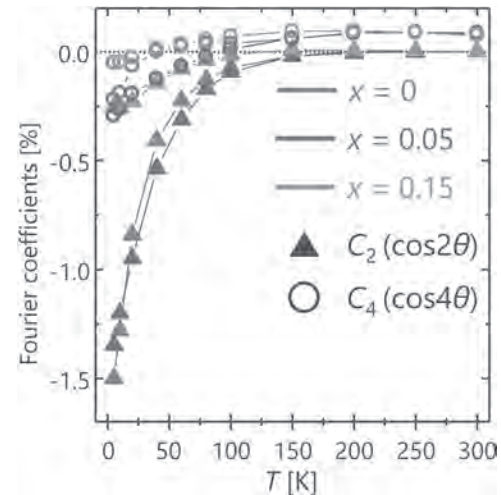


Fig. 2 Fourier coefficients C_2 and C_4 of AMR curves of $Mn_{4-x}Ni_xN$.

IF-03. Anomalous Hall Effect in Anisotropic Weyl Semimetals.

C. Yesilyurt¹, Z. Siu², F. Ozaydin³ and M.B. Jalil²

1. Department of Physics, Istanbul University, Istanbul, Turkey;
 2. Electrical and Computer Engineering, National University of Singapore, Singapore; 3. Institute for International Strategy, Tokyo International University, Tokyo, Japan

Various types of Anomalous Hall effects have been widely investigated in recent years [1, 2]. In most of the cases, the predicted or measured Hall signal has been attributed to spontaneous magnetic moment arisen from the dynamics of the current flow [1]. In this work, we aim to investigate the role of anisotropic band dispersion of chiral Weyl fermions in generating a transverse current resulting in a Hall signal. For this purpose, the simplest Weyl semimetal phase consisting of two Weyl nodes with opposite chirality is adopted and the angular dependence of conductance is calculated [3, 4]. Multi-terminal devices with circular geometry as illustrated in Fig. 1 are commonly used to probe the dependence of the signal on transport direction in experiments [1, 3]. Therefore, in the proposed model, we adopt the circular channel geometry and calculate the conductance for arbitrary transport directions. The Hamiltonian of the simplest Weyl system is as follows, $H = V_0 + \sum_i \hbar k_i \tau (v_i \sigma_i + w_i)$, where σ 's are Pauli matrixes, v 's are velocities and their sign ($\tau = \pm$) carry the chirality of Weyl nodes. We assume symmetric velocities equal to $v_F = 10^6$ m/s. The dispersion of Weyl fermion can be tilted along all three directions, and the strength of the tilt is denoted by w_i . In the current work, two Weyl nodes having opposite chirality are also tilted along opposite directions. The tilt direction is chosen to lie along the high anisotropy axis, which is close to one of the crystal axes in most of the Weyl semimetals reported up to date [e.g., Refs. 3, 5]. The angular dependence of the conductance [3, 4, 5] can be calculated based on transmission probability along an arbitrary direction and integrated over all transverse wave vectors based on the following equation, $G\beta = G_0 \int -(\partial f / \partial E) dE \iint dS_{FS} T \phi \gamma \cos \phi \cos \gamma$. In the above equation, γ is the angle between Fermi wave vector k and the x-y plane, ϕ is the azimuthal angle with respect to the x-axis, G_0 is the quantum conductance, dS_{FS} is the infinitesimal element of the elliptical Fermi surface per unit variation of the coordinates ϕ and γ . The anisotropy in crystal symmetry and the bandstructure make the conductance dependent on the angle between the transport direction and the crystal axis. Based on the conductance profile, the voltage difference between the transverse electrodes can be found as follows, $V_t = V_{t1} - V_{t2} \propto (S/\rho)[(G_{t1} - G_{t2})/(L/\sqrt{2})]$, where $G_{t1} = G\beta_{t1}(\pi/4)$ and $G_{t2} = G\beta_{t2}(\pi/4)$. The longitudinal potential difference can be calculated similarly by replacing the respective conductance value and distance between the voltage probes. As shown in Fig. 2 and predicted by the above equation, transverse voltage emerges at some angles which are related to the imbalance of G_{t1} and G_{t2} . The highest V_t occurs at the maximum imbalance, where G_{t1} and G_{t2} coincide with the lowest and highest conductance points in the conductance profile shown in Fig. 1 (right). On the other hand, the conductance between source and drain is minimum in this direction as seen in Fig. 2. Our predicted results are quite consistent with the experimental results presented recently in literature [1] thus revealing a possible origin of the measured Hall signals in Weyl semimetals in the absence of a magnetic field.

[1] Kang, K., Li, T., Sohn, E. *et al.* Nonlinear anomalous Hall effect in few-layer WTe₂. *Nat. Mater.* 18, 324–328 (2019). [2] Ma, Q., Xu, SY., Shen, H. *et al.* Observation of the nonlinear Hall effect under time-reversal-symmetric conditions. *Nature* 565, 337–342 (2019). [3] Qisheng Wang, Can Yesilyurt, Fucai Liu, Zhuo Bin Siu, Kaiming Cai, Dushyant Kumar, Zheng Liu, Mansoor B. A. Jalil, and Hyunsoo Yang *Nano Letters* 2019 19 (4), 2647-2652 [4] Yesilyurt, C., Siu, Z.B., Tan, S.G. *et al.* Electrically tunable valley polarization in Weyl semimetals with tilted energy dispersion. *Sci Rep* 9, 4480 (2019). [5] Soluyanov, A., Gresch, D., Wang, Z. *et al.* Type-II Weyl semimetals. *Nature* 527, 495–498 (2015).

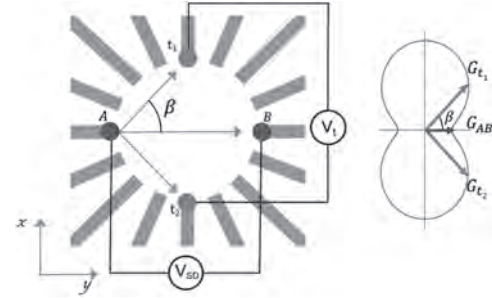
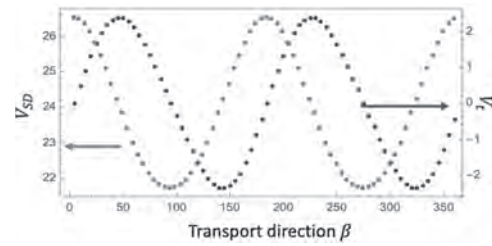


Illustration of the adopted model, i.e., circular multi-terminal circuit (left). Terminal A and B denote source and drain electrodes respectively, and the Hall signal is calculated as the voltage difference at two transverse points t_1 and t_2 . Normalized anisotropic conductance profile of the Weyl system with two opposite chirality Weyl nodes (right). Blue (Red) arrow(s) indicates the conductance between the source and drain (transverse electrodes).



Angular dependence of anomalous Hall effect, where the Hall voltage V_t is calculated as the voltage difference between the points t_1 and t_2 (i.e., shown in Fig. 1). The longitudinal voltage V_{SD} is calculated as the voltage difference between points A and B (i.e., shown in Fig. 1)

IF-04. Large Anomalous Hall Angle in a Topological Semimetal Candidate TbPtBi.

J. Chen^{1,2}, H. Li², B. Ding², H. Zhang², X. Xi² and W. Wang^{2,1}

1. Songshan Lake Materials Laboratory, Dongguan, China; 2. Chinese Academy of Sciences Institute of Physics, Beijing, China

Magnetotransport properties of magnetic materials receive considerable interests, because of they make an important role in basic science and technological applications[1]. Anomalous Hall Effect (AHE), as an important topic in condensed matter, contains extensive physics for their many different mechanisms, such as intrinsic mechanism associated with the Berry curvature in entangled Bloch electronic bands, extrinsic mechanism including skew scattering and side jump scattering[2]. In this study, the magnetotransport properties in antiferromagnetic half-Heusler single crystals of TbPtBi, a magnetic-field-induced topological semimetal with simple band structure, were investigated. We found a non-monotonic dependence of the anomalous Hall resistivity on the magnetic field in a strong magnetic field ($B > 7\text{T}$), which comes from the change of band structure caused by the Zeeman-like splitting when an external magnetic field is applied. The experimental results show that credible anomalous Hall resistivity and conductivity reach up to $0.68\text{m}\Omega\text{cm}$ and $125\Omega^{-1}\text{cm}^{-1}$, respectively. A large anomalous Hall angle (AHA) up to 33% is achieved in TbPtBi, which is comparable to a typical ferromagnetic Weyl semimetal $\text{Co}_3\text{Sn}_2\text{S}_2$ [3]. The analysis of the results shows that this should be attributed to topological band around E_F and low carrier density.

[1] Science advances 4 : eaar7880 (2018). [2] Rev. Mod. Phys. 82 (2), 1539 (2010); Physical Review 95 (5), 1154 (1954); Physica 24, 39 (1958); Physica 21, 877 (1955); Phys. Rev. B 2 (11), 4559 (1970). [3] Nat. Phys. 14, 1125 (2018); Adv. Funct. Mater., 2000830 (2020); Nano Lett. 7476–7481, (2020).

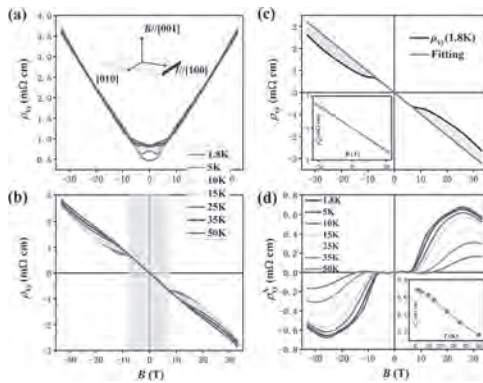


Figure 1. Dependence of the longitudinal resistivity ρ_{xx} (a) and Hall resistivity ρ_{xy} (b) on magnetic field B at temperatures from 1.8K to 50K. (c) Separation progress of normal Hall resistivity ρ_{xy}^N and anomalous Hall resistivity ρ_{xy}^A at 1.8K. The inset shows the normal Hall resistivity obtained by linear fitting for low magnetic field curves at corresponding T . (d) The anomalous Hall resistivity ρ_{xy}^A after subtracting the fitting normal Hall resistivity ρ_{xy}^N . The inset is the maximum value of ρ_{xy}^A at different temperatures.

IF-05. Efficient Tuning of Electronic, Transport, and Thermoelectric Properties of Weyl Semimetal $\text{Co}_2\text{MnAl}_{1-x}\text{Si}_x$ Composition-Spread Thin Film.

R. Modak¹, Y. Miura¹, S. Ueda¹, K. Uchida^{1,2} and Y. Sakuraba^{1,3}

1. Research Center for Magnetic and Spintronic Materials, National Institute for Materials Science, Tsukuba, Japan; 2. Institute for Materials Research, Tohoku University, Sendai, Japan; 3. PRESTO, Japan Science and Technology Agency, Saitama, Japan

The thermoelectric generation based on the anomalous Nernst effect (ANE) has become one of the promising approaches to realize efficient energy harvesting from waste heat and heat flux sensor due to its several advantages over conventional devices based on the Seebeck effect (SE)^{1,2}. However, till date, the observed ANE thermopower is very small and a systematic material investigation to realize large anomalous Nernst coefficient is necessary. Recent theoretical and experimental investigations identified a Weyl semimetal as a potential material having giant ANE which can be achieved by a little tuning of Fermi level (E_F) near Weyl points^{3,4,5}. However, systematic tuning of E_F and investigation of thermoelectric properties based on many films with different compositions are time-consuming. Furthermore, in this process, one loses many intermediate compositions due to the limitation of number of films that can be prepared. In this regard, we introduce an efficient approach to tune E_F for Weyl semimetals and demonstrate the approach through a layer-by-layer combinatorial deposition of a $\text{Co}_2\text{MnAl}_{1-x}\text{Si}_x$ (CMAS) thin film with x varied from 0 to 1 on a single substrate. The fabrication procedure is represented schematically in Fig.1 (a). The structural characterization reveals the formation of single-phase CMAS alloys throughout the composition range. Hard X-ray photoemission spectroscopy (HAXPES) directly confirmed a continuous shifting of E_F from Co_2MnAl to Co_2MnSi with a maximum shift of 0.4 eV (see Fig.1. (b)), which is consistent with the theoretical prediction. We also measured the anomalous Ettingshausen effect (AEE), the reciprocal of ANE, for the all x range using a single strip along the composition gradient (see Fig.1. (c)) by means of the lock-in thermography technique^{6,7}. Only one LIT image tells us that large AEE is obtained between $x = 0.06$ to 0.12 , which well agrees with the composition dependence of the ANE signals (see Fig.1. (d)), measured by making many parallelly aligned Hall bars elongated to the orthogonal direction to the composition gradient (see Fig.1. (c)). The findings clearly demonstrate that the AEE measurement using the composition spread film is an effective approach to investigate the composition dependence of ANE and find the highest performance without fabricating many films and performing systematic measurements. These demonstrations will enable the optimization of the composition in Weyl semimetals and exploration of new materials to obtain giant ANE/AEE, which is essential to realize applications based on the transverse thermoelectric effects.

[1] Y. Sakuraba *et al.*, Appl. Phys. Express 6, 033003 (2013) [2] W. Zhou *et al.*, Appl. Phys. Express 13, 043001 (2020) [3] K. Sumida *et al.*, Commun. Mater. 1, 89 (2020) [4] J. Noky *et al.*, NPJ Comput. Mater. 6, 77 (2020) [5] Y. Sakuraba *et al.*, Phys. Rev. B 101, 134407 (2020) [6] S. Daimon *et al.*, Nat. Commun. 7, 13754 (2016) [7] T. Seki *et al.*, Appl. Phys. Lett. 112, 152403 (2018)

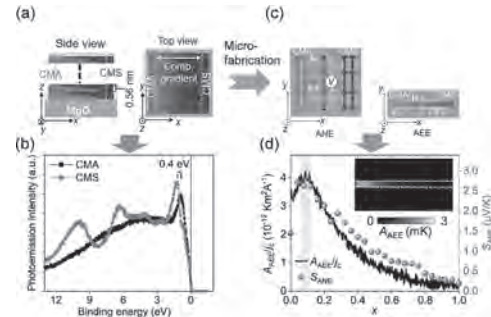


Fig.1 (a) Schematic representation of composition-spread CMAS combinatorial film deposited with wedge shaped layer by layer deposition (b) Valence band HAXPES spectra for CMAS composition-spread film at Co_2MnAl (CMA) and Co_2MnSi (CMS) side (c) Schematic measurement configuration used for ANE and AEE (d) A_{AEE}/j_c and S_{ANE} as a function of x . Where A_{AEE} is the amplitude of temperature modulation due to AEE, j_c is the charge current density and S_{ANE} is anomalous Nernst coefficient. The inset shows observed A_{AEE} image in LIT.

IF-06. Micromagnetic Study of Strain-Induced Magnetization Switching in FeGaB Nanomagnets for Self-Biased MRAM Applications.

P. Pathak¹ and D. Mallick¹

¹Department of Electrical Engineering, Indian Institute of Technology Delhi, New Delhi, India

Lately, Magnetic Random-Access Memory (MRAM) has stimulated significant interests compared to traditional semiconductor memory devices due to its non-volatility combined with expeditious read and write endurance. In the preceding studies, conventional methods that had been investigated widely include spin-orbit torque (SOT)¹, spin-transfer torque (STT)² and current-driven switching. However, magnetization switching in MRAM utilizing such techniques fall short to observe the desired switching and inevitably supplemented by thermal issues, leading to inefficient functionality. Recently, considerable endeavour towards a new paradigm of straintronic devices (STR)³ for efficient magnetization switching is explored. A magnetoelectric STR constitutes of ferromagnetic and piezoelectric order parameters, in which an applied electric field across the piezoelectric order parameter instigate mechanical strain at the heterostructure interface giving rise to the magnetization switching due to the Villari effect. Though both out-of-plane and in-plane magnetization switching are examined in the aforementioned studies to explore the STR devices, magnetization switching in the in-plane direction is obscured on account of thermal instability in smaller element size and multi-domain formation in larger element size. Also, the self-biased STR-MRAM device that extinguishes the external bias magnetic field is still undiscovered. In this work, we investigated the size-dependent in-plane magnetization switching of FeGaB/PMN-PT (ferromagnetic/piezoelectric) heterostructure (Fig. 1(a)) using micromagnetic finite element method (FEM) coupled with electrodynamic and elastic analysis. Three elliptical nanodiscs of FeGaB magnetoelastic material having cross-sectional areas $100 \times 90.9 \text{ nm}^2$, $100 \times 66.67 \text{ nm}^2$, and $100 \times 50 \text{ nm}^2$ are investigated by varying the thickness from 2 nm to 28 nm on a $10 \times 10 \times 0.5 \text{ mm}^3$ single-crystal PMN-PT (011) piezoelectric substrate. Initially, minimum thickness (d_{\min}) at pre-stress condition for three elliptical nanodiscs are investigated (Fig. 1(b)) using in-plane induced energy well (ΔE) scaled by $k_b T$ (where k_b is Boltzmann constant and T is the temperature in Kelvin). $\Delta E/k_b T \leq 70$ is an assumed condition for thermal instability to ensure d_{\min} for STR-MRAM devices. To explore the maximum thickness related to self-biasing (d_{sb}), pre-stress equilibrium exchange and demagnetization energies associated with the three elliptical nanodiscs are analyzed against thickness. The larger size magnets make an effort to minimize the energy by aligning the magnetization with the elliptical nanodisc boundary and gives rise to vortex state. On contrary, smaller size magnets minimize the energy by aligning the magnetization along the easy axis (0° or 180°) of the elliptical FeGaB nanomagnets without applying the external magnetic bias field (Fig. 2). This result is pivotal as such self-biasing would give primacy to future STR-MRAM devices by omitting the necessity for an extrinsic magnetic bias field. Although the above analysis is performed to obtain optimum size where STR-MRAM device is stable and self-biased, the maximum thickness (d_{\max}) for in-plane 180° magnetization switching is limited by the critical stress requirement. It is observed that d_{sb} is not necessarily the same as d_{\max} for in-plane 180° magnetization switching. When compressive strain equal or greater than the critical compressive strain is applied from the pre-stress state, where magnetization is along the easy axis, in-plane 90° magnetization switching (along 90° or 270°) is observed. This happens as exchange and stress anisotropy energies are almost negligible and the demagnetization energy rises as the magnetization is switched from the easy to the hard axis. Magnetic precession is used to obtain in-plane 180° switching. When the magnetization component along the x-axis is negative during the precession, removal of external strain causes another 90° switching because the ferromagnet tries to reduce its total energy by gravitating to its nearest easy axis. In-plane fastest 180° magnetization switching time and associated external strain are investigated also. For fixed thickness, compressive strain requirement rises with increasing cross-sectional area. As the thickness is increased, tradeoff between fastest switching time and associated switching energy is observed for the same cross-sectional area. Whereas faster switching time and lesser switching energy are required for larger cross-sectional nanodiscs

having the same thickness. This work can be potentially useful in the future STR-MRAM devices that eliminates the necessity of extrinsic magnetic field bias and completes in-plane 180° magnetization switching.

¹C. Zhang, S. Fukami, H. Sato, F. Matsukura, H. Ohno, Appl. Phys. Lett., 107, 012401 (2015). ²C.F. Pai, L. Liu, Y. Li, H. W. Tseng, D. C. Ralph, R. A. Buhrman, Appl. Phys. Lett., 101, 122404 (2012). ³K. Roy, S. Bandyopadhyay, J. Atulasimha, Appl. Phys. Lett., 99, 063108 (2011).

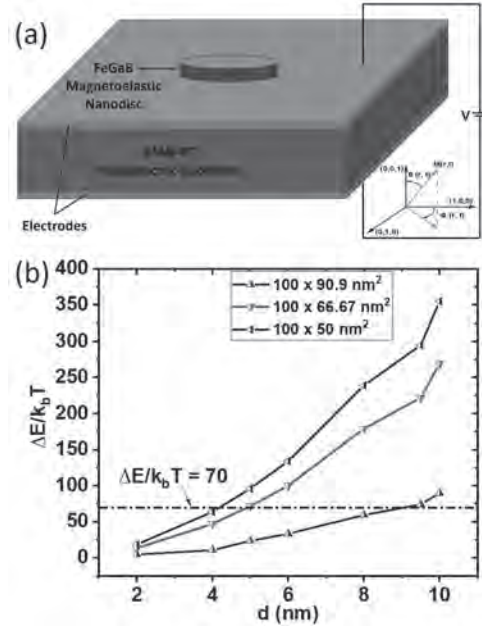


FIG 1: (a) Proposed structure consists of FeGaB/PMN-PT (ferromagnetic/piezoelectric) heterostructure and corresponding magnetization components. (b) $\Delta E/k_b T$ vs thickness curve to examine the minimum thickness (d_{\min}) requirement for thermal stability.

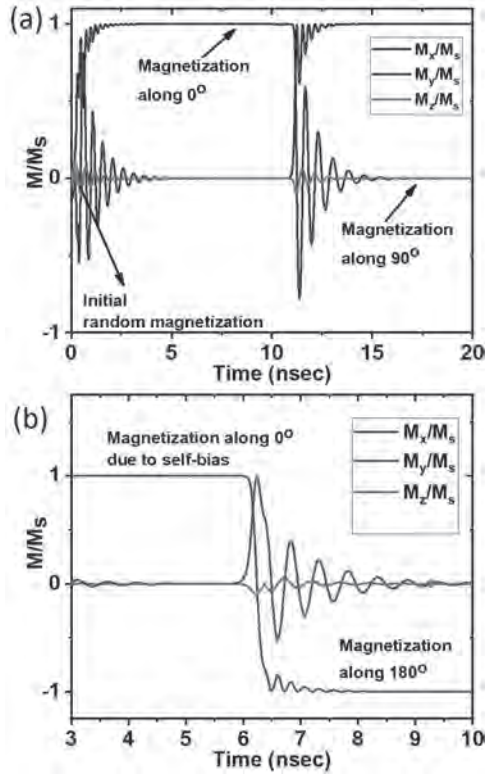


FIG 2: (a) Simulated in-plane 90° magnetization switching from initial random magnetization state after applying critical stress. (b) Simulated in-plane 180° magnetization switching after magnetization switches to in-plane easy axis for $100 \times 90.9 \times 9.5 \text{ nm}^3$ nanodisc.

IF-07. Huge Room Temperature Negative Magneto Capacitance in $\text{La}_{0.7}\text{Pb}_{0.3}\text{Mn}_{0.4}\text{Fe}_{0.6}\text{O}_{3-\delta}$ and Positive Magneto Capacitance in $\text{La}_{0.7}\text{Pb}_{0.3}\text{Mn}_{0.4}\text{Ti}_{0.6}\text{O}_{3-\delta}$.

P. Singh¹ and B. Singh¹

¹ University of Allahabad Centre of Material Sciences, Allahabad, India

In this study, we report room temperature negative magneto capacitance due to 60% Fe doping and positive magneto capacitance due to 60% Ti doping at Mn site in $\text{La}_{0.7}\text{Pb}_{0.3}\text{MnO}_3$. We have studied the structural, mixed valence studies using synchrotron X-ray absorption spectroscopy (XAS), magnetic and magneto capacitance properties of $\text{La}_{0.7}\text{Pb}_{0.3}\text{Mn}_{0.4}\text{Fe}_{0.6}\text{O}_{3-\delta}$ and $\text{La}_{0.7}\text{Pb}_{0.3}\text{Mn}_{0.4}\text{Ti}_{0.6}\text{O}_{3-\delta}$. $\text{La}_{0.7}\text{Pb}_{0.3}\text{Mn}_{0.4}\text{Fe}_{0.6}\text{O}_{3-\delta}$ and $\text{La}_{0.7}\text{Pb}_{0.3}\text{Mn}_{0.4}\text{Ti}_{0.6}\text{O}_{3-\delta}$ were synthesized by solid state method. The x-ray diffraction (XRD) patterns show (i) successful substitution of Fe and Ti at Mn site and (ii) change in lattice parameters of $\text{La}_{0.7}\text{Pb}_{0.3}\text{Mn}_{0.4}\text{Fe}_{0.6}\text{O}_{3-\delta}$ and $\text{La}_{0.7}\text{Pb}_{0.3}\text{Mn}_{0.4}\text{Ti}_{0.6}\text{O}_{3-\delta}$. L edge absorption studies using synchrotron XAS show the presence of mixed valence states in these compositions. $\text{La}_{0.7}\text{Pb}_{0.3}\text{Mn}_{0.4}\text{Fe}_{0.6}\text{O}_{3-\delta}$ show maximum ~64 % negative magneto capacitance at 500 gauss(G) magnetic field, ~60 % at 5kG magnetic field and -56 % at 10 kG magnetic field at 300 K. $\text{La}_{0.7}\text{Pb}_{0.3}\text{Mn}_{0.4}\text{Fe}_{0.6}\text{O}_{3-\delta}$ show ~51% negative magneto capacitance at 15 kG magnetic field while $\text{La}_{0.7}\text{Pb}_{0.3}\text{Mn}_{0.4}\text{Ti}_{0.6}\text{O}_{3-\delta}$ show ~ 12 % positive magneto capacitance at 15 kG magnetic field. Magneto capacitance values in these compositions at room temperature in accordance with the Maxwell Wagner effect, which was explained by Catalan et al. Interaction between Mn^{+3} and Mn^{+4} via oxygen atom in the lattice originates the local magnetic region in the middle of non magnetic regions which originated negative magneto capacitance while Ti doped samples show positive magneto capacitance due to the presence quantum interference and coulombic interaction effects. Presence of unpaired electrons in the d orbitals of Fe, Mn and Ti dictates the magneto capacitance properties of these materials.

1. G. Catalan Appl Phys Lett 88, 102902 (2006) 2. P. Chen, D. Y. Xing and Y. W. Du *Phys. Rev. B* 64, 104402 (2001) 3. S. S. Manoharan, B. Singh, R.K. Sahu, et al. *J. Phys.: Condens. Matter* 20, 235205 (2008) 4. B. Singh Mater. Let. 156, 76 (2015)

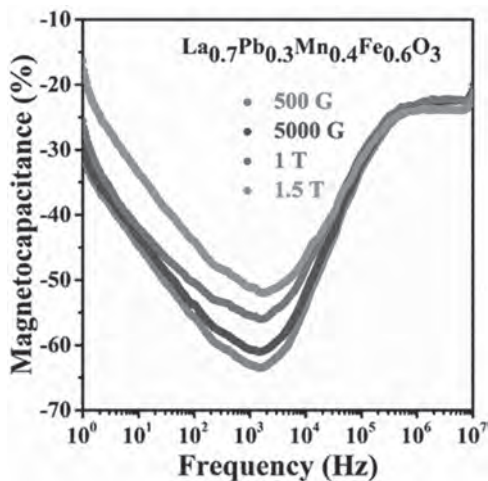


Fig. 1 Magneto capacitance vs frequency plots at different applied Magnetic field for $\text{La}_{0.7}\text{Pb}_{0.3}\text{Mn}_{0.4}\text{Fe}_{0.6}\text{O}_{3-\delta}$ polycrystalline sample.

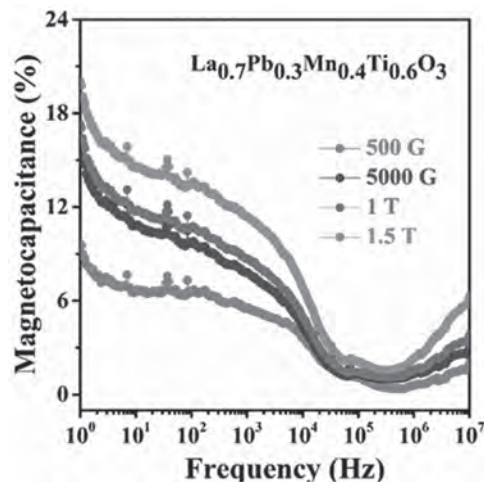


Fig. 2 Magneto capacitance vs frequency plots at different applied Magnetic field for $\text{La}_{0.7}\text{Pb}_{0.3}\text{Mn}_{0.4}\text{Ti}_{0.6}\text{O}_{3-\delta}$ polycrystalline sample.

Session IG

MULTILAYERED AND PATTERNED FILMS, AND EXCHANGE BIAS

Aidan Hindmarch, Chair

University of Durham, Durham, United Kingdom

CONTRIBUTED PAPERS

IG-01. Nanoscale Manipulation of Magnetic Domains by Interfacial Strain-Induced Proximity.

J. Rodríguez Alvarez¹, I. Valmianski², A. Fraile Rodríguez¹, M. García del Muro¹, C. Wolowiec², F. Kronast³, J. Ramírez⁴, I.K. Schuller², A. Labarta¹ and X. Batlle¹

1. *Departament de Física de la Matèria Condensada i Institut de Nanociència i Nanotecnologia (IN2UB), Universitat de Barcelona, Barcelona, Spain;* 2. *Department of Physics and Centre for Advanced Nanoscience, University of California San Diego, La Jolla, CA, United States;* 3. *Helmholtz-Zentrum Berlin für Materialien und Energie GmbH, Berlin, Germany;* 4. *Department of Physics, Universidad de los Andes, Bogotá, Colombia*

Coupling lattice and spin degrees of freedom without the use of external magnetic fields allows for energy-efficient spintronic devices. In this context, hybrid materials composed of an oxide layer undergoing a first-order, structural phase transition (SPT), such as V_2O_3 , and a ferromagnetic layer, such as Ni, constitute a very promising paradigm for the development of such applications. In the case of a Ni/ V_2O_3 heterostructure, the structural domains inherent to the first-order phase transition in the V_2O_3 cause a differential strain pattern in the Ni layer. By virtue of the inverse magnetostrictive effect, this strain pattern is converted into a magnetic anisotropy distribution in the Ni. This offers a promising alternative to voltage-controlled magnetism or other switching mechanisms without a magnetic field [1,2]. Here we show by direct imaging of the thermal evolution of the Ni spin structure that the magnetic domains can be tuned in both size and orientation upon crossing the structural phase transition (SPT) of the proximal V_2O_3 layer [3]. We find a drastic temperature-driven reorientation of the Ni magnetic domains across the SPT which is responsible for an abrupt increase in the coercive field (up to 500%). By synchrotron-based X-ray microscopy we show a reconfiguration of the ferromagnetic domain pattern in the Ni layer across the V_2O_3 SPT together with changes in magnitude and direction of the magnetic anisotropy. These observations are in good agreement with both angular dependent ferromagnetic resonance measurements and micromagnetic simulations. Our simulations successfully replicate the change in the coercivity as well as the reorientation of the magnetization of the Ni domains after the implementation of a simple model of strain-dependent magnetic anisotropies. Furthermore, simulations also exhibit a phase coexistence of different magnetic domains across the SPT in the V_2O_3 . Direct observations of the lateral correlation length of the Ni domains show an increase of almost an order of magnitude at the SPT compared to room temperature as well as a broad spatial distribution of the local transition temperatures. This corroborates the phase coexistence of Ni anisotropies due to the V_2O_3 structural domains coexistence across the SPT. Our data reveal that the reorientation of Ni domains is controlled by the reconfiguration of the structural domains of the oxide layer across the SPT [4,5], due to strain induced proximity. Our findings reveal a novel pathway to control magnetic domains without a magnetic field through proximity to a material undergoing a first-order structural phase transition, which allows for engineering of coercive fields for novel data storage architectures and novel device concepts based on “straintronics”. Acknowledgements: This work was supported by the Spanish MINECO projects MAT2015-68772-P and PGC2018-097789-B-I00 and European Union FEDER funds. A.F.R. and M.G.M acknowledge financial support from the EU CALIPSO Transnational Access programme. J.G.R. acknowledges support from Colciencias under grant 120471250659. The work by I.V., C.W. and I.K.S. at UCSD were supported by the Office of Basic Energy Science, U.S. Department of Energy, BES-DMS funded by the Department of Energy’s Office of Basic Energy Science, DMR under grant DE FG02 87ER-45332.

[1] de la Venta, J., Wang, S., Ramirez, J. G., et al., Appl. Phys. Lett. 102, 1 (2013); [2] de la Venta, J., Wang, S., Saerbeck, T., et al., Appl. Phys. Lett. 104, 062410 (2014). [3] Valmianski, I., Fraile Rodríguez, A., Rodríguez-Alvarez, J., et al., (in review). [4] McLeod, A. S., Van Heumen, E., Ramirez,

J. G., et al. Nat. Phys. 13, 80 (2017). [5] Gilbert, D. A., Ramirez, J. G., Saerbeck, T., et al., Sci. Rep. 7 13471 (2017).

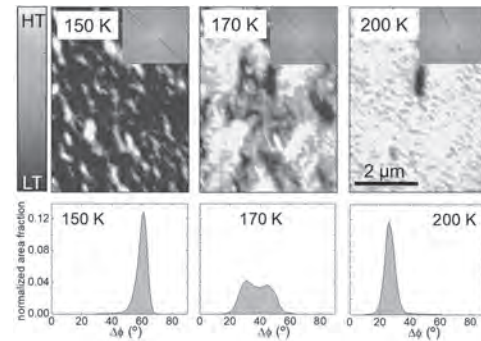


Fig. 1. Top row panels show representative XMCD-PEEM images recorded at temperatures below (150 K), across (170 K) and above (200 K) the SPT of V_2O_3 . The insets show their Fourier transforms. The initial state (blue contrast) at low temperature (LT) splits into a pattern of small domains (yellow) which progressively rotate and grow across the V_2O_3 SPT as the high-temperature (HT) phase is reached. Bottom row panels show histograms of the absolute value of the average rotation angle of the Ni magnetization, Df , at selected temperatures (calculated from the images in the top row). Sharp Df distributions are found for the LT (150 K) and HT (200 K) phases in contrast to broader distributions in the middle of the V_2O_3 SPT (170 K).

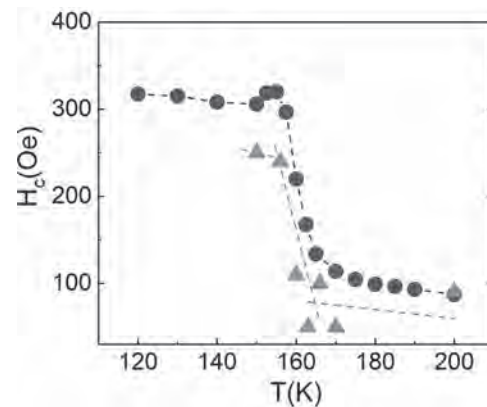


Fig. 2. Coercivity as a function of temperature of Ni(10 nm)/ V_2O_3 (100 nm) across the V_2O_3 SPT recorded while cooling the sample from 300 K to 120 K (only data from 200 K are shown). A sharp rise in the coercive field, H_c , of about a factor of four, is found as the temperature goes below the V_2O_3 SPT. The garnet circles represent the coercivity values obtained from the experimental loops while the green triangles correspond to those obtained from micromagnetic simulations.

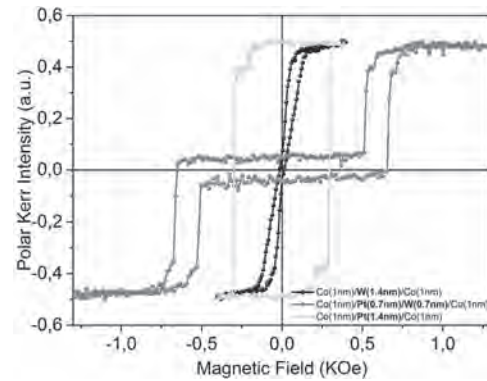
IG-02. Magnetic Anisotropy, Interlayer Coupling and Dzyaloshinskii-Moriya Interaction in Epitaxial W/Co/Pt Multilayers.

S.K. Jena¹, M.M. Jakubowska¹, E. Milinska¹, A. Pietruczik¹,
P. Aleszkiewicz¹ and A. Wawro¹

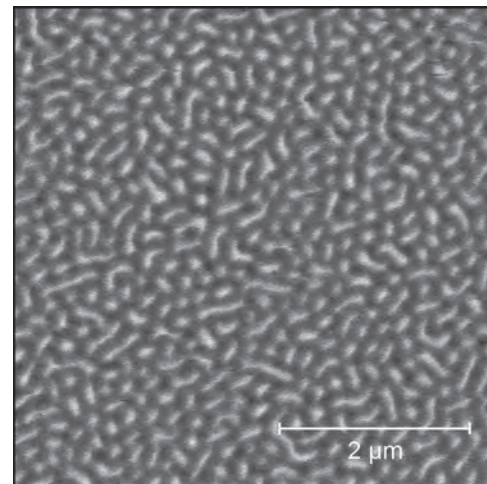
¹. Institute of Physics, Polish Academy of Sciences, Warsaw, Poland

Systematic studies of magnetic properties observed in epitaxial W/Co/Pt layered structures grown by molecular beam epitaxy are discussed. In this system contributions to interfacial Dzyaloshinskii-Moriya interaction (DMI) from the asymmetric interfaces between ferromagnet (Co) and non-magnetic heavy metals with high spin-orbit coupling (W or Pt) are of additive nature. DMI can stabilize the chiral magnetic texture, vortex and skyrmions, being promising in future data storage technology. Presented progressive investigations encompass layered structures containing: a single Co layer (magnetic anisotropy), two Co layers (interlayer coupling) and multilayers (dipolar interactions, complex domain structure). Layered structures containing a single Co layer exhibit spin reorientation transition (SRT) with increasing thickness, d_{Co} , from perpendicular (perpendicular magnetic anisotropy, PMA) to in-plane aligned magnetisation. The range of d_{Co} with PMA and the critical thickness d_{SRT} depend on the type and sequence of adjacent covers. In the Pt/W/Co/Pt system d_{Co} range with PMA shifts towards higher values (from 0.6-0.9 nm to 2.1-2.4 nm) with increasing bottom W layer thickness, d_W , from 2.4 nm to 8.0 nm. This behaviour differs from the similar system with Mo component layer, studied earlier [1]. Hysteresis loops measured by polar magneto-optical Kerr effect (PMOKE) magnetometry exhibit shapes typical of fine domain structure with perpendicular magnetisation. In the W/Co(1.0 nm)/Pt(d_{Pt})/W(d_W)/Co(1.0 nm)/Pt interlayer antiferromagnetic coupling of perpendicular magnetization with the strength as high as 0.6 kOe is very distinct for the component spacers of equal thickness, $d_{Pt} = d_W$, in the range between 0.7 and 1.1 nm. For $d_W \neq d_{Pt}$ (keeping the same total thickness $d_W + d_{Pt}$) the coupling strength decreases. Particularly, the single spacer systems (Pt or W; d_{Pt} or d_W kept in the corresponding range from 1.4 nm to 2.0 nm) do not exhibit such feature, indicating a crucial role of the complex spacer structure affecting both coupling and PMA (Figure 1). The multilayer structures W/Co($0.6 < d_{Co} < 1.0$ nm)/Pt (10-20 repetitions) are magnetised in perpendicular direction to the film plane and display at the remanent state typical labyrinth domain structure with tendency towards bubble domains formation with diameter of around 75 nm (Figure 2). DMI strength determined form (aligned) domain structure reaches the value of $D = 2.49$ mJ/m² [2]. Such high value of D is a result of high quality crystalline structure characteristic for epitaxial systems and additive contribution to DMI from asymmetric well-defined interfaces. The above discussed structures are compared to those with different component layer thickness and opposite sequence (i.e. Pt/Co/W). This work is supported by IEEE educational seed funding 2020 (beneficiary:-Sukanta Kumar Jena), Foundation for Polish Science (FNP) under the European Regional Development Fund – Program REINTEGRATION 2017 OPIE 14-20 and by the National Science Centre in Poland, projects no: 2016/23/G/ST3/04196 and 2020/37/B/ST5/02299.

[1] A Wawro *et al. J. Phys. D: Appl. Phys.* 50 215004 (2017). [2] S.K. Jena *et al.* to be submitted (2021).



“Fig.1” Hysteresis PMOKE loop from W/Co/Pt/W/Co/Pt layered structures composed of two Co (1nm) layers separated by the Pt/W spacer with total thickness of 1.4 nm showing distinct antiferromagnetic coupling (red). Corresponding structures with a single spacer: W (black) or Pt (green) 1.4 nm thick do not exhibit such coupling.



“Fig.2” Magnetic force microscopy image from as grown W/Co/Pt multilayer with basic trilayer repetition number equal to 20.

IG-03. Structural and Magnetic Characterization of Epitaxial Co(10.0)/Pt(110) Multi-Layers for Future Anisotropic DMI Systems Based on C_{2v} Symmetry.

M.D. Kitcher¹, Y. Liu¹, M. De Graef¹ and V.M. Sokalski¹

¹. Materials Science & Engineering, Carnegie Mellon University, Pittsburgh, PA, United States

The interfacial Dzyaloshinskii-Moriya Interaction has had profound consequences on the possible magnetic configurations that can be stabilized in multi-layer thin films, most notably chiral Neel skyrmions and domain walls. [1] More recently, there have been theoretical calculations and experimental work confirming the existence of an appreciable anisotropic DMI in epitaxial thin films with further reduced symmetry – namely the C_{2v} (or $mm2$) point group. [2] However, so far the systems under consideration have been based on cubic crystals where the magnetocrystalline anisotropy is nearly isotropic. Here, we identify a new epitaxial relationship with C_{2v} symmetry based on HCP Co(10.0)/FCC Pt(110). Although it is quite common to grow FCC Co(111)/Pt(111), for the case of a Pt(110) underlayer, the lattice mismatch is actually smaller for the HCP Co(10.0) orientation [as opposed to FCC Co(110)] where the c-axis lies along a single direction in the plane of the film (figure 1). Such an orientation is expected to offer some degree of anisotropic DMI based on the heavy metal Pt and reduced symmetry as well as the added feature of significant uniaxial in-plane magnetocrystalline anisotropy. Samples were prepared by DC magnetron sputtering on HF-etched Si(110) single crystal substrates. Following the work of Yang et al., we use a Ag (10nm) buffer layer, which is known to grow with (110) orientation on Si(110) at room temperature, thereby avoiding further unwanted interface diffusion. [3] This is followed by deposition of the Pt (10nm) /Co (10-50nm) bilayers, which are the focus of this work. All depositions were done in an Ar atmosphere with the working pressure fixed at 2.5 mTorr. The films were characterized structurally by standard $\theta/2\theta$ x-ray diffraction (XRD) measurements and phi-scans to characterize the epitaxial relationship. The XRD scan shows primarily Ag(220), Pt(220), and Co(10.0) peaks with no identifiable Co(220) peak suggesting the film is predominantly HCP. Phi scans (figure 2) on Pt(111), Ag(111), and Co(10.1) confirm the epitaxial relationship shown in figure 1. Moreover, reciprocal space q-scans on the HCP Co spots were leveraged to characterize directional peak broadening due to stacking faults. As it is known that stacking faults cause broadening only of certain peaks ($h-k \neq 3m$) along the c^* direction (with breadth also determined by the parity of l), it is possible to extract the density of growth and deformation faults in the Co layer, which are found to be approximately 10% and 3% respectively in 50nm Co films. Details on how these stacking fault densities are calculated will be presented in detail. Alternating gradient field magnetometry was used to measure M-H loops along different crystallographic directions in the plane of the film. A clear in-plane easy axis is identified along Si[001] (parallel to Co[0001]). The hard axis saturation field of 1.5 kOe suggests a notably smaller magnetocrystalline anisotropy than would be expected for bulk cobalt, likely due to the aforementioned stacking faults. Although the relatively thick Co layer in these films makes any interface induced DMI unlikely, the epitaxial relationship is expected to be preserved in thinner samples along with the reported uniaxial anisotropy. Together with the expected interfacial anisotropic DMI, this in-plane anisotropy makes the proposed material system an interesting playground for exploring new chiral magnetic ground states.

[1] Thiaville, A., Rohart, S., Jué, É., Cros, V. and Fert, A., 2012. Dynamics of Dzyaloshinskii domain walls in ultrathin magnetic films. *EPL (Europhysics Letters)*, 100(5), p.57002. [2] Hoffmann, M., Zimmermann, B., Müller, G.P., Schürhoff, D., Kiselev, N.S., Melcher, C. and Blügel, S., 2017. Antiskyrmions stabilized at interfaces by anisotropic Dzyaloshinskii-Moriya interactions. *Nature communications*, 8(1), pp.1-9. [3] Yang, W., Lambeth, D.N. and Laughlin, D.E., 1999. Unicrystal Co-alloy media on Si (110). *Journal of applied physics*, 85(8), pp.4723-4725.

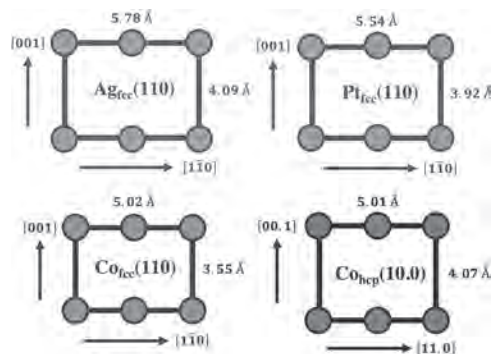


Fig 1. Schematic of the lattice matching for Ag(110)/Pt(110) with bottom left) FCC Co(110) or bottom right) HCP Co(10.0). The HCP (10.0) orientation has a better match along the Pt [001] direction.

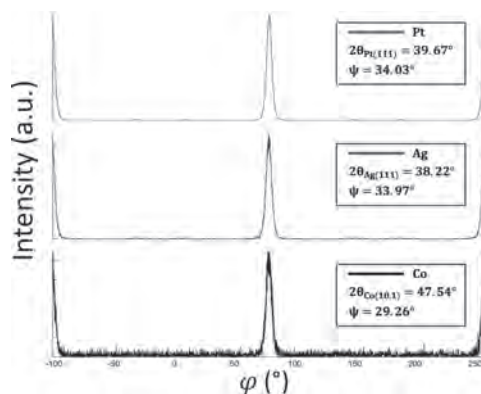


Fig 2. Phi scans for Pt (111), Ag (111), and Co (10.1) confirming the epitaxial relationship shown in figure 1.

IG-04. Skyrmions in 3D Soft Magnetic Nanodots With no Dzyaloshinskii-Moriya Interactions.

E. Berganza², J. Fernandez-Roldan³, M. Jaafar⁴, A. Asenjo¹, K. Gusliencko⁵ and O. Chubykalo-Fesenko¹

1. Instituto de Ciencia de Materiales de Madrid, Madrid, Spain; 2. Institute of Nanotechnology, Eggenstein-Leopoldshafen, Germany; 3. Universidad de Oviedo, Oviedo, Spain; 4. Universidad Autonoma de Madrid, Madrid, Spain; 5. Universidad del Pais Vasco - Campus Gipuzkoa, Donostia, Spain

Skyrmions typically appear in systems with perpendicular magnetic anisotropy (PMA) and Dzyaloshinskii-Moriya interactions (DMI). Bloch skyrmion states can be stabilized in magnetic dots with no need of DMI [1]. However, PMA is typically considered to be necessary. Nanoparticle geometry is an additional important factor for the skyrmion stabilization due to the influence of magnetostatic energy. Therefore, the sample shape (e.g. spherical) can result in stabilization of the skyrmions [2]. Recently, stabilization of the half-hedgehog skyrmions in soft magnetic (Permalloy) hemispherical dots by the MFM tip was demonstrated [3]. Here we conduct micromagnetic simulations in 3D soft magnetic dots with planar (cylindrical) or curved (spherical cap) geometry with neither PMA nor DMI. The geometries of both magnetic elements correspond to the base radius 60-120 nm and the aspect ratio thickness/ radius ranged from 0.4 to 2 and magnetic parameters of permalloy. In a wide range of the dot sizes, we observed the co-existence of multiple magnetic states. Particularly, in the spherical caps we stabilized for the same geometry, the in-plane, the out-of-plane (flower-like), the 3D vortex-like (Bloch skyrmion), the 3D Néel skyrmion -like (see Fig.1) and the Bloch point-like states. The Bloch skyrmion is characterized by a vortex configuration in the basal plane while the Néel-like skyrmion - by the radial vortex configuration and is similar to the half hedgehog structure. The existence of magnetic skyrmions without DMI or PMA in cylindrical nanodots was demonstrated by analytical calculations using the Belavin-Polyakov ansatz [4]. Both Néel and Bloch (vortex-like) skyrmions structures have been proven to be metastable or stable states in some range of dot sizes. The Néel skyrmion always has larger energy than the Bloch skyrmion. Direct micromagnetic simulations confirm the co-existence of both types of skyrmions, although in a smaller range of geometrical parameters than predicted by analytical calculations. In spherical caps, the curved geometry provides an additional factor for the Néel skyrmion stabilization which was obtained for a wide range of geometrical parameters. Typically, the Néel skyrmion has the largest energy of all structures, however its energy decreases as a function of the cap basal diameter and aspect ratio. Consequently, for some geometrical parameters we found a Néel skyrmion having smaller energy than that of the Bloch skyrmion. The spherical geometry also leads to a coupling between the skyrmion polarization and radial magnetization components, so that only the skyrmions with positive Polarity (P) and outward chirality (Q) or negative polarity and inward chirality are possible, see Fig. 1 Finally, we present the state diagram for skyrmions in soft magnetic caps and nanopillars. We have also calculated 2D topological charges and the gyrovectors values, both depending on the geometrical parameters.

[1] K. Gusliencko, K. Y. IEEE Magn. Lett. Vol. 6, p.4000104 (2015) [2] V.P. Kravchuk et al Phys. Rev. B, Vol. 85, p.144433 (2012). [3] E. Berganza et al, Nanoscale, Vol.12, p.18646 (2020) [4] A. A. Belavin and A. M. Polyakov, Pis'ma Zh. Eksp. Teor. Fiz. Vol. 22, p. 503 (1975).

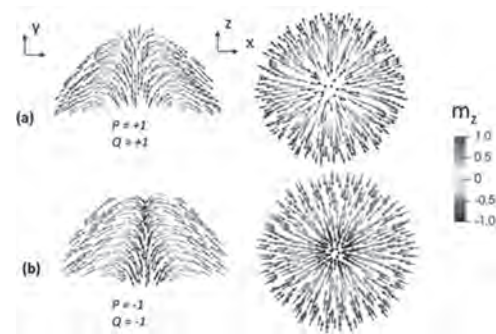


Figure.1 (a-b) Chiral (Neel-like) skyrmion magnetic configurations in permalloy caps with diameter 60 nm and height 30 nm colored by the axial-component m_z . Left and right figures are cross sections in the XZ plane and in the XY basis plane respectively. P and Q stand for the polarity and the chirality of the skyrmion respectively.

IG-05. Exchange Spring Co-Rich CoP Nanomagnetic Thin Films.

A. Samanta^{1,2} and S. Roy^{1,2}

1. Micropower Systems & Nanomagnetics Group, Micro-Nano-Systems Center, Tyndall National Institute, Cork, Ireland; 2. Department of Physics, University College Cork, Cork, Ireland

Exchange-spring nanomagnets [1–3] are composed of the interaction of the magnetic exchange coupling between magnetically hard and soft phases. Such frameworks are promising for cutting edge perpetual magnetic applications, as they have a high energy product - the mix of permanent magnetic field and magnetization - contrasted with the conventional, single-phase magnetic materials. Hence, for the last three decades, these exchange spring nanomagnets have taken the keen attention of the scientific community. However, the necessary condition that both the hard and soft phases are controlled at the nanometer scale, to ensure effective exchange coupling, has posed significant preparation challenges. In pursuit of preparing multi-nano-layered-structured nanomagnetic material, sputtering, electron beam lithography/ evaporation (EBL/EBE) have inspired a wealth of experimental results. However, to date, there is a very limited experimental understanding of preparing *in situ* multilayered nanomagnetic material using electrodeposition technique and the elucidation of their magnetic behavior. Towards this end, using electrodeposition technique with a modified and stable acidic bath chemistry at room temperature, we have prepared *in situ* multilayered nanomagnetic cobalt phosphorus (CoP) thin film and investigated its characteristics structurally and magnetically combined with micromagnetic simulation utilizing MuMax³. Despite the availability of various techniques, the electrodeposition technique [4–7] has been chosen for the preparation of the nanomagnetic cobalt phosphorous thin films at room temperature using acidic bath chemistry due to its relatively higher deposition rate and low cost. Here, the crossover from the exchange spring structure to exchange coupled structures by the manipulation of thickness in nanometer level in a single amorphous system of cobalt phosphorus nanomagnetic thin film has been demonstrated. We have characterized the developed smooth, stress-free, and shiny electroplated samples structurally by XRD (shown in FIG. 1), SEM, and magnetically by the hysteresis loop tracer (ShB Instruments, USA). The SEM micrographs confirm the fine grain surface morphology of the cobalt phosphorous nanomagnetic thin films. The XRD analysis further ensures the amorphousness of the thin film, as in the XRD pattern, the three dominating peaks only appears from the substrate, i.e., the largest peak near $2\theta = 69.22^\circ$ is due to the Si-wafer and the rest of the two peaks near $2\theta = 38^\circ$ and 83° are from the top conducting seed layer of gold (Au). The elemental analysis by energy dispersive X-Ray (EDX) yields the stoichiometry of the electrodeposited cobalt phosphorous. An optimum exchange coupling can be obtained by tuning the spin configuration with respect to the multi-nano layer thicknesses. The static in-plane magnetic measurement by the hysteresis loop tracer shown in FIG. 2 reveals different hysteresis loops of electrodeposited CoP thin film. FIG. 2(a) confirms the exchange spring amorphous cobalt phosphorus films with a relatively higher coercivity of ~ 197 Oe for $0.68 \mu\text{m}$ CoP thin film while the FIG. 2(b) affirms the flat hysteresis loop with a coercivity of 162 Oe for the $11.54 \mu\text{m}$ thick CoP thin film which signifies the exchange coupled structure. Utilizing the finite difference method-based freely available GPU-accelerated micromagnetic simulator, MuMax³ [8], we have also verified the experimentally obtained results further by doing a micromagnetic simulation. Considering the typical magnetic material parameters (i.e., Saturation Magnetization (M_s) as obtained from the static measurement, Exchange Stiffness Constant (A_{ex}), Anisotropy Constant (K_{eff})), MuMax³ solves the well-known Landau-Lifshitz-Gilbert (LLG) equations, and so forth gives the static micromagnetic evolution of the nanomagnetic thin films. To proceed with the simulation, we have discretized the overall amorphous cobalt phosphorous thin film into the cells of dimension $5 \times 5 \times 5 \text{ nm}^3$. To include all the exchange interactions in the static magnetization of nanoscale thin film, this cell size in each direction is considered lower than the exchange length ($l_{\text{ex}} = 5.1 \text{ nm}$) of the system, as well as to precisely reproduce the nanomagnetic impression of the thin film under study. The dimensions of the whole atlas we used for the simulation are ($l \times w \times t = 8000 \times 6000 \times 5400 \text{ nm}^3$), where l , w , and t are the length, width, and thickness of the atlas, respectively. Finally, we report the micromagnetic spin configuration at every coordinate point within the

nanomagnetic thin film at every instant of field determined by the simulator, which confirms the formation of a multidomain state from a single domain state (shown in FIG. 2(e))

- [1] E. F. Kneller and R. Hawig, IEEE Trans. Magn. 27, 3560 (1991). [2] E. E. Fullerton, J. S. Jiang, M. Grimsditch, Phys. Rev. B 58, 12193 (1998). [3] H. Zeng, J. Li, J. P. Liu, Z. L. Wang, Nature 420, 395 (2002). [4] P. McCloskey, B. Jamieson, T. O'Donnell, J. Magn. Mater. 320, 2509 (2008). [5] P. McCloskey, B. Jamieson, T. O'Donnell, J. Magn. Mater. 322, 1536 (2010). [6] P. McCloskey, T. O'Donnell, B. Jamieson, in *Handb. Nanoelectrochem. Electrochem. Synth. Methods, Prop. Charact. Tech.*, 2016, pp. 1–27. [7] S. Roy, A. Connell, M. Ludwig, J. Magn. Mater. 290–291, 1524 (2005). [8] A. Vansteenkiste, J. Leliaert, M. Dvornik, AIP Adv. 4, 107133 (2014).

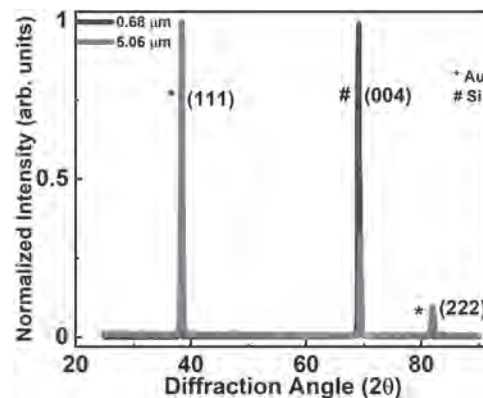


FIG. 1. XRD of $0.68 \mu\text{m}$, $5.06 \mu\text{m}$ thick electrodeposited thin films having only the substrate peaks (i.e., Au and Si) confirms the amorphousness of the samples.

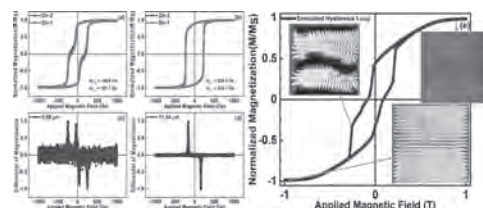


FIG. 2. Hysteresis loop of the electrodeposited CoP thin films measured in XY plane, and here, $\text{dir-1} + 90^\circ = \text{dir-2}$. The thickness of the films is (a) $0.68 \mu\text{m}$, (b) $11.54 \mu\text{m}$. (c)–(d) The differential of the magnetization of the (a) $0.68 \mu\text{m}$, (b) $11.54 \mu\text{m}$ thick CoP thin films, respectively. (e) Simulated Hysteresis Loop and different micromagnetic spin configurations at different coordinates of the hysteresis loop.

IG-06. Competing Magnetic Anisotropies and Spin Reorientation in Phase-Segregated Single Layer Ferrimagnetic FeGd Films.

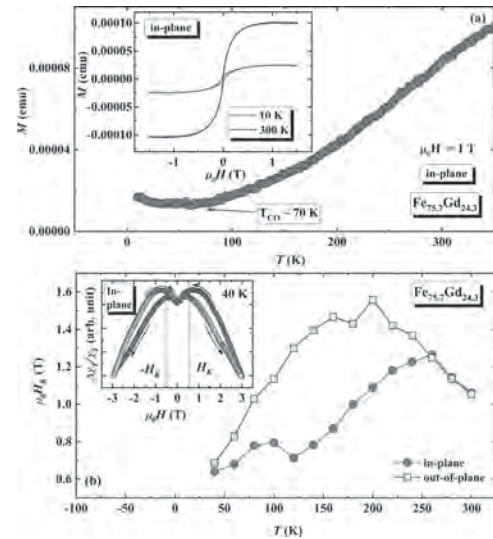
A. Chanda¹, J.E. Shoup¹, N. Schulz¹, D. Arena¹ and H. Srikanth¹

1. Physics Department, University of South Florida, Tampa, FL, United States

Controlled manipulation of spin texture in magnetic materials by external means, e.g., magnetic and electric fields, temperature etc., is a prerequisite for the cutting-edge spintronic applications. Magnetic materials with perpendicular magnetic anisotropy (PMA) are of special interest because of their wide-ranging functionalities starting from applications in magnetoresistive random access memory (MRAM) devices to modulation of topological spin textures. Recently, there has been a growing interest in rare earth (RE)-transition metal (TM) alloy thin films due to their tunable spin configurations as a function of temperature and RE content. For example, GdFeCo shows in-plane spin configuration at room temperature, but PMA occurs near the compensation temperature (T_{CO}). [1] Such spin reorientation is generally attributed to competition between PMA and shape anisotropy. In order to understand the behaviour of magnetic anisotropy around the spin reorientation temperature, several indirect methods were employed to determine the temperature dependence of anisotropy fields, e.g., longitudinal and polar MOKE, FMR etc. [1] Here, we examined the spin reorientation in single layer ferrimagnetic alloy thin films of FeGd by dc magnetometry and radio frequency transverse susceptibility measurement, which is a direct method to determine the effective anisotropy fields. The FeGd system belongs to the RE-TM family and is particularly interesting as T_{CO} of this system can be tuned by varying the chemical composition. We prepared the Fe_xGd_{100-x} (90 nm)/Ta(8 nm) films onto a Si substrate coated with a 10 nm Ta layer using RF and DC sputtering; we focus below on a nominal composition of $Fe_{75.7}Gd_{24.3}$. From the temperature dependence of the in-plane magnetization $M(T)$ curve, T_{CO} for the $Fe_{75.7}Gd_{24.3}$ film was estimated to be ~ 70 K (main panel of Fig. 1(a)). Inset of Fig. 1(a) depicts the in-plane $M(H)$ loops for this film measured at $T = 10$ and 300 K. While the in-plane saturation magnetization has drastically dropped between 300 and 10 K, the coercivity is enhanced significantly. In addition, the ratio of remanent magnetization to the saturation magnetization is an order of magnitude higher at 10 K than at 300 K. These observations indicate the occurrence of spin reorientation between 10 and 300 K. In order to probe the spin reorientation, we performed magnetic field dependent transverse susceptibility (TS) measurements for both in-plane and out-of-plane configurations at different temperatures between $T = 300$ and 10 K. Our TS measurement set up exploits a self-resonant ultra-sensitive tunnel diode oscillator circuit with a resonant frequency of 13 MHz and is a highly sensitive technique to precisely determine the effective anisotropy fields. [2] The inset of Fig. 1(b) shows the magnetic field dependence of the relative change in TS at 40 K for the $Fe_{75.7}Gd_{24.3}$ for in-plane configuration. As the dc magnetic field is swept from positive to negative saturation, the first (second) peak to positive (negative) anisotropy field (H_K). As shown in the main panel of Fig. 1(b), H_K remains the same for in-plane and out-of-plane configurations but begins bifurcating below 250 K. At lower temperatures, the out-of-plane H_K shows a broad maximum between 200-150 K and then decreases smoothly. On the other hand, the in-plane H_K continues to decrease down to 100 K below which it shows a small plateau around T_{CO} and then decreases gradually. These observations indicate that the spin configuration in the system changes from a combination of in-plane and out-of-plane spins with equal contributions above 250 K, to a combination of in-plane and out-of-plane spins with a major contribution by the out-of-plane spins below 250 K. The origin of such temperature-driven spin reorientation might be related to phase-segregation. With the help of scanning transmission electron microscopy equipped with energy dispersive x-ray spectroscopy (STEM-EDS) and x-ray reflectivity (XRR) measurements, a recent study shows that modulation of chemical composition occurs in FeGd films with thickness more than 20 nm where Fe is partially diffused to the adjacent Ta layer. [3] Since the thickness of our film is ~ 90 nm, it is possible that there are different Fe-deficient (Gd-rich) regions which are separated by regions with nominal chemical composition. In such a hybrid phase-segregated spin system, different regions have distinct spin configurations and hence, different orientations of magnetic anisotropy. We have also performed out-of-plane $M(H)$ measurements on

the $Fe_{75.7}Gd_{24.3}$ film that showed a double-step reversal behaviour below 250 K and hence, confirms the chemical phase-segregation in our system. The spin reorientation in our system is thus determined by the competition between local magnetic anisotropy energies of adjacent phase-segregated regions. Our TS technique determines the average behaviour of the local anisotropy field and hence effectively probes the spin reorientations in these micron-scale phase-segregated magnetic systems. Results for other Fe/Gd compositions will also be discussed.

[1] W. He, H. -L. Liu, H.-Y. Wu, J. -W. Cai, and Z. -H. Cheng, Appl. Phys. Lett. 106, 042401 (2015). [2] V. Kalappattil, R. Geng, R. Das, M. Pham, H. Luong, T. Nguyen, A. Popescu, L. M. Woods, M. Kläui, H. Srikanth and M. H. Phan, Mater. Horiz. 7, 1413-1420 (2020). [3] E. Kirk, C. Bull, S. Finizio, H. Sepehri-Amin, S. Wintz, A. K. Suszka, N. S. Bingham, P. Warnicke, K. Hono, P. W. Nutter, J. Raabe, G. Hrkac, T. Thomson and L. J. Heyderman, Phys. Rev. Mater. 4, 074403 (2020).



(a) Main panel: in-plane $M(T)$ of $Fe_{75.7}Gd_{24.3}$ measured in 1 T field and inset: in-plane $M(H)$ loops at 10 and 300 K, (b) main panel: in-plane and out-of-plane $H_K(T)$, inset: field dependent TS curve at 40 K for in-plane configuration.

IG-07. Beating the Limit of Ordering Temperature of FeO With Antiferromagnetic Proximity in FeO/CoO.

M. Szpytma¹, A. Koziol Rachwal¹, J. Korecki^{1,2}, M. Slezak¹, P. Drozd¹, W. Janus¹, H. Nayyef¹, M. Zajac³ and T. Slezak¹

1. AGH University of Science and Technology, Krakow, Poland; 2. Polish Academy of Sciences, Institute of Catalysis and Surface Chemistry, Krakow, Poland; 3. National Synchrotron Radiation Centre Solaris, Jagiellonian University, Krakow, Poland

Antiferromagnets (AFMs), due to their unique set of properties, are promising candidates for future spintronic materials. However, their low ordering temperature makes a wide group of AFM materials not applicable. Hence, tuning ordering temperature and spin configuration due to magnetic proximity effect in AFM/AFM systems has been recently identified as an important field of research [1]. In our studies we investigated how the proximity of antiferromagnetic layer with a higher ordering temperature (Néel temperature, T_N) influences the T_N of FeO in FeO/CoO bilayer. The layers were grown by molecular beam epitaxy on MgO(001) substrate coated with a 5 nm-thick homoepitaxial MgO buffer. CoO layer with a thickness of 2 nm was prepared by reactive deposition of Co in a molecular oxygen atmosphere under a pressure of 1×10^{-6} mbar. FeO layer was deposited by reactive deposition of 1 nm of Fe under oxygen pressure of 5×10^{-8} mbar, which corresponds to about 1.7 nm of stoichiometric wüstite (FeO). To enable Mössbauer spectroscopy (MS) studies we used ^{57}Fe isotope during FeO deposition. The sample was capped with 3 nm of MgO. To compare magnetic properties of wüstite in FeO/CoO bilayer with a single FeO layer a MgO/FeO/MgO sample was prepared. The magnetic properties of FeO were studied with Conversion Electron Mössbauer Spectroscopy (CEMS). CEMS measurements were obtained in temperature controlled cryostat under UHV conditions with use of a channeltron detector connected to a standard Mössbauer spectrometer and a $^{57}\text{Co}(\text{Rh})$ source irradiating the sample at normal incidence. Figure 1 shows CEMS spectra collected at 240 K for MgO/ ^{57}FeO /MgO (Fig. 1(a)) and MgO/ ^{57}FeO /CoO/MgO (Fig. 1(b)). The temperature of 240 K is far above the T_N of FeO (198 K) [2]. The spectrum of FeO (Fig. 1(a)) is characteristic for bulk wüstite in paramagnetic state [3]. It was fitted by two quadrupole sites, which describe the octahedrally coordinated Fe^{2+} (Q_1) atoms and Fe^{2+} atoms neighbouring defects (Q_2). Interestingly, proximity of CoO causes a serious modification of the spectrum, it becomes magnetically split. Similar spectrum was recorded for MgO/FeO/MgO under the T_N (not shown). Systematic measurement of CEMS spectra recorded as a function of temperature for FeO/CoO revealed that the magnetic character of spectrum is preserved up to 260 K. Thus, proximity of CoO layer induces enhancement of the T_N of FeO up to 260 K. To determine T_N of CoO in FeO/CoO bilayer we performed X-ray Magnetic Linear Dichroism (XMLD) measurements [4]. X-ray absorption spectra (XAS) were collected using a linearly polarized x-rays for two grazing incident angles (0° and 60°) as a function of temperature. XMLD effect observed at the Co L_3 edge can be attributed to the AFM ordering in CoO. Thus, R_{L_3} difference (ΔR_{L_3}) described as $\Delta R_{L_3} = R_{L_3}^{0^\circ} - R_{L_3}^{60^\circ}$, where $R_{L_3}^{0^\circ}$ and $R_{L_3}^{60^\circ}$ are defined as the ratio of the intensities of the XAS peaks at 777 eV and 779.6 eV for grazing incident angles of 0° and 60° , respectively is a measure of AFM ordering in CoO. The AFM contribution to $\Delta R_{L_3}(T)$ decreases with an increase of temperature and vanishes above T_N . The inset in Figure 1 shows $\Delta R_{L_3}(T)$ dependence obtained for CoO in MgO/FeO/CoO/MgO multilayers. We noted positive ΔR_{L_3} values, which indicates in-plane alignment of CoO AFM spins in FeO/CoO/MgO [5,6]. Dependence of ΔR_{L_3} on temperature is negligible for $T \geq 290$ K. Thus, the ordering temperature of CoO layer in FeO/CoO/MgO stack is comparable to the T_N of bulk CoO (293 K). Enhancement of ordering temperature of FeO should result in increase in exchange interaction between ferromagnetic (FM) layer and FeO in FM/FeO/CoO multilayer. To elucidate how AFM proximity effect influence exchange interaction with FM a dedicated sample was prepared for which Fe(1 nm)/FeO bilayer was grown on wedge shaped CoO. Figure 2 presents the product of exchange bias field (defined as $H_{\text{EB}} = (H_{\text{C1}} - H_{\text{C2}})/2$, where C1 and C2 represent respectively the coercive fields of ascending and descending branches of hysteresis loop) and CoO layer thickness d_{CoO} as a function of temperature obtained for different CoO thicknesses. The values of H_{EB} were determined from the magnetic hysteresis loops measured with longitudinal magneto-optic Kerr

effect (LMOKE). While for Fe/FeO/CoO(0.7 nm) we noted vanishing of $H_{\text{EB}} \cdot d_{\text{CoO}}$ at around 220 K (so called blocking temperature, T_B), for $d_{\text{CoO}} > 2$ nm T_B was established at around 260 K, which is much greater than a blocking temperature of Fe/FeO bilayer (160 K). Our study demonstrates the feasibility of tailoring the magnetic properties of AFM layer with a proximity of other AFM. This work was supported by the "Antiferromagnetic proximity effect and development of epitaxial bimetallic antiferromagnets – two routes towards next-generation spintronics" project, which is carried out within the Homing programme of the Foundation for Polish Science co-financed by the European Union under the European Regional Development Fund.

[1]. S. Fukami et al., Journal of Applied Physics 128 070401 (2020) [2] K. Koike, T. Furukawa, Physical Review Letters 77 3921 (1996) [3] A. Koziol-Rachwal et al., Applied Physics Letters 108 041606 (2016) [4] https://synchrotron.uj.edu.pl/en_GB/linie-badawcze/peem-xas [5] J. Zhu et al., Physical Review B 90 054403 (2014) [6] Q. Li et al., Scientific Reports 6 22355 (2016)

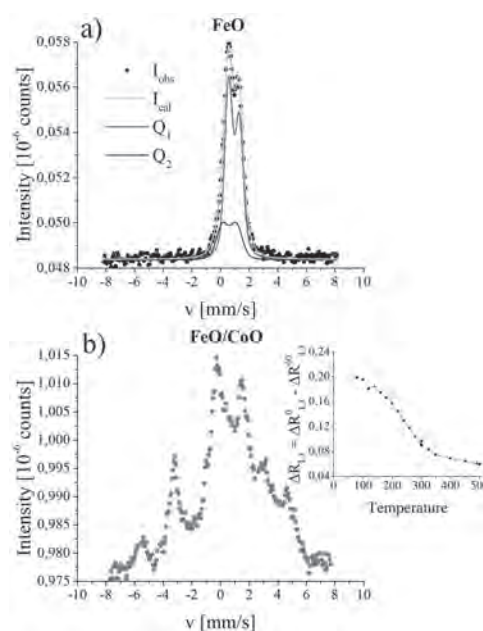


Fig. 1 CEMS measurements of FeO (black points) in MgO/FeO/MgO and MgO/FeO/CoO at 240 K. Inset represents $\Delta R_{L_3}(T)$ dependence for CoO in FeO/CoO/MgO(001).

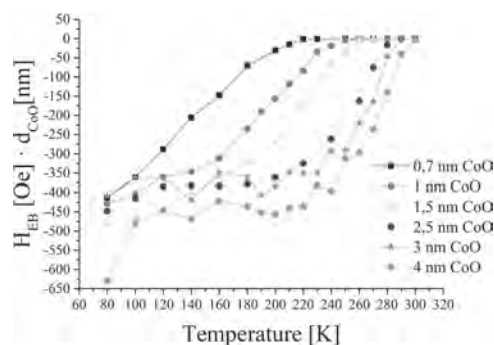


Fig. 2 $H_{\text{EB}} \cdot d_{\text{CoO}}(T)$ obtained from LMOKE measurements for MgO/Fe/FeO/CoO/MgO(001) for different CoO thicknesses. Lines are guides for the eye.

IG-08. Disorder by Design in an Artificial Spin Ice With Dipolar Interactions: an Energetic Analysis.

M. Di Pietro Martínez¹

1. Physique du Métal, Sciences et Ingénierie des Matériaux et des Procédés, Saint Martin d’Hères, France

Artificial spin ice (ASI) consists of a lithographically manufactured two-dimensional array of ferromagnetic nanoislands with a strong shape anisotropy resulting in single-domains that behave like giant Ising spins. In natural spin ices, such as, for example, the rare earth pyrochlore $\text{Ho}_2\text{Ti}_2\text{O}_7$, the local ordering of magnetic moments is particularly difficult to measure [1]. Despite the extraordinary advances in imaging techniques in the last decade, which allows us now to access the three-dimensional magnetic nanostructure of micrometric bulk samples [2], we still need to work together with simplified models to understand more about the underlying physics that governs these highly complex systems. In that direction, artificial frustrated magnetic systems allow us to test and reproduce theoretical models as well as to understand more about their three-dimensional analogs. But even more importantly, it allows us to design a system rather than discover it [3]. Here we study a squared artificial spin ice, with dipolar interactions, where there is a height separation h between the magnetic islands which are oriented perpendicularly [3, 4] (see Fig. 1). In a tetrahedral lattice, such as the one found in natural spin ices, the distance between any pair of spins (belonging to the same tetrahedron) is the same, and therefore, the dipolar energy has the same value for any pair. On the contrary, in the square ASI, the distance between collinear spins is different from the distance between perpendicular spins. Hence, the need to add this height parameter. In this way, this system is halfway between three-dimensional (natural) and two-dimensional (artificial) spin ices. The effect of disorder is still an open question and a field to study in ASI [1,4]. Budrikis *et al* (2012) study from the point of view of theory, simulations and experiments the influence of disorder on the response of the system to an external field [5]. To do this, in the simulations, they propose that each spin had an internal (coercive) field given by a Gaussian distribution. With this model, they manage to estimate the strength of disorder in a sample. There are several works that quantify the disorder, what is new in Budrikis’ work is that they also study how disorder affects the dynamics of ASI. Chern *et al* (2014) take this same idea to model disorder and study the avalanches and critical behavior in square and kagome ASI when a magnetic field is applied in-plane [6]. This system shows a phase transition out-of-equilibrium induced by disorder strength. Reichhardt *et al* (2015) show that the avalanche distributions of this process follow a power law [7]. Another way to include disorder in the system is to disconnect the islands by eliminating a given percentage of them at random. Greenberg *et al* (2018) show through simulations that this system changes its thermal behavior as the percentage of holes increases [8]. These results coincide with what was observed experimentally in diluted spin ice, once again showing that the study of ASI allows modeling and better understanding of the behavior of spin ice. Our aim is to study, through simulations and an energetic analysis, the effect of a geometrical quenched disorder by design on a square ASI. To do this, we propose to include disorder in the length of the magnetic islands. In this way, the strength of disorder could be easily controlled experimentally. As the system behavior depends on its geometrical parameters (a , h and d in Fig. 1), we focus on studying it in the proximity of the ice regime, where Type I and II vertices are equally likely (see Fig. 2). This regime is quite difficult to thermalize both in experiments and simulations. In this work, we show how length disorder affect the antiferromagnetic (all Type I vertices) and locally ferromagnetic (all Type II vertices) ordering, by inducing the system, in the case of weak disorder, to intermediate or mix states. An important result is that this means that disorder strength can be chosen and tuned to thermalize the ice regime. Moreover, in the case of strong disorder, ferromagnetic vertices prevail regardless of whether the mean length of the islands corresponds to an antiferromagnetic ordering. The energetic analysis let us understand the intermediate regimes that we found and also why disorder does not permit defects (Type III and IV vertices) at low temperatures in this model, contrary to expectations. Also, with this analysis, we show in detail how the ferromagnetic–antiferromagnetic transition with h is rounded by quenched disorder. Finally, we

found that disorder in the geometry causes a slowdown in the dynamics of the system which increases with disorder.

[1] C. Nisoli, R. Moessner and P. Schiffer, *Rev. Mod. Phys.*, Vol. 85, p. 1473 (2013) [2] C. Donnelly, M. Guizar-Sicairos, V. Scagnoli *et al*, *Nature*, Vol. 547, p. 328–331 (2017) [3] R. F. Wang, C. Nisoli, R. S. Freitas *et al*, *Nature*, Vol. 439, p. 303 (2006) [4] G. Möller and R. Moessner, *Phys. Rev. Lett.*, Vol. 96, p. 237202 (2006) [5] Z. Budrikis, J. P. Morgan, J. Akerman *et al*, *Phys. Rev. Lett.*, Vol. 109 p. 037203 (2012) [6] G. W. Chern, C. Reichhardt and C. Nisoli, *Appl. Phys. Lett.*, Vol. 104, p. 013101 (2014) [7] C. J. O. Reichhardt, G. W. Chern, A. Libál and C. Reichhardt, *J. Appl. Phys.*, Vol. 117, p. 172612 (2015) [8] N. Greenberg and A. Kunz, *AIP Adv.*, Vol. 8, p. 055711 (2018)

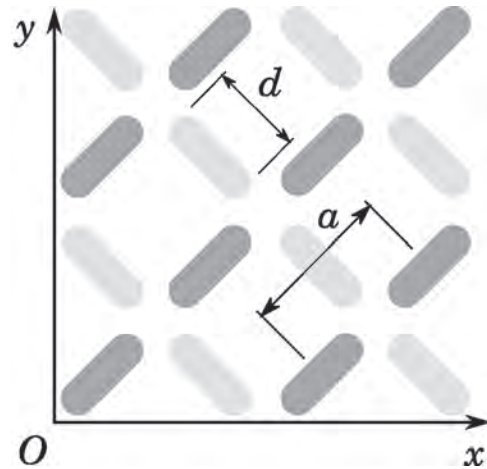


Fig. 1: Square artificial spin ice array with dipolar interactions: a is the lattice spacing and d is the island length; in this model, the width is considered negligible. There is a height separation h between the position of islands which are oriented in perpendicular directions; this means that dark-gray shaded islands are located at height $z = h$ while light-gray shaded islands are located at height $z = 0$.

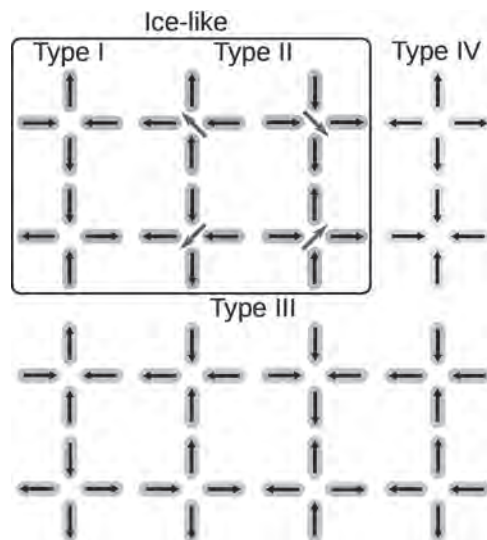


Fig. 2: The point where four islands concur is called a *vertex*. There are 16 possible configurations for each vertex of an squared ASI, according to the orientation of its spins. Furthermore, these can be classified into four different topological groups. Type I and II satisfy the so called *ice rule* (two spins point inwards the vertex and two point outwards), while Type III and IV do not. Type II and III vertices have a non-trivial net magnetization.

IG-09. Magnetisation Asymmetry in Exchange Bias Systems.

J. Gompertz¹, R. Carpenter², S. Hassan³ and K. O'Grady¹

1. Physics, University of York, University of York, York, North Yorkshire, GB, York, United Kingdom; 2. IMEC, Leuven, Belgium; 3. Seagate Technology LLC, Cupertino, CA, United States

There have been reports for different systems that there is an asymmetry in the saturation magnetisation in exchange bias systems [1, 2]. This report contains the first comprehensive study of these effects in the CoFe/IrMn system which is used in the read head of almost all HDDs [3]. The magnetic behaviour of exchange bias systems has two quasi-independent contributions [3]. The first contribution derives from the ferromagnetic (F) layer which in device applications is in the range 2 to 5 nm. This thickness produces the maximum loop shift when the structure is field cooled. However, it has been shown that there can be a further significant contribution to the magnetisation from spins lying at the interface which can have their origin either from the F layer or the antiferromagnetic (AF) layer. It has been shown that ordering of interface spins increases the loop shift by increasing the coupling between the F and AF layers and that doping the interface in the CoFe/IrMn system with atomic layers of the high-moment Mn can increase the spin ordering significantly [3, 4]. In this work the asymmetry in the saturation moment (m_s) and its temperature (T) dependence to <4.2 K have been measured for sputtered polycrystalline multilayer Si/Ta (2)/Ru (2)/IrMn (10)/Mn (d_{Mn})/CoFe (5)/Ru (5) (thicknesses in nm) thin films where $0 \leq d_{Mn} \leq 0.2$ nm in a LakeShore 8600 Series VSM. The York Model of Exchange Bias was used to separate and interpret the effect of the F/AF interface [3]. Low-temperature measurements were undertaken to ensure that the bulk of the AF grains remained magnetically frozen. Thus there was no reorientation of the magnetic moments in the bulk of the AF grains in subsequent measurements. The magnetisation of an exchange bias system undergoes an athermal training effect whereby the first and second magnetisation loops exhibit different loop shifts after the initial field cooling, even when the temperature of measurements is such that the moment of the bulk of the AF grain does not vary. This effect on the coercivity, which is defined as half loop width, has been shown to originate in the interfacial spins [5]. Figure 1 shows the measured hysteresis loop, the structure of which is shown in the inset, at 5.5 and 300 K. For the system measured we established by separate measurements (not shown) that the loop shift for the system shown was thermally stable at $T = 300$ K by holding the magnetisation at reverse saturation for a period of 30 mins after which time the hysteresis loop show at 300 K reproduced. In figure 1 the difference between the loops measured was due to changes in the orientation and ordering of interfacial spin clusters. The increase in the measured loop shift comes from ordering of spins at the interface. Furthermore, the first loop training effect is very small at $T = 300$ K but becomes significant at $T = 5.5$ K. This shows that the training effect is caused by interfacial spins, as is the coercivity. There is an asymmetry in the magnetisation. This data was obtained for the same sample without it being removed from the magnetometer. A significant increase in m_s occurs at 5.5 K, which is greater at negative saturation than is the case in a positive field. We designate this difference in m_s in positive (m_s^+) and negative (m_s^-) fields as $\Delta m_s = |m_s^+| - |m_s^-|$. (1) Figure 2 shows the temperature dependence of Δm_s for samples where there is a variation in the thickness of the Mn interface doping layer (d_{Mn}). It has been found that the optimum loop shift for this structure is affected by d_{Mn} and has been found to be a layer of subatomic thickness of the order of 1/6 of an atom. The use of layers of an atomic thickness or greater were found to result a reduction in Δm_s [4]. Figure 2 shows Δm_s for the first (i) and second (ii) loops measured immediately after the field annealing process. There is a change in the interfacial spin ordering which gives rise to the interface training effect but also effects the change in Δm_s . For all films figure 2 shows that the increase in Δm_s is small at $T > 100$ K. We attribute this to the interface spins not being ferromagnetically ordered and hence not responding to the modest fields used to measure the loops. Below 100 K the change in Δm_s with T becomes more rapid as it appears these spins become F ordered, probably in a spin cluster structure similar to a spin glass [6]. It appears that at <6 K Δm_s goes through a peak for all samples which is consistent with a spin cluster structure. It would be expected that d_{Mn} would not be optimum for a layer of subatomic thickness. It is most likely that the Mn layer is making a compositional adjustment

at the interface. In studies of a similar system by Baltz *et al.* using 3-D atom probe tomography on an exchange bias system containing Co and Mn significant diffusion was found to occur [7]. CoMn alloys have complex properties existing in both F, AF and superparamagnetic phases dependent on composition and temperature but no high resolution phase diagram has been determined [8]. In the production of an exchange bias system the field annealing requires up to 600 K which promotes interfacial diffusion [3, 7]. We conclude that the role of the Mn interface layer is to replace Mn deficiencies in the bulk of the AF.

[1] U. Nowak *et al.*, Phys. Rev. B, Vol. 66(1), p. 014430 (2002) [2] J. Keller *et al.*, Phys. Rev. B, Vol. 66(1), p. 014431 (2002) [3] K. O'Grady *et al.*, J. Magn. Magn. Mater., Vol. 322(8), p. 883-899 (2010) [4] R. Carpenter *et al.*, IEEE Trans. Magn., Vol. 48(11), p. 4351-4354 (2014) [5] R. Carpenter *et al.*, J. Appl. Phys., Vol. 115(17), p. 17D715 (2014) [6] J. L. Tholence and R. Tournier, Phys. B+C, Vol. 86-88, p. 873-874 (1977) [7] F. Letellier, *et al.*, J. Appl. Phys., Vol. 116, p. 203906 (2014) [8] A. Z. Men'shikov, *et al.*, Sov. Phys. JETP, Vol. 62, p. 734 (1985)

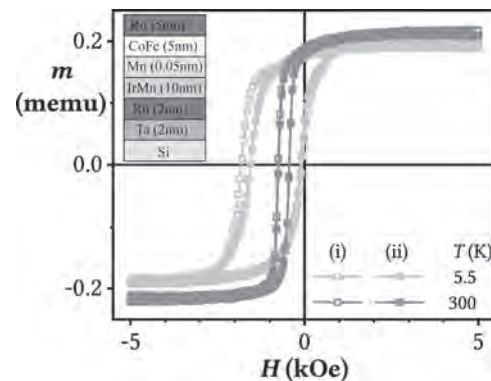


Figure 1: The first (i) and second (ii) hysteresis loops at 5.5 and 300 K for a film with structure shown inset.

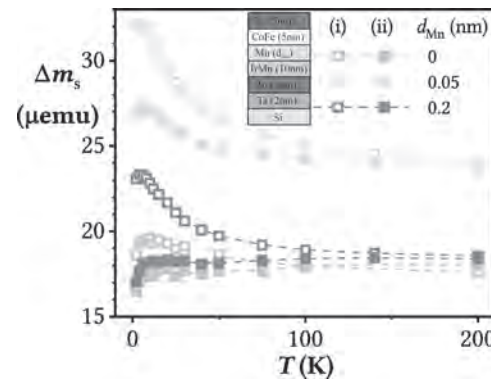


Figure 2: The temperature dependence of the magnetisation offset (Δm_s) measured at ± 5 kOe shown for the first (i) and second (ii) magnetisation reversal for the thin films shown inset where $0 \leq d_{Mn} \leq 0.2$ nm.

IG-10. Large Exchange Bias in FeCr Spinel Oxide Nanoparticles With Embedded Fe_xO Clusters.

C.E. Bulbucan^{1,2}, C. Preger^{2,3}, A. Kostanyan^{4,5}, K.M. Jensen⁶, E. Kokkonen⁷, C. Piamonteze⁵, M.E. Messing^{2,3} and R. Westerström^{1,2}
 1. Synchrotron Radiation Research, Lunds Universitet, Lund, Sweden; 2. NanoLund, Lunds Universitet, Lund, Sweden; 3. Solid State Physics, Lunds Universitet, Lund, Sweden; 4. Physik-Institut, Universitat Zurich, Zurich, Switzerland; 5. Swiss Light Source, Paul Scherrer Institut, Villigen, Switzerland; 6. Chemistry, Kobenhavns Universitet, Kobenhavn, Denmark; 7. MAX IV-laboratoriet, Lund, Sweden

Here we present an X-ray, magnetometry, and electron microscopy study of novel 40 nm FeCr spinel oxide nanoparticles (NPs) containing ~4 nm FeO clusters occupying up to 20% of the volume. The unique structure provides a large effective interface area between the antiferromagnetic (AFM) FeO clusters and the ferrimagnetic (FiM) spinel structure, leading to one of the largest exchange bias (EB) observed in FeO-based NP systems. Nanoparticles composed of Wüstite FeO and Magnetite Fe₃O₄ have been studied extensively and exhibit a wide range of magnetic properties [1-3]. Both oxides share the same fcc oxygen lattice and differ only in the occupancy and valence of the Fe cations in the tetrahedral (A) and octahedral (B) interstitial sites. Wüstite has a rock salt (RS) structure with Fe²⁺ occupying B-sites in the fcc O-lattice. In bulk, FeO is not stoichiometric and thermodynamically stable under ambient conditions, which results in a defect Fe_xO RS structure. The Fe²⁺ ions in the RS structure can diffuse and oxidize into Fe³⁺ at the surface, forming the inverse spinel structure of Magnetite, where Fe³⁺ occupies the A-lattice while the B-lattice is equally shared by the Fe²⁺ and Fe³⁺ cations. At the nanoscale, the transformation of Wüstite into Magnetite leads to Fe_xO/Fe₃O₄ core/shell (CS) NPs where exchange coupling between the AFM core and the FiM shell leads to the emergence of EB [1-6], which manifests as a horizontal shift of the hysteresis and coercivity increase. Here, NPs with an average diameter of 40 nm are generated using an aerosol technique based on spark ablation [7-9] where the material is evaporated from stainless steel grade 430 electrodes containing 97.4% FeCr with a 4:1 ratio of Fe:Cr [9]. The evaporated material is transported where adiabatic expansion and mixing with the carrier gas cool down the vapor, which condensates into sub 10 nm primary particles that form larger agglomerates as they collide. The agglomerates are transported through a furnace where they are compacted at 1200 °C before being size-selected and deposited onto a substrate using an electric field. The structural characterization was performed by high-resolution electron microscopy (HRTEM) and the compositional analysis was carried out with energy dispersive X-ray spectroscopy (EDXS) in scanning transmission electron microscopy (STEM) mode, see Figure 1 (a and b), along with X-ray photoelectron spectroscopy (XPS) performed at the Species beamline, MAX IV [10]. The NPs appear to have a single crystalline phase with a spinel oxide structure, and homogeneously distributed Fe and Cr within the NP with the expected Fe:Cr ratio of 4:1. However, X-ray diffraction (XRD) acquired at the 11-ID-B beamline of the Advanced Photon Source [11] reveals the co-existence of up to 20% RS crystallites with a size (~4 nm) about one order of magnitude smaller than the spinel phase (~40 nm). The significant volume fraction and the small size of the RS phase rule out a CS structure and point to Fe_xO RS clusters embedded in the spinel structure as schematically illustrated in Fig. 1 c). In stainless steel, Cr prevents the corrosion of metallic Fe by forming an oxide that blocks further diffusion and oxidation of Fe at the surface. We propose that Cr plays a similar role here, but now preventing the full transformation from Fe_xO → Fe₃O₄, both in the primary particles and during compaction. X-ray magnetic circular dichroism (XMCD) data, acquired at the X-treme beamline of the Swiss Light Source [12] shows the FM interaction between the Fe²⁺/Fe³⁺ and Cr³⁺ ions in the B-lattice, and an AFM coupling to the Fe³⁺ ions in the A-lattice. Differences observed in XMCD spectra recorded at 2 K and 300 K at the Fe L₃-edge indicate an AFM to paramagnetic transition, further supporting the presence of Fe_xO in the NPs. Element and site specific m(H) curves were recorded and the differences between Fe and Cr will be discussed, along with a more precise determination of the individual ions' magnetic contribution by means of multiplet simulations. Temperature-dependent magnetization measurements also indicate the presence of Fe_xO, where a rapid increase in magnetization is observed around the Néel

temperature of FeO (T_N ~ 200 K - Fig.2 left-panel). The magnetic moment as a function of applied magnetic field at a temperature of 2 K after cooling in a field of 1 T is shown in the right-panel of Figure 2. As can be seen, the hysteresis is significantly shifted with respect to the field axis. The observed shift of μ₀H = 460 mT is among the highest values ever reported for Fe-oxide NPs, and significantly larger than the typical values for Fe_xO/Fe₃O₄ NPs [13] (a record high of 860 mT was reported by Lottini *et al* [14] after Co doping). Furthermore, a 38% increase in the coercivity at 2 K (580 mT) after cooling in a magnetic field is also observed. That the EB is the result of interactions with the AFM Fe_xO clusters is also corroborated by the temperature dependence of the H_{EB} which vanishes above the FeO T_N, immediately followed by a rapid coercivity decrease. The large EB is attributed to the unique structure in which the embedded AFM clusters have an increased effective AFM-FiM interface area compared to AFM/FiM core/shell structures.

[1] Sun, Xiaolian, et al. "Tuning exchange bias in core/shell FeO/Fe₃O₄ nanoparticles." *Nano letters* 12.1 (2012): 246-251. [2] Estrader, Marta, et al. "Origin of the large dispersion of magnetic properties in nanostructured oxides: Fe_xO/Fe₃O₄ nanoparticles as a case study." *Nanoscale* 7.7 (2015): 3002-3015. [3] Wetterskog, Erik, et al. "Anomalous magnetic properties of nanoparticles arising from defect structures: topotaxial oxidation of Fe_{1-x}O|Fe_{3-δ}O₄ core|shell nanocubes to single-phase particles." *ACS nano* 7.8 (2013): 7132-7144. [4] Iglesias, Oscar, Amilcar Labarta, and Xavier Batlle. "Exchange bias phenomenology and models of core/shell nanoparticles." *Journal of nanoscience and nanotechnology* 8.6 (2008): 2761-2780. [5] Meiklejohn, William H., and Charles P. Bean. "New magnetic anisotropy." *Physical review* 102.5 (1956): 1413. [6] Nogués, Josep, et al. "Exchange bias in nanostructures." *Physics reports* 422.3 (2005): 65-117. [7] R. Hallberg, L. Ludvigsson, C. Preger, B. Mueller, K. Dick, and M. Messing, "Hydrogen-assisted spark discharge generated metal nanoparticles to prevent oxide formation," *Aerosol Science and Technology*, vol. 52, no. 3, pp. 347-358, 2018. [8] B.O. Mueller, M.E. Messing, D.L.J. Engberg, et al. "Review of spark discharge generators for production of nanoparticle aerosols" *Aerosol Sci. Technol.*, 46, 1256, 2012. [9] C. Preger et al., "Controlled Oxidation and Self-Passivation of Bimetallic Magnetic FeCr and FeMn Aerosol Nanoparticles", *The Journal of Physical Chemistry C*, vol. 123, no. 26, pp. 16083-16090, 2019. [10] S. Urpelainen, C. Sâthe, W. Grizolli, M. Agâker, A. R. Head, M. Andersson, S.-W. Huang, B. N. Jensen, E. Wallén, H. Tarawneh, et al., "The species beamline at the max iv laboratory: a facility for soft x-ray rixs and apxps", *Journal of synchrotron radiation*, vol. 24, no. 1, pp. 344-353, 2017. [11] U. Rütt, M. Beno, J. Stremper, G. Jennings, C. Kurtz, and P. Montano, "Diffractometer for high energy x-rays at the APS", *Nuclear Instruments and Methods in Physics Research Section A: Accelerators, Spectrometers, Detectors and Associated Equipment*, vol. 467, pp. 1026-1029, 2001. [12] C. Piamonteze, U. Flechsig, S. Rusponi, J. Dreiser, J. Heidler, M. Schmidt, R. Wetter, M. Calvi, T. Schmidt, H. Pruchova, et al., "X-treme beamline at sls: X-ray magnetic circular and linear dichroism at high field and low temperature", *Journal of synchrotron radiation*, vol. 19, no. 5, pp. 661-674, 2012. [13] Phan, Manh-Huong, et al. "Exchange bias effects in iron oxide-based nanoparticle systems." *Nanomaterials* 6.11 (2016): 221. [14] Lottini, E., et al. "Strongly exchange coupled core|shell nanoparticles with high magnetic anisotropy: a strategy toward rare-earth-free permanent magnets." *Chemistry of Materials* 28.12 (2016): 4214-4222.

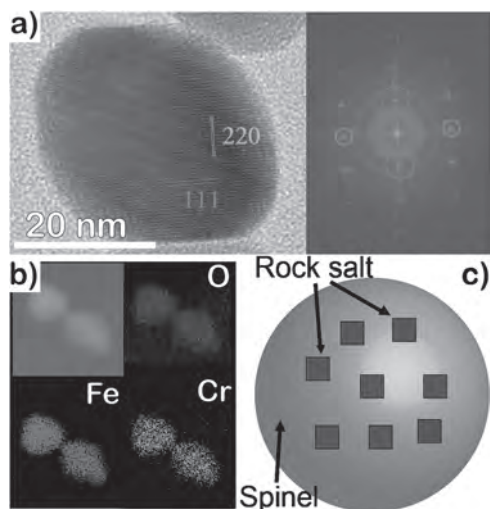


Fig 1. a) left: HRTEM image of a NP; right: FFT indicating spinel; b) EDXS showing Fe, Cr and O distribution; c) Schematic model of a spherical spinel NP containing cubic FeO clusters (brown).

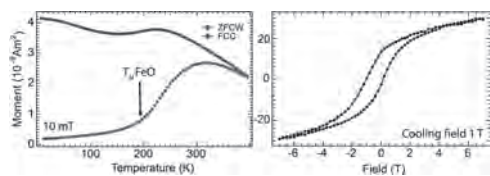


Fig 2. Left: temperature susceptibility in a 10 mT field in ZFC and FC cases; right: 1 T FC $m(H)$ showing the horizontal hysteresis shift.

IG-11. Tailoring Interfacial Phenomena in Hybrid v_2O_3 /Co Bilayers.

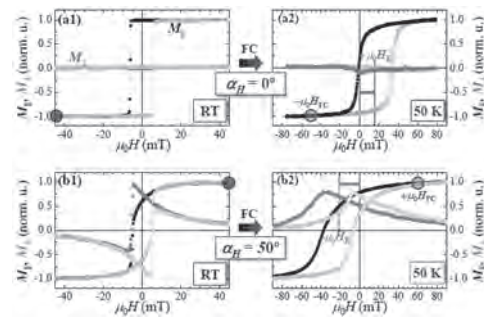
J.M. Diez^{1,2}, J.L. Fernández Cuñado¹, P. Perna², P. Lapa³, A. Bollero², R. Miranda^{1,2}, I.K. Schuller³ and J. Camarero^{1,2}

1. Física de la Materia Condensada, Universidad Autónoma de Madrid, Madrid, Spain; 2. Fundacion IMDEA Nanociencia, Madrid, Spain;

3. Department of Physics and Center of Advanced Nanoscience, University of California San Diego, La Jolla, CA, United States

The research on hybrid systems combining dissimilar materials with artificial interfaces is among the major challenges of the nanotechnology during the last decades. Different functionalities may be engineered by combining dissimilar materials. To this regard, bilayers composed of a ferromagnetic (FM) layer interfaced with a transition-metal-oxide (TMO) layer can be considered as model hybrid systems V_2O_3 is an archetypical TMO system exhibiting a first-order metal insulator transition (MIT) when the temperature is decreased below $T_{MIT} = 170$ K [1], from a paramagnetic metallic state to an antiferromagnetic (AFM) insulating phase, accompanied simultaneously by a structural phase transition [2]. We are provided with an additional degree of freedom in order to control the FM properties at the FM/TMO interface. Below T_{MIT} , several interfacial exchange-coupling effects have already been found in similar FM/ V_2O_3 bilayers [3], ranging from moderate to negligible exchange bias fields, enhanced giant coercive fields and unique dynamical effects. To understand these interesting effects it is important to investigate in detail the temperature dependence of the magnetic anisotropies of this system. Here we present a detailed angular and temperature dependent angle-resolved vector magnetometry study of the model FM/TMO system mentioned across the MIT. This provides fundamental insights on how to tailor and control the interfacial exchange effects. More specifically, we investigated the magnetic anisotropy landscape of Co/ V_2O_3 bilayers, where the Co layer has a well-defined uniaxial magnetic anisotropy at room temperature (see Fig. 1a1 y Fig. 1b1). We have studied the effects using different magnetic anisotropy configurations by setting a magnetic orientation of the FM layer across the MIT transition. Different field cooling (FC) procedures strongly affect the magnetic configuration of the hybrid bilayer. Just after the FC, the low temperature (50 K) loops display strong interfacial exchange coupling effects (see Fig. 1a2 y Fig. 1b2), i.e., enhanced coercive field, clear exchange bias, and asymmetric magnetization reversal [4]. In general, depending on the FC procedure, different angle-dependent and temperature evolutions are found, which are ascribed to the modifications of the anisotropy configuration. Our findings demonstrate that we have an effective control of the interfacial exchange phenomena in the FM/TMO heterostructures, especially across the MIT, which enables the development of novel magnetic devices with specific functionalities. This research was partially supported by the Spanish Ministry of Economy and Competitiveness (MINECO) (grant numbers FIS2016-78591-C3-1-R, RTI2018-097895-B-C42, and SEV-2016-0686) and by the Regional Government of Madrid (through project NANOMAGCOST-CM). JMD acknowledges support from MINECO through FPI program (BES-2017-080617). Work at UCSD supported by the Office of Basic Energy Science, U.S. Department of Energy, BES-DMS funded by the Department of Energy's Office of Basic Energy Science, DMR under grant DE FG02 87ER-45332. We thank C. Urban, and J. Trastoy for initial work and discussions on this problem.

[1] Imada, M., Fujimori, A. and Tokura, Y. Rev. Mod. Phys. 70, 1039-1263 (1998). [2] De La Venta, J., Wang, S., Ramirez, J. G., and Schuller, I. K. Applied Physics Letters, 102(12), 122404 (2013). [3] E. Jiménez, J. Camarero, J. Sort, J. Nogués, A. Hoffmann, N. Mikuszeit, J. M. Garcia-Martín, B. Dieny, and R. Miranda. Phys. Rev. B. 80, 014415 (2009). [4] J. Camarero, J. Sort, A. Hoffmann, J. M. Garcia-Martín, B. Dieny, R. Miranda, and J. Nogués. Phys. Rev. Lett. 95, 057204 (2005)



Representative v-MOKE loops of a V_2O_3 (100 nm)/Co (15 nm) heterostructure above (a1,b1) and below (a2,b2) the MIT transition using different field-cooling (FC) conditions: a) Negative-FC along the easy axis and b) Positive-FC around 50° off the easy axis. Note that after FC, the hysteresis field-shift (indicated with arrows) is opposite to the FC direction, while the reversal pathways are very different [notoriously in $M_x(H)$].

IG-12. Observation of Training Effect in Fe Thin Film Implanted With F+ Ions.

S. Sen^{1,2}, A. Gupta³, V. Reddy⁴ and R. Gupta¹

1. School of Instrumentation, Devi Ahilya University, Indore, India;

2. Department of Physics, Maharaja Bhoj Government P.G. College, Dhar-454001, India, Dhar, India; 3. Centre for Spintronic Devices, Amity University, Noida, India., Noida, India; 4. UGC DAE CSR Indore Centre, Khandwa Road, Indore-452017, India, Indore, India

Introduction: Exchange Bias(EB) originates from the interfacial interaction between a ferromagnetic (FM) and an Antiferromagnetic (AFM) material, after cooling the sample in a magnetic field below the Neel temperature (T_N) of the AFM [1]. The main feature of EB is training effect which is a gradual reduction of EB field when hysteresis loop (n) measured many times at constant temperature. The training effect is inversely dependence on FM layer thickness and interface structure, etc [2]. We have carried out the Kerr microscopy measurements to get direct information about magnetization irreversible of FM layers along with hysteresis loops. Experimental details: Thin films of Al(10nm)/Fe(30nm)/Fe⁵⁷(10nm)/Fe(30nm)/Si substrate were deposited using Ion-beam sputtering technique. The films were implanted with 35 keV Fluorine ions. With this ion energy, the maximum energy has been deposited only at the centre of the Fe film to obtain FeF₂ at the center, which is an antiferromagnet and its Neel temperature is 78 K. For magnetic characterization, the measurements were done using in-plane Magneto-optic Kerr effect microscope (MOKE) at 50 K after field cooling from room temperature. Results and discussions Fig. 1(a) shows the hysteresis loop as function of number of loops. It clearly shows the exchange bias and it becomes quite constant. Similar observation has also been showed for the sample irradiated with 5×10^{16} F-ions/cm². Magnetic domain evolution during the magnetization irreversible and the training effect have been studied after F-ion implantation at 50 K. Kerr microscopy measurements were carried out at different temperatures after the field-cooling across the Neel temperature of the antiferromagnetic (AFM) FeF₂ layer. It is observed that with the increasing anti-ferromagnetic (AFM) FeF₂ layer thickness, the exchange bias increase and the training effect becomes weaker. Analysis of the temperature variation of the exchange bias field indicates the disorder decreases at the FM-AFM interface with the increasing F-Ion fluences. Higher fluence specimen indicates a behavior that is changing from non-equilibrium state to equilibrium state and behavior of training effect is suggesting step-like. For 1×10^{17} ions/cm² sample, change in the exchange bias field after measuring the 6th cycle is 4.42% while in case of 5×10^{16} ions/cm² 27.32%. Remarkably, for the largest fluences, the relative training becomes smaller than the one for the lower fluence. It indicates higher ion fluence EB system is suitable for device application.

[1] W. H. Meiklejohn and C. P. Bean, Phys. Rev. 102, 1413(1956). [2] M. Gruyters and D. Riegel, Phys. Rev. B 63, 052401 (2000).

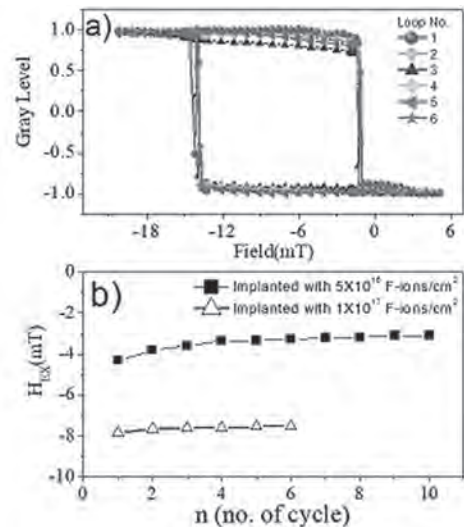


Figure 1: (a) The hysteresis loops as a function of number of loops (n) for the specimen 1×10^{17} ions/cm² (b) Value of Exchange bias for both the films implanted with ion fluences 5×10^{16} ions/cm² and 1×10^{17} ions/cm² at 50 K.

Session IH
THIN FILMS AND SURFACE EFFECTS
Hideto Yanagihara, Chair
Tsukuba University, Tsukuba, Japan

CONTRIBUTED PAPERS

IH-01. Giant Perpendicular Magnetic Anisotropy in Mo-Based Double-Interface Free Layer Structure for Advanced Magnetic Tunnel Junctions.

H. Cheng^{1,2}, J. Chen¹, S. Peng^{1,2}, B. Zhang¹, Z. Wang¹, D. Zhu¹, K. Shi¹, S.R. Eimer^{1,2}, X. Wang¹, Z. Guo¹, Y. Xu^{1,2}, D. Xiong¹, K. Cao¹ and W. Zhao^{1,2}

1. Fert Beijing Institute, Beijing Advanced Innovation Center for Big Data and Brain Computing, School of Integrated Circuit Science and Engineering, Beihang University, Beijing, China; 2. Hefei Innovation Research Institute, Beihang University, Hefei, China

Magnetic tunnel junctions (MTJs) with perpendicular magnetic anisotropy (PMA) have advantages of high packing density due to their high thermal stability, efficient current-induced magnetic switching, and unrestricted cell aspect ratio.[1] Therefore, PMA-based MTJs (p-MTJs) have broad application prospects on high-density and non-volatile spin-transfer torque magnetic random access memories (STT-MRAMs) and other spintronics devices.[2-4] In particular, p-MTJs with CoFeB/MgO structures show high tunnel magnetoresistance ratio.[4] In the W/CoFeB/MgO stacks, the interfacial magnetic anisotropy (K_i) of 1.98 mJ/m² is acquired after annealing at 350 °C.[5] To further improve K_i , it is an effective way to use MgO/CoFeB/X/CoFeB/MgO double-interface free layer structures, where the X represents the spacer material. [6] However, higher K_i is needed to scale down the MTJs devices and maintain high thermal stability.[7] In this work [8], we study the magnetic anisotropy of the double-interface free layer stacks with different annealing temperatures and different spacer materials. The samples of Ta(5)/MgO(2)/Co₂₀Fe₆₀B₂₀(t)/X(0.4) /Co₂₀Fe₆₀B₂₀(1.2)/MgO(2)/Ta(3) are deposited by sputtering system, where the numbers in parentheses indicate the thickness in nanometers, X including Ta, W, and Mo. The thickness of the bottom CoFeB layer t ranges from 0.4~3.2 nm. The films with Mo spacer layer exhibit the highest K_i of 4.06 mJ/m² compared with the Ta- and W-based films. Furthermore, the K_i of Mo-based films remains at 2.93 mJ/m² even after annealing at 500 °C for 1 h. Fig.1a and 1b show the structures with bottom CoFeB thickness of 0.8 nm and with spacer materials of Mo and W. As shown in the M - H (Magnetization M versus magnetic field H) curves, all the films show good PMA. Fig.1c and 1d show the corresponding high-resolution transmission electron microscopy (HR-TEM) and energy-dispersive X-ray spectroscopy (EDX) images. Saturation magnetization M_s and the total thickness of magnetic dead layer t_{DL} can be extracted from the curves (M/A versus t_{CoFeB} curves), where A is the area of the sample and t_{CoFeB} is the total thickness of CoFeB layers. The K_i can be extracted from the intercept of the $K_{eff}^*t_{eff}$ versus t_{eff} curves, where K_{eff}^* is effective magnetic anisotropy energy density and $t_{eff} = t_{CoFeB} - t_{DL}$. As shown in Fig.2a and 2b, K_i of 2.15±0.11 mJ/m² and 2.90±0.34 mJ/m² can be obtained for Ta- and W-based stacks, respectively. More importantly, the maximum of 4.06±0.14 mJ/m² is acquired for the Mo-based structure after annealing at 350 °C as shown in Fig.2c. According to previous study, when the required thermal stability factor is 70, if the K_i reached 4 mJ/m², the device size can be reduced to 10 nm.[8] It can be shown in Fig.2d- 2f that the K_i decreases with the increase of annealing temperature. Note that the K_i reaches 2.93 mJ/m² even after annealing at 500 °C for 1 h, which demonstrates the high thermal stability of this structure. Revealed by the HR-TEM and EDX images, the sharper interface, weaker interdiffusion, better interfacial uniformity and higher crystallinity can be seen in the Mo-based stack than the W-based stack. These results show that Mo plays an important role in improving the film quality. When the annealing temperature increases, the interfacial mixing intensifies, which leads to the decrease of K_i in Mo-based films. In summary, we study the dependence of magnetic anisotropy and film quality of the MgO/CoFeB/X/CoFeB/MgO double-interface free layer structures on the spacer material and the annealing temperature. We find that, the Mo-based structure exhibits the strongest PMA (4.06 mJ/m²). Furthermore, K_i in the Mo-based stack is still as strong as 2.93 mJ/m² even after annealing at 500 °C. The HR-TEM and EDX images of W- and Mo-based stacks show that the high thermal stability can be attributed to the high film quality in

the Mo-based films. Our work provides a practical solution to scale down MRAM device while maintaining a high thermal stability.

[1] Ikeda, S., Miura, K., Ohno, H. Nature materials, 9(9), 721-724 (2010). [2] Wang, M., Cai, W., Zhao, W. Nature electronics, 1(11), 582-588 (2018). [3] Peng, S., Zhu, D., Zhao, W. Nature Electronics, 1-8 (2020). [4] Wang, M., Cai, W., Zhao, W. Nature communications, 9(1), 1-7 (2018). [5] An, G. G., Lee, J. B., Hong, J. P. Acta Materialia, 87, 259-265 (2015). [6] Hwang, C. S. Advanced Electronic Materials, 1(6), 1400056 (2015). [7] Peng, S., Kang, W., Zhao, W. IEEE Magnetics Letters, 8, 1-5 (2017). [8] Cheng, H., Chen, J., Zhao, W. Advanced Electronic Materials, 6(8), 2000271 (2020).

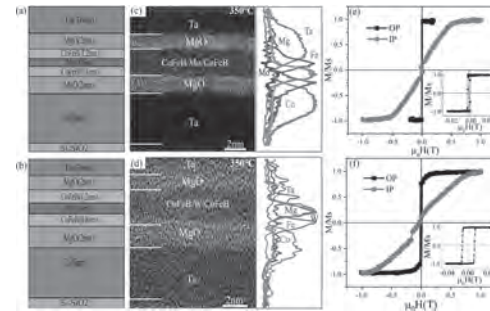


Fig.1. (a,b) The schematic of Ta(5)/MgO(2)/Co₂₀Fe₆₀B₂₀(0.8)/X(0.4) / Co₂₀Fe₆₀B₂₀(1.2)/MgO(2)/Ta(3) with spacer material of (a) X=Mo and (b) X=W. (c,d) The corresponding HR-TEM images and EDX line profiles with spacer material of (c) X=Mo and (d) X=W. (e,f) The corresponding hysteresis loops with the in-plane (IP) field (red line) and out-of-plane (OP) field (black line) for different spacer materials of (e) X=Mo and (f) X=W. In the inset of (e) and (f), a M - H image under the small OP field with spacer material of (e) X=Mo and (f) X=W.

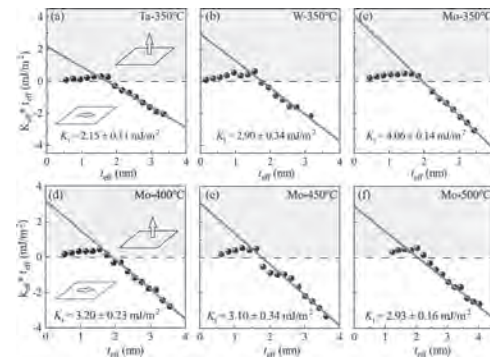


Fig.2. (a-c) The K_i fittings for MgO (2)/Co₂₀Fe₆₀B₂₀(t)/X(0.4) / Co₂₀Fe₆₀B₂₀(1.2)/MgO(2) stacks under annealing at 350 °C with spacer layer X of (a) Ta, (b) W, and (c) Mo. (d-f) The K_i fittings for MgO(2)/Co₂₀Fe₆₀B₂₀(t) / Mo(0.4) / Co₂₀Fe₆₀B₂₀(1.2) / MgO(2) stacks with the annealing temperature of (d) 400 °C, (e) 450 °C, and (f) 500 °C.

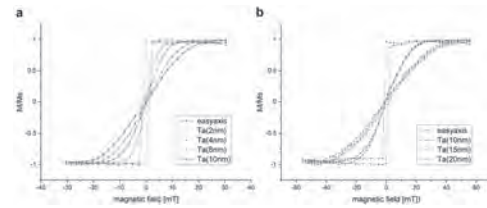
IH-02. Tuning the Inplane Anisotropy of CoFeB Films.

S. Scheibler^{1,2}, O. Yildirim¹, A. Mandru¹ and H.J. Hug^{1,3}

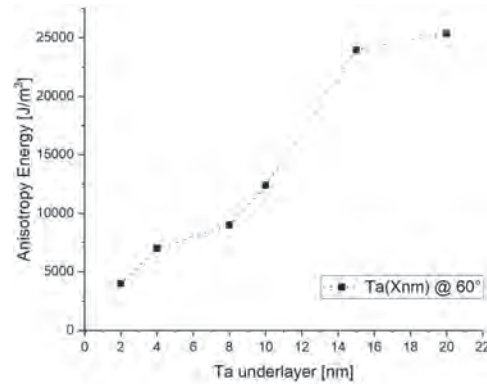
1. Magnetic & Functional Thin Films Lab 203, Empa, Swiss Federal Laboratories for Materials Science and Technology, Dübendorf, Switzerland; 2. ETH Zurich, Zurich, Switzerland; 3. Department of Physics, University of Basel, Basel, Switzerland

Soft magnetic films consisting of CoFeB alloys are widely applied in magnetic sensor [1] and MRAM devices [2], but also used as cores for microfabricated transformers used to power specific subunits on microprocessors [3]. These applications typically require a well-defined in-plane uniaxial anisotropy axis which aligns the magnetic moments and permits operation modes where a field is applied either along the anisotropy axis to obtain a domain wall motion easy axis or a magnetization rotation governed magnetization process. Several implementations have been discussed in literature to obtain a well-defined uniaxial in-plane anisotropy axis and to tune the anisotropy. Apart from the geometry of a sensor element which can be chosen to obtain a shape anisotropy, oblique sputtering of seed layers for the successively deposited magnetic layer(s) [4], sputter deposition or post-deposition annealing in a magnetic field [5] have been employed. Here, we deposit CoFeB layers on Ta seed layers grown by oblique sputtering and compare the resulting anisotropies to those obtained by deposition of the magnetic layer in an applied field. Moreover, for the CoFeB layers on the oblique-sputtered seeds we compare the anisotropies obtained for different CoFeB-thicknesses to distinguish between a surface or interface induced anisotropy or a bulk anisotropy term. Specifically, we deposited Ta(2nm)/CoFeB(6nm)/Ta(Xnm)-seed films onto a Si-wafer covered by its native oxide using angles of 40°, 50° and 60° between the sample normal and the Ta source, and Ta-seed layer thicknesses from 2nm to 10nm. For an angle of 60° the Ta-seed layer was additionally deposited with a thickness of 15nm and 20nm. In addition, we deposited 4nm, 8nm, 16nm and 32nm CoFeB films on 4nm-thick Ta-seed layer deposited at an angle of 50°. Selected systems were deposited in fields of 4mT and 40mT, applied parallel to the substrate surface. VSM was then used to obtain the magnetization of the CoFeB films. Hard- and easy axis magnetization loops were measured with a Kerr Microscope to determine the in-plane anisotropy (see figure 1 & figure 2). We find that the in-plane anisotropy increases with the deposition angle and also the seed layer thickness. For a deposition angle of 60° the anisotropy increases from 4kJ/m³ to 25kJ/m³ with thicknesses from 2nm to 20nm. For smaller deposition angles, we measure a much smaller increase of in-plane anisotropy. Concerning the scientific question whether the anisotropy arises from a surface or a bulk effect, our analysis of CoFeB films with thicknesses from 4nm to 32nm revealed that the anisotropies stemming from the oblique-sputtered Ta-seed layers is well modeled by a surface anisotropy term. While with oblique sputtering, a wide range of in-plane anisotropies can be covered, the anisotropies remain much smaller when films are deposited in fields. However, it has already been demonstrated that with CoSm-alloys much larger anisotropies have been obtained [5]. To correlate the seed-layer morphology with the in-plane anisotropy, high resolution AFM imaging on the Ta-seed layer was performed. Our work shows that in-plane anisotropies in magnetically soft systems can be tuned over a wide range by oblique seed-layer depositions. However, the anisotropy arises from an interface effect and thus decays as 1/t with CoFeB film layers thickness “t”. The anisotropy of CoFeB films deposited in an applied field does not depend on film thickness and remains rather small. We propose that alloying Sm into the CoFeB films may increase the field-induced anisotropy, while keeping the soft magnetic properties of the CoFeB films.

[1] T. Ogasawara, M. Oogane and M. Al-Mahdawi; Sci. Rep. 9, 17018 (2019) [2] S. Zhanga, Y. Sua and X. Li; Appl. Phys. Lett. 114, 042401 (2019) [3] J. Michel et al. IEEE Transactions on Magnetics 55, 7, pp. 1-7, (2019) [4] R. D. McMichael, C. G. Lee and J. E. Bonevich; Journal of Applied Physics 88, 5296 (2000) [5] F. Magnus, R. Moubah and A. H. Roos; Appl. Phys. Lett. 102, 162402 (2013)



Hard- and easy axis magnetization loops measured with Kerr Microscope of deposited Ta(2nm)/CoFeB(6nm)/Ta(Xnm)-seed layer at an angle of 60°



In-plane anisotropy of deposited Ta(2nm)/CoFeB(6nm)/Ta(Xnm)-seed layer at an angle of 60°

IH-03. Magnetization Processes and Magnetic Domain Structures in Ta/CoFeB/MgO Stacks.

A.K. Dhiman¹, T. Dohi², W. Dobrogoski¹, Z. Kurant¹, I. Sveklo¹, S. Fukami², H. Ohno² and A. Maziewski¹

1. Department of Physics, Uniwersytet w Białymstoku, Białystok, Poland;
2. Tohoku University Denki Tsushin Kenkyujo, Sendai, Japan

In this work, we present the results of polar magneto-optical Kerr effect (PMOKE) magnetometry and microscopy study of Ta/CoFeB/MgO stacks with a prototypical perpendicular easy axis system in spintronics applications [1]. Multilayer films with a structure of Ta (5 nm)/(Co_{0.25}Fe_{0.75})₇₅B₂₅ ($d=1.24\div 1.60$ nm)/MgO (2 nm)/Ta (2 nm) were deposited by dc/rf magnetron sputtering on thermally-oxidized Si substrates and after were annealed at 300 °C for 1 h under a perpendicular magnetic field 0.4 T in vacuum [2,3]. The magnetization processes statics, magnetization reversal dynamics and domain structures evolution driven by magnetic field were studied as a function of CoFeB thickness d . Magnetization curves are measured for samples with various d applying PMOKE magnetometry. For $d=1.24$ to 1.36 nm square-shaped hysteresis loops with full remanence, indicating an out-of-plane magnetization easy axis, are observed. For $d=1.40$ nm the shape of magnetization curve corresponds to the transitional state (at the edge of out-of-plane and in-plane magnetization states). For $d=1.44$ nm the magnetization curves demonstrate no hysteresis, which indicates on the reversible magnetization rotation and in-plane magnetization. The values of magnetic anisotropy parameters were deduced from the fitting of hard axis hysteresis curves using macrospin approximation model. In the case of the samples without in-plane magnetization additional 0.05 T magnetic field was applied to prevent domain structure formation. In the case of square hysteresis loop ($d=1.24\div 1.36$ nm) magnetization reversal dynamics was studied exploiting PMOKE microscopy imaging technique driven by sequential magnetic field pulses (duration 200 ms) with a constant amplitude. Magneto-optical images were acquired in zero field after each pulse. The derived normalized magnetization m can be obtained as a function of number of field pulses expressed as time t using image processing techniques [4]. The dependence of magnetization m for direct process (starting from full saturated state) on time t for the sample with $d=1.24$ nm is shown in Fig. 1. The logarithm of time $t_{1/2}$, time when the sample has magnetization $m=0$, depends linearly on amplitude of pulses, which indicates on thermal activation of jump-like domain wall motion [5] and allows to calculate Barkhausen length $l_B \gg 120$ nm [6]. Magnetization reversal in the stacks with out-of-plane anisotropy ($d=1.24\div 1.36$ nm) goes through domain nucleation and domain wall propagation. In the case of the samples with $d=1.24, 1.28$ nm, while increasing H few nucleation point appears initially in the field of view and later quickly expands covering all the area excluding narrow domain between neighboring expanding domains named as narrow stripe domains (NSDs). NSDs are stabilized due to magnetostatic repulsion between there opposite domain walls and finite value of coercivity [7]. The increase of thickness d lead to significant reduction of straight cuts of NSDs, and for $d=1.32, 1.36$ nm (close to d_{SRT}) NSDs network is converted to the more complex dendrite like structures. The evolution of NSDs network in external out-of-plane magnetic field was studied exploiting PMOKE microscopy imaging technique driven by sequential magnetic field pulses (duration 500 ms) with a growing amplitude. The digital image processing of acquired images yielded normalized magnetization and NSDs length in the field of view. The obtained dependences of normalized magnetization and NSDs length for the stack with $d=1.24$ nm are presented in Fig. 2 as the functions of the amplitude of applied field pulses. NSDs appear after beginning of nucleation process at 1.25 mT, quickly reach maximum at 1.45 mT (when normalized magnetization $m_L \gg 0.92$), then gradually annihilate and disappear after 5.5 mT. So saturation field is few times bigger than coercivity due to the NSDs. In conclusion, we have performed an experimental study of the static and dynamic magnetization processes in ultrathin FeCoB films depending on their thickness. We find that magnetization reversal is occurred via thermal activated domain wall motion and is influenced by NSDs. The dependence of NSDs network length on applied out-of-plane magnetic field was studied.

[1] S. Ikeda, K. Miura, H. Yamamoto, K. Mizunuma, H. D. Gan, M. Endo, S. Kanai, J. Hayakawa, F. Matsukura and H. Ohno, A perpendicular-anisotropy

CoFeB–MgO magnetic tunnel junction, Nature Mater. 9, 721–724 (2010), 10.1038/nmat2804 [2] S. Fukami, T. Suzuki, Y. Nakatani, N. Ishiwata, M. Yamanouchi, S. Ikeda, S. Kasai, and H. Ohno, Current-induced domain wall motion in perpendicularly magnetized CoFeB nanowire, Appl. Phys. Lett. 98, 082504 (2011), 10.1063/1.3558917 [3] C. Burrowes, N. Vernier, J.-P. Adam, L. Herrera Diez, K. Garcia, I. Barisic, G. Agnus, S. Eimer, Joo-Von Kim, T. Devolder, A. Lamperti, R. Mantovan, B. Ockert, E. E Fullerton, and D. Ravelosona, Low depinning fields in Ta-CoFeB-MgO ultrathin films with perpendicular magnetic anisotropy, Appl. Phys. Lett. 103, 182401 (2013), 10.1063/1.4826439 [4] M. Kisielewski, Z. Kurant, M. Tekielak, W. Dobrogowski, A. Maziewski, A. Wawro, L.T. Baczewski, Magneto-optical micromagnetometry of ultrathin Co wedges, Physica Status Solidi (A), vol.196, No.1, 129-132 (2003), 10.1002/pssa.200306370. [5] J. Ferré, V. Grolier, P. Meyer, S. Lemerle, A. Maziewski, E. Stefanowicz, S. V. Tarasenko, V. V. Tarasenko, M. Kisielewski, and D. Renard, Magnetization-reversal processes in an ultrathin Co/Au film, Phys Rev B 55, 15092–102 (1997), 10.1103/PhysRevB.55.15092. [6] A. K. Dhiman, T. Dohi, W. Dobrogowski, Z. Kurant, I. Sveklo, S. Fukami, H. Ohno, A. Maziewski, Magnetization processes and magnetic domain structures in Ta/CoFeB/MgO stacks, accepted in JMMM. [7] N. Vernier, J.-P. Adam, S. Eimer, G. Agnus, T. Devolder, T. Hauet, B. Ocker, F. Garcia, and D. Ravelosona, Measurement of magnetization using domain compressibility in CoFeB films with perpendicular anisotropy, Appl. Phys. Lett. 104, 122404 (2014), 10.1063/1.4869482

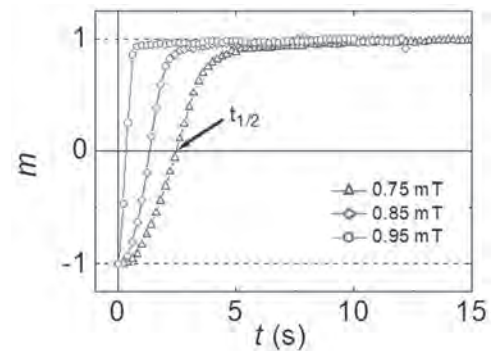


Fig. 1 The dependence of normalized magnetization m (derived from domains area) on total duration of magnetic field pulses t for the stack with $d=1.24$ nm. The amplitudes of magnetic field pulses in series are 0.75, 0.85 and 0.95 mT.

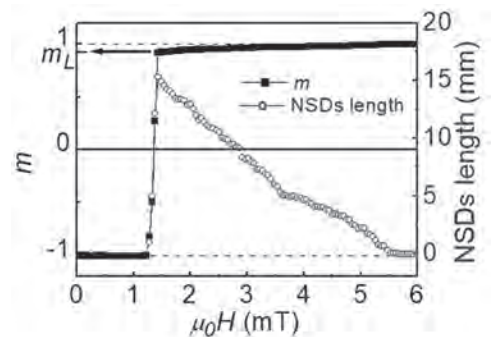


Fig. 2 The dependence of the normalized magnetization m (left Y-axis) and total length of NSDs, extracted from the field of view 1.4 mm² (right Y-axis) on amplitude of magnetic field pulses $m_0 H$ (pulse duration 500 ms) for the stacks with $d=1.24$ nm.

IH-04. Effect of Annealing Temperature on Spectroscopic g Factor at CoFeB/MgO Interface.

S. Tamaru¹, T. Yamamoto¹, T. Nozaki¹, K. Yakushiji¹, H. Kubota¹, A. Fukushima¹ and S. Yuasa¹

1. RCECT, National Institute of Advanced Industrial Science and Technology (AIST), Tsukuba, Japan

Magnetic properties of an ultra-thin CoFeB film, particularly at the CoFeB/MgO interface, are of critical importance for the development of magnetic tunnel junction based magnetoresistive random access memory (MRAM) such as spin transfer torque MRAM (STT-MRAM) and voltage-controlled MRAM (VC-MRAM), because these MRAM cells have a CoFeB free layer with a thickness of around 1 nm in direct contact with a MgO tunnel barrier layer. In STT-MRAM cells, the CoFeB free layer is magnetized perpendicularly to the film plane by taking advantage of interfacial perpendicular magnetic anisotropy (PMA) induced at the interface with MgO [1,2]. Larger interfacial PMA is advantageous for shrinking the cell size while maintaining a sufficiently large thermal stability factor of the free layer magnetization. In VC-MRAM cells, the interfacial PMA is not only used to perpendicularly magnetize the free layer, but also actively modulated by the application of electric fields to trigger the so-called precessional toggle switching [3]. Therefore, thorough understanding of the physical mechanism of interfacial PMA is indispensable for material/process engineering of these MRAM technologies. The source of the interfacial PMA is considered to be preferential occupation of the d_{xy} electron orbit that lies in-plane due to broken symmetry at the interface and spin-orbit interaction [4,5], which revives the orbital angular moment of the d-electrons that is almost completely quenched in the bulk. The magnitude of the orbital angular moment can be evaluated by the deviation of spectroscopic g factor from 2, i.e., $g=2+L/S$, where S and L are the spin and orbital angular moments, respectively. It has been observed that the magnitude of interfacial PMA is strongly dependent on the annealing temperature, suggesting that the crystalline state affects the electronic structure at the CoFeB/MgO interface, thus changing the interfacial PMA. According to these considerations, the spectroscopic g factor is expected to increase at the CoFeB/MgO interface with an annealing temperature dependence similar to that of the interfacial PMA. To examine this notion, we studied static and dynamic magnetic properties of CoFeB/MgO film stacks as a function of CoFeB thickness and annealing temperature. The samples are Ta(5) / CoFeB (t) / MgO(2) / Ta(5) / Ru(5) film stacks sputter deposited on a thermally oxidized Si substrate (from bottom to top, number in parentheses is the thickness of each layer in nm), where t is the nominal CoFeB thickness ranging from 1.1 nm up to either 1.5 or 5 nm for different annealing temperatures. These films were left as deposited or annealed between 150°C and 350°C for 1 hour in vacuum. We performed vibrating sample magnetometry (VSM) measurement for static characterization, and broadband ferromagnetic resonance (FMR) measurement for dynamic characterization, respectively. The CoFeB films have a magnetically dead layer at the Ta/CoFeB interface due to Ta diffusion with thicknesses depending on the annealing temperature, and the saturation magnetization M_s also varies on annealing temperature due to different degrees of crystallization. From the static M-H loop obtained by VSM, M_s as a function of t was first plotted, from which the effective thickness t_{eff} (t minus dead layer thickness) and effective M_s of the CoFeB layer were estimated for each annealing temperature. Next, the total PMA energy was calculated by integrating the static M-H loop. The interfacial PMA energy was estimated from the linear regression on the plot of total PMA energy as a function of t_{eff} for each annealing temperature. Figure 1 shows the interfacial PMA energy as a function of annealing temperature, which becomes maximum at 250°C. In the dynamic magnetic characterization, the broadband FMR measurement performed under out-of-plane bias magnetic field H_B observed a Kittel mode FMR spectrum. The FMR frequency showed a liner relation on H_B , from the slope of which the spectroscopic g factor was determined. The value of g factor showed a significant increase as t_{eff} decreased. Figure 2 shows the increase of g factor at the CoFeB/MgO interface from the bulk value as a function of annealing temperature, which becomes maximum at 200°C, and exhibits a very similar dependence on the annealing temperature to the interfacial PMA. These results support the notion that the increase of g factor and interfacial PMA have the same physical origin, i.e., revival

of the orbital angular moment due to broken symmetry at the CoFeB/MgO interface. In the talk, we will present the detailed experimental and analytical procedures for studying the static and dynamic magnetic properties of the ultra-thin CoFeB film at MgO interface performed in this work, and possible physical origin to explain the observation results. This presentation was partly based on results obtained from a project, JPNP16007, commissioned by the New Energy and Industrial Technology Development Organization (NEDO), Japan, and JSPS KAKENHI 18K14118.

[1] S. Yakata et al., J. Appl. Phys. 105, 07D131 (2009). [2] S. Ikeda et al., Nat. Mater. 9, 9, 721 (2010). [3] Y. Shiota et al., Nat. Mater. 11, 1, 39 (2012). [4] S. Miwa et al., J. Phys. D 52, 6, 063001 (2018). [5] B. Dieny and M. Chshiev, Rev. Mod. Phys. 89, 2, 025008 (2017).

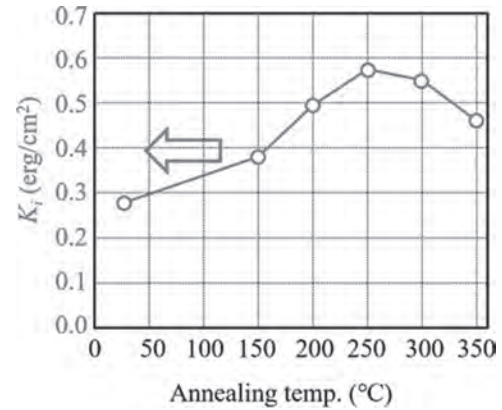


Fig. 1, Interfacial PMA at CoFeB/MgO interface as a function of annealing temperature.

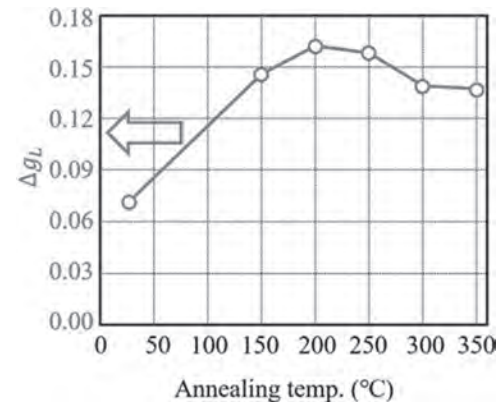


Fig. 2, Increase of g factor at CoFeB/MgO interface as a function of annealing temperature.

IH-05. Low Gilbert Damping and High Thermal Stability of Ru-Seeded $L1_0$ -Phase FePd Perpendicular Magnetic Thin Films at Elevated Temperatures.

D. Zhang¹, D. Huang², R. Wu³, D. Lattery², J. Liu¹, X. Wang^{1,4}, D.B. Gopman⁴, A.K. Mkhoyan³, J. Wang¹ and X. Wang²

1. Electrical and Computer Engineering, University of Minnesota Twin Cities, Minneapolis, MN, United States; 2. Department of Mechanical Engineering, University of Minnesota Twin Cities, Minneapolis, MN, United States; 3. Chemical Engineering and Materials Science, University of Minnesota Twin Cities, Minneapolis, MN, United States; 4. Materials Science and Engineering Division, National Institute of Standards and Technology, Gaithersburg, MD, United States

Bulk perpendicular magnetic anisotropy materials are proposed to be a promising candidate for next-generation ultra-high density and ultralow energy-consumption spintronic devices (1~5). In this presentation, we will report the experimental investigation on the structure, thermal stability, and magnetic properties of FePd thin films seeded by a Ru layer. An *fcc*-phase Ru layer induces the highly-ordered $L1_0$ -phase FePd thin films with perpendicular magnetic anisotropy ($K_u \sim 10.1$ Merg/cm³). The thermal stability of FePd samples is then studied through the annealing process. It is found that a $K_u \sim 6.8$ Merg/cm³ can be obtained with the annealing temperature of 500 °C. In addition, the damping constant α , an important parameter for switching current density, is determined as a function of the testing temperature. We observe that α increases from 0.006 to 0.009 for the as-deposited FePd sample and from 0.006 to 0.012 for the FePd sample annealed at 400 °C as the testing temperature changes from 25 °C to 150 °C (6). These results suggest that Ru-seeded FePd provides great potential in scaling perpendicular magnetic tunnel junctions below 10 nm for applications in ultralow energy-consumption spintronic devices.

1. M. Weisheit, S. Fähler, A. Marty, Y. Souche, C. Poinignon, and D. Givord, *Science* 315, 349-351 (2007). 2. S. Iihama, A. Sakuma, H. Naganuma, M. Oogane, T. Miyazaki, S. Mizukami, and Y. Ando, *Appl. Phys. Lett.* 105, 142403 (2014). 3. S. Iihama, A. Sakuma, H. Naganuma, M. Oogane, S. Mizukami, and Y. Ando, *Phys. Rev. B* 94, 174425 (2016). 4. D.-L. Zhang, K. B. Schliep, R. J. Wu, P. Quarterman, D. R. Hickey, Y. Lv, X. Chao, H. Li, J.-Y. Chen, Z. Zhao, M. Jamali, K. A. Mkhoyan, and J.-P. Wang, *Appl. Phys. Lett.* 112, 152401 (2018). 5. D.-L. Zhang, C. Sun, Y. Lv, K. B. Schliep, Z. Zhao, J.-Y. Chen, P. M. Voyles, and J.-P. Wang, *Phys. Rev. Applied* 9, 044028 (2018). 6. D.-L. Zhang, D. Huang, R. J. Wu, D. Lattery, J. Liu, X. Wang, D. B. Gopman, K. A. Mkhoyan, J.-P. Wang, and X. Wang, *Appl. Phys. Lett.* 117, 082405 (2020)

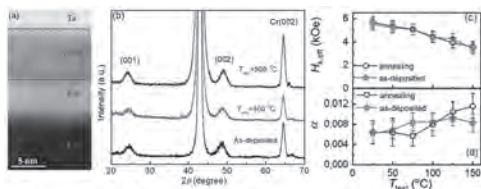


FIG. 1. (a) Atomic-resolution HAADF-STEM image of the as-deposited Ru-seeded FePd thin film. (b) The out-of-plane (θ - 2θ scans) XRD patterns as a function of the annealing temperatures for Ru-seeded FePd thin films. The very clear (001) and (002) peaks of $L1_0$ -phase are observed, indicating the high-ordered FePd thin films. (c), (d) The temperature-dependent effective anisotropic field ($H_{k,eff}$) and damping constant extracted from TR-MOKE measurements for both as-deposited and 400 °C-annealed samples.

IH-06. Creep of Domain Walls in Epitaxial Pd/Co/Pd(111) Trilayers.

*N. Sarnavskiy¹, A. Kozlov¹, M. Steblyi¹ and A. Davydenko¹
1. Far Eastern Federal University, Vladivostok, Russian Federation*

Investigation of a creep of domain walls (DWs) in a combination of the in-plane and out-of-plane magnetic fields may give useful information about the Dzyaloshinskii-Moriya interaction in magnetic films. The first approach of the definition of the DMI field implied simple searching for the minimum in the dependence of the velocities of the DWs on the in-plane magnetic field, $v(H_x)$ [1]. It was considered that when the in-plane magnetic field compensates the DMI field, the energy density of the DW is maximal and the velocity of the DW is minimal. However, papers were published in which the DMI fields measured by other methods like Brillouin light spectroscopy were very different from the magnetic fields of minima in the velocity curves $v(H_x)$ [2]. To explain the shape of strongly asymmetric $v(H_x)$ dependencies different extended models of the creep of DWs were introduced [3, 4]. In this study, we investigate the DMI in the epitaxial Si(111)/Cu/Pd/Co(0.7 nm)/Pd system with the thickness of the bottom Pd layer varying from 0 to 3 nm. Since we measured non-zero DMI in the symmetric Pd/Co/Pd system in the previous paper [5], present study is aimed to understand the origin of the DMI in the symmetric Pd/Co/Pd system. The velocity curves $v(H_x)$ were fitted by the extended dispersive stiffness model [4, 6] and the energy of DMI was derived from the fittings. We carried out the investigation of strains in the interfaces depending on the thickness of the Pd bottom layer, d_{Pd} , by a reflection high energy electron diffraction during the process of fabrication of the samples. We found a large asymmetry of the strains between the bottom Pd/Co and top Co/Pd interfaces in the samples. The bottom Pd layer is initially largely strained when it grows on the Si/Cu(2 nm) surface. Stress is gradually relaxed by the introduction of misfit dislocations in the Pd layers. Co layers grown on the top of Pd underlayers are strained. Strains are partially relaxed during growth of the Co layers. Therefore, strains in the bottom and in the top of Co layers depend on the thickness of the Pd bottom layer. Magnetic hysteresis loops of the samples were measured by a vibrating sample magnetometer and the energy of a perpendicular magnetic anisotropy was defined in the series of samples. We investigated the creep of domain walls by means of a Kerr-microscope equipped with in-plane electromagnet and home-made perpendicular coil. Measured velocity curves of the samples were strongly asymmetric. They may be fitted well only by using a variable velocity prefactor in the creep law, $v = v_0 \exp(-\Delta E/kT)$, $v_0 = v_0^*(1 + \chi^* \cos(\varphi_{eq}))$, where ΔE is an energy barrier, χ^* is the weight of a chiral damping effect, φ_{eq} is an azimuthal angle of the magnetization in the DW. Strictly speaking the nature of the dependence of the velocity prefactor on the in-plane magnetic field is still under debate. In some studies, this effect is named chirality-induced or additional asymmetry effect. The dependence of the chiral damping weight on the Pd bottom layer thickness is shown in Fig. 1. The absolute value of the chiral damping weight increases up to 0.95 at the thickness of the bottom Pd layer of 1 nm and oscillates near this value with further increasing of the thickness of Pd. This behavior of the chiral damping weight is correlated with the dependence of the asymmetry of the strains between the bottom and top interfaces on the thickness of the Pd bottom layer. Therefore, we assume that the possible origin of the strong asymmetry of the velocity curves may be related with strains gradient in the Co layers. The energy of the effective DMI, D_{eff} , as a function of the thickness of the bottom Pd layer is outlined in Fig. 2. The negative energy of effective DMI slightly increases when $d_{Pd} = 0.2$ nm. It may be explained by a structural inhomogeneity of the bottom interface and possible intermixing of Pd and Cu. With further increasing of d_{Pd} , the magnitude of $|D_{eff}|$ decreases. D_{eff} changes a sign at the thickness of Pd layer of 0.8 nm and increases with an increase in the thickness of the Pd bottom layer. The overall dependence of D_{eff} on the d_{Pd} may be explained by the dependence of strains in the interfaces on the thickness of Pd bottom layer. A kink in the $D_{eff}(d_{Pd})$ dependence correlates well with the kink in the dependence of the elastic strains on the d_{Pd} . For the first sight the change in the sign of D_{eff} may be easily explained by the growing influence of the contribution to the DMI from the bottom Pd/Co interface. However, we prepared asymmetric Pd(3 nm)/Co(0.7 nm)/Cu sample with the same strains distribution as in the Pd(3 nm)/Co(0.7 nm)/Pd sample but with near zero DMI. Therefore, the non-zero DMI in the symmetric Pd(3 nm)/Co/Pd(3 nm) sample is caused mainly by the contribu-

tion to the DMI from the top Co/Pd interface. We may conclude that unequal elastic strains in the bottom Pd/Co and top Co/Pd interfaces cause non-zero DMI in symmetric Pd/Co/Pd system. Authors acknowledge the financial support of the Russian Ministry of Science and Higher Education under the state task (0657-2020-0013), the Grant program of the Russian President (Grant No. MK-1384.2021.1.2) and Russian Foundation for Basic Research according to the research project No.19-02-00530.

1. S.-G. Je, D.-H. Kim and S.-C. You, Phys. Rev. B., Vol. 88, p. 214401 (2013).
2. R. Soucaille, M. Belmeguenai, J. Torrejon, Phys. Rev. B., Vol. 94, p. 104431 (2016).
3. J. P. Pellegren, D. Lau and V. Sokalski, Phys. Rev. Lett., Vol. 119, p. 027203 (2017).
4. D.M.F. Hartmann, R. A. Duine, M.J. Meijer, Phys. Rev. B., Vol. 100, p. 094417 (2019).
5. A.V. Davydenko, A.G. Kozlov, A.G. Kolesnikov, Phys. Rev. B., Vol. 99, p. 014433 (2019).
6. D. Lau, J. P. Pellegren, H. T. Nembach, Phys. Rev. B., Vol. 98, p. 184410 (2018).

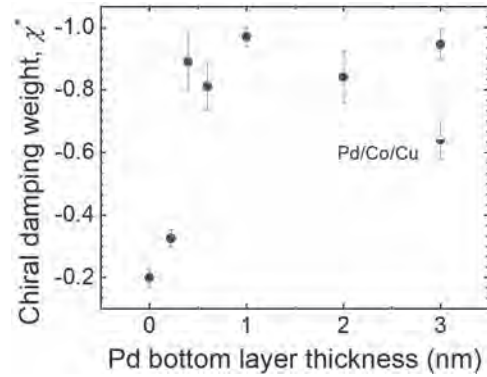


Fig. 1. The Pd thickness dependence of the chiral damping weight in the Si(111)/Cu/Pd(0–3 nm)/Co(0.7 nm)/Pd(3 nm) samples.

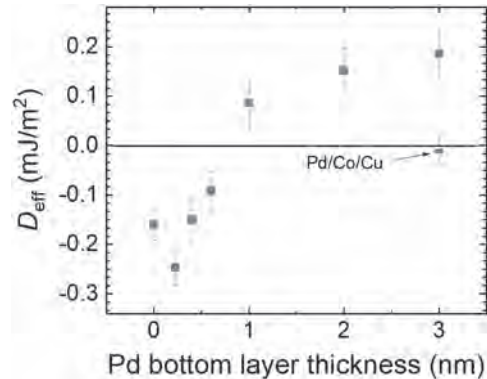


Fig. 2. The Pd thickness dependence of the energy of the effective DMI in the Pd/Co/Pd films.

IH-07. Tailoring of Magnetic Anisotropy in Co and Amorphous CoFeB Thin Films Through Glancing Angle Deposition.

K. Bukharia¹, A. Gupta¹ and P. Pandit²

1. Amity University, Noida, India; 2. Deutsches Elektronen-Synchrotron, Hamburg, Germany

The technique of glancing angle deposition (GLAD) has been widely used in the literature in order to produce thin films with controlled microstructure at nanometer length scale. Glancing angle deposition in general leads to anisotropy in the microstructure resulting in anisotropy in physical properties. The technique has been used in a wide variety of fields like magnetic and optical devices, sensor technologies, photovoltaic cells etc. [1-2] In the present work we have used the GLAD technique to produce controlled magnetic anisotropy in thin films of Co and amorphous CoFeB. Thin films were deposited using ion-beam sputtering. Several depositions were done by varying the angle of deposition between 40° to 80° from surface normal. Figure 1 shows some representative longitudinal MOKE results for CoFeB films deposited at the glancing angles of 60° with applied magnetic field along the tilt axis and normal to it. It has been seen that in the case of Cobalt, upto a glancing angle of 60° the direction of the tilt axis of deposition is the easy magnetization direction. Along the direction normal to the tilt axis, a significantly higher magnetic field is needed to saturate the sample. However, for glancing angle of 70° and above the easy direction gets reverse, making the tilt axis as hard direction. This behavior has been seen in the earlier studies as well. [3] The anisotropy in the magnetization behavior can be understood in the terms of the surface topography of the film and the interplay between magneto static and magnetic exchange energies Interestingly, in the case of amorphous CoFeB film, the results are contradictory to that those in Co films. The easy axis is normal to the tilt axis for lower angle of deposition, and reverses the direction for deposition angle of 70° and above. In order to understand the possible origin of this opposite behavior of magnetic anisotropy in the two samples, we have done a detailed microstructure study using grazing incidence small angle x-ray scattering (GISAXS) measurements at the beamline P03 of PETRA III, Hamburg. Figure 2 show a representative GISAXS image of CoFeB film deposited at glancing angle of 60° . A plume like feature marked by dotted rectangle in Fig. 2 is seen, which has also been observed in earlier studies, and has been attributed to the specific morphology of the film consisting of nano-columnar structure with the longitudinal axis of the columns tilted with respect to the surface normal. Average separation between the nanocolumns, D , which gives rise to the maximum in the intensity in the plume, is obtained using the relation [4]: $D=2\pi/q_{y_{max}}$... (1) where $q_{y_{max}}$ is the magnitude of the y-component of the scattering vector corresponding to the position of the maximum of the intensity in the plume. The angle which q_{max} makes from the vertical $q_y=0$ axis gives the tilt angle of tilt of the nanocolumns. A broad peak around the $q_{y_{max}}$ value obtained from the intensity profile extracted by taking a horizontal strip along the q_y direction reveals that there is a large distribution in the inter-columnar separation around the mean value. It has been observed that the inter-columnar distance D , as measured from GISAXS increases with the increasing glancing angle and is almost double for Co as compared to that for CoFeB. The inter columnar distance D for various glancing angles are:- for Co, (D for $55^\circ=11.2\text{nm}$, $60^\circ=12.7\text{nm}$, $65^\circ=13.5\text{nm}$, $70^\circ=19.9\text{nm}$, $75^\circ=29.5\text{nm}$) and for CoFeB (D for $40^\circ=5.5\text{nm}$, $50^\circ=5.6\text{nm}$, $60^\circ=6.5\text{nm}$, $70^\circ=8.1\text{nm}$, $80^\circ=17.8\text{nm}$). It has been found that the columnar tilt with respect to surface normal is higher for Co than that of CoFeB. This suggests that microstructures formed by the ballistic shadowing of the flux are very different in the two cases. The deposition of films of both Co and CoFeB results in nano-columnar growth but the length scale of the growth in the two cases is different. The opposite behavior of easy magnetization direction in CoFeB and cobalt may be related to the modified inter-columnar magneto-static interaction due to difference in the columnar structures of cobalt and amorphous CoFeB.

[1] Michael. T. Taschuk et al. Glancing Angle Deposition, P.M. Martin (Ed.), Handbook of deposition technologies for films and coatings (3rd ed.), Elsevier, Oxford, UK, pp. 621-651 (2010) [2] Matthew M. Hawkeye and Michael J. Brett, Journal of Vacuum Science & Technology A 25, 1317

(2007) [3] C. Quirós et al., Nanotechnology. 25 335704 (2014) [4] L. González-García, et al., ChemPhysChem. 11, 2205 (2010)

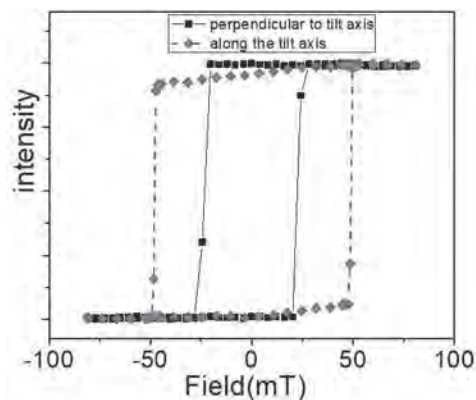


Fig 1 (a) Hysteresis loop of CoFeB film deposited at 60° from the surface normal for i) along the tilt axis (dotted line) and ii) perpendicular to the tilt axis (continuous line)

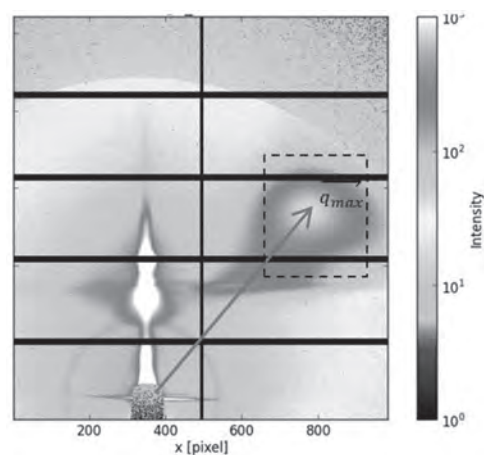


Fig 2-Experimental GISAXS pattern of nanocolumn deposited at oblique angle of 60° from the surface normal. The plume arising due to the tilted columns is marked by dotted rectangle

IH-08. High-Coercive Hexagonal MnBi Micro-Islands With Tunable Magnetic Anisotropy and Stripe Magnetic Domain Patterns.

M. Villanueva¹, C. Navío¹, E. Sanchez², P. Pedraz¹, P. Olleros-Rodríguez¹, L. Zha⁴, P. Perna¹, J. Camarero^{1,3}, J. Yang⁴, P.S. Normile², J. de Toro² and A. Bollero¹

1. *Fundacion IMDEA Nanociencia, Madrid, Spain*; 2. *IRICA, Universidad de Castilla-La Mancha, Ciudad Real, Spain*; 3. *Condensed Matter Physics Department, Universidad Autonoma de Madrid, Madrid, Spain*; 4. *State Key Laboratory for Mesoscopic Physics, School of Physics, Peking University, Beijing, China*

Permanent micro-magnets are widely used in many devices such as MEMS and diverse biological applications. However, their fabrication typically includes several complex processing steps. MnBi is an intermetallic ferromagnetic alloy that possesses good permanent magnet properties such as a high Curie temperature of 711 K, a high magnetocrystalline anisotropy of 1.6 MJ/m³ at room temperature, a relatively high (BH)_{max} of around 20 MGOe and, remarkably, an unusual positive temperature coefficient of the coercivity [1,2], which makes MnBi an attractive rare earth-free alternative for high temperature applications. In this study, a one-step route has allowed for the fabrication of highly crystalline hexagonal MnBi micro-islands (lateral dimension of 30 μm and thickness of 0.2 – 2.1 μm), by RF-sputtering of a composite target onto glass substrates at different deposition temperatures (T_D) [3]. A strong impact of T_D on the magnetic properties has been proven. Specifically, magnetic anisotropy could be tuned from out-of-plane (T_D < 375 K) to in-plane (T_D = 475 K), remarkably, without applying any external magnetic field during the deposition. High values of coercivity have been obtained: 13.1 kOe at 400 K along the out-of-plane direction for the sample grown at 375 K and 14.1 kOe at 400 K along the in-plane direction for the sample grown at 475 K. The sample topography and the magnetic domain structure have been studied, observing a strong perpendicular anisotropy in micro-islands with a crater-like shape as shown in the scheme of Figure 1. It has been observed that the periodicity of stripe domains obeys the $D = 1.18 \cdot \sqrt{T}$ law [4] in good agreement with theoretical predictions (data points and red line in Figure 1). We have validated the dependency of D vs T in MnBi thin films previously reported in literature, which has been possible through the MFM study (Fig. 1) of the crater-like shape of our MnBi micro-islands [3]. Moreover, this study has allowed us to extend the dependency of D vs T for MnBi in a thickness range well beyond previously published results. Acknowledgements IMDEA acknowledges financial support from the EU M-ERA.NET Network and MINECO through “NEXMAG” (Project Success Case at H2020 M-era.Net, Ref. PCIN-2015-126) and “3D-MAGNETOH” (Ref. MAT2017-89960-R); and from CM through “NANOMAGCOST” (Ref. P2018/NMT-4321).

[1] K. Patel *et al.*, *Nanoscale* 10, 11701 (2018) [2] E. Céspedes *et al.*, *J. Alloys Compd.* 729, 1156 (2017); M. Villanueva *et al.*, *AIP Adv.* 9, 035325 (2019) [3] M. Villanueva *et al.*, Submitted for publication (2021) [4] C. Kittel, *Physical Review* 70, 11-12 (1946)

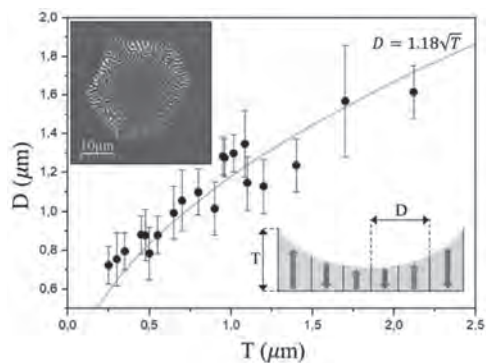


Figure 1. Dependence of domain width (D/2) on the thickness (T) of the MnBi micro-islands from MFM images (inset) measured at remanence after sample demagnetization. The $D = 1.18 \cdot \sqrt{T}$ law is obtained by fitting the data points (red line).

IH-09. Epitaxial Ferrimagnetic Mn_4N Thin Films on GaN by Molecular Beam Epitaxy.

Z. Zhang¹, Y. Cho¹, M. Gong¹, S. Ho¹, J. Singhal¹, J. Encomendero¹, X. Li¹, H. Lee¹, H.G. Xing¹ and D. Jena¹

1. Cornell University, Ithaca, NY, United States

The III-nitride family of wide bandgap semiconductors GaN, AlN, and their alloys are important for diverse applications ranging from solid-state lighting to RF and power electronics [1]. The long spin lifetimes in nitride semiconductor platform [2] makes it attractive for exploiting the spin degree of freedom of conducting electrons. The ferromagnet/semiconductor heterostructure is crucial for fundamental spin-related device building blocks such as spin injection, spin transport, spin detection [3] and spin to charge conversion [4]. Memory devices utilizing spin-orbit torques require *smooth* interfaces between ferromagnets and the heavy metal or topological insulator layers on top for efficient spin transmission [5]. Epitaxial growth of magnetic layers with *smooth* surfaces on GaN hosting desirable properties for spintronic applications will provide a path towards spintronic devices for energy-efficient memory applications, and its integration with GaN-based RF, photonic, and wide-bandgap CMOS platforms [6]. Mn_4N , a metallic nitride ferrimagnet, is an attractive candidate for direct epitaxial integration with GaN and AlN for all-nitride ferromagnet/semiconductor heterostructures. MBE grown Mn_4N thin films on cubic substrates such as MgO and SrTiO₃ (STO) exhibit desirable properties for spintronic applications such as a high critical temperature ($T_N \sim 740$ K), large spin polarization ($P \sim 70\%$), strong perpendicular magnetic anisotropy ($K_u = 1.1 \times 10^5$ J/m³), low saturation magnetization ($M_s = 7.1 \times 10^4$ A/m on STO), large domains (\sim millimeter size on STO) and high domain wall velocities (up to 900 m/s) [7, 8]. Through exploration of nucleation and growth conditions, we uncover plasma-assisted MBE growth conditions needed for significantly improved epitaxial growth of c-axis aligned Mn_4N on GaN with smooth surface morphologies. A series of four samples were grown in which the growth temperature of the 80 nm Mn_4N layer was varied from $T_s = 150$ C to $T_s = 375$ C, after the deposition of 100 nm homoepitaxial undoped GaN buffer layers at $T_s = 670$ C, as shown in Fig. 1. Instead of out-of-plane [111] orientation of Mn_4N on GaN as found in reactive MBE [9], Mn_4N layers grown using plasma-assisted MBE in this work are dominated by [001] orientation, and exhibit 12-fold in-plane symmetry in the diffraction pattern. Smooth Mn_4N layers are obtained at low growth temperatures of $T_s \leq 300$ C, though deep pits with depth ~ 10 nm measured by atomic force microscopy are present in the film grown at $T_s = 300$ C. The magnetic properties of Mn_4N grown on hexagonal GaN are comparable to those in earlier reports on cubic substrates such as MgO, and can be tailored by varying the growth temperature. For example, with the increase of growth temperature, the anomalous Hall resistance hysteresis loop (Fig. 2) not only becomes squarer but also exhibits an interesting sign-flip from n-type to p-type between $T_s = 225$ C and $T_s = 300$ C. Details about the structural and magnetic properties of Mn_4N on GaN will be presented.

[1]. D. Jena, *et al.*, Japanese Journal of Applied Physics 58, SC0801 (2019).

[2]. S. Krishnamurthy, *et al.*, Applied physics letters 83, 1761 (2003).

[3]. A. Song, *et al.*, Applied Physics Express 13, 043006 (2020). [4]. W.

Stefanowicz, *et al.*, Physical Review B 89, 205201 (2014). [5]. Q. Shao,

et al., Nature communications 9, 1 (2018). [6]. S. J. Bader, *et al.*, IEEE

Electron Device Letters 39, 1848 (2018). [7]. T. Gushi, *et al.*, Nano Letters

19, 8716 (2019). [8]. T. Gushi, *et al.*, Japanese Journal of Applied Physics

57, 120310 (2018). [9]. S. Dhar, *et al.*, Applied Physics Letters 86, 112504

(2005).

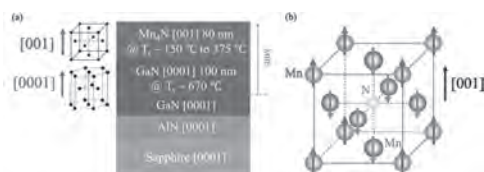


Fig. 1 (a) Schematic of the epitaxial structures in this study and (b) Crystal and magnetic structure of Mn_4N .

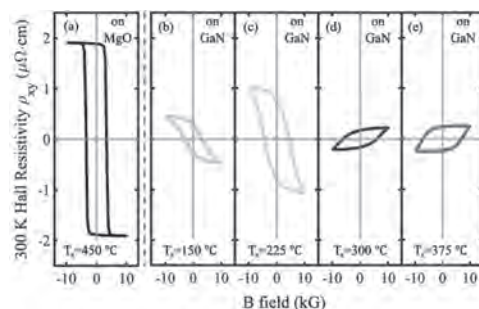


Fig. 2 Anomalous Hall resistance hysteresis loops at 300 K for Mn_4N layers grown on MgO at (a) 450 C and on GaN at (b) 150 C (c) 225 C (d) 300 C and (e) 375 C. Note the flip in the loop orientation from (c) to (d), indicating n-type to p-type conversion.

IH-10. Strain and Ferromagnetic Proximity Induced Spin Reorientation Transition in NiO.

W. Janus¹, A. Koziol-Rachwał¹, M. Slezak¹, M. Zajac², P. Drozdzi¹, M. Szpytma¹, H. Nayyef¹ and T. Slezak¹

1. Faculty of Physics and Applied Computer Science, AGH University of Science and Technology, Krakow, Poland; 2. National Synchrotron Radiation Centre SOLARIS, Jagiellonian University, Krakow, Poland

Ability to control the spin orientation in antiferromagnets (AFMs) has recently attracted a lot of attention [1]. In our recent work we performed systematic studies on magnetic properties of NiO in Fe/NiO/Cr/MgO multilayers for various Cr thicknesses [2]. We proved existence of a continuous strain-induced spin reorientation transition (SRT) in NiO from nearly out-of-plane direction in Fe/NiO/MgO to the in-plane direction in Fe/NiO/Cr. For ultrathin NiO layers the in plane direction of AFMs spins was determined to be perpendicular to Fe spins due to spin-flop interaction. In this contribution we studied magnetic properties of NiO in NiO/MgO(d_{MgO})/Cr(20 nm)/MgO(001) for different MgO thicknesses, d_{MgO} . We also investigated how the adjacent ferromagnetic coverage layer influence the spin structure in NiO. X-ray Magnetic Linear Dichroism (XMLD) technique was used to determine magnetic ordering in NiO. The XAS spectra were collected using a linearly polarized x-ray beam for the Ni²⁺ L₂ edge at normal ($\gamma = 0^\circ$) and grazing ($\gamma = 60^\circ$) x-ray incident angles. The XAS spectra were measured as a function of MgO buffer layer thickness for NiO/MgO/Cr, MgO/NiO/MgO/Cr and Fe/NiO/MgO/Cr. Figure 1 shows L₂ ratio difference, defined as $\Delta RL_2 = RL_2(\gamma = 0^\circ) - RL_2(\gamma = 60^\circ)$, as a function of d_{MgO} for NiO with different capping layers. For both, capped and non-capped NiO layers we noted an increase in ΔRL_2 with an increase in d_{MgO} . According to the previous studies [3] increase of ΔRL_2 can be interpreted as enhancement of the out-of-plane component of NiO spins. Thus, our results show that insertion of MgO layer between NiO and Cr leads to development of out-of-plane NiO spin direction, which can be understand in terms of tensile strain exerted by MgO buffer layer on NiO. Interestingly, while there are no significant differences between $\Delta RL_2(d_{MgO})$ dependences for MgO-capped and uncapped NiO layers (Fig. 1, circles, triangles), a change of ΔRL_2 as a function of MgO thickness is much more pronounced for Fe/NiO/MgO/Cr (Fig. 1, stars). Moreover, only for Fe/NiO/MgO/Cr ΔRL_2 changes a sign with an increase of d_{MgO} which indicates that NiO spins undergo an SRT from in-plane to out-of-plane direction. To investigate the influence of Fe/NiO interactions on SRT in NiO a dedicated sample was prepared. Wedge-shaped Fe layer was grown on NiO(2 nm)/MgO(8.5 nm)/Cr(20 nm)/MgO(001), where the d_{MgO} layer was chosen to be near the critical thickness of MgO for which SRT in NiO was observed. To elucidate if modulation of magnetic structure in NiO is influenced by magnetic properties of Fe or rather by strains from capping layer, half of the sample was capped with wedge-shaped Cr. Due to the small lattice mismatch between Cr and Fe (1.5%) strain-induced changes in magnetic properties of NiO should be similar for Cr/NiO/MgO and Fe/NiO/MgO. Prior to XAS measurement the sample was magnetized along the Fe[001] (NiO[110]) in-plane direction ($\phi = 0^\circ$) to study the influence of Fe magnetization on NiO spin structure. Figure 2(a) shows ΔRL_2 dependence on $d_{Fe/Cr}$ for two azimuthal angles, ϕ . In case of Cr/NiO, for both $\phi = 0^\circ$ and $\phi = 90^\circ$ we noted no considerable ΔRL_2 changes as a function of Cr thickness (d_{Cr}) (Fig. 2(a) circles, triangles). For Fe/NiO we noted a drastic difference in $\Delta RL_2(d_{Fe})$ dependence for $\phi = 0^\circ$ and $\phi = 90^\circ$. Strong ΔRL_2 dependence on d_{Fe} observed for $\phi = 90^\circ$ and a lack of change in ΔRL_2 as a function of d_{Fe} for $\phi = 0^\circ$ was noted for Fe/NiO/MgO/Cr, which brings two conclusions. First, a change of sign in $\Delta RL_2(d_{Fe})$ obtained for $\phi = 90^\circ$ proves that SRT from in-plane to out-of-plane direction in NiO can be obtained as a function of Fe thickness. Dependence of $\Delta RL_2(d_{Fe})$ on azimuthal angle in Fe/NiO/MgO together with a lack of ΔRL_2 dependence on d_{Cr} in Cr/NiO/MgO prove that reorientation of NiO spins is not related to the strains exerted by capping layer, but to the magnetism of Fe layer. Second, a difference between $\Delta RL_2(d_{Fe})$ for $\phi = 0^\circ$ and $\phi = 90^\circ$ indicates that together with an increase in Fe thickness an in-plane anisotropy of NiO is developed. This conclusion was confirmed in XAS measurements collected as a function of ϕ (γ was set to 0) for different Fe thicknesses (Fig. 2(b)). While for $d_{Fe} = 2 \text{ \AA}$ no change in the $RL_2(\phi)$ was observed, for $d_{Fe} \geq 8 \text{ \AA}$ we noted well-pronounced extrema in the $RL_2(\phi)$ dependence for the NiO[110] and [1-10]. According to the previous studies

[3], if the RL_2 reaches an extremum when the polarization vector is parallel to the [110] NiO direction, the AFM spin alignment is determined from the maximum of the RL_2 . Thus, an in-plane component of NiO spins is perpendicular to the spins of Fe. Our results show that spin structure of antiferromagnet can be modulated by strain induced by the buffer layer and emphasize the role of adjacent ferromagnetic layer on the magnetic structure in AFM. This work was supported by the "Antiferromagnetic proximity effect and development of epitaxial bimetallic antiferromagnets – two routes towards next-generation spintronics" project, which is carried out within the Homing programme of the Foundation for Polish Science co-financed by the European Union under the European Regional Development Fund.

- [1] C. Song, Y. You and X. Chen, *Nanotechnology*, Vol.29, p.112001(2018)
 [2] A. Koziol-Rachwał, M. Slezak, M. Zajac, *APL Mater.*, Vol.8, p.061107 (2020) [3] W. Kim, E. Jin, J. Wu, *Phys. Rev. B.*, Vol.81, p.174416 (2010)

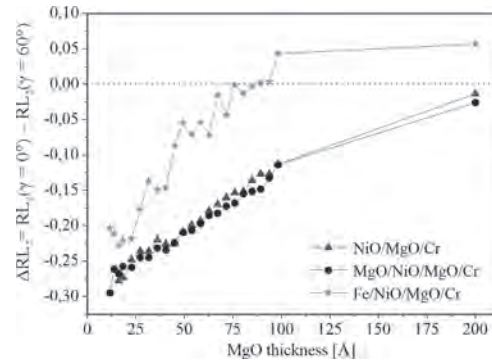


Fig. 1. XLD magnitudes of NiO in the NiO/MgO/Cr, MgO/NiO/MgO/Cr, Fe/NiO/MgO/Cr.

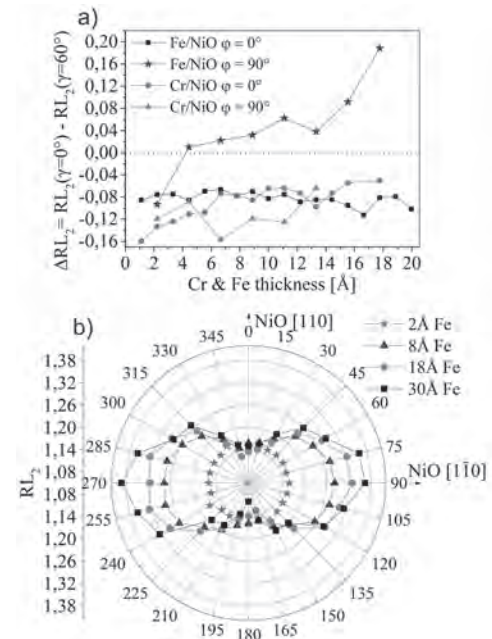


Fig. 2. a) XLD magnitudes of NiO in the Fe/NiO and Cr/NiO as a function of $d_{Fe/Cr}$, b) Ni $RL_2(\phi)$ as a function of polarization angle ϕ for Fe(2 Å)/NiO, Fe(8 Å)/NiO, Fe(18 Å)/NiO and Fe(30 Å)NiO.

IH-11. Tailoring the Magnetic Anisotropy and Controlling the Spin Orientation in Antiferromagnetic NiO(111) Films on Fe(110).

H. Nayyef¹, M. Slezak¹, P. Drozd¹, W. Janus¹, A. Koziol Rachwal¹, M. Szpytma¹, M. Zajac², T. Mentès³, F. Genuzio³, A. Locatelli³ and T. Slezak¹

1. Faculty of Physics and Applied Computer Science, AGH University of Science and Technology, Krakow, Poland; 2. National Synchrotron Radiation Centre SOLARIS, Jagiellonian University, Krakow, Poland; 3. Elettra - Sincrotrone Trieste, Basovizza, Italy

The ability to modify the magnetic anisotropy and to control spin state of AFM materials is interesting from both a fundamental and an application point of view. By taking advantage of AFM/FM coupling, magnetic anisotropy of AFM sublayer can be tailored either by appropriate choice of FM thickness or in uniform thickness system by temperature induced processes [1]. Additionally, magnetic state of the AFM can be controlled by small external magnetic field. Here, we follow the magnetic properties of epitaxial NiO(111)/Fe(110) bilayers on W(110) substrate using XMCD and XMLD spectroscopy together with PEEM microscopy. We find that the magnetic spins in NiO are rotatable within the NiO(111) plane and both NiO magnetic anisotropy and orientation of AFM spins are determined by the magnetic properties of underlying ferromagnetic Fe layer. Specifically, magnetic state and anisotropy of antiferromagnetic NiO can be modified by tuning the thickness of Fe, changing the temperature or applying small external magnetic field. A special sample was prepared for X-PEEM measurements in order to image the magnetic domain pattern below and above the critical Fe thickness of in-plane Spin Reorientation Transition (SRT). The sample consisted two 50Å and 200Å thick Fe(110) regions, covered by homogeneous (40Å) layer of NiO(111). Fig. 1 a shows XMCD-PEEM and XMLD-PEEM images of the border spot between the two Fe thicknesses. The photon helicity k is aligned parallel to the Fe[1-10] direction which is easy axis of thin Fe and perpendicular to the bulk-like Fe[001] easy axis of 200Å thick Fe(110) region. The zig-zag pattern indicates the 90° in-plane rotation of Fe magnetization across the Fe (50/200Å) boundary. XMLD-PEEM image acquired at the Ni L₂ edge (Fig. 1 a, middle panel, “XMLD Ni L₂V POL”), with the linear polarization of incoming X-rays oriented in the Fe(110) || NiO(111) surface plane shows that magnetic domain structure of Fe in the vicinity of SRT is directly imprinted into the antiferromagnetic NiO overlayer. The transition between orthogonally oriented ferromagnetic Fe regions is reflected in the shape of the magnetic domain structure of AFM NiO. In XMLD-PEEM image acquired with horizontal polarization of incoming beam (bottom panel of Fig. 1 a, “Ni L₂H POL”) magnetic contrast totally vanishes because the X-ray polarization is along the surface normal. This confirms that the NiO spins are confined within NiO(111) plane and no out-of-plane magnetic components are present. In case of NiO, the magnitude of XMLD effect is usually defined by the ratio of the two characteristic peaks at L₂ absorption edge of Ni (R_{L2}). We define R_{L2} as the higher-energy peak intensity divided by the intensity of the lower one. R_{L2} ratios were determined for both normal ($\gamma = 0^\circ$) and grazing ($\gamma = 60^\circ$) incidence geometries and we define their difference as $|\Delta R_{L2}| = |R_{L2}(\gamma = 0^\circ) - R_{L2}(\gamma = 60^\circ)|$. Fig. 1 b shows polar plots $\Delta R_{L2}(\varphi)$ of ΔR_{L2} as a function of the azimuthal in-plane angle φ between polarization and Fe[1-10] direction. Instead of three-fold in-plane symmetry observed for bulk NiO(111) in pioneering works [2], exchange coupling with neighboring Fe layer makes the in-plane magnetic anisotropy of NiO two-fold with its easy axis determined by the magnetic anisotropy of ferromagnet. Specifically, NiO and Fe spins couple collinearly at the interface and so the easy axis of NiO is parallel to Fe[1-10] or Fe[001] on 50 and 200Å thick regions, respectively. In Fig. 1 c we show element sensitive magnetic hysteresis loops measured by means of XMCD and XMLD for ferromagnetic Fe and antiferromagnetic NiO sublayers, respectively. Typical square hysteresis curve is observed for thin Fe region which is below SRT critical thickness, while hard axis loop with almost zero magnetization in remanent state is presented for 200Å thick Fe. In case of NiO, on 50Å thin Fe region, external magnetic field makes no changes in XMLD as it is insensitive to 180° reversal of AFM spins. Contrary, on thick Fe one can clearly see a change of R_{L2} as a function of small external magnetic field (~ 500 Oe). Recently we showed that in a uniform thickness NiO(111)/Fe(110) epitaxial bilayer system, at given temperature near 300 K, two magnetic states with orthogonal spin orienta-

tions can be stabilized in antiferromagnetic NiO [1]. Field-free, reversible switching between these two AFM states was demonstrated. Here we present results of systematic investigations of such field-free, temperature induced switching of AFM NiO spins. A sample prepared for that purpose contained several 300 μm wide Fe stripes with different thickness in the range of (92Å – 113Å). Fig. 2 shows temperature dependence of R_{L2} ratio for various thicknesses of Fe (only heating branch is shown for clarity). It is clear that depending on the Fe thickness a critical temperature of SRT in AFM NiO can be tuned. With increasing Fe thickness the critical temperature, at which NiO spins rotate in-plane by 90° towards Fe[1-10] direction, continuously increases. This provides possibility to cover wide temperature window ~ (250 – 380 K) for field-free, reversible switching of AFM spins.

References [1] M. Slezak, P. Drozd, W. Janus, H. Nayyef, A. Koziol-Rachwal, M. Szpytma, M. Zajac, T.O. Mentès, F. Genuzio, A. Locatelli and T. Slezak. *Nanoscale* 2020, 12, 18091. [2] K. Kurosawa, M. Miura, S. Saito, *J. Phys. C: Solid St. Phys.* 13 (1980) 1521-7

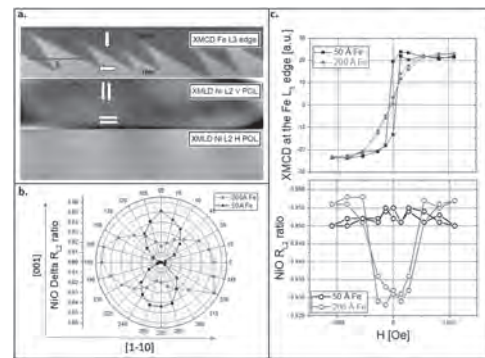


Fig. 1 (a) XMCD-PEEM and XMLD-PEEM images at the border between thick (up) and thin (down) Fe (110) regions (200 and 50Å). (b) polar plot of XMLD for NiO (111) sublayer as a function of azimuthal in-plane angle (c) XMCD and XMLD magnetic hysteresis loops for Fe and NiO respectively.

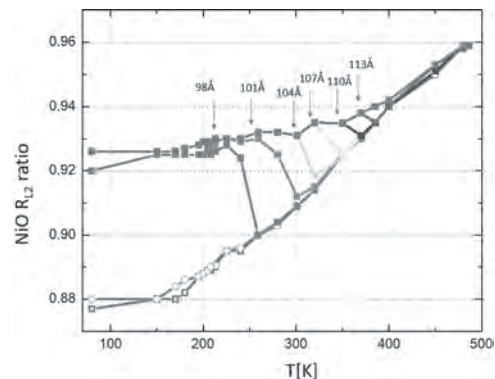


Fig. 2. Temperature dependence of XMLD (R_{L2}) shows SRT in AFM NiO during heating process for various Fe(110) thicknesses.

IH-12. Domain Wall Pinning in Epitaxial Spinel Ferrites Grown on Ru.

S. Ruiz Gómez¹, A. Mandziak^{1,2}, C. Munuera³, A. Quesada³, J. Prieto³,
M. Foerster¹, L. Aballe¹ and J. De La Figuera³

1. *Alba Synchrotron, Cerdanyola del valles, Spain*; 2. *SOLARIS National Synchrotron Radiation Center, Cracow, Poland*; 3. *Consejo Superior de Investigaciones Científicas, Madrid, Spain*

In the last decades, transition metal oxides are growing in importance in spintronic applications. There are many different magnetic oxides, all of them very stable, with a wide range of properties that could allow broadening the range of spintronic applications [1]. Furthermore, the physical properties of these materials can be tuned by reducing the material to the nanoscale, tuning the composition, and/or incorporating it to heterostructures. However, in many cases, growth defects such as antiphase boundaries can strongly affect their magnetic properties, acting as pinning centers for magnetic domain walls. Considering their potential, it is essential to develop growth methods that allow engineering high quality oxide-based epitaxial nanostructures with customizable functionalities [2], as well as to develop the tools to fully characterize them. Extremely high-quality oxide films can be obtained by depositing metals by molecular beam epitaxy on a hot substrate, while the sample is exposed to an oxidizing agent such as molecular oxygen. We have used this method to fabricate ultrathin spinel islands of up to 100 μm^2 area, with nanometer thickness and atomically flat surfaces. By this method many spinel islands (CoFe₂O₄ [3], Fe₃O₄ [4] and NiFe₂O₄ [5]) grow from single crystallographic nuclei and are thus expected to be antiphase boundaries-free. The extremely low defect concentration leads to a robust magnetic order and exceptionally large magnetic domains. Different microscopy techniques can be used to explore the magnetic configuration of these nanoobjects but few provide information about the vector configuration of the magnetic moments. In this work we use PhotoEmission Electron Microscopy with X-Ray Magnetic Circular Dichroic contrast (XMCD-PEEM) in order to obtain 3D information of the magnetic configuration of in-situ grown single crystal nanometer-thick islands, by acquiring images at different photon beam incidence angles. The 3D magnetization maps were used as the initial magnetization configuration for micromagnetic simulations of islands with the same lateral and vertical dimensions as the experimental ones. A careful analysis of the magnetic configuration was done by combining XMCD-PEEM with atomic force microscopy and Low Energy Electron Microscopy (LEEM) maps in order to tackle which effects might be responsible for the differences between measured and simulated experimental domain landscape. We will show how the combination of XMCD-PEEM, LEEM and modelling is a very powerful tool for the study of magnetic configurations of nanometer sized objects, and how the atomic steps in the Ru substrate give rise to efficient pinning sites for the domain walls in the particular case of ultrathin CoFe₂O₄ ferrites.

[1] S. Gariglio, et al. Rep. Prog. 82, 012501, (2019) [2] S. Farokhipoor et al. Nature, 515, 379, (2015). [3] L. Martín-García et al. Adv. Mater. 27, 5955, (2015) [4] S. Ruiz-Gómez, et al. Nanoscale 10, 5566 (2018). [5] A. Mandziak et al. Scientific reports 8, 1, (2018).

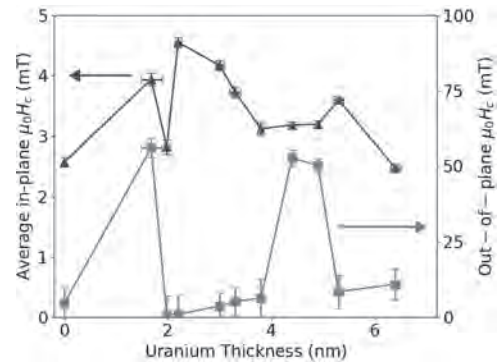
IH-13. Uranium-Based Spintronics.

E.R. Gilroy^{1,2}, M. Wu², M. Gradhand², R. Springell² and C. Bell²

1. The University of Sheffield, Sheffield, United Kingdom; 2. University of Bristol, Bristol, United Kingdom

Large spin orbit coupling (SOC) is at the heart of many magnetic phenomena important for spintronic systems such as magnetic anisotropy, the spin Hall effect (SHE), and the Dzyaloshinskii-Moriya interaction. In a simple picture, the SOC of a material increases $\sim Z^2$, where Z is the atomic number [1]. Therefore there has recently been intense focus on systems containing heavy non-magnetic metals such as Pt, Au and Ir. However, heavy metals may also result in undesirable effects within these systems, such as enhanced spin damping in the ferromagnetic layer [2], and proximity-induced magnetism, which may inhibit the efficiency of spin current detection through the inverse SHE [3]. Understanding the influence of the interfacial induced moment and the large SOC is an important challenge. To understand and disentangle the roles of induced moment and large SOC, the study of uranium - with the largest Z for a naturally occurring element - may be of considerable interest. Earlier X-ray magnetic circular dichroism studies of U/FM (FM = Fe, Ni, Co) superlattices observed negligible induced moment in U when grown on FM = Ni, Co, but a relatively large moment when U is grown on Fe [4,5]. Through comparing and contrasting studies of Fe/U and Ni/U, the phenomena related to proximity induced moment and SOC may potentially be identified. Bilayer films with the structure glass/Fe(~ 8 nm)/U(0-6.5 nm)/Nb(~ 10 nm) were fabricated by dc magnetron sputtering. Both the in-plane and out-of-plane magnetic anisotropy was investigated through vibrating sample magnetometry. The average in-plane coercive field for each sample provides a quantitative measure of the in-plane magnetic anisotropy and the effect uranium has. Fig.1 illustrates the non-monotonic behaviour of the average coercive field of each sample as a function of uranium thickness (triangles). Given that the iron layers thicknesses are not in the ultra-thin limit, it is not expected that any perpendicular magnetic anisotropy (PMA) would be observed. However, as seen in Fig.1 (squares), a small subset of samples do exhibit PMA. It does not appear that there is significant correlation between the in-plane anisotropy and the samples which display out-of-plane behaviour. Out-of-plane measurements revealed perpendicular magnetisation for samples with thicknesses $d_U = 1.7, 4.4$ and 5.0 nm. The unexpected presence of PMA in these relatively thick films can not be easily explained and significant further study would be required to pinpoint its origin. This non-monotonic behaviour of the in-plane anisotropy is likely linked to quantum well states which form in the uranium overlayers. Computational calculations of the Bloch spectral functions for α -U indicate possible regions in the electronic structure which might drive this behaviour. Magnetometry studies on Ni/U also reveal non-monotonic behaviour in the in-plane anisotropy with uranium thickness, though on a smaller scale, most likely due to the weaker hybridisation of Ni and U.

[1] Y. Tserkovnyak, *et al.* Rev.Mod. Phys., 77, 1375 (2005) [2] S. Mizukami, Y. Ando, and T. Miyazaki, Phys. Rev. B., 66, 104413 (2002) [3] S. Y. Huang, *et al.*, Phys. Rev. Lett., 109, 107204 (2012) [4] R. Springell, *et al.*, Phys. Rev. B., 77, 064423 (2008) [5] F. Wilhelm, *et al.*, Phys. Rev. B., 76, 024425 (2007)



Average in-plane coercive field (triangles) as a quantitative measure of in-plane magnetic anisotropy in comparison with the out-of-plane coercive field measurements (squares).}

IH-14. Thermally Activated Processes for Ferromagnet Intercalation in Graphene-Heavy Metal Interfaces.

A. Gudín Holgado^{2,1}, J.M. Diez^{2,1}, A. Anadón², C. Ayani², P. Olleros-Rodríguez², F. Ajejas^{2,1}, I. Arnay², R. Guerrero², F. Calleja², J. Camarero^{2,1}, R. Miranda^{2,1} and P. Perna²

1. Instituto Nicolás Cabrera & IFIMAC, Universidad Autónoma de Madrid, Madrid, Spain; 2. Nanoscience, Instituto Madrileño de Estudios Avanzados, Madrid, Spain

The future sensing and data storage technologies will be based on the exploitation of the spin-orbit physics in ferromagnetic-heavy metal systems. Graphene (Gr), a single atomic layer of graphite, is considered an ideal material for room temperature spintronics because of its unique and intrinsically tuneable electronic properties [1]. However, its technological development for this purpose relies on the capability to engineer high-quality interfaces in which the negligible intrinsic spin-orbit interaction in Gr would be modified to allow for efficient room-temperature spin injection, detection, manipulation, or gating [2]. We have introduced a novel methodology based on the combined use of ultrahigh vacuum growth, metal intercalation, spectroscopy, and tunneling microscopy to fabricate and characterize in situ high-quality Gr-based, perpendicular magnetic anisotropy systems [3]. By combining a collection of surface science ultra-high vacuum techniques, including XPS, LEED and STM, and performing experiments as functions of the annealing temperature, the team has discerned the processes of Co intercalation underneath Gr grown epitaxially on two different heavy metal surfaces, Pt and Ir, which were deposited onto (111)-oriented insulating oxides. The experiments show that the thermally activated Co intercalation occurs in two steps in which the deposited atoms penetrate in Gr either via direct Co-C exchange or through surface defects and edges. The intercalated atoms diffuse then in 2D underneath Gr and form flat, homogeneous, and crystalline layers. These processes are characterized by a low activation temperature. The Co intercalation occurs at lower temperature and is more efficient in Gr/Pt interfaces than Gr/ Ir. Higher temperatures promote the intermixing between the FM and the metallic buffer. This research demonstrated that the metal intercalation allows for efficient tuning of the structural and electronic properties of Gr and enables the growth of high-quality flat layers with tailored magnetic properties.

[1] W. Han, R.K. Kawakami, M. Gmitra and J. Fabian, Graphene Spintronics, Nat. Nanotech. 9, 794 (2014). [2] F. Ajejas, *et al.*, *Unravelling Dzyaloshinskii–Moriya interaction and chiral nature of Graphene/Cobalt interface*, Nano Lett. 18(9), 5364-5372 (2018). [3] F. Ajejas, *et al.* ACS Applied Materials & Interfaces 12 (3), 4088-4096 (2020).

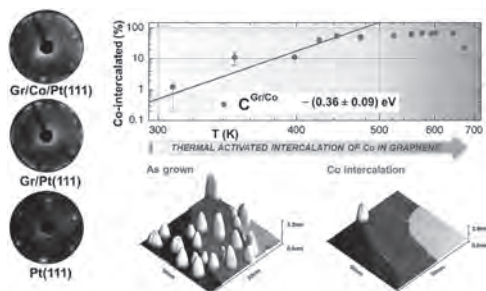


Figure 1. The thermally activated Co intercalation underneath Graphene occurs in two steps in which the deposited atoms penetrate in Gr either via direct Co-C exchange or through surface defects and edges. The intercalated atoms diffuse then in 2D underneath Gr and form flat, homogeneous and crystalline layers [3].

IH-15. Withdrawn

Session IP

**DOMAIN WALLS, ENERGY-ASSISTED RECORDING AND RECORDING PHYSICS
(Poster Session)**

Tomoya Nakatani, Chair
National Institute for Materials Science, Tsukuba, Japan

IP-01. Effects of Static Magnetic Fields and Temperature on 3D Magnetic Storage in Heated Dot Magnetic Recording.

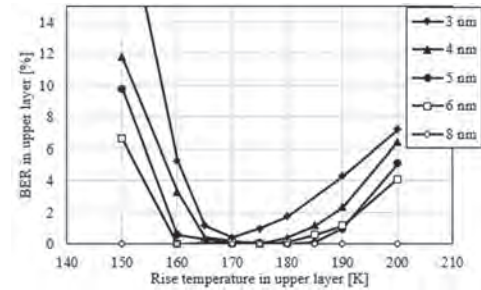
F. Akagi¹, Y. Sakamoto¹ and N. Matsushima¹

¹ Kogakuin Univ., Tokyo, Japan

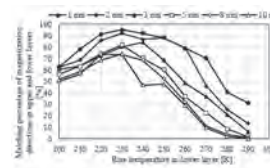
1. Background Heat assisted magnetic recording technology combining L10-FePt-based bit-patterned media (BPM) has been investigated to realize terabit data storage density in hard disk drives. This technology has been referred to as heated dot magnetic recording (HDMR). The size of the magnetic dot of the BPM must be reduced to no greater than 5 nm to achieve areal recording density of 8.0 Tbps or more [1]. However, the critical size for L10-ordering of FePt layers was evaluated as 3 nm, below which the respective long-range order parameter degraded [2]. Then, 3D magnetic storage technology, where data are written in multi-recording layers in the depth direction of a magnetic medium, can be employed to increase the areal recording density. This technology could enable magnetic recording over 10 Tbps, even if the dot size is large. Some recording methods that use this technology have been proposed, including a method in which data are written in order from the lower layer with the higher Curie temperature to the upper layer with the lower Curie temperature in the multi-layers. Here, the intensities of the static magnetic fields between multi-layers and rise temperatures in the layers via near-field optics are important factors for writing different data in each layer. Thus, in this study, the effects of static magnetic fields and temperatures on 3D magnetic storage in HDMR was investigated using micromagnetic simulation. 2. Calculation Method and Conditions The recording process was calculated using the Landau-Lifshitz-Gilbert equation [1] while considering thermal fluctuations as a first-stage analysis. In this study, the magnetic media had double recording layers with 8-nm dot arrays and 16-nm dot pitch corresponding to areal recording density of 5.0 T bpsi. The saturation magnetizations (M_s) of the upper and lower layer were 1.1 T and 1.2 T, and the anisotropy fields (H_k) were 3374 kA/m and 3965 kA/m at room temperature, respectively. The Curie temperatures of the upper and lower layers were 550 K and 600 K, respectively. Here the temperature (T) dependence of M_s was calculated by the Brillouin function. The temperature dependence of the magnetic anisotropy constant ($K_u(T)$) was $K_u(T)/K_u(0) = \{M_s(T)/M_s(0)\}^{2.1}$. The spacing between the recording head and medium was 4 nm, and the thickness of the recording layers was 4 nm. The thermal profiles in the recording layers were assumed to be the same as the Gaussian distribution with a full-width at half-maximum of 20 nm. The head-field strengths of the upper and lower layers were 926 and 810 kA/m at the center of the thermal profile and were constant regardless of the spacing value between the recording layers. The relative velocity between the head and medium was set to 10 m/sec. 2. Results Figure 1 shows the temperature dependence of the bit error rate (BER) in the upper layer. Here, the BER was determined as the ratio of the number of error bits to the number of on-track bits. The upper layer was recorded after the lower layer was recorded at 260 K. The spacing between the upper and lower layers was changed from 3 to 8 nm. As shown, the BER was very small (less than 0.1%) when the spacing between layers was 4 nm or greater and the temperature was approximately 175 K. As mentioned previously, the minimal spacing depends on the static magnetic fields between the recording layers. The magnetization directions in the upper layer are determined by the static magnetic fields from the lower layer during the cooling process of the medium. Therefore, the magnetization directions in the upper layer when the lower layer was recorded according to the change of the head fields were examined. Then, the temperature dependence of the matching percentage of the magnetization directions in the upper and lower layers was calculated by changing the spacing between layers. We found that the matching percentage decreased as the spacing between layers increased but did not change when the spacing was greater than 8 nm, as shown in Fig. 2. Therefore, the static magnetic fields between layers become nearly zero at the 8-nm spacing. We also found that the matching percentage of the magnetizations was the highest at 230 K. The differences in the matching percentage among temperatures were due to thermal fluctuations. At 230 K, thermal stability was high; however, the lower layer could not be recorded due to the poor temperature. Note that the lower layer was recorded without errors at 260 K. 3. Conclusion The minimal spacing for recording nearly without error was 4 nm for 3D magnetic storage in HDMR. This gives the critical

value of the static magnetic fields for recording different data in each layer. Acknowledgment We thank Hitachi Corporation for the use of the simulator. We also thank Dr. Yamakawa from the Akita Industrial Technology Center for calculating the head fields.

[1] J. Ushiyama, F. Akagi, A. Ando, and H. Miyamoto: *IEEE Trans. Magn.* 49(7), pp. 3612-3615 (2013). [2] T. Miyazaki, O. Kitakami, S. Okamoto, and Y. Shimada: *PHYSICAL REVIEW B* 72, 144419 (2005).



Temperature dependence of BER in upper layer



Matching percentage of magnetization directions in upper and lower layers

IP-02. Correlation Among Lattice Strain of MgO Underlayer at Hetero-Interface Between MgO/ FePt, Degree of Order, and Ratio of *c*-Axis Parallel to Normal for FePt Granular Film.

T. Saito¹, K. Tham², R. Kushibiki², T. Ogawa¹ and S. Saito¹

1. Tohoku University, Sendai, Japan; 2. Tanaka Kikinzoku Kogyo Kabushiki Kaisha, Chiyoda-ku, Japan

As a next-generation technology for heat-assisted magnetic recording (HAMR), L1₀ typed FePt granular film with a *c*-plane sheet texture deposited on a flat MgO underlayer is a promising candidate [1]. Although it has been reported that there existed FePt grains whose *c*-axes are parallel to the film plane (in-plane grains) with FePt grains whose *c*-axes are normal to the film plane (normal grains) in a FePt granular film [2 - 4], a dominant factor affecting the *c*-axis orientation of FePt grains with cubic (disorder) and/or tetragonal (order) system was not clarified yet. Therefore, we evaluated the volume ratio of in-plane grains to normal grains in the FePt granular films with various GBMs (GBMs: B₂O₃, MoO₃, SnO, WO₃, Nb₂O₅, TiO₂, MnO, Y₂O₃, MgO, C) and discussed about an effect of the volume ratio and degree of order on perpendicular magnetic anisotropy for the granular films. First of all, we have proposed a new approach to the evaluation of the volume ratio of in-plane grains to normal grains, R_{parallel} , using in-plane XRD profiles. R_{parallel} is defined as follows; $R_{\text{parallel}} = (I_{002}^{\text{Meas}} / I_{002}^{\text{Calc}}) / (I_{200}^{\text{Meas}} / I_{200}^{\text{Calc}} + I_{002}^{\text{Meas}} / I_{002}^{\text{Calc}})$. (1) Here, $I_{\text{hkl}}^{\text{Meas}}$ and $I_{\text{hkl}}^{\text{Calc}}$ are experimentally obtained and calculated values of the integrated intensity of the (hkl) diffractions from FePt phase, respectively. In in-plane XRD profiles, I_{200} and I_{002} were observed, which meant there existed not only normal grains but also in-plane grains in the granular films. Fig. 1 (a) shows the dependence of R_{parallel} on lattice constant of the MgO layer just under the FePt granular layer in the films with various GBMs. There was negative correlation between R_{parallel} and the lattice constant of the MgO underlayer. Especially in the FePt-C granular film, R_{parallel} is about 0. The lattice constants were expanded and contracted from literature value (4.213 Å) depending on GBMs. These results mean that the stack of the FePt granular layer with the GBM causes the lattice strain of the MgO underlayer since the lattice constant of MgO underlayer is the same before the FePt-GBM granular layer stacking, which suggests interdiffusion of GBM elements to the MgO underlayer. Fig. 1 (b) shows R_{parallel} as a function of the degree of order (S_{in}) for the FePt granular films with various GBMs. The negative correlation between R_{parallel} and S_{in} was observed. This result indicates that ordering into L1₀ structure results in *c*-axis orientation of FePt grains. From the results of Fig. 1 (a) and (b), the lattice constant of the MgO underlayer has the positive correlation with S_{in} , which suggests that the lattice strain affects S_{in} . Fig. 2 shows (a) $L_{2\theta}^{\text{sat}} / (L_{2\theta}^{\text{sat}} + L_{4\theta}^{\text{sat}})$ and (b) $L_{4\theta}^{\text{sat}} / (L_{2\theta}^{\text{sat}} + L_{4\theta}^{\text{sat}})$ plotted against R_{parallel} . Here, $L_{2\theta}^{\text{sat}}$ and $L_{4\theta}^{\text{sat}}$ are the saturated torque coefficient of the twofold components and the fourfold components measured by 90 kOe torqueometry [5], respectively. We considered that the fourfold components of the torque curves were induced by an overlap of the torque curve with a 90° phase shift which was due to in-plane grains [5]. Therefore, $L_{4\theta}^{\text{sat}}$ is index for in-plane grains and $L_{4\theta}^{\text{sat}} / (L_{2\theta}^{\text{sat}} + L_{4\theta}^{\text{sat}})$ reflects the volume ratio of in-plane grains, while $L_{2\theta}^{\text{sat}} / (L_{2\theta}^{\text{sat}} + L_{4\theta}^{\text{sat}})$ reflects that of normal grains. $L_{2\theta}^{\text{sat}} / (L_{2\theta}^{\text{sat}} + L_{4\theta}^{\text{sat}})$ and $L_{4\theta}^{\text{sat}} / (L_{2\theta}^{\text{sat}} + L_{4\theta}^{\text{sat}})$ had negative and positive correlation with R_{parallel} , which means $L_{2\theta}^{\text{sat}} / (L_{2\theta}^{\text{sat}} + L_{4\theta}^{\text{sat}})$ and $L_{4\theta}^{\text{sat}} / (L_{2\theta}^{\text{sat}} + L_{4\theta}^{\text{sat}})$ also had correlation with S_{in} . This result is consistent with the relationship between R_{parallel} and S_{in} and it indicates that there is a significant correlation with *c*-axis orientation and degree of order.

[1] D. Weller, O. Mosendz, G. Parker, S. Pisana, and T. S. Santos, *Phys. Status Solidi A*, 210, 1245 (2013). [2] T. Saito, K. K. Tham, R. Kushibiki, T. Ogawa, and S. Saito, *Jpn. J. Appl. Phys.*, 59, 045501 (2020). [3] T. Shiroyama, T. Abe, Y. Takahashi, and K. Hono, *IEEE Trans. Magn.*, 49, 3616 (2013). [4] J. Wang, H. Sepehri-Amin, H. Tajiri, T. Nakamura, K. Masuda, Y.K. Takahashi, T. Ina, T. Uruga, I. Suzuki, Y. Miura, and K. Hono, *Acta Materialia*, 166, 413 (2019). [5] T. Saito, K. K. Tham, R. Kushibiki, T. Ogawa, and S. Saito, *IEEE Trans. Magn.* (in press) (DOI: 10.1109/TMAG.2020.3015515).

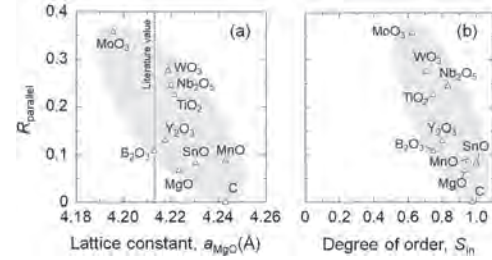


Fig.1 Volume ratio of FePt grains with the *c*-axes parallel to the film plane, R_{parallel} plotted against (a) lattice constant of the MgO layer under the FePt granular layer with various GBMs and (b) degree of order of FePt grain.

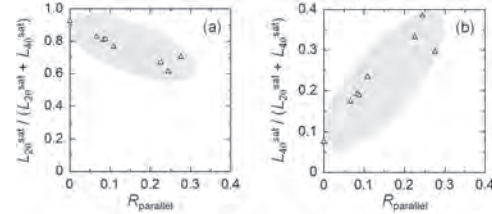


Fig. 2 (a) $L_{2\theta}^{\text{sat}} / (L_{2\theta}^{\text{sat}} + L_{4\theta}^{\text{sat}})$ and (b) $L_{4\theta}^{\text{sat}} / (L_{2\theta}^{\text{sat}} + L_{4\theta}^{\text{sat}})$ plotted against R_{parallel} . $L_{2\theta}^{\text{sat}}$ is the saturated torque coefficient of the twofold components and $L_{4\theta}^{\text{sat}}$ is that of fourfold component.

IP-03. Effect of FePt-C Nucleation Layer on Magnetic Properties and Nanostructure for FePt-Oxide / FePt-C Stacked Media.

K. Tham¹, T. Saito², R. Kushibiki¹, T. Ogawa² and S. Saito²

1. Tanaka Kikinzoku Kogyo Kabushiki Kaisha, Chiyoda-ku, Japan;

2. Tohoku University, Sendai, Japan

LI₀ FePt has drawn attention from a lot of researches as the most probable material for the next generation magnetic recording media due to its high magnetocrystalline anisotropy of $\sim 5\text{--}7 \times 10^7$ erg/cm³ at room temperature. Realization of columnar small magnetic grains with granular structure and good isolation, strong perpendicular (001) texture, and high degree of ordering still remain challenging for its commercial applications. In order to achieve these requirements, many studies regarding the addition of various grain boundary materials (GBMs), such as C^{1,2}, MgO³, TiO₂⁴, Ta₂O₅⁵, and SiO₂⁶ into the FePt magnetic thin films which is expected to separate the magnetic grains to promote the exchange decoupling have been done. To obtain columnar growth magnetic grains, the employment of FePt-C as a granular nucleation layer (NL) due to well separated in-plane granular structure has been widely studied.⁷ Furthermore, it was reported that the in-plane (001) texture component was observed when FePt-oxide granular film was directly deposited on MgO underlayer.^{8,9} One of the methods to reduce the in-plane (001) texture component is by introducing a granular NL in between MgO underlayer and FePt-oxide granular layer. However, the effect of the granular NL on nanostructure, including the heteroepitaxial growth and crystal orientation in relation with magnetic properties has not been clarified. Therefore, in this paper, we have quantitatively evaluated grain diameter (*GD*), degree of ordering (*S_{in}*), and size effect of FePt-GBM granular films with various thickness deposited on FePt-C granular film as the granular NL. As a typical FePt-oxide granular film, Fig. 1(a) shows in-plane XRD profile of FePt-SnO (0-8 nm) deposited on FePt-C (2 nm) granular NL. For references, powder pattern diffractions of FePt, and MgO are shown in the figure. In the in-plane XRD profile, at diffraction angle of around 33° and 69°, FePt(110) and FePt(220) diffractions, respectively, are observed which indicates that the granular films have *c*-plane sheet texture with ordered phase. Furthermore, at angle of around 24° FePt(001) diffraction is observed which reveals that the granular films have in-plane (001) texture component. Dependence of FePt(001) diffraction integral intensity of the granular films with granular NL against the film thickness is shown in Fig. 1(b). For the reference, the integral intensity of FePt(001) diffraction for FePt-SnO granular film without granular NL are also shown in the figure. There is almost no integral intensity of FePt(001) diffraction observed for FePt-C (2 nm) granular NL. Integral intensity of FePt(001) diffraction for FePt-SnO granular film with granular NL is reduced linearly against granular layer thickness and the amount the reduction increases with thicker granular layer thickness. FePt-oxide granular films with other GBM also show the same tendency with different amount of reduction which suggests that in-plane (001) texture component in the FePt-oxide / FePt-C stacked media depends on the GBM. Fig. 2 shows dependence of degree of ordering (*S_{in}*) on the grain diameter (*GD*) of FePt granular layers of various GBMs with and without granular NL. The GBMs are B₂O₃, MoO₃, SnO, GeO₂, WO₃, Nb₂O₅, SiO₂, TiO₂, MnO, Y₂O₃, ZrO₂, and MgO. *S_{in}* is evaluated from in-plane X-ray diffraction from the LI₀ FePt(110) and FePt(220) diffractions.¹⁰ *GD* is determined from the translation of crystal lattice along an in-plane direction in a FePt grain and was evaluated according to Scherrer's equation⁹ derived by the LI₀ type FePt (200) diffraction of the in-plane XRD profiles. Depends on the GBM, *GD* for FePt-GBM granular film, becomes smaller or larger with range changes from around 3-8 to 5-8 nm when the granular NL is introduced which indicates that magnetic grain of the stacked media is not growing in one-on-one mode. Focusing on the *S_{in}*, *S_{in}* enhancement is observed for FePt-GBM granular film with the granular NL. From the film thickness dependence analysis, it was found that from the disordered and ordered part of the film, the *S_{in}* for the ordered part was improved. In the conference, the detail analysis of *S_{in}* and magnetic properties will be discussed.

1) J. S. Chen, B. C. Lim, J. F. Hu, B. Liu, G. M. Chow, and G. Ju, *Appl. Phys. Lett.*, 91, 132506 (2007). 2) A. Perumal, Y. K. Takahashi, and K. Hono, *J. Appl. Phys.*, 105, 07B732 (2009). 3) Y. Peng, J.-G. Zhu, and D. E.

Laughlin, *J. Appl. Phys.*, 99, 08F907 (2006). 4) Y. F. Ding, J. S. Chen, B. C. Lim, J. F. Hu, B. Liu, and G. Ju, *Appl. Phys. Lett.*, 93, 032506 (2008). 5) B. C. Lim, J. S. Chen, J. F. Hu, P. W. Lwin, Y. F. Ding, K. M. Cher, and B. Liu, *J. Appl. Phys.*, 105, 07A730 (2009). 6) E. Yang and D. E. Laughlin, *J. Appl. Phys.*, 104, 023904 (2008). 7) B. S. D. Ch. S. Varaprasad, M. Chen, Y. K. Takahashi, and K. Hono, *IEEE Trans. Magn.*, 49, 718 (2013). 8) J. Wang, S. Hata, Y. K. Takahashi, H. Sepehri-Amin, B. S. D. Ch. S. Varaprasad, T. Shiroyama, T. Schrefl, and K. Hono, *Acta Mater.*, 91, 41 (2015). 9) T. Saito, K. K. Tham, R. Kushibiki, T. Ogawa, and S. Saito, *Jpn. J. Appl. Phys.*, 59, 045501 (2020). 10) P. Scherrer, *Göttinger Nachr. Ges.* 2, 98 (1918).

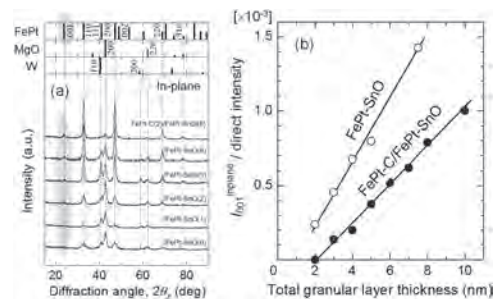


Fig.1 (a) In-plane XRD profile for Sub./CoW(80 nm)/MgO(5 nm)/FePt-C(2 nm)/FePt-SnO(0-8 nm)/C(7 nm) and (b) dependence of FePt(001) diffraction integral intensity of the granular films on the film thickness.

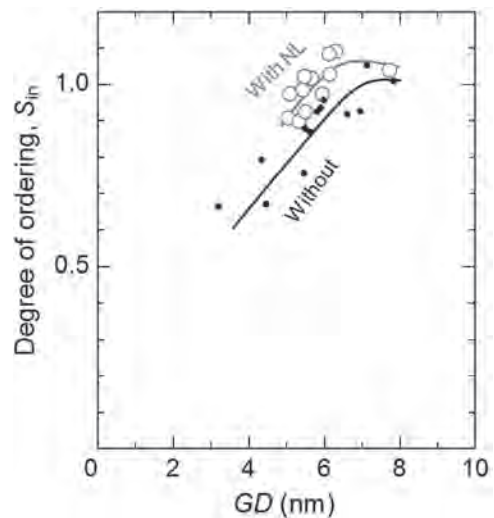


Fig. 2 Dependence of degree of ordering (*S_{in}*) on the grain diameter (*GD*) of FePt granular layers of various GBMs with and without granular NL.

IP-04. Two-Stage Signal Processing Schemes for Heated Dot Magnet-Recording With Polar Coding and Double-Layered Bit Patterned Media.

H. Saito¹ and F. Akagi²

1. Department of Electrical and Electronic Engineering, Faculty of Engineering, Kogakuin University, Shinjuku-ku, Japan; 2. Department of Applied Physics, School of Advanced Engineering, Kogakuin University, Shinjuku-ku, Japan

I. INTRODUCTION It is expected that a heated-dot magnetic recording (HDMR) is a significant future technology to attain the areal density over 5 Tdpsi with bit-patterned media (BPM) [1], [2]. In this research, a two-stage signal processing scheme for the HDMR system with polar coding schemes and double-layered BPM is proposed. This approach assumes to be applicable to a HDMR system with areal density of up to 5Tdpsi. This proposed scheme uses two independent log-likelihood ratio (LLR) detectors which are cascaded and able to detect each recorded data sequence recorded on each layer in order. A high rate polar encoding scheme is used for the error-correcting scheme for the second layer. In generally, the effective rate of the HDMR system with double-layered BPM can be improved twice of that of a HDMR system with single-layered BPM. II. TWO-STAGE SIGNAL PROCESSING SCHEME FOR HDMR Fig.1 shows the block diagram of the proposed signal processing scheme for a HDMR system using double-layered BPM. In Fig.1, double-layered recording is assumed for the HDMR system. In this read/write system, a raw data sequence $\{a_k\}$ is input into each modulation encoder which gives a run length limited (RLL) constraint sequence $\{b_{i,k}\}$ for the down-track direction. One of the RLL constraint sequence is transformed into the precoded sequence $\{c_{0,k0'}\}$ and is recorded on the first layer. The other RLL constraint sequence is encoded into the polar codeword sequence and transformed into the precoded sequence $\{c_{1,k1'}\}$ with 16 CRC bits. The sequence $\{c_{1,k1'}\}$ is recorded on the second layer. The sequence $\{c_{i,k1'}\}$ is NRZ-recorded on islands made of the discrete double layered perpendicular magnetic medium with a soft under layer. These islands are arranged on a circular grid in the surface of recording media. We assume head/medium conditions and modeling with FePt granular magnetic media to achieve areal density of 2.5Tdpsi using micro-magnetic simulation [3],[4]. Both of magnetic dots are called "upper dot" and "lower dot" in this research. In the recording process, it is assumed that magnetization is calculated by use of the Landau-Lifshitz-Gilbert equations for both of magnetic dots. For the readback HDMR channel, the readback signal of BPM is represented by our evaluated 2D pulse response and the normalized peak amplitude is A_p . In this system, the parallel readback signal sequence $\{r'_k\}$ is obtained by combining readback signal sequences from the pair of upper and lower dots. In Fig. 1, $r'_k = r_{0,k} + r_{1,k} + n_k$, where the sequence $\{r_{i,k}\}$ is the readback signal sequence from the k -th dot of the $i+1$ -th layer and the noise sequence $\{n_k\}$ is added at the reading point. The sequence $\{n_k\}$ is additive white Gaussian noise (AWGN) with zero mean and variance. The reproducing waveform corresponding to the recording sequences readback by the reading head is input into the equalizer which consists of a 2D low-pass filter (LPF) and the 2D transversal filter (TVF). The equalization is performed so that the overall characteristic between the input of recording head and the output of the equalizer is equal to the aimed 2D generalized partial response (GPR) targets. The equalizer output sequence $\{y_k\}$ is obtained which sums equalizer output sequences from the pair of two upper and lower dots. In the equalizing process, tap-gain coefficients in the 2D TVF are evaluated by minimizing the expectation of the mean square error (MSE) $E\{e_k\}$, where the sequence $\{e_k\}$ is the equalized error sequence between the ideal GPR target output sequence $\{d_k\}$ and the sequence $\{y_k\}$. The signal-to-noise ratio (SNR) at the reading point is defined as the ratio of A_p and the noise power of AWGN. In decoding process, the equalizer output sequence $\{y_k\}$ is decoded by the one-dimensional (1D) multi-level LLR detector. Both of the estimated RLL codeword sequence $\{b'_{0,j}\}$ and readback signal waveforms corresponding to the sequence $\{c'_{0,k0'}\}$ are given as the detector output. Using this estimated readback signal waveforms $\{r_{0,k}\}$, it is able to estimate the readback signal waveforms $\{r'_{1,k}\}$. The estimated readback signal waveforms $\{r'_{1,k}\}$ is input into 1D TVF and equalized to generate the aimed 1D GPR target output sequence and detected by the 1D LLR detector and CRC-aided successive cancellation list (SCL) decoder [5]. The

output sequence from this decoder is the estimated RLL codeword sequence $\{b'_{1,j}\}$. The sequences $\{b'_{i,j}\}$ are decoded by RLL decoders and we get the estimated data sequence $\{a'_k\}$ is obtained after demodulation. The block error rate (BER) performance is evaluated by computer simulation between the sequences $\{a_k\}$ and $\{a'_k\}$. III. ERROR RATE PERFORMANCES In Fig.2, the solid line shows the BER performance of the proposed coding GPR scheme with the double-layered BPM. The dashed and dotted lines show the performances of the compared 64/65(0,8) coding schemes using the single-layered, double-layered BPM. These coding schemes have the effective transmission rate $r_{eff} = 1.96, 1.97, 0.985$, respectively. The recording condition of the proposed scheme corresponds to the areal density of 5.0Tdpsi. As can be seen Fig.2, the proposed scheme outperforms that of the compared 1D scheme by about 6.0 dB of SNR gains at a BER of 10^{-6} . IV. CONCLUSIONS In this digest, we propose a two-stage signal processing scheme for a HDMR system with polar coding and double-layered BPM. Our proposed scheme shows the possibility of development of the advanced signal processing scheme with multi-layered recording.

[1] T. R. Albrecht, et al., *IEEE Trans. Magn.*, 51, 5, 0800342, May 2015. [2] J. K. W. Yang, et al., *Nanotechnology*, 38501, Aug. 2011. [3] F. Akagi, et al., *J. Appl. Phys.*, 101, 09H5011, Apr. 2007. [4] F. Akagi, et al., *J. Magn. Mater.*, 324, pp.309–313, Apr. 2012. [5] I. Tal and A. Vardy, *IEEE Trans. Inf. Theory*, 61, 5, 2213–2226, May 2015.

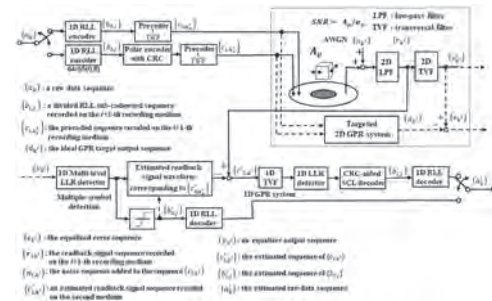


Fig.1 Block diagram of the proposed HDMR system.

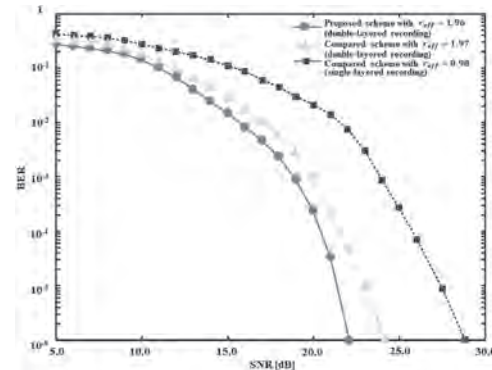


Fig.2 BER performances.

IP-05. Reliability Ratio-Based Serial Scheduling of LDPC Decoder for Turbo Equalization Schemes.

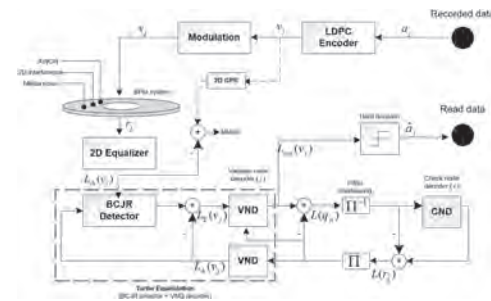
S. Khittiwitayakul¹, W. Phakphisut¹ and P. Supnithi¹

¹. School of engineering, King Mongkut's Institute of Technology Ladkrabang, Bangkok, Thailand

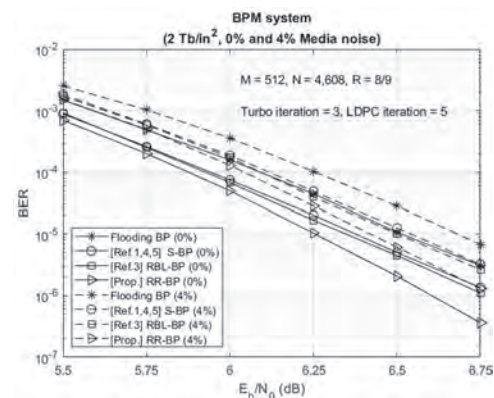
1) Introduction: Low-density parity-check (LDPC) codes have been known to exhibit good error-correcting performance by using the belief propagation (BP) decoding algorithm. The BP algorithm commonly updates all variable nodes simultaneously, known as “flooding BP” schedule. However, the flooding BP schedule has drawback on convergence speed required in high-speed applications. Alternatively, the “sequential” schedules of variable node updates, e.g., Shuffled-BP (S-BP) [1], V-to-C Residual BP (VCR-BP) [2], and Reliability-based-Layered BP (RBL-BP) [3] are shown that the convergence speed is twice faster than flooding BP schedules. Previously, the S-BP schedule is applied in the turbo equalization of magnetic recording system [4], the results on bit patterned media (BPM) system show that the S-BP schedule can achieve some coding gains over the flooding BP schedule. The paper [5] also proposed the stopping criterion of S-BP schedule in BPM system to reduce the number of updated variable nodes per iteration. Motivated by the fact that the previous works [4,5] utilize the S-BP schedule straightforwardly in BPM systems, in this work, we then propose the sequential schedules, namely the “Reliability ratio-based BP (RR-BP)” schedule in the turbo equalization of BPM system. The update sequences of RR-BP schedule may differ at each iteration according to the *extrinsic* LLR. Our results show that the RR-BP schedule applied in BPM system gives better performance than the S-BP [1,4,5] and RBL-BP [3]. 2) Turbo equalization of BPM system: The read channel of BPM system is shown in Fig. 1. The encoded bits v_j are modulated and recorded on the patterned media. On the receiver side, the readback r_j is passed to 2D MMSE equalizer to handle the 2D interference effect, and the output LLR $L_{ch}(v_j)$ will be sent to the turbo equalization consisting of BCJR detector and LDPC decoder. The BCJR detector is performed corresponding to the received LLR $L_{ch}(v_j)$, and *extrinsic* LLR $L_A(v_j)$ from LDPC decoder. Then, the *extrinsic* LLR $L_E(v_j)$ is sent to LDPC decoder. The LDPC decoder consists of N variable nodes, $v = [v_1, v_2, \dots, v_j, \dots, v_N]$, representing the codeword bits, and M check nodes, $c = [c_1, c_2, \dots, c_j, \dots, c_M]$, representing the parity-check equation. The LDPC decoder uses the BP algorithm to exchange the variable-to-check message $L(q_{ji})$ and check-to-variable message $L(r_{ij})$ at each iteration. The flooding BP schedule is a conventional schedule of BP algorithm, whereby the simultaneous update of all $L(q_{ji})$ is followed by simultaneous update of $L(r_{ij})$ at each iteration. After the maximum number of iteration is reached, the LDPC decoder will send back the *extrinsic* LLR $L_A(v_j)$ to the BCJR detector. 3) Sequential schedule: 3.1) Previous schedules: S-BP [1] introduced the ordering of message updates resulting in the best convergence speed and/or decoding performance. An iteration consists of the sequential update of all $L(q_{ji})$ by ascending or descending order. For each variable node v_j to generate the message $L(q_{ji})$, the message $L(r_{ij})$ from its connected check nodes is required. Even though the convergence speed of S-BP schedule is twice as fast as that of the flooding BP schedule, the convergence speed can be further increased by using dynamic schedules. The VCR-BP updates have been presented in [2] to update the messages according to the difference between the message $L(q_{ji})$ in current and previous iterations. The drawback of VCR-BP schedule is the high complexity of the residual operations. Therefore, in paper [3], the RBL-BP schedule is proposed to omit the residual computations, the absolute of LLR values from the channel $|L_{ch}(v_j)|$ is used to measure the reliability of variable nodes instead of the residual values. The variable nodes with low $|L_{ch}(v_j)|$ will start to update at early iterations, and those with high $|L_{ch}(v_j)|$ will start later. The performances of RBL-BP schedule is comparable to VCR-BP schedule. However, in MR systems, only the fixed schedule, such as S-BP, is studied [4-5]. In this work, we then propose the dynamic schedules for BPM system with high-level interferences and media noise in which the ordering of message updates will be generated based on the reliability ratio of *extrinsic* LLR. 3.2) Proposed RR-BP schedule: Based on our observation and study in the recent works, the received $|L_{ch}(v_j)|$ introduced in [3] cannot indicate the reliabilities of variable nodes in the MR system due to the high-level interferences and media noise. Therefore, in this work, we then propose the RR-BP schedule which utilizes the *extrinsic* LLR $L_A(v_j)$

combined with syndrome checking to indicate the reliability of each variable node instead of channel information. Here we will introduce the update criterion in terms, $E_j = (1/|L_A(v_j)|) \sum_{i \in N(j)} (2s_i - 1) \sum_{c \in M(i)} |L_A(v_j)|$, where s_i is the syndrome bit associated with the i^{th} check node, the set $N(j)$ denotes the j^{th} check nodes connected to the variable node v_j and the set $M(i)$ denotes the i^{th} variable nodes connected to the check node c_i . The variable node has a large E_j , which means that it has not converged yet (may be in error). Hence, at any iteration, the variable nodes with the largest E_j will be firstly updated and followed by the remaining variable nodes. Fig. 2 shows the BER performance comparisons of the RR-BP, RBL-BP, S-BP, and flooding BP schedules in BPM system with 2Tb/in². The results show that the RR-BP schedule offers about 0.13, 0.14, and 0.25 dB coding gains compared to RBL-BP, SBP, and flooding BP schedules, respectively.

[1] J. Zhang, and *et al.*, “Shuffled iterative decoding,” *IEEE Transactions on Communications*, vol. 53, no. 2, pp. 209–213, 2005. [2] J. H. Kim, and *et al.*, “Variable-to-check residual belief propagation for ldpc codes,” *Electronics Letters*, vol. 45, no. 2, pp. 117–119, 2009. [3] R. Sun, and *et al.*, “Reliability-Based-Layered Belief Propagation for Iterative Decoding of LDPC Codes,” 2018 *IEEE International Symposium on Information Theory (ISIT)*, Vail, CO, 2018, pp. 1156-1160 [4] W. Phakphisut, and *et al.*, “Serial Belief Propagation for The High-Rate LDPC Decoders and Performances in The Bit Patterned Media Systems with Media Noise,” in *IEEE Transactions on Magnetics*, vol. 47, no. 10, pp. 3562-3565, Oct. 2011. [5] X. Liu, and *et al.*, “Improved Decoding Algorithm of Serial Belief Propagation with a Stop Updating Criterion for LDPC Codes and Applications in Patterned Media Storage,” in *IEEE Transactions on Magnetics*, vol. 49, no. 2, pp. 829-836, Feb. 2013.



Read channel of BPM systems.



BER performance comparisons.

IP-06. An Improvement to Factor Graph-Based Detector for Bit Patterned Media Recording.

T. Sopon¹, P. Supnithi² and S. Pilabutr³

1. Department of Electronic Engineering, Rajamangala University of Technology Isan, Nakhon Ratchasima, Thailand; 2. Department of Telecommunication Engineering, King Mongkut's Institute of Technology Ladkrabang, Bangkok, Thailand; 3. Department of Information Technology, Nakhon Ratchasima College, Nakhon Ratchasima, Thailand

Abstract: A Factor graph-based detector (FGB) is one of the promising for the two-dimensional (2-D) detection which can mitigate the 2-D interference channel. In this paper, we present the modified FGB (MFGB) detection of a 2-D interference channel on bit patterned media recording (BPMR) system. The 2-D interference channel with 3×3 matrix is separated into the three sub-windows with 1×3 matrix in horizontal direction and three sub-windows with 3×1 matrix in vertical direction. After that, the joint outputs are averaged of each sub-window in horizontal and vertical directions. This simulation results show that compared with MFGB method achieves lower bit error rate (BER) performances than the original FGB detector and generalized belief propagation (GBP) algorithm on BPMR system at an areal density of 4 Tb/in². In currently, because of an enlargement in data growth thus the requirement for high areal density storage system has increased. Bit patterned media recording (BPMR) system is one of the most promising choices to continue magnetic recording storage density [1]. The significant issue for very high areal density of BPMR system is the small grain sizes with thermal fluctuation effect of magnetic grains. However, the reduction of grain sizes in both across track and along track directions has become the 2-D interference in read channel of BPMR system that constitute inter-symbol interference (ISI) and inter-track interference (ITI) from the adjacent tracks [2]. More recently, the researchers have works on the method of the impairments in the 2-D interference channel and mitigating their effects using signal processing for communication techniques. A graph based detector has received much attention due to its intrinsic 2-D detection, particularly, for multihead multitrack processing [3], as an alternative to the soft-output Viterbi algorithm (SOVA) method. In this system model, the write head of BPMR system with multihead multitrack processing assumes the five input bit sequences recorded on five adjacent tracks. such the read head will be received three readback signal sequences which are caused by combination of noiseless received signal with additive white Gaussian noise. After that, the readback signal sequences are sent to two 2-D equalizer with horizontal and vertical directions. The output bits of horizontal equalizer and vertical equalizer are processed for two FGB detectors with horizontal and vertical directions of the summation which then produce the estimated input bits, as shown in Figure 1. In this paper, we consider the 2-D interference channel 3 by 3 matrix arrays into three sub-windows for horizontal direction and vertical direction. The coefficients of 2-D interference channel represent the weight of the current pixel. Thus, the MFGB detector in the 2-D interference channel separates the 3×3 matrix arrays into two sections for message passing on factor graph. Section one is three sub-windows with 1×3 matrix in horizontal direction. Section two is three sub-windows with 3×1 matrix in vertical direction. After that, the output of each FGB detectors in horizontal and vertical directions are determined the summation of joint outputs detections. The method of the MFGB detector divides the factor graph into three steps. The first step, the 2-D interference channel separates the 3×3 matrix array into 1×3 matrix for sub-window $f_{h1} = [h_{k-1,j-1}, h_{k,j-1}, h_{k+1,j-1}]$ of the first horizontal direction and the first vertical direction with 3×1 matrix for sub-window $f_{v1} = [h_{k-1,j-1}, h_{k-1,j}, h_{k-1,j+1}]$, as shown in Figure 2. As for, the second step is the sub-window sliding in second horizontal direction $f_{h2} = [h_{k-1,j}, h_{k,j}, h_{k+1,j}]$ and the vertical direction $f_{v2} = [h_{k,j-1}, h_{k,j}, h_{k,j+1}]$, as shown in Figure 3. Finally, the third step is similar to the both previous steps. The sub-window slides to the third horizontal direction $f_{h3} = [h_{k-1,j+1}, h_{k,j+1}, h_{k+1,j+1}]$ and the vertical direction $f_{v3} = [h_{k+1,j-1}, h_{k+1,j}, h_{k+1,j+1}]$, as shown in Figure 4. In this simulation, we consider the BPMR system at areal density of 4 Tb/in². Corresponding to bit period and track pitch are 12.7 nm, PW_{50} of along-track and PW_{50} across-track are considered with 4.2 nm and 8.4 nm, respectively [4]. Therefore, the 2-D interference channel resultant of coefficients matrix H with a size of 3×3 can be written as $H_{4Tb} = [0.0163 \ 0.4008 \ 0.0163; 0.0408 \ 1.0000 \ 0.0408; 0.0163 \ 0.4008 \ 0.0163]$. In this work, we compare

BER performance of the MFGB detector, the original FGB detector [5], and generalized belief propagation (GBP) algorithm detector [6]. From the graph considerations in Figure 5, BER performance of the MFGB detector performs better than the original FGB detector. Furthermore, the MFGB detector achieves the gain of about 3.6 dB over the GBP algorithm detector at BER = 10^{-4} after three iterations of all detectors.

[1] G. F. Hughes, *IEEE Transactions on Magnetics*, vol.35, no.5, pp. 2310-2312, (1999) [2] P. W. Nutter, I. T. Ntokas, B. K. Middleton and D. T. Wilton, *IEEE Transactions on Magnetics*, vol.41, no.10, pp. 3214-3216, (2005) [3] J. Hu, T.M. Duman and M.F. Erden, *EURASIP Journal on Advances in Signal Processing*, vol.2008. 10.1155/2008/738281, (2009) [4] Y. Wang and B. V. K. Vijaya Kumar, *IEEE Transactions on Magnetics*, vol.53, no.10, ID.3000710, (2017) [5] T. Sopon, P. Supnithi and K. Vichienchom, *IEEE Transactions on Magnetics*, vol.50, no.11, ID. 3101704, (2014) [6] J. S. Yedidia, W. T. Freeman and Y. Weiss, *IEEE Transactions on Information Theory*, vol. 51, no. 7, pp. 2282-2312, (2005)



Fig.1. Block diagram of BPMR system with 2-D interference channels, 2-D equalizers and FGB detectors

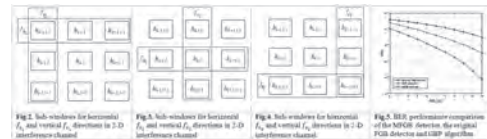


Fig. 2. Sub-windows for horizontal f_{h1} and vertical f_{v1} directions in 2-D interference channel. Fig. 3. Sub-windows for horizontal f_{h2} and vertical f_{v2} directions in 2-D interference channel. Fig. 4. Sub-windows for horizontal f_{h3} and vertical f_{v3} directions in 2-D interference channel. Fig. 5. BER performance comparison of the MFGB detector, the original FGB detector and GBP algorithm.

IP-07. A Study on Iterative Decoding by Neural Network Detector in SMR System.

M. Nishikawa¹, Y. Nakamura¹, Y. Kanai², H. Osawa¹ and Y. Okamoto¹
 1. Ehime University Kogakubu Universityin Rikogaku Kenkyuka, Matsuyama, Japan; 2. Niigata Koka University, Kashiwazaki, Japan

Introduction We study the low-density parity-check (LDPC) coding [1] and iterative decoding system, as signal processing for the shingled magnetic recording (SMR) [2] in two-dimensional magnetic recording (TDMR). Previously we have reported waveform equalization using a two-dimensional finite impulse response (TD-FIR) filter [3] and an inter-track interference (ITI) canceler [4] and showed the influence of ITI is reduced. Also, we have proposed a neural network detector (NND) and evaluated the performance of the first decoding by the NND [5]. In this study, the NND iteratively calculates the log-likelihood ratio (LLR) as the decoding reliability using the returned sum-product (SP) decoder [6] output sequence as well as using TD-FIR filter [3] output sequence. Furthermore, we compare the iterative decoding using an NND with a soft-output Viterbi algorithm (SOVA) detector with the signal-dependent noise predictor [7], [8].

Read/write system The input sequence passes through a 128/130 (0, 16/8) run-length limited (RLL) encoder and a (3, 30)-regular LDPC encoder to be changed into the recording sequence and is recorded on a granular medium model [4] under the specification of 4 Tbit/inch². In the reading process, the decoding target track and both adjacent tracks are read composed by the array head with three readers at the same time [1], [2], and the different additive white Gaussian noise (AWGN) sequence is added to each waveform as the system noise. The signal-to-noise ratio (SNR_S) for the system noise at the reading point is defined as $\text{SNR}_S = 20\log_{10}(A/\sigma_S)$ [dB], where A is the positive saturation level of the waveform reproduced from an isolated magnetic transition and σ_S is the root-mean-square (RMS) value of the system noise in the bandwidth of the channel bit rate f_c . A channel bit response including read/write (R/W) process on the intended track is equalized to the partial response class-I (PR1) target by the equalizer composed of three low-pass filters (LPFs) having cut-off frequency x_b normalized by the f_c and TD-FIR filter with N_t taps, where N_t is the number of taps [3] for a reader. We assume that these parameters are set to $x_b = 0.4$ and $N_t = 15$. Then, the output waveform from the PR1 channel is iteratively decoded by the turbo equalization performed between an NND and an SP decoder [6]. The SP decoder also iteratively decodes using the constraint of LDPC code until the maximum iteration number i_{sp} times. Furthermore, the SP decoder returns the reliability sequence including the parity bits of LDPC code to the NND again. In this way, the turbo equalization for the target track is performed with the maximum iteration number i_{global} times. After the given number of iterations in the turbo equalization, the output sequence is obtained by the posterior probability sequence except parity passing through a hard decision unit and the RLL decoder. Then, the bit error rate (BER) is calculated by comparing the input sequence with the output sequence.

Neural network detector Figure 1 shows the block diagram of the turbo equalization. In the figure, D is the delay operator for a bit interval, N_m ($m = 1 \sim 3$) is the number of elements in the m^{th} layer. We adopt $N_1 = 30$, $N_2 = 10$ and $N_3 = 1$. The NND consists of the neural network, the memory, the selector, and the LLR calculator. The neural network provides outputs for 3-bit patterns in the down-track direction for the TD-FIR filter and the returned SP decoder outputs, and stores the output in the memory. In the training process by back-propagation algorithm, we set the training signal to be "1" for the target bit pattern and "0" for the others, in order to obtain connection weight sets $w_{ij}^{(m)(n)}$ between the i^{th} element at the m^{th} layer and the j^{th} ($j = 1 \sim N_{m-1}$) element at the $(m-1)^{\text{th}}$ layer for the n^{th} pattern ($n = 1 \sim 8$). Furthermore, the LLR calculator provides the logarithmic ratio of the maximum values for the center bit "1" and "0" from the selector. **Performance evaluation** Figure 2 shows the BER performances for SNR_S. The marks of circle and triangle show the performances of the NND and the SOVA detector, respectively. Here, the LLR of the SOVA detector is provided by the metric of the PR1 channel, where the metric is calculated considering the external LLR obtained by the SP decoder output [5]-[7]. The turbo equalization parameters i_{sp} and i_{global} adopt the optimum values for minimizing the BER in each detector. As can be seen from the figure, the system with the NND improves about 5.5 dB in the required SNR to achieve no-errors compared to the system with the SOVA detector. **Acknowledg-**

ments This work was supported in part by the Advanced Storage Research Consortium (ASRC).

[1] R. G. Gallager, IRE Trans. Inform. Theory, Vol.IT-8, pp.21-28 (1962). [2] R. Wood, M. Williams, A. Kavcic, and J. Miles, IEEE Trans. Magn., Vol.45, No.2, pp.917-923 (2009). [3] R. Suzuto *et al.*, IEEE Trans. Magn., Vol.52, No.7, 3001604 (2016). [4] M. Yamashita *et al.*, IEICE Trans. Electron., Vol. E96-C, No.12, pp.1504-1507 (2013). [5] M. Nishikawa, Y. Nakamura, Y. Kanai, H. Osawa, and Y. Okamoto, IEEE Trans. Magn., Accepted. [6] P. Robertson *et al.*, Proc. IEEE Int. Conf. Commun. (ICC 1995), pp.1009-1013, Seattle, USA (1995). [7] J. Hagenauer *et al.*, in Proc. IEEE Global Telecommun. Conf. 1989, Dallas, Texas, pp. 1680-1686 (1989). [8] Y. Okamoto *et al.*, IEEE Trans. Magn., Vol.38, No.5, pp.2349-2351 (2002).

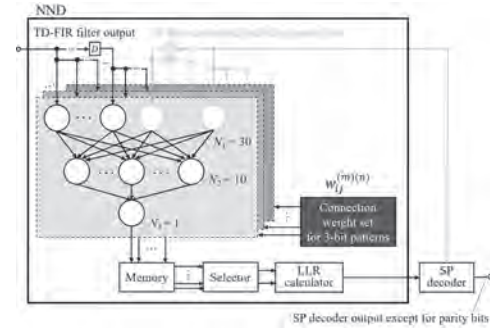


Fig. 1 Block diagram of turbo equalization.

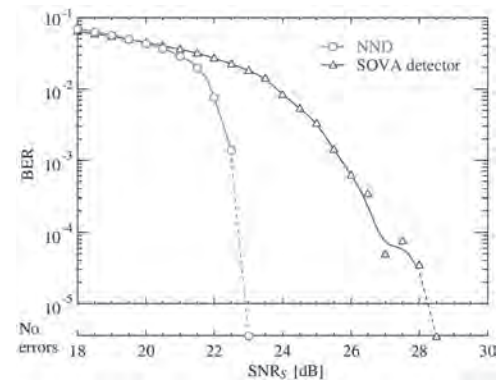


Fig. 2 BER performances for SNR_S.

IP-08. A Study of Multi-Dimensional Magnetic Recording System With Double Recording Layers.

Y. Nakamura¹, M. Nishikawa¹, Y. Kanai² and Y. Okamoto¹

1. Graduate School of Science and Engineering, Ehime University, Matsuyama, Japan; 2. Department of Information and Electronics Engineering, Niigata Koka University, Kashiwazaki, Japan

I. INTRODUCTION To further increase areal recording density in hard disk drives, we study a three-dimensional magnetic recording system with double recording layers and the magnetoresistive (MR) read-sensors [1]. We constructed the read/write channel model which combines double recording layers with MR reading sensors to evaluate a three-dimensional magnetic recording. In this study, we evaluate the bit error rate (BER) performance of the generalized partial response (GPR) maximum likelihood (ML) (GPRML) system [2] under each areal recording density of 4 Tbits/inch² on a dual recording layers medium. II. READ/WRITE CHANNEL MODEL WITH DOUBLE RECORDING LAYERS The two input sequences for 1st and 2nd recording layers are recorded on double recording layers medium without the jitter like medium noise, phase error, grain size fluctuation, and so on. The R/W simulations are started at each areal density corresponding to 4 Tbit/inch² with bit length l_c of 7.3 nm and track pitch l_{tp} of 22.1 nm. The full-shielded reader [3] is assumed. The width between side shields, the shield gap of the individual reader are set to 30 nm and 22 nm, and the width and thickness of the magneto-resistive element are set to 17 nm and 2 nm, respectively. We define the magnetic spacing between the bottom of the reader and the top of each recording layer as Δ_1 and Δ_2 , respectively. In this study, we assume the $\Delta_1 = 2.0$ nm and $\Delta_2 = 5.0$ nm. Figure 1 shows the distributions of reproducing waveforms from 1st and 2nd recording layers at the reading point without the system noise obtained by the sensitivity functions of the MR read sensor. In this figure, the dotted and solid lines show the distributions of samples captured at phases of the bit center and boundary, respectively. As can be seen from the figure, the distribution at the phase of the bit boundary is clearer than that at the bit center. A channel bit response on the double recording layer medium is adjusted to the GPR-target by the equalizer composed of a low-pass filter (LPF) having cut-off frequency $x_h = 0.4$ normalized by the channel bit rate f_c , a finite impulse response (FIR) filter with $N_f = 15$ taps, and an M^{th} ($M : 0\sim 3$) order noise predictor [2]. The GPR channel output is decoded by the Viterbi detector for double recording layers. III. SIMULATION RESULTS AND DISCUSSION Figure 2 shows BER performances of the GPRML systems for the double recording layer medium. The open and filled symbols show the performances for samples at phases of the bit center and boundary, respectively. The horizontal axis shows the correlation length for the signal given by the GPR system. As can be seen from the figure, the performance improves by the introduction of GPR for the samples at the bit boundary. It is certified that the GPRML system for the reproducing waveforms captured at phases of the bit boundary offers better BER performance compared with that of the bit center.

[1] S. Greaves, K. S. Chan, and Y. Kanai, "Optimization of dual-structure recording media for microwave-assisted magnetic recording," *IEEE Trans. Magn.*, vol.55, no.7, 3001305, July 2019. [2] N. Shinohara, H. Osawa, Y. Okamoto, Y. Nakamura, K. Miura, H. Muraoka, and Y. Nakamura, "Performance of GPRML-AR system in perpendicular magnetic recording channel with thermal decay," *J. Magn. Magn. Mat.*, vol.320, no.22, pp.3140-3139, Nov. 2008. [3] Y. Nakamura, H. Osawa, Y. Okamoto, Y. Kanai, and H. Muraoka, "Bit error rate performance for head skew angle in shingled magnetic recording using dual reader heads," *J. Appl. Phys.*, vol.117, no.17, pp.17A901-1-17A901-4, May 2015.

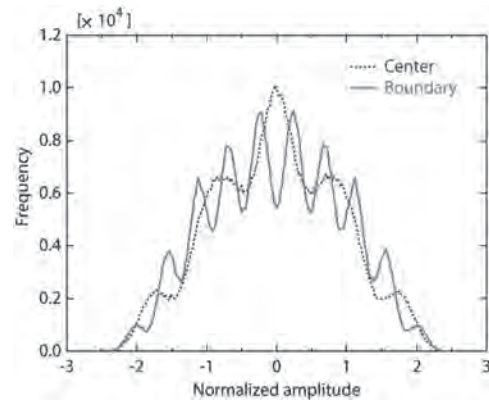


Fig.1 Distributions of reproducing waveforms.

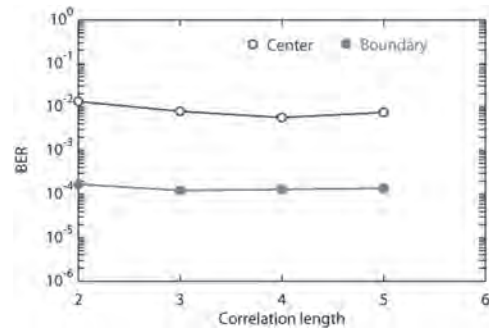


Fig.2 BER performances.

IP-09. Investigation of Ferrimagnetic Domain Wall Motion Behavior in GdFeCo Through the Anomalous Hall Effect.

N. Hai¹, Z. Chen¹, R.C. Bhatt², L. Ye², T. Wu², L. Horng¹ and J. Wu¹

1. Physics, National Changhua University of Education, Changhua, Taiwan; 2. Graduate School of Materials Science, National Yunlin University of Science and Technology, Douliou, Taiwan

Magnetic domain wall (DW) manipulation has been widely investigated because of its potential applications for information processing, storage, and transport. Probably the best-known concept device is the racetrack memory, which was proposed by IBM based on the current induced domain wall motion (CIDM) effect [1]. Recently, experimental investigations on GdFeCo exhibits fast domain wall motion (DWM) in the vicinity of the angular momentum compensation temperature [2]. To date, most of the achievements of DWM and the dynamic of DW are based on the Magneto-optical Kerr effect (MOKE) technique. In this work, we investigate ferrimagnetic DWM behavior in GdFeCo by anomalous Hall signal. Multilayers of Hf(4nm)/GdFeCo(7nm)/SiN(4nm) are deposited by means of a high vacuum RF magnetron sputtering method on the thermally oxidized silicon substrate. Using the X-Ray Fluorescence (XRF) spectroscopy technique, we determine that the GdFeCo composition of our sample is 25% of Gd and 75% of FeCo by content. As displayed in Fig.1(a), at room temperature (RT), the magnetic compensation point is observed at a composition of higher Gd content (27%), indicating that the sample possesses TM-rich ferrimagnetic properties. The square-shaped hysteresis loop in the inset of Fig.1(a) measured by the Alternating Gradient Magnetometer (AGM) exhibits high bulk PMA. The Hall bar with a width of 10 μm and length of 65 μm is fabricated using standard photolithography, electron-beam lithography, and Ar ion-beam etching technique. A 150 nm copper (Cu) wire thickness is deposited as probing pads. The experimental setup and Hall bar device schematic is shown in Fig.1(b). The measurements are performed simultaneously with two nanovoltmeters: Voltmeter 1 measures the anomalous Hall voltage at cross PQ, whereas voltmeter 2 measures the longitudinal voltage along the current channel. The AHE resistance and magnetoresistance of the sample are examined as a function of the perpendicular magnetic field with various input DC currents (DCs). As displayed in Fig. 2(a), Fig. 2. (b), and Fig. 2. (c), the magnetoresistance (MR) varies significantly (resulting in MR peaks) as AHE resistance crosses the switching path of the hysteresis loop. Unlike well known MR effects such as the anisotropy MR (AMR) [3], giant MR (GMR) [4], spin Hall MR (SMR) [5], and Rashba MR [6], the anomalous MR observed here exhibits only two sharp peaks that are asymmetric with respect to the applied field and relates to switching path. It should be noted that the magnitude of the MR peak is equal to the AHE resistance ($R_{H1} \approx 8.23 \Omega$). Therefore, the curve switching path (Fig. 2(c)) relates to the origin of the MR peak (Fig. 2(a) and Fig. 2(b)) and is attributed to the magnetization switching behavior of the sample. We further investigate the magnetization reversals by MOKE and observe that as the DW runs along the Hall bar, as shown in Fig. 2(d)), it divides the area of the bar into 2 domains with opposite magnetization alignment which generates intermediate AHE resistances increasing along the curve switching path. Utilizing this fact, we propose a new approach to measuring the DW motion velocity over the hall bar channel. We first realize that the average DW velocity measured at crossbar of width w is given $|v_{DW}| = w/(t_s - t_N)$, where t_N , t_s are time corresponding to the nucleation and saturation points detected by AHE hysteresis, respectively. Our measurement results indicate that the external field sweeping speed changes $|v_{DW}|$ significantly. The DW propagation can be manipulated in the wide range from a low rate of 0.09 $\mu\text{m/s}$ (corresponding to field sweep of 0.24 Oe/s) to a high rate of 138.6 $\mu\text{m/s}$ (corresponding to field sweep of 200 Oe/s). The measurement results exhibit the trend that average DW velocity increases linearly with increasing field sweep speed. Furthermore, from the experiment data, we deduce that DW velocity displays an exponential growth function of $H-H_n$, thus: $V_{DW} = \alpha V_{\text{sweep field}} \times (e^{\beta(H-H_n)} - \gamma)$. Fitting the expression to experimental data we deduce α , β , and γ . The linear dependence of DW velocity on the field sweep speed and exponential growth of it in the field suggest that DWs have effective mass and thus have inertia. These findings provide further insight into the DWM behavior at the nucleation stage.

- [1] S. S. P. Parkin, M. Hayashi, and L. Thomas, Science 320 (2008) 190-194. [2] K. J. Kim, S. K. Kim, Y. Hirata, and S. H. Oh, Nat. Mater. 16, 1187 (2017). [3] T. McGuire, R. Potter, IEEE Trans. Magn. 11 (1975) 1018. [4] M.N. Baibich, J.M. Broto, and A. Fert, Phys. Rev. Lett. 61 (1988) 2472. [5] H. Nakayama, M. Althammer, and Y.-T. Chen, Phys. Rev. Lett. 110 (2013) 206601. [6] K. Narayanapillai, G. Go, R. Ramaswamy, and K. Gopinadhan, Phys. Rev. B 96 (2017) 064401.

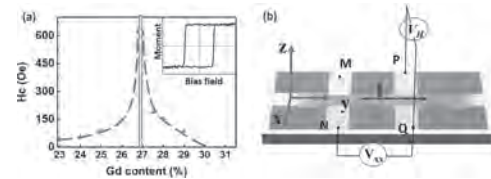


Figure 1: (a) Coercive field H_c as a function of Gd content in the GdFeCo composition. Inset: the out-of-plane hysteresis loops of the sample, measured by an AGM; (b) Optical image of Hall bar devices and schematic illustration of the measurement setup.

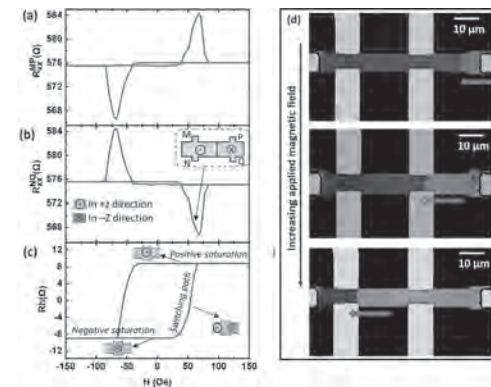


Figure 2: MR as a function of the perpendicular field at (a) lower edge across N and Q, and (b) upper edge across M and P. (c) the AHE resistance measured at the transverse cross bar. The inset illustrates the reversal domain mechanism corresponding to the switching path of hysteresis. (d) the MOKE image of DW motion on Hall bar.

IP-10. Very Fast Current Driven and Reverse Domain Wall Motion in a Rare-Earth Free Compensated Ferrimagnetic $Mn_{4-x}Ni_xN$.

S. Ghosh^{1,2}, T. Komori², A. Hallal¹, J.A. Peña Garcia³, T. Gushi^{2,1}, T. Hirose², H. Mitarai², H. Okuno⁴, J. Vogel³, M. Chshiev¹, J. Attané¹, L. Vila¹, T. Suemasu² and S. Pizzini³

1. Univ. Grenoble Alpes, CEA, CNRS, Grenoble INP, IRIG-Spintec, Grenoble, France; 2. Institute of Applied Physics, Graduate School of Pure and Applied Sciences, University of Tsukuba, Tsukuba, Japan; 3. Univ. Grenoble Alpes, CNRS, Institut Néel, Grenoble, France; 4. Univ. Grenoble Alpes, CEA, IRIG-MEM, Grenoble, France

Current induced domain wall motion is a crucial part of spintronics that has received large attention in the last 15 years and has resulted in memory as well as logic applications. Spin transfer torques (STT) and Spin orbit torques (SOT) are the two mechanisms through which the current induced domain wall motion takes place. In the case of STT, the electron spins get polarized through exchange interaction within the ferromagnetic layer and then transfers its angular momentum into the local magnetic moment of the domain walls thereby resulting in its motion. On the other hand, in the case of spin orbit torque, the spin current is generated by Spin Hall effect and Rashba effect in an adjacent heavy metal layer or interface and then diffuses into the magnetic layer applying a torque on the domain wall magnetic moments. Here, we will focus on spin transfer torque driven domain wall motion in ferrimagnetic Ni doped Mn_4N thin films. Recent work on domain wall motion has focused on ferrimagnets in which angular or spin moment compensation can be obtained by either changing the temperature of the material or the composition. Very fast domain wall velocities have been shown at the angular momentum compensation point where the precessional motion of the local spin is negligible thus resulting in faster domain wall motion. Mn_4N is a class of rare-earth free ferrimagnetic material with a low magnetization and a high perpendicular magnetic anisotropy. It has an anti-perovskite crystal structure with antiferromagnetically coupled magnetic Mn atoms at the corner sites Mn(I) and at the face centered sites Mn(II). Very high current driven domain wall velocities have already been demonstrated in thin Mn_4N films epitaxially grown on $SrTiO_3$ [1]. Since in these systems domain walls have Bloch internal structure, the driving mechanism is the classical spin-transfer torque. The compensation point is not achieved by varying the temperature of the material. However, by doping of Ni in Mn_4N the magnetic compensation can be achieved at room temperature [2]. The Ni atoms replace the Mn(I) atom at the corner sites and their moments align parallel to that of Mn(II) leading to a decrease in the net magnetization and a magnetic compensation or around 3.6% of Ni concentration [3]. On these epitaxially grown $Mn_{4-x}Ni_xN$ thin films on $SrTiO_3$ substrates, due to the reduction of the angular momentum originating from the Ni doping and the large spin-polarization of conduction electrons, very high velocities approaching 3000 m/s have been achieved for compositions close to the magnetic compensation point. Moreover, a reversal of the domain wall motion direction was observed after crossing the angular momentum (and magnetization) compensation point where the domain walls move in the opposite to the electron flow. This unique phenomenon is in agreement with the analytical 1D model applied to ferrimagnetic systems and is due to the switch of the sign of the angular momentum with respect to that of the spin polarization after the compensation point. This is supported by the results of *ab-initio* calculations.

1. T. Gushi, M.J. Klug, J.P. Garcia, NanoLetters.,19, 8716–8723(2019) 2. T. Komori, A. Anzai, T. Gushi, Journal of Crystal Growth., 507, 163-167 (2019) 3. T. Komori, T. Hirose, T. Gushi, Journal of Applied Physics 127, 043903 (2020)

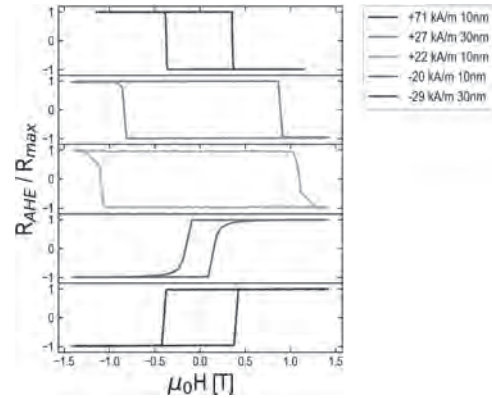


Fig 1: Anomalous Hall Effect curves showing a change of sign from negative to positive when crossing the magnetic compensation point. The magnetization decreases towards the compensation point and has been shown as negative after the crossing the compensation point.

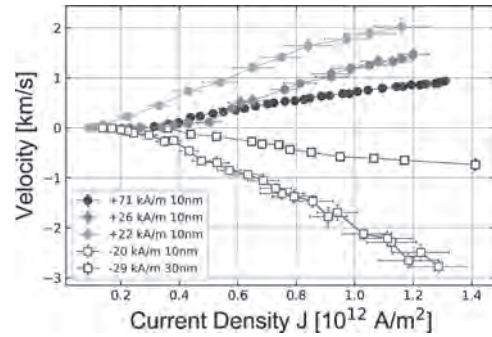


Fig 2: Domain wall velocity vs current density for $Mn_{4-x}Ni_xN$ thin films of different compositions below and above the compensation point; full symbol show velocities parallel to the electron flow before the compensation point and empty symbols show velocity after the compensation point in the opposite direction. Here, the highest velocity of 3000 m/s is achieved for the lowest magnetization with a composition after the compensation point.

IP-11. Nonvolatile Spintronic 2-to-1 Multiplexer Based on Current-Driven Domain Wall Propagation.

X. Zhang¹ and Z. Lu¹

*1. School of Materials Science and Engineering, Tsinghua University
School of Materials Science and Engineering, Beijing, China*

Reconfigurable logic device represented by field-programmable gate array (FPGA) has been widely used in various fields of applications including digital signal processing, image processing, cryptography and so on [1]. The logic programmability makes it possible to deal with varieties of different computing tasks with limited number of devices. Because SRAM-based FPGA suffers from static power dissipation and volatility issues, numerous studies have been conducted on nonvolatile reconfigurable spintronic logic devices [2][3]. Although the logic devices proposed in these studies could perform multiple Boolean logic operations, they could not cover all logic functions. In order to perform all combinational logic functions in a reconfigurable way, look-up tables (LUTs) are used in FPGA and the function of LUT could be realized by cascading multiplexers. Hence, reconfigurable spin logic covering all combinational logic functions could be realized if spintronic multiplexers are demonstrated. Here, we proposed a nonvolatile spintronic 2-to-1 multiplexer based on propagation of domain wall in Ta/CoFeB/MgO multilayer with perpendicular magnetic anisotropy (PMA). The device could operate at room temperature with no external magnetic field required for the function of multiplexer. The schematics of the nonvolatile spintronic multiplexer were shown in the inset of Fig. 1 and Fig. 2. Ta/CoFeB/MgO multilayer with PMA was patterned with “H” shape. The magnetization of the magnetic multilayer located at the vertical wires of “H” was manipulated by external out-of-plane magnetic field. The magnetization of the H-shaped magnetic film was first saturated by an external magnetic field applied on all parts of the film. After removing the saturation field, magnetic field of opposite direction was applied only on the left vertical wire of “H” to reverse the magnetization. Thus, a domain wall was generated. When current was applied in the horizontal wire, the domain wall would propagate and the direction of the domain wall movement was determined by the direction of the applied current. No external field was required for the current-driven domain wall motion. When the domain wall propagated from one end to the other end of the horizontal wire, the magnetization of the magnetic multilayer passed through by the domain wall would be reversed. Thus, the magnetization of the horizontal wire was determined by two factors: the initial magnetization state of the device and the direction of the write current applied. The experiment results of the device were shown in Fig. 1 and Fig. 2. The magnetization of the horizontal wire was represented by anomalous Hall voltage. When the write current flow leftwards, the magnetization of the horizontal wire would be the same with the left vertical wire, and vice versa when the write current flow rightwards. If the magnetization states of the two vertical wires were considered as two data inputs and the direction of write current as the selection input, the magnetization of the horizontal wire would be the output of the 2-to-1 multiplexer. In our proposed device, both the data inputs and the output were in the form of spin directions of ferromagnetic multilayer which would retain after power off. Such property not only made this device nonvolatile, but also provided the possibility for cascading because the output could be used as the data input of the multiplexer in the next step. The cascading feature was necessary for reconfigurable combinational logic. Above all, the proposed device consisted of H-shape ferromagnetic multilayer Ta/CoFeB/MgO with PMA realized the function of nonvolatile 2-to-1 multiplexer experimentally at room temperature and was expected to performing full sets of combinational logic with programmability by cascading.

[1] C. Katherine and H. Scott, *ACM Computing Surveys.*, Vol. 34, p.171-210 (2002) [2] Z. Luo, Z. Lu, X. Zhang, et al., *Advanced Materials.*, Vol. 29, p.1605027(2017) [3] X. Wang, C. H. Wan and X. F. Han, et al., *Advanced Materials.*, Vol. 30, p.6 (2018)

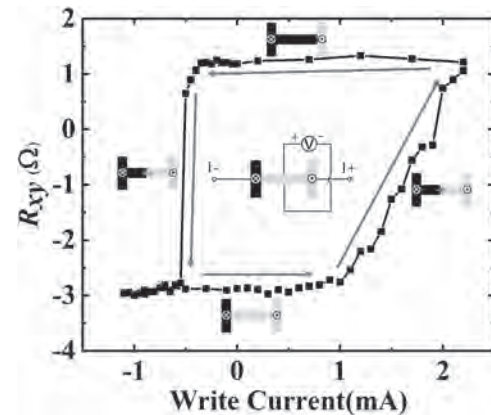


Fig. 1 Current-driven domain wall propagation when the left vertical wire was magnetized downward and right vertical wire magnetized upward. When current flow leftwards in the horizontal wire, the domain wall moved rightwards and the magnetization of the horizontal wire was reversed to downward. When current flow rightwards, the propagation of domain wall and the reversal of magnetization in the horizontal wire were both in the opposite direction.

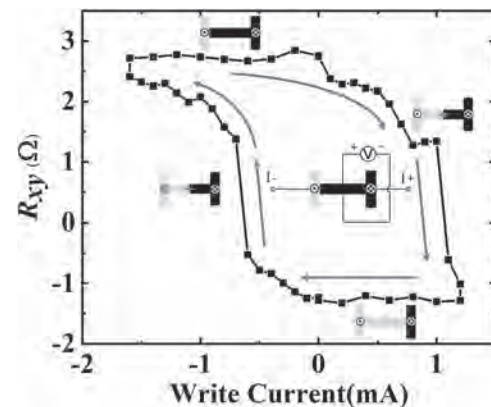


Fig. 2 Current-driven domain wall propagation when the left vertical wire was magnetized upward and right vertical wire magnetized downward. Compared with the case in Fig. 1, the direction of applied write current was still opposite to the direction of domain wall propagation. As a result, the chirality of magnetization switching was reversed. The magnetization state of the horizontal wire was determined by both write current and the magnetization of vertical wires on the left and right side.

IP-12. Domain Wall Pinning Probability in Different Width of sub-Micron-Wire With a Notch.

D. Shiu¹, C. Wei¹, K. Lai¹, Z. Gao¹, Y. Li², Y. Kao¹ and L. Horng¹

1. Physics, National Changhua University of Education, Changhua, Taiwan; 2. Graduate Institute of Photonics, National Changhua University of Education, Changhua, Taiwan

We report simulation results of vortex domain wall (VDW) dynamics pinning behavior magnetic wire with 20-nm-thick 100-nm, 200-nm, and 300-nm-wide wires with a triangular notch that depth ratio(R_d) is 30%. The R_d is the depth of notch divide by wire width. The transverse domain wall(TDW) dynamics pinning behavior in 100-nm wide wire has reported by Ref. [2]. Ref. [2] shows the pinning and depinning of DW in the Walker breakdown state(WB). Therefore we are interested in VDW depinning behavior and probability. The method of our study are running the simulation software Mumax³. Our simulation parameters of saturation magnetization(M_s), damping constant, exchange stiffness (A), and cell size of simulation parameters are 860 kA/m, 0.01, 13 pJ/m, and $5*5*5$ nm³, respectively. Our results show the width of wire influence dynamic pinning probability, as shown in Fig. 1 and Fig. 2. Figure 1 and Fig. 2 show the relation between dynamics VDW pinning probability and applied field. We employed the different separations from notch sharp to VDW starting positions to simulate the DW initial states in the WB. The data points of Figures 1 and 2 are averaged fields per 5 Oe, this averaged fields mean DW passing notch probability in a field range. The insert of Fig. 1 shows the type of DW pinning at notch. The type of DW pinning is influenced by pinning potential energy barrier or side well of the notch. It indicates that the shape of the notch influences the DW dynamics pinning probability. The applied field gives the magnetic energy to overcome the notch pinning potential. Figure 1 shows VDW in the 100-nm-wide wire is easier pinning as TDW type than 200-nm and 300-nm wide wire. The wire width influences the DW energy density, DW structure, and notch pinning potential energy. To make comparison with Fig. 1, we run the simulation with different wire widths, as shown in Fig. 2. Figure 2 shows the VDW type pinning probability of 200-nm and 300-nm wide wire has more than 100-nm-wide wire. It is caused by the wire width influences. The DW energy density influences by wire width and DW energy density also influences by a notch. The DW potential energy landscape is different at the differently wide wire. The wide wire has more space to release DW energy, and more space can lead DW to transform the structure of itself. In figure 2, 200-nm-wide wire shows unique behavior in the range of 200 Oe. In 200-nm-wide wire and 300-nm-wide wire, wide wires caused by wire width is not large enough to lead DW release metastable state DW energy, the DW energy is lower in the VDW chirality. The topological defects moving are also important for DW chirality changing in DW depinning behavior. The pinning potential of notch also influenced the DW depinning behavior. Those results show the applications of DW structures controlling and placing using notch.

[1]. L. J. Chang, Y.D. Yao, Pang Lin, IEEE Transactions on Magnetics., Vol. 47, No 10, (2011) [2]. Burn, D. M., & Atkinson, D. Scientific reports, 6, 34517 (2016). [3]. L. K. Bogart and D. Atkinson, Physics Review B., Vol. 79, p.054414 (2009) [4]. Y. Gao, B. You, X. Z. Ruan, Scientific Reports., Vol. 6, Article number: 32617 (2016) [5]. J. Brandão, R. L. Novak, H. Lozano., Journal of Applied Physics., Vol. 116, p.193902 (2014) [6]. D. M. Burn, D. Atkinson, Scientific Reports., Vol. 6, Article number: 34517 (2016) [7]. K. A. Omari, T. J. Hayward, Scientific Reports., Vol. 7, Article number: 17862 (2017) [8]. Y. Li a, Z. Lu, C. Chen, M. Cheng, Journal of Magnetism and Magnetic Materials., Vol. 456, p.341 (2018)

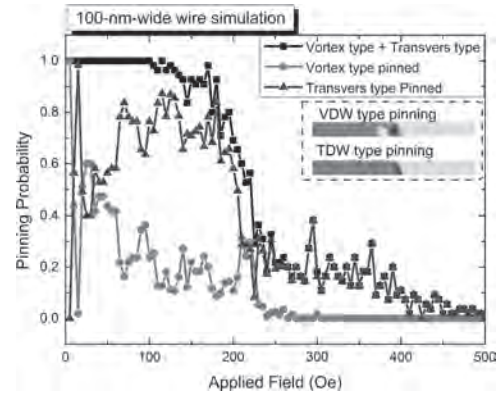


Fig. 1. Dynamics domain wall pinning probability of 100-nm-wide and 200-nm-wide wires. Insert shows the pinning types image of vortex domain wall(VDW) pinning and transverse domain wall(TDW).

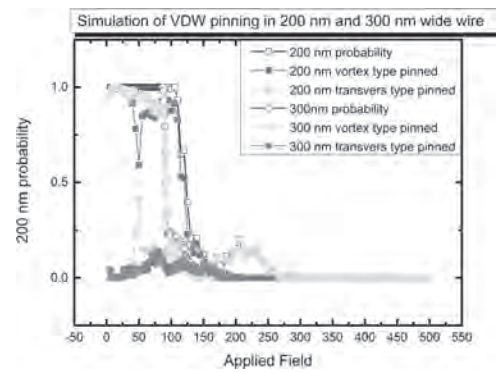


Fig. 2. The curve shows VDW and TDW types pinning probability in 200-nm-wide wire and 300-nm-wide. The square symbol shows the 200-nm-wide wire simulation results. The circle symbol shows the 300-nm-wide wire simulation results. The open symbols show the probability of DW depinning.

Session IQ
ELECTRIC FIELD EFFECTS AND MAGNETORESISTANCE
(Poster Session)

Hélène Béa, Chair
CEA-SPINTEC, Grenoble, France

IQ-01. Low-Voltage-Pulse Control of the Transport Properties of Antiferromagnetic $\text{La}_{0.35}\text{Sr}_{0.65}\text{MnO}_3$ Thin Film via Ferroelectric P(VDF-TrFE) Copolymer.

X. Zhao¹, H. Wong¹, Y. Liu^{1,2}, S. Ng¹, J. Liang¹, K. Lam¹, W. Cheng¹, C. Mak¹ and C. Leung¹

1. Applied Physics, The Hong Kong Polytechnic University, Kowloon, Hong Kong; 2. College of Electronic Information and Mechatronic Engineering, Zhaoqing University, Zhaoqing, China

Antiferromagnetic spintronics have been blooming in both fundamental science and practical application in recent few years due to the low sensitivity to external perturbation and ultrafast spin dynamics in antiferromagnetic materials. How to detect and manipulate the magnetic state of antiferromagnets efficiently has been a long-term outstanding question (1, 2). Among various regulation methods, electric-field control of antiferromagnetism is a promising way for realizing ultrafast and high density antiferromagnetic spintronics without considering Joule heating effect. Based on ferroelectric P(VDF-TrFE) copolymer, low-voltage-pulse modulation of ferromagnetic $\text{La}_{0.7}\text{Sr}_{0.3}\text{MnO}_3$ (FM-LSMO) thin films via oxygen vacancy has been demonstrated (3, 4). Here, we investigated low-voltage-pulse modulation of antiferromagnetic $\text{La}_{1-x}\text{Sr}_x\text{MnO}_3$ ($x = 0.65$) (AFM-LSMO) thin films. Positive 10-volt pulses can increase the resistance at low temperature (Fig. 1), which is ascribed to the oxygen vacancies induced by positive voltage pulses at 300K. This effect was further demonstrated to be related with oxygen vacancy by x-ray photoelectron spectra (XPS) results (Fig. 2). The XPS results suggest that positive pulses can induce more oxygen vacancy and reduce the valence state of Mn ions in AFM-LSMO thin films, thus changing the electrical and magnetic properties of antiferromagnetic layer. Exchange bias effect was established in bilayer FM-LSMO/AFM-LSMO structure and regulated by low-voltage pulses. Both exchange bias field and coercivity show voltage-polarity dependence, suggesting that low-voltage-pulse induced oxygen vacancy dominates the tuning process. Our findings provide a new way for exploring electric-field modification of antiferromagnetic spintronics.

1. T. Jungwirth, X. Marti, P. Wadley, J. Wunderlich. Nat Nanotechnol 11, 231-241 (2016). 2. P. Nėmec, M. Fiebig, T. Kampfrath, A. V. Kimel. Nat Phys 14, 229-241 (2018). 3. H. F. Wong, S. M. Ng, W. F. Cheng et al. Solid-State Electronics 138, 56-61 (2017). 4. H. F. Wong, S. M. Ng, W. Zhang et al. ACS Appl Mater Interfaces 12, 56541-56548 (2020).

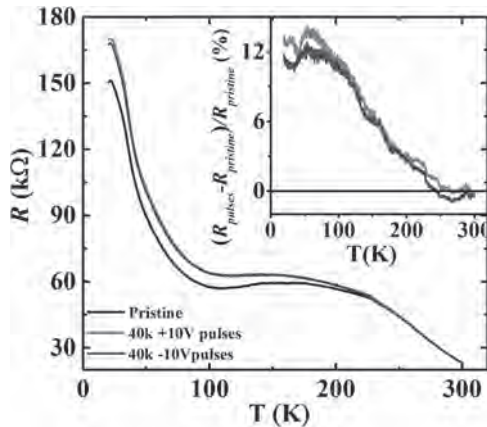


Fig. 1 Temperature dependent resistance of 7-nm AFM-LSMO thin film at pristine, positive pulses gated and negative pulses gated states, respectively. Inset: resistance change as a function of temperature. R_{pulses} and $R_{pristine}$ represent the resistance of pulses gated state and pristine state, respectively. Note that all pulses are applied at 300K in vacuum by Kiethley 2400 multimeter and the resistance is recorded after removing pulses.

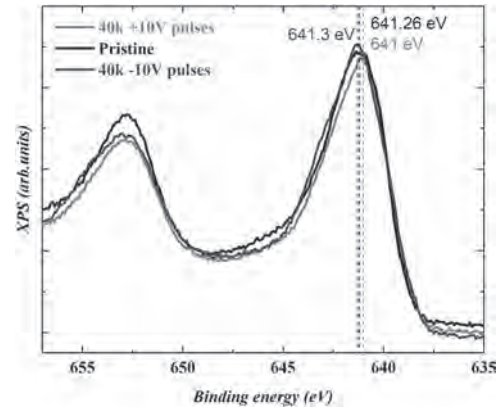


Fig. 2 Mn 2p core-level spectra of AFM-LSMO thin films at pristine, positive pulses gated and negative pulses gated states, respectively.

IQ-02. Influence of BiFeO₃ Phase on Perpendicular Magnetic Anisotropy in Co/Pt.

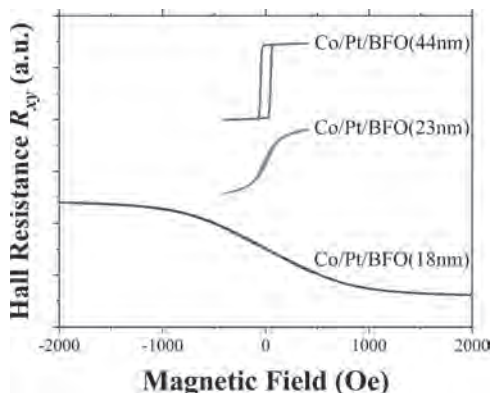
Y. Ji^{1,2}, P. Shepley¹, Z. Xu², L. Chen² and T. Moore¹

1. Physics and Astronomy, University of Leeds, Leeds, United Kingdom;

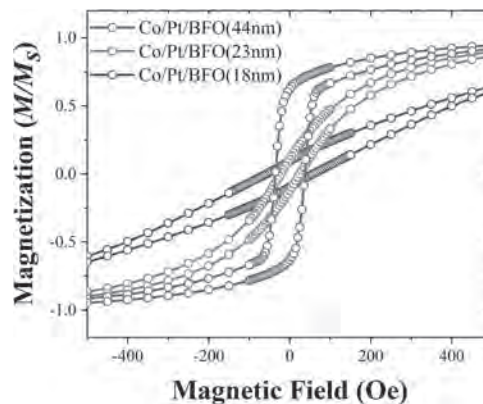
2. Physics, Southern University of Science and Technology, Shenzhen, China

Using LaAlO₃ (100) substrates and a 17-nm thick Ca_{0.96}Ce_{0.04}MnO₃ (CCMO) buffer layer, we grew BiFeO₃ (BFO) thin films with various thicknesses (18nm, 23nm, and 44nm) via pulsed laser deposition (PLD). X-Ray diffraction (XRD), Reciprocal Space Mapping (RSM) and Atomic Force Microscopy (AFM) techniques are employed to characterize the thickness, structure and surface morphology of the films. The large misfit of lattice constants between BFO films and LAO substrates exerts a large compressive strain on the BFO film, which initially stabilizes BFO in the tetragonal (T-) phase. A mixture of T-phase and rhombohedral (R-) phase emerges when the BFO thickness exceeds 20nm. As the BFO film thickness increases, the proportion of R-phase BFO increases as verified by AFM and XRD. Using DC magnetron sputtering, magnetic multilayers of Pt(4nm)/Co(0.8nm)/Pt(1.5nm) were deposited on top of these BFO films. Both Anomalous Hall Effect (AHE) and SQUID-VSM measurements reveal that the mixed-phase BFO favours a perpendicular magnetic anisotropy (PMA) of the upper Pt/Co/Pt multilayers, while the pure T-phase BFO film with smaller thickness suppresses the PMA (Fig.1 and Fig.2). Considering the R-phase BFO at the surface of the mixed-phase BFO film can change reversibly to T-phase BFO when applying electric field across BFO, this finding may provide a new route for realizing the electrical control of PMA in hybrid ferromagnetic-multiferroic structures.

[1] Zuhuang Chen, *et al.*, *Phys. Rev. B* 84, 094116 (2011). [2] He, Q., *et al.*, *Nat Commun* 2, 225 (2011). [3] R. J. Zeches, *et al.*, *Science* 326, 977-980 (2009) [4] Huang, Y., *et al.*, *Nat Commun* 11, 2836 (2020).



Room temperature anomalous Hall resistance R_{xy} for Co(0.8nm)/Pt(1.5nm)/BFO(44nm), Co(0.8nm)/Pt(1.5nm)/BFO(23nm), and Co(0.8nm)/Pt(1.5nm)/BFO(18nm).



Room temperature out-of-plane hysteresis curves for Co(0.8nm)/Pt(1.5nm)/BFO(44nm), Co(0.8nm)/Pt(1.5nm)/BFO(23nm), and Co(0.8nm)/Pt(1.5nm)/BFO(18nm).

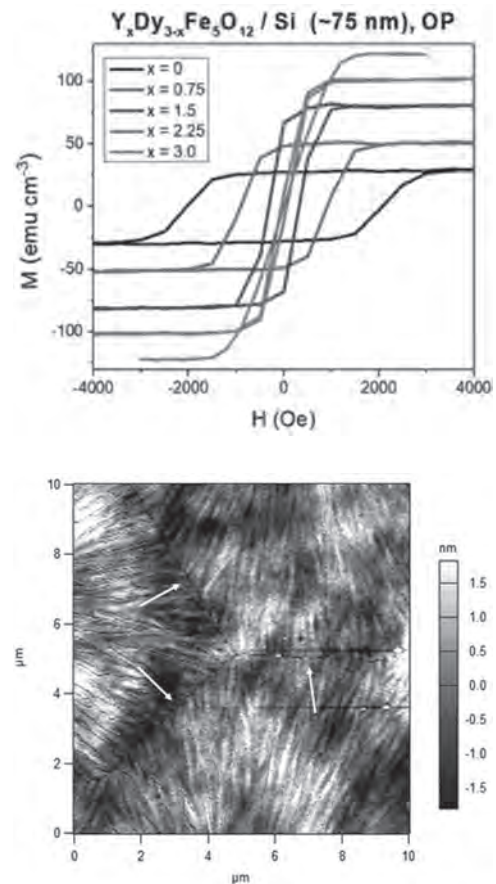
IQ-03. Dysprosium Iron Garnet Films on Silicon and Piezoelectric Substrates With Perpendicular Magnetic Anisotropy.

M. Gross¹, J. Bauer² and C. Ross²

1. *Electrical Engineering and Computer Science, Massachusetts Institute of Technology, Cambridge, MA, United States*; 2. *Materials Science and Engineering, Massachusetts Institute of Technology, Cambridge, MA, United States*

Rare earth iron garnets (REIGs) are magnetic insulators that can be grown as nanometer thickness films with perpendicular magnetic anisotropy (PMA), making them attractive for studies of spin orbit torques (SOT) and chiral spin textures. PMA has been achieved in epitaxial films of several REIGs on garnet substrates due to magnetoelastic anisotropy from epitaxial lattice mismatch strain¹⁻². However, it is of interest to develop PMA garnet films on non-garnet substrates, such as silicon for practical spintronic devices and piezoelectric substrates to investigate the effects of modulating the piezoelectric strain. PMA garnet has been grown directly on silicon, enabling integration of garnet-based spintronics into a conventional CMOS ecosystem. The films are polycrystalline, and PMA is due to the thermal expansion mismatch between the film and substrate following a high temperature anneal to crystallize the film³. Here, we report the growth of garnet films on Si and on piezoelectric substrates. Piezoelectric substrates allow modulation of the film strain through application of a voltage. This allows for tuning of the film anisotropy through magnetoelastic anisotropy, which may be used to manipulate domain walls with voltage-induced strain⁴. Dysprosium iron garnet (DyIG) was chosen because its two magnetostriction coefficients have the same sign. Pulsed laser deposition is then used to deposit the DyIG, which is then crystallized by a rapid thermal anneal (850 °C/5 min). DyIG grown on Si crystallized without a seed layer for thicknesses over 25nm. Atomic force microscopy of the DyIG/Si films indicates sub-nanometer surface roughness with large grain sizes on the order of 10 μm in a 41 nm thick film. DyIG on Si has a large in plane tensile strain leading to PMA with a coercivity of 4.5kOe at 41 nm thickness compared with 2.5kOe at 75nm thickness, and a room temperature saturation magnetization of 20 emu cm⁻³. The film coercivity can be tuned from 2.5-6 kOe by varying the annealing temperature. The anisotropy was reduced while retaining PMA by substitution of yttrium for dysprosium. We show that thinner films of DyIG may be crystallized using an underlayer of a nonmagnetic garnet Gd₃Ga₅O₁₂ coated with ~2nm Pt to prevent interdiffusion. This allowed 10 nm polycrystalline DyIG films to be formed on Si with bulk-like magnetization and PMA. Films were also grown on PMN-PT (011) substrates by first sputtering a thin layer of Pt onto the substrates to prevent interdiffusion. The modulation of the magnetic properties of DyYIG/Pt/PMN-PT will be described as a function of voltage applied to the PMN-PT which produces a strain in the garnet. Fig. 1. Out of plane VSM hysteresis loop for a 75 nm DyIG/Si film substituting the dysprosium with varying amounts of yttrium. Fig. 2. AFM image of large grains in a 41 nm DyIG/Si film. Grain boundaries are indicated by the arrows.

1. A. Quindeau, C. Avci, W. Liu, *Adv. Elec. Mater.*, Vol. 3, 1600376 (2017).
2. E. Rosenberg, L. Beran, C. Avci, *Phys. Rev. Mater.*, Vol. 2, 094405 (2018).
3. J. Bauer, E. Rosenberg, C. Ross, *APL*, Vol. 114, 052403 (2019).
4. M. Azam, et al. *Nanotechnology*, Vol. 31, 145201 (2020).



IQ-04. Field-Free Switching of Perpendicular Magnetization and Memristive Properties Through Spin-Orbit Torque in FePt/[TiN/NiFe]₅ Multilayers.

C. Sun¹, Y. Tao¹, L. Zhu¹, Y. Jiao¹, X. Hu¹, Y. Hui¹, F. Jin¹ and K. Dong¹
 1. China University of Geosciences, Wuhan, China

The electrical manipulation of the magnetization in ferromagnetic (FM) nanostructures through current-induced spin-orbit torque (SOT) is one of the representative phenomena based on the spin-orbit coupling. Very recently, centrosymmetric L1₀ FePt is reported to achieve the room temperature SOT switching in single layer and a new type of inversion asymmetry called composition gradient is responsible for the observed SOT. Till now, current-induced magnetization-based switching in L1₀ FePt requires the application of an additional external in-plane magnetic field to break the mirror symmetry and field-free switching is rarely investigated. The objective of this work is to study the effect of interlayer exchange coupling on the field-free magnetization switching performance by SOT of FePt based multilayer devices. The AHE and VSM results show that FePt/[TiN/NiFe]₅ multilayers perform large perpendicular magnetocrystalline anisotropy and XRD results show very clear FePt (001) peak since the fabrication conditions keep the same, indicating good L1₀ FePt structure. Moreover, only high temperature deposited NiFe exhibits (200) peak while that with room temperature performs amorphous phases. Current-induced partial magnetization-based switching with different external fields H_x from +500 Oe to -500 Oe for FePt/[TiN/NiFe]₅ is shown in Fig. 1g, h and it can be seen that field-free switching is realized for both devices. Interestingly, the transition from clockwise to counterclockwise switching can be observed once for RT devices while that changes three times for HT devices, which may be due to RKKY effect. Furthermore, SOT-induced tunable multistate memristors have been observed even for that without external field (Fig. i-l) and these results pave the way for developing SOT-based energy-efficient neuromorphic systems.

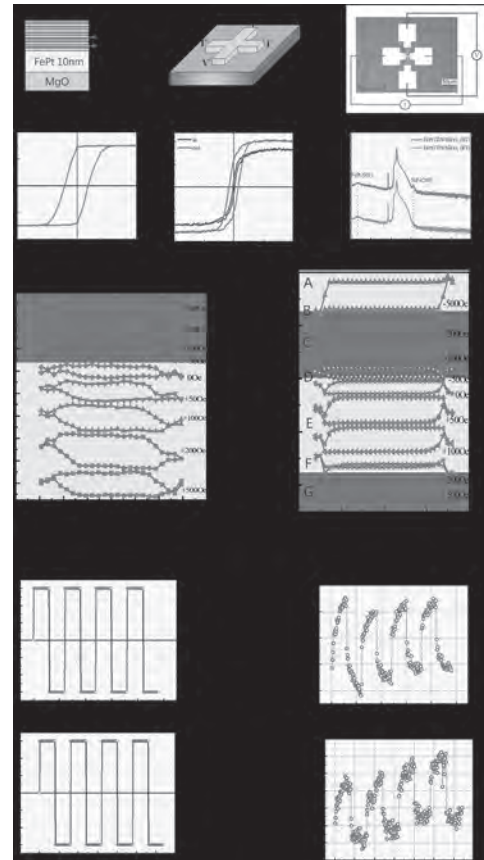


Fig.1The structures of SOT devices(a, b, c), AHE and VSM of FePt/[TiN/NiFe]₅ (HT) (d, e), XRD of FePt/[TiN/NiFe]₅ both for RT and HT (f), Current-induced magnetization switching of FePt/[TiN/NiFe]₅ with different external fields H_x for RT and HT, respectively (g, h), the applied consecutive current pulses and corresponding resistance modulation for FePt/[TiN/NiFe]₅ (HT) with external +200 Oe fields H_x (i, j), the same measuring results for devices without external fields (k, l).

IQ-05. Electric Field Modulation of Interfacial Magnetic Anisotropy in Magnetron-Sputtered Pt/Co/MgO Ultra-Thin Structure With Chemically Tailored top Co Interface.

R. One^{1,2}, S. Mican¹, A. Mesaros², M. Gabor², T. Petrisor Jr², M. Joldos², L.D. Buda-Prejbeanu³ and C. Tiusan^{1,2}

1. Faculty of Physics, Department of Solid State Physics, Universitatea Babeş-Bolyai, Cluj-Napoca, Romania; 2. Universitatea Tehnica din Cluj-Napoca, Cluj-Napoca, Romania; 3. SPINtronique et Technologie des Composants, Grenoble, France

The electric field manipulation of magnetization [1,2] became a subject of acute interest, since it provides a low energy consumption and sub-nano-second switching time. The yield of such process depends on the anisotropy energy variation in response to the applied electric field and therefore a wide variety of studies have been dedicated to this topic. In this work we present a combined experimental-theoretical study of the perpendicular magnetic anisotropy (PMA) electric field modulation in magnetron-sputtered epitaxial Pt(111)/Co/MgO type systems. *Ab-initio* calculations of voltage-controlled PMA have been performed using the *Full Potential Linear Augmented Plane Wave FP-LAPW* code *Wien2k* [3]. A supercell model has been used to describe the multilayer configuration and the electric field has been applied using a zig-zag additional potential in the Hamiltonian. The anatomy of PMA and its electric field dependence has been theoretically analyzed within the framework of two main mechanisms: the surface charge doping which alters the relative occupation of electronic orbitals at the interface and the intrinsic interfacial dipole field. The main issue of our calculation is the prediction that the adjunction of Pt at top Co/MgO interface in Pt/Co/MgO ultrathin structures enhances the perpendicular anisotropy by about 84% and its electric field variation rate (Fig.1 (a), (b)). These theoretical predictions have been further used to design, grow by sputtering samples and pattern spintronic devices dedicated for the experimental analysis of the voltage response of magnetic anisotropy. As expected, in both standard Pt/Co(1nm)/MgO and top interface tailored Pt/Co(1nm)/Pt/MgO samples, the room-temperature magnetometry experiments demonstrated the out-of-plane remanent magnetization configuration related to surface PMA. The electric field influence on the PMA has been then studied on Hall-bridge patterned samples with a top-gating insulator (Fig.2 (a)), suitable for Anomalous Hall Effect magnetometry. In these devices, a qualitative agreement between the theoretical predictions and experimental results has been observed. The asymmetric variation of the anisotropy energy dependent on the polarity of the electric field, which was deduced from the *ab-initio* calculations is also reflected in the asymmetric variation of the coercive field as a response to the applied voltage (Fig.2 (b)). Supplementary insight into the anatomy of the mechanisms involved in the electric field effect on the coercive field, driven by the electric field modulation of the surface anisotropy, is further provided within a macrospin approach.

References [1] W-G. Wang et al, Nature Mater., vol. 11, pp. 64-68, 2012. [2] Y. Shiota et al, Nature Mater., vol. 11, pp. 39-43, 2012. [3] P. Blaha et al, J. Chem. Phys., vol. 152, p. 074101, 2020.

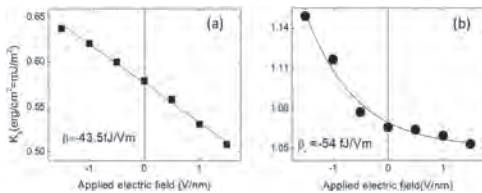


Fig.1 *Ab-initio* calculation of electric field variation of the surface perpendicular anisotropy K_s for Pt/Co/MgO (a) and Pt/Co/Pt(1ML)/MgO (b) supercells

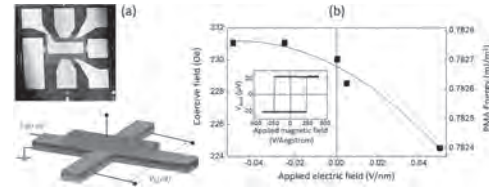


Fig.2 (a) Hall-bridge UV lithographically patterned devices; (b) Variation of coercive field, surface anisotropy with the applied electric field.

IQ-06. Origin of the Large Voltage-Controlled Magnetic Anisotropy in Cr/Fe/MgO Junction With an Ultrathin Fe Layer: First-Principles Investigation.

W. Chen¹, L. Jiang¹, Z. Yan¹, Y. Zhu¹, C. Wan¹ and X. Han¹

1. Institute of Physics, University of Chinese Academy of Sciences, Chinese Academy of Sciences, Beijing, China

Voltage-controlled magnetic anisotropy (VCMA) has attracted broad interests due to its high efficiency in switching magnetization. Large VCMA was experimentally observed in Cr/Fe/MgO junction with ultrathin Fe layer [T. Nozaki et al., Phys. Rev. Applied 5, 044006 (2016)], whose underlying mechanism was still not clear however. The Cr/Fe/MgO/Fe magnetic tunnel junction (MTJ) is also well known for its quantum-well (QW) states and as-induced spin-dependent resonant tunneling [F. Greullet et al, Phys. Rev. Lett. 99, 187202 (2007)]. Here, in order to uncover the relation between the large VCMA and the QW states, we developed a *k*-resolved VCMA calculation method combined with the second-order perturbation theory to investigate it. We find the VCMA coefficient reaches -290 fJ/Vm matching well with the previous experiment with 3 monolayers (MLs) of Fe. The coefficient oscillates strongly and even changes its sign with increasing the number of Fe MLs. Comparing the *k*-resolved VCMA with Fermi surface of the interfacial Fe atom, the screening charges theory for VCMA was verified. For 2~9 MLs Fe, interestingly, the QW states of Δ_1 electron at Γ point provide large (no) contribution to the VCMA with odd (even) MLs. Moreover, the change of the orbital-resolved Fermi surface at the interfacial Fe atom also plays an important role on VCMA oscillation, which as well as the QW states result in the largest VCMA for 3 MLs Fe. Our results deepen understanding of the large VCMA in Cr/Fe/MgO junction, which would be helpful to design practical MTJ with large VCMA.

[1] W. Z. Chen, L. N. Jiang, Z. R. Yan, Y. Zhu, C. H. Wan, and X. F. Han, Phy. Rev. B 101, 144434 (2020)

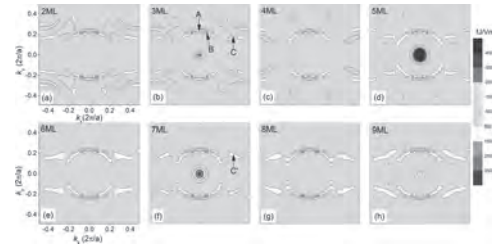


Fig. 2. *k*-resolved VCMA in the two dimensional Brillouin zone for Cr/Fe/MgO junctions with different number of Fe MLs from 2MLs to 9MLs (a)~(h).

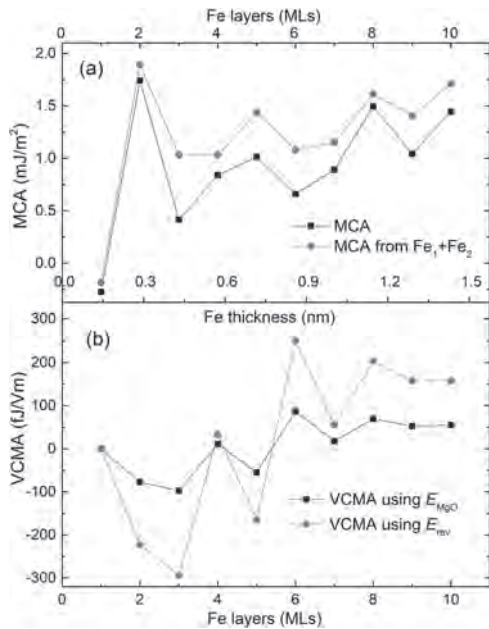


Fig. 1. (a) MCA and (b) VCMA for Cr/Fe/MgO junctions with different number of Fe MLs. The blue stars are the VCMA coefficient measured in Ref [Takayuki Nozaki, etc PRA 5, 044006 (2016)].

IQ-07. Control of Electrical Resistance and Magnetoresistance by Electric Field-Driven Oxygen Ion Migration in a Single GdO_x Wire.

J. Kang¹, S. Lee², T. Lee¹, J. Yang¹, J. Lee², C. Tae⁴, J. Jeong⁴, S. Park³, B. Park² and K. Kim¹

1. Physics, Korea Advanced Institute of Science and Technology, Daejeon, The Republic of Korea; 2. Materials Science and Engineering, Korea Advanced Institute of Science and Technology, Daejeon, The Republic of Korea; 3. Korea Basic Science Institute, Daejeon, The Republic of Korea; 4. Chungnam National University, Daejeon, The Republic of Korea

Electric field-driven ion migration can significantly modulate the electric- and magnetic- properties of solids, which creates new opportunities for electromagnetic devices with ultralow power consumption. Earlier works used vertically stacked structures, e.g., ferromagnet/oxide heterostructures, in which the magnetic properties of ferromagnet are controlled by the electric-field-driven oxygen ion migration along the vertical direction [1,2]. However, the existence of an interface obscures the detailed understanding of how the oxygen ion migration occurs and how it affects the electrical and magnetic properties of a ferromagnet. Instead of stacked structures, here we investigate the oxygen ion migration effect in a single ferromagnetic GdO_x wire with lateral electric field application [3]. We directly visualize the electric-field-driven lateral motion of oxygen ions by an optical microscope (Fig. 1). The oxygen ions are found to migrate along the electric field direction by thermal activation. By exploiting the electric-field-driven oxygen ion migration, we succeed to increase or decrease the resistivity of GdO_x in a controllable way, which allows mimicking the functional behavior of biological synapse (Fig. 2). Large negative magnetoresistance is observed in GdO_x wire of which magnitude is significantly enhanced up to 20% by 9 T by oxygen ion control. Our results suggest that the electrical and magnetic properties of a single GdO_x can be efficiently controlled by an electric field, which paves the way towards fully functional electromagnetic devices such as artificial synapses.

1. Uwe Bauer, Lide Yao and Geoffrey S. D. Beach, *Nature Materials*, Vol. 14, p.174 (2015) 2. Mantao Huang, Aik Jun Tan and Geoffrey S. D. Beach, *Scientific Report*, Vol. 7, p.7452 (2017) 3. Jun-Ho Kang, Soogil Lee and Kab-Jin Kim, *NPG Asia Materials*, Vol. 12, p.44 (2020)

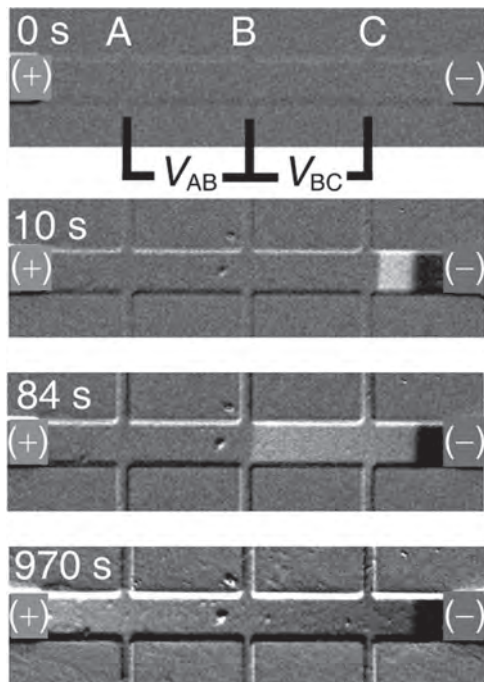


Fig. 1. Real-time images of the migration of accumulated oxygen ions in a GdO_x device.

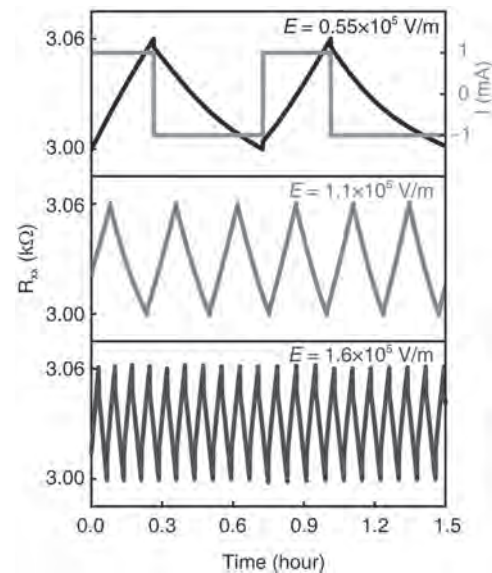


Fig. 2. Longitudinal resistance (R_{xx}) with repeated switching of the current (I) direction.

IQ-08. Magnetic Tunnel Junctions Based on Photoswitchable Self Assembled Monolayers.

L. Jerro¹, B. Quinard¹, S. Delprat¹, F. Godel¹, S. Collin¹, A. Sander¹, A. Vecchiola¹, K. Bouzehouane¹, R. Mattana¹, P. Seneor¹ and F. Petroff¹
 1. *Unité Mixte de Physique CNRS-Thales, Université Paris Saclay, 91177 Palaiseau, France, Palaiseau, France*

Magnetic tunnel junctions (MTJs) are known to be one of the main building blocks of spintronics. In these devices, the integration of molecular layers as tunnel barrier is envisioned as an opportunity to allow the engineering of spintronics at the molecular scale. Actually, thanks to the spin-dependent hybridization at ferromagnet/molecule interfaces, spin polarization and thus tunnel magnetoresistance can now be tailored by molecules. For example, it was shown that spin polarization could be inverted or enhanced depending on the hybridization coupling strength [1]. In this direction, among molecular systems, self-assembled monolayers (SAMs) appear as one of the most promising tool to tailor MTJs properties. Indeed, the anchoring group, body and head of molecules can be changed to tune the coupling strength of both ferromagnetic electrodes independently and at will. However, up to now, only basic “passive” molecules such as alkane chain have been integrated into MTJs [2-4]. These molecules could be defined as “passive” since their electronic properties cannot be switched by external stimulus. In this talk we will present molecular MTJs integrating “active” molecules from the diarylethene molecule family. These molecules can be switched between two stable states corresponding to an open and a closed form of its central part. As the electron delocalization, energy gap and coupling strength to the electrodes depend on the molecule state, the tunnel resistance and tunnel magnetoresistance (TMR) is expected to be tuned by switching the molecule. We will then discuss the magnetotransport properties of NiFe/diarylethene/Co MTJs (cf. Figure 2(a)). After presenting the fabrication process of the molecular MTJs, we will first show that the diarylethene molecules grafting over the NiFe ferromagnetic bottom electrode do not alter its surface properties. We will in particular show X-Ray Photoelectron Spectroscopy (XPS) measurements with spectra recorded at Ni and Fe 2p edges (figure 1) ruling out any trace of oxidation and validating our surface recovery protocol [5]. We will then focus on the transport results. We will show that we have been able to obtain non-linear $I(V)$ and parabolic conductance curves in both open and closed forms. In addition, we have performed inelastic electron tunneling spectroscopy (IETS) in order to detect molecular vibrations inside the tunnel barrier. Those measurements confirm that these active molecules act as an effective tunnel barrier in our MTJs. We will also show magnetoresistance curves that have been recorded at different bias voltages, temperatures and magnetic field directions. We have obtained magnetoresistance effects in both open and closed formed of diarylethene molecules (result shown for the open form in figure 2(b)). The angular dependence of the magnetoresistance reveals that both TMR and tunneling anisotropic magnetoresistance effects coexist and allows us to disentangle them. All these studies demonstrate for the first time that switchable active molecules can be successfully integrated into MTJs to build multifunctional spintronic devices electrically and/or optically controllable.

[1] C. Barraud et al., Nat. Phys. 6, 615 (2010) [2] J. R. Petta et al., Phys. Rev. Lett., 93, 136601 (2004) [3] W. Wang et al., Appl. Phys. Lett. 89, 153105 (2006) [4] M. Galbiati et al., Adv. Mater. 24, 6429 (2012) [5] M. Galbiati et al., AIP Advances. 5, 057131 (2015)]

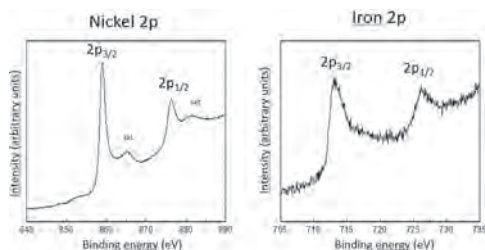


Figure 1: XPS spectra at nickel and iron 2p edges of diarylethenes SAMs grafted on a NiFe electrode.

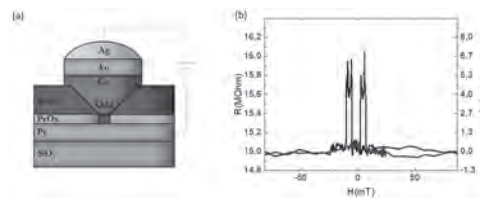


Figure 2: (a) Schematic representation of the molecular MTJ (b) Magnetoresistance curve of a NiFe/diarylethene/Co MTJ at 50 K obtained for the open form of the diarylethene molecules

IQ-09. Atomistic Simulations for TAMR Applications.

B.W. Wilson¹, J.N. Scott¹, W. Hendren¹ and R. Bowman¹

¹. School of Mathematics and Physics, Queen's University Belfast, Belfast, United Kingdom

The areal density of hard disk drives (HDD) must be increased to meet the needs of today's society and its ever-increasing data creation. This requires both the writability of smaller bits and the ability to read these bits. This can only be achieved by reducing the size of conventional tunnelling magnetoresistance (TMR) sensors. A possible solution to this is tunnel anisotropic magnetoresistance (TAMR) which arises due to a change of density of states at the Fermi level when a magnetic sublattice rotates with respect to the crystal field. It is particularly present in materials which possess large spin-orbit (SO) interactions such as CoPt [1]. Very large TAMR signals have been observed at low temperatures consisting of an IrMn based magnetic tunnel junction (MTJ) [2] which if optimised at room temperature would remove the requirement for a second ferromagnetic electrode and thus reducing the size of the sensor. VAMPIRE [3] brings together a simple user interface through the use of plain text files to produce an open-source atomistic spin simulation software. The software is used in conjunction with vibrating sample magnetometry (VSM) and ferromagnetic resonance (FMR) to investigate the bilayer system of Ni₈₀Fe₂₀/Co₇₀Fe₃₀ deposited via magnetron sputtering, in order to optimise the ferromagnetic layer of the MTJ. Simulation parameters are achieved directly from experiment and supplied to VAMPIRE. Integration of simulation and experiment in this manner can yield insight into the magnetisation dynamics on the atomic scale and guide experimental development. The inclusion of the thin layer of Co₇₀Fe₃₀ within simulations of a permalloy thin film has been found to enhance the coercive field of ferromagnetic layer of the MTJ which can be seen in figure 1. This has been experimentally confirmed in addition to an increase in magnetisation saturation. Building on this, we found that there is an increase in exchange with 1nm of CoFe on top of NiFe through FMR analysis as shown in figure 2. Further research has been carried out on Ta, Ru and Pd seed layers to assess whether or not they would make viable seed layers for the FM layer of the MTJ. VSM measurements, FMR analysis and X-Ray diffraction (XRD) scans have been carried out to further analyse the stacks. As each layer of the TAMR structure is simulated, experimentally confirmed and finally optimised; it will pave the way for the future of data storage.

[1] - Phys. Rev. Letts 100, 087204 (2008) [2] - Nature Mat. 10, 347 (2011)
 [3] - R. F. L. Evans et al., Appl. Phys. Lett. 104, 082410 (2014)

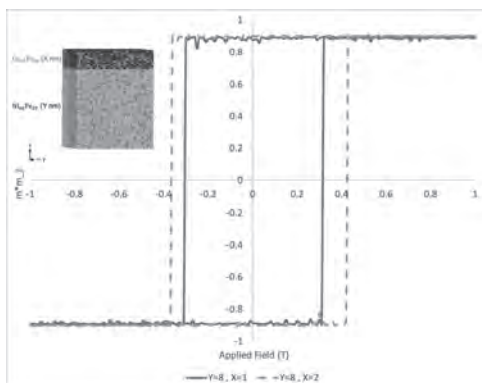


Fig.1 VAMPIRE hysteresis loop Ni₈₀Fe₂₀(Y)/Co₇₀Fe₃₀(X) of normalised magnetisation against applied field. Inset is the visual representation of the generated system with a total z height of x + y

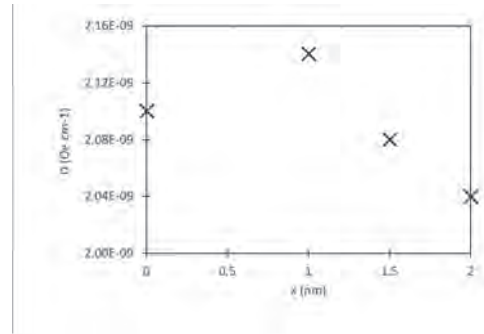


Fig.2 Spin wave stiffness, D against CoFe thickness, x for Ta(5)/NiFe(70)/CoFe(x)/Ta(5) sample set.

IQ-10. Direct Observation of Spin Polarization in Amorphous CoFeB Thin Film.

Q. Liu¹, X. Lu¹, C. Fu², Y. Yan¹, Q. Gao¹, H. Li², Y. Nie¹, J. Wu³, L. He¹, R. Zhang¹ and Y. Xu¹

1. Nanjing University, Nanjing, China; 2. Shandong University, Jinan, China; 3. University of York, York, United Kingdom

CoFeB-based magnetic tunnel junctions (MTJ) is one of the most studied spintronic devices[1] due to its high tunneling magnetoresistance (TMR) [2] and low switching current density[3]. Here, using a direct characterization technique of spin-resolved photoemission, the spin polarization of an amorphous Co₄₀Fe₄₀B₂₀ thin film prepared by magnetron sputtering is obtained. The spin-resolved photoemission measurement consists of a UVS 300 unpolarized helium lamp () and a SPECS PHOIBOS 150 hemisphere energy analyzer equipped with 3D Micro-Mott detector operated at a scattering energy of 25 kV. As shown in Fig. 1, the measured spin polarization at Fermi level is as high as 60%, which is comparable to the values obtained by other techniques. It is shown that our experimental value of spin polarization at is positive while the calculated spin polarization at ground state using first-principle calculation has a negative spin polarization at. Fig. 2 displays the density of states after considering the photoionization cross section, thermal broadening and experimental resolution broadening. The modified calculated spin polarization indicates a positive spin polarization at which is consistent to the experimental results. Moreover, we find that the maximum spin polarization is located at ~0.2 eV above, supported by the modified calculated spin polarization spectrum.

1. C. Fu, X. Zhang, and Y. Duan. Magn. Magn. Mater. 492, 165657 (2019).
2. S. Ikeda, J. Hayakawa, and Y. Ashizawa, Appl. Phys. Lett. 93 (8), 082508 (2008). 3. B. Liu, X. Ruan, Z. and Y. Xu, Appl. Phys. Lett. 109 (4), 042401 (2016).

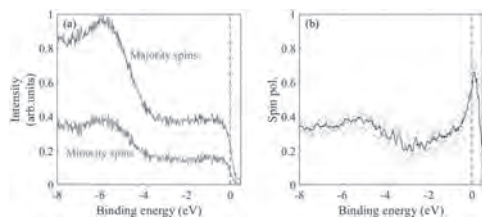


Fig. 1 (a) Spin-resolved photoemission spectra of the CoFeB thin film. (b) Corresponding spin polarization curve, with the black line is a guide to eyes.

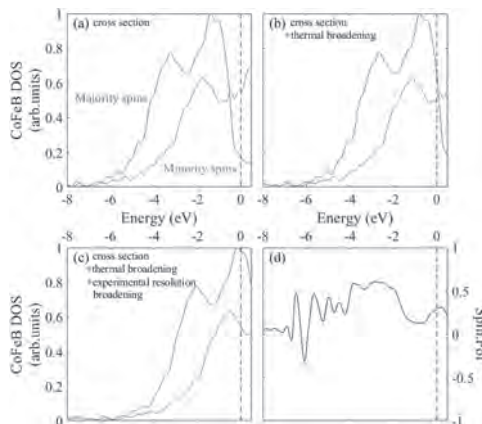


FIG. 2 Calculated density of states after considering (a) the photoionization cross sections, (b) temperature and (c) experimental resolution. (d) Spin polarization curve corresponds to (c).

Session IR
THIN FILMS AND INTERFACE EFFECTS
(Poster Session)

Yu Shiratsuchi, Co-Chair
Osaka University, Osaka, Japan

Maciej Dabrowski, Co-Chair
University of Exeter, Exeter, United Kingdom

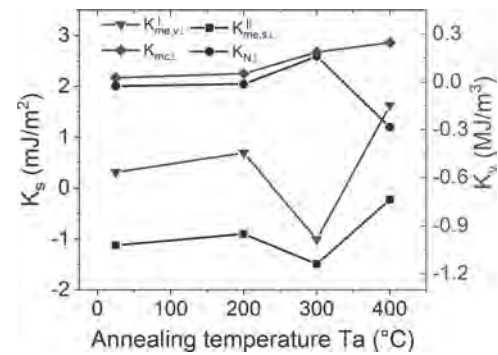
IR-01. Annealing Temperature and Thickness Dependencies of Perpendicular Magnetic Anisotropy and Dzyaloshinskii-Moriya Interaction of Pt/Co/MgO Thin Film.

D. Ourdani¹, Y. Roussigné¹, S.M. Cherif¹, M. Gabor² and M. Belmeguenai¹
 1. Université Sorbonne Paris Nord, Villetaneuse, France; 2. Universitatea Tehnica din Cluj-Napoca, Cluj-Napoca, Romania

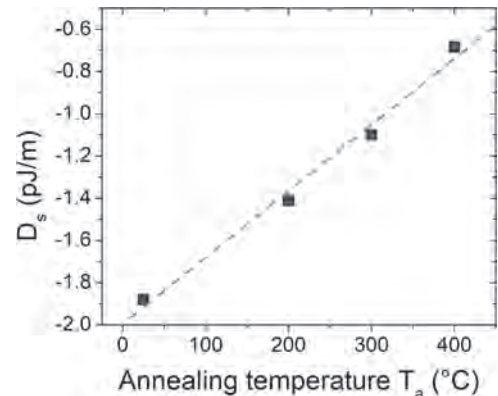
At the interface of a heavy metal (HM) with a strong spin-orbit coupling (SOC) and a ferromagnetic material (FM), a break in inversion symmetry arises leading to the appearance of several phenomena. One of them is the antisymmetric exchange interaction called the Dzyaloshinskii-Moriya Interaction (iDMI). It is responsible for the stabilization of chiral magnetic structures such as skyrmions and for the non-reciprocity of spin wave propagation. Another interface phenomenon, subject of extensive research in magnetic heterostructures (e.g. for HM/FM/metal oxide (MOx) type stacks) is interfacial Perpendicular Magnetic Anisotropy (iPMA) [2]. This originates from the level of oxidation, from the interface roughness and from the SOC [3]. These two quantities are of considerable interest because of their crucial importance for applications in spintronic devices, such as non-volatile magnetic memories and hard disk recording [4]. As an example, an MgO layer is often used as a tunnel barrier in magnetic tunnel junctions (MTJs), providing high spin transfer torque (SST), or in tunnel magnetoresistance (TMR), which are key properties for such devices. In order to optimize the magnetic properties at the interfaces of thin films, a thermal treatment is often used because it yields structural changes and atomic rearrangement and thus induces phase transition or alloys formation. However, annealing at high temperatures can also induce oxidation thus reducing the volume magnetic moment or increasing the magnetic anisotropy. In this work, we investigate the effect of the annealing temperature on iPMA and iDMI in Pt/Co/MgO stacks, with variable Co thickness ($1 \leq t_{Co} \leq 6$ nm). These stacks were deposited by magnetron sputtering on a Si substrate and annealed at different temperatures (T_a), up to 400°C. For all the studied films, the saturation magnetic moment per unit area was measured by Vibrating Sample Magnetometry (VSM) for each Co thickness. This allowed us to accurately determine the saturation magnetization M_s and the dead layer thickness t_d which are necessary to evaluate iDMI and iPMA. These quantities have been measured using the Brillouin light scattering (BLS) in the Damon-Eshbach (DE) configuration. Effective magnetizations (M_{eff}) were deduced from measurements with fixed wave vector ($k_{sw} = 8.08 \mu\text{m}^{-1}$) and variable magnetic fields. The presence of the DMI in the studied structures induces a frequency shift between the two Stokes and anti-Stokes modes, this allowed us to quantify the iDMI effective constant (D_{eff}) which is proportional to this shift. The variation of M_{eff} as a function of the inverse of the Co thickness, shows the presence of two different linear regimes separated by a critical thickness (t_c), which depends on T_a . This is generally observed in the case of epitaxial growth with a lattice misfit between the constituents, the strain can contribute to $K_{v\perp}$ (regime I: $t < t_c$), or to $K_{s\perp}$ (regime II: $t_c < t$). In order to separate the different surface/interface anisotropies (magnetocrystalline, magnetoelastic and Neel type) from the volume anisotropies, we have used an adapted model [1]. In figure (1), we can see the evolution of these different anisotropies as a function of the annealing temperature. For T_a above 200°C, a variation in the different contributions of the surface and volume anisotropies is observed. Similar to the iPMA, the evolution of the iDMI interaction was investigated as a function of the annealing temperature and the thickness of the effective magnetic layer. The measurements show that the effective iDMI constant (D_{eff}) is proportional to the inverse effective magnetic thickness. Therefore, for low thicknesses we find that the values of D_{eff} deviate from the linear regime probably due to the reduction of magnetic thickness (effect of dead layer). The iDMI surface constant D_s is then deduced from D_{eff} which decreases linearly (with absolute value) with the annealing temperature T_a (see figure(2)). It varies from (-1.9pJ/m) at room temperature to (-0.7pJ/m) at 400°C annealing temperature. We then conclude the possibility to modulate the strength of the iDMI by changing the annealing temperature.

[1] M. T. Johnson, P. J. H. Bloemenz, F. J. A. den Broeder, and J. J. de Vries, Rep. Prog. Phys. 59, 1409 (1996). [2] B. Dieny and M. Chshiev, Rev. Mod. Phys. 89, 025008 (2017). [3] N.-H. Kim, et al, AIP Adv. 7, 035213

(2017). [4] Xueying Zhang, et al *ACS Applied Materials & Interfaces* 2018 10 (19), 16887-16892 [5] J. H. Moon, et al, Phys. Rev. B 88, 184404 (2013)



Variation of the different anisotropy constants magnetocrystalline (K_{mcl}), volume ($K_{me,v,l}^I$) magnetoelastic, Neel-type interface (K_{Nl}) and the surface ($K_{me,s,l}^I$) magnetoelastic as a function of annealing temperature.



iDMI surface constant D_s as a function of annealing temperature.

IR-02. Interfacial Dzyaloshinskii-Moriya Interaction and Perpendicular Magnetic Anisotropy in CoFeB/PtO_x Based Systems.

I. Benguettat^{1,2}, Y. Roussigné¹, S. Chérif¹, L. Chahed², F. Kail², S. Auffret³, C. Baraduc³, H. Béa³ and M. Belmeguenai¹

1. Université Sorbonne Paris Nord, LSPM CNRS UPR 3407, Villetaneuse, France; 2. Université Oran1, laboratoire de physique des couches minces et matériaux pour l'électronique, Oran, Algeria; 3. Université Grenoble Alpes, CEA, CNRS, Grenoble INP, IRIG, SPINTEC, Grenoble, France

Over the past few years, spintronic devices have attracted considerable attention due to their potential application compared to the classical electronics. Recently, a new concept of racetrack memory (RM) is developed, where domain walls (DW_s) are replaced by magnetic chiral spin textures (skyrmions) [1] stabilized in the presence of the interfacial Dzyaloshinskii-Moriya interaction (iDMI). Their small size, high speed, and low energy consumption make skyrmions good candidates for future spintronic data storage. Skyrmion-RM will allow to considerably increasing storage densities and information transfer speed [1, 2]. Therefore such devices performance depends significantly on the proper modulation of the Nonmagnetic/Ferromagnetic (FM) interface and interfacial associated phenomena. In addition to the Heavy-metal (HM)/ (FM) interfaces and related spin-orbit coupling (SOC) interaction, it has recently been demonstrated the presence of the perpendicular magnetic anisotropy (PMA) and the iDMI in the FM/ Metal Oxide (Mo_x) interfaces. The PMA in such interface is due to the hybridization between the ferromagnetic metal and oxygen ions [3]. Recently, density functional theory has predicted the controlling of the iDMI sign and magnitude by changing the oxygen coverage of the FM layer [4]. However, knowing that these effects are dependent on the interface configuration, the study of the iDMI in the FM/MO_x is still lacking. An efficient way to determine the role and the contribution of such interface is to investigate a FM/MO_x system with or without a HM underlayer. Thus, in this work we propose the investigation of the PMA and, the iDMI as a function of the annealing temperature, the PtO_x thickness and the oxidation state in CoFeB/PtO_x interfaces. We expect to obtain overoxidation state for the thinner Pt films, where oxygen penetrates the underlying magnetic layer, whereas underoxidized and optimally oxidized states are obtained for thicker Pt layers. Two categories of samples were grown by DC magnetron sputtering on thermally oxidized silicon, with or without Ta (3 nm) buffer layer. In the first category, the Co₈Fe₇₂B₂₀ (CFB) thickness was varied up to 10 nm (2nm ≤ t_{CFB} ≤ 10 nm) and capped by TaO_x (0.8 nm). In the second category, CFB thickness was kept at 1.5 nm and was capped by variable thicknesses of PtO_x (0.7nm ≤ t_{Pt} ≤ 1.6 nm). Both as grown and 225 °C annealed are studied for this second category. For this experimental investigation, Vibrating sample magnetometer (VSM), Brillouin light scattering (BLS) in Damon-Esbach (DE) configuration and Microstrip line ferromagnetic resonance (MS-FMR) were combined. The VSM was used to investigate the static magnetic properties (magnetization at saturation (M_s) and magnetic dead layer thickness (t_d)). The FMR was used for the determination of the gyromagnetic ratio, and for the investigation of the PMA in the thicker films. The BLS was employed for the study of the PMA (thinner films) and the iDMI. For the PMA, the spectra were measured at spin wave (SW) vector (k_{sw} = 8.08 μm⁻¹) under variable in-plane applied magnetic fields, while for the iDMI measurements, BLS spectra were measured as a function of the k_{sw} under in-plane saturating magnetic field. VSM measurement revealed that t_d is approximately the same for the CFB/TaO_x (t_d ≈ 0.7 nm) and CFB/PtO_x (t_d ≈ 1 nm) systems. For the CFB/PtO_x stacks we notice slightly higher value for the samples with Ta buffer layer due to the supplement of intermixing at the bottom interface. The larger value of the t_d (≈ 1 nm) obtained for CFB/PtO_x compared to CFB/TaO_x samples may be due to the fact that the Pt does not oxidize, the oxygen penetrates more into the CFB films thus increasing the thickness of the magnetic dead layer. M_s is also approximately the same for all the samples (around 1510 emu/cm³) which is in good agreement for systems of CFB rich on Fe [5]. The PMA investigation in the CFB/TaO_x samples has shown the degradation of the interface anisotropy by inserting a Ta buffer layer. Indeed, the surface anisotropy constant (K_s) in the Ta/CFB/TaO_x is twice weaker for the samples without Ta buffer layer confirming the degradation of the interface anisotropy by the Ta buffer layer. The PMA and iDMI measurements as a function of the Pt thickness have shown that the effective magnetization

(M_{eff}) and the effective iDMI constant (D_{eff}) have the same trend for all the systems. D_{eff} and M_{eff} increase with increasing t_{Pt} thus allowing characterizing the strength of the iDMI and PMA for the CFB/PtO_x interface. In the as deposited CFB/PtO_x films, the thinnest Pt (t_{Pt} = 0.7 nm) sample is perpendicularly magnetized. The increasing of M_{eff} as Pt thickness increases suggested that the oxidation of CoFeB decreases. The experimental data of M_{eff} and D_{eff} were then fitted using exponential growth function, to extract a decay thickness (λ). It is found that, λ for the M_{eff} is higher compared to that of D_{eff} for as grown CFB/PtO_x stacks, confirming that the iDMI is slightly more localized at the first monolayers at the interface compared to the PMA. Measurements of spin pumping induced damping have also been performed by FMR and BLS will also be presented.

[1] R. Tomasello, E. Martine, R. Zivieri et al., Sci Rep 4, 6784, (2014) [2] W. Kang, X. Chen, D. Zhu et al., IEEE 7th Non-Volatile Memory Systems and Applications Symposium (NVMSA), Hakodate, pp. 7-12, (2018) [3] S. Monso, B. Rodmacq, S. Auffret, et al. Applied Physics Letters, 80, n° 22, pp 4157, (2002) [4] A. Belabbes, G. Bihlmayer, S. Blügel, et al. Scientific Reports 6, 24634, (2016). [5] T. Ogasawara, M. Oogane, M. Al-Mahdawi et al. AIP Adv. 9, 125053, (2019).

IR-03. Effect of Oxidation of Top Interface on Magnetic Parameters of Epitaxial Films With Dzyaloshinskii-Moriya Interaction.

G.S. Suslin¹, V. Shatilov¹ and A. Kozlov¹

1. School of Natural Sciences, Far Eastern Federal University, Vladivostok, Russian Federation

In this work, we investigate the influence of interface parameters on the magnetic energies such as the perpendicular magnetic anisotropy (PMA) and the interfacial Dzyaloshinskii-Moriya interaction (DMI) [1, 2] of Pd(111)/Co_x/CoO_{1-x}/Pd ultrathin epitaxial films with different oxidation depths. Epitaxial Pd(3 nm)/Co(1 nm) films were grown on a Si(111)/Cu(2nm) surface by molecular beam epitaxy in ultrahigh vacuum chamber, and after that, films were exposed the procedure of artificial oxidation. We varied the oxide thickness and this way we changed ferromagnetic thickness. The lattice parameters of bulk Pd and Co materials are mismatched by about 9,7%, which leads to the appearance of significant elastic strains on the bottom interface, which induced strong perpendicular magnetic anisotropy [3]. Oxidation in heavy metal(HM)/ferromagnetic metal(FM)/Oxide polycrystalline trilayers leads to significant changes of the magnetic properties [4]. The lattice period of the metal layers during growth and their structure were analyzed by means of RHEED. Magnetic hysteresis loops of the samples were measured using a vibrating sample magnetometer (VSM). Magnetic structure was investigated by a magneto-optical Kerr effect (MOKE) microscope. The MOKE microscope was equipped with a hand-made coil applying out-of-plane magnetic fields and an in-plane electromagnet. The out-of-plane coil was used in pulse mode and produced magnetic fields with an amplitude up to 50 mT and a width down to 2 msec. Artificial oxidation of magnetic layer leads to symmetry breaking on the bottom and top magnetic interfaces, which reduces compensation of interfacial DMI. Determination of the thickness of the magnetic layers carried out by measuring the saturation magnetization with vibrating samples magnetometry. Increasing of oxidation time leads to decreasing of volume of magnetic material and to increasing of effective PMA energy. The reported study was partially funded by Council for Grants of the President of the Russian Federation (project - MK-1384.2021.1.2) and the Russian Ministry of Science and Higher Education (the state task 0657-2020-0013).

[1] Dzyaloshinsky I., Journal of Physics and Chemistry of Solids, Vol. 4.4, p.241-255 (1958) [2] Moriya T., Physical review, Vol. 120, p. 91 (1960) [3] Davydenko A. V., et al., Phys. Rev. B, Vol. 95, 064430 (2017) [4] Feng, Junxiao, et al., Physical Review Applied, Vol. 13.4, 044029 (2020)

IR-04. Ultrathin CoFe_2O_4 Films Grown by Molecular Beam Epitaxy on Pt(111).

G. Delgado Soria¹, K. Freindl², J. Prieto¹, A. Quesada³, J. De La Figuera¹, N. Spiridis², J. Korecki^{2,4} and J. Marco¹

1. Instituto Química Física Rocasolano, CSIC, Madrid, Spain; 2. Jerzy Haber Institute of Catalysis and Surface Chemistry, Polish Academy of Sciences, Krakow, Poland; 3. Instituto de Cerámica y Vidrio, Madrid, Spain; 4. AGH University of Science and Technology, Faculty of Physics and Applied Computer Science, Krakow, Poland

Cobalt ferrite (CoFe_2O_4 , CFO) is a material used for technological applications such as permanent magnets, spintronic devices and recording media. This is due to its high magnetocrystalline anisotropy, large saturation magnetization in comparison to other ferrites, elevated Curie temperature and large magnetostrictive constant. Structurally, the ideal CFO corresponds to an inverse spinel (AB_2O_4), i.e. with all the cobalt cations (Co^{2+}) and half of the iron ions (Fe^{3+}) located in octahedral sites (B), and the other half of the Fe^{3+} occupying tetrahedral sites (A). However, in the case of thin films, depending on the growth conditions and subsequent annealing treatments, a fraction of the cobalt cations can be forced to move to tetrahedral sites. The subject of cationic distribution in cobalt ferrite thin films has been already addressed in the past, with Mössbauer spectroscopy playing a fundamental role. In most cases, however, the films have been grown on oxide substrates whilst films grown on metallic substrates have been scarcely studied. In this work, we have studied the properties of ultrathin CoFe_2O_4 films grown by oxygen assisted molecular beam epitaxy on a Pt(111) single crystal. The deposition was performed at 523 K temperature, and the resulting film was subsequently annealed at intermediate temperatures (up to 773 K) in order to prevent the formation of multiphase films, island growth or dewetting phenomena. Samples were grown from a few nanometers thickness to 20 nm. We characterized their composition and structural properties after each step of the growth process by Conversion Electron Mössbauer and Auger electron spectroscopies (CEMS and AES, respectively), low energy electron diffraction (LEED), and scanning tunneling microscopy (STM). An important particularity of this work was that both the growth and the characterization of the films were performed *in-situ*, i.e. in the same ultra high vacuum chamber, without exposure of the samples to the laboratory atmosphere in order to avoid any chemical transformations resulting from such exposure.

V.A.M. Brabers, Handbook of Magnetic Materials, Vol. 8, pp.189–324 (1995) J. Smit and H. Wijn, Philips' technical library, Vol. 278, pp. 136-172 (1959) M. De Santis et al, Acta Cryst B, Vol. 75, pp. 8-17 (2019)

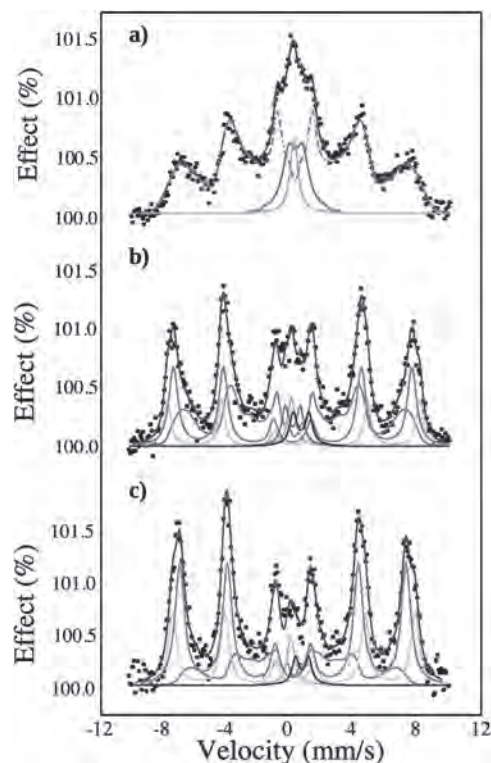


Fig 1. Mössbauer spectra obtained for the 5 nm cobalt ferrite thin film for the different stages: a) as grown measured at room temperature, b) and c) annealed to 673 K and 773 K measured at room temperature and 125 K, respectively.

IR-05. Superconducting Properties of Epitaxial Films of Superconducting NbN and Highly Spin Polarized Co₂FeSi Under High Magnetic Fields.

I. Shigeta¹, T. Kubota^{2,3}, S. Kimura², S. Awaji², K. Takanashi^{2,3} and M. Hiroi¹

1. Department of Physics and Astronomy, Kagoshima University, Kagoshima, Japan; 2. Institute for Materials Research, Tohoku University, Sendai, Japan; 3. Center for Spintronics Research Network, Tohoku University, Sendai, Japan

The properties of superconductor/ferromagnet multilayers and junctions have been intensively studied from the standpoint of the interplay between superconductivity and ferromagnetism. Though in a special case superconductivity and ferromagnetism can coexist and exhibit novel phenomena such as π state in superconductor/ferromagnet/superconductor junctions [1], in general, the superconducting order parameter is expected to suppress in the superconducting layer but to penetrate into the ferromagnetic layer. A number of the studies have been carried out with ferromagnetic component consisting of 3d transition metals like Fe, Co and Ni [2]. In contrast, only few reports exist for epitaxial NbN/Heusler alloy layered films and their devices so far; for example, giant coercivity enhancement in NbN/Co₂FeSi bilayers [3], efficient injection of pure spin currents in NbN/Co₂MnSi devices [4], superconductivity in NbN/Co₂(Fe,Mn)Si/Au trilayers [5,6], and spin polarization measurements of Co₂FeSi by the epitaxial contact Andreev reflection spectroscopy [7]. Therefore, we focus on superconducting properties of epitaxial films of a superconducting NbN layer attached to a highly spin polarized Heusler alloy Co₂FeSi layer, where the superconductivity of the NbN layer penetrates into the ferromagnetic Co₂FeSi layer. We investigate how the Co₂FeSi layer with the high spin polarization affects the superconductivity of the NbN layer in epitaxial NbN/Co₂FeSi/Au films through their interface. We have fabricated NbN/Co₂FeSi/Au epitaxial films on an MgO-substrate by an ultrahigh-vacuum (UHV)-compatible magnetron sputtering system. The thickness of the CFMS film was 5 nm while the thickness of the NbN film was fixed to 100 nm. Considering the NbN film was thicker enough than its coherence length $\xi_{\text{NbN}}(0)$ at 0 K, the superconductivity of the layered film should be in the three-dimensional (3D) regime, due to satisfying $d_{\text{NbN}} \gg \xi_{\text{NbN}}(0)$. Superconducting properties of the epitaxial films were evaluated by resistivity measurements with the standard four-terminal technique under both parallel and perpendicular magnetic fields up to 17 T. The superconducting transition temperature T_c of NbN/Co₂FeSi/Au trilayer films was determined to be 16.1 K in the absence of magnetic field. Temperature dependence of the resistivity $\rho(T)$ was measured in both magnetic fields parallel and perpendicular to the surface of NbN/Co₂FeSi/Au trilayer films. Figure 1 shows the field dependence of the pinning potential $U_0(H)$ for both applied magnetic field directions deduced from the Arrhenius plots for the $\rho(T,H)$ curves. As shown in Fig. 1, $U_0(H)$ was well described by $H-\alpha(1-H/H^*)^\beta$ above 5 T by the similar model with the exponents in the field dependence of the pinning force density, where H^* is a characteristic field representing the irreversibility field at 0 K. Temperature dependence of the upper critical field $\mu_0 H_{c2}(T)$ was evaluated from the $\rho(T)$ measurements. Figure 2 represents the upper critical fields $\mu_0 H_{c2}^{\parallel}(T)$ and $\mu_0 H_{c2}^{\perp}(T)$ of a NbN/Co₂FeSi/Au trilayer film in two magnetic field directions applied parallel and perpendicular to the surface of the trilayer. From Fig. 2, the upper critical field $H_{c2}(0)$ at 0 K was also deduced to be $\mu_0 H_{c2}^{\parallel}(0) = 23.2$ T for the parallel magnetic field and $\mu_0 H_{c2}^{\perp}(0) = 16.2$ T for the perpendicular magnetic field, respectively. The experimental results under magnetic fields revealed the superconductivity of the NbN layer was affected by the interplay between the superconducting NbN layer and the highly spin polarized Co₂FeSi layer.

[1] T. Kontos, M. Aprili, J. Lesueur, F. Genêt, B. Stephanidis, R. Boursier, Phys. Rev. Lett. 89 (2002) 137007. [2] L. Lazar, K. Westerholt, H. Zabel, L. R. Tagirov, Y. V. Goryunov, N. N. Garif'yanov, I. A. Garifullin, Phys. Rev. B 61 (2000) 3711. [3] A. Gupta, G. Singh, D. Kumar, H. Kishan, and R. C. Budhani, Appl. Phys. Lett. 103 (2013) 182602. [4] D. Kumar, P. C. Joshi, Z. Hossain, and R. C. Budhani, Appl. Phys. Lett. 102 (2013) 112409. [5] I. Shigeta, T. Kubota, K. Makise, S. Kimura, S. Awaji, B. Shinozaki, K. Koyama, K. Takanashi, and M. Hiroi, IEEE Magn. Lett. 8 (2017) 3305605.

[6] I. Shigeta, T. Kubota, Y. Sakuraba, S. Kimura, S. Awaji, K. Takanashi, and M. Hiroi, Physica B 536 (2018) 310. [7] I. Shigeta, T. Kubota, Y. Sakuraba, C. G. Molenaar, J. N. Beukers, S. Kimura, A. A. Golubov, A. Brinkman, S. Awaji, K. Takanashi, and Masahiko Hiroi, Appl. Phys. Lett. 112 (2018) 072402.

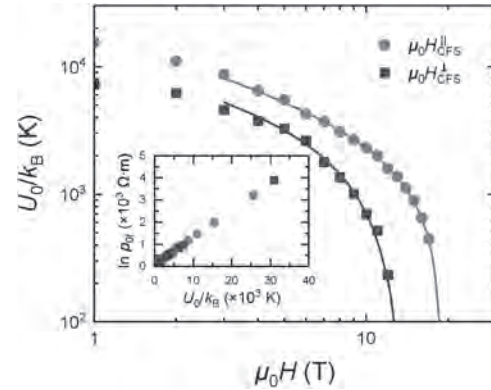


Fig. 1. Pinning potential $U_0(H)$ as a function of magnetic field H . The blue circles are $U_0(H)$ parallel magnetic fields H^{\parallel} to the surface for the NbN/Co₂FeSi/Au trilayer film and the red squares are perpendicular magnetic fields H^{\perp} . Inset: Relationship between $\ln \rho_{0r}$ and U_0 for both magnetic fields H^{\parallel} and H^{\perp} .

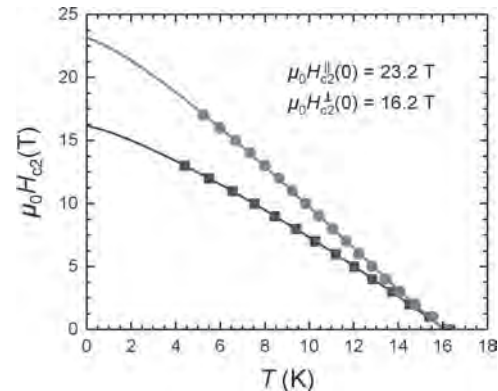


Fig. 2. Temperature dependence of the upper critical field $H_{c2}(T)$ for both directions deduced from $\rho(T)$ measurements at various magnetic fields.

IR-06. Observation of Antiferromagnetic Coupling Between Ferrimagnetic Garnet Thin Films.

J. Liang¹, X. Zhao¹, S. Ng¹, H. Wong¹, Y. Liu², C. Mak¹ and C. Leung¹
 1. Applied Physics, The Hong Kong Polytechnic University, Hong Kong, China; 2. College of Electronic Information and Mechatronic Engineering, Zhaoqing University, Zhaoqing, China

Antiferromagnetic coupling between magnetic films has long been studied for the design and tuning of spin structures, and is a core issue in spintronics research. Such a coupling has been widely reported in metallic multilayers, but the effect is seldom seen in the more complex multilayer film interfaces [1]. Here we studied the antiferromagnetic coupling at the interface between terbium iron garnet ($Tb_3Fe_5O_{12}$, TbIG) and yttrium iron garnet ($Y_3Fe_5O_{12}$, YIG) thin films, being manifested in form of an inverted hysteresis loop at low temperatures. TbIG (7 nm)/YIG (23 nm) was deposited on $Y_3Al_5O_{12}$ (YAG) substrates with (110) orientation by pulsed laser deposition at 437 K under 100 mTorr oxygen pressure. As a control, a sample with 5 nm $Gd_3Ga_5O_{12}$ (GGG) spacer between the two iron garnet layers was also prepared. The crystal structure of the films was characterized by a high-resolution X-ray diffractometer (HRXRD). The surface morphology of samples was characterized by atomic force microscopy (AFM). The microstructures and thickness of the samples were examined by high-resolution transmission electron microscopy (HRTEM). For transport measurements, Pt (5 nm) Hall bar patterns were deposited on the garnet samples by rf sputtering. Anomalous-Hall effect (AHE) of samples was measured by a physical property measurement system (PPMS). The magnetic properties of the samples were measured by the vibrating sample magnetometer (VSM) option of the PPMS. Fig. 1(a) shows the HRXRD pattern of TbIG (7 nm)/YIG (23 nm), demonstrating epitaxial growth of the films on YAG with strong (110) orientation (rocking curve with a full width at half maximum (FWHM) of 0.064° , Fig. 1(b)). AFM scan indicates a small root mean square roughness of 0.38 nm, with clear atomic terraces. Fig. 1(c) and (d) show the in-plane magnetic hysteresis loops of single layer YIG (30 nm) and TbIG (30 nm) measured at 10 K, respectively; both films were deposited on YAG (110) substrates under the aforementioned conditions. Due to the strong contribution from the Tb at low temperatures, the TbIG monolayer film exhibited much stronger magnetization than YIG of the same thickness did. A strong magnetocrystalline anisotropy was observed in the TbIG monolayer as evidenced by the high coercivity ($H_{c-TbIG} = 5.5$ kOe; $H_{c-YIG} = 0.19$ kOe) [2]. As shown in Fig. 2(a), the hysteresis loop of the TbIG (7 nm)/YIG (23 nm) sample measured at 10 K shows an obvious soft/hard magnetic coupling phenomenon, supported by the appearance of double coercivity behavior. The switching at the low field was mainly attributed to YIG, while the reversal at the high field was attributed to TbIG. The most characteristic feature of the hysteresis curve was the inversion under the low magnetic field (Inset of Fig. 2(a)): when the external field decreased from the positive saturation, the YIG layer first reversed its magnetization at a small positive field, while the magnetization of TbIG remained undisturbed. This clearly indicated the antiferromagnetic coupling between the TbIG/YIG at the interface [3]. In the case of the control sample, when a 5 nm GGG spacer is present at the TbIG/YIG interface, one could only observe the normal magnetic hysteresis loop as shown in Fig. 2(b). The inverted loop at the low field disappeared but the double coercivity could still be clearly observed, indicating the inverted loop at the low field was caused by the antiferromagnetic coupling at the interface of two different ferrimagnets. In summary, the antiferromagnetic coupling effect has been observed between two neighboring ferrimagnets, manifested in the form of an inverted hysteresis loop at the low magnetic field. Temperature-dependence of such an antiferromagnetic coupling effect and the anomalous-Hall effect of samples would be conducted to further elucidate the nature of the coupling effect. Financial support by the RGC, HKSAR (PolyU 15302320) is acknowledged.

[1] T. Maity, D. Kepaptsoglou and S. Roy, "Observation of complete inversion of the hysteresis loop in a bimodal magnetic thin film," Physical Review B., 95(10):100401, 2017. [2] R. F. Pearson, "Magnetocrystalline Anisotropy of Rare-Earth Iron Garnets," Journal of Applied Physics., 33(3):1236-1242, 1962. [3] H. Zhang, J. Zhang and J. R. Sun,

"Antiferromagnetic interlayer coupling of (111)-oriented $La_{0.67}Sr_{0.33}MnO_3/SrRuO_3$ superlattices," Chinese Physics B., 28(3):037501, 2019.

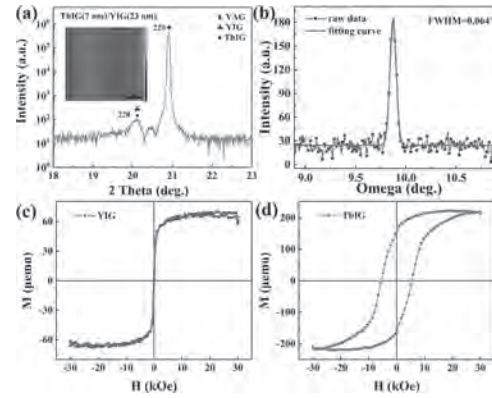


Fig.1. (a) $\theta/2\theta$ scan and (b) rocking curve of TbIG (7 nm)/YIG (23 nm)/YAG (110) sample. Inset of (a) shows the AFM image (scan height = 10 nm). In-plane magnetic hysteresis loops of YIG (30 nm) and TbIG (30 nm) single layer films at 10 K are shown in (c) and (d), respectively.

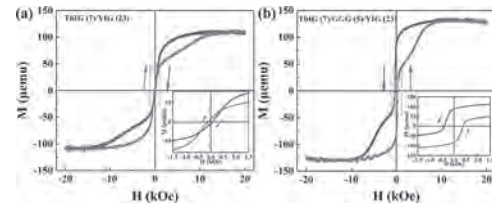


Fig 2. In-plane magnetic hysteresis loops of (a) TbIG (7 nm)/YIG (23 nm) and (b) TbIG (7 nm)/GGG (5 nm)/YIG (23 nm) samples at 10 K. The insets in each figure show the corresponding enlarged images at low field. The arrows indicate the field sweep directions.

IR-07. Modulated in-Plane Uniaxial Magnetic Anisotropy and Permeability Spectrum of NiFe Films by Sapphire Substrates With Periodical Ripples.

X. Xu¹, Y. Han¹, L. Jin¹, T. Wen¹, Y. Liao¹, X. Tang¹, H. Zhang¹ and Z. Zhong¹

1. State Key Laboratory of Electronic Thin Films and Integrated Devices, University of Electronic Science and Technology of China, Chengdu, China

As one of the methods to induce uniaxial magnetic anisotropy in magnetic films, the method of “periodically patterning of films” has attracted more and more research interest because of its promising application in magnetic electronic devices. It has been confirmed that in-plane uniaxial anisotropy of magnetic films can be induced by substrate with ripple patterns, and the direction of easy axis of induced anisotropy is parallel to the ripple direction [1]. Ki in Ref. 2 produced strong in-plane uniaxial anisotropy in NiFe films by annealing the sapphire substrate to form substrate of periodical ripple patterns; the anisotropy in samples is from the dipole effect by surface magnetic charge and shape anisotropy by rippled surface morphology [2]. However, the relationship between annealing-time dependent faceting and coarsening mechanisms of substrate on permeability spectrum of films has not been clarified. In our work, we fixed the annealing temperature at 1400 degrees centigrade and changed the annealing time of substrate to prepare rippled sapphire substrates with different periodicity. Then, we deposited Ta (5 nm)/NiFe (50 nm)/Ta (2 nm) three-layer films on these substrates to investigate the annealing-time dependent faceting and coarsening mechanism of substrate on permeability spectrum of film. The surface morphology of substrates was characterized by atomic-force microscopy, see Fig. 1. The effective modulation of substrate ripple is confirmed. Fig. 2 (a)-(f) show the permeability spectra of real parts μ' and imaginary parts μ'' at no external field for films deposited on substrates annealed for 0-10 h. The results show both μ' and μ'' of NiFe films that were deposited on substrates with periodical ripples are smaller than the film on substrate not annealed. The magnitude of permeability can be modulated by annealing time of substrate and it is related to the number of ripples per unit area and the geometric size of the ripples. The resonance frequency of films on substrates with periodical ripples is higher than that of film on substrate not annealed because of the in-plane uniaxial magnetic anisotropy induced by rippled patterns. This work provides an optimized annealing time to obtain high natural resonance frequency and a method to design permeability of magnetic films. This work would be helpful for film-based magnetic devices on ripple substrate.

[1] Sarathlal K V, Kumar D, Gupta A, Appl. Phys. Lett. 98, 123111 (2011).

[2] Ki S and Dho J, Appl. Phys. Lett. 106, 212404 (2015).

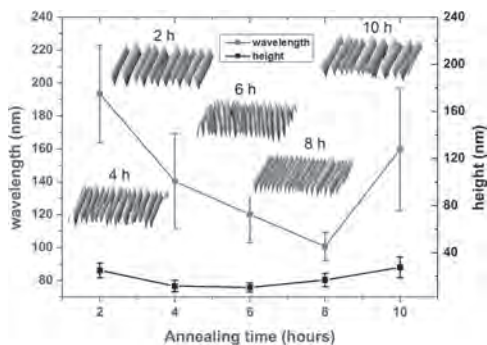


Fig. 1 Dependence of wavelength and height of substrate ripples on different annealing time. The inset maps are surface morphologies of these annealed substrates characterized by atomic-force microscopy.

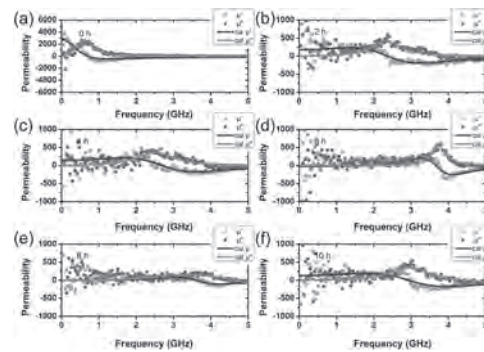


Fig. 2 Permeability spectra of real parts μ' and imaginary parts μ'' at no external field for films deposited on substrates annealed for different time: (a) 0 h, (b) 2 h, (c) 4 h, (d) 6 h, (e) 8 h, (f) 10 h.

IR-08. Withdrawn

IR-09. Influence of ion-Irradiation and Annealing on Magnetic Properties of FeCo/NiO Exchange Biased Thin Film.

R. Gupta¹, S. K¹, F. Singh², V. Reddy³ and A. Gupta⁴

1. School of Instrumentation, Devi Ahilya University, Indore, India;

2. Inter-University Accelerator Centre, New Delhi, India; 3. University

Grants Commission Department of Atomic Energy Consortium for Scientific

Research, Indore, India; 4. Center For Spintronics, Amity University,

Noida, India

Introduction: The exchange bias (EB) effect is caused due to the interface coupling between a ferromagnet (FM) and an antiferromagnet (AFM). To explain the EB phenomenon, several models have been proposed. [1-2] Interfacial origin is the basis of all models to explain the EB effect. Hence, it is sensitive to the microstructure of the bilayer and also to its interface. Hence, one might expect that small structural modifications across the interface could cause considerable changes in the EB field (H_{EB}) and in the coercive field (H_c). Annealing and ion irradiations are known to be an excellent tool to tailor the magnetic properties of thin films. **Experimental details:** Ion-beam sputtering technique has been used for the deposition of thin-film Al(10nm)/FeCo(30nm)/NiO (80nm)/Si substrate at room temperature. During the deposition of NiO partial pressure of oxygen has been used. The films were irradiated with 100 MeV Au ions and annealed in ultra-high vacuum condition at a different temperature ranging from 473 K to 673 K. For magnetic characterization, the measurements were done using an in-plane Magneto-optic Kerr effect microscope (MOKE) at 300 K after field cooling from 523 K, which is the Neel temperature of NiO antiferromagnet. **Results and Discussion:** Fig 1(A) shows the magnetic hysteresis loop of the as-deposited specimen at room temperature (300 K) after the field cooling from 523 K to 300 K. The sample exhibit the exchange bias at 300 K. Fig. 1(B) shows the value of H_{EB} and H_c before and after ion-irradiation with different ion-fluences. A perusal of fig. 1(B) clearly shows that the value of H_c is increasing with ion-fluence while the H_{EB} value has been decreasing. The increase in the value of H_c is due to the creation of defects and roughness of the film which has been increasing due to ion-irradiation. Fig. 1(B) clearly states that the ion-irradiation reduces the value of HEB as a function of ion-fluences. Annealing of FeCo/NiO film enhances the value of H_{EB} . The decrease in the value of HEB due to ion-irradiation and the value of HEB increasing with annealing temperature will be correlated with its interface roughness obtained from X-ray reflectivity.

(1) Meiklejohn, W.H.; Bean, C.P. *Phys. Rev.* 1956, 102, 1413–1414. (2) Mauri, D.; Siegmann, H.; Bagus, P.S.; Kay, E. *J. Appl. Phys.* 1987, 62, 3047–3049.

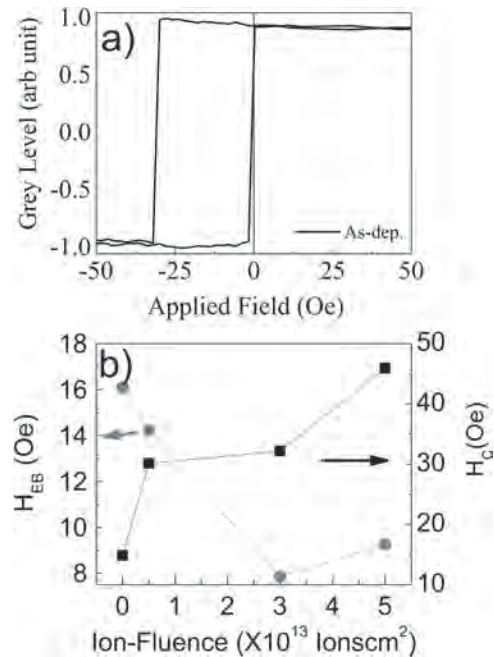


Fig.1 (a) Hysteresis curve of FeCo/NiO thin film at 300 K using Kerr Microscope (b) The Value of H_{EB} and H_c as a function of ion-fluence.

IR-10. Estimating the Anisotropy Constant in an Antiferromagnet Through Exchange Bias in Polycrystalline Ni-Mn/Fe-Ni Films.

M. Moskalev¹, E. Kudryukov¹, A. Gorkovenko¹, V. Lepalovskij¹ and V. Vas'kovskiy^{1,2}

1. Department of Magnetism and Magnetic Materials, Ural Federal University, Ekaterinburg, Russian Federation; 2. Mikheev Institute of Metal Physics, Ekaterinburg, Russian Federation

The exchange bias effect, which manifests itself as a shift of the hysteresis loop of a ferromagnet when it is adjacent to an antiferromagnet, is a key feature used in such technological spheres as magnetic recording and storage as well as magnetic sensorics [1,2]. The exchange bias field H_{ex} – an amount by which the loop is shifted along the magnetic field axis – as well as the coercivity H_c are very sensitive to the temperature. Changes in both of these characteristics are directly connected with changes of magnetic properties of the layers, mainly, the anisotropies of the layers. Directly determining this parameter for an antiferromagnet is often a demanding task, especially dealing with a nanostructure. This task, however, is not only of fundamental, but of applied interest too. By systemizing a collection of data on currently used antiferromagnets it is then possible to propose brand new ones, suitable for technological applications. The industrial standards currently are Pt- and Ir-based antiferromagnets, in which the presence of precious metals substantially affects the overall cost of manufacturing. Recently scientists have been studying nitrides, oxides and Heusler-type compounds as affordable alternatives, but those come with their own limitations, such as relatively low Néel temperatures or high interdiffusion tendency. In this regard use of machine learning for prediction of possible new antiferromagnets seems rather promising, although it requires a dataset on existing antiferromagnets. For example, one of the most crucial properties of any magnetic material, and especially of an antiferromagnet is its anisotropy constant [3]. One way of obtaining this data is by using different measurement protocols. For instance, the York protocol [3,4] has proven itself as a useful tool that by subsequent measurements of the hysteresis loops (Fig. 1) of an ferromagnet/antiferromagnet bilayer estimate the anisotropy constant of the antiferromagnet. All the measurements are conducted at 100 K, but between them the sample is activated: it is maintained at subsequently raising temperatures T_{act} during the activation time t in a field of the sign opposite to that in which the sample was set initially. This approach is based on the fact that magnetron-sputtered films, such as those considered in this work, have a grain-size distribution of crystallites. Due to this distribution at any finite temperature the whole antiferromagnetic layer divides into three categories: 1) stable grains, which pin the ferromagnet's magnetization thus contributing to H_{ex} ; 2) unstable grains, which irreversibly follow the ferromagnet's magnetization thus contributing to H_c ; 3) paramagnetic and superparamagnetic grains, which do not contribute to the hysteresis. This segregation is due to the fact that the energy of a grain depends on its volume and when it equals the thermal energy, a grain becomes unstable. The equation is as follows: $K_{AF} V = k_B T \ln(2)$, where K_{AF} is the anisotropy constant of an antiferromagnet, V is the volume of a grain, k_B is the Boltzmann's constant and T is temperature. Through a series of field-cooling procedures alternating with hysteresis loop measurements it is possible to estimate the median blocking temperature $\langle T_B \rangle$ at which exactly one half of the type 1 grains pin the magnetization in one direction while the other half does so in the opposite direction so that the net shift of the loop is zero (Fig. 2). The value of the anisotropy constant K_{AF} at this particular temperature can be calculated by using the following equation: $K_{AF} (\langle T_B \rangle) = (K_B \langle T_B \rangle \ln(2 f_0)) / V_m$ (2), where t is the time for which the setting field was applied, set to be 30 min in our experiment, f_0 is switching attempt frequency from the Néel-Arrhenius law taken to be $2.1 \cdot 10^{12} \text{ s}^{-1}$ [5], V_m is the median volume of the grains, which was estimated by using the X-ray diffractometry and electron microscopy. In this work by using the York protocol and employing a vibrating sample magnetometer with a temperature chamber we estimate the anisotropy constants of the antiferromagnetic Ni-Mn in a series of magnetron-sputtered Fe-Ni/Ni-Mn films of different thickness of the Ni-Mn layer. Ni-Mn is a metallic antiferromagnet, systems based on which are capable of sustaining exchange bias up to temperatures as high as 700 K [6]. Using this approach, we estimated that a 20-nm thick Ni-Mn has $K_{AF}(320 \text{ K}) = 2.1 \cdot 10^6 \text{ erg/cc}$. Our results can help to form a dataset on the anisotropy constants of antiferromagnets and

can also be used to study the finite-size scaling effect in Ni-Mn. This work was financially supported by the Russian Science Foundation (RSC), project No. 18-72-10044.

F. Radu, H. Zabel, Magnetic heterostructures, Springer, 97 (2008) J. Nogués, J. Sort, V. Vanglajs, et al., Phys. Rep., Vol. 422, p.65 (2005) K. O'Grady, J. Sinclair, K. Elphick, et al., J. Appl. Phys., Vol. 128, p.040901 (2020) K. O'Grady, L.E. Fernandez-Outon, G. Vallejo-Fernandez, JMMM, Vol. 322, p.883 (2010) S. Jenkins, R.W. Chantrell, T.J. Clemmer, et al., Phys. Rev. B, Vol. 100, p.220405(R) (2019) V.O. Vas'kovskiy et al., J. Alloys Compd., Vol. 777, p.264 (2019)

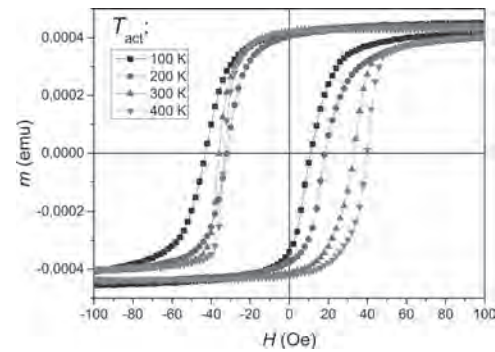


Fig. 1. Hysteresis loops of a Fe₂₀Ni₈₀ (40 nm)/Ni₃₀Mn₇₀ (20nm) film obtained at 100 K following the York protocol after being set at an activation temperature T_{act} .

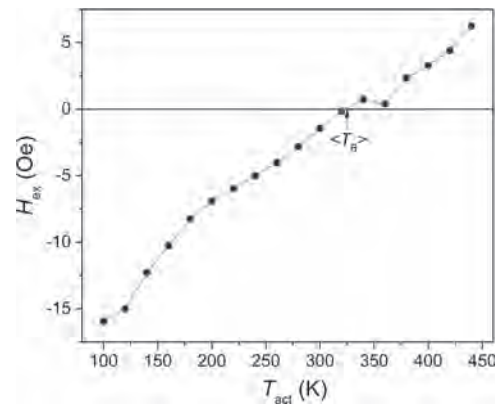


Fig. 2. Measurement of the blocking temperature for a Fe₂₀Ni₈₀ (40 nm)/Ni₃₀Mn₇₀ (20nm) film. The arrow denotes the median blocking temperature $\langle T_B \rangle$.

IR-11. Spin Reorientation Transition and Exchange Bias in Hard/Soft Tb-Co/FeNi Films.

A. Svalov¹, V. Lepalovskij¹, A. Gorkovenko¹, I. Makarochkin¹, E. Stepanova¹, A. Larrañaga², G.V. Kurlyandskaya^{3,1} and V. Vas'kovskiy^{1,4}
 1. Institute of Natural Sciences and Mathematics, Ural Federal University, Ekaterinburg, Russian Federation; 2. Servicios Generales de Investigación, Universidad del País Vasco (UPV/EHU), Leioa, Spain; 3. Departamento de Electricidad y Electrónica, Universidad del País Vasco (UPV/EHU), Bilbao, Spain; 4. Institute of Metal Physics, Ural Branch of Russian Academy of Sciences, Ekaterinburg, Russian Federation

Ferrimagnetic films of rare earth-transition metal (RE-TM) alloys are successfully used as an effective source of internal magnetic bias in exchange-coupled magnetically hard/soft bilayers, including those which demonstrate a hysteresis-free magnetization process. The last feature is in demand for many applications, for example, magnetic sensors [1]. It is known that the magnetic properties of RE-TM films are largely determined by their chemical composition. In particular, amorphous Tb-Co films with the Tb content in the range of 15-40 at. % can display a perpendicular magnetic anisotropy [2]. Within a certain temperature range, the shape anisotropy becomes dominant, and the magnetization orients in the film plane. Thus, the spontaneous spin reorientation transition takes place [3]. Therefore, in these exchange-spring systems, the magnetizations of adjacent soft magnetic and hard magnetic layers can lie in the plane of the film, be perpendicular to the plane, or be orthogonal to each other. Models of the magnetization reversal processes for both planar and perpendicular exchange-spring systems are successfully developed [1,4,5]. At the same time, the reason for the onset of exchange interaction between layers, the magnetizations of which are orthogonal to each other, is not entirely clear. Several models have been proposed to explain this phenomenon. Within one of them, the RE-TM layer is considered as a heterophase system, the magnetizations of different phases are oriented parallel or perpendicular to the film plane [6]. The second model assumes that there is a transition region in the RE-TM layer, within which a gradual reversal of spins occurs from an orientation parallel to the interface of the layers to a perpendicular one [7]. The third model assumes that the exchange bias effect originates from the chiral spin texture of the interfacial domain wall. The creation of the chiral interfacial domain wall is a consequence of the interplay between Dzyaloshinskii-Moriya-interaction in Dy-Co and ferromagnetic exchange coupling between the Ni-Fe and Dy-Co layers [8]. Investigation of changes in the magnetic properties of hard/soft bilayers near the spin reorientation transition of ferrimagnetic hard layer can provide additional information on the exchange bias mechanism in the systems with orthogonal orientation of layer magnetizations. This work presents the results of a study of the magnetic properties of exchange-coupled Tb-Co/FeNi films with different composition of Tb-Co layer in a wide temperature range. Ta(5 nm)/Tb-Co(20 nm)/FeNi(40 nm)/Ta(5 nm) multilayered films were prepared by magnetron sputtering. The films were deposited on Corning glass substrates in the presence of a constant magnetic field of 250 Oe oriented in the plane of the substrate. Magnetic measurements of the multilayered films were carried out in the temperature range of 5-350 K by means of MPMS-XL7 and PPMS DynaCool 9T devices. It was found that a relatively small change in the composition of the Tb-Co layer results in a sizeable change in the hysteresis loops of bilayers measured both along and perpendicular to the plane of the samples (Fig. 1). A change in the temperature of the sample is accompanied by a change in the sequence of magnetization reversal of the layers. In addition, at a certain temperature, the value of which depends on the composition of the Tb-Co layer, instead of layer-by-layer switching, magnetization reversal of the Tb-Co/FeNi film occurs as a whole structure magnetization reversal. An analysis of the obtained results suggests that in the course of deposition of the Tb-Co layer onto the FeNi layer, an interlayer magnetic boundary is formed, the parameters of which depend on the composition of the Tb-Co layer. The features of this boundary determine the value of the exchange bias and its temperature dependence. This work was financially supported by the Russian Science Foundation (RSF), project No. 18-72-10044.

[1] C. Vogler, M. Heigl, A.-O. Mandru, *et al.* Phys. Rev. B 102 (2020) 014429. [2] K. Umadevi, A. Talapatra, J. Arout Chelvane, *et al.* J. Appl.

Phys. 122 (2017) 065108. [3] V.O. Vas'kovskii, A.N. Gor'kovenko, *et al.* Phys. Met. Metallogr. 120 (2019) 1055. [4] E.E. Fullerton, J.S. Jiang, S.D. Bader. J. Magn. Magn. Mater. 200 (1999) 392. [5] D. Chumakov, R. Schäfer, D. Elefant, *et al.* Phys. Rev. B 66 (2002) 134409. [6] G.I. Frolov, V.Yu. Yakovchuk, *et al.* Tech. Phys. 50 (2005) 1605. [7] W.C. Cain, M.H. Kryder. J. Appl. Phys. 67 (1990) 5722. [8] K. Chen, A. Philippi-Kobs, V. Lauter, *et al.* Phys. Rev. Appl. 12 (2019) 024047.

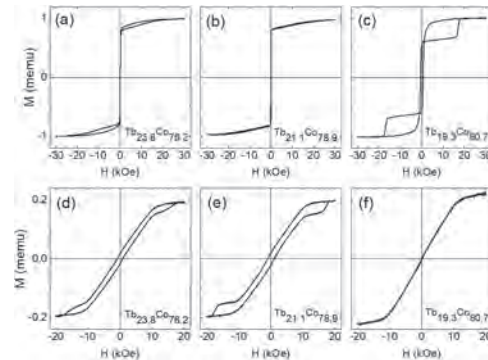


Figure 1. The hysteresis loops measured at $T = 5$ K in the field oriented along (a,b,c) and perpendicular (d,e,f) to film plane for Tb-Co/FeNi films with different Tb-Co layer composition.

[1] C. Vogler, M. Heigl, A.-O. Mandru, *et al.* Phys. Rev. B 102 (2020) 014429. [2] K. Umadevi, A. Talapatra, J. Arout Chelvane, *et al.* J. Appl.

IR-12. Angular Deviation of the Exchange Bias in Bilayer CoFe/IrMn Under Rotating Magnetic Field.

N. Strelkov¹, A. Timopheev¹, C. Ducruet¹ and J.R. Childress¹

1. Isere, Crocus Technology Grenoble, Grenoble, France

A model of exchange bias in polycrystalline bilayers based on a thermal fluctuations [1] was extended to account for an arbitrary magnetization angle of the FM layer. It allows a more accurate description of the behavior of the thermally activated reversal of the Néel vector of a grain since the extended model takes into account a variation of barrier height relative to the magnetization angle of the FM layer. Field annealing (setting of the exchange bias) and further relaxation of the FM/AFM bilayer was simulated using a sequence of iterations based on this model. At each iteration step we tracked the average value of exchange bias field amplitude and its angle, until a convergence was reached. We defined the array of grains in an AFM layer as having a lognormal distribution of grain volumes [2] and a uniform in-plane distribution of the uniaxial anisotropy axis. We have chosen the parameters of the lognormal distribution based on the fit to the experimentally-measured temperature dependence of exchange bias in our FM/AFM samples. We observed a small angle deviation from the initial field annealing direction due to the relaxation of exchange bias in a finite ensemble of AFM grains. Applying a relatively strong magnetic field at an angle to exchange bias (i.e. non-collinear depinning) for a certain time and then releasing it, gives rise to a shift of the final angle of exchange bias and a slight variation of its amplitude. Generally, the direction of the exchange bias is more affected by the FM layer non-collinear depinning than its amplitude, which recovers within a certain time interval upon release of the external field. Sweeping the angle of applied field from - to and back we observed the hysteretic behavior of exchange bias. Again, the exchange bias angle is mainly affected, rather than its amplitude. Angular variation of the exchange bias degradation and its time, field and temperature dependencies were also simulated and analyzed in the framework of this extended model.

[1] H. Xi and R. M. White, *J. Appl. Phys.* 94, 5850 (2003). [2] K. O'Grady, L. E. Fernandez-Outon, and G. Vallejo-Fernandez, *J. Magn. Magn. Mater.* 322, 883 (2010).

IR-13. Severe Plastically Deformed, Supersaturated FeCr Alloys – a Candidate Material for Exchange Bias and Enhanced Magnetostriction.

L. Weissitsch¹, S. Wurster¹, M. Stücker¹, A. Paulischin¹, H. Krenn², R. Pippan¹ and A. Bachmaier¹

1. Erich Schmid Institute of Materials Science, Austrian Academy of Science, Leoben, Austria; 2. Institute of Physics, University of Graz, Graz, Austria

High-pressure torsion (HPT) as a severe plastic deformation (SPD) technique is a well-known method of material processing [1,2]. A key feature of SPD techniques per se is the constancy of sample's volume and shape during the deformation process and therefore allowing the production of nanocrystalline samples exhibiting *bulk* dimensions. One of its further advantages is the avoidance of many processing limits of binary and ternary systems that exhibit large miscibility gaps in their thermodynamic equilibrium. It allows the production of alloys with non-equilibrium compositions at low temperatures [3]. In this study, different compositions of Fe and Cr are processed with the principal goal of having a bulk material of alternating phases of ferromagnetic Fe and antiferromagnetic Cr on the nanoscale, enabling exchange bias. By HPT, the production of a supersaturated nanocrystalline FeCr alloy is possible. During a subsequent annealing treatment, decomposition might occur in closely spaced phases of separated Fe and Cr. Thus, it offers the possibility to induce exchange bias phenomena after field cooling below the Néel temperature. The nanocrystalline microstructure of the HPT-deformed samples increases the amount of interfaces; thus, increasing the effect. In a previous study of Weissitsch et al. [4] on Fe-Cr materials, it has been shown that homogeneous nanocrystalline microstructures can be produced by HPT at room temperature for compositions inside the miscibility gap. The nanocrystalline nature of the material and the identical crystal structure of Fe and Cr at room temperature (body centred cubic) with almost identical lattice parameters, make the microstructural investigation of the HPT-deformed material very challenging. Synchrotron results are ambiguous in peak deconvolution due to peak broadening and the above mentioned similarity in crystal structure. Scanning electron microscopy, including space-resolved chemical characterization, is difficult to perform due to the strongly refined microstructure. Still, the initial state has to be characterized before any further annealing treatments. An alternative characterization way is the measurement of magnetostrictive properties of the as-deformed alloys. Bormio-Nunes et al. [5] measured a large, positive magnetostriction for arc-melted supersaturated single phase FeCr alloys with up to 30 at% Cr. An increase in saturation magnetostriction with increasing Cr-content is further reported. Thus, it is of interest to study magnetostrictive properties of materials with even higher Cr-content. The saturation magnetostriction of Fe with 30% Cr ($3/2\lambda_s \sim +30$ to $+70$ ppm) found in [5], is slightly higher compared to our measurements (see Figure 1), bearing in mind the completely different involved microstructures. In the present study, the maximum saturation magnetostriction is found for 30 at% Cr as well. For an even higher Cr content of 50at%, a positive but decreasing saturation magnetostriction was measured. For a material only containing 30at%Fe, magnetostriction is about zero, which is in accordance with the very small values reported on pure Cr [6]. Due to this findings, the largest magnetostriction would have to be searched for compositions close to 30 at% Cr. Figure 1 depicts the pronounced difference magnetostrictive behaviour of FeCr compared with of pure Fe ($3/2\lambda_s \sim -14$ ppm). Thus, it can be stated that Fe and Cr are in a supersaturated state after HPT deformation at room temperature. To achieve an exchange bias coupled material, an improved understanding of the decomposition behaviour of the HPT-deformed FeCr alloys is crucial. Therefore, the influence of annealing treatments on the microstructural evolution and magnetostrictive properties is further investigated in this study. Annealed samples (1h at 500°C) do not show pronounced changes in magnetostrictive behaviour, i.e. the supersaturated state seems to prevail. To achieve the goal of exchange coupling, a proper concatenation of annealing treatments at even higher temperatures and subsequent HPT-deformation, producing a nanocrystalline microstructure again, is the next step. This study demonstrates that magnetostrictive measurements are an efficient tool to characterize the microstructure of nanocrystalline FeCr alloys deformed by HPT deformation, which are difficult to investigate by other

techniques. Large magnetostriction is found in the as-deformed and annealed states of Fe-rich materials. HPT deformation combined with subsequent annealing treatments is a first step towards processing of Fe-Cr composites showing exchange bias phenomena. *This project has received funding from the European Research Council (ERC) under the European Union's Horizon 2020 research and innovation programme (grant agreement No 757333).*

[1] R. Valiev, R. Islamgaliev, I. Alexandrov, *Progress in Materials Science*. 45 (2000) 103–189. [2] R. Pippan, S. Scheriau, A. Taylor, M. Hafok, A. Hohenwarter, A. Bachmaier, *Annual Review of Materials Research*. 40 (2010) 319–343. [3] K.S. Kormout, R. Pippan, A. Bachmaier, *Advanced Engineering Materials*. 19 (2017). [4] L. Weissitsch, M. Stücker, S. Wurster, R. Pippan, A. Bachmaier, *Materials Science Forum*. 1016 (2021) 1603–1610. [5] C. Bormio-Nunes, J.P. Serra, F.S. Barbosa, M.B.S. Dias, R.S. Turtelli, M. Atif, R. Grossinger, *IEEE Trans. Magn.* 52 (2016) 1–4. [6] E.I. Kondorskii, T.I. Kostina, V. Yu. Galkin, *Sov. Phys. JETP* 42 (890) 890-891.

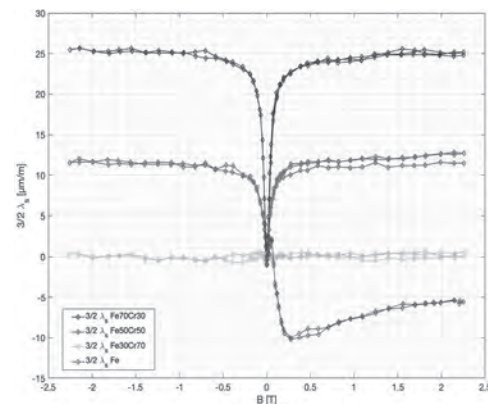


Figure 1: Magnetostriction as a function of applied field, measured for HPT-deformed FeCr materials, spanning the composition range from 30at% to 70at% Fe. A comparison with the markedly different magnetostrictive behaviour of pure Fe is given.

IR-14. Influence of Extrinsic Factors on FMR Linewidth in Systems With Exchange Bias.

N.G. Chechenin¹, I.O. Dzhun¹, G.V. Babaytsev¹, M.G. Kozin¹, A.V. Makunin¹ and I.L. Romashkina¹

1. Skobeltsyn Institute of Nuclear Physics, Lomonosov Moscow State University, Moscow, Russian Federation

We study the extrinsic factors influence on FMR LW in polycrystalline systems F/AF with exchange bias, by varying AF layer thickness for different sequence of F and AF layers deposition. We observe that the exchange bias has a negligible effect on FMR LW. Instead, the contributions of uniaxial anisotropy, microstructure and F/AF interface roughness can be of major extrinsic factors. Using DC magnetron sputtering, Ta(30nm)/NiFe(10nm)/IrMn(t_{AF})/Ta(30nm) (TS) and Ta(30nm)/IrMn(t_{AF})/NiFe(10nm)/Ta(30nm) (BS) multilayers on silicon substrate were prepared with the AF thickness $t_{AF} = 10, 20, 30$ and 40 nm. A permanent in-plane magnetic field of 420 Oe was applied during the deposition. Sample surface morphology was investigated by atomic force microscopy to obtain the mean square roughness σ_{rms} . The magnetic characteristics were investigated using FMR at a constant frequency $\omega/2\pi = 9, 65$ GHz and with magnetic field H directed along the sample surface and scanned in the range up to 6 kOe. The main magnetic characteristics of the samples were obtained from the angular dependences (AD) of the resonant magnetic field, $H_r(\alpha)$, where α is the angle between the direction of the FMR field and the direction of the magnetic field applied during the deposition of the sample. Despite some quantitative differences, the qualitative form of the dependency of the exchange bias on the AF layer thickness is the same for both TS and BS structures. However, there is a significant discrepancy in the widths of the FMR lines for TS and BS structures: ΔH_{TS} is smaller than ΔH_{BS} . In addition, in the case of TS, the values of ΔH for $\alpha = 0^\circ$ and $\alpha = 90^\circ$ coincide within the experimental accuracy and synchronously repeat the variations with thickness. These observations indicate that the effect of the exchange bias on the FMR LW is negligible small compared to the influence of other factors. The roughness, σ_{rms} , for TS samples is greater than for BS, the dependence $\sigma_{rms}(t_{AF})$ is nonmonotonous and is in antiphase for TS and BS structures. The effect of the sample surface roughness on the FMR LW is quite noticeable. The experimental data can be approximated for TS samples by the dependence $\Delta H_{TS} \sim (\sigma_{rms} S)^{1/3}$, where S is the average area of defects and the FMR line width is proportional to the average linear size of defects on TS sample surface. This tendency is qualitatively consistent with the known results [1], where a linear relationship between ΔH and the pore radius on the sample surface was predicted. In BS samples, as compared with TS, the picture is quite different. The roughness is weaker while the LW is larger. That assumes that the roughness does not play a dominant role in LW of BS samples. Evidently, the features of the layers growth lead to different magnetic properties of AF/F and F/AF samples at the same chemical content of the F and AF layers. When the F layer grows on the AF layer, the microstructure of the AF layer can affect the properties of the F layer deposited on it. An increase in the AF layer thickness can lead, for example, to an increase in the size of AF grains in the bulk and at the AF/F interface. The F layer deposited on top takes on a typical AF grain size, i.e., the F grain size, possibly, increases with increasing AF layer thickness. In this case, the uniaxial magnetocrystalline anisotropy H_K becomes the dominant factor affecting the broadening ΔH . Taking into account that the samples have a polycrystalline structure, we assume that the approximation of strongly bonded grains with $H_K \ll 4\pi Ms$ works. In this approximation, a polycrystal is regarded as a homogeneous medium with an inhomogeneous effective field, which is affected by the presence of grains with different crystallographic orientations. The magnetic fluctuations of the grains are coupled to each other through demagnetizing fields [2], which leads to uncompensated crystallographic anisotropy, which enhances uniaxial anisotropy and causes smooth spatial oscillations of magnetization. Spatially fluctuating magnetization, the so-called “micromagnetic ripple” observed in Lorentz transmission microscopy [3, 4], correlates with the grain size [3] and can be, if not the main, then an important additional source of broadening of the FMR line [5]. We show that FMR LWs in the BS samples decrease with increase of AF layer thickness, approximately, as $1/t_{AF}\beta$, with $\beta = 2 \pm 1$ and the difference in LW values measured along HA and EA in BS samples varies proportionally to the square of H_K .

1. M. Sparks, R. Loudon, and C. Kittel, Phys.Rev. vol. 122, p.791 (1961) 2. A.G. Gurevich, G.A. Melkov. Magnetization Oscillation and Waves, CRC Press, New York (1996). 3. N.G. Chechenin, C.B. Craus, A. Chezan, *et al* IEEE Trans. Magn. MAG 38, p. 3027 (2002). 4. N.G. Chechenin. J. Magn. Mater. Vol. 300, 198 (2006). 5. N.G. Chechenin, Phys. Solid State vol. 46, p. 479 (2004)

IR-15. Design of a Spin Filter Device Based on Graphene Free-Standing Membranes.

L. Nessi¹, C. Rinaldi¹, R. Bertacco¹ and M. Cantoni¹

¹. Politecnico di Milano, Milano, Italy

Ultrathin free-standing magnetic layers are promising candidates to efficiently detect the spin of the electrons by means of the selective transmission of spin parallel or anti-parallel to a magnetization axis [1]. The capability to control the direction of this quantization axis joined to the engineering of a device able to guarantee spatial resolution allow to completely reconstruct the spin configuration of an electron beam. This could represent an outstanding tool integrable in electron spectroscopy experiments, where the spin resolution may be added to the E-k mapping in Angle-Resolved Photoemission Spectroscopy (ARPES) [2]. This task was tackled first by defining a proper fabrication process to obtain a bidimensional matrix of free-standing membranes. Then, in order to guarantee a sufficiently high transmission of the electrons (larger than 3×10^{-2}), the film thickness was chosen not to exceed 10nm. A suitable heterostructure was designed, consisting in a mechanically robust layer, a buffer layer, the active magnetic layer and finally a capping layer. Graphene was chosen for the former aim (see Fig. 1a) and a variable number of monolayers (MLs) was tested (from 2 to 8 MLs). Also the buffer layer was selected according to its mechanical properties and measured with Atomic Force Microscope (AFM) to infer information about the Young modulus and the film roughness (see Fig. 1b). The desired direction of the magnetization was defined using different magnetic materials (or stacks). Co was chosen for in-plane (IP) configuration, while Ta/CoFeB/MgO for the out-of-plane (OOP) one. Finally, the devices were capped with Au or Ru. The growth was performed comparing two different techniques: Magnetron Sputtering and Molecular Beam Epitaxy (MBE). The magnetic properties were measured both on micrometric patterned structures on rigid substrates by Vibrating Sample Magnetometer and Kerr microscopy and on ultrathin membranes by Faraday effect. The key features of sufficiently high coercive field and magnetic remanence are obtained (see Fig. 1c). The mechanical properties were measured by Force Spectroscopy with the AFM, probing the robustness of these devices. The final aim is the characterization of the spin-filtering efficiency exploiting a spin polarized electron beam at low energy (0-30 eV) produced by a GaAs photocathode with negative electron affinity and recording the transmission of the membranes for different orientations of the beam polarization [3]. In this way we plan to probe the Figure of Merit (FOM) of the device and to infer the Sherman function, i.e. the asymmetry factor, which should be larger than 0.5.

[1] D. Oberli *et al.*, Phys. Rev. Lett. 81, 4228 (1998). [2] Övergaard T. *et al.*, arXiv:1709.03838v3 (2017). [3] M. Cantoni and R. Bertacco, Rev. Sci. Instrum. Vol. 75(7), pp. 2387-2392 (2004).

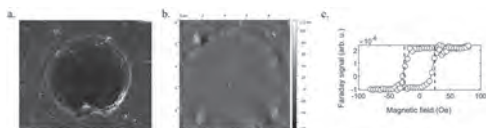


Fig. 1: a. Scanning Electron Microscopy image of a suspended graphene membrane; b. AFM topography of the free-standing magnetic stack; c. Magnetic hysteresis loop measured probing the Faraday effect for the OOP configuration of the magnetization.

IR-16. Tuning Work Function in Graphene by Thermally Assisted Metal Intercalation.

I. Aray¹, A. Gudín Holgado¹, A. Guedeja-Marron Gil^{1,3}, J.M. Diez^{1,2}, A. Anadón¹, R. Guerrero¹, M. Varela³, J. Camarero^{1,2}, R. Miranda^{1,2} and P. Perna¹

1. *Fundacion IMDEA Nanociencia, Madrid, Spain*; 2. *Departamento de Física de la Materia Condensada, Instituto Nicolás Cabrera, and Condensed Matter Physics Center (IFIMAC), Universidad Autonoma de Madrid, Madrid, Spain*; 3. *Departamento de Física de Materiales & Instituto Pluridisciplinar, Universidad Complutense de Madrid, Madrid, Spain*

Graphene (Gr) is one of the most outstanding materials for room temperature (RT) spintronics due to its unique and intrinsically tunable electronic properties [1,2]. Some important effects such as high spin injection efficiency, anti-ferromagnetic coupling, Rashba, spin filtering, TMR or enhanced PMA have been found when Gr is coupled with ferromagnetic materials. Its electronic properties can be tuned by proximity with heavier metallic atoms, which may allow for the technological development of more efficient devices based on spin-orbit effects. However, the development of Gr-based hybrid structures requires the capability of engineering high-quality interfaces, as it has a direct impact in the functional properties of the system [3]. On this regard, metal intercalation has been widely used for the fabrication of functional Gr/FM/HM heterostructures. Gr promotes a layer-by-layer growth of the metal at the interface with a heavy metal substrate, resulting in high quality epitaxial interfaces. Moreover, Gr protects the intercalated material from air exposition avoiding its oxidation and preserving its physical properties. It has been recently demonstrated by the authors that if the intercalated species is a FM, one can prepared highly perfect and flat hybrid Gr/FM/HM epitaxial heterostructures onto insulating oxides with enhanced perpendicular magnetic anisotropy (PMA), large DMI and stable Néel-type chiral magnetic nanometer sized objects [4]. In the present work we report on the fabrication of high quality epitaxial Gr/Fe/Pt asymmetric magnetic structures with extremely abrupt interfaces. Samples were fabricated entirely in UHV following a methodology previously established [5]. Thermal intercalation of Fe in Gr/Pt(111) interfaces is studied in detail by means of X-ray photoelectron spectroscopy, observing a shift of the C1s core level main contribution to higher binding energies due to the transition from n-doped to p-doped graphene due to graphene-iron interaction. High surface and interface quality is demonstrated by means of HR-TEEM, LEED and XRR. Atomic resolution images prove an epitaxial and commensurate growth of Fe on Pt(111) with a characteristic ABC stacking of the fcc structure. EELS elemental mapping of the heterostructures confirms the good chemical differentiation of all the layers in the system. Magnetic characterization was performed by MOKE at ambient conditions varying Fe thickness in a range between 1 to 4 MLs. Our results show the presence of PMA in the system for 1 ML of Fe, with a complete transition to in plane magnetization for thicknesses above 3 MLs.

- [1] A. H. Castro Neto et al., *Rev. Mod. Phys.* 81, 109-162 (2009) [2] W. Han et al., *Nature Nanotech* 9, 794–807 (2014) [3] W. J. Wells et al., *Phys. Rev. B* 95, 054428 (2017) [4] F. Ajejas et al., *Nano Lett.* 18, 9, 5364-5372 (2018) [5] F. Ajejas et al., *ACS Appl. Mater. Interfaces.* 12, 4088-4096 (2020)

IR-17. Layered Ni/Ge Thin Films: the Ni-Ge Interface Effect in the Films Magnetic Properties.

A. Chernichenko¹ and Y.E. Samoshkina¹

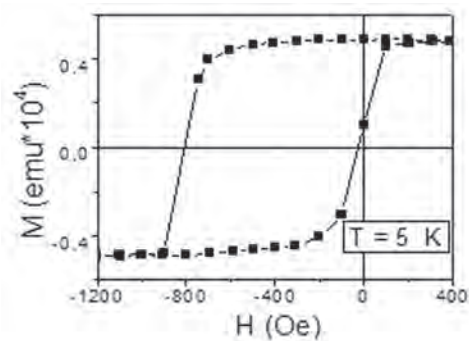
1. FGBNU, Federal Research Center Krasnoyarsk Scientific Center of the Siberian Branch of the RAS, Krasnoyarsk, Russian Federation

It has been shown that a number of phases are formed in the interface between Ni and Ge layers. Main peculiarities of these properties: the low temperature hysteresis loop shift and the difference between FC and ZFC magnetization temperature dependences are explained satisfactory by the magnetic order appearance in the interface layers. According to the modern tendencies in industry, Ge is a proper candidate to replace Si in some spintronic devices. Ge demonstrates the higher carrier mobility [1] and has a larger exciton Bohr radius comparing to Si [2]. Nickel germanide Schottky contacts are ideal for p-channel Ge metal-oxide-semiconductor field-effect transistor (MOSFET): the highest Schottky barrier for electrons combined with the close to zero barrier for holes were obtained with rapid thermal annealing technique [3]. These features attract the growing interest to the thin film structures based on Ge and its compounds with some metals, especially, with Ni (e.g., [4-7]). Along with the special electrical properties, magnetic characteristics of the films can be of interest because of their contribution to the structures functionality. Recently, we revealed several peculiarities in the temperature and magnetic field dependences of the layered Ni/Ge films magnetization [8] that were ascribed to the effect of the interface between Ni and Ge layers. The present work is aimed to elucidate the interface structure and the mechanism of its interaction with Ni layers. Ni/Ge and Ge/Ni/Ge/Ni/Ge films with different thicknesses of the component layers were fabricated with the ion-plasma sputtering technique described in Ref [8]. Insert Table 1 – The interplanar distances, d , obtained from SAED data for the Ni/Ge (9nm/14nm) film in comparison with data for Ni (Fm3m) and several NiGe compounds. The X-ray fluorescent analysis (X-ray spectrometer S4 PIONEER, Bruker), EXAFS/XANES spectroscopy and X-ray reflectometry using synchrotron radiation station in the National Research Center «Kurchatov Institute», transmission electron-microscope (JEOL JEM-2100 (LaB6), energy dispersive X-ray spectrometer (Oxford Instruments INCA x-sight), and selected-area electron diffraction (SAED) were used to characterize films. Magnetic properties of the film samples were studied with a SQUID magnetometer, operating in the 4.2–300 K temperature range at a maximum applied magnetic field $H = 1$ kOe. Structural data have shown that Ni layers were polycrystalline of Fm3m face centered phase, Ge layers were amorphous, Ni and Ge oxides were detected in trace amounts. Intermediate layers of about 9 nm in thickness were shown to form between Ni and Ge layers. Micro-diffraction images of the layered samples cross-section images revealed not only all the reflections characteristic for Ni but also reflexes, which can be compared with some Ni oxides. According to the interplanar distances presented in Table 1, these could be Ni₃Ge, Ni₅Ge₂, Ni₂Ge₃. At that, Ni₃Ge and Ni₅Ge₃ are ferromagnetic with different temperature dependences of magnetization. In particular, the Ni₃Ge magnetization increases almost five times in the range 290 - 77 K. Therefore, the data obtained do not allow determining the interface structure unambiguously. However is clear that Ni layers border with Ni_xGe_y layers but not with Ge layers. This neighborhood can effect in the layered films magnetic behavior essentially. Insert Fig. 1. Hysteresis loop of Ni/Ge film at $T = 5$ K. One of the most pronounced features of the layered films investigated is the low temperature hysteresis loop broadening and shift along the magnetic field axis (Fig. 1). The magnetization loop shift is observed usually in the film structures consisting of a ferromagnetic (FM) and the antiferromagnetic (AFM) layers or including magnetic soft and hard layers and explained by the exchange interaction between these layers [9, 10]. One can assume that the hard FM layer (for example, Ni₃Ge) in the boundary adjacent to a soft nickel layer, and the observed hysteresis loop shift is due to the exchange interaction between these layers. The processes of Ni layer magnetization in such situation depend on the direction of an external field with respect to the direction of the magnetic moment of the adjacent interface layer. When the magnetic moment of the hard FM layer and the external magnetic field are oriented in the same direction, the soft magnetic layer magnetized homogeneously in the same direction in relatively low magnetic field. The change of the external magnetic field direction leads to the formation of the

helical structure in the soft FM layer similar to the Bloch wall [11]. The helix pitch depends on the thickness of the soft layer and on the magnitude of the exchange interaction between adjacent layers. The increase in thickness of the soft FM reduces a degree of an influence of the hard FM layer on the soft layer magnetic state. It has been shown that a number of phases are formed in the interface between Ni and Ge layers. These phases are close to Ni₃Ge, Ni₅Ge₂, and Ni₅Ge₃, influencing on the magnetic properties of the films. Main peculiarities of these properties: the low temperature hysteresis loop shift and the difference between FC and ZFC magnetization temperature dependences are explained satisfactory by the magnetic order appearance in the interface layers.

1. S.M. Sze and K.K. Ng, Physics of Semiconductor Devices, Wiley, New York, (2007) 789. 2. Y. Maeda, N. Tsukamoto, Y. Yazawa, Y. Kanemitsu, and Y. Masumoto, Appl. Phys. Lett. 59 (1991) 3168. 3. D.R. Gajula, D.W. McNeill, B.E. Coss, H. Dong, S. Jandhyala, J. Kim, R.M. Wallace, and B.M. Armstrong, Appl. Phys. Lett. 100 (2012) 192101. 4. B. De Schutter, W. Devulder, A. Schrauwen, K. van Stiphoub, T. Perkisas, S. Bals, A. Vantomme, C. Detavernier, Microelectronic Engineering 120 (2014) 168. 5. S. Kazan, B.Kocaman, A.Parabas, F.Yildiz, B.Aktas, J. Magn. Magn. Mater. 73(2015)164. 6. Yunsheng Deng, Osamu Nakatsuka, Jun Yokoi, Noriyuki Taoka, Shigeaki Zaima, Thin Solid Films 557 (2014) 84. 7. Phyllis S. Y. Lim, Dong Zhi Chi, Poh Chong Lim, Xin Cai Wang, Taw Kuei Chan, Thomas Osipowicz, and Yee-Chia Yeo, Appl. Phys. Lett. 97 (2010) 182104. 8. I.S. Edelman, D.A. Velikanov, A.V. Chernichenko, D.A. Marushchenko, E.V. Eremin, I.A. Turpanov, G.V. Bondarenko, Yu.E. Grebenkova, and G.S. Patrin, Physica E 42 (2010) 2301. 9. W.H Meiklejohn, C.P. Bean, Phys. Rev.105 (1957) 904. 10. J. Nogues, J. Sort, V. Langlais, V. Skumryev, S. Surinach, J.S. Munoz, and M.D. Baro, Physics Reports 422 (2005) 65. 11. A. Hubert and R.Schäfer, Magnetic Domains: The Analysis of Magnetic Microstructures. Springer (2008) 216.

d, Å experiment	Ni (Fm3m) 00-004-0850	Ni ₃ Ge (Fm3m) 00-035-1359	Ni ₅ Ge ₂ (F63cm) 04-007-4194	Ni ₅ Ge ₃ (C2) 04-007-1419
2.797				
2.814				
2.027	2.034	2.062	2.003	2.013
2.018				2.016
1.933			1.970	1.945
1.954				
1.784	1.762	1.786		
1.413				
1.408				
1.362	1.246	1.262		
1.136				
1.056	1.062	1.077		
0.886	0.881	0.819		



IR-18. Study of the Schottky Contacts of Ultrathin Fe₃O₄ Films Schottky Contacts on GaAs Substrates.

J. Zhou¹, Z. Zhang¹, Y. Yan¹, X. Lu¹ and Y. Xu^{1,2}

1. School of Electronic Science and Engineering, Nanjing University, Nanjing, China; 2. York-Nanjing Joint Center in Spintronics, Department of Electronic Engineering, University of York, York, United Kingdom

We have successfully fabricated Fe₃O₄/GaAs Schottky barrier on n-type GaAs (100) substrates with high carrier concentrations (3X10¹⁸cm⁻³) by photolithography and mesa etching. 10ML Fe was deposited on GaAs substructure and annealed in an oxygen environment. Current-Voltage measurements were carried on over the temperature range of 80- 290K in Nonlocal and Local device structure. We extracted ideality factor *n* and barrier height Φ_B from I-V curves which are fitted with the equation based on Thermionic Emission Diffusion theory and Back to back Schottky diodes theory. In local structure, there are Fe₃O₄/GaAs/Fe₃O₄ back to back diode model. Barrier height with Symmetric distribution in local device and the ideality factor is closer to unity in low temperature. In the Nonlocal device structure, we annealed Indium in vacuum atmosphere base pressure with 10⁻⁸ torr. When temperatures over 200k, the experimental I-V curves obey the ideal thermionic emission model, and the ideality factors near a constant 1.88. However, the apparent barrier heights decrease with decreasing temperature. This abnormal behavior is interpreted by the assumption of a Gaussian distribution of barrier heights when we used Gaussian distribution to modified Richardson plot, the experimental data are fitted well by the modified Richardson equation and we got a constant barrier value 0.55ev. Finally, we find from the temperature dependence of Fe₃O₄/GaAs Schottky barrier in different device structures that and the barrier heights decrease with decreasing temperature (>200K), which is attributed to a Gaussian distribution of barrier heights.

1. Chiquito AJ, Amorim CA and Berengue OM. *J Phys Condens Matter* 24, 225303 (2012). 2. Karata, Altındal. *Materials Science and Engineering: B* 122, 133-139 (2005).

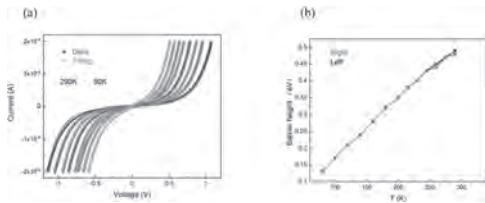


Fig.1 Local device :(a) The forward bias current-voltage characteristics of Fe₃O₄ on GaAs substrates at various temperatures. All these curves are fitted with the equation based on back to back diode theory. (b) The left and right Fe₃O₄/GaAs barrier heights as a function of temperature.

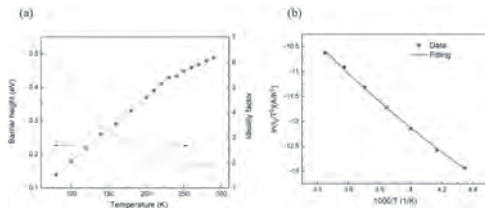


Fig.2 Nonlocal device :(a)Schottky barrier height and ideality factor derived from the fitting as function of temperature for Fe₃O₄ contacts on GaAs substrates. (b) The experimented data are fitted by the modified Richardson equation.

Session IS
MAGNETIC FIELD SENSORS II
(Poster Session)

Pavel Ripka, Co-Chair
Ceske vysoké učení technické v Praze, Prague, Czechia

Dirk Meyners, Co-Chair
University of Kiel, Kiel, Germany

IS-01. A Wide-Bandwidth Impedance Measurement Technique With Small Perturbation Injection Based on Magnetic Sensing.

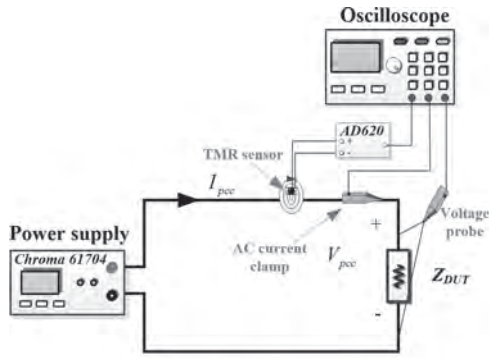
J. Liu¹, H. Liu¹, C. Lee¹ and P. Pong²

1. *Electrical and Electronic Engineering, University of Hong Kong, Hong Kong*; 2. *Department of Electrical and Computer Engineering, New Jersey Institute of Technology, Newark, NJ, United States*

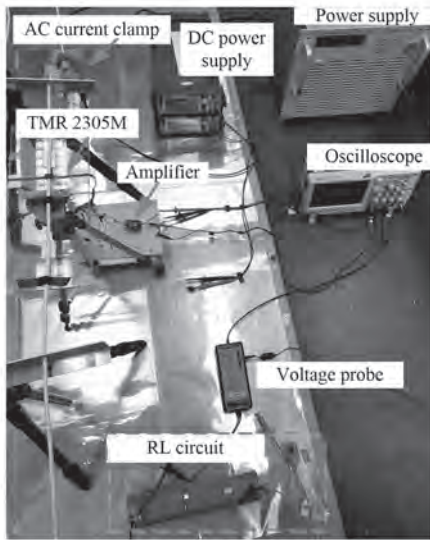
1. Introduction With the increasing penetration of power electronic devices, wide-bandwidth oscillation events are frequently reported in recent years [1]. To meet the demand of analyzing wide-bandwidth oscillation without prior knowledge of detailed parameters of the concerned system, the impedance-based stability method [2] is now a widely used technique. However, the accuracy of the impedance-based stability method heavily relies on the precise measurement of the impedance of the concerned system, which is determined by following three critical factors. 1) Response Signal Sensing: The limited bandwidth of sensor can jeopardize the accuracy of impedance measurement over a wide bandwidth. In [3], shunt resistor is used to measure the current response from 1 Hz to 1 kHz. The drawback of shunt resistor is that the resistance shifts with ambient temperature, frequencies and rated current. Besides, the Hall-effect current transducers can be used to obtain the current response. However, the narrow bandwidth of Hall-effect current transducers makes them not suitable for wide bandwidth impedance measurement [4]. 2) Perturbation Injection: Most existing work sets the current or voltage injection as 10% of rated value to obtain a good signal-to-noise ratio [5]. However, for certain concerned systems, especially under weak grid, even 10% disturbance can make the system deviates from the equilibrium point and interferes with the normal operation of the system. Besides, it is also costly and challenging to design an injection source with high injection capacity and broadband injection at the same time in high-power application. 3) Response Components Extraction: Another inevitable problem is the inaccurate response components extraction due to the spectral leakages of FFT-based algorithm. A Hanning window in [6] is applied to improve the accuracy of measured impedance by solve the spectral leakages in Fourier analysis. However, the impedance measurement results vary significantly with the selection and design of window function. To overcome these limitations, this paper proposes a wide bandwidth impedance measurement technique with a small perturbation injection based on magnetic sensing and Prony-FFT extraction algorithm. Firstly, a low-cost tunnel magnetoresistance (TMR) sensor is applied to measure the desired impedance result over a wide bandwidth. Besides, the high sensitivity of TMR sensor enables the impedance measurement with small perturbation injection. Finally, to extract the magnitude and phase of the response component precisely from the sensing response signal, an improved algorithm based on Prony-FFT is developed to avoid the spectral leakages and lighten the computation burden in high frequency band. Hence, the proposed measurement technique can potentially be an effective tool in modern power system because of its wide bandwidth, high sensitivity, light computation burden. 2. Experiments For a selected frequency band of interest, the impedance of a RL circuit was measured experimentally by proposed impedance measurement technique. The result was compared with the one measured with a commercial AC current clamp (i400s, FLUKE). Meanwhile, the reference impedance value of the RL was obtained by a vector network analyzer (VNA, E5061B, Keysight). A programmable AC power source (61704, Chroma) was used to inject a wide-bandwidth perturbation into the RL circuit as shown in Fig. 1. Thirty injection frequencies were spaced between 10 Hz to 2 kHz. Then, the voltage of the RL was measured by a differential voltage probe (A042, PICO). Meanwhile, a TMR sensor (TMR2305M, MultiDimension Technology) with high sensitivity of 25 mV/V/Oe was selected to measure the input current of the RL circuit. The output of TMR sensor was amplified by a differential amplifier (AD620). The frequency response of TMR sensor with amplifier was investigated as shown in Fig. 2(a). The gain deviation of the TMR sensor was within 0.2 dB over the bandwidth whereas the variation of phase was within 3 degree. Thus, the TMR sensor could enable wideband impedance measurement with constant gain and negligible phase shift. Then, the impedance measurement results with 10% injection magnitude based on the proposed technique and AC current clamp were compared in Fig. 2(b). Compared with the impedance measured by the VNA, the average magnitude deviation measured by the TMR sensor was 0.9 Ω whereas that measured by

the AC current clamp was 1.6 Ω . Besides, the phase deviation of impedance based on TMR sensor was within 2 degree, while the maximum phase deviation of the result measured by the AC current clamp reached 8 degree over the wide frequency band of measured. Furthermore, the impedance measurement with 3% injection magnitude based on proposed technique was compared with the 10% injection magnitude based on AC current clamp in Fig. 2(c). The measured result with 3% injection magnitude based on TMR sensor had maximum phase deviation of 3 degree, which was still smaller than the result measured by the AC current clamp with 10% injection magnitude. 3. Results and Discussion Compared with the impedance measured by the AC current clamp, the proposed impedance measurement technique based on TMR sensor achieved higher accuracy in magnitude and less phase shift over a wide bandwidth. Meanwhile, the proposed technique can measure the impedance under smaller injection magnitude without sacrificing the measurement accuracy. In the full paper, the details of the impedance extraction algorithm based on Prony-FFT and more experimental results will be presented.

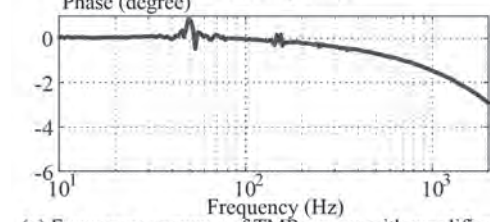
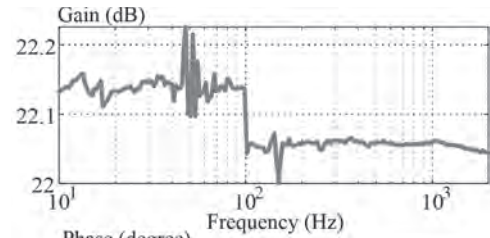
[1] M. Amin, M. Molinas, and L. Jing, "Oscillatory phenomena between wind farms and HVDC systems: The impact of control," *IEEE*, 2015, pp. 1-8. [2] S. Jian, "Impedance-Based Stability Criterion for Grid-Connected Inverters," *TPEL*, vol. 26, no. 11, pp. 3075-3078, 2011. [3] D. A. Howey, P. D. Mitcheson, V. Yufit, G. J. Offer, and N. P. Brandon, "Online Measurement of Battery Impedance Using Motor Controller Excitation," *TVT*, vol. 63, no. 6, pp. 2557-2566, 2014. [4] A. Patel, and M. Ferdowsi, "Current Sensing for Automotive Electronics-A Survey," *TVT*, vol. 58, no. 8, pp. 4108-4119, 2009. [5] T. Roinila, M. Vilkkko, and S. Jian, "Online Grid Impedance Measurement Using Discrete-Interval Binary Sequence Injection," *JESTPE*, vol. 2, no. 4, pp. 985-993, 2014. [6] C. Xin, Z. Yang, W. Shanshan, C. Jie, and G. Chunying, "Impedance-Phased Dynamic Control Method for Grid-Connected Inverters in a Weak Grid," *TPEL*, vol. 32, no. 1, pp. 274-283, 2017.



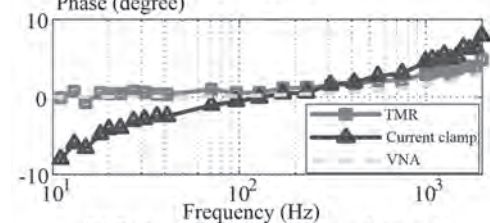
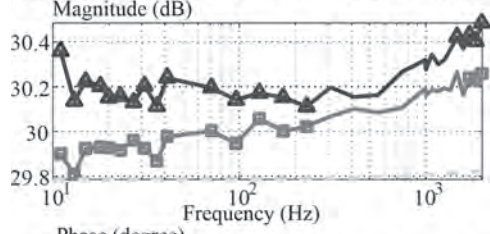
(a) Schematic of the setup



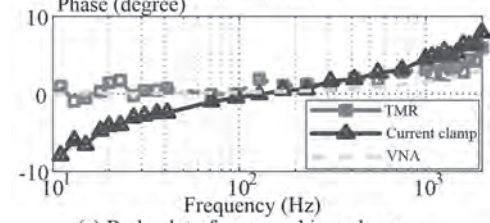
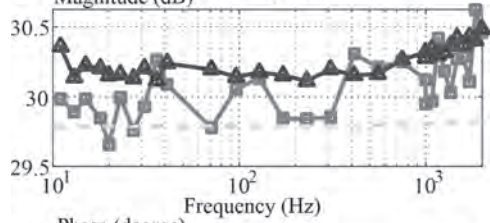
(b) Photograph of the setup



(a) Frequency response of TMR sensor with amplifier



(b) Bode plot of measured impedance with Magnitude (dB) 10% injection



(c) Bode plot of measured impedance. TMR: 3% injection ; Current clamp: 10% injection

IS-02. Semi-Analytical Modeling of High Frequency Eddy Current Sensor in Ferromagnetic Steel With DC Bias.

D. Um¹, H. Nam¹, M. Kim¹, J. Jo¹, D. Kim², H. Yoo² and G. Park¹
 1. Pusan National University, Kumjeong-ku, The Republic of Korea;
 2. Korea Gas Corp Research and Development Division, Incheon, The Republic of Korea

Pipelines have played an essential role in transporting basic energy sources such as oil, natural gas and hydrogen. In recent years, non-destructive testing (NDT) technology for the structural integrity of various pipes has increased their demands due to the increase and deterioration of the energy resource network. There are various types of NDT methods, and magnetic flux leakage (MFL) and eddy current testing (ECT) technologies are most widely used for evaluating the integrity of pipelines, steam generator tube and aircraft components [1], [2]. Both MFL and ECT have inherent several weaknesses from their operation principle. A defect signals by MFL inspection have an ambiguity in distinguishing between defects in the inner surface and outer surface. ECT inspection must consider the effect of skin effect, thus the driving frequency is strictly limited by material and thickness of specimen. Consequently, each limit greatly affects the inspection performance and speed, so that this makes the bottleneck for the precise and versatile evaluation. In order to overcome constraints of conventional MFL and ECT, many research and development have been conducted by combining MFL and ECT into a single sensor [3]. This method inspects the ferromagnetic steel by applying DC biased magnetic field to the steel and measuring the outer surface or subsurface of steel wall with an ECT sensor. If the DC magnetic flux is distorted due to the existence of the defect, the magnetic permeability changes based on the nonlinear and hysteretic characteristics of the ferromagnetic material. Then, the defect signal can be measured as the perturbation of the permeability. Consequently, the skin effect no longer limits to the measurement of specific defects at the given frequency. Compared to other NDT methods, DC-biasing ECT is relatively recently introduced so that detailed descriptions of methodologies for the design and analysis are still short including optimal operating conditions, and signal analysis. To estimate the operating performance of DC-biasing ECT, both static magnetic field by permanent magnet or electromagnet, and time-harmonic magnetic field must be considered simultaneously. The finite element method (FEM) can compute the problem accurately, but the fine discretization of near surface, which requires high computational resources and time. The driving conditions are different depending on the application environment of the sensor, and a design is required for this, which causes a large time and cost aspect for development. In this paper, a semi-analytical method using finite element method for static magnetic field computation and analytical method for eddy current problem is suggested. The time consumption for determining the operating condition of DC-biasing ECT sensor can be greatly reduced by using the suggested approach. Fig. 1 illustrates the traditional method and proposed method to evaluate the performance of DC-biasing ECT. Both methods requires the calculation of static magnetic field by permanent magnet (PM) or electromagnet (EM), and the subsequent calculation of time-harmonic magnetic field by sensor coil. The ferromagnetic specimen includes both nonlinear and hysteretic characteristics, but this study would not consider the effect of magnetic hysteresis, which will be dealt in a future research. The magnetic flux density in each element is calculated by inputting the magnetization curve of the specimen, and the permeability determined by the magnetic flux density is stored for time-harmonic field problem. Since the amplitude of time-varying magnetic field by sensor coil is very small compared to the magnitude of static magnetic field, the permeability can be considered as the derivatives of the magnetization curve at the operating point of static field. Computation of high frequency magnetic field by using FEM requires very large number of discretization due to severe skin effect near surface of sensor coil. The performance of DC-biasing ECT sensor depends on many parameters such as static field and, frequency and the material of specimen. Thus, the computational time and cost should be reduced for the efficient sensor design. In this study, analytical method is used as an alternative to the calculation of time-harmonic field problem. The transformer model is formulated in analogy with the interaction between the sensor coil and eddy currents. Then, the different permeability distribution on the specimen is transformed in

to a homogenized plane to reduce computational complexity. The detailed formulation of the transformer model and homogenization will be included in the full manuscript. Fig. 2(a) shows the schematic diagram of DC-biasing ECT. The electromagnet was used to control DC magnetic field and reflection probe constructed with coaxial driving coil and sensing coil. The impedance response is calculated and results are shown in Fig. 2(b). The number of turns of electromagnet is 400 and exciting current is 3.5A. The calculated values of both normal and defective specimen are compared, and measurement setup and result will be dealt to complement the correspondence with the prototype. When the frequency increases, the normalized value of imaginary part of sensing voltage decreases while the real part of voltage increases. The proposed method can estimate the response of the sensor throughout the wide frequency range.

[1] J. Wu et al, IEEE Transactions on Magnetics, vol. 54, pp. 1-8 (2018) [2] Y. Xu, Y. Yang and Y. Wu, IEEE Sensors Journal, vol. 20, pp. 10502-10510 (2020) [3] J. Wu, J. Zhu, H. Xia, C. Liu, IEEE Transactions on Industrial Informatics, vol. 15, pp. 6252-6259 (2019)

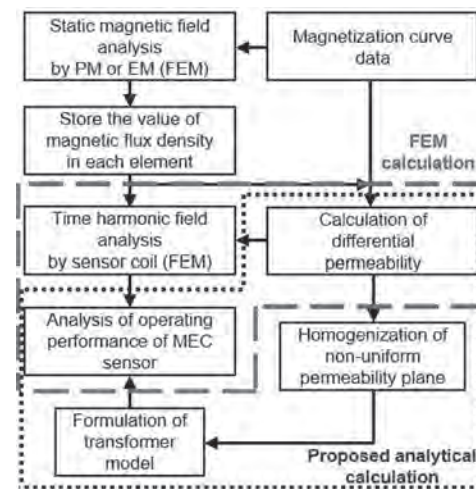


Fig. 1. Comparison of calculation scheme between traditional and proposed method

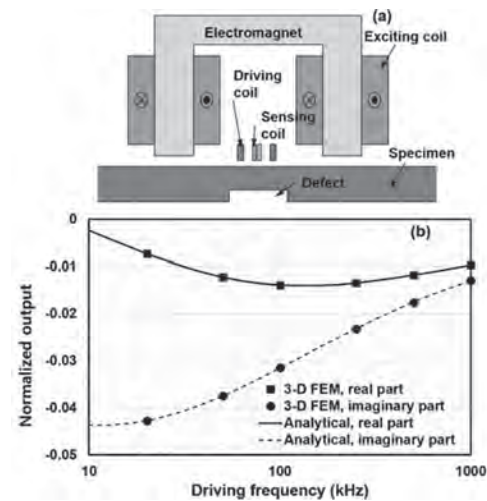


Fig. 2. (a) Schematic diagram of DC-biasing ECT and (b) comparison of two calculated results

IS-03. RTD Fluxgate Sensors Based on Current Induced Magnetization Reversal in Twisted Glass-Coated Microwires.

S. Corodeanu¹, C. Henschl^{1,2}, A. Damian¹, H. Chiriac¹, N. Lupu¹ and T.A. Ovari¹

1. National Institute of Research and Development for Technical Physics, Iasi, Romania; 2. Alexandru Ioan Cuza University, Faculty of Physics, Iasi, Romania

Fluxgate sensors are among the most sensitive devices for the detection of weak magnetic fields (in the range of 10^{-6} T) with resolutions of 100 pT at room temperature [1]. In conventional configuration, a fluxgate magnetometer consists of two ferromagnetic cores around which two coils for excitation and two coils for detection are wound and differentially connected. The residence times difference (RTD) fluxgate sensor first proposed by Bruno Andò, et al [1] consist of a single soft ferromagnetic core and two coils (one for excitation and one for detection). The sensor detects the external magnetic field strength through its corresponding relationship with the residence times difference of the induced peaks that appear when the excitation field cycles the magnetization of the core. One of the materials showing potential for the development of RTD sensors is represented by the glass-coated microwires exhibiting large Barkhausen effect, i.e., magnetization switching in a single step when the external excitation field is reversed. Recently, a new method to switch the axial magnetization in bistable glass-coated microwires has been reported [2, 3]. The method, detailed in [2], consists in applying a current directly through a magnetic sample subjected to controlled torsion. Using this method as a basis, we report here the development of a new RTD magnetic sensor that does not require an excitation coil. The sensor electronics was built using a dsPIC microcontroller which generates the signal for sensor excitation and measures the time difference between induced peaks (Fig.1). The time resolution of the electronics is about $1/(384 \times 10^6)$ s. The sensor performance was studied comparatively using as sensitive elements glass-coated microwires with nominal compositions of the magnetic core $\text{Fe}_{77.5}\text{Si}_{7.5}\text{B}_{15}$, $\text{Co}_{68.18}\text{Fe}_{4.32}\text{Si}_{12.5}\text{B}_{15}$ and $\text{Fe}_{73.5}\text{Si}_{13.5}\text{B}_9\text{Cu}_1\text{Nb}_3$ (FINEMET), having metallic core diameters (Φ_{metal}) of 10, 20 and 30 μm , respectively, and 7 mm glass coating thickness. The transfer functions (time difference versus applied field) were measured for different configuration of the sensor excitation current and torsion values. The value of the sensor sensitivity (S) decreases, and the dynamic range (DR) increases when the excitation current amplitude (I) increases. For annealed $\text{Co}_{68.18}\text{Fe}_{4.32}\text{Si}_{12.5}\text{B}_{15}$ microwires, having a metallic core diameter of 20 μm , we obtained a sensitivity value of 84 $\mu\text{s}/(\text{A}/\text{m})$, with a dynamic range of 17 A/m, for an excitation current amplitude of 10 mA. For an excitation current with an amplitude of 40 mA we obtained a sensitivity value of 11.7 $\mu\text{s}/(\text{A}/\text{m})$ and a dynamic range of 180 A/m. For current amplitudes of 50 mA and above, the dynamic range decreases due to the fact that the induced peaks become poorly defined, with low amplitudes, and cannot be easily distinguished by the electronic detection system. The annealed $\text{Co}_{68.18}\text{Fe}_{4.32}\text{Si}_{12.5}\text{B}_{15}$ microwires show wider measuring range and higher linearity of the transfer function as compared to all the other analyzed compositions (DR = ± 130 A/m for $\Phi_{\text{metal}} = 20 \mu\text{m}$ and I=30 mA). The $\text{Fe}_{77.5}\text{Si}_{7.5}\text{B}_{15}$ microwires show a fairly high noise on the measured transfer graph and lower dynamic range as compared to the $\text{Co}_{68.18}\text{Fe}_{4.32}\text{Si}_{12.5}\text{B}_{15}$ microwires (DR = ± 32 A/m for $\Phi_{\text{metal}} = 20 \mu\text{m}$ and I=30 mA). The annealed $\text{Fe}_{73.5}\text{Si}_{13.5}\text{B}_9\text{Cu}_1\text{Nb}_3$ wires show an extremely low linear variation transfer function (± 9 A/m for $\Phi_{\text{metal}} = 20 \mu\text{m}$ and I=30 mA) as compared to the other compositions analyzed. For annealed $\text{Co}_{68.18}\text{Fe}_{4.32}\text{Si}_{12.5}\text{B}_{15}$ microwires with different core diameters, we observed that for the same excitation current of 30 mA and the same torsion of 483 Rad/m, the sensitivity of the sensor decreases from 27.7 $\mu\text{s}/(\text{A}/\text{m})$ for wires with a diameter of 10 μm , to 12.7 $\mu\text{s}/(\text{A}/\text{m})$ for wires having 30 μm in diameter, the dynamic range increasing at the same time from 41 A/m for wires with 10 μm in diameter, to 200 A/m for the samples with 30 μm in diameter (Fig 2). This behavior follows the evolution of the switching field of the same samples, which decreases from 45 A/m for wires with a diameter of 10 μm to 21 A/m for wires with a diameter of 30 μm . The influence of torsion on the transfer function of the sensor is relatively low. Thus, for $\text{Co}_{68.18}\text{Fe}_{4.32}\text{Si}_{12.5}\text{B}_{15}$ wires with a diameter of 30 μm we obtained a sensitivity of 12 $\mu\text{s}/(\text{A}/\text{m})$ for a torsion of 120 Rad/m (one end rotation of 45° on a wire with a length of 6.5 mm) and 12.7 $\mu\text{s}/(\text{A}/\text{m})$ for

483 Rad/m (one end rotation 180° on a wire with a length of 6.5 mm). For higher torsion values, a sharp decrease in field sensitivity is observed, most likely due to the strong increase of the mechanical stresses induced in the wire. Work supported by the Nucleu Programme (Project PN 19 28 01 01) and Contract No. 11PFE/16.10.2018 financed by the Romanian Ministry of Education and Research.

1. B. Andò, S. Baglio, A.R. Bulsara et al., IEEE Instrum Meas Mag, Vol.8(4), 2005 2. S. Corodeanu, H. Chiriac, A. Damian et al., Scientific Reports, Vol. 9, No. 5868, 2019. 3. V. Zhukova, J. M. Blanco, A. Chizhik et al., AIP Adv. 7, 056026, 2017.

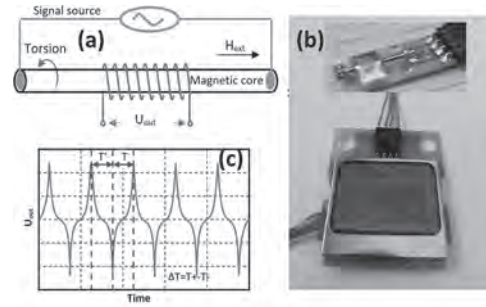


Fig. 1. Schematic representation (a) and picture (b) of the RTD fluxgate sensor and the typical output voltage for a sinusoidal excitation signal (c).

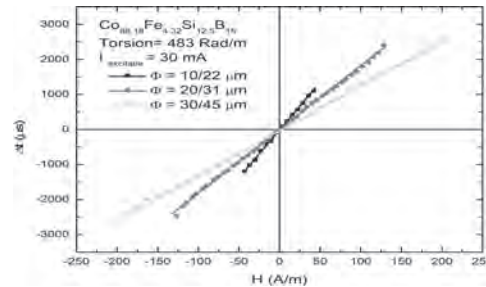


Fig. 2. The transfer graph obtained for $\text{Co}_{68.18}\text{Fe}_{4.32}\text{Si}_{12.5}\text{B}_{15}$ microwires, annealed at 300°C -1h, having different diameters of the metallic core.

IS-04. High-Bandwidth Current Sensing Technique Based on Magnetic-Field Sensing Using a Wire Loop and a Differential Amplifier Calibration Circuit.

W.C. Miao¹, F. Wang¹, Q. Xu² and P.W. Pong³

1. School of Mechatronic Engineering and Automation, Shanghai University, Shanghai, China; 2. Electrical and Electronic Engineering, University of Hong Kong, Hong Kong; 3. Department of Electrical and Computer Engineering, New Jersey Institute of Technology, Newark, NJ, United States

I. Introduction To achieve a higher power density of power electronic modules, the switching frequency of the power electronic devices is increasing significantly. Especially, the next-generation power electronic devices utilizing wide-bandgap semiconductor materials such as SiC and GaN which can realize the switching frequency in megahertz [1]. The current sensing is essential for the control purpose, condition monitoring, protection, and power management in power electronic modules. Although the shunt resistor can be used to measure the current, it is non-isolated and the parasitic impedance introduced may incur extra power losses and jeopardize the reliability of power electronic modules [2]. The Hall-effect current transducers are extensively exploited for current measurement in power electronic modules. Nevertheless, they are inapplicable in high-bandwidth current sensing due to the limited bandwidth of typically less than 200 kHz [3]. Since the magnetic sensor such as magnetoresistive (MR) sensor can measure current up to several megahertz non-invasively [4], there are researches on using the MR sensors for current measurement in power electronics [5-8]. Due to the skin effect, the high-bandwidth current tends to be distributed on the surface of a conductor and the skin depth decreases with the frequency. Thus, the main challenge is that the magnetic field of current varies with frequency causing the nonlinearity of MR sensors. It was studied that the frequency response can be improved by placing a copper sheet around the MR sensor [5]. Although the planar copper concentrator can concentrate the magnetic field [6], the magnetic flux density (B) still varies with the frequency. The copper foil is used to wrap the MR sensor to achieve a unity normalized gain until 83.3 kHz, but the gain increases for higher frequency [7]. Besides, the field summing and decoupling methods are adopted to reduce the phase shift and extend the bandwidth to 1 MHz with an error of 5 % by using two MR sensors [8]. Therefore, the technique for a single magnetic sensor to measure a high-bandwidth current is still lacking. In this paper, a technique using a specially designed wire loop and differential amplifier based calibration circuit is developed for the magnetic sensor to measure high-bandwidth current. The skin effect of rectangular wire on the printed circuit board (PCB) is analyzed mathematically. The effects of concentrators in various structures on B are investigated based on simulation results. The effectiveness of the proposed wire loop on concentrating magnetic field of current up to 10 MHz is evaluated. The experimental results verify that the proposed technique using the wire loop and differential amplifier based calibration circuit can sense the high-bandwidth current in high accuracy. II. Analysis of High-Bandwidth Current Sensing Technique Generally, the PCB trace of a power electronic module is rectangular as shown in Fig. 1 (a). Considering a 1 oz copper trace in a width of 2.54 mm, the height is 35 μm which is much less than the width. Thus, magnetic vector potential (A) of the position (x, y) can be calculated by [9] $A = \mu_0 / 8\pi w \{ (w+x) \log[(w+x)^2 + y^2] + (w-x) \log[(w-x)^2 + y^2] + 2y [\tan^{-1}(w+x)/y + \tan^{-1}(w-x)/y] - 4w \}$ where $2w$ and $2h$ are the width and height of the PCB wire respectively, μ_0 is the vacuum permeability. When the trace is carrying a high-bandwidth current, the skin effect should be considered. The skin depth can be calculated by $\delta = \sqrt{2\rho/\omega\mu_0}$ where δ is the skin depth, ρ is the electrical resistivity of copper, ω is the angular frequency. The skin depth decreases with the frequency. This affects the A and thus the B since $B = \nabla \times A$. As shown in Fig. 1 (b) and (c), the magnetic sensor is located on the top layer of the PCB and the trace with a current of 1 A is on the bottom layer, the average B of the magnetic sensor located region (B_{avg}) decreases from 0.0746 mT to 0.0725 mT when the frequency increases from 1 kHz to 1 MHz. A copper sheet of 25.4 μm can be used to concentrate the B_{avg} to 0.141 mT at 1 MHz as shown in Fig. 1 (d). However, in this case, the B_{avg} increases with the frequency. The problem that B_{avg} varies with frequency still exists. A wire loop is designed to reduce the variation of B_{avg} with frequency as

shown in Fig. 2 (a). The bottom-layer current passes through a rectangular wire with a cross-section of 0.2 mm \times 0.2 mm located 0.35 mm above the magnetic sensor and then passes to the top layer. In this way, the B_{avg} is 0.242 mT when the frequency is 1 kHz and 100 kHz as shown in Fig. 2 (b) and (c). It only decreases by 0.826 % to 0.240 mT at 10 MHz. Thus, a stable B can be achieved by this method, and thus current can be sensed accurately by the magnetic sensor despite the high frequency. In the full paper, the influence of skin effect on high-bandwidth current sensing will be analyzed. The effects of concentrators in various structures on B will be investigated and presented. The principle of the proposed wire loop and differential amplifier based calibration circuit will be elaborated. The effectiveness of the proposed technique for high-bandwidth current sensing will be verified and evaluated experimentally.

[1] E. Santi, K. Peng, and H. A. Mantooth, IEEE Transactions on Electron Devices., Vol. 62, pp. 434-442 (2015). [2] S. Ziegler, R. C. Woodward, and H. H.-C. Iu, IEEE Sensors Journal., Vol. 9, pp. 354-376 (2009). [3] A. Patel and M. Ferdowsi, IEEE Transactions on Vehicular Technology., Vol. 58, pp. 4108-4119 (2009). [4] J. Lenz and S. Edelstein, IEEE Sensors Journal., Vol. 6, pp. 631-649 (2006). [5] P. E. Schneider, M. Horio, and R. D. Lorenz, IEEE Transactions on Industry Applications., Vol. 48, pp. 1432-1439 (2012). [6] S. J. Nibir and B. Parkhideh, IEEE Transactions on Industrial Electronics., Vol. 65, pp. 2766-2774 (2018). [7] S. Shao, N. Yu, and X. Xu, IEEE Transactions on Power Electronics., Vol. 35, pp. 10930-10944 (2020). [8] M. Sheng, M. H. Alvi, and R. D. Lorenz, IEEE Journal of Emerging and Selected Topics in Power Electronics., (2020). [9] K. J. Binns and P. J. Lawrenson, Analysis and Computation of Electric and Magnetic Field Problems. Elsevier (2013).

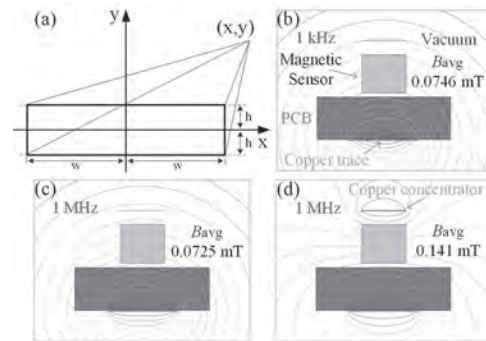


Fig. 1. PCB trace. (a) Cross-section. Magnetic flux at (b) 1 kHz, (c) 1 MHz, and (d) 1MHz with a copper concentrator.

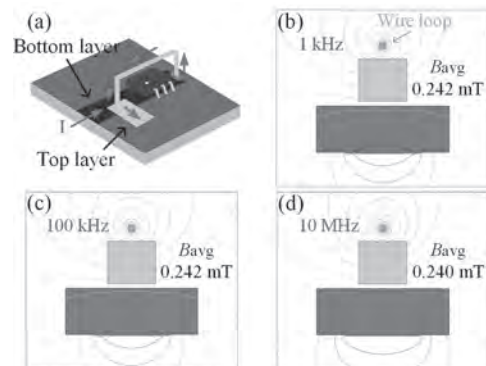


Fig. 2. Wire loop. (a) Layout. Magnetic flux at (b) 1 kHz, (c) 100 kHz, and (d) 10 MHz.

IS-05. Ultra-Lower Anisotropy Magnetic Field Sensor in Ferrite/Piezoelectric Toroidal Magnetolectric Composites.

J. Zhang¹, G. Bingfeng¹, J. Liu¹, Q. Zhang¹, H. Zhao¹, Z. Wang¹ and K. Li¹
¹. College of Electrical and Information Engineering, Zhengzhou University of Light Industry, Zhengzhou, China

In recent years, magnetolectric (ME) composites consisting of magnetostrictive and piezoelectric phases mechanically coupled to each other have received widely attention due to the tremendous potential applications for functional devices such as magnetic sensors, phase shifters, transformers or gyrators, current sensors and energy harvesters. In the field of magnetic sensors, the ME magnetic sensors are composed of ME composites that show many excellent advantages, such as low cost, high sensor performances (sensitivity, linearity, resolution), small volume perfect and simplified electronic circuits [1]. These advantages offer the potential of ME magnetic sensor to be a new generation of magnetic sensors. There are enormous investigations activities in recent years on ME magnetic sensor. Previous research shows that ME magnetic sensor exhibit high AC/DC magnetic sensor performances at room temperature under resonance conditions [2]. Additionally, the ME magnetic field sensors have been drawn significant interests for numerous applications, such as bio-magnetism detecting apparatuses, earth magnetic field detection, non-destructive material testing, and aerospace instruments[3]. However, these ME magnetic sensor need to be strictly parallel to the magnetic field when measuring the magnetic field due to the ME laminates of configurations of square, or rectangular geometries have high anisotropy, otherwise will cause enormous deviation and affect the stability of ME magnetic sensors. It is thus desirable to develop ME magnetic sensor with ultra-lower anisotropy, along with high sensor performances. In this study, a toroidal ME magnetic sensor in composite of strictly concentric ferrites/piezoelectric rings with toroidal solenoid wound around was fabricated and developed. Compared with the previously reported ME magnetic sensor of configurations of square, or rectangular geometries, the toroidal ME magnetic sensor has ultra-lower shape-induced anisotropy, high stability and high sensor performances, which voltage output is almost unaffected by the angle between the ME magnetic sensor and the magnetic field. These excellent stability and sensor performances characteristics offer unique possibilities for possible use of ME magnetic sensor.

[1] J. Zhai, Z. Xing, S. Dong, Appl. Phys. Lett. Vol. 88, p.062510 (2006). [2] H. Xi, M. Lu, Q. Yang, Sensor Actuat A-Phys. Vol. 311, p.112064 (2020). [3] J. Gao, L. Shen, Y. Wang, J. Appl. Phys. Vol. 109, p.074507 (2011).

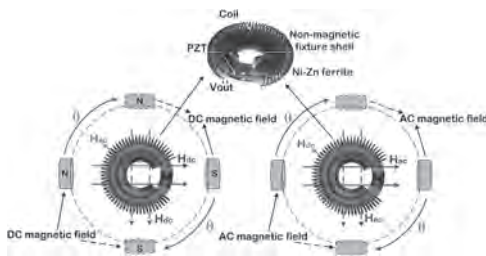


Fig.1. Schematic diagram of the presented magnetic field sensor.

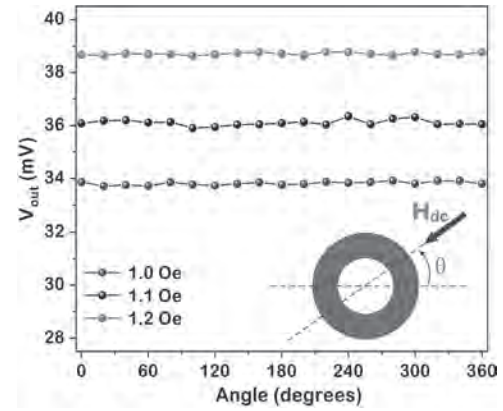


Fig.2. The effect of DC magnetic field angle on the ME output voltage measured for toroidal ME sensor. The inset indicates the direction of the DC magnetic fields in a top view

IS-06. New Eddy Current Probe for Vibration Signal Suppression.

D. Kosaka¹, Y. Kumakura², F. Kojima³ and H. Yamasaki²
 1. Polytechnic University, Kodaira-shi, Japan; 2. Tex Riken Co., Ltd.,
 Nishinomiya-shi, Japan; 3. Kobe University, Kobe, Japan

1. Background and problem considered Metal tube and wire are used in variety parts of infrastructures. Defects like holes and cracks in the products can cause serious accidents. They are inspected in manufacturing processes by using Non-Destructive Techniques (NDTs). The inspection speed and sensitivity are important because the tube and wire are long. The Eddy Current Testing (ECT) is one of NDTs and widely used in the processes. The ECT is better than the ultrasonic testing, the X-ray testing and other NDTs on the speed and sensitivity. However tube and wire manufacturers need faster inspection speed and better inspection sensitivity, because the speed is closely related to the production speed. The speed is determined by the vibration of the inspection sample caused by the transport of the sample. The vibration has an impact on detection signals of the ECT^[1]. In previous studies, signals caused by vibration are removed from the detection signal by suppressing the vibration of the transport device, and/or signal processing^[2-4]. We propose a new ECT probe to suppress the vibration component in the detection signal. The novelty of the proposed probe is that it has two outer coils for electromagnetically suppressing the vibration components outside of the two inner coils for flaw detection. The principle that the proposed method reduces the detection signal due to the vibration is explained. 2. Vibration Signal Suppression Probe The proposed probe has four coils and is used with a variable amplifier and a phase shifter which is known as an all-pass filter. It is possible that effect of the vibration in the detection signal can be equal to zero by using the variable amplifier and phase shifter which adjust the amplitude and the phase of the excitation current flowing through the outer coil. Fig. 1 shows the structure of the probe with four coils. L₂ and L₃ are defined as the inner coils. L₁ and L₄ are defined as the outer coils. The inside coils form a self-induced differential sensor. The outer and inner coils form a mutually induced differential sensor with the outer coil as excitation and the inner coil as detection. The detection signals of the sensors due to the displacement of the rod is defined as the displacement signal. The displacement signal of the probe is equal to the total output of the self-induced and mutual-induced sensors. We simplify discussion by limiting static displacement. The displacement is defined the offset between axes of the rod and coils and rotation of the rod. As shown in Fig. 1, axis of the rod has the offset from axis of coils to the radius direction. The rod rotates around a point on the plane containing the axes of the rod and coil. To demonstrate the effectiveness of the method, the displacement signals of the ECT were simulated by the 3D finite element method. In the simulation, excitation current was 10 mA at 16 kHz, a brass rod with a conductivity of 1.26×10^7 S/m was used, and d_{Coils} was 6 mm. Simulated detection signals are shown in Fig. 2. The detection signal of the ECT is obtained as a point on the complex plane. The horizontal and vertical axes of the plane represent in-phase and quadrature components of the signals for the excitation current. The solid and dotted lines in Fig. 2 show simulated results of displacement signals when the inner or outer coils are used as the excitation coils. The lines show the displacement signals generated when the balance of the electromotive force was lost due to the displacement. The phases of the displacement signals were constant. The amplitudes of the displacement signals were proportional to the rod of offset and rotation. The dash dot line shows that displacement signal with the amplitude and phase of the outer excitation signal adjusted using a variable amplifier and phase shifter. The amplitude and phase were adjusted so that it is equal to the inverted phase of the inner excitation signal and the amplitude of the inner excitation signal. The displacement signals cancel each other when inner and outer coils are used as excitation coil at the same time. In this case, the gain of the amplifier was 4.59 and the phase of the phase shifter was -44.8 degrees. The detail of the experimental method and results will be presented in our presentation.

& E International, Vol. 38, No. 6, pp. 508-515(2005) [4] W. Yin, and A. J. Peyton, NDT & E International, Vol. 40, No. 1, pp. 43-48(2007)

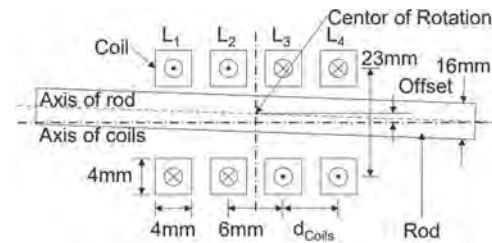


Fig. 1. Structure of the vibration suppression probe. The inside coils, L₂ and L₃, form a self-induced differential sensor. The outer, L₁ and L₄, and inner coils form a mutually induced differential sensor with the outer coil as excitation and the inner coil as detection.

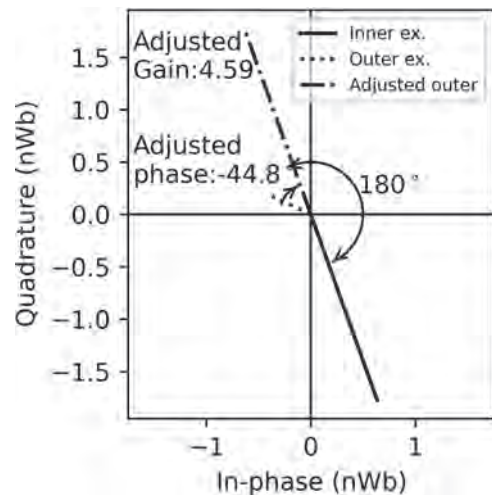


Fig. 2. Simulated displacement signals. The solid line is the signal with the inner excitation. The dot line is the signal with the outer excitation. The dash dot line is the signal adjusted from the outer excitation signal. The total signal of inner and adjusted outer signals is equal to zero.

[1] C. Reboud, D. Prémel, G. Pichenot, and D. Lesselier, International Journal of Applied Electromagnetics and Mechanics, Vol. 25, No. 1-4, pp. 313-317(2007) [2] Cheng-Chi Tai, James H. Rose, and John C. Moulder, In Review of Progress in Quantitative Nondestructive Evaluation, pp. 1593-1600(1997). [3] L. Janousek, Z. Chen, N. Yusa, and K. Miya, NDT

IS-07. Magnetic Target Motion Monitoring Based on Weighted Route Fitting.

J. Qiu¹ and D. Xie¹

1. College of Optoelectronic Engineering, Chongqing University, Chongqing, China

Many ferromagnetic substances are naturally magnetized under the influence of the geomagnetic field, and information about the corresponding objects can be obtained based on the analysis of monitoring the magnetic fields generated around magnetic targets. The detection and tracking of magnetic targets is the current research hotspot, and the target monitoring based on magnetic signals as well as widely used in various fields. Currently, the magnetic target localization method is commonly used to obtain the relative position of the target by inversion of the magnetic field gradient tensor matrix. However, this method has a detection blind spot, and even if the final results are corrected by mean filtering, there is still a certain amount of error. Therefore, the correction of the localization results needs to be based on the information of the magnetic field gradient matrix collected at the detection point. This paper uses the magnetic field gradient tensor target localization algorithm as the basis of single-point localization, analyzes its error in detection, and proposes a weighted route fitting method based on magnetic field gradient matrix information for the characteristics of route calculation which is vulnerable to great errors. After simulation experiments, the method can reduce the fluctuation of detection results to a certain extent, and can effectively propose the influence of the extreme error generated by the detection blind area on the positioning results. To investigate the sources of error in target localization, we designed a series of experiments for the magnetic field gradient matrix-based localization method. The location of the detection blind zone is verified by changing the relative position of the magnetic target to the detection point. When the position vector is perpendicular to the magnetic moment vector, the error rate increases significantly. The experimental results are consistent with the theoretical formula, and the higher the accuracy of the magnetic sensor, the smaller its detection blind zone. When the detection point out is in the detection blind area, its magnetic field gradient matrix is a non-full-rank matrix, so the accuracy of target detection is often inversely proportional to the dispersion of its matrix eigenvalues. Therefore, by introducing a weighted fitting method based on the gradient matrix, the detection error can be reduced to a certain extent and the interference caused by abnormal data can be eliminated. Experiments are designed to verify the feasibility of the method. The schematic diagram of the positioning detection experiment is shown in Figure 1 below, where ABCED represents the location of different detection points, and the oval dashed line is its detection range. The magnetic target is set to come out from the coordinates (-0.5m,0m) and advance along a straight line to (0.5m,0m), and the comparison of its route monitoring results is shown in Figure 2 below. Based on the results, it can be concluded that the error-corrected route is closer to the set simulation route.

Zhao G, Han Q, Tong X, et al. Adaptive filtering method for magnetic anomaly detection[J]. *Journal of Applied Remote Sensing*, 2018, 12(2):1-10. Kim K Y, Jeong E, Kim S, et al. Magnetic Anomaly Detection Using Continuous Angle Alignment of Three-Axis Magnetic Signal[J]. *IEEE sensors journal*, 2019, 19(2):743-750. Zheng J, Fan H, Zhang Q, et al. Magnetic Anomaly Target Recognition Based on SVD and SVMs[J]. *IEEE Transactions on Magnetics*, 2019, 55(9):1-8. Shen Y, Wang J, Shi J, et al. Interpretation of Signature Waveform Characteristics for Magnetic Anomaly Detection Using Tunneling Magnetoresistive Sensor[J]. *Journal of Magnetism and Magnetic Materials*, 2019, 484(AUG.):164-171. Huang Y, Wu L H, Sun F. Underwater Continuous Localization Based on Magnetic Dipole Target Using Magnetic Gradient Tensor and Draft Depth[J]. *IEEE Geoscience and Remote Sensing Letters*, 2014, 11(1):178-180. Nara T, Ito W. Moore-Penrose generalized inverse of the gradient tensor in Euler's equation for locating a magnetic dipole[J]. *Journal of Applied Physics*, 2014, 115(17PT.3):3646-3648.

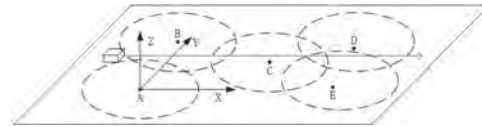


Fig.1 Schematic diagram of magnetic target movement route monitoring

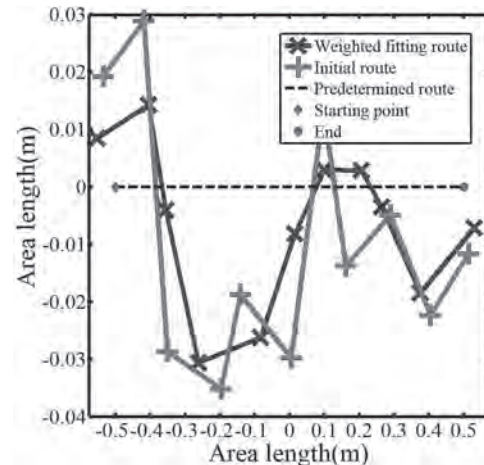


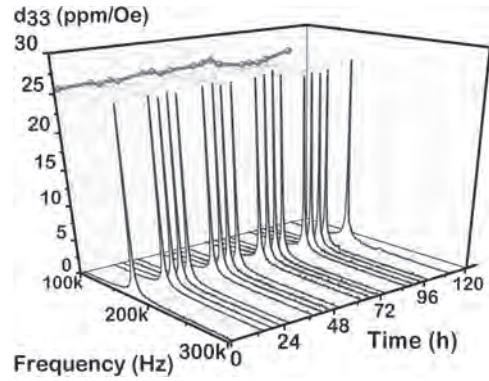
Fig.2 Comparison chart of route fitting correction results

IS-08. High-Stability Magnetic Sensors in Permalloy/Piezoelectric Magnetolectric Heterostructure Using Inappreciable Hysteresis.

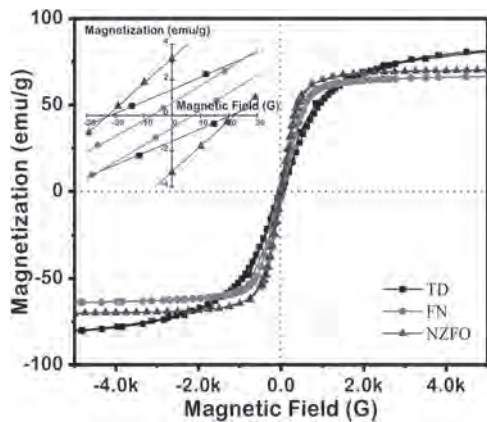
J. Zhang¹, J. Liu¹, G. Bingfeng¹, Z. Wang¹, K. Li¹, H. Zhao¹ and Q. Zhang¹
 1. College of Electrical and Information Engineering, Zhengzhou University of Light Industry, Zhengzhou, China

Low frequency and weak magnetic field sensors based on magnetolectric effect have received extensive attention due to their valuable characteristics, such as low-cost materials and fabrication, room-temperature response, low size, self-powered and non-contact sensing, high sensing resolution and large dynamic range¹. In order to improve the sensitivity of magnetolectric sensors, it is necessary to use soft magnetic materials (such as magnetic amorphous alloys, nickel, permendur, galfenol, Terfenol, ferrites) with low coercivity, low residual magnetization and high permeability as magnetostrictive phase². The characteristics of soft magnetic field determine that the magnetolectric sensor can quickly respond to the change of the external magnetic field, obtain the induced electromotive force, and timely recover to the state of complete demagnetization when the external magnetic field disappears. However, the output voltage generated by the magnetolectric composite is an ambiguous function of the applied DC magnetic field due to non-negligible hysteresis loss in soft magnetic materials. The intrinsic hysteresis loop of magnetic materials is a multivalued function, which causes the magnetolectric composites to output an uncertain voltage under the same external DC magnetic field. The non-negligible hysteresis behavior of magnetic media leads to the absolute measurement error of DC magnetic field sensor and reduces the signal-to-noise ratio (SNR). This will limit the measurement stability and accuracy of magnetolectric sensors. Therefore, the use of magnetostrictive materials with smaller remanence may be a way to further improve the working stability of magnetolectric sensors. In this study, by comparing three typical magnetostrictive materials with different properties, the effect of intrinsic hysteretic properties of the materials on the stability of the sensor will be studied. Furthermore, the advantages of permalloy such as low coercivity and low remanence have been used to fabricate a ME sensor with high stability. Each vibration mode of permalloy shows consistency for at least 110 hours without any demagnetization. The stable vibration mode indicates that the stability of magnetolectric sensor based on permalloy will reach a higher order of magnitude than NZFO and Terfenol-D. Compared to previously reported counterparts, this ME sensor can achieve higher precision measurement and produce higher stability signal.

¹ Hu J M, Chen L Q and Nan C W, Adv. Mater., Vol. 28, p.15-39 (2016)
 Burdin D A, Chashin D V and Ekonomov N A, J. Magn. Magn. Mater., Vol. 449, p.152-156 (2018)



The dynamic d_{33} spectrum which sampled under the condition of resonance and the same applied magnetic field for 120h.



Three different magnetostrictive material magnetization curves. The insert shows initial part of the curve in expanded scale.

IS-09. Simulation of Wave Mode of Flexible SAW Magnetic Sensor Based on ZnO/FeGa/PI Structure.

J. Qiu¹ and J. Du¹

¹. Chongqing University College of Optoelectronic Engineering, Chongqing, China

With the development of the Internet of things, the demand for wearable flexible sensors is increasing. In order to research the new type of flexible magnetic sensors, in this paper, aiming at the vacancy of the application surface acoustic wave(SAW) devices in the field of wearable flexible magnetic sensors, the SAW magnetic sensors with ZnO/FeGa/PI structure are modeled and simulated^[1,2], and the resonant characteristics and wave modes are studied. The frequency domain analysis of four kinds of devices with different thickness of 1.2 μm , 2 μm , 3.4 μm and 4 μm is carried out respectively. It is found that the device has multiple wave modes in each case, and the resonance peak of the device shifts to high frequency with the increase of the thickness of the piezoelectric layer. By comparing the modal deformation figure, it is found that the main modes of piezoelectric film with different thickness are various. For example, for 1.2 μm , the main mode is mode 2, while for 2 μm , the main mode is mode 4. The reason is that the device is composed of multi-layer thin films, in which the acoustic wave is not only affected by the piezoelectric medium, but also by the magnetostrictive layer and flexible substrate. Therefore, the optimal working mode is different for different thickness devices. In this paper, the flexible magnetic sensor is designed according to different thickness structure, and its optimal working mode is studied. When the maximum resonant mode is used as the working mode, the linear region of the magnetic sensor is basically unchanged, which is between 2 and 10 Oe. When the thickness of ZnO is 2 μm , the sensitivity in the linear region is the largest, about 253.3 kHz/Oe, and the working frequency is about 70MHz. When the thickness of ZnO is 3.4 μm , the sensitivity is only 30.5 kHz/Oe, but the working frequency is the highest, about 106MHz. This provides a theoretical basis for the development and application of flexible magnetic sensors. It is also found that when the thickness of ZnO is 1.2 μm , the maximum absolute value of admittance is only 0.0564, while for the structure with 4 μm , the maximum absolute value of admittance is 10.3413, which is of great significance for the subsequent design of impedance matching of wireless SAW magnetic sensor.

[1] Datta S, Atulasimha J, Mudivarthi C, et al. Stress and magnetic field-dependent Young's modulus in single crystal iron-gallium alloys[J]. Journal of Magnetism and Magnetic Materials, 2010, 322(15): 2135-2144. [2] Chung G S, Phan D T. Finite Element Modeling of Surface Acoustic Waves in Piezoelectric Thin Films[J]. Journal of the Korean Physical Society, 2010, 57(3): 446-450.

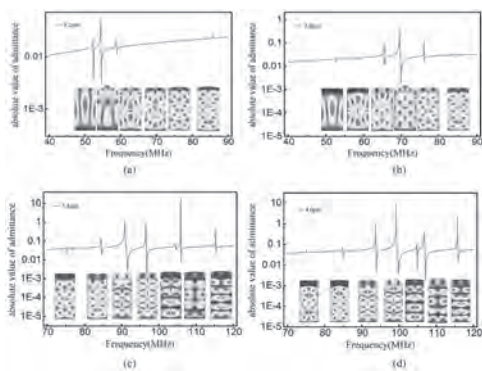


FIG. 1 Absolute value of admittance and deformed shape plot of piezoelectric layers with different thickness (a) 1.2 μm (b) 2 μm (c) 3.4 μm (d) 4 μm .

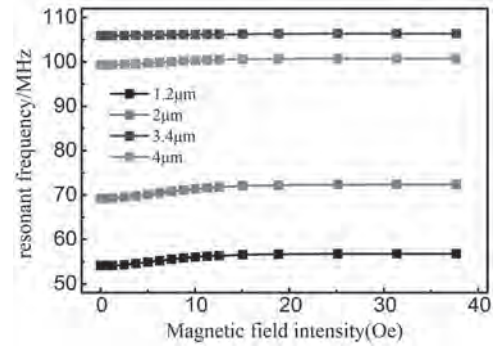


FIG. 2 (a) Relationship between resonant frequency of main mode and magnetic field intensity when the thickness of ZnO is 1.2 μm . (b) Sensitivity of main modes corresponding to different ZnO thickness.

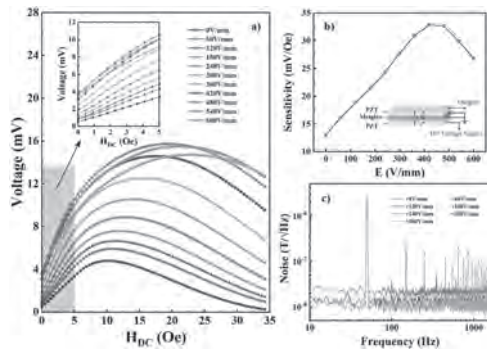
IS-10. Optimization of Equivalent Noise in the DC Magnetic Field Sensor Based on Magnetolectric Effect.

J. Luo¹, Y. Qiu¹, H. Yang¹, G. Yu¹, M. Zhu¹ and H. Zhou¹

1. Key Laboratory of Electromagnetic Wave Information Technology and Metrology of Zhejiang Province, China Jiliang University, Hangzhou, China

Magnetic field sensors using the magnetolectric (ME) effect in the composite multiferroic structures have attracted intensive attention due to their convenient operating at room temperature and high sensitivity. Large works have focused on the improvement of sensitivity and linearity by designing novel device structures but put rare attention on the optimization of equivalent noise that is also an important parameter for actual device application. In this work, we present a DC magnetic field sensor consisting of PZT/Metglas/PZT composites. With applying a voltage bias on the bottom PZT piezoelectric layer, the ME coefficient of the top PZT/Metglas bilayers can be increased obviously, as shown in Fig.1(b). This effective increase of ME coefficient will benefit the improvement of the magnetic field-to-voltage transfer coefficient and the reduction of the noise in the magnetolectric sensor that have been shown in Fig.1(b). By increasing the electric field from 0 V/mm to 360 V/mm, the sensitivity of the sensor can increase from 13.04 mV/Oe to 32.85 mV/Oe at the resonant frequency of 131.6 kHz, and the equivalent magnetic noise of the sensor will decrease from 20 nT/ $\sqrt{\text{Hz}}$ to 9.8 nT/ $\sqrt{\text{Hz}}$, as shown Fig.1(c). This three times increase of sensitivity and two times reduction of equivalent noise in the DC magnetic field detection by using ME effect may offer a new route for the development of novel magnetic field sensors or arrays.

1. J. L. Hockel, T. Wu, and G. P. Carman, Journal of Applied Physics, Vol. 109, p. 064106 (2011). 2. V. N. Serov, Y. K. Fetisov, and A. A. Berzin, IEEE Sensors Journal, Vol. 18, p. 8256 (2018). 3. Y. Shen, D. Ma, and J. Gao, IEEE Electron Device Letters, Vol. 39, p. 1417 (2018).



(a) Dependence of the output voltage with the DC magnetic field at different bias voltages; (b) Dependence of the sensitivity with the bias electric field for the proposed magnetic field sensor; (c) Frequency dependent equivalent noise density spectra at different bias electric fields of the proposed sensor.

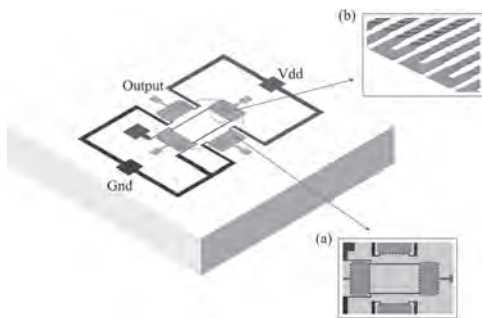
IS-11. A Sensitive, 2-Axis Magnetic Sensor Based on Anisotropic Magnetoresistance Effect.

Q. Jiang¹ and Y. Jiang¹

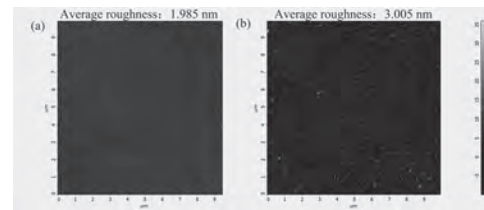
¹. Jiangnan University, Wuxi, China

Nowadays, the detection of the ultra-weak magnetic fields (< 1 mOe) in micro- or nano-scope (< 100 nm) is a hot research field. The magnetic sensor based on the principle of anisotropic magnetoresistance effect is attractive in the application of detecting the ultra-weak magnetic field in a contactless manner [1]. In this paper, a sensitive, 2-axis magnetic sensor based on anisotropic thin-film structure is proposed and fabricated. As the sensor's induction layer, the anisotropic films of permalloy Ni (80%) Fe (20%) with different thicknesses (20 nm and 50 nm) are deposited by means of magnetron sputtering [2]. Seed layer under NiFe layer is used to control the grain size in the NiFe layer, which is an important parameter for magnetoresistance. In order to obtain the NiFe layer with good performance, tantalum is deposited as the seed layer, making the NiFe layer with $\langle 111 \rangle$ crystallographic texture with suitable grain size [3]. Figure 1 shows the schematic structure of the designed sensor for the ultra-weak magnetic field detection. The characterizations are conducted on the prepared layer, including surface roughness by atomic force microscope (AFM) and the crystalline structure by X-ray diffraction (XRD). According to the test results of AFM, it is found that the film with a thickness of 20 nm has a smoother surface with an average roughness of 1.985 nm, which is less than that of the film with a thickness of 50 nm with an average roughness of 3.005 nm. With the difference of surface roughness, the coercivity of the two thickness films is also different, and it ultimately has an effect on the film properties. Figure 2 shows the characterization results of the surface roughness of the deposited NiFe thin film. Based on the characterized results, the magnetoresistance related to the anisotropic effect is demonstrated and analyzed. The influence of the thickness of the anisotropic film on the characteristics of the magnetization and the dynamic range of the sensors, as well as the range of the magnetic field sensitivity is studied and analyzed in the paper [4]. The deposited film with 20 nm thickness shows obvious anisotropy with low coercivity, resulting in high sensitivity and outstanding detecting ability in the weak magnetic field.

[1] N. A. Djuzhev, N. S. Mazurkin, and V. S. Pozdnyakov, *Semiconductors*, Vol. 49, no. 13, pp. 1739-1742 (2015) [2] M. Y. Chinenkov et al., *NANOCON 2010 - 2nd International Conference, Conference Proceedings*, pp. 270-273 (2010) [3] S. V. Luong, A. T. Nguyen, T. L. Nguyen, and A. T. Nguyen, *IEEE Transactions on Magnetics*, Vol. 54, no. 99, pp. 1-4 (2018) [4] D. Murzin, V. Belyaev, and F. Groß, *Japanese Journal of Applied Physics*, Vol. 59 (2019)



The model of the magnetic sensor. Internal figure (a) Local top view of the model. (b) Enlarged view of permalloy stripes and parallelograms which are biased



Results of $\text{Ni}_{80}\text{Fe}_{20}$ films' surface roughness with different thicknesses tested by atomic force microscope (AFM). (a) The thickness is 20nm. (b) The thickness is 50nm.

IS-12. Heterogenous Integrated Displacement Sensor With Grooved Ferrite.

M.G. Kisic¹, A. Stefanov¹, M. Lukovic², O. Aleksic², M. Damjanovic¹ and L. Zivanov¹

1. Faculty of Technical Sciences, University of Novi Sad, Novi Sad, Serbia;

2. The Institute for Multidisciplinary Research, Belgrade, Serbia

There are many different ways and methods for measuring displacement. The influence of the magnetic material on the inductance of the inductor in its vicinity has been well investigated and used for the realization of various sensors, as well as displacement sensors [1, 2]. However, it has been shown that an improvement in the inductance of the inductor can be achieved if the grooves are realized on the surface of the magnetic film [3], which gives the great potential for the realization of magnetic sensors with better characteristics. With advances in development of materials in recent years, 3D printing technology allows a very fast fabrication of prototypes. It can be used for development of electronic components, sensors and actuators. It is a very simple, high-quality and precise way to create complex geometric structures using different materials which enable the realization of sensors of different characteristics. This paper presents a wireless magnetic displacement sensor realized in heterogeneous integration technology. The sensor is realized using additive 3D printing technology and magnetic disc with improved design. The wireless measurement method enables simpler and more precise measurement and data collection compared to the classic wired method. The exploded 3D model of the sensor is shown in the Fig. 1. The proposed sensor consists of three parts: the inductor, the sensor's casing with spacer and the ferrite disk with grooves. The inductor windings are turned downwards towards the ferrite. The inductor is realized in Printed Circuit Board Technology, in the form of a spiral with an outer diameter of 25 mm and 22 turns (the width of the conducting lines is 500 μm and the conductor spacing is 730 μm). Using the $\text{Mn}_{0.5}\text{Zn}_{0.5}\text{Fe}_2\text{O}_4$ powder, the ferrite disc with grooves is pressed and sintered at a temperature of 1275 $^{\circ}\text{C}$ for 2 hours in a chamber furnace. The ferrite disc has a diameter of 25 mm. It has three concentric rings and a circle in the center on its surface. The part of the sensor that allows the sensor to be sensitive to displacement is the spacer. The spacer is printed using a 3D technology. It was made of Ninjaflex, one of the leading flexible 3D filaments. It is in the shape of the ring with the thickness of 500 μm . Using a Polylactic acid (PLA) filament, the sensor's housing is 3D printed in which the sensor parts are connected and fixed. The applicator of displacement that acts on the surface of the sensor is also 3D printed. Displacement measurement is performed wirelessly using an impedance analyzer HP4194A. A coil (antenna) is placed around the sensor and the impedance and the phase of the antenna-sensor system are measured, from which the resonant frequency is determined. The displacement operation on the sensor is performed using a manual translation stage which enables the precise movement of the sensor surface in the steps of 50 μm . The characteristic of the antenna-sensor is shown in the Fig. 2. During the action of the displacement, the spacer is compressed and the ferrite approaches the inductor, which causes an increase in inductance, i.e. a decrease in the resonant frequency of the antenna-sensor system.

1. M. Kisic, N. Blaz, Lj. Zivanov and M. Damjanovic, AIP Advances, Vol. 10, paper no. 015017, p. 1-4 (2020) 2. M. G. Kisic, N. V. Blaz, Lj. D. Zivanov and M. S. Damjanovic, IEEE Transactions on Magnetics, Vol. 53, no. 11, Art no. 4004104, p. 1-4 (2017) 3. X. Zhou, Y. Wen, Y. Mu and P. Li, 64th Annual Conference on Magnetism and Magnetic Materials, MMM2019, November 4-8. 2019, Las Vegas, Nevada, Book of abstracts, paper no. DV-05, p. 437-438 4. Available online at: <https://ninjatek.com/ninjaflex/>, accessed 05.01.2021.



Fig.1. The exploded 3D view of the sensor.

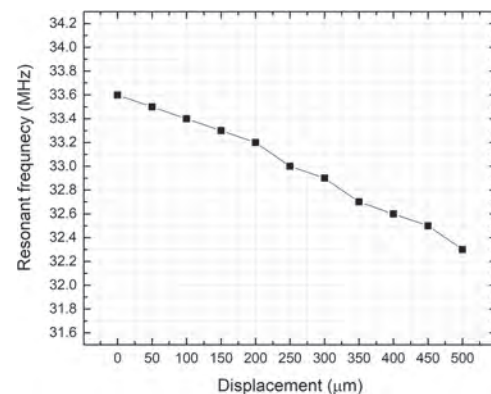


Fig. 2. The dependence of the resonant frequency on the displacement.

IS-13. Selection of Applied Magnetic Field for Optimal Detectability in Eddy Current Testing With DC Bias.

H. Nam¹, D. Um¹, H. Yoo², D. Kim², C. Heo¹, M. Kim¹, J. Jo¹ and G. Park¹
 1. Pusan National University, Kumjeong-ku, The Republic of Korea;
 2. Korea Gas Corp Research and Development Division, Incheon, The Republic of Korea

1. INTRODUCTION The non-destructive testing technology is appropriate to inspect high-priced product because it can inspect while maintaining the shape of the structure. And as the structure of the inspection body becomes complex and diversified with the development of the industrial society, the demand for non-destructive inspection is increasing mainly in developed countries. These techniques investigate structures of inspection by detecting energy deformation caused by the defects or constitution of products using specific physical energy to the target. Depending on the type of energy used for investigation, non-destructive testing is divided into technologies such as magnetic-particle testing, eddy-current testing, ultrasonic testing, radiation transmission testing, liquid-penetration testing and is applied to a wide range of application such as automobiles, nuclear power, steel structures, and pipelines [1]. Oil and gas pipes are mostly buried underground, so it is necessary to regularly manage corrosion or internal defects in pipes. Non-destructive testing is mainly used for safe long-distance transportation of oil and gas, among which Eddy-Current Testing (ECT), which does not have direct contact with the test object, is widely used. In ECT, operating frequencies have a significant impact on detecting faults. Traditional ECT mostly operates within the frequency range of a few kHz to MHz [2]. When the following high frequencies applied at the structure of the inspection, there is some difficulty to detect defects under pipe because eddy current does not flow to the bottom of the pipe due to the skin effect. In order to compensate for these limitations, the industry recently started to use the Magnetic Eddy Current technique that combines the principle of eddy current testing and magnetic flux leakage testing. The principle of this technology is based on the change in the pipe permeability due to defects by applying a certain amount of magnetic flux to the pipe using a permanent magnet or an electromagnet. In this technique, the magnetic flux used here does not need to go to the saturation point like MFL. In general, the magnetic field size required for MFL is at least 10 KA/m, but in MEC, a magnetic field of 3 KA/m is sufficient [3]. In the MEC technique, the value of magnetization level applied to the structure of the inspection has a significant influence on the defect determination performance. If the magnetic field is too small, it is impossible to determine the defects on the outer part of the pipe, and if the magnetic field is too large, defects of various sizes cannot be distinguished. Therefore, it is important to properly apply magnetic flux to the pipe so that defects can be found with high resolution in a given driving condition and the defect position can be distinguished. However, it has not been long since MEC technology has been introduced and researched, so there are insufficient papers on what driving conditions the sensor should operate under for optimal defect detection performance. For this reason, in this paper, a study was conducted to compare the defect detection performance according to the applied magnetic field point and to find the optimal applied magnetic field under a given driving condition. In order to analyze the distribution of the magnetic field around the defect according to the applied magnetic field value, a 3D model is set as shown in Fig.1-(a) and analyzed using 3D FEM. The defect underneath the pipe increases the density of magnetic flux in the pipe, thereby the permeability of pipe decreases and the impedance of the coil changes accordingly to generate a defect signal. The thickness of the defect used in the simulation is fixed at 1.5mm, which is 30% of the pipe thickness, and the diameter of the defect is fixed at 20mm. The value of magnetic field applied within the pipe was changed by changing the current value using an electromagnet. Fig.1-(b) show the respective magnetic field point of the pipe when 1A, 2A, 3A, 4A current is applied to the electromagnet coil. When a current of 1A is passed, it is difficult to determine the defects outside the pipe due to the large permeability value, and at 3A and 4A, the magnetic field applied to the pipe reaches almost saturation and the magnetic permeability is close to 1, making it inappropriate for detection of various size of defects. However, at 2A, it has a permeability, which is the middle value of the previous values, so it can detect various size of defects. Thus, using MEC techniques allows optimal defect detection performance

at lower magnetic flux than MFL. In order to compare the defect detection performance in a real situation according to the applied magnetic field value, a prototype was made as shown in Fig.2-(a) and the experiments were conducted to verify compare to the simulated values. As shown in Fig.2-(b_Above), a specimen with artificial defects was produced and an actual MEC driving experiment was conducted. The specimens consist of defects of 10%, 30%, and 50% depth of the pipe thickness, where the solid line represents the external defect of the pipe and the dotted line represents the internal defect of the pipe. And defects were detected by using coils as shown in Fig.2-(b_Below). The setting and procedures of experiments and the discussion of the results will be covered in the manuscript.

[1] Seung-Seok Lee, Ki-Bok Kim, Journal of the Korean Society for Nondestructive Testing, vol. 24, pp. 64-85 (2015) [2] K.Reber, A.Boenisch, Stefanie Asher, PPSA Seminar in Scotland, pp.1-12 (2015) [3] Mohd Aufa Hadi Putera Zaini, Mohd Mawradi Saari, Nurul Ain Nadzri, 2020 11th IEEE Control and System Graduate Research Colloquium (ICSGRC 2020), Malaysia, pp.1-4 (2020)

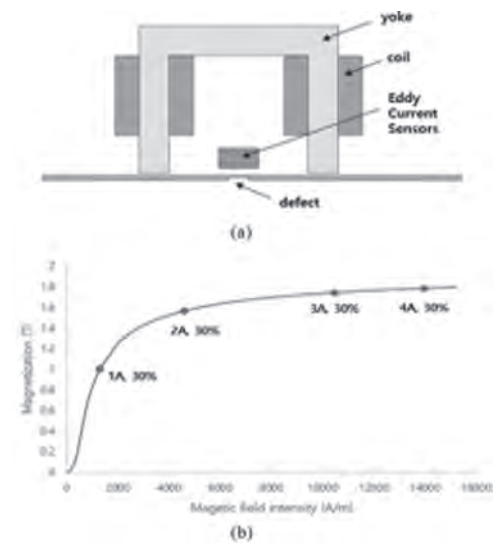


Fig. 1. (a) MEC simulation models. (b) Magnetic field points according to the applied magnetic flux.

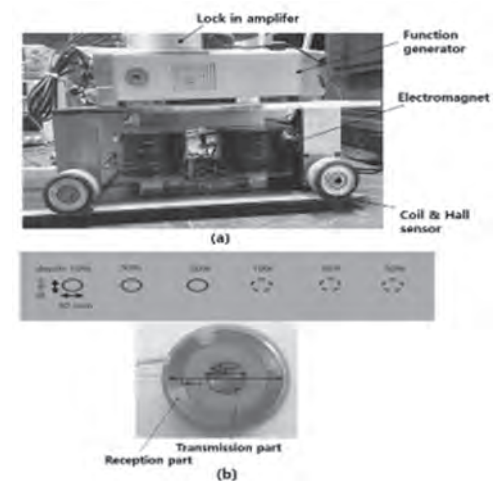


Fig.2. (a) MEC prototype. (b) specimen with artificial defects(Above) and MEC coil(Below).

IS-14. A Study of Hysteresis Reduction of Small AC Magnetic Field Modulated Tunneling Magnetoresistive Sensor.

H. Huang¹, S. Liao¹, Y. Yang², A. Sokolov³, Y. Liu^{2,3}, X. Yin⁴ and S. Liou^{2,3}

1. Institute of Electro-Optical Engineering, National Taiwan Normal University, Taipei, Taiwan; 2. Department of Physics and Astronomy, University of Nebraska-Lincoln, Lincoln, NE, United States; 3. Nebraska Center for Materials and Nanoscience, University of Nebraska-Lincoln, Lincoln, NE, United States; 4. Western Digital Corporation, Fremont, CA, United States

Tunneling magnetoresistive (TMR) sensors can easily be used for magnetic sensing due to high sensitivity, small size, and low power consumption. [1] They also have extremely short response times and are suitable for precise sensing applications. The magnetic hysteresis in the sensing layer of TMR sensors usually has a negative effect on the linearity and reversibility of the sensors. Therefore, reduced magnetic hysteresis, as well as low power and low noise, is favored in low magnetic field measurement. Previous research has shown that the magnetic hysteresis in TMR sensors can be reduced using AC modulation magnetic fields. [2] In this study, a much smaller AC modulation amplitude is used for lower overall power consumption of TMR sensors and the linear response range of the sensors under a small modulation field is investigated. The magnetic tunnel junction (MTJ) stack in the studied TMR sensor was designed as Si/150 SiO₂/ 1.5 Ta/25 Ru/7 Ir₂₀Mn₈₀ / 2.2 Co₃₀Fe₇₀ /0.85 Ru/ 2.8 Co₄₀Fe₄₀B₂₀/ 2 MgO /1.3 Co₄₀Fe₄₀B₂₀ / 0.6 MgO/ 50 Co₄₀Fe₄₀B₂₀/2 Ta/15 Ru (in nm). The TMR ratio is about 180 % and the coercivity of the free layer is about 0.5 mT after magnetic annealing at 340 °C for 2 hour. The MTJs were connected into a Wheatstone bridge to form a sensor. An alternating current driven modulation coil was added surrounding the TMR sensor during magnetic field measurement with the AC modulation field applied along the sensing direction. The DC voltage output of the TMR sensor with different measurement conditions is shown in Fig. 1. The sensor was powered by a 1.5 Volt battery and a sinusoidal modulation field was applied with a frequency of 1 kHz and an amplitude of 0.3 mT. The output voltage of the sensor was measured in these DC magnetic field ranges: (a) -3 mT to 3 mT, marked in black in the figure, (b) -1.8 mT to 1.8 mT, marked in green, (c) -0.6 mT to 0.6 mT, marked in blue, and (d) -0.1 mT to 0.1 mT, marked in red. The figure shows that magnetic hysteresis in TMR sensor was effectively reduced if measured in a small range of DC magnetic field. With the amplitude of AC modulation field being as small as 0.3 mT, the sensor exhibits a linear response in the range of -0.6 mT to 0.6 mT, where the sensitivity is 20.6%/mT. It's demonstrated that based on a simple construction, TMR sensors with small AC modulation fields can be used for low field sensing with good linearity. ACKNOWLEDGMENT This work was supported by Ministry of Science and Technology of Taiwan under grant number: 108-2314-B-003 -001 and 109-2314-B-003 -004. The MTJ samples were prepared in the Nebraska Nanoscale Facility: National Nanotechnology Coordinated Infrastructure and the Nebraska Center for Materials and Nanoscience, which are supported by the National Science Foundation under Award ECCS: 2025298, and the Nebraska Research Initiative.

[1] Zheng, C. et al. Magnetoresistive Sensor Development Roadmap (Non-Recording Applications). IEEE Trans. Magn. 2019, 55, 1–30. [2] S. Liao et al., "Hysteresis Reduction in Tunneling Magnetoresistive Sensor with AC Modulation Magnetic Field," IEEE Transactions on Magnetics,(2020) doi: 10.1109/TMAG.2020.3009900.

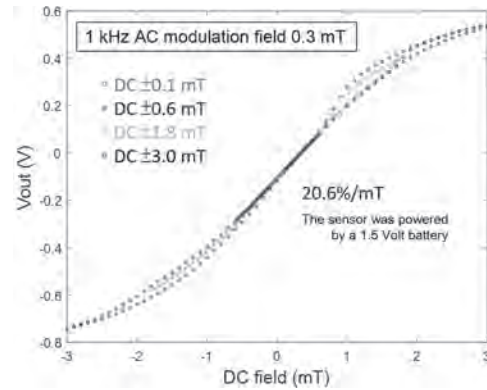


Fig.1 The output voltage of the sensor as a function of the applied DC magnetic field in the range of four conditions: -0.1 mT to 0.1 mT, -0.6 mT to 0.6 mT, -1.8 mT to 1.8 mT, and -3 mT to 3 mT. The sensor was powered by a 1.5 Volt battery and a AC modulation field was applied with a frequency of 1 kHz and an amplitude of 0.3 mT for all conditions of DC field range.

IS-15. Proposal of Inspection Method for Lift-Off and Surface Hardened Depth of Induction Hardened Steel Plate Using by Alternating Magnetic Field.

T. Yoshinaga¹, K. Murai², Y. Gotoh², S. Onita³, T. Horino³ and Y. Misaka³
 1. Mechanical and Energy Systems Engineering, Oita University, Oita, Japan; 2. Department of Innovative Engineering, Oita University, Oita, Japan; 3. Research and Development Headquarters, Koshuha Netsuren Kabushiki Kaisha, Hiratsuka-shi, Japan

Introduction Induction hardening treatment is used for a variety of steels because of its short hardening time and ability to hardened steel with complex shapes. In this research, the non-destructive inspection method for the hardened depth in surface of the induction hardened steel plate by an electromagnetic sensor is investigated. The hardened depth in surface of the steel plate is measured by detecting the difference in the permeability and the conductivity between the hardened and the non-hardened layers inside the steel plate by the electromagnetic sensor [1,2]. On the other hand, the detection signal in the electromagnetic sensor is also affected by the changing in the distance (L_o : Lift-off) between the surface of the induction hardened steel plate and the sensor. Therefore, the method for simultaneously measuring the surface hardened depth in the hardened steel plate and the lift-off is proposed. The model and the evaluation method Fig.1 shows the 1/2 region of the proposal inspection model for detecting the surface hardened depth in the surface hardened steel plate of SCM440 steel material. The proposal electromagnetic sensor is consisted of an electromagnetic yoke made of laminated silicon steel plate, an alternating excitation coil, and two types of detection coils. The z-direction of the flux density (B_z) inside the magnetic yoke is detected by the z-direction detection coil on one leg of the yoke, and the x-direction magnetic field distributed (B_x) between the two legs of the yoke is detected by the x-direction detection coil. Since the permeability and conductivity in the hardened layer are lower than that of the non-hardened layer, the flux density in the x- and z- direction of these detection coils is changed when the hardened depth is changed. However, even if the depth of the hardened layer is constant, their detected magnetic flux in these detection coils is changed when the lift-off is changed. Therefore, both the lift-off and the surface hardened depth are estimated by the B_x and B_z . 3-D electromagnetic FEM considering the nonlinearity of magnetic properties The flux density and eddy current inside the surface hardened steel plate are calculated by 3-D nonlinear finite element method (FEM) taking account of the initial magnetization curve and conductivity of the hardened and non-hardened layers in the steel. In an induction hardened steel plate, there is an intermediate layer called a heat-affected zone between the hardened and non-hardened layers. Therefore, in this analysis, the initial magnetization curves and conductivity inside the intermediate layer are calculated by linear interpolation of the initial magnetization curves and conductivity of the hardened and non-hardened layers. Measurements results and estimates Fig.2 shows the obtained values of B_x and B_z in the two detection coils when the hardened depth (D) and L_o are changed, respectively. This figure denotes that if L_o is constant, B_x is increased and B_z is decreased when D is increased. This is, because the flux density B_z inside the magnetic yoke is decreased, and the B_x distributed between both feet of the yoke is increased, since the permeability and conductivity in surface domain of the steel plate is decreased when the D is increased. On the other hand, if D is constant, B_x is increased and B_z is decreased when L_o is increased. This is, because the flux density B_z in the closed magnetic path between the sensor and the steel plate is reduced when the L_o is increased, and the magnetic flux B_x distributed between both feet of the yoke is increased. The figure shows that the signals of B_x and B_z due to the changes of D and L_o are distinguished. Therefore, Both D and L_o are inspected by the linear interpolation using measured B_x and B_z . Table 1 shows the interpolated results of D and L_o using the $B_x - B_z$ plane of Fig.2. The measured values are almost in agreement with the obtained ones. The table illustrates that both D and L_o can be detected from the B_x and B_z in two detection coils. Conclusions The results obtained are summarized as follows: (1)It is possible to estimate the depth (D) of surface hardened steel plate by detecting the change of flux density in two detection coils due to the difference of the permeability and the conductivity in the steel with and without hardened layers. However, the flux density detected by the search coil is influenced by the change of both lift-off and depth of surface hardened steel.

(2)The flux density (B_x) in the detection coil of x-direction is increased and the flux density (B_z) in the detection coil of z-direction is decreased when the surface hardened depth (D) of the induction hardened steel or the lift-off (L_o) are increased. However, the signals of B_x and B_z in two detection coils due to the changes of D and L_o are distinguished. Therefore, it is possible to inspect the D of the surface hardened steel without the influence of L_o by detecting both the B_x and B_z of two detection coils in the proposed inspection sensor.

[1] Y. Gotoh, S. Onita, T. Horino, and Y. Misaka, "Detecting Method of Hardened Depth in Surface Hardened Steel by Magnetic Field on Steel", *IEEE Transactions on Magnetics*, vol.54, no.11, Article Sequence Number:6202404, 2018. [2] Y. Gotoh, K. Sakurai, N. Takaoka, Y. Misaka, K. Kawasaki, and N. Takahashi, "Proposal of Electromagnetic Inspection Method of Hardened Depth of Steel using 3-D Nonlinear FEM Taking Account of Hysteresis", *IEEE Transactions on Magnetics*, vol.47, no.10, pp.3546-3549, 2011.

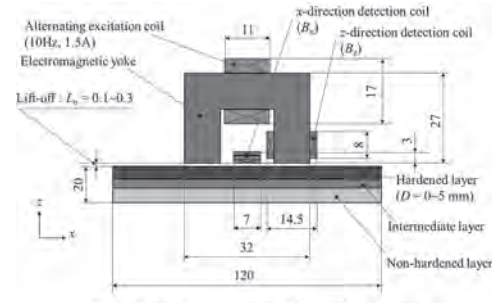


Fig.1. Proposal inspection model (x-z plane 1/2 region).

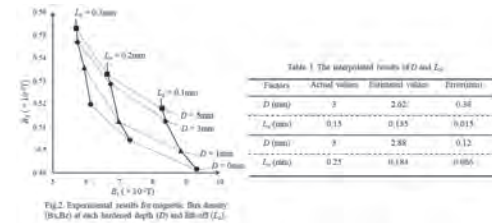


Fig.2. Experimental results for magnetic flux density (B_x, B_z) at each hardened depth (D) and lift-off (L_o).

Factors	Actual values	Interpolated values	Errors(mm)
D (mm)	3	2.82	0.18
L_o (mm)	0.15	0.145	0.015
D (mm)	3	2.88	0.12
L_o (mm)	0.25	0.184	0.066

Fig.2. Experimental results for magnetic flux density (B_x, B_z) at each hardened depth (D) and lift-off (L_o). Table 1. The interpolated results of D and L_o .

IS-16. Voltage Tuning of a Bridge-Structured Spin Valve Magnetoresistance Sensor With Enhanced Output Performance.

L. Liu¹, Y. Hui¹, H. Jiang¹, K. Wang¹, K. Dong¹, W. Mo¹, J. Song¹ and F. Jin¹

1. China University of Geosciences School of Automation, Wuhan, China

In this letter, a bridge-structured spin valve giant magnetoresistance (SV-GMR) sensor design that allows for voltage tuning of the output performance is proposed by the micro-magnetic simulation. The bridge structured ferromagnet (FM)/Cu/NiFe/IrMn SV-GMR sensor on a piezoelectric substrate is investigated. We made a systematic study for uniaxial magnetic anisotropy constant (K) and spin polarization (P) on the influence for the sensor properties. When K varies between 2×10^4 J/m³ and 10×10^4 J/m³, the output performance can be significantly manipulated. The linear range alters from 350 Oe to 690 Oe, the linearity error is reduced from -0.945% to -0.977%, and the sensitivity is tuned by almost 5 times, by applying an electric field of 14 kV/cm. When P varies between 0.2 to 1.0, the sensitivity increases linearly from 6.48×10^{-5} to 3.38×10^{-4} with a decrease of linearity error from -0.96% to -0.797%. The electrically tunable GMR sensor integrates the advantages of materials properties with magnetostrictive and spin polarizability, which is sensitive to output performance, therefore exhibiting great potential for applications in the internet of things.

Session IT
NON-DESTRUCTIVE EVALUATION & OTHER SENSORS II
(Poster Session)

Nicholas Jones, Chair
Naval Surface Warfare Center, Carderock Division, Bethesda, MD, United States

IT-01. High Spatial Resolution Flaw Detector Based on the GMR Eddy-Current Probe.

H. Nguyen¹, J. Jeng¹, V. Doan¹, C. Dinh¹, D. Dao¹ and T. Pham¹
 1. Department of Mechanical Engineering, National Kaohsiung University of Science and Technology, Kaohsiung City 807618, Taiwan

In recent years, the non-destructive inspection (NDI) method based on the eddy-current (EC) effect is increasingly playing an important role in many applications. The advancement in the EC NDI techniques with the miniature magnetic field sensors enables the size estimation of small magnetic particles and the detection of deep-lying defects, such as cracks, metal loss, and other mechanical damages, in highly conductive metals. Several solutions of the field-detection based EC NDI have been developed based on the combination of an excitation coil and magnetic sensors such as Hall, giant-magnetoresistance (GMR), or superconducting quantum interference device (SQUID) sensors. The high-sensitivity and cost-effect solutions are the technique with GMR sensors, which are suitable for many different applications, including the defect evaluation in the related industries [1]-[3] and the electronic compass in consumer electronics [4]. The reliability and capability of GMR sensors for defect detection have been demonstrated by using the eddy-current probe with packaged GMR sensor arrays [2] or a single chip having double-coil excitation [3]. However, the usage of the GMR sensor with a big excitation coil is not suitable for the applications for which the space for scanning the probe is small. Furthermore, the linear arrangement of elements in the array [3] makes it suitable only to the specimen with a flat surface. Further improvement in the design of the GMR EC probe should be made to enhance the sensitivity and accuracy in flaw characterization. In this work, we proposed a novel design of miniature differential EC probes consist of a GMR bare-die sensor and a tiny coil. The schematic diagram for the high spatial resolution GMR EC probe is shown in Fig. 1. This probe consists of a tiny excitation coil with a small feature size of less than 3 mm. The GMR sensor is the GF708 bare die from Sensitex GmbH. The chip layout is a Wheatstone bridge circuit with four spin-valve magnetoresistance elements, as shown in the inset of Fig. 1. The sensitivity of the two active elements, R_1 and R_2 , are enhanced by the soft magnetic flux concentrator films, while the two reference elements, R_0 , are shielded by the same soft magnetic films. The output voltage of the GMR bridge sensor can be expressed as: $V_{ab} = V_{cc} \{R_0/[R(H)+R_0] - R(H)/[R_0+R(H)]\}$ (1) where $R(H)$ is the transfer curve modeled as a hyper-tangent function of the magnetic field H on R_1 and R_2 [4]. The GMR chip is 1 mm in width and 1.4 mm in length, and the sensing axis is along the width of the chip. It is mounted on the edge of a printed circuit board (PCB). A special aluminum wire bonding technique is developed to connect the terminals of the GMR sensor onto both sides of the PCB. With this technique, the distance from the chip surface to the sample surface can be reduced to within 0.2 mm. The sensor surface is perpendicular to the PCB and parallel to the sample surface. The sensing direction of the GMR chip is parallel to the specimen surface and perpendicular to the vertical excitation field. With this arrangement, the GMR chip acts like a gradiometer sensitive to the gradient of the defect field. The miniature chip-and-coil assembly and the short lift-off distance effectively enhance the spatial resolution in flaw detection with the GMR EC probe. To test the spatial resolution in the detection of the defect signal, the sample was placed on the translation stage controlled by the 08TMC-2 motor controller from Unice E-O Services Inc. To scan for the simulated defect in the sample. The GMR EC probe is driven by a 100-kHz sine wave voltage provided by a function generator. The differential output of the probe is measured by a low noise preamplifier and transmitted to the lock-in amplifier to analyze the amplitude and phase of the EC signal. The spatial distribution of the signals was digitized in real-time by a data acquisition (DAQ) module USB-6216 from National Instruments and recorded by the computer. An in-house developed C# program is used to set the scanning range, velocity, and step size as well as to receive the eddy-current signal taken by the DAQ device. The experiment is performed on an aluminum plate with machined slots to simulate the cracks of different depths of 0.1, 0.3, 0.5, 1.0, 1.5 and 1.8 mm and the same width of 0.2 mm. The B-scan image with a lift-off distance of 0.2 mm between the probe and the specimen is shown in Fig. 2. It can be seen that the cracks on the aluminum plate are detected and the position of cracks coincides with the change in the in-phase (Re) and quadrature (Im)

of the output voltage (V_{out}). The amplitude for the integration of V_{out} over the spatial coordinate x is roughly proportional to the depth of cracks. The full width at half maximum of each peak near the crack is less than 2 mm, which has achieved the physical limit set by the lateral size of the probe. The phase plot shows that all of the surface cracks deeper than 0.1 mm can be clearly identified. The result shows that the developed EC probe is suitable for the quantitative evaluation of the geometrical characteristics, such as shapes, sizes and positions of the machined defects on the metallic sample, with a high-spatial resolution. This work is supported by the Ministry of Science and Technology of Taiwan under Grant Nos. MOST108-2221-E992-083MY2 and MOST 107-2221-E-992-094.

[1] D. Rifai, A. N. Abdalla, K. Ali, & R. Razali, "Giant magnetoresistance sensors: A review on structures and non-destructive eddy current testing applications", *Sensors*, 16(3), 298 (2016). [2] O. Postolache, A. L. Ribeiro, and H. G. Ramos, "GMR array uniform eddy current probe for defect detection in conductive specimens", *Measurement*, 46(10), 4369-4378 (2013). [3] Andrea Bernieri, Luigi Ferrigno, Marco Laracca, and Antonio Rasile, "Eddy Current Testing Probe Based on Double-Coil Excitation and GMR Sensor", *IEEE Transactions on Instrumentation and measurement*, vol. 68, no. 5, pp. 1533 – 1542(2019). [4] V. S. Luong, Y.-H. Su, C.-C. Lu, J.-T. Jeng, J.-H. Hsu, M.-H. Liao, J.-C. Wu, M.-H. Lai, C.-R. Chang, "Planarization, Fabrication and Characterization of Three-dimensional Magnetic Field Sensors", *IEEE Transactions on Nanotechnology*, Vol. 17, no. 1, pp.11 - 25 (2018).

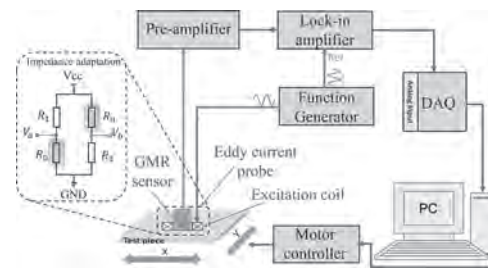


Fig. 1. High spatial resolution GMR EC probe.

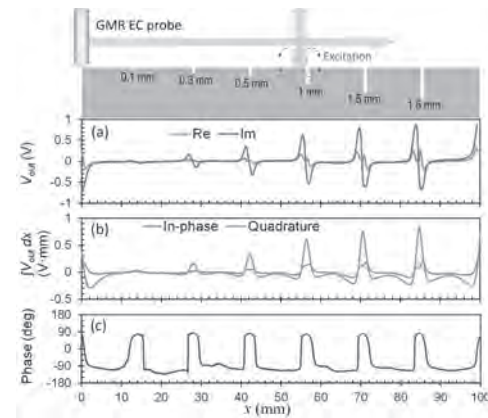


Fig. 2. The integral phase for the output voltage of EC probe when scanning on the aluminum plate.

IT-02. Inspection Device Using MFL Sensors for Buried Pipe Inspection to Find all Cracks Regardless of Direction.

C. Heo¹ and G. Park¹

1. Pusan National University, Kumjeong-ku, The Republic of Korea

Energy sources used in industries, such as gas and oil, are mainly transported through buried pipes. If an energy source leaks out from the pipe due to corrosion or cracks, an accident such as an explosion may occur, so it is very important to periodically inspect the buried pipes. Since cracks have the risk of the pipe being torn, it is important to look for cracks in pipe inspection. There are several methods for inspecting buried pipe, such as ultrasonic testing(UT), and magnetic flux leakage testing(MFL). UT method is often used for various inspections including pipe inspection due to their very high accuracy, but has the disadvantage of slow inspection speed and high battery consumption. Buried pipes are connected up to tens to hundreds of kilometers at a time, so long-distance inspections are required for pipe inspection. UT, which has a slow inspection speed and high battery consumption, has limitations in the inspection of buried pipes. On the other hand, the MFL method using MFL sensors has little battery consumption except for the power used for the sensor, the inspection speed is relatively fast, and the defect detection accuracy is high. However, because the width of the crack is very narrow, the crack in the same direction as the magnetic field direction hardly affects the flow of magnetic flux, and there is almost no leaked magnetic flux due to the crack in the same direction as the magnetic field direction. That is, conventional MFL inspection devices such as axial MFL(AMFL) and circumferential MFL(CMFL), which allow magnetic flux to flow in only one direction in the pipe, hardly find cracks in the same direction as the magnetic flux direction[1]-[2]. Fig.1 is here Conversely, if the MFL inspection device is used to allow magnetic flux to flow in various directions in the pipe, it has the advantage of MFL method and can find all cracks regardless of direction. This paper proposes an MFL inspection device that allows magnetic flux to flow through a pipe in various directions and can find all cracks regardless of the direction. Fig. 2 shows the comparison of the magnet placement and magnetic flux direction of the AMFL, CMFL, and the proposed MFL inspection device. Fig.2 is here As shown in Fig. 2(a) and (b), the magnetic flux flows only in the axial and circumferential directions of the conventional MFL inspection devices, AMFL and CMFL, respectively. In contrast, the proposed MFL inspection device arranges the magnets differently from the conventional MFL inspection device, so that the magnetic flux flows in the diagonal and circumferential directions. When the magnetic flux flows through the pipe in two directions using the proposed MFL inspection device, the cracks in the circumferential direction can be detected at the section where the magnetic flux flows in the diagonal direction, and the cracks in the diagonal direction can be detected at the section where the magnetic flux flows in the circumferential direction. In other words, even if there are cracks that can't be found in the section where the magnetic flux flows in a specific direction, the cracks can be found in the section where the magnetic flux flows in the other direction. As a result, all cracks can be found regardless of the direction using the proposed MFL inspection device. The reason why the MFL method can't find cracks in the same direction as the magnetic flux direction and details of the proposed MFL inspection device will be covered in full paper.

[1] M. Rostami Kandroodi, B. Nadjar Araabi, and M. Nili Ahmadabadi, in *IEEE Transactions on Magnetics*, Vol. 53, No. 3, pp.1-10(2017) [2] H. M. Kim, C. G. Heo, and G. S. Park, in *IEEE Transactions on Magnetics*, Vol. 54, No. 11, pp.1-5(2018)



Fig. 1. The magnetic flux leakage pipe inspection devices. (a) AMFL[1] (b) CMFL[2].

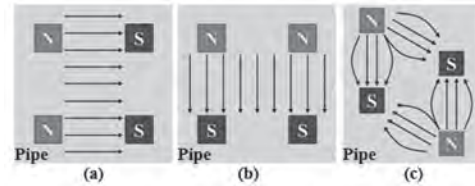


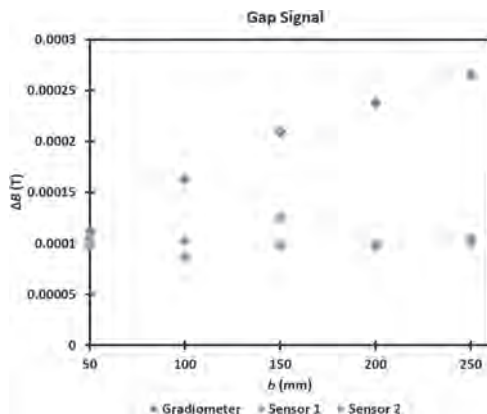
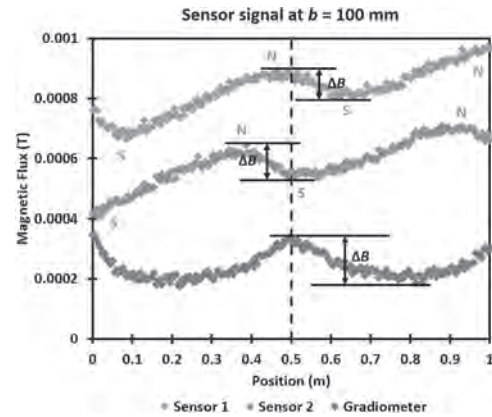
Fig. 2. The magnet placement and the magnetic flux direction of (a) AMFL. (b) CMFL. (c) the proposed MFL inspection device.

IT-03. Detection of Gap in Steel Bars by Magnetic Tunnel Junction Sensor Gradiometer Based Magnetic Flux Leakage Testing Method.

M.b. Mohd Noor Sam¹, J. Zhenhu¹, M. Oogane¹ and Y. Ando¹
 1. Applied Physics, Tohoku University, Sendai, Japan

Magnetic flux leakage (MFL) testing is a widely used method for detection of defects such as the metal loss due to the corrosion in steel bars located in reinforced concrete. The magnetic flux leak caused by the defect is then measured by a magnetic sensor, which gives information to the user of the presence of the defect [1]. For small defects, it is difficult for the sensor to determine the presence and location of the defects. Therefore, we propose a gradiometer measurement setup [2] using highly sensitive magnetic tunnel junction (MTJ) sensors, which is based on the tunnel magnetoresistance (TMR) effect, to increase the magnitude of the measured signal. In this work, 2 MTJ sensor modules were used to measure a gap of 0.1 mm between two steel bars (diameter = 20 mm, length = 500 mm). The length of the overall specimen is 1000 mm, where the gap is at the 500 mm mark (touching point of the two steel bars). The MTJ sensor modules consist of each sensor connected in a full-bridge circuit [3]. The signal is then passed through an amplifier circuit and low pass filter to further reduce noise in the measured signal. A robot is then used to move the sensor along the steel bars at a speed of 50 mm/s, measuring the magnetic flux signal. The lift-off value for the overall measurement is set at 50 mm. Before each measurement, the steel bars are magnetized using a solenoid (approximately 1.52 mT). A planar gradiometer setup was used, whereby the MTJ modules are placed in the same x-axis. The effect of the baseline (b), the distance between the first and second MTJ sensor module, was investigated ($b = 50, 100, 150, 200$ mm). From the results, the overall magnitude of the gradiometer sensor signal showed an increase, almost twice as large as the single sensor module signal (Figure 1). Furthermore, the gradiometer sensor signal produced a single peak response (gap is right above the peak), in contrast to the single sensor signal which produced a sine-like wave response (gap is between the peak and trough) (Figure 2). This is helpful in terms that the location of the gap can be determined in real time. For the estimated gap location, a loss in accuracy was observed in all the signals, with the most accurate location determined for $b = 100$ mm. We demonstrated that a planar gradiometer setup consisting of 2 MTJ sensors could improve the overall signal value of the measurement setup resulting in an easier way to determine the location of a 0.1 mm gap at 50 mm lift-off. The results obtained from this research are expected to contribute to the further application of MTJ sensors not only in MFL testing but in other fields of magnetic-based non-destructive testing. This work was partly supported by the Center of Innovative Integrated Electronic Systems (CIES) and the Center for Spintronics Research Network (CSRN). The sensors were provided by Mr. Kosuke Fujiwara from Spin Sensing Factory (SSF).

[1] Hirose, M, Maeda, T, Matsuda, K, Yokota, M, Hattori, A, and Miyagawa, T, J. Stru. Eng., 58A, p.867-878 (2012). [2] W. Dehui, S. Lingxin, W. Xiaohong, and L. Zhitian, J Nondestruct Eval., 36, p.24 (2017). [3] J. Cao, and P.P Freitas, J. Appl. Phys., 107, 09E712 (2010).



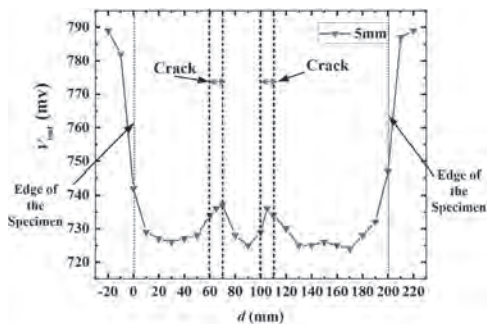
IT-04. An Electromagnetic non-Destructive Method for Crack Detection Based on Magnetolectric Sensors.

C. Leung¹ and K. Wu¹

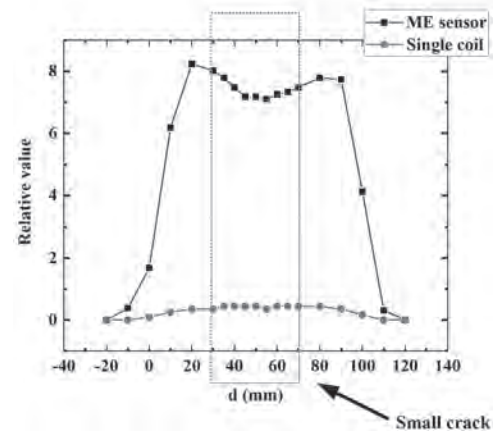
1. Harbin Institute of Technology Shenzhen, Shenzhen, China

Non-destructive detection methods are widely used in the industry and science in order to evaluate the injuring and aging conditions of materials using in various applications of aircraft, gas pipes, and cables without causing any physical damages [1]. While many methods of non-destructive testing such as eddy current, magnetic particle, or radiographic and ultrasonic can detect the failure and cracks in conductive metals, the most efficient and effective method is based on eddy current testing [2]. Without the safety flaws and coupling agent, eddy current testing allows technicians to perform rapid and convenient inspections of the crack problems in conductive metals without sacrificing accuracy. Accordingly, for the past few decades, many researchers' attention was focused on improving the design structure of traditional coil sensors to improve the accuracy of the eddy current testing. However, among many well-known methods, it is impossible to find a small-size, low power consumption, low-noise, and giant output magnetic detection coils, which motivates engineers to look for new devices. Compared with the coil sensors using in eddy current typed non-destructive testing, Magnetolectric (ME) laminate-made sensors have advantages of higher sensitivity, higher linearity, lower noise, lower dimension size, and simpler structure of sensors which make it most promising for magnetic field detection in eddy current testing [3]. In this paper, a ME sensor composited of Metglas/PZT laminate has been proposed to replace the traditional detection coil for non-destructive eddy current testing. In detail, two types of ferromagnetic and nonferromagnetic conductive metals were used in the experiments for comparing the detection ability of failure and crack in materials between our proposed ME laminate and traditional coil sensors. Under the same excitation current of 10mA and lift-off distance of 5 mm between target and sensor, the non-destructive detection system based on our proposed ME sensors produced 10 times higher detection ability compared with a traditional single detection coil at the crack size <5mm in length. Besides, the length and depth of cracks can be determined by using a numerically analyzing technique based on the output signal of the ME non-destructive system. These findings enabled the possibility of the ME sensors in the high resolution and rapid detection for the finding and analysis of the crack problem in conductive metals.

[1] Janousek, L., Capova, K., Yusa, N., & Miya, K. (2008). Multiprobe inspection for enhancing sizing ability in eddy current nondestructive testing. *IEEE transactions on magnetics*, 44(6), 1618-1621. [2] García-Martín, J., Gómez-Gil, J., & Vázquez-Sánchez, E. (2011). Non-destructive techniques based on eddy current testing. *Sensors*, 11(3), 2525-2565. [3] Ripka, P., & Janosek, M. (2010). Advances in magnetic field sensors. *IEEE Sensors journal*, 10(6), 1108-1116.



The output voltage (V_{out}) of the crack detection based on the magnetolectric (ME) sensor working in linear-mode searching.



The comparison of relative output detection value between the magnetolectric (ME) laminate and single-coil sensor under the same excitation condition.

IT-05. A Study on the Estimation of the Shapes and Distance of External Metal Around Underground Pipeline Using Magnetic Flux Leakage Sensors.

C. Heo¹, H. Jeong¹ and G. Park¹

1. Pusan National University, Busan, The Republic of Korea

Non-destructive testing(NDT) is a method that detects discontinuous boundaries or defects that exist inside and outside of pipes without damaging or destroying pipe[1]. The magnetic flux leakage(MFL) method, one of the most representative NDT methods, uses permanent magnets to saturate the ferromagnetic pipe by applying a large magnetic field to the pipe and measure the leakage magnetic flux signal around the defect. Because the MFL signal contains information about the size and shape of the defect, an algorithm can be created to estimate the shape of the defect through analysis[2]-[3]. In general, many studies on non-destructive testing, including the MFL method, mainly focus on detecting defects or cracks in pipeline. However, not only defects but also metal objects outside the pipe affect the condition of the pipe. When external metal contact with the pipe wall, corrosion is more prone to the metal contact area on the pipe. In addition, pipes used in industry are coated with thick plastic to block contact with oxygen or external metal, However, the external metal damages the plastic coating. If a hole is made in the plastic coating of the pipe due to external metal, it is more prone to corrosion by contacting the pipe with oxygen as well as the external metal. Therefore, it is necessary to study not only defects but also detection of metal existing outside the pipe. Analysis of external metals requires research not only to prevent corrosion but also to prevent theft of energy sources in pipes such as oil and gas. People who steal energy sources eventually drill holes in pipes through which the energy source flows, and use metal pipes to steal the energy source. Metal pipe for theft can eventually be found through external metal analysis, so analysis of external metal also helps prevent theft of energy sources. Because the MFL method uses a large magnetic field, it is easier to detect and analyze external metals than other NDT methods. Fig.1 is here This paper analyzes the MFL sensor signals according to the shape and distance of external metal around underground pipeline, and presents an algorithm that estimates the shape and the distance of the external metal to the pipe using the MFL sensor signal. Fig. 2 shows the magnetic flux and the magnetic flux density distribution when there is a defect or external metal, respectively. Fig.2 is here When a defect occurs in the pipe, the cross-sectional area through which the magnetic flux passes decreases, and the magnetic flux flowing through the pipe leaks out of the pipe. In other words, when a defect occurs in the pipe, the magnitude of the signal detected by MFL sensors increases. Conversely, when external metal contacts the pipe, the cross-sectional area through which the magnetic flux passes increases, and the amount of magnetic flux leaking out of the pipe decreases. That is, when external metal contacts the pipe, the magnitude of the signal detected by MFL sensors decreases. In addition, like defects, when the shape or distance of the external metal changes, the size or shape of the signal detected by the MFL sensors also changes. As a result, the shape and distance of the external metal can be estimated by applying the signal change tendency and the defect shape estimation algorithm[2]-[3].

[1] M. Rostami Kandroodi, B. Nadjar Araabi, and M. Nili Ahmadabadi, in *IEEE Transactions on Magnetics*, Vol. 53, No. 3, pp.1-10(2017) [2] H. M. Kim, C. G. Heo, and G. S. Park, in *IEEE Transactions on Magnetics*, Vol. 54, No. 11, pp.1-5(2018) [3] H. M. Kim, and G. S. Park, in *IEEE Transactions on Magnetics*, Vol. 50, No. 2, pp.109-112(2014)

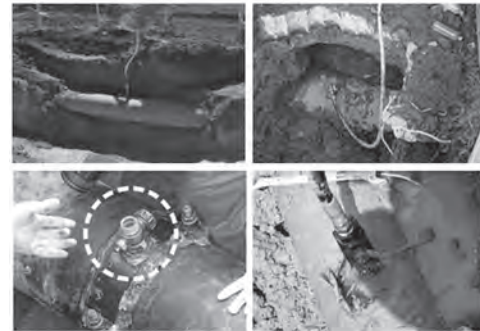


Fig.1. Photographs of external metal and pipes

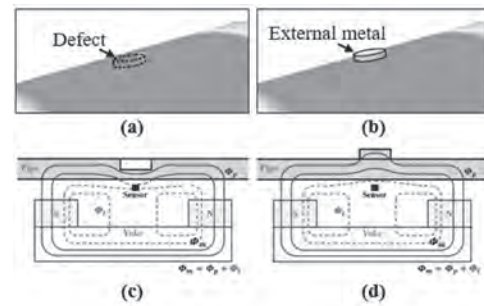


Fig.2. Distribution of magnetic flux density around (a) the defect. (b) the external metal. Diagram of magnetic flux line around (c) the defect. (d) the external metal.

IT-06. Multimodal Magneto-optic Sensing of Magnetic Field, Electric Current and Temperature.

F. Klingbeil¹, S. Stölting¹ and J. McCord¹

¹. Institute for Materials Science, Kiel University, Kiel, Germany

Temperature measurements are vital in laboratory and industry settings. For that reason, many different measurement methods exist. Common temperature sensors are based on thermistors, resistance temperature detectors, thermocouples, semiconductors and fiber optics. Optical sensor technologies possess advantages for electrical measurements and analysis in high voltage applications like monitoring in smart grids, ranging from several Hz to some kHz in frequency. In general, in such systems current measurements are based on sensing the magnetic field generated by the electric current rather than the current itself. By this, possible electric hazards are eliminated, and a natural galvanic separation is built into the sensing system. Optical magnetic field or direct current measurement systems have been realized through fiber-optic current sensors, based on an optical fiber around a current conductor¹, bulk magnetic garnet materials², or single or stacked garnet thin films³. We demonstrate magneto-optical measurement schemes based on the Faraday effect for relating magnetic and micromagnetic features to magnetic field, electrical current and temperature⁴. For that, we use magneto-optical active only micrometer thin iron garnet film. The garnet film has a large Verdet constant (Faraday effect) together with a low absorption coefficient. The magneto-optical Faraday effect sensitivity of the magneto-optical indicator film is $1.8^\circ/\text{mT}$ at room temperature. The polarimetric magneto-optical read-out is realized in a non-contact optical arrangement. For the measurements, the magnetic state of the garnet sensor is modulated through a low noise current amplifier and the magneto-optical response signal is acquired through a lock-in amplifier. The thin film sensor element has the ability for high sensitivity magnetic field and naturally electrical current sensing capabilities over a many magnitudes of field and current. High-resolution magnetic field sensitivities down to the nanotesla regime are demonstrated as shown in Fig. 1. For the micrometer thick garnet films we demonstrate a magnetic field detection limit of better than $20 \text{ nT/Hz}^{0.5}$ and an electrical current detection limit of $3 \text{ mA/Hz}^{0.5}$. These values are achieved over several orders of magnitude of magnetic field frequencies into the kHz regime. The magneto-optical response at small magnetic field amplitudes originates from small magnetic angle rotations inside the magnetic domain walls. Different schemes for the measurements of temperature are evaluated. In all cases the range of application is defined by the Néel temperature of the sensing garnet material⁵. Exemplary results of temperature sensing based on variations in the magnetic domain wall susceptibility with temperature, from analyzing the resulting magneto-optical signal amplitude in a magnetic modulation field, are shown in Fig. 2. Temperatures are derived with high accuracy of 0.1°C across a wide temperature range. Overall, we propose and demonstrate a multimode magneto-optical temperature sensor relying on combined magneto-optical Faraday effect amplitude variations with the related physical properties. The sensing range spans many orders of signal amplitude and a wide frequency range with equal sensitivity and a limit of detection. Temperatures are derived with high accuracy across a wide temperature range. The measurement schemes can be extended to the use of other magnetic sensing materials. These include ferromagnetic and ferromagnetic films with lower or higher Néel temperatures or Curie temperatures. The magneto-optical sensor allows for measuring magnetic field, direct electrical current, and temperature without electrical connection and will therefore be especially useful in applications requiring resistance to electrical noise. This work was funded by the German Research Foundation (DFG) through grant no. MC 9/20-1.

1. R. Silva, H. Martins, I. Nascimento et al., *Applied Sciences*, Vol. 2, p. 602-628(2012) 2. B.J.H. Stadler, and T. Mizumoto, *IEEE Photonics Journal*, Vol. 6, p.1-15(2014) 3. A. Garzarella, M.A. Shinn, and D.H. Wu, *Appl. Phys. Lett.*, Vol. 108, p.241101 (2016) 4. F. Klingbeil, S. D. Stölting and J. McCord, *Appl. Phys. Lett.*, (under review) 5. M. Kustov, R. Grechishkin, M. Gusev et al, *Adv. Mater.*, Vol. 27, p.5017 (2015)

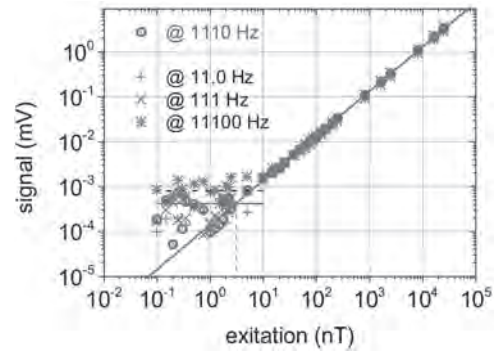


Fig. 1 Exemplary limit of detection plot for a base-to-peak magnetic field H_{ac} amplitude with a frequency of $f_H = 1110 \text{ Hz}$.

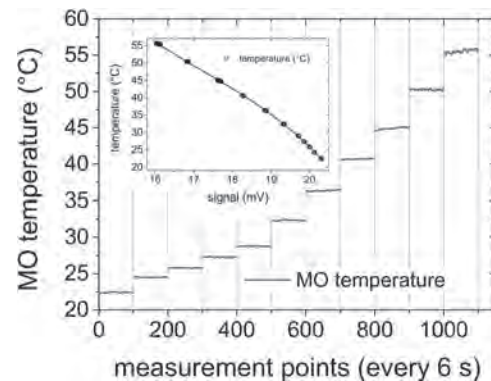


Fig. 2 Magneto-optically measured temperature derivation with varying temperature. The inset shows the corresponding change of the magneto-optical signal amplitude versus a thermocouple temperature used for calibration.

IT-07. Tunnel Magnetoresistance Sensors for Real-Time Detection of Magnetic Nanoparticles.

C. Ghemes¹, M. Tibu¹, O. Dragos-Pinzaru¹, M. Lostun¹, N. Lupu¹ and H. Chiriac¹

1. National Institute of Research and Development for Technical Physics, Iasi, Romania

Due to their special features such as low background noise, high sensitivity, and the possibility of nanoscale fabrication, magnetoresistive (MR) sensors present a great interest for the scientific community, being used especially in biomedical applications [1]. Among MR sensors, those based on tunnel magnetoresistance (TMR) effect exhibit the highest magnetoresistance value, higher sensitivity, and lower power consumption [2, 3]. However, shortcomings as weak linearity in the variation of electric resistance with the applied magnetic field, high coercive field, or quite complicated fabrication process, make the TMR sensors less investigated for biosensing applications. The purpose of this work is to develop a model of TMR based sensor, with small size and high sensitivity, capable of real-time detection of magnetic particles, with possible applications in the detection of magnetic particles from tissues in hyperthermia. The operation of the sensor will be done without magnetic flux concentrators or permanent magnets, therefore no additional steps in the technological process are required. In order to obtain a TMR structure with high values of magnetoresistance and sensitivity, the thicknesses of the component layers were optimized reaching the final configuration: Ta (5 nm)/Ru (20nm)/Ta (5 nm)/CoFe (3 nm)/IrMn (20 nm)/CoFe (2.5 nm)/Ru (0.85 nm)/CoFeB (3 nm)/MgO (1.8 nm)/CoFeB (3 nm)/Ta (10 nm). The thin layers were deposited on Si/SiO₂ support (18 x 18 mm²), using the ATC 2200 / AJA International deposition system, which allows both magnetron sputter deposition and electron beam evaporation. Excepting the MgO barrier layer, which was deposited by electron beam evaporation, all other thin layers were obtained by magnetron sputter deposition at a working pressure of 3 mTorr. To induce an in-plane easy axis in the ferromagnetic layers, a magnetic field (100 Oe) parallel to the plane of the thin films, was applied during the deposition. As a detection element, we proposed a structure with a low aspect ratio in the shape of a cylindrical pillar with 4 μm diameter. The total size of each device (sensor and contacts) is 400x250 μm², as depicted in Fig. 1(a). These small dimensions allow the fabrication of 100 sensors onto single support of 18x18 mm², leading to a simplification of the technological process. In the first step of the sensor microfabrication, rectangular structures of 40x80 μm² (Fig. 1(b)) were patterned by e-beam lithography, then ion beam milling and removing of e-resist. The detection element (pillar) and contact surfaces, were defined by electron beam lithography and ion beam milling. In order to passivate the lateral sides of the pillar, 60 nm of insulating layer (SiO₂) was sputter-deposited, then the resist and SiO₂ from the top of the pillar and contact surfaces were removed by lift-off technique. For measurements, the CPP (“current perpendicular to plane”) configuration was used by passing the electric current perpendicular to the plane of the thin layers. For this step, the electrical contacts with coplanar waveguide geometry (ground-signal-ground), were defined by laser beam lithography followed by Ta (10 nm)/Cu (200 nm) deposition and then lift-off. The coplanar waveguide geometry consists of a middle pad which is the signal strip and two lateral pads that are used as ground lines. The middle pad is connected to the top of the pillar and the two outer pads are connected to the bottom part of the pillar. After microfabrication, TMR sensors were annealed at a temperature of 320 °C in an external magnetic field of 5 kOe, in the direction of anisotropy induced during the deposition. For the as-fabricated TMR sensor, we obtained a magnetoresistance value of 37.5 % and 0.26 %/Oe for the sensitivity. In order to test the TMR sensor, detection experiments were performed using FeCrNbB magnetic particles with a diameter of 50-500 nm obtained by high-energy ball milling from melt-spun ribbons (MSRs) precursors [4]. The magnetic nanoparticles were dispersed in cyanoacrylate adhesives in order to obtain solutions with concentrations of 20 % and 80 %. Then, a glass support was partially covered with these solutions and used to demonstrate the detection capability of the MR sensor. During the measurements, a magnetic field of 20 Oe was applied perpendicular to the direction of the sensor, in order to generate a dipole magnetic field of magnetic particles. The output voltage variation was measured for different concentrations of magnetic

particles. As shown in Fig. 2, an output voltage variation of 0.044 mV was obtained for a magnetic particles concentration of 20 %. Increasing the particles concentration to 80%, the variation of the sensor output voltage also increased to 0.161 mV. We demonstrated a dependent relationship between the sensor output voltage and the concentration of magnetic particles. It should also be noted that the values of electrical resistances remain constant over time, indicating the stability of the sensor. **Acknowledgment** This work was supported by the Romanian Ministry of Research and Innovation (MCI) under the NUCLEU programme, Project PN 19 28 01 01.

[1] D. Su, K. Wu, R. Saha et al., *Micromachines*, Vol. 11, p. 1 (2020) [2] D. D. Djayaprawira, K. Tsunekawa, M. Nagai et al., *Applied Physics Letters*, Vol. 86, p. 092502-1 (2005) [3] S. Cardoso Freitas, D. C. Leitao, L. Gameiro et al., *Microsystem Technologies*, Vol. 20, p. 793 (2014) [4] H. Chiriac, N. Lupu, M. Lostun et al., *Journal of Applied Physics*, Vol. 115, p.17B520-1 (2014)

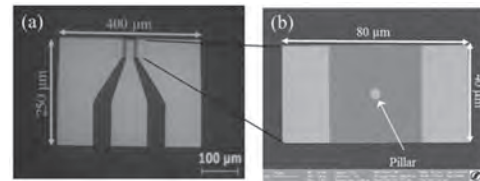


Fig. 1. (a) Optical microscope image of a device with G-S-G type electrical contacts and (b) SEM image of a rectangular structure.

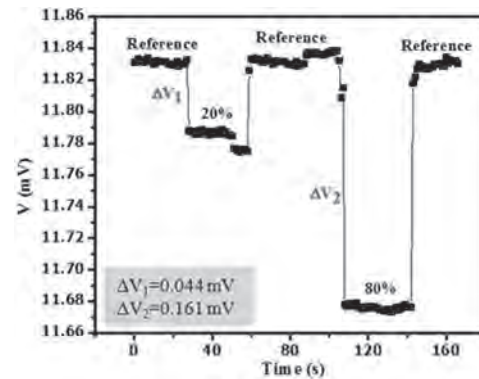


Fig. 2. Real-time signal of the TMR sensor for different magnetic particles concentrations.

IT-08. Modelling Magnetostrictive Materials for Structural Health Monitoring of Carbon Fibre Composite.

N. Ahmed¹, R. Deffley^{1,2} and N. Morley¹

1. Materials Science and Engineering, The University of Sheffield Faculty of Engineering, Sheffield, United Kingdom; 2. Royce Translational Centre, The Henry Royce Institute, Sheffield, United Kingdom

The aerospace industry has become increasingly reliant on carbon fibre composite (CFC) as a structural component in aircraft, due to his strength to weight ratio. One of the disadvantages of CFC are their vulnerability to impact damage and external environment changes during flight, which causes barely visible damage to the structure. One solution to this is structural health monitoring (SHM), which monitors the composite structure to provide early detection for damage. Previous work has found that magnetostriction ribbons used as sensors have good resolution to detect damage but are time consuming to attach to the composite surface [1]. To solve this issue, research has focused on additive layer manufacturing to produce 3D printed sensors, which can be directly attached to the surface of the composite. To evaluate the magnetic performance of the 3D printed sensors, this project focused on the design and development of 3D printed magnetostrictive materials using computer simulations in parallel with experimental research to measure the magnetic and mechanical performance. The design of the magnetostrictive sensors was simulated using COMSOL multiphysics, to determine how design parameters such as thickness, track length and gap changed the magnetic response with and without applied force. A desktop bound metal deposition printer at the Royce Translational Centre, was then used to print the metal with a polymer binder (polypropylene) to create the chosen 3D structures (Fig 1). The magnetic material chosen for this work was stainless steel 17/4ph. The initial work assessed the current performance of the printer at each stage. The designed structure goes through two stages of printing and heat treatment processes. The development of the feedstock to the heat treated structure could affect the final performance of the magnetostrictive material. For example, after printing the printed part (green body) goes through a debinder and a sintering stage which ultimately changes the microstructure and allows grain growth, which could affect the saturation magnetisation magnitude and direction. Using a MPMS3-SQUID magnetometer, in-plane magnetisation hysteresis loops were measured of different track lengths taken from structures at the different processing stages (green body and sintering). The results show that there is an increase in saturation magnetisation from green body to sintered sample. The sintered sample showed isotropic magnetisation within the track while the green body showed an anisotropic magnetisation. This may be due to the homogenous grain growth. To evaluate the grid design performance as a strain sensor, a weight was applied to the sintered structure and the change in magnetic flux density was measured. The COMSOL simulations were used to validate the results by using the in-built magnetostriction module. Both simulations and experimental works show comparable results (Fig 2). Demonstrating the larger the track gap the larger the response to an applied force. Future work will explore a range of printable magnetostrictive materials such as nickel and magnetite. The work will explore different designs based on COMSOL simulations including mechanical and magnetic performance. Acknowledgements: We wish to acknowledge the Henry Royce Institute for Advanced Materials, funded through EPSRC grants EP/R00661X/1, EP/S019367/1, EP/P02470X/1 and EP/P025285/1, for the financial support and the Desktop Metal Studio+ system and MPMS3-SQUID access at The University of Sheffield.

[1] Z. Leong, W. Holmes, J. Clarke, A. Padki, S. Hayes, and N. A. Morley, *IEEE Trans. Magn.*, 55, 7, 1–6, 2019.

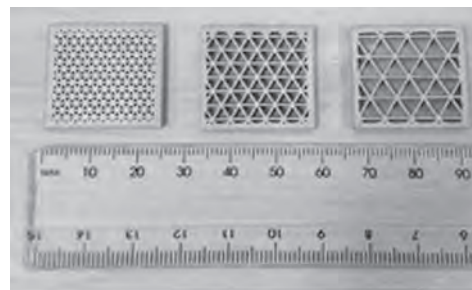


Fig 1. Additive manufacture sintered samples with track gap of 1.5mm, 3mm and 5mm (left to right)

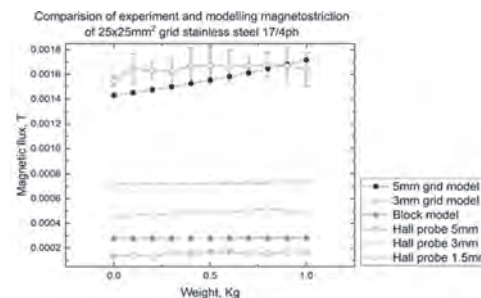


Fig 2. Comparison of COMSOL model and experimental data

IT-09. Rogowski Coil With Ferromagnetic Core.

V. Grim¹, P. Ripka¹, M. Mirzaei¹ and K. Draxler²

1. Department of Measurement, Ceske vysoké uceni technické v Praze
 Fakulta elektrotechnická, Praha, Czechia; 2. Department of electromagnet-
 ic quantities, Cesky metrologický institut, Praha, Czechia

Introduction Rogowski coils (RC) are used for the measurement of large alternating current, particularly as a short circuit detector in electric substations. Another application is in electricity meters. A regular, air-core RC cannot be saturated and therefore its dynamic range is limited only by noise voltage and supply voltage of the accompanying integrator or ADC [1]. An RC used for precise current measurement should have a consistent cross-sectional area and turn-to-turn spacing, limiting the winding arrangement to a single layer. The sensitivity of such coils is poor, causing a low signal-to-noise ratio [2]. Our proposed design adds a low-permeability ferromagnetic core to improve the sensitivity and thus reduce the required number of turns. Ferromagnetic core has been already tested for different types of RC, e.g. self-integrating RCs which are used for measurement of short current pulses. In this case increasing the core permeability decreases the low frequency limit of self-integrating operation [3]. Contrary to that, our target application is precise current sensing at the mains frequency and its harmonics. Such a sensor should be able to work with high accuracy (typical requirement is 0.5% or 0.2%) in the nominal range, as well as above this range with reduced accuracy with partly saturated core as a fault current detector [4]. Because the coil does not require a load resistor on its winding, there is no concern about overheating during overload conditions. However, there are some open questions, how will the ferromagnetic core affect the frequency characteristics of the RC, its ability to suppress external currents and resistance against the position deviations of the measured (primary) conductor. Several different materials, either in the form of a finished toroidal core or a 3-D printer filament filled with magnetic particles were tested, both theoretically by a FEM simulation and practically by measurement. **FEM Simulation** We have made a series of 3D FEM simulations to evaluate the effect of the core permeability on rejection of external currents and position of the measured conductor. In both cases the perfectly homogenous coil would be absolutely immune against both these influences. Practical coil always has uneven winding density, in particular between the first and last turn [5]. Also the cross-sectional area of individual turns varies slightly. We simulated the role of these imperfections in crosstalk from an external conductor as a function of its position and core permeability. In general, the error is diminishing with increasing permeability due to demagnetization effect. However, for practical permeability of 20 the error reduction is only very small (from 0.23 % to 0.15 %). The permeability effect on the resistance against the position deviations of the measured (primary) conductor is even lower and for permeability of 20 it is negligible. The effect of nonuniformity of the core permeability along its circumference was found to be insignificant as well. **Samples used for measurement** The first batch of test specimens (labeled A, B, C) are toroidal powder cores with an outer diameter of 79 mm and rated relative permeability of 26 (Kool Mju and Sendust materials) or 14 (Sendust). The winding is electrostatically shielded by a copper adhesive tape, care was taken to avoid the creation of a short-circuited turn. We also tested 3D printed cores from two types of plastic filament filled with magnetic particles and for the full paper we plan to test resin-based cores of various sizes. **Measurement procedure** Two important sensor characteristics were measured: linearity and frequency response. Test current was provided by a Techron 7548 power amplifier with an additional step-down transformer. Reference current measurement was done by a LEM Ultrastab current sensor (IT60S for frequency response, IT1000S for linearity). Two different measurement approaches were tested: either integrating the induced voltage with a Lakeshore 480 fluxmeter in AC mode, or measuring the voltage directly with a HF2LI lock-in amplifier. Both methods give similar results in amplitude, but the phase can only be measured by a lock-in amplifier. A primary conductor with a loop length of 10 meters was passed once through the measured coil to minimize the influence of the return current. Fig. 1 shows the frequency dependence: there is no observable sensitivity drop due to frequency dependence of the permeability. The sensitivity increase at high frequencies is due to the resonance with parasitic coil capacitance and its amplitude could be reduced by a parallel damping resistor [6] at the

expense of heat being generated in the associated circuitry. Fig. 2 shows the measured linearity error at 93 Hz, which is in a good agreement with the catalogue values of permeability vs. flux density in the core. A nominal flux line length of 0.196 m was used to convert flux density to primary current. **Conclusion** We have demonstrated that adding a ferromagnetic core to a RC of the classical dl/dt type is beneficial for its sensitivity, which would allow the design of very precise RCs for lower currents. The RC linearity is decreased, but remains acceptable for most applications. The amplitude error caused by self-resonance can be reduced by standard methods such as a damping resistor, or by using a different material with high core loss. **Acknowledgement** This study was supported by the Grant Agency of the Czech Republic within the Nanofluxgate project (GACR GA20-27150S).

[1] S. Tumanski, *Meas. Sci. Technol.* 18, p. R31, 2007 [2] J. D. Ramboz, *IEEE Trans. Instrum. Meas.* 45, p. 515, 1996. [3] J. D. Zhu, Q. G. Zhang, J. B. Jia et al., *Plasma Sci. Tech.* 8, p. 4571, 2006. [4] L. A. Kojovic, M. T. Bishop, and D. Sharma, *IEEE Trans. Ind. Appl.* 49, pp. 8, 2013. [5] L. Ferkovic, D. Ilic, and R. Malaric, *IEEE Trans. Instr. Meas.* 58, p. 122, 2009. [6] M. H. Samimi, A. Mahari, M. A. Farahnakian et al., *IEEE Sens. J.* 15, p. 651 (2015).

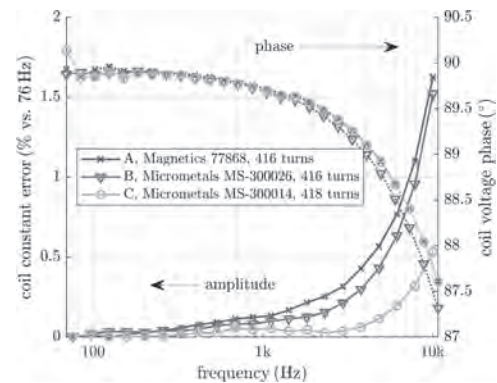


Fig. 1 Frequency response

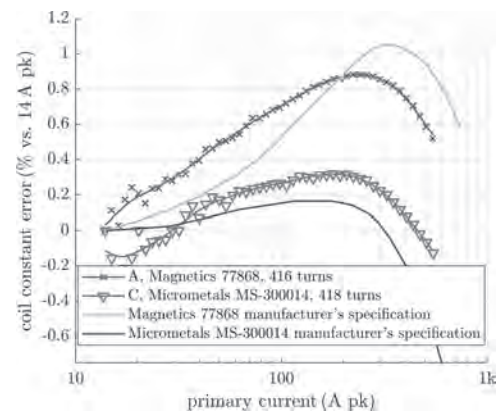


Fig. 2 Linearity

Session JA

AMORPHOUS AND NANOCRYSTALLINE SOFT MAGNETS AND APPLICATIONS

Rastislav Varga, Chair

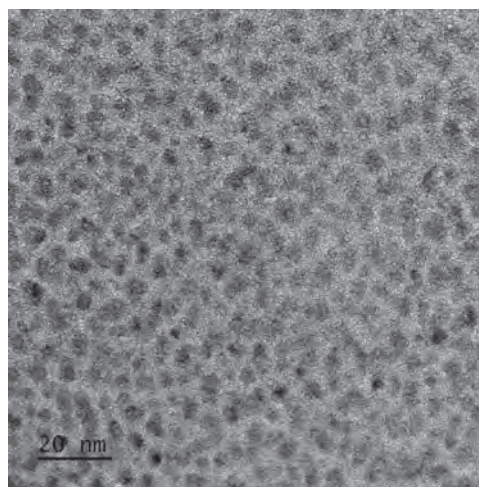
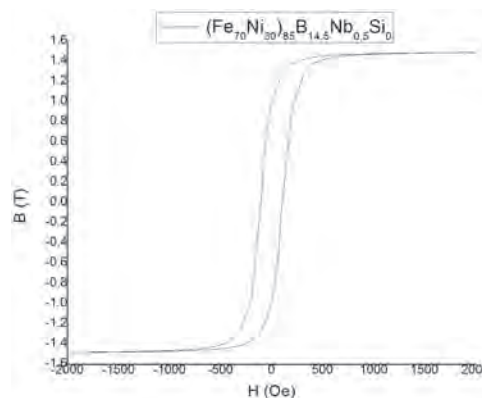
Univerzita Pavla Jozefa Safarika v Kosiciach, Kosice, Slovakia

CONTRIBUTED PAPERS

JA-01. Development of High Saturation Induction Fe-Ni Based Metal Amorphous Nanocomposite by Optimization of Glass Forming Ability.Y. Krimer¹, A. Barberis¹ and M. McHenry¹*1. Materials science, Carnegie Mellon University, Carnegie Mellon University, Pittsburgh, PA, US, academic, Pittsburgh, PA, United States*

A growing interest in electric vehicles challenges soft magnetic materials to improve efficiency and power density. Metal amorphous nanocomposites (MANCs) have lower coercivities and eddy current losses, allowing for greater efficiency and higher switching frequency. The later allows for high motor speeds and improved power density. However, commercially available and laboratory demonstrated MANCs have shortcomings. Fe-based MANCs, such as FINEMET have excellent magnetic properties, but mechanical properties limit their application in high speed electric motors (HSMs). Fe-Co based MANCs, such as HITPERM, have high saturation inductions and good mechanical properties, but elevated magnetostrictive losses. Co-based MANCs and more recent Fe-Ni based MANCs have low losses and good mechanical properties, but lower saturation inductions (1-1.2 T), that limit power density in HSMs. Recently, much work has explored improving saturation induction in MANCs by increasing the content of magnetic elements, which comes at the cost of glass-forming ability (GFA). These efforts were generally limited to trial and error testing. Additionally, all work to date has focused on Fe-based alloys. In this work, a method of using Thermocalc simulation to locate near-eutectic compositions has been applied to Fe-Ni based alloys. Minima in liquidus temperature and solidification range were found for a ternary composition range and used to identify compositions that retain good GFA as the percentage of magnetic elements is increased. The $(\text{Fe}_{70}\text{Ni}_{30})_x(\text{B-Si-Nb})_{100-x}$ alloy system for $x=82\%$ and $x=85\%$ was explored by Thermocalc simulations. This is an increase in magnetic element content compared to previously developed $x=80\%$ alloys. 3 compositions in the $x=82\%$ system, and 1 alloy in the $x=85\%$ system were identified and successfully cast as amorphous ribbon. The amorphous nature of the ribbon was confirmed by a bend test and XRD. Magnetic testing was performed by PPMS to measure saturation induction and Curie temperature of the amorphous material. The Curie temperatures increased to 407-438 °C for the $x=82\%$ alloys, and 462 °C for the $x=85\%$ alloy. Saturation induction increased to 1.28-1.36 T for the $x=82\%$ alloy and 1.48 T for the $x=85\%$ alloy, which is a significant improvement over the ~370 °C Curie temperature and 1.2 T saturation of previous Fe-Ni alloy. Crystallization behavior was studied by XRD for the $x=85\%$ alloy, showing that crystallization process follows a 2-step process of Amorphous \rightarrow BCC+FCC+Amorphous \rightarrow BCC+FCC+ Fe_3B + Fe_{23}B_6 . Post annealing magnetic properties were studied by strip testing, and saturation induction as high as 1.48 T was seen after optimal annealing. TEM was used to study structure of as cast and annealed material. 2 alloys with $x=82\%$ compositions were identified with an optimal crystalline size of 10-20 nm, while the $x=85\%$ alloy had this structure in the as cast state. This opens the possibility of using the alloy in the as cast state, without requiring annealing. In conclusion, alloys with good GFA and improved magnetic properties were identified by Thermocalc simulation.

N. Aronhime, V. DeGeorge, V. Keylin, JOM. 69 (2017) 2164–2170 N. Aronhime, E. Zoghlin, V. Keylin, Scr. Mater. 142 (2018) 133–137 J.M. Silveyra, A. Leary, V. DeGeorge, J. Appl. Phys. 115 (2014) 17A319 J.M. Silveyra, P. Xu, V. Keylin, J. Electron. Mater. 45 (2015) 219–225 A. Urata, H. Matsumoto, S. Sato, J. Appl. Phys. 105 (2009) 2007–2010 C. Wang, A. He, A. Wang, J. Pang, Intermetallics. 84 (2017) 142–147 A. Wang, C. Zhao, A. He, J. Alloys Compd. 656 (2016) 729–734 Y. Krimer, N. Aronhime, P. Ohodnicki, J. Alloys Compd. 814 (2020) 1-9



JA-02. Development of an (Fe, Sn)-Based Nanocrystalline Soft Magnetic Alloy.

P. Wang¹ and M. Willard¹

1. Material Science and Engineering, Case Western Reserve University, Cleveland, OH, United States

The $D0_3$ Fe_3Sn phase shows higher magnetization and smaller magnetocrystalline anisotropy compared to Fe_3Si based on the comprehensive first principles calculations. For this reason, it is important to develop nanocrystalline soft alloys which have $D0_3$ Fe_3Sn phase as primary crystallite. A new alloy design method, motivated by the work of Villars, was used to choose the alloy composition. Element Co was found to stabilize the $D0_3$ Fe_3Sn phase. In this work, a new alloy system $(Fe_{1-x-y}Co_xSn_y)_{87}Nb_3B_9Cu_1$ was studied to achieve $D0_3$ Fe_3Sn phase with the help of the non-equilibrium processing method. Differential scanning calorimetry was used to determine the primary crystallization temperatures of the amorphous ribbons. The amorphous ribbons were annealed in tube furnace at 723K, 773K, and 823K for 3600 seconds after encapsulating them in a fused quartz ampoule. X-Ray Diffraction (XRD) has been used to analyze structural properties of as-spun and heat-treated ribbons of all alloy compositions. The single broad peak of $Fe_{60}Co_{20}Sn_{7}Nb_3B_9Cu_1$ as-spun ribbons' XRD diffractograms indicates an amorphous phase due to their lack of long-range order. The rest as-spun ribbons' XRD diffractograms shows partial crystalline during melt-spinning process due to the low glass-forming ability of these series of alloys. XRD diffractogram of the heat-treated ribbons are comprised of a B2 phase, which has a BCC structure. The crystallite sizes for each heat-treated sample were estimated by Scherrer broadening to have values between 7 and 10 nm. The magnetic properties of as-spun and heat-treated ribbons were studied by vibrating sample magnetometry. Saturation magnetization and coercivity were determined from room temperature magnetic hysteresis loops. The highest magnetization value achieved was 161.7 Am²/kg for the $Fe_{75}Co_4Sn_{8}Nb_3B_9Cu_1$ ribbon annealed at 723K.

P. Villars, "Three-dimensional structural stability diagrams for 648 binary AB₃ and 389 binary A₃B₅ intermetallic compounds: III," *J. Less-Common Met.*, vol. 102, no. 2, pp. 199–211, 1984 P. Villars, "A three-dimensional structural stability diagram for 998 binary AB intermetallic compounds," *J. Less-Common Met.*, vol. 92, pp. 215–238, 1983 Alex Zunger, "Systematization of the stable crystal structure of all AB-type binary compounds: A pseudopotential orbital-radii approach," *Phys. Rev. B*, vol. 22, no. 12, pp. 5839–5872, 1980 S.S. Batsanov, "Dielectric Methods of Studying the Chemical Bond and the Concept of Electronegativity," vol. 51, no. 7, 1982.

JA-03. Reducing the Core Losses of Fe-Si-B Amorphous Ribbons by High Cooling Rate Planar Flow Casting.

D. Li¹ and Z. Lu¹

1. School of Electrical Engineering, Beijing Jiaotong University, Beijing, China

INTRODUCTION Fe-based amorphous ribbons play an important role in high efficiency energy conversion devices and have been widely used in the field of electric power, power electronics and renewable energy as transformers [1], inductors [2] and reactors [3]. Small improvements in core losses can have large energy savings [4]. The demands of high efficiency and energy saving pose a challenge to further reduce the core losses of amorphous ribbons. To date, numerous studies have been investigated on materials development [5], subsequent annealing and structure design of magnetic cores [6] to further reduce the core losses of Fe-based amorphous cores and components. However, few reports are found on the influence of process parameters on core losses of Fe-based amorphous ribbon produced by planar flow casting (PFC) process. The objectives of this work are to study the influence of the thermal conductivity of cooling wheel substrate on cooling rate of Fe-based amorphous ribbon, to investigate the effect of cooling rate on core losses of Fe-Si-B amorphous ribbons. **MATERIALS AND METHODS** A batch of copper beryllium (Cu-2Be) cylindrical rings with different thermal conductivity was manufactured. A cooling wheel system is composed of a stainless steel wheel core and the cylindrical ring. Amorphous alloy ribbons with nominal composition of Fe₈₀Si₉B₁₁ (at. %) were produced by using the Cu-2Be as the substrate of cooling wheel, the ribbon width is 50±0.5 mm and the ribbon thickness is 25±0.5 mm. The core losses were measured using IWATSU SY-8232 B-H analyzer. All the measured samples are toroidal cores with inner diameter of 30 mm, outer diameter of 35 mm and height of 50 mm subjected to heat treatment at 365 °C for 60 minutes with applied longitudinal field of 400 A/m. A 2D numerical model was established to calculate heat and mass transfer during PFC process by using ANSYS FLUENT software, the parameters used in the numerical calculation were the same as that of practical casting of Fe-Si-B alloy ribbons. **RESULTS AND DISCUSSIONS** The PFC process was simulated and the thermal conductivity of 175.3 W/m×K and 206.5 W/m×K for the Cu-2Be rings as a substrate of cooling wheel were used. The main process parameters employed for the simulation are as the follows: the applied pressure at the bottom of nozzle is 45 kPa, the cooling wheel outer diameter is 300 mm, the thickness of the Cu-2Be ring is 10 mm, the linear velocity of cooling wheel surface is 20 m/s, the nozzle slit width is 0.3 mm, the nozzle wheel gap distance is 0.15 mm, the temperature of molten alloy 1420 °C, the initial temperature of Cu-2Be substrate and circumferential air is 32 °C, the glass formation temperature of Fe-Si-B alloy is assumed to be 750 °C. Fig. 1 shows the simulation results of upstream meniscus, downstream meniscus and growth of liquid/solid interface at the 130th revolution for substrate thermal conductivity of 175.3 W/m×K and 206.5 W/m×K, respectively. In Fig. 1, upstream meniscus and down meniscus are plotted by the line of volume fraction of melt=1 and the liquid/solid interface is plotted by the isothermal line of glass formation temperature T_g=750 °C. The growth of liquid/solid interface is from P₃ to P₄ for this case. The solidification time is t=L/U and the average cooling rate is h=(T_g-T_s)/t, where L is the puddle length from P₃ to P₄, U is the linear velocity of cooling wheel surface and T_s is the surface temperature of cooling wheel beneath the puddle (not shown). Based on the data extracted from the liquid/solid interface of the puddle and the surface temperature of cooling wheel beneath the puddle, the average cooling rates are 1.26e-6 K/s and 1.44e-6 K/s for k=175.3 W/m×K and 206.5W/m×K, respectively. The cooling rate increases by 14.3% due to the increase of substrate thermal conductivity. To investigate the cooling rate on core losses of Fe-Si-B alloy during PFC process, Cu-2Be rings with thermal conductivity of 175.3 W/m×K and 206.5 W/m×K were shrink fitted onto the wheel core as the substrate of cooling wheel. Fig. 2 shows the core losses at 50 Hz as a function of induction for Fe-Si-B ribbons produced by cooling wheel with different thermal conductivity. The increase of thermal conductivity of cooling wheel from 175.3 W/m×K to 206.5 W/m×K results in the decrease of core losses from 0.171 W/kg to 0.133 W/kg, with the core losses reduction up to 22.1%. **CONCLUSIONS** The influence of thermal conductivity of cooling wheel substrate on cooling rate during PFC process

was simulated by numerical method and the results show that the increase of thermal conductivity of cooling wheel substrate from 175.3 W/m×K to 206.5 W/m×K leads to the increase of cooling rate from 1.26e-6 K/s to 1.44e-6 K/s in PFC process. The effect of cooling rate on structure and soft magnetic properties of Fe-Si-B alloy ribbons was investigated. The results show that the increase of thermal conductivity of cooling wheel substrate from 175.3 W/m×K to 206.5 W/m×K during PFC process results in the decrease of core losses from 0.171 W/kg to 0.133 W/kg, with the core losses reduction up to 22.1%.

[1] D. Azuma, R. Hasegawa, IEEE Trans. Magn., 44, 4104-4106 (2008) [2] R. Hasegawa, J. Non-Cryst. Solids, 387, 405-412 (2001) [3] N. Kurita, K. Onda, K. Nakanoue, IEEE Trans. Power Electr., 29, 3657-3668 (2014) [4] O. Gutfleisch, M. A. Willard, E. Brück, Adv. Mater., 23, 821-842 (2011) [5] C. Dong, A. Inoue, X. H. Wang, J. Non-Cryst. Solids, 500, 173-180 (2018) [6] D. Azuma, N. Ito, M. Ohta, J. Magn. Magn. Mater., 501, 166373 (2020)

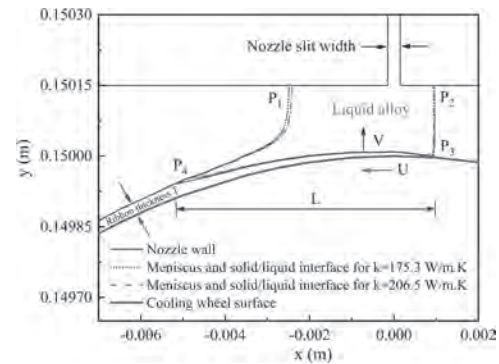


Fig. 1 The simulation results of upstream meniscus, downstream meniscus and growth of liquid/solid interface in quasi-static process for substrate thermal conductivity of 175.3 W/m×K and 206.5 W/m×K.

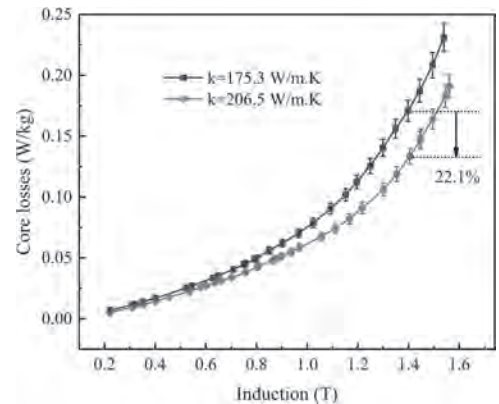


Fig. 2 Core losses at 50 Hz as a function of induction for Fe-Si-B ribbons produced by cooling wheel with different thermal conductivity.

JA-04. Laser Processing of Soft Magnetic Metal Amorphous Nanocomposites.

A. Talaat¹, D.W. Greve^{2,3}, Y. Liu¹, K. Byerly⁴, M. McHenry⁴, J. Wieszorek¹ and P. Ohodnicki^{1,5}

1. Mechanical Engineering & Materials Science, University of Pittsburgh, Pittsburgh, PA, United States; 2. DWGreve Consulting, Sedona, AZ, United States; 3. Electrical and Computer Engineering, Carnegie Mellon University, Pittsburgh, PA, United States; 4. Materials Science and Engineering, Carnegie Mellon University, Pittsburgh, PA, United States; 5. Electrical and Computer Engineering, University of Pittsburgh, Pittsburgh, PA, United States

Crystallization from an amorphous precursor has been historically exploited to synthesize metastable soft magnetic nanocomposite systems comprised of transition metal rich ferromagnetic nanocrystals embedded within an intergranular amorphous phase [1,2]. Subsequent thermal processing steps are designed to produce a highly refined microstructure with grain sizes in the nm-range to enable effective exchange averaging and highly reversible magnetization processes as described by the random anisotropy model [3,4]. Successful realization of superior soft magnetic properties results from ubiquitous nucleation and self-limiting growth of nanocrystals due to expulsion of glass formers to the intergranular amorphous matrix, thereby requiring significant amounts of metalloids and early transition metals which reduce the effective saturation magnetization. Recent work has discovered the balance between nucleation and growth can alternatively be optimized through highly controlled thermal processing steps involving extremely rapid heating and subsequent cooling rates on the order of 10^2 - 10^3 K/s referred to as “flash annealing”, such that a high density of nucleation sites can be achieved with limited nanocrystal growth even for alloy chemistries which do not produce nm-scale microstructures for conventional annealing [5]. High heating and cooling rates generated during laser radiation have offered great advantages for rapid thermal processing and surface treatment of ferromagnetic amorphous ribbons [6–8]. In this work, we report on pulsed-laser processing of a series of Fe-based and Co-based amorphous ribbons with emphasis being placed on phase transformations within the laser-irradiated regions as well as impacts on surrounding regions due to the detailed thermal effects associated with the laser pulse. Amorphous ribbons with nominal compositions $\text{Fe}_{73.5}\text{Si}_{13.5}\text{Nb}_3\text{B}_9\text{Cu}_1$ and $\text{Co}_{77.2}\text{Fe}_{1.4}\text{Mn}_{1.4}\text{Nb}_4\text{B}_{14}\text{Si}_2$ were used for laser experiments. Laser annealing has been carried out using a Q-smart pulsed Nd-YAG (wavelength of 1064 nm) and laser beam diameter around 0.6 mm. The laser power was varied from 50-150 mJ and the time delay associated with each laser power has been calculated using the FWHM of the laser output pulse. Microstructure and crystalline phases after laser annealing were characterized using both XRD and SEM. Temperature profiles achieved during laser annealing have been estimated using FEA heat transient analysis. Fig. 1 shows XRD patterns of as-cast and laser annealed Fe- and Co-based ribbons at different laser power. As can be seen, as-cast and samples annealed at 60 mJ are fully amorphous, whereas samples treated at higher laser power (i.e., at 100mJ and above) present a mixture of boride and α -Fe phases with an average grain size of the latter being on the order of 8-10 nm estimated from the FWHM of the corresponding crystalline peak. In conventional annealing methods, the formation of boride phases are typically observed only after reaching secondary crystallization temperatures in these alloy systems. Because the borides are already observed in laser annealed samples with significant volume fraction for the lowest pulse power levels at which crystalline peaks can be detected, a need exists to revisit the crystallization mechanism in light of the detailed thermal histories experienced across and surrounding the irradiated region and the Gaussian distribution of the laser beam across the irradiated surface. Laser energy density decreases exponentially in the radial direction and has a maximum at the center of the laser spot leading to greater temperature values at the center and a temperature gradient from the center towards the edges. In addition, laser beam intensity also produces a stress distribution which can be associated with its Gaussian profile resulting in an inhomogeneous stress across the beam diameter, tensile at the center and compressive at the edges. Such temporally and spatially dependent temperature and stress profiles can alter free volume, nucleation rate, and diffusion kinetics leading to rapid crystallization events and alternative pathways towards the crystalline phase. Temperature as

a function of time of a simulated laser-irradiated spot at the top surface and below the top surface of an amorphous ribbon is shown in Fig. 2. The temporal temperature profile suggests temperatures above 2000K at the top surface which is beyond the melting point and most likely results in a local melting at the top surface layer with crystallization possible upon cooling. Temperatures estimated approximately 2 microns below the surface (within the skin penetration depth of Fe at the optical wavelength of Nd-YAG) are on the order of 1000K and likely not to reach melting temperatures, consistent with the surface deformation observed as illustrated in the SEM images of Fig. 2c. These temperatures significantly decrease within the distance from the center towards the edge of the laser spots suggesting diffusion of heat from the centers outwards and therefore different crystallization kinetics are expected.

[1] M. E. McHenry, M. A. Willard, and D. E. Laughlin, *Progress in Materials Science*, vol. 44, no. 4, pp. 291–433, Oct. 1999 [2] A. Talaat, D. W. Greve, M. V. Suraj, and P. R. Ohodnicki, *Journal of Alloys and Compounds*, vol. 854, p. 156480, Feb. 2021 [3] G. Herzer, *Acta Materialia*, vol. 61, no. 3, pp. 718–734, Feb. 2013, doi: 10.1016/j.actamat.2012.10.040. [4] Y. Yoshizawa, S. Oguma, and K. Yamauchi, *Journal of Applied Physics*, vol. 64, no. 10, pp. 6044–6046, Nov. 1988 [5] K. Suzuki *et al AIP Advances*, vol. 9, no. 3, p. 035311, Mar. 2019, doi: 10.1063/1.5079778. [6] S. Katakam *et al., Scripta Materialia*, vol. 66, no. 8, pp. 538–541, Apr. 2012 [7] C. Smith *et al., Materials Letters*, vol. 122, pp. 155–158, May 2014 [8] L. Lanotte and V. Iannotti, *Journal of Applied Physics*, vol. 78, no. 5, pp. 3531–3533, Sep. 1995

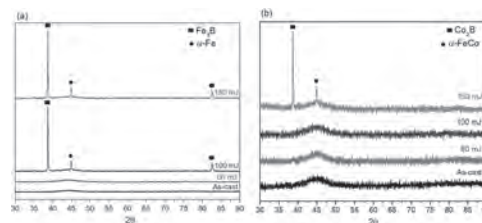


Fig. 1 XRD patterns of as-cast and laser-annealed Fe-based (a), and Co-based ribbons (b)

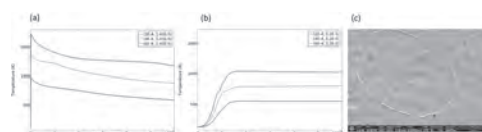


Fig. 2. FEA simulations of temperature as a function of time at a laser power of 100mJ for (a) top surface and (b) below top surface of an amorphous ribbon. Red (0.6 mm), green (0.4 mm), and blue (0.2 mm) lines represent the distance from the center towards the edge of the laser spot. (c) SEM image of the ribbon surface layer showing evidence for local surface melting at the center of the laser irradiated region.

JA-05. Effect of Process Parameters on the Properties of Compositionally Graded FeCoNi Films: a High Throughput Strategy.

Z. Tsakadze¹, V. Chaudhary¹, S.P. Padhy¹, W. Gan², G.J. Lim², W. Lew² and R. Ramanujan¹

1. School of Materials Science and Engineering, Nanyang Technological University, Singapore, Singapore; 2. School of physical and mathematical sciences, Nanyang Technological University, Singapore, Singapore

Abstract: Fe-Co-Ni magnetic thin films with continuously varying compositions have been fabricated by the magnetron co-sputtering method. The films were characterized by high-throughput techniques. The results reveal the correlation between a range of compositions and the electrical properties of the films fabricated at various process parameters. **Introduction:** Soft magnetic materials are essential elements of electro-magnetic energy transformation technologies and they are widely used in various distribution, conversion, generation devices, such as transformers, motors, converters, generators, actuators, sensors etc. However, it usually takes long time for a new material before its acceptance for commercial application. Therefore, it is very crucial to speed up the discovery of new materials and incorporate them into various systems. High-throughput methods are efficient research methods [1-3] to explore this immense search space to identify new or optimized materials. Fe-Co based alloys received great attention due to high saturation magnetization. And what makes them even more fascinating is that their magnetic and electric properties can be tuned by controlling the alloy composition and microstructure. Among these compositions, Fe-Co-Ni films revealed significant induced magnetic anisotropy, low coercivity and high anisotropy of magnetoresistivity, what makes them a good candidate for technical applications. The resistivity is an important parameter to determine power loss in many soft magnetic applications. In this work we studied the effect of process parameters on the structure and resistivity of compositionally graded Fe-Co-Ni films to find process conditions at which optimum properties are obtained. **Experimental details:** Fe-Co-Ni films with continuously varying alloy compositions were fabricated by the magnetron sputtering method. Two experimental procedures were designed: a) Fe-Co-Ni films were deposited on SiO₂/Si substrates by co-sputtering of permalloy and Co target materials using DC sources at different substrate temperatures (T_s): in particular, ambient temperature, 300 °C and 500 °C; b) the film was deposited at ambient temperature and annealed for 2 hours in vacuum at 500 °C. The base pressure in the chamber was controlled at 4×10^{-4} Pa. Depositions were performed in argon gas environment while the pressure was kept approximately at 0.3 Pa. For compositional, structural and electrical properties high-throughput Electron Probe Micro-Analysis (EPMA), X-ray Diffraction, four-point probe measurements were performed to determine chemical compositions, structure and resistivities of the films. **Results and discussion:** Fe-Co-Ni films with continuously varying alloy compositions were fabricated by magnetron sputtering method. The results of high-throughput Electron Probe Micro-Analysis measurements across Fe-Co-Ni films (Fig.1) revealed that atomic composition of Ni was highest, while Co was lowest in the film fabricated at $T_s = 300$ °C. The ratios of Co and Ni atomic compositions in deposited graded films were calculated as well. We found that Fe-Co-Ni film fabricated at $T_s = 300$ °C shows the lowest ratio as compared to other films. XRD measurements and analysis of multiple selected areas on Fe-Co-Ni film fabricated at ambient substrate temperature exhibited amorphous structure. As the substrate temperature increased diffraction peaks appeared, showing a clear change in structure. The diffraction patterns showed that only one FCC phase appeared. The peak intensity increased with temperature and the grain sizes became larger. The increase of peak intensity and average grain size indicated that increasing the substrate temperature from room temperature to 500 °C enhances the crystallinity of Fe-Co-Ni films. As for the annealed samples the intensity of the peak was low, and peak shifted towards lower angles indicating crystal lattice expansion. In addition, oxide peaks have been observed. Fig. 2 shows the measured resistivities as a function of composition of various process parameters. Resistivities of the graded film deposited at $T_s = 300$ °C exhibited higher values than resistivities of the films deposited at ambient, 500 °C, and at ambient temperature followed by annealing at 500 °C. These results indicate that Ni plays important role in tuning resistivities of the films. **Conclusion:** Fe-Co-Ni films with continuously varying compositions

have been fabricated by magnetron sputtering and characterized by high-throughput experimentation methods. The results revealed the correlation between continuously varying alloy compositions and selected properties of the films fabricated at various process parameters. Acknowledgement: This work is supported by the AME Programmatic Fund by the Agency for Science, Technology and Research, Singapore under Grant No. A1898b0043

[1] Sean W. Fackler, Vasileios Alexandrakis, Dennis König, A. Gilad Kusne, Tieren Gao, Matthew J. Kramer, Drew Stasak, Kenny Lopez, Brad Zayac, Apurva Mehta, Alfred Ludwig and Ichiro Takeuchi, *Science and Technology of Advanced Materials* 2017, Vol.18, No.1, 231–238 [2] H. Koinuma, I. Takeuchi: *Nat. Mater.* 3 (2004) 429 –438. [3] Alfred Ludwig, *npj Computational Materials* (2019) 5:70

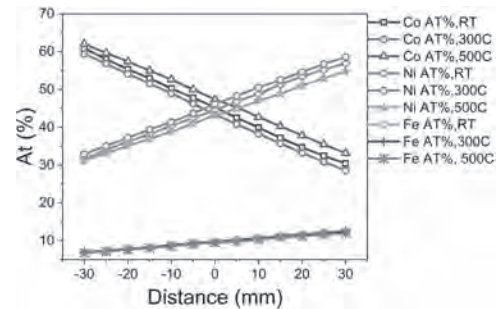


Fig. 1 Elemental compositions of the graded Fe-Co-Ni films

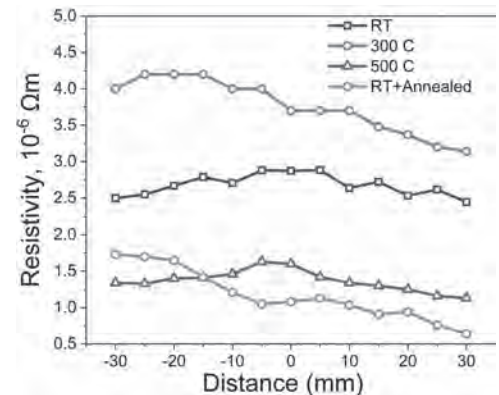


Fig. 2 Resistivities of Fe-Co-Ni films with continuously varying alloy compositions fabricated at different process parameters

JA-06. Soft Magnetic Properties of Severely Drawn Pearlitic-Ferritic Wires With Nanocrystalline Microstructure.

S. Wurster¹, M. Stückler¹, L. Weissitsch¹, H. Krenn², A. Hohenwarter³, R. Pippan¹ and A. Bachmaier¹

1. Erich Schmid Institut für Materialwissenschaft, Leoben, Austria;

2. Institute of Physics, Karl Franzens Universität Naturwissenschaftliche Fakultät, Graz, Austria; 3. Department of Materials Physics,

Montanuniversität Leoben, Leoben, Austria

Recently, pearlitic wires, which experienced large drawing strains awoke the interest of material scientists due to their astonishing high strength of up to 7 GPa [1]. Because of the large amount of deformation applied during wire drawing, the grain size refines into the nanocrystalline regime and microstructural sizes of 10 nm and below are reported. The present study focusses on the capabilities to magnetically soften pearlitic steel by this “top-down”, conventional metal-forming process, as these length scales are already below the ferromagnetic exchange length of pure Fe. To do so, volume saturation magnetization and temperature dependent coercivities of wires experiencing high drawing strains ($\epsilon > 5$) were investigated. The results are compared to the ones of the initial wire, having more than twenty times the diameter and consequently a much coarser microstructure. To investigate the magnetic softening upon wire drawing, SQUID magnetometry and VSM measurements were performed. For the accurate determination of the volume saturation magnetization, the precise determination of the volume of the small samples is necessary. A confocal laser scanning microscope was used – the results allow the 3D reconstruction of the surfaces of the samples, for an example see inset in Figure 1. From the surface reconstruction the volume can be calculated. It was found that the volume saturation magnetization is higher for the very thin wires in comparison to the initial state. While the thick, non-deformed wire shows a saturation magnetization very close to the one of pure pearlite, the saturation values for the thin wires are close to the one of pure body centred cubic (bcc) Fe (Figure 1). The slightly higher values, even in comparison to pure Fe, can be explained by C being supersaturated in the Fe matrix. The C necessary for supersaturation originates from the dissolution of cementite (Fe_3C) during the wire drawing process [1]. Regarding the potential of wire drawing for magnetic softening, a decrease in coercivity was indeed found. The measured coercivities of the thin wires, determined with VSM, are smaller (24 μm : 520 A/m, 36 μm : 610 A/m) compared to the thick wire (1510 A/m). It is evident from magnetic measurements that there is a small but no substantial further refinement in grain size upon drawing the wire from 36 μm to 24 μm , although this constitutes a large degree of further deformation. Restoration mechanisms, as they are also known from other techniques involving severe deformation, seem to keep the grain size almost constant. For the thin wires, the grain size is calculated from the room temperature coercivity measurements. The grain size is found to be below the ferromagnetic exchange length of pure Fe, thus the random anisotropy model is applied. Using magnetic constants of pure Fe yields a grain size of 11 nm. This is in excellent agreement with atom probe tomography studies on the same material, where a subgrain size of 10 nm and below was found [2]. To further confirm the finding of dissolving cementite, the coercivity was determined as a function of temperature. Figure 2 includes calculated coercivities based on temperature dependent magnetocrystalline anisotropies for pure bcc Fe from [3–5]. Comparison reveals a very good match of measured and literature data; thus it can be safely assumed that the cementite has largely dissolved. Residual stresses, which might prevail from the drawing process would lead to an increased coercivity. Thus, a further softening of the drawn wires can be expected after thermal treatment, as it was the case for severe plastically deformed material, presented in [6]. One of the thin wires was annealed at 150°C for 30 min, which resulted in a decrease in coercivity by about 76 A/m or 12%. This proves the temperature stability of the microstructure at that temperature, as an increase in grain size would result in an increase in coercivity. The decrease in coercivity can be explained by reduced magneto-elastic effects, as residual stresses after wire drawing increase the effective anisotropy. In summary, pearlitic material was drawn to very high strains, resulting in very thin wires with nanocrystalline microstructure. Results of magnetic measurements indicate grain sizes close to 10 nm, the dissolution of cementite and a supersaturation of bcc Fe with C. It was possible to magnetically soften

the coarse grained pearlitic steel from $\sim 1500\text{A/m}$ to $\sim 500\text{A/m}$ by this wire drawing process. However, the almost constant coercivity and grain size for very high drawing strains demonstrates that the magnetic softening seems to be maxed out. *This project received funding from the European Research Council (ERC) under the European Union's Horizon 2020 research and innovation programme (Grant No. 757333).*

[1] Y.J. Li, P. Choi, C. Borchers, et al., Atom probe tomography characterization of heavily cold drawn pearlitic steel wire, *Ultramicroscopy*. 111 (2011) 628–632. [2] Y. Li, D. Raabe, M. Herbig, et al., Segregation Stabilizes Nanocrystalline Bulk Steel with Near Theoretical Strength, *Physical Review Letters*. 113 (2014). [3] H.-P. Klein, E. Kneller, Variation of Magnetocrystalline Anisotropy of Iron with Field and Temperature, *Phys. Rev.* 144 (1966) 372–374. [4] B. Westerstrand, P. Nordblad, L. Nordborg, The Magnetocrystalline Anisotropy Constants of Iron and Iron-silicon Alloys, *Phys. Scr.* 11 (1975) 383–386. [5] I.M. Puzei, V.V. Sadchikov, Dependence of the magnetic-anisotropy energy in iron on the magnetic field, *Sov. Phys. JETP*. 70 (1990) 137–139. [6] M. Stückler, L. Weissitsch, S. Wurster, et al., Magnetic dilution by severe plastic deformation, *AIP Advances*. 10 (2020) 015210.

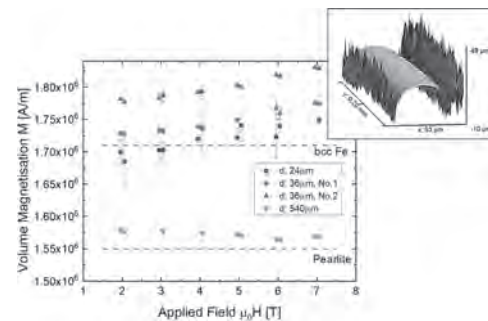


Figure 1: Saturation magnetization for all investigated wires, measured at applied fields ≥ 2 T, taking into account the individual sample volume determined by confocal laser scanning microscopy. The values of pure bcc Fe and pearlite are included. As an inset, the 3D-reconstruction of the wire surface of a small section of one of the 36 μm -wires is shown.

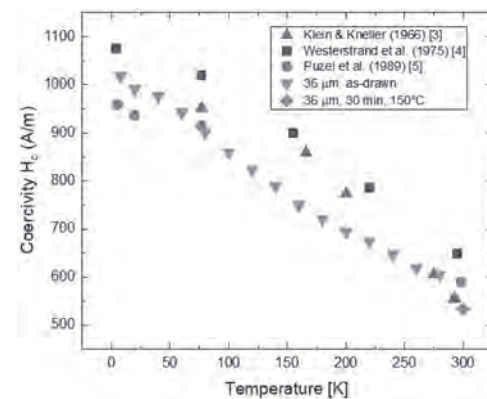


Figure 2: Measured and corrected temperature-dependent coercivity of one of the 36 μm -wire as a function of temperature. Results are compared with coercivities calculated according to literature [3–5] on temperature dependent magneto-crystalline anisotropy. The coercivity of the annealed 36 μm -wire is also shown.

JA-07. Detection of Diazinon Organophosphates Using Magnetoelastic Sensor.

S. Atalay¹, O. Inan¹, B. Ates², S. Balcioglu², S. Kolak², M. Simsek², V. Kolat¹, S. Koytepe² and T. Izgi¹

1. Physics, Inonu Universitesi, Malatya, Turkey; 2. Chemistry, Inonu Universitesi, Malatya, Turkey

Organophosphates (OP) have been used to kill insects in many areas such as homes and workplaces, especially in agricultural pest control [1]. In many people, the remains of OP can lead to many health problems to range from paralysis to death. For this reason, it is very important to detect OPs, which is the most important way of passage to the human organism, as a sensitive, fast, and cheap way. Nowadays, conventional OP detection is carried out by techniques such as mass spectroscopy, gas chromatography, and high-performance liquid chromatography. Although these methods give accurate and sensitive results, they require time-consuming processes such as sample preparation, solid-phase extraction, and comparison of sample peaks with references. Moreover, the cost of these methods is quite high. Therefore, the development of an alternative method as sensitive, fast, practical and cheap for detection of OPs was carried out in this study. The system used in the detection of OPs is a magnetoelastic sensor (MES). Magnetoelastic sensors are preferred because of their low cost, disposable application, wireless and easier to use. Magnetoelastic materials begin to vibrate (shorten and elongate) when exposed to a time-varying (AC) magnetic field. The vibration frequency of such samples varies depending on the geometry, elastic coefficient and mass (density) of the sample [2]. In magnetoelastic sensors, the amount of mass usually deposited on the sensor surface causes a shift in the resonance frequency and the shift in the magnetoelastic measurement system is measured. In this way, the mass accumulated on the sensor surface can be measured. It is important that the sensor surface is functionalized according to the type of molecule being detected. The magnetoelastic sensor will be more precise and superior if it measures a very low mass change. Therefore, enlarging the sensor surface area makes a significant contribution to the sensitivity of the sensor. In this context, electrospun nanofibers were coated on the sensor surface in order to increase the surface area of magnetoelastic sensors for the first time within this study. Within the scope of this project, 2826MB ($\text{Fe}_{40}\text{Ni}_{38}\text{Mo}_4\text{B}_{18}$) amorphous ferromagnetic ribbons with 35 mm long and 5 mm in width were used as MES. Then, the nanofibers were functionalized with glutaraldehyde (GA) in order to covalently bind acetylcholinesterase (AChE) enzyme to the surface. The resonance frequency of the functionalized amorphous strip was measured to be around 59 000 Hz. OP in the 10% EtOH solution was dripped with a micropipette on the surface of the functionalized MES then allowed drying. It was observed that the EtOH solution evaporate and the remaining OP covalently binds the acetylcholinesterase (AChE) enzyme. When 50 ppm OP in 10% EtOH solution were dropped, a decrease of approximately 22 Hz was observed in the resonance frequency at 500 A/m DC bias magnetic field. Figure 1 shows the measured resonance frequency change when different amounts of OP were dropped onto the MES. As can be seen, MES shows a linear change according to the amount of OP measured in the range of 0-150 ppm in 10% EtOH solution. To determine whether the frequency shift comes only from the OP, only 10% EtOH solution was dripped onto the functionalized MES surface in different amounts and it was found that no shift in the frequency had occurred. Acknowledgment This work was supported by TUBITAK with 119F144 project number.

[1] M. Eddleston, M.R. Phillips, *BMJ*. 328, 42 (2004). [2] C.A. Grimes, P.G. Stoyanov, D. Kouzoudis, K.G. Ong, *Rev. Sci. Instrum.*, 70, 4711 (1999).

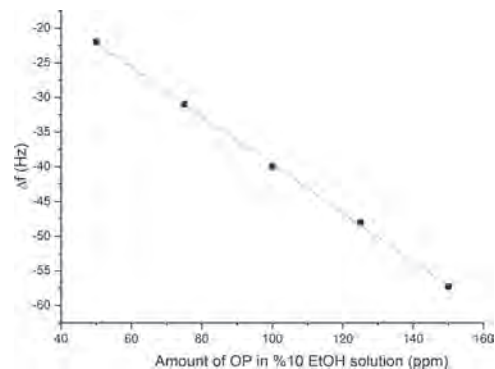


Fig.1. Variation of resonance frequency as a function of diazinon organophosphates amount.

JA-08. Magnetic Substrate Coupled Broadband and Miniaturized Electromagnetic Interference Shielding Structure Using Deep Neural Network.

V. Chaudhary¹ and R. Panwar¹

1. PDPM Indian Institute of Information Technology Design and Manufacturing Jabalpur, Jabalpur, India

Owing to the augmentation of wireless communication, the development of electromagnetic interference (EMI) shielding structures is an open area for research. The devices working at microwave frequencies are hazardous to human health and can also result in the malfunctioning of various sensitive equipments. Various techniques are reported by the researchers for the development of an efficient EMI shielding structure, some of them are composite materials, nanocomposites, metamaterials, and frequency selective surfaces (FSSs) [1]-[3]. FSSs are an array of periodic slots or apertures having excellent electromagnetic (EM) wave filtering properties. Major challenges across the research community are to create a miniaturized, angular stable, wideband, polarization-insensitive, and flexible EMI shielding structure. Multiband structures are often used by researchers to get a wide bandwidth. Whereas, miniaturization is attained either by techniques like 3-D, convoluted geometries, and lumped capacitances. All these methods of bandwidth improvement and miniaturization result in complex design and therefore fabrication becomes tedious. Almost all reported EMI shielding structures uses pure dielectric substrates like FR4 and Rogers. However, bandwidth and miniaturization can be improved by increasing the overall inductance of the shielding structure. The introduction of lumped inductors can be a solution but it not only increases the fabrication complexities but also may result in unwanted parasitic capacitance. Also introducing active or reactive components limits the conformal applications of shielding structures. One possible solution is to use magnetic substrates, which will increase the overall inductance of the shielding structure. Therefore, in this work electromagnetic properties of two magnetic substrates (Ferrite and magnetic silicon rubber) are measured and investigated to improve the bandwidth and miniaturization of an EMI shielding structure. Further, a polarization-insensitive, angular stable FSS is designed and the equivalent circuit model (ECM) is developed to have a physical insight into the structure. Moreover, a competent deep neural network (DNN) approach is employed for fast and accurate optimization of the shielding structure. At last, a prototype is developed and measured for validation of the proposed technique. The schematic of the proposed shielding structure is depicted in Figure 1(a). It comprises an array of periodic unit cells, a magnetic ferrite substrate, and a silicon rubber sheet. Figure 1(b) demonstrates an FSS unit cell with corresponding geometrical design variables. Here, r_o is the radius of the outer circle and r_i corresponds to the radius of the inner circle. d is the length of the patch, w is the width, and periodicity of the unit cell is represented by p . The electromagnetic properties of magnetic substrates are measured using a waveguide-based microwave measurement technique. Figure 1(c) depicts the measured relative permittivity (ϵ_r) and permeability (μ_r) of both the substrates. The real part of μ_r varies between 2.10 and 1.49 and the imaginary part varies between 0.34 and 0.0025 for magnetic silicon rubber when the frequency changes from 8.2 to 12.4 GHz. The real part of ϵ_r is 5.50 and the imaginary part varies between 0.20 and 0.005. On the other hand, the ferrite substrate real part of μ_r changes varies between 1.17 and 1.13 and the imaginary part varies between 0.04 and 0.001. Moving a step further, ECM of the FSS backed substrates is developed and the overall impedance is calculated. A huge database is created using the ECM and a deep neural network is trained using the Levenberg-Marquardt algorithm. The entire dataset is divided into three sections randomly for training, validation, and testing in the proportion of 70%, 15%, and 15%. Once the training, testing, and validation of the network is done, the shielding structure is optimized for resonant frequency and bandwidth. A prototype is then fabricated from the optimized parameters using the printed circuit board (PCB) technique. Figure 2(a) shows the image of the fabricated prototype. Meanwhile, the effect of the magnetic properties of the substrates on the transmission performance of the shielding structure is investigated. When the permittivity of the substrates dominates, a bandwidth of 2.75 GHz is obtained with resonant frequency at 10.42 GHz as shown in Figure 2(b). The bandwidth of surfaces with quite high impedance is directly proportional to the square root of overall induc-

tance. To increase the bandwidth and to achieve miniaturization substrates with dominant magnetic properties are used. The overall inductance of the structure is increased by using substrates with dominant μ_r . Figure 2(b) depicts when substrates with dominant permeability are used in place of permittivity dominant substrates resonance shifts to lower value as the overall inductance of the structure increased. Also, the bandwidth obtained from such magnetic substrate increased to 3.37 GHz from 2.75 GHz. Therefore, it can be concluded that using magnetic substrates bandwidth enhancement and miniaturization of the shielding structure can be achieved.

[1] M. Sonehara, T. Sato, M. Takasaki, H. Konishi, K. Yamasawa and Y. Miura, "Preparation and Characterization of Nanofiber Nonwoven Textile for Electromagnetic Wave Shielding," IEEE Transactions on Magnetics, vol. 44, no. 11, pp. 3107-3110, Nov. 2008. [2] J. Lee, B. M. Jung, S. B. Lee, S. Lee and K. H. Kim, "FeCoNi-Coated Glass Fabric/Polycarbonate Composite Sheets for Electromagnetic Absorption and Shielding," IEEE Transactions on Magnetics, vol. 53, no. 11, pp. 1-4, Nov. 2017. [3] R. Panwar, S. Puthucheri, D. Singh and V. Agarwala, "Design of Ferrite-Graphene-Based Thin Broadband Radar Wave Absorber for Stealth Application," IEEE Transactions on Magnetics, vol. 51, no. 11, pp. 1-4, Nov. 2015.

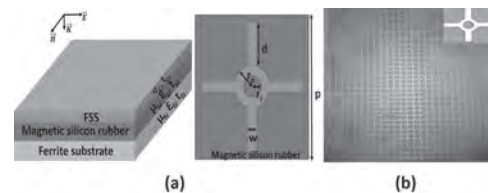


Figure 1. Proposed shielding structure (a) Schematic and FSS unit cell, and (b) Fabricated prototype

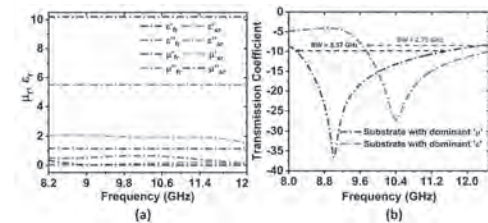


Figure 2. EMI shielding characteristics (a) Frequency-dependent electromagnetic characteristics of silicon rubber and ferrite substrates, and (b) Transmission performance for different configurations of FSS and substrates.

JA-09. Withdrawn

JA-10. Fe-SiC Composite Constituted Multilayer Gradient Perforated Microwave Absorbing Structure for Stealth Applications.

R. Yadav¹ and R. Panwar¹

1. PDPM Indian Institute of Information Technology Design and Manufacturing Jabalpur, Jabalpur, India

Microwave absorbers are advanced electromagnetic structures that can competently deplete the incident electromagnetic (EM) wave, and widely utilized for stealth and electromagnetic interference mitigation applications. There have been enormous strides in the broadening of absorption bandwidth (BW) using thin and lightweight functional materials. Apart from functional materials, the shape and loading of the absorber are equally responsible for attenuating the EM wave. There are various potential structures capable of altering the equivalent EM properties of the material to achieve excellent absorption BW [1]-[2]. The simultaneous achievement of wide absorption bandwidth and lower coating thickness of the absorber layer is a very challenging task. In this work, an effort is made towards the design of thin and broadband triple-layer absorber by incorporating gradient air perforation into the absorbing sheets constituted of iron (Fe)-silicon carbide (SiC) composites synthesized by robust top-down fabrication technique. The gradient air perforation prompts viable absorption BW if the period and diameter of perforations are equivalent to the wavelength. Fe-SiC composites in distinct compositions (i.e., FS1, FS2, FS3, FS4, FS5, FS6, and FS7) have been utilized in the development of microwave absorber. The composites have been developed using a top-down fabrication technique accomplished via a high-energy planetary ball mill (Model: Insmart device, MBM-07, India). The milling process has been initiated by loading stainless steel containers with hard 20 mm and 10 mm diameter steel balls. The powder to ball weight ratio (PBR) of 1:10 was taken with the rotor speed to 400rpm. The EM properties of the composite were measured in the range of 8.2 to 12.4 GHz (i.e., X-band) using a waveguide-based microwave measurement technique. Further, Jaya's-Grey Wolf based hybrid multiobjective optimization technique has been utilized for the modelling of a perforated multi-layered absorber using the measured EM parameters. The mathematical model of air perforation is integrated with the transmission line equations such that the developed structure appears like a gradient perforated triple-layer structure. The fitness function of maximum BW below -10dB with minimum thickness is organized in the hybrid optimization algorithm. An optimal sample has been fabricated using epoxy coating and drilling techniques based on the optimal design variables obtained using the algorithm. The schematic of 3D topology and fabricated prototype of perforated absorber constituted of Fe-SiC composites is shown in Figs. 1 (a) and (b), respectively. Fig. 2 shows the reflection coefficient curve (RC) of single-layer absorber at their optimal thicknesses. Among all Fe-SiC composite database, FS-7 composite achieves a minimum RC value of -24.7dB at 11.1 GHz at an optimal thickness of 1.7mm, covering an absorption BW of 3.1 GHz below -10dB threshold in X-band. Furthermore, FS-4 composite exhibits an absorption BW of 1.7GHz with a minimum RC value of -10.9 dB at 9.3 GHz at an optimal thickness of 1.7 mm. However, FS-3 composite achieves a minimum RC value of -9dB at 8.2 GHz demonstrating no absorption BW. In the proposed gradient structure, the hybrid optimization algorithm chooses composite FS-4 for layer 1 with an optimal thickness of 0.4 mm backed with a perfect electrical conductor. Consecutively, layers 2 and 3 (i.e., air absorber interface) are structured using FS-7 and FS-3 composites with an optimal thickness of 0.9 mm and 0.3 mm, respectively. The optimum air perforation diameter is 6 mm, 5mm, 4mm for FS-3, FS-7, and FS-4, respectively with a period of 20 mm. The magneto-dielectric properties of composite FS-3 are high as compared to FS-4 and FS-7 composites. Due to the larger diameter of air perforation, the effective magneto-dielectric properties are supervised to act as an impedance matching layer. A 1.6 mm multilayer structure (without hole) is compared with the proposed structure as shown in Fig. 2 (b). Due to gradient air perforation in the layered structure, the EM parameters are altered, which leads to the shift of resonance frequency. The obtained result reveals a better -10 dB absorption BW of 3.4 GHz with a minimum RC of -19.9 dB at 10.8 GHz. An exceptional microwave absorption is achieved in terms of peak RC and BW with a substantial reduction in the total coating thickness of 1.6 mm in comparison to a single-layer absorber. Moreover, due to perforation, the weight of the structure is also reduced. The gradient

impedance alignment within the structure improves the other mechanisms of absorption, such as phase cancellation, internal reflection, and frequency dispersion within the structure which results in improved absorption BW.

1. R. Panwar, S. Puthucheri, D. Singh and V. Agarwala, *IEEE Transactions on Magnetics.*, vol. 51, no. 11, pp. 1-4 (2015). 2. L. Zhang, P. Zhou, H. Zhang, L. Lu, G. Zhang, H. Chen, H. Lu, J. Xie, and L. Deng, *IEEE transactions on magnetics.*, vol. 50, no. 5, pp. 1-5 (2013).

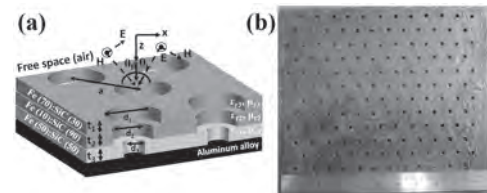


Fig. 1. Schematic of perforated absorber (a) 3D topology and (b) fabricated prototype.

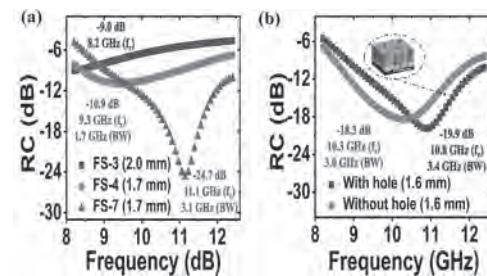


Fig. 2. Frequency-dependent RC curve of the absorber (a) single layer and (b) gradient perforated multilayered absorber in X-band.

JA-11. Experimental Investigation and Comparison of Magnetic Properties at High Frequency Between Non-Annealed and Annealed 1 μm-Thick Steels.

G. Nguyen^{2,1}, J. Tanase¹, K. Nambu¹, K. Fujisaki¹ and E. Tsuchida³
 1. Toyota Technological Institute, Nagoya, Japan; 2. Nagoya University, Nagoya, Japan; 3. Maruyoshi Kogyo Co., Ltd., Kakamigahara, Japan

The μm-thick steels made by the rolling process may be promising magnetic materials for inductor and transformer cores utilized in power applications at high frequency [1]. From [2],[3], the annealing process can be used to enhance the magnetic characteristics of electrical steels, but the characteristics at high frequency of the annealed μm-thick steels have not yet been considered. To try reducing the core loss and improving the permeability of the 1 μm-thick steel significantly, we are researching and implementing a suitable annealing process for this thin steel. This abstract is the first work to investigate advantages of the annealed 1 μm-thick steel compared to the non-annealed 1 μm-thick steel of the same material in terms of the core loss and relative permeability in experiments where the excitation frequency is up to 1 MHz. Moreover, a measurement method for determining the core loss and relative permeability of the non-annealed and annealed steel parts attached in ring cores under test are concisely described in this study. The composition of the considered 1 μm-thick steel is 99.63% Fe, 0.003% C, 0.35% Mn, 0.009% P, and 0.007% S. The annealing process is performed at 450 °C in the atmosphere of Ar. The temperature was raised from the room temperature to 450 °C within one hour, and then held for one hour; last, the material was cooled in a furnace. For evaluation, there are three separate ring cores made and measured in this research. The first ring core is with the annealed 1 μm-thick steel part, the second ring core is with the non-annealed 1 μm-thick steel part, and the third one is a plastic core without a steel part for reference aim. All the ring cores have the same dimension and number of turns of copper coils as given in Fig. 1. The B-H analyzer Iwatsu SY-8219 [4] is utilized for measurement with the sinusoidal excitation method. The primary current I_1 and secondary open-circuit voltage V_2 of a ring core are measured to compute the magnetic field strength H and flux density B as shown in (1) and (2), respectively; then, the core loss per weight P_{cm} is calculated by (3). $H = (N_1 I_1)/L$ (1) $B = (\int V_2 dt)/(N_2 S)$ (2) $P_{cm} = f \cdot (\int H dB) / (\rho \cdot W_m)$ (3) Where $N_1 = N_2 = 23$ is the number of coil turns, $L = 0.05$ m is the average magnetic path length, S is the ring cross section area (and $S_{Ring1} = S_{Ring2} = S_{Ring3}$), $\rho = 7874$ kg/m³ is the steel density and W_m is the weight of steel part. The measurement method has four key steps as follows. STEP 1: The first ring core with the annealed 1 μm-thick steel part is connected to the B-H analyzer for measurement, where the excitation frequency is altered from $f = 10, 50, 100, 200$ kHz and up to 1 MHz. STEP 2: The third ring core without a steel part is connected to the B-H analyzer for another measurement. In this step, the maximum magnetic field strength $H_{Ring3,m}$ of the third ring core is chosen to be equal to $H_{Ring1,m}$ of the first ring core in Step 1 at each frequency. STEP 3: From the six known parameters $B_{Ring1,m}$, $H_{Ring1,m}$, S_{Ring1} , $B_{Ring3,m}$, $H_{Ring3,m}$ and S_{Ring3} , where $H_{Ring1,m} = H_{Ring3,m}$, the maximum flux density through the annealed steel part $B_{Fe,Ring1,m}$ and its relative permeability $\mu_{Fe,Ring1,r}$ in the first ring core at each frequency are estimated by (4) and (5). We note that $H_{Ring1,m}$ is suitably set in Step 1 to force $B_{Fe,Ring1,m}$ to be fixed at 0.3 T in all the frequencies. STEP 4: Repeat Step 1 with the second ring core including the non-annealed 1 μm-thick steel part, and then repeat Step 2 with the third ring core where $H_{Ring3,m} = H_{Ring2,m}$. Similar to Step 3, the maximum flux density through the non-annealed steel part $B_{Fe,Ring2,m}$ and its relative permeability $\mu_{Fe,Ring2,r}$ in the second ring core are estimated by (4) and (5). $H_{Ring2,m}$ is suitably chosen to cause $B_{Fe,Ring2,m}$ to be fixed at 0.3 T. $B_{Fe,Ring[i],m} \approx (B_{Ring[i],m} \cdot S_{Ring[i]} - B_{Ring3,m} \cdot S_{Ring3}) / S_{Fe,Ring[i]}$ (4) $\mu_{Fe,Ring[i],r} = B_{Fe,Ring[i],m} / (\mu_0 \cdot H_{Ring[i],m})$ (5) Where $\mu_0 = 4\pi \times 10^{-7}$ H/m, $S_{Ring[i]} = S_{Ring3}$, and index $i = 1$ for the first ring core in Step 3, or $i = 2$ for the second ring core in Step 4. As depicted in Fig. 2(a), at the frequency $f = 700$ kHz, the core losses per weight P_{cm} of the non-annealed and annealed 1 μm-thick steels are 55.41 W/g and 28.71 W/g, respectively; furthermore, at $f = 1$ MHz, P_{cm} of the annealed steel is 43.95 W/g, while the core loss of the non-annealed steel maybe around 80 W/g as forecasted in the red dashed line. In addition, at $f = 700$ kHz, the relative permeability values $\mu_{Fe,r}$ of the non-annealed and annealed steels are 216 and 401, respectively, as shown in Fig. 2(b); besides, at $f = 1$ MHz, $\mu_{Fe,r}$ of the annealed steel is slightly

reduced to 375. This research has assessed the magnetic properties of the annealed 1 μm-thick steel, where the excitation frequency is varied from $f = 10, 50, 100$ kHz and up to 1 MHz. In details, the core loss per weight P_{cm} and relative permeability $\mu_{Fe,r}$ of the annealed and non-annealed steels at the maximum flux density of $B_{Fe,m} = 0.3$ T were measured and compared. The measured results showed that P_{cm} of the annealed 1 μm-thick steel is around 48.2% smaller than that of the non-annealed steel, and $\mu_{Fe,r}$ of the annealed steel is around 185.6% larger than that of the non-annealed one. Thus, the 1 μm-thick steel implemented in an appropriate annealing process, which has the much better magnetic characteristics than that of the non-annealed steel, is potentially used for inductor cores in power electronic applications at high frequency.

[1] M. Komatsubara, K. Sadahiro, O. Kondo, et al., "Newly Developed Electrical Steel for High-Frequency Use", J. of Magnetism & Magnetic Materials, Vol. 242–245, Part 1, pp. 212-215 (2002). [2] M. C. Guimaraes, F. L. Alcantara, R. U. C. Moreira, et al., "Improvement of Magnetic Properties of a Reversible Hot Rolled Grain-oriented Electrical Steel," IEEE Trans. on Magnetics, Vol. 52, No. 5, ID: 2002704 (2016). [3] J.-Y. Soh, K.-Y. Shin, H. Jung and S.-B. Kim, "Iron Loss Influenced by Magnetic Annealing in 0.1-mm-Thick Grain-Oriented High-Silicon Steels," IEEE Trans. on Magnetics, Vol. 47, No. 10, pp. 3208-3211 (2011). [4] B-H Analyzer SY-8219, Iwatsu Electric Co., Ltd., www.iti.iwatsu.co.jp/en/pdf/BH_catalog14055E-108.pdf.

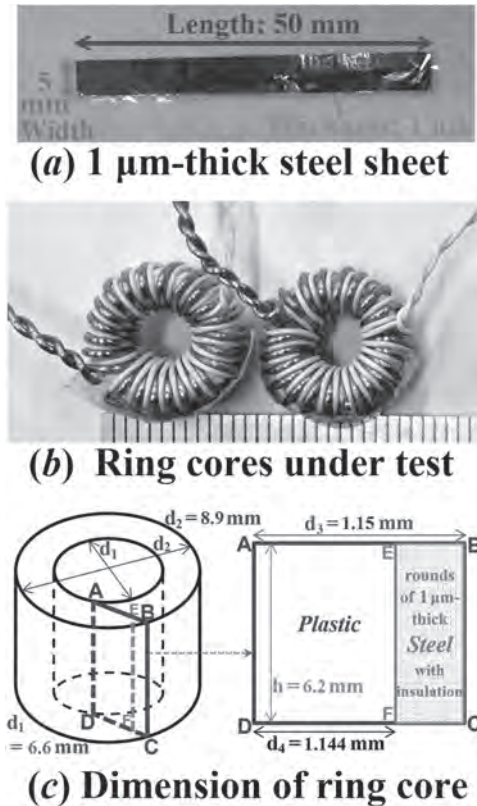


Fig.1: Dimension of 1 μm-thick steel and ring core

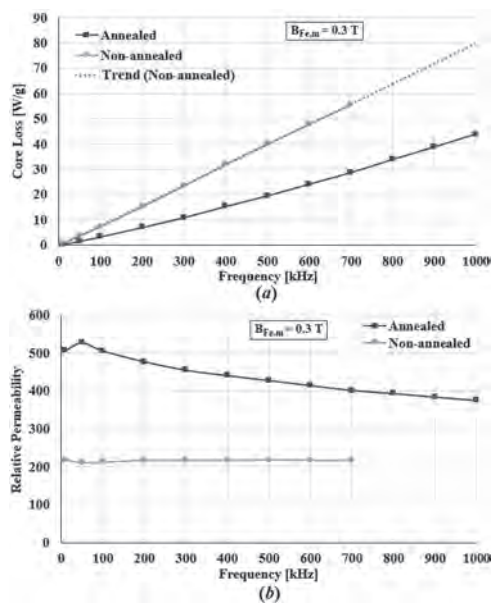


Fig.2: Measured results; (a) Core loss, (b) Relative permeability

JA-12. Fine Tuning of the Magnetic Anisotropy Results in Temperature Independent Ferromagnetic Resonance Frequency for Bi-YIG Thin Films Grown by Pulsed Laser Deposition.

D. Gouéré¹, H. Merbouche¹, C. Carrétéro¹, J. Ben Youssef², E. Jacquet¹, R. Lebrun¹, P. Bortolotti¹, V. Cros¹ and A. Anane¹

1. *Unité Mixte de Physique CNRS, Thales, Université Paris Saclay, Palaiseau, France;* 2. *LabSTICC-UMR 6285/CNRS, Université de Bretagne Occidentale, Brest, France*

Yttrium Iron Garnet (YIG) is the benchmark material for ferromagnetic resonance; it is up to today the only magnetic material that is being integrated in on-shell electronic devices for its radiofrequency properties that combine high resonance quality factor (10^4) and frequency tunability. It is the goal of YIG magnonics to utilize this potential for a large variety of applications ranging from beyond complementary metal-oxide semiconductor (CMOS) computation to radiofrequency front-end and back-end analogue signal processing. YIG devices have however a severe drawback that is that they should include thermal stabilization. This is a necessity since YIG has a relatively low Curie temperature ($\sim 550\text{K}$) which results in a high sensitivity of its magnetization to temperature (~ 4 Gauss/Kelvin). Here, we present a novel approach to solve this long standing issue by engineering the magnetic anisotropy in Bi substituted YIG. We evidence for those films that a vanishing effective magnetization yields high thermal stability over very wide temperature range: from 260K to 400K, where the frequency thermal drift is 50 times smaller than that of YIG. These types of properties can be leveraged for new applications where the temperature dependence of YIG is detrimental, while keeping the extremely low damping and insulating character of YIG^[1]. For instance, this was key for the excitation of coherent spin-waves using SOT^[2]. We anticipate that fabricating a material whose FMR frequency is temperature independent open new opportunities for the field of spintronics. In his seminal article^[3] of 1948 Charles Kittel established the Ferromagnetic resonance (FMR) conditions of magnetic samples with arbitrary shapes stressing the importance of correcting the effective magnetic field that sets the Larmor frequency by taking into account the demagnetization field and the effect of uniaxial anisotropy. In today notations the FMR frequency can hence be written for a thin film in the in-plane magnetization configuration as: $f = \gamma * (H_a * (H_a + (M_s - H_u)))^{1/2}$. Where γ is the gyromagnetic factor, H_a is the applied magnetic field, M_s is the saturation magnetization and H_u is the out-of-plane magnetization and the effective magnetization is defined as $M_{eff} = M_s - H_u$. It arises from this equation that the only temperature dependent terms are $M_s(T)$ and $H_u(T)$. For most ferromagnetic materials H_u depends on M_s with power law dependence defined by Callen and Callen theory^[4]. Nonetheless, by engineering the magnetic anisotropy in Bi-YIG films, we were able to balance the saturation magnetization with the uniaxial anisotropy between 260K and 400K. These measurements were done on thin $\text{Bi}_1\text{Y}_2\text{Fe}_5\text{O}_{12}$ films of 21nm grown on (111)-oriented sGGG substrates with Pulsed Laser Deposition. We varied the substrate growth temperature within a range of 100°C and probed the films effective magnetization using FMR: we evidenced a magnetization state transition from in-plane to out-of-plane as the substrate growth temperature decreases from 500°C to 400°C. To ensure the nominal Bi content as well as the magneto-elastic anisotropy were maintained over all the growth temperature range, X-Ray Diffraction measurements were done and evidenced a perfect structural match between thin $\text{Bi}_1\text{Y}_2\text{IG}$ films. Magneto-Optical Kerr Effect (MOKE) measurements were performed complementary to visualize not only the magnetic domains but also the magnetic anisotropy transition. With room temperature FMR measurements, we obtained the optimal substrate growth temperature range to be 420°C to 430°C: temperatures for which the effective magnetization $M_{eff} \approx 0\text{G}$. Interestingly, for thin films closest to the compensation, FMR measurements performed at lower temperatures evidenced that effective magnetization stay constant in a range of 140K: suggesting $H_u(T) = M_s(T)$ contradictory with Callen and Callen theory^[4]. Finally we measured the frequency thermal drift was about 1mT between 260K and 400K for films close to the compensation, FMR frequency is temperature independent.

[1] L. Soumah, N. Beaulieu, L. Qassym, Nature Communication 9, 3355 (2018) [2] M. Evelt, L. Soumah, A.B. Rinkevich, Physical Review Applied 10, 041002 (2018) [3] C. Kittel, Physical Review 73, 155 (1948) [4] H. B. Callen and E. Callen, Journal of Physics and Chemistry of Solids 27, 1271 (1966).

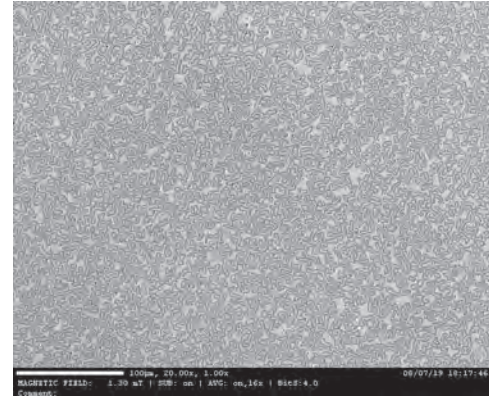


Fig. 1 Polar Magneto-Optical Kerr Effect (MOKE) measurement for a Bi-YIG thin film close to the compensation evidences the presence of magnetic domains.

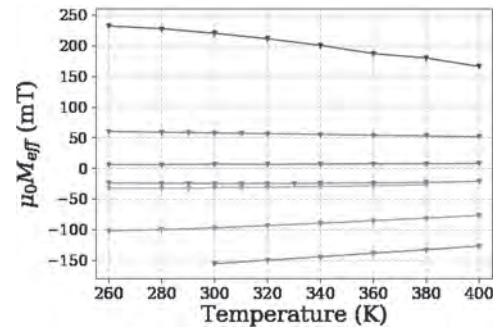


Fig. 2 Variation of the effective magnetization Meff(T) for Bi₁YIG thin films within a range of 140K probed by Ferromagnetic Resonance (FMR) measurement.

JA-13. Microwave Synthesis of Magnetic Hollow Nanosystem and Shape Anisotropy Contribution on Enhancement of the Heating Efficiency.

G. Niraula¹, J.A. Coaquira², G. Zoppellaro³, D. Muraca⁴ and S.K. Sharma^{1,5}

1. Physics, Universidade Federal do Maranhao, Sao Luis, Brazil;

2. Physics, Universidade de Brasilia, Brasilia, Brazil; 3. Regional Centre

of Advanced Technologies and Materials, Faculty of Science, Univerzita

Palackeho v Olomouci Prirodovedecka fakulta, Olomouc, Czechia;

4. Physics, Universidade Estadual de Campinas, Campinas, Brazil;

5. Physics, Central University of Punjab, Bathinda, India

The use of microwave-assisted synthesis (in water) of α - Fe_2O_3 nanomaterials followed by their transformation onto core-shell $\text{Fe}_3\text{O}_4@ \gamma$ - Fe_2O_3 hollow nanosystems encoding well-defined sizes and shapes (nanorings and nanotubes) is henceforth described. The impact of experimental variables such as the concentration of reactants, the volume of solvent employed, and reaction times/temperatures during the shape-controlled synthesis revealed that the key factor that gated generation of the morphologically diverse nanostructures was associated with the initial concentration of phosphate anions employed in the reactants mixture. All the nanomaterials presented were fully characterized by powder X-ray diffraction, FESEM, FTIR, Mössbauer spectroscopy, and SQUID. The core-shell nanostructures that expressed the most promising magnetic responses, nanotubes (NTs) and nanorings (NRs), were further tested in terms of efficiencies in controlling the hyperthermia phenomena, in view of their possible use for biomedical applications, a possibility supported by their excellent viability as screened by in-vitro cytotoxicity tests. These systems NTs and NRs expressed very good magneto-hyperthermia properties, results that were further validated by micromagnetic simulations. The observed specific absorption rate (SAR) and intrinsic loss power (ILP) of the NRs and NTs peaked at the values of 340 W/g and 2.45 $\text{nH m}^2 \text{kg}^{-1}$ (NRs) and 465 W/g and 3.3 $\text{nH m}^2 \text{kg}^{-1}$ (NTs) respectively, at maximum clinical field 450 Oe and under the frequency of 107 kHz, and are the highest values among those reported so far in the hollow iron-oxide family. The higher SAR in NTs accounts for the importance of magnetic shape anisotropy, which is well predicted by the modified dynamic hysteresis (β -MDH) theoretical model. Keywords: $\text{Fe}_3\text{O}_4@ \gamma$ - Fe_2O_3 hollow nanostructures, shape anisotropy, heating efficiency, micromagnetic simulation, Modified dynamic hysteresis model

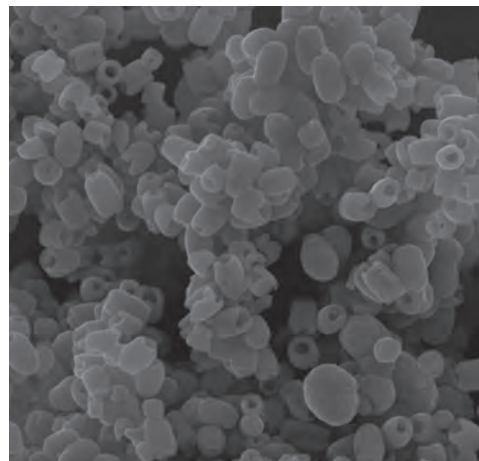


Fig 2: FESEM image of magnetic nanotubes

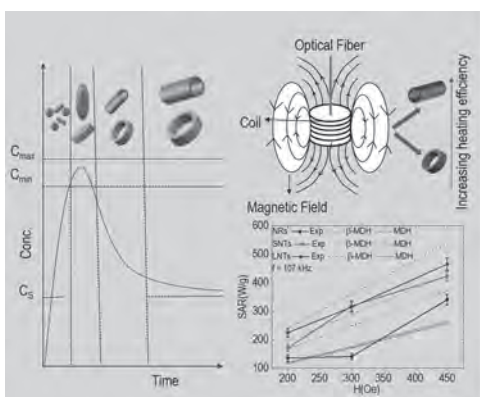


Fig 1: Formation and growth mechanism of hollow nanosystem and specific absorption rate (SAR)

Session JB

CRYSTALLINE SOFT MAGNETS

Paul Ohodnicki, Chair

University of Pittsburgh, Allison Park, PA, United States

INVITED PAPER

JB-01. Flexible Ferromagnetic and Magnetoelectric Thin Films With Excellent Tunability INVITED.

Z. Zhou¹, Y. Zhao¹, G. Dong¹ and M. Liu¹

1. Electronic Materials Research Laboratory, Key Laboratory of the Ministry of Education, School of Electronic and Information Engineering, State Key Laboratory for Mechanical Behavior of Materials, Xi'an Jiaotong University, Xi'an, China

The high demand for flexible spintronics makes growing high-quality flexible ferromagnetic and magnetoelectric thin films urgently. Low-damping flexible $Y_3Fe_5O_{12}$ (YIG) thin films by pulsed laser depositing (PLD)¹ prepared for strain-tunable RF/microwave applications. A noticeable ferromagnetic resonance (FMR) field shift of 180 Oe was obtained along the out-of-plane direction via the flexible tunable factor $f(R)$, which shows a greater FMR tuning frequency shift as much as 550 MHz. Furthermore, we fabricated ultra-flexible and malleable Fe/BaTiO₃ (BTO) magnetoelectric thin films via a damage-free lifting-off process for voltage tunable flexible spintronics. The Fe/BTO magnetoelectric thin films indicated strong in-plane magnetic anisotropy (~1000 Oe), large magnetoelectric (ME) coupling coefficient of 120 Oe/°C along the out-of-plane direction during the heating process, and excellent bending tunability with a 690 Oe FMR field shift along the out-of-plane direction under the flexible tuning ($R=5$ mm). Lastly, we synthesized single-crystalline BTO/LSMO bi-layer magnetoelectric thin films, which shows a self-assembled spring shape due to the lattice mismatch as free-standing. Such spring exhibits record-high elongation/compression capability up to 300% with remarkable resilience and an excellent ME coupling effect. These flexible ferromagnetic and magnetoelectric heterostructures could open a door toward flexible sensors, memories, and spintronics in the future.

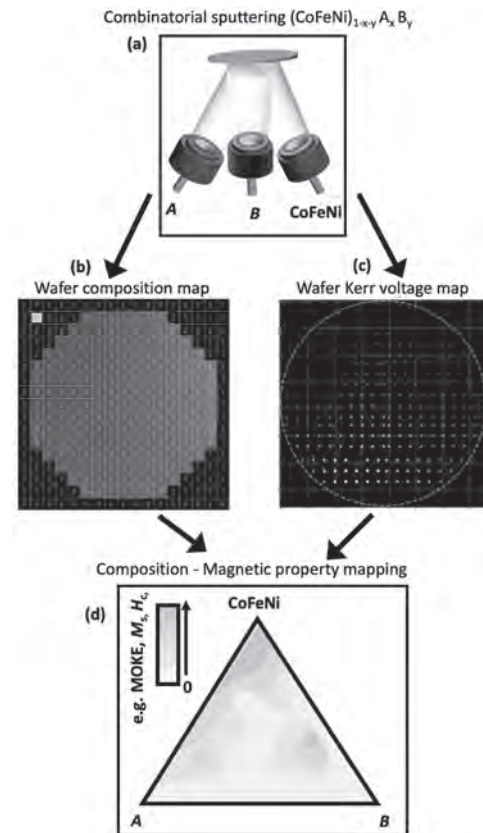
1. G. Dong et al., *Science*, 366, 475-479 (2019) 2. Y. Zhao, et al., *Mater. Horiz.*, 7, 1558-1565 (2020)

CONTRIBUTED PAPERS

JB-02. High-Throughput Studies of Magnetic High Entropy Alloys.R. Rowan-Robinson¹, Z. Leong¹ and N. Morley¹¹. Materials Science and Engineering, The University of Sheffield, Sheffield, United Kingdom

The typical timescale for material discovery is remarkably long, taking between 10 – 20 years to propagate through idea conception, experimentation, optimisation, and deployment¹. Existing global challenges such as the climate emergency require rapid development of new materials on timescales that are incompatible with the traditional *linear* material discovery approach. High-throughput approaches can be applied as a *parallel* material discovery methodology, for which a single sample contains a library of different material compositions that can be rapidly screened for the realisation of new magnetic materials. We apply the high-throughput material discovery approach to the new class of materials known as High Entropy Alloys (HEAs). HEAs often consist of five or more constituent elements mixed in near equal quantities. The name is owed to the resulting high configurational entropy of the alloy, which contributes to suppressing the formation of intermetallic phases and stabilises simple FCC and BCC solid solutions. HEAs occupy the unexplored central regions of phase diagrams, and as such, have potential to provide disruptive materials. Already HEAs have exhibited promising soft magnetic properties such as high saturation magnetisation alongside high electrical resistivity, as well as obtaining nanocrystalline textures^{2,3}. However, the number of constituent elements and the various chemical compositions mean HEAs can be found in a very broad parameter space making it difficult to localise the search for useful compositions. This work has used combinatorial sputtering, to fabricate sample libraries containing composition variations of up to 35 at.% on a single Silicon wafer (Figure 1a). We investigate the $(\text{CoFeNi})_{1-x-y}\text{A}_x\text{B}_y$ series, where A and B are 3d/4d transition metals (with the addition of Si and Al). Systems studied include CoFeNiMnAl, CoFeNiMnSi, and CoFeNiMnV. We implement a program to model the composition variation across a 3" Silicon wafer with three sputter sources at different incidence angles with concurrent deposition (Figure 1b). The resulting sample library is characterised using a high-throughput magneto-optical Kerr effect (MOKE) magnetometer which has been developed to automatically map the Kerr voltage (which is proportional to the magnetic moment) and coercive field across this sample library as function of HEA composition (Figure 1c). These can then be combined to achieve magnetic property mapping within the chemical composition space (Figure 1d). Following this, XRD, SQUID magnetometry, FMR and magneto-transport are used to generate a complete structural and functional property description of selected compositions. The resulting methodology not only provides a scalable process for magnetic HEA fabrication and characterisation, but can also be paired with data driven machine learning material discovery strategies such as Materials 4.0⁴. The large datasets necessary for machine learning are costly to procure and so far lacking in functional magnetic properties (e.g. M_s , H_c) for which these high-throughput methods could provide.

1. Y. Liu, T. Zhao, W. Ju and S. Shi, *J. Materiomics* 3, 159–177 (2017). 2. Y. Zhang, T. Zuo, Y. Cheng and P. K. Liaw, *Sci. Rep.* 3, 1455 (2013). 3. T. Zuo *et al.*, *Acta Mater.* 130, 10–18 (2017). 4. R. Jose and S. Ramakrishna, *Appl. Mater. Today* 10, 127–132 (2018).



Schematic representation of the high-throughput thin film methodology applied to magnetic material discovery, including (a) combinatorial sputtering, (b) modelling the composition across the wafer, (c) a measured Kerr Voltage map, and (d) mapping of magnetic properties as a function of chemical composition.

JB-03. Accelerated Development of Soft Magnetic Alloys.R. Ramanujan¹, V. Chaudhary¹, S.P. Padhy¹, L. Tan¹ and Z. Tsakadze¹¹. School of Materials Science and Engineering, Nanyang Technological University, Singapore, Singapore

Abstract: The accelerated development of new soft magnetic materials is urgently required to address the challenges of next generation high frequency rotating electrical machines. We used high-throughput experimental and characterization techniques as well as thermodynamic modeling and machine learning (ML) to develop novel soft magnetic materials based on the Fe-Co-Ni alloy system. The experimental methods include (i) Direct energy deposition based additive manufacturing of compositionally graded bulk materials, (ii) Magnetic thin films with a range of compositions, (iii) Chemical flow synthesis of magnetic nanoparticles, (iv) Spark plasma sintered compositionally graded magnetic alloys. The structural, magnetic, mechanical, and electrical properties were determined. The feasibility of our strategy to develop new soft magnetic alloys has been demonstrated. **Introduction:** Soft magnetic materials are the key component for various applications such as electric motors and generators, magnetic shielding, robotics, electromagnets, sensors, etc [1, 2]. Such systems utilize a significant fraction of the total energy consumption of the world, hence increasing their efficiency will have a significant impact on the urgent need for energy conservation. High frequency rotating electrical machines require magnetic materials with a balance of magnetic, mechanical, and electrical properties. The traditional methods of developing such materials are costly and time consuming, limiting the opportunity to discover new excellent materials. Hence, high throughput methods are of high demand for accelerated discovery of novel materials and to improve the properties of existing materials. We present experimental and computational high throughput approaches to design new magnetic materials. **Methods:** Compositionally graded Fe-xNi [3], Fe-xCo, Fe-xNi-yMo, Fe-xCo-yNi samples were prepared by a DED process. High purity spherical Fe, Co, Ni, Mo powders with sizes ranging from 50 to 150 nm were employed. Thin film libraries of Fe-Co-Ni were prepared by co-sputtering of Ni-21Fe and Co targets using magnetron sputtering at a base pressure of 10^{-8} torr. Thermodynamic modeling was found to be very helpful to identify the heat treatment conditions [4]. The following characterization methods were employed: XRD for crystal structure and phase fraction, EPMA-WBS and EDX for composition, PPMS and magnetic field assisted TGA for magnetic properties, four-point probe for electrical resistivities, and nano(micro)-indentation for mechanical properties. A neural network model was trained on the data to predict the magnetic, mechanical and electric properties. Figure 1 shows the methods and the properties of our interest.

Results and discussion: Additive manufacturing was utilized to explore a range of compositions. Iron rich ternary Fe-Co-Ni (Fe > 75%, Co < 20%, Ni < 25%) alloys exhibit saturation magnetization (M_s), coercivity (H_c), Curie temperature (T_c) and hardness values ranging from 167 to 218.4 emu/g, 19.6 to 10.2 Oe, 534 to 940 °C, 185 to 359 Hv, respectively. Fe-8Co-9.1Ni and Fe-7.4Co-11.3Ni were found to have optimum magnetic and mechanical properties with M_s of 218.4 and 217 emu/g, H_c of 10.2 and 13 Oe, T_c of 765 and 741 °C, hardness of 334 and 359 Hv, respectively. In spark plasma sintered compositionally graded Ni-21Fe-xCo alloys, the largest M_s , H_c , T_c and HV were observed in Co rich samples while the resistivity was found to be larger in Ni rich samples. As an example, the compositions along the diameter of 7.6 cm sample of a co-sputtered thin film is shown in figure 2. Thus, the feasibility to accelerate the development of novel soft magnets has been demonstrated in the Fe-Co-Ni system. **Acknowledgement:** This work is supported by the AME Programmatic Fund by the Agency for Science, Technology and Research, Singapore under Grant No. A1898b0043.

[1] V. Chaudhary, S.A. Mantri, R.V. Ramanujan, R. Banerjee, Progress in Materials Science 114 (2020) 100688. [2] J.M. Silveyra, E. Ferrara, D.L. Huber, T.C. Monson, Science 362 (2018) eaao0195. [3] V. Chaudhary, N.M. Sai Kiran Kumar Yadav, S.A. Mantri, S. Dasari, A. Jagetia, R.V. Ramanujan, R. Banerjee, Journal of Alloys and Compounds 823 (2020) 153817. [4] S. Dasari, V. Chaudhary, B. Gwalani, A. Jagetia, V. Soni, S. Gorsse, R.V. Ramanujan, R. Banerjee, Materialia 12 (2020) 100755.

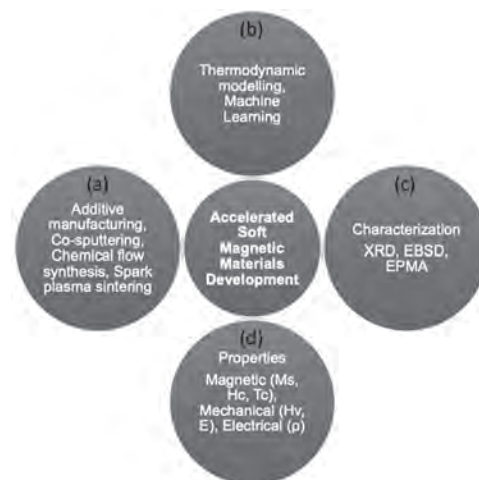


Fig. 1 Soft magnetic materials development using accelerated (a) experimental, (b) computational and (c) characterization techniques, (d) measured/predicted properties

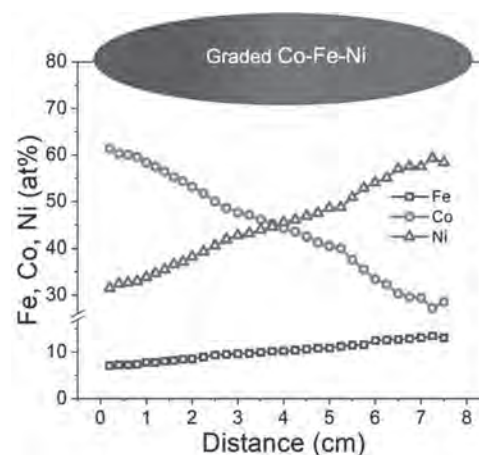


Fig. 2 Change in composition across the diameter of circular graded thin film

JB-04. Compositionally Graded Fe/Co/Ni/NiFe/FeCoV Soft Magnetic Materials.

V. Chaudhary¹, Z. Tsakadze¹ and R. Ramanujan¹

¹. School of Materials Science and Engineering, Nanyang Technological University, Singapore, Singapore

Abstract: Compositionally graded materials are attractive since the properties can be optimized according to the spatial requirement. We report the use of spark plasma sintering for the processing of compositionally graded magnetic materials. Magnetic, mechanical and electrical properties were screened using high throughput characterization techniques. A significant change in all these properties, e.g., saturation magnetization (M_s) ranging from 57 to 224 emu/g, Curie temperature (T_c) ranging from 358 to 1116 °C, and Vickers hardness ranging from 91 to 195 HV across the length of a single cylindrical sample was observed. **Introduction:** Elemental Fe, Co, Ni exhibit ferromagnetic behavior, and their alloys such as Fe-Co-2V (hiperco) and Ni-21Fe (permalloy) are well established commercially available soft magnetic materials. Fe-Co-2V exhibits an attractive combination of high saturation magnetization, high Curie temperature, high yield strength, and is very useful for high temperature magnetic applications. On the other hand, Permalloys exhibit low coercivity, high permeability, and moderate saturation magnetizations and are of high interest for transformers, electric motors and other electromagnetic devices. Magnetic components of a power electronic converters functioning at high frequency can be >50 % of total weight of the system[1]. It has been demonstrated that graded properties of soft magnetic materials are beneficial for next generation power converters/generators[2, 3]. Therefore, developing magnetic components with spatially optimized properties is of high interest[1]. This work demonstrates the use of spark plasma sintering (SPS) for the accelerated preparation of a compositionally graded magnetic materials. Fe/Co/Ni/NiFe/FeCoV have been prepared using gas atomized spherical powders of Fe, Co, Ni, Ni-21Fe and Fe-Co-2V. This graded SPS technique produces a dense bulk metallic sample with discrete changes in composition, resulting in tunable, spatially optimized structural and functional properties. **Experiment:** Gas atomized prealloyed Fe-Co-2V and Ni-21Fe, and elemental Co, Fe and Ni, from Tosoh SMD Inc. were used as starting powders. The purity of all the powders is >99.9%. The 5 compositions were loaded layer by layer in a graphite die. Sintering of compositionally graded Fe/Co/Ni/NiFe/FeCoV soft magnetic materials was performed using a Spark Plasma Sintering (SPS) equipment (Fuji Electronic Industrial, SPS-211LX) at a vacuum level below 8 Pa. The sample was vertically cut in two sections, one section was annealed at 800 °C for 4 h. The crystal structure of graded samples was determined by X-ray diffraction (XRD) using a Bruker D8 discover diffractometer (CuK α radiation). Elemental mapping was performed by an energy dispersive X-ray spectrometer attached to the SEM. The magnetic properties were measured using a physical property measurement system (PPMS) (EverCool-II, Quantum Design), equipped with a vibrating sample magnetometer. The microhardness of the graded samples was measured by a Vickers hardness tester (Future-Tech). **Results and conclusion:** Saturation magnetization (M_s), Curie temperature (T_c) and Vickers hardness (HV) of a typical compositionally graded Fe-Co-Ni-NiFe-FeCoV sample are shown in figure 1. Both ends (Fe and FeCoV) of the sample exhibit M_s of >200 emu/g, while the central region, which is Ni, exhibits the minimum M_s of ~57 emu/g. The Curie temperature of the compositionally graded sample measured by employing a permanent magnet placed near the TGA pan. The Co region exhibits the highest T_c , with the T_c following the sequence of Co > FeCoV > Fe > NiFe > Ni. These M_s and T_c values closely matched with the values reported in earlier references. A significant change in mechanical properties across the sample was observed with a maximum Vickers hardness of 195 HV in the FeCoV region. Thus, SPS processed samples with spatially varying compositions were developed, relevant to the urgent need for magnetic components with spatially optimized properties. **Acknowledgement:** This work is supported by the AME Programmatic Fund by the Agency for Science, Technology and Research, Singapore under Grant No. A1898b0043.

[1] D. Rodriguez-Sotelo, M.A. Rodriguez-Licea, A.G. Soriano-Sanchez, A. Espinosa-Calderon, F.J. Perez-Pinal, IEEE Access 8 56238-56252, (2020).
[2] V. Chaudhary, S.A. Mantri, R.V. Ramanujan, R. Banerjee, Progress in

Materials Science 114, 100688 (2020). [3] K. Byerly, P.R. Ohodnicki, S.R. Moon, A.M. Leary, V. Keylin, M.E. McHenry, S. Simizu, R. Beddingfield, Y. Yu, G. Feichter, R. Noebe, R. Bowman, S. Bhattacharya, JOM 70, 879-891 (2018).

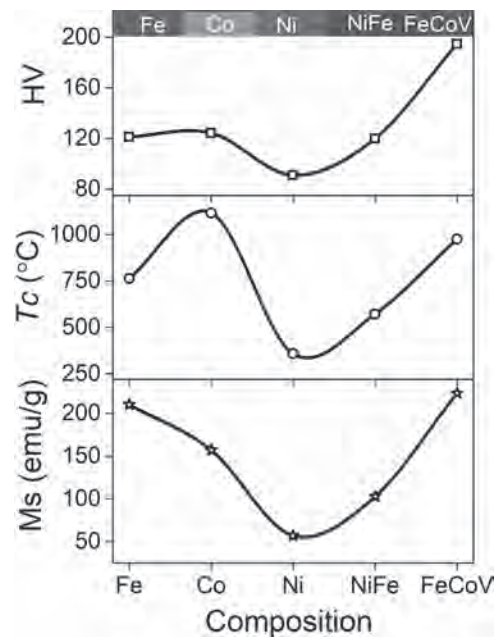


Fig. 1 Change in saturation magnetization (M_s), Curie temperature (T_c) and Vickers hardness (HV) across the length of a compositionally graded cylindrical sample

JB-05. Parametric Semi-Empirical Design of Magnetic Properties in Complex Concentrated Alloys: Curie Temperature and Saturation Magnetisation.

Z. Leong¹, R. Rowan-Robinson¹, A. Quintana-Nedelcos¹ and N. Morley¹
 1. The University of Sheffield, Sheffield, United Kingdom

Alloy systems of the past tend towards single principal component alloy systems. In present research, the stoichiometry of alloy systems with large number of alloying components (>4) can be adjusted to stabilise near-ideal solid solution phases (termed High-entropy alloys, HEAs due to their high configurational entropy), or to possess some mixture of ordered intermetallic phases and the near-ideal solid solution phase (termed Complex Concentrated Alloys, CCAs). HEA and CCA possess many design degree-of-freedom. Precise control over stoichiometry and thermomechanical history lead to exciting magnetic properties; *e.g.* through the formation of nano-composite microstructures [1] in CCAs can achieve good magnetic softness by allowing exchange averaging of the magnetic anisotropy. A major challenge to general application is the vast compositional design space; if ignoring stoichiometry: restricting the number of elements to 1) 3d transition metals, and 2) Si and B, there are $10C5 = 792$ [RRR1] possible equimolar combinations. Millions more are possible if stoichiometry is relaxed. Appropriate strategies to filter out good candidate families for study are thus essential. Alloy design can be generalised to two approaches: data-driven discovery (DDD) and functionality-driven discovery (FDD). For DDD experimental data obtained from exploratory and characterisation frameworks are extrapolated for design and prediction; in FDD search and optimisation methods are used to achieve targeted properties. Prediction models (*e.g. ab-initio*) are used in conjunction with FDD to determine microscopic parameters that govern material properties. FDD is useful in exploring materials with large numbers of degree-of-freedom such as HEA/CCA systems as extrapolation from experimental data is not a good predictor of quantum mechanical behaviour (*i.e.* electronic structure interactions). *Ab-initio* models can calculate potential properties of new compositions, iterating over shedloads[RRR2] of stoichiometries using search and optimisation methods. Although computationally efficient, significant computational power is still required. Applying reasonably accurate low-fidelity pre-filters derived from quantum principles reduces the computational resources required. This work uses two such low-fidelity pre-filters using a parametric semi-empirical approach for determining the saturation magnetisation and mean Curie temperature of HEA/CCA systems. The Curie temperature can be expressed as a function alloyed system (*i.e.* the number of impurity atoms). At the electronic level these changes are due to 1) Variations of the local moments, and/or 2) Changes in interaction strength between moments represented by the molecular field coefficient (dependent on interatomic distances and local environment effects) [2]. Since the uniaxial pressure experienced by the valence electrons upon interatomic distance changes leads to electronic density compression [3], the rectangular band model [4] can be used to explore the onset of ferromagnetism by evaluating the bulk modulus, B with respect to the Stoner criterion. From this, the ratio B/E_F (where the Fermi energy E_F is approximated by the Mulliken electronegativity, X_M) is used to predict the Curie temperature in HEAs and CCAs (*cf.* Fig. 1). The predictions are validated through synthesised as-cast HEA/CCA compositions that are characterised on a SQUID-VSM and are found to be dependent on the amount of antiferromagnetic Cr alloying in the system. The Bethe-Slater curve forms part of the early understanding of magnetism and the electronic-structure-driven magnetic ordering of 3d transition metals. Slater Rules [5] are used to evaluate the 4s:3d orbital radius ratio to reconstruct the Bethe-Slater curve (*cf.* Fig. 2a) using synthesised HEA/CCA compositions from literature, predictions, and our own experiments. Deviations in the 3d Bethe-Slater curve due to electronic interactions lead to curve shifts and model multiplicities, making predictions non-trivial. Orbital radius changes and valence symmetry-breaking are thus evaluated in a parametric function derived from rule-of-mixtures X_M and valence electron values as a supplement to the modified Beth-Slater curve. Plotted using the same dataset, this function in Fig. 2b shows good parameterisation of M_S with no model multiplicities making it suitable for design predictions. Both models show reasonable accuracies when compared to the experimental data and data from literature. One benefit of both models is that they are

derived from common parameters (Bulk modulus, Mulliken electronegativity, atomic number, and d-electron count). This means that the predictive calculations can be obtained by using the rule-of-averages to determine the weighted mean of these parameters for various alloy systems. In order to further test the validity of these models, the models are used with an evolutionary algorithm to design a HEA/CCA with targeted Curie temperature and saturation magnetisation. The results of this prediction are synthesised and characterised through x-ray diffraction and SQUID-VSM and will be presented here.

[1] N.A. Morley, B. Lim, J. Xi, A. Quintana-Nedelcos, Z. Leong, *Sci. Rep.*, Vol. 10, 14506 (2020). [2] J.P. Gavigan, D. Givord, H.S. Li, in: *Concert. Eur. Action Magn. CEAM*, p.163–173 (1989). [3] S.A. Serebrinsky, J.L. Gervasoni, J.P. Abriata, V.H. Ponce, *J. Mater. Sci.*, Vol. 33, 167–171 (1998) [4] D.G. Pettifor, *Bonding and structure of molecules and solids* (1995). [5] J.C. Slater, *Phys. Rev.*, Vol 36, p.57–64 (1930).

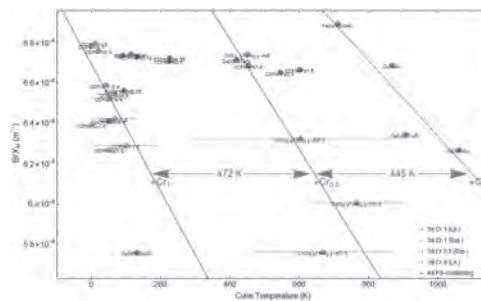


Fig. 1. Plot of a dimensionless number, B/X_M against the Curie temperature for experimental values as well as values taken from literature. The lines represent a guide to the eye for the various amounts of Cr addition to the composition.

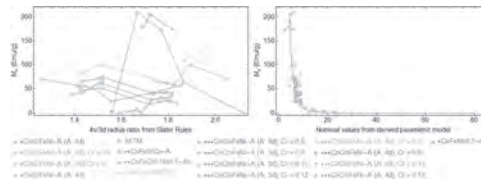


Fig. 2. Saturation magnetisation plotted against the 4s:3d ratio calculated using Slater Rules. *New results presented here **Experimental results from literature, ***Simulated results from literature.

JB-06. Data Mining Based Development of Fe-Co-Ni Soft Magnetic Material.

S.P. Padhy¹, V. Chaudhary¹, G.J. Conduit², V. Sharma¹, L. Tan¹ and R. Ramanujan¹

1. Materials Science and Engineering, Nanyang Technological University, Singapore, Singapore; 2. Physics, University of Cambridge, Cambridge, United Kingdom

Abstract: Accelerated materials development has gained interest in the research community as this approach can generate large amount of data in short period of time, and models built from this data can optimize the properties of the material for specific engineering applications. One such material is soft magnetic material which are widely used in electric motors, generators, transformers, inductors, etc. To model and optimize the properties, machine learning can be deployed. We present preliminary findings of the data mining of the literature for the Fe-Co-Ni alloy system. The processing conditions, properties, and compositions were obtained from the literature. The use of a machine learning tool to predict the properties based on composition, processing parameters, and structural information is described. **Introduction:** Globally, in the past two decades, total energy consumption has increased exponentially and electric motors account for a significant fraction of the total power consumption[1]. Soft magnetic materials play an important role in energy conversion and are widely used in electric motors, transformer cores, electric vehicles, inductors, etc [2]. However, commercially available soft magnetic materials do not have the optimum balance of properties needed in high frequency electric motors operating in extreme environments. Hence, machine learning based magnetic property prediction, optimization and design of soft magnetic materials has gained attention [3-5]. We build a Fe-Co-Ni based metallic soft magnetic materials database from literature and use a neural network algorithm [6, 7] to optimize properties. **Database and Machine Learning:** A database of 891 data entries comprising magnetic, mechanical, and electrical properties of various composition of Fe-Co-Ni alloys processed at various conditions was compiled from relevant literature. To curate this database, 55 references were compiled, including standard books, handbooks, and relevant publications. The atomic % of other elements in the alloys was restricted to maximum of 10%. Further, the database was preprocessed to convert the weight % to atomic % of the elements, to convert alphanumeric type of material and processing condition entries to numerical, and to calculate grain size from coercivity and yield strength of the alloys. This preprocessed database was used to train the machine learning tool with input variables: (a) composition, (b) type of material (categorical), (c) processing parameters like treatment temperature and time, cooling rate, % reduction in area (% r.a.) either by cold rolling or hot rolling, reheating temperature and time, etc., (d) grain size, and (e) volume fraction of phases (FCC, BCC, HCP). The output properties were saturation magnetization, log(coercivity), log(maximum permeability), log(electrical resistivity), yield strength, tensile strength, log(elongation), Vickers hardness, and cost of the material. The quality of fit, coefficient of determination (R^2) values was determined through cross-validation. Using the trained model, properties of various compositions were predicted. **Results and Discussion:** Figure 1 shows the R^2 values from cross-validation and the uncertainty in prediction for the output parameters. The algorithm was able to predict the properties in good agreement with the literature data. However, the prediction for electrical resistivity and elongation were not as good as that of other properties. This can be attributed to the lack of the data and complex behavior of the properties with the input parameters. The trained model was used to predict the properties of various Fe-Co-Ni alloys with the following conditions: cold rolled sheets with 95% r.a., annealed at 1000°C for 2 hours, and furnace cooled. The predicted saturation magnetization for the above specified conditions reveals a complex interplay between the properties, hence there it could be possible to design a soft magnetic material with improved mechanical strength. **Conclusion:** Using this robust neural network model and data mining, preliminary results relevant to the development of a Fe-Co-Ni based soft magnetic material with optimal combination of properties could be obtained. **Acknowledgement:** This work is supported by the AME Programmatic Fund by the Agency for Science, Technology and Research, Singapore under Grant No. A1898b0043, and the Royal Society.

[1] R. Saidur, Renewable and Sustainable Energy Reviews, vol. 14, no. 3, p. 877-898 (2010) [2] V. Chaudhary, S.A. Mantri, R.V. Ramanujan, et. al., Progress in Materials Science, vol. 114, p. 100688 (2020) [3] Y. Wang, Y. Tian, T. Kirk, et. al., Acta Materialia, vol. 194, p. 144-155 (2020) [4] J. Nelson, and S. Sanvito, Physical Review Materials, vol. 3, no. 10, p. 104405 (2019) [5] J. Konieczny, L. Dobrzański, B. Tomiczek, et. al., Archives of Materials Science, vol. 106, p. 106 (2008) [6] B.D. Conduit, N.G. Jones, H.J. Stone, et. al., Scripta Materialia, vol. 146, p. 82-86 (2018) [7] B. Conduit, N.G. Jones, H.J. Stone, et. al., Materials & Design, vol. 131, p. 358-365 (2017)

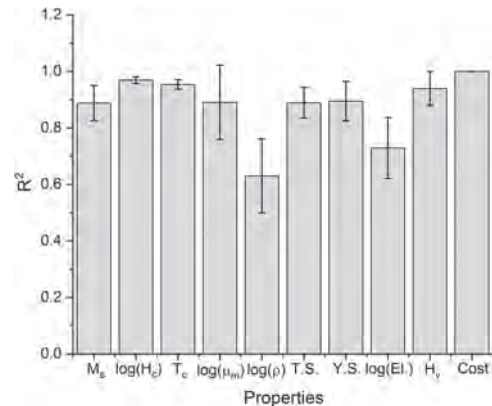


Figure 1: Coefficient of determination (R^2) values and the uncertainty in prediction of the properties, i.e., saturation magnetization (M_s), coercivity (H_c), Curie temperature (T_c), maximum permeability (μ_m), tensile strength (T.S.), yield strength (Y.S.), elongation (EI), Vickers hardness (H_v), and cost (from left to right).

JB-07. Data Mining Approach to Development of Iron-Silicon Soft Magnetic Alloys.

L. Tan¹, V. Chaudhary¹, S.P. Padhy¹, V. Sharma¹, G.J. Conduit² and R. Ramanujan¹

1. School of Materials Science and Engineering, Nanyang Technological University, Singapore, Singapore; 2. Department of Physics, University of Cambridge, Cambridge, United Kingdom

Abstract: There has been renewed interest in recent years to accelerate materials development beyond traditional approaches. A combination of both machine learning and high-throughput experiments can be used for predicting material properties and designing compositions beyond what is currently known. Herein we report the use of a computational tool, Alchemite™, to mine for important processing parameters of Fe-Si-Al alloys from a data set curated from published experimental results. The preliminary calculations suggest that this is a viable method to develop new Fe-Si based alloys. **Introduction:** Silicon steels (Fe-Si) are an important class of materials as they are widely used in applications like electric motors and transformers. Currently, 3.2 wt.% Si is widely used due to (i) good balance of electrical and magnetic properties, and (ii) ductility requirements in traditional processing methods.¹ Recent trends have pointed to higher Si content of up to 10 wt.%, with an addition of small amounts of aluminum (Al) to improve material performance. Due to the small literature, it is imperative that we use machine learning to explore higher Si compositions and their processing methods to obtain a good balance of soft magnetic properties, electrical properties and mechanical properties. **Data Set and Machine Learning Model:** A typical machine learning model comprises three parts: training data, attributes for describing the material, and the machine learning algorithm to map the attributes to properties. The Fe-Si-Al data set was compiled of reported experiment values from 40 references (IEEE Ferromagnetism Handbook² and 39 journal references, published between 2000 – 2020), resulting in a total of 572 entries. The attributes that were selected as input parameters to describe the material were (i) Composition, (ii) Type of material – like ingots, sheets or powder etc., (iii) Final thickness of the material, heat treatment conditions (iv) Treatment temperature, (v) Treatment time and (vi) Cooling rate, (vii) Frequency and (viii) Magnetic flux density. The output parameters comprised various soft magnetic, electrical and mechanical properties. Alchemite™ is a machine learning technology commercialized for materials and industrial chemicals design through Intellegens.³ The artificial neural network trains from the data set provided and predicts the selected material properties. The coefficient of determination (R^2) values was obtained to determine the consistency of the data and predictions. **Results and Discussion:** Figure 1 shows the R^2 values for the input parameters. The machine learning tool showed good predictions for most properties, although mechanical properties were not as well predicted ($R^2 < 0.8$). This is expected as there is a gap in the reported literature. More work will be done to address this gap, by means of improving the data set through theoretical calculations and high-throughput experimental methods. We studied the machine learning model parameters to reveal the most important variables for each output parameter: The frequency of operation affects total core loss greatly, like observations in alternating current (AC) applications – core loss is higher at increased operating frequency. To mitigate such effects, electrical resistivity must be increased – by controlling material thickness, grain size, and composition. Next, the type of material strongly affects the coercivity. The coercivity is affected by the grain size and composition, and this is in turn is affected by the method of fabrication and subsequent processing. The tensile strength is sensitive to the cooling rate because it affects the formation of different phases (A2, B2, and D03). It is reported that the ordering of phases (in B2 and D03) can interact with dislocations, resulting in a strengthening effect which decreases ductility.¹ The phases formed also depend on the Si content, as reflected by the correlation between yield strength and Si content. The above highlights how the various input attributes are interrelated in affecting the output properties, and physical insights this can deliver. This underpins the main difficulty in traditional trial and error experiments and the mammoth task to undertake if it is to be done manually. **Conclusions:** The results show that the use of Alchemite™ for the development of Fe-Si-Al alloys are robust and promising, as it can capture property-processing relationships and highlight gaps in the data set. More work will be focused

on improving the data set and high-throughput experiments performed to compare the results obtained with the predicted values. This will enable us to add to knowledge on achieving optimized and balanced properties in Fe-Si based alloys. This work is supported by the AME Programmatic Fund by the Agency for Science, Technology and Research, Singapore under Grant No. A1898b0043 and the Royal Society.

[1] G. Ouyang, X. Chen, and Y. Liang, Journal of Magnetism and Magnetic Materials, Vol. 481, p.234–250 (2019) [2] RM Bozorth, Ferromagnetism. (IEEE Press, 1993) [3] <https://intellegens.ai/> (accessed January 2021)

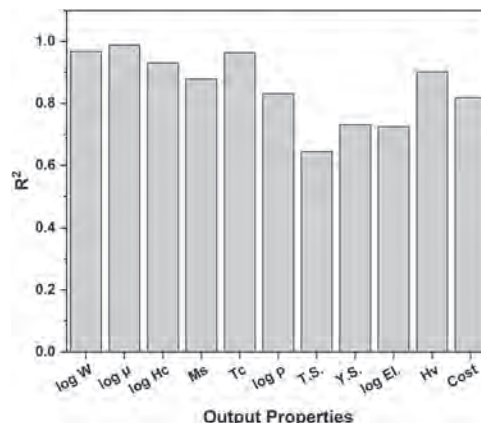


Fig. 1: Coefficient of determination values of output properties from machine learning predictions. The properties from left to right are: W – Total core loss, μ – Permeability, Hc – Coercivity, Ms – Saturation magnetisation, Tc – Curie temperature, ρ – Electrical resistivity, T.S. – Tensile strength, Y.S. – Yield strength, El. – Elongation, Hv – Hardness and Cost.

JB-08. Effect of Cutting Methods on Magnetic Properties of Electrical Steel.

H. Wang¹, J. Chen¹, Y. Jiang¹ and D. Wang¹

1. The Key Laboratory of Science and Technology on Vessel Integrated Power System, Naval University of Engineering, Wuhan, China

Introduction Manufacturing of electrical machines, in general, involves cutting of electrical steel sheets to appropriate sizes. Different cutting techniques such as punching, electrical discharge machining (EDM) and laser cutting are popular. These methods cause damage inside the material close to the cutting edge, which results in deterioration of magnetic properties [1]. Existing studies are based on measurement result by Epstein frame, Ring sample and single-sheet tester. However, these methods do have problems, causing error when analyzing influence of manufacture on material properties[2]. For example, the such non-ideal factors as overlapping joint causes significant eddy current loss especially at high frequency, which may make effect of manufacture effect negligible. In order to obtain more accurate measurement results, this paper aims to propose a new method to clarify the cutting effect on magnetic properties of silicon steel, eliminating those non-ideal factors, and to find out mechanism behind the deterioration of magnetic properties based on macroscopic magnetic measurement and microstructure observation.

2Effect of Cutting Methods on Magnetic Properties of Electrical Steel

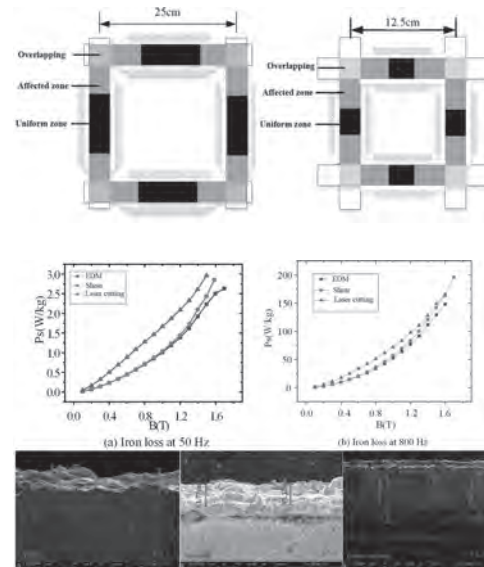
2.1Macroscopic Magnetic Measurement The effect of cutting on the electrical steel sheets is analyzed by magnetic measurement on steel strips of different widths. The magnetic test samples were 35WW270 electrical steel lamination (300 mm×30 mm×0.35 mm). Half of the samples were cut along rolling direction while the other half were in the transverse direction. Then the samples have been cut along their length into different width by shearing, EDM, laser cutting, and glued up with polyimide tapes. Magnetic measurements are usually performed on electrical steel samples with Epstein frame. Nevertheless, the Epstein frame has some intrinsic weaknesses. One of them is that the flux density and specific total loss is uneven near the corners. The Epstein frame can be divided as uniform area, transitional area and overlapping area. In order to eliminate the impact of overlapping area and transitional area, two Epstein frames were designed as Fig 1, E(25), 25cm (standard) and E(12.5), 12.5cm (non-standard) Epstein frames, which have identical corner areas and transitional areas. The only difference in size is that the uniform area of E(12.5) is shorter than E(25). The same steel sheet (300mm length *30mm width) were used in both Epstein frames and their total absolute loss was measured. Magnetic measurement are performed following standard IEC: 604004-2. It can be assumed the absolute loss of corner and affected area of E(25) and E(12.5) is equal because of the identical corners and affected area. Then the only difference in absolute power loss between the two Epstein frames is due to the difference in absolute loss of the different uniform areas. The magnetic properties of the samples were measured at 50-800 Hz, and the results at 50 Hz were shown in Fig 2. When $B = 1$ T and frequency is 50 Hz, compared with EDM, the iron loss of samples with shearing increased by 5.6% and that with laser cutting increased by 32.6%. It can be found that the difference decreased at a higher frequency. The iron loss can be divided into static loss and dynamic loss. With the frequency increasing, dynamic loss takes more share of total iron loss[3]. Therefore, it can be assumed that the effect of cutting stresses on static loss is greater than that on dynamic loss.

2.1.1Microstructure Observation The steel samples were prepared by grinding on 400, 800, and 1200 grit SiC papers and polishing using 3 μ m diamond paste to obtain a mirror-like surface. Specimen microstructure was examined by scanning electron microscopy (SEM). Fig 2 shows the microstructure of the samples with different cutting methods observed by SEM. There are different contrast effects due to the plastic deformation near the cutting edge. It can be seen that the width of damaged area of EDM is about 20 μ m, smaller than that of shearing (83 μ m). And it is obvious that there is melting or heat affect zone (108 μ m) in the immediate proximity of the cut edge due to laser cutting procedure, which leads to the worst magnetic properties of samples with laser cutting.

3Conclusion This paper has compared and analyzed the effect of different cutting methods on the magnetic properties of electrical steel by double Epstein frames. It is found that EDM has the least influence on the sample, followed by shearing, and laser cutting has the greatest influence. The laser cutting effect is the worst, that is beca-

use that there is no cooling in the cutting process, while EDM has coolant flow. The microstructure of the samples was observed by SEM. The results show that the macro measurement results are consistent with the micro observation results.

[1] H. Naumoski, "Investigation of the influence of different cutting procedures on the global and local magnetic properties of non-oriented electrical steel," Journal of Magnetism and Magnetic Materials, vol. 392, pp. 126-133, 2015. [2] Z. Xiaoyang, "Study on Measurement and Simulation Method of Magnetic Properties of Electrical Steel Sheets Considering Influence of Cutting Method," Shenyang University of Technology, 2016. [3] W. D. Chen J, Cheng S, "Modeling of Temperature Effects on Magnetic Property of Nonoriented Silicon Steel Lamination," IEEE Transactions on Magnetics, vol. 51, no. 11, pp. 1-4, 2015.



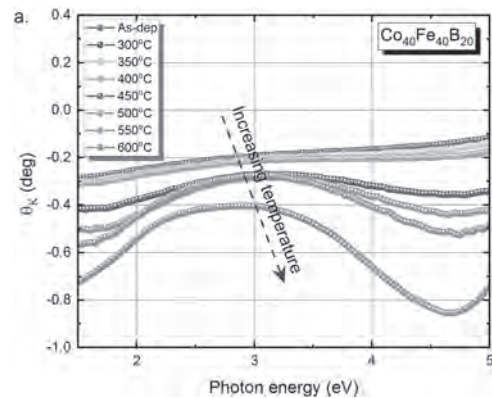
JB-09. Crystallisation of Optically Thick Films of $\text{Co}_x\text{Fe}_{(80-x)}\text{B}_{20}$: Evolution of the (Magneto-) Optical and Structural Properties.

A. Sharma¹, M.A. Hoffmann², P. Matthes³, O. Hellwig^{1,4}, C. Kowol³, S.E. Schulz³, D.R. Zahn^{1,5} and G. Salvan^{1,5}

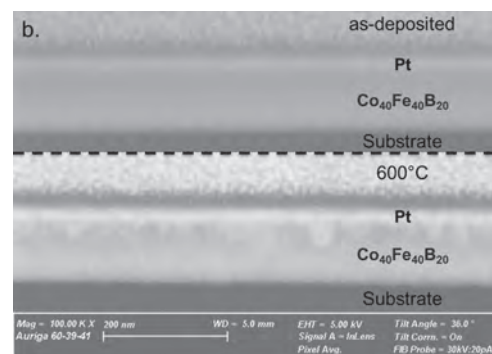
1. Institute of Physics, Technische Universität Chemnitz, Chemnitz, Germany; 2. Center for Microtechnologies, Technische Universität Chemnitz, Chemnitz, Germany; 3. Fraunhofer Institute for Electronic Nanosystems, Chemnitz, Germany; 4. Institute of Ion Beam Physics and Materials Research, Helmholtz-Zentrum Dresden-Rossendorf, Dresden, Germany; 5. Center for Materials, Architecture, and Integration of Nanomembranes (MAIN), Technische Universität Chemnitz, Chemnitz, Germany

CoFeB is one of the most extensively studied magnetic materials due to its atypical properties such as structurally smooth growth [1], soft magnetic properties [2], high spin polarization [3], and very low Gilbert damping [4], which makes it especially suitable for magnetic tunnel junction devices [5]. Numerous researches have proclaimed that thermal annealing is a decisive measure for a high performance of CoFeB based magnetic tunnel junction devices. Therefore, it is of utmost importance to understand the influence of thermal annealing on this alloy. In this work, the crystallisation of Co-Fe-B alloys triggered by thermal annealing was investigated by X-ray diffraction techniques and scanning electron microscopy, as well as spectroscopic ellipsometry and magneto-optical Kerr effect spectroscopy for annealing temperatures ranging from 300°C to 600°C. The transformation of ~100 nm thick $\text{Co}_x\text{Fe}_{(80-x)}\text{B}_{20}$ films from amorphous to polycrystalline was revealed by the sharpening of spectral features observed in optical and magneto-optical dielectric function spectra. These features are ascribed to direct inter-band transitions due to the hybridization of *p*- and *d* orbitals of Co-Fe alloys in bcc crystalline phase. Cross-sectional scanning electron microscopy of Co-Fe-B layers annealed at 600°C further confirmed that in the case of a Pt capping layer, the crystallization starts at the interface of CoFeB and Pt, and expands for a thickness, which is consistent with the vertical coherence length of the crystallites determined from XRD. The influence of B on the dielectric function was assessed both experimentally and by optical modeling. By analysing the Drude component of the optical dielectric function, a consistent trend between the charge carrier scattering time/resistivity and the annealing temperature was observed, in agreement with the electrical investigations by means of the four-point-probe method. The result obtained from this study were recently published in ref. [6].

1. D. D. Djayaprawira, K. Tsunekawa, M. Nagai, H. Maehara, S. Yamagata, N. Watanabe, S. Yuasa, Y. Suzuki, and K. Ando, *Appl. Phys. Lett.* 86, 92502 (2005). 2. H. Hauser and R. Grössinger, *J. Appl. Phys.* 85, 5133 (1999). 3. S. X. Huang, T. Y. Chen, and C. L. Chien, *Appl. Phys. Lett.* 92, 242509 (2008). 4. C. Bilzer, T. Devolder, J.-V. Von Kim, G. Counil, C. Chappert, S. Cardoso, and P. P. Freitas, *J. Appl. Phys.* 100, 053903 (2006). 5. T. Devolder, J.-V. Kim, L. Nistor, R. Sousa, B. Rodmacq, and B. Diény, *J. Appl. Phys.* 120, 183902 (2016). 6. A. Sharma, M. A. Hoffmann, P. Matthes, O. Hellwig, C. Kowol, S. E. Schulz, D. R. T. Zahn, and G. Salvan, *Phys. Rev. B* 101, 054438 (2020).



The polar Kerr effect measured polarisation rotation (θ_K) spectra for a Pt capped 100 nm thick $\text{Co}_{40}\text{Fe}_{40}\text{B}_{20}$ film before and after annealing at various temperatures.



SEM micrograph collage of substrate/ $\text{Co}_{40}\text{Fe}_{40}\text{B}_{20}$ / Pt before and after annealing at 600°C, recorded in a FIB trench at 36° stage tilt.

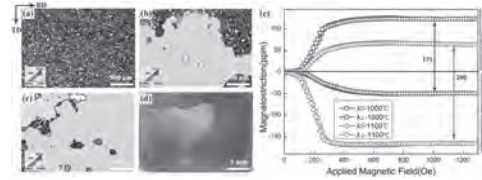
JB-10. The Secondary Recrystallization Texture and Magnetostriction in Fe-Ga Alloy Ultra-Thin Sheet.

Z. He^{2,1}, Y. Sha¹, F. Lei¹, H. Du², F. Zhang¹, L. Chen² and L. Zuo¹

1. Key Laboratory for Anisotropy and Texture of Materials (Ministry of Education), Northeastern University, Shenyang, China; 2. School of Materials Science and Engineering, Shenyang University of Technology, Shenyang, China

Fe-Ga alloy is an advanced magnetostrictive material for actuators and sensors in terms of combining excellent mechanical and magnetostrictive properties. It is desirable to produce η ($\langle 100 \rangle // RD$) textured Fe-Ga sheets due to the magnetostriction anisotropy with the largest coefficient along $\langle 100 \rangle$ direction and the serious eddy current loss in high-frequency use^{1,2}. The secondary recrystallization Goss ($\{110\} \langle 001 \rangle$) texture and large magnetostriction coefficient were mainly achieved in Fe-Ga alloy thin sheet with the thickness of 0.3–0.5 mm, by the combination of micron-sized NbC particles and surface energy effect in high-temperature annealing^{3,4}, as well as the initial sharp $\langle 100 \rangle$ -oriented columnar grains by directional solidification⁵. Since the eddy current loss is proportional to the square of the sheet thickness, the thinning of the sheet thickness can improve the energy conversion efficiency significantly. However, the secondary recrystallization of Goss texture significantly deteriorated in the Fe-Ga alloy sheet with a thickness of less than 0.3 mm due to the insufficient pinning force from the micron-sized NbC particles⁶. The introduction of surface energy effect from H₂S or S element, as well as the initial columnar crystals by directional solidification⁷, cannot guarantee the complete secondary recrystallization in Fe-Ga alloy sheet with the thickness less than 0.3 mm. Qi et al⁸ supposed the 0.10-mm Fe-Ga alloy ultra-thin sheets were prepared by rolling the 0.3 mm secondary recrystallized sheets, the strong cube texture and magnetostriction of 140 ppm were obtained after annealed for 2 h at 1200 °C under a flowing argon–hydrogen mixture. However, the preparation process is complicated and the incomplete secondary recrystallization restricts the magnetostriction coefficient. Therefore, it is necessary for the realization of complete secondary recrystallization in the Fe-Ga alloy sheet with a thickness of less than 0.3 mm. In the present study, the Fe-Ga ultra-thin sheets with the thickness of 0.10–0.25 mm were prepared via two-stage cold rolling method. The composite inhibitors composed of nanometer-sized sulfide and carbonitride are dispersedly precipitated during hot rolling and subsequent annealing, which provides effective pinning force for the normal growth of matrix grains. The gradually dissipated inhibition force during high-temperature annealing promotes a few exact Goss grains to grow abnormally by consuming primary recrystallized matrix grains textured by γ -fiber. Centimeter-sized secondary recrystallization Goss grains and large magnetostriction coefficient as high as 240 ppm is obtained in Fe-Ga alloy ultra-thin sheet without surface energy effect. The result indicates that complete secondary recrystallization can be realized based on the precise design and control of nano-sized composite precipitates and primary recrystallization microstructure/texture in Fe-Ga alloy ultra-thin sheet by conventional rolling and annealing methods.

¹ S. M. Na and A. B. Flatau, *Scripta Mater.* Vol., 66, p.307-310 (2012). ² J. H. Li, X. X. Gao, J. Zhu, T. Xia and M. C. Zhang, *Scripta Mater.* Vol., 63, p.246-249 (2010). ³ C. Yuan, J. H. Li, X. Q. Bao and X. X. Gao, *J Magn Magn Mater.* Vol., 391, p.145-150 (2015). ⁴ S. M. Na, K. M. Atwater and A. B. Flatau, *Scripta Mater.* Vol., 100, p.1-4 (2015). ⁵ C. Yuan, J. H. Li, X. G. Bao and X. X. Gao, *J Magn Magn Mater.* Vol., 374, p.459-462 (2015). ⁶ S. M. Na and A. B. Flatau, *AIP Adv.* Vol., 7, p.056406 (2017). ⁷ J. H. Li, C. Yuan, Q. L. Qi, X. Q. Bao and X. X. Gao, *Metals.* Vol., 7, p.36 (2017). ⁸ Q. Qi, J. Li, X. Mu, Z. Ding, X. Bao and X. Gao, *J Mater Sci.* Vol., 55, p.2226–2238 (2019).



Orientation image maps of Fe-Ga ultra-thin sheets annealed at 950°C (a), 1000°C (b), 1100°C (c), and macrostructure after final annealing (d), as well as the variation of magnetostriction coefficients ($\lambda_{//}$, λ_{\perp}) with magnetic field annealed at 1000°C and 1100°C (e)

JB-11. The 2D Magnetization Process in HGO Fe-Si Sheets.

E. Ferrara¹, C. Appino¹, C. Ragusa², O. de la Barrière³ and F. Fiorillo¹
 1. *Advanced Materials Metrology and Life Science Division, Istituto Nazionale di Ricerca Metrologica, Torino, Italy;* 2. *Department of Energy, Politecnico di Torino, Torino, Italy;* 3. *Systemes et Applications des Technologies de l'Information et de l'Énergie, Saclay, France*

Grain-oriented (GO) steel sheets increasingly face novel applications, like the ones enforced by the emerging *smart grid* technologies and the related medium-to-high frequencies *conversion devices* and those connected with the development of highly efficient low-noise rotating machines [1-3]. Comprehensive knowledge of the material behavior, going beyond the standard assessment of its properties at power frequencies along the rolling direction (RD), is therefore appreciated in the practice of machine design. This requires both experiments made upon broader than usual range of frequencies [4] and the investigation of the complex anisotropic response of the GO sheets and the related 2D magnetization process [5]. Such a process is shown to consist in the balanced contributions by moving [001] directed 180° domain walls (dws) and 90° dw transitions towards the [100] and [010] phases. It is then observed that, with the applied field leaving the RD, not only the magnetic losses suffer a sharp increase, but also a strong geometry dependent effect, under both static and dynamic regimes. This descends from the interference of the demagnetizing field, invariably arising in Fe-Si single crystals, but for closed samples cut along the <100>, <110>, and <111> axes. Consequently, the popular approach to GO characterization using Epstein strips cut at different angles θ to RD can provide the intrinsic properties of the material only for $\theta = 0^\circ$ (RD) and $\theta = 90^\circ$ (TD). This is ill-suited to straightforward use in those cases, like the rotating machine cores, where directions other than RD and TD are involved. However, the experimental knowledge of the geometry-independent RD and TD magnetization curves can be usefully exploited, following the lines of the Néel's phase theory, to reconstruct the same curves measured on Epstein strips cut along a generic angle θ [6]. The same applies to the DC hysteresis loops and their area, once the fundamental role of the demagnetizing field is recognized. One can also emulate an infinitely extended sheet, the ideal configuration leading to the intrinsic material response, by adopting an X-stacked sheet configuration, where flux continuity across the sheet edges can be achieved, resulting in a net magnetization variation both along the applied field (i.e., the strip edges) and orthogonal to it. Also in this case the DC properties become predictable by starting from the RD and TD magnetic properties [6]. Any other sample geometry will then be fully represented by or will be intermediate between the Epstein and the X-stack configurations. In this work, we provide a general approach to DC and AC (1 Hz - 200 Hz) magnetic hysteresis loop and losses in Epstein and X-stacked HGO sheets. The experiments are made using either the standard Epstein frame or a single sheet tester, where 120 mm wide 300 mm long X-stacked sheet samples are inserted in a laminated flux-closing yoke. A phenomenological predicting method is devised, which relies on the pre-emptive knowledge of the behavior of hysteresis loop and energy loss independently measured under sinusoidal induction in the RD- and TD-cut Epstein strips. We treat, in accordance with magneto-optical observations, the magnetization process unfolding for generic angle θ as the result, dictated by applied, demagnetizing, and eddy current fields, of two mechanisms: 1) Displacement of the 180° dws, the process pertaining to the RD cut sheets and strips; 2) Motion of 90° dws, converting the antiparallel slab-like [001] domains into [010] and [100] domains, and vice versa. The frames in Fig. 1 qualitatively show an example of domain structure in an X-stacked sheet at two instants of time along a major hysteresis loop (peak polarization $J_p = 1.45$ T). The antiparallel [001] domain structure observed at $J = 0$, largely disappears upon attaining $J = 0.87$ T. With this configuration, only a faint demagnetizing field is expected to arise at the sample edges and a net 2D magnetization variation is observed. By taking then, for a given J_p , the experimental energy loss and the hysteresis loops pertaining to the RD and TD samples, obtained at $J_{pRD} = J_p \cos(\theta)$ and $J_{pTD} = J_p \sin(\theta)$, and realizing that the fractional sample volume $v_{180}(t)$ occupied by the [001] phase is related to the same quantity $v_{90}(t) = \sqrt{2} J_{TD} / J_s$ associated with the [010] and [100] domains as $v_{180}(t) = 1 - v_{90}(t)$, we calculate loss and loop for any given θ value. An example of so-obtained energy loss $W(f)$ at 50 Hz across a range of J_p values on 0.288 mm thick high-permeability GO Epstein strips cut at

different angles θ to RD is provided in Fig. 2. The experiments show that $W(\theta)$ peaks around $\theta = 75^\circ$. The predicting approach to $W(\theta)$ is based on the experimental knowledge of the energy loss measured at the same frequency in the RD and TD strips for $J_{pRD} = J_p \cos(\theta)$ and $J_{pTD} = J_p \sin(\theta)$. This associates with the calculation of the hysteresis loop. A more involved approach is required by the $W(\theta)$ prediction in the X-stacked samples, where the simplifying assumption of zero magnetization across the sheet width does not hold.

[1] T. Belgrand, R. Lemaître, A. Benabou, J. Blazkowski et C. Wang, *AIP Advances* 8, 047611 (2018). [2] G. Parent, R. Penin, J. P. Leconte, J. F. Brudny, and T. Belgrand, *IEEE Trans. Magn.* 49, 1977 (2013). [3] S. Lopez, B. Cassoret, J. Brudny, L. Lefebvre, and J. Vincent, *IEEE Trans. Magn.* 45, 4161(2009). [4] M. A. Shamsuddin, F. Rojas, R. Cardenas, J. Pereda, M. Diaz, and R. Kennel, *Energies* 13, 2319 (2020). [5] W. Pluta, *IEEE Trans. Magn.* 52, 6300912 (2016). [6] F. Fiorillo, L. R. Dupré, C. Appino, and A. M. Rietto, *IEEE Trans. Magn.* 38, 1467 (2002).

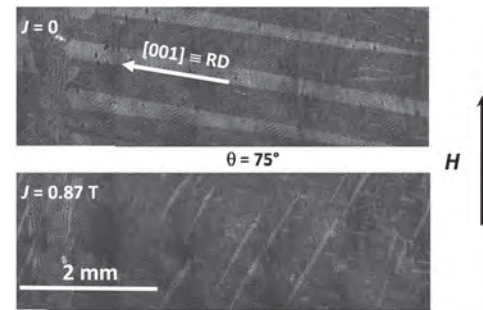


Fig. 1. X-stacked GO sheet, cut at 75° with respect to the RD. The [001] antiparallel slab-like domain structure found in the demagnetized state ($J = 0$) is converted by 90° dw motion into symmetric [100] and [010] structures under increasing applied field ($J_p = 1.45$ T).

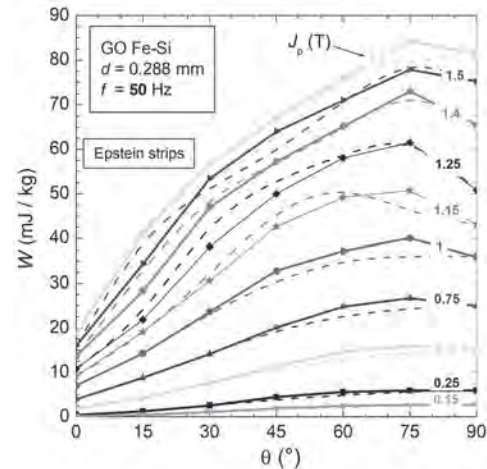


Fig. 2. Energy loss at 50 Hz measured versus J_p and θ in Epstein strips. Solid lines and symbols: experiments. Dashed lines: prediction by a weighted combination of the 50 Hz RD and TD loss figures.

JB-12. Impact of Pulsed Laser Irradiation, Scribing and Ablation on 2-D Scalar and Vector Magnetic Losses and General Properties of Grain-Oriented Electrical Steels.

P. Dupont^{1,2}, M. Nesser^{2,3}, O. Maloberti^{4,2}, J. Dupuy⁵, M. Lamblin⁵, M. Ployard¹, D. Laloy¹ and J. Fortin^{4,2}

1. Jeumont Electric, Jeumont, France; 2. Laboratoire des Technologies Innovantes (LTI), Amiens, France; 3. Universite de Picardie Jules Verne, Amiens, France; 4. UniLaSalle, Amiens, France; 5. Multitel A.S.B.L., Mons, Belgium

Increasing the efficiency of electrical machines is a global objective. One way to contribute to its fulfilment is to reduce iron losses of soft magnetic materials within their magnetic circuits (stator, rotor, core, ...). Improvement of soft magnetic material properties, especially Grain-Oriented Electrical Steels (GOES) based on iron and 3% silicon, is possible using surface laser treatments through the magnetic domain refinement technic and introduction of favorable stress [1-2]. These improvements are classically obtained for unidirectional excitation fields parallel to the rolling direction, the pronounced easy magnetic axis of GOES. However, in appliances such as rotating electrical machines, the flux lines are not always parallel to this preferred configuration (ex: in the teeth) and can also rotate (ex: in the yoke). In the literature, papers address the development of the expression and measurements of 2-D-magnetic properties [3], but the behavior of laser treated GOES under rotational and parallel to transverse direction fields remains slightly explored [4] and can be investigated further. Indeed, advanced pulsed laser technologies have been proven to improve magnetic [5-6] and magneto-mechanical [7] properties significantly under unidirectional field along the rolling direction. They include irradiation and scribing processes but also a new laser process called ablation with ultra-short laser pulses [5]. Therefore, in this research work, the effects of pulsed laser irradiation, scribing and ablation on GOES under transverse and rotational fields are presented. The objective is to optimize the vector behavior of GOES. The study focuses on power losses and B-H curves. The considered material is a laboratory grade of 0,28mm thickness with a CARLITE coating of 3-4µm thickness. The experimental plan includes 6 laser sets of parameters. The selection was made to enable comparisons between the types of laser processes (irradiation, scribing or ablation) and regarding the power loss reductions in the rolling direction. The main configurations were based on reference [5] in which the study was conducted with unidirectional excitation field parallel to the rolling direction on 150x150mm² samples. In the present work, power losses have been measured in both rolling and transverse directions with a Single Sheet Tester (SST) and in rotational field with a Rotational Power loss Tester (RPT). An accuracy study will be detailed in the extended paper. So as to avoid any sample dispersion, measurements were carried out systematically on the same samples before and after laser treatment with the same setups (SST for 150x150mm² samples and RPT for 60x60mm² samples). The rotational power losses were obtained by considering the average of Clock-Wise (CW) and Counter-Clock-Wise (CCW) measurements and compared to the sum of unidirectional power losses. Thanks to loss model and B-H curve representation, while separating each direction but also the static and dynamic contributions, the impact of various laser parameters will be analyzed separately on scalar and vector magnetic properties as a function of working conditions. Additionally, all samples have been observed at each step (before and after laser treatment) with a Magneto-Optic Indicator Film technic (MOIF), which is very adapted for GOES's magnetic domains observations. This will be illustrated in the final paper. Both macroscopic and microscopic analysis will be helpful to understand the reasons for opposite or simultaneous improvements in case of unidirectional or rotational fields. Concerning RPT measurements, rotational power losses reductions are reported for several laser sets of parameters (to be compared) and for several Polarization/Frequency couples as shown in figures 1 and 2. By using the pre-selected laser treatments, magnetic properties have been improved with iron losses reduction rate up to -12% at 50Hz&1T and up to -7% at 500Hz&0.5T in comparison with non-laser treated material for one of the selected sets of parameters. Further measurements will be carried out by the authors by improving the laser parameters (laser power and patterns), which might enhance the actual results and reduce even more significantly power losses. In the extended paper, measurement results (SST, RPT) will be

presented with more details. Comparisons and discussions about the impact of considered laser treatments on GOES measured in both unidirectional and rotational fields on magnetic properties will be proposed as well. Acknowledgments: This work was supported by JEUMONT Electric and was carried out with the help of financing from the Association Nationale Recherche Technologie (ANRT). It was carried out in parallel with the ESSIAl project, which the authors would like to thank. The ESSIAl project is funding from the European Union's Horizon 2020 research and innovation program under grant agreement No 766437. The authors would also like to thank the Aperam-Brazil company for having supplied the samples.

[1] Y. Huang, W. Ming, M. Li et al., The International Journal of Advanced Manufacturing Technology, vol. 70, p. 1-9 (2014) [2] I. Petryshynets, F. Kováč, V. Puchý et al., AIP Advances, vol. 8, p. 047604 (2018) [3] Y. Maeda, H. Shimoji, T. Todaka and M. Enokizono, Journal of Magnetism and Magnetic Materials, vol. 320, p. e567-e570 (2008) [4] T. Kajiwara and M. Enokizono, IEEE Transactions on Magnetics, vol. 50, p. 1-4 (2014) [5] M. Nesser, O. Maloberti, J. Dupuy et al., Journal of Magnetism and Magnetic Materials, vol. 504, p. 166696 (2020) [6] E. Salloum, O. Maloberti, M. Nesser et al., Journal of Magnetism and Magnetic Materials, vol. 503, p. 166613 (2020) [7] E. Salloum, M. Nesser, O. Maloberti et al., conference MMM2019, Las Vegas, USA (2019)

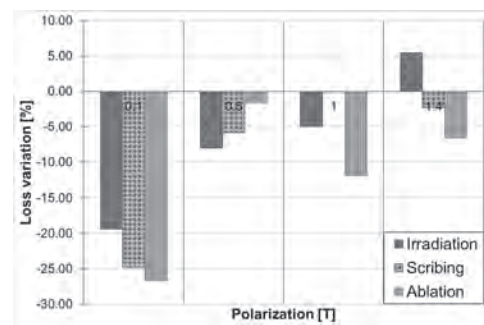


Fig.1 - Rotational power loss variation [%] after laser treatment at 50Hz for various polarizations (0.1T, 0.5T, 1T and 1.4T)

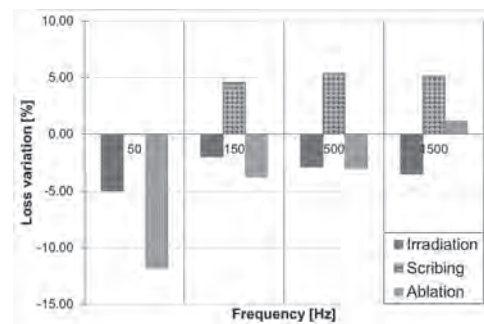


Fig.2 - Rotational power loss variation [%] after laser treatment at 1T for various frequencies (50Hz, 150Hz, 500Hz and 1500Hz)

JB-13. Iron Loss Modeling of Anisotropic Soft Magnetic Steels in FEM Simulation Environment.

L.A. Millan Mirabal^{1,2}, O. Messal¹, A. Benabou¹, Y. Le Menach¹, J. Roger² and J. Ducreux²

1. Univ. Lille, Arts et Metiers Institute of Technology, Centrale Lille, Yncrea Hauts-de-France, ULR 2697 - L2EP, Lille, France; 2. EDF Lab Saclay, Palaiseau, France

Due to their texture, the magnetic characteristics of grain oriented (GO) steels depend on the angle between the applied magnetic field and the rolling direction RD. These GO steels exhibit advantageous magnetic characteristics, such as high permeability in the RD and relatively poor properties in the transverse direction TD. In order to obtain a better electromagnetic modeling of the electrical energy conversion systems using GO steels, the dissipative phenomena and the anisotropy must be reliably represented. One example is the case of the GO electrical steels used in stators of turbo-generators. In order to create an appropriate model, the associated magnetic losses have to be taken into account for any angle between the applied field and the RD. However, the problem of computing iron losses whatever the angle between the applied field and the RD has remained unsolved especially within the finite element method (FEM) framework. In this paper, a phenomenological iron loss model, recently proposed in [1], taking into account the anisotropy and nonlinearity of GO sheets has been successfully implemented in the L2EP FEM software baptized code_Carmel [2]. The model relies on the ‘loss separation’ approach. In this approach, which is based on the traditional decomposition proposed by Bertotti [3], the total losses are decomposed into three terms (hysteresis, classical and excess losses). The originality of the model concerns the first loss term i.e., the quasi-static losses dissipated per magnetization cycle, depending on the polarization level J_p and on the angle θ between the applied field and RD. The proposed quasi-static loss model considers the magnetization process and the evolution of the domain wall structure (dws) with the angle θ [4]. It is built from the two sets of W - J_p quasi-static experimental data obtained in the principal directions RD and TD and is based on the interactions between the main classes of magnetic domains, 180° and 90° dws, known as ‘Néel phases’ [5] through a single analytical relationship involving the volumic fraction occupied, for any direction of the magnetic field, by these classes. This same principle is applied for the determination of the excess losses. At this stage, the corresponding input data are the excess losses measured in both RD and TD. Concerning the classical loss term, it simply takes the expression resulting from the classical eddy current theory which is independent of the angle θ . Indeed, the case of an infinite sheet of thickness e , with a linear constitutive law (μ independent of H) and conductivity σ , under a sinusoidal field of frequency f , allows an entirely analytical resolution of the magnetic diffusion equation. Finally, we get a description of the total losses $W(f, J_p)$ as a function of the angle θ , without any adjustable parameter. The model has been validated on industrial sheets of EDF turbo-generators by means of simple study cases under periodic (cyclic) waveforms. Thus, we dispose of an efficient and reliable tool for modeling the magnetic losses of GO sheets within the FEM simulation environment. In order to validate the implementation of the developed model, a finite element analysis (FEA) has been performed using code_Carmel. A 3D linear magnetostatic simulation has been done using the magnetic vector potential formulation. A diagonal permeability tensor has been used to represent the anisotropic properties of the GO material. This tensor is formed assuming non-diagonal terms. The values of the tensor for the axes x and y were obtained from the characterization of the industrial GO steel C150-35S in the RD and TD, while for the axis z a very low relative permeability of ≈ 30 is assumed, as measured in [6]. Furthermore, the analyzed geometry corresponds to a GO sheet with dimensions of 10 cm x 10 cm and a thickness of 0.35 mm, surrounded by a coil along the x -axis. The iron loss calculation is performed in a section at the center of the sheet with an area of 1 cm x 1 cm. The elements at the center are subjected to a sinusoidal waveform of J_p of 0.5 T. Thirteen values of θ have been evaluated in this study (0° , 5° , 10° , 15° , 20° , 25° , 30° , 42° , 54.7° , 65° , 75° , 82.5° and 90°). They correspond to the angles characterized experimentally using the Epstein frame method with Epstein strips cut at different angles from the industrial GO steel sheet. Finally, from the distribution of H and J obtained in the FEA, the iron losses have been calculated in post-treatment. The main

entries for the iron loss model were the hysteresis and excess losses in the RD and TD. In Table 1, an example comparing the static and dynamic losses obtained from the FEA against the experimental losses is given for some angles at 0.5 T. Further validations, analysis and discussions are envisaged in the extended version of the paper.

[1] Carlo Appino, Enzo Ferrara, Fausto Fiorillo, et al., *Journal of Magnetism and Magnetic Materials*, vol. 500, (2019). [2] code_Carmel. [Online]. Available: <https://code-carmel.univ-lille.fr/?q=fr/node/15>, accessed 2021 [3] G. Bertotti, *IEEE Transactions on Magnetics*, vol. 24, no. 1, pp. 621–630, (1988) [4] F. Fiorillo, L. R. Dupré, *IEEE Trans. on Mag.*, vol. 38, no. 3, (2002) [5] L. Néel, *J. Phys. Rad.*, vol. 5, pp. 241, (1944) [6] N. Hihat, J. P. Lecointe, O. Ninet, et al., *International Journal of Applied Electromagnetics and Mechanics*, vol. 46, pp. 349 - 354, (2014)

Angle	Experimental quasi-static losses (W/m ³)	Computed quasi-static losses (W/m ³)	Experimental excess losses (W/m ³)	Computed excess losses (W/m ³)
0°	272.79	274.41	400.16	402.21
10°	338.91	327.26	459.66	441.86
25°	526.40	478.50	557.58	563.19
42°	969.90	900.86	898.73	862.41
82°	3112.54	3182.72	2156.27	2436.50

Table 1. Comparison of computed and experimental losses at 0.5 T

Session JC

RE-BASED PERMANENT MAGNETS

Hossein Sepehri-Amin, Chair
Busshitsu Zairyo Kenkyu Kiko, Ibaraki, Japan

CONTRIBUTED PAPERS

JC-01. Advancing Additive Manufacturing of Bonded Permanent Magnets via *in-Situ* Magnetic Field Alignment During 3D Printing.

A. Sarkar¹, M. Somashekara², P.M. Paranthaman³, M.J. Kramer⁴ and C.I. Nlebedim¹

1. Critical Materials Institute, Ames Laboratory, Ames, IA, United States;

2. Mechanical Engineering, Indian Institute of Technology Dharwad,

Dharwad, India; 3. Oak Ridge National Laboratory, Oak Ridge, TN,

United States; 4. Division of Materials Science and Engineering, Ames Laboratory, Ames, IA, United States

Additive manufacturing (AM) via 3-D printing technologies have become a frontier in materials research, including its application in the development and recycling of permanent magnets^{1,2}. The increasing criticality in availability of the rare earth minerals in magnets present a demanding challenge to the losses from conventional or subtractive manufacturing. AM allows for a minimal waste production and re-utilization of recovered rare earths in the magnet processing. *In-situ* alignment during 3D printing of magnetic materials has opened new horizons for manufacturing of complex permanent magnets^{3,4}. The introduction of functionalized magnetic 3D printing (Fig. 1a) as an AM process yields several unique advantages including rapid prototyping of multi-directionally aligned magnetic systems, and reduced energy requirement due to the elimination of post-production alignment³. In this work, we have developed a mechanism to align magnetic materials using fused filament 3D printer with a novel magnetic field source architecture (Fig. 1b). The work addresses opportunities to integrate magnetic field into 3D printing process to enable printing, and alignment of anisotropic permanent magnets, without requiring further processing. The principle behind the analysis is rotation of magnetic particles in a molten matrix under low magnetic field. The alignment architecture was designed and optimized for weight and applied field. An in-depth finite element modeling and CAD was performed followed by prototyping of the magnetic field source (Fig. 1c-d). Several electromagnetic core models were developed using finite element modeling to obtain a field strength of > 1 T with a magnetic material in the nozzle. The electromagnetic simulations were coupled with thermal analysis to obtain realistic transient thermal profiles. Design modifications were incorporated to improve the thermal performance of the models without compromising the electromagnetic output. The results predict models that could be operated over prolonged durations (> 10 hours) at less than the rated temperature (80 °C) and at the rated current (5 A), while producing field strength of > 1 T. As a future prospective, the model would be implemented as a prototype to be incorporated with the 3D printer. Magnetization vs. field measurements of extruded and printed Sm-Co (15 vol.%) in PLA and Nd-Fe-B/Sm-Fe-N composite (65 vol.%) in Nylon-12, prepared with and without magnetic field, confirmed alignment of magnetic particles (Fig. 2a-b). Field vs. alignment and printer temperature vs. alignment analyses were performed to understand the effects of process variables on the degree of alignment of the samples. Finally, a multiphysics model was developed, that couples fluid dynamics and electromagnetic interactions, to predict the degree of alignment (DoA) of a polymer bonded magnet printed under applied field. The model predicts the flow of magnetic particles in a viscous fluid through a nozzle under applied magnetic field. A particle-fluid interactive flow simulation was performed to model the flow regime of molten bonded magnet. The interactions between the drag, inertial, and magnetophoretic forces were analyzed to predict the particle trajectory. A torque balance was performed between the drag torque, magnetic torque on particles from the applied field, and torque from particle-particle interactions. The analysis was used to predict the degree of rotation of magnetic particles during printing. The simulated DoA of 0.68 compares well with the experimentally obtained for 65 vol.% NdFeB+SmFeN in Nylon-12. For 15 vol.% Sm-Co in PLA, the simulated DoA of 0.86 also compared well with the 0.83 obtained experimentally (Fig.2c-d). This process can be used for any permanent magnet composition or hybrid magnets and presents a benchmark for application of this technology in industrial and commercial applications. This work is supported by the Critical Materials Institute (CMI), an Energy Innovation Hub funded by the U.S. Department of Energy (DOE), Office of

Energy Efficiency and Renewable Energy, Advanced Manufacturing Office. Ames Laboratory is operated for the U.S. Department of Energy by Iowa State University of Science and Technology under Contract No. DE-AC02-07CH11358.

1. C. Huber et al., *Appl. Phys. Lett.*, 109, 162401 (2016) <http://arxiv.org/abs/1605.07309>. 2. L. Li, B. Post, V. Kunc, A. M. Elliott, and M. P. Paranthaman, *Scr. Mater.* (2017). 3. A. Sarkar et al., *Addit. Manuf.*, 34, 101289 (2020) <https://linkinghub.elsevier.com/retrieve/pii/S2214860420306618>. 4. Y. Kim, H. Yuk, R. Zhao, S. A. Chester, and X. Zhao, *Nature*, 558, 274–279 (2018) <http://www.nature.com/articles/s41586-018-0185-0>.

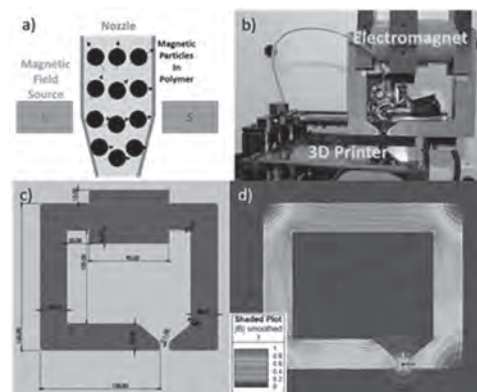


Figure 1. a) Schematic of in-situ alignment mechanism for magnetic 3D printing, b) Representation of the prototyped 3D printer, c) Novel EM-core design with advanced cooling technology, and d) FEM simulation of c-core @ 5A current.

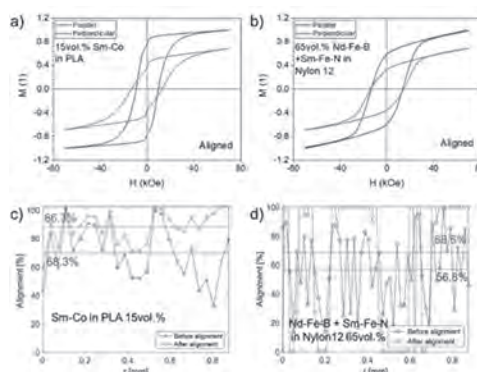


Figure 2. a-b) MH loop for aligned magnetic samples, and c-d) Simulation validation.

JC-02. High Coercivity in Bulk Pr-Fe-Cu-B Alloys as a Stable Precursor for Permanent Magnets by Additive Manufacturing.

L. Schäfer¹, K. Skokov¹, J. Liu¹, F. Maccari¹, T. Braun¹, S. Riegg¹, I. Radulov¹, J. Gassmann², H. Merschroth³, J. Harbig³, M. Weigold³ and O. Gutfleisch¹

1. *Functional Materials, Technische Universität Darmstadt Fachbereich Material- und Geowissenschaften, Darmstadt, Germany*; 2. *Fraunhofer-Einrichtung für Wertstoffkreislaufe und Ressourcenstrategie IWKS, Hanau, Germany*; 3. *Technische Universität Darmstadt Institut für Produktionstechnik und Umformmaschinen, Darmstadt, Germany*

Today, the 3D-printing technology faces a new challenge - the Additive Manufacturing (AM) of functional magnetic materials, especially permanent magnets. AM should provide very good functional properties of the printed magnets, namely locally tailored remanent magnetization M_r and coercivity H_c . The highest magnetic performance is reached for Nd-Fe-B magnets based on the hard magnetic $Nd_2Fe_{14}B$ phase, and on extrinsic properties (micro and nanostructure) mastered during the production. Ideal microstructure consists of magnetically decoupled grains of the hard magnetic $RE_2Fe_{14}B$ ($RE =$ Rare earth element) phase. The main challenge for Nd-Fe-B magnets, which arises during direct AM techniques, consists of an unsuitable microstructure appearing after re-melting of Nd-Fe-B precursor by the laser, followed by a fast solidification of the alloy. This usually leads to a very low coercivity in magnets made from commonly used commercial Nd-Fe-B alloy powders. Thus, one of the main obstacles in successful 3D printing of full-dense hard magnetic materials, is the engineering of a desired phase composition and the mastering of an appropriate microstructure. In the contrast to conventional Nd-Fe-B-based bulk alloys, a large H_c has been found in annealed Pr-Fe-Cu-B compounds. The $Pr_2Fe_{14}B$ phase is isostructural to $Nd_2Fe_{14}B$ and the Pr-Fe-B and Nd-Fe-B ternary phase diagrams exhibit the same phases. By doping the system with Cu, additional phases can be formed in the sample and some of them affecting drastically the hard-magnetic properties of the magnet. Kajitani et al. [4] found a new grain-boundary phase with tetragonal structure (space group $I4/mcm$) and $Pr_6Fe_{13}Cu$ stoichiometry in hot-pressed $Pr_{17}Fe_{76}B_{5.5}Cu_{1.5}$ alloys. Annealing at 500 °C leads to an increase in H_c of 50 % compared to the hot-pressed state, which was associated to the formation of the antiferromagnetic grain-boundary phase. Further investigations by Marcondes et al. [5] proved the occurrence of the antiferromagnetic $Pr_3Fe_{13}Cu$ phase and it was found that annealing at 500 °C improves the H_c drastically due to the formation of the $Pr_3Fe_{13}Cu$ phase at the expense of the Pr,Cu-rich grain-boundary phase. Recently, the occurrence of the $RE_6(Fe,Ga)_{14}$ within the grain boundary [6]–[8] of Nd-Fe-B permanent magnets was reported. The magnets show good hard-magnetic properties, but the role of the $RE_6Fe_{13}(Cu,Ga)$ phase is not clear yet. Our studies explore the applicability of Pr-Fe-Cu-B based alloys for the use in Additive Manufacturing (AM) techniques to produce fully dense permanent magnets. Induction molten $Pr_{17}Fe_{76}B_{5.5}Cu_{1.5}$ alloys were annealed at high temperature (1000 °C for 5 hours), followed by a low temperature annealing (500 °C for 3 hours). The samples show the formation of soft magnetic Pr_2Fe_{17} phase at high temperature accompanied by low coercivity. After a low temperature annealing, the mentioned $Pr_6Fe_{13}Cu$ is forming (see Fig. 1) and an increase of coercivity can be observed. Based on these experiments, the composition has been optimized regarding the coercivity. For this, three pre-alloys ($Pr_6Fe_{13}Cu$, $Pr_2Fe_{14}B$, FeB) were prepared by induction melting and two compositional series by mixing the $Pr_6Fe_{13}Cu$ with FeB or $Pr_2Fe_{14}B$ were prepared by arc melting. The heat treatments were the same for all samples and the development of coercivity was characterized. The shape of the hysteresis is drastically changing within the sample series. High amount of the $Pr_6Fe_{13}Cu$ phase leads to a shoulder and decreasing saturation magnetization, which indicates the non-ferromagnetic properties of the phase. The combination of $Pr_6Fe_{13}Cu + FeB$ shows the largest coercivity of ~1250 kA/m which is comparable to a sintered magnet (without heavy Rare Earth elements). In both sample series, the formation of the reported $Pr_6Fe_{13}Cu$ phase could be observed by SEM-EDX. The large coercivity in the bulk state makes this material interesting to use as stable precursors for AM of fully dense magnets. The material needs to be in powder form for techniques like SLM. Therefore, the hydrogen decrepitation (HD) process was successfully applied on high coercive samples. Afterwards, the material

was suction casted which simulates the remelting and rapid solidification during the SLM process. After the aforementioned annealing, the coercivity is equal to the as-cast condition which demonstrates that the magnetic hardening mechanism is stable throughout the different preparation steps and the material will exhibit large coercivity after SLM. We thank the German Research Foundation (DFG) and the Collaborative Research Center/Transregio 270 HoMMage, Project ID No. 405553726, TRR 270, for making this work possible.

[1] O. Gutfleisch, "Controlling the properties of high energy density permanent magnetic materials by different processing routes," *J. Phys. D. Appl. Phys.*, vol. 33, no. 17, pp. R157–R172, Sep. 2000. [2] T. G. Woodcock et al., "Understanding the microstructure and coercivity of high performance NdFeB-based magnets," *Scripta Materialia*, vol. 67, no. 6, pp. 536–541, 2012. [3] G. Hrkac et al., "Impact of different Nd-rich crystal-phases on the coercivity of Nd-Fe-B grain ensembles," *Scr. Mater.*, vol. 70, no. 1, pp. 35–38, 2014. [4] T. Kajitani, K. Nagayama, and T. Umeda, "Microstructure of Cu-added Pr-Fe-B magnets: Crystallization of antiferromagnetic $Pr_6Fe_{13}Cu$ in the boundary region," *Magn. Magn. Mater.*, vol. 117, no. 3, pp. 379–386, Dec. 1992. [5] P. V. P. Marcondes and R. N. Faria, "Microstructural studies on Pr-Fe-B-Cu magnets produced by upset forging of cast ingot," *Mater. Sci. Eng. A*, vol. 272, no. 2, pp. 245–249, 1999. [6] K. Niitsu et al., "Magnetization measurements for grain boundary phases in Ga-doped Nd-Fe-B sintered magnet," *J. Alloys Compd.*, vol. 752, pp. 220–230, 2018. [7] G. Ding et al., "Coercivity enhancement in Dy-free sintered Nd-Fe-B magnets by effective structure optimization of grain boundaries," *J. Alloys Compd.*, vol. 735, pp. 795–801, 2018. [8] T. T. Sasaki et al., "Formation of non-ferromagnetic grain boundary phase in a Ga-doped Nd-rich Nd-Fe-B sintered magnet," *Scr. Mater.*, vol. 113, pp. 218–221, 2016.

as-cast (Laser Powder Bed Fusion)

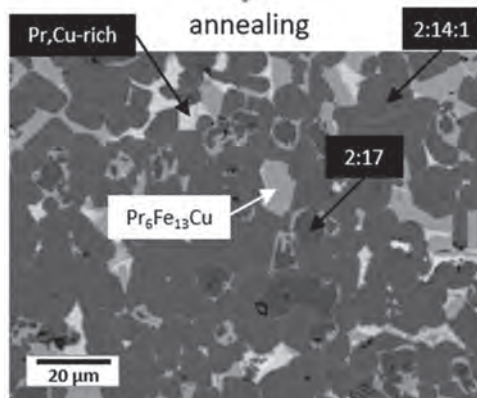
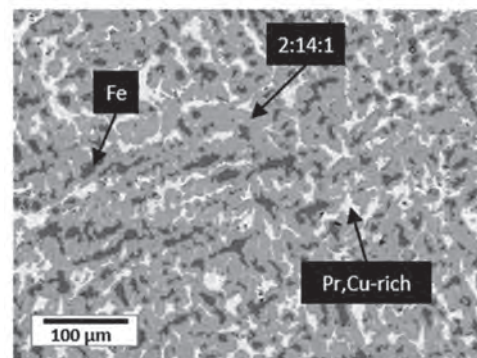


Fig. 1: Microstructural evolution during the annealing treatment of Pr-Fe-Cu-B alloys. The sample is shown in as-cast condition (top) and annealing (bottom).

JC-03. Unexpected Coercivity Enhancement > 1 T for Nd-Fe-B Permanent Magnets With 20 wt.% Nd Produced by Laser Powder bed Fusion.

F. Bittner¹, J. Thielsch¹ and W. Drossel^{1,2}

1. Additive Manufacturing, Fraunhofer-Institut für Werkzeugmaschinen und Umformtechnik IWU, Dresden, Germany; 2. Technical University of Chemnitz, Chemnitz, Germany

Current production of dense Nd-Fe-B permanent magnets is restricted to the powder metallurgical way consisting of powder production, pressing and magnet field alignment, sintering and post processing. This method allows the production of simple shaped magnets with superior magnetic performance. Bonded magnets show a higher geometrical flexibility on the expense of magnetic performance due the mixing with non-magnetic polymer with a volume content of up to 50%. Additive Manufacturing by means of laser powder bed fusion (LPBF) offers the opportunity to overcome design restrictions of conventional production techniques and allows new strategies for the application-oriented product development. LPBF is characterized by a layer-by-layer local melting of powder on a built platform by a focused laser beam, which is scanned across the powder. New powder is applied on top of melted material afterwards and the melting process is continued. Local melting, rapid solidification, directional heat transfer and several re-melting and re-heating cycles control the microstructural development of metals during LPBF. For this reason, achievable microstructures and properties differ in general significantly from such ones, which can be obtained from conventional fabrication processes. We applied laser powder bed fusion to commercial Nd-lean MQPTM-S powder from Magnequench for the additive manufacturing of Nd-Fe-B bulk permanent magnets. Samples were manufactured on a “M2 cusing” machine from Concept Laser GmbH under protective Argon atmosphere and an Oxygen content below 0.2%. Nd-Fe-B behaves very different compared to established materials during LPBF and the resulting magnetic performance is mainly controlled by the energy input from the laser beam and depends on the processing parameter laser power P_L , laser scan velocity v_L and hatch distance h_y . The latter one represents the offset of neighbouring laser scan lines [1]. The impact of processing parameter laser power and scan velocity on coercivity is shown in Figure 1 (a). It is obvious, that H_c is enhanced, when laser power increases or scan velocity decreases – in other words, if the energy input raises. A similar behaviour was observed for remanence B_r and maximum energy product $(BH)_{max}$. However, the enhancement of magnetic performance is limited by a material specific maximum allowed limit of processibility, at which the samples will be increasingly destroyed. For optimized processing parameter a coercivity of 920 kA/m (1.16 T), a remanence of 0.63 T and a maximum energy product of 63 kJ/m³ is obtained. Thereby, B_r and $(BH)_{max}$ represent the highest reported values for additively manufactured permanent magnets so far. The demagnetization branch of the hysteresis curve for a magnet with optimized magnetic properties is shown in Figure 1 (b) and compared to the initial MQPTM-S powder and a polymer bonded magnet from the powder, which is produced by injection molding with a loading factor of 60 vol.%. The coercivity of the powder is 700 kA/m and is slightly reduced by injection molding. However, LPBF leads to an unexpected enhancement of coercivity and the value of the powder is exceeded by 30% without the addition of any rare earth containing eutectics or other post processes. The composition of the used material exhibits 20 wt.% of rare earth, which is equivalent to 8 at.% and is in the range of α -Fe/Nd₂Fe₁₄B nanocomposites [2]. These are typically prepared by melt spinning and show coercivities of 400 – 600 kA/m for comparable compositions [2,3], e.g rare earth content between 8 and 9 at.%. These values are clearly exceeded by our LPBF-processed Nd-Fe-B magnets. The link between LPBF-processing and enhanced magnetic performance is the microstructure of the magnets and the microstructural development is controlled – as described above – by several factors. In the case of LPBF-processed Nd-Fe-B magnets we obtained a unique fine-grained microstructure with a grain size between 60 and 600 nm. Our results demonstrate, that improved magnetic performance can be achieved by LPBF of Nd-Fe-B bulk permanent magnets with an optimized coercivity, which is unexpected high for the given Nd-lean composition. This offers new perspectives for the development of new manufacturing processes for the production of improved Nd-Fe-B permanent magnets.

[1] F. Bittner, J. Thielsch and W.-G. Drossel: Progress in Additive Manufacturing, Vol. 5, p. 3-9 (2020) [2] G.C. Hadjipanayis: Journal of Magnetism and Magnetic Materials, Vol. 200, p. 379-391 (1999) [3] C. Wang, M. Yan and Q. Li: Materials Science and Engineering B, Vol. 150, p. 77-82 (2008)

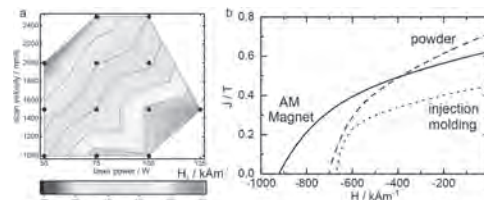


Figure 1: Magnetic performance of additively manufactured Nd-Fe-B permanent magnets produced by laser powder bed fusion: (a) dependence of H_c on laser power and scan velocity and (b) demagnetization curve of additively manufactured magnet (“AM Magnet”, solid line), initial MQPTM-S powder (“powder”, dashed line) and injection molded magnet from MQPTM-S with loading of 60 vol.% (“injection molding”, dotted line).

JC-04. Batch Fabrication of 50 μm Thick Anisotropic NdFeB Micro-Magnets.

F.O. Keller¹, R. Haettel¹, T. Devillers¹ and N. Dempsey¹
 1. Institut Néel, UGA-CNRS, Grenoble, France

Excellent hard magnetic properties have been achieved in rare earth transition metal films (Nd-Fe-B, Sm-Co) produced by sputtering, pulsed laser deposition and molecular beam epitaxy. Such films can serve as model systems to probe intrinsic magnetic properties or to study the link between microstructure and extrinsic magnetic properties. They can also be used to produce miniaturized magnetic field sources for applications. In the latter case, the films must be patterned at a length scale comparable to the film thickness, because of the demagnetising field effect. The choice of film thickness will depend on the targeted application, nm-sized field sources require nm-thick films while μm -sized sources require μm -thick films. The film deposition rate becomes very relevant as the film thickness is increased, especially if the ultimate aim is for commercial production. What is more, deposition on large surface areas is needed to allow batch fabrication and integration of micro-magnets. We have previously reported on triode sputtering of 5 μm thick Nd-Fe-B films at deposition rates of up to 18 $\mu\text{m}/\text{h}$ [1]. We then demonstrated how such films could be physically patterned at the micro-scale using a topographic approach based on pre-patterning of the substrate or post-deposition etching of the magnetic layer [2]. We also showed that localised heating by laser irradiation through a mask can be exploited to produce magnetisation reversal at the μm -scale in the so-called thermo-magnetic patterning approach [3]. Small arrays of micro-magnets produced using these approaches have already been used in a range of bio-medical experiments [4]. In this work we will demonstrate the potential that triode sputtering holds for batch fabrication of even thicker micro-magnets, for future integration into micro-scaled devices. Deep Reactive Ion Etching (DRIE) was used to anisotropically etch 55 μm deep trenches into Si substrates of diameter 100 mm and thickness 525 μm . Patterns consisting of squares with lateral size varying from 20 to 400 μm , and 4 mm long stripes with width varying from 20 to 400 μm , were used as test structures (Fig 1). Ta (100 nm) / Nd-Fe-B (50 μm) / Ta (100 nm) trilayers were deposited onto these topographically patterned substrates heated to a temperature of 500°C or 700°C. The NdFeB layer deposited at 500°C was amorphous, while that deposited at 700°C was crystallised. Post-deposition crystallisation of the former was achieved by annealing the full wafer in a Rapid Thermal Annealing (RTA) furnace, under secondary vacuum (10^{-6} mbar) at 600 °C, with a heating rate of 20°C/s and a dwell time of 10 minutes. Hereafter the samples will be referred to as 1-step processed ($T_{\text{dep}} = 700^\circ\text{C}$) or 2-step processed ($T_{\text{dep}} = 500^\circ\text{C} + T_{\text{anneal}} = 600^\circ\text{C}$). Despite the relatively large thickness of the NdFeB layers, film peel-off does not occur. It should be noted that NdFeB films deposited onto non-patterned Si substrates start to peel off the substrate at a film thickness greater than 10 μm . The stress relief afforded by topographic patterning of the substrate depends on the dimensions of the pattern features and the film thickness, and some peel off was observed in 50 μm thick NdFeB layers deposited on square structures of width 500 μm prepared in another study. For the samples detailed here, some cracking of the deposit was observed in expansive regions far from etched features. SEM images of fractured cross-sections of stripes of two different width (200 μm and 30 μm) of each sample type are compared in Fig 2. Deposition on the sidewalls of the etched trenches leads to the deposition on the “hills” being wider than the underlying Si pillars. A shadowing effect results in the profiles of the deposit in the “valleys” being different to that on the neighbouring “hills”, and the effect becomes stronger as the feature size is reduced. The shadowing effect can be enhanced by increasing the depth of the trenches, as will be shown elsewhere. SEM imaging at higher resolution reveals that the NdFeB grains of the 1-step processed sample are columnar and have widths as large as 1 μm while those of the 2-step processed film are almost equiaxed with diameters in the range of 200 – 500 nm (not shown). Hysteresis loops measured on pieces taken from each sample are shown as insets to Fig 2. The 1-step sample has a coercivity of 1.2 T and an $M_{0T}/M_{7.5T}$ of 0.79 while the corresponding values for the 2-step sample are 2.2 T and 0.85. The higher coercivity of the latter is due to its much finer microstructure and the 2-stage initial magnetization curve may be explained by easy domain wall motion in

grains coarser than 300 nm, the single domain particle size of $\text{Nd}_2\text{Fe}_{14}\text{B}$, and domain wall pinning in finer grains. An in-house developed Scanning Hall Probe Microscope (SHPM) equipped with a Hall cross of active area size $4 \times 4 \mu\text{m}^2$ [5], was used to measure the stray magnetic field produced at different heights above out-of-plane magnetized pieces of each sample. In this presentation we will provide full details of structural and magnetic characterization and will compare measured field profiles with simulated profiles. We will finish by discussing future prospects for the fabrication, integration and use of high-performance NdFeB micro-magnets.

[1] N.M. Dempsey et al., “High performance hard magnetic NdFeB thick films for integration into Micro-Electro-Mechanical-Systems”, Appl. Phys. Lett. 90 092509 (2007) [2] A. Walther et al., “Micro-patterning of NdFeB and SmCo magnet films for integration into Micro-Electro-Mechanical-Systems”, J. Magn. Mag. Mat. 321 (2009) 590–594 [3] F. Dumas-Bouchiat et al., “Thermo-magnetically patterned micro-magnets”, Appl. Phys. Lett. 96, 102511 (2010). [4] N.M. Dempsey, “Magnetism and Biology” in “Handbook of Magnetic Materials”, J.M.D. Coey et al. (eds), Springer, in-press [5] Gorky Shaw et al., “A Scanning Hall Probe Microscope for high resolution, large area, variable height Magnetic Field Imaging”, Rev Sci Inst 87 (2016) 113702

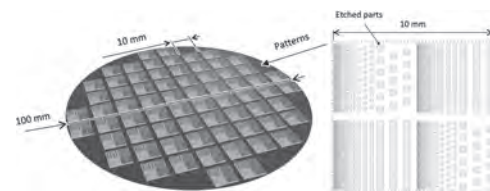


Fig 1: Schematic of the pre-patterned substrates.

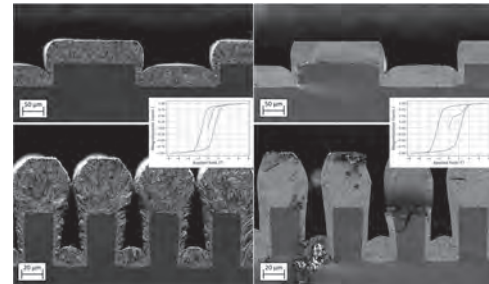


Fig 2: SEM images of fractured cross-sections of stripes of width 200 μm (top) and 30 μm (bottom) prepared using 1-step (left) and 2-step processing. Insets: M(H) loops of pieces taken from 1-step (left) and 2-step processed samples.

JC-05. Magnetic Properties and Microstructure of $\text{Sm}_5\text{Fe}_{17}$ -Based Two-Phase Magnets.

I. Dirba¹, H. Sepehri-Amin², K. Skokov¹, Y. Skourski³, K. Hono² and O. Gutfleisch¹

1. *Functional Materials, Technische Universität Darmstadt Fachbereich Material- und Geowissenschaften, Darmstadt, Germany*; 2. *Research Center for Magnetic and Spintronic Materials, National Institute for Materials Science, Tsukuba, Japan*; 3. *Helmholtz-Zentrum Dresden Rossendorf, Dresden, Germany*

I. INTRODUCTION A phase with extraordinarily high room-temperature coercivity in the Sm-Fe-Ti system was first observed in thin films crystallized from an amorphous precursor where $\mu_0 H_c$ reached 3.85 T for a $\text{Sm}_2\text{Fe}_7\text{Ti}_1$ composition [1]. Giant room-temperature coercivities up to 5.03 T were reported later [2] in a ‘new and possibly metastable phase’ with $\text{Sm}_2\text{Fe}_7\text{Ti}_1$ composition prepared by mechanical alloying. The reason for the maximum in coercivity at the $\text{Sm}_2\text{Fe}_7\text{Ti}_1$ composition has been a subject of debate. The observed unit cell expansion is smaller than expected when replacing the respective Fe atoms with Ti, which led to the conclusion that the amount of Ti in the $\text{Sm}_5\text{Fe}_{17}$ phase has to be smaller than weighted and thus the remaining Ti must form a secondary phase [3]. The interesting question arises then, whether the high coercivity is caused solely by the intrinsic magnetic properties of the $\text{Sm}_5\text{Fe}_{17}$ phase or is a result of a multi-phase microstructure. To answer this, in this work we have performed a detailed microstructural investigation of samples with varying Ti contents and correlated our findings with the observed magnetic properties. **II. EXPERIMENTAL** Mechanical alloying of Sm-Fe-Ti samples was carried out by high energy ball milling (SPEX 8000D) under argon atmosphere from elemental Fe (74–149 μm , 99.9%, Alfa Aesar), Ti (–74 μm , 99%, Alfa Aesar) powders and Sm pieces (3–4 mm, 99.9%, ChemPUR). The resultant powders were subsequently compacted, and heat treated in a horizontal tube furnace at different temperatures. The samples were handled in an Ar filled glovebox ($p(\text{O}_2) < 0.1$ ppm, MBraun) to avoid oxidation. Magnetic measurements were performed using a Quantum Design Physical Property Measurement System (PPMS) vibrating sample magnetometer (VSM). The magnetization measurements were extended up to 43 T using a non-destructive pulsed-field coil at the Dresden High Magnetic Field Laboratory. A single 1.44 MJ capacitor bank was used. When fully charged, it could produce a maximum magnetic field of 60 T with a rise time of about 7 ms and a total pulse duration of 25 ms. In our experiments, the capacitor module was charged to about two thirds. The magnetization was detected by the induction method using a coaxial pick-up coil system surrounding the sample. All pulsed-field data were calibrated against the magnetization recorded in steady fields. **III. RESULTS AND DISCUSSION** As shown in Fig. 1a, ultrahigh coercivities, 7.18 T at room temperature (8.86 T at 10 K), were achieved for the $\text{Sm}_{20}\text{Fe}_{70}\text{Ti}_{10}$ alloy. The coercivity as high as 2.18 T is maintained even at 500 K. Anisotropy field $\mu_0 H_a$ of 20.7 ± 0.8 T determined from high-field pulse measurements demonstrates that H_c reaches 35% of the H_a at room temperature. Large switching field of around 7 T is visible in the initial magnetization curve. This behavior is similar to fine-grained (below the critical single-domain grain size) Nd-Fe-B alloys. The Curie temperature T_C of $\text{Sm}_{20}\text{Fe}_{70}\text{Ti}_{10}$ is 577 K and calculated exchange stiffness parameter A is 7.72 pJ/m. Because of high rare earth content as well as presence of a nonmagnetic secondary phase, the magnetization was only $60 \text{ A m}^2 \text{ kg}^{-1}$, which is roughly 0.58 T. Detailed transmission electron microscopy investigations presented in Fig. 1b show two-phase microstructure consisting of the $\text{Sm}_5\text{Fe}_{17}$ -based hard magnetic matrix phase with size below 200 nm and fine, <100 nm, Fe_2Ti grains. Majority of the Fe_2Ti secondary phase grains are located at the grain boundaries as well as inside of the 5:17 grains. No distinct segregation of any element at the grain boundaries can be seen. Despite high areal fraction of the Fe_2Ti grains, near single-phase demagnetization loops are observed. Aiming at enhancing M_s by realizing $\text{Sm}_5\text{Fe}_{17}/\alpha\text{-Fe}$ composite magnets, the effect of Ti content on the phase constitution, magnetic properties and microstructure was investigated in detail for $\text{Sm}_{20}\text{Fe}_{70}\text{Ti}_x$ with $4 \leq x \leq 10$. The fraction of Fe_2Ti phase decreases with x and for $x=4$ $\text{Sm}_2\text{Fe}_{17}$ phase appears. M_s increases and H_c decreases for the Ti-lean compositions. Based on the microstructural investigations, it is concluded that the reduced coercivities are the consequence of both intrinsic

and extrinsic factors, such as the lower anisotropy field, larger grain size and smaller volume fraction of the Fe_2Ti precipitates. **ACKNOWLEDGEMENTS** We acknowledge funding by the Deutsche Forschungsgemeinschaft (DFG, German Research Foundation), Project ID No. 40553726-TRR 270, and Elements Strategy Initiative Center for Magnetic Materials (ESICMM), Grant Number JPMXP0112101004, through the Ministry of Education, Culture, Sports, Science and Technology (MEXT), Japan. We also acknowledge the support of the HLD at HZDR, member of the European Magnetic Field Laboratory (EMFL).

1. N. Kamprath, N.C. Liu, H. Hegde, F.J. Cadieu, J. Appl. Phys. 64 (1988) 5720–5722. 2. L. Schultz, K. Schnitzke, J. Wecker, J. Magn. Magn. Mater. 83 (1990) 254–256. 3. H. Stadelmaier, G. Schneider, E.T. Henig, M. Ellner, Mater. Lett. 10 (1991) 303–309.

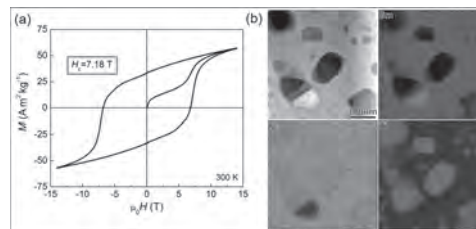


Fig. 1 (a) Room temperature hysteresis loop and (b) the corresponding microstructure of the $\text{Sm}_{20}\text{Fe}_{70}\text{Ti}_{10}$ sample. Two-phase microstructure consisting of the $\text{Sm}_5\text{Fe}_{17}$ -based hard magnetic matrix phase with fine Fe_2Ti grains is visible.

JC-06. Microstructure and Hard Magnetic Properties of $\text{Sm}_{1-x}\text{Zr}_x(\text{Fe},\text{Co})_{11.3-y}\text{Ti}_{0.7}\text{B}_y$ Ingots and Thick Melt-Spun Ribbons.

A. Gabay¹ and G. Hadjipanayis¹

¹ University of Delaware, Newark, DE, United States

Revived interest on SmFe_{12} -based compounds of the ThMn_{12} type as the permanent magnet materials has brought into focus the $\text{Sm}_{1-x}\text{Zr}_x(\text{Fe},\text{Co})_{11+\delta}\text{Ti}_{1-\delta}$ alloys remarkable by their high Curie temperature, large magnetization and strong magnetic anisotropy. However, attempts to develop practically useful coercivity in these alloys has encountered considerable difficulties. As most of the ongoing efforts rely on pulverization or on creation of a nanostructure in powders or melt-spun ribbons, relatively unexplored remain the massive cast alloys and “thick” ribbons melt-spun at a low solidification rate, even though they can be utilized as magnets without the need for costly compaction. In this study, alloys of $\text{Sm}_{1.1-x}\text{Zr}_x(\text{Fe}_{0.8}\text{Co}_{0.2})_{11.3-y}\text{Ti}_{0.7}\text{B}_y$ with $0 \leq x \leq 0.6$ and $0 \leq y \leq 0.9$ were subjected to structural, microscopic, thermomagnetic and isothermal magnetic characterization in samples immediately after arc-melting and after melt-spinning at a low wheel speed of 0.75–6.0 m/s. Slower solidification rates and Zr were found to generally promote the ThMn_{12} -type crystal structure, whereas higher solidification rates and B tend to suppress the 1:12 structure in favor of the TbCu_7 -type one. When added simultaneously, B and Zr can alter the morphology of the 1:12 phase thus noticeably affecting the coercivity (Fig. 1). In particular, this alloying was found to generate in the arc-melted ingots a microstructure of isolated 1:12 crystallites 1–3 μm in size (Fig. 2); a better control of the minority phases, at least some of which are ferromagnetic, would be needed, however, to obtain in the alloy with such microstructure a H_c greater than 0.5–0.7 kOe. A moderately accelerated solidification can refine the 1:12 crystallites and increase the H_c ; a $\text{Sm}_{0.7}\text{Zr}_{0.4}(\text{Fe},\text{Co})_{10.8}\text{Ti}_{0.7}\text{B}_{0.5}$ alloy exhibited a H_c of 1.5 kOe and a maximum energy product $(BH)_{\text{max}}$ of 2.5 MGOe when it was melt-spun at 1.5 m/s into a 0.26-mm-thick ribbon. However, a more rapid solidification was found to suppress the 1:12 phase in favor of the magnetically softer 1:7 phase. After annealing at 800–900 °C, the alloys with the large B and Zr substitutions develop reasonably high H_c and $(BH)_{\text{max}}$ values even if melt-spun at the moderate wheel speed of 6 m/s. The respective values for the $\text{Sm}_{0.7}\text{Zr}_{0.4}(\text{Fe},\text{Co})_{10.8}\text{Ti}_{0.7}\text{B}_{0.5}$ alloy were 4.1 kOe and 7.8 MGOe, whereas for a very Sm-lean $\text{Sm}_{0.5}\text{Zr}_{0.6}(\text{Fe},\text{Co})_{10.6}\text{Ti}_{0.7}\text{B}_{0.7}$ alloy they were 3.6 kOe and 7.4 MGOe. In comparison, the parent $\text{Sm}_{1.1}(\text{Fe},\text{Co})_{11.3}\text{Ti}_{0.7}$ alloy subjected to the same processing developed a H_c of only 0.4 kOe. The work was supported by the U.S. Department of Energy under Grant DE-FG02-90ER45413.

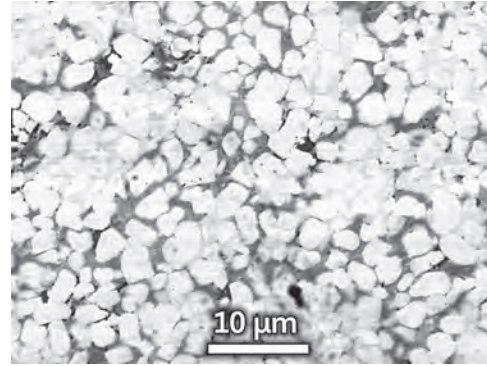


Fig. 2. Microstructure of arc-melted $\text{Sm}_{0.5}\text{Zr}_{0.6}(\text{Fe}_{0.8}\text{Co}_{0.2})_{10.8}\text{Ti}_{0.7}\text{B}_{0.5}$ alloy features fine well-separated crystallites of the 1:12 phase.

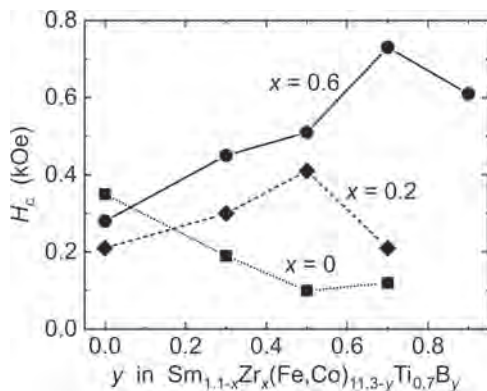


Fig. 1. Coercivity of bulk arc-melted alloys controlled through B and Zr substitutions.

JC-07. “Artificial Elements” Based on High Entropy Alloys as “Building Blocks” for Novel Magnetic Alloys Suitable for Permanent Magnets: Special Case SmFe₃CoNi.

D. Niarchos^{1,2}, E. Devlin¹, V. Psycharis¹ and M. Gjokas¹

1. INN, Ethniko Kentro Ereunas Physikon Epistemon Demokritos, ATHENS, Greece; 2. R&D, AMEN New Technologies, Aghia paraskevi, Attikis, Greece

Demand for rare earths or cobalt is set to soar the next decade boosted especially by demand for valuable NdPr or SmCo magnets used in electric motors (electric vehicles, wind turbines, consumer electronics, military & aerospace applications). The global permanent magnet market size is expected to reach €30 billion by 2030 from the current €20 billion. It is predicted that by 2030 a) Market for rare-earth oxides will increase 5-fold, b) annual NdFeB shortages of 48,000 tonnes expected by 2030, c) annual Dy oxide Shortages of 1850 tonnes is expected by 2030. Extending the forecasting Dr. M.Sagawa had predicted that by 2050 every one on earth will be served by at least 2 robots each one having at least 10 magnets, a market that has to be served by novel groundbreaking approaches [1]. In Fig. 1. the opportunities that exist for novel permanent magnets are shown. For centuries the design concepts of alloys has been based on only one or two principle elements, while minor fraction of other elements are added for property enhancement. This classical approach was broken in 2004 by Yeh et al. [2] who suggested of a new alloy design concept, which he called high entropy alloys. The original definition was “multiprincipal elements alloys composed of five or more elements in equal or near-atomic percentages”. Most of the current dominant (PMs) are intermetallic compounds containing rare earth elements e.g. NdPr or Sm and Co, both expensive and originating mainly from either China or Congo. These natural elements from the periodic table have a fixed atomic radii, fixed valence electron configuration and specific electronegativity, parameters that are crucial for the formation of intermetallic compounds. By creating artificial elements of the type of HEAs based on multicomponent rare-earth elements (RE-HEAs) and HEAs based on multicomponent transition metal elements (TM-HEAs), we have created a library of elements with tunable atomic radii, valence electron configuration and electronegativity. This approach enhances the opportunities for discovering novel permanent magnets [3]. The concept of using artificial elements based on either rare-earths or transition metals is depicted in Fig. 2. for the case of SmCo₅-type alloys, an approach that we followed for the stabilization of the SmFe₃CoNi magnetic phase [4,5]. We have extended this substitutional approach to the class of RFe_{12-x}T_xa and R₂Fe₁₄B alloys and the results so far are very promising. For example: Sample M_s (emu/g) H_A (T) T_c (K) (BH)_{max}^{Theory} (MGOe) (RE-HEAs)-Co₅ 75-90 >10 >800 8-18 Sm(TM-HEAs)₅ 65-80 >8 >800 8-15 (RE-HEAs)-Fe₁₁T 120-135 >5 570-600 8-18 (RE-HEAs)₂-Fe₁₄B 125-145 4-6 550-600 10-25 We will present a general approach by unlocking the new possibilities of using artificial elements to create new magnetic alloys that can be processed towards (PMs) to address the opportunities that are shown in Figure 1. This approach also works not only with metallic alloying but with oxides, pnictides, nitrides etc. We can also use the configurational entropy to stabilize metastable phases, since entropy is increased and competes with enthalpy towards negative Gibbs energy.

1. J.M.D.Coey, Engineering 6 (2020) 119–131. 2. Yeh, J. W et al, Adv. Eng. Mater. 6, 299-303 (2004) 3. PCT/EP2019/074449, approved June 2020, Rare Earth Based High Entropy Alloys (RE-HEAs) as building blocks for novel materials: Rare-Earth-HEAs permanent Magnets 4. P. Soderlind, et al. Phys. Rev. B 96, 100404(R) – Published 14 September 2017 5. Landa et al. Journal of Alloys and Compounds 765 (2018) 659-663.

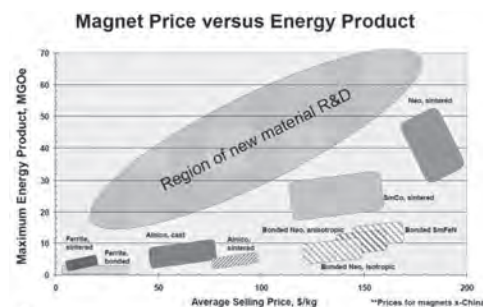


Figure 1. Opportunities for novel magnet alloys, suitable for permanent magnets, as a function of (BH)_{max} vs cost (Arnold Engineering)

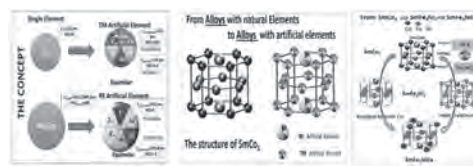


Figure 2. Three steps towards HEA-Magnetic Alloys. Step1 is the fabrication of the artificial elements RE-HEAs and TM-HEAs with variable atomic radii and valence electron concentration, Step2 use these artificial elements to synthesize model structures as counter-alloys of existing structures e.g. SmCo₅ and in Step3 with proper heat treatment stabilize through entropy optimization a phase e.g. SmFe₃CoNi, that otherwise is not possible because the formation energy is just slightly positive.

JC-08. Magnetic Alignment in Anisotropic Nd-Fe-B Bonded Magnets.X. Liu¹, K. Gandha¹, P.M. Paranthaman² and C.I. Nlebedim¹¹. Ames Laboratory, Ames, IA, United States; ². Oak Ridge National Laboratory, Oak Ridge, TN, United States

Nd-Fe-B bonded magnets have been widely applied in data storage and consumer electronic devices [1-3]. Theoretically, the maximum energy product of anisotropic magnets is four times as that of isotropic magnets, hence making anisotropic bonded magnets attractive. To produce bonded magnets, magnetic powders are mixed with thermoset- or thermoplastic-polymers for compression or injection molding methods, respectively. In addition to the specific performance of the magnetic powder used, a higher remanent magnetization, hence high energy product, can be achieved with a higher loading fraction of magnetic powder. For anisotropic bonded magnets, a high degree of magnetic alignment (DOA) of the powders in polymer matrix is important. However, the desire for higher loading fraction needs to be balanced with the requirement for good mechanical properties which decreases with loading fraction. As part of our endeavor to develop high-performance Nd-Fe-B bonded magnets, we studied different processing parameters that contribute to the resultant magnetic alignment and hence magnetic properties of anisotropic Nd-Fe-B bonded magnets. We select Nylon12 as binder and Magfine Nd-Fe-B powder to fabricate bonded magnets. Magfine powder is a commercial Nd-Fe-B anisotropic magnetic powder produced by hydrogenation, disproportionation, desorption, and recombination (HDDR). Different loading fractions of Nd-Fe-B powder were mixed with binder and warm-compacted (450 K) into bonded magnets with a diameter of 8mm and a length of 5mm. To magnetically align Nd-Fe-B powder in the as-prepared bonded magnets, a post-compaction magnetic field alignment was performed with an applied external magnetic field of up to 30 kOe. Samples were heated in magnetic fields from 300 to 530 K (Nylon-12) with a dwell time of 15 min at 530 K, and then cooled down to 300 K. After each alignment process, the magnetic hysteresis loops were measured again at 300 K using a Quantum Design Versalab VSM magnetometer. For Nd-Fe-B bonded magnet with 70% loading fraction of magnetic powder, the magnetic remanence increases from 4.8 kGs to 7.2 kGs, while the intrinsic coercivity remains almost unchanged (12 kOe) upon magnetic alignment (Fig. 1). The enhancement of remanence is due to the magnetic alignment of magnetic powder in bonded magnets. Thermomagnetic measurement data shown in Fig. 2 reveal a jump of magnetization at 480-490 K during post-compaction annealing under external applied fields. This temperature is slightly higher than the melting point of Nylon-12 (450 K), which means the binder (Nylon-12) is melted and at a low viscous state. The low viscosity of binder reduces friction between binder and particle and facilitates the magnetic powder alignment under magnetic field. This is a necessary condition for achieving alignment of magnetic particles in Nd-Fe-B bonded magnets during post-compaction magnetic alignment process. We performed magneto-static calculations which show that the DOA are determined mainly by the interplay between the Zeeman energy (E_{app}) and the inter-particle magnetic-static energy (E_{stat}) at the chosen alignment temperature and the applied magnetic fields. The good alignment can be achieved by an alignment magnetic field which is twice as its coercivity in anisotropic Nd-Fe-B bonded magnet.

1. J. M. D. Coey and K. O'Donnell, *J. Appl. Phys.*, vol. 81, no. 8 PART 2B, pp. 4810-4815, 1997. 2. J. Ormerod and S. Constantinides, *J. Appl. Phys.*, vol. 81, no. 8 PART 2B, pp. 4818-4820, 1997. 3. M. P. Paranthaman *et al.*, *Jom*, vol. 68, no. 7, pp. 1978-1982, 2016.

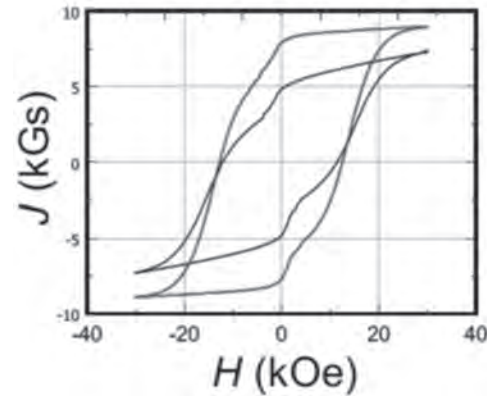


Fig. 1. Magnetic hysteresis of J-H of nonaligned- and aligned samples for 75 vol% Magfine Nd-Fe-B Nylon bonded magnets.

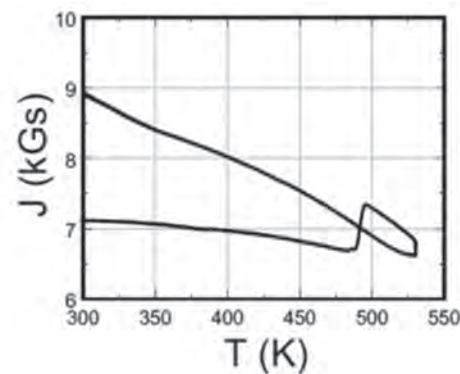


Fig. 2. Thermomagnetic curve of J-T for 75 vol% Magfine Nd-Fe-B Nylon bonded magnets

JC-09. Anisotropic Fractal Dimension of Nd-Fe-B Permanent Magnets Fracture Surface.

Q. Sun^{1,2}, M. Zhu¹ and J. Bai²

1. Central Iron and Steel Research Institute Group, Beijing, China;

2. School of Materials Science and Engineering, Northeastern University, Shenyang, China

Abstract: In this work, SEM image analysis and fractal dimension calculations are carried out on the fractures obtained under the same conditions for N50-type with high remanence, 30EH-type with high coercivity, and isotropic commercial Nd-Fe-B permanent magnets. It is further proved that the fractal dimensions of the fractures parallel and perpendicular to the c-axis for Nd-Fe-B permanent magnets are different. In other words, there is anisotropy in fractal dimension. In addition, it was discovered for the first time that the difference between the fractal dimensions D_{\perp} and D_{\parallel} of N50-type magnet with high remanence is large, and the difference between the fractal dimensions D_{\perp} and D_{\parallel} of the 30EH-type magnet with high coercivity is small, indicating that both remanence and coercivity are sensitive parameters with the microstructure. The difference in the fractal dimension of the fracture will provide new insights for studying the relationship between the magnetic properties and the microstructure of permanent magnetic materials. The anisotropic fractal dimension of the fracture will serve as a new performance parameter in the research of Nd-Fe-B permanent magnets. **Keywords:** Nd-Fe-B, Fractal dimension, Anisotropy, Performance parameter Introduction The magnetic properties of permanent magnets are closely related to the microstructure. However, researchers have seldom focused on the fractal characteristics of fractures in Nd-Fe-B permanent magnets. In fact, it is significant to study the fractal dimension of the fractured microstructure of permanent magnets with statistical self-similarity. Zhu et al. [1] reported the line-measuring dimension of fracture cracks of N50-type permanent magnets, and pointed out that the fractal dimension perpendicular to the c-axis and parallel to the c-axis has some anisotropic trends, but the difference in anisotropy is not obvious. In this work, N50-type, 30EH-type, and isotropic magnets are selected as the research objects. The anisotropic characteristics in fractal dimension of permanent magnets fractures parallel and perpendicular to the c-axis are explored. Experimental N50-type, 30EH-type, and isotropic commercial Nd-Fe-B permanent magnets were selected as the research specimens. A Zeiss field emission scanning electron microscope (FE-SEM) was used to observe the fracture morphology of all samples. The fractal dimensions of the fractures were calculated by the method of box counting dimension based on the image processing function of MATLAB. **Results and Discussion** The fractal dimensions of different types of magnet fractures parallel and perpendicular to the c-axis are summarized in Fig. 1. The difference ΔD between the fractal dimension D_{\perp} and D_{\parallel} of N50-type and 30EH-type magnets are 0.0856 and 0.0311, respectively. However, there is almost no difference in the fractal dimension of the isotropic magnet. In a word, the fractal dimension of the magnet oriented by the magnetic field has obvious anisotropy. The fractal dimension can be used as a research method to prove the anisotropy of magnets. The internal microstructure of magnet has a great influence on the magnetic parameters such as remanence, coercivity, and maximum energy product. Comparing the difference in fractal dimensions between N50-type and 30EH-type magnets, it can be found that N50-type magnet with higher remanence has larger anisotropic fractal dimensions, while 30EH-type magnet with higher coercivity has smaller anisotropic fractal dimension. The difference in ΔD of different magnets is inherently related to remanence and coercivity, which indirectly indicates that remanence and coercivity are sensitive parameters of microstructure. **Conclusions** The calculation on fractal dimensions of the fractures for the N50-type and 30EH-type commercial Nd-Fe-B permanent magnets along different crystalline axes demonstrates that the fractal dimensions of the fracture of the permanent magnet are anisotropic. So that the fractal dimension of the fracture can be used as a method to characterize the anisotropy of Nd-Fe-B magnet, which specifically characterizes whether the magnet has anisotropy, the magnitude of remanence and coercivity, and even the level of magnetic properties.

[1] M.G. Zhu, W. Li, Y.K. Fang, et al. Fractal study for the fractured surface of Nd-Fe-B permanent magnets. *J. Appl. Phys.* 2011, 109, 07A706.

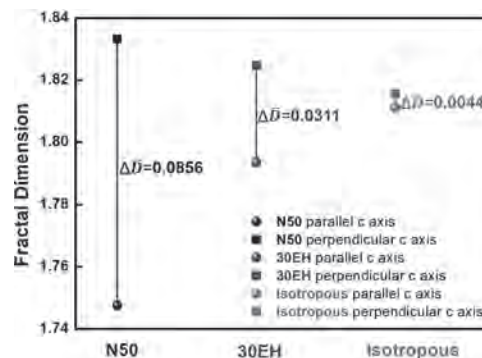


Figure 1 Fractal dimensions of fractures parallel and perpendicular c-axis for different types of magnets

JC-10. Influence of Reducing Agent to Recovery of Nd2Fe14B Sludge Waste by Calcium Reduction Diffusion Method.

H. Xu¹, Q. Lu¹, W. Liu^{1,2}, X. Yi² and M. Yue^{1,2}

1. Key Lab of Advanced Functional Materials, Beijing University of Technology, Beijing, China; 2. State Key Laboratory of rare earth permanent magnetic materials, Hefei, China

I. INTRODUCTION With the increasing risk of global rare earth supply and the growing environmental cost of recycling Nd2Fe14B waste by conventional hydrometallurgical technology, development of green and efficient recycling technology has become particularly important [1]. Recently, the reduction diffusion (RD) technology has been developed as an eco-friendly method for recycling Nd2Fe14B sludge waste [2]. At present, researchers mainly use granular calcium or CaH2 as reducing agent, and the amount of reducing agent will affect the phase, morphology, and magnetic properties of recycled powders [3]. Owing to the differences in physical and chemical properties of different reducing agents, the phase, morphology, and magnetic properties of the powders are substantially different in the recovery process. However, the influence of different reducing agents to the recovery of Nd2Fe14B sludge waste by RD method is rarely reported. In this paper, we respectively used granular calcium and CaH2 as reducing agents to recycled Nd2Fe14B sludge waste by RD method. The effect of different reducing agents on the phase, microstructure, and magnetic properties of the recycled powder were investigated. II. EXPERIMENTAL The multi-wire cutting sludge waste was collected from Anhui Earth-Panda Advance Magnetic Material Co. Ltd. The sludge was purified and then mixed with appropriate amount of Ca or CaH2. The mixtures compacted and heated to 1073 K, 1123 K, 1173 K, and 1323 K under high purity argon atmosphere for 2 h. Finally, deionized water was used to wash the powder for removing CaO and then vacuum dried at room temperature to obtain the recycled powders. The phase and orientation were characterized by X-ray diffraction meter (XRD). Microscopic morphology was observed by scanning electron microscopy (SEM). The magnetic properties of the samples at room temperature were measured by a vibrating sample magnetometer (VSM) with a maximum magnetic field of 3T. III. RESULTS AND DISCUSSIONS The XRD patterns of the recycled powders at different reaction temperatures are shown in Fig. 1. The results show that single phase Nd2Fe14B powder can be obtained with granular calcium as the reducing agent at 1323 K. However, when CaH2 is used as the reducing agent, single phase Nd2Fe14B powder can be obtained at 1123 K. This indicates that the latter can carry out the RD reaction at lower reaction temperature. In addition, Fig.1(a) shows that the diffraction peak of Nd2O3 is detected at 1073 K, which indicates that the Ca has not completely reacted with Nd2O3, but the diffraction peak of Nd2O3 is not detected at 1073 K with CaH2 as reducing agents. This proves that CaH2 is more prone to reduction reactions since the melting point of CaH2 (948 K) is lower than that of Ca (1115 K), so the former can be liquefied at lower temperature and thus liquid-solid RD reactions can occur more easily. In addition, since the size of CaH2 powder is smaller than that of granular calcium, it can be better mixed with sludge waste, which is beneficial to promote the RD reaction. On the other hand, the magnetic properties of the recovered powder of the latter (M3T=141.55 emu/g) are higher than that of the former (M3T=137.00 emu/g). And the M3T is increased by 12.9% compared with the purified sludge raw material (M3T=125.38 emu/g). To explore the reason, we observed the morphology of the cross section and powder of the products, and the results are shown in Fig. 2. Since CaH2 releases hydrogen during the RD process, there are many pores in the cross section as shown in Fig.2(c), instead of the dense and smooth cross section shown in Fig. 2(a). From Fig.2(b), it can be seen that the powder has severe sintering and agglomeration, but the dispersion of the powder is better and the powder particle size is more uniform in Fig. 2(d). Owing to the better dispersibility, it is easier to remove CaO during the washing process, so the non-magnetic phase and oxygen content in the corresponding washed magnetic powder are lower, which is also the reason for the better magnetic performance. IV. CONCLUSIONS In summary, using CaH2 as a reducing agent can obtain a single-phase Nd2Fe14B powder at 1123 K by RD method, which is lower than the 1323 K with Ca as the reducing agent. Besides, the dispersion of the powder is better and the powder particle size is more uniform. The magnetic properties of the recovered powder of the former

(M3T=141.55 emu/g) are higher than that of the latter (M3T=137.00 emu/g). And the M3T is increased by 12.9% compared with the purified sludge. ACKNOWLEDGEMENT This work was supported by the National key R & D project (2018YFC1903405, No. 2016YFB0700902), and by State Key Laboratory of Rare Earth Permanent Magnetic Materials Opening Foundation (No. SKLREPM170F02).

[1] O. Takeda, T.H. Okabe. Metall. Mater. Trans. E. 1 (2014) 160-173. [2] S.K. Haider, J.Y. Lee, D. Kim, Y.S. Kang. ACS Sustainable Chem. Eng. 8 (2020) 8156-8163. [3] C.Q. Chen, D. Kim, C. Choi. J. Magn. Magn. Mater. 355 (2014) 180-183.

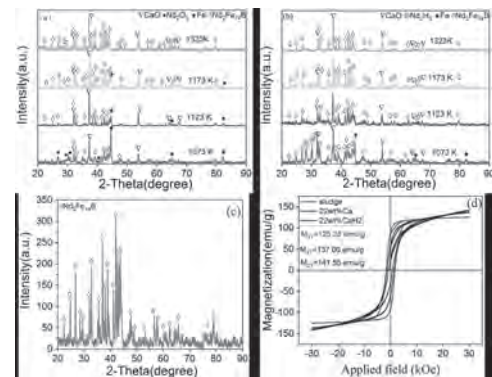


Fig. 1 XRD patterns of recycled powder obtained at different temperatures with Ca (a) or CaH2(b) as reducing agent, and recycled powder after washing (c) and the hysteresis loop of recycled powder (d)

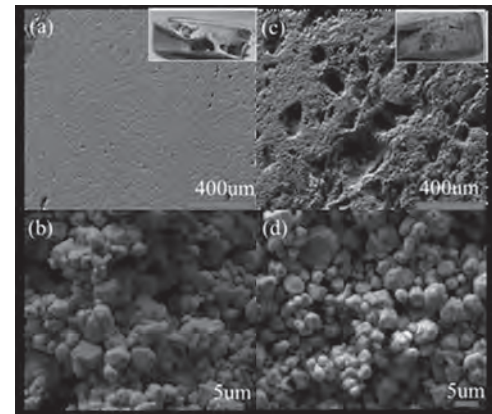


Fig.2. SEM micrograph of the cross section and recycled powder of the reaction products with Ca (a and b) or CaH2 (c and d) as reducing agent

JC-11. Anisotropic Nd-Fe-B Magnets Prepared From Recycled Jet-Milled Powders With Spark-Plasma Sintering Technique.

T. Tomše¹, B. Podmiljšak¹, K. Zuzek Rozman¹, S. Šturm¹, C. Burkhardt² and S. Kobe¹

1. Department for Nanostructured Materials, Institut Jozef Stefan, Ljubljana, Slovenia; 2. Institute for Precious and Technology Metals, Hochschule Pforzheim, Pforzheim, Germany

The world is progressively shifting from a fossil-fuel-based energy-and-transportation system to more environmentally friendly and energy-efficient technologies. The transport sector currently presents a quarter of Europe's CO₂ emissions. The European "Green Deal", presented in December 2019, aims at reaching net-zero greenhouse gas emissions by 2050. The emergence of electric vehicles and electricity production from renewable sources like wind power are necessary steps towards resolving contemporary environmental issues like climatic changes and air pollution in larger cities. However, the state-of-the-art traction motors and wind turbine generators often depend on Nd-Fe-B magnets to provide the strong and constant magnetic fields required to convert electrical to mechanical energy and vice versa. The rapid growth of the market for electric vehicles and advancements in green technologies development are inevitably related to the increasing demand for Nd and other rare-earth (RE) elements (RE = Nd, Pr, Dy, Tb). The rare-earth elements are considered most critical for Europe due to the high supply risk and their impact on the economy. Less than 1 % of all magnets are recycled after the magnet-containing device has been put out of use. It is thus necessary to develop cost-effective and sustainable reprocessing routes for end-of-life (EOL) permanent magnets. The hydrogen decrepitation (HD) of sintered magnets, combined with jet-milling, is used to obtain anisotropic Nd-Fe-B powders for further processing [1]. However, each reprocessing step exposes the material to oxidation, limiting its potential for the processing of high-coercivity magnets. Moreover, an increase in the oxygen content reduces the amount of the secondary Nd-rich phases, which can hinder the densification and evolution of microstructure during sintering when conventional powder metallurgy approaches are considered. Spark-plasma sintering (SPS) is a pulsed-current-activated, pressure-assisted sintering technique characterised by fast sintering kinetics. The technique exploits the Joule heating effect to consolidate a powder compact under non-equilibrium conditions. SPS offers a high potential for the net-shape manufacture of dense sintered bodies from various materials [2]. Recently, an SPS route was provided as an alternative to the conventional sintering of Nd-Fe-B jet-milled powders. By exploiting the SPS-specific sintering mechanisms, it is possible to densify such material without risking extensive grain growth or oxidation [3]. We have taken the spark-plasma sintering approach to synthesise anisotropic, fully-dense magnets from a heavily-oxidised Nd-Fe-B jet-milled powder. The powder that could not be sintered by conventional methods was obtained through hydrogen decrepitation and jet-milling of a magnet scrap and contained 0.8 wt.% of oxygen. Small additions of Nd-Cu eutectic alloy (up to 5 wt.%) were beneficial for developing the hard-magnetic properties in bulk magnets. We studied the effect of the sintering parameters such as heating rate and dwell time on magnetic properties and microstructure formation. The as-sintered samples' intrinsic coercivity exceeded 1000 kA/m, and the properties could be further tuned with post-sinter annealing.

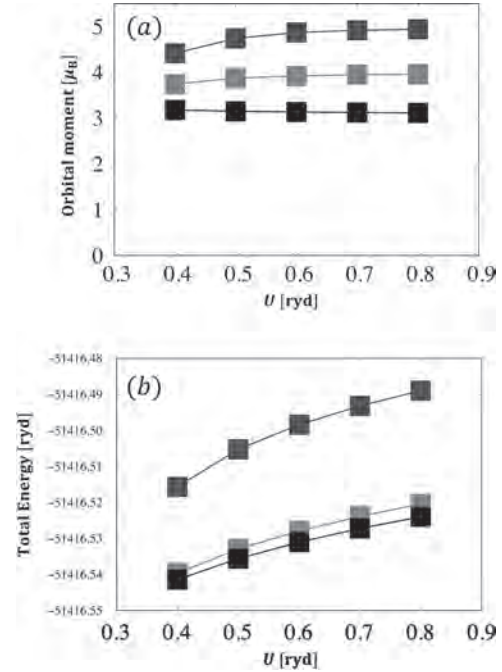
[1] A. Walton, H. Yi and N. A. Rowson, *Journal of Cleaner Production*, Vol. 104, p.236-241 (2015) [2] O. Guillon, J. Gonzalez Julian and B. Dargatz, *Advanced Engineering Materials*, Vol. 16, p.830-849 (2014) [3] T. Tomše, Z. Samardžija and L. Scherf, *Journal of Magnetism and Magnetic Materials*, Vol. 520, p.166504 (2020)

JC-12. Theoretical Investigation of the Orbital Moment of the Sm Ions in SmFe₁₂ With the GGA+U Method.

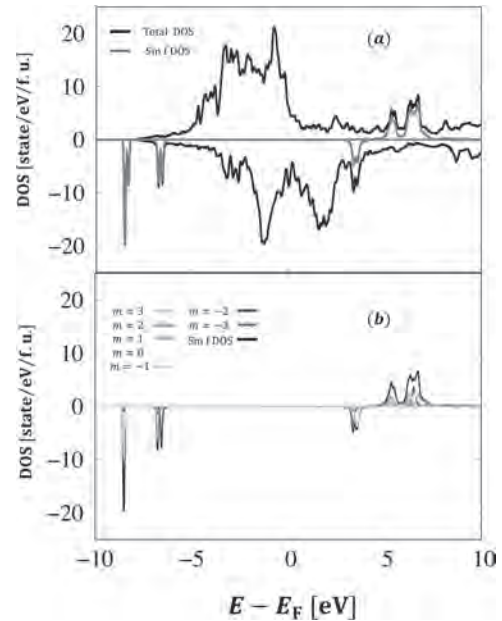
S. Yamashita¹, T. Yoshioka¹, H. Tsuchiura¹ and P. Novák²
 1. Tohoku University, Sendai, Japan; 2. Czech National Academy of Science, Praha, Czechia

Some rare-earth intermetallic compounds are superior in magnetic properties such as saturation magnetization and magnetocrystalline anisotropy, and are suitable for permanent magnetic materials. This is due, at least in part, to the orbital magnetic moment of the 4f shell, and also to its interaction with the crystal field. Thus it is important to know the 4f orbital magnetic moment of rare-earth ions in those compounds in order to theoretically search for novel permanent magnets. However, first-principles calculations based on density functional theory (DFT) still have a problem with the treatment of 4f orbital magnetic moments: even for 3d transition metals, they are often underestimated in DFT calculations. Therefore some additional corrections such as the so-called DFT+U method [1] [2] or the self-interaction correction (SIC) are necessary to describe the strongly correlated 4f electronic states adequately. Of course, comparison with experimental inputs is inevitable to validate these corrections. A suitable material to study the 4f orbital magnetic moment with reference to experimental information is SmFe₁₂ with ThMn₁₂ structure [3] [4]. This is due to its relatively simple crystal structure, and also the abundance of recent detailed experimental results, as it has received renewed attention as a promising candidate for new permanent magnet materials in the last few years. Of course it is well known that this system is thermodynamically unstable, but also that Ti substitution for Fe can stabilize the crystal structure. In the resulting crystal structure, the volume of the so-called interstitial region is larger than in other well-known rare-earth intermetallics such as Nd₂Fe₁₄B or SmCo₅. Thus we can expect that the 4f electrons of Sm ions are well localized enough to form the well-defined 4f orbital magnetic moment. We calculate the electronic structure of SmFe₁₂ and orbital moment of the Sm ions with the DFT+U method (GGA+U). In the frame work of the first-principles method, we have to investigate ground state properties, however, the DFT+U method sometimes might converge to metastable states [5]. Therefore, we examine several initial conditions and investigate the properties of a possible ground state. In present study, we use three initial conditions to approach the true ground state. The initial conditions are reflected in the orbital potential for 4f states of the Sm ions, the matrix elements of which are specified by the magnetic quantum number m. First one is set so that m=3,2,1,0,-1 states are occupied (Condition 1). Second one is set so that m=3,2,1,0,-2 states are occupied (Condition 2). The final one is set so that mainly m=3,2,1,0,-2 states are occupied, however, these states include the hybridization between different m reflecting four-fold symmetry (Condition3). We tested these conditions and search the true ground states. According to the calculated U dependence of the orbital moment and total energy shown in Figure 1, the third one (Condition 3) yields the lowest energy regardless of the U value. The calculated orbital moment of the Sm ions is about 3.0μ_B which is smaller than the maximum value expected from 4f⁶ configuration regardless of the U value. This implies that the orbital moment of the Sm ions is partially quenched due to the crystal field. The calculated 4f charge density has the four-fold symmetry which reflects the symmetry of the crystal. The calculated total, f-partial, and m-resolved f-partial density of states (DOS) are shown in Figure 2 (a) and (b). In Figure 2 (a), DOS is mainly composed by the Fe states and the down spin Sm f-states are well localized below the fermi level. Increasing U value, the gap between upper and lower Hubbard part of Sm f states becomes larger. In our calculation, we have confirmed that the anti-parallel spin configuration between Fe and Sm becomes stable. From the calculated f-partial density of states in Figure 2 (b), m=3,2,1,0,-2 states are mainly occupied. It yields the orbital moment roughly 4.0μ_B. In addition, hybridized states between m=3 and m=-1, m=2 and m=-2, and m=1 and m=-3 are also realized according to the initial condition. These states cause the reduction of the orbital moment from 4.0μ_B to 3.0μ_B due to the partial quenching of the orbital moment. In our DFT+U calculation, the quenching of the orbital moment is predicted, the comparison with the experimental data such as XMCD is expected. For future work, we are going to investigate the effect of the quenching of the orbital moment to magnetocrystalline anisotropy energy.

[1] V. I. Anisimov, J. Zaanen, and O. K. Andersen, Phys. Rev. B., Vol. 44, p. 943 (1991). [2] A. I. Liechtenstein, V. I. Anisimov, and J. Zaanen, Phys. Rev. B., Vol. 52, p. 5467 (1995). [3] Y. Hirayama *et al.*, Scripta Mater., Vol. 138 p.62-65 (2017). [4] Y. Harashima *et al.*, JPS Conf., Proc. 5 011021 (2015). [5] P. Larson, I. I. Mazin, D. A. Papaconstantopoulos, Phys. Rev. B., Vol. 67, p. 214405 (2003).



The U dependence of the calculated (a) orbital moment and (b) total energy including spin-orbit coupling. Blue, red and black plots correspond to the initial conditions Condition1, Condition2 and Condition3 (see text). The magnetization axis is set (001) direction.



The calculated density of states (DOS) of SmFe₁₂ with U=0.8 Ryd and J=0.0615 Ryd. (a) Black line corresponds to total DOS and red line corresponds to Sm f-partial DOS. (b) Sm f-partial DOS and m-resolved Sm f-partial DOS. The magnetization axis is set the (001) direction with spin-orbit coupling.

Session JD

RE-FREE PERMANENT MAGNETS

Yusuke Hirayama, Chair

National Institute of Advanced Industrial Science and Technology (AIST), Nagoya, Japan

INVITED PAPER

JD-01. Correlation Between Atomic Ordering and Magnetic Properties in $L1_0$ Alloys INVITED.S. Laureti¹¹ Institute for Structure of Matter, Consiglio Nazionale delle Ricerche, Roma, Italy

Magnetic binary alloys with a CuAu-I type chemically ordered face centered tetragonal (fct) structure, mainly known as $L1_0$ structure, have attracted a special attention in the last decades due to their peculiar physical properties and excellent chemical stability, which arise from the particular arrangement of the atoms that alternate in composition along the c-axis direction of the fct unit cell [1]. Among the $L1_0$ alloys, ferromagnetic (e.g. FePt, FePd, CoPt, CoPd, NiPt, MnAl, FeNi) and antiferromagnetic (e.g. MnPt, MnPd, MnNi, CrPt) nanostructured materials are of particular interest in view of their potential applications in many technological fields. The extraordinary high uniaxial magnetic anisotropy of $L1_0$ FePt(Pd) and CoPt makes such alloys of particular importance for next generation ultra-high density magnetic recording media, magnetic hyperthermia and catalysis. High-anisotropy $L1_0$ MnAl and FeNi alloys are excellent and cost-effective alternative to materials containing rare-earths and other critical elements for both permanent magnets and spintronic applications. Many studies have been carried out to find the optimum conditions for the preparation of $L1_0$ -ordered alloys that are commonly obtained by post-deposition high-temperature treatments for a few hours in order to favour the conversion from the chemically disordered fcc (A1) phase into the chemically ordered fct ($L1_0$) phase. However, in the last decade advanced chemical synthesis strategies have been proposed, allowing highly-ordered $L1_0$ magnetic alloys to be synthesized at a much milder conditions than usual; this is the case of the *Pre-ordered Precursor Reduction* (PPR) method [2] where the desired MPt phase (M=Fe, Co, Ni) is obtained by a thermal decomposition in a reductive atmosphere of a pre-ordered $M(H_2O)_6PtCl_6$ crystalline precursor salts consisting of alternating planes of pure Me and Pt atoms, which mimic the atomic structure in the alloy (fig.1). Among the characterization techniques applied to investigate the structural properties at the local-scale, XAS is an effective tool to probe the chemical environment around an absorber element, and to get information on the average structural features of the materials, thus being complementary to conventional X-ray diffraction techniques. Due to its peculiar characteristics, i.e. selectivity and high sensitivity, Extended X-ray Absorption Fine Structure (EXAFS) analysis represents the main technique to investigate the local properties in many systems whose behaviour is strongly affected by the atomic arrangement, as in the case of the $L1_0$ chemically ordered alloys, where the degree of chemical order influences significantly the final magnetic properties. In this paper, recent studies based on a combination of *ex-situ* and *in-situ* X-ray Absorption Spectroscopy (XAS) experiments suitably set-up to describe the local environment around the metals during the synthesis processes of different $L1_0$ alloys are presented. In particular, by comparing *PPR*-synthesised $L1_0$ alloys by means of EXAFS, X-ray diffraction results, TGA-DTA analysis and magnetic measurements, we could firstly formulate a general and comprehensive explanation of the process at the basis of the thermal treatment that brings to the reduced alloys with such a high ordering degree ($S > 0.9$). This allows a greater control on the synthesis method, which can be exploited, by properly choosing the starting salt, to synthesize other binary alloys, such as $L1_0$ -FeNi, $L1_0$ -MnAl and $L1_0$ -MnPt that are of great interest for many technological applications but extremely challenging to be obtained.

[1] A. Cebollada et al., Magnetic nanostructures, H. Nalwa (Ed), American Scientific Publishers, 2002, ch. 3, p.93 (2002) [2] G. Varvaro et al., Journal of Alloys and Compounds, Vol. 846, p.643 (2020)

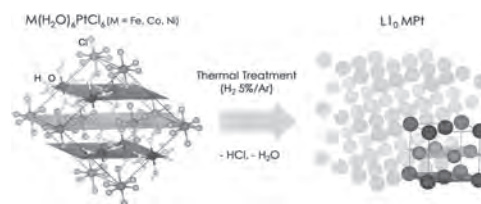


Fig. 1. Schematic illustration of the Pre-ordered Precursor Reduction strategy.

CONTRIBUTED PAPERS

JD-02. High-Throughput and Data-Mining Search for Rare-Earth-Free Permanent Magnets.

A. Vishina¹, H.C. Herper¹ and O. Eriksson^{1,2}

1. Uppsala Universitet, Uppsala, Sweden; 2. School of Science and Technology, Örebro University, Örebro, Sweden

High-performance permanent magnets are needed for a large number of applications, especially 'green' energy conversion, such as electric motors and windmills, which require them in extremely large quantities. At the same time, the heavier rare-earth elements which are necessary for obtaining the good magnetic characteristics of these materials (such as Pr, Nd, Sm, Tb, or Dy), are often mined with methods that leave an environmental footprint, quite expensive, and are rapidly decreasing in availability. We are using a high-throughput and data-mining approach to the search of rare-earth free permanent magnets by filtering through a large number of known structures from ICSD database [1]. Using a full-potential linear muffin-tin orbital method with the relativistic formulation as implemented in the RSPT electron structure code [2] we calculate the magnetic moment (M), magnetic anisotropy energy (MAE), and Curie temperature, looking for the materials with high $M > 1$ T, uniaxial MAE > 1 MJ/m³, and $T_c > 300$ K to identify the suitable replacement for rare-earth containing materials. To test the method, we investigated the materials containing a 3d-, a 5d-, and one extra element of the periodic table and found several candidates that have characteristics suitable for a good permanent magnet (Pt₂FeCu, Pt₂FeNi, W₂FeB₂, etc). Based on this result we have also proposed two new materials, not existing in ICSD database - Pt₂FeCo and Pt₂CoNi [3]. The second run was performed for the materials that contain at least two 3d- metals (with no restriction on the number of elements). Based on this run, new material was found (that had not been used as a permanent magnet before) and consequently synthesized, that has the high magnetization, MAE, and T_c . Hence, a new class of rare-earth-free permanent magnets has been proposed. We would like to acknowledge the financial support of the SSF and SNIC for the computation resources.

1. http://www2.fiz-karlsruhe.de/icsd_home.html 2. John M. Wills *et al.*, arXiv:cond-mat/9912173 (1999) 3. A. Vishina, O. Yu. Vekilova, T. Björkman, A. Bergman, H. C. Herper and O. Eriksson *Phys. Rev. B* 101, 094407 (2020)

JD-03. Fcc-Co Clusters in $L1_0$ -FePt Matrix as Graded-Interface Magnetic Nanocomposite.

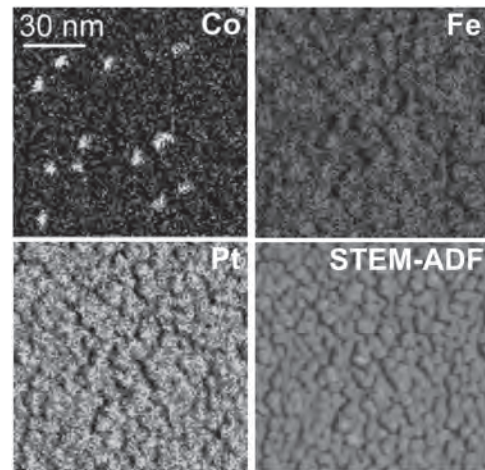
C. Paleo¹, V. Dupuis¹, F. Wilhelm², T. Epicier³, N. Dempsey⁴ and D. Le Roy¹

1. Institut Lumiere Matière, Villeurbanne, France; 2. ESRF, Grenoble, France; 3. Institut National des Sciences Appliquées de Lyon, Villeurbanne, France; 4. Institut NEEL, Grenoble, France

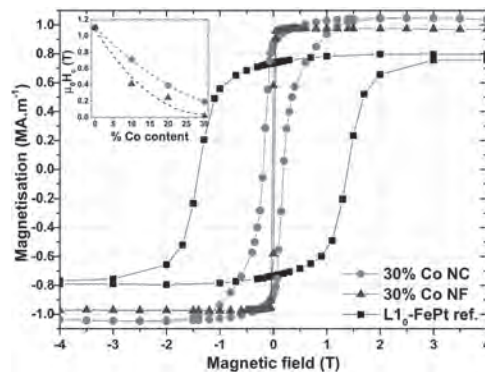
Hard magnetic nanocomposites, consisting of a fine mixture between a large magneto crystalline anisotropy phase and a large magnetization phase, are attractive materials both for integration of hardness-tuned magnets in microsystems and for building next-generation high performance permanent magnets for energy conversion technologies. Instead of relying on the hypothetical discovery of new hard magnetic compound, this approach is based on the mastering of the microstructure in a mixture of already known magnetic phases. Theoretical descriptions predicted a potential energy product of 1 MJ/m^3 , which is twice as large as the one of best $\text{Nd}_2\text{Fe}_{14}\text{B}$ magnets produced today [1]. However, exploiting their full potential has appeared to be very challenging since the first reports on exchange spring structures in the 90's. Indeed, calculations pointed out the absolute necessity to confine the softer phase in nano-sized grains, smaller than twice the domain wall width of the hard phase. In parallel, to maximize the magnetization, the hard phase volume fraction should be restricted to the minimum needed to develop enough coercivity. These requirements cannot be obtained with conventional process for mass scale material fabrication. In this context, investigations of model systems in films can give insights about the interplay between the nanoscale microstructure and the magnetic properties [2]. In particular, the degree of interdiffusion at the soft-hard interface is expected to significantly impact the magnetization reversal but is difficult to address experimentally. Here we focus on the impact of a graded soft-hard interface on magnetic properties. To do so, we recently prepared Co@FePt transition metal-based nanocomposite (NC) films from mass-selected low energy cluster beam deposition technique (MS-LECBD) of Co clusters, in situ embedded in FePt matrix independently produced by alternative electron gun evaporation on the same substrate [3,4,5]. The Co cluster inclusions can be selected in size prior to their deposition, between 1 and 10 nm. The cluster to matrix volume ratio is adjusted controlling the thickness of each Co, Fe, Pt individual layers. The as-prepared Co clusters have been observed by transmission electron microscopy (TEM) and found to crystallise in magnetically soft fcc phase. In this study, we focused on 8 nm Co clusters. The Co to FePt volume fraction was varied from 0 to 50%. Post-deposition annealing of the whole stack is a crucial step to drive the initial Fe and Pt multilayers to the high-magnetic anisotropy $L1_0$ phase. However, this inevitably comes with partial intermixing at the interface between the clusters and the matrix. We systematically compared the nanoclusters-based film with same stoichiometry and alloyed films (NF), obtained by sequential evaporation of Co, Fe, Pt thin and continuous layers. Local atomic structures have been thoroughly investigated using polarization-dependent hard x-ray absorption and element-specific spectroscopies (EXAFS, XLD). Transmission electron microscopy (TEM) equipped with energy-dispersive x-ray spectroscopy (EDX) was used to explore the local chemical profile of the composite films (figure 1). The macroscopic magnetic properties were measured in a Superconducting quantum interference device (SQUID) magnetometer together with local and element specific characterisations using circular dichroism (XMCD). We demonstrate the persistence of soft and hard regions and rule out the fully diluted hypothesis. Magnetic measurements (figure 2) showed a very different behaviour upon annealing between NF and NC films. Using a combinatorial approach, we investigated the coercive magnetic field decay when increasing the Co content. The magnetic coercivity is found to be systematically higher in the NC samples, over the whole range of studied composition. EXAFS spectra fitting and numerical modelling of the diffusion mechanism show that magnetically soft Co-rich inclusions remain after annealing, even at the high temperature required to obtain the $L1_0$ phase of the matrix. In the case of multilayer nanofilms with Co thin layers, the diffusion leads to homogeneous alloying. Local XMCD revealed the evolution of spin and orbital moments of Fe and Co as a function of the composition, further distinguishing the NC system with respect to fully homogeneous alloy. Studying these materials in model systems synthesised by nanofab-

rication routes provides interesting insights into the interplay between the microstructure and the magnetic performances in view to develop mass-scale production of such materials. This work is supported by the ANR collaborative project "SHAMAN": Soft in Hard Magnetic Nanocomposites (2017-2020).

1. Skomski R. and Coey J. M. D. Phys. Rev. B 48, 15812 (1993). 2. Balasubramanian B. et al, Scientific reports 4, 6265 (2014) 3. Tournus F. et al, Journal of Magnetism and Magnetic Materials, vol. 323, p. 1868 (2011) 4. Liu Y. et al, Appl. Phys. Lett. 99, 172504 (2011) 5. Paleo C. et al, Interplay between local structure and magnetic properties of graded exchange-coupled Co@FePt nanocomposite films. Phys. Rev. B 7 (2020).



Energy-dispersive x-ray images of a FePt/Co cluster/FePt sample on a Si_3N_4 substrate, along with the scanning transmission electron microscopy-annular dark-field (STEM-ADF) image.



Hysteresis loops at 300 K for two samples with the same Co content and a $L1_0$ -FePt sample without Co. The NC sample has higher saturation magnetization than the bare $L1_0$ -FePt ref., which is brought by the Co but retains a sizeable coercivity, whereas the NF is magnetically soft. Inset: Dependence of the coercive field $\mu_0 H_c$ on the Co content for the NF and NC.

JD-04. Tuning Magnetic Anisotropy of MnBi Permanent Magnet With Sn*

M. Choi¹, Y. Hong¹, H. Won¹, T. Lee² and J. Lee²

1. Electrical and Computer Engineering, The University of Alabama, Tuscaloosa, AL, United States; 2. Institute of Fundamental and Advanced Technology (IFAT), Hyundai Motor Company, Uiwang-si, The Republic of Korea

Low-temperature phase (LTP) MnBi has the hexagonal NiAs structure and retains its ferromagnetic phase up to 613 K [1]. Above 613 K, some Mn atoms from the octahedral sites diffuse into the trigonal-bipyramidal sites, resulting in the antiferromagnetic coupling between Mn at the octahedral and Mn at the trigonal-bipyramidal interstitial sites. Therefore, the magnetic moment sharply drops before reaching the Curie temperature (T_C) of 720 K. Spin reorientation of LTP MnBi occurs at about 90 K from *ab*-plane (0 - 90 K) to *c*-axis ($T > 90$ K) [2]. The spin orientation and magnetocrystalline anisotropy of LTP MnBi can be tuned by partially replacing Bi of MnBi with the third element. Sakuma et al. have performed first-principles calculations on Sn-doped MnBi ($\text{MnBi}_{1-x}\text{Sn}_x$) and found that the K_u increases to about 3 MJ/m³ at $x = 0.1$ from -0.5 MJ/m³ at $x = 0$ and then remains unchanged up to $x = 0.3$, and T_C is 580 K for $x = 0$ [3]. These calculated K_u and T_C for $x = 0$ are much larger and lower than experimental -0.2 MJ/m³ and 720 K, respectively. Sakuma et al. did not relax $\text{MnBi}_{1-x}\text{Sn}_x$ ($x > 0$) to estimate lattice constants, but used the lattice constants ($x = 0$) for $\text{MnBi}_{1-x}\text{Sn}_x$ ($x > 0$). Therefore, the calculated K_u and magnetic moment for $x > 0$ would be inaccurate. In this study, hexagonal crystal structures of LTP MnBi and Sn-doped MnBi in Fig. 1 were used. The LTP MnBi unit cell has two Mn atoms at the octahedral $2a$ sites of (0, 0, 0) and (0, 0, 1/2) and two Bi atoms at the $2c$ sites of (1/3, 2/3, 1/4) and (2/3, 1/3, 3/4) [4]. We have relaxed $\text{MnBi}_{1-x}\text{Sn}_x$ ($x = 0, 0.5$) unit cell to obtain lattice constants a and c . Doped Sn decreases the a and c from 4.287 and 6.118 Å for $x = 0$ to 3.954 and 5.456 Å for $x = 0.5$, respectively. Accordingly, the volume and c/a ratio also decrease from 97.37 Å³ and 1.43 ($x = 0$) to 73.87 Å³ and 1.38 ($x = 0.5$), respectively. These relaxed lattice constants ($x = 0$) are in good agreement with the experimental lattice constants [5, 6]. The WIEN2k package based on density functional theory (DFT) and using the full-potential linearized augmented plane wave (FP-LAPW) method was used to conduct the first-principles calculations [7]. In order to calculate spin-polarization and spin-orbit coupling, we used the DFT within the local-spin-density approximation (LSDA) and $19 \times 19 \times 27$ k-point mesh generating 1400 k-points in the irreducible part of the Brillouin zone. Figure 2 shows density of states for $\text{MnBi}_{1-x}\text{Sn}_x$ ($x = 0, 0.5$). The net magnetic moments per formula unit is 3.613 $\mu_B/f.u.$ for $x = 0$ and 2.517 $\mu_B/f.u.$ for $x = 0.5$. The net magnetic moment decreases as the Sn concentration increases. The corresponding saturation magnetization in the unit of Tesla (T) monotonically decreases to 0.794 from 0.865 T as the Sn concentration increases to $x = 0.5$. Calculated magnetic moment of 3.613 $\mu_B/f.u.$, K_u of -0.2 MJ/m³ and T_C of 711 K for $x = 0$ are in good agreement with the previously reported results [8]. We will present K_u and magnetic moment as a function of Sn concentration and discuss the discrepancy between Sakuma's results and this work.

[1] A. F. Andersen, *Acta Chemica Scandinavica* 21, 1543 (1967). [2] Michael A. McGuire, Huibo Cao, Bryan C. Chakoumakos, and Brian C. Sales, *Phys. Rev. B* 90, 174425 (2014). [3] Akimasa Sakuma, Yuki Manabe, and Yohei Kota, *Journal of the Physical Society of Japan* 82, 073704 (2013). [4] http://materials.springer.com/isp/crystallographic/docs/sd_1823960, 2020 (accessed 11 November 2020). [5] B. W. Roberts, *Phys. Rev.* 104, 607 (1956) [6] Wenyong Zhang et al., *APL Mater.* 7, 121111 (2019) [7] P. Blaha, et al., WIEN2K: An Augmented Plane Wave + Local Orbitals Program for Calculating Crystal Properties (Karlheinz Schwarz, Techn. Universitat, Wien, Austria, 2001) [8] J. Köhler et al., *J. Phys.: Condens. Matter* 8, 8681(1996)

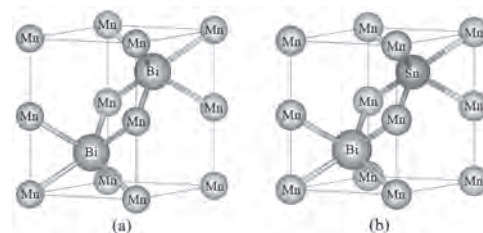


Fig. 1. Crystal structure for (a) MnBi and (b) $\text{MnBi}_{0.5}\text{Sn}_{0.5}$

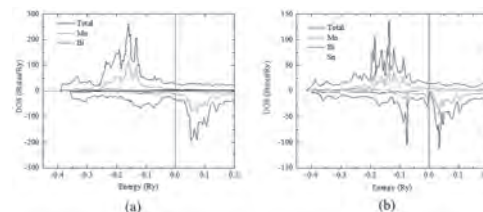


Fig. 2. Density of states for (a) MnBi and (b) $\text{MnBi}_{0.5}\text{Sn}_{0.5}$

JD-05. Effects of Composition on the Ordered Phase Formation in Mn-Al and Mn-Ge Alloy Thin Films Grown on Cr(001) Single-Crystal Underlayers.

S. Noro¹, K. Nakano¹, M. Ohtake¹, M. Futamoto¹, T. Kawai¹, F. Kirino² and N. Inaba³

1. Faculty of Engineering, Yokohama National University, Yokohama, Japan; 2. Faculty of Fine Arts, Tokyo University of the Arts, Tokyo, Japan; 3. Faculty of Engineering, Yamagata University, Yonezawa, Japan

[Introduction] Hard magnetic materials with high K_u , low M_s , and low α have attracted much attention to MRAM application. MnAl alloy with $L1_0$ (Pearson symbol: $tP4$, prototype: CuAu) phase and Mn_3Ge alloy with $D0_{22}$ (Pearson symbol: $tI8$, prototype: Al_3Ti) phase have (K_u , M_s , α) = (1.5×10^7 erg/cm³ [1], 500 emu/cm³ [2], 0.006-0.0175 [3,4]) and (1.2×10^7 erg/cm³, 100 emu/cm³ [5], 0.03 [6]), respectively. However, these phases are metastable and crystallographic phases other than $L1_0$ or $D0_{22}$ may be involved in Mn-Al and Mn-Ge films [3,5]. The formation of ordered phases is delicately influenced by the film composition. In the present study, Mn-Al and Mn-Ge films are prepared by using a molecular beam epitaxy system with a reflection high-energy electron diffraction (RHEED) facility, which can reveal the crystallographic property during film formation. The effects of composition on the structural and magnetic properties are investigated. [Experimental Procedure] 20-nm-thick Mn_xAl_{100-x} and Mn_yGe_{100-y} (at. %) films were formed on Cr(001) single-crystal underlayers at 300 °C. The Mn contents, x and y , were varied from 40 to 100 at. %. The crystal structure and the crystallographic orientation relationship between film and underlayer were determined by RHEED. The order degrees of $L1_0$ and $D0_{22}$ phases were estimated by XRD. The surface morphology was observed by AFM. The magnetization curves were measured by VSM. [Results and Discussion] Fig. 1(a) shows the RHEED patterns observed for Mn-Al films with different compositions. Diffraction patterns from $L1_0(001)$ and $A12(001)$ surfaces [Fig. 1(b-1)] are overlapped for the films with $x \leq 50$, which involves the $L1_0$ -MnAl stoichiometry ($x = 50$), as shown for example in Fig. 1(a-1). Although metastable $L1_0$ phase is formed, $A12$ (Pearson symbol: $cI58$, prototype: α -Mn) phase is coexisting with $L1_0$ phase in the films. Diffraction pattern from only $L1_0(001)$ surface [Fig. 1(b-2)] is observed for the films with Mn-rich compositions of $x = 58-72$, as shown in Fig. 1(a-2). The result shows that $L1_0(001)$ single-crystal films with the c -axis perpendicular to the substrate surface are successfully obtained. The formation of $L1_0$ ordered phase is promoted by using Mn-rich compositions. However, the order degree determined by XRD (not shown here) decreases with increasing the Mn content. With further increasing the Mn content ($x = 80-100$), diffraction pattern from only $A12(001)$ surface is recognized. Fig. 1(c) summarizes the compositional dependence on crystal structure. Fig. 1(d) shows the crystallographic orientation relationships of $L1_0(001)$ and $A12(001)$ crystals with respect to Cr(001) underlayer, which are also determined by RHEED. Fig. 1(e) shows the RHEED patterns observed for Mn-Ge films. Diffraction pattern from $D0_{22}(001)$ surface [Fig. 1(f-2)] is obtained for the films with $y = 68-75$ including the $D0_{22}$ - Mn_3Ge stoichiometry ($y = 75$). Metastable $D0_{22}(001)$ single-crystal films are epitaxially grown on the Cr underlayers. For the films with Mn-rich compositions of $y = 83-100$, diffraction pattern from $A12(001)$ surface [Fig. 1(f-3)] is recognized, similar to the case of Mn-Al films. For the films with Ge-rich compositions of $y = 43-60$, diffraction pattern from (001) single-crystal surface with simple cubic structure (Pearson symbol: cP , lattice parameter: $a = 0.85$ nm) [Fig. 1(f-1)], which does not exist in the bulk Mn-Ge phase diagram, is appearing. In order to determine the crystal structure, characterization by neutron diffraction is necessary. The crystal structures and the epitaxial orientation relationships of Mn-Ge films are summarized in Figs. 1(g) and (h), respectively. Figs. 2(a) and (b) show the compositional dependences on surface roughness values (R_a) of Mn-Al and Mn-Ge films. Flat surfaces with $R_a \leq 0.3$ nm are realized for the Mn-Al films with $x = 58-72$ and the Mn-Ge films with $y = 68-75$ which are respectively composed of $L1_0$ and $D0_{22}$ phases. Fig. 2(c) shows the magnetization curves measured for Mn-Al films. The $Mn_{58}Al_{42}$ film consisting of $L1_0$ phase shows strong perpendicular magnetic anisotropy [Fig. 2(c-2)]. The magnetization does not saturate at 10 kOe. The magnetic property is apparently reflecting the magnetocrystalline anisotropy of $L1_0$ phase. Isotropic magnetization curves are observed for the $Mn_{65}Al_{35}$ film [Fig. 2(c-3)], though the $Mn_{65}Al_{35}$

film is consisting of only $L1_0$ phase. The reason is due to an influence of low order degree. The $Mn_{50}Al_{50}$ film also shows isotropic magnetic property due to an influence of coexistence of $L1_0$ and $A12$ phases. Fig. 2(d) shows the magnetization curves of Mn-Ge films composed of only $D0_{22}$ phase. These films do not show perpendicular magnetic anisotropies, since the order degrees are not so high. In the present study, $L1_0$ -MnAl and $D0_{22}$ - Mn_3Ge films are prepared under similar experimental conditions. Although flat surfaces which are required for practical applications are realized for both MnAl and Mn_3Ge films, strong perpendicular anisotropy is observed only for a MnAl film. The present study shows that it is important achieving a high order degree in addition to obtaining a single phase of $L1_0$ or $D0_{22}$ in order to enhance strong perpendicular magnetic anisotropy.

[1] A. Sakuma: *J. Phys. Soc. Jpn.* 63, 1422 (1994). [2] J. H. Park, Y. K. Hong, S. Bae, J. J. Lee, J. Jalli, G. S. Abo, N. Neveu, S. G. Kim, C. J. Choi, J. G. Lee: *J. Appl. Phys.* 107, 09A731 (2010). [3] M. Hosoda, M. Oogane, M. Kubota, T. Kubota, H. Saruyama, S. Iihama, H. Naganuma, Y. Ando: *J. Appl. Phys.* 111, 07A324 (2012). [4] S. W. Mao, J. Lu, L. Yang, X. Z. Ruan, H. L. Wang, D. H. Wei, Y. B. Xu, J. H. Zhao: *Chn. Phys. Lett.* 37, 058501 (2020). [5] A. Sugihara, S. Mizukami, Y. Yamada, K. Koike, T. Miyazaki: *Appl. Phys. Lett.* 104, 132404 (2014). [6] S. Mizukami, A. Sugihara, S. Iihama, Y. Sasaki, K. Z. Suzuki, T. Miyazaki: *Appl. Phys. Lett.* 108, 012404 (2016).

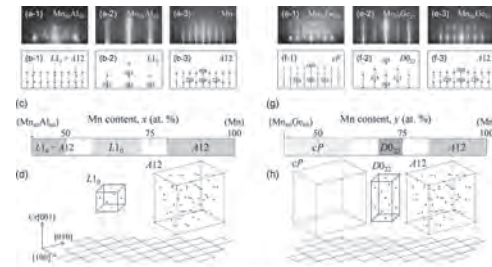


Fig. 1. [(a), (e)] RHEED patterns observed for (a) Mn-Al and (e) Mn-Ge films formed on Cr(001) underlayers. [(b), (f)] Schematic diagrams of simulated RHEED patterns. [(c), (g)] Compositional dependences of crystal structures of (c) Mn-Al and (g) Mn-Ge films. [(d), (h)] Crystallographic orientation relationships with respect to Cr(001) underlayer.

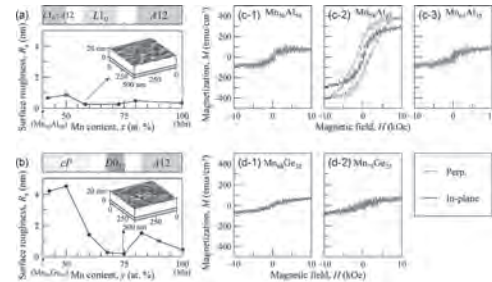


Fig. 2. [(a), (b)] Compositional dependences on surface roughness, R_a of (a) Mn-Al and (b) Mn-Ge films. The insets show the AFM images observed for (a) $Mn_{58}Al_{42}$ and (b) $Mn_{68}Ge_{32}$ films. [(c), (d)] Magnetization curves measured for (c) Mn-Al and (d) Mn-Ge films.

JD-06. The Dependence of the Intrinsic Magnetic Properties of Mn_3AlC on its Chemical Composition.

F. Jürries^{1,2}, K. Nielsch^{1,2} and T. Woodcock¹

1. Leibniz IFW Dresden, Dresden, Germany; 2. Technische Universität Dresden, Dresden, Germany

The $L1_0$ structured τ -phase of the Mn-Al-C system gained interest for the potential use as a rare earth free hard magnetic material [1]. It has been reported that the formation of a small fraction of Mn_3AlC precipitates leads to an increase in coercivity of the τ -phase [2]. Mn_3AlC is also of interest because it is ferromagnetic, has a wide phase field in the Mn-Al-C equilibrium diagram and shares a two-phase region with the ϵ -phase of MnAl, which is the origin of τ -MnAl-C. Despite its broad homogeneity range, the Curie temperature (T_C) of Mn_3AlC is often reported to be at around 290 K [3,4]. There are only few reports of the influence of composition on the T_C [5,6,7] and one has demonstrated a dramatic increase in T_C up to 880 K with increasing Mn-content [5]. Furthermore, it has been reported that a full substitution of Al with Mn is possible, while retaining the ferromagnetic properties, resulting in Mn_4C with a T_C of 870 K [8]. The aim of the current work is to carry out a systematic investigation of the intrinsic magnetic properties of Mn_3AlC in order to confirm the dramatic results presented in the literature and to assess the possible influence of Mn_3AlC precipitates on the properties of MnAl-C permanent magnets. Two series of Mn-Al-C alloys have been prepared: in one series the Mn-content was constant while Al was substituted with C (compositions: $Mn_{58}Al_{34-x}C_{8+x}$, $x = 0, 5, 10$) and in the other series the C-content was constant, while Al was substituted with Mn (compositions: $Mn_{60+x}Al_{21-x}C_{19}$, $x = 0, 5, 10$). The alloys were arc-melted in 10 g ingots, followed by a homogenisation at 1100°C in Ar-atmosphere for 5 days and were finally quenched into water. The chemical composition of the homogenised materials was determined using Inductively Coupled Plasma Optical Emission Spectroscopy for Mn- and Al-contents and by carrier-gas hot-extraction for C-content. In Fig. 1 and Fig. 2 the measured values of Mn-content were used for alloys produced in this study. Structural information about the phases in the alloys was gathered from XRD measurements, using a Bruker diffractometer with a Co-K α radiation. Analysis of the XRD patterns was done using FullProf Suite software. Local chemical analysis of the microstructure was done by EDX-measurements using a Gemini Leo 1530 SEM. The magnetic properties of the alloys were measured using the VSM-mode of a Quantum Design PPMS. $M(T)$ -curves were measured at an applied field of 0.1 T in a temperature range from 10 K to 900 K with a heating and cooling rate of 5Kmin⁻¹. Furthermore, hysteresis loops up to an applied field of 14 T were measured at room temperature and at 100 K. In Fig.1 the T_C of Mn_3AlC is plotted against the Mn content of the phase from various sources. The Mn-content is related to the Mn_3AlC formula unit containing 5 atoms. The curves represent the work of different groups that investigated the influence of composition on the T_C . The results of the current work are shown in separate branches, since the two different series of alloys focus on different changes of the composition. The substitution of Al with C in the current work (solid black squares) shows a nearly constant T_C at around 290 K, despite the change of the overall Mn-content. The same kind of substitution was done by Tong et al. [7], who reported a somewhat larger influence on T_C : a change of 60 K was found in going from a composition of 2.75 to 3.0 Mn atoms per formula unit. Contrary to that, the substitution of Al with Mn in the current work (unfilled black squares) shows a drastic increase of the T_C from around 355 K to 765 K. This behaviour of the T_C is similar to the increase of the T_C shown by the work of Wang et al. [5] and Butters et al. [6], who substituted Al with Mn as well. The work of Si et al. [8] focused on the properties of Mn_4C , which shows a similar crystal structure to Mn_3AlC . The T_C of the Mn_4C phase seems to fit well to the dependence of T_C of Mn_3AlC , which could confirm that a full substitution of Al with Mn is possible. Fig. 2 shows the magnetisation (M) as a function of Mn-content measured in the current work and data taken from Wang et al. [5]. The data for M was taken at 1.5 T, for which the samples are close to saturation. The Mn-content is related to the Mn_3AlC formula unit. The M values are taken at 100 K. The curves represent the work of our group and the work of Wang et al. Compared to Fig. 1 we do not consider alloys of the first series, since they do not contain Mn_3AlC only which means a change of M is connected to the phase fraction of Mn_3AlC and not only connected

to a change of composition. The alloy series in which Al was replaced by Mn shows a maximum of 92 Am²kg⁻¹ at 3.4 Mn atoms per unit formula. Compared to the work of Wang et al. [5], who found a maximum for M of 90 Am²kg⁻¹ for a stoichiometric composition the maximum of magnetisation is shifted to higher values of Mn atoms per unit cell. In the current work two different alloy series were used to study the effect of composition on the T_C and M of Mn_3AlC . The results confirm the dramatic increase in T_C on substituting Al with Mn reported in the literature [5] and the decrease in M of Mn_3AlC on increasing Mn content. The ferromagnetic nature of the Mn_3AlC phase may influence the magnetic properties of τ -MnAl-C magnets, particularly for low temperature applications. To investigate this in more detail, further studies are needed.

[1] Feng, L. et al. Acta Materialia 199, 155-168 (2020) [2] Ohtani, T. et al. IEEE Transactions on Magnetics 13, 1328-1330 (1977) [3] Dierkes, H. et al. Inorganic Chemistry 56, 1045-1048 (2017) [4] Wang, B. et al. Journal of Applied Physics 108, 093925 (2010) [5] Wang, X. et al. Journal of Magnetics 24 123-127(2019) [6] Butters, R. P.; Myers H.P. Cl. The London, Edinburgh, and Dublin Philosophical Magazine and Journal of Science 46, 895-902 (1955) [7] Tong, P. et al. Solid State Communications 138, 64-67 (2006) [8] Si, P. et al. Applied Physics Letter 112 192407 (2018)

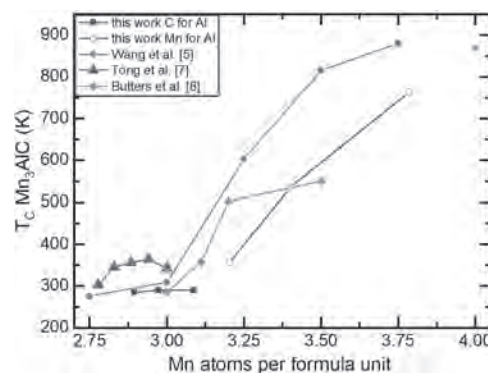


Fig. 1: Curie temperature of Mn_3AlC depending on the Mn content per formula unit.

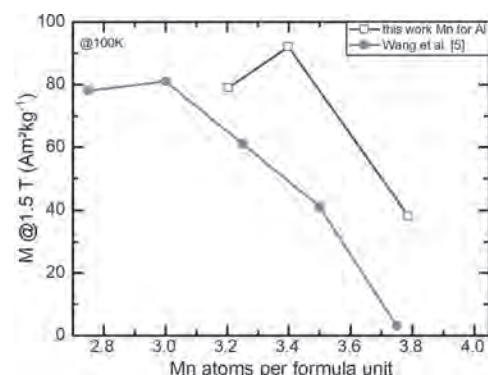


Fig. 2: Measured magnetisation at an applied field of 1.5 T at 100 K for different MnAlC-alloys.

JD-07. Tuning Spin and Magnetocrystalline Anisotropy of $L1_0$ -Ordered MnAl With Transition Metal Elements (TM = Mn, Fe, Co, Ni)*.

M. Choi¹, Y. Hong¹, H. Won¹, C. Yeo², S. Kim³, H. Lee³ and W. Lee³
 1. Electrical and Computer Engineering and Materials Science Ph.D. Program, The University of Alabama, Tuscaloosa, AL, United States;
 2. Mechanical Engineering, Texas Tech University, Lubbock, TX, United States;
 3. Materials Science & Engineering, Yonsei University, Seoul, The Republic of Korea

$L1_0$ -ordered MnAl shows a high magnetic moment of $2.4 \mu_B/f.u.$ and magnetocrystalline anisotropy constant (K) of 1.5 MJ/m^3 [1,2]. The magnetocrystalline anisotropy and spin direction can be tuned by either the axial ratio c/a or substituting the Mn of MnAl by transition metals. Sakuma calculated K_u of $L1_0$ -ordered equiatomic MnAl as a function of the axial ratio c/a ranging from 0.60 to 1.2 by first-principles calculation [1]. It was found that the spin direction changes to the out-of-plane direction (uniaxial) from the in-plane direction at $c/a = 0.7071$ by changing the magnetocrystalline anisotropy sign to positive from negative. The calculated magnetocrystalline anisotropy constant is 1.5 MJ/m^3 at $c/a = 0.9058$. Sakuma used the lattice constants of $a = 3.93 \text{ \AA}$ and $c = 3.56 \text{ \AA}$ measured at 300 K in his first-principles calculations. On the other hand, Manchanda *et al.* have performed the first-principles calculation on Fe-substituted $L1_0$ -ordered MnAl to investigate magnetocrystalline anisotropy constant and found that Fe increases the magnetocrystalline anisotropy constant to 2.5 MJ/m^3 from 1.5 MJ/m^3 of non-substituted MnAl. However, the total magnetic moment decreased, and the spin direction did not change [3]. Neither Sakuma nor Manchanda reported the Curie temperature for various c/a MnAl and Fe-substituted MnAl and relaxed the studied MnAl system. In this paper, we have systematically investigated the effects of transition metals (Fe, Co, Ni) on magnetization, magnetocrystalline anisotropy, and Curie temperature of $L1_0$ -ordered MnAl. We used the WIEN2k package based on density functional theory (DFT) and the full-potential linearized augmented plane wave (FP-LAPW) method to conduct the first-principles calculations [4]. All calculations used $19 \times 19 \times 27$ k-point mesh generating 1400 k-points in the irreducible part of the Brillouin zone to obtain electronic structures of $\text{Mn}_{0.5}\text{TM}_{0.5}\text{Al}$ (TM = Mn, Fe, Co, and Ni). Each TM has the following valence electrons (n): 7 for Mn ($3d^5 4s^2$), 8 for Fe ($3d^6 4s^2$), 9 for Co ($3d^7 4s^2$), and 10 for Ni ($3d^8 4s^2$). After having relaxed $L1_0$ -ordered $\text{Mn}_{0.5}\text{TM}_{0.5}\text{Al}$ (TM = Mn, Fe, Co, and Ni), we obtained the lattice constants, volumes, and c/a ratios in Table 1. It is found that the c/a ratio and volume decrease with an increase in n from 7 (Mn) to 10 (Ni) in Table 1. Figure 1 shows the density of states (DOS) for $\text{Mn}_{0.5}\text{TM}_{0.5}\text{Al}$ (TM = Mn, Fe, Co, and Ni) with spin configuration. DOS significantly changes with the TM substitution. It is striking that Ni-substituted MnAl shows the ferrimagnetic spin configuration, as seen in Fig. 1(d). However, the ferromagnetic spin configuration is set in $\text{Mn}_{0.5}\text{TM}_{0.5}\text{Al}$ (TM = Mn, Fe, and Co). As summarized in Table 1, the total magnetic moment decreases as the valence electron increases in the order of Ni, Co, and Fe. In order to calculate the K of the $\text{Mn}_{0.5}\text{TM}_{0.5}\text{Al}$ system, the magnetocrystalline anisotropy energy (MAE) was calculated using the total energy difference between $\langle 001 \rangle$ and $\langle 100 \rangle$ spin configurations ($\Delta E = E_{\langle 001 \rangle} - E_{\langle 100 \rangle}$). The Fe substitution leads to a significant increase in K from 1.34 MJ/m^3 to 2.98 MJ/m^3 . When either Co or Ni replaces Fe, the K becomes negative and is -0.3 MJ/m^3 for Co or -0.18 MJ/m^3 for Ni in Table 1. This implies the magnetization (Co, Ni) direction changes to the in-plane direction from the out-of-plane direction, *i.e.*, uniaxial (Mn and Fe). Curie temperature (T_C) was calculated by the mean-field approximation (MFA). The T_C dramatically decreases from 685 K(Mn) to 20 K(Ni). Alloying the MnBi with transition elements could tune the spin direction and magnetocrystalline anisotropy of $L1_0$ -ordered MnAl. However, magnetization and Curie temperature are negatively affected by the alloying. We will discuss all these findings in detail in this presentation. * This work was supported in part by the E. A. "Larry" Drummond Endowment at the University of Alabama.

[1] A. Sakuma, *J. Phys. Soc. Jpn.* 63, 1422 (1994) [2] J. H. Park, Y. K. Hong, *et al.*, *J. Appl. Phys.* 107, 09A731 (2010) [3] P. Manchanda, *et al.*, *J. Magn. Magn. Mater.* 365, 88-92 (2014) [4] Blaha, P. and Schwarz, K., WIEN2k: An Augmented Plane Wave + Local Orbitals Program for Calculating Crystal Properties (Karlheinz Schwarz Techn. Universität Wien, Vienna, Austria, 2001)

Lattice parameters				
	a (Å)	c (Å)	Volume	c/a ratio
MnAl	3.94	3.54	49.26	0.90
Mn _{0.5} Fe _{0.5} Al	3.83	3.21	47.43	0.84
Mn _{0.5} Co _{0.5} Al	3.81	3.17	46.97	0.83
Mn _{0.5} Ni _{0.5} Al	3.83	3.12	45.81	0.79

Magnetic Properties (Magnetic moment, anisotropy magnetization (AM), and magnetocrystalline anisotropy constant (K))										
Material	Spin Moment (μ _B)			Orbital Moment (μ _B)			Total Moment (μ _B)	M (μ _B /f.u.)	MAE (meV/f.u.)	K (MJ/m ³)
	Mn	Fe	Al	Mn	Fe	Al				
MnAl	2.18	2.18	-0.04	0.03	0.03	-0.01	4.34	617.68	0.41	1.34
Mn _{0.5} Fe _{0.5} Al	1.99	1.36	-0.01	0.04	0.07	-0.00	3.32	646.16	0.48	2.98
Mn _{0.5} Co _{0.5} Al	1.49	0.01	-0.02	0.02	0.00	-0.00	1.49	201.25	-0.04	-0.30
Mn _{0.5} Ni _{0.5} Al	0.93	-0.08	-0.01	0.02	-0.00	-0.00	0.89	179.16	-0.03	-0.18

Table 1. Lattice parameters and magnetic properties of $L1_0$ - $\text{Mn}_{0.5}\text{TM}_{0.5}\text{Al}$ (TM = Mn, Fe, Co, Ni).

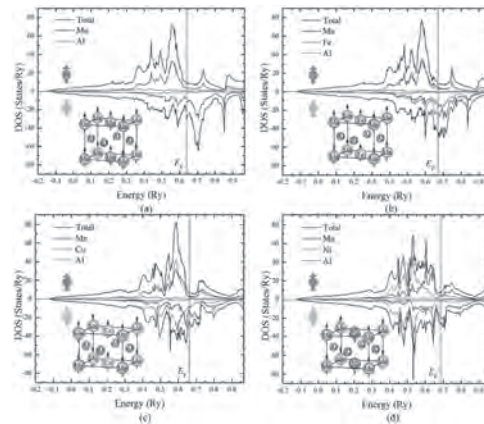


Figure 1. Density of states (DOS) for (a) MnAl, (b) $\text{Mn}_{0.5}\text{Fe}_{0.5}\text{Al}$, (c) $\text{Mn}_{0.5}\text{Co}_{0.5}\text{Al}$, and (d) $\text{Mn}_{0.5}\text{Ni}_{0.5}\text{Al}$ based relaxed lattice constants.

JD-08. MnAlC Permanent Magnets Obtained Directly From ϵ -Phase Gas-Atomized and Milled Powder by Hot-Pressing.

C. Muñoz Rodríguez¹, E.M. Palmero¹, J. Rial¹, L. Feng², T. Mix², B. Skårman³, H. Vidarsson³, P. Larsson³, T. Woodcock² and A. Bollero¹
 1. Division of Permanent Magnets and Applications, Fundacion IMDEA Nanociencia, Madrid, Spain; 2. Leibniz-Institut für Festkörper- und Werkstofforschung Dresden eV Institut für Metallmaterialien, Dresden, Germany; 3. Höganas AB, Höganas, Sweden

Nowadays the use of permanent magnets (PMs) plays a key role in different applications such as energy and electromobility. In order to obtain a high magnetic performance, the most extended choice is PMs containing rare-earths (REs). Alternative RE-free PM materials are investigated to plug the gap between ferrites and NdFeB magnets [1]. MnAlC alloy is a promising RE-free PM candidate, but further optimization is required in order to achieve a proper combination of saturation magnetization (provided by the only ferromagnetic phase of the system: L1₀ or τ -MnAl) and coercivity. Studies on MnAl alloys typically focus on obtaining a maximum content of τ -phase, which results in an optimized saturation magnetization [2]. We have recently shown the possibility of developing coercivity in gas-atomized MnAl powder by applying milling times as short as 30-270 s via the self-developed “flash milling” method [3]. A successful combination of nanostructuring and a controlled phase transformation process is behind the observed increase in coercivity [3]. In this study we have used ϵ -phase MnAlC powder produced by gas-atomization and flash-milling (60 s) to fabricate MnAlC bulk magnets, with no need to transform previously the ϵ into τ phase. Under the optimal combination of pressure (300 MPa) and temperature (600 °C), hot-pressing applied to ϵ -phase MnAlC alloy has been able to manage simultaneously the ϵ -to- τ transformation and the powder compaction to end with a high-density (93%) MnAlC magnet [4]. Figure 1(a) shows the X-ray diffraction pattern of the precursor ϵ -phase loose powder and the successful transformation into τ -phase after the hot-pressing process. The room temperature hysteresis loops measured for the hot-pressed magnet showed an enhancement of the coercivity of up to 25 % and a slightly superior magnetization at remanence by comparison with the annealed gas-atomized loose powder (Fig. 1 (b)). The large coercivity obtained for the magnet may be explained based on the formation of both β -Mn and Mn₃AlC phases together with a reduced mean crystallite size (27 nm) and the induced strain during compaction [4]. On this basis, we have demonstrated that coercivity of the compacted magnet can be further increased in about 15% by starting from flash-milled gas-atomized powder, due to a larger content of β -Mn and Mn₃AlC phases. We have obtained comparable magnetization and coercivity values when compacting the starting material with a crystallographic structure based on τ -phase (i.e., involving two steps: annealing for managing ϵ into τ phase transformation followed by hot-pressing), thus validating our single-step process. This is a promising cost-efficient route which opens the path to new possibilities for the fabrication of MnAlC-based magnets. Acknowledgements IMDEA acknowledges financial support from EU M-ERA.NET and MINECO through the projects “NEXMAG” (Project Success Case at H2020 M-era. Net Programme, Ref. PCIN-2015-126) and “3D-MAGNETOH” (Ref. MAT2017-89960-R); Regional Government of Madrid through “NANOMAGCOST” project (Ref. P2018/NMT-4321); and Höganas AB through the industrial collaboration “ECNanoManga”.

[1] J.M.D. Coey, IEEE Trans. Magn., 47, 4671 (2011) [2] V. Øygarden et al., J. Alloys Compd., 779, 776 (2019) [3] J. Rial et al., Acta Mater., 157, 42 (2018); Engineering, 6 (2), 173 (2020) [4] C. Muñoz-Rodríguez et al., J. Alloys Compd., 847, 156361 (2020)

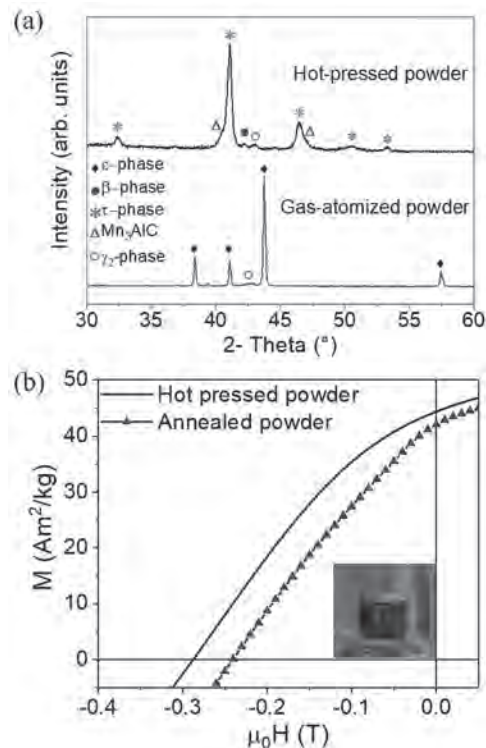


Fig. 1. (a) X-ray diffraction pattern of the ϵ -phase gas-atomized loose powder and hot-pressed powder. (b) Room temperature hysteresis loops (second quadrant) of the loose annealed powder (ϵ transformed into τ -phase) and the magnet obtained by hot-pressing the ϵ -phase powder. Inset shows an image of the resulting compacted MnAlC magnet.

JD-09. Additive Manufacturing of Rare Earth-Free and Hybrid Permanent Magnets: From Composites Synthesized by Solution Casting to Magnetic Filament and 3D-Printing of Magnets.

E.M. Palmero¹, D. Casaleiz¹, J. de Vicente¹ and A. Bollero¹

1. Group of Permanent Magnets and Applications, Fundacion IMDEA Nanociencia, Madrid, Spain

Nowadays multi-material additive manufacturing (AM) is attracting much interest in many high technological sectors such as automotive, energy, electronics, aeronautics and medicine. The combination of AM technology with the synthesis of composite materials allows for designing and fabricating objects with complex shapes and tuned properties for reaching high performance [1]. For permanent magnet (PM) applications, a present challenge is developing magnets by AM with no geometrical constrictions, high filling factor (FF) to avoid diluting their magnetic properties, and no deterioration of their PM properties during processing [2]. The industrial fabrication of PM/polymer composites (typically in the shape of pellets) is done by mechanical methods. We showed recently, and for the very first time, the possibility of producing a continuous PM-based filament (meters long) using as a precursor a highly loaded PM/polymer composite synthesized by solution casting [3]. This technique allows for the synthesis of customized composites making possible the choice of the polymer according to the requirements dictated by the final application. Moreover, it is an easily scalable route, which opens a new path to the AM technology of PMs. In this study, different composites (PM particles/polymer) have been analyzed consisting on several PM materials: gas-atomized τ -MnAlC (Fig. 1(a)), Sr-ferrite, NdFeB, and hybrid (NdFeB/Sr-ferrite) powders embedded in different polymer matrix. It is of large scientific and technological interest to consider rare earth (RE)-free PM alternatives such as improved ferrites, and the promising MnAl-based alloys [4]. The starting powders showed different mean particle size ranging from the 5 μm of Sr-ferrite to the 50 μm of NdFeB powders. MnAlC powders showed an intermediate mean particle size between 15 and 30 μm . This work will show the effect of particle size (with special attention to the benefits of combining dissimilar sizes), polymer and fabrication parameters on the properties of the final products, showing that they are key factors to be considered and optimized for obtaining flexible and continuous filaments with a high FF. Particle size plays a key role when extruding the composites in order to obtain flexible filaments with a high FF [3,5,6]. It has been observed that if the mean particle size is larger than 20 μm (coarse particles), the extrusion process is affected by the composite rheology under the exerted pressures and, consequently, the FF of the extruded filament is reduced [5,6]. A key result from this study is the demonstration that, by mixing particles with different size and optimizing the fine-to-coarse particles ratio, it is possible to obtain flexible filaments with increased FF (up to 90%), i.e., leading to an enhanced effectiveness of the extrusion process [5,6]. MnAlC-based composites were synthesized by solution casting (Fig. 1(a)) making possible to tune the FF, reaching extremely high values above 85% [3]. Composites were extruded into continuous and flexible filaments with PM properties (Fig. 1(b)), with a length over 10 m [3,6]. The homogeneity of the composites and filaments has been determined by scanning electron microscopy, SEM (Fig. 1(b)). Processing of SEM images allowed for obtaining the FF of the composites and filaments. Vibrating sample magnetometry (VSM) has been used for accurately determining the FF of composites and filaments, being positioned as a faster technique in comparison with image processing. Moreover, and important in view of practical applications, this technique has demonstrated the no deterioration of PM properties of the starting particles after composite synthesis and filament extrusion processes (Fig. 1(b)) [3,5,6]. We will compare these results with those obtained in the preparation of filament prepared from composites based on: Sr-ferrite ($H_c \sim 3$ kOe, FF=92%), NdFeB ($H_c=10.2$ kOe, FF=83%) and hybrid composites containing fine (Sr-ferrite) and coarse (NdFeB) particles ($H_c=8$ kOe, FF=90%). Optimized MnAlC-based filament (with a high MnAlC content above 80 wt.%) was used for 3D-printing objects as a proof-of-concept (Fig. 2). Magnetic measurements performed on the printed objects (Fig. 2) have proved that alternative PM materials can be efficiently synthesized and processed for developing novel PMs by AM under controlled processing temperature, which might be used in sensing devices [6]. Acknowledgements Authors acknowledge fruitful collaboration and discussions with B.

Skårman, H. Vidarsson and P.-O. Larsson from Höganäs AB (Sweden), and A. Nieto and R. Altimira from IMA S.L.U. (Spain). Authors additionally acknowledge financial support from EU M-ERA.NET and MINECO through the projects “NEXMAG” (M-ERA.NET Project Success Case, Ref. PCIN-2015-126) and “3D-MAGNETOH” (Ref. MAT2017-89960-R); Regional Government of Madrid through “NANOMAGCOST” project (Ref. P2018/NMT-4321); and Höganäs AB through the industrial contract “GAMMA”.

[1] S.A.M. Tofail et al., *Mater. Today*, 21, 22 (2018) [2] C. Huber et al., *Appl. Phys. Lett.*, 109, 162401 (2016) [3] E.M. Palmero et al., *Sci. Technol. Adv. Mater.*, 19, 465 (2018) [4] A. Bollero et al., *ACS Sustainable Chem. Eng.*, 5, 3243 (2017); J. Rial et al., *Acta Mater.*, 157, 42 (2018); J. Rial et al. *Engineering*, 6 (2), 173; C. Muñoz-Rodríguez et al., *J. Alloys Compd.*, 847, 156361 (2020) [5] E.M. Palmero et al., *IEEE Trans. Magn.*, 55, 2101004 (2019) [6] E.M. Palmero et al., *Addit. Manuf.*, 33, 101179 (2020)

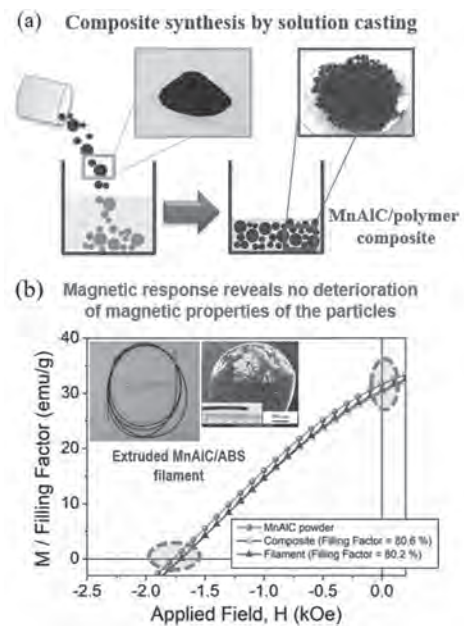


Fig. 1. (a) Composite synthesis by solution casting with representative images of the starting MnAlC powders and the resulting MnAlC/polymer composite. (b) Second quadrant of the hysteresis loops measured at room temperature for the gas-atomized MnAlC particles, MnAlC/polymer composite and extruded filament. Inset shows an extruded MnAlC-based filament together with an SEM image of its circular cross section.

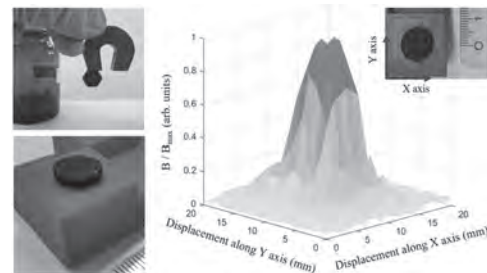


Fig. 2. Magnetic pieces obtained by additive manufacturing using an extruded filament based on MnAlC particles, together with the magnetic flux density measured at the surface of a 3D-printed disc.

JD-10. Morphology, Structure and Magnetic Coupling Relationship in Hard-Soft SrFe₁₂O₁₉-CoFe₂O₄ Nanostructures.

P. Maltoni¹, T. Sarkar¹, G. Barucca², G. Varvaro³, F. Locardi⁴, D. Peddis^{4,3} and R. Mathieu¹

1. of Materials Science and Engineering, Solid State Physics, Uppsala Universitet, Uppsala, Sweden; 2. Universita Politecnica delle Marche, Ancona, Italy; 3. Istituto di Struttura della Materia Consiglio Nazionale delle Ricerche Sede secondaria di Montelibretti, Montelibretti, Italy; 4. DCCI, Universita degli Studi di Genova, Genova, Italy

In recent years, magnetic nanocomposites (NCs) have obtained an ever-increasing attention, due to the possibility to finely control and modify their features at the nanoscale, which is fundamental for extending their applicability as permanent magnets in a multitude of energy-related technological areas [1,2]. In this regard, ferrites have shown to be a promising class of materials, in particular M-type SrFe₁₂O₁₉ (SFO) and spinel CoFe₂O₄ (CFO) nanoparticles (NPs): their respective hard and soft magnetic properties make them interesting candidates for hard-soft exchange-coupled nanostructures. Effectively, the combination of two prototypical phases with different extrinsic properties expands the potentiality and hence the suitability of such nanosystems [3]. Our main focus here is on the investigation of the synthesis strategy in controlling the magnetic coupling, through the optimization of the interface between the hard-soft magnetic phases, thus achieving efficiently strongly coupled nanostructures. This work addresses a systematic investigation of the magnetic interaction in SFO-CFO hard-soft NCs. Several samples were synthesized through a self-combustion sol-gel approach, with compositions ranging from 50/50 to 90/10 w/w %, in step of 10%. In order to elucidate the synthesis method, a thermogravimetric/differential thermal analysis (TG/DTA) was performed, showing a first evidence that the reaction proceeds in a symbiotic way, where the formation of CFO after-combustion assists the evolution of SFO precursors, when the CFO % is increased [4]. The subsequent investigation on the inner structure of the NCs, by transmission electron microscopy (TEM) technique, revealed that SFO NPs are in the form of platelets, with CFO nanocrystals confined between the SFO ones. This clearly suggests a strong interaction between the two structures [5]. The evidence of a symbiotic growth was furtherly confirmed by X-ray powder diffraction (XRPD): the crystallite size extracted by Rietveld refinement shows an evident dependence of SFO crystallite size on the amount of inserted soft phase. When CFO increases, the d_c (size extracted along the c-axis) and d_{ab} (size extracted along the ab-plane) for SFO drop from 104 to 51 nm from 132 to 77 nm, respectively. Hence, we illustrate here for the first time that the CFO grains act as nucleation sites for the SFO phase, resulting in an effect of confinement, which restricts the growth of one phase by the other. To clarify the relationship between the morphological-structural features and magnetic coupling, the static magnetic properties of NCs were investigated at 300 K using a superconducting quantum interference device (SQUID) magnetometer. The analysis of field-dependent magnetization loops shows that the two magnetic phases are homogeneously dispersed and strongly coupled (as reported in Figure 1). Furthermore, the switching field distributions clearly exhibit a single reversal process of magnetization, confirming that the SFO and CFO phases are strongly coupled in the composite (as shown in Figure 2). As expected, the variation of coercivity (H_C) is consistent with the increasing amount of soft CFO phase, as it decreases from ~463 to 178 kA/m, within the limit of exchange-coupling, whereas the saturation moment (M_S) increases up to ~74 Am²/kg. Our study shows that it is possible to control and limit the decrease of the coercivity of hard-soft bi-magnetic NCs to our desire by controlling the size and distribution of the hard-soft regions, and their interface. We thank the Swedish Energy Agency and Swedish Research Council (VR) for financially supporting this work.

[1] R. Skomski, P. Manchanda, P. K. Kumar, B. Balamurugan, A. Kashyap, D. J. Sellmyer, *IEEE Trans. Magn.*, 49 (7), 3215, (2013) [2] K. P. Skokov, O. Gutfleisch, *Scr. Mater.*, 154, 289, (2018) [3] G. Muscas, P. Anil Kumar, G. Barucca, G. Concas, G. Varvaro, R. Mathieu, D. Peddis, *Nanoscale*, 8, 2081, (2016) [4] F. Sayed, G. Kotnana, G. Muscas, F. Locardi, A. Comite, G. Varvaro, D. Peddis, G. Barucca, R. Mathieu, T. Sarkar, *Nanoscale Adv.*, 2 (2), 851, (2020) [5] P. Maltoni, T. Sarkar, G. Varvaro, G. Barucca, S. Ivanov, D. Peddis, R. Mathieu, *J. Phys. D: Appl. Phys.*, in print, (2020), doi:10.1088/1361-6463/abd20d

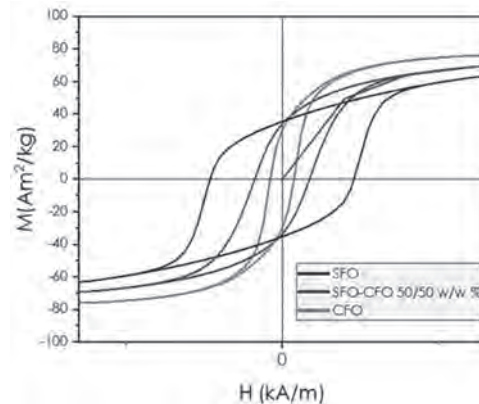


Fig.1 Magnetization M vs. magnetic field H curves for SFO, SFO-CFO 50/50 w/w % and CFO at 300K

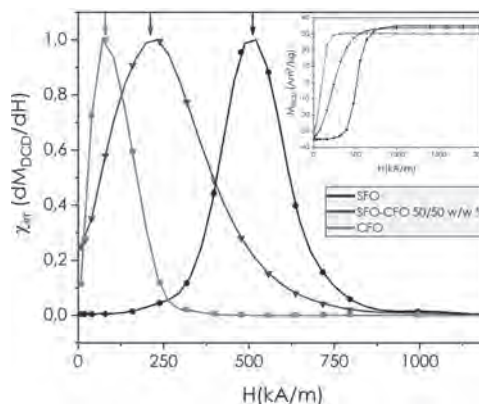


Fig.2 Normalized irreversible susceptibility χ_{irr} vs reverse magnetic field H for SFO, SFO-CFO 50/50 w/w % and CFO at 300K; the inset shows the M_{DC} vs H .

JD-11. Metal Nanowire–Strontium Ferrite Composites for Free Rare-Earth Magnets.

J. Guzmán Mínguez¹, S. Ruiz Gómez², L. Vicente Arche¹, C. Granados Miralles¹, C. Fernández González³, F. Mompeán⁴, M. García Hernández⁴, S. Erohkin⁵, D. Berkov⁵, D. Mishra^{6,7}, L. Pérez García², A. Quesada¹ and C. de Julian Fernandez⁷

1. Instituto de Cerámica y Vidrio - CSIC, Madrid, Spain; 2. Departamento de Física de Materiales, Universidad Complutense de Madrid, Madrid, Spain; 3. Instituto Madrileño de Estudios Avanzados, Madrid, Spain; 4. Instituto de Ciencia de Materiales de Madrid, Madrid, Spain; 5. General Numerics Research Lab, Jena, Germany; 6. Department of Physics, Indian Institute of Technology Jodhpur, Jodhpur, India; 7. IMEM - CNR, Parma, Italy

Permanent magnets are receiving an increasing economical impact due to their role in the Low Carbon Green Transition being employed for energy generation (wind generators), energy storage (flywheels) and electric transport. However, the most performing magnets, composed by rare earth (RE) elements, are in the head of the list of the Critical Raw Materials due to the recent uncertainty in supply and the increase of the costs of the RE. This last question has pushed the research of alternatives to RE magnets. Between the different solutions, the improvement of the performances of the hard ferrites is receiving an increasing interest [1-4]. In fact, ferrite magnets constitute by far the most widely used permanent magnet by weight [2,3] and any improvement of the performances is expected to have an important impact [4]. The most promising approach to improve the performances of ferrite magnets is the development of nanocomposites formed by magnetically coupled high magnetization and hard magnetic nanophases [4]. We present a research on a novel class of hybrid magnet composed by micrometric nanowires (NWs) and micrometric ferrites that exhibit improved hard magnetic properties. We have investigated the properties of composites containing micrometric FeCo nanowires and micrometric SrFe₁₂O₁₉ powders [5] to produce bonded magnets. FeCo NWs were prepared by template-assisted electrochemical deposition using nanoporous templates and polycarbonate nanoporous membranes to obtain NWs with different diameters (30, 50, and 100 nm). FeCo NWs–strontium ferrite mixture composites in the powder form were fabricated by mixing each phase. The evolution of the magnetic properties of the mixtures considering the different diameter of the NWs and the soft-hard ratio will be shown. The coercive field of the composites decreases as the soft content is larger, while remanence magnetization remains almost constant but also increases depending on NWs size. The magnetic coupling between the two phases has been investigated using remanence measurements. Even the soft nature of the NWs, the hard and soft phases are magnetically coupled up to a 20%wt of the soft phase in the case of the NWs of 50 nm of diameter. A 20% increase in remanence together with a weak decrease in coercivity, as consequence of the magnetodipolar interaction between ferrite particles and FeCo NWs, is observed. In fact, the oriented bonded composites magnets exhibit a larger energy product up to 40% larger than the corresponding ferrite ones. The magnetic properties of these magnets will be discussed considering the magnetic configuration of the Nanowires. This research was supported by EU- H2020 AMPHIBIAN Project (H2020-NMBP-2016-720853) and by the JECs Trust.

[1] EU-H2020, AMPHIBIAN Project. Website : amphibianproject.eu. [2] R. C. Pullar, *Progress in Materials Science* 57, 1191 (2012). [3] S H Mahmood and I Abu-Aljarayesh *Hexaferrite Permanent Magnetic Materials*. Materials Research Forum LLC, (2016) [4] C. de Julián Fernández et al., *J. Applied Phys. D: Applied Physics*, (2020) in press

Session JE
MAGNETO-CALORIC MATERIALS AND DEVICES I
Radhika Barua, Chair
Virginia Commonwealth University, Richmond, VA, United States

INVITED PAPER

JE-01. Overcoming the Limitations of Magnetocaloric Rare-Earth-Free High-Entropy Alloys INVITED.J. Law¹, Á. Díaz-García¹, L.M. Moreno-Ramírez¹ and V. Franco¹¹. Department of Condensed Matter Physics, ICMS-CSIC, Universidad de Sevilla, Sevilla, Spain

The design and development of alloys are typically based on one or two main constituents since the Bronze age, whereby the search for new materials using this millennia-old technique is reaching limits. Today, a new class of materials, using a different design approach of alloying multiple elements (five or more) to form compositions without dominant elements and therefore having high entropy of mixing, can discover materials with excellent properties, some of them being superior or unique compared to the conventional materials. This is also known as the high-entropy alloy (HEA) design concept where its multi-principal-element composition encompasses a vast compositional space, which further indicates many opportunities for materials design. While HEA research expands at a rapid growth since its first report in 2004 and has evolved from 1st to 2nd generation HEAs, most of the efforts focus on structural applications while their functional reports are scarce in comparison to their mechanical properties. Furthermore, when compared to conventional functional materials, they underperform due to their modest functional properties. One of their most reported functional properties, the magnetocaloric effect (MCE), only shows large values among HEAs for those compositions containing rare-earth elements. The rare-earth-free HEAs, on the other hand, typically exhibit very small MCE instead. In this talk, we will show that it is possible to enhance the MCE of rare-earth-free HEAs by at least one order of magnitude upon introducing a magneto-structural phase transition: isothermal entropy change increases from 1.7 to 13.1 J kg⁻¹ K⁻¹ (for 2.5 T) [1,2]. The significant improvement in the MCE performance is further shown in Fig. 1 when comparing the isothermal entropy change and the temperature averaged entropy change, *TEC*(10), to the literature. Instead of sampling the huge HEA compositional space by brute force, we have followed a directed search procedure to develop FeMnNiGe_xSi_{1-x} HEAs that enabled us to put the functionality of HEAs comparable to some of the high-performance traditional materials. The variation of Ge/Si ratio enables the tuning of the thermomagnetic phase transitions (magneto-structural transformation and Curie transitions), leading to a further enhancement in the MCE. Our work is also found to merge the gap between magnetocaloric HEAs versus conventional magnetocaloric materials. These findings demonstrate the promising potential of HEAs for magnetocaloric applications. Work supported by AEI/FEDER-UE (grant PID2019-105720RB-I00), US/JUNTA/FEDER-UE (grant US- 1260179), Consejería de Economía, Conocimiento, Empresas y Universidad de la Junta de Andalucía (grant P18-RT-746), Army Research Laboratory under Cooperative Agreement Number W911NF-19-2-0212.

[1] J.Y. Law, L.M. Moreno-Ramírez, Á. Díaz-García, A. Martín-Cid, S. Kobayashi, S. Kawaguchi, T. Nakamura, V. Franco, *J. Alloy. Compd.* 855 pp. 157424 (2021). [2] J.Y. Law, Á. Díaz-García, L.M. Moreno-Ramírez, V. Franco, Submitted (2021). [3] M.C. Gao, D.B. Miracle, D. Maurice, X. Yan, Y. Zhang, J.A. Hawk, *J. Mater. Res.* 33(19) pp.3138-3155 (2018).

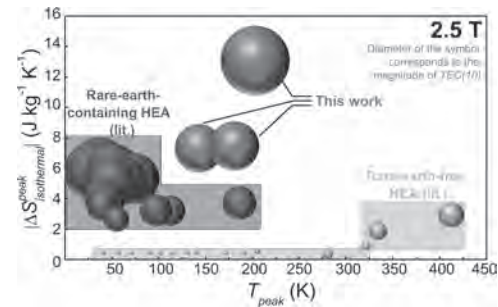


Fig 1. Performance comparison of magnetocaloric HEAs for 2.5 T based on isothermal entropy change peak, its corresponding temperature and temperature averaged entropy change over a 10 K span, *TEC*(10). Each data point represents a single material, with a diameter size proportional to its *TEC*(10). Literature data are collected from refs. [1 - 3].

CONTRIBUTED PAPERS

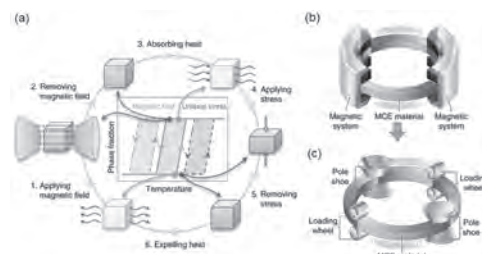
JE-02. Designing Multicaloric Materials for Using Thermal Hysteresis in a Novel Multi-Stimuli Cooling Cycle.

A. Taubel¹, F. Scheibel¹, L. Pfeuffer¹, B. Beckmann¹, W. Liu¹, J. Lemke¹, M. Töllner¹, T. Gottschall², S. Ener¹, K. Skokov¹ and O. Gutfleisch¹
 1. Materials Science, Technical University of Darmstadt, Darmstadt, Germany; 2. Dresden High Magnetic Field Laboratory (HLD-EMFL), Helmholtz Zentrum Dresden-Rossendorf, Dresden, Germany

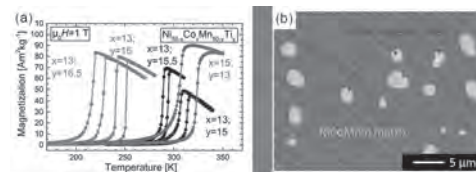
In the age of climate change and the global goal of reducing CO₂ emissions, the increase of energy efficiency becomes an important aspect of material and device development in many industrial sectors. The energy spent for cooling and air conditioning in industry and households represents a significant part of the global energy consumption. Furthermore, it is predicted that the amount of energy needed for cooling will rise drastically within this century [1]. Magnetocaloric (MC) refrigeration attracts a lot of attention since it can be more energy efficient and environmentally friendly than current vapor compression technology [2]. It uses a solid-state magnetic material that heats up and cools down cyclically when exposed to a changing magnetic field. Many efforts are guided towards a reduction of the thermal hysteresis to enhance the cyclic magnetocaloric effect (MCE) in first-order materials [3]. An alternative solution has been proposed, which benefits from the thermal hysteresis by using two stimuli to trigger the phase transition in a multicaloric material [4]. In a first step, the application of a magnetic field induces the high-magnetization state which leads to a negative adiabatic temperature change for the case of an inverse MC material. The large thermal hysteresis prevents the back transformation and locks the material in its high-magnetization phase, which allows an efficient heat exchange in zero field. In order to transform the material back, an external stress is applied as a second stimulus leading to a conventional elastocaloric effect (ECE). The use of two stimuli enables a complete first-order transformation under cyclic conditions. Therefore, the drawback of the thermal hysteresis which limits the cyclic performance in a MC cycle can be overcome by using a second stimulus. Furthermore, the amount of permanent magnets to generate the magnetic field can be significantly reduced in a multi-stimuli cycle because the material needs to be magnetized only for a short time and in a small volume. The caloric material for the new multi-stimuli cycle requires a large sensitivity of the phase transition towards both stimuli as well as a good mechanical stability. In this work, we present the concept of the new multi-stimuli cooling concept including potential material systems and methods to tailor their functional and mechanical properties. The main objective is adapting the properties for a classical MC cycle towards the extended needs of the multi-stimuli cycle and tailoring the desired properties by intrinsic and extrinsic means. The most promising materials are Ni-(Co)-Mn-based Heusler alloy due to their adjustable transition temperature and large MCE [5]. We studied these alloy systems with respect to their MC response in low and high magnetic fields as well as for varying field-sweep rates. For the second applied stimulus, the behavior under uniaxial stress application has been investigated for arc-molten and suction-cast alloys. The influence of microstructural modifications, such as grain refinement and precipitates, were studied regarding mechanical stability and caloric performance. Especially the microstructure has an influence on the thermal hysteresis and caloric functionality. Thus, we studied the possibility of tailoring the thermal hysteresis as well as improving the mechanical stability by the addition of secondary phases. We could show that the doping with Gd introduces Gd-rich precipitates into a Ni-(Co)-Mn-In matrix. The alloy shows a magnetic entropy change of 9 Jkg⁻¹K⁻¹ and an adiabatic temperature change of 4 K in 2 T, comparable with values for phase-pure Ni-Mn-In alloys. Compression tests show that the strength is increased significantly for samples with Gd-rich precipitates. In parallel, the development of new Heusler systems opened up broad perspectives since the realization of all-*d*-Heusler alloys [6]. Recently, the system of Ni-Co-Mn-Ti is investigated intensively because of large MCE and good mechanical properties for a single-phase microstructure. In addition, a large volume change during the martensitic phase transition leads to a large ECE. By optimizing the heat treatment, we could enhance the sharpness of the phase transition

and reach large isothermal entropy changes of up to 40 Jkg⁻¹K⁻¹ in 2 T [7]. A systematic study of different Co- and Ti-contents results in a phase diagram, from which the transition temperature can be estimated by the *e/a* ratio. In addition, the magnetic-field-sensitivity as well as the stress-sensitivity of the phase transition and the thermal hysteresis can be designed precisely by tuning the stoichiometry. The mechanical stability required for a cyclic application of stress can be tailored by the microstructure, e.g. by variation of the processing route. In order to evaluate general design rules for magnetocaloric compounds, the novel all-*d* Heusler system is compared to the well-characterized Ni-Mn-X alloys with X being a main group element. Significant differences could be attributed to the preferred state of atomic order, which has been analysed by combining the experimental results with theoretical calculations. This work was supported by the ERC Advanced Grant “CoolInnov” (No 743116), and the CRC/TRR 270 “HoMMage” (DFG).

[1] M. Isaac, D. P. van Vuuren, Energy Policy 37, 507 (2009) [2] O. Gutfleisch et al., Adv. Mater. 23, 821-842 (2011) [3] F. Scheibel et al., Energy Technol. 6, 1397-1428 (2018) [4] T. Gottschall et al., Nature Mat. 17, 929-934 (2018) [5] A. Taubel et al., Phys. Status Solidi B 255, 1700331 (2018) [5] Z. Y. Wei et al., Appl. Phys. Lett. 107, 022406 (2015) [6] A. Taubel et al., Acta Mater. 201, 425-434 (2020)



Schematic of the six-step multi-stimuli cycle, which makes use of a large thermal hysteresis [4].



Tailoring the functional properties of Ni-Co-Mn-Ti by varying the stoichiometry (a) and tuning mechanical properties of Ni-Mn-In by introducing secondary phases (b).

JE-03. Machine Learning Strategies for Screening Mn-T-X (T=Co, Fe, Ni; X=Si, Ge, Sn) Multicaloric Materials.

T. Hartnett¹, P. Balachandran^{1,2}, R. Barua³ and V. Sharma³

1. *Materials Science Engineering, University of Virginia, Charlottesville, VA, United States*; 2. *Mechanical Engineering, University of Virginia, Charlottesville, VA, United States*; 3. *Mechanical and Nuclear Engineering, Virginia Commonwealth University, Richmond, VA, United States*

Solid-state cooling devices based on the “caloric” class of functional materials are considered a promising alternative to conventional vapor compression technologies as they allow complete elimination of high-global warming potential (GWP) refrigerants and have high energy efficiency that is theoretically equivalent to 60% of Carnot efficiency. [1] By definition, multicaloric materials exhibit reversible thermal changes that can be driven concurrently or in sequence by more than one type of external energy sources (magnetic field, electric field, strain/pressure). The use of multiple driving forces can bring about larger thermal changes with smaller field magnitudes over broader operating temperature ranges, while reducing energy losses due to hysteresis in one control parameter by shifting it to another. Multicaloric materials under current investigation are fraught with issues related to the inclusion of strategically-limited and toxic elements (e.g., $\text{Gd}_2(\text{GeSi})_4$, FeRh, MnAs; bold=problematic element) or require complex synthesis and processing to realize an acceptable, or even marginal, functional response. Against this backdrop, the MnTX family of compounds [T = transition metal elements (Fe, Ni, or Co); X = main group p-block element (Si, Ge, or Sn)] are poised to overcome these limitations since they are made of earth-abundant, non-toxic elements, are scalable for powder production using low-cost, conventional solid-state processing techniques. Select MnTX alloys demonstrate tunable, room-temperature, first-order magnetic phase transition (i.e., magnetostructural transition from a low temperature TiNiSi -type ferromagnetic orthorhombic phase to a high temperature Ni_2In -type paramagnetic hexagonal phase) with promising magnetic fields and pressure-driven caloric responses. Though one can tune the magnetic and caloric properties through careful choice of chemical elements that occupy T- and X-sites or their relative concentrations, large chemical diversity presents formidable combinatorial challenges for experimental and theoretical studies. To accelerate the discovery of new MnTX materials with low hysteresis magneto-structural phase transitions near room temperature, we apply a machine learning (ML) approach utilizing data from published literature to construct data-driven ML models as illustrated in figure one. To this end, we start by performing a literature review and constructing a database representative of the MnTX materials that undergo the Pnma to $\text{P6}_3/\text{mmc}$ magneto-structural transition. [2]-[21] We found 87 unique observations that have been experimentally synthesized and whose Pnma to $\text{P6}_3/\text{mmc}$ transition temperature on heating (T_H) and $\text{P6}_3/\text{mmc}$ to Pnma transition temperature on cooling (T_C) have been characterized. The difference between $|T_H - T_C|$ is indicative of the hysteresis associated with the phase transition. From these 87 observations, we created 2 different methods of representing the data for machine learning. The first was created using element specific features (e.g., valence electron concentration, electronegativity, and size), where each composition is described as a weighted average of these individual elemental properties. In the second method, we performed density functional theory (DFT) to calculate certain properties (e.g., magnetic moment, bond lengths, and unit cell parameters) of end-point compositions for each compound using the open source electronic structure code quantum espresso.[22]-[24] Each alloy or solid solution was then described as a weighted average of the properties of each end point composition. Models were trained using bootstrapped LASSO, support vector regression (SVR), gaussian process regression and random forest methods implanted in the statistical computing language, R.[25] Of these algorithms SVR was the most accurate on the validation set for both the elemental feature space and the DFT feature space. The performance of this model is shown in figure two. When compared to each other the model trained on the DFT generated features out-performed the model trained on the features generated from elemental properties. Promising candidates are recommended for experimental validation and feedback for iterative model improvement.

[1] J. Lyubina, “Magnetocaloric materials for energy efficient cooling,” *Journal of Physics D: Applied Physics*, 2017, doi: 10.1088/1361-6463/50/5/053002. [2] A. Biswas *et al.*, “Designed materials with the giant magnetocaloric effect near room temperature,” *Acta Mater.*, 2019, doi: 10.1016/j.actamat.2019.09.023. [3] J. H. Chen *et al.*, “Tuning martensitic transitions in $(\text{MnNiSi})_{0.65}(\text{Fe}_2\text{Ge})_{0.35}$ through heat treatment and hydrostatic pressure,” *J. Appl. Phys.*, 2018, doi: 10.1063/1.5051551. [4] J. Liu *et al.*, “Realization of magnetostructural coupling by modifying structural transitions in MnNiSi-CoNiGe system with a wide Curie-temperature window,” *Sci. Rep.*, 2016, doi: 10.1038/srep23386. [5] P. Lloveras *et al.*, “Giant reversible barocaloric response of $(\text{MnNiSi})_{1-x}(\text{FeCoGe})_x$ ($x = 0.39, 0.40, 0.41$),” *APL Mater.*, 2019, doi: 10.1063/1.5097959. [6] T. Samanta *et al.*, “Effects of hydrostatic pressure on magnetostructural transitions and magnetocaloric properties in $(\text{MnNiSi})_{1-x}(\text{FeCoGe})_x$,” *J. Appl. Phys.*, 2015, doi: 10.1063/1.4916339. [7] F. R. Shen *et al.*, “Neutron diffraction study on hydrostatic pressure regulated magnetostructural transition and magnetocaloric effect in $\text{MnNi}_{1-x}\text{Fe}_x\text{Si}_{1-y}\text{Ge}_y$ alloys,” *J. Appl. Phys.*, 2020, doi: 10.1063/5.0003056. [8] Y. Si *et al.*, “Magnetostructural transformation and magnetocaloric effect of Sn-bonded $\text{Mn}_{0.66}\text{Fe}_{0.34}\text{Ni}_{0.66}\text{Fe}_{0.34}\text{Si}_{0.66}\text{Ge}_{0.34}$ composite,” *Sci. Rep.*, 2018, doi: 10.1038/s41598-017-18240-x. [9] Z. Y. Wei *et al.*, “Unprecedentedly Wide Curie-Temperature Windows as Phase-Transition Design Platform for Tunable Magneto-Multifunctional Materials,” *Adv. Electron. Mater.*, 2015, doi: 10.1002/aeml.201500076. [10] C. L. Zhang *et al.*, “Tunable magnetostructural coupling and large magnetocaloric effect in $\text{Mn}_{1-x}\text{Ni}_x\text{Fe}_2\text{Si}_{1-x}\text{Gax}$,” *J. Magn. Magn. Mater.*, 2017, doi: 10.1016/j.jmmm.2017.02.046. [11] C. L. Zhang *et al.*, “Magnetostructural transition and magnetocaloric effect in $\text{MnNiSi-Fe}_2\text{Ge}$ system,” *Appl. Phys. Lett.*, 2015, doi: 10.1063/1.4936610. [12] C. L. Zhang *et al.*, “The tunable magnetostructural transition in MnNiSi-FeNiGe system,” *Appl. Phys. Lett.*, 2013, doi: 10.1063/1.4823510. [13] J. Q. Zhao *et al.*, “Tunable magnetostructural phase transition and magnetocaloric effect in $\text{Mn}_{1-x}\text{Ni}_x\text{Co}_2\text{Si}_{1-x}\text{Gex}$ system,” *J. Alloys Compd.*, 2017, doi: 10.1016/j.jallcom.2016.12.156. [14] K. Deepak and R. V. Ramanujan, “Magnetocaloric properties of low-cost Fe and Sn substituted mnnisi-based alloys exhibiting a magnetostructural transition near room temperature,” *IEEE Trans. Magn.*, 2018, doi: 10.1109/TMAG.2018.2832090. [15] K. Deepak and R. V. Ramanujan, “Near room temperature giant magnetocaloric effect in $(\text{MnNiSi})_{1-x}(\text{Fe}_2\text{Ge})_x$ alloys,” *J. Alloys Compd.*, 2018, doi: 10.1016/j.jallcom.2018.02.018. [16] P. Dutta, S. Pramanick, S. Chattopadhyay, D. Das, and S. Chatterjee, “Observation of colossal magnetocaloric effect and its dependence on applied hydrostatic pressure in thermally cycled $\text{Mn}_{0.53}\text{Fe}_{0.47}\text{Ni}_{0.53}\text{Ge}_{0.47}$ alloy,” *J. Alloys Compd.*, 2018, doi: 10.1016/j.jallcom.2017.11.379. [17] S. Ghosh, A. Ghosh, P. Sen, and K. Mandal, “Giant Room-Temperature Magnetocaloric Effect across the Magnetostructural Transition in $(\text{MnNiSi})_{1-x}(\text{FeCoGa})_x$ Alloys,” *Phys. Rev. Appl.*, 2020, doi: 10.1103/PhysRevApplied.14.014016. [18] S. Ghosh, P. Sen, and K. Mandal, “Magnetostructural transition and large magnetocaloric effect in $(\text{Mn}_{0.6}\text{Fe}_{0.4})\text{NiSi}_{1-x}\text{Al}_x$ ($x = 0.06-0.08$) alloys,” *J. Magn. Magn. Mater.*, 2020, doi: 10.1016/j.jmmm.2019.166345. [19] D. Kasimov, J. Liu, Y. Gong, G. Xu, F. Xu, and G. Lu, “Realization of magnetostructural coupling in a high temperature region in $\text{Mn}_{0.85}\text{Co}_{0.3}\text{Ni}_{0.85}\text{Si}_{1-x}\text{Gax}$ system,” *J. Alloys Compd.*, 2018, doi: 10.1016/j.jallcom.2017.10.295. [20] L. Lei *et al.*, “The magnetostructural transition and magnetocaloric properties in $\text{Fe}_{0.6}\text{Mn}_{0.4}\text{NiSi}_{1-x}\text{Al}_x$ alloys,” *J. Appl. Phys.*, 2020, doi: 10.1063/5.0003261. [21] Y. Li *et al.*, “Windows open for highly tunable magnetostructural phase transitions,” *APL Mater.*, 2016, doi: 10.1063/1.4955214. [22] P. Giannozzi *et al.*, “Advanced capabilities for materials modelling with Quantum ESPRESSO,” *J. Phys. Condens. Matter*, 2017, doi: 10.1088/1361-648X/aa8f79. [23] P. Giannozzi *et al.*, “Quantum ESPRESSO toward the exascale,” *J. Chem. Phys.*, 2020, doi: 10.1063/5.0005082. [24] P. Giannozzi *et al.*, “QUANTUM ESPRESSO: A modular and open-source software project for quantum simulations of materials,” *J. Phys. Condens. Matter*, 2009, doi: 10.1088/0953-8984/21/39/395502. [25] R. R Development Core Team, *R: A Language and Environment for Statistical Computing*, 2011.

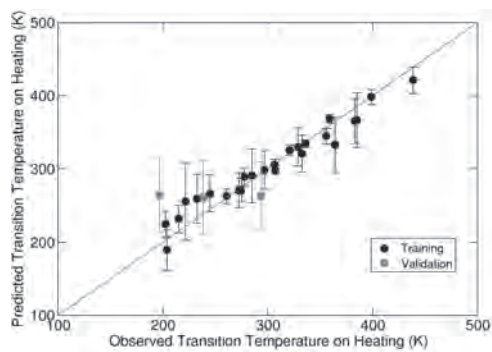


Figure 1: DFT model performance, phase transition temperature predicted is plotted against the observed experimental data.



Figure 2: Workflow of machine learning optimization of MTX alloys.

JE-04. Influence of Short-Range Correlation on Magnetocaloric Properties of Tb₂Ni_{0.94}Si_{3.2} Alloy.

R. U D¹, A. K¹, S. S¹, A. Dzubinska², M. Reiffers^{3,4} and N. R¹
 1. PHYSICS, National Institute of Technology Tiruchirappalli, Tiruchirappalli, India; 2. CPM-TIP, Univerzita Pavla Jozefa Safarika v Kosiciach, Kosice, Slovakia; 3. Science, Presovska univerzita v Presove Fakulta humanitnych a prirodnych vied, Presov, Slovakia; 4. Institute of Experimental Physics, Slovenska akademia vied, Bratislava, Slovakia

To get more insight into fundamental physical properties and their application relevance, the studies on Rare-earth intermetallic compounds are always remarkable. One of such systems that vastly studied is R₂TX₃ series (R- Rare-earth element, T- Transition element, and X-p-block element), which shows magnetic properties like spin glass, Kondo interaction, Heavy fermion, skyrmions, etc^{1,2}. Also, the good magnetocaloric properties of the series make them relevant for magnetic cooling applications as well³. In this work, Tb₂Ni_{0.94}Si_{3.2} alloy from the same series has been prepared using the arc melting technique followed by annealing at 1073 K for one week. And magnetic, magnetocaloric, and magnetoresistance properties of the alloy have been investigated. Tb₂Ni_{0.94}Si_{3.2} alloy crystallizes in AlB₂-type structure (space group = P6/mmm) with lattice parameters, $a = b = 3.9210(3)$ Å, and $c = 4.0044(5)$ Å, respectively, which are determined from the Rietveld refinement of room temperature powder XRD studies. The magnetic state of the alloy consists of spin-glass behavior around $T_f = 5.2$ K and an antiferromagnetic transition at $T_N = 12.7$ K (See Fig.1). Anomalies corresponding to these magnetic transitions are clearly observed in the variation of DC magnetization with temperature in an applied magnetic field of 0.01 T. Further, the appearance of small thermomagnetic irreversibility at higher temperature ($T_N < T < 55$ K) denotes the presence of short-range ferromagnetic correlation in the alloy. It is concordant with the positive Curie Weiss temperature ($\theta_p = 3.13$ K) and slight higher effective magnetic moment of Tb atom ($\mu_{eff} = 9.78 \mu_B$ / Tb atom) from the Curie-Weiss fit (@ $B=1$ T). The spin-glass behavior around T_f can be confirmed from the variation of AC magnetic susceptibility with temperature for different frequencies ($f=10, 100, \text{ and } 1000$ Hz). As shown in inset of Fig.1.a, the peak corresponding to T_f shows a frequency dependence and shifted to higher temperatures as the AC frequency increases, confirms spin-glass behavior. Along with the reentrant spin glass behavior of the alloy, the magnetic state is marked with successive metamagnetic transitions around $B_{C1} = 1$ T and $B_{C2} = 2.5$ T in isothermal magnetization data. Studies on magnetocaloric properties of the alloy are done by calculating isothermal entropy change ($-\Delta S_M$) and Relative Cooling Power (RCP) from the isothermal magnetization studies. As demonstrated in Fig.2, $-\Delta S_M$ has reached peak values of 12 J/kg K and 8 J/kg K for a magnetic field change of 9T and 5T, respectively, which is comparable with the other magnetocaloric material in the R₂TX₃ series like Pr₂CuSi₃ and Gd₂CuSi₃ compounds⁴. Calculated RCP values of the alloy are 504 J/kg and 330 J/kg for $\Delta B = 9$ T and 5T, respectively, which are higher than the other compounds⁵ having the same $-\Delta S_M$. Enhanced magnetocaloric effect (MCE) of the alloy is the result of the presence of the short-range correlation, which increases the working temperature span of the material. As an extension to the analysis, the magnetoresistance properties of the alloy were studied. Alloy is noted with a magnetoresistance(MR) of -22% for $T = 4$ K in $B = 9$ T. Also, the influence of metamagnetic transition and short-range correlation is reflected in the variation of MR with the applied magnetic field. It denotes the strong correlation between the magnetic and lattice state of the alloy. In conclusion, magnetic, magnetocaloric, and magnetoresistance properties of Tb₂Ni_{0.94}Si_{3.2} alloy shows reentrant spin glass behavior with good MR and enhanced MCE property. Acknowledgment: This research work was supported partially by VEGA 1/0611/18, 1/0705/20 and APVV-16-0079, and project No. 001PU-2-1/2018.

¹ P. Zhi-Yan, C. Chong-De, B. Xiao-Jun, S. Rui-Bo, Z. Jian-Bang, and D. Li-Bing, Chinese Phys. B 22, 056102 (2012). ² R. Kumar, K.K. Iyer, P.L. Paulose, and E. V. Sampathkumaran, Phys. Rev. B 101, 144440 (2020). ³ V. Franco, J.S. Blázquez, J.J. Ipus, J.Y. Law, L.M. Moreno-Ramírez, and A. Conde, Prog. Mater. Sci. 93, 112 (2018). ⁴ F. Wang, F. Yuan, J. Wang, T. Feng, and G. Hu, J. Alloys Compd. 592, 63 (2014). ⁵ L. Li, D. Huo, Z. Qian, and K. Nishimura, J. Phys. Conf. Ser. 263, 2 (2011).

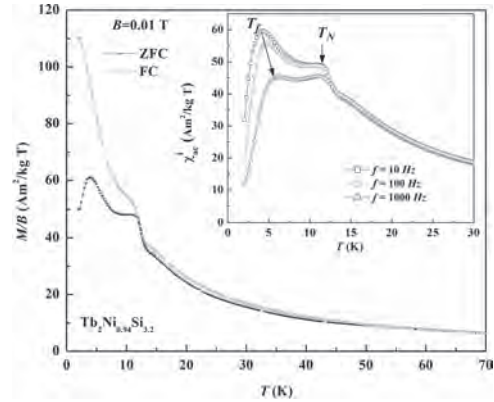


Fig.1. Variation of DC magnetic susceptibility (M/B) as a function of temperature in applied magnetic field $B = 0.01$ T. Inset shows AC magnetic susceptibility for frequencies 10,100 and 1000 Hz.

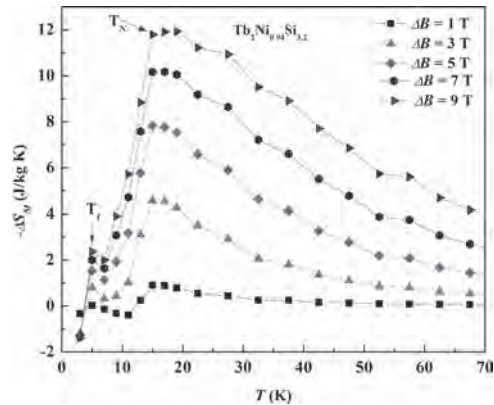


Fig.2. Variation of isothermal entropy as a function of temperature

JE-05. Temperature-Induced Successive Martensitic and Inter-Martensitic Phase Transformations of $Ni_{2.15}Mn_{0.85}Ga$ Heusler Alloy.

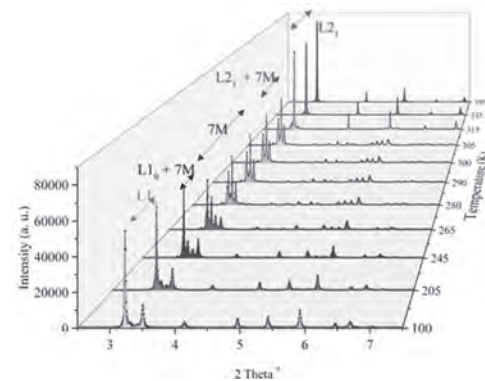
A.S. Madiligama¹, P. Ari-Gur², Y. Ren³, V. Shavrov⁴, V. Koledov⁴, Y. Ge⁵ and J. George⁶

1. Science/Physics, Penn State DuBois, DuBois, PA, United States; 2. Department of Mechanical and Aerospace Engineering, Western Michigan University, Kalamazoo, MI, United States; 3. X-ray Science Division, Argonne National Laboratory Advanced Photon Source, Lemont, IL, United States; 4. Laboratory of Magnetic Phenomena in Microelectronics, Kotelnikov Institute of Radio-engineering and Electronics of RAS, Moscow, Russian Federation; 5. Aalto-yliopisto, Aalto, Finland; 6. Department of Biomedical Engineering, University of Michigan, Ann Arbor, MI, United States

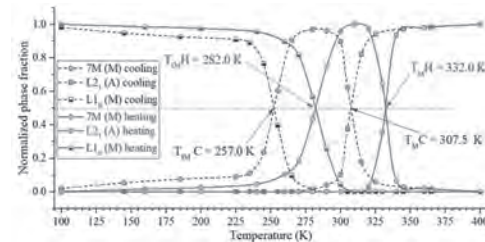
1. Abstract Entropy change of successive martensitic transformations in Ni-Mn-Ga Heusler alloys can be utilized to realize enhanced magnetocaloric properties. A detailed study of phase transformations of $Ni_{2.15}Mn_{0.85}Ga$, ($\Delta Q = 4900$ J/kg at 343 K and 140 kOe) is reported here. Upon cooling, paramagnetic austenite ($L2_1$) transforms into a ferromagnetic 7M monoclinic martensitic phase. This phase is stable in a narrow temperature range and, upon further cooling, transforms into a non-modulated ferromagnetic tetragonal ($L1_0$) phase. The separation between the equilibrium temperatures of the $L2_1$ and the $L1_0$ phases is only ~ 50 K. The alloy undergoes reversible temperature-induced martensitic and inter-martensitic phase transformations with thermal hysteresis about 25 K. The conclusions from the detailed study of the phase transformations lead to new possibilities to enhance the magnetocaloric effect by utilizing the entropy associated with multi-structural transformations. 2. Introduction Magnetic cooling based on the giant magnetocaloric effect (GMCE) is a proposed solution to the low-efficiency and eco-adverse refrigerant of current technologies [1]. Developing a material that produces a GMCE near room temperature is key to the more efficient and economical cooling technology. Ni-Mn-X alloys are under the spotlight because they are inexpensive and non-toxic. The isothermal entropy changes exhibited by some Ni-Mn-Ga alloys are in close range or even higher than those reported in Gd and La-based compounds [2]. Several techniques are available to enhance the GMCE demonstrated by Ni-Mn-X alloys. Combining magnetocaloric and elastocaloric effects by applying stress to the refrigerants is one technique [3]. The latest trend is to utilize the two consecutive structural transformations of these alloys [4]. Here we report a study of the inter-martensitic phase transformations of such an alloy. The analysis of the structures, phase transformation temperatures, and the thermal hysteresis will support the search for new avenues to enhance the magnetocaloric effect by utilizing the entropy associated with multi-structural transformations [5]. 3. Experimental A polycrystalline sample was prepared by arc-melting in an argon atmosphere and then annealed at 1073 K for 50 hours [6]. The chemical composition, $Ni_{2.15}Mn_{0.85}Ga$, was determined by energy dispersive spectroscopy. In-situ synchrotron diffraction data were collected at beamline 11-ID-C of the Advanced Photon Source at Argonne National Laboratory ($\lambda = 0.010804$ nm). Diffraction data were analyzed using the General Structure Analysis System EXPGUI [7]. Magnetization measurements were done using a SQUID magnetometer. 4. Results and Discussion The diffraction data (Fig. 1) at selected temperatures (400-100 K) shows that the alloy undergoes martensitic and inter-martensitic transformations and mixtures of phases in different temperature intervals. The austenitic structure is cubic $L2_1$ (Fm-3m space group). Upon cooling, the alloy transforms into a 7M monoclinic (P 1 2/m 1 space group). Upon further cooling, it transforms into a non-modulated tetragonal $L1_0$ structure (I 4/m m m space group). The thermograms (Fig. 2) were constructed by the calculated phase fractions obtained from Rietveld refinements. The alloy undergoes martensitic transformation around 310 K from austenite to 7M modulated martensite. Upon further cooling (~ 260 K), the inter-martensitic phase transformation [8] occurs from monoclinic to tetragonal phase. The reverse-phase transformations occur while heating (see fig. 2). The characteristic temperatures of the austenitic ($T_M H$), martensitic ($T_M C$), and inter-martensitic transformations ($T_{IM} H$ and $T_{IM} C$) were defined at 50% phase fraction of the respective phases upon cooling and then heating, respectively. Thermal hystereses of the transformations, calculated by the differences between $T_M H$ & $T_M C$ and between $T_{IM} H$ & $T_{IM} C$, respectively, are very

close (~ 25 K). Because of the similar hysteresis, the separation between the martensitic and inter-martensitic transformation temperatures, while heating and cooling, are the same and is ~ 50 K. The austenitic phase is paramagnetic, and the martensitic phases are ferromagnetic. The austenitic phase transformation temperature (332 K) and Curie temperature (337 K) are very close. Under a suitable field, these two transformations could coincide to give a much higher MCE. 5. Conclusions and Future work The alloy undergoes two successive phase transformations with narrow separation between them (~ 50 K). The hystereses are less than 25 K. These conditions suggest that utilizing two successive phase transformations may result in higher GMCE. To optimize the GMCE, extensive knowledge of two transformations is required. The magnetic phase transformation temperature increases with increasing magnetic field [6]. However, the behavior of the crystalline phase transformation temperatures under magnetic fields is unknown and essential to study. Also, isothermal magnetization measurements could reveal the possible magnetic phase transformations.

1. D. R. Brown, N. Fernandez, J. A. Dirks, U.S. Department of Energy, (2010) 2. J. Liu, T. Gottschall, K. P. Skokov, nature materials, Vol. 11.7, p.620-626 (2012) 3. Y. Hu1, Z. Li, B. Yang, APL Materials Vol.5, p.046103 (2017) 4. Z. Li, K. Xu, Y. Zhang, Scientific Reports, Vol. 5, p.15143 (2015) 5. Z. Li, Y. Zhang, C. F. Sanchez-Valdes, Appl. Phys. Lett., Vol.104, p.044101 (2014) 6. A. Kamantsev, V. Koledov, A. Mashirov, J. Appl. Phys., Vol. 117, p.163903 (2015) 7. B. H. Toby, J. Appl. Cryst., Vol. 34, p.210-213 (2001) 8. S.M. Konoplyuk, V.V. Kokorin, Ukr. Phys. J. Vol.43, p.1275 (1998)



Diffraction patterns collected while cooling from 395 to 100 K. At 395 K, the alloy is austenitic, and upon cooling, it transforms into a 7M monoclinic phase. Upon further cooling, it transforms into a tetragonal $L1_0$ structure.



Variation of the three phases' phase fractions upon heating (red) and cooling (blue). Characteristic temperatures of the martensitic and inter-martensitic phase transformations were determined by the intersections as shown.

JE-06. Chemical Stability of Magnetocaloric $\text{La}(\text{Fe}_x\text{Co}_y\text{Si}_{1-x-y})_{13}$ Particles.

V. Sharma¹, K. Javed¹, S. Gupta², A. Biswas², V. Pecharsky^{2,3}, R. Barua¹ and R.L. Hadimani^{1,4}

1. Department of Mechanical and Nuclear Engineering, Virginia Commonwealth University, Richmond, VA, United States; 2. Division of Materials Science and Engineering, Ames Laboratory, Ames, IA, United States; 3. Department of Materials Science and Engineering, Iowa State University, Ames, IA, United States; 4. Department of Electrical and Computer Engineering, Iowa State University, Ames, IA, United States

Introduction: Magnetocaloric refrigeration is an emerging technology that shows significant potential to reduce the dependence on traditional vapor compression systems that support most of the cooling and refrigeration needs. Unlike significant body of work on the development of magnetocaloric materials, only a limited number of reports address their functional and chemical stability. This study focuses on a known refrigerant – intermetallic compound of lanthanum, iron, and silicon with minor amounts of cobalt, $\text{La}(\text{Fe}_{0.84}\text{Co}_{0.07}\text{Si}_{0.08})_{13}$, and its stability in a standard heat exchange fluid, that is, water [1]–[3]. **Experimental Details:** An alloy with a nominal composition of $\text{La}(\text{Fe}_{0.84}\text{Co}_{0.07}\text{Si}_{0.08})_{13}$ weighing 20 g was prepared by arc-melting of the elements under argon atmosphere on a water-cooled Cu-hearth. The ingot was re-melted four times, being turned over each time to achieve homogeneity. The total measured weight loss was less than 0.5 wt. %. The as-cast ingot was broken into smaller pieces, which were wrapped in a tantalum-foil, sealed inside a fused-silica tube under vacuum, and annealed at 1050°C for one week, followed by quenching in ice-cold water. Powders from the annealed pieces were prepared by crushing and grinding in an agate mortar with an agate pestle inside an argon-filled glove box and screened to particle sizes of 100 μm and below. Thus, prepared powder was divided into two samples. One sample was stored in deionized water and another in air, both for 14 days. Magnetic measurements were carried out using the Physical Property Measurement System (PPMS) VersaLab and PPMS Dynacool, whereas heat capacity was measured using PPMS Dynacool [4], [5]. **Results and Discussions:** Figure 1 presents ΔS vs. T calculated from magnetization isotherms and Fig. 2 shows the same calculated from heat capacity data after ground powders were stored in water and air. Both sets of data are in good agreement. The powders stored in water exhibit larger magnetocaloric effects by ~40% when compared to the same after stored in air. The most likely reason is nearly complete dissolution of the smallest particles in water, leaving behind only the largest particles with relatively low concentration of surface reaction products. Storing in air, on the other hand, likely leads to severe oxidation of the smallest particles but does not remove them from the material, thus effectively reducing the measured magnetocaloric effect. Further analysis of the powders to confirm this hypothesis is underway and the results will be reported in due time. **Acknowledgment:** Ames Laboratory is operated for the U.S. Department of Energy (DOE) by Iowa State University of Science and Technology under contract No. DE-AC02-07CH11358. Work at Ames Laboratory was supported by the U.S. DOE, Office of Science, Office of Basic Energy Sciences, Materials Sciences and Engineering Division.

[1] F. Hu, B. Shen, J. Sun, Z. Cheng, G. Rao, and X. Zhang, “Influence of negative lattice expansion and metamagnetic transition on magnetic entropy change in the compound $\text{LaFe}_{11.4}\text{Si}_{1.6}$,” *Appl. Phys. Lett.*, vol. 78, no. 23, pp. 3675–3677, Jun. 2001, doi: 10.1063/1.1375836. [2] F. X. Hu *et al.*, “Magnetocaloric effect in itinerant electron metamagnetic systems $\text{La}(\text{Fe}_{1-x}\text{Co}_x)_{11.9}\text{Si}_{1.1}$,” *J. Appl. Phys.*, vol. 97, no. 10, p. 10M303, May 2005, doi: 10.1063/1.1847071. [3] L. Mañosa *et al.*, “Inverse barocaloric effect in the giant magnetocaloric La-Fe-Si-Co compound,” *Nat. Commun.*, vol. 2, p. 595, Jan. 2011, doi: 10.1038/ncomms1606. [4] K. Javed, S. Gupta, V. K. Pecharsky, and R. L. Hadimani, “Stability of magnetocaloric $\text{La}(\text{Fe}_x\text{Co}_y\text{Si}_{1-x-y})_{13}$ in water and air,” *AIP Adv.*, vol. 9, no. 3, p. 035239, Mar. 2019, doi: 10.1063/1.5080108. [5] D. Clifford, V. Sharma, K. Deepak, R. V. Ramanujan, and R. Barua, “Multicaloric Effects in $(\text{MnNiSi})_{1-x}(\text{Fe}_2\text{Ge})_x$ Alloys,” *IEEE Trans. Magn.*, pp. 1–1, 2020, doi: 10.1109/TMAG.2020.3025002.

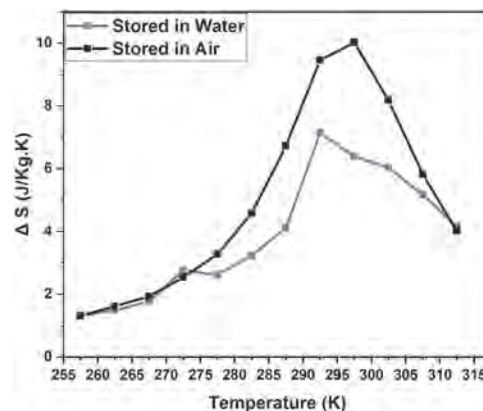


Fig.1: Comparison of ΔS vs T calculated using Maxwell's equation for samples stored in air and water for $\Delta H = 3T$.

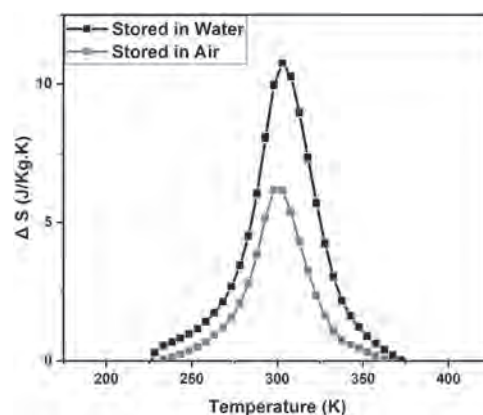


Fig. 2 Comparison of ΔS vs T calculated using heat capacity measurements for samples stored in air and water for $\Delta H = 3T$.

JE-07. Analysis of the Magnetic Field Dependence of the Isothermal Entropy Change of Inverse Magnetocaloric Materials.

L.M. Moreno-Ramírez¹, J. Law¹, S. Pramana², A. Giri³ and V. Franco¹
 1. Universidad de Sevilla, Sevilla, Spain; 2. Newcastle University, Newcastle upon Tyne, United Kingdom; 3. US CCDC Army Research Laboratory, Aberdeen Proving Ground, MD, United States

Power law to express the field dependence of the isothermal entropy change ($\Delta s_T \propto \Delta H^n$) has been widely employed for obtaining information of the thermomagnetic second-order phase transitions (e.g. critical exponents [1] or Curie temperatures [2]). Recently, the analysis of this field dependence has been extended to materials undergoing thermomagnetic first-order phase transitions, the most promising magnetocaloric materials up to the moment. It has been shown that the value of the exponent n overshoots above 2 for first-order phase transitions, while it does not overshoot for the second-order case, allowing to establish a quantitative criterion for determining the order of the phase transitions [3]. This is in excellent agreement with previous phenomenological observations, supporting the validity of the proposed criterion. For direct magnetocaloric effect (MCE), the overshoot feature for fingerprinting first-order transitions can be validated in the frame of the Bean-Rodbell model [4], obtaining an excellent agreement between experiments (e.g., for $\text{La}(\text{Fe},\text{Si})_{13}$ which undergoes a ferromagnetic (FM) to paramagnetic (PM) magnetoelastic transition [5]) and the model. However, for inverse MCE, the validity of the proposed criterion and the characteristics of the field dependence have only been studied experimentally. In this work, the magnetic field dependence of the inverse MCE is analyzed using a mean field approach for describing antiferromagnetic (AF) to FM magnetoelastic transitions. The model is able to describe both second- and first-order phase transitions through the introduction of a magnetovolume energy term according to the Callen-Callen theory [6] (having a Gibbs energy term of the form $-\beta\omega M^2/4$, being ω the relative volume change, M the magnetization and β an introduced magnetoelastic coupling parameter). Using this model, we are able to reproduce the experimentally observed features for the exponent n , showing the existence of the characteristic overshoot for first-order transitions (which corresponds to $\beta > 0$) and its absence for second-order ones ($\beta = 0$), as shown in Fig. 1. We explore the influence of different parameters of the model on exponent n , such as the transition temperature and Curie temperature separation or the exchange constant between the moments of the different sublattices. The existence of the overshoot feature is corroborated for all the different cases. This supports the extension of the quantitative criterion to AF-FM phase transitions and set the basis for the analysis of exponent n in these materials. A main difference with respect to direct MCE is that negative values of the exponent n are obtained at temperatures close to the transition. This is ascribed to the reduction of the inverse MC response due to the influence of the unavoidable FM to PM transition at higher temperatures. The obtained features for exponent n (field dependence and temperature dependence) are qualitatively compared to those of $\text{GdBaCo}_2\text{O}_6$ [7] (AF to FM magnetoelastic transition), showing a good agreement between both the experiment and the model. The obtained results are extrapolated to understand the behavior of the exponent n for a $\text{Ni}_{49}\text{Mn}_{36}\text{In}_{15}$ sample [8] (low magnetization to high magnetization magnetostructural transition). Work supported by AEI/FEDER-UE (grant PID2019-105720RB-I00), US/JUNTA/FEDER-UE (grant US-1260179), Consejería de Economía, Conocimiento, Empresas y Universidad de la Junta de Andalucía (grant P18-RT-746), Army Research Laboratory under Cooperative Agreement Number W911NF-19-2-0212 and Sevilla University under VI PPIT-US program.

[1] V. Franco, A. Conde, Int. J. Refrig. Vol. 33 pp. 465–473 (2010) [2] L.M. Moreno-Ramírez, J.S. Blázquez, V. Franco et al., IEEE Magn. Lett. Vol. 7 Art no. 6102004 (2016) [3] J.Y. Law, V. Franco, L.M. Moreno-Ramírez et al., Nat. Commun. Vol. 9 Art no. 2680 (2018) [4] C.P. Bean, D.S. Rodbell, Phys. Rev. Vol. 126 pp. 104–115 (1962) [5] L.M. Moreno-Ramírez, C. Romero-Muñiz, J.Y. Law et al., Acta Mater. Vol. 175 pp. 406–414 (2019) [6] E. Callen, H.B. Callen, Phys. Rev. Vol. 139 p. A455–A471 (1965) [7] J.Y. Law, V. Franco, A. Conde et al., J. Alloys Compd. Vol. 777 pp. 1080–1086 (2019) [8] J.Y. Law, Á. Díaz-García, L.M. Moreno-Ramírez et al., Acta Mater. Vol. 166 pp. 459–465 (2019)

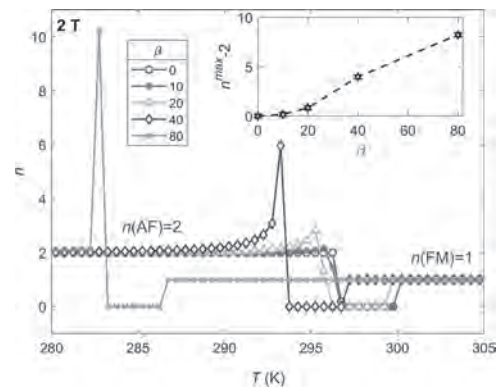


Fig. 1. Temperature dependence of exponent n for different magneto-volume coupling parameter β . Inset: maximum value of the overshoot above 2 as a function of β .

JE-08. Deconvolution of First and Second Order Phase Transitions Using the Scaling Laws of the Magnetocaloric Effect.

Á. Díaz-García¹, J. Law¹, A. Giri² and V. Franco¹

1. Condensed Matter Physics, Universidad de Sevilla, Sevilla, Spain; 2. US CCDC Army Research Laboratory, Aberdeen Proving Ground, MD, United States

Magnetocaloric effect (MCE) receives an increasing interest for its promising applicability in energy efficient refrigerators. Among the different magnetocaloric materials having potential applications for cooling devices that operate near room temperature, those exhibiting a first-order phase transition (FOPT) usually show larger responses than those exhibiting a second-order phase transition (SOPT), but the intrinsic hysteresis could be deleterious for cyclic operations [1]. Some FOPT materials such as Heusler alloys can also exhibit the Curie transition of their magnetic phases, thus leading to alloys exhibiting both direct (positive isothermal entropy change, ΔS_{iso}) and inverse MCE (negative ΔS_{iso}). However, the close proximity of the two types of transitions can produce a convoluted and compensated global response due to the different nature, direct and inverse, of their MCEs [2]. In order to evaluate the potential of the FOPT for magnetocaloric applications and, therefore, ascertain the usefulness of tuning the Curie temperature of the alloy by compositional modifications, it is necessary to be able to deconvolute its responses. It has previously been shown that concurrent SOPTs can be deconvoluted by applying the scaling laws of the MCE [3]. In this work, we propose an extension of the methodology to deconvolute concurrent FOPT and SOPT. For this purpose, a Heusler alloy with stoichiometry $\text{Ni}_{48.1}\text{Mn}_{36.5}\text{In}_{15.4}$ has been used as a model case. Upon heating, this sample exhibits a FOPT from a low magnetization martensite to an austenite with higher magnetization. This magneto-structural transition produces an inverse MCE that is immediately followed by the Curie transition of the austenite, with its corresponding conventional MCE. With increasing the magnetic field, two different behaviors are observed: 1) the onset of the FOPT shifts to lower temperatures, with a peak ΔS_{iso} value that increases abruptly at the beginning, reaches a maximum for ~ 5 T and subsequently decreases, and 2) a Curie transition whose response increases gradually in height and width, with a peak position that remains almost field independent. Due to the proximity of these two competing transitions, the overlapping of their responses increases with increasing field. The application of the scaling laws for the SOPT magnetocaloric response allows us to deconvolute the contributions of the two transitions. Top panel of Fig. 1 shows the experimental ΔS_{iso} of the sample together with its reconstructed response. The separated contributions of the two phase transitions are presented in the bottom panel of Fig. 1. The good agreement between experimental and reconstructed curves allows us to reach the following conclusions: - Universal scaling can be used to deconvolute overlapping first and second order phase transitions. - The broadening of the SOPT with increasing field causes a larger overlap between transitions despite the shift of the FOPT to lower temperatures. - The experimental decrease of the inverse MCE peak above ~ 5 T is due to the competing contribution of the SOPT and is not intrinsic to the FOPT. This deconvolution methodology allows to extract the information of the different phase transitions in the material without having to experimentally synthesize new alloys with different compositions. Work supported by AEI/FEDER-UE (grant PID2019-105720RB-I00), US/JUNTA/FEDER-UE (grant US-1260179), Consejería de Economía, Conocimiento, Empresas y Universidad de la Junta de Andalucía (grant P18-RT-746), and Army Research Laboratory under Cooperative Agreement Number W911NF-19-2-0212.

[1] V. Franco, J.S. Blázquez, J.J. Ipus, J.Y. Law, L.M. Moreno-Ramírez, A. Conde, Prog. Mater. Sci. 93 (2018) 112–232. [2] J. Y. Law, Á. Díaz-García, L. M. Moreno-Ramírez, V. Franco, A. Conde, A. K. Giri, Acta Mater. 166 (2019) 459. [3] Á. Díaz-García, J. Y. Law, P. Gebara, V. Franco, JOM 72 (2020) 2845–2852.

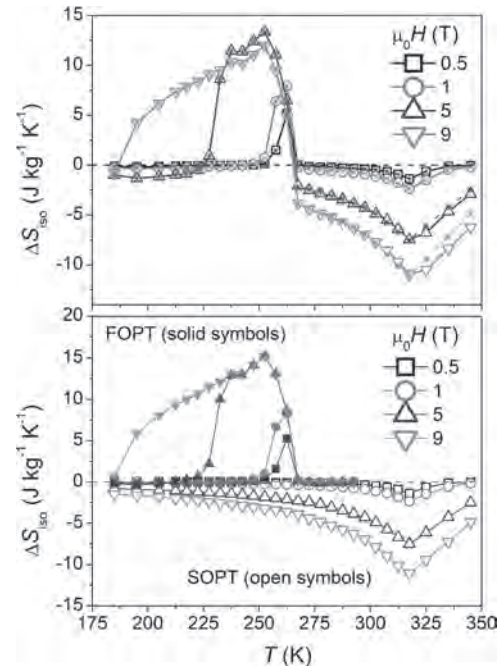


Fig. 1 (Top panel) Experimental temperature dependence of ΔS_{iso} of $\text{Ni}_{48.1}\text{Mn}_{36.5}\text{In}_{15.4}$ Heusler alloy for different magnetic fields (open symbols) and its reconstructed ΔS_{iso} response (stars symbols). (Bottom panel) Temperature dependence of ΔS_{iso} for different fields of the deconvoluted responses of the SOPT (open symbols) and the FOPT (solid symbols).

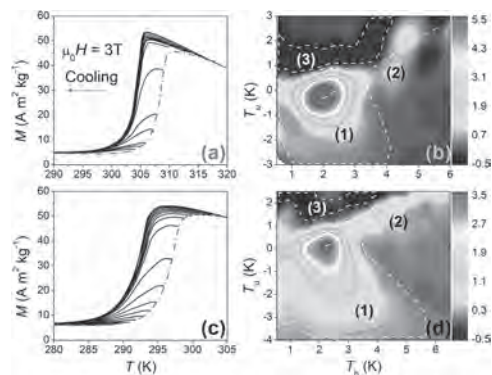
JE-09. T-FORC as a Tool for the Characterization of Magnetocaloric Materials: From Experiments to Models.

V. Franco¹, Á. Díaz-García¹, L.M. Moreno-Ramírez¹, J. Law¹, S. Fabbri² and F. Albertini²

1. Universidad de Sevilla, Sevilla, Spain; 2. Istituto dei Materiali per l'Elettronica e il Magnetismo, Consiglio Nazionale delle Ricerche, Parma, Italy

Magnetocaloric materials with a first order phase transition exhibit thermal hysteresis, which is one of the key limiting factors that prevent their efficient implementation in magnetic refrigerators. This problem has to be tackled in a twofold way: a) understanding the different sources of thermal hysteresis of technologically relevant materials in order to minimize them, and b) predicting the response of the materials upon an arbitrary sequence of excitations, so that the trajectories of the minor loops in the $M(T,H)$ space is known and their behavior in a magnetic refrigerator can be suitably modeled. To achieve those, in the recent years, the temperature variant of the first order reversal curves technique (T-FORC) has been proposed as a fingerprinting method for the characterization of thermal hysteresis in magnetocaloric materials [1]. This initial approach has been expanded in two complementary directions: the implementation of a faster characterization technique that makes use of an effective temperature approach (T*FORC) [2], and the development of models of the phase transformation that provide a physical meaning to the distinct features observed in experimental T-FORC distributions [3]. In this presentation we will show an overview of the T-FORC technique and highlight its potential for the characterization of hysteretic thermomagnetic phase transitions by applying it to two different Heusler alloys of the $\text{Ni}_{50}\text{Mn}_{34}\text{In}_{16}$ family, with similar Curie temperatures but different temperatures of the martensitic transition (see figure). Experiments have been performed upon cooling and heating for different fixed values of magnetic field. The different relative distance between transitions leads to different features in their T-FORC distributions. The comparison of the experimental distributions with those obtained from the model of the magneto-structural transitions allows us to associate the distinct T-FORC features to different characteristics of the transformations. The existence of different rates during the transition is what mainly defines the features of the T-FORC distributions. The model also allows us to separate the effects of the structural transformation and the temperature dependence of magnetization of the martensitic and austenitic phases, making us conclude that T-FORC distributions mainly reveal the characteristics of the structural component of the hysteretic transition. The appearance of a negative elongation in the cooling mode T-FORC (and positive in the heating one) is associated to the significant temperature dependence of the magnetization of both pure phases. Work supported by AEI/FEDER-UE (grant PID2019-105720RB-I00), US/JUNTA/FEDER-UE (grant US-1260179), Consejería de Economía, Conocimiento, Empresas y Universidad de la Junta de Andalucía (grant P18-RT-746), Army Research Laboratory under Cooperative Agreement Number W911NF-19-2-0212, Sevilla University under VI PPIT-US program, and by the FRIMAG project, funded by Emilia Romagna region within the 2014-20 POR-FESR program (CUP E32F16000190007). The authors thank Dr. Cecilia Bennati for her contributions on the synthesis of the samples.

[1] V. Franco, T. Gottschall, K.P. Skokov, O. Gutfleisch, IEEE Magn. Lett. 7 (2016) 6602904. [2] L.M. Moreno-Ramírez, V. Franco, Metals 10 (2020) 1039. [3] V. Franco, J. Appl. Phys. 127 (2020) 133902.



Magnetothermal hysteresis loops for (a) $\text{Ni}_{49.65}\text{Mn}_{34.19}\text{In}_{16.17}$ and (c) $\text{Ni}_{49.42}\text{Mn}_{34.35}\text{In}_{16.23}$ alloys with their corresponding T-FORC distributions, (b) and (d) respectively, where white dashed lines indicate schematically the most relevant features: (1) main peak distorted downwards; (2) elongation along the $+45^\circ$ direction that forms a ridge; (3) sinking to negative values.

JE-10. Half-Metallic Fe₂CoAl Heusler Nanoparticles: a Hunt for Spintronics and Magnetic Refrigeration Application.

A. Ahmad¹, S. Mitra¹, S.K. Srivastava¹ and A.K. Das¹

1. Physics, Indian Institute of Technology Kharagpur, Kharagpur, India

A significant enhancement over conventional electronics is possible with spintronics, where aside from the charge of the electrons, its spin also plays an important role in order to transfer and storage of the information [1]. Numerous Heusler compounds showing a half-metallic character, low Gilbert damping together with the high T_c and magnetic moment have proven their potential for spintronics applications [2-5]. Their unusual half-metallic property arises due to their unique electronic band structures at the Fermi energy (E_F) of which one-spin band behaves as metal while the other behaves as a semiconductor and unveils an energy-gap at the E_F [3, 5]. HAs have attracted enormous interest to the researchers due to their unique and multifunctional properties such as half-metallicity [6], magnetocaloric effects [7], thermoelectric behavior [8], catalytic behavior [9], shape memory effect [10], spin injection [11] and spin filtering [12]. In this report, spherical nanoparticles (NPs) made of intermetallic Fe₂CoAl (FCA) Heusler alloy are synthesized via co-precipitation method and its structural, magnetic, and magnetocaloric properties are explored, for the first time. The basic structural characterizations have revealed an A2-disordered cubic Heusler structure. HRTEM with the SAED pattern analysis revealed the crystalline nature of the FCA-NPs with a mean diameter of around 14 nm. Field and temperature-dependent magnetization (M) study shows that the NPs are soft ferromagnetic with a high saturation magnetization (M_s) and Curie temperature (T_c) of 831 K. We also observed that FCA-NPs do not follow the Slater Pauling (SP) rule possibly because of the disorder present in this system. We further investigate its phase transition and magnetocaloric properties. The peak value of entropy change vs T curve at a magnetic field change of 20 kOe corresponds to about 2.65 J/Kg-K, and the observed value of refrigeration capacity (RCP) was as large as 44 J/Kg, suggesting a large heat conversion in the magnetic refrigeration cycle. To analyze the magnetic phase transition (MPT), magnetization property is studied in detail. The Arrott plot and the nature of the universal curve accomplish that the ferromagnetic (FM) to paramagnetic (PM) phase transition in FCA-NPs is of second order. The present study suggests that the FCA-NPs system is found to be proficient/useful/a good candidate not only for spintronics applications but also suitable in multistage magnetic refrigeration technology.

[1] J.P. DeGrave, A.L. Schmitt, R.S. Selinsky, et al., *Nano Letters*, 11 (2011) 4431-4437. [2] M. Jourdan, J. Minár, J. Braun, et al., *Nature Communications*, 5 (2014) 1-5. [3] C. Felser, L. Wollmann, S. Chadov, et al., *APL materials*, 3 (2015) 041518. [4] S. Idrissi, R. Khalladi, S. Ziti, et al., *Physica B*, 562 (2019) 116-123. [5] T. Graf, C. Felser, et al., *Heusler Compounds: Applications in Spintronics*, (2016) 335-364. [6] I. Galanakis, P. Dederichs, N. Papanikolaou, *Physical Review B*, 66 (2002) 174429. [7] X. Zhang, H. Zhang, M. Qian, L. Geng, *Scientific Reports*, 8 (2018) 1-11. [8] T. Graf, J. Barth, B. Balke, et al., *Scripta Materialia*, 63 (2010) 925-928. [9] T. Kojima, S. Kameoka, A.-P. Tsai, *Science Techn. Advanced Materials*, 20 (2019) 445-455. [10] P. Devi, M.G. Zavareh, C.S. Mejía, et al., *Physical Review Materials*, 2 (2018) 122401. [11] S. Datta, B. Das, *Applied Physics Letters*, 56 (1990) 665-667. [12] K. Kilian, R.H. Victora, *J. Applied Physics*, 87 (2000) 7064-7066.

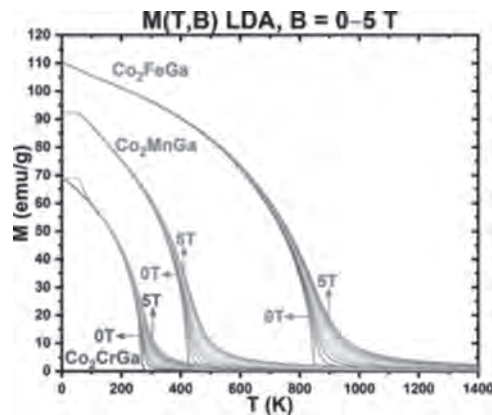
JE-11. In-Silico Thermodynamic Description of Heusler Compounds Applied to Magnetocalorics by Monte Carlo Simulations Starting From ab-Initio.

C. Amorim¹, J.N. Gonçalves¹, V.S. Amaral¹ and J.S. Amaral¹

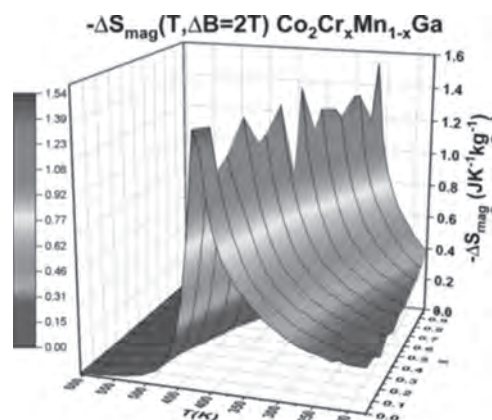
1. Physics, Universidade de Aveiro CICECO, Aveiro, Portugal

Heusler compounds are intermetallic ternary materials which can display a huge variety of physical phenomena, hence being potential: superconductors, gap tunable semiconductors, topological insulators, thermoelectrics, magnetoelectrics, magnetocalorics, etc. For this reason, it comes without surprise that since the discovery of its first compound (Cu_2MnAl) more than 1500 Heusler compounds have been discovered [1]. Still, the unguided search for new and better properties is truly a demanding task, especially if done through the careful, time-consuming and often expensive production of all possible compounds. A popular approach to perform this arduous task is to resort to an in-silico approach, namely through DFT calculations considering possible elements and respective stoichiometries [2]. DFT is a powerful tool to search for new Heusler compounds and better understanding their inherent. However, DFT calculations give a physical description of the studied system at $T = 0\text{K}$, which is particularly handicapping for magnetocaloric materials whose region of interest is located around their Curie temperature. A well-established approach to simulate the thermodynamic properties of Heuslers from ab initio results, consists these results as the starting point to perform mean field approximations (MFA) [3], or Monte Carlo simulations such as the popular Metropolis method [4]. However, MFA tends to be conceptionally too simplistic, whilst the Metropolis method performs a too narrow sampling of the partition function and requires a new set of simulations for each new pair of temperature and magnetic fields, being quite expensive from a computational point of view. New Monte Carlo methods, based on the sampling of the energy and magnetization joint density of states (JDOS) to calculate the partition function, show quite promising results in the description of magnetic material using a pure in-silico methodology [5-6]. In particular, the Random Path Sampling (RPS) method samples the partition function through random paths of spin flipping which begin and end in full oriented spins, assuring a magnetization flat sampling [6]. Using the RPS method to determine the JDOS of a $L2_1$ system, we present a full in-silico study of several Heusler compounds, namely the ternary Co_2CrGa , Co_2FeGa and Co_2MnGa compounds, and the quaternary $\text{Co}_2\text{Cr}_x\text{Y}_{1-x}\text{Ga}$ ($Y=\text{Fe}$ and Mn) stoichiometry families. We show that it is possible to predict relevant thermodynamic quantities, such as the temperature and magnetic field dependence of the magnetization, the Curie temperature, and the isothermal magnetic entropy change. This is achieved simply by applying statistical mechanics concepts, after determining the partition function of each studied system from a microscopic classical Hamiltonian, such as the Heisenberg Hamiltonian, whose exchange coupling constants were obtained from DFT ab initio calculations [7].

[1] T. Graf, C. Felser, and S. S. Parkin, "Simple rules for the understanding of Heusler compounds," *Progress in Solid State Chemistry*, vol. 39, no. 1, pp. 1–50, 2011. [2] S. Sanvito, et al., "Accelerated discovery of new magnets in the heusler alloy family," *Science advances*, vol. 3, no. 4, p. e1602241, 2017. [3] J. Gonçalves, et al. "Volume dependence of magnetic properties in $\text{Co}_2\text{Cr}_x\text{Y}_{1-x}\text{Ga}$ ($Y=\text{Ti-Ni}$) heusler alloys: A first-principles study," *Journal of Magnetism and Magnetic Materials*, vol. 428, pp. 362–367, 2017. [4] D. P. Landau, "The metropolis monte carlo method in statistical physics," in *AIP Conference Proceedings*, vol. 690, pp. 134–146, AIP, 2003. [5] D. Landau, et al. "A new approach to monte carlo simulations in statistical physics: Wang-landau sampling," *American Journal of Physics*, vol. 72, no. 10, pp. 1294–1302, 2004. [6] J. Amaral, et al. "Thermodynamics of the 2-d ising model from a random path sampling method," *IEEE Transactions on Magnetics*, vol. 50, no. 11, pp. 1–4, 2014. [7] C. O. Amorim, et al. "In silico Thermodynamic description of Heusler compounds applied to magnetocalorics by Monte Carlo simulations starting from ab initio." *European Journal of Inorganic Chemistry*.



M–T curves for the three Heusler alloys considering several magnetic fields (using the J_{ij} from LDA). The magnetic fields are presented between $B = \mu_0 H = 0 - 5\text{ T}$ with a step $\Delta B = 0.5\text{ T}$.



Temperature and Cr fraction dependence of the isothermal magnetic entropy change of the $\text{Co}_2\text{Cr}_x\text{Mn}_{1-x}\text{Ga}$ quaternary Heusler compound, around T_C , for $\Delta B = 2\text{ T}$.

JE-12. Unit Cell Volume Reduction of $Gd_5(Si,Ge)_4$ Nanoparticles Controlled by Bulk Compressibility.

V.M. Andrade¹, J.H. Belo¹, N. Checca², A. Rossi², F. Garcia², B. Gonçalves Almeida³, J. Tedesco⁴, A. Poulain⁵, A. Pereira¹, M.S. Reis⁶ and J. Pedro Esteves de Araújo¹

1. *Physics and Astronomy, (a) IFIMUP - Institute of Physics for Advanced Materials, Nanotechnology and Photonics of University of Porto, Porto, Portugal*; 2. *Centro Brasileiro de Pesquisas Físicas - CBPF, Rio de Janeiro, Brazil*; 3. *Department of Physics, Department of Physics, Minho, Portugal*; 4. *Polytechnic Institute - Rio de Janeiro State University, Rio de Janeiro, Brazil*; 5. *ESRF, Grenoble, France*; 6. *Instituto de Física, Universidade Federal Fluminense, Niteroi, Brazil*

Since the discovery of the Giant Magnetocaloric Effect (MCE) on $Gd_5Si_2Ge_2$ by Pecharsky and Gschneidner [1], the $Gd_5(Si_{1-x}Ge_x)_4$ family compounds have been intensively studied for applications in magnetic refrigeration (MR) at room temperature. The vast investigation at the macroscale on these alloys up to this time revealed many other important properties, such as giant magnetoresistance and colossal magnetostriction (CMS) [2]. Such behaviors arise from a strong magneto-volume coupling extreme sensitivity to variation of external (e.g., temperature, magnetic field, and pressure) and internal (e.g., stoichiometry, dimensionality, and doping) parameters. For this reason, this family compound presents a rich phase diagram that, for example, gives a wide range of temperatures for device operations. However, the low mechanical stability and oxidations issues are some drawbacks for long periods of appliance operation. Reducing it to the micro and nanoscales can improve the alloys' properties and also find novel properties. In the last years, some experimental approaches have been used to produce micro/nanostructures of $Gd_5(Si,Ge)_4$ [3]. It is possible to mention high-energy ball milling, RF magnetron sputtering, and laser ablation techniques, being the most promising. Using a femtosecond pulsed laser deposition, our group successfully obtained $Gd_5Si_{1.3}Ge_{2.7}$ nanogranular film composed of 80 nm particles presenting a magnetostructural transition [4] and a negative thermal expansion [5]. Although this evidence revealed the great potential of ultra-short laser ablation, a more conventional and low-cost technique should be pursued aiming practical applications of these compounds. For example, Tarasenko et al. were able to produce colloidal suspensions of Gd-Si-Ge nanoparticles in liquid with a more accessible Nd:YAG nanosecond pulsed laser [6]. Although the NPs presented fine crystalline features, the formation of silicon carbide and particle segregation after an additional laser ablation occurs. Given this, in addition to finding the most appropriate experimental technique, reasonable control of the intrinsic structures is essential to optimize the material production on a large scale. Here, we demonstrate that a more simple gas-phase synthesis using a Nd:YAG and KrF Excimer nanosecond pulsed lasers can be used to produce $Gd_5(Si_{1-x}Ge_x)_4$ nanostructures with $x = 0, 0.45$ and 0.60 . The stoichiometries were selected to cover all the possible structures adopted by this family: orthorhombic-II [O(II)] for $x = 0$; monoclinic (M) of $x = 0.45$; and orthorhombic-I [O(I)] for $x = 0.60$. It is worth mentioning that $x = 0.45$ and 0.60 are in the vicinity of the phase-mixed region to show the feasibility of this method along with the family phase-diagram. In particular, the KrF Excimer was chosen due to the laser wavelength that presents higher penetration depth and reduced reflectance in metals. The nanostructures were obtained by ablating the polished surface of ingots produced by tri-arc melting with 10 Hz of frequency and maximum energy of 550 mJ and 200 mJ, for Nd:YAG and KrF Excimer lasers, respectively. The chamber was pumped several times down to a base pressure of 10⁻⁶ Torr to prevent oxidation. During the deposition, Argon inert gas was used in a continuous flux in constant pressure of 1 Torr inside the chamber. From this process, $Gd_5(Si,Ge)_4$ grains with an average particle size between 10-30 nm were achieved with good crystalline features, as can be seen in Fig.1(a). Synchrotron X-ray Diffraction confirmed the great level of the structures crystallinity and revealed a change in symmetry for $x = 0$ and 0.45 respectively from O(II) and M to O(I). The structural shrinkage was found to be around 2% for the Si-rich compositions and less than 1% for Gd_5Ge_4 ($x=0$). Given the lower unit cell volume for the O(I) structure, a shortening between the Si(Ge)-Si(Ge) distances is responsible for a change in the transition order from a first to a second one for $x = 0.45$. Also, the magnetic transition occurs at 290 K for this 0.45 composition

nanostructure, see Fig.1(b), confirming the XRD analysis. Distinctly, for $x = 0$, the reduction to the nanometric scale leads to a superparamagnetic-like behavior that leads to a maximum of 8 J/kgK at 5 K that drastically reduces to null values as the temperature increases. Furthermore, the reduction of the unit cell volume was found to be directly related to the bulk target volumetric compressibility that is due to intrinsic surface tension (σ) rising from the nanostructuring process. Thereby, we can conclude that the nanosecond PLD successfully produces dispersed crystalline nanoparticles of $Gd_5(Si_{1-x}Ge_x)_4$ family compounds. This technique allows the formation of NPs with particles size under 30 nm without loss on the stoichiometry of the targets, as observed through Synchrotron XRD [7]. Notwithstanding, the direct relation between bulk compressibility and nanoparticle size due to an intrinsic surface pressure might be the path to understand the particles' growth from pulsed laser deposition techniques under inert gas in the chamber.

[1] V. K. Pecharsky and K. A. Gschneidner Jr., *Phys. Rev. Lett.*, vol. 78, p. 4494 (1997); [2] L. Morellon, *et al.*, *Phys. Rev. B*, vol. 58, p. R14721(R) (1998); [3] J. H. Belo, *et al.*, *J. of Mater. Res.*, vol. 34, p. 134 (2019); [4] R. L. Hadimani, *et al.*, *Appl. Phys. Lett.*, v. 106, p. 032402 (2015); [5] J. H. Belo, *et al.*, *PRB*, vol. 100, p. 134303 (2019); [6] N. Tarasenko, *et al.*, *J. Nanosci. Nanotechnol.*, vol. 16, p. 7451 (2016); [7] V. M. Andrade, *et al.*, *J. Alloys Compd.*, vol. 849, p. 156384 (2020[AP1]).

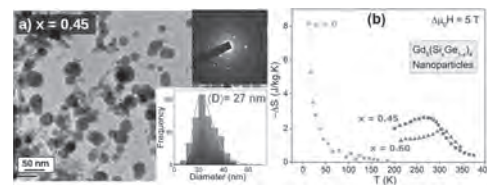


Figure 1: (a) TEM images for $x = 0.45$ nanoparticles with 27 nm of the mean size where the SAED reveals the good crystalline features of the structures. (b) Magnetic entropy change curves for all produced samples for an applied field of 5 T.

Session JF

MAGNETO-ELASTIC AND MAGNETO-OPTIC MATERIALS AND DEVICES

Nicola Morley, Co-Chair

University of Sheffield, Sheffield, United Kingdom

Lei Bi, Co-Chair

University of Electronic Science and Technology of China, Chengdu, China

INVITED PAPER**JF-01. All-Dielectric Magnetophotonics INVITED.***V.I. Belotelov¹**I. Lomonosov Moscow State University, Moscow, Russian Federation*

Faraday effect was a first demonstration of magnet influence on the light. Since then many generations of scientists tried to strengthen it. A decade ago, a breakthrough based on plasmonics was proposed for a significant enhancement of the magneto-optical interaction. However, all metals, even noble ones, introduce rather notable absorption which worsen quality factor of the optical resonances and constrains their role in the magneto-optical enhancement. Here we demonstrate that low lossy all-dielectric magnetic structures are more advantageous in this respect. We propose a specially designed all-dielectric magnetic meta-surface allowing a novel mechanism of the magneto-optical intensity effect [1]. It consists of a 2D array of iron-garnet nanopillars on an ultrathin iron-garnet slab. The nanostructure exhibits high transparency and superior quality-factor resonances followed by multifold increase of the magneto-optical intensity modulation. Unlike the magneto-optical intensity effects in smooth films and plasmonic gratings the photonic crystal metasurface provides the magnetically induced modulation of light intensity not only in a single light polarization, e.g. p-polarization, but also in the orthogonal one (s-polarization). It is due the wide variety of the excited mode types in the all-dielectric nanostructure. It is very promising for sensing, magnetometry and light modulation applications. This work was financially supported by the Russian Ministry of Education and Science, Megagrant project N 075-15-2019-1934.

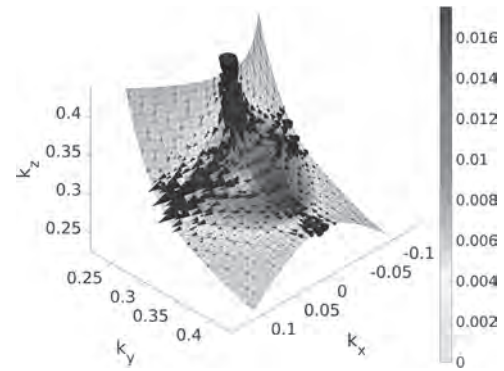
[1] D.O. Ignatyeva et al., Nature Communications 11, 5487 (2020).

CONTRIBUTED PAPERS

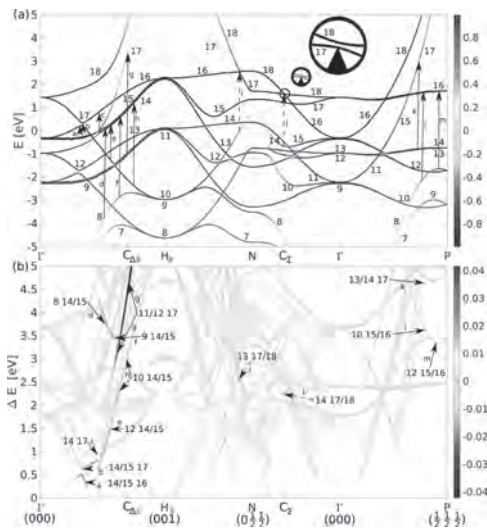
JF-02. Magneto-Optical Effect in bcc Fe: Microscopic Origin and Topological Aspects.O. Stejskal¹, M. Veis¹ and J. Hamrle¹¹ Univerzita Karlova Matematicko-fyzikalni fakulta, Praha, Czechia

We present analysis of microscopic origin of magneto-optical spectra from the electronic structure of bcc Fe. The magneto-optical (MO) permittivity spectra are obtained by the WIEN2k code [1] and compared to the corresponding experimental MO Kerr effect spectra. The ab-initio spectra are given by the Kubo formula, i.e., as a result of summation over all pairs of electronic bands and integration over the Brillouin zone that all sum up to the single MO spectrum. We investigate what features of electronic structure contribute to the outgoing total MO spectrum. We have also developed several novel ways of visualizing MO-related phenomena in the Brillouin zone. It turns out that strong MO signal comes from several isolated k-points in the Brillouin zone, where the band degeneracy is avoided by the spin-orbit interaction (Fig.1). There are two major types of MO contributions determined by the nature of the avoided degeneracy (given by topology of the approaching bands), that contribute differently to the total MO spectrum. Both types are visualized and their contributions to the total spectrum are demonstrated in the form of local MO spectra. K-points, where the strong MO signal is originated, also give rise to strong Berry curvature. We show the flow of the Berry curvature in the vicinity of those k-points (Fig.2) and in the full Brillouin zone.

[1] P. Blaha, K. Schwarz, G. Madsen, D. Kvasnicka and J. Luitz, WIEN2k



Flow of the Berry curvature in the vicinity of k-point with strong magneto-optical response.



(a) Band structure of bcc Fe with colors corresponding to the d -character of bands with spin-up being positive and spin-down negative. (b) Joint band structure with colors representing the strength of the magneto-optical response. Strong magneto-optical transitions are marked by arrows and labelled by the corresponding band indices.

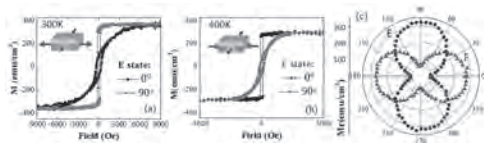
JF-03. Magnetic Anisotropy Switching Induced by Shape Memory Effect in NiTi/Ni Bilayer.

A. Kyianytsia¹, M. Poncot¹, E. Gaudry¹, P. Boulet¹, S. Migot¹,
J. Ghanbaja¹, B. Kierren¹ and T. Hauet¹

1. Institut Jean Lamour, Institut Jean Lamour, Nancy, Grand Est, FR, academic/chem, Nancy, France

In the last decade, a huge amount of work has been devoted to constructing a composite thin film where magnetic anisotropy becomes tunable by coupling ferromagnetic layer to a functionalized layer. Electrical control of interfacial anisotropy with an insulator and interfacial strain transferred from an electrically controlled piezoelectric or ferroelectric material are still heavily pursued. In 2016, Feng et al. [1] proposed a novel approach to manipulate magnetic anisotropy by interfacial strain transferred from a thermally controlled NiTiNb shape memory alloy (SMA). They obtained pioneering results in showing small variation of interfacial anisotropy in NiTiNb (0.5mm)/FePt (10–20 nm) with in-plane anisotropy. This innovative architecture benefits from the shape memory effect, in particular, from the two-way shape memory effect (TWSME). The TWSME consists in a reproducible hysteretic transformation of shape memory alloys from a strained B19' structure (at low temperature) to a differently strained B2 structure (at high temperature) during the thermal cycle. NiTi-based alloys are among the most used shape memory alloys within a wide range of applications in industry, military technologies, health care, etc. [2]. They are metallic and may be grown by regular microelectronics industry deposition techniques. NiTi-based SMAs can produce as much as 4% of TWSME strain and recover up to 10% of the initial deformation [3]. The transformation temperatures can be easily tuned from 250 K to 1000 K [2]. In our talk, we demonstrate that the NiTi alloy can be used to reproducibly switch by 90° the in-plane uniaxial anisotropy of a 20 nm thick Ni thin film during a thermal cycle between room temperature and 100°C (as shown in Figure 1) [4]. We first properly quantify NiTi sample longitudinal strain and transverse strain produced by an external uniaxial tensile stress followed by a thermal cycle, required to setup the TWSME. We demonstrate that NiTi is a Pauli paramagnetic material and explain temperature variations of its magnetic susceptibility by comparing experimental data with ab-initio calculations [5]. We show that both martensitic transition temperature and magnetic susceptibility depend on NiTi lattice structure, which we tuned through strain and characterized by TEM and XRD techniques. Secondly, we characterize magnetic anisotropy of the Ni layer, deposited by PVD on top of NiTi after tensile deformation. As shown in Fig. 1, when NiTi is in its martensite (respectively, austenite) phase, Ni anisotropy points along (respectively, perpendicular to) the initial tensile axis. Variation of Ni anisotropy up to 1.10^5 J.m^{-3} was achieved. It is a promising result since the strain transfer at NiTi/Ni interface is not yet optimized. Indeed during the TWSME strain in NiTi varies from 0% to 2.7% whereas Ni strain varies only from 0% to 1.3. We performed transmission electron microscopy and reveal that a thin oxidized interface layer is the main origin of strain loss at the NiTi/Ni interface.

[1] C. Feng et al., Appl. Phys. Lett. 109, 212401 (2016) [2] J. Mohd Jani, et al., Mater. Des. (1980–2015) 56, 1078 (2014) [3] O. Benafan, et al., J. Appl. Phys. 112, 093510 (2012) [4] A. Kyianytsia et al., Appl. Phys. Lett. 115, 222402 (2019) [5] A. Kyianytsia et al., Appl. Phys. Lett. 117, 122411 (2020)



(a–b) Magnetization vs magnetic field when the field is applied along the x-axis (0°), and y-axis (90°), when NiTi is in martensite state (E state) and austenite state (F state). (c) Remanent magnetization of NiTi/Ni as a function of magnetic field angle for E and F state.

JF-04. Influence of Additive Manufacturing Processes on the Microstructure and Magnetic Properties of Co-Ni-Ga Shape Memory Alloy.

F. Scheibel¹, C. Lauhoff², S. Riegg¹, P. Krooß², T. Niendorf² and O. Gutfleisch¹

1. Institute of Materials Science, Technische Universität Darmstadt, Darmstadt, Germany; 2. Institute of Materials Engineering, Universität Kassel, Kassel, Germany

High-temperature shape memory alloys (HT-SMAs) are required in specific automotive, aerospace or energy applications [1], [2]. Common binary Ni-Ti SMAs are characterized by a limited transformation temperature and, thus, cannot be used for applications operating at 100°C or above. Ternary elements (Pt, Au, Hf, Zr) can be added to increase the transformation temperature [3]. The ternary Ni-Ti-Hf alloy is currently the most promising candidate material, however, pronounced brittleness and high costs due to the significant amount of Hf hinders its technological breakthrough. Alternative HT-SMAs are Co-Ni-Ga Heusler alloys. These materials undergo a first-order magnetostructural transformation (FOMST) from high-temperature B2-ordered austenite to tetragonal L1₀ low-temperature martensite [4]. A fully reversible superelastic response up to 500°C as well as excellent cyclic stability up to temperatures of 100°C have been reported for single-crystals [5]. However, polycrystalline Co-Ni-Ga suffers from intergranular cracking and a premature failure after several transformation cycles due to the anisotropic volume change of randomly crystallographic orientated grains. Many efforts in the fields of grain boundary and microstructure engineering have been done to synthesize HT-SMAs with favorable grain boundary configuration in order to fully prevent intergranular cracking and premature failure. It was reported that a columnar-grained microstructure with strong <001> texture and straight low-angle grain boundaries can overcome the structural and functional limitations in Cu-based SMAs [6]. Additive manufacturing (AM) is a very promising technique to synthesize HT-SMA since it allows a direct microstructure design. Selective laser melting (SLM) and directed energy deposition (DED) are two common AM techniques for metallic alloys. During the SLM process, pre-alloyed powder is molten layer-by-layer using a laser system operating under inert gas atmosphere to prevent oxidation. Microstructure can be directly tailored by different processing parameters like laser power, scanning velocity and scanning path. In contrast to the powder-bed based SLM, DED is a powder-stream based process using nozzles to directly transfer the powder material into a focused laser beam. Similar to the SLM process the microstructure can be directly tailored by varying the processing parameters such as laser power and scanning speed. In our present work, we compare the microstructure and magnetic properties of Co₄₉Ni₂₁Ga₃₀ alloys processed by SLM and DED with single crystals as well as polycrystalline material prepared by conventional casting. The preferred columnar-grained microstructure could be obtained by proper choice of processing parameters for the different AM techniques [7], [8]. Fig. 1 shows the microstructure of Co-Ni-Ga fabricated by SLM. The electron backscatter diffraction (EBSD) analysis of the cross-section shows a polycrystalline columnar-grained microstructure along the building direction (BD) [7]. A similar columnar-grained microstructure is also observed in the DED processed material [8]. In addition, the DED sample is characterized by a strong <001> texture along BD. Due to these highly anisotropic microstructures, AM processed Co-Ni-Ga obtained by both, SLM and DED, shows excellent HT-SMA properties without any post-processing [7], [8]. To study the FOMST in more detail, temperature and field-dependent magnetization measurements were performed. Fig. 2 shows the temperature-dependent magnetization of additively processed samples, polycrystalline material in the as-cast condition and in a single crystalline state for different orientations. The SLM sample reveals the largest transition width and thermal hysteresis while the DED sample provides for a transformation behavior being very similar to the cast and single crystalline counterparts. Since the transformation behavior depends on parameters such as grain size, residual stresses, defects and precipitates [9] the influence of the processing parameters on these parameters is essential to understand the FOMST and functional properties in Co-Ni-Ga in more detail. This work was supported by the ERC Advanced Grant “CoolInnov” (No 743116), the CRC/TRR 270 “HoMMage” (DFG). TN acknowledges funding by DFG (No 398899207).

[1] J. Ma, I. Karaman, R. D. Noebe, International Materials Reviews, vol. 55, pp. 257-315, (2010) [2] K. Otsuka, Ed., *Shape memory materials*, Cambridge Univ. Press, (1999) [3] M. Elahinia *et al.*, Scripta Materialia, vol. 145, pp. 90-94, (2018) [4] A. Reul *et al.*, Shap. Mem. Superelasticity, vol. 4, pp. 61-69, (2018) [5] P. Krooß *et al.*, Shap. Mem. Superelasticity, vol. 1, pp. 6-17, (2015) [6] J.-L. Liu, H.-Y. Huang, J.-X. Xie, Materials & Design, vol. 64, pp. 427-433, (2014) [7] C. Lauhoff *et al.*, Metall and Mat Trans A, vol. 51, pp. 1056-1061, (2020) [8] C. Lauhoff *et al.*, Materials Research Letters, vol. 8, pp. 314-320, (2020) [9] F. Scheibel *et al.*, Energy Technol., vol. 6, pp. 1397-1428, (2018)

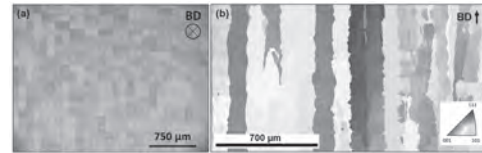


Fig. 1: Microstructure of Co-Ni-Ga processed by SLM: (a) optical micrograph, the building direction is perpendicular to the surface, (b) EBSD inverse pole figure map of the cross-section revealing a polycrystalline columnar-grained microstructure along the building direction (BD)

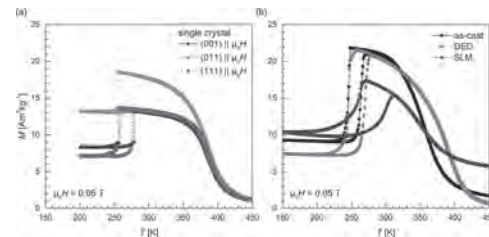


Fig. 2: Temperature dependent magnetization of (a) Co-Ni-Ga single crystals, (b) cast polycrystalline Co-Ni-Ga and Co-Ni-Ga alloy processed by SLM and DED.

JF-05. Dynamic Response of Fe-Ga for Multiferroic Magnetic Field Transmitters.

T.R. Mion¹, M. Staruch¹, J. Yoo², N. Jones² and P. Finkel¹

1. *Material Science & Technology, US Naval Research Laboratory, Washington, DC, United States;* 2. *Naval Surface Warfare Center Carderock Division, West Bethesda, MD, United States*

Recent progress in multiferroic antenna shows high promise for communication in rf-denied environment for transmitting signals in lossy electrically conductive media. The antenna utilizes the ultra-low (ULF/VLF) frequency band (1 – 30 kHz) while also maintaining a compact design [1]. In such multiferroic antennas, containing magnetostriuctive materials that are mechanically actuated, becoming a near-field magnetic field transmitter. This transduction mechanism is based on magnetization changes inside the magnetostrictive material, due to the application of time-variable stresses generated by an electrically-driven piezoelectric material (which is elastically coupled with the magnetostrictor). Magnetolectric coupling between the piezoelectric driving element and magnetostrictive material allows for modulation of a large magnetic signal from the multiferroic antenna [2]. Of particular importance is the material with a high piezomagnetic coefficient coupled with a large change in the internal flux density. Iron-gallium alloys, $\text{Fe}_{1-x}\text{Ga}_x$ (Galfenol) with $0.12 < x < 0.30$, are promising magnetostrictive, transducer materials that combine highly desirable tensile and compressive mechanical excitation with superior magnetic properties [3]. Doping studies of Galfenol show a maximum in the magnetostrictive response when the Ga composition is $x = 0.16 - 0.19$; while there is an additional peak at higher gallium compositions, this range maintains a large internal flux response [3,4]. This work investigates the mechanically-driven magnetic response of several Galfenol compositions as a function of driving frequency. A solid and laminated rod of similar size are also compared to determine the effect of eddy current losses on the flux response of the rod. The laminated rod is composed of 12 μm , epoxy bonded Galfenol sheets with $x = 0.186$. Magnetostrictive transducer elements under test were placed in a nonmagnetic frame with an applied, axial static prestress and permanent magnets placed above the Galfenol rods. When placed in an optimal magnetic bias field and compressively actuated through driving with a $\text{Pb}[\text{Zr},\text{Ti}]\text{O}_3$ (PZT) stack the magnetostrictive Galfenol changes magnetic states depending upon the applied stress. The bias magnetic field was optimized by determining the distance where the permanent magnets would allow for the highest Galfenol flux density response. A fluxgate magnetometer at 1 m and search coil surrounding the Galfenol rods determined the radiated magnetic field and changing internal flux, respectively; both showed similar frequency responses. Figure 1 shows the near-field (1 m) response of 3 samples (2 solid rods and 1 laminated) revealing an improved response at the lower Ga composition. Interestingly, a larger signal was measured from the laminated sample at all frequencies despite being a higher composition (18.4 at. % Ga); it also showed little variation with increasing frequency over the measured range. The laminated sample showed better operational properties compared with the solid samples that decreased with increasing frequency. Mechanically driven laminated Galfenol samples showed an improved dynamic response when compared with solid rods. Additional optimizations to the device configuration are possible as variations in production quality, heat treatments, and microstructural properties such as grain size and domain boundaries can affect the magnetostrictive and magnetic response of the material. Further investigations are needed to verify if any additional improvements are possible through annealing.

[1] Joseph D. Schneider, John P. Domann, and Gregory P. Carman, *Journal of Applied Physics* 126, 224104 (2019) [2] Junran Xu, Chung Ming Leung, and Dwight Viehland, *Sensors*, 19(4), 853 (2019) [3] G. Petculescu, K. B. Hathaway, and A. E. Clark, *Journal of Applied Physics* 97, 10M315 (2005) [4] A. Mahadevan, P. G. Evans, and M. J. Dapino, *Appl. Phys. Lett.* 96, 012502 (2010)

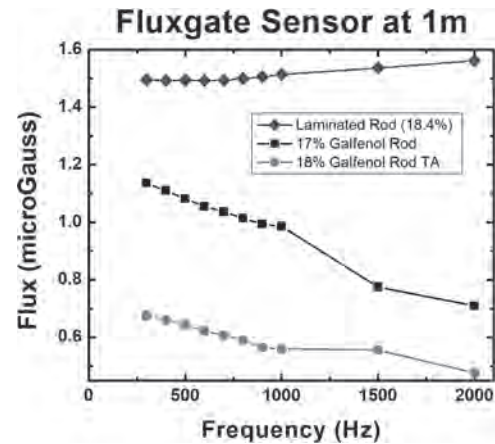


Figure 1: Frequency response of the fluxgate magnetometer 1 meter from the actuated Galfenol rods (solid: 17 and 18 at. % Ga; laminated: 18.4 at. % Ga), showing a nearly flat frequency response for the laminated rod from 300Hz to 2kHz. Both solid rods decrease with increasing frequency. The 18% solid rod has been annealed under tension.

JF-06. Validation of a Reduced Order Magnetoelastic Beam Model.M.E. Goforth¹, J.P. Domann¹ and A.N. Imhof¹¹. Biomedical Engineering and Mechanics, Virginia Polytechnic Institute and State University, Blacksburg, VA, United States

There has been a recent interest in the use of magnetoelastic materials to develop new magnetic antenna technologies [1,2,3]. Magnetic antennas show promise for surpassing shortcomings in current technologies, such as communicating in lossy environments (e.g., underground or underwater). One commonly proposed design is a resonant composite multiferroic beam consisting of magnetoelastic, elastic, and piezoelectric layers. Applying a voltage to the piezoelectric layer causes the beam to bend, straining the magnetoelastic layer, modulating the magnetic field around the antenna, thereby transmitting information. Current analytical and finite element magnetoelastic beam models [4,5,6] appear to work well for sufficiently long and thin structures, however the analytical models often neglect or overly simplify the magnetostatic field (i.e. demag) or spatially distributed material properties such as Young's modulus or piezomagnetic coupling coefficients. Therefore, an analysis of under what conditions reduced-order analytical models are valid is needed before they can be used as a tool for analyzing general geometries where complex magnetic field distributions are expected. This work presents a detailed comparison of a finite element model and an analytical reduced order Euler-Bernoulli beam model with the goal of determining under what conditions the reduced order model is valid, and which foundational assumptions are responsible for any discrepancies. Both the finite element model and the analytical reduced order Euler-Bernoulli beam are set up to solve the same geometry, governing equations, and boundary conditions. The antenna has a simple geometry composed of three rectangular plates; with a linear elastic layer sandwiched between piezoelectric and magnetoelastic layers. The governing equations consist of the equations of magnetostatics, electrostatics, and linear elasticity (i.e., suitable for a near-field antenna operating at low kHz frequencies). The mechanical boundary conditions are setup to model a free-free Euler Bernoulli beam. The finite element analysis is conducted in a series of steps. First, a uniform magnetic field is applied, and the bias state of the antenna is solved for using a coupled, nonlinear, magnetoelastic constitutive model (along with linear elastic, and piezoelectric behaviors). A linearized modal analysis is then performed around this bias state to determine the dynamic eigenmodes of the mechanical vibrations. Once found, the first eigenmodes is subsequently used to model the mechanical deformation, which is then fed into the nonlinear magnetic material model to obtain the dynamic magnetization changes (i.e., a one-way coupled model, with mechanics driving the magnetics). The reduced order Euler-Bernoulli beam model is constructed using a similar approach. A bias strain distribution for a composite Euler-Bernoulli beam is first computed. In contrast to the FEA model, this assumes a spatially uniform demag factor, and spatially uniform material properties. A linearized eigenmode analysis is then performed that utilizes a linear piezomagnetic approximation to obtain a fully-coupled linearized solution. Both the finite element model and the analytical model have their strengths and weaknesses. The finite element model produces more accurate results utilizing spatially non-uniform and nonlinear material properties, and an accurate description of demag. However, the speed of the analytical model greatly outperforms the finite element model making it more suitable for understanding design alternatives and optimization. This work will examine how the assumption of uniform material properties and demag fields affects the accuracy of the analytical model and determine under what conditions the approximations are valid. Fig. 1 shows an example, from the finite element model, of the spatially distributed piezomagnetic coupling in the magnetoelastic material where the maximum coupling is found to be at the end of the beam. A specific focus will be made on examining the validity of using an analytical model to optimize the geometry of a magnetic antenna.

J. Domann, and G. Carman. *Journal of Applied Physics* Vol. 121(4), p.044905 (2017) J. Xu, C. Leung, X. Zhuang et al. *Sensors* Vol.19(4), p.853 (2019) C. Dong, Y. He, M. Li et al. *IEEE Antennas and Wireless Propagation Letters* Vol. 19(3), p.398–402 (2020) L. Shu, M. Dapino, P. Evans, et al. *Journal of Intelligent Material Systems and Structures* Vol. 22(8), p.781–93 (2011) H. Zhou, and Y. Zhou. *Smart Materials and Structures* Vol. 16(1), p.198–206 (2007) V. Guerrero, and R. Wetherhold. *Journal of Applied Physics* Vol. 94(10), p.6659–66 (2003)

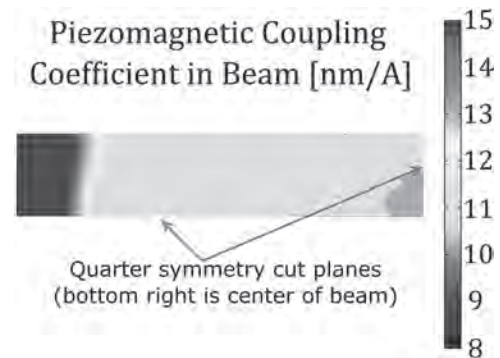


Fig. 1. Spatially distributed piezomagnetic coupling coefficient in the magnetoelastic layer of the beam. Note that the image is from the finite element model where quarter symmetry is utilized (center of the beam is the bottom right corner).

JF-07. Design and Analysis of a Fuel Injector Based on a Magnetostrictive Actuator.

L. Allocca¹, D. Davino², A. Montanaro¹ and C. Visone³

1. Istituto di Scienze e Tecnologie per l'Energia e la Mobilità Sostenibili (STEMS) - CNR, Napoli, Italy; 2. Dipartimento di Ingegneria, Università degli Studi del Sannio, Benevento, Italy; 3. DIETI, Università degli Studi di Napoli Federico II, Napoli, Italy

The paper presents the steps that brought the authors to design and implement the proof of principle of a fuel injector based on a custom Terfenol-D actuator. Magnetostrictive actuators play a relevant role in the perception of usefulness of smart materials and devices. Their applications are potentially wider than that of piezoelectric actuators because of the higher energy density and intrinsic robustness [1]. This activity is aimed to investigate the basic elements related to the fuel injection by fully controlling the injection rate. This would contribute to the NOx emission reduction that is a crucial goal for internal combustion engines. The study provides the design, development and a feasibility analysis of a magnetostrictive actuator for fuel injection, by providing both magneto-static numerical analysis of the actuator, the adaptation of a commercial fuel injector and its final experimental testing. Commercial fuel injectors work under on/off conditions and the modulation of the fuel rate is made over time. Recent developments make use of piezo-stacks to control the fuel injector needle [2] but the system is rather complex because the piezo-stacks cannot directly withstand the fuel high pressures. Indeed, the use of magnetostrictive materials would allow to have a simpler device with a full direct control of the injection and with higher achievable injection pressures [3]. The first step in the proof of principle has been the accurate design and analysis of the actuator employing a Terfenol-D magnetostrictive alloy aimed for the needle driving of a commercial fuel diesel injector with hydraulic drive. To this aim, a custom actuator employing a magnetostrictive alloy and fulfilling reasonable constraints for fuel injection (needle Lift of 50 - 200 μm, injection Pressure of 250-1000 bar, rise Time of 100 μs and a duty Cycle of 1/20 ms/ms) has been designed. The scheme of the magnetostrictive actuator, mechanically coupled with the modified injector, is shown in Fig. 1-left. The mechanical frame is acting also as a magnetic circuit and can accommodate different magnetostrictive rods. It is equipped with embedded force and displacement force sensors. The Fig. 1-right shows the realized prototype ready for injection tests. The magnetic circuit includes permanent magnets aimed to provide a bias magnetic field able to force the MS rods to the maximum stroke at zero current in the coil. In this condition the injector's holes are closed at zero current. The coil is designed to reduce magnetization in the rod driving back the needle and allowing the fuel injection. The system has been assembled and successfully tested with different driving signals. The Fig.2 shows the trigger signal (A), needle displacement (B), flow rate (C) and coil current (D) in case of square (red curves) and triangular (black curves) references and it is apparent that the flow rate sufficiently follows the reference signal shape. In the complete paper more details about the design, the numerical analysis and the experimental tests will be given.

[1] Apicella, V.; Clemente, C.S.; Davino, D.; Leone, D.; Visone, C. Review of Modeling and Control of Magnetostrictive Actuators. *Actuators* 2019, 8, 45. [2] H. Nouraei, R. Ben-Mrad and A. N. Sinclair, Development of a Piezoelectric Fuel Injector, *IEEE Transactions on Vehicular Technology*, 65(3),1162-1170, 2016, doi: 10.1109/TVT.2015.2410136. [3] G. Xue et al, A review of giant magnetostrictive injector (GMI), *Sensors and Actuators A: Physical*, 273 (2018), 159-181, <https://doi.org/10.1016/j.sna.2018.02.001>.

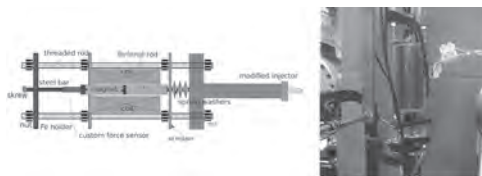


Fig.1: Scheme of the custom actuator (left) and of the assembled prototype (right).

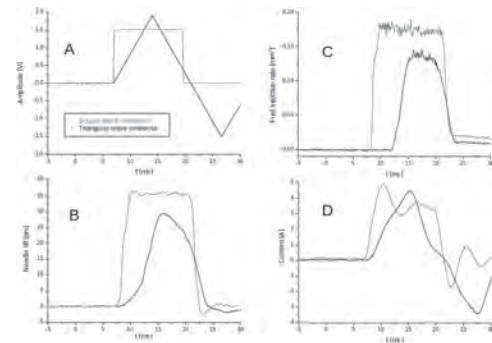


Fig.2: Reference signal (A), needle displacement (B), flow rate (C) and coil current (D) in case of square (red curves) and triangular (black curves) references at a 500-bar injection pressure.

JF-08. Approximation Methods for Hybrid Constitutive Model of Magnetostriction.

A.N. Imhof¹, J.P. Domann¹ and M.E. Goforth¹

1. Biomedical Engineering and Mechanics, Virginia Polytechnic Institute and State University, Blacksburg, VA, United States

Coupling piezoelectric and magnetoelastic materials together enables the electrical control of magnetism. However, the lack of an accurate non-linear magnetoelastic constitutive model complicates designing macroscale devices with these multiferroic composites. While micromagnetic simulations are the gold standard for mesoscale magnetic modeling, their use is limited to very small systems (i.e., typically below 10s of cubic microns). The focus of this research is on generating an accurate constitutive model for macroscale magnetoelastic materials that is consistent with micromagnetics. Multiple different constitutive models are currently used to describe macroscale magnetoelastic materials [1,2,3]. Two common approaches, polynomial and statistical energy models, each have their own strengths and limitations. For example, series expansion models that use polynomial expansions are straightforward to setup, however they are not capable of capturing the saturating behavior of magnetic materials. Additionally, to obtain nonlinear material properties well-controlled experiments to curve fit the models are required [4], which can be prohibitively challenging, time consuming, and expensive for anisotropic materials. Alternatively, statistical models can overcome the inherent limitations of polynomial expansions. These models utilize Boltzmann statistics to calculate the average magnetization and magnetostriction. These calculations account for the Zeeman, magnetoelastic, and magnetocrystalline anisotropy energies. A challenge of this statistical approach is that the requisite integral expressions do not possess general closed form solutions and therefore require numerical solutions. The first of these integrals is the partition function, which is dependent on the micromagnetic energies of the system u , and the thermal energy. In the title of Figure 1 the partition function includes beta which is used as a nondimensional term representing the magnitude of the micromagnetic energies in u . The other integral to consider is the average magnetization, which is derived from the partition function. While standard numerical integration methods can be utilized, they are computationally expensive, limiting their use in finite element models. In this work a constitutive model utilizing statistical physics to bridge micromagnetics to the macroscale is developed, and the accuracy and computational complexity of several integration methods are analyzed to produce a model suitable for use in high fidelity numerical models. The two methods for approximating the partition function that were examined are a partial series expansion and Laplace's method. Conceptually a series expansion is asymptotically exact at the point its expanded about, conversely Laplace's method is asymptotically exact at higher energy values (i.e., the methods are complimentary). The accuracy of each method was compared to an accurate, but computationally expensive numerical integral with relative error set at machine precision. The average magnetization, and therefore the partition function, has a closed form solution when only the Zeeman energy is included. If the additional micromagnetic energies are small compared to the Zeeman energy, they can be expanded in a Maclaurin series, which maintains integrals with exact solutions. Figure 1(a) shows the absolute error of this partial series expansion method as the magnitude of the applied energies (beta) increase. The inset graph also plots the absolute error, but beta 1 represents when only Zeeman energy is applied, and beta 2 shows when only the other micromagnetic energies are applied. Figure 1(b) shows the absolute error of Laplace's method as the magnitude of the applied energies increase. The inset graph again considers the main contributor to the energy of the system. These two figures show that the two methods are indeed complimentary and so a hybrid model would maintain low relative errors for the entire range of beta values. Additionally, Laplace's method only requires a small number of points (e.g., between two and six) to approximate integrals, making it more computationally efficient compared to standard integration methods. To conclude, we will use this model to simulate both the magnetization and magnetostriction of Galfenol subjected to magnetic fields up to 20 mT and mechanical stresses between -50 and 50 MPa. The results will be compared to experimental data from the literature [5].

[1] P. G. Evans and M. J. Dapino, Journal of Applied Physics., Vol. 107, (2010) [2] Yining Li et al. Journal of Magnetism and Magnetic Materials., Vol. 472, p. 59–65 (2019) [3] Z. Xiao et al. ACS Applied Materials & Interfaces., Vol 12.5, p. 6752–6760 (2020) [4] Z. Xiao and S. Le, Journal of Applied Physics., Vol 100.6, (2006) [5] A. Mahadevan, P.G. Evans, and M.J. Dapino, Applied Physics Letters., Vol. 96, (2010)

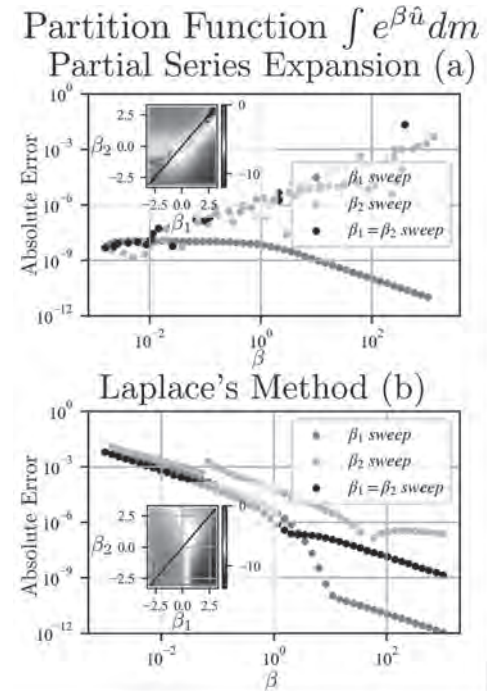


Figure 1: Absolute error of both approximation methods. (a) Results for partial series expansion (b) Results for Laplace's method

JF-09. Prediction of Magnetic Field Strength in Magnetorheological Elastomers Using Feedforward Neural Network.

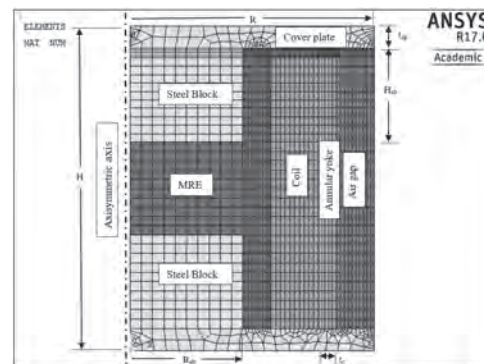
M. Keshav¹ and S. Chandramohan²

1. Mechanical Engineering, Pandit Deendayal Petroleum University School of Technology, Gandhinagar, India; 2. Dept. of Mechanical Engineering, Indian Institute of Technology Madras, Chennai, India

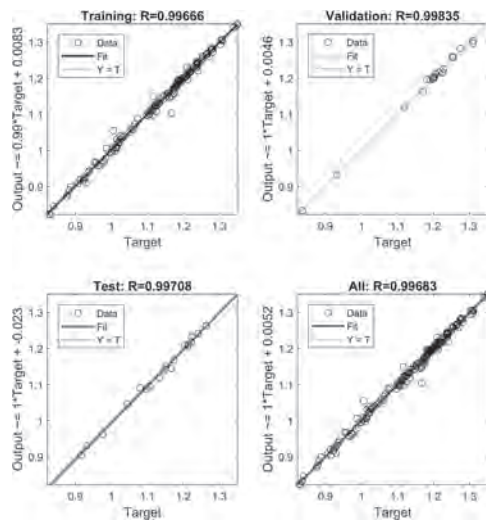
Introduction A magnetorheological elastomer (MRE) is a composite material with magnetic particles suspended or arranged within a non-magnetic elastomer matrix [1]. On the application of the magnetic field, it exhibits controllable stiffness and damping properties. When compared to a magnetorheological fluid, MRE has added advantage that it is leak-proof, deposition resistant, has a wide range of controllable properties, compatibility to mechanical components, and has a fast response and low power requirements. These advantages make it a very good option in various engineering applications. Changes in composition, shape and size of the MRE has led to a wide range of applications in vibration absorber, adaptive base isolator, and sandwich beams [2]. The magnetic field generated inside the MRE plays an important role in evaluating its properties based on the external load. However, due to non-availability of B-H curve data for MRE, it becomes cumbersome to numerically model it. If this data is available, the MRE and its magnetic circuit can be modelled in finite element (FE) software. B-H curve data for MRE can be found experimentally at a particular composition and size of MRE [3]. Li and Li [4] did FE analysis of adaptive base isolators utilizing laminated base MRE layers proposed by Li *et al* [5] and studied the magnetic field distribution in MRE layers in the deformed position. Therefore, FE modelling of MRE device can be an effective way to determine its optimal geometry and shape to draw the maximum magnetic field through it. However, all possible geometric combinations cannot be made every time to find out the maximum magnetic field through it. Data-driven modelling paves the way for it. In literature, most of the authors have applied the data-driven technique to model the dynamic behaviour of MRE [6][7]. However, predicting the magnetic field inside MRE using neural network data-driven technique has not been reported till now. In this study, a single-hidden layered feedforward neural network (FNN) is fitted for the magnetic flux data generated from FE model for different dimensions of the magnetic circuit and the study proposes an optimal dimension of it that will generate maximum magnetic flux density inside the MRE region of the magnetic circuit. The data fitting has been done using Neural Net Fitting toolbox and the optimization has been carried out using SQP method in optimization toolbox of MATLAB® 2017a. **Methodology: FE modelling and FNN architecture** An effective magnetic circuit is very important to maintain a strong magnetic in the MRE region. An axisymmetric FE model of the magnetic circuit is developed in ANSYS-APDL software which is shown in Fig. 1. For the FE analysis, the magnetic field is calculated in terms of magnetic flux density generated in the mid-section of the MRE and this has been set as an output parameter for a given geometry and applied current. Nodal solution for magnetic flux density at 3 A of current is fetched. After the FE model is developed, a log file is generated, which is later modified to include defined geometric variables. These geometric parameters are the same as the design variables (DVs) for the optimization problem. In the present work, the FNN is fitted to predict the magnetic flux density in the MRE region [8]. Training data for the FNN are generated from the results of the FE model encoded in a log file for different values of geometric variables taken between the bounds. The total training data have been divided as 80% for training, 10% for validation and 10% for testing. **Results** The number of activation units (or nodes) in the hidden layer is decided through error analysis. It is found that 8 activation units would be most suitable as it gives minimal mean square error (MSE) of all data sets as compared to other activation units. At this architecture, MSE for training data, validation data and testing data are 9.73×10^{-5} , 4.3×10^{-5} , and 8.21×10^{-5} respectively. The optimal weights obtained can be fed in MATLAB® software for a given number of inputs and activation units and the magnetic flux density can be predicted for any set of geometric input. Fig. 2 shows the regression analysis for the same where training data achieve the fitness value, $R=0.9967$, validation as $R=0.9984$ and testing as $R=0.9971$. Optimization problem aims at maximising magnetic flux density in the MRE region of the magnetic circuit for the given constraints on the geometric variables of the magnetic circuit. From the optimal results it is

observed that the height of the steel block, H_{sb} , coil thickness, t_c and annular yoke thickness, t_{ay} tend to take on their upper bound values, whereas the radius of the steel block, R_{sb} takes on the lower bound, for the magnetic flux density in the MRE region to be maximum. **Conclusion** The study presents the way to analyse the distribution of magnetic field in the MRE for different geometric dimensions of the magnetic circuit using the data-driven model and 30-50% of what it predicts that would be considered as approximate for real-time application. The application of data-driven modelling in MRE can be extended to decide the optimization of the geometric configuration of the magnetic circuit with the constraint on magnetic saturation limit and also to be able to predict the magnetic field inside the MRE when it is in a deformed shape. This would help in evaluating the performance of MRE at its different shapes and configurations of the magnetic circuit.

[1] Carlson J D and Jolly M R, “MR fluid, foam and elastomer devices”, *Mechatronics*, 10(4-5), 555-69, 2000. [2] Li Y, Li J, Li W and Du H, “A state-of-the-art review on magnetorheological elastomer devices”, *Smart Mater. Struct.*, 23, 123001, 2014. [3] Zeng J, Guo Y, Li Y, et al., “Two-dimensional magnetic property measurement for magneto-rheological elastomer”, *Journal of Applied Physics*, 113(17), 919, 2013. [4] Li Y and Li J, “ Finite element design and analysis of adaptive base isolator utilizing laminated multiple magnetorheological elastomer layers” in *14th Int. Conf. on Electrorheological Fluids and Magnetorheological Suspensions*, Granada, July 2014, 26(14), 1861-70, 2014. [5] Li Y, Li J, Li W, et al., “Development and characterization of a magnetorheological elastomer based adaptive seismic isolator”, *Smart Mater. Struct.*, 22(3), 035005, 2013. [6] Jie Fu, Guanyao Liao, Miao Yu, Peidong Li and Junjie Lai, “NARX neural network modeling and robustness analysis of magnetorheological elastomer isolator”, *Smart Mater. Struct.*, 25, 125019, 2016. [7] Dingxin Leng, Kai Xu, Yong Ma, Guijie Liu and Lingyu Sun, “Modeling the behaviors of magnetorheological elastomer isolator in shear-compression mixed mode utilizing artificial neural network optimized by fuzzy algorithm (ANNOFA)”, *Smart Mater. Struct.*, 27, 115026, 2018. [8] Manjeet Keshav and Sujatha Chandramohan, “Geometric optimization of magnetorheological valve using feedforward neural networks for distribution of magnetic flux density inside the valve”, *Smart Mater. Struct.*, 28, 105018, 2019.



1. Axisymmetric 2D FE model of magnetic circuit of MRE.



2. Regression analysis of the fitted FNN model.

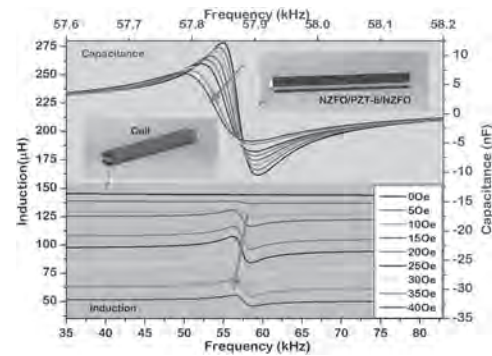
JF-10. Mutual Conversion Effect of Induction and Capacitance on the Magnetolectric Gyrator Consisting of Ferrite/PZT-8/Ferrite Laminate.

J. Zhang¹, K. Li¹, Q. Zhang¹ and G. Srinivasan²

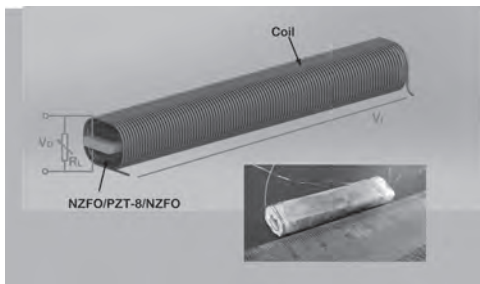
1. Zhengzhou University of Light Industry, Zhengzhou, China; 2. Oakland University, Rochester, MI, United States

Traditionally, the gyrator can be achieved by utilizing amplifier or RC circuits to construct two port net, accomplishing the transform from inductance to capacitance, or vice versa. This device assembled on RC resonators, oscillators, filters and inverters has been received in versatile and highly sophisticated fields including space, military, telecom, test/measurement, and medical electronic industries. Nevertheless, there are some drawbacks in their performance of larger redundant power dissipation bulky and complex of wiring connection due to using multi-element consisting of inductors and capacitors. Similarly, this device comprised by amplifier has an adverse influence of high consumption related to with leakage current and short channel effects, resulting in overheating imposed and ever-increase worse with time[1]. Tellegen proposed an ideal conception that a passive linear lossless electronic device, gyrator, based on transduction of magnetic flux and electric charge to address this issue. This device, with the merits of passive, linear, lossless, can theoretically accomplish conversion between voltage and current as well as between inductance and capacitance. Subsequently, the gyrator involved in the conversion between voltage and current with high power efficiency has been achieved taking advantage of magnetolectric (ME) composite and substantially reported and researched[2]. However, the issue of energy loss in the transformation process between inductance and capacitance and lower conversion ratio are still challenges. Therefore, research on the ME gyrator involved in conversion between inductance and capacitance to achieve lower energy loss and compact can be beneficial to the extensive applications. In this work, a ME gyrator consisting of the symmetrical Ni-Zn ferrite/PZT-8/Ni-Zn ferrite laminates and solenoid wound around it was proposed and characterized, as shown in Fig1. Through manipulating external magnetic field, inducing the permeability variation and strain in magnetostriction phase and then the strain transfer to the piezoelectric phase arise to permittivity variation, or vice versa, thereby achieving conversion between inductance and capacitance. Figure 2 presents the frequency dependence of the inductance of coil and the capacitance of piezoelectric in ME composite in the near of resonance frequency under various magnetic fields. With frequency increasing, the capacitance and inductance exhibit a climb to its peaks and then a sharp drop to minimum value, followed by a rise reaching a steady state. The result demonstrates the maximum Capacitance (C)/inductance (L) conversion ratio (C/ΔL) reaching 15.6 μH/nF in 25 Oe whereas the highest L/ΔC ratio of 0.06 occurs in 25 Oe. The proposed ME gyrator provides the potential to gain conversion between inductance and capacitance with lower energy loss and higher ratio.

[1] J.T. Zhang, D.Y. Chen, D.A. Filippov, K. Li, Applied Physics Letters, 113 113502 (2018). [2] X. Zhuang, C.M. Leung, J.F. Li, G. Srinivasan, IEEE Transactions on Industrial Electronics, 66 24992505 (2019).



The frequency dependence of the inductance of coil and the capacitance of piezoelectric in ME composite in the near of resonance frequency under various magnetic field.



Schematic diagram and photograph of the presented ME gyrator.

JF-11. Phase Transformation and Magnetostriction in Fe_{100-x}Ga_x Bulk Alloys.

M. Coisson¹, K.D. N'Dri², L. Diallo³, E.S. Olivetti¹, L. Martino¹, C.P. Sasso¹, F. Celegato¹, G. Barrera¹, M. Pasquale¹, P. Tiberto¹, J. Juraszek³, S. Bahamida⁴ and A. Fnidiki³

1. *Advanced Materials and Life Sciences, Istituto Nazionale di Ricerca Metrologica, Torino, Italy*; 2. *Universite de Lorraine Faculte des Sciences et Technologies, Vandoeuvre-les-Nancy, France*; 3. *Groupe de Physique des Materiaux, Sainte Etienne du Rouvray, France*; 4. *Universite M'Hamed Bougara Boumerdes, Boumerdes, Algeria*

Large magnetostriction and magnetoelastic coupling are properties extensively sought after because of their exploitability in low power consumption devices, energy conversion, and spintronics. Many alloys displaying large magnetostriction coefficients contain rare earths, whereas Fe-Ga systems, being rare earths free, have attracted attention because of their significant magnetostrictive response, coupled with good corrosion resistance and mechanical hardness [1]. Magnetostriction is particularly significant in Fe-rich alloys, with Ga content approximately equal to 19% and 27%. However, in this range of compositions, the Fe-Ga binary system is characterised by the possible presence of multiple phases, whose complex interplay strongly affects the magnetostrictive response. The stabilisation of the A2 phase by means of suitable thermal treatments turns out to be an effective way to obtain remarkable magnetostrictive properties. In this work, Fe-Ga alloys, containing 18, 21 and 23 at.% of Ga, were prepared in bulk form by arc melting. In their as-cast state they display a small magnetostriction, that is strongly improved after annealing at 1000 °C for 24 h, and subsequent rapid cooling. Multiple characterisation techniques, such as X-ray diffraction, Differential scanning calorimetry, Mössbauer spectroscopy, temperature-dependent magnetisation curves, hysteresis loops, magnetic force microscopy and magnetostriction measurements were exploited in synergy to gain a deep understanding of the structure-properties relationships in the studied alloys, before and after annealing. The A2 phase, which is favoured in the lower range of compositions and is promoted at the expense of the D0₃ one by the annealing, is responsible for characteristic dendritic and maze magnetic domains, shown in Figure 1, reporting domains patterns acquired with a magnetic force microscope on as-cast and annealed samples of the three compositions. Conversely, the lower-contrast regions, especially in the Ga23 as-cast sample, are due to the D0₃ phase. The transformation of the D0₃ phase into the A2 one with annealing, followed through extensive microstructure investigations, is responsible for the strong improvement of the magnetostriction, which almost reaches 240 ppm (transverse configuration) in the alloys with 18 at.% of Ga, after annealing (Figure 2).

[1] J. Atulasimha, A.B. Flatau, *Smart Mater. Struct.*, Vol. 20, p.043001 (2011).

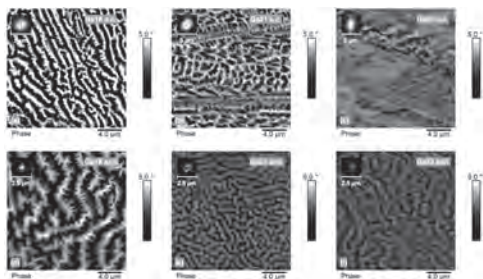


Fig. 1. MFM images of as-cast and annealed Fe-Ga bulk alloys with 18, 21 and 23 at.% of Ga. In the insets, FFT transforms of the same images.

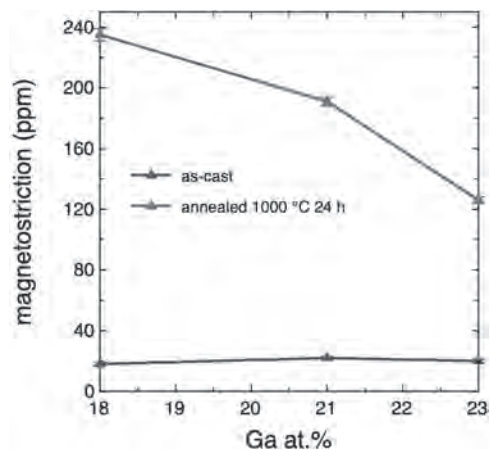


Fig. 2. Transverse magnetostriction as a function of Ga at.% for as-cast (blue curve) and annealed (red curve) samples.

JF-12. Real Time Monitoring of the Precipitation of Calcium Oxalate by Using Corrosion Resistant Magnetoelastic Resonance Sensors.

B. Sisniega Soriano¹, A. Sagasti¹, J. Gutiérrez^{1,2} and A. García-Arribas^{1,2}

1. *Electricidad y Electrónica, Universidad del País Vasco, Bilbao, Spain;*

2. *Fundación BCMaterials - Basque Center for Materials Applications and Nanostructures, Leioa, Spain*

Magnetoelastic sensors are typically amorphous ferromagnetic ribbons in which mechanical and magnetic properties are coupled, so an acoustic wave can be excited in these materials by the application of an alternating magnetic field and detected by the magnetic changes induced in it. The magnetoelastic ribbon can enter in resonance at certain frequencies of excitation, compatible with the dimensions and elastic properties of the material. These resonance frequencies are sensitive to different external parameters, which can be used to design different types of sensors [1], in particular, differences in ribbon mass loading cause a shift of the resonance frequency of the sensor. This sensitivity and its ability to query and detect remotely, made these devices especially interesting for sensing biological and chemical agents. In the present work, we have used magnetoelastic sensors to monitor the precipitation reaction of calcium oxalate crystals (CaC_2O_4), one of the most common minerals which form calcifications in the urinary track. The formation of these crystals was measured in real-time by tracking the changes in the resonant frequency of the sensor, which decreases as the precipitate is deposited on its surface (Figure 1), changing its total mass [2]. Previous works by Bouropoulos et al. have used magnetoelastic sensors based on the commercial material Metglas® 2826 for monitoring the kinetics of different precipitation reactions [3]; in this work a different amorphous ferromagnetic alloy ((Fe-Cr)-Based metallic glass of composition $\text{Fe}_{73}\text{Cr}_5\text{Si}_{10}\text{B}_{12}$) that has shown to have an improved corrosion resistance has been used [4]. This composition contains a small amount of chromium that allows the formation of a passivation layer on the material, thus favoring its corrosion-resistant behavior, which allows it to be used in biomimetic environments without any pre-treatment of its surface and avoid possible changes in the resonance frequency due to the corrosion of the ribbon. The precipitation reaction of calcium oxalate was carried out by mixing equal parts of solutions at the same concentration of oxalic acid and calcium chloride, and the formation of the insoluble salt crystals was monitored in a 500 s time interval. Solutions of different concentration (1, 5, 10, 30, 50 and 100 mM) were used in order to observe its effect on the rate of reaction (Figure 1). In addition, the monitoring of the reaction was complemented with the numerical fittings of the obtained resonance curves (Figure 2) to an analytical expression that describes the behavior of the resonance [5]. These numerical fittings improve the observation of the temporal evolution of the different parameters that characterize the response of the sensor (such as the resonance frequency, the damping parameters or the quality factor Q), and can be used to monitor the precipitation reaction, since in addition to a decrease in the resonance frequency, the deposition of calcium oxalate crystals on the ribbon causes an increase in the damping experienced by the sensor and therefore, a decrease in its quality factor. The numerical fittings made allowed to obtain this quality factor of the sensor with more accuracy than with traditional methods, which are unreliable when working with damped signals, such as when the sensor is immersed in a liquid and subject to mass loads. In addition, these fittings allow to get rid of the noise associated with the experimental measurements, which facilitates the calibration and use of the sensor. These fittings allow to follow the evolution of the precipitation reaction of calcium oxalate in a more reliable, precise and noiseless way.

[1] C. Grimes, C. S. Mungle and K. Zeng, *Sensors*, Vol. 2, no 7, p. 294-313 (2002). [2] B. Sisniega, A. Sagasti, J. Gutiérrez and A. García-Arribas, *Sensors*, Vol. 20, no 10, p. 2802 (2020). [3] N. Bouropoulos, D. Kouzoudis and C. Grimes, *Sensors and Actuators B: Chemical*, Vol. 109, no 2, p. 227-232 (2005). [4] A. Sagasti, V. Palomares, J. M. Porro, *Materials*, vol. 13, no 1, p. 57 (2020). [5] B. Sisniega, J. Gutiérrez, V. Muto and A. García-Arribas, *Materials*, vol. 13, no 21, p. 4708 (2020).

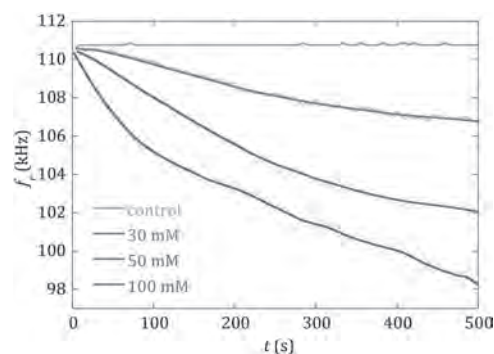


Fig. 1: Temporal evolution of the resonance frequency of the magnetoelastic sensor as the precipitation reaction progresses, for different concentration of reactants in the reaction (30, 50 and 100 mM) and a control measurement (sensor in a vial with distilled water).

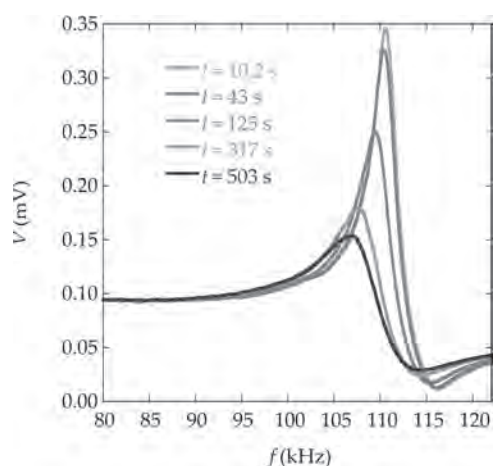


Fig. 2: Temporal evolution of the resonance curves of the magnetoelastic sensor during the precipitation reaction of calcium oxalate for the case of 30 mM concentration of reagents. As the reaction progresses, the resonant frequency and the quality factor Q of the curves decrease.

JF-13. A Calculation of Magneto-Mechanical Sensitivity for Various Compositions of Galfenol.

J. Yoo¹, N. Jones¹, P. Finkel² and M. Staruch²

1. Naval Surface Warfare Center Carderock Division, West Bethesda, MD, United States; 2. US Naval Research Laboratory, Washington, DC, United States

Magnetostrictive materials are distinguished by an inherent coupling between their mechanical and magnetic processes which is manifested as a direct (actuator) and an inverse (sensor) effect. Iron-gallium alloys (Galfenol, $Fe_{100-x}Ga_x$ with $12 < x < 30$) are a particularly promising magnetostrictive, transducer material that combines highly desirable tensile and compressive mechanical attributes with superior magnetic properties. These characteristics make it possible to design robust structural sensors and energy harvesters. However, the behavior of the mechanical and magnetic phenomena is essentially non-linear, making it difficult to develop analytical models to find an optimal operational condition. Because the magnetostriction strongly depends on both the pre-stress and magnetic field, the characterization of the material is usually conducted under controlled conditions for normalizing the parameters with respect to each other. In this study, large-grained, highly textured, polycrystalline Galfenol samples with 15, 17, 18, and 19 at. % Ga were evaluated. As shown in Figure 1(a), standard magnetic hysteresis loops were measured at various applied compressive stresses. Changes in the flux density, B , as a function of applied stress were determined as the intercept values at specific applied magnetic fields, shown by the red dotted line for the 50 Oe bias magnetic field condition. Figure 1(b) shows an example of the flux density as a function of the mechanical pre-stress at constant magnetic fields of 30, 50, 80, 100, 120, and 150 Oe for 18% Galfenol sample (colored dot symbols). To estimate the response of the magnetic flux density as a function of applied stress, a hyperbolic tangent function was used with 4-nonlinear parameters (a , b , c and d) which are functions of magnetic field, as defined below: $B(T, H) = a(H) \times \tanh[b(H) \times (T + c(H))] + d(H)$ (1) The calculated magnetization based on the fitted parameters is plotted in Figure 1(b) with solid lines, which fits the experimental data well. The continuous magneto-mechanical sensitivity, defined as the slope of the magnetization versus stress data, was calculated from the fitted equation (1) and the magneto-mechanical sensitivity results are depicted in Figure 2 for various bias magnetic fields. The same data process procedure was applied for the experimental characterization data of 15, 17 and 19% Ga specimens and Figure 3 shows the maximum value of the magneto-mechanical sensitivity as a function of applied bias field for the various compositions of Galfenol. As can be seen in Figure 3, 17% Galfenol shows higher magneto-mechanical sensitivity than 18% Galfenol, which usually shows higher magnetostriction values. Based on the results in Figure 3, 17% Galfenol will give better performance for sensor and energy harvester applications as compared to 18% alloys, which are used for actuation.

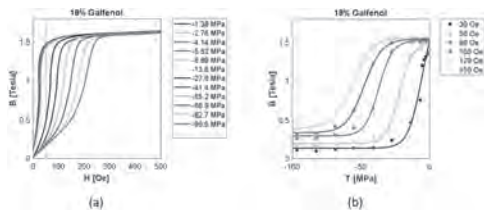


Figure 1. (a) Flux-density (B) versus external applied magnetic field (H) at various pre-stress values (T). (b) Magnetic induction (B) versus external compressive stress (T) at various bias fields (H) and curve-fit results based on hyperbolic tangent function.

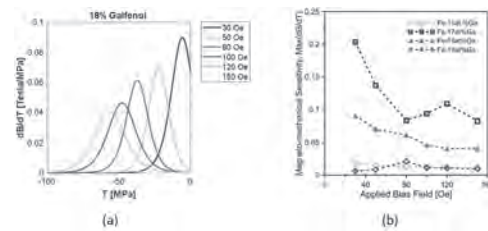


Figure 2. (a) Magneto-mechanical sensitivity at various bias magnetic fields (30, 50, 80, 100, 120 and 150 Oe). (b) Magneto-mechanical sensitivity at various bias magnetic fields for various composition.

Session JG

BIO-APPLICATIONS OF MAGNETISM I

Yuko Ichiyanagi, Chair

Yokohama National University, Yokohama, Japan

CONTRIBUTED PAPERS

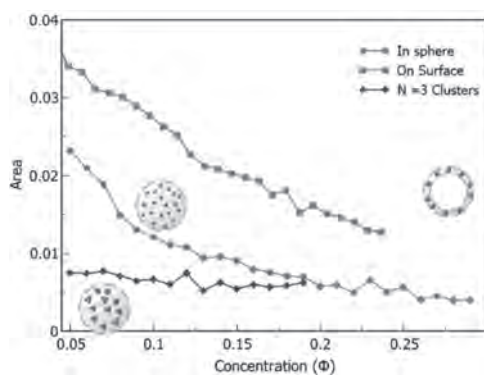
JG-01. Aggregates and Dipolar Interactions in Nanoparticle Assemblies for Magnetic Hyperthermia.O. Iglesias^{1,2}

1. Condensed Matter Physics, Universitat de Barcelona, Barcelona, Spain;

2. IN2UB, Barcelona, Spain

Magnetic hyperthermia is one of the most promising biomedical applications of magnetic nanoparticles (NP) and is intended to be alternative to cancer therapies based on drug delivery and radiotherapy. It is based on the fact that magnetic NP dissipate heat when an oscillating magnetic field is applied to them in a quantity (specific absorption rate, SAR) that is closely related to the area of the hysteresis loop. The main problem in the field has become to find the suitable range of parameters that maximize SAR for a given material [1], SAR depends of course on the amplitude of the applied magnetic field and its frequency, but also on intrinsic parameters of the NP such as saturation magnetization, anisotropy, shape and size [2]. Although the role of external parameters is somehow well contrasted, there is still ongoing controversy on the role that dipolar interactions (DI) and aggregation state of the assemblies play on SAR. We will present results of Monte Carlo simulations of hysteresis loops of interacting NP assemblies in the macro-spin approximation [3]. We will present first results of different regular spatial arrangements of NP, showing the influence of interparticle separation and particle size on SAR. Next, we will study the case of randomly placed NP with varying concentrations mimicking experimentally found situations [4] (inside and at the surface of liposomes/cells, clusters). It is found that formation of chain-like arrangements or assemblies with prolate shapes, lead to considerable increases in SAR due to DI. Acknowledgements: Work supported by Spanish MINECO (PGC2018-097789-B-I00), Catalan DURSI (2017SGR0598) and EU FEDER funds (Una manera de hacer Europa) also CSUC for supercomputer facilities.

[1] S.-H. Noh, et al. *Nano Today* 13, 61 (2017); R. Hergt et al. *Nanotechnology* 21, 015706 (2010). [2] B. Mehdaoui, et al. *Phys. Rev. B* 87, 174419 (2013); R. P. Tan et al. *Phys. Rev. B* 90, 214421 (2014); P. Hasse and U. Nowak *Phys. Rev. B* 85, 045435 (2012); P. V. Melenev et al. *Phys. Rev. B* 86, 104423 (2012). [3] C. Martínez-Boubeta et al. *Scientific Reports* 3, 1652 (2013). [4] Brollo et al., *Phys. Chem. Chem. Phys.* 20, 17829 (2018); D. Niculaes et al., *ACS Nano* 11, 12121 (2017)



Concentration dependence of the hysteresis loop area for different kinds of NP random assemblies.

JG-02. Shimming Design of Magnetic Shield Room Using Ferromagnetic Plates.

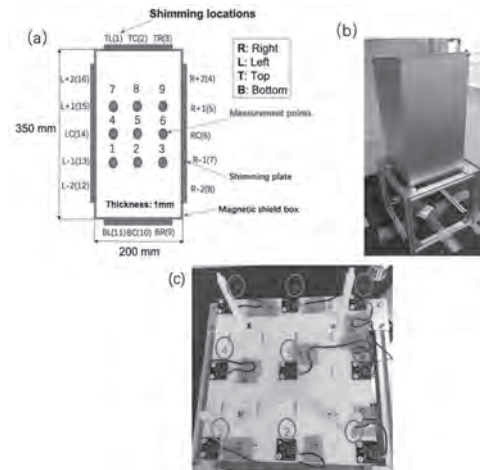
S. Jin¹, A. Kuwahata¹, S. Chikaki¹, M. Hatano² and M. Sekino¹

1. Department of Electrical Engineering and Information Systems, Graduate School of Engineering, Tokyo University, Tokyo, Japan;

2. Department of Electrical Engineering and Information Systems, Graduate School of Engineering, Tokyo Institute of Technology, Tokyo, Japan

Recent wearable ultrasensitive magnetometers opened novel applications of magnetoencephalography (MEG) to brain machine interface. In a recent study, the subject was allowed to move the head in a limited area of approximately 40 x 40 x 40 cm³ having a uniform magnetic field produced by a set of active shimming coils⁽¹⁾. The significant challenge of such wearable MEG systems is to improve the uniformity of magnetic field in the entire space in the magnetic shield room (MSR) and to suppress motion artifacts in MEG signals. A typical approach of realizing high field uniformity has been to make MSRs with highly symmetric shapes such as cylinder and polyhedron. However, these MSRs still require additional adaptive techniques to improve residual non-uniformity. The purpose of this study is to develop a new method of passive shimming for an MSR using ferromagnetic plates attached to its walls. The concept of this study is to optimize the spatial distribution of the magnetic field inside MSR with combination of ferromagnetic plates attached to the surface of MSR. The method mainly consists of two steps. In the forward problem, firstly, we calculated the spatial distributions of magnetic fields with the ferromagnetic plates of 601 mm (1 mm thickness) attached at 16 locations on the surface of a downsized magnetic shield box (MSB) of 200x350 mm (1 mm thickness) (Fig. 1(a)). The uniformity was evaluated by obtaining the standard deviation for 9 measurement points inside the MSB. We established the relationship between the individual shimming plates and the resulting magnetic field uniformity inside MSR. Secondly, by solving the inverse problem based on the forward solution, we identified the optimum number of plates to be attached at each location. We used the Tikhonov regularization⁽²⁾ to solve the ill-posed inverse problem, and the L-curve method⁽³⁾ to determine its optimal parameters. In the experiments, we measured and evaluated the spatial distribution of magnetic fields using nine magneto-impedance (MI) sensors (ROHM BM1422AGMV), as shown in Figs. 1(b) and (c). We found one shimming steel plate caused magnetic field variation of 50 ~ 300 nT inside MSB in the forward problem. And then we let the value of magnetic field of 9 measurement points equal to zero and solve the inverse problem to find the number of shimming plates. Figure 2(a) shows the combination of the shimming plates optimized by the inverse problem. Figures 2(b) and (c) show the magnetic field distribution in the area of 120 x 120 mm inside MSB with and without the combination of shimming plates, respectively. The shielding factor increased 131% of MSB, from ~5 to ~8, by the proposed method. We also evaluated magnetic field uniformity by calculating the standard deviation of 9 measurement points inside MSB. The standard deviation is 0.211 and 0.379 with and without the shimming method, indicating the magnetic field uniformity inside MSB has improved 44% by the shimming method. Figures 2(d) and (e) show the magnetic field distribution measured by nine MI sensors in the area of 160 x 160 mm without MSB and with MSB, respectively. The experimental shielding factor is ~7, which is comparable to the simulation results. In conclusion, the proposed methods of passive shimming for an MSR using ferromagnetic plates demonstrates the feasibility of improving the magnetic field uniformity and is applicable to wearable MEG system in the future. This work was supported by MEXT Q-LEAP with the Grant Number JPMXS0118067395.

(1) H. Niall, *et al.*, NeuroImage 181: 760-774 (2018). (2) D. Calvetti, *et al.*, Journal of Computational and Applied Mathematics 123.1-2: 423-446 (2000). (3) H. Christian, *et al.*, "The L-curve and its use in the numerical treatment of inverse problems." (1999): 119-142.



(a) Schematic of 16 shimming location and 9 measurement points of shimming design (b) Magnetic shield box assembled by steel. (c) Image of MI sensors setup. We used 9 MI sensors fixed on a resin board to measure the magnetic field distribution, distance of each sensor is 80 cm.

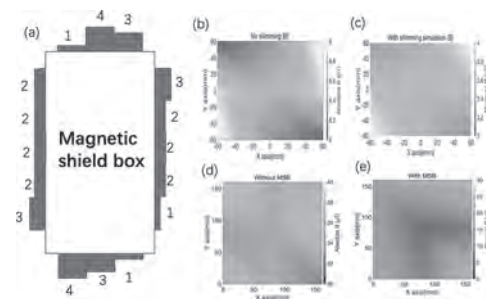


Figure.2 (a) Number of plates on each shimming location. 2D Simulation results of (b) no shimming case and (c) with shimming case solved by inverse problem, Experiment results of (d) magnetic field distribution without MSB (Magnetic Shield Box) and (e) magnetic field distribution with MSB (Magnetic Shield Box)

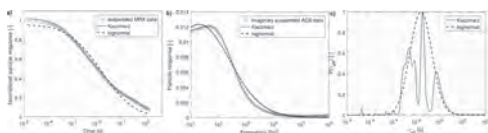
JG-03. Advanced Analysis of Magnetic Nanoflower Measurements to Leverage Their use in Biomedicine.

A. Karpavicius¹, A. Coene^{2,3}, P. Bender^{4,5} and J. Leliaert¹

1. Dept. of Solid State Sciences, Universiteit Gent Faculteit Wetenschappen, Gent, Belgium; 2. Dept. of of Electromechanical, Systems and Metal Engineering, Universiteit Gent Faculteit Ingenieurswetenschappen en Architectuur, Gent, Belgium; 3. Cancer Research Institute (CRIG), Universiteit Gent, Gent, Belgium; 4. Dept. of Physics and Materials Science, Universite du Luxembourg, Luxembourg, Luxembourg; 5. Heinz Maier-Leibnitz Zentrum (MLZ), Technische Universitat Munchen, Munchen, Germany

Magnetic nanoparticles are an important asset in many biomedical applications ranging from the local heating of tumours[1] to targeted drug delivery towards diseased sites[2]. Recently, magnetic nanoflowers showed a remarkable heating performance[3,4] in hyperthermia experiments thanks to their complex structure leading to a broad range of magnetic dynamics. To grasp their full potential and to better understand the origin of this unexpected heating performance, we propose the use of Kaczmarz' algorithm[5] in interpreting magnetic characterisation measurements[6]. It has the advantage that no a priori assumptions need to be made on the particle size distribution, contrasting current magnetic interpretation methods that often assume a lognormal size distribution. Both approaches are compared on DC magnetometry, magnetorelaxometry and AC susceptibility characterisation measurements of the nanoflowers. We report that the lognormal distribution parameters vary significantly between data sets, whereas Kaczmarz' approach achieves a consistent and accurate characterisation for all measurement sets. Additionally, we introduce a methodology to use Kaczmarz' approach on distinct measurement data sets simultaneously. It has the advantage that the strengths of the individual characterisation techniques are combined and their weaknesses reduced, further improving characterisation accuracy. Our findings are important for biomedical applications as Kaczmarz' algorithm allows to pinpoint multiple, smaller peaks in the nanostructure's size distribution compared to the monomodal lognormal distribution. The smaller peaks permit to fine-tune biomedical applications with respect to these peaks to e.g. boost heating or to reduce blurring effects in images. Furthermore, the Kaczmarz algorithm allows for a standardised data analysis for a broad range of magnetic nanoparticle samples. Thus, our approach can improve the safety and efficiency of biomedical applications of magnetic nanoparticles, paving the way towards their clinical use.

[1] A. Espinosa, R. Di Corato, J. Kolosnjaj-Tabi, et al, ACS Nano, Vol. 10, p. 2436–2446 (2016) [2] K. T. Al-Jamal, J. Bai, J. T.-W. Wang, et al, Nano Letters, Vol. 16, p. 5652–5660 (2016) [3] P. Bender, J. Fock, C. Frandsen, et al, J. Phys. Chem. C, Vol.122, p. 3068–3077 (2018) [4] C. Blanco-Andujar, D. Ortega, P. Southern, et al, Nanoscale, Vol. 7, p. 1768–1775 (2015) [5] S. Kaczmarz, Bulletin International de l'Academie Polonaise des Sciences et des Lettres, Vol. 35, p. 355–357 (1937) [6] J. Leliaert, D. Schmidt, O. Posth, et al, Journal of Physics D: Applied Physics, Vol. 50, p.195002 (2017)



Best combined fit to a) the magnetorelaxometry measurement data and b) imaginary part of the AC-susceptibility measurement data of suspended nanoflowers using a lognormal distribution and using Kaczmarz' method. c) The obtained relaxation time distributions corresponding to the fits in panel a) and b).

JG-04. Low Frequency Induction Heating of a Ferromagnetic Catheter for the Varicose Veins Treatment: Study of Feasibility.

Y. Liu^{1,2}, Z. Xiang¹, B. Ducharme^{2,1}, J. Garcia³, B. Newell³ and M. Le¹
 1. LGEF INSA Lyon, Villeurbanne, France; 2. ElyTMax UMI 3757, CNRS – Université de Lyon – Tohoku University, International Joint Unit, Tohoku University, Sendai, Japan, Sendai, Japan; 3. Purdue University, West Lafayette, IN, United States

Additive manufacturing of smart materials is a novel field in engineering. The ability to produce adaptable materials in varying geometries opens the door to the creation of a tremendous variety of new sensors, actuators and applications in domains including, transportation, energy production and medicine [1][2]. In this work, our objective is to build a ferromagnetic catheter by using additive manufacturing principles employed for the creation of smart materials (Fig. 1). Induction heating phenomena takes place in the ferromagnetic catheter due to the influence of a varying magnetic excitation field. This contactless heat source can be used to heal locally and destroy damaged blood vessels. According to medical specialists, thermal ablation of varicose veins requires a temperature close to 120°C and time constants lower than a few seconds [3]. First investigation results showed great potential for success using the low frequency induction heating (LFIH) method but further surveys and validation steps are still needed before in vivo testing can commence. Fig. 1 – Illustration of the ferromagnetic catheter. In this study, multi-physics simulation results, including ferromagnetic, thermal and fluid mechanics domains were compared to experimental data, then conclusions are proposed to establish the most adapted magnetic waveform (frequency) and its influence on the human tissues. In our process, heat is transferred through a contactless method. The flexible 3D printed ferromagnetic catheter is subjected to an alternating magnetic excitation. Under the influence of the magnetic excitation, eddy currents are generated through the catheter creating heat. First published results [4][5] describing this technique have experimentally demonstrated the feasibility of heat generation but the conditions tested and simulated were still far from the in vivo environment. In this study, we go deeper into the investigation process, we propose simulation results (magnetic, thermal ...) under much realistic experimental conditions. In [4], the authors limit the magnetic excitation signal to a few kHz. The purpose is to avoid undesired charge displacements in the surrounding tissue, but this restriction is strictly assumption based and further investigations must be under-taken to determine the optimal value for ablation while minimizing charge displacement. No further investigations have been proposed to establish a significant cutoff frequency. In this new research, a ferromagnetic model for the simulation of the ferromagnetic composite magnetic behavior is developed first. This model is based on previous work on the same topic [6]-[8] and it investigates the frequency dependence of the composite hysteresis area, i.e. the heat generated through the LFIH influence. Next, comparisons between the model and experimental situations are investigated to set the ferromagnetic model parameters and to establish the most efficient LFIH frequency. Finally, multi-physics simulation results combined with experimental tests are reviewed to predict the ferromagnetic composite's behavior on living tissues under the influence of the optimized magnetic excitation. Before validating the ferromagnetic catheter as a realistic treatment method for varicose veins, special attention must be given to the undesired charges or ionic displacements in the healthy surrounding tissues causing local temperature elevations and degradations. A compromise between treatment and negative effects on surrounding tissue must be made to establish the best working frequency. Numerical simulations are proposed to establish the optimized configuration of the magnetic source (frequency, amplitude) and of the ferromagnetic catheter behavior, these results constitute a huge step toward a first medical test.

[1] Standard A. F2792, Pa, USA: ASTM International (2012) [2] G.N. Levy & al., CIRP Annals-Manuf. Technol., vol. 52 iss.2, pp. 589-609 (2003) [3] S. Nehemiah & al., Cochrane Library, iss. 13 (2013) [4] Z. Xiang & al., polymers 2020, 12(2), 386 (2020) [5] Z. Xiang & al., Mat. & Des., Vol. 174, 107804 (2019) [6] M. A. Raulet & al., IEEE Transactions on Magnetics, vol. 40, n° 2, pp. 872 – 875 (2004) [7] Z. Xiang & al., IEEE Trans. on Mag, IEEE int. Mag. Conf. (INTERMAG), Singapore (2018) [8] B. Gupta & al., Proc. of the 21st int. conf. on the comp. of electromag. fields COMPUMAG, Daejeon (S. Korea), (2017)



JG-05. Cation Leaching Alters the Properties of Mn Nanoferrites for Biomedical Applications.

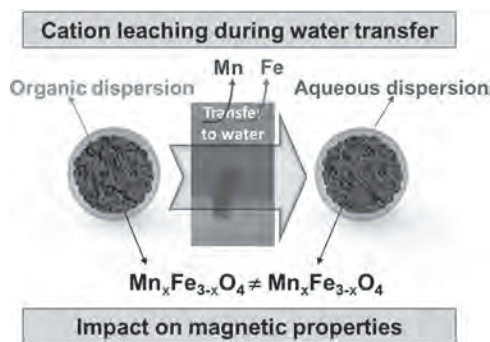
D. García-Soriano¹, N. Lafuente-Gómez¹, P. Milán-Rois¹, Á. Somoza^{1,2}, C. Navío¹, F. Herranz³, L. Gutiérrez⁴ and G. Salas^{1,2}

1. *Fundación IMDEA Nanociencia, Madrid, Spain*; 2. *Unidad Asociada de Nanobiotecnología (CNB-CSIC e IMDEA Nanociencia), Madrid, Spain*;

3. *Instituto de Química Médica, Consejo Superior de Investigaciones Científicas, Madrid, Spain*; 4. *Universidad de Zaragoza Instituto de Nanociencia de Aragón, Zaragoza, Spain*

Mn-doped ferrite nanoparticles are promising materials for applications in biomedicine as they exhibit better properties for some biomedical applications than non-doped magnetite or maghemite. [1] The thermal decomposition of metal precursors in an organic solvent is arguably the best method in terms of size control and the magnetic properties of the so-obtained materials. It provides hydrophobic nanoparticles that must be transferred to water through surface modification procedures before their use in biomedicine. In this work, Mn-doped ferrite nanoparticles have been synthesized by thermal decomposition changing systematically the Mn/Fe ratio of the metal precursors. Then, they have been transferred to the aqueous phase through ligand substitution with dimercaptosuccinic acid and dopamine. We show that the synthesis and post-synthesis manipulations lead to changes in the composition. During the thermal decomposition process, Mn is incorporated in the nanoparticles in a relatively lower amount than Fe and, then, during the surface modification step both Mn and Fe ions leach out from the nanoparticles (Figure 1). This alteration of the chemical identity of the nanoparticles have substantial implications for their subsequent application because small variations in the Mn/Fe ratio have a strong impact on properties like the saturation magnetization, blocking temperature, contrast enhancement for magnetic resonance imaging, magnetic heating, as well as on the cytotoxicity.[2]

[1] L. Yang *et al.*, *Chem. Mater.*, Vol. 29, p.3038 (2017). [2] D. García-Soriano *et al.*, *J. Colloid Interf. Sci.*, Vol. 578, p.510 (2020).



Scheme illustrating the changes in composition when the nanoparticles are transferred from an organic dispersion to an aqueous one.

JG-06. Vortex Nano-Discs: From Micromagnetic Simulations to Cancer Cells Internalization for Magneto-Mechanically Induced Damage Applications.

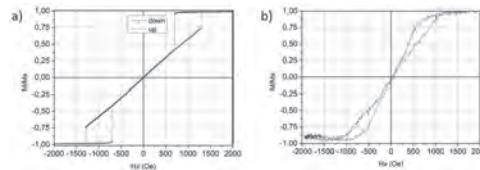
C. Sousa¹, R. Magalhães¹, S. Caspani¹, S. Moraes¹, L. Peixoto¹, D. Navas², C. Redondo³, R. Morales^{4,5}, S. Lima⁶, C. Nunes⁶, S. Reis⁶ and J. Pedro Esteves de Araújo¹

1. IFIMUP and DFA, Faculdade de Ciências da Universidade do Porto, Porto, Portugal; 2. Instituto de Ciencia de Materiales de Madrid, ICMM-CSIC, Madrid, Spain; 3. Dpto. de Química-Física, Universidad del País Vasco UPV/EHU, Madrid, Spain; 4. Dpto. de Química-Física & BCMaterials, Universidad del País Vasco UPV/EHU, Bilbao, Spain; 5. IKERBASQUE, Basque Foundation for Science, Bilbao, Spain; 6. LAQV, REQUIMTE, Faculty of Pharmacy of Porto University, Porto, Portugal

The advances in synthesis methods and the research of new magnetic effects have been the driving forces propelling the use of magnetic nanostructures in several research fields. In biomedical applications, magnetic nanoparticles, usually in the superparamagnetic state, are mainly used in magnetic fluid hyperthermia (MFH) and as contrast agents. In contrast, the novel magnetic nanostructures (MNS) studied in this work present a unique spin arrangement in the magnetic ground state, namely spin-vortex or synthetic antiferromagnetic state. MNS are mainly produced using top-down lithography techniques and physical vapour deposition methods. They are not spherical, rather disc-shaped, like coins with nanometer dimensions. MNS showed promising results in cell separation, as a contrast enhancing agents in MRI and in magneto-mechanically induced cell annihilation. Magneto-mechanically induced cell annihilation is a comparable technique with MFH for cancer therapy, where instead of superparamagnetic particles, micro/nano-discs in the spin-vortex state or synthetic antiferromagnetic nanostructures are employed. The main advantages of this novel approach are the usage of weaker magnetic fields with lower frequencies, as well as the need for a lower concentration of particles. This scenario opens new possibilities in cancer therapy, having triggered a scientific interest for MNS with unique spin configurations suitable for biomedical applications [1]. In this work, we developed one subset of biocompatible magnetic nanostructures that exhibit a spin-vortex state with interest in analysing their application in magneto-mechanically induced cell death [2]. First, micromagnetic simulations, using mumax3 of sub-micron iron discs, were performed for different interdot distance and aspect-ratio (thickness/diameter), to better understand the magnetic behaviour of these nanostructures. Two sets of samples were studied: ideal circular discs and disc-shaped nanostructures (based on images of real samples). By analysing the nucleation and annihilation fields, as well as the magnetic susceptibility, it was found that the (ideal) discs could be considered as isolated for interdot distances greater than twice the radius of the disc (2R) [3]. We also found that discs with an aspect ratio between 5 and 15 should sustain the vortex state in remanence. Iron nano-discs, with a diameter of about 500 nm, were fabricated by electron beam evaporation on a Si substrate pre-patterned by interference lithography [4]. The discs, protected by bottom and top gold layers, were fully characterized with scanning electron microscopy (SEM), X-ray diffraction (XRD), superconducting quantum interference device (SQUID), magneto-optic Kerr effect (MOKE) and ferromagnetic resonance (FMR) techniques. The synthesized nanostructures showed the desired vortex state configuration. The obtained magnetic measurements are in good agreement with the micromagnetic simulations (Fig. 1). Then, the magnetic vortex nano-discs were released from the substrate by chemical etching of a sacrificial layer. Subsequently, cell viability and uptake assays were performed in a human leukaemia monocyte cell line (THP-1). Several concentrations of nano-discs were studied by flow cytometry. As a result, the discs were internalized by the cells and found to be innocuous to them, in the absence of an external magnetic field. Work supported by Horizon 2020 MSCA grant agreement No 734801, AEI PID2019-104604RB, IT1162-19, IF/01159/2015, SFRH/BD/148563/2019, POCI-01-0145-FEDER-028676/PTDC/CTM-CTM/28676/2017 and POCI-01-0145-FEDER-031302/PTDC/FIS-MAC/31302/2017.

[1] L. Peixoto, R. Magalhães, D. Navas, S. Moraes, C. Redondo, R. Morales, J. P. Araújo, C.T. Sousa, Magnetic nanostructures for emerging biomedical applications. *Appl. Phys. Rev.*, 7 (2020) 011310., [2] Y. Cheng,

M. E. Muroski, D.C.M.C. Petit, R. Mansell, T. Vemulkar, R. A. Morshed, Y. Hana, I. V. Balyasnikova, C.M. Horbinski, X.Huang, L. Zhangc, R. P. Cowburn, M. S. Lesniak, *J. Control. Release* 223 (2016) 75. [3] L. Peixoto, C. Sousa, D. Navas, and J. P. Araújo, Micromagnetic study of the vortex state in sub-micron iron discs. *EPJ Web of Conferences* 233 (2020) 05002. [4] B. Mora, A. Perez-Valle, C. Redondo, M.D. Boyano, R. Morales, *ACS Appl. Mater. Interfaces* 10 (2018) 8165.



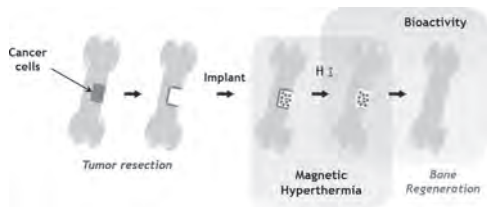
JG-07. Superparamagnetic and Bioactive Nanoparticles for Bone Cancer Treatment.

F. Vergnaud¹, C. Vichery¹ and J. Nedelec¹

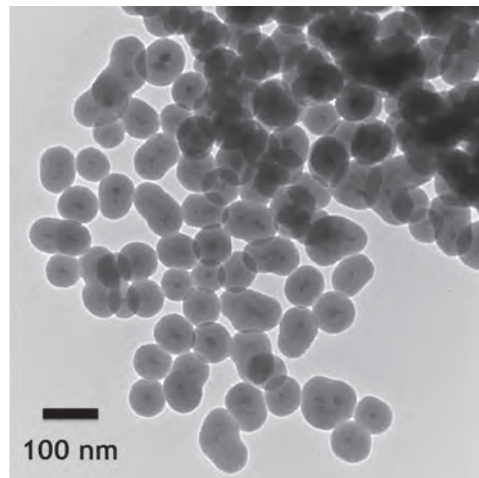
¹. SIGMA Clermont Grande école d'ingénieurs, Aubiere, France

Most patients who develop primary bone tumors require surgical intervention. In this respect, the design of a multifunctional material, used as bone substitute, is of high clinical interest to simultaneously treat cancer and promote bone regeneration. Bioactive glass (BG) nanoparticles are a promising material for bone tissue regeneration because when implanted, a hydroxyapatite layer is quickly formed onto their surface, bonding them to natural bone tissue [1,2]. By coupling the high bioactivity of large specific surface area bioactive glass particles with the heating ability of superparamagnetic iron oxide nanoparticles (SPIONs) under an alternating magnetic field [3], a multifunctional material could be designed and used to selectively destroy remaining or resurging cancer cells through hyperthermia treatment before promoting bone regeneration. In this scope, heterostructures consisting of SPIONs encapsulated in BG have been synthesized by sol-gel synthesis and characterized. The $\gamma\text{-Fe}_2\text{O}_3\text{@SiO}_2\text{-CaO}$ core-shell nanoparticles show promising hyperthermia and bioactivity properties, with a specific loss power (SLP) of 159 W/g_{Fe} and hydroxyapatite growth within 3 days [4]. At a concentration of 1 mg_{Fe}/mL, a temperature rise of 4 °C was achieved within 3 minutes, which could be suitable for cancer treatment. However, the heating power of these core-shell nanoparticles can still be improved, for example by increasing the SPIONs size. Indeed, the presence of a non-negligible amount of SPIONs with a diameter under 10 nm due to size dispersion is not optimal for hyperthermia [3]. Moreover, as evidenced in Figure 2, this sample present magnetic cores clustering, that is known to induce a decrease of the SLP value due to magnetic dipolar interactions [5]. Single-core NPs with a larger core size would thus be a better candidate for more efficient heating. In that respect, the core-shell particle structure has been modified in order to study the impact of core size and clustering on the hyperthermia properties. Using larger SPIONs led to an increase in SLP and an increasing percentage of single-core heterostructures. Magnetic core aggregation was also controlled by varying SPIONs concentration. The BG shell thickness was also modified, by varying the ratio between the magnetic cores and the silica precursor, because it could affect the heat dissipation of the magnetic particles in fluids [6].

[1] J. R. Jones, *Acta Biomaterialia*, Vol. 9, p. 4457 (2013) [2] C. Vichery and J.-M. Nedelec, *Materials*, Vol. 9, p. 288 (2016) [3] F. Gazeau, M. Lévy and C. Wilhelm, *Nanomedicine*, Vol. 3 (6), p. 831 (2008) [4] X. Kesse, C. Vichery and J.-M. Nedelec, *ACS Applied Materials & Interfaces*, Vol. 12, p. 47820 (2020) [5] D. F. Coral, P. M. Zélis and M. B. Fernández van Raap, *Langmuir*, Vol. 32, p. 1201 (2016) [6] M. Hu, X. Wang and G. V. Hartland, *Chemical Physics Letters*, Vol. 372, p. 767 (2003)



Schematic representation of bone repair coupled with hyperthermia treatment



TEM image of $\gamma\text{-Fe}_2\text{O}_3\text{@SiO}_2\text{-CaO}$ core-shell nanoparticles

JG-08. Unidirectional Transport of Superparamagnetic Beads and Biological Cells Along an Oval Shaped Magnetic Element Path.

F. Block¹, F. Klingbeil¹, U. Sajjad¹, D. Seidler¹, C. Arndt^{2,3}, S. Sindt^{2,3}, C. Selhuber-Unkel^{2,3} and J. McCord¹

1. *Nanoscale Magnetic Materials - Magnetic Domains, Institute for Materials Science, Kiel University, Kiel, Germany;* 2. *Biocompatible Nanomaterials, Institute for Materials Science, Kiel University, Kiel, Germany;* 3. *Institute for Molecular Systems Engineering (IMSE), Heidelberg University, Heidelberg, Germany*

Achieving new possibilities of cell manipulation or of other microbiological species is one of the most important tasks of the latest lab-on-a-chip devices [1-3]. High throughput and precise movement control are the figures of merit for new tools or chip designs. Common concepts consist of labeling biological cells or other biological entities with magnetic nanoparticles to achieve transport by timely and spatially varying magnetic field gradients [4]. In this context, superparamagnetic microbeads (MB) are widely used to imitate the properties of tagged cells or act as carriers for smaller biological species like DNA-strings or proteins. The particles or MBs can be manipulated on top of hard magnets [5] or soft magnetic thin film structures [6]. Recent research has shown many differently designed patterned thin film structures, featuring multiple advantages for the transport of MBs. One of the transport concepts relies on the interaction of their magnetic moment with a stray magnetic field gradient of arranged soft-magnetic thin film elements. Magnetic field sequences create varying potential states, enabling specific MB trajectories. In narrow soft magnetic tracks, magnetic microstructures that exhibit strong local stray field gradients are moved to drag the MBs along certain directions. For example, two-dimensional arrays of soft magnetic elements with various magnetization states varying with applied magnetic fields enable complex MB manipulation [2]. In every case, the maximum speed of the MB is limited by the hydrodynamic drag force, the surface friction, and by the magnetic force. This links the magnetic moments of the thin film elements and the MB, the friction coefficients, and the MB size. Beneficial and applicable unidirectional movement of a MB and a magnetically labeled rat embryonic fibroblast cell is demonstrated. We show the unidirectional transport of MBs and cells independent of the sign of the magnetic stimuli. Oval shaped elements made from a soft magnetic amorphous iron-based alloy are arranged in a one-dimensional chain, allowing MB transport whether clockwise or counter-clockwise in-plane rotating magnetic fields are applied. A directional motion scheme is achieved by exploiting the stray field dependence of the curvature radius of the facing magnetic elements. Three dimensional simulations [7] are used to forecast the motion of a particle along a chain of ovals and provide the theoretical background to the experimental results. Magnetic potential energy landscapes are calculated between the MB anticipated as magnetic dipoles and the micromagnetic structure of the oval elements simulated using mumax³ [8]. We find that an overlap of the potential minima of two neighboring elements for a spacing similar to the diameter of the MB enables a handover of MBs between magnetic elements. The agreement between the numerical simulated bead trajectories and the experimental movement path is shown in Fig. 1. The unidirectional motion scheme of the beads is demonstrated for different starting conditions for clockwise and counterclockwise rotating fields. The motion is independent of the sense of field rotation. The same manipulation options are obtained with a MB engulfed rat embryonic fibroblast cell as shown in Fig. 2. The robust diode-like particle guidance along predefined tracks, formed by chains of elements, holds also great potential for lab-on-a-chip applications, including cell sorting or highly controllable manipulation of biological carriers. The diode-like behavior of the oval elements leaves the direction of magnetic field rotation as a degree of freedom unexploited, permitting its usage for adding-on other application relevant manipulation schemes. Various aspects and options of the motion rectifying magnetic structures will be discussed. J.M., F.B., and U.S. acknowledge funding through the Deutsche Forschungsgemeinschaft grants DFG MC 9/13-1 and MC 9/13-2. C.A. and C.S. thank the Volkswagen Foundation for funding the project "Molecularly controlled, stimuli-sensitive hydrogels for dynamically adjustable biohybrid actuators". S.S. and C.S. acknowledge funding of the Research Training Group RTG 2154 "Material for Brain" through the Deutsche Forschungsgemeinschaft.

J.M. thanks S. Gutekunst for stimulating discussions. The authors thank L. Thormählen for magnetic thin film deposition.

[1] S. Rampini, P. Li, and G. U. Lee, *Lab Chip* 16, 3645-3663 (2016). [2] U. Sajjad, E. Lage, and J. McCord, *Adv. Mat. Int.* 5, 1801201 (2018). [3] B. Lim, P. Vavassori, R. Sooryakumar, et al., *J. Phys. D: Appl. Phys.* 50, (2016). [4] T. Henighan, A. Chen, G. Vieira, et al., *Biophys. Jour.* 98, 412-417 (2010). [5] J. Pivetal, D. Royet, G. Ciuta, et al., *J. Magn. Magn. Mat.* 380, 72-77 (2015). [6] U. Sajjad, R. B. Holländer, F. Klingbeil, et al., *J. Phys. D: Appl. Phys.* 50, (2017). [7] F. Klingbeil, F. Block, U. Sajjad, et al., *Sci. Rep.* 10, 1-12 (2020). [8] A. Vansteenkiste, J. Leliaert, M. Dvornik, et al., *AIP Adv.* 4, 107133 (2014).

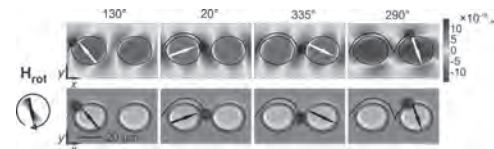


Fig. 1: Simulation data of a single MB motion for clockwise magnetic field rotation. Snapshots of the unidirectional motion together with the corresponding potential landscape are shown for four magnetic field angles. The corresponding matching experimental behavior for the same parameters are shown. The calculations and experiments were performed at clockwise rotating magnetic fields of 40 mT with a rotation frequency of 1.0 Hz.

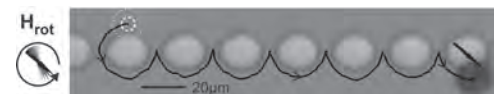


Fig. 2: Forward transport of a microbead engulfed by a rat embryonic fibroblast cell. The initial position of the cell and the microbead on the upper side of an oval structure is marked, demonstrating a forward motion even under the condition of a starting velocity in the backward direction. Here a counterclockwise rotating magnetic field of 40 mT with a rotation frequency of 0.3 Hz is applied.

JG-09. In-Vitro Manipulation and Bio-Imaging of Cells Using Magnetic Nanodiamond.

R. Selvam¹, E. Perevedentseva^{1,2}, A. Karmenyan¹ and C. Cheng¹

1. Department of physics, National Dong Hwa University, Shoufeng, Taiwan; 2. P.N. Lebedev Physics Institute of Rus. Acad. Sci, Moscow, Russian Federation

Nanoparticles are one of the potential carriers of drug for the treatment of cancer due to their multifunctionality. Among those nanoparticles, nanodiamond is a well known biocompatible multifunctional material with promising physiochemical properties and has the ability to fluoresce without photo bleaching which allows us to track the particle with one- or two-photon excitations [1]. In this work, nanodiamond with unknown nature of magnetism (MND, Ray Technique, Israel) is used and characterized based on the structural and magnetic properties. Raman spectroscopy reveals the characteristic peak of the well-defined diamond structure with respect to the phonon confinement of the 5 - 10 nm crystalline size diamond [2]. And the soft ferromagnetism was determined using SQUID measurement. The strong fluorescence of the MND is visualized using the fluorescence spectra recorded using the single photon excitation wavelength of 488 nm and 512 nm CW laser. Strong emission is also detected at two-photon excitation using femto-second laser with excitation wavelength of 760 - 800 nm with pulse duration of 140 fs, at the rate of 80 MHz repetition rate, and signal collection in the range of 450-650 nm. To utilize the nanodiamonds magnetic property in bio-medical applications, first, the MND biocompatibility was tested using Baby Hamster Kidney cells. Then the cells were incubated with the MND, trypsinized and dispersed in the phosphate buffer solution. The dispersed cells were manipulated using externally magnetized needle and visualized under the optical microscope for about 2 min [3]. The particle interaction with the cells with and without magnetic field was visualized with the help of Confocal fluorescence microscopy and Two photon Fluorescence Lifetime Imaging. In this experiment, 5×10^3 cells per well was seeded and incubated. When the cells confluence reaches 50 - 60 %, the particle of concentration 20 mg/ml was dispersed and incubated for 10 min under the presence and absence of external magnetic field. Afterwards, the unpenetrated particles were washed away and the samples were fixed using 4 % PFA and used for images recording. The results show that the magnetic nanoparticle is not cytotoxic. Labelling of cells with MND allows magnetic manipulation of the cells using external magnetic field. Hence, MND can be used as a promising agent for controlled drug delivery, cells manipulation and filtration, etc. and the well distinguishable lifetimes of the nanodiamond and the cells allow tracking of the particle in the cells. We appreciate the Ministry of Science and Technology (MOST) of Taiwan (MOST 106-2112-M-259-009-MY3)

1. Perevedentseva, E., Y.C. Lin, and C.L. Cheng, Expert Opinion on Drug Delivery, 2020. 2. Mermoux, M., Chang, S., Girard, H. A., et al., Diamond and Related Materials., vol. 87: p. 248-260 (2018) 3. Perevedentseva, E., Karmenyan, A., Lin, Y. C., et al., Journal of Biomedical Optics vol 23, 091404 (2018).

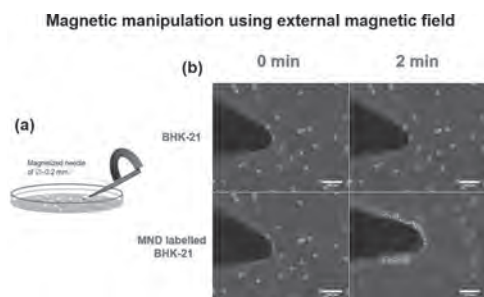


Fig.1.(a) Schematic representation of the experiment. (b) Microscopic images of the magnetized needle in PBS with and without suspended MND labelled cells. Images indicate the magnetophoretic movement of MND labelled cells towards the magnetic field

JG-10. Concentration Gradients of Magnetic Nanoparticles in non-Magnetic Fluids and non-Magnetic Particles in Magnetic Fluids for Rapid Toxicity Screening.

L. Abelmann^{1,2}, E. Gwag¹ and B. Sung¹

1. Korea Institute of Science and Technology Europe

Forschungsgesellschaft mbH, Saarbrücken, Germany; 2. Universiteit Twente, Enschede, Netherlands

We demonstrate the realisation of nanoparticle concentration gradients by means of Halbach arrays positioned below channels dedicated for cell culture studies. The nanoparticles can be magnetic as well as non-magnetic if a biocompatible chelated Gadolinium carrier fluid is used. These gradients are extremely helpful for the dose-response analysis of nano-particle toxicity. Conventionally, concentration ranges are prepared in individual containers (wells). Even though precise, this method is labour intensive both in preparation and analysis and requires considerable space inside the incubator. The use of gradients allows for rapid scanning of the concentration range of interest at small form factor. The Halbach array was realized using 48 commercially available 1.0x1.5x5.0 mm NdFeB magnets. Analytical solutions are given for the forces on magnetic nanoparticles and non-magnetic spheres in a paramagnetic solution. We demonstrate this method on human liver cells inside Ibidi micro-Slide channels of 400 μm height using Fe₂O₃ and silver nanoparticles.

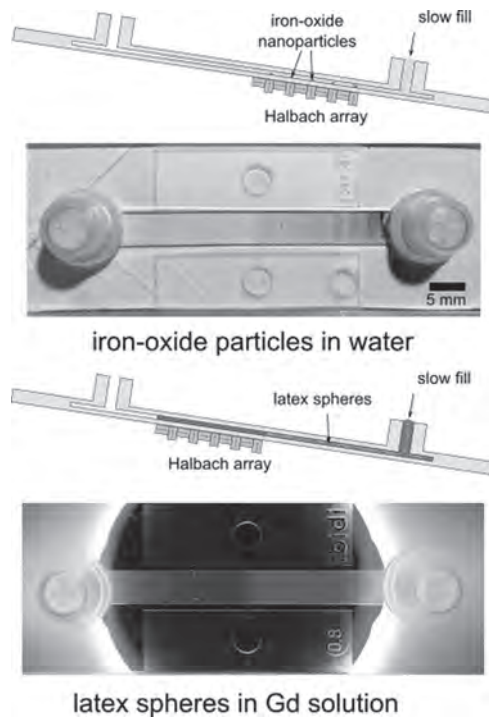


Fig. 1. Top: Concentration gradient of oxide nanoparticles of 5 nm diameter inside a channel slide dedicated for cell culture analysis. Bottom: Using a paramagnetic fluid, also concentration gradients of non-magnetic particles can be realized.

JG-11. EPR Characterization of the Mixed Radiation Field of a Boron Neutron Capture Therapy Irradiation Facility: a Dual Natural Lithium Formate/L-Alanine Dosimeter.

G. Alejandro^{1,2}, J.M. Longhino³, N.R. Álvarez¹, E. Pawlak⁴ and A. Butera^{2,3}

1. Centro Atómico Bariloche - Comisión Nacional de Energía Atómica (CNEA), San Carlos de Bariloche, Argentina; 2. Consejo Nacional de Investigaciones Científicas y Técnicas (Conicet), San Carlos de Bariloche, Argentina; 3. Centro Atómico Bariloche - Comisión Nacional de Energía Atómica (CNEA) and Instituto Balseiro (UNCuyo), San Carlos de Bariloche, Argentina; 4. Centro Atómico Ezeiza - Comisión Nacional de Energía Atómica (CNEA), Ezeiza, Argentina

Electron paramagnetic resonance (EPR) is a non-destructive technique widely used to estimate doses of ionizing radiation [1] in radiological emergencies, medical therapies, industrial processes, etc. An EPR dosimeter detects and quantifies point paramagnetic defects, usually free radicals, that are created by ionizing radiation (photons, neutrons, electrons) incident on an adequate material. The intensity of the EPR signal is a reliable measure of the number of paramagnetic centers induced, which is proportional to the received dose. Several compounds [2] can be used as EPR dosimeters: L-alanine, hidroxyapatite, 2-methyl alanine, lithium formate, glucose, etc. The election depends on the sensitivity, time stability, linearity, and the dose interval of interest (from mGy to kGy). L-alanine [3] is widely used in industrial medium dose applications (50 Gy–10 kGy) or high dose applications (10–50 kGy). The widespread use of alanine in low-dose (below 5 Gy) biomedical applications is due to its tissue equivalent properties. The induced free radicals responsible for the five-line EPR spectrum are very stable and produce a signal that can remain unchanged for years. Its response is reasonably linear in a wide range of doses. The optimal range of detection for alanine commercial sensors is 10 Gy–100 kGy [4]. It is almost insensitive to thermal neutrons and for this kind of radiation it is usual to dope alanine with boron or lithium, with a large neutron capture cross section, to enhance the response [5]. Lithium formate monohydrate (abbreviated ‘LiFo’) is EPR sensitive and has several advantages [6]. LiFo’s atomic composition is closer to that of water, what makes it more similar to organic tissues, has a higher sensitivity (5–6 times), and a simpler (single line) EPR spectrum than alanine’s. LiFo is receiving considerable attention due to its ability to capture thermal neutrons through the reaction ${}^6\text{Li} + n \rightarrow {}^4\text{He} + {}^3\text{H}$. The cross section for thermal neutrons capture of the ${}^6\text{Li}$ isotope (natural abundance 7.5%) is roughly $2 \cdot 10^4$ times larger than the majority isotope ${}^7\text{Li}$. Thus, the irradiation of LiFo with thermal neutrons produces the emission of alpha particles and tritium atoms which generate paramagnetic defects that could be detected and quantified by EPR [7]. This is relevant for medical applications that use mixed radiation fields of photons and thermal neutrons, as Boron Neutron Capture Therapy (BNCT). An adequate characterization of a BNCT mixed field implies the simultaneous determination of the gamma photon dose and the thermal neutron fluence in a certain position, which is crucial to manage the therapy [8]. A dual dosimeter that would combine the EPR readings of natural Li and ${}^6\text{Li}$ -enriched LiFo was proposed in the past [7]. In this work we investigate the factibility of a L-alanine/LiFo dosimeter without requiring ${}^6\text{Li}$ isotopic enrichment. The γ -doses in our BNCT source go from ~7 Gy to 150 Gy, while the thermal neutron fluences range is $10^{12} - 2 \cdot 10^{13}$ neutrons cm^{-2} . For calibration purposes we used a ${}^{60}\text{Co}$ auxiliary source ranging from 0.1 to 50 kGy γ -doses. We used commercial L-alanine pellets and specially prepared (milling and sieving) natural lithium formate powder samples of specific granulometry, that were irradiated in the ${}^{60}\text{Co}$ irradiation plant (PISI) and in the mixed flux of the BNCT facility (Fig. 1) placed in the RA6 experimental reactor (Bariloche, Argentina). The EPR study of the irradiated samples was performed by determining the intensity of the spectrum relative to a reference standard constituted by Mn^{2+} impurities diluted into a MgO single crystal. As expected, L-alanine has revealed to be largely insensitive to thermal neutrons in the investigated range. On the contrary, the EPR intensity of irradiated natural LiFo powders is clearly sensitive to thermal neutrons and has a linear dependence on the γ -dose (Fig. 2). Based on these results we propose a dual dosimeter by combining L-alanine pellets and LiFo powders that would allow to determine the γ -dose and thermal neutron fluence in a selected position. Moreover, we demonstrate that the ${}^6\text{Li}$ enrichment that has been proposed in the past to enhance the

performance of Li-based EPR dosimeters is not crucial here. The natural isotopic abundance is enough to obtain a satisfactory sensibility to thermal neutrons in our BNCT irradiation facility for fluences $> 10^{12}$ neutrons cm^{-2} . This work was supported by Conicet, ANPCyT and UN Cuyo (Argentina). The technical support from R. Benavides, C. Pérez and M. Guillén is deeply acknowledged.

[1] A. Lund and M. Shiotani, *Applications of EPR in Radiation Research* (Springer) (2014). [2] A. Lund, S. Olsson, M. Bonora et. al., *Spectrochim. Acta A* 58, 1301 (2002). [3] D. F. Regulla and U. Deffner, *Int. J. Appl. Radiat. Isot.* 33, 1101 (1982). [4] www.harwell-dosimeters.co.uk [5] F. Ureña-Núñez, S. Galindo and J. Azorín, *Appl. Radiat. Isot.* 50, 763 (1999). [6] E. Waldeland, J. Helt-Hansen and E. Malinen, *Radiat. Meas.* 46 213 (2011). [7] E. Lund, H. Gustafsson, M. Danilczuk et al., *Spectrochim. Acta A* 60, 1319 (2004). [8] S. Bortolussi, N. Protti, M. Ferrari et al., *Nucl. Instrum. Methods Phys. Res. B* 414, 113 (2018).

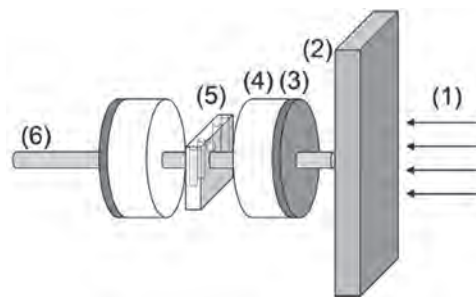


Fig. 1. BNCT irradiation set-up. (1) Incoming neutron–photon radiation (2) Bismuth shield (65 cm diameter) to reduce the gamma photon component. (3) Removable cadmium disc for the absorption of thermal neutrons, 2 cm apart from bismuth shield. The other cadmium disc is fixed. (4) Polyethylene disc for the thermalization of neutrons. (5) Sample holder (10 cm × 5 cm × 1.9 cm), in direct contact with the polyethylene discs (not to scale). It holds four quartz tubes and an alanine monitor at the center. (6) Aluminum rod to hold the discs and the sample holder.

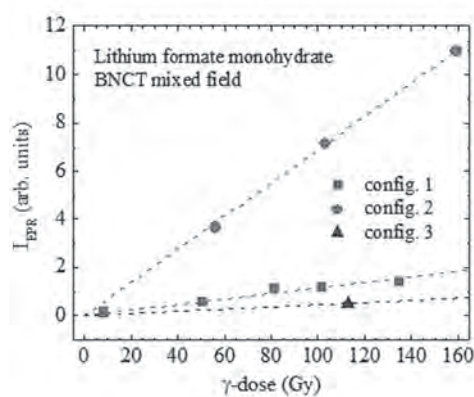


Fig. 2. EPR intensity measured on LiFo samples irradiated at the BNCT facility. Average neutron fluences are 1.75 and 12.6 for configurations #1 and #2 respectively, in units of 10^{12} neutrons cm^{-2} . The triangle corresponds to a LiFo sample irradiated with γ photons at the ${}^{60}\text{Co}$ source. The line for configuration #3 is a straight line passing through the experimental point and the origin of coordinates. The maximum relative uncertainty in the γ -dose is 6%.

INVITED PAPER

JG-12. A Novel Magnetic Respiratory Sensor for Real-Time Tracking of Coronavirus Progress INVITED.K. Hwang¹, V. Jimenez¹, B. Muchharla¹ and M. Phan¹*1. Department of Physics, University of South Florida College of Arts & Sciences, Tampa, FL, United States*

Corona virus 2019 (COVID-19) has already killed more than 1.93 million people around the world, a number which continues to increase daily. This outbreak represents an unprecedented global public health challenge. To limit the spread of COVID-19 and help doctors in clinical decision-making, the detection and real-time monitoring of their symptoms and growth at all (early, intermediate and severe) states is critical. Common symptoms of COVID-19 include: (i) shortness of breath or difficulty breathing, (ii) cough and (iii) fever. Current detectors provide limited information and possess lengthy processing time, or are physically contacted to patients. Therefore, there is an urgent need for developing contactless devices that enable early and fast detection of COVID-19 and track their growth rates in real time. In this study, we have integrated an ultrasensitive magneto-LC resonance (MLCR) sensor technology based on an ultrasoft ferromagnetic microwire [1] with machine learning to develop an innovative, contactless diagnostic device that can sense the breathing symptoms of COVID-19 at multiple stages of disease progress and provide crucial information on the growth rate by patient of this deadly virus. The MLCR sensor can precisely measure and track patients' breathing patterns and respiratory rates in real-time, thus providing efficient screening and monitoring at a clinic or at home. The sensor converts magnetic oscillations generated from a person's breathing into impedance spectra, which allows for a deep analysis of one's breath variation to identify patients being infected by COVID-19 or other types of virus. We add predictive analytics, with the help of machine learning, to provide a good understanding of what can and cannot be said about a patient's health condition status and a possible treatment plan, based on the available data. Actual tests were performed on various subjects. We have demonstrated that the MLCR sensor can track a person's breathing pattern very precisely in real time over the course of multiple states (normal breathing, holding breath, and sleeping). Owing to its ultrahigh sensitivity, the sensor yielded a distinct breathing pattern for each person tested and revealed abnormal breathing, which is superior to existing respiratory monitoring devices. Figure 1 shows how we explored the ultrahigh sensitivity of the MLCR sensor for real-time tracking of a patient's breathing in multiple/complex states from holding breath (Stage 1) to the release of breath (Stage 2) and the return to normal breathing (Stage 3). We have found that when getting older, one usually manifests weaker breathing marked by an increasing breathing rate. He/she tends to hold his/her breath for a shorter period of time and often experiences more with respiratory issues than younger people. People become more relaxed, thus breath more regularly and slowly while sleeping as compared to the wake-up mode. Our highly sensitive magnetic respiratory monitor provides not only valuable information on a patient's current health status, but also a novel breathing control tool for improving our health and physical performance. Finally, we have demonstrated the integration of the MLCR sensor with machine learning for the fast screening and real-time monitoring of COVID-19 progress.

O. Thiabgoh, T. Eggers, and M. H. Phan, A new contactless magneto-LC resonance technology for real time respiratory motion monitoring, *Sensors and Actuators A* 265, 120 (2017)

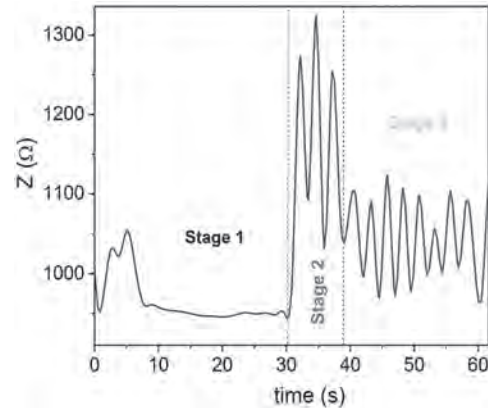


Figure 1. Breathing patterns of a tested subject at three different stages; Stage 1: breath holding, Stage 2: breath releasing, and Stage 3: normal breathing. A detailed analysis of the complex breathing stages provides valuable information on the patient's health status.

Session JH

MAGNETIC PARTICLES, MAGNETIC FLUIDS, AND SEPARATION

Jungjin Park, Co-Chair

University of Maryland at College Park, College park, MD, United States

Oscar Iglesias, Co-Chair

University of Barcelona, Barcelona, Spain

CONTRIBUTED PAPERS

JH-01. High Magnetic Sorting Efficiency in a Microfluidic Device.

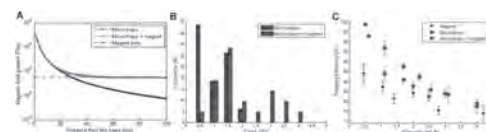
L. Descamps¹, S. Mekkaoui¹, J. Howard¹, M. Audry¹, A. Deman¹ and D. Le Roy²

1. Institut des Nanotechnologies de Lyon, Villeurbanne, France; 2. Institut Lumiere Matiere, Villeurbanne, France

Implementing magnetophoresis in microsystems inspired vivid interest in biomedical applications as it meets a need for trapping and separation methods enabling specific and continuous isolation of biological objects for further analysis. Magnetophoresis, referring to the motion of an object in a magnetic field gradient, is a highly selective and versatile sorting method and, contrary to concurrent methods such as immunoaffinity or dielectrophoresis, it doesn't depend on the medium properties (pH, temperature, ionic strength...). Downscaling the size of the magnetic flux source considerably increases the generated magnetic field gradients generated [1], but inevitably reduces the interaction distance. Therefore integrating micrometric magnetic structures, within a microfluidic system is the best compromise, while offering portable and compact systems. Permanent micro-magnets generate their own stray magnetic field and gradient at remanence state, leading to autonomous systems. However, the fabrication of microscale permanent magnets by conventional thin-film techniques requires a precise control over the shape, size and material microstructure and involves complex and expensive processes. In addition, their implementation in polymer-based devices brings up heterogeneous integration issues. To overcome this technological challenge, we present a simple fabrication process based on NdFeB particle self-ordering in a polymer matrix. The NdFeB@polydimethylsiloxane (PDMS) microstructure was simulated on Comsol® to determine the generated magnetic forces. The calculations were consistent with colloidal probe atomic force microscopy (AFM) measurements and showed magnetic forces up to few nN at contact. In particular, we showed that enhanced magnetic forces could be achieved at large distance by adding an external permanent magnet (25x8x2 mm³). Finally, the micro-magnets were integrated at the bottom of a microfluidic channel and efficient magnetic bead trapping was demonstrated thanks to the beneficial effect of two-scale permanent magnets. The integrated permanent micro-magnet array inside a polymer membrane was obtained using a previously described method [2]. The principle rests on an organized agglomeration of magnetic powder inside a polymer matrix by submitting the composite to an external magnetic field pattern during the polymer reticulation. NdFeB particles organize in chain-like agglomerates characterized by a diameter of 5 μm, a length of 75 μm and an areal density of 1500 agglomerates/mm². The composite membrane was then sealed to a microfluidic channel by O₂ plasma bonding. In addition, magnetic force measurements were conducted by colloidal probe AFM to assess magnetic performances of the permanent micro-magnets. Finally, magnetophoretic trapping ability of the micro-magnets, acting as micro-traps, was demonstrated with 12-μm superparamagnetic beads at increasing flow rates (0.5-4 mL/h). In particular, we investigated the effect of adding an external permanent magnet (25x8x2 mm³) at the bottom of the micro-traps on the system magnetic performances. Magnetic field gradients generated by the NdFeB agglomerates were estimated from numerical simulations (Comsol Multiphysics®) and the effect of an external permanent magnet was studied. As illustrated in Figure 1-A, micro-traps alone generate magnetic gradients as high as 10⁵ T/m at contact, 10⁴ times higher than the gradients produced by the external magnet alone, whereas the external magnet permits to reach higher magnetic gradient values for larger distances from the traps (20 μm). These observations were confirmed by colloidal probe AFM measurements. As shown in Figure 1-B, magnetic forces generated by the micro-magnet at contact are comprised between 0.5 and 2 nN, while adding an external magnet permits to widen the force range to 4 nN, which surpasses forces of several pN usually encountered in microfluidic devices. Finally, the micro-traps were integrated in a microfluidic channel and successful capture of superparamagnetic beads was achieved. Trapping efficiency measurements as a function of flow rate are depicted in Figure 1-C. At 1 mL/h, trapping efficiency reached 75% with the micro-traps and the additional external magnet, while it was 50% and 35%, with the

micro-traps alone and the magnet alone, respectively. Results demonstrate the benefit of combining micrometer-scale and millimeter-scale permanent magnets to enhance magnetic performances. Indeed, the high magnetic force range of the external magnet attracts beads located in the upper part of the channel while the high localized gradients generated by the micro-traps lead to their trapping. We have presented a low-cost and easy-to-handle fabrication process to integrate large density arrays of permanent micro-magnets in a microfluidic system. In particular, we highlighted the beneficial effect of combining two-scale magnetic sources as strong magnetic field gradients are produced by the micro-magnets and large magnetic force ranges are obtained with an additional external magnet. This novel approach could lead to autonomous and compact magnetophoretic trapping devices.

[1] O. Cugat, J. Delamare, and G. Reyne, IEEE Trans. on Magn. 39, 3607-3612 (2003). [2] L. Descamps, S. Mekkaoui, M.-C. Audry, A.-L. Deman and D. Le Roy, AIP Adv., 10, 015215 (2020).



JH-02. Development and Characterization of Magnetically Actuated Milli-Robots by Stereolithography.

B.H. Domac¹, H. Alshammari¹, N. Gunduz Akdogan² and O. Akdogan¹
 1. Bahcesehir Universitesi, Istanbul, Turkey; 2. Piri Reis Universitesi, Istanbul, Turkey

* Corresponding Author: ozan.akdogan@eng.bau.edu.tr Magnetically actuated milli swimmers/robots, especially in biomedical field, are used in many applications such as cargo delivery and sensing applications. In this study, magnetically actuated small-scale swimmers have been developed by using Fe flakes embedded in photocurable polymeric resin. Our future aim will be to merge the developed small-scale swimmers with minimally invasive biomedical applications. The 3D printed structures were fabricated using a photocurable polymeric resin acquired from Wanhao (China). In addition to monomers and oligomers, the chemical composition of this resin includes a photo initiator that responds to a certain wavelength of UV light (405nm) to change the polymerization conformation of the resin into a solid state. Then, structures were printed by using the Anycubic Photon digital light processing (DLP) 3D printer with an exposure time of 10 seconds and a layer thickness of 0.05 mm. Different sizes and shapes of (length of the ship1, ship2 and square, 5.6 mm, 2.7 mm and 0.6mm, respectively) the magnetically actuated swimmers were 3D printed; two ellipsoid shaped swimmers with different sizes and a cubic shaped swimmer. An ellipsoid and cubic shape were chosen for its unique morphology that gives it hydrodynamic superiority over traditional spheres [1]. The combination of polymeric materials such as resins with magnetic particles expand the robot's functionality [2]. The Fe flakes have been previously tested with functional polymer composites for extrusion-based 3D printing [3]. In this study, Fe flakes (100-200nm thickness and ~10µm lateral size) were incorporated into the photocurable resin to actuate robots in response to the magnetic field. The X-Ray Diffraction and vibrating sample magnetometer analysis of Fe flakes showed that Fe flakes have BCC crystal symmetry and soft ferromagnetic response, respectively. (Fig 1a and b). A 0.2 g of Fe flakes and 40 ml of the polymeric resin were mixed to synthesize 0.5% wt/vol concentration. The printed structures were cured by UV light exposure. The incorporated Fe flakes were visualized by a light microscope (Fig.1c, d and e). The movement characteristics of the swimmers in a magnetic field gradient were tested by a homemade electromagnetic setup with a maximum field of 336 Gauss. The 3D printed magnetic structures' movement speed in DI water were calculated experimentally as 12.27±1.89 mm/s, 11.92±1.9mm/s and 8.29±1.5mm/s for milli ship1, milli ship 2 and sub-mm square, respectively. The theoretical swimming speed values were calculated according to the equations below; the magnetic force acting on the robots by a gradient, in which m and B are the magnetic moment and the field, respectively (3) and the drag force (Stoke's Law), in which, η , the viscosity of DI water (8.9×10^{-4} Pa.s), R and v are the hydrodynamic radius and velocity of the objects, respectively (4). $F_m = \nabla (m \cdot B)$ [3] $F_d = 6\pi \eta R v$ [4] Theoretical speeds calculated for milli ship1, milli ship2 and sub-mm square were 13.54 mm/s, 9.9 mm/s and 10 mm/s, respectively. The different shaped milli swimmers were actuated by electromagnetic system and tracked (Fig.2). Magneto-responsive robots movement abilities will be tested against specific obstacles with different shapes and magnetic materials as well. Acknowledgements This work was supported by BAP.2019-03.11(Bahcesehir University).

1. Carrasco, B. et al., Hydrodynamic Properties of Rigid Particles: Comparison of Different Modeling and Computational Procedures., *Biophysical Journal*, 76, 3044–3057, (1999) 2. Song, S. W., Jeong, Y. & Kwon, S., Photocurable polymer nanocomposites for magnetic, optical, and biological applications., *IEEE J. Sel. Top. Quantum Electron.* 21, 324–335, (2015) 3. Zirhli, O. et al. Fabrication and Characterization of Fe16N2 Micro-Flake Powders and Their Extrusion-Based 3D Printing into Permanent Magnet Form., *Adv. Eng. Mater.* 22, (2020) 4. Pankhurst, Q. A. et al., Applications of magnetic nanoparticles in biomedicine., *J. Phys. D. Appl. Phys.* 36, 167-181, (2003) 5. L.D. Landau, I. Akhiezer, M. Lifshitz, Chapter XV-Viscosity, *General Physics*, 341-366, (1967)

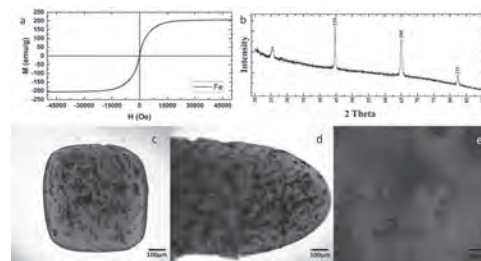


Figure 1. a) VSM and b) XRD analysis of Fe flakes given. Light microscopy image of Fe flakes nanoparticle distribution 3D-printed structures c) Milli square. d) Milli ship. e) Texture of printed structures.

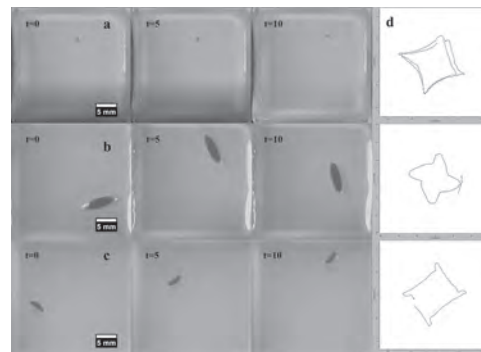


Figure2. The swimming pathway of structures in the DI water are shown in the figure respectively. a) Square, b) Ship 1 and c) Ship 2 (0.6 mm 5.6 mm, 2.7 mm, respectively). d) The swimming trajectory snapshots of robots under the magnetic field.

JH-03. A Study on the Effects of Graphite Flakes on Torque Transmission of a Magnetorheological Fluid Clutch.

M.A. Fernández¹ and J. Chang¹

1. Power Mechanical Engineering, National Tsing Hua University, Hsinchu, Taiwan

The transmittable torque of magnetorheological fluid (MRF) clutches can be adjusted by controlling the magnetic field inside the clutch. In order to increase their maximum transmittable torque while decreasing their volume and mass, geometry optimization is often carried out, such as in [1]. Additionally, the MRF used in them can be designed to have a higher yield stress, resulting in a higher transmittable torque. In [2], this was studied by adding micrometer-sized graphite flakes to an in-house created MRF; it was found that the inclusion of graphite flakes led to an increased yield stress. The present research aims to further study this, by investigating the effects that including graphite flakes in a commercially available MRF may have on the transmittable torque of an MRF clutch. Clutch design. The MRF clutch utilized in this research is a drum-type, permanent magnet-based clutch, made from two concentric cylinders. The external cylinder was fabricated from low carbon steel and the internal cylinder was fabricated from aluminum. A cavity for the MRF is formed between these cylinders, with a width of 0.75 mm. The external cylinder formed the main body of the output stage of the MRF clutch. The magnet assembly used to magnetize the clutch consisted of four magnets which have a hollowed-out cylinder shape when assembled together. These magnets were magnetized in the radial direction, with two of them having their south poles in the outer face, while the other two had them in the inner face. The internal cylinder formed the main body of the input stage of the clutch, driven by a DC motor. A mechanism called field blocker, presented in [3], was used to adjust the magnetization level of the MRF inside the clutch. MRF. A commercially available MRF, the LORD MRF-140CG, was used in this study. Four mixtures with 20 μm graphite flakes (282863, Sigma-Aldrich) were prepared, with a graphite content of 0.5% w/w, 1.0% w/w, 2.0% w/w, and 3.0% w/w. Experimental set-up. The MRF clutch was driven by a velocity-controlled DC motor, and its output stage was connected to one end of a 5 Nm T22 HBM torque meter. A lever was attached to the other end of this torque meter, which contacted the testing bench when rotated in one or the other direction. After contacting the bench, this lever forced the output stage of the MRF clutch to remain stationary while the input stage continued rotating. A stepper motor moved the field blocker in or out of the MRF clutch by means of a ball-screw mechanism, covering and uncovering the magnet assembly. The testing set-up is shown in Figure 1 a). Experimental procedure. The testing of the four MRF mixtures together with the MRF without graphite were carried out the following way: 1) The torque output was measured during one second without driving the clutch and with the lever in a free position. 2) The clutch was then driven at the velocity under test for a duration equal to 2 s plus the time required for the clutch to complete a rotation. 3) The clutch was driven backward at a low angular velocity for one second, in order to leave the lever in a free position. This procedure was repeated three times for each combination of five angular velocities, six field blocker positions, with and without the magnet assembly, for a total of 180 measurements per MRF mixture. The average torque value was calculated from the torque recorded during the second testing step, after the first two seconds had passed. The effects on torque due to seal friction and viscosity on the measured torque values were then removed. Results. The results of these tests are summarized in Table 1, Figure 1 b) and c). In Figure 1 b) and c), the average torque values of the tests carried out with the field blocker not covering and covering the magnets are shown (two out of the six positions tested). The torque values are higher in the case where the magnet assembly is uncovered than when it is covered. It is also seen that the difference in torque caused by the graphite content increases as the input angular velocity increases. Higher magnetization levels decrease the difference in torque (the field blocker does not block the magnetic field entirely). The mean, maximum, and minimum torque values over the six magnetization cases are shown in Table 1. It can be seen that on average, the transmittable torque increases with both graphite content and angular velocity, achieving up to 70% torque increase. Conclusion. The inclusion of graphite flakes in a commercially available MRF can be used to increase the output torque of an MRF clutch, a result which aligns to those

of [2]. This effect in a clutch with aluminum cylinders is more evident at higher angular velocities.

[1] R. M. Andrade, A. B. Filho, C. B. S. Vímieiro, and M. Pinotti, “Optimal design and torque control of an active magnetorheological prosthetic knee,” *Smart Mater. Struct.*, vol. 27, no. 10, p. 105031, 2018. [2] M. K. Thakur and C. Sarkar, “Influence of Graphite Flakes on the Strength of Magnetorheological Fluids at High Temperature and its Rheology,” *IEEE Trans. Magn.*, vol. 56, no. 5, pp. 1–10, 2020. [3] M. A. Fernandez, J. Y. Chang, and C. Y. Huang, “Development of a passive magnetorheological fluid clutch with field-blocking mechanism,” *IEEE Trans. Magn.*, vol. 54, no. 11, pp. 1–5, 2018.

Graphite content (% w/w)	Velocity (rev/s)	Mean (%)	Max (%)	Min (%)
0.5	0.10	7.7	17.1	-1.8
	0.35	12.3	20.4	2.4
	0.60	14.8	21.7	6.8
	0.85	15.8	19.5	10.2
	1.10	15.7	21.1	11.4
1.0	0.10	12.3	24.8	1.2
	0.35	14.0	25.7	2.6
	0.60	17.1	26.2	8.3
	0.85	19.7	26.3	12.4
	1.10	19.8	27.7	13.4
2.0	0.10	4.2	14.6	-6.1
	0.35	19.5	35.9	4.2
	0.60	25.6	41.3	9.2
	0.85	31.8	46.8	17.4
	1.10	35.2	47.1	23.6
3.0	0.10	6.4	21.5	-3.2
	0.35	19.5	43.0	3.0
	0.60	28.1	55.4	7.7
	0.85	35.9	60.3	11.6
	1.10	44.1	70.0	22.7

Table 1. Percentage of the average torque values obtained using MRF with graphite above or below the average torque value obtained with the MRF without graphite.

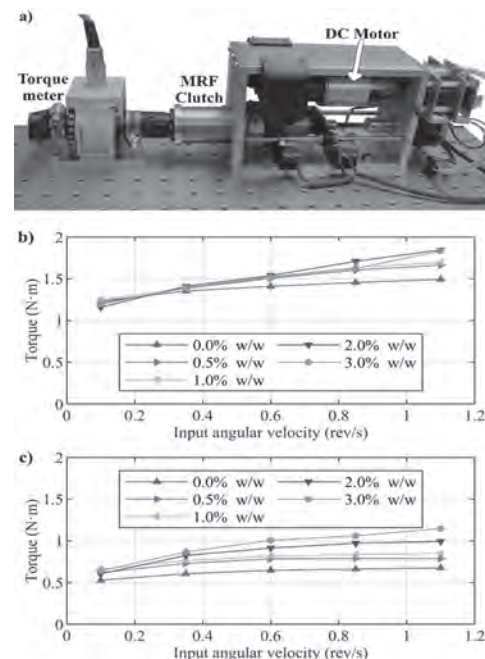


Figure 1. The testing set-up is presented in a). The plotted torque values when the magnet assembly was uncovered and covered are shown in b) and c), respectively.

JH-04. A Novel Sealing Method Using Nano-Micron Magnetic Powders and its Leakage Rate Analysis.

Z. Li¹ and D. Li¹

1. State Key Laboratory of Tribology, Beijing, China

Magnetic fluid sealing is a high-performance sealing technique compared to traditional sealing methods, but is limited to a few working conditions. Here we present a novel sealing method using nano-micron magnetic powders as sealing medium. Nano and micron-sized magnetic particles of different materials and size distribution were prepared and mixed. Packing process of magnetic particles was simulated by DEM. Leakage rate was calculated by Darcy's Law. Finally, the static sealing experiment showed a high pressure resistance and a rather low leakage rate of this novel sealing method.

1. Introduction Sealing with magnetic fluids has been a commonly used high-performance sealing technique with its unique advantages like low friction torque, no leakage and long lifetime. However, it is not capable of resisting high pressure difference or working under extreme temperatures. Magnetic powders are mixture of nano- and micron-sized particles which can be magnetized by an external magnetic field. This research prepared nano-micron magnetic powders of great magnetic and rheological properties. Then the packing process of magnetic powders was simulated and leakage rate was calculated. A static sealing device was designed to test the sealing behavior of this novel sealing method. 2. Methods 2.1 Preparation of magnetic powders Chemical precipitation was used to prepared magnetic nanoparticles. Experimental conditions were adjusted to acquire nanoparticles of different materials, sizes and magnetic intensity. Micron particles were prepared by high-energy ball milling method. Surfactants were coated on particles to control the interparticle forces. 2.2 Simulation of packing process Interparticle forces of magnetic particles are complex and so is the packing process of magnetic powders. In this research, packing process of nano-micron magnetic powders was simulated by DEM using Hertzian-Mindlin model with JKR. Fraction, sizes, magnetization and surfactants of powder preparation, leads to changes of interparticle forces, especially cohesive and magnetic forces. Magnetic particles follow the basic equation: $m_i dv_i(t)/dt = m_i g + F_{i,d}(t) + F_{i,c}(t) + F_{i,m}(t)$ $v_i(t)$ is the i th particle's velocity at time t ; $F_{i,d}(t)$, $F_{i,c}(t)$, $F_{i,m}(t)$ are the total drag force, net contact force and magnetic force of the i th particle, respectively. 2.3 Calculation of leakage rate by Darcy's Law Darcy's law is commonly used to describe the flow of a fluid through a porous medium. We established a microscopic model to estimate the permeability for calculation of leakage rate of the sealing device. The permeability κ is calculated by the equation: $\kappa = \mu \dot{U} h / \Delta p$ μ is the fluid viscosity; \dot{U} is the outlet velocity; h is the computational zone height; Δp is the pressure difference. 2.4 Design and experiments of static sealing device A static sealing device was designed, where magnetic field distribution was simulated to maximize the magnetic flux density in the sealing gap. For each magnetic powder example, sealing capacity and leakage rate were measured. 2.5 Results The simulation results showed that the permeability decreased rapidly with the decrease of particle sizes, and appropriate mixture of nano- and micron-sized particles further decreased the permeability. For the powders prepared, the permeability could be as low as $5.09E-18 \text{ m}^2$. Considering the size of the sealing device, the calculated leakage rate was $2.22E-9 \text{ m}^3/\text{s}$. Experiments indicated a sealing capacity $\geq 0.5 \text{ MPa}$ and leakage rate $\leq 1E-6 \text{ Pa} \times \text{m}^3/(\text{s} \times \text{cm})$. 3. Discussion By selecting magnetic materials, mixture of particles of different sizes and coating particles with surfactants, nano-micron magnetic powders can possess great magnetic and rheological properties. Proper size distribution and interparticle forces lead to a denser packing of magnetic powders. Further, a denser packing leads to a rather low leakage rate, which is verified by both simulation and sealing experiments. A novel sealing method using nano-micron magnetic powders shows distinctive property and may be a promising sealing technique.

[1] J. Kafashan, J. Wiacek and N. Abd Rahman, *Granular Matter*, Vol. 21, p.80 (2019) [2] R.A. Sperling, W.J. Parak, *Philosophical Transactions of the Royal Society A: Mathematical, Physical and Engineering Sciences*, Vol. 368, p.1333-1383 (2010) [3] M. Neouze, U. Schubert, *Monatshefte für Chemie - Chemical Monthly*, Vol. 139, p.183-195 (2008) [4] R. About Hosn, L. Sibille and N. Benahmed, *Computers and Geotechnics*, Vol. 95, p.30-39(2018) [5] K. Chen, Y. Tian and L. Shan, *Smart Materials and Structures*, Vol. 22, p.97001 (2013)



Fig.1 Prepared magnetic powders

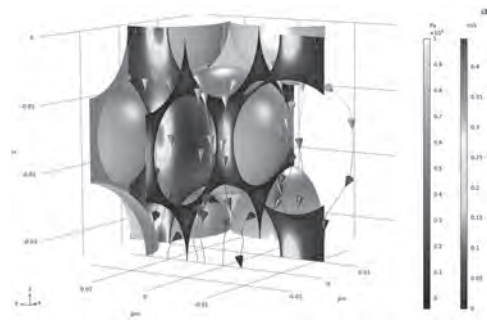


Fig.2 A microscopic model to calculate permeability

JH-05. A Novel Magnetofluidic System to Cool Solar Cells.

V.B. Varma^{1,2}, S. Cheekati^{1,2}, M.S. Pattanaik^{1,2} and R. Ramanujan^{1,2}

1. School of Materials Science and Engineering, Nanyang Technological University, Singapore, Singapore; 2. Singapore-HUJ Alliance for Research and Enterprise (SHARE), Nanomaterials for Energy and Energy-Water Nexus (NEW), Campus for Research Excellence And Technological Enterprise, Singapore, Singapore

Magnetofluidic cooling (MFC) is a heat transfer technology to transfer heat using thermomagnetic convection (TMC) of a ferrofluid[1, 2]. The temperature-dependent response of the ferrofluid leads to TMC[2] under the combined effect of thermal and magnetic field gradients. Practical applications require application-specific device design and materials. Solar cells can exhibit significant performance degradation with increasing temperature[3]. Methods reported for cooling, e.g., forced water/air circulation, water spraying, floating tracking concentrating, phase-change materials, and water immersion, show several limitations[4]. Here, we report a novel MFC device for the cooling of solar cells. We first developed a simulation model to investigate the ferrofluid flow needed to cool solar cells. Studying the effect of magnetic field strength, field distribution, channel size, and hydrodynamic properties of the fluid resulted in a novel design (Figure 1). We developed a novel ferrofluid and integrated it with our MFC system. We then built a setup for quantitative measurements of the solar cell performance. As expected, the solar cells showed decreasing performance with increasing temperature without MFC. On the other hand, with MFC (yellow band regions in Figure 2), we observed significant performance improvement. Interestingly, the MFC device demonstrated a higher relative performance enhancement at higher initial solar cell temperatures due to the self-regulating behavior of the MFC device. Hence, the current MFC system offers a novel, versatile, green, energy-efficient, environmentally friendly, noise-free, and vibration-free approach for passive cooling of solar cells. Acknowledgments This research is supported by grants from the National Research Foundation, Prime Minister’s Office, Singapore, under its Campus of Research Excellence and Technological Enterprise (CREATE) programme.

[1] V. B. Varma, M. S. Pattanaik, S. K. Cheekati, and R. V. Ramanujan, “Superior cooling performance of a single channel hybrid magnetofluidic cooling device,” *Energy Convers. Manage.*, vol. 223, p. 113465, 2020. [2] M. S. Pattanaik, V. B. Varma, S. K. Cheekati, G. Prasanna, N. M. Sudharsan, and R. V. Ramanujan, “A self-regulating multi-torus magneto-fluidic device for kilowatt level cooling,” *Energy Convers. Manage.*, vol. 198, p. 111819, 2019. [3] P. Singh and N. M. Ravindra, “Temperature dependence of solar cell performance—an analysis,” *Sol. Energy Mater. Sol. Cells*, vol. 101, pp. 36-45, 2012. [4] J. Siecker, K. Kusakana, and B. Numbi, “A review of solar photovoltaic systems cooling technologies,” *Renewable Sustainable Energy Rev.*, vol. 79, pp. 192-203, 2017.

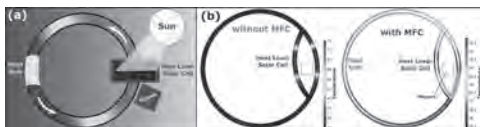


Figure 1: (a) Schematic of the application-specific MFC device for Solar cell cooling. (b) Numerical simulations of the MFC device showing temperature profile with and without MFC.

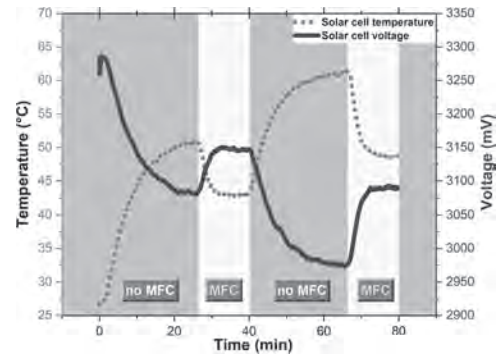


Figure 2: Solar cells surface temperature and generated voltage with and without magnetofluidic cooling (MFC). Yellow bands denote the MFC of the solar cell under an applied magnetic field of 550 mT. Gray bands show the performance without MFC.

JH-06. Magnetic Manipulation of Hydrogel Droplets in Culture Media for Biological Applications.

S. Yuan¹, A. Shum² and P. Pong^{3,1}

1. Department of Electrical and Electronic Engineering, University of Hong Kong, Hong Kong; 2. Department of Mechanical Engineering, University of Hong Kong, Hong Kong; 3. Department of Electrical and Computer Engineering, New Jersey Institute of Technology, Newark, NJ, United States

Introduction The manipulation of cell laden droplets in the bulk culture media is essential for precise analysis and screening of cells, drugs, or other biological objects, which can lead to various applications. With the rapid growth of microfluidic technology, the physical and chemical properties of the droplets can be controlled much more uniformly. This breakthrough leads to more targeted manipulation and handling of the cell-laden objects. Different methods have been proposed using electrical, optical, or magnetic principles [1]. Among all these methods, magnetic force manipulation is of great interests because it is non-contact, non-thermal, and insensitive to the dielectric properties [2]. The manipulation of magnetic and non-magnetic objects with magnetic fields in various applications have been studied [3]. However, most studies focused on the handling on a single nanoparticle. Little work has been done regarding the tweezing of particle with microscale diameter. Besides, the kinematics mechanism underlying the manipulation of magnetic objects is still not fully studied. This work aimed at developing a platform that can generate and manipulate magnetic-nanoparticle-laden hydrogel droplets with more controllable manner. The relation between the magnetic force and the behavior of hydrogel droplets was also studied. This work can provide more in-depth understanding of the coupling between magnetic force and fluidic mechanics in handling microfluidic droplets, which can be a guideline in designing magneto-microfluidic platforms for biological applications. **Experiments** The hydrogel droplets were generated using a microfluidic platform following standard processes [3]. The fabrication of the microfluidic device followed typical soft lithography replica molding technique, by using maskless photolithography and PDMS prepolymer curing [4]. Superparamagnetic nanoparticles (DynaBeads Myone Carboxylic Acid, Purchased from ThermoFisher) was added into the hydrogel solution and mixed completely before the generation of the droplets. The magnetic beads were used as the medium to respond to the external magnetic field; thus the hydrogel droplets can be manipulated remotely. The flow rates of the oil (HFE 7500) and hydrogel solution were carefully adjusted to generate droplets with desired diameter, about 55 μm . The generation of the hydrogel droplet is illustrated in Fig. 1a. After the droplets were solidified with fixed shape, the droplets were released into cell culture media, as shown in Fig. 1b. An external magnetic field was exerted using an electromagnet to manipulate the magnetic-nanoparticle-laden hydrogel droplets within the culture media. The magnetic field could be controlled by adjusting the current of the DC power source. The magnetic manipulation setup and the movement of hydrogel droplets in the culture media are shown in Fig. 1c, Fig. 1d and Fig. 1e. **Results and discussion** The microfluidic device was successfully fabricated, and the magnetic-nanoparticle-laden hydrogel droplets were generated using the droplet microfluidic platform. The diameter of the droplet was approximately 55 μm , which is suitable for cell encapsulation and other biological applications. After the hydrogel droplets were released into cell culture media, an external magnetic field was exerted to manipulate the droplets. The results showed that the droplets could be moved in the culture media through magnetic force (Fig. 2a and Fig. 2b). By adopting superparamagnetic nanoparticles, the droplets could be moved rapidly, at a speed of 200 $\mu\text{m/s}$, as shown in Fig. 2c). Since there is no remanence in the superparamagnetic nanoparticles after each manipulation, the hydrogel droplets could be manipulated for several times as desired, which is also favorable for biological applications in which multiple steps are required. In the experiments, the droplets sank to the bottom after 5 min, due to the higher density of the hydrogel droplets relative to water. The moving speed of the hydrogel droplet was much slower than when the droplets were suspended in the media. A detailed kinetics analysis of the movement of hydrogel droplets will be addressed in the full paper.

References [1] Yi, Changqing, et al. "Microfluidics technology for manipulation and analysis of biological cells." *Analytica chimica acta* 560.1-2 (2006): 1-23. [2] Pamme, Nicole. "Magnetism and microfluidics." *Lab on a Chip* 6.1 (2006): 24-38. [3] Utech, Stefanie, et al. "Microfluidic generation of monodisperse, structurally homogeneous alginate microgels for cell encapsulation and 3D cell culture." *Advanced healthcare materials* 4.11 (2015): 1628-1633. [4] Nan, Lang, et al. "Oil-mediated high-throughput generation and sorting of water-in-water droplets." *Microsystems & Nanoengineering* 6.1 (2020): 1-10. **Acknowledgements** Yuan Shuai and Prof. Shum provided the idea. Yuan Shuai did the experiments in Microfluidics and Soft Matter Group, the University of Hong Kong. Yuan Shuai composed the paper. Prof. Shum and Dr. Pong directed the project and revised the paper. **Information of the authors:** Shuai Yuan is with the Department of Electrical and Electronic Engineering, The University of Hong Kong, Hong Kong (ysthoth@connect.hku.hk). Anderson H. C. Shum is with the Department of Mechanical Engineering, The University of Hong Kong, Hong Kong (ashum@hku.hk). Philip W. T. Pong is with the Department of Electrical and Computer Engineering, New Jersey Institute of Technology, and the Department of Electrical and Electronic Engineering, The University of Hong Kong (philip.pong@njit.edu).

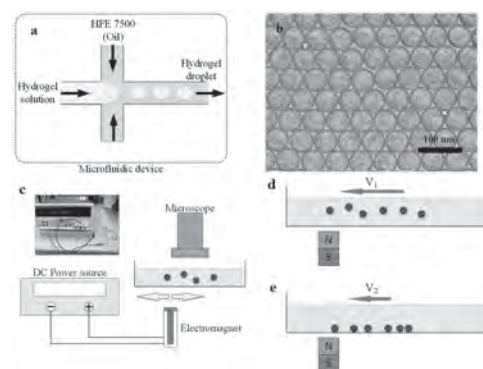


Fig. 1. a) Generation of magnetic nanoparticle laden hydrogel droplets using microfluidic platform, b) Release of the hydrogel droplets into the cell culture media. c) Setup of the magnetic manipulation platform. d) Illustration of the movement of hydrogel droplets suspended in the culture media in response to the external magnetic field. e) Movement of hydrogel droplets that sank to the bottom.

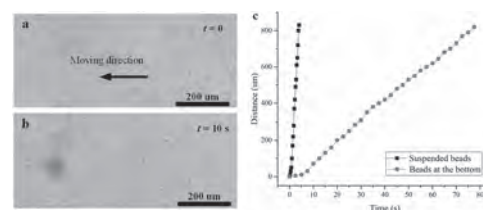


Fig. 2. a) and b) Movement of the magnetic-nanoparticle-laden hydrogel droplets under magnetic field. The hydrogel droplets at the bottom of the Petri dish moved much more slowly than the floating droplets. c) Moving speed of the suspended and sank hydrogel droplets, respectively. The measurement of the suspended droplets stopped at 5 s because the droplets moved outside the scope.

JH-07. Crucial Role of the Co Cations on the Destabilization of the Ferrimagnetic Alignment in Co-Ferrite Nanoparticles With Tunable Structural Defects.

C. Moya^{1,2}, A. Fraile Rodríguez¹, M. Escoda-Torroella¹, M. García del Muro¹, S.R. Avula³, C. Piamonteze³, X. Batlle¹ and A. Labarta¹

1. *Física de la Matèria Condensada, Institut de Nanociència i Nanotecnologia (IN2UB), Universitat de Barcelona, Universitat de Barcelona, Barcelona, Catalunya, ES, academic, Barcelona, Spain;*
 2. *Engineering of Molecular Nanosystems, Universite Libre de Bruxelles, Bruxelles, Belgium;*
 3. *Swiss Light Source, Paul Scherrer Institut, Villigen, Switzerland*

Cobalt ferrite nanoparticles (NPs) are competitive candidates in nanomedicine and biomedical applications, especially in the fields of magnetic drug delivery, magnetic resonance imaging, and separation and detection of biomolecules [1,2]. The reason behind is a suitable combination of excellent chemical and magnetic characteristics, such as a high chemical stability, surface active sites, and ease of synthesis and functionalization, together with a high anisotropy constant, a high coercivity, and a moderate saturation magnetization. However, in order to control the functional response of cobalt ferrite NPs, one of the biggest challenges is to quantitatively disentangle the dependence of the composition, structure, or surface chemistry onto the overall magnetic response. In this study we unravel the key role played by the Co^{2+} cations on the destabilization of the collinear ferrimagnetism in cobalt ferrite NPs, by combining an advanced synthesis approach with a broad set of world-class complementary local probes. A set of samples of monodispersed, 8 nm cobalt ferrite NPs of identical stoichiometry but with a progressive inclusion of structural defects was prepared [3,4]. SQUID magnetometry results show a rapid degradation of the collinear ferrimagnetism as the structural disorder increases within the NPs, and even samples that are almost free from crystallographic defects exhibit relatively large values of the high-field susceptibility suggesting the occurrence of canting at least for some of the cations and sites [5]. As local characterization probes, synchrotron-based, element-, valence- and site- specific X-ray spectroscopy and magnetometry on ensembles of NPs was combined with high resolution transmission electron microscopy of selected, individual NP (Fig. 1) [5]. The analysis of element-specific X-Ray Magnetic Circular Dichroism (XMCD) spectra and hysteresis loops for all cationic sites reveals that the collinear alignment of the Co^{2+} cations in octahedral sites is significantly more affected by the structural disorder than in any other cation. This is because structural defects cause local distortions of the crystal field acting on the orbital component of the cations, yielding effective local anisotropy axes that cause a prevalent Co^{2+} spin canting through the spin-orbit coupling, owing to the relatively large value of the partially unquenched moment of these cations, as found by XMCD. As the number of structural defects increases, the rest of the cations are progressively dragged off the ferrimagnetic alignment, being the Fe^{3+} cations in tetrahedral sites the last ones to be affected by the disorder because the canting takes place first in octahedral sites thanks to their smaller number of next-nearest neighbors in the tetrahedral sublattice [5]. Our results demonstrate the key role of the Co^{2+} cations on the destabilization of the collinear ferrimagnetism in Co-ferrite NPs as their crystalline quality worsens and may help clarify the often conflicting, large variability of magnetic properties in the literature of Co-ferrite NPs with slightly different structural features. Our work may provide new avenues to interpret and control the functional response of Co-ferrite NPs, of relevance in the fields of rare-earth free permanent magnets, biological separation and detection, or nanomedicine. Acknowledgements The work was supported by Spanish MCIU and AEI (MAT2015-68772-P; PGC2018-097789-B-I00) and European Union FEDER funds. M.E.T. acknowledges Spanish MINECO for the Ph.D. contract BES-2016-077527. A.F.R. and C.M. acknowledge the financial support from the EU CALIPSO Transnational Access programme. Part of this work was performed at the Swiss Light Source, Paul Scherrer Institut, Switzerland. The measurements at FEI TITAN3 of the Laboratorio de Microscopias Avanzadas (LMA), Instituto de Nanociencia de Aragon (INA), Universidad de Zaragoza, are also gratefully acknowledged. S.R.V.A. thanks the Swiss National Science Foundation for financial support under project Nr. 169467.

[1] S. Y. Srinivasan, K.M. Paknikar, D. Bodas, et al. Applications of Cobalt Ferrite Nanoparticles in Biomedical Nanotechnology. *Nanomedicine*. Future Medicine Ltd. May 2018, pp 1221–1238. <https://doi.org/10.2217/nmm-2017-0379>. [2] S. Amiri, H. Shokrollahi, The Role of Cobalt Ferrite Magnetic Nanoparticles in Medical Science. *Materials Science and Engineering C*. Elsevier January 2013, pp 1–8. <https://doi.org/10.1016/j.msec.2012.09.003>. [3] C. Moya, M. D. P. Morales, X. Batlle, A. Labarta, *Phys. Chem. Chem. Phys.* 17, 13143 (2015). [4] C. Moya, G. Salas, M. D. P. Morales, et al. *J. Mater. Chem. C* 3, 4522 (2015). [5] C. Moya, A. Fraile Rodríguez, M. Escoda-Torroella, et al., *J. Phys. Chem. C* (2020) (in press). <https://dx.doi.org/10.1021/acs.jpcc.0c06657>.

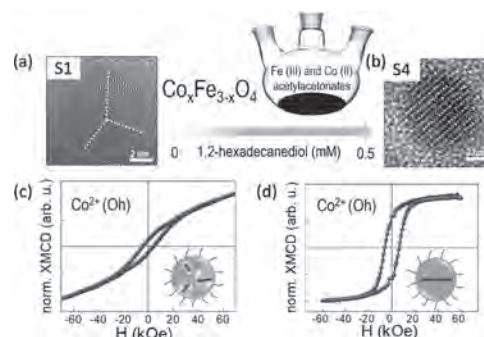


Fig. 1. Monodisperse samples of 8 nm NPs with a tunable amount of structural defects prepared by thermal decomposition of Fe(III) and Co(II) acetylacetonates with a variable concentration of 1,2-hexadecanediol. HRTEM images and element-specific XMCD loops of the Co^{2+} cations corresponding to highly defective (a, c) and highly crystalline nanoparticles (b, d).

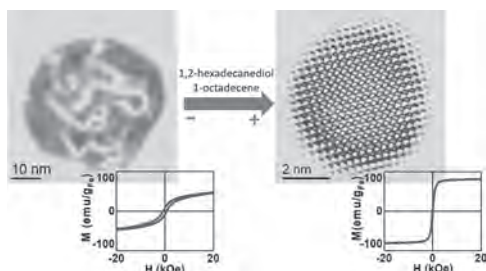
JH-08. Selective Control of Reagents as a Tuning Knob for Iron Oxide Nanoparticles With Controlled Morphology, Oxidation State and Magnetic Response.

M. Escoda-Torroella^{1,2}, C. Moya^{2,3}, A. Fraile Rodríguez^{1,2}, X. Batlle^{1,2} and A. Labarta^{1,2}

1. Física de la Matèria Condensada, Universitat de Barcelona, Barcelona, Spain; 2. Institut de Nanociència i Nanotecnologia, Universitat de Barcelona, Barcelona, Spain; 3. Engineering of Molecular Nanosystems, Université Libre de Bruxelles, Bruxelles, Belgium

Iron oxide nanoparticles (NPs) have attracted a great attention for biomedical and environmental applications due to their good biocompatibility and magnetic performance. The control over the crystal structure and oxidation state are of paramount importance to optimize their properties [1, 2]. In this work we studied the effect of the amount of both 1,2-hexadecanediol and the solvent 1-octadecene on the thermal decomposition method with iron (III) acetylacetonate. On the one hand, a higher amount of one of the reagents gives rise to single-phase, single-crystal Fe₃O₄ NPs with diameters below 10 nm and narrow size distributions but with moderate reaction yields. On the other hand, low amounts of either of the two reagents result in large NPs containing both Fe₃O₄ and FeO phases but with high values of the reaction yield. Consequently, the samples exhibited two distinct magnetic behaviors depending on the amount of these two reagents. The hysteresis loops at room temperature for the small NPs showed the typical features of superparamagnetism: values of the saturation magnetization close to the bulk one for magnetite with no coercive field. On the contrary, larger NPs showed ferrimagnetic behavior with reduced values of the saturation magnetization, as well as shifted hysteresis loops at 5 K after field cooling the sample at 1 T. Zero-field cooling-field cooling (ZFC-FC) curves below 200 K for the small NPs exhibited a peak below room temperature corresponding to the blocking temperature, while those curves for the larger particles displayed two peaks at higher temperatures which can be associated with the Verwey and Neel transitions of magnetite and wüstite phases, respectively. This shows the biphasic nature of the large NPs. With this accurate monitoring of the reaction conditions we have added an extra level of optimization to the synthesis of these NPs. In particular, we have found that, for 1 mmol of iron (III) acetylacetonate, the minimum amounts of 1,2-hexadecanediol and 1-octadecene for the preparation of monophasic, single-crystalline Fe₃O₄ NPs are 2.5 mmol and 5 mL, respectively. This allows us to tune the properties of each sample of iron oxide NPs to its specific application. [3] Acknowledgements The work was supported by Spanish MCIU and AEI (MAT2015-68772-P; PGC2018-097789-B-I00) and European Union FEDER funds. M.E-T. acknowledge Spanish MCIU for BES-2016-077527.

[1] A. Fraile Rodríguez, C. Moya, M. Escoda-Torroella, A. Romero, A. Labarta and X. Batlle. *J. Mater. Chem. C*, 6, 4, 875–882 (2018). [2] C. Moya, M. P. Morales, X. Batlle and A. Labarta. *Phys. Chem. Chem. Phys.*, 17, 19, 13143–13149 (2015). [3] M. Escoda-Torroella, C. Moya, A. Fraile Rodríguez, X. Batlle and A. Labarta. *Langmuir* (2020) doi.org/10.1021/acs.langmuir.0c02221



Colored HRTEM images of two samples synthesized with increasing amounts of 1,2-hexadecanediol and 1-octadecene and their respective magnetization curves, showing the correlation between low amount of both reagents and a defective crystal structure and a poorer magnetic behavior.

JH-09. Tailored Magnetic Field Sequences for Improved Magnetic Nanoparticle Characterization and Imaging.

A. Coene^{1,2} and J. Leliaert³

1. Department of Electromechanical, Systems and Metal Engineering, Universiteit Gent, Gent, Belgium; 2. Cancer Research Institute, Universiteit Gent, Gent, Belgium; 3. Department of solid state sciences, Universiteit Gent, Gent, Belgium

Magnetic nanoparticles (MNPs) exhibit many properties that make them very useful in a broad range of biomedical applications [1]. For example, their small size allows them to reach virtually every region in the human body and to directly interact with various biological entities such as viruses and cells. By attaching so-called biomarkers to the MNPs they can bind with specific entities, useful in disease detection. When the particles act as medicine carriers, this is referred to as magnetic drug targeting in which they are guided to specific sites in the human body through the application of magnetic field gradients. Medicine release can be done by using external stimuli such as pH and temperature changes. Another biomedical application is magnetic hyperthermia in which the MNPs are exposed to specific time-dependent magnetic fields that result in the heating of the MNPs. By bringing the particles towards malignant tissues targeted destruction can be achieved, while sparing the healthy tissues. In order for previous applications to be safe and efficient, accurate characterization and localization of the MNPs are required. For instance, the generated heat in magnetic hyperthermia experiments critically depends on the chosen frequency of the applied magnetic fields, which is associated with the particles' sizes. Moreover, the particles' coercivity values determine their ability to heat up at that specific frequency. Current magnetic characterization techniques require the use of *a priori* assumptions or complex postprocessing procedures which make an accurate determination of particle size very hard. Additionally, it is not straightforward to find the particles' coercivity values because a coercivity measurement is often performed on immobilized particles, while in most applications, the particles are suspended in a liquid, resulting in coercivity values that do not reflect reality. Another issue is that the coercivity of the MNPs also depends on the nanoparticle size, which results in the coercivity values being averaged out over the size distribution of the sample. Therefore, several samples typically need to be prepared in order to analyze the coercivity values. In this digest, an innovative magnetic field sequence is introduced that allows to directly determine the size distribution and magnetic coercivity of magnetic nanoparticles without the disadvantages mentioned before [2]. This is accomplished by exploiting the interplay between the magnetic and rotational dynamics of the MNPs, through the application of specific magnetic fields, so only particles with a specific coercivity are excited by the applied field. Once the field is removed, a decaying magnetic signal originating from the excited MNPs, similar as in magneto-relaxometry (MRX) [3], can be measured using sensitive sensors such as SQUIDs, fluxgates, or optical magnetometers. The difference with 'traditional' MRX is that only a subset of the particles, those having a specific coercivity value, will be captured in the decaying signal. From this decaying signal, the particle size associated with the specific coercivity can be determined. By changing the properties of the applied magnetic field, the selected particle coercivity, and therefore associated size, can be shifted, resulting in a series of measurements that intrinsically contain particle size information without the need to decompose the resulting measurement data in size-dependent functions in postprocessing. Figure 1 depicts an overview of the presented technique for a MNP sample consisting of three MNP types. In this case, three AC magnetic field pulses are applied each exciting a specific subset of particle types. By subtracting subsequent measurement signals (e.g. the measurements in panels c and b), particle types with a specific coercivity can be excited and their associated size determined. Additionally, the presented magnetic field sequences are also of value for MNP imaging as they allow to selectively excite specific particle types. This way functional imaging using MNPs can be realized as environmental changes such as differences in temperature, viscosity, and inter-particle reactions can be directly mapped to a specific color, referred to as multi-color/multi-contrast imaging. Previously, complex procedures in multi-color MRX were required to allow the decomposition of the measurement signal into its constituting colors [4]. The developed technique advances current magnetic nanoparticle

characterization possibilities and opens up exciting pathways for biomedical applications and particle imaging procedures.

[1] Q. Pankhurst, et al., J. Phys. D Appl. Phys., Vol. 36, p.R167–R181 (2003) [2] A. Coene and J. Leliaert, Sensors., Vol. 20, p.3882 (2020) [3] F. Ludwig, et al., Rev. Sci. Instrum., Vol. 76, p.106102 (2005) [4] A. Coene, et al., Phys. Med. Biol., Vol. 62, p.3139 (2017)

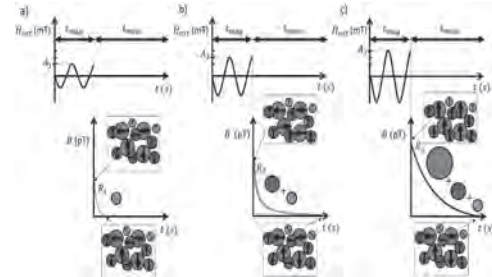


Fig. 1. Overview of the technique for the specific case of a sample consisting of 3 MNP types. a) First the sample is exposed to an AC magnetic field pulse of amplitude A_1 for a duration of t_{mag} . Only particles with a coercivity lower than the pulse amplitude will align themselves to the pulse (see the inset at the end of the pulse). In this example, only the first particle type (in green) fulfills the requirement. When the pulse is removed, a decaying magnetic signal will be observed which is measured for a duration of t_{meas} , as the particles of the first type relax towards a random orientation again (second subset at the end of the measurement). b) Next, a second pulse is applied with amplitude A_2 , which excites the first and second MNP type (in blue). Hence, the decaying signal contains the response of both particle types. c) Finally, a pulse with amplitude A_3 is generated that evokes a decaying signal of all MNP types. Reprinted from [2].

JH-10. Time-Dependent AC Magnetometry of Magnetite Nanoparticles in the Monodomain-Multidomain Limit.

I. Morales Casero¹, P. de la Presa^{1,2}, N. Mille^{3,4}, J. Carrey^{3,4}, P. Morales^{5,6} and A. Hernando¹

1. Universidad Complutense de Madrid Instituto de Magnetismo Aplicado, Madrid, Spain; 2. Departamento de Materiales, Universidad Complutense de Madrid Facultad de Ciencias Físicas, Madrid, Spain; 3. Laboratoire de Physique et Chimie des Nano-objets, Toulouse, France; 4. INSA Toulouse, Toulouse, France; 5. Instituto de Ciencia de Materiales de Madrid, Madrid, Spain; 6. Consejo Superior de Investigaciones Científicas, Madrid, Spain

The heating ability of magnetic nanoparticles when subjected to alternating magnetic fields is a topic of interest for biomedical applications, as in the case of magnetic hyperthermia, and more recently in the area of induction heating in heterogeneous catalysis [1-2]. In particular, AC magnetometry stands out as a powerful technique to study the dynamic hysteresis loops of the nanoparticles in the desired medium and to quantify their heating efficiency, which is proportional to the area of the cycles. When properly calibrated, this device provides more accurate and reproducible measurements than the most widespread calorimetric method, giving also information about the magnetic properties of the system such as the coercive field, magnetization saturation and susceptibility. The study of the dynamic behaviour of systems of magnetic nanoparticles under radiofrequency fields is still being investigated both experimentally and theoretically [3-5], in particular the influence of nanoparticle dipolar interactions and chain formation, due to the huge increase in the heating efficiency reported in the literature. In this work, we perform an experimental systematic study of three samples of magnetite with sizes of 12 nm, 30 nm and 50 nm as a function of the applied field, the initial temperature of the sample and of the acquisition time. Time-dependent high-frequency hysteresis loop measurements are presented, showing that, in some cases, the hysteresis strongly depends on the acquisition time of the cycle, effect that can be associated to the chain formation. In the case of the 30 nm sample, there is a strong dependence of the hysteresis cycle shape with the acquisition time, increasing the area as well as the susceptibility as the acquisition time increases; whereas the 50 nm nanoparticles show always the same hysteresis cycles independently of the acquisition time (see Fig. 1). This effect is associated to the time required for the chain formation. Similar results have been already observed by Asensio et al., in iron carbide nanoparticles [1].

[1] J.M. Asensio, et al., *Nanoscale.*, Vol. 11(12), p.5402-5411 (2019) [2] B. Rivas-Murias, et al., *Angewandte Chemie.*, Vol. 132(36), p.15667-15672 (2020) [3] I. Morales, et al., *Nanomaterials.*, Vol. 8(12), p.970 (2018) [4] I. Rodrigo, I. Castellanos-Rubio, E. Garaio, et al., *International Journal of Hyperthermia.*, Vol. 31(1), p.976-991 (2020) [5] D.P. Valdés, E. Lima Jr, R.D. Zysler, E. De Biasi, *Physical Review Applied.*, Vol. 14, p.014-023 (2020)

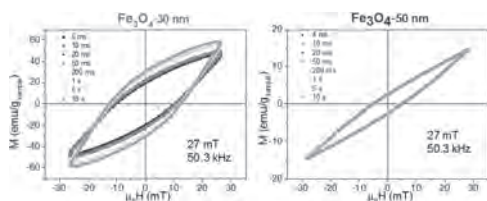


Fig. 1. Evolution of the cycles as a function of the acquisition time between 5 ms and 10 s, for an applied field of 27 mT and 50.3 kHz.

JH-11. Chain Formation of PNIPAM Coated Magnetic Nanoparticles in an External Magnetic Field and the Effect of Temperature.

N. Taib^{1,2}, R. Woodward³, K. Iyer⁴ and T. St. Pierre²

1. Faculty of Applied Sciences, Perak Branch, Tapah Campus, 35400, Universiti Teknologi MARA, Tapah Road, Malaysia; 2. School of Physics, Mathematics, and Computing, The University of Western Australia, Perth, WA, Australia; 3. John Forrest Secondary College, Morley, WA, Australia; 4. School of Molecular Sciences, The University of Western Australia, Perth, WA, Australia

Over the past decade, magnetic field-induced self-assembly of magnetic inorganic nanoparticles has been studied extensively for particles having different sizes and compositions. However, relatively little attention has been devoted to how the surface chemistry of polymer nanoparticles affects their self-assembly properties. Self-assembly of nanoparticles becomes more important because novel collective and exceptional properties can be produced in the ordered array of nanoparticles [1-3]. More recently, methods using external fields such as magnetic fields have emerged as key methods to direct the assembly of inorganic nanoparticles effectively [4, 5]. In this work, we present the first direct observation of polymer nanoparticle chain formation in a magnetic field based on temperature induced surface properties of the PNIPAM layer. The colloidally stable PNIPAM coated Iron Oxide Nanoparticles were successfully synthesized by using 7-nm magnetic iron oxide nanoparticles embedded in a PNIPAM-g-PGMA shell. This temperature responsive polymer (PNIPAM-g-PGMA) was synthesized by a simple polymerization reaction at 80 °C involving the anchoring of poly(N-isopropylacrylamide) (PNIPAM) chains onto the surface of poly(glycidyl methacrylate) (PGMA). The PGMA was used because it has been explicitly shown to have the epoxide functional groups groups [6] located in the loops and tails of the core macromolecule. This work was concerned with the capability of thermoresponsive polymer nanoparticles forming chains in an external magnetic field at 25 °C and 45 °C. Chain length and width information was measured using SEM and TEM. The time-series experiment performed enabled the measurement of proton transverse relaxation rates with the magnitude of the fractional reduction in R_2 being observed to decrease as the concentration of iron in polymer nanoparticles decreased for both temperatures. At 45 °C, we obtained more nanosized chain-like structures of PNIPAM-g-PGMA-NPs, which contain wider and longer chain-like substructures, owing to the hydrophobic properties of PNIPAM chain as shown in Fig. 1 (c). It is important to note that the magnetic properties of all the synthesized nanoparticles presented as superparamagnetic even after the surface was coated with PNIPAM- PGMA. The relevance of this work is that many applications of PNIPAM- PGMA coated magnetic nanoparticles are likely to involve the particles being exposed to strong magnetic fields. As such, a knowledge of the rates of chain formation and sizes of chains could be critical to predicting the behaviour of the flow of the particles in the blood stream, for example.

[1] A.T. Ngo, M.P. Pileni, Nanoparticles of cobalt ferrite: Influence of the applied field on the organization of the nanocrystals on a substrate and on their magnetic properties, *Advanced Materials*, 12 (2000) 276-279. [2] S.H. Sun, C.B. Murray, Synthesis of monodisperse cobalt nanocrystals and their assembly into magnetic superlattices *Journal of Applied Physics*, 85 (1999) 4325-4330. [3] S. Wirth, S. von Molnar, M. Field, D.D. Awschalom, Magnetism of nanometer-scale iron particles arrays *Journal of Applied Physics*, 85 (1999) 5249-5254. [4] L.G. Paterno, E.H.C.P. Sinnecker, M.A.G. Soler, J.P. Sinnecker, M.A. Novak, P.C. Morais, Tuning of magnetic dipolar interactions of maghemite nanoparticles embedded in polyelectrolyte layer-by-layer films, *Journal of Nanoscience and Nanotechnology*, 12 (2012) 6672-6678. [5] C. Hoffmann, E. Mazari, S. Lallet, R.L. Borgne, V. Marchi, C. Gosse, Z. Gueroui, Spatiotemporal control of microtubule nucleation and assembly using magnetic nanoparticles, *Nature Nanotechnology*, 8 (2013) 199-205. [6] N.I. Taib, Vipul Agarwal, Nicole M. Smith, Robert C. Woodward, Timothy G. St Pierre, and K. Swaminathan Iyer., Direct correlation of PNIPAM thermal transition and magnetic resonance relaxation of iron oxide nanoparticles., *Materials Chemistry Frontiers* 1(2017) 2335-2340.

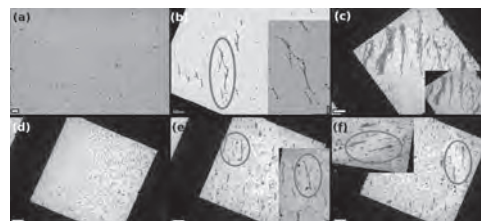


Fig. 1. TEM micrograph of the nanoparticles: (a) PNIPAM-PGMA-NPs and (d) PGMA-NPs in the absence of external magnetic field at 25 °C. Chain-like structures of PNIPAM-PGMA-NPs and PGMA-NPs at 25 °C (b and e) and 45 °C (c and f) in the presence of external magnetic field. Insets showing the details of the chain-like structures of nanoparticles. Scale bar: (a) 2 μm , (b) 5 μm , (c), (d), (e) and (f) 10 μm , (insets: (b), (e) and (f) 2 μm ; (c) 5 μm).

Session JI
NANOPARTICLES AND NANOWIRES
Tomoyuki Ogawa, Chair
Tohoku University, Sendai, Japan

INVITED PAPER

JI-01. Engineered Self-Assembled Magnetic Nanochains INVITED.

M. Sedrpooshan^{1,2}, C. Preger^{2,3}, C.E. Bulbucan^{1,2}, P. Ternero^{2,3}, M. Josefsson^{2,3}, S. Finizio⁴, A.M. Burke^{2,3}, M.E. Messing^{2,3} and R. Westerström^{1,2}

1. Synchrotron Radiation Research, Lunds Universitet, Lund, Sweden; 2. NanoLund, Lunds Universitet, Lund, Sweden; 3. Solid State Physics, Lunds Universitet, Lund, Sweden; 4. Swiss Light Source, Paul Scherrer Institut, Villigen, Switzerland

Bottom-up fabrication of magnetic nanostructures composed of particles with desired sizes and composition can result in significant magnetic properties desired for practical applications in high performing magnetics, spintronics, and magnetic sensors [1, 2]. Magnetic and magneto-transport properties are strongly size-dependent, and the ability to adjust nanoparticle size leads to a high control on nanostructures' behavior [3, 4]. Generation of nanoparticles by aerosol methods provides great control of particle formation, size and deposition [5, 6]. Here, we present a novel bottom-up approach for generating self-assembled magnetic nanostructures [7]. The method uses an aerosol technique based on spark ablation to produce nanoparticles (NPs) with tunable compositions guided onto any substrate of choice using combined electric and magnetic fields. Using external magnetic fields, magnetic NPs can be assembled one-by-one along any direction to form 1, 2, or 3-D structures, see Fig. 1. In these systems, both shape and magneto-crystalline contributions play a key role in the magnetic anisotropy resulting in enhanced magnetic properties such as higher coercivity [8]. The presented technique provides a new approach for self-assembly of 1, 2, and 3-D magnetic nanostructures with building blocks that can be tailored for a specific application. Fig. 1 (a-c) shows the magnetic-field-induced self-assembly of vertical and in-plane structures. The magnetic field used to control the self-assembly also aligns the easy axis of the NPs, resulting in a higher anisotropy compared to a chain with randomly oriented particles. Fig. 1 (d) shows the possibility of particle size modulation, which is similar to diameter modulation in magnetic nanowires [9]. As illustrated in Fig. 1 (e), these structures can be directly integrated on the suitable substrates for, e.g., transport measurements or practical applications, which suggests a great advantage over the common solution-based methods [10]. Furthermore, the particle generation technique can be used to generate a vast number of material systems that can be used as building blocks. We have produced nanochains (NCs) composed of Ni, Fe, Co [7, 11], and as shown in Fig. 1 (f, g), CoPd (alloy) and CoAu (segmented/1D granular) structures. By tuning the segmented structures or chemical composition of alloys, a variety of systems can be achieved with possible applications in magnetism and spintronics [5]. Fig. 2 shows the NCs transferred to a carbon-supported copper grid where they were imaged using SEM (a & d) and by Scanning Transmission X-ray Microscopy (STXM) using circular polarized X-rays. The measurements were performed at the PolLux beamline at the Swiss light source (SLS) [12]. X-ray magnetic circular dichroism (XMCD) provides magnetic contrast (b-c & e-f) with a resolution approaching that of a single particle when combined with SEM images from the same NC. Applying a strong *ex-situ* magnetic field produces a mostly homogeneous remanent magnetization along the NCs with only minor indications of domain formation. Applying an *in-situ* field of -140 mT resulted in that the XMCD contrast of several more regions along the NC turned bright. These results demonstrate that an *ex-situ* field can produce a strong remanent magnetization and that the weak *in-situ* fields can be used to switch the magnetization in some regions. It is argued that these observations are due to larger multi-domain particles that behave as nucleation centers to initiate domain formation. As shown in Fig. 2 (g), micromagnetic simulations on NCs show that the magnetization is energetically favorable along the long axis of the chains and in the same direction (single domain). However, when there is a particle with a diameter larger than the single domain size, the NC breaks up into two domains. Magneto-transport in these structures is of interest since the magnetized and demagnetized states of the chains can result in a magnetoresistance response, and also, the segmented chains composed of different materials (Such as

Co/Au in Fig. 1) can act as 1-D magnetic multilayers. To investigate the magneto-transport in these systems, NCs are self-assembled directly onto the surface of a Si-chip insulated with SiO₂ and pre-patterned with aligned markers. Contacts to the NCs are defined via electron beam lithography and thermal evaporation, and magneto-transport properties along with micro-magnetic simulations will be discussed.

[1] H. Wang, Y. Yu, Y. Sun, *Nano*, Vol. 6, p. 1-17 (2011) [2] D. Lisjak, A. J. P. i. M. S. Mertelj, *Progress in Materials Science*, Vol. 95, p. 286-328 (2018) [3] J. Mohapatra, M. Xing, J. Elkins, *Journal of Physics D*, Vol. 53, p. 504004 (2020) [4] Z. Xiang, Y Song, D Pan, *Journal of Alloys and Compounds*, Vol. 744, p. 432-437 (2018) [5] C. Preger, C. Bulbucan, B. O. Meuller, *The Journal of Physical Chemistry C*, Vol. 123, p. 16083-16090 (2019) [6] J. Fang, L Schlag, SC Park, *Advanced Materials*, Vol. 28, p. 1770-1779 (2016) [7] C. Preger, M. Josefsson, R. Westerström, M. E. Messing, *Nanotechnology* (Submitted Article) (2021) [8] S. Singamaneni, V. N. Bliznyuk, C. Binek, *Journal of Materials Chemistry*, Vol. 21, p. 16819-16845 (2011) [9] L. A. Rodríguez, C. Bran, D Reyes, "ACS nano", Vol. 10, p. 9669-9678 (2016) [10] X. Chen, Z. Zhou, H. E. Karahan, Small, Vol. 14, p. 1801929 (2018) [11] A. Schmidt-Ott, *Spark Ablation: Building Blocks for Nanotechnology*. CRC Press (2019) [12] J. Raabe, G Tzvetkov, U Flechsig, *Review of scientific instruments*, Vol. 79, p. 113704 (2008)

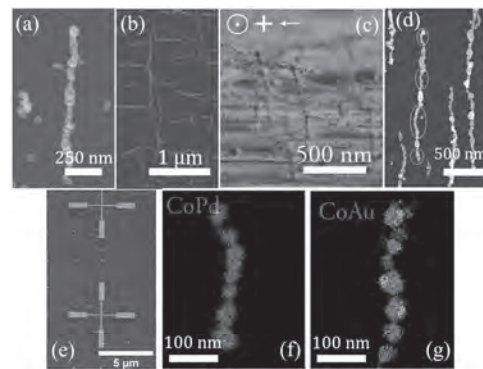


Fig. 1. SEM image of a single vertical nanochain (NC) (a), 2-D chains along the surface of the substrate (b), and 3-D self-assembly of Co nanoparticles (c). Nanochains with particle-size modulation (d), direct integration of NCs on a Chip (e). EDS (energy-dispersive X-ray spectroscopy) mapping of a CoPd alloy (f) and CoAu segmented (g) nanochain.

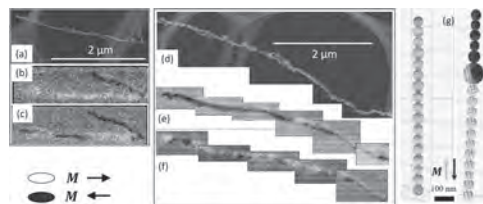


Fig. 2. SEM image of a nanochain (a) and corresponding XMCD contrast in a field of +140 mT (b) and -140 mT (c). SEM (d) and remnant XMCD contrast after magnetizing ex-situ in +1.5 T (e). XMCD contrast after applying an in-situ field of -140 mT (f). Micromagnetic simulation of a chain composed of magnetic single-domain particles and a chain including a particle larger than the single-domain size.

CONTRIBUTED PAPERS

J1-02. Controlled Magnetization by Magnetic Fields in Multisegmented Cylindrical Nanowires.

C. Bran¹, J. Fernandez-Roldan^{1,2}, E. Saugar¹, R. del Real¹, A. Asenjo¹, A. Fraile Rodríguez³, M. Foerster⁴, L. Aballe⁴, O. Chubykalo-Fesenko¹ and M. Vázquez¹

1. Instituto de Ciencia de Materiales de Madrid (ICMM-CSIC), Madrid, Spain; 2. Universidad de Oviedo Departamento de Física, Oviedo, Spain; 3. Departament de Física de la Matèria Condensada, Universitat de Barcelona, Barcelona, Spain; 4. ALBA Synchrotron Light Facility, Barcelona, Spain

Cylindrical magnetic nanowires (NWs) are promising candidates for building blocks of 3D nanoarchitectures and 3D nanotechnologies [1,2]. They present great potential for 3D applications, offering responses to many external (electrical, magnetic, mechanical, thermal, etc.) stimuli [3]. The emerging interest toward cylindrical magnetic NWs is related to the fact that their geometry promotes topologically non-trivial 3D magnetic structures such as Bloch-point domain walls, complex configurations that connect vortex domains with opposite chirality, vortices or skyrmion tubes [4,5]. Here, we present a study on multisegmented NWs formed by ferromagnetic (FM) segments separated either by a different FM material or a non-magnetic (NM) one. On one hand we have alternating CoNi/Ni segments (Fig. 1 (a)), where the domain structure can be tailored by alternating magnetocrystalline anisotropy and the length of each segment. On other hand, FeCo ferromagnetic layers separated by thin Cu NM layers (Fig. 1 (c)). The multisegmented NWs were prepared by electroplating filling the pores of anodic aluminum oxide membranes. The HRTEM analysis confirms the multisegmented morphology with a uniform diameter, and periodic and sharp interfaces. Quantitative analysis reveals that the diameter of CoNi/Ni NWs is about 140 nm with lengths between 0.6 μm and 1.4 μm for CoNi and 1 μm for Ni segments while FeCo/Cu wires with 165 nm in diameter are formed by FeCo segments with 250 nm in length separated by 50 nm Cu layers. XMCD-PEEM imaging of multisegmented CoNi/Ni NWs reveals that the magnetic structure in Ni segment is in a dominantly axial magnetic state while in CoNi segments it depends on their length. In NWs with the shortest CoNi segments (0.6 μm), we observed single vortex domains, in longer segments of 1.2 μm we observed one to three vortex domain states (Fig. 1 (a)), while in the NWs with the longest CoNi segments either multi-vortex or multi-transverse domains were observed. The micromagnetic simulations show that the remanent magnetic structure of CoNi segments depends on the direction of the previously applied field. If the direction is perpendicular to both the NW and the magnetization easy axis, the vortex domains simply expand inside the segment following the structures formed at the interfaces and resulting in one vortex domain for short segments and two or more vortex structures for longer segments. In turn, when the field is applied perpendicular to the NW but along the magnetization easy axis, transverse domains are formed. They are separated by vortex domain structures with core at the surface pointing perpendicular to it. Furthermore, although Ni segments are in an almost single-domain state, they are not completely saturated, and present a small magnetization curling on the NW surface. Their chirality is formed prior to formation of magnetic structures in CoNi and imprints the chirality along the next CoNi segments (Fig. 1 (b)) [5]. The second investigated multisegmented system, FeCo/Cu (Fig. 1 (c-d)), presents a tilt at the interface between FM/NM layer. From the XMCD-PEEM images (Fig. 1 (c)) we determined that each FeCo segment presents a single vortex state which switches its magnetization under the influence of perpendicular magnetic fields. This switching is sequential and each segment has a slightly different switching field. The simulations (Fig. 1 (d)) unveil the main differences between magnetization states when the field is applied along different directions with respect to the NW axis. The tilt between adjacent segments breaks the rotational symmetry providing different magnetic potentials for vortices moving in a certain direction under the influence of applied magnetic field. The proper design of segments anisotropy and geometry (e.g., surface tilting) in cylindrical multisegmented nanowires opens multiple opportunities for advanced nanotechnologies in 3D magnetic nanostructures.

[1] Fernández-Pacheco, A.; Streubel, R.; Fruchart, O.; Hertel, R.; Fischer, P.; Cowburn, R. P., *Nat. Commun.* 2017, 8, 15756. [2] Hertel, R, *Spin* 2013, 03 (03), 1340009. [3] "Magnetic Nano- and Microwires: Design, Synthesis, Properties and Applications", Elsevier 2020, edited by M. Vazquez. [3] Da Col, S.; Jamet, S.; Rougemaille, N.; Locatelli, A.; Mentès, T. O.; Burgos, B. S.; Afid, R.; Darques, M.; Cagnon, L.; Toussaint, J. C.; et al., *Phys. Rev. B* 2014, 89 (18), 180405. [4] Fernandez-Roldan, J. A.; Perez del Real, R.; Bran, C.; Vazquez, M.; Chubykalo-Fesenko, O., *Nanoscale* 2018, 10 (13), 5923–5927. [5] Bran, C.; Fernandez-Roldan, J.A.; P Del Real, R.; Asenjo, A.; Chen, Y.-S.; Zhang, J.; Zhang, X.; Fraile Rodríguez, A.; Foerster, M.; Aballe, L.; et al., *ACS Nano* 2020, 14, 12819.

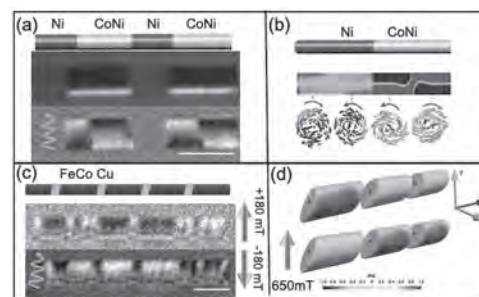


Figure 1. Schematic illustrations of multisegmented NWs (top panels) (a) Chemical contrast and XMCD-PEEM images of a CoNi (1.2 μm)/Ni (1 μm) multisegmented NWs (b) Modelled magnetization state of the CoNi/Ni NW presented in (a), (c) XMCD-PEEM images of FeCo/Cu NWs measured in remanence after perpendicular magnetic fields were applied, (d) Simulated magnetization configurations of FeCo/Cu NW before (upper panel) and after (bottom panel) magnetic fields were applied in y-direction. Scale bar 1 μm .

JI-03. Phase Diagram of Magnetization Reversal Modes in Cylindrical Ni Nanowires.

M.P. Proenca^{1,2}, J. Rial¹, J. Pedro Esteves de Araújo¹ and C. Sousa¹

1. Departamento de Física e Astronomia, Faculdade de Ciências da Universidade do Porto, IFIMUP - Institute of Physics for Advanced Materials, Nanotechnology and Photonics of University of Porto, Porto, Portugal; 2. Instituto de Sistemas Optoelectrónicos y Microtecnología (ISOM), Universidad Politécnica de Madrid, Madrid, Spain

Cylindrical magnetic nanostructures are attracting much interest in a wide range of applications (biomedical imaging, drug delivery, 3D memory storage devices, sensors, etc.). The ability to tune their magnetic properties by changing the geometry (disks, dots, wires, tubes), combined with low-cost and high-yield template fabrication methods, makes these nanostructures highly attractive for implementation in emerging technologies. However, most applications require a full understanding of the magnetization reversal mechanisms. Although it is a well-known topic, thoroughly studied for the past two decades, recent advances in characterization and micromagnetic simulation techniques renewed the attention of the scientific community towards the complete understanding of such magnetic 3D nano-elements [Bran2016, Fernández-Pacheco2017, Charilaou2018, Ruiz-Gómez2020]. In particular, Ni nanowires have been the most reported nanostructures fabricated in nanoporous alumina templates so far [Sousa2014, Proenca2012]. But, nanodisks and low-aspect ratio nanowires are still less explored, particularly regarding the full understanding of the magnetization reversal mechanisms. In this work, we have analyzed the magnetization response of cylindrical Ni nanostructures with 15 to 100 nm in diameter and 12 to 230 nm in length and compared our results with experimental data for periodic arrays. Our simulations show the presence of a critical diameter ($d \approx 30$ nm) that determines the type of domain wall nucleated (transverse or vortex/skyrmion tube); and a critical length ($L \approx 100$ nm) that limits the number of domain walls formed (one or two). By adjusting the diameter/length of the Ni nanocylinders, different magnetic remanent states and reversal mechanisms were observed (Figure 1). Moreover, vortex DWs were found to originate from 3D skyrmion tubes, which have been reported as one of the best configurations for magnetic storage devices. By increasing the diameter and aspect ratio (L/d) of nanowires with $L > 100$ nm, three distinct reversal modes were observed: i) simultaneous propagation of two vortex DWs with opposite chirality; ii) propagation of only one vortex DW, or iii) spiral rotation of both DWs through the “corkscrew” mechanism (Figure 2). Only for very low aspect ratio structures (nanodisks), no skyrmion tubes were observed and reversal occurred by spiral rotation of one vortex DW. The broad range of dimensions studied in this work allowed the creation of the first complete magnetic phase diagram in cylindrical nanostructures [Proenca2021]. This universal phase diagram will be highly important for the future choice of nanoscaled dimensions in the development of novel nano-devices. This work has been supported by the European Union’s Horizon 2020 research and innovation program under the Marie Skłodowska-Curie Grant Agreement No. 734801; by the Portuguese *Fundação para a Ciência e Tecnologia* (FCT) through the *Investigador FCT program* (Contract No. IF/01159/2015); by FCT and COMPETE 2020 (FEDER) under the projects POCI-01-0145-FEDER-028676, POCI-01-0145-FEDER-031302, POCI-01-0145-FEDER-032527, POCI-01-0145-FEDER-032257 and UIDB/04968/2020; and by the Spanish *Ministerio de Ciencia e Innovación* under the project MAT2017-87072-C4-3-P.

C. Bran, E. Berganza, E. M. Palmero, *et al.*, *J. Mater. Chem. C*, Vol. 4, p.978 (2016) A. Fernández-Pacheco, R. Streubel, O. Fruchart, *et al.*, *Nat. Commun.*, Vol. 8, p15756 (2017) M. Charilaou, H. B. Braun and J. F. Löffler, *Phys. Rev. Lett.*, Vol. 121, p.97202 (2018) S. Ruiz-Gómez, C. Fernández-González, E. Martínez, *et al.*, *Nanoscale*, Vol. 12, p.17880 (2020) C. T. Sousa, D. C. Leitao, M. P. Proenca, *et al.*, *Appl. Phys. Rev.*, Vol. 1, p.031102 (2014) M. P. Proenca, C. T. Sousa, J. Ventura, *et al.*, *Electrochim. Acta*, Vol. 72, p.215 (2012) M. P. Proenca, J. Rial, J. P. Araujo and C. T. Sousa, *Magnetic reversal modes in cylindrical nanostructures: from disks to wires*, submitted (2021)

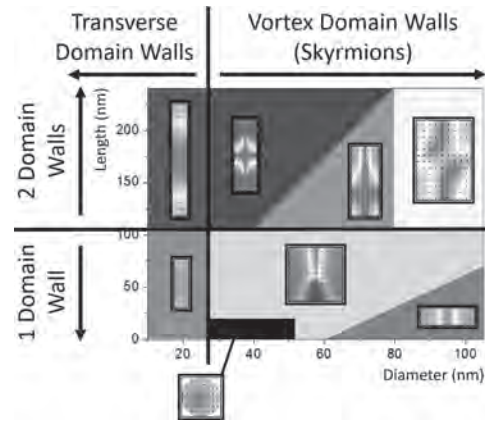


Figure 1: Phase diagram of the magnetization reversal modes in individual Ni nanocylinders with different lengths and diameters, when applying the magnetic field along the nanocylinder’s length (parallel direction). Insets show selected cross-sectional representations of the magnetic configuration during reversal.

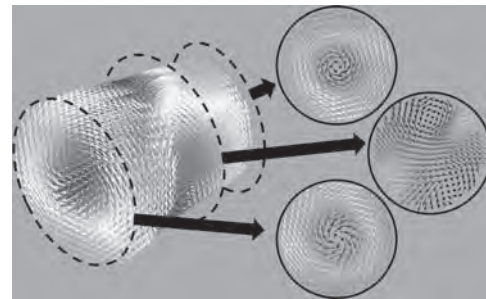


Figure 2: 3D representation of the magnetic configuration during reversal of the simulated Ni nanowire with 100 nm in diameter and 130 nm in length illustrating the spiral rotation of two vortex domain walls (skyrmion tubes) through the “corkscrew” mechanism when applying the magnetic field along the z-direction (parallel to the nanowires’ long axis).

J1-04. Ferromagnetism of Single Vertical Cobalt Nanotubes Grown by Focused Electron Beam Induced Deposition.

J. Pablo-Navarro^{1,2}, L. Rodríguez³, I. Andersen⁴, D. Sanz Hernandez⁵, A. Fernandez-Pacheco⁵, C. Gatel⁴, E. Snoeck⁴, J. De Teresa² and C. Magén²

1. Institute of Ion Beam Physics and Materials Research, Helmholtz-Zentrum Dresden-Rossendorf, Dresden, Germany; 2. Instituto de Nanociencia y Materiales de Aragón (INMA), CSIC-University of Zaragoza, Zaragoza, Spain; 3. Centro de Excelencia de Nuevos Materiales, Universidad del Valle, Cali, Colombia; 4. Centre d'Elaboration de Matériaux et d'Etudes Structurales-CNRS, Toulouse, France; 5. Cavendish Laboratory, University of Cambridge, Cambridge, United Kingdom

Three-dimensional (3D) nanomagnets provide a great potential to be implemented in future spintronic devices for high-density magnetic memories, nano-sensing or logic. Among these appealing architectures, ferromagnetic nanotubes (NTs) are currently being investigated for their fast and low-power domain wall conduit properties [1]. The development of novel 3D nanostructures typically requires complex synthetic methods. Moving forward in this challenging task, Focused Electron Beam Induced Deposition (FEBID) has been explored for the growth of 3D ferromagnetic NTs. This unique one-step nanolithography technique, based on the decomposition of organometallic precursor gas molecules in the vicinity of a substrate [2,3], has demonstrated great versatility in terms of shape, composition and magnetic properties [4]. Following the strategy developed for the fabrication of core-shell nanowires [5], the growth of 3D Co NTs by FEBID has been performed for the first time [6]. The heterostructured design is composed by a vertical Pt-C nanowire (≤ 100 nm in diameter) acting as a core, and a Co coating forming the shell with a thickness down to ~ 11 nm. These are exotic magnetic nanostructures in which unconventional domain walls are formed, presenting high domain wall velocities without Walker breakdown phenomenon and where great stability during propagation has been predicted. Furthermore, Transmission Electron Microscopy (TEM) experiments reveal that these NTs present a nanocrystalline structure and a metallic content of ~ 70 at. %. In addition, a coercivity of ~ 16 mT has been obtained by Magneto-Optical Kerr Effect magnetometry, and magnetic characterization performed by Electron Holography evidences the ferromagnetic behaviour, estimating a remanent magnetic induction up to 1.3 T and detecting complex head-to-head magnetic domain walls. The application of magnetic fields inside the TEM has allowed the pinning and imaging of domain walls in these nanostructures. Finally, micromagnetic simulations have been performed for a deeper understanding of the magnetization dynamics [6].

[1] R. Hertel, *J. Phys.: Condens. Matter*, 28, 483002 (2016). [2] J. Pablo-Navarro, S. Sangiao, C. Magén, et al., *Nanofabrication: Nanolithography techniques and their applications*. Edited by J. M. De Teresa, IOP Publishing (2020). [3] A. Fernández-Pacheco, L. Skoric, J. M. De Teresa, et al., *Materials*, 13, 3774 (2020). [4] J. Pablo-Navarro, D. Sanz-Hernández, C. Magén, et al., *J. Phys. D: Appl. Phys.*, 50, 18LT01 (2017). [5] J. Pablo-Navarro, C. Magén and J. M. De Teresa, *Nanotechnology*, 27, 285302 (2016). [6] J. Pablo-Navarro, et al., *manuscript in preparation*.



Fig. 1. (a) HAADF-STEM image of a Co-FEBID NT cross-section. (b,c) Experimental and simulated magnetic phase shift around a domain wall obtained by Electron Holography and micromagnetic simulations, respectively. (d) Spin configuration obtained from micromagnetic simulations.

J1-05. Non-Planar Geometrical Effects on the Magnetoelectrical Signal in a 3D Nanomagnetic Circuit.

F. Meng^{1*}, C. Donnelly¹, C. Abert², L. Skoric¹, S. Holmes³, Z. Xiao¹, J. Liao¹, P. Newton¹, C. Barnes¹, D. Sanz Hernandez², A. Hierro Rodriguez⁵, D. Seuss², R. Cowburn¹ and A. Fernandez-Pacheco⁶

1. University of Cambridge, Cambridge, United Kingdom; 2. Universitat Wien, Wien, Austria; 3. London Centre for Nanotechnology, London, United Kingdom; 4. Unite Mixte de Physique CNRS/Thales, Palaiseau, France; 5. Universidad de Oviedo, Oviedo, Spain; 6. University of Glasgow, Glasgow, United Kingdom

Bringing nanomagnetism into the third dimension is of growing interest due to many advantages that three-dimensional (3D) structures provide. The introduction of 3D geometrical effects such as curvature and chirality¹, as well as the high density and enhanced device connectivity, lead to many opportunities for new physics and applications^{2,3}. When we combine this promising field of 3D nanomagnetism with the well-established field of spintronics, a number of proposals ranging from the ultra-high-density 3D racetrack memory⁴ to 3D interconnected memristors for neuromorphic computing⁵ appear. However, before we can fully exploit the promise of 3D spintronics, significant advances in both the integration of 3D nanomagnets into 2D microelectronic circuits, and the understanding of the influence of a 3D geometry on the magnetotransport properties, are required. The implementation of 3D nanomagnetic circuits faces great challenges regarding the fabrication of a 3D nanostructure and its interconnectivity to the electronic components. Until recently, most magnetotransport experiments have concerned cylindrical nanowires, with complex micromanipulations needed to electrically contact them⁶. In this work, we employ 3D nano-printing capabilities provided by Focused Electron Beam Induced Deposition (FEBID)⁷, to directly fabricate a high-quality 3D Cobalt nanobridge with well-defined leads on pre-synthesized electrical contacts (Figure 1a). The SEM image shown in Figure 1b demonstrates the successful integration of this complex, high-aspect-ratio 3D nanostructure onto lithographically patterned electrodes. This printed 3D nanomagnetic circuit allows four-probe transport measurements with which we can probe the magnetotransport properties of the 3D nanostructure - and determine the influence of the three-dimensionality on these properties. To fully characterise the magnetotransport (MT) properties of the 3D magnetic nanobridge, we measured MT hysteresis loops for fields applied in different directions in three-dimensions (Figure 2a, b). These magnetotransport measurements, in combination with macrospin and finite element simulations, reveal that the three-dimensional structure of the nanobridge directly affects the magnetotransport in several ways. Firstly, the non-collinear current path in the 3D geometry results in a complex superposition of different MT effects, leading to an unusual angular dependence of well-known effects such as the Anomalous Hall effect. Secondly, we also identify a significant angular-dependence of the magnetoelectric signal due to the magnon magnetoresistance. This strong angular dependence occurs due to the strong influence of the demagnetising field within the non-collinear regions of the 3D geometry, highlighting the importance of magneto-statics in 3D nanostructures⁸. These new insights into the influence of a 3D geometry on the magnetotransport effects reported in this work provide the basis for the future study of new spintronic effects in 3D magnetic nanostructures, as well as the realization of 3D spintronic technologies. This methodology shown here combining FEBID 3D printing and standard planar lithography can be extended to more complicated geometries and other materials, opening the door to the fundamental study of new phenomena that exploit the interplay between 3D geometry and magnetotransport and may find applications in the future of areas such as magnonics, frustrated magnetic systems, and magnetic neural networks.

(1) R. Streubel, P. Fischer and F. Kronast, *J Phys D Appl Phys.*, Vol. 49, p.363001(2016) (2) A. Fernández-Pacheco, R. Streubel and O. Fruchart, *Nat Commun.*, Vol. 8, p.15756 (2017) (3) P. Fischer, D. Sanz-Hernández and R. Streubel, *Apl Mater.*, Vol. 8, p.15756 (2017) (4) S. Parkin, M. Hayashi and L. Thomas, *Science.*, Vol. 320, p.190-194 (2008) (5) A. May, M. Hunt and A. Berg, *Commun Phys.*, Vol. 2, p.13 (2019) (6) M. Schöbitz, A. Riz and S. Martin, *Phys Rev Lett.*, Vol. 123, p.217201 (2019) (7) L. Skoric, D. Sanz-

Hernández and F. Meng, *Nano Lett.*, Vol. 20, p.184-191 (2019) (8) F. Meng, C. Donnelly and C. Abert, *Arxiv.*, arXiv:2011.09199 (2020)

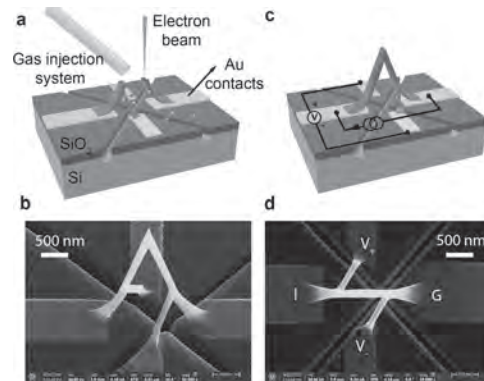


Fig.1 (a) 3D nano-printing of the bridge via Focused Electron Beam Induced Deposition (FEBID) on pre-patterned electrical contacts. (b) The SEM image of the as-fabricated nanomagnetic circuit. (c) Four-probe magnetotransport measurement configuration. (d) The SEM image of the top view of the nanobridge.

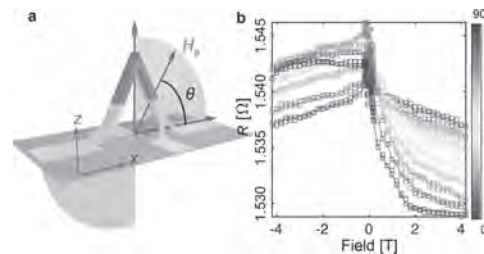


Fig.2 (a) The schematic shows how the field was applied relative to the 3D nanobridge, θ is the angle between the applied field and the substrate (b) Magnetotransport hysteresis loop obtained from -4 T to 4 T and 4 T to -4 T for each field angle θ , from $\theta = 0^\circ$ to $\theta = 90^\circ$ (from violet to red).

J1-06. Magnetocuring and Magnetorheology of Composites.R. Chaudhary¹, V. Chaudhary¹, R. Ramanujan¹ and T.W. Steele¹¹. School of Materials Science and Engineering, Nanyang Technological University, Singapore, Singapore

Abstract: Magnetocuring of carbon and glass fibers was performed using Curie temperature tuned magnetic nanoparticles (CNP) embedded in adhesives, aka magneto-adhesive. Interestingly, these fibers were cured under alternating magnetic field (AMF) within a few minutes. *In-situ* heating of the magneto-adhesive were controlled by CNP loading and AMF strength. The heating of the CNP switches off above its Curie temperature, which prevents overheating. For the first time, custom made AC-magnetorheometry was employed to understand the kinetics of curing of the magneto-adhesive under AMF. The storage modulus of the magnetocured adhesive exceeded 10 MPa at shear strain of < 10%. **Introduction:** Magnetic field activated adhesive curing, aka magnetocuring have recently been reported[1]. Magnetocuring overcomes the limitations of available curing techniques e.g. photocuring[2], snap-curing[3], and electrocuring[4], etc, it allows the adhesive to be activated on-demand when an alternating magnetic field is applied. Carbon fiber is increasingly being used to make lighter and stronger parts in many industries including aviation, automobile, marine, sports, defence, IT, etc. [5] However, in most of the applications, these fibers need to bond with suitable thermosets/thermoplastics in order to achieve high stiffness, for which thermal curing is required. Magnetocuring of carbon and glass fibers can be applied in a range of commercial applications. The present work addresses the design and application of one-pot epoxy adhesives by the ‘modifier’ methodology for on-demand contactless curing under alternating magnetic field (AMF). **Material and Methods:** Curie nanoparticles (CNP) were synthesized by the hydrothermal method and functionalized using oleic acid and epoxy [1]. Functionalized CNP were mixed into commercial 1C epoxy adhesive and cured under an alternating magnetic field (AMF, 400 kHz, 140 Oe). The kinetic parameters, real-time properties of the adhesive and composite were evaluated using a custom made AC magneto-rheometry setup. **Results and Conclusions:** Magneto-adhesive applied carbon and glass fibers were passed through the magnetic field generated solenoid coil and cured within 5 min (Fig. 1A). This fast curing is important for *in-line* manufacturing of fiber based components. The magneto-adhesive property under AMF and at room temperature were studied using AC-magnetorheometry. The gelation point of the magneto-adhesive with 30wt.% CNP was achieved within 70 s of AMF exposure (Fig. 1B and 1C). On applying the magnetic field, a decrease in the loss modulus (G'') and increase in the storage modulus (G') was observed due to the initiation of crosslinking and composite hardening. The storage modulus of the magnetocured adhesive was observed to be >10 MPa at shear strain of < 10% (Fig. 1C). These results suggest that magnetocuring is an attractive technology for in the sports goods, automotive, aerospace and medical industries. It offers an energy efficient, remote, and wireless method of on-demand adhesion by exploiting self-regulating Curie nanoparticles (CNP). Real time magnetorheology measurements were used to determine the properties, fast gelation within 70 s was observed. **Acknowledgement:** Authors acknowledge the financial support from the Agency for Science, Technology and Research (A*Star) for the grant IRG17283008 “Microprocessor- based methods of composite curing.

[1] R. Chaudhary, V. Chaudhary, R.V. Ramanujan, T.W.J. Steele, Applied Materials Today 21, 100824 (2020). [2] S.C. Ligon-Auer, M. Schwentenwein, C. Gorsche, J. Stampfl, R. Liska, Polymer Chemistry 7, 257-286 (2016). [3] X.K. Hillewaere, R.F. Teixeira, L.T.T. Nguyen, J.A. Ramos, H. Rahier, F.E. Du Prez, Advanced Functional Materials 24, 5575-5583 (2014). [4] J. Ping, F. Gao, J.L. Chen, R.D. Webster, T.W. Steele, Nature communications 6, 1-9 (2015). [5] C. Soutis, Materials Science and Engineering: A 412, 171-176 (2005).

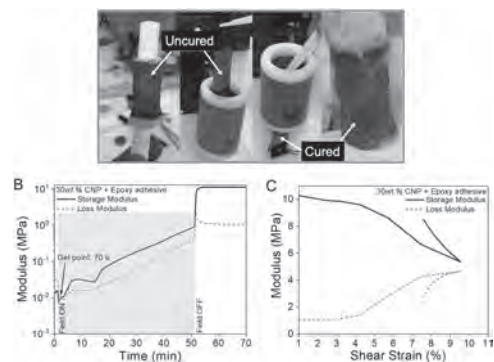


Fig.1 Magnetocuring and AC-magnetorheology of composites. (A) Magnetocuring of carbon and glass fibers for *in-line* manufacturing, (B-C) Oscillation and amplitude sweep of 30wt.% CNP within epoxy adhesive.

JJ-07. Long-Range Exchange Interaction Between Ferromagnetic Nanoparticles Embedded in Carbon Nanotubes.

S.L. Prischepa^{1,2}, A.L. Danilyuk¹ and A.V. Kukharev¹

1. Belarusian State University of Informatics and Radioelectronics, Minsk, Belarus; 2. National Research Nuclear University MEPhI, Moscow, Russian Federation

Investigation of magnetic properties of nanostructured ferromagnets, such as oriented arrays of carbon nanotubes (CNTs) containing ferromagnetic nanoparticles (FNPs), is still relevant. In addition to attractive applications in magnetoelectronics, CNTs with embedded FNPs are also a very useful model object for studying magnetic interaction of the latter through a conducting medium. For this, it is important to establish a relation between macroscopic and microscopic parameters of the system. In nanostructured ferromagnets, this dependence is described within the random magnetic anisotropy model (RAM), in which the spin system and, consequently, the main macroscopic characteristics (coercivity, susceptibility, saturation magnetization) are determined by such microscopic parameters as the exchange interaction constant, FNP magnetization, local magnetic anisotropy constant and grain size $2R_c$ [1]. Recently, magnetic parameters like the exchange and anisotropy fields, effective magnetic anisotropy constant, Bloch and exchange constants in aligned CNT arrays containing FNPs were determined within the RAM by analyzing law of the approach to saturation magnetization and corresponding modeling of the correlation functions of the magnetic anisotropy axes of the FNPs [2,3]. Presence of the interplay between the exchange interaction and magnetic anisotropy, as well as the contribution of not only random, but also coherent anisotropy, was established [3]. In addition, the important role of magnetoelastic anisotropy in the case when a single FNP is localized inside a CNT has been revealed. [4]. It was shown also that aligned CNT arrays with a low concentration of FNPs embedded only inside CNT have relatively high values of exchange fields, random and coherent anisotropy. They are manifested in CNT arrays, in which the average distance between the FNPs significantly exceeds the size of the latter, reaching hundreds of nanometers. These effects, which do not currently have a convincing explanation, are mainly associated with the presence of the exchange interaction between FNPs through the CNT matrix. However, there is still no reasonable mechanism of the long-range exchange interaction in CNT arrays. In our work [5], it was assumed that these effects are related to the indirect exchange coupling of the RKKY type via the conducting electrons of CNTs. The obtained preliminary estimations have shown that the RKKY exchange interaction is enhanced by the presence of spin-orbit coupling (SOC) and could propagate up to a micrometer scale [5]. In this contribution a multi-wall CNT (MWCNT) with embedded FNPs is considered. We present the results of modeling of the RKKY interaction in MWCNT depending on its diameter, chirality, chemical potential and SOC constant within the Klinovaya-Loss model [6]. The influence of the external longitudinal magnetic field is also studied. It is assumed that the main contribution to the RKKY interaction is caused by the conduction electrons of the inner wall of CNTs which is in contact with the FNP. In addition, spin-orbit interaction (SOI) in CNT is also considered. The SOI in a nanotube can occur due to the curvature effect, which significantly increases its contribution in comparison with a flat graphene. It can also be enhanced by FNP, CNT defects or impurity states. The spin susceptibility of CNT conduction electrons χ/χ_0 is evaluated ($\chi_0 = a^2 k_G / \hbar v_F$, where v_F is the Fermi velocity, k_G is the circumferential direction, a is the lattice constant). Fast oscillations are excluded and only slowly changing envelopes of spin susceptibility are considered. The chemical potential is tuned inside the gap opened by SOI. It is shown that the decay of the amplitude of the χ/χ_0 oscillations depends strongly on the chemical potential: the higher the Fermi energy of the CNT (ϵ_F), the more significant is the decay. The frequency of spin susceptibility oscillations increases with the increase of the ϵ_F (Fig. 1). This is due to the fact that with the increase of the Fermi energy of CNTs, the discrepancy between the gap opened by SOI and the value of chemical potential increases. Finally, the proposed approach allows evaluating the energy of the exchange interaction between FNPs belonging to the same CNT. The work is supported by the COST Action CA19118.

[1] E.M. Chudnovsky, J. Appl. Phys., Vol. 64, p. 5770 (1988). [2] A.L. Danilyuk, A.L. Prudnikava, I.V. Komissarov, et al. Carbon, Vol. 68, p. 337 (2014). [3] A.L. Danilyuk, I.V. Komissarov, V.A. Labunov, et al. New J. Phys. Vol. 17, p. 023073 (2015). [4] S.L. Prischepa, A.L. Danilyuk, A.V. Kukharev, et al. IEEE Trans. Magn. Vol. 55, p. 2300304 (2019). [5] A.L. Danilyuk, I.V. Komissarov, A.V. Kukharev, et al. Europhys. Lett. Vol. 117, p. 27007 (2017). [6] J. Klinovaya and D. Loss, Phys. Rev. B, Vol. 87, p. 045422 (2013).

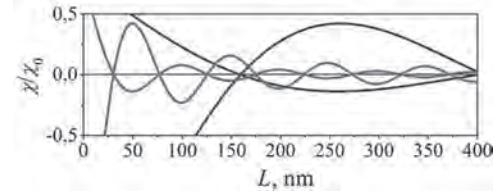


Fig. 1. Decay of the oscillation amplitude of the spin susceptibility χ/χ_0 along the axis of the semiconductor CNT of diameter of 25 nm with chiral indices (235,129) and $\epsilon_F=18$ (blue) and 30 (red) meV. The chirality angle is 39.54° and $k_G=0.053 \text{ nm}^{-1}$.

J1-08. Advanced Size Distribution Determination of Superparamagnetic Nanoparticles.

R. Shao¹, C. Zambrzycki², R. Güttel² and U. Herr¹

1. Institute of Functional Nanosystems, Ulm University, 89081 Ulm, Germany; 2. Institute of Chemical Engineering, Ulm University, 89081 Ulm, Germany

Superparamagnetic nanoparticles are drawing increasing interests because of their special physical properties and potential applications in magnetic-supporting catalysts, water purification, ferrofluids, and medical diagnostics [1,2]. For most applications, an accurate determination of the particle size distribution is required since the magnetic properties of the particles directly depend on the particle size. Transmission electron microscopy (TEM) and X-ray diffraction (XRD) are widely used to determine the particle size. However, both methods have limitations. For TEM, normally only a limited amount of particles contribute to the result, and the precise determination of extremely small particles is difficult due to the limit of the TEM image contrast and resolution. For XRD, the evaluation is based on the Scherrer equation, the result of which is the average size of the particles, more detailed information of the size distribution is not available. Furthermore, this method assumes that the peak broadening is solely due to the crystallite size, other effects such as microstrain are neglected. Besides, neither TEM nor XRD are suitable for embedded nanoparticles. Above the blocking temperature T_B , the magnetic moment versus external magnetic field curve (m-H curve) of superparamagnetic particles is described by $m = m_s L(x)$, with $x = \mu_0 m_p(d) H / k_B T$, where m is the magnetic moment, m_s is the saturation magnetic moment, μ_0 is the vacuum permeability, m_p is the magnetic moment of one particle of size d , H is the external field, k_B is the Boltzmann constant, T is the temperature in Kelvin, $L(x)$ is the Langevin function: $L(x) = \coth(x) - 1/x$. Since the m-H curve is dependent on the size d , the particle size could be determined by fitting the measured m-H curve with the Langevin function. Note that the realistic particle size normally includes a distribution. In 1978, Chantrell et al. [3] presented a method to determine the mean value and standard deviation of the particle size distribution. This method fits the measured m-H curve to a weighted sum of Langevin functions using a pre-assumed lognormal size distribution. Since then, this method has been used in many works for decades [4-6]. However, the assumption that the size distribution is always lognormal might not be accurate for particles synthesized by all the techniques. In this work, we present a fitting method without a pre-assumed distribution. The measured m-H curve is fitted to a superposition of Langevin functions with corresponding fractions, and the combination of these fractions is the size distribution. In the fitting procedure, three constraints are considered: 1) The method of least squares is used to obtain a well fitted m-H curve; 2) The smoothness of the distribution is a criterion to judge whether the fit is valid, since a realistic distribution should be relatively smooth; 3) Saturation magnetic moment should be fitted since the small particles cannot be saturation magnetized. To obtain a fitted distribution under all these three constraints with optimized weights, we apply the method of Lagrange multipliers. This fitting method is used to determine the size distribution of five different superparamagnetic $\gamma\text{-Fe}_2\text{O}_3/\text{SiO}_2$ core-shell nanoparticle samples. The m-H curves were measured by VSM and then fitted with a superposition of Langevin functions. The fitting results of selected samples are shown in Fig. 1 and Fig. 2. The fitted mean values and standard deviations of the particle size distributions agree well with the results of TEM and XRD [1].

[1] C. Zambrzycki, R. Shao, A. Misra, C. Streb, U. Herr, R. Güttel, *Catalysts*. 2021; 11(1):72. [2] V. Wu, E. Huynh, S. Tang, V Uskoković, *Acta biomaterialia* 88 (2019): 422-447. [3] R. Chantrell, J. Popplewell, S. Charles, *IEEE Transactions on Magnetics* 14.5 (1978): 975-977. [4] E. Ferrari, F. Da Silva, M. Knobel, *Physical Review B* 56.10 (1997): 6086. [5] F. C. Fonseca, et al., *Physical review B* 66.10 (2002): 104406. [6] D. Henrard, et al., *Journal of Nanomaterials* 2019 (2019).

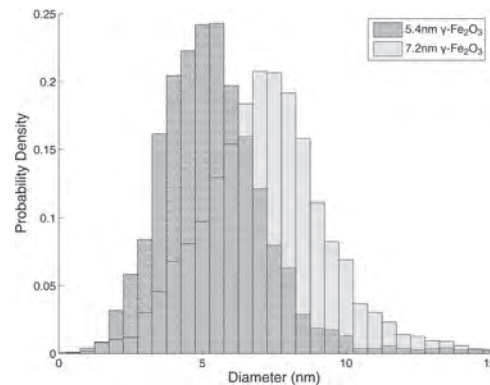


Fig. 1: Core size distributions of two selected as-made $\gamma\text{-Fe}_2\text{O}_3/\text{SiO}_2$ core-shell particle samples fitted from corresponding m-H curves with a superposition of Langevin functions.

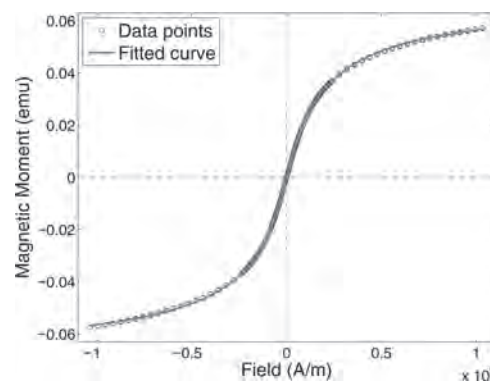


Fig. 2: m-H curve of as-made 5.4nm $\gamma\text{-Fe}_2\text{O}_3/\text{SiO}_2$ core-shell particles measured by VSM together with fitted curve with a superposition of Langevin functions.

J1-09. Revealing Magnetic Morphologies and Spin Disorder in Ferrite Nanoparticles Using Polarized SANS.

D. Zákutná^{1,2}, D. Honecker³ and S. Disch¹

1. Universität zu Köln, Köln, Germany; 2. Institut Laue-Langevin, Grenoble, France; 3. Rutherford Appleton Laboratory, Didcot, United Kingdom

Magnetic nanoparticles reveal unique magnetic properties making them relevant for data storage, electronic and mechanical engineering, and biomedical applications. Despite the considerable technological relevance and fundamental importance, a key challenge in magnetic nanoparticle research remains in the quantitative interpretation of the three-dimensional magnetic configuration and the nanoscale distribution of magnetization and spin disorder. Disorder effects - being intrinsic to nanomaterials - crucially determine the magnetization properties such as the heating performance of magnetic nanoparticles [1-4]. In this regard, the main aspects of fundamental interest are the effective magnetic anisotropy and the magnetization distribution within individual nanoparticles. Polarized, magnetic contrast-enhanced small-angle neutron scattering (SANS) is a versatile technique to investigate the chemical morphology and magnetization with nanoscale spatial resolution [5]. Addressing structural and magnetic inhomogeneities on the nanoscopic length scales of 1-300 nm, magnetic SANS is highly relevant for a variety of materials classes ranging from permanent magnets, magnetic steels and alloys to vortex lattices, skyrmions, and ferrofluids. For monodisperse nanoparticles, magnetic SANS has the unique potential to isolate core and surface-related effects of magnetization and spin disorder. In this contribution, we will present our recent results on the spin disorder in ferrite nanoparticles induced during synthesis. For the synthesis of iron oxide nanoparticles via thermal decomposition of iron oleates [7], the initial formation of FeO nanoparticles followed by topotaxial oxidation to magnetite and maghemite is well established [8,9]. Polarized SANS offers a great potential for the understanding of the microstructure in such heterostructured nanoparticles and allows to disentangle the magnetic field response of core and shell magnetization. For cobalt ferrite nanoparticles, our polarized SANS study reveals even in the wuestite-like nanoparticle core a significant magnetization contribution at ambient temperature (Fig. 1), in contrast to the conventionally assumed paramagnetic or AFM behavior. This FiM@FiM core-shell morphology explains the origin of the low-temperature exchange-bias phenomenon. Despite the overall homogeneous Co:Fe distribution within the nanoparticles, the sensitivity of SANS to nanoscale density variations enables us to verify the chemical core-shell morphology for as-prepared cobalt ferrite nanoparticles. We analyze the progressive oxidation of the core and the aging process into single-phase ferrite nanoparticles with nearly homogeneous magnetization distribution. This process occurs within years and does not compromise the size distribution or stability of the dispersion. In an idealized picture, one would consider such single-crystalline magnetic nanoparticles as defect-free nanocrystals with a collinearly magnetized core. In real systems, however, the internal spin structure exhibits a greater complexity, e.g., at the surface where compositional and structural defects are ubiquitous. As a result, the surface region is described as a shell of magnetically disordered surface spins. Polarized SANS has the necessary sensitivity to resolve the spatial distribution of spin disorder in fine detail. We have recently shown that the magnetization configuration inside magnetic nanoparticles may not be static – as often presumed – but rather susceptible to magnetic fields with the occurrence of field-dependent magnetization processes [6]. We have established a significant field-induced growth of the total particle moment by a magnetic ordering transition at the structurally disordered surface (Fig. 2). In our study, polarized SANS extends the traditional macroscopic magnetic characterization and reveals the local magnetization response. This approach allows us to quantitatively separate surface-spin disorder from intra-particle disorder contributions. Finally, we have elucidated the intra-particle spin-disorder energy, giving indirect insight into the structural defect profile in magnetic nanoparticles.

[1] P. Bender *et al.*, J. Phys. Chem. C, 122, 3068 (2018). [2] A. Lak *et al.*, Nano Lett., 18, 6856 (2018). [3] A. Lappas *et al.*, Phys. Rev. X, 9, 041044. [4] A. Lak, S. Disch, P. Bender, Adv. Science, accepted (2020). [5] S. Mühlbauer, D. Honecker, S. Disch, A. Michels *et al.*, Rev. Mod. Phys.,

91, 015004 (2019). [6] D. Zákutná, D. Honecker, S. Disch *et al.*, Phys. Rev. X, 10, 031019 (2020). [7] T. Hyeon, Chem. Comm., 927 (2003). [8] E. Wetterskog *et al.*, ACS Nano, 7, 7132 (2013). [9] R. Ichikawa *et al.*, Small, 14, 1800804 (2018).

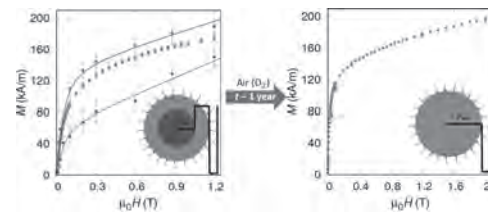


Fig. 1: Polarized SANS reveals distinct magnetization in the wuestite-like core (green) and spinel-type shell (red) of as-synthesized ferrite nanoparticles. The volume average magnetization (orange) is in excellent agreement with macroscopic magnetization (blue). Ageing (right panel) leads to the single-phase behavior of homogeneous ferrite nanoparticles.

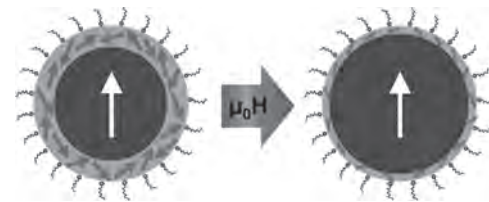


Fig. 2: In a strong magnetic field, the collinearly magnetized cores of ferrite nanoparticles grow due to the gradual alignment of initially disordered surrounding spins [6].

JJ-10. Epitaxially Grown Single-Crystalline Cobalt Nanowires With High Coercivity.

J. Mohapatra¹, M. Xing¹ and P. Liu¹

¹. Department of Physics, The University of Texas at Arlington, Arlington, TX, United States

I. INTRODUCTION Although ferromagnetic particles can nowadays be grown in various size and shapes, controlling the crystallinity and microstructure parameters have remained challenging.[1,2] Nanomagnets with single-crystalline structures are particularly important because they typically exhibit reduced crystalline defects. Motivated by these prospects, our group has been established efforts in producing single-crystal and single-domain nanowires (NWs) through chemical process.[3-5] The single-domain structure led to changes in the magnetization reversal mechanism from the complicated domain-wall-motion-related process to a magnetic moment rotation mechanism that found to results in record high coercivity. Having a technique at hand that could extend growth to oriented magnetic NW array films would be highly desirable. Thin films of magnetic materials with high perpendicular anisotropy and coercivity have great application potential in ultrahigh-density perpendicular magnetic recording, permanent magnets, and spintronic and magnetoresistance sensors.[6] However, to synthesize and organize magnetic NWs to a vertically oriented structure is still a challenging task because of its dipolar interaction between neighboring NWs. In this work, we demonstrate bottom-up epitaxial solution growth of ferromagnetic Co NW arrays on crystalline metal surfaces. It is found that the coercivity of the NW arrays is strongly related to the wire diameter, film thickness, and orientation. This study provides a simple procedure to achieve recording media with ultra-high-recording densities. II. EXPERIMENTAL SECTION Single step chemical approach was used to fabricate the vertically aligned Co NW array films. In a typical synthesis, silicon substrates sputtered with Pt (111) film were kept in the solution of 1,2-butanediol, cobalt (II) laurate, and hexadecylamine (HDA). The growth was allowed for 12 h at 180 C in a Teflon-lined stainless-steel hydrothermal reactors. The diameter of Co NWs was controlled by varying the Pt film thickness from sub-10 nm to 100 nm. III. RESULTS AND DISCUSSION Figures 1a-c show top view scanning electron microscopy image of Co NW arrays having wire diameter of 12-20 nm. The NW array film is highly dense, and nanowires are uniformly distributed over large wafer-scale area (25 x 25 mm) with an areal density up to 5.6×10^{12} wires/in². The cross-sectional view (inset of Figures 1a-c) of the as-grown film demonstrates that the NWs are vertically aligned.

High-resolution TEM imaging and X-ray diffraction (XRD) measurements demonstrate the epitaxial growth of cobalt on platinum, with c-axis along the long-axis of NWs (i.e perpendicular to the film). As one would expect, the 6-fold symmetry of the Pt(111) surface favors Co crystal growth along the hexagonal (0001) wire basal planes and hence with a single in-plane orientation. Figures 1d-e shows the room temperature magnetic hysteresis loops of the Co NWs arrays of wire diameters 12-20 nm. It is found that the coercivity for the NW arrays along the wires axis (||) increases from 3.4 kOe to 7 kOe with the decrease of diameter. In addition, it can also be seen from Figures 1d-e that the squareness in hysteresis loop and coercivity in the parallel direction of NWs are larger than those in the perpendicular direction, which reveals that the easy axis of the Co NWs is parallel to the wire axis. Although the NW array film shows a typical perpendicular anisotropic behavior with high coercivity along NW axis, the squareness ratio of $M_R/M_S < 0.9$. The low value of squareness could be due to the closely packed NW array, which induces a demagnetizing field along the plane of the film. The effective magnetic anisotropy of the NWs in an array film can result from the interplay of three major effects: 1) the macroscopic demagnetization field, $H_d = -6\pi M_s p$, where p is the porosity of the film and M_s is bulk value of the saturation magnetization for Co; 2) the shape anisotropy of individual nanowire $H_{sh} = 2\pi M_s$; and 3) magnetocrystalline anisotropy field, $H_m = -2K_1/M_s$, where K_1 is the magnetocrystalline anisotropy constant for Co.[7] Thus, the theoretical effective coercive field of the nanowires is given by $H_d + H_{sh} + H_m$. The calculated effective anisotropy field for Co NWs is ~ 12.5 kOe, which is much higher than the experimental coercivity values. The observed low coercivity in the prepared Co NW arrays is due to the strong magnetostatic coupling among the NWs, which is in agreement with those reported in the literature.[8] IV. CONCLUSIONS In conclusion, highly

ordered Co NW arrays with coercivity comparable to magnetocrystalline anisotropy have been successfully fabricated via a simple chemical synthesis process. Magnetic measurements show that the as-prepared Co NWs with different diameters display magnetic anisotropy with the easy magnetization direction parallel to the axis of Co NW. The coercivity measured along the wire axis increases with decreasing nanowires diameter, which reveals the role of shape anisotropy in enhancing coercivity. In addition, this study opens an interesting option in tuning the magnetic properties of NW arrays and their applications in perpendicular recording media.

[1] Y. Soumare, C. Garcia, T. Maurer, G. Chaboussant, F. Ott, F. Fiévet, J. Y. Piquemal, G. Viau, Adv. Funct. Mater. 2009, 19, 1971. [2] A. Ramazani, M. Almasi Kashi, A. H. Montazer, J. Appl. Phys. 2014, 115, 113902. [3] K. Gandha, K. Elkins, N. Poudyal, X. Liu, J. P. Liu, Sci. Rep. 2014, 4. [4] K. Gandha, J. Mohapatra, J. P. Liu, J. Magn. Magn. Mater. 2017, 438, 41. [5] J. Mohapatra, M.Y. Xing, J. Elkins, J. Beatty, J. P. Liu, Adv. Funct. Mater. 2021, doi:10.1002/adfm.202010157. [6] N. Liakakos, T. Blon, C. Achkar, V. Vilar, B. Cormary, R. P. Tan, O. Benamara, G. Chaboussant, F. Ott, B. Warot-Fonrose, E. Snoeck, B. Chaudret, K. Soulantica, M. Respaud, Nano Letters 2014, 14, 3481. [7] J. Mohapatra, J. P. Liu, in *Handbook of Magnetic Materials*, Vol. 27 (Ed: E. Brück), Elsevier, 2018, 1. [8] A. Encinas-Oropesa, M. Demand, L. Piraux, I. Huynen, U. Ebels, Phys. Rev. B 2001, 63, 104415.

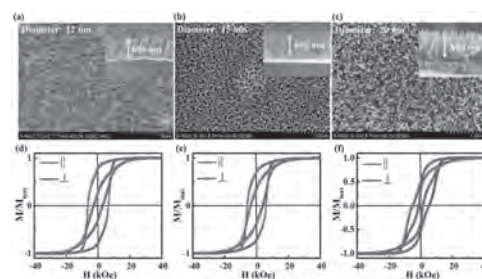


Figure 1 (a,b,c) SEM images of Co/CoO NWs array film with different wire diameters prepared via hydrothermal decomposition of cobalt carboxylate and inset shows the cross-section view of the nanowire array film. (d,e,f) The respective room temperature hysteresis loops by applying the magnetic field parallel (||) and perpendicular (⊥) to the NW axis.

J1-11. On Metamagnetic Phase Transition in 150 nm B2-Like FeRh Film of Nanoclusters Assembled.

G.A. Herrera Huerta¹, A. Robert¹, V. Dupuis¹, I. Cañero Infante², P. Rojoromero², B. Vilquin², E. Otero³, P. Ohresser³, O. Boisron¹, C. Albin¹, L. Bardotti¹, D. Le Roy¹, F. Tournus¹ and A. Tamion¹

1. Institut Lumiere Matiere, Villeurbanne, France; 2. Institut des Nanotechnologies de Lyon, Villeurbanne, France; 3. Synchrotron SOLEIL, Gif-sur-Yvette, France

The FeRh alloy in CsCl-type (B2) phase is well-known for its metamagnetic transition from antiferromagnetic (AFM) to ferromagnetic (FM) state when the temperature increases over 370 °C, which comes with a volume expansion of 1% [1,2]. Nowadays, magneto-structural transition near room temperature are of great interest for potential applications to the control of nanostructures, magnetocaloric refrigeration and antiferromagnetic spintronics [3,4]. However, there are still open questions at nanoscale, including the finite size effects on magnetic FeRh phase transition, which require to continue efforts. The aim of this work is to explore the magnetic behavior of a 150 nm-thick FeRh nano-structured film prepared from Low Energy Cluster Beam Deposition (LECBD). Using a laser vaporization source, the initial diameter of the deposited FeRh nanoparticles is ranging from 2 nm to 10 nm in a log-normal distribution according to previous transmission electron microscopy observations [5]. The sample was annealed at 700 °C for 3 hours under vacuum in order to achieve the chemically ordered B2 phase. Then X-ray Diffraction spectrum reveals all α' -bcc peaks with a lattice parameter of 2.98 Å as expected in the B2-FeRh phase for a concentration of 48%-56% of Rh. The full width at half maximum (FWHM) of the α' (001) peak gives us an estimated crystallite size of about 30 nm in agreement with a limited coalescence upon annealing, leading to a surface granular thick-sample as observed from Atomic Force Microscope observations (Fig. 1). To study the magnetic behavior, various SQUID magnetometry measurements have been performed, including thermal dependence magnetization $m(T)$ in the heating and cooling mode, for different values of applied magnetic field. As reported in Fig. 2, one can observe a broad and asymmetric metamagnetic transition with a significant fraction of residual magnetization at low temperature. This persistent FM state is attributed to the presence of non-switchable FM Grains. By increasing the external field, the metamagnetic transition is pushed to lower temperature following a linear correlation which is observed from the temperatures of maximum and minimum magnetization evolution as a function of field (insert Fig. 2). From Hysteresis magnetization $m(H)$ loops a decreasing coercive field as the temperature increases has also been observed sustaining the evidence of FM regions down to low temperature. This behavior supports the coexistence of these two magnetic orders in thick nanogranular B2-like FeRh film. Moreover, field cooling - zero field cooling (FC-ZFC) susceptibility measurements have revealed the presence of single FM domains with a superparamagnetic (SPM) like-transition at temperatures higher than 130K. But because there is no exchange bias measured in $m(H)$ loops at low temperature, there is no strong FM-AFM exchange coupling as could be expected for FM core@AFM shell morphology. In this work, the magnetic behavior of such thick nanogranular B2-like FeRh film will be described as a competition between different magnetic orders as a function of nanoparticle size, temperature and applied magnetic field. Several thermal regimes in the heating and cooling modes will be proposed as 1) Low temperature regime for $T < 50K$ where small persistent FM nanoparticles co-exist with large AFM nanoparticles, 2) Intermediate regime with AFM-FM switching events and 3) at $T > 300K$ the whole film is in the FM state. In the cooling mode, the FM dragging effect will be related to the applied magnetic field. A simple model could be considered with two distinct nanoparticles populations: one with smaller nanoparticles (FM/SPM) where relaxation effects avoid reaching AFM states at low temperature, and one with larger nanoparticles with AFM-compressed core@FM-relaxed shell morphology up to room temperature. To go a step further, X-ray magnetic circular dichroism results on mass-selected FeRh nanoparticles embedded in matrix recently measured at DEIMOS-SOLEIL will be discussed to illustrate finite size and surface/interface effects on metamagnetic FeRh transition.

[1] V. L. Moruzzi and P. M. Marcus. Antiferromagnetic-ferromagnetic transition in FeRh. Phys. Rev. B 46, 2864 (1992) [2] M. R. Ibarra and P. A. Algarabel. Giant volume magnetostriction in the FeRh alloy. Phys. Rev. B 50, 4196 (1994) [3] Y. Liu, L. Phillips, R. Mattana et al. Large reversible caloric effect in FeRh thin films via a dual-stimulus multicaloric cycle. Nat. Commun. 7, 11614 (2016). [4] Y. Wang, M. M. Decker, T. N. G. Meier et al. Spin pumping during the antiferromagnetic-ferromagnetic phase transition of iron-rhodium. Nat. Commun. 11, 275 (2020). [5] V. Dupuis, A. Hillion, G. Khadra., N. Blanc, D. Le Roy, F. Tournus, C. Albin, O. boisron and A. Tamion. Cubic chemically ordered FeRh and FeCo nanomagnets prepared by mass-selected low-energy cluster-beam deposition: a comparative study. Beilstein J. Nanotechnol. 7, 1850 (2016).

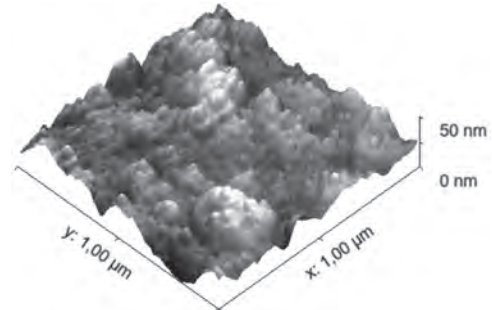


Fig 1: Atomic Force Microscope image of the FeRh 150nm sample taken on tapping mode.

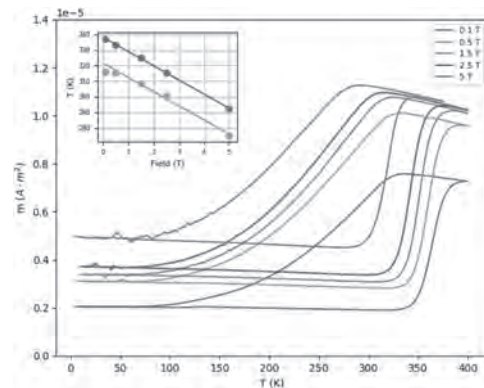


Fig 2: Magnetization as function of the temperature for FeRh 150 nm at different external field. Inserted the temperature of maximum magnetization which follow $T=338.1 K-9.11 \cdot H \mu_0 K/T$ (blue), and temperature of minimum magnetization which follow $T=321.6 K-9.11 \cdot H \mu_0 K/T$ (yellow).

J1-12. Hybrid Metallic Nanowires: Tailoring Magnetic and Plasmonic Properties by Pulsed Laser Deposition.

T. Tran¹, D. Demaille¹, B. Gallas¹, G. Patriarche², Y. Zheng¹ and F. Vidal¹
 1. Institut des NanoSciences de Paris, Sorbonne Université, Paris, France;
 2. Centre de Nanosciences et de Nanotechnologies, Université Paris-Saclay, Saint-Aubin, France

Hybrid nanomaterials, combining ferromagnetic and plasmonic metals, are potential model systems for the study of emergent magnetoplasmonic phenomena, which motivate the development of new nanoarchitectures through top-down and bottom-up approaches. Vertically aligned nanocomposites (VANs) consist of two functional phases embedded in a matrix as illustrated on Fig. 1. Such epitaxial systems can be grown by pulsed laser deposition (PLD); the embedded nanowires (NWs) are formed by self-assembly during the growth. In this contribution, we report on the growth and study of the structural and physical properties of new VANs consisting of hybrid NWs with ferromagnetic and plasmonic parts embedded in an epitaxial oxide thin film. Cobalt and gold, compounds that show low bulk miscibility, are a typical material choice for the growth of hybrid NWs [1]. However, at room temperature pure Co has a hexagonal close-packed structure, which is detrimental to the uniaxial anisotropy of the NWs, and thus would not permit to obtain a bistable magnetic system. In order to get hard uniaxial magnetic properties, the ferromagnetic NWs were made of a CoNi alloy. A compromise of 80% of cobalt and 20% of nickel was chosen to retain an optimal anisotropy with the face-centered cubic phase (fcc) [2]. The plasmonic NWs were made of Au, known to be able to sustain localised plasmon resonances, collective oscillations of the free electrons, in the visible-near infrared range. Au/Co_{0.8}Ni_{0.2} nanowires embedded in a SrTiO₃ matrix were grown on a SrTiO₃(100) substrate at a substrate temperature of 600 °C and high vacuum (< 10⁻⁵ mbar) by sequential pulsed laser deposition, leveraging self-assembly mechanisms driven by metal-oxide phase segregation. Sequential PLD, based on the repetition of a basic sequence, is well suited to get a precise nanoarchitecture; as it offers control over the structure (morphology, epitaxy) and the composition. Such control is crucial for future magnetoplasmonic studies, given that both magnetic and plasmonic properties are significantly affected by the structural properties. The structural properties of the NWs were investigated by transmission electron microscopy (TEM) and x-ray diffraction (XRD) using synchrotron radiation. TEM images (Fig. 1) in plan view show circular sections with a diameter of ≈ 4 nm, whereas scanning transmission electron microscopy images in high-angle annular dark field mode in cross-sectional view reveal elongated segregated ribbons, thus proving the growth of VANs displaying phase segregation in oxide matrix. Further TEM investigations show the proneness of gold NWs to grow onto cobalt-nickel NWs with a proportion of ≈ 80%. XRD indicates a fcc structure with a predominant cube-on-cube epitaxy of Au, Co_{0.8}Ni_{0.2} and SrTiO₃ lattices; in addition, an axial strain up to 5% is measured, pointing a stretch of the Co_{0.8}Ni_{0.2} NWs along the growth axis. The magnetic hysteresis of hybrid NWs were recorded by vibrating sample magnetometry. As shown on Fig. 2, the response is anisotropic and the easy axis of magnetisation is along the long axis of the NW, with a coercive field H_c ≈ 1 T at 10 K; such significant anisotropy stems from the elongated shape of the NWs (shape anisotropy) and the axial strain induced by the epitaxy with the STO matrix (magnetoelastic anisotropy). Furthermore, spectroscopic ellipsometry measurements display two absorption bands at visible and near-infrared wavelengths, attributed to the transverse and longitudinal localised plasmon resonances (LPRs). Such LPRs can be shifted to a suitable wavelength by control of the morphology of the Au NWs. Due to the Joule effect, the plasmon excitation would provoke the heating of the Au NWs, which would act as nanosources of heat for future heat-assisted magnetisation reversal experiments. The separate control of the structure of Au and CoNi NWs enables the tuning of highly anisotropic magnetic and optical properties. This establishes hybrid metallic NWs embedded in an oxide matrix grown by PLD as promising systems for future magnetoplasmonic studies.

[1] M. Hennes, X. Weng, E. Fonda, B. Gallas, G. Patriarche, D. Demaille, Y. Zheng and F. Vidal. "Phase separation and surface segregation in Co-Au-SrTiO₃ thin films: Self-assembly of bilayered epitaxial nanocolumnar composites". Phys. Rev. Materials 3 (3), p. 035002 (2019). doi: 10.1103/

PhysRevMaterials.3.035002 [2] X. Weng, M. Hennes, T. Tran, N. Casaretto, D. Demaille, F. Vidal and Y. Zheng. "Orientation and lattice strain matching of CoNi nanowires embedded in SrTiO₃: unveiling novel strain relaxation mechanisms in vertically aligned nanocomposites". CrystEngComm 22 (28), pp. 4730-4739 (2020). doi: 10.1039/d0ce00574f

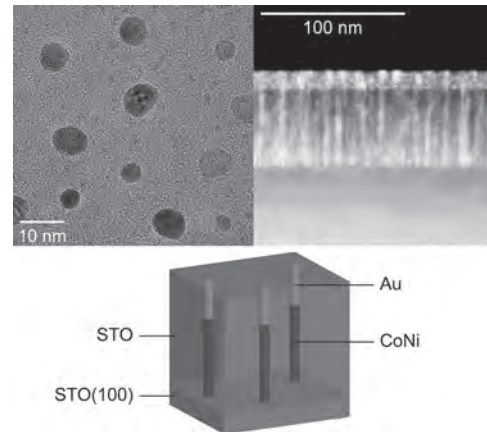


Fig. 1 : (top left) High-resolution transmission electron microscopy image of Au/CoNi nanowires (NWs) embedded in a SrTiO₃ matrix in plan view and (top right) scanning transmission electron microscopy image in high-angle annular dark field mode in cross-sectional view show the ability to grow segregated hybrid NWs. (bottom) Illustration of the metallic hybrid NWs in an oxide matrix; the gold phase sustains localised plasmon resonances, whereas the alloy phase is ferromagnetic.

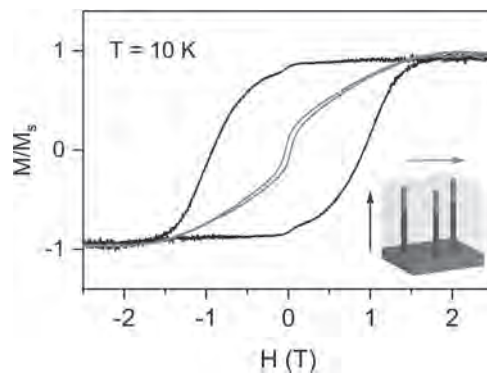


Fig. 2 : Magnetic hysteresis cycles at low temperature (T = 10 K), recorded along the easy axis (black curve) and the hard axis (grey curve) of magnetisation.

J1-13. A Roadmap Toward Expanding Magnetic Nanobarcode Signatures.

M. Zamani Kouhpanji¹, J. Um¹ and B. Stadler¹

1. University of Minnesota, Minneapolis, MN, United States

Magnetic nanowires (MNWs) have been proposed for nanobarcoding and biolabeling for decades, but surprisingly, they have never been successfully realized for these applications due to the lack of reliable decoding strategies. Here, several types of MNWs were electrodeposited into track-etched polycarbonate templates for application as nanobarcode. The coercivity (H_c) and interaction fields (H_u) of the MNWs were engineered using the composition, dimensions, and spatial distributions to tune the remanence spectra¹ of each barcode. This remanence spectrum is the irreversible switching field distribution measured at zero applied field after applying a pre-defined field sequence. It is therefore a complex function of both coercivity and interaction field. An automated algorithm was also introduced to reliably decode unknown remanence spectra measured in unknown combinations of the magnetic nanobarcode^{2,3}. Up-to-date, H_c and H_u distributions themselves have been the most popular magnetic signatures using in decoding, usually measured using the first-order reversal curve (FORC) method^{1,4}. Despite numerous works on tuning H_c and H_u , these parameters can only be independently decoded for a limited number of unique signatures. For instance, H_u for arrays of non-interacting MNWs is always zero, which limits signatures to simply H_c and its distribution. Typical decoding is even harder when both non-interacting and highly interacting magnetic nanobarcode are at the readout simultaneously³. Although the H_c distribution may be inherently distinct for each MNW; fully decoupling the interaction field effects from the coercivity distribution is a very tedious procedure⁵. Our recently proposed approach of decoding via the remanence spectra⁶ has overcome these limitations while also using orders of magnitude fewer measurement points compared to FORC leading to a significantly faster decoding procedure. Figure 1 shows the remanence spectra of a combined measurement with two barcodes: 30nm-diameter Ni MNWs and 100nm-diameter Ni MNWs. The automated algorithm makes a best fit assuming the number of barcodes presence are 1, then 2, then 3. The root-mean-square (RMS) error between the fit and the measurement is calculated at each step. At “n” steps (here 3), the RMS error is not significantly improved, so the number of barcodes is determined to be “n-1” (here 2). This presentation will demonstrate how to expand the number of magnetic nanobarcode remanence spectra using coercivity and interaction field as independent encoding parameters tuned through various strategies. We will also describe our automated algorithm to reliably and rapidly decode unknown remanence spectra, which is also capable to decode other nanobarcode including magneto-optic nanobarcode. In summary, remanence spectra are promising for decoding nanobarcode for three reasons. First, the coercivity and interaction field can be tailored individually to expand the number of remanence spectra encoded magnetic nanobarcode. Second, the decoding can reliably be done even when one of these parameters is zero or negligible and also when the number of nanobarcode presence is unknown. Third, remanence spectra are much faster to measure and less tedious to decouple than standard signatures.

1 Y. G. Velázquez, A. L. Guerrero, J. M. Martínez, E. Araujo, M. R. Tabasum, B. Nysten, L. Piroux and A. Encinas, *Sci. Rep.*, 2020, 10, 21396. 2 M. R. Zamani Kouhpanji and B. Stadler, *Part. Part. Syst. Charact.*, 2020, 2000227. 3 M. R. Zamani Kouhpanji and B. J. H. Stadler, *Nanoscale Adv.*, 2021, DOI:10.1039/D0NA00924E. 4 D. A. Gilbert, G. T. Zimanyi, R. K. Dumas, M. Winklhofer, A. Gomez, N. Eibagi, J. L. Vicent and K. Liu, *Sci. Rep.*, 2014, 4, 1–5. 5 C.-I. Dobrotă and A. Stancu, *J. Appl. Phys.*, 2013, 113, 043928. 6 M. R. Zamani Kouhpanji, A. Ghoreyshi, P. B. Visscher and B. J. H. Stadler, *Sci. Rep.*, 2020, 10, 15482.

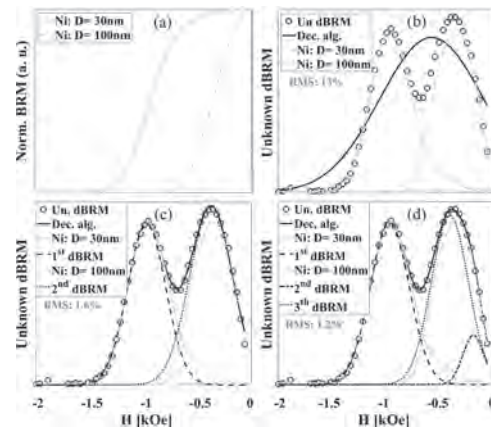


Figure 1: shows encoding and decoding remanence spectra of magnetic nanowires (MNWs) for nanobarcoding. (a) depicts the normalized backward remanence (BRM) spectra of the individual MNWs “encoded” using their dimensions, and (b-d) illustrate the decoding of an unknown BRM spectrum composed of Ni MNWs with diameters of 30nm and 100nm. The reduction percentage of the root-mean-square (RMS) error is the convergence criteria for identifying the number and type of magnetic nanobarcode in the unknown BRM spectra.

Session JP
BIO-APPLICATIONS OF MAGNETISM II
(Poster Session)

Arantxa Fraile Rodríguez, Co-Chair
Universitat de Barcelona, Universitat de Barcelona, Barcelona, Catalunya, ES, academic, Barcelona, Spain

Jonathan Leliaert, Co-Chair
Ghent University, Ghent, Belgium

JP-01. Neural Network Model for Estimation of the Induced Electric Field During Transcranial Magnetic Stimulation.

O.F. Afuwape^{1,2}, O.O. Olafasakin² and D.C. Jiles¹

1. Department of Electrical and Computer Engineering, Iowa State University, Ames, IA, United States; 2. Department of Mechanical Engineering, Iowa State University, Ames, IA, United States

Transcranial Magnetic Stimulation (TMS) is a non-invasive technique of modulating the neurons of the brain. TMS is a tool in cognitive neuroscience for studying neuronal connectivity and brain mapping. It is also approved for the treatment of neuropsychiatric disorders [1]. It functions on the principle of electromagnetic induction in inducing electric field in the neurons of the brain. With TMS studies, accurate estimation of the induced E-Field is usually necessary. This, however, requires a lot of processes, which include the three-dimensional head model generation from magnetic resonance imaging (MRI) scans using the SimNIBS software [2] and finite element analysis to calculate the induced E-Field (Fig. 1). These processes are time-consuming and computationally expensive. Additionally, with each head model's uniqueness, outcomes cannot be generalized across a particular population as the intensity of E-Field is subject-specific [3], [4]. A few studies have explored the use of artificial neural networks to estimate the electric field from T1 MR images [5], [6], [7]; however, none has considered the effect of different coil geometry in their estimation. In this research, the authors develop a deep neural network (DNN) model to determine the induced E-Field directly from the patient's MRI scan and across different coil types. We trained neural network models from realistically anatomic head models' and across 16 different coil type to predict the induced electric field in the brain and scalp (E-Max brain and scalp) and the volume of stimulation of the brain and scalp (V-half brain and scalp) from T1 MR images and specific coil type. Using Deep Neural Network (DNN), the processing and estimation time for the induced E-Field is measurably reduced, which is helpful both to clinicians and researchers as the need to create subject-specific anatomical head structures is eliminated. This will also be beneficial to the TMS patients as there will be no need for additional stimulation sessions with the different coil types as the DNN network is able to predict the outcome from each coil type. The other advantage of the DNN model is that the E-Field from the different coil types can be compared simultaneously. Preliminary results for the E-Max brain report a correlation coefficient of 0.93 for the training dataset and 0.88 on the test dataset, as shown in the parity plot in Fig. 2.

[1] L. J. Gomez, S. M. Goetz, and A. V. Peterchev, "Design of transcranial magnetic stimulation coils with optimal trade-off between depth, focality, and energy," *J. Neural Eng.*, vol. 15, no. 4, p. 046033, Aug. 2018, doi: 10.1088/1741-2552/aac967. [2] M. Windhoff, A. Opitz, and A. Thielscher, "Electric field calculations in brain stimulation based on finite elements: An optimized processing pipeline for the generation and usage of accurate individual head models," *Human Brain Mapping*, vol. 34, no. 4, pp. 923–935, 2013, doi: 10.1002/hbm.21479. [3] F. Syeda, H. Magsood, E. G. Lee, A. A. El-Gendy, D. C. Jiles, and R. L. Hadimani, "Effect of anatomical variability in brain on transcranial magnetic stimulation treatment," *AIP Advances*, vol. 7, no. 5, p. 056711, Jan. 2017, doi: 10.1063/1.4974981. [4] P. C. Miranda, L. Correia, R. Salvador, and P. J. Basser, "The Role of Tissue Heterogeneity in Neural Stimulation by Applied Electric Fields," in *2007 29th Annual International Conference of the IEEE Engineering in Medicine and Biology Society*, Aug. 2007, pp. 1715–1718, doi: 10.1109/IEMBS.2007.4352640. [5] J. A. Livezey, K. E. Bouchard, and E. F. Chang, "Deep learning as a tool for neural data analysis: Speech classification and cross-frequency coupling in human sensorimotor cortex," *PLoS Comput Biol*, vol. 15, no. 9, p. e1007091, Sep. 2019, doi: 10.1371/journal.pcbi.1007091. [6] Tatsuya Yokota, Toyohiro Maki, Tatsuya Nagata, Takenobu Murakami, Yoshikazu Ugawa, Ilkka Laakso, Akimasa Hirata, Hidekata Hontani, Real-time estimation of electric fields induced by transcranial magnetic stimulation with deep neural networks, *Brain Stimulation*, Volume 12, Issue 6, 2019, Pages 1500-1507, ISSN 1935-861X, doi: <https://doi.org/10.1016/j.brs.2019.06.015>. [7] A. S. Lundervold and A. Lundervold, "An overview of deep learning in medical imaging focusing on MRI," *Zeitschrift für Medizinische Physik*, vol. 29, no. 2, pp. 102–127, May 2019, doi: 10.1016/j.zemedi.2018.11.002.



Fig. 1. Conventional Process for Induced Electric Field Estimation during TMS

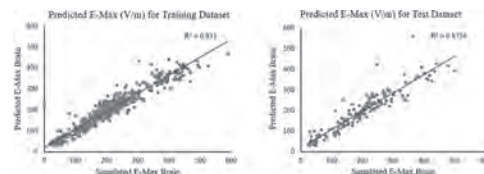


Fig. 2. Parity Plots of the E-Max Brain for the Test and Training dataset.

JP-02. Low Temperature Synthesis of Functionalized Magnetic Nanoparticles Engineering for Cancer Theranostics.

K. Chinnasamy² and V. Harris¹

1. *Electrical and Computer Engineering, Northeastern University, Boston, MA, United States*; 2. *Manheim Township High School, Lancaster, PA, United States*

In the medical world, today's challenge is to kill and control tumors at a cellular level, allowing a more localized (confined) treatment for the eradication of malign cells. Due to this localized treatment, secondary harmful effects induced on healthy cells would be significantly reduced. In fact, different approaches have been used to apply hyperthermia in tumor regions, but with the harmful side effects it defeats the purpose. Hence, the author selected to engineer biocompatible magnetic nanoparticles, which are much smaller than the pore size of the cells, for hyperthermia and drug delivery applications. In order to achieve this goal, one has to produce biocompatible magnetic nanoparticles that are controlled regarding size and shape for hyperthermia treatment. Furthermore, FeCo nanoparticles have superior magnetic properties (230-240 emu/g) than iron oxide nanoparticles (60-80 emu/g). However, this idea is not yet fully explored because of the commercial unavailability of nanoparticles that are size and shape controlled; toxicity also plays a key role in regards to the commercial unavailability. Here, the author presents a cheap, economical, and environmentally friendly approach to prepare the surfactant coated FeCo nanoparticles in the size range of 15-25 nm with a decent amount of dispersity. The FeCo nanoparticles are prepared by using the "mixed glycol process," with which Fe and Co metal salts are used as precursors. Mixed polyols can increase the viscosity of the solution and can reduce the migration rate of metal ions in the solution. First, the ethylene glycol, trimethylene glycol, and polyethylene glycol were used in different ratios, and then the metal precursors were added as well. To increase the reaction rate, sodium hydroxide (NaOH) was used. Further, the surfactants (i) polyvinylpyrrolidone (PVP) and (ii) a mixture of oleylamine and oleic acid were used to control the particle size, shape and dispersity. The experiment was carried out at different temperatures between 70 and 110° C. Once the temperature was raised to 60° C, the solution started to change from a pink to green color. At 110° C, the solution also became a dark green color as well. After an hour, the reaction was completed, the mantle heater was switched off, and left for cooling. After cooling, the reaction flask was taken out and the viscous solution was poured into four centrifuge tubes; this is to centrifuge the samples at 2500 rotation per minute using a small lab scale centrifuge set up for 10 minutes. The following are the observations and data seen in the experiment. The particles that were prepared without surfactants had agglomerated (clustered) particles with an irregular shape. However, the PVP and oleylamine/oleic acid coated samples had a cubic shape for the particles, with average particle sizes in the range of 15 and 20-25 nm respectively. The X-ray diffraction analysis characterized that the structure was the single phase body centered cubic structure. The magnetization value is about 210 emu/g, which is higher than the iron oxide nanoparticles. The nanoparticles with surfactants show well dispersion in ethanol. Since these nanoparticle sizes are smaller than the size of the cell, it is possible to use these particles for hyperthermia and drug delivery applications.

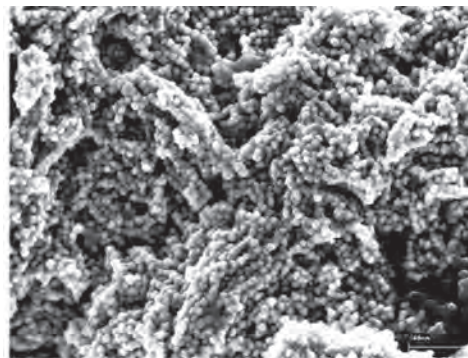


Fig. 1. SEM image of the low temperature synthesized FeCo nanoparticles through mixed glycol process

JP-03. Cancer Cells Death Induced by Magneto-Mechanical Actuation of Fe-Cr-Nb-B Magnetic Particles Carried by Stem Cells to the Cancer Cells Area.

H. Chiriac¹, A. Minuti^{1,2}, C. Stavila^{1,2}, L. Labusca¹, D. Herea¹ and N. Lupu¹
 1. Dept. of Magnetic Materials & Devices, National Institute of R&D for Technical Physics, Iasi, Romania; 2. Faculty of Physics, "Alexandru Ioan Cuza" University, Iasi, Romania

Magnetic particles (MPs) found their usefulness in different cancer treatment applications, such as magnetic hyperthermia, magnetic controlled delivery and release of antitumoral drugs at the targeted site of a tumor, or through magneto-mechanical actuation. Recently, we have introduced a new type of magnetic particles (MPs), prepared by wet milling of superferromagnetic Fe-Cr-Nb-B precursor glassy ribbons, for cancer treatment by magneto-mechanical actuation in low magnetic fields (1 ± 20 Oe) [1]. The rectangular shapes of newly developed MPs and the superferromagnetism of the glassy alloys of which they are made induce important magnetic shape anisotropies which, in association with a large saturation magnetization, generate an improved torque in a rotating magnetic field, producing important damages on the cellular viability of MG-63 human osteosarcoma (HOS) cells, a form of bone cancer. In this work we studied the possibility of transporting Fe-Cr-Nb-B MPs to areas with cancer cells (HOS), using adipose derived stem cells (ADSC) as carriers, considering their tumor-targeting capacity [2], and the effect of magneto-mechanical actuation of the MPs on HOS viability. Fe-Cr-Nb-B MPs have dimensions between 5 and 100 nm. The Fe-Cr-Nb-B MPs prepared by wet milling were used to obtain a ferrofluid (FF) that was added to the cell culture media before adding it in the cell cultures. Afterwards, HOS and ADSC cells were incubated for 24h with the MPs, and cellular viability assay was performed with MTT (3-(4,5-dimethylthiazolyl-2)-2,5-diphenyltetrazolium bromide). We performed the tests by measuring the cell proliferation rate for 1 mg/ml of particles on both cell types (HOS and ADSC). No cytotoxic effect was observed, the cell proliferation being improved in cell culture incubated with particles. At the same time we performed two tests to confirm the presence of MPs inside both cell types. This was accomplished using transmission electron microscopy (TEM) and colorimetric Ferrozine assay, the latter evaluating the quantity of iron inside the cell. MPs upload by HOS was confirmed using TEM, the particles can be seen both in the extracellular and intracellular medium, being incorporated as single or aggregated particles. Iron quantity per cell was evaluated 48h after adding the MPs to the culture media. We calculated the iron content per cell after subtracting the normal quantity of iron in similar culture condition. ADSC, being larger cells, incorporated larger quantities of MPs (1.12 ng per cell) than HOS (0.31 ng per cell). ADSC cellular migration, both loaded and non-loaded with MPs, was recorded by time-lapse imaging performed using an Evos optical microscope while cells were inside a self-made mini-incubator. Before evaluation, the two cell population (ADSC-MPs and tumor cells) were separated by a free space of about 0.5 mm made mechanically in the co-culture by using a pipette tip ("wound healing" model). The traveled distance of loaded ADSCs towards the zone of the tumor cells was the highest among the evaluated ones. The recorded films showed that MPs-loaded ADSC were able to easily target osteosarcoma cells, moving at twice the speed of the MPs-free ADSC (control sample) in similar cultures (Fig. 1). Magneto-mechanical actuation was performed in a system consisting of four coils placed in cross, which can produce low magnetic field (1 ± 20 Oe). The destruction of HOS co-incubated with MPs-loaded ADSC was performed through controlled magneto-mechanical actuation (MMA). Magneto-mechanical actuation led to the destruction of ADSC and to the release of MPs on HOS cells, the latter incorporating the released MPs (Fig. 2). By magneto-mechanical actuation, the HOS viability dropped down to $21 \pm 22\%$. The rotational motion of the irregular shaped MPs produced in the rotating magnetic led to irreversible damages on the cells membranes and organelles, and, subsequently, the cells death. We have successfully showed that Fe-Cr-Nb-B magnetic particles (MPs) are highly biocompatible *in vitro*. MPs were easily incorporated by ADSC and HOS cells, results confirmed through TEM imaging and Ferrozine assay. MPs loaded ADSCs display increased motility towards tumor cells, compared with their unloaded counterparts. The scope of the study, the destruction of HOS through MMA of the MPs released from ADSC

was confirmed through MTT assay. MMA led to the release of the MPs towards tumor cells, the latter being destroyed in high proportion (about 80%) by immediate applying of the MMA. Consequently this method could be successfully implemented in the treatment of bone cancer. *Acknowledgements* - Work supported by the Romanian Executive Agency for Higher Education, Research, Development and Innovation Funding (UEFISCDI) under contract no. 502PED/2020 (project PN-III-P2-2.1-PED-2019-3442/OPTIMAG).

[1] H. Chiriac et al., Scientific Report, Vol. 8, Article Number 11538 (2018).
 [2] M.G. Scioli et al., International Journal of Molecular Sciences, Vol. 20, p. 3296 (2019).

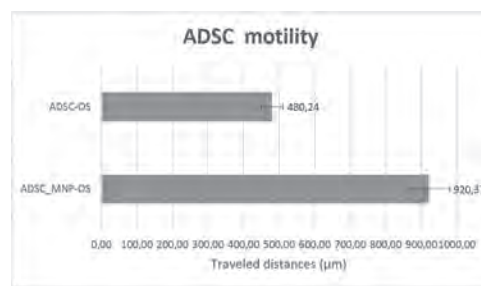


Fig. 1. *In vitro* cell migration of ADSC loaded and non-loaded, respectively, with MPs towards tumor cells.

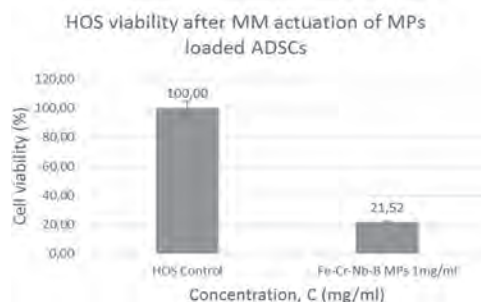


Fig. 2. Cell viability of HOS and ADSC cells, controls and cells with MPs after MM actuation.

JP-04. Observation of Red Blood Cell Membrane Charge Using Magnetic Beads Under Pulsed Magnetic Field.

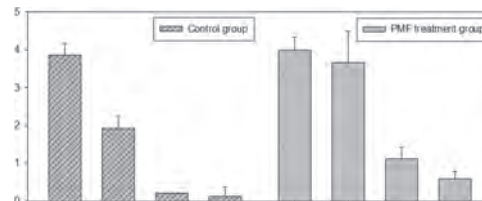
Y. Choi¹, S. Bang¹ and H. Lee¹

1. Oriental Biomedical Engineering, Sangji University, Wonju, The Republic of Korea

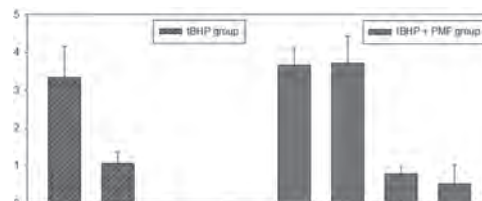
Introduction: Red blood cell(RBC), which passes through capillaries and exchanges O₂ and CO₂ with surrounding tissues, plays a very important in the blood circulation in the human body. Imbalance in blood circulation could lead to various cardiovascular related diseases such as high blood pressure, arteriosclerosis, diabetes, and stroke.[1] This is closely related to RBC aggregation. Negatively charged RBC membrane arranges a compact layer of positive ions around the membrane by electrical attraction with cations in plasma. The rearranged ions layer in plasma forms zeta potential with compact layer. When the electrostatic interaction between RBCs, i.e., zeta potential increases, RBC aggregation is improved. It is known that zeta potential depends on electronegativity of the RBC membrane, the dielectric constant of the medium and ionic strength [2]. Since pulsed magnetic field (PMF) influences human physiology, many clinical studies demonstrated the effect of PMF for wound healing, reducing pain, increasing angiogenesis, as well as improving blood circulation.[3-5] In this study, we have tried to elucidate the effect of PMF on RBC aggregation by indirectly observing zeta potential using negatively-charged magnetic beads(MB). Our hypothesis is that the increase of negative charges on RBC membrane results in the increase of cations in the compact layer, thus the increase of the zeta potential. As a result, the number of MB attached to the RBC increases, as the binding force between MB and compact layer increases. **Experimental Method:** Blood needed for experiment was obtained from Korean Red Cross after reviewing IRB exemption in Sangji University Bioethics Committee. Whole blood of 6 ml was centrifuged at 3000 rpm for 5 min in 4 °C for separating RBCs and plasma. MB used this experiment has diameter 1 μm with OH⁻ groups (SiMAG-Silanol, Chemicell). To clearly see the MB attached to RBCs and, in addition, to avoid blood clots caused by proteins in plasma, RBC suspension of hematocrit (Ht) of 10% was prepared using PBS(phosphate buffer saline). The amount of MB added to RBC suspension was 0.5 mg. RBCs were also oxidative stressed with tBHP(Tert-Butyl hydroperoxide) in 0.4 mM at 37 °C incubator for 30 min, in order to confirm the change of RBCs membrane charge due to oxidative stress under PMF stimulus. In oxidative stressed RBCs, hemoglobin(Fe²⁺) is altered to methemoglobin(Fe³⁺) because of loss an electron, thereby, electronegativity of RBC membrane will be changed.[6] Each sample was exposed to PMF for 3 min. Our PMF stimulator system consisted of single layered coil of 10 turns with an elliptical shape of 12.0 x 4.5 cm. The maximum intensity is 0.27 T at a transition time of 0.102 ms, with pulse intervals of 1 Hz. The numbers of RBC attached MB were compared with control group and PMF treatment group. Only RBCs with a distance of about 1 μm between the MB and the surface of RBC were counted using hemocytometer. **Results and Discussion:** Fig.1. shows the numbers of RBCs according to the number of attached MB in the control and PMF treatment group. The numbers of RBCs attached MB increased after PMF treatment. The more the number of MBs attached to RBCs, the thicker the compact layer surrounding RBC membranes. This phenomenon might be inferred due to an increase of zeta potential, thereby, increase of negative charges on the RBC membrane. Thus, it can be interpreted that MB having hydroxide OH⁻ group are more attached to RBCs via binding force between MB and compact layer. Also the numbers of MB in the group treated tBHP and the group exposed to PMF after tBHP treatment (tBHP+PMF) were compared in Fig.2. Although the number of MB attached to RBCs was 1~2 in tBHP group, after PMF stimulus, i.e. in tBHP+PMF group it appears the number of MB attached to RBCs increased up to 3~4. This might be explained that PMF affects the increase of RBC membrane charge on not only normal RBCs but also oxidative stressed RBCs. Therefore, it can be deduced that high instantaneous flux change of PMF improves the aggregation of RBCs by increasing the zeta potential, due to the increase of the membrane charge.

[1] H. L. Goldsmith, G. R. Cokelet, and P. Gaechtgens, *Am. J. Physiol.* 257, H1005 (1989) [2] H. P. Fernandes, C. L. Cesar and M. D. L. Barjas-Castro, *Rev. Bras. Hematol. Hemoter.* 33(4), 297(2011) [3] N. M. Shupak, J. C.

McKay, W. R. Nielson, G. B. Rollman, F. S. Prato and A. W. Thomas, *Pain Res Manag.* 11(2), 85(2006) [4] L. X. Alvarez, J. McCue, N. K. Lam, G. Askin and P. R. Fox, *J. Am. Anim. Hosp. Assoc.* 55, 83(2019) [5] J. W. Mok, S. H. Han and H. S. Lee, *AIP Advances* 10, 015005(2020) [6] A. Knishita, Y. Nakayama, T. Kitayama and M. Tomita, *The FEBS Journal* 274(6), 1449(2007)



The numbers of RBCs according to the number of attached MB in the control and PMF treatment group



The numbers of RBCs according to the number of attached MB in the tBHP treated group and tBHP+PMF treatment group

JP-05. Multifunctional Fe-Au Nanostructures for Biomedical Applications.

S.C. Freitas¹, J.H. Belo¹, C. Sousa¹, R. Magalhães¹, H. Crespo¹, M. Canhoto¹, M.P. Almeida², E. Pereira², B. Gonçalves Almeida³, B. Machado da Silva³ and J. Pedro Esteves de Araújo¹

1. IFIMUP, Universidade do Porto Faculdade de Ciências, Porto, Portugal; 2. LAQV/REQUIMTE, Universidade do Porto Faculdade de Ciências, Porto, Portugal; 3. CF-UM-UP, Universidade do Minho, Braga, Portugal

Cancer is the leading cause of death in Europe after cardiovascular disease, accounting for about 20% of deaths on that continent [1]. In recent years, hyperthermia emerged as a promising treatment approach in oncology consisting in raising the temperature of cancer cells to 40-45°C to reach apoptosis i.e., programmed cell death. Differences in the vasculature of tumors and healthy tissues leads to different heat-induced damage responses. At temperatures up to 45°, the vasculature of healthy tissues allows an effective heating dissipation, while the tumor's lumpy and disorganized ones makes them less efficient in heat dissipation. Therefore, for the same thermal dose, the healthy tissue adjacent to the tumor can remain at lower temperatures than the tumor itself [2]. One way to reach local and controlled hyperthermia is via functionalizable nanostructures that are activated by external stimuli, such as magnetic fields or electromagnetic radiation. In this context, gold nanostructures (Au-NS) have been the subject of much attention in the academic and clinical environment, due to their biocompatibility and high absorption of electromagnetic radiation in the near-infrared range caused by its surface plasmon resonance [3]. In parallel, magnetic nanostructures based on iron (Fe-NS) have also been gaining attention, since they can combine the diagnostic (as contrast agents for magnetic resonance imaging) and therapy (magnetic hyperthermia) properties [4]. Although the Fe-oxide NS are the most reported in the literature, Fe-NS are a promising alternative. The high magnetic moment of Fe-NS can improve the heat dissipation phenomena produced by the magnetic hysteresis, due to the irreversible magnetization/ demagnetization processes induced by an applied alternating magnetic field [5]. The main goal of this work is to combine the "best of both worlds" producing multifunctional Iron-Gold nanostructures (Fe-Au-NS) with high heating performance when stimulated with radiation (500-1000nm) and with alternating magnetic fields, for applications in controlled and localized hyperthermia. Fe-Au-NS were produced by two methods: 1) through the ablation of Iron and Gold targets with a femto-second pulsed laser in liquids (such as ethanol) and 2) by electrodeposition in self-organized alumina matrices. The first technique is particularly interesting for the development of NS-Fe-Au with complex structures such as the core-shell structure [4]. In turn, the second technique allows a controlled growth of nanowires, nanotubes, and more complex morphologies such as segmented Fe-Au-Fe nanowires [6]. The Fe-Au-NS have been fully characterized with scanning electron microscopy (SEM), X-ray diffraction (XRD) and superconducting quantum interference device (SQUID) techniques. The morphological analysis showed a narrow distribution in diameter and length of the obtained structures with improved robustness and high yield, making these techniques versatile approaches strongly compatible with large scale production. Finally, we show the possibility to tune accurately the size of the nanostructures and consequently provide an easy control over the magnetic properties of these nanostructures ultimately enabling reaching the superparamagnetic regime.

[1] World Health Organization, Regional office for Europe: <http://www.euro.who.int/en/health-topics/noncommunicable-diseases/cancer/data-and-statistics> [2] A. Espinosa, *et al*, "Magnetic (Hyper)Thermia or Photothermia? Progressive Comparison of Iron Oxide and Gold Nanoparticles Heating in Water, in Cells, and In Vivo", *Advanced Functional Materials*, 28, 37 (2018) [3] Huang, *et al* "Cancer Cell Imaging and Photothermal Therapy in the Near-Infrared Region by Using Gold Nanorods", *Journal of American Chemical Society*, 128, 2115-2120 (2004) [4] P. Wagener, *et al* "Solvent-surface interactions control the phase structure in laser generated iron-gold core-shell nanoparticles", *Scientific Reports*, 6, 23352 (2016) [5] L. Peixoto, *et al*, "Magnetic nanostructures for emerging biomedical applications", *Applied Physics Reviews*, 7 (2020) [6] C. Sousa, *et al*, "Nanoporous alumina

as templates for multifunctional applications" *Applied Physics Reviews*, 1, 031102 (2014)

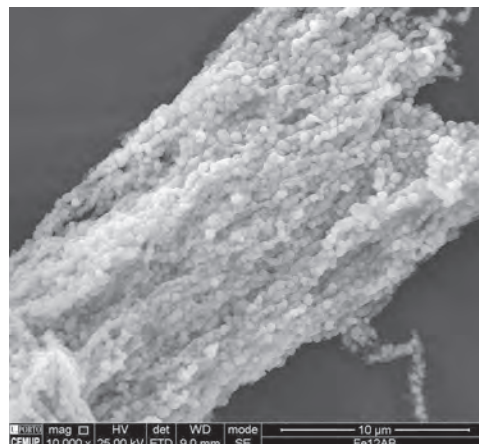


Fig 1. Fe-NPs synthesized via ablation of an iron target by femtosecond laser in ethanol, in the presence of magnetic field applied post LAL

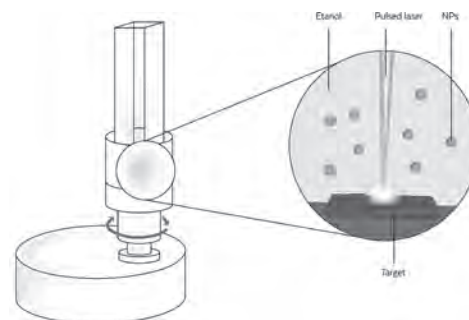


Fig 2. Laser Ablation in Liquids Set-up

JP-06. Possibilities of Registration of Biological Molecules via Magnetic Particles.

L.P. Ichkitidze^{2,1}, M. Belodedov³, A. Gerasimenko^{2,1}, D. Telyshev^{2,1}, Y. Rezvantseva¹ and S. Selishchev²

1. I.M. Sechenov First Moscow State Medical University, Moscow, Russian Federation; 2. National Research University of Electronic Technology, MIET, Zelenograd, Moscow, Russian Federation; 3. National Research University of Technology (BMSTU), Moscow, Russian Federation

For all materials in the form of particles of micron, submicron, and nanosize, there is a significant transformation of their magnetic parameters in comparison with bulk samples of these materials. In this case, the ferromagnetic material becomes a superparamagnetic. In this state, per atom, the magnetization, magnetic moment, and magnetic anisotropy of magnetic particles (MPs) significantly exceed the analogous parameters of a bulk material. Therefore, MP is often used as a tool as an addition to various methods of registration and isolation of molecules in biological media, including DNA and RNA. Undoubtedly, DNA extraction is an important platform in various fields of research, such as biotechnology, diagnostics and therapy, forensic medicine, determination of paternity, etc. One of the modern techniques is based on the use of spherical MPs coated with active substances for the extraction of DNA and RNA. The use of MPs can significantly increase the storage life of nucleic acid samples. In our work, we investigate the methods of using magnetic particles in a biological environment and the possibility of their registration with modern magnetic field sensors (MFS). Figure 1 shows the interaction of an external magnetic field with a spherical MP in a biological environment, as well as with a set of such MPs, that is, with an aggregate of magnetic particles. It also lists the main parameters of the MP and the aggregate created from many magnetic particles. An estimate is obtained for the maximum possible distance that ensures reliable detection of the unit: $l \approx 0.01 D \Delta (J^* \times \rho n)^{1/2}$, (1) where δB is the threshold magnetic sensitivity of the MFS, J^* is the magnetic moment per mass of the magnetic material, and ρ is the density of the magnetic material. All values of the considered quantities are given in the system of reporting units in SI. It has been established that magnetite (Fe_3O_4) particles with a specific magnetization of $J^* \sim 50 \text{ A} \times \text{m}^2/\text{kg}$ with a size of $\Delta \sim 50 \text{ nm}$ and a concentration of $n \sim 10^{18} \text{ m}^{-3}$ can be detected by a commercial superconducting magnetometer (SQUID MGreen) at distances of $l \leq 0.1 \text{ m}$ [1]. This estimate follows from (1), where the following are taken into account: $\delta B \sim 10^{-14} \text{ T}$, $D \sim 10^{-3} \text{ mm}$, $\rho \sim 5 \times 10^3 \text{ kg/m}^3$. Note that the existing research combined magnetic field sensors (CMFS) can have better magnetically sensitive parameters than commercial SQUID magnetometers [2-4]. Therefore, their application will make it possible to decrease the values of and, and to increase them relative to the above estimates. Therefore, CMFS can be more efficient with respect to SQUIDS. Thus, single molecules of DNA, RNA, etc., (or their combination) attached to MPs in small ($\sim 10^{-3} \text{ mm}$) aggregates can be non-invasively recorded by modern magnetometers and further isolated. Let us emphasize the fact that carbon nanotubes (CNTs), which are present at their ends, of catalytic ferromagnetic particles or encapsulated inside nanotubes, can serve as magnetic particles. In this case, after binding surface active substances to CNTs, they can also be used to fix and isolate DNA, RNA, and other biological molecules, along with magnetic particles. This work was supported by the Ministry of Science and Higher Education of the Russian Federation (project no.075-03-2020-216 from 27.12.2019). δB

1. <http://www.supracon.com/en/msgreen.html> 2. L.P. Ichkitidze AIP Adv., 3, pp. 062125–062128 (2013) 3. L.P. Ichkitidze and A.N. Mironyuk J. Phys.: Conf. Ser., 400, no. 2, Art. no. 022032 (2012) 4. M. Pannetier, C. Fermon, G. Le Goff et al. Science, 304, pp. 1648–1650 (2004)

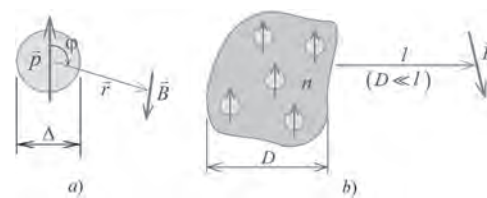


Fig. 1. Spherical MP in a biological environment: (a) – isolated MP; (b) – aggregate of MPs. Here are the notation: Δ – the diameter of the MP, D – the average size of the MPs, p – the magnetic moment of the MP, r – the distance between the MP and the MFS, B – the magnetic field induction at the point where is the MFS, ϕ – the angle between the vectors p and r , n – the concentration of MPs in the aggregate, l – the distance from the unit to the MFS. It is assumed that an external magnetic field magnetizes the MP.

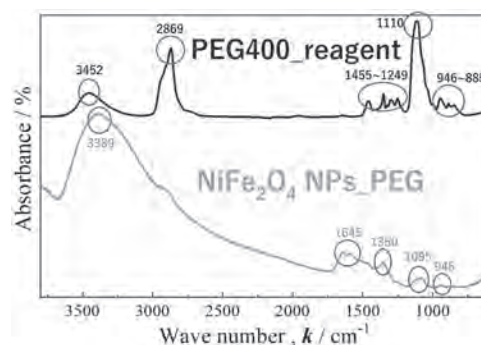
JP-07. PEGylation of Ni_{1-x}Zn_xFe₂O₄ Nanoparticles With Heat Dissipation Based on Néel and Brownian Relaxation.

K. Kodama¹, S. Hamada¹, K. Nashimoto¹, K. Aoki² and Y. Ichiyangi^{1,3}

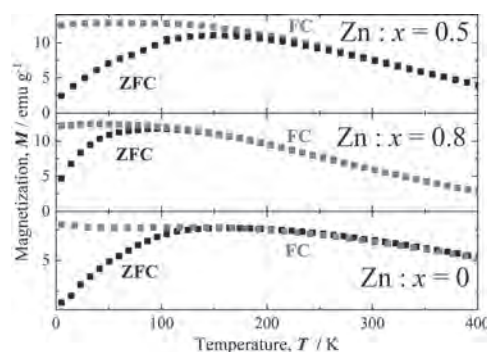
1. Engineering, Yokohama Kokuritsu University, Yokohama, Japan;
2. Environmental information, Yokohama Kokuritsu University, Yokohama, Japan; 3. Research Center for Thermal and Entropic Science, Osaka University, Suita, Japan

Ferrite nanoparticles (NPs) have demonstrated considerable potential for use in biomedical applications such as magnetic resonance imaging, magnetic particle imaging, and magnetic hyperthermia treatment (MHT)[1,2]. In the medical application of ferrite NPs, biocompatibility must be ensured. To enhance the biocompatibility, we modified the NPs by using polyethylene glycol (PEG), which is highly hydrophilic and biocompatible. Furthermore, in the heat dissipation of the magnetic NPs, caused by the relaxation mechanism, the imaginary part of the magnetic susceptibility χ'' at the room temperature is a key parameter. Moreover, *M*-Zn ferrite NPs (*M* = Ni, Co, Mn, Fe) are multielement ferrites, whose magnetization can be increased by doping with nonmagnetic Zn ions. The purpose of this study was to develop a sample with improved biocompatibility by PEGylation, to clarify the change in magnetization characteristics due to the Zn doping effect, and to clarify the heat generation mechanism of the sample for MHT application. This study was focused on Ni-Zn ferrite NPs, and NPs with different contents of Zn ions were prepared. Ni_{1-x}Zn_xFe₂O₄ (*x* = 0, 0.2, 0.5, 0.8) NPs coated with PEG were synthesized using our original method[2]. The crystal structures of these particles were examined through X-ray diffraction and X-ray absorption spectroscopy. The particle diameters were controlled to be between 5–20 nm by controlling the amount of water, and the samples with different Zn doping amounts were adjusted to have a particle size of 10 nm. PEGylation in the particles was confirmed through the Fourier-transform infrared spectrometry technique (Fig. 1) and by using a thermogravimeter-differential thermal analyzer. The magnetization curves of all the samples were obtained at 300 K in a ± 10 kOe field. All the samples exhibited superparamagnetic behavior with no coercive force, and the magnetization values ranged between 39 and 43 emu g⁻¹ with only a slight difference. The field-cooled/zero-field-cooled measurement showed that, in terms of the temperature dependence of the magnetization, the blocking temperature T_B ranged between 105 and 150 K (Fig. 2). χ'' exhibited a peak value in the *x* = 0.5 sample at room temperature, and the most effective temperature rise was expected in this composition because the heat dissipation of superparamagnetic particles depends on the value of χ'' . Moreover, we measured the increase in the temperature in the AC magnetic field of 15 kHz, 130 Oe for all the samples. The temperature of the samples was measured using an optical fiber thermometer. The value of heat dissipation could be attributed to the Néel relaxation system. To clarify if the heat generation mechanism pertained to the Néel relaxation or Brownian relaxation, the heating effect in silicone oil and water was evaluated at a frequency of 210 kHz. It was noted that the Néel relaxation and Brownian relaxation were dominant for particle sizes of approximately 10 nm and more than 20 nm, respectively. Thus, we successfully developed highly biocompatible magnetic NPs and experimentally clarified the contribution of the Néel and Brownian relaxation depending on the particle size.

[1]Shigeoka, D., Yamazaki, T., Ishikawa, T., Miike, K., Fujiwara, K., Ide, T., Oshima, A., Hashimoto, T., Aihara, D., Kanda, K., Usui, A., Hosokai, Y., Saito, H. and Ichiyangi, Y., 2018. Functionalization and magnetic relaxation of ferrite nanoparticles for theranostics. *IEEE Transactions on Magnetics*, 54(11), p.6100707. [2]Oshima, A., Kanda, K., Fujiwara, K., Ide, T., Takano-Kasuya, M., and Ichiyangi, Y., 2020. PEGylation of Co-Zn Ferrite Nanoparticles for Theranostics. *Journal of Nanoscience and Nanotechnology*, 20(12). Pp.7255–7262.



FT-IR spectra for PEG400 reagent and NiFe₂O₄ NPs coating with PEG400.



Temperature dependence of magnetization of both field-cooled (FC) and zero-field-cooled (ZFC) magnetization under 100 Oe field for *x* = 0, 0.5, 0.8 samples.

JP-08. Influence of ELF Magnetic Field on Thyroxine-Inducing Forced Metamorphosis of Axolotl (*Ambystoma Mexicanum*).

H. Nakagawa¹, S. Fujiwara² and T. Tadokoro¹

1. Department of Electrical and Electronic Engineering, Tokyo Denki University, Tokyo, Japan; 2. Division of Clinical Research, CPCC, Tokyo, Japan

Background Over a long period of time, the Mexican axolotl (*Ambystoma mexicanum*) has been used as an invaluable model for regenerative capacity [1]–[3]. On the other hand, there are no reported studies of the observation of the capacity under exposure to extremely low frequency (ELF) magnetic fields. Our previous report already provided a precious finding about the influences of a gradient/ELF magnetic field on axolotl metamorphosis induced forcibly with a thyroid hormone [4]. In this research, we investigated the ELF magnetic effects on axolotl-tailfin regeneration, as well as the survival rates of the axolotls influenced by the presence of thyroxine (T_4). **Experimental** Twenty axolotls (about 120 mm) were bred under the same condition as group feeding. Before performing this experiment, axolotls were individually kept in 0.85-L square boxes containing a de-chlorinated water (0.7 L) without aeration under illumination of $250 \mu\text{Em}^{-2}\text{s}^{-1}$ on a 12 : 12 h L : D photocycle. Employing an original water-renewing system [4], the water temperature was strictly controlled at 24°C. Exposures of axolotls to ELF fields (10 mT at 10–100 Hz) were performed using an air-cored coil system. The regenerations of the axolotl-tailfins were monitored every day, and the survival rates were evaluated minutely. **Results** As it turned out, we found that the initiation timings of ELF field exposure did affect the rapidity of the axolotl-tailfin regeneration, as well as the metamorphic rapidity of the T_4 -administrated axolotls (Fig. 1). In addition, there were a few distinct patterns that revealed a serious indigestion in each of the salamanded bodies (Fig. 2). Our data could prove to be helpful for future reference with respect to a magnetic control study of tissue-regeneration.

1) T. Demircan *et al.*, Proteomics 17, 1600338 (2017). 2) L. Alibardi, J. Exp. Zool. A, Ecol. Genet. Physiol. 323, 757 (2015). 3) K. Mitogawa *et al.*, PLoS ONE 10, e0133375 (2015). 4) H. Nakagawa and M. Ohuchi, IEEE Trans. Magn. 54, 5000405 (2018).

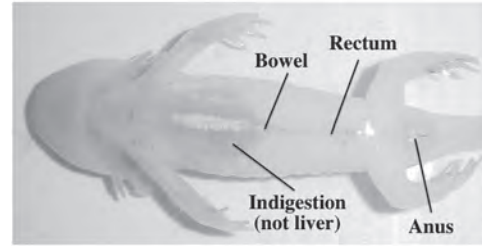


Fig. 2. Mexican axolotl with serious indigestion.

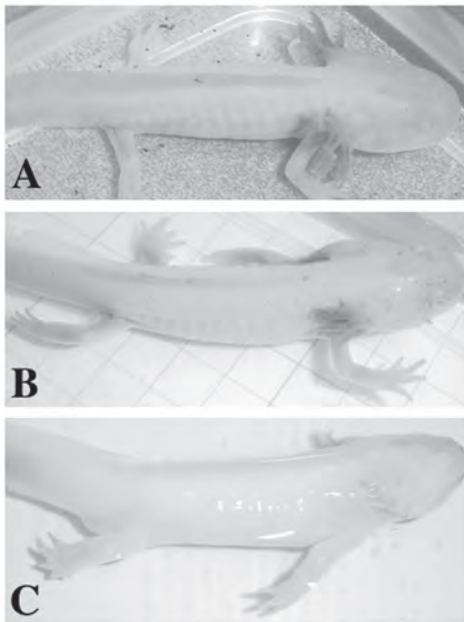


Fig. 1. Timeframe of morphological changes in T_4 -administrated axolotls. (A) Day 0. (B) Day 7. (C) Day 14.

JP-09. Research on X-Shape Quad Helix Coil for Transcranial Magnetic Stimulation.

N. Zhang¹, J. Shi¹, Y. Zhang¹, P. Song¹, B. Lai³, T. Zhu¹, S. Ning² and S. Wang¹

1. School of Electrical Engineering, Xi'an Jiaotong University, Xi'an, China; 2. School of Electronic Information and Artificial Intelligence, Shaanxi University of Science and Technology, Xi'an, China; 3. Quanzhou Experimental Middle School, Quanzhou, China

I. Introduction Nowadays, the bio-effect of the magnetic field has been confirmed, and the magnetic stimulations on human tissues have drawn a considerable interest around the world. Magnetic stimulation has many advantages. For instance, it is easier to achieve a deeper region beneath the skin without causing any trauma or pain. The magnetic stimulation will not leave any residue in tissue either. However, the stimulated area and intensity were still limited by the signal generator system and the design of the stimulation coil. The depth and the focality are the most critical performance indicators of magnetic stimulation on brain tissue. Because the depth of the stimulus should be fit with the location of the target area, and the stimulus should avoid affecting the neighboring regions around the target nerve. Li studied the double butterfly coil for transcranial magnetic stimulation. The focality of the coil was better than the typical coil [1]. Liu proposed a pulsed magnetic-field generator, which provided a noncontact way for functional nerve stimulation. The magnetic field and the induced electric field were produced by a figure-8 coil under the excitation of the pulsed discharging current [2]. Based on our previous work, a solenoid was proposed to stimulate the injured sciatic nerves of rats. The regeneration process of injured sciatic nerves was facilitated by pulsed magnetic stimulation [3]. Peterchev compared 50 coil designs and studied the tradeoff between the depth and the focality [4]. Despite the great progress of the magnetic field on human tissue stimulation, the performances of the magnetic stimulation still need to be improved. In this research, a novel type of magnetic stimulation coil based on the big-little structure quad helix coil was proposed. A three-dimensional human head model was established to simulate the stimulus. The magnetic field distribution was calculated, and a measurement coil was designed to verify the simulations. A comparison between the figure-8 coil and the coil proposed in this paper was also carried out. The result showed that the big-little quad helix coil could obtain higher stimulation strength and a better focality. The directivity of the proposed coils was also better than that of the figure-8 coil. More details of the analysis and the experiments of the magnetic stimulation system will be presented in the extended paper. II. The design of the quad helix coil and the magnetic stimulation system The design of the stimulation coil should take many issues into consideration. Based on previous researches, there are various coils for magnetic stimulation have been proposed. Such as the figure-8 coil, coil array, cap coil, and so on. In order to obtain a deeper stimulus, the coil should be designed with larger dimensions. On the other hand, the higher focality depends on the smaller radius of the coil. Therefore, the stimulation coil should subject to a depth-focality tradeoff. In the present research, as shown in Fig. 1, the coils are designed in Big-Little form and are arranged in X-shape. The coils close to the stimulation target (Little coils) could improve the focality of the stimulations, and the coils away from the target (Big coils) could intensify the depth of the stimulation. The signal of stimulation is the decaying sinusoidal current in the stimulation coil. The pulsed current frequency is 13 kHz, and the repeat frequency is 100 Hz. The magnetic field system consists of a control microprocessor, an insulated gate bipolar translator (IGBT), a resistor and a capacitor. The capacitor is charged by power source and control by a microprocessor. The IGBT will switch to the discharge loop through the coil for magnetic stimulations. In the present research, a measurement coil is also proposed to measure the magnetic field distribution. The magnetic field strength can be expressed in terms of the induced voltage. The turns of the measurement coil is 80, and the diameter was 5 mm. III. Theoretical Analysis and Field Distribution According to Biot Savart's law, the magnetic flux density of one of the stimulation coils can be calculated. By MATLAB programming, the calculation of magnetic flux density at the location of the brain (10 cm beneath the calvarium) is 50 mT, and the magnetic flux density measured by measurement coil is 44 mT. Fig. 2 shows the comparison of magnetic flux density between big-little quad helix coil

and figure-8 coil with the same radius and excitation signal. The focality is evaluated by the half power region. Therefore, the result shows that the big-little quad helix coils not only have higher focality but also achieve higher stimulation strength. IV. Conclusion In this research, a big-little quad helix coil for transcranial magnetic stimulation was proposed. As simulated by programming and finite element method, the depth and the focality were studied and verified by measurement. Comparing with the typical stimulation coil, the big-little quad helix coil has higher stimulation strength and a better focality. This approach may suggest a new way of designing the coils for transcranial magnetic stimulation.

[1] J. Li, Z. Liang, Q. Ai, et al., *IEEE Transactions on Magnetics*, Vol. 48, pp. 3509(2012) [2] C. Liu, J. Zhu, J. Li, et al., *IEEE Transactions on Magnetics*, Vol. 49, pp. 1853(2013) [3] N. Zhang, S. Wang, X. Chen, et al., *IEEE Transactions on Magnetics*, Vol. 51, pp.e5000704(2015) [4] Z. Deng, S. H. Lisanby, A. V. Peterchev, *Brain Stimulation*, Vol. 6, pp. 1(2013)



Fig. 1 The prototype of the quad helix coil for TMS

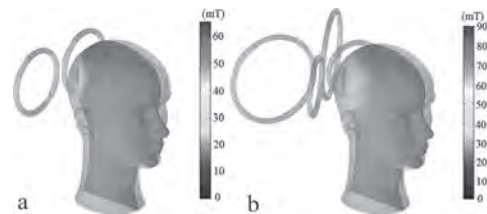


Fig. 2 The comparison of magnetic flux density between big-little quad helix coil and figure-8 coil. (a) Figure-8 coil. (b) Big-little quad helix coil.

JP-10. Transcranial Magnetic Stimulation: the Effect of Age and Other Factors on the Intensity of the Quadruple Butterfly Coil.

O.F. Afuwape^{1,2}, J. Runge¹ and D.C. Jiles¹

1. Department of Electrical and Computer Engineering, Iowa State University, Ames, IA, United States; 2. Department of Mechanical Engineering, Iowa State University, Ames, IA, United States

Transcranial Magnetic Stimulation (TMS) is a non-invasive technique that is approved by the U.S. Food and Drug Administration (FDA) for the treatment of certain neurological disorders [1]. When comparing TMS to techniques with similar desired outcomes such as conventional brain surgery, TMS has far fewer risks due to its non-invasive nature. TMS works by inducing an electric field that polarizes or depolarizes brain tissues depending on treatment mode. TMS researchers have proposed different coil designs to achieve higher focality and increased depth of penetration of the induced electric field [2]. The Quadruple Butterfly Coil (QBC) is a novel coil design with increased focality when compared to the commercially available Figure-of-eight (FOE) coil [3]. The human brain reaches 90% of its adult volume at age six and does not reach full maturity until approximately the age of 25, and throughout adolescence, the brain is still maturing [4]. The differences in the brain from adolescents to adults could affect the effectiveness of TMS, mainly because the coils have been designed for use on adult patients [5], [6]. Comparing the efficacy of TMS coils across age groups to determine if the difference in brain volume is enough to warrant specific TMS treatment protocols for adolescents is of the essence in advancing TMS research [7]. In this research, the authors compare the use of the Quadruple Butterfly Coil (QBC) across different age groups to test the effectiveness of the coil on various stages of brain development. Simulations were run using a finite element analysis software, Sim4Life. The models used in this study were sourced from the Computable Virtual Population Models from the IT'IS Foundation. The models have well defined anatomy and were selected to each represent a different age group. The adult models used as the control are 34 years old male (34M) and 26 years old female (26F), as they both fall in the typical age range of models (25 to 35 years) used for TMS studies. The models used to represent the pediatric population are 14 years old male (14M), 11 years old female (11F), 8 years old female (8F), 8 years old male (8M), 6 years old male (6M), and 5 years old female (5F) [8]. Fig. 1 presents the distribution of the induced electric field intensity with depth across the different models. Besides age and brain volume, other factors such as the brain – scalp distance (BSD), cerebrospinal fluid (CSF) thickness, scalp thickness, and skull thickness of the models were also considered in the analysis. This study provides an understanding of the various factors contributing to the response from TMS. The maximum electric field intensity on the scalp (E-Max scalp), maximum electric field intensity on the brain (E-Max brain) and the proportion of the E-Max scalp to E-Max brain are parameters considered in this analysis.

[1] M. Hallett, "Transcranial magnetic stimulation and the human brain", *Nature*, vol. 406, no. 6792, pp. 147-150, 2000. Available: <https://www.nature.com/articles/35018000>. [2] M. Hallett, "Transcranial Magnetic Stimulation: A Primer", *Neuron*, vol. 55, no. 2, pp. 187-199, 2007. Available: <https://www.sciencedirect.com/science/article/pii/S0896627307004606>. [3] P. Rastogi, E. G. Lee, R. L. Hadimani, and D. C. Jiles, "Transcranial Magnetic Stimulation-coil design with improved focality," *AIP Adv.*, vol. 7, no. 5, p. 056705, May 2017, doi: 10.1063/1.4973604. [4] J. Stiles and T. Jernigan, "The Basics of Brain Development", *Neuropsychology Review*, vol. 20, no. 4, pp. 327-348, 2010. Available: <https://www.ncbi.nlm.nih.gov/pmc/articles/PMC2989000/>. [5] L. Crowther, R. Hadimani and D. Jiles, "A numerical dosimetry study for pediatric transcranial magnetic stimulation", 2013 6th International IEEE/EMBS Conference on Neural Engineering (NER), 2013. Available: <https://ieeexplore.ieee.org/abstract/document/6695916/authors#authors>. [Accessed 10 September 2020]. [6] J. Weissman, C. Epstein and K. Davey, "Magnetic brain stimulation and brain size: relevance to animal studies", *Electroencephalography and Clinical Neurophysiology/ Evoked Potentials Section*, vol. 85, no. 3, pp. 215-219, 1992. Available: <https://www.sciencedirect.com/science/article/pii/016855979290135X>. [7] M. Garvey and V. Mall, "Transcranial magnetic stimulation in children", *Clinical Neurophysiology*, vol. 119, no. 5, pp. 973-984, 2008. Available:

<https://www.sciencedirect.com/science/article/pii/S1388245707007353>. [8] M. Gosselin et al., "Development of a new generation of high-resolution anatomical models for medical device evaluation: The Virtual Population 3.0", *Physics in Medicine and Biology*, vol. 59, no. 18, pp. 5287-5303, 2014. Available: 10.1088/0031-9155/59/18/5287.

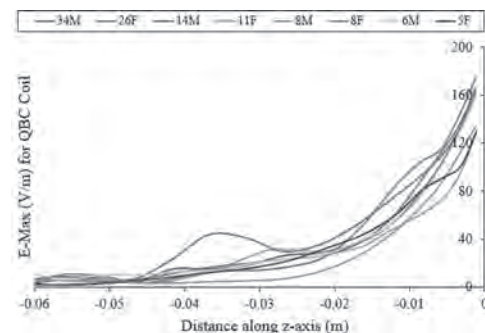


Fig. 1. Variation of the Induced Electric Field (V/m) with depth across the different subjects.

JP-11. The Series Study of the $\text{CoZnFe}_2\text{O}_4\text{Ag}$ in the MRI Contrast.

V. Sabie¹, C. Constantin¹, O. Caltun¹ and R. Danila²

1. *Universitatea Alexandru Ioan Cuza Facultatea de Fizica, Iasi, Romania;*

2. *Faculty of Chemistry, Universitatea Alexandru Ioan Cuza, Iasi, Romania*

Nuclear magnetic resonance imaging is the most used technique for investigating human tissue. This is a noninvasive technique for the patient, based on the use of an intense magnetic field and radiofrequency pulses applied at certain angles. The application of the radiofrequency pulse has the effect of disrupting the equilibrium state of nuclear atomic moments of atoms, induced signals being described by longitudinal relaxation time (T1) and transverse relaxation time (T2). For a better view of tumor tissues, there are used contrast agents; a dose of contrast agent distributed throughout the body can be used to quickly view extensive areas of anatomy. Most of the NMR contrast agents are either complex paramagnetic ions or superparamagnetic loadstone particles (iron oxide). However, the most used agents in NMR investigations are based on Gadolinium chelates. These are less toxic and present positive contrast in the T1 sequence. Superparamagnetic loadstone particles (iron oxide) are at an experimental stage; the sensitivity of these techniques is currently not suitable for clinical applications, new significant relaxation agents targeted to specific tissues or disease processes being required. In this study, the $\text{CoZnFe}_2\text{O}_4\text{Ag}$ nanoparticle series was dispersed in distilled water, thus forming dilutions, and the same amounts of ferrite were stabilized in agar gels. The obtained dilutions and agar phantoms were scanned with the MRI medical facilities with the intensity of the magnetic field of 1.5 T and 0.4 T respectively. For these, the basic sequences, T1 and T2, were obtained. The contribution of $\text{CoZnFe}_2\text{O}_4\text{Ag}$ nanoparticles on the contrast of nuclear magnetic resonance images obtained from scanning of two medical MRI installations as compared to images obtained by scanning several commercial contrast agents used in medical imaging. The resulting images were analyzed using a commercial graphics program to highlight the influence of particles on the contrast of the images. The analyzed images indicate that the $\text{CoZnFe}_2\text{O}_4\text{Ag}$ ferrites show positive contrast in the T1 sequence. Small ferrite concentrations (0.05, 0.08, 0.1) have better contrast compared to higher concentrations (0.5, 1). Large concentrations of ferrite have the effect of decreasing magnetization and, implicitly, of lowering the signal (contrast). The $\text{CoZnFe}_2\text{O}_4\text{Ag}$ series could be used as a possible contrast agent for MRI investigations, only if they are compatible by coating with polymers compatible with the human body. In this respect, severe toxicity tests should be carried out.

Rinck, Peter A *MAGNETIC RESONANCE IN MEDICINE - A Critical Introduction*. 12th edition (2018) Chrysikopoulos, Haris S, *Clinical MR Imaging and Physics.*, (2009) J. Lohrke, T. Frenzel *25 Years of Contrast-Enhanced MRI: Developments, Current Challenges, and Future Perspectives*, (2016) Yu-Dong Xiao, Ramchandra Paudel, *MRI contrast agents: Classification and application.*, Vol. 38 (2016) Perry Sprawls, *Magnetic Resonance Imaging- Principles, Methods, and Techniques*. (2000) Alshowiman, Sami S, *MRI Contrast Agents: Developments, Challenges, and Future Trends.*, Vol. 8 (2018) C. P. Constantin, A. Iordana, O. F. Caltun, *CoxZnx-1Fe2O4 nanoparticles ferrite series as magnetic resonance imaging contrast agents*. (2012)

JP-12. The Effect of Silica Shell Thickness on Magnetic and Proton Relaxometric Properties: Fe₃O₄@mSiO₂ Nanoparticles.

N. Taib^{1,2}, T. St. Pierre² and R. Woodward³

1. Faculty of Applied Sciences, Perak Branch, Tapah Campus, 35400, Universiti Teknologi MARA, Tapah Road, Malaysia; 2. School of Physics, Mathematics, and Computing, The University of Western Australia, Perth, WA, Australia; 3. John Forrest Secondary College, Morley, WA, Australia

Over the past decade, superparamagnetic iron oxide (Fe₃O₄) nanoparticles have drawn significant attention for different applications such as contrast agents for magnetic resonance imaging (MRI), drug delivery or magnetic hyperthermia (MRI) [1-3]. Due to their negative contrast enhancement effect on T₂ and T₂* weighted images, they have played a role as contrast agents in MRI [4]. They provide the most change in signal per unit of metal particularly on T₂* weighted images as each particle is composed of thousands of iron atoms and defeats the inherent low contrast agent sensitivity of MRI [5]. However, the contrast enhancing effectiveness of a superparamagnetic nanoparticle depends on size of the iron oxide crystal, the composition, the charge, the nature of the coating, the hydrodynamic size of the coated nanoparticle, magnetization and aggregation state in the biological environment as these parameters influence the longitudinal and transverse proton relaxivities [6, 7]. The surface properties of the magnetic NPs play an important role in their efficiency as MRI contrast agents. Therefore, they require a surface coating in order to improve their dispersion and stability in aqueous media. This work was related to the effect of silica shell thickness on proton relaxivities and magnetic properties of superparamagnetic iron oxide nanoparticles. It is possible to predict and finely tune the silica shell thickness by varying the amount of TEOS used to adjust the magnetic properties and proton relaxometric properties. Core-shell structures of the form Fe₃O₄@mSiO₂ with different silica shell thicknesses i.e 45, 63 nm and 73 nm were synthesized by a surfactant template sol-gel method. The silica-coated magnetic iron oxide nanoparticles were found to be spherical in TEM images with a core shell structure with average diameters of 136, 155, and 175 nm for 45, 63 nm and 73 nm shell thickness coatings, respectively. A decrease in M_s value was found with decreasing silica shell thickness. Both r₁ and r₂ proton relaxivities inversely correlated with the increasing silica shell thickness and size of the particles. The r₂ relaxivities were found to be much higher than the r₁ relaxivities, which reflects the fact that the T₂ proton relaxation is mainly influenced by outer sphere processes. All the Fe₃O₄@mSiO₂ particles are relatively weak T₁ contrast agents. While, as T₂ contrast agents, they showed higher relaxivity with decreasing silica coating of the magnetic core. It is interesting to note that the changes in r₁ and r₂ due to silica shell thickness indicate that it is an important factor to take into consideration when designing magnetic nanoparticle probes for molecular imaging applications using MRI. It is crucial to develop an understanding of the structure and properties of the nanoparticle since the different silica shell thicknesses around magnetite have an effect on the proton transverse relaxivity.

[1] R. Qiao, C. Yang, M. Gao, Superparamagnetic iron oxide nanoparticles: from preparations to in vivo MRI applications, Journal of Materials Chemistry, 19 (2009) 6274-6293. [2] M. Mahmoudi, S. Sant, B. Wang, S. Laurent, T. Sen, Superparamagnetic iron oxide nanoparticles (SPIONs): development, surface modification and applications in chemotherapy, Adv Drug Deliv Rev, 63 (2011) 24-46. [3] Q.A. Pankhurst, J. Connolly, S.K. Jones, J. Dobson, Applications of magnetic nanoparticles in biomedicine, Journal of Physics D: Applied Physics, 36 (2003). [4] D.-X. Chen, N. Sun, Z.-J. Huang, C.-M. Cheng, H. Xu, H.-C. Gu, Experimental study on T₂ relaxation time of protons in water suspensions of iron-oxide nanoparticles: Effects of polymer coating thickness and over-low 1/T₂, Journal of Magnetism and Magnetic Materials, 322 (2010) 548-556. [5] D.W. McRobbie, E.A. Moore, M.J. Graves, M.R. Prince, MRI from picture to proton, Second ed., Cambridge University Press, UK, 2003. [6] S.H. Koenig, K.E. Kellar, Theory of 1/T₁ and 1/T₂ NMRD profiles of solutions of magnetic nanoparticles, Magn Reson Med, 34 (1995) 227-233. [7] P.H. Qiu, C. Jensen, N. Charity, R. Towner, C.B. Mao, Oil Phase Evaporation-Induced Self-Assembly of Hydrophobic Nanoparticles into Spherical Clusters with Controlled Surface Chemistry in an Oil-in-Water Dispersion and Comparison of Behaviors of Individual and Clustered Iron

Oxide Nanoparticles, Journal of the American Chemical Society, 132 (2010) 17724-17732.

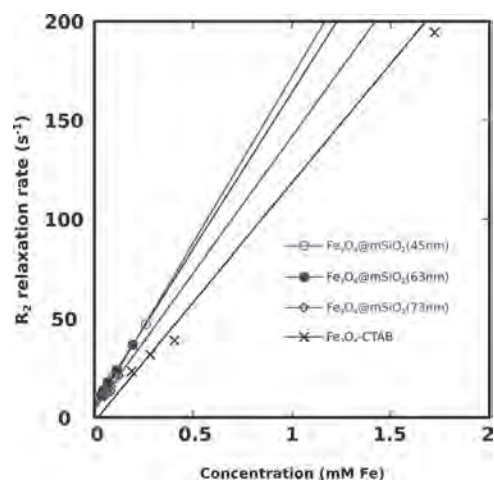


Fig. 1. Plot of transverse relaxation rates (1/T₂), at different iron oxide concentrations for Fe₃O₄@mSiO₂ with different silica shell thickness, measured at 25 °C and 60 MHz; number in the brackets indicate the thickness of the silica shell.

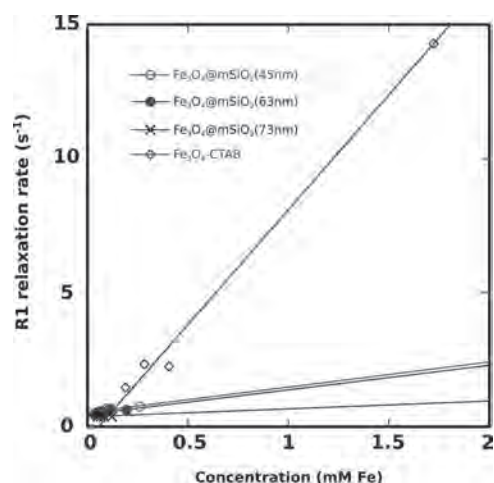


Fig. 2. Plot of longitudinal relaxation rates (1/T₁) at different iron oxide concentrations for Fe₃O₄@mSiO₂ with different silica shell thickness, measured at 25 °C and 60 MHz; number in the brackets indicate the thickness of the silica shell.

JP-13. A Simple Localization Method of Magnetic Particles for Hyperthermia Therapy Using Figure-8 Coil.

L. Ton That¹, R. Hirota¹, T. Kitamura¹, K. Okita² and S. Yabukami^{1,2}

1. Department of Electrical Engineering, Tohoku University, Sendai, Japan; 2. Graduate School of Biomedical Engineering, Tohoku University - Aobayama Campus, Sendai, Japan

Magnetic hyperthermia is a promising cancer therapy gaining great interest in recent years using heat generation ascribed to magnetic particles subjected to a high-frequency magnetic field. To make this therapy feasible in clinical settings, in addition to magnetic particles, important elements include techniques for detecting their position and temperature in a tumor region in determining the effectiveness of therapeutic heating. In previous studies, we developed thermosensitive magnetic micro/nanoparticles with high heating efficiency and considerable permeability change around the therapeutic temperature range of 42-45°C [1]. We also proposed a wireless temperature measurement method for monitoring the tumor temperature using pickup coils to detect the temperature-dependent stray magnetic field caused by the magnetic particles [2]. A challenge remains when the particles injected into the tumor region deviate from the longitudinal axis of drive coil (heating coil). As a result, the heating generation of the particles and the accuracy of the proposed thermometry are decreased. To solve this problem, by taking the advantage of the fact that the induced voltage in pickup coil depends on the position of the particles, we developed a localization system using three pickup coils symmetrically installed inside drive coil. The position of particles could be automatically localized by using a robot arm to operate the unit composed of drive coil and pickup coils in two modes of coarse adjustment (rotary scanning) and fine adjustment (linear scanning) [3]. In this study, we propose a simpler, faster and more cost-effective localization method by using only figure-8 coil instead of three pickup coils (loop type coils) and operating the unit of drive coil and figure-8 coil (hereafter the unit) only in linear scanning mode. Fig. 1 shows the conceptual diagram of the proposed localization method using figure-8 coil. Figure-8 coil consists of two reverse-winding loop coils and is adjusted so that its initial bias (the voltage without sample) close to 0 V and fixed to the center of drive coil. As a result, the induced voltage changes depending on the relative position of the implant (i.e., magnetic particles) as seen from the unit when the implant moves along the longitudinal axis of figure-8 coil (x-axis) on xz-plane. Here, xyz and x'y'z' are the coordinate systems of the unit (known) and the implant (unknown), respectively. That is, in actual localization, by monitoring the voltage during moving the unit linearly over the existence possibility area of the implant, it is possible to specify the symmetry plane of the implant (e.g., y'z'-plane which is perpendicular to the moving x-axis when the voltage is at the inflection point). Similarly, as shown in Fig. 1(b), by simply rotating the unit 90° counter-clockwise on xy-plane, and then moving the unit along the longitudinal axis of figure-8 coil, it is possible to specify the symmetry plane x'z'. Finally, for specifying the symmetry plane x'y', rotating the unit 90° around y-axis counter-clockwise, and the resulting three symmetry plane intersect at the position of the implant. Next, we verified the validity of the proposed method using the constructed experimental setup as shown in Fig. 2(a). The strength and frequency of magnetic field applied at the center of drive coil (pancake coil, 40 turns, internal diameter 28.1 mm, external diameter 113.5 mm) were 2.88 mT and 2 kHz, respectively. The induced voltage in figure-8 coil (each loop 1 turn, diameter 10 mm) without the sample was subtracted from the induced voltage with the sample. The sample (1 g of magnetic particles dispersed in 1mL of deionized water) used in the following experiments was our previously-developed micromagnetic particles with a Curie point of 45°C [1]. As shown in Fig. 2(b), when the sample moved manually along the x-axis (z = 10 mm; y = 0 mm or -10mm), the average voltage (all experiments were repeated three times) changed depending on the position of sample, and the voltage was at the inflection point when the sample was directly above the intersection of two loops of figure-8 coil. In Fig. 2(c), when the sample moved along the y-axis (z = 10 mm; x = 0 mm), the voltage (almost 0 V) was extremely small compared to the one when the sample moved along the x-axis around the intersection of two loops of figure-8 coil (z = 10 mm; y = 0 mm). This means that the symmetric plane of the implant can be specified with high accuracy by using figure-8 coil. As shown in Fig. 2(d), with our currently constructed experimental setup, it

is possible to detect the sample up to 5 cm from the unit. Future studies are needed to investigate the optimal design of drive coil and figure-8 coil to extend the detectable distance for deeper tumor.

[1] L. Tonthat, Y. Yamamoto, F. Aki et al, IEEE Trans. Magn., Vol. 54(7), p. 5400506 (2018) [2] F. Aki, L. Tonthat, H. Saito et al, Electron. Comm. Jpn., Vol. 101 (6), p. 58–66 (2018) [3] L. Tonthat, K. Mitobe, S. Yabukami, IEEE Trans. Magn., Vol. 57(2), doi: 10.1109/TMAG.2020.3008490 (early access).

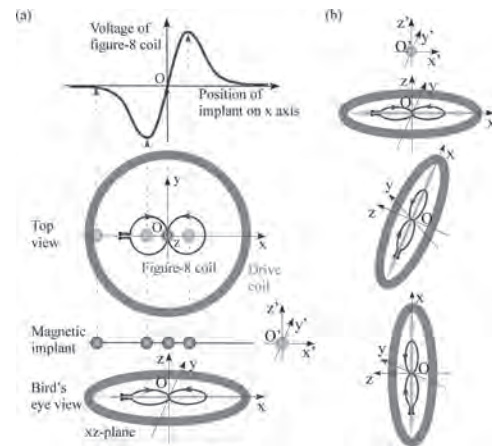


Fig. 1 The conceptual diagram of the proposed localization method for magnetic particles using a figure-8 coil. (a) The voltage changes depending on the relative position of the implant as seen from the unit when the implant moves along x-axis on xz-plane. (b) By simply rotating the unit 90° counter-clockwise on xy-plane, it is possible to specify the symmetry plane x'z' and rotating the unit 90° around y-axis counter-clockwise for specifying the symmetry plane x'y'.

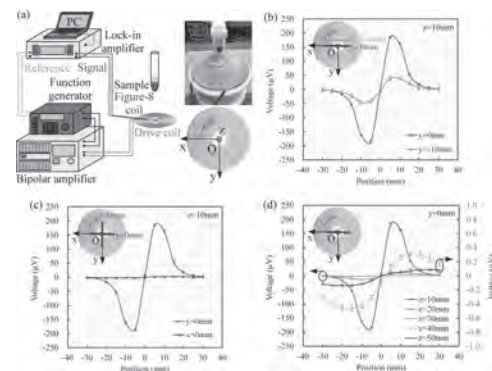


Fig. 2 (a) The constructed experimental setup and (b), (c), (d) the relationship between the average voltage (n=3) and the position of the sample when the sample moved manually above the fixed unit.

JP-14. Study on Non-Thermal Intervention of Lung Tumor by $\text{Fe}_3\text{O}_4@/\text{SiO}_2$ Nanoparticles in a Magnetic Field.

N. Zhang^{1,2}, Z. Wang¹, S. Ning³, S. Wang¹, B. Lai⁴, C. Zhang², S. Wang¹ and H. Qiu¹

1. School of Electrical Engineering, Xi'an Jiaotong University, Xi'an, China; 2. Department of Oncology, Johns Hopkins University School of Medicine, Baltimore, MD, United States; 3. School of Electronic Information and Artificial Intelligence, Shaanxi University of Science and Technology, Xi'an, China; 4. Quanzhou Experimental Middle School, Quanzhou, China

I. Introduction Lung tumor with the K-Ras mutation is one of the most deadly tumors, and there is a lack of drugs that can effectively target mutant K-Ras. Both chemotherapy and radiation are harmful to normal tissues. Hence, it is urgent to find a new way to treat K-Ras lung tumors with higher efficiency and fewer side effects. As a novel material, the intervention of cell proliferation by magnetic nanoparticles (MNPs) has attracted more attention [1-3]. In 2017, Wilhelm studied the killing function of MNPs on cells. The tumor cells were killed due to the thermal effect of MNPs with a magnetic field [4]. However, the thermal effects will affect normal tissues adjacent to tumor cells. To avoid this disadvantage, the use of non-thermal effects of MNPs by mechanical force to interfere with tumor cells has shown great potentials. However, the internal mechanism have not been fully discovered. Herein, the $\text{Fe}_3\text{O}_4@/\text{SiO}_2$ core-shell NPs were prepared and synergized with the magnetic field to intervene in the proliferation and migration of lung tumor A549 cell line (K-Ras driven). The MNPs were characterized by TEM and XRD. By numerical simulations, the force and thermal analysis of the MNPs are studied. Upon light microscopic examination and cell counting, the proliferation of tumor cells was slowed down. The result of the wound healing assay showed that the migration of tumor cells was also suppressed. This research may suggest a new way treat K-Ras driven lung tumors by using the non-thermal effect of MNPs without the side effect caused by hyperthermia. More details will be presented in the extended paper. II. Magnetic nanoparticles and experiment platforms In this research, the process flow of $\text{Fe}_3\text{O}_4@/\text{SiO}_2$ is shown in Fig. 1. The diameter of MNPs is around 20 nm and were characterized by TEM. According to the frequency of the magnetic field, the experiment platform consists of a signal generator, a stimulation coil, and a confocal microscope. Due to the optical path and imaging modality, a planar coil with a central hole to allow the light going through has been designed and realized on the PCB. By numerical calculation, the maximum magnetic flux density at the position of the targeting area is 2.2 mT. III. Field calculation of magnetic nanoparticles Due to the influence of the magnetic field, when the MNPs are placed in the magnetic field, the magnetic force is experienced. Based on the endocytosis of the cells, the MNPs could go inside the cell, and exert the magnetic force to the organelle [5]. a. Force analysis Considering the dimension of the MNPs, the magnetic field generated by the coil around the MNPs can be considered as a uniform field in calculation. The magnetic force is calculated by the Maxwell stress tensor method. The Maxwell stress tensor is a second rank tensor used in classical electromagnetism to represent the interaction between electromagnetic forces and mechanical momentum [6]. Based on the Maxwell stress tensor method, the magnetic force is calculated, the maximum magnetic force of MNPs induced by the applied magnetic field is around 1.5 nN. According to the previous research [7], the magnetic force could influence the cellular activities and would lead to intervention in cell activities. b. Thermal analysis To utilize the non-thermal effect of the MNPs, the frequency of the magnetic field should be relatively lower and the significant rise of the temperature should be avoided. In this section, the temperature rise of the MNPs is calculated by the bioheat equation [8]. The response surface is established to reflect the relationship among concentrations of MNPs, frequency of the applied magnetic field, and thermal effect. The response surface indicates that the higher concentrations of MNPs were in cells, the higher thermal effect occurred. In this research, the temperatures of each group are not exceeding 37.2 centigrade over the past 24 hours. IV. Cell Experiments The cell experiment was based on the A549 cell line. The tumor cells are divided into three groups, such as Group A, Group B, and Group C. Group A is stimulated by the magnetic field, the Group B are stimulated by the magnetic field and synergized with the MNPs, and

the Group C is the control group for contrast. After 72 hours, as shown in Fig. 2(a), the ratio of cell proliferation in Group A is suppressed by the magnetic field. Besides, the ratio of cell proliferation of Group B is 13.9% lower than Group A. Comparing with the group A, the result indicates that the MNPs with magnetic field achieve a higher suppression effect. To discover the inhibition effect on the migration of tumor cells, the scratch wound healing assay is carried out. By cell counting, the level of cell migration of Group B is 16.6% lower than Group A in Fig. 2(b). It shows that the MNPs synergized with the magnetic field could suppress the migration of the A549 tumor cells. V. Conclusions In this paper, with the magnetic field stimulation, the non-thermal effect of MNPs in the magnetic field is studied by numerical analysis and verified by experiments. The core-shell based MNPs in the magnetic field could not only suppress the proliferation of tumor cells without ambustion caused by hyperthermia but also strengthen the inhibitory effect of the magnetic field stimulation on lung tumors related to K-Ras mutations.

- [1] W. Chen, G. Lin, S. Lin, *et al.*, *Plos One*, Vol. 13, p. e0191078(2018)
 [2] E. D. Kirson, V. Dbaly, F. Tovarys, *et al.*, *Proceedings of the National Academy of Sciences of the United States of America*, Vol. 104, pp. 10152(2007) [3] S.G. Turner, T. Gergel, H. Wu, *et al.*, *World journal of surgical oncology*, Vol. 12, pp. 162(2014) [4] A. Espinosa, C.R. Di, J. Kolosnjaj-Tabi, *et al.*, *Acs Nano*, Vol. 10, pp. 2436(2016) [5] D. H. Kim, E. A. Rozhkova, I. V. Ulasov, *et al.*, *Nature Materials*, Vol. 9, pp.165(2010)
 [6] F. P. Miller, A. F. Vandome, M. John. Maxwell Stress Tensor. *VDM Publishing* (2010) [7] C. Y. Tay, P. Cai, M. I. Setyawati, *et al.*, *Nano Letters*, Vol. 14, pp. 83(2014) [8] S. Weinbaum and L. M. Jiji, *J. Biomech.Eng.*, Vol. 114, pp. 539(1992)

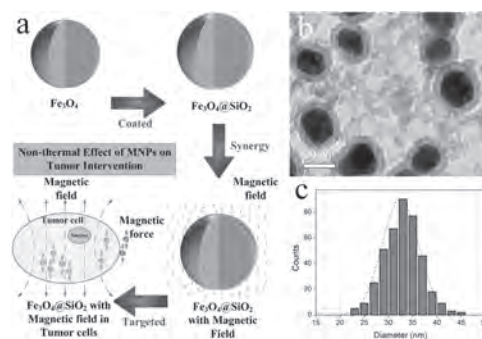


Fig. 1 The process flow of $\text{Fe}_3\text{O}_4@/\text{SiO}_2$ MNPs and the characterizations of the MNPs

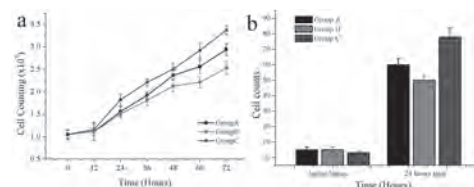


Fig. 2 The counting of cell experiments and the wound healing assay

JP-15. Optically Powered Diamagnetically Levitated Robots for Biomedical Applications.

M. Beauchamp¹, S. Yee¹, I. O'Carroll¹, E. Chapman¹ and H. ElBidweihy¹
 1. US Naval Academy, Annapolis, MD, United States

Introduction: Delivery of biological fluids and agents requires precision and can benefit from separation between substance and user for accurate results and safety, for example, in studies involving contagious organisms or viruses or when experimenting on sensitive cellular behaviors. Using a robot that contacts only the substance to be loaded and the unloading site provides that degree of separation needed for safety and study integrity. In this work, we demonstrate the use of optically powered diamagnetically levitated pyrolytic graphite robots with end effector micropipettes for a contact-free fluid delivery solution for use in biological studies. Specifically, we demonstrate loading, transporting, and releasing dyed water into agarose gel with autonomous control. Optical control of diamagnetically levitated PyG has been demonstrated in our previous work [1]. Using projector-based optical sources or independent control of laser beams, multiple samples may be controlled in parallel in an unsegmented workspace [2, 3]. An unsegmented workspace allows multiple robots to collaborate in a factory set-up with no extra circuitry or boundaries specific to each robot. All that is needed is a light source for each sample, which can be provided with a projector setup or a laser-splitting device. The alternative system design is the actuation of Neodymium-Iron Boron (NdFeB) magnets levitated on top of graphite [4, 5]. Control is achieved using active current traces in printed circuit boards under the graphite. This arrangement has segmented work surfaces, limited motion in close proximity, and requires extensive changes to expand the workspace. It also requires continuous power to ensure levitation and movement. In our work, the experimental setup includes PyG samples passively levitating on top of a checkerboard permanent magnet array. Instead of complicated circuitry, the displacement of the PyG robot is controlled using single laser sources for individual control. Given the low levitation height of the PyG, the load mass is constrained, which limits the end effectors and manipulators employed. With the contactless design, static end effectors, such as the micropipettes used in this study, are preferable. These micropipettes work on pressure differences, which keeps the system as autonomous as possible. The advantages that arise from a passively levitated, optically actuated platform are accompanied by loading and handling challenges and limitations. **System Design:** PyG, an artificial graphite, has the strongest known diamagnetism at room temperature, allowing it to levitate over an array of checkerboard permanent magnets at room temperature. Its large out-of-plane temperature-dependent diamagnetic susceptibility allows it to be actuated by localized temperature changes. Optical irradiation, such as that from a laser or projector, increases the local temperature, which decreases its local diamagnetic susceptibility, resulting in an in-plane force due to asymmetric out-of-plane forces and an induced tilting in the sample. In this study, a vision-based autonomously controlled laser source on a motorized stage irradiates the PyG sample, moving it towards the laser spot. The end effector micropipette is placed on the PyG sample, which is levitated on top of a magnet array, as shown in Fig. 1. The micropipette loads fluids from droplets placed on a glass slide via capillary action. A coefficient of penetration is used to determine the loadable fluids, while also considering adhesion between the glass slide and fluid to facilitate the retreat of the micropipette. To ensure liquid forces on the micropipette do not draw the PyG onto the droplet, a plastic barrier with holes that allow passage of the micropipette but not the PyG is placed at the edge of the magnet array. During the unloading process, the fluid diffuses when the micropipette penetrates an agarose gel. **Experiment:** Photographs taken during operation are shown in Fig. 2. In response to joystick user input, a motorized stage translates and moves the laser and levitated robot carrying a glass micropipette end effector (25-100 μ m dia.) fixed to the PyG with vacuum grease. The robot's pipette approaches the fluid and loads within <10 seconds for the liquid solutions tested (5% xylene cyanol, 1% bromophenol blue, 0.1M NaCl). To retreat, the stage for the fluid droplet is lowered mechanically, releasing the pipette. Laser power is insufficient to retreat the PyG from the fluid droplet after loading due to high surface tension forces. Once free of the droplet, the PyG is moved by the laser to the agarose at the unloading site. After penetration, diffusion of the fluid into the agarose is visible within 30s and takes several minutes to

completely unload the pipette. The main focus for future work is process automation. Currently, the process is executed by a user with a joystick, but the future goal is to develop a single input program that will complete the whole process, including finding the robot and executing the loading and unloading procedure.

[1] M. Ewall-Wice, et al., IEEE Transactions on Magnetics 55.7 (2019): 1-6. [2] J. Young, et al. AIP Advances 9.12 (2019): 125038. [3] J. Young, et al. Proc. SPIE 112930S (2020). [4] E. E. Hunter, et al., IEEE Robotics and Automation Letters 4.2 (2019): 997-1004. [5] A. Hsu, et al., IEEE Robotics and Automation Letters 5.2 (2020): 2913-2920.

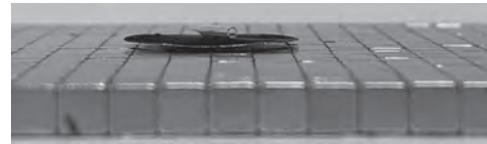


Figure 1. Photograph of a micropipette (50 μ m inner diameter tip, overall length 10mm) placed on top of a levitated 15mm \varnothing PyG sample.

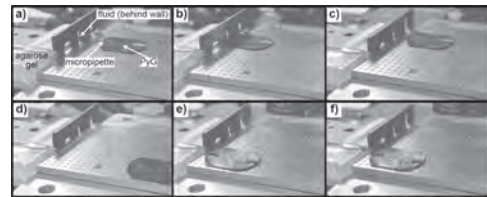


Figure 2. Photographs of the operation. The PyG sample is counterbalanced with a tip of toothpick. a) PyG approaches the fluid behind the wall. b) Micropipette loads the fluid, which is placed on a glass slide and a tilting stage. c) PyG retreats after the tilting stage is lowered. d) PyG moves towards agarose. e) Micropipette penetrates agarose. f) Fluid diffuses into agarose.

Session JQ
BIO-MAGNETISM, MAGNETIC FLUIDS, AND SEPARATION
(Poster Session)

Horia Chiriac, Chair

National Institute of Research and Development for Technical Physics, Iasi, Romania

JQ-01. Capture of Magnetic Particulate Matter Directly From air on Silicon Substrates.

L. Abelmann^{1,2}

1. Korea Institute of Science and Technology Europe Forschungsgesellschaft mbH, Saarbrücken, Germany; 2. Universiteit Twente, Enschede, Netherlands

A major fraction of airborne particulate matter is magnetic. The origin of these magnetic particles is anthropogenic (industry, traffic), and often accompanied by traces of very toxic heavy metal pollutants. The magnetic fraction of airborne particulate matter is therefore a good indicator for the amount of air pollution, and can serve as a first indicator for toxicity. We collected airborne magnetic particulate matter directly onto silicon substrates by means of a stack of permanent NdFeB magnets (Figure 1). Collection was performed in open air along a campus road for a period of 2-4 weeks. For comparison, a control substrate was mounted in a similar fashion, nearby but not on a magnet. The silicon substrates can be readily used in a variety of surface analysis techniques. The morphology of the captured particles was analyzed by optical and electron microscopy, as well as by AFM. The substrate that was on the magnet stack showed an increased amount of particles. The particle size varied from 50 micrometer down to diameters below 100 nm. Many of the particles are perfectly round spheres with a diameter of a few up to tens of micrometers. SEM-EDX analysis showed that particles that are captured magnetically mainly consist of iron-oxide. VSM analysis showed that the substrate that was on the magnet has a magnetic moment that is six times higher than the substrate that was not in the magnetic field gradient (Figure 2). The average collection of magnetic particulate matter on the 5mm×5mm area is approximately 4 nAm²/day, which translates to 46 ng/day if the particles are made entirely of iron-oxide. These experiments show that one can collect magnetic particulate matter directly from the air, without using filters and complex post-treatment procedures that change the particle composition and cause clustering. Magnetic particulate matter sampling is therefore a promising complementary technique that can be applied in for instance air quality monitoring stations.

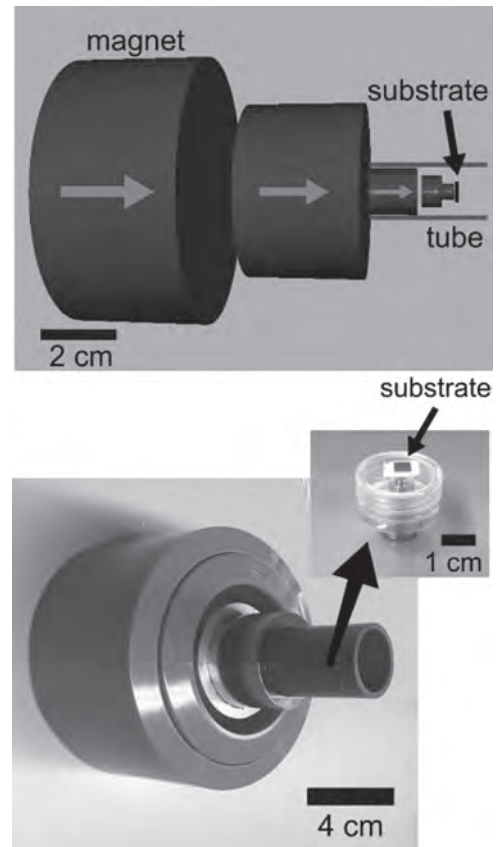


Fig 1. A stack of NdFeB magnets ranging in diameter from 70 down to 4 mm is used to attract magnetic particulate matter onto a 5 mm x 5 mm silicon substrates. The substrate is shielded from rain by a tube, and the magnets are protected by a PVC enclosure.

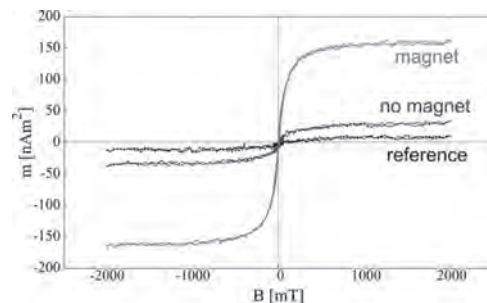


Fig. 2. The magnetic moment of the substrate that was outside on the magnet stack for a month (red curve) is at least six times higher than that of a substrate that was outside for the same period, but not on a magnet (blue curve). The reference (black curve) is the signal of a substrate that was kept in a box.

JQ-02. Hybrid Coil Design for Shapeable Magnetic Field for Transcranial Magnetic Stimulation.

J. Boldrey¹, G. Goss¹, Z. Higgs¹ and D.C. Jiles¹

1. Electrical and Computer Engineering, Iowa State University, Ames, IA, United States

Transcranial Magnetic Stimulation (TMS) has proven in recent years to be an effective method for neuromodulation without surgical interventions. Such non-invasive stimulation treatment has been approved by the U.S. Federal Drug Administration (FDA) for treating major depressive disorder (MDD), obsessive compulsive disorder (OCD) and certain types of migraine headaches [1]. Current research is investigating the use of TMS for treating Parkinson's Disease (PD) and Post-Traumatic Stress Disorder (PTSD) [2] [3]. Despite the promise that TMS offers for non-invasive neuromodulation, most commercial TMS coils deliver a uniform H field to the brain. In the process of delivering a sufficiently strong H field to the targeted region, surrounding areas of the brain can be stimulated unnecessarily. Stimulating non-target areas can result in side effects ranging from tingling sensations in the scalp to seizures [4]. Due to this, the ability for conventional TMS coils to treat a wider variety of systemic neurological disorders is limited. We have developed a novel hybrid coil design that incorporates a traditional single circular coil with a group of 8 solenoids. This design, shown in Fig. 1, allows for a shapeable H field HHH in order to target a specific area for stimulation through selective activation of the solenoid architecture. By activating the solenoids with either a clockwise or counter-clockwise current of varying intensity, the H field of the overall coil can be shaped in a non-uniform manner. This shapeable architecture allows localized stimulation of various neural structures with less risk of stimulating non-target regions. This coil design also presents the possibility for patient-specific customized focality of the H field.

[1] "FDA permits marketing of transcranial magnetic stimulation for treatment of obsessive compulsive disorder | FDA." [Online]. Available: <https://www.fda.gov/news-events/press-announcements/fda-permits-marketing-transcranial-magnetic-stimulation-treatment-obsessive-compulsive-disorder>. [Accessed: 010-Jun-2020]. [2] C. Fricke et al., "Dual-Site Transcranial Magnetic Stimulation for the Treatment of Parkinson's Disease," *Front. Neurol.*, vol. 10, no. March, pp. 1–9, 2019, doi: 10.3389/fneur.2019.00174. [3] R. J. Koek et al., "Neuromodulatory treatments for post-traumatic stress disorder (PTSD)," *Prog. Neuro-Psychopharmacology Biol. Psychiatry*, vol. 92, no. December 2018, pp. 148–160, 2019, doi: 10.1016/j.pnpbp.2019.01.004. [4] S. Rossi et al., "Safety, ethical considerations, and application guidelines for the use of transcranial magnetic stimulation in clinical practice and research," *Clin. Neurophysiol.*, vol. 120, no. 12, pp. 2008–2039, 2009.



Fig. 1. Hybrid circular-solenoid coil and simulation head model in Sim4Life software.

JQ-03. Optimum Design of the Eccentric Trapezoidal Magnetic Stimulation Coil With Trade-off Between Stimulation Effect and Heat Dissipation.

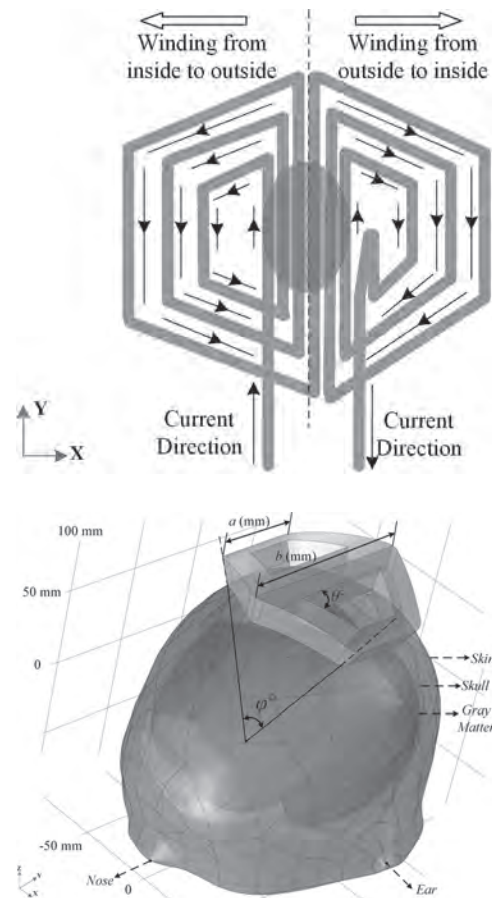
X. Fang¹, W. Liu¹, Y. Luo¹, C. Liu² and Z. He²

1. College of Nuclear Technology and Automation Engineering, Chengdu University of Technology, Sichuan, China; 2. State Key Laboratory of Advanced Electromagnetic Engineering and Technology, Huazhong University of Science and Technology, Wuhan, China

Abstract In order to improve the spatial distribution characteristics of induced electromagnetic field, the eccentric trapezoidal magnetic coil (ETM coil) is designed based on the inspiration of special shaped magnets. And to overcome the overheat problem during repetitive stimulation, the inner cooling cycle is designed for the ETM coil as well. The proposed ETM coil consists of two identical coil units and each unit is in the shape of eccentric trapezoid when projected onto the plane parallel to stimulating target plane. The two coil units are placed adjacent or overlapped which is referred to as Type I-ETM coil and Type II-ETM coil in this paper, respectively. To limit the induced electromagnetic field within a smaller domain, the ETM coil is bent along the symmetrical axis at specific angles. Results show that the ETM coil can produce the same stimulation intensity as the traditional FOE coil with less driving current, and it can also significantly improve the intracranial stimulation focalization while reducing the risk of side effects. Because of the internal cooling design, the temperature of the ETM coil could be maintained at room temperature after 3000 effective pulses were applied, while the temperature rise of the FOE coil is over 40K. To verified our method, an anatomically realistic human head model with different electrical properties assigned to each tissue of the brain is employed in this paper. **Index Terms-** induced electromagnetic field, Magnetic Coil, stimulation intensity. **Introduction** Transcranial magnetic stimulation (TMS) has been proved to be an effective tool in medical researches[1], [2]. The stimulated volume or stimulated area within human brain need to be limited into a smaller domain to avoid unnecessary side effects [3]-[7]. Also, The geometry of the magnetic coil not only influences to the spatial distributions of induced field but also relates to the heating problem [8]. In order to provide reliable and efficient experimental conditions for scientific exploration, the eccentric trapezoidal magnetic coil (ETM coil) is introduced and optimized in this paper. Results prove that the ETM coil is superior to the traditional FOE coil in terms of stimulation performance and continuous working performance. **Method A. The Geometry of ETM coil** The ETM coil can be obtained by bending two eccentric trapezoidal coils along an axis of symmetry. When the two coil units are placed adjacent, the coil is referred as Type I-ETM coil and when the two coil units are placed overlapped, the coil is referred as Type II-ETM coil. In this paper, all ETM coil is described as a (mm), b (mm), θ° and φ° . a (mm) represents the length of upper side of the trapezoid. b represents the length of bottom side of the trapezoid. θ° represents the bottom corner of the trapezoid. φ° stands for the bending angle of the eccentric trapezoidal coil pair. The geometry the of Type I-ETM coil when projected to XY plane is shown in Fig. 1. The transparent red circle in Fig.1 represents the targeted plane below the ETM coil. The relative position between Type I-ETM coil and human head is shown in Fig.2. **B. Real Human Head Model** The real human head model used in this study is model numbered 101309 in the Population Head Model (PHM) Repository (<https://itis.swiss/virtual-population/regional-human-models/phm-repository/>). The PHM repository was developed by Lee et al. using the SimNIBS pipeline, which was utilized to segment anatomical regions from Human Connectome Project MRI images. **C. Optimization Steps** Firstly, multiple Type I-ETM coil and Type II-ETM coils are construct under the power loss constraint. Both the Type I-ETM coil experimental group and Type II-ETM coil experimental group are divided into three sets including the a/b set, the θ° set and the φ° set. Secondly, the influence of coil geometry parameters on the spatial distribution of intracranial induced electromagnetic field was analyzed qualitatively. A mathematical model reflecting the mapping relationship between the geometric parameters of the coil and the spatial distribution characteristics of the intracranial induced electromagnetic field is established. Thirdly, the particle swarm optimization method (PSO) is adopted to obtain the optimized values of the ETM coil geometric parameters. Results prove that the overall performance of the optimum ETM coil is

improved by about 40% comparing to the traditional FOE coil. Fourthly, the copper wire used in the optimum ETM coil is replaced with hollow copper wire and the central hollow part is used to circulate low-temperature deionized water. The pressure and temperature distribution on the cooling water channel is simulated based on non-isothermal water pipe model. Finally, the induced neurologic damage which may be caused during a typical treatment are calculated. Results In this paper, we have proposed and verified the ETM coil design for magnetic stimulation. Type I-ETM coil is advantageous in generating stronger induced field while the Type II-ETM coil is beneficial to improving the stimulation focalization. The bending structure of the ETM coil helps to reduce the risk of side effects. The overall performance of the optimum ETM coil is improved by about 40% comparing to the traditional FOE coil. And the inner cooling cycle of the optimum ETM coil makes it possible to work continuously without overheat. In conclusion, the proposed ETM coil is superior to the traditional FOE coil in terms of stimulation performance and continuous working performance which may bring more possibilities for the applications of TMS.

References: [1] B. J. Hand, G. M. Opie, S. K. Sidhu, et al. *Brain Res.*, vol.1746, no.147027, July 2020. [2] C. C. Sanchez, M. R. Cabello, A. Q. Olozabal, *J. Neural. Eng.*, vol. 17, no.016056, 2020. [3] Y. Wu, H. Yu, Z. Liu, *IEEE Trans. Magn.*, vol. 54, no. 11, pp. 1–5, 2018. [4] Z. Zhang, W. Ai, B. Deng, *IEEE Trans. Magn.*, vol. 53, no. 11, Nov. 2017, Art. no. 9100605 [5] S. Chang, et al. *IEEE Trans. Magn.*, vol. 54, no. 11, pp. 1–5, 2018. [6] A.V. Peterchev, T.A. Wagner, *Brain Stimul.*, vol. 5, pp.435–453, 2012. [7] G. Yi, J. Wang, X. Wei, *Appl. Math. Comput.* vol.231, pp.100-110, 2014. [8] V. Novickij, A. Grainys, J. Novickij, and A. Lucinskis, *IEEE Trans. Magn.*, vol. 50, no. 11, Nov. 2014, Art. no. 5101004



JQ-04. Enhanced Magnetorheological Response of Particle Added Carbonyl Iron Suspension.

H. Kim¹ and H. Choi¹

¹ Inha University, Incheon, The Republic of Korea

I. INTRODUCTION Magnetorheological (MR) fluids are suspensions of soft-magnetic particles dispersed in a non-magnetic liquid medium, such as silicone oil and mineral oil [1]. Their rheological behaviors can be tuned depending on either the presence or the absence of the applied magnetic field strength. Without an applied magnetic field, they behave like a Newtonian fluid while in the presence of the magnetic field, they become a solid-like state [2], due to the fact that the dispersed magnetic particles are magnetically polarized and then form a chain structure [3]. When the external magnetic field is removed, they return to an original liquid-like state immediately. Based on this tunable and reversible characteristics, their potential applications cover the areas of robotics, haptic devices, and mechanical systems [4]. As for the MR material, carbonyl iron (CI) microspheres have been widely used because of their high saturation magnetization. However, their high density intrinsically possesses a sedimentation problem [5]. To improve this problem, several methods have been employed such as an introduction of additive particles and coating the CI with either polymers or inorganics [6]. In this work, as an additive material, zinc ferrite nanoparticles were synthesized by a surfactant-assistant solvothermal method and then added into CI-based MR fluid. By adding these particles with high magnetism to MR fluid consisting of fine CI particles, the MR effect is expected to be improved [7]. **II. EXPERIMENT** The ZnFe_2O_4 nanoparticles were synthesized by solvothermal synthesis method. Ferric chloride hexahydrate (5.4g) and zinc chloride (1.36g) were put into 200 ml ethylene glycol with stirring using a magnetic bar. After 45 min, the solution turned to be transparent yellow. Both sodium acetate (14.4g) and polyethylene glycol(4g) were then added, and reacted in an autoclave at 200°C for 12 h. The particles were separated using a magnet and washed several times with ethanol. Finally, the synthesized zinc ferrite nanoparticles were dried in a vacuum oven for a day. Morphology of nanoparticles was observed by scanning electron microscope. The CI particles (CM grade, BASF, average particle size: 4.5 μm , density: 7.8 g/cm^3) were then used as a main component for the MR fluids. The 0.5wt% of ZnFe_2O_4 was added into 50wt% of CI based MR fluid, while CI-based MR fluid (50 wt%) dispersed in silicone oil (viscosity of 100cS) was also prepared for the comparison. Their MR characteristics were measured using a rotational rheometer under various magnetic field strengths. **III. RESULT AND DISCUSSION** Figure 1 presents SEM image of the morphology of particles, with a smooth surface and particle size distribution in 300-500nm range. The density of zinc ferrite particles was measured to be 4.8 g/cm^3 by a pycnometer. Rheological response of shear stress as a function of shear rate of both MR fluids is presented in Figure 2 under a magnetic field strength range from 0 to 341 kA/m. Without a magnetic field, the MR fluid behaves like a Newtonian fluid. However when magnetic field strength was applied, the shear stress increased as the shear rate increased. MR properties of the CI/ ZnFe_2O_4 based MR fluid (50/0.5wt %) showed a higher shear stress than that of CI-based MR fluid. Under the magnetic field applied, both MR fluids with and without an additive show similarly a wide plateau region which is attributed to the formed columns due to the strong dipole-dipole interaction among the magnetic particles. Additionally, we also measured the sedimentation ratio to confirm the role of zinc ferrite as an additive material for MR fluids through a Turbiscan optical analyser system. The CI-based MR fluid had a faster sedimentation rate than the CI/ ZnFe_2O_4 based MR fluid, indicating that the dispersion stability of CI/ ZnFe_2O_4 based MR fluids increased as compared to the CI based MR fluids. Improved dispersion stability is thought due to the fact that the nanoparticles fill the free space between the CI particles at the same time partially being coated on the surface of the CI particles, contributing to flow resistance. Therefore, in this work, the positive role of zinc ferrite as a proper additive for the CI based MR fluid is confirmed.

[1] S. E. Premalatha, R. Chokkalingam and M. Mahendran, Am. J. Polym. Sci, 2, 50 (2012). [2] J. de Vicente, D. J. Klingenberg and R. H. Alvarez, Soft Matter, 7, 3701 (2011) [3] M. J. Hato, H. J. Choi and H. H. Sim, Colloids Surf. A-Physicochem. Eng. Asp, 377, 103 (2011) [4] C. Y. Gao, M. W. Kim,

D. H. Bae, Polymer, 125, 21 (2017) [5] J. E. Kim, H. J. Choi, IEEE Trans. Magn, 47, 3173 (2011) [6] Y. Z. Dong, W. J. Han and H. J. Choi, J. Ind. Eng. Chem. 93, 210 (2021) [7] S. H. Piao, H. S. Chae, and H. J. Choi, IEEE Trans. Magn. 51,4600704 (2015)

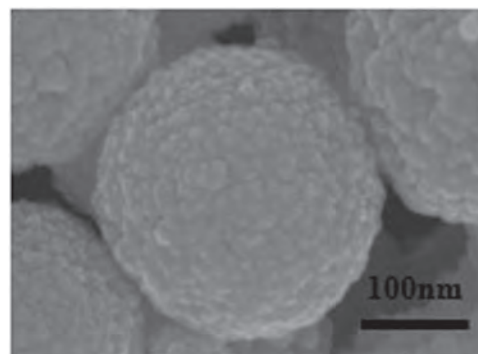


Fig. 1 SEM images of ZnFe_2O_4

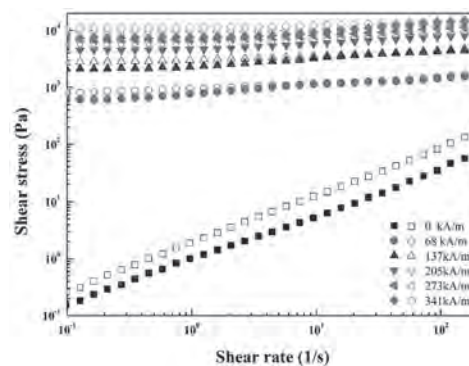


Fig. 2 Shear stress curves of both pure CI (closed) and CI/ ZnFe_2O_4 (open) MR fluids at different magnetic field strengths

JQ-05. Fabrication and Magnetorheological Characteristics of Core-Shell Typed Poly(2-Methylaniline)/Carbonyl Iron Microspheres.

Q. Lu¹ and H. Choi¹

1. Inha University, Incheon, The Republic of Korea

I. INTRODUCTION Actively tunable smart magnetorheological (MR) fluids consisting of soft-magnetic particles suspended in nonmagnetic liquids like mineral oil or silicone oil [1], [2], have drawn extensive attentions with their many potential applications in mechanical engineering, biomedicine, pigments, and even in aerospace devices due to their controllable capability. They exhibit reverse and tunable rheological properties from Newtonian fluid-like to solid-like through applied magnetic field strengths employed within milliseconds order. Among extensive potential magnetic particles for their MR applications, soft-magnetic carbonyl iron (CI) microspheres possessing a large saturation magnetization value, proper size, and large permeability have brought lots of interests [3], [4]. However, CI particles are known to intrinsically possess the limitation of their usage with their much higher particle density than of the non-magnetic fluids, which may easily cause the sedimentation in the MR fluids. In this study, poly(2-methylaniline)(PMAN)-CI core-shell structured particles were synthesized by a chemical grafting method with dopamine hydrochloride as a grafting agent to enhance repulsive interaction or to decrease distance among CI microspheres. Dopamine was coordinated on the surface of magnetic particles by electro-donating bidentate enediol, combined with magnetic particles through a bidentate ligand reaction [5]. At this point, the amine groups of dopamine-modified CI particles can be further modified as functional groups. The morphology of the fabricated core-shell structured particles was examined by transmission electron microscopy and scanning electron microscopy. In addition, the rheological properties of MR fluids were measured by using a rotational rheometer under various magnetic field strengths.

II. EXPERIMENT Before PMAN coating, the surface of CI particles was modified with dopamine hydrochloride to improve the affinity between magnetic CI particles and PMAN coated shell. At first, CI particles were dispersed in DI-water, and dopamine hydrochloride was mixed with ultrasonic stirring reaction solution for 12 h to promote dopamine coating. The unattached dopamine was then flushed with excess deionized water and hexane. The CI particles of the surface coating were dried in vacuum for 24 h. The dopamine-modified CI particles were dispersed in deionized water under ultrasonication for 30 min. PMAN was coated by polymerizing 2-methylaniline via a chemical oxidation process induced by ammonia peroxide in an acidic environment. We then added the mixture to poly(vinyl alcohol) dissolved in di-water, transferred the reaction solution to the reactor, and cooled it down. Aniline and ammonia peroxide were added to the reactor. The reaction was kept for 24 h and stirred at 300 rpm. When the reaction was complete, the resulting product was separated using a magnet and dried in a vacuum for 24 h.

III. RESULTS AND DISCUSSION The SEM images of CI/PMAN core-shell particles are shown in Figure 1, in which the CI/PMAN particles exhibit a larger particle size because of the PMAN coated shell, compared to a smooth surface of the pristine CI particles. The MR behaviors of CI/PMAN based MR suspension were carried out using a rotational rheometer in a controlled shear rate mode under a series of applied magnetic field strengths from 0 to 342 kA/m. The shear stress increases with increasing shear rate, which implies that the MR fluid exhibits a Newtonian fluid-like behaviour without an external magnetic field as shown in Fig. 2. When the magnetic field was applied, the shear stress demonstrated a significant improvement because of the change from a liquid-like to solid-like behaviour of the MR fluid, followed by stepwise growth with the increase of magnetic field. For each magnetic field strength, the shear stress of MR suspension displayed a wide plateau region over the entire shear rate range. In addition, the shear stress with the external magnetic field of MR suspensions was also fitted with the Herschel-Bulkley model [6], [7] as follows: $\tau = \tau_0 + K\dot{\gamma}^n$ where τ is the shear stress, τ_0 represents the dynamic yield stress, is the shear rate, K and n represent the consistency index and power-law exponent, respectively. The relationship between the dynamic yield stress of PANI/CI and the magnetic field strength was observed by measuring the universal yield stress. Even though the saturation magnetization and density of the PMAN/CI particles were reduced by the introduction of a non-magnetic PMAN shell, their dispersion stability was observed to be improved according to the

Turbiscan test by synthesizing the PMAN-coated CI particles. These results were attributed to the rough surface and low density of the core-shell structure PMAN/CI particles.

[1] M. Mrlik, M. Ilcikova and V. Pavlinek, *J. Colloid Interf. Sci.*, 396, 146 (2013). [2] D. J. Klingenberg and J. C. Ulicny, *Int. J. Mod. Phys. B*, 25, 911 (2011). [3] I. Bica, E. M. Anitas and L. Chirigiu, *J. Ind. Eng. Chem.* 56, 407 (2017). [4] F. F. Fang, Y. D. Liu and H. J. Choi, *ACS Appl. Mater. Inter.* 3, 3487 (2011). [5] C. J. Xu, K. M. Xu and H. W. Gu, *J. Am. Chem. Soc.* 126, 9938 (2004). [6] K. J. Son, *Korea-Austral. Rheol. J.* 30, 29 (2018). [7] Y. Seo and H. J. Choi, *Korea-Austral. Rheol. J.* 30, 317 (2018).

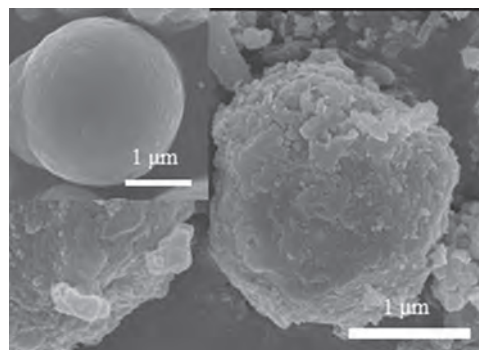


Fig.1 SEM images of CI (inset) and CI/PMAN core-shell particles

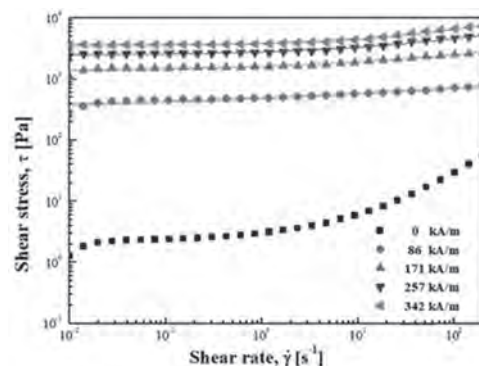


Fig.2 Flow curve of shear stress for CI-PMAN MR fluid under various magnetic field strengths as a function of shear rate

JQ-06. Development of Individualized Brain Model and Physical Phantom of Small Animals for Experimental Verification of Transcranial Magnetic Stimulation.

C. Nimonkar^{1,2}, E. Knight¹, H.A. Magsood¹, I.C. Carmona¹ and R.L. Hadimani^{1,3}

1. Department of Mechanical and Nuclear Engineering, Virginia Commonwealth University, Richmond, VA, United States; 2. Mills E. Godwin High School, Richmond, VA, United States; 3. Department of Electrical and Computer Engineering, Iowa State University, Ames, IA, United States

Transcranial magnetic stimulation (TMS) is a neuromodulation therapy that can be used to treat neurological and psychiatric conditions and has been approved by the FDA for certain disorders [1]–[4]. Since TMS trials with humans are not always feasible, brain phantoms have been developed as ways of testing without actually stimulating the patient. Although a brain phantom has been developed for humans, a comparable brain phantom for rats or mice has not been created specifically for TMS or other neuromodulation techniques. An individualized brain phantom for rats is needed to accelerate the study of neuromodulation techniques, especially the measurement of induced electric field and voltages in the brain regions when stimulated by a time-varying magnetic field. The main objective of this paper is to develop an individualized, anatomically-accurate rat brain model for finite element simulation and a physical model for experimental measurement of stimulation strengths. We initially obtained magnetic resonance images (MRIs) from public databases to create the anatomically accurate brain models. The Waxholm Space Atlas of the Sprague Dawley rat brain was chosen as the MRI to be created into the preliminary phantom. Using the Skull Stripping tool from the BrainSuite software package, the brain was separated from the surrounding skull and skin. Both the original and skull-stripped brain NIFTI files were downsampled using AFNI software tools. The skull-stripped brain was then inputted as a reference mask into the Skull Stripper Python program, along with the downsampled original MRI [5]. The output was the final file, containing 3D information of the chosen rat brain. Using the 3D Slicer program, the final brain file was converted into a 3-dimensional STL file. The program Meshmixer was then used to reduce the file size and fix any model errors. The anatomically accurate individualized brain model was combined with a TMS coil designed for small animals in SolidWorks. An enclosure was also made that surrounded the coil and brain (serving as air in the simulation). The Maxwell 3D module in ANSYS finite element simulation software was then used to simulate the magnetic flux density and induced electric fields in the rat brain models. Fig. 1 inset shows the orientation of the brain and coil in the simulation. Fig. 1 and Fig. 2 show preliminary results of what is predicted for the physical phantom, with all the layers (skin, skull, and other tissues) hidden except the brain. We had assigned uniform conductivity of 0.2 S/m for the entire brain, a relative permeability of 1, and a relative permittivity of 12,000. A figure of eight coil was used on the top of the rat's head with 1000A current supplied to the coil. The peak magnetic field of 1.22 T and $2.5 \times 10^{-6} \text{A/m}^2$ occurs on the surface of the brain below the center of the coil. We are currently in the process of developing a physical individualized, anatomically-accurate physical brain phantom using the above computation models. Work to consider white and grey matter separately in the model is currently in progress. We will use similar techniques as used in the development of our existing human brain phantoms [6], [7]. Using the phantom, we will systematically measure the stimulations strengths in different regions of the brain using several coils types. Acknowledgement: Authors would like to thank funding from Dean's Early Researcher Initiative (DERI) program at College of Engineering of Virginia Commonwealth University, Richmond, VA, USA.

[1] E. M. Wassermann and S. H. Lisanby, "Therapeutic application of repetitive transcranial magnetic stimulation: a review," *Clin. Neurophysiol.*, vol. 112, no. 8, pp. 1367–1377, Aug. 2001, doi: 10.1016/S1388-2457(01)00585-5. [2] L. Carmi, U. Alyagon, N. Barnea-Ygael, J. Zohar, R. Dar, and A. Zangen, "Clinical and electrophysiological outcomes of deep TMS over the medial prefrontal and anterior cingulate cortices in OCD patients," *Brain Stimulat.*, vol. 11, no. 1, pp. 158–165, Sep. 2017, doi: 10.1016/j.brs.2017.09.004. [3] R. B. Lipton *et al.*, "Single-pulse transcranial magnetic stimulation for acute treatment of migraine with aura: a randomised,

double-blind, parallel-group, sham-controlled trial," *Lancet Neurol.*, vol. 9, no. 4, pp. 373–80, Apr. 2010, doi: 10.1016/S1474-4422(10)70054-5. [4] M. S. George and R. H. Belmaker, *Transcranial Magnetic Stimulation in Clinical Psychiatry*. American Psychiatric Pub, 2007. [5] A. Delora *et al.*, "A simple rapid process for semi-automated brain extraction from magnetic resonance images of the whole mouse head," *J. Neurosci. Methods*, vol. 257, pp. 185–193, Jan. 2016, doi: 10.1016/j.jneumeth.2015.09.031. [6] H. Magsood and R. L. Hadimani, "Development of anatomically accurate brain phantom for experimental validation of stimulation strengths during TMS," *Mater. Sci. Eng. C*, p. 111705, Nov. 2020, doi: 10.1016/j.msec.2020.111705. [7] H. Magsood, F. Syeda, K. Holloway, I. C. Carmona, and R. L. Hadimani, "Safety Study of Combination Treatment: Deep Brain Stimulation and Transcranial Magnetic Stimulation," *Front. Hum. Neurosci.*, vol. 14, p. 123, Apr. 2020, doi: 10.3389/FNHUM.2020.00123.

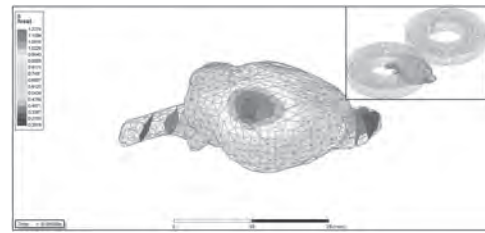


Figure 1. Magnetic flux density (B) plot of rat brain surface. Inset: Coil and rat brain orientation (scalp, skull and cerebrospinal fluid layers are hidden)

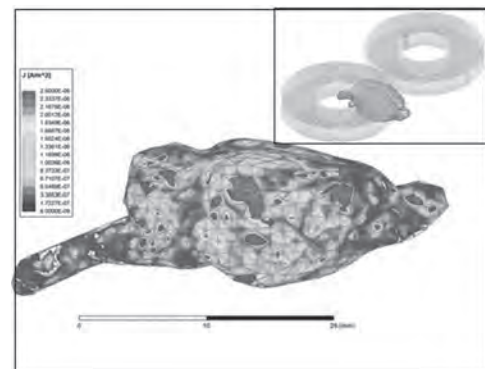


Figure 2. Electric current density (J) plot of rat brain surface. Inset: Coil and rat brain orientation (scalp, skull and cerebrospinal fluid layers are hidden)

JQ-07. Structure and Magnetic Properties of Maghemite Nanoparticles for DNA Extraction.

S. Stolyar¹, S.V. Komogortsev², R. Yaroslavtsev¹, A. Gorbenko¹, I. Olkhovskiy¹, D.S. Neznakhin³ and R. Iskhakov²

1. FGBNU, Federal Research Center Krasnoyarsk Scientific Center Siberian Branch of the RAS, Krasnoyarsk, Russian Federation; 2. Kirensky Institute of Physics, Krasnoyarsk, Russian Federation; 3. Ural Federal University, Ekaterinburg, Russian Federation

In recent years, magnetic nanoparticles based on iron oxides have found increasing interest in practical applications in the field of biotechnology and biomedicine. Surface modified magnetic nanoparticles can be used for selective isolation of certain biomolecules, such as nucleic acids and proteins. The method, commonly known as “magnetic separation”, has gained popularity in performing tests for diagnostic purposes. The aim of this work was to develop a nanomagnetic construction based on iron oxide nanoparticles for efficient separation of DNA molecules and subsequent investigation by polymerase chain reaction. The magnetic particles were prepared by coprecipitation from a solution of FeCl₃ and FeCl₂ salts in a molar ratio of 2:1 at room temperature. With constant stirring, an NH₄OH solution (25%) was injected into the solution of iron salts until pH = 10 was reached. At the end of the reaction, the magnetic nanoparticles were collected using a magnet and washed several times in distilled water until pH = 7.0. To use nanoparticles in magnetic separation of DNA, we treated them with a solution containing 1.25 M sodium chloride and 10% PEG 6000 to inhibit free radical oxidation. For biomedical applications of magnetic nanoparticles, an important role is played by the blocking temperature - the temperature separating the hysteresis and hysteresis-free responses of an ensemble of particles. For applications such as bio-separation, blocking temperatures close to ambient (body temperature) are considered optimal. This choice is due to a compromise between the better colloidal stability of an ensemble of superparamagnetic particles (hysteresis-free behavior) and the high magnetic susceptibility of blocked nanoparticles (response with hysteresis). For magnetic characterization of our particles, we performed measurements of magnetization curves at various temperatures (Fig. 1). According to Fig. 1, the magnetic hysteresis disappears at temperatures above 100 K. The distribution of particles by size and by the magnitude of magnetic anisotropy can lead to inhomogeneity of the blocking temperature in the ensemble of particles. To quantify this inhomogeneity (blocking temperature distribution), we calculated the data in Fig. 1 by different methods. The temperature behavior of the coercive force in Fig. 2 does not follow the power-law dependence $H_c(T) = H_c(0) * (1 - (T/T_B)^\alpha)$, (1) usually discussed for single-domain non-interacting nanoparticles at temperatures below the blocking temperature (T_B) [1,2]. The power exponent α , in this case, is in the range from 0.67 to 1.00 [3,4]. This deviation may be due to the inhomogeneity of the blocking temperature in the system of the studied nanoparticles. Therefore, to describe the coercive force, we used averaging [5]: $H_c(T) = H_c(0) * (\int H_c(T) * f(T_B) dT_B) / (\int f(T_B) dT_B)$ (2) where the parameter $H_c(0)$ is the average coercive force at $T = 0$ K. Describing the experimental behavior of the coercive force by expression (2), we can determine the parameters of the distribution function $f(T_B)$ corresponding to the best description of the experiment. The best agreement is achieved using the lognormal distribution function: $f(T_B) = 1 / (T_B \sigma \sqrt{2\pi}) * \exp(-\ln^2(T_B/T_{B0}) / 2\sigma^2)$ with the parameters $T_{B0} = 80$ K, $\sigma = 0.77$. The study of the nanoparticles ability to isolate nucleic acids was carried out as follows. Leukocyte lysate from a blood sample obtained from a patient with chronic myeloproliferative disease was added to the nanoparticle suspension. Then, the nanoparticles bound to DNA molecules were separated using a magnet. Subsequent washing of DNA from nanoparticles was carried out with 70% ethanol at room temperature, then elution was carried out in 50 μ l of TE buffer for 5 minutes at 65 °C. Real-time PCR reaction was performed using the resulting eluate to detect the JAK2 gene. As a comparison, a parallel reaction was carried out with DNA samples isolated by the sorption method using a commercial kit “DNA-Sorb-B” (Amplisens, Russia). The comparative concentration of the isolated DNA was 3.9 ng/ μ l with standard isolation and 2.4 ng/ μ l with isolation using magnetic nanoparticles. It follows from the PCR results that the proposed method for isolating DNA from human blood samples is not inferior in efficiency to the standard isolation method and does not affect the efficiency of PCR amplification. This work was supported by

Russian Foundation for Basic Research, Government of Krasnoyarsk Territory, Krasnoyarsk Region Science and Technology Support Fund to the research projects No. 20-42-242902 and by the Council of the President of the Russian Federation for State Support of Young Scientists and Leading Scientific Schools (project no. MK-1263.2020.3). We are grateful to the Center of collective use of FRC KSC SB RAS for the provided equipment.

[1] R.S. Iskhakov, S.V. Komogortsev, S.V. Stolyar et al. *Met. Metallogr.*, 88, 261–269 (1999) [2] S. V. Komogortsev, R.S. Iskhakov, A.D. Balaev et al. *Phys. Solid State*. 49, 734–738 (2007) [3] H. Pfeiffer, *Phys. Status Solidi*. 118, 295–306 (1990) [4] I.S. Poperechny, Y.L. Raikher, V.I. Stepanov, *Phys. B Condens. Matter.*, 435, 58–61 (2014) [5] S. V. Komogortsev, R.S. Iskhakov, A.D. Balaev et al., *Phys. Solid State*. 51, 2286–2291 (2009)

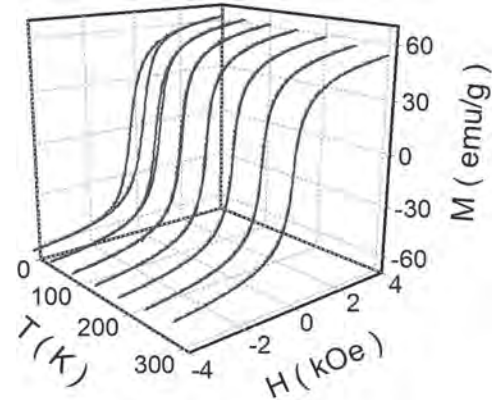


Fig. 1 Magnetization curves

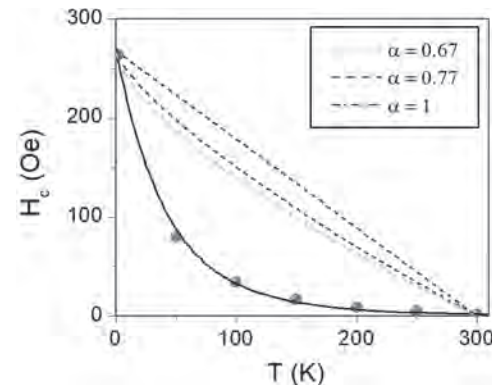


Fig. 2. The temperature behavior of the coercive force (red symbols) is not described by equation (1) - dashed lines, but is described by equation (2) - solid line.

JQ-08. Design and Analysis of High-Gradient Magnetic Field Source at Micro-Scale for Microfluidic Magnetophoresis Applications.

V.K. Yadav¹, S. Das² and D. Mallick¹

1. Department of Electrical Engineering, Indian Institute of Technology Delhi, New Delhi, India; 2. Centre for Applied Research in Electronics, Indian Institute of Technology Delhi, New Delhi, India

To separate magnetically coupled particles on lab-on-a-chip devices, microfluidic magnetophoresis plays a pivotal role [1]. It can be useful for biomedical applications like cancer detection, drug delivery, screening, clinical diagnostics [2, 3]. When subjected to a non-uniform magnetic field, small-sized (μm - nm) particles suspended in a fluidic medium will translate toward either the maxima or minima of the gradient of the magnetic field. However, it is very difficult to produce high-gradient magnetic field at micro-scale due to several issues such as non-availability of integratable, high energy product permanent magnets and the detrimental effect of strong demagnetization field of the thin film magnets. Therefore, patterning the magnetic surface is required to produce high flux density with micro-scale resolution over large areas. The efficient design and optimization of such micro-magnetic structures along with their magnetic interaction play an important role in the development of the devices for microfluidic magnetophoresis applications. In our work, comparative FEM analysis is performed to show the advantages of using micro-patterned magnets over bulk rectangular magnet for microfluidic magnetophoresis applications, which is also validated using an analytical framework. The width (x-axis) and height (y-axis) of microfluidic channel were considered $1200\ \mu\text{m}$ and $100\ \mu\text{m}$ respectively with varying gap distance from the permanent magnetic structures (Fig. 1(a)). We have considered bulk rectangular magnetic structure of $1000\ \mu\text{m}$ width and a variation in the height from 100 to $500\ \mu\text{m}$. Micro patterned rectangular magnets, with $50\ \mu\text{m}$ fixed gap distance between successive patterns, across the width of microfluidic channel are also analyzed to study the advantage of micro-patterned magnets over bulk rectangular magnet as shown comparatively in Fig. 1(b) and (c). All proposed magnetic structures were concocted using a nano-composite of NdFeB magnetic powder embedded in Polydimethylsiloxane (PDMS) matrix. Geometric optimization of the entire structure including the separation size, height, and width of the separate features are explored using FEM and analytical models to efficiently control the particle trajectories within the microfluidic channel. Effect of different geometries (rectangle, square, triangular etc.) of the micro-patterned magnets are also determined by a factor $(\mathbf{H} \cdot \nabla) H$, which is proportional to the magnetic force and describe the range of impact of magnets [4]. At the various height ($w_g = 50\ \mu\text{m}, 80\ \mu\text{m}, 110\ \mu\text{m}$) from the micro-magnet structure, the magnetic flux densities H_x and H_y were extracted and subsequently used in an customized MATLAB code to determine the force F_x and F_y for describing the motional behavior of magnetic particles in the channel with the help of Newton's second law. A wide magnet comparable to the microfluidic channel can yield a pseudo magnetic field which can magnetize the micro/nano particles in the channel but does not cause cumulative forces, being exerted on them which can be greatly enhanced by using optimized micro-patterns as shown in Fig. 2. Proof-of-concept prototype of the proposed device is being fabricated using standard micro-fabrication processes. Overall, an effective design methodology for developing highly efficient micro-magnetic flux sources is described which can be useful in many micro-scale applications including biological particle separation and mixing.

1. R. Zhou, Q. Yang, F. Bai, J. A. Werner, H. Shi, Y. Ma, C. Wang, *Microfluid. Nanofluid.*, 20, 110 (2016). 2. R. Zhou, A. N. Surendran, M. Mejulu, Y. Lin, *Micromachines*, 11,129. 25 (2019). 3. F. Alnaimat, S. Karam, B. Mathew, B. Mathew, *IEEE Nanotech. Mag.*, 14(3), 24-41 (2020). 3. E. P. Furlani, *J. Appl. Phys.*, 99, 024912 (2006).

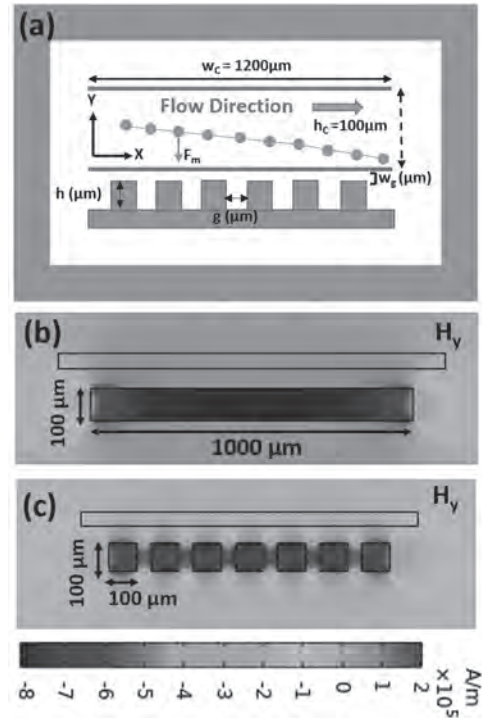


Fig. 1: (a) Proposed device architecture. FEM simulation results of the y component of magnetic flux density in the microfluidic channel due to rectangular magnet of size (b) $1000 \times 100\ \mu\text{m}^2$ (bulk magnet) and (c) $100 \times 100\ \mu\text{m}^2$ (micro-patterned magnets) with $50\ \mu\text{m}$ pattern gap. A thin film (b) produces magnetic field only at the edges whereas the magnetic flux density vis-à-vis the magnetic flux gradient can be significantly improved through micro-patterning (c) of the magnetic surface.

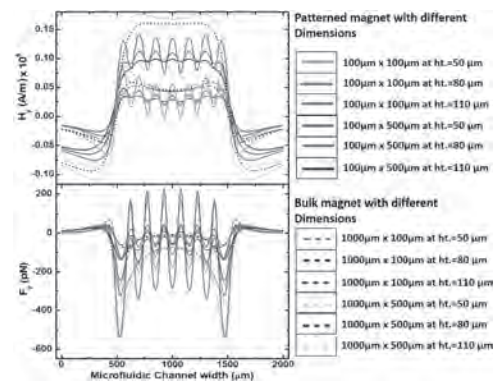


Fig. 2: The Y component of (a) magnetic field intensity (H_y) and (b) Force (F_y) exerted on the particles inside the microfluidic channel at different height (ht.) due to single bulk and patterned micro-magnets.

JQ-09. Research on Cell Proliferation Model Based on A549 Cell Line With Magnetic Field Intervention.

N. Zhang^{1,2}, Z. Wang¹, S. Ning³, S. Wang¹, B. Lai⁴, T. Zhu¹ and H. Qiu¹
 1. School of Electrical Engineering, Xi'an Jiaotong University, Xi'an, China; 2. Department of Oncology, Johns Hopkins University School of Medicine, Baltimore, MD, United States; 3. School of Electronic Information and Artificial Intelligence, Shaanxi University of Science and Technology, Xi'an, China; 4. Quanzhou Experimental Middle School, Quanzhou, China

I. Introduction In recent years the K-Ras gene mutations are more malignant than others in lung cancer [1]. Although radiation therapy and chemotherapy can slow the growth of some kinds of lung cancer cells, such as non-small cell lung cancer. The effects of these treatments on K-Ras gene mutation were still not desirable. The survival rate of K-Ras driven lung cancer was lower than that of the other lung cancer [2]. Therefore, it is important to find a new way to treat lung cancers. Many researchers found that the magnetic field could disturb the proliferation of cancer cells. It suggested a novel therapy for cancer treatment. However, the mechanism was still not been fully determined. Quantifying the cancer cell proliferation and establish the proliferation model could make a contribution to revealing the mechanism of the magnetic field on the cancer cells. In addition, the model could suggest useful information from the proliferation of the cancer cell to help further steps. In 1997, Pilkington studied the models of the brain tumor in both vitro and vivo [3]. Swanson quantified the glioma cell in vitro. A mathematical model was developed to describe the proliferation of the brain tumor. The model was based on the brain tumor without magnetic field stimulations [4]. Although extensive work has been done to characterize the proliferation of the cancer cell in vitro, the cell proliferation model based on K-Ras mutations, considering magnetic field stimulation has not been developed. Herein, a cancer cell proliferation model based on A549 cell line considering sensitive magnetic stimulation was proposed. Based on our previous studies [5]-[6], the magnetic field stimulation with sensitive frequency was applied to the A549 cancer cells. The data of cell proliferation was obtained during the cell experiment with magnetic field stimulations. In addition, the parameters of the cell proliferation model were regressed by the finite difference method [7]. As simulated by the established model, the density of the cancer cell was fit well with the cell experiment. II. Cell Experiment and Cell Proliferation Model A. The cell experiments The A549 cancer cells are adenocarcinomic human alveolar basal epithelial cells. Mutations on K-Ras of A549 cancer cells were obtained from the American Tissue Culture Collection. The cells are divided into the experimental group and the control group. The frequency of the magnetic field is 2 kHz, and the magnetic flux density at the cells is 0.5 mT. The density of cells is chosen as the variable to describe cell proliferation. During the cell experiments, in order to monitor the situation of the cell proliferation, the cell is counted by an automated cell counter (TC10, BIO-RAD, USA) every 12 hours, and captured every 6 hours. B. The proliferation model of A549 cancer cells It is well known that most of the normal cells are stable. By contrast, with sufficient nutrients, the cancer cells can multiply indefinitely and become immortal. In order to describe the feature of the infinite proliferation, the diffusion equation is proposed and it could represent the behavior of the cancer cells well. The cell proliferation model is shown in equation (1). In equation (1), c is the density of the cancer cell, x is the one-dimensional coordinate, t is the time, D is the diffusion coefficient, and ρ is the rate of cell proliferation. The boundary conditions of equation (1) were set as c_0 due to the initial density of cancer cells. During the magnetic field stimulation, the effect of the magnetic field will rise due to the proliferation of A549 cancer cells. To take the influence of the magnetic field into consideration, the power function would reflect the magnetic field well. The relationship between the magnetic field stimulation and the proliferation of the A549 cancer cells can be obtained by equation (2). The parameters of a and b are controlled by the parameters of the magnetic field stimulations. According to the cell experiments, the exponent of the power function is set as 0.5. The parameters will be regressed from the cell experiment. III. Parameters Regression and Numerical Simulation Due to the cell proliferation in the culture dish, the cells are diffused from the center to the periphery. Therefore, the cancer cell proliferation model is established in the one-dimensional coordinate. The finite difference method

is based on definite solution problems. As shown in equation (3), the finite difference method in the time domain is based on the problem of a definite solution, and the parameters of the proliferation model can be obtained by equation (4). The parameters of the cancer cell proliferation model are obtained by solving multivariate regression equations. As shown in Fig. 2 (a), (b), (c), and (d), the density of A549 cells was fit well with measured data from the electron microscope. IV. Conclusion In this paper, a proliferation model based on the A549 cancer cell line was proposed. The inhibitory effect of the magnetic field was taken into account. It is believed that the contributions of this approach not only helps to reveal the mechanism of magnetic field on the cell but also suggests a new way to predict the effect of magnetic stimulation on cancer inhibition.

[1] V. S. Veena, P. S. George, K. Jayasree, et al., *Proc. Int. J. Sci. Res. Publ.* Vol. 2 pp. 1(2013) [2]R.H. Mak, E. Doran, A. Muzikansky, et al., *International Journal of Radiation Oncology Biology Physics*, Vol. 78, pp. S36(2010) [3] G.J. Pilkington, R. Bjerkvig, L.R. De, et al., *Anticancer research*, Vol. 17, pp. 4107(1997) [4]K.R. Swanson, *Mathematical and Computer Modelling*, Vol. 47, pp. 638(2008) [5] N. Zhang, S. Wang, S. Wang, et al., *IEEE Transactions on Applied Superconductivity*, Vol.26, pp. 0607504 (2016) [6] N. Zhang, S. Ning, S. Wang, et al., *IEEE Transactions on Magnetics*, Vol. 54, pp. 5001004(2018) [7] T.L. Baker, *The Finite Difference Method in Partial Differential Equations*, John Wiley and Sons, (1980)

$$\frac{\partial c}{\partial t} = D \frac{\partial^2 c}{\partial x^2} + \rho c \tag{1}$$

$$\frac{\partial c}{\partial t} = D \frac{\partial^2 c}{\partial x^2} + \rho c - [at^{0.5} + b]c \tag{2}$$

$$\frac{\partial u(t,x)}{\partial t} - a^2 \frac{\partial^2 u(t,x)}{\partial x^2} = 0 \quad 0 < x < L_x, \quad 0 < t < T \tag{3}$$

$$\frac{c(t_{i+1},x_j) - c(t_i,x_j)}{\tau} = D \frac{c(t_i,x_{j+1}) - 2c(t_i,x_j) + c(t_i,x_{j-1}))}{h^2} + \rho c(t_i,x_j) - [at_i^{0.5} + b]c \tag{4}$$

Fig. 1 Equations

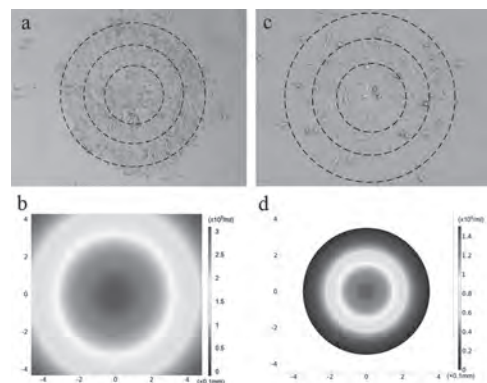


Fig. 2 (a) The A549 cancer cell without MF. (b) The A549 cancer cell with MF. (c) Numerical simulation of the A549 cell proliferation model without MF. (d) Numerical simulation of the A549 cell proliferation model with MF.

Session JR
NANOPARTICLES AND NANOWIRES
(Poster Session)

Mariana P Proenca, Chair
IFIMUP (Portugal) and ISOM-UPM (Spain), Porto, Portugal

JR-01. Magnetic Vortex Formation of Cubic Fe_3O_4 Submicron Particles.

E. Nomura¹, M. Chiba¹, S. Matsuo¹, S. Kobayashi¹, J. Manjanna², Y. Kawamura³, J. Suzuki³, K. Ohishi³ and K. Hiroi⁴

1. Iwate University, Morioka, Japan; 2. Rani Channamma University, Belagavi, India; 3. Ippan Zaidan Hojin Sogo Kagaku Kenkyu Kiko, Tsuchiura, Japan; 4. Nihon Genshiryoku Kenkyu Kaihatsu Kiko, Naka-gun, Japan

Ferromagnetic particles showing a spin vortex (SV) structure have received considerable attentions in the biomedical field, because of the possibility of such as high efficient heating properties [1], higher magnetomechanical effects [2]. Extensive investigations revealed that a SV state appears at low fields for many types of nanoscale-to-submicron-sized ferromagnets and its stability changes depending on the morphology (size, shape, structure etc.); for instance, in the case of cubic nanoparticles, zero-field critical single-domain/vortex size is smaller as compared with that of sphere and a behavior of SV core drastically changes with size [1,3]. Despite its relatively simple shape and its superior magnetic property for biomedical applications [1], the magnetic nature of a SV state for submicron cubic particles was not fully understood in detail. In this study, we have performed first-order reversal curves (FORCs) measurements and small-angle neutron scattering (SANS) experiments for cubic Fe_3O_4 submicron particles to microscopically understand the SV behavior under magnetic fields. For Fe_3O_4 cubes with a side length of 265 nm, we measured FORCs at several temperatures between 10 and 300 K using SQUID magnetometer. The FORC distribution as a function of magnetic field H and reversal field H_r was calculated [4]. We also carried out SANS experiments at the Japan Proton Accelerator Research Complex (J-PARC). The Fourier coefficients of magnetization under magnetic fields were determined from magnetic SANS intensities in the direction parallel and perpendicular to the magnetic field [5]. Fig.1 shows the temperature dependence of the FORC diagram below and above the Verwey transition temperature of 120 K. At the lowest measuring temperature of 10 K, two strong FORC distribution peaks were clearly observed as shown Fig.1(a), indicating the formation of a SV structure at low fields; the two peaks reflect irreversible magnetization changes due to SV nucleation and annihilation [4]. As the temperature increases, the two peaks approach each other, associated with the development of the sharp central peak between them, and disappear at around $T = 90$ K below T_v as shown in Fig. 1(b). Above $T \sim 90$ K, only a sharp single peak was observed in the FORC diagram as shown in Fig. 1(c). These results imply that the switching of a SV core domain [6] dominates irreversibility of magnetization process at higher temperatures, whereas at low temperatures irreversible magnetization reversal which occurs between single domain and SV states dominates the FORC distribution. Nucleation and annihilation fields of SV, estimated from the position of the FORC distribution peak at $T = 10$ K are ~ 0 and -1100 Oe, respectively; the former is very weakly temperature dependent, whereas the latter slightly increases to -800 Oe at $T = 70$ K. Such a large negative annihilation field and the appearance of the central FORC distribution peak were not observed in the hollow Fe_3O_4 spheres with a SV structure [4] and might be responsible for the cubic shape. Analysis of magnetic SANS intensities showed that a Fourier coefficient of magnetization components parallel to magnetic field decreases as the magnetic field is reduced from a high field, whereas that perpendicular to field increases and maximizes in a SV state. The latter is in contrast to our expectation assuming a simple SV structure, indicating the presence of spin disorder in the SV structure due to the cubic particle geometry.

[1] N. A. Usov, et al., Scientific Reports, 8, 1224 (2018) [2] L. Peixoto et al., Appl. Phys. Rev., 7, 011310 (2020). [3] W. Williams et al., J. Geophys. Res., 100, 3859 (1995) [4] M. Chiba, et al., J. Mag. Mag. Mater., 512, 167012 (2020) [5] A. Michels, J. Phys.: Condens. Matter, 26, 383201 (2014) [6] W. Williams et al., J. Geophys. Res., 111, B12S13 (2006)

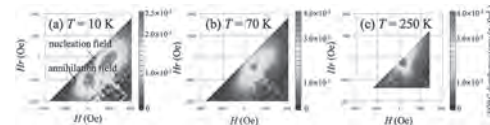


Fig.1 Temperature dependence of the FORC diagram at (a) $T = 10$ K, (b) $T = 70$ K, and (c) $T = 250$ K. Red and blue denote the FORC distribution with higher and lower intensities, respectively.

JR-02. Size-Specific Magnetic Configurations in Epitaxial Iron Nano-Cuboids.

S. Guo¹, M. Henschel¹, V. Neu¹, T. Blon², D. Pohl³ and K. Leistner¹
 1. Leibniz-Institut für Festkörper- und Werkstoffforschung Dresden eV, Dresden, Germany; 2. Laboratoire de Physique et Chimie des Nano-Objets, Université de Toulouse, Toulouse, France; 3. Dresden Center for Nanoanalysis (DCN), Center for Advancing Electronics Dresden (cfaed), TU Dresden, Dresden, Germany

Magnetic nanostructures attract considerable scientific and technological efforts in diverse applications, such as magnetic recording, magnetic sensors, biomedicine, etc.^[1,2] Whereas patterned nanomagnets are mostly 2D planar structures, recently research has been expanded into 3D aspect. In 3D nanomagnets, more delicate and complicated magnetic configurations, with novel properties, become possible.^[3,4] Imaging and understanding the magnetic configurations in 3D nanomagnets is an increasingly important issue for a wide range of modern applications. Here, aligned, isolated iron nano-cuboids [Fig. 1 (a)] have been fabricated by taking advantage of epitaxial, three-dimensional-island growth on GaAs(001) during electrodeposition at low deposition rates.^[5] The nanoparticles exhibit lateral size between 10 and 250 nm and heights below 80 nm. Surface {100} facets predominate with a thin crystalline oxide shell that protects the nanoparticles during prolonged storage in air [Fig. 1 (b)]. The magnetic configurations inside the cuboids are systematically investigated by combining quantitative magnetic force microscopy (qMFM) with micromagnetic simulations [Fig. 1 (c, d)]. Experimental results and micromagnetic simulations give evidence for a transition from single-domain state to vortex state, and even to Landau pattern with increasing the size of the cuboids, demonstrating the key importance of nanometric size control of magnetic nanoparticles. The simulated and experimental magnetic charge profiles are compared and show good agreement [Fig. 1 (e-h)]. Such measurements open the door to fine tuning the magnetic configuration of nano-objects that will find applications in fields of sensor, magnetic recording, and biomedicine.

1. C. Gatel, F. J. Bonilla, A. Meffre, et al. *Nano Lett.* 2015, 15, 6952–6957.
 2. M. Bode, A. Wachowiak, J. Wiebe, et al. *Appl. Phys. Lett.* 2004, 84, 948–950.
 3. L. A. Fomin, I. V. Malikov, S. V. Pyatkin, et al. *J. Magn. Magn. Mater.* 2010, 322, 851–857.
 4. F. J. Bonilla, L.-M. Lacroix, T. Blon, J. Magn. Magn. Mater. 2017, 428, 394–400.
 5. K. Leistner, M. Yang, C. Damm, et al. *Nanoscale*, 2017, 9, 5315–5322.

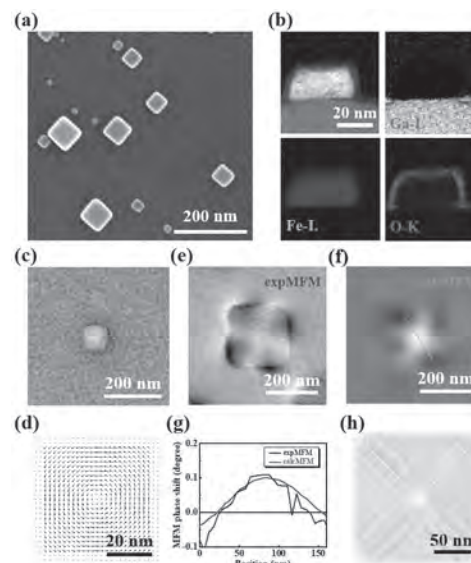


Fig.1 (a) SEM image showing isolated iron cuboids with different size distribution. (b) EELS mapping of Ga, Fe and O elements in iron cuboid. (c) qMFM scan of one cuboid with a lateral size of 54 nm, and the related micromagnetic simulation showing vortex state (d). Experimental MFM phase of one cuboid with a lateral size of 170 nm (e) and the calculated MFM phase (f). (g) Extracted profiles from (e) and (f), (h) Simulation of (e) showing Landau pattern.

JR-03. Temperature-Dependent FORC Investigation of Electrodeposited Magnetic Shape Memory Nanowires Array.

M. Varga^{1,2}, L. Galdun¹, B. Kunca³, K. Saks⁴, P. Diko³ and R. Varga¹
 1. TIP, CPM-TIP, P.J. Safarik University in Kosice, Košice, Slovakia;
 2. Department of Condensed Matter Physics, Univerzita Pavla Jozefa Safarika v Kosiciach Prirodovedecka fakulta, Košice, Slovakia;
 3. Institute of Experimental Physics, Slovenska Akademia Vied v Kosiciach, Košice, Slovakia;
 4. Institute of Materials Research, Slovenska Akademia Vied v Kosiciach, Košice, Slovakia

We aim to prepare a multifunctional application-ready material, which could be used as a sensing and simultaneous actuating device driven by shape memory processes. One of the most promising ways to expand the application possibilities of a well-known material is the down-sizing. Therefore, we have prepared Ni₂FeGa Heusler-based nanowires and studied their magnetic properties. The Ni₂FeGa Heusler alloy has a L₂ structure and undergoes a martensitic transformation [1]. The martensitic transformation temperature of the Ni₂FeGa Heusler alloy can be tuned by changing its chemical composition [2]. It also shows a shape memory and a multi-caloric behaviour. The nanowires that we have studied were prepared by a galvanostatic electrochemical deposition, using the anodized aluminium oxide (AAO) membrane with the nanopores diameter of 60 nm. The deposition time was adjusted to obtain nanowires of an appropriate length, which was 7.5 μm. The chemical composition of the prepared nanowires is Ni₅₅Fe₄₃Ga₂. The deviation from the X₂YZ Heusler chemical composition is probably due to the difficult determination of the effective deposition area of the AAO membrane. During the isothermal magnetization measurement (Fig. 1), a magnetic shape memory temperature region was defined. Between the temperatures of 290 and 360 K, an unusual magnetization increase was observed within each magnetization isotherm. The magnetization increase within the isothermal measurement or within the measurement of the hysteresis loops was ascribed to the magnetic shape memory behaviour within previous research of shape memory materials, such as the Ni₂MnGa or Ni₂MnSn [3, 4]. The observed magnetization increase occurs at different values of the applied transformation magnetic field. A deeper analysis shows that the transformation fields are temperature dependent. The temperature dependence of the transformation magnetic field can be described according to the Clausius-Clapeyron equation and a fitting model of the experimental data shows that the transformation temperature is ≈285 K and is also dependent on the system pressure. The shape memory behaviour of the prepared nanowires made them interesting for further analysis. Therefore, we have performed the First-Order Reversal Curve (FORC) analysis of the magnetic shape memory nanowires. The measurements of the individual FORCs were performed at four different temperatures, following the cooling behaviour of the isothermal magnetization measurement. The FORC measurements were performed at 395, 300, 200 and 100 K (Fig. 2). Each measurement shows a diverging FORC distribution, which was defined by Pike, et al. [5]. The contours within such diagram diverge from the H_u axis and intersect the H_c = 0 axis. The FORC distribution with the diverging shape shows that the nanowires array is a multi-domain and highly interacting system, as stated by Muxworthy, et al. [6]. In the hysteresis loops measurements, we show that the main contribution to the nanowires array magnetization process consists of the magnetostatic interactions of the neighbouring nanowires. The vertical spread of the FORC distribution is a function of the internal demagnetization field (magnetostatic interactions within the neighbouring nanowires), but it depends on several domain properties (domain cancellation, domain shape and domain wall interactions) [7]. However, the vertical spread of the diverging FORC distribution should increase with the system volume, which points to the shape changes that occur within the Ni₅₅Fe₄₃Ga₂ nanowires. This was shown in the case of multi-domain magnetic nanoparticles with a strong domain wall pinning. During the investigation of a structure transformation of CoNi alloy nanowires, the structural change from *hcp* to *fcc* was accompanied by a change of the FORC distribution shape, where it became more symmetric [8]. Therefore, to describe the changes within the FORC investigation of the Ni₅₅Fe₄₃Ga₂ nanowires, a detailed analysis of the obtained results is necessary. We have shown that the Ni₅₅Fe₄₃Ga₂ nanowires show a magnetic shape memory behaviour. The magnetization increase within the isothermal measurement is temperature- and magnetic

field dependent. The diverging FORC distribution shows that the nanowires array behaves as a multi-domain and highly interacting system and the vertical spread of the divergence narrows with respect to the H_c axis of the FORC density contour plot. To determine the origin of the FORC distribution change at different temperatures, further analysis of the FORC measurements is necessary. However, the current results show that the Ni₅₅Fe₄₃Ga₂ nanowires show an elongation within the low-temperature measurements, below the transformation temperature region that was determined during the isothermal magnetization measurements. Acknowledgement: This work was supported by Slovak Grant Agency VEGA 1/0053/19, Slovak Grant Agency grant number APVV-16-0079, VVGS-2019-1231 and VVGS-PF-2020-1420.

[1] Y. Li, D. Zhao, and J. Liu, *Sci. Rep.*, vol. 6, pp. 1–11 (2016) [2] M. Hennel, L. Galdun, T. Ryba, *J. Magn. Magn. Mater.*, vol. 511, p. 166973 (2020) [3] P. Cejpek et al., *J. Alloys Compd.*, vol. 775, pp. 533–541 (2019) [4] B. Hernando et al., *Appl. Phys. Lett.*, vol. 92, pp. 12–14 (2008) [5] C. R. Pike, et al., *Phys. Earth Planet. Inter.*, vol. 126, pp. 11–25 (2001) [6] A. R. Muxworthy, A. P. Roberts, *Encycl. Geomagn. Paleomagn.*, pp. 266–272 (2007) [7] A. P. Roberts, D. Heslop, X. Zhao, *Rev. Geophys.*, vol. 52, pp. 557–602 (2014) [8] A. S. Samardak et al., *J. Alloys Compd.*, vol. 732, pp. 683–693 (2018)

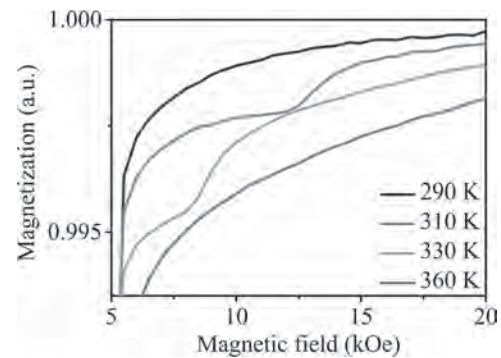


Fig. 1: Isothermal magnetization measurements at different temperatures

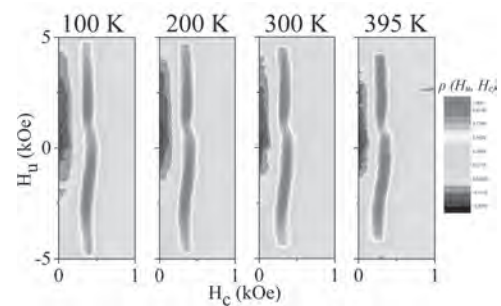
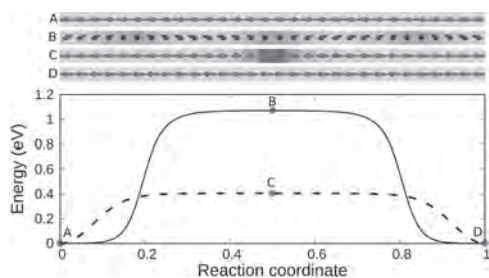


Fig. 2: FORC density distribution of the Ni₅₅Fe₄₃Ga₂ nanowires at different temperatures

JR-04. Optimal Control of Magnetization Switching in Nanowires.M. Badarneh¹, G. Kwiatkowski¹ and P. Bessarab^{1,2}¹. Science Institute, University of Iceland, Haskoli Islands, Reykjavik, IS, academic, Reykjavik, Iceland; ². National Research Saint Petersburg State University of ITMO, St. Petersburg, Russian Federation

Bistable magnetic nanowires hold great promise as a basis of novel devices for data transmission, storage and processing where information can be encoded by domains with opposite magnetization [1]. Development of this technology depends critically on the knowledge about energy-efficient manipulation of the magnetization. In this study, we apply optimal control theory to predict energy-efficient protocols of external magnetic field pulses for the magnetization reversal in Co nanowires [2]. We calculate optimal control paths (OCPs) of the magnetization reversal, i.e. reversal trajectories minimizing the energy cost of magnetization switching, and explore how the OCPs depend on various parameters such as the switching time, nanowire length and Gilbert damping. We obtain time- and space-resolved shape and amplitude of optimal switching pulses from calculated OCPs by solving the inverse problem in the Landau-Lifshitz-Gilbert equation. The OCP calculations demonstrate that short nanowires reverse their magnetization via coherent rotation which can be induced by applying uniform external magnetic field with frequency defined by a collective in-phase precession of the magnetization [3]. If the length of the wire exceeds a certain critical length, standing spin wave emerges and effectively assists the magnetization reversal (see Fig. 1). We find that the critical length at which the crossover between the coherent rotation of magnetization and spin wave assisted switching occurs depends on the switching time and damping parameter. Spin wave assisted magnetization switching has recently attracted much attention as a promising technique to reduce the switching field for magnetic recording [4-5]. Our results provide a valuable insight into this phenomenon, contributing to the development of low-power technologies. The calculated OCPs are very different from minimum energy paths (MEPs) of the magnetization reversal (see Fig. 1). In contrast to MEPs, OCPs demonstrate dependence on dynamical parameters such as switching time and damping. Moreover, analysis of the energy variation along the OCPs and MEPs demonstrates that the highest energy point along an OCP is typically higher than the energy barrier derived from an MEP (see Fig. 1), suggesting that energy-efficient control of magnetization switching does not necessarily translate into the minimization of the energy barrier between the target states. This work was funded by the Russian Science Foundation (Grant No.19-72-10138) and the Icelandic Research Fund (Grant No. 184949-052).

[1] S.S.P. Parkin, M. Hayashi, L. Thomas, *Science* 320, 190 (2008). [2] M.H.A. Badameh, G.J. Kwiatkowski, P.F. Bessarab, *Nanosyst.: Phys. Chem. Math.* 11, 294 (2020). [3] G.J. Kwiatkowski, M.H.A. Badarneh, D.V. Berkov, P.F. Bessarab, under review at: *Phys. Rev. Lett.* Manuscript available online: <https://arxiv.org/abs/2004.02146> [4] T. Seki *et al.*, *Nat. Commun.* 4, 1726 (2013). [5] T. Seki *et al.*, *Appl. Phys. Lett.* 103, 122403 (2013).



Variation of the energy of a Co nanowire along the minimum energy path (dashed line) and the optimal control path. Reaction coordinate is defined as a normalized displacement along the path. The letters label the states for which magnetic configurations are shown in the upper panel.

JR-05. Isotropic Magnetic Behavior of Multi-Segmented FeCo Nanowire Arrays.

V.M. Andrade¹, S. Caspani¹, J. Pedro Esteves de Araújo¹, C. Sousa¹ and M.P. Proenca^{1,2}

1. Universidade do Porto Instituto de Física dos Materiais Instituto de Nanociência e Nanotecnologia, Porto, Portugal; 2. (b) ISOM - Institute of Optoelectronic and Microtechnology Systems, Technical University of Madrid (UPM), Madrid, Spain

The study of 1D-nanostructures has been intensified in the last few decades due to the development of fabrication methods of metallic, semiconductors and insulator materials aiming applications in several areas [1]. In particular, multi-segmented magnetic nanowire (NW) arrays are prospective candidates for an extensive range of applications such as racetrack memory devices, spintronic, and drug delivery [1, 2, 3]. These possibilities are due to the number of degrees of freedom related to the intrinsic shape anisotropy combined with the potential to introduce different materials along the NW's length. Concerning practical applications, understanding the role of layers with distinct structural and magnetic properties can be a path to avoid some issues such as system overheating and Walker breakdown in racetrack devices. For instance, micromagnetic simulations revealed that the combination of Co segments with different structures, bcc and hcp, promotes a faster way of writing information in 3D racetrack memory devices [2]. This observation results from the high magnetocrystalline anisotropy along the wire length induced by the Co-hcp structure. Although these evaluations seem promising, thorough experimental research of multi-segmented NWs with low and high anisotropy components still needs to be performed. Here, we present the FeCo layer properties' evaluation onto multi-segmented NW arrays produced through DC electrodeposition into ordered porous alumina templates with 40 nm of pore diameter and 60 μm of length. For each layer's deposition, a Pt electrode was used as the counter electrode, Ag/AgCl as the reference electrode, and an Au layer as the working electrode [5]. Two samples were prepared: 1) Au [200 nm] / Fe₃₃Co₆₇ [24 μm] / Au [10 nm] and 2) Au [200 nm] / Ni₉₀Cu₁₀ [1 μm] / (Fe₃₃Co₆₇ [13 μm] / Au [10 nm])₃, where the indicated length was obtained from scanning electron microscopy (SEM) images and the alloy's stoichiometry from energy dispersive spectroscopy (EDS). X-ray diffraction (XRD) measurements at room temperature revealed the formation of bcc structure of FeCo with the (110) preferential orientation for both samples and an additional hcp phase with the (110) preferential orientation for FeCo tri-segmented NWs (Figure 1). The magnetic hysteresis loops acquired at room temperature for the Au/FeCo/Au arrays present the easy magnetization axis along the parallel direction, evidencing a typical strong shape anisotropy [5]. Distinctly, when three FeCo segments of 13 μm are deposited along the NW's length, the arrays present an isotropic magnetic behavior with an increase of the coercive field when applying the magnetic field perpendicular to the nanowires' axis (Figure 2). This change in magnetic behavior for the segmented NWs might be related to the presence of an hcp phase that induces a perpendicular magnetocrystalline anisotropy. However, further research should be performed to better comprehend the interplay between the NiCu and FeCo layers into the NW arrays. In summary, multi-segmented NWs of FeCo alloys were successfully achieved through the electrodeposition process into porous templates. The growth of FeCo segments leads to the formation of hcp structures and the observation of an isotropic magnetic behavior. This can be related not only to the structural properties but also to the interplay between FeCo segments along the NW's length. A more complete evaluation of the magnetic properties of the produced samples should be performed to fully understand the role of the different layers in the magnetocrystalline anisotropy of the arrays. This work was financially supported by projects POCI-01-0145-FEDER-028676 and UIDB/04968/2020 from Portuguese FCT and COMPETE 2020 (FEDER) and IF/01159/2015, POCI-01-0145-FEDER-031302/PTDC/FIS-MAC/31302/2017. .

References: [1] C. T. Sousa et al., Appl. Phys. Rev., vol.1, p. 031102 (2014); [2] J. Rial and M. P. Proenca, Nanomaterials, vol. 10, p. 2403 (2020); [3] D. Wang et al., Materials, vol. 12, p. 3908 (2019); [4] C. Bran et al., J. Phys. D: Appl. Phys., vol. 48, p. 145304 (2015); [5] E. M. Palmero et al., Nano Research, vol. 12, p. 1547 (2019).

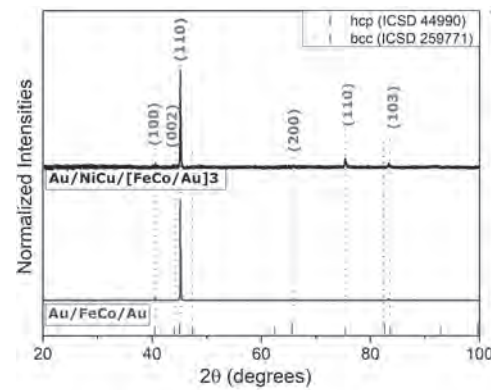


Figure 1: XRD patterns for Au/FeCo/Au and Au/NiCu/[FeCo/Au]₃ segmented nanowires with the Bragg peak positions for bcc (green) and hcp (red) structures.

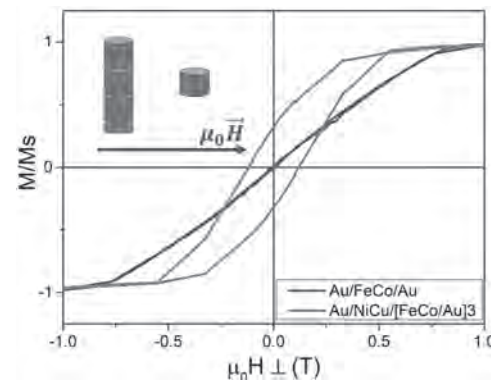


Figure 2: Hysteresis loops obtained by applying the magnetic field perpendicular to the NWs' length

JR-06. Core-Shell and Bi-Segmented Cobalt-Nickel Nanorods Prepared by Electroless Deposition.

E. Denisova^{1,2}, L. Chekanova¹, S.V. Komogortsev¹, M.V. Rautskii¹, I.V. Nemtsev^{1,2}, R. Iskhakov¹, V.V. Tkachev³, V.S. Plotnikov³ and M.V. Dolgoplova²

1. Kirensky Institute of Physics, Federal Research Center KSC SB RAS, Krasnoyarsk, Russian Federation; 2. Siberian Federal University, Krasnoyarsk, Russian Federation; 3. Far Eastern Federal University, Vladivostok, Russian Federation

Striving for create ultrafast electronics led to the development of three-dimensional compact architectures in many disciplines including magnetism. Coercivity, squareness, and magnetic anisotropy can be tailored by varying the geometry and/or spatial distribution of the magnetic functional units [1, 2]. Elongated elements (nanowires and nanotubes) have been used in the number of technologies. The problems concerned with the complicated dipole-dipole interactions in arrays of such elements motivates in researching new designs for these elements. Two-phase nanowires with a coaxially combined or varied along axis phases could generate additional applied advances. In this work, we describe experimental results concerning the bi-segmented and coaxial Co/Ni rods in porous of track etched polycarbonate membranes (PCTE) and focus on the comparison of their magnetic properties. The 3D coaxial nanostructures investigated consist of a cylindrical cobalt core that is completely surrounded by a shell of nickel layer. The bi-segmented (BS) rods contain two coupled rods of nickel and cobalt. The magnetic anisotropy of the bi-segmented and core-shell rods electroless deposited to the pores of PCTE was studied. The Co and Ni deposition into the PCTE membranes pores is carried out by electroless reduction of metal-salt solution with sodium hypophosphite as reducing agent. In a first step in the case of coaxial rods, the inner pore walls were treated with palladium chloride used as a nucleating agent. In the next step the pores are coated with nickel by electroless deposition. The deposited Ni tubes are shown in Fig. 1a. Then the Ni tubes were filled with cobalt by electroless deposition. The coaxial rods are shown in Fig. 1b. The cobalt core has a diameter of about 200 nm, which is determined by the PCTE pore diameter and the thickness of the Ni shell layers. The reference tube and rod samples consisting of “shell only” or “core only” was prepared using the same technique. For the synthesis of bi-segmented rods one side of the membrane was coated by a thin layer of thermal-sputtered copper to create an electrochemical potential that promotes the metal deposition inside PCTE channels along the pore axis. Then Co/Ni rods (along-axis) were prepared by electroless deposition. The employed rods growth method allows for tuning both the composition and crystalline structure of each individual Co and Ni segments. The magnetic properties and structure of the rods are characterized by scanning electron microscopy, X-ray diffraction, ferromagnetic resonance (FMR) and vibrating sample magnetometer. Information on local magnetic anisotropy is obtained using the approach to magnetic saturation curves. The X-ray powder diffraction shows that the Ni and Co alloys for the rods of the both types were crystalline with fcc structure. The local magnetic anisotropy field of Co/Ni rods was estimated to be in the range from 0.9 to 2 kOe. The core/shell geometry of Co@Ni rods transpires in their physical properties. A staggering difference is observed between the FMR spectra measured on arrays of Co/Ni core/shell rods, Co/Ni BS rods and the “parent” samples, namely, Ni tubes without core and Co rods without Ni shell (fig.2). The FMR spectrum for Co core and Ni tube consists of a single absorption line. For Co/Ni and Co@Ni rods the FMR spectrum consists of two wide absorption lines corresponding to different layers. The presence of graded Co or Ni content at layer boundaries could give rise to graded anisotropy effects (that is, local variations of the effective magnetic anisotropy along the rod axis). Such variations in magnetic anisotropy could manifest in variations of resonance fields for different rod segments and could increase FMR linewidth. The measurements of FMR spectrum and magnetization curves at different orientations of an external field allow us to obtained data about macroscopic magnetic anisotropy of synthesized rods. It was found that for Co rods easy magnetization axis lying along the long axis of the rod, and its value is close to magnetic shape anisotropy of elongated column pM_s . The overall magnetic anisotropy of the array is mainly determined by the following three contributions: the anisotropy results from the shape effect of the indi-

vidual rods, which will induce a magnetic easy axis parallel to the wire axis; magnetostatic coupling among the rods, which tends to develop a magnetic easy axis perpendicular to the rod axis; and the local anisotropy field, which consists of magnetocrystalline anisotropy and anisotropy of intrinsic strain. In the case of BS rods for distribution density of rods more than 20% the contribution from dipole-dipole interaction was comparable to those for shape anisotropy. The room temperature magnetic behavior of the core-shell Co/Ni nanorod arrays is also studied and correlated with their structural and morphological properties. The successful synthesis of the bi-segmented rods with coaxial (Co@Ni) and along-axis (Co/Ni) segmentation was demonstrated. The magnetic anisotropy field, ferromagnetic resonance field, linewidth and the coercivity are mainly determined by the artificially created interface boundaries for two types of bi-segmented rods with coaxial (Co@Ni) and along-axis (Co/Ni) segmentation. This work was funded by the RFBR, the Government of the Krasnoyarsk Territory, the KRFS (project no. 20-43-240003)

1. R. Streubel, J. Lee, D. Makarov et al, J. Phys. D, 49, 363001, (2016) 2. E. Y. Vedmedenko, R. K. Kawakami, D. D. Sheka et al., J. Phys. D. Appl. Phys. 53, 453001 (2020)

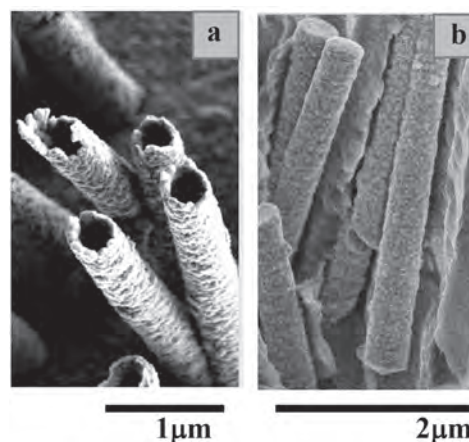


Fig.1 SEM image of Ni tube (a) and Co@Ni core/shell rods (b).

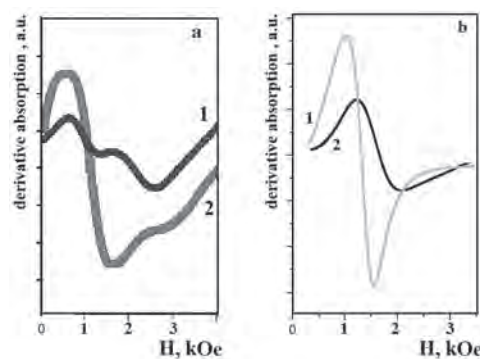


Fig.2 a - FMR spectra for Co/Ni core-shell rods (1) and BS rods (2); b-Co rods (1), Ni tubes (2).

JR-07. Unexpected Longitudinal Kerr Rotation in two Dimensional Magneto Plasmonic Structure.

S. Sadeghi¹ and S. Hamidi¹

¹. Laser and Plasma research Institute, Shahid Beheshti University, Tehran, The Islamic Republic of Iran

Properties of two-dimensional spatially periodic nanostructures formed by a corrugated 2D structured as substrate which covered by gold and Ce:YIG films were studied by magneto-optical spectroscopy techniques. It was shown that the structures exhibit a considerable magneto optical response to longitudinal Kerr effect at wavelength of 450 nm and this enhancement seems to be related to excitation of localized surface plasmon-polaritons (LSPR) in the array of nanorods created in this structure. Recent achievements in photonics and optoelectronic require the advanced magneto-photon microdevice with ability of control the magneto-optical response in micron and submicron scales. The Advanced magneto-optical devices tend to miniature the components, which requires strong magneto-optical effect in small scale. Combination of magnetic and plasmonic materials with different functionalities into a magneto-plasmonic structure is considered as a promising route to enhance the magneto-optical activity [1]. On the one hand, plasmonics allows for extreme electromagnetic field enhancement and subwavelength localization. On the other hand, MO materials bring optical non-reciprocity properties in the presence of magnetic field. Early studies on magneto-plasmonic structures addressed propagating surface plasmon-polariton (SPP) along the smooth surface of a metallic film [2]. In parallel to the studies on SPPs, the rapid developments in nanofabrication, enable extending studies of optics in nanoscale with nanostructures also supporting localized surface plasmon (LSPR) [3,4]. In the recent work, we investigate the magneto-optical response of a 2D magnetoplasmonic nanostructure which can support LSPR. A two-dimensional 2D magneto-plasmonic nanostructure was prepared by nanoimprint lithography method. For this purpose, a 2D charge coupled device (CCD) separated from a camera was used as stamp and the poly-dimethylsiloxane (PDMS) substrate was patterned as 2D substrate. First, the substrate was covered by gold layer of 30 nm thickness as plasmonic material by using a PVD coating device. Then it was coated by a Ce:YIG layer with an approximate thickness about 100 nm as magnetic material by using of pulsed laser deposition method. Actually this structure composed of 2D array of cubic holes with width and length of 3 μm and depth of 500 nm. these cubic holes were arranged in 2D with a distance about 170 nm. The Schematic of this structure is shown in Fig. 1a. Also, the periodicity of the sample and its surface has been examined by scanning electron microscopy (SEM) and shown in Fig. 1b. The nanometric distance between holes well creates nanorods which can support LSPR in the structure and this surface lattice resonance. Investigation of MO activity of the prepaid sample was carried out by a home-made longitudinal spectral Kerr effect set up with applying a DC magnetic field in the plan of sample and parallel to the incidence plane. The linear polarized light was incident on the sample at incidence angle of 30°. In our set up, the linear polarized light was achieved by passing the unpolarized broadband light from a polaroid sheet which can linearly polarized the light in the wavelength range of 400-700 nm. Thereafter, the reflected spectra of the sample were recorded for positive and negative directions of magnetic field in rotational analyzer method. Finally, the recorded spectra were analyzed by a Labview program. The longitudinal Kerr effect spectrum showed a sharp peak at the wavelength of 450 nm which is related to Ce:YIG magneto-optical response.

[1] Maccaferri, N., Zubritskaya, I., Rzdolski, I., Chioar, I. A., Belotelov, V., Kapaklis, V., & Dmitriev, A. 2020. *J. Appl. Phys.*, 127, 8, 080903. [2] D. Martin-Becerra, J.B. Gonzalez-Diaz, V.V. Temnov, A. Cebollada, G. Armelles, T. Thomay, A. Garcia-Martín and M. Ujue Gonzalez, 2010, *Appl. Phys. Lett.* 97, 183114. [3] V. I. Belotelov, I. A. Akimov, M. Pohl, V. A. Kotov, S. Kasture, A. S. Vengurlekar, Achanta Venu Gopal, D. R. Yakovlev, A. K. Zvezdin, M. Bayer (2011), *Nature Nanotechnol.*, 6, 370. [4] B. Sepúlveda, J. B. Gonzalez-Diaz, A. Garcia-Martín, L. M. Lechuga, and G. Armelles, 2010, *Phys. Rev. Lett.* 104, 147401.

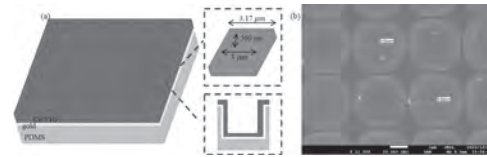


Fig1. (a) schematic of 2D magneto-plasmonic structure composed of PDMS corrugated substrate covered by gold layer with thickness of 30 nm and Ce:YIG layer with approximate thickness of 100 nm. (b) SEM image of prepaid magneto-plasmonic structure.

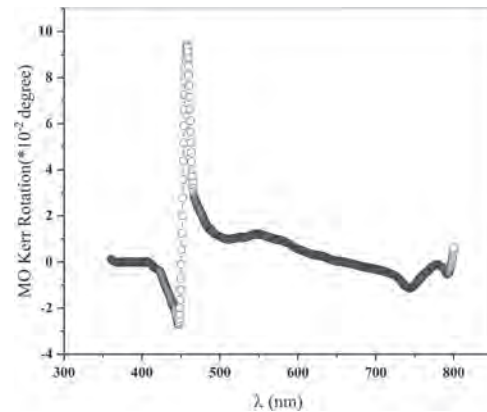


Fig.2: MO spectrum of the 2D grating sample composed of Gold and Ce:YIG layer measured at incident angle of 30° by home-made spectral longitudinal Kerr set up.

JR-08. The Annealing Effect on Domain Wall Dynamics in Wires With Induced Gradient of the Perpendicular Anisotropy.

L. Fecova^{1,2}, K. Richter^{1,3} and R. Varga²

1. Department of Condensed Matter Physics, Univerzita Pavla Jozefa Safarika v Kosiciach, Kosice, Slovakia; 2. CPM-TIP, Univerzita Pavla Jozefa Safarika v Kosiciach, Kosice, Slovakia; 3. Institute for Materials Science, Christian-Albrechts-Universitat zu Kiel, Kiel, Germany

Amorphous glass-coated microwires are among the excellent material that can be used in sensor and spintronic devices. The magnetization process is realized due to the fast domain wall propagation. The studies on domain wall dynamics showed that additional perpendicular magnetic field changes domain wall velocity [1, 2]. Moreover, after the rotation of the microwire in the perpendicular magnetic field the difference in the domain wall velocity is even more significant [3]. However, the obtained results are contrary to the expectations based on previous knowledge. Due to the cylindrical shape of the wires, no change in domain wall velocity was expected for different rotations. The results are explained in terms of the gradient of the perpendicular magnetic anisotropy in the cross-section of the wire. The gradient is induced to the microwire during the fabrication process. The water stream causes additional induced stresses due to the cooling of the microwire from one side (Fig. 1a). The direct observation of such stresses in the cross-section of the wire is not possible due to the amorphous structure of the microwires. However, it is clearly visible when the sample is annealed above the crystallization temperature (Fig. 1b). In this work, we present the domain wall (DW) dynamics studies on the sample ($\text{Fe}_{76}\text{Si}_9\text{B}_{10}\text{P}_5$) as-cast and annealed below the crystallization temperature (at 450 °C) (Fig. 2). The DW velocity v is described by the following relation [4]: $v = S(H - H_0)$ (1) where S is DW mobility, and H_0 critical magnetic field. The DW velocity of the as cast sample is linearly increasing for different angles of rotation θ (Fig.2a). For $\theta = 180^\circ$, DW velocity increases up to 350 A/m with mobility $S = 1.44 \text{ m}^2\text{s}^{-1}\text{A}^{-1}$. From 350 A/m, the DW mobility is $S = 24.9 \text{ m}^2\text{s}^{-1}\text{A}^{-1}$. However, after annealing, the DW motion is observed from $H_{\text{axial}} = 550 \text{ A/m}$ with the mobility $S = 1.73 \text{ m}^2\text{s}^{-1}\text{A}^{-1}$ up to 700 A/m (Fig.2b). DW mobility from $H_{\text{axial}} = 700 \text{ A/m}$ is incomparably smaller in comparison to the case before annealing, with the value $S = 6.79 \text{ m}^2\text{s}^{-1}\text{A}^{-1}$. When the sample is annealed, it leads to the release of the stresses induced in the cross-section of the microwire. Annealing causes the homogenization of the sample, and as a result, a significant decrease in DW mobility is observed. Thus, an effective mechanism for suppressing the angular dependence of DW mobility in a perpendicular magnetic field is annealing under suitable conditions. Acknowledgements: This work was supported by Slovak Grant Agency VEGA 1/0053/19, VEGA 1/0195/17; Slovak Grant Agency grant number APVV-16-0079, APVV-17-0184, APVV SK-FR-2017-024 and Pavol Jozef Šafárik University internal grant system VVGS-2016-320.

[1] R. Varga et al., Physica Status Solidi A, Vol. 213, p. 356–362 (2016).
 [2] K. Richter et al., Applied Physics Letters, Vol. 96, 182507 (2010). [3] L. Fecova, K. Richter, and R. Varga, Acta Physica Polonica A, Vol. 137 (5), p. 849-851 (2020). [4] V. Zhukova et al, Journal of Applied Physics, Vol. 111, 07E311-1 (2012).

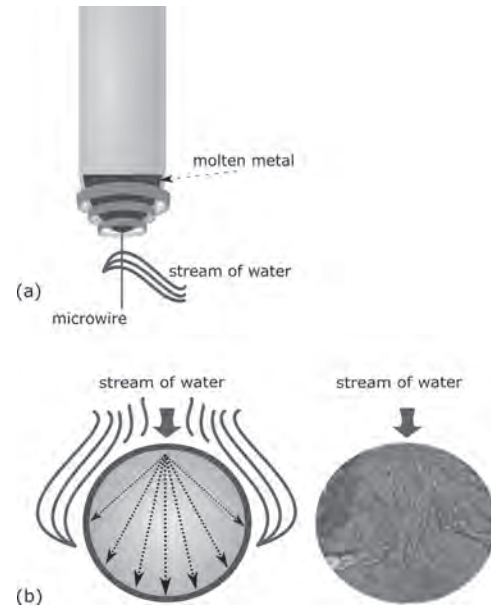


Fig.1 Taylor-Ulitovski method of drawing the glass-coated microwire $\text{Fe}_{76}\text{Si}_9\text{B}_{10}\text{P}_5$, which is quenched by the water jet from one side in order to obtain the amorphous structure (a), and the stress distribution in the section of the amorphous wire annealed above crystallization temperature (b).

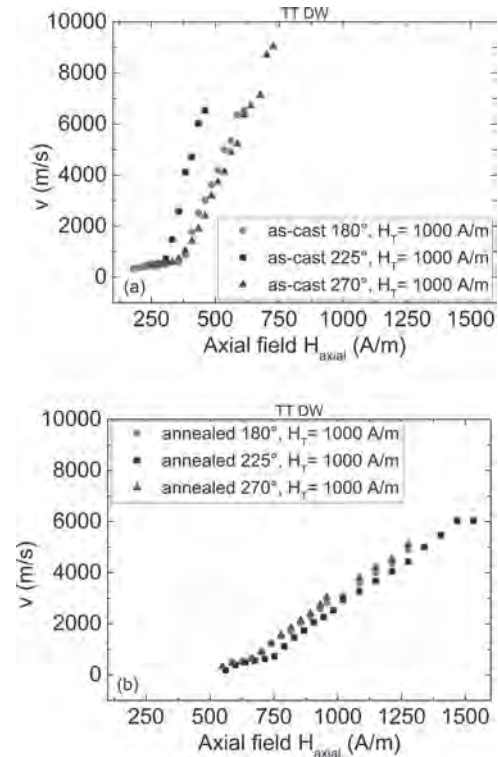


Fig.2 Domain wall velocity as a function of the axial magnetic field in the perpendicular magnetic field for the as-cast sample (a) and sample annealed below the crystallization temperature (b).

JR-09. Superparamagnetic Nanosphere Arrays: Self-Assembly and the Effect of Applied Magnetic Fields.

A. Mourkas¹, A. Zarlaha¹, N. Kourkoumelis² and I.V. Panagiotopoulos¹

1. *Materials Science and Engineering, University of Ioannina, Ioannina, Greece*; 2. *Faculty of Medicine, University of Ioannina, Ioannina, Greece*

Introduction Modern magnetic material applications require homogeneous microstructures consisting of monodisperse magnetic entities. A facile route towards such microstructures is to exploit other materials as templates of model nanostructures via a “bottom-up”, low-cost approach. To that end, monodisperse nanosphere single-layers which tend to form 2D-hexagonal close packed patterns can be utilized either as templates for the deposition of “nanocaps” or as masks for the formation of triangular-like islands [1]. Although a lot of work has been devoted to the optimization these arrays [2,3] little progress has been made towards the use of self-assembly magnetic materials [4–7]. Here, we explore the effect of in-plane and perpendicular magnetic fields on the spatial arrangement of superparamagnetic nanoparticles. Thus, we add the long range magnetic dipolar interactions to the competing nanoparticle-surface (substrate hydrophobicity-hydrophilicity) and the nearest neighbor nanoparticle-nanoparticle interactions which control order and agglomeration. We present the optimization of the self-assembly of paramagnetic polystyrene nanospheres (0.25 nm - 1.43 nm) obtained by spin coating and drop casting, with respect to monolayer formation, substrate coverage, 2D hexagonal packing, and size of ordered areas. Arrays prepared under zero field by drop casting and spin coating were compared with those obtained under the effect of an in plane or perpendicular magnetic field. Experimental Methods - Results We utilize PS nanospheres with different sizes (0.270 μm , 0.536 μm and 1.43 μm) which incorporate superparamagnetic Fe₃O₄ nanoparticles. Thermally oxidized silicon wafers, with approximately 500nm oxidation layer, are used as substrates. Prior to the deposition, the substrate’s hydrophilicity is improved using piranha solution. Contact angle measurements were performed to determine the hydrophilicity of the substrates, before and after the surface treatment. After the surface treatment, contact angle was measured as low as 9.3deg compared to 46deg of the untreated wafer. The different methods utilized are summarized in Table 1. In the drop casting experiments droplets of an aqueous suspension were mixed with tritonX – 100 and methanol (1:400) were deposited on the hydrophilic surface. A small electromagnet was used to generate the magnetic field. This method has two main geometrical control parameters, substrate inclination and angle of the applied magnetic field. In spin coating experiments under perpendicular field the surface-treated substrate is rotated on the platform of the spin coater which is placed in the middle of a coil. For in-plane field application, the sample is rotated until the solution expands on the surface; then it is removed from the spin coater and left to settle under the field on horizontal platform inside a coil. As surface wettability is an important parameter, two different surfactants have been employed and the results are compared. For the tritonX-100 treated samples rotation speeds up to 8000 rpm with a standard acceleration rate of 200rpm/s were used. For the SDS treated samples experiments, lower rotation speeds up to 800 rpm are optimal. For the observation of the macroscopic and microscopic surface morphologies of the samples, we used a Zeiss AxioImager A1 optical microscope fitted with a Canon 80D DSLR and a Scanning Electron Microscope (SEM, JEOL Ltd). During spin coating, competing forces like gravity, centrifugal, magnetic dipolar interactions and surface tension have a significant impact on the NPs self-assembly. Without magnetic fields the arrays can be optimized for monolayer formation, substrate coverage, 2D hexagonal packing, and size of ordered areas. The use of in-plane magnetic fields permits the organization of NPs in directional arrays along the direction of the field. Perpendicular fields tend to create 3D structures in competition to the hydrophilicity of the substrates. Acknowledgement: This research is co-financed by Greece and the European Union (European Social Fund-ESF) through the Operational Programme «Human Resources Development, Education and Lifelong Learning 2014-2020» in the context of the project “Dynamic Response of Magnetically organized nanoelements (DAMON) (MIS5047646).

- [1] T.C. Ulbrich, D. Assmann, M. Albrecht, Magnetic properties of Co/Pt multilayers on self-assembled particle arrays, *J. Appl. Phys.* 104 (2008) 084311. <https://doi.org/10.1063/1.3003064>. [2] A. Chandramohan, N. V. Sibirev, V.G. Dubrovskii, M.C. Petty, A.J. Gallant, D.A. Zeze, Model for large-Area monolayer coverage of polystyrene nanospheres by spin coating, *Sci. Rep.* 7 (2017) 9–11. <https://doi.org/10.1038/srep40888>. [3] B. Park, S.Y. Na, I.-G. Bae, Uniform two-dimensional crystals of polystyrene nanospheres fabricated by a surfactant-assisted spin-coating method with polyoxyethylene tridecyl ether, *Sci. Rep.* 9 (2019) 11453. <https://doi.org/10.1038/s41598-019-47990-z>. [4] J.D. Feldmann, G.J. Kalman, P. Hartmann, M. Rosenberg, Ground state of magnetic dipoles on a two-dimensional lattice: Structural phases in complex plasmas, *Phys. Rev. Lett.* 100 (2008) 085001. <https://doi.org/10.1103/PhysRevLett.100.085001>. [5] V. Håkonsen, G. Singh, P.S. Normile, J.A. De Toro, E. Wahlström, J. He, Z. Zhang, Magnetically Enhanced Mechanical Stability and Super-Size Effects in Self-Assembled Superstructures of Nanocubes, *Adv. Funct. Mater.* 29 (2019) 1904825. <https://doi.org/10.1002/adfm.201904825>. [6] C. Jiang, Synthesis, Assembly, and Integration of Magnetic Nanoparticles for Nanoparticle-Based Spintronic Devices, Tesis. (2018). <https://doi.org/10.13140/RG.2.2.17523.22563>. [7] M. Hu, H.-J. Butt, K. Landfester, M.B. Bannwarth, S. Wooh, H. Thérien-Aubin, Shaping the Assembly of Superparamagnetic Nanoparticles, *ACS Nano.* 13 (2019) 3015–3022. <https://doi.org/10.1021/acsnano.8b07783>

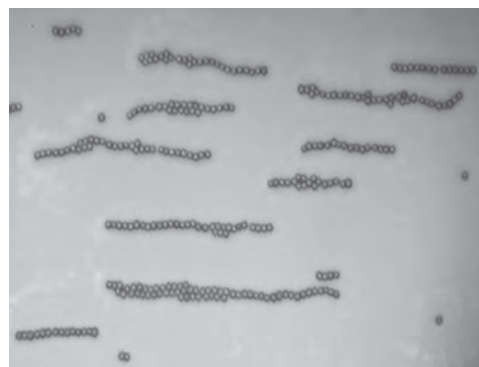


Figure 1 - Optical microscopy image of 1,43 μm superparamagnetic PS spheres deposited on a tritonX-100 treated surface, under an in-plane magnetic field.

METHOD	No Field	
	Drop Casting with TritonX-100	In Plane Field
No Field		
In Plane Field		Perpendicular Field
Spin Coating with TritonX-100	No Field	
	Field	

Table 1 - Methods utilized for drop casting and spin coating experiments

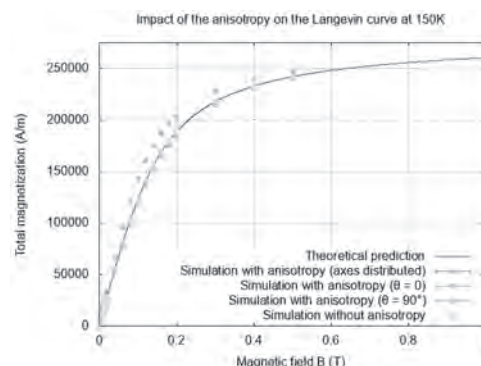
JR-10. Monte Carlo and Experimental Study of the Magnetic Relaxation of Superparamagnetic Nanoparticle Ensembles.

É. Martin¹, Q. Vuong¹ and Y. Gossuin¹

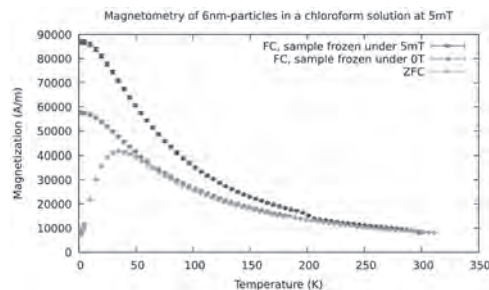
1. Service de Physique Biomédicale, Université de Mons Faculté de Médecine et Pharmacie, Mons, Belgium

Superparamagnetic Iron Oxide Nanoparticles (SPION) are nanosize beads of iron oxides. Their peculiar magnetic behaviour makes them particularly suited for a variety of biomedical applications, ranging from cellular imaging to cancer treatment by hyperthermia. The usual theory used to describe their magnetic behaviour is that developed by Paul Langevin [1], which only applies to idealized (isotropic, monodisperse in size and non-interacting) nanoparticles at high temperatures. Reality however usually deviates from that theoretical framework. First, real samples are polydisperse in size, which impacts the particles' magnetic moments and therefore their behaviour. Second, particles usually have at least one easy magnetization axis, which adds a term to their Hamiltonian. Finally, particularly in biological media, they tend to aggregate, leading to locally high particle volumic fractions and therefore dipolar interaction between their magnetic moments [2]. Moreover, as demonstrated by Néel and Brown [3], at low temperatures the particles' magnetic moments and anisotropy axes appear effectively blocked at their initial directions. Under the Néel blocking temperature, the particles are unable to reorganize their internal moments to change the resulting moment's direction, and under the Brown blocking temperature they are unable to rotate so as to align their easy axis with their moment and/or the external field. All those phenomena impact the magnetization of particle ensembles in a non-trivial way and are impossible to study simultaneously theoretically. In this work, these deviations from the Langevin law are studied numerically, at thermodynamic equilibrium, using a Metropolis algorithm, and compared with experimental data obtained on a Vibrating Sample Magnetometer. The Metropolis algorithm is adapted to take into account the Néel and Brown blocking of the particles, as those time-dependant effects are not explained by free energy minimization. Its Hamiltonian is also chosen to take into account the particles' magnetic anisotropy and the dipolar interactions between the particles as well as the interaction of their moments with the magnetic field. Thorough tests were led on the simulation program to ensure correct convergence of the algorithm. Notably, the temperature step used in the ZFC curve does not impact the simulation results, as expected from a robust computation. Convergence was tested with respect to all of the simulation parameters, and the impact of the magnetic anisotropy on the MH curves was validated by comparing to previous theoretical results obtained by M. Respaud et al [4]. Various other validation tests were conducted. The interest of using numerical simulation is that it allows to discriminate the effects of each tweak to the theory, leading to a better understanding of their various impacts. Curves studying the effect of varying each parameter were obtained, as can be seen in figure 1, where the effect of the magnetic anisotropy on the MH curve is compared in different situations. The ultimate goal being to replicate by numerical simulation the experimental results, it is important to understand how each effect impacts the shape of the curves, to have a clear sense of which experimental parameters impact the results and which don't. In terms of experimental data, two types of magnetization curves in particular are obtained: so called MH curves, where the magnetization is plotted versus the external magnetic field that is applied, and magnetization vs temperature curves. These can be obtained following different protocols, leading to different types of curves, the most common being the zero field cooled (ZFC) curve and the field cooled (FC) curve. Their shape is, naturally, impacted by the different effects at play, and by the precise experimental protocol, as can be seen in figure 2, where a ZFC curve is compared with two FC curves: one obtained after freezing the sample under no magnetic field and one after freezing it under a 5 mT magnetic field. FC/ZFC curves and MH curves (at various temperatures) of three different particle samples were obtained and compared. In particular, PolyMAG particles, which are commercialized for transfection protocols, were studied, and revealed a very unusual ZFC curve, showing no peak nor the usual bell shape of those graphs. One of the future goals of the numerical simulation will be to explain, at least qualitatively, this peculiar behaviour.

[1] P. Langevin, J. Phys. Theor. Appl., Vol. 4 (1), p. 678, (1905) [2] M. Lévy, C. Wilhelm, et al., Nanoscale, Vol. 3, p. 4402 (2011) [3] W.F. Brown, Jr, Physical Review, Vol. 130(5), p. 1677 (1963) [4] M. Respaud, J. App. Phys., Vol. 86, p. 556 (1999)



Simulated MH curve of the system in different cases : without considering magnetic anisotropy, and considering magnetic anisotropy with various dispositions of the particles' anisotropy axes ; aligned with the external field ($\theta = 0$), perpendicular to it ($\theta = 90^\circ$) or randomly oriented ("distributed" case).



Experimental ZFC and FC curves of a 6nm sample under different freezing protocols: freezing the sample under 0T to 2K (ZFC), freezing it under 5mT to 2K, and freezing it under 5mT to 175K and then under 0T to 2K.

JR-11. Magnetic Hardening of Cobalt Ferrite Nanoparticles by a Controlled Solvent-Mediated Annealing.

A. López-Ortega^{1,3}, B. Muzzi^{2,4}, E. Lottini⁷, D. Peddis⁵, G. Bertoni⁶,
C. Sangregorio^{2,7} and C. de Julian Fernandez⁸

1. *Universidad Publica de Navarra Departamento de Ciencias, Pamplona, Spain*; 2. *I.C.C.O.M. - C.N.R., Sesto Fiorentino, Italy*; 3. *Institute for Advanced Materials and Mathematics INAMAT2, Universidad Pública de Navarra, Pamplona, Spain*; 4. *Dept. of Biotechnology, Chemistry and Pharmacy, University of Siena, Siena, Italy*; 5. *Universita degli Studi di Genova, Genova, Italy*; 6. *NANO - C. N. R., Modena, Italy*; 7. *University of Florence and INSTM, Sesto Fiorentino, Italy*; 8. *I.M.E.M.- C.N.R., Parma, Italy*

The magnetic anisotropy and the coercive field (H_C) are key properties of the magnetic nanoparticles (NPs) considering their applications in biomedicine, for drug delivery and magnetic hyperthermia, and for the development of free-rare-earth magnets. Cobalt ferrite ($\text{Co}_x\text{Fe}_{3-x}\text{O}_4$) nanoparticles exhibit the largest coercive field between all the Fe oxides nanoparticles with spinel structure. The large coercive property is correlated to the Co^{2+} contain, that gives rise to the single ion- anisotropy, but the role of other parameters like: cationic occupancy, structural quality, magnetic order, structure, particle size and morphology and surface properties, have been considered very important [1-4]. In general, to optimize and tailoring the magnetic properties of NPs annealing treatments are employed fruiting the thermal induced structural magnetic properties of Cobalt ferrite nanoparticles that is induced by an alternative solvent mediated annealing process in mild temperatures. $\text{Co}_{0.4}\text{Fe}_{2.6}\text{O}_4$ nanoparticles of average size of 32 (8) nm were synthesized by thermal decomposition technique and further solvent mediated annealing at temperatures between 150-320° C. We obtain an important change of the coercive field but not of the remanence ratio neither the specific magnetization as function of the treatment temperature. The NPs annealed at 210 °C exhibit maximum H_C of 0.19 T with high specific magnetization (79 Am²/kg) being the H_C almost 50% larger than the value of the as-prepared NPs ($H_C=0.12\text{T}$). A wide structural (XRD), morphological (HRTEM), chemical (Mossbauer) and magnetic characterization was performed to determine the main mechanism that gives rise to the coercive improvement. These characterizations exclude the role of the particle size, the particle morphology or the inversion degree in the magnetic changes. The analysis of the temperature dependence of the hysteresis and the remanence measurements do not evidence changes in the reversal process. Herein we demonstrate that a solvent mediated annealing treatment in mild conditions permits the reduction of the concomitant internal stresses generated during the nanocrystal growth. Therefore, the increase in the coercive field observed in the post treatment process in a solvent media increase substantially the performances of this type of material for the development of novel rare-earth free permanent magnets. This research was supported by EU- H2020 AMPHIBIAN Project (H2020-NMBP-2016-720853).

[1] C. Moya et al. *J. Mater. Chem. C* 3, 4522 (2015) [2] A. López-Ortega et al., *Chem. Mater.* 27, 4048 (2016). [3] E. Lottini et al., *Chem. Mater.* 28, 4214 (2016). [4] A. López-Ortega, E. Lottini, G. Bertoni, C. de Julián Fernández, C. Sangregorio, *Chem. Mater.* 29, 1279 (2017).

JR-12. Field Dependence of Blocking and Irreversibility Temperature in Fe₃O₄ Magnetic Nanoparticles Coated by Oleic and Citric Acid.

A. Galluzzi^{1,2}, M. Modestino¹, S. Pace^{1,2}, M. Iuliano³, P. Ciambelli³, M. Sarno^{1,4} and M. Polichetti^{1,2}

1. Department of Physics "E.R. Caianiello", Università degli Studi di Salerno, Fisciano, Italy; 2. CNR-SPIN, Consiglio Nazionale delle Ricerche, Fisciano, Italy; 3. Department of Industrial Engineering, Università degli Studi di Salerno, Fisciano, Italy; 4. NANO_MATES Research Centre, Università degli Studi di Salerno, Fisciano, Italy

The magnetic nanoparticles can develop superparamagnetic properties in certain conditions¹ and this feature attracted the researchers that began to study this class of materials in order to exploit their magnetic properties for applications. The main magnetic peculiarities which make these samples so interesting are the high magnetization and near zero coercive field that allow to use the magnetic nanoparticles for biomedical purposes^{2,3}. Among all the magnetic nanoparticles, the Fe₃O₄ (magnetite) ones are very attractive due to their biocompatibility and because they show a low toxicity suggesting their possible use in different scopes^{4,5}. Unfortunately, the magnetite nanoparticles are very sensitive to the action of oxygen, thus some of them might undergo oxidation to ferric hydroxide (Fe(OH)₃) or to maghemite (γ-Fe₂O₃) phases. To limit this undesired effect and also the aggregation of primary nanoparticles of low dimension (10-30 nm), specific surface treatments and techniques of encapsulation are currently used to allow their utilization⁶. In this work, two samples of Fe₃O₄ magnetic nanoparticles coated with oleic acid (Fe₃O₄-OA) and citric acid (Fe₃O₄-CA) have been studied by means of DC magnetization measurements as a function of temperature (T) in Zero Field Cooling (ZFC) and Field Cooling (FC) conditions at different magnetic fields. The measurements have been performed by means of a Quantum Design PPMS equipped with a VSM option. The M(T) measurements have shown a superparamagnetic behavior in both the samples although with different characteristics which have been highlighted studying the field dependence of the blocking and irreversibility temperature. These two temperatures give important information on the nanoparticles distribution and their dispersion together with information on the diameter of the nanoparticles. In particular, the blocking temperature T_B can be identified by taking the maximum of the ZFC curve which, in the case of superparamagnetic samples, has a dome shape behavior. The maximum M value of the ZFC curve can be considered as the blocking temperature of the entire sample, which, of course, differs from the blocking temperatures of the various nanoparticles of different sizes present in the sample. It can be considered as a sort of average blocking temperature of the sample useful when these materials are considered in view of applications. On the other hand, to estimate the T_B distribution of the sample it is possible to use the procedure reported in our previous paper⁷. In this work, the attention has been focused only on the T_B obtained from the maximum of ZFC curves. In Fig. 1, an example of M(T) measurement at H = 700 Oe has been reported. The panel(a) and (b) show the M(T) behavior of Fe₃O₄-OA and Fe₃O₄-CA, respectively. It can be noted in the insets that both the ZFC curves show a dome shape behavior with the presence of the maximum which identifies the T_B of the samples. For the sample Fe₃O₄-OA, T_B ≈ 160 K while for the sample Fe₃O₄-CA T_B ≈ 145 K. In this framework, it is worth to underline that, for H = 700 Oe, the samples are in a superparamagnetic state at room temperature since T_{room} > T_B in both the cases. The temperature value where the ZFC and FC curves separate identifies the irreversibility temperature T_{irr}. In an ideal case where the nanoparticles are of the same dimensions, the T_B and the T_{irr} are equal. Usually, this is quite uncommon and, in the real case, the T_{irr} represents the temperature at which all the nanoparticles are certainly unblocked, as the reversible phase occurs after it. Specifically, T_{irr} represents the unblocking moment of the particles with larger dimensions, which, given the bigger volume than the particles with lower dimensions, unblock at higher temperatures. It is evident that in our case T_B ≠ T_{irr} for both the samples which indicates that the nanoparticles have different diameters. In particular, the temperature difference ΔT between T_{irr} and T_B for Fe₃O₄-OA is lower respect to the Fe₃O₄-CA one. In fact, Fe₃O₄-OA has T_{irr} ≈ 197 K while Fe₃O₄-CA has T_{irr} ≈ 282 K, so giving ΔT(Fe₃O₄-OA) = 37 K and ΔT(Fe₃O₄-CA) = 137 K indicating a bigger diameters difference among the nanoparticles of the Fe₃O₄-CA than the Fe₃O₄-OA. Finally,

performing M(T) measurements at several magnetic fields, the magnetic field dependence of T_B and T_{irr} has been determined and fitted with power and exponential equations extracting interesting samples peculiarities.

¹C.P. Bean and J.D. Livingston, J. Appl. Phys. 30, S120 (1959). ²O. Veiseh, J.W. Gunn, and M. Zhang, Adv. Drug Deliv. Rev. 62, 284 (2010). ³R. Hergt, S. Dutz, R. Müller, and M. Zeisberger, J. Phys. Condens. Matter 18, S2919 (2006). ⁴H. wang Zhang, Y. Liu, and S. heng Sun, Front. Phys. China 5, 347 (2010). ⁵J. Huang, L. Bu, J. Xie et al, ACS Nano 4, 7151 (2010). ⁶A. Ali, H. Zafar, M. Zia et al, Nanotechnol. Sci. Appl. 9, 49 (2016). ⁷M. Polichetti, M. Modestino, A. Galluzzi et al, Mater. Today Proc. 20, 21 (2020).

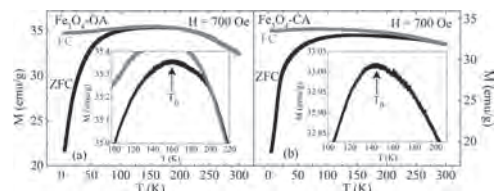


Fig. 1 M(T) ZFC-FC curves for Fe₃O₄-OA (a) and Fe₃O₄-CA (b) at H = 700 Oe. The insets show an enlargement of the region near the maximum of ZFC curves and the arrows indicate the blocking temperatures of the samples.

JR-13. Deducing Uniaxial Anisotropy for Various NiCr Nanostructures.M. Bohra¹, S. Battula² and V. Alman¹*1. Physics, Mahindra Ecole Centrale, Hyderabad, India; 2. Electrical and Electronics, Mahindra Ecole Centrale, Hyderabad, India*

A vital problem of technological interest is in the behavior of magnetically disordered M-Cr nanoalloys. The problem arises due to the onset of ferromagnetic order that is complicated by the random distribution of short-range and long-range magnetic interactions. These interactions are ferromagnetic (FM) or antiferromagnetic (anti-FM) along with size induced superparamagnetic behavior [1]. On this note, using a phenomenological model that considers various magnetically interacting NiCr nanostructures, a comparative magnetic study was carried out [2]. These NiCr nanostructures (nano-clusters, nano-thin films, and nano-composites) were synthesized using a magnetron sputtering system on silicon substrates. The phenomenological model which we used in the current study is based on an interactive modified random anisotropy model that takes into account the concentration, size of the nanostructure, field dependence of the correlation length [2]. By employing magnetic field dependence of blocking temperatures, we deduced uniaxial anisotropy constant (K_u) that is in the range of 10^4 to 10^5 J/m³, compared to the bulk Ni of 10^4 J/m³, giving reasonable K_u values compared to non-interacting models. Further, the M-H curves were well-fitted by superparamagnetic (SPM), paramagnetic (PM), and ferromagnetic (FM) based component models above the blocking temperatures [3], demonstrating a mixture of SPM and FM behaviors. This analysis is rudimentary to understand, prove, and verify the physics behind these complex NiCr nano-systems which is necessary for numerous applications.

1. M. Bohra, P. Grammatikopoulos and R.E Diaz, Chemistry of Materials, 27(9) (2015) 2. W. C. Nunes, L. M. Socolovsky and J. C. Denardin, Physical Review B, 72(21) (2005) 3. V. Singh, V. Srinivas and M. Ranot, Physical Review B, 82(5) (2010)

Session JS
MAGNETO-CALORIC AND MAGNETO-OPTIC MATERIALS AND DEVICES
(Poster Session)

Lei Bi, Co-Chair

University of Electronic Science and Technology of China, Chengdu, China

Karl G Sandeman, Co-Chair

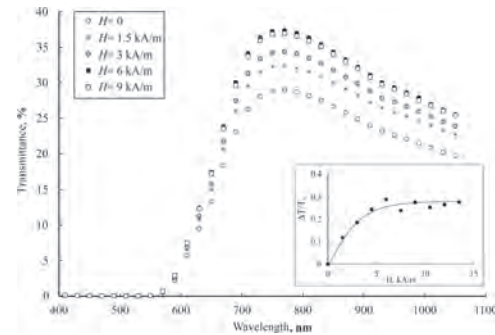
Brooklyn College, Brooklyn, NY, United States

JS-01. Magnetic Emulsions as Prospective Magneto-Optical Media.C.V. Yerin¹ and S.S. Belykh¹*1. Physical and Technical Faculty, North Caucasus Federal University, Stavropol, Russian Federation*

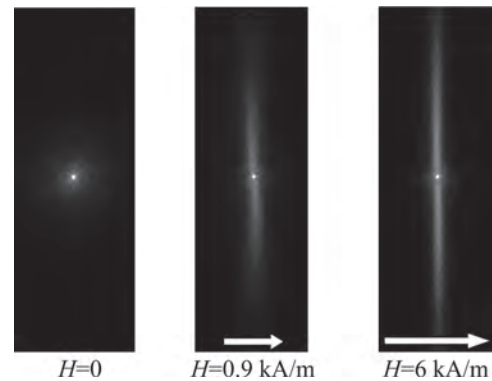
Recently, studies of structured systems based on magnetic fluids have become popular. These media include magnetic emulsions, magnetorheological suspensions, magnetic elastomers, ferrogels [1]. Due to significant changes in magnetic, mechanical, rheological, optical, and other properties under the action of a field, such systems are referred to as Smart Materials. One of the most typical representatives of such systems are magnetic emulsions - dispersed systems in the form of droplets of a magnetic fluid of micron and submicron size, suspended in other immiscible and non-magnetic fluid media [2,3]. In this work, we present the results of studying the possibilities of using magnetic emulsions with low interfacial tension as magneto-optical media. Low interfacial tension magnetic emulsions were produced as follows. Magnetic fluid based on kerosene with magnetite nanoparticles was mixed with AMG-10 hydraulic oil. The volume concentration of magnetite in the initial magnetic fluid was 5%. The size range of magnetite nanoparticles is 8–20 nm. Depending on the preparation conditions, the size of microdroplets in the magnetic emulsion could vary from 1000 to 10000 nm. To study the optical effects in magnetic emulsions, we used an optical setup consisting of a helium-neon laser with a radiation wavelength of 633 nm. The sample under study was placed in two types of cuvettes: in the form of a cylinder and in the form of a thin flat layer. Transmission spectra of the magnetic emulsion were studied using an ELLIPS-1891 spectral ellipsometer in the spectrophotometer mode in the wavelength range of 400–1050 nm. Exposure to a magnetic field leads to a rapid (within 0.1–0.3 s) drawing of microdroplets of the magnetic emulsion into long needle-like structures. This effect leads to a significant change in the transparency of the magnetic emulsion (Fig. 1), which opens up prospects for the use of such systems as magnetically controlled optical filters. The most pronounced effect is achieved in the longitudinal field (the relative change in transparency reaches 25–30%). In this case, the magnitude of the change in transparency can be controlled not only by the magnitude of the field strength but also by its orientation relative to the light beam. The effect of changing transparency has a pronounced saturation at a magnetic field strength of over 5 kA/m. For light with a wavelength of less than 550 nm, the magnetic emulsion is practically opaque and therefore has a characteristic yellow-brown color. The mechanism for changing the transparency of magnetic emulsions under the action of a field seems to be quite simple. The transparency of the system T is determined by the concentration of particles and the cross-section of light scattering by an individual particle. When the emulsion droplets are stretched along the direction of the field (and the light beam in this case), the attenuation cross-section significantly decreases at a practically unchanged concentration of particles, which leads to a pronounced effect of changing the transparency. When exposed to a magnetic field perpendicular to the direction of propagation of light, a pronounced effect of small-angle anisotropic scattering of light on elongated needle-shaped microdroplets appears in magnetic emulsions (Fig. 2). A qualitative interpretation of the effect of diffraction scattering in polydisperse magnetic emulsions can be based on the representation of the system in a magnetic field as an irregular diffraction grating, which is formed from microdroplets of a magnetic emulsion elongated in a magnetic field. In the absence of a field, the microdroplets have a spherical shape and the intensity of light diffracted by polydisperse drops smoothly decreases from the center to the periphery of the diffraction pattern without pronounced minima. The action of the field in the direction perpendicular to the light beam leads to a strong elongation of the emulsion droplets and the appearance of pronounced anisotropy of small-angle light scattering (light is scattered mainly in the plane perpendicular to the direction of droplet extension). In a magnetic field, the optical properties of magnetic emulsions change significantly. Deformation of drops of a magnetic emulsion in a magnetic field creates an oriented structure in the emulsion, in which pronounced effects of anisotropic attenuation and diffraction scattering of light are observed. A magnetic field directed along the light beam increases the transparency of the emulsion without changing the transmission spectrum. This allows magnetic emulsions with low interfacial tension to be used as neutralizing filters with fine-tuning of light transmission by the magnetic

field. The effect of diffraction by needle-shaped microdroplets can be used in magneto-optical sensors to determine the orientation and strength of the magnetic field. The use of magnetic emulsions can significantly expand the range of applications of liquid magnetic nanostructures [4–6]. This work was financially supported by the Ministry of Science and Higher Education of Russia (project no. 0795-2020-007).

S. Odenbach, Arch. Appl. Mech., Vol. 86, p. 269 (2016). A.R. Zakinyan and Y.I. Dikansky, J. Magn. Magn. Mater., Vol. 431, p. 103 (2017). I.M. Subbotin and A.O. Ivanov, Magnetohydrodynamics, Vol. 52, No. 1, p. 269 (2016). J. Philip and J.M. Laskar, J. Nanofluids., Vol. 1, p. 3 (2012). V. Mahendran and J. Philip, Appl. Phys. Lett., Vol. 100, 073104 (2012). P. Das, M. Colombo, and D. Prosperi, Colloids and Surfaces B: Biointerfaces., Vol. 174, p. 42 (2019).



The transmission spectrum of a magnetic emulsion under the action of a magnetic field



Diffraction light scattering in a magnetic emulsion

JS-02. Design Improvements for a Magnetic Field Pulser: a Look Into Switching Device and Circuit Effects.

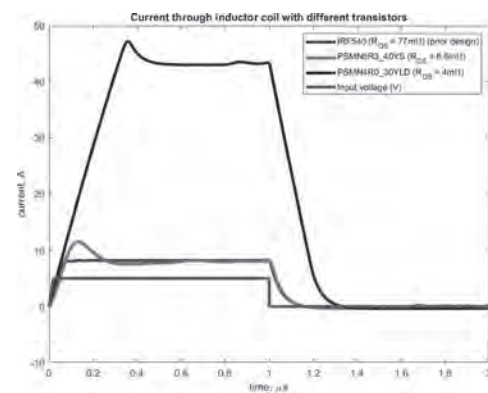
W. Theh¹, N. Prabhu Gaunkar¹ and M. Mina¹

1. Electrical and Computer Engineering, Iowa State University, Ames, IA, United States

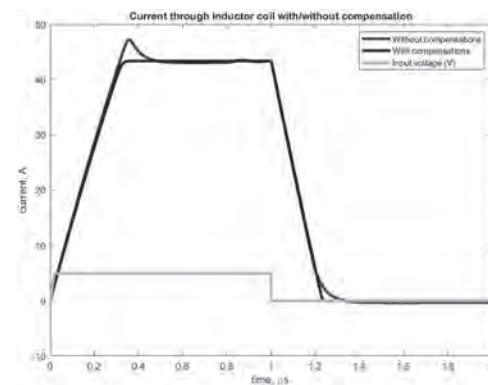
A magnetic field pulser works by feeding a pulsed signal to a switching device which drives current through an inductor to generate magnetic field. These pulsers can be designed to output different levels of magnetic field intensity depending on its application. At the same time, a short switching time, on both the rise and fall end, is preferred to keep the outputted magnetic field clean and in sync with the initial pulsed signal. This is especially important in some use cases. In application of the magnetic field pulser is in an all-optical communication system. The pulser generates a magnetic field which causes a polarization rotation in the light signal as per the theory of Faraday rotation [1]. In this situation, the ideal magnetic field intensity is relatively high to ensure sufficient polarization rotation for the end sensors to detect and a short switching time to prevent signal deterioration or contamination. Another application of the magnetic field pulser is to perform transcranial magnetic stimulation, a medical treatment for certain mental disorders [2]. Small, controlled pulses of magnetic field are targeted at parts of the brain to stimulate it without the need to perform open surgery. The noninvasive nature of this treatment is safer and more accessible for the patients. For this application, the pulser generates a magnetic field with much lower intensity and a shorter pulse width. These are some of the many fields where a variant of magnetic field pulser is found. The mechanics behind a magnetic field pulser can be perceived as simple on paper. The pulser design can be broken into four parts: 1. Switching device 2. Inductor coil 3. Dissipation loop 4. Capacitor banks These are by no means complicated systems. However, applications such as the all-optical communication system requires a magnetic field pulser with high magnetic field intensity and fast switching. That factor coupled with the restrictions in physical dimensions mean the pulser is using a relatively large inductor coil. This introduces a fair amount of reactance into the circuit hence affecting the switching time. Hence, a balance between the magnetic field intensity and switching time is needed. The larger reactance and parasitic effects also affect the natural response of the circuit. This investigation will look to tackle several of these factors to bring improvements to an aging design. Firstly, this investigation will examine the switching device of the magnetic field pulser. In most cases, a silicon-based transistor is used as the switching device. Recent developments in transistor technologies have enabled production of transistors with higher drain current, superfast switching, and smaller on-resistance. Compared to transistors from yesteryears, these new products are better replacements to achieve the balance as mentioned above. A quick comparison between several pre-selected transistors can be seen in Figure 1 attached below. These are based on the same magnetic field pulser design by Pritchard, Weber, and Mina (2013) albeit with different transistors [3]. Alternately, the technology behind gallium nitride-based (GaN) transistors has made it another potential candidate as the switching device. Compared to silicon-based (Si) transistors, GaN transistors show higher electron mobility. This means a similarly sized GaN transistor (compared to a Si transistor) will have higher drain current, faster switching time, and smaller on-resistance [4]. By comparing the different parameters in the transistor technologies, this investigation looks to present a better pulser design that can output a higher magnetic field intensity with faster switching time compared to prior published designs. Next, this investigation also analyzes the natural response of the magnetic field pulser. As previously mentioned, the natural response of the circuit is affected by the presence of the relatively big inductor coil. As a result, it is common to see either underdamped or overdamped response on either or both rise and fall ends. This investigation will consider ideal compensation components to mitigate these effects. For better understanding, the investigation looks at the rise and fall end as separate RLC circuits. As a result, the new pulser design can produce a magnetic field pulse that is clean on the rise, fall, and steady-state sides as shown in Figure 2 attached below. In the case of the all-optical communication system, the cleaner magnetic field output prevents cross signal contaminations which results in bad light signal to the end sensors. On the other hand, in the case of the transcranial magnetic stimulation, the cleaner magnetic field output ensures no accidental

over or under-stimulation of the patient's brain. In conclusion, this investigation seeks to improve upon the magnetic field pulser design that has been around for a while. The authors will present a design that shows a significant improvement over previously published designs and a paper that shows the procedure of achieving it. The authors are confident the paper can be of tremendous help to readers who are looking into creating their own magnetic field pulser to fit into their individual requirements.

1. J. W. Tioh, M. Mina, and R. J. Weber, "All-optical integrated switch utilizing Faraday rotation," *IEEE Trans. Magn.*, vol. 46, no. 6, pp. 2474–2477, Jun. 2010. 2. J. Selvaraj, P. Rastogi, N. P. Gaunkar, R. L. Hadimani, and M. Mina, "Transcranial magnetic stimulation: Design of a stimulator and a focused coil for the application of small animals," *IEEE Transactions on Magnetics*, no. 99, pp. 1–5, 2018. 3. J.W. Pritchard, M. Mina, and R.J. Weber, "Magnetic Field Generator Design for Magneto-Optic Switching Applications," *IEEE Transactions on Magnetics*, Vol. 49, No. 7, pp. 4242–4244, 2013. 4. L. F. Eastman and U. K. Mishra, "The toughest transistor yet [GaN transistors]," *IEEE Spectrum*, vol. 39, no. 5, pp. 28–33, May 2002, doi: 10.1109/6.999791.



Comparing magnetic field pulsers using three different transistors including one from previously published paper



Comparing magnetic field pulser before and after adding compensation components

JS-03. Photonic Crystal Nanostructures With the Magnetic Layer of Gradient Thickness for Optical Magnetic Switching.

O. Borovkova¹, M. Kozhaev^{2,3}, A. Kalish^{1,2} and V.I. Belotelov^{1,2}

1. Lomonosov Moscow State University, Faculty of Physics, Moscow, Russian Federation; 2. Russian Quantum Center, Moscow, Russian Federation; 3. Institute of Physics, Moscow, Russian Federation

Among a variety of magneto-optical effects we focus on the inverse Faraday effect (IFE) that plays a crucial role for optical magnetic switching. The IFE is the emergence of magnetization in a transparent medium illuminated by a circularly polarized high-frequency electromagnetic wave [1]. It provides a new way for efficient control of magnetization at GHz and THz rates. Quantitatively the IFE magnetic field is determined by the distribution of the electric field inside the magnetic layer [2]: $H_{IFE} \sim [E \times E^*]$. Recently it has been demonstrated that optical confinement of light in the magnetophotonic crystals (MPC) or in magnetophotonic microcavity leads to the significant increase of the IFE [2-4]. It happens due to the photonic crystal (PC) defect mode existing in such magnetophotonic crystals or microcavities. These states are spectrally located inside the band gaps and reveal themselves as a sharp peaks in transmittance spectra of a nanostructure. These defect modes also provide strong localization of light inside the magnetic layer that leads to the significant enhancement of the IFE. In this work we propose the novel design of the MPC nanostructures with gradual variation of the magnetic layer thickness. So, the spectral position of the defect mode of the MPC nanostructure depends on the spatial position of input light spot on the sample surface. Therefore, the resonant enhancement of the IFE associated with the peak in transmittance band gap also changes with the input light spot position. Besides that, the design of the MPC nanostructure with perforated magnetic layer provide a spatially localized emergence of the IFE in the spots of several microns that seems very promising for practical applications. The principle scheme of the PC nanostructure with smooth magnetic layer consist of the magnetic layer sandwiched between two non-magnetic Bragg mirrors (Fig. 1). Iron-garnet films doped with bismuth (or BIG films) provide a large Faraday effect and have a relatively low optical absorption in the long-wavelengths visible spectral range [2]. Illuminating this nanostructure by the circularly polarized light at the normal incidence one can observe a defect mode, when the resonance peak appears in the bandgap of the transmittance spectrum. The spectral position and amplitude of this peak depend on the thickness of the magnetic layer h . The spectral position of the defect mode changes from $0.6 \mu\text{m}$ for 120nm-thick magnetic layer to $0.675 \mu\text{m}$ for 180nm-thick one. So, the gradual tuning of the resonance spectral position can be realized in sample with the gradient change of the BIG layer thickness. The IFE is determined by the electromagnetic field intensity localized in magnetic layer. In Fig. 2 the spectral dependence of the total energy in the BIG layer normalized by the layer thickness is presented for several values of h . Therefore, the magnitude of the inverse Faraday effect can also be detuned by moving the input beam along the gradient direction of the sample. Besides the smooth gradient magnetic layer, the PC nanostructure with the magnetic layer with etched discs is proposed. In the BIG magnetic layer with the constant thickness the discs with diameter of dozen microns are etched. The etching depth is different for various discs. As a result, the thickness of the magnetic layer is smaller in the area of these discs. Therefore, the enhanced IFE occurs at the different frequencies for each disc. This approach allows us to achieve spatial localization of the IFE limited just by the disc diameter. To sum up, we propose two designs of the MPC nanostructures with gradient of the magnetic layer thickness for tunable inverse Faraday effect. The spectral position and amplitude of the transmittance peak and resonant IFE depend on the thickness of the magnetic layer. The first design of the MPC nanostructure has smooth magnetic layer with thickness gradient that allows to tune the spectral position of peak in transmittance spectra and the IFE gradually. The second design has perforated magnetic layer and provide spatially localized emergence of the IFE in the spots of several microns. The sample fabrication and the experimental verification of the reported results is expected. This study was supported by Russian Science Foundation (project No. 19-72-10139).

A. Kirilyuk, A.V. Kimel, and T. Rasing, Rev. Mod. Phys. Vol. 82, pp. 2731 (2010). M.A. Kozhaev, A.I. Chernov et al., Sci. Rep. Vol. 8, p. 11435 (2018). T. Goto, A.V. Baryshev, M. Inoue et al., Phys. Rev. B, Vol. 79, p. 125103 (2009). M. Inoue, et al., J. Phys. D. Appl. Phys. Vol. 39, p. R151 (2006).

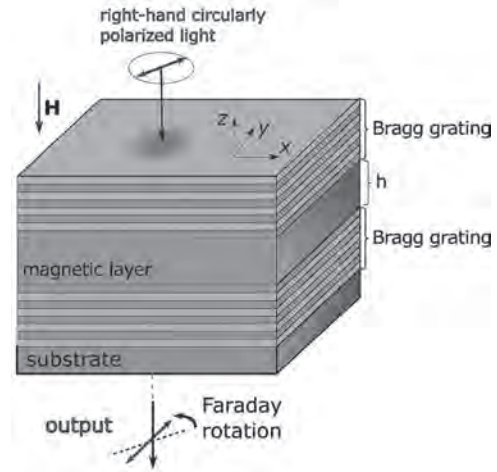


Fig. 1. The principle scheme of the photonic crystal nanostructure with smooth magnetic layer (the gradient of the magnetic layer thickness isn't shown).

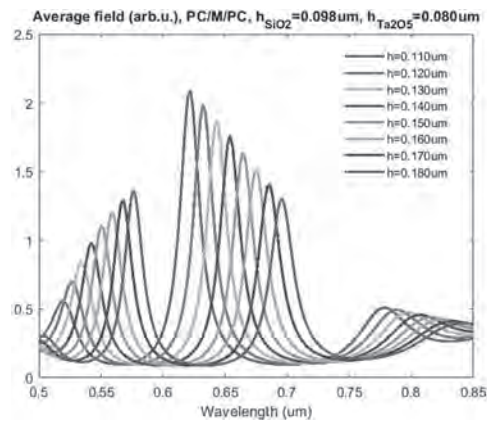


Fig. 2. Spectra of the total energy localized in the magnetic layer of the MPC for various values of h .

JS-04. Enhancement of a Diffracted Beam by Optimizing an Incident Beam and Cap Layer Thickness in a Domain-Wall-Motion Type Light Modulator Array.

R. Higashida¹, N. Funabashi¹, K. Aoshima¹ and K. Machida¹
 1. Nihon Hoso Kyokai, Shibuya-ku, Japan

Introduction We have been trying to develop magneto-optical spatial light modulators (MO-SLMs) driven by current-induced domain wall motion (CIDWM) because MO-SLMs offer a high-frame rate and high-resolution adequate for holographic display applications [1-3]. Each pixel consists of a magnetic nanowire that modulates the beam by MO Kerr effect (MOKE) and two hard magnets (HMs) embedded at both ends of the nanowire. When a pulse current is injected into the nanowire, a magnetic domain of the nanowire expands and shrinks according to the direction of electron flow. We fabricated a single light modulator with a dimension of $1\ \mu\text{m} \times 2\ \mu\text{m}$ and successfully demonstrated magnetization reversal by pulse current injection [2]. Using the fact that the reversal magnetic field of the nanowires changes depending on the presence or absence of HMs, we fabricated an array device that displays a magnetic grating pattern with different magnetization directions for each pixel row by applying an external magnetic field and succeeded in measuring diffraction characteristics [3]. The SLM should have high diffraction efficiency because the diffracted beam's intensity provides the brightness of reproduced images. The intensity of the diffracted beam by the magnetic grating is proportional to the MO figure of merit (FOM), which is the product of the reflectivity and the square of the complex Kerr rotation angle of the nanowire. In this study, we optimized the device structure and the incident angle and polarization direction of the incident beam to amplify the FOM and enhance the diffracted beam's intensity. Experimental method Figure 1(a) shows the structure of the array device. The nanowire material was $\text{Gd}_{24}\text{Fe}_{76}$, which was expected to provide large MOKE and magnetization reversal at low current density. The HMs material was a Co/Pd multilayer with perpendicular magnetic anisotropy. The HMs' magnetization directions were fixed anti-parallel using the different coercivity. The red dotted line indicates a single pixel. The light modulators were arranged at a pitch of $1\ \mu\text{m} \times 2\ \mu\text{m}$. HM1 and the nanowires were partially shared with adjacent pixels to expand the aperture ratio. The width and length of the nanowires was $0.5\ \mu\text{m}$ and $3.8\ \mu\text{m}$, respectively. The widths of HM1 and HM2 were $0.1\ \mu\text{m}$, and the lengths were 600 and $0.8\ \mu\text{m}$, respectively. The coercivity of HM1 and HM2 was controlled by fabricating them at different lengths [2]. When the external magnetic field is applied to the array device, only the magnetization direction of the nanowire with HM2 is reversed. Figure 1(b) shows a two-dimensional magnetic grating pattern displayed on the array. Figure 1(c) shows a cross-sectional illustration of the nanowire. Inside the nanowire, the beam is reflected complexly at each interface. We calculated the dependence of the FOM on the thickness of the Si-N cap layer and the incident beam angle using an optical analysis simulator for multilayers (Multilayer from MM Research, Inc. [4]). The thickness of the cap layer was set at $5\ \text{nm}$ steps from 5 to $30\ \text{nm}$, and the incident angle was set at 1° steps from 0° to 89° in the vertical direction of the film surface. Figure 1(d) shows the optical setup for measuring the diffracted beam. A linearly polarized laser beam with a wavelength of $532\ \text{nm}$ was incident at a tilt in the x-axis direction. The first-order diffracted beam's intensity was measured using a laser power meter. The magnetic grating pattern was turned on and off by applying an external magnetic field from an electromagnet placed at the back of the array device. The incident angle was set to be between 0° and 15° since the first-order diffraction angle of the array device is 15.4° . The polarization direction of the incident beam was set to p-polarization and s-polarization, and the diffracted beam's intensity was measured, respectively. Results and discussions Figure 2(a) shows the FOM calculated by the simulator. The FOM is larger when the thickness of the cap layer is thinner, and it has a maximum at an incident angle of around 50 degrees in this device. It is worth noting that the FOM does not depend on the polarization direction. Figures 2(b) and (c) show the diffraction efficiency of the array device when p- and s-polarized beams were incident, respectively. The diffraction efficiency behaved differently depending on the polarization direction of the incident beam. This is attributed to the pixel shape, which is $1\ \mu\text{m} \times 2\ \mu\text{m}$ and not square. For s-polarized beam, the diffraction efficiency showed the same behavior as that of the FOM, i.e., it was maximum when

the thickness of the cap layer was thin, and the incident angle was large. When the thickness of the cap layer was $5\ \text{nm}$, the diffraction efficiency increased by a factor of 5.9 by optimizing the incident angle and polarization direction. These results showed that the diffracted beam's intensity can be enhanced by amplifying the FOM of Gd-Fe film, including cap and under layers in MO-SLMs. Also, it showed that the maximum intensity of the diffracted beam can be obtained by considering the polarization direction in MO-SLMs with non-square pixel shapes.

[1] K. Aoshima et al., Jpn. J. Appl. Phys., Vol.57, p.09TC03 (2018) [2] R. Higashida et al., Jpn. J. Appl. Phys., Vol.59, p.053001 (2020) [3] R. Higashida et al., Opt. Eng., vol. 59(6), p.064104 (2020) [4] M. Mansuripur, J. Appl. Phys., vol. 67, p.6466 (1990)

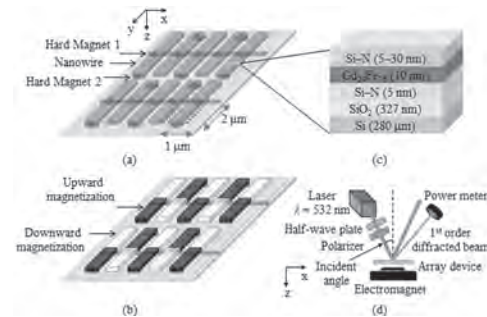


Fig. 1 (a) Domain wall motion type light modulator array (b) illustration of the two-dimensional magnetic grating (c) cross-sectional illustration of the nanowire (d) optical setup for measuring the diffracted beam

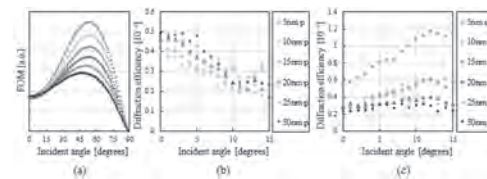


Fig. 2 (a) Calculated FOM of the Gd-Fe film including cap and under layers, (b) diffraction efficiency of the fabricated array device in the p-polarized incident beam, and (c) s-polarized incident beam

JS-05. Amplification of Faraday Rotation in Iron Garnets Using a Multilayer Fabry-Perot Cavity.

A. Schwarz¹

¹. Electrical and Computer Engineering, University of Minnesota Twin Cities, Minneapolis, MN, United States

Rare-earth transition metal garnets are known for their strong magneto-optical properties such as the Faraday effect. Substituted yttrium iron garnet has one of the highest reported figures of merit near -4500 deg/cm. In an effort to increase the effective optical path length of light passing through the garnet material, yttrium iron garnet was both simulated and experimentally tested as the defect layer of a thin film Fabry-Perot cavity. The Q factor of the Fabry-Perot cavity and the peak transmittance can be used to theoretically determine the number of times light passes through the material, increasing the overall rotation of the material without increasing the thickness of the garnet. This idea grew from the concept behind lasers, but instead of light amplification, we amplify Faraday rotation. Thin-film Fabry-Perot cavities consist of two stacked distributed Bragg reflectors, with a low-index defect layer in between. Thin film Fabry-Perot cavities have been well demonstrated using many different materials. We started with simulations using alternating {Si / SiO₂} layers and hoped to find a simple design with a high Q factor. We used a Python based transfer-matrix method algorithm to solve for the transmission spectra of several different device designs. Our device is being developed for telecommunication applications and our designs are centered at the wavelength at 1550 nm. The optimal application for our design is optical isolation. There is an optimal trade-off with these devices. Increasing the number of layers in the mirrors has been simulated to greatly increase the Q factor of the cavity. Garnet, however, requires high temperature annealing process that has been known to distort the reflectivity of a Bragg mirror. The annealing lowers the Q-factor and overall transmittance. With this knowledge, we looked to balance the number of layers with the overall Q-factor. This would hopefully minimize the effect of the annealing on the overall transmittance of the cavity. To test our simulations, we decided to fabricate the simple device in Fig. 1. We call each {Si / SiO₂} stack one “bilayer”. The simulation predicts 100% transmission for this device, and our first rough attempt reached 90% transmittance, but can easily be improved with careful fabrication. This project is still in progress. Next steps include polarization rotation studies after successful spectrometer peaks and optimization of mirror reflectivity to achieve 45 degrees of net rotation as required for optical isolation.

Srinivasan, K., Radu, C., Bilardello, D., Solheid, P., & Stadler, B. J. H. (2020). Interfacial and Bulk Magnetic Properties of Stoichiometric Cerium Doped Terbium Iron Garnet Polycrystalline Thin Films. *Advanced Functional Materials*, 30(15). <https://doi.org/10.1002/adfm.202000409>
 Gomi, M., Satoh, K., Furuyama, H., & Abe, M. (1990). Sputter Deposition of Ce-Substituted Iron Garnet Films with Giant Magneto-Optical Effect. *IEEE Translation Journal on Magnetism in Japan*, 5(4), 294–299. <https://doi.org/10.1109/TJM.1990.4564118>
 Stadler, B. J. H., & Hutchings, D. C. (2018). Sputter-deposited magneto-optical garnet for all-mode (transverse electric/transverse magnetic) Faraday rotators. *MRS Bulletin*, 43(6), 430–435. <https://doi.org/10.1557/mrs.2018.121>

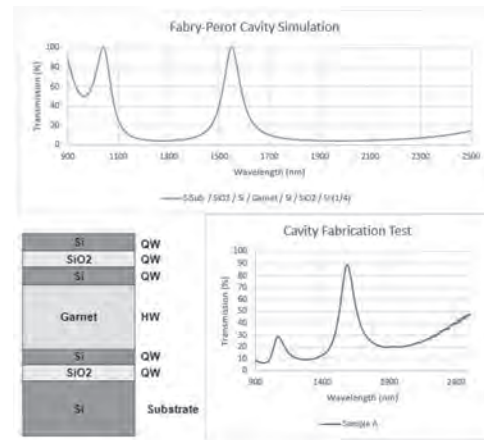


Figure 1 Simulation vs. experiment for the thin film structure given above. Notice the shape of the curves are nearly identical. The experimental structure has a peak near 90% and the simulation has a peak at 100%.

JS-06. Inverse Magnetocaloric Effect and the Magnetostructural Transition in $\text{Pr}_{0.15}\text{Ca}_{0.85}\text{MnO}_3$ Manganite.

K. Thangavel^{1,2}, A.V. Morozkin³, M. V R K¹, S. Rayaprol⁴, A. Pöpl² and N. R¹

1. Physics, Indian Institute of Technology Madras, Chennai, India; 2. Felix Bloch Institute for Solid State Physics, Leipzig University, Leipzig, Germany; 3. Chemistry, Moscow Lomonosov State University, Moscow, Russian Federation; 4. Mumbai Centre, UGC-DAE Consortium for Scientific Research, Mumbai, India

Perovskite manganites $\text{R}_x\text{A}_{1-x}\text{MnO}_3$ (R = Rare earth, A = alkaline earth; $0 < x < 1$) are well-known for their correlated charge, spin and lattice degrees of freedom [1]. While studies on hole-doped manganites are almost complete, the physical properties of electron-doped manganites are still being understood. Recent studies on $\text{R}_{0.15}\text{Ca}_{0.85}\text{MnO}_3$ ($\text{R} = \text{Y}, \text{Gd}$ and Dy) revealed interesting metamagnetic transition in the antiferromagnetically ordered state across which the samples show insulator to metal-like change in the electrical resistivity and also switches from an inverse magnetocaloric effect (MCE) to normal MCE [2]. In this work, magnetic and magnetocaloric properties of electron-doped $\text{Pr}_{0.15}\text{Ca}_{0.85}\text{MnO}_3$ are studied in order to understand the effect of light rare earth substitution at the Ca-site of antiferromagnetic CaMnO_3 . Polycrystalline $\text{Pr}_{0.15}\text{Ca}_{0.85}\text{MnO}_3$ has been prepared by solid state reaction. The X-ray diffraction (XRD) data were collected at several temperatures (T) from 300 K down to 25 K (Cu Ka, Rigaku). It is found that $\text{Pr}_{0.15}\text{Ca}_{0.85}\text{MnO}_3$ crystallizes in orthorhombic structure (space group $Pnma$, no. 62, $oP20$) at 300 K and orders antiferromagnetically at 147 K (T_N). Paramagnetic susceptibility follows Curie-Weiss law. The effective paramagnetic moment (m_{eff}) and paramagnetic Curie temperature (q_p) values are $4.47 m_B/\text{f.u}$ and $+118$ K respectively. The positive q_p value indicates the presence of coexisting ferromagnetic interactions in the system. The field dependent magnetization measured at 5 K in fields up to 70 kOe is almost linear suggesting the presence of dominant antiferromagnetic interactions. The magnetization value at 5 K in 70 kOe field is about $0.11 m_B/\text{f.u}$. only. From low temperature XRD, it is observed that the crystal structure changes to monoclinic (space group $P2_1/m$, no.11-2, $mP20$) across the magnetic transition. No metamagnetic transition is evidenced in $\text{Pr}_{0.15}\text{Ca}_{0.85}\text{MnO}_3$ at 5 K in fields up to 70 kOe suggesting robust antiferromagnetic state. Magnetocaloric effect (MCE) has been estimated in terms of isothermal magnetic entropy change (ΔS_m) using magnetization vs field (M-H) isotherms measured around T_N . Positive MCE (i.e. inverse MCE) is observed below T_N [Fig. 1a]. The maximum ΔS_m value is about $6.4 \text{ J/kg}\cdot\text{K}^{-1}$ at 137.5 K for 70 kOe field change. The peak in inverse magnetocaloric effect coincides with the magnetostructural transition temperature. The maximum value of isothermal magnetic entropy change, ΔS_m^{max} , at 142.5 K is plotted as a function of magnetic field change (ΔH) and is fitted to a power law, i.e. $\Delta S_m^{\text{max}} \propto (\Delta H)^n$ [Fig. 1b] and the 'n' value is found to be 1.75. It is recalled that a value of $n = 2$ is expected for antiferromagnets [3] and the decrease in the 'n' value could be indicative of the coexistence of ferromagnetic interactions in the system. Though $\text{Pr}_{0.15}\text{Ca}_{0.85}\text{MnO}_3$ shows a strong electrical resistivity value in the antiferromagnetically ordered state, the electrical resistivity value decreased by several order below T_N . Non adiabatic polaron hopping conduction is observed above T_N and polaron activation energy is found to be ~ 40 meV. Electron spin resonance studies were performed from 300 K to down to 7 K reveal Dysonian broadening as a result of the intrinsic electrical conductivity of the material. The g-value observed at 300 K is less than the free electron g-value and it increases with decreasing temperature down to T_N . Thermopower measurements showed strong temperature dependence near T_N and a large negative thermopower of ~ 40 mV/K was obtained around 100 K.

1. Y. Tokura, Rep. Prog. Phys. 69 (2006) 797 2. Lakshman Dhal, Eesha Andharia, N. Shukla, T. Geetha Kumary, A. K. Nigam, S. K. Malik, P. N. Santhosh and R. Nirmala, J. Magn. Magn. Mater. 474 (2019) 215 3. A. Biswas, S. Chandra, T. Samanta, M. H. Phan, I. Das and H. Srikanth, J. Appl. Phys. 113 (2013) 17A902

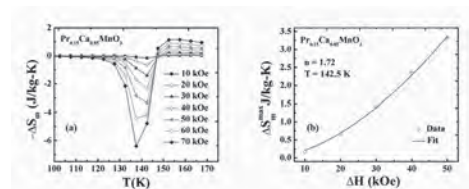


Fig. 1 (a) Isothermal magnetic entropy change (ΔS_m) vs temperature for various field changes and (b) Maximum magnetic entropy change vs ΔH at T_N and the fit to power law, $(\Delta H)^n$, with $n = 1.75$.

JS-07. Magnetocaloric Study of $\text{La}_{0.45}\text{Nd}_{0.25}\text{Sr}_{0.3}\text{MnO}_3/\text{MO}$ ($\text{MO}=\text{CuO}$, CoO and Ni) Nanocomposites.

D. Neupane¹, A. Pathak² and S.R. Mishra¹

1. *Physics and Materials Science, The University of Memphis, Memphis, TN, United States*; 2. *Physics, SUNY Buffalo State College, Buffalo, NY, United States*

Recently, solid-state magnetic refrigeration (MR) technique has great interest of research as a promising technology based on magnetocaloric effect to replace the conventional cooling techniques. Many literature reviewed $\text{La}_{0.45}\text{Nd}_{0.25}\text{Sr}_{0.3}\text{MnO}_3/5\%\text{CuO}$ composite shows convincing magnetocaloric properties. The present study investigate the detail magnetocaloric study of $\text{La}_{0.45}\text{Nd}_{0.25}\text{Sr}_{0.3}\text{MnO}_3/x \text{ Wt}\% (\text{M})\text{O}$, ($x=0.0, 0.25, \text{ and } 0.50$, $\text{M} = \text{Cu, Co and Ni}$) nano-composite samples. Pure phase exchange coupled nanocomposites of magnetically soft oxides were prepared via one-pot autocombustion method and heat treated in air at 1100°C for 12 h. The influence of wt% of transition metal oxide to the composite on the structural, morphology, magnetic and magnetocaloric properties have been investigated using X-ray diffraction, SEM and SQUID. XRD pattern of the composite reveals the presence of a distinct pure and single-phase rhombohedral structure of perovskite-based material $\text{La}_{0.45}\text{Nd}_{0.25}\text{Sr}_{0.3}\text{MnO}_3$ (LNSMO) with space group R-3c and monoclinic structure of metal oxide(MO) with the ICDD numbers (LNSMO: 01-082-1152). No trace of secondary phase was detected within the sensitivity limit of the experiment. Rietveld refinement was performed using fullprof software to calculate prepared sample's mass ratio, lattice parameter and cell volume. The lattice parameters aren't much effected due to presence of very small amount of metal oxide and values are matched with published literature. The SEM techniques were used to identify the obtained nano-structural morphologies. The NiO/CoO/CuO material were located at the grain boundaries with uniform homogeneity due to the uniaxial pressure effect. Temperature dependence of field-cooled (FC) curve exhibits second-order transition with T_c near room temperature. The temperature depending of magnetization as a function of applied field for all the samples set were measured and conformed the paramagnetic behavior above the transition temperature and ferromagnetic behavior below the transition temperature. The isothermal magnetic entropy change (ΔS_m) was calculated to evaluate the magnetocaloric property of the material. The ΔS_m have a maximum value around the vicinity of the transition temperature and decrease with any further increase of the temperature. The maximum value of ΔS_m for 5T field were found near room temperature. All the values of ΔS_m are higher than ferrites oxides. The reason could be the grain size and particle distribution. The uniform distribution of NiO and CoO particles in the grain boundaries than CuO gives the enhance value of entropy change with CoO and NiO compare to CuO. Also, the grain size of $\text{La}_{0.45}\text{Nd}_{0.25}\text{Sr}_{0.3}\text{MnO}_3$ for CoO has higher as compare to CuO. This is the effectiveness of one pot autocombustion technique in achieving effective growth of fine grains of respective phases. Cooling efficiency can be calculated from the peak position of ΔS_m called relative cooling power (RCP). RCP values of our nanoparticle samples being the maximum for 5wt%CoO. These results make our compounds promising materials for magnetic refrigeration technology. Our study suggests that the $\text{La}_{0.45}\text{Nd}_{0.25}\text{Sr}_{0.3}\text{MnO}_3/x \text{ Wt}\% (\text{A})\text{O}$, ($x=0.0, 0.25, \text{ and } 0.50$, $\text{A} = \text{Cu, Co and Ni}$) nano-composite materials with various morphologies could exhibit interesting magnetocaloric properties near room temperatures

1. Tishin, A. M., & Spichkin, Y. I. (2016). *The magnetocaloric effect and its applications*. CRC Press. 2. Gschneidner Jr, K. A., Pecharsky, V. K., & Tsokol, A. O. (2005). Recent developments in magnetocaloric materials. *Reports on progress in physics*, 68(6), 1479. 3. Gschneidner Jr, K. A., & Pecharsky, V. K. (2000). Magnetocaloric materials. *Annual Review of Materials Science*, 30(1), 387-429. 4. Fkhar, L., Mahmoud, A., Boschini, F., Schrijnemakers, A., Hamedoun, M., Benyoussef, A., ... & Mounkachi, O. (2020). A study of magnetic and magnetocaloric properties of 0.95 ($\text{La}_{0.45}\text{Nd}_{0.25}\text{Sr}_{0.3}\text{MnO}_3$)/0.05 CuO composites prepared by spray drying. *Inorganic Chemistry Communications*, 119, 108129. 5. Fkhar, L., Lamouri, R., Mahmoud, A., Boschini, F., Hamedoun, M., Ez-Zahraouy, H., ... & Mounkachi, O. (2020). Enhanced Magnetic and Magnetocaloric Properties of $\text{La}_{0.45}\text{Nd}_{0.25}\text{Sr}_{0.3}\text{MnO}_3/\text{CuO}$ Composite. *Journal of*

Superconductivity and Novel Magnetism. 6. Kallel, N., Kallel, S., Hagaza, A., & Oumezzine, M. (2009). Magnetocaloric properties in the Cr-doped $\text{La}_{0.7}\text{Sr}_{0.3}\text{MnO}_3$ manganites. *Physica B: Condensed Matter*, 404(2), 285-288. 7. Kumaresavanji, M., Sousa, C. T., Pires, A., Pereira, A. M., Lopes, A. M. L., & Araujo, J. P. (2014). Room temperature magnetocaloric effect and refrigerant capacitance in $\text{La}_{0.7}\text{Sr}_{0.3}\text{MnO}_3$ nanotube arrays. *Applied Physics Letters*, 105(8), 083110. 8. Fang, Y. K., Yeh, C. C., Chang, C. W., Chang, W. C., Zhu, M. G., & Li, W. (2007). Large low-field magnetocaloric effect in $\text{MnCo}_{0.95}\text{Ge}_{0.1}$ alloy. *Scripta materialia*, 57(6), 453-456.

JS-08. Structural and Electronic Properties on $Gd_3Fe_{5-x}Al_xO_{12}$ ($x=0.25, 0.5, 1.0$) Using Rietveld, Maximum Entropy Method (MEM).

D. Neupane¹, K.S. Ali² and S.R. Mishra¹

1. *Physics and Materials Science, The University of Memphis, Memphis, TN, United States*; 2. *Harmony School of Excellence, Houston, TX, United States*

The precise study of the bonding in materials is an important part of material characterization. The Maximum Entropy Method (MEM) is a powerful tool for deriving accurate electron density distribution in crystalline materials using experimental data. The MEM provides us with the least biased deduction, which is compatible with certain given information. The bonding nature and the distribution of electrons in the bonding region can be clearly visualized using this technique. MEM electron densities are always positive and even with the limited number of data, one can evaluate reliable electron densities resembling true densities. In this present work, the attention is focused on the growth, structural, and electron density distribution of $Gd_3Fe_{5-x}Al_xO_{12}$ ($0 \leq x \leq 1$) using X-ray powder data. $Gd_3Fe_{5-x}Al_xO_{12}$; $x = 0.0, 0.25, 0.50$ and 1.0 samples were synthesized via auto combustion method and heat-treated in air at $1100^\circ C$ for 12 h. The phase identification and lattice parameter of the powders performed using X-ray diffraction data. The Rietveld analysis was performed for the present analysis, which proves the synthesized material of $Gd_3Fe_{5-x}Al_xO_{12}$ ($0 \leq x \leq 1$) stays in high-crystalline with single-phase garnet structure, the structural and profile parameter were compared with the reported results from JCPDS-48-0077. The Rietveld analysis was performed using JANA 2000 software package, the results show that the lattice parameters and the cell volume decrease with the increasing the Al, this is clearly evidencing the Al content is replacing the Fe. From this analysis, we observed that a gradual shift in the peaks from the lower angle to the higher angle as compared to the pure $Gd_3Fe_5O_{12}$. The lattice parameters for $Gd_3Fe_{5-x}Al_xO_{12}$ decreases from 12.50Å to 12.44Å due to smaller ionic radii of Al^{3+} ion (0.535Å) replacing Fe^{3+} ions (0.645Å). The atomic site occupancy and bond distance analysis for each site were derived from Rietveld refinement for $Gd_3Fe_{5-x}Al_xO_{12}$, the Al is preferred to the tetrahedral site for $x \leq 0.5$ and prefers both sites; tetrahedral and octahedral thereafter. The structure factors from the Rietveld analysis were further taken to determine the electron density distribution analysis by MEM method. The bonding nature and radii of atoms/ions and interaction between the atoms were clearly analyzed and represented by 3D, 2D, and 1D MEM maps. The mid bond electron densities between atoms were analyzed. The two-dimensional MEM electron density maps on the (001) and (202) planes, and the one-dimensional electron density profiles along Fe-O, Gd-O, and O-O directions were calculated. From this analysis, the substitution of Al^{3+} ions actually reduces the lattice parameter and volume of the $Gd_3Fe_{5-x}Al_xO_{12}$. The 2D map shows the depletion of charge density in the valence regions are clearly seen. Our study suggests that the Al^{3+} doped $Gd_3Fe_5O_{12}$ nano-materials could exhibit interesting electronic properties for data storage applications.

1. Lassri, H., Hlil, E. K., Prasad, S., & Krishnan, R. (2011). Magnetic and electronic properties of nanocrystalline $Gd_3Fe_5O_{12}$ garnet. *Journal of solid state chemistry*, 184(12), 3216-3220. 2. Nakamoto, R., Xu, B., Xu, C., Xu, H., & Bellaiche, L. (2017). Properties of rare-earth iron garnets from first principles. *Physical Review B*, 95(2), 024434. 3. Ali, K. S., Saravanan, R., Israel, S., & Arda, L. (2010). Localized ferromagnetic charge ordering through charge density analysis in nano sized diluted magnetic semiconductor Co^{2+} : ZnO. *Physica B: Condensed Matter*, 405(7), 1763-1769. 4. Ali, K. S., Saravanan, R., Pashchenko, A. V., & Pashchenko, V. P. (2010). Local distortion in Co-doped LSMO from entropy-maximized charge density distribution. *Journal of Alloys and Compounds*, 501(2), 307-312. 5. Saravanan, R., & Rani, M. P. (2011). *Metal and alloy bonding-an experimental analysis: Charge density in metals and alloys*. Springer Science & Business Media.

JS-09. On the Real Potential of $R_{1-x}A_xMnO_3$ Oxides in Magnetic Cooling: $Pr_{0.6}Sr_{0.4}MnO_3$ as a Case of Study.

O. Chdil¹, M. Balli¹, O. Mounkachi² and K. El maalam³

1. AMEEC team, LERMA, College of Engineering and Architecture, Université Internationale de Rabat, Sale, Morocco; 2. LaMCSel Laboratory, B.P. 1014, Faculty of science, Université Mohammed V de Rabat, Rabat, Morocco; 3. Materials and Nanomaterials Center, Moroccan Foundation for Advance Science Innovation and Research, Rabat, Morocco

The family of manganese oxides with the general formula $R_{1-x}A_xMnO_3$ (R=lanthanide and A=divalent alkaline earth) has a non-negligible potential in magnetic cooling particularly because of the high chemical stability and interesting magnetocaloric properties at room temperature [1]. In this work, we report a detailed study of the thermodynamic performance of $Pr_{0.6}Sr_{0.4}MnO_3$ in a functional magnetic cooling system up to the theoretical limit of its magnetocaloric effect. In this context, a one-dimensional numerical model of the AMR cycle is developed, while the required magnetocaloric properties of the oxide are calculated in the framework of Mean Field Theory (MFT). The obtained results are deeply analyzed and then compared with the reference Gadolinium (Gd) metal. Moreover, it is revealed that using $Pr_{0.6}Sr_{0.4}MnO_3$ as refrigerant requires high magnetic fields to generate reasonable temperature spans for application. Under a magnetic field of 8 T, the studied oxide can generate an AMR temperature span of 33 K. However, such a span can be achieved by employing Gd and using only a magnetic field source of 1.45 T. The thermodynamic efficiency was evaluated by directly considering the involved magnetic forces between the $Pr_{0.6}Sr_{0.4}MnO_3$ regenerator and the magnetic field source. The associated magnetic work is numerically calculated by using Altair Flux 3D software. Particularly, it was found that the coefficient of performance (COP) can be enhanced by a factor of two when balancing magnetic forces (Fig. 1) despite of the moderate magnetocaloric effect shown by $Pr_{0.6}Sr_{0.4}MnO_3$ under practical fields (1 to 2 T). On the other hand, the hidden thermodynamic performances of this compound are also pointed out by investigating its magnetocaloric properties in the theoretical limit zone. In this way, our calculations unveil that is possible to reach cold source temperatures under -22°C even when using helium as heat transfer fluid (Fig. 2). Finally, a magnetic cooling device working with $Pr_{0.6}Sr_{0.4}MnO_3$ as refrigerant and fully powered by solar cells is proposed.

[1] M. Balli, S. Jandl, P. Fournier, and A. Kedous-Lebouc, Appl. Phys. Rev. 4, 021305 (2017).

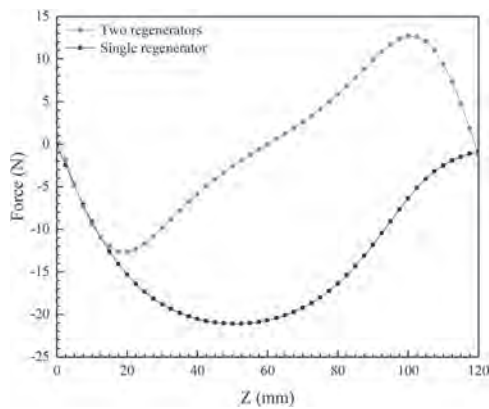


Fig. 1 The simulated magnetic forces in the case of one and two separated regenerators of $Pr_{0.6}Sr_{0.4}MnO_3$.

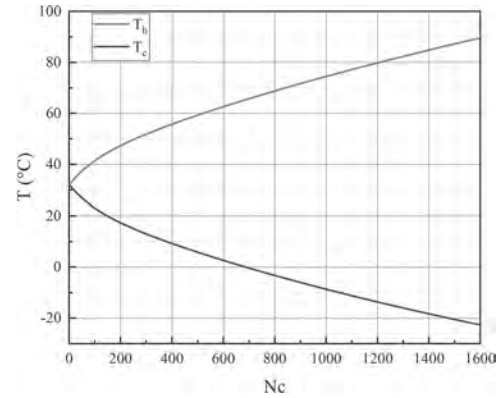


Fig. 2 Temperature evolution of the hot and cold ends as a function of the number of cycles for using helium as transfer fluid

JS-10. Multiferroic Electroactive Polymer Blend/Ferrite Nanocomposite Film for Cooling Devices.

P. Thandapani¹, F. Béron¹, R. Aepuru², M. Ramalinga Viswanathan^{3,4}, F. Luis Zabotto⁵, J. A Jiménez⁶ and J. C Denardin⁷

1. Materials and Low-temperature Laboratory, Institute of Physics Gleb Wataghin, Universidade Estadual de Campinas, Campinas, Brazil; 2. Department of Mechanical Engineering, Faculty of Engineering, Universidad Tecnológica Metropolitana, Santiago, Chile; 3. Advanced Ceramics and Nanotechnology Laboratory, Department of Materials Engineering, Faculty of Engineering, Universidad de Concepcion, Concepcion, Chile; 4. Technological Development Unit (UDT), Universidad de Concepcion, Concepcion, Chile; 5. Physics Department, Universidade Federal de Sao Carlos, Sao Carlos, Brazil; 6. Department of Physical Metallurgy, Consejo Superior de Investigaciones Científicas, Madrid, Spain; 7. Department of Physics, Universidad de Santiago de Chile, Santiago de Chile, Chile

The materials that exhibit mutual control of more than one property by external stimuli such as magnetic, electric and stress fields are known as multifunctional material. They are useful to design smart sensors and can be extended as a functional refrigerant for cooling. The magnetic refrigerator is an alternative to the conventional refrigerators as they do not emit toxic greenhouse gases to the environment. However, the product cost of a magnetic refrigerator is expensive due to the raw material and magnetic components required to achieve the maximum entropy change at a given magnetic field strength (≤ 1.5 T). Assuming the combination of electric and magnetic properties may yield adiabatic temperature change at low (magnetic/electric) field, the piezoelectric/magnetic nanocomposites are proposed. Poly(methyl methacrylate)/Poly(vinylidene fluoride-co-hexafluoropropylene) (PMMA/PVDF-HFP) blend and PMMA/PVDF-HFP/ $Zn_{0.5}Cu_{0.5}Fe_2O_4$ flexible nanocomposites were fabricated by solution casting method. Pristine polymer blend and PMMA/PVDF-HFP/ferrite nanocomposite are having 67 and 62% of F(b), respectively. $Zn_{0.5}Cu_{0.5}Fe_2O_4$ and PMMA/PVDF-HFP/ $Zn_{0.5}Cu_{0.5}Fe_2O_4$ nanocomposite show superparamagnetic nature with the saturation magnetization of 44 and 5.3 emu/g, respectively. The composite film is thermally stable up to 753 K and later it shows 80% of weight loss. The magnetic entropy change (DS_M) of $Zn_{0.5}Cu_{0.5}Fe_2O_4$ and PMMA/PVDF-HFP/ $Zn_{0.5}Cu_{0.5}Fe_2O_4$ show interesting table-like flat variation with respect to magnetic field (0 to 40 kOe) and temperature (100 to 400 K). The DS_M (refrigerant capacity) at 300 K is found to be -0.69 (293 J/kg) and -0.094 (40 J/kg) J/kg/K for $Zn_{0.5}Cu_{0.5}Fe_2O_4$ and PMMA/PVDF-HFP/ $Zn_{0.5}Cu_{0.5}Fe_2O_4$, respectively. Ferroelectric polarization change as a function of electric field is analysed at room temperature. The composite film exhibiting both magnetism and ferroelectricity is proved and would be attractive to design different compositions to increase the temperature variation for cooling devices.

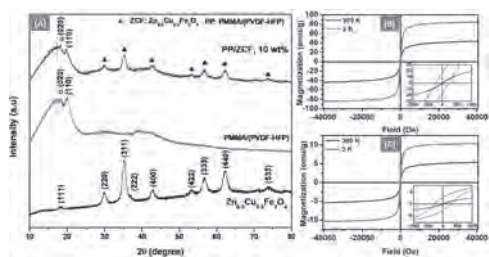


Figure 1 (A) X-ray diffraction patterns, (B) and (C) M-H hysteresis loops of $Zn_{0.5}Cu_{0.5}Fe_2O_4$ and PP/ $Zn_{0.5}Cu_{0.5}Fe_2O_4$ nanocomposite respectively.

Session JT
MAGNETO-CALORIC MATERIALS AND DEVICES II
(Poster Session)

Jia-Yan Law, Chair
Universidad de Sevilla, Sevilla, Spain

JT-01. Elastocaloric and Magnetocaloric Effects Through the Martensitic Transformation in Bulk $\text{Ni}_{55}\text{Fe}_{11}\text{Mn}_7\text{Ga}_{27}$ Alloys Produced by Arc-Melting and Spark Plasma Sintering.

J.D. Navarro-García¹, J.P. Camarillo-García², F. Alvarado-Hernández², J.L. Sánchez Llamazares¹ and H. Flores-Zúñiga¹

1. Potosino Institute of Scientific and Technological Research, San Luis Potosí, Mexico; 2. Universidad Autónoma de Zacatecas, Zacatecas, Mexico

The current interest in developing solid-state refrigeration devices has encouraged the investigation of caloric effects linked to first-order phase transitions in different families of solids [1]. Among them, (Ni, Mn)-based Heusler-type magnetic shape memory alloys have deserved particular attention due to their multicaloric nature [2]. For properly chosen compositions, martensitic transformation (MT) in Ni-Fe-Ga alloys appears around room temperature (RT) [1]. This, together with their good mechanical properties in comparison with other (Ni,Mn)-based alloys (improved with the precipitation of γ phase [3]), and the facts that with the partial replacement of Fe by Mn in the $\text{Ni}_{55}\text{Fe}_{19}\text{Ga}_{26}$ alloy γ phase remains in a low concentration, increases the entropy of the MT, not significantly modifying the MT temperature [3], motivated present investigation. Two bulk $\text{Ni}_{55}\text{Fe}_{11}\text{Mn}_7\text{Ga}_{27}$ samples were prepared from pure elements ($\geq 99.9\%$) by arc-melting and spark plasma sintering (SPS) (bulk and SPS samples, respectively), and their phase constitution, as well as magnetocaloric (MC) and elastocaloric (eC) effects studied across the MT. The SPS sample was a dense disc ($\rho \approx 8.4 \text{ g.cm}^{-3}$; $\sim 99\%$ in respect of theoretical), with diameter and height of 15 and 2.2 mm, sintered from a powdered arc-melted ingot at constant pressure of 30 MPa in a Labox-210 SPS system. The time evolution of vertical displacement and temperature during the process is given in Fig. 1(a). Samples received homogenization annealing at 1273 K for 24 h, followed by a chemical ordering treatment at 773 K (1 h). Start and finish temperatures of the structural transition were determined from the 5 and 95 %, respectively, of the DSC peak area. RT phase constitution was determined by X-ray diffraction (XRD). As Fig. 1(b) shows, the structural transition for both samples is close to RT with similar temperatures. This highlights the effectiveness of SPS technique for consolidating (Ni-Fe-Ga)-based alloys. XRD patterns, shown in Figs. 1(c) and (d), respectively, were obtained with the X-ray beam impinging on a plane perpendicular to the gradient during solidification and on the surface of the sintered disc. In both patterns, a $L2_1$ -type austenite (AST) is the major phase, while cubic γ phase [4] is also detected ($\sim 6\%$ vol.). However, notice that the peak intensities in the XRD pattern for the SPS sample correspond to an isotropic polycrystal, whereas for the bulk arc melted one AST grains preferentially grow with the $[100]$ direction oriented along the thermal gradient during solidification. Partial preferential and non-preferential grain orientation in both samples was confirmed by SEM observations (not shown). Magnetization measurements were done by VSM in a PPMS Dynacool system. $M(T)$ curves, under 5 mT and 5 T following zero-field-cooling (ZFC) and field-cooling (FC) regimens (1.0 Kmin^{-1}), are depicted in Fig. 2(a). The magnetic entropy change ΔS_M was estimated from the Maxwell relation through the reverse MT from a set of $M(T)$ curves (shown in Fig. 2(b)), measured up to an applied magnetic field $\mu_0 H_{\text{max}}$ of 5 T. As shown in Fig. 2(c), bulk sample exhibits a moderate $|\Delta S_M|_{\text{max}}$ value of 8.2 ($12.9 \text{ Jkg}^{-1}\text{K}^{-1}$ under $\mu_0 H_{\text{max}} = 2$ (5) T (though $|\Delta S_M|_{\text{max}}$ values measured are the largest reported for alloy studied [3]). The eC effect adiabatic temperature change $\Delta T_{\text{ad}}^{\text{me}}$ was determined in a home-made facility under a compression uniaxial load change of 120 MPa for parallelepiped-shaped samples cut from the bulk and SPS samples; uniaxial stress for the bulk sample was applied along thermal gradient during solidification. Fig. 2(d) gives the $\Delta T_{\text{ad}}^{\text{me}}(T)$ curves for both samples loading and unloading the uniaxial stress. The bulk sample exhibits a $|\Delta T_{\text{ad}}^{\text{me}}|_{\text{max}}$ of 2.4 K at a load removal of 120 MPa, whereas this magnitude significantly decreases for the SPS sample. This result agrees with the around 1/3 reduction of the eC effect expected for the direction $[100]$ [5,6]. Hence, the above-mentioned partial crystallographic texture and isotropic nature of the samples, explain the significant difference observed in the eC effect value. In summary, apart from probing the efficacy of SPS technique for the shaping and consolidation of Ni-Fe-Ga alloys exhibiting similar phase transformation temperatures than those obtained for the bulk sample, the MC and eC effects were assessed for bulk samples of the Heusler alloy $\text{Ni}_{55}\text{Fe}_{11}\text{Mn}_7\text{Ga}_{27}$. Whereas the MC effect is moderate in comparison

with the reported for (Ni-Mn-X)-based alloys ($X = \text{Ga, In, Sn, Sb}$), our results underline their good mechanical strength and the relevant role of crystallographic texture on the eC effect.

[1] L.I. Mañosa, A. Planes, Adv. Mater. 29 (2017) 1603607. [2] L.I. Mañosa, A. Planes, Phil. Trans. R. Soc. A 374 (2016) 20150310. [3] S. Kumar Sarkar, A. Biswas, P.D. Babu, S.D. Kaushik, A. Srivastava, V. Siruguri, M. Krishnan, J. Alloys Compd. 586 (2014) 515–523. [4] T. Omori, N. Kamiya, Y. Sutou, K. Oikawa, R. Kainuma, K. Ishida, Mater. Sci. Engin. A 378 (2004) 403–408. [5] F. Xiao, M. Jin, J. Liu, X. Jin, Acta Mater. 96 (2015) 292–300. [6] F. Hernández-Navarro, J.P. Camarillo-García, C.O. Aguilar-Ortiz, H. Flores-Zúñiga, D. Ríos, J.G. González, P. Álvarez-Alonso, Appl. Phys. Lett. 112 (2018) 164101.

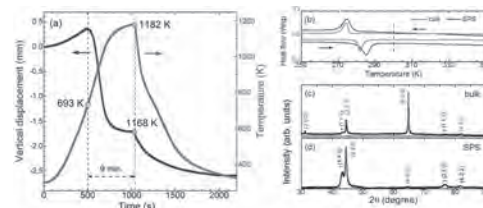


Fig. 1. (a) Vertical displacement and temperature versus time along the SPS process. (b) DSC curves for bulk and SPS samples (10 K.min^{-1}). Starting and finishing MT temperatures for the bulk (SPS) sample were $M_S = 276$ (278) K, $M_F = 269$ (262) K, $A_S = 277$ (279) K, and $A_F = 286$ (290) K. (c) and (d) indexed XRD patterns for bulk and SPS samples, respectively ($\text{CuK}\alpha$).

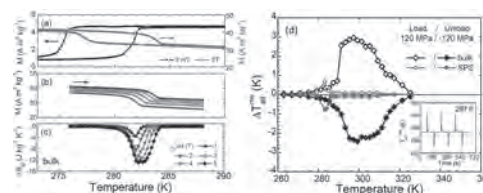


Fig 2. ZFC and FC $M(T)$ curves under 5 mT and 5 T across the structural transition (a), isofield $M(T)$ curves under fields from 1 to 5 T (b), and $\Delta S_M(T)$ curves (c) through the reverse MT for the bulk arc melted alloy. (d) $\Delta T_{\text{ad}}^{\text{me}}(T)$ curves for both samples under a load and unload applied stress of 120 MPa. Inset: $\Delta T_{\text{ad}}^{\text{me}}$ as a function of time at 297 K for the bulk sample.

JT-02. Enhancement of Curie Transition by Substituting Sb in MnCo_{1-x}Sb_xGe (x=0, 0.2, 0.4, 0.6) Alloys and its Structural, Morphological, Magnetic, Magneto Caloric Investigations.

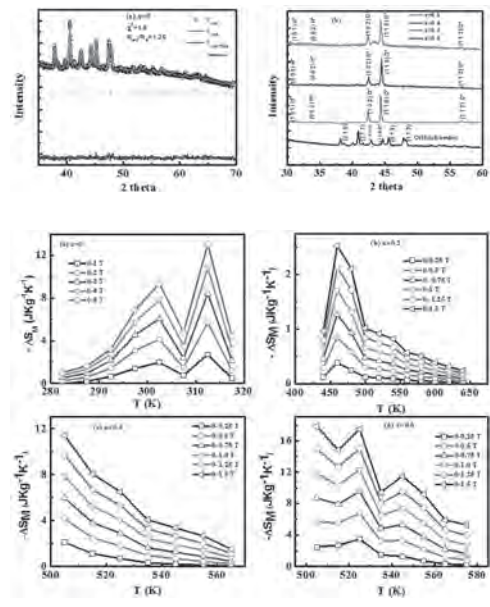
D. U^{1,3}, M. S² and V. C¹

1. Department of Nuclear Physics, University of Madras, Chennai, India; 2. Physics and Materials Chemistry Division, National Chemical Laboratory CSIR, Pune, India; 3. Department of Physics, Indian Institute of Science Education and Research, Pune, India

Abstract: We investigate on structure, surface morphology, magnetic and magnetocaloric properties of MnCo_{1-x}Sb_xGe (x=0, 0.2, 0.4, 0.6) alloys. The MnCoGe exhibits doublet-orthorhombic at ambient conditions, after substituting Sb in MnCoGe which are completely crystallized and form mixture of Orthorhombic and Hexagonal structure. The surface morphology of alloys are analyzed by viewing images which exhibits spherical and dumb-bell shape particles. The spherical shaped particles are enhanced with Sb doped samples. The magnetic properties are changed from martensitic-T_M (x=0) to Curie's transformations-T_C (x=0.2, 0.4, 0.6) of alloys. The T_c are enhanced with Sb doped samples in the order of 489.6 K, 519.1 K, 536.4 K which corresponding to x=0.2, 0.4, 0.6 alloys respectively. The change in magnetic entropy (ΔS_M) are calculated around transformation temperatures for these alloys from the isothermal [M (H)] curves for all samples. The (ΔS_M) values are 11.8, 2.5, 11.6, 16.1 JKg⁻¹K⁻¹ for x=0, 0.2, 0.4, 0.6 alloys respectively. However, gradual decreasing trend of MCE are observed in x=0.4, 0.6 alloys. These observations will be highly benefit applications for this class of magneto response materials which is used for magnetic refrigeration technology near room temperature. **Introduction:** The recent trends in magnetic materials are more emphasized in solid state cooling which are environmental friendly comparable to gas refrigeration. They are many materials exhibits magnetocaloric effect such as Ni-Mn-X (X=In, Ga, Sn, P). MnCOGe is regarded an excellent alternative magnetic refrigeration material by its outstanding magnetic, magnetocaloric properties [1-3]. It under goes structural transition at 420 K high temperature Ni₂In type hexagonal structure (space group P63/mmc) to low temperature orthorhombic structure (space group: Pnma). The Curie temperature (T_C) of hexagonal and orthorhombic structure are 275 and 345 K respectively [4-5]. The giant MCE observed in these alloys by adding interstitial impurities, changing composition and applying hydrostatic pressure. By doping Cu for MnCo_{1-x}Cu_xGe and large ΔS_M of 53.3 JKg⁻¹K⁻¹ is observed at 5T [6]. Further, more substitution of Nd for Mn [7] Zn for Co [8] Ga for Ge [9] and B (or) Cr into MnCoGe [10-11] also show the appreciable MCE with an excellent thermal and magnetic reversibility. In the present study, MnCo_{1-x}Sb_xGe (x=0, 0.2, 0.4, 0.6) alloys with various Sb contents are studied. Structural, Morphological, magnetic and magnetocaloric properties are discussed. We anticipate that can open up some possibilities for magnetic refrigerants for room temperature applications. **Experimental details:** The polycrystalline MnCo_{1-x}Sb_xGe (x=0, 0.2, 0.4, 0.6) alloys are prepared by arc melting stoichiometric amounts of Mn, Co, Ge and Sb (>99.95 wt%) in an argon arc furnace with 3% excess of Mn added to compensate for the mass loss of Mn during sample preparation. The ingot is re-melted five times to improve sample homogeneity. The quality of the sample and its crystallographic structure are studied by X-ray powder diffraction measurements at room temperature in glass substrate with Cu-Kα radiation. The orthorhombic and hexagonal structures are found to be present in the sample at ambient temperature as expected with no discernible impurity. The surface morphology of samples are captured and compositions are identified by Scanning Electron Microscope (SEM) attach with Energy Dispersive X-ray Analysis (EDAX) respectively. Temperature dependent magnetization measurements are performed for x=0 alloy in a constant magnetic field of 0.005 T from 10 to 320 K using a Quantum Design Magnetic Properties Measurement System (MPMS) with different (ZFC, FC, FW) modes and field dependence of magnetization (0-5-0 T) collected over the temperature range across the transition in 5 K interval steps. the magnetic measurements for remaining x=0.2,0.4,0.6 alloys are carried out by EG&G PAR 4500 vibrating sample magnetometer (VSM). The high-temperature measurements are done with an electrically heated oven attached to the VSM which can heated the sample up to 973 K. The field dependent magnetization are measured up to magnetic field of 1.5 T at ambient temperature using the VSM. the thermo-magnetization measurements are made by heating

the sample with heating rate of 2 K /minute in the presence of a constant magnetic field 0.001 T. The isothermal measurements are done using same instruments at constant temperature intervals. **Result and Discussion:** Structural studies: The phase confirmation of MnCoGe compound is illustrated by Rietveld refinement with double Orthorhombic phases are shown in Figure.1.1. The Orthorhombic phase-I has (S.G: Pnma, lattice parameters a=5.934, b=3.828, c=7.06, V=160.4 Å³ and Orthorhombic phase-II has (S.G: Pnma, lattice parameter: a=5.319, b=4.09, c=7.072, V=154Å³ which in match with existing reports [12].The phase fraction of Orthorhombic-I, II is seen to be are 89.6 and 10.4% respectively at room temperature. The figure.1.2 (a) reveals that powder X-ray pattern of MnCo_{1-x}Sb_xGe (x=0, 0.2, 0.4, 0.6) system. While, doping Sb in Co site of MnCoGe system exhibits Orthorhombic phase changes into mixed phase of Orthorhombic and Hexagonal. The phase and lattice parameters are significantly changed with Sb which are shown in figure. 1 (b). Calculation of MCE: Figure.5 (a, b, c, d): Temperature dependence of ΔS_M for MnCo_{1-x}Ni_xGe (x=0, 0.2, 0.4, 0.6) alloys at various magnetic fields (0-5 T). From the isothermal magnetization curves, magnetic entropy is calculated using Maxwell relation.

1. V. K Sharma, M. A. Manekar and S. B. Roy., *J. Phys. D: Appl. Phys.*, 49 50LT01 (2016). 2. L. Caron, Z. Ou and E. Bruck, *J. Mag. Magn. Mater.*, 321 3559 (2009). 3. U. Devarajan and Sunil Nair, *Mater. Res. Express.*, 6 106117 (2019). 4. D. Choudhury, T. Suzuki and Y. Taguchi, *Scientific Reports.*, 4 7544 (2014). 5. S.C. Ma, Y.X. Zheng, H.C. Yuan and Y.W. Du., *J. Magn. Magn. Mat.*, 324 135-139 (2012). 6. J. B. A. Hamer, R. Daou, S. Ozcan, N. D. Mathur, D. J. Fray and K. G. Sandeman, *J. Magn. Magn. Mater.*, 321 3535 (2009). 7. J. Shen, J.L. Zhao, F.X. Hu., *Appl. Phys. A Mater. Sci. Process.*, 99 853-858 (2011). 8. T. Krenke, E. Duman, M. Acet, *Nat. Mater.*, 4 450 (2005). 9. C. L. Zhang, H. F. Shi and E. J. Ye, *Appl. Phys. Lett.* 107 212403 (2015). 10. Ya Wei Li, Hu Zhang, Kun Tao, YiXu Wang, MeiLing Wu, Yi Long, *Materials and Design.*, 114 410-415 (2017). 11. Xiaodong Si, Yongsheng Liu, Xiaofei Lu, Wenli Wang, Wei Lei, Jia Lin, Tao Zhou, and Yan Xu, *J. Appl. Phys.* 119 215104 (2016).



JT-03. Magnetocaloric Effect in the Alloy $\text{Ni}_{45}\text{Mn}_{44}\text{In}_{11}$ Subjected to the Thermobaric Treatment.

S. Emelyanova¹, T. Dyachkova², A. Tyutyunnik², Y. Zainulin², E. Marchenkova¹ and V. Marchenkov^{1,3}

1. *Mikheev Institute of Metal Physics Ural Branch of the Russian Academy of Sciences, Ekaterinburg, Russian Federation;* 2. *Institute of Solid State Chemistry Ural'sky branches of the Russian Academy of Sciences, Ekaterinburg, Russian Federation;* 3. *Ural Federal University, Ekaterinburg, Russian Federation*

Recently so-called shape-memory ferromagnets based on Heusler alloys Ni-Mn-Z (Z = Ga, In, Sn, Sb) began to be considered as a promising materials for magnetic cooling technology. These alloys can exceed compounds with gadolinium in the value of the magnetocaloric effect (MCE) for magnetic field of the same magnitude, because the giant values of the MCE are achieved in them due to the structural transformation accompanying the magnetic transition. The electrical and magnetic properties of the alloy are closely related with the state of its microstructure, which can be changed using various methods of intense plastic deformation (e. g. equal channel angular pressing, intense torsional plastic deformation) or thermobaric treatment (TBT) which is the processing of materials under conditions of high temperature (up to 2000 K) and high quasi-hydrostatic pressure (up to 10 GPa). Ingots of $\text{Ni}_{45}\text{Mn}_{44}\text{In}_{11}$ alloy were prepared by arc melting in an inert atmosphere and subsequently subjected to annealing at 1100 K for 24 h followed by furnace cooling. The temperature dependence of the electrical resistivity $\rho(T)$ were measured by the standart method. The magnetic properties were measured using an MPMS XL7 (Quantum Design) SQUID magnetometer. The magnetic properties were measured in magnetic fields of up to 70 kOe in the temperature range 150-330 K. Thermobaric treatment has a significant effect on both electrical (changing the type of temperature dependence of electrical resistivity from “semiconductor” to “metallic”) and magnetic properties of the $\text{Ni}_{45}\text{Mn}_{44}\text{In}_{11}$ alloy. In addition, as a result of TBT, the maximum value of electrical resistivity increases in 1,7 times. Despite this the value of the entropy change ΔS before and after TBT practically was not changed ($\Delta S \approx 3.6 \text{ J}/(\text{kg}\cdot\text{K})$), but its maximum shifted along the temperature scale from 200 K to 300 K. The results of this work were obtained within the state assignment of Minobrnauki of Russia (theme “Spin” No. AAAA-A18-118020290104-2) and “New functional materials for promising technologies: synthesis, properties, spectroscopy and computer simulation” (No. AAAA-A19-119031890025-9), supported in part by the Government of Russian Federation (Decree No. 211, Contract No. 02.A03.21.0006).

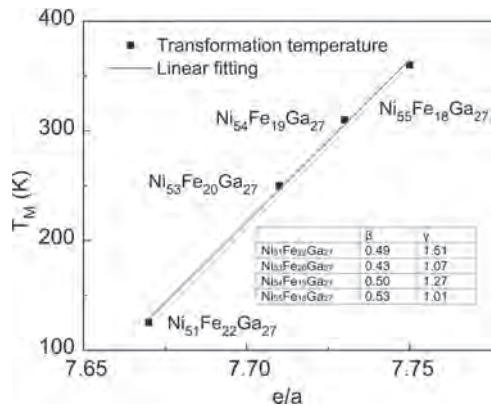
JT-04. Modified Arrott Plot and Critical Exponent Study on Series of Magnetocaloric Ni_2FeGa Based Heusler Glass-Coated Microwires.

M. Henne^{1,2}, L. Galdun^{1,3}, T. Ryba³ and R. Varga^{1,3}

1. CPM - TIP, Univerzita Pavla Jozefa Safarika v Kosiciach, Kosice, Slovakia; 2. Institute of physics, Univerzita Pavla Jozefa Safarika v Kosiciach, Kosice, Slovakia; 3. RVmagnetics, a. s., Košice, Slovakia

Heusler alloys are promising candidates for micro-magnetic cooling applications thanks to their desirable behavior. The possibility of tuning the structural transformation temperature by changing the stoichiometry of compounds is one of the most favorable properties in the presented group of alloys. Modulation of valence electron concentration ratio can be used to produce microwires with the required transformation temperature. Preparation by the Taylor-Ulitovsky technique allows easy and fast production of microwires with protective glass coating. In this work, Heusler alloys in the form of glass-coated microwires with different valence electron concentration ratio (e/a) are analyzed. The effect of e/a tuning on martensitic transformation temperature has been studied using indirect magnetocaloric measurements and their proper analysis. Modified Arrott plot and critical exponent analysis point to the fact that the series of Ni_2FeGa microwires belong to the same universality. Hence transformation temperature in this series of alloys has been estimated from transformation temperature vs. e/a dependence using the interpolation method. This research was supported by Slovak Grant Agency VEGA 1/0053/19, Slovak Grant Agency grant number APVV-16-0079.

V. Franco and A. Conde, International Journal of Refrigeration, Vol. 33(3), p. 465–473 (2010) A. Kharrat and W. Boujelben, Journal of Low Temperature Physics, Vol. 197, p. 357–378 (2019)



JT-05. Functional Heusler Nanowires.

L. Galdun¹, M. Varga^{1,2}, P. Szabo³, V. Vega⁴, V. Prida⁴ and R. Varga¹

1. CPM-TIP, Univerzita Pavla Jozefa Safarika v Kosiciach, Kosice, Slovakia; 2. Condensed matter physics, Univerzita Pavla Jozefa Safarika v Kosiciach, Kosice, Slovakia; 3. Institute of Experimental Physics, Slovenska Akademia Vied v Kosiciach, Kosice, Slovakia; 4. Universidad de Oviedo, Oviedo, Spain

Heusler alloys X_2YZ are well-known materials for their various properties which depend on their chemical composition and structure [1]. Their unique features such as shape memory effect, magnetocaloric effect, superconductivity, or spin polarisation have been observed and well described in the form of bulk, rapidly quenched ribbons, glass-coated microwires, or thin films [2]. Therefore, one fundamental question arises: whether the peculiar properties of Heusler alloys will also remain in the nanoscale? There are several technology areas that may be enhanced using Heusler alloys, especially in the field of spintronics, sensors and actuators, biological application based on hypo- or hyperthermia, or drug delivery [3]. The preparation of a large amount of Heusler alloys in the form of nanomaterials with a well-defined shape remains still a challenge. Here, one of the best possible methods consists of the fast and straightforward electrochemical approach [4-5]. With the presented template-assisted deposition using nanoporous anodic alumina membrane, it is possible to prepare a considerable amount (10^9 nanowires/cm²) of nanodisks or 1D nanowires with uniform morphology and chemical composition. Thanks to the possibility of co-deposition of various metals such as Fe, Co, Ni, Mn, In, Ga, Sn, etc., many types of ternary and quaternary Heusler alloys can be prepared via electrochemical deposition in the various form [6]. We present the possibility of the preparation of Heusler nanowires via electrochemical deposition in nanoporous anodic alumina template with well-defined shape and morphology. Depending on the chemical composition, the prepared Heusler nanowires show different physical properties such as high spin polarisation (Co₂FeZ based Heusler alloys) and magnetocaloric or shape memory effect (Ni₂FeZ-based). Electrodeposited Co₂FeSn nanowires with a diameter of 60 nm and length 10 μ m exhibit *B2* disordered phase, high curie temperature (>1000 K) and easy magnetization axis parallel to the nanowires axis. Point Contact Andreev Reflection spectroscopy (PCAR) performed with Nb superconductive tip revealed high spin polarisation up to 100 %. The presented approach allows the preparation of promising nano scaled Heusler alloys suitable for applications in spintronics or high-density magnetic data recording [7]. On the other hand, Ni₂FeGa-based Heusler alloys are well known as shape memory or magnetocaloric materials. Electrodeposited nanowires with a diameter of 60 nm and length of 7.5 μ m show unusual magnetic behavior which points to the structural transformation in the temperature range of 340-395 K. Magnetic nanowires with shape memory effect offer new opportunities in various areas of research such as drug delivery or nanorobotics. Template-assisted electrochemical deposition enables the preparation of a large amount of uniform Heusler nanowires with various chemical composition and related physical properties. Acknowledgments: This research was supported by Slovak Grant Agency VEGA 1/0053/19, Slovak Grant Agency grant number APVV-16-0079.

[1] T. Graf, C. Felser, S.S.P. Parkin, *Prog. Solid State Chem.*, 39, 1–50 (2011). [2] J. Alam, C. Bran, et al., *J. Magn. Magn. Mater.*, 513, 167074 (2020). [3] I. Koh, L. Josephson, *Sensors*, 9, 8130 (2009). [4] L. Galdun, et al., *ACS Appl. Nano Mater.*, 1 (12), 7066–7074 (2018). [5] S. Khan, et al., *J. Magn. Magn. Mater.*, 465, 462–470 (2018). [6] M. Sharma, et al. *AIP Advances*, 9, 125054 (2019). [7] L. Galdun et al., *ACS Appl. Nano Mater.*, 3, (8), 7438-7445 (2020).

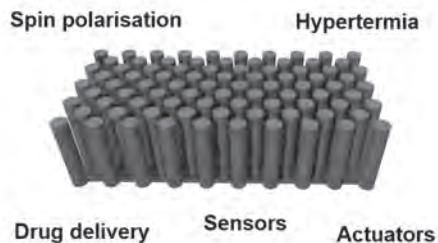


Figure 1, Representation of free-standing Heusler nanowires whose properties and application possibilities strongly depend on their chemical composition.

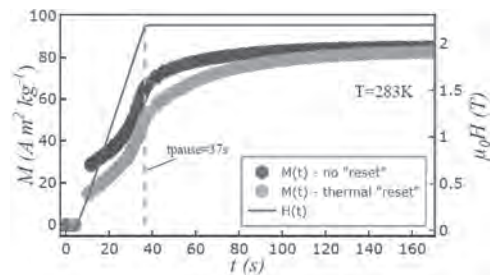
JT-06. Kinetics of First-Order Phase Transitions in Magnetocaloric Materials.

R. Almeida⁵, J.H. Belo⁵, R. Costa⁵, C. Amorim³, J.S. Amaral³, T. Del Rose⁴, Y. Mudryk⁴, V. Pecharsky^{4,6}, L. Pfeuffer¹, B. Beckmann¹, K. Skokov¹, O. Gutfleisch¹, E. Lovell², A. Pereira⁵ and J. Pedro Esteves de Araújo⁵
 1. Technical University of Darmstadt, Institute of Materials Science, Darmstadt, Germany; 2. Blackett Laboratory, Imperial College, London, London, United Kingdom; 3. CICECO-Aveiro Institute of Materials and Department of Physics University of Aveiro, Aveiro, Portugal; 4. The Ames Laboratory U.S. Department of Energy, Iowa State University, Ames, Ames, IA, United States; 5. IFIMUP Institute of Physics for Advanced Materials, Nanotechnology and Photonics, Physics and Astronomy Department, University of Porto, Porto, Portugal; 6. Department of Materials Science and Engineering, Iowa State University, Ames, Ames, IA, United States

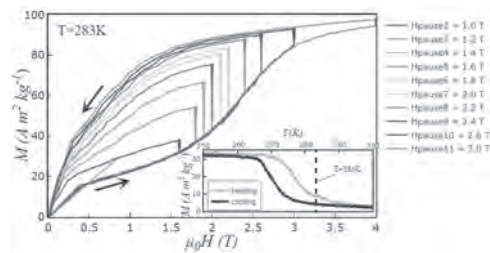
Materials with a giant magnetocaloric effect near ambient temperature have been a subject of intense investigation in the last 20 years due to their high technological potential as magnetic refrigerators or heat pumps, and as thermomagnetic regenerators for thermal energy harvesting¹. HVAC (heating, ventilation and air conditioning) technologies based on the magnetocaloric effect could lead to more environmentally friendly systems, due to higher energy efficiency and the lack of greenhouse gases¹. These materials are characterized by their strong spin-lattice coupling that manifests itself in first-order phase transitions (FOPT) during which the materials undergo simultaneous or closely coupled magnetic and structural transitions. These transitions may be controlled by extrinsic (temperature, magnetic field, pressure, time) and intrinsic (composition, morphology) parameters. In the referred applications, the devices require relatively high operating frequencies (of the order of 10 Hz) in order to maximize their efficiency. Such a technological requirement implies the utilized materials should complete their FOPT rapidly (for 10Hz operating frequencies, the FOPT timescale should be in the order of few milliseconds), however, unfortunately, there are relatively few studies dedicated to these materials transition kinetics²⁻⁸. From the few reports dedicated to this topic, the ones focused on the La-Fe-Si family stand out. In these, it has been shown that the shape and the interactions between particles influence the magnetic hysteresis and the time-scale of the transitions significantly⁴. In the Gd-Si-Ge family of materials, the Gd₅Ge₄ composition has been subject of relevant kinetic studies which unveiled its magnetic glass state and a kinetically arrested AFM-FM transition⁵. To our knowledge there is only one preliminary study for the Gd₅Si₂Ge₂ composition, where it has been shown that the FOPT transition can last up to 300 seconds to be completed - an impressively long time considering the required operating frequencies mentioned above⁶. Heusler alloys such as Ni-Mn-In exhibit a giant inverse-magnetocaloric effect along their AFM-PM transition, and display typically faster transition kinetics⁷. Our work will thus fit in an effort to shed light on the kinetics of the FOPTs which occur in these most prominent giant magnetocaloric material families. To accomplish this, we will thoroughly study the kinetics of FOPT, encompassing the magnetic transitions (through time-dependent SQUID measurements) and the (de) coupled structural transitions time-dependencies, their electron transport kinetics as a function of temperature, magnetic field, composition and microstructure and then attempt to theoretically model the observed phenomena. The growing surge of interest in these unusual transitions is not only due to the pursuit of application-ready materials, but also to attempt to provide answers to purely scientific questions such as how the transition kinetics of the different material families compare and how they change with different magnetovolume couplings and different morphologies (macro, micro and nanostructured). Bulk samples of the above mentioned materials families were produced and their single-phase nature, magnetic and structural properties were assessed via Scanning Electron Microscopy, SQUID magnetometry and X-ray Diffraction. As preliminary work, we have followed the time dependent magnetic field (SQUID) measurement protocol done in⁸ for a bulk (6x2.5x2 mm) Gd₅Si₂Ge₂ sample. We analyze the evolution of the magnetization of the sample through time, while subjected to initially increasing and then paused fields: the fields are increased with a constant sweep rate of 70 mT/s until a given H_{pause} value, which is maintained for 300 seconds. Not only is magnetic hysteresis detected, but also a significant difference is

observed between magnetization vs time curves obtained by two different measurement protocols: 1) a thermal “reset”, where in between measurements the sample is heated up to 45K above T_c=270K and cooled down again before the following measurement, and 2) no thermal “reset”, where the sample temperature is unchanged before subsequent measurements (see figure 1). In both, one can see once the field is stopped (at t=t_{pause}), the rate of increase of the magnetization slows down, but keeps evolving in time. We made measurements for different temperatures a few degrees above T_c (T=283K in the presented results) so that the sample begins in its paramagnetic state and the transition to the high magnetization state must be induced by the applied field. At the given temperature, the field is increased at 70 mT/s rate until a given field value is reached (H_{pause}) and the M(H) curves show a relaxation behavior - vertical lines in figure 2. As can be seen, the relaxation has non monotonous behaviour, increasing until a maximum at the critical field value around 2 T, and then decreasing again for higher H_{pauses}. The measurements followed protocol 1, where the relaxation is more significant.

- 1) V. Franco, J. S. Blázquez and J. J. Ipus, Prog. Mater. Sci. Vol. 93 p. 112–232 (2018) 2) V. Basso, M. Piazza and C. Bennati, Physica Status Solidi B Vol. 255, Issue 2 (2017) 3) A. Biswas, Y. Mudryk and A. K. Pathak, J. Appl. Phys. 126, 243902 (2019) 4) M. G. Zavareh, Y. Skourski and K. P. Skokov, Phys. Rev. Applied 8, 014037 (2017) 5) J. D. Moore, G. K. Perkins and K. Morrison, J. Phys.: Condens. Matter Vol. 20, 465212 (2008) 6) J. Leib, J. E. Snyder and T. A. Lograsso, J. Appl. Phys. 95, 6915 (2004) 7) L. Pfeuffer, T. Gottschall and T. Faske, Phys. Rev. Materials 4, 111401(R) (2020) 8) E. Lovell, A. M. Pereira and A. D. Caplin, Adv. Energy Mater. Vol. 5, Issue 6 (2015)



The evolution of the magnetization for a measurement with protocol 1) (M(t) - thermal “reset”) and another with protocol 2) (M(t) - no “reset”) and the applied field H(t) increasing at 70mT/s and pausing at H_{pause}=2.2 T.



The M vs H curves for different maximum paused fields, H_{pause}. In the inset, the M vs T curves (for constant field of 0.1 T) are shown. The vertical bar at 283K highlights the temperature at which the M vs H curves were obtained.

JT-07. Predicting the Performance of Magnetocaloric Heat Pumps Using Statistical Learning Algorithms.

D. Silva¹, J. Ventura¹ and J. Pedro Esteves de Araújo¹

1. Universidade do Porto Faculdade de Ciências, Porto, Portugal

The use of a significant share of consumed energy is dedicated to refrigeration and heating systems. Hence, innovating the current state of refrigeration and heating systems to improve their efficiencies is a critical challenge to be tackled, especially under the quest of global warming mitigation. Magnetocaloric (MC) systems are one of the most promising innovations, as their theoretical coefficient of performance (COP) is significantly larger than that of vapor-compression systems. MC systems rely on the reversible magnetocaloric effect where applying (or removing) magnetic fields (H) changes the thermodynamic state of the material in such a way that, in adiabatic processes, the temperature increases (or decreases) [1]. Although the development of magnetocaloric systems is now in a relatively mature phase, the geometrical and operating optimization is still a time consuming task. One way of optimizing a system is by predicting what are the performance values if using a set of geometrical and operating parameters. In that respect, the recent interest of artificial intelligence lead to the development of several statistical learning techniques and respective algorithm implementations [2]. These techniques have recently been used in a wide number of research fields. One specific class of statistical techniques concerns supervised learning, where regressors (or classifiers) are trained based on datasets with continuous (or boolean) output values [2]. In this work, different statistical learning regressors are applied, and critically compared, in predicting the three main performance values for a generic magnetocaloric heat pump: no load temperature span, heating power and COP [4]. Four different regressors were used: ordinary least squares (ols), ridge, lasso, and K-nearest neighbors (KNN). The used dataset was obtained with the recently developed heatrapy framework to compute caloric systems [5]. The minimum average relative error of the temperature span, heating power and COP were 23%, 29% and 31%, respectively, as can be seen in Fig. 1. The Lasso regressor shows the best performance with the order of the polynomials. The best order of polynomials range between 3, for the heating power, to 5, for the COP. The worse performance in predicting the three performance values occurs when using the KNN regressor. Furthermore, the application of regressors to the dataset is more adequate to evaluate the temperature span rather than energetic performance values.

[1] A. Kitanovski et al., Magnetocaloric Energy Conversion. Springer (2015). [2] C. M. Bishop, Pattern recognition and machine learning. Springer (2006). [3] C. Aprea et al., Int. J. Refrig. 82 (2017) 238. [4] D. J. Silva et al., Energy and AI, 2 (2020) 100030. [5] D. J. Silva et al., SoftwareX 7 (2018) 373.

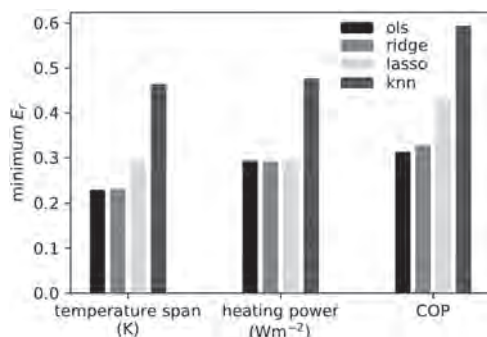


Figure 1: Minimum average relative error of the temperature span, heating power and COP for the different used regressors.

JT-08. High Efficient Magnetic Refrigeration Using Static Bias Magnetic Field.

H. Mamiya¹, N. Terada¹ and H. Kitazawa¹

1. Busshitsu Zairyo Kenkyu Kiko, Tsukuba, Japan

Magnetic refrigeration, which is a way to cool a matter with a magnetic field, was discovered more than 100 years ago. For the last several decades, the magnetic refrigeration has been intensively studied for possible application of refrigeration near room temperature. More recently, the magnetic refrigeration research field was also opened for low target temperature for the purpose of hydrogen liquefaction with condensation temperature of 20 Kelvin. However, in most of the studies, high magnetic fields, which is not lower than several Tesla, were necessarily used to obtain a large entropy change, leading to large energy costs to operate a superconducting magnet. Alternatively, we here propose high efficient cooling technique where small magnetic field changes superimposed on a static bias magnetic field can obtain one order magnitude higher cooling efficiency than the typical magnetocaloric materials. In the case of Ho, the cooling efficiency reaches $\Delta S_M/\Delta\mu_0H = -31 \text{ J kg}^{-1}\text{K}^{-1}\text{T}^{-1}$. The temperature range with high efficiency can be adjusted by varying the bias magnetic field. We hope that the presently provided small field controlled magnetic refrigeration technique will be a standard method, equipped with permanent magnets, for hydrogen liquefaction as an alternative to conventional gas compression-based cooling.

JT-09. Substitution of Fe by Ti and Mn in GdFeSi.

S. Platonov¹, A. Kuchin¹, A. Lukoyanov^{1,2}, A. Volegov^{1,2}, V. Gaviko^{1,2} and M. Yakovleva¹

1. Mikheev Institute of Metal Physics, Ekaterinburg, Russian Federation;
2. Ural Federal University, Ekaterinburg, Russian Federation

The RTX compounds, where R is a 4f-metal, T and X are d- and p-elements, exhibit various physicochemical properties and have potential for practical application [1]. The GdFeSi, GdTiSi and GdMnSi compounds crystallize into the same tetragonal CeFeSi ($P4/nmm$)-type structure [1,2]. This structure is composed of alternating (001) layers with the sequence: Gd-Si-T2-Si-Gd-Gd-Si-T2-Si-Gd (T = Fe, Co, Ti, Mn). This is why the exchange interactions between atoms Gd-Gd, Gd-T, T-T in GdTSi depend on the lattice parameter c , whereas interaction T-T depends on the lattice parameter a as well. The hybridization of Si p and T $3d$ states causes filling of the $3d$ band and results in the absence of magnetic moment of T = Fe or Co in the GdTSi compound [1-5]. Mn is a unique example of the $3d$ -transition metal T with a magnetic moment in the GdTSi compounds. Significant changes in the magnetic and structural parameters of these compounds were observed upon a mutual partial substitution of d-metals. In this work, the intermetallic compounds GdTi_{0.05}Fe_{0.95-x}Mn_xSi, $x=0-0.95$ with a tetragonal crystal structure of the CeFeSi ($P4/nmm$)-type have been studied. It is shown in Fig.1 that the lattice parameter c and the Curie temperature T_C increase, whereas the lattice parameter a is almost unchanged in the GdTi_{0.05}Fe_{0.95-x}Mn_xSi system when the concentration of Mn increases. The similar variations of the lattice parameters and T_C were earlier obtained for the GdFe_{1-x}Mn_xSi system [3], although c and T_C are noticeably smaller as compared with GdTi_{0.05}Fe_{0.95-x}Mn_xSi, whereas a is about the same. Hence, an increase of T_C in the systems is caused by short-range Mn-Mn exchange interactions in the basal plane, whereas higher T_C in GdTi_{0.05}Fe_{0.95-x}Mn_xSi is caused by stronger indirect exchange interactions Gd-Gd. The increase in the interatomic distances along the c axis due to large Ti substitution atoms should weaken the Gd-Gd, Gd-T and T-T exchange interactions and should decrease T_C in GdTi_{0.05}Fe_{0.95-x}Mn_xSi as compared with GdFe_{1-x}Mn_xSi. At the same time, the partial substitution of Ti for Fe or Mn decreases a number of the $3d$ "spin-down" electrons in the system, because Ti, Mn and Fe atoms have 2, 5 and 6 of the $3d$ electrons, respectively. As a result, a number of the $3d$ electrons with "spin up" non-compensated by the $3d$ electrons with "spin down" increases. Owing to this, indirect exchange interactions between Gd ions become stronger, because they are realized through polarization of the conduction electrons. The difference between the numbers of the $3d$ electrons for Ti (2) and Mn (5) or Fe (6) is less for the compositions $x > 0.5$, where the concentration of Mn prevails, than for the compositions $x < 0.5$, where the concentration of Fe prevails. As a result, T_C for GdTi_{0.05}Fe_{0.95-x}Mn_xSi exceeds T_C for GdFe_{1-x}Mn_xSi by 10-15 K for the compounds with $x > 0.5$ and by 50-70 K for the compounds with $x < 0.5$. Fig.2 shows that the saturation magnetization M_{sat} decreases non-monotonically in the GdTi_{0.05}Fe_{0.95-x}Mn_xSi system with a minimum at intermediate compositions. Usually, the R-T intermetallic compounds with a heavy rare earth element R are characterized by strong negative R-T exchange interaction [1]. From this point of view, one should expect the antiparallel arrangement of Gd and Mn moments and a linear decrease in magnetization in the GdTi_{0.05}Fe_{0.95-x}Mn_xSi system with an increase in Mn concentration. It is obvious that this model cannot explain the existence of the minimum on the dependence $M_{sat}(x)$. A similar change of $M_{sat}(x)$ with a minimum was published for the GdFe_{1-x}Mn_xSi system [4]. It was shown that the GdMnSi compound is characterized by strong exchange interactions inside the Gd and Mn subsystems and weaker Gd-Mn interaction, since the atoms of different types are stacked in isolated (001) layers [2,6]. As a result, a non-collinear ferrimagnetic structure is formed in GdMnSi in which the moments of Gd ions are oriented along the tetragonal axis of the compound and the moments of Mn ions are oriented at an angle to it. Apparently, a similar structure exists in the GdFe_{1-x}Mn_xSi and GdTi_{0.05}Fe_{0.95-x}Mn_xSi systems. Variations of Mn concentration or strength of external magnetic field can produce an essential change in the relative orientation of magnetic moments of the Gd and Mn sublattices and non-monotonic variation of $M_{sat}(x)$. The isothermal magnetic entropy change $-\Delta S_M$ (i.e. the magnetocaloric effect MCE) was calculated from the magnetization isotherms $M(H)$ using the well-known Maxwell

relation [1]. The peak value of $-\Delta S_M$ decreases with the appearance Mn in the GdTi_{0.05}Fe_{0.95-x}Mn_xSi system and varies within a narrow range of 1.2-1.6 J/kgK at 17 kOe field for all Mn contents. At the same time, T_C varies in a wide range around room temperature: from 220 to 360 K. Thus, the MCE of the GdTi_{0.05}Fe_{0.95-x}Mn_xSi compounds can be of practical interest. Acknowledgements Support by RSF (Project No. 18-72-10098) is acknowledged.

[1] S. Gupta and K.G. Suresh, J. Alloys Comp., Vol. 618, p.562 (2015) [2] R. Welter, G. Venturini and B. Malaman, J. Alloys Comp., Vol. 189, p.49 (1992) [3] S.A. Nikitin, T.I. Ivanova and I.A. Tskhadadze, J. Alloys Comp., Vol. 280, p.16 (1998) [4] S.A. Nikitin, T.I. Ivanova and I.A. Tskhadadze, Acta Phys. Pol., Vol. A 91, p.463 (1997) [5] M. Napolitano, F. Capera and P. Manfrinetti, J. Mater. Chem., Vol. 10, p.1663 (2000) [6] I.A. Ovtchenkova, S.A. Nikitin and T.I. Ivanova, J. Alloys Comp., Vol. 451, p.450 (2008)

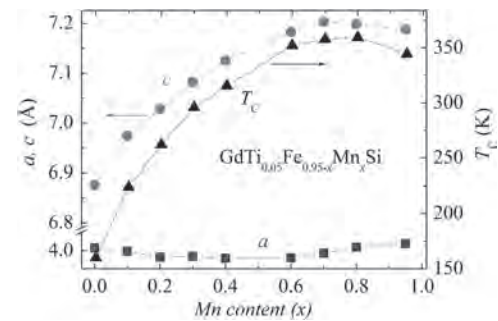


Fig.1. Dependences of the lattice parameters a (■) and c (●) and the Curie temperature T_C (Δ) of the GdTi_{0.05}Fe_{0.95-x}Mn_xSi compounds versus Mn content.

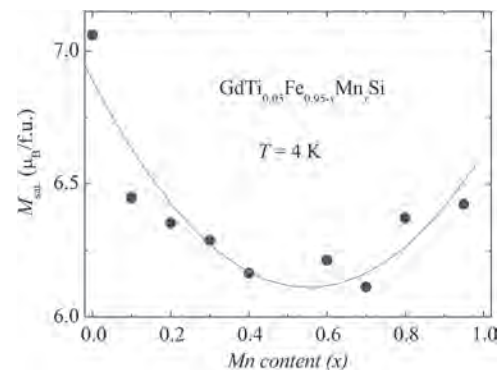


Fig.2. Concentration dependence of the saturation magnetization M_{sat} measured on free powder samples of the GdTi_{0.05}Fe_{0.95-x}Mn_xSi compounds at $T = 4$ K. Points (●) – experiment, line – interpolation.

JT-10. Breaking the Magnetic Symmetry by Reorientation Transition Near 50 K in Multiferroic, Magnetocaloric HoFeO₃.

A. Ovsianikov^{1,5}, H. Thoma², V. Hutanu¹, T. Chatterji³, P. Brown⁶, S. Barilo⁴, L. Peters¹ and O. Usmanov⁵

1. Rheinisch-Westfälische Technische Hochschule Aachen Institut für Kristallographie, Aachen, Germany; 2. Forschungszentrum Julich GmbH Julich Centre for Neutron Science, Julich, Germany; 3. Institut Laue-Langevin, Grenoble, France; 4. GO National Science and Practice Center Academy of Sciences of Belarus in Materials Science, Minsk, Belarus; 5. FGBU Petersburg Institute of Nuclear Physics, Gatchina, Russian Federation; 6. University of Cambridge, Cambridge, United Kingdom

HoFeO₃ is one of the most interesting representatives of the rare-earth orthoferrites RFeO₃ with orthorhombic structure possessing different useful for potential applications physical properties. Dzyaloshinskii-Moriya interaction (DMI) which leads to a weak ferromagnetic (WF) moment in the Fe sublattice, might play an essential role in their occurrence. A spontaneous electric polarization occurs in HoFeO₃ at ~ 210 K [1]. At lower temperatures, strong magneto-caloric effect makes the compound to a promising candidate for the magnetic cooling in the cryogenic gases liquefying technology. Three peaks in the entropy-change occur for field variation 0-7 T: ΔSM=9 J/Kg K at 53 K, ΔSM=15 J/Kg K at 10 K and ΔSM=18 J/Kg K at 3 K [2]. The first peak is associated with a spin reorientation in the Fe subsystems. Below 53 K the Fe sublattice starts to polarize the Ho. Thus, the second and third peaks should be associated with some processes related also to the Ho subsystem. The crystal structure of HoFeO₃ is described by space group Pbnm. Below 637 K, the Fe sublattice orders antiferromagnetic (AFM) along the a-axis, and WF moment along c-axis (magnetic phase Gm4). At zero field, the compound has two spin reorientation transitions: at 53 K where the Fe moments rotate from a to b-axis (magnetic phase Gm1) and at 35 K where the magnetic moments align almost along c-axis (magnetic phase Gm2). Ho orders at a temperature of 4 K [3]. Polarized Neutron diffraction (PND) experiments were performed at the Heinz Maier-Leibnitz Zentrum (Garching, Germany) on the diffractometer POLI [4]. The used instrumental setup with a 2.2 T cryogen-free, compact high-Tc superconducting magnet is presented in Ref. [5]. The evolution of the magnetic structure in HoFeO₃ with temperature and magnetic field in the range of 300-47 K and 0.15-2.2 T was investigated. In particular, the effect of the magnetic field on the reorientation transition from Gm4 to Gm1 symmetry, which takes place in zero field at 53 K, has been studied in detail. Originating from the mmm Laue class of HoFeO₃, the Bragg reflections to which the Fe sublattice contributes can be separated in four sets: F: (h + k even, l even), A: (h + k even, l odd), C: (h + k odd, l even) and G: (h + k odd, l odd). The asymmetry values $A = (I^{-} - I^{+}) / (I^{-} + I^{+})$ for 275 Bragg reflections were measured at 65 K. Here, I^{\pm} is the measured intensity for the two antiparallel spin orientations of the incoming neutron beam. Using these values, we could refine the precise orientation of the AFM moments in HoFeO₃ in the Gm4 phase (Fig. 1). Our results are in good agreement with the previously published structure at 70 K [6] but superior in details. To follow the magnetic phase transition explicitly, the asymmetries of 70 selected peaks (mostly of G-type) were measured in 2 K steps between 67-47 K. Below 53 K in the lowest field (0.15 T), the magnitude of the x-component of the Fe moment decreases abruptly whilst that of the y-component increases. This behavior is consistent with the reorientation transition to the Gm1 structure observed in zero field. Further increasing the applied field lowers the temperature of the transition, until it does not occur within the scanned temperature range for 2.2 T. However, an attempt to fit the intermediate phase (Fig. 1-2) as a linear combination of different volume fractions of Gm1 and Gm4 phases did not lead to a converging solution. In particular, the observed presence of significant asymmetry values for G type reflections below 53 K suggests, that the applied field may introduce some distortion of the purely AFM Gm1 structure. This is confirmed by the occurrence of a G-type z-component in the intermediate phase, which is forbidden in both Gm1 and Gm4. Taking also into account the occurrence of magnetic moments on the Ho positions, we can finally conclude that the observed intermediate state is a correlated phase with monoclinic symmetry. Additionally, in the Gm4 phase the magnetic field aligns the WF moment along its direction. This lifts the degeneracy between 180 degrees AFM domains, since the orientation of the AFM structure to the WF moment is

fixed by the DMI. Conversely, the sign of the DMI can be determined by the refined precise orientations of the AFM moments in the Gm4 phase from PND data (Fig. 2). By performing a proper averaging over the four Fe sublattices of the Gm4 structure, we could reduce the DMI interaction to two independent parameters D_{12} and D_{14} , pointing in y-direction. D_{nm} denotes the interaction of the Fe sublattice n to m, with sublattice notations from Ref. [6]. With this clear convention, positive signs for D_{12} and D_{14} could be deduced. Corresponding DMI and exchange interactions magnitudes were determined in our previous work by inelastic neutron scattering [7]. One may conclude that the competition between the external magnetic field, the DMI and the exchange interactions between different magnetic sublattices leads to a complex picture of phase transitions in rare-earth orthoferrites causes also their useful functionality.

1. K. Dey, A. Indra, S. Mukherjee, S. Majumdar, J. Stempfer, O. Fabelo, E. Mossou, T. Chatterji, and S. Giri. Phys. Rev. B 100, 214432 (2019)
2. M. Shao et al. / Solid State Communications 152 (2012)
3. T. Chatterji, M. Meven, P. J. Brown, AIP ADVANCES 7, 045106 (2017)
4. V. Hutanu, M. Meven, S. Masalovich, G. Heger, and G. Roth, J. Phys.: Conf. Ser. 294 12012 (2011)
5. H. Thoma, W. Lubertetter, J. Peters, and V. Hutanu, J. Appl. Cryst. 51 17-26 (2018)
6. T. Chatterji et al., J. Phys.: Condens. Matter 29 385802 (2017)
7. A.K. Ovsianikov, I.A. Zobkalo, W. Schmidt, S.N. Barilo, S.A. Guretskii, V. Hutanu, JMMM, Volume 507, 166855 (2020)

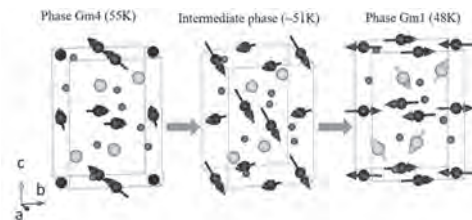


Fig.1: Magnetic structure evolution by the reorientation phase transition in HoFeO₃ near 50 K with magnetic field along [001]. An intermediate phase breaking orthorhombic symmetry occurs between the magnetic phases Gm4 and Gm1. Here: blue balls - Fe ions, green - Ho, red - O, colored arrows denote ordered magnetic moments.

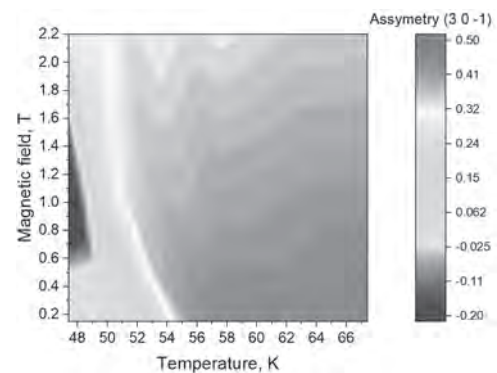


Fig. 2: Temperature/field map for the measured asymmetry of G-type peak (3 0 -1). Redish area denotes magnetic phase Gm4, blue - Gm1, celestial-greenish - intermediate monoclinic phase.

JT-11. Magnetocaloric Effect in $\text{Hf}_{1-x}\text{Ta}_x\text{Fe}_2\text{B}_z$.K. Matsumoto¹, K. Ishihara¹, J. Gouchi², Y. Uwatoko² and K. Hiraoka¹¹. Ehime University, Matsuyama, Japan; ². Institute for Solid State Physics, University of Tokyo, Kashiwa, Japan

Magnetic refrigeration based on magnetocaloric effect (MCE) is attractive cooling technology because of its high energy efficiency and environmental friendliness. MCE is defined as the changes in temperature and entropy by changing a magnetic field. Magnetic refrigeration for near room temperature needs the magnetocaloric materials with large magnetic entropy change (ΔS_m) near room temperature. $\text{Hf}_{1-x}\text{Ta}_x\text{Fe}_2$ crystallizes the hexagonal structure. The magnetism of $\text{Hf}_{1-x}\text{Ta}_x\text{Fe}_2$ changes by Ta substitution. For example, $\text{Hf}_{1-x}\text{Ta}_x\text{Fe}_2$ for $0.1 < x < 0.3$ shows the successive transitions from ferromagnetic order to antiferromagnetic order on cooling [1]. For $x=0.17$, large ΔS_m at 225 K is reported [2]. The magnetic transition temperature (T_M) decreases with applying pressure [3]. On the contrary, the volume expands by inserting the interstitial atom, T_M would be decrease. In this work, we study the B doping effect on the magnetic properties of $\text{Hf}_{1-x}\text{Ta}_x\text{Fe}_2$. The $\text{Hf}_{0.83}\text{Ta}_{0.17}\text{Fe}_2\text{B}_z$ ($z=0, 0.1$, and 0.5) alloys were synthesized by arc-melting under Ar atmosphere. The crystal structure was confirmed by the powder X-ray diffraction (XRD) technique. Magnetic properties were measured in the range of $150 \leq T \leq 270$ K up to 5 T. The XRD pattern of $\text{Hf}_{0.83}\text{Ta}_{0.17}\text{Fe}_2$ indicates a single phase as the hexagonal structure. For $z=0.1$, the minor phases as HfO_2 and HfB_2 were observed. For $z=0.5$, the intensity of the peak of HfB_2 phase increased and is comparable to those of $\text{Hf}_{0.83}\text{Ta}_{0.17}\text{Fe}_2$ phase. The scattering angles of $\text{Hf}_{0.83}\text{Ta}_{0.17}\text{Fe}_2$ shifted higher, indicating the volume shrinking. These results suggest that the unit cell volume decreased due to deficiency of Hf by forming HfB_2 in B-doped $\text{Hf}_{0.83}\text{Ta}_{0.17}\text{Fe}_2$. Figure 1 shows the temperature dependence of magnetization (M) of $\text{Hf}_{0.83}\text{Ta}_{0.17}\text{Fe}_2\text{B}_z$ ($z=0$ and 0.1) in a magnetic field of 0.1 T. For $z=0$, M increased suddenly at 215 K with decreasing temperature. The values of M for $z=0.1$ increased at 200 K. The obtained data indicate that the T_M decreased by B-doping. The result is consistent with the volume reduction. The maximum values of ΔS_m for $z=0$ and 0.1 are both 5 J/K kg, which is approximately one-third of the previously reported data [2]. In summary, introducing B into $\text{Hf}_{1-x}\text{Ta}_x\text{Fe}_2$, B elements reacted Hf atoms to form HfB_2 . The volume and T_M decreased due to the deficiency of Hf.

[1] Y. Nishihara and Y. Yamaguchi, J. Phys. Soc. Jpn. Vol. 51, p.1333 (1982). [2] J. F. Herbst, C. D. Fuerst and R. D. McMichael, J. Appl. Phys. Vol. 79, p.5998 (1996). [3] K. Hoshi, J. Phys. Soc. Jpn. Vol. 57-9, p.3112 (1988).

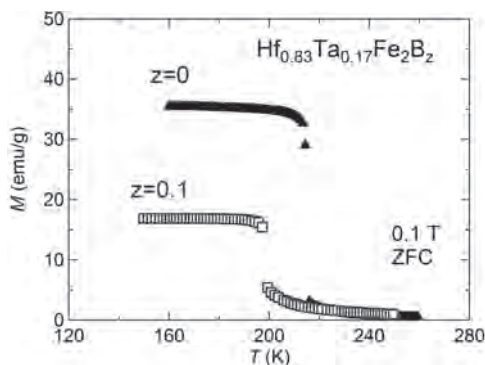


Fig. 1. Magnetization versus temperature of $\text{Hf}_{0.83}\text{Ta}_{0.17}\text{Fe}_2\text{B}_z$ ($z=0$ and 0.1) in a magnetic field of 0.1 T.

JT-12. Magnetocaloric Properties of Ball Milled Gd Powder Subjected to Heat Treatments.

A.V. Arkhipov¹, D.S. Neznakhin¹, S.V. Andreev¹, A. Larrañaga², G.V. Kurlyanskaya^{1,3} and A. Svalov¹

1. Institute of Natural Sciences and Mathematics, Ural Federal University, Ekaterinburg, Russian Federation; 2. Servicios Generales de Investigación, Universidad del País Vasco (UPV/EHU), Leioa, Spain; 3. Departamento de Electricidad y Electrónica, Universidad del País Vasco (UPV/EHU), Bilbao, Spain

One of the possible practical applications of magnetocaloric effect (MCE) is eco-friendly magnetic refrigeration [1]. A condition for the successful operation of a magnetic refrigerator is a high efficiency of heat transfer between the working body and the surroundings. This is facilitated by an increase in the surface to the volume ratio for the working body. The material in the form of powder meets this requirement [2]. Therefore, the features of MCE in powder samples are the subject of active research [3-5]. Ball milling is a well-established technique for producing different materials in powder shape. This process contributes to the reduction of the crystal size down to nanometric scales and the accumulation of defects in grain boundaries [6]. For magnetic materials, this causes a decrease in magnetization and slow change in magnetization near the phase transition temperature. This lowers the MCE [3]. On the other hand, nanostructuring causes the effect of a Curie temperature distribution. In turn it leads to a broadening of the peak of the temperature change of the magnetic entropy (ΔS_M) and an increase in a refrigeration capacity (RC) value, which can be defined as the product of the maximum value of the peak of magnetic entropy change and the width of ΔS_M peak at its half-height [1]. In addition, nanostructuring can enhance the field dependence of the magnetocaloric effect [5-7]. Appropriate annealing of polycrystalline materials can to some extent restore the perfection of their crystal structure and magnetization behavior, thereby establishing an advantageous balance between the height and width of ΔS_M peak, which determine the RC value [8]. In this work, we present the result of detailed study of influence of thermal treatment on structure, magnetic and magnetocaloric properties of Gd powder obtained by ball milling. Ball milling was performed with a mixer/mill using hardened-steel vials in acetone. Gd powder samples were annealed in vacuum at different temperatures up to 600 K. The structure of the samples was studied by X-ray diffraction technique using automatic PHILIPS X'PERT PRO diffractometer operating with Cu-K α radiation. The magnetic entropy change was calculated using the Maxwell relation follow the standard procedure [1]. The temperature dependence of the magnetic entropy change measured for Gd powder samples annealed at different temperature shows that ΔS_M peak is constricted in each case (Fig. 1). The value of the ΔS_M peak height and the RC values are decreased with the increase of the temperature (Fig. 2). Observed MCE behavior was understood taking into account the changes in the crystal structure including strain values and contribution of the partial surface oxidation as a result of the heat treatment. At the same time, heat treatment at the temperature of 500 K results in the shift of MCE peak exactly for the room temperature point that might be very useful for applications. This study was supported by the Ministry of Science and Higher Education of the Russian Federation (project No. FEUZ -2020-0051) and Elkartek AVANSITE grant of the Basque Government.

[1] V. Franco, J.S. Blázquez, J.J. Ipus, et al. Prog. Mater. Sci. 93 (2018) 112. [2] Q. Gao, B.F. Yu, C.F. Wang, et al. Int. J. Refrig. 29 (2006) 1274. [3] J.S. Blázquez, J.J. Ipus, L.M. Moreno-Ramírez, et al. Metall. Mater. Trans. E 2 (2015) 131. [4] S. Wolf, T.M. Riedemann, J. Barclay, et al. Powder Technol. 359 (2020) 331. [5] A.V. Svalov, A.V. Arkhipov, S.V. Andreev, et al. Mater. Lett. 284 (2021) 128921. [6] J.S. Blázquez, J.J. Ipus, L.M. Moreno-Ramírez, et al. J. Mater. Sci. 52 (2017) 11834. [7] D. Doblas, L.M. Moreno-Ramírez, V. Franco, et al. Mater. Design 114 (2017) 214. [8] S.V. Taskaev, V.D. Buchelnikov, A.P. Pellenen, et al. J. Appl. Phys. 113, (2013) 17A933.

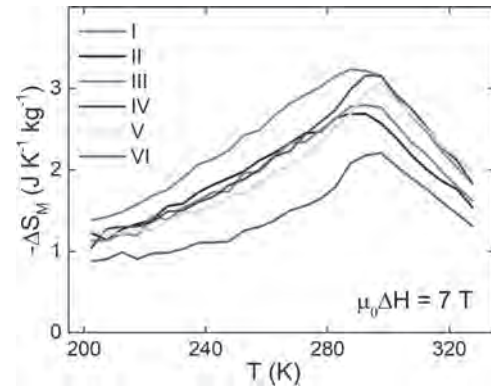


Fig 1. The magnetic entropy changes versus the temperature for Gd powder samples in initial state (curve I) and after annealing at different temperatures (curves II, III, IV, V and VI for 350 K, 450 K, 500 K, 550 K and 600 K, respectively). Magnetic field changes from 0 to 7 T.

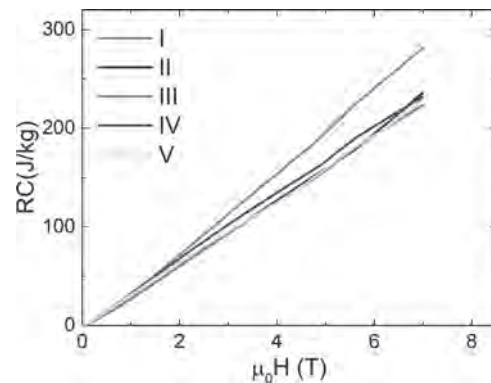


Fig 2. RC versus the magnetic field for Gd powder samples in initial state (curve I) and after annealing at different temperatures (curves II, III, IV and V for 350 K, 450 K, 500 K and 550 K, respectively).

JT-13. Magnetic and Transport Properties of Multicomponent Laves Phase Intermetallic Compound $Gd_{0.2}Tb_{0.2}Dy_{0.2}Ho_{0.2}Er_{0.2}Al_2$.

J. P. K¹, A. J², A. Nigam³ and N. R¹

1. Indian Institute of Technology Madras, Chennai, India; 2. DRDO Defence Metallurgical Research Laboratory, Hyderabad, India; 3. Tata Institute of Fundamental Research, Mumbai, India

Recent studies on multicomponent systems and high entropy alloys offer enormous motivation and scope to study the magnetic and magnetocaloric properties of a multicomponent Laves phase intermetallic compound, RA_2 , where R site is occupied by five equiatomic heavy rare earth elements [1]. Polycrystalline intermetallic compound $Gd_{0.2}Tb_{0.2}Dy_{0.2}Ho_{0.2}Er_{0.2}Al_2$ has been prepared by arc-melting under argon atmosphere and the single phase nature was confirmed by powder X-ray diffraction (XRD) study carried out at room temperature. DC magnetization has been measured in the temperature range of 2 K to 300 K in applied magnetic fields up to 70 kOe. Electrical resistivity, heat capacity and thermoelectric power have been measured as a function of temperature from 300 K to about 4 K. Magnetization data reveal that $Gd_{0.2}Tb_{0.2}Dy_{0.2}Ho_{0.2}Er_{0.2}Al_2$ compound orders ferromagnetically at ~ 80 K (T_C) [Fig. 1]. This ordering temperature is approximately equal to the mean value of the ferromagnetic ordering temperatures of the single rare earth component compounds $GdAl_2$, $TbAl_2$, $DyAl_2$, $HoAl_2$ and $ErAl_2$ respectively. The Arrot plots and the nature of the temperature variation of magnetization suggest second order nature for this transition at 80 K. In the present work, electrical resistivity, thermopower and specific heat of the title compound are studied. Electrical resistivity shows metallic behaviour and one does see an anomaly around T_C . Electrical resistance vs field is measured at a few selected temperatures in fields up to 50 kOe. A weak, negative magnetoresistance is observed below T_C . The heat capacity vs temperature plot shows a weak second order transition around 80 K. However, thermoelectric power did not register the magnetic anomaly strongly. The isothermal magnetic entropy change calculated using the magnetization-field data near T_C reveal a broad magnetocaloric effect around T_C , as one would expect for ferromagnetic material showing a second order transition. These results are compared with that of the individual heavy rare earth Laves phase dialuminides in order to understand the collective behavior of magnetic rare earth moments in such a multicomponent system. This along with the studies on high entropy alloys should pave a new way in the materials design for magnetics and magnetocalorics.

P. K. Jesla, J. Arout Chelvane, A. K. Nigam and R. Nirmala, AIP conference proceedings 2265 (2020) 030565

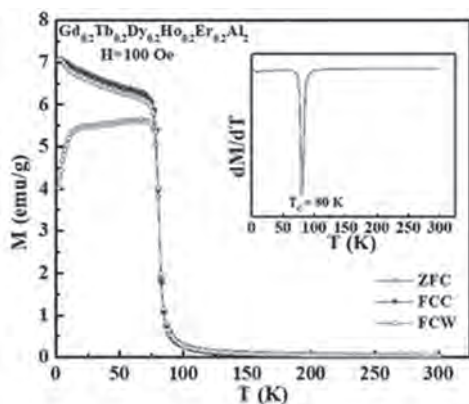


Fig. 1 Zero-field-cooled (ZFC) and field-cooled cooling and warming (FCC and FCW) Magnetization vs temperature data of $Gd_{0.2}Tb_{0.2}Dy_{0.2}Ho_{0.2}Er_{0.2}Al_2$ measured in 100 Oe field [Inset dM/dT vs T plot]

Session JU
MAGNETO-ELASTIC MATERIALS AND DEVICES
(Poster Session)

Dhritiman Bhattacharya, Chair
Georgetown University, Washington, DC, United States

JU-01. The Design and Output Characteristics of Ultrasonic Transducer Based on Rare-Earth Giant Magnetostrictive Material.

Y. Li¹, W. Huang² and B. Wang²

1. School of Electrical Engineering and Automation, Qilu University of Technology, Jinan, China; 2. State Key Laboratory of Reliability and Intelligence of Electrical Equipment, Hebei University of Technology, Tianjin, China

Abstract—A new type of rare-earth giant magnetostrictive transducer, working in ultrasonic frequencies, is designed by the structural dynamic model and the dynamic coupling model. Based on the vibration, wave and frequency equations, the structural dynamic model of the transducer is established. By using COMSOL Multiphysics software parametric design method, considering the influence of materials, shapes and dimensions on the output characteristics of the transducer, the optimum mechanical structure of the ultrasonic transducer is determined. The magnetic circuit structure is analyzed by the dynamic coupling model based on the Jiles-Atherton model, Maxwell's equations and magneto-mechanical coupling effect. The prototype of the ultrasonic transducer is fabricated. The relationship between the output characteristics and the frequency is studied. The results demonstrate that the ultrasonic transducer can work in the range of 18–22 kHz, and exhibits higher magneto-mechanical conversion efficiency at the frequency of 19.5 kHz. I. Introduction The rare-earth giant magnetostrictive transducer has the advantages of high power, large amplitude and high response speed and it can be used in the fields of accurate actuation and ultrasonic machining [1]. At present, the transducers used in ultrasonic applications are mainly piezoelectric ceramic transducer [2]. Compared with piezoelectric materials, rare-earth giant magnetostrictive material, Terfenol-D ($Tb_{0.7}Dy_{0.3}Fe_2$), has greater strain, smaller hysteresis, and lower saturation magnetic field. Wang designed a giant magnetostrictive transducer (GMT) with a resonant frequency of 2 kHz [3]. Karunanidhi designed a GMT. The resonant frequency was 3 kHz. The transducer with mechanical amplifier and permanent magnet biasing was designed and realized [4]. Sheykholeslami proposed an approach to design a GMT. The resonant frequency was 8.25 kHz. This approach can make the transducer have high mechanical quality factor [5]. Fang introduced a design and finite element analysis method of a GMT. The working frequency of the transducer is 15.2 kHz [6]. Karafi designed a new hybrid longitudinal–torsional GMT with a resonant frequency of 20.6 kHz. The output displacement of the transducer was $0.6 \mu\text{m}$ [7]. References [3]–[5] studied the design method and output characteristics at relatively lower frequency magnetostrictive transducers. Reference [7] designed the giant magnetostrictive ultrasonic transducers, but the output displacement is small. So, how to design and manufacture a rare-earth giant magnetostrictive transducer with large output displacement, working in ultrasonic frequencies, is still a crucial problem for the development of transducers. II. The magnetic circuit and mechanical structure design of the ultrasonic transducer The magnetic circuit design needs to improve the magnetic flux density of magnetostrictive rod and reduce losses of the magnetic circuit. Based on the Jiles-Atherton model, Maxwell's equations and magneto-mechanical coupling effect, the magnetostrictive rod, magnetic yoke and magnetic circuit structure of the ultrasonic transducer are designed. It is found that the magnetic circuit structure of two Terfenol-D rods with coils in series connection is more suitable for the ultrasonic transducer. The radius of the Terfenol-D rod is 7.5 mm, and the length is 102 mm. To reduce the effect of dynamic losses, the Terfenol-D rod is machined into 2 mm slices and glued together by epoxy resin. The width of the magnetic yoke is 16 mm and the length is 60 mm. Based on the vibration, wave and frequency equations, the structural dynamic model of the ultrasonic transducer is established. By using COMSOL Multiphysics software parametric design method, considering the influence of materials, shapes and dimensions on the output characteristics of the ultrasonic transducer, the optimum mechanical structure of the ultrasonic transducer is determined. The whole mechanical structure of the transducer is analyzed, and the resonant frequency of the transducer is obtained. A detailed and complete design scheme is given and the main body of the ultrasonic transducer consists of two Terfenol-D rods, driving coils, disc spring, adjusting nut, vibrating horn, magnetic yoke and shell, as shown in Fig.1. III. Experimental results The prototype of the ultrasonic transducer was fabricated. The relationship between the output characteristics and

the frequency is experimentally studied by using laser displacement sensor (LK-H008, KEYENCE). Output displacement amplitude versus frequency is shown in Fig.2. The amplitudes of exciting current are 1A and 2A. The frequencies are 16.5 kHz–22.5 kHz. The experimental results have obvious resonance peaks, and their changing tendencies are consistent. When $f < 19.5$ kHz, the amplitudes of vibration increase with increasing frequencies; When $f = 19.5$ kHz, the output amplitude reaches the maximum value, the amplitude reaches $6.07 \mu\text{m}$ at 1A and $9.46 \mu\text{m}$ at 2A exciting current respectively; When $f > 19.5$ kHz, the amplitudes of vibration decrease with frequency increasing. It can be seen that the measured resonant frequency is 19.5 kHz, and the resonant frequency almost does not change at the different applied magnetic field.

[1] J. J. Scheidler and V. M. Asnani, *Smart Materials and Structures*, vol. 26, p. 035057 (2017) [2] X. Wei, Y. Yang and W. Yao, *Sensors*, vol. 17, p. 2253, (2017) [3] W. Wang and P. J. Thomas, *Sensors and Actuators A: Physical*, vol. 263, p. 113, (2017) [4] S. Karunanidhi and M. Singaperumal, *Sensors and Actuators A: Physical*, vol. 157, p. 185, (2010) [5] M. R. Sheykholeslami, Y. Hojjat and S. Cinquemani, *Smart Structures & Systems*, vol. 17, p. 313, (2016) [6] S. Fang, Q. Zhang and H. Zhao, *Micromachines*, vol. 9, p. 98, (2018) [7] M. R. Karafi, Y. Hojjat and F. Sassani, *Smart Materials & Structures*, vol. 22, p. 065013, (2013)

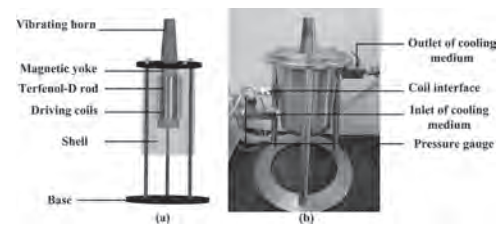


Fig.1 (a) Structure of the ultrasonic transducer (b) Prototype of the ultrasonic transducer

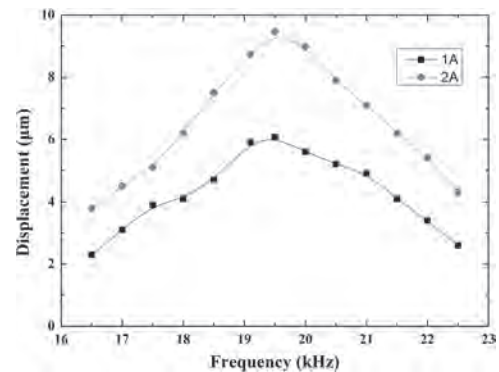


Fig.2 Output displacement amplitude versus frequency at different exciting current

JU-02. Structural and Magnetic Phase Transitions in $\text{Fe}_{100-x}\text{Al}_x$ Alloys: an *ab Initio* Studies.

A. Koshkin¹, M. Zagrebin¹, M. Matyunina¹, V. Sokolovskiy¹ and V. Buchelnikov¹

1. Celabin State University, Celyabinsk, Russian Federation

Fe-Al-based functional materials are a perspective for industrial application due to the unique combination of properties such as high strength, corrosion stability, low density, and low cost [1,2]. The right framework for such materials development is the knowledge of the binary Fe-Al phase diagram. The full concentration range was considered by Kubaschewski [3]. In this paper, experimentally observed phase transitions were studied for wide temperature ranges (200–1600°C). It is seen from this diagram that the most well-determined area is one above 500°C. While in the area below 500°C, phase boundaries are inexact. Different ways of sample preparation and measurements lead to different transition temperatures and phase coexistence areas [4-6]. It would be interesting to estimate structural and magnetic phase transition temperatures in the most questionable area of 10–30 at.% of Fe-Al with different structures. The present work is devoted to theoretical studies of the structural and magnetic phase transitions of binary $\text{Fe}_{100-x}\text{Al}_x$ ($15 \leq x \leq 25$ at.%) alloys with different crystal structures. To study the ground state and magnetic properties of $\text{Fe}_{100-x}\text{Al}_x$ ($15 \leq x \leq 25$ at.%), the Korringa-Kohn-Rostoker method was used as implemented in SPR-KKR [7] computational package. The geometry optimization was performed for crystal structures observed experimentally in Fe-Al alloys. These structures are ordered $D0_3$ (space group Fm-3m no. 225), partially disordered $B2$ (space group Pm-3m no. 221), and fully disordered $A2$ (space group Im-3m no. 229). The disorder in $D0_3$, $B2$, and $A2$ phases was produced with the coherent potential approximation. Computations were performed with the help of the spin-polarized scalar-relativistic Dirac-Hamiltonian in general gradient approximation in the form of Perdew-Burke-Ernzerhof [8]. According to the Birch-Murnaghan equation of state, the equilibrium lattice parameters a_0 and the total energies E_0 were evaluated for all considered phases. To obtain temperatures of the structural phase transitions the crude approximation $\Delta E \approx k_B T$ was used ($\Delta E = E_0 - E_{\min}$, E_{\min} is the energy of the favorable phase, k_B is the Boltzmann constant). Obtained optimized lattice constants were used for the exchange interaction parameters J_{ij} calculations. Using exchange interaction constants, we can estimate the Curie temperature T_C through the well-known Heisenberg model in the framework of MFA [9]. Let us further discuss the results of calculations for $\text{Fe}_{100-x}\text{Al}_x$ ($15 \leq x \leq 25$ at.%). Lattice constants of $A2$, $B2$, and $D0_3$ structures as a function of Al concentration are presented in Fig.1. It was found from the geometry optimization that lattice constants a_0 of $A2$ and $D0_3$ structures increase with the increasing Al concentration. While a_0 of the $B2$ phase does not demonstrate the dependence on Al content. It is also found from geometry optimization that the $D0_3$ structure is energetically favorable for the all considered concentration range. The energy difference relative to the energetically favorable structure allows us to obtain temperatures of the structural phase transitions. Estimated structural and magnetic phase transition temperatures allow us to construct the complex phase diagram for $\text{Fe}_{100-x}\text{Al}_x$ ($15 \leq x \leq 25$ at.%) depicted in Fig.2. Note, the structural phase transition temperature is the temperature, above which the corresponding phase exists. According to this diagram, depending on concentration, two areas with different phase transition sequences were determined. The first area of the phase diagram corresponds to Al concentration $15 \leq x \leq 20$ at.%. In this area, the magnetic transition from ferromagnetic (FM) to paramagnetic (PM) state is realized in the $A2$ crystal structure. The same sequence of phase transitions is experimentally observed for $\text{Fe}_{80}\text{Al}_{20}$ [6]. In the second area ($20 < x \leq 25$ at.%) magnetic phase transition is occurring in the $B2$ phase. It should be noted, that in considering the concentration range, temperatures of transitions to $B2$ and $A2$ structures increase with increasing Al concentration. At the same time, Curie temperature decreases with the increasing Al content. Based on these studies, it seems justified to conclude that the behavior of the phase transition temperatures is found to be in qualitative agreement with the available experimental diagram for $\text{Fe}_{100-x}\text{Al}_x$. To provide more accurate phase transition temperatures, which are taking place in $\text{Fe}_{100-x}\text{Al}_x$, finite temperature calculations should be performed. These calculations include electronic, vibrational, and magnetic excitations. In conclusion, it should be said that

$\text{Fe}_{100-x}\text{Al}_x$ might be promising for technological applications. This work was supported by the Ministry of Science and Higher Education of the Russian Federation within the framework of the Russian State Assignment under contract No. 075-00250-20-03.

[1] J.R. Knibloe, R.N. Wright, C.L. Trybus et al., *J Mater Sci.*, Vol. 28, p. 2040 (1993). [2] M. Johnson, D.E. Mikkola, P.A. March et al., *Wear*, Vol. 140, p. 279 (1990). [3] O. Kubaschewski. *Iron-binary phase diagrams*. Berlin: Springer-Verlag; 1982. [4] H. Okamoto (ed). *Phase diagrams of binary iron alloys*. Materials Park (OH): ASM International; 1993. [5] M. Palm, *Intermetallics*, Vol. 13, p. 1286 (2003). [6] O. Ikeda, I. Ohnuma, R. Kainuma et al., *Intermetallics*, Vol. 9, p. 755 (2001). [7] H. Ebert, D. Ködderitzsch, J. Minár, *Rep Prog Phys.*, Vol. 74, p. 096501 (2011). [8] J.P. Perdew, K. Burke, M. Ernzerhof, *Phys Rev Lett.*, Vol. 77, p. 3865 (1996). [9] P.W. Anderson, *Solid State Phys.*, Vol. 14, p. 99 (1963).

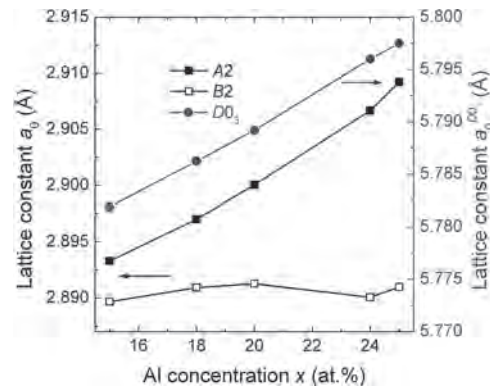


Fig.1. Lattice parameters a_0 (in Å) $A2$, $B2$, and $D0_3$ structures as a function of Al concentration.

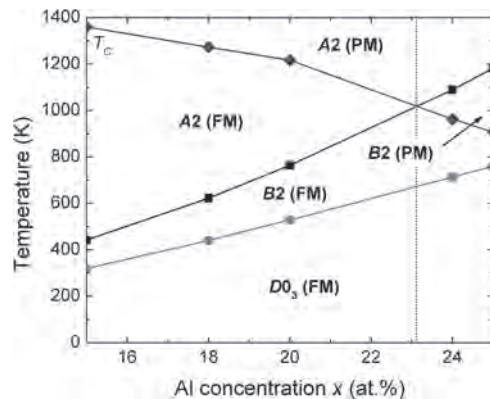


Fig.2. Phase diagram of the magnetic (T_C) and structural phase transition temperatures for $\text{Fe}_{100-x}\text{Al}_x$ ($15 \leq x \leq 25$ at.%).

JU-03. Effects of Geometrical and Physical Parameters on a Cantilever Beam Energy Harvester in Periodic Steady State Conditions.

V. Apicella¹, D. Davino¹ and C. Visone²

1. Dipartimento di Ingegneria, Università degli Studi del Sannio, Benevento, Italy; 2. DIETI - Dipartimento di Ingegneria Elettrica e Tecnologie dell'Informazione, Università degli Studi di Napoli Federico II, Napoli, Italy

Magneto-elastic beams in a cantilever configuration represents a quite common layout for a vibration energy harvester and its design is aimed to increase performances in terms of geometrical characteristic and power conversion [1-4]. Cantilever-like harvesters are employed when a quite constant vibration source is available, dealing to periodic steady state conditions. But the analysis of such a system is still a *multiphysics* problem, involving the mechanical deformation of the elastic body coupled with the electromagnetic problem through the magneto-elastic characteristics of the active material. In [1] and [4] the importance of cantilever's geometry has been outlined, showing the importance of the neutral axis location for the output power optimization, also providing [4] a qualitative analysis describing the phenomenon. In the same contribution, the focus was on the design and development of the harvester through an experimental analysis of several layouts. The effort was so addressed on the identification of the converted electrical source supplying the output electrical circuit by the standard tools of circuit's theory (Thevenin's theorem), which was designed to optimize load resistance and efficiency for the whole device. The modeling of the harvester as a magneto-mechanical converter requires more effort, e.g. coupling the beam's dynamics through the Euler-Bernoulli equation and the magneto-elastic characteristics of the beam. Despite interesting contributions exploiting 3-D FEM algorithms to describe the beam dynamics [3],[5],[6], in the present contribution attention is focused on the definition of a semi-coupled model where the mechanical behavior (in periodic steady state conditions) is taken into account through a model, described synthetically in Fig. 1b, and referred to the cantilever beam, described in Fig. 1a, supplied by a vertical sinusoidal acceleration on the left tip, in AC sinusoidal steady state, with amplitude a . The well-known solution (not provided for brevity) describes the behavior of the beam deformation $w(z,t)$ which provides the moment bending and therefore the longitudinal stress and the strain along the cantilever, [7] and, through the assumed linear magneto-elastic coupling of the magnetostrictive alloy, the flux linkage and the *emf* at the coil terminals, the as shown in Fig. 2. The detailed derivation of eqns. requires some algebra and will be detailed in the paper. The *emf* measured at coil's ends is related to the beam's deformation dynamics and to the cantilever's geometry. In particular, when the neutral axis is exactly in the middle of the magnetostrictive sheet ($x_1 = -x_2$) the total *emf* is zero. This result seems to fit with the experimental evidence of. In Fig. 2b where the output power on a 5.6Ω resistive load is plotted vs frequency, with $a = 1g, 2g, 3g, 4g$, for three different cantilever layouts. In the first one a magnetostrictive (Fe-Ga) lamination is "sandwiched" by two Al sheets (C2) and realizes a configuration with neutral axis at almost the middle of the active alloy. The second is conversely realized by an Al sheet "sandwiched" by two Fe-Ga laminations (C1), while in the last a single Al sheet is stucked to a Fe-Ga lamina (C3). In both C1 and C3 cases, the neutral axis lays outside the magnetostrictive laminas. All configurations share the same two bias magnets on the upper side of the cantilever. In linear assumptions, the RMS power in the plot is proportional to ε^2 and according to the model shows a much lower converted power of C2 case with respect to other configurations. An accurate analysis on the influence of geometric and physical parameters of the cantilever by the proposed modeling will be discussed in the paper. Such plot confirms that a simplified magnetostrictive cantilever's modeling could provide information on the parameters that impact the harvester design and represents a simple but effective generalization of [4]. Further, without significative effort, a natural introduction of a nonlinear magneto-elastic behavior could be plugged in.

[1] T. Ueno, S. Yamada, Performance of energy harvester using iron-gallium alloy in free vibration, IEEE Trans. Magn. 47 (10) (2011) 2407–2409. [2] J.-H. Yoo, A.B. Flatau, A bending-mode Galfenol electric power harvester, J. Intell. Mater. Syst. Struct. 23 (6) (2012) 647–654. [3]

Z. Deng, M.J. Dapino, Modeling and design of Galfenol unimorph energy harvesters, Smart Mater. Struct. 24 (12) (2015) 125019. [4] V. Apicella, C. S. Clemente, D. Davino, D. Leone, C. Visone, Magneto-mechanical optimization and analysis of a magnetostrictive cantilever beam for energy harvesting, J. of Magnetism and Magnetic Materials, 475, (2019), 401–407. [5] Mojtaba Ghodsi, Hamidreza Ziaiefar, Morteza Mohammadzahari, Amur Al-Yahmed, Modeling and characterization of permenur cantilever beam for energy harvesting, Energy, 176 (2019), 561–569. [6] M. Borowiec, A. Syta, G. Litak, Energy Harvesting Optimizing with a Magnetostrictive Cantilever Beam System, International Journal of Structural Stability and Dynamics Vol. 19, No. 05, 1941002 (2019). [7] S. H. Crandall, Mechanics of Solids, McGraw-Hill, Third Edition.

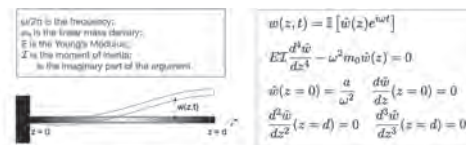


Figure 1. a) Sketch of the cantilever beam and its parameters. b) Model for the Euler-Bernoulli equation in AC conditions.

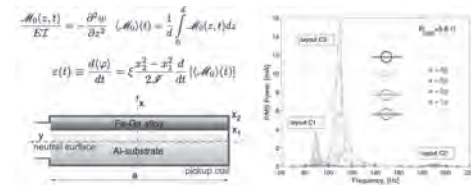


Figure 2. a) Cross section of the cantilever. b) Output power vs. frequency in different harvester's layout

JU-04. Improvement of Gyration Effects by Dysprosium Doping in Spinel Ferrite/Piezoelectric Magnetolectric Gytrators.

J. Zhang¹, Z. Wang¹, Q. Zhang¹, H. Zhao¹, K. Li¹, J. Liu¹, G. Bingfeng¹ and L. Cao²

1. College of Electrical and Information Engineering, Zhengzhou University of Light Industry, Zhengzhou, China; 2. International Education College, Zhengzhou University of Light Industry, Zhengzhou, China

As a single solid element, the magnetolectric (ME) gytrator has verified Tellegen's conjecture about the gytrator. In recent years, a number of attempts have been made to reduce losses in the energy conversion process. It is well known that the properties of spinel ferrites are dependent on such as composition, cation substitutions. A small contents of rare earth doping can modify the magnetic and magnetostrictive properties by replacing the tetrahedral (A) or octahedral (B) sites, which is beneficent to ME coupling¹. It has been reported that Dy elements possess high magnetocrystalline anisotropy due to the strong anisotropy of the 4f electron cloud, thus inducing strong magnetostriction². However, due to the high loss in the energy conversion process of the pure spinel ferrite ME gytrator, it is necessary to improve the ability of energy capture by means of the change of magnetic properties caused by Dy³⁺ doping. Therefore, the research on the improvement of gyration properties caused by high magnetostriction induced by Dy³⁺ doped ferrite has been initiated. Here, a variety of ME gytrators composed of nickel zinc ferrite and piezoelectric ceramic under various Dy³⁺ concentration were fabricated with coil around it and systematically characterized of magnetic properties, dynamic piezomagnetic coefficient, resonance ME response, V/I-I/V conversion ratio and power conversion efficiency, and each stage involved in the magneto-mechanical-electric energy conversion process under influences of Dy³⁺ concentration was clarified. Fig.1 shows the V/I conversion spectra of the ME gytrators with frequency, applied field and Dy³⁺ concentration, respectively. It can be clearly seen that under the resonant frequency and optimal bias, the maximum V/I of 1610 V/A occurring at sample with x=0.04 while the minimum of 998 V/A occurring at the one with x=0. Compared with pure spinel ferrite, the conversion effect of the ME gytrators is improved by 161% by Dy³⁺ doping. The experimental results attributed to the strong ME coupling is caused by the high magnetocrystalline anisotropy of Dy³⁺. Therefore, it can be concluded that Dy³⁺ doping reduces the loss in the energy conversion process of ME gytrator and promotes the improvement of gyration properties. Consequently, the high gyration properties of ME gytrator has important potential application for miniaturized V/I converters for power electronics.

¹ A. Anwar, S. Zulfiqar, and M. A. Yousuf, Journal of Materials Research and Technology-Jmr&T. Vol. 9, p.5313-5325 (2020) ² T. Y. Jin, W. Wu, and C. B. Jiang, Scripta Materialia. Vol. 74, p.100-103 (2014)

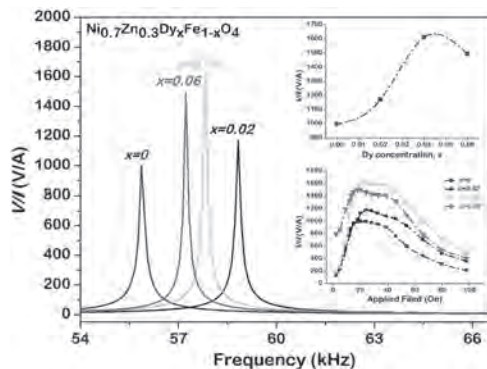


Fig.1 V/I conversion of the ME gytrators with different Dy³⁺ concentrations under optimal bias in the frequency range of 54kHz-66kHz. The insets are the V/I as a function of the Dy³⁺ concentration and Applied Field respectively.

JU-05. A Dual-Output Magnetolectric Energy Harvester in Ferrite/ Piezoelectric Toroidal Magnetolectric Composites.

J. Zhang¹, G. Bingfeng¹, J. Liu¹, Z. Wang¹, H. Zhao¹, K. Li¹ and Q. Zhang¹
 1. College of Electrical and Information Engineering, Zhengzhou University of Light Industry, Zhengzhou, China

In recent years, energy harvester around power lines have received widely attention due to the convenient power supply for monitoring devices around power lines such as vibration and conductor temperature sensors, fault diagnosis and prediction devices, intelligent sensor monitoring devices *etc.* Generally, energy harvested from near power lines includes solar energy, wind energy, sound energy, vibration and magnetic field, and so on. In terms of reliability and stability, energy harvesting using magnetic fields has been reported as optimum mode to provide energy to monitoring devices around power lines. Compared to solar and wind energy sources, magnetic field energy is almost unaffected by the environment or weather conditions. Traditional magnetic energy harvesters are the best represented by electromagnetic induction energy harvesters. While featuring low cost and wide applicability, these electromagnetic induction energy harvesters are generally limited by large volume, heavy weight and low output power density^[1]. The recent development of magnetolectric (ME) materials enables novel electromagnetic devices. The ME energy harvester are composed of ME composites that show many excellent advantages, such as low cost, small volume perfect and high output power density^[2]. These advantages offer the potential of ME energy harvesters to be a new generation of magnetic energy harvesters. Over the past decade, considerable reports have been published using ME materials to realize magnetic energy harvest. Previous investigations have focused on ME laminates whose piezoelectric/magnetostrictive layers are some simple configurations of disk, square, or rectangular shapes. However, for harvesting the magnetic energy around power lines, these geometries cannot make full use of the magnetic energy. In this case, the ME sample best geometry is the toroidal configuration. It is thus desirable to develop ME energy harvester with toroidal configuration, along with high output power density. This paper is on a high power density, dual-output ME energy harvester. It consisted of strictly concentric ferrites/piezoelectric rings with toroidal solenoid wound around that was operated in C-C mode. The electrode lead of the piezoelectric ring is port 1 and the coil lead is port 2 forming dual port. The ferrite in the collector senses the alternating magnetic field and transforms it into circumferential dynamic strain, which is transferred to the piezoelectric ring and finally output in the form of voltage from port 1. At the same time, according to the principle of electromagnetic induction, due to the existence of closed loop alternating magnetic field, the coil will produce induced electromotive force and output in the form of voltage from part 2. This dual-output ME energy harvester can ample harvest of the magnetic field energy produced by power lines and offer unique possibilities for possible use of ME energy harvester.

[1] J. Ryu, J. Kang, and Y. Zhou, Energy & Environmental Science. Vol. 7, P.2402-2408 (2015) [2] D. Zhao, N. Han, Energy Convers Manage. Vol. 178, p.311-21 (2018)

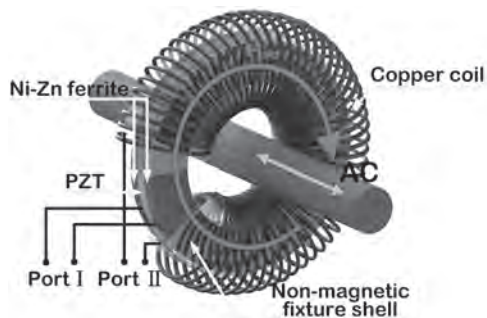


Fig.1. Schematic diagram of the presented dual-output magnetolectric energy harvester

JU-06. Magnetic Properties of FeGa on Rigid and Flexible Substrates.G. Pradhan^{1,2}, M. Coisson¹, F. Celegato¹, G. Barrera¹ and P. Tiberto¹¹. Istituto Nazionale di Ricerca Metrologica, Torino, Italy; ². Department of Chemistry, Università degli Studi di Torino, Torino, Italy

Magnetostrictive materials possess the potential to be used in wide variety applications such as sensing, straintronic, spintronic devices etc due to the coupling between the strain and the magnetization. In this context, FeGa which has a very high magnetostrictive constant, high tensile strength and low coercivity proves to be an efficient material for current research. Commercial producibility of FeGa is cheaper and easier compared to the rare earth alloy families since it does not include any rare earth elements. Fe_{100-x}Ga_x with x = 19% has the highest magnetostriction constant with a value of around $3/2 \times \lambda_{100} = 400$ ppm [1]. A thin film with this composition is attributed to the formation of next-nearest-neighbours (NNN) Ga-Ga pairs along [100] directions which leads to the formation of ordered D0₃ lattice structure [2]. In our report, we characterized the magnetic properties of Fe₇₀Ga₃₀ deposited on Si/SiO₂ substrate (rigid material) and Kapton substrate (flexible material) by measuring room-temperature hysteresis loops by AGFM and MFM characterisation as a function of magnetic field. The magnetic hysteresis behaviour is quite different for Fe₇₀Ga₃₀ sputtered Si/SiO₂ and Kapton as shown in Fig. 1(a, b). The coercive field obtained for Fe₇₀Ga₃₀/Kapton is approximately 20 times higher than that of Fe₇₀Ga₃₀/SiO₂/Si. This can be referred to the interface induced strain which results in higher anisotropy for Fe₇₀Ga₃₀/Kapton. MFM results reveal linear stripe domains for the both Fe₇₀Ga₃₀/SiO₂/Si and Fe₇₀Ga₃₀/Kapton shown in Fig. 1(c, d). The periodicity of domains is higher for the samples on Kapton due to high anisotropy. The substrate induced effect largely changes the properties of FeGa. We further try to measure the properties of Fe₈₁Ga₁₉ deposited on both Si/SiO₂ and Kapton for comparison. The dependence of strain percentage with magnetic anisotropy will be studied for Fe₈₁Ga₁₉/Kapton.

[1] A. E. Clark et al. *Journal of Applied Physics* 93, 8621 (2003). [2] H. Yangkun et al. *Adv. Funct. Mater.* 28 (20) 1800858 (2018).

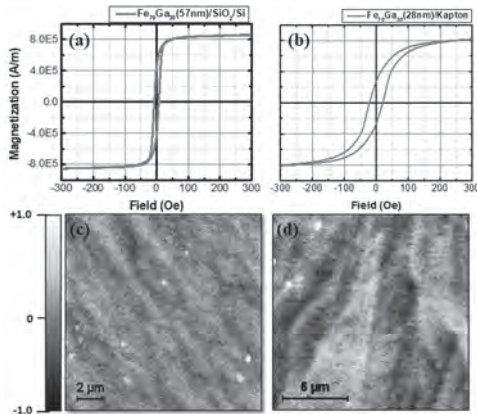


Fig. 1 Hysteresis loops and MFM domain patterns of Fe₇₀Ga₃₀/SiO₂/Si (a, c) and Fe₇₀Ga₃₀/Kapton (b, d), respectively.

JU-07. High-Frequency Losses Calculating Model for Magnetostrictive Materials Considering Variable DC Bias.

P. Guo¹, W. Huang¹, W. Guo¹ and L. Weng¹

1. Hebei University of Technology School of Electrical Engineering, Tianjin, China

Under high-frequency excitation, the large magnetic energy losses of magnetostrictive materials have limited the output characteristic of the magnetostrictive transducer [1]. Many magnetostrictive transducers are usually operated under DC bias to eliminate the frequency doubling effect and optimize the output performance. Based on the Steinmetz losses model, Ref. [2] proposed an improved total iron losses model considering DC bias, however, the separated losses compositions were not explored. Ref. [3] established a separated core losses model with the DC pre-magnetization, however, the model is more suitable for rectangular excitation and it was not about the giant magnetostrictive materials. Ref. [4] measured the magnetic energy losses on Terfenol-D material at different frequency f and peak flux magnetic density B_m , variable coefficients separated losses model without biased magnetic field had been shown. However, the effect of DC bias on magnetic energy losses of Terfenol-D cannot be ignored due to the max losses deviation will reach 27.6% when $f=10$ kHz and $B_m = 0.06$ T by losses measuring. Therefore, it is not suitable to use the losses model of an unbiased magnetic field to predict the operation condition with a bias magnetic field. On this basis, an improved magnetic energy losses separation model on giant magnetostrictive materials considering DC bias excitation at high-frequency is emphatically studied here. In this paper, according to the actual operation conditions, a kind of high-frequency losses testing system for magnetostrictive materials under DC bias is built. The dynamic hysteresis loops of Terfenol-D samples at different magnetic frequencies and exciting magnetic densities are studied experimentally under the condition of variable DC bias excitation. The total magnetic energy losses are obtained from these dynamic hysteresis loops aimed to provide the data basis for the establishment of a high-frequency magnetic energy losses model. The three-variables magnetic energy loss matrix is established by these measured data. Based on the Bertotti losses separation theory, the high-frequency losses calculating model of magnetostrictive materials considering variable DC bias excitation is established by using the algorithm of Levenberg-Marquard and the method of matrix transformation. In this model, according to the multivariate parametric regression, the losses coefficients are modified by introducing DC bias-related terms. The comparison of computed and experimental data of losses at different operating conditions are compared and analyzed. By comparing the experimental data, it is proved that the computed results in this proposed model are in good agreement with the experimental results. Based on the built dynamic magnetic characteristic testing system, the dynamic hysteresis loops of Terfenol-D samples at different f (1 kHz~20 kHz), B_m (0.01 T~0.06 T), and H_{dc} (0 A/m~5000 A/m) can be measured. And the trend of hysteresis loops varying with different DC bias excitation can be shown in Fig.1. It can be seen that the dynamic hysteresis loops will be seriously distorted and asymmetric when the different DC bias applied. This phenomenon is caused by the increase of the magnetization working point and the change of the relative permeability of the material. And the losses can be computed based on the measured hysteresis loops. Using the proposed variable coefficients losses model, the losses could be separated into magnetic hysteresis, eddy-current, and anomalous losses. In fig.2, the bar graphs of the losses changing with DC bias frequency are obtained. The magnetic energy losses decrease with the DC bias. When the $f=15$ kHz and $B_m=0.05$ T, the measured losses change from 513.74 W/kg to 409.022 W/kg with the DC bias changing from 0 to 5000 A/m. Based measured losses matrix and the method of multivariate parametric regression, an improved losses separation model is proposed to calculate the losses components when the Terfenol-D samples under DC bias excitation. The computed losses in this proposed model have high accuracy over the measured results (average percentage error<5.6%). It shows that the suitable DC bias can decrease the losses for the magnetostrictive materials. This research could provide significant theoretical guidance and experimental data support for the giant magnetostrictive device structure optimization and thermal analysis at high-frequency excitation.

[1] Rudd, Jonathan, Myers, et al. Experimental fabrication and nondestructive testing of carbon fiber beams for delaminations using embedded Terfenol-D particles. Journal of intelligent material systems and structures, 29(4):600-609 (2018). [2] W. Chen, X. Huang, S. Cao, et al. Predicting Iron Losses in Soft Magnetic Materials Under DC Bias Conditions Based on Steinmetz Premagnetization Graph. IEEE Transactions on Magnetics, 52, (7):1-4 (2016) [3] Y. Zhou and Q. Chen, Predicting core losses under the DC bias based on the separation model, IEEE Journal of Emerging and Selected Topics in Power Electronics 5, 833 (2017). [4] W. M. Huang, X. Q. Wu, and P. P. Guo, Variable Coefficient Magnetic Energy Losses Calculation Model for Giant Magnetostrictive Materials, IEEE Transactions on Magnetics, Aug.2020. DOI: 10.1109/TMAG.2020.3013393, 2020.

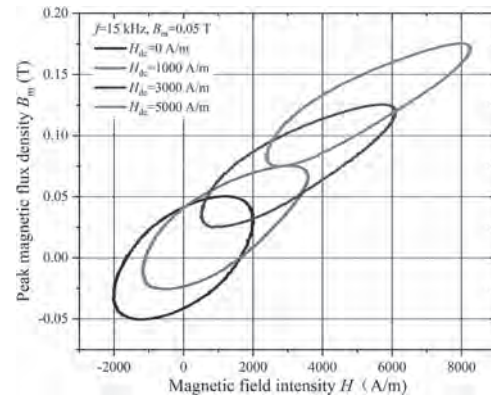


Fig.1. Measured dynamic hysteresis loops at different DC bias excitation)

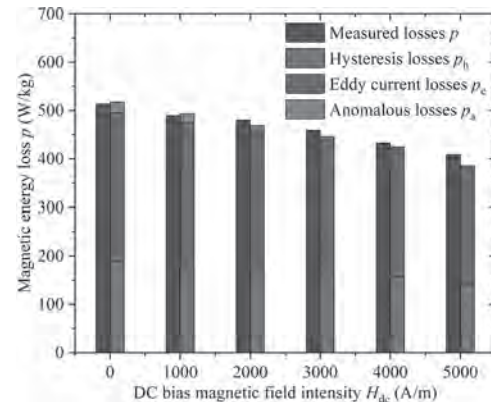


Fig.2 Calculated loss components and measured values with different DC bias ($f=15$ kHz, $B_m=0.05$ T)

JU-08. High Frequency Characteristic Test and Loss Calculation of TbDyFe Alloy Under Variable Temperature.

W. Huang¹, Z. Xia¹ and P. Guo¹

1. Hebei University of Technology, Tianjin, China

The giant magnetostrictive material TbDyFe alloy is considered to be an ideal material for making the core drive components of high-power, high-frequency magnetostrictive transducers. It has the characteristics of fast output response and large output displacement. Under high-frequency excitation conditions, the accurate calculation of TbDyFe alloy magnetic energy loss is a major and difficult point, and it is also an important step in the design of high-power magnetostrictive devices. Reference [1] improves the traditional loss separation formula based on high-frequency loss test data of TbDyFe alloy. Reference [2] analyzed the dynamic magnetic characteristic parameters of the TbDyFe alloy laminations, and conducted an in-depth study on the loss mechanism in the high frequency range. The above studies all assume that the temperature of the sample remains unchanged, but in actual work, the magnetostrictive transducer will produce serious hysteresis loss, eddy current loss and coil copper loss under high-frequency excitation, which will change the temperature distribute of the device. Considering the temperature-sensitive characteristics of TbDyFe alloy [3], the novelty of this article is mainly to study the change trend of the magnetic properties and loss characteristics of TbDyFe alloy at different temperatures. On the basis of the existing research, a temperature-controllable high-frequency magnetic characteristic test platform is built with AMH-1M-S dynamic magnetic characteristic tester and temperature box, so as to obtain the dynamic magnetic characteristic curve and loss of TbDyFe alloy at different temperatures. When the magnetic density amplitude and frequency are constant, the dynamic hysteresis loop of the sample at different temperatures is shown in Figure 1. As the temperature increases, the dynamic hysteresis loop narrows laterally, the required magnetic field strength decreases, and the coercive force gradually decreases. When the magnetic density amplitude is constant, the magnetic loss of the sample at different temperatures at different frequencies is shown in Figure 2. In the classic Bertotti loss separation model, the loss is a binary function of the magnetization frequency f and the magnetic density amplitude B_m . The formula assumes that under a fixed magnetization condition, no matter what the temperature of the sample is, the calculation results of the loss model will not change, which is obviously inconsistent with the experimental results. At the same time, because the TbDyFe alloy is significantly affected by the eddy current skin effect and dynamic hysteresis under high frequency conditions, the loss coefficient is no longer constant. Hence, the traditional calculation method is no longer accurate and must be improved. In order to solve the above problems, a high-frequency loss calculation model of magnetostrictive materials under variable temperature conditions is proposed. The model corrects the loss coefficient by introducing temperature-related terms. In addition, considering the effects of high-frequency hysteresis characteristics and skin effect, a loss-added magnetic flux density term and loss-added frequency term are introduced. The hysteresis, eddy current and residual loss coefficients k_h , k_c and k_a are all regarded as ternary functions of $\Delta T, f, B_m$. Combining the experimental test data, analyze the influence weights of the three free variables of temperature, frequency and magnetic density amplitude on the loss coefficient through curve fitting, and obtain the changes of hysteresis loss, eddy current loss and residual loss with $\Delta T, f, B_m$. Thus an improved loss calculation model that can effectively consider the temperature effect is established. The results show that the calculation method can accurately calculate the high-frequency magnetic energy loss of magnetostrictive materials under variable temperature conditions. The average error between the calculated value and the measured value is 2.29%.

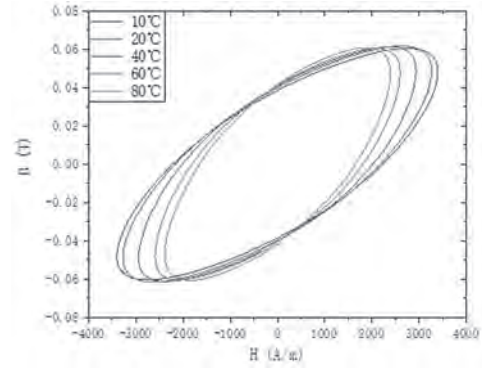


Fig.1. Dynamic hysteresis loop at different temperatures ($f=10\text{kHz}$, $B_m=0.06\text{T}$)

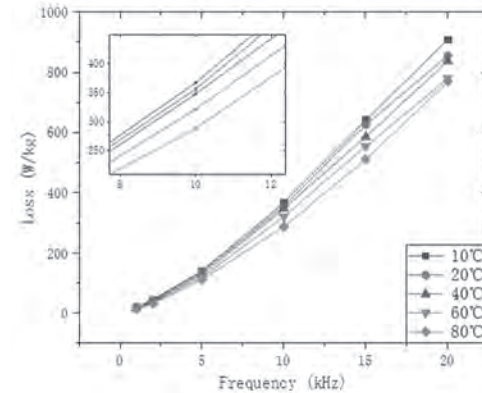


Fig.2. Variation of loss with frequency at different temperatures ($B_m=0.05\text{T}$)

[1] W. M. Huang, C.Y. Gao, et al. Experimental and Calculating Analysis of High Frequency Magnetic Energy Losses for Terfenol-D Magnetostrictive Material. IEEE Trans. Magn, 99 (2018): 1-4. [2] W. M. Huang, X.Q. Wu, et al. Analysis of high frequency dynamic magnetic characteristics and loss characteristics of TbDyFe alloy[J]. Chinese Journal of Scientific Instrument, 2020, 41(01): 215-222. [3] Jin K, Kou Y, et al. A nonlinear magneto-thermo-elastic coupled hysteretic constitutive model for magnetostrictive alloys[J]. Journal of Magnetism & Magnetic Materials, 2012, 324(12):1954-1961.

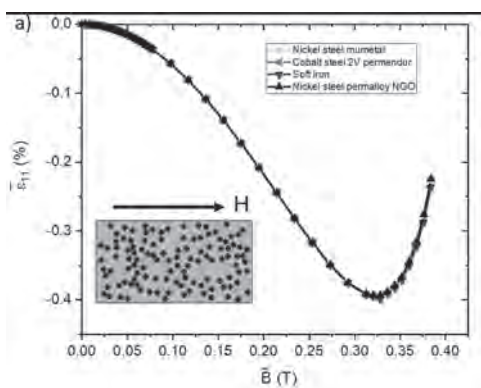
JU-09. Effective Magneto-Deformation Behavior of Soft Magnetically Susceptible Elastomer Composites.

W.M. Kiarie¹, D. Sitarski² and D.C. Jiles^{3,1}

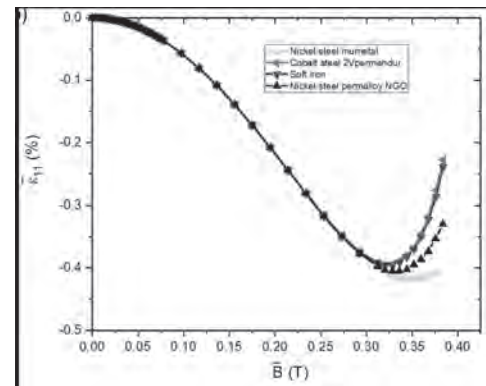
1. *Materials Science and Engineering, Iowa State University, Ames, IA, United States*; 2. *Aerospace Engineering, Iowa State University, Ames, IA, United States*; 3. *Electrical and Computer Engineering, Iowa State University, Ames, IA, United States*

We report on an investigation of the effect of different types of magnetic particles on the effective magneto-induced strain behavior of magnetorheological elastomers (MREs). MREs are composites consisting of magnetically permeable particles dispersed in a nonmagnetic polymeric matrix [1]. Under the action of an externally applied magnetic field, a large deformation change occurs in these materials [2]. Such deformation changes the mechanical properties of these materials. This is often attributed to the magnetic interaction among the magnetic filler particles [3]. In this study, we determined the effect of different types of magnetic filler particles on the effective magneto-induced strain of these materials. Four types of magnetic particles including nickel steel mumetal, nickel steel permalloy nongrain oriented (NGO), soft iron (without losses), and cobalt iron 2V permendur were selected from the computational software COMSOL Multiphysics magnetic materials library. With the assumption of constant shape and size for the selected particles, microscale modeling using a finite element analysis (FEA) based on continuum field theory was used in the study of the macroscopic behavior of the MREs. Without the simplifying assumption of magnetic dipoles, the magnetic and mechanical behavior was resolved by considering the polymer matrix and magnetic fillers as continua of distinct material properties. A suitable computational homogenization scheme [4] was used to relate the microscopic behavior to the composite's effective macroscopic properties. Here, both linear and nonlinear magnetic constitutive relationships were considered. The simulations were performed for isotropic microstructures with a constant particle-volume fraction ($\phi \approx 20\%$) and varying magnetic fillers. From the analysis, only a small change is observed in the effective magneto-induced strain (ϵ) parallel (ϵ_{11}) and transverse (ϵ_{22}) to the direction of the applied magnetic field for the different magnetic particles, particularly in the effective smaller magnetic flux density ($B < 0.3\text{T}$) region as shown in Figs. 1 (a) and (b). As seen from Figs. 1 (a) and (b) at higher $B > 0.3\text{T}$, a reversal in the magneto-induced deformation which for the nonlinear magnetization significant differences in magneto-induced strain for the different magnetic particles is observed. This can be attributed to saturation magnetization effects in this region.

[1] W. M. Kiarie, E. J. Barron, A. P. S. Baghel, I. C. Nlebedim, M. D. Bartlett and D. C. Jiles, *IEEE Transactions on Magnetics*, doi: 10.1109/TMAG.2020.3024878. [2] D. Borin, G. Stepanov, and P. Storozhenko, *Polymers (Basel)*, vol. 12, no. 10, pp. 1–25, 2020. [3] M. R. Jolly, J. D. Carlson, and B. C. Muñoz, *Smart Mater. Struct.*, vol. 5, no. 5, pp. 607–614, 1996. [4] C. Spieler, M. Kästner, J. Goldmann, J. Brummund, and V. Ulbricht, *Acta Mech.*, vol. 224, no. 11, pp. 2453–2469, 2013.



Effective magneto-induced strain behavior for isotropic MRE with particle-volume fraction ($\phi \approx 20\%$) and varying magnetic particles assuming a) linear



b) nonlinear magnetization.

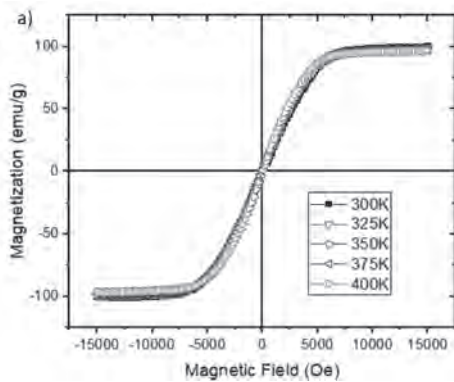
JU-10. Temperature-Dependent Magnetic Properties of Magnetorheological Elastomers.

W.M. Kiarie¹, K. Gandha², I.C. Nlebedim² and D.C. Jiles^{3,1}

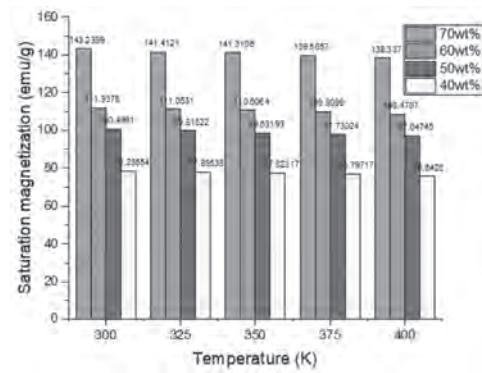
1. *Materials Science and Engineering, Iowa State University, Ames, IA, United States*; 2. *Critical Materials Institute, Ames Laboratory, Ames, IA, United States*; 3. *Electrical and Computer Engineering, Iowa State University, Ames, IA, United States*

We report on an investigation of the temperature-dependent magnetic properties of magnetorheological elastomers (MREs). These are a class of composites that consist of magnetically permeable particles dispersed in a nonmagnetic polymeric matrix [1,2]. When subjected to an external magnetic field, a large deformation occurs altering the mechanical properties of these materials. Due to their magnetoelastic coupling response, these materials are finding increasing interest among the scientific community. The performance of these polymer-based composites depends on many factors [3,4], which temperature is one of the biggest influencing factors requiring further investigations. In this work, the magnetic properties of isotropic polyurethane-based MRE with varying iron (Fe) particle loading fractions (40, 50, 60 and 70% by weight) were investigated under different temperatures. From the analysis, the magnetization response of these materials is observed to almost overlap for all the measured temperature values as shown in Fig. 1a. Although, zooming in the saturation magnetization is observed to decrease with an increase in temperature (See Fig. 1a). Figure 1b shows the saturation magnetization for varying temperature and particle loading fractions. Generally, ~ 3% decrement in the saturation magnetization is obtained for each of the loading fraction between the lowest (300K) and the highest (400K) measured temperature. Hence, as it can be seen the magnetization response of these materials is only slightly sensitive to temperature changes. This can be attributed to the measured temperature being below the curie temperature (T_c) of Fe. Further, the magnetization response is observed to increase with the increase in the particle loading fraction (See Fig. 1b).

[1] Bastola A K and Hossain M 2020 *Compos. Part B* 108348 [2] W. M. Kiarie, E. J. Barron, A. P. S. Baghel and D. C. Jiles, *IEEE Transactions on Magnetics*, doi: 10.1109/TMAG.2020.3024878. [3] Kallio M 2005 *The elastic and damping properties of magnetorheological elastomers* [4] Jin Q, Xu Y G, Di Y and Fan H 2015 *Mater. Sci. Forum* 809–810 757–63



a) Magnetization curve for 50wt. % iron in polyurethane for different temperatures



b) Saturation magnetization for varying temperature and particle loading fraction

JU-11. Measurement of Built-in Magnetic Anisotropy After Load Cycle for Polymer Composite Embedded Magnetostrictive Particles.

J. Yoo¹, N. Jones¹, A.J. Hall² and M.D. Coatney²

1. Naval Surface Warfare Center Carderock Division, West Bethesda, MD, United States; 2. Vehicle Technology Directorate, US Army Research Laboratory, Aberdeen Proving Ground, MD, United States

Composite materials, in the form of laminated and polymer matrix composites, are being increasingly used in manned and unmanned vessels and aircraft structures mainly due to their high strength and high stiffness to weight ratios. Composite structures are susceptible to degradation due to prolonged use, exposure to severe service environments, fatigue, sand abrasion as well as operator abuse, and neglect. This degradation increases the risk of operation and the cost of maintenance. Over the last two decades, progress has been made in structural state awareness using various sensing techniques such as acoustic emission, eddy current, and ultrasonic pitch hatch to diagnose damage and predict remaining life of the composite. Despite this progress, reliable detection and quantification of composite damage, particularly in the early stage, has remained a major challenge. Structural damage may be considered as a process that compromises the integrity of a structure. Delamination and cracking, two of the most common safety concerns of airframe structures, propagate rather slowly in the early stage but grow at a much faster rate in the later stage. Since early stage damage is not detectable using current technologies, it may be possible that by the time this damage is detected, the remaining life of a structure or its capacity has been severely degraded. The objective of this study is to show the feasibility of early stage damage detection utilizing embedding magnetic particles (Terfenol-D powder, a magnetostrictive material) into the composite structure, which is affected by the compressive stress surrounding them. Magnetostrictive materials exhibit dimensional changes in response to external magnetic fields. The inverse is also true; magnetization changes due to applied external stresses. When a composite material is cured, the particles are brought into compression due to shrinking of the resin, which provides a localized magnetic response. In this study, Terfenol-D ($Tb_{0.3}Dy_{0.7}Fe_{1.92}$) was embedded between layers of a composite structure. A laminated panel, 8 inches by 8 inches, was fabricated from thirteen 0.01 inch thick unidirectional plies of a pre-impregnated AS4/3501-6 carbon/epoxy material system. The panel was pressed in an aluminum mold and cured in autoclave at 175 °C under vacuum pressure for about 3.5 hours. The Rectangular panels were cut to a nominal size of 8 inch by 1-inch tensile specimens. A pair of tapered fiber glass tabs was attached at both ends of the rectangular specimens in accordance with the ASTM standard D-3039/D3479. Figure 1(a) shows the test specimen and a disk cut out of the specimen for built-in anisotropy measurement using a VSM (Vibrating Sample Magnetometer). The specimen was then subjected to a quasi-static load up to 70% of the UTS (ultimate tensile strength/ultimate tensile stress to failure). Figure 1(b) shows the magnetization measurement within the VSM system and shows the reference measurement angle for the built-in anisotropy. Figure 2 shows the magnetization results for the different measurement angles, showing the built-in anisotropy before (2a) and after (2b) the load cycle. Following unidirectional loading, the sample clearly shows a change in built-in anisotropy. The slope of the hysteresis loop is now dependent upon angle, demonstrating a possible way to detect early stage damage using magnetostrictive particles embedded in a composite structure. Additionally, it appears to also provide information on the major load direction.

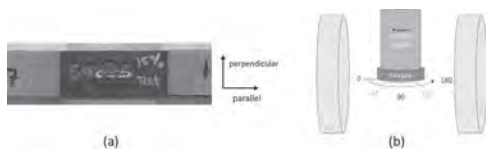


Figure 1. (a) Tensile test specimen and a disk cut for magnetic characterization out of the Terfenol-D powder embedded composite panel. (b) Schematic of the magnetization measurement angle with respect to the tensile specimen loading direction.

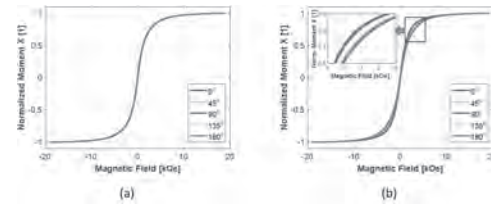


Figure 2. Magnetic hysteresis loop measurement of the Terfenol-D embedded composite panel measured (a) before loading, and (b) after loading to 70% of UTS (Ultimate Tensile Strength).

JU-12. Enhanced Power and Energy Conversion of Magnetolectric Laminate Heterostructures Based on High-Permeability FeCuNbSiB Nanocrystalline.

L. Liu¹, J. Qiu¹, Y. Huang¹, Q. Chang¹ and H. Liu¹

1. Chongqing University College of Optoelectronic Engineering, Chongqing, China

In recent years, magnetolectric composite materials have received more attention in the field of energy and power conversion. Many kinds of research have been devoted to improving magnetolectric composite materials for energy and power conversions, including transformers, energy harvesters, and ME gyrators [1]. However, numerous researches are mainly focused on how to maximize the power conversion efficiency. Studies have shown that the bias magnetic field has an important effect on many types of magnetolectric composite materials. And the bias magnetic field also affects the energy conversion characteristics [2]. Generally, the power conversion efficiency of piezoelectric materials is defined as the ratio of output electrical power to input mechanical energy. Correspondingly, the energy conversion process of ME composites introduces the influence of magnetoelastic energy [3]. The efficiency of the entire energy conversion is affected by the process of converting magnetic field energy into mechanical energy and mechanical energy into electrical energy. Therefore, we have introduced nanocrystalline FeCuNbSiB as a functional layer in the magnetolectric composite material to converge the space magnetic field energy with its extremely high magnetic permeability. The introduction of this functional layer reducing the bias magnetic field demand of the composite material and improving the energy conversion efficiency. Fig. 1 shows the effect of different layers of FeCuNbSiB on the magnetolectric voltage coefficient of the Galfenol-PZT laminate structure. It can be observed that after the introduction of multilayer FeCuNbSiB, the optimal magnetic bias of the magnetolectric composite material is reduced from 200 Oe to 110 Oe. This optimal bias reduction is due to the introduction of the high magnetic permeability layer has a certain convergence effect on the magnetic field. Fig. 2 shows the influence of the frequency of the alternating magnetic field on the magnetolectric voltage coefficient after the FeCuNbSiB layer is introduced. The test of energy conversion efficiency shows that the power conversion efficiency of the magnetolectric composite material is increased by 8.7% under the optimal load resistance and the optimal bias magnetic field. A series of results show that the introduction of high-permeability layers can significantly improve the magnetic deflection characteristics of the magnetolectric composite material and increase its power conversion efficiency.

[1] C. Q. Zhao, M. J. PourhosseiniAsl and S. Dong, Journal of Physics D: Applied Physics., Vol. 51, p.243001(2018). [2] Z. Xin, C.M. Leung and J. Li, IEEE Transactions on Industrial Electronics., Vol. 66, 2499-2505(2018). [3] Z. Xin, M. Gao and X. Tang, IEEE Sensors Journal., Vol. 20, p.752-759(2020).

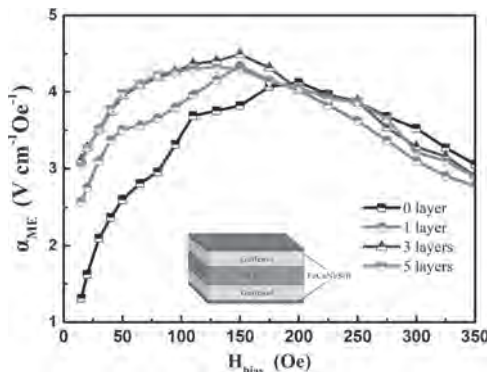


Fig.1 Variation of magnetolectric voltage coefficient with bias magnetic field introducing different layers of FeCuNbSiB

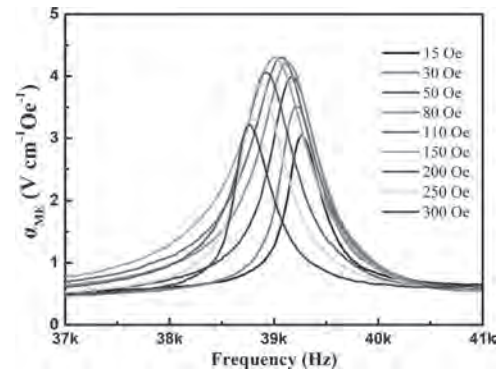


Fig.2 The influence of alternating magnetic field frequency on magnetolectric voltage coefficient under different bias magnetic fields after introducing 5 layers of FeCuNbSiB

Session JW
RE-BASED AND RE-FREE PERMANENT MAGNETS
(Poster Session)

Alberto Bollero, Co-Chair
IMDEA Nanoscience, Madrid, Spain
Kinjal Gandha, Co-Chair
Iowa State University, Ames, IA, United States

JW-01. Anisotropic Nanocrystalline SmCo₅ Permanent Magnet Prepared by Hot Extrusion.

H. Wang¹, D. Zhang¹, Y. Tang¹, Y. Li¹, W. Liu¹ and M. Yue¹

1. Faculty of Materials and Manufacturing, Beijing University of Technology, Beijing, China

I. INTRODUCTION As the first generation of rare earth transition metal based permanent magnet, SmCo₅ has a high anisotropy field of more than 240 kOe, and the coercivity of its nanocrystalline magnet is as high as 50 kOe [1]. Hot deformation technology is an effective way to prepare anisotropic SmCo₅ nanocrystalline magnets. A.M.Gabay et al found that the texture in (00l) direction can be obtained for the SmCo₅ magnets after upsetting deformation[2]. Yue et al prepared anisotropic nanocrystalline magnets by upsetting deformation. When the deformation reaches 90%, a strong c-axis texture appears in the crystals[3]. However, the upsetting deformation method can not achieve large-scale continuous production. In addition, the magnetic properties of the magnet at different positions are quite different. A.S. Kim et al prepared anisotropic cylindrical NdFeB magnets by hot extrusion, but there is still a large space to improve the magnetic properties[4]. Up to now, there is no detailed report on the preparation of SmCo₅ magnets by hot extrusion. In this paper, a new hot deformation method was designed. The anisotropic SmCo₅ nanocrystalline magnet was prepared by hot extrusion. The microstructure, texture and magnetic properties of the hot extruded (HE) SmCo₅ magnet were systematically studied, and the deformation mechanism is analyzed in detail. II. EXPERIMENTAL SmCo₅ ingot was prepared by induction melting method with 99.9% pure elements, excess Sm of 5 wt.% was added to compensate the Sm losses due to evaporation. The as-cast ingot was crushed into blocks that were subjected to high energy ball milling, which was carried out under argon atmosphere for 5 h in a high energy mill. Then the milled powder was put into WC-Co mold, hot pressed (HP) by spark plasma sintering (SPS) at 700 degree Celsius under 500MPa. Then the HP magnet was extruded by extrusion die with extrusion aperture of 10 mm*2.5 mm. The phase composition and texture of the samples were analyzed by X-ray diffraction (XRD). The alignment of the samples was measured by electron backscattered diffraction (EBSD). The microstructure of the samples was observed by scanning electron microscopy (SEM) and transmission electron microscopy (TEM). Magnetic measurement of the samples was carried out in a Quantum Design physical properties measurement system magnetometer with a maximum magnetic field of 9 T. III. RESULTS AND DISCUSSION Fig. 1 (a) shows a schematic diagram, which explains the test direction and regions of the HE magnet. Fig. 1(b) shows the XRD results of the HE magnet in different directions. When the test direction is parallel to the X and Z direction, the HE magnet does not show obvious c-axis texture, the relative intensity ratio between the diffraction peaks of (002) and (111) [$I_{(002)}/I_{(111)}$] is low, and the diffraction pattern is almost the same as that of the HP magnet. But when the test direction is Y direction, the (00l) peaks in the XRD diffraction pattern is significantly enhanced, along with the decrease of other peaks. Meanwhile, the $I_{(002)}/I_{(111)}$ increases significantly. This result shows that the HE magnet forms a strong c-axis texture in the Y direction. The cross-section of the HE magnet (Fig. 1a, pink section) was observed by SEM. It is worth to note that the grains in the region 1 are aligned along the Y direction (Fig. 2a), indicating a strong c-axis texture. The grains in the region 2 tend to be aligned along the X direction (Fig. 2b), which is perpendicular to the direction of grains in the region 1, indicating that the aligned direction of the grains has changed when approaching the region 2. Furthermore, it is not conducive to the formation of the Y-direction texture. A small amount of grains in the region 3 are aligned along the Y direction (Fig. 2c), the most grains have no obvious alignment. Therefore, the results show that the Y direction is the main alignment direction of the HE magnet. Besides, The XRD results of the three regions show that the value of the $I_{(002)}/I_{(111)}$ follows a sequence: region 1>region 2>region 3. In addition, the remanence of the three regions also show the same trend. The poor remanence of the region 3 is due to the change of grains alignment, which is related to the deformation mechanism during the HE process. The deformation mechanism of the HE magnet will be further investigated. IV. CONCLUSIONS The anisotropic nanocrystalline SmCo₅ permanent magnet with strong c-axis texture can be prepared by hot extrusion, which provides a promising protocol to fabricate high performance nanocrystalline SmCo₅

magnets. Meanwhile, it will be a potential method for improving production efficiency of the anisotropic SmCo₅ nanocrystalline magnets.

[1] J. Ding, P. G. McCormick, and R. Street, *J. Alloys Compounds*, 191, 197, (1993). [2] A. M. Gabay, et al., *Journal of Magnetism and Magnetic Materials*, 321, 3318-3323, (2009). [3] M. Yue, J. H. Zuo, W. Q. Liu, *Journal of Applied Physics*, 109, 07A711, (2011). [4] A.S. Kim, et. al., *Materials Engineering*, 12, 93-100, (1990).

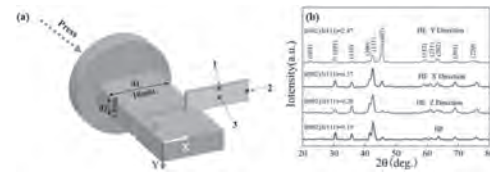


Fig. 1. (a) Schematic diagram of the HE SmCo₅ magnet, (b) XRD patterns of the HP and HE SmCo₅ magnets in different directions.

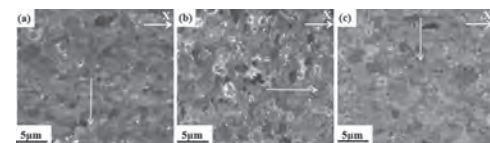


Fig. 2. BSE images of the HE SmCo₅ magnet in different regions, (a) region 1, (b) region 2, (c) region 3. The red and yellow arrows represent the different directions of the HE SmCo₅ magnet, The green arrows represent the alignment of the grains.

JW-02. Magnetic Properties of (Sm,Zr)Fe₁₀ Melt-Spun Ribbons.

T. Saito¹

¹ Chiba Institute of Technology, Narashino, Japan

There are several Sm-Fe intermetallic compounds such as Sm₂Fe₁₇, SmFe₂, SmFe₃ phases in the Sm-Fe alloys.¹ Among them, the Sm₂Fe₁₇ intermetallic compound has been studied for permanent magnet application.²⁻⁴ The Sm₂Fe₁₇N₃ compound possesses a large anisotropy field and a high saturation magnetization and has been prepared in Sm₂Fe₁₇N₃ powder. Sm-Fe-N bulk magnets cannot be produced by the sintering of Sm-Fe-N powder, however, due to the poor thermal properties of the powder.⁵ Therefore, it would be desirable if the magnetic properties of the Sm₂Fe₁₇ phase could be increased without the need for nitrogenation. Although several studies were carried out on the Sm₂Fe₁₇ phase at the early stage of such research, relatively little attention has been paid to this material due to their easy-plane anisotropy. We have continued to study the Sm₂Fe₁₇-type phase with the additions of both Ti and Zr to Sm₂Fe₁₇-type alloys. The structures and magnetic properties of (Sm,Zr)Fe₁₀ and (Sm,Zr)(Fe,Ti)₁₀ melt-spun ribbons are discussed. (Sm_{1-x}Zr_x)Fe₁₀ (x = 0–0.3) and (Sm_{1-x}Zr_x)Fe_{9.5}Ti_{0.5} (x = 0–0.3) alloy ingots were prepared by induction melting in an argon atmosphere. Small amounts of the alloy ingots were induction melted under an argon atmosphere in a quartz crucible and then ejected through an orifice with argon onto a chromium-coated copper wheel rotating at a surface velocity of 50 m/s. The pulverized melt-spun ribbons were annealed at 973–1273 K for 1 h under an argon atmosphere. The phases in the specimens were examined by X-ray diffraction (XRD). The hysteresis loops of the specimens were measured at room temperature using a vibrating sample magnetometer (VSM). The SmFe₁₀ melt-spun ribbon showed a narrow hysteresis loop with a coercivity less than 1 kOe. The substitution of Zr for Sm in the SmFe₁₀ melt-spun ribbon did not change the structure and magnetic properties. Thus, heat treatment of these specimens was carried out to increase the coercivity. Annealing resulted in an increase in coercivity of the (Sm_{1-x}Zr_x)Fe₁₀ (x = 0–0.3) specimens. Figure 1 shows the hysteresis loops of the (Sm_{1-x}Zr_x)Fe₁₀ (x = 0–0.3) melt-spun ribbons annealed at 1073 K. The maximum coercivity of 1.8 kOe was obtained in the (Sm_{0.9}Zr_{0.1})Fe₁₀ melt-spun ribbon when annealed at 1073 K. Next, (Sm_{1-x}Zr_x)Fe_{9.5}Ti_{0.5} (x = 0–0.3) melt-spun ribbons were prepared and the effect of the substitution of Ti for Fe in the SmFe₁₀ alloy was investigated. The substitution of Ti for Fe in the (Sm_{1-x}Zr_x)Fe₁₀ (x = 0–0.3) melt-spun ribbon resulted in the formation of the amorphous phase. The (Sm_{1-x}Zr_x)Fe_{9.5}Ti_{0.5} (x = 0–0.3) melt-spun ribbons showed a narrow hysteresis loop with a coercivity less than 0.5 kOe, regardless of the Zr content. However, heat treatment of these specimens resulted in a large increase in coercivity. Figure 2 shows the hysteresis loops of the (Sm_{1-x}Zr_x)Fe_{9.5}Ti_{0.5} (x = 0–0.3) melt-spun ribbons annealed at 1173 K. The maximum coercivity of 4.5 kOe was obtained in the (Sm_{0.7}Zr_{0.3})Fe_{9.5}Ti_{0.5} melt-spun ribbon when annealed at 1173 K. The XRD study revealed that the annealed specimen mainly consisted of the Th₂Zn₁₇-type phase. In conclusion, the specimens with higher Zr and Ti content tended to exhibit a higher coercivity than those with lower Zr and Ti content. The highest coercivity of 4.5 kOe was achieved in the annealed (Sm_{0.7}Zr_{0.3})Fe_{9.5}Ti_{0.5} melt-spun ribbon with the h₂Zn₁₇-type phase.

[1] K. H. J. Buschow, *J. Less-Common Metals* 25, 131 (1971). [2] J. M. D. Coey and H. Sun, *J. Magn. Magn. Mater.* 87, L251 (1990). [3] T. Iriyama, K. Kobayashi, N. Imaoka, T. Fukuda, H. Kato, and Y. Nakagawa, *IEEE Trans. Magn.* 28, 2835 (1992). [4] M. Katter, J. Wecker, C. Kuhrt, L. Schultz, and R. Grössinger, *J. Magn. Magn. Mater.* 117, 419 (1992). [5] F. A. O. Cabral, S. Gama, E. de Morais, N. L. Sanjurjo, C. A. Rubeiro, and C. C. Colucci, *IEEE Trans. Magn.* 32, 4365 (1996).

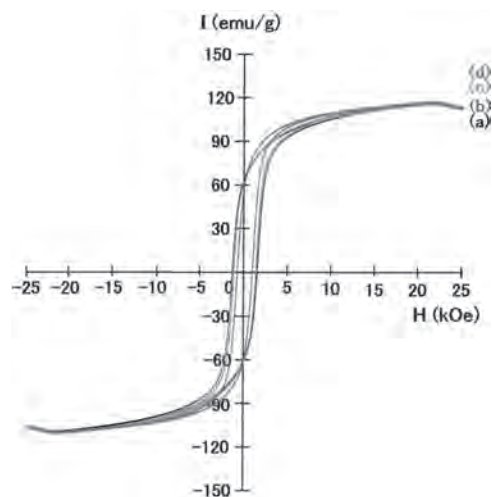


Fig. 1 Hysteresis loops of the (a) SmFe₁₀, (b) (Sm_{0.9}Zr_{0.1})Fe₁₀, (c) (Sm_{0.8}Zr_{0.2})Fe₁₀, and (d) (Sm_{0.7}Zr_{0.3})Fe₁₀ melt-spun ribbons annealed at 1073 K.

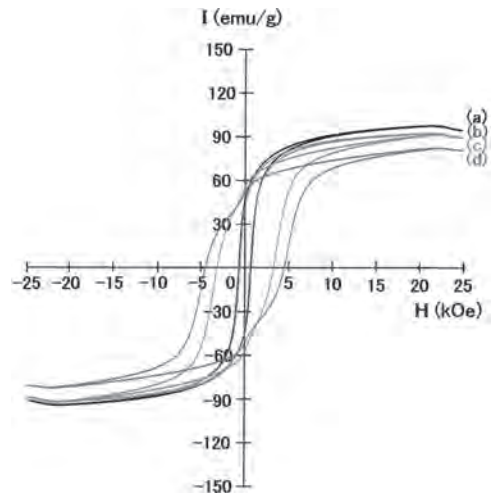


Fig. 2 Hysteresis loops of the (a) SmFe_{9.5}Ti_{0.5}, (b) (Sm_{0.9}Zr_{0.1})Fe_{9.5}Ti_{0.5}, (c) (Sm_{0.8}Zr_{0.2})Fe_{9.5}Ti_{0.5}, and (d) (Sm_{0.7}Zr_{0.3})Fe_{9.5}Ti_{0.5} melt-spun ribbons annealed at 1173 K.

JW-03. Preparation of SmCo_5 and Fe Magnetic Precursor for Realizing Anisotropic Bulk Nanocomposite Magnet by low Oxygen Powder Metallurgy Process.

K. Park^{1,2}, Y. Hirayama², W. Yamaguchi², M. Kobashi¹ and K. Takagi²

1. Department of Materials Process Engineering, Nagoya University, Nagoya, Japan; 2. Magnetic Powder Metallurgy Research Center, National Institute of Advanced Industrial Science and Technology (AIST), Nagoya, Japan

1. Introduction Anisotropic nanocomposite (NC) magnet which utilizes the exchange coupling effect between the hard and soft magnetic phase is attracting a lot of attention as a next-generation permanent magnet [1]. However, the realization of anisotropic NC magnet is still experiencing many difficulties, and its maximum energy product (BH_{max}) is less than that of a single-phase permanent bulk magnet [2, 3] since its microstructures are not well-controlled in the nanoscale. In order to realize the nanoscale-controlled microstructure with an effective exchange coupling effect, the grain size of the soft magnetic phase needs to be smaller than twice the domain wall width of the hard magnetic phase [4]. In this work, we attempted to prepare the anisotropic bulk NC magnet with the nanoscale-controlled microstructure by using the powder metallurgy process. SmCo_5 compound as a hard magnetic phase which has a high anisotropy field [5] and Fe with high saturation magnetization as a soft magnetic phase were chosen as a preliminary work. The precursor needs to satisfy with the following requirements: (1) anisotropic hard magnetic powder, (2) fine soft magnetic powder. In addition to these requirements, the surface oxide of hard and soft magnetic powder should be as thin as possible for effective exchange coupling effect. Therefore, the preparation and handling of the micro-sized SmCo_5 and nano-sized Fe powder have been done in low oxygen atmosphere. Using the mixture of these powders, we have synthesized an anisotropic bulk NC magnet and evaluated its microstructure and magnetic properties. 2. Experimental procedure SmCo_5 ingot was prepared by the arc-melting process. The ingot was roughly crushed to around 100 μm powder by a blender. SmCo_5 powder was more refined by the jet-milling process in a glove box. Fe nanopowder was prepared by the induction thermal plasma process. The detail experimental set up and condition were described elsewhere [6]. The prepared nano-sized Fe powder was handled in a glove box to prevent the oxidation. Then, SmCo_5 powder and Fe nanopowder were mixed with as SmCo_5 -10 wt.% Fe by a homogenizer in heptane. The mixture was magnetically aligned under 2 T at 300 K, then consolidated at 600 °C under 300 MPa by the direct current sintering process. The phase of SmCo_5 powder and SmCo_5/Fe NC magnet was analyzed by X-ray diffractometer (XRD). Magnetic measurement was carried out by a vibrating sample magnetometer (VSM). The microstructure of the NC magnet was observed by scanning electron microscope (SEM). 3. Results and discussion In the XRD profile, the compound prepared by the arc-melting was single phase of SmCo_5 . Even after the jet-milling process, the peaks of single phase SmCo_5 without oxides were also detected. The peaks of the jet-milled SmCo_5 powder were slightly broadened because the particles were damaged by large mechanical energy during the jet-milling. The median particle size (D_{50}) of the jet-milled powder was measured as 2.5 μm . In Fig. 1(a), the black line represents the hysteresis loop measured along an easy direction of magnetically aligned the jet-milled SmCo_5 powder. The coercivity of 12.8 kOe was obtained. The magnetizations at 9 T were almost saturated, and its values were measured as 100 emu/g, which is similar with the intrinsic properties of SmCo_5 compound [7]. The red line in Fig. 1(a) shows the hysteresis loop measured along an easy direction of magnetically aligned SmCo_5 -10 wt.% Fe bulk NC magnet. An anisotropic magnetic behavior was clearly confirmed by the magnetic measurement. The magnetization at 9 T was measured about 10 % higher than that of SmCo_5 powder because of the addition of 10 wt.% Fe nanopowder, indicating that the SmCo_5 and Fe powders were consolidated without a formation of another intermetallic compounds. The XRD profile also showed the peaks of only SmCo_5 and Fe. The recoil loop clearly represented a non-linear spring back effect, indicating that the nano-sized Fe powder with negligibly thin oxide film was partially exchange-coupled with anisotropic SmCo_5 powder. Another evidence of exchange-coupling is that the remanent magnetization was increased by the exchange-coupled Fe. In consequence, we realized the exchange-coupled anisotropic SmCo_5/Fe

bulk nanocomposite magnet by the low oxygen powder metallurgy process. This work proposed the strategy to achieve an improved anisotropic bulk NC magnet. Fig. 1(b) shows the cross-sectional image of SmCo_5 -10 wt.% Fe bulk NC magnet. There are many pores in the magnet, which leads to the reduction of the effective exchange interaction. In order to obtain the more densified magnet, the higher sintering temperature and/or pressure is effective. Moreover, there is a possibility to refine the Fe nanoparticle by controlling the conditions of thermal plasma such as counterflow gas and radial injection of cooling gas [8]. It is expected that the finer Fe nanoparticle could be more effectively exchange-coupled with a hard magnetic phases. 4. Conclusion In this study, SmCo_5 powder was prepared by the jet-milling process, and coercivity of 12.8 kOe and magnetization of 100 emu/g were obtained. Fe nanopowder with average particle size of 100 nm, was synthesized by ITP process. The magnetic measurement revealed the anisotropic magnetic behavior of SmCo_5/Fe NC magnet.

[1] E. F. Kneller and R. Hawig, IEEE Transactions on Magnetics, Vol. 27, p.3588 (1991) [2] M. Ito, K. Majima and H. Nagai, Journal of alloys and compounds, Vol. 329, p.272 (2001). [3] J. Zhang, S. Y. Zhang and B. G. Shen, Journal of Applied Physics, Vol. 89, p.5601 (2001) [4] R. Fischer, T. Leineweber and H. Kronmüller, Physical Review B, Vol. 57, p.10723 (1998). [5] H. Nakamura, Scripta Materialia, Vol. 154, p.273 (2018). [6] Y. Hirayama and K. Takagi, Journal of Alloys and Compounds, Vol. 792, p.594 (2019). [7] S. Liu, Chinese Physics B, Vol. 28, p.017501 (2019) [8] X. Zhang, Z. Liu and T. Watanabe, Chemical Engineering Science, Vol. 230, p.116217 (2020).

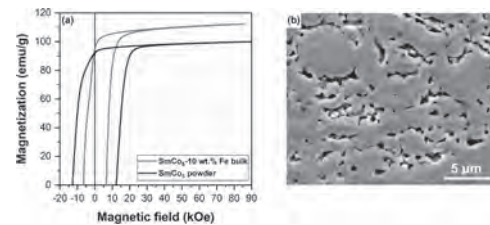


Fig. 1. (a) Hysteresis loops measured along an easy direction of magnetically aligned SmCo_5 powder (black line) and SmCo_5 -10 wt.% Fe bulk NC magnet (red line). (b) Cross sectional image of SmCo_5 -10 wt.% Fe bulk NC magnet.

JW-04. Measurement and Analysis of Temperature-Dependent AC Loss of $\text{Sm}_2\text{Co}_{17}$ Magnets.

Y. Li¹, Z. Fan¹, C. Zhang¹ and H. Geng¹

1. State Key Laboratory of Reliability and Intelligence of Electrical Equipment, Hebei University of Technology, Tianjin, China

1. Introduction Permanent magnet synchronous motors (PMSMs) are widely used in traction, robot, aerospace and other industrial automation fields. According to statistics, the loss of permanent magnets (PMs) can account for up to 20% of the total loss^[1]. And the increasing temperature of the PM is mainly caused by eddy current loss. In high-power PMSMs, the working temperature of rotor PM can reach 150 centigrade under normal working condition, which will be higher in case of fault^[2]. Too high temperature may cause failure of demagnetization and changes in conductivity of PMs. Therefore, when designing PMSMs, the loss of PMs must be considered, especially including the influence of temperature and frequency. The sintered Sm-Co PMs have larger maximum magnetic energy product and coercivity, as well as better temperature and chemical stability^[3]. This paper measures and analyzes the eddy current loss and hysteresis loss of $\text{Sm}_2\text{Co}_{17}$ magnets under variable temperature conditions using the customized heatable AC loss measurement system and the physical properties measurement system (PPMS). 2. Measurement System Setup The customized heatable AC loss measurement system is designed to measure the loss of PMs under sinusoidal excitation in different frequencies and temperatures, as shown in Fig.1. It contains excitation system, data acquisition system, and temperature control system. The excitation system is composed of a double C-shaped closed magnetic circuit, a PM sample, four flexible excitation windings connected to a signal generator, a power amplifier and an impedance matcher. The data acquisition is completed by the oscilloscope collecting the induced voltage of the H-coil and the circular B-coil sensors attached to the sample surface. The temperature control system includes a DC power supply, a temperature controller, an alumina ceramic heating fixture, heating rods, and aluminum silicate ceramic insulation layers. Four heating rods inserted around the heating fixture heat the sample embedded in the center of the fixture. The thermostat controls the on and off of the heating circuit according to the feedback of the thermocouple, so as to realize the precise control of the sample temperature. The temperature control accuracy can reach 0.1 centigrade. The sample is a $10 \times 10 \times 10$ mm saturated magnetized XG-28A $\text{Sm}_2\text{Co}_{17}$ PM. During the test, first turn on the temperature control system, wait for the sample to reach the set temperature and keep it for 20 minutes. Then start the excitation system and data acquisition system to measure the B - H loop of the PM. The total loss of PM is obtained by multiplying the frequency by the area of the B - H loop. Test bench for measurement of the hysteresis loss of PMs consists of a PPMS with up to 9 Tesla superconducting magnet with a P525 VSM and data acquisition system. The sample is an axially magnetized $\Phi 3 \times 1$ mm cylindrical $\text{Sm}_2\text{Co}_{17}$ PM. The hysteresis loss of the sample at different temperatures is obtained by integrating the measured local hysteresis loop of the sample. 3. Measurement Results and Discussion The change rate of AC loss with temperature of the $\text{Sm}_2\text{Co}_{17}$ PM is shown in Table 1. The percentage is obtained by dividing the AC loss at different temperatures by the AC loss at 25 centigrade. When the frequency is 50 Hz, the AC loss of the $\text{Sm}_2\text{Co}_{17}$ PM increases with an increase in temperature. When the frequency is greater than 200Hz, the AC loss of the $\text{Sm}_2\text{Co}_{17}$ PM decreases with an increase in temperature. By using the PPMS to measure the local hysteresis loop, it is concluded that the hysteresis loss of the $\text{Sm}_2\text{Co}_{17}$ PM increases with an increase in temperature. And at the same temperature, when the PM works in the second quadrant, the hysteresis loss of the $\text{Sm}_2\text{Co}_{17}$ PM is very small. But when the applied magnetic field causes the magnetic flux density of the $\text{Sm}_2\text{Co}_{17}$ PM to exceed the B axis and reach the first quadrant, the hysteresis loss will increase significantly. The AC loss of PMs contains three components: hysteresis loss, eddy current loss and residual loss. The residual loss is negligible. Hysteresis loss is proportional to frequency, and eddy current loss is proportional to the square of frequency. Therefore, the AC loss of PMs at high frequency is mainly eddy current loss. Eddy current loss can be expressed as: $P_e = \int_V \gamma E^2 dV$ (1) Where E is the electric field strength in the PM and γ is the electrical conductivity of the PM. As the temperature increases, the eddy current loss of the $\text{Sm}_2\text{Co}_{17}$ PM decreases as its electrical conductivity decreases. Therefore, the AC loss

at high frequency decreases as the temperature increases. At low frequencies, hysteresis loss is the main component of AC loss. Therefore, when the frequency is 50 Hz, the AC loss increases as the temperature increases. 4. Conclusion This paper measures and analyzes the change rate of AC loss with temperature of $\text{Sm}_2\text{Co}_{17}$ PMs. The results show that when the frequency is 50Hz, the AC loss at 150 centigrade increases by about 13% compared to that at 25 centigrade. When the frequency is greater than 200Hz, the AC loss at 150 centigrade is reduced by about 9% compared to that at 25 centigrade. When the frequency is greater than 500Hz, the AC loss at 150 centigrade is reduced by about 12% compared to that at 25 centigrade. The measurement results provide an important reference for the optimization and design of motors working at different frequencies and temperatures.

[1] N. Zhao, Z. Q. Zhu and W. Liu, IEEE Transactions on Magnetics., Vol. 47, p.4199-4202 (2011) [2] R. Wrobel, P. H. Mellor and N. McNeill, IEEE Transactions on Energy Conversion., Vol. 25, p.403-411 (2010) [3] H. Machida, T. Fujiwara and C. Fujimoto, IEEE Transactions on Magnetics., Vol. 55, p.1-4 (2019)

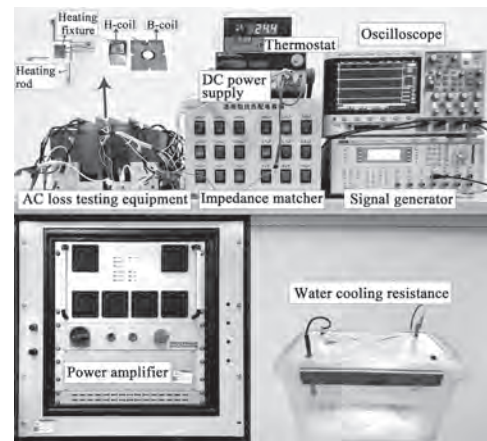


Fig.1. The customized heatable AC loss measurement system

	50Hz	200Hz	500Hz	1000Hz	1500Hz	2000Hz
50°C	105.27%	97.90%	97.67%	97.78%	97.26%	98.25%
75°C	108.58%	95.92%	94.85%	95.98%	95.60%	95.72%
100°C	109.50%	93.17%	92.13%	93.33%	92.88%	93.38%
125°C	110.06%	91.75%	89.58%	90.43%	90.02%	90.78%
150°C	115.88%	90.58%	86.38%	87.92%	87.70%	87.97%

Table 1. The change rate of AC loss of $\text{Sm}_2\text{Co}_{17}$ magnets with temperature at different frequencies

JW-05. Development of a Modified Mechanochemical Process for High-Performance Sm-Co Particles.

G. Lee¹, M. Kang¹, C. Bae¹, K. Lee¹ and J. Kim¹

¹. Materials Science and Chemical Engineering, Hanyang University - Ansan Campus, Ansan, The Republic of Korea

[Introduction] Among permanent magnets applying to various industries such as automobiles, power plants, electronics, etc., the Sm-Co hard magnetic materials have been attracted much attention recently due to their high magnetocrystalline anisotropy ($\sim 10^7$ J/m³) and saturation magnetization (~ 1.2 T) as well as high curie temperature (~ 1190 K)[1]. There have been many efforts to increase the high coercivity of permanent magnet materials in order to improve the maximum magnetic energy further. Since the coercivity depends on the microstructure of the magnet materials, the control of their particle size can be an effective strategy to form single-domain or anisotropic oriented grains through the powder metallurgical approach. For example, the high-energy ball milling process has been used to obtain the fine particles from crushing the casted ingots or ribbons produced by a rapid solidification process[2], although it could result in the inflow of the grinding medium or the oxidation of materials including the rare-earth elements by thermal energy. Recent studies have also reported that the nanoscale Sm-Co nanoparticles can be produced through a chemical or physical combination of Sm and Co precursors with CaO before the reduction diffusion process with metallic calcium as a reductant[3, 4]. However, the toxic compounds can be generated under the chemical process, and there are limitations to industrial applications because of difficulties in mass production. Therefore, in this study, we report the improved method for synthesis of high-performance Sm-Co particles by introducing Ca(ac)₂ powder and calcination process, and also aim to understand the relation between the magnetic properties and microstructures of Sm-Co nanoparticles. [Experimental procedures] Sm₂O₃, CoO, and Ca(ac)₂ powder were used for the synthesis of Sm-Co hard magnetic materials. The Sm₂O₃, CoO, and Ca(ac)₂ powder were mixed in an atomic ratio of 1: 5~8: 8~48. The mixture was crushed roughly using the zirconia ball with a diameter of 3 mm. The mass ratio of balls to powder was about 10: 1. The calcination process of the crushed mixture was carried out in the temperature range of 700 to 1000 °C in order to improve homogeneity between elements and decompose from Ca(ca)₂ to CaO. After that, these calcinated specimens were reduced to Sm₂Co₁₇ or SmCo₅ particles at 900 °C for 1 hr under Ar atmosphere using metallic calcium. The reduced products were washed using 0.1 M NH₄Cl-methanol solution to remove the residual CaO. [Results and discussion] It was found that the calcination before the reduction diffusion process was a significant step to manufacture successfully Sm-Co particles with high coercivity and squareness (M_r/M_s). As shown in Fig. 1, the Sm-Co particles after the reduction process without the ball milling process showed low coercivity of 1.7 kOe while the mixture crushed by the ball milling had an increased coercivity of 6.6 kOe, and the XRD results showed that both Sm₂Co₁₇ and SmCo₅ phases were observed. In the condition under the calcination process at 800 °C after the ball milling, the reduced Sm-Co particles showed the coercivity of 7.2 kOe and the magnetization of 93 emu/g under the applied field of 2.5 T. In addition, it was fully composed of the typical Sm₂Co₁₇ phase. These results confirmed that the proper condition of milling and calcination is required in order to obtain effectively the targeted phase and advantages for inhibition of the grain growth by addition of Ca(ac)₂. Fig. 2a shows the magnetic properties of the aligned Sm₂Co₁₇ particles with the amount of Ca(ac)₂. In the fixed atomic ratio of Sm: Co to be 1: 8, the atomic ratio of Ca was controlled from 8 to 40. It was observed that all the particles, regardless of the amount of Ca(ac)₂, were reduced into the Sm₂Co₁₇ phase through the optimized calcination and reduction process. Thus the magnetization values remained relatively constant in the range of 91 to 95 emu/g. However, other magnetic properties such as coercivity, squareness gradually improved as the amount of Ca(ac)₂ increased, indicating that the particle size reached toward the single domain size (~ 300 nm) of Sm₂Co₁₇(Fig. 2b), and the fraction of isolated single crystal particles increased. Under the optimal condition, the Sm₂Co₁₇ hard magnetic particles were found to have a high alignment of 86% and a maximum energy product of 14.5 MGOe. A more detailed analysis of the microstructural characteristics will be discussed.

[1] R. Skomski and D. J. Sellmyer, Springer US, pp. 1-57 (2006). [2] Y. Wang, Y. Li, C. Rong, and J. P. Liu, *Nanotechnology*, vol. 18, p. 465701 (2007). [3] W. Liu and P. G. McCormick, *Journal of Magnetism and Magnetic Materials*, vol. 195, p. L279 (1999). [4] B. Shen *et al.*, *Angew Chem Int Ed Engl*, vol. 58, p. 602 (2019).

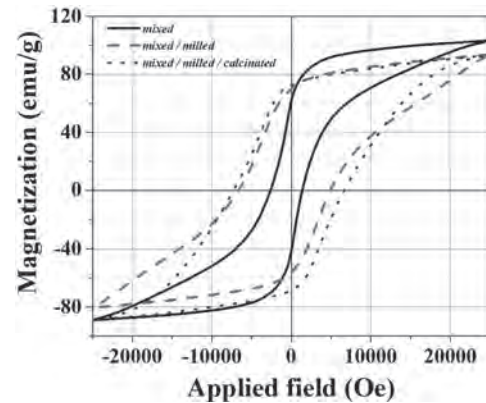


Fig. 1. The hysteresis loops of the Sm-Co particles reduced at 900 °C for 1 hr with different conditions.

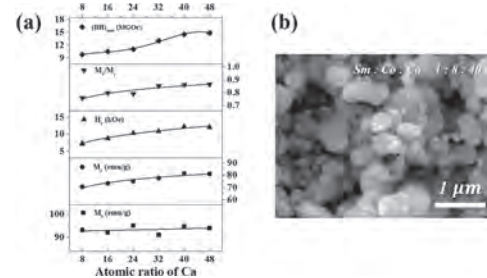


Fig. 2. (a) The magnetic properties of Sm₂Co₁₇ particles with the amount of Ca(ac)₂ and (b) the SEM images of the particles in an atomic ratio of Sm: Co: Ca = 1: 8: 40.

JW-06. Magnetic Properties of Sm(FeTi)₁₂ hot Deformed Magnets.T. Saito¹, Y. Ogawa¹ and D. Nishio-Hamane²¹ Chiba Kogyo University, Chiba, Japan; ² The University of Tokyo, Bunkyo-ku, Japan

In recent years, much efforts has been paid to synthesize new compounds having the potential for permanent magnet application. One of the new compounds is the RFe₁₂ (R = rare earth) intermetallic compound.¹⁻³ Although the binary RFe₁₂ intermetallic compounds with the ThMn₁₂-type structure are not thermodynamically stable and do not exist in bulk form, it has been found that the substitution of T (T = Ti, V, Cr, Mo) for Fe in the RFe₁₂ intermetallic compound stabilizes the ThMn₁₂-type structure.⁴⁻⁶ The objective of the present study was to produce anisotropic Sm(Fe,Ti)₁₂ magnets. In the case of Nd-Fe-B magnets, anisotropic Nd-Fe-B magnets have been produced by either the sintering of Nd-Fe-B powder or hot deformation of hot-pressed Nd-Fe-B magnets. In this study, we attempted to produce anisotropic Sm(Fe,Ti)₁₂ magnets by the hot deformation of hot-pressed Sm(Fe,Ti)₁₂ magnets. The magnetic properties of the hot-deformed Sm(Fe,Ti)₁₂ magnets are discussed. Sm(Fe,Ti)₁₂ alloy ingots were prepared by induction melting in an argon atmosphere. The alloy ingots were induction melted and then ejected through an orifice with argon onto a copper wheel. The resultant melt-spun ribbons were comminuted into powders and then hot-pressed by the spark plasma sintering (SPS) method. Hot deformation of the hot-pressed Sm(Fe,Ti)₁₂ magnets was performed in a vacuum at 973–1173 K under a pressure of ~200 MPa by the SPS method. The specimens were examined by X-ray diffraction (XRD), a scanning electron microscope (SEM), a transmission electron microscope (TEM), and a vibrating sample magnetometer (VSM). The hot-pressed Sm(Fe,Ti)₁₂ magnets were successfully hot deformed to an 80% reduction without cracking. The magnetic properties of the resultant hot deformed Sm(Fe,Ti)₁₂ magnets were examined. Figure 1 shows the hysteresis loops of the hot-deformed Sm(Fe,Ti)₁₂ magnets, measured parallel and perpendicularly to the pressing direction. The magnetic anisotropy of the hot-deformed Sm(Fe,Ti)₁₂ magnets was confirmed by the existence of a higher remanence in the parallel direction than in the perpendicular direction. This indicates that anisotropic Sm(Fe,Ti)₁₂ magnets were successfully produced by the hot deformation of hot-pressed Sm(Fe,Ti)₁₂ magnets. In order to examine the crystallographic alignment of the Sm(Fe,Ti)₁₂ phase, the surface of the SmFe₁₁Ti magnets were examined by XRD. The results are shown in Figure 2. The XRD patterns of the hot-deformed Sm(Fe,Ti)₁₂ magnets show clear diffraction peaks of the Sm(Fe,Ti)₁₂ phase, but the XRD pattern of the Sm(Fe,Ti)₁₂ magnet hot-deformed at 1173 K was slightly different from that of the Sm(Fe,Ti)₁₂ magnet hot-deformed at 973 K. It was found that the hot-deformed Sm(Fe,Ti)₁₂ magnets contained a small amount of the α-Fe phase together with the Sm(Fe,Ti)₁₂ phase. Although the magnetic measurements revealed that the hot-deformed Sm(Fe,Ti)₁₂ magnets exhibited slight magnetic anisotropy, they did not show clear crystallographic alignment of its Sm(Fe,Ti)₁₂ phase. In conclusion, Sm(Fe,Ti)₁₂ magnets were successfully produced by the hot deformation. Magnetic measurements revealed that the hot-deformed Sm(Fe,Ti)₁₂ magnets exhibited a relatively low coercivity value but were slightly magnetically anisotropic. However, no clear crystallographic alignment of its Sm(Fe,Ti)₁₂ phase was observed in the XRD studies.

[1] F. R. De. Boer, et al. *J. Less-Common Met.* 135, 199 (1987). [2] L. X. Liao, Z. Altounian, and D. H. Ryan, *J. Appl. Phys.* 70, 6006 (1991). [3] L. Shultz and J. Wecker, *J. Appl. Phys.* 64, 5711 (1988). [4] Y. Wang, et al. *J. Appl. Phys.* 67, 4954 (1990). [5] Y. Otani, H. S. Li, and J. M. D. Coey, *IEEE Trans. Magn.* 26, 2658 (1990). [5] J. Yang, Ph. Oleinek, K.-H. Müller, *J. Appl. Phys.* 88, 988 (2000). [6] E. Tomey, et al. *J. Alloys Compd.* 231, 195 (1995).

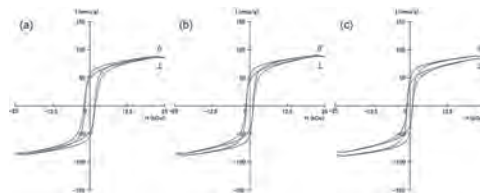


Fig. 1 Hysteresis loops of the hot-deformed Sm(Fe,Ti)₁₂ magnets produced at (a) 973 K, (b) 1073 K, and (c) 1173 K.

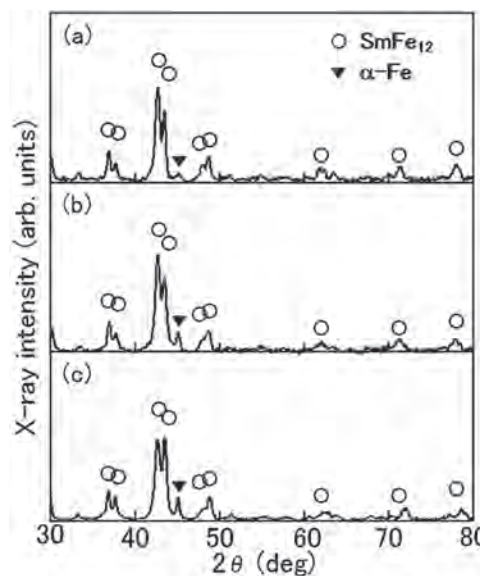


Fig. 2 XRD patterns of the hot-deformed Sm(Fe,Ti)₁₂ magnets produced at (a) 973 K, (b) 1073 K, and (c) 1173 K.

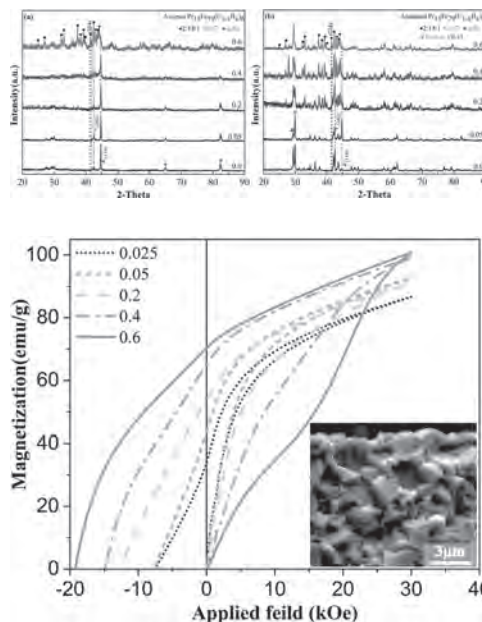
JW-07. Phase and Magnetism Evolution in $\text{Pr}_2\text{Fe}_{14}\text{C}$ System Upon B Doping and Heat Treatment.

H. Yao¹, H. Zhang¹, W. Liu¹ and M. Yue¹

¹. Beijing University of Technology, Beijing, China

At present, rare-earth-based permanent magnet (REPM) $\text{R}_2\text{Fe}_{14}\text{B}$ is one of the most widely used permanent magnets with excellent performance. However, improving this material's properties is still the main topic so far in this field [1]. For $\text{R}_2\text{Fe}_{14}\text{B}$ alloys, it needs to use heavy rare earth elements to obtain high coercive force, which is not conducive to the balanced application of rare earth resources. In contrast, $\text{R}_2\text{Fe}_{14}\text{C}$ system has the same tetragonal structure as $\text{R}_2\text{Fe}_{14}\text{B}$ but a larger magnetic anisotropy field, especially when R is a light rare earth element [2]. This means a great potential to obtain high coercive force in this system, which is necessary for developing medium performance and high coercive force magnets based on high abundance light rare earth elements [3]. However, the $\text{R}_2\text{Fe}_{14}\text{C}$ system suffers from the low phase stability of the tetragonal phase produced by a sluggish solid-state reaction process. Therefore, in this study, we carried on a thorough investigation in the $\text{Pr}_2\text{Fe}_{14}\text{C}$ system considering the effects of element doping and heat treatment on the phase evolution. Fig.1 shows the XRD patterns of the as-spun and annealed samples of $\text{Pr}_{15}\text{Fe}_{79}(\text{C}_{1-x}\text{B}_x)_6$ ($x = 0, 0.05, 0.2, 0.4$ and 0.6) series. In the as-spun flakes, only $\alpha\text{-Fe}$ and $\text{Pr}_2\text{Fe}_{17}$ phase are found in the samples with $x = 0, 0.05, 0.2$ and 0.4 , while the $\text{Pr}_2\text{Fe}_{14}\text{C}$ phase were not observed until $x = 0.6$. It suggests that, without enough amount of B doping, $\alpha\text{-Fe}$ and $\text{Pr}_2\text{Fe}_{17}$ can not form 2:14:1 phase via solid-state transformation in Pr-Fe-C system. On the other hand, after the annealing process at 750°C , the 2:14:1 phase starts to form even in the $x = 0.05$ sample. As shown in Fig. 1(b), the amount of the 2:14:1 phase is small then, but it becomes dominant when the B content is 0.2. The amount of $\alpha\text{-Fe}$ dramatically decreases at the same time. Due to the high rare-earth content in these samples, there is also a pronounced peak at $2\theta = 30^\circ$ of the Pr-rich phase crystallized during the annealing. The oxidation of the rare-earth-rich phase during the annealing process causes the other peak at $2\theta = 29^\circ$. More importantly, the lower limit of the solid-state reaction temperature of the 2:14:1 phase decreases continuously with the doping of B, from 950°C to 600°C . It means that the B doping reduces the forming energy of the 2:14:1 phase. Fig.2 shows the initial magnetization and demagnetization curves for the annealed samples with different B contents. With the increase of B content, both the remanent magnetization (M_r) and the coercivity field (H_c) exhibit an overall enhancement. This is consistent with the XRD results, indicating that the content of the 2:14:1 phase is increased. There is also a waist-like feature on the demagnetization curve of the samples with low B content, which is a sign of the coexistence of soft and hard magnetic phases. Even though the magnetization is not saturated at 3 T, the M_r and H_c are still as high as 70.5 emu/g and 19.1 kOe , respectively, in the sample with $x=0.6$. This considerable value of coercivity may be related to the fine microstructure of the samples. As can be seen from the inset of Fig.2, the average grain size is about $2\text{ }\mu\text{m}$ and does not change too much with the increase of annealing temperature. This is because the main phase is surrounded by a rare-earth-rich phase, limiting the growth of the main phase grains. This is another advantage of the $\text{R}_2\text{Fe}_{14}\text{C}$ system. We systematically investigated the phase evolution of the $\text{Pr}_2\text{Fe}_{14}\text{C}$ system and established an effective way to obtain a relatively large percent of 2:14:1 phase. By optimizing the composition and process, we can also control the microstructure of the main phase and obtain promising magnetic properties. The $\text{Pr}_2\text{Fe}_{14}\text{C}$ material has great potential to be used for bonded magnets and hot deformed magnets. Acknowledgments This work was supported by the Beijing Natural Science Foundation (No. 2182006), the General Program of Science and Technology Development Project of Beijing Municipal Education Commission of China (No. KM201710005006), the National Natural Science Foundation of China [No.51401002], and Program of Top Disciplines Construction in Beijing (PXM2019_014204_500031).

[1] Buschow, K. H. J., New developments in hard magnetic materials. Reports on Progress in Physics 1991, 54 (9), 1123. [2] Burzo, E., Permanent magnets based on R-Fe-B and R-Fe-C alloys. Reports on Progress in Physics 1998, 61 (9), 1099. [3] Coey, J. M. D., Permanent magnets: Plugging the gap. Scripta Materialia 2012, 67 (6), 524-529.



JW-09. Study on Magnetization Reversal Processes of Anisotropic HDDR Pr₂Fe₁₄B-Type Magnetic Materials.

Z. Lin¹, J. Han¹, Y. Zhang¹, X. Zhang¹, S. Liu¹, C. Wang¹, J. Yang¹ and Y. Yang¹
 1. Peking University, Beijing, China

HDDR process can not only refine the coarse R₂Fe₁₄B grains (~ 100 μ m) into fine grains (~300 nm), but also induce these fine grains to be oriented along the c-axis. The grain refinement can improve the coercivity of the magnetic materials, and the grain orientation is helpful to obtain high remanence, so the anisotropic R₂Fe₁₄B materials with high coercivity, remanence and maximum energy products can be obtained after HDDR process. Recent researches show that the coercivity of HDDR R₂Fe₁₄B magnetic materials can be enhanced to ~20 kOe by refining the grain size of the materials or by diffusion of the eutectic alloys with the low melting point, but there is still a big gap between the coercivity and its anisotropic field (70 kOe). This indicates that the coercivity of HDDR magnetic materials still has a lot of room to improve, especially the grain size of HDDR powder is close to that of R₂Fe₁₄B single domain particles. In order to further improve the coercivity, it is necessary to study the coercivity mechanism of HDDR magnetic materials. In this study, the initial magnetization curve of thermally demagnetized HDDR anisotropic Pr-Fe-B sample was firstly investigated. The results show that the magnetization increase moderately with external magnetic field, but it is not only different from the rapid rise of magnetization of sintered R-Fe-B magnets but also different from the slow increase of melt-spun R-Fe-B powders at the beginning and then the sudden rapid increase at a certain critical field. Therefore, it is not easy to determine the type of the coercivity mechanism for the powders. In order to study the coercivity mechanism of the above HDDR anisotropic powders in detail, the temperature dependence of coercivity of the sample was measured. The coercivity decrease monotonically with the increase of temperature. According to the micromagnetic model, the coercivity H_c can be generally expressed $H_c = \alpha\phi\alpha_k 2K_1/M_S - N_{eff}M_s$. Due to the preferential nucleation of inhomogeneous regions in the magnetic powder, a correction factor α_k should be introduced. In addition, because the grain alignment in the magnetic powder is not completely consistent, the correction factor $\alpha\phi$ is also introduced. The dependence of the anisotropy constants K_1 , and saturation magnetization (M_s) of the main phase Pr₂Fe₁₄B on the temperature are all from the literature. The measured data of HDDR Pr-Fe-B and the theoretical formula were compared to analyze that the coercivity mechanism is controlled by the nucleation of the reversed domain or by the uniform rotation of the magnetic moment. (1)Uniform rotation model: Firstly, in order to analyze whether the coercivity mechanism belongs to uniform rotation of the magnetic moments, the dependence of H_c/M_s on $2K_1/M_s^2$ was investigated. It is found that the experimental data only fall on a straight line in a part of the temperature region. Even in the section of the line, the slope of the line is not 1, which does not meet the theoretical requirements of uniform rotation. So we can exclude the possibility that the magnetization process is uniform rotation of the magnetic moments. (2)Strongly correlated reverse domain nucleation model When the grains in the magnetic powder are strongly magnetically coupled, a reversion of a misaligned grain would drive the reversion of the neighboring grains. Therefore, the coercivity of the material depends on the grains with the smallest nucleation field. In this case, $\alpha\phi = \alpha\phi^{min}$. The coefficient can be calculated for a given temperature. The value of this angle is about 40 ~ 60 degrees on the basis of the calculation results of the external field angle corresponding to the minimum nucleation field $\alpha\phi^{min}$ at 50K ~ 350K. Fig.1 shows the H_c/M_s vs $2\alpha\phi^{min}K_1/M_s^2$ curve of the powder. The purpose of this curve is to analyze whether the coercivity mechanism of the above powder is the nucleation mechanism of strongly magnetically coupled grains. It can be seen from the figure that the experimental data points basically fall on a straight line, which means that under the framework of micromagnetism, the nucleation mechanism with the magnetically coupled grains can describe the magnetization reversal process of the HDDR powder. Fig.2 shows magnetic domain patterns of the HDDR treated Pr-Fe-B alloys. In the case of the HDDR treated alloys, very fine maze-like magnetic domains were observed and these domains extend over more than 1 μ m in the original large single particles with the mean size of 10 μ m (Fig.2 (b) and (c)). This domain pattern shows a characteristic of

interaction domains, and each domain consists of several fine grains, which are magnetically coupled to form large interaction domains. The evolution of the magnetic domain of HDDR anisotropic Pr-Fe-B magnetic powder under the external applied magnetic field (0 T → 2 T → 0 T → -2 T → 0 T → 2 T) was also investigated. Only the disappearance of the labyrinth domain composed of multiple grains and the appearance of the magnetic domain under the condition of positive magnetization field and negative reverse magnetization field were observed, while the domain wall movement was not observed, which further implies that the nucleation of demagnetization is the main mechanism controlling the coercivity of anisotropic HDDR Pr-Fe-B powder.

[1] T. Takeshita, R. Nakayama, in 11th Workshop on Rare Earth Magnets and their Applications, Pittsburg, USA, 49 (1990). [2] K. D. Durst and H. Kronmüller, J. Magn. Magn. Mater. 68, 63 (1987). [3] H. Kronmüller, K. D. Durst, and M. Sagawa, J. Magn. Magn.Mater. 74, 291(1988). [3] W. L. Chen, W. Liu, and Z. D. Zhang, Phy. Rev. B, 72,224419 (2005)

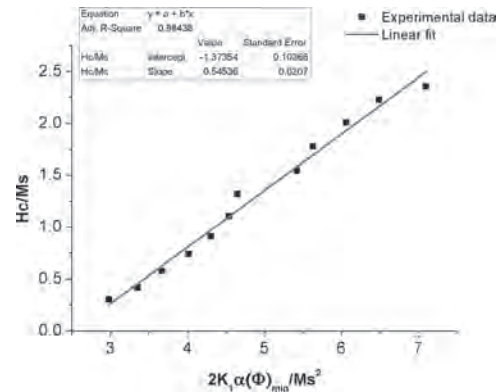


Fig.1 The dependence of H_c/M_s on $2\alpha\phi^{min}K_1/M_s^2$ of HDDR powders

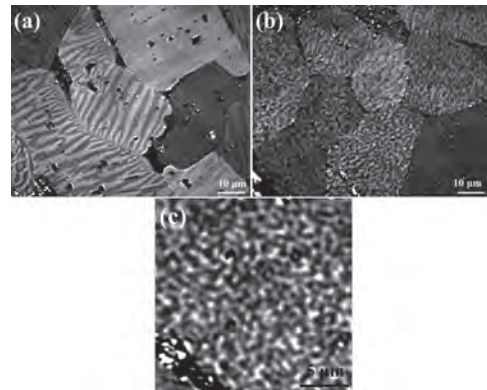


Fig. 2 Magnetic domain Kerr images of Pr-Fe-B alloys (a) before and (b) after the HDDR treatment. (c) zoom in of red rectangle region in the figure (b)

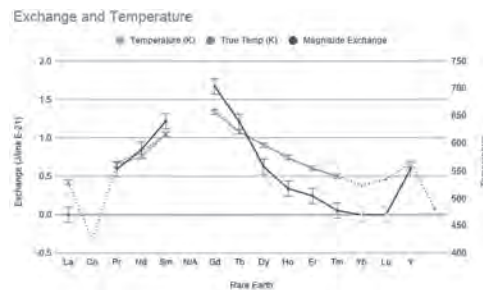
JW-10. Optimisation of Atomistic Modelling Parameters for Nd₂Fe₁₄B-Type Rare Earth Ferromagnets, Using the Curie Temperature and First Order Magnetic Phase Transitions as Figures of Merit.

A. Naden¹, R.W. Chantrell¹ and R.F. Evans¹

¹ Physics, University of York, York, United Kingdom

Cobalt as a substitute for Iron, and combinations of different rare earths in alloy can increase the Curie temperature and coercivity of Nd₂Fe₁₄B type ferromagnets[1]. Complex ferromagnets, with atomic scale ordering, require high resolution simulations which are computationally expensive due to individual treatment of atoms. The compromise of the atomistic model[2], allows nanometer scale simulations with reasonable efficiency, but requires input parameters often derived from ab initio calculations, or Density functional theory, creating a multi-scale model. Complex materials often have several input parameters, such as magnetic exchange and magnetocrystalline anisotropy constants, which cannot be easily evaluated using these methods. As a result, often the requirement is to fit the exchange parameter to macroscopic experimental data. For simple materials this can be evaluated with few test simulations, as the relationship between exchange and macroscopic properties behaves linearly for single element materials, as in the mean field model. Complex materials can have complex relationships between exchange and macroscopic properties, so many test simulations are often required to perform a full sweep of the parameter space. This body of work details the evaluation of exchange and anisotropy constants for 2:14:1, or Nd₂Fe₁₄B type rare earth ferromagnets, using the VAMPIRE atomistic software modelling package. Treating this as an optimisation problem reduces the number of atomistic simulations required for a given numerical precision of constant. Evaluation of exchange constants was performed using the Curie temperature as a figure of merit with several different methods of evaluating the Curie temperature compared for robustness and consistency, with the optimisation of these exchange constants performed with a combination of linear searching and root finding algorithms. These methods have often been compared for various rock magnets[3]. The search uses a locally linear assumption, to prime the low temperature quantum rescaling in VAMPIRE, and to better parallelise the initial stages of the search. Similar approaches are taken to calculate the anisotropy constants of Nd₂Fe₁₄B to reproduce the First Order Magnetic Phase Transition[4] at high external fields and low temperatures. The exchange constant of various rare-earth ferromagnets is reproduced, yielding the correct macroscopic Curie temperatures without reliance on density functional theory/ab initio calculations. Lanthanum was used as the prototype for the Fe-Fe exchange, and this was fixed throughout the other ferromagnets. The Curie temperatures calculated are in good agreement with J.F.Herbst, 1991 [5]. The First Order Magnetic Phase Transition was effectively reproduced, but requires additional tuning for a complete analysis of the relationship between second and fourth order anisotropy constants and the subsequent macroscopic magnetic behaviour.

[1] Wei, L, et al. J. Less Common Metals 126 (1986); [2] R. F. L. Evans, W. J. Fan, P. Churemart, T. A. Ostler, M. O. A. Ellis and R. W. Chantrell, Journal of Physics: Condensed Matter, vol. 26, 103202, (2014); [3] K. Fabian, V. P. Shcherbakov, S.A. McEnroe, Geochemistry, Geophysics, Geosystems, 14, 947, (2013); [4] J. M. Cadogan, J. P. Gavigant, D. Givordt and H. S. Li, J. Phys. F: Met. Phys. 18 779 (1988); [5] J. F. Herbst Rev. Mod. Phys. 63, 819 (1991)



The exchange parameters calculated using the optimisation method result in appropriate Curie temperatures when evaluated using the VAMPIRE atomistic modelling software package. The Curie temperature calculated from this simulation compares well to the values from literature[5] (Herbst, 1991). Ce₂Fe₁₄B has not been calculated, as the rare earth behaves sufficiently differently to Lanthanum as to prevent using Lanthanum as the base of Cerium's Fe-Fe exchange in this manner. The magnitude of the exchange is presented, the heavier rare earths are ferrimagnetic in the 2:14:1 phase.

JW-11. Nano-Sized Anisotropic Sm-Fe-N Particle Preparation by Induction Thermal Process.Y. Hirayama¹, L. Zheng¹ and K. Takagi¹*1. National Institute of Advanced Industrial Science and Technology, Nagoya, Japan*

High-performance, high-efficiency motors are indispensable for the development of electric vehicles and the realization of electric aircraft. The key is the development of permanent magnets that can withstand use even at high temperatures. The reported Sm-Fe-based magnet compounds [1-3] have a high Curie temperature, and the values of the magnetic anisotropy field and saturation magnetization are higher or comparable to those of Nd₂Fe₁₄B. In this work, we focused on the Induction thermal plasma (ITP) process as a new process for obtaining anisotropic nano-sized powder of these permanent magnet compounds. The ITP process is a physical bottom-up process that can synthesize nano-sized single-crystal powders due to the high quenching effect during the process [4, 5]. When this process can be applied to prepare a fine permanent magnet anisotropic powder of around 100 nm, which is difficult to obtain by the conventional method, can be synthesized, leading that an anisotropic magnet having a large coercive force can be obtained. Therefore, as the first step, we tried to produce nano-sized anisotropic Sm-Fe-N alloy powder and to evaluate the feasibility of preparing the nano-sized powder by the ITP process. The mixed powder of Sm powder ($D_{50} = 18 \mu\text{m}$) and Fe powder (particle size about $3 \mu\text{m}$, High Purity Chemical Laboratory) was used as a starting powder for the ITP process. The ITP process was performed under the condition of process pressure of 100 kPa. The input power was 6 kW. Since Sm metal powder as a starting material is not commercially available, we prepared micron-sized Sm powder by using a crucible-less skull gas atomizing device (manufactured by Sinfonia Technology Co., Ltd.). Though the ITP process, the obtained nano-sized powder was sealed in a quartz capillary in a glove box, and the crystal structure was evaluated by a powder X-ray diffraction experiment with Aichi Synchrotron BL5S2 without oxidizing the powder. In addition, SEM and STEM were used for microstructure analysis. From the XRD profile, SmFe₂ and Sm-Fe with TbCu₇-type structure were identified as Sm-Fe alloy phases. From the SEM image, the average particle size of the SmFe alloy was about 100 nm. The Sm-Fe alloy particles were found to be single crystals by high-resolution STEM observation. In addition, many particles consist of Fe-core/Sm-shell and Fe-core/SmFe-shell were also observed. Combine the results obtained from the XRD measurement and the STEM observation, it was found that the Fe detected by XRD is not the Fe particle but the Fe core in the core-shell structure. This is because the vapor pressure of Sm is more than 10000 times higher than that of Fe, so in the thermal plasma process, Fe nucleates first and then Sm and Fe or Sm agglomerates around the Fe particles. After the nitriding process by the heat treatment at an elevated temperature of 400C in N₂ flow for 15min, nitrogen was surely introduced into the Sm-Fe lattice, which is confirmed from the lattice expansion. For the first time in this study, we succeeded in synthesizing Sm-Fe-N anisotropic particles with a particle size of 100 nm or less using the ITP process. Especially, the preparation of the anisotropic particle with TbCu₇-type structure will lead to the next generation high-performance permanent magnet.

[1] T Iriyama, K Kobayashi, N Imaoka et al., IEEE Trans. Magn., Vol.28, p.2326 (1992) [2] S. Sakurada, A. Tsutai, T. Hirai et al., J. Appl. Phys., Vol.79, p4611 (1996) [3] Y. Hirayama, Y.K. Takahashi, S. Hirose et al., Scr. Mater., Vol.138, p.62 (2017) [4] Y. Hirayama and K. Takagi, J. Alloys. Compd., Vol.792, p.594 (2019) [5] Y. Hirayama, M. Shigeta, Z. Liu et al., Available at <http://dx.doi.org/10.2139/ssrn.3692994>

JW-12. Fabrication and Characterisation of Polymer-Bonded Flexible Anisotropic Micro-Magnet Arrays.

*E. Fontana*¹, *L. Motyckova*¹, *F.O. Keller*¹, *G. Groza*¹, *M. Bonfim*²,
*L. Ranno*¹, *T. Devillers*¹ and *N. Dempsey*¹

1. Institut Néel, UGA-CNRS, Grenoble, France; 2. DELT, Universidade Tecnológica Federal do Paraná, Curitiba, Brazil

Permanent magnets are a key component of a wide range of everyday devices, including motors, actuators, transducers and sensors. Depending on the application needs, magnets are based on high performance rare-earth transition metal phases or on more moderate performance hard ferrite phases, and they may be sintered or polymer bonded. While the remanence of bonded magnets is necessarily limited by dilution of the magnetic material in a non-magnetic matrix, they are cheaper in both material and fabrication costs. What is more, the mechanical properties of the magnets can be tuned according to the choice of matrix. Traditional fabrication routes for polymer bonded magnets include calendaring, injection moulding, extrusion, and compression bonding [1] and there has been much recent activity concerning 3D printing of polymer bonded magnets [2,3,4]. Down-sizing magnets opens new opportunities for their use in micro-scaled devices with applications in fields as diverse as telecommunications, energy management and bio-medicine. Sputtering combined with micro-patterning has been used to make fully dense magnets which are a micro-scale equivalent to sintered magnets while various techniques including casting and screen printing combined with photo-lithography have been used to make polymer bonded micro-magnets [5]. Sputtered films may be isotropic or textured, depending on the deposition temperature, whereas micro-scaled polymer bonded magnets reported to date are isotropic. Here we present a process developed to fabricate arrays of anisotropic, flexible bonded micro-magnets. The study focuses on micro-magnets prepared using commercial single crystalline hard ferrite (B_c : 195 mT, H_c : 123 kA/m) or Sm-Fe-N (B_c : 1.31 T, H_c : 889 kA/m) powders mixed with polydimethylsiloxane (PDMS). This binder was chosen so as to have flexible micro-magnets that can be used to study the influence of mechanical forces on cell development [6]. The innovative aspect of this process, schematized in Fig. 1, consists in the possibility to transfer a specific pattern from a silicon mould, made by deep reactive ion etching (DRIE), to a magnetically aligned powder-polymer composite. The composite is maintained within the mould during the alignment step by coverage with a glass slide. A first soft curing step is performed with the cover-slide in place, then a final curing is performed to attach the micro-magnets to a PDMS base. The procedure has been used to fabricate arrays of micro-magnets of thickness ranging from 50 μm to 300 μm and width in the range from 20 μm to 4000 μm . As a magnetic field source, bulk magnets, a superconductive coil and pulsed magnetic field systems were tested. The degree of alignment was assessed by measuring the hysteresis loops of fully cured micro-magnet arrays with the measuring field applied parallel or perpendicular to the direction of the alignment field. Note that these measurements were made prior to removal of the arrays from the Si mould, to prevent distortion of the flexible micro-magnets under the torque induced by the measuring field. As an example, easy and hard axes hysteresis loops made on an array of SmFeN-bonded square micro-pillars with in-plane dimensions of 200x200 μm^2 and a height of 300 μm , aligned in a magnetic field of 800 mT, are compared in Fig. 2 a. As can be expected, higher intensity fields were needed to align the SmFeN particles compared to the ferrite particles. The stray fields produced by aligned and non-aligned micro-magnet arrays were measured using an in-house developed Scanning Hall Probe Microscope [7]. In Fig. 2 b we present the z-component of the stray field produced at a height of 50 μm above the SmFeN micro-magnet array featured in Fig. 2 a. In this presentation, we will give details of structural and magnetic characterisation as well as simulations of arrays of ferrite and SmFeN bonded micro-magnets. We will also report on the actuation of these micro-magnets under the influence of a 3D magnetic field. Finally, we will present prospects for the further development and use of such micro-magnet arrays.

[1] J. Ormerod and S. Constantinides, *Journal of Applied Physics*, Vol. 81, p.4816 (1997) [2] C. Huber, C. Abert and F. Bruckner, *Appl. Phys. Lett.*, Vol. 109, p.162401 (2016) [3] L. Li, A. Tirado and I. C. Nlebedim, *Scientific Reports*, Vol. 6, p.36212 (2016) [4] K. Sonnleitner, C. Huber and I. Teliban,

Appl. Phys. Lett., Vol. 116, p.092403 (2020) [5] N.M. Dempsey, “Nanoscale Magnetic Materials and Applications”, J.P. Liu et al.(eds), p.661, (Springer 2009) [6] N.M. Dempsey, “Handbook of Magnetic Materials”, J.M.D. Coey et al. (eds), Springer, (in-press) [7] G. Shaw, R.B.G. Kramer and N. M. Dempsey, *Rev Sci Inst*, Vol.87, p.113702 (2016)

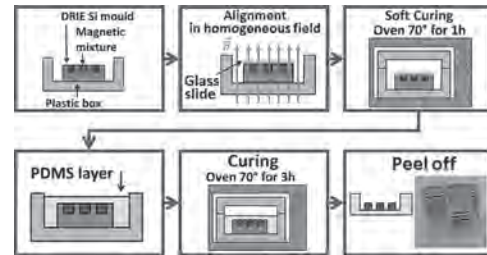


Fig. 1 Schematic of the process developed for the fabrication of arrays of flexible, anisotropic bonded micro-magnets.

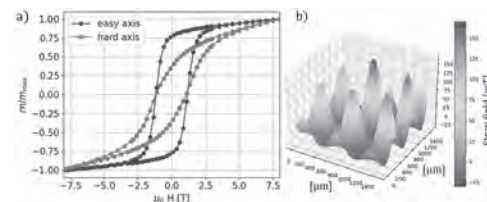


Fig. 2 (a) Hysteresis loops of an array of SmFeN (30 vol %) - PDMS (70 vol %) bonded micro-magnet pillars with in-plane dimensions of 200x200 μm^2 and a height of 300 μm . (b) Z-component of the stray magnetic field produced by this array, measured using a micro-Hall probe scanned at a height of 50 μm above the magnet array.

JW-13. Magnetic Anisotropy of Chemically Ordered CoPt and FePt Nanoparticles, why is it so Different?

F. Tournus¹, A. Tamion¹, A. Rogalev², F. Wilhelm², J. Gutierrez³, L.E. Diaz-Sanchez³, G.M. Pastor⁴ and V. Dupuis¹
 1. Institut Lumiere Matiere, Villeurbanne, France; 2. ESRF, Grenoble, France; 3. Universidad Autonoma del Estado de Mexico, Toluca, Mexico; 4. Institut fur Theoretische Physik, Universitat Kassel, Kassel, Germany

The CoPt and FePt alloys, when chemically ordered in the L1₀ phase [1], are among the magnetic materials displaying the highest magnetic anisotropy constant. Therefore, they are perfect candidates for ultra-high density magnetic storage applications, provided nanoparticles can be prepared in such a high anisotropy phase. In the bulk L1₀ phase both alloys exhibit close magnetic and structural properties. Indeed, the tetragonalization of the unit cell, measured by the c/a ratio is almost the same and equal to 0.97 for both alloys while their anisotropy constant is equal to 5 and 7 MJ.m⁻³ respectively for CoPt and FePt [1]. The first part of this work is then to determine and compare the intrinsic magnetic anisotropy constant of CoPt and FePt L1₀ nanoparticles. For this purpose, we dilute, as far as possible, mass-selected nanoparticles (around 3 nm diameter) in an inert carbon matrix to avoid coalescence and to make magnetic interactions negligible. To promote the chemically L1₀ ordered phase the samples have to be annealed at 600°C during two hours. The magnetic properties are then determined using SQUID magnetometer and a global fitting procedure of the entire set of magnetic measurements [2,3] (see Fig. 1). In a second part we try to explain their significant differences using extended X-ray absorption fine structure measurements and atomic relaxation calculations (see Fig. 2). We conclude that the very high magnetic anisotropy measured in FePt nanoparticles [4] is related to the weak atomic relaxation in this alloy, while for chemically ordered CoPt nanoparticles the strong atomic relaxation in the Co plans [5] seems to reduce drastically the magnetic anisotropy.

[1] P. Andreazza et al., Surf. Sci. Rep. 70, 188 (2015) [2] A. Tamion et al., Phys. Rev. B 85, 134430 (2012) [3] A. Hillion et al., Phys. Rev. B 88, 094419 (2013) [4] P. Capiod et al., Phys. Rev. Lett. 122, 106802 (2019) [5] N. Blanc et al., Phys. Rev. B 87, 155412 (2013)

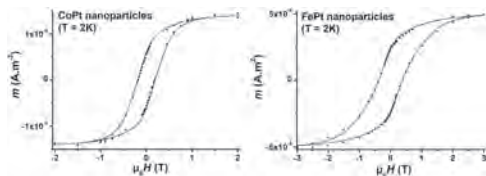


Fig. 1: Low temperature hysteresis loop measured for a diluted assembly of CoPt nanoparticles (left) and FePt nanoparticles (right), after annealing. The dots correspond to measurements while the line is obtained with a global fit taking into account the particle size and magnetic anisotropy distributions. Note that despite the particles are similar (around 3.5 nm diameter), the coercivity is much larger for FePt nanoparticles.

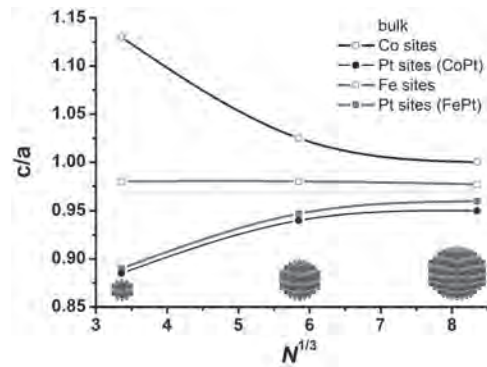


Fig. 2: Comparison between the mean c/a ratio (computed from inter-atomic distances: homoatomic and heteroatomic bonds) around transition metal atoms and Pt atoms, from density functional calculations of relaxed CoPt or FePt clusters. N represents the number of atoms used to build perfect truncated octahedrons. The lines are guide to the eye, while the dashed line indicates the c/a ratio in the bulk L1₀ phase.

JW-14. Manipulation of Phase Transformation and Microstructure in Mn_3Ga Using Magnetic Field Annealing.

G. Kirshte¹, C. Blum¹, J. Freudenberger¹, S. Wurmehl¹ and B. Büchner¹

¹ IFW Dresden, Leibniz-Institut für Festkörper- und Werkstofforschung Dresden eV, Dresden, Sachsen, DE, academic/physics, Dresden, Germany

In the 1980s ferrous materials were the first subject of extensive investigation on magnetic field annealing (MFA). Hereby, the potential of using high external magnetic fields as an additional degree of freedom for materials synthesis and tailoring of microstructures in solid state was demonstrated. Since then, due to the progression in magnetic materials and superconducting magnets, processing in magnetic field has become both less costly and more viable. Hence, MFA is achieving renewed attention nowadays. The processing technique might even evolve into a valuable tool on broad industrial level, since it provides the opportunity to save energy by lowering heat treatment temperatures and shortening processing times. Furthermore, the application of an external high magnetic field as an additional independent processing parameter allows for stabilization of metastable phases and creation of texturized microstructures that are not accessible on zero-field conditions. Nevertheless, a lot of experimental work and modeling is still required to entirely unveil the mechanisms of MFA for gaining control on such material manipulation. Mn_3Ga is a very interesting and highly suitable candidate for exploring MFA. The intermetallic compound occurs in three different crystal structures, all of them possessing rich magnetic properties attractive for different kinds of application. Regarded as a rare-earth-free permanent magnet in potential application, especially the tetragonal phase meets the particular requirements of being exceptionally prone to manipulation by MFA. Due to the ferrimagnetic ordering it exhibits a much higher magnetic moment compared to the other Mn_3Ga polymorphs. Therefore, it is supposed to be thermodynamically favored in its formation under influence of an external magnetic field. Additionally, the tetragonal structure shows high anisotropy in susceptibility, which is conditional to establish a texture upon MFA. As already reported by *Ener et al.*, the phase transition from hexagonal to tetragonal $Mn_{70}Ga_{30}$ can be accelerated remarkably by combining severe plastic deformation and MFA [1]. In contrast, the study at hand adds the investigation of the influence of different degrees of deformation plus the impact of MFA on the phase transformation starting from a predominantly cubic structure of the parent material Mn_3Ga . For this purpose annealing was performed at 400°C, lasting for at least 0.5 hours and up to 14 days. In the case of MFA samples, a magnetic flux density of 7 T was applied. By X-ray diffraction the different stages of phase transformation were observed. Further characterization regarding microstructure and magnetic properties was achieved using light and electron microscopy as well as SQUID magnetometry. The results indicate that the properties after long-term annealing are very similar, independent of previous state of deformation and use of magnetic field. More specifically, after 14 days of annealing samples attained a phase-pure tetragonal structure and show equal remanence. Nevertheless, within the first 24 hours of annealing the differences are enormous with respect to phase formation, microstructure and magnetic properties. In case of zero-field annealing of highly deformed samples or MFA of undeformed samples, reaching the tetragonal structure is postponed by a pronounced intermediate formation of the hexagonal phase. Apart from that, combining previous deformation and MFA accelerates the phase transformation effectively. Furthermore, with increasing degree of deformation the coercivity can be increased stepwise. However, the development of coercivity over annealing time is complex for both zero-field annealing and MFA. An attempt to solve this complex behavior by relating microstructure and coercivity is presented. Finally, the phase transformation behavior of Mn_3Ga under influence of an external magnetic field is correlated to changes in defect mobility and development of local deviations in composition (see Fig. 1).

[1] S. Ener, K.P Skokov, D.Y. Karpenkov, M.D. Kuz'min and O. Gutfleisch, *Journal of Magnetism and Magnetic Materials*, 382, 265-270 (2015)

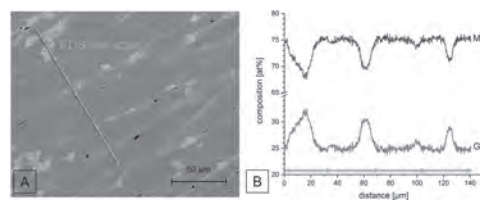


Fig. 1: EDS line scan of highly deformed sample after 1 h of MFA A) SEM picture showing local course of scan (bright areas in hexagonal, grey areas in tetragonal structure) B) compositional mismatch along line scan

JW-15. Magnetic Properties of Bulk Magnets Manufactured by the Cryo-Milled $Mn_{54}Bi_{46}$ Powder.

C. Bae¹, H. Lee¹, G. Lee¹, M. Kang¹ and J. Kim¹

1. Materials Science and Chemical Engineering, Hanyang University - Ansan Campus, Ansan-si, The Republic of Korea

Recently, the topic of rare-earth-free permanent magnets has received considerable attraction for the alternative to rare-earth magnets due to the resource crisis and the high cost of rare-earth metals. Among rare-earth-free permanent magnetic materials, the low-temperature phase (LTP) of MnBi has been considered as a potential alternative because it exhibits an unusual positive temperature coefficient of coercivity in the temperature range 153-550 K. Because of the above magnetic property, the MnBi-LTP has a higher coercivity compared to $Nd_2Fe_{14}B$ permanent magnetic material at elevated temperature, and it was recently reported that the coercivity of MnBi-LTP reached up to 28.3 kOe at 530K. According to previous researches, this excellent coercivity characteristic of the MnBi-LTP is attributed to its high magneto-crystalline anisotropy ($K_1 \approx 1.6 \times 10^6$ J/m³ at 300 K)[1]. In spite of such excellent intrinsic magnetic properties, the MnBi-LTP bulk magnets practically fabricated have a significantly lower energy product compared to its theoretical value ($BH_{max} \approx 16$ MGOe at 300 K) due to engineering issues that occur during the mechanical milling process such as decomposition of the magnetic phase, manganese oxidation, and agglomeration. At present, several approaches including high or low energy ball-milling (HEBM or LEBM), surfactant-assisted ball-milling (SABM) have been reported to avoid those issues. However, those approaches based on a ball milling process at room temperature have inevitably a restriction in reducing the powder size as well as agglomerating the powder by cold welding phenomenon. Consequently, this leads to the degradation of the energy product by lowering the total anisotropic characteristics of the MnBi-LTP bulk magnets. Therefore, it is essential to synthesize the particle size of the MnBi-LTP to be close to that of its single magnetic domain (≈ 500 nm) in order to achieve the MnBi-LTP bulk magnets with improved anisotropic characteristics. In this regard, it has been proposed that the cryo-milling method is able to be one of the approaches to synthesize the MnBi-LTP particle satisfying the above-required size. It is well known that the cryo-milling method is able effectively to reduce the particle size as well as to avoid cold welding and agglomeration of the powder because it carried out at a temperature lower than 123 K, where materials become brittle and friable[2]. It has been reported that the cryo-milling method is successfully synthesized nanocrystalline structures in ductile materials such as Fe, Ni, Al, Zn, etc. However, researches into the cryo-milling of MnBi alloys have been rarely conducted. In this study, the $Mn_{54}Bi_{46}$ -LTP powders were synthesized by the cryo-milled method combined with the addition of a surfactant (stearic acid) as well as calcium, and a schematic illustration of the process is shown in figure 1. As shown in the figure, a stainless-steel vial containing a mixture of powder, balls, surfactant, and calcium was vibrated with a certain frequency, and the temperature was maintained at 77 K during the milling process by the flow of liquid nitrogen. In addition, surfactant (stearic acid) and calcium were added in order to suppress the particle agglomeration and manganese oxidation, respectively. Figure 2 shows the Hysteresis loops for the cryo-milled $Mn_{54}Bi_{46}$ powder according to the addition of surfactant and calcium. All of the milling conditions have an identical ball-to-powder ratio of 18:1, and stearic acid and calcium were added 0.225g and 0.01g to $Mn_{54}Bi_{46}$ powder of 0.9 g, respectively. As shown in the figure, the cryo-milled $Mn_{54}Bi_{46}$ powder without any addition has a H_c of 14.1 kOe with a remanence (M_r) of 40.7 emu/g and a magnetization ($M_{s,2.5T}$) of 40.7 emu/g, while the cryo-milled $Mn_{54}Bi_{46}$ powders with the addition of stearic acid have a higher both M_r of 51.0 emu/g and $M_{s,2.5T}$ of 53.2 emu/g. These results, especially the increase of $M_r/M_{s,2.5T}$ ratio, indicate that the powders were effectively separated by the addition of stearic acid during the milling process. In addition, the result of improved $M_{s,2.5T}$ means that the decomposition rate of the magnetic phase decreases as the impact energy received by the powder is alleviated by the stearic acid on the powder surface. Furthermore, from the result of magnetic properties under the calcium addition conditions, it is found that calcium addition plays an important role in the purification of $Mn_{54}Bi_{46}$ -LTP powder by suppressing manganese oxidation. Based on these results, further investigation on the optimization of the cryo-milling process

and the magnetic properties of bulk magnets manufactured with cryo-milled powders will be discussed.

[1] V. N. Antonov and V. P. Antropov, *Low Temperature Physics*, vol. 46, no. 1, p.1 (2020) [2] N. K. Katiyar, K. Biswas, and C. S. Tiwary, *International Materials Reviews*, p.1 (2020)

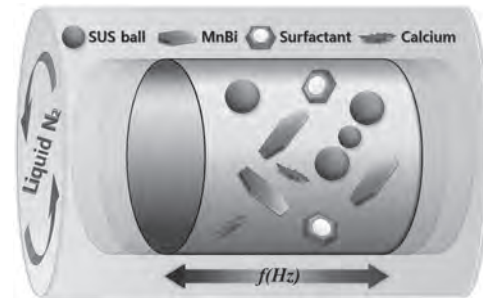


Fig. 1. A schematic illustration of the cryo-milling process used in this study.

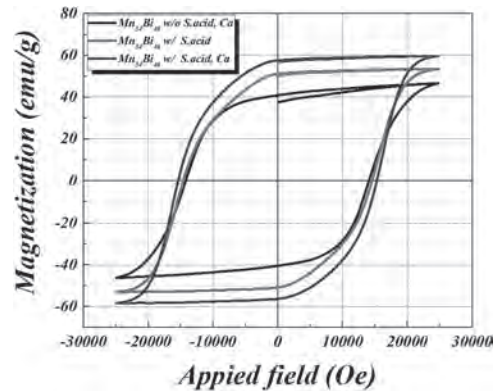


Fig. 2. Hysteresis loops for the cryo-milled $Mn_{54}Bi_{46}$ powder measured parallel to the alignment direction.

JW-16. Temperature Dependence of Magnetic Properties of Sb Substituted LTP-MnBi Alloy Ribbons.

M. Kang¹, H. Lee¹ and J. Kim¹

1. Hanyang University Department of Materials Science and Chemical Engineering, Ansan, The Republic of Korea

In recent years, growing concerns about energy and environment issues strongly demand that electro-magnetic devices, especially motors, are required to increase their energy conversion efficiency and performance. Thus, the development of inexpensive permanent magnets with high energy product have been attracted much attention because they can economically reduce the energy consumption and miniaturize the motor. In order to satisfy these requirements, the development of new rare earth free magnetic alloys with high remanence magnetization values and coercivity have been strongly required. A low-temperature phase (LTP) MnBi intermetallic compound alloy has higher maximum energy product than ferrite magnets and it has higher coercivity than Nd-Fe-B magnets at high temperature. Because of these advantages, the MnBi alloy has been scientifically and technically considered to be one of excellent candidates for a "gap-magnet" to fill the large magnetic property difference between Nd-Fe-B and ferrite magnets. However, the LTP-MnBi alloy has the positive coercivity temperature coefficient. Thus it is well-known that the coercivity of the alloy sharply decreases as the operating temperature decreases below 273 K. This temperature dependency limits the use of the LTP-MnBi alloy in motors. To overcome this limitation, many researches have been conducted to increase the coercivity of the MnBi alloy by adding new alloy elements as well as optimizing the conditions of the powder fabrication and post-heat treatment processes. The first-principle calculation results of Mn-Bi ternary alloys suggested that the change of the Mn atomic distance by adding interstitial and substitutional atoms could increase the magnetic moment and anisotropy property of the MnBi alloy [1], [2]. Bi and Sb atoms have the same number of valence electrons and the similar atomic size. This indicates that, while maintaining its crystal structure, Sb atoms can substitute the Bi site of the Mn-Bi alloy, resulting in the atomic distance change of Mn atoms. Therefore, in this study, we focused on the effect of the Sb addition on the crystalline structure and temperature dependence of the magnetic properties of the Mn-Bi alloy. In this experiment, MnBi-Sb ribbons were prepared in a arc-melting and a melt-spinning process followed by an annealing. High purity Mn, Bi and Sb chips were weighed according to the $Mn_{54}Bi_{46-x}Sb_x$ ($x = 0.0, 1.5, 3.0, 5.0$) ratio, and then the arc melting was carried out. Induction melting was used for the melt-spinning process and MnBi-Sb melt-spun ribbons were produced using a copper roller. In order to obtain the LTP-MnBi crystal structure, the melt-spun ribbons were annealed in a tube furnace at 270 ~ 330°C for 6 ~ 48 hr in Ar atmosphere. The crystal structure of annealed LTP-MnBi alloy ribbons were analyzed by an X-ray diffractometer (XRD, Rigaku, D/MAX-2500) and the relative weight fraction and lattice parameter were calculated using a Rietveld refinement by JADE 9.5 (Materials Data, Inc.). The magnetic properties of the ribbons were measured by SQUID-VSM (Quantum Design, MPMS-3) with a maximum applied field of 5 T at 223, 248, 298, 378 K. In the magnetic property measurement, the annealed ribbons were measured without any magnetic alignment process. Fig. 1. (a) shows the XRD patterns of annealed $Mn_{54}Bi_{46-x}Sb_x$ ($x = 0 \sim 5$) ribbons at 285°C for 24 hr. When $x = 0$, only XRD peaks of the single LTP-MnBi phase were observed. However, the XRD peaks of the $Bi_9Mn_{10}Sb$ phase, i.e. antiferromagnetic phase, began to appear when x was 1.5. Only $Bi_9Mn_{10}Sb$ phase peaks were found when x reached 5. It is also noticeable that the (101) XRD peak position of the LTP-MnBi phase increased with increasing the Sb content. This means that the lattice parameter of the LTP-MnBi crystal structure was reduced by adding Sb atoms. Figure 1 (b) shows changes in the lattice parameters of the $Mn_{54}Bi_{46-x}Sb_x$ ($x = 0 \sim 3$) ribbons by the Rietveld refinement method. As the amount of Sb increased, the lattice parameters of a and c and the lattice volume were monotonically decreased. This should be due to that the radius of the Bi and Sb atoms is 156 pm and 140 pm, respectively, and the Sb atoms occupy the Bi sites. Change in the coercivity of the $Mn_{54}Bi_{46-x}Sb_x$ ($x = 0 \sim 3$) annealed ribbons with temperature are shown in Fig. 2. (a). The coercivity of the single phase LTP- $Mn_{54}Bi_{46}$ ribbon dramatically decreased from 2886 to 265 Oe when measured at 378K and 223K, respectively. This shows that the coercivity

measured at 223K was reduced to less than 10% compared to the value measured at 378K. However, by the addition of Sb atoms, the coercivity of the $Mn_{54}Bi_{46-x}Sb_x$ ribbons increased significantly over the entire temperature range. When $x=3$, the coercivity at 223K still had a value of 3608 Oe. On the contrary, the addition of Sb atoms ($x=3$) reduced the saturation magnetization value measured at 223K from 83.6 to 64.1 emu/g. Despite the drop in the saturation magnetization, the above results showed that the $Mn_{54}Bi_{46-x}Sb_x$ ($x = 1.5 \sim 3$) alloy had the excellent magnetic properties as a hard magnetic material even at low temperature due to the improvement of its coercivity. In order to fabricate bulk magnets, the development of powdering and magnetic alignment processes of the MnBiSb annealed ribbons is in progress, and detailed results will be presented.

[1] J. Park et al., *Metals* 4(3), 455 (2014) [2] T.X. Nguyen et al., *Physica B* 552, 190 (2019)

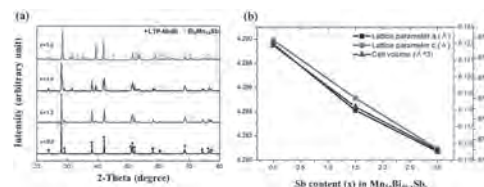


Fig. 1. (a) XRD patterns and (b) lattice parameters of $Mn_{54}Bi_{46}Sb_x$ ($x = 0.0 \sim 5.0$) annealed ribbons

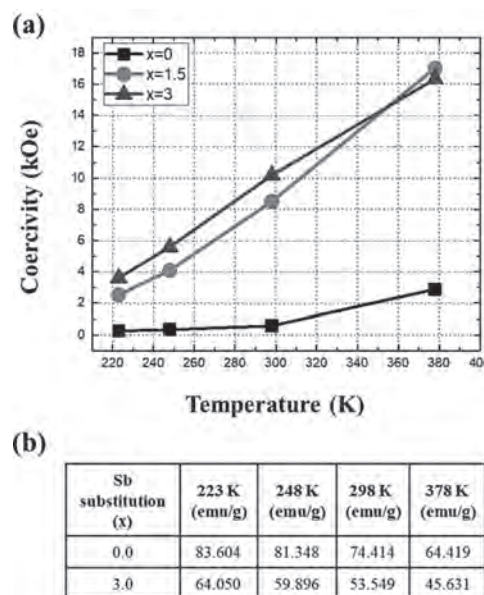


Fig. 2. Magnetic properties changes of $Mn_{54}Bi_{46}Sb_x$ ($x = 0.0, 1.5, 3.0$) annealed ribbons with temperature

JW-17. Synthesis of α'' -(Fe, M)₁₆N₂ Nanoparticles Obtained by Hydrogen Reduction and Subsequent Nitridation Starting From α -(Fe, M)OOH (M= Co, Al).

M. Tobise¹ and S. Saito¹

¹. Electronic engineering, Tohoku University, Sendai, Japan

Introduction The metastable α'' -Fe₁₆N₂ is considered as a candidate for rare earth free semi-hard magnetic materials [1]. It is necessary to improve magnetocrystalline anisotropy of α'' -Fe₁₆N₂ to obtain higher coercivity H_c [2]. Many theoretical calculations and thin film experiments substituting Fe with some elements such as Co, Ni, Mn, Al, etc. have been done. For example, Co is suggested to increase in magnetocrystalline anisotropy [3]. As one of the synthesis methods of α'' -Fe₁₆N₂ nanoparticles, it is well known that the nitridation of α -Fe nanoparticles produced by reduction of iron hydroxide such as α -FeOOH. Previously, we have reported that the influence of substituting Co, Al for Fe by synthesizing α'' -(Fe, Co)₁₆N₂ or α'' -(Fe, Al)₁₆N₂ nanoparticles [5] and revealed that Co substitution results in the temperature regimes for reduction and nitridation were confirmed to very narrow limits, on the other hand Al substitution brings the wider temperature regimes. In this paper, in order to investigate the complex substitution effect of Fe by Co and Al, we challenged to the synthesis of α'' -(Fe_{0.95}Co_{0.02}Al_{0.03})₁₆N₂ nanoparticles by hydrogen reduction of α -(Fe_{0.95}Co_{0.02}Al_{0.03})OOH as a starting material and subsequent nitridation. Experimental We used commercially available α -(Fe_{1-x}M_x)OOH (M= Co, Al, x= 0, 0.02, 0.05) and α -(Fe_{0.95}Co_{0.02}Al_{0.03})OOH nanoparticles as a starting material. The conditions for reduction and nitridation were systematically examined to obtain higher yield of α'' -(Fe_{1-x}M_x)₁₆N₂ or α'' -(Fe_{0.95}Co_{0.02}Al_{0.03})₁₆N₂ according to the following procedure. The α -(Fe_{1-x}M_x)OOH nanoparticles were first reduced at 300 - 500 °C for 4 hours in a H₂ gas flow. Nitridation was subsequently performed at 150 - 180 °C for 5 hours in an NH₃ gas flow. Crystallite diameter D_c of reduced α -Fe_{1-x}M_x nanoparticles was measured as average diameter of nanoparticles using Scherrer's formula based on X-ray diffraction (XRD) with Co K α radiation. Morphological changes were observed using transmission electron microscopy (TEM). For magnetic properties measurements, these nanoparticles were packed into a disk shape (6 mm diameter, 1 mm thick) with resin. Magnetization M_{15k} and coercivity H_c were measured using vibrating sample magnetometer (VSM) with a maximum applied magnetic field of 15k Oe. Results Fig. 1 (a) shows the regions in the nitridation temperature versus reduction temperature diagrams corresponding to where the α'' -phase was produced. M_{15k} and H_c values of the assembled nanoparticles are also indicated. α'' -phase was produced under the limited conditions of reduction temperature of 340 °C and nitridation temperature of 170 °C for starting from α -(Fe_{0.98}Co_{0.02})OOH. On the contrary, α'' -phase was produced under broad conditions of reduction temperatures of 400 - 500 °C and nitridation temperatures of 155 - 170 °C for starting from α -(Fe_{0.98}Al_{0.02})OOH. In the case of starting from α -(Fe_{0.95}Co_{0.02}Al_{0.03})OOH, α'' -phase was produced under the conditions of reduction temperatures of 400 - 500 °C and nitridation temperature of 160 °C. The conditions of α'' -phase production were broadened by Al addition to Co. Fig. 1 (b) shows TEM images for the nanoparticles after nitridation starting from α -(Fe_{0.98}Co_{0.02})OOH, α -(Fe_{0.95}Al_{0.05})OOH and α -(Fe_{0.95}Co_{0.02}Al_{0.03})OOH. These nanoparticles are synthesized with hydrogen reduction at 340 °C for 4 hours and subsequent nitridation at 170 °C for 5 hours for α -(Fe_{0.98}Co_{0.02})OOH, and with hydrogen reduction at 400 °C for 4 hours and subsequent nitridation at 160 °C for 5 hours for α -(Fe_{0.98}Co_{0.02})OOH and α -(Fe_{0.95}Co_{0.02}Al_{0.03})OOH, respectively. The particle size of nanoparticles after nitridation starting from α -(Fe_{0.98}Co_{0.02}Al_{0.03})OOH are between the ones of starting from (Fe_{0.98}Co_{0.02})OOH and α -(Fe_{0.95}Al_{0.05})OOH. This result suggested that Al was effective to avoid sintering during reduction. Fig. 2 (a) shows the relationship between M_{15k} and H_c for the nanoparticles after nitridation starting from α -(Fe_{0.98}Co_{0.02})OOH, α -(Fe_{0.95}Al_{0.05})OOH and α -(Fe_{0.95}Co_{0.02}Al_{0.03})OOH. In the case of starting from α -FeOOH was also shown. Higher H_c were obtained by the complex of Co and Al compared to Co or Al alone. Fig. 2 (b) shows H_c change as a function of D_c of those nanoparticles. This result indicates that there is a good relationship between H_c and D_c regardless additive composition. H_c increases with decrease in D_c . In the case of nanoparticles after nitridation starting from α -(Fe_{0.95}Co_{0.02}Al_{0.03})OOH gives the smallest D_c of

22 nm and highest H_c of 1800 Oe. It is assumed that Al addition to Co is effective to prevent crystalline growth which leads to high H_c of α'' -phase. To clarify the reason of increase in H_c , further precise investigation of the distribution of Al and the relationship between anisotropy field of nanoparticles after nitridation will be presented in this conference.

[1] R. Skomski et al., Scr. Mater., 112 (2016) 3 [2] M. Tobise et al., J. Magn. Soc. Jpn, 41 (2017) 58 [3] Y. Jiang et al., AIP Adv., 6 (2016) 056007 [4] L. Ke et al., Phys. Rev. B, 88 (2013) 024404 [5] M. Tobise et al., AIP Adv., 9 (2019) 035233

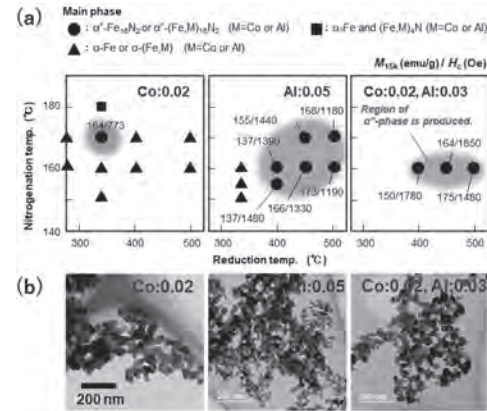


Fig. 1. (a) The regions in the nitridation temperature versus reduction temperature diagrams corresponding to where the α'' -phase was produced and M_{15k} and H_c values of the nanoparticles are also indicated. (b) TEM images for the nanoparticles after nitridation starting from the material α -(Fe_{0.98}Co_{0.02})OOH, α -(Fe_{0.95}Al_{0.05})OOH and α -(Fe_{0.95}Co_{0.02}Al_{0.03})OOH.

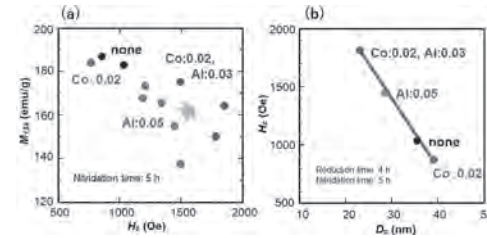


Fig. 2. (a) The relationship between M_{15k} and H_c for the nanoparticles after nitridation starting from the material α -(Fe_{0.98}Co_{0.02})OOH, α -(Fe_{0.95}Al_{0.05})OOH and α -(Fe_{0.98}Co_{0.02}Al_{0.03})OOH. (b) H_c change as a function of crystalline diameter D_c of those nanoparticles.

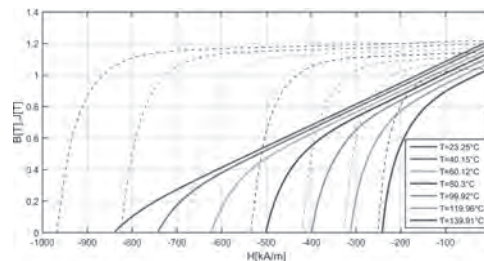
JW-18. Permanent Magnet Non-Linear Demagnetization Model for FEM Simulation Environment.

W. Bekir¹, O. Messal¹ and A. Benabou¹

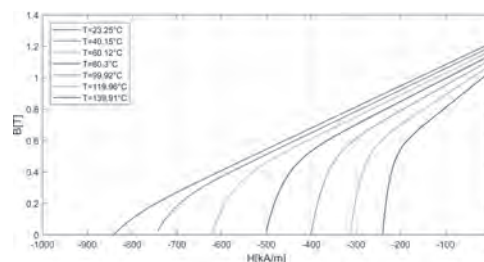
¹. Univ. Lille, Arts et Metiers Institute of Technology, centrale Lille, Junia, ULR 2697 – L2EP, F-59000 Lille, France, Lille, France

Abstract— In this paper, a toolbox baptized “PM-Demag” taking into account the permanent magnet (PM) demagnetization phenomenon has been developed. It is based on a nonlinear demagnetization model which considers the thermal state of the PM and reproduces the knee rounded shape of the $B(H)$ curve. Validations against experimental measurements performed on commercial NdFeB PM are presented. **Index Terms**— Demagnetization, electrical machines, finite element method, permanent magnet. Nowadays, permanent magnets (PM) are widely used in industry, especially in electrical machines. Their use is expected to grow especially in the context of the energy transition of the 21st century. Like soft magnetic materials, they exhibit nonlinear behavior and hysteresis. The part of the curve situated in the second quadrant of the hysteresis cycle, commonly called the demagnetization curve is of interest because it defines the PM properties and operation. It mainly depends on the temperature and on the applied external field. These two parameters strongly influence the magnetic properties of the PM and can cause reversible or irreversible demagnetization [1]. In the special case of a PM electrical machine, an overheating or a short circuit could lead to partial or total demagnetization of the magnets [2]. In this framework, considering the demagnetization phenomena is necessary to precisely predict the change in the PM characteristics and then the machine performances. The knee in the PM demagnetization curve is crucial for a good knowledge of the magnet state. This state depends on the position of the system operating point (intersection between the load line and the demagnetization curve) with respect to the position of the knee. When the operating point is located in the linear zone, above the knee point (reversible part), the PM keeps its initial performances. However, if the operating point is situated below the knee point (irreversible part), the PM must be considered to be partially demagnetized, the remanent flux density decreases and the PM will operate along a minor hysteresis loop which is often approximated by a recoil line [3]. This phenomenon often occurs in electrical machines (especially on the PM surfaces and edges) and could degrade their performances. The degradation degree depends on the temperatures that the machine could reach and on the PM quality. In this work, a toolbox baptized “PM-Demag” based on a non-linear exponential demagnetization model is developed. The model considers the thermal state and it is expressed as a function of the remanent flux density B_r , the coercive field H_c , the relative permeability μ_r , as well as an adjustable coefficient K . All these parameters are themselves expressed as functions of the temperature T . The model parameters are identified from the measurements carried out on a dedicated PM hysteresis meter (HyMpulse of Metis®) for different NdFeB magnets. For example, Fig. 1.a shows the measured $B(H)$ and $J(H)$ demagnetization curves for the N35 NdFeB PM and for different temperatures ranging from room temperature (RT) to 140°C. Figure 1.b shows the simulated $B(H)$ demagnetization curves. The developed “PM-Demag” toolbox will be implemented in code_Carmel, which is a home-made finite element method (FEM) software. Application to an electrical machine is envisaged for the extended paper.

[1] Furlani, E.P. (2001) Permanent Magnet and Electromechanical Devices: Materials, Analysis, and Applications. Academic Press, Waltham. [2] P. Zhou, D. Lin, Y. Xiao, N. Lambert and M. A. Rahman, “Temperature-Dependent Demagnetization Model of Permanent Magnets for Finite Element Analysis,” in *IEEE Transactions on Magnetics*, vol. 48, no. 2, pp. 1031-1034, Feb. 2012, doi: 10.1109/TMAG.2011.2172395. [3] S. Hamidzadeh, N. Alatawneh, R. R. Chromik and D. A. Lowther, “Comparison of Different Demagnetization Models of Permanent Magnet in Machines for Electric Vehicle Application,” in *IEEE Transactions on Magnetics*, vol. 52, no. 5, pp. 1-4, May 2016, Art no. 2100304, doi: 10.1109/TMAG.2015.2513067.



Experimental results [B(H) in solid line].



Simulated B(H) demagnetization curves.

Session JX
SOFT MAGNETIC ALLOYS AND OXIDES
(Poster Session)

Tianxiang Nan, Co-Chair
Tsinghua University, Beijing, China
Raju Ramanujan, Co-Chair
Nanyang Technological University, Singapore, Singapore

JX-01. Magnetic and Structural Properties Analysis of Cerium Substituted Nickel Zinc Ferrites.

R. Dosoudil¹, M. Šoka¹, M. Ušáková¹, E. Ušák¹, V. Jančárik¹ and E. Dobročka²

1. Institute of Electrical Engineering, Faculty of Electrical Engineering and Information Technology, Slovak University of Technology in Bratislava, Slovenska technicka univerzita v Bratislave, Bratislava, SK, academic, Bratislava, Slovakia; 2. Institute of Electrical Engineering, Slovenska akademia vied, Bratislava, Slovakia

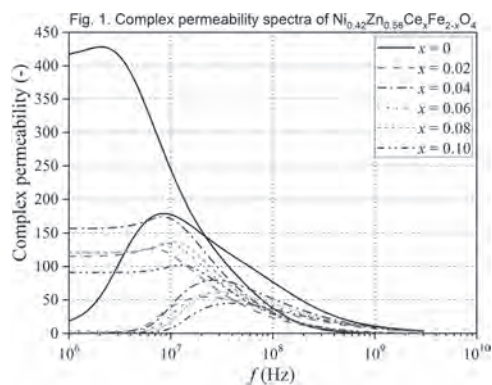
Abstract The influence of Ce³⁺ ions substitution for Fe³⁺ ions in Ni_{0.42}Zn_{0.58}Ce_xFe_{2-x}O₄ (x = 0, 0.02, 0.04, 0.06, 0.08, 0.10) compounds on the selected magnetic properties and structure were investigated. The samples were synthesized by means of wet glycine-nitrate technology annealed at the temperature 1200°C for 6 hours. The wide spectrum of characterization methods were used for the study of relevant properties of synthesized materials. X-ray diffraction patterns were recorded by a diffractometer using conventional X-ray tube (CuK α radiation, $\lambda = 1.5418 \text{ \AA}$). EDAX were performed by the SEM JEOL 7600-F equipped with both EDX and WDX system. Temperature dependences of magnetic susceptibility was measured using bridge method. The hysteresis loops were recorded using computer controlled digital hysteresisgraph at the same amplitude of applied field $H_{max} = 1500 \text{ A/m}$, measured at the frequency $f = 50 \text{ Hz}$ and at room temperature. The determination of real μ' and imaginary μ'' parts of complex (relative) permeability have been performed by means of an impedance analysis procedure using a vector network analyser Keysight E5063A in the frequency range from 1 MHz to 3 GHz. Results and Discussion XRD results indicate a presence of multi-phase structure. The major is found to be spinel phase and secondary, increasing with the addition of Ce³⁺ ions, corresponds to CeO₂. The final number of possible substitution of Ce³⁺ ions for Fe³⁺ ions in the B sites, and the difference in their ionic radii, is the cause of the formation of aggregates on the grain boundary as secondary phase [1]. The distribution of elements and their amounts in weight percentages for NiZnCe samples were studied by means of EDAX analysis. The real content of Ni²⁺, Zn²⁺, Ce³⁺, Fe³⁺ and O²⁻ shown in Tab. I confirmed the substitution of Fe³⁺ ions by Ce³⁺ ions, since the increase of Ce³⁺ content decreases the amount of Fe³⁺. Temperature dependences of magnetic susceptibility were recorded within the range from room temperature up to 450°C at rise of 4°C/min. Ferrite powder specimens of amount approximately 50 mg were measured; susceptibility values were related to the same weight (1 mg) for all cases. These dependences are decreasing monotonously and they exhibit one strong drop to paramagnetic state. From that, we can conclude that no unwilled phase is present in the ferrite to a significant extent. Curie temperature T_C was determined from the point of inflexion at strong decrease of temperature dependence. Even the paramagnetic substituent (Ce³⁺) ions occupy B-sites dominantly at expense of Fe³⁺ ions, it does not change the A-B exchange interactions, because T_C remains almost constant [2]. The hysteresis loops exhibit quite complicated behavior. By adding larger amount of Ce³⁺ ions, the maximum flux density B_{max} at given maximum applied field sometimes raises and sometimes decreases comparing to the non-substituted ferrite. Note that the value of B_{max} at given maximum applied field $H_{max} = 1500 \text{ A/m}$ approaches the largest value for $x = 0.08$ (only slightly larger than for $x = 0.04$). The differences can be explained by the fact that the saturation magnetization is an intrinsic parameter (thus, structurally independent) meanwhile the B_{max} corresponds to structurally sensitive behavior of material when magnetizing and approaching the saturation. In addition, coercive field is nearly linearly increasing with increment of x . This behavior is similar to that observed in case of Cu-substituted ferrites with the similar chemical formula (except for Cu instead of Ce), [3]. This may be justified by the complexity of the spinel structure, presence of other crystalline phases, etc. In Fig. 1 the frequency dependences of real μ' and imaginary μ'' parts of complex (relative) permeability $\mu = \mu' - j\mu''$ are presented for prepared spinel ferrites. The obtained frequency dispersion of complex permeability is caused by the domain wall and ferrimagnetic (or spin precession) resonance [4], [5]. The achieved results may be explained as follows. Magnetic properties of nickel-zinc ferrites as representatives of spinel-like ferrites are affected not only by the method of preparation and chemical structure (and composition), but also by properties such as porosity, crystallite size

(or grain size), lattice impurities (or defects), concentration of cations, etc. Also the super exchange interactions may strongly change the resultant properties: in spinel ferrite system AA and BB interactions are poorer than AB interaction. In the prepared ferrites, the shrinkage of lattice is present because of the larger ionic radius of cations such as Ce³⁺ (1.143Å), Zn²⁺ (0.74Å) and Ni²⁺ (0.69Å) in comparison with Fe³⁺ (0.65Å). The magnetic moments of these cations are as follows (in Bohr magnetons): 2.5 μ_B , 0 μ_B , 2.3 μ_B and 5 μ_B . Values of magnetic moments relates the cation distribution of Ni_{0.42}Zn_{0.58}Ce_xFe_{2-x}O₄ ferrite system (Ce³⁺ ions have preference on B sites): (Zn_{0.58}²⁺Fe_{1-x}³⁺)_A[Ni_{0.42}²⁺Ce_x³⁺Fe_{1-x}³⁺]_BO₄²⁻. Due to the values of ionic radius and magnetic moment, Ce³⁺ ions replace more Fe³⁺ ions in the crystal lattice and this leads to the raise of coercive field which in turns changes the value of permeability [5], [6]. Conclusion From the above experimental results, it can be seen that adding even a small amount of cerium element has evident influence on selected properties. Consequently, by adding defined amount of Ce³⁺ ions, the desired parameters can be easily controlled by a straightforward way and thus tailored for any particular application required in industrial practice.

[1] R. S. Yadav, J. Havlica, J. Masilko, J. Magn. Magn. Mater., Vol. 399, pp. 109-117 (2016) [2] M. A. Ahmed, S. F. Mansour, S. I. El-Dek, Solid State Ionics, Vol. 181, pp. 1149-1155 (2010) [3] J. Sláma, A. Grusková, M. Ušáková, J. Magn. Magn. Mater., Vol. 321, pp. 3346-3351 (2009) [4] M. Šoka, R. Dosoudil, M. Ušáková, Acta Phys. Pol. A, Vol. 131, pp. 690-692 (2017) [5] R. Dosoudil, M. Ušáková, A. Grusková, IEEE Trans. Magn., Vol. 50, no. 4 (2014) [6] M. N. Akhtar, M. A. Khan, J. Magn. Magn. Mater., Vol. 460, pp. 268-277 (2018)

TABLE I.
EDAX ANALYSIS OF Ni_{0.42}Zn_{0.58}Ce_xFe_{2-x}O₄

Substitution amount x	w _{Ni} (%)	w _{Zn} (%)	w _{Ce} (%)	w _{Fe} (%)	w _O (%)
0	11.61	17.83	—	49.02	21.56
0.02	10.31	15.92	1.51	49.13	22.95
0.04	10.67	15.75	2.41	47.31	23.38
0.06	10.51	15.52	4.08	46.67	23.02
0.08	10.41	15.13	4.93	46.68	22.84
0.10	10.20	15.31	6.00	45.32	22.98



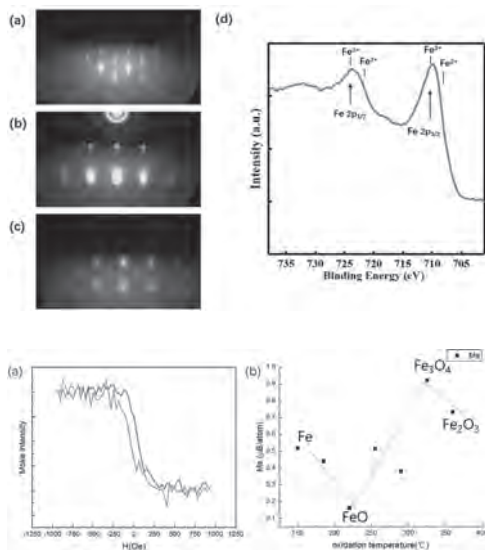
JX-02. Oxidation Process of FeO_x Films and the Growth Conditions of Epitaxial Fe_3O_4 on GaAs(100).

Z. Zhang¹, X. Lu¹ and Y. Xu¹

¹. Nanjing University, Nanjing, China

Magnetite(Fe_3O_4) has attracted great attention recently for spintronics as it is a half-metal material. Fe_3O_4 has high polarization at the Fermi level and the theoretically calculated spin polarization rate is -100% ¹. In addition, Fe_3O_4 has a high Curie temperature and a relatively high electronic conductivity at room temperature, so it has been demonstrated to be a promising material as a spin injector for spintronic devices². The quality of the film is very important for spin injection. Here, we report our detailed study of the oxidation process and their properties of the Fe films on GaAs. The base pressure of the MBE growth chamber is 2×10^{-10} mbar, and the GaAs substrate is annealed at 320 for 40 minutes to obtain a flat and clean surface. Then grow 10 ML Fe at room temperature with a growth rate of 0.02 Å/s. After the growth is completed, oxygen is introduced into the chamber, and the grown single crystal Fe film is oxidized in an oxygen-rich environment for 3 minutes and 45 seconds to obtain a single crystal Fe_3O_4 film. The pressure of the growth chamber during oxidation is 6×10^{-4} Torr and the oxidation temperature is 325. Figure 1 shows the RHEED patterns of GaAs (100), Fe and Fe_3O_4 film, and the XPS spectrum of Fe_3O_4 film. This result is consistent with the previously reported literature³. Subsequently, Fe_3O_4 films of different thickness were successfully grown by the same method, and the single oxidation depth was about 7 nm (50 ML Fe). Figure 2 shows hysteresis loop of Fe_3O_4 measured by MOKE at room temperature and the saturation magnetization of FeO_x at different oxidation temperatures. The Fe oxides of different compositions are found to form under different annealing temperatures.

1Dedkov, Y. S., Rüdiger, U. & Güntherodt, G. Evidence for the half-metallic ferromagnetic state of Fe_3O_4 by spin-resolved photoelectron spectroscopy. *Physical Review B* 65, doi:10.1103/PhysRevB.65.064417 (2002). 2Li, Y. et al. Oscillatory spin polarization and magneto-optical Kerr effect in Fe_3O_4 thin films on GaAs(001). *Phys Rev Lett* 105, 167203, doi:10.1103/PhysRevLett.105.167203 (2010). 3Lu, Y. X. et al. Epitaxial growth and magnetic properties of half-metallic Fe_3O_4 on GaAs(100). *Physical Review B* 70, doi:10.1103/PhysRevB.70.233304 (2004).



JX-03. Modeling Stray-Field Distribution Generated by Domain-Walls in Rare-Earth Substituted Iron Garnets.

A. Napolitano^{2,1}, C. Ragusa³ and F. Laviano^{2,1}

1. Istituto Nazionale di Fisica Nucleare Sezione di Torino, Torino, Italy;
2. Department of Applied Science and Technology, Politecnico di Torino, Torino, Italy; 3. Department of Energy, Politecnico di Torino Dipartimento di Energia, Torino, Italy

Rare earth substituted iron garnets (REIG) are characterized by a high magnetic susceptibility that results in a large magnetization in the presence of small magnetic fields [1]. The magnetic microstructures are influenced by natural or artificial defects; in particular, domain walls (DWs) undergo to nucleation, segmentation and pinning in correspondence to them. In REIG with in-plane spontaneous magnetization, the Néel spike domain structure is one of the most common magnetic microstructure nucleated at microdefects and its charged DWs can produce not negligible stray fields above the REIG. These DWs are interesting both for fundamental studies and for innovative applications such as micro positioning by contactless actuators [2]. To make the most out of this, performing a quantitative analysis is crucial. The experimental characterization by means of quantitative magneto-optical imaging with an indicator film [3] showed that stray fields are detectable above the surface of (Lu, Bi) substituted iron garnets, characterized by a spontaneous in-plane magnetization around 150 kA/m, in correspondence of DWs delimiting a Néel spike that is generated by a micro-crack [4]. In order to understand how the externally detected stray fields are correlated to the pattern of the internal magnetization, here we propose 2D and 3D models based on FEM developed through the COMSOL Multiphysics[®] software. These models take into account the magnetic microstructure of the Néel spike, i.e., either single DWs that run parallel into the bulk of the domain and a couple of DWs at the Néel spike tip (2D) or DWs that merge in a single point (3D). This approach allows us to describe the magnetic microstructure by means of CAD defined patterns, whose complex structure can be implemented easily in the FEM simulation. It turns out that the results are in agreement both with experiments and with previous numerical calculations performed with a simplified model in MATLAB[®] [4]. The comparison with experiments allowed us also to determine the distance of measurement between the indicator film of MOI experiments and the REIG under investigation. Figure 1 shows linear profiles across the DWs, along with experimental data. The distance of measurement is about 7 μm and the magnetic induction at the tip of the Néel spike is twice the value found for the single charged DW at the domain boundary. The simplicity of the 2D model limits the computational cost required; on the other hand, the 3D simulation can be useful for reproducing in detail the stray field distribution generated by the complex structure of the Néel spike domain, as shown in Figure 2. In summary, we validated these models for reproducing the stray field distribution above charged DWs, opening the way for the design of artificial structures in order to obtain controlled magnetic patterns, thanks to the powerful 3D engine of the COMSOL Multiphysics[®] software.

[1] L. E. Helseth, M. Kurniawan, R. W. Hansen, and T. H. Johansen, PHYSICAL REVIEW B 77, 064433 (2008) [2] L. E. Helseth, R. W. Hansen, T. H. Johansen, and T. M. Fischer, Appl. Phys. Lett. 85, 2556 (2004) [3] F. Laviano, D. Botta, A. Chiodoni, R. Gerbaldo, G. Ghigo, L. Gozzelino, S. Zannella and E. Mezzetti, 16, (2003) 71; Physica B 403 (2008) 293 [4] A. Napolitano, C. Ragusa, S. Guastella, S. Musumeci, P. Rivolo, F. Laviano, JMMM, Vol 504, 2020, 166556 [5] O. Khan, C. Ragusa, and F. Khan, IEEE transactions on magnetics, vol. 50, no. 11, November 2014

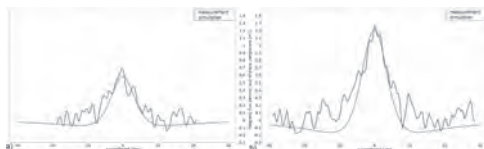


Figure 1. Cross sectional profiles of the stray field, simulated and experimental values, for a single DW (a) and the tip of the Néel spike (b).

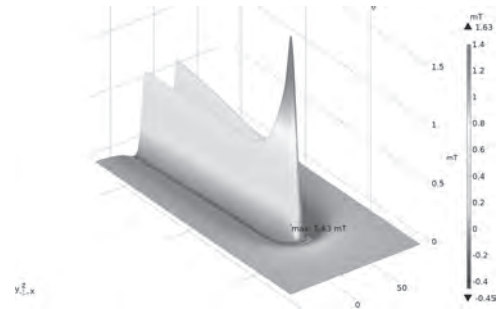


Figure 2. Magnetic field distribution of the stray field above a Néel spike: 3D plot of the magnetic induction intensity that clearly shows the stray field peak in correspondence to the tip of the Néel spike. The distance of measurement was chosen on the basis of the previous comparison between experimental data and 2D simulations.

JX-04. Quantitative Retrieving of the Magnetic Moment of Iron Oxide Nanoparticles Through Structural Characterizations.

M.S. Darcheville¹, C. Boscher¹, A. Adenot-Engelvin¹, J. Greneche², C. Lefevre³, C. Sanchez⁴ and A. Thiaville⁵

1. Commissariat à l'énergie atomique et aux énergies alternatives Direction des applications militaires Le Ripault, Monts, France; 2. Institut des Molécules et Matériaux du Mans, Le Mans, France; 3. Institut de Physique et Chimie des Matériaux de Strasbourg, Strasbourg, France; 4. UPMC-CNRS-Collège de France, Paris, France; 5. Laboratoire de Physique des Solides, Orsay, France

Intensive research on soft magnetic nanoparticles has been attracted by biomedical applications such as MRI markers and cancer therapy by magnetic hyperthermia. These nanoparticles can also be used in additive manufacturing processes, such as inkjet printing, to elaborate magnetic coatings to meet emerging needs such as RFID antenna shielding or wireless power transfer. The nanoparticles are synthesized by thermal decomposition with organic solvents. Two different ways of heating are employed: the conventional one using a heating mantle and the other one using a microwave oven[1]. A good control of the particle size of Fe₃O₄ through the addition of ethylene glycol has been reported². Other groups have used this technique to synthesize core-shell Fe₃O₄ nanoparticles. We have synthesized nanoparticles of mixed oxides Zn_xFe_{3-x}O₄, where the magnetic and dielectric properties can be tuned by the Zn/Fe ratio[2]. The two processing methods were compared in order to determine the most appropriate way to control the size and morphology spread of the obtained nanoparticles. The influence of the microstructure on the magnetic properties of Zn_{0.4}Fe_{2.6}O₄ and Zn_{0.2}Fe_{2.8}O₄ (theoretical compositions) nanoparticles was studied by X-ray diffraction analysis and ⁵⁷Fe Mössbauer spectrometry, under zero field and in-field. Experimental details: The conventional way in a heating mantle allows obtaining various morphologies: cubes, octahedra... However, it induces heterogeneity in terms of size and shape in a batch, due to insufficient monitoring of the temperature during the reaction. The microwave-assisted thermal decomposition enables a fast and more uniform heating, leading reproducibly to nanoparticles with homogeneous size and shape. The difference lies in the choice of solvents and surfactants: respectively benzyl ether and oleic acid for the conventional thermal decomposition, and octadecene for the solvent with a combination of oleic acid and oleylamine for the surfactant for the microwave reactor. These surfactants have two complementary functions in the synthesis. Oleic acid stimulates the growth of nanoparticles along a preferential axis while oleylamine, in addition to redox possibilities, slows down the nanoparticle growth[3]. Tuning their compositional ratio yields a good control of the nanoparticle morphology. Results: The morphology and the size were observed by scanning electron microscopy and transmission electron microscopy. Two different morphologies are highlighted. While 5 nm-nanoparticles (written SP(F)M) are quite spherical, the 35 nm-particles (FM) have a “raspberry” morphology (Fig. 1). These observations are consistent with those of Y-J. Liang’s¹ on 50 nm particles. It should be assimilated to a binding between crystallites and the continuity of the crystal planes in a raspberry structure is noticed, as observed by S. Begin-Colin’s group[4] with structures of about 250 nm. The phase purity was probed by X-ray diffraction (XRD). The size of the coherent diffraction domains was calculated with two different methods: using Scherrer’s formula, and through a Rietveld refinement. The results are compared and correlated to TEM observations. The saturation magnetization was determined through the hysteresis cycles measured with a vibrating sample magnetometer (VSM) at room temperature. The superparamagnetism is observed for the 5 nm particles. The magnetization curve has been fitted with a Langevin function[5] which allows recovering the intrinsic saturation magnetization and an apparent size of 5 nm, close to that observed by TEM. The intrinsic saturation magnetization (85.6 emu/g) from the model is in good agreement with that determined at 2 K with a VSM/SQUID (85 emu/g). The saturation magnetization of the two types of nanoparticles is lower (85.6 emu/g for the 5 nm and 80.6 emu/g for the 35 nm) than that of the bulk ferrite Zn_{0.4}Fe_{2.6}O₄ which is about 98.8 emu/g. Several contributions have to be taken into account to explain this discrepancy: - A surface spin-canting effect[6] could impact the magnetic moment of particles, especially for the smallest ones. The thickness of the surface spin-canting

was estimated and the magnetic moments were thus corrected (Fig. 2). - A cationic disorder with a fraction of Zn²⁺ ions at the octahedral sites of the spinel structure, and not only at the tetrahedral (A) ones, can be deduced from a Rietveld analysis of X-ray patterns, and in-field Mössbauer spectra. Indeed, these techniques have made it possible to quantify the distribution of cations at the tetrahedral (A) and octahedral (B) sites of the spinel, and thus to calculate the magnetization according to a molecular field model[7] (Fig. 2). - Oxidation of the nanoparticles with conversion of Fe²⁺ into Fe³⁺ could lead to the reduction of the saturation magnetization[8]. The analysis of Mössbauer spectra enables to recover values close to the measured magnetic moments, which makes the cations distribution reliable. It therefore makes it possible to predict a magnetic moment close to the experimental one, keeping a spinel-type chemical formula with presence of vacancies to take into account the oxidation of the theoretical composition. The understanding of the effect of the microstructure on the magnetic moment opens up possibilities by tuning magnetic properties of iron oxide nanoparticles.

[1] Y-J. Liang, F. Fan and M. Ma, Colloids and Surfaces A, Vol. 530, p.191-199 (2017) [2] A. Fujiwara, M. Tada and T. Nakagawa, J. Magn. Magn. Mater., Vol. 320, p.L67-L69 (2008) [3] S. Mourdikoudis and L. M. Liz-Marzán, Chem. Mater., Vol. 25, no. 9, p.1465–1476 (2013) [4] O. Gerber, B. Pichon, and C. Ulhaq, J. Phys. Chem. C., Vol. 119, p.24665-24673 (2015) [5] J.L. Dormann, D. Fiorani and E. Tronc, Adv. Chem. Phys., Vol. 98, p.283-494 (1997) [6] E. Tronc, P. Prené, J.P. Jolivet, J.L. Dormann and J-M. Greneche, Hyper. Inter., Vol. 112, p.97-100 (1997) [7] P. G. Bercoff and H. R. Bertorello, J. Magn. Magn. Mater., Vol. 169, p.314–322 (1997) [8] A. Demortiere, P. Panissod and B.P. Pichon, Nanoscale., Vol. 3, p.225-232 (2011)

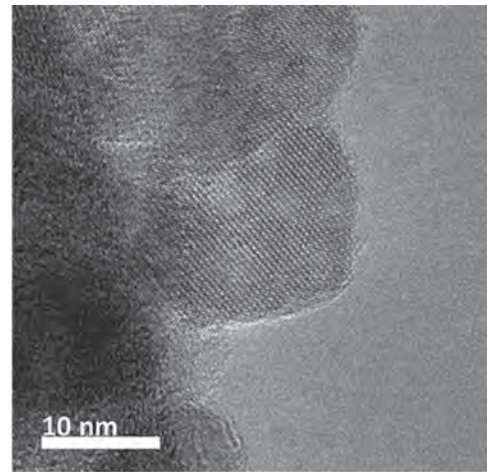


Fig. 1. TEM picture of raspberry-like nanoparticles

Case	SP(F)M	FM (0.2)	FM (0.4)
Experimental moment corrected from surface spin-canting	3.71 μg	2.71 μg	4.16 μg
Cationic disorder	Rietveld analysis	(Zn _{0.4} Fe _{2.6}) _{1-x} (Fe _{2.6}) _x O ₄	(Zn _{0.2} Fe _{2.8}) _{1-x} (Fe _{2.8}) _x O ₄
	Mössbauer	random Zn distribution	(Zn _{0.2} Fe _{2.8}) _{1-x} (Fe _{2.8}) _x O ₄
Repartition of Fe ³⁺ and Fe ²⁺ on A and B sites (from Mössbauer)		35.6 % Fe ³⁺ (A) 64.4 % Fe ²⁺ (B)	32.5 % Fe ³⁺ (A) 49.1 % Fe ²⁺ (B)
		3.74 μg	3.29 μg
	1 % of gap with exp.	15% of gap with exp.	12 % of gap with exp.

Fig. 2. Magnetic moments predicted from microstructural characterizations for SP(F)M and FM particles with different Zn contents (0.2 and 0.4).

JX-05. Soft Magnetic Properties of $\text{Ni}_{81}\text{Fe}_{19}$ and its Domain Structure by Micromagnetic Simulation.

Z. He¹, C. Wu¹, Y. Wang¹, X. Jiang¹, Z. Yu¹, Z. Lan¹ and K. Sun¹

1. University of Electronic Science and Technology of China, Chengdu, China

As the integration of circuit gradually increases, the demand for miniaturization of magnetic device become more urgent. The miniaturization and integration of the inductor with electronic circuits are the key to realize electronic products with high performance, small size, light weight, high saturation current, high efficiency, and low lost [1]. Due to high saturation magnetization, low coercivity and better high frequency performance, soft magnetic thin film has widely used in on-chip inductor, magnetic storage and magnetic sensing devices [2-3]. Many efforts have been done to investigate factors that may influence soft magnetic properties. G. Chai et al [4] through changing thickness of Ta in $[\text{Co}_{90}\text{Nb}_{10}/\text{Ta}]_n$ multilayers have obtained an improvement in resonance frequency from 1.4GHz to 6.5GHz. M. Belusky et al [5] have studied magnetic anisotropy of $\text{Ni}_{80}\text{Fe}_{20}$ thin film induced by substrate roughness, and they obtained a 233% coercivity increasing when using PVDF substrate. They have latter used a modified micromagnetic theory confirming the correlation between surface roughness and anisotropy field. By using micromagnetic simulation, P.N. Solovev et al [6] investigate magnetic domain structure and magnetization process in 200nm permalloy thin film. Their study reveals the relationship between domain width and film thickness. In this work, $\text{Ni}_{81}\text{Fe}_{19}$ (NiFe) thin film with different thickness from 110nm to 140nm have been prepared by electron beam evaporation method on Si (100) substrate with base pressure lower than 8.010^{-5} Pa. The microstructure, static magnetic properties, and coercivity distribution of $\text{Ni}_{81}\text{Fe}_{19}$ have been investigated in detail. Moreover, we study the formation of domain structure and magnetization reversal in thin permalloy films with uniaxial in-plane and perpendicular magnetic anisotropy. The static magnetic properties of films have been measured by vibrating sample magnetometer which are shown in Fig.1. It is clear that NiFe thin film with thickness of 120nm has the lowest coercivity both in in-plane and out-of-plane, and this value increase with thickness of film. FORC diagram has been further utilized to explore the distribution of in-plane coercivity. Fig.2 shows the FORC diagrams of thin film with thickness from 110nm to 140nm. The peak values of four thickness films in FORC diagrams are all lying around $H_u=0$ axis which indicate there is no exchange field. Film with thickness of 120nm has the narrowest coercivity distribution from 1.2Oe to 1.4Oe, and the distribution of coercivity gradually increase with the thickness of thin film.

[1] K. Mallik, A. Abuelgasim, N. Hashim, P. Ashburn, Analytical and numerical model of spiral inductors on high resistivity silicon substrates. *Solid-State Electron.*, 93(2014) 43-48. [2] Elsherbini, A.; Braunisch, H.; O'Brien, K. Circuit modeling of nonlinear lossy frequency dependent thin-film magnetic inductors. In *Proceedings of the 2012 IEEE 21st Conference on Electrical Performance of Electronic Packaging and Systems (EPEPS)*, Tempe, AZ, USA, 21-24 October 2012; pp. 105-108. [3] C.D. Meyer, S.S. Bedair, B.C. Morgan, D.P. Arnold, A micromachined wiring board with integrated microinductor for chip-scale power conversion. *IEEE Trans. Power Electron.*, 29(2014) 6052-6063. [4] G. Z. Chai, Y. C. Yang, J. Y. Zhu, M. Lin, W. B. Sui, D. W. Guo, X. L. Li, and D. S. Xue, Adjust the resonance frequency of $(\text{Co}_{90}\text{Nb}_{10}/\text{Ta})_n$ multilayers from 1.4 to 6.5 GHz by controlling the thickness of Ta interlayers, *Appl. Phys. Lett.*, 96(2010) 012505. [5] M. Belusky, S. Lepadatu, J. Naylor, M.M. Vopson, Evidence of substrate roughness surface induced magnetic anisotropy in $\text{Ni}_{80}\text{Fe}_{20}$ flexible thin films, *J. Magn. Magn. Mater.*, 478 (2019) 77-83. [6] P.N. Solovev, A.V. Izotov, B.A. Belyaev, N.M. Boev, Micromagnetic simulation of domain structure in thin permalloy films with in-plane and perpendicular anisotropy, *J. Phys. B: Condensed Matter* (2020) 412699.

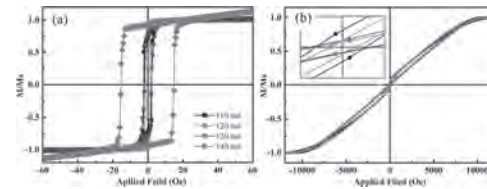


Fig.1. The static magnetic properties of NiFe for (a) the in-plane magnetic hysteresis loop, (b) the out-of-plane magnetic hysteresis loop.

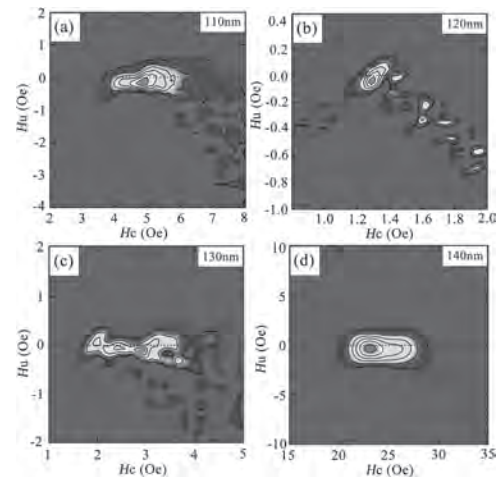


Fig.2. FORC diagrams of NiFe thin film with thickness of (a) 110nm, (b) 120nm, (c) 130nm and (d) 140nm.

JX-06. $\text{La}_6\text{Pd}_{2+x}\text{Sb}_{15}$ ($x = 0.28$): a Rare-Earth Palladium Intermetallic Compound With Extended Pnictogen Ribbons.

M.I. Sturza¹, M. Amigó¹, J. Facio², F. Caglieris³, S. Wurmehl¹ and B. Büchner⁴

1. *Synthesis and Crystal Growth, Leibniz-Institut für Festkörper- und Werkstofforschung Dresden eV, Dresden, Germany*; 2. *Institute for Theoretical Solid State Physics, Leibniz-Institut für Festkörper- und Werkstofforschung Dresden eV, Dresden, Germany*; 3. *Transport and Scanning Probe Microscopy Research Team, Leibniz-Institut für Festkörper- und Werkstofforschung Dresden eV, Dresden, Germany*; 4. *Institute for Solid State Research, Leibniz-Institut für Festkörper- und Werkstofforschung Dresden eV, Dresden, Germany*

A new intermetallic ternary compound $\text{La}_6\text{Pd}_{2.28}\text{Sb}_{15}$ was synthesized from the reaction of lanthanum and palladium metals in a molten antimony flux. The compound crystallizes in the orthorhombic space group $Immm$ with $a = 4.3082(9)$ Å, $b = 15.399(3)$ Å, and $c = 19.689(4)$ Å. The crystal structure contains a three-dimensional framework of Sb squares and ribbons that extend along the a axis, including complex Sb–Sb bonding. Magnetization measurements indicate that the intrinsic magnetic behavior of $\text{La}_6\text{Pd}_{2+x}\text{Sb}_{15}$ ($x = 0.28$) is diamagnetic, which we associate with Landau diamagnetism slightly larger than Pauli paramagnetism in this compound. The resistivity (ρ) decreases when lowering the temperature, indicating metallic behavior, and at low temperatures ρ depends quadratically on T . Interestingly, both the Hall resistivity and magnetoresistance present a nonlinear dependence on the applied magnetic field, suggesting a multiband behavior. This is supported by density-functional electronic structure calculations which show a complex Fermi surface originated in the antimonide substructures and containing both electron and hole pockets as well as open sheets.

M. I. Sturza, M. L. Amigó, J. I. Facio et al., *Journal of Solid State Chemistry*, Vol. 291, pp. 121578 (2020)

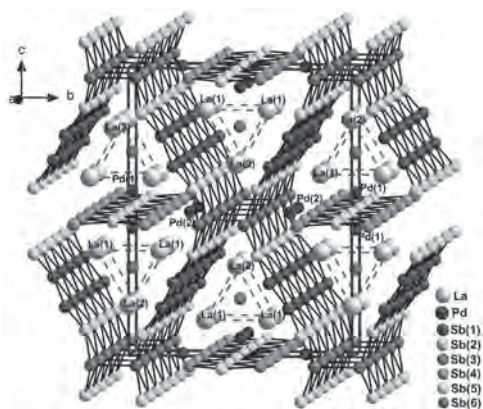


Fig 1. Ball-and-stick representations of three-dimensional structure of $\text{La}_6\text{Pd}_{2+x}\text{Sb}_{15}$ ($x = 0.28$) viewed down the crystallographic a -axis. The red dashed lines outline the La_6 trigonal prisms.

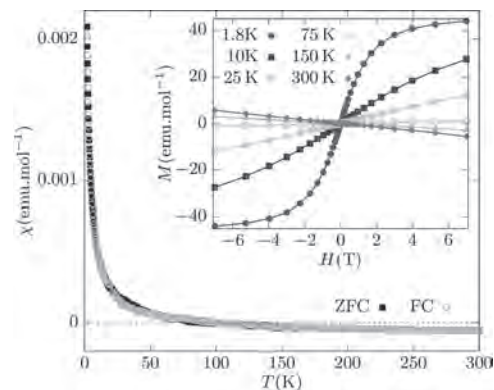


Fig 2. Temperature dependence of the susceptibility for zero field cooling (ZFC) and field cooling (FC) procedures. Inset: Field dependence of the magnetization for several temperatures. In all cases, the background of the glue and the sample holder was subtracted, as well as, the core diamagnetic contribution.

JX-07. Pressure Effect on Magnetization of Heusler Alloy FeCoCrAl.

S. Tsujikawa¹, I. Shigeta¹, J. Gouchi², T. Kanomata³, R. Y. Umetsu⁴, Y. Uwatoko² and M. Hiroi¹

1. Department of Physics and Astronomy, Kagoshima University, Kagoshima, Japan; 2. Institute for Solid State Physics, University of Tokyo, Kashiwa, Japan; 3. Research Institute for Engineering and Technology, Tohoku Gakuin University, Tagajo, Japan; 4. Institute for Materials Research, Tohoku University, Sendai, Japan

Half metal (HM) is suitable for developing electrode materials in spintronics devices because they possess a bandgap at the Fermi energy E_F only for its minority spin band, achieving 100% spin polarization at E_F . Spin-gapless semiconductor (SGS) was recently reported as one of possible functional materials for spintronics devices, as well as HM. For SGS, the valence band edge and conduction band edge are touched at E_F in the majority spin band, and there is a bandgap at E_F in the minority spin band. Reflecting this unique band structure, the characteristics of both low carrier and high spin polarization are realized in SGS. The Heusler alloy FeCoCrAl was predicted to be SGS by the first-principles band calculations [1], and experimental results suggesting that it has high spin polarization have been reported [2]. In this study, we focus on Heusler alloy FeCoCrAl as a potential candidate of SGS, and investigated its crystal structure and pressure effect on magnetization. Polycrystalline FeCoCrAl samples were synthesized by arc-melting high-purity constituent elements under high purity Ar atmosphere. Powder X-ray diffraction measurements were performed with monochromatic Cu-K α radiation to evaluate the crystal structure. The magnetization measurements at high pressure up to 1.17 GPa were performed using a superconducting quantum interferometer (SQUID) and a piston-cylinder-type pressure cell made by BeCu alloy. The superlattice peaks (111) and (200) were observed in the powder X-ray diffraction patterns, exhibiting that the synthesized sample has the highly ordered L2₁ structure. From the temperature dependent magnetization $M(T)$, the Curie temperature T_C was determined to be 522 K, which is higher enough than room temperature. The spontaneous magnetization M_s was estimated to be 2.01 μ_B /f.u. at ambient pressure from the magnetization curve $M(H)$ at $T = 7.5$ K. The magnetic moment of FeCoCrAl was in good agreement with that expected from the Slater-Pauling rule, suggesting that FeCoCrAl is a half-metal [3]. Figure 1 shows that the pressure dependence of $M(H)$ curve up to 1.17 GPa at $T = 7.5$ K. It is seen that the five curves obtained under different pressures are completely overlapped in FeCoCrAl. As shown in Fig. 1, the magnetization curves were characteristic for soft ferromagnets. The magnetization at 7.5 K was saturated in the magnetic field at about 0.5 T, indicating that the magnetocrystalline anisotropy energy of FeCoCrAl is small. The inset shows the pressure dependence of the spontaneous magnetization M_s obtained from Fig. 1. The M_s value is almost independent of applying pressure, exhibiting that FeCoCrAl possesses the half-metallic electric structure, i.e., only the majority spin band exists at E_F [4]. Figure 2 shows the pressure dependence of the spontaneous magnetization M_s in the wide temperature range from 7.5 K to 300 K. It was found that the M_s value is almost independent of pressure even at 300 K, suggesting that the half-metallic electric structure is kept up to 300 K in FeCoCrAl. In summary, we have investigated the pressure effect of Heusler alloy FeCoCrAl under pressure up to 1.17 GPa with the high-pressure cell. The experimental results obtained in the study reveal that FeCoCrAl possesses half metallic electric structure. At present, since the information of the density of state at E_F in the majority spin band is not enough to discuss if FeCoCrAl possesses the SGS electric structure, further experimental and theoretical works are needed.

[1] J. Nehra, V. D. Sudheesh, and N. Lakshmi, Phys. Status Solidi RRL 7 (2013) 289. [2] L. Bainsla, A. I. Mallick, and A. A. Coelho, J. Magn. Mater. 394 (2015) 82. [3] I. Galanakis, P. H. Dederichs, and N. Papanikolaou, Phys. Rev. B 66 (2002) 174429. [4] T. Kanomata, Y. Chieda, and K. Endo, Phys. Rev. B 82 (2010) 144415.

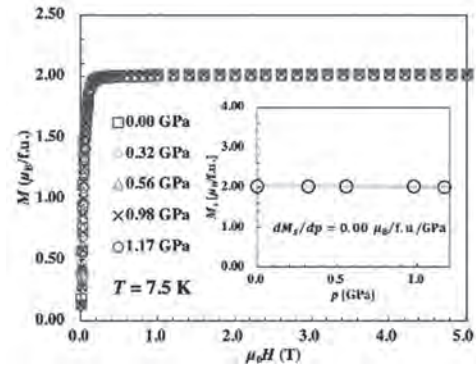


Fig.1 Magnetization curve $M(H)$ of FeCoCrAl under various pressures. Inset: Pressure dependence of the spontaneous magnetization M_s .

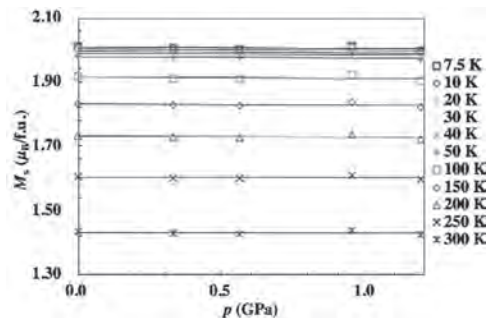


Fig.2 Pressure dependence of the spontaneous magnetization M_s at various temperatures.

JX-08. Critical Behavior of the Magnetization in Heusler Alloy **$\text{Co}_2\text{TiGa}_{0.8}\text{Sn}_{0.2}$.**

T. Yokoyama¹, I. Shigeta¹, A. Nomura², K. Yubuta², T. Yamauchi³,
T. Kanomata⁴, H. Nishihara⁵, R. Y. Umetsu² and M. Hiroi¹

1. Department of Physics and Astronomy, Kagoshima University, Kagoshima, Japan; 2. Institute for Materials, Tohoku University, Sendai, Japan; 3. Institute for Solid State Physics, University of Tokyo, Kashiwa, Japan; 4. Research Institute for Engineering and Technology, Tohoku Gakuin University, Tagajo, Japan; 5. Faculty of Science and Technology, Ryukoku University, Otsu, Japan

Heusler alloys have been intensively investigated to develop functional materials as half-metals, shape memory alloys, and thermoelectric conversion materials. Heusler alloy Co_2TiZ ($Z = \text{Si}, \text{Ge}, \text{Sn}$) was expected to be a half-metal with characteristics of Weyl fermions by first-principles band calculations [1]. The Weyl semimetals are of great interest materials, due to their unusual magnetoelectronic and magnetothermal properties. In the case of magnetic materials, the spatial and temporal correlations of the magnetization $M(r,t)$ show a tendency to diverge at the critical temperature. The phenomenon in which magnetic properties show peculiar temperature and magnetic field dependence at the critical temperature is called a critical phenomenon. The critical exponent δ is defined at $T = T_C$ by $H = DM(T, H)\delta$. (1) In later work, to find the critical exponent δ , the temperature at which the plot, taking logarithms on both sides of equation (1), is linear in $\log(M)$ - $\log(H)$ scale is defined as the Curie temperature T_C [2]. Theoretically, the molecular field theory predicts $\delta = 3.0$, the three-dimensional Heisenberg model $\delta = 4.80$ [2], the three-dimensional Ising model $\delta = 4.82$ [2], and the spin fluctuation theory by Takahashi $\delta = 5.0$ [3]. For half-metals with characteristics of Weyl fermions, there are few reports of systematic analyses of the critical exponents. Therefore, we focus on the element substitution effect between Co_2TiSn and Co_2TiGa . Co_2TiSn possesses characteristics of both half-metal and Weyl fermions, and Co_2TiGa is the itinerant electron ferromagnet with the high spin polarization. We measured the magnetization in the mixed crystal compound $\text{Co}_2\text{TiGa}_{0.8}\text{Sn}_{0.2}$ and investigated the critical exponent δ near T_C . Polycrystalline $\text{Co}_2\text{TiGa}_{0.8}\text{Sn}_{0.2}$ samples were synthesized by arc-melting high-purity constituent elements under high purity Ar atmosphere. To homogenize the synthesized sample, it was annealed at 1100°C for 3 days and then quenched in water. The magnetization of $\text{Co}_2\text{TiGa}_{0.8}\text{Sn}_{0.2}$ was measured using a superconducting quantum interference device (SQUID) (Quantum Design MPMS-XL). From the magnetization measurements of $\text{Co}_2\text{TiGa}_{0.8}\text{Sn}_{0.2}$, the spontaneous magnetization M_s was estimated to be $M_s = 0.907 \mu_B/\text{f.u.}$ The critical exponent δ was analyzed from the magnetic field dependence of the magnetization near T_C using equation (1). The magnetization curves obtained at each temperature were plotted for $\log(M/M_{\max})$ against $\log(H/H_{\max})$ in Fig.1. The values of δ and its fitting error, obtained from the analysis of the magnetization curves in Fig.1, are shown in Fig.2. Since the temperature at which the fitting error is minimized agrees best with equation (1), that temperature can be considered as the Curie temperature T_C . From Fig.2, $T_C = 105 \text{ K}$ and $\delta = 4.45$ were obtained. The δ value obtained in this study was different from the value 3 by the molecular field theory, but was close to the value 5 predicted by the spin fluctuation theory for a weakly ferromagnetic itinerant electron system. Therefore, we also reanalyzed the magnetization below 10 kOe, where the magnitude of the applied magnetic field is 1/5 of 50 kOe, because the strong magnetic field may suppress the spin fluctuations. From the analysis of the data below 10 kOe, $T_C = 104 \text{ K}$ and $\delta = 4.82$ were obtained. Thus, a change of δ due to the suppression of the critical fluctuation by the strong applied magnetic field seems to be likely at least in this case. The discrepancy between our results and the theoretical models seem to arise from a distribution of the Curie temperatures in the samples since the δ value changes even at 1 K.

[1] G. Chang *et al.*, Sci. Rep. 6, 38839 (2016). [2] M. Seeger *et al.*, Phys. Rev. B 51, 12585 (1995) and references cited therein. [3] K. Shimizu *et al.*, J. Phys. Soc. Jpn. 59, 305 (1990).

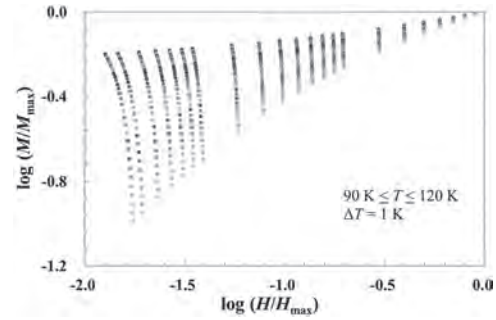


Fig.1. The $\log(M/M_{\max})$ - $\log(H/H_{\max})$ plots of $\text{Co}_2\text{TiGa}_{0.8}\text{Sn}_{0.2}$ near T_C .

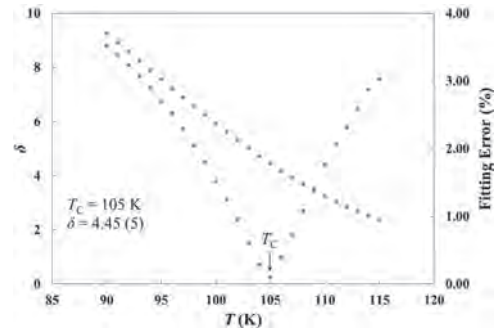


Fig.2. The critical exponent δ and its fitting error of $\text{Co}_2\text{TiGa}_{0.8}\text{Sn}_{0.2}$.

JX-09. Antisite Disorder and Defect Phase Segregation and its Role in Magnetic Properties of Mn_2NiSn .

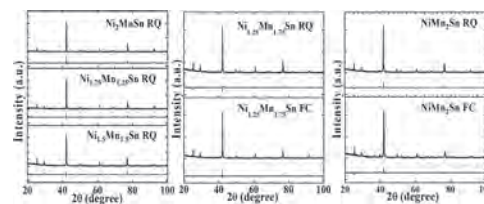
S.V. Malik¹, A. Nigam² and K. Priolkar¹

1. School of Physical and Applied Sciences, Goa University, Taleigao, India; 2. Tata Institute of Fundamental Research, Mumbai, India

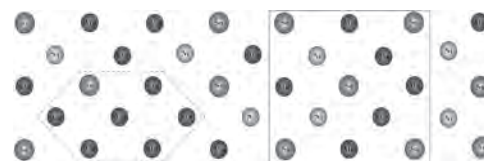
Mn_2YZ based inverse Heusler alloys with cubic or tetragonal structures and high Curie temperature (T_C) display exceptional tunability of their properties either by controlling the degree and the type of atomic ordering [1] or by controlling the total valence electron concentration (VEC) of the alloy [2]. Here the Mn atoms occupy both the (0,0,0) or $(\frac{1}{2}, \frac{1}{2}, \frac{1}{2})$ and $(\frac{1}{4}, \frac{1}{4}, \frac{1}{4})$ or $(\frac{3}{4}, \frac{3}{4}, \frac{3}{4})$ sites in the Heusler structure with antiparallel spins of different magnitude resulting in a ferrimagnetic order. Several theoretical and experimental studies on Mn_2YZ alloys have predicted interesting properties like half-metallicity, spin gapless semiconductor with a high magnetic ordering temperature, anomalous hall effect and even zero field exchange bias, spin valve behaviour [3,4] etc. Mn_2NiSn is one such cubic ferrimagnetic Heusler alloy with a moderately high magnetic moment of $\sim 2.5 m_B$ [5]. Density functional calculations as well as neutron diffraction studies have shown that the magnetic moment of Mn_2NiSn can be tuned by controlling antisite disorder [5,6]. There are also reports suggesting a strong relation between the magnetic moment and the VEC controlled essentially by the Z element in Mn_2NiZ alloys [7]. In the present work we aim to understand the role of antisite disorder on the magnetic properties of Mn_2NiSn . We have employed two routes to introduce the antisite disorder. Firstly, we have systematically replaced Ni by Mn at the X site in Ni_2MnSn by preparing alloys of the type $Ni_{2-x}Mn_{1+x}Sn$ (where $x = 0, 0.25, 0.5, 0.75$ and 1) Secondly, the two alloy compositions, $Ni_{1.25}Mn_{1.75}Sn$ ($x = 0.75$) and Mn_2NiSn ($x = 1$) were subjected to an additional thermal treatment. The alloys were prepared by arc melting constituent elements in argon atmosphere and subsequently annealed at 800 °C for 72 hours in evacuated quartz tubes and quenched in ice cold water (referred to as rapid quenched (RQ)). The arc melted $Ni_{1.25}Mn_{1.75}Sn$ and Mn_2NiSn were cut into two halves and were sealed in four different quartz tubes. While two of these tubes containing the respective alloys were quenched from 800°C in ice water, the temperature of the other two tubes with the same compositions as that of the RQ alloys was lowered from 800°C to 427°C after 72 hours of annealing and were annealed at this lower temperature for the next 28 hours and cooled in furnace (referred as FC). All the alloys were characterized by x-ray diffraction (XRD) and SEM-EDX for the determination of their structure and composition. SEM-EDX indicated the compositions to be within 1% of their starting values. Rietveld refinement of the XRD patterns for the RQ alloys showed them to be largely single phase with a cubic L2₁ Heusler structure (SG: Fm-3m). Small percentage ($\sim 1 - 2\%$) of the MnO impurity phase was noticed in a few compositions. In the case of FC alloys, while $Ni_{1.25}Mn_{1.75}Sn$ alloy was cubic, Mn_2NiSn was biphasic with major L2₁ phase ($\sim 93\%$) and minor ($\sim 7\%$) Mn_3Sn type hexagonal phase (SG: P6₃/mmc) (Fig 1). Magnetization measurements as a function of temperature (3 K to 390 K) were carried out in 100 Oe applied magnetic field employing zero-field cooling and field cooling protocols. T_C increased from 340 K in $x = 0$ to above the highest measured temperature for all alloys with $x = 0.5$ and above. Isothermal magnetization at 5 K was measured in the field interval of ± 7 T to determine the saturation magnetic moment. All the compositions showed ferromagnetic like M(H) loop with very low coercivity. The saturation magnetization in Ni_2MnSn gave an effective moment of 4.06 $m_B/f.u.$ good agreement with reported values [8]. In the RQ alloys, with increase in Mn content, the magnetic moment decreases steadily from 4.06 $m_B/f.u.$ to 1.93 $m_B/f.u.$ in $Ni_{1.25}Mn_{1.75}Sn$ and then increased to 2.80 $m_B/f.u.$ in $NiMn_2Sn$. The FC $Ni_{1.25}Mn_{1.75}Sn$ showed a significant increase in its magnetic moment to 3.31 $m_B/f.u.$ This increase is surprising considering its structure to be the same as that of its RQ counterpart. In the phase separated Mn_2NiSn the magnetic moment showed a marginal increase to 2.83 $m_B/f.u.$ To understand the above magnetic properties, local structures of Ni, Mn and Sn in all the alloys were studied by employing extended x-ray absorption fine structure (EXAFS) spectroscopy. In all the alloys EXAFS data were analysed together using a model based on their respective crystal structure. Excellent fits were obtained for RQ alloys with $x = 0, 0.25$ and 0.5. In case of $Ni_{1.25}Mn_{1.75}Sn$, only Ni EXAFS could be well described with the crystal structure model. Both Mn and Sn

EXAFS could not be fitted and relaxation of structural constraints indicated a much lower value for the Mn – Sn bond distance than the predicted 3.025 Å from its crystal structure. Introduction of additional Mn – Sn and Mn – Mn correlations derived from hexagonal Mn_3Sn resulted in a good fit to the EXAFS data of $x = 0.75$ and 1 RQ and FC alloys. Mn_3Sn like environment can exist in Mn_2NiSn type alloys if, in addition to the A2 type disorder, there is also an antisite disorder between Mn and Sn atoms (Fig 2). EXAFS analysis indicated a defect concentration $\sim 20 \pm 7\%$ in RQ and FC Mn_2NiSn and much less in $Ni_{1.25}Mn_{1.75}Sn$. Such a segregation of defect within the overall Heusler structure due to antisite disorder seems to be the reason for the increased magnetic moment in Mn_2YZ alloys.

[1] T. Graf, C. Felser, S. Parkin, Prog. Solid State Chem. 39, 1 (2011). [2] C. Felser, L. Wollmann, S. Chadov, Chem Int Ed. 46:668-99, (2007). [3] S. Ouardi, G. Fecher, C. Felser, Phys. Rev. Lett. 110, 100401 (2013). [4] A. K. Nayak, M. Nicklas, S. Chadov et al, Phys. Rev. Lett. 110, 127204 (2013). [5] R. B. Helmholtz and K. H. J. Buschow, J. Less-Common Met. 128, 167 (1987). [6] S. Paul, A. Kundu, B. Sanyal, J. Appl. Phys. 116, 133903 (2014). [7] H. Luo, G. Liu, F. Meng, J. of Magn. Magn. Mater. 321, 4063–4066 (2009). [8] M. Nazmunnahar, T. Ryba, J. J. deVal, J. of Magn. Magn. Mater. 386, 98–101 (2015).



X-ray diffraction patterns for $Ni_{2-x}Mn_{1+x}Sn$ series of RQ alloys where ($x = 0, 0.25, 0.5, 0.75, 1$) and $Ni_{1.25}Mn_{1.75}Sn$, $NiMn_2Sn$ FC alloys.



Schematic diagram of the ab plane of Mn_2NiSn showing the segregation of Mn_3Sn -type Hexagonal defect phase.

JX-10. High Entropy Alloys: the Next big Thing in Functional Magnetic Alloys.

J. Harris¹, M. Anis¹, R. Osman¹, R. Rowan-Robinson¹, A. Quintana-Nedelcos^{1,2}, Z. Leong¹ and N. Morley¹

1. The University of Sheffield, Sheffield, United Kingdom; 2. New Model Institute for Technology and Engineering (NMITE), Hereford, United Kingdom

The search for new functional magnetic materials has led to the exploration into multi-component alloys (MCAs), which contain four or more elements with percentages between 12.5 % and 33 %. These include the sub-class of high entropy alloys (HEAs) which often exhibit single phases, thought to be stabilised by the high entropy of mixing of these compounds amongst other competing thermodynamic contributions. The resulting alloys often have interesting functional properties, which are linked to their structure. This work has explored a number of different compositions ($\text{CoFeNi}_{0.5}\text{Cr}_{0.5}\text{Al}_x$, $\text{CoFeNi}_{0.5}\text{Cr}_x\text{Al}$ $\text{CoFeNiCr}_y\text{Cu}_x$) in both bulk form, to understand how the phases present in the alloys influence the magnetic properties. The work has also used semi-empirical models to predict the different phases within the compositions and machine learning has been used to predict the saturation magnetisation. For example, in bulk $\text{CoFeNi}_{0.5}\text{Cr}_{0.5}\text{Al}$ it was found that Fe-Cr nanoparticles formed in a weakly magnetic CoNiAl matrix [1]. This formation of round nanoparticles increased the magnetisation of the $\text{CoFeNi}_{0.5}\text{Cr}_{0.5}\text{Al}$ alloy by a factor 4 at room temperature. For all the $\text{CoFeNi}_{0.5}\text{Cr}_{0.5}\text{Al}_x$ samples, the coercive field was small and the saturation magnetisation comparable with NiFe. While for the bulk $\text{CoFeNi}_{0.5}\text{Cr}_x\text{Al}$ samples, nanoparticles formed in all the samples containing Cr, with the $\text{CoFeNi}_{0.5}\text{Cr}_{1.0}\text{Al}$ sample having square nanoparticles. Thus the amount of Cr in $\text{CoFeNi}_{0.5}\text{Al}$ dominates the geometry of the FeCr nanoparticles that form. Plus encapsulating the Cr in Fe-Cr nanoparticles meant that the Curie Temperatures for all the alloys containing Cr and Al were above 300 K (Fig. 1a). While for bulk $\text{CoFeNiCr}_y\text{Cu}_x$ ($x = 0.0 - 1.5$ and $y = 0.0 - 1.0$) samples, it was found that the addition of Cu could be used to tune the Curie Temperature over a 100 K range, with less than a 30 % reduction in the saturation magnetisation at 10 K, while the addition of Cr changed the Curie Temperature by 700 K and reduced the saturation magnetisation by 60 % at 10 K. By tuning the Cu to Cr ratio it is possible to achieve a Curie temperature around room temperature. The magnetocaloric effect (MCE) was studied in these materials, as the compositions tend to involve cheaper, more widely available elements, plus careful tuning of the composition will allow for the Curie Temperature to be around 300 K. It was found that the refrigeration capacity for the $\text{CoFeNiCr}_y\text{Cu}_x$ alloys was ~ 70 J/kg and for the $\text{CoFeNi}_{0.5}\text{Cr}_{0.5}\text{Al}_x$ alloys was ~ 75 J/kg at 2 T (Fig. 1b) [2]. Although these are smaller than existing materials such as LaFeSi, these HEAs still have advantages due to the presence of second order transitions, and having a wider operational temperature range for the MCE. In conclusion, the MCAs studied have promising functional magnetic properties, with small coercive fields, and reasonable saturation magnetisations. The phases present can be tuned via the composition, allowing for two-magnetic phase systems to be fabricated, that improve the magnetic properties compared to a single solid solution. The research carried out is only the tip of the iceberg, but these alloys are showing encouraging results.

[1] N. A. Morley, C. R. B. Lim, J. Xi, A. Quintana-Nedelcos, and Z. Leong, Scientific Reports, 10, 14506, (2020) [2] A. Quintana-Nedelcos, Z. Leong, and N.A. Morley, Materials Today Energy, (accepted 2021)

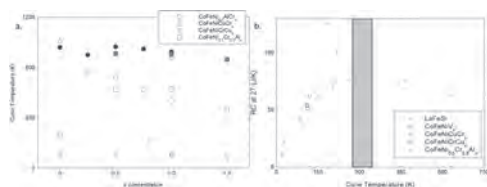


Figure 1a. Curie Temperature for $\text{CoFeNi}_{0.5}\text{Cr}_{0.5}\text{Al}_x$, $\text{CoFeNi}_{0.5}\text{Cr}_x\text{Al}$ and $\text{CoFeNiCr}_y\text{Cu}_x$ alloys. 1b. Refrigeration capacity at 2 T for $\text{CoFeNi}_{0.5}\text{Cr}_{0.5}\text{Al}_x$, $\text{CoFeNi}_{0.5}\text{Cr}_x\text{Al}$ and $\text{CoFeNiCr}_y\text{Cu}_x$ alloys. Shaded area useful temperature range.

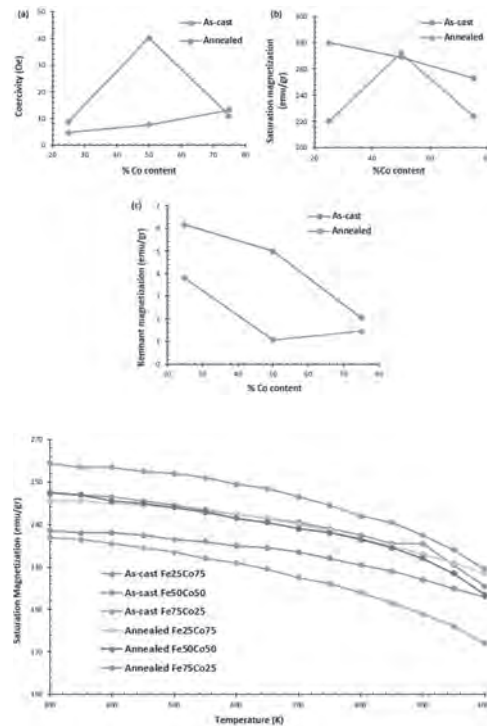
JX-11. Heat Treatment Investigations of Fe-Based Alloys.

M.G. Ozden¹, Z. Leong¹ and N. Morley¹

1. The University of Sheffield, Sheffield, United Kingdom

Fe-Co alloys have been ideal materials for various applications where high saturation magnetization (M_s), high permeability (μ) and low coercivity (H_c) are needed, especially for the applications where the minimization of mass and volume is a design parameter, such as aerospace industries [1-6]. In addition, their high Curie temperature makes them competitive candidates for high temperature applications [4]. In this study, in order to fully understand the compositional effect of Fe-Co alloys on their magnetic behaviour, Fe₂₅Co₇₅, Fe₅₀Co₅₀ and Fe₇₅Co₂₅ alloys were produced by using arc melting technique and characterized with the help of X-ray diffraction (XRD) analysis and superconducting quantum interference magnetometer (SQUID). XRD analysis indicated that all the samples were single phase (BCC), proving that oxidation did not occur during the manufacturing process. Furthermore, from their hysteresis loops, their magnetic saturations, remnant magnetizations and coercivities were found in the ranges 253-280 emu/gr, 2.06-6.15 emu/gr and 8.67-40.24 Oe, [4] respectively (Fig. 1). It was observed that as the % Co (wt.) content increases, saturation and remnant magnetization decreases, thus the Fe-rich alloys have higher magnetic properties. Also, after arc melting, stress-relief annealing was employed at 1073 K for 1 hr, resulting in reduction of the magnetic saturation (220-272 emu/gr), remnant magnetization (1.08-3.8 emu/gr) and coercivity (4.73-13.28 Oe) [5] due to the microstructural refinement, as it can be seen clearly in Fig.1. This study confirms that arc melting helps to improve the magnetic properties of Fe-Co alloys, because their magnetic properties is higher than the magnetic properties of those fabricated by mechanical alloying (M_s : 150-225 emu/gr, H_c : 25-70 Oe) [4] and cold rolling (M_s : 217.8 emu/gr, H_c : 87.7 Oe) [3]. Curie temperatures of the as-cast samples (1097-1181 K), are slightly lower than the values in the literature [5], also decreased slightly to the value range of 1071-1107 K after the heat treatment. By looking at Fig. 2, for the high temperature magnetic performances of as cast and annealed specimens, it can be seen that the annealed samples have a higher saturation magnetisation as a function of temperature. Further study has been undertaken to design and develop a new Fe-based amorphous alloy, with similar properties to Fe-Co alloys. The alloy of Fe₄₅Co₁₅B₂₈Al₁₀B₂ was arc-melted followed by stress-relief annealing at 573 K for 1 hr to achieve the desired magnetic properties and amorphous morphology. Using DCS and temperature dependence magnetisation measurements up to 1000 K, the temperature dependence structural and magnetic behaviour was studied. DSC analysis indicates that the sample has glassy phase with the melting point of 1200 K and glass transition temperature of 800 K. Moreover, its Curie temperature was found as 940 K. Thus, this composition has promising results as a new soft magnetic material for high temperature applications.

[1] S. Bergheul, A. Haddad, H. Tafat and M. Azzaz, "Magnetic, Microwave and Absorbing Properties Fe-Co of Alloy Synthesized by Mechanical Alloying Process," in *Application of Contemporary Non-Destructive Testing in Engineering*, Portoroz, Slovenia, 2005. [2] R. Fingers and G. Kozlowski, "Microstructure and magnetic properties of Fe-Co alloys," *Journal of Applied Physics*, vol. 81, no. 8, pp. 4110-4111, 1997. [3] S. Honjo, S. Kikuchi, A. Sakuma, S. Ishio and J. Balachandran, "Preparation of magnetic Fe-Co alloy using texture controlled technique," *Journal of Magnetism and Magnetic Materials*, vol. 465, pp. 64-69, 2018. [4] F. Sanchez-De Jesus, A. Bolarin-Miro, C. Cortes Escobedo, G. Torres-Villasenor and P. Vera-Serna, "Structural Analysis and Magnetic Properties of FeCo Alloys Obtained by Mechanical Alloying," *Journal of Metallurgy*, vol. 2016, p. 8347063, 2016. [5] R. Sundar and S. Deevi, "Soft magnetic FeCo alloys: alloy development, processing, and properties," *International Materials Reviews*, vol. 50, no. 3, pp. 157-192, 2005. [6] Y. Zhang, R. Ma, S. Feng, L. Cheng, P. Davies and P. Yu, "Microstructures and magnetic properties of Fe-35%Co alloy fabricated by metal injection molding," *Journal of Magnetism and Magnetic Materials*, vol. 497, p. 165982, 2020.



JX-12. Withdrawn

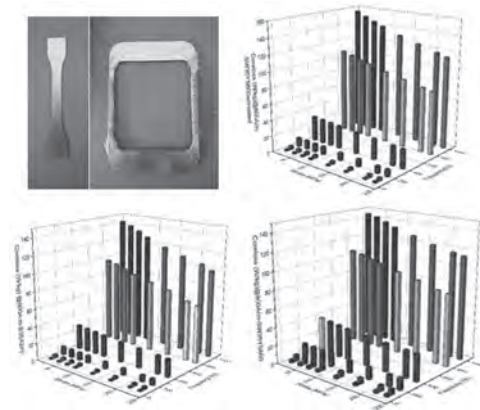
JX-13. Magnetic Performance Improvement Caused by Tensile Stress in Equivalent Iron Core Fabricated by High-Strength Non-Oriented Electrical Steel.

R. Pei¹, H. Zhang¹ and L. Gao²

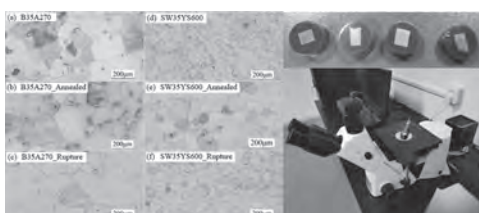
1. Electrical Engineering, Shenyang University of Technology, Shenyang, China; 2. Suzhou InnMag New Energy Ltd., Suzhou, China

Permanent Magnet Synchronous Machines (PMSM) have gradually become the mainstream solution for drive motors. One main trend for advanced PMSM optimization is focused on new material application. Conventional PMSM iron core is fabricated by Non Grain-Oriented (NGO) silicon steel sheet lamination, based on traditional technic, the high-strength NGO silicon steel uses solid solution strengthening and precipitation strengthening methods to enhance mechanical strength [1]. As mentioned in [2-3], due to the increase in mechanical strength of high-strength NGO steel, a narrower magnetic bridge design can be applied in the rotor design. Thereby reducing the leakage flux to increase the output torque and the overall efficiency. Even though the high-strength NGO had higher iron loss, counting the reduction in the rotor bridge width, the overall performance can be significantly enhanced. The maximum speed of advanced PMSM is mostly greater than 12000rpm, thus the rotor sustains significant tensile stress due to centrifugal force. It's easier to form the striped 180° domain with higher permeability under tensile stress [4]. While the frequency influence and thermal condition has not been discussed in [4]. In this paper, we designed an equivalent sample to simulate the condition of an iron core, similarly in [5], with different excitation and manufacture parameter such as laminated number and thermal condition. Three types of high-strength NGO (SW35YS600\SW35YS900\B35AHS500) and a controlled group (conventional NGO B35A270) has been tested. Magnetic performance of equivalent sample is measured by ring sample method. Two narrow sides of the sample are subjected to large tensile stress concentration, the lamination number is 5, 10, and 20. At high excitation frequencies, the level of iron loss improvement caused by tensile stress is significant. Four materials have also been annealed respectively at 720°C for 10 hours under argon atmosphere. After annealing, the tensile stress has lower effect on the magnetic properties for B35AHS500 and B35A270, but is significant for SW35YS600 and SW35YS900. Therefore, it is speculated that a large proportion of heat treatment process has been adopted during SW35YS600 and SW35YS900. In addition, we also conduct metallographic experimental observations on the material of the sample and the tensile fracture, and analyze the reasons for this result at the grain level. And in the subsequent experiment process, we further explored the influence of different environmental temperatures and different tensile stresses on the magnetic properties of these four NGO materials.

[1] GONG, Jian, and Hai-wen LUO. "Progress on the research of high-strength non-oriented silicon steel sheets in traction motors of hybrid/electrical vehicles." *Journal of Materials Engineering* 43.6 (2015): 102-112.
 [2] Tietz, Marco, et al. "Effects and advantages of high-strength non grain oriented (NGO) electrical steel for traction drives." 2013 3rd International Electric Drives Production Conference (EDPC). IEEE, 2013. [3] Tanaka, Ichiro, et al. "Application of high-strength nonoriented electrical steel to interior permanent magnet synchronous motor." *IEEE transactions on magnetics* 49.6 (2012): 2997-3001. [4] Senda, Kunihiro, et al. "Magnetic properties and domain structure of non-oriented electrical steel under stress." *IJTFM* 131.10 (2011): 884-890. [5] Gao, Lingyu, et al. "Application of grain-oriented electrical steel used in super-high speed electric machines." *AIP Advances* 10.1 (2020): 015127.



sample of the tensile experiment and result of the magnetic test



metallographic experimental observations

JX-14. Influence of Size and Position of Stacking-Hole on Local Vector Magnetic Properties of Grain-Oriented Steel Sheet.

R. Dou¹, Y. Li¹, Z. Lin¹, M. Yang¹ and L. Yang¹

1. State Key Laboratory of Reliability and Intelligence of Electrical Equipment, Hebei University of Technology, Tianjin, China

Grain-oriented (GO) electrical steel sheets, as a core material used in power transformers broadly, often holed at particular and suitable regions to make the stacking of the sheet easier. The magnetic properties around the hole will be deteriorated, and the local magnetic domain structure will be impacted [1]. These phenomena will significantly influence the performance of the transformer [2]. It is necessary to accurately measure and study the influence of hole on local vector magnetic properties to optimize the core structure. Some studies use the search coils wound by drilling through the sample to analyze the flux orientations [3]-[4]. Yet the distributions of local magnetic properties around the hole have not been clarified. To obtain a more comprehensive and accurate distribution of local vector magnetic properties, and avoid damaging the sample to wind the search coils, the needle probes and double *H*-coils, which were discussed in [5] and [6], are adopted and developed. In this paper, a novel local magnetic property testing system using an accurately-movable *B-H* sensor is designed and constructed to study the local vector magnetic properties around the hole in a transformer type core made of grain-oriented electric steel sheets. The influence of sizes and positions of the holes on the properties is compared and analyzed at 50-400 Hz. In addition, the changes of the magnetic domain are observed and analyzed. Fig. 1 shows the local testing system with an accurately-movable *B-H* sensor and sample with 300 mm × 300 mm studied in this paper. The distance between the needles of *B* sensor is 3.5 mm, and *H*-sensor coil is 2 mm × 2 mm assembled using wire with 0.01 mm diameter. The number of turns is 600. The sensor is mounted to a XYZ-precise-positioning device, hence, the magnetic flux density, *B*, magnetic field strength, *H*, and core loss, *P*, of each point in the local area can be measured. Eight holes with diameter of *D* and interval of 100 mm are punched in the transformer sheets. *W* is the distance of the center of hole to the inner edge. Different *D* and *W* are studied in the paper. Single layer grain-oriented steel sheet (namely, B30P120) is tested. To study the vector magnetic properties around the hole, the square area (47 × 47 mm²) centered at the hole is measured and studied. The $H = H(x, y)$, $B = B(x, y)$ and $P = P(x, y)$ are measured when the sensor is moved 1 mm in interval along the *x*-, or *y*-directions and the total number of measured points are 2000. As a criterion of measurements, the peak flux density is measured and controlled with a search coil, which wound uniformly around the sample. Fig. 2 shows *P* distributions around the hole with *D* = 4 mm and *W* = 25 mm when *B* is controlled to be 50 Hz sinusoidal waveform with 1.5 T amplitude. The domain structures at particular areas *A*₁ and *A*₂ are also shown in Fig. 2. The results show that the core loss *P* around the hole is much larger than that around points far to the hole. It could be attributed to the non-uniform flux density distributions, in particular, increasing flux density close to the hole. It is consistent with the observation of domain structure around the hole. The domain structure is disordered close to the hole due to strain introduced by hole punching while it is uniform at the point far to the hole. In addition, the distribution of the flux density *B*, field strength *H*, and core loss *P* around the hole with different diameters (*D* = 4, 6, 8, 10 mm) and different positions (*W* = 20, 25, 30 mm) are measured and analyzed in the flux density ranges of 0.1 – 1.5 T at 50 – 400 Hz. The experiment results show that the local *B* and *H* distributions are altered by the hole. The domain pattern is also restructured due to strain introduced by hole punching. As a result, the local losses are increased. In addition, the losses around the hole increase to 150 – 300 % compared with the losses at the far point depending on *D* value of 4 – 10 mm. However, the location of hole has minor influence on the losses, in particular, when the hole is located at the symmetrical position (*W* = 25 mm). In conclusion, small size of the hole and symmetrical position of the hole during stacking of the core can minimize the deterioration of local magnetic properties and improve the performance of the stacked electrical steel sheets ultimately.

N.Derebasi and C.Erdonmez, IEEE Transactions on Magnetics., Vol. 51, p.1-4 (2015) [4] N Derebasi, C Erdonmez, Journal of Superconductivity and Novel Magnetism., Vol. 30, p.3309-3313 (2017) [5] S. Imamori, S. Aihara and H. Shimoji, Journal of Magnetism and Magnetic Materials., Vol. 500 (2020) [6] S Aihara, H Shimoji and T TodakaM, IEEE Transactions on Magnetics., Vol. 48, p.4499-4502 (2012)

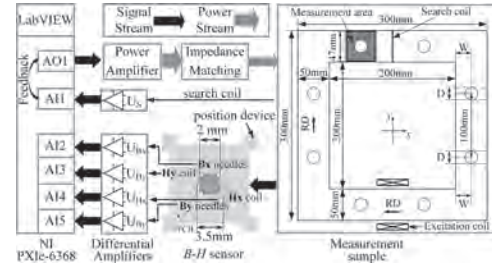


Fig. 1. Novel local measurement system and measurement sample.

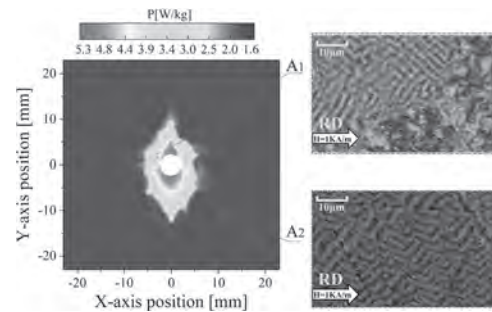


Fig. 2. Distributions of the core loss around the hole and magnetic domain structure at area *A*₁, *A*₂.

[1] T.Gunes, R. Schäfer and N.Derebasi, IEEE Transactions on Magnetics., Vol. 54, p.1-8 (2018) [2] G. teNyenhuis, S. Giris and F. Mechler, IEEE Transactions on Power Delivery., Vol. 16, p.648-653 (2001) [3] T.Gunes,

JX-15. Effect of Punching on Magnetic Properties of Non-Oriented Electrical Steel.

C. Zhang^{2,1}, L. Yang^{2,1}, Y. Li^{2,1}, Y. Dou^{2,1} and Q. Yang³

1. Hebei University of Technology, Tianjin, China; 2. Hebei University of Technology State Key Laboratory of Reliability and Intelligence of Electrical Equipment, Tianjin, China; 3. Tianjin University of Technology, Tianjin, China

Introduction: Non-oriented silicon steel is widely used in the manufacture of motors and other equipments due to its excellent magnetic properties. In the production process, non-oriented electrical steel often needs to be punched to form the required shape. During the punching process the magnetic properties of silicon steel sheets will be deteriorated due to the mechanical stress [1-4]. As a result, the plastic deformation and residual stress emerge around the area of cutting edge, which have a significant impact on the magnetic properties and magnetic domain structure of electrical steel sheets. In this paper the effects of punching on the magnetic properties and magnetic domain structure of non-oriented electrical steel are studied. And the deterioration degree of the magnetic properties caused by different punching load are analyzed quantitatively. **I Test samples and methods** The test samples of cold-rolled non-oriented electrical steel B35A270 are punched on the precision punching machine by the 25-ton and 80-ton punching load, respectively. Then, two kinds of samples with a size of 49.5*49.5*0.35mm are obtained. The sample processed by 25 tons of punching load is denoted as sample A, and the one processed by 80 tons of punching load is denoted as sample B. The 2D magnetic properties measurement apparatus consists of two single C-shaped yokes, excitation windings and silicon steel sheet samples. An AC magnetic field with a frequency of 50 ~ 200Hz is applied along the rolling direction of the sample. The samples supported by the sample holder are placed in the gap between the two yokes, and the yoke air gap matches the size of the sample. The sensing system is specially designed to measure the local magnetic properties in different position of the sample. In the sensing system, the micro-size H coil is wound on a 0.05mm thick PCB substrate with a length of 3mm to measure the H signal in the rolling direction of the sample. Two retractable B probes are fixed on a 1.5mm thick PCB with a spacing of 3.5mm to measure the B signal in the rolling direction of the sample. Taking the midline of the sample along the tangential direction as the measurement characteristic sampling line, the micro-size composite B - H sensor can be moved smoothly along the characteristic sampling line with a 2 mm distance step. **II Experimental results and analysis** The core loss curves of the two samples measured at 50Hz sinusoidal signals are depicted in Fig.1 (a) and (b). The loss of the sample A increases by 0.9% ~ 15.25% in the range of 8 mm from the edge, especially in the range of 6 mm. The loss of the sample B increases by 6.8 % ~ 29.55%, while the deteriorated area expands to 14 mm. According to the Bertotti loss separation, the hysteresis, eddy current and excess loss coefficient are identified by the experimental results. It is concluded that the punching process cause an increase of the hysteresis loss. It can be attributed to plastic deformation and residual stress around the punching edge. The moving of magnetic domains can be hindered with the increase of the width of plastic deformation area. During the magnetization process, the movement resistance of the edge domain increases, so the hysteresis loss increases, which increases the iron loss of the sample. At the edge of the sample A, the magnetic coercivity increases by 5.5%, the magnetic remanence and permeability decreases by 11.7% and 29.2%. The magnetic coercivity increases by 24.3%, the remanence and the permeability decreases by 35.9% and 47.9% at the edge of the sample B. **III Observation of magnetic domain structure** In order to investigate the mesoscopic properties of punching effect, the 8*8mm sample need to be prepared for Kerr microscope, which is cut by wire electrical discharge machining from the above sample A and B in the edge and center area of the samples. After sanding, mechanical polishing and other steps, shiny mirror-like samples are obtained. Using a Kerr microscope to observe the magnetic domains of the sample, as shown in Fig. 2(a), the center of the sample A is dominated by sheet-like magnetic domains, while there are a large number of labyrinth domains near the punching edge as shown in Fig. 2 (b). The size and shape of the domains also change. In addition, the magnetic domain in the center is parallel to the rolling direction, while the direction of the magnetic domain at the edge changes, which makes it difficult to magnetize. This leads to the

increase of iron loss and the deterioration of magnetic properties. **IV Conclusion** Based on the local 2D magnetic measurement and magnetic domain observation, the magnetic properties of non-oriented electrical steel deteriorate by the punching processing. Furthermore, the deterioration degree of the magnetic properties become more significant by larger punching load.

[1] Campos M F D, Sablik M J, and Landgraf F J G. Journal of Magnetism & Magnetic Materials., Vol.320, p.e377-e380(2008) [2] René Siebert, Wetzig A, and Beyer E. IEEE Electric Drives Production Conference., (2013) [3] Nakata T. IEEE Translation Journal on Magnetics in Japan., (2008) [4] Senda K, Ishida M, and Nakasu Y. Journal of Magnetism and Magnetic Materials., Vol.304, p.e513-e515, (2006)

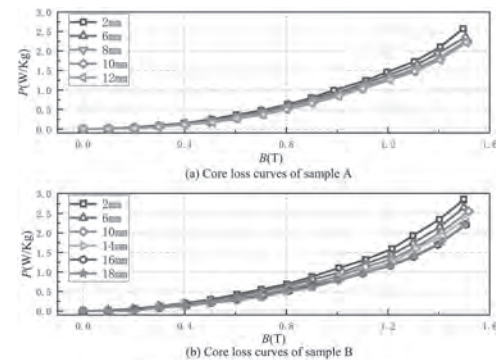


Fig.1. Core loss curves of sample A and B

Fig.1 Core loss curves of sample A and B

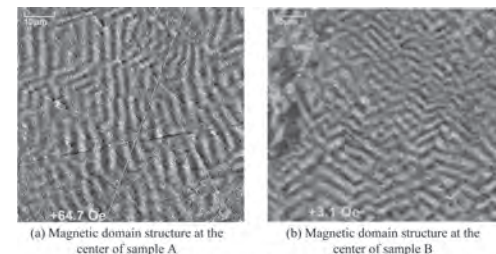


Fig.2. Magnetic domain structure of sample A

Fig.2 Magnetic domain structure of sample A

Session JY
SOFT MAGNETIC MATERIALS AND APPLICATIONS
(Poster Session)

Paola Tiberto, Co-Chair
INRIM, Torino, Italy

Carlo Stefano Ragusa, Co-Chair
Politecnico di Torino, Torino, Italy

JY-01. Time-Resolved Observation of a Domain Wall Motion in Microwires With Positive Magnetostriction.

K. Richter^{2,1}, O. Vahovsky², R. Varga² and J. McCord¹

1. Christian-Albrechts-Universität zu Kiel, Kiel, Germany; 2. Univerzita Pavla Jozefa Safarika v Kosiciach, Kosice, Slovakia

Thin magnetic cylindrical wires attract considerable attention due to interesting features of a domain wall motion like absence of the Walker breakdown that prevents fast domain wall dynamics [1]. Amorphous glass-coated microwires are composite material, in which very high domain wall velocities have been observed [2-3]. Owing to the amorphous state of wires, the magnetocrystalline anisotropy vanishes. Recently, it was shown that the axial magnetic anisotropy resulting from rapid quenching has comparable strength, leading to a tilted domain wall orientation [4]. It is an open question of how the tilted domain wall in cylindrical wires moves at high velocities and the origin of the so-called unidirectional effect [5]. An essential prerequisite for understanding the magnetic domain walls dynamics is a detailed knowledge of its spin structure in static. While several experimental techniques allow for well controllable deposition of magnetic structures with complex geometries [6], a reliable determination of a surface magnetization usually meets several obstacles in case of sample with curved surface. In the first part, we extend our analytical model of the Magneto-Optical Kerr Effect (MOKE) contrast [7] for cylinders with reduced diameter. Understanding the underlying mechanisms allows devising a new approach for interpretation of magneto-optical observations of thin magnetic cylinders. It is shown that the cylindrical shape of sample surface gives rise to a spatial distribution of the planes of incidence that are all tilted each to other. Phase diagrams of a magneto-optical contrast are calculated for various angles of incidence, extinction angles between polarizer and analyzer and as a function of thickness of a glass coat. In particular, it is shown that additional layer of a glass coat changes remarkably the circumferential dependence of light intensities. Our framework is used to optimize the LASER MOKE setup for direct visualization of a surface shape of domain wall in thin magnetic cylinders [4]. Stabilization of a domain wall is achieved by two opposite magnetic fields, resulting in effective one-dimensional potential well. Periodic back-and-forth motion of the well is used to synchronize the domain wall position with MOKE imaging and direct time-resolved images of a surface magnetism are performed. In contrary to previous measurements, a small pick-up coil is wound around a thin glass capillary in order to detect spin dynamics inside the wire (Fig. 1). A direct comparison between surface domain wall position detected by MOKE and a signal from pick-up coils is given. It is shown that the voltage induced in pick-up coil has two sources: a, the voltage from spatially dependant magnetic field controlling the domain wall position and b, the signal from the domain wall. Employing simulations based on finite element method, the shape of a magnetic potential well is calculated. The profile of the magnetic domain wall potential well is then used to calculate the contribution from domain wall. At slow motion of a domain wall potential well, the signal from pick-up coils is well synchronized with a surface domain wall motion. The result implies almost planar structure of a domain wall. At high domain wall velocities, the signal in pick-up coil is induced earlier than surface boundary arrives to the position of a pick-up coil. The findings show that the tilted domain wall in microwires is not planar during the propagation. Our time-resolved observations of a domain wall depinning process show domain wall strongly distorts at pinning centres (Fig. 2). The finding is important for correct interpretation of a domain wall velocities measured by Sixtus-Tonks method. Finally, we propose a single scheme for wireless magneto-optical sensor based on domain wall motion in thin magnetic cylinders.

[1] M. Yan, A. Kákay, S. Gliga, et al., Phys. Rev. Lett., Vol 104, p.057201 (2010) [2] P. Klein, R. Varga, M Vázquez, J. Alloy. Compd., Vol 550, p.31 (2013) [3] R. Varga, K. L. Garcia, M. Vazquez, P. Vojtanik, Phys. Rev. Lett., Vol 94, p.017201 (2005) [4] K. Richter, A. Thiaville, R. Varga, J. McCord, J. Appl. Phys., Vol. 127, p.193905 (2020) [5] J. Onufer, J Ziman, M. Kladvivova, J. Magn. Magn. Mater., Vol 396, p.313 (2015) [6] A. Fernandez-Paecho, et al., Sci. Rep., Vol 3, p.1492 (2013) [7] K. Richter, A. Thiaville, and R. Varga, Phys. Rev. B, Vol. 96, p.064421 (2017)

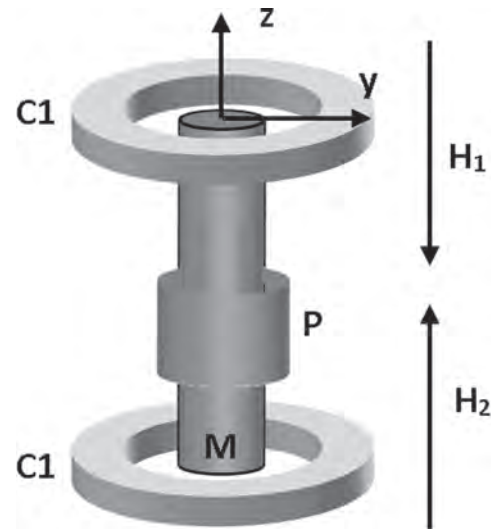


Fig. 1 Stabilization of a domain wall by potential well. Microwire (M) is placed between coils. Pair of driving coils (C1 and C2) generates opposite magnetic fields H_1 and H_2 . The domain wall is moved back-and-forth by ramping the current in one coil. Surface magnetization is detected by two LASER spots (red lines). Inner magnetization dynamics is sensed by pick-up coil (P).

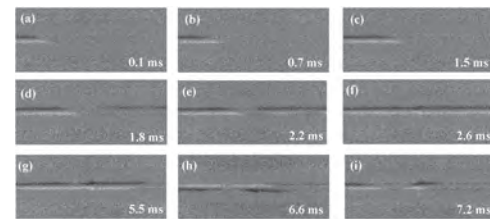


Fig. 2 Time-resolved observation of a domain wall depinning process in amorphous glass-coated microwire. Images are performed by time-resolved MOKE microscopy.

JY-02. Magneto-Impedance Behavior of Soft Ferromagnetic Microwires at GHz-Frequency for the Application of High-Performance Magnetic Sensory Devices.

J. Alam¹, M.G. Nematov², N.A. Yudanov¹ and L. Panina^{1,2}

1. *Technology of Electronics Materials, National University of Science and Technology, MISIS, Moscow, Russian Federation;* 2. *Immanuel Kant Baltic Federal University, Kaliningrad, Russian Federation*

Abstract—The idea of the present work is devoted to improving the SOLT calibration standard by specially designed microstrip cells as a PCB SOLT standard for VNA calibration and measuring the high-frequency magneto-impedance (MI) for the development of various high-performance micro-sensor devices. The high-frequency sensitivity of MI was enhanced by the current annealing of partially crystalline wires. In the past few years, soft ferromagnetic amorphous wires have attracted growing attention in research due to their miniature dimensions, excellent soft magnetic properties, and giant-magnetoimpedance (MI) effect [1,2]. The MI effect which is referred to as a large and sensitive change in the complex-valued impedance of a magnetic conductor in the presence of an external magnetic field and/or mechanical stress is of particular interest for the development of various high-performance micro-sensor devices [3]. To optimize sensing operation regimes, it is important to measure the impedance characteristics of the individual wire which may present considerable problems at higher frequencies in the GHz range. This is related to uncertainties occurring due to the calibration of measuring devices (Network Analyzer). In the present work, we suggest an application-specific calibration technique with a specially designed microstrip cell for the impedance measurement for frequencies up to 6 GHz. We also demonstrate that the MI plots change their shape with increasing frequency and high sensitivity range caused by the directional change in the dc magnetization vanishes at frequencies of about 2 GHz for Co-rich wires with a circumferential anisotropy. The frequency range of high MI sensitivity can be enhanced by inducing a surface anisotropy in partially crystallized wires. Coaxial and microstrip transmission lines are widely used as sample holders, however, in the case of the impedance measurements when the sample is subjected to mechanical stress, coaxial lines are not convenient. Here we discuss the calibration procedures for microstrip lines. In the microwave de-embedding methods, the electrical reference planes are shifted to the sample location. This requires the use of dummy sample holders with specific terminations, for example, three reflection standards (open, short, and match load) and two ports connected together (thru). This calibration procedure is known by its name as short-open-load-thru (SOLT) or thru-open-short-match (TOSM). Accurate calibration standards can be fabricated on customized PCB, then, the complex impedance Z is calculated from the S_{21} -parameter using a simple formula without solving any equations. Fig. 1 shows the MI characteristics at different frequencies of amorphous $\text{Co}_{66.6}\text{Fe}_{4.28}\text{B}_{11.51}\text{Si}_{14.48}\text{Ni}_{1.44}\text{Mo}_{1.69}$ microwires in an as-prepared state (total diameter $D=25.8\ \mu\text{m}$ metal core diameter $d=25\ \mu\text{m}$ and $d=14.2\ \mu\text{m}$). The wire has a well-defined circular anisotropy with an anisotropy field of about 7.5 Oe. The wires of this composition are of particular interest due to low Curie temperature, so they can be used as embedded temperature sensors. It is seen that the high sensitivity of MI due to the dc magnetization re-orientation is preserved for frequencies below 2 GHz. When the dc magnetization is along the wire and does not change by the field, only the permeability parameter determines the field behavior of the impedance: for high frequencies, it increases with a much lower slope: the sensitivity of the impedance change is about few percent per Oe. In the case of wires with partial crystallization, the current annealing establishes a stronger surface anisotropy which improves the MI behavior at higher frequencies. Moreover, it is possible to realize a strong stress dependence of MI at zero fields as demonstrated in Fig. 2. Acknowledgment: This work was supported by the Russian Foundation for Basic Research (RFBR 19-32-90129) and the part from the Ministry of Education and Science of the Russian Federation in the framework of the Increase Competitiveness Program of MISIS.

[1] L. V. Panina, K. Mohri, T. Uchiyama, Giant Magneto-Impedance in Co-Rich Amorphous Wires and Films, IEEE Trans. Magn. Vol. 31, p. 1249-1260 (1995). [2] M. Vázquez, Soft magnetic wires, in: Phys. B Condens. Matter. Vol 299, p. 302-313 (2001). [3] J. Alam, C. Bran, H. Chiriac, et al, Cylindrical micro and nanowires: Fabrication, properties and applications, J. Magn and Magnetic Mater. Vol. 513 (2020) 167074.

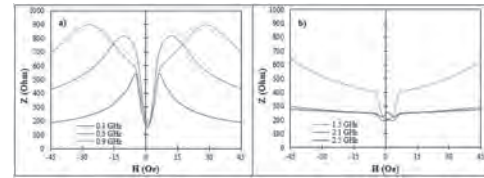


Fig. 1: MI vs magnetic field of amorphous $\text{Co}_{66.6}\text{Fe}_{4.28}\text{B}_{11.51}\text{Si}_{14.48}\text{Ni}_{1.44}\text{Mo}_{1.69}$ microwires in as-prepared state at GHz frequency range a) 0.1 GHz to 0.9 GHz and b) 1.5 GHz to 2.5 GHz

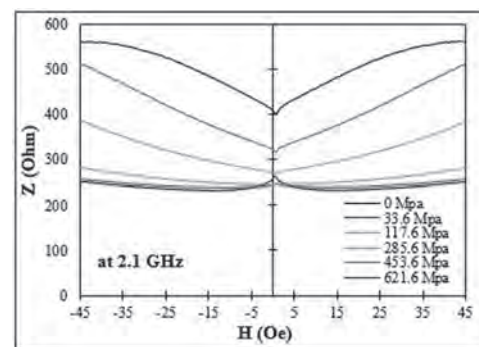


Fig. 2: Effect of tensile stress on the MI vs. magnetic field of $\text{Co}_{71}\text{Fe}_5\text{B}_{11}\text{Si}_{10}\text{Cr}_3$ (total diameter, a metal core diameter, partially crystalline) microwires after DC current annealing at 50 mA for 30 minutes. The frequency is 2.1 GHz.

JY-03. Transformation of the Magnetostriction of Amorphous Microwires by Heat Treatment.

S. Evstigneeva¹, M.G. Nematov², I. Baraban², V. Rodionova² and L. Panina^{1,2}
 1. National University of Science and Technology, MISiS, Moscow, Russian Federation; 2. Immanuel Kant Baltic Federal University, Kaliningrad, Russian Federation

Thermal treatments of amorphous alloys are known to cause structural relaxation which is followed by an evaluation of the magnetic anisotropy and saturation magnetostriction. In this work we investigated the effect of annealing with a temperature close to the onset of the crystallization on the magnetic hysteresis properties of glass-coated amorphous microwires of Co-rich compositions with a nearly zero magnetostriction. The annealing process was performed on the wires by two methods: dc current annealing and conventional annealing in furnace (at 475-490 °C for 30 min). The current intensities were chosen such to ensure similar annealing conditions. The annealing temperatures were higher than the Curie temperature (~360 °C) and slightly lower than the primary crystallization temperature (510 °C). We have demonstrated a sharp change in the shape of the magnetic hysteresis after annealing which is caused by the change in the magnetostriction. Typically, amorphous microwires of Co-rich compositions with negative magnetostriction are regarded as excellent soft magnetic materials suitable for large and sensitive magnetoimpedance (MI) [1]. A well-defined circumferential anisotropy could be established in these wires by a proper choice of composition, geometry and annealing treatments, which increases the MI ratio up to hundred percent in characteristic fields of few Oersted [2]. The high sensitivity of impedance to low magnetic fields makes amorphous ferromagnetic microwires a promising material for the construction of different sensor systems. In the present work, the transformation of the sign of magnetostriction in amorphous microwires of composition: $\text{Co}_{71}\text{Fe}_5\text{B}_{11}\text{Si}_{10}\text{Cr}_3$ (diameter: $D/d = 29/25 \mu\text{m}$) and $\text{Co}_{66.6}\text{Fe}_{4.28}\text{B}_{11.51}\text{Si}_{14.48}\text{Ni}_{1.44}\text{Mo}_{1.69}$ (diameter: $D/d = 35/25 \mu\text{m}$) was established after annealing in a narrow temperature range near the crystallization onset. This restores soft magnetic properties and ensures high temperature stability of all magnetic parameters. The wires under the study were produced by quenching and drawing technique (also referred to as modified Taylor-Ulitovskiy method). The choice of composition is justified by specific magnetoelastic properties with near zero magnetostriction of the order. It is known that annealing without applied stress can produce short-range order relaxation and consequently releases some frozen-in stresses and improves soft magnetic properties. In the present paper, we propose current and conventional annealing at relatively high temperatures slightly lower than the primary crystallization temperature. This causes nano crystallization and sharp change in the saturation magnetostriction. Therefore, we proposed a method of controllable change in magnetic anisotropy by changing the sign of magnetostriction. In particular, this results in a change in the shape of magnetic hysteresis and enhances the sensitivity of MI at microwave frequencies. The hysteresis loop of samples annealed by dc current and by conventional annealing are shown in Figures 1, 2. The annealing at temperatures higher than the Curie temperature increases the saturation magnetostriction and induces an axial easy anisotropy. A sharp change in the behavior of the hysteresis loops occurs after annealing with temperatures near the crystallization point, which can be explained by a change in the sign of the magnetostriction constant. Acknowledgment: This work was supported by the Russian Foundation for Basic Research (RFBR: 19-32-50097; 20-32-90145)

[1] M. G. Nematov, I. Baraban, N.A. Yudanov et al., *Journal of Alloys and Compounds*, 837, 155584 (2020) [2] A. Zhukov and V. Zhukova, *Nova Science Publishers*, New York (2009)

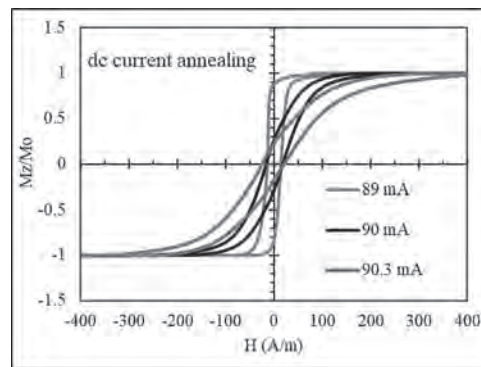


Fig. 1. Hysteresis loops of amorphous $\text{Co}_{71}\text{Fe}_5\text{B}_{11}\text{Si}_{10}\text{Cr}_3$ (diameter: $D/d = 29/25 \mu\text{m}$) microwires after dc current of which approximately corresponds to 490°C.

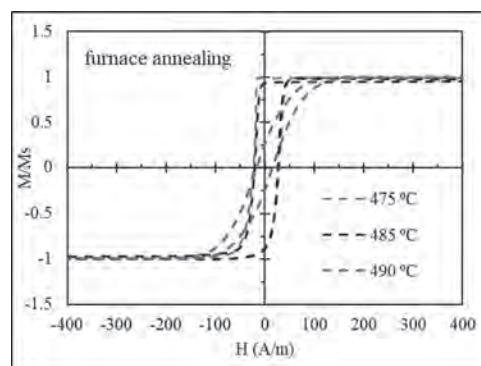


Fig. 2. Hysteresis loops of amorphous $\text{Co}_{71}\text{Fe}_5\text{B}_{11}\text{Si}_{10}\text{Cr}_3$ (diameter: $D/d = 29/25 \mu\text{m}$) microwires after annealing at furnace (475°C, 485°C, 490°C)

JY-04. Correlation Between Structural Relaxation and Magnetic Behavior in Amorphous Submicron Magnetic Wires.

S. Corodeanu¹, C. Rotarescu¹, C. Hlenschi¹, H. Chiriac¹, N. Lupu¹ and T.A. Ovari¹

1. Dept. of Magnetic Materials & Devices, National Institute of R&D for Technical Physics, Iasi, Romania

Submicron and nanosized cylindrical amorphous $\text{Fe}_{77.5}\text{Si}_{7.5}\text{B}_{15}$ and $(\text{Co}_{0.94}\text{Fe}_{0.06})_{72.5}\text{Si}_{12.5}\text{B}_{15}$ wires with diameters between 100 and 900 nm have been successfully cast by means of an upgraded variant of the glass-coated melt spinning technique [1]. Amorphous samples with both compositions show a magnetically bistable behavior, i.e., a single step axial magnetization reversal with a characteristic rectangular hysteresis loop. This reversal consists in the displacement of a 180-degree domain wall along the wire axis when the applied field is equal to or larger than the switching field. The values of the switching field are significantly different, with the positive magnetostrictive amorphous submicron wires ($\text{Fe}_{77.5}\text{Si}_{7.5}\text{B}_{15}$) displaying one to two orders of magnitude larger values than the nearly zero magnetostrictive $(\text{Co}_{0.94}\text{Fe}_{0.06})_{72.5}\text{Si}_{12.5}\text{B}_{15}$ ones. This emphasizes the importance of the types and magnitudes of the intrinsic magnetic anisotropies. Here we report on the study of structural relaxation within the amorphous submicron wires using measurements of the 180-degree domain wall velocity, in order to gain deeper insights into the roles played by the various types of magnetic anisotropy in amorphous submicron wires with different magnetostriction, such as $\text{Fe}_{77.5}\text{Si}_{7.5}\text{B}_{15}$ with the magnetostriction constant of 25×10^{-6} and $(\text{Co}_{0.94}\text{Fe}_{0.06})_{72.5}\text{Si}_{12.5}\text{B}_{15}$ with the magnetostriction constant of -1×10^{-7} , respectively. The samples have been furnace annealed in vacuum at 200°C and 350°C for 1h, in order to induce structural relaxation phenomena in the amorphous phase without crystallization. Domain wall velocity measurements have been performed on as-cast and annealed samples with both compositions and different diameters, using a method developed specifically for such ultrathin cylindrical wires [2]. Fig. 1 shows the dependence of the domain wall velocity on the annealing temperature for highly magnetostrictive amorphous $\text{Fe}_{77.5}\text{Si}_{7.5}\text{B}_{15}$ samples with diameters between 230 and 850 nm. Fig. 2 illustrates the same dependence in the case of nearly zero magnetostrictive $(\text{Co}_{0.94}\text{Fe}_{0.06})_{72.5}\text{Si}_{12.5}\text{B}_{15}$ samples with 300 and 770 nm in diameter, respectively. The domain wall velocity increases monotonically with the annealing temperature for all the highly magnetostrictive samples. The slope of the curves decreases with the increase in the wire diameter. This behavior originates in the stress relief that accompanies the structural relaxation and shows the important role played by the magnetoelastic anisotropy in the $\text{Fe}_{77.5}\text{Si}_{7.5}\text{B}_{15}$ samples. The effect is more pronounced in the thinner samples, due to their stronger intrinsic magnetoelastic interaction. A completely different behavior has been observed in the nearly zero $(\text{Co}_{0.94}\text{Fe}_{0.06})_{72.5}\text{Si}_{12.5}\text{B}_{15}$ samples. For a wire with 770 nm in diameter, a monotonic decrease of the domain wall velocity with the annealing temperature was observed. For a thinner one, with 300 nm in diameter, a change of slope was observed: the wall velocity slightly increases after annealing at 200°C, and then drops below the value of as-cast sample after annealing at 350°C. This behavior is consistent with a diminished role of the magnetoelastic anisotropy and a more prevalent role of the shape anisotropy. Only the latter is important in the thicker sample. In the thinner one, the magnetoelastic anisotropy contributes to the magnetic behavior until a sufficiently large annealing temperature is used, so that the residual stresses are decreased. The results show that measuring the domain wall velocity of amorphous submicron wires with different magnetostriction constants can provide essential information on the structural relaxation effects by means of the dominant magnetic anisotropy type and its changes triggered by the low temperature annealing process. This analysis is important for the future application of cylindrical amorphous submicron wires. Acknowledgements - Work supported by the Romanian Executive Agency for Higher Education, Research, Development and Innovation Funding (UEFISCDI) under contract no. 511PED/2020 (project PN-III-P2-2.1-PED-2019-0586/NanoCylCon).

[1] T.-A. Óvári, N. Lupu, and H. Chiriac, Recent trends in magnetic nanowires and submicron wires prepared by the quenching and drawing technique, in *Magnetic Nano- and Microwires (Second Edition)*, edited by M. Vázquez (Woodhead Publishing, Cambridge, 2020), pp. 221-253. [2] S.

Corodeanu, H. Chiriac, and T.-A. Óvári, Accurate measurement of domain wall velocity in amorphous microwires, submicron wires and nanowires, *Rev. Sci. Instrum.* 82 (2011) 094701.

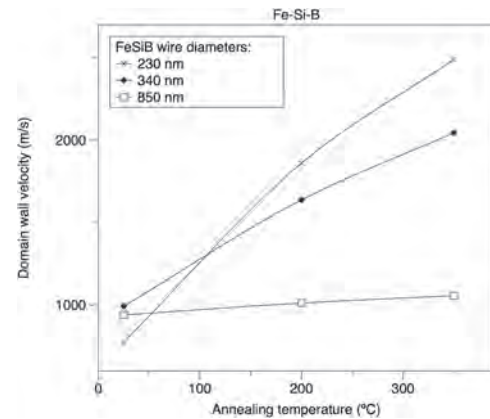


Fig. 1. Domain wall velocity vs. annealing temperature for highly magnetostrictive amorphous $\text{Fe}_{77.5}\text{Si}_{7.5}\text{B}_{15}$ glass-coated submicron wires.

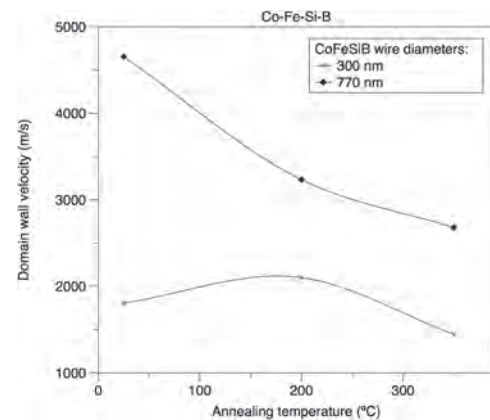


Fig. 2. Domain wall velocity vs. annealing temperature for nearly zero magnetostrictive amorphous $(\text{Co}_{0.94}\text{Fe}_{0.06})_{72.5}\text{Si}_{12.5}\text{B}_{15}$ glass-coated submicron wires.

JY-05. Study on the Soft and High-Frequency Magnetic Properties of Amorphous Co-Fe-B Thin Films With Various Co Compositions.

Y. Endo¹, H. Tanaka¹, S. Hashi² and T. Miyazaki³

1. Graduate School of Engineering, Tohoku University, Sendai, Japan;

2. Research Institute of Electrical Communication, Tohoku University,

Sendai, Japan; 3. Technical Division, School of Engineering, Tohoku University, Sendai, Japan

I. INTRODUCTION With the rapid development of new, ultra-low power spin-based devices such as magnetic random access memory (MRAM), spin logic, and so on, the magnetization dynamics in amorphous Co-Fe-B thin films has been studied intensively both from the fundamental and application points of view. In particular, a Gilbert damping constant (α), which describes the strength of damping torque, is one of the most important parameters to understand the dynamics. Until now, other groups reported α of amorphous Co-Fe-B thin films with various thicknesses and B compositions [1],[2], while details about the effect of Co compositions on α of these films have not been understood fully. In addition, the correlation between α and other magnetic parameters such as magnetic anisotropy, magnetostriction and so on still remains unclear. Herein, we evaluate the soft and high-frequency magnetic properties of Co-Fe-B thin films with various Co compositions, and discuss in detail the effect of Co composition on these magnetic properties of these films. III. EXPERIMENTAL PROCEDURES 10-nm thick $\text{Co}_x\text{Fe}_{80-x}\text{B}_{20}$ (Co-Fe-B) thin films ($0 \leq x \leq 80$) were fabricated by RF sputtering onto glass substrates. Co composition (x) was determined by energy dispersive x-ray spectroscopy (EDX) and the saturation magnetization estimated from VSM. The identification of the crystallographic structure of Co-Fe-B films was performed using the high-angle XRD analysis and TEM observation. These analyses indicated that every film structure is amorphous regardless of Co composition. The soft magnetic properties of Co-Fe-B films and the in-plane M-H curves were measured by VSM. The measurement of magnetostriction was performed using a thin-film magnetostriction measurement system (Toei Scientific Industrial Co., Ltd), which used an optical-cantilever method to detect sample deflection caused by magnetostrictive effect. The saturation magnetostriction (λ_s) of these films was evaluated using this system in an external magnetic field of 0.0 - +13.5 kA/m, which was sufficiently strong to magnetically saturate the films. The high-frequency magnetic properties were evaluated using a broadband ferromagnetic resonance (B-FMR) measurement technique with a coplanar waveguide (CPW) and a vector network analyzer (VNA). These measurements were performed at room temperature. III. RESULTS AND DISCUSSION Figure 1(a) shows the dependence of saturation magnetostriction (λ_s) on Co composition (x) for Co-Fe-B thin films. λ_s increased when Co composition increased up to 15 at.%, kept constant when Co composition was 15–40 at.%, and further decreased markedly when Co composition was above 40 at.%. This feature was almost similar to that of the Co-Fe-B bulk alloy, while their values were higher than those of these alloys [3]. The reason for this may be attributed to the compressive stress induced in the film plane during the film deposition. To understand the high-frequency magnetic properties of Co-Fe-B thin films, the parameters related to these properties [e.g., effective in-plane damping constant (α_{\parallel}) and magnetic inhomogeneous broadening at zero frequency ($\Delta H(0)$)] were estimated and are summarized in Fig. 1(b) as a function of Co composition (x). α_{\parallel} decreased to a minimum at the Co composition of 15 at.%, increased to approximately 0.0096 when Co composition was increased up to 30 at.%, again decreased to approximately 0.0062 for the Co composition between 40–50 at.%, and further markedly increased to a maximum at 80 at.%. The α_{\parallel} values for the Co composition of 30 and 80 at.% were twice or three times as high as those for other Co compositions, respectively. On the other hand, for $\Delta H(0)$, the trend was almost similar to that of α_{\parallel} . The values for the Co compositions of 30 and 80 at.% were much higher than those for other Co compositions. Therefore, these results suggest that the magnetic inhomogeneities such as the anisotropic dispersion, two-magnon scattering, and so on mainly influences on the high-frequency magnetic properties of Co-Fe-B thin films. ACKNOWLEDGEMENT The authors thank Prof. Satoshi Okamoto, and Associate Prof. Nobuaki Kikuchi at Tohoku University for performing the photo lithography and measuring XRD diffraction patterns, and Mr. Osamu Mori, Mr. Takashi Oizumi, Mr. Shigeyuki Sato, and Mr. Ryoichi Utsumi of Toei Scientific Industrial Corpo-

ration for measuring magnetostriction. This work was supported in part by KAKENHI (JP17H03226) from MEXT, Japan. This work was supported in part by CSIS, CSRN, and CIES, Tohoku University. This work was also supported in part by the ASRC in Japan.

[1] M. Oogane et al., Jpn. J. Appl. Phys. 45, 3889 (2006). [2] X. Liu et al., J. Appl. Phys. 110, 033910 (2011). [3] R.C. O'Handley, Solid State Comm. 21, 1119 (1977).

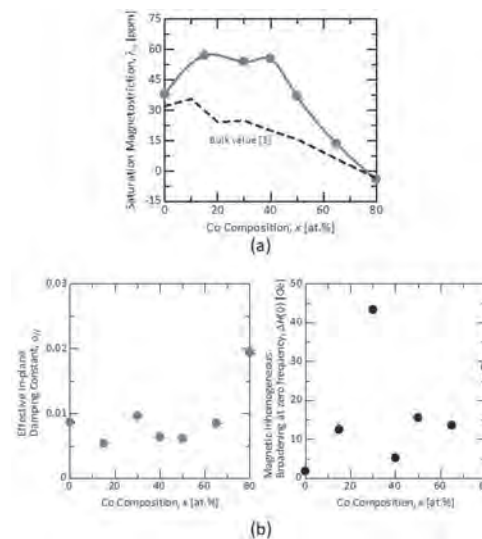


Fig. 1. (a) Dependence of saturation magnetostriction (λ_s) on Co composition (x) for Co-Fe-B thin films. The dotted line shows λ_s of the Co-Fe-B bulk alloy reported in Ref.[3]. (b) Change in the effective in-plane damping constant (α_{\parallel}) and magnetic inhomogeneous broadening at zero frequency ($\Delta H(0)$) of Co-Fe-B thin films with Co composition (x).

JY-06. Anisotropy Field Change With Piezoelectric Strain in Ultrathin Pt/Co(Fe)B/Ir Films.

K.N. Alshammari¹, M. Ali¹ and T. Moore¹

1. School Of Physics and Astronomy, University of Leeds, Leeds, United Kingdom

The magnetostrictive materials in the form of thin films have become increasingly vital in the development of actuators and sensors. Applying a strain to the magnetostrictive ferromagnet offers a degree of control over the material's magnetic anisotropy energy. In the recent past, there has been continued interest in having control of perpendicular magnetic anisotropy in the thin films through strain from piezoelectric material [1-4]. The induction of strain during the measurement allows the introduction of various strains. In addition, the measurement of the ensuing magnetic anisotropy changes permits an accurate calculation of magnetostriction. The magnetostriction constant λ is calculated from the changes of the magnetic anisotropy field induced by strain with applied stress. We report on our study of multilayers of Ta(3)/[Pt(2.3)/Co₆₈Fe₂₂B₁₀(0.7)/Ir(0.5)]_n/Pt(2.3) and Ta(3)/[Pt(2.3)/Co₆₈B₃₂(0.8)/Ir(0.5)]_n/Pt(2.3) with perpendicular magnetic anisotropy deposited by dc magnetron sputtering onto a glass substrate. Here, the layer thicknesses are displayed in nm and 'n' is the number of Pt/CoFeB/Ir or Pt/CoB/Ir trilayer. The polar MOKE was used in the characterisation of all the samples to display perpendicular magnetic anisotropy due to a large interface contribution Fig.1.(a). Also, we measure the magnetic anisotropy using a technique based on the Anomalous Hall Effect. The anisotropy measurement was done under strain applied perpendicular to plane using a biaxial piezoelectric transducer. A voltage of 150 V applied to the transducer generates a maximum strain of ~0.1%. This results in a decrease of the perpendicular anisotropy field in the films up to 12 mT as shown in Fig.1.(b). The Pt/CoFeB/Ir and Pt/CoB/Ir magnetostriction constant is found from a least-squares fit of the change in anisotropy field as shown in Fig 1.(c).

[1] Lee J-W et al., Appl. Phys. Lett. 82 2458 (2003). [2] Kim J-H et al., Appl. Phys. Lett. 97 252508 (2010). [3] Lei N et al., Phys. Rev. B 84 012404 (2011). [4] De Ranieri E et al., Nat. Mater. 12 808–14 (2013).

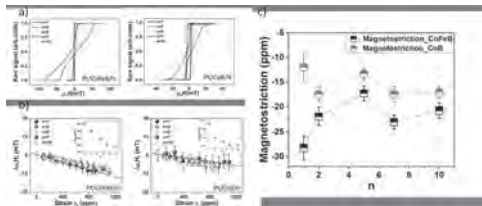


Fig.1.(a) Polar MOKE measurement for [Pt/CoFeB/Ir]_n and [Pt/CoB/Ir]_n multilayers on glass substrates. (b) The change in the anisotropy field of Pt/CoFeB/Ir and Pt/CoB/Ir with different repeats is due to out-of-plane strain ϵ_z and the solid line is a fit of the data. (c) Magnetostriction constant of Pt/CoFeB/Ir and Pt/CoB/Ir with different repeats.

JY-07. Effect of Meander Structure on Magnetoimpedance Characteristics in FeNi/Cu/FeNi Films.

J. Jiang^{1,2}, F. Jin^{1,2}, K. Dong^{1,2}, W. Mo^{1,2}, Y. Hui^{1,2}, J. Song^{1,2}, L. Xu^{1,2} and Y. Biao^{1,2}

1. School of Automation, China University of Geosciences, Wuhan, China;

2. Hubei key Laboratory of Advanced Control and Intelligent Automation for Complex Systems, China University of Geosciences, Wuhan, China

The giant magnetoimpedance (GMI) effect is the change of the total impedance under the application of an external DC field when alternating current flows through the ferromagnetic conductor. The three-layered film structure with a non-magnetic conductive center layer seems to be promising for future GMI sensor applications. Furthermore, it was reported that the meander structure allows one to improve the GMI effect of the sensor [1], and also can enhance the spatial resolution of the sensor [2]. However, the experimental and theoretical research concerning the influence of the meander structure on the GMI behavior in three-layered film is very limited, which needs further study. In this work, the three-dimensional physical models for NiFe/Cu/NiFe films with two different structures which are linear and meander are developed (as shown in Fig.1). Firstly, the magnetization process of the soft magnetic film of these structures is simulated by the Landau–Lifshitz equation for the magnetization motion. And then the electromagnetic distribution of these structures is calculated in the presented simulation model. Finally, we obtained the relationship between the impedance of the film and the applied magnetic field or excitation frequency. The influence of geometric parameters and structures of the films on the GMI is also analyzed. As shown in Fig.2(a), the GMI effect in meander structures appears to be much stronger compared with that in linear structure films, and the maximum values of the GMI ratio are more than 150% within the frequency range from 100MHz to 250MHz. For further analysis, Fig.2(b) shows the frequency dependence of the imaginary part of impedance ($\text{Im}(Z)$) with different values of the external magnetic field (H_{ext}). It presents that the mutual inductance of each parallel line in the meander structure will reduce the total inductance and decrease frequency response. The results obtained could be useful both for a better understanding of the GMI effect of the meander structure film and for designing a high-sensitivity magnetic field sensor.

[1] Rivero M A, Maicas M, Lopez E, et al. Influence of the sensor shape on permalloy/Cu/permalloy magnetoimpedance[J]. *Journal of magnetism and magnetic materials*, 2003, 254: 636-638. [2] Kikuchi H, Tanii M, Umezaki T. Effects of parallel and meander configuration on thin-film magnetoimpedance element[J]. *AIP Advances*, 2020, 10(1): 015334.

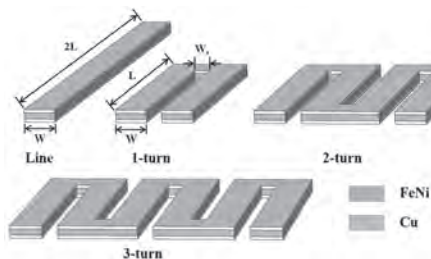


Fig. 1 Schematic description of linear structure and meander structure FeNi/Cu/FeNi films.

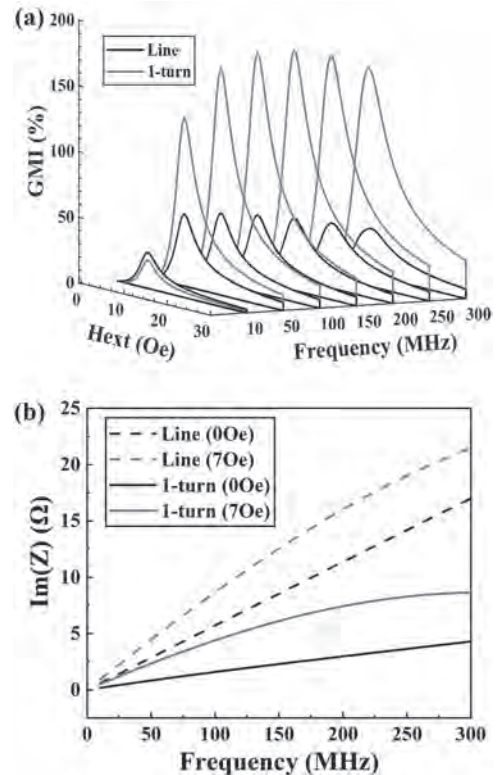


Fig. 2 (a) The GMI ratio for linear and meander FeNi/Cu/FeNi films. (b) Frequency dependence of the imaginary part of impedance.

JY-08. Magnetic Properties Evolution During Thermal Ageing of High Permeability Nanocrystalline FeSiCuNbB Alloys Annealed With Longitudinal Field.

R. Saoudi¹, L. Morel¹ and M. Raulet¹

1. Ampère laboratory, UMR 5005, University of Lyon1, Villeurbanne, France

Nanocrystalline materials are soft magnetic materials discovered by the Yoshizawa teamwork in 1988[1]. These materials are amorphous alloys which have been partially crystallized using rapid cooling technique. Their interesting magnetic high characteristics, such as high saturation flux density ($B_s > 1.25$ T), low coercivity ($H_c < 10$ A/m) and low dynamic losses, are owing to their two-phase nature nanosize randomly oriented Fe(Si) crystals in the amorphous matrix [2][3]. Ultra soft magnetic characteristics can be reached by applying a magnetic field during their thermal annealing which induces a field uniaxial anisotropy that allows controlling hysteresis loop shape [4][5]. A round hysteresis loop (R type) is obtained by applying a thermal annealing in the temperature range of 500-600°C, a flat B-H curve (F type) can be obtained by applying a transverse magnetic field during the thermal annealing, whereas a longitudinal magnetic field allows having a square hysteresis loop (Z type). The variety of B-H hysteresis loops makes these materials suitable for many applications operating whether with high permeability materials like transformers, current sensors, CEM filter and magnetic shielding or with low permeability like smoothing inductance and current transformers. In aircraft applications and electric vehicles industry, the compactness of electrical systems is very important to increase energy efficiency but this reduction of mass and volume exposes magnetic components to high temperatures and decreases their magnetic properties over time. There are several works deal with studying magnetic materials behavior under high temperature but few of them discuss the magnetic ageing (temperature+time) which is a very serious issue concerns many industries. The study presented in [6] is based on monitoring magnetic characteristics evolution under thermal ageing of two nanocrystalline nuances: $\mu 30\ 000$ (F type) and $\mu 500\ 000$ (R type). Many measurements have been done which proved that there were no microstructures changes to make correlation with the noticed ageing in both nuances. However, some of these measurements proved that the total anisotropic energy in the material has increased which lead to the following hypothesis; a new anisotropic energy was introduced during ageing process which disturbs the domain walls displacement and magnetic domains rotation[7]. The current work is based on studying nanocrystalline FeSiCuNbB magnetic behavior during thermal ageing at four temperatures (-55, 110, 150 and 200°C). The ageing study has been performed on high permeability $\mu 1000\ 000$ (Z type) toroidal wound cores where the magnetization process is determined by domain walls displacement. To monitor ageing evolution, quasi-static B-H loops were measured with applying a 300 mHz sinusoidal magnetic field. All the following characteristics were measured: coercive force H_c , maximal permeability μ_{max} , saturation flux density B_s , hysteresis losses P_{hys} and E_k the total anisotropic energy developed during the magnetization process. Finally, a comparison between nanocrystalline (Z type) ageing evolution and other nuances presented in work [6] will be analysed and discussed in paper.

[1] Y. Yoshizawa, S. Oguma, and K. Yamauchi, "New Fe-based soft magnetic alloys composed of ultrafine grain structure," *J. Appl. Phys.*, vol. 64, no. 10, pp. 6044–6046 (1988). [2] G. Herzer, "Grain structure and magnetism of nanocrystalline ferromagnets," *IEEE Trans. Magn.*, vol. 25, no. 5, pp. 3327–3329 (1989). [3] S. Flohrer, R. Schäfer, and G. Herzer, "Magnetic microstructure of nanocrystalline FeCuNbSiB soft magnets," *J. Non. Cryst. Solids*, vol. 354, no. 47–51, pp. 5097–5100 (2008). [4] K. Yoshizawa, Y. Yamauchi, "Effect of magnetic field annealing on magnetic properties in ultrafine crystalline Fe-Cu-Nb-Si-B Alloys," *IEEE Trans. Magn.*, vol. 25, no. 5, pp. 3324–3326 (1989). [5] Y. Yoshizawa and K. Yamauchi, "Induced Magnetic Anisotropy and Thickness Dependence of Magnetic Properties in Nanocrystalline Alloy 'Finemet,'" *IEEE Transl. J. Magn. Japan*, vol. 5, no. 11, pp. 1070–1076 (1990). [6] A. Lekdim, L. Morel, and M. Raulet, "Magnetic ageing study of high and medium permeability nanocrystalline FeSiCuNbB alloys," *J. Magn. Mater.*, vol. 428, no. December 2016, pp. 260–268 (2017). [7] A. Lekdim, L. Morel,

and M. A. Raulet, "Magnetic properties evolution of a high permeability nanocrystalline FeCuNbSiB during thermal ageing," *EPJ Appl. Phys.*, vol. 79, no. 2 (2017).

JY-09. Nb Effects on the Magnetic and Microstructural Properties of Fe-Based Nano-Crystalline Alloys.

K. Lee¹, J. Ahn¹ and J. Kim¹

¹ Hanyang University - Ansan Campus, Ansan, The Republic of Korea

Fe-based soft magnetic materials have been widely used in electrical devices, such as motors, transformers, and inductors, due to their high saturation magnetic flux density. These Fe-based materials generally have a cubic crystal structure with the $\langle 100 \rangle$ easy axis of magnetization and fairly high intrinsic crystalline anisotropy constants. Thus, in order to improve their soft magnetic properties, nano-crystalline Fe-based alloy ribbons have been fabricated by rapid solidification and subsequent annealing processes. Because nano-crystalline grains with isotropic and homogeneous microstructures are known to reduce the coercivity (H_C) effectively. However, the saturation magnetization (M_S) of nano-crystalline alloy ribbons is reduced by adding glass forming elements. Thus it is always required to increase the M_S of the Fe-based alloy ribbons without deteriorating their coercivity. Our previous study showed that $\text{Fe}_{84.3}\text{B}_{13.7}\text{C}_1\text{Cu}_1$ amorphous ribbons could be fabricated by the rapid solidification process (RSP) and their crystallization procedures during the subsequent annealing process were discussed in terms of the nucleation and crystal growth of α -Fe grains [1]. In these ribbons, square shaped Fe grains were found to be formed and the growth rate of them were shown to be too fast to control the grain size below the exchange length of Fe [2]. Thus, despite their high Fe concentration, the permeability of the ribbons was limited by their H_C . This means that it is required to develop the method for inhibiting the grain growth rate and controlling the morphology of annealed Fe grains. In this paper, $\text{Fe}_{82.3}\text{B}_{13.7}\text{C}_1\text{Cu}_1\text{Nb}_2$ as-quenched ribbons were fabricated and annealed to understand the effect of Nb addition on the magnetic properties and microstructures during the annealing process. In this experiment, the ingots of $\text{Fe}_{82.3}\text{B}_{13.7}\text{C}_1\text{Cu}_1\text{Nb}_2$ alloy were prepared by an arc melt process. As-quenched alloy ribbons were fabricated by the RSP under Ar atmosphere. The thermal properties of the as-quenched ribbons were analyzed by a differential thermogravimetric analyzer (DTA, TG-DTA2000SA) at a heating rate of 10 °C/min under Ar atmosphere. The annealing process was conducted using a rapid thermal process (RTP, IA-1240) equipment. During RTP, the ribbons were heated at a heating rate of 80 °C/min under Ar atmosphere. The M_S and H_C were measured by a vibrating sample magnetometer (VSM, LakeShore 7410). The microstructures of samples were analyzed by X-ray diffractometer (XRD, D/MAX-2500/PC) with CuK α radiation and atom probe tomography (APT, LEAP 4000X HR) analysis. The APT samples were prepared in the form of needles of 6060200 nm using a focused ion beam (FIB, Helios nanolab G3 UC). The XRD and compositional analysis of as-quenched ribbons confirmed the successful fabrication of $\text{Fe}_{82.3}\text{B}_{13.7}\text{C}_1\text{Cu}_1\text{Nb}_2$ amorphous ribbons with a thickness of 21 μm and a width of 2 mm. The average M_S and H_C of the amorphous ribbons, measured at 10 kG, were 150.2 emu/g and 0.42 Oe, respectively. The DSC analysis of the amorphous ribbons showed that the first exothermic peak (T_{x1}) started at 400 °C and its maximum peak intensity appeared at 420 °C. In addition, the secondary crystallization temperature of the ribbons was increased up to 550 °C. Compared to $\text{Fe}_{84.3}\text{B}_{13.7}\text{C}_1\text{Cu}_1$ amorphous alloy, the higher peak temperatures indicate that the addition of Nb element improved the thermal stability of the ribbons. Figure 1 shows changes in the magnetic properties of $\text{Fe}_{84.3}\text{B}_{13.7}\text{C}_1\text{Cu}_1$ and $\text{Fe}_{82.3}\text{B}_{13.7}\text{C}_1\text{Cu}_1\text{Nb}_2$ as-quenched ribbons annealed at their own T_{x1} with increasing the annealing time. As shown in the figure, the low M_S of Fe-B-C-Cu-Nb as-quenched ribbon confirms that the Nb addition effectively stabilize the thermal stability of the Fe-B-C-Cu ribbon. Despite the high thermal stability, the M_S and H_C values of the Fe-B-C-Cu-Nb ribbon are shown to be sharply increased after annealing for 60 seconds. However, as the annealing time increased further, the increasing rate of the H_C sharply drops, which is much lower than that of the Fe-B-C-Cu ribbon. These changes in magnetic properties should be caused by that the Nb addition changes the crystal nucleation and growth rate of the as-quenched ribbon and the crystalline shape of Fe grains during the annealing. In order to understand the microstructural effect of the Nb addition, the compositional changes at the interfaces of amorphous/crystalline grain during the annealing were measured by APT and their elemental distributions with the annealing time are shown in Figure 2. These figures confirm that B and C atoms, known

as amorphous forming elements, were continuously pushed out of the α -Fe grain with increasing the annealing time. On the other hand, Cu atoms are known to act as nucleation sites of nanocrystals but evenly distributed in the α -Fe grain and the amorphous matrix. However, the diffusion of Nb atoms into the matrix is clearly observed when the annealing time is longer than 300 sec. This Nb diffusion behavior in the annealing time is in well accord with the coercivity change of the $\text{Fe}_{82.3}\text{B}_{13.7}\text{C}_1\text{Cu}_1\text{Nb}_2$ ribbon. The change in the morphology of the α -Fe grain behavior was also confirmed by TEM. These results clearly show the role of Nb atoms in the fabrication of nano-crystalline α -Fe grains and more detailed analysis results will be presented.

[1] K. Lee, M. Choi, G. Lee, M. Kim, and J. Kim, "Changes in Microstructure and Magnetic Properties of Fe-B-Cu Ribbons According to Annealing Conditions," *IEEE Transactions on Magnetics*, vol. 55, no. 2, pp. 1-4, 2019. [2] H. Lashgari, D. Chu, S. Xie, H. Sun, M. Ferry, and S. Li, "Composition dependence of the microstructure and soft magnetic properties of Fe-based amorphous/nanocrystalline alloys: a review study," *Journal of Non-Crystalline Solids*, vol. 391, pp. 61-82, 2014.

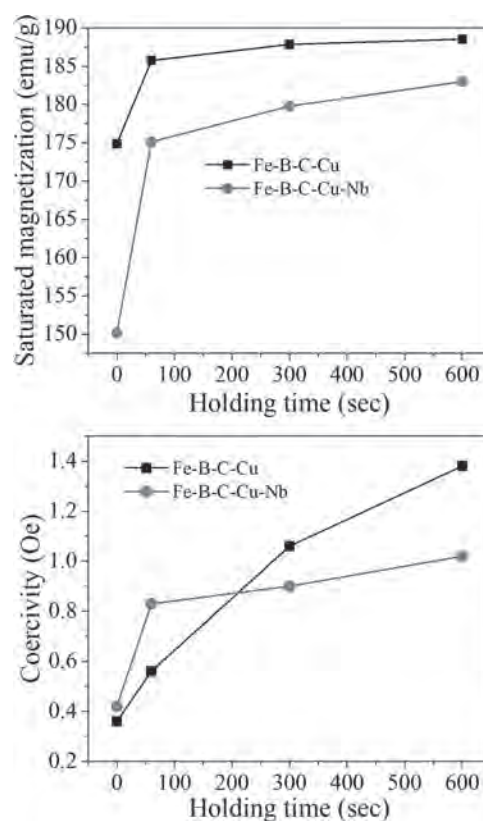


Fig 1. Changes in the magnetic properties of $\text{Fe}_{84.3}\text{B}_{13.7}\text{C}_1\text{Cu}_1$ and $\text{Fe}_{82.3}\text{B}_{13.7}\text{C}_1\text{Cu}_1\text{Nb}_2$ ribbons annealed at T_{x1} for different annealing times

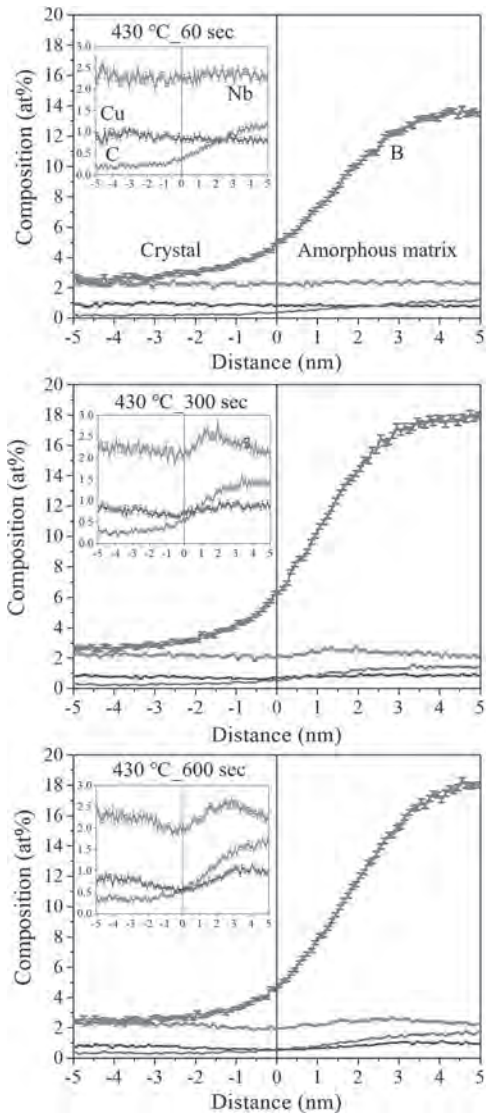


Fig 2. Changes in element distributions of the $Fe_{82.3}B_{13.7}C_1Cu_1Nb_2$ ribbon at the interface during annealing

JY-10. Magnetic Properties Measurement and Loss Calculation of the High-Frequency Core With Air Gap.

Y. Li¹, H. Liu¹, H. Sun¹ and Z. Wan¹

1. State Key Laboratory of Reliability and Intelligence of Electrical Equipment, Hebei University of Technology, Tianjin, China

Due to high permeability, low coercivity, high resistivity, and low eddy current loss, amorphous and nanocrystalline materials with their excellent magnetic properties are attractive for high-frequency high-power applications, such as transformers, reactors and inverters to achieve high power density transmission. However, some electrical applications include inductors and transformers for multi-kilowatt power converters often necessary to add air gap in the magnetic core. The reasons are as follow: (a) reducing the equivalent permeability μ_{re} of the core, (b) increasing the excitation current for saturation, (c) effectively improve the anti-saturation ability of the core, (d) improve the capacity of the energy storage of magnetic components. The desired functions achieved from magnetic characteristic changes due to the air gap including: maintaining the stability of the inductance value of the reactor, increasing the power density of the inductor and the optimized design of the high frequency transformer, etc. Moreover, air gap may also increase the core loss. It is of great significance to study the magnetic properties of the cores with different air gaps. In this paper, dynamic magnetic properties of C-type amorphous (AMCC025) and nanocrystalline (F3CC0125) cores are measured with different air gap lengths (0-6mm) and frequencies (5-20 kHz) based on a novel designed magnetic tester. The tester can restrain the C-type core from six directions to ensure the stability of the testing sample. The air gap between the two cores can be accurately adjusted by the screw fixed on the precision displacement stage. The minimize air gap length can be fixed on 0.01mm. The effect of air gap length and frequency on the magnetic properties of different materials are compared. Moreover, the corresponding core losses of the samples in a wide range of frequency are analyzed. The traditional Steinmetz empirical formula is revised, and the core loss is calculated in sections according to the air gap length, and compared with experimental values. The hysteresis loops of the amorphous and nanocrystalline alloy cores at the same frequency of 20 kHz, different magnetic densities and different air gap lengths are shown in Fig. 1. As the air gap length increases, the slope of the $B-H$ loops is reduced more and the slope of inclination is smaller slowly. Moreover, the effect of the air gap on the magnetic properties of nanocrystalline cores is more obvious than that of amorphous cores. It can be found that the nanocrystalline alloy is more sensitive to air gap than amorphous alloy due to its ultra-high relative permeability. According to the intensity of the fringing effect caused by the air gap length, two cases are concerned in the loss calculation. One is that the air gap is small enough to ignore the fringing effect, the other is that the air gap length is too large to ignore the fringing effect of the loss. Generally speaking, when $l_g/l_c < 0.5\%$, where l_g is the air gap length and l_c is the equivalent magnetic circuit length, the influence of the fringing magnetic flux caused by the air gap on the inductance of the core can be ignored. But when $l_g/l_c > 1.0\%$, due to the fringing diffusion of the air gap magnetic flux, the magnetic area of the air gap increases and the effective length of the air gap becomes shorter. Therefore, the influence of the fringing magnetic flux for core loss must be considered. Therefore, a modified Steinmetz empirical formula considering fringing flux is proposed, in which, the air gap length is used as a variable in the calculation and the precision is improved. Fig. 2. shows the variation in core loss density between the experimental and calculated results at given frequency with the different air gap lengths and magnetic density. From the ratio of the air gap length to the magnetic circuit length, it can be seen that for amorphous core, the fringing effect does not need to be considered when the air gap length is less than 1 mm. Similarly, the air gap length boundary point of the nanocrystalline core is 1.6 mm. It can be seen that most of the calculated results well agree with the experimental results. The average percentage errors of the modified Steinmetz formula with fringing effect are all within 10% for amorphous and nanocrystalline core. It is proved that the influence of the fringing magnetic flux can be minimized under an optimized air gap length, and the loss will be reduced accordingly. Moreover, the modified Steinmetz formula can predict the core loss of the C-type core under different air gap lengths well. The

modified core loss calculation model can provide theoretical guidance for the high frequency inductor and transformer cores design and optimization.

[1] Ayachit, Agasthya, and M. K. Kazimierzuk, IET Circuits Devices & Systems, Vol. 11.3, p. 209-215(2017). [2] G. Calderon-Lopez, Y. Wang and A. J. Forsyth, IEEE Transactions on Power Electronics, vol. 34, p. 4656-4664, (2019). [3] Y. Wang, G. Calderon-Lopez, and A. J. Forsyth, IEEE Transactions on Power Electronics, vol. 32.6, p. 4683-4690(2019).

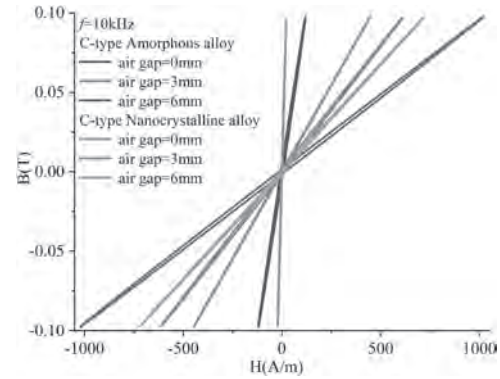


Fig. 1. The hysteresis loops of core under different air gap lengths ($B = 0.1T$, $f = 10kHz$).

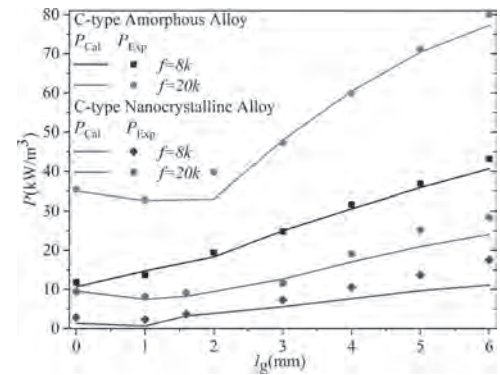


Fig. 2. Core loss under different magnetic density and air gap lengths at fixed frequency.

JY-11. Temperature Dependence of Powder Cores Magnetic Properties for High Frequency Applications.

W. Zhang¹, Y. Li¹, Q. Yang², Z. Lin¹ and M. Yang¹

1. State Key Laboratory of Reliability and Intelligence of Electrical Equipment, Hebei University of Technology, Tianjin, China; 2. School of Electrical and Electronic Engineering, Tianjin University of Technology, Tianjin, China

I. INTRODUCTION With the rapid development of the power electronics industry, electrical equipment is tending towards high-power, high-frequency, and miniaturization, in particular for the inductors, chokes, and transformers [1]. The magnetic material becomes a hinder to improve the device performance further [2]. At present, soft magnetic ferrite is widely used in high frequency applications due to the lower conductivity and core loss at the high operating frequency. However, the saturation flux density of ferrite is usually less than 0.5 T, which is much lower than that of alloy soft magnetic materials [3]. Nanocrystalline and amorphous alloys have excellent magnetic properties, such as low coercive force, high permeability, and saturation flux density, but these materials have high conductivity which causes great eddy current loss P_{ed} . Magnetic cores fabricated by amorphous and nanocrystalline alloy powders can effectively reduce the P_{ed} due to their lowered conductivity [4]. Consequently, these powder cores are gradually used in high-frequency and high-power applications. In fact, it is inevitable that the core and winding losses will lead to the temperature increase of the core, in particular, at high frequency [5]. Therefore, it is significant to study the temperature dependence of the magnetic properties of powder cores at high frequency. The results can be used to optimize the performance of electrical devices. II. MEASUREMENT PRINCIPLE AND SYSTEM In this article, the magnetic properties and loss characteristics of nanocrystalline powder core, amorphous powder core, ferrite, X-Flux (Fe-Si), and Kool-M μ (Fe-Si-Al) are measured and analyzed in the range of 25 °C to 125 °C from 20 kHz to 100 kHz. The magnetic properties measurement system for the toroidal powder core sample is constructed, as shown in Fig.1. The toroidal powder core is placed in a thermotank for heating, and the internal temperature in the thermotank can be controlled by PID adjustment. The magnetic field intensity H and the magnetic flux density B are calculated by Ampere law and Faraday's law of induction, respectively. The core loss is calculated by the Poynting equation and analyzed by the Steinmetz equation. III. EXPERIMENTAL RESULTS OF POWDER CORES The magnetic properties of the above materials as a function of temperature are investigated, such as coercive force, remanence, complex permeability, inductance factor, saturation flux density, and core loss. The properties are discussed using the micro-magnetism theory. Meanwhile, the material properties of the above materials are compared and summarized. A. Magnetic properties at different conditions The inductance factor, AL , of Kool-M μ decreases with the increasing temperature. When the temperature rises from 25 °C to 50 °C, the AL of Kool-M μ only changed by 0.383% from 156.7 nH/N² to 156.1 nH/N² at 100 kHz, 30 mT, which is a very little variation. But it decreased by 7.367% from 156.1 nH/N² to 144.6 nH/N² with the temperature rising from 50 °C to 125 °C. The saturation flux density B_s of the ferrite is also affected by temperature and frequency. The saturation flux density presents a downward trend with the increasing temperature or frequency, as shown in Fig.2 (a). The experimental results indicate that the saturation flux density of ferrite decreased from 0.479 T to 0.453 T while the operating frequency is from 20 kHz to 100 kHz at room temperature, which decreased by 5.428%. From 25 °C to 125 °C, the saturation flux density of ferrite decreased from 0.453 T to 0.319 T at 100 kHz, which decreased by 29.581%. B. Core loss analysis at different conditions When the temperature is increased from 25°C to 125 °C, the loss of Kool-M μ increases from 48.68 W/kg to 75.368 W/kg by 54.823% at operating frequency $f=100$ kHz, and magnetic flux density $B = 80$ mT. However, the core loss of X-Flux and amorphous powder cores shows a decrease with increasing temperatures. The loss of X-Flux decreases from 199.708 W/kg at 25 °C to 175.805 W/kg at 125 °C by 11.969% while the loss of amorphous powder cores decreases from 118.165 W/kg at 25 °C to 107.127 W/kg at 125 °C. It is found that the amorphous powder cores have better temperature stability, as shown in Fig.2 (b). The nanocrystalline powder core shows the relative temperature stability compared with other samples since the loss values are similar

at the experimental temperatures. On the other hand, the Kool-M μ shows clearly temperature dependent loss property among the five samples. In addition, the core loss of the X-Flux is the largest, then followed by amorphous powder core, Kool-M μ , nanocrystalline powder core, and ferrite at different frequencies over the experimental temperature range. In summary, the magnetic properties of five samples of different materials are measured at high frequencies over the temperature range from 25 °C to 125 °C. The physical characteristic of different materials exhibits an opposite trend with increasing temperature. The detailed comparison of results for five powder core materials will be shown in the full paper.

[1] C. Jiang, X. Li, S. Ghosh, IEEE Transactions on Power Electronics., Vol. 35, p.10821-10830 (2020) [2] J. Millan, P. Godignon, X. Perpina, IEEE Transactions on Power Electronics., Vol. 29, p.2155-2163 (2014) [3] M. Yang, Y. Li, Q. Yang, IEEE Transactions on Applied Superconductivity., Vol. 30, p.1-5 (2020) [4] T. Suzuki, P. Sharma, L. Jiang, IEEE Transactions on Magnetics., Vol. 54, p.1-5 (2018) [5] N. Takahashi, M. Morishita, D. Miyagi, IEEE Transactions on Magnetics., Vol. 46, p.548-551 (2010)

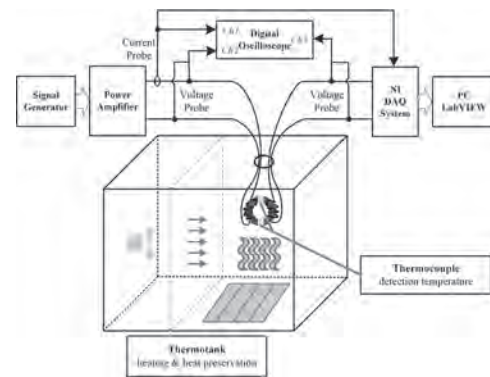


Fig. 1 Schematic diagram of experimental system for magnetic properties measurement with the effect of temperature.

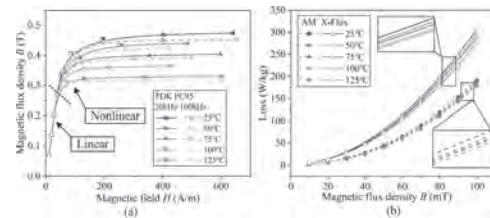


Fig. 2 The fundamental magnetization curve of TDK PC95 at different temperature (a), and core loss characteristic curves of amorphous (AM) and X-Flux powder cores at 100 kHz and different temperatures (b).

JY-12. Comprehensive Analysis of Nanocrystalline Ribbon Cores in High-Power-Density WPT Pads for Electric Vehicles.

W. Zhang¹, Y. Li¹, Q. Yang², Z. Lin¹, M. Yang¹ and M. Mi¹

1. State Key Laboratory of Reliability and Intelligence of Electrical Equipment, Hebei University of Technology, Tianjin, China; 2. School of Electrical and Electronic Engineering, Tianjin University of Technology, Tianjin, China

I. INTRODUCTION The wireless power transfer (WPT) systems, that is the contactless electrical power transfer, by electromagnetic coupling are of interest in charge of electric vehicles (EVs). However, a fraction of electromagnetic energy generated by the primary coil is lost due to loosely-coupled characteristics of the WPT system^[1]. The stray flux will harm the human body and interfere with other electromagnetic equipment. Hence, it is necessary to effectively shield the leaking magnetic flux and improve the efficiency of coupling in the WPT system^[2]. Generally, ferrite is used in WPT systems to concentrate the magnetic flux, and plays a role of shielding because of its high resistivity and permeability^[3]. It is beneficial to reducing the core loss of the ferrite at high frequency. However, the effectiveness of shielding will be degraded by the low saturation flux density B_s of ferrite. And it is decreased drastically with the increasing temperature or frequency, usually between 0.2 and 0.5 T^[4]. The thickness of the ferrite has to be increased for high power density WPT systems. Compared with ferrite, the nanocrystalline alloy has higher permeability and saturation flux density, which can improve the shielding effect. The use of alloy also reduces the weight and volume of the shielding pad. However, its high conductivity will lead to more eddy current losses, and the reduction of the power transmission efficiency. Conclusively, core material and structure are of importance to the transmission efficiency and power level of the WPT system. II. INVESTIGATION OF MAGNETIC MATERIAL PROPERTIES In this article, the nanocrystalline ribbons processed by the refinement crushing process and alternating seamless stitching process show an advantage in WPT since the eddies are restricted to the smaller areas and less eddy current loss of. Three types of ribbon with $\mu = 1000, 3000, 6000$ respectively are simulated for the WPT system. The nanocrystalline ribbon of 1k107B, and PC95 ferrite are studied as well to optimize the design of WPT. The comparison involves permeability, conductivity, saturation flux density, and Curie temperature. The system performance, such as the leakage magnetic flux B , self inductances of secondary coil L_2 , mutual inductances M , coupling factor k , and transmission efficiency η are simulated using $LCC-LCC$ topology and 1.5 kW at 85 kHz based on the above materials to summarize the influence of material characteristics on system performance. The results show that the PC95 pad shows the highest η of 98.07% among all the magnetic cores. The η of processed nanocrystalline alloy pad increases with the increased permeability, which is 96.10%, 97.86%, and 98.02%, respectively. The ferrite pad and nanocrystalline alloy pad with $\mu = 6000$ have a similar η , but the latter shows a better shielding effect. The η of 1k107B pad is only 95.92%. The nanocrystalline alloy pad with $\mu = 1000$ shows the lowest k value of 0.1002 due to its low permeability. III. OPTIMIZED DESIGN OF SHIELDING PAD To balance the efficiency of power transmission, shielding, and eddy current losses, the novel embedded magnetic shielding structure is proposed according to the magnetic flux distribution. It is composed of nanocrystalline alloy and ferrite, as shown in Fig.1. The ferrite pattern is designed to block the eddies. It found that the k and η of this novel structure show great improvement compared with the nanocrystalline ribbon cores. For example, the η of the embedded structure with 1k107B and PC95 is increased to 98.10% while it is 95.92% in pure 1k107B. In addition, ferrite frames with different heights are used in order to reduce the magnetic flux leakage at the edge of the shielding pad. The results using the 3-D finite element method indicate that the shielding effect and system performance are improved with the increasing the frame height Fig. 2 shows that flux densities along the centerline over 10 cm above the embedded pad decrease with increasing the height where the pad is composed of the nanocrystalline ribbon with $3\mu = 6000$ and ferrite. The L_2 and M increased by 6.84% and 13.80% with a height of 5 cm while the L_2 and M are 248.23 μ H and 28.85 μ H without the ferrite frame. However, η is almost unchanged, that is about 98.03%. The experimental WPT system for 85 kHz, 1.5 kW with a 24 cm air gap has been built to validate the simulation. The transmission performance with different

shielding structures is compared, including PC 95 ferrite pad only and the novel structure composed of ferrite with the three nanocrystalline alloys with permeability $\mu = 1000, 3000, \text{ and } 6000$, respectively. Within the acceptable range of error, the experimental results are consistent with that of simulation. But the experimental efficiency η is lower than that of simulation due to the connecting line loss and switching loss. The former is generated by serious skin effect at a high operating frequency. The experimental results will be presented and discussed in detail in the full paper.

[1] H. Kim, C. Song and D. Kim, IEEE Transactions on Microwave Theory and Techniques., Vol. 64, p.383-400(2016) [2] M. Pearce, G. A. Covic and J. T. Boys, IEEE Transactions on Power Electronics., Vol. 34, p. 6062-6075 (2019) [3] K. Elnail, X. Huang and C. Xiao, Energies., Vol. 11, p.1-17 (2018) [4] M. Yang, Y. Li, Q. Yang, IEEE Transactions on Applied Superconductivity., Vol. 30, p.1-5 (2020)

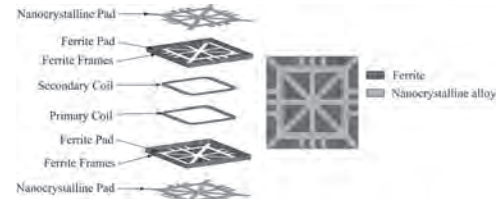


Fig. 1 The geometry of embedded shielding pattern.

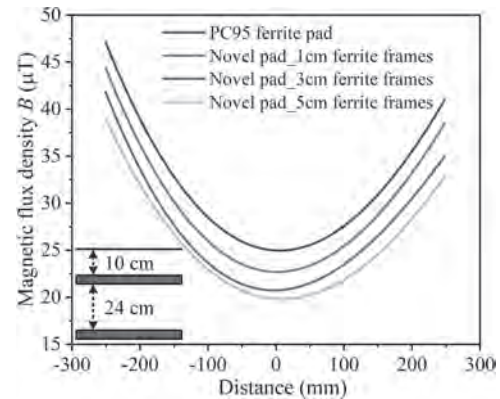


Fig. 2 Simulated the flux densities distributions along the centerline at 10 cm over the secondary shielding pattern, transmitting current $i_1 = 10\sqrt{2}\sin(2\pi \times 85000t)$ A, $t = 2.88 \times 10^{-6}$ s.

JY-13. The Microwave Absorption Properties of Fe_{16}N_2 Nanoparticles.

Y. Wang¹, Z. Lin¹, G. Qiao², Z. Liu¹, P. Zhang¹, K. Li¹, W. Yang¹, J. Han¹, S. Liu¹, C. Wang¹, L. Qiao³ and J. Yang¹

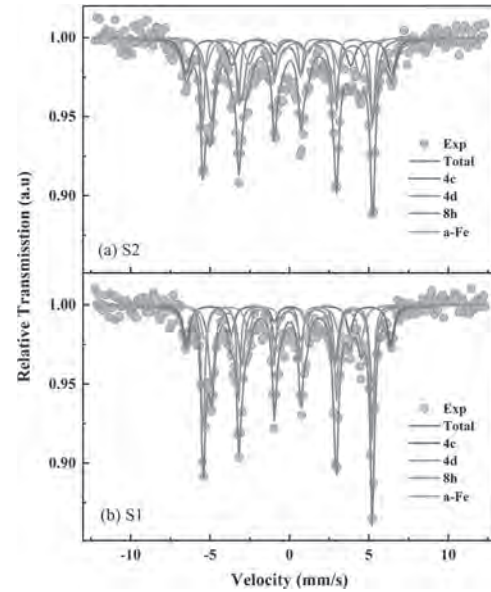
1. Physics, Peking University, Beijing, China; 2. Peking University, Beijing, China; 3. Physics, Lanzhou University, Lanzhou, China

Using Fe nanoparticles as raw material, we manufactured Fe_{16}N_2 nanoparticles by hydrogen reduction and ammonia nitriding process. XRD and Mossbauer spectroscopy analyses show that the prepared nanoparticles are composed of Fe_{16}N_2 and $\alpha\text{-Fe}$. The proportion of Fe_{16}N_2 phase could reach 79%, and the saturation magnetization of the nanoparticles could reach 197emu/g. The Fe_{16}N_2 nanoparticles are mixed with paraffin, and the microwave absorption properties of the composites are measured. The reflection loss (RL) of the Fe_{16}N_2 nanoparticles can reach -18.3dB@4.82GHz, which shows it is a potential candidate for microwave absorbing materials.

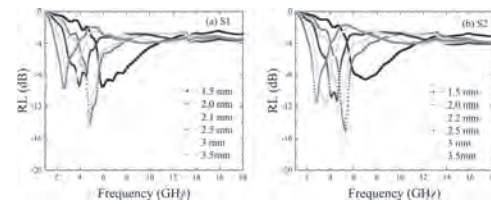
I. Introduction Fe_{16}N_2 is a special kind of FeN compound because its saturation magnetization can be higher than that of $\alpha\text{-Fe}$. Depending on the preparing methods, Fe_{16}N_2 could have different morphologies including foils, wires, and nanoparticles. The saturation magnetization of Fe_{16}N_2 nanoparticles could reach 245emu/g as previous research reported, exceeding the saturation magnetization of Fe. The high saturation magnetization of Fe_{16}N_2 nanoparticles makes it possible for some practical use. In this work, the Fe_{16}N_2 nanoparticles are prepared and the microwave absorption properties were measured. II. Experimental Fe nanoparticles with average diameters of 65nm were used as the raw material. The Fe nanoparticles were firstly heated to 450°C in an H_2 atmosphere and kept for 3h. Then, the samples were then cooling down to 160°C and kept for 22h (sample S1) or 39h (sample S2) in NH_3 . Every three hours the sample has been flipped. III. Result and Discussion The XRD of S1 and S2 were measured using $\text{Cu}_K\alpha$ X-rays. Both S1 and S2 show the main peak of the Fe_{16}N_2 phase at $2\theta=42.8^\circ$. The intensity of the main peak of S2 is higher than that of S1. Both samples have an XRD peak at 44.8° which is contributed by the overlap of the Fe_{16}N_2 secondary peak and the peak of $\alpha\text{-Fe}$. So both samples are a mixture of Fe_{16}N_2 and $\alpha\text{-Fe}$, and from the relative peak intensity, it can be inferred that the Fe_{16}N_2 phase content in S2 is higher than in S1. To determine the Fe_{16}N_2 phase content in S1 and S2 samples, the Mossbauer spectroscopy of the two samples are carried out.

The experimental data and the fitting curve of the Mossbauer spectroscopy are shown in Fig. 1. The fitting result shows that S1 contains 69% Fe_{16}N_2 phase and S2 contains 79% Fe_{16}N_2 phase. This result is consistent with the judgment based on the relative peak intensity of XRD. The hysteresis loops of the samples are measured, and the saturation magnetization of S1 and S2 were 185emu/g and 197emu/g, respectively. As the Fe_{16}N_2 phase content increases, the saturation magnetization of the samples increase. This shows that Fe_{16}N_2 might have a higher saturation magnetization than $\alpha\text{-Fe}$. The nanoparticles are mixed with paraffin with a mass ratio of 3:1 to form composites (also named S1 and S2). Then the composites are pressed into a toroidal shape with an inner diameter of 3.04 mm and an outer diameter of 7 mm. A vector network analyzer (VNA) is used to measure the high-frequency permittivity ϵ and permeability μ of the torus samples. Then, the reflection loss (RL) of the composite materials with different thicknesses is calculated by the transmission line theory depending on the measured ϵ and μ . The reflection losses of S1 and S2 are shown in Figure 2 (a) and (b), respectively. It can be seen that the microwave absorbing performance of S2 is slightly better than that of S1. When the thickness of the absorber is 2.2mm, the maximum RL of S2 could reach -18.5dB at 4.8GHz.

1. J. P. Wang, Journal of Magnetism and Magnetic Materials., Vol. 497, p.165962 (2020) 2. Z. Liu, W. Yang, R. Wu, Journal of Magnetism and Magnetic Materials., Vol. 516, p.167332 (2020)



The Mossbauer Spectrum of sample S2 (a) and S1 (b).



The Reflection Loss (RL) of sample S1 (a) and S2 (b).

JY-14. Design and Simulation of Electromagnetic Metamaterial Unit for High-Frequency Transformer.

Y. Wang¹, Y. Wang¹, S. Wu¹ and W. Fu²

1. School of Mechanical Electronic & Information Engineering, China University of Mining and Technology - Beijing Campus, Beijing, China;

2. Department of Electrical Engineering, The Hong Kong Polytechnic University, Kowloon, Hong Kong

0 Introduction As the operating frequency of the switching power supply continues to increase to MHz, the loss of various magnetic materials will increase rapidly with frequency and magnetic induction. The magnetization performance and the loss of magnetic materials limit the increase in power density. A metamaterial unit composed of resonant coils and resonant capacitors in series is printed on the FR-4 panel to form a metamaterial structure that can produce considerable equivalent permeability at a specific frequency. The relevant structural parameters and their optimization methods are analyzed, and the electromagnetic simulation software is used to verify the correctness of the electromagnetic metamaterial designed. Since the metamaterial unit only has a significantly increased equivalent permeability at a specific frequency, the metamaterial unit is designed to work at a fixed frequency or within a fixed frequency range. 1 Design and optimization of metamaterial units The metamaterial unit is printed on the FR4 board in the form of a matrix, and a total of 10 layers are printed to form a metamaterial structure, which is used to replace the central column part of the traditional transformer core. Figure 1 shows the two-dimensional model of the transformer based on the metamaterial structure and its flux distribution. This article uses controlled experimental methods to design and optimize the coil unit layout, size, shape, number of turns and resonant capacitance and other parameters. The window is defined as the ratio of the area of the FR4 board to the total area of the FR4 board after the metamaterial coil unit is removed. When only the arrangement of metamaterial units is changed, it is found through analysis that each metamaterial unit works independently instead of in series or parallel, and has better permeability and higher transmission efficiency. First, design the line width of the coil unit. The study found that as the line width increases, the line loss of the metamaterial unit will increase and the transmission efficiency of the transformer will decrease. Therefore, the wire width of the metamaterial unit should be as small as possible. Due to different technical levels, the minimum width of the coil is also different. The minimum line width used in this article is 0.3mm. When other parameters remain unchanged, when the number of turns n of the metamaterial unit is less than or equal to 3 or the window is greater than 72.25%, the energy transmission efficiency of the transformer will be much lower than that of the traditional transformer. When the number of turns of the coil is greater than 4, the metamaterial structure can provide a higher equivalent magnetic permeability, which can significantly improve the energy transmission efficiency compared with traditional transformers. When the value of n gradually increases, the equivalent permeability of the metamaterial continues to increase, and the transmission efficiency of the transformer also continues to increase. However, when the number of turns of the metamaterial unit is greater than 7, the transmission efficiency is basically unchanged. Blindly increasing the number of turns will increase the complexity of printing special material coil units. This leads to unnecessary waste of resources and increased costs. Therefore, when the number of coil turns is 7, the metamaterial structure has the best effect. Figure 2 is a graph of the dielectric parameters of the metamaterial when the number of coil turns is 7. Finally, the influence of different layers of the resonant capacitor on the metamaterial unit is studied. It is found that when the resonance capacitance of each layer is the same, the equivalent permeability coefficient of the intermediate metamaterial unit is lower than that of the mutual metamaterial unit. Therefore, the capacitance of the capacitors of the metamaterial units on both sides can be slightly enhanced, and the energy transmission efficiency of the transformer can be improved. 2. Simulation analysis of metamaterial unit Ansys electromagnetic simulation software is used to simulate the designed metamaterial unit structure. Based on the metamaterial structure and the 1:1 size of the traditional transformer, a two-dimensional model was established, and simulated and compared. The simulation parameters are not listed here. It is found through simulation that when the metamaterial coil unit has 7 turns, the transformer of the metamaterial structure has a

higher equivalent permeability in the frequency range of 298-301kHz, and the degree of suppression of the magnetic flux is obvious. Compared with traditional magnetic cores, its energy efficiency is also higher. This verifies the correctness of the above-mentioned metamaterial structure design. 3. Conclusion This paper designs a metamaterial structure for high-frequency transformers. The new metamaterial structure design makes the transformer more efficient. The electromagnetic field simulation analysis of two different transformer models is carried out through the control experiment method. The results show that when the number of turns of the metamaterial unit is 7 turns and the operating frequency is about 300kHz, the equivalent permeability is higher and the energy transmission efficiency is better than that of the traditional transformer. Achieve the desired effect. The metamaterial structure designed in this paper does not require high circuit components and has obvious advantages in a certain frequency range.

[1]SMITHDR, VIERDC, KOSCHNYT, etal. Electromagnetic parameter retrieval from inhomogeneous metamaterials [J]. Physical Review E Statistical Nonlinear&Soft Matter Physics, 2005, 71 (3):036617.

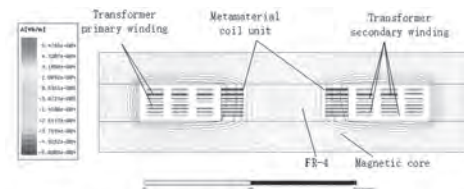


Fig.1 the two-dimensional model of the transformer based on the metamaterial structure and its flux distribution

Fig.1

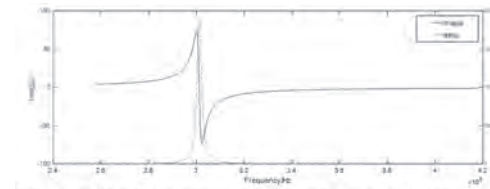


Fig.2 the graph of the dielectric parameters of the metamaterial when the number of coil turns is 7

Fig.2

JY-15. Linear-to-Circular Polarization Converter Based on Meander-Line Metasurfaces.

Y. Zhao¹, J. Fu¹, W. Chen¹, B. Lv² and Z. Wang¹

1. Harbin Institute of Technology, Harbin, China; 2. Harbin Engineering University, Harbin, China

I. Introduction Metasurfaces can be seen as two-dimensional metamaterial, which has been attracting attention for researchers these years [1]-[3]. In the early years, metasurfaces was considered as special frequency selective surfaces, the structure may be split-ring resonator, complementary split-ring resonator [4] or isotropic elements [5]. However, most researchers regard the metasurfaces as a novel periodic structure, that is different from frequency selective surfaces [2]. And metasurfaces can be using in many different and important applications such as reflection surface [2]-[4], perfect absorber [6]-[7] and holographic imaging. Polarization conversion surfaces are commonly used electromagnetic surfaces, which can be designed into reflective surfaces or transmissive surfaces [3], [4]. A traditional method to design polarization conversion surfaces is using birefringent materials, which can change the polarization state of incident wave and wavefront phase in each cardinal planes. Recently, research discovered that birefringent materials can be realized by anisotropic frequency selective surfaces. For all types of polarization conversion surfaces, the type which can converts linear polarization (LP) wave into circular polarization (CP) wave, is the most popular one. This type of metasurfaces converts an incident LP wave into a CP transmitted or reflected wave. In recent years, linear-to-circular polarization converter has great application prospect in satellite [5]-[6] and communication systems [7]. In this paper, a novel linear-to-circular polarization converter based on meander-line metasurfaces is presented. The proposed metasurfaces is a two-dimensional periodic structure which consists of two metallic layers separated by dielectric substrate. The structure of each unit is meander-line which is printed on the top and bottom metallic layers. By controlling different phase for vertical and horizontal electric field components of incident wave, the phase difference is 90° between two components, after passing through the metasurfaces. The metasurfaces converts the LP wave to CP wave with the bandwidth of 10.5~11.5 GHz. The simulation results show the metasurfaces is valuable for polarization conversion application.

II. Metasurfaces Structure Design and Analysis

A. Metasurfaces Structure The geometry of the metasurfaces is presented in Fig. 1. The structure is composed of two metallic layers and one dielectric substrate. The structure of two metallic layers is shown in Fig. 1(b). And the size of the metasurfaces unit is 6.2*6.2 mm². Two metallic layers are printed on Rogers RT5880 substrate with the relative permittivity of $\epsilon_r = 2.2$ and the thickness of $h = 0.762$ mm. The structure of the top metallic layer is meander-line which have different resonance characteristics to vertical and horizontal electric field components. And the bottom metallic layer is exactly the same as top layer. The geometric parameters of the metasurfaces are $a = 6.2$ mm, $p = 0.9$ mm and $g = 0.65$ mm.

B. Analysis of Metasurfaces To the vertical electric field, the meander-line can be equivalent to a shunt inductance. But, to the horizontal electric field, the meander-line will be equivalent to a shunt capacitance. Therefore, the incident wave with the 45° linear polarized, it can be divided into vertical and horizontal electric field components. Next, by controlling the phase difference between two components to 90°, the structure will convert LP wave to CP wave. The bandwidth of the metasurfaces can be increased by cascading several metasurfaces screen, and the additional dielectric layer can improve the oblique incidence stability. Equivalent circuit model (ECM) can be used to analyse the physical principle of the metasurfaces. Fig. 2(b) shows the ECM of the metasurfaces for vertical electric field. And Fig. 2(c) shows the ECM of the metasurfaces for horizontal E-field. Thus, adjusting the phase difference between two electric field components ($|\varphi_1 - \varphi_2|$) is 90°, and a linear polarized wave can be converted into circular polarized wave.

III. Simulation Results and Discussions The proposed metasurfaces can realize LP to CP conversion. For different electric field components, the metasurfaces has different functions. Fig. 3 and Fig. 4 show the simulated transmission coefficient of the metasurfaces with vertical and horizontal electric field. And TABLE I shows the amplitude and phase of transmission coefficient at 10.5 GHz and 11.5 GHz. Under two polarization waves and oblique incidence angles from 0° to 30°, the phase difference of vertical component and horizontal component is approximately 90°, and the transmissivity is

over 50%. The polarization conversion bandwidth covers 10.5~11.5 GHz. The simulation results show that the proposed metasurfaces can convert linear polarization wave to circular polarization wave, and has good angular stability.

IV. Conclusion A novel linear-to-circular polarization converter based on meander-line metasurfaces with angular stability is presented. The linear-to-circular polarization conversion bandwidth of the metasurfaces is 10.5~11.5 GHz for the transmissivity is over 50%. By controlling different phase for vertical and horizontal electric field components of incident wave, the phase difference between two electric field components can be adjusted to 90° after passing through the metasurfaces. The simulation results show the metasurfaces is valuable for linear-to-circular polarization conversion application.

[1] J. Zhu and G. V. Eleftheriades, IEEE Antennas Wireless Propag. Lett., Vol. 8, pp. 295–298 (2009) [2] C. L. Holloway, E. F. Kuester and J. A. Gordon, IEEE Antennas Propag. Mag., Vol. 54, no. 2, pp. 10–35 (2012) [3] M. Euler, V. Fusco and R. Dickie, IEEE Trans. Antennas Propag., Vol. 59, no. 8, pp. 3103–3106 (2011) [4] B. A. Munk, Frequency Selective Surfaces: Theory and Design. Hoboken, NJ, USA: Wiley, 2005. [5] N. Yogesh, T. Fu, F. Lan and Z. Ouyang, IEEE Photon. J., Vol. 7, no. 3 (2015) [6] H. L. Zhu, S. W. Cheung and K. L. Chung, IEEE Trans. Antennas Propag., Vol. 61, no. 9, pp. 4615–4623 (2013) [7] M. Euler, V. Fusco and R. Cahill, IET Microw., Antennas Propag., Vol. 4, no. 11, pp. 1764–1772 (2010)

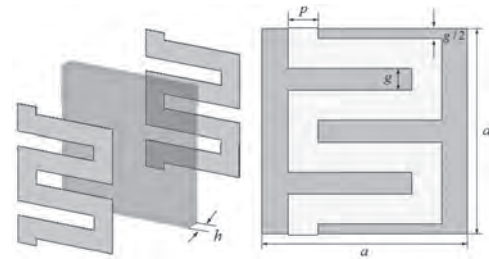


Fig. 1. Geometry of the metasurfaces

	θ	E_v		E_h		$ \varphi_1 - \varphi_2 $
		σ_r (dB)	φ_1	σ_r (dB)	φ_2	
$f = 10.5$ GHz	0	-2.8	34°	-2.5	-55°	89°
	10	-2.9	34°	-2.5	-54°	88°
	20	-3.0	36°	-2.3	-53°	89°
	30	-3.0	38°	-2.0	-50°	88°
	0	-1.9	27°	-2.7	-58°	85°
$f = 11.5$ GHz	10	-2.0	27°	-2.7	-58°	85°
	20	-2.0	28°	-2.5	-57°	85°
	30	-2.1	30°	-2.2	-54°	84°

Table 1. Amplitude and Phase for Two Electric Field Components

JY-16. Design of a Rectenna With Metamaterial Grounding Plane.

F.L. Souza¹ and Ú.d. Resende¹

1. Electrical engineering, Centro Federal de Educacao Tecnologica de Minas Gerais, Belo Horizonte, Brazil

In recent years wireless systems have experienced a rapid and wide expansion. Although these services provide an expressive amount of electromagnetic energy in the environment, a large amount of this energy is actually wasted. Despite the low electromagnetic power density available ambient, it is permanent and can be harvested, by using a rectenna, in order to supply small electrical devices, such as Wireless Sensor Networks (WSNs) used in the Internet of Things (IoT) devices. The RF-based energy harvesting technology is especially suitable to power WSNs because if a compact rectenna is used it can be completely integrated in the distributed hosting sensors structure, reducing its cost, maintenance and environmental impact. The contribution of this work is to present a compact rectenna, which employs a patch antenna with a Metamaterial Unit Cell (MUC) as grounding plane, called Metamaterial Antenna (MA). The proposed rectenna is composed of a square patch antenna with a MUC operating as grounding plane and a double voltage rectifier circuit. Both were built by using a double-sided copper fiberglass substrate, FR-4, with thickness $t=1.5\text{mm}$ and characterized relative electric permittivity $\epsilon_r=4.15$ and tangent of losses $\delta=0.026$. The initial antenna geometry was defined by using transmission line theory. The MUC geometry, composed of a Complementary Split Ring Resonator (CSRR) [1]-[2], was designed and optimized by using Computer Simulation Software (CST[®]) in order to obtain the value $\epsilon_r < 0$ in 2.45GHz. Then, the antenna geometry was optimized together the obtained MUC geometry in order to find values of $S_{11} < -10\text{ dB}$ in the range from 2.4 to 2.5GHz. The final topology of the optimized MA is shown in Fig. 1(a) and 1(b). A Conventional Antenna (CA), Fig. 1(c), with a perfect conductor grounding plane, also was designed and optimized by using the same goal of the MA, in order to process comparisons. The obtained results for CA and MA are 6.69dBi and 3.01dBi (simulated directivity) and -24.93dB and -20.58dB (measured S_{11} parameter), respectively. The rectifier circuit is composed of an open stub for impedance matching, a schottky diode HSMS-2852 and two 100uF capacitors. It was projected and optimized by using Advanced Design Software (ADS[®]) in order to obtain values of $S_{11} < -10\text{ dB}$ in 2.45GHz for input power $P_{in} = -20\text{dBm}$. In order to experimentally evaluate the proposed rectenna performance it was positioned at a variable distance d from an internet router and a 10 kW resistive load was fed. The values of the measured voltage on the load (V_L) are presented in Fig. 2. As can be observed the energy harvested by CA and MA rectennas is enough to supply low consumption loads, such as WSNs. As expected, CA is able to harvest more energy than MA, once it is more directive and larger (3.19 times bigger). However, since MA is more compact it can be more easily incorporated in the WSN structure. In the full paper, rectenna association results will be presented.

[1] Y. Lee, Y. Hao, Characterization of microstrip patch antennas on metamaterial substrates loaded with complementary split-ring resonators, *Microwave and Optical Technology Letters*, vol. 50, no. 8, pp. 2131-2135, Aug. 2008. [2] P. D. Tung, P. H. Lam, N. T. Q. Hoa, A miniaturization of microstrip antenna using negative permittivity metamaterial based on csrr-loaded ground for wlan applications, *Journal of Science and Technology*, vol. 54 (6), pp.689-697, 2016.

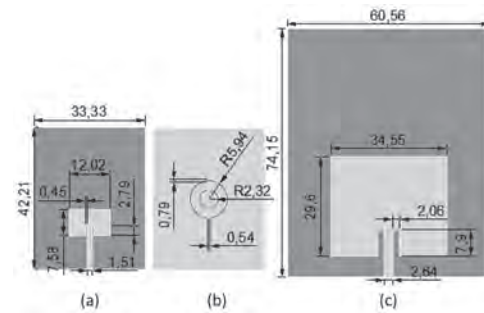


Figure 1. Antennas Geometry: (a) MA, (b) MUC grounding plane and (c) CA.

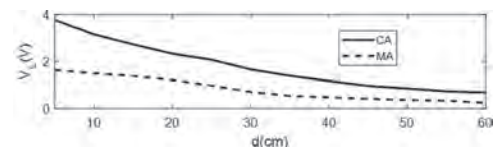


Figure 2. Output voltage for CA and MA rectennas.

JY-17. Fabrication of Polyindole Coated Zinc Ferrite Particles and Their Dual Rheological Response Under Magnetic and Electric Fields.

S. Kang¹ and H. Choi¹

1. Inha University, Incheon, The Republic of Korea

1. INTRODUCTION A variety of smart materials have been focused on a broad range of engineering applications. Among several kinds of smart materials, magnetorheological (MR) fluids inducing a reversible change in rheological behavior under an external magnetic field are suspensions of soft-magnetic particles randomly dispersed in a non-magnetic liquid medium [1]. MR fluids enable rapid switching and proper control between a liquid-like and a solid-like structure by controlling the magnetic field strength. Soft-magnetic carbonyl iron (CI) microspheres have been extensively studied as a major material in MR fluids due to their appropriate particle size and magnetic properties but possess a serious sedimentation problem due to their high particle density [2]. On the other hand, spinel ferrites can be a good alternative to CI particles because of their low density [3]. In particular, spinel zinc ferrite of super-paramagnetic behavior with high magnetic susceptibility, saturation magnetization, low coercivity, and low remanent magnetization is seen as a promising candidate for the use as a dispersed particle in MR fluids [4]. In this work, ZnFe₂O₄ particles were coated with polyindole (PI_n), a conducting polymer with high thermal stability, redox activity, and stable degradation rate [5]. By combining an inorganic with a conductive polymer, the density was lowered, showing better sedimentation improvement. Furthermore, these particles can be also responsive under an applied electric field strength in addition to magnetic fields. 2. EXPERIMENT ZnFe₂O₄ nanoparticles were synthesized by a solvothermal method, and the PI_n was followed to be coated as a shell onto the core ZnFe₂O₄ nanoparticles during oxidation polymerization. A proper amount of ferric chloride hexahydrate and zinc chloride were mixed in ethylene glycol solvent by magnetic stirring. Sodium acetate and polyethylene glycol 400 were slowly poured into the solution. The vigorously stirred mixture was placed in an autoclave and heated at 200 °C for 12 h. After that, the product was washed several times and dried to obtain particles. In the next step, ZnFe₂O₄ was coated by a polymerization process of indole monomer using ammonium persulfate as an initiator. The final particles were collected using an external magnet. For rheological analysis, a smart fluid responding to both magnetic and electric fields was prepared by dispersing the synthesized ZnFe₂O₄/PI_n particles in silicone oil (100cSt, 5 vol%) under sufficient sonication. Morphology and chemical elements of the ZnFe₂O₄/PI_n were examined by the field emission transmission electron microscope in combination with an energy-dispersive X-ray spectroscopy, respectively. Rheological properties of the MR fluid were measured using a rotational rheometer via either a parallel-plate geometry under the magnetic field or a concentric cylinder geometry under the electric field. 3. RESULT AND DISCUSSION Figure 1 shows the FE-TEM image and line scan profiles of core/shell structured ZnFe₂O₄/PI_n particles. The main elements of ZnFe₂O₄ were found abundantly in the center of the particle, and C was confirmed as the main element on the outside of the particle. This result definitively demonstrates that the particles consist of ZnFe₂O₄ as the core material and PI_n composed of C and N as the shell material. In addition, as the detection amount of the core elements increased gradually toward the center of the line drawn along the particle diameter for line scan, it was clearly revealed that the ZnFe₂O₄ core had a spherical morphology. Figure 2 shows the shear stress as a function of shear rate for ZnFe₂O₄/PI_n based on MR fluid under various magnetic field strengths up to 239 kA/m. Without the magnetic field strength, shear stress of MR fluids increased in proportion to shear rate showing a Newtonian fluid-like behaviour, but as the magnetic field was applied, shear stress was relatively maintained within a certain shear rate range and displayed non-Newtonian fluid-like behaviour. When the magnetic field strength was increased, the interaction between magnetic particles was formed more strongly compared to the hydrodynamic force, resulting in a strong chain-like structure of the particles leading to an increase in yield stress. The solid lines in Figure 2 were fitted by Herschel-Bulkley model expressed as $\tau = \tau_0 + K\dot{\gamma}^n$ to explain the rheological behaviour of non-Newtonian fluids [6]. In the given model, τ_0 is the yield stress of materials, K is the consistency factor and n is the flow behaviour index. The n of pseudo-plastic materials is generally known to be between 0 and 1. [7]. The chain-like structure of

ZnFe₂O₄/PI_n particles formed by the magnetic field is destroyed as the shear rate increases, resulting in a shear thinning behaviour. In addition to steady shear test, dynamic test was also performed to examine dynamic moduli under a magnetic field strength. Rheological properties of this smart fluid under an applied electric field strength were further tested to confirm the dual characteristics of the synthesized ZnFe₂O₄/PI_n particles.

[1] J. S. Oh and S. B. Choi, J. King Saud Univ. Sci., 29, 390 (2017). [2] B. Sim, H. S. Chae and H. J. Choi, Express Polym. Lett., 9, 736 (2015). [3] G. Wang, Y. Ma and Y. Tong, J. Intell. Mater. Syst. Struct., 28, 2331 (2017). [4] Y. Xu, D. Sun and H. Hao, RSC Adv., 6, 98994 (2016). [5] I. H. Park, S. H. Kwon and H. J. Choi, J. Magn., 24, 155 (2019). [6] G. Mullineux, Appl. Math. Model., 32, 2538 (2008). [7] C. H. Jeon and B. R. Hodges, Nat. Hazards Earth Syst. Sci., 18, 303 (2018).

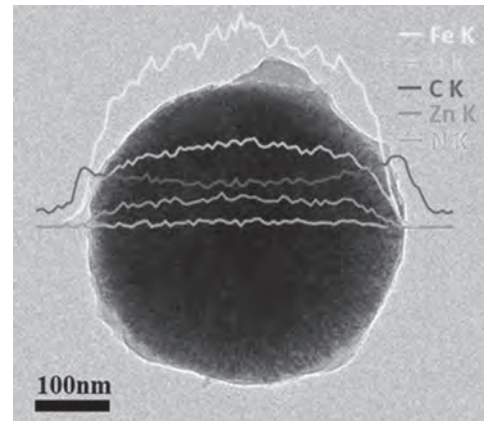


Fig. 1 FE-TEM image of ZnFe₂O₄/PI_n particle

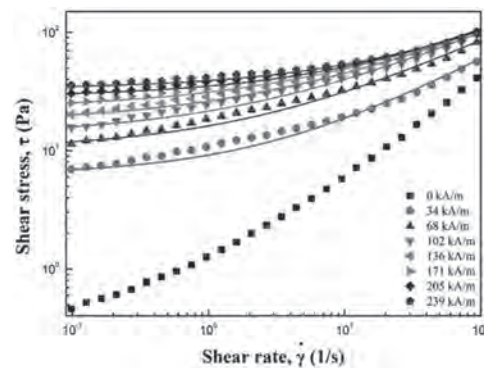


Fig. 2 Shear stress curve of ZnFe₂O₄/PI_n particle based MR fluid under various magnetic field strengths

JY-18. Fabrication and Shear Response of Conducting Polymer Coated Zinc Ferrite Particles Under Magnetic/Electric Field.

T. Kim¹ and H. Choi¹

¹. Inha University, Incheon, The Republic of Korea

1. INTRODUCTION While magnetorheological (MR) fluids consisting of soft-magnetic particles in non-magnetizable carrier fluid draw a huge attention with their active tune-ability under a magnetic field strength, electro/magnetorheological (E/MR) fluids prepared with conducting polymer and magnetic particle composite particles dispersed in a non-conducting carrier fluid exhibit a dual response under both magnetic and electric fields. The smart dual electro/magneto-responsive characteristics of fine tuning and the quick response make them appropriate candidates in wide engineering areas such as clutches, optical finishing systems, medical therapies, actuators, haptic master, micro-fluidic control which have been already adopted separately for either ER fluids or MR fluids [1]. Meanwhile, soft-magnetic carbonyl iron (CI) particles have been widely used in MR fluids, but possess several disadvantages such as their high density and low dispersion stability. Therefore, spinel ferrites with low density and sufficient magnetic behavior are also introduced as a new family of MR materials [2]. In this work, $ZnFe_2O_4$, a magnetic particle constituting the core, was synthesized in a spherical shape using the solvothermal method, and poly(diphenylamine) (PDPA), which has low density and suitable electrical conductivity, was coated through radical polymerization. $ZnFe_2O_4$ /PDPA based MR fluid showed appropriate MR property due to the spinel structure of $ZnFe_2O_4$. Furthermore, it showed improved sedimentation stability because of the advantage of low density of particle [3]. 2. EXPERIMENT First of all, $ZnFe_2O_4$ was synthesized using the surfactant-assistant solvothermal method. 1.35g iron chloride hexahydrate ($FeCl_3 \cdot 6H_2O$) (5mmol) and 0.34g Zinc chloride ($ZnCl_2$) (2.5mmol) were added to 50ml of ethylene glycol, and agitation was performed using a magnetic bar. After stirring, sodium acetate of 3.6g (40mmol) as a weak base and polyethylene glycol 400 (1g) as a surfactant were slowly added to the prepared solution. After vigorously stirring the solution for about 1 h, it was transferred to a Teflon-lined stainless-steel autoclave, and the reacted at 200 for 12 h. After making the reactor to room temperature, black solid particles were obtained using magnets after several washing with ethanol and DI-water. Then, 0.75g $ZnFe_2O_4$ was added to a mixture of methanol and water 40ml/10ml, and then reaction was proceeded at 40 and 1ml of N-[(3-trimethoxysilyl)propyl] aniline was added as a grafting agent, followed by stirring for 18 h. Modified $ZnFe_2O_4$ and diphenylamine (3mmol) were mixed with ethanol. Subsequently, HCl 1M 40ml was added and stirred at 5 for 30 min. Ammonium persulfate (4mmol) dissolved in 1M 10ml HCl was added to the solution, the reaction was carried out for 5 h, and the particles were obtained using a magnet and dried for 12h. 3. RESULT AND DISCUSSION TEM image of Fig. 1 for $ZnFe_2O_4$ /PDPA particle synthesized shows that the size of synthesized material is about 300nm with its morphology of a core-shell structure. The thickness of the shell is about 14 nm, and by coating the polymer on the magnetic particle, the density of the particle is reduced, and the dispersion stability of its MR fluid can be improved. Figure 2 shows flow curve of MR fluid made by dispersing the synthesized core-shell particles in 100 cs silicone oil at 5 vol%. From the controlled shear rate test mode, the shear rate from 0.01s⁻¹ to 200s⁻¹ was applied, depending on the strength of the magnetic field up to 205kA/mm. In the absence of a magnetic field, the fluid behaves like a Newtonian fluid in which the shear stress increases lineary as the shear rate increases. This is because MR fluid behaves like a simple particle suspension following an Einstein equation behavior. On the other hand, when an external magnetic field is applied, the shear stress rises sharply and shows a certain specific yield. This behavior is due to the fact that the attractive force between magnetic particles becomes strong when a magnetic field is applied, and the particles form a chain-like structure in the fluid. As the strength of the magnetic field increases, the attractive force between particles also increases, so the shear stress value increases gradually [4]. To fit the curves representing non-Newtonian fluid properties of MR fluid, a solid line was drawn using the Herschel-Bulkley equation, which is expressed as $\tau = \tau_0 + K\dot{\gamma}^n$. Here, τ means shear stress and τ_0 is the yield stress exhibited by the chain-like structure when a magnetic field is applied. The K value of the consistency index refers to the viscosity of the fluid and n is the

power law index [5]. As the solid lines fit well with the graph, it can be seen that Herschel-Bulkley equation interprets the behavior of MR fluid well over a wide shear rate range. In this work, we synthesized a core-shell structured magnetic particles and conducting polymer and confirmed MR properties such as yield stress and shear thinning under external magnetic field along with ER characteristics under an applied electric field.

[1] M. T. Ramesan, Adv. Polym. Technol., 302, 21362 (2013) [2] G. S. Wang, Y. Y Ma, Yu Tong and J. Intell. Mater. Syst. Struct., 28, 2331 (2017) [3] J. H. Lee, H. J. Choi, Colloid Polym. Sci., 296, 1857 (2018) [4] Y. Z. Dong, H. J. Choi, IEEE Trans. Magn., 54, 4601004 (2018) [5] M. Zubieta, S. Eceolaza and M. J. Elejabarrieta, Smart Mater. Struct., 18, 095019 (2009)

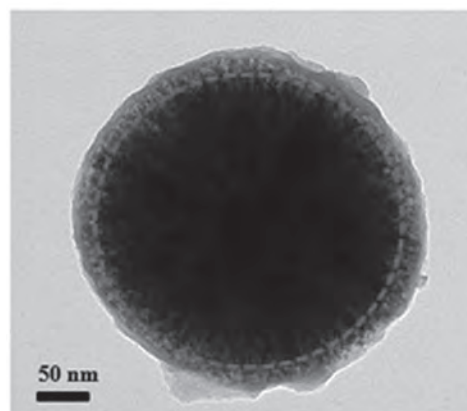


Fig 1. TEM image of core shell structure coated with PDPA on $ZnFe_2O_4$

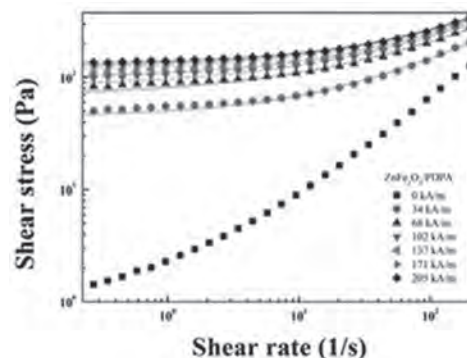


Fig 2. Flow curve of $ZnFe_2O_4$ coated with PDPA under the external magnetic field of $ZnFe_2O_4$ coated with PDPA

JY-19. Modelling of the Intracrystalline Interactions in Trigonal Weak Ferromagnets With Zero Orbital Moment.

K. Seleznyova¹, Y. Mogilenec¹, S. Yagupov¹, M. Strugatsky¹ and J. Kliava²
 1. Physics and Technology Institute, V.I. Vernadsky Crimean Federal University, Simferopol, Russian Federation; 2. LOMA, Universite de Bordeaux, Talence, France

During the last decade, iron borate FeBO₃ based crystals have been attracting an increased interest of scientific community, mainly for the following reasons: (i) these materials can be applied in modern technical devices, e.g. serving as sensitive instruments for measuring magnetic field, pressure, etc., or as monochromators for use with synchrotron radiation [1]; (ii) mixed iron gallium borate Fe_xGa_{1-x}BO₃ crystals are quite suitable objects for studying properties of trigonal weak ferromagnets with zero orbital moment [2, 3]. We have recently shown that with decreasing iron contents the magnetic state of Fe_xGa_{1-x}BO₃ crystals shows a gradual passage from easy-plane weak ferromagnet to diluted paramagnet, passing through magnetic clusters at intermediate iron contents [2]. Thus, by isomorphously substituting paramagnetic Fe³⁺ ions in iron borate, FeBO₃, by diamagnetic Ga³⁺ ions one can synthesize a series of isostructural single crystals allowing not only fine-tuning their magnetic characteristics, thus creating new materials with sought-for properties, but also studying the nature of magnetic state, magnetocrystalline anisotropy, etc. [2, 3]. Such crystals can be synthesized using well-known flux growth technique [4]. However, obtaining high quality Fe_xGa_{1-x}BO₃ crystals in wide range of substitutions, 0 ≤ x ≤ 1, has required many trials in order to find out optimal regimes for crystallization at different concentrations and a considerable improvement of the standard synthesis technique [1]. In this work, we have focused on microscopic characterization of certain magnetic properties of Fe_xGa_{1-x}BO₃ borates by considering in detail *intracrystalline* interactions in these materials. The density of the magnetic energy for Fe_xGa_{1-x}BO₃ crystals can be expressed as follows [5]: $E = 1/2 Em^2 + D(l_x m_x - l_y m_y) + 1/2 al_z^2 + d(3l_x^2 - l_y^2)l_z + e(l_x^4 - 14l_x^2 l_y^2 + l_y^4)(l_x^2 - l_y^2)$ (1) where *m* and *l* are reduced ferromagnetic and antiferromagnetic vectors, *D* and *E* are the Dzyaloshinskii-Moriya and exchange constants, *a* is the uniaxial anisotropy constant, and *d* and *e* are the basal anisotropy constants. Different mechanisms responsible for the magnetic properties have different dependences on the concentration of paramagnetic ions and temperature; therefore, experimental studies of the latter dependences and a subsequent modelling based on eq. (1) could, on the one hand, single out dominating mechanisms of the magnetic transitions observed and, on the other hand, get better insight in the nature of intracrystalline interactions in trigonal weak ferromagnets. Since the Dzyaloshinskii-Moriya and exchange constants characterize pair interactions between paramagnetic ions, we have assumed that the corresponding *microscopic* constants for a pair of Fe³⁺ ions in mixed crystals remain the same as those in unmixed crystal. Thus, we can express both constants for mixed iron-gallium borates through the *macroscopic* *D* and *E* constants for unmixed iron borate and obtain an analytical expression of the macroscopic constants for mixed crystals. We have put forward a computer code modelling the diamagnetically diluted crystal lattice by the Monte-Carlo technique [6] and implementing a summation, first, over the nearest-neighbouring Fe³⁺ for a reference Fe³⁺ ion and, next, over all sites occupied by Fe³⁺ ions. As a result, we have shown that the dependences of both *D* and *E* constants on *x* (at 0 K) follow a parabolic law. In calculating the magnetocrystalline anisotropy for Fe_xGa_{1-x}BO₃ crystals one should take into account only crystal field and dipole-dipole contributions. Indeed, the 3d⁵ electronic configuration of Fe³⁺ has zero orbital moment; therefore, the exchange energy in a good approximation is isotropic [7]. Recently we have calculated the dipole-dipole interaction energy in the model of “extended dipoles” [8], having non-negligible dipole size. Unlike the point dipoles, the extended dipoles bring a non-zero dipole-dipole contribution to the basal magnetocrystalline anisotropy, and earlier we have evaluated it for unmixed iron borate [3]. In the model of extended dipoles, a calculation of the Ampérian current, i.e., a circular current loop of a radius *R*, results in two possible sizes of the magnetic dipole represented by a Fe³⁺ ion: *R*₁ = 0.2189 and *R*₂ = 0.0797 Å [3]. In this work, we have applied the model of extending dipoles to evaluating the dipole-dipole contributions to the magnetocrystalline anisotropy constants of mixed iron-gallium borates. To this purpose, we have put forward a computer code implementing the lattice-sum method [3]

and modelling the diamagnetically diluted crystal lattice using the Monte Carlo technique in the same way as in calculating *D* and *E* constants, *vide supra* [6]. Resultantly, the dependences on *x* of the dipole-dipole contribution to the magnetocrystalline constants for Fe_xGa_{1-x}BO₃ crystals have been obtained, see Figures 1 and 2. The dipole-dipole contributions to the basal anisotropy constants have been calculated at 0 K for different *x* using both possible effective dipole sizes, *R*₁ and *R*₂, determined for Fe³⁺ ions. This work was partially supported by the V.I. Vernadsky Crimean Federal University Development Program for 2015-2024 Grant no. VG04/2019; and by the RFBR projects Grants No. 19-32-90054 and 18-42-910008.

1. E.S. Smirnova, N.I. Snegirev, I.S. Lyubutin *et al.*, Acta Cryst., Vol. B76, p. 1100 (2020)
2. K. Seleznyova, M. Strugatsky, S. Yagupov *et al.*, J. Appl. Phys., Vol. 125, p. 223905 (2019)
3. M. Strugatsky, K. Seleznyova, S. Yagupov *et al.*, J. Magn. Magn. Mater., Vol. 442, p. 417 (2017)
4. S. Yagupov, M. Strugatsky, K. Seleznyova *et al.*, Appl. Phys. A, Vol. 121, p. 179 (2015)
5. E.A. Turov and N.G. Guseinov, Soviet Physics JETP, Vol. 11, p. 955 (1960)
6. L. Devroye, *Non-Uniform Random Variate Generation*, Springer, 843 pp. (1986)
7. J. Kanamori, in: *Magnetism*, eds., G.T. Rado, H. Suhl, Acad. Press, Vol 1, pp. 127 (1963)
8. K. Seleznyova, M. Strugatsky and J. Kliava, Eur. J. Phys., Vol. 37, p. 025203 (2016)

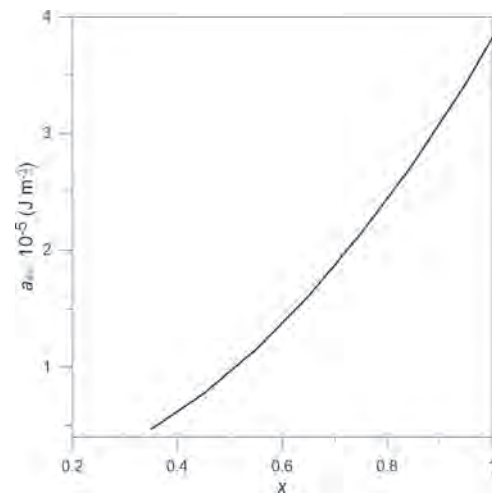


Fig.1 Dipole-dipole contribution to *a* vs. *x* in Fe_xGa_{1-x}BO₃ crystals at 0 K.

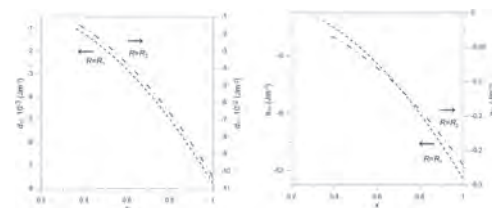


Fig.2 Dipole-dipole contributions to *d* (left) and *e* (right) vs. *x* in Fe_xGa_{1-x}BO₃ crystals, calculated for two possible effective dipole sizes: *R*₁ (dashed curves) and *R*₂ (dash-dotted curves) at 0 K.

- A -

- A Jiménez, J. (JS-10) 1360
 Ababei, R.V. (GB-09) 932
 Abad, L. (DF-02) 654
 Aballe, L. (DD-07) 637
 Aballe, L. (FH-06) 889
 Aballe, L. (GA-02) 915
 Aballe, L. (GB-03) 925
 Aballe, L. (HA-04) 970
 Aballe, L. (HD-04) 1006
 Aballe, L. (IH-12) 1113
 Aballe, L. (JI-02) 1298
 Abd-El-Hafiz, S. (CS-08) 590
 Abelmann, L. (AC-10) 50
 Abelmann, L. (JG-10) 1281
 Abelmann, L. (JQ-01) 1327
 Abert, C. (GD-04) 954
 Abert, C. (JI-05) 1301
 Adachi, Y. (BJ-03) 291
 Adachi, Y. (CQ-01) 559
 Adelman, C. (EC-07) 738
 Adenot-Engelvin, A. (JX-04) 1411
 Adeyeye, A.O. (ED-01) 746
 Adly, A. (CS-08) 590
 Aepuru, R. (JS-10) 1360
 Afanasyev, K. (ID-05) 1065
 Afrasiabi, S. (BG-12) 259
 Afsar, M. (ID-11) 1071
 Afuwape, O.F. (CQ-10) 568
 Afuwape, O.F. (JP-01) 1311
 Afuwape, O.F. (JP-10) 1320
 Agarwal, N. (FD-05) 853
 Ageron, B. (CF-06) 518
 Aggarwal, S. (CF-01) 513
 Aguirre, M. (FC-04) 842
 Agustsson, S. (FH-13) 896
 Ahmad, A. (JE-10) 1253
 Ahmad, G. (BD-01) 211
 Ahmad, H. (AC-07) 47
 Ahmad, H. (BB-05) 196
 Ahmad, H. (BG-08) 255
 Ahmad, M. (BI-10) 286
 Ahmed, N. (IT-08) 1186
 Ahn, J. (AR-12) 127
 Ahn, J. (JY-09) 1432
 Ait Oukaci, K. (EB-03) 718
 Ajejas, F. (CC-11) 481
 Ajejas, F. (DB-09) 613
 Ajejas, F. (HC-02) 991
 Ajejas, F. (HC-09) 999
 Ajejas, F. (IH-14) 1115
 Akagi, F. (IP-01) 1118
 Akagi, F. (IP-04) 1121
 Akaki, M. (DP-04) 682
 Akano, Y. (IA-09) 1034
 Akbar, S. (DE-08) 650
 Akdogan, O. (JH-02) 1286
 Åkerman, J. (FB-08) 831
 Akinola, O.G. (GB-02) 924
 Al Ma'mari, F. (HA-01) 967
 Al Mamoori, M. (GA-02) 915
 Al-Mahdawi, M. (CP-15) 556
 Alam, J. (JY-02) 1425
 Alamdar, M. (GB-02) 924
 Albertini, F. (JE-09) 1252
 Albin, C. (JI-11) 1307
 Albrecht, M. (FA-05) 819
 Albuquerque, G. (IA-10) 1035
 Alejandro, G. (FB-06) 829
 Alejandro, G. (JG-11) 1282
 Alekhina, I.A. (ID-04) 1064
 Alekseev, S. (FB-03) 824
 Aleksic, O. (IS-12) 1173
 Aleszkiewicz, P. (IG-02) 1089
 Algarin, J. (YA-01) 6
 Ali, K.S. (JS-08) 1358
 Ali, M. (DP-09) 687
 Ali, M. (JY-06) 1429
 Ali, Q. (BB-08) 199
 Alia, M. (DC-12) 628
 Alimi, R. (GC-08) 945
 Allende, S. (ED-10) 756
 Allia, P. (YA-04) 9
 Allocca, L. (JF-07) 1263
 Allwood, D. (GA-02) 915
 Allwood, D. (GB-03) 925
 Allwood, D. (GB-04) 926
 Allwood, D. (GB-09) 932
 Allwood, D. (GB-11) 934
 Alman, V. (JR-13) 1349
 Almeida, M.P. (JP-05) 1315
 Almeida, R. (JT-06) 1367
 Alonso, J. (YA-01) 6
 Alotibi, S. (DP-09) 687
 Alshammari, H. (JH-02) 1286
 Alshammari, K.N. (JY-06) 1429
 Alshammari, S.J. (AU-02) 163
 Althammer, M. (CE-05) 504
 Althammer, M. (FG-10) 877
 Alvarado-Hernández, F. (JT-01) 1362
 Alvarez Prado, L. (EC-05) 736
 Alvarez-Héault, J. (IB-07) 1045
 Álvarez, N.R. (JG-11) 1282
 Álvaro Gómez, L. (DD-07) 637
 Amann, A. (BK-05) 308
 Amara, S. (GB-06) 929
 Amara, Y. (BA-06) 190
 Amara, Y. (BD-11) 223
 Amaral, J.S. (DF-10) 663
 Amaral, J.S. (IC-07) 1059
 Amaral, J.S. (JE-11) 1254
 Amaral, J.S. (JT-06) 1367
 Amaral, V.S. (DF-10) 663
 Amaral, V.S. (IC-07) 1059
 Amaral, V.S. (JE-11) 1254
 Ambrose, T. (CG-05) 531
 Amemiya, K. (DG-07) 673
 Amigó, M. (JX-06) 1413
 Amorim, C. (DF-10) 663
 Amorim, C. (IC-07) 1059
 Amorim, C. (JE-11) 1254
 Amorim, C. (JT-06) 1367
 An, K. (EA-04) 712
 An, K. (ED-04) 750
 Anadón, A. (DB-09) 613
 Anadón, A. (IH-14) 1115
 Anadón, A. (IR-16) 1157
 Anane, A. (EB-02) 717
 Anane, A. (ED-02) 748
 Anane, A. (ED-03) 749
 Anane, A. (ED-07) 753
 Anane, A. (FH-12) 895
 Anane, A. (JA-12) 1201
 Andersen, I. (AA-04) 23
 Andersen, I. (DD-07) 637
 Andersen, I. (JI-04) 1300
 Ando, K. (CE-12) 511
 Ando, Y. (CP-03) 543
 Ando, Y. (CP-15) 556
 Ando, Y. (IT-03) 1181
 Andrade, V.M. (JE-12) 1255
 Andrade, V.M. (JR-05) 1341
 Andreev, N. (DP-08) 686
 Andreev, S.V. (JT-12) 1373
 Andrew, J. (ID-02) 1062
 Andrews, B. (BE-03) 227
 Andrews, B. (BE-04) 228
 Andrieu, S. (DD-10) 640
 Andrieu, S. (DE-01) 642
 Andrieu, S. (DE-03) 644
 Andrieu, S. (ID-01) 1061
 Androvitsaneas, P. (CB-03) 466
 Ang, C.C. (HB-04) 978
 Anghel, L. (GB-05) 928
 Anis, M. (JX-10) 1417
 Ansalone, P. (EB-11) 727
 Ansalone, P. (GC-04) 941
 Ansermet, J. (FC-02) 840
 Antonov, G. (CS-02) 584
 Antonov, V. (GA-05) 919
 Aoki, K. (JP-07) 1317
 Aoshima, K. (JS-04) 1354
 Apicella, V. (JU-03) 1378
 Appino, C. (JB-11) 1214
 Aquino, H.O. (EE-11) 774
 Arena, D. (IG-06) 1093
 Ari-Gur, P. (JE-05) 1248
 Arkhipov, A.V. (JT-12) 1373
 Armay, I. (DB-09) 613
 Armay, I. (IH-14) 1115
 Armay, I. (IR-16) 1157
 Arndt, C. (JG-08) 1279
 Arnold, D. (ID-02) 1062
 Arora, N. (ED-15) 762
 Arregi Uribeetxebarria, J.A. (FD-05) 853
 Arriola Córdoba, A.Y. (CC-08) 478
 Arriola Córdoba, A.Y. (HB-01) 975
 Artemchuk, P. (EB-10) 726
 Artemova, A. (ER-13) 813
 Asa, M. (FG-14) 881
 Asam, N. (IA-01) 1025
 Asenjo, A. (AA-05) 24

Asenjo, A. (IG-04)	1091	Back, C.H. (EB-09)	725	Baraduc, C. (HB-07)	981
Asenjo, A. (JI-02)	1298	Back, C.H. (FD-05)	853	Baraduc, C. (HP-04)	1016
Asselberghs, I. (GD-09)	959	Backes, D. (FG-06)	873	Baraduc, C. (IB-07)	1045
Atalay, S. (JA-07)	1195	Badarneh, M. (JR-04)	1340	Baraduc, C. (IR-02)	1143
Atallah, K. (AU-02)	163	Badelin, A. (DP-06)	684	Barakat, G. (BA-06)	190
Atallah, K. (BF-03)	235	Badura, A. (FG-08)	875	Barakat, G. (BD-11)	223
Atallah, K. (BF-04)	236	Badura, A. (FH-08)	891	Barberis, A. (JA-01)	1189
Atcheson, G. (AD-02)	61	Bae, C. (JW-05)	1393	Barbour, A. (AB-05)	31
Ates, B. (JA-07)	1195	Bae, C. (JW-15)	1403	Bardotti, L. (JI-11)	1307
Attané, J. (CB-02)	465	Baek, M. (AR-12)	127	Barilo, S. (DF-09)	662
Attané, J. (CD-02)	487	Baek, Y. (AU-08)	171	Barilo, S. (JT-10)	1371
Attané, J. (CD-06)	491	Bagschik, K. (HA-02)	968	Baringthon, L. (FB-01)	822
Attané, J. (CD-11)	496	Bahamida, S. (JF-11)	1268	Barker, C. (AE-11)	81
Attané, J. (CD-13)	498	Bahl, C.R. (BE-07)	231	Barnes, C. (JI-05)	1301
Attané, J. (DC-11)	627	Bahl, C.R. (BK-03)	306	Barrera, G. (JF-11)	1268
Attané, J. (DG-07)	673	Bai, B. (AS-11)	146	Barrera, G. (JU-06)	1381
Attané, J. (FE-02)	859	Bai, B. (AS-13)	148	Barrera, G. (YA-04)	9
Attané, J. (GD-02)	952	Bai, B. (AS-14)	149	Barrett, R. (BF-03)	235
Attané, J. (IP-10)	1127	Bai, B. (AS-15)	150	Barrett, R. (BF-04)	236
Atxitia, U. (FG-02)	869	Bai, B. (AS-16)	151	Bartell, J. (AB-05)	31
Aubert, A. (CR-05)	575	Bai, H. (DC-08)	624	Barthélémy, A. (ED-02)	748
Audry, M. (JH-01)	1285	Bai, H. (HA-05)	971	Barton, C. (HC-06)	996
Auffret, S. (CF-06)	518	Bai, J. (BF-06)	238	Barua, R. (JE-03)	1245
Auffret, S. (CF-07)	519	Bai, J. (BT-02)	383	Barua, R. (JE-06)	1249
Auffret, S. (CF-11)	524	Bai, J. (JC-09)	1226	Barucca, G. (JD-10)	1240
Auffret, S. (ER-06)	806	Bailleul, M. (EB-03)	718	Baryshev, A. (ID-05)	1065
Auffret, S. (FE-02)	859	Bairagi, K. (HD-04)	1006	Bas, D.A. (EC-11)	742
Auffret, S. (FH-02)	885	Bal, M. (FG-09)	876	Basit, A. (BD-07)	218
Auffret, S. (HB-07)	981	Balachandran, P. (JE-03)	1245	Basso, V. (CC-14)	484
Auffret, S. (HC-05)	995	Balachandran, T. (BB-07)	198	Basso, V. (EB-11)	727
Auffret, S. (HD-04)	1006	Balakrishnan, P.P. (DE-07)	649	Basu, D. (BJ-02)	289
Auffret, S. (IR-02)	1143	Balcioglu, S. (JA-07)	1195	Basumatary, H. (FB-04)	826
Avci, C. (CC-06)	476	Bald, C. (IB-02)	1040	Battle, X. (IG-01)	1088
Avci, C. (CC-13)	483	Baldrati, L. (FG-04)	871	Battle, X. (JH-07)	1291
Avci, C. (CD-11)	496	Baldrati, L. (FG-06)	873	Battle, X. (JH-08)	1292
Avci, C. (FE-01)	858	Balédent, V. (EC-12)	743	Battula, S. (JR-13)	1349
Avilés, L. (FB-06)	829	Bali, R. (FB-02)	823	Bauer, G.E. (EA-04)	712
Avula, S.R. (JH-07)	1291	Bali, R. (IA-03)	1028	Bauer, J. (CE-08)	507
Awaji, S. (IR-05)	1146	Ballet, P. (DC-11)	627	Bauer, J. (IQ-03)	1133
Awano, H. (CD-05)	490	Balli, M. (JS-09)	1359	Bauer, M. (ID-02)	1062
Awano, H. (CP-15)	556	Baltz, V. (CD-11)	496	Baumgaertl, K. (EC-03)	734
Ayani, C. (IH-14)	1115	Baltz, V. (FG-08)	875	Baumgaertl, K. (ED-12)	759
Aydin, M. (BE-02)	226	Baltz, V. (FH-02)	885	Baumgaertl, K. (ED-14)	761
Aydin, M. (BG-04)	251	Baltz, V. (FH-08)	891	Bayzi Isfahani, V. (DB-01)	605
Aydin, M. (BG-07)	254	Bang, S. (JP-04)	1314	Bazrov, M. (CB-01)	464
Aydin, M. (BH-06)	269	Bang, T. (AP-12)	96	Béa, H. (FE-08)	865
Azevedo, A. (FB-07)	830	Bang, T. (AQ-07)	105	Béa, H. (HB-07)	981
Azuma, T. (AV-01)	179	Bang, T. (AU-08)	171	Béa, H. (HP-04)	1016
		Bang, T. (BQ-05)	334	Béa, H. (IR-02)	1143
		Bang, T. (BQ-09)	338	Beach, G. (AB-05)	31
		Bang, T. (BQ-10)	339	Beach, G. (FE-05)	862
		Bang, T. (BR-06)	352	Beach, G. (FE-06)	863
		Bang, T. (BS-02)	366	Beach, G. (FH-04)	887
		Bang, T. (BS-04)	369	Beach, G. (FH-07)	890
		Bang, T. (BV-09)	435	Beach, G. (HA-02)	968
		Bao, X. (AP-10)	94	Beauchamp, M. (JP-15)	1325
		Bao, X. (AQ-05)	103	Beaulieu, N. (EA-04)	712
		Bao, X. (AU-09)	172	Beaulieu, N. (ED-04)	750
		Bao, X. (BW-02)	439	Beaulieu, N. (EE-08)	771
		Bao, X. (CR-03)	573	Beaulieu, N. (FP-06)	904
		Baraban, I. (JY-03)	1426	Beckmann, B. (JE-02)	1244
Ba, S. (AC-18)	58				
Babaytsev, G.V. (IR-14)	1155				
Babenkov, S. (FH-13)	896				
Babu, N.K. (EC-08)	739				
Bachmaier, A. (IR-13)	1154				
Bachmaier, A. (JA-06)	1194				
Bachmann, J. (DD-05)	635				
Bachmann, J. (DD-06)	636				
Back, C.H. (CC-03)	473				

- B -

- Beckmann, B. (JT-06) 1367
- Becle, E. (GB-05) 928
- Becnel, A. (YB-06) 18
- Bedoya Pinto, A. (DB-04) 608
- Beg, M. (DD-04) 634
- Beg, M. (GC-05) 942
- Begari, K. (FP-10) 908
- Beginin, E. (EC-04) 735
- Beginin, E. (EP-09) 789
- Beginin, E. (EQ-04) 794
- Beginin, E. (EQ-06) 796
- Beginin, E. (EQ-07) 797
- Behbahani, R. (AD-03) 62
- Beik Mohammadi, J. (CF-10) 523
- Bekir, W. (JW-18) 1406
- Belguerras, L. (BA-03) 187
- Belkhou, R. (DD-07) 637
- Belkhou, R. (GD-02) 952
- Bell, C. (IH-13) 1114
- Bello, J. (CC-08) 478
- Bellouard, C. (ID-01) 1061
- Belmeguenai, M. (FE-09) 866
- Belmeguenai, M. (GD-01) 951
- Belmeguenai, M. (HD-04) 1006
- Belmeguenai, M. (IR-01) 1142
- Belmeguenai, M. (IR-02) 1143
- Belo, J.H. (JE-12) 1255
- Belo, J.H. (JP-05) 1315
- Belo, J.H. (JT-06) 1367
- Belodedov, M. (JP-06) 1316
- Belotelov, V.I. (EB-14) 730
- Belotelov, V.I. (FP-04) 902
- Belotelov, V.I. (FP-07) 905
- Belotelov, V.I. (JF-01) 1257
- Belotelov, V.I. (JS-03) 1353
- Belykh, S.S. (JS-01) 1351
- Ben Ahmed, H. (BA-06) 190
- Ben Youssef, J. (EA-04) 712
- Ben Youssef, J. (ED-04) 750
- Ben Youssef, J. (EE-08) 771
- Ben Youssef, J. (FP-06) 904
- Ben Youssef, J. (JA-12) 1201
- Ben, T. (BE-01) 225
- Benabou, A. (BJ-11) 299
- Benabou, A. (JB-13) 1216
- Benabou, A. (JW-18) 1406
- Bender, P. (JG-03) 1274
- Bendjeddou, I. (ID-07) 1067
- Bendjeddou, I. (ID-08) 1068
- Benetti, L. (DD-09) 639
- Benguettat, I. (IR-02) 1143
- Benitez, L.A. (DA-03) 600
- Benlloch, J. (YA-01) 6
- Bennett, C.H. (GB-02) 924
- Bennett, S.P. (IB-03) 1041
- Bensmann, J. (FA-05) 819
- Berganza, E. (AA-05) 24
- Berganza, E. (IG-04) 1091
- Berger, F. (YA-02) 7
- Berger, H. (HC-07) 997
- Berges, L. (AE-10) 80
- Berges, L. (FH-06) 889
- Berges, L. (HD-08) 1010
- Bergholdt, J. (AC-11) 51
- Berkov, D. (JD-11) 1241
- Bernand-Mantel, A. (FE-08) 865
- Bernot, F. (BI-07) 283
- Bernstein, G.H. (EE-11) 774
- Béron, F. (JS-10) 1360
- Bertacco, R. (DB-06) 610
- Bertacco, R. (IR-15) 1156
- Bertoni, G. (JR-11) 1347
- Bertran, F. (DE-01) 642
- Bespas, J. (AD-02) 61
- Bessarab, P. (JR-04) 1340
- Bessonov, S. (HP-11) 1023
- Betsunoh, R. (BS-09) 374
- Bevis, C. (EA-06) 714
- Bhat, V. (ED-14) 761
- Bhat, V. (EE-03) 766
- Bhatt, R.C. (IP-09) 1126
- Bhatti, I. (IB-05) 1043
- Bhatti, S. (HB-11)* 985
- Bhowmik, D. (GB-01) 922
- Bi, Y. (AQ-03) 101
- Biacchi, A. (AC-13) 53
- Bialek, M. (FC-02) 840
- Bian, Z. (GB-08) 931
- Biao, Y. (JY-07) 1430
- Bibes, M. (ED-02) 748
- Bibes, M. (FE-02) 859
- Biela, J. (BJ-01) 288
- Bierhance, G. (DC-12) 628
- Binda, F. (CD-11) 496
- Bingfeng, G. (IS-05) 1166
- Bingfeng, G. (IS-08) 1169
- Bingfeng, G. (JU-04) 1379
- Bingfeng, G. (JU-05) 1380
- Bingham, N. (AA-03) 22
- Bir, A.S. (ER-01) 801
- Bird, J. (BA-04) 188
- Bird, J. (BF-10) 242
- Birge, N.O. (FH-04) 887
- Birge, N.O. (FH-07) 890
- Biroska, M. (DC-13) 629
- Biroska, M. (DG-03) 669
- Biswas, A. (JE-06) 1249
- Bitla, Y. (CP-05) 545
- Bittner, F. (JC-03) 1220
- Bjørk, R. (BE-07) 231
- Bjørk, R. (BH-01) 264
- Bjørk, R. (BK-03) 306
- Bjørk, R. (GC-09) 946
- Blanc, B. (AC-06) 46
- Blanco-López, M.C. (YA-05) 10
- Block, F. (JG-08) 1279
- Blon, T. (JR-02) 1338
- Blügel, S. (CE-12) 511
- Blügel, S. (FD-04) 852
- Blügel, S. (FH-10) 893
- Blum, C. (JW-14) 1402
- Bobrovskii, S. (ER-13) 813
- Bocher, L. (FH-06) 889
- Boddapati, L. (DB-01) 605
- Bodnar, S. (FH-13) 896
- Bogy, D. (IA-08) 1033
- Bohra, M. (JR-13) 1349
- Boiron, O. (JI-11) 1307
- Bokor, J. (GD-08) 958
- Bokor, J. (HB-01) 975
- Boldrey, J. (JQ-02) 1328
- Bollero, A. (IG-11) 1099
- Bollero, A. (IH-08) 1109
- Bollero, A. (JD-08) 1238
- Bollero, A. (JD-09) 1239
- Bolyachkin, A. (GC-07) 944
- Bommanaboyena, S. (FH-11) 894
- Bommanaboyena, S. (FH-13) 896
- Bonetti, S. (FA-02) 816
- Bonetti, S. (FD-08) 856
- Bonfim, M. (JW-12) 1400
- Bonnet, C. (ID-01) 1061
- Bono, D. (FH-04) 887
- Borders, W.A. (FC-09) 847
- Borders, W.A. (GB-10) 933
- Borel, S. (ID-03) 1063
- Borisenko, I. (EA-02) 710
- Borisov, K. (AD-02) 61
- Borodavka, F. (DF-07) 659
- Borovkova, O. (FP-04) 902
- Borovkova, O. (JS-03) 1353
- Borreguero, J. (YA-01) 6
- Bortolotti, P. (ED-02) 748
- Bortolotti, P. (ED-03) 749
- Bortolotti, P. (ED-07) 753
- Bortolotti, P. (IB-04) 1042
- Bortolotti, P. (ID-08) 1068
- Bortolotti, P. (JA-12) 1201
- Bosch, R. (YA-01) 6
- Boscher, C. (JX-04) 1411
- Böse, H. (YB-04) 16
- Boselli, M. (CD-08) 493
- Bostrem, I.G. (EQ-08) 798
- Botsch, L. (GC-11) 949
- Böttcher, M. (HA-02)
- 976 Bottegoni, F. (CB-05)
- 468 Bouckaert, W. (HP-09)
- 1021 Bouda, N. (CR-11)
- 581 Boulet, P. (JF-03)
- 1259 Boule, O.
- (CD-06) 491 Boule, O.
- (HB-07) 981 Boule, O.
- (HD-04) 1006 Boule, O.
- (HP-04) 1016
- Boumesbah, A. (BH-05) 268
- Bourdel, S. (ID-08) 1068
- Bouzehouane, K. (AB-11) 38
- Bouzehouane, K. (DB-02) 606
- Bouzehouane, K. (DD-10) 640
- Bouzehouane, K. (GA-01) 914
- Bouzehouane, K. (HC-02) 991
- Bouzehouane, K. (HC-09) 999
- Bouzehouane, K. (IQ-08) 1138
- Boventer, I. (ED-02) 748

- Boventer, I. (ED-03) 749
 Boventer, I. (FH-12) 895
 Bowen, D. (BJ-02) 289
 Bowman, R. (FC-08) 846
 Bowman, R. (IQ-09) 1139
 Boynov, K.O. (BI-04) 278
 Bozhko, D. (CA-02) 458
 Bracher, D. (HA-01) 967
 Brächer, T. (ED-11) 757
 Brächer, T. (EE-04) 767
 Bradley, H. (ED-08) 754
 Bran, C. (JI-02) 1298
 Brandl, G. (AC-17) 57
 Brataas, A. (EB-06) 721
 Brataas, A. (FH-12) 895
 Brataas, A. (HB-10) 984
 Bratschitsch, R. (FA-05) 819
 Braun, T. (JC-02) 1219
 Breitbach, D. (ED-11) 757
 Brems, M. (FG-05) 872
 Brems, M. (HC-10) 1000
 Brenac, A. (CD-06) 491
 Brenac, A. (CD-11) 496
 Brenac, A. (DC-11) 627
 Breth, L. (AD-04) 63
 Briático, J. (FC-04) 842
 Brink, J. (DC-06) 622
 Brock, J. (HD-09) 1011
 Broomhall, T.J. (GA-02) 915
 Brown, P. (JT-10) 1371
 Brückel, T. (AC-17) 57
 Brückl, H. (AD-04) 63
 Brunn, O. (DQ-09) 700
 Brunn, O. (DQ-11) 702
 Brus, P. (DB-02) 606
 Buchanan, K. (AE-12) 82
 Buchelnikov, V. (JU-02) 1377
 Büchner, B. (JW-14) 1402
 Büchner, B. (JX-06) 1413
 Buda-Prejbeanu, L.D. (CF-11) 524
 Buda-Prejbeanu, L.D. (CG-03) 529
 Buda-Prejbeanu, L.D. (ED-10) 756
 Buda-Prejbeanu, L.D. (HB-07) 981
 Buda-Prejbeanu, L.D. (HD-04) 1006
 Buda-Prejbeanu, L.D. (HP-04) 1016
 Buda-Prejbeanu, L.D. (IQ-05) 1135
 Buettner, F. (AB-05) 31
 Buettner, F. (HA-02) 968
 Bui, T.Q. (AC-13) 53
 Bukhari, S. (BW-04) 441
 Bukharia, K. (IH-07) 1108
 Bulbucan, C.E. (IG-10) 1097
 Bulbucan, C.E. (JI-01) 1297
 Bull, C. (FB-13) 836
 Bunyaev, S.A. (FC-07) 845
 Burke, A.M. (JI-01) 1297
 Burkhardt, C. (JC-11) 1228
 Burnell, G. (HA-01) 967
 Busch, O. (FG-01) 868
 Busel, O. (EE-07) 770
 Bussmann, K. (DF-04) 656
 Bussmann, K. (IB-03) 1041
 Butera, A. (FB-06) 829
 Butera, A. (FC-04) 842
 Butera, A. (JG-11) 1282
 Büttel, G. (ER-11) 811
 Butterling, M. (DF-02) 654
 Butterling, M. (IA-03) 1028
 Buzdakov, A. (FP-14) 912
 Buzdin, A. (FH-02) 885
 Buznikov, N.A. (ID-04) 1064
 Byeon, C. (AP-03) 87
 Byerly, K. (JA-04) 1192
 Bykov, I. (ID-05) 1065
 Bykova, I. (HB-05) 979
- C -
- C Denardin, J. (JS-10) 1360
 C, L. (BP-01) 310
 C, V. (JT-02) 1363
 Caçoilo, N. (CG-03) 529
 Cagliaris, F. (JX-06) 1413
 Cagnon, L. (DD-07) 637
 Cai, F. (BU-11) 414
 Cai, F. (BU-18) 422
 Cai, H. (GB-08) 931
 Cai, J. (FC-05) 843
 Cai, K. (IA-05) 1030
 Cai, S. (BC-01) 204
 Cai, T. (AR-04) 118
 Cai, W. (FG-07) 874
 Cai, Z. (AU-07) 170
 Cai, Z. (CS-13) 595
 Calarco, R. (DB-06) 610
 Calleja, F. (IH-14) 1115
 Calo, C. (ED-07) 753
 Caltun, O. (JP-11) 1321
 Calverley, S.D. (BF-03) 235
 Calverley, S.D. (BF-13) 246
 Camacho, G. (YB-01) 13
 Camarero, J. (AE-08) 78
 Camarero, J. (DB-09) 613
 Camarero, J. (IB-05) 1043
 Camarero, J. (IG-11) 1099
 Camarero, J. (IH-08) 1109
 Camarero, J. (IH-14) 1115
 Camarero, J. (IR-16) 1157
 Camarillo-Garcia, J.P. (JT-01) 1362
 Camley, R.E. (HA-06) 973
 Camosi, L. (HB-08) 982
 Canals, B. (DG-11) 677
 Canals, B. (DQ-09) 700
 Canals, B. (DQ-11) 702
 Canals, B. (GA-01) 914
 Cañero Infante, I. (JI-11) 1307
 Canhota, M. (JP-05) 1315
 Canon Bermudez, G. (IB-01) 1038
 Cantoni, M. (DB-06) 610
 Cantoni, M. (FG-14) 881
 Cantoni, M. (IR-15) 1156
 Cao, G. (BC-02) 205
 Cao, G. (BQ-02) 330
 Cao, H. (BC-04) 207
 Cao, H. (DP-12) 690
 Cao, J. (BQ-07) 336
 Cao, K. (IH-01) 1102
 Cao, L. (BU-12) 415
 Cao, L. (BV-05) 431
 Cao, L. (JU-04) 1379
 Cao, S. (AV-04) 182
 Cao, W. (AP-08) 92
 Cao, X. (AS-14) 149
 Capotondi, F. (FD-03) 851
 Cardoso de Olivero, R. (FB-10) 833
 Caretta, L.M. (FE-05) 862
 Carley, R. (FD-05) 853
 Carlotti, G. (EC-05) 736
 Carlotti, G. (HC-06) 996
 Carmona, I.C. (CQ-10) 568
 Carmona, I.C. (JQ-06) 1332
 Carpenter, R. (CF-12) 525
 Carpenter, R. (CG-13) 539
 Carpenter, R. (IG-09) 1096
 Carpentieri, M. (FD-02) 850
 Carpentieri, M. (HA-05) 971
 Carpentieri, M. (HC-11) 1001
 Carreira, S. (FC-04) 842
 Carrétéro, C. (ED-02) 748
 Carrétéro, C. (JA-12) 1201
 Carrey, J. (JH-10) 1294
 Caruana, A. (IA-03) 1028
 Carver, K. (BE-03) 227
 Casaleiz, D. (JD-09) 1239
 Casanova, F. (CC-01) 471
 Casanova, F. (CE-04) 503
 Caspani, S. (JG-06) 1277
 Caspani, S. (JR-05) 1341
 Castell-Queralt, J. (GC-03) 940
 Castro, M. (ED-10) 756
 Cating-Subramanian, E. (EA-06) 714
 Cecchi, B.M. (DG-01) 667
 Cecchi, S. (DB-06) 610
 Cecchini, R. (DC-01) 617
 Cecchini, R. (DC-12) 628
 Celegato, F. (JF-11) 1268
 Celegato, F. (JU-06) 1381
 Centala, G. (EC-08) 739
 Céspedes-Berrocal, D. (CC-08) 478
 Céspedes, O. (DP-09) 687
 Ceylan, D. (BI-04) 278
 Chahed, L. (IR-02) 1143
 Chai, F. (AQ-03) 101
 Chai, F. (BP-09) 318
 Chai, F. (BQ-12) 341
 Chai, F. (BV-01) 426
 Chai, S. (BP-13) 323
 Chakraborty, A. (DC-02) 618
 Chambard, M. (GA-02) 915
 Chan, J. (CE-06) 505
 Chanda, A. (IG-06) 1093
 Chandramohan, S. (JF-09) 1265

- Chang, J. (BE-06) 230
- Chang, J. (FE-05) 862
- Chang, J. (IC-04) 1056
- Chang, J. (IC-05) 1057
- Chang, J. (JH-03) 1287
- Chang, K. (DB-04) 608
- Chang, L. (DF-12) 665
- Chang, Q. (JU-12) 1387
- Chang, T. (BU-07) 409
- Chang, T. (DC-03) 619
- Chang, Y. (CC-12) 482
- Chantrell, R.W. (FD-06) 854
- Chantrell, R.W. (FG-02) 869
- Chantrell, R.W. (HB-03) 977
- Chantrell, R.W. (JW-10) 1398
- Chao, W. (HA-05) 971
- Chao, X. (FP-03) 901
- Chapman, E. (JP-15) 1325
- Charipar, N. (AD-06) 65
- Charipar, N. (CS-03) 585
- Charipar, N. (CS-04) 586
- Charlier, J. (DB-02) 606
- Charlier, J. (DC-07) 623
- Charlton, T. (BE-04) 228
- Chashin, D.V. (AU-01) 162
- Chatelain, C. (ID-01) 1061
- Chatterjee, J. (GD-08) 958
- Chatterji, T. (JT-10) 1371
- Chatzimpaloglou, K. (CB-03) 466
- Chau, K. (AS-02) 136
- Chau, K. (AU-03) 164
- Chau, K. (BU-12) 415
- Chau, K. (BV-05) 431
- Chau, K. (BW-14) 452
- Chau, K. (BW-16) 454
- Chaudhary, R. (JI-06) 1302
- Chaudhary, V. (JA-05) 1193
- Chaudhary, V. (JA-08) 1196
- Chaudhary, V. (JB-03) 1206
- Chaudhary, V. (JB-04) 1207
- Chaudhary, V. (JB-06) 1209
- Chaudhary, V. (JB-07) 1210
- Chaudhary, V. (JI-06) 1302
- Chauleau, J. (CD-08) 493
- Chavent, A. (AC-06) 46
- Chdil, O. (JS-09) 1359
- Che Lah, N. (AC-07) 47
- Che, P. (ED-12) 759
- Che, P. (HC-07) 997
- Checceca, N. (JE-12) 1255
- Chechenin, N.G. (IR-14) 1155
- Checkati, S. (JH-05) 1289
- Cheenkundil, R. (AE-04) 74
- Chekanova, L. (JR-06) 1342
- Chen, B. (BW-11) 449
- Chen, C. (BT-04) 385
- Chen, D. (AS-11) 146
- Chen, D. (AS-13) 148
- Chen, D. (AS-14) 149
- Chen, D. (AS-15) 150
- Chen, D. (AS-16) 151
- Chen, G. (AT-05) 157
- Chen, G. (AU-09) 172
- Chen, G. (FG-03) 870
- Chen, H. (AB-02) 28
- Chen, H. (DG-04) 670
- Chen, H. (EQ-09) 799
- Chen, H. (FH-01) 884
- Chen, H. (GB-04) 926
- Chen, H. (HP-09) 1021
- Chen, J. (AP-04) 88
- Chen, J. (BB-04) 195
- Chen, J. (BJ-12) 300
- Chen, J. (CF-08) 520
- Chen, J. (ED-12) 759
- Chen, J. (GB-08) 931
- Chen, J. (IB-12) 1050
- Chen, J. (IF-04) 1082
- Chen, J. (IH-01) 1102
- Chen, J. (JB-08) 1211
- Chen, K. (AC-09) 49
- Chen, L. (BE-01) 225
- Chen, L. (BQ-02) 341
- Chen, L. (IQ-02) 1132
- Chen, L. (JB-10) 1213
- Chen, M. (BD-01) 211
- Chen, M. (BF-07) 239
- Chen, M. (BV-02) 427
- Chen, Q. (AR-17) 132
- Chen, S. (BE-05) 229
- Chen, T. (BP-09) 318
- Chen, T. (CC-02) 472
- Chen, T. (CC-10) 480
- Chen, T. (CC-12) 482
- Chen, T. (FH-05) 888
- Chen, W. (CS-07) 589
- Chen, W. (IQ-06) 1136
- Chen, W. (JY-15) 1439
- Chen, X. (BW-17) 455
- Chen, X. (FB-12) 835
- Chen, X. (HB-12) 987
- Chen, X. (HC-04) 994
- Chen, Y. (AQ-04) 102
- Chen, Y. (AR-04) 118
- Chen, Y. (AS-09) 144
- Chen, Y. (AU-11) 174
- Chen, Y. (AV-05) 183
- Chen, Y. (BR-09) 355
- Chen, Y. (BU-03) 405
- Chen, Y. (BU-04) 406
- Chen, Y. (BU-05) 407
- Chen, Y. (CF-09) 522
- Chen, Y. (CS-09) 591
- Chen, Z. (AR-06) 120
- Chen, Z. (FA-03) 817
- Chen, Z. (FC-05) 843
- Chen, Z. (IP-09) 1126
- Cheng, C. (BW-03) 440
- Cheng, C. (JG-09) 1280
- Cheng, H. (CC-03) 473
- Cheng, H. (CF-08) 520
- Cheng, H. (IH-01) 1102
- Cheng, J. (CP-12) 553
- Cheng, L. (BE-06) 230
- Cheng, L. (BR-02) 348
- Cheng, L. (BR-07) 353
- Cheng, Q. (IA-08) 1033
- Cheng, S. (AQ-02) 100
- Cheng, W. (BC-02) 205
- Cheng, W. (BQ-02) 330
- Cheng, W. (IQ-01) 1131
- Cheng, X. (AE-12) 82
- Cheng, Y. (FG-15) 882
- Cheng, Z. (CS-06) 588
- Chengkun, S. (HC-10) 1000
- Chérif, S. (IR-02) 1143
- Cherif, S.M. (IR-01) 1142
- Cherkasskii, M. (FD-07) 855
- Chernichenko, A. (IR-17) 1158
- Chernov, S.V. (FH-13) 896
- Chernyshov, D. (DF-06) 658
- Cherubini, G. (IA-09) 1034
- Chiba, M. (JR-01) 1337
- Chichkov, V. (DP-08) 686
- Chigarev, S. (FP-02) 900
- Chikaki, S. (JG-02) 1273
- Childress, J.R. (IB-07) 1045
- Childress, J.R. (IR-12) 1153
- Chin, J. (AU-10) 173
- Ching, T. (BT-05) 386
- Ching, T. (BV-05) 431
- Chinnasamy, C. (BE-03) 227
- Chinnasamy, K. (JP-02) 1312
- Chiriac, H. (IS-03) 1164
- Chiriac, H. (IT-07) 1185
- Chiriac, H. (JP-03) 1313
- Chiriac, H. (JW-08) 1396
- Chiriac, H. (JY-04) 1427
- Chistyakov, V. (DB-11) 615
- Cho, H. (AQ-07) 105
- Cho, H. (BQ-10) 339
- Cho, H. (BR-06) 352
- Cho, H. (BS-04) 369
- Cho, H. (BV-09) 435
- Cho, K. (DC-02) 618
- Cho, Y. (IH-09) 1110
- Choi, G. (CP-14) 555
- Choi, H. (DQ-06) 697
- Choi, H. (DQ-07) 698
- Choi, H. (JQ-04) 1330
- Choi, H. (JQ-05) 1331
- Choi, H. (JY-17) 1441
- Choi, H. (JY-18) 1442
- Choi, J. (AP-12) 96
- Choi, J. (AQ-07) 105
- Choi, J. (AU-08) 171
- Choi, J. (BQ-05) 334
- Choi, J. (BQ-06) 335
- Choi, J. (BQ-09) 338
- Choi, J. (BQ-10) 339
- Choi, J. (BR-06) 352
- Choi, J. (BS-01) 365
- Choi, J. (BS-02) 366

Choi, J. (BS-04)	369	Constantin, C. (JP-11)	1321	da Costa Neves, C.G. (BF-08)	240
Choi, J. (BS-07)	372	Cooke, G. (BF-04)	236	da Costa Neves, C.G. (BG-14)	261
Choi, J. (BV-07)	433	Cooke, G. (BF-13)	246	da Costa Neves, C.G. (BG-15)	262
Choi, J. (BV-09)	435	Cooper, J.F. (GA-02)	915	Dai, L. (BR-03)	349
Choi, M. (JD-04)	1234	Cooper, N.R. (AA-03)	22	Dai, L. (BR-11)	357
Choi, M. (JD-07)	1237	Corodeanu, S. (IS-03)	1164	Dai, Q. (IA-08)	1033
Choi, S. (DP-03)	681	Corodeanu, S. (JY-04)	1427	Dalganan, A. (BE-04)	228
Choi, W. (CC-01)	471	Coronado, E. (DB-03)	607	Damas, H. (CC-08)	478
Choi, Y. (CB-03)	466	Correa, D.C. (ER-05)	805	Damian, A. (IS-03)	1164
Choi, Y. (DP-03)	681	Correa, E. (AC-13)	53	Damnjanovic, M. (IS-12)	1173
Choi, Y. (DP-05)	683	Cortés, D. (HP-07)	1019	Dang, T. (FB-01)	822
Choi, Y. (JP-04)	1314	Cosset-Cheneau, M. (CD-06)	491	Daniels, B. (BI-04)	278
Choi, Y. (YB-03)	15	Cosset-Cheneau, M. (CD-11)	496	Daniels, M. (GA-04)	918
Chopdekar, R. (FG-15)	882	Cosset-Cheneau, M. (CD-13)	498	Daniels, M. (GB-12)	935
Chowdhury, B. (ID-09)	1069	Cosset-Cheneau, M. (DC-11)	627	Danila, R. (JP-11)	1321
Chshiev, M. (CB-02)	465	Cosset-Cheneau, M. (FE-02)	859	Danilyuk, A.L. (JI-07)	1303
Chshiev, M. (CB-05)	468	Costa-Krämer, J. (DF-02)	654	Dao, D. (CQ-11)	569
Chshiev, M. (CF-04)	516	Costa, R. (JT-06)	1367	Dao, D. (CR-09)	579
Chshiev, M. (DF-02)	654	Costache, M.V. (DA-03)	600	Dao, D. (IT-01)	1179
Chshiev, M. (IP-10)	1127	Couet, S. (CF-12)	525	Darcheville, M.S. (JX-04)	1411
Chchelkatchev, N. (DG-09)	675	Couet, S. (CG-13)	539	Das, A.K. (JE-10)	1253
Chubykalo-Fesenko, O. (AE-08)	78	Couet, S. (GD-09)	959	Das, P. (ED-15)	762
Chubykalo-Fesenko, O. (FD-06)	854	Cowburn, R. (JI-05)	1301	Das, P. (HP-08)	1020
Chubykalo-Fesenko, O. (FG-02)	869	Cramer, J. (FD-03)	851	Das, S. (JQ-08)	1334
Chubykalo-Fesenko, O. (HB-03)	977	Crespo, H. (FC-07)	845	Dash, S.P. (DC-04)	620
Chubykalo-Fesenko, O. (HP-07)	1019	Crespo, H. (JP-05)	1315	Datskaya, Z. (DP-06)	684
Chubykalo-Fesenko, O. (IG-04)	1091	Cros, V. (CC-08)	478	Davies, J. (IB-08)	1046
Chubykalo-Fesenko, O. (JI-02)	1298	Cros, V. (CC-11)	481	Davino, D. (JF-07)	1263
Chue, E. (HB-12)	987	Cros, V. (DD-10)	640	Davino, D. (JU-03)	1378
Chuhan, L. (FP-13)	911	Cros, V. (EB-02)	717	Davydenko, A. (CB-01)	464
Chumak, A. (ED-11)	757	Cros, V. (ED-03)	749	Davydenko, A. (IH-06)	1107
Chumak, A. (EE-04)	767	Cros, V. (ED-07)	753	Dawidek, R. (GA-02)	915
Chung, H. (CE-06)	505	Cros, V. (HC-02)	991	Dawidek, R. (GB-03)	925
Churikova, A. (FH-04)	887	Cros, V. (HC-09)	999	De Graef, M. (AB-08)	34
Churikova, A. (FH-07)	890	Cros, V. (IB-04)	1042	De Graef, M. (GD-06)	956
Ciambelli, P. (JR-12)	1348	Cros, V. (ID-08)	1068	De Graef, M. (IG-03)	1090
Cideciyan, R.D. (IA-09)	1034	Cros, V. (JA-12)	1201	de Julian Fernandez, C. (JD-11)	1241
Ciftija, O. (DQ-05)	696	Crotti, D. (CF-12)	525	de Julian Fernandez, C. (JR-11)	1347
Ciprian, C. (HC-04)	994	Crotti, D. (CG-13)	539	de la Barrière, O. (JB-11)	1214
Ciubotaru, F. (EC-07)	738	Cubukcu, M. (DC-09)	625	De La Figuera, J. (IH-12)	1113
Clark, A.T. (AE-12)	82	Cubukcu, M. (HC-06)	996	De La Figuera, J. (IR-04)	1145
Clement, S. (YA-06)	11	Cui, C. (GB-02)	924	de la Presa, P. (JH-10)	1294
Clendenning, S. (DA-04)	601	Cui, C. (HD-01)	1003	de Loubens, G. (EA-04)	712
Clénet, S. (BH-05)	268	Cui, S. (HP-01)	1013	de Loubens, G. (EB-02)	717
Coaquira, J.A. (JA-13)	1202	Cui, W. (BG-11)	258	de Loubens, G. (ED-04)	750
Coatney, M.D. (JU-11)	1386	Cui, X. (AS-15)	150	de Loubens, G. (FP-06)	904
Coene, A. (JG-03)	1274	Cui, X. (AS-16)	151	de Loubens, G. (HC-09)	999
Coene, A. (JH-09)	1293	Curtí, M. (AS-10)	145	de Matos Gomes, E. (DB-01)	605
Coester, B. (CD-03)	488	Curto, D. (BD-04)	215	de Melo, C. (DD-10)	640
Cogulu, E. (CF-09)	522	Cussac, S. (AC-06)	46	de Melo, C. (DE-03)	644
Cogulu, E. (FG-15)	882	Cutugno, F. (FD-02)	850	De Moro do Carmo, C. (ER-10)	810
Coisson, M. (JF-11)	1268	Czettel, C. (AD-04)	63	De Riz, A. (DD-05)	635
Coisson, M. (JU-06)	1381			De Riz, A. (DD-06)	636
Collin, S. (CC-11)	481			De Riz, A. (DD-08)	638
Collin, S. (DB-02)	606			de Rojas, J. (DF-02)	654
Collin, S. (HC-02)	991			de Souza Batalha, R.M. (ER-05)	805
Collin, S. (IQ-08)	1138			de Souza Batalha, R.M. (ER-10)	810
Collingwood, J. (YA-03)	8	d'Aquino, M. (EB-11)	727	De Teresa, J. (EB-02)	717
Conduit, G.J. (JB-06)	1209	d'Aquino, M. (FD-08)	856	De Teresa, J. (JI-04)	1300
Conduit, G.J. (JB-07)	1210	d'Aquino, M. (GC-04)	941	de Toro, J. (IH-08)	1109
Connell, L. (AE-06)	76	d'Aquino, M. (GC-10)	948	de Vicente, J. (JD-09)	1239
		D'Souza, S. (FH-13)	896		

- de Vicente, J. (YB-01) 13
- De Zoysa Karunathilaka, V. (CC-09) 479
- Deflley, R. (IT-08) 1186
- DeHerrera, M. (CF-01) 513
- Del Pizzo, A. (BJ-14) 302
- del Real, R. (JI-02) 1298
- Del Rose, T. (JT-06) 1367
- Del-Valle, N. (GC-03) 940
- Delgado Soria, G. (IR-04) 1145
- Delprat, S. (IQ-08) 1138
- Demaille, D. (JI-12) 1308
- Deman, A. (JH-01) 1285
- Demeter, L. (BP-15) 325
- Demidov, V.E. (EA-02) 710
- Demidov, V.E. (ED-07) 753
- Demidov, V.E. (EE-08) 771
- Demidov, V.E. (FB-05) 828
- Demidov, V.E. (FG-03) 870
- Demir, J. (ER-11) 811
- Demir, Y. (BG-04) 251
- Demokritov, S. (EA-02) 710
- Demokritov, S. (ED-07) 753
- Demokritov, S.O. (EE-08) 771
- Demokritov, S.O. (FB-05) 828
- Demokritov, S.O. (FG-03) 870
- Dempsey, N. (JC-04) 1221
- Dempsey, N. (JD-03) 1233
- Dempsey, N. (JW-12) 1400
- Dendooven, J. (DF-02) 654
- Deng, C. (BQ-13) 342
- Deng, H. (AC-17) 57
- Deng, H. (DG-04) 670
- Deng, J. (AS-01) 135
- Deng, Z. (BC-02) 205
- Deng, Z. (BE-05) 229
- Deng, Z. (BQ-02) 330
- Denisova, E. (JR-06) 1342
- Dennis, C. (AC-13) 53
- Derzhavin, I. (DP-06) 684
- Descamps, L. (JH-01) 1285
- Desplat, L. (GC-01) 938
- Desplat, L. (HA-06) 973
- Detavernier, C. (DF-02) 654
- Devillers, T. (JC-04) 1221
- Devillers, T. (JW-12) 1400
- Devlin, E. (JC-07) 1224
- Devolder, T. (DD-10) 640
- Devolder, T. (HB-06) 980
- Devolder, T. (HC-09) 999
- Dhesi, S. (GA-02) 915
- Dhesi, S. (GB-03) 925
- Dhillon, S. (FB-01) 822
- Dhiman, A.K. (IH-03) 1104
- Di Pietro Martinez, M. (IG-08) 1095
- Di Ventra, M. (GB-13) 936
- Di, C. (AP-10) 94
- Di, C. (AQ-05) 103
- Di, C. (AU-09) 172
- Di, C. (BW-02) 439
- Di, C. (CR-03) 573
- Diab, H. (BD-11) 223
- Diallo, L. (JF-11) 1268
- Diao, K. (BW-07) 444
- Díaz-Caballero, E. (YA-01) 6
- Díaz-García, Á. (JE-01) 1243
- Díaz-García, Á. (JE-08) 1251
- Díaz-García, Á. (JE-09) 1252
- Díaz-Sánchez, L.E. (JW-13) 1401
- Díaz, J. (EC-05) 736
- Díaz, S.A. (HC-08) 998
- Dieny, B. (AE-07) 77
- Dieny, B. (CF-04) 516
- Dieny, B. (CF-06) 518
- Dieny, B. (CF-07) 519
- Dieny, B. (CF-11) 524
- Dieny, B. (CG-03) 529
- Dieny, B. (ED-10) 756
- Dieny, B. (ER-06) 806
- Dieny, B. (ID-07) 1067
- Diep, H.T. (HD-07) 1009
- Diez, J.M. (DB-09) 613
- Diez, J.M. (IG-11) 1099
- Diez, J.M. (IH-14) 1115
- Diez, J.M. (IR-16) 1157
- Diez, L.H. (FE-09) 866
- Diko, P. (JR-03) 1339
- Dimier, T. (BJ-01) 288
- Dimoulas, A. (DC-01) 617
- Din, E. (CG-05) 531
- Ding, B. (HB-09) 983
- Ding, B. (IF-04) 1082
- Ding, H. (CP-10) 551
- Ding, H. (CP-12) 553
- Ding, J. (CP-12) 553
- Ding, S. (FG-06) 873
- Ding, X. (ER-07) 807
- Ding, Y. (AR-04) 118
- Ding, Z. (AT-08) 160
- Dinh, C. (CQ-11) 569
- Dinh, C. (CR-09) 579
- Dinh, C. (IT-01) 1179
- Diop, L. (DQ-04) 695
- Dirba, I. (JC-05) 1222
- Disch, S. (JI-09) 1305
- Dittrich, F. (HC-10) 1000
- Divinskiy, B. (EA-02) 710
- Divinskiy, B. (ED-07) 753
- Divinskiy, B. (EE-08) 771
- Divinskiy, B. (FB-05) 828
- Divinskiy, B. (FG-03) 870
- Dizhur, S. (FB-03) 824
- Dlubak, B. (DB-02) 606
- Dlubak, B. (DB-03) 607
- do Carmo Resende, Ú. (ER-05) 805
- Doan, V. (CQ-11) 569
- Doan, V. (CR-09) 579
- Doan, V. (IT-01) 1179
- Dobročka, E. (JX-01) 1408
- Dobrogoski, W. (IH-03) 1104
- Dobrovolskiy, O. (EC-02) 733
- Dobrovolskiy, O. (ED-11) 757
- Dohi, T. (FG-05) 872
- Dohi, T. (HC-10) 1000
- Dohi, T. (IH-03) 1104
- Dolezal, P. (FG-08) 875
- Dolgoplova, M.V. (JR-06) 1342
- Dolisy, B. (BA-03) 187
- Doludenko, I. (FP-02) 900
- Domac, B.H. (JH-02) 1286
- Domann, J.P. (JF-06) 1262
- Domann, J.P. (JF-08) 1264
- Domozhirova, A. (DB-11) 615
- Dong, G. (JB-01) 1204
- Dong, H. (IB-09) 1047
- Dong, J. (CP-07) 547
- Dong, K. (CP-02) 542
- Dong, K. (CP-08) 548
- Dong, K. (GP-05) 965
- Dong, K. (HP-06) 1018
- Dong, K. (IQ-04) 1134
- Dong, K. (IS-16) 1177
- Dong, K. (JY-07) 1430
- Dong, X. (BU-10) 413
- Dong, Y. (HA-05) 971
- Donnelly, C. (AA-03) 22
- Donnelly, C. (JI-05) 1301
- Dorrell, D.G. (AS-01) 135
- Doshita, H. (IA-09) 1034
- Dosoudil, R. (JX-01) 1408
- Dou, R. (JX-14) 1421
- Dou, Y. (CQ-06) 564
- Dou, Y. (CQ-07) 565
- Dou, Y. (JX-15) 1422
- Doucet, M. (BE-04) 228
- Dounia, S. (IB-07) 1045
- Dragan, R. (BF-03) 235
- Dragan, R. (BF-04) 236
- Dragan, R. (BF-13) 246
- Dragos-Pinzaru, O. (IT-07) 1185
- Draxler, K. (IT-09) 1187
- Drossel, W. (JC-03) 1220
- Drouhin, M. (GA-02) 915
- Drozd, P. (IG-07) 1094
- Drozd, P. (IH-10) 1111
- Drozd, P. (IH-11) 1112
- Du, B. (CR-07) 577
- Du, H. (JB-10) 1213
- Du, J. (FC-05) 843
- Du, J. (IS-09) 1170
- Du, W. (AR-11) 126
- Du, Y. (AU-12) 175
- Du, Y. (BQ-13) 342
- Du, Y. (BR-05) 351
- Du, Y. (CR-08) 578
- Duan, N. (CS-10) 592
- Dubois, S.M. (DB-02) 606
- Dubs, C. (ED-11) 757
- Dubs, C. (EE-04) 767
- Ducharme, B. (AD-09) 68
- Ducharme, B. (AD-10) 69
- Ducharme, B. (JG-04) 1275
- Ducreux, J. (JB-13) 1216
- Ducruet, C. (IR-12) 1153

Dumas, R.K. (IC-07)	1059
Dumesnil, K. (ID-01)	1061
Dupé, B. (HA-06)	973
Dupé, B. (HA-02)	968
Dupont, P. (JB-12)	1215
Dupuis, V. (JD-03)	1233
Dupuis, V. (JI-11)	1307
Dupuis, V. (JW-13)	1401
Dupuy, J. (JB-12)	1215
Duquesne, J. (FB-10)	833
Durbha, R. (ID-11)	1071
Durin, G. (FE-09)	866
Durr, H. (FD-05)	853
Durrenfeld, P. (FB-08)	831
Dutta, R. (DF-06)	658
Dutta, T. (FH-03)	886
DuttaGupta, S. (CC-09)	479
DuttaGupta, S. (FG-05)	872
Dyachkova, T. (JT-03)	1364
Dzhun, I.O. (IR-14)	1155
Dzubinska, A. (DQ-01)	692
Dzubinska, A. (JE-04)	1247

- E -

Eames, P. (IB-08)	1046
Ebels, U. (EA-04)	712
Ebels, U. (ED-10)	756
Ebels, U. (ER-06)	806
Ebels, U. (IB-04)	1042
Ebels, U. (ID-07)	1067
Ebels, U. (ID-08)	1068
Ebermann, P. (IA-09)	1034
Ebert, H. (CD-04)	489
Eda, G. (DA-06)	603
Eda, G. (DC-03)	619
Eggert, B. (IA-03)	1028
Ehrler, J. (FB-02)	823
Ehrlich, A. (AD-06)	65
Ehrlich, J. (YB-04)	16
Eichenberger, L. (DQ-04)	695
Eimer, S.R. (IH-01)	1102
Eisebitt, S. (AB-05)	31
Eisebitt, S. (HA-02)	968
Ekomasov, A. (CS-02)	584
Ekomasov, E.G. (CS-02)	584
Ekomasov, E.G. (EQ-08)	798
El Hamdi, A. (CD-08)	493
El Kanj, A. (ED-03)	749
El maalam, K. (JS-09)	1359
ElBidweihy, H. (JP-15)	1325
Ellis, M.O. (FD-06)	854
Ellis, M.O. (GA-02)	915
Ellis, M.O. (GB-04)	926
Ellis, M.O. (GB-09)	932
Ellis, M.O. (GB-11)	934
Elmers, H. (FH-13)	896
Elphick, K. (CE-03)	502
Elphick, K. (CG-06)	532
Elphick, K. (IE-02)	1074

Emelyanova, S. (JT-03)	1364
Emerenciano Santos, H. (BG-14)	261
Encica, L. (BA-02)	186
Encomendero, J. (IH-09)	1110
Endo, H. (DP-04)	682
Endo, Y. (CC-09)	479
Endo, Y. (EE-05)	768
Endo, Y. (FB-09)	832
Endo, Y. (FP-11)	909
Endo, Y. (JY-05)	1428
Endoh, T. (CC-09)	479
Endoh, T. (CF-03)	515
Endoh, T. (CF-05)	517
Endoh, T. (CG-07)	533
Ener, S. (JE-02)	1244
Engel, D. (HA-02)	968
Enger, L. (IB-05)	1043
Ensinger, W. (GD-02)	952
Epicier, T. (JD-03)	1233
Eremin, E. (DQ-08)	699
Eremin, M. (DF-11)	664
Eriksson, O. (JD-02)	1232
Eroglu, A. (ID-09)	1069
Erohkin, S. (JD-11)	1241
Escoda-Torroella, M. (JH-07)	1291
Escoda-Torroella, M. (JH-08)	1292
Eserig, J. (HP-07)	1019
Esien, K. (AE-06)	76
Esien, K. (DG-10)	676
Eskandari, H. (BH-04)	267
Espanet, C. (AC-12)	52
Esquinzai, P.D. (GC-11)	949
Estemirova, S. (DP-06)	684
Evans, R.F. (FD-06)	854
Evans, R.F. (FG-02)	869
Evans, R.F. (JW-10)	1398
Everaert, K. (AC-08)	48
Evstigneeva, S. (JY-03)	1426
Exl, L. (GC-06)	943
Ezawa, M. (HD-07)	1009

- F -

Fabbrici, S. (JE-09)	1252
Fabian, J. (DC-13)	629
Facio, J. (JX-06)	1413
Fagan, P. (AD-09)	68
Fan, D. (AQ-12)	111
Fan, D. (BB-01)	192
Fan, W. (BP-08)	317
Fan, X. (BJ-06)	294
Fan, X. (FH-09)	892
Fan, Y. (BG-13)	260
Fan, Z. (JW-04)	1392
Fang, C. (CB-01)	464
Fang, C. (CP-07)	547
Fang, C. (CP-11)	552
Fang, C. (FB-12)	835
Fang, C. (GP-02)	962
Fang, D. (AS-11)	146

Fang, S. (BT-03)	384
Fang, X. (JQ-03)	1329
Fang, Y. (BI-06)	281
Fang, Y. (BU-13)	417
Fang, Y. (BU-15)	419
Fangohr, H. (DD-04)	634
Fangohr, H. (GC-05)	942
Faria Junior, P.E. (DC-13)	629
Fariborzi, H. (GB-06)	929
Farle, M. (FB-02)	823
Farle, M. (FD-07)	855
Fassatoui, A. (FE-08)	865
Fassatoui, A. (HB-07)	981
Fassatoui, A. (HB-08)	982
Fassbender, J. (GD-04)	954
Faupel, F. (IB-02)	1040
Favaro, F. (AB-11)	38
Fecher, G. (IA-11)	1036
Fecova, L. (JR-08)	1344
Fedchenko, O. (FH-13)	896
Felser, C. (CA-05)	461
Felser, C. (DC-06)	622
Felser, C. (HP-02)	1014
Felser, C. (IA-11)	1036
Felton, S. (AE-06)	76
Felton, S. (DG-10)	676
Feng, J. (CC-05)	475
Feng, L. (BW-05)	442
Feng, L. (JD-08)	1238
Feng, S. (BU-10)	413
Feng, X. (BS-10)	375
Feng, Y. (AB-09)	36
Feng, Y. (AP-07)	91
Feng, Y. (AQ-01)	99
Feng, Z. (AS-01)	135
Fermon, C. (IB-04)	1042
Fernández Cuñado, J.L. (IG-11)	1099
Fernández González, C. (DD-07)	637
Fernández González, C. (JD-11)	1241
Fernandez Scarioni, A. (GA-05)	919
Fernandez-Pacheco, A. (JI-04)	1300
Fernandez-Pacheco, A. (JI-05)	1301
Fernandez-Roldan, J. (IG-04)	1091
Fernandez-Roldan, J. (JI-02)	1298
Fernández, M.A. (JH-03)	1287
Ferrara, E. (JB-11)	1214
Ferreira, A.H. (ER-05)	805
Ferreira, R. (DD-09)	639
Ferreira, R. (ER-08)	808
Ferreira, R. (ID-08)	1068
Ferrer, S. (CQ-08)	566
Ferroudj, A. (DQ-02)	693
Fert, A. (CB-05)	468
Fert, A. (CC-08)	478
Fert, A. (CC-11)	481
Fert, A. (DB-02)	606
Fert, A. (HC-02)	991
Fetisov, L.Y. (AU-01)	162
Fetisov, Y.K. (AU-01)	162
Fiebig, M. (CE-04)	503
Fil'chenkov, I. (EQ-04)	794

- Filianina, M. (FG-06) 873
 Filipe Horto Belo da Silva, J. (DB-01) 605
 Fillion, C. (HB-07) 981
 Fillion, C. (HP-04) 1016
 Finazzi, M. (CB-05) 468
 Finco, A. (AB-11) 38
 Finizio, S. (AA-03) 22
 Finizio, S. (DD-05) 635
 Finizio, S. (ED-05) 751
 Finizio, S. (HA-01) 967
 Finizio, S. (JI-01) 1297
 Finkel, P. (DF-04) 656
 Finkel, P. (IB-03) 1041
 Finkel, P. (JF-05) 1261
 Finkel, P. (JF-13) 1270
 Finocchio, G. (FD-02) 850
 Finocchio, G. (FG-06) 873
 Finocchio, G. (HA-03) 969
 Finocchio, G. (HA-05) 971
 Finocchio, G. (HC-11) 1001
 Fiorillo, F. (JB-11) 1214
 Fischbacher, J. (AD-04) 63
 Fischer, H. (ID-01) 1061
 Fischer, J. (AB-11) 38
 Fisher, E. (GC-08) 945
 Fix, M. (FA-05) 819
 Flajšman, L. (ED-05) 751
 Flament, S. (IB-05) 1043
 Flatau, A. (YB-06) 18
 Flores Filho, A.F. (BF-08) 240
 Flores Filho, A.F. (BG-14) 261
 Flores Filho, A.F. (BG-15) 262
 Flores-Zúñiga, H. (JT-01) 1362
 Fnidiki, A. (JF-11) 1268
 Foerster, M. (DD-07) 637
 Foerster, M. (FH-06) 889
 Foerster, M. (GA-02) 915
 Foerster, M. (GB-03) 925
 Foerster, M. (HD-04) 1006
 Foerster, M. (IH-12) 1113
 Foerster, M. (JI-02) 1298
 Fong, C. (DP-11) 689
 Fontana, E. (JW-12) 1400
 Forestier, G. (FH-02) 885
 Forment-Aliaga, A. (DB-03) 607
 Förster, J. (ED-05) 751
 Fortin, J. (JB-12) 1215
 Foury, P. (EC-12) 743
 Fraile Rodríguez, A. (IG-01) 1088
 Fraile Rodríguez, A. (JH-07) 1291
 Fraile Rodríguez, A. (JH-08) 1292
 Fraile Rodríguez, A. (JI-02) 1298
 Francis, F. (DP-02) 680
 Franco, V. (DP-01) 679
 Franco, V. (JE-01) 1243
 Franco, V. (JE-07) 1250
 Franco, V. (JE-08) 1251
 Franco, V. (JE-09) 1252
 Francoual, S. (AC-11) 51
 Franke, K.J. (FE-03) 860
 Franklin, J.D. (DC-10) 626
 Franzitta, V. (BD-04) 215
 Freimuth, F. (FD-03) 851
 Freimuth, F. (FD-04) 852
 Freimuth, F. (FH-10) 893
 Freindl, K. (IR-04) 1145
 Freitas, P.P. (DD-09) 639
 Freitas, S.C. (JP-05) 1315
 Freudenberger, J. (JW-14) 1402
 Friedman, J.S. (GB-02) 924
 Frost, W. (CG-06) 532
 Fruchart, O. (CG-03) 529
 Fruchart, O. (DD-05) 635
 Fruchart, O. (DD-06) 636
 Fruchart, O. (DD-07) 637
 Fruchart, O. (DD-08) 638
 Fruchart, O. (GD-02) 952
 Fruchart, O. (HB-08) 982
 Fry, P. (GA-02) 915
 Fry, P. (GB-03) 925
 Fu, C. (IQ-10) 1140
 Fu, J. (CS-07) 589
 Fu, J. (ER-07) 807
 Fu, J. (JY-15) 1439
 Fu, W. (AP-01) 85
 Fu, W. (BS-03) 367
 Fu, W. (BU-03) 405
 Fu, W. (BU-04) 406
 Fu, W. (BU-05) 407
 Fu, W. (BU-11) 414
 Fu, W. (BU-16) 420
 Fu, W. (BU-17) 421
 Fu, W. (BU-18) 422
 Fu, W. (JY-14) 1438
 Fu, Y. (CD-11) 496
 Fu, Y. (CQ-06) 564
 Fu, Y. (CQ-07) 565
 Fu, Y. (DC-11) 627
 Fuad, A. (EA-04) 712
 Fuhrmann, F. (FG-06) 873
 Fujii, J. (DB-06) 610
 Fujisaki, K. (JA-11) 1199
 Fujisaki, K. (TU-02) 3
 Fujiwara, K. (CD-09) 494
 Fujiwara, S. (JP-08) 1318
 Fukami, S. (CC-09) 479
 Fukami, S. (CG-01) 527
 Fukami, S. (CG-02) 528
 Fukami, S. (FC-09) 847
 Fukami, S. (FD-01) 849
 Fukami, S. (FG-05) 872
 Fukami, S. (GB-10) 933
 Fukami, S. (IH-03) 1104
 Fukushima, A. (CD-10) 495
 Fukushima, A. (GB-07) 930
 Fukushima, A. (IB-04) 1042
 Fukushima, A. (IH-04) 1105
 Fulara, H. (FB-08) 831
 Fullerton, E. (HD-09) 1011
 Funabashi, N. (JS-04) 1354
 Funatsu, T. (GB-10) 933
 Furrer, S. (IA-09) 1034
 Fusil, S. (AB-11) 38
 Fusil, S. (ED-02) 748
 Futamoto, M. (JD-05) 1235
- G -
- G. V., V. (DP-02) 680
 Gabay, A. (JC-06) 1223
 Gabor, M. (IQ-05) 1135
 Gabor, M. (IR-01) 1142
 Gabsi, M. (BA-06) 190
 Gaida, J. (HA-02) 968
 Galanakis, I. (DP-01) 679
 Galbiati, M. (DB-02) 606
 Galbiati, M. (DB-03) 607
 Galceran, R. (DB-03) 607
 Galdun, L. (DQ-01) 692
 Galdun, L. (IC-03) 1055
 Galdun, L. (JR-03) 1339
 Galdun, L. (JT-04) 1365
 Galdun, L. (JT-05) 1366
 Gallas, B. (JI-12) 1308
 Galluzzi, A. (JR-12) 1348
 Galve, F. (YA-01) 6
 Gambardella, P. (CC-06) 476
 Gambardella, P. (CC-13) 483
 Gambardella, P. (CD-11) 496
 Gambardella, P. (CE-04) 503
 Gambardella, P. (HB-06) 980
 Gambarelli, S. (CD-11) 496
 Gamecova, J. (IC-03) 1055
 Gan, Q. (BU-13) 417
 Gan, W. (CD-03) 488
 Gan, W. (HB-04) 978
 Gan, W. (JA-05) 1193
 Gandha, K. (JC-08) 1225
 Gandha, K. (JU-10) 1385
 Gao, J. (AR-11) 126
 Gao, J. (BP-16) 326
 Gao, J. (BR-03) 349
 Gao, J. (BR-11) 357
 Gao, J. (CE-04) 503
 Gao, L. (AR-17) 132
 Gao, L. (JX-13) 1420
 Gao, P. (ED-12) 759
 Gao, Q. (IQ-10) 1140
 Gao, T. (CE-12) 511
 Gao, X. (BJ-04) 292
 Gao, Y. (CS-11) 593
 Gao, Z. (IP-12) 1129
 García del Muro, M. (IG-01) 1088
 García del Muro, M. (JH-07) 1291
 García Hernández, M. (JD-11) 1241
 García-Arribas, A. (JF-12) 1269
 García-Sánchez, F. (GA-05) 919
 García-Soriano, D. (JG-05) 1276
 García, C. (FC-04) 842
 García, C. (FC-07) 845
 García, F. (JE-12) 1255
 García, J. (JG-04) 1275

Garcia, J.H. (CB-06)	469	Gillon, F. (BJ-11)	299	Gosavi, T. (CC-01)	471
Garcia, J.H. (DA-03)	600	Gilroy, E.R. (IH-13)	1114	Gosavi, T. (DA-04)	601
Garcia, V. (AB-11)	38	Giordano, A. (HA-03)	969	Goss, G. (JQ-02)	1328
Garcia, V. (ED-02)	748	Giordano, A. (HC-11)	1001	Gossuin, Y. (JR-10)	1346
Garello, K. (AC-06)	46	Giraud, A. (BJ-08)	296	Goto, M. (GA-03)	917
Garello, K. (CF-12)	525	Giri, A. (JE-07)	1250	Gotoh, Y. (IC-02)	1054
Garello, K. (CG-13)	539	Giri, A. (JE-08)	1251	Gotoh, Y. (IS-15)	1176
Garello, K. (FE-02)	859	Gjokas, M. (JC-07)	1224	Gottschall, T. (JE-02)	1244
Garello, K. (GD-09)	959	Gladii, O. (FH-02)	885	Gouchi, J. (JT-11)	1372
Gargiani, P. (DB-04)	608	Gliga, S. (AA-03)	22	Gouchi, J. (JX-07)	1414
Gariglio, S. (CD-08)	493	Gliniors, B. (CD-04)	489	Gouéré, D. (EB-02)	717
Garst, M. (HB-10)	984	Gloskovskii, A. (FH-13)	896	Gouéré, D. (ED-02)	748
Garten, L. (DF-04)	656	Glowinski, H. (EC-08)	739	Gouéré, D. (ED-03)	749
Gassmann, J. (JC-02)	1219	Go, D. (CE-12)	511	Gouéré, D. (ED-07)	753
Gatel, C. (GA-05)	919	Go, D. (FH-10)	893	Gouéré, D. (JA-12)	1201
Gatel, C. (JI-04)	1300	Go, G. (EC-10)	741	Goux, L. (CF-12)	525
Gaudin, G. (HB-07)	981	Göbel, B. (FG-01)	868	Grachev, A. (EC-04)	735
Gaudin, G. (HC-05)	995	Göbel, B. (HD-03)	1005	Grachev, A. (EQ-04)	794
Gaudin, G. (HD-04)	1006	Göbel, B. (HP-02)	1014	Grachev, A. (EQ-07)	797
Gaudry, E. (JF-03)	1259	Godel, F. (DB-02)	606	Graczyk, P. (EC-08)	739
Gaviko, V. (JT-09)	1370	Godel, F. (DB-03)	607	Gradhand, M. (IH-13)	1114
Gavriloaea, P.I. (HB-03)	977	Godel, F. (IQ-08)	1138	Gräfe, J. (AA-01)	20
Gavrilov, S. (DF-09)	662	Godinho, J. (AB-04)	30	Graham, D. (FB-13)	836
Ge, H. (BP-17)	327	Goennenwein, S.T. (FG-08)	875	Graham, S. (BF-04)	236
Ge, J. (IB-09)	1047	Goennenwein, S.T. (FH-08)	891	Gramage, C. (YA-01)	6
Ge, Q. (BS-08)	373	Goforth, M.E. (JF-06)	1262	Granados Miralles, C. (JD-11)	1241
Ge, Y. (BH-02)	265	Goforth, M.E. (JF-08)	1264	Grassi, M. (EB-03)	718
Ge, Y. (FG-05)	872	Goldys, E. (YA-06)	11	Grau-Ruiz, D. (YA-01)	6
Ge, Y. (HC-10)	1000	Golubeva, E. (IB-02)	1040	Graulich, D. (AC-11)	51
Ge, Y. (JE-05)	1248	Gomes Rolo, A. (DB-01)	605	Greaves, S. (GP-03)	963
Gegenwart, P. (DG-04)	670	Gomez-Perez, J. (CE-04)	503	Greenblatt, M. (DF-07)	659
Géhanne, P. (AE-02)	72	Gomez, C. (FH-02)	885	Greer, J.A. (FH-04)	887
Geilen, M. (EB-03)	718	Gomez, G. (CR-05)	575	Greer, J.A. (FH-07)	890
Geng, H. (JW-04)	1392	Gómez, J. (FB-06)	829	Greneche, J. (JX-04)	1411
Geng, L. (BV-01)	426	Gómez, J. (FC-04)	842	Greve, D.W. (JA-04)	1192
Geng, W. (AR-05)	119	Gomonay, O. (FD-04)	852	Grezes, C. (CD-11)	496
Geng, W. (BV-04)	429	Gomonay, O. (FG-04)	871	Grezes, C. (CD-13)	498
Genuzio, F. (HB-08)	982	Gomonay, O. (FG-11)	878	Grezes, C. (DC-11)	627
Genuzio, F. (IH-11)	1112	Gompertz, J. (IG-09)	1096	Grezes, C. (FE-02)	859
George, J. (CB-05)	468	Gonçalves Almeida, B. (DB-01)	605	Griggs, W. (IA-03)	1028
George, J. (CC-11)	481	Gonçalves Almeida, B. (DE-06)	648	Grigoras, M. (JW-08)	1396
George, J. (FB-01)	822	Gonçalves Almeida, B. (JE-12)	1255	Grim, V. (IB-06)	1044
George, J. (JE-05)	1248	Gonçalves Almeida, B. (JP-05)	1315	Grim, V. (IC-06)	1058
Geprägs, S. (CE-05)	504	Gonçalves, J.N. (JE-11)	1254	Grim, V. (IT-09)	1187
Geprägs, S. (FG-10)	877	Gong, M. (IH-09)	1110	Grimaldi, E. (HB-06)	980
Gerasimenko, A. (JP-06)	1316	Gong, Y. (BP-14)	324	Grimes, M. (IA-03)	1028
Gerasimova, N. (FD-05)	853	Gong, Y. (FC-05)	843	Grishin, S.V. (EB-04)	719
Gerken, M. (IB-02)	1040	González-Gómez, L. (GC-03)	940	Grishin, S.V. (ER-01)	801
Gerlach, T. (YB-04)	16	Gonzalez-Hernandez, R. (FG-08)	875	Grochot, K. (CC-14)	484
Gerlinger, K. (HA-02)	968	González, J. (YA-01)	6	Groen, I. (CC-01)	471
Ghanbaja, J. (CC-08)	478	Gonzalez, T. (IB-05)	1043	Grollier, J. (GA-01)	914
Ghanbaja, J. (JF-03)	1259	Goovaerts, E. (FB-06)	829	Gross, M. (IQ-03)	1133
Ghandour, M. (BD-11)	223	Gopal, R.K. (DP-10)	688	Gross, R. (CE-05)	504
Ghemes, C. (IT-07)	1185	Gopman, D.B. (IH-05)	1106	Gross, R. (FG-10)	877
Ghosh, A. (HD-05)	1007	Gorbenko, A. (JQ-07)	1333	Groza, G. (JW-12)	1400
Ghosh, S. (CB-02)	465	Gorchon, J. (FD-01)	849	Gruber, R. (FG-05)	872
Ghosh, S. (FD-04)	852	Gorchon, J. (HB-01)	975	Gruber, R. (HC-10)	1000
Ghosh, S. (IP-10)	1127	Gorchon, J. (ID-01)	1061	Grundler, D. (EC-03)	734
Giebultowski, M. (AC-03)	42	Gorkovenko, A. (IR-10)	1151	Grundler, D. (ED-12)	759
Gilbert, D. (FG-07)	874	Gorkovenko, A. (IR-11)	1152	Grundler, D. (ED-14)	761
Gillon, F. (AP-06)	90	Gort, R. (FD-05)	853	Grundler, D. (EE-03)	766

- Grundler, D. (HC-07) 997
- Gruszecki, P. (EB-07) 722
- Gruszecki, P. (EC-05) 736
- Gruszecki, P. (EE-07) 770
- Gruszecki, P. (EE-14) 778
- Grutter, A. (DE-07) 649
- Grutter, A. (FG-07) 874
- Grzybowski, M. (FG-09) 876
- Gu, C. (CS-05) 587
- Gu, X. (AU-10) 173
- Gu, X. (BQ-01) 329
- Guan, W. (CS-11) 593
- Guang, Y. (CC-05) 475
- Guang, Y. (HB-05) 979
- Gubanov, V. (EP-03) 783
- Gubanov, V. (EP-09) 789
- Gubbiotti, G. (EE-10) 773
- Gückelhom, J. (CE-05) 504
- Gückelhom, J. (FG-10) 877
- Gudín Holgado, A. (DB-09) 613
- Gudín Holgado, A. (IH-14) 1115
- Gudín Holgado, A. (IR-16) 1157
- Gueckstock, O. (CD-04) 489
- Gueckstock, O. (DC-12) 628
- Guedaja-Marron Gil, A. (IR-16) 1157
- Guendouz, W. (BU-14) 418
- Guenther, G. (DG-04) 670
- Guerrero, R. (AE-08) 78
- Guerrero, R. (DB-09) 613
- Guerrero, R. (IH-14) 1115
- Guerrero, R. (IR-16) 1157
- Gui, Y. (EC-01) 732
- Guillemard, C. (DD-10) 640
- Guillemard, C. (DE-01) 642
- Guillemard, C. (DE-03) 644
- Guillet, B. (IB-05) 1043
- Guillet, T. (CB-05) 468
- Guin, S. (DC-06) 622
- Guizar-Sicarios, M. (AA-03) 22
- Gulec, M. (BH-06) 269
- Guller, A. (YA-06) 11
- Gumerov, A. (CS-02) 584
- Gunduz Akdogan, N. (JH-02) 1286
- Günther, C.M. (AB-05) 31
- Günther, C.M. (HA-02) 968
- Guo, B. (BP-17) 327
- Guo, C. (CP-07) 547
- Guo, C. (CP-11) 552
- Guo, C. (ED-12) 759
- Guo, C. (EP-06) 786
- Guo, C. (GP-02) 962
- Guo, J. (BC-03) 206
- Guo, J. (DG-09) 675
- Guo, J. (HP-03) 1015
- Guo, L. (AC-18) 58
- Guo, L. (BI-05) 279
- Guo, L. (CR-07) 577
- Guo, M. (HA-05) 971
- Guo, P. (JU-07) 1382
- Guo, P. (JU-08) 1383
- Guo, S. (JR-02) 1338
- Guo, W. (JU-07) 1382
- Guo, Y. (BD-10) 222
- Guo, Z. (IH-01) 1102
- Gupta, A. (DP-01) 679
- Gupta, A. (IG-12) 1100
- Gupta, A. (IH-07) 1108
- Gupta, A. (IR-09) 1150
- Gupta, M. (CG-13) 539
- Gupta, R. (IG-12) 1100
- Gupta, R. (IR-09) 1150
- Gupta, S. (JE-06) 1249
- Gurleyen, H. (BF-09) 241
- Gusakova, D. (CD-13) 498
- Gusakova, D. (DD-05) 635
- Gusakova, D. (DD-06) 636
- Gusakova, D. (DD-07) 637
- Gusakova, D. (DD-08) 638
- Gusakova, D. (GD-02) 952
- Gushi, T. (CB-02) 465
- Gushi, T. (IP-10) 1127
- Guslienko, K. (EB-07) 722
- Guslienko, K. (IG-04) 1091
- Gutfleisch, O. (CR-05) 575
- Gutfleisch, O. (JC-02) 1219
- Gutfleisch, O. (JC-05) 1222
- Gutfleisch, O. (JE-02) 1244
- Gutfleisch, O. (JF-04) 1260
- Gutfleisch, O. (JT-06) 1367
- Gutfleisch, O. (TU-01) 2
- Gutiérrez, J. (JF-12) 1269
- Gutierrez, J. (JW-13) 1401
- Gutiérrez, L. (JG-05) 1276
- Gutkelch, D. (AC-08) 48
- Gutt, C. (FD-03) 851
- Güttel, R. (JI-08) 1304
- Guzmán Mínguez, J. (JD-11) 1241
- Gwag, E. (JG-10) 1281
- Gypens, P. (GB-13)* 936
- Gyselinck, J. (BH-04) 267
- Gyselinck, J. (BI-01) 275
- Hallal, A. (CB-05) 468
- Hallal, A. (CF-04) 516
- Hallal, A. (IP-10) 1127
- Haltz, E. (AE-10) 80
- Haltz, E. (AE-11) 81
- Haltz, E. (FH-06) 889
- Haltz, E. (HD-08) 1010
- Hamada, S. (JP-07) 1317
- Hamidi, S. (JR-07) 1343
- Hamrie, J. (JF-02) 1258
- Hamzehbahmani, H. (BJ-09) 297
- Hamzehbahmani, H. (CS-11) 593
- Han, G. (BQ-14) 343
- Han, H. (DC-02) 618
- Han, H. (HA-05) 971
- Han, J. (BG-10) 257
- Han, J. (JW-09) 1397
- Han, J. (JY-13) 1437
- Han, W. (AS-02) 136
- Han, W. (AU-03) 164
- Han, W. (HA-05) 971
- Han, X. (CB-01) 464
- Han, X. (CC-05) 475
- Han, X. (CG-10) 536
- Han, X. (CP-07) 547
- Han, X. (CP-11) 552
- Han, X. (DB-05) 609
- Han, X. (ED-12) 759
- Han, X. (EP-05) 785
- Han, X. (EP-06) 786
- Han, X. (FP-09) 907
- Han, X. (GP-02) 962
- Han, X. (HB-05) 979
- Han, X. (IQ-06) 1136
- Han, Y. (IR-07) 1148
- Hane, Y. (BI-02) 276
- Hane, Y. (BI-03) 277
- Hanke, J. (FH-10) 893
- Hantila, I. (BP-15) 325
- Haran, K. (BB-07) 198
- Harau, P. (DQ-04) 695
- Harbig, J. (JC-02) 1219
- Harris, J. (JX-10) 1417
- Harris, V. (JP-02) 1312
- Hartmann, U. (ER-11) 811
- Hartnett, T. (JE-03) 1245
- Harvey, T. (HA-02) 968
- Hasan, M. (FE-06) 863
- Hasegawa, S. (HC-03) 993
- Hashi, S. (FB-09) 832
- Hashi, S. (JY-05) 1428
- Haspot, V. (ED-02) 748
- Hassan, S. (IG-09) 1096
- Hatano, M. (JG-02) 1273
- Hauet, T. (ID-01) 1061
- Hauet, T. (JF-03) 1259
- Haupt, J. (AD-02) 61
- Hawacker, J. (FB-01) 822
- Hayakawa, K. (FC-09) 847
- Hayakawa, K. (GB-10) 933
- Hayashi, M. (HC-03) 993

Haykal, A. (AB-11)	38	Hierro Rodriguez, A. (CQ-08)	566	Honkura, S. (ID-06)	1066
Hayward, T. (GA-02)	915	Hierro Rodriguez, A. (EC-05)	736	Honkura, Y. (IB-11)	1049
Hayward, T. (GB-03)	925	Hierro Rodriguez, A. (JI-05)	1301	Honkura, Y. (ID-06)	1066
Hayward, T. (GB-04)	926	Higashida, R. (JS-04)	1354	Honnali, S. (DF-03)	655
Hayward, T. (GB-09)	932	Higgs, Z. (JQ-02)	1328	Hono, K. (DE-05)	646
Hayward, T. (GB-11)	934	Hight Walker, A.R. (AC-13)	53	Hono, K. (IE-04)	1076
He, C. (CC-05)	475	Higo, T. (FH-05)	888	Hono, K. (JC-05)	1222
He, K. (CP-12)	553	Higuchi, M. (CQ-01)	559	Horino, T. (IS-15)	1176
He, L. (FC-05)	843	Hikishima, M. (ID-06)	1066	Hornig, L. (IP-09)	1126
He, L. (IQ-10)	1140	Hillebrands, B. (CA-02)	458	Hornig, L. (IP-12)	1129
He, P. (IF-01)	1079	Hillebrands, B. (EB-08)	723	Hou, J. (BV-04)	429
He, Y. (IA-11)	1036	Hillebrands, B. (ED-11)	757	Hou, M. (BC-05)	208
He, Z. (JB-10)	1213	Hiraoka, K. (JT-11)	1372	Hou, Z. (HD-07)	1009
He, Z. (JQ-03)	1329	Hirata, K. (BB-06)	197	Houshmand Sharifi, S. (CF-12)	525
He, Z. (JX-05)	1412	Hirata, K. (BD-02)	212	Houzet, M. (FH-02)	885
Hecquet, M. (AP-06)	90	Hirata, K. (BD-08)	219	Howard, J. (JH-01)	1285
Hecquet, M. (BJ-11)	299	Hirata, K. (BD-09)	220	Hrabec, A. (AA-03)	22
Hedrich, N. (DF-01)	653	Hirata, K. (BK-02)	305	Hrabec, A. (ED-05)	751
Hehn, M. (CC-08)	478	Hirata, Y. (CP-04)	544	Hrakova, D. (IB-06)	1044
Hehn, M. (EB-03)	718	Hirayama, Y. (JW-03)	1391	Hsiao, Y. (CC-02)	472
Hehn, M. (FD-01)	849	Hirayama, Y. (JW-11)	1399	Hsieh, M. (AR-03)	117
Hehn, M. (GA-01)	914	Hiremath, B. (CP-05)	545	Hsieh, M. (BC-06)	209
Hehn, M. (HB-01)	975	Hirohata, A. (CE-03)	502	Hsieh, M. (BP-07)	316
Hehn, M. (ID-01)	1061	Hirohata, A. (CG-06)	532	Hsin, Y. (AC-09)	49
Heinz, B. (ED-11)	757	Hirohata, A. (IE-02)	1074	Hsu, C. (AU-14)	177
Heinz, B. (EE-04)	767	Hiroi, K. (JR-01)	1337	Hsu, C. (BR-10)	356
Heistracher, P.T. (HA-03)	969	Hiroi, M. (IR-05)	1146	Hsu, C. (CG-04)	530
Hellwig, O. (JB-09)	1212	Hiroi, M. (JX-07)	1414	Hsu, C. (DC-03)	619
Henderick, L. (DF-02)	654	Hiroi, M. (JX-08)	1415	Hu, C. (CC-04)	474
Hendren, W. (FC-08)	846	Hirosawa, T. (HC-08)	998	Hu, C. (EC-01)	732
Hendren, W. (IQ-09)	1139	Hirose, T. (CB-02)	465	Hu, H. (BP-08)	317
Hennel, M. (JT-04)	1365	Hirose, T. (DG-07)	673	Hu, J. (AP-05)	89
Hennequin, D. (ID-01)	1061	Hirose, T. (IP-10)	1127	Hu, J. (BP-01)	310
Henneron, T. (BH-05)	268	Hirota, R. (JP-13)	1323	Hu, J. (BQ-08)	337
Henry, Y. (EB-03)	718	Hirschmann, E. (IA-03)	1028	Hu, M. (BD-01)	211
Henschel, M. (JR-02)	1338	Hisayoshi, K. (CR-04)	574	Hu, M. (BQ-08)	337
Heo, C. (IS-13)	1174	Hisayoshi, K. (CR-06)	576	Hu, M. (BV-02)	427
Heo, C. (IT-02)	1180	Hlenschi, C. (IS-03)	1164	Hu, M. (CE-07)	506
Heo, C. (IT-05)	1183	Hlenschi, C. (JY-04)	1427	Hu, W. (AB-05)	31
Herea, D. (JP-03)	1313	Hlioui, S. (BA-06)	190	Hu, X. (GP-05)	965
Hermann, F. (EE-09)	772	Ho, P. (HC-04)	994	Hu, X. (IQ-04)	1134
Hermann, S. (AC-12)	52	Ho, P. (HD-06)	1008	Hu, Y. (BQ-03)	331
Hermosa, J. (CQ-08)	566	Ho, S. (BU-03)	405	Hu, Y. (BW-11)	449
Hernandez, S. (IA-10)	1035	Ho, S. (BU-04)	406	Hua, W. (BH-09)	271
Hernando, A. (JH-10)	1294	Ho, S. (BU-05)	407	Hua, W. (BQ-08)	337
Herper, H.C. (JD-02)	1232	Ho, S. (IH-09)	1110	Hua, W. (BT-11)	395
Herr, U. (JI-08)	1304	Hoefer, M. (CE-07)	506	Hua, Y. (BG-02)	249
Herranz, F. (JG-05)	1276	Hoffmann, A. (AE-12)	82	Hua, Y. (BI-09)	285
Herrera Diez, L. (GD-01)	951	Hoffmann, M.A. (JB-09)	1212	Hua, Z. (AU-03)	164
Herrera Diez, L. (HC-06)	996	Hohenwarter, A. (JA-06)	1194	Huang, C. (BP-14)	324
Herrera Huerta, G.A. (JI-11)	1307	Hohlfeld, J. (FD-01)	849	Huang, C. (DG-09)	675
Hertel, R. (AE-04)	74	Hohlfeld, J. (HB-01)	975	Huang, D. (IB-08)	1046
Heuraux, S. (ID-01)	1061	Holanda, J. (FB-07)	830	Huang, D. (IH-05)	1106
Hewett, S. (FB-13)	836	Holler, M. (AA-03)	22	Huang, G. (BV-08)	434
Heya, A. (BD-02)	212	Holmes, S. (JI-05)	1301	Huang, H. (BT-01)	382
Heya, A. (BD-09)	220	Honecker, D. (JI-09)	1305	Huang, H. (BU-01)	402
Heyderman, L. (AA-03)	22	Hong, Y. (JD-04)	1234	Huang, H. (BU-07)	409
Heyderman, L. (ED-05)	751	Hong, Y. (JD-07)	1237	Huang, H. (IS-14)	1175
Hibino, Y. (CD-10)	495	Honjo, H. (CF-03)	515	Huang, J. (BG-10)	257
Hicken, R.J. (CB-03)	466	Honjo, H. (CF-05)	517	Huang, J. (BU-16)	420
Hickey, B. (DP-09)	687	Honkura, S. (IB-11)	1049	Huang, J. (BU-17)	421

- Huang, J. (DB-11) 615
Huang, L. (BD-01) 211
Huang, L. (BV-02) 427
Huang, L. (CG-08) 534
Huang, M. (AB-05) 31
Huang, M. (FE-05) 862
Huang, M. (FE-06) 863
Huang, M. (IA-04) 1029
Huang, P. (AR-03) 117
Huang, P. (BU-07) 409
Huang, R. (BG-03) 250
Huang, R. (BG-09) 256
Huang, R. (BU-02) 403
Huang, R. (DP-11) 689
Huang, S. (AP-07) 91
Huang, S. (AQ-01) 99
Huang, S. (BP-16) 326
Huang, S. (BQ-16) 345
Huang, S. (BR-01) 347
Huang, S. (BR-03) 349
Huang, S. (BR-11) 357
Huang, W. (BR-09) 355
Huang, W. (JU-01) 1376
Huang, W. (JU-07) 1382
Huang, W. (JU-08) 1383
Huang, Y. (JU-12) 1387
Huebl, H. (CE-05) 504
Huebl, H. (FG-10) 877
Hueso, L. (CC-01) 471
Hueso, L. (CE-04) 503
Hug, H.J. (AB-09) 36
Hug, H.J. (FH-03) 886
Hug, H.J. (HA-03) 969
Hug, H.J. (IH-02) 1103
Hughes, B. (CF-01) 513
Hui, Y. (CP-02) 542
Hui, Y. (CP-08) 548
Hui, Y. (HP-06) 1018
Hui, Y. (IQ-04) 1134
Hui, Y. (IS-16) 1177
Hui, Y. (JY-07) 1430
Hurdequint, H. (EA-04) 712
Hurdequint, H. (EB-02) 717
Hurdequint, H. (FP-06) 904
Hurst, J. (DD-05) 635
Hurst, J. (DD-06) 636
Hurst, J. (DD-07) 637
Hurst, J. (DD-08) 638
Hurst, J. (GD-02) 952
Hutanu, V. (AC-17) 57
Hutanu, V. (DF-06) 658
Hutanu, V. (DF-08) 661
Hutanu, V. (DF-09) 662
Hutanu, V. (DG-04) 670
Hutanu, V. (JT-10) 1371
Huxtable, A. (HA-01) 967
Huynh, T. (AR-03) 117
Huynh, T. (BC-06) 209
Hvizdos, L. (IC-03) 1055
Hwang, K. (JG-12) 1283
Hwang, S. (BS-11) 376
Hwang, S. (BS-12) 377
Hwang, Y. (CP-09) 549
- I -
- Iacocca, E. (CE-07) 506
Ibarra Gomez, M. (ED-10) 756
Ibrahim, F. (CF-04) 516
Ibrahim, F. (DF-02) 654
Ichinose, T. (IE-02) 1074
Ichinose, T. (IE-05) 1077
Ichiyanagi, Y. (JP-07) 1317
Ichkitidze, L.P. (JP-06) 1316
Igarashi, J. (CG-01) 527
Igarashi, J. (CG-02) 528
Igarashi, J. (FD-01) 849
Igarashi, J. (GB-10) 933
Iglesias, O. (DD-03) 633
Iglesias, O. (JG-01) 1272
Ignatyeva, D. (EB-14) 730
Ignatyeva, D. (FP-04) 902
Ignatyeva, D. (FP-07) 905
Iguchi, R. (CE-09) 508
Iihama, S. (CD-12) 497
Iihama, S. (ED-06) 752
Iihama, S. (ED-13) 760
Iihama, S. (FD-01) 849
Imori, R. (CP-13) 554
Ikeda, S. (CC-09) 479
Ikeda, S. (CF-03) 515
Ikeda, S. (CF-05) 517
Ikegawa, S. (CF-01) 513
Im, M. (HA-05) 971
Im, S. (BQ-01) 329
Imaoka, N. (IA-09) 1034
Imbaquingo, C. (BK-03) 306
Imhof, A.N. (JF-06) 1262
Imhof, A.N. (JF-08) 1264
Inaba, N. (JD-05) 1235
Inan, O. (JA-07) 1195
Incorvia, J.C. (GB-02) 924
Incorvia, J.C. (HD-01) 1003
Incorvia, J.C. (IE-03) 1075
Inoue, M. (CE-03) 502
Insinga, A.R. (BK-03) 306
Insinga, A.R. (GC-09) 946
Ionel, D.M. (AP-08) 92
Isella, G. (CB-05) 468
Iserna, N. (GC-10) 948
Ishak, D. (BI-10) 286
Ishibashi, K. (CD-12) 497
Ishihara, K. (JT-11) 1372
Ishikawa, R. (GA-03) 917
Iskhakov, R. (JQ-07) 1333
Iskhakov, R. (JR-06) 1342
Isshiki, H. (FH-05) 888
Ito, K. (BF-02) 234
Ito, K. (DE-04) 645
Ito, K. (DG-07) 673
Ito, Y. (CE-03) 502
Itoh, Y. (BS-05) 370
Iuliano, M. (JR-12) 1348
Iurchuk, V. (ID-07) 1067
Ivry, A. (GC-08) 945
Iwahori, T. (CE-10) 509
Iwai, M. (CQ-05) 563
Iwai, M. (CR-01) 571
Iwasaki, C. (ER-12) 812
Iwata, S. (FC-06) 844
Iyer, K. (JH-11) 1295
Izgi, T. (JA-07) 1195
Izmozherov, I. (CS-01) 583
Izmozherov, I. (CS-12) 594
Izquierdo, M. (FD-05) 853
- J -
- J, A. (JT-13) 1374
Jaafar, M. (AA-05) 24
Jaafar, M. (IG-04) 1091
Jaber, M. (GD-02) 952
Jacko, P. (IC-03) 1055
Jacques, V. (AB-11) 38
Jacquet, E. (JA-12) 1201
Jacquot, J. (CD-11) 496
Jadaun, P. (HD-01) 1003
Jadaun, P. (IE-03) 1075
Jaffari, G. (DE-08) 650
Jaffrès, H. (CB-05) 468
Jaffrès, H. (CC-11) 481
Jaffrès, H. (CD-13) 498
Jaffrès, H. (FB-01) 822
Jakob, G. (CG-09) 535
Jakubowska, M.M. (IG-02) 1089
Jalil, M.B. (IF-03) 1081
Jamet, M. (CB-05) 468
Jamil, M. (DE-08) 650
Jančárik, V. (JX-01) 1408
Janda, T. (AB-04) 30
Janesky, J. (CF-01) 513
Jang, G. (AU-08) 171
Jang, G. (BQ-06) 335
Jang, G. (BS-07) 372
Jang, G. (BS-13) 378
Jang, H. (GD-08) 958
Janus, W. (IG-07) 1094
Janus, W. (IH-10) 1111
Janus, W. (IH-11) 1112
Javed, K. (JE-06) 1249
Jayacody, A. (DC-10) 626
Je, S. (HA-05) 971
Jena, D. (IH-09) 1110
Jena, J. (HD-03) 1005
Jena, J. (HP-02) 1014
Jena, S.K. (IG-02) 1089
Jeng, J. (CQ-11) 569
Jeng, J. (CR-09) 579

- Karamanis, E.K. (AP-13) 97
- Karampuri, Y. (EC-13) 744
- Karashitin, E. (ID-10) 1070
- Kardasz, B. (CF-09) 522
- Karki, D. (FP-07) 905
- Karki, S. (IE-03) 1075
- Karki, U. (DP-01) 679
- Karmenyan, A. (JG-09) 1280
- Karnaushenko, D. (AB-07) 33
- Karpasyuk, V. (DP-06) 684
- Karpavicius, A. (JG-03) 1274
- Kästner, B. (AB-04) 30
- Kateel, V. (CG-13) 539
- Katine, J. (CB-03) 466
- Kato, M. (BD-06) 217
- Kato, M. (BD-08) 219
- Kato, M. (BK-02) 305
- Kato, T. (FC-06) 844
- Katsaras, J. (BE-04) 228
- Kawaguchi, M. (HC-03) 993
- Kawahara, T. (CG-11) 537
- Kawai, T. (JD-05) 1235
- Kawamura, Y. (JR-01) 1337
- Kazakova, O. (DC-09) 625
- Kazakova, O. (GA-05) 919
- Kazakova, O. (HC-06) 996
- KC, S. (DP-01) 679
- Ke, M. (CG-11) 537
- Ke, Z. (AQ-05) 103
- Ke, Z. (CR-03) 573
- Keatley, P.S. (CB-03) 466
- Keebaugh, S. (CG-05) 531
- Kehayias, P. (AB-03) 29
- Keller, F.O. (JC-04) 1221
- Keller, F.O. (JW-12) 1400
- Kemer, S.B. (BH-11) 273
- Kent, A. (FG-15) 882
- Kent, A.D. (CA-01) 457
- Kent, A.D. (CF-09) 522
- Kent, A.D. (CF-10) 523
- Kentsch, U. (IA-03) 1028
- Keogh, A.M. (GA-02) 915
- Kerber, N. (FD-03) 851
- Kerber, N. (FG-05) 872
- Kerber, N. (HC-10) 1000
- Kern, L. (HA-02) 968
- Kersulis, S. (IB-13) 1051
- Keshav, M. (JF-09) 1265
- Khajetoorians, A.A. (GA-06) 920
- Khan, B. (BB-02) 193
- Khan, B. (BG-06) 253
- Khan, F. (BB-02) 193
- Khan, F. (BD-07) 218
- Khan, F. (BG-06) 253
- Khan, S. (DC-09) 625
- Khanjani, M.V. (CC-14) 484
- Kharlamova, A. (ER-09) 809
- Khittiwitachayakul, S. (IP-05) 1122
- Khodadadi, M. (DF-12) 665
- Khoo, K. (HC-04) 994
- Khurana, B. (CE-08) 507
- Kiarie, W.M. (JU-09) 1384
- Kiarie, W.M. (JU-10) 1385
- Kichin, G. (ER-08) 808
- Kief, M.T. (IA-10) 1035
- Kierren, B. (JF-03) 1259
- Kikuchi, E. (ID-06) 1066
- Kim, C. (AR-07) 121
- Kim, C. (BQ-06) 335
- Kim, C. (BQ-15) 344
- Kim, C. (BS-01) 365
- Kim, C. (BS-07) 372
- Kim, C. (BV-07) 433
- Kim, C. (DQ-06) 697
- Kim, C. (DQ-07) 698
- Kim, D. (AS-05) 140
- Kim, D. (BP-11) 321
- Kim, D. (BQ-01) 329
- Kim, D. (BR-04) 350
- Kim, D. (EP-04) 784
- Kim, D. (IS-02) 1163
- Kim, D. (IS-13) 1174
- Kim, H. (AR-10) 125
- Kim, H. (AR-15) 130
- Kim, H. (AR-16) 131
- Kim, H. (BQ-15) 344
- Kim, H. (BR-13) 359
- Kim, H. (BR-14) 360
- Kim, H. (BW-12) 450
- Kim, H. (JQ-04) 1330
- Kim, J. (AC-05) 44
- Kim, J. (AV-03) 181
- Kim, J. (BG-05) 252
- Kim, J. (DD-10) 640
- Kim, J. (DP-03) 681
- Kim, J. (DP-05) 683
- Kim, J. (GC-01) 938
- Kim, J. (GC-02) 939
- Kim, J. (HA-06) 973
- Kim, J. (HC-09) 999
- Kim, J. (JW-05) 1393
- Kim, J. (JW-15) 1403
- Kim, J. (JW-16) 1404
- Kim, J. (JY-09) 1432
- Kim, K. (AC-05) 44
- Kim, K. (BG-05) 252
- Kim, K. (BR-16) 362
- Kim, K. (CB-06) 469
- Kim, K. (CP-04) 544
- Kim, K. (IQ-07) 1137
- Kim, M. (IS-02) 1163
- Kim, M. (IS-13) 1174
- Kim, S. (BR-04) 350
- Kim, S. (BR-14) 360
- Kim, S. (CP-04) 544
- Kim, S. (CP-14) 555
- Kim, S. (EC-10) 741
- Kim, S. (EP-04) 784
- Kim, S. (FP-12) 910
- Kim, S. (JD-07) 1237
- Kim, T. (CG-12) 538
- Kim, T. (JY-18) 1442
- Kim, W. (AR-18) 133
- Kim, W. (BR-04) 350
- Kim, W. (BR-12) 358
- Kim, W. (BR-13) 359
- Kim, W. (BR-15) 361
- Kim, W. (BR-16) 362
- Kim, W. (BR-17) 363
- Kim, W. (BS-01) 365
- Kim, W. (CF-12) 525
- Kim, W. (CG-13) 539
- Kim, Y. (AR-10) 125
- Kim, Y. (AS-08) 143
- Kim, Y. (BU-08) 410
- Kim, Y. (BW-15) 453
- Kimel, A. (FA-06) 820
- Kimel, A. (FB-11) 834
- Kimura, S. (IR-05) 1146
- Kimura, T. (CE-10) 509
- Kimura, T. (CP-13) 554
- Kinane, C. (IA-03) 1028
- Kindiak, I. (ER-08) 808
- Kipp, J. (FH-10) 893
- Kirchhof, C. (IB-02) 1040
- Kirilyuk, A. (FB-14) 837
- Kirino, F. (JD-05) 1235
- Kirste, G. (JW-14) 1402
- Kiryukhin, V. (DP-03) 681
- Kishi, Y. (CG-11) 537
- Kishine, J. (EQ-08) 798
- Kisic, M.G. (IS-12) 1173
- Kitamura, T. (JP-13) 1323
- Kitayama, F. (BD-06) 217
- Kitayama, F. (BS-14) 379
- Kitazawa, H. (JT-08) 1369
- Kitcher, M.D. (HD-09) 1011
- Kitcher, M.D. (IG-03) 1090
- Kladas, A.G. (AP-13) 97
- Klaur, M. (CG-09) 535
- Kläui, M. (FD-03) 851
- Kläui, M. (FG-04) 871
- Klaur, M. (FG-05) 872
- Kläui, M. (FG-06) 873
- Klaur, M. (FH-11) 894
- Kläui, M. (FH-12) 895
- Klaur, M. (FH-13) 896
- Klaur, M. (HC-10) 1000
- Kleibert, A. (HA-01) 967
- Klein, O. (EA-04) 712
- Klein, O. (EB-02) 717
- Klein, O. (ED-04) 750
- Klein, O. (EE-08) 771
- Kliava, J. (JY-19) 1443
- Klingbeil, F. (IT-06) 1184
- Klingbeil, F. (JG-08) 1279
- Klos, J.W. (EC-08) 739
- Klos, J.W. (EE-07) 770
- Klose, C. (AB-05) 31
- Klyukin, K. (FE-05) 862
- Kmita, A. (AC-14) 54
- Knauer, S. (ED-11) 757
- Knight, E. (JQ-06) 1332

Kobashi, M. (JW-03)	1391	Kounta, I. (FG-08)	875	Kumakura, Y. (IS-06)	1167
Kobayashi, K. (CQ-05)	563	Kounta, I. (FH-08)	891	Kumar, A. (DC-01)	617
Kobayashi, K. (CR-01)	571	Kourkoumelis, N. (JR-09)	1345	Kumar, A. (DC-12)	628
Kobayashi, K. (FC-09)	847	Kovacs, A. (AA-04)	23	Kumar, D. (CE-06)	505
Kobayashi, S. (JR-01)	1337	Kovacs, A. (AD-04)	63	Kumar, D. (CP-01)	541
Kobe, S. (JC-11)	1228	Kowalik, M. (AC-03)	42	Kumar, D. (DC-03)	619
Koda, T. (EE-05)	768	Kowol, C. (JB-09)	1212	Kumar, R. (HB-07)	981
Koda, T. (FB-09)	832	Koytepe, S. (JA-07)	1195	Kumar, S. (CP-05)	545
Kodama, K. (JP-07)	1317	Kozhaev, M. (JS-03)	1353	Kumar, V. (HP-02)	1014
Koh, C. (AD-07)	66	Koziej, D. (AC-14)	54	Kumar, Y. (HP-08)	1020
Koh, C. (AD-08)	67	Kozin, M.G. (IR-14)	1155	Kunca, B. (JR-03)	1339
Köhler, L. (HB-10)	984	Koziol Rachwal, A. (IG-07)	1094	Kundu, S. (CF-12)	525
Kohno, R. (EA-04)	712	Koziol Rachwal, A. (IH-10)	1111	Kunimatsu, K. (IE-02)	1074
Kohno, R. (ED-04)	750	Koziol Rachwal, A. (IH-11)	1112	Kurant, Z. (IH-03)	1104
Koike, T. (IA-09)	1034	Kozlov, A. (IH-06)	1107	Kurebayashi, H. (DC-09)	625
Koike, Y. (ED-06)	752	Kozlov, A. (IR-03)	1144	Kurebayashi, H. (ED-06)	752
Koike, Y. (ED-13)	760	Kramer, M.J. (JC-01)	1218	Kurebayashi, H. (ED-13)	760
Kojima, F. (IS-06)	1167	Krarcha, H.K. (DQ-02)	693	Kurebayashi, H. (HC-06)	996
Koki, K. (EP-01)	781	Kravchuk, V. (GD-04)	954	Kurihara, K. (EP-01)	781
Kokkonen, E. (IG-10)	1097	Krawczyk, M. (AE-09)	79	Kurimune, Y. (EC-06)	737
Kolak, S. (JA-07)	1195	Krawczyk, M. (EB-07)	722	Kurlyandskaya, G.V. (ER-09)	809
Kolat, V. (JA-07)	1195	Krawczyk, M. (EC-05)	736	Kurlyandskaya, G.V. (IR-11)	1152
Koledov, V. (JE-05)	1248	Krawczyk, M. (EE-02)	765	Kurlyandskaya, G.V. (JT-12)	1373
Kolesnikov, A. (CB-01)	464	Krawczyk, M. (EE-07)	770	Kurniawan, I. (DE-05)	646
Koliada, M. (IB-13)	1051	Krawczyk, M. (EE-14)	778	Kuroe, H. (DP-04)	682
Komine, T. (IA-02)	1027	Krawczyk, M. (EP-07)	787	Kurokawa, Y. (EP-01)	781
Komineas, S. (FH-14)	897	Krenn, H. (IR-13)	1154	Kurokawa, Y. (FP-13)	911
Komlev, A.E. (EQ-02)	792	Krenn, H. (JA-06)	1194	Kurta, R. (FD-05)	853
Komogortsev, S.V. (JQ-07)	1333	Krichevsky, D. (FP-07)	905	Kuschel, T. (AC-11)	51
Komogortsev, S.V. (JR-06)	1342	Kriegner, D. (FG-08)	875	Kuschel, T. (CE-01)	500
Komori, T. (CB-02)	465	Kriegner, D. (FH-08)	891	Kushibiki, R. (IP-02)	1119
Komori, T. (DG-07)	673	Krimer, Y. (JA-01)	1189	Kushibiki, R. (IP-03)	1120
Komori, T. (IF-02)	1080	Krishnia, S. (CC-11)	481	Kushwaha, V.K. (DE-05)	646
Komori, T. (IP-10)	1127	Krishnia, S. (FH-06)	889	Kutuzau, M. (DF-03)	655
Kondo, R. (BS-14)	379	Krist, T. (AC-17)	57	Kuwahara, H. (DP-04)	682
Kondou, K. (CP-09)	549	Krizakova, V. (HB-06)	980	Kuwahata, A. (JG-02)	1273
Kong, J. (HB-12)	987	Kroha, J. (DG-08)	674	Kwiatkowski, G. (JR-04)	1340
Kong, J. (HC-04)	994	Kronast, F. (GD-04)	954	Kwon, D. (BQ-06)	335
Kong, W. (AT-07)	159	Kronast, F. (IG-01)	1088	Kwon, D. (BS-07)	372
Kong, W. (BQ-14)	343	Krooß, P. (JF-04)	1260	Kwon, D. (BV-07)	433
Kong, W. (CG-10)	536	Krop, D. (AD-05)	64	Kyianytsia, A. (JF-03)	1259
Kong, X. (BG-02)	249	Ksenzov, D. (FD-03)	851	Kyle, S. (GA-02)	915
Kong, X. (BI-09)	285	Kubota, H. (CD-10)	495	Kyle, S. (GB-03)	925
Koo, B. (AP-09)	93	Kubota, H. (GB-07)	930	Kyle, S. (GB-11)	934
Koo, H. (CP-14)	555	Kubota, H. (IA-01)	1025		
Koo, H. (FP-12)	910	Kubota, H. (IB-04)	1042		
Koopmans, B. (FG-09)	876	Kubota, H. (IH-04)	1105		
Korecki, J. (IG-07)	1094	Kubota, T. (DE-04)	645		
Korecki, J. (IR-04)	1145	Kubota, T. (FG-13)	880		
Korenistov, P. (DE-09)	651	Kubota, T. (IR-05)	1146		
Kori, B. (CP-05)	545	Kuchin, A. (JT-09)	1370		
Korol, A.O. (DG-06)	672	Kuchko, A. (EE-07)	770		
Kosaka, D. (IS-06)	1167	Kuciakowski, J. (AC-14)	54		
Kosel, J. (AC-02)	41	Kudo, K. (ID-06)	1066		
Koshelev, A. (GC-07)	944	Kudryavtsev, R. (CS-02)	584		
Koshkin, A. (JU-02)	1377	Kudyukov, E. (IR-10)	1151		
Kostanyan, A. (IG-10)	1097	Kuepferling, M. (CC-14)	484		
Kosub, T. (DF-01)	653	Kühne, I.A. (DG-10)	676		
Kotur, K. (DG-03)	669	Kukharev, A.V. (JI-07)	1303		
Kou, B. (AT-02)	154	Kulesh, N. (GC-07)	944		
Kou, B. (BS-08)	373	Kulikova, D. (ID-05)	1065		

- L -

L'vov, V.S. (EB-08)	723
Labarta, A. (IG-01)	1088
Labarta, A. (JH-07)	1291
Labarta, A. (JH-08)	1292
Labusca, L. (JP-03)	1313
Lachowicz, D. (AC-14)	54
Lacour, D. (EB-03)	718
Lacour, D. (FD-03)	851
Lacour, D. (GA-01)	914
Lacour, D. (ID-01)	1061
Lafuente-Gómez, N. (JG-05)	1276
Lafuerza-Bielsa, S. (AC-14)	54
Lagarriue, A. (CP-09)	549

- Lägel, B. (ED-11) 757
 Lägel, B. (EE-04) 767
 Lai, B. (CQ-09) 567
 Lai, B. (JP-09) 1319
 Lai, B. (JP-14) 1324
 Lai, B. (JQ-09) 1335
 Lai, C. (BG-12) 259
 Lai, K. (IP-12) 1129
 Laloy, D. (JB-12) 1215
 Lam Chok Sing, M. (IB-05) 1043
 Lam, K. (IQ-01) 1131
 Lamard, N. (ID-07) 1067
 Lambert, C. (CC-06) 476
 Lambert, C. (CC-13) 483
 Lambert, C. (CD-11) 496
 Lambert, C. (CE-04) 503
 Lambert, C. (HB-06) 980
 Lamblin, M. (JB-12) 1215
 Lamichhane, T. (BE-03) 227
 Lamichhane, T. (BE-04) 228
 Lammel, M. (FG-08) 875
 Lan, Z. (JX-05) 1412
 Landeros, P. (DD-02) 632
 Lang, J. (BF-06) 238
 Lang, M. (DD-04) 634
 Lang, M. (GC-05) 942
 Langer, J. (CC-14) 484
 Langer, J. (CG-09) 535
 Langer, J. (FE-09) 866
 Langer, J. (ID-07) 1067
 Lantz, M. (IA-09) 1034
 Lapa, P. (IG-11) 1099
 Laref, S. (CB-06) 469
 Larrañaga, A. (ER-09) 809
 Larrañaga, A. (IR-11) 1152
 Larrañaga, A. (JT-12) 1373
 Larsson, P. (JD-08) 1238
 Lattery, D. (FC-01) 839
 Lattery, D. (IH-05) 1106
 Lau, Y. (DE-04) 645
 Lau, Y. (FG-13) 880
 Lau, Y. (GD-07) 957
 Laughlin, D.E. (IA-04) 1029
 Lauhoff, C. (JF-04) 1260
 Laureti, S. (JD-01) 1231
 Lauria, D. (BJ-14) 302
 Laurson, L. (AE-03) 73
 Lauter, V. (BE-04) 228
 Laviano, F. (JX-03) 1410
 Lavrijsen, R. (FB-14) 837
 Law, J. (DP-01) 679
 Law, J. (JE-01) 1243
 Law, J. (JE-07) 1250
 Law, J. (JE-08) 1251
 Law, J. (JE-09) 1252
 Lazari, P. (AU-02) 163
 Lazarski, S. (CC-14) 484
 le Guyader, L. (FD-05) 853
 Le Menach, Y. (JB-13) 1216
 Le Roy, D. (JD-03) 1233
 Le Roy, D. (JH-01) 1285
 Le Roy, D. (JI-11) 1307
 Le-Guennec, Y. (ID-08) 1068
 Le, M. (JG-04) 1275
 Le, W. (BB-03) 194
 Le, W. (BT-15) 399
 Lebargy, S. (IB-05) 1043
 Lebrun, L. (AC-06) 46
 Lebrun, R. (ED-02) 748
 Lebrun, R. (ED-03) 749
 Lebrun, R. (FB-01) 822
 Lebrun, R. (FG-04) 871
 Lebrun, R. (FH-12) 895
 Lebrun, R. (IB-04) 1042
 Lebrun, R. (ID-08) 1068
 Lebrun, R. (JA-12) 1201
 LeClair, P. (DP-01) 679
 Lee, B. (AU-04) 166
 Lee, B. (BP-13) 323
 Lee, C. (AU-04) 166
 Lee, C. (BP-04) 313
 Lee, C. (BP-11) 321
 Lee, C. (BU-12) 415
 Lee, C. (BW-14) 452
 Lee, C. (BW-16) 454
 Lee, C. (IS-01) 1161
 Lee, D. (AR-09) 124
 Lee, D. (BB-07) 198
 Lee, D. (EP-04) 784
 Lee, D. (FP-12) 910
 Lee, G. (JW-05) 1393
 Lee, G. (JW-15) 1403
 Lee, H. (AP-12) 96
 Lee, H. (BQ-05) 334
 Lee, H. (BR-06) 352
 Lee, H. (CE-12) 511
 Lee, H. (IH-09) 1110
 Lee, H. (JD-07) 1237
 Lee, H. (JP-04) 1314
 Lee, H. (JW-15) 1403
 Lee, H. (JW-16) 1404
 Lee, H.K. (CF-01) 513
 Lee, J. (AP-03) 87
 Lee, J. (AR-15) 130
 Lee, J. (AR-16) 131
 Lee, J. (BQ-09) 338
 Lee, J. (BQ-15) 344
 Lee, J. (BR-06) 352
 Lee, J. (BR-13) 359
 Lee, J. (BR-14) 360
 Lee, J. (BW-12) 450
 Lee, J. (IQ-07) 1137
 Lee, J. (JD-04) 1234
 Lee, K. (AR-14) 129
 Lee, K. (BR-12) 358
 Lee, K. (BR-15) 361
 Lee, K. (BR-17) 363
 Lee, K. (BS-04) 369
 Lee, K. (CP-14) 555
 Lee, K. (EC-10) 741
 Lee, K. (EP-04) 784
 Lee, K. (FE-05) 862
 Lee, K. (FP-12) 910
 Lee, K. (HA-05) 971
 Lee, K. (JW-05) 1393
 Lee, K. (JY-09) 1432
 Lee, M. (AP-09) 93
 Lee, N. (DP-03) 681
 Lee, N. (DP-05) 683
 Lee, S. (AP-03) 87
 Lee, S. (BD-08) 219
 Lee, S. (BG-05) 252
 Lee, S. (BK-02) 305
 Lee, S. (BQ-01) 329
 Lee, S. (BR-12) 358
 Lee, S. (BR-16) 362
 Lee, S. (BS-04) 369
 Lee, S. (CP-04) 544
 Lee, S. (HA-05) 971
 Lee, S. (IQ-07) 1137
 Lee, T. (IQ-07) 1137
 Lee, T. (JD-04) 1234
 Lee, W. (BS-13) 378
 Lee, W. (CP-14) 555
 Lee, W. (JD-07) 1237
 Lefevre, C. (JX-04) 1411
 Lefèvre, P. (FB-01) 822
 Lefler, B. (IB-03) 1041
 Legrand, W. (HC-02) 991
 Lei, F. (JB-10) 1213
 Lei, G. (BD-10) 222
 Leistner, K. (AB-07) 33
 Leistner, K. (DF-03) 655
 Leistner, K. (FE-04) 861
 Leistner, K. (FE-06) 863
 Leistner, K. (JR-02) 1338
 Leiviska, M. (FG-08) 875
 Leiviska, M. (FH-02) 885
 Lekshmi, P. (DE-06) 648
 Leliaert, J. (AC-08) 48
 Leliaert, J. (EC-07) 738
 Leliaert, J. (GB-13) 936
 Leliaert, J. (JG-03) 1274
 Leliaert, J. (JH-09) 1293
 Lemaître, A. (HB-01) 975
 Lemesh, I. (AB-05) 31
 Lemke, J. (JE-02) 1244
 Lengaigne, G. (ID-01) 1061
 Lentfert, A. (EE-04) 767
 Lenz, K. (FB-02) 823
 Leonard Deepak, F. (DB-01) 605
 Leonard Deepak, F. (DE-06) 648
 Leonard, T. (GB-02) 924
 Leong, J. (BI-10) 286
 Leong, Z. (JB-02) 1205
 Leong, Z. (JB-05) 1208
 Leong, Z. (JX-10) 1417
 Leong, Z. (JX-11) 1418
 Lepalovskij, V. (IR-10) 1151
 Lepalovskij, V. (IR-11) 1152
 Lepetit, M. (EC-12) 743
 Lequeux, S. (CG-03) 529
 Létang, J. (DD-10) 640

Leung, C. (IQ-01)	1131	Li, W. (FG-07)	874	Liao, Y. (IR-07)	1148
Leung, C. (IR-06)	1147	Li, W. (YB-05)	17	Lichtenstein, A. (FD-05)	853
Leung, C. (IT-04)	1182	Li, X. (AS-09)	144	Liebl, M. (AC-08)	48
Leupold, O. (AC-11)	51	Li, X. (BW-11)	449	Liedke, M. (DF-02)	654
Lévêque, J. (BA-03)	187	Li, X. (DB-08)	612	Liedke, M. (IA-03)	1028
Levy, A. (GB-04)	926	Li, X. (FE-07)	864	Lien, H. (IC-04)	1056
Levy, M. (FP-07)	905	Li, X. (IH-09)	1110	Liensberger, L. (CD-04)	489
Lew, W. (CD-03)	488	Li, Y. (AP-05)	89	Lim, D. (AR-08)	122
Lew, W. (HB-04)	978	Li, Y. (AP-07)	91	Lim, D. (AR-12)	127
Lew, W. (JA-05)	1193	Li, Y. (AQ-01)	99	Lim, D. (AR-14)	129
Lezaic, M. (FH-10)	893	Li, Y. (AQ-04)	102	Lim, G.J. (JA-05)	1193
Li, B. (BF-11)	243	Li, Y. (AR-02)	115	Lim, M. (AU-10)	173
Li, C. (BP-16)	326	Li, Y. (AS-04)	139	Lim, M. (AV-03)	181
Li, D. (AD-08)	67	Li, Y. (AS-07)	142	Lim, M. (BG-05)	252
Li, D. (AS-03)	138	Li, Y. (AS-09)	144	Lim, M. (BQ-01)	329
Li, D. (AT-07)	159	Li, Y. (AU-11)	174	Lim, N.C. (HD-06)	1008
Li, D. (BT-01)	382	Li, Y. (BD-01)	211	Lim, S. (CE-06)	505
Li, D. (BT-04)	385	Li, Y. (BF-11)	243	Lim, S. (CG-08)	534
Li, D. (BT-09)	392	Li, Y. (BJ-05)	293	Lim, S. (HB-11)	985
Li, D. (BU-01)	402	Li, Y. (BP-10)	319	Lima, S. (JG-06)	1277
Li, D. (JA-03)	1191	Li, Y. (BT-06)	387	Lin, C. (CC-01)	471
Li, D. (JH-04)	1288	Li, Y. (BT-08)	391	Lin, C. (DA-04)	601
Li, G. (EB-12)	728	Li, Y. (BV-02)	427	Lin, C. (FB-13)	836
Li, G. (FA-06)	820	Li, Y. (CQ-06)	564	Lin, H. (AR-02)	115
Li, G. (FB-11)	834	Li, Y. (CQ-07)	565	Lin, H. (BB-09)	201
Li, H. (CC-07)	477	Li, Y. (CS-06)	588	Lin, H. (BH-02)	265
Li, H. (DA-04)	601	Li, Y. (EB-13)	729	Lin, H. (BH-10)	272
Li, H. (HB-09)	983	Li, Y. (ED-12)	759	Lin, H. (BJ-13)	301
Li, H. (IF-04)	1082	Li, Y. (FC-03)	841	Lin, H. (BP-10)	319
Li, H. (IQ-10)	1140	Li, Y. (IP-12)	1129	Lin, H. (BV-10)	436
Li, J. (AQ-05)	103	Li, Y. (JU-01)	1376	Lin, M. (BB-03)	194
Li, J. (AU-09)	172	Li, Y. (JW-01)	1389	Lin, M. (BT-15)	399
Li, J. (BR-09)	355	Li, Y. (JW-04)	1392	Lin, Q. (BU-11)	414
Li, J. (IB-10)	1048	Li, Y. (JX-14)	1421	Lin, Q. (BU-18)	422
Li, K. (BP-01)	310	Li, Y. (JX-15)	1422	Lin, S. (HA-05)	971
Li, K. (IS-05)	1166	Li, Y. (JY-10)	1434	Lin, X. (FH-09)	892
Li, K. (IS-08)	1169	Li, Y. (JY-11)	1435	Lin, Y. (AC-09)	49
Li, K. (JF-10)	1267	Li, Y. (JY-12)	1436	Lin, Y. (BC-01)	204
Li, K. (JU-04)	1379	Li, Z. (AU-07)	170	Lin, Z. (CS-06)	588
Li, K. (JU-05)	1380	Li, Z. (BQ-12)	341	Lin, Z. (JW-09)	1397
Li, K. (JY-13)	1437	Li, Z. (BS-03)	367	Lin, Z. (JX-14)	1421
Li, L. (AR-05)	119	Li, Z. (BT-11)	395	Lin, Z. (JY-11)	1435
Li, L. (AS-01)	135	Li, Z. (CC-03)	473	Lin, Z. (JY-12)	1436
Li, L. (AS-12)	147	Li, Z. (DB-08)	612	Lin, Z. (JY-13)	1437
Li, L. (BJ-05)	293	Li, Z. (HB-09)	983	Lindner, J. (FB-02)	823
Li, L. (BW-11)	449	Li, Z. (JH-04)	1288	Linfield, E. (HA-01)	967
Li, M. (AD-07)	66	Liang, D. (BU-10)	413	Ling, Z. (BW-03)	440
Li, M. (BC-02)	205	Liang, G. (DC-03)	619	Liou, S. (AT-05)	157
Li, M. (BQ-02)	330	Liang, H. (BS-10)	375	Liou, S. (IS-14)	1175
Li, M.P. (AB-08)	34	Liang, J. (IQ-01)	1131	List, F. (BE-03)	227
Li, M.P. (GD-06)	956	Liang, J. (IR-06)	1147	Litsardakis, G. (CP-06)	546
Li, Q. (AR-05)	119	Liang, P. (AP-02)	86	Litvinenko, A. (EA-04)	712
Li, Q. (BV-04)	429	Liang, T. (AU-06)	168	Litvinenko, A. (ED-10)	756
Li, Q. (BW-10)	448	Liang, Z. (BT-09)	392	Litvinenko, A. (ER-06)	806
Li, R. (DC-08)	624	Liao, C. (EA-06)	714	Litvinenko, A. (ID-07)	1067
Li, S. (AQ-06)	104	Liao, H. (DB-08)	612	Litvinenko, A. (ID-08)	1068
Li, V.Z. (HB-11)	985	Liao, J. (JI-05)	1301	Litvinov, D. (DF-12)	665
Li, W. (BJ-06)	294	Liao, S. (IS-14)	1175	Litzius, K. (FD-03)	851
Li, W. (CC-03)	473	Liao, W. (CC-02)	472	Liu, C. (AC-04)	43
Li, W. (CC-08)	520	Liao, W. (CC-10)	480	Liu, C. (BD-10)	222
Li, W. (CF-08)	520	Liao, Y. (EP-08)	788	Liu, C. (BF-11)	243
Li, W. (FE-07)	864				

- Liu, C. (BG-03) 250
 Liu, C. (BG-09) 256
 Liu, C. (BJ-04) 292
 Liu, C. (BR-08) 354
 Liu, C. (BU-02) 403
 Liu, C. (ED-12) 759
 Liu, C. (FP-05) 903
 Liu, C. (JQ-03) 1329
 Liu, E. (DC-06) 622
 Liu, F. (AP-05) 89
 Liu, F. (AV-02) 180
 Liu, F. (BB-10) 202
 Liu, F. (BP-03) 312
 Liu, F. (BP-05) 314
 Liu, F. (BP-06) 315
 Liu, F. (BP-12) 322
 Liu, G. (BF-12) 245
 Liu, G. (BT-02) 383
 Liu, H. (IB-09) 1047
 Liu, H. (IS-01) 1161
 Liu, H. (JU-12) 1387
 Liu, H. (JY-10) 1434
 Liu, J. (AT-07) 159
 Liu, J. (BB-04) 195
 Liu, J. (BF-06) 238
 Liu, J. (BF-12) 245
 Liu, J. (BT-02) 383
 Liu, J. (IH-05) 1106
 Liu, J. (IS-01) 1161
 Liu, J. (IS-05) 1166
 Liu, J. (IS-08) 1169
 Liu, J. (JC-02) 1219
 Liu, J. (JU-04) 1379
 Liu, J. (JU-05) 1380
 Liu, K. (BH-09) 271
 Liu, K. (BQ-08) 337
 Liu, K. (DF-02) 654
 Liu, L. (HP-06) 1018
 Liu, L. (IS-16) 1177
 Liu, L. (JU-12) 1387
 Liu, M. (JB-01) 1204
 Liu, P. (BS-15) 380
 Liu, P. (JI-10) 1306
 Liu, Q. (CP-10) 551
 Liu, Q. (CP-12) 553
 Liu, Q. (HC-10) 1000
 Liu, Q. (IQ-10) 1140
 Liu, S. (DB-07) 611
 Liu, S. (ED-12) 759
 Liu, S. (JW-09) 1397
 Liu, S. (JY-13) 1437
 Liu, T. (ED-12) 759
 Liu, W. (AS-02) 136
 Liu, W. (BV-10) 436
 Liu, W. (DB-07) 611
 Liu, W. (JC-10) 1227
 Liu, W. (JE-02) 1244
 Liu, W. (JQ-03) 1329
 Liu, W. (JW-01) 1389
 Liu, W. (JW-07) 1395
 Liu, X. (BQ-04) 332
 Liu, X. (BU-15) 419
 Liu, X. (CS-13) 595
 Liu, X. (HD-07) 1009
 Liu, X. (JC-08) 1225
 Liu, Y. (AT-02) 154
 Liu, Y. (BD-01) 211
 Liu, Y. (BF-07) 239
 Liu, Y. (BG-02) 249
 Liu, Y. (BJ-04) 292
 Liu, Y. (BP-03) 312
 Liu, Y. (BP-05) 314
 Liu, Y. (BP-06) 315
 Liu, Y. (BS-08) 373
 Liu, Y. (BV-02) 427
 Liu, Y. (CC-05) 475
 Liu, Y. (CC-12) 482
 Liu, Y. (HB-05) 979
 Liu, Y. (HP-06) 1018
 Liu, Y. (IG-03) 1090
 Liu, Y. (IQ-01) 1131
 Liu, Y. (IR-06) 1147
 Liu, Y. (IS-14) 1175
 Liu, Y. (JA-04) 1192
 Liu, Y. (JG-04) 1275
 Liu, Z. (IB-09) 1047
 Liu, Z. (IB-12) 1050
 Liu, Z. (JY-13) 1437
 Lloyd, D. (CE-03) 502
 Lo Conte, R. (HB-01) 975
 Lo, T. (CC-12) 482
 Lo, Y. (EA-06) 714
 Locardi, F. (JD-10) 1240
 Locatelli, A. (HB-08) 982
 Locatelli, A. (IH-11) 1112
 Locatelli, L. (DC-01) 617
 Locatelli, L. (DC-12) 628
 Lofink, F. (IB-02) 1040
 Lofland, S. (IB-03) 1041
 Lombard, L. (IB-07) 1045
 Lomonova, E. (AD-05) 64
 Lomonova, E. (AS-10) 145
 Lomonova, E. (BI-04) 278
 Lone, A.H. (GB-06) 929
 Longhino, J.M. (JG-11) 1282
 Longo, E. (DC-01) 617
 Longo, E. (DC-12) 628
 Longo, M. (DC-01) 617
 Longo, M. (DC-12) 628
 Lopeandia, A. (DF-02) 654
 Lopes Seeger, R. (EA-04) 712
 Lopes Seeger, R. (FG-08) 875
 Lopes Seeger, R. (FH-02) 885
 Lopes Seeger, R. (FH-08) 891
 Lopes, A.L. (DE-06) 648
 López-Ortega, A. (JR-11) 1347
 Lopez-Quintas, I. (FD-03) 851
 Loss, D. (HC-08) 998
 Lostun, M. (IT-07) 1185
 Lostun, M. (JW-08) 1396
 Lottini, E. (JR-11) 1347
 Loughran, T. (CB-03) 466
 Louis, S. (ED-08) 754
 Louis, S. (ER-06) 806
 Lourembam, J. (CG-08) 534
 Lovell, E. (JT-06) 1367
 Loving, M. (CG-05) 531
 Lu, J. (CC-03) 473
 Lu, J. (CF-08) 520
 Lu, J. (FE-07) 864
 Lu, J. (FG-07) 874
 Lu, Q. (AT-03) 155
 Lu, Q. (BD-03) 214
 Lu, Q. (DE-07) 649
 Lu, Q. (JC-10) 1227
 Lu, Q. (JQ-05) 1331
 Lu, W. (FP-05) 903
 Lu, X. (EA-06) 714
 Lu, X. (FC-05) 843
 Lu, X. (IQ-10) 1140
 Lu, X. (IR-18) 1159
 Lu, X. (JX-02) 1409
 Lu, Y. (AQ-11) 109
 Lu, Z. (IP-11) 1128
 Lu, Z. (JA-03) 1191
 Luberstetter, W. (AC-17) 57
 Lubin, T. (BA-03) 187
 Lubk, A. (AA-04) 23
 Luis Zabotto, F. (JS-10) 1360
 Lukovic, M. (IS-12) 1173
 Lukoyanov, A. (DE-09) 651
 Lukoyanov, A. (JT-09) 1370
 Luo, J. (IS-10) 1171
 Luo, Y. (JQ-03) 1329
 Lupu, N. (IS-03) 1164
 Lupu, N. (IT-07) 1185
 Lupu, N. (JP-03) 1313
 Lupu, N. (JW-08) 1396
 Lupu, N. (JY-04) 1427
 Lux, F. (FH-10) 893
 Luzanov, V. (FB-03) 824
 Lv, B. (JY-15) 1439
 Lysne, E. (HB-10) 984
 Lyu, S. (BJ-13) 301
 Lyubchanskii, I. (EB-07) 722

- M -

- Ma, B. (AP-07) 91
 Ma, B. (AQ-01) 99
 Ma, J. (BU-15) 419
 Ma, T. (CP-07) 547
 Ma, T. (GP-02) 962
 Ma, Y. (BH-03) 266
 Ma, Y. (BW-03) 440
 Ma, Z. (CR-08) 578
 Ma, Z. (CS-14) 596
 Maccari, F. (JC-02) 1219
 Maccariello, D. (CC-08) 478
 Maccherozzi, F. (FG-06) 873
 Maccherozzi, F. (GA-02) 915
 Maccherozzi, F. (GB-03) 925

Machado da Silva, B. (DE-06)	648	Manipatruni, S. (CC-01)	471	Matsumura, T. (CQ-03)	561
Machado da Silva, B. (JP-05)	1315	Manjanna, J. (JR-01)	1337	Matsuo, M. (CA-06)	462
Machida, K. (JS-04)	1354	Manna, K. (DC-06)	622	Matsuo, M. (CE-03)	502
Madhavan, A. (GA-04)	918	Mansueto, M. (CF-07)	519	Matsuo, M. (EC-06)	737
Madhavan, A. (GB-12)	935	Mantovan, R. (DC-01)	617	Matsuo, S. (JR-01)	1337
Madiligama, A.S. (JE-05)	1248	Mantovan, R. (DC-12)	628	Matsuo, T. (BH-04)	267
Madrid Aguilar, C. (ER-09)	809	Manzin, A. (GA-05)	919	Matsushima, N. (IP-01)	1118
Maekawa, S. (EC-03)	734	Marangolo, M. (FB-10)	833	Matsuyama, K. (EP-01)	781
Magalhães, R. (JG-06)	1277	Marault, J. (AP-06)	90	Mattana, R. (IQ-08)	1138
Magalhães, R. (JP-05)	1315	Marchenkov, V. (DB-11)	615	Mattauch, S. (AC-17)	57
Magén, C. (JI-04)	1300	Marchenkov, V. (DE-09)	651	Mattevi, C. (DB-02)	606
Magni, A. (CC-14)	484	Marchenkov, V. (JT-03)	1364	Matthes, P. (JB-09)	1212
Magnitskaya, M. (DG-09)	675	Marchenkova, E. (DB-11)	615	Matveeva, A. (DF-09)	662
Magrez, A. (HC-07)	997	Marchenkova, E. (JT-03)	1364	Matveyev, Y. (FH-13)	896
Magsood, H.A. (JQ-06)	1332	Marchionni, A. (CB-05)	468	Matyunina, M. (JU-02)	1377
Mah, W. (CP-01)	541	Marco, J. (IR-04)	1145	Mausser, N.J. (GC-06)	943
Mahat, R. (DP-01)	679	Mardegan, J.R. (AC-11)	51	Mawass, M. (GD-04)	954
Mahendiran, R. (HB-11)	985	Maria Ferreira Baptista, R. (DB-01)	605	Mayr, S. (AA-03)	22
Mailly, D. (GD-01)	951	Maricarú, M. (BP-15)	325	Mayr, S. (ED-05)	751
Mailly, D. (HD-04)	1006	Marinella, M.J. (GB-02)	924	Mayr, S. (HA-01)	967
Maior, D. (FB-07)	830	Marques de Andrade Júnior, K. (BF-08)	240	Mazaleyrat, F. (BA-01)	185
Majetich, S. (HP-09)	1021	Marques de Andrade Júnior, K. (BG-14)	261	Mazet, T. (DQ-04)	695
Mak, C. (IQ-01)	1131	Marques de Andrade Júnior, K. (BG-15)	262	Maziewski, A. (IH-03)	1104
Mak, C. (IR-06)	1147	Marqués, J.L. (YA-05)	10	Mazraati, H. (FB-08)	831
Makarochkin, I. (IR-11)	1152	Marrows, C. (AE-11)	81	Mazurek, P. (CR-02)	572
Makarov, A. (DG-06)	672	Marrows, C. (FE-03)	860	Mazzoli, C. (AB-05)	31
Makarov, D. (DD-02)	632	Marrows, C. (HA-01)	967	McClelland, J.J. (GB-12)	935
Makarov, D. (DF-01)	653	Marshall, D.S. (IE-03)	1075	McCord, J. (AB-01)	27
Makarov, D. (GD-04)	954	Martin, E. (CC-08)	478	McCord, J. (IB-02)	1040
Makhnev, A. (DB-11)	615	Martin, E. (HB-01)	975	McCord, J. (IT-06)	1184
Makhnev, A. (DE-09)	651	Martin, É. (JR-10)	1346	McCord, J. (JG-08)	1279
Makunin, A.V. (IR-14)	1155	Martin, J. (CQ-08)	566	McCord, J. (JY-01)	1424
Makushko, P. (GD-04)	954	Martin, J. (EC-05)	736	McHenry, M. (JA-01)	1189
Malathi, M. (EE-13)	777	Martin, M. (DB-03)	607	McHenry, M. (JA-04)	1192
Maletinsky, P. (AB-11)	38	Martin, N. (DG-09)	675	McMaster, M.R. (FC-08)	846
Maletinsky, P. (DF-01)	653	Martin, V. (BJ-11)	299	Méchin, L. (IB-05)	1043
Malik, S.V. (JX-09)	1416	Martínez-García, J.C. (YA-05)	10	Meckenstock, R. (FB-02)	823
Malinowski, G. (FD-01)	849	Martini, M. (CC-13)	483	Medapalli, R. (HD-09)	1011
Malinowski, G. (HB-01)	975	Martino, L. (JF-11)	1268	Medjanik, K. (FH-13)	896
Mallick, D. (IF-06)	1084	Martins, L. (DD-09)	639	Medvedeva, T.M. (EB-04)	719
Mallick, D. (JQ-08)	1334	Marty, A. (CB-05)	468	Mei, L. (BE-05)	229
Mallick, S. (AE-10)	80	Marty, A. (CC-01)	471	Meier, D. (HB-10)	984
Mallick, S. (HB-13)	988	Marty, A. (CD-06)	491	Meinert, M. (CD-04)	489
Maloberti, O. (JB-12)	1215	Marty, A. (CD-13)	498	Mekkaoui, S. (JH-01)	1285
Maltoni, P. (JD-10)	1240	Marty, J. (CF-06)	518	Memon, A. (BW-04)	441
Mamiya, H. (JT-08)	1369	Martyshkin, A.A. (EQ-06)	796	Menéndez, E. (DF-02)	654
Manago, T. (CB-03)	466	Maruyama, T. (AV-01)	179	Meng, D. (BP-14)	324
Mañas-Valero, S. (DB-03)	607	Masaki, S. (CP-16)	557	Meng, F. (JI-05)*	1301
Manchon, A. (CB-06)	469	Masell, J. (HB-10)	984	Meng, N. (BC-03)	206
Mancilla, D. (ED-10)	756	Masseboeuf, A. (CB-05)	468	Meng, Y. (BT-03)	384
Mancoff, F.B. (CF-01)	513	Masseboeuf, A. (DD-07)	637	Mentes, T. (HB-08)	982
Mandru, A. (AB-09)	36	Masseboeuf, A. (GD-02)	952	Mentes, T. (IH-11)	1112
Mandru, A. (FH-03)	886	Massey, J. (HA-01)	967	Mentink, J. (HA-02)	968
Mandru, A. (HA-03)	969	Massouras, M. (GA-01)	914	Merbouche, H. (EB-02)	717
Mandru, A. (IH-02)	1103	Masuda, T. (DF-06)	658	Merbouche, H. (ED-02)	748
Mandziak, A. (IH-12)	1113	Mathews, S.A. (AD-06)	65	Merbouche, H. (ED-03)	749
Manescu Paltanea, V. (BP-15)	325	Mathews, S.A. (CS-03)	585	Merbouche, H. (ED-07)	753
Mangin, S. (CC-08)	478	Mathews, S.A. (CS-04)	586	Merbouche, H. (JA-12)	1201
Mangin, S. (FD-01)	849	Mathieu, R. (JD-10)	1240	Mercadier, L. (FD-05)	853
Mangin, S. (HB-01)	975	Matsuda, R. (CE-10)	509	Mercurio, G. (FD-05)	853
Mangin, S. (ID-01)	1061	Matsumoto, K. (JT-11)	1372	Mercurio, G. (HA-02)	968

Merschroth, H. (JC-02)	1219	Mirzadeh Vaghefii, P. (FH-03)	886	Montaigne, F. (GA-01)	914
Merte, M. (FH-10)	893	Mirzaei, M. (IB-06)	1044	Montaigne, F. (ID-01)	1061
Mertig, I. (FG-01)	868	Mirzaei, M. (IC-06)	1058	Montanaro, A. (JF-07)	1263
Mertig, I. (HD-03)	1005	Mirzaei, M. (IT-09)	1187	Moon, J. (AR-09)	124
Mertig, I. (HP-02)	1014	Misaka, Y. (IS-15)	1176	Moon, J. (DP-03)	681
Mesaros, A. (IQ-05)	1135	Mishra, D. (JD-11)	1241	Moore, T. (HA-01)	967
Messal, O. (JB-13)	1216	Mishra, R. (CG-12)	538	Moore, T. (IQ-02)	1132
Messal, O. (JW-18)	1406	Mishra, S.R. (JS-07)	1357	Moore, T. (JY-06)	1429
Messing, M.E. (IG-10)	1097	Mishra, S.R. (JS-08)	1358	Moraes, S. (JG-06)	1277
Messing, M.E. (JI-01)	1297	Mitani, S. (IE-04)	1076	Morales Casero, I. (JH-10)	1294
Metlov, K. (AA-03)	22	Mitarai, H. (CB-02)	465	Morales, P. (JH-10)	1294
Meunier, T. (DC-11)	627	Mitarai, H. (DG-07)	673	Morales, R. (JG-06)	1277
Mewes, C. (CA-03)	459	Mitarai, H. (IF-02)	1080	Morche, D. (ID-08)	1068
Mewes, T. (CA-03)	459	Mitarai, H. (IP-10)	1127	Morel, L. (JY-08)	1431
Meyners, D. (IB-02)	1040	Mitra, S. (JE-10)	1253	Morel, R. (AE-07)	77
Mezani, S. (AQ-08)	106	Mitsuya, K. (BI-02)	276	Moreno-Ramirez, L.M. (JE-01)	1243
Mezani, S. (BA-03)	187	Miura, A. (CE-09)	508	Moreno-Ramirez, L.M. (JE-07)	1250
Mi, M. (AS-04)	139	Miura, D. (CE-11)	510	Moreno-Ramirez, L.M. (JE-09)	1252
Mi, M. (JY-12)	1436	Miura, K. (EC-03)	734	Moreno, J.A. (AC-02)	41
Mi, W. (DC-05)	621	Miura, S. (CF-03)	515	Moreu, J. (BF-03)	235
Mi, W. (DC-08)	624	Miura, S. (CF-05)	517	Morgan, G.G. (DG-10)	676
Mi, W. (DE-02)	643	Miura, Y. (CE-09)	508	Morikawa, H. (BH-07)	270
Miao, B. (CP-10)	551	Miura, Y. (IF-05)	1083	Morillas, J.R. (YB-01)	13
Miao, B. (CP-12)	553	Mix, T. (JD-08)	1238	Moriyama, T. (FA-04)	818
Miao, J. (EA-06)	714	Miyazaki, T. (FP-11)	909	Moriyama, T. (FB-11)	834
Miao, W.C. (IS-04)	1165	Miyazaki, T. (JY-05)	1428	Morley, N. (IT-08)	1186
Mican, S. (IQ-05)	1135	Mizokami, K. (CE-10)	509	Morley, N. (JB-02)	1205
Michaelis De Vasconcellos, S. (FA-05)	819	Mizrahi, A. (GA-04)	918	Morley, N. (JB-05)	1208
Michel, J. (ID-03)	1063	Mizukami, S. (CD-12)	497	Morley, N. (JX-10)	1417
Michez, L. (FG-08)	875	Mizukami, S. (ED-06)	752	Morley, N. (JX-11)	1418
Michez, L. (FH-08)	891	Mizukami, S. (ED-13)	760	Morozkin, A.V. (JS-06)	1356
Mielcarek, S. (EC-08)	739	Mizukami, S. (FB-11)	834	Morozova, M. (EA-05)	713
Mieszczak, S. (EC-08)	739	Mizukami, S. (IE-02)	1074	Morshed, M. (HD-05)	1007
Mieszczak, S. (EE-07)	770	Mizukami, S. (IE-05)	1077	Moshkina, E. (DQ-08)	699
Migot, S. (CC-08)	478	Mkhoyan, A.K. (IH-05)	1106	Moskalenko, O.I. (EB-04)	719
Migot, S. (JF-03)	1259	Mo, L. (BW-13)	451	Moskalev, M. (IR-10)	1151
Mihajlović, G. (CB-03)	466	Mo, W. (CP-02)	542	Moskvin, A. (DQ-03)	694
Mikami, T. (ER-03)	803	Mo, W. (CP-08)	548	Mosseri, I. (GC-08)	945
Mikhaylovskiy, R.V. (FB-11)	834	Mo, W. (HP-06)	1018	Motiejuitis, K. (IB-13)	1051
Miki, S. (GA-03)	917	Mo, W. (IS-16)	1177	Motyckova, L. (JW-12)	1400
Milán-Rois, P. (JG-05)	1276	Mo, W. (JY-07)	1430	Mougin, A. (AE-10)	80
Milinska, E. (IG-02)	1089	Moalic, M. (EP-07)	787	Mougin, A. (FH-06)	889
Millan Mirabal, L.A. (JB-13)	1216	Modak, R. (IF-05)	1083	Mougin, A. (HD-08)	1010
Mille, N. (DD-07)	637	Modestino, M. (JR-12)	1348	Moulin, J. (IB-04)	1042
Mille, N. (JH-10)	1294	Moeller, M. (HA-02)	968	Mounkachi, O. (JS-09)	1359
Miller, D. (CG-05)	531	Mogilenc, Y. (JY-19)	1443	Mourkas, A. (JR-09)	1345
Min, J. (AR-18)	133	Mohapatra, J. (JI-10)	1306	Moutafis, C. (FC-03)	841
Mina, M. (CR-11)	581	Mohd Noor Sam, M.b. (IT-03)	1181	Moya, C. (JH-07)	1291
Mina, M. (JS-02)	1352	Mohd Shafiqi, S.A. (BI-10)	286	Moya, C. (JH-08)	1292
Minamitani, M. (AT-06)	158	Mohseni, F. (IC-07)	1059	Moyano, A. (YA-05)	10
Minar, J. (FH-13)	896	Mokrousov, Y. (CE-12)	511	Mruczkiewicz, M. (AE-09)	79
Minciunescu, P. (BP-15)	325	Mokrousov, Y. (FD-03)	851	Mucchietto, A. (EE-03)	766
Minuti, A. (JP-03)	1313	Mokrousov, Y. (FD-04)	852	Muchharla, B. (JG-12)	1283
Mion, T.R. (IB-03)	1041	Mokrousov, Y. (FH-10)	893	Mudryk, Y. (JT-06)	1367
Mion, T.R. (JF-05)	1261	Molho, P. (ID-01)	1061	Muduli, P.K. (GB-01)	922
Miranda, R. (DB-09)	613	Molodtsov, S. (FD-05)	853	Muechler, L. (DC-06)	622
Miranda, R. (IB-05)	1043	Molokeev, M. (DQ-08)	699	Mugerman, K. (TU-03)	4
Miranda, R. (IG-11)	1099	Mompeán, F. (JD-11)	1241	Mukherjee, B. (BI-07)	283
Miranda, R. (IH-14)	1115	Mondal, D. (DB-06)	610	Mulkers, j. (EC-07)	738
Miranda, R. (IR-16)	1157	Monga, S. (DP-10)	688	Mulkers, j. (GC-02)	939
Miron, I. (HC-05)	995	Monma, R. (IE-05)	1077	Mullen, A. (GA-02)	915

Nlebedim, I.C. (JU-10)	1385
Noack, T.B. (EB-08)	723
Noda, M. (DP-04)	682
Noël, P. (CD-11)	496
Noël, P. (DC-11)	627
Noël, P. (FE-02)	859
Nogarede, B. (BJ-08)	296
Noguchi, y. (CF-03)	515
Nogues, J. (DF-02)	654
Noky, J. (DC-06)	622
Nomdedeu, M. (BJ-08)	296
Nomura, A. (JX-08)	1415
Nomura, E. (JR-01)	1337
Nomura, H. (GA-03)	917
Normile, P.S. (IH-08)	1109
Noro, S. (JD-05)	1235
Novák, P. (JC-12)	1229
Novak, V. (AB-04)	30
Novati, A. (DB-06)	610
Novotny, J. (IB-08)	1046
Nozaki, T. (GA-03)	917
Nozaki, T. (IH-04)	1105
Nozaki, Y. (EC-06)	737
Nozawa, K. (ER-12)	812
Nsibi, M. (HC-05)	995
Nunes, C. (JG-06)	1277
Nuss, J. (DP-03)	681
Nutter, P. (FB-13)	836

- O -

O' Sullivan, B. (CF-12)	525
O'Carroll, I. (JP-15)	1325
O'Grady, K. (IG-09)	1096
Obinata, S. (CP-13)	554
Och, M. (DB-02)	606
Ocker, B. (CG-09)	535
Odintsov, S. (EP-02)	782
Odintsov, S. (EQ-05)	795
Oezelt, H. (AD-04)	63
Ogami, H. (EP-01)	781
Ogasawara, S. (BP-02)	311
Ogawa, T. (IP-02)	1119
Ogawa, T. (IP-03)	1120
Ogawa, Y. (JW-06)	1394
Ognev, A. (CB-01)	464
Ognev, A. (GP-02)	962
Ogrin, F. (EP-02)	782
Oguz, K. (DA-04)	601
Oh, D. (DP-03)	681
Oh, D. (DP-05)	683
Oh, S. (AR-15)	130
Oh, S. (AR-16)	131
Oh, S. (BQ-15)	344
Oh, S. (BR-14)	360
Oh, S. (BW-12)	450
Oh, S. (EP-04)	784
Oh, S. (FP-12)	910
Ohashi, S. (AT-06)	158
Ohashi, S. (AV-01)	179

Ohashi, S. (BD-05)	216
Ohashi, S. (BS-09)	374
Ohishi, K. (JR-01)	1337
Ohkubo, T. (IE-04)	1076
Ohldag, H. (FG-15)	882
Ohnishi, K. (CE-10)	509
Ohno, H. (CG-01)	527
Ohno, H. (CG-02)	528
Ohno, H. (FC-09)	847
Ohno, H. (FD-01)	849
Ohno, H. (FG-05)	872
Ohno, H. (GB-10)	933
Ohno, H. (IH-03)	1104
Ohodnicki, P. (JA-04)	1192
Ohresser, P. (JI-11)	1307
Ohtake, M. (JD-05)	1235
Okamoto, Y. (IP-07)	1124
Okamoto, Y. (IP-08)	1125
Okamura, N. (CQ-04)	562
Okita, K. (ER-12)	812
Okita, K. (JP-13)	1323
Okuno, H. (CB-02)	465
Okuno, H. (CB-05)	468
Okuno, H. (IP-10)	1127
Olafasakin, O.O. (JP-01)	1311
Oliveira, J. (DE-06)	648
Oliveros Mata, E. (GD-04)	954
Olivetti, E.S. (JF-11)	1268
Olkhovskiy, I. (JQ-07)	1333
Ollefs, K. (CR-05)	575
Olleros-Rodríguez, P. (AE-08)	78
Olleros-Rodríguez, P. (DB-09)	613
Olleros-Rodríguez, P. (HB-03)	977
Olleros-Rodríguez, P. (IH-08)	1109
Olleros-Rodríguez, P. (IH-14)	1115
One, R. (IQ-05)	1135
Ong, H. (BI-10)	286
Onita, S. (IS-15)	1176
Ono, S. (FE-09)	866
Ono, T. (CP-04)	544
Ono, T. (FB-11)	834
Ono, Y. (CQ-05)	563
Onsal, M. (BG-04)	251
Oogane, M. (CP-03)	543
Oogane, M. (CP-15)	556
Oogane, M. (IT-03)	1181
Opel, M. (FG-10)	877
Orikawa, K. (BP-02)	311
Orue, I. (ER-09)	809
Osawa, H. (IP-07)	1124
Oshima, D. (FC-06)	844
Osipov, A. (ER-13)	813
Osman, R. (JX-10)	1417
Ostatnicky, T. (AB-04)	30
Otani, Y. (CP-09)	549
Otani, Y. (EC-03)	734
Otani, Y. (FH-05)	888
Otero, E. (JI-11)	1307
Otxoa, R.M. (FG-02)	869
Ou, J. (CR-10)	580
Ouazir, Y. (AQ-08)	106

Oue, D. (CE-03)	502
Ourdani, D. (FE-09)	866
Ourdani, D. (IR-01)	1142
Ovari, T.A. (IS-03)	1164
Ovari, T.A. (JY-04)	1427
Ovchinnikov, A.S. (EQ-08)	798
Ovsianikov, A. (JT-10)	1371
Oyama, D. (CQ-01)	559
Ozaydin, F. (IF-03)	1081
Ozden, M.G. (JX-11)	1418
Ozdincer, B. (BE-02)	226

- P -

P K, J. (JT-13)	1374
P.S., A.K. (GP-04)	964
Pablo-Navarro, J. (JI-04)	1300
Pace, S. (JR-12)	1348
Pachat, R. (FE-09)	866
Pachlhofer, J. (AD-04)	63
Padalko, M. (DG-06)	672
Padhy, S.P. (JA-05)	1193
Padhy, S.P. (JB-03)	1206
Padhy, S.P. (JB-06)	1209
Padhy, S.P. (JB-07)	1210
Page, M. (EC-11)	742
Pai, C. (CC-02)	472
Pai, C. (CC-04)	474
Pai, C. (CC-10)	480
Pai, C. (CC-12)	482
Paikaray, B. (CD-07)	492
Paikaray, B. (HP-05)	1017
Pakdelian, S. (BU-09)	411
Pala, J. (CD-07)	492
Paleo, C. (JD-03)	1233
Palin, V. (DE-03)	644
Pallás, E. (YA-01)	6
Palmero, E.M. (JD-08)	1238
Palmero, E.M. (JD-09)	1239
Palomino, A. (CF-06)	518
Palomino, A. (CF-07)	519
Palomino, A. (CG-03)	529
Paltanea, G. (BP-15)	325
Pan, Z. (BT-03)	384
Panagiotopoulos, I.V. (JR-09)	1345
Panagopoulos, C. (CC-08)	478
Pandey, N. (GD-06)	956
Pandey, S. (DQ-10)	701
Pandeya, A. (DB-04)	608
Pandit, P. (IH-07)	1108
Pang, H. (AS-02)	136
Pang, H. (AU-03)	164
Panigrahi, B. (FB-04)	826
Panina, L. (JY-02)	1425
Panina, L. (JY-03)	1426
Pannetier-Lecoer, M. (IB-04)	1042
Panov, Y. (DQ-03)	694
Panwar, R. (JA-08)	1196
Panwar, R. (JA-10)	1198

Papin, J. (DC-11)	627	Peddis, D. (JD-10)	1240	Perumkunnil, M. (CG-13)	539
Paranthaman, P.M. (BE-03)	227	Peddis, D. (JR-11)	1347	Pesteri, M. (BP-15)	325
Paranthaman, P.M. (BE-04)	228	Pedersoli, E. (FD-03)	851	Peters, J. (AC-17)	57
Paranthaman, P.M. (JC-01)	1218	Pedraz, P. (IH-08)	1109	Peters, L. (AC-17)	57
Paranthaman, P.M. (JC-08)	1225	Pedro Esteves de Araújo, J. (DB-01)	605	Peters, L. (JT-10)	1371
Park, B. (IQ-07)	1137	Pedro Esteves de Araújo, J. (DE-06)	648	Peters, T. (ER-11)	811
Park, D. (AC-05)	44	Pedro Esteves de Araújo, J. (JE-12)	1255	Petit-Watlot, S. (CC-08)	478
Park, E. (BU-08)	410	Pedro Esteves de Araújo, J. (JG-06)	1277	Petit-Watlot, S. (DD-10)	640
Park, G. (AS-08)	143	Pedro Esteves de Araújo, J. (JI-03)	1299	Petit-Watlot, S. (DE-01)	642
Park, G. (AU-08)	171	Pedro Esteves de Araújo, J. (JP-05)	1315	Petit-Watlot, S. (DE-03)	644
Park, G. (IS-02)	1163	Pedro Esteves de Araújo, J. (JR-05)	1341	Petit-Watlot, S. (HB-01)	975
Park, G. (IS-13)	1174	Pedro Esteves de Araújo, J. (JT-06)	1367	Petit-Watlot, S. (ID-01)	1061
Park, G. (IT-02)	1180	Pedro Esteves de Araújo, J. (JT-07)	1368	Petit, S. (EC-12)	743
Park, G. (IT-05)	1183	Pei, R. (BV-03)	428	Petricek, V. (DG-04)	670
Park, H. (AQ-07)	105	Pei, R. (JX-13)	1420	Petricek, V. (FG-08)	875
Park, H. (BQ-10)	339	Pei, T. (AT-07)	159	Petrisor Jr, T. (IQ-05)	1135
Park, J. (AV-03)	181	Pei, Y. (AQ-03)	101	Petroff, F. (DB-02)	606
Park, J. (BG-05)	252	Peiro, J. (DB-02)	606	Petroff, F. (IQ-08)	1138
Park, J. (BP-02)	311	Peixoto, L. (JG-06)	1277	Petrov, D. (ER-13)	813
Park, J. (BP-13)	323	Peña García, J.A. (CB-02)	465	Pfau, B. (AB-05)	31
Park, J. (CG-12)	538	Peña García, J.A. (FE-08)	865	Pfau, B. (HA-02)	968
Park, J. (CP-04)	544	Peña García, J.A. (HB-08)	982	Pfeuffer, L. (JE-02)	1244
Park, J. (YB-06)	18	Peña García, J.A. (IP-10)	1127	Pfeuffer, L. (JT-06)	1367
Park, K. (BS-11)	376	Penedo, M. (HA-03)	969	Pfister, P. (BI-06)	281
Park, K. (BS-12)	377	Peng, C. (BE-05)	229	Pfister, P. (BU-13)	417
Park, K. (JW-03)	1391	Peng, C. (CC-10)	480	Phakphisut, W. (IP-05)	1122
Park, S. (AR-12)	127	Peng, H. (AQ-10)	108	Pham, T. (CQ-11)	569
Park, S. (AV-03)	181	Peng, H. (BV-08)	434	Pham, T. (CR-09)	579
Park, S. (BG-05)	252	Peng, J. (AR-03)	117	Pham, T. (IT-01)	1179
Park, S. (CP-04)	544	Peng, K. (IC-05)	1057	Pham, V. (CC-01)	471
Park, S. (IQ-07)	1137	Peng, S. (CC-03)	473	Pham, V. (CD-06)	491
Park, Y. (AR-15)	130	Peng, S. (CF-08)	520	Pham, V. (CD-13)	498
Park, Y. (AR-16)	131	Peng, S. (FE-07)	864	Pham, V. (HD-04)	1006
Park, Y. (BQ-15)	344	Peng, S. (FG-07)	874	Phan, M. (JG-12)	1283
Park, Y. (BR-13)	359	Peng, S. (IH-01)	1102	Phatak, C. (AB-08)	34
Park, Y. (BR-14)	360	Pepper, R. (GC-05)	942	Philippe, S. (AE-07)	77
Park, Y. (BW-12)	450	Pereira, A. (JE-12)	1255	Phuoc, C. (CP-04)	544
Parkin, S. (DA-01)	598	Pereira, A. (JT-06)	1367	Piamonteze, C. (IG-10)	1097
Parkin, S. (DB-04)	608	Pereira, E. (JP-05)	1315	Piamonteze, C. (JH-07)	1291
Parkin, S. (DC-02)	618	Pereiro, E. (CQ-08)	566	Picozzi, S. (DB-06)	610
Parkin, S. (HD-03)	1005	Perevedentseva, E. (JG-09)	1280	Pierre, D. (ID-01)	1061
Parkin, S. (HP-02)	1014	Perevozchikova, Y. (DE-09)	651	Pierron, V. (IB-05)	1043
Pasquale, M. (JF-11)	1268	Pérez García, L. (DD-07)	637	Pietro, A.D. (FE-09)	866
Pastor, G.M. (JW-13)	1401	Pérez García, L. (JD-11)	1241	Pietruczik, A. (IG-02)	1089
Pathak, A. (JS-07)	1357	Permyakov, N. (GC-07)	944	Pilabutr, S. (IP-06)	1123
Pathak, P. (IF-06)	1084	Perna, P. (AE-08)	78	Pilidi, A. (CP-06)	546
Patriarche, G. (JI-12)	1308	Perna, P. (DB-09)	613	Pinarbasi, M. (CF-09)	522
Pattabi, A. (GD-08)	958	Perna, P. (HB-03)	977	Pinna, D. (GB-13)	936
Pattabi, A. (HB-01)	975	Perna, P. (IB-05)	1043	Pippan, R. (IR-13)	1154
Pattanaik, M.S. (JH-05)	1289	Perna, P. (IG-11)	1099	Pippan, R. (JA-06)	1194
Paul, K. (BK-05)	308	Perna, P. (IH-08)	1109	Piquemal-Banci, M. (DB-03)	607
Paulides, J.J. (BA-02)	186	Perna, P. (IH-14)	1115	Piramanayagam, S. (CE-06)	505
Paulischin, A. (IR-13)	1154	Perna, P. (IR-16)	1157	Piramanayagam, S. (CP-01)	541
Pauly, C. (DG-10)	676	Perna, S. (BJ-14)	302	Piramanayagam, S. (GP-04)	964
Pavilonis, D. (IB-13)	1051	Perna, S. (EB-11)	727	Piramanayagam, S. (HB-11)	985
Pavlov, A.N. (EB-04)	719	Perna, S. (FD-08)	856	Pirola, K. (DG-01)	667
Pawlak, E. (JG-11)	1282	Perna, S. (GC-04)	941	Pirro, P. (EB-03)	718
Pazzocco, R. (FG-14)	881	Perna, S. (GC-10)	948	Pirro, P. (ED-11)	757
Pecharsky, V. (JE-06)	1249	Perov, N.S. (ID-04)	1064	Pirro, P. (EE-04)	767
Pecharsky, V. (JT-06)	1367	Perrin, Y. (DQ-09)	700	Pistono, E. (ID-08)	1068
Peda, M. (GP-04)	964	Perumkunnil, M. (CF-12)	525	Pitala, K.T. (AC-14)	54

- Pizzini, S. (CB-02) 465
Pizzini, S. (FE-08) 865
Pizzini, S. (HB-07) 981
Pizzini, S. (HB-08) 982
Pizzini, S. (HC-02) 991
Pizzini, S. (IP-10) 1127
Platonov, S. (JT-09) 1370
Plausinaitiene, V. (IB-13) 1051
Plombon, J. (DA-04) 601
Plotnikov, V.S. (JR-06) 1342
Ployard, M. (JB-12) 1215
Plumer, M.L. (AD-03) 62
Podevin, F. (ID-08) 1068
Podgornik, B. (AB-01) 27
Podgornykh, S. (DB-11) 615
Podmiljšak, B. (JC-11) 1228
Poh, C. (CE-06) 505
Pohl, D. (JR-02) 1338
Pokrovsky, V. (EB-12) 728
Polichetti, M. (JR-12) 1348
Polinder, H. (BG-01) 248
Pollard, S. (HC-01) 990
Polley, D. (GD-08) 958
Pollok, S. (BH-01) 264
Polzikova, N. (FB-03) 824
Pomyalov, A. (EB-08) 723
Poncot, M. (JF-03) 1259
Pong, P. (HP-03) 1015
Pong, P. (IS-01) 1161
Pong, P. (JH-06) 1290
Pong, P.W. (IS-04) 1165
Ponomareva, S. (AE-07) 77
Pöppel, A. (JS-06) 1356
Porod, W. (EE-11) 774
Potzger, K. (FB-02) 823
Poulain, A. (JE-12) 1255
Pourkeivannour, S. (AS-10) 145
Povzner, A. (HP-11) 1023
Powell, D. (BF-04) 236
Powell, D. (BF-13) 246
Pownall, R. (CG-05) 531
Prabhakar, A. (EE-13) 777
Prabhu Gaunkar, N. (CR-11) 581
Prabhu Gaunkar, N. (JS-02) 1352
Pradhan, G. (HB-13) 988
Pradhan, G. (JU-06) 1381
Pramana, S. (JE-07) 1250
Prat, J. (GA-02) 915
Pratt, J. (GB-03) 925
Préault, V. (AC-12) 52
Preger, C. (IG-10) 1097
Preger, C. (JL-01) 1297
Prejbeanu, I. (CF-06) 518
Prejbeanu, I. (CF-07) 519
Prejbeanu, I. (CF-11) 524
Prejbeanu, I. (GB-05) 928
Prejbeanu, I. (IB-07) 1045
Prejbeanu, I.L. (CG-03) 529
Prejbeanu, I.L. (ID-07) 1067
Prenat, G. (GB-05) 928
Prida, V. (JT-05) 1366
Prieto, J. (IH-12) 1113
Prieto, J. (IR-04) 1145
Priolkar, K. (JX-09) 1416
Prischepa, S.L. (JI-07) 1303
Proenca, M.P. (GD-03) 953
Proenca, M.P. (JI-03) 1299
Proenca, M.P. (JR-05) 1341
Psaroudaki, C. (HC-08) 998
Psycharis, V. (JC-07) 1224
Pu, W. (AR-13) 128
Pu, Y. (BT-16) 400
Puebla, J. (CP-09) 549
Puebla, J. (EC-03) 734
Pufall, M.R. (GB-12) 935
Puliafito, V. (AE-05) 75
Puttock, R. (GA-05) 919
Pylypovskiy, O. (DD-02) 632
Pylypovskiy, O. (DF-01) 653
Pylypovskiy, O. (EB-01) 716
Pylypovskiy, O. (GD-04) 954
Pyo, H. (BR-15) 361
Pyo, H. (BR-17) 363
- Q -
- Qaid, M. (ER-11) 811
Qaiumzadeh, A. (HB-10) 984
Qi, J. (FP-05) 903
Qian, C. (BH-10) 272
Qiao, G. (AV-02) 180
Qiao, G. (BB-10) 202
Qiao, G. (BP-03) 312
Qiao, G. (BP-05) 314
Qiao, G. (BP-06) 315
Qiao, G. (BP-12) 322
Qiao, G. (JY-13) 1437
Qiao, L. (JY-13) 1437
Qiao, M. (AC-18) 58
Qin, H. (EE-09) 772
Qin, L. (BT-03) 384
Qin, W. (AT-01) 153
Qin, W. (BI-08) 284
Qin, X. (BC-01) 204
Qin, Y. (IA-06) 1031
Qiu, H. (CR-08) 578
Qiu, H. (CS-14) 596
Qiu, H. (JP-14) 1324
Qiu, H. (JQ-09) 1335
Qiu, J. (CG-08) 534
Qiu, J. (CR-10) 580
Qiu, J. (IS-07) 1168
Qiu, J. (IS-09) 1170
Qiu, J. (JU-12) 1387
Qiu, L. (BU-15) 419
Qiu, X. (BP-17) 327
Qiu, Y. (EQ-01) 791
Qiu, Y. (HP-01) 1013
Qiu, Y. (IS-10) 1171
Qu, G. (BG-13) 260
Qu, R. (AS-03) 138
Qu, R. (AT-07) 159
Qu, R. (BT-01) 382
Qu, R. (BT-04) 385
Qu, R. (BT-09) 392
Qu, R. (BU-01) 402
Qu, T. (FC-01) 839
Quaegebeur, P. (BJ-11) 299
Quan, L. (AQ-11) 109
Quan, L. (AR-13) 128
Querlioz, D. (GA-01) 914
Quesada, A. (IH-12) 1113
Quesada, A. (IR-04) 1145
Quesada, A. (JD-11) 1241
Quinard, B. (IQ-08) 1138
Quinata-Nedelcos, A. (JB-05) 1208
Quinata-Nedelcos, A. (JX-10) 1417
Quintana, A. (DF-02) 654
Quiros, C. (CQ-08) 566
Quiros, C. (EC-05) 736
- R -
- R, M. (CP-05) 545
R, N. (JE-04) 1247
R, N. (JS-06) 1356
R, N. (JT-13) 1374
Raab, K. (FG-05) 872
Raab, K. (HC-10) 1000
Raabe, J. (AA-03) 22
Raabe, J. (DD-05) 635
Raabe, J. (ED-05) 751
Raabe, J. (HA-01) 967
Radu, F. (DB-04) 608
Radu, I. (GD-09) 959
Radulov, I. (CR-05) 575
Radulov, I. (JC-02) 1219
Raevskiy, A. (FB-03) 824
Rafin, S.H. (BB-08) 199
Ragusa, C. (JB-11) 1214
Ragusa, C. (JX-03) 1410
Raimondo, E. (HC-11) 1001
Raja, M.M. (FB-04) 826
Rajauria, S. (IA-08) 1033
Rallabandi, V. (AP-08) 92
Rama-Eiroa, R. (FG-02) 869
Ramalinga Viswanathan, M. (JS-10) 1360
Ramanujan, R. (JA-05) 1193
Ramanujan, R. (JB-03) 1206
Ramanujan, R. (JB-04) 1207
Ramanujan, R. (JB-06) 1209
Ramanujan, R. (JB-07) 1210
Ramanujan, R. (JH-05) 1289
Ramanujan, R. (JI-06) 1302
Ramesh, A. (AC-09) 49
Ramirez, J. (IG-01) 1088
Ramos, R. (FG-04) 871
Ramos, R. (FG-06) 873
Rana, A. (EA-06) 714
Rana, B. (EC-03) 734
Rana, K. (HD-04) 1006

Ranjbar, M. (FB-08)	831	Rezende, S.M. (FB-07)	830	Rosch, A. (HB-10)	984
Ranjbar, S. (CP-15)	556	Rezvantseva, Y. (JP-06)	1316	Roschewsky, N. (CG-04)	530
Ranno, L. (FE-08)	865	Rezzoug, A. (BA-03)	187	Ross, A. (FG-06)	873
Ranno, L. (HB-07)	981	Rial, J. (GD-03)	953	Ross, C. (CE-08)	507
Ranno, L. (JW-12)	1400	Rial, J. (JD-08)	1238	Ross, C. (IQ-03)	1133
Rao, J. (EC-01)	732	Rial, J. (JI-03)	1299	Ross, K. (DG-04)	670
Rao, S. (CF-12)	525	Ribeiro, L. (ER-10)	810	Rossi, A. (JE-12)	1255
Rao, S. (CG-13)	539	Richter, K. (JR-08)	1344	Rotarescu, C. (JY-04)	1427
Rasly, M. (IB-10)	1048	Richter, K. (JY-01)	1424	Roth, G. (AC-17)	57
Rath, C. (DF-05)	657	Rieger, R. (IB-02)	1040	Rothörl, J. (FG-05)	872
Raulet, M. (JY-08)	1431	Riegg, S. (IC-02)	1219	Rothörl, J. (HC-10)	1000
Rautskii, M.V. (DP-08)	686	Riegg, S. (JA-04)	1260	Rothuizen, H. (IA-09)	1034
Rautskii, M.V. (JR-06)	1342	Rigla, J. (YA-01)	6	Rott, K. (ER-11)	811
Ravelosona, D. (CG-09)	535	Rimal, B.P. (GB-02)	924	Rougemaille, N. (DG-11)	677
Ravelosona, D. (FE-09)	866	Rimoldi, M. (DC-01)	617	Rougemaille, N. (DQ-09)	700
Ravelosona, D. (GD-01)	951	Rinaldi, C. (CD-11)	496	Rougemaille, N. (DQ-11)	702
Ravelosona, D. (HB-11)	985	Rinaldi, C. (DB-06)	610	Rougemaille, N. (GA-01)	914
Ravelosona, D. (HC-06)	996	Rinaldi, C. (FG-14)	881	Roussigné, Y. (FE-09)	866
Ravelosona, D. (HD-04)	1006	Rinaldi, C. (IR-15)	1156	Roussigné, Y. (GD-01)	951
Rawat, R. (DP-10)	688	Ríos, A. (YA-01)	6	Roussigné, Y. (HD-04)	1006
Rawat, R. (DQ-10)	701	Riault, M. (GD-02)	952	Roussigné, Y. (IR-01)	1142
Rayaprol, S. (JS-06)	1356	Ripka, P. (IB-06)	1044	Roussigné, Y. (IR-02)	1143
Raymenants, E. (GD-09)	959	Ripka, P. (IC-06)	1058	Rovillain, P. (FB-10)	833
Rebelo, T. (DE-06)	648	Ripka, P. (IT-09)	1187	Rowan-Robinson, R. (JB-02)	1205
Reddy, V. (IG-12)	1100	Rippard, W.H. (GB-12)	935	Rowan-Robinson, R. (JB-05)	1208
Reddy, V. (IR-09)	1150	Ritzinger, P. (FG-08)	875	Rowan-Robinson, R. (JX-10)	1417
Redies, M. (FH-10)	893	Ritzmann, U. (HA-06)	973	Roy, P. (EC-12)	743
Redondo, C. (JG-06)	1277	Rivas, M. (YA-05)	10	Roy, S. (BK-05)	308
Reeve, R. (FH-11)	894	Rizzo, N. (CG-05)	531	Roy, S. (DP-02)	680
Rehm, L. (CF-09)	522	Rizzolo, M. (CF-02)	514	Roy, S. (EE-10)	773
Reichlova, H. (AB-04)	30	Ro, J. (BW-04)	441	Roy, S. (IG-05)	1092
Reichlova, H. (FG-08)	875	Roberjot, P. (EE-02)	765	Roy, T. (IE-02)	1074
Reichlova, H. (FH-08)	891	Robert, A. (JI-11)	1307	Rozanov, K. (ER-13)	813
Reiffers, M. (DQ-01)	692	Rocha-Rodrigues, P. (DE-06)	648	Ruan, X. (FC-05)	843
Reiffers, M. (JE-04)	1247	Roche, S. (CB-06)	469	Rubanskyi, V. (AC-17)	57
Reis, M.S. (JE-12)	1255	Roche, S. (DA-03)	600	Rubi, K. (FG-09)	876
Reis, S. (JG-06)	1277	Rodionova, V. (JY-03)	1426	Rubio-Roy, M. (FH-02)	885
Reiss, G. (ER-11)	811	Rodriguez Alvarez, J. (IG-01)	1088	Rudokas, V. (IB-13)	1051
Reitz, D. (ED-04)	750	Rodriguez, L. (AA-04)	23	Rudolf, P. (DE-08)	650
Rékioua, T. (BU-14)	418	Rodriguez, L. (JI-04)	1300	Ruiz Gómez, S. (DD-07)	637
Remy, Q. (FD-01)	849	Rogalev, A. (CR-05)	575	Ruiz Gómez, S. (IH-12)	1113
Ren, I. (AU-07)	170	Rogalev, A. (JW-13)	1401	Ruiz Gómez, S. (JD-11)	1241
Ren, L. (BG-11)	258	Roger, J. (JB-13)	1216	Runge, J. (JP-10)	1320
Ren, X. (BT-01)	382	Rogers, V.C. (IE-03)	1075	Russina, M. (DG-04)	670
Ren, X. (BT-09)	392	Rohart, S. (AE-02)	72	Ruta, S. (FD-06)	854
Ren, Y. (AC-04)	43	Rohart, S. (AE-10)	80	Ruta, S. (HB-03)	977
Ren, Y. (CQ-02)	560	Rohart, S. (HB-08)	982	Ryan, S. (EA-06)	714
Ren, Y. (HC-04)	994	Rohart, S. (HB-13)	988	Ryba, T. (JT-04)	1365
Ren, Y. (JE-05)	1248	Rojas-Sanchez, J. (CC-08)	478	Rybin, A. (DG-06)	672
Renshaw, W. (GP-04)	964	Rojas-Sanchez, J. (DE-03)	644	Rychly, J.N. (EE-14)	778
Repaka, D.M. (CG-08)	534	Rojas-Sanchez, J. (HB-01)	975	Ryu, J. (AU-10)	173
Resende, Ú.d. (ER-10)	810	Rojas-Sanchez, J. (ID-01)	1061		
Resende, Ú.d. (JY-16)	1440	Rojo-romero, P. (JI-11)	1307		
Restrepo, J. (DD-03)	633	Romanenko, D.V. (EB-04)	719		
Retuerto, M. (DF-07)	659	Romanenko, D.V. (ER-01)	801		
Reyren, N. (CB-05)	468	Romashkina, I.L. (IR-14)	1155		
Reyren, N. (CC-11)	481	Rongione, E. (FB-01)	822	S, M. (JT-02)	1363
Reyren, N. (FB-01)	822	Ronnow, H.M. (HC-07)	997	S, S. (JE-04)	1247
Reyren, N. (GA-01)	914	Ropers, C. (HA-02)	968	S. K. Hasanain, S. (DE-08)	650
Reyren, N. (HC-02)	991	Rosamond, M. (GA-05)	919	Sá, S. (FC-07)	845
Reyren, N. (HC-09)	999	Rosamond, M. (HA-01)	967	Saari, M. (AC-07)	47
				Saari, M. (IC-01)	1053

- Sabariago, R. (BI-01) 275
- Sabie, V. (JP-11) 1321
- Sadeghi, S. (JR-07) 1343
- Sadovnikov, A.V. (EB-04) 719
- Sadovnikov, A.V. (EC-04) 735
- Sadovnikov, A.V. (EP-02) 782
- Sadovnikov, A.V. (EP-03) 783
- Sadovnikov, A.V. (EP-09) 789
- Sadovnikov, A.V. (EQ-04) 794
- Sadovnikov, A.V. (EQ-05) 795
- Sadovnikov, A.V. (EQ-06) 796
- Sadovnikov, A.V. (EQ-07) 797
- Sadovnikov, A.V. (HA-01) 967
- Saeedi Ilkhchy, K. (FB-14) 837
- Safarpour, R. (BU-09) 411
- Safeer, C. (HC-05) 995
- Safi Samghabadi, F. (DF-12) 665
- Safin, A. (FB-14) 837
- Safranski, C. (CA-01) 457
- Sagasta, E. (CC-01) 471
- Sagasti, A. (JF-12) 1269
- Sagkovits, D. (DC-09) 625
- Sagkovits, D. (HC-06) 996
- Saha, R. (ER-02) 802
- Saha, S. (AE-09) 79
- Sahoo, S.K. (FB-04) 826
- Sahu, U. (GB-01) 922
- Saika-Voivod, I. (AD-03) 62
- Saito, H. (CQ-03) 561
- Saito, H. (IP-04) 1121
- Saito, S. (IP-02) 1119
- Saito, S. (IP-03) 1120
- Saito, S. (JW-17) 1405
- Saito, T. (IP-02) 1119
- Saito, T. (IP-03) 1120
- Saito, T. (JW-02) 1390
- Saito, T. (JW-06) 1394
- Saito, Y. (CC-09) 479
- Saitoh, E. (FG-04) 871
- Saitoh, E. (FG-06) 873
- Sajjad, U. (JG-08) 1279
- Sakakibara, M. (BJ-03) 291
- Sakamoto, Y. (IP-01) 1118
- Sakoguchi, A. (FC-06) 844
- Saksl, K. (JR-03) 1339
- Sakuma, A. (CE-11) 510
- Sakuraba, Y. (CE-09) 508
- Sakuraba, Y. (DE-04) 645
- Sakuraba, Y. (DE-05) 646
- Sakuraba, Y. (IA-01) 1025
- Sakuraba, Y. (IB-10) 1048
- Sakuraba, Y. (IF-05) 1083
- Sala, G. (HB-06) 980
- Salahuddin, S. (BK-04) 307
- Salahuddin, S. (CG-04) 530
- Salahuddin, S. (GD-08) 958
- Salamatin, D. (DG-09) 675
- Salas, G. (JG-05) 1276
- Salguero, J. (DF-02) 654
- Salimy, S. (AC-06) 46
- Salinas, H. (DD-03) 633
- Sall, M. (CG-09) 535
- Sall, M. (GD-01) 951
- Sall, M. (HB-11) 985
- Sall, M. (HC-06) 996
- Sall, M. (HD-04) 1006
- Salvador, M. (YA-05) 10
- Salvan, G. (JB-09) 1212
- Samanta, A. (EE-10) 773
- Samanta, A. (IG-05) 1092
- Samanta, K. (FH-10) 893
- Samardak, A.S. (CB-01) 464
- Samardak, A.S. (GP-02) 962
- Sami, I. (BB-05) 196
- Sami, I. (BG-08) 255
- Samiepour, M. (CG-06) 532
- Samoshkina, Y.E. (DP-08) 686
- Samoshkina, Y.E. (IR-17) 1158
- Sampaio, J. (AE-10) 80
- Sampaio, J. (FH-06) 889
- Sampaio, J. (HD-08) 1010
- Samsonov, K. (CS-02) 584
- San Emeterio Alvarez, L. (DD-09) 639
- Sanchez Hazen, D. (CF-11) 524
- Sánchez Llamazares, J.L. (JT-01) 1362
- Sánchez-Tejerina, L. (AE-05) 75
- Sánchez-Tejerina, L. (FD-02) 850
- Sanchez-Tejerina, L. (FG-06) 873
- Sanchez, C. (JX-04) 1411
- Sanchez, E. (IH-08) 1109
- Sander, A. (IQ-08) 1138
- Sangiao, S. (EB-02) 717
- Sangregorio, C. (JR-11) 1347
- Santos, O. (FB-07) 830
- Sanz Hernandez, D. (GA-01) 914
- Sanz Hernandez, D. (JI-04) 1300
- Sanz Hernandez, D. (JI-05) 1301
- Saoudi, R. (JY-08) 1431
- Saren, H. (HP-08) 1020
- Sarkar, A. (JC-01) 1218
- Sarkar, T. (JD-10) 1240
- Sarker, M. (EE-15) 779
- Sarnavskiy, N. (IH-06) 1107
- Sarno, M. (JR-12) 1348
- Sasaki, T. (DE-05) 646
- Sasaki, Y. (FB-11) 834
- Sasayama, T. (CQ-04) 562
- Sassi, Y. (CC-11) 481
- Sassi, Y. (HC-02) 991
- Sassi, Y. (HC-09) 999
- Sasso, C.P. (JF-11) 1268
- Sato, M. (ER-12) 812
- Saugar, E. (JI-02) 1298
- Savary, M. (AC-12) 52
- Savelev, D.V. (AU-01) 162
- Savero Torres, W. (DA-03) 600
- Sawa, T. (HC-03) 993
- Sawayashiki, Y. (IA-09) 1034
- Sayed, S. (BK-04) 307
- Sayed, S. (CG-04) 530
- Sazonov, A. (DF-09) 662
- Sbiaa, R. (CE-06) 505
- Scagnoli, V. (AA-03) 22
- Scalera, V. (EB-11) 727
- Scalera, V. (FD-08) 856
- Scalera, V. (GC-04) 941
- Scalera, V. (GC-10) 948
- Schäfer, L. (JC-02) 1219
- Schäfer, R. (AB-07) 33
- Schäfer, R. (FE-04) 861
- Schaffner, S. (GC-06) 943
- Schanilec, V. (DG-11) 677
- Schänilec, V. (GA-01) 914
- Scheibel, F. (JE-02) 1244
- Scheibel, F. (JF-04) 1260
- Scheibler, S. (IH-02) 1103
- Scheike, T. (IE-04) 1076
- Scherz, A. (FD-05) 853
- Scherz, A. (HA-02) 968
- Scheuerlein, M. (GD-02) 952
- Schippers, C.F. (FB-14) 837
- Schippers, C.F. (FG-09) 876
- Schlappa, J. (FD-05) 853
- Schlauder, C. (ID-01) 1061
- Schlitz, R. (FG-08) 875
- Schlitz, R. (FH-08) 891
- Schlueter, C. (FH-13) 896
- Schmalhorst, J. (ER-11) 811
- Schmalz, J. (IB-02) 1040
- Schmid, A.K. (FE-03) 860
- Schmidt, G. (ER-11) 811
- Schmidt, G. (IB-02) 1040
- Schmitt, C. (FG-04) 871
- Schmitt, C. (FG-06) 873
- Schmitt, P. (ID-01) 1061
- Schmoranzarová, E. (FG-08) 875
- Schmoranzarová, E. (FH-08) 891
- Schneider, M. (AB-05) 31
- Schneider, M. (ED-11) 757
- Schneider, M. (EE-04) 767
- Schneider, M. (HA-02) 968
- Schneider, R. (FA-05) 819
- Schneider, S. (AA-04) 23
- Schneider, S. (DF-03) 655
- Schöbitz, M. (DD-05) 635
- Schöbitz, M. (DD-06) 636
- Schöbitz, M. (DD-07) 637
- Schöbitz, M. (GD-02) 952
- Schoenherr, G. (FH-13) 896
- Schoenherr, P. (HB-10) 984
- Schoenke, D. (FH-11) 894
- Schönenberger, T. (HC-07) 997
- Schreck, E. (IA-08) 1033
- Schrefl, T. (AD-04) 63
- Schrefl, T. (GC-06) 943
- Schreiber, F. (FG-06) 873
- Schuller, I.K. (IG-01) 1088
- Schuller, I.K. (IG-11) 1099
- Schuller, I.K. (ZA-01) 705
- Schultheiss, H. (AA-06) 25
- Schultheiss, K. (AA-06) 25
- Schulz, N. (IG-06) 1093
- Schulz, S.E. (JB-09) 1212

- Schumacher, H.W. (GA-05) 919
- Schütz, G. (AA-01) 20
- Schütz, G. (HB-05) 979
- Schwarz, A. (JS-05) 1355
- Schwarz, M. (AD-04) 63
- Schwingenschlogl, U. (CB-06) 469
- Scipioni, L. (FH-04) 887
- Scipioni, L. (FH-07) 890
- Scott, J. (FC-08) 846
- Scott, J.N. (IQ-09) 1139
- Sebald, G. (AD-10) 69
- Sedrhooshan, M. (JI-01) 1297
- Seidler, D. (JG-08) 1279
- Seifert, T. (CD-04) 489
- Seki, M. (EE-15) 779
- Seki, T. (DE-04) 645
- Seki, T. (GD-07) 957
- Sekino, M. (JG-02) 1273
- Seleznev, E.P. (EB-04) 719
- Seleznyova, K. (JY-19) 1443
- Selhuber-Unkel, C. (JG-08) 1279
- Selishchev, S. (JP-06) 1316
- Selvam, R. (JG-09) 1280
- Semiannikova, A. (DE-09) 651
- Semisalova, A. (FB-02) 823
- Semisalova, A. (FD-07) 855
- Sen, S. (IG-12) 1100
- Seneor, P. (DB-02) 606
- Seneor, P. (DB-03) 607
- Seneor, P. (IQ-08) 1138
- Seng, B. (FD-03) 851
- Seng, B. (FG-05) 872
- Seng, B. (HC-10) 1000
- Seo, H. (AC-05) 44
- Sepehri-Amin, H. (IA-01) 1025
- Sepehri-Amin, H. (IB-10) 1048
- Sepehri-Amin, H. (JC-05) 1222
- Serga, A.A. (CA-02) 458
- Serga, A.A. (EB-08) 723
- Serga, A.A. (ED-11) 757
- Serha, R. (ED-11) 757
- Serokurova, A. (EQ-07) 797
- Serpico, C. (EB-11) 727
- Serpico, C. (FD-08) 856
- Serpico, C. (GC-04) 941
- Serpico, C. (GC-10) 948
- Serrano-Pertierra, E. (YA-05) 10
- Servet, B. (DB-02) 606
- Sessi, P. (DB-04) 608
- Seuss, D. (JI-05) 1301
- Sha, Y. (JB-10) 1213
- Shafer, P. (FG-07) 874
- Shah, P. (EC-11) 742
- Shah, S. (DE-08) 650
- Shahbazi, K. (HA-01) 967
- Shalygina, E. (ER-09) 809
- Shan, S. (EE-03) 766
- Shang, J. (BP-01) 310
- Shao, D. (AP-01) 85
- Shao, R. (JI-08) 1304
- Sharavskii, Y.P. (EB-04) 719
- Sharda, J. (GB-01) 922
- Sharma, A. (JB-09) 1212
- Sharma, R. (DC-03) 619
- Sharma, S.K. (JA-13) 1202
- Sharma, V. (JB-06) 1209
- Sharma, V. (JB-07) 1210
- Sharma, V. (JE-03) 1245
- Sharma, V. (JE-06) 1249
- Shatilov, V. (IR-03) 1144
- Shavrov, V. (JE-05) 1248
- Shaw, J. (GD-06) 956
- She, X. (DP-11) 689
- Sheka, D.D. (DD-01) 631
- Sheka, D.D. (DD-02) 632
- Sheka, D.D. (DF-01) 653
- Sheka, D.D. (GD-04) 954
- Shekhar, C. (CA-05) 461
- Shen, J. (BC-01) 204
- Shen, J. (BC-04) 207
- Shen, K. (EA-03) 711
- Shen, S. (AS-06) 141
- Shen, Y. (BT-06) 387
- Shen, Y. (BT-08) 391
- Shendrikova, L.A. (ID-04) 1064
- Shepard, A. (FH-04) 887
- Shepard, A. (FH-07) 890
- Shepley, P. (IQ-02) 1132
- Sheshukova, S. (EQ-05) 795
- Sheshukova, S.E. (EC-04) 735
- Sheshukova, S.E. (EP-03) 783
- Sheshukova, S.E. (EQ-07) 797
- Shevchenko, Y. (DG-06) 672
- Shi, D. (AB-02) 28
- Shi, D. (AQ-10) 108
- Shi, D. (BQ-11) 340
- Shi, D. (BV-08) 434
- Shi, J. (BW-11) 449
- Shi, J. (JP-09) 1319
- Shi, K. (IH-01) 1102
- Shi, T. (BI-05) 279
- Shi, X. (HB-01) 975
- Shi, Y. (BT-05) 386
- Shields, B.J. (DF-01) 653
- Shigeta, I. (IR-05) 1146
- Shigeta, I. (JX-07) 1414
- Shigeta, I. (JX-08) 1415
- Shima, M. (CP-16) 557
- Shimon, G. (CF-01) 513
- Shin, D. (BR-12) 358
- Shin, D. (BR-16) 362
- Shin, H. (AU-04) 166
- Shin, H. (AU-08) 171
- Shin, H. (BP-04) 313
- Shin, H. (BP-11) 321
- Shin, H. (BQ-06) 335
- Shin, H. (BS-01) 365
- Shin, H. (BS-07) 372
- Shin, H. (DP-03) 681
- Shin, H. (DP-05) 683
- Shin, J. (AC-05) 44
- Shin, K. (AP-12) 96
- Shin, K. (AQ-07) 105
- Shin, K. (BQ-09) 338
- Shin, K. (BQ-10) 339
- Shin, K. (BR-06) 352
- Shin, K. (BS-02) 366
- Shin, K. (BS-04) 369
- Shin, K. (BV-07) 433
- Shin, K. (BV-09) 435
- Shin, S. (BQ-01) 329
- Shirai, M. (IE-02) 1074
- Shirasaki, T. (DP-04) 682
- Shirata, M. (IA-09) 1034
- Shirokura, T. (CD-09) 494
- Shiryaev, A. (ER-13) 813
- Shiu, D. (IP-12) 1129
- Shoup, J.E. (IG-06) 1093
- Shreder, E. (DB-11) 615
- Shreder, E. (DE-09) 651
- Shu, H. (FP-13) 911
- Shuai, K. (BW-03) 440
- Shum, A. (JH-06) 1290
- Sidi El Valli, A. (ER-06) 806
- Sidi El Valli, A. (ID-07) 1067
- Sidi El Valli, A. (ID-08) 1068
- Sidorov, A. (CG-05) 531
- Sidorov, V. (DG-09) 675
- Sierra, J.F. (DA-03) 600
- Sikora, M. (AC-14) 54
- Silva, A.S. (FC-07) 845
- Silva, D. (JT-07) 1368
- Sim, M. (HD-06) 1008
- Simensen, H.T. (FH-12) 895
- Simon, G. (ID-03) 1063
- Simsek, M. (JA-07) 1195
- Sindt, S. (JG-08) 1279
- Singh, B. (IF-07) 1086
- Singh, F. (IR-09) 1150
- Singh, P. (AC-09) 49
- Singh, P. (IF-07) 1086
- Singh, S. (CP-05) 545
- Singhal, J. (IH-09) 1110
- Sinitsyn, V.E. (EQ-08) 798
- Sinova, J. (FG-04) 871
- Sinova, J. (FG-08) 875
- Sinova, J. (FH-13) 896
- Sinova, J. (HA-02) 968
- Sireus, V. (DF-02) 654
- Siruguri, V. (DQ-10) 701
- Sisniga Soriano, B. (JF-12) 1269
- Sisodia, N. (GB-01) 922
- Sisodia, N. (HD-04) 1006
- Sitarski, D. (JU-09) 1384
- Siu, Z. (IF-03) 1081
- Sivakumar, I. (DP-02) 680
- Sivanesarajah, I. (ER-11) 811
- Siwak, N. (CG-05) 531
- Skarlatos, A. (AD-09) 68
- Skárman, B. (JD-08) 1238
- Skiadopoulou, S. (DF-07) 659
- Skirdkov, P. (ER-08) 808
- Skirdkov, P. (FP-14) 912

Skokov, K. (CR-05)	575	Song, I. (BP-11)	321	Statuto, N.N. (FG-15)	882
Skokov, K. (JC-02)	1219	Song, J. (CP-02)	542	Stavila, C. (JP-03)	1313
Skokov, K. (JC-05)	1222	Song, J. (CP-08)	548	Stebliy, E. (CB-01)	464
Skokov, K. (JE-02)	1244	Song, J. (HP-06)	1018	Stebliy, M. (CB-01)	464
Skokov, K. (JT-06)	1367	Song, J. (IS-16)	1177	Stebliy, M. (GP-02)	962
Skoric, L. (JI-05)	1301	Song, J. (JY-07)	1430	Stebliy, M. (IH-06)	1107
Skourski, Y. (FH-13)	896	Song, P. (CS-14)	596	Steele, T.W. (JI-06)	1302
Skourski, Y. (JC-05)	1222	Song, P. (JP-09)	1319	Stefanov, A. (IS-12)	1173
Skowronski, W. (CC-14)	484	Song, S. (BR-04)	350	Steinke, N. (GA-02)	915
Slavin, A.N. (CA-02)	458	Song, S. (BR-16)	362	Stejskal, O. (JF-02)	1258
Slavin, A.N. (EA-01)	709	Song, Z. (BG-03)	250	Stepanov, S. (CS-02)	584
Slavin, A.N. (EA-04)	712	Song, Z. (BG-09)	256	Stepanova, E. (DP-08)	686
Slavin, A.N. (EB-10)	726	Song, Z. (BI-05)	279	Stepanova, E. (IR-11)	1152
Slavin, A.N. (ED-11)	757	Song, Z. (BU-02)	403	Stepanova, M. (HB-10)	984
Slavin, A.N. (ER-06)	806	Sopon, T. (IP-06)	1123	Steren, L. (FC-04)	842
Slezak, M. (IG-07)	1094	Soree, B. (EC-07)	738	Stiles, M. (GA-04)	918
Slezak, M. (IH-10)	1111	Sorrentino, A. (CQ-08)	566	Stiles, M. (GB-12)	935
Slezak, M. (IH-11)	1112	Sort, J. (DF-02)	654	Stoeffler, D. (EB-03)	718
Slezak, T. (IG-07)	1094	Soumyanarayanan, A. (HB-11)	985	Stognij, A. (EC-04)	735
Slezak, T. (IH-10)	1111	Soumyanarayanan, A. (HB-12)	987	Stognij, A. (EQ-07)	797
Slezak, T. (IH-11)	1112	Soumyanarayanan, A. (HC-04)	994	Stoian, G. (JW-08)	1396
Smaili, I. (CB-06)	469	Soumyanarayanan, A. (HD-06)	1008	Stoll, H. (ED-05)	751
Smejkal, L. (FG-08)	875	Souriau, J. (ID-03)	1063	Stöltz, S. (IT-06)	1184
Smejkal, L. (FH-08)	891	Souriau, L. (CF-12)	525	Stolyar, S. (JQ-07)	1333
Smejkal, L. (FH-13)	896	Sousa, C. (JG-06)	1277	Storf, C. (AD-04)	63
Smigaj, W. (EE-14)	778	Sousa, C. (JI-03)	1299	Strelkov, N. (CG-03)	529
Smith, R. (IA-08)	1033	Sousa, C. (JP-05)	1315	Strelkov, N. (IR-12)	1153
Snoeck, E. (GA-05)	919	Sousa, C. (JR-05)	1341	Stremoukhov, P. (FB-14)	837
Snoeck, E. (JI-04)	1300	Sousa, R. (AC-06)	46	Strocov, V. (FH-13)	896
Soares, G. (CC-14)	484	Sousa, R. (CF-06)	518	Strugatsky, M. (JY-19)	1443
Soban, Z. (AB-04)	30	Sousa, R. (CF-07)	519	Strungaru, M.S. (FD-06)	854
Sobucki, K. (EE-14)	778	Sousa, R. (CF-11)	524	Strungaru, M.S. (HB-03)	977
Sochnikov, I. (DC-10)	626	Sousa, R. (CG-03)	529	Strusch, T. (FB-02)	823
Sofronova, S.N. (DQ-08)	699	Sousa, R. (ID-07)	1067	Stuart, A. (AE-12)	82
Sohier, T. (ID-03)	1063	Souza, F.L. (JY-16)	1440	Stückler, M. (IR-13)	1154
Šoka, M. (JX-01)	1408	Sowman, P. (YA-06)	11	Stückler, M. (JA-06)	1194
Sokalski, V.M. (AB-08)	34	Speliotis, T. (CP-06)	546	Šturm, S. (JC-11)	1228
Sokalski, V.M. (AE-01)	71	Spetzler, B. (IB-02)	1040	Sturza, M.I. (JX-06)	1413
Sokalski, V.M. (GD-05)	955	Spiridis, N. (IR-04)	1145	Su, D. (ER-02)	802
Sokalski, V.M. (GD-06)	956	Springell, R. (IH-13)	1114	Su, J. (FC-05)	843
Sokalski, V.M. (HD-09)	1011	Srikanth, H. (IG-06)	1093	Su, J. (IB-02)	1040
Sokalski, V.M. (IG-03)	1090	Srinivasan, G. (JF-10)	1267	Su, P. (BT-06)	387
Sokolov, A. (IS-14)	1175	Srivastava, S.K. (JE-10)	1253	Su, P. (BT-08)	391
Sokolovskiy, V. (JU-02)	1377	Srivastava, T. (EB-02)	717	Su, P. (BT-11)	395
Sola, A. (CC-14)	484	Srivastava, T. (HC-09)	999	Subramanian, A. (DP-02)	680
Sola, Í.J. (FC-07)	845	St. Pierre, T. (JH-11)	1295	Sud, A. (ED-06)	752
Soldatov, I. (AB-07)	33	St. Pierre, T. (JP-12)	1322	Sud, A. (ED-13)	760
Soldatov, I. (FE-04)	861	Stackhouse, G. (BJ-02)	289	Sud, A. (HC-06)	996
Soldatov, K. (DG-06)	672	Stadler, B. (AD-01)	60	Suemasu, T. (CB-02)	465
Solignac, A. (IB-04)	1042	Stadler, B. (CS-09)	591	Suemasu, T. (DG-07)	673
Solis, L.M. (FC-04)	842	Stadler, B. (JI-13)	1309	Suemasu, T. (IF-02)	1080
Somashekara, M. (JC-01)	1218	Stamenov, P.S. (AD-02)	61	Suemasu, T. (IP-10)	1127
Somoza, Á. (JG-05)	1276	Stamps, R. (GC-01)	938	Suess, D. (GC-01)	938
Son, J. (AR-14)	129	Stankevic, V. (IB-13)	1051	Suess, D. (GC-06)	943
Son, K. (DP-03)	681	Stano, M. (DD-08)	638	Suess, D. (HA-03)	969
Song, C. (BP-04)	313	Stark, A. (AB-11)	38	Sugimoto, S. (ER-12)	812
Song, C. (HA-05)	971	Staruch, M. (DF-04)	656	Sugiura, S. (CR-06)	576
Song, G. (IA-05)	1030	Staruch, M. (IB-03)	1041	Sui, Y. (BF-12)	245
Song, I. (AU-04)	166	Staruch, M. (JF-05)	1261	Sui, Y. (BR-02)	348
Song, I. (BP-04)	313	Staruch, M. (JF-13)	1270	Sui, Y. (BR-07)	353

- T -

Sukegawa, H. (IB-10)	1048	Tang, X. (IR-07)	1148
Sukegawa, H. (IE-04)	1076	Tang, Y. (AU-07)	170
Sulaiman, E. (BB-02)	193	Tang, Y. (BP-09)	318
Sulaiman, E. (BG-06)	253	Tang, Y. (DP-12)	690
Sulaiman, M. (AC-07)	47	Tang, Y. (JW-01)	1389
Sulaiman, M. (IC-01)	1053	Taniguchi, T. (CD-10)	495
Sun, C. (GP-05)	965	Taniguchi, T. (EB-09)	725
Sun, C. (IQ-04)	1134	Tao, R. (YB-02)	14
Sun, H. (JY-10)	1434	Tao, W. (AQ-02)	100
Sun, J. (CF-01)	513	Tao, W. (EC-13)	744
Sun, J. (DB-07)	611	Tao, Y. (GP-05)	965
Sun, J.Z. (CA-01)	457	Tao, Y. (IQ-04)	1134
Sun, K. (JX-05)	1412	Tatay, S. (DB-03)	607
Sun, L. (BC-05)	208	Tateno, S. (EC-06)	737
Sun, L. (BF-12)	245	Taubel, A. (JE-02)	1244
Sun, L. (BW-10)	448	te Velthuis, S.G. (AE-12)	82
Sun, L. (CP-10)	551	Tedesco, J. (JE-12)	1255
Sun, L. (CP-12)	553	Teichert, N. (AD-02)	61
Sun, L. (DG-09)	675	Teichmann, M. (FD-05)	853
Sun, Q. (JC-09)	1226	Teixeira de Paula, G. (BF-08)	240
Sun, R. (AQ-10)	108	Teixeira de Paula, G. (BG-14)	261
Sun, R. (BQ-11)	340	Teixeira de Paula, G. (BG-15)	262
Sun, R. (BV-08)	434	Tejo, F. (HP-07)	1019
Sun, W. (BW-10)	448	Telyshev, D. (JP-06)	1316
Sun, W. (CQ-05)	563	Terada, K. (CR-04)	574
Sun, W. (CR-01)	571	Terada, K. (CR-06)	576
Sun, X. (BW-05)	442	Terada, N. (JT-08)	1369
Sun, X. (BW-06)	443	Teresi, S. (IB-07)	1045
Sun, X. (BW-07)	444	Terkel, M.B. (YB-01)	13
Sun, X. (BW-08)	445	Ternero, P. (JI-01)	1297
Sun, Y. (AR-17)	132	Tetik Girgin, M. (BG-07)	254
Sun, Y. (BC-01)	204	Tew, W. (AC-13)	53
Sun, Y. (BJ-06)	294	Tey, N. (HC-04)	994
Sun, Y. (CA-05)	461	Tham, K. (IP-02)	1119
Sun, Y. (DC-06)	622	Tham, K. (IP-03)	1120
Sun, Z. (AR-01)	113	Thandapani, P. (JS-10)	1360
Sung, B. (JG-10)	1281	Thangavel, K. (JS-06)	1356
Supnithi, P. (IP-05)	1122	Theh, W. (CR-11)	581
Supnithi, P. (IP-06)	1123	Theh, W. (JS-02)	1352
Suslin, G.S. (IR-03)	1144	Thian, D. (HD-06)	1008
Suto, H. (IA-01)	1025	Thiaville, A. (AE-02)	72
Suzuki, H. (BB-06)	197	Thiaville, A. (FH-06)	889
Suzuki, H. (IA-09)	1034	Thiaville, A. (HB-08)	982
Suzuki, J. (JR-01)	1337	Thiaville, A. (JX-04)	1411
Suzuki, K. (IE-05)	1077	Thielsch, J. (JC-03)	1220
Suzuki, Y. (GA-03)	917	Thiery, N. (ED-04)	750
Svalov, A. (ER-09)	809	Thiery, N. (EE-08)	771
Svalov, A. (IR-11)	1152	Thirion, C. (DD-05)	635
Svalov, A. (JT-12)	1373	Thirion, C. (DD-06)	636
Sveklo, I. (IH-03)	1104	Thirion, C. (DD-07)	637
Swagten, H. (FG-09)	876	Thoma, H. (AC-17)	57
Syskaki, M.A. (FE-09)	866	Thoma, H. (DF-06)	658
Sysoev, I.V. (EB-04)	719	Thoma, H. (DF-08)	661
Syvorotka, I. (CA-02)	458	Thoma, H. (JT-10)	1371
Szabo, P. (JT-05)	1366	Thomson, T. (FB-13)	836
Szpytma, M. (IG-07)	1094	Thomson, T. (FC-03)	841
Szpytma, M. (IH-10)	1111	Thomson, T. (IA-03)	1028
Szpytma, M. (IH-11)	1112	Thormählen, L. (AB-01)	27
Szule, K. (EC-05)	736	Tian, X. (BW-14)	452
Szule, K. (EE-02)	765	Tian, X. (BW-16)	454
Tabata, H. (EE-15)	779		
Tacchi, S. (CC-13)	483		
Tacchi, S. (EC-05)	736		
Tacchi, S. (HC-06)	996		
Tadokoro, T. (JP-08)	1318		
Tae, C. (IQ-07)	1137		
Tafti, F. (DC-10)	626		
Taib, N. (JH-11)	1295		
Taib, N. (JP-12)	1322		
Takagi, K. (JW-03)	1391		
Takagi, K. (JW-11)	1399		
Takahara, K. (BB-06)	197		
Takahashi, H. (EC-03)	734		
Takahashi, S. (ER-12)	812		
Takahashi, Y. (GD-07)	957		
Takanashi, K. (DE-04)	645		
Takanashi, K. (FG-13)	880		
Takanashi, K. (GD-07)	957		
Takanashi, K. (IR-05)	1146		
Takemoto, M. (BP-02)	311		
Takimura, S. (AT-06)	158		
Talaat, A. (JA-04)	1192		
Talatchian, P. (GA-04)	918		
Talatchian, P. (GB-12)	935		
Talluri, M. (CD-07)	492		
Tam, M. (ED-13)	760		
Tamaru, S. (IA-01)	1025		
Tamaru, S. (IH-04)	1105		
Tamion, A. (JI-11)	1307		
Tamion, A. (JW-13)	1401		
Tamura, E. (GA-03)	917		
Tan, A.K. (HD-06)	1008		
Tan, C. (BI-10)	286		
Tan, H. (HB-11)	985		
Tan, H. (HB-12)	987		
Tan, H. (HD-06)	1008		
Tan, L. (JB-03)	1206		
Tan, L. (JB-06)	1209		
Tan, L. (JB-07)	1210		
Tan, P. (BD-01)	211		
Tan, P. (BV-02)	427		
Tan, X. (AU-07)	170		
Tan, X. (BS-10)	375		
Tanabe, J. (ID-06)	1066		
Tanabe, K. (CD-05)	490		
Tanabe, K. (CP-15)	556		
Tanabe, K. (HC-03)	993		
Tanaka, H. (JY-05)	1428		
Tanaka, M. (ER-03)	803		
Tanaka, T. (EP-01)	781		
Tanaka, Y. (GA-03)	917		
Tanase, J. (JA-11)	1199		
Tang, C. (BI-06)	281		
Tang, J. (CD-03)	488		
Tang, P. (CC-08)	478		
Tang, S. (YB-05)	17		
Tang, X. (BW-08)	445		
Tang, X. (EP-08)	788		

- Tian, Y. (CS-06) 588
 Tiang, T. (BI-10) 286
 Tiberto, P. (JF-11) 1268
 Tiberto, P. (JU-06) 1381
 Tiberto, P. (YA-04) 9
 Tibu, M. (IT-07) 1185
 Timopheev, A. (IR-12) 1153
 Tiusan, C. (IQ-05) 1135
 Tiwari, D. (FP-08) 906
 Tiwari, D. (GD-02) 952
 Tiwari, P. (DF-05) 657
 Tkachev, V.V. (JR-06) 1342
 Tobise, M. (JW-17) 1405
 Toh, Y. (CG-08) 534
 Tohara, M. (IC-02) 1054
 Tokarz, W. (AC-03) 42
 Toko, K. (DG-07) 673
 Toko, K. (IF-02) 1080
 Tokura, Y. (HB-10) 984
 Töllner, M. (JE-02) 1244
 Tomas, A. (FG-08) 875
 Tomasello, R. (FD-02) 850
 Tomasello, R. (FH-14) 897
 Tomasello, R. (HA-03) 969
 Tomasello, R. (HA-05) 971
 Tomasello, R. (HC-11) 1001
 Tomilo, A.V. (DF-01) 653
 Tomše, T. (JC-11) 1228
 Ton That, L. (JP-13) 1323
 Tong, C. (BB-10) 202
 Tong, C. (BF-06) 238
 Tong, W. (AQ-06) 104
 Tong, W. (BC-05) 208
 Tounzi, A. (AP-06) 90
 Tounzi, A. (BU-14) 418
 Tournus, F. (JI-11) 1307
 Tournus, F. (JW-13) 1401
 Toussaint, J. (DD-05) 635
 Toussaint, J. (DD-06) 636
 Toussaint, J. (DD-07) 637
 Toussaint, J. (DD-08) 638
 Tran, T. (JI-12) 1308
 Trapanese, M. (BD-04) 215
 Tretiakov, O. (HD-03) 1005
 Tretiakov, O. (HD-07) 1009
 Trevillian, C. (EA-01) 709
 Trevillian, C. (EC-09) 740
 Tria, A. (ID-03) 1063
 Trier, F. (FE-02) 859
 Triscone, J. (CD-08) 493
 Troncoso, R. (EB-06) 721
 Trzaskowska, A. (EC-08) 739
 Tsai, M. (BU-07) 409
 Tsai, T. (CC-12) 482
 Tsakadze, Z. (JA-05) 1193
 Tsakadze, Z. (JB-03) 1206
 Tsakadze, Z. (JB-04) 1207
 Tseng, Y. (AC-09) 49
 Tserkovnyak, Y. (ED-04) 750
 Tshipas, P. (DC-01) 617
 Tsuchida, E. (JA-11) 1199
 Tsuchiura, H. (JC-12) 1229
 Tsuchiya, T. (IE-02) 1074
 Tsujikawa, M. (IE-02) 1074
 Tsujikawa, S. (JX-07) 1414
 Tsujimoto, S. (IA-09) 1034
 Tsukada, K. (AC-07) 47
 Tsukada, K. (IC-01) 1053
 Tsukamoto, A. (CP-04) 544
 Tsunata, R. (BP-02) 311
 Tsunegi, S. (GB-07) 930
 Tsunegi, S. (IB-04) 1042
 Tsunoda, M. (CP-03) 543
 Tsvyashchenko, A. (DG-09) 675
 Tu, R. (BB-09) 201
 Tu, R. (BJ-13) 301
 Tu, S. (ED-12) 759
 Tung, M. (GP-02) 962
 Turenne, D. (FD-05) 853
 Tyberkevych, V. (CA-02) 458
 Tyberkevych, V. (EA-01) 709
 Tyberkevych, V. (EA-04) 712
 Tyberkevych, V. (EB-10) 726
 Tyberkevych, V. (EC-09) 740
 Tyberkevych, V. (ED-08) 754
 Tyberkevych, V. (ED-11) 757
 Tyberkevych, V. (ER-06) 806
 Tyutyunnik, A. (JT-03) 1364
- U -
- U D, R. (JE-04) 1247
 U, D. (JT-02) 1363
 Uchida, H. (CE-03) 502
 Uchida, K. (CA-04) 460
 Uchida, K. (CE-09) 508
 Uchida, K. (IF-05) 1083
 Ueda, S. (IF-05) 1083
 Uehara, G. (BJ-03) 291
 Uehara, G. (CQ-01) 559
 Ueyama, T. (IA-09) 1034
 Uhlir, V. (FD-05) 853
 Ulitko, V. (DQ-03) 694
 Ullah, B. (BB-02) 193
 Ullah, N. (BD-07) 218
 Ullah, W. (BB-02) 193
 Ullah, W. (BG-06) 253
 Um, D. (AS-08) 143
 Um, D. (IS-02) 1163
 Um, D. (IS-13) 1174
 Um, J. (JI-13) 1309
 Umair, M. (BG-06) 253
 Urazhdin, S. (EA-02) 710
 Urazhdin, S. (FB-05) 828
 Urazhdin, S. (FG-03) 870
 Urbánek, M. (ED-05) 751
 Ušák, E. (JX-01) 1408
 Ušáková, M. (JX-01) 1408
 Usmanov, O. (JT-10) 1371
 Ustinov, A.B. (DQ-02) 792
 Uwatoko, Y. (JT-11) 1372
 Uwatoko, Y. (JX-07) 1414
 Uyeda, C. (CR-04) 574
 Uyeda, C. (CR-06) 576
- V -
- V R K, M. (JS-06) 1356
 Vadim, D. (DF-06) 658
 Vagner, M. (IB-13) 1051
 Vahovsky, O. (JY-01) 1424
 Vakili, H. (HD-05) 1007
 Valdes Bango, F. (EC-05) 736
 Valenzuela, S.O. (DA-03) 600
 Vallobra, P. (CC-08) 478
 Valmianski, I. (IG-01) 1088
 Valmispild, V. (FD-05) 853
 Valvidares, M. (DB-04) 608
 Van Beek, S. (CF-12) 525
 Van Beek, S. (CG-13) 539
 van der Jagt, J.W. (FE-09) 866
 van der Jagt, J.W. (GD-01) 951
 van Dijken, S. (EE-09) 772
 Van Kuiken, B.E. (FD-05) 853
 van Landeghem, M. (FB-06) 829
 Van Waeyenberge, B. (AC-08) 48
 Van Waeyenberge, B. (EC-07) 738
 Van Waeyenberge, B. (GB-13) 936
 Vanderveken, F. (EC-07) 738
 Vannier, J. (BI-07) 283
 Varaprasad, B. (IA-04) 1029
 Varaticeanu, B. (BP-15) 325
 Varela, M. (IR-16) 1157
 Varga, M. (DQ-01) 692
 Varga, M. (JR-03) 1339
 Varga, M. (JT-05) 1366
 Varga, R. (DQ-01) 692
 Varga, R. (IC-03) 1055
 Varga, R. (JR-03) 1339
 Varga, R. (JR-08) 1344
 Varga, R. (JT-04) 1365
 Varga, R. (JT-05) 1366
 Varga, R. (JY-01) 1424
 Varma, V.B. (JH-05) 1289
 Varotto, S. (CD-11) 496
 Varvaro, G. (JD-10) 1240
 Vas'kovskiy, V. (GC-07) 944
 Vas'kovskiy, V. (IR-10) 1151
 Vas'kovskiy, V. (IR-11) 1152
 Vasilaki, E. (GA-02) 915
 Vasilaki, E. (GB-04) 926
 Vasilaki, E. (GB-09) 932
 Vasilaki, E. (GB-11) 934
 Vasiliev, E. (DG-06) 672
 Vasilyev, D. (FH-13) 896
 Vasin, K. (DF-11) 664
 Vaskivskiy, I. (FD-05) 853
 Vasyuchka, V.I. (EB-08) 723
 Vaunat, A. (EC-12) 743
 Vázquez, M. (JI-02) 1298
 Vecchiola, A. (DB-02) 606

- Wang, W. (CP-02) 542
- Wang, W. (DB-08) 612
- Wang, W. (HB-09) 983
- Wang, W. (HD-07) 1009
- Wang, W. (IF-04) 1082
- Wang, X. (AE-12) 82
- Wang, X. (CB-01) 464
- Wang, X. (CC-05) 475
- Wang, X. (CG-10) 536
- Wang, X. (CP-07) 547
- Wang, X. (CP-10) 551
- Wang, X. (CP-11) 552
- Wang, X. (EB-06) 721
- Wang, X. (FC-01) 839
- Wang, X. (GP-02) 962
- Wang, X. (IB-09) 1047
- Wang, X. (IH-01) 1102
- Wang, X. (IH-05) 1106
- Wang, Y. (AC-04) 43
- Wang, Y. (AP-11) 95
- Wang, Y. (AS-14) 149
- Wang, Y. (BC-04) 207
- Wang, Y. (BD-10) 222
- Wang, Y. (BE-01) 225
- Wang, Y. (BF-07) 239
- Wang, Y. (BF-12) 245
- Wang, Y. (BT-02) 383
- Wang, Y. (BT-06) 387
- Wang, Y. (BT-08) 391
- Wang, Y. (CC-03) 473
- Wang, Y. (EB-13) 729
- Wang, Y. (EC-01) 732
- Wang, Y. (HP-10) 1022
- Wang, Y. (JX-05) 1412
- Wang, Y. (JY-13) 1437
- Wang, Y. (JY-14) 1438
- Wang, Z. (AQ-09) 107
- Wang, Z. (AS-01) 135
- Wang, Z. (AT-03) 155
- Wang, Z. (AT-04) 156
- Wang, Z. (BI-05) 279
- Wang, Z. (BW-13) 451
- Wang, Z. (HA-05) 971
- Wang, Z. (IH-01) 1102
- Wang, Z. (IS-05) 1166
- Wang, Z. (IS-08) 1169
- Wang, Z. (JP-14) 1324
- Wang, Z. (JQ-09) 1335
- Wang, Z. (JU-04) 1379
- Wang, Z. (JU-05) 1380
- Wang, Z. (JY-15) 1439
- Wani, F. (BG-01) 248
- Warin, P. (CD-11) 496
- Waring, H.J. (FC-03) 841
- Warisam, C. (IA-07) 1032
- Wartelle, A. (EB-09) 725
- Watanabe, K. (AR-01) 113
- Watanabe, K. (CG-02) 528
- Watanabe, S. (ED-14) 761
- Watanabe, S. (EE-03) 766
- Watanabe, T. (CF-03) 515
- Watts, J.D. (IB-08) 1046
- Wawro, A. (IG-02) 1089
- Weber, A. (AC-17) 57
- Wei, C. (IP-12) 1129
- Wei, G. (FH-09) 892
- Wei, J. (AC-09) 49
- Wei, J. (CC-05) 475
- Wei, J. (CC-12) 482
- Wei, J. (CP-11) 552
- Wei, J. (DB-05) 609
- Wei, J. (FP-09) 907
- Wei, Q. (BK-01) 304
- Wei, Y. (HP-06) 1018
- Wei, Z. (FP-05) 903
- Weigand, M. (AA-01) 20
- Weigand, M. (ED-05) 751
- Weigold, M. (JC-02) 1219
- Weil, R. (FH-06) 889
- Weil, R. (HD-08) 1010
- Weiler, M. (CD-04) 489
- Weiß, E. (EE-04) 767
- Weissitsch, L. (IR-13) 1154
- Weissitsch, L. (JA-06) 1194
- Welbourne, A. (GA-02) 915
- Welbourne, A. (GB-04) 926
- Welbourne, A. (GB-11) 934
- Welleweerd, M. (AC-10) 50
- Wen, H. (AU-12) 175
- Wen, T. (EP-08) 788
- Wen, T. (IR-07) 1148
- Wen, Z. (IE-04) 1076
- Wende, H. (CR-05) 575
- Wende, H. (IA-03) 1028
- Weng, L. (JU-07) 1382
- Wereley, N. (YB-03) 15
- Wereley, N. (YB-06) 18
- Wernsdorfer, W. (AD-02) 61
- Weßels, T. (HA-01) 967
- Westerström, R. (IG-10) 1097
- Westerström, R. (JI-01) 1297
- Wi, C. (AR-08) 122
- Wiegand, P. (IB-02) 1040
- Wiekhorst, F. (AC-08) 48
- Wiesendanger, R. (ZA-02) 706
- Wiczorek, J. (JA-04) 1192
- Wijaya, T. (CE-03) 502
- Wilhelm, F. (CR-05) 575
- Wilhelm, F. (JD-03) 1233
- Wilhelm, F. (JW-13) 1401
- Wilkins, S.B. (AB-05) 31
- Willard, M. (JA-02) 1190
- Wilson, B.W. (IQ-09) 1139
- Wilson, R.B. (HB-01) 975
- Wimmer, S. (CD-04) 489
- Wimmer, T. (CE-05) 504
- Wimmer, T. (FG-10) 877
- Wintz, S. (AA-01) 20
- Wintz, S. (ED-05) 751
- Wintz, S. (HA-01) 967
- Wittmann, A. (FH-04) 887
- Wittmann, A. (FH-07) 890
- Wittmann, A. (HA-02) 968
- Wittrock, S. (IB-04) 1042
- Witz, J. (BJ-11) 299
- Wójcik, K.P. (DG-08) 674
- Wolf, D. (AA-04) 23
- Wolf, D. (DF-03) 655
- Wolf, G. (CF-09) 522
- Wolowicz, C. (IG-01) 1088
- Won, C. (EQ-09) 799
- Won, H. (JD-04) 1234
- Won, H. (JD-07) 1237
- Wong, G.D. (CD-03) 488
- Wong, G.D. (HB-04) 978
- Wong, H. (BF-10) 242
- Wong, H. (IQ-01) 1131
- Wong, H. (IR-06) 1147
- Wong, K. (BT-10) 393
- Wong, K. (BT-12) 396
- Wong, K. (BT-13) 397
- Wong, K. (BT-14) 398
- Wong, T. (GD-05) 955
- Woo, J. (AP-12) 96
- Woo, J. (BQ-05) 334
- Woo, S. (AV-03) 181
- Woodcock, T. (JD-06) 1236
- Woodcock, T. (JD-08) 1238
- Woods, S. (AC-13) 53
- Woodward, R. (JH-11) 1295
- Woodward, R. (JP-12) 1322
- Wrona, J. (ID-07) 1067
- Wu, C. (JX-05) 1412
- Wu, D. (BJ-05) 293
- Wu, D. (FG-12) 879
- Wu, G. (AP-07) 91
- Wu, G. (AQ-01) 99
- Wu, H. (AP-01) 85
- Wu, H. (CC-03) 473
- Wu, H. (FE-07) 864
- Wu, H. (FG-07) 874
- Wu, H. (HA-05) 971
- Wu, J. (AP-08) 92
- Wu, J. (AQ-11) 109
- Wu, J. (AQ-12) 111
- Wu, J. (AS-07) 142
- Wu, J. (BQ-14) 343
- Wu, J. (FC-05) 843
- Wu, J. (IP-09) 1126
- Wu, J. (IQ-10) 1140
- Wu, K. (ER-02) 802
- Wu, K. (IT-04) 1182
- Wu, L. (AU-12) 175
- Wu, L. (BR-05) 351
- Wu, L. (BU-15) 419
- Wu, M. (CP-12) 553
- Wu, M. (ED-12) 759
- Wu, M. (FH-05) 888
- Wu, M. (IH-13) 1114
- Wu, Q. (BJ-06) 294
- Wu, Q. (BU-15) 419
- Wu, Q. (ER-07) 807
- Wu, R. (IH-05) 1106

Wu, S. (AQ-06).....	104
Wu, S. (AT-04).....	156
Wu, S. (BC-05).....	208
Wu, S. (BD-03).....	214
Wu, S. (BI-05).....	279
Wu, S. (JY-14).....	1438
Wu, T. (IP-09).....	1126
Wu, W. (AR-17).....	132
Wu, X. (DP-12).....	690
Wu, X. (FB-12).....	835
Wu, Y. (AB-02).....	28
Wu, Y. (AS-06).....	141
Wu, Y. (BQ-12).....	341
Wu, Y. (CG-13).....	539
Wu, Y. (EQ-09).....	799
Wu, Y. (FA-03).....	817
Wu, Y. (FP-01).....	899
Wu, Y. (FP-05).....	903
Wunderlich, J. (AB-04).....	30
Wurmehl, S. (JW-14).....	1402
Wurmehl, S. (JX-06).....	1413
Wurster, S. (IR-13).....	1154
Wurster, S. (JA-06).....	1194
Wytrwal-Sama, M. (AC-14).....	54

- X -

Xi, X. (DB-08).....	612
Xi, X. (IF-04).....	1082
Xia, H. (EQ-09).....	799
Xia, H. (FP-01).....	899
Xia, H. (FP-05).....	903
Xia, J. (AB-02).....	28
Xia, J. (HD-07).....	1009
Xia, J. (HP-03).....	1015
Xia, Y. (BW-17).....	455
Xia, Z. (JU-08).....	1383
Xiang, Q. (IE-04).....	1076
Xiang, Z. (BB-01).....	192
Xiang, Z. (BP-08).....	317
Xiang, Z. (BR-03).....	349
Xiang, Z. (BT-16).....	400
Xiang, Z. (JG-04).....	1275
Xiao, J.Q. (HP-10).....	1022
Xiao, L. (BC-02).....	205
Xiao, L. (BQ-02).....	330
Xiao, T.P. (GB-02).....	924
Xiao, Y. (BA-05).....	189
Xiao, Y. (BH-03).....	266
Xiao, Y. (BJ-04).....	292
Xiao, Y. (BW-11).....	449
Xiao, Z. (JI-05).....	1301
Xie, D. (AD-07).....	66
Xie, D. (AD-08).....	67
Xie, D. (IS-07).....	1168
Xie, Y. (AU-06).....	168
Xin, Z. (AS-11).....	146
Xing, H.G. (IH-09).....	1110
Xing, M. (JI-10).....	1306
Xing, Y. (CP-11).....	552

Xing, Y. (FP-09).....	907
Xing, Y. (GP-02).....	962
Xiong, D. (CC-03).....	473
Xiong, D. (CF-08).....	520
Xiong, D. (FE-07).....	864
Xiong, D. (FG-07).....	874
Xiong, D. (IH-01).....	1102
Xiu, F. (DB-07).....	611
Xu, B. (BU-15).....	419
Xu, B. (DC-10).....	626
Xu, C. (IA-04).....	1029
Xu, D. (BW-02).....	439
Xu, D. (DB-08).....	612
Xu, G. (AC-18).....	58
Xu, G. (BF-01).....	233
Xu, G. (BF-05).....	237
Xu, G. (CR-07).....	577
Xu, H. (CC-05).....	475
Xu, H. (DB-05).....	609
Xu, H. (JC-10).....	1227
Xu, J. (AB-02).....	28
Xu, J. (CA-01).....	457
Xu, L. (JY-07).....	1430
Xu, M. (CP-09).....	549
Xu, M. (EC-03).....	734
Xu, Q. (DC-06).....	622
Xu, Q. (IS-04).....	1165
Xu, T. (HA-05).....	971
Xu, W. (AU-09).....	172
Xu, W. (CS-10).....	592
Xu, X. (AR-01).....	113
Xu, X. (CR-08).....	578
Xu, X. (CS-14).....	596
Xu, X. (IR-07).....	1148
Xu, Y. (AR-13).....	128
Xu, Y. (BK-01).....	304
Xu, Y. (BQ-11).....	340
Xu, Y. (BR-08).....	354
Xu, Y. (BW-02).....	439
Xu, Y. (CC-08).....	478
Xu, Y. (FC-05).....	843
Xu, Y. (IH-01).....	1102
Xu, Y. (IQ-10).....	1140
Xu, Y. (IR-18).....	1159
Xu, Y. (JX-02).....	1409
Xu, Z. (IQ-02).....	1132
Xue, K. (AE-13).....	83
Xue, L. (GB-02).....	924

- Y -

Y. Umetsu, R. (JX-07).....	1414
Y. Umetsu, R. (JX-08).....	1415
Ya, X. (EP-01).....	781
Yablonovitch, E. (BK-04).....	307
Yabukami, S. (ER-12).....	812
Yabukami, S. (JP-13).....	1323
Yacoby, A. (AA-02).....	21
Yadav, R. (JA-10).....	1198
Yadav, V.K. (JQ-08).....	1334

Yagmur, A. (CD-05).....	490
Yagmur, A. (CP-15).....	556
Yaguchi, H. (BS-05).....	370
Yagupov, S. (JY-19).....	1443
Yahagi, Y. (CE-11).....	510
Yakovleva, M. (JT-09).....	1370
Yakushiji, K. (CD-10).....	495
Yakushiji, K. (GB-07).....	930
Yakushiji, K. (IB-04).....	1042
Yakushiji, K. (IH-04).....	1105
Yamada, A. (CG-11).....	537
Yamada, K. (CP-16).....	557
Yamada, K. (HC-03).....	993
Yamaguchi, W. (JW-03).....	1391
Yamahara, H. (EE-15).....	779
Yamamoto, K. (CE-09).....	508
Yamamoto, K. (EC-03).....	734
Yamamoto, R. (BS-09).....	374
Yamamoto, T. (IH-04).....	1105
Yamasaki, H. (IS-06).....	1167
Yamashita, S. (JC-12).....	1229
Yamauchi, T. (JX-08).....	1415
Yamonoi, K. (EC-06).....	737
Yan, J. (AP-10).....	94
Yan, J. (AQ-05).....	103
Yan, R. (AV-04).....	182
Yan, X. (AC-01).....	40
Yan, Y. (FC-05).....	843
Yan, Y. (IQ-10).....	1140
Yan, Y. (IR-18).....	1159
Yan, Z. (CP-11).....	552
Yan, Z. (EP-05).....	785
Yan, Z. (FP-09).....	907
Yan, Z. (GP-02).....	962
Yan, Z. (HB-05).....	979
Yan, Z. (IQ-06).....	1136
Yang, D. (AQ-10).....	108
Yang, D. (BQ-11).....	340
Yang, F. (CS-05).....	587
Yang, F. (FG-15).....	882
Yang, H. (AR-02).....	115
Yang, H. (BB-09).....	201
Yang, H. (BH-02).....	265
Yang, H. (BH-10).....	272
Yang, H. (BJ-13).....	301
Yang, H. (BP-10).....	319
Yang, H. (BU-19).....	424
Yang, H. (BV-06).....	432
Yang, H. (BV-10).....	436
Yang, H. (CG-12).....	538
Yang, H. (DA-05).....	602
Yang, H. (DC-03).....	619
Yang, H. (DC-10).....	626
Yang, H. (EQ-01).....	791
Yang, H. (HC-05).....	995
Yang, H. (HP-01).....	1013
Yang, H. (IF-01).....	1079
Yang, H. (IS-10).....	1171
Yang, I. (BR-04).....	350
Yang, J. (AS-03).....	138
Yang, J. (BQ-16).....	345

- Zhan, X. (CD-03) 488
- Zhan, Y. (BF-01) 233
- Zhan, Y. (BF-05) 237
- Zhang, A. (DP-12) 690
- Zhang, B. (IH-01) 1102
- Zhang, C. (AP-01) 85
- Zhang, C. (AQ-04) 102
- Zhang, C. (AS-09) 144
- Zhang, C. (AU-11) 174
- Zhang, C. (CQ-06) 564
- Zhang, C. (CQ-07) 565
- Zhang, C. (JP-14) 1324
- Zhang, C. (JW-04) 1392
- Zhang, C. (JX-15) 1422
- Zhang, D. (CC-07) 477
- Zhang, D. (EP-08) 788
- Zhang, D. (FC-01) 839
- Zhang, D. (IH-05) 1106
- Zhang, D. (JW-01) 1389
- Zhang, F. (JB-10) 1213
- Zhang, H. (AQ-04) 102
- Zhang, H. (AS-07) 142
- Zhang, H. (AT-02) 154
- Zhang, H. (BH-09) 271
- Zhang, H. (BS-08) 373
- Zhang, H. (BV-03) 428
- Zhang, H. (IF-04) 1082
- Zhang, H. (IR-07) 1148
- Zhang, H. (JW-07) 1395
- Zhang, H. (JX-13) 1420
- Zhang, J. (AS-07) 142
- Zhang, J. (BQ-14) 343
- Zhang, J. (BU-15) 419
- Zhang, J. (BW-17) 455
- Zhang, J. (EB-13) 729
- Zhang, J. (ED-12) 759
- Zhang, J. (FC-02) 840
- Zhang, J. (IS-05) 1166
- Zhang, J. (IS-08) 1169
- Zhang, J. (JF-10) 1267
- Zhang, J. (JU-04) 1379
- Zhang, J. (JU-05) 1380
- Zhang, K. (CQ-06) 564
- Zhang, K. (CQ-07) 565
- Zhang, K. (ER-07) 807
- Zhang, M. (BW-17) 455
- Zhang, N. (CQ-09) 567
- Zhang, N. (CR-08) 578
- Zhang, N. (CS-14) 596
- Zhang, N. (JP-09) 1319
- Zhang, N. (JP-14) 1324
- Zhang, N. (JQ-09) 1335
- Zhang, P. (AS-04) 139
- Zhang, P. (AS-12) 147
- Zhang, P. (JY-13) 1437
- Zhang, Q. (BB-04) 195
- Zhang, Q. (BF-07) 239
- Zhang, Q. (BG-11) 258
- Zhang, Q. (BQ-14) 343
- Zhang, Q. (CS-07) 589
- Zhang, Q. (FA-03) 817
- Zhang, Q. (HD-04) 1006
- Zhang, Q. (IS-05) 1166
- Zhang, Q. (IS-08) 1169
- Zhang, Q. (JF-10) 1267
- Zhang, Q. (JU-04) 1379
- Zhang, Q. (JU-05) 1380
- Zhang, R. (DP-11) 689
- Zhang, R. (FC-05) 843
- Zhang, R. (IQ-10) 1140
- Zhang, S. (AS-14) 149
- Zhang, S. (AV-02) 180
- Zhang, S. (BP-12) 322
- Zhang, S. (HC-06) 996
- Zhang, S. (IF-01) 1079
- Zhang, S.F. (CC-08) 478
- Zhang, T. (AP-11) 95
- Zhang, T. (AQ-09) 107
- Zhang, T. (AT-03) 155
- Zhang, T. (AT-04) 156
- Zhang, T. (AT-08) 160
- Zhang, W. (AS-04) 139
- Zhang, W. (BP-16) 326
- Zhang, W. (BR-11) 357
- Zhang, W. (JY-11) 1435
- Zhang, W. (JY-12) 1436
- Zhang, X. (AB-02) 28
- Zhang, X. (BS-03) 367
- Zhang, X. (BT-07) 389
- Zhang, X. (BU-19) 424
- Zhang, X. (BV-06) 432
- Zhang, x. (CS-13) 595
- Zhang, X. (FA-03) 817
- Zhang, X. (GP-02) 962
- Zhang, X. (HC-06) 996
- Zhang, X. (HD-07) 1009
- Zhang, X. (HP-03) 1015
- Zhang, X. (IP-11) 1128
- Zhang, X. (JW-09) 1397
- Zhang, Y. (AD-07) 66
- Zhang, Y. (AD-08) 67
- Zhang, Y. (AP-01) 85
- Zhang, Y. (AS-03) 138
- Zhang, Y. (AV-05) 183
- Zhang, Y. (BC-04) 207
- Zhang, Y. (CP-07) 547
- Zhang, Y. (CP-10) 551
- Zhang, Y. (CQ-09) 567
- Zhang, Y. (CR-08) 578
- Zhang, Y. (CS-14) 596
- Zhang, Y. (FE-07) 864
- Zhang, Y. (FP-03) 901
- Zhang, Y. (JP-09) 1319
- Zhang, Y. (JW-09) 1397
- Zhang, Z. (AS-02) 136
- Zhang, Z. (AS-06) 141
- Zhang, Z. (BE-01) 225
- Zhang, Z. (BF-05) 237
- Zhang, Z. (BG-02) 249
- Zhang, Z. (BG-10) 257
- Zhang, Z. (BI-09) 285
- Zhang, Z. (BQ-08) 337
- Zhang, Z. (BV-04) 429
- Zhang, Z. (BW-17) 455
- Zhang, Z. (DE-02) 643
- Zhang, Z. (IH-09) 1110
- Zhang, Z. (IR-18) 1159
- Zhang, Z. (JX-02) 1409
- Zhao, C. (AV-04) 182
- Zhao, C. (IB-09) 1047
- Zhao, F. (AP-11) 95
- Zhao, F. (BQ-07) 336
- Zhao, G. (BT-11) 395
- Zhao, G. (HD-07) 1009
- Zhao, H. (BF-01) 233
- Zhao, H. (BF-05) 237
- Zhao, H. (BG-03) 250
- Zhao, H. (BG-09) 256
- Zhao, H. (BU-02) 403
- Zhao, H. (CS-11) 593
- Zhao, H. (FB-12) 835
- Zhao, H. (IS-05) 1166
- Zhao, H. (IS-08) 1169
- Zhao, H. (JU-04) 1379
- Zhao, H. (JU-05) 1380
- Zhao, H.B. (EQ-09) 799
- Zhao, H.B. (FP-01) 899
- Zhao, H.B. (FP-05) 903
- Zhao, J. (BI-08) 284
- Zhao, K. (DG-04) 670
- Zhao, L. (HA-05) 971
- Zhao, M. (CB-01) 464
- Zhao, M. (CP-07) 547
- Zhao, S. (AR-11) 126
- Zhao, W. (CC-03) 473
- Zhao, W. (CF-08) 520
- Zhao, W. (CG-09) 535
- Zhao, W. (FB-12) 835
- Zhao, W. (FE-07) 864
- Zhao, W. (FG-07) 874
- Zhao, W. (FH-09) 892
- Zhao, W. (IH-01) 1102
- Zhao, X. (BT-10) 393
- Zhao, X. (BT-12) 396
- Zhao, X. (BT-13) 397
- Zhao, X. (BT-14) 398
- Zhao, X. (BU-06) 408
- Zhao, X. (BU-11) 414
- Zhao, X. (BU-18) 422
- Zhao, X. (BW-09) 446
- Zhao, X. (CG-09) 535
- Zhao, X. (IQ-01) 1131
- Zhao, X. (IR-06) 1147
- Zhao, Y. (AQ-02) 100
- Zhao, Y. (CS-07) 589
- Zhao, Y. (JB-01) 1204
- Zhao, Y. (JY-15) 1439
- Zhao, Z. (ER-07) 807
- Zheng, H. (AU-07) 170
- Zheng, J. (AV-04) 182
- Zheng, J. (BW-03) 440
- Zheng, L. (EP-08) 788
- Zheng, L. (JW-11) 1399

Zheng, P. (AV-02)	180	Zhou, Y. (AB-02)	28	Zhu, Y. (IQ-06)	1136
Zheng, P. (BB-10)	202	Zhou, Y. (ED-09)	755	Zhu, Z. (BA-05)	189
Zheng, P. (BF-06)	238	Zhou, Y. (HD-07)	1009	Zhu, Z. (BH-03)	266
Zheng, P. (BF-12)	245	Zhou, Y. (HP-03)	1015	Zhu, Z. (BJ-13)	301
Zheng, P. (BP-03)	312	Zhou, Z. (AT-08)	160	Zhuang, B. (AP-08)	92
Zheng, P. (BP-05)	314	Zhou, Z. (JB-01)	1204	Zhuo, L. (AQ-10)	108
Zheng, P. (BP-06)	315	Zhu, D. (FG-07)	874	Zhuo, L. (BQ-11)	340
Zheng, P. (BP-12)	322	Zhu, D. (IH-01)	1102	Zhuo, L. (BR-08)	354
Zheng, P. (BR-02)	348	Zhu, J. (AP-07)	91	Zhuo, L. (BV-08)	434
Zheng, P. (BR-07)	353	Zhu, J. (AQ-01)	99	Zimnyakova, P. (FP-07)	905
Zheng, P. (BT-02)	383	Zhu, J. (BD-10)	222	Zivanov, L. (IS-12)	1173
Zheng, S. (BP-08)	317	Zhu, J. (BF-11)	243	Zivieri, R. (HD-02)	1004
Zheng, Y. (JI-12)	1308	Zhu, J. (BW-05)	442	Zobkalo, I. (DF-09)	662
Zheng, Z. (AR-11)	126	Zhu, J. (BW-06)	443	Zografos, O. (EC-07)	738
Zhenhu, J. (IT-03)	1181	Zhu, J. (BW-07)	444	Zollitsch, C.W. (ED-06)	752
Zhong, H. (AB-11)	38	Zhu, J. (BW-08)	445	Zollitsch, C.W. (ED-13)	760
Zhong, X. (IA-05)	1030	Zhu, J. (CS-10)	592	Zoppellaro, G. (JA-13)	1202
Zhong, Z. (EP-08)	788	Zhu, J. (FC-01)	839	Zou, J. (BK-01)	304
Zhong, Z. (IR-07)	1148	Zhu, J. (IA-04)	1029	Zou, J. (BQ-11)	340
Zhou, B. (IA-04)	1029	Zhu, J. (IA-06)	1031	Zou, J. (BR-08)	354
Zhou, C. (AB-02)	28	Zhu, J. (IB-09)	1047	Zou, X. (IB-12)	1050
Zhou, H. (CF-08)	520	Zhu, L. (BC-03)	206	Zou, Y. (BS-06)	371
Zhou, H. (EQ-01)	791	Zhu, L. (IQ-04)	1134	Zou, Y. (DP-11)	689
Zhou, H. (HA-05)	971	Zhu, M. (EQ-01)	791	Zucchetti, C. (CB-05)	468
Zhou, H. (HP-01)	1013	Zhu, M. (HP-01)	1013	Zuo, L. (JB-10)	1213
Zhou, H. (IS-10)	1171	Zhu, M. (IS-10)	1171	Zuo, Y. (BG-12)	259
Zhou, J. (BG-11)	258	Zhu, M. (JC-09)	1226	Zurauskiene, N. (IB-13)	1051
Zhou, J. (DC-07)	623	Zhu, R. (AU-09)	172	Zuzek Rozman, K. (JC-11)	1228
Zhou, J. (IR-18)	1159	Zhu, T. (CQ-09)	567	Zverev, V. (GC-07)	944
Zhou, L. (AT-02)	154	Zhu, T. (JP-09)	1319	Zverev, V.V. (CS-01)	583
Zhou, L. (BH-03)	266	Zhu, T. (JQ-09)	1335	Zverev, V.V. (CS-12)	594
Zhou, L. (BW-03)	440	Zhu, X. (AQ-12)	111	Zvezdin, A. (EB-14)	730
Zhou, W. (BP-16)	326	Zhu, X. (AR-04)	118	Zvezdin, K. (CS-02)	584
Zhou, W. (CE-09)	508	Zhu, X. (AU-05)	167	Zvezdin, K. (ER-08)	808
Zhou, W. (DE-04)	645	Zhu, X. (BB-01)	192	Zvezdin, K. (FP-14)	912
Zhou, W. (IA-01)	1025	Zhu, X. (BP-08)	317		
Zhou, X. (AU-05)	167	Zhu, X. (BT-16)	400		